REPORT DOCUMENTATION PAGE

Form Approved
OMB No. 0704-0188

Public reporting burden for this collection of information is estimated to average 1 hour per response, including the time for reviewing instructions, searching existing data sources, gathering and maintaining the data needed, and completing and reviewing the collection of information. Send comments regarding this burden estimate or any other aspect of this collection of information, including suggestions for reducing this burden, to Washington Headquarters Services, Directorate for Information Operations and Reports, 1215 Jefferson Davis Highway, Suite 1204, Arlington, VA 22202-4302, and to the Office of Management and Budget, Paperwork Reduction Project (0704-0188), Washington, DC 20503.

1. AGENCY USE ONLY (Leave blank)

2. REPORT DATE
1996

3. REPORT TYPE AND DATES COVERED
FINAL APRIL 95-MARCH 95

4. TITLE AND SUBTITLE
"TWENTY-~~SIXTH~~ FIFTH SYMPOSIUM (INTERNATIONAL) ON COMBUSTION"

5. FUNDING NUMBERS
F49620-95-1-0278

6. AUTHOR(S)
BRUGESS & DRYER (EDITORS)
MULTIPLE

7. PERFORMING ORGANIZATION NAME(S) AND ADDRESS(ES)
THE COMBUSTION INSTITUTE
5001 BAUM BOUELVARD, SUITE 635
PITTSBURGH PA 15213-1851 USA
(ROBERT F SAWYER)

8. PERFORMING ORGANIZATION REPORT NUMBER

9. SPONSORING/MONITORING AGENCY NAME(S) AND ADDRESS(ES)
AFOSR/PKA
110 DUNCAN AVENUE ROOM B115
BOLLING AIR FORCE BASE DC 20332-8050
(M. BIRKAN)

10. SPONSORING/MONITORING AGENCY REPORT NUMBER

11. SUPPLEMENTARY NOTES

12a. DISTRIBUTION/AVAILABILITY STATEMENT
Approved for public release;
distribution unlimited.

12b. DISTRIBUTION CODE

13. ABSTRACT (Maximum 200 words)

THE "TWENTY-SIXTH SYMPOSIUM (INTERNATIONAL) ON COMBUSTION IS A TWO VOLUME SET CONTAINING THE COMPLETE TEXT OF THE 400 PAPERS GIVEN ORALLY OR AS POSTER PRESENTATIONS AT THE 26TH INTERNATIONAL SYMPOSIUM ON COMBUSTION HELD AT THE UNIVERSITY OF NAPLES, ITALY, JULY 28-AUGUST 2, 1996. ALSO CONTAINED ARE THE QUESTIONS AND REPLIES WHICH FOLLOWED THE PRESENTATIONS. THE VOLUMES ALSO HAVE A FULL AUTHOR AND SUBJECT INDEX. THE CONTENTS IS AN ARCHIVAL RECORD OF CURRENT COMBUSTION RESEARCH RESULTS.

14. SUBJECT TERMS
COMBUSTION RESEARCH

15. NUMBER OF PAGES
3449

16. PRICE CODE

17. SECURITY CLASSIFICATION OF REPORT	18. SECURITY CLASSIFICATION OF THIS PAGE	19. SECURITY CLASSIFICATION OF ABSTRACT	20. LIMITATION OF ABSTRACT
UNCLASSIFIED	UNCLASSIFIED	UNCLASSIFIED	UL

TWENTY-FIFTH SYMPOSIUM
(International)
ON
COMBUSTION

At The University of California
Irvine, California
July 31–August 5, 1994

Organized By

THE COMBUSTION INSTITUTE

Pittsburgh, Pennsylvania

1994

DISTRIBUTION STATEMENT A
Approved for public release
Distribution Unlimited

DTIC QUALITY INSPECTED 4

19971002 026

COPYRIGHT © 1994 BY THE COMBUSTION INSTITUTE

ALL RIGHTS RESERVED

No part of this book may be reproduced in any form
by photostat, microfilm, or any other means,
without written permission from the publishers.
Brief quotations from this book for purposes of scientific
discussion will be permitted.

THE COMBUSTION INSTITUTE
5001 Baum Boulevard
Suite 635
Pittsburgh, Pennsylvania 15213-1851 USA

ISSN 0082-0784

Type composed at Edwards Brothers, Inc., Ann Arbor, Michigan

PRINTED IN THE UNITED STATES OF AMERICA

PREFACE

The University of California at Irvine was host to the Twenty-Fifth International Symposium on Combustion held on July 31–August 5, 1994. Chancellor Laural L. Wilkening welcomed the 1218 scientists, which included 367 students, to the UCI campus. Along with 181 accompanying visitors, the registration represented a new record for Symposium attendance. The attendance, representing 38 countries, is as follows: Argentina 1, Armenia 1, Australia 9, Austria 3, Belgium 4, Bulgaria 1, Byelrus 4, Canada 27, China 4, China-Taipei 10, Denmark 10, Finland 12, France 53, Germany 101, Hong Kong 2, Hungary 9, India 5, Ireland 2, Israel 11, Italy 30, Japan 66, Kazhakhstan 1, Korea 9, Malaysia 1, Mexico 3, New Zealand 1, Norway 11, Poland 7, Portugal 8, Russia 26, Spain 3, Sweden 13, Switzerland 11, The Netherlands 17, Ukraine 3, United Kingdom 83, USA 646 and Venezuela 1.

The Institute was proud to honor its founder, Dr. Bernard Lewis, who died May 23, 1993, by presenting the "In Celebration of the Life and Work of Bernard Lewis." Dr. Lewis' widow, Eunice Norton-Lewis, was present for the occasion. A committee chaired by Dr. C. William Shipman collected pictures, correspondence, stories and other mementos from Bernard Lewis' life and organized the celebration. "An Appreciation of Bernard Lewis" gave the overflowing auditorium a composite view of this dynamic individual who brought the family of The Combustion Institute together. The establishment of The Bernard Lewis Endowment Fund was announced and the 25th Symposium was dedicated to the Institute's founder.

The Gold Medal Awards Committee, chaired by Professor Graham Dixon-Lewis, selected the following award recipients for 1994:

Professor Klaus-Heinrich Homann of the Technische Hochschule Darmstadt, Germany was presented The Bernard Lewis Gold Medal "for brilliant research in the field of combustion, particularly on flame structure and soot formation" by Professor Jack B. Howard.

Dr. Hartwell F. Calcote of AeroChem Research Laboratories, Inc, USA was presented The Alfred C. Egerton Gold Medal "for distinguished, continuing and encouraging contributions to the field of combustion" by Professor Heinz Gg. Wagner.

Professor Amable Liñán of the Universidad Politécnica de Madrid, Spain was presented The Ya. B. Zeldovich Gold Medal "for outstanding contributions to the theory of combustion" by Professor Forman A. Williams.

The Silver Medal Awards Committee, chaired by Professor A. D'Alessio, selected two papers for recognition "for an outstanding paper presented at the Twenty-Fourth International Symposium on Combustion, The University of Sydney, Australia, 1992." The medals were presented by Professor D'Alessio to:

Klaus H. Homman, Matthias Hausmann and Peter Hegen for their paper entitled "Radicals in Flames: Analysis via Scavenging Reaction."

M.D. Smooke, Y. Xu, R.M. Zurn, P. Lin, J.H. Frank and M.B. Long for their paper entitled "Computational and Experimental Study of OH and CH Radicals in Axisymmetric Laminar Diffusion Flames."

The Institute extends its gratitude to the members of the Local Arrangements Committee co-chaired by Professors William A. Sirignano and C. Scott Samuelsen for their time and energy in organizing the logistics of the technical sessions and the social events. An outdoor welcome reception in front of the newly constructed engineering complex afforded an opportunity for attendees to renew acquaintances and partake of sumptuous food. Many attended the Pageant of the Masters, a unique depiction of master artworks, held under the stars at the Festival of the Arts, Laguna Beach on Tuesday evening. A barbecue at Newport Dunes Beach Park made Wednesday afternoon a tropical break of frolic and camaraderie. The annual Awards Banquet was held at the Hyatt Regency on Thursday. Following a superb meal and presentation of the 1994 Combustion Institute Medals, all had a chance to enjoy dancing. The farewell reception was held outdoors on the UCI campus offering an opportunity to relax and to say goodbyes.

The Institute extends its appreciation to Dr. Elaine Oran, her staff, the Naval Research Laboratory, the colloquia organizers, session chairs, authors, the members of the Program Committee for the excellent technical program, and to Dr. William Pitz, Professor G.M. Faeth, Professor Derek Bradley and the members of the Publication Committee who are responsible for the publishing the proceedings and the special issues of *Combustion and Flame*.

The Institute recognizes and thanks the following US government agencies and organizations for their generous financial support of the Twenty-Fifth International Symposium on Combustion:

Air Force Office of Scientific Research
Department of Energy
National Aeronautics & Space Administration
National Institute of Standards & Technology
National Science Foundation
Office of Naval Research

AeroChem Research Laboratories, Inc.

Arthur D. Little
AUS Combustion Company
BOC Group
Chevron Research and Technology Company
CONSOL
Cummins Engine Company, Inc.
Elsevier Science Publishing Co., Inc.
Energy and Environmental Research
Engineering Research Corporation
Exxon Research and Engineering Company
Factory Mutual Research Corporation
Flame Research, Inc.
Fossil Energy Research Corporation
Gas Research Institute
GE Aircraft Engines
General Electric Company
Gordon & Breach Publishers, Inc.
John Deere Product Engineering Center
MetroLaser
Philip Morris Corporation
Research Industries Incorporated
Rockwell International Corporation
Southern California Gas Company
Texaco, Inc. Research & Development
The MITRE Corporation
Thermo Electron
United Technologies Research Center

Sue Terpack
Executive Secretary

Bernard Lewis
Ph.D. Sc.D. (Cantab)
1899-1993

Scientist, Colleague, Leader, Counsellor, and Friend
who devoted his life
to bringing science to combustion research,
combustion science to practical problems
combustion researchers to fruitful
intercommunication and friendships,
and two generations of his neighbors
and his colleagues
to a lively appreciation of the musical arts.

THE COMBUSTION INSTITUTE

OFFICERS

President ..... Robert F. Sawyer
Vice President/President Elect ..... Daniel J. Seery
International Vice President ..... Robert W. Bilger
Treasurer ..... Robert F. Chaiken
Assistant Treasurer ..... Charles Hwang
Secretary ..... Craig T. Bowman
International Secretary ..... K. N. C. Bray

EXECUTIVE COMMITTEE

Robert F. Sawyer, *Chair*
Robert W. Bilger
Craig T. Bowman
K. N. C. Bray
Hartwell F. Calcote
Robert F. Chaiken
Chung K. Law
Daniel J. Seery
William A. Sirignano

EXECUTIVE OFFICE

The Combustion Institute
5001 Baum Boulevard, Suite 635, Pittsburgh, PA 15213-1581 USA
Sue Terpack, Executive Secretary
Ann Steffy, Assistant to the Executive Secretary
Phone: (412) 687-1366; Fax: (412) 687-0340
E-Mail: combust@telerama.lm.com

BOARD OF DIRECTORS

Prof. Robert W. Bilger ..... University of Sydney, Australia
Dr. Roland Borghi ..... CNRS 230 – CORIA, France
Prof. A. A. Borisov ..... Russian Academy of Sciences, Russia
Dr. Craig T. Bowman ..... Stanford University, USA
Dr. Derek Bradley ..... The University of Leeds, England
Prof. K. N. C. Bray ..... Cambridge University, England
Dr. Nancy J. Brown ..... Lawrence Berkeley Laboratory, USA
Dr. Hartwell F. Calcote ..... AeroChem Research Labs Inc, USA
Dr. Sébastien Candel ..... Ecole Centrale, Paris, France
Dr. Robert F. Chaiken ..... Bureau of Mines, USA
Prof. Antonio D'Alessio ..... Lab Ricerche Comb CNR, Italy
Prof. Gerard M. Faeth ..... University of Michigan, USA
Dr. Raymond Friedman* ..... Factory Mutal Research Corp, USA
Prof. Irvin Glassman ..... Princeton University, USA
Dr. Newman A. Hall* ..... Consultant, USA
Dr. Dan L. Hartley ..... Sandia National Laboratories, USA
Prof. Toshisuke Hirano ..... University of Tokyo, USA
Prof. Hoyt C. Hottel* ..... Massachusetts Inst of Technology, USA
Prof. Hiroshi Jinno ..... Kyoto University, Japan
Dr. Th. Just ..... DLR, Inst Physikalische Chemie Verb, Germany
Prof. Chung K. Law ..... Princeton University, USA
Prof. John H. S. Lee ..... McGill University, Canada
Dr. Robert S. Levine* ..... Natl Inst of Standards & Tech, USA
Prof. John P. Longwell* ..... Massachusetts Inst of Tech, USA
Dr. Walter T. Olson* ..... Consultant, USA
Dr. Elaine S. Oran ..... Naval Research Laboratory, USA

Prof. Howard B. Palmer° ..... Pennsylvania State University, USA
Prof. Robert F. Sawyer ..... Univ of California, Berkeley, USA
Dr. Daniel J. Seery ..... United Technologies Research Ctr, USA
Dr. William A. Sirignano ..... Univ of California, Irvine, USA
Prof. L. Douglas Smoot ..... Brigham Young University, USA
Dr. Bernard M. Sturgis° ..... Consultant, USA
Prof. Heinz Gg Wagner ..... Universität Göttingen, Germany
°Honorary

THE COMBUSTION INSTITUTE COMMITTEE

Dr. Robert Bilger, Chair ..... University of Sydney, Australia
Dr. K. N. C. Bray, Vice Chair/Secretary ..... Cambridge Univ, UK

Prof. O. Borat ..... Marmar Universitesi, Turkey
Prof. R. Borghi ..... Université de Rouen, France
Prof. D. Bradley ..... University of Leeds, England
Prof. A. Cavaliere ..... Universita di Napoli, Italy
Dr. R. F. Chaiken ..... US Bureau of Mines, USA
Prof. D. Durao ..... Univ Tecnica de Lisboa, Spain
Prof. G. M. Faeth ..... University of Michigan, USA
Dr. Ö. L. Gülder ..... Nat'l Research Council Canada, Canada
Dr. J. Hansson ..... Sekt. f Detonik Och Forbranning, Sweden
Prof. B. S. Haynes ..... University of Sydney, Australia
Prof. Toshisuke Hirano ..... University of Tokyo, Japan
Prof. Th. Just ..... Universität Stüttgart, Germany
Prof. M. M. Kamel ..... Cairo University, Egypt
Dr. J. Keller ..... Sandia National Laboratories, USA
Dr. Nickolai I. Kidin ..... Russian Academy of Sciences Russia
Prof. C. K. Law ..... Princeton University, USA
Dr. H. B. Levinsky ..... NGR, The Netherlands
Dr. Assa Lifshitz ..... Hebrew University, Israel
Prof. A. M. Mellor (CSS) ..... Vanderbilt University, USA
Dr. A. A. Merzhanov ..... Russian Academy of Sciences, Russia
Dr. G. Millan ..... SENER, Spain
Dr. L. J. Muzio (WSS) ..... Fossil Energy Research, Corp, USA
Dr. T. Niioka ..... Tohoku University, Japan
Dr. K. Remenyi ..... Inst for Electric Power Res, Hungary
Prof. R. J. Santoro (ESS) ..... Pennsylvania State University, USA
Dr. U. S. P. Shet ..... ITT, Madras, India
Prof. S.-X. Shi ..... Tianjin University, China
Prof. H. D. Shin ..... Korea Adv Inst of Science & Tech, Korea
Dr. D. Stepowski ..... Université de Rouen, France
Dr. J. Sykes ..... AEA, England
Prof. J. Tomeczek ..... Institute of Fuel Energy, Poland
Prof. C. Treviño ..... Univ Nacl Autonoma de Mexico, Mexico
Dr. H. Tsuji ..... Tokyo Denki University, Japan
Dr. J. Vandooren ..... Univ Catholique de Louvain, Belgium
Prof. H. Gg. Wagner ..... Universität Göttingen, Germany
Prof. J.-C. Yang ..... ITRI, Taiwan

FINANCE COMMITTEE

William A. Sirignano, Chair ..... Univ of California, Irvine, USA

K. N. C. Bray ..... Cambridge University, UK
Robert F. Chaiken ..... US Bureau of Mines, USA
Alan Eckbreth ..... United Technologies Research Center, USA
Donald R. Hardesty ..... Sandia National Laboratories, USA
Toshisuke Hirano ..... University of Tokyo, Japan
L. Douglas Smoot ..... Brigham Young University, USA
Jürgen Warnatz ..... Universität Stüttgart, Germany

NOMINATING COMMITTEE FOR DIRECTORS

Daniel J. Seery, Chair ..... United Technologies Res Ctr, USA

Derek Bradley ..... University of Leeds, UK
Irvin Glassman ..... Princeton University, USA
Thomas Just ..... Universität Stüttgart, Germany
William A. Sirignano ..... University of California, Irvine, USA

NOMINATING COMMITTEE FOR OFFICERS

Chung K. Law, Chair ..... Princeton University, USA

Roland Borghi ..... Université de Rouen, France
John H. S. Lee ..... McGill University, Canada
L. Douglas Smoot ..... Brigham Young University, USA
Heinz Gg. Wagner ..... Universität Göttingen, Germany

SITE SELECTION COMMITTEE

Craig T. Bowman, Chair ..... Stanford University, USA

Nicholas Cernansky ..... Drexel University, USA
Toshisuke Hirano ..... University of Tokyo, Japan
David B. Smith ..... British Gas plc, UK
Jürgen Warnatz ..... Universität Stüttgart, Germany

TWENTY-FIFTH SYMPOSIUM COMMITTEES

Technical Program Committee

Chair
Elaine S. Oran, Naval Research Laboratories

Program Advisory Subcommittee

Pamela K. Barr, Sandia National Laboratories, USA
Jay P. Boris,* Naval Research Laboratory, USA
Craig T. Bowman, Stanford University, USA
Derek Bradley, University of Leeds, UK
Sébastien Candel,* Ecole Centrale, Paris, France
Norman Chigier, Carnegie Mellon University, USA
Antonio D'Alessio, University of Naples, Italy
Gabrielle Dupre,* CNRS/LCSR, France
Gerard M. Faeth, University of Michigan, USA
Richard G. Gann,* Natl Inst of Standards & Tech, USA
Toshisuke Hirano,* University of Tokyo, Japan
Jack B. Howard,* Massachusetts Inst of Technology, USA
Thomas Just, Universität Stüttgart, Germany
K. Kailasanath,* Naval Research Laboratory, USA
Herman Krier, Univ of Illinois, Urbana-Champagne, USA
Chung K. Law, Princeton University, USA
William J. Pitz, Lawrence Livermore National Labs, USA
G. Scott Samuelsen, University of California, Irvine, USA
Adel F. Sarofim,* Massachusetts Inst of Technology, USA
Robert F. Sawyer, University of California, Berkeley, USA
Daniel J. Seery,* United Technologies Research Ctr, USA
Martin Sichel,* University of Michigan, USA
William A. Sirignano, University of California, Irvine, USA
L. Douglas Smoot,* Brigham Young University, USA
Ian Smith,* University of Sydney, Australia
Charles K. Westbrook,* Lawrnce Livermore Natl. Labs, USA

Committee Members

Prof. John Abraham, University of Minnesota
Dr. Andrew A. Adamczyk, Ford Motor Company
Prof. G. Adomeit, RWTH, Aachen
Dr. George Adams, US Army Research Laboratory
Dr. P. K. Agarwal, University of Wyoming
Prof. Suresh K. Aggarwal, University of Illinois, Chicago
Dr. Tanvir Ahmad, GM Research Laboratories
Prof. Marcus Aldén, Lund Institute of Technology
Prof. Ralph Aldredge, University of California
Dr. Mark G. Allen, Physical Sciences Inc
Prof. Robert A. Altenkirch, Mississippi State University
Prof. Elmar R. Altwicker, Rensselaer Polytechnic Institute
Dr. Paul R. Amyotte, Technical University of Nova Scotia
Dr. William R. Anderson, US Army Research Laboratory
Dr. Richard W. Anderson, Ford Motor Company
Prof. K. Annamalai, Texas A & M University
Prof. Umberto Arena, University of Naples
Prof. Verdat S. Arpaci, University of Michigan
Prof. Katsuo Asato, Gifu University
Prof. Nasser Ashgriz, SUNY at Buffalo
Dr. W. T. Ashurst, Sandia National Lababoratories
Prof. Dennis N. Assanis, University of Illinois
Dr. R. M. Asseva, Russian Academy of Sciences
Prof. Arvind Atreya, University of Michigan
Prof. C. Thomas Avedisian, Cornell University
Prof. Richard L. Axelbaum, Washington University
Dr. V. S. Babkin, Russian Academy of Sciences
Dr. William D. Bachalo, Aerometrics Inc
Prof. Seung W. Baek, Korea Adv Inst of Science & Tech
Dr. Mel Baer, Sandia National Laboratory
Dr. M. Y. Bahadori, Science Applications International Corp
Mr. Donald W. Bahr,* GE Aircraft Engines
Dr. Graham J. Ball, University of Southampton
Prof. Dilip R. Ballal, University of Dayton
Dr. Ezra Bar-Ziv, Nuclear Research Center, Negev
Dr. Thierry A. Baritaud, Inst Francais du Petrole
Dr. Robert Barlow, Sandia National Laboratories
Dr. F. Baronnet, INPL-ENSIC-CNRS, France
Dr. Pamela K. Barr, Sandia National Laboratories
Ir. H. Bartelds, TNO Inst of Environmental and Energy Tech
Dr. William Bartok, Consultant
Prof. Vadim V. Barzykin, Russian Academy of Sciences
Prof. Simon H. Bauer, Cornell University
Prof. D. L. Baulch, University of Leeds
Dr. Howard R. Baum, Natl Inst of Standards and Technology
Dr. Larry L. Baxter, Sandia National Laboratories
Dr. J. Bechtold, Princeton University
Prof. Henry A. Becker, Queen's University
Prof. Janos M. Beér, Massachusetts Inst of Technology
Dr. Josette Bellan,* Jet Propulsion Laboratory

Dr. Frank Belles, Consultant
Dr. P. Bennett, BP-Sunbury Research Center
Dr. Steve Benson, Arthur D. Little Inc
Dr. Federico Beretta, Inst di Ricerche sulla Comb
Prof. A. L. Berlad, University of California, San Diego
Prof. Al. Al. Berlin, Russian Academy of Sciences
Prof. Philip E. Best, University of Connecticut
Dr. Craig L. Beyler, Hughes Associates Inc
Prof. S. Bhattacharjee, San Diego State Univeristy
Prof. Robert W. Bilger, University of Sydney
Dr. Aviezer Birk, Ballistic Research Laboratory
Dr. Mitat Birkan, Air Force Office of Scientific Research
Dr. Richard J. Blint, General Motors Research Laboratory
Prof. Henning Bockhorn, Universität Kaiserslautern
Prof. Roland P. Borghi, CORIA, Fac. des Sci. de Rouen
Dr. Jay P. Boris, Naval Research Laboratory
Prof. Anatolii A. Borisov, Russian Academy of Sciences
Prof. Gary L. Borman, University of Wisconsin
Prof. Craig T. Bowman, Stanford University
Prof. Joseph W. Bozzelli, New Jersey Inst of Technology
Prof. Derek Bradley, University of Leeds
Prof. Melvyn C. Branch, University of Colorado
Prof. K. N. C. Bray, Cambridge University
Prof. M. Quinn Brewster, University of Illinois
Dr. Kenneth Brezinsky, Princeton University
Prof. T. Brill, University of Delaware
Prof. Jacques Brossard, Lab de Recherche Universitaire
Dr. Nancy J. Brown, Lawerence Berkeley Laboratory
Prof. Claudio Bruno, CRS4, Sardinia
Prof. Richard O. Buckius, University of Illinois
Prof. John Buckmaster, University of Illinois
Dr. Mary Bui-Pham, Sandia National Laboratories
Prof. E. M. Bulewicz, Cracow University of Technology
Prof. David Bull, Thorton Research Centre
Prof. Alexander Burcat, Technion
Prof. A. R. Burgess, University College London
Prof. Barry P. Butler, University of Iowa
Dr. Hartwell F. Calcote, AeroChem Research Labs Inc
Prof. Sebastien Candel, Ecole Centrale, Paris
Dr. R. Stewart Cant, UMIST
Dr. John M. Card, Sandia National Laboratories
Prof. M.G. Carvalho, Technical University of Lisbon
Mr. Kenneth L. Cashdollar, U.S. Bureau of Mines
Dr. Kent H. Casleton, US DOE/METC
Dr. Michel Cathonnet, LCRS-CNRS, Orleans
Prof. Jerald A. Caton, Texas A & M University
Dr. Leonard H. Caveny, SDIO/IST
Prof. Nicholas P. Cernansky, Drexel University
Prof. Baki M. Cetegen, Yale University
Dr. Robert Chaiken, Bureau of Mines
Prof. S. H. Chan, University of Wisconsin, Milwaukee
Dr. Calvin Chan, AECL
Prof. Richard Chang, Yale University
Prof. T. T. Charalampopoulos, Louisiana State University
Prof. M. David Checkel, University of Alberta
Prof. Harsha K. Chelliah, University of Virginia
Prof. Lea D. Chen, University of Iowa
Dr. J. Y. Chen, University of California, Berkeley
Prof. Chiun-Hsun, Chen National Chiao Tung University
Dr. J.H. Chen, Sandia National Laboratories
Dr. Robert K. Cheng, Lawrence Berkeley Laboratories
Prof. Norman Chigier, Carnegie Mellon University
Prof. Wallace Chinitz, Cooper Union
Dr. Riccardo Chirone, Inst di Ricerche sulla Comb, CNR
Prof. Peck Cho, Michigan Technical University
Prof. Kyung-Kook Cho, Seoul National University
Prof. S. Y. Cho, Inha University
Prof. Sangmin Choi, Korea Adv Inst of Science & Tech
Prof. P. Roy Choudhury, University of Southern California
Prof. Suk-Ho Chung, Seoul National University
Prof. Stuart W. Churchill, University of Pennsylvania
Dr. Anna Ciajolo, ICNR Naples
Prof. Paul Clavin, Université de Provence
Dr. Larry Cloutman, Lawrence Livermore National Lab
Dr. C. M. Coats, University of Leicester
Dr. Terence P. Coffee, US Army Research Laboratory
Dr. Aldo Coghe, Politecnico de Milano
Mr. Arthur Cohen, US Army Research Laboratory
Dr. Norman Cohen, Aerospace Corporation
Mr. Jerald A. Cole, Energy and Environmental Research Corp
Dr. Meredith B. Colket, United Technologies Research Ctr.
Dr. Gaetano Continillo, CNR, Istituto Ricerche Combustione
Dr. Denis K. Cook, Midlands Research Station
Prof. Terrill A. Cool, Cornell University
Dr. Richard A. Copeland, SRI International
Dr. C. Corre, ELF ANTAR FRANCE
Dr. Sanjay M. Correa, General Electric Research Ctr.
Prof. M. J. Cottereau, University de Rouen
Mr. T. A. Coultas, W. J. S. A.
Prof. G. Cox, Fire Research Station
Dr. David R. Crosley, SRI International
Prof. Fred E. C. Culick, California Institute of Technology
Prof. Vic A. Cundy, Louisiana State University
Prof. Antonio D'Alessio, Università de Napoli

Prof. E. K. Dabora, University of Connecticut
Dr. Philippe Dagaut, CNRS/LSCR
Prof. Werner J. A. Dahm, University of Michigan
Prof. J. D. Dale, University of Alberta
Dr. Nasser Darabiha, Ecole Centrale
Dr. David F. Davidson, Stanford University
Dr. Ronald W. Davis, Natl Inst of Standards & Technology
Dr. John de Ris, Factory Mutual Research
Dr. Anthony M. Dean, Exxon Research and Engineering Co
Dr. John E. Dec, Sandia National Laboratories
Dr. S. Deevi, Philip Morris
Dr. M. A. Delichatsios, Factory Mutual Research Corp
Prof. Barry Dellinger, University of Dayton Research Institute
Dr. J.-P. Delplanque, Societé Européenne de Propulsion
Prof. J. C. Dent, Loughborough University of Technology
Prof. Michel Destriau, Université de Bordeaux I
Prof. Robert Dibble,* University of California, Berkeley
Prof. Colomba DiBlasi, Università di Napoli
Prof. G. Dixon-Lewis, University of Leeds
Dr. K. Döbbeling, ABB Dept. CHCRC T4
Prof. Richard A. Dobbins, Brown University
Dr. Sandor Dóbé, Central Research Inst for Chem
Mr. Willard J. Dodds, Consultant
Prof. J. W. Dold, University of Bristol
Prof. Cesar Dopazo, University of Zaragoza
Prof. Michael C. Drake, General Motors Research Laboratory
Prof. James F. Driscoll, University of Michigan
Prof. Frederick L. Dryer, Princeton University
Prof. D. D. Drysdale, University of Edinburgh
Prof. Derek Dunn-Rankin,† University of California, Irvine
Dr. Gabrielle Dupre, CNRS/LCSR, France
Prof. Harry A. Dwyer, University of California, Davis
Dr. Alan C. Eckbreth, United Tech. Research Ctr.
Dr. R. Edelman, Consultant
Prof. D. H. Edwards, The University of Wales, Aberystwyth
Dr. John C. Edwards, US Bureau of Mines
Dr. Fokion Egolfopoulos, University of Southern California
Prof. Heinrich Eickhoff, DLR, Koln
Dr. Shmuel Eidelman, Science Applications Intl
Dr. Sherif H. El Tahry, General Motors Research Labs
Prof. S. E. Elghobashi, University of California-Irvine
Prof. Janet Ellzey, University of Texas
Prof. Howard W. Emmons, Harvard University
Prof. E. Esposito, Ecole Centrale
Prof. R. H. Essenhigh, Ohio State University
Prof. Gerard M. Faeth, University of Michigan
Prof. Baochun Fan Nanjiing, Univ of Science and Technology
Dr. T. D. Fansler, General Motors Research Laboratories
Prof. Bakhtier Farouk, Drexel University
Prof. P. V. Farrell, University of Wisconsin
Dr. Roger L. Farrow, Sandia National Laboratories
Dr. Alan S. Feitelberg, GE Corporate R&D
Frank Fendell, TRW
Prof. C. Fernandez-Pello, University of California, Berkeley
Prof. Elizabeth M. Fisher, Cornell University
Dr. James Fleming, Naval Research Laboratory
Prof. Edward A. Fletcher, University of Minnesota
Dr. Thomas H. Fletcher, Brigham Young University
Prof. Arthur Fontijn, Rensselaer Polytechnic Institute
Dr. Jerry W. Forbes, Naval Surface Weapons Center
Dr. Peter Frank, DLR, Stuttgart
Dr. Roydon A. Fraser, University of Waterloo
Prof. M. Frenklach, Pennsylvania State University
Dr. Raymond Friedman, Factory Mutual Research Corp
Dr. Vladimir A. Frost, Russian Academy of Science
Prof. Wei Biao Fu, Tsinghua University
Dr. David Fyfe, Naval Research Laboratory
Dr. Stephen B. Gabriel, Southampton University
Prof. Dezso Gal, Hungarian Academy of Sciences
Prof. V. Ganesan, Indian Institute of Technology
Dr. Richard G. Gann, Natl Institute Standards & Technology
Dr. W.C. Gardiner, University of Texas, Austin
Dr. Nancy Garland, Naval Research Laboratory
Prof. Boris E. Gelfand, Russian Academy of Science
Mr. Randall S. Gemmen, Morgantown Energy Tech Ctr
Prof. Ahmed Ghoniem, Massachusetts Inst of Technology
Dr. P. Gilot, ENSC Mulhouse
Prof. Peyman Givi, State University of New York
Dr. Peter Glarborg, Technical University of Denmark
Prof. Irvin Glassman, Princeton University
Prof. George Gogos, University of Nebraska
Dr. Iskender Gokälp, LCSR-CNRS, Orléan
Dr. David M. Golden, SRI International
Prof. S. R. Gollahalli, University of Oklahoma
Prof. J. P. Gore, Purdue University
Prof. A. D. Gosman, Imperial College of Science & Tech
Dr. Larry P. Goss, Systems Research Laboratories Inc
Dr. Daniel T. Gottuk, Hughes Associates Inc
Prof. F. C. Gouldin, Cornell University
Prof. Peter Gray, Gonville & Caius College
Dr. Robert M. Green, Sandia National Laboratories

Prof. D. A. Greenhalgh, Cranfield Institute of Technology
Prof. Ralph Greif, University of California, Berkeley
Dr. John F. Griffiths, University of Leeds
Dr. Fernando Grinstein, Naval Research Laboratories
Dr. W. L. Grosshandler, Natl Inst of Standards & Technology
Dr. H.-H. Grotheer, DFVLR-Institut-442
Dr. C. Guirao, Natural Sciences & Eng. Council of Canada
Dr. O. L. Gülder, National Research Council of Canada
Prof. Ashwani K. Gupta, University of Maryland
Dr. Effie Gutmark, Naval Air Warfare Center
Prof. W. Hack, Max-Planck-Institut für Stromungsforschung
Mr. Robert Hall, United Technologies Research Center
Prof. M. J. Hall, University of Texas, Austin
Dr. Anthony Hamins, Natl Inst of Standards & Technology
Dr. G. Hancock, Oxford University
Prof. Ronald K. Hanson, Stanford University
Dr. David J. Harris, CSIRO, Div. of Coal & Energy Tech.
Dr. Dan L. Hartley, Sandia National Laboratories
Dr. Daniel C. Haworth, General Motors Research Labs
Dr. A. Koichi Hayashi, Nagoya University
Dr. A. N. Hayhurst, Cambridge University
Prof. Brian S. Haynes, University of Sydney
Prof. William C. Hecker, Brigham Young University
Prof. Paul O. Hedman, Brigham Young University
Dr. Uday Hegde, Sverdrup Technology Inc
Prof. Klaus R. G. Hein, Technische Universiteit Delft
Prof. M. Heitor, Technical University of Lisbon
Dr. Joseph J. Helble, PSI Technology Corporation
Dr. Charles B. Henderson, Consultant
Dr. James C. Hermanson, United Technologies Research Ctr
Dr. M. Hertzberg, Lock Haven University
Prof. Jean Hertzberg, University of Colorado
Dr. Gunnar Heskestad, Factory Mutual Research Corporation
Dr. Scott Hill, Brigham Young University
Prof. Toshisuke Hirano, University of Tokyo
Prof. Hiro Hiroyasu, Hiroshima University
Prof. Bjorn H. Hjertager, Telemark Institute of Technology
Prof. Vladimir Hlavacek, SUNY
Prof. Simone Hochgreb, Massachusetts Inst of Technology
Prof. K. H. Homann, Technische Hochschule Darmstadt
Prof. M. Hori, Takushoku Universtiy
Prof. Jack B. Howard, Massachusetts Inst of Technology
Dr. John R. Howell, University of Texas
Prof. K. Hoyermann, Institut für Physikalische Chemie
Dr. Robert Hurt, Sandia National Laboratories
Dr. J. Hustad, Norwegian Institute of Technology
Dr. Makoto Ikegami, Kyoto University
Prof. Satoru Ishizuka, University of Tokyo
Dr. T. Jackson, ICASE
Prof. J. I. Jagoda, Georgia Institute of Tech.
Prof. Yogesh Jaluria, Rutgers University
Prof. Johannes Janicka, Technische Hochschule Darmstadt
Dr. Peter Jansohn, ASEA BROWN BOVERI
Dr. Jay B. Jeffries, SRI International
Dr. Robert G. Jenkins, University of Cincinnati
Prof. In-Seuck Jeung, Seoul National University
Dr. A. D. Johnson, Shell Research Ltd.
Dr. David Jones, Materials Research Laboratory
Dr. W. P. Jones, Imperial College
Dr. P. Joulain, University of Poitiers,
Prof. Thomas Just, Universität Stüttgart
Dr. K. Kailasanath,* Naval Research Laboratory
Dr. E. W. Kaiser, Ford Motor Co.
Prof. Takeyuki Kamimoto, Tokyo Institute of Technology
Prof. A. M. Kanury, Oregon State University
Dr. A. K. Kapila, Rensselaer Polytechnic Institute
Dr. Carolyn Kaplan,* Naval Research Laboratory
Prof. Ann R. Karagozian, Univ of California, Los Angeles
Dr. George E. Karniadakis, Brown University
Dr. Oleg E. Kashireninov, Russian Academy of Sciences
Dr. Takashi Kashiwagi, Natl Inst of Standards & Technology
Prof. David R. Kassoy, University of Colorado
Prof. C. W. Kauffman, University of Michigan
Prof. Osamu Kawaguchi, Keio University
Prof. James C. Keck, Massachusetts Inst of Technology
Dr. Robert J. Kee, Sandia National Laboratories
Dr. Jay O. Keller, Sandia National Laboratories
Dr. J. T. Kelly, ALTEX
Dr. R. M. Kendall, Alzeta Corporation
Prof. Lawrence A. Kennedy, Ohio State University
Prof. Ian M. Kennedy, University of California, Davis
Prof. Ralph Donald Kern, University of New Orleans
Dr. Alan R. Kerstein, Sandia National Laboratories
Mr. J. A. Kezerle, Gas Research Institute
Dr. B. M. Khusid, Scientific Laboratories, Inc
Prof. N. I. Kidin, Russian Academy of Sciences
Prof. Hiroyuki Kido, Kyushu University
Prof. John H. Kiefer, University of Illinois-Chicago
Dr. Jim Kilgroe, Res Triangle NC/ Combustion Res Branch

Prof. Sang-Soo Kim, Korea Adv Inst of Science & Technology
Prof. Itsuro Kimura, Tokai University
Dr. Merrill K. King, NASA
Prof. K. King, University of Adelaide
Dr. Michael Klassen, Purdue University
Dr. Rudolf Klemens, Warsaw University of Technology
Dr. R. Bruce Klemm, Brookhaven National Laboratory
Prof. Omar M. Knio, The Johns Hopkins Unviersity
Prof. K. F. Knoche, Lehrstuhl fur Technische
Dr. V. G. Knorre, Moscow State Technical University
Prof. Eldon L. Knuth, University of California, Los Angeles
Prof. Seiichiro Koda, University of Tokyo
Dr. K. Kohse-Höinghaus, DLR Institut f Physikalische Chemie
Dr. Thomas Kolb, BASF AG, Germany
Prof. W. Kollmann, University of California, Davis
Prof. Michikata Kono, University of Tokyo
Dr. Douglas E. Kooker, US Army Research Laboratory
Prof. V. P. Korobeinikov, Russian Academy of Science
Prof. Catherine P. Koshland,* Univ of California, Berkeley
Prof. A. Kowalewicz, Aviation Institute
Prof. John C. Kramlich, Energy & Environmental Res Corp
Dr. Thomas G. Kreutz, Princeton University
Prof. Herman Krier, Univ of Illinois at Urbana-Champaign
Prof. Jerry C. Ku, Wayne State University
Dr. N. Kubota, Japan Defense Agency
Dr. Allen L. Kuhl, Lawrence Livermore National Laboratory
Prof. Seiichiro Kumagai, University of Tokyo
Dr. T. W. Kuo, General Motors Research Laboratory
Prof. S. H. Lam, Princeton University
Prof. Juan C. Lasheras, University of California, San Diego
Dr. Allan H. Laufer, US Department of Energy
Prof. N. M. Laurendeau, Purdue University
Dr. Moshe Lavid, Energia Inc
Dr. George A. Lavoie, Ford Motor Company
Prof. Chung K. Law, Princeton University
Dr. C. J. Lawn, Rolls Royce PLC
Prof. Bo Leckner, Chalmers Technical University
Dr. Albert Lee, National Inst of Standards & Technology
Prof. Denz Lee, National Cheng Kung University
Prof. Shih-Tuen Lee, National Taiwan University
Dr. Su-Ryong Lee, Hyundai Motor Company
Prof. Michel Lefebvre, Royal Military Academy, Belgium
Dr. Christopher B. Leger, Paraxair Inc
Dr. P. Lemieux, Combustion Research Branch, US-EPA
Prof. B. Lenze, Universität Karlsruhe
Dr. W. Leppard, General Motors Research Laboratory
Prof. Wolfgang Leuckel, Universität Karlsruhe
Prof. Yiannis A. Levendis, Northeastern University
Dr. Robert S. Levine, Natl Inst of Standards & Technology
Dr. H.B. Levinsky, Nederlandse Gasunie Research
Mr. Arthur Levy, Consultant
Prof. J.C. Leyer, ENSMA Poitiers
Dr. Chiping Li, Naval Research Laboratory
Dr. Shui-Chi Li, University of California, San Deigo
Paul A. Libby, University of California, San Diego
Prof. Assa Lifshitz, The Hebrew University
Dr. P. D. Lightfoot, ICI Explosives Canada
Prof. JoAnn S. Lighty, University of Utah
Prof. Pier Giorgio Lignola, University of Calabria
Prof. Ming Chang Lin, Emory University
Dr. William P. Linak, US EPA
Dr. R. P. Lindstedt, Imperial College
Dr. Gregory T. Linteris, Natl Inst of Standards & Technology
Prof. A. M. Lipanov, Russian Academy of Sciences
Prof. Thomas A. Litzinger, Pennsylvania State University
Dr. Jia Cong Liu, Xian Modern chemistry Institute
Prof. John Lloyd, Michigan State University
Prof. Fred C. Lockwood, Imperial College
Mr. Steve B. Londerville, Coen Company Inc
Prof. Marshall B. Long, Yale University
Prof. John P. Longwell, Massachusetts Inst of Technology
Prof. Eric Loth, University of Illinois
Dr. Donald Lucas, Lawrence Berkeley Laboratories
Prof. Robert P. Lucht, Sandia National Laboratories
Dr. Andrew E. Lutz, Sandia National Laboratories
Dr. R. K. Lyon, EEA Co.
Dr. Valerie J. Lyons, NASA Lewis Research Ctr.
Prof. Hsiao-Kang Ma, National Taiwan University
Dr. Ulrich Maas, Institute für Tech. Verbrennung
Dr. Andrej Macek, National Inst of Standards & Technology
Dr. J. MacInnes, University of Sheffield
Prof. John C. Mackie, University of Sydney
Dr. Daniel W Mackowski, Auburn University
Prof. S. Mahalingam, University of Colorado
Prof. G. Makhviladze,* University of Central Lancashire
Prof. Atsushi Makino, Shizuoka University
Dr. Daniel J. Maloney, Morgantown Energy Technology Ctr.
Prof. Philip C. Malte, University of Washington
Dr. Rudolf R. Maly, Daimler-Benz AG
Dr. David Mann, U.S. Army Research Office
Prof. Mohy Saad Mansour, Cairo University

Dr. C. P. Mao, Delavan Inc
Prof. Frank E. Marble, California Institute of Technology
Dr. S. B. Margolis, Sandia National Laboratories
Prof. Jay K. Martin, University of Wisconsin-Madison
Prof. Assaad R. Masri, University of Sydney
Prof. M. Matalon, Northwestern University
Prof. Hiroyuki Matsui, University of Tokyo
Prof. Ronald D. Matthews, University of Texas, Austin
Prof. Jim McDonough, University of Kentucky
Dr. John S. McFeaters, Auckland University
Prof. J. McGuirk, Loughborough University
Dr. Edward T. McHale, SAIC
Dr. A. C. McIntosh, Leeds University
Prof. J. Thomas McKinnon, Colorado School of Mines
Dr. W. J. McLean, Sandia National Laboratories
Prof. C. Megaridis, University of Illinois
Prof. Eckart Meiburg, University of Southern California
Dr. Carl Melius, Sandia National Laboratories
Prof. A. M. Mellor, Vanderbilt University
Prof. M. Pinar Menguc, University of Kentucky
Dr. Suresh Menon, Georgia Institute of Technology
Prof. Charles Merkle, Pennsylvania State University
Prof. John D. Mertens, Trinity College
Dr. A. G. Merzhanov, Russian Academy of Sciences
Prof. Ralph Metcalfe, University of Houston
Prof. Mohamad Metghalchi, Northeastern University
Dr. Richard Miake-Lye, Aerodyne Research Inc
Dr. Joe V. Michael, Argonne National Laboratories
Prof. K. Clark Midkiff, University of Alabama
Prof. David W. Mikolaitis, University of Florida
Dr. Paul C. Miles, Sandia National Laboratories
Dr. R. B. Miles, Princeton University
Prof. J. Houston Miller, The George Washington University
Dr. Martin S. Miller, US Army Research Laboratory
Dr. James A. Miller, Sandia National Laboratories
Prof. Rodolphe Minetti, Univ des Sciences et Tech de Lilles
Dr. T. Mitani, Kakuda Research Center
Prof. Reginald E. Mitchell, Stanford University
Prof. Toshio Miyauchi, Tokyo Institute of Technology
Dr. Andrzej W. Miziolek, US Army Research Laboratory
Prof. Masahiko Mizomoto, Keio University
Prof. Y. Mizutani, Osaka University
Dr. I. O. Moen, Defense Research Establishment, Canada
Dr. Penelope Monkhouse, University of Heidelberg
Dr. James H. Morehart, Edwards Air Force Base
Dr. Chris Morley, Shell Research Limited
Prof. J. B. Moss, Cranfield Institute of Technology
Prof. Jacob Moulijn, Delft University of Technology
Dr. Alexander S. Mukasyan, Russian Academy of Sciences
Prof. Hanasoge S. Mukunda, Indian Institute of Science
Dr. Edward J. Mularz, NASA Lewis Research Center
Prof. J. A. Mulholland, Georgia Institute of Technology
Prof. Godfrey Mungal, Stanford University
Prof. Z. Munir, University of California-Davis
Prof. S. N. B. Murthy, Purdue University
Dr. Lawrence J. Muzio, Fossil Energy Research Corporation
Dr. Jeffrey D. Naber, Sandia National Laboratories
Dr. Habib N. Najm, Sandia National Laboratories
Dr. Mehdi Namazian, Altex Technologies Co.
Dr. Ichiro Naruse, Toyohashi University of Technology
Dr. Peter F. Nelson, CSIRO, Australia
Dr. R. Nelson, US Forest Service
Prof. Andras Nemeth, Inst for Science Mgt & Informatics
Dr. David C. Newey, BP Oil
Prof. J. K. Nieuwenhuizen, Technische Universiteit
Prof. Takashi Niioka, Tohoku University
Dr. Stephen Niksa, SRI International,
Dr. Gary L. North, NASA-Lewis Research Center
Dr. T. S. Norton, Morgantown Energy Technology Center
Prof. B. V. Novozhilov, Chemical Physics Institute, RAS
Dr. Peter O'Rourke, Los Alamos National Laboratory
Prof. Kazutomo Ohtake, Toyohashi University of Technology
Dr. Ken Okazaki, Tokyo Institute of Technology
Dr. Sandra L. Olson, NASA Lewis Research Center
Dr. Douglas B. Olson, New Mexico Tech.
Prof. Anthoni K. Oppenheim, Univ of California, Berkeley
Dr. Lawrence Orloff, Factory Mutual Research Corporation
Dr. Peter J. Padley, University College of Swansea
Prof. Patrick J. Pagni, University of California, Berkeley
Prof. Claude Paillard, CNRS, France
Prof. Howard B. Palmer, Pennsylvania State University
Dr. John Pan, US Air Force Phillips Laboratory
Prof. Dimitri Papamoschou, University of California, Irvine
Dr. Gopal Patnaik, Naval Research Laboratory
Dr. P. J. Paul, Indian Institute of Science
Dr. C. A. J. Paulson, CSIRO Div. of Coal and Energy Tech.
Prof. Robert E. Peck, Arizona State University

Prof. Jozef L. Peeters, University of Leuven
Dr. Michael J. Pegg, Technical University of Nova Scotia
Prof. David W. Pershing, University of Utah
Prof. James E. Peters, University of Illinois
Prof. Norbert Peters,* RWTH Aachen
Prof. Tom Peterson, University of Arizona
Prof. Richard B. Peterson, Oregon State University
Prof. L. D. Pfefferle, Yale University
Prof. M. J. Pilling, University of Leeds
Dr. William M. Pitts, National Inst of Standards and Tech
Prof. Robert W. Pitz, Vanderbilt University
Dr. William J. Pitz, Lawrence Livermore Laboratories
Dr. John H. Pohl, Energy International
Dr. Thierry Poinsot, Inst de Mec des Fluides de Toulouse
Prof. S. B. Pope, Cornell University
Dr. Gilles Prado, EENSC, Mulhouse
Prof. Norman H. Pratt, University of Southampton
Dr. Cary Presser, National Inst of Standards & Technology
Prof. Edward W. Price, Georgia Institute of Technology
Dr. C. H. Priddin, Rolls Royce plc.
Dr. R. Primus, Cummins Engine Co.
Prof. D. Puechberty, INSA, Rouen
Prof. Ishwar K. Puri, University of Illinois at Chicago
Prof. J. A. Puszynski, SDSM&T
Prof. Mardson Queiroz, Brigham Young University
Prof. James Quintiere, University of Maryland
Dr. R. Ragucci, IRC-CNR, Italy
D.J. Rakestraw, Sandia National Laboratory
Prof. Juan I. Ramos, Carnegie-Mellon University
Prof. Roger H. Rangel, University of California, Irvine
Prof. Fred Reardon, CA State University, Sacramento
Prof. R. Reitz, University of Wisconsin
Dr. Karoly Remenyi, Institute for Electrical Power Research
Dr. David L. Reuss, General Motors Research Laboratories
Dr. James J. Reuther, Battelle Columbus Operations
Dr. Jean-Robert Richard, CNRS, France
Dr. George A. Richards, U.S. Department of Energy
Prof. Cecilia Richards, Washington State University
Dr. Wolfgang Richter, Consultant
Dr. Edward Ritter, Villanova University
Dr. William L. Roberts, Lockheed Engineering Science
Dr. Richard J. Roby, Hughes Associates Inc
Prof. Larry Roe, Virginia Polytechnic Inst & State University
Dr. Eric A. Rohlfing, Sandia National Laboratories
Prof. Paul D. Ronney, University of Southern California
Dr. W. M. Roquemore, Wright-Patterson AFB
Dr. Tom Rosfjord, United Technologies Research Center
Dr. Howard Ross, NASA Lewis Research Center
Prof. Paul Roth, University of Duisburg
Prof. C. J. Rutland, University of Wisconsin-Madison
Dr. Kurt R. Sacksteder, NASA Lewis Research Center
Prof. Kozo Saito, University of Kentucky
Prof. Piero Salatino, University of Naples
Prof. G. Scott Samuelsen, University of California-Irvine
Dr. J. J. Sangiovanni, United Technologies Research Center
Prof. Taeko Sano, Tokai University
Prof. Robert J. Santoro, Pennsylvania State University
Prof. Adel F. Sarofim, Massachusetts Inst of Technology
Dr. Hamid Sarv, Babcock & Wilcox
Dr. Jun'ichi Sato, Ishikawajima-Harima Heavy Ind. Co.
Prof. J. P. Sawerysyn, Univ des Sciences de Lille
Prof. Robert F. Sawyer, University of California, Berkeley
Prof. Alan W. Scaroni, Pennsylvania State University
Dr. Klaus Schadow, Naval Air Warfare Center
Dr. Robert Schefer, Sandia National Laboratories
Prof. Joseph Schetz, Virginia Polytechnic Inst and State Univ
Dr. Keith Schofield, University of California, Santa Barbara
Dr. Garry L. Schott, Retired-Los Alamos Laboratory
Dr. G. Searby, Université de Provence, CNRS, France
Dr. Wm. Randall Seeker, Energy & Environment Res Corp
Dr. Daniel J. Seery, United Technologies Research Center
Dr. Connie Senior, PSI Technology Company
Prof. Selim M. Senkan, University of California, Los Angeles
Prof. Lee H. Sentman, University of Illinois
Dr. Michael A. Serio, Advanced Fuel Research
Prof. K. Seshadri, University of California, San Diego
Dr. S. M. Shahed, Southwest Research Institute
Prof. S. P. Sharma, Indian Institute of Technology
Prof. Benjamin D. Shaw, University of California-Davis
Dr. Yu. N. Shebeko, Russian Sci Res Inst for Fire Protection
Prof. J. E. Shepherd, CA Institute of Technology
Dr. Ian G. Shepherd, Lawrence Berkeley Laboratories

Dr. C. G. W. Sheppard, University of Leeds
Prof. Vladimir G. Shevchuk, Odessa State University
Dr. C. William Shipman, Consultant
Prof. Wei Shyy, University of Florida
Prof. Merwin Sibulkin, Brown University
Prof. Martin Sichel, University of Michigan
Prof. G. D. Silcox, University of Utah
Dr. R. F. Simmons, UMIST
Prof. William A. Sirignano, University of California-Irvine
Prof. G. I. Sivashinsky, Tel-Aviv University
Dr. Y. R. Sivathanu, Purdue University
Dr. John P. Smart, National Power, Netherlands
Prof. Owen I. Smith, University of California, Los Angeles
Dr. Gregory Smith, SRI International
Mr. Ian W. Smith, CSIRO, Australia
Dr. David B. Smith, Gas Research Centre
Prof. Philip J. Smith, University of Utah
Prof. Mitchell D. Smooke, Yale University
Prof. L. Douglas Smoot, Brigham Young University
Dr. Kermit C. Smyth, Natl Inst of Standards & Technology
Dr. David R. Snelling, National Research Council of Canada
Prof. Andrzej Sobiesiak, Queen's University
Prof. S. H. Sohrab, Northwestern University
Prof. Paul E. Sojka, Purdue University
Dr. William A. Sowa, University of California Irvine
Dr. Sten H. Stårner, The University of Sydney
Dr. W. P. Stricker, DLR Stüttgart
Prof. D. S. Stewart, University of Illinois
Dr. Dennis Stepowski, Université de Rouen
Mr. Steve Stein, National Institute of Standards & Technology
Dr. Frank Sun, Parker Hannifin Corp
Dr. James W. Sutherland, Brookhaven National Laboratory
Prof. Eric Suuberg, Brown University
Prof. Takuji Suzuki, Ibaraki University
Prof. J. Swithenbank, Sheffield University
Prof. N. Syred, University of Wales at Cardiff
Dr. Rodney J. Tabaczynski, Ford Motor Company
Prof. Toshimi Takagi, Osaka University
Dr. Fumiaki Takahashi, Univ of Dayton Research Institute
Dr. Hisahiro Takeda, American Pacific Corporation
Prof. Tadao Takeno, Nagoya University
Dr. Douglas G. Talley, US Air Force Phillips Laboratory
Prof. R. Tam, Purdue University at IUPUI
Dr. Franco Tamanini, Factory Mutual Research Corporation
Prof. Ming-Jun Tang, East China Institute of Technology
Prof. Hiroshi Taniguchi, Hokkaido University
Dr. R. S. Tankin, Northwestern University
Dr. Pat Tatem, Naval Research Laboratory
Dr. Simon C. Taylor, British Gas PLC
Dr. Alex M.K.P. Taylor, Imperial College
Dr. Philip H. Taylor, University of Dayton
Dr. F. Temps, Max-Planck-Institut für Strömungsforschung
Dr. A. Teodorczyk, Warsaw University of Technology
Dr. A. Tewarson, Factory Mutual Research Corporation
Dr. I. W. R. Thevenin, Univ of Heidelberg
Prof. James S. Tien, Case Western Reserve University
Dr. Julian M. Tishkoff, Air Force Ofc. of Scientific Research
Prof. Leonardo Tognotti, Università di Pisa
Prof. Jerzy Tomeczek, Politechnika Slaska KEP
Dr. Rowena J. Torres-Ordonez, Amoco Oil Company
Prof. Cesar Trevino, Univ Nacional Autonoma de Mexico
Prof. J. Troe, Institut f. Physik. Chemie der Universität
Dr. Arnaud Trouvé, Institut Français du Pétrole
Dr. John S. Truelove, BHP Research Newcastle Laboratories
Dr. Wing Tsang, Natl Inst of Standards & Technology
Prof. Shunichi Tsuge, University of Tsukuba
Prof. Hiroshi Tsuji, Tokyo Denki University
Dr. Takashi Tsuruda, The University of Tokyo
Dr. Allen J. Tulis, ITT Research Institute
Dr. F. P. Tully, Sandia National Laboratories
Prof. Stephen R. Turns, Pennsylvania State University
Dr. B. J. Tyler, UMIST
Prof. Akira Umemura, Yamagata University
Dr. Erdem A. Ural, Factory Mutual Research Corporation
Dr. David Urban, NASA Lewis Research Center
Prof. P. J. Van Tiggelen, Univ Catholique de Louvain
Dr. J. Vandooren, Univ Catholique de Louvain
Prof. Uri Vandsburger, Virginia Polytechnic Inst & State Univ
Dr. Jean-Pierre Vantelon, Université de Poitiers
Dr. Philip Varghese, University of Texas, Austin
Dr. M. Vedha-Nayagam, NASA Lewis Research Center
Dr. Luc Vervisch, CNRS, France
Prof. Denis Veynante, Ecole Centrale Paris
Dr. Bernard Veyssiere, ENSMA and CNRS, France
Dr. Tamas Vidoczy, Central Research Institute for Chemistry
Prof. Raymond Viskanta, Purdue University
Dr. Steven R. Vosen, Sandia National Laboratories
Dr. Jakob I. Vovchuk, Odessa State University
Dr. Christian Vovelle, CRCCHT-CNRS
Dr. Alexander Vranos, A. B. Associates

Dr. R. H. W. Waesche, Science Applications Intl Corp
Dr. Albert Wagner, Argonne National Laboratories
Prof. Heinz Georg Wagner, Universität Göttingen
Dr. Dick Waibel, John Zink Company
Prof. G. C. Wake, Massey University
Prof. R. W. Walker, University of Hull
Prof. T. F. Wall, University of Newcastle
Dr. Peter M. Walsh, EER
Prof. Jürgen Warnatz, Universität Stüttgart
Prof. Brent W. Webb, Brigham Young University
Dr. Roman Weber, International Flame Research Foundation
Prof. E. J. Weckman, University of Waterloo
Prof. Joseph A. Wehrmeyer, University of Missouri, Columbia
Prof. Felix Weinberg, Imperial College (Retired)
Prof. Jost O. L. Wendt, University of Arizona
Dr. Charles K. Westbrook, Lawrence Livermore Natl. Labs
Prof. P. R. Westmoreland, University of Massachusetts
Prof. James H. Whitelaw, Imperial College
Prof. Indrek S. Wichman, Michigan State University
Prof. Richard D. Wilk, Union College
Prof. Forman A. Williams, University of California, San Diego
Prof. Alan Williams, Leeds University
Dr. Bradley A. Williams, Naval Research Laboratory
Prof. Robert B. Williamson, University of California, Berkeley
Dr. Michael Winter, United Technologies Research Center
Dr. Sigmar Wittig, Universität of Karlsruhe
Prof. Stanlislaw Wojcicki, Washington State University
Prof. Piotr Wolanski, Warsaw University of Technology
Dr. Hans G. Wolfhard, Inst for Defense Analyses
Dr. J. Wolfrum, Universität Heidelberg
Prof. Cheng-kang Wu, Chinese Academy of Sciences
Prof. Xuchang Xu, Tsinghwa University
Prof. Vigor Yang, Pennsylvania State University
Prof. K. T. Yang, University of Notre Dame
Prof. P. Garcia Ybarra UNED-Fisica Fundamental
Dr. Lisa Yeh, Exxon Research and Engineering
Dr. Richard A. Yetter, Princeton University
Prof. Akira Yoshida, Tokyo Denki University
Dr. Brian Young, University of North Dakota, EERC
Dr. Hong-Zeng Yu, Factory Mutual Research Corporation
Prof. Saburo Yuasa, Tokyo Metropolitan Inst of Technology
Dr. Martin F. Zabielski, United Technologies Research Ctr
Dr. Michael Zachariah, Natl Inst of Standards & Technology
Dr. Vladimir Zamansky, Energy and Environmental Res Corp
Dr. Vladimir E. Zarko, Russian Academy of Sciences, Siberia
Dr. Nikolaos Zarzalis, MTU-Munchen
Prof. Igor S. Zaslonko, Russian Academy of Sciences
Prof. Lixing Zhou, Tsinghua University
Prof. Jingyi Zhu, University of Utah
Prof. Ben T. Zinn, Georgia Institute of Technology
Dr. Giorgio Zizak, Istituto Propulsione Ed Energetica
Prof. Andrey N. Zolotko, Odessa State University
Prof. E. E. Zukoski, California Institute of Technology

*Colloquia Organizers
°Poster Organizers
†Reading Room Coordinator

Publication Committee

Dr. William A. Pitz, Chair, Lawrence Livermore Natl Labs, USA
Prof. P. R. Westmoreland, University of Massachusetts, USA
Prof. L. D. Pfefferle, Yale University, USA
Prof. Joseph W. Bozzelli, New Jersey Inst of Tech, USA
Prof. Paul D. Ronney, Univ of Southern California, USA
Dr. Peter M. Walsh, EER, USA
Dr. Anthony Hamins, Natl Inst of Standards & Tech, USA
Dr. William P. Linak, US Environ Protection Agency, USA
Prof. Kozo Saito, University of Kentucky, USA
Dr. Howard Ross, NASA Lewis Research Center, USA
Dr. Michael C. Drake, General Motors Research Lab, USA
Prof. Thomas H. Fletcher, Brigham Young University, USA
Prof. Fokion Egolfopoulos, Univ of Southern California, USA
Dr. Gregory Smith, SRI International, USA
Dr. Larry L. Baxter, Sandia National Laboratories, USA
Dr. Robert Hurt, Sandia National Laboratories, USA
Dr. Jay O. Keller, Sandia National Laboratories, USA
Dr. Donald Lucas, Lawrence Berkeley Laboratories, USA
Prof. Ian M. Kennedy, University of California, Davis, USA
Prof. Simone Hochgreb, Massachusetts Inst of Tech, USA
Prof. John C. Kramlich, University of Washington, USA

Prof. M. Quinn Brewster, University of Illinois, USA
Prof. Suresh Menon, Georgia Institute of Technology, USA
Dr. Richard A. Yetter, Princeton University, USA
Dr. Habib N. Najm, Sandia National Laboratories, USA
Prof. Mary Judy Wornat, Princeton University, USA

English-Editing Subcommittee

Dr. Sanjay Correa, General Electric Research Center, USA
Prof. P. V. Farrell, University of Wisconsin, USA
Dr. Edward J. Mularz, NASA Lewis Research Center, USA
Dr. Mary Bui-Pham, Sandia National Laboratories, USA
Dr. Steve Niksa, SRI International, USA

Gold Medal Awards Committee

G. Dixon-Lewis, Chair, University of Leeds, England
Robert W. Bilger, University of Sydney, Australia
William J. McLean, Sandia National Laboratories, USA
A. G. Merzhanov, Russian Academy of Sciences, Russia
Gérard de Soete, Institut Français du Petrole, France
Hiroshi Tsuji, Tokyo Denki University, Japan
Heinz Gg. Wagner, Universität Göttingen, Germany

Silver Medal Awards Committee

Antonio D'Alessio, Chair, Università di Napoli, Italy
Alan C. Eckbreth, United Technologies Research Ctr, USA
Irvin Glassman, Princeton University, USA
Jack B. Howard, Massachusetts Inst of Technology, USA
Michikata Kono, University of Tokyo, Japan
Norbert Peters, RWTH, Aachen, Germany
Paul Roth, Universität of Duisburg, Germany
Scott Samuelsen, University of California, Irvine, USA

Planning Committee

Scott Samuelson, Co-Chair, Univ of California, Irvine, USA
William Sirignano, Co-Chair, Univ of California, Irvine, USA
Stephanie Beck, Coordinator, Univ of California, Irvine, USA
Candice Reimers, Ass't Coordinator, UC, Irvine, USA
Debbie Hart, Special Arrangements Coordinator, UCI, USA
Derek Dunn-Rankin, University of California, Irvine, USA
Said Elgobashi, University of California, Irvine, USA
John LaRue, University of California, Irvine, USA
Dmitri Papamoschou, University of California, Irvine, USA
Roger Rangel, University of California, Irvine, USA

CHAIRS OF TECHNICAL SESSIONS

Hottel Plenary Lecture
Elaine S. Oran

Invited Lecture on Incineration
Catherine P. Koshland

Invited Lecture on Soot
K. H. Homann

Invited Lecture on Chemical Kinetics
Daniel J. Seery

Invited Lecture on Turbulent Combustion
Robert Dibble

Supersonic Combustion
Gabrielle Dupre
Martin Sichel

Active Control of Combustors
Ben T. Zinn
Janet Ellzey

Incineration—Halogen Combustion
Elizabeth M. Fisher
Donald Lucas

Laminar Flames
Paul D. Ronney
V. S. Babkin

Turbulent Flame Structure
W. Kollmann

NO_x Chemistry
Peter Glarborg
Joe V. Michael

Supersonic Combustion
Chiping Li
Michael Shur

Pool Fires
C. Fernandez-Pello
Takashi Kashiwagi

Spark Ignition Engines
Charles K. Westbrook
Michael C. Drake

Laminar Flames
Jakob I. Vovchuk
G. Dixon-Lewis

N_2O from Fluidized Bed Combustion
Peter M. Walsh
Roman Weber

Soot Formation
T. T. Charalampopoulos
J. Thomas McKinnon

Biomass
P. J. Paul
Kim Dam-Johansen

Hydroperoxy Chemistry
John H. Kiefer
K. Hoyermann

Spark Ignition Engines
John S. McFeaters
Marcus Aldén

Laminar Flame Extinction
A. C. McIntosh
M. J. Linevsky

Flame Spread over Thin Fuels
Robert A. Altenkirch
Colomba DiBlasi

Simulations of Turbulent Flames
Denis Veynante
S. B. Pope

The Fate of Metals in Incineration
Adel F. Sarofim
Catherine P. Koshland

Gas Turbines
Sanjay M. Correa
J. J. Sangiovanni

Turbulent Combustion
Robert W. Bilger
Arnaud Trouvé

Chemistry of Aromatics
Ming Chang Lin
Ritsu Dobashi

Reaction Mechanisms in Coal
Judy Wornat
Larry L. Baxter

Gaseous Detonation
Michel Lefebvre
I.O. Moen

Modeling
Jay P. Boris
G. Makhviladze

Experimental Diagnostics
Alan C. Eckbreth
J. Wolfrum

Reduced Chemistry Mechanisms
Ulrich Maas
John F. Griffiths

Ignition
Takashi Niioka
P.J. Van Tiggelen

Two-Phase Combustion Dynamics
David Jones
Gerard M. Faeth

Nitrogen Radical Kinetics
H.-H. Grotheer
Joseph W. Bozzelli

Turbulent Combustion
Derek Bradley
Robert W. Pitz

Turbulent Combustion
K. N. C. Bray
Norbert Peters

Two-Phase Ignition & Liquid Propellents
Herman Krier
Mitat Birkan

Incineration
E. I. Kauppinen
Owen I. Smith

Supersonic Combustion and Detonations
Frank E. Marble
Michael Kh. Strelets

Laminar Flames
M. Matalon
Chung K. Law

Laminar Flames
W. M. Roquemore
Howard B. Palmer

Solid-Fuel Flammability
P. Joulain

Chemistry of Combustion
A. R. Burgess
Arthur Fontijn

Chemistry of Combustion
T. Brill

Fire Suppression
Robert B. Williamson
Andrzej W. Miziolek

Reactivity and Soot Suppression
K. H. Homann
Jack B. Howard

Fire Hazards
Richard G. Gann
Toshisuke Hirano

Solid Propellant Combustion
Takuo Kuwahara
Edward W. Price

Simulations of Turbulent Reactive Flow
Gabriel Roy
Roland P. Borghi

Nitrogen Radicals // CO in Flames
Frederick L. Dryer
Michel Cathonnet

Sprays
Suresh K. Aggarwal
Antoni Cavaliere

Hydrocarbon Radical Chemistry
Christian Vovelle
Daniel J. Seery

Global Environmental Effects
Nancy J. Brown
David M. Golden

Laminar Flames
Fokion Egolfopoulos
Takashi Tsuruda

Diesel Engines
S. M. Shahed
C. J. Rutland

Soot Formation
P. Gilot
Henning Bockhorn

Fluid Dynamic Effects on Turbulent Flames
Forman A. Williams
Ann R. Karagozian

Heterogeneous Detonations
Allen J. Tulis
Boris E. Gelfand

Detailed Chemical Mechanisms
Jurgen Warnatz
James A. Miller

Flame-Vortex Interactions
Thierry Poinsot
Pamela K. Barr

Sprays
Josette Bellan
Norman Chigier

Turbulent Flame Experiments
Michael Winter
James F. Driscoll

Soot Formation
Richard A. Dobbins
Heinz Georg Wagner

Engines and Combustors
Edward T. McHale
G. Scott Samuelsen

Engines and Combustors
Jay O. Keller
Jean Hertzberg

Sprays and Drops
Julian M. Tishkoff
Sigmar Wittig

NO_x Formation and Control
Lawrence J. Muzio

Soot Formation
Brian S. Haynes
Meredith B. Colket

Materials Synthesis
Lawrence A. Kennedy

Microgravity
Howard Ross

Ignition
Nicholas P. Cernansky

Coal-Reaction Mechanisms
Robert Chaiken

Coal Pyrolysis
Reginald E. Mitchell
Piero Salatino

Pulverized Coal & Fluidized Beds
Umberto Arena

Chemistry of Combustion
Anthony M. Dean
J. Vandooren

Turbulent Combustion
Sebastien Candel
Robert Dibble

Coal Pyrolysis
L. Douglas Smoot
Janos M. Beér

Materials Synthesis
Oleg E. Kashireninov
Hartwell F. Calcote

Microgravity Diffusion Flames
Merrill K. King
Andrzej Sobiesiak

Fluidized Bed Combustion
Matteo D'Amore
Andrej Macek

Chemistry of Aromatics
Wing Tsang
Igor S. Zaslonko

Explosions
Allen L. Kuhl
Piotr Wolanski

Chemistry of Aromatics
Kenneth Brezinsky
John C. Mackie

Droplet Combustion
Seiichiro Kumagai
Robert S. Levine

Pulse Combustion
Robert Serauskas
C. Fureby

Pulverized Fuel Flames
Peter F. Nelson
Donald Hardesty

Turbulent Flame Structures
Anthoni K. Oppenheim
Paul Clavin

CONTENTS

	Page
PREFACE	iii
BERNARD LEWIS TRIBUTE	v
THE COMBUSTION INSTITUTE	vii
TWENTY-FIFTH SYMPOSIUM COMMITTEES	xi
CHAIRPERSONS OF TECHNICAL SESSIONS	xxi
INTRODUCTION	xxxix

HOTTEL PLENARY LECTURE

Gasdynamic Enhancement of Nonpremixed Combustion. *Frank Marble* 1

SUPERSONIC COMBUSTION

Navier-Stokes Numerical Simulation of Supersonic Hydrogen-Flourine Combustion in CW Chemical Lasers. *M. Rotinian, M. Shur and M. Strelets* 13

Numerical Modeling of Combustion Processes Induced by a Supersonic Conical Blunt Body. *M. H. Lefebvre and T. Fujiwara* 85**

Numerical Simulation of Supersonic Mixing and Combustion. *P. Gerlinger, D. Brüggemann and J. Algermissen* 21

The Influence of Equivalence Ratio and Sorêt Effect on the Ignition of Hydrogen-Air Mixtures in Supersonic Boundary Layers. *L. F. F. da Silva and B. Deshaies* 29

Cavity-Actuated Supersonic Mixing and Combustion Control. *K. Yu and K. C. Schadow* 295*

The Application of New Combustion and Turbulence Models to H_2—Air Non-premixed Supersonic Combustion. *L. L. Zheng and K. N. C. Bray* 440*

Reduced Kinetic Mechanism of Ignition for Non-Premixed Hydrogen/Air in a Supersonic Mixing Layer. *Y. Ju and T. Niioka* 240*

DETONATIONS AND EXPLOSIONS

Accumulating Sequence of Ignitions from a Propagating Pulse. *J. W. Dold, M. Short, J. F. Clarke and N. Nikiforakis* 465**

On Deviations from Ideal Chapman-Jouguet Detonation Velocity. *H. K. Brüls, M. H. Lefebvre and J. Berghmans* 37

Theoretical and Numerical Analysis of the Photochemical Initiation of Detonations in Hydrogen-Oxygen Mixtures. *L. He and P. Clavin* 45

H_2-Air and CH_4-Air Detonations and Combustions behind Oblique Shock Waves. *C. Viguier, C. Guerraud and D. Desbordes* 53

Collision of a Shock Wave with Obstacles in a Combustible Mixture. *C. K. Chan* 341**

Weak and Strong Ignition Within the Scope of Spontaneous Flame Concept. *A. M. Bartenev and B. E. Gelfand* 61

Shock Tube Study of Ignition Delays and Detonation of Gaseous Monomethylhydrazine/Oxygen Mixtures. *L. Catoire, X. Bassin, G. Dupre and C. Paillard* 573*

Detonation Cell Size Measurements and Predictions in Hydrogen-Air-Stream Mixtures at Elevated Temperatures. *G. Ciccarelli, T. Ginsberg, J. Boccio, C. Economos, K. Sato and M. Kinoshita* ... 212*

Critical Diameter for the Transmission of a Detonation Wave into a Porous Medium. *A. Makris, T. J. Oh, J. H. S. Lee and R. Knystautas* 65

*Combustion and Flame, Vol. 99, 1994.

**Combustion and Flame, Vol. 100, 1995.

Initiation of Upstream-Directed Detonation Induced by the Venting of Gaseous Explosion. *S. P. Medvedev, A. N. Polenov, S. V. Khomik and B. E. Gelfand* 73
Phenomenological Aspects in Explosive Powder/Gas Two-Phase Detonations. *A. J. Tulis, W. K. Sumida, R. P. Joyce, D. C. Heberlein and D. L. Patel* 79
Investigation of Organic Dust Detonation in the Presence of Chemically Inert Particles. *R. Klemens, M. Kapuscinski, M. Wolinski, P. Wolanski and M. Sichel* 742*
Experimental Study of Deflagration to Detonation Transition Supported by Dust Layers. *Y.-C. Li, C. W. Kauffman and M. Sichel* 505**
Effect of Diethylenetriamine Sensitization on Detonation of Nitromethane in Porous Media. *J. J. Lee, M. Brouillette, D. L. Frost and J. H. S. Lee* 292**
Physical and Chemical Observations in Underwater Explosion Bubbles. *Warren C. Strahle and S. G. Liou* 89
Surface Erosion by High Speed Combustion Waves. *R. Klein, H. Breitbach, K. J. Geratz and W. Senger* 95
Prediction of the Maximum Turbulence Intensities Generated by Grid-Plate Obstacles in Explosion-Induced Flows. *H. Phylaktou and G. E. Andrews* 103

INTERNAL COMBUSTION ENGINES

State of the Art and Future Needs in S.I. Engine Combustion **(Invited Topical Review).** *R. R. Maly* 111
Develoment and Demonstration of 2D-LIF for Studies of Mixture Preparation in SI Engines. *H. Neij, Bengt Johansson and Marcus Aldén* 449*
Cars Temperature Measurements and the Cyclic Dispersion of Knock in Spark Ignition Engines. *D. Bradley, G. T. Kalghatgi, C. Morley, P. Snowden and Jinku Yeo* 125
Detection of Hot Spots in the End Gas of an Internal Combustion Engine Using Two-Dimensional LIF of Formaldehyde. *B. Bäuerle, F. Hoffmann, F. Behrendt and J. Warnatz* 135
Simultaneous 2D-Single Shot Imaging of OH Concentrations and Temperature Fields in a SI Engine Simulator. *A. Orth, V. Sick, J. Wolfrum, R. R. Maly and M. Zahn* 143
Chemical Kinetic Modeling of Exhaust Hydrocarbon Oxidation. *K.-C. Wu, S. Hochgreb and M. G. Norris* 193**
Hydrocarbon Oxidation in the Exhaust Port and Runner of a Spark Ignition Engine. *Kristine Drobot, Wai K. Cheng, Frederick H. Trinker, E. William Kaiser, Walter O. Siegl, David F. Cotton and Joel Underwood* 422*
In-Cylinder Crank Angle Resolved Imaging of Fuel Concentration In a Firing Spark-Ignition-Engine Using Planar Laser-Induced Flourescence. *M. Berckmüller, N. P. Tait, R. D. Lockett, D. A. Greenhalgh, K. Ishii, Y. Urata, H. Umiyama and K. Yoshida* 151
Analysis of In-Cylinder Flow Processes by LDA. *F. E. Corcione and G. Valentino* 387*
Numerical Modeling of Spark Ignition and Flame Initiation in a Quiescent Methane-Air Mixture. *T. Kravchik and E. Sher* 635*
A Thermochemical Phase Space for Combustion in Engines. *A. K. Oppenheim and J. A. Maxson* 157
Fuel and Soot Oxidation in Diesel-like Conditions. *A. Cavliere, R. Barbella, A. Ciajola, A. D'Anna and R. Ragucci* 167
Effects of Natural Gas Composition on Ignition Delay Under Diesel Conditions. *J. D. Naber, D. L. Siebers, S. S. Di Julio and C. K. Westbrook* 192*
The Droplet Group Microexplosions in Water-in-Oil Emulsion Sprays and Their Effects on Diesel Engine Combustion. *H. Z. Sheng, L. Chen, Z. P. Zhang, C. K. Wu, C. An and C. Q. Cheng* 175
Structure of a Spray Flame Stabilized on a Production Engine Combustor Swirl Cup. *F. Takahashi, W. J. Schmoll, G. L. Switzer and D. T. Shouse* 183

PRACTICAL ASPECTS OF COMBUSTION

Determination of Flue Gas Alkali Concentrations in Fluidized-Bed Coal Combustion by Excimer Laser Induced Fragmentation Fluorescence. *K. T. Hartinger, P. B. Monkhouse, J. Wolfrum, H. Baumann and B. Bonn* 193

*Combustion and Flame, Vol. 99, 1994.
**Combustion and Flame, Vol. 100, 1995.

A Field Study on the Trace Metal Behavior in Atmospheric Circulating Fluidized Bed Combustion. *T. Lind, E. I. Kauppinen, J. K. Jokiniemi and W. Maenhaut* 201
The Oxidation of Calcium Sulphide at the Temperatures of Fluidised Bed Combustors. *N. H. Davies, K. M. Laughlin and A. N. Hayhurst* 211
Primary and Secondary Fragmentation of Coals in a Circulating Fluidized Bed Combustor. *U. Arena, A. Cammarota and R. Chirone* 219
Ignition and Combustion of a Packed Bed in a Stagnation Point Flow. *D. Reinelt, A. Laurs and G. Adomeit* ..... 395°
The Effect of Hydrogen and Propane Addition on the Operation of a Natural Gas-Fired Pulsed Combustor. *H. R. N. Jones and J. Leng* ..... 404°
Heat Release Timing in a Non-Premixed Helmholtz Pulse Combustor. *Y. M. Tang, G. Waldherr, J. I. Jagoda and B. T. Zinn* ..... 251°°
NO_x and CO Emissions from a Pulse Combustor Operating in a Lean Premixed Mode. *J. O. Keller, T. T. Bramlette, P. K. Barr and J. R. Alvarez* ..... 460°
The Nonlinear Dynamics of Intrinsic Acoustic Oscillations in a Model Pulse Combustor. *Stephen B. Margolis* ..... 311°
Comparison of Measurements and Predictions of Wall Heat Flux and Gas Composition in an Oil-Fired Utility Boiler. *M. G. Carvalho, P. J. Coelho, A. L. N. Moreira, A. M. C. Silva and T. F. Silva* 227
Effect of Radiation on Nitrogen Oxides Emissions From Non-Sooty Swirling Flames of Natural Gas. *A. Sayre, N. Lallemant, J. Dugué and R. Weber* 235
Phase Averaging of the Precessing Vortex Core in a Swirl Burner Under Piloted and Premixed Combustion Conditions. *D. Froud, T. O'Doherty and N. Syred* ..... 407°°
On the Effects of Fuel Leakage on CO Production from Household Burners as Revealed by LIF and CARS. *C. E. van der Meij, A. Mokhov, R. A. A. M. Jacobs and H. B. Levinsky* 243
Turbulent Velocity and Temperature Measurements from a Gaseous Fueled Technology Combustor with a Practical Fuel Injector. *P. O. Hedman and D. L. Warren* ..... 185°°
On the Aero-thermal Characteristics of Gasifier-Fuelled Gas Turbine Combustors with Complex Geometries. *N.H. Kandamby and F.C. Lockwood* 251
A Spark Ignition Model for Relight Problems in Aircraft Gas Turbines. *D. Liou and D. A. Santavicca* 261
Fuel Saving by Heat-Recirculating Combustion Using Fibre Mats. *Sunao Nakamura and Felix Weinberg* 269

INVITED LECTURE

Combustion Science for Incineration Technology. *Jost Wendt* 277

INCINERATION AND WASTES

The Homogeneous, Gas-Phase Formation of Chlorinated and Brominated Dibenzo-P-Dioxins from 2,4,6-Trichloro- and 2,4,6-Tribromophenols. *S. S. Sidhu, L. Maqsud, B. Dellinger and G. Mascolo* ..... 11°°
Kinetic Interactions of CO, NO_x, and HCl Emissions in Post-Combustion Gases. *J. F. Roesler, R. A. Yetter and F. L. Dryer* ..... 495°°
Burning Rate Enhancement and Soot Reduction Through Blending in Chlorinated Waste Incineration. *T. X. Li and C. K. Law* 291
The Fate of Arsenic in a Laminar Diffusion Flame. *Scott Chesworth, GoSu Yang, Daniel P. Y. Chang, A. Daniel Jones, Peter B. Kelly and Ian M. Kennedy* ..... 259°°°
Modeling Heterogeneous/Homogeneous Reactions and Transport Coupling for Catalytic Combustion of Methyl Chloride over a Mn-based Catalyst. *H. Karim, L. D. Pfefferle, P. Markatou and M. Smooke* 299
TACCOS—A Thermography-Assisted Combustion Control System for Waste Incinerators. *F. Schuler, F. Rampp, J. Martin and J. Wolfrum* ..... 431°

°Combustion and Flame, Vol. 99, 1994.
°°Combustion and Flame, Vol. 100, 1995.
°°°Combustion and Flame, Vol. 98, 1994.

Active, Optimal Control of a Model, Industrial, Natural Gas-Fired Burner. *D. St. John and G. S. Samuelsen* 307
An Adaptive Optimal Combustion Control Strategy. *K. T. Padmanabhan, C. T. Bowman and J. D. Powell* 101**
Sorbent Capture of Nickel, Lead and Cadmium in a Laboratory Swirl Flame Incinerator. *W. P. Linak, R. K. Srivastava and J. O. L. Wendt* 241**
Biosludge Incineration in FBCs: Behavior of Ash Particles. *K. K. Rink, J. A. Kozinski and J. S. Lighty* 121**
Mixing and Chemical Kinetic Constraints on PIC Production during Chlorocarbon Combustion. *J. Brouwer, G. Sacchi, J. P. Longwell and A. F. Sarofim* 231*
Destruction of Liquid and Gaseous Waste Surrogates in an Acoustically Excited Dump Combustor. *J. W. Willis, C. Cadou, M. Mitchell, A. R. Karagozian and O. I. Smith* 280*
Experimental and Numerical Study of an Incinerator- and Furnace-Related Flow. *D. K. Heist, M. Ravichanran and F. C. Gouldin* 339*
Cold-Flow Simulation of Municipal Waste Incinerators. *S. Choi, J. S. Lee, S. K. Kim and D. H. Shin* 317
In Situ Detection of Hazardous Waste. *Charles S. McEnally, Robert F. Sawyer, C. P. Koshland and D. Lucas* 325

SPRAYS AND DROPLET COMBUSTION

Injection, Dispersion, and Combustion of Liquid Fuels **(Invited Topical Review).** *W. D. Bachalo* 333
Influence of Ambient Pressure on Drop-Size and Velocity Distributions in Dense Sprays. *Arvind K. Jasuja and Arthur H. Lefebvre* 345
Analysis of Droplet Arrival Statistics in a Pressure-Atomized Spray Flame. *J. T. Hodges, C. Presser, A. K. Gupta and C. T. Avedesian* 353
2D Laser Diagnostics of Liquid Methanol for Investigation of Atomization and Vaporization Dynamics in a Burning Spray Jet. *R. Bazile and D. Stepowski* 363
Flame Stabilization and OH Fluorescence Mapping of the Combustion Structures in the Near Field of a Spray Jet. *D. Stepowski, A. Cessou and P. Goix* 516*
Effect of Gravity on the Structure of an Unsteady Spray Diffusion Flame. *T. W. Park, S. K. Aggarwal and V. R. Katta* 767*
The Structure of the Dense Core Region in Transient Diesel Sprays. *G. J. Smallwood, Ömer L. Gülder and David R. Snelling* 371
Similarity Analysis of Spray Diffusion Flames in a Unidirectional Shear-Layer Flow. *Y. Tambour and D. Katoshevski* 381
Heat, Mass, and Momentum Transfer About Arbitrary Groups of Particles. *H. A. Dwyer, H. Nirschl, P. Kerschl and V. Denk* 389
Vaporization of a Dense Spherical Cloud of Droplets at Subcritical and Supercritical Conditions. *T. L. Jiang and W.-T. Chiang* 355*
Entrainment and Evaporation of Drops in the Laminar Part of a Two-Dimensional Developing Mixing Layer. *F. Fichot, J. Bellan and K. Harstad* 397
Vortex Pairing and Droplet Dispersion in a Turbulent, Free Shear Layer. *K. T. Kiger and J. C. Lasheras* 407
Application of an Integrated Phase Doppler Interferometer/Rainbow Thermometer/Point Diffraction Interferometer for Characterizing Burning Droplets. *S. V. Sankar, D. H. Buermann, K. M. Ibrahim and W. D. Bachalo* 413
The Effect of Initial Diameter on Free Droplet Combustion with Spherical Flame. *H. Hara and S. Kumagai* 423
Interactive Combustion of Two Droplets in Microgravity. *M. Mikami, H. Kato, J. Sato and M. Kono* 431
Clarification of the Flame Structure of Droplet Burning Based on Temperature Measurement in Microgravity. *M. Mikami, M. Niwa, H. Kato, J. Sato and M. Kono* 439
Ignition Experiment of a Fuel Droplet in High-Pressure High-Temperature Ambient. *R. Nakanishi, H. Kobayashi, S. Kato and T. Niioka* 447

*Combustion and Flame, Vol. 99, 1994.
**Combustion and Flame, Vol. 100, 1995.

Effects of Natural Convection on Two Stage Ignition of an n-Dodecane Droplet. *M. Tanabe, M. Kono, J. Sato, J. Koenig, C. Eigenbrod and H. J. Rath* 455

COAL AND ORGANIC SOLIDS COMBUSTION

Impact of Coal Pyrolysis on Combustion **(Invited Topical Review).** *P. R. Solomon and T. H. Fletcher* 463
An Experimental Study of High-Temperature, Oxidative Pulverized Coal Devolatilization. *L. H. Sorensen, O. Biede and R. E. Peck* 475
Volatile Matter Release, Particle/Cloud Ignition and Combustion of Near-Stoichiometric Suspensions of Pulverized Coal. *J. A. Lucas and T. F. Wall* 485
The Effect of Pulverized Coal Injection and Volatile Matter Content of Coal on Combustion Characteristics Around the Raceway Zone in the Blast Furnace. *H. Tsuge, T. Yoshida, H. Aoki and T. Miura* 493
The Influence of Burner Injection Mode on Pulverised Coal and Biomass Co-Fired Flames. *T. Abbas, P. Costen, N. H. Kandamby, F. C. Lockwood and J. J. Ou* ..... 617°
Performance Predictions of Pulverized-Coal Flames of Power Station Furnace and Cement Kiln Types. *F. C. Lockwood and B. Shen* 503
The Partitioning of Iron during the Combustion of Pulverized Coal. *L. E. Bool III, T. W. Peterson and J. O. L. Wendt* ..... 262°°
Radiative Heat Transfer in Pulverized-Coal-Fired Boilers—Development of the Absorptive/Reflective Character of Initial Ash Deposits. *G. H. Richards, J. H. Harb, L. L. Baxter, S. Bhattacharaya, R. P. Gupta and T. F. Wall* 511
Influence of Initial Particle Density on the Reaction Mode of Porous Carbon Particles. *Robert H. Essenhigh* ..... 269°
Ignition and Combustion of Isolated and Binary Arrays of Coal Particles. *E. Kharbat, K. Annamalai and C. Gopalakrishnan* ..... 413°°
Characterization of Mass and Density Distributions of Sized Coal Fractions. *E. R. Monazam and D. J. Maloney* ..... 733°
Evolution of Char Chemistry, Crystallinity, and Ultrafine Structure during Pulverized-Coal Combustion. *K. A. Davis, R. H. Hurt, N. Y. C. Yang and T. J. Headley* ..... 31°°
Evolution of Porosity and Thermal Conductivity during Char Oxidation. *Y. Weiss, Y. Benari, I. I. Kantorovich, E. Bar-Ziv, G. Krammer, A. Modestino and A. F. Sarofim* 519
A Transient Kinetics Study of the Combustion Reactivity of a Coal Char. *P. Salatino, F. Zimbardi and M. Paulicelli* 527
Fragmentation and Attrition of Coal Char Particles Undergoing Collisions During Combustion at Temperatures From 900 to 1100 K. *P. M. Walsh and Tong Li* ..... 749°
Predicting the Evolution of Fuel Nitrogen From Various Coals. *Stephen Niksa* 537
Combustion Roles of Bubble and Emulsion Phase in Bubbling Fluidized Bed Coal Combustion Elucidated by Conditional Gas Sampling. *Ichiro Naruse, Kazuhiro Koizumi, Koji Kuramoto, Guo-Quing Lu and Kazutomo Ohtake* 545
Predicting the Devolatilization Behavior of Any Coal From its Ultimate Analysis. *S. Niksa* ..... 384°°
A Method of Predicting Coal Devolatilization Behavior Based on the Elemental Composition. *Y. Zhao, M. A. Serio, R. Bassilakis and P. R. Solomon* 553
Decreases in the Swelling and Porosity of Bituminous Coals during Devolatilization at High Heating Rates. *T. K. Gale, C. H. Bartholomew and T. H. Fletcher* ..... 94°°
Near-Extinction and Final Burnout in Coal Combustion. *R. H. Hurt and K. A. Davis* 561
Gas-Particle Flows and Coal Combustion in a Burner/Combustor With High-Velocity Jets. *L. X. Zhou, W. Y. Lin, W. W. Luo and X. Q. Huang* ..... 669°
Application of Multiple Opposed Jets to Coal Flame Stabilization. *H. F. Zhao* ..... 653°
Catalytic Oxidation of an Amorphous Carbon Black. *P. Ciambelli, M. D'Amore, V. Palma and S. Vaccaro* ..... 413°
Structural and Compositional Transformations of Biomass Chars During Combustion. *M. J. Wornat, R. H. Hurt, N. Y. C. Yang and T. J. Headley* ..... 131°°

°Combustion and Flame, Vol. 99, 1994.
°°Combustion and Flame, Vol. 100, 1995.

Pyrolysis and Combustion of Corncobs in a Fluidized Bed: Measurement and Analysis of Behavior. *J.-L. Lin and H. M. Keener* 271**
On the Combustion of Wood-Char Spheres in O_2/N_2 Mixtures—Experiments and Analysis. *S. Dasappa, H. V. Sridhar, P. J. Paul, H. S. Mukunda and U. Shrinivasa* 569

SOOT AND POLYCYCLIC AROMATIC HYDROCARBONS

Soot Mass Growth and Coagulation of Soot Particles in C_2H_4/Air Flames at 15 Bar. *S. Hanisch, H. Jander, Th. Pape and H. Gg. Wagner* 577
Suppression of Soot Formation in Ethene Laminar Diffusion Flames by Chemical Additives. *T. Ni, S. B. Gupta and R. J. Santoro* 585
Iron/Soot Interaction in a Laminar Ethylene Nonpremixed Flame. *J. Zhang and C. M. Megaridis* 593
Effect of Flame Structure and Soot-Particle Inception in Diffusion Flames. *J. Du and R. L. Axelbaum* 367**
Detailed Modeling of Soot Formation in Laminar Premixed Ethylene Flames at a Pressure of 10 Bar. *A. Kazakov, H. Wang and M. Frenklach* 111**
Quantitative Measurements of Enhanced Soot Production in a Flickering Methane/Air Diffusion Flame. *C. R. Shaddix, J. E. Harrington and K. C. Smyth* 723*
Soot Formation in Weakly Buoyant Acetylene-Fueled Laminar Jet Diffusion Flames Burning in Air. *P. B. Sunderland, Ü. Ö. Köylü and G. M. Faeth* 310**
Nonluminous Diffusion Flame of Diluted Acetylene in Oxygen Enriched Air. *G. Sugiyama* 601
Soot Formation in Turbulent Non-Premixed Kerosine-Air Flame Burning at Elevated Pressure: Experimental Measurement. *K. J. Young, C. D. Stewart and J. B. Moss* 609
Experimental and Theoretical Study of Diesel Soot Reactivity. *F. Marcuccilli, P. Gilot, B. Stanmore and G. Prado* 619
Soot Formation at Elevated Pressures and Carbon Concentrations in Hydrocarbon Pyrolysis. *St. Bauerle, Y. Karasevich, St. Slavov, D. Tanke, M. Tappe, Th. Thienel and H. Gg. Wagner* ... 627
Thermal and Chemical Influences on the Soot Mass Growth. *M. Bachmann, W. Wiese and K. H. Homann* 635
Inception and Growth of Soot Particles in Dependence on the Surrounding Gas Phase. *Fabian Mauss, Thomas Schäfer and Henning Bockhorn* 697*
Laser Microprobe Analysis of Soot Precursor Particles and Carbonaceous Soot. *R. A. Dobbins, R. A. Fletcher and W. Lu* 301**
Optical Characterization of Rich Premixed CH_4/O_2 Flames Across the Soot Formation Threshold. *A. D'Alessio, G. Gambi, P. Minutolo, S. Russo and A. D'Anna* 645
Agglomeration of Soot Particles in Diffusion Flames under Microgravity. *Hiroyuke Ito, Osamu Fujita and Kenichi Ito* 363*
Some Physico-Chemical Parameters of Soot Formation During Pyrolysis of Methane and Methane-Acetylene and Methane-Benzene Mixtures. *P. A. Tesner and S. V. Shurupov* 653
Thermal Decomposition of Propargyl Bromide and the Subsequent Formation of Benzene. *R. D. Kern, H. Chen, J. H. Kiefer and P. S. Mudipalli* 177**
Shock Wave Study of the Thermal Decompostion of Benzyl Alcohol. *S. Frisch, H. Hippler, H. Neunaber and J. Troe* 254*
High Temperature Pyrolsis and Oxidation of Fullerene C_{60} Behind Shock Waves. *S. von Gersum and P. Roth* 661
Further Testing of the Fullerene Formation Mechanism With Predictions of Temperature and Pressure Trends. *C. J. Pope and J. B. Howard* 671
The Formation of Aromatic Carbon in Sooting Ethylene Flames. *A. Ciajolo, A. D'Anna, R. Barbella and A. Tregrossi* 679

INVITED LECTURE

Multichannel Reactions in Combustion. *Th. Just* 687

*Combustion and Flame, Vol. 99, 1994.
**Combustion and Flame, Vol. 100, 1995.

REACTION KINETICS

Thermal Decomposition of CH_2 Verified by Product Concentration Measurements of C, H, and CH. *M. W. Markus, A. M. Tereza and P. Roth* 705
The Thermal Reactions of CH_3. *K. P. Lim and J. V. Michael* 713
The Reaction System CH_3 + OH at Intermediate Temperatures. Appearance of a New Product Channel. *R. Humpfer, H. Oser, H.-H. Grotheer and Th. Just* 721
Bifurcation Analysis of Methyl Radical Oxidation in Open Systems. The Low Pressure Regime. *M. A. Grela and A. J. Colussi* 733
A Shock Tube Study of the CO + OH → CO_2 + H Reaction. *M. S. Wooldridge, R. K. Hanson and C. T. Bowman* 741
The Use of Carbon Monoxide/Hydrogen Burning Velocities To Examine the Rate of the CO + OH Reaction. *I. C. McLean, D. B. Smith and S. C. Taylor* 749
New Results on Moist CO Oxidation: High Pressure, High Temperature Experiments and Comprehensive Kinetic Modeling. *T. J. Kim, R. A. Yetter and F. L. Dryer* 759
Experimental and Numerical Comparison of Extractive and In-Situ Laser Measurements of Non-Equilibrium Carbon Monoxide in Lean-Premixed Natural Gas Combustion. *Q. V. Nguyen, B. L. Edgar, R. W. Dibble and A. Gulati* 395**
A Study of Carbon Monoxide in a Series of Laminar Ethylene/Air Diffusion Flames using Tunable Diode Laser Absorption Spectroscopy. *R. R. Skaggs and J. H. Miller* 430**
Kinetic Parameters for the Initiation Reaction RH + O_2 → R + HO_2. *T. Ingham, R. W. Walker and R. E. Woolford* 767
Formation of Methoxy and Hydroxymethyl Free Radicals in Selected Elementary Reactions. *S. Dóbé, T. Bérces. F. Temps, H. Gg. Wagner and H. Ziemer* 775
The Reaction of Hydroperoxy-Propyl Radicals with Molecular Oxygen. *J. W. Bozzelli and W. J. Pitz* 783
Reaction of Hydroperoxy t-Butyl Radicals and t-Butyl Peroxy t-Butyl Radicals in Relation To Chain Propagation in Combustion. *L. Batt, M. A. Khan and T. J. Mitchell* 793
Thermal Decomposition of HCl Measured by ARAS and IR Diode Laser Spectroscopy. *G. N. Schading and P. Roth* 467*
Experimental Studies of Cl-Atom Reactions at High Temperatures: Cl + H_2 → HCl + H from 291 to 1283 K. *G. Y. Adusei and A. Fontijn* 801
Thermal Decomposition of CH_2Cl_2 *K. P. Lim and J. V. Michael* 809
The Unimolecular Decomposition of 1-Chloroethyl Radical. *V. D. Knyazev, Á. Bencsura, I. A. Dubinsky, D. Gutman and S. M. Senkan* 817
Decay Mechanism of CF_3H or CF_2HCl in H_2/O_2/Ar Flames. *H. Richter, J. Vandooren and P. J. Van Tiggelen* 825
High Temperature Reactions of Phenyl Oxidation. *P. Frank, J. Herzler, Th. Just and C. Wahl* 833
Kinetics of the Phenyl Radical Reaction with Ethylene: An RRKM Theoretical Analysis of Low and High Temperature Data. *T. Yu and M. C. Lin* 169**
Reactions of Phenoxy Radicals in the Gas Phase. *R. Buth, K. Hoyermann and J. Seeba* 841
A Direct Study of the Reaction of Benzyl Radicals With Molecular Oxygen: Kinetics and Thermochemistry. *K. Hoyermann and J. Seeba* 851
Detailed Kinetic Modelling of Premixed Benzene Flames. *R. P. Lindstedt and G. Skevis* 551*
Laser Ionization Time-Of-Flight Mass Spectrometry Combined With Residual Gas Analysis for the Investigation of Moderate Temperature Benzene Oxidation. *G. Bermudez and L. Pfefferle* 41**
The Reactions of Phenylacetylenes With $O(^3P)$ in the Gas Phase. *M. Eichholtz, A. Schneider, D.-V. Stuchen, J.-T. Vollmer and H. Gg. Wagner* 859
Hydrogen Atom Attack on 1-Phenylpropene at High Temperatures. *W. Tsang and J. A. Walker* 867
Pyrolysis of p-Xylene and of 4-Methylbenzyl Radicals. *H. Hippler, S. Seisel and J. Troe* 875
Reaction Mechanisms for Toluene Pyrolysis. *M. B. Colket and D. J. Seery* 883
Kinetics of the Thermal Decomposition and Isomerisation of Pyrazine (1,4 Diazine). *A. Doughty, J. C. Mackie and J. M. Palmer* 893
An Experimental and Computational Study of Methanol Oxidation in the Intermediate and High Temperature Regimes. *T. J. Held and F. L. Dryer* 901

*Combustion and Flame, Vol. 99, 1994.
**Combustion and Flame, Vol. 100, 1995.

C_1/C_2 Chemistry in Fuel-Rich Post-Flame Gases: Detailed Kinetic Modelling. *I. T. Woods and B. S. Haynes* 909
A New Comprehensive Reaction Mechanism for Combustion of Hydrocarbon Fuels. *E. Ranzi, A. Sogaro, P. Gaffuri, G. Pennati, C. K. Westbrook and W. J. Pitz* 201*
Kerosene Combustion at Pressures up to 40 Atm: Experimental Study and Detailed Chemical Kinetic Modeling. *P. Dagaut, M. Reuillon, J.-C. Boettner and M. Cathonnet* 919
Laser-Induced Fluorescence Study of Manganese Fuel Additive Effects in a Propane/Air Flame. *U. Westblom, F. Fernandez-Alonso, G. P. Smith, J. B. Jeffries and D. R. Crosley* 261*
Cool Flames and Oscillations in Hydrocarbon Oxidation. *A. A. Mantashyan* 927
A Reduced Thermokinetic Model For The Autoignition of Fuels With Variable Octane-Ratings. *M. Schreiber, A. Sadat Sakak, A. Lingens and J. F. Griffiths* 933
A Unified Approach to the Reduced Kinetic Modelling of Alkane Combustion. *J. F. Griffiths, K. J. Hughes, M. Schreiber and C. Poppe* 533*
Reduced Mechanism of Soot Formation—Application to Natural Gas Fueled Diesel Combustion. *Y. Yoshihara, A. Kazakov, H. Wang and M. Frenklach* 941
Application of Repro-Modeling For the Reduction of Combustion Mechanisms. *Tamás Turányi* 949
Analysis of a Systematical Reduction Technique. *L. M. T. Somers and L. P. H. de Goey* 957

NO_x

Analysis of the Reactions H + N_2O and NH + NO: Pathways and Rate Constants Over a Wide Range of Temperature and Pressure. *J. W. Bozzelli, A. Y. Chang and A. M. Dean* 965
The Reactions of $NH(X^3\Sigma^-)$ with the Water Gas Components CO_2, H_2O and H_2. *M. Röhrig and Hg. Wagner* 975
Mechanism and Modeling of Hydrogen Cyanide Oxidation in a Flow Reactor. *P. Glarborg and J. A. Miller* 475*
A Shock Tube Study of the Reactions of CN and NCO with NO_2. *S. T. Wooldridge, J. D. Mertens, R. K. Hanson and C. T. Bowman* 983
Kinetic Investigation of the Reactions of NCO Radicals With Alkanes in the Temperature Range 294 K to 1113 K. *Alexander Schuck, Hans-Robert Volpp and Jürgen Wolfrum* 491*
A Shock Tube Study of the Reaction $H_2 + NO \rightarrow HNO + H$. *K. Natarajan, H. J. Mick, D. Woiki and P. Roth* 610*
Kinetic Studies of the Reactions $NH(X^3\Sigma^-) + NO$ and $NH(X^3\Sigma^-) + O_2$ at Elevated Temperatures. *H. Lillich, A. Schuck, H.-R. Volpp, J. Wolfrum and P. D. Naik* 993
Kinetics of Homogeneous Nitrous Oxide Decomposition. *P. Glarborg, J. E. Johnsson and Kim Dam-Johansen* 523*
NO_x and N_2O in Lean-Premixed Jet-Stirred Flames. *Robert C. Steele, Philip C. Malte, David G. Nicol and John C. Kramlich* 440**
Flame Structure Studies of a Lean $H_2/N_2O/Ar$ Flame Employing Molecular Beam Mass Spectrometry and Modeling. *D. C. Dayton, C. M. Faust, W. R. Anderson and R. C. Sausa* 323*
An Experimental and Modeling Study of the Selective Noncatalytic Reduction of NO by Ammonia in the Presence of Hydrocarbons. *R. Hemberger, S. Muris, K.-U. Pleban and J. Wolfrum* 660*
Hydrocarbon-NO_x Interactions at Low Temperatures—1. Conversion of NO to NO_2 Promoted by Propane and the Formation of HNCO. *P. F. Nelson and B. S. Haynes* 1003
Aspects of Nitrogen Flame Chemistry Revealed By Burning Velocity Modelling. *M. J. Brown and D. B. Smith* 1011
NO_x Formation in Lean Premixed Non-Catalytic and Catalytically Stabilized Combustion of Propane. *A. Schlegel, S. Buser, P. Benz, H. Bockhorn and F. Mauss* 1019
NO_x Formation in Geometrically Scaled Gas-Fired Industrial Burners. *A. D. Al-Fawaz, L. M. Dearden, J. T. Hedley, M. Missaghi, M. Pourkashanian, A. Williams and L. T. Yap* 1027
Influence of Gasodynamics on NO_x Emission From Large Diffusion Natural Gas Flames. *J. Tomeczek, J. Góral and B. Gradon* 1035
Study of NOx Emission Characteristics In Pressurized Staged Combustor Concepts. *J. Meisl, R. Koch, R. Kneer and S. Wittig* 1043
NO and N_2O Decomposition Over Coal Char at Fluidized-Bed Combustion Conditions. *J. Rodriguez-Mirasol, A. C. Ooms, J. R. Pels, F. Kapteijn and J. A. Moulijn* 499*

*Combustion and Flame, Vol. 99, 1994.
**Combustion and Flame, Vol. 100, 1995.

Effect of NO and O_2 Concentration on N_2O Formation during Coal Combustion in a Fluidized Bed Combustor: Modeling Results. *S. K. Goel, A. Morihara, C. J. Tullin and A. F. Sarofim* 1051
Impact of Air Staging on the Fate of NO and N_2O in a Circulating Fluidized-Bed Combustor. *X. S. Wang, B. M. Gibbs and M. J. Rhodes* .... 508°

INVITED LECTURE

Transition and Structure of Jet Diffusion Flames. *T. Takeno* 1061

TURBULENT FLAMES

Modeling Turbulent Flame Propagation **(Invited Topical Review).** *W. T. Ashurst* 1075
Chemical Closure and Burning Rates in Premixed Turbulent Flames. *F. C. Gouldin and P. C. Miles* .... 202°°
The Production of Premixed Flame Surface Area in Turbulent Shear Flow. *A. Trouvé* .... 687°
Dynamics of the Flame Surface Area in Turbulent Non-Premixed Combustion. *W. Kollmann and J. H. Chen* 1091
Partially Premixed Turbulent Flame Propagation in Jet Flames. *C. M. Müller, H. Breitbach and N. Peters* 1099
A Lagrangian Model For Predicting Turbulent Diffusion Flames With Chemical Kinetic Effects. *M. Obounou, M. Gonzalez and R. Borghi* 1107
Two-Dimensional Non-Stationary Causal Stochastic Model for Turbulence/Radiation Interactions in Flames. *S. H. Chan, X. C. Pan and J. Zhang* 1115
Effects of Molecular Transport on Turbulence-Chemistry Interactions in a Hydrogen-Argon-Air Jet Diffusion Flame. *S. Menon, W. H. Calhoon, Jr., G. Goldin and A. R. Kerstein* 1125
Experimental Identification of Mixing Regimes in the Analysis of Turbulent Diffusion Flames. *A. Cavaliere, M. El-Naggar and R. Ragucci* .... 679°
Measurements of Scalar Dissipation in the Reaction Zones of Turbulent Nonpremixed H_2-Air Flames. *S. P. Nandula, T. M. Brown and R. W. Pitz* .... 775°
Conserved Scalar Measurements in Turbulent Diffusion Flames by a Raman and Rayleigh Ribbon Imaging Method. *S. H. Starner, R. W. Bilger, K. M. Lyons, J. H. Frank and M. B. Long* .... 347°
Simultaneous Measurement of Conserved and Reactive Scalars in Turbulent Diffusion Flames for Assessment of PDF Models. *T. S. Cheng and R. W. Pitz* 1133
Wide Field Conserved Scalar Imaging in Turbulent Diffusion Flames By a Raman and Rayleigh Method. *J. B. Kelman, A. R. Masri, S. H. Stårner and R. W. Bilger* 1141
Simultaneous NO and Temperature Imaging Measurements in Turbulent Nonpremixed Flames. *M. Namazian, J. Kelly and R. Schefer* 1149
Laser Raman Scattering Measurements of Differential Molecular Diffusion in Turbulent Nonpremixed Jet Flames of H_2/CO_2 Fuel. *L. L. Smith, R. W. Dibble, L. Talbot, R. S. Barlow and C. D. Carter* .... 153°°
Mixture Fraction Imaging in Turbulent Nonpremixed Hydrocarbon Flames. *J. H. Frank, K. M. Lyons, D. F. Marran, M. B. Long, S. H. Stårner and R. W. Bilger* 1159
Raman Measurements and Joint PDF Modeling Of a Non-Premixed Bluff-Body-Stabilized Methane Flame. *S. M. Correa, A. Gulati and S. B. Pope* 1167
Flame Stabilization in the Wake Flow Behind a Slit V-Gutter. *Jing-Tang Yang, Chang-Wu Yen and Go-Long Tsai* .... 288°
Interactions Between Nonsymmetrical Wake Structure and Turbulent Diffusion Flames Behind a Rear-Facing Semicircular Cylinder. *Norio Ohiwa, Yojiro Ishino and Shigeki Yamaguchi* .... 302°
Effect of Dilution on the Liftoff of Non-Premixed Jet Flames. *B. J. Lee, J. S. Kim and S. H. Chung* 1175
Stabilization Mechanism of Lifted Jet Diffusion Flames. *C. R. Kaplan, E. S. Oran and S. W. Baek* 1183
Modeling of Extinction in Turbulent Diffusion Flames by the Velocity-Dissipation-Composition PDF Method. *A. T. Norris and S. B. Pope* .... 211°°

°Combustion and Flame, Vol. 99, 1994.
°°Combustion and Flame, Vol. 100, 1995.

The Effect of Turbulence on Extinction of Counterflow Diffusion Flame. *H. Tsuji, A. Yoshida and N. Endo* 1191
Strain Effects on the Structure of Counterflowing Turbulent Premixed Flames. *C. Mounaïm-Rousselle and I. Gökalp* 1199
Experimental Investigation of a Premixed Flame in an Impinging Turbulent Stream. *S. C. Li, P. A. Libby and F. A. Williams* 1207
Lewis Number Effects on Premixed Flames Interacting with Turbulent Kármán Vortex Streets. *J. G. Lee, T.-W. Lee, D. A. Nye and D. A. Santavicca* 161**
Flame Propogation Through Periodic Vortices. *J. W. Dold, O. S. Kerr and I. P. Nikolova* 359**
Experiments on the Interaction Between a Vortex and a Strained Diffusion Flame. *J. C. Rolon, F. Aguerre and S. Candel* 422**
Mixing Characteristics of Compressible Vortex Rings Interacting with Normal Shock Waves. *B. M. Cetegen and J. C. Hermanson* 232**
The Formation and Destruction of Aromatic Compounds in a Turbulent Flame. *J. H. Thijssen, M. A. Toqan, J. M. Beér and A. F. Sarofim* 1215
Experimental Study of Premixed Flames in Intense Isotropic Turbulence. *B. Bédat and R. K. Cheng* 485**
Temporal Evolution of Turbulence/Chemistry Interactions in Lifted, Turbulent-Jet Flames. *R. W. Schefer, M. Namazian, E. E. J. Filtopoulos and J. Kelly* 1223
Fine Structure of Small-Scale and High-Intensity Turbulent Premixed Flames. *J. Furukawa and T. Hirano* 1233
Comparative Experimental and Numerical Investigation of a Piloted Turbulent Natural-Gas Diffusion Flame. *T. W. J. Peeters, P. P. J. Stroomer, J. E. de Vries, D. J. E. M. Roekaerts and C. J. Hoogendoorn* 1241

TURBULENT COMBUSTION

Experimental Analysis of Flamelet Models for Premixed Turbulent Combustion. *D. Veynante, J. M. Duclos and J. Piana* 1249
Large Eddy Simulations of Bluff Body Stabilized Flames. *C. Fureby and C. Löfström* 1257
The Vorticity Dynamics of an Exothermic, Spatially-Developing, Forced, Reacting Shear Layer. *M. C. Soteriou and A. F. Ghoniem* 1265
Three-Dimensional Numerical Simulations of Unsteady Reactive Square Jets. *F. F. Grinstein and K. Kailasanath* 2**
Strain Rate Modelling for a Flame Surface Density Equation with Application to Non-premixed Turbulent Combustion. *F. Fichot, B. Delhaye, D. Veynante and S. M. Candel* 1273
Numerical Simulation of Local Extinction Effects in Turbulent Combustor Flows of Methane and Air. *I. R. Gran, M. C. Melaaen and B. F. Magnussen* 1283
Strained Dissipation and Reaction Layer Analyses of Nonequilibrium Chemistry in Turbulent Reacting Flows. *E. S. Bish and W. J. A. Dahm* 457**
Large-Eddy Simulations of Turbulent Reacting Flows in a Chamber With Gaseous Ethylene Injecting Through the Porous Wall. *T. M. Liou, W. Y. Lien and P. W. Hwang* 591*
Turbulent Broadening of Autoignition Limits. *S. M. Correa and A. J. Dean* 1293
The Structure of the Recirculation Zone of a Bluff-Body Combustor. *A. R. Masri, B. B. Dally, R. S. Barlow and C. D. Carter* 1301
Afterburning in Spherical Premixed Turbulent Explosions. *Derek Bradley, M. Lawes, M. J. Scott, E. M. J. Mushi and M. J. Scott* 581*

LAMINAR FLAMES

Rich Methane/Air Flames: Burning Velocities, Extinction Limits and Flammability Limit. *M. N. Bui-Pham and J. A. Miller* 1309
Laminar Flame Speeds and Extinction Strains Rates of Mixtures of Carbon Monoxide with Hydrogen, Methane, and Air. *C. M. Vagelopoulos and F. N. Egolfopoulos* 1317
Aspects of Laminar Premixed Flame Extinction Limits. *G. Dixon-Lewis* 1325

*Combustion and Flame, Vol. 99, 1994.
**Combustion and Flame, Vol. 100, 1995.

Effects of Pressure and Dilution on the Extinction of Counterflow Nonpremixed Hydrogen-Air Flames. *P. Papas, I. Glassman and C. K. Law* 1333
Further Considerations on the Determination of Laminar Flame Speeds With the Counterflow Twin Flame Technique. *C. M. Vagelopoulos, F. N. Egolfopoulos and C. K. Law* 1341
Laminar Flame Calculations Using Simplified Chemical Kinetics Based on Intrinsic Low-Dimensional Manifolds. *U. Maas and S. B. Pope* 1349
Numerical Investigation of Steady Laminar Flame Propagation in a Circular Tube. *S. T. Lee and C. H. Tsai* 484*
Laminar Counterflow Mixing of Acetylene Into Hot Combustion Products. *H. Breitbach, J. Goettgens, F. Mauss, H. Pitsch and N. Peters* 1357
Response of Counterflow Diffusion Flames To Oscillating Strain Rates. *H. G. Im, C. K. Law, J. S. Kim and F. A. Williams* 21**
Dynamics and Structure of Unsteady, Strained, Laminar Premixed Flames. *F. N. Egolfopoulos* ... 1365
Geometric and Radiation Effects on Steady and Unsteady Strained Laminar Flames. *F. N. Egolfopoulos* 1375
Stretch Effects Extracted from Propagating Spherical Premixed Flames with Detailed Chemistry. *D. P. Mishra, P. J. Paul and H. S. Mukunda* 379*
On the Structure of Stretched/Compressed Laminar Flamelet—Influence of Preferential Diffusion. *V. R. Katta and W. M. Roquemore* 61**
Effects of Curvature and Unsteadiness in Diffusion Flames. Implications for Turbulent Diffusion Combustion. *B. Cuenot and T. Poinsot* 1383
Effect of Unsteady Stretch Rate on OH Chemistry During a Flame-Vortex Interaction: To Assess Flamelet Models. *C. J. Mueller, J. F. Driscoll, D. J. Sutkus, Wm. L. Roberts, M. C. Drake and M. D. Smooke* 323**
On Adiabatic Stabilization and Geometry of Bunsen Flames. *C. J. Sun, C. J. Sung and C. K. Law* 1391
Effects of Rotation on the Stability and Structure of Tubular Flame. *Kazuhiro Yamamoto, Satoru Ishizuka, Toshisuke Hirano* 1399
The Initial Development of a Tulip Flame. *M. Matalon and J. L. McGreevy* 1407
An Evolution Equation Modelling Inversion of Tulip Flames. *J. W. Dold and G. Joulin* 450**
The Development of Instabilities in Laminar Explosion Flames. *Derek Bradley and C. M. Harper* 562*
Temperature Field on a Laminar Diffusion Dust Flame. *J. I. Vovchuk and N. I. Poletaev* 706*
Flame Front Disturbance Induced by a Weak Pressure Wave. *R. Dobashi, T. Hirano and T. Tsuruda* 1415

FLAME SPREAD, FIRE AND HALOGENATED FIRE SUPPRESSANTS

Polymer Combustion and Flammability—Role of the Condensed Phase **(Invited Topical Review).** *T. Kashiwagi* 1423
Creeping Flame Spread: Some New Results and Interpretation for Material Flammability Characterization. *T. Chen and M. A. Delichatsios* 601*
Upward Flame Spread along PMMA Vertical Corner Walls. Part II: Mechanism of "M" Shape Pyrolysis Front Formation. *C. Qian, H. Ishida and K. Saito* 331*
Behavior of Fires Spreading Downward Over Thick Paper. *M. Suzuki, R. Dobashi and T. Hirano* 1439
Flame Spread over Thin Solid Fuels in Partially Premixed Atmospheres. *P. D. Ronney, J. B. Greenberg, Y. Zhang and E. V. Roegner* 474**
An Instrument for Characterization of the Thermal and Optical Properties of Charring Polymeric Materials. *M. A. Serio, D. S. Pines, A. S. Bonanno, P. R. Solomon and G. A. Simmons* 1447
Carbon Monoxide Formation in Fires By High-Temperature Anaerobic Wood Pyrolysis. *W. M. Pitts, E. L. Johnsson and N. P. Bryner* 1445
Simulation of Smoke Plumes from Large Pool Fires. *H. R. Baum, K. B. McGrattan and R. G. Rehm* 1463
Air Entrainment Flow Field Induced by a Pool Fire. *X. C. Zhou and J. P. Gore* 52**
Simultaneous Optical Measurement of Soot Volume Fraction, Temperature, and CO_2 in Heptane Pool Fire. *M. Y. Choi, A. Hamins, H. Rushmeier and T. Kashiwagi* 1471

*Combustion and Flame, Vol. 99, 1994.
**Combustion and Flame, Vol. 100, 1995.

Boilover Burning of Heating Oil Spilled on Water. *J. P. Garo, J. P. Vantelon and A. C. Fernandez-Pello* 1481
Autoignition of Combustible Fluids in Porous Insulation Materials. *A. C. McIntosh, M. Bains, W. Crocombe and J. F. Griffiths* 541*
The Inhibiting Effect of CF_3Br on the Reaction $CH_4 + O_2$ at 1070 K. *F. Battin-Leclerc, G. M. Come and F. Baronnet* 644*
Experimental and Computational Study of the Effect of C_2F_6 on Premixed Methane Flames. *O. Sanogo, J.-L. Delfau, R. Akrich and C. Vovelle* 1489
Extinction of Nonpremixed Flames with Halogenated Fire Suppressants. *A. Hamins, D. Trees, K. Seshadri and H. K. Chelliah* 221*
Suppression of High-Speed C_2H_4 / Air Flames with C_1—Halocarbons. *G. Gmurczyk and W. Grosshandler* 1497
Fluoromethane Chemistry and Its Role in Flame Suppression. *P. R. Westmoreland, D. R. F. Burgess, M. R. Zachariah and W. Tsang* 1505

GLOBAL ENVIRONMENTAL EFFECTS

Combustion's Impact on the Global Atmosphere **(Invited Topical Review).** *M. J. Prather and J. A. Logan* 1513

IGNITION

A Bifurcation Analysis of High-Temperature Ignition of H_2-O_2 Diffusion Flames. *A. L. Sánchez, A. Liñán and F. A. Williams* 1529
The Role of Kinetic Versus Thermal Feedback in Nonpremixed Ignition of Hydrogen Versus Heated Air. *T. G. Kreutz, M. Nishioka and C. K. Law* 758*
Effect of the Initial Temperature and Composition of a Hot Transient Jet on the Ignition of H_2-Air-Diluent Mixtures. *N. Djebaili, R. Lisbet, G. Dupre and C. Paillard* 1539
Diffusion and Premixed Flame Ignition Dynamics in a Field of Variable Strain Rate. *D. Thevenin and S. Candel* 1547
Self Ignition of Expanding High Temperature H_2-Air and CH_4-Air Mixtures. *H.-J. Weber, A. Mack and P. Roth* 1555
Natural Gas and Blends Oxidation and Ignition: Experiments and Modeling. *Y. Tan, P. Dagaut, M. Cathonnet, J. Cl. Boettner, J. S. Bachman and P. Carlier* 1563
Shock Initiated Ignition in Ethylene Oxide, Propylene Oxide, 1,2-Epoxybutane and 2,3-Epoxybutane. *A. Lifshitz and A. Suslensky* 1571
Shock-Tube Investigation on the Self-Ignition of Hydrocarbon-Air Mixtures at High Pressures. *K. Fieweger, R. Blumenthal and G. Adomeit* 1579
Pressure and Concentraion Dependences of the Autoignition Temperature for Normal Butane + Air Mixtures in a Closed Vessel. *M. R. Chandraratna and J. F. Griffiths* 626*

TWO-PHASE COMBUSTION

Ignition and Combustion of Magnesium in Carbon Dioxide Streams. *S. Yuasa and A. Fukuchi* ... 1587
Ignition Process of a Heated Iron Block in High Pressure Oxygen Atmosphere. *J. Sato, H. Ohtani and T. Hirano* 376**
Modelling of Partially Confined Hot Fragment Conductive Ignition. *T. H. Huang, S. T. Thynell and K. K. Kuo* 1595
Solid- Fuel Regression During Ignition Transient in a Ramjet. *J.-T. Yang and C. Y. Y. Wu* 1603
Supercritical and Subcritical Combustion of LOX with Hydrogen in an Axisymmetric Laminar Diffusion Flame. *A.-S. Yang, K. K. Kuo and W. H. Hsieh* 1609
Analyses of Liquid Rocket Instabilities Using a Computational Testbed. *J. M. Grenda, S. Venkateswaran and C. L. Merkle* 1619

*Combustion and Flame, Vol. 99, 1994.
**Combustion and Flame, Vol. 100, 1995.

Superadiabatic Combustion of Methane Air Mixtures under Filtration in a Packed Bed. *S. Zhdanok, L. A. Kennedy and G. Koester* 221**
Modeling of Combustion Wave Propagation in Carbon Dust/Gas Mixture. *Piotr M. Krishenik, Eduard N. Rumanov and K. G. Shkadinskii* 713*
Characteristics of Water-Base Foam Combustion. *V. S. Babkin, N. A. Kakutkina and V. V. Zamaschikov* 1627

SOLID PROPELLANT COMBUSTION

RDX Flame Structure. *D. Hanson-Parr and T. Parr* 1635
Laser Recoil, Plume Emission, and Flame Height Combustion Response of Oxidizers HMX and RDX at Atmospheric Pressure. *J. C. Finlinson, T. Parr and D. Hanson-Parr* 1645
Unsteady Combustion of Homogeneous Energetic Solids Using the Laser-Recoil Method. *S. F. Son and M. Q. Brewster* 283**

MATERIALS SYNTHESIS

Combustion Synthesis of ZnS in Microgravity. *S. Goroshin, J. H. S. Lee and D. L. Frost* 1651
Nonoxide Ceramic Powder Synthesis. *B. W. Gerhold and K. E. Inkrott* 144**
Nanoscale Unagglomerated Nonoxide Particles from a Sodium Coflow Flame. *D. P DuFaux and R. L. Axelbaum* 350**
Propagation and Diffusion Limited Extinction of Nonadiabatic Heterogeneous Flame in the SHS Process. *A. Makino and C. K. Law* 1659
A DMS Kinetic Study of the Boron Oxides Vapor in the Combustion Front of SHS System Mo + B. *O. E. Kashireninov and I. A. Yuranov* 1669
Stochastic Modeling of Multi-State Combustion of Condensed Heterogeneous Systems. *B. M. Khusid, B. B. Khina, E. P. Podvoisky and I. S. Chebotko* 371*
Theory of Spin and Spiral Gasless Combustion. *Boris V. Novozhilov* 1677

MICROGRAVITY

Buoyant Downward Diffusion Flame Spread and Extinction in Partial-Gravity Accelerations. *K. R. Sacksteder and J. S. T'ien* 1685
The Behavior of Flames Spreading over Thin Solids in Microgravity. *P. A. Ramachandra, R. A. Altenkirch, S. Bhattacharjee, L. Tang, K. Sacksteder and M. K. Wolverton* 71**
Predictions of Wind-Opposed Flame Spread Rates and Energy Feed Back Analysis For Charring Solids in a Microgravity Environment. *C. Di Blasi* 332**
Flame Propagation Experiment of PMMA Particle Cloud in a Microgravity Environment. *H. Kobayashi, N. Ono, Y. Okuyama and T. Niioka* 1693
The Effect of Gravity on a Laminar Diffusion Flame Established over a Horizontal Flat Plate. *J. L. Torero, L. Bonneau, J. M. Most and P. Joulain* 1701
Numerical Simulations of Burner-Stabilized Hydrogen-Air Flames in Microgravity. *G. Patnaik and K. Kailasanath* 247*
On Burner-Stabilized Cylindrical Premixed flames in Microgravity. *J. A. Eng, C. K. Law and D. L. Zhu* 1711
An Experimental and Numerical Investigation on the Hot Surface Ignition of Premixed Gases Under Microgravity Conditions. *H. Nagata, H. M. Kim, J. Sato and M. Kono* 1719

EXPERIMENTAL DIAGNOSTICS

Determination of Temperature From N_2 and O_2 Cars Spectra at Very High Pressure. *T. Dreier, M. Ridder, G. Schiff, A. Saur and A. A. Suvernev* 1727

*Combustion and Flame, Vol. 99, 1994.
**Combustion and Flame, Vol. 100, 1995.

Dual-Broadband Rotational CARS Measurements in an IC Engine. *P.-E. Bengtsson, L. Martinsson, M. Aldén, B. Johansson, B. Lassesson, K. Marforio and G. Lundholm* 1735
Double-Pulsed Imaging Using Simultaneous OH/Acetone PLIF For Studying the Evolution of High-Speed, Reacting Mixing Layers. *J. M. Seitzman, M. F. Miller, T. C. Island and R. K. Hanson* 1743

AUTHOR INDEX 1751
SUBJECT INDEX 1761

INTRODUCTION

The growing number of papers submitted to the International Combustion Symposia has created new challenges, opportunities, and demands on the paper selection and publication processes. To accomodate this growth, the Program Committee made a number of changes in the procedures for the Twenty-Fifth Symposium. For example: most of the papers presented appear in this volume, but some appear in special issues of *Combustion and Flame*; there were six parallel sessions of contributed papers; we tried a new procedure in which authors of controversial papers had a chance for rebuttal; we attempted to obtain more reviews for each paper; about one third of the contributed papers were given in poster format; and electronic communications were encouraged to facilitate communications with authors and reviewers. In this Introduction, I try to explain some of these in more detail.

This volume contains about two thirds of the papers accepted for presentation at the Twenty-Fifth Symposium, including the Hottel Lecture, three of the Invited Lectures, and all of the Topical Reviews. The other third of the papers presented appear in special issues of *Combustion and Flame*, the journal of The Combustion Institute. In order to present a complete listing of all of the papers presented at the Symposium, the table of contents of this volume lists *all* of the invited and contributed papers, but indicates those papers that appear in *Combustion and Flame*. In addition to the papers themselves, this volume and the issues of *Combustion and Flame* include comments and questions from the audience, and the responses to these from the authors.

The five invited presentations and six Topical Reviews represent the diversity of combustion research, ranging from basic chemical kinetics to the operation of automobile engines, to the global effects of combustion on our atmosphere. The Hottel Lecture that opened the meeting was given by Frank E. Marble, who spoke on "Gasdynamic Enhancement of Nonpremixed Combustion." The Invited Lectures were "Multichannel Reactions in Combustion Chemistry" by Thomas Just, "Combustion Science for Incineration Technology" by Jost Wendt, "Smoke, Diamonds, and Stardust" by Antonio D'Alessio, and "Transition and Structure of Jet Diffusion Flames" by Tadeo Takeno. The six Topical Reviews were "Combustion Modeling and Turbulence Structure," by William T. Ashurst, "Role of the Condensed Phase in Polymer Combustion and Flammability," by Takashi Kashiwagi, "State of the Art and Future Needs in S.I. Engine Combustion," by Rudolf R. Maly, "Injection, Dispersion, and Combusion of Liquid Fuels" by William D. Bachalo, "Impact of Coal Pyrolysis on Combustion" by Thomas H. Fletcher and Peter R. Solomon, and "Global Atmospheric Effects of Combustion Sources" by Michael Prather and Jennifer Logan.

There were ten Colloquia, which consisted of a series of papers grouped according to topic and usually associated with an Invited Lecture or a Topical Review. These were: *Coal and Organic Solids*, organized by L. Douglas Smoot and Ian W. Smith; *Combustion Modeling*, organized by Jay P. Boris, and Georgy Makhviladze; *Detonations and Supersonic Combustion*, organized by Martin Sichel and Gabrielle Dupr'e; *Incineration and Wastes*, organized by Adel F. Sarofim and Catherine P. Koshland; *Large-Scale Fires*, organized by Toshisuke Hirano and Richard G. Gann; *Practical Aspects of Engine Combustion*, organized by Charles K. Westbrook and Don W. Bahr; *Reaction Kinetics*, organized by Daniel J. Seery and Norbert Peters; *Soot and PAH*, organized by Jack B. Howard and Klaus H. Homann; *Spray Combustion*, organized by Norman Chigier and Josette Bellan; and *Turbulent Reacting Flows*, organized by Robert Dibble and S'ebastien Candel.

The contributed papers were given as either oral or poster presentations. The oral contributed papers were given as 25-minute talks with a five-minute question and answer period. The poster contributed papers were available for viewing for at least a day, and there was a two-hour period in which the authors were present for discussions.

All of the contributed papers were thoroughly reviewed, with over 99% of the papers receiving three or more reviews. The review process was particularly stringent: approximately 40% of the contributed papers were accepted for presentation. All of the contributed papers should be considered to have submission dates of December 15, 1993, which was the last day submitted papers were considered for review. All invited and contributed papers should be considered to have acceptance dates of August 1, 1994, which is the first day of the technical program of the Symposium. By this date, all authors' revisions were completed, the final version was approved for publication by the Program Committee and the Publications Committee, and copies of the final version were deposited in the Symposium Reading Room. Furthermore, since all papers were available for reading when the Reading Room was opened to the Symposium attendees on August 1, 1994, the technical information of the individual papers was first made public on that date, rather than on the publication date of this Volume.

The Work-in-Progress Poster Sessions were organized by Carolyn Kaplan and K. Kailasanath. Ap-

proximately 450 of these papers were presented in the technical session. The title and abstracts of these papers are published in a separate volume available at the meeting and subsequently from The Combustion Institute headquarters. The large number of WIP Posters meant that each poster was available for viewing for less than one full day, while the authors were available for discussion during fixed periods of time.

The Symposia volumes have always been a valuable source of timely and high-quality technical information for combustion researchers. Consequently, publication in these volumes has been highly valued and there have always been more submissions than can be accomodated in the program. A critical and fair review processs is therefore needed for the selection of papers for inclusion in the technical program. This, in turn, requires solicitation of as many reviews per paper as possible, from reviewers whose expertise is as close to the subject area of the paper as possible. The following is a brief accounting of how the review process was conducted for this Symposium.

In order to identify the most appropriate reviewers, suggestions were solicited from members of the Program Advisory Subcommittee (PAS). For most papers, the abstract and reference pages of each paper were sent to one or two members with expertise in the area of submitted papers, asking them to suggest four or five potential reviewers. Each PAS member was also supplied with a summary of the technical profiles of the members of the Program Review Subcommittee (PRS) provided in questionnaires returned in an earlier survey. The PAS members could then select reviewers either from this compilation, or suggest new reviewers. The reviewers were selected based on suggestions by members of the PAS and my own selections after reading through the paper.

A record number of papers, 730, were sent out for review. Each paper was sent to between three and five reviewers. Over 3200 review requests were sent out, and over 2800 were returned. This is truly an impressive performance by the over 700 members of the PRS, especially since they had to respond under a very tight schedule and with difficult mailing situations, and many reviewed a large number of papers. The entire review process extended over a two and half month period. This year we experimented with a limited rebuttal for papers in which there was clear disagreement among the reviewers. Before a final decision was made, the reviews were faxed to these selected authors, and they were asked to provide a one-page rebuttal within one week. The authors of approximately 120 papers were asked to provide rebuttals. All of this had to be done before the PAS met and made final decisions in early March. The PAS met for three days at the Naval Research Laboratory in Washington, DC, to evaluate the reviews, recommend papers for acceptance, and to prepare the session format. This process led to acceptance of 317 papers.

This rigorous paper selection procedure is outlined here because many research and academic institutions do not consider symposium volumes at the same level as refereed journal articles. Those authors who wish to have their Symposium papers receive appropriate recognition should consider attaching copies of these Introduction pages to their evaluation packages as additional supporting material.

Throughout the paper selection and evalution process, every effort was made to incorporate and test advances in electronic communication. We found that e-mail was particularly effective, especially when dealing with countries for which using the telephone and fax were difficult. For example, we had excellent communication with Russia, the Ukraine, and Armenia by e-mail, whereas sending faxes or telephoning was only occasionally successful. By the end of the Symposium, we were also receiving e-mail from the Peoples' Republic of China and South Africa. Meeting Announcements were sent by e-mail, reviews were sent here by e-mail, and the PAS communicated primarily by e-mail. During peak periods, I had daily e-mail communication with hundreds of authors and reviewers. Besides transferring information quickly and efficiently, their e-mail was a source of much humor, good news, and sadness.

Organizing a Symposium program required the participation of and support from many individuals. I am greatly indebted to the members of the Program Committee and PAS for their help in every aspect of the process. Their names, as well as the extensive list of members of the Program Review Subcommittee, appear elsewhere in this Volume. The NRL Local Program Subcommittee worked long, hard hours to make the operation efficient and reliable. Betsy Reid, my other self, organized us into an extremely efficient team.

The Local Arrangements Committee in Irvine, chaired jointly by G. Scott Samuelsen and William A. Sirignano, did a superb job of arranging the meeting in Irvine. The facilities were excellent and all of the special needs for the technical presentations were met cheerfully and efficiently. The Reading Room was organized by Derek Dunn-Rankin. Much of the general planning and detailed work was carried out by Debbie Hart, Stephanie Beck, and Candy Reimers. We are all indebted to them for their effort and for being such gracious hosts.

Production of the Volume was handled by the Publications Committee, chaired by William J. Pitz. This work required a great deal of effort, which ranged from verifying the adequacy of the revisions to editing the discussions of the papers. It has truly been a pleasure to work with Bill.

Finally, I wish to express my most sincere thanks to Sue S. Terpack and Ann E. Steffy of The Combustion Institute for their tremendous support throughout the process. I wish to thank all of my

colleagues at NRL who took on parts of my regular work during the time when most of the work on the Symposium had to be done. In this regard, I particularly want to thank Jay Boris. Finally, I would like to thank my husband, Dan, for his patience and support during this process. Not only was he patient and supportive, but many of his organizational ideas helped the process to run smoothly.

Elaine S. Oran
Chair, Program Committee

The preparation of the volume was an enormous task that required the assistance of many people: The members of the Publication Committee, authors, reviewers, and secretarial staff at Lawrence Livermore National Laboratory (LLNL). The Publications Committee was responsible for ensuring that all the papers in this Volume satisfy the technical comments made by the reviewers, as well as meet the length and style requirements established by The Combustion Institute. This committee also screened comments submitted to the papers at the Symposium so that only substantive discussions were included.

The members of the Publications Committee were Larry L. Baxter, Joseph W. Bozzelli, M. Quinn Brewster, Michael C. Drake, Folkion Egolfopoulos, Thomas H. Fletcher, Anthony P. Hamins, Simone Hochgreb, Robert Hurt, Jay O. Keller, Ian M. Kennedy, John C. Kramlich, William P. Linak, Donald Lucas, Suresh Menon, Habib N. Najm, L. D. Pfefferle, Paul D. Ronney, Howard Ross, Kozo Saito, Gregory Smith, Peter M. Walsh, P. R. Westmoreland, Mary J. Wornat, and Richard A. Yetter. The great effort of these members is very much appreciated.

An English-editing subcommittee was formed to handle papers that needed special revision. Their names appear on committee lists on previous pages. I wish to thank them for their work.

I greatly enjoyed working with Elaine Oran, The Program Chair, and Sue Terpack, Executive Secretary of The Combustion Institute office, in coordinating the publication activities. Our office at LLNL was responsible for sorting and filing the submitted manuscript materials, requesting missing materials, mailing manuscripts to committee members and the printer, faxing comments to authors, final proofing of the papers and comments, and preparation of the table of contents and index of this Volume. I am greatly indebted to Deede Landon, Kerry O'Connor, and Kathy Poeckert of LLNL for accomplishing these time-consuming, detailed tasks. I wish to thank Charlie Westbrook and the combustion group at Lawrence Livermore Laboratory for providing the time and resources for accomplishing the publication work. Finally, this Volume would not have made it into print in such a timely and accurate fashion without the support of Paula Gensch and her staff at Edwards Brothers, Inc.

William J. Pitz
Chair, Publications Committee

Twenty-Fifth Symposium (International) on Combustion/The Combustion Institute, 1994/pp. 1–12

HOTTEL PLENARY LECTURE

GASDYNAMIC ENHANCEMENT OF NONPREMIXED COMBUSTION

FRANK E. MARBLE
California Institute of Technology
Pasadena, CA 91125, USA

To promote efficient performance of very high speed air-breathing propulsion systems, the combustor Mach number must be of the order of six for a flight Mach number of 18. Because of this high gas speed through the combustor, mixing rates of hydrogen fuel with air must be very rapid in order to allow a combustor of reasonable length. It is proposed to enhance the rate of mixing and combustion of hydrogen and air, and thereby reduce combustor length, through the introduction of streamwise vorticity generated by the interaction of a weak oblique shock wave with the density gradient between air and a cylindrical jet of hydrogen.

Because of the high Mach number flow in the combustor, the oblique shock traverses the jet at a small angle with respect to the free stream direction, and the principle of slender body theory allows one conceptually to replace the three-dimensional steady flow with a two-dimensional unsteady flow. As a consequence, two-dimensional time-dependent computational studies and an extensive experimental shock tube investigation were employed to assess mixing rates for the steady flow in the combustor. The results indicated that under realistic conditions, adequate mixing could be accomplished within 1 ms, a rate that was technologically interesting.

Encouraged by these experiments, a "practical" injector, utilizing shock-enhanced mixing, was designed for a combustor having a free stream Mach number of 6.0. A detailed aerodynamic and mixing investigation was carried out in the Mach 6 High Reynolds Number Tunnel at the NASA-Langley Research Center. The results confirmed both the details and the overall effectiveness of the shock-enhanced mixing concept.

Introduction

Today, in addition to inaugurating the 25th International Symposium on Combustion, we have the opportunity to honor Hoyt Hottel, whose remarkable career of technological innovation, academic research, and pedagogy commands our deepest respect.

I met Hoyt Hottel shortly after World War II when academia was rebuilding its structure, and he was fresh from experiences that had led him into areas of fluid mechanics remote from his home base of chemistry. It was his belief that combustion might profit through more expertise in fluid mechanics that led to our initial meeting.

As Hoyt and I became better acquainted, I recognized his unusual ability to abstract, from his wide contacts with industrial technology, fundamental issues appropriate to academic research. This process of distilling fundamental scientific issues from one's technological activities is not only key to a vital academic program but is essential to the health of the science itself. But the results of Hoyt's scientific research have gone one step further. They have returned again and again to enrich the technological source from which they sprang.

Guided by these observations, I have chosen to deviate from the usual format of the Hottel lectures and to describe my own experience with a scientific issue, drawn from current technology, to form a fruitful academic research program, the results of which made their way back toward the parent technology. It is the problem of hydrogen injection, mixing, and combustion in the very high speed air-breathing engine, the so-called Supersonic Combustion Ram Jet.

Origins of the Supersonic Combustion Problem

Air-breathing propulsion at speeds exceeding 4 km/s that is, Mach numbers of 12 or higher, encounters some novel and troublesome constraints on the combustion problem, e.g., Ferri [1], Kumar et al. [2]. To keep structural loads at acceptable levels, flight at such speeds is confined to altitudes of 30 km or higher, and in order to support reasonable combustion, the air pressure must be increased in the diffuser to about 1 atm from its ambient value of 1/100th atm.

To be specific, travelling at Mach number 18 at 31.5-km altitude requires decelerating the air to Mach number 6.0 to achieve a combustion pressure of 1 atm, using a good diffuser and accounting for deviations from ideal gas. At the same time, the temperature of the air, initially at 231 K, has risen to 1499

K, a range where substantial structural cooling is necessary. Air enters the combustor with a velocity of 5185 m/s, and for hydrogen fuel at a stoichiometry of 1.2, the products leave the combustor with a temperature of 2612 K. For chemical equilibrium at this temperature and pressure, the mole fraction of OH at the combustor discharge is 0.011 and the resulting fuel-specific impulse is 1068 s. It is this high specific impulse that establishes the value of the air-breathing hypersonic engine.

At this velocity, a combustion residence time of only 1 ms involves a flow length of 5 m and a correspondingly large surface area to be cooled. Even a modest additional reduction in this velocity results in an increase in air pressure and temperature that seriously increases the surface cooling load. But the most compelling reason to avoid further velocity reduction is the increase in nozzle entrance temperature and the molar fraction of OH that accompanies this temperature rise.

To illustrate this point, consider the significant changes that would take place* if we chose to drop the combustor inlet Mach number to 4.5. First, in order to keep the combustor pressure at 1 atm, the flight altitude must be increased to nearly 53.7 km with the attendant effect that the ambient air temperature is increased from 231 K to 271 K. This Mach number reduction, in addition to the increase in ambient temperature, leads to a much higher diffuser exit temperature and a 400 K increase in combustor discharge temperature over that for the Mach 6 combustor. As a consequence, the mole fraction of OH in the combustion products increases dramatically to 0.039 and the fuel-specific impulse drops to 658 s. This value is barely interesting and would not justify the attending complication of an air-breathing engine. To make matters worse, the combustor inlet velocity is scarcely changed by the Mach number reduction and remains at a value such that a combustor length of 5 m provides a residence time of only 1 ms. The combustor length must be recognized as a serious issue because the gas temperature we have found requires intensive wall cooling, which in turn mandates large heat capacity of the fuel. If the time required for fuel injection, mixing, and chemical reaction requires a long combustor, the cooling load exceeds the heat capacity available in the liquid hydrogen fuel used for the 1.2 times stoichiometric mixture. The additional hydrogen, regardless of how cleverly it is used, further reduces the fuel-specific impulse and correspondingly compromises the performance of the scramjet.

The foregoing factors set the injection, mixing, and reaction constraints on the scramjet. Above all, the mixing must be very rapid; the injection must be accomplished with very low drag penalty, and the fuel must be distributed reasonably well over the burner cross section.

*The numerical results quoted in this section were calculated using a procedure and code developed by Serdengecti [3].

Generation of Streamwise Vorticity

The mixing of two parallel gas streams in a shear layer and the augmentation of this mixing rate by the introduction of streamwise vorticity are among the classical problems of fluid mechanics. Throughout the development of technical fluid mechanics, a wide variety of devices, vortex generators, have been employed to create streamwise vorticity, usually to promote mixing within boundary layers to delay or avoid separation. When, however, such devices are placed further away from the wall in a very high velocity stream, their survival may be jeopardized by very high heating rates even when they are cooled through their function as fuel injectors. Such devices may further introduce significant total pressure losses into the engine flow stream and deteriorate its performance, considerably so at combustor Mach numbers of 2.5 and above. In spite of these obstacles, very effective combined fuel injectors and vortex generators that span the combustor stream have been developed and have proven very effective for combustors appropriate to flight Mach numbers as high as 10 [4].

The difficulties encountered in proceeding to higher speeds encourage the exploration of other techniques, preferably noninvasive techniques, to generate streamwise vorticity. The most promising mechanism of vorticity generation for our purposes results from the interaction between variable density and pressure fields. We propose to generate streamwise vorticity utilizing the density gradient at the interface between air and hydrogen fuel interacting with the pressure gradient created by an oblique shock wave. To fix our ideas, consider the configuration shown in Fig. 1. Air flows supersonically over the combustor wall, which, at one point, bends sharply into the flow through a small angle δ, creating a weak oblique shock wave. Ahead of the shock wave, a cylindrical stream of hydrogen flows parallel with the air stream and at the elliptical intersection with the shock turns slightly upward. It is at this intersection that the pressure and density gradients coexist, and the progress of the two gradient vectors as the shock passes through the jet is shown in several cross sections, looking upstream into the flow. The density gradient lies in the plane and is radial to the slightly diffused air-hydrogen interface; the pressure gradient, normal to the shock wave front, lies slightly out of the plane. The vorticity generated at the intersection of these two regions is predominantly in the streamwise direction. The small azimuthal component of vorticity, lying on the surface of the hydrogen cylinder, will be neglected in our discussion because

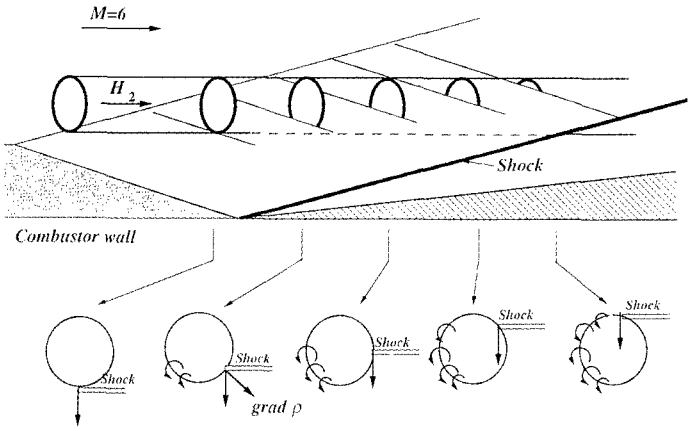

FIG. 1. Progression of shock through the hydrogen jet.

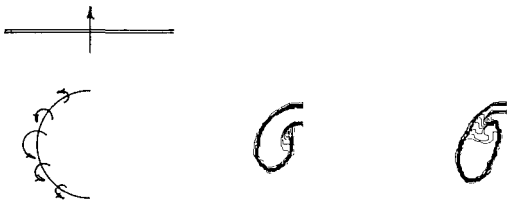

FIG. 2. Distortion of hydrogen cylinder after shock passage and subsequent formation of vortex pair.

for air Mach numbers of interest the shock angle is very flat and this vorticity component correspondingly small.

As the shock intersection moves up through the jet, the magnitudes of the gradient vectors remain constant, but the angle between them, equal to the angle of the radial line from the jet axis to the point of intersection, increases from 0 as the shock enters the jet to π as it passes out at the top. The magnitude of the vorticity deposited at the intersection of the property gradients is proportional to the sine of this angle. The resulting distribution of vorticity at the air-hydrogen interface is shown in a set of diagrams immediately below the sketch in Fig. 1. From this view, clockwise vorticity is accumulated on the right half of the cross section and counterclockwise vorticity on the left half. The mixing enhancement contributed by the streamwise vorticity manifests itself as the induced distortion of the hydrogen jet. The progress of this distortion is sketched qualitatively in Fig. 2 as it proceeds from the distribution of vorticity, as it exists immediately after the shock has passed through the hydrogen jet, to the distortion induced by this vorticity a short time subsequent to shock passage. Because the vorticity distribution is antisymmetric about the vertical axis, the velocity field is antisymmetric also and the composition contours symmetric. The configuration is suggestive of a vortex pair and can be expected, in first approximation, to behave like one. Air is swept from below to the interior of the jet while the hydrogen in the upper portion of the field is stretched into a thin sheet joining the two vortices. Accompanying this is the large increase of interfacial area through which the diffusion requisite for molecular mixing takes place.

Because the cross-plane velocities introduced by the shock interaction are small in comparison with the free stream velocity, the flow directions deviate only slightly from that of the undisturbed main stream. As a consequence, sections normal to the flow remain approximately plane, and the flow in such a section may be analyzed by following the flow downstream. This transformation of certain steady three-dimensional flow fields into two-dimensional unsteady flows, known as slender body theory, is widely used in aerodynamic analysis. Therefore, the essential information concerning the shock-induced flow may be obtained through (1) two-dimensional Euler calculations of the progressive distortion of the shape and of the entire gas-dynamic field, and (2) shock tube experiments of the distortion and mixing of cylindrical light gas masses subjected to weak shock waves.

Recognition of this possibility brought the problem within modest experimental and computational resources without requiring extensive and expensive facility investment. It was our good fortune that these virtues were also recognized by Dr. Julian Tishkoff, AFOSR, to whom we are grateful for both enthusiasm and financial support.

Shock Tube Experiments

A substantial portion of the experimental investigation was performed in the Galcit 17-inch Shock Tube [5]. A smaller facility was utilized by Haas and Sturtevant [6] in their study of shock interaction with gas inhomogeneities, and our initial work benefited substantially from their experience. As our

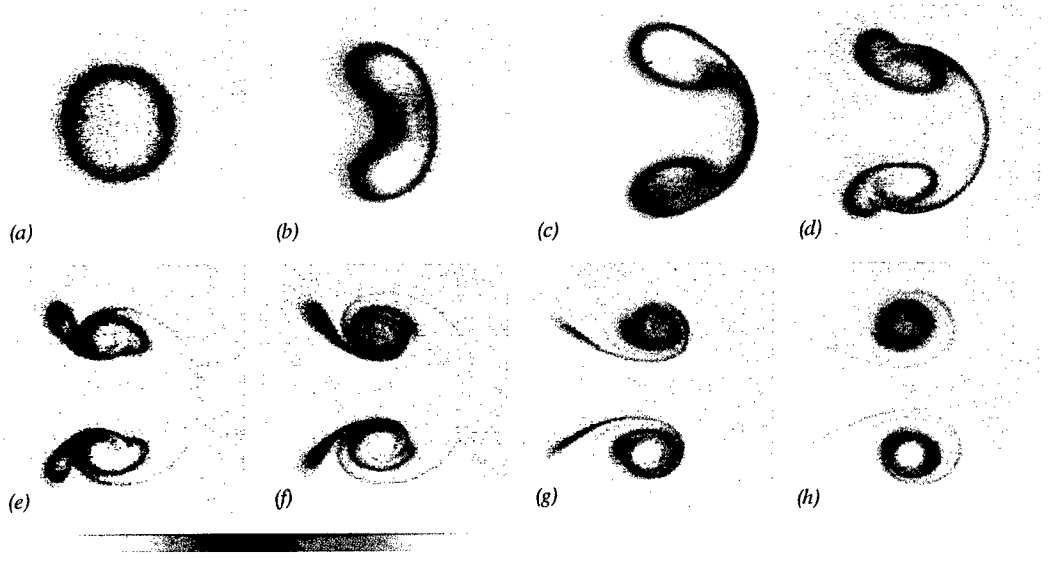

FIG. 3. Time sequence of PLIF images of the distortion and mixing of helium jet after encounter with $M_s = 1.093$ shock. (a) The initial jet, (b) 0.123 ms, (c) 0.273 ms, (d) 0.373 ms, (e) 0.473 ms, (f) 0.573 ms, (g) 0.773 ms and (h) 0.973 ms.

investigation developed, however, a quite different and novel technique for introducing light gas was developed by Jacobs [7].

These experiments utilized planar laser-induced fluorescence (PLIF) in which helium was seeded with a small amount of biacetyl, a gaseous fluorescent dye [8], induced to fluoresce with a sheet of laser light. A laminar circular jet of helium was introduced into the lower portion of the test section and allowed the jet to convect vertically upward within the view of the window. A second opening was situated directly above the jet to collect the light gas and avoid accumulation of helium in the test section. A portion of the helium was bubbled through liquid biacetyl, seeding the helium with nearly saturated vapor. Using a ratio of 10 parts pure helium to 1 part biacetyl-laden helium assured that the addition of biacetyl to the helium stream would not increase the mixture density by more than 10%. A flashlamp-pumped dye laser produced 100-mJ pulses of 0.7-μs duration at 430 nm, finally providing a sheet of laser light that bisected the biacetyl-seeded helium jet, illuminating a 1-mm-thick cross section. A complete description of the experimental arrangement is given by Jacobs [7].

Figure 3 shows the PLIF images of the distorted helium cylinder, initially of 0.66-cm diameter, resulting from interaction with a shock of Mach number 1.093, corresponding to a Mach wave in a combustor having a throughflow Mach number of 6.0. The false coloring, as indicated in the color bar, extends from white, representing the lowest fluorescent intensity, to yellow, representing the highest. The images at 0.123 and 0.273 ms after the encounter confirm that the vorticity deposited at the boundary rolls up into a distinct vortex pair, the individual lobes moving apart extending the fine "umbilical cord" that joins them. From the viewpoint of mixing, the extension of the interfacial area and the thinning of the interfacial zone due to straining are the crucial items.

Beginning with frame (d), 0.373 ms, a second lobe develops, further extending the interfacial area. This second lobe appears to mix much more rapidly than the original vortices, essentially disappearing by 0.773 ms after the encounter. After 0.973 ms, the secondary lobes and the umbilical cord are thoroughly mixed, but a remnant of the original vortex persists. A simple estimate using the areas and intensities indicates that when the two lobes are first discernible, the primary lobe contains about 60% of the helium, the secondary lobe containing the remainder. After about 1 ms, the secondary lobe is completely mixed and the primary lobe is about 40% mixed.

One concern about the experiments employing the biacetyl dye has to do with the differences in diffusion rates of the relatively heavy biacetyl molecule compared with that of helium. As a consequence, the diffusion component will be underestimated. To discern significant effects, Budzinski et al. [9] used Rayleigh scattering, which differentiates between air and helium through the very much larger scattering cross section of oxygen and nitrogen compared with that of helium. As a result, the molar concentrations of the species themselves may be followed without relying upon a foreign tracer molecule, thereby provid-

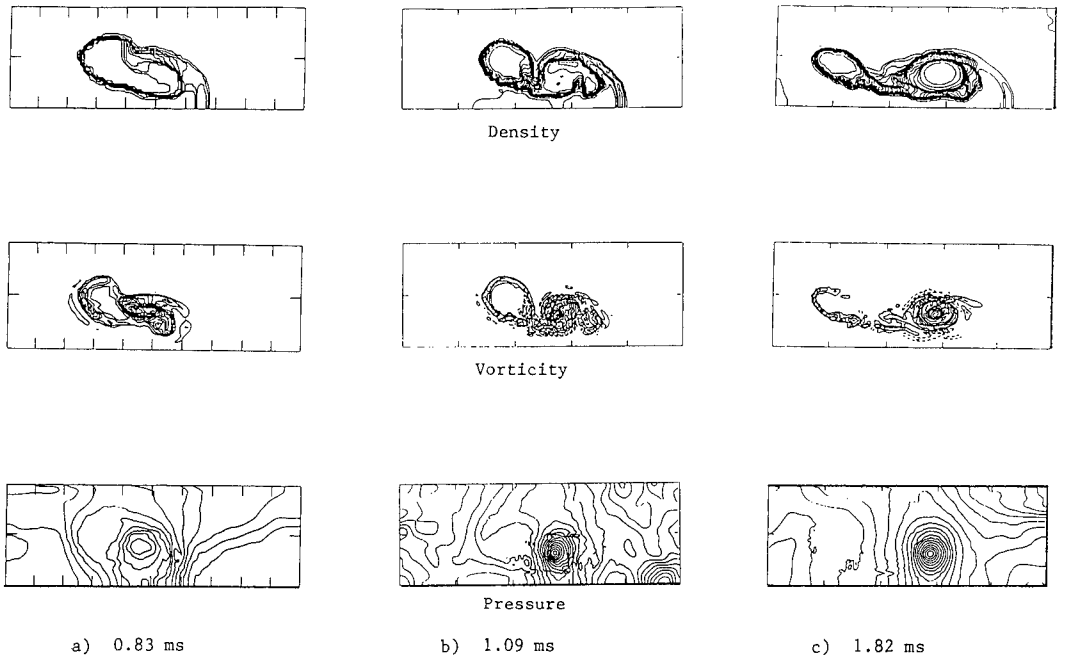

FIG. 4. Computed density, vorticity, and pressure contours, $M_s = 1.22$. (a) $t = 0.83$ ms, (b) $t = 1.09$ ms, and (c) $t = 1.82$ ms.

ing a quantitative measure of the helium distribution and mixing. The general course of the distortion and rolling up process recorded by Jacobs is well confirmed. However, the extent of the diffusion zones is somewhat greater than suggested by the PLIF images.

Computational Investigation

An extensive computational program, undertaken in parallel with experiments, provided both a guide to the experimental effort and determination of pressure and vorticity distributions that could only be qualitatively inferred from the experiments. This investigation used a code that originated at the Naval Research Laboratory and employed the Flux Corrected Transport algorithm developed by Boris and Book [10] and Boris et al. [11].

In keeping with the use of slender body theory, the three-dimensional steady problem is replaced by a two-dimensional unsteady problem. Further, the computations employed an inviscid, nondiffusive formulation, and consequently any diffusive component to the results is purely numerical. Although the use of an Euler code in this investigation suppresses some features of the real process, it does calculate, and indeed emphasize, certain structural features of the flow that are key to a deeper understanding of the experiments. These calculations, carried out by G. J. Hendricks during the spring of 1987, have been previously published only in part [12] but were essential in understanding the mixing phenomenon.

Figure 4 shows a sequence of composition (density) distributions from Hendricks' numerical calculations for a Mach 1.22 shock passing over an initially circular cylinder of helium in air. Because of its symmetry with respect to the horizontal centerline, only the upper half of the vortex pair is shown. The stages of development in these three diagrams have been selected to show the formation of the two lobes and their further development in correspondence with the PLIF images in Fig. 3. Specifically, Fig. 4a corresponds approximately to Fig. 3d, Fig. 4b to Fig. 3e, and Fig. 4c to Fig. 3g. In the density distribution, one sees evidence of the tendency to form two lobes beginning in Fig. 4a and quite developed in Fig. 4c. Figure 4c illustrates the stretching of the rearward lobe, but because diffusive mixing is absent, this lobe does not disappear as in the PLIF images, but retains its strong density boundary.

The mechanism of the process is clarified by examination of the pressure and vorticity diagrams corresponding to the composition plots of Fig. 4. Quite early in the development, Fig. 4a shows the vorticity to be moving to the forward position of the structure, and the closed contours of the pressure distribution suggest a well-formed vortex. The forward movement of the highly vortical portion is thus associated with the motion of the corresponding vortex pair.

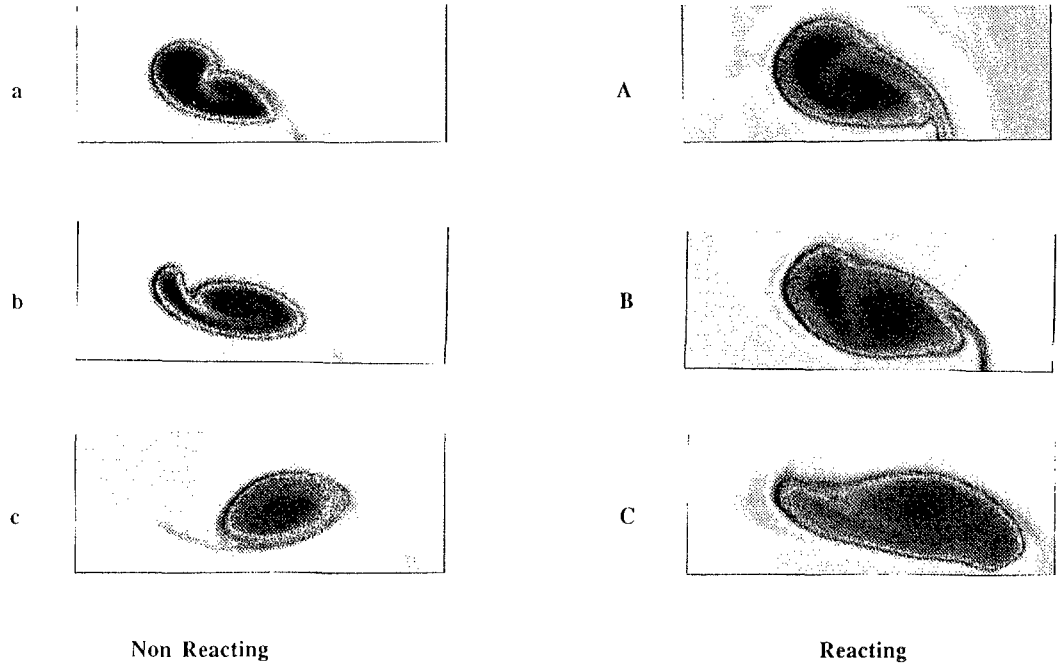

FIG. 5. Computed density contours for reacting and nonreacting flow: initial temperature 1000 K, $M_s = 1.22$.

The composition distribution of Fig. 4b shows the distinct separation of the two lobes, and the corresponding vorticity distribution exhibits the continued differentiation between the vorticity concentrations on the two lobes. The pressure distribution emphasizes the vortex structure of the forward lobe, continuing to pull away from its trailing counterpart. The final set of diagrams (Fig. 4c) shows the weak trailing "wake," which in physical reality would be experiencing the diffusive mixing shown in the PLIF images. The vorticity is now well formed into a relatively stable circular vortex structure. The pressure distribution shows this even more convincingly; the field of the forward portion is very much that of a classical vortex pair while the rear lobe has effectively vanished dynamically. The reason for the longevity of the forward lobe is now quite clear; it has formed a very stable stratified vortex and will maintain itself over a long period, mixing and dissipating relatively slowly. From a mixing point of view, it is interesting to speculate on the merit of another disturbance to alter the flow before the vortex has stabilized.

Numerical calculations for reacting flow fields have frequently been troubled by oscillations due to "stiffness" associated with the differential equations containing the chemical reaction terms. Recently, several methods have been advanced to avoid this difficulty, one of which, the ENO (Essentially Non-Oscillatory) scheme [13,14], has been applied to study the combustion of hydrogen in air for the problem we have been discussing.

For this computation, the cylinder of hydrogen was situated in air at 1 atm and at the same initial temperature; the kinematic conditions were similar to both calculations and experiments that have been described. For hydrogen chemistry, eight chemical species were followed (H_2, H, O_2, O, H_2O, OH, HO_2, and H_2O_2) using the set of 37 reactions described by Maas and Warnatz [15]. The details of the formulation, including the determination of local transport properties, are described by Ton et al. [16].

Figure 5 shows the rather striking dispersion of the density distribution by the reaction. Figures 5a, 5b, and 5c, the computations for nonreacting flow, correspond approximately to Figs. 4a, 4b, and 4c of Hendricks. The corresponding calculations for reacting flow (Figs. 5A, 5B, and 5C) show clearly the "source effect" of the heat release, described in a rudimentary way by Karagozian and Marble [17]. In addition, those features observed in diagrams for nonreacting mixing, due only to variation in composition, are obscured here by those density variations controlled by temperature. For example, the separation into two lobes (Figs. 5b and 5c), so evident in the nonreacting development, is largely obscured by the hot products outside the structure but may be discerned by the darkest contours within the diagram.

A second important feature shown by these computations is the effect upon the ignition and the ensuing combustion processes of increasing the initial temperature from 1000 to 1500 K. At stages of de-

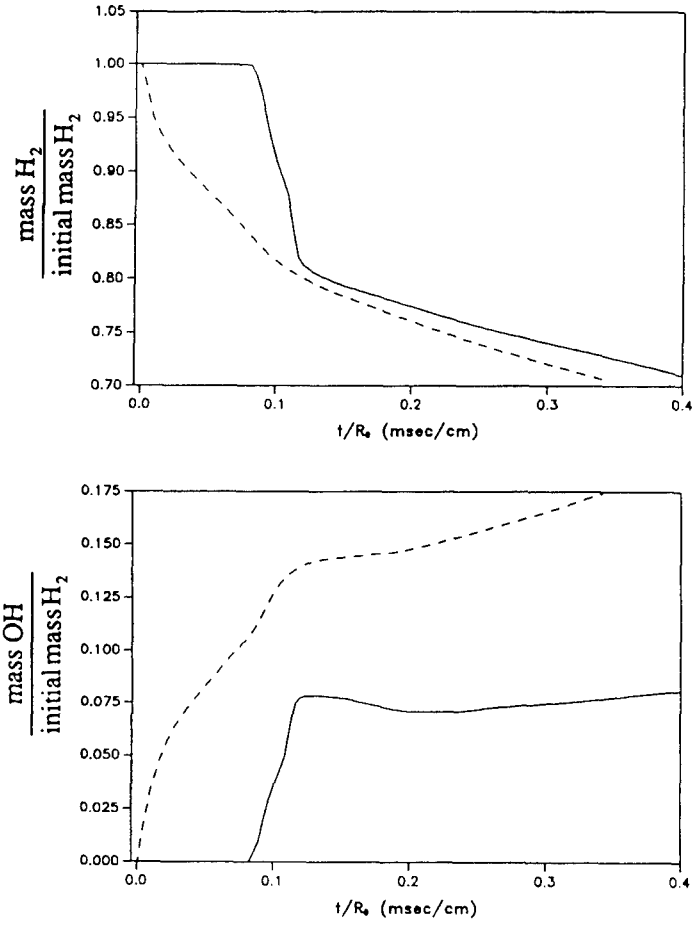

FIG. 6. Consumption/growth histories of H_2 and OH: initial temperature 1000 K, solid line; initial temperature 1500 K, broken line; and R_0 = radius of jet.

velopment corresponding to Figs. 4a, 4b, and 4c at each temperature, very significant differences are evident in the point of ignition and the rates of flame growth. It is evident that the higher temperatures in the outer portions of the burning vortex are counteracting the stable stratification due to composition that was observed in the nonreacting computations and experiments. Indeed, if this observation is valid, the contribution of combustion may go a long way toward reducing the mixing and combustion times for the forward-moving vortex pair.

Finally, from the viewpoint of combustor performance, the production and consumption rates of certain species are of interest. Figure 6 shows the time histories of the concentrations of H_2 and OH for each of the initial temperatures, their masses integrated over the computational domain. The consumption of hydrogen shows clearly the ignition delay occurring at the lower initial temperature, the subsequent rapid reaction and consumption of hydrogen at a rate no longer sensitive to initial temperature. The ignition delay might be expected simply on the basis of temperature, but it seems likely that a more complex process is involved. The very rapid reaction subsequent to the time delay suggests that a considerable amount of surface extension has taken place during the time and that reaction has been suppressed by the high straining rates involved in extending the hydrogen-air interface. Recent analytical studies of the effect of strain rate on ignition support this interpretation, and the straining rates in the experiments and computations described are well in the range to play a role in the observed phenomenon.

Toward a Practical Injector

At this stage of the investigation, it appeared that the principle of shock-enhanced mixing through generation of streamwise vorticity had been well demonstrated, but its application in the harsh environment of a scramjet engine was yet another matter. It was evident that some innovation was required, and a rudimentary sketch of our concept is shown in Fig. 7.

Air moves at a Mach number 6.0 parallel to the

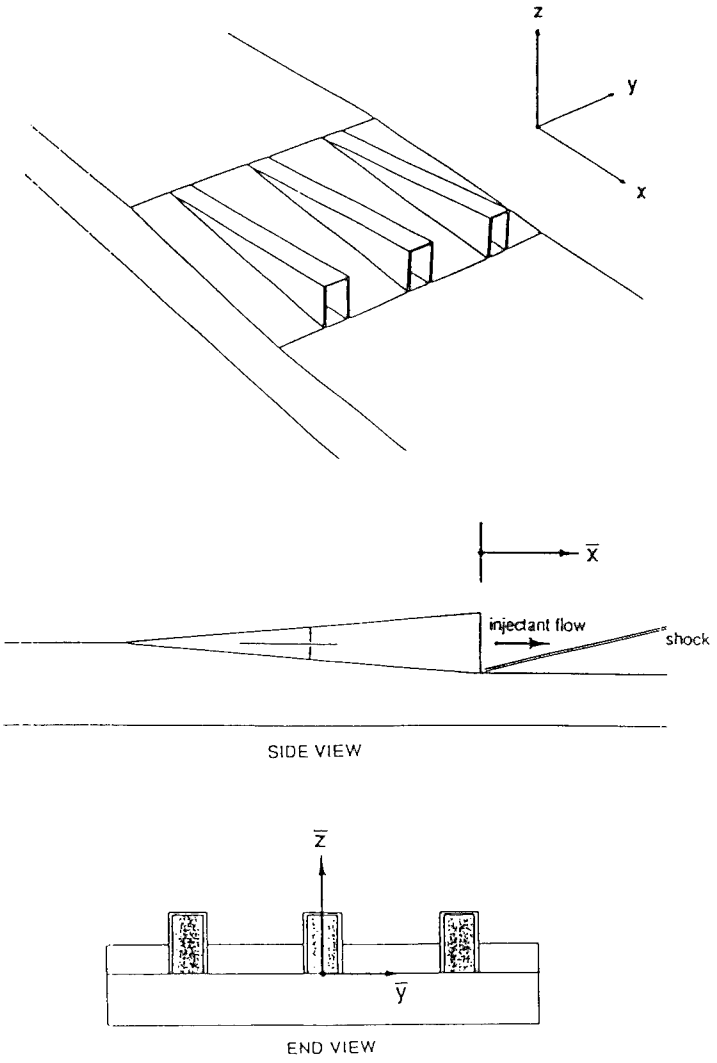

FIG. 7. Sketch of wall-mounted hydrogen injector utilizing shock-enhanced mixing.

combustor wall, which, at one position, divides into alternating ramps and troughs; the air expands to a higher velocity within the troughs but generates weak compression waves above the ramps. The ramps also serve as channels guiding the hydrogen jets to discharge into the chamber. At the point of discharge, there is a shearing motion between the downward-moving air and the upward-moving hydrogen, creating a vertical shear layer at the interface where the hydrogen and the air merge. This motion corresponds to a significant amount of streamwise vorticity at the hydrogen-air interface, and care must be taken to insure that the shock enhancement augments rather than cancels this vorticity. At the point of hydrogen discharge, the combustor wall returns to its original direction, creating a weak oblique shock in the air leaving each trough. These shocks, in turn, establish locally high pressures that propagate into and upward through the hydrogen, driving it upward to create a recognizable analog of the shock-cylinder interaction studied in the shock tube.

Because the trough and ramp angles are very small, this flow may again be analyzed as a two-dimensional nonsteady one; computations were again performed by G. J. Hendricks. The computational domain consisted of one geometric cycle parallel to the y axis in Fig. 7. The motion generated in the cross plane, while the plane is still within the injector, was modeled by stepping up the height of the ramps and stepping down the height of the troughs in time increments. Because of the pressure difference caused by the compression shock and the expansion wave, air flows from the top of the ramp, around the sharp corner, and into the trough. These two corner flows

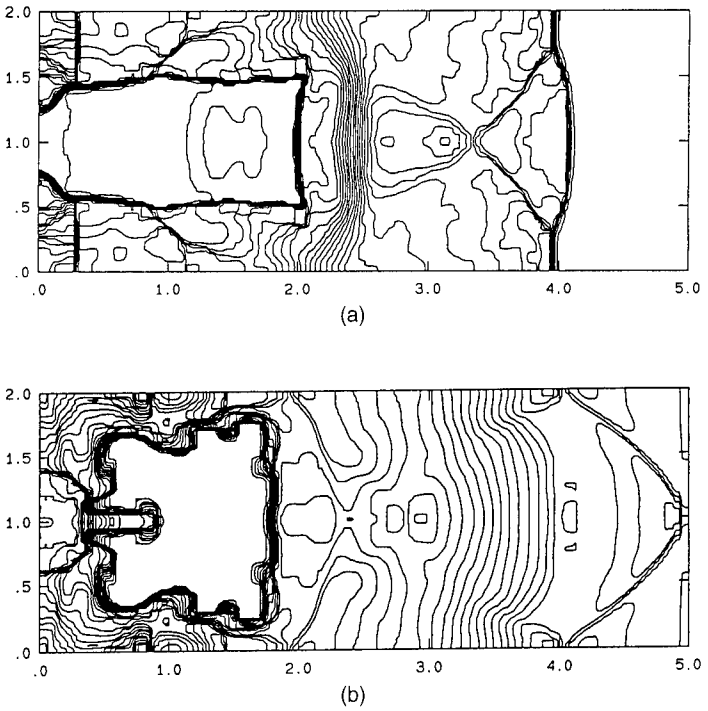

FIG. 8. Computed development of the streamwise vortex pair downstream of the injector. (a) $x = 14$, and (b) $x = 20$.

overexpand and subsequently shock to move parallel with the channel walls.

Beyond the plane at which the injector ends, the restraints of the walls are removed so that the air and hydrogen are set in motion, relieving the pressure difference previously existing across the injector walls, and the oblique shock shown in the side view of Fig. 7 is formed, causing an abrupt pressure increase below it. In Fig. 8a, two injector widths downstream of the discharge, the shock wave generated in the air at the lower part of the trough is seen propagating upward. At the same time, the higher pressure created under this shock is moving air under the hydrogen and displacing it upward. Figure 8b, eight injector widths downstream of the discharge, shows that the symmetric shock waves under the hydrogen have reflected at the center point, further increasing the pressure under the hydrogen and creating a vertical jet that penetrates into the hydrogen flow, dividing it into two halves and generating the vortex pair corresponding to those observed in the shock tube studies. The concept of creating a vortex pair in the hydrogen flow and generating streamwise vorticity is now clear [18]. By configuring the injector to build a shock that penetrates under the hydrogen jet, the shock then moves up through the hydrogen, producing an almost identical phenomenon to that generated in the shock tube.

With the guidance of such numerical studies, an injector corresponding to that shown in Fig. 7 was designed and built for installation in the One Foot, Mach 6 High Reynolds Number tunnel at Langley Memorial Aeronautical Laboratory. Use of this facility gave us an opportunity to measure performance of the injector in a physical situation duplicating the actual event in all ways except actual combustion. The success of this effort was assured by the good offices of Dr. Dennis Bushnell, who enthusiastically supported the effort and more than once extracted us from bureaucratic tar pits, and by Ian Waitz, a Caltech graduate student, who brought two years of valuable experience at Langley.

The wind tunnel model, described in detail in Waitz [19] and Waitz et al. [20], was identical in concept to the original design except for a spacing between injector ramps of three injector widths rather than one. The most compelling reason for this change was that both initial experiments and computations suggested that the flow of boundary layer air from the compression ramps into the troughs was sufficient to "soften" the compression shock at the injector outlet. Because this would compromise the performance, the spacing between injector lobes was increased by a factor of 3, greatly reducing the possibility of boundary layer contamination. The model injectors were installed as inserts on the flat plate rig, helium flowing into the individual injectors from a plenum supplied through the mounting strut supporting the plate. Two geometrically similar injector inserts were used in the experiments, one having an injector height of 2.54 cm at the discharge plane, the

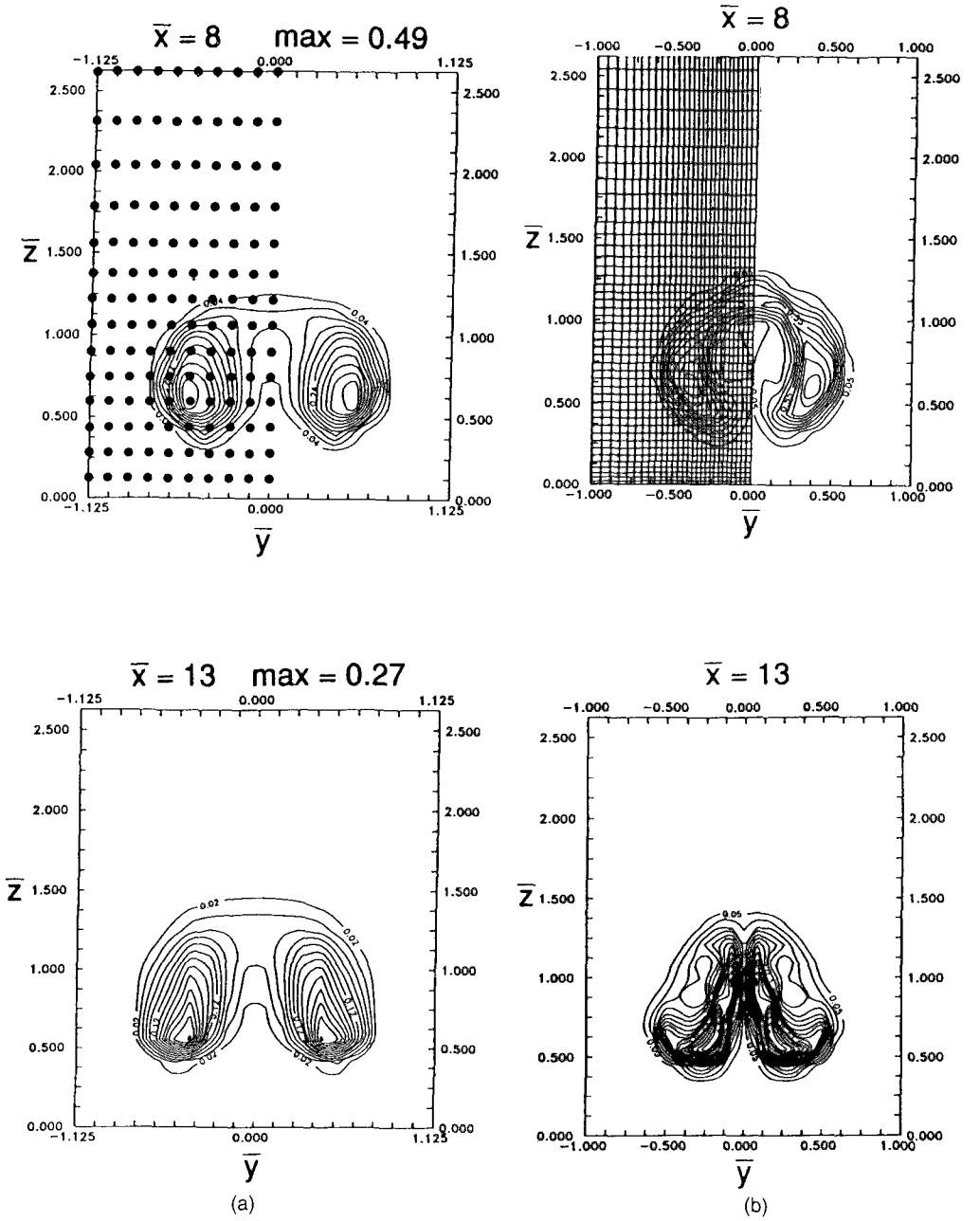

FIG. 9. Experimental and computational contours of helium mass fraction. (a) Experimental, and (b) computational.

other having an injector height of 1.27 cm. The desirability of two models resulted from the maximum allowable length of the model in the tunnel, and since the position downstream from the injector was measured in injector heights, the smaller model provided greater effective length of the mixing region while the larger model provided better resolution for measurements in the near field.

To obtain a good estimate of the experimental mixing performance we should expect and to determine bounds on the range of densities and pressures to be measured, a detailed computational study was un-

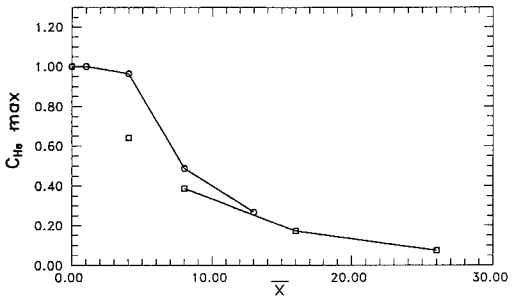

FIG. 10. Measured decay of maximum helium concentration along flow direction: circles, full-size injector; and squares, half-size injector.

dertaken using the SPARK3D code [21], provided by the Computational Methods Branch of NASA Langley Research Center. This code allowed solution for three-dimensional multispecies flows using Navier–Stokes, energy, and species conservation equations. The results of these computations [20] show remarkable similarity with time development of the flow observed in the shock tube, including formation of the vortex pair, the development of the trailing lobes, and the motion of the strong vortex pair away from the wall.

Data acquired during the wind tunnel experiments consisted of three-dimensional surveys by four rake-mounted probes: a composition probe, a cone static probe, a pitot probe, and a total temperature probe. The positioning of the probe rake, the pressure and temperature data, and the helium sampling were automated. Helium concentration measurements were made with a composition probe (see Waitz [19]) based upon the response of a hot film anemometer sensor in a binary gas mixture. The error in helium concentration measurements was less than $\pm 3\%$ over the range of application.

Figure 9a shows experimental contours of helium concentration at two locations downstream of the larger, or full-scale, injector [20,22]. The experimental sampling grid is shown superposed on the contour plot for $x = 8$. This experimental confirmation of the formation and development of the vortex pairs is again quite remarkable. For rough comparison with the sequence of density images (Fig. 3) obtained in the shock tube, the density distribution at $x = 13$ occurs at a time of approximately 0.36 ms after leaving the injection plane at which time the maximum concentration was found to be 0.27, about a quarter of the original.

The corresponding computational helium concentration contours (Fig. 9b) compare very favorably with the measurements. The projection of the computational grid on the cross section is shown superposed on the contour plot for $x = 8$. The far field lifting of the vortex pair appears to be computed with reasonable accuracy. Finally, utilizing data from both the full-size and half-size models, it is possible to trace the decay of maximum helium concentration along the flow path from the injector discharge to a point 26 injector heights downstream. These data are shown in Fig. 10; the different symbols identify from which injector the data came. If we interpret this final point of Fig. 10, at which 10% of the original helium concentration has been reached, in terms of the full-size injector, the elapsed time at wind tunnel conditions would be about 0.6 ms. At the flight condition proposed in the second section of this article ("Origins of the Supersonic Combustion Problem"), this translates to a length under 3 m, a distance well within the range of our initial goal for shock-enhanced mixing.

Concluding Remarks

I can mention with some satisfaction that a few preliminary experiments on our injector-mixer model, with hydrogen injection, were run in the Caltech Piston Shock Tunnel, T-5, with appropriate flight enthalpy levels and combustor Mach numbers. Rayleigh scattering measurements of the OH radical demonstrated ignition and indicated the vortex pair formation and lifting found in the wind tunnel experiments. And, although hypersonic flight has given ground to what some consider more relevant activities, this technology is here for its next incarnation!

Let me return for a moment to our honoree. Some time ago, at the Leeds Symposium to be exact, Hoyt Hottel introduced me to his handsome young grandson and told me he made it a practice to bring one of his grandchildren to each Symposium. Moreover, he would continue attending so long as the supply of grandchildren held out! Well, I think we can safely assume that supply to be exhausted, and so, in addition to continued good health and vigor, let us wish him a plentiful crop of great-grandchildren for future Symposia!

REFERENCES

1. Ferri, A., "Mixing-Controlled Combustion," *Annu. Rev. Fluid. Mech.* 5:301–338 (1973).
2. Kumar, A., Bushnell, D. M., and Hussaini, M. Y., "Mixing Augmentation Technique for Hypervelocity Scramjets," *AIAA J. Prop. Power* 5(5):514–522 (1989).
3. Serdengecti, S., "A General Computational Analysis of Scramjet Performance," Unpublished Notes, California Institute of Technology, Pasadena, CA, 1992.
4. Northam, G. B., Greenberg, I., and Byington, C. S., "Evaluation of Parallel Injector Configurations for Supersonic Combustion," AIAA Paper No. 89-2525, 1989.

5. Liepmann, H. W., Roshko, A., Coles, D., and Sturtevant, B., "A 17-inch Diameter Shock Tube for Studies in Rarified Gas Dynamics," *Rev. Sci. Instrum.* 33:625–631 (1962).
6. Haas, J.-F. L., and Sturtevant, B., "Interaction of Weak Shock Waves with Cylindrical and Spherical Gas Inhomogeneities," *J. Fluid Mech.* 181:41–76 (1987).
7. Jacobs, J. W., "Shock Induced Mixing of a Light Gas Cylinder," *J. Fluid Mech.* 234:629–649 (1992).
8. Epstein, A. H., "Quantitative Density Visualization on a Transonic Compressor Rotor," *ASME J. Eng. Power Trans. ASME,* Vol. 99, Ser. A, No. 3, 460–475 (1977).
9. Budzinski, J. M., Zukoski, E. E., and Marble, F. E., "Rayleigh Scattering Measurements of Shock Enhanced Mixing," AIAA Paper No. 92-3546, 1992.
10. Boris, J. P., and Book, D. L., "Flux Corrected Transport. I. SHASTA, a Fluid Transport Algorithm that Works," *J. Comput. Phys.* 11:38–69 (1973).
11. Boris, J. P., Book, D. L., and Hain, K., "Generalization of the Flux-Corrected Transport-Technique," *J. Comput. Phys.* 18:284 (1975).
12. Marble, F. E., Hendricks, G. J., and Zukoski, E. E., "Progress toward Shock Enhancement of Supersonic Combustion Processes," AIAA Paper No. 87-1880, 1987.
13. Harten, A., Osher, S. J., Engquist, B. E., and Chakravarthy, S. R., "Some Results on Uniformly High-Order Accurate Essentially Non-Oscillatory Schemes," *J. Appl. Numer. Math.* 2:347–377 (1986).
14. Shu, C. W., and Osher, S. J., "Efficient Implementation of Essentially Non-Oscillatory Shock Capturing Schemes, II," *J. Comput. Phys.* 83:32–78 (1989).
15. Maas, U., and Warnatz, J., "Ignition Processes in Hydrogen-Oxygen Mixtures," *Combust. Flame* 74:53–69 (1988).
16. Ton, V. T., Karagozian, A. R., Marble, F. E., Osher, S. J., and Engquist, B. E., "Numerical Simulation of High Speed Chemically Reacting Flow," *Theor. Comput. Fluid Dyn.*, 6:161–179 (1994).
17. Karagozian, A. R., and Marble, F. E., "Study of a Diffusion Flame in a Stretched Vortex," *Combust. Sci. Technol.* 45:65–84 (1986).
18. Marble, F. E., Zukoski, E. E., Jacobs, J. W., Hendricks, G. J., and Waitz, I. A., "Shock Enhancement and Control of Hypersonic Mixing and Combustion," AIAA Paper No. 90-1981, 1990.
19. Waitz, I. A., "An Investigation of Contoured Wall Injectors for Hypervelocity Mixing Augmentation," Ph.D. Thesis, California Institute of Technology, Pasadena, CA, 1994.
20. Waitz, I. A., Marble, F. E., and Zukoski, E. E., "An Investigation of a Contoured Wall Injector for Hypervelocity Mixing Augmentation," *AIAA J. Prop. Power* 31(6):1014–1021 (1993).
21. Eklund, D. R., Northam, G. B., and Fletcher, D. G., "A Validation Study of the Spark Navier Stokes Code for Nonreacting Scramjet Flowfields," AIAA Paper No. 90-2360, 1990.
22. Waitz, I. A., Marble, F. E., and Zukoski, E. E., "A Systematic Experimental and Computational Investigation of a Class of Contoured Wall Fuel Injectors," AIAA Paper 92-0625, 1992.

Twenty-Fifth Symposium (International) on Combustion/The Combustion Institute, 1994/pp. 13–19

NAVIER–STOKES NUMERICAL SIMULATION OF SUPERSONIC HYDROGEN-FLUORINE COMBUSTION IN CW CHEMICAL LASERS

M. ROTINIAN,* M. SHUR** AND M. STRELETS+
Chemical Gas Dynamics Laboratory
Federal Russian Scientific Center "Applied Chemistry"
14 Dobrolyubov ave., Saint Petersburg 197198, Russia

Results are presented of numerical simulations of nonpremixed supersonic combustion with an account of nonequilibrium vibration energy exchange and stimulated radiation in the continuous-wave (CW) HF chemical lasers with different fuel/oxidant mixing devices. The main goal of the study was to obtain better insight into the mechanism of coupling between the processes in the combustion region (laser cavity) and in the supersonic supply system (nozzle array). In order to take into account this effect, which is caused by the upwind influence of the cavity processes on the nozzle array flow, a coupled one-domain approach is used, i.e., a simultaneous Navier–Stokes simulation of both nozzle and cavity flows. The results of the computations clearly show that coupling or, more exactly, the feedback mentioned above, is explained mainly by the fuel and oxidant nozzle flows interaction due to propagation of the pressure disturbances from one nozzle to another through the nozzle array base recirculation zone and subsonic part of the nozzle boundary layers. It causes significant deformation of the mixing zone and flame configuration and turns out to be crucial when the difference between the nozzle exit pressure levels is large. In this case, separation of the nozzle boundary layer may occur, which leads to the ignition of the mixture inside the nozzle array. The results illustrate also the influence of the regime parameters and the design of the nozzle array on the flow wave pattern, flame configuration, structure of the base recirculation zones, and the laser output characteristics.

Introduction

The conventional, and the simplest, approach to the numerical simulation of nonpremixed supersonic combustion chambers is based on the successive computation of the supply nozzles flow and the mixing/combustion flow, i.e., using the flow parameter values at the exit plane of the fuel and oxidant nozzles, obtained by the computation of the nozzle flows, as the inflow boundary conditions for the combustion chamber. The same is true for the supersonic continuous-wave (CW) chemical laser, which is, in fact, a low-pressure supersonic combustion chamber with a supply system realized as an array of Laval nozzles. Irrespective of the level of the gasdynamic model used for the laser simulation (one-dimensional [1], parabolic [2], or the full Navier–Stokes equations [3–5]), such an approach does not permit description of the upwind influence of the supersonic mixing and combustion processes in the laser cavity on the nozzle flow, which may be of great significance in real-life devices [6]. In particular, without taking this influence into consideration, it is impossible to describe adequately the processes in the recirculation zone in the nozzle array base region, which might affect strongly the evolution of the supersonic mixing layers and flame fronts in the cavity and consequently control the combustion rate and the whole system efficiency.

The only possible way to describe all these phenomena is, obviously, by using another, more sophisticated, approach, based on a coupled simulation of the flow in the domain of complex geometry that includes, along with the cavity region, the fuel and oxidant nozzles as well. Besides, probably only the full Navier–Stokes equations can provide an adequate description of the strong interaction of the complicated flow wave pattern, recirculation zones, and boundary and mixing layers typical for the flows under consideration. As far as the authors are aware, the sole attempt to implement such an approach was undertaken in Ref. 7, where an example is presented of the DF CW chemical laser flow calculation with the help of the APACHE code [8].

In the present work, apparently for the first time, an analysis is performed, on the basis of the above approach, of the flow fields and combustion processes in the HF CW supersonic chemical lasers with different types of fuel and oxidant mixing organization (see Fig. 1). For the numerical solution of the

*Head of Laboratory.
**Senior Research Scientist.
+Principal Scientist.

governing Navier–Stokes equations, we use a finite-difference technique that has been developed during the last several years in the Chemical Gas Dynamics Laboratory of the Federal Russian Scientific Center "Applied Chemistry" [Compressibility Scaling Method (CSM) [9–11]]. The main advantage of the CSM over the conventional numerical methods for the compressible Navier–Stokes equations is the insensitivity of its computational efficiency to a wide-range variation of the flow Mach number (from supersonic $M > 1$ down to hyposonic $M << 1$ and fully incompressible $M = 0$ flows). This feature of the CSM is of great importance for the flows considered because of their "multiscale" character, i.e., the presence of supersonic, large subsonic, and recirculation zones.

First, we present the governing Navier–Stokes equations and briefly dwell upon some specific features of the chemical laser flow modeling connected with the description of the vibration relaxation processes and stimulated radiation transfer. Then we discuss the results of some preliminary numerical experiments, which were performed to evaluate the "depth" of the upwind influence of the exhaust conditions on the supply nozzles flow. Finally, we describe the results of the numerical study of the mechanism of coupling between the processes in the combustion region and in the nozzle array, and discuss the influence of the regime parameters and the nozzle array design on the flow pattern and laser output characteristics.

Governing Equations

The Navier–Stokes equations for the 2D multicomponent chemically reacting, vibrationally nonequilibrium gas mixture flow, which are used for the description of the processes in the HF CW chemical laser nozzles and optical cavity, may be written in the following form:

$$\partial\rho/\partial t + \nabla\cdot(\rho\mathbf{V}) = 0 \tag{1}$$

$$\partial\rho\mathbf{V}/\partial t + \nabla\cdot(\rho\mathbf{V}\mathbf{V}) = -\nabla p + \nabla\cdot\hat{\tau} \tag{2}$$

$$\partial(\rho H - p)/\partial t + \nabla\cdot(\rho\mathbf{V}H) = -\nabla\cdot\mathbf{q} + \nabla\cdot(\hat{\tau}\cdot\mathbf{V}) - \sum_{k=1}^{N_v} a_k I_k \tag{3}$$

$$\partial\rho c_k/\partial t + \nabla\cdot(\rho\mathbf{V}c_k) = -\nabla\cdot\mathbf{J}_k + \sum_{s=1}^{N_r} \dot{w}_{ks} + (m_{\mathrm{HF}}/\hbar N_A)\cdot(a_k I_k/\nu_k - a_{k-1} I_{k-1}/\nu_{k-1}),$$
$$k = 1, 2, \ldots, N_v + 1 \tag{4}$$

$$\partial\rho c_k/\partial t + \nabla\cdot(\rho\mathbf{V}c_k) = -\nabla\cdot\mathbf{J}_k + \sum_{s=1}^{N_r} \dot{w}_{ks},$$
$$k = N_v + 2, \ldots, N_s \tag{5}$$

$$\rho = pm/(RT), \qquad m^{-1} = \sum_{k=1}^{N_s} c_k/m_k \tag{6}$$

$$\int_0^{L_{\mathrm{opt}}} a_k dy = -\frac{1}{2}\ln r_1 r_2,$$
$$k = 1, 2, \ldots, N_v. \tag{7}$$

Here N_v is the number of transitions between the vibrational levels $\mathfrak{v}$ of the exited hydrogen-fluorine molecules HF($\mathfrak{v}$) ($\mathfrak{v} = 0, 1, \ldots, N_v$) that are considered as the individual chemical species (their numbers are $k = 1, 2, \ldots, N_v + 1$, respectively); N_s is the total number of species; N_r is the number of elementary reactions including the processes of V-V and V-T relaxation of the HF($\mathfrak{v}$) molecules (these processes are considered as the individual reactions); $\dot{w}_{ks}$ are the chemical source terms for the species k in the reaction s; c_k and m_k are the mass fraction and the molar mass of the species k; m, ρ, p, T, and H are the molar mass, density, pressure, temperature, and total enthalpy of the mixture; $\hbar$ is the Plank constant; N_A is the Avogadro number; a_k, I_k, and ν_k are, respectively, the optical gain coefficient, the intensity, and the frequency of the radiation generated in the P branch of the vibration-rotational spectral lines of the HF($\mathfrak{v}$) molecules ($\mathfrak{v} + 1, j - 1) \rightarrow (\mathfrak{v}, j)$, where j is the rotational quantum number determined taking into account the so-called "J-shift" effect [1,6].

The quantities $\hat{\tau}$, $\mathbf{q}$, and $\mathbf{J}_k$ in Eqs. (2) through (5) are the viscous stress tensor, the heat flux vector, and the diffusive flux vector for species k in the multicomponent gas mixture, respectively.

The integral equations (7), the so-called steady-state lasing conditions for the laser with a plane-parallel-mirrors cavity [6], are used for the evaluation of the radiation intensities I_k, since the optical gain coefficients a_k in these equations depend implicitly on I_k. Finally, L_{opt} in Eq. (7) is the length of the optical path, and r_1 and r_2 are the resonator mirrors reflectivities.

The system (1) through (7) is supplemented by the equations for the determination of the diffusive fluxes $\mathbf{J}_k$ (the so-called Stephan–Maxwell equations), which were solved by an efficient (without matrix inversion) algorithm [12].

For the numerical solution of the governing equations, an implicit nonlinear-upwind second-order finite-difference scheme of approximate factorization based on the CSM approach [9–11] was used, coupled with an efficient fully implicit algorithm of the radiation intensities calculation [4].

Results of Preliminary Numerical Experiments

As has been already mentioned, the simulation of nonpremixed supersonic combustion in the CW chemical lasers, generally speaking, requires the computations to be performed in the domain of complex geometry that contains not only the mixing and combustion zone itself, but the supply fuel and oxidant nozzles as well. However, one can expect that the upwind influence of the supersonic mixing and combustion processes on the nozzle flow is tangible only in some limited neighborhood of the nozzle array exit plane. If the "depth" of this influence is not too large, the computational costs might be decreased significantly. That is why a set of special preliminary numerical experiments was carried out for the evaluation of the minimum size of the nozzle areas that have to be included in the computational domain in order to achieve the main goal of the present work, that is, to describe adequately the feedback between the processes in the combustion zone and in the supersonic supply system. These experiments included calculations of the chemically nonequilibrium F + H_2 + DF + He mixture flow in the nozzles in a wide range of the wall pressure value p_{out}, prescribed at the nozzle exit plane, and modeling the variation of the exhaust conditions and therefore the strength of the upwind influence of the laser cavity processes on the nozzle flow.

The results of these numerical experiments (some of them can be found in Ref. 11 and are not included here because of the space limitations) show that, in the range of practically meaningful p_{out} values (2 torr $\leq p_{out} \leq$ 30 torr), the influence of this parameter on the nozzle flow does not exceed the supersonic (divergent) part of the nozzle even in the case of a highly overexpanded regime of the nozzle performance when a developed separation of the nozzle boundary layer occurs. Hence, the numerical simulation of the supersonic combustion in the cavity of the CW chemical lasers, as well as in any other similar supersonic combustors, may be organized as follows.

At the first stage, the independent computations of the fuel and oxidant nozzle flows should be carried out with the "soft" (extrapolating) outflow boundary conditions for all the flow variables including pressure ("nominal" nozzle flow regime). The flow parameters, determined at this stage for some cross sections in the supersonic parts of the fuel and oxidant nozzles close to their throats, can be used as the inflow boundary conditions for the Navier–Stokes equations at the second stage of simulation, i.e., while computing mixing and combustion processes in the cavity.

Exactly this two-stage approach was employed in the present work. The corresponding configurations of the computational domains used at the second stage for the coupled computation of the flow in the supersonic parts of the nozzles and in the laser cavity

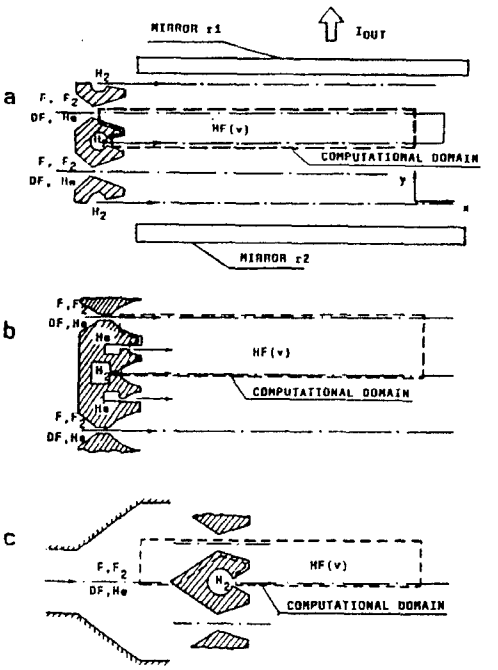

FIG. 1. Schematic of the flow and computational domains for the lasers with (a) two-slot nozzle array; (b) three-slot nozzle array; (c) wedge-shaped fuel injectors placed at the exit plane of the oxidant mono-nozzle.

for different designs of the nozzle array are shown in Fig. 1. It should be mentioned that, taking into account the periodic nature of the flow under consideration, these computational domains include only the area between the symmetry planes of two neighboring fuel and oxidant nozzles.

Results and Discussion

Within the framework of the above strategy, the simulation of the supersonic hydrogen-fluorine combustion in the laser cavity was performed for three types of mixing devices presented schematically in Fig. 1. Though the finite-difference grids used in the calculations (see Fig. 2) are relatively coarse, it was shown that they provide for an acceptable resolution of both the subsonic parts of the nozzle array boundary layers and the base recirculation zones that is crucial from the standpoint of the goals of the present study. They also permit virtually grid-independent results to be obtained for all the laser output characteristics.

The kinetic model of the processes in the oxidant nozzles included the gas-phase finite-rate recombi-

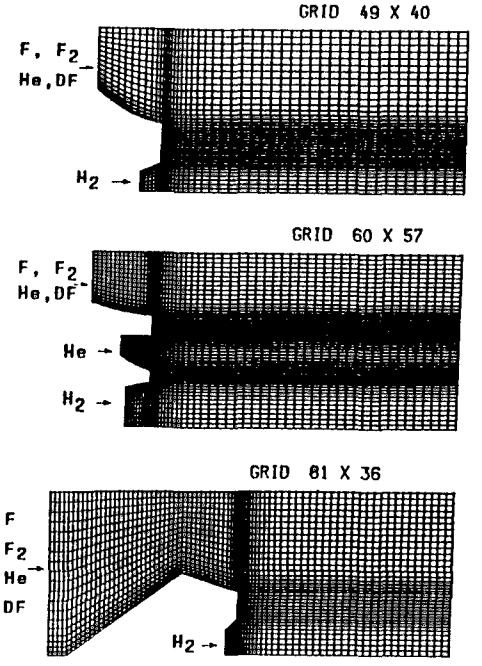

FIG. 2. Typical finite-difference grids used in computation.

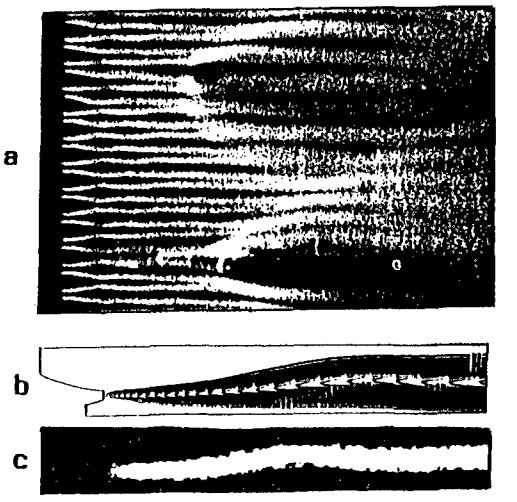

FIG. 3. Photograph of the flow pattern in the laser cavity (a), and comparison of the numerical and experimental data on the flame configuration (b) and (c): (b) computed field of the total HF mass fraction $HF_{\Sigma} = \Sigma\ HF(\upsilon)$; (c) enlarged fragment of (a).

nation of the fluorine atoms and their catalytic recombination on the nozzle walls.

For the description of the finite-rate hydrogen-fluorine chemistry in the cavity, the kinetic model [6] was used, which included the so-called "cold" and "hot" pumping reactions $F + H_2 = HF(\upsilon) + H$ ($\upsilon = 1, 2, 3$), $H + F_2 = HF(\upsilon) + F$ ($\upsilon = 1, 2, \ldots, 6$), the reactions of dissociation-recombination, and the reactions of *V-V* and *V-T* energy exchange with the participation of the vibrationally excited molecules $HF(\upsilon)$. The total number of the elementary reactions taken into account was 165, and the total number of the species was 13 [H, H_2, F, F_2, He, DF, $HF(\upsilon)$ $0 \leq \upsilon \leq 6$].

All the computations were performed using a local choice of the CSM preconditioning parameter in accordance with the local Mach number value (see Ref. 11 for more details) coupled with a spatially varying time-stepping strategy. The steady-state solutions (five orders of magnitude drop of the maximum residual) were obtained in 200–1000 iterations, the CFL values being equal to 3–5. This required 1–10 h on PC AT 486/66MHz.

Two-Slot Nozzle Array (Fig. 1a):

This type of mixing device was used in the first constructions of the CW chemical lasers [6], so it is the most studied device. Nevertheless, even for this relatively simple case, the only successful predictions reported till now have been for the integral laser output parameters.

Figure 3 illustrates the correspondence between the experimental data and the numerical prediction of the flame configuration in the laser cavity obtained in the present work. The white regions in the photo (see Fig. 3a and its enlarged fragment, Fig. 3c) are obviously the hydrogen-fluorine flame fronts obtained in the experiment. Corresponding computational results are presented in Fig. 3b in the form of the contours of the total HF mass fraction C_{HF} (the white region in this picture is the line of the C_{HF} maximum values, which may be treated as the computational flame front configuration). One can see that the agreement between the experiment and the numerical prediction is rather good, which demonstrates the validity of the approach used here. It should be emphasized that, when using the conventional, uncoupled approach (the successive computation of the nozzle flows and combustion in the cavity), it turned out to be impossible to achieve even a qualitative correspondence of the numerical and experimental data on the flame configuration. Thus, only the coupled computations of the nozzle array flows and mixing/combustion processes in the laser cavity provide a realistic evaluation of the local characteristics of the flow in the laser cavity.

This conclusion is confirmed by the results of the numerical experiments presented in Fig. 4, which elucidate also the mechanism of the feedback between the processes in the laser cavity and in the nozzle array. In these experiments, the hydrogen supply pressure value p_{H_0} was varied in a wide range,

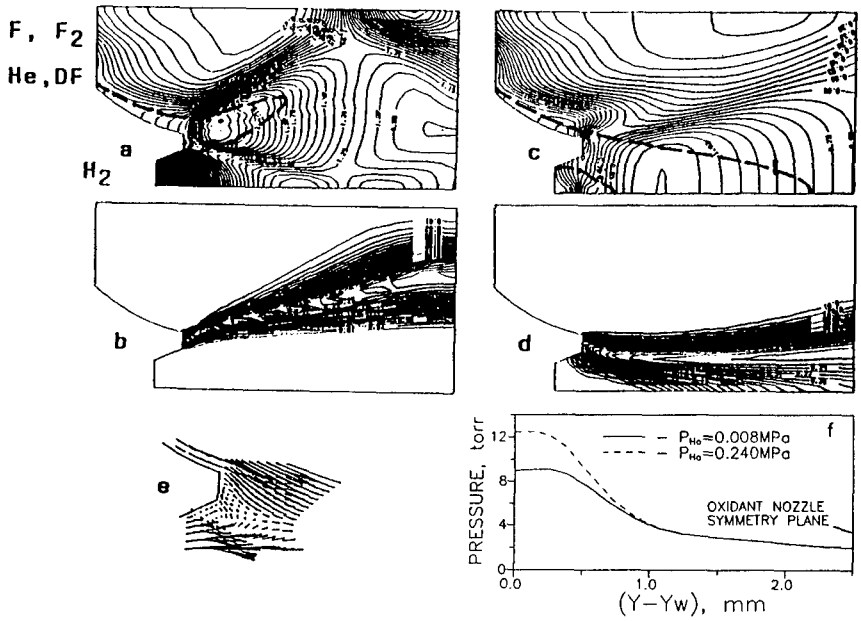

FIG. 4. Influence of the hydrogen supply pressure p_{H_0} on the cavity flow pattern for the nozzle array with the hydrogen and fluorine nozzles throats 0.4 and 0.45 mm, expansion ratios 4.5 and 11.0, and fluorine nozzle supply pressure 0.12 MPa: (a) and (b) p_{H_0} = 0.24 MPa; (c) through (e) p_{H_0} = 0.008 MPa; (a) and (c) pressure contours; (b) and (d) HF mass fraction contours; (e) the fragment of the velocity vector field in the vicinity of the nozzle array base; (f) fluorine nozzle exit pressure profiles; dashed curve is the sonic line.

while the oxidant supply pressure was kept constant. From comparison of the pressure fields in Figs. 4a and 4c and the pressure profiles in Fig. 4f, it is seen clearly that, in spite of the same boundary conditions at the inlet of the oxidant nozzle for both presented cases, the flow wave pattern near the wall at the vicinity of the exit plane of the oxidant nozzle for these cases is rather different, or in other words, it depends significantly upon the value of the hydrogen supply pressure p_{H_0}. This is obviously explained by the pressure disturbances propagation from one nozzle to another, through the base recirculation zone and through the subsonic part of the nozzle boundary layer. For the flow under consideration, this effect turns out to be important, since the boundary layer at the nozzle wall is rather thick as a result of the low Reynolds number value, typical for the CW chemical lasers.

At some point, the difference between the oxidant and fuel nozzles exit pressures becomes large enough to induce the separation of the hydrogen nozzle boundary layer (see Fig. 4e). In this case, fluorine penetrates into the separation bubble, which causes ignition of the mixture and starts the combustion directly inside the hydrogen nozzle (see Fig. 4d). This, in turn, leads to significant deformation of the mixing zone and turns out to affect crucially the flame configuration, the structure of the base recirculation zone, and the laser output power, which decreases sharply at low p_{H_0} values.

Three-Slot Nozzle Array (Fig. 1b) and Wedge-Shaped Fuel Injectors Placed at the Exit of Oxidant Mono-Nozzle (Fig. 1c):

These types of HF CW chemical lasers are known to have significant advantages over the conventional design considered above, from the point of view of the manufacturing technology and/or operational control. The present work seems to be the first attempt at Navier–Stokes simulation of the flows in such lasers.

Figure 5 illustrates the complicated flow structure and the space distribution of the HF mass fraction in the neighborhood of the nozzle array exit for the laser under consideration. When analyzing these results, one can see that, unlike in the case considered in the previous section, the combustion in the three-slot laser cavity starts at a rather long distance downstream from the nozzle array. This is caused by the effect of the intermediate helium jet and results in a long lasing zone, typical for the three-slot laser. Also, varying this jet parameter, it is possible to control efficiently the combustion processes and hence the laser performance. It should be mentioned also that the combustion in such lasers occurs in the region

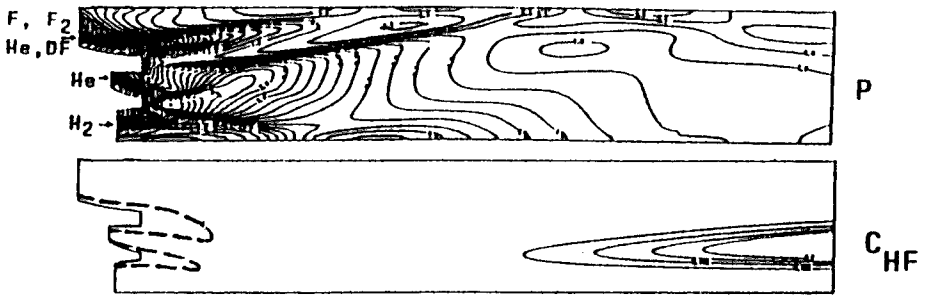

FIG. 5. Typical flow pattern for the three-slot laser; dashed curve is the sonic line.

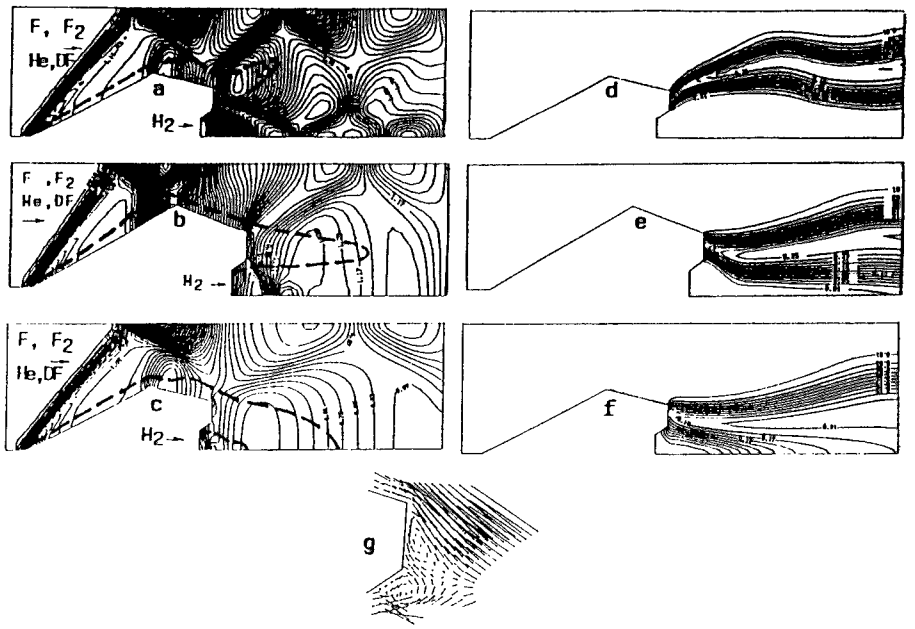

FIG. 6. Hydrogen supply pressure p_{H_0} and distance between hydrogen injectors h effect on the flow field in the laser with Mach 5 oxidant mono-nozzle (hydrogen nozzle as in Fig. 4): (a) through (c) pressure field; (d) through (f) HF mass fraction; (g) the fragment of velocity vector field in the vicinity of injector base; (a) and (d) $p_{H_0} = 0.2$ MPa, $h = 4$ mm; (b) and (e) $p_{H_0} = 0.025$ MPa, $h = 3$ mm; (c), (f), and (g) $p_{H_0} = 0.008$ MPa, $h = 4$ mm; dashed curve is the sonic line.

where the pressure gradients caused by the interaction of the shock waves become much weaker than in the entrance region of the cavity. This obviously permits the optical quality of the laser beam to be increased drastically.

The last mixing device considered in the present work is an oxidant mono-nozzle with a system of wedge-shaped hydrogen supersonic injectors placed at its exit plane. Such a design is much easier to manufacture than the two previous designs. Besides, it permits the viscous losses in the supply system to be reduced significantly.

Figure 6 illustrates the influence of the hydrogen supply pressure level and the distance between the neighboring hydrogen injectors on the local flow characteristics and combustion processes for this type of nozzle array. The distinguishing feature of the flow pattern presented in these pictures is the interaction between the bow oblique shock, symmetry plane, rarefaction fan generated by the obtuse angle of the injector, and combustion zone. This interaction results in the formation of a complicated diamond-shaped system of shock waves, whose intensity depends strongly upon the value of the hydrogen supply pressure, and leads to a significant distortion of the flame front. As to the combustion processes/supply system flow feedback and the effect of the fuel and oxidant nozzle flows interaction, their mecha-

nism is exactly the same as discussed above for the two-slot nozzle array. In particular, just as in that case, the separation of the boundary layer in the hydrogen nozzle can be induced by the pressure disturbance propagating from the high-pressure oxidant flow through the injector base region, which leads to the ignition of the mixture inside the injector (see Figs. 6f and 6g).

Finally, it should be mentioned that decreasing the distance between the fuel injectors, rather profitable from the viewpoint of intensification of the reactants mixing rate, may, at some point, have a dramatic effect on the flow structure and hence on the overall device performance. We mean "choking" of the supersonic oxidant flow as a result of the interaction of intensive oblique shocks in the interinjector space with formation of the straight shock. For the considered design, a situation quite close to the latter one takes place when $h = 3$ mm, as can be clearly seen from the pressure field presented in Fig. 6c.

Conclusions

Numerical study of nonpremixed supersonic combustion in continuous-wave HF chemical lasers with different fuel/oxidant mixing devices, using the coupled Navier–Stokes simulation of the mixing/combustion region and supersonic supply system, has permitted elucidation of the mechanism of the feedback between the processes in the laser cavity and nozzle array. It is shown, in particular, that this effect is caused by the upwind influence of the mixing/combustion processes on the nozzle array flow, and by the fuel and oxidant nozzle flows interaction due to the propagation of the pressure disturbances from one nozzle to another through the nozzle array base recirculation zone and subsonic part of the nozzle boundary layers. The coupled approach provides for correct description of these effects, and thus permits significant improvement of the correspondence between the numerical predictions and experimental data on the flame structure in the laser cavity, especially for regimes with the supply nozzle boundary layer separation.

REFERENCES

1. Emanuel, G., *J.Q.S.R.T.* 11:1481–1520 (1971).
2. Ratliff, A. W., and Thoens, J., AIAA Paper No 74–225, 1974.
3. Ramshaw, J. D., Mjolsness, R. C., and Farmer, O. A., *J.Q.S.R.T.* 17:149–164 (1977).
4. Lapin, Yu. V., Strelets, M. Kh., and Shur, M. L., *Combust. Explos. Shock Waves* 18(5):573–579 (1982) (translated from Russian).
5. Imbert, M., Zeitoun, D., and Brun, R., *Tenth International Colloquium on Dynamics of Explosions and Reactive Systems,* 1985, pp. 429–440.
6. *Handbook on Chemical Lasers* (R. W. F. Gross and J. F. Bott, Eds.), Wiley Interscience, New York, 1976.
7. Rapagnani, N. L., and Lankford, D. W., AIAA Paper No 81–1135, 1981.
8. Ramshaw, J. D., and Dukowicz, J. K., *APACHE: A Generalized-Mesh Eulerian Computer Code for Multicomponent Chemically Reactive Fluid Flow,* Los Alamos National Laboratory Report No LA-7427, 1979.
9. Strelets, M. Kh., and Shur, M. L., *U.S.S.R. Comput. Math. Math. Phys.* 28(1):165–173 (1988) (translated from Russian).
10. Kuznetsov, A. E., Strelets, M. Kh., and Shur, M. L., *U.S.S.R. Comput. Math. Math. Phys.* 31(2) (1991) (translated from Russian).
11. Shur, M. L., *Seventh International Conference on Numerical Methods in Laminar and Turbulent Flow,* Pineridge Press, Swansea, Wales, 1991, pp. 1526–1536.
12. Strelets, M. Kh., and Shur, M. L., *Seventh International Conference on Numerical Methods in Thermal Problems,* Pineridge Press, Swansea, Wales, 1991, pp. 858–867.

Twenty-Fifth Symposium (International) on Combustion/The Combustion Institute, 1994/pp. 21–27

NUMERICAL SIMULATION OF SUPERSONIC MIXING AND COMBUSTION

P. GERLINGER, D. BRÜGGEMANN AND J. ALGERMISSEN
Institut für Thermodynamik der Luft- und Raumfahrt
Universität Stuttgart, 70550 Stuttgart, Germany

Problems of hydrogen mixing and combustion in supersonic air streams are numerically investigated. An implicit lower-upper (LU) scheme is used for solving the full, averaged, two-dimensional Navier–Stokes and species transport equations. For turbulence closure, a two-equation low-Reynolds-number q-ω turbulence model is employed. While the chemical source terms are treated fully coupled with the fluid motion, the conservation equations for q and ω are integrated in a decoupled way. This is done by the same LU algorithm as for the main flow equations. The combustion process in chemical nonequilibrium is based on a 20-step, 9-species finite-rate chemistry model. Because of the short residence times of the gas in supersonic combustors, the kind of hydrogen supply is very important for combustion process. This paper investigates hydrogen injections axial to the main stream at subsonic, sonic, and supersonic injection velocities. In addition to an optimal mixing that is strongly influenced by the shear layer behind the injector, it is important that the main stream remains supersonic. This results in a diverging geometry that compensates for the increase in boundary-layer thickness and rise in temperature due to combustion. There is also a strong interaction with shock waves, which often induce subsonic regions. The turbulent shear flow of hydrogen and air enables the gases to interpenetrate and can improve mixing.

Introduction

With increasing interest in air-breathing propulsion systems for hypersonic flight, the demand on CFD (computational fluid dynamics) in this field also is growing strongly. This tendency is emphasized by the lack of experimental test facilities that are able to treat combustion problems in high-speed flows. The phenomena in supersonic combustion are quite complicated and include a variety of problems, each of which alone is already difficult to treat in CFD. These are, for example, complicated shock structures that have to be resolved, shock-wave boundary-layer interactions as well as turbulent mixing and combustion. Therefore, there is a need for reliable experimental data to calibrate the CFD codes. At lower Mach numbers, it is easier to perform experiments to validate numerical codes that can be extended to predict flow structures at higher Mach numbers. In this work, turbulence-combustion interactions are not treated yet. In addition to the need for an exact description of turbulent effects in compressible flows, the numerical stability and economy are also very important. This was the reason for using a two-equation low-Reynolds-number q-ω turbulence model [1]. We have shown previously [2] that this turbulence closure is superior with respect to stability and economy to other two-equation low-Reynolds-number models. Similar results have been reported by others [1,3]. In this paper, cases are investigated that are dominated by mixing shear flows, both sub- and supersonic. These mixing layers, and the diffusive transport of oxygen and hydrogen, are responsible for a good combustion. Because diffusion is dominated by turbulent effects in such regions, not only chemical kinetics but also the turbulent transport coefficients are of great importance. For finite-rate chemistry modeling, we used a 9-species 20-step hydrogen-air reaction scheme [4].

Governing Equations

Reactive flows are treated using the averaged compressible Navier–Stokes and species transport equations. Because the continuity equation is included in the set of governing equations, only $N_k - 1$ different species transport equations have to be considered if N_k is the total number of different species. For the density ρ and the pressure p, conventional time averaging is used, while for the remaining variables we use mass-weighted averaging. For simplicity, the bar and tilde notations have been omitted from averaged variables. Expressed in Cartesian tensor form, the modeled transport equations are as follows.

Continuity:

$$\frac{\delta \rho}{\delta t} + \frac{\delta}{\delta x_j}(\rho u_j) = 0 \tag{1}$$

Momentum:

$$\frac{\delta(\rho u_i)}{\delta t} + \frac{\delta}{\delta x_j}(\rho u_i u_j) = -\frac{\delta p}{\delta x_i} + \frac{\delta}{\delta x_j}(\tau_{ij}) \qquad i = 1,2 \tag{2}$$

Energy:

$$\frac{\delta(\rho E)}{\delta t} + \frac{\delta}{\delta x_j}(u_j[\rho E + p]) = \frac{\delta}{\delta x_j}(u_i \tau_{ij} - q_j) \quad (3)$$

Species:

$$\frac{\delta(\rho Y_i)}{\delta t} + \frac{\delta}{\delta x_j}(\rho u_j Y_i) = -\frac{\delta}{\delta x_j}(\rho \check{u}_i Y_i) + w_i \quad (4)$$

where u_i are the velocity components, E is the specific total energy, τ_{ij} is the stress tensor, Y_i is the mass fraction, and w_i the chemical source term of species i, due to chemical reactions. The heat flux vector q_j due to conduction and diffusion is given by

$$q_j = -\lambda \frac{\delta T}{\delta x_j} + \rho \sum_{k=1}^{N_k} h_k Y_k \check{u}_{j,k} \quad (5)$$

and the diffusion velocities $\check{u}_{j,k}$ are calculated using Fick's law by

$$Y_k \check{u}_{j,k} = -D_{k,m} \frac{\delta}{\delta x_j} Y_k. \quad (6)$$

Gradient transport is involved for modeling the turbulent correlations in the heat flux vector. The turbulent transport coefficients are calculated using the turbulent Prandtl and Schmidt numbers, which are both taken as constants of 0.9 [5]. The Boussinesq approximation is used to relate the turbulent Reynolds stresses to the main strain rate. With this approximation, the stress tensor $\tau_{ij} = \tau_{ij}^M + \tau_{ij}^T$ is calculated from

$$\tau_{ij} = -(\mu + \mu_t)\left(\frac{\delta u_i}{\delta x_j} + \frac{\delta u_j}{\delta x_i} - \frac{2}{3}\delta_{ij}\frac{\delta u_k}{\delta x_k}\right) - \frac{2}{3}\rho k \delta_{ij} \quad (7)$$

where τ_{ij}^M is the molecular stress tensor, τ_{ij}^T is the Reynolds stress tensor, and k is the turbulent kinetic energy. The closure of this system of averaged equations is achieved by the low-Reynolds-number q-ω turbulence model. In addition, we assumed ideal gas for our calculations.

The LU-SGS Algorithm

The governing equations are discretized by means of a finite-volume method that facilitates the application in general curvilinear coordinates. The program is held in a block structured form to allow for a coupling of different computing domains. Every block itself has to consist of a structured grid. All calculations in this paper are performed with a two-block grid. For time integration, an implicit LU-SGS (lower-upper symmetric Gauss–Seidel) method is used, both for the main flow and the turbulence transport equations [5,6,2]. The chemical source terms are treated implicitly and fully coupled with the fluid motion. Because the LU scheme leads to block diagonal operators, it is also fully vectorizable in the implicit part. This is a great advantage, especially if reactive flows, which often have a large number of species conservation equations, are treated. For high-Reynolds-number flows, it is often sufficient to use only the inviscid Jacobians in the implicit operator, even if the full Navier–Stokes equations are treated. Low-Reynolds-number turbulence models require very fine grids in near-wall regions. Here it is advantageous also to include the viscous Jacobians in the implicit operator. We use a simplified form that is based on the thin-layer Navier–Stokes equations [6]. The numerical scheme has proven to be efficient and very stable. Because central differences are used in the explicit part, we had to add some kind of artificial dissipation. This is done by a second- and fourth-order matrix dissipation [7,8,9,10]. In contrast to the ordinary scalar dissipation where every equation is scaled by the spectral radius of the inviscid Jacobian, every equation is scaled here by an individual value to allow the reduction of artificial dissipation.

Turbulence Modeling

To close the averaged Navier–Stokes equations, we investigated three different turbulence models, as follows: an algebraic Baldwin–Lomax model [11], a low-Reynolds-number k-ε model with wall functions from Launder and Sharma [12,13], and a two-equation low-Reynolds-number q-ω model developed by Coakley [1,14,15]. For high-speed flows and supersonic combustion, we have chosen the q-ω model because of its good numerical stability and economy. In contrast to many other two-equation low-Reynolds-number turbulence models, the q-ω model is numerically very stable and shows good convergence rates comparable to the algebraic Baldwin–Lomax model. This is achieved by the way in which the low-Reynolds terms are modeled.

While we have not obtained converged solutions with the k-ε model for wall injection at high total pressure ratios (between the injected stream and the main flow) [2], this problem vanishes using the q-ω model. In our calculations as well as in calculations of Coakley [15], the accuracy is comparable to that of the k-ε model. In addition to its much better numerical behavior, this closure is also advantageous as it may be started with constant free-stream values of q and ω. A complicated calculation of initial profiles is not necessary. These features may be of increasing value in future three-dimensional (3D) calculations.

Instead of the turbulent kinetic energy k and the

dissipation rate ε, the q-ω model uses $q = s_1 = \sqrt{k}$ and $\omega = s_2 = \varepsilon/k$ as turbulent transport variables. The modeled governing equations are given by

$$\frac{\delta(\rho s_i)}{\delta t} + \frac{\delta}{\delta x_j} \cdot \left(\rho u_j s_i - (\mu + \mu_t/\sigma_i)\frac{\delta s_i}{\delta x_j}\right) = H_i \rho \omega s_i \qquad i = 1,2. \tag{8}$$

With the divergence of the velocity field $\mathcal{D}$ and the strain invariant $\mathcal{S}$

$$\mathcal{D} = \frac{\delta u_k}{\delta x_k} \qquad \mathcal{S} = \left(\frac{\delta u_i}{\delta x_j} + \frac{\delta u_j}{\delta x_i}\right)\frac{\delta u_i}{\delta x_j} - \frac{2}{3}\mathcal{D}^2 \tag{9}$$

we can express the turbulent source function by

$$H_i = C_{i1}\left(C_\mu f_i \frac{\mathcal{S}}{\omega^2} - C_{i3}\frac{\mathcal{D}}{\omega}\right) - C_{i2}. \tag{10}$$

While $f_2 = 1$ is a constant, the eddy viscosity damping function f_1

$$f_1 = 1 - \exp(-0.022\, R_T) \tag{11}$$

depends on the turbulent Reynolds number $R_T = \rho q y/\mu$, which itself depends on the distance y from the wall. The turbulent Reynolds number takes a value of one in fully developed turbulent flow, while it approaches zero in laminar regions or within the viscous sublayer [16]. The damping function for the ω equation C_{21}

$$C_{21} = 0.5 f_1 + 0.055 \tag{12}$$

has a finite value even if f_1 approaches zero. From the calculated values of q and ω, the eddy viscosity is calculated by

$$\mu_t = C_\mu f_1 \frac{\rho q^2}{\omega}. \tag{13}$$

The constants of this model are [15].

$$C_{1i} = 0.5, \qquad C_{22} = 0.833, \qquad C_{i3} = 2/3$$
$$\sigma_1 = 0.8, \qquad \sigma_2 = 2.0, \qquad C_\mu = 0.09. \tag{14}$$

This standard model has been modified by two corrections [15]. The first one is to improve the prediction of the surface heat transfer and results in a limitation on the turbulent length scale l_t (in our calculations for $y^+ \leq 20$). We have used this as a constraint for the variable ω

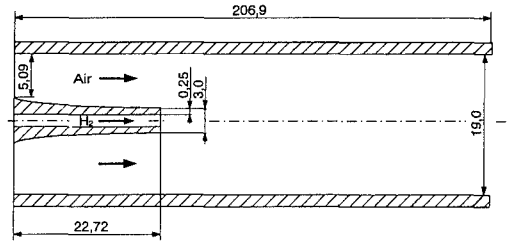

FIG. 1. Geometry of test cases 1 through 4 (sizes in mm).

$$l_t = \min(2.5y, q/\omega), \qquad \omega = q/l_t. \tag{15}$$

The second modification is a compressibility correction to improve predictions of shock-wave boundary-layer interactions that results in a new multiplicator for the dilatation term ($C_{23} = 2.4$). In a detailed study [17], we have investigated the effects of these corrections and have obtained the best agreement with experimental data if both corrections are used simultaneously.

Results

The numerical code has been investigated at different test cases with and without combustion [2,9,17,10]. Calculations of shock-induced premixed hydrogen-air combustion agree very well with those of other researchers [9]. For comparison with experimentally obtained data, we have calculated the Burrows–Kurkov mixing and combustion experiment in which pure hydrogen is injected at a wall step axially to the main stream. In our results, the diffusion process seems to be too slow in comparison to the experiment [17], but the overall agreement is good. One reason for the remaining discrepancy may be the use of a constant turbulent Schmidt number of 0.9, which might be too high for the diffusion of hydrogen in vitiated air. Libby and Williams [18] reported that, for binary mixtures of gases with large and small molecular weights, the turbulent Schmidt number may be as small as 0.25.

Mixing Investigations:

Mixing of hydrogen axially injected to the main stream is investigated for different injection conditions and geometries. The assumed configurations correspond to experimental studies that have been started at the ITLR. The channel geometry for the first four cases is shown in Fig. 1. Hydrogen is injected through the blunt end of a central body that simultaneously serves as a nozzle for the main flow. We start the calculation at the smallest cross section with sonic conditions. Downstream, the air accelerates up to flow Mach numbers of about 2. The blunt

TABLE 1
Inflow conditions for the air at the smallest cross section

Air main stream	p (bar)	T (K)	Ma	Y_{O_2}	Y_{N_2}
cases 1 through 3 and 5, 6	1.53	241	1.0	0.2336	0.7664
case 4	1.53	1450	1.0	0.2336	0.7664
cases 7, 8	3.0	1400	1.0	0.2336	0.7664

TABLE 2
Injection conditions for the hydrogen

Hydrogen	case 1	case 2	case 3	case 4	case 5	case 6	case 7	case 8
p (bar)	0.5	0.36	0.57	0.65	0.6	0.47	1.6	1.6
T (K)	270	240	240	540	240	240	1200	1200
Ma	0.47	0.84	1.0	1.0	1.0	1.2	1.0	1.2

end of the central body has a height of 3 mm and a wall thickness of 0.25 mm. Because of the injection and the wall thickness of the injector lip, we get a system of shocks and expansion fans that has a strong influence on the flow behavior. Tables 1 and 2 show the flow conditions for air in the smallest cross section and for hydrogen at the injector, respectively. The last two calculations include combustion. For cases 1 and 2, hydrogen is injected at subsonic conditions with different Mach numbers but with about the same total pressure. This results in nearly the same flow fields. For constant total pressure, the variance in static pressure and Mach number is of minor influence. Figure 2 shows pressure contours for case 1. Because, with the exception of the central body wall thickness, there is no divergence in the channel cross section, the flow speed of the hydrogen remains subsonic at the channel center. Shocks and expansion fans are reflected at the subsonic region near the channel center. The highest values of the turbulent intensity are obtained at the corners of the blunt end of the central body. In this case, the hydrogen is injected with about the air stream velocity, which is disadvantageous for the mixing. In case 3, hydrogen is injected at sonic conditions and with an increased static pressure of 0.57 bar. Now a supersonic flow behind the injector appears, but, as a result of the reflection of the shock waves at the channel walls, a small normal shock at the channel center is formed, resulting again in subsonic regions (Fig. 3). However, the flow is now supersonic at the channel end. Figure 4 shows the mixing efficiency for the channel cross sections. This parameter is defined as that part of the hydrogen mass flow that could react with available oxygen in relation to the total hydrogen mass flow. A second performance parameter shown in Fig. 5 is the total pressure, which is averaged by the mass flow for every cross section and is related to the value at the flow entrance. The better mixing efficiency and the larger loss in total pressure for case 3 result from the larger difference between the flow velocities of the hydrogen jet and the air. If we further increase the total pressure ratio between the hydrogen and the incoming air above values of about 0.4, the shocks induce large subsonic regions, or the flow is totally subsonic as in case 4. For further calculations (cases 5 and 6), we have opened the channel at the end of the central body with an angle of 1.5°. Again, a variation of static pressures and Mach numbers at a constant total pressure results in nearly the same flow fields. The divergent channel geometry now compensates for the increase in boundary-layer thickness and losses due to shocks, and the flow is everywhere supersonic.

Combustion Investigations:

A similar channel with a total length of 21.2 cm and an opening angle of 5° is used for the combustion investigations. The divergent part of the channel starts 9.2 cm behind the smallest cross section. The inflow and injection conditions for these cases (7 and 8) are given in Tables 1 and 2. The wall temperature is assumed to be $T_W = 700$ K. The calculated pressure, Mach number, and temperature contours for the upper channel part are shown in Figs. 6 through 8. We can observe that the combustion starts about 5.5 cm downstream of the blunt end of the central body. In front of the ignition zone, an oblique shock is formed in the upper part and a normal one in the lower. Therefore, a small subsonic region again appears behind the normal shock (see Fig. 7). With the

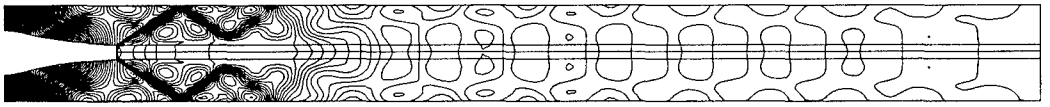

FIG. 2. Pressure contours of case 1.

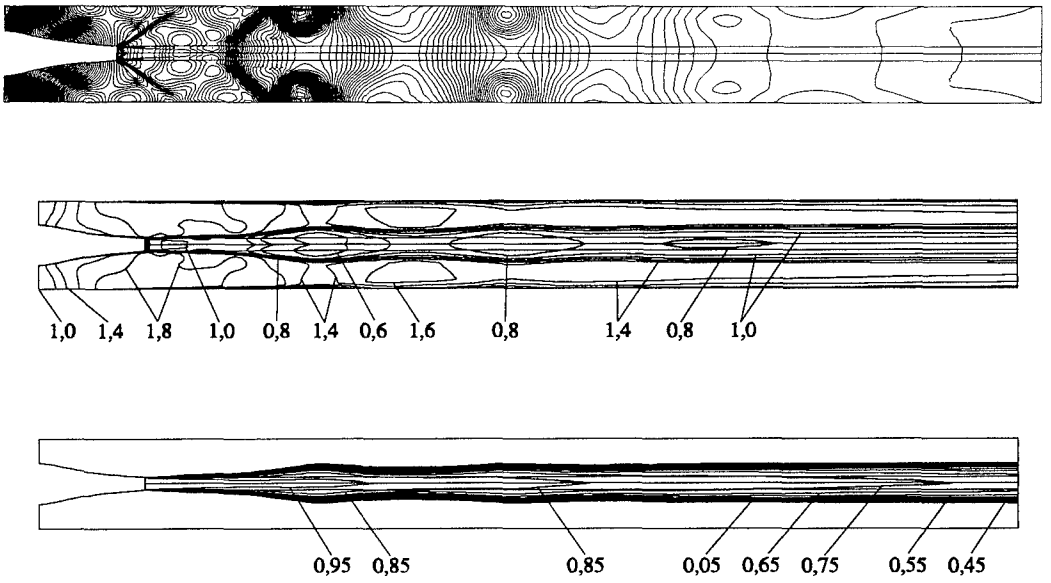

FIG. 3. Pressure, Mach number, and H_2 mole fraction contours of case 3.

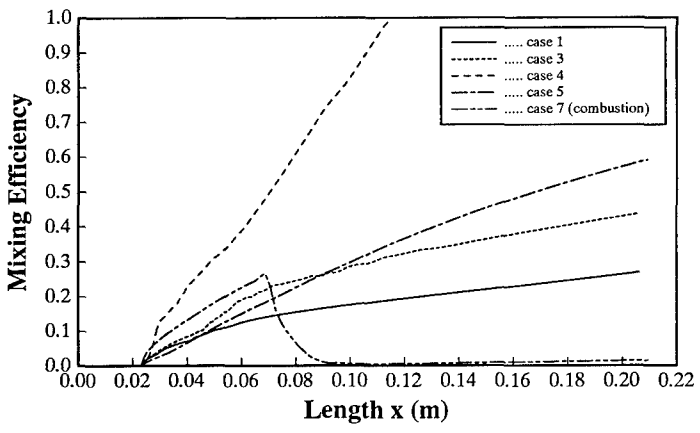

FIG. 4. Mixing efficiencies for channel cross sections.

beginning of the divergent part, the flow accelerates, and the combustion process is supersonic. In a further calculation, we tried to reduce the size of the subsonic region and have increased the channel opening up to an angle of 7.5°, hoping that a stronger expansion could have an upwind influence on the subsonic region. Although not shown here, the results in this case are nearly the same up to the divergent channel part. The subsonic region does not disappear. Because of the stronger expansion, Mach numbers of about 2.6 appear at the channel end. The constant cross section of the first channel part is used as a flame holder. If the channel is opened directly at the central body end, it is more difficult to find an optimum angle that allows the reactions to start and the flow to remain supersonic. The mass fraction con-

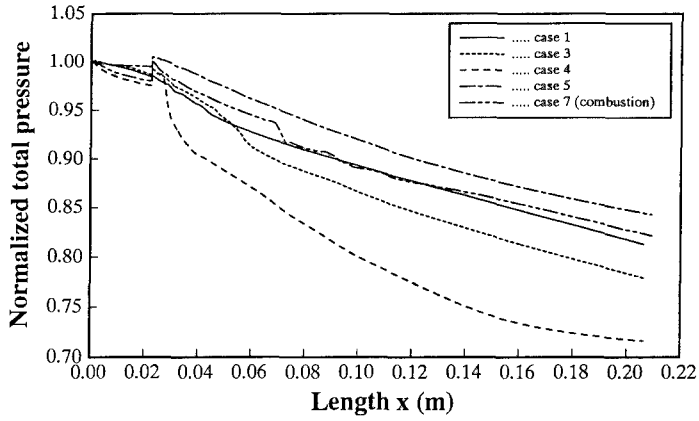

FIG. 5. Normalized mass weighted total pressure.

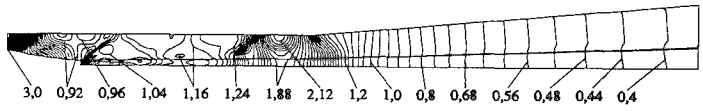

FIG. 6. Pressure contours of case 7.

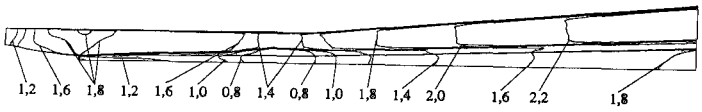

FIG. 7. Mach number contours of case 7.

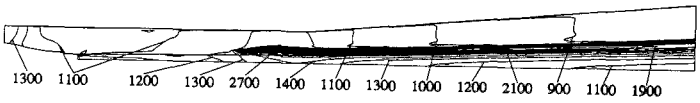

FIG. 8. Temperature contours of case 7.

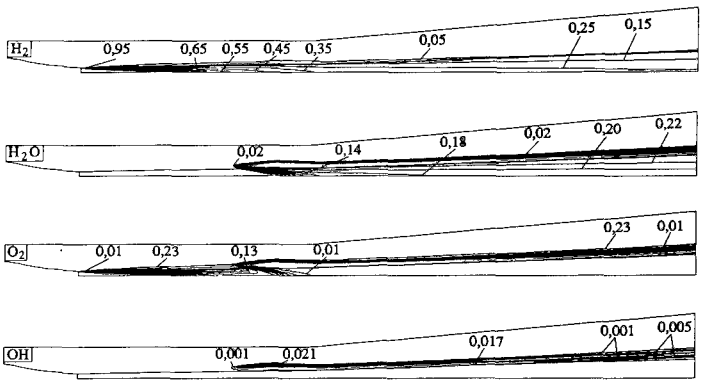

FIG. 9. Contours of H_2, O_2, H_2O, and OH mass fractions of case 7.

tours of H_2, H_2O, O_2, and OH are shown in Fig. 9. The OH distribution reveals a very small reaction zone, but it has to be considered that the total length of this channel is only 21 cm. For the divergent channel part, the mixing efficiency shows only a small nearly constant hydrogen fraction that is able to react. The maximum H_2 mass fraction decreases from $Y_{H_2} = 0.36$ at $x = 9$ cm to $Y_{H_2} = 0.26$ at $x = 20$ cm.

Conclusions

With the same geometry, an increase in injection total pressure results in better mixing, caused by

more extreme shear layers and stronger expansion fans. On the other hand, stronger shocks are induced, which lead to losses in total pressure and may lead to a breakdown of the supersonic stream. Numerical investigations may help here to find optimal values for the total pressure ratio. This is also the case for combustion problems where we used a constant cross section of the first channel part to start combustion. The low-Reynolds-number q-ω turbulence model has proven to be numerically very stable and is simple to use even for complex geometries.

Acknowledgment

We would like to thank the Deutsche Forschungsgemeinschaft (DFG) for the financial support of this work within the special research program SFB 259 at the University of Stuttgart.

REFERENCES

1. Coakley, T. J., AIAA Paper 83-1693, 1983.
2. Gerlinger, P., and Algermissen, J., AIAA Paper 93-5021, 1993.
3. Martelli, F., and Michelassi, V., in *Advanced Applied Computational Fluid Dynamics* (O. Baysal, Ed.), ASME, New York, 1990.
4. Jachimowski, C. J., NASA TP 2791, 1988.
5. Shuen, J. S., and Yoon, S., *AIAA J.* 27:9 (1989).
6. Shuen, J. S., *J. Comp. Phys.* 99:233 (1992).
7. Swanson, R. C., and Turkel, E., *J. Comp. Phys.* 101:292 (1992).
8. Jorgenson, P., and Turkel, E., *J. Comp. Phys.* 107:297 (1993).
9. Gerlinger, P., and Algermissen, J., *J. Comp. Phys.*, submitted.
10. Gerlinger, P., Algermissen, J., and Brüggemann, D., AIAA Paper 94-3181, 1994.
11. Baldwin, B. S., and Lomax, H., AIAA Paper 78-257, 1978.
12. Launder, B. E., and Sharma, B. I., *Letters in Heat and Mass Transfer*, 1974, Vol. 1, p. 325.
13. Gerolymos, G. A., *AIAA J* 28:10 (1990).
14. Vuong, S. T., and Coakley, T. J., AIAA Paper 87-0286, 1987.
15. Coakley, T. J., and Huang, P. G., AIAA Paper 92-0436, 1992.
16. Marvin, J. G., and Coakley, T. J., NASA TM 101079, 1989.
17. Gerlinger, P., Algermissen, J., and Brüggemann, D., AIAA Paper 94-2247, 1994.
18. Libby, P. A., and Williams, F. A., in *Topics in Applied Physics* (P. A. Libby and F. A. Williams, Eds.), Vol. 44, "Turbulent Reacting Flows," Springer, Berlin, 1980, p. 5.

Twenty-Fifth Symposium (International) on Combustion/The Combustion Institute, 1994/pp. 29–36

THE INFLUENCE OF EQUIVALENCE RATIO AND SORÊT EFFECT ON THE IGNITION OF HYDROGEN-AIR MIXTURES IN SUPERSONIC BOUNDARY LAYERS

LUÍS FERNANDO FIGUEIRA DA SILVA AND BRUNO DESHAIES
Laboratoire d'Energétique et de Détonique-URA 193 au CNRS-ENSMA
Site du Futuroscope, B.P. 109, 86960 Futuroscope Cedex, France

As a result of viscous heating, spontaneous ignition of a supersonic flow of premixed combustible gases can occur in boundary layers. In a previous numerical study, the main structure of the reacting flow related to this specific type of ignition was given in the case of a laminar boundary layer of hydrogen and air developing over a flat plate.

To complete the first mapping of the ignition as a function of the boundary conditions, we present in this paper the results of a specific study of the influence of the equivalence ratio of the mixture on ignition. The equivalence ratio is found to modify the chemical induction time in the boundary layer as follows: (1) in a direct way, (2) via the dependence of the wall temperature on the composition. Because of these combined effects, the minimum induction length is obtained for unusually lean mixtures. As it modifies local composition, the Sorêt effect is also found to change the boundary-layer induction length.

Introduction

It can be expected that, within boundary layers developing in supersonic flows of premixed combustible gases, viscous dissipation heating can result in an ignition of the mixture.

A mapping of the critical conditions that ignition requires is of great importance for practical systems such as scramjet engines and ram accelerators. In particular, some working regimes of the ram accelerator seem to be partially controlled by a boundary-layer ignition along the projectile [1]. It is thus essential to understand the basic underlying physical mechanisms controlling boundary-layer ignition, in order to (1) prevent undesirable effects such as the slowing of the projectile by an early ignition along the forebody, and (2) control efficient ignition in the superdetonative mode.

In a previous work [2], we have identified the basic features of viscous–dissipation-controlled ignition within a supersonic H_2-air laminar boundary layer developing over a flat plate. A first mapping of the influence of the external flow (temperature and Mach number) and wall conditions on the ignition length that can be associated with such boundary-layer ignition was given. This problem has recently been addressed by Im et al. [3] in the framework of an overall chemical reaction and asymptotic analysis.

In the present paper, additional computations are performed to further specify the nontrivial influence of the mixture equivalence ratio of the external flow and of the Sorêt transport effect on the critical ignition parameters and on the induction length. The equivalence ratio will be found to affect the induction length via the sensitivity of the chemical induction time to both equivalence ratio and boundary-layer temperature, the latter being also a function of composition. As a consequence, the minimum induction length is found at very lean equivalence ratios.

Moreover, the inclusion of the diffusion of species due to temperature gradients (Sorêt effect), that also contributes to a modification of the local composition is found to substantially change the induction length in the case of H_2-air mixtures.

Mathematical Formulation of the Problem

As shown previously, both from the point of view of an order-of-magnitude analysis [2,4] and from a comparison with two-dimensional full Navier–Stokes calculations, classical boundary-layer approximations remain valid for a multicomponent reactive gas when the flow is supersonic. Under such an assumption, the conservation equations for total mass momentum, energy, and species read as follows [5]:

$$\frac{\partial \rho u}{\partial x} + \frac{\partial \rho v}{\partial y} = 0 \tag{1}$$

$$\rho u \frac{\partial u}{\partial x} + \rho v \frac{\partial u}{\partial y} = -\frac{\partial p}{\partial x} + \frac{\partial}{\partial y}\left(\mu \frac{\partial u}{\partial y}\right); \qquad \frac{\partial p}{\partial y} = 0 \tag{2}$$

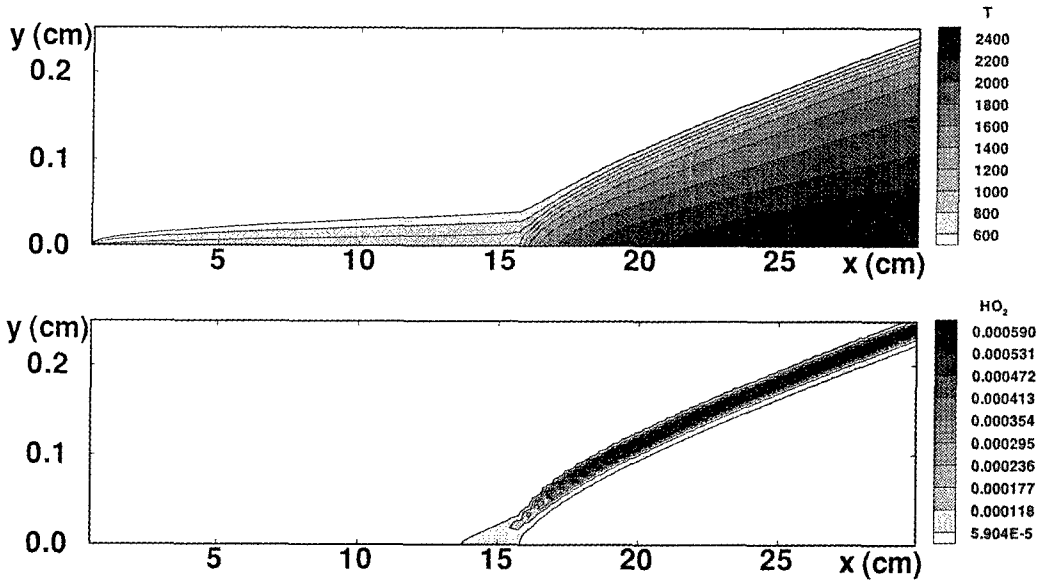

FIG. 1. Fields of temperature and mass fractions of H_2 and HO_2, in the (x,y) plane, freestream conditions $T_\infty = 400$ K, $M = 4$, $\phi = 1$, $p_\infty = 0.1$ MPa, adiabatic plate, with Sorêt effect.

$$\rho u c_p \frac{\partial T}{\partial x} + \rho v c_p \frac{\partial T}{\partial y} = u \frac{\partial p}{\partial x} + \frac{\partial}{\partial y}\left(\lambda \frac{\partial T}{\partial y}\right) - \sum_{k=1}^{K} \rho Y_k V_k c_{pk} \frac{\partial T}{\partial y} + \mu\left(\frac{\partial u}{\partial y}\right)^2 - \sum_{k=1}^{K} h_k \omega_k \quad (3)$$

$$\rho u \frac{\partial Y_k}{\partial x} + \rho v \frac{\partial Y_k}{\partial y} = -\frac{\partial}{\partial y}(\rho Y_k V_k) + \omega_k \qquad k = 1, \ldots, K \quad (4)$$

$$p = \rho R T \sum_{k=1}^{K} \frac{Y_k}{M_k}; \qquad h_k = h_k^0 + \int_{T_0}^{T} c_{pk} dT. \quad (5)$$

In these equations, classical terminology is employed. We will retain in the expression for the relative velocity V_k only transport due to species gradient (Fick's law) and temperature gradient (Sorêt effect) [5,6]:

$$V_k = -D_k \frac{1}{X_k}\frac{\partial X_k}{\partial y} + \frac{D_k \theta_k}{X_k}\frac{1}{T}\frac{\partial T}{\partial y} + V_c \quad (6)$$

where V_c is a correction velocity [6,8]. The chemical production rates are expressed in the form of Arrhenius laws. Results presented in our previous work [2,4] show that, for some flow conditions, the induction length value can be dependent on the choice of the chemical kinetics scheme. The present calculations will be performed on the basis of the chemical kinetics scheme (9 species, 18 reactions) given by Kee et al. [6,7]. Thermodynamic and transport properties are calculated as functions of local values of temperature, composition, and pressure [8]. The equations above are discretized in the physical space by finite differences and solved by a modified Newton method. Such a calculation procedure is based on the one provided by Kee et al. [6,7,8] and is described in our previous work [2,4]. Initial conditions for the calculation are the compressible boundary-layer velocity and temperature profiles [2,9]. The boundary conditions used are fixed freestream conditions for the external flow and adiabatic, noncatalytic wall. Consistent with the boundary-layer approximation, the static pressure for all the calculations is fixed at 0.1 MPa.

Brief Recall of the Structure of Combustion within a Supersonic Boundary Layer:

For sufficiently high freestream Mach numbers, and for an external flow in which the temperature remains low enough for the mixture to be chemically frozen, viscous heating may become sufficiently large for the mixture to start reacting within the boundary layer.

A first study of the structure of the reacting flow in the boundary layer in a case where such ignition and development of the combustion process occurs is given by Figueira da Silva et al. [2]. As illustrated in Fig. 1, where the fields of temperature and mass fraction of HO_2 are plotted, three regions can be identified within the flow along the streamwise direction:

1. An *induction region*, where the heat released by the chemical process remains very small compared to viscous heating and the structure of the boundary layer is quite similar to the corresponding nonreactive one.
2. A *thermal runaway region*, where a rapid increase of the heat released by the combustion process, and thus of temperature, is observed. This increase in temperature goes with a thickening of the boundary layer.
3. An *oblique flame region*, corresponding in Fig. 1 to the maximum of HO_2 mass fraction, which develops from the thermal runaway region and is positioned at the outer edge of the boundary layer, thus separating the external flow of unburned mixture from the boundary-layer flow of burned gases.

Both the critical conditions for boundary-layer ignition to occur and the spatial extent of the induction region are sensitive functions of the temperature reached in the induction region and therefore, for given wall boundary conditions, of the external flow Mach number and temperature.

Results and Discussion

The process that fixes the induction length of the chemical kinetics in the boundary-layer ignition is a result of the competition between the induction time of the mixture within the boundary layer, and both streamwise convection and transverse transports. Therefore, it can be, in a crude approximation, related to the product of the characteristic chemical time and a typical velocity of the flow (for instance, the freestream velocity $\ell_{ch} = u_\infty \cdot \tau_{ch}$). The chemical time is a function of both the equivalence ratio and of local pressure and temperature. At the beginning of the boundary layer, the temperature (for instance, the wall temperature) is essentially fixed by viscous heating. Therefore, the chemical time at the beginning of the boundary layer depends on the equivalence ratio in two ways: (1) as an explicit function, and (2) via the corresponding change of the wall temperature at the beginning of the boundary layer, since, as shown later on, viscous heating is also a function of the equivalence ratio.

We will first investigate the change of the wall temperature as a function of the equivalence ratio and Mach number of the flow. The corresponding variation of the induction time at constant pressure of the mixture will be computed and the expected induction length compared with the results obtained with the boundary-layer calculation.

In all the calculations, the induction length is taken to be the distance along the plate where the H_2O mass fraction reaches 10% of its final equilibrium value. The induction time is defined similarly.

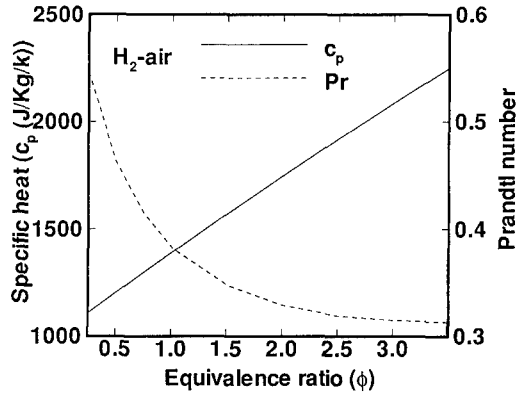

FIG. 2. Specific heat at constant pressure and Prandtl number for an H_2-air mixture as a function of the equivalence ratio, $T = 300$ K.

Influence of the Equivalence Ratio on the Temperature at the Early Beginning of the Boundary Layer:

The temperature at the wall in the induction region is dependent on the viscous dissipation heating, and thus on the freestream flow conditions of temperature and equivalence ratio, which also determine the transport properties across the boundary layer. Since the chemical heat release remains very small, temperature is fixed as in a nonreactive supersonic boundary layer by a balance between viscous dissipation, thermoconductive heat transport, and streamwise convection. This temperature is given in a first approximation, assuming constant c_p, by [9]

$$T_w = T_\infty + \sqrt{Pr}\,\frac{u_\infty^2}{2c_p} = T_\infty\left(1 + \sqrt{Pr}\,\frac{\gamma - 1}{2}\,M_\infty^2\right). \qquad (7)$$

This relation shows that an increase of the temperature in a boundary layer will be obtained, at fixed velocity of the external flow, by decreasing c_p and/or increasing the Prandtl number, while, at fixed Mach number, a temperature increase is only related to an increase of the Prandtl number. Figure 2 shows that increasing the equivalence ratio results in a decrease of the mixture's Prandtl number and in an increase of the specific heat at constant pressure. Thus, in accordance with Eq. (7), increasing the equivalence ratio at fixed M_∞ and T_∞ always results in an decrease of the wall temperature, as illustrated in Fig. 3.

Figure 3 also shows a comparison between the temperature at the wall in the beginning of the boundary layer, calculated from the above relation using the values of c_p and Pr given in Fig. 2, and the

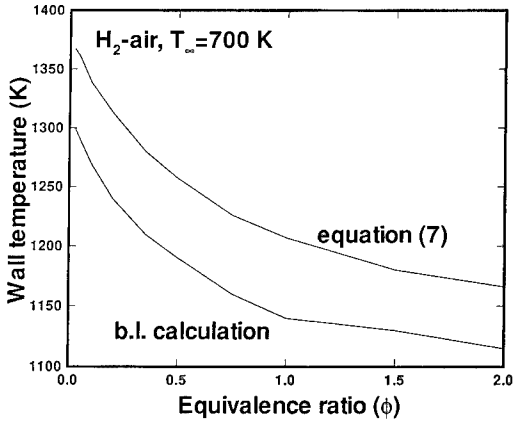

FIG. 3. Wall temperature as a function of the equivalence ratio as calculated by the boundary-layer code and the approximate relation (7), $T_\infty = 700$ K, $M_\infty = 2.5$.

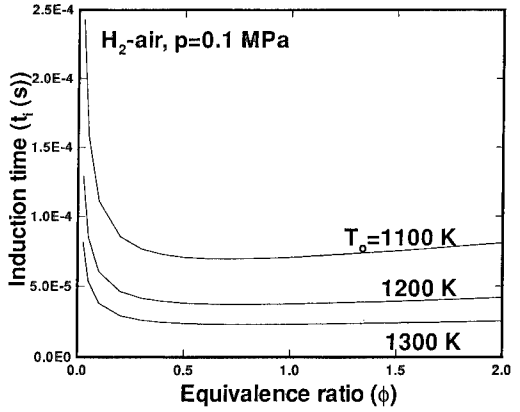

FIG. 4. Induction time of the chemical kinetics as a function of the equivalence ratio for different initial temperatures, $p = 0.1$ MPa.

temperature calculated by the boundary-layer code in a chemically frozen multispecies medium. The complete calculation leads to a smaller temperature than the approximate computation. This discrepancy is due to the increase in c_p that goes with the increase in temperature through the boundary layer. Such a change of c_p is taken into account by the boundary-layer calculation, while the use of Eq. (7) requires the assumption of a constant c_p (taken to be equal to its value in the freestream flow). Even if the difference between the two computed temperatures is found to be small (~60 K), it should be already noticed that it may lead eventually to a drastic change in the evolution of the induction length.

Influence of the Equivalence Ratio on the Induction Time of a Constant-Pressure Thermal Explosion:

The induction time of a constant-pressure thermal explosion (Semenov explosion) is a function of initial pressure, temperature, and equivalence ratio of the mixture. At a given pressure and equivalence ratio, increasing initial temperature is a way to decrease the induction time. For given initial pressure and temperature, the induction time for H_2-air mixtures has minimum value around an equivalence ratio of 0.8. Such a result is shown in Fig. 4, where we have plotted the induction time for the thermal explosion problem as a function of the equivalence ratio for the initial temperatures of 1100, 1200, and 1300 K. These temperatures are in the range of those found in the boundary layers we study. We can also see in this figure that only a very small variation of the induction time is evidenced in the range of equivalence ratios $0.2 < \phi < 2$. Therefore, the major effect of the equivalence ratio on the typical induction time in the boundary layer will be provided by the corresponding change of the wall temperature. We anticipate that, in this range, the increase in the chemical induction time observed for $\phi < 0.2$ affects more drastically the ignition characteristics in the boundary layer.

It can therefore be expected that the combined effects of the equivalence ratio on both wall temperature and characteristic induction time will lead to a nontrivial behaviour of the induction length.

The Influence of the Equivalence Ratio on the Induction Length:

In Fig. 5, the wall temperature profiles are shown for different equivalence ratios, $\phi = 0.5$, 1, and 2, and for freestream temperature and Mach number of $T_\infty = 400$ K, $M_\infty = 5$, respectively. It is clear that, for these compositions, the lower the equivalence ratio, the shorter the induction length. Such a behaviour is independent of both the Mach number and the freestream temperature for the three aforementioned equivalence ratios. This is illustrated in Fig. 6 where the curves giving the boundary in the (M_∞, T_∞) plane for which ignition is obtained on a 10-cm plate are plotted. In these cases, the predominant effect on the induction length is the increase of wall temperature with the decrease of equivalence ratio that goes with a decrease of the chemical induction time.

Such reasoning is correct as long as the change of the characteristic chemical induction time is controlled by the equivalence ratio via the wall temperature. This is no longer true when, for very lean mixtures, the explicit dependence of the characteristic chemical time with the equivalence ratio exhibits a very rapid change, as is described in the preceding section (cf. Fig. 4).

In order to clarify this point, we have plotted in

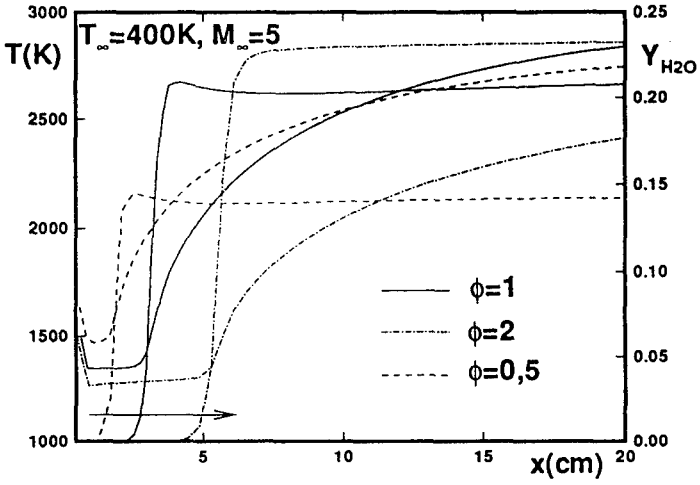

FIG. 5. Temperature and H_2O mass fraction profiles at the plate for different equivalence ratios, T_∞ = 400 K and M_∞ = 5, p_∞ = 0.1 MPa, adiabatic plate.

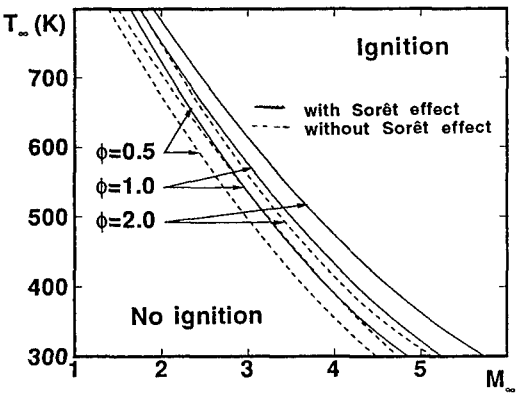

FIG. 6. Ignition curves in the (M_∞, T_∞) plane, for equivalence ratios of ϕ = 0.5, 1, and 2, p_∞ = 0.1 MPa, with and without inclusion of the Sorêt effect.

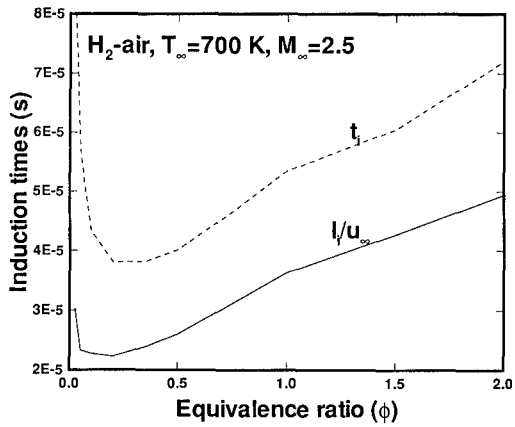

FIG. 7. Boundary-layer induction length divided by the freestream velocity and induction time calculated at the initial wall conditions as a function of the equivalence ratio, for M_∞ = 2.5, T_∞ = 700 K, p_∞ = 0.1 MPa.

Fig. 7, as a function of the equivalence ratio (ϕ), the boundary layer (b.l.) induction length divided by the freestream velocity (ℓ_i/u_∞) and the induction time (t_i) for the thermal explosion problem in which the initial temperature is that of the wall of the corresponding nonreactive boundary layer. Freestream conditions for the boundary-layer computation are M_∞ = 2.5, T_∞ = 700 K, and p_∞ = 0.1 MPa. We can see in Fig. 7 that, in the limit of very small equivalence ratios ($\phi < 0.2$), the induction length increases as ϕ decreases, although the wall temperature increases (as explained above). This is due to the steep increase in the chemical induction time for very lean H_2-air mixtures that occurs, at a fixed initial temperature (cf. Fig. 4), for $\phi < 0.2$. It is also observed in Fig. 7 that the chemical induction time calculated using the nonreactive wall temperature gives an upper bound for the ratio between the b.l. induction length and the flow freestream velocity. Moreover, both curves have minima around $\phi \sim 0.2$ and the same overall behaviour, which indicates that the chemical induction time (t_i) calculated at the initial wall conditions largely influences the ratio ℓ_i/u_∞. The latter parameter is always smaller than t_i. This difference can have two origins: (1) the choice of the velocity u_∞, which is larger than the velocity experienced by the reacting flow within the boundary layer, and/or (2) the transverse transport effects that on one hand evacuate heat from the boundary layer but on the other hand feed the reaction zone near the wall with fresh unburnt reactants. As a consequence, the accuracy of the prediction of the values of ℓ_i/u_∞ by calculating t_i can be expected to depend on the Lewis number of the mixture.

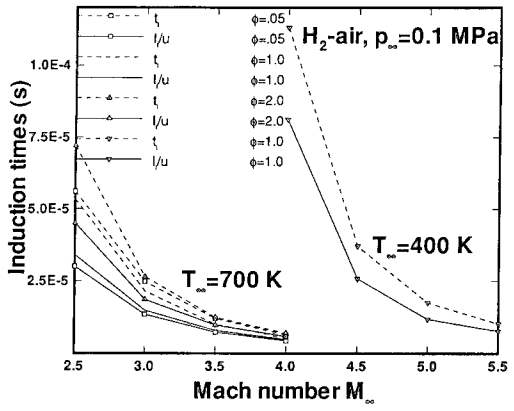

FIG. 8. Induction time calculated at the initial wall conditions and boundary-layer induction length divided by the freestream velocity as a function of the Mach number, for the equivalence ratios of 0.05, 1, and 2, $p_\infty = 0.1$ MPa.

To determine the exact origin of the difference between t_i and ℓ_i/u_∞, we have plotted in Fig. 8 the ratio ℓ_i/u_∞ for equivalence ratios of 0.05, 1, and 2 as a function of the external flow Mach number, and the chemical induction time t_i for the thermal explosion, taking as initial temperature the corresponding wall temperature. It should be noticed that, as the freestream Mach number increases, the ratio $(\ell_i/u_\infty)/t_i$ approaches unity, thus indicating that the induction length can be predicted only on the basis of a simple calculation of the thermal explosion time.

It can be noticed that (1) increasing the freestream Mach number leads to an increase in the boundary-layer thickness, which shields the ignition region from transverse molecular transport, and (2) increasing the velocity of the flow should lead to an increase of the overestimation by u_∞ of the reference velocity. Since closer values of t_i and ℓ_i/u_∞ can be found when increasing M_∞, mechanism (1) must be the predominant one.

The Influence of the Sorêt Effect on the Induction Length:

The Sorêt effect, which is the diffusion of species due to temperature gradients, is known to play a significant role in H_2-air combustion as a result of the presence of species of different molecular weights. More specifically, this effect modifies the diffusion velocity of the light species H and H_2, which tend to concentrate on the hot regions of the flow. In the case considered here of a supersonic boundary layer over an adiabatic plate, a strong temperature gradient exists between the plate and the freestream. This results, for a fixed equivalence ratio of the mixture of the external flow, in an increase of H_2 mass fraction near the wall, and therefore of the equivalence ratio, as can be seen in Fig. 9. In this figure, we present the fields of H_2 mass fraction in cases computed with and without inclusion of the Sorêt effect.

In Fig. 10, we show plots of temperature and mass

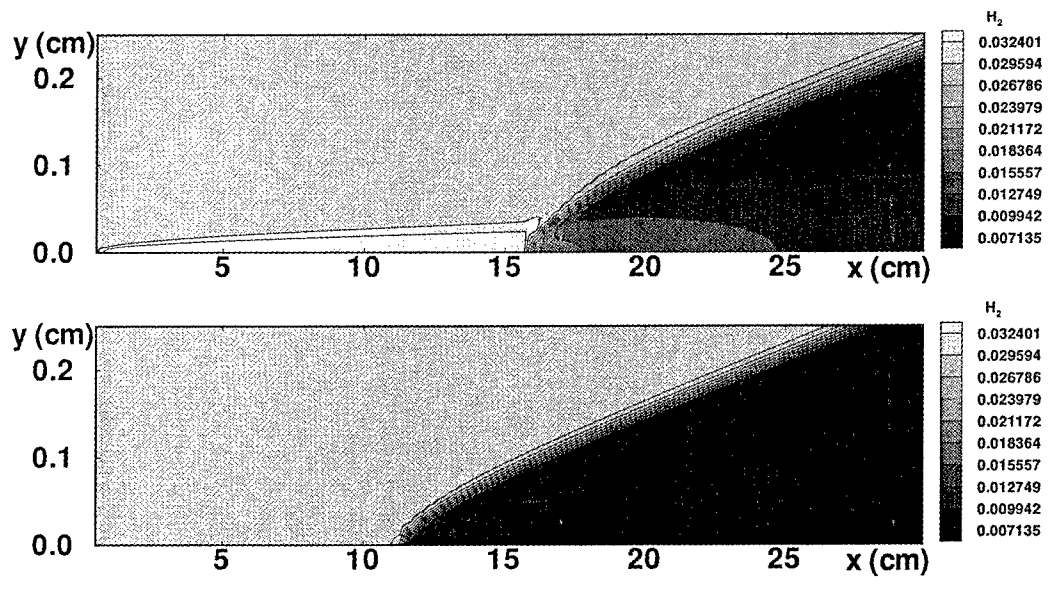

FIG. 9. Fields of H_2 mass fraction in the (x,y) plane, freestream conditions $T_\infty = 400$ K, $M_\infty = 4$, $\phi = 1$, $p_\infty = 0.1$ MPa, adiabatic plate, with and without inclusion of the Sorêt effect.

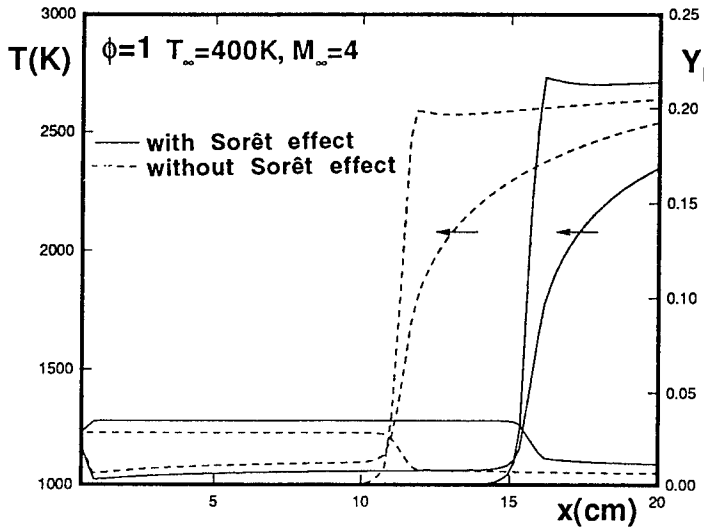

FIG. 10. Temperature and H_2O mass fraction profiles at the plate with and without the Sorêt effect, $T_\infty = 400$ K and $M_\infty = 4$, $p_\infty = 0.1$ MPa, adiabatic plate.

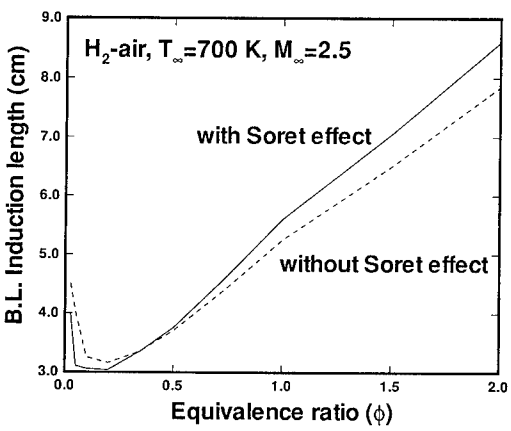

FIG. 11. Boundary-layer induction length as a function of the equivalence ratio, with and without inclusion of the Sorêt effect, for $M_\infty = 2.5$, $T_\infty = 700$ K, $p_\infty = 0.1$ MPa.

fractions of H_2 and H_2O at the wall, in cases computed with and without including the Sorêt effect. For the case where we have included the Sorêt effect, an increase of the induction length is observed. This increase of the induction length is due to the decrease of the wall temperature that accompanies the increase of the equivalence ratio, as explained previously. A more general plot of the influence of the Sorêt effect is given in Fig. 6, where the ignition boundary for a 10-cm plate is given in the (M_∞, T_∞) plane. The influence of the Sorêt transport effect is always to increase the induction length for equivalence ratios ranging from 0.5 to 2.

This effect is reversed for very lean mixtures ($\phi <$ 0.3), when the boundary-layer induction length behaves as a decreasing function of the equivalence ratio. This is illustrated in Fig. 11, where the boundary-layer induction length corresponding to the case $M_\infty = 2.5$, $T_\infty = 700$ K, and $p_\infty = 0.1$ MPa, already presented above, is plotted as a function of the equivalence ratio, both with and without the Sorêt effect.

As illustrated in Fig. 9, a second consequence of the Sorêt effect is the presence of unburned hydrogen in the vicinity of the wall.

Acknowledgments

This work was accomplished under Contract No. 93-053, "Combustion Supersonique PREPHA," of the Direction des Recherches et Etudes Techniques DRET/DGA.

REFERENCES

1. Auzias de Turenne, J., Chew, G., and Bruckner, A. P., *Recent Results from the University of Washington's 38 mm Ram Accelerator*, AIAA/SAE/ASME/ASEE 28th Joint Propulsion Conference and Exhibit, AIAA Paper 92-3782, 1992.
2. Figueira da Silva, L. F., Deshaies, B., and Champion, M., *AIAA J.* 31:884–890 (1993).
3. Im, H. G., Bechtold, J. K., and Law, C. K., *J. Fluid Mech.* 249:99–120 (1993).
4. Figueira da Silva, L. F., Deshaies, B., Champion, M., and René-Corail, M., *Combust. Sci. Technol.* 89:317–333 (1993).
5. Williams, F. A., *Combustion Theory*, 2nd ed., Chap. 12, Benjamin/Cummings Publishing Company, Inc., Menlo Park, CA, 1985.
6. Kee, R. J., Grcar, J. F., Smooke, M. D., and Miller, J. A., *A Fortran Program for Modeling Steady Laminar One-Dimensional Premixed Flames*, Sandia National

Laboratories Technical Report SAND85-8240/UC-4, 1985.

7. Kee, R. J., Miller, J. A., and Jefferson, T. H., *CHEMKIN: A General-Purpose, Problem-Independent, Transportable, Fortran Chemical Kinetics Code Package*, Sandia National Laboratories Technical Report SAND80-8003/UC-4, 1980.
8. Kee, R. J., Warnatz, J., and Miller, J. A., *A Fortran Computer Code Package for Evaluation of Gas-Phase Viscosities, Conductivities, and Diffusion Coefficients*, Sandia National Laboratories Technical Report SAND83-8209/UC-32, 1983.
9. Schlichting, H., *Boundary-Layer Theory*, 7th ed., McGraw-Hill Book Company, New York, 1979.

COMMENTS

Jerry C. Finlinson, Naval Air Warfare Center, USA. Why not compare your results to experimental data points? Are there any such data? If not, how do you verify your model?

Author's Reply. To our knowledge, there are no experimental results available concerning viscous heating ignition of hydrogen-air mixtures in boundary layers. Therefore, there is no possibility of performing a direct comparison between our calculations and experimental results. Nevertheless, as already noted in our paper, this type of ignition is expected to play an important role in both the transdetonative and superdetonative regimes of ram accelerators, as stated by Auzias de Turenne et al. [1].

The aim of the paper is to identify the mechanisms and the parameters that control this type of ignition. The calculations we perform take into account all aspects of the ignition process, including detailed thermochemical properties (functions of both local temperature and composition) and chemical kinetics scheme. The only phenomenon that can modify quantitatively the results is turbulence, our calculations being performed in the laminar case. But the choice and/or the development of turbulence models requires first, in our opinion, a clear identification in the laminar regime of (1) the basic physicochemical mechanisms, and (2) the dependence on the flow conditions and mixture composition of the time and length scales that in fact control boundary layer ignition.

Twenty-Fifth Symposium (International) on Combustion/The Combustion Institute, 1994/pp. 37–44

ON DEVIATIONS FROM IDEAL CHAPMAN–JOUGUET DETONATION VELOCITY

H. K. BRÜLS AND M. H. LEFEBVRE
Département de Chimie
30 Avenue de la Renaissance
1040 Bruxelles, Belgium
Ecole Royale Militaire

AND

J. BERGHMANS
Departement Werktuigkunde
Celestijnenlaan 300 A
3001 Heverlee, Belgium
Katholieke Universiteit Leuven

Experimental data shows that under certain conditions, measured detonation velocities exhibit deviations from theoretical values computed according to the Chapman–Jouguet (CJ) model. The purpose of this paper is to investigate why in some circumstances such deviations occur. A Zeldovitch-von Neuman-Doring model (ZND) taking into account the specific chemical kinetics of the mixture enables us to identify a critical parameter: the effective chemical reaction length. This parameter is mainly related to the chemical composition of the reactive mixture. It is shown that the ratio of this parameter to the dimension of the tube where the velocity measurements are carried out can explain deviations from ideal values. This simple model has been applied to a series of existing experimental data characterized by such deviations. Different initial conditions, namely, (1) mixtures near detonation limits, (2) low initial pressures, and (3) mixtures containing halogenated hydrocarbons, are investigated. All data show that the velocity deficit, ΔD_{CJ}, is an increasing, but not necessarily linear, function of the ratio reaction length/dimension of the tube, d_{rea}/d_{tube}. To support this statement, a detailed one-dimensional numerical computation has been performed, taking into account both nonstationary hydrodynamics and detailed chemical kinetics. These computations end up with a detonation wave traveling at the ideal Chapman–Jouguet velocity. This suggests that the deviation from the CJ values ought to be explained by parameters taking into account the relative size of the surrounding of the detonation wave; d_{rea}/d_{tube} is such a parameter.

Introduction

Detonation is a particular mode of propagation of a chemical reaction front. Chapman and Jouguet independently developed a steady model that is able to predict the propagation velocity of a detonation wave. According to this model, the wave velocity is only dependent on the physical and chemical properties of the reactive mixture, i.e., pressure, temperature, and chemical composition. This first model has been extensively tested on experimental data, and an excellent agreement is obtained, when correct thermodynamic values are used for the reaction products [1]. The Zeldovitch-von Neuman-Doring (ZND) model refines the Chapman–Jouguet (CJ) one by dividing the detonation wave into a shock wave and a chemical reaction zone, while maintaining the assumption of a stationary model. Despite the general good validity of this one-dimensional model, the experimental detonation velocity differs under certain conditions from the theoretical value. An overview of experimental conditions showing important velocity deficits is given in Ref. 2 and more recently in Ref. 3. In the present paper, the following mixtures are investigated: (1) hydrogen-oxygen mixtures near the detonation limits [4]; (2) H_2, CO, O_2, and Ar mixtures at low pressures [5]; and (3) hydrogen-oxygen-argon mixtures containing halogenated hydrocarbons (CF_3H) [6]. Although many parameters influencing the structure of the detonation wave have been put forward, no theory provides a quantitative method for computing a detonation velocity different from the Chapman–Jouguet value. On the other hand, the multidimensional character of detonation waves has been clearly established, both experimentally [7] and through numerical computations [8,9]. The multidimensional structure leads to the formation of detonation cells, whose dimensions play a ma-

jor role in shaping the detonation front. Although numerical modeling, taking into account detailed chemical mechanisms and multidimensional geometry, exists [10], the computation of a detonation velocity by a model capturing both aspects is still at the limit of present computation power (especially for complex reactive mixtures). The purpose of this paper is to identify a computed parameter related to the discrepancies between experimental detonation velocities and the Chapman–Jouguet values. In the first section, stationary ZND computations are carried out for different reactive mixtures, and a relation is established between the transversal dimension of the tube and both the induction and the reaction lengths. In the second part, detonation velocities are computed using a one-dimensional nonstationary numerical model, including a full set of chemical equations to better quantify the influence of the chemical mechanism on the steady detonation velocity.

ZND Model

The ZND model we use is the classical set of algebraic equations describing the flow field coupled with a complete set of ordinary differential equations describing the reaction mechanism of the mixture studied. The equations are as follows:

$$\rho u = \rho_1 u_1 \tag{1}$$

$$P + \rho u^2 = P_1 + \rho_1 u_1^2 \tag{2}$$

$$u_1^2 - u^2 = 2 \cdot \Delta H \tag{3}$$

$$\frac{dn_i}{dt} = \sum_{k=1}^{n} \zeta_{kj} A_k T^m e^{-E_k/RT} \prod_j n_j^{\nu_{kj}} \tag{4}$$

where $\rho, u, P, H, n_i, \zeta_{kj}, A_k, T, t, E_k$, and ν_{kj} represent the density, relative velocity of the gas in a frame fixed to the detonation wave, pressure, total enthalpy, molar concentration of the ith species, stoichiometric coefficient, pre-exponential factor, temperature, time, activation energy, and order of the reaction, respectively. The index 1 refers to the initial conditions, while no index is used to describe an arbitrary point in the detonation wave. Indexes i and j refer to species, index k to the kth chemical reaction. The ideal gas law is assumed and a temperature dependent specific heat capacity is used to calculate the enthalpy. The set of Eqs. (1) through (4) can readily be computed by a time-step splitting technique, i.e., alternatively solving the algebraic Eqs. (1) through (3) by a Newton–Raphson scheme and the differential Eq. (4) by the selective asymptotic integration method [11]. The time step is adapted by the latter method. The integration provides the stationary profiles for all physicochemical quantities behind the detonation front. The analysis of the profiles enables us to define two main parameters: a characteristic of the chemical kinetics, i.e., the induction time, t_{ind}, and the effective reaction time, t_{rea}. No precise definition for both parameters exists, and the following criteria have been used. The induction time is the time necessary for the reactive mixture to increase its temperature by 20 K. This definition is consistent with the idea that the induction period is thermoneutral. The reaction time is the period during which the chemical reaction takes place. The reaction ends when the chemical composition reaches equilibrium. Since pressure and temperature continuously change in the detonation wave due to both chemical and aerodynamic effects, it is ambiguous to characterize chemical equilibrium from the species density profiles. We may define reaction time as the time necessary to reach the equilibrium free energy within 1%. On the other hand, the fact that the flow is choked at the sonic plane leads to another definition of the effective reaction time: the time required to reach the sonic plane. We therefore define the effective reaction time as the time at which chemical equilibrium is achieved (within 1%) or the time at which the flow becomes sonic, whichever comes first. We also define the induction and reaction lengths, d_{ind} and d_{rea} as the induction and reaction time multiplied by the average detonation velocity, respectively.

ZND computations have been performed for various reactive mixtures according to available data. We successively study (1) H_2-O_2 mixtures at different fuel ratios, (2) H_2-CO-O_2-Ar mixtures at different initial pressures, and (3) H_2-O_2-Ar mixtures with variable amount of CF_3H. Existing experimental data related to these cases are summarized in Table 1. The thermodynamic data used are from the JANAF tables [12].

A typical calculation starts with the theoretical von Neumann values for the physical quantities and the CJ velocity for the value of u_1 in Eqs. (1) through (3).

H_2-O_2 Mixture Approaching the Rich Limit:

The computation is carried out with an H_2-O_2 mixture at initial pressure and temperature of 0.1 MPa and 298 K, respectively. This reactive system has one of the most simple kinetic mechanisms, which is currently well established. The mechanism proposed by Westbrook [13] is used in our computation and includes the following species H_2, O_2, H, OH, O, H_2O, and HO_2. For the H_2-O_2 system, several experimental data are available. In most circumstances, good agreement is found between experimental detonation velocities and the CJ values. However, near the detonation limits, deviations from CJ values arise. Near the lean limit (around 17% H_2), a very rapid deviation from the CJ detonation velocity is noted resulting ultimately in detonation failure [4]. Near the rich limit (around 90% of hydrogen), the phe-

TABLE 1
Theoretical CJ detonation velocity and deviation[a] of the experimental velocity from the CJ value in percent

Mixture (1)	% H_2	D_{CJ} (m/s)	ΔD_{CJ} (%)[b]	
H_2/O_2	66	2818	1.6	
P = 100 kPa	80	3408	2.0	
T = 298 K	85	3638	5.0	
	87	3720	6.0	
	88	3755	7.0	
Mixture (2)	**P (kPa)**	**D_{CJ} (m/s)**	**ΔD_{CJ} (%)[c]**	
$H_2/CO/O_2/Ar$	33.3	1629	3.7	
3.3/30/16.7/50	26.7	1623	4.5	
T = 298 K	20.0	1615	5.4	
	13.3	1603	7.3	
Mixture (3)	**% CF_3H**	**D_{CJ} (m/s)**	**ΔD_{CJ} (%)[c]**	**ΔD_{CJ} (%)[d]**
$H_2/O_2/CF_3H/Ar$	0.0	1874	2.3	4.6
33.3/16.7/x/50 − x	2.5	1895	1.7	3.3
P = 26.7 kPa	5.0	1913	1.9	3.7
T = 298 K	7.5	1930	1.75	3.7
	10.0	1945	1.5	3.6
	12.5	1959	—	4.6
	15.0	1970	2.3	—
	20.0	1987	3.5	—
	25.0	1996	3.9	—

[a] Calculation of the deviations are based on experimental data from mixture (1) [4], mixture (2) [5], and mixture (3) [6].
[b] Cylindrical tube.
[c] Rectangular tube.
[d] Square tube.

nomenon is similar but less abrupt [4] (Table 1). This observation is investigated here, focusing on the influence of the effective reaction time and length. Table 2 gives the calculated induction and reaction lengths for different mixtures ranging from the stoichiometric composition to the rich detonation limit (fuel mole fraction equal to 66, 80, 85, 87, and 88%). The table shows an increase in both induction and reaction lengths near the limit. This can be readily explained by the Arrhenius type of mechanism, which states that the reaction rate is proportional to the product of the concentrations of the reactants. When the concentration of the limiting species, in this case oxygen, is lowered, an overall decrease in reaction rate is observed. This explains the long induction and reaction lengths but does not explain deviations from CJ velocity.

H_2-CO Mixture at Low Pressure:

Similar computations have been performed with reactive systems containing H_2, CO, O_2, and Ar (mole fraction equal to 3.3, 30.0, 16.7, and 50.0). We use the same kinetic mechanism as before. Chemical rates specific to the CO mechanism are added, according to Westbrook [13]. Experimental data for the low-pressure system are provided by Libouton and Van Tiggelen [5]. Since pressure has only a limited influence on the equilibrium composition of the burnt gases, the CJ detonation velocity remains quasi constant over the whole pressure range (13–33 kPa). Experimentally, however, an increasing deviation from the ideal CJ detonation speed is observed when the pressure drops (Table 1). Table 2 shows an increase in both induction and reaction length, when the pressure drops from 33.3 to 13.3 kPa. The increase is similar to the previous case. A decrease in pressure yields an equivalent decrease in the concentrations of the reactive species, and thus, the reaction rate drops according to the Arrhenius equation.

Mixtures Containing Fluorocarbons:

The ZND computations have also been performed with a reactive system containing halogenated hydro-

TABLE 2
Computed values of d_{ind} and d_{rea} for the mixtures studied

Mixture (1)	% H_2	d_{ind} (mm)	d_{rea} (mm)
H_2/O_2	66	0.20	0.60
P = 100 kPa	80	0.34	1.09
T = 298 K	85	0.72	2.40
	87	1.16	4.27
	88	1.40	6.19
Mixture (2)	**P (kPa)**	**d_{ind} (mm)**	**d_{rea} (mm)**
$H_2/CO/O_2/Ar$	33.3	1.65	22
3.3/30/16.7/50	26.7	1.95	28
T = 298 K	20.0	2.90	44
	13.3	4.50	80
Mixture (3)	**% CF_3H**	**d_{ind} (mm)**	**d_{rea} (mm)**
$H_2/O_2/CF_3H/Ar$	0.0	0.79	8.0
33.3/16.7/x/50 − x	2.5	0.76	5.0
P = 26.7 kPa	5.0	0.76	6.1
T = 298 K	7.5	0.80	4.5
	10.0	0.85	5.7
	12.5	0.90	8.5
	15.0	0.90	11.8
	20.0	1.18	24
	25.0	1.50	50

carbons, namely, CF_3H. This system has been extensively investigated [14,6]. According to the CJ model, CF_3H acts as a promoter for the detonation; i.e., the substitution of inert Ar by reactive CF_3H results in an increase of the detonation velocity (Table 1). Experimental data [6] in a rectangular tube of 9.2 × 3.2 cm show the following behaviour. Without any CF_3H, the detonation velocity approaches the CJ value by about 2%. When the CF_3H content goes from 0 to 15%, by substitution of Ar, the detonation speed increases and a rather constant discrepancy in velocity is noticed (Table 1). When more CF_3H is added (up to 28%), an increasing deviation from the CJ value is observed. At a mole fraction of 30% of CF_3H, no detonation was observed for the considered experimental conditions. In a small square tube of 3.2 × 3.2 cm, a similar behaviour is observed. However, in that case, the deviations from the ideal CJ are larger, and no detonation can be recorded beyond 12.5% of CF_3H (Table 1).

In the present calculation, we use the same kinetic mechanism as the one used for the oxidation of H_2-CO. The steps to convert CF_3H into CO_2 and HF are described by Westbrook [15]. The mechanism takes into account the following additional species: CF_3H, CF_3, CF_2O, CF_2, CFO, CF, CO, CO_2, HOF, FO, HF, F, and F_2. Table 2 gives the induction and reaction lengths for different fractions of CF_3H in the mixture. The conversion of CF_3H interferes with the oxidation of hydrogen, from both a thermal and a kinetic point of view [6]. But none of these aspects can fully explain the observations. When the mixture contains less than 15% of CF_3H, the induction and reaction lengths vary little. For the cases above 15% of CF_3H, both induction and reaction lengths increase. The increase is most pronounced for the reaction length. Moreover, the global heat release increases, accounting for an increasing detonation speed.

Discussion:

Increasing the fuel content, decreasing the initial pressure, or adding CF_3H to a H_2-O_2-Ar mixture influences the process of heat release in the same way. It results in increasing induction and reaction lengths. Moreover, the absolute values of both induction and reaction characteristics are quite different for the mixtures presented above. The H_2-O_2 mixture has reaction lengths ranging from 0.6 to 6 mm. This is one order of magnitude smaller than the values calculated for mixtures containing carbon monoxide. Mixtures containing CF_3H are also characterized by relatively large values of d_{ind} and d_{rea}.

This is directly related to the kinetic mechanism, but discussion about the chemical mechanism does

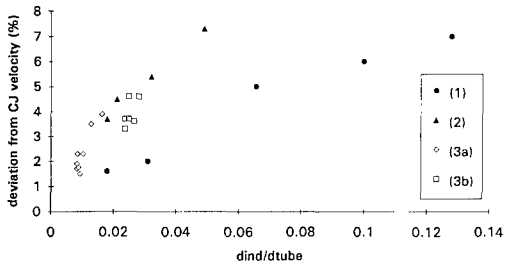

FIG. 1. ΔD_{CJ} as a function of d_{ind}/d_{tube} for the mixtures studied: (1) H_2/O_2 near the rich limit in the cylindrical tube, (2) $H_2/CO/O_2/Ar$ at low pressure in the rectangular tube, (3a) $H_2/O_2/Ar/CF_3H$ in the rectangular tube, and (3b) $H_2/O_2/Ar/CF_3H$ in the square tube.

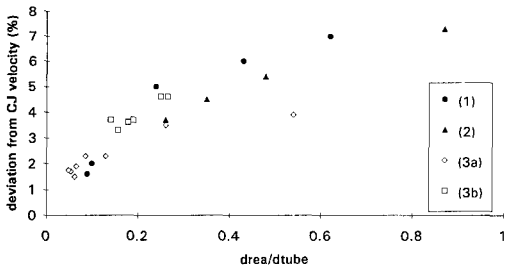

FIG. 2. ΔD_{CJ} as a function of d_{rea}/d_{tube} for the mixtures studied: (1) H_2/O_2 near the rich limit in the cylindrical tube, (2) $H_2/CO/O_2/Ar$ at low pressure in the rectangular tube, (3a) $H_2/O_2/Ar/CF_3H$ in the rectangular tube, and (3b) $H_2/O_2/Ar/CF_3H$ in the square tube.

not answer the question why deviations from the CJ model increase. From a kinetic point of view, there is no strong evidence that the gap between experimental data and the CJ model should increase when (1) the fuel content increases, (2) the pressure decreases, or (3) CF_3H is added to the mixture.

Figure 1 shows, for all mixtures studied, the deviation from CJ velocity as function of the ratio d_{ind}/d_{tube}, where d_{tube} is a characteristic transversal dimension of the tube. For a cylindrical tube, it is its diameter. In the case of a square and rectangular tube, d_{tube} represents the channel width. Figure 2 shows the deviation from CJ velocity vs the ratio d_{rea}/d_{tube}.

For the mixtures containing H_2-O_2 and H_2-CO-O_2-Ar, Figs. 1 and 2 show that the velocity deficit is an increasing function of both ratios d_{ind}/d_{tube} and d_{rea}/d_{tube}. For the mixtures containing CF_3H, no significant relation between ΔD_{CJ} and d_{ind}/d_{tube} is noticed (Fig. 1). Indeed, induction length varies little when CF_3H is added. On the other hand, a relation between ΔD_{CJ} and d_{rea}/d_{tube} is noticed on Fig. 2. The latter figure shows that an overall increase of ΔD_{CJ} with d_{rea}/d_{tube} exists for all mixtures studied. It suggests that the dominant parameter influencing deviation from ideal CJ velocity is the reaction length relative to the channel size. The actual relationship depends, however, on the specificity of the mixture and the geometry of the tube. This leads us to consider that the velocity deficit cannot be attributed only to chemical effects. An interaction between chemical characteristics and the geometry of the tube can well account for it.

When the transversal dimension of the detonation tube is sufficiently large, the detonation cells can develop freely, and the cell size is a characteristic of the reactive mixture. The average detonation velocity is then close to the CJ speed. When the size of both the tube and the detonation cell are of the same order of magnitude, the structure of the detonation front is largely influenced by its boundary, and, to some extent, the cellular structure has to adjust to the channel geometry. Only specific acoustic modes can propagate. The interaction between the geometry of the tube and the natural reaction length leads to a reduction of the detonation velocity and, accordingly, to an increasing deviation from the ideal detonation, resulting eventually in detonation failure. A parameter closely related to d_{rea} has been proposed in Ref. 16, and a correlation has been established between this parameter and the critical tube diameter for detonation failure. In the limiting case of a very large tube, no detonation velocity deficit should be observed. This has been established by Tsugé [17]. This is also suggested by Fig. 2, where the deviations from CJ approach zero as the ratio d_{rea}/d_{tube} approaches zero. Note that a global influence of the kinetic mechanism did not vanish. The overall effect of reaction rates is included in the parameter d_{rea}.

Nonstationary Model

The major drawback of the ZND model coupled with a set of reaction rates is the assumption of steady state and the requirement of an input detonation velocity. Nonstationary models of supersonic reactive flow are described by the conservation equations for mass, momentum, total energy, and chemical species densities. Because of the speed of the phenomenon involved, one usually neglects relatively slow molecular phenomena like molecular and thermal diffusion of chemical species, viscosity, and heat conduction [18]. The governing equations for a one-dimensional model are

$$\frac{\partial \rho}{\partial t} = -\frac{\partial \rho v}{\partial x} \tag{5}$$

$$\frac{\partial \rho v}{\partial t} = -\frac{\partial \rho v^2}{\partial x} - \frac{\partial P}{\partial x} \tag{6}$$

$$\frac{\partial E}{\partial t} = -\frac{\partial E v}{\partial x} - \frac{\partial P v}{\partial x} \tag{7}$$

TABLE 3
Comparison between detonation velocity from CJ theory and one-dimensional nonstationary model

Mixture	Composition	P (kPa)	D_{CJ} (m/s)	D_{1d} (m/s)	ΔD_{CJ} (%)[a]
(1)	H_2/O_2:85/15	100	3638	3658	0.5
(2)	$H_2/CO/O_2/Ar$:3.3/30/16.7/50	20.0	1615	1603	0.7
(3)	$H_2/O_2/Ar$:33.3/16.7/50	26.7	1874	1880	0.3
	$H_2/O_2/Ar/CF_3H$:33.3/16.7/35/15	26.7	1970	1990	1.0

[a]Relative deviation between D_{CJ} and D_{1d}.

$$\frac{\partial n_i}{\partial t} = -\frac{\partial n_i v}{\partial x} + \sum_{k=1}^{n} \zeta_{kj} \prod_j n_j^{\nu_{kj}} A_k e^{-E_k/RT} \quad (8)$$

where x, v, and E denote the space coordinate, the velocity of the gas, and the total density of total energy, respectively. The same equations of state, thermodynamic data, and reaction mechanism are used as in the previous section. The set of differential equations is solved using a time-step splitting technique. Equations (5) through (7) and the first term of Eq. (8), i.e., the convective term, are solved using the flux corrected transport algorithm developed by Boris and coworkers [19,20]. This monotone, conservative, positivity-preserving algorithm ensures fourth-order phase accuracy and minimum residual diffusion. The last term of Eq. (8), i.e., the change in chemical species, is solved using the selected asymptotic integration method developed by Young and coworkers [11,21]. The algorithm identifies the stiff equations for treatment with a stiffly stable method. The remaining equations are treated with a standard classical method. The algorithm is a very low-overhead method that is particularly efficient when coupled with fluid dynamic calculation. The main time step is chosen according to the Courant number criterion, and subcycling is performed for the chemical part. The numerical grid is eulerian with constant numerical cell size. The Courant number we use is equal to 0.35. To ignite a detonation wave, the calculation starts as a diaphragm problem. A detailed description is given by Boris et al. [17]. The velocity of the developing detonation front is recorded up to its stabilization.

Results and Discussion:

The simulation has been performed on several mixtures representative of the aforementioned experimental data. Table 3 gives the initial chemical and physical conditions of the mixtures modeled. The initial temperature for all mixtures is 298 K. A typical example of the stabilization process of a detonation wave is shown in Fig. 3. The asymptotic value of the detonation velocity D_{1d} is always close to the theoretical CJ value. The calculated values of D_{1d} are given in Table 3 and compared to the theoretical one, D_{CJ}. Comparison between D_{1d} and D_{CJ} shows no significant deviations from the CJ value when a one-dimensional nonstationary model is used. Transient stages of the developing detonation wave always converge to steady conditions. Figure 4 compares the heat release curves obtained with the ZND model and the one obtained with the one-dimensional model. Both curves result in an almost identical final value. The sharp heat release curve in the nonstationary model can be attributed to the limited spatial resolution of the grid, which influences the coupling between aerodynamic and chemical phenomena. The one-dimensional model we use takes efficiently

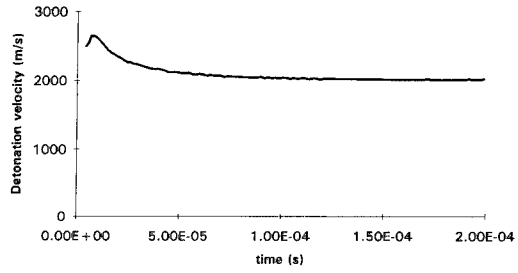

FIG. 3. Evolution of the detonation velocity as a function of time for mixture $H_2/O_2/Ar/CF_3H$: 33.3/16.7/35/15. Initial conditions are T = 298 K and P = 26.7 kPa.

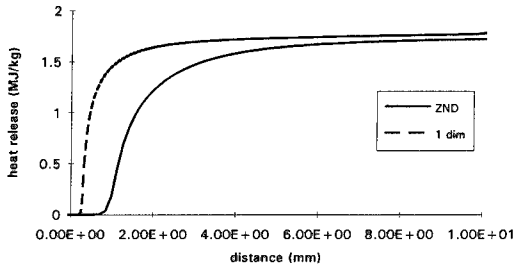

FIG. 4. Heat release curve computed according to the ZND model and the one-dimensional model for mixture $H_2/O_2/Ar$: 16.7/33.3/50. Initial conditions are T = 298 K and P = 26.7 kPa.

into account the specific chemical characteristics of the mixture but does not integrate either multidimensional or boundary effects. Numerical modeling of a two-dimensional detonation structure, using a parametric model for the heat release, has been reported by Lefebvre et al. [22]. This simulation models a H_2-O_2-Ar mixture at an initial pressure of 6.7 kPa and ends up with an average detonation velocity very close to the CJ value. Moreover, a similar recent two-dimensional calculation carried out by Weber [10] and using a full set of chemical reactions for tracking the change in species result again in an average detonation velocity close to the CJ one (within 0.5%). The good overall agreement between D_{CJ} and all our calculated D_{1d} and the mentioned two-dimensional simulations supports the statement in the previous section: In the absence of boundary and wall effects, the detonation wave travels at the ideal CJ value. Chemical kinetics alone cannot account for discrepancies from CJ detonation velocities.

Conclusions

The results from the one-dimensional nonstationary computation support the information obtained from the ZND model. For the mixtures studied, kinetic effects alone cannot account for discrepancies between experimental detonation velocities and CJ values. When the length of the chemical reaction becomes comparable to the channel size, the interaction between chemical kinetics and tube geometry plays a major role. The magnitude of this interaction can be characterized by the ratio d_{rea}/d_{tube}. Deviations from ideal CJ detonation velocity increase when this ratio increases. However, the presented analysis does not provide a direct method for computing a nonideal detonation velocity. The computation of the detonation velocity deficit would require the development of a multidimensional model including submodels for phenomena such as heat losses at the wall and momentum losses due to shock wave–boundary layer interaction. We think that such a model is necessary to gain better insight into complex phenomena like initiation and failure of detonation for given geometry and reactive mixture.

Acknowledgment

This work was sponsored by the Department of Defence of Belgium under Contract CGMC 93–03.

REFERENCES

1. Lewis, B., and von Elbe, G., *Combustion, Flames and Explosions of Gases,* Academic Press, New York, 1961, pp. 524–528.
2. Zeldovich, I. B., and Kompaneets, A. S., *Theory of Detonation,* Academic Press, New York, 1960.
3. Vasil'ev, A. A., *Fiz. Goreniya Vzryva* 23(3):121–126 (1987).
4. Berets, D. G., Greene, E. F., and Kistiakowski, G. B., *J. Am. Chem. Soc.* 72:1080–1086 (1950).
5. Libouton, J. C., and Van Tiggelen, P. J., *Acta Astronaut.* 3:759–769 (1976).
6. Lefebvre, M. H., Nzeyimana, E., and Van Tiggelen, P. J., Progress in Astronautics and Aeronautics, AIAA, Inc., Washington, 1993, Vol. 153, pp. 144–161.
7. Denisov, Y. H., and Troshin, Y. K., *Dokl. Akad. Nauk. SSSR* 125:110 (1959).
8. Kailasanath, K., Oran, E. S., Boris, J. P., and Young, T. R., *Combust. Flame* 61:199–209 (1985).
9. Lefebvre, M. H., Oran, E. S., Kailasanath, K., and Van Tiggelen, P. J., *Combust. Flame* 95:206–218 (1993).
10. Weber, J. W., "The Efficient Simulation of Gas Detonation Physics on a Massively Parallel Connection Machine," Ph.D. Dissertation, University of Maryland, College Park, MD, UM-AERO 94–01, 1994.
11. Young, T. R., and Boris, J. P., *J. Phys. Chem.* 81:2424–2427 (1977).
12. *JANAF Thermochemical Tables,* U.S. Department of Commerce, NBS, Washington DC, 1985.
13. Westbrook, C. K., *Combust. Flame* 46:191–210 (1982).
14. Nzeyiama, E., "Rôle de la Cinétique Chimique dans les Détonations, Approches Théorique et Expérimentale," Doctoral Dissertation, UCL, Belgium, 1991.
15. Westbrook, C. K., *Comb. Sci. Technol.* 34:201–225 (1983).
16. Westbrook, C. K., and Urtiew, P. A., *Nineteenth Symposium (International) on Combustion,* The Combustion Institute, Pittsburgh, 1982, pp. 615–623.
17. Tsugé, S., *Comb. Sci. Technol.* 3:195–205 (1971).
18. Oran, E. S., and Boris, J. P., *Numerical Simulation of Reactive Flow,* Elsevier, New York, 1987.
19. Boris, J. P., and Book, D. L., *Methods Comp. Phys.* 16:85–129 (1976).
20. Boris, J. P., Landsberg, A. M., Oran, E. S., and Gardner, J. H., *LCPFCT—Flux-Corrected Transport Modules for Solving Generalized Continuity Equations,* NRL Memorandum Report 6410, 1993.
21. Young, T. R., *CHEMEQ—A Subroutine for Solving Stiff Ordinary Differential Equations,* NRL Memorandum Report 4091, 1980.
22. Lefebvre, M. H., Oran, E. S., Kailasanath, K., and Van Tiggelen, P. J., Progress in Astronautics and Aeronautics, AIAA, Inc., Washington, 1993, Vol. 153, pp. 64–77.

COMMENTS

Aris Makris, McGill University, Canada. It is surprising to see the authors choosing to correlate the velocity deficits they measured with the ZDN reaction zone length. Several authors over the past decade (Moen et al., Laberge et al., Makris) have successfully correlated the detonation velocity deficit with the nondimensional ratio comprised of the tube diameter and a dynamic parameter for the detonation length scale (i.e., cell size or critical diameter d_c). The ZDN reaction zone does not correlate well with λ or d_c. Why do the authors use a length scale computed from a physically unrealistic model to describe the very unstable and 3D near-limit behavior, where velocity deficits are typically measured for obstacle-free propagation, when established practice makes use of a dynamic experimentally measured parameter?

Author's Reply. The purpose of the work is to correlate velocity deficits with computed parameters and not with an experimentally measured parameter. The correlation mentioned in the question requires performing experiments in order to assess the detonation cell size. Consequently, the velocity deficit is de facto observed. In this work, the nonideality is predicted by (1) performing a relatively simple numerical calculation, and (2) using the initial conditions (pressure, temperature, composition, and tube geometry) as the only input data.

•

A. C. McIntosh, Leeds University, UK. (Similar comment submitted by D. Desbordes, Laboratoire d'Energetique et de Detonique, France.) The velocity deficit between real detonations (near propagation limits) and theoretical C-J detonation speeds will be affected by three-dimensional effects (not just overall curvature and heat loss to the walls, but the well-known diamond structure). Could you comment on this please?

Author's Reply. Three-dimensional effects are certainly major effects and must be taken into account to fully understand detonation phenomena. So far, very few 3D numerical simulations have been performed, and the cost in CPU time does not allow (for the time being) sets of simulations to be run to better understand the influence of various physical (pressure) and chemical (stoichiometry, additives, etc.) parameters. We agree with the comment that one-dimensional calculations are, to some extent, "partial and incomplete." Nevertheless, such modeling still contains some useful information. Note that the one-dimensional Cartesian model we used does not properly model spherical detonations. The diverging effect of a spherical geometry should be taken into account by using spherical coordinates. Since it is not the case here, our calculations must be related to detonation in tubes.

•

Martin Sichel, University of Michigan, USA. (Similar comment submitted by A. Milne, University of St. Andrews, Scotland.) Does the grid size in your unsteady calculation affect the final detonation velocity you obtain?

Author's Reply. The numerical cell size used in our calculation is about 0.1 mm. Coarse grid size does not properly resolve the induction and reaction zones. Using the mentioned grid size, the induction zone is described by at least five numerical cells. The reaction zone always contains more than 20 numerical cells. Since smaller grid size does not influence the final detonation velocity, we assume that the grid size we used is adequate to describe the coupling between the shock and the reaction zones.

Twenty-Fifth Symposium (International) on Combustion/The Combustion Institute, 1994/pp. 45–51

THEORETICAL AND NUMERICAL ANALYSIS OF THE PHOTOCHEMICAL INITIATION OF DETONATIONS IN HYDROGEN-OXYGEN MIXTURES

LONGTING HE AND PAUL CLAVIN

Laboratoire de Rechereche en Combustion, URA 1117, CNRS & Université d'Aix-Marseille 1
Service 252, Centre St-Jérôme, 13397 Marseille CEDEX 20, France

A theoretical study of the formation of planar detonations in hydrogen-oxygen mixtures irradiated by a strong light pulse has been carried out for different types of distribution of light intensity, yielding different types of initiation criteria and showing that the Zeldovich criterion for the formation of detonations by nonuniform conditions may not be sufficient. The critical conditions are first estimated using a reduced two-step reaction mechanism for hydrogen-oxygen mixtures. The conditions thus obtained involve parameters that characterize the laser beam (energy, power, and geometry) and the kinetics of hydrogen-oxygen mixtures, including not only the induction time but also the exothermal reaction rate at the final stage of combustion. These critical conditions are also determined by direct numerical simulations involving detailed chemistry coupled with full gas dynamics mechanisms. Particular attention is devoted to elucidating the transition phenomena that develop in the vicinity of the critical conditions where the initiation of detonations is not spontaneous. The temperature gradient, which is responsible for the birth of a shock-reaction wave complex, may later prevent the detonation formation.

Introduction

It has been known for a long time that, in the absence of any external shock waves, a detonation may be initiated spontaneously in a mixture inhomogeneously irradiated by a strong light flash [1]. Direct initiation of detonations in gaseous mixtures of H_2—Cl_2, H_2—O_2, and C_2H_2—O_2 has been obtained by Lee et al. [2] using flash photolysis. This photochemical initiation was interpreted as a mechanism of synchronization of the chemical energy release to the shock wave as it propagates through the nonuniform mixture (SWACER mechanism [2]). An approximate condition for the direct initiation of detonations in reactive mixtures with an initial gradient of induction time was proposed by Zeldovich [3]: A detonation is spontaneously initiated when the apparent velocity of the induction front has the same order of magnitude as the local sound speed. Further developments have been carried out recently by Dold et al. [4]. Moreover, as exhibited in one of our previous theoretical analyses [5], temperature gradients in the initial mixture with the same order of magnitude as the one responsible for the spontaneous initiation at high temperature may also produce detonation quenching at a lower temperature.

One of the characteristics of the photochemical initiation is that it does not require a powerful shock wave as in blast initiation. Blast initiation is now fairly well understood [6], and a recent theory [7] is available to give quantitative predictions of the blast energy required. Another characteristic of the photoinitiation is that the detonation wave is initiated on a much shorter length scale than the one usually involved in the mechanism of transition from deflagration to detonation. It is known from early experiments [2] and a more recent numerical calculation [11] in H_2—Cl_2 mixtures that an appropriate gradient of the free radical distribution generated by the photodissociation is required. But the critical conditions for the formation of detonations are not yet known.

The present paper is a first step to bridge this gap by investigating theoretically the critical conditions of photochemical initiation of detonations in H_2—O_2 gaseous mixtures. The critical conditions of the spontaneous formation of detonations are investigated in two cases, a Gaussian and an exponential distribution of the intensity of the laser beam, yielding two different types of criteria and showing that the Zeldovich criterion may not be sufficient.

Critical Conditions for a Uniformly Irradiated Mixture

As the gradient of the induction delay is the key mechanism of the photochemical initiation of detonations, the induction delay of an uniformly irradiated H_2—O_2 mixture will be determined first. Consider a mixture that is sensitized by addition of few percent of NH_3 and irradiated by a strong flash or a powerful laser beam with the appropriate energy in the UV spectrum. Let's assume that the photodissociation produces H radicals; the case of production

of O or OH radicals may be treated in a similar way. Then, the elementary reactions controlling the induction period in the presence of the H radicals that are produced by photodissociation, are as follows

$$H + O_2 \rightarrow OH + O \quad (1f)$$

$$O + H_2 \rightarrow OH + H \quad (2f)$$

$$OH + H_2 \rightarrow H_2O + H \quad (3f)$$

$$H + O_2 + M \rightarrow HO_2 + M \quad (5f)$$

$$H + HO_2 \rightarrow OH + OH \quad (6f)$$

$$H + HO_2 \rightarrow H_2 + O_2 \quad (7f)$$

$$H + HO_2 \rightarrow H_2O + O \quad (8f)$$

The other elementary reactions are neglected because their reaction rate is smaller in the induction period. Because of the large activation energy of (1f), the chain branching mechanism producing H radicals through (1f) (2f) (3f) is dominated at low temperature by the H consumption rate controlled by (5f), which has a small activation energy. The quasi-steady-state approximation may be applied to OH, O, and HO_2 radicals, and the well-known two-step reduced mechanism is derived [8,9]

$$H + O_2 + (3H_2) = 2H_2O + 3H + Q_I \quad (I)$$

$$H + H + M = H_2 + M + Q_{II} \quad (II)$$

with $Q_I = 11.37$ Kcal/mole and $Q_{II} = 104$ Kcal/mole and with the following semiglobal reaction rates:

$$\omega_I = (k_{1f} + a[M]k_{5f})[H][O_2] \quad (1a)$$

$$\omega_{II} = [M]k_{5f}[H][O_2] \quad (1b)$$

with

$$a = \frac{k_{7f} + k_{8f}}{k_{6f} + k_{7f} + k_{8f}}, \quad \text{and } [M] = [H_2] + 0.4[O_2] + 6.5[H_2O] \quad (1c)$$

Let τ_f and ω_H be the total duration of the irradiation and the production rate of H radicals per mole of irradiated mixture, respectively. The laser-induced production term Ω_H in the conservation equation of mole fraction X_H of H radicals can be written as follows:

$$\Omega_H = \begin{cases} \omega_{II}, & 0 \le t \le \tau_f \\ 0, & t > \tau_f. \end{cases} \quad (2)$$

The corresponding equations for the evolution of temperature T and H radical concentration X_H are

$$\frac{C_v}{Q_{II}}\frac{dT}{dt} = \frac{X_H}{\tau_T}, \quad \text{with } \tau_T \equiv \frac{W}{\rho X_{O_2}}\{(k_{1f} + a[M]k_{5f})Q_I/Q_{II} + [M]k_{5f}\}^{-1} \quad (3a)$$

$$\frac{dX_H}{dt} = -\frac{X_H}{\tau_H} + \Omega_H, \quad \text{with} \quad \tau_H \equiv \frac{W}{2\rho X_{O_2}}\{(1 - a)[M]k_{5f} - k_{1f}\}^{-1} \quad (3b)$$

where the reaction is assumed to proceed at constant volume. Equations are similar at constant pressure. Equations (3a) and (3b) yield

$$dX_H/dt = -(\tau_T/\tau_H)(C_v/Q_{II})dT/dt + \Omega_H \quad (4a)$$

to give the following relation between $X_H(t)$, $T(t)$, and t

$$X_H = -\int_{T_u}^{T} \frac{\tau_T}{\tau_H}\frac{C_V}{Q_{II}}dT + \int_0^t \Omega_H dt \quad (4b)$$

with $T = T_u$ at $t = 0$. Notice that, according to Eqs. (3a) and (3b), both τ_T and τ_H are temperature dependent through k_{1f}. $1/\tau_H$ is positive at low temperature, $T < T^*$, and crosses zero when the temperature reaches a cross-over temperature T^*, corresponding to the extended second limit of explosion, defined by

$$k_{1f}(T^*) - (1 - a)k_{5f}(T^*)[M] = 0. \quad (5a)$$

Here $T^* \approx 1100$ K at 1 atm. During the induction period, $T < T^*$, H radicals are produced by photodissociation and consumed by (I) + (II) to warm up the mixture. As soon as T^* is crossed, H production by (I) takes over the consumption by (II), and a rapid chain branching explosion develops with a very short characteristic reaction time, $\tau_r \approx W/(k_{1f}\rho X_{O_2}) \approx 10^{-7}$ s. The induction delay τ_e corresponds to the time required to warm up the mixture from T_u to T^*, and it may be easily computed from Eqs. (3a) and (3b). The computation is simplified by anticipating a two time-scales behavior. When $T < T^*$, k_{1f} is negligible, and τ_H and τ_T are almost constant like k_{5f}, $\tau_T \approx \tau_H \approx 10^{-7}$ s. During the first 10^{-7} s of irradiation, the mole fraction of H radicals reaches a plateau value corresponding to the quasi-steady-state approximation in Eq. (3b), $X_H \approx \tau_H\omega_H$. When the H production rate by photo-dissociation, ω_H, is assumed to be constant, X_H stays almost constant during the induction period $\tau_H < t < \tau_e$ while the temperature keeps increasing almost linearly with time. The term τ_e is then given from Eq. (3a)

$$\tau_e = X_H^*/\omega_H \quad (5b)$$

where X_H° is a characteristic of the H_2—O_2 kinetics and is defined as

$$X_H^\circ \equiv \int_{T_u}^{T^\circ} \frac{\tau_T(T)}{\tau_H(T)} \frac{C_v}{Q_{II}} dT$$

$$X_H^\circ \approx 10^{-2} \quad \text{at } T_u \approx 300 \text{ K and } p \approx 1 \text{ atm.} \tag{5c}$$

The two time-scales approximation is valid when $\tau_H << \tau_e$, yielding a X_H plateau value, $(\tau_H/\tau_e)X_H^\circ$, much smaller than X_H°. If the duration of irradiation is not long enough, $\tau_f < \tau_e$, the temperature stops increasing at $t = \tau_f$, X_H decreases from its plateau value to zero in a short time delay τ_H, and the simplified kinetic scheme (I) (II) cannot predict further evolution. In real mixtures, a secondary reaction path involving H_2O_2 radicals may lead to a thermal explosion, but after a much longer time delay (typically 10^{-1} s at 900 K and 1 atm), which is no more relevant for the problem considered here. A parametric numerical study based on the detailed chemistry of Maas and Warnatz [10] in the pressure and initial temperature ranges of 0.1–10 atm and 100–500 K with a deposition rate ω_H of few hundred per second has confirmed these results, yielding typical values of the plateau and of the induction time, $X_H = O(10^{-5})$ and $\tau_e \approx 10^{-4}$ s.

Critical Conditions for the Formation of Detonations

The temperature at which the explosion proceeds, $T = T^\circ$, as well as X_H°, is prescribed for a H_2—O_2 mixture by Eqs. (5a) and (5b). The H production rate by photodissociation, ω_H, is proportional to the intensity of the irradiating light. When this last quantity is nonuniform, $\omega_H = \omega_H(x/L)$, a spatial distribution of induction time is produced according to Eq. (5b), $\tau_e(x/L) = X_H^\circ/\omega_H(x/L)$. As a consequence, an induction front will propagate at an apparent velocity $u = (d\tau_e/dx)^{-1}$, and according to Zeldovich, a necessary condition for a detonation to be formed spontaneously requires that u becomes the same order of magnitude as the sound velocity c° at T°, $u/c^\circ = O(1)$, while a quasi-constant volume explosion develops in the region when $u/c^\circ >> 1$.

When the induction delay is much shorter (larger) than the acoustic time, the constant volume (pressure) approximation is valid during the induction period. A detailed analysis requires the solution of the compressible reactive flow fields, but here we will limit our attention to an order-of-magnitude analysis in the one-dimensional case. The results are compared in the following section with the direct numerical solutions of the compressible flow fields with a complex chemistry.

The criterion for the formation of detonation depends on the type of distribution $\omega_H(x/L)$ that is used. This is illustrated here by considering two cases, a Gaussian and an exponential distribution, yielding two different criteria:

$$\omega_H = \omega_0 \exp(-x^2/L^2) \quad \text{and}$$

$$\omega_H = \omega_0 \exp(-|x|/L). \tag{6}$$

The first one is representative of the radial distribution of the light intensity in a cylindrical beam. The second one represents the longitudinal gradient due to the photon absorbtion and was already studied by Yoshikawa and Lee [11] for H_2—Cl_2 mixtures. The Gaussian distribution yields

$$\tau_e \approx \tau_{e,0} \exp(x^2/L^2) \Rightarrow$$

$$u \approx (L^2/2\tau_{e,0}x) \exp(-x^2/L^2) \tag{7a}$$

where $\tau_{e,0} \equiv X_H^\circ/\omega_0$ is the time delay at which the ignition started at the origin $x = 0$ and u is the velocity of the point $T = T^\circ$ followed immediately by the runaway. When the duration of irradiation is sufficiently long, $\tau_f > \tau_{e,0}$, the explosion propagates from the origin $x = 0$, and because of the zero slope of $\omega_H(x/L)$ at the origin, the apparent velocity of the induction front u starts with an infinite value at $x = 0$ and decreases with the distance x. The condition $u = c^\circ$ is always verified at a position $x = l_Z$ given by Eq. (7a).

$$l_Z = L^2/(2c^\circ\tau_{e,0}) \tag{7b}$$

where we have assumed that $l_Z << L$. But clearly, a detonation can only be spontaneously formed if the distance from the origin is not too small, and a necessary condition for the formation of detonation at l_Z is that the time elapsed from the ignition at the centre be larger than the reaction time, $\{\tau_e(l_Z/L) - \tau_{e,0}\} \approx (l_Z^2/L^2)\tau_{e,0} > \tau_r$. This yields the following critical conditions for the spontaneous formation of a detonation:

$$\tau_r\tau_{e,0} < L^2/4c^{\circ 2} \quad \text{with } \tau_f > \tau_{e,0}. \tag{7c}$$

The term L/c° is a characteristic acoustic time based on the size of the light distribution. Condition (7c) involves the size L, the kinetic of the chain branching reaction through τ_r, the power of the light source, and the kinetic of the induction period through X_H° in Eq. (5b) for $\tau_{e,0}$. The additional condition $\tau_f > \tau_{e,0}$ defines a minimal energy of the light source.

The condition is much simpler for the exponential distribution and is directly obtained from the Zeldovich condition to give

$$\tau_{e,0} < L/c^\circ \quad \text{with } \tau_f > \tau_{e,0}. \tag{7d}$$

The reason for such simplicity is that the explosion

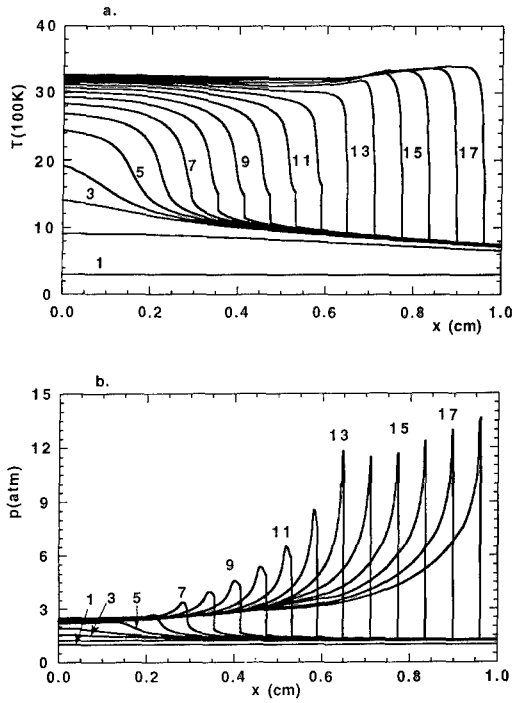

FIG. 1. Temperature and pressure profiles at different instants in time for a Gaussian distribution. $\omega_0 = 216\ s^{-1}$, $\tau_f = 1.82\ 10^{-4}$ s, $L = 1.25$ cm. $t_1 = 0$, $t_3 = 0.12012$ ms, $t_5 = 0.18000$ ms, $t_7 = 0.18103$ ms, $t_9 = 0.18183$ ms, $t_{11} = 0.18253$ ms, $t_{13} = 0.18316$ ms, $t_{15} = 0.18370$ ms, $t_{17} = 0.18418$ ms.

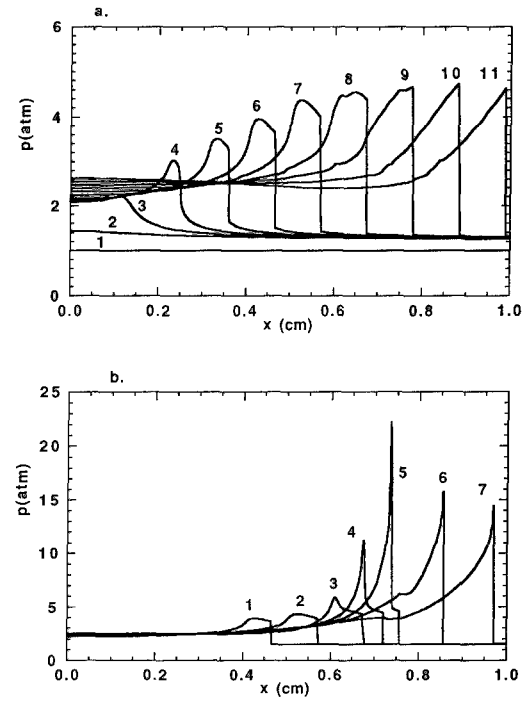

FIG. 2. (a) Pressure profiles at different instants in time for a Gaussian distribution. $\omega_0 = 216\ s^{-1}$, $\tau_f = 1.82\ 10^{-4}$ s, $L = 0.9$ cm. $t_1 = 0$, $t_2 = 0.17926$ ms, $t_3 = 0.18018$ ms, $t_4 = 0.18093$ ms, $t_5 = 0.18165$ ms, $t_6 = 0.18234$ ms, $t_7 = 0.18301$ ms, $t_8 = 0.18369$ ms, $t_9 = 0.18438$ ms, $t_{10} = 0.18508$ ms, $t_{11} = 0.18580$ ms. (b) Pressure profiles at different instants in time, obtained with the results represented by curve 6 in Fig. 2a as initial conditions with removing the temperature gradient in the mixture ahead of the shock. $t_1 = 0.18234$ ms, $t_2 = 0.18301$ ms, $t_3 = 0.18367$ ms, $t_4 = 0.18393$ ms, $t_5 = 0.18415$ ms, $t_6 = 0.18451$ ms, $t_7 = 0.18491$ ms.

starts from the origin with a finite value of the apparent velocity of the induction front u, which decreases with the distance x. Thus, the critical condition is simply given by $u(x = 0) \approx c^*$, and the finite duration of the heat release τ_r does not modify significantly the criterion when $\tau_r << \tau_{e,0}$.

Numerical Results

The time-dependent solutions of the compressible reactive flow fields generated by the deposition of free radicals are obtained by solving a system of reactive Euler equations [5] with a numerical code recently developed by He and Larrouturou [12]. The reaction scheme consists of 37 elementary reactions and 8 species [10]. The temperature dependence of the specific heat of each species is taken to be in the form of polynomial fits of data from the JANAF table [13]. The numerical method combines a second-order upwind Total Variation Diminishing (TVD) shock-capturing method with a treatment of the shock wave and nonuniform gridding. This combination treats the shock as a real discontinuity and allows us to capture perfectly the Neumann spike. This numerical code has been proved to be able to solve unsteady detonation problems with high precision, such as the one-dimensional instability of detonations propagating in hydrogen-oxygen mixtures [12]. We investigate here the critical conditions of the formation of detonation in the planar geometry for a stoichiometric hydrogen-oxygen mixture initially at uniform temperature and pressure (at $t = 0$, $T_u = 298$ K and $p_u = 1$ atm) and irradiated by a nonuniform light source.

It is instructive to look first to the transition phenomena occurring in the vicinity of the critical conditions. The numerical simulations presented in Figs. 1 and 2 are performed with a Gaussian distribution with $\omega_0 = 216\ s^{-1}$ and $\tau_f = 1.82\ 10^{-4}$ s and for two different values of L (1.25 and 0.9 cm) separating the critical condition. The duration of irradiation τ_f is

slightly larger than the minimum duration for producing a rapid self-explosion $\tau_{e,0} = 1.62\ 10^{-4}$ s. The results for $L = 1.25$ cm are shown in Figs. 1 and represent a successful formation. The development of the detonation may be divided into four stages:

1. A hot pocket with nonuniform temperature is formed as a result of the deposition of free radicals (see curve 3 in Fig. 1a).
2. A volume explosion takes place in the region $0 \leq x < 0.3$ cm where the temperature is higher than $T^* = 1100$ K, and this explosion leads to the birth of a shock wave near $x = 0.3$ cm with an intensity much smaller than that of CJ detonation (see curve 7).
3. Then a shock-reaction wave complex is developed that consists of a relatively weak leading shock followed by an unsteady induction zone and a rapid reaction zone (see curves 7 through 11). As this complex propagates, the leading shock is amplified, and an overdriven detonation is formed near $x = 0.65$ cm (see curve 13).
4. Then the overdriven detonation relaxes quickly to a quasi-steady CJ detonation propagating in a nonuniform temperature field (curves 13 through 18).

The results for $L = 0.9$ cm in Fig. 2a show an amplification of shock followed by an attenuation. The events in the early stage are very similar to the case shown in Figs. 1, but the propagation of the shock-reaction wave complex does not lead to the formation of a strong detonation. The attenuation of the shock begins from $x = 0.5$ cm. The structure of the shock-reaction complex is very different during the two stages of amplification and attenuation. During the amplification stage, the pressure increases in the induction zone as the chemical reactions proceed, while during the attenuation stage, the shock intensity is continuously weakened by the rarefaction wave that follows the leading shock. The temperature gradient in the mixture ahead of the leading shock is responsible for this damping. If this gradient is removed when the leading shock reaches $x = 0.45$ cm, a strong detonation is formed at $x = 0.75$ cm (see Fig. 2b). These results show that, close to the critical condition, the formation of detonation is not spontaneous and that the temperature gradient that is responsible for the birth of a shock-reaction wave complex may later prevent the formation of detonation. As for the detonation quenching by a thermal gradient [5], this is a consequence of the high sensitivity of the reaction rate to temperature. Sufficiently far above the critical conditions, the detonation is formed spontaneously at $x = l_Z$. Far below, the intensity of the shock produced by the volume explosion near $x = 0$ is very weak, and the amplification phenomenon is not observed. The shock wave amplification mechanism requires the primitive shock

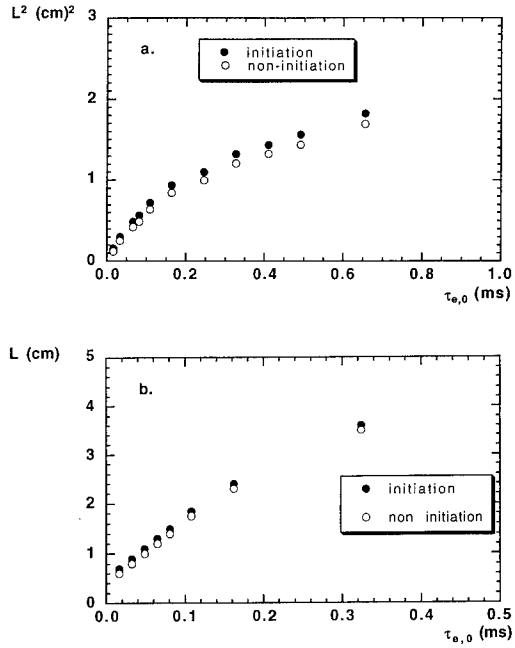

FIG. 3. Critical sizes as a function of the induction time, (a) Gaussian distribution, (b) exponential distribution.

resulting from the volume explosion to be sufficiently large.

A parametric study is carried out to determine the critical size L_c for the successful formation of detonations for different values of ω_0. Figure 3a shows L_c^2 as a function of the induction time $\tau_{e,0}$ for the Gaussian distribution. The critical size is about 1 cm for an induction time $\tau_{e,0} = 0.5$ ms. A linear relation between L_c^2 and $\tau_{e,0}$, as predicted by condition (7c), is verified for $\tau_{e,0} < 0.2$ ms. But, because of the transition phenomenon described in Fig. 1, the formation of the detonation occurs before the theoretical limit (7c) for $\tau_{e,0} > 0.2$ ms, and condition (7c) appears to be too restrictive. Figure 3b shows L_c as a function of the induction time $\tau_{c,0}$ for the exponential distribution of the production rate ω_{II}. A linear relation between L_c and $\tau_{e,0}$, as predicted by condition (7d), is well verified.

Finally, we should stress here that the results given in Figs. 3a and 3b concern only the critical condition for the formation of detonations at high temperature. Well-formed detonations may quench later at a lower temperature [5]. Figure 4a shows the pressure at the Neumann state as a function of the position of the leading shock for an exponential distribution with $L = 0.65$ cm and $\omega_0 = 21600\ \mathrm{s}^{-1}$. The detonation is formed spontaneously near $x = 0.1$ cm, producing an overpressure of the order of 30 atm. As the detonation propagates in the mixture with a decreasing temperature, the propagating detonation is first sta-

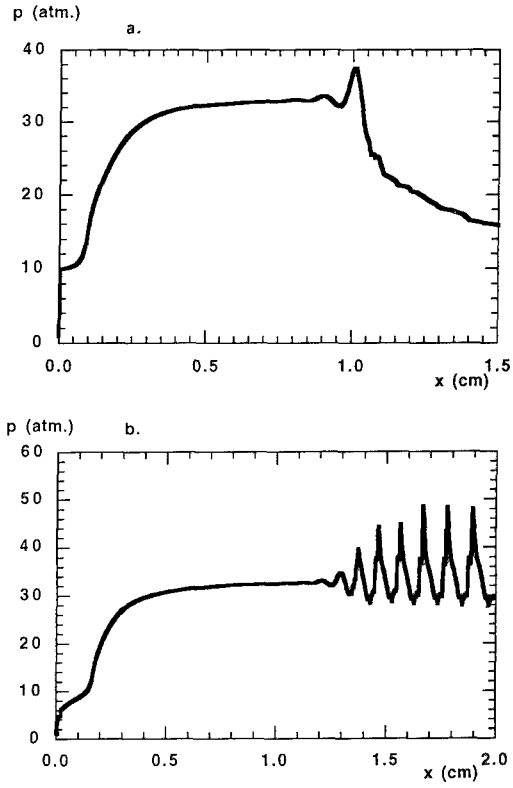

FIG. 4. (a) Detonation quenching. $\omega_0 = 21{,}600\ s^{-1}$, $\tau_f = 3 \cdot 10^{-6}$ s, $L = 0.65$ cm. (b) Detonation transmission. $\omega_0 = 21{,}600\ s^{-1}$, $\tau_f = 2 \cdot 10^{-6}$ s, $L = 1.0$ cm.

ble, then a galloping instability [14,15] appears, and finally, the overpressure decreases suddenly, showing the quenching of detonation. In this case, no detonation is transmitted in the surrounding cold mixture. This quenching mechanism has been described in a previous work [5]. In order to transmit a detonation, a larger size L is needed. Figure 4b shows the pressure trace of a successful transmission for an exponential distribution with $L = 1.0$ cm and $\omega_0 = 21600\ s^{-1}$. Oscillations appear with a very large amplitude when the detonation front arrives at $x = 1.2$ cm. For a stoichiometric H_2/O_2 mixture at 1 atm, such a one-dimensional galloping instability appears systematically for temperature of the fresh mixture below a critical value that is about 400 K, leading in real experiments to the formation of the well-known cellular detonation fronts.

Conclusion

The critical conditions for the spontaneous formation of detonation by a strong light pulse have been studied analytically and numerically for different distributions of light intensity. For a Gaussian distribution, the Zeldovich criterion is not sufficient. The critical conditions involve parameters that characterize the laser beam (energy, power, and geometry) and the kinetics of the H_2-O_2 mixture, including not only the induction time but also the high rate at which the heat is released at the end of the induction delay. As shown by direct numerical simulations, the transition regime that develops in the vicinity of the critical conditions is more complex than in the case of the spontaneous formation of detonation.

Nomenclature

c^*	acoustic velocity
C_v	specific heat at volume constant
k_i	chemical reaction constant of the elementary reaction i
L_c	critical size
l_z	position of the formation of detonation
p	pressure
Q_I, Q_{II}	heat release parameters
R	gas constant
T	temperature
t	time
u	apparent velocity
W	molecular weight of the gas
X_H^*	critical mole fraction of the radical H
X_H	mole fraction of the radical H
X_{O_2}	mole fraction of O_2
x	spatial coordinate

Greek

ρ	density
τ_H, τ_T	characteristic times given in Eqs. (3a) and (3b)
τ_e	induction time [Eq. (5b)]
τ_f	duration of irradiation
Ω_H	production rate of H radicals given in Eq. (1)
ω_{II}	production rate of H radicals
ω_I,ω_{II}	chemical reaction rates (1a) and (1b)

Subscripts

u	initial states in the surrounding gas mixture
0	value at $x = 0$

REFERENCES

1. Norrish, R. G. W., *Tenth Symposium (International) on Combustion*, The Combustion Institute, Pittsburgh, 1965, pp. 1–18.
2. Lee, J. H., Knystautas, R., and Yoshikawa, N., *Acta Astronaut.* 5:971 (1978).
3. Zeldovich, Ya. B., *Combust. Flame* 39:211 (1980).

4. Dold, J. W., Kapila, A. K., and Short, M., in *Dynamic Structure of Detonation in Gaseous and Dispersed Media* (A. A. Borissov, Ed.), Kluwer Academic Publishers, Dordrecht, The Netherlands, 1991, pp. 109–141.
5. He, L. T., and Clavin, P., *Twenty-Fourth Symposium (International) on Combustion,* The Combustion Institute, Pittsburgh, 1992, pp. 1861–1867.
6. Lee, J. H., *Annu. Rev. Fluid Mech* 16:311–336 (1984).
7. He, L. T. and Clavin, P., *J. Fluid Mech.* 277:227–248.
8. He, L. T., and Clavin, P., *Combust. Flame* 93:391–420 (1993).
9. Peters, N., in *Reduced Kinetic Mechanisms and Asymptotic Approximations for Methane-Air Flames* (M. D. Smooke, Ed.), Springer-Verlag, Berlin, Heidelberg, 1991, pp. 48–67.
10. Maas, U., and Warnatz, *Combust. Flame* 74:53–69 (1988).
11. Yoshikawa, N., and Lee, J. H., "Dynamic Aspects of Detonations." *Prog. Astronaut. Aeronaut.* 153:95–104 (1993).
12. He, L. T., and Larrouturou, B., *J. Comput. Phys.*, submitted (1994).
13. Stull, D. R., and Propret, H. (Eds), *JANAF Thermochemical Tables,* U.S. Department of Commerce, Washington DC, 1971.
14. Erpenbeck, J. J., *Twelfth Symposium (International) on Combustion,* The Combustion Institute, Pittsburgh, 1967, p. 711.
15. Fickett, N., and Davis, W. C., *Detonation,* University of California Press, Berkeley, 1979.

COMMENTS

S. Dorofeev, RRC-Kurchatov Institute, Russia. It is inadequate to consider Zel'dovich's criterion as a criterion for detonation onset. This criterion gives the conditions for strong blast wave formation. Suggested critical conditions (7a) and (7d) can serve only as conditions for strong blast formation. Critical conditions for the onset of detonation should take into account mixture properties. They cannot include only reaction times at the center of disturbance.

Author's Reply. As explained in Ref. 3, Zel'dovich's condition corresponds to the birth of a shock-reaction complex consisting of a leading shock wave followed by an unsteady induction zone and a rapid reaction zone as shown in Fig. 1b. The amplification of the shock wave and the formation of detonation take place only when the initial leading shock is strong enough. If the conditions (7c) and (7d) are not satisfied, the initial shock wave is too weak and the detonation formation cannot be observed. The intensity of the shock wave produced by the volume explosion at the center is mainly determined by the conditions (7c) and (7d) and depends only weakly on the mixture properties. It should also be recalled that these conditions can only be used as order of magnitude for estimating the critical conditions.

•

Yu-Chen Li, Energia, Inc., USA. Have you determined, in your model, that the photochemical process is due to single or multiphoton effect?

Author's Reply. We have assumed that the photochemical process is a single-photon process, $h\nu + NH_3 \rightarrow H + NH_2$, and that NH_2 is much less reactive with O_2 than H.

Twenty-Fifth Symposium (International) on Combustion/The Combustion Institute, 1994/pp. 53–59

H_2-AIR AND CH_4-AIR DETONATIONS AND COMBUSTIONS BEHIND OBLIQUE SHOCK WAVES

C. VIGUIER, C. GUERRAUD AND D. DESBORDES
Laboratoire d'Energétique et de Détonique
URA 193 CNRS, ENSMA
Site du Futuroscope, B.P. 109, 86960 Futuroscope Cedex, Poitiers, France

Two stoichiometric reactive mixtures (H_2-air and CH_4-air) at initial conditions of temperature and pressure, $T_0 = 293$ K and $p_0 < 1$ bar, respectively, very different from the point of view of their detonability, are used in order to study the conditions of the onset of combustion and/or detonation when submitted to the action of an oblique shock wave (OSW) at Mach number M of about 6 and at various angles of inclination θ. Generation of an OSW in the reactive mixture at rest is obtained via lateral expansion of the detonation products of a normal CJ detonation wave propagating in a bounded gaseous detonable mixture separated from the mixture under test by a 6-μm-thick mylar film. Different steady combustion regimes are observed depending on θ and on the reactive mixture. Based on simple polars analysis, the possibility of observing an oblique detonation wave (ODW) are checked for the two mixtures.

In the case of H_2-air mixtures, ODWs are obtained with small degrees of overdrive (D/D_{CJ}) ($\cong 1$) of the detonation (where D is the normal detonation velocity of the ODW) after a predetonation zone, where the OSW is followed by an oblique flame initiated at the beginning of the interaction between the two media. Minimal conditions for detonative combustion are deduced, which correspond to a postshock temperature $T_s \cong 1000$ K, while the minimal condition for combustion as an oblique flame behind the OSW is $T_s \cong 800$ K.

For CH_4-air mixtures, no detonation appears even when the degree of overdrive of the theoretically possible solutions of stable ODW is increased up to 1.1 and beyond for T_s up to 1480 K. Only the OSW and oblique flame configuration are observed. For $T_s < 1000$ K, no combustion occurs behind the shock wave. Thus, this mixture appears to be especially difficult to detonate.

Introduction

In the past few years, the study of supersonic combustion has gained considerable importance in connection with the use of SCRAM jets for hypersonic vehicle propulsion and RAM accelerator for accelerating projectiles to high-speed motion. For both, detonation regimes [1–6] may be involved, especially for high Mach number. Oblique detonations in RAM accelerators [4–6] have a dominant role in the supersonic motion of the projectile (see Ref. 6). The feasibility of the detonation RAM jet is thus indirectly demonstrated, even though the detonation regime presents many disadvantages compared to lower-rate combustion processes having theoretically higher propulsive efficiency. Nevertheless, detonative combustion exhibits an important advantage, as liberation of the chemical energy is complete and takes place in a very narrow region without losses. In order to generate oblique detonation waves (ODWs), a kind of "oblique shock tube" is used in this study [7–10]. It consists essentially of a chamber divided in two by a very thin mylar film (cf. Fig. 1). Part A of the chamber is a booster section containing a detonative mixture, where a normal quasi-CJ detonation wave propagates. Detonation products expand as a wedge of angle δ, inducing an oblique shock wave (OSW) of inclination angle θ in the reactive mixture B in the upper section. The entire structure propagates at a uniform Mach number M.

Classical stable solutions for the OSW are given in the P, δ (pressure, deflection angle) plane by the intersection between the shock polar of B and the Prandtl–Meyer expansion polar of the detonation products of A, starting from $P = P_{CJ}(A)$ and $\delta = 0$ (displayed in Fig. 1). (This intersection gives, in fact, two solutions, only the lower of which has a physical meaning.) The oblique detonation regime in mixture B is then possible but requires that several conditions be satisfied:

1. The value of the Mach number M defined by $M = D_{CJ}(A)/a_0(B)$ (where $a_0(B)$ is the velocity of sound of the mixture B at T_0, p_0) must be larger than Mach number $M_{CJ}(B)$ defined by the CJ conditions of the mixture B. If this condition is fulfilled, a detonation polar exists in the P, δ plane, which is open at the CJ point.
2. The intersection of the expansion polar for the

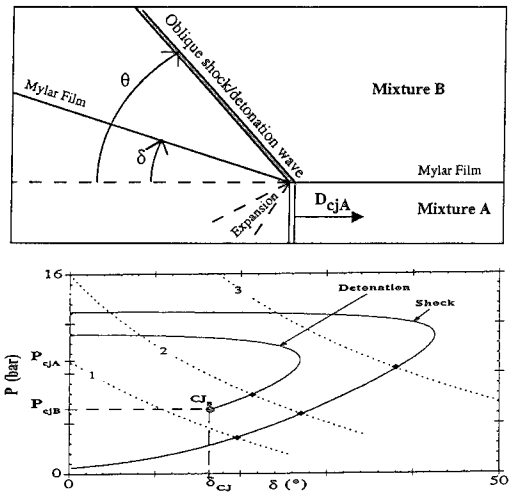

FIG. 1. Schemes of interaction between mixtures A and B and of possible solutions of interaction in P, δ.

detonation products of A with the detonation polar for B (only the lower solution is physical) requires a minimal (and a maximal) value for the detonation pressure of A, i.e., $P_{CJ}(A)$, and consequently for the initial pressure $p_0(A)$ (cf. Fig. 1).

The lowest regime obtained for the stable ODW is the CJ condition, in which case normal velocity $D(B)$ of the ODW is equal to $D_{CJ}(B)$, and deflection and inclination angles $\delta_{CJ}(B)$ and $\theta_{CJ}(B)$ are minimal. Other regimes (overdriven ODW) of stable ODW may be obtained with $D(B)/D_{CJ}(B) > 1$, i.e., $\delta > \delta_{CJ}$ and $\theta > \theta_{CJ}$.

In a previous paper (see Ref. 10), where the above conditions have been achieved, stable ODWs are observed in a very detonable mixture such as C_2H_2 + $2.5O_2$ + 10.5 Ar. This mixture exhibits in its CJ detonation regime a cellular structure of a size λ_{CJ} of about 1 mm for p_0 = 1 bar and T_0 = 293 K. Then, used in the range of p_0 from 0.1 to 1 bar, this mixture has supported stable ODW for the minimum solution given by the polar analysis (the CJ regime) and also a fortiori for overdriven detonation regimes of degree of overdrive D/D_{CJ} defined as

$$D/D_{CJ} = \frac{\sin\theta}{\sin\theta_{CJ}} \tag{1}$$

up to 1.48.

For less detonable fuel/air mixtures, recent experiments in H_2-air mixtures (see Ref. 11) show the possibility of observing an ODW with quasi-CJ regime, generally obtained after a "predetonation" zone of combustion consisting in an OSW followed by an oblique flame initiated at the apex of the wedge. The initial pressure $p_0(B)$ of the mixture is 0.5 bar, corresponding to a detonation cell size of $\lambda_{CJ} \sim 35$ mm.

In stoichiometric CH_4-air mixtures at ambient conditions, where free-field detonations were never observed, the detonation cell size λ_{CJ} would be about 300 mm (λ_{CJ} was estimated as 320 mm in Ref. 12, and the size measured in Ref. 17 was about 280 mm). Therefore, the detonation regime near the CJ condition would be difficult to obtain, but it might be expected for the overdriven regime.

The purpose of this paper is to investigate the conditions of the onset of ODWs in H_2-air and CH_4-air mixtures. These mixtures were chosen as representative of common fuel-air mixtures, the first one being a very detonable mixture, the second one being much less detonable.

Concerning the technique for obtaining OSW (see above), we have looked more carefully at the problem of the initial separation between the two media. As shown recently, the very beginning of interaction between the two media and the delay for obtaining a constant lateral rate of expansion of the detonation products of A depend drastically on the film thickness. In the present experiments, following the results given in Ref. 13, we have decreased the thickness of the mylar film from 10 to 18 μm of our previous experiments [10,11,14] to 6 μm in order to reduce the delay for establishing an OSW of constant slope.

The Mach number M for this study is fixed at about 6. Normal detonation Mach numbers M_{CJ} for stoichiometric H_2-air and CH_4-air mixtures are roughly 5, which allowed the existence of detonation polars for these mixtures and thus the possibility to observe ODWs.

Experimental Details

The oblique shock tube used here is composed of one chamber separated into two sections, each containing a reactive mixture [10,11,14]. The upper section contains the driven mixture B and is 50-cm long, 3-cm thick, and 19-cm high. The lower section is the same length and thickness and 5-cm high; it contains the driving detonable mixture A. The two sections are separated by a mylar film 6-μm thick, in order to maintain different initial pressures without diffusion across the separation plane. The channel of the driver section is connected to a 3-m-long detonation tube of 5.2-cm i.d. The normal quasi-CJ detonation wave propagation in section A is triggered at the end of this tube by an exploding wire source. The upper section is equipped with glass windows of 80 × 130 mm. The structures of the OSW, ODW, and oblique flame produced are examined using Schlieren photography. A long duration flash (about 500 μs) is used, coupled with a high-speed streak-framing camera, Thomson TSN506. Sequences of OSW and ODW propagation in the upper section are thereby obtained with a frequency of 100 kHz.

Piezoelectric pressure transducers are mounted vertically above the mylar film and face four ionization or optical probes used to measure pressure evolutions and different angles of oblique shocks, flames, and detonations.

Several mixtures A are used:

1. C_2H_2 + 2.5 O_2 for H_2-air mixture as B, at M = 6.
2. C_2H_2 + 2.5 O_2 + 2Ar and C_2H_2 + 2.5 O_2 + 5 Ar for CH_4-air mixture as B, at respectively, M = 6 and 5.5.

The gas mixtures are prepared by the partial pressure method in separated tanks where they are left quiet for at least 2 h before being used for the experiments.

Results and Discussion

For each mixture B tested (H_2-air and CH_4-air) at given initial conditions T_0 and p_0, the first value of initial pressure p_0(A) for mixture A (respective to mixture B) is given by the polar analysis when the ODW is very close to the expected CJ regime. Starting from that value, p_0(A) is progressively increased for successive shots. For the same initial conditions T_0 and p_0, systematic experiments are also performed by using air as the mixture B. Generally the OSW and the contact surface with constant angles are observed on schlieren pictures. The contact surface exhibits a narrow region where some distortions appear resulting from the breaking of the mylar film and lateral contact between the detonation products of A and the inert mixture B. Experimental values of θ, δ and p are typically a few percent lower than those given by theory.

H_2-Air Mixtures:

For the H_2-air mixture at p_0 = 0.5 bar and T_0 = 293 K, the critical onset of the ODW is observed for solution close to the CJ regime and is induced by the action of the detonation of C_2H_2 + 2.5 O_2 mixture at p_0 = 0.8 bar, T_0 = 293 K (p_{CJ} = 27.3 bar and D_{CJ} = 2413 m/s). This onset is displayed in Fig. 2a by schlieren sequence of propagating oblique waves. The detonation appears after a predetonation zone. This predetonation zone is stable and consists of the initial OSW generated by the wedge of the detonation products of mixture A followed by what we call an oblique turbulent flame having a different angle θ_f. Combustion of mixture B is initiated at the beginning of the interaction between the two media (the apex of the wedge).

The new characteristics of the OSW (pressure jump p, angle θ) and the contact surface (angle δ) are very close to the solution given by theory, assuming there is no combustion in mixture B and shown in P, δ, and θ, δ planes in Fig. 2b. In such a situation, the oblique flame creates a very small wedge of burnt gases of B ($\theta_f - \delta \cong 3°$; cf. Fig. 2a), which corresponds to a normal mean burning velocity of about 70 m/s [15] and which does not change significantly the position of the OSW if no combustion arises [11].

The detonation regime (a transient ODW regime followed by a stable ODW) happens suddenly. The motion of the triple point is parallel to the direction of wave propagation (cf. Fig. 2a).

The theoretical ODW is characterized by a degree of overdrive of D/D_{CJ} = 1.02. Because the ratio of cellular sizes of overdriven detonation waves to the CJ wave, i.e., λ/λ_{CJ}, varies roughly as (cf. Ref. 16)

$$\lambda/\lambda_{CJ} \sim \frac{D}{D_{CJ}} \exp \frac{E_A}{RT_{ZND}} \left[\left(\frac{D_{CJ}}{D} \right)^2 - 1 \right] \quad (2)$$

where T_{ZND} is the postshock temperature of the OSW propagating in the H_2-air mixture with velocity D_{CJ} (T_{ZND} = 1560 K) and E_A is the apparent activation energy of the mixture (= 19 kcal/mole); the cell size λ is 20% lower than the CJ size. Thus, the cellular structure under CJ conditions in H_2-air mixture (p_0 = 0.5 bar, T_0 = 293 K), i.e., $\lambda_{CJ} \cong 35$ mm, is reduced for the overdriven ODW observed to $\lambda \cong$ 28 mm. The temperature behind the shock wave is about 1000 K (slightly lower than that—1100 K—obtained in Ref. 11 with a larger thickness mylar film of 10–12 μm).

For lower conditions of interaction corresponding to D/D_{CJ} = 1 for the theoretical ODW, only the OSW followed by an oblique flame of slightly lower characteristics than the predetonation zone of the previous case is observed. In that case, it may be possible to obtain the onset of detonation, but this would require an upper chamber of very large size.

For conditions of higher initial pressure p_0(A) in the driver mixture, the predetonation zone is reduced drastically and quickly becomes indistinguishable. The ODW takes place rapidly with a constant slope and with characteristics very close to those given by the polar method, as shown previously with a very detonable mixture [10].

Previous experiments have shown that the oblique flame disappears when T_s becomes lower than 800 K [11].

CH_4-Air Mixtures:

In order to obtain ODWs in the stoichiometric CH_4-air mixture at p_0 = 0.3 bar and T_0 = 293 K, for M = 6, C_2H_2 + 2.5O_2 + 2Ar mixtures are used at different initial pressures p_0(A), namely, p_0(A) = 0.5, 0.7, 1.0, and 1.5 bar, corresponding to cases 1, 2, 3, and 4, respectively, on P, δ, and θ, δ planes displayed in Fig. 3.

For p_0(A) = 0.5 bar in C_2H_2 + 2.5O_2 + 2Ar

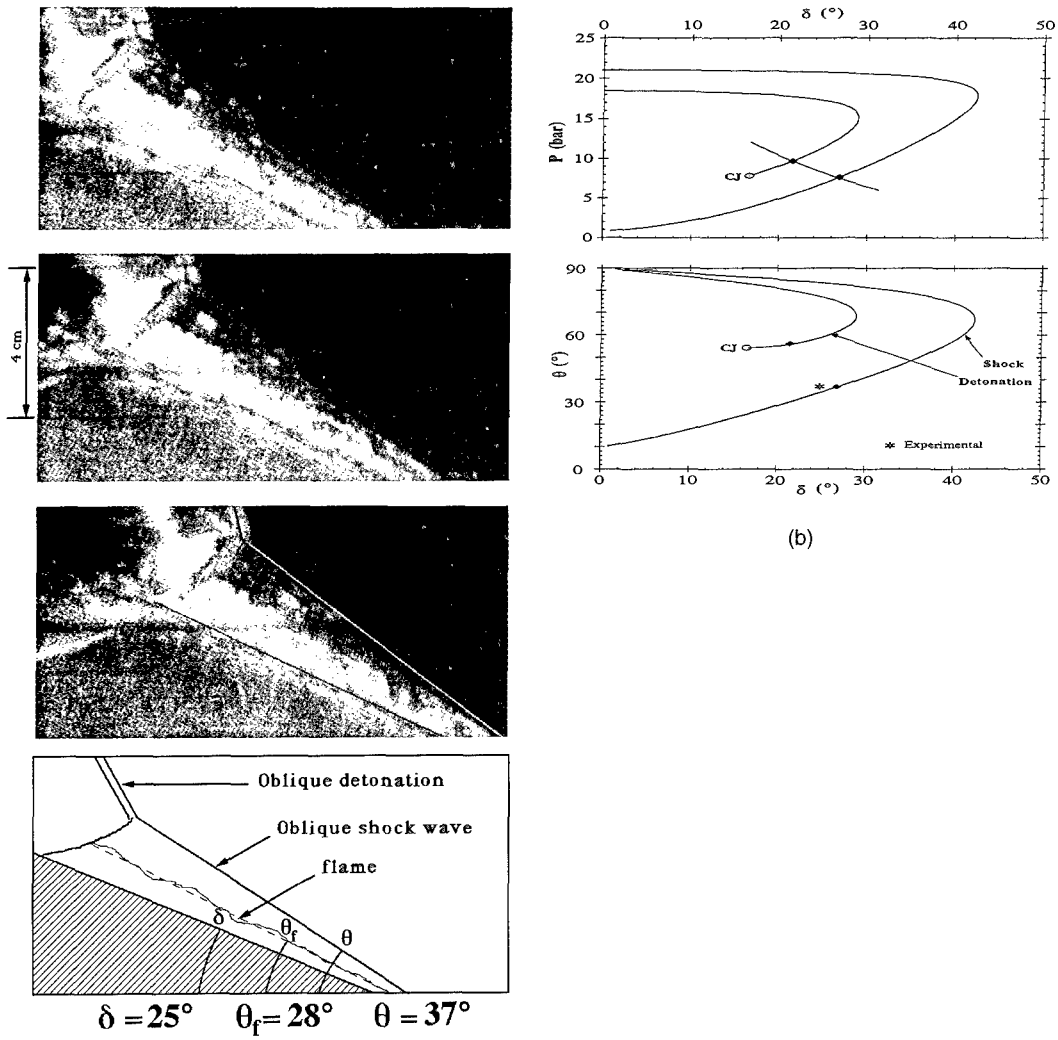

FIG. 2. (a) Schlieren photographs of the onset of an H_2-air (p_0 = 0.5 bar, T_0 = 293 K) oblique detonation wave for M = 6 (A = C_2H_2 + 2.5O_2, p_0(A) = 0.8 bar). (b) Solutions in P, δ, and θ, δ planes corresponding to (a).

mixtures, conditions are fulfilled to obtain expected quasi-CJ detonation regime (in fact, D/D_{CJ} = 1.01). In that case, neither an oblique detonation nor a flame is observed in mixture B, except for the OSW, in agreement with the polar solution (Fig. 3, case 1). The postshock temperature T_s is then about 900 K.

For p_0(A) ≅ 0.7 bar, an oblique flame appears behind the OSW, initiated at the apex of the wedge in a manner similar to the H_2-air mixtures. Figure 4 shows an example of such a configuration. In that case, T_s is about 1050 K. Polar analysis gives a possible overdriven detonation regime of D/D_{CJ} = 1.02 (Fig. 3, case 2).

For p_0(A) = 1 bar, the preceding configuration is observed (cf., Fig. 5), except with a stronger coupling between the OSW and the flame near the apex, where the phenomena are very complex. The oblique flame propagating just behind the OSW progressively separates from it. The OSW at the beginning is undoubtedly strengthened by combustion but recovers an inclination angle θ according to the interaction model without combustion.

The wedge angle $\theta_f - \delta$ for the burnt gases of B is then not negligible (8° to 10°) and corresponds to a normal flame burning velocity of about 100–120 m/s. Experimental δ appears slightly reduced in com-

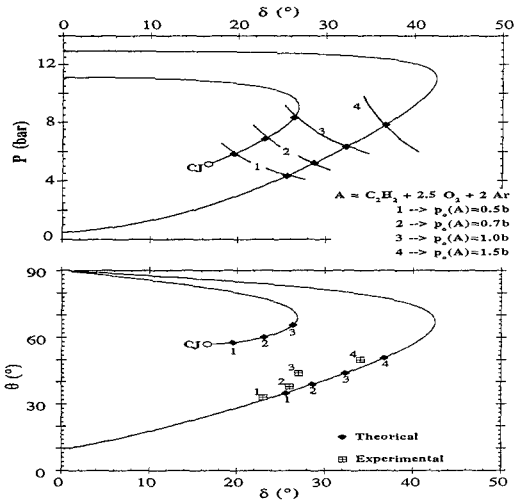

FIG. 3. Scheme of different solutions of interaction in P, δ, and θ, δ planes between CH_4-air mixture (p_0 = 0.3 bar, T_0 = 293 K) and C_2H_2 + 2.5O_2 + 2Ar mixture (T_0 = 293 K) at different initial pressures p_0(A) = 0.5 (case 1), 0.7 (case 2), 1.0 (case 3), and 1.5 (case 4).

parison with lateral expansion of A in a nonreactive mixture (cf. Fig. 3, case 3). The temperature T_s is 1220 K, and the degree of overdrive of possible ODW is D/D_{CJ} = 1.085.

For p_0 = 1.2 bar, which corresponds to the possible upper limit condition for obtaining ODW with $D/D_{CJ} \cong 1.1$, because the expansion polar of A is tangent to the detonation polar of B, the same behavior as the previous case is observed with $T_s \cong$ 1300 K. Beyond this last value of p_0(A), no possible stable ODW supported by an oblique piston can be achieved for the lack of intersection between the expansion polar of A and the detonation polar of B. Nevertheless, detonation may exist but cannot be explained by the postulated mechanism. An example of such a situation is given in Fig. 3 (case 4) and in Fig. 6, where p_0(A) = 1.5 bar. The phenomenon shows the same features as in the cases considered above. The flame remains very close to the OSW for a long time and progressively deviates from it. T_s is roughly 1480 K and remains too low to induce the detonation regime.

The λ_{CJ} cell size of the CJ detonation in the CH_4-air stoichiometric mixture at p_0 = 0.3 bar and T_0 = 293 K can be estimated to be in the order of 1 m, starting from the value of 0.3 m given at p_0 = 1 bar, T_0 = 293 K, and assuming that λ_{CJ} varies as p_0^{-1}. Possible ODW regimes expected in our experiments exhibit variations of D/D_{CJ} ranging from 1 to 1.1. Based on Eq. (2) with T_{ZND} = 1640 K and $E_A \cong 44$ kcal/mole for the CH_4-air mixture, cell size may be reduced to a maximum factor of 10, corresponding

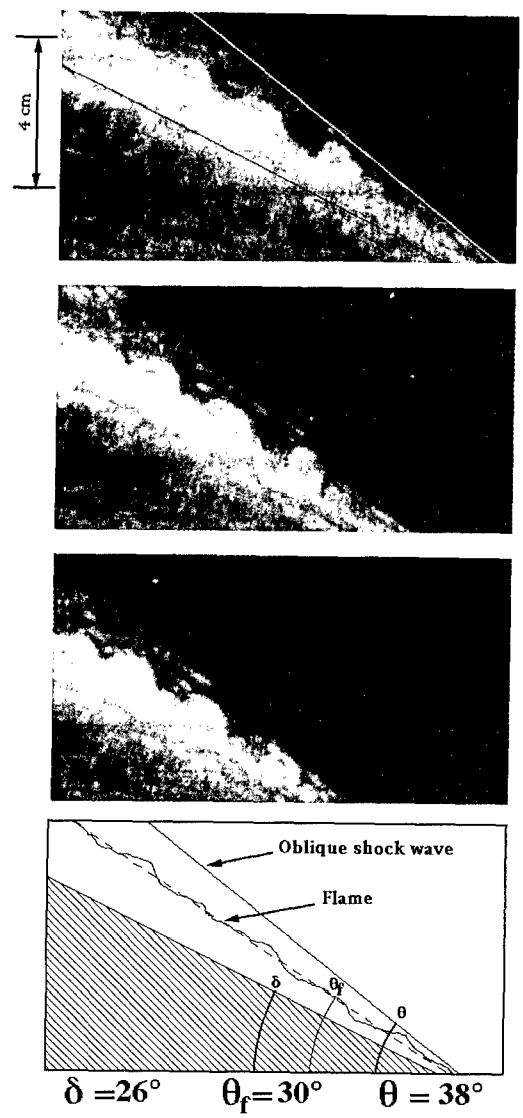

FIG. 4. Schlieren photographs of oblique shock waves with oblique flames in CH_4-air mixtures (p_0 = 0.3 bar, T_0 = 293 K) for M = 6 (A = C_2H_2 + 2.5O_2 + 2Ar, p_0(A) = 0.7 bar).

to λ = 0.1 m, which remains very large in comparison to the H_2-air system used ($\lambda \sim$ 28 mm).

A few experiments were performed with the same mixture with M = 5.5. The range of possibility of detonation is narrower in this case. The phenomena follow the same trend as for M = 6. The oblique flame behind the OSW is observed when T_s is about 1000–1050 K. Finally, we never observed an ODW in the two cases at M = 5.5 and M = 6.

Thus, we can conclude, for intermediate flow

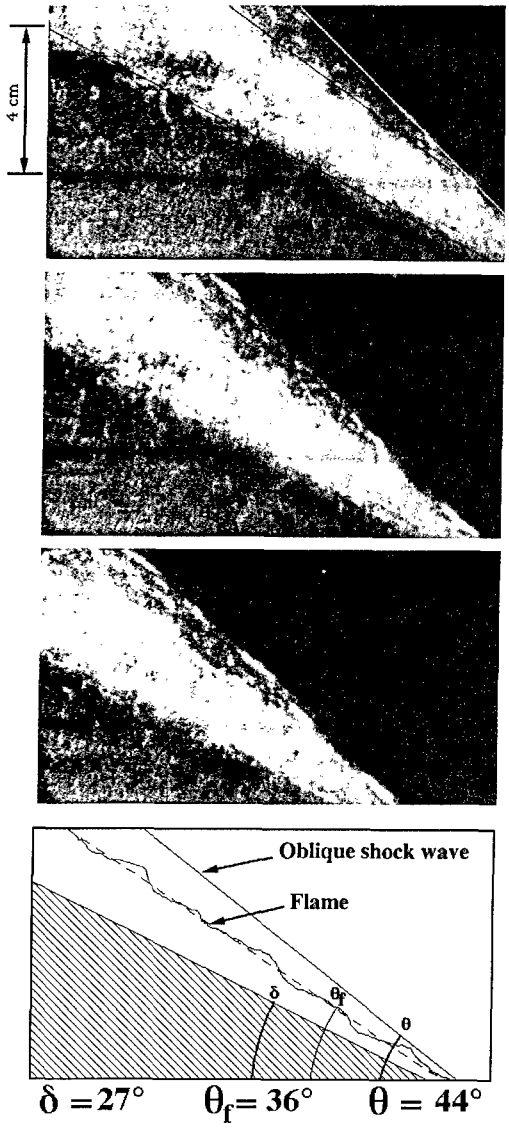

FIG. 5. Schlieren photographs of oblique shock waves with oblique flames in CH_4-air mixtures (p_0 = 0.3 bar, T_0 = 293 K) for M = 6 (A = C_2H_2 + 2.5O_2 + 2Ar, p_0(A) = 1 bar).

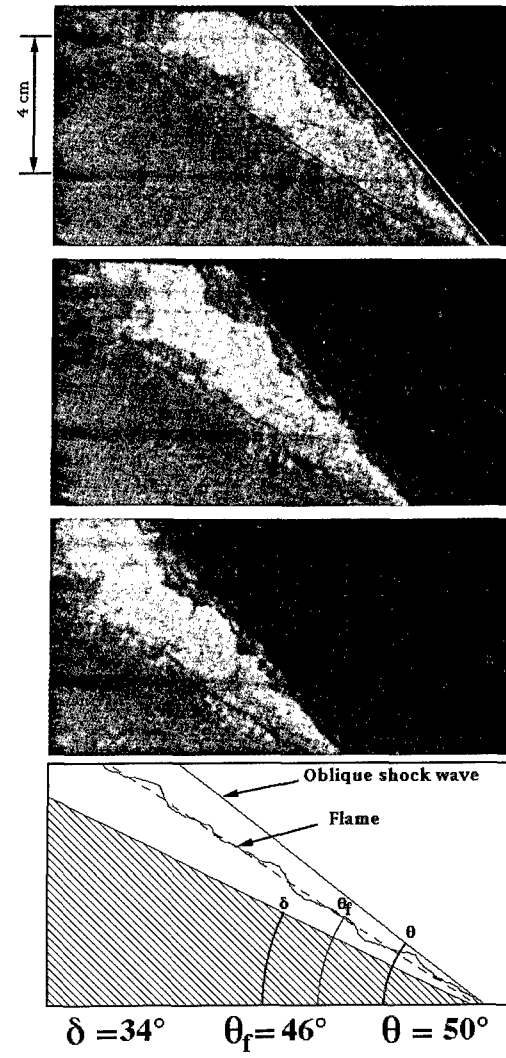

FIG. 6. Schlieren photographs of oblique shock waves with oblique flames in CH_4-air mixtures (p_0 = 0.3 bar, T_0 = 293 K) for M = 6 (A = C_2H_2 + 2.5O_2 + 2Ar, p_0(A) = 1.5 bar).

Mach number M = 6, that the onset of the detonation regime stabilized as an ODW in C_nH_m-air or H_2-air mixtures where the normal CJ detonation propagates with $M_{CJ} \cong 5$ depends drastically on the sensitivity to detonation of the mixture used. The ODW of H_2-air stoichiometric mixture is very easy to obtain; however, this is not the case for the CH_4-air mixtures.

Conclusions

Conditions for the emergence of combustion behind an oblique shock wave (OSW) created by an artificial wedge in stoichiometric H_2-air and CH_4-air mixtures at initial pressure p_0, respectively, of 0.5 and 0.3 bar and temperature T_0 = 293 K are studied for Mach number M = 6 and for different inclination angles θ of the shock.

Depending on the strength of the OSW (i.e., the angle θ), two regimes of stabilization of combustion were observed:

1. The OSW followed by an oblique flame initiated at the apex of the wedge for postshock temperature $T_s \geq 800$ K and 1000–1050 K for H_2-air and CH_4-air mixtures, respectively.

   The normal burning velocity of mixtures ranges from 50 to 120 m/s, which does not significantly alter the characteristics of the OSW obtained without combustion.
2. The ODW regime that appears in H_2-air mixtures for $T_S \geq 1000$ K and that corresponds to conditions close to the CJ points among the possible solutions given by the detonation polar of the mixture.

No ODWs have been observed in CH_4-air mixtures, despite the large possibility of solutions belonging to the detonation polar of that mixture. Temperature T_s has been increased up to 1480 K without initiating the detonation regime. Once more, this mixture (well known as very difficult to detonate) was not initiated in detonation regime in our experiments.

Nevertheless, for higher Mach number M, detonation in CH_4-air mixtures may be obtained, because the range of the degree of overdrive can be larger, and then, λ may be considerably shortened.

Acknowledgments

This work was supported by the *Direction des Recherches, Etudes et Techniques* (DRET) of the French military organization *Délégation Générale pour l'Armement* (DRG).

REFERENCES

1. Adelman, H. G., Cambier, J. L., Menees, G. P., and Balboni, J. A., AIAA Paper No. 88-0097, Jan., 1988.
2. Wang, Y. Y., Fujiwara, T., Aoki, T., Arawaka, J., and Ishiguro, T., AIAA Paper No. 88-0478, 1988.
3. Pratt, D. T., Humphrey, J. W., and Genn, D. E., *J. Propul. Power*, 7:837 (1991).
4. Hertzberg, A., Bruckner, A. P., and Bogdanoff, D. W., *AIAA J:* 26:195–203 (1988).
5. Li, C., Kailasanath, K., and Oran, E. S., AAIA Meeting, 92-0089, 1992.
6. Li, C., Kailasanath, K., and Oran, E. S., *Progr. Astronaut. Aeronaut.* 153:231–240 (1991).
7. Dabora, E. K., Nicholls, J. A., and Morisson, R. B., *Tenth Symposium (International) on Combustion*, The Combustion Institute, 1965, p. 81.
8. Liu, J. C., Liou, J. J., Sichel, M., Kauffman, C. W., and Nicholls, J. A., *Twenty-First Symposium (International) on Combustion*, The Combustion Institute, Pittsburgh, 1986, pp. 1639–1647.
9. Dabora, E. K., Desbordes, D., Guerraud, C., and Wagner, H. G., *Progr. Astronaut. Aeronaut.* 133:187–201 (1991).
10. Dabora, E. K., Wagner, H. G., and Desbordes, D., *Ann. Phys. Fr.* 14:637–639 (1989).
11. Desbordes, D., Hamada, L., and Guerraud, C., *Preprints of the 14th ICDERS*, Coimbra, Portugal, 1993.
12. Bull, D. C., Elsworth, J. E., Shuff, P. J., and Metcalfe, E., *Combust. Flame* 45:7–22 (1982).
13. Broda, J. C., and Dabora, E. K., *Preprints of the 14th ICDERS*, Coimbra, Portugal, 1993.
14. Hamada, L., PH.D. Thesis, University of Poitiers, France, 1992.
15. Foster, R., and Clarke, J. F., *Aeronaut. Q.* 516:80–90 (1968).
16. Desbordes, D., *Progr. Astronaut. Aeronaut.* 114:170–184 (1988).
17. Moen, I. O., Funk, J. W., Ward, S. A., Rude, G. M., and Thibault, P. A., *Progr. Astronaut. Aeronaut.* 94:55–79 (1983).

Twenty-Fifth Symposium (International) on Combustion/The Combustion Institute, 1994/pp. 61–64

WEAK AND STRONG IGNITION WITHIN THE SCOPE OF SPONTANEOUS FLAME CONCEPT

A. M. BARTENEV AND B. E. GELFAND
Institute of Chemical Physics, Russian Academy of Sciences
117977 ul. Kosygina, 4 Moscow, Russia

The concept of spontaneous onset of detonation was applied to the problem of distinguishing mild and strong regimes of ignition. It was assumed that the strong ignition is connected with the coupling between spontaneous reaction front and gasdynamic perturbations inside the initiating exothermic center. The initiating center was considered as a region with increased temperature distributed according to the Gaussian law. Critical conditions for strong-mild ignition cutoff were found. The results show a good quantitative agreement with experimental and theoretical studies on ignition in an hydrogen-oxygen stoichiometric mixture. A decisive role of temperature fluctuations on the order of 10–20 K is pointed out. It was shown that these fluctuations may result from the heating in sound waves at the initial stage of shock-wave reflection.

Introduction

The process of combustible gaseous mixture self-ignition is usually investigated using a shock-tube facility. Sharp heating up to high temperature behind reflected shock waves permits the measurement of self-ignition delays as well as the study of specific features of explosion development. Depending on the initial conditions behind a shock wave, two different cases of ignition can be indicated, namely strong (sharp) and mild (weak) ignition. The regimes were revealed in hydrogen and hydrocarbon mixtures with air or pure oxygen [1,2,16]. Strong regimes are characterized by a sharp increase in pressure and temperature after ignition, and in the case of mild ignition, the pressure increase is smooth and substantially lower. Experimental observations allow the distinction of the following specific features of ignition phenomena [1–4].

In the case of strong ignition, the reaction initiates in the vicinity of the end wall. It occupies practically the whole cross section of the tube. The reaction front coupled with the shock front propagates into the direction of the leading shock. Having detonation-like structure, the front overtakes the primary shock, and a Chapman–Jouguet detonation is established.

Another situation exists in the case of mild ignition. Schlieren photographs clearly show that the reaction waves originate from spatially distributed exothermic initiating centers. These centers have an elevated temperature with respect to the surroundings and are often referred to as "hot spots." Such centers can be formed in various ways, for example, as a result of irregularities in the shock front, nonideal reflection, etc. Two-dimensional calculations performed in Ref. 12 show the possibility of temperature fluctuations because of boundary layer effects.

Studies have been performed experimentally and theoretically [see overview in Refs. 1 through 4] to obtain the cutoff conditions that divide different regimes of self-ignition. On the basis of the chemical nature of the process, it was proposed in Ref. 13 that the boundary be the second ignition limit extended to the domain of high pressures. The gasdynamic aspect of explosions was taken into account in Refs. 1 and 2 where a dividing line in pressure-temperature coordinates was drawn to suit the experimental data obtained. It was also found in Refs. 1 and 2 that condition $(\partial\tau_i/\partial T)_p = -2$ μs/K fits the experimental curve. Numerical calculations in Refs. 3 and 4 showed the importance of chemical induction sensitivity to sound-wave perturbations and, hence, to the process of self-ignition and character of pressure escalation.

Recently, a concept of spontaneous detonation initiation in nonuniformly preheated gas mixtures was formulated [5–11]. This idea assumes that the coupling between gasdynamic and chemical processes starts when the velocity of the spontaneous flame attains a certain characteristic value. The following velocities were specified in Ref. 5 as being responsible for explosive processes: spontaneous flame velocity $u_{sp} = \mathrm{grad}(\tau_i)/\mathrm{grad}^2(\tau_i)$, sound velocity a, and detonation velocity D. The relation between these velocities provides the conditions for detonation escalation in combustible mixtures. Numerical calculations in Refs. 6 through 10 showed that detonation onset in various systems with spatially distributed ignition delays occurs when the spontaneous flame velocity be-

comes equal to the local sound velocity. The distribution of ignition delay can be formed as a result of non uniform preheating or concentration gradient. At the point of chemical and gasdynamic processes coupling, a strong shock wave arises. This shock wave accelerates rapidly and finally escalates into detonation. The onset of detonation according to the mechanism of spontaneous flame acceleration proceeds within a certain spatial domain. Characteristic sizes of the domain are approximately in the same order as the sizes of nonuniformities resulting from nonideal premixing or temperature fluctuations. Due to the fact that a spotty character is a specific feature of mild ignition, it seems reasonable to consider the onset of detonation in terms of the spontaneous flame concept.

To apply the concept of spontaneous flames to the problem of distinguishing mild and strong ignition, we assume the following hypothesis. If the spontaneous flame velocity is much greater than sound velocity in the exothermic center, then no shock wave forms inside this center. The combustible mixture inside the exothermic center burns out almost instantaneously and serves as a heat source from spark ignition. Maximal pressure during combustion slightly exceeds explosion pressure. If the condition of shock formation is satisfied, then the shock wave will appear in the initiating center, and the ignition will be strong. Formation of a shock wave causes the mechanism of amplification and onset of detonation.

The probabilistic character of fluctuations should be noted. If most of the initiating centers do not satisfy the conditions of shock formation, then the initiation will be mild, although some amplification of pressure waves from several neighboring centers is plausible.

Problem Formulation

We assume the initiating center has a temperature profile distributed according to Gaussian law.

$$T = T_0 + \frac{1}{\sigma\sqrt{2\pi}} e^{-x^2/2\sigma^2}$$

Here T is the temperature inside the exothermic center, T_0 is the base temperature, and σ is the dispersion of the distribution. This distribution was chosen with the aim of describing mathematically the greatest possible arbitrary energy sources. In fact, most of temperature fluctuations resulting from heat conduction processes obey this distribution (Gaussian law is the basic solution of the heat conduction problem). Moreover, acoustic perturbation will take a Gaussian shape if we take into account dissipation processes or the effect of sound-wave energy absorption under reflection conditions [15].

We can substitute the maximal overtemperature ΔT for the dispersion parameter. Then the distribution takes the form

$$T = T_0 + \Delta T e^{-x^2 \Delta T^2 \pi}. \tag{1}$$

This assumption guarantees that the total heat flux into the initiating center remains the same, independent of the method of heat addition. It means that the value of the integral

$$2 \int_0^\infty \Delta T e^{-x^2 \Delta T^2 \pi}\, dx$$

is constant.

The average temperature in the exothermic region remains uniform because of the low value of the integral (1 K m). Then the velocity of spontaneous flame propagation in one-dimensional geometry is defined by the formula

$$\mu_{sp}^{-1} = \frac{\partial \tau_i}{\partial x} = \frac{\partial \tau_i}{\partial T}\frac{\partial T}{\partial x}. \tag{2}$$

Using Eq. (1), one can write the following expression for the temperature gradient:

$$\frac{\partial T}{\partial x} = -2\Delta T(T - T_0)\left[\pi \ln\left(\frac{\Delta T}{T - T_0}\right)\right]^{1/2}. \tag{3}$$

We use Meyer and Oppenheim's [1] approach for $(\partial \tau_i/\partial T)_p$ to evaluate the spontaneous flame velocity:

$$\ln(\tau_i) = A + B/T + Cp_0^n e^{D/T} - \ln(Ep_0/T)$$

$$(\partial \tau_i/\partial T)_p = \tau_i(T - B - CDp^n e^{(D/T)})/T^2. \tag{4}$$

Coefficients are as follows: $A = -10.7$ ln (μs mole/L), $B = 9130$ (K) ln(μs mole/L). $C = 3\ 10^9$ (atm)$^{-2}$ ln(μs mole/L), $D = 19{,}000$ (K), $n = 2$, $E = 4.06$ (mole K/L atm). Formulas (4) were derived from numerical modeling of the explosion process in a stoichiometric hydrogen-oxygen mixture using a detailed kinetics mechanism. The results of calculations were fitted to experimental data on ignition delays.

The dependence $u_{sp}(x)$ is shown in Fig. 1 for $T_0 = 1000$ K and $P_0 = 1$ atm. At $x = 0$, the velocity of the spontaneous flame is infinite because $dT/dx = 0$. The minimum value of $u_{sp}(x)$ corresponds to the point of inflection on curve $T(x)$. This point shifts to the right if we take into account the effect of pressure wave precompression [11]. However, this fact will not affect the results significantly.

According to the spontaneous flame concept, the condition of shock formation can be written in two ways:

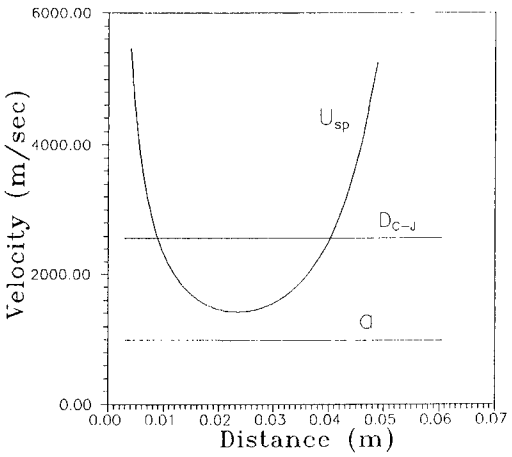

FIG. 1. Distribution of characteristic velocities (spontaneous flame u_{sp}, Chapman–Jouguet detonation D, and sound velocity a) inside initiating center.

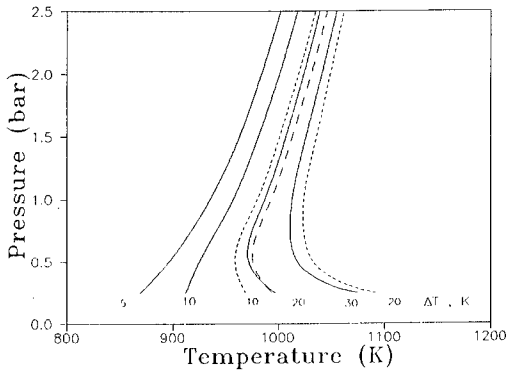

FIG. 2. Calculated boundary curves separating the domains of strong and mild ignition. Solid lines—sound condition (5), dotted lines—detonation condition (5′), dashed line—Myer and Oppenheim condition $(\partial\tau_i/\partial T)_p = -2$ μs/K. Parameter is maximal overtemperature inside exothermic center ΔT (K).

$$u_{sp}(x) = a(x) \tag{5}$$

or

$$u_{sp}(x) = D(x). \tag{5'}$$

Here a is a local sound speed and D is a local velocity of Chapman–Jouguet detonations. Both sound velocity and detonation velocity are functions of temperature, and therefore, they are spatially distributed inside the initiating center. We assume the following expressions for a and D:

$$a(T) = \sqrt{\gamma RT}$$
$$D^2(T) = a^2(T) + (\gamma + 1)Q \cdot\left(1 + \sqrt{1 + \frac{2a^2(T)}{(\gamma + 1)Q}}\right). \tag{6}$$

Here Q is the heat of combustion and γ is the specific heat ratio.

On the basis of the Hugoniot diagram analysis, Short and Dold [11] found that the second condition is responsible for shock formation. However, calculations performed in Refs. 9 and 10 show that the spontaneous flame velocity, being originally infinite, falls below the speed of detonation, and shock formation begins at the point where the first condition is satisfied. In Ref. 14, both conditions were used for evaluation, but an intermediate value was obtained throughout the numerical calculations.

The velocities of detonation and sound are drawn in Fig. 1. One can see that condition (5) as well as condition (5′) can be satisfied in two points. We assume that a boundary between mild and strong ignition corresponds to the case when a unique solution for (5) or (5′) exists.

Results

Thus, we can separate domains of strong and mild ignition on a P-T diagram, as was done in Refs. 1 through 4. Solid lines in Fig. 2 correspond to condition (5), and dotted lines correspond to condition (5′). The ΔT value was taken as a parameter. Equations (2), (3), (4), and (6) were used for the calculations. Strong ignition arises on the right-hand side of the separated curves, and the mild ignition domain is on the left. Also presented in Fig. 2 is a boundary obtained in Refs. 1 and 2. This boundary agrees with the condition $(\partial\tau_i/\partial T)_p = -2$ μs/K found in Refs. 1 and 2 by fitting experimental results. The theoretical background of the condition was given in Ref. 2. Clearly seen is a good agreement between present results and the Meyer and Oppenheim boundary for $\Delta T = 20$ K for (5) and for $\Delta T = 10$ K for (5′). It should be emphasized that the present results were obtained on the basis of the spontaneous flame concept rather than the energy pulse deposit [2].

The increase of fluctuation expands the domain of mild ignition regimes. It confirms the fact that mild ignition has a spotty nature.

From Fig. 2, it follows that the values of $\Delta T =$ 10–20 K become important for dividing regimes of ignition. Values of the same order were obtained in Ref. 14 by numerical calculations using a detailed chemistry mechanism and a full set of gasdynamic equations. Fluctuations of such intensity may be obtained in the case of nonideal reflection or boundary effects. We also propose that these temperature fluctuations can result from the heating in acoustic per-

turbations. Calculations in Refs. 3 and 4 showed that, at the beginning of shock-wave reflection, maximum velocity perturbations are about 60 m/s, and attenuate fast down to values of 1–10 m/s or less. We can evaluate the temperature increase due to velocity perturbations using the following equation [15]:

$$\Delta T = \frac{a\beta T_0}{C_p} v.$$

Here β is the thermal expansion coefficient and v is the amplitude of a sound wave. For $v = 60$ m/s, we can assess that ΔT is about 30 K. This temperature rise corresponds to the critical values obtained (taking into account the decrease in fluctuation amplitude).

Conclusions

This study shows the importance of spontaneous detonation initiation for the problem of mild and strong ignition phenomena. The critical conditions correspond to the possibility of shock-wave formation inside the initiating center. Further escalation of explosion in the case of strong ignition occurs due to the spontaneous initiating detonation mechanism. The boundary condition derived on the basis of the spontaneous flame concept fits experimental and theoretical results obtained by other investigators. It was shown that temperature fluctuations of 10–20 K are the crucial factor for the transition between mild and strong regimes of ignition. This level of temperature fluctuations can be built up as a result of heating in sound waves just after shock-wave reflection.

Nomenclature

a	sound velocity
D	detonation velocity
P	pressure
Q	heat of combustion
T	temperature
ΔT	overtemperature
u	velocity
x	coordinate
$\beta = -(dp/dT)_p$	the thermal expansion coefficient
γ	specific heat ratio
v	amplitude of a sound wave
σ	standard deviation
τ	ignition delay

Indexes

i	ignition
0	initial (basic values)
sp	spontaneous

Acknowledgment

This study was supported by Russian Fund of Fundamental Research.

REFERENCES

1. Meyer, J. W., and Oppenheim, A. K., *Thirteenth Symposium (International) on Combustion*, The Combustion Institute, Pittsburgh, 1977, pp. 1153–1164.
2. Oppenheim, A. K., *Phil. Trans. R. Soc. Lond. A* 3115:471–508 (1985).
3. Oran, E. S., Young, T. R., and Boris, J. P., *Combust. Flame* 48:135–148 (1982).
4. Oran, E. S., and Boris, J. P., *Combust. Flame* 48:149–161 (1982).
5. Zel'dovich, Ya. B., *Combust. Flame* 39:211–214 (1980).
6. Zel'dovich, Ya. B., Librovich, V. B., Makhviladze, G. M., and Sivashinsky, G. I. *Astronaut. Acta* 15:313–321 (1970).
7. Gelfand, B. E., Polenov, A. N., Frolov, S. M., and Tsyganov, S. A., *Fiz. Gorenia Vzriva* 21:118–123 (1985).
8. Gelfand, B. E., Makhviladze, G. M., Rogatykh, D. I., and Frolov, S. M., *Spontaneous Explosive Regimes in the Areas with Temperature and Concentration Nonuniformities*, I, Preprint Institute of Applied Mechanics, USSR Academy of Science, No. 358, 1988.
9. Zel'dovich, Ya. B., Gelfand, B. E., Tsyganov, S. A., Frolov, S. M., and Polenov, A. N., *Eleventh Colloquium (International) on Dynamics of Explosions and Reactive Systems*, Warsaw University of Technology, Warsaw, 1988, p. 89.
10. Gelfand, B. E., Frolov, S. M., and Tsyganov, S. A., *Khim. Fiz.* 8:655 (1989).
11. Short, M., and Dold, J. W., in *Dynamic Aspects of Explosion Phenomena* (A. L. Kuhl, J. C. Leyer, A. A. Borisov, W. A. Sirignano, Eds.), American Institute of Aeronautics and Astronautics, 1993, Vol. 154, pp. 59–75.
12. Takano, Y., in *Shock Waves* (K. Takayama, Ed.) Springer-Verlag, Japan, 1991, Vol. 2, p. 869.
13. Voevodsky, V. V., and Soloukhin, R. I., *Tenth Symposium (International) on Combustion*, The Combustion Institute, Pittsburgh, 1965, p. 279.
14. Frolov, S. M., Mack, A., and Roth, P., *Fourteenth International Colloquium on Dynamics of Explosions and Reactive Systems*, University of Coimbra, Portugal, Vol. 2, 1993, C1.4.1.
15. Landau, L. D., and Lifshitz, E. M., *Theoretical Physics, Hydrodynamics*, Nauka Publishers, Moscow, Vol. 6, 1986.
16. Fieweger, K., Yao, J., Ciezki, H., and Adomeit, G., *Kolloquium des sonderforschungs-bereich 224, Motorishe verbrannung*, RWTH Aachen, Germany, 1993, p. 81.

Twenty-Fifth Symposium (International) on Combustion/The Combustion Institute, 1994/pp. 65–71

CRITICAL DIAMETER FOR THE TRANSMISSION OF A DETONATION WAVE INTO A POROUS MEDIUM

ARISTIDIS MAKRIS, TAE J. OH, JOHN H. S. LEE AND ROM KNYSTAUTAS
McGill University
Montreal, Canada

An experimental investigation has been undertaken to elucidate the existence of a critical diameter for the transmission of gaseous detonation into a porous medium. A Chapman–Jouguet (CJ) detonation is first established in a tube and allowed to transmit through an orifice plate into a porous medium comprised of inert spheres of equal diameter. It is found that detonation can successfully transmit past the orifice for diameters much smaller than the normal critical diameter (d_c) of the mixture. An immediate transition from detonation to quasi-detonation normally takes place upon wave entry in the porous medium. Failure of detonation is observed to take place downstream of the orifice in the near-limit regime and is followed by deflagration to detonation transition (DDT) within the porous medium. Wave velocities in the porous medium are found to be identical to the corresponding values measured for direct transmission (without an orifice). For subcritical conditions, there is complete quenching of combustion in the pores. The critical composition (lean and rich) for mixtures with high activation energy is found to be practically the same as the propagation limits in the porous medium without an orifice. This indicates that the phenomenon is governed by the smallest physical dimension of the pore size, and thus a local failure mechanism exists. In mixtures highly diluted with argon, i.e., (C_2H_2-O_2) + 75% Ar, which have a lower activation energy and for which the "$d_c = 13\lambda$" correlation (where λ is the cell size) is known to break down, the critical composition appears to depend on the orifice diameter. The orifice now introduces a larger controlling length scale at the limits compared to the pore size, indicating that a global failure mechanism may prevail for such mixtures. Present findings are consistent with a local and global failure mechanism for normal detonation failure recently proposed by Lee.

Introduction

The transmission of a detonation wave from a circular tube into a sudden area enlargement has been studied extensively for the past decade [1–4]. It was found for most mixtures that the critical tube diameter (d_c) scales with the detonation cell size (λ) according to the $d_c = 13\lambda$ correlation. Exceptions to this correlation were mixtures with high argon dilution [5]. Lee [6] recently forwarded an explanation for this discrepancy by proposing different failure mechanisms, i.e., local failure mechanism for the high activation energy mixtures where the 13λ correlation applies, and a global failure mechanism for mixtures where the 13λ correlation breaks down. Detonation limits in tubes also appear to be governed by a local and a global failure mechanism for the different types of mixtures.

When a gaseous detonation transmits into a porous medium, Makris and coworkers [7–9] found that the ensuing propagation phenomenon is governed by the relative length scales describing the sensitivity of the detonable mixture (i.e., λ or d_c) and the properties of the porous medium [i.e., the average pore size (d_p) or, equivalently, the channel size connecting the pores]. In fact, the quasi-detonation velocity, normalized with respect to the Chapman–Jouguet (J) value (V/V_{CJ}), in different gaseous fuel-oxidizers over a broad range of particle sizes was shown to correlate with the ratio d_c/d_p. The pore size is a local length scale controlling the detailed diffraction processes of the detonation wave in the voids. Thus, one may consider the detonation in a porous medium to be controlled by the local phenomenon of transmission through the passages interconnecting the pores. It would be of great interest to investigate the critical diameter for the transmission of a detonation into a porous medium. If the critical diameter is greater than the pore size, this would imply the existence of a larger global length scale controlling detonation failure in the porous medium. However, if the smaller dimension of the pore still dominates, then wave propagation would appear to be an entirely local phenomenon. This could imply that the propagation limits in the porous medium are governed by the smallest length scale, and consequently, a critical diameter does not exist. It is also of interest to investigate mixtures with high argon dilution, for which a global mechanism of failure determines the limits [6] of normal gaseous detonation in a tube.

This paper investigates the transmission of a detonation into a porous medium through an orifice, to elucidate on the limit mechanism of local vs global failure. Experimental results are presented for different gaseous fuel-oxidizers, including a case of high argon dilution, (C_2H_2-O_2) + 75% Ar. All tests are conducted at atmospheric initial pressure, and the mixture sensitivity is controlled by the equivalence ratio. A limited study of the critical tube diameter (d_c) for the different fuel mixtures was also undertaken to provide a basis for comparing the critical orifice diameter for detonation transmission in the porous medium.

Experimental Details

The apparatus used for the present investigation is a vertical detonation tube with inner diameter of 146.05 mm and is comprised of two sections. The lower section contains the porous medium and is 1.1-m long. It is attached to the upper section (2.575 m in length), which contains only detonable mixture, by adjoining flanges. Orifice plates can be secured within a central adjoining flange situated immediately upstream of the interface with the porous medium. The orifice plates are made of steel (9.5-mm thick) and have a circular hole in the center. Porous media consist of alumina (ceramic) spheres of equal diameter (D = 12.7 mm). A few of the common detonable mixtures were tested (C_3H_8-O_2, H_2-O_2, CH_4-O_2, C_2H_4-O_2), including (C_2H_2-O_2) + 75% Ar. The mixture composition is varied by changing the equivalence ratio from lean to rich. For each test, the detonation tube is evacuated to better than 100 Pa, and fuel-oxidizer mixtures are prepared by partial pressures to a total initial pressure of 1 atm. A recirculation pump is then used to mix the fuel in a closed loop, for a duration nominally equivalent to displacing at least seven tube volumes. To ensure careful control of the pore size, the spheres comprising the porous medium are thoroughly washed and dried on a frequent basis. In the determination of the critical tube diameter (d_c) for the different fuels, the porous medium downstream of the orifice plate was replaced entirely with detonable mixture. By varying the mixture composition for each orifice diameter, it was then possible to determine the variation of d_c over a range of Φ, provided that the ratio of tube to orifice diameter was at least greater than 4–5.

Direct initiation of detonation in the mixture at the top end of the tube was effected by a high-energy spark from a 0.6-μF capacitor bank, charged to 24-kV DC. For the less sensitive mixtures near the detonability limits, a solid explosive detonator (#12 blasting cap), sometimes wrapped with various lengths of primachord (booster), was used to initiate detonation. To ensure that a steadily propagating CJ wave enters the porous bed, the velocity was monitored over a length of tube immediately upstream ($\approx$0.6 m) of the interface with the particles using two phototransistors (0.499 m apart). PCB piezoelectric pressure transducers (1-μs rise time), placed 150-mm apart and starting at a distance of 120 mm downstream of the orifice plate, were also used to measure the combustion wave velocities and the pressure profiles in the porous medium. The diagnostic probes were all connected through appropriate power supplies to a four-channel computer scope, having a total sampling capability of 1 MHz (i.e., 4-μs sampling period per channel).

Results and Discussion

It is not presently clear whether the limits for detonation transmission into a porous medium are governed by a local or a global mechanism. Normal detonation in a tube is known to fail when subjected to an abrupt area expansion if the tube diameter (d) is below a certain critical value, i.e., $d < d_c$, where $d_c = 13\lambda$ for most mixtures [1–4]. The existence of a critical diameter for the case of a porous medium has not been previously established. A porous medium is known to attenuate the propagation of normal detonation, as evidenced by the detriment that is measured in the velocity and pressure associated with the wave compared with the corresponding Chapman–Jouguet values. At the same time, however, a porous medium assists the propagation of detonation via quasi-detonation, and allows for a gradual transition (as opposed to abrupt in rough tubes [15]) to a high-speed deflagration predominating near the limits [7–10]. This provides for a much wider and continuous velocity range ($0.25 < V/V_{CJ} < 1$), with values substantially below the lowest observed prior to normal detonation failure in a tube (0.80–$0.85V_{CJ}$) [5,11]. It is thus not apparent how a critical diameter for detonation transmission in a porous medium would scale relative to the normal value of d_c for the mixture. Information on d_c itself, in fuel-oxygen mixtures at atmospheric initial pressure, is very limited. To provide a basis for comparison, the critical tube diameter experiment has been repeated for different fuel mixtures of interest.

A CJ detonation is established at the top end of the tube and allowed to transmit across an orifice plate. The mixture composition (Φ) is varied to get the critical condition for each orifice diameter. The variation of d_c with Φ for selected mixtures is presented in Fig. 1. Also plotted on the same set of axes are d_c data at $\Phi = 1$, based on direct measurements [3] and extrapolation from low initial pressures [4]. These data at $\Phi = 1$ satisfy the 13λ correlation and agree with present measurements that cover a much wider range of Φ. Although the validity of this correlation is not yet proven for mixtures of H_2-O_2, C_3H_8-O_2, C_2H_4-O_2 across their entire detonability

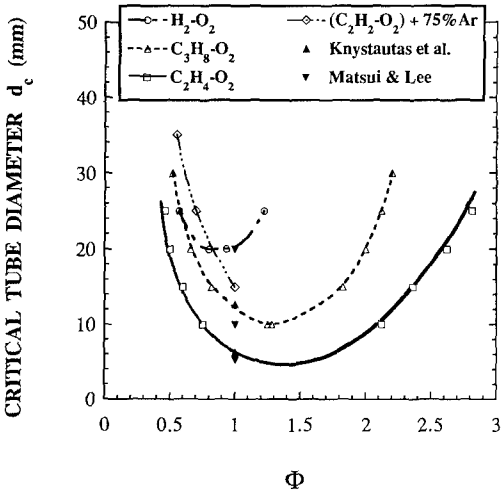

FIG. 1. Variation of critical tube diameter (d_c) with equivalence ratio (Φ) for the following mixtures: H_2-O_2, C_3H_8-O_2, C_2H_4-O_2, and (C_2H_2-O_2) + 75% Ar at P_0 = 1 atm. Also plotted are data for d_c at Φ = 1.0, based on direct measurements by Knystautas et al. [3], and extrapolation by Matsui and Lee [4].

range, the corresponding fuel-air mixtures satisfy $d_c = 13\lambda$ for all Φ [12], suggesting that the same may apply for fuel-oxygen mixtures as well. On the other hand, it is firmly established that $d_c = 13\lambda$ breaks down for (C_2H_2-O_2) + 75% Ar. Values for d_c in fuel-oxygen mixtures are at least an order of magnitude smaller than the corresponding values in fuel-air mixtures. For instance, $d_c \approx 20.5$ mm in a mixture of H_2-O_2 at $\Phi = 1$, while for the same composition in H_2-air, $d_c \approx 190$ mm [13]. Except for the case of H_2-O_2, the minimum d_c (or most sensitive composition) corresponds to a mixture composition slightly on the rich side ($\Phi > 1$), rather than at stoichiometric. This is consistent with what is observed for fuel-air mixtures by Knystautas et al. [12] and agrees with theoretical predictions based on the 1-D ZND induction length by Westbrook and Urtiew [13]. Note that, for fuel-O_2 mixtures, the relative sensitivities of the various fuels are different from those of the corresponding fuel-air mixtures [12]. For example, in fuel-air mixtures, H_2 is more sensitive than C_2H_4, which in turn is more sensitive than C_3H_8. However, for fuel-O_2 mixtures, C_2H_4 is more sensitive than both C_3H_8 and H_2, while the argon-diluted mixtures appear to be the least sensitive (at least for $\Phi < 0.8$). Because of the large value of d_c in CH_4-O_2 (i.e., $d_c \approx 51$ mm at $\Phi = 1$ [4]) compared with the diameter of the detonation tube, it was not possible to study the variation of d_c with Φ for this fuel.

Having established the critical diameter for the various mixtures, we proceed to determine the critical orifice diameter for transmission of a CJ detonation into a porous medium. The mixture on both sides of the orifice plate (i.e., detonation tube upstream and porous bed downstream) is the same. There are essentially three variables in this problem: the mixture composition (Φ), which determines a detonation length scale (d_c), the orifice diameter, and a characteristic length scale describing the porous medium (d_p). For convenience in carrying out the experiments, the porous medium was fixed, and for each orifice size, the mixture composition was varied to establish the critical condition. Figure 2a shows a typical pressure record downstream of the orifice plate, for the case of successful transmission into the porous medium, in a mixture of CH_4-O_2 at $\Phi = 0.25$

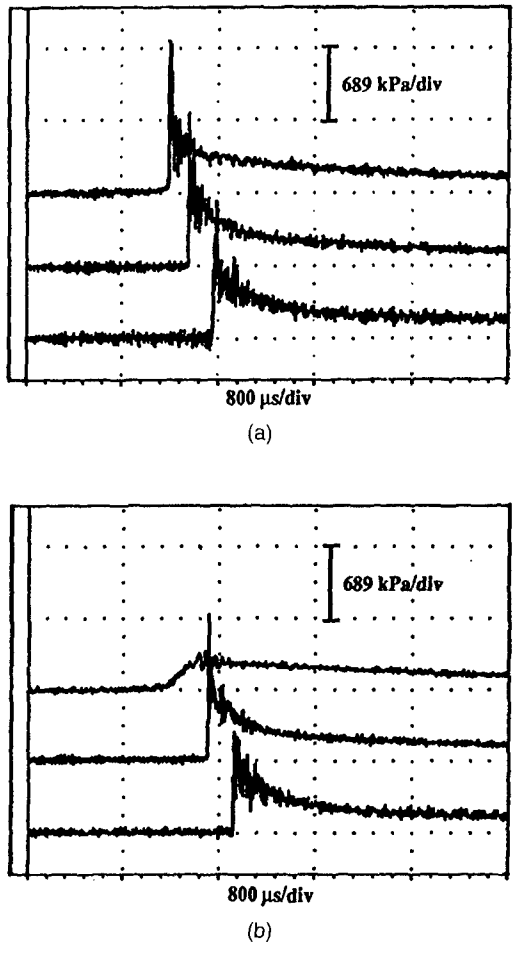

FIG. 2. Pressure profile of a transmitted detonation in CH_4-O_2 mixture across an orifice (3 mm in diameter), in a porous medium comprised of inert spheres (D = 12.7 mm): (a) immediate transmission to quasi-detonation at Φ = 0.25, (b) detonation failure and retransition within porous medium at Φ = 0.225.

and an orifice diameter of 3 mm. The pressure profile indicates a quasi-steady wave propagation of non-decaying amplitude. The wave shape is qualitatively similar to that for normal detonation waves, i.e., sharp pressure rise followed by the expansion in the Taylor wave. Velocities for successful transmission across the orifice are identical to those previously measured [7,8] for direct transmission into the porous medium without an orifice (i.e., $0.3 < V/V_{CJ} < 1$). An estimate of the velocity in the initial segment of the porous bed (120 mm) downstream of the orifice, based on the elapsed time between detonation arrival at the orifice and the onset of the pressure rise at the position of the first pressure transducer within the porous medium, indicates that there is an immediate transition from detonation to quasi-detonation at the interface. It should be noted that the critical tube diameter for CH_4-O_2, at a far more sensitive composition of $\Phi = 1$, is approximately 51 mm [4], which is at least an order of magnitude greater than the orifice diameter of 3 mm.

As the composition limits for direct transmission into the porous medium [8,9] are approached, the detonation fails immediately downstream of the orifice plate. This is illustrated by the absence of a sharp pressure rise in the top trace of the pressure record presented in Fig. 2b, corresponding to a mixture of CH_4-O_2 at $\Phi = 0.225$ and an orifice diameter of 3 mm. The lean propagation limit reported by Makris and coworkers [8,9] for CH_4-O_2 in the same porous medium (without an orifice) is $\Phi = 0.2$. Figure 2b also indicates that the failed detonation retransits back to quasi-detonation in the porous medium, and sharp pressure jumps are once again detected at subsequent locations along the tube (traces 2 and 3). Velocities measured after retransition were found to be in full accord with values reported for direct transmission into the medium in the same mixture [7,8]. We justify the use of the term "retransition" to detonation rather than "reinitiation" (as in the case of normal transmission across an area expansion for supercritical conditions), because the time interval between failure and reappearance of detonation is long. This strongly supports the existence of a definite deflagration regime. Indeed, if one estimates the averaged wave velocity in this initial segment of the porous medium, it is found to be even below that for quasi-detonation, e.g., 50–300 m/s. In the normal case of detonation transmission through an orifice, transition back to detonation is not observed once the detonation has failed, or completely decoupled. Apparently, the presence of a porous medium downstream of an abrupt area expansion assists the retransition to quasi-detonation (or high-speed turbulent deflagration) within a relatively short distance. It has been illustrated [7,9] that shock-wave–particle interactions within the medium are able to generate sites of very high temperature, or "hot spots," to reinitiate detonation at discrete points across the wave front and thereafter sustain the propagation of quasi-detonation.

It is interesting to note that, if a weak spark is used to ignite the near-limit mixture described in Fig. 2b, rather than ignition via transmission through the orifice, transition from deflagration to detonation (DDT) is not observed over the length of the porous medium. This suggests that the strong jet ignition of the transmission through the orifice (for subcritical conditions) induces DDT, whereas a weak spark ignition failed to cause significant flame acceleration leading to DDT in the porous medium. It is also of interest to note that, when transmission was not successful (including DDT), there is no combustion at all detected in the porous medium. This is characterized by a rapid decay in the pressure profile, rather than the emergence of a sharp pressure front. If a weak spark is used to ignite the same mixture without the orifice, a slow flame (5–50 m/s) can propagate over the full length of the porous medium; however, for subcritical transmission of detonation through the orifice, all combustion is quenched in the pores. This indicates that the strong jet ignition provides a different quenching mechanism compared with that for slow laminar flame quenching, where conductive heat losses dominate [14]. A recent study by Makris [7] illustrates that ignition transfer near the limits for direct detonation transmission into a porous medium is via turbulent jetting of hot combustion products through the interstitial sites and the subsequent entrainment of the unburnt mixture. Excessive cooling from the turbulent mixing processes in the pores can lead to the complete extinction of combustion. The quenching mechanism in this case is essentially described by the "gasdynamic quenching regime" [14,15].

For the case of a porous medium ($D = 12.7$ mm), the results for C_3H_8-O_2, CH_4-O_2, and H_2-O_2 are given in Figs. 3a through 3c, respectively. In Fig. 3, the velocity of the transmitted waves downstream of the orifice is plotted against Φ for different orifice diameters (25, 10, and 3 mm). Also plotted is a curve fit of the velocity data for direct transmission (without an orifice) in the same porous medium [7,8]. The limiting compositions (lean and rich) are denoted as the left and right extremities of the solid curve in Fig. 3. For successful transmission, it can readily be observed that velocities appear to be independent of orifice diameter (up to a minimum size of 3 mm), and agree with the curve fit of velocity data for the case of direct transmission. This indicates that the propagation phenomenon is governed by the local environment, and the dynamics of the combustion products do not really influence propagation. The ability to correlate quasi-detonation velocities in porous media using d_c/d_p [8] suggests that the pore size may instead be the controlling physical dimension rather than a more global length scale. For a sphere diameter $D = 12.7$ mm, the average pore size, es-

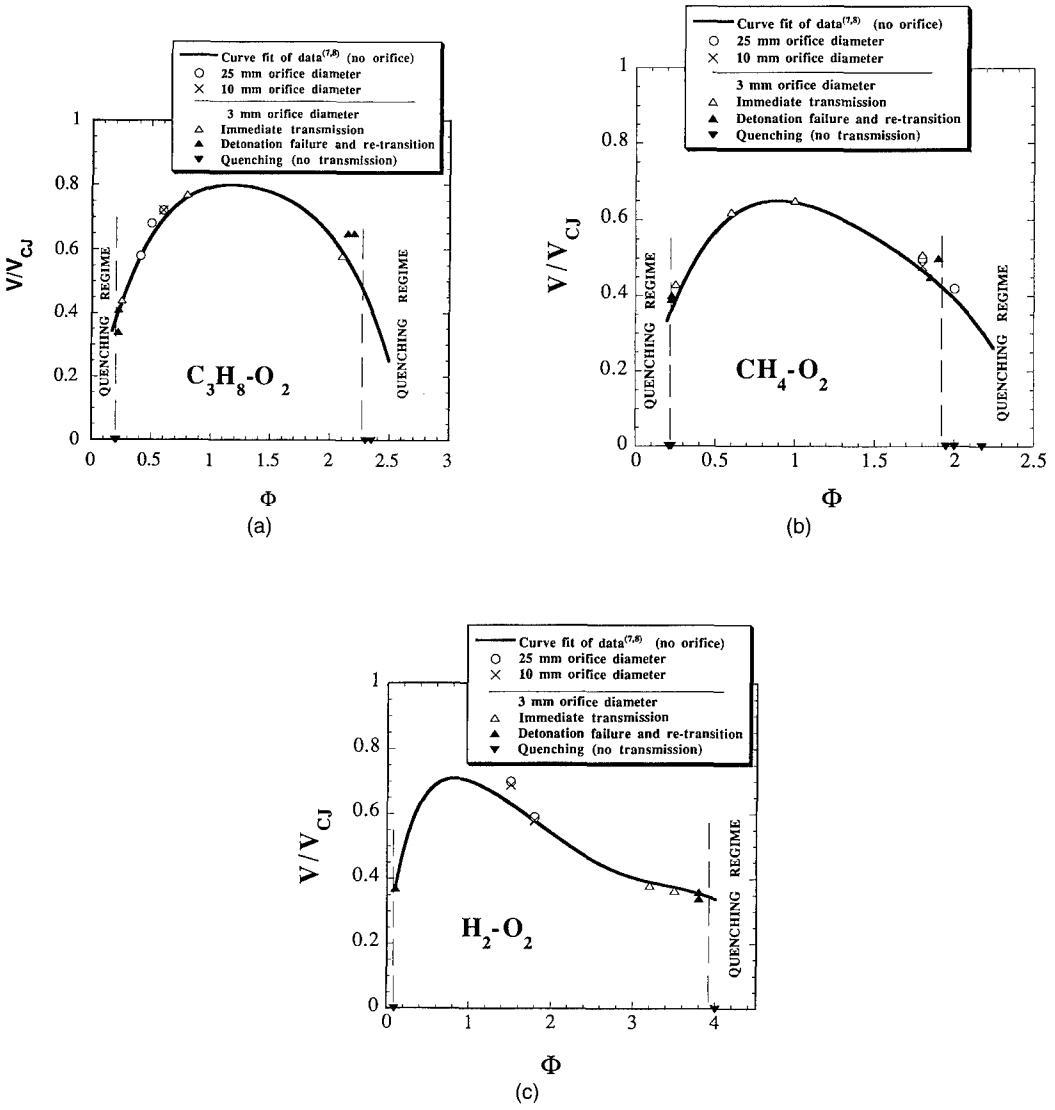

FIG. 3. Variation of transmitted velocity in the porous medium (D = 12.7 mm) with mixture composition, through different orifice diameters: (a) C_3H_8-O_2, (b) CH_4-O_2, and (c) H_2-O_2. Curve fit represents velocity data in the same porous medium for direct transmission without an orifice [7,8]. The dashed lines define the range of compositions for which successful detonation transmission is possible.

timated as $d_p \approx D/3$, corresponds to ≈4 mm. This value is smaller than the orifice diameters of 25 and 10 mm and very close to the smallest orifice tested.

The dashed vertical lines in Fig. 3 denote the composition boundaries (lean and rich) beyond which a failed detonation downstream of the orifice does not undergo DDT. Similar to the critical composition limits for direct transmission (no orifice), the limits in the present case are characterized by the complete quenching of combustion within a short distance downstream of the orifice (≈120 mm). For purposes of graphical display, quenching is identified in Fig. 3 by assigning a zero velocity to the transmitted wave. Following Refs. 14 and 15, the range of compositions outside the region bounded by the dashed lines is denoted as the "quenching regime." The quenching limits of the different fuels for detonation transmission across the 3-mm orifice occur very close to the critical compositions for transmission without an orifice. This is a significant observation in that it pro-

vides clear evidence that the smallest physical dimension indeed controls transmission into the porous medium for these mixtures. The slightly narrower range of Φ for successful transmission with the orifice, compared to the detonability range for direct transmission denoted by the solid curve, may perhaps be accounted for by taking note that the 3-mm orifice is a marginally smaller dimension than the effective pore diameter ($\approx$4 mm) for this sphere bed. It should also be noted that the critical orifice diameter is at least an order of magnitude less than the critical tube diameter (d_c) of the mixture at the same composition (refer to Fig. 1), pointing to a local failure mechanism [6] for these mixtures.

It is of interest to examine next the transmission phenomenon for a mixture of (C_2H_2-O_2) + 75% Ar, for which the $d_c = 13\lambda$ correlation is known to break down. Based on observations of the near-limit detonation phenomenon in such mixtures [16], Lee [6] proposed that detonation failure is governed by a global mechanism, as opposed to a local mechanism for mixtures with a high activation energy, considered in Fig. 3. If detonation transmission into a porous medium for mixtures highly diluted with argon is similarly governed by a global mechanism, then the phenomenon should be controlled by the orifice diameter and not by the smallest physical dimension. Velocity data in the porous medium (D = 12.7 mm) corresponding to a mixture of (C_2H_2-O_2) + 75% Ar are presented in Fig. 4 for cases of transmission across orifice diameters of 3 and 10 mm, as well as for the case of direct transmission. The solid curve represents a curve fit of the transmitted velocity data plotted. Similar to the other mixtures tested (Fig. 3), quasi-detonation velocities (for successful transmission) do not appear to be a function of the orifice diameter. A failed detonation downstream of the 3-mm orifice can once again retransit to quasi-detonation in the porous medium (as in Fig. 2b). The lean limit (or quenching boundary) in this case of high argon dilution appears to be clearly a function of the orifice diameter. Quenching occurs at a more sensitive Φ for an orifice of 10 mm in diameter, compared with the case of direct transmission. Moreover, a reduction in orifice diameter to 3 mm brings about a shift in the lean quenching limit to a more sensitive composition. The orifice introduces a larger length scale into the problem, thereby providing evidence supporting the existence of a global failure mechanism. If the failure mechanism were local, as in the mixtures with high activation energy, then the smallest physical dimension of the pore would dominate.

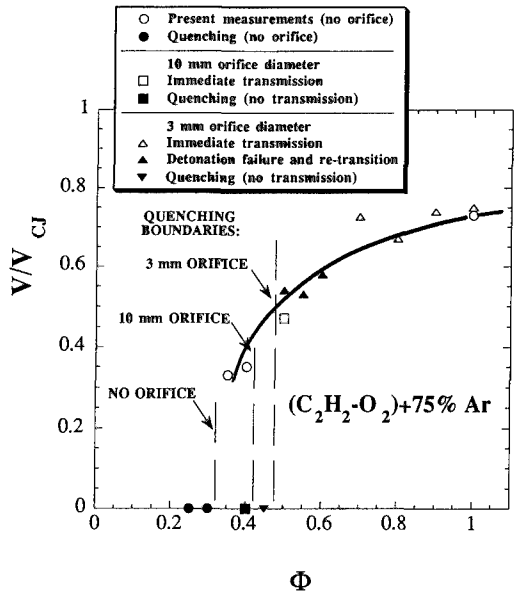

FIG. 4. Variation of transmitted velocity with mixture composition in (C_2H_2-O_2) + 75% Ar through different orifice diameters. Critical conditions for transmission are dependent on orifice diameter, suggesting a global failure mechanism [6].

Conclusions

It is conclusively demonstrated that a CJ detonation can transmit into a porous medium through an orifice, for orifice diameters much smaller than the normal critical tube diameter (d_c) for the mixture. The transmitted wave is independent of the orifice diameter and propagates as a quasi-detonation, with a velocity identical to the normal value for direct transmission without an orifice [7,8]. For well-detonable mixtures, transition from detonation to quasi-detonation is immediate at the interface of the porous medium. In the near-limit regime, the detonation wave fails downstream of the orifice and undergoes deflagration to detonation transition (DDT) within a relatively short distance of travel in the porous medium. This is in sharp contrast to the normal case of detonation transmission through an orifice, where retransition to detonation is not observed once the wave has failed. A porous medium can artificially generate "hot spots" from shock-wave–particle interactions [7,9] and thus can assist the retransition process to a quasi-detonation. It appears that DDT is only possible for strong jet ignition through the orifice and not for weak flames characterized by low flame accelaration. For subcritical transmission of detonation through the orifice, a turbulent jetting mechanism seems to be responsible for the complete and abrupt extinction of combustion that takes place within the pores. The quenching limits for mixtures with relatively high activation energy occur very close to the critical compositions for detonation quenching in the porous medium without an orifice. This strongly suggests that transmission in

such mixtures is governed by the smallest physical dimension (e.g., the pore), and thus, a local failure mechanism prevails. In mixtures for which the activation energy is not as high and the $d_c = 13\lambda$ correlation is known to break down, e.g., (C_2H_2-O_2) + 75% Ar, the limiting composition for successful transmission appears to be dependent on the orifice diameter. The larger length scale introduced by the orifice indicates that a global failure mechanism may exist in this case. The present results therefore seem to confirm the existence of a local and global failure mechanism proposed by Lee [6] for normal detonations, depending upon the activation energy of the mixture and the applicability of the $d_c = 13\lambda$ correlation.

REFERENCES

1. Mitrofanov, V. V., and Soloukhin, R. I., *Sov. Phys. Dokl.* 9(12):1055–1058 (1964).
2. Edwards, D. H., Thomas, G. O., and Nettleton, M. A., *J. Fluid Mech.* 95:79–96 (1979).
3. Knystautas, R., Lee, J. H. S., and Guirao, C., *Combust. Flame* 48:63–83 (1982).
4. Matsui, H., and Lee, J. H. S., *Seventeenth Symposium (International) on Combustion*, The Combustion Institute, Pittsburgh, 1979, pp. 1269–1280.
5. Moen, I., Sulmistras, A., Thomas, G. O., Bjerketvedt, D., and Thibault, P.A., *Progress in Astronautics and Aeronautics*, AIAA Inc., New York, 1986, Vol. 106, p. 220.
6. Lee, J. H. S., in *Combustion Science and Technology* (W. A. Sirignano, Ed.), 1993, in press.
7. Makris, A., "The Propagation of Gaseous Detonations in Porous Media," Ph.D. Thesis, Department of Mechanical Engineering, McGill University, Montreal, Quebec, Canada, 1993.
8. Makris, A., Shafique, H., Zhang, F., Lee, J. H. S., and Knystautas, R., 14th ICDERS, Coimbra, Portugal, August 1993, submitted for publication in *Shock Waves* (in press).
9. Makris, A., Papyrin, A., Kamel, M., Kilambi, G., Lee, J. H. S., and Knystautas, R., *Progress in Astronautics and Aeronautics*, AIAA Inc., New York, 1992, Vol. 153, p. 363.
10. Lyamin, G. A., Mitrofanov, V. V., Pinaev, A. V., and Subbotin, V. A., in *Dynamic Structure of Detonation in Gaseous and Dispersed Media* (A. Borisov, Ed.), Kluwer Academic Publishers, 1991, p. 51.
11. Laberge, S., Atanasov, M., Knystautas, R., and Lee, J. H. S., *Progress in Astronautics and Aeronautics*, AIAA Inc., New York, 1993, Vol. 153, p. 381.
12. Knystautas, R., Guirao, C., Lee, J. H. S., and Sulmistras, A., *Progress in Astronautics and Aeronautics*, AIAA Inc., New York, 1985, Vol. 94, p. 23.
13. Westbrook, C. K., and Urtiew, P. A., *Nineteenth Symposium (International) on Combustion*, The Combustion Institute, Pittsburgh, 1982, pp. 615–623.
14. Thibault, P., Liu, Y. K., Chan, C., Lee, J. H. S., Knystautas, R., Guirao, C., Hjertager, B., and Fuhre, K., *Nineteenth Symposium (International) on Combustion*, The Combustion Institute, Pittsburgh, 1982, pp. 599–606.
15. Lee, J. H. S., Knystautas, R., and Chan, C. K., *Twentieth Symposium (International) on Combustion*, The Combustion Institute, Pittsburgh, 1984, pp. 1663–1672.
16. Dupre, G., Joannon, J., Knystautas, R., and Lee, J. H. S., *Twenty-Third Symposium (International) on Combustion*, The Combustion Institute, Pittsburgh, 1990, pp. 1813–1820.

Twenty-Fifth Symposium (International) on Combustion/The Combustion Institute, 1994/pp. 73–78

INITIATION OF UPSTREAM-DIRECTED DETONATION INDUCED BY THE VENTING OF GASEOUS EXPLOSION

S. P. MEDVEDEV, A. N. POLENOV, S. V. KHOMIK AND B. E. GELFAND
Institute of Chemical Physics, Russian Academy of Sciences
Kosygina 4, Moscow 117977, Russia

An experimental study to demonstrate the possibility of nontraditional trends of vented explosion has been performed. The experiments have been carried out using a cylindrical horizontally placed 4-L explosion chamber. One of the end flanges of the explosion chamber was equipped with a centrally located opening. Initially, it was covered by a hermetically mounted diaphragm. Various configurations of short vent pipes were available for attachment to the opening. The explosion was initiated by an electrical spark at the closed end flange of the explosion chamber. Two mixtures under investigation were stoichiometric hydrogen-oxygen and acetone-oxygen mixtures diluted with nitrogen at initial pressures of 3 and 2 bar, respectively. Pressure and ionization measurements, streak camera photographs, and smoked plate records indicated that, under certain conditions, a detonation wave propagates upstream from the vent opening into the explosion vessel. The presence of at least a short duct is a necessary condition for the upstream-directed detonation event. The interpretation of the experimental results is based on the consideration of the intense mixing of the hot combustion products with the unburned gas in the vent duct. It was shown that a gradient of ignition delay of fresh mixture is set along the initial run of the vent pipe. As a result, upstream-directed detonation is initiated as a result of the shock wave amplification by coherent energy release (SWACER) mechanism.

INTRODUCTION

Pressure release at the initial stage of the gaseous explosion in a closed vessel is widely used as a method for explosion mitigation. Normally, practical recommendations are based on experimental data and theoretical grounds for spherical or cylindrical vessels of length/diameter ratio less than 3:1. An examination of numerous experimental results [1] from the point of view of the value of p_{max}, i.e., the largest pressure inside the vented vessel during depressurization, showed that p_{max} usually does not exceed the pressure of diaphragm rupture p_v by more than a factor of 4–6. Only in specific cases are the largest measured values of p_{max} comparable with the maximum pressure p_m of the constant volume explosion. In particular, it is known that the pressure history inside the explosion chamber is affected by the presence of a duct connecting the opening with the environment [2,3]. The possibility of the onset of a detonation in a long duct joined to the opening of an explosion vessel recently has been demonstrated [2]. Nevertheless, this process does not influence the maximum pressure value inside the vented chamber. It should be noted finally that almost all conceivable venting experiments have been performed with the fuel-air mixtures at initial pressure $p_0 = 1$ bar.

Analysis of the conventional experimental data [1–3] does not answer the question of great practical importance: Is it possible that, in some instances of vented explosions, a detonation will initiate and strong shock waves will propagate into the vented chamber? As mentioned above, the present study concerns vessels with small length to diameter ratios. Taking into account that the explosion is initiated by a weak source (e.g., electrical spark), there is only a very low probability that a deflagration to detonation transition will occur in a manner similar to that observed in elongated tubes. A more suitable mechanism is fast turbulent mixing of hot combustion products with reactants [4,5]. This can lead to the onset of detonation at very short distances. Setting aside the mechanism of this phenomenon [known as the shock wave amplification by coherent energy release (SWACER) mechanism] for later consideration, it should be noted here that, in spite of obvious differences of experimental setups [4,5] from traditional vented explosion vessel design, the mixing process of combustion products with unburned gas takes place during a vented explosion when the flame front reaches the opening. So there is no reason to rule out the possibility of detonation onset for some mixture under proper conditions.

The aim of the present work is to demonstrate the possibility of upstream-directed detonation onset as a result of explosion venting. Experiments have been carried out using a cylindrical 4-L explosion chamber with a ratio of length to diameter of 2.2. In accor-

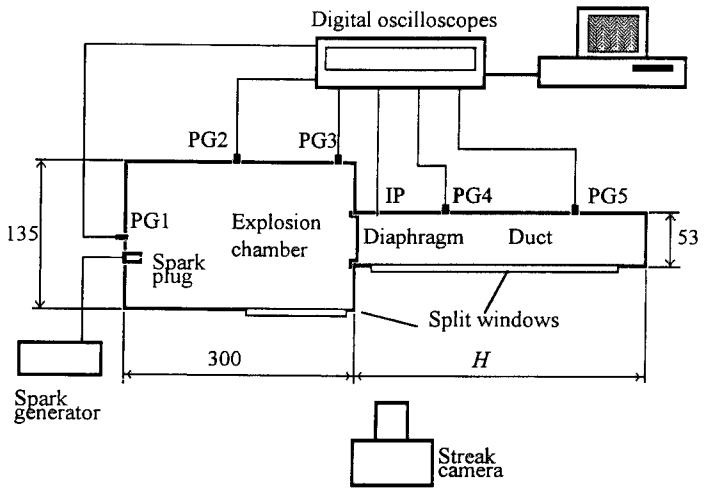

FIG. 1. Schematic diagram of the basic experimental apparatus and data acquisition system.

dance with the above analysis, the essential features required of the experimental setup and combustible mixture are as follows:

1. Mixture: more reactivity than conventional hydrocarbon-air mixtures.
2. Initial pressure: greater than barometric pressure.
3. Ducting: the possibility of the variation of the vent-pipe length.

Experimental Details

The general arrangement of the experimental apparatus and the data acquisition system are shown in Fig. 1. One of the ends of the explosion chamber was equipped with a centrally located opening 53 mm in diameter. Initially, it was capped by a hermetically mounted aluminum or copper diaphragm. Four vent tubes of the same diameter as the opening and of lengths H = 50, 100, 150, and 340 mm were available for attachment to the opening.

The burning of the mixture under investigation was initiated by an electrical spark at the closed end flange of the explosion chamber. The pressure rise inside the explosion chamber leads to rupture of the diaphragm at a preset pressure p_v. The pressure history both before and after beginning of the depressurization was recorded by means of piezoelectric gauges PG1–PG5 placed as shown in Fig. 1. The explosion chamber, as well as the duct of 340 mm in length, is equipped with split windows for the visualization by means of high-speed streak camera FK-1M. Finally, in some experiments, additional information could be obtained by using an ionization probe (IP) mounted flush with the duct wall, at a distance of 25 mm from the diaphragm. Pressure gauges were spaced along the explosion chamber as follows: PG1—centrally located at the close end of the explosion chamber; PG2 and PG3—respectively at distances of 155 and 290 mm from the closed end flange. The locations of the pressure gauges mounted outside the explosion chamber depended on the duct used. Normally, the distance between the diaphragm and the first of the external gauges was no more than 65 mm. The two mixtures under investigation were stoichiometric hydrogen-oxygen and acetone-oxygen mixtures diluted with nitrogen ($2H_2 + O_2 + N_2$ and $C_3H_6O + 4O_2 + 3.3N_2$) at initial pressures of 3 and 2 bar, respectively. Pressure of diaphragm rupture and duct length were varied in the present experiments.

Experimental Results

The main attention of the present investigation was focused on the gas-dynamic effects of the venting process. Systematic experiments on the depressurization of the burning mixture have revealed an interesting result. It was established that proper combinations of pressure p_v and length H inevitably give rise to a violent pressure buildup within the vented explosion chamber.

As an illustration of the foregoing, consider the selected runs that are presented in Figs. 2 and 3. Figure 2 gives an example of typical pressure-time histories inside the explosion chamber in the experiments with the hydrogen mixture. The lowest traces numbered 1 are useful in visualizing a trend in a combustion process without depressurization, i.e., constant volume burning. This preliminary experiment gives an important parameter—the maximum constant volume explosion pressure p_m, which approximately equals 23 bar. The records 2 and 3 illustrate typical pressure histories inside the explosion chamber that were observed during vented experiments. Both experiments presented here were performed

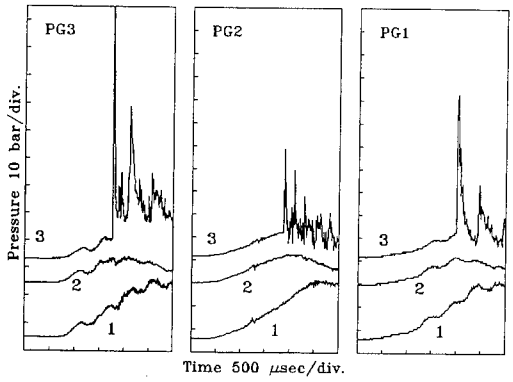

FIG. 2. Pressure histories inside the explosion chamber. (1) Constant volume burning; (2) $H = 0$; (3) $H = 50$ mm.

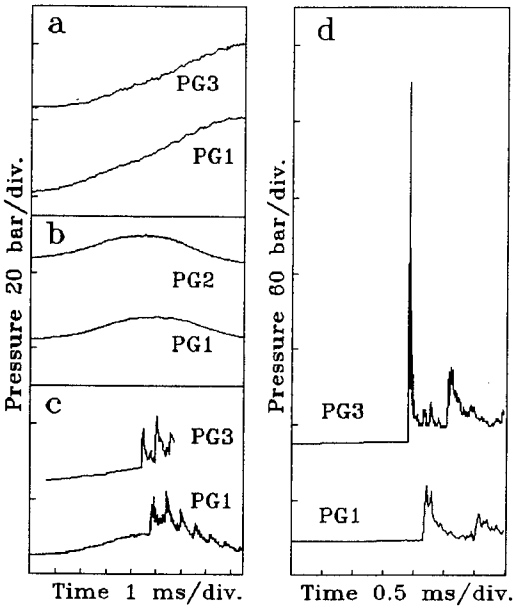

FIG. 3. Typical pressure records for acetone mixture. $p_v = 3.5$ bar. (a) Constant volume burning; (b) $H = 0$; (c) $H = 100$ mm; (d) $H = 340$ mm.

under identical pressure, $p_v = 7$ bar. The only difference between the described cases consists in the length of the venting duct. It is readily seen that the absence of the duct leads to attenuation of the explosion (see curves 2 in Fig. 2). The pressure falls smoothly and uniformly throughout the explosion volume after diaphragm rupture. The addition of the short duct results in both qualitative and quantitative changes. In the specific case of Fig. 2 (curves 3), at some instant of time after diaphragm rupture, the pressure suddenly increases and reaches a value that is greater than the value p_m by more than an order

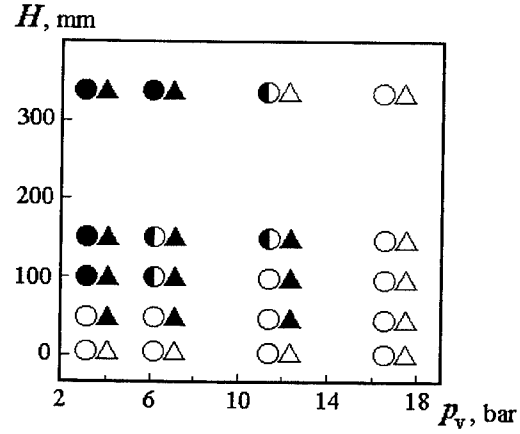

FIG. 4. Graphical summary of the experimental outcomes. ○—Acetone mixture; Δ—hydrogen mixture. Open circles—smooth depressurization; semisolid circles—depressurization with oscillations; solid circles—DD regime.

of magnitude. The observed strong shock wave of short duration is propagated from the opening into the explosion chamber. The characteristic features of this process are similar to those of detonation onset. We denote this phenomenon by means of the short abbreviation DD, i.e., Detonation due to Depressurization.

The above phenomenology is applicable to the experiments with the acetone mixture presented in Fig. 3. The only addition lies in the fact that, as illustrated in Fig. 3c, for some intermediate length of the vent duct one observes the emergence of relatively weak pressure disturbances that are superimposed on the smooth pressure traces. Nevertheless, the maximum pressure in this case does not exceed the value p_m.

An analytical treatment of more than 100 experiments for different values of pressure p_v and length H shows that the described modes of pressure change within the explosion chamber are characteristically different. For the sake of convenience, one can introduce the following short summary of possible venting regimes:

1. Smooth depressurization: $p_v < p_{max} < p_m$
2. Depressurization with pressure oscillations: $p_{max} \approx p_m$
3. DD regime: $p_{max} > (6\text{–}10)p_m$.

The experimental outcomes are summarized in Fig. 4. As seen from this diagram, the probability of the third regime increases with both decreasing pressure of diaphragm rupture and increasing duct length. It is significant that the presence of at least a short duct is a necessary condition for the DD advent. Thus, present experiments demonstrate a possibility of unusual trends in vented explosion. To clarify the details of the DD phenomenon, some additional experiments were performed.

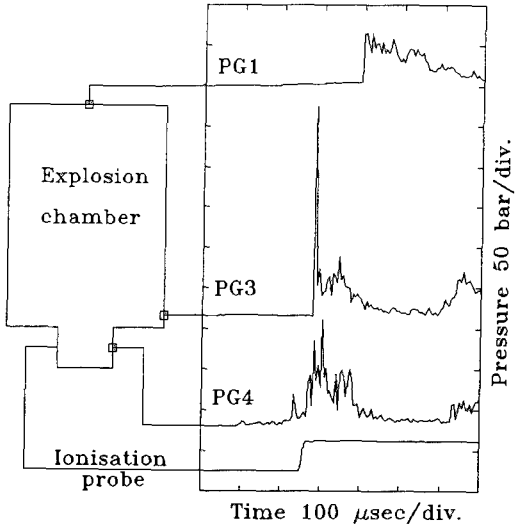

FIG. 5. Pressure and ionization records. Hydrogen mixture. p_v = 7 bar, H = 50 mm.

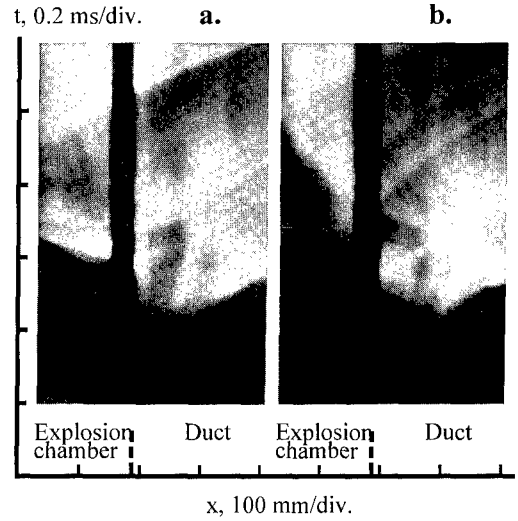

FIG. 6. Streak camera photographs under DD regime (a) and without DD regime (b). Acetone mixture. p_v = 3.5 bar.

Pressure and Ionization Measurements:

An example of simultaneous pressure and ionization records is presented in Fig. 5. As seen from this figure, a strong shock wave suddenly arises within the explosion chamber shortly after the emergence of hot burning products in the duct. Then the observed wave propagates into the explosion chamber. It should be noted that the pressure inside the explosion chamber is higher than that in the duct.

Streak Camera Photographs:

Figure 6 presents two typical streak camera records of a venting process. Self-luminosity of the flame inside the explosion chamber until the moment the flame enters into the duct is negligible. Under DD-regime conditions (Fig. 6a), a bright line is easily observed that appears in the vicinity of the diaphragm and moves into the explosion chamber. Its visible velocity is equal to approximately 1800 m/s. Simultaneously, a detonation wave is initiated inside the duct at a distance of about 150–200 mm from the diaphragm.

Figure 6b illustrates the flow pattern without the DD regime. The experiments shown were performed at the same conditions for the setup and the initial pressure. To avoid the onset of the DD regime, a less sensitive mixture (C_3H_6O + $9O_2$ + $6.6N_2$) was used. As seen from Fig. 6b, the main features of the flame propagation in the duct are quite similar to those presented in Fig. 6a. Considering the explosion chamber, it should be mentioned that, as opposed to the case of Fig. 6a, there is no line that can be identified as a strong gas-dynamic disturbance. In

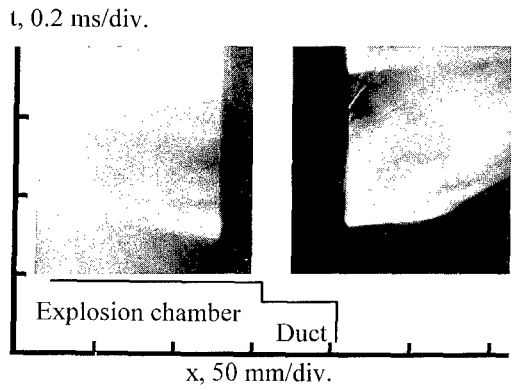

FIG. 7. Streak camera photographs of hydrogen mixture with a duct attached to the chamber. H = 50 mm, p_v = 7 bar.

this case, the pressure measurements indicate that the process under investigation is one of depressurization with oscillations.

Another illustration of the process under study is presented in Fig. 7. Contrary to the above example (Fig. 6), the right part of Fig. 7 is a streak photograph of the process in the unconfined space outside of the explosion chamber and duct. As seen from Fig. 7, the detonation-like wave propagates both inward and outward of the explosion chamber. A likely place of origin of these waves is inside the duct. Taking into account that the observed waves are propagated upstream and downstream, respectively, one can estimate the outflow speed as one-half of the difference

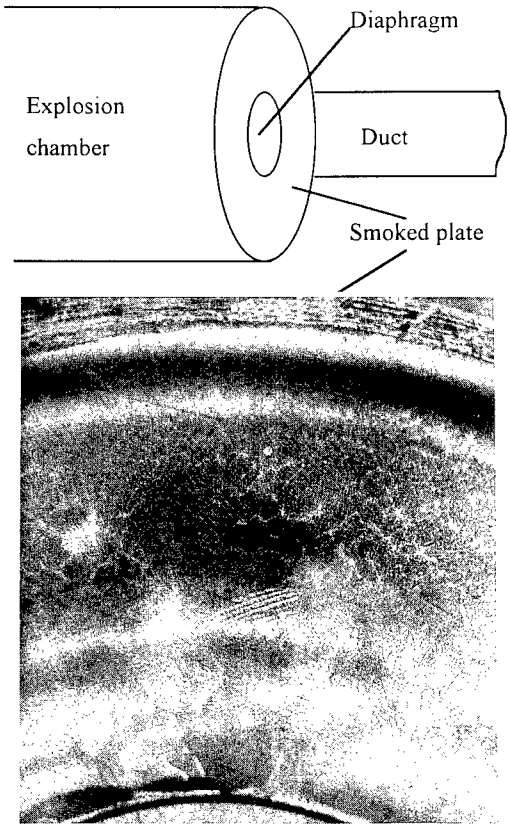

FIG. 8. Schematic of the smoked plate location and typical smoked print under DD regime. Acetone mixture.

between the visible wave velocities. This comes to a value of about 1100 m/s. Thus, the velocities of the waves relative to the flow are approximately equal to 2450 m/s. This is in good agreement with the theoretical (Chapman–Jouguet) CJ value of 2465 m/s (at initial pressure 12 bar and temperature 440 K, which correspond to the state of the unburned mixture at the instant of the DD-regime onset). In the absence of any duct extension, the ignition outside the explosion chamber is observed. However, it does not substantially influence the flow pattern inside the explosion chamber.

Smoked Plate Records and Aluminum Foil Tests:

As mentioned above, pressure measurements and streak camera photographs show that the inwardly directed strong shock wave has much in common with a detonation wave. So additionally, in some experiments, a smoked plate was placed around the opening inside the explosion chamber, as shown in Fig. 8. A typical smoked print under DD conditions is given by Fig. 8. The cellular structure indicating a detonation process is clearly seen. The trend of cell shape and size variation shows that the detonation, if any, is directed from the opening. An essential feature of the DD regime is its destructive effect. The proof of its mechanical action was not difficult to visualize by replacing the smoked plate with a thin aluminum foil. It was shown that only the DD regime inevitably gives rise to full disintegration of the foil into numerous small fragments.

Discussion

First and foremost, it is pertinent to note that the DD regime is not due to the flame acceleration after rupture of the diaphragm. This is evident from the pressure histories before DD advent, which are not dissimilar in aspect from those in a closed volume explosion even at relatively low values of p_v (see, e.g., Figs. 2 and 3). The experimental results show that the detonation wave propagating into the vented chamber is initiated shortly after the arrival of the flame front at the vent opening. By this instant of time, only a small portion of the unburned mixture is exhausted into the atmosphere. Hence, the DD onset is preceded by a concurrent outflow of combustion products and fresh mixture. In view of the fact that the transition to detonation takes place in a short time interval, it is reasonable to suggest that the most appropriate mechanism of the observed phenomenon is fast turbulent mixing of the hot combustion products with unburned mixture at the short section of the duct immediately adjacent to the opening. This mixing keeps pace with the critical outflow through the duct because of the sufficiently high pressure difference between the explosion chamber and the environment. So the transient ignition delay t_i of the unburned mixture governed by the turbulent mixing with the combustion products will have elapsed at some distance H_i from the opening. These parameters are interrelated by means of an obvious equation,

$$H_i = a_c t_i \tag{1}$$

where a_c is critical velocity of the outflow. On the other hand, the ignition time t_i can be estimated by the relationship [6]

$$\int_0^{t_i} \frac{dt}{\tau(t)} = 1. \tag{2}$$

Here τ is the chemical induction time. For a hydrogen-oxygen mixture, it can be written as follows [7]

$$\tau = 1.85 \times 10^{-6} \frac{T}{[O_2]} \exp\left(\frac{9130}{T}\right) \tag{3}$$

where τ is in μs, $[O_2]$ is partial pressure (in bar) of the oxygen in the explosible mixture, and the temperature T is in K.

The present approach is similar to that of Ref. 4. Following Ref. 4, one can assume that, for a short mixing time, the temperature of the combustion products T_p changes negligibly. So the induction time of the unburned mixture will depend only on the oxygen concentration, which is given by the linear relationship [4]

$$[O_2] = [O_2]_0 kt \tag{4}$$

where $[O_2]_0$ is the initial partial pressure of oxygen in the unburned mixture at the beginning of the mixing and k denotes mixing rate.

Solving the set of Eqs. (1) through (4), we obtain the condition on the distance at which self-ignition is to occur: $H_i = (2\tau_0 a_c^2 k^{-1})^{0.5}$ (τ_0 is the induction time at temperature T_p). On the other hand, it is easy to show that there exists a distribution of ignition delays along the vent duct given by $\tau(x) = \tau_0 a_c (kx)^{-1}$ (x is measured from the opening of the explosion chamber). This distribution is essentially steady state because of sonic flow inside the duct. It can play a crucial role in the realization of the SWACER mechanism of the detonation onset. Omitting the details here, we can use the condition of strong shock wave and detonation onset in systems with nonuniform distribution of induction time [8]: $|d\tau/dx|^{-1} \approx a_p$ (a_p is speed of sound in the combustion products). This gives a distance from the opening to the location of detonation onset: $H_d = (\tau_0 a_c a_p k^{-1})^{0.5}$. It should be particularly emphasized that the detonation wave, if any, has to be propagated to the opening and further into the explosion chamber. So it can be referred to as an upstream-directed detonation. It is well to bear in mind that all of the preceding does not rule out the possibility of the onset of a detonation that propagates out of the duct to the environment.

In spite of a number of simplifications, the present consideration is attractive for estimation of the minimum length of the duct for the upstream-directed detonation advent: $H_{\min} \geq H_i \geq H_d$. This criterion imposes, among other things, the necessary condition on the outflow velocity: $a_c \geq a_p/2$.

For the sake of comparison with the present experimental results, one can take into account an estimation of the most uncertain parameter k given in Ref. 4: $k = (0.51\text{–}4.6) \times 10^3$ 1/s. Assuming $T_p \sim 1800$ K and recalling that the DD regime takes place when approximately one-half of the initial mixture has reacted, one has $\tau_0 \sim 4\ \mu$s for the hydrogen mixture used. The velocity estimated above of the outflow ($a_c \approx 1100$ m/s) is obviously higher than the value $a_p/2$. Thus, $H_{\min} = H_i \sim 46\text{–}138$ mm, which compares satisfactorily with the experimental value of 50 mm.

Conclusion

The present work has revealed the distinctive features of the vented explosion of mixtures of relatively high reactivity at elevated initial pressures. An upstream-directed detonation onset was observed under proper conditions. The described destructive process can be realized even in a small-scale compact vessel with the ratio of length to diameter less than 3. It was shown that the presence of at least a short smooth duct can give rise to the qualitative changes in the pressure histories inside the vented chamber. Close inspection of the experimental evidence and theoretical estimations indicate that the mechanism of the transition to detonation is most likely to be the SWACER mechanism. From the point of view of further inquiry into the problem of direct initiation of detonation without a powerful source, the present experimental arrangement can be suitable for the practical realization of the desired gradient of induction time.

Acknowledgment

This work was supported by the Russian Fund of Fundamental Research.

REFERENCES

1. Bradley, D., and Mitcheson, A., *Combust. Flame* 32:237–255 (1978).
2. Bouhard, F., Veyssiere, B., Leyer, J.-C., and Chaineaux, J., in *Progress in Astronautics and Aeronautics* (A. L. Kuhl, J.-C. Leyez, A. A. Borisov, W. A. Sirignano, Eds.), AIAA, Washington, DC, 1990, Vol. 134, p. 85.
3. Kordylewski, W., and Wach, J., *Combust. Flame* 66:77–79 (1986).
4. Knystautas, R., Lee, J. H., Moen, I. O., and Wagner, H. Gg., *Seventeenth Symposium (International) on Combustion,* The Combustion Institute, Pittsburgh, 1979, pp. 1235–1244.
5. Carnasciali, F., Lee, J. H. S., Knystautas, R., and Fineschi, F., *Combust. Flame* 84:319–330 (1991).
6. Strehlow, R. A., *Fundamentals of Combustion,* International Textbook Company, 1968.
7. Schott, G. L., and Kinsey, J. L., *J. Chem. Phys.* 29:1177–1182 (1958).
8. Zel'dovich, Y. B., Gelfand, B. E., Tsyganov, S. A., Frolov, S. M., and Polenov, A. N., in *Progress in Astronautics and Aeronautics* (A. L. Kuhl, J. R. Bowen, J.-C. Leyez, A. Borisov, Eds.), AIAA, Washington, DC, 1988, Vol. 114, p. 99.

Twenty-Fifth Symposium (International) on Combustion/The Combustion Institute, 1994/pp. 79–87

PHENOMENOLOGICAL ASPECTS IN EXPLOSIVE POWDER/GAS TWO-PHASE DETONATIONS

ALLEN J. TULIS, WILLIAM K. SUMIDA AND RICHARD P. JOYCE
IIT Research Institute
10 West 35th Street, Chicago, IL 60616–3799, USA

AND

DAVID C. HEBERLEIN AND DIVYAKANT L. PATEL
U.S. Army, Mine and Countermine, NVESD
Fort Belvoir, VA 22060, USA

Attempts were made to detonate a special ball-milled TNT powder of about 30-μm particle size that was dispersed in air, oxygen, and nitrogen at nominally 1 kg/m^3 in a highly instrumented 152-mm-diameter 7.31-m-long horizontal detonation tube. Results were successful in both air and oxygen, but not in nitrogen. New modifications to the detonation tube for this work included implementation of two-color temperature-measuring instrumentation, and the repositioning of some piezoelectric pressure transducers and fiber-optic light-detector probes so that phenomena such as spinning detonation and multiple-front detonations could be better identified and quantified. TIGER Code Chapman–Jouguet (CJ) computations were made for TNT, RDX, and mixtures of TNT and RDX in air, oxygen, and nitrogen at concentrations up to 100 kg/m^3. The computed results for TNT in air and oxygen at a concentration of 1 kg/m^3 for the detonation velocities, pressures, and temperatures were 2.00 km/s, 4.00 MPa, 3250 K in air and 2.05 km/s, 4.40 MPa, 3740 K in oxygen. Experimental results for TNT powder were 1.82 km/s, 4.06 MPa, 3245 K in air and 1.90 km/s, 4.61 MPa, 4240 K in oxygen; the experimental concentrations, which were monitored with laser optics, were determined to be 1 kg/m^3 with an estimated error of $\pm 10\%$. Subsequent experiments were conducted with RDX, alone and in mixtures with TNT, in attempts to achieve detonation in nitrogen. These were successful except when the RDX percentage fell below 20% by weight. Results of successful detonations of RDX/TNT mixtures indicated multiple-front detonations, suggesting that the TNT was reacting behind the RDX detonation front in such a manner that it supported the overall detonation.

Introduction

The achievement and phenomenology of heterogeneous two-phase solid particulate/gas detonations have become subjects of considerable interest and investigation in recent years, involving fuel, energetic material, and molecular explosive powders dispersed in air (as well as in other gaseous media). However, the phenomenological aspects of these heterogeneous detonations remain as causes of considerable controversy with regard to classical homogeneous Chapman–Jouguet (CJ) detonation theory. Confined detonations of fuel powders dispersed in air have been documented over a decade ago, e.g., detonation of aluminum (Al) powder [1] and grain dust [2], achieved in one-dimensional detonation/shock tubes. (Although not an issue in this paper, the *unconfined* detonation of Al powder dispersed in air has also been unequivocally demonstrated [3].) The criteria, however, are very severe. The solid fuel particles must burn sufficiently fast and effectively to support propagation of detonation, and are therefore critically dependent upon stoichiometry, homogeneity, and particle size. Hence, fuel powders dispersed in air are very difficult to detonate, even in one-dimensional detonation tube studies, in which case they generally manifest spinning detonation [4].

However, about two decades ago, it was discovered that molecular explosive powders such as PETN, RDX, and TNT could be dispersed in air and readily detonated, yielding stable detonation characteristics that correlated quite well with analytical thermochemical CJ computations [5]. Because stoichiometry in molecular explosives is essentially intrinsic, particle size and homogeneity would appear to be inconsequential, except for minimum concentrations required to sustain propagation of detonation.

Subsequent studies demonstrated that the severe criteria for achieving stable detonation of Al particles dispersed in air are considerably relaxed by sensitization with small amounts of molecular explosive powders such as RDX [6]. Computations and experiments conducted with Al and carbohydrate powders

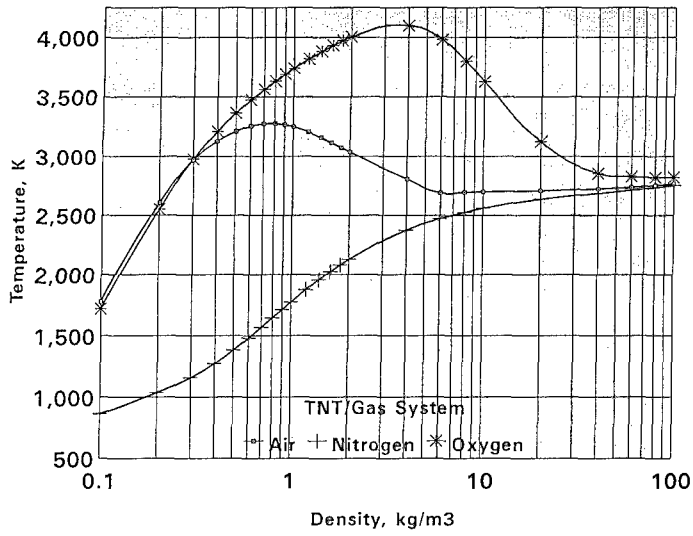

FIG. 1. TIGER Code CJ detonation temperature computations for TNT/air, TNT/oxygen, and TNT/nitrogen systems.

to which molecular explosives were added demonstrated extensive mitigation of the severe stoichiometry and detonability requirements, respectively [7], both for dispersions in air and in bulk formulations.

In other experimental investigations conducted to gain better insight into the mechanisms of heterogeneous two-phase solid powder/gas detonations, the molecular oxidizers ammonium perchlorate and potassium perchlorate were dispersed and detonated in a gaseous fuel of ethylene [8]. The achievement of detonation in the case of potassium perchlorate was especially significant, in that it demonstrated detonation could proceed by the sequential mechanisms of (1) decomposition of this solid molecular compound to potassium chloride with the attendant release of gaseous oxygen (net heat of reaction about zero), and (2) subsequent combustion of gaseous ethylene in the gaseous oxygen, within the time frame of a stable, propagating detonation.

Organic molecular explosives such as TNT, RDX, and PETN can respond by alternate mechanisms under different stimuli, dependent upon their particular chemical structure. For instance, TNT will readily burn in air, usually uneventfully without transition to detonation, whereas both RDX and PETN will not burn per se but will immediately transition to detonation if exposed to flame or sufficient heat. Hence, TNT is highly fuel rich and, if combusted in oxygen, will release almost three times as much heat of reaction as it will in detonation; RDX is essentially fuel oxidizer balanced, and PETN is somewhat oxidizer rich.

In this paper, results of recent studies of confined, one-dimensional detonation tube experiments to assess and characterize the detonation of TNT and RDX in air, oxygen, and nitrogen are presented. Further improvements in the detonation tube facility used in these experiments have been implemented, including provision to monitor detonation *temperatures* as well as detonation pressures, velocities, and induction times. Modifications have also been made to allow better assessment of phenomena such as spinning detonation and multiple-front detonations.

Analytical TIGER Code CJ computations, using the most recent upgraded version of this code for CHNO and other species [9], were also conducted to assess the detonation characteristics of the various heterogeneous systems investigated and for comparative purposes in regard to experimental results that have been obtained.

Analytical Results

Figures 1 through 3 present the analytical TIGER Code computational CJ results for detonation temperatures, pressures, and velocities for TNT in air, oxygen, and nitrogen, as a function of concentration. Similar computations were also conducted for various mixtures of TNT and RDX in nitrogen, and are presented in Figs. 4 through 6.

In Fig. 1, it is evident that, in the case of TNT, the gaseous phase is quite influential in regard to detonation temperature, up to concentrations of about 10 and 50 kg/m^3 in the case of air and oxygen, respectively, as would be expected. However, there is extensive variability in the lower concentrations; the influence of the amount of oxygen is paramount. Similar observations are noted in Figs. 2 and 3 for the case of detonation pressures and velocities, but to a much lesser degree. Enhancement of detonation characteristics by the improvement of stoichiometry

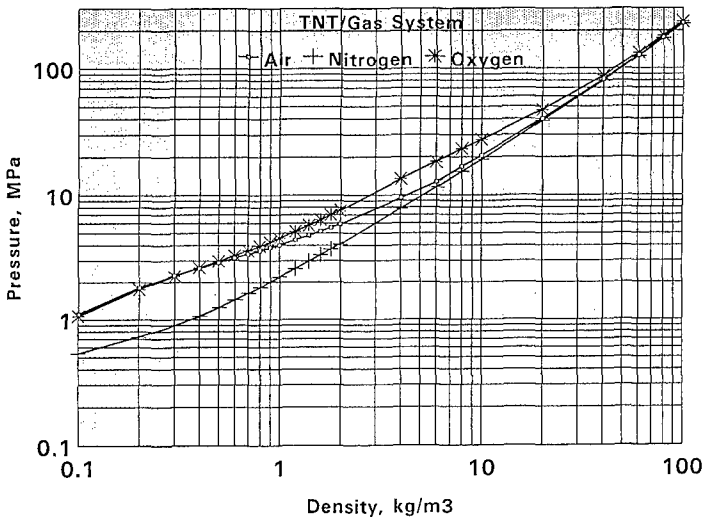

FIG. 2. TIGER Code CJ detonation pressure computations for TNT/air, TNT/oxygen, and TNT/nitrogen systems.

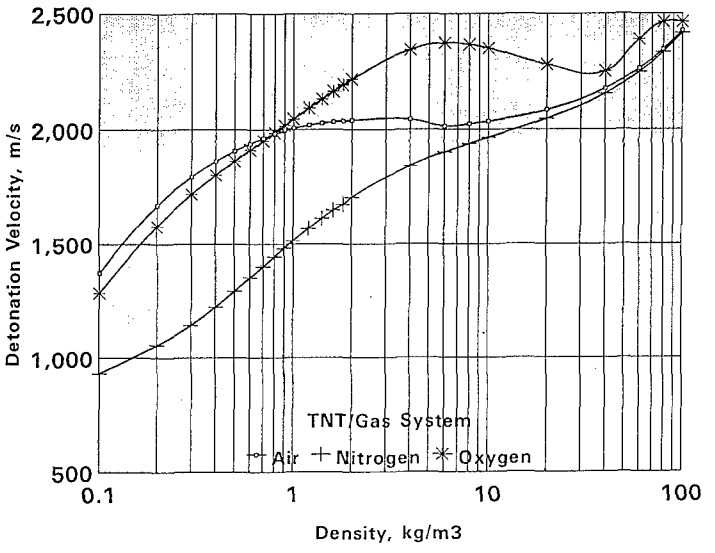

FIG. 3. TIGER Code CJ detonation velocity computations for TNT/air, TNT/oxygen, and TNT/nitrogen systems.

available from oxygen is manifested mainly in detonation temperatures.

Figures 4 through 6 illustrate that detonation characteristics of RDX are considerably better than those of TNT when detonated in nitrogen, as would be expected based on the fact that TNT is so fuel rich and that RDX is essentially stoichiometrically balanced in regard to its fuel/oxidizer structure.

Detonation Tube Facility

Figure 7 illustrates the latest modified and instrumentally improved IITRI detonation tube facility. The instrumented section is constructed of stainless steel and, as illustrated, contains one set each of diametrically opposed piezoelectric pressure transducers and fiber-optic light-detector probes at each of the 11 stations. However, to better assess phenomena such as spinning detonation and multiple-front detonations, the five sensor locations at four of the 11 stations were altered so that Station Nos. 2 and 8 consisted of five pressure sensors for each, and similarly, Station Nos. 3 and 9 consisted of five light sensors for each.

Ratio two-color radiometry was selected for providing the basis for measurement of two-phase detonation temperatures. This technique for temperature measurements is based on the relative relationship of incident radiation at one wavelength

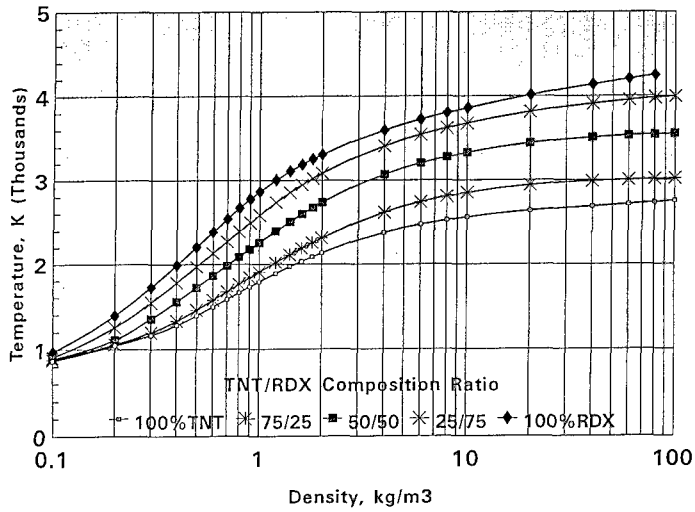

FIG. 4. TIGER Code CJ detonation temperature computations for various TNT/RDX mixtures in nitrogen.

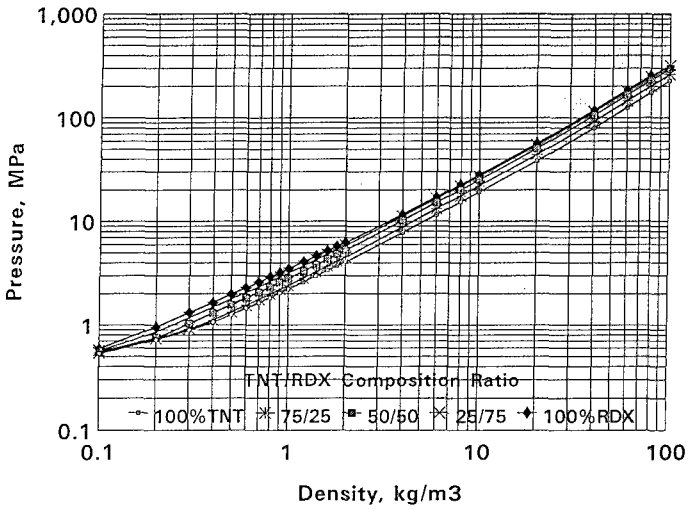

FIG. 5. TIGER Code CJ detonation pressure computations for various TNT/RDX mixtures in nitrogen.

to that at another wavelength, i.e., Plank's law for spectral emissive power of a blackbody radiator at relatively short wavelengths. Fiber optics were used to receive and transmit the radiation from the detonation front to appropriate detectors and signal conditioning circuitry. For more comprehensive assessment of this methodology, the temperature-measuring instrumentation (TMI) involved three color wavelengths to provide three independent measurements and to cover a larger portion of the radiation spectrum.

The TMI system consists of a quartz lens, a trifurcated bundle made from glass fibers, bandpass filters, and silicon photodiodes. The fiber optics, in conjunction with the bandpass filters, are used to provide the three different color outputs from the temperature source. The fiber bundles used are comb randomized to produce evenly divided outputs. When light is uniformly incident onto the large unified input, the trifurcated bundle transmits 30% of the total to each leg. Approximately 4% is reflected at the input and output. The transmittance of glass fiber over a 1-m length is about 48%, and remains relatively constant over the wavelength range 400–1300 nm. The numerical aperture is 0.56, thus providing an acceptance cone angle of 68°. The bandpass filters are three-cavity interference filters, pass a narrow band of visible light, and reject out-of-band wavelengths in the UV and IR range. The center wavelengths of 500, 600, 700, and 800 nm were selected. Two units were fabricated and implemented into the instrumented section of the detonation tube. Unit No. 1 has center wavelengths of 500, 600, and 700 nm, and Unit No. 2 has center wavelengths of 600,

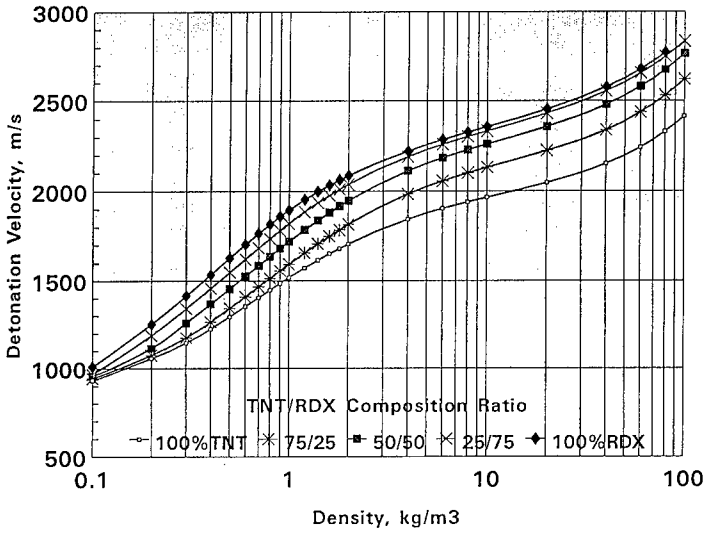

FIG. 6. TIGER Code CJ detonation velocity computations for various TNT/RDX mixtures in nitrogen.

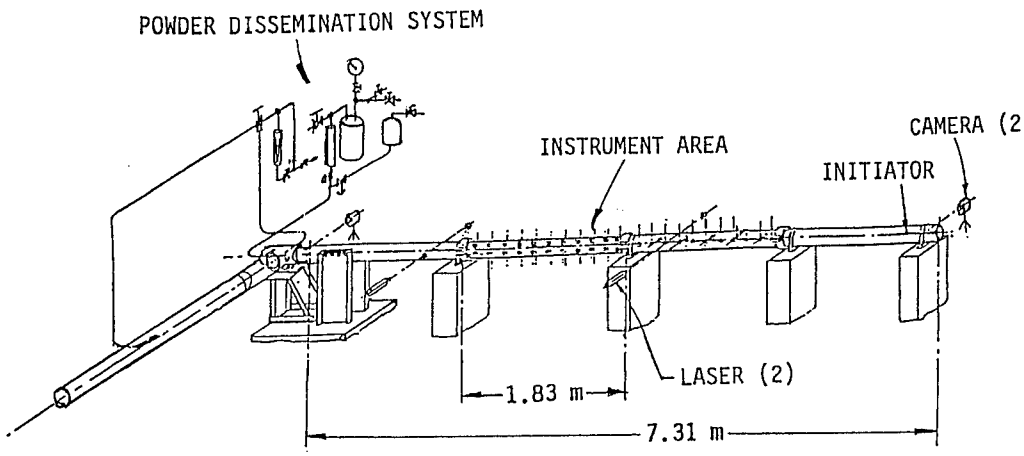

FIG. 7. Schematic of the detonation tube.

700, and 800 nm. All filters have a bandwidth of 70 nm. The transmittance for these filters is in the range of 50–60%. The filters were selected to cover the visible and near-IR range and have one color pair in common, 600 and 700 nm. This selection was made to provide information on response as a function of location as well as on the consistency of the measurements.

The photodiodes have a radiant sensitivity of about 0.35 A/W in the range of interest. The radiant sensitivity is nil in the UV and IR range and somewhat wavelength dependent in the band of interest. The photodiodes are operated in the photoelectric mode and provide for a rise time (10–90%) of 0.25 μs with a linear response range extending over five orders of magnitude.

Results of pretest calibrations and the data from the first detonation tube experiment showed that the use of a collimating beam probe was a desirable feature; hence, all three channels of each unit were equipped with collimating probes for all subsequent experiments. In addition, the line amplifiers used for the initial experiments were removed from the system after it was determined that the amplitude of the signals generated by the photodiodes was of a suitable level for recording.

The radiated energies are not measured directly; they are conducted through the optical fibers and, in turn, through the filters to the sensing elements of the photodiodes. The radiated energies cause current flows in the photodiode circuits, which are detected by measuring the voltages developed across appropriate load resistors. These voltages are linearly related to the radiated energies, but their amplitude is

TABLE 1
Experimental detonation characteristics of TNT powder dispersed in various gases

Gas	Velocity (km/s)	Pressure (MPa)	Temperature (K)	Induction Time (μs)
Air	1.82	4.06	3245	18
Oxygen	1.90	4.61	4240	15
Nitrogen	—	—	—	—

influenced by the overall system characteristics. This TMI system is explicitly described elsewhere [10].

Experimental Procedure

The experimental procedures in these studies were essentially identical to those previously reported [5,8], with some modifications/improvements. Two lasers were used as depicted in Fig. 7 for monitoring concentration of the powders as well as establishing the timing for the initiation of the explosive charge used to initiate detonation in these heterogeneous systems. The reason for the extension of the detonation tube is that, although in most experiments the initiation charge consisted of a detonator and a small 2.8-g booster pellet (A4), the initiation of detonation in many experiments required substantially larger initiation charges, e.g., 10 to over 30 g of total explosive charge. Calibration studies indicated that the shorter detonation tube did not allow sufficient attenuation of the blast output to preclude interference to the pressure and light sensors; i.e., in some experiments, blast enhancements were obtained that could have been misconstrued to be nonideal detonations. Calibration experiments with the present extended detonation tube using explosive initiation charges up to 30 g C4 indicated complete attenuation of light output signals and decaying blast pressures below 0.5 MPa in the instrumented section.

The most difficult aspect of these dispersed powder experiments was, and remains, the achievement of homogeneous concentrations throughout the detonation tube. Calibration experiments were always conducted prior to detonation testing in order to obtain concentration information as well as timing requirements.

Experimental Genesis and Results

It is known that PETN and RDX, which are not combustible as is TNT, detonate individually as discrete particles when dispersed in a gaseous medium such as air [11]. However, it is also known that the addition of flaked Al powder to PETN and RDX dispersions in air provides considerably improved detonation characteristics [12]. Hence, it became evident that the Al is reacting within the detonation zone in such a manner that the overall detonation and blast output are enhanced. In other words, the Al participates in the detonation mechanism.

Because TNT is an excellent fuel as well as an explosive, studies were conducted with specially ball-milled TNT of about 30-μm average particle size, dispersed in air, oxygen, and nitrogen in the detonation tube. The concentrations were about 1 kg/m^3. The TNT readily detonated in air and in oxygen, but it did not detonate in nitrogen. Certainly TNT powder dispersed in nitrogen, if of sufficient concentration and suitable size and confinement, will detonate. Numerous additional experiments were conducted, i.e., with initiation explosive charges up to 30 g C4 or Detasheet, and at concentrations in excess of 2 kg/m^3. All failed to detonate. Evidently, the presence of oxygen was requisite to propagate detonation under the experimental conditions imposed.

Results of representative experiments, i.e., those that had the most uniform concentration as well as incremental pressures and velocities throughout the instrumented section of the detonation tube, are included in Table 1. These values can be compared to the TIGER Code analytical computations at the approximately equivalent concentration of 1 kg/m^3, as presented in Table 2.

To further investigate this phenomenology, experiments were conducted with about 22 μm RDX alone and as mixtures of RDX and TNT dispersed in nitrogen. The RDX alone, as expected, readily detonated in nitrogen. Mixtures of RDX and TNT of 75:25, 50:50, 25:75, and 10:90 by weight RDX:TNT were also tested. Detonations were achieved in all of these ratios except the 10:90 ratio; subsequently, ratios of 15:85 and 20:80 were also tested; the 15:85 ratio failed, but the 20:80 ratio detonated.

Figure 8 illustrates the TMI responses at the three wavelengths monitored at Station No. 8, along with a piezoelectric pressure transducer response at the same location, for RDX dispersed and detonated in nitrogen gas. Figure 9 illustrates the same responses,

TABLE 2
Analytical TIGER code detonation characteristics of TNT powder dispersed in various gases at 1 kg/m

Gas	Velocity (km/s)	Pressure (MPa)	Temperature (K)	Induction Time μs
Air	2.00	4.00	3250	NA[a]
Oxygen	2.05	4.40	3740	NA
Nitrogen	1.50	2.10	1775	NA

[a]NA = not applicable.

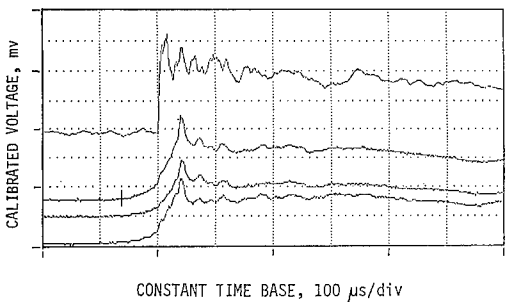

FIG. 8. TMI responses at three wavelengths of 600, 700, and 800 nm in the detonation of RDX powder dispersed in nitrogen along with a piezoelectric pressure transducer response (top trace), all at Station No. 8 and on the same time base.

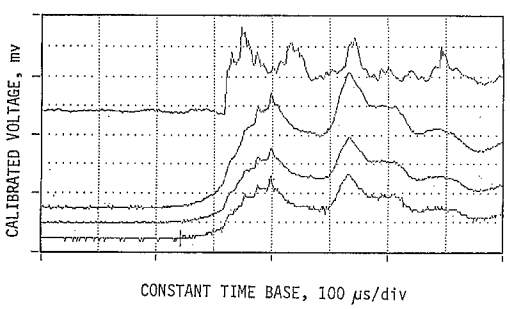

FIG. 9. TMI responses at three wavelengths of 600, 700, and 800 nm in the detonation of 50:50 weight ratio mixtures of RDX and TNT powders dispersed in nitrogen along with a piezoelectric pressure transducer response (top trace), all at Station No. 8 and on the same time base.

at the same location, for a mixture of 50:50 RDX:TNT by weight also dispersed and detonated in nitrogen. For comparative purposes, Fig. 10 is included here to illustrate the much "cleaner" and essentially singular responses of temperature, pressure, and light sensors for the denotation of TNT powder in oxygen. The TMI Unit 1, pressure, and light responses are at Station No. 6; the TMI Unit 2 response

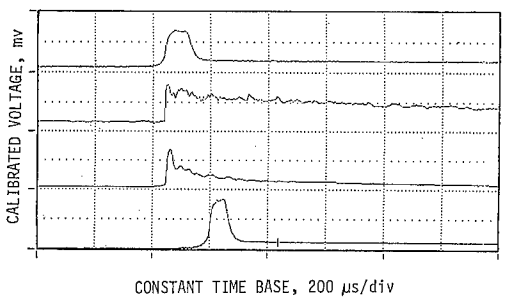

FIG. 10. Temperature, pressure, and light sensor responses in the detonation of 30-μm TNT powder dispersed in oxygen in the detonation tube. First (top) trace: TMI Unit No. 1 response; 2nd trace: piezoelectric pressure transducer response; 3rd trace: fiber-optic light-detector response; and 4th (bottom) trace: TMI Unit No. 2 response. Top three responses at Station No. 6; bottom trace at Station No. 8, with all traces on the same time base.

is at Station No. 8. All responses are on the same time scale.

Conclusions

It is premature to make definitive conclusions regarding this work, but the following observations will suffice for now. Under the constraints of the experimental conditions imposed by the detonation tube size, concentrations investigated, and initiation techniques used, the nominal 30-μm average particle size TNT does not appear to be detonable in nitrogen. There can be a number of implications regarding this.

First, from Table 2 it is observed that, at a TNT concentration of 1 kg/m^3 in nitrogen, the detonation temperature and pressure are about 50% less, and the detonation velocity is about 25% less, than that in air or oxygen. Hence, energetically this concentration may be too low to propagate detonation in nitrogen; below certain minimum concentrations, even RDX and PETN will fail to detonate whether dispersed in air or any other gaseous medium.

Second, this would suggest that TNT detonation in a gaseous medium, at very low concentrations, is dependent on a burning mechanism such as is the case for fuels, e.g., Al. Both analytical and experimental results confirm that TNT dispersions in air provide superior detonation characteristics to those of RDX or PETN at low concentrations wherein the oxygen from the air enhances the TNT energy release [4].

Third, based on the detonation of RDX/TNT mixtures in nitrogen, as readily indicated in the sensor responses of pressure, light, and TMI records, it would appear that the RDX is detonating and that the TNT is "reacting" behind the RDX detonation front so as to extend the reaction zone, i.e., a "second front" detonation.

Finally, in all of these experiments involving TNT and RDX in various gaseous media, detonations that were achieved did not involve spinning detonation. The detonation fronts were generally classical, such as for homogeneous fuel/oxidizer gaseous systems, with the exception noted above regarding mixtures of RDX and TNT.

Regarding the particle size of the TNT, in previous detonation tube experiments involving TNT particles dispersed and detonated in air [4], smaller, average 30-μm particle size TNT detonation characteristic results correlated very well with analytically predicted values, whereas for larger, average 200-μm particle size TNT, the results were considerably lower than those of the smaller particles. This was attributed to the fact that when the smaller particles detonated they were much more readily enhanced by oxygen from the air. However, in a nitrogen atmosphere, it is quite possible that larger particles would be more readily detonated.

REFERENCES

1. Tulis, A. J., and Selman, J. R., *Nineteenth Symposium (International) on Combustion,* The Combustion Institute, Pittsburgh, 1982, pp. 655–663.
2. Kauffman, C. W., Wolanski, P., Arisoy, A., Adams, P. R., Maker, B. N., and Nicholls, J. A., *Dynamics of Shock Waves, Explosives, and Detonations* (J. R. Bowen, N. Manson, A. K. Oppenheim, and R. I. Soloukhin, Eds.), AIAA, New York, 1984, Vol. 94, p. 221.
3. Tulis, A. J., *First (International) Colloquium on Explosivity of Industrial Dusts,* Polish Academy of Sciences, Warsaw, 1984, pp. 178–186.
4. Tulis, A. J., Sumida, W. K., Heberlein, D. C., Patel, D. L., and Egghart, H., *Fifth (International) Colloquium on Dust Explosions,* Oficyna Wydawnicza Politechniki Warszawskiej, Warsaw, 1993, pp. 391–400.
5. Tulis, A. J., Austing, J. L., and Heberlein, D. C., *Fourteenth (International) Symposium on Shock Tubes and Waves,* New South Wales University Press, Kingston, New South Wales, Australia, 1983, pp. 447–454.
6. Tulis, A. J., *International Symposium on Intense Dynamic Loading and Its Effects,* Beijing Science Press, Beijing, P. R. China, 1986, pp. 213–218.
7. Tulis, A. J., Austing, J. L., Sumida, W. K., Baker, D. E., and Hrdina, D. J., *Ninth Symposium (International) on Detonation, Office of the Chief of Naval Research, Arlington, Virginia* OCNR-113291-7, 1989, pp. 972–983.
8. Egghart, H., Heberlein, D. C., Tulis, A. J., and Sumida, W. K., *Eighteenth (International) Pyrotechnics Seminar,* IIT Research Institute, Chicago, 1992, pp. 1083–1107.
9. Hobbs, M. L., and Baer, M. R., *EUROPYRO 93—5th Congres (International) de Pyrotechnie du Groupe de Travail, Association Francaise de Pyrotechnie, Vaires-sur-Marne, France,* 1993, pp. 53–59.
10. Tulis, A. J., Sumida, W. K., and Joyce, R. P., *Advanced Detonation Tube Studies of Hybrid Solid-Gas Dispersions,* IIT Research Institute Report No. E06661–17, October 1993.
11. Tulis, A. J., *Advanced Concepts for Chemical Energetics Manifestations,* IIT Research Institute Report No. H01105-F; unclassified volume, 1988.
12. Tulis, A. J., *Development and Demonstration of a Bimodal Mine Clearing Munition,* U.S. Army BRDEC, IIT Research Institute Final Report No. CO6705, March 1993.

COMMENTS

Martin Sichel, The University of Michigan, USA. Professor Hertzberg has commented on the influence of particle size on detonability. We observed this effect in the case of RDX dust about 10 years ago. For a given loading ratio, the finer dust particles were more difficult to detonate or, in fact, transition to detonation failed to occur. Modeling suggested that the reason for this behavior is that the finer dust absorbs heat more rapidly so that the temperature of the gas around the particles is lower. This results in an increase in ignition delay or a failure of ignition altogether.

Author's Reply. Your previous findings regarding the influence of particle size, as well as the comments made by Professor Hertzberg, are relevant and have also been observed by us in other studies in which particle size was specifically investigated. Your suggestion based on your modeling work is very reasonable; however, we believe that mass transport also plays an important role; i.e., finer particles are readily accelerated into the high-temperature convective gas flow behind the incident shock wave whereas more massive particles will "resist" and induce considerable convective, viscous heating of the surface of

these larger particles. In the case of monopropellants such as RDX, this may be sufficient to induce ignition, or possibly direct detonation, of such larger particles much more quickly than the smaller particles that are entrained in the gas flow and depend on slower, mainly conductive heating. The influence of particle size is a complex matter, involving factors such as particle geometry, chemical kinetics, and the type of particles; i.e., ignition, and particularly detonation, of starch, aluminum, and RDX particles could be expected to involve differing phenomena.

•

A. A. Borisov, Institute of Chemical Physics, Russia. What was the minimum TNT concentration in detonable mixtures with air? We performed similar experiments with TNT, RDX, and HMX suspensions in air and found that TNT mixtures detonated at 0.25 kg/m^3, whereas HMX and RDX mixtures detonated starting with 1 kg/m^3. We found that the TNT mixtures were more detonable than HMX and RDX. How did you define the induction time?

Author's Reply. We did not specifically investigate the lower concentration limits for detonation of TNT, RDX, and PETN in air but did achieve detonations of all three at concentrations in the range of 0.5 kg/m^3. Your finding that TNT would detonate in air down to 0.25 kg/m^3, in particular at a concentration considerably lower than those for RDX and HMX, is not surprising; analytical computations indicate that TNT has much greater detonation performance at 0.25 kg/m^3 in terms of detonation temperature, pressure, and velocity, than RDX or HMX, or PETN for that matter, since the presence of oxygen from air contributes substantially to the overall energy release at this near-stoichiometric concentration for TNT in air.

The induction time was obtained by measuring the time difference between the arrival of the shock front (pressure response signal) relative to the flame front (light response signal) at each monitoring station. Since 11 stations were used in each experiment, both stability and accuracy of induction times as well as the detonation were determined.

•

Herman Krier, University of Illinois, USA. I'm not so sure that if you could have suspended greater concentrations of TNT in nitrogen (i.e., greater than 1–2 kg/m^3) that you would have seen a detonation. Clearly, a richer concentration of your 30-μm particles if promptly shock ignited would detonate, even in nitrogen.

Author's Reply. You are absolutely correct; and we did state in the paper: "Certainly TNT powder dispersed in nitrogen, if of sufficient concentration and suitable size and confinement, will detonate. . . . In fact, we have achieved the detonation of TNT powder dispersed in air, in an unconfined state, at concentrations in excess of 20 and perhaps as high as 50 kg/m^3. Obviously, at these concentrations the influence of oxygen from the air is inconsequential; hence, it can be inferred that detonation would have been achieved in the absence of oxygen altogether.

Twenty-Fifth Symposium (International) on Combustion/The Combustion Institute, 1994/pp. 89–94

PHYSICAL AND CHEMICAL OBSERVATIONS IN UNDERWATER EXPLOSION BUBBLES

WARREN C. STRAHLE AND S. G. LIOU
School of Aerospace Engineering
Georgia Institute of Technology
Atlanta, GA 30332, USA

Underwater explosion bubbles are created by nearly constant volume explosions of gaseous explosives in the C-H-O-diluent system. Contained initially in glass globes at 0.1 MPa pressure, the explosions create an oscillating bubble in two modes. First, the explosions are created in a free field, and second, the explosion takes place near a flat plate. These bubbles are intended as a subscale model of the actual bubbles created by detonation of a solid explosive in an underwater configuration. Of primary interest are the bubble energy loss mechanisms in the cycle-to-cycle oscillations in the free field explosions and the impact pressure of the water jet created when exploding near a flat plate. Using CO and H_2 with stoichiometric O_2 and various diluents, the curious fact emerges in the free field explosions that the molecular weight of the product gases has a primary effect upon the loss mechanism. In addition, the molecular weight strongly influences the impact pressure in the flat plate tests. In particular, the lower the molecular weight, the lower the loss and the higher the impact pressure. Alternatively, the water vapor mass fraction in the product gases has a primary effect upon the loss mechanism. Indicated are the presence of evaporative and Birkhoff instability but not Rayleigh-Taylor instability.

Introduction

The gas bubble formed in water after a detonation of a solid explosive is an oscillating one that may consist of many oscillation cycles. When formed in an essentially free field, the oscillating pressure imparted to the water may interact destructively with a nearby structure. Alternatively, when formed near an adjacent body, the bubble, now asymmetric, will form a water jet upon the first collapse cycle with very large impact pressure upon the target body [1,2]. In the free field case, however, the bubble loses symmetry after the first cycle and loses energy in each cycle. The question is why the energy loss takes place and upon which fluid mechanical or chemical properties does the loss depend. In the jet impact case, there has been no systematic determination of the factors influencing the strength of the impact.

In a prior paper [3], many potential types of bubble instabilities have been discussed. These occur primarily upon collapse and initial rebound of the bubble cavity. Figure 1 shows a sketch, based on the image recorded in an actual event, of the appearance of the bubble during the first cycle collapse. The corrugations developing on the bubble are due to some instability. Exactly which kind of instability, or which combination of several kinds of instability, is currently open to question and will be addressed in this paper. This paper is experimental and observational in nature. For some of the instability analysis, see Ref. 3.

Experiment

The experiment is conducted by igniting an explosive mixture in a glass globe, shown with its pressure instrumentation in Fig. 2. The wall thickness of the glass globe is about 0.1 mm. The water tank is a 4.5-m^3, 1.5-m-deep vessel open to the atmosphere. The explosive mixtures used here are gaseous hydrogen and carbon monoxide with oxygen; helium and nitrogen are added as diluents in some cases. Using various combinations of these gases, independent control over pressure, temperature, molecular weight, and adiabatic exponent may be attained. The initial pressure is 0.1 MPa. The closest approximation to the explosion type is a constant volume explosion, even after the glass globe burst, because based on the examination on the test results, combustion is completed before the water appreciably moves outward. The explosion and subsequent unsteady bubble motion is intended as a model for the bubble behavior of a real solid explosive detonation. As discussed in Ref. 3, while there is a great discrepancy in explosion pressure between the real case and the experiment here (10,000 vs 1 MPa), this is a reasonable subscale model. Briefly, the reason is that all instability mechanisms rely on linear dimensions of the bubble, which is only weakly dependent upon pressure ($p^{1/3}$). Other parameters of temperature and gas composition are comparable. However, because several phenomena that occur in a real deto-

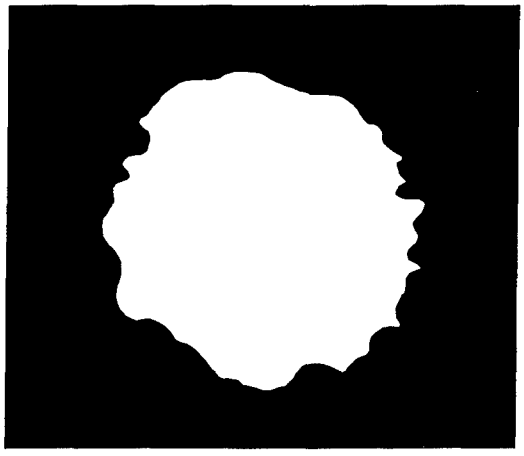

FIG. 1. Sketch of bubble appearance under collapse.

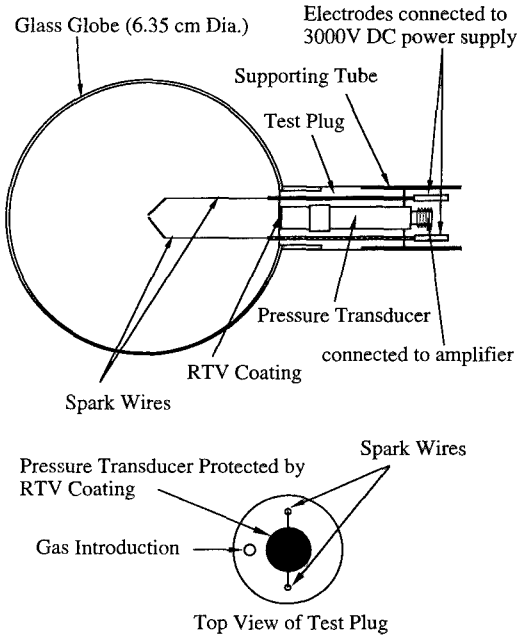

FIG. 2. Schematic of the glass globe assembly.

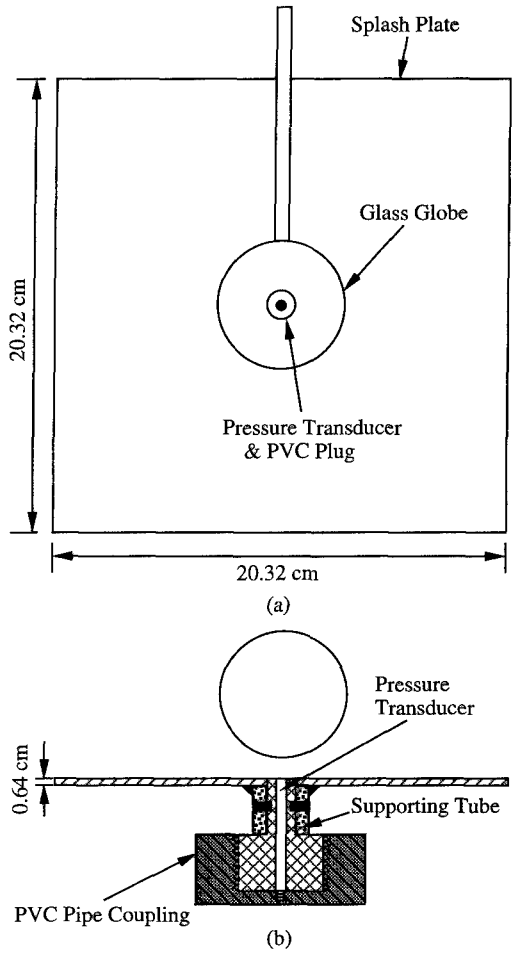

FIG. 3. Sketch of the splash plate assembly: (a) top view, (b) side view, with glass globe also shown.

nation are not present in the globe experiment, test results should not be implied to the real solid detonation directly, that is, not until a set of proper equations are developed and solved for the real detonation and differences and similarities compared with the globe results are noted, as were planned for future work.

A second configuration investigated here is that of the explosion interaction with a "splash plate," shown in Fig. 3. Upon bubble collapse, a jet is formed, shooting toward the plate with extremely high pressure upon impact.

Most of the experiments here will focus upon stoichiometric mixtures of both hydrogen and carbon monoxide with oxygen. There is an interesting fact for such mixtures in that the heat release is almost identical on a molar basis (not a mass basis) for the two fuels (284 kJ/mol for CO and 242 kJ/mol for H_2). Moreover, the primary products are triatomic. Consequently, the use of these two explosives in conjunction with diluents is a way to fix all explosion parameters while varying only the molecular weight of the products.

Figure 4 shows typical pressure records within the bubble and within the water about 0.54 m away from the bubble. The hydrophone record is used as an event marker and to monitor the strength of the wall-reflected waves. Over most of the bubble cycle, the reflected waves are much weaker than the primary

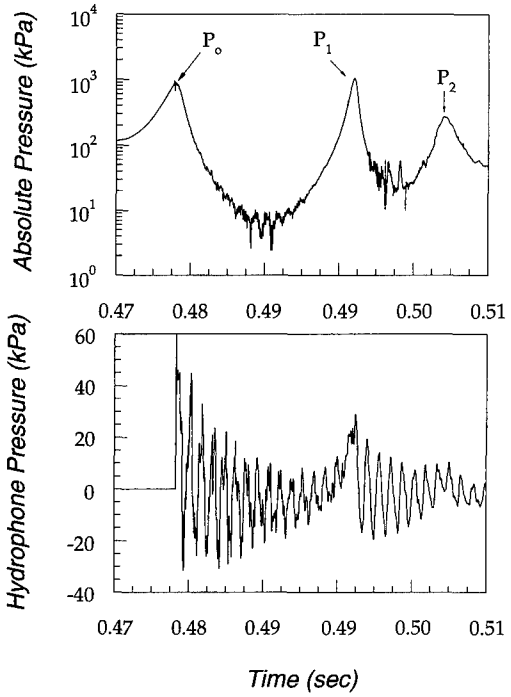

FIG. 4. Typical trace for bubble pressure and hydrophone pressure (Po: explosion pressure; P_1, P_2, . . .: subsequent pressure peaks corresponding to bubble minima).

bubble pressure, while near the bubble pressure minimum, there is some interference. However, the interference does not affect the long time average pressure in the vicinity of the pressure minimum. It should be noted that the successive pressure maxima get weaker and weaker in each cycle. This is a well-known indication of [1] bubble energy loss and is a focus of this paper.

Results and Interpretation

Figure 5 shows the experimental results of six tests, where the ratio of successive pressure peaks to the peak explosion pressures are shown. In all cases, the mixture ratio of the carbon monoxide and hydrogen is stoichiometric with oxygen. In four cases, either nitrogen or helium is used as a diluent to alter the gas properties, primarily the molecular weight. Viewing the table to the right of Fig. 5, the theoretical gas properties (using the NEWPEP [4] program from NWC) are shown for the instant after the explosion is complete. Note that the pressures, temperatures, and adiabatic exponent, γ, are all comparable. Of course, the temperatures are slightly depressed with diluents, but the temperatures are all between 3038 and 3372 K. The dominant variation is in molecular weight, which runs from 12.98 to 36.33. This is what was desired from these runs and, again, occurs because of the nearly equal energetics from CO and H_2.

Within the hydrogen group, the lower the molecular weight, the less the energy loss for the first two cycles. Within the carbon monoxide group, the same phenomena occur, except the case with nitrogen. Then, comparing the hydrogen and carbon monoxide groups, it still appears that, in general, the lower the molecular weight, the greater the energy retention. The discrepancy noticed in the second and, especially, the third cycle is believed to be associated with the bubble migration and breakup. Besides, the difference on pressure ratio among the cases also gets smaller in the subsequent cycles.

Another curious fact in the hydrogen sequence is that in two cases, the pressure is *higher* in the second maximum (P_1) than in the first (the explosion pressure, P_0). There may be two reasons why this is so. First, there is some residual energy deposition from the spark (<10%) while the bubble has already started its pressure decline after the explosion. This is considered minor. Second, the dominant combustion product is water vapor. Moreover, the interface temperature* is 339 K. Under these conditions, using the Hertz–Knudsen evaporation/condensation kinetic equation [5], during the time interval shortly after the explosion, condensation is occurring, not evaporation. This is an exothermic process insofar as the bubble gases are concerned. In the carbon dioxide case, since no water vapor is generated by the explosion, evaporation occurs, which is endothermic. Coupled with the molecular weight effect, the subsequent pressure peaks are always lower than the explosion pressure in the carbon monoxide cases.

In all cases, the cycle-to-cycle loss in pressure runs between 50 and 70%. This loss is of the same magnitude as reported for real detonation-induced bubbles [1]. The bubble internal energy is directly proportional to the residual pressure so that it is evident that strong energy losses occur between cycles. Using the Trilling–Herring equation for bubble dynamics [6], as done in Ref. 3, the only loss for a spherically symmetric bubble is an acoustic radiation loss to the water. However, it cannot explain the magnitude of loss observed here. The loss must come from the instability and breakup of the bubble and the generation of "turbulence." Moreover, molecular weight does not appear as a parameter in the standard bubble equation, but it does in several of the equations of various instabilities. Only through these instability mechanisms can the above molecular weight effects enter.

The possible instabilities were discussed in Ref. 3. There, the so-called Rayleigh–Taylor instability (in-

*This comes from a heat transfer calculation which will be presented in a forthcoming paper together with full evaporation/condensation calculations.

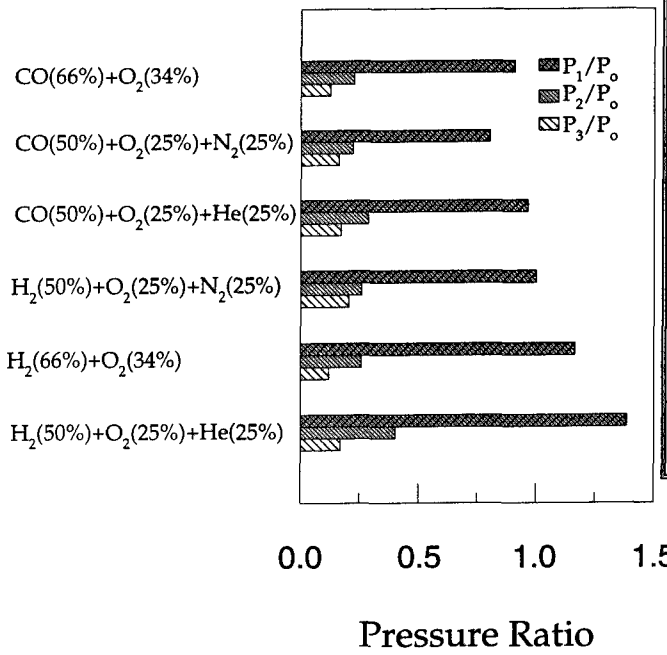

T_0(°K)	Po_a(kPa)	W_0(g)	γ
3230	858.5	36.33	1.20
3038	820.5	35.40	1.21
3113	855	29.15	1.23
3165	834	19.15	1.22
3372	869	15.51	1.21
3242	862	12.98	1.24

FIG. 5. Sequential pressure ratio for different gas mixtures. Also shown is the table containing analytical results for maximum temperature, maximum pressure, molecular weight, and specific heat ratio for the corresponding mixture.

stability under acceleration at a light fluid–heavy fluid interface) [7] was ruled out as a possibility because no exponential growth on disturbance amplitude was observed in the period when the instability was operative. Moreover, a high wave number of the spatial corrugations was required, and the experimental evidence favors low wave number. It is further ruled out here because analysis reveals no molecular weight dependence in the disturbance growth rate.

Considered in Ref. 3 were also the Birkhoff [8] (B) instability and the Landau–Darrieus [9] (LD) evaporative/condensation instability. Both of these involve density of the product gases, which depends upon molecular weight. In particular, the critical evaporation rate for the LD instability onset is raised as the molecular weight increases. There is an unconditional instability criterion in the case of the LD instability. For the mass flow per unit area, j, above the value below, there exists a range of wave numbers for which instability is guaranteed:

$$j^4 > 4g\rho_1\rho_2^2\sigma.$$

Here σ is the surface tension, g is the acceleration (gravitational or unsteady interface acceleration), and ρ_1 and ρ_2 are the liquid and gas densities, respectively. The formula has never been substantiated experimentally and should probably be given limited credence. In any event, recall the hydrogen-carbon monoxide comparison above, with the remarks about condensation/evaporation and molecular weight. Detailed calculations concerning the B and LD instabilities are required and are currently underway.

Turning now to the splash plate tests, Fig. 6 shows the bubble gas and the plate pressures as functions of time for a particular hydrogen-oxygen case. The peak plate pressure always comes near the end of the bubble cycle, although the pressure signature can become extremely complex, depending upon the proximity of the glass globe to the plate. The plate pressure transducer has a range of 0–3.5 MPa. The extreme range of the pressure oscillation shows a slightly negative pressure on the plate for a short time interval, which is clearly impossible; this deviation from zero should be considered an indicator of the accuracy of the pressure measurements.

Shown in Fig. 7 are the peak plate pressures as a function of globe distance from the splash plate. Extremely high pressures are shown if the globe is sufficiently near the plate. Seen is an amplification of the explosion pressure by a factor of 5; hence, the usefulness in applications is clear. At large separation distances, the peak pressure falls off as 1/(distance), as it should from acoustic principles. However, as the separation distance decreases, the peak pressure reaches a maximum first and then starts falling again.

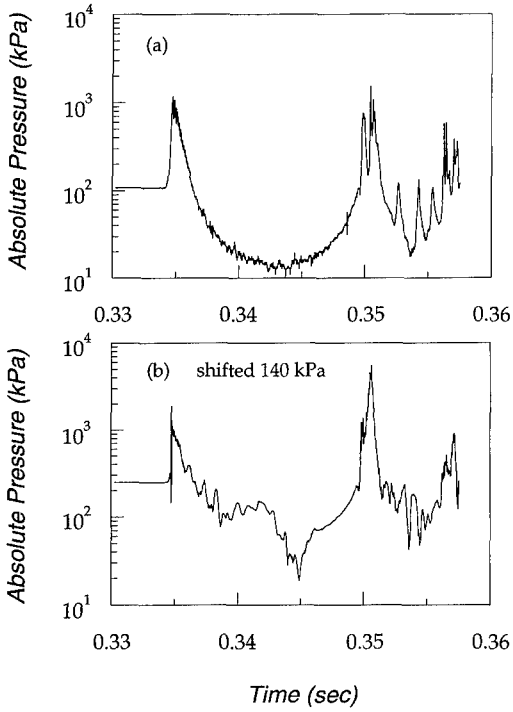

FIG. 6. Trace of (a) bubble pressure and (b) splash plate pressure for stoichiometric H_2-O_2, with $d/R = 1.6$.

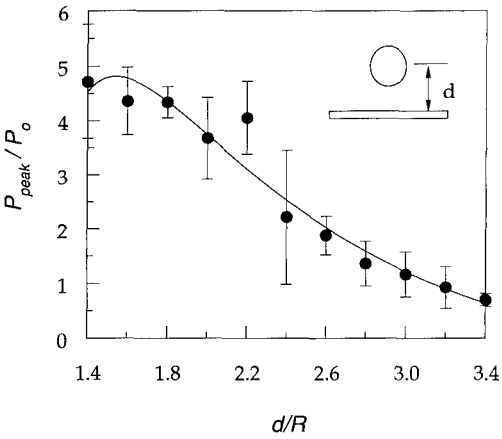

FIG. 7. Normalized splash plate peak pressure vs separation distance for stoichiometric H_2-O_2.

The scatter in the results is fairly large, precisely because of bubble instability, which is also present here. It is difficult to tell precisely where the jet is going to impact, even though from the event recording, it seems that the jet hits the plate right underneath the center of the bubble every time. Therefore, each data point consists of three runs.

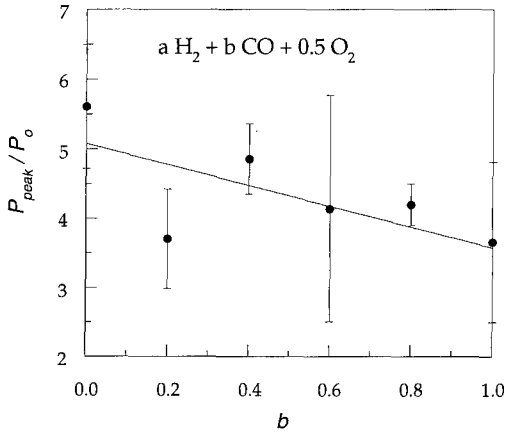

FIG. 8. Normalized splash plate peak pressure vs volume ratio of CO, with $d/R = 1.6$.

Another curious molecular weight effect is seen here. Figure 8 shows the peak (optimum spacing) pressure attained when a mixture of hydrogen and carbon monoxide, stoichiometric with oxygen, is used. Varied is the CO mole number, b, where $a + b = 1$ has been maintained. As b goes from 0 to 1, the energetics per mole are nearly the same, but the molecular weight of the product gases rises, from approximately 18 to 44. As the molecular weight rises, the peak pressure falls. Again, low molecular weight products give a more favorable result.

This result is, perhaps, more understandable than in the case of the free field bubbles. In any fluid mechanical scheme where force generation is required, the ratio of T/W, (where T the temperature and W is the molecular weight) occurs, being proportional to the square of the mean molecular speed in the gas.** This is also proportional to the stagnation enthalpy. As b is varied, the variation in the pressure result is greater than the mild energetics variation and so appears to indeed be a molecular weight result.

Conclusions

Underwater explosion bubbles created by low-pressure gas explosions can simulate many of the aspects of the detonation of real solid explosives that produce underwater explosion bubbles. Investigated here were energy losses in successive oscillation cycles and the jetting impact pressure when explosions take place near solid boundaries. Typical bubble energy loss per cycle was 50–70%. Typical impact pressures were of the order of five times the explosion pressure under optimum conditions of explosive

**See Ref. 5 (p. 25).

placement. For fixed energy release, the molecular weight of the product gases was found to have an important effect in both cases: increasing the energy loss and decreasing the impact pressure as molecular weight increases. Indications were given that water-gas interface evaporation and/or condensation plays a role in the energy loss mechanism. Detailed calculations are warranted for the unsteady evaporation/condensation problem in this configuration.

Acknowledgments

This work was supported by the Office of Naval Research. The Contract Monitor is Dr. Judah Goldwasser.

REFERENCES

1. Cole, R. H., *Underwater Explosions*, Princeton University Press, Princeton, NJ, 1948, pp. 270–352.
2. Snay, H. G., *Hydrodynamics of Underwater Explosions*, Naval Hydrodynamics, NAS-NRC Publication 515, 1957, pp. 325–351.
3. Strahle, W. C., and Liou, S. G., *Combust. Sci. Technol.*, 1994 (in review).
4. Cruise, D. R., *Theoretical Computations of Equilibrium Compositions, Thermodynamic Properties, and Performance Characteristics of Propellent Systems*, NWC TP-6037. The code used here was modified by Chan Price and dated April, 1988.
5. Kennard, E. H., *Kinetic Theory of Gases*, Chap. III, McGraw-Hill, New York, 1938.
6. Trilling, L., *J. Appl. Phys.* 23:14–17 (1952).
7. Sturtevant, B., in *16th Int. Symposium on Shock Tubes and Waves* (H. Groenig, Ed.), 1988, pp. 89–100.
8. Birkhoff, G., *Q. Appl. Math.* 13:451–453 (1956).
9. Landau, L. D., and Lifshitz, E. M., *Fluid Mechanics*, Pergamon Press, London, 1959, p. 498.

Twenty-Fifth Symposium (International) on Combustion/The Combustion Institute, 1994/pp. 95–102

SURFACE EROSION BY HIGH-SPEED COMBUSTION WAVES

R. KLEIN, H. BREITBACH, K. J. GERATZ, AND W. SENGER
Institut für Technische Mechanik
Rheinisch-Westfälische Technische Hochschule Aachen
Templergraben 64, 52056 Aachen, Germany

Violent high-speed combustion events lead to erosive destruction of piston surfaces under knocking conditions in internal combustion engines. The details of the damaging mechanism are the subject of an extensive controversy. In this paper, we present and support a new theoretical model for one possible mechanism causing erosive destruction due to high-speed combustion waves. The theory involves the initiation and resonant amplification of Rayleigh surface waves in the elastic piston material. Intense peak stresses develop very close to the material surface and may explain the erosive nature of the observed damage. We support the proposed theory by research engine experiments as well as by direct numerical simulations for a simplified two-dimensional model problem. The model computations include the gas-phase high-speed combustion and the elastic wave propagation in the solid. In this paper, we focus on mechanical stresses, while we leave a detailed investigation of and comparison with thermal loads for future work.

Introduction

A multitude of experimental as well as theoretical investigations [1–9] indicate that very fast shock and combustion waves develop under knocking conditions in an internal combustion engine. Wave speeds as large as 1700 m/s have been measured. Even faster processes cannot be excluded, since a suitable sequential autoignition in the end gas can lead to a rapid pressure wave amplification [9] that may culminate in the establishment of detonations [3,8,10,15], achieving velocities as large as 2000 m/s. Knocking combustion induces erosive surface destruction [5,8], and in this paper, we propose an explanation that provides a link between high-speed combustion and surface erosion.

Order-of-magnitude estimates for thermal and mechanical loads induced by high-speed combustion fronts in Refs. 8 and 9 indicated that both effects may lead to stresses close to the yield threshold of typical piston materials. These estimates were based, however, on quasi-static considerations for the solid, and thus they neglected the fact that the wave speeds associated with knocking combustion can be comparable to the elastic wave velocities in the piston alloy. Of particular interest in this context are elastic Rayleigh surface waves. They not only have the slowest propagation speed (typically 2800 m/s), but in addition, their stress distributions are concentrated near the material surface. Here we analyse excess mechanical stresses due to inherently unsteady effects. Thermal loads will be considered in future work.

When a fast combustion or shock front hits the piston material surface under a suitable angle of incidence, the point of reflection may attain effective propagation speeds along the surface that are comparable to the Rayleigh wave velocity and, so we emphasize, much larger than the normal velocity of the incident wave in the gas phase. In this situation, a dynamical resonant Rayleigh wave excitation occurs, and local stresses close to the surface may considerably exceed the nominal stresses obtained from a quasi-static estimate. Stresses beyond the yield threshold of typical piston materials can easily occur by this mechanism. Even if the local stresses are not critical, further stress amplifications may occur during material wave reflections at sharp edges of the piston geometry. In fact, very often the erosive damage is observed to begin close to the upper edge of the piston top land.

We support our theory by a scaling analysis based on theoretical results of Miles [11] and a combination of experimental and computational evidence. The analysis reveals two factors that crucially contribute to stress amplification due to Rayleigh wave resonances: One is a slow passage through the resonance; the other factor is short characteristic lengths of the wall pressure signature. The latter is of particular interest in connection with reflected detonations where a narrow reaction zone imposes a short characteristic length. In the experiments, we consider metallographic cuts of slices of damaged piston material and observe characteristic changes of the microstructure in a thin layer underneath the piston surface. In modern eutectic piston materials, a ductile, saturated aluminum-silicon matrix encloses brittle silicon crystals. These enclosures show fractures in the damaged sur-

face layer, indicating extreme stress concentrations in this region.

In preparation for extended simulations for more realistic geometries, we present here a series of numerical computations for a two-dimensional model problem. These computations involve direct numerical simulations of high-speed combustion in the gas phase based on the reactive Euler equations combined with finite-element computations of elastic wave propagation in an adjacent solid body. By appropriate initial data, we create a cylindrical detonation in the combustible gas some distance above the plane surface of the solid. The detonation wave expands and reaches the surface after a short time. In the sequel, the detonation shock reflection point moves along the material surface. The theoretical speed of this reflection point is infinite at the instant of the first contact between the detonation shock and the solid surface, and it decreases continuously thereafter as the angle of incidence and the lead shock strength change with time. Asymptotically, the detonation shock becomes normal to the surface, and the reflection point moves at the Chapman–Jouguet detonation speed. During this process, the reflection point velocity will for a limited interval of time be comparable to the Rayleigh wave speed, and we expect and compute a considerable amplification of stresses near the surface at this time. By suitable variations of the model parameters, we find that the most severe stress amplification occurs when the conditions for Rayleigh wave resonance are most favourable.

We are aware that the autoignition in the end gas under knocking conditions does not necessarily produce fully developed detonations, but that mostly transient processes dominate in reality. In this sense, our computations should be understood as model computations with a well-defined set of parameters and a reproducible setup. We hope to investigate more realistic examples in the future.

Experimental Setup

In our experiments, we used a single-cylinder water-cooled four-stroke spark ignition engine. The engine has a disk-shaped combustion chamber with two valves and the spark plug in typical positions. The displacement is 500 cm^3, the cylinder bore 84 mm, and the compression ratio $\varepsilon = 10$. As fuel, we used commercial unleaded premium-grade gasoline with a Research Octane Number RON = 98. The engine parameters and the combustion chamber geometry have intentionally been chosen to closely resemble typical production engines.

Inlet air temperature and pressure (25°C, 101.3 kPa) and fuel temperature at the injection nozzle (25°C), as well as oil and water temperature (both 90°C), are controlled independently to minimize the influence from ambient and engine operation conditions. Injection and ignition timing can be electronically controlled in steps of 1° crank angle; the electromechanical injector injects directly into the inlet valve port. In this investigation, we used a commercially available production engine piston. The piston material is an eutectic aluminum-silicon alloy with 12% silicon and copper, magnesium and nickel about 1% each.

FIG. 1. Metallographic cut of area with onset of material damage visible.

We observed typical knock damage on the piston crown and in the ring belt area. As expected, the knock damage occurs in the end-gas region opposite to the spark plug position. The pistons show typical surface erosion phenomena that have often been observed and discussed as knock damage [4,5,12]. To cause the damage, we had the engine running at 2500 rpm under full load and with an equivalence ratio of $\phi = 1$ for 30 min. The ignition timing was 32° crank angle before top dead center (BTDC), which is 7° beyond the threshold of 25° CA when first slightly knocking cycles occur under these conditions.

Metallographic cuts of material from the damaged areas were prepared and examined. Figure 1 shows a cut of 210 × 140 μm in the radial direction and perpendicular to the piston crown surface from a slightly damaged part of the piston top land area. The dark structures represent silicon crystals; the slightly grey structures are eutectica. As can be seen, the silicon crystals beneath the surface show cracks down to a depth of about 15–20 μm, whereas deeper crystals are completely unaffected. The appearance of these cracks directly beneath the surface was a motivation for us to search for mechanisms causing mechanical stresses in thin surface layers.

Since we later employ a theoretical model for possible damage mechanisms that assumes the presence of strong pressure waves, we will now present pressure measurements from locations adjacent to the surface damage region.

We have installed three pressure transducers, two in the cylinder wall and one in the cylinder head, with

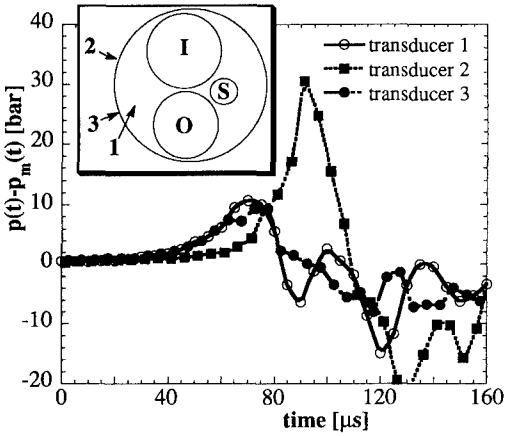

FIG. 2. Pressure signals measured in the ring crevice (pressure traces 2, 3) and cylinder head (pressure trace 1) adjacent to the surface damage area of the piston. The insert indicates the positions of the pressure transducers (I: inlet valve; O: outlet valve; S: spark plug).

positions as marked in the insert in Fig. 2. Transducer 1 is mounted in the cylinder head. Transducers 2 and 3 are mounted in the ring crevice; with the piston at top dead center, the distance from the transducer center to the first piston ring is 3 mm and to the piston crown 6 mm. The distance between transducers 2 and 3 is 30 mm, and 9 mm between transducers 1 and 3. The transducers' membranes were flush mounted to the cylinder wall and cylinder head surface to avoid resonances in gas volumes between cylinder and transducer. The sensitive area of the transducer membranes has a diameter of 4 mm.

It is known from many investigations that pressure pulses with frequencies up to 50 kHz occur during knocking combustion [13]. Therefore, we used pressure transducers with a natural frequency of about 400 kHz and a rise time of 1 μs, so that measurements of pressure oscillations with frequencies up to about 150 kHz would have been possible. For data acquisition, we use a personal computer; transducer signals are acquired with a sampling rate of 200 kHz each.

Figure 2 shows typical transducer signals for a knocking cycle under the above-mentioned conditions. The signal is high-pass–filtered with a Butterworth filter and a cutoff frequency of 2 kHz. It indicates a pressure wave in the ring crevice and cylinder, propagating clockwise. The propagation speed calculated from the pressure maxima is about 1450 m/s; the amplitude of the pressure wave, as well as the gradient, is increasing with time. This kind of development of a pressure pulse with increasing amplitude closely resembles the pressure history of a developing detonation by the SWACER mechanism [3,9,10]. With the experimental techniques used here, the verification of such an assumption is not yet possible, but existence and propagation speed of the pressure pulse are a motivation for us to use the model problem presented in the subsequent sections.

Theoretical Estimates

Miles [11] analyses the elastic wave propagation in a half-space due to the pressure load of a half-spherical blast wave, initiated on its surface. The paper concentrates on cases where the blast wave velocity is larger than the Rayleigh wave velocity to begin with and then decays so that resonant excitation occurs over a limited time interval. Using Fourier–Bessel transformation techniques, Miles derives exact solution formulas that involve complex integrations. The integrals are evaluated approximately by asymptotic methods based on the following simplifying assumptions:

1. The spatial structure and amplitude of the moving pressure distribution are slowly varying on the time scale ℓ_{ref}/D, where D is a typical propagation speed of the moving load and ℓ_{ref} is a characteristic length scale of the pressure signature.
2. Only points far away from the blast wave origin are considered, so that lines of constant surface pressure are approximately straight on the scale of ℓ_{ref}.
3. The temporal Fourier transform, $\hat{p}(x,\omega)$, of the pressure signature satisfies the equation

$$\frac{\partial}{\partial x} x^{1/2}\hat{p}(x, \omega) = 0. \tag{1}$$

The first assumption allows a stationary phase approximation of the solution integrals. It seems to be particularly justified when the pressure load is due to a detonation that is driven by a chemical reaction that introduces a short reaction zone thickness as a typical reference length (see Fig. 3 for illustration). The second assumption allows a quasi–two-dimensional approximation with the effects of three-dimensionality entering mainly through the space-time dependence of the pressure load. Assumption three is mainly introduced for convenience in the analysis, but it is motivated, e.g., by G. I. Taylor's [14] strong shock theory. We do not expect the last assumption to crucially affect the scaling results derived in this section, even though this is hard to prove rigorously.

Miles succeeds in separating explicitly the effects of resonant Rayleigh wave excitation from those effects that would also occur without it. Besides other results, he derives the following formula for the tangential displacement of mass elements at the solid surface induced by the Rayleigh wave resonance alone.

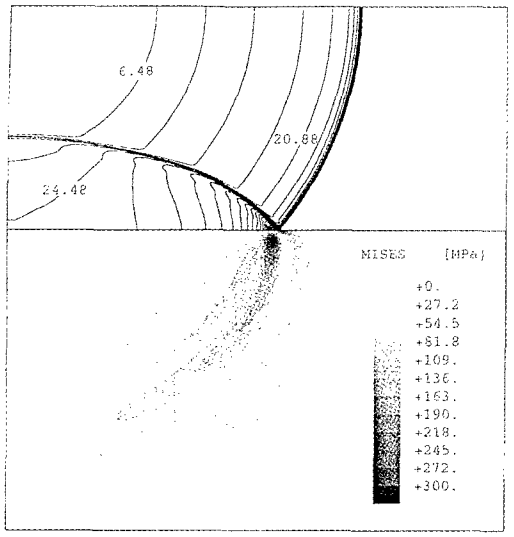

FIG. 3. Pressure contours in the gas phase and contours of the von Mises equivalent stress for the elastic material, exhibiting the detonation-induced Rayleigh wave structure.

$$q_0(x,t) = \frac{A^* E^{-1}}{2[2t_0''(x)]^{1/2}} \int_0^t \frac{p(x,\tau)}{t - \tau^{1/2}} d\tau \tag{2}$$

where $t_0(x)$ denotes the inverse of the leading shock location function, $x_{sh}(t)$, A^* is a nondimensional material constant and E is young's modulus.

To obtain an order-of-magnitude estimate for the damage potential due to the Rayleigh wave resonating with a reflected detonation, we evaluate the formula in Eq. (2) with

$$p(x,t) = p_{max}(t) \left\{ \tilde{p}\left(\frac{x - x_{sh}}{\ell_r}, t\right) + \bar{p}\left(\frac{x - x_{sh}}{x_{sh}}, t\right) \right\} \tag{3}$$

where ℓ_r characterizes the reaction zone thickness of the detonation and where $\tilde{p}$ and $\bar{p}$ are scaled to be of order $O(1)$ and, just as $p_{max}(t)$, are slowly varying on the time scale ℓ_r/D. The short-scale pressure, $\tilde{p}$, stands for the pressure signature of the detonation reaction zone, while $\bar{p}$ represents long-range pressure variations, e.g., the Taylor wave behind a detonation receding from a wall.

An asymptotic evaluation of Eq. (3) for $\ell_r/x_{sh} << 1$ yields an approximate expression for the tangential stresses at the material surface of the form

$$\sigma_{xx}^{max} = E \frac{\partial q_0}{\partial x} \approx \frac{A^*}{\Delta D/D^{1/2}} a p_{max} \tag{4}$$

where

$$\Delta D \approx \ell_r \frac{dD}{dx} \tag{5}$$

characterizes the change of the blast wave velocity while it passes a distance comparable to the detonation reaction length, and

$$a = \max_{\xi} \int_{-\xi}^{0} \frac{d\tilde{p}}{d\eta}(\eta) \frac{1}{\xi + \eta^{1/2}} d\eta \tag{6}$$

is a scalar factor that depends on the detailed shape of the narrow pressure peak. The estimate in Eq. (4) shows that, for a given maximum of the pressure signature, arbitrarily large stresses can be generated as a result of the resonance phenomenon, provided that the speed of the pressure pulse passes through the Rayleigh wave speed sufficiently slowly, so that $\Delta D/D << 1$. Notice also that the shape factor, a, itself can be extremely large if the gradient $d\tilde{p}/d\eta$ is large near $\eta = 0$. In fact, if the effective pressure on the wall is discontinuous, as it is for a moving shock wave, then $d\tilde{p}/d\eta(0)$ approaches a δ peak, and the theory predicts infinite stresses. Boundary-layer effects or the fact that the piston surface is not exactly plane and smooth may shield the effect of this discontinuity in reality, but we emphasize that intolerable surface stresses will always occur, provided that $\Delta D/D$ is sufficiently small.

Gas-Phase Computation

High-speed combustion events after the onset of knock in internal combustion engines can be modeled in a first approximation by the reactive Euler equations, neglecting all dissipative mechanisms [8]. The goal of the present work is to exhibit by direct numerical simulation that high-speed combustion events induce inherently unsteady elastic material deformations associated with extremely high stress amplitudes. For the gas-phase computations, a simple chemico-thermodynamic model is sufficient to begin with. In this work, we use an irreversible one-step Arrhenius reaction with an activation energy E^+ and an ideal gas equation of state with constant specific heat ratio γ.

Gasdynamic Solver:

The computer code used for the present direct numerical simulation is a higher order shock-capturing scheme in combination with Strang-type operator splitting to cope with the reaction model. The shock-capturing scheme is a Godunov-type method modified to second-order accuracy following Harten and Yee (see Ref. 16). For the numerical fluxes, we use Roe's approximate Riemann solver [17] with a modification for the fluxes of the passively transported

mass fractions according to Larrouturou [18]. The chemical source term is discretized explicitly with a time-step restriction that combines the Courant condition for stability of the gasdynamic solver with the constraint that the internal and kinetic energy in any grid cell may not change during a time step by more than a prechosen fraction of the total energy due to the progress of the chemical reaction [19]. The numerical resolution in our computations is about five grid cells per half-reaction length of a Chapman–Jouguet detonation. For the purposes of this paper, it is sufficient to consider stably propagating detonations with relatively low activation energy reactions. To simulate reliably these systems, higher resolution or more sophisticated numerical tools [20] are not needed.

Calculation of Elastic Wave Propagation

We employ the finite-element program ABAQUS, version 5.2.1, for the simulation of elastic wave propagation. ABAQUS is a commercial program designed for linear and nonlinear structure analyses and is specially suited for general-purpose applications as well as for nonlinear problems [21,22].

We use square elements containing four nodes each and a linear ansatz function for the material displacement. The stress wave calculations are performed running ABAQUS' "dynamic analysis option," which means that the full dynamic equations of motion are integrated. The program involves an implicit time integration operator with artificial damping called HILBER–HUGHES–TAYLOR operator. We use constant time increments and automatic solution control tolerances. Comparison of results for several sample problems obtained with a new explicit version of the code and the implicit version did not show any noticeable difference, provided the implicit code was not forced to operate with extremely large time steps.

The model problem to be discussed in the next section involves the collision of a cylindrical detonation with an elastic half-space. We simulate this configuration by using special "infinite elements" that efficiently mimic reflectionless boundaries and allow us to focus all computational power in the active solution region where the Rayleigh surface waves need to be resolved.

Results

To exhibit by direct numerical simulation the Rayleigh wave resonance effect predicted by the theory, we consider a cylindrical detonation wave that expands from a center located 5.8 mm above an aluminum surface. We emphasize again the model character of this setup. A detonation wave is characteristic for high-speed gas-phase combustion, and it has the advantage that it can be set up easily and reproducibly in the numerical simulation. The predetonation state corresponds to the precompressed unburnt end gas in an internal combustion engine just before the onset of knock. Thus, we assume an initial pressure of 3 MPa and an initial gas density of 11.5 kg/m^3. The heat release of the assumed one-step Arrhenius reaction is $(-\Delta h) = 3.86 \cdot 10^3$ kJ/kg, which is in the range of the heat of reaction of a typical hydrocarbon-air mixture. The Chapman–Jouguet detonation velocity for this gas mixture, when an ideal gas equation of state with constant specific heats and $\gamma = c_p/c_v = 1.2$ is assumed, evaluates to $D_{CJ} = 2000$ m/s. Thus, the detonation speed is large enough to render a resonant Rayleigh wave excitation possible. An activation energy was assumed for the present computation, so that $E^+/RT_0 = 1$, where T_0 is the temperature in the predetonation gas. This low value is chosen to guarantee stable propagation of the simulated detonation and highly reproducible results for this comparison of theory and direct simulation. More realistic chemical kinetic and thermodynamic models will be considered in future work.

We initiate the detonation by assuming an initial radius of the leading shock front of 4 mm and by imposing the data of a plane Chapman–Jouguet (ZND) detonation on radial rays through the blast wave origin. Averaged values of the conserved quantities for each numerical cell within the initial shock radius are obtained by averaging the CJ-ZND data for 10×10 equally spaced subcells per cell. This procedure reproducibly initiates a detonation with minimal start-up noise.

The detonation then expands and is subsequently reflected at the material surface. The choice of the material constants is guided by realistic values for piston alloys [23] at a temperature of about 500 K. Thus, we set Young's modulus $E = 7.4 \cdot 10^{10}$ Pa and the Poisson's ratio $\nu = 0.33$.

Figure 3 shows a combined graph of pressure contours in the gas phase and a grey-shade representation of the von Mises equivalent stresses in the solid at time $t = 0.28$ μs. One clearly can identify the expanding detonation front and the reflected shock in the burnt gases, and we observe a strong pressure peak at the reflection point.

The van Mises stresses exhibit the characteristic comma-shaped distribution that results from a local impulsive load [24] and indicates that a Rayleigh wave has been generated. Very close to the surface and next to the detonation reflection point, the maximum stresses are achieved. Figure 4 shows the time history of the maximum tangential stress at the material surface, and we find that the absolute maximum achieved in this first computation (black solid circles) is about 278 MPa. This exceeds the maximum pressure by a factor of 2.7.

In the following, we present the results of two ad-

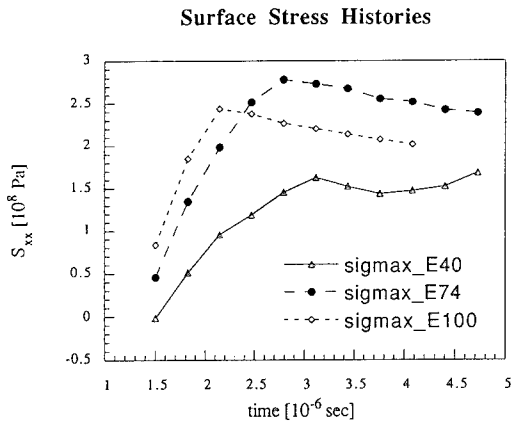

FIG. 4. Time histories of the maximum tangential surface stress for the three computational runs: $E = 4.0 \cdot 10^{10}$ Pa; $E = 7.4 \cdot 10^{10}$ Pa; $E = 10.0 \cdot 10^{10}$ Pa.

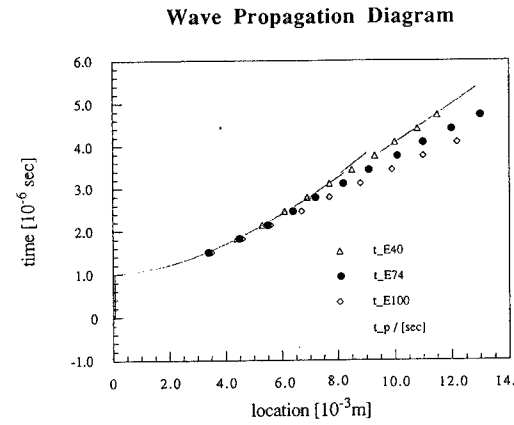

FIG. 5. Wave propagation diagram showing the motion of the peak pressure along the wall (dotted), and the locations of maximum tangential stresses at the material surface for the different values of the elastic moduli: $E = 4.0 \cdot 10^{10}$ Pa; $E = 7.4 \cdot 10^{10}$ Pa (realistic); $E = 10.0 \cdot 10^{10}$ Pa.

ditional computations that are set up to prove that these extreme stresses are due mainly to resonant excitation of the Rayleigh wave. If this claim is correct, then, under the given wall pressure history, the peak stresses in the material should be reduced when the elastic wave speeds are either decreased or increased. In both cases, the Rayleigh wave initiated during the first head-on collision of the detonation shock would be out of tune with the shock reflection point.

With these considerations in mind, we have performed two further computations, one with a reduced Young's modulus of $E = 4.0 \cdot 10^{10}$ Pa, and a second one with $E = 10.0 \cdot 10^{10}$ Pa. The key results are presented in Figs. 4 and 5. Figure 5 is a wave propagation diagram. The dotted line is the time-dependent location of the maximum wall pressure from the gas phase. Its speed decreases from being close to infinite to about 2300 m/s towards the end of the computation. The solid circles indicate the location of the maximum tangential stresses in the solid for the first computation discussed above. We observe that it moves in close junction with the pressure maximum between the locations $x = 3$ mm and $x = 7$ mm, but that the paths diverge thereafter. The Rayleigh wave speed for this case is 3000 m/s, and the divergence of the paths of extreme stresses indicates that, after an initial resonant excitation, the Rayleigh wave leaves the pressure peak behind, thereby approximately maintaining its amplitude. The corresponding time history of the maximum surface stresses in Fig. 4 shows an abrupt end of the stress growth at the time when the resonance condition is no longer satisfied.

The triangle- and diamond-signed traces in Figs. 4 and 5 are the corresponding results for the decreased and increased values of the elastic modulus, respectively. The Rayleigh wave speeds for these data are 2300 and 3500 m/s. For the former calculation, the pressure peak moves faster than the Rayleigh wave for $x < 8$ mm. The maximum surface stress does occur approximately at the location of the maximum pressure, but as a result of the lack of resonance, the stress amplification is much less pronounced than in the previous case. Only at a later stage does the tangential stress again increase, when the pressure wave has slowed down so that resonance occurs. An amplification is seen, even though by this time the pressure amplitude has reduced by a factor of 3 (not shown), so that the residual amplification is weak. For the last computation, the stress amplification is very rapid initially, as indicated by the diamonds in Fig. 4. This amplification ceases abruptly at $x = 2.3$ mm. Only over a very short distance do the Rayleigh wave and the pressure peak move in tandem, but as soon as they separate, the stress amplification stops. Notably, the stresses do not increase in this case again at later times. This is in contrast to the situation of the second example with reduced Young's modulus, and it lends additional support to our earlier interpretation of this case.

Conclusions

The speed of high-velocity combustion fronts can be comparable to the elastic wave speeds of the piston material of internal combustion engines. This observation led us to consider detonation-induced resonant excitation of Rayleigh surface waves as a potential mechanism for the erosive surface damage often seen under knocking combustion conditions. Experimental evidence supports this idea, since the

observed damage is not only located close to the material surface, but in addition, the brittle cracking of silicon crystals in a thin surface layer points towards a pure mechanical destruction rather than to thermal problems. Theoretical estimates predict very high stress amplification as soon as the proposed resonance mechanism becomes active, and direct numerical simulations of a simplified two-dimensional model problem clearly exhibit the expected effect. The computed maximum tangential stresses in the elastic solid exceed the maximum wall pressures by a factor of 2–3 under certain conditions. These most suitable conditions occurred for the parameter set most similar to the conditions in a knocking internal combustion engine.

Acknowledgments

The authors wish to thank Mrs. Monika Zeevaert-Senger for her active support in producing the high-quality metallographic cuts of the damaged piston material. We could not have presented the experimental evidence in this work without her help. We also thank Professor Norbert Peters for his continuous encouragement and generous financial support.

REFERENCES

1. Miller, C. D., "Roles of Detonation Waves and Autoignition in SI-Engines," *SAE Quart. Trans.* 1:88–143 (1947).
2. Downs, D., and Wheeler, R. W., "Recent Developments in Knock Research," *Proceedings of the Automotive Division of the Institute of Mechanical Engineers*, 1951, pp. 88–99.
3. Zeldovich, Y., Librovich, B., Makhviladze, G. M., and Sivashinsky, G. I., "On the Development of a Detonation in a Non-Uniformly Preheated Gas," *Astronaut. Acta* 15:313–321 (1970).
4. Lee, W., and Schäfer, H. J., *Analysis of Local Pressures, Surface Temperatures and Engine Damages under Knock Conditions*, SAE Paper 830508, 1983.
5. Adolph, N., and Pischinger, F., *Mechanismus der Klopfschädigung an Ottomotoren und Möglichkeiten zu deren Vermeidung*, FVV—Abschlußbericht zum Vorhaben No. 301, 1984.
6. Hayashi, T., Take, M., Kojima, S., and Kond, T., *Photographic Observation of Knock with a Rapid Compression and Expansion Machine*, SAE Paper 841336, 1984.
7. Cuttler, D. H., and Grigis, N. S., *Photography of Combustion during Knocking Cycles in Disk and Compact Chambers*, SAE Paper 880195, 1988.
8. Maly, R. R., Klein, R., Peters, N., and König, G., *Theoretical and Experimental Investigation of Knock Induced Surface Destruction*, SAE Paper 900025, 1990.
9. König, G., Maly, R. R., Bradley, D., Lau, A. K. C., and Sheppard, C. G. W., *Role of Exothermic Centres on Knock Initiation and Knock Damage*, SAE Paper 902136, 1990.
10. He, L., Ph.D. Thesis, Université d'Aix-Marseille, Marseille, France, 1991.
11. Miles, J. W., "On the Response of an Elastic Half-Space to a Moving Blast Wave," *J. Appl. Mech.* December, 1960.
12. *Knocking of Combustion Engines* (Volkswagen Research Division, Ed.), International VW-Symposium, Volkswagenwerk AG, Wolfsburg, Germany, November, 1981.
13. Adolph, N., "Messung des Klopfens an Ottomotoren," Ph.D. Thesis, RWTH-Aachen, Aachen, Germany, 1984.
14. Courant, R., and Friedrichs, K. O., *Supersonic Flow and Shock Waves*, Interscience Publishers, Inc., New York, 1948, p. 422.
15. Lee, J. H., and Moen, I. O., "The Mechanism of Transition from Deflagration to Detonation in Vapor Cloud Explosions," *Prog. Energy Combust. Sci.* 6:359–389 (1980).
16. Yee, H. C., *A Class of High Resolution Explicit and Implicit Shock Capturing Methods*, The von Karman Institute, Rhode-Saint-Genése, Belgium, 1989, Lecture Series 1989-04.
17. Roe, P. L., "Approximate Riemann Solvers, Parameter Vectors, and Difference Schemes," *J. Comput. Phys.* 43:357–372 (1981).
18. Larrouturou, B., "How to Preserve the Mass Fractions Positivity when Computing Compressible Multi-component Flows," *J. Comput. Phys.* 95(1): 59–84 (1991).
19. Oran, E. S., and Boris, J. P., *Numerical Simulation of Reactive Flow*, Elsevier, New York, 1987.
20. Bourlioux, A., and Majda, A. J., "Theoretical and Numerical Structure for Unstable Two-Dimensional Detonations," *Combust. Flame* 90:211–229 (1992).
21. Hibbitt, H. D., "ABAQUS/EPGEN—A general purpose finite element code with emphasis on nonlinear applications," *Nucl. Eng. Design* 77:271–297 (1984).
22. Sorensen, E. P. "ABAQUS Applications in the Automotive Industry," *International Conference on Supercomputer Applications in the Automotive Industry*, Computational Mechanics Publications, Southampton, England, 1986, pp. 183–191.
23. Mahle GMBH, *Kleine Kolbenkunde*, Mahle GMBH, D 7000 Stuttgart 50, Germany, 1991.
24. Kim, S. K., *Spannungswellen an Grenzflächen in linearelastischen Scheiben*, VDI-Verlag Düsseldorf, Reihe 18: Mechanik, Bruchmechanik, Fortschrittberichte VDI, 91, 1991.

COMMENTS

J. W. Dold, Bristol University, UK. Pressure waves of almost any speed could be generated by self-ignition processes in the end gas. Supposing that one of these has exactly the speed that causes the most damage, can you estimate the least amplitude of pressure rise in the gaseous wave that would succeed in damaging the solid?

Author's Reply. The theoretical estimates from linear elasticity theory in the section "Theoretical Estimates" of this paper show that the stress amplitudes in the Rayleigh wave are proportional to the spatial gradient of the pressure trace on the solid surface. Hence, the most severe are shock fronts (with formally infinite gradients), while smooth distributions are less prone to damage the material. Also, the stress amplitudes in the solid, under conditions of resonance, rise linearly with time, so that another factor to be accounted for is the duration of the (approximate) resonance. The key observation is that even very short time passages through resonance of impinging shocks (or detonations) will, in general, be sufficient to cause damage, due to the dependence of the maximum stresses on the gradient of the pressure trace.

Twenty-Fifth Symposium (International) on Combustion/The Combustion Institute, 1994/pp. 103–110

PREDICTION OF THE MAXIMUM TURBULENCE INTENSITIES GENERATED BY GRID-PLATE OBSTACLES IN EXPLOSION-INDUCED FLOWS

H. PHYLAKTOU AND G. E. ANDREWS
Department of Fuel and Energy
University of Leeds
Leeds LS2 9JT, UK

A method is presented to predict the maximum turbulence levels generated downstream of a grid-plate obstacle by an explosion-induced flow. From theoretical considerations, it is shown that the turbulence intensity, defined as the ratio of the root-mean-square (rms) turbulence velocity u' to the mean velocity of the flow U, is simply given by the equation

$$u'/U = C_T \sqrt{K}$$

where K is the pressure-loss coefficient and C_T is a constant (equal to 0.58 in theory). Established techniques for the prediction of flow-pressure-loss coefficient K across obstacles in steady-state flows were used, and practical values of the constant C_T were determined by using measured data of the peak turbulence downstream of grid plates in steady-state flows. The applicability of such steady-state flow concepts was supported by experimental evidence. Two practical values of C_T were determined: 0.225 for "thin" or sharp-edged obstacles and 0.076 for "thick" or round-edged ones. The model was shown to predict available turbulence measurements in both transient (explosion-generated) and steady-state flows.

Introduction

The interaction of the explosion-induced unburnt gas flow with an obstacle results in the generation of turbulence downstream of the obstacle and the acceleration of the flame when it reaches this turbulence. Extremely fast explosion flames can be generated by this mechanism, giving rise to severe overpressures. Prediction of these phenomena is of concern to process industries. Many obstacles in practice can be treated as grid-plate obstacles, and there have been numerous explosion studies using grid plates. However, the findings from these works are of limited use because the data are not presented in terms of fundamental turbulent flow and combustion parameters, as these parameters are particularly difficult to measure under harsh transient conditions.

The objective of this work was to develop and validate a model through which the explosion-induced maximum turbulent intensity downstream of an obstacle could be quantified. This information can be used in conjunction with a turbulent burning velocity correlation to predict the maximum overpressures generated in explosions.

Established steady-state flow techniques for the prediction of flow pressure loss across obstacles will be used. The use of pressure-loss data is preferred to that of drag coefficients, used by other researchers [1], as the pressure loss determines the turbulence, whereas drag coefficients are related to the forces induced on the structures by the explosion.

Model Development

Summary Review of Orifice Flow:

Pressure-loss characteristics of constrictions in ducts have been the subject of many experimental and theoretical studies, reviewed by Ward Smith [2,3]. In particular, single-hole sharp-edged orifices under incompressible, high Reynolds number conditions have been investigated (for flow-metering applications). Fewer studies of multihole grid plates have been carried out, and it is generally assumed that they behave as single-hole orifices of equivalent area.

The main factor affecting the pressure loss (and hence the turbulence generation) for both orifice and perforated plates is the degree of flow restriction given by the blockage ratio (BR), also expressed as the porosity ratio ($p = 1 - \mathrm{BR}$). The hole aspect ratio, t/d (orifice thickness/orifice diameter), the flow Reynolds number, compressibility, and the approach flow-velocity uniformity are also found to be important factors. At Reynolds numbers above 4000, the discharge characteristics of the orifice plate and the general flow patterns are insensitive to the value of

Reynolds number [2]. The following discussion applies to these practical turbulent flows.

As the flow passes through the orifice plate, it separates from the upstream face of the orifice to form a discrete jet, which contracts to a minimum cross-sectional area A_v, known as the *vena contracta.* The coefficient of contraction, C_c, is defined by the ratio

$$C_c = A_v/A_2. \tag{1}$$

On the wall of the duct, there is a step change in pressure across the orifice plate. It is this large change in pressure that is used for flow-metering purposes, and it is given by

$$\Delta P_d = P_1 - P_2 \tag{2}$$

where subscript 1 refers to the upstream pipe and 2 to the *vena contracta.* The total pressure loss caused by the presence of the plate is given by

$$\Delta P_T = P_1 - P_3 \tag{3}$$

where P_3 is the static pressure after the flow expansion from the *vena contracta.*

This overall pressure loss ΔP_T indicates that there has been some energy loss from the flow. It is this balance of energy that is first turned into turbulent motion, and it is then dissipated as heat and randomised molecular motion in the system.

This pressure loss is characteristic of the geometry of the constriction and the velocity of the flow, and it is usually expressed in a nondimensional form as either the discharge coefficient C_d or the pressure-loss coefficient K. The latter is defined by

$$K = \frac{\Delta P_T}{\frac{1}{2}\rho U^2}. \tag{4}$$

For incompressible flow, K can also be expressed in terms of the geometry alone [3] as

$$K = \left(\frac{1}{C_c}\frac{A_1}{A_2} - 1\right)^2. \tag{5}$$

Equation (5) can be rewritten in terms of the fractional blockage ratio ($\mathrm{BR} = 1 - A_2/A_1$)

$$K = \left(\frac{1}{C_c(1 - \mathrm{BR})} - 1\right)^2. \tag{6}$$

For a sharp-edged orifice of high blockage, $C_c \approx 0.61$ (equal to C_d), but its actual value depends on the blockage ratio and on the aspect ratio (t/d) of the orifice.

An empirical correlation of C_c [2] was combined with Eq. (6) to produce expressions for K independent of C_c and dependent only upon the geometrical characteristics of the orifice, the porosity ratio, p ($= 1 - \mathrm{BR}$), and the aspect ratio, t/d. These are

$$K = \left[\frac{1}{0.608p(1 - p^{2.6})[1 + (t/d)^{3.5}] + p^{3.6}} - 1\right]^2 \tag{7}$$

for data in the ranges $0 < t/d < 0.6$, $0 < p < 0.75$, $0.57 < K < 35{,}000$, and

$$K = \left[\frac{1}{p[0.872 - 0.015(t/d) - 0.08(d/t](1 - p^{3.3}) + p^{4.3}[1 + 0.134(t/d)^{0.5}]^{-1}} - 1\right]^2 \tag{8}$$

for data in the ranges $0.98 < t/d < 7.1$, $0 < p < 0.48$, $2.4 < K < 63{,}400$.

The major difference between Eq. (7) and Eq. (8) is in the different application range for the orifice aspect ratio t/d. For $t/d > 1$, reattachment of the flow to the orifice wall occurs, before the flow exits the orifice [2], and this reduces the baffle pressure-loss characteristics. For $t/d < 0.6$, no reattachment of the flow occurs. Within the transition range of $0.6 < t/d < 1$, the flow may reattach or it may not; that is why this range is excluded from the above equations.

Turbulence Generation:

The amount of turbulence generated is dependent upon the flow velocity and the geometry of the confinement. There is very little data on the turbulence generated in transient flows, so the following model is based on information from steady-state studies. The available data on turbulence generation in explosions will be used to validate the model.

The pressure energy loss ΔP_T must appear as turbulence energy prior to dissipation as molecular motion. Therefore, ΔP_T can be equated to the isotropic turbulent kinetic energy as in Eq. (9) [4,5].

$$\Delta P_T = \frac{3}{2}\rho u'^2. \tag{9}$$

Combining Eqs. (4) and (9) produces an equation for the turbulence intensity given by

$$u'/U = C_T\sqrt{K} \tag{10}$$

where C_T is a constant. In theory, this constant should be equal to 0.58, but in practice will be less than that because not all pressure loss through a constriction is translated to isotropic, turbulent, kinetic

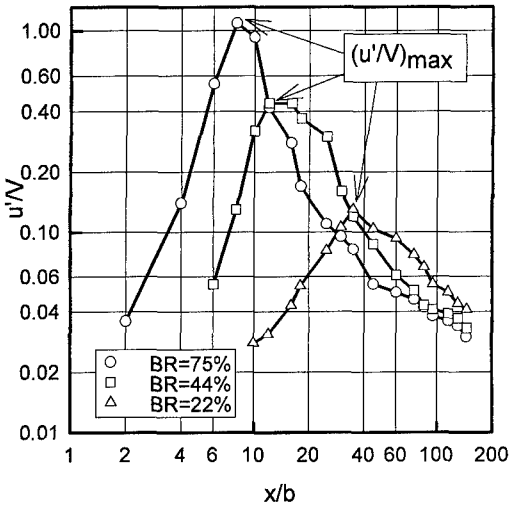

FIG. 1. Variation of the centreline turbulence intensity produced by perforated plates of different blockage ratios [8]. It should be noted that the temporal mean velocity V is used in this plot as opposed to the spatial mean velocity U, however, at the position where u'/V is maximum $V \approx U$ [8,11].

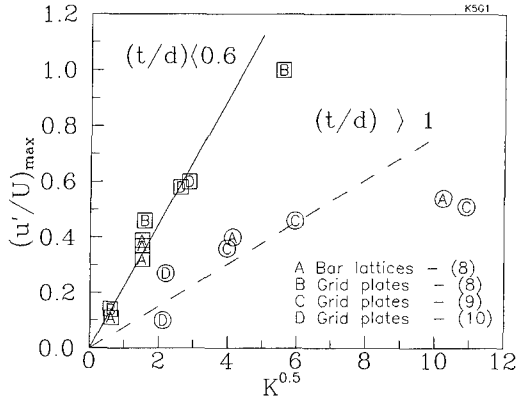

FIG. 2. The maximum turbulence intensity measured behind screens [8,9,10] as a function of the pressure-loss coefficient, K.

energy. In order to determine the validity of Eq. (10) and evaluate the practical value of the constant C_T, available experimental data need to be considered.

Most measurements of grid-induced turbulence have been made well downstream of the grid plate, in the turbulent decay period, where the turbulence is isotropic, i.e., 40–50 hole diameters downstream of the grid [6]. This is well beyond the region of interest in the explosion hazards field since the maximum combustion rate generally takes place within a distance of 3–20 obstacle-hole diameters from the obstacle [7].

Measurements of the turbulence intensity, u'/U, in the region immediately downstream of the grid are scant, and only limited data could be found from cold-flow wind-tunnel studies [8–10]. An example of these near grid measurements of turbulence is reproduced in Fig. 1 from the work of Baines and Peterson [8]. This is a plot of the turbulence intensity (measured on the centreline of the grid holes) as a function of the axial distance normalised by the characteristic grid scale b (b is defined as the width of the solid material between the grid holes [8]). It shows that the turbulence intensity increases downstream of the grid, reaches a maximum value some distance after it, and then begins to decay at a more or less steady rate, over a relatively long distance.

The region of major concern in explosion hazards is the region of maximum turbulence that is shown to occur at some distance downstream of the grid. In an explosion scenario, the maximum burning rate (and therefore the highest rate of generation of overpressure) will occur at the position of maximum turbulence intensity, and it is therefore this region that should guide the protection and mitigation requirements in a system.

In order to obtain a practical value for C_T in Eq. (10), the maximum turbulence intensity, $(u'/U)_{max}$ as measured by the above workers was correlated to the pressure-loss coefficient K [calculated using Eq. (7) or Eq. (8)] of the grid employed, as shown in Fig. 2. The turbulence intensity was found to be roughly proportional to the square root of K, as predicted by Eq. (10), and the results were found to fall on two lines depending on the thickness-to-diameter ratio (t/d, aspect ratio) of the grid holes.

The influence of $t/d > 1$ on the flow characteristics through an orifice is to reduce the value of K (as discussed earlier), and therefore, this would reduce the amount of turbulence generated. However, since this influence is taken into account in the calculation of K, then the results of the plot in Fig. 2 should have been independent of t/d. The fact that they are not indicates that there is an additional (negative) influence of t/d directly on the turbulence levels. The mechanism of this influence is not clear, and more data are needed in order to investigate this influence and confirm whether this effect is real or not and to improve the correlations shown in Fig. 2.

The equations of the fitted lines in Fig. 5 are as follows:

$$(u'/U)_{max} = 0.225\sqrt{K} \qquad (11)$$

for $t/d < 0.6$ and

$$(u'/U)_{max} = 0.076\sqrt{K} \qquad (12)$$

for $t/d > 1$.

These equations show that the maximum turbu-

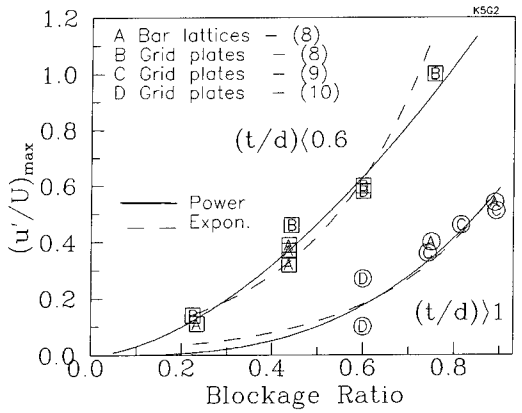

FIG. 3. The maximum turbulent intensity [8,9,10] as a function of the blockage ratio. Dashed lines are an exponential correlation; solid lines are a power correlation.

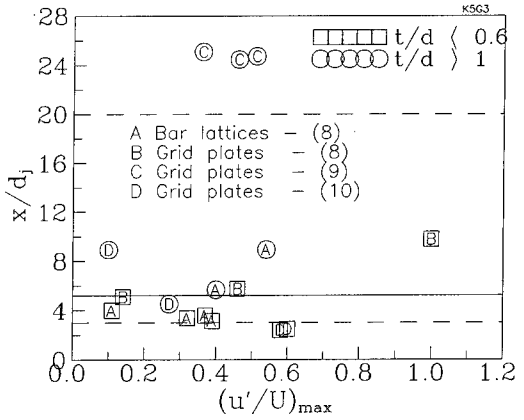

FIG. 4. The position of maximum turbulence intensity in terms of number of jet diameters downstream of the obstacle. The solid line is the average position excluding the data of Robinson and Covitz [9]. The dashed lines envelop the range of position of maximum flame speeds in explosions in tubes with grid-plate obstacles [7].

lence intensity downstream of an obstruction depends solely on the characteristic pressure-loss coefficient of the obstacle and on its aspect ratio. If it is a thin or a sharp-edged obstruction, then Eq. (11) could be applied. If it is a thick or round-edged obstruction, then Eq. (12) could be applied. The pressure-loss coefficient K could be determined in simple steady-flow, small-scale experiments, or it could be calculated from Eqs. (7) and (8).

Equations (11) and (12) suggest that the optimum layout of structures within a vented enclosure would be that which would give the lower pressure-loss characteristics; therefore, in order to determine this layout, a scaled model could simply be placed in a wind tunnel, and the model layout could be rearranged until minimum pressure loss is obtained. This would then be the optimum layout for minimising the overall large-scale turbulence levels.

These are interesting implications, but before they can be explored, the correlations in Fig. 2 need to be confirmed and/or improved and validated in a more detailed study, first for grid plates and then for obstacle shapes directly relevant to the onshore process industries and the offshore petroleum sector.

The maximum turbulence intensity data in Fig. 2 were also plotted against the blockage ratio in Fig. 3. Again the data separated into "thick" and "thin" geometries. For each type of geometry, a strong dependence of the maximum turbulence intensity on the blockage ratio is indicated. It was difficult to choose between an exponential or a power fit to the data, shown as dashed and solid lines, respectively, in Fig. 3. The equations of the exponential correlations are given below. For $t/d < 0.6$,

$$(u'/U)_{\max} = 0.059e^{3.95(\mathrm{BR})} \tag{13}$$

and for $t/d > 1$,

$$(u'/U)_{\max} = 0.016e^{4.10(\mathrm{BR})}. \tag{14}$$

Position of Maximum Turbulence:

Following the lead of Baines and Peterson [8], other researchers [9,10] also presented their turbulence measurements as a function of the axial distance nondimensionalised by the characteristic obstacle scale b. Although this presentation correlates the data well in the isotropic turbulence decay region, as shown in the example of Fig. 1, it does not correlate the position of maximum turbulence intensity, which is shown to occur at different relative distances from the grids.

From jet theory [12], it is expected that the maximum turbulence on the centreline will occur after the end of the potential core of the jet, where the inner edges of the surrounding shear region meet. The length of the potential core is usually expressed in terms of the diameter of the jet at the origin (d_j). The diameter of the jet for a flow through an orifice is the diameter of the *vena contracta.*

From the calculated K values of the geometries in Fig. 2 and using Eq. (6), the appropriate C_c for each geometry was calculated. The diameter of the jet was determined from Eq. (1), and the position of maximum turbulence intensity was expressed in terms of jet diameters. The results are plotted as a function of the maximum turbulence intensity in Fig. 4. It is shown that the position of maximum turbulence was independent of the intensity of the turbulence, and furthermore, all the data (with the exception of those of Robinson and Covitz [9]) fell in the region of 2.5–10 jet diameters. The majority of the data were between 3 and $6dj$. The average position of maximum

turbulence intensity, excluding the data of Robinson and Covitz, was at 5.2 d_j and is shown as a solid line through the data in Fig. 4. This compares well with the expectation of the maximum turbulence being at or after the end of the potential core, which is usually taken to be 4–5 jet diameters long [12].

In a series of explosion tests in tubes with grid-plate obstacles, the authors [7,13] have shown that the maximum flame speeds occurred at a distance of between 3 and 20 jet diameters from the obstacle. This range is indicated by the dashed lines in Fig. 4. It was also shown that the position of the maximum flame speed downstream of the obstacle for the near stoichiometric mixtures moved increasingly farther away from the obstacle as the blockage ratio was increased. This is against expectations because, as the blockage was increased, the hole diameter was reduced, and therefore, the position of maximum turbulence (and hence of maximum flame speed) should have moved nearer to the obstacle. A possible explanation for this apparent discrepancy is that, as the turbulence levels were increased by the increasing blockage ratio, the tubular geometry prevented the turbulence from spreading radially and forced it to spread axially over a long distance downstream of the obstacle. This scenario could also be used to explain the findings of Robinson and Covitz [9] in Fig. 4; these researchers carried out their turbulence measurements in a tube 102 mm in diameter. In contrast, the measurements of Checkel [10], and those of Baines and Peterson [8] were carried out in large wind tunnels (6-ft wide and 4-ft high for the latter research group).

Limited Validation of the Turbulence Generation Model

There is very little data on which to validate the maximum turbulence generation equations. As noted earlier, measurements in steady flows have concentrated on the region of isotropic turbulence decay, well downstream of the position of maximum turbulence intensity that is of concern in explosions. Almost no measurements of turbulence generated in explosions are available. To the authors' knowledge, the only published set of data (of the latter type) is that of Hjertager et al [14].

These researchers carried out an experimental study of flame and pressure development in a large-scale 50-m^3 tube of diameter 2.5 m and length 10 m, with one end closed and the other open to the atmosphere. Methane/air and propane/air mixtures were ignited at the closed end with either a point source or a planar ignition. The explosion was accelerated in the tube by five regularly spaced (pitch = 2 m) single-hole orifice plates having a fixed blockage ratio of 32.1% (d = 2.06 m).

In addition to pressure and flame-arrival probes, some of the tests included hot-wire probes for flow and turbulence measurements. They found that there was a close correlation between the flame speed and the flow velocity along the centreline. The flow velocity was 10–20 m/s lower than the flame speed. They measured flow velocities in the range of 8–600 m/s—increasing with the distance from the ignition plane. In general, the root-mean-square (rms) turbulent velocity u' was higher in the shear region than in the centreline. This is not contradictory to the preceding discussion on the position of the maximum turbulence. In these experiments, the orifice plates were placed too close to each other (less than one hole diameter, d, apart). This meant that the end of the potential core of the generated jets was never reached within the vessel; only the potential core of the last orifice would have had the required distance to converge, and this would have occurred outside the vessel. The centreline region along the length of the vessel was therefore, in effect, one long potential core, and hence all the u' centreline measurements were inside this potential core. The wind-tunnel experiments reviewed earlier indicated that the maximum u' occurs at or after the end of the potential core, and therefore, the measurements of u' on the vessel centreline by Hjertager et al. [14] are not the maximum possible values; this would explain why their u' measurements on the centreline were not as high as those in the shear regions.

It can be argued that since in the steady flow tests, reviewed earlier, the position of maximum centreline turbulence was in the region where the shear spreads to the centre, then these measurements effectively represent the turbulence in the shear region. These experimental values of u' [14] were plotted against the corresponding measured values of the centreline explosion-induced flow velocities, S_g, in Fig. 5. The symbol S_g is used for the flow velocity in order to differentiate this explosion-induced transient flow from steady-state flow velocities, U. A linear dependence of u' on S_g is exhibited by most of the measurements. This is in agreement with the predictive Eqs. (11) through (14), which show that, for a fixed geometry, u' would be linearly (and solely) dependent on flow velocity.

It was assumed that the orifice aspect ratio in Ref. 14 was small (t/d was taken as equal to 0.1), and the pressure-loss coefficient K was calculated to be equal to 0.92 [using Eq. (7)]. Then using Eq. (11), the turbulence levels generated by this geometry were calculated for the range of the experimental flow velocities. The predicted rms velocities are shown as a solid line in Fig. 5 and are seen to be in good agreement with the experimental values. Three experimental data on the high side of the flow velocity range, were underpredicted. These points did not follow the trend set by the rest of the experimental data either. These rms velocities were measured to-

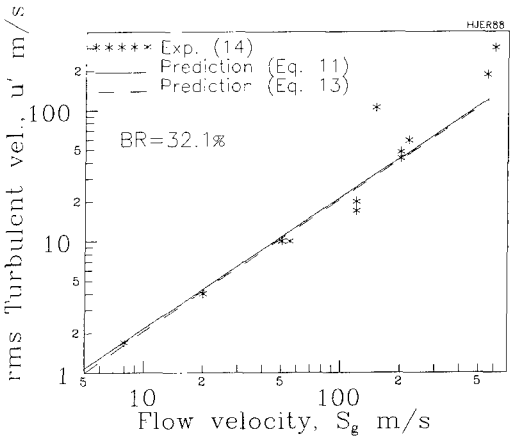

FIG. 5. Experimental measurements [14] of u' as a function of the explosion-induced flow velocity and present predictions.

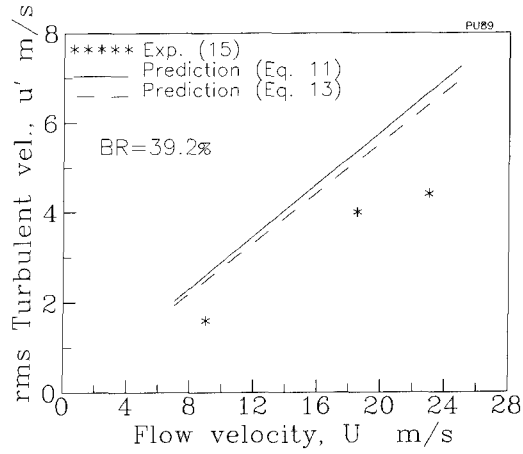

FIG. 6. Experimental measurements [15] of u' in steady-state flow tests as a function of the flow velocity and present predictions.

wards the end of the vessel when ignition was planar. With planar ignition, higher flow velocities were measured, and it is possible that compressibility effects became significant and were responsible for the observed deviations.

The correlation between the predictions and the experimental results was good (86% if all data are considered, 92% if the three odd points are excluded). This demonstrates the efficacy of the present approach for the prediction of the turbulence levels, and it validates Eq. (11) for one value of K over a wide range of flow velocities. Similar data over a range of geometries (K values) are needed for a complete validation of this predictive equation. Also shown in Fig. 5, as a dashed line, are the predictions of Eq. (13), which is simpler to use as it is based directly on the blockage ratio. These predictions are in close agreement with those of Eq. (11).

Pu et al. [15] measured the turbulence levels in a *steady flow* tubular rig (D = 200 mm, L = 1 m) filled with "concentric rings" of blockage ratio 39.2%, in close spacing (pitch = $0.68d$). Measurements were made with three mean flow velocities, 9, 18.5 and 23 m/s. The maximum rms velocities, u'were measured in the shear region and are plotted against the mean flow velocities U in Fig. 6. Also shown in this figure are the predictions of Eqs. (11) and (13), which are shown to overpredict the experimental data by as much as 50%. The geometry of the obstacles was not well defined; they were described as concentric rings, and their thickness was not given. In the predictive equations, they were assumed to be thin sharp-edged orifices. The assumption of the obstacles being thick or round-edged orifices would lead to under prediction of the turbulence levels. Overall, this data set was not well defined, and it was too small for any definite conclusions. Nevertheless, experiment and predictions followed roughly the same trend, and the actual values were of the same order.

No set of data could be found on which to test the predictive equations for thick ($t/d > 1$) obstacles. One encouraging point comes from the large scale-explosion tests by Shell Research [16]. Grids of horizontal pipes 315 mm in diameter and of 40% grid blockage ratio were used to accelerate the flame. Catlin and Johnson [17] approximated u' in these experiments as being 10% of the flame speed. Using Eq. (12), u' is calculated to be 8.1% of the flow velocity, while Eq. (14) gives u' as being 9.6% of the flow velocity.

From the preceding limited validation exercise, it can be concluded that the proposed maximum-turbulence-generation equations predict the available experimental data well, but more data are needed, particularly in terms of geometrical variation, for a more complete validation. The good agreement between the predictions and the experimental measurements in explosion tests [14] further demonstrates that steady-state flow concepts can be successfully applied to explosion-induced transient flows.

However, before u' can be calculated, the explosion-induced flow velocities through the obstacle are required. If the upstream explosion is laminar, then a reliable estimate of flow velocity can be made from simple knowledge of the laminar burning velocity and expansion factor of the mixture. This was demonstrated by the authors [18] in spherical explosions with spherical grid-plate obstacles. If the upstream explosion is not laminar, or the flame shape is distorted by the geometry, then knowledge of the flame speed (through experiments, perhaps) is required. There is strong experimental evidence [7,14] that the

induced flow velocity is a fraction of the flame speed (~80% [7]).

Conclusions

A turbulence-generation model has been developed in terms of the pressure-drop characteristics of the obstacle geometry and the velocity of the flow in the form of a simple theoretical equation that was calibrated using steady-state measurements of maximum turbulence generated behind grids. The applicability of such steady-state flow concepts was supported by experimental evidence. It was shown that the position of maximum burning rate downstream of the obstacle corresponds with the expected position of maximum turbulence from steady-state cold-flow studies. Hence, the turbulence can be considered to be fairly developed, and experimental data on continuous flow turbulence and turbulent burning velocity may be used to interpret the transient explosion data. The model was shown to predict available turbulence measurements in both transient (explosion-generated) and steady-state flows. However, available data are limited, and this turbulence-generation model needs a more rigorous validation over a wider range of conditions.

Nomenclature

A_1	cross-sectional area of the pipe
A_2	area of the orifice
A_v	area of the *vena contracta*
b	characteristic obstacle scale; width of the solid material between the grid holes
BR	blockage ratio
C_c	contraction coefficient
C_d	discharge coefficient
C_T	constant
d	diameter of orifice
D	diameter of tube
d_j	diameter of jet at origin
K	pressure-loss coefficient
L	length
p	porosity ratio (1 − BR)
P	pressure
S_g	explosion-induced unburnt gas flow velocity
t	orifice (or plate) thickness
t/d	orifice aspect ratio
U	mean velocity of the flow
u'	root-mean-square (rms) turbulent velocity
ΔP_d	pressure difference across the obstacle
ΔP_T	overall pressure loss
ρ	density of the fluid

Acknowledgements

We thank the Science and Engineering Research Council for supporting this work (Research Grants GR/F 30286 and GR/H 40914).

REFERENCES

1. Cates, A. T., and Samuels, B., *J. Loss Prevention Proc. Ind.* 4:287 (1991).
2. Ward Smith, A. J., *Pressure Losses in Ducted Flows,* Butterworths, London, 1971.
3. Ward Smith, A. J., *Internal Fluid Flow,* Clarendon Press, Oxford, UK, 1980.
4. Al-Dabbagh, N. A., and Andrews, G. E., *Combust. Flame* 55:31 (1984) .
5. Swithenbank, J., in *Combustion Technology—Some Modern Developments* (H. B. Palmer and J. M. Beer, Eds.), Academic Press, New York, 1974, p. 103.
6. Comte-Bellot, G., and Corrsin, S., *J. Fluid Mech.* 25(4):657 (1966).
7. Phylaktou, H., and Andrews, G. E., *Combust. Flame* 85:363 (1991).
8. Baines, W. D., and Peterson, E. G., *Trans. ASME* 73:167 (1951).
9. Robinson, G. F., and Kovitz, A. A., *AAIA J.* 13:1488 (1975).
10. Checkel, M. D., "Turbulence Enhanced Combustion of Lean Mixtures," Ph.D Thesis, Cambridge University, Cambridge, UK, 1981.
11. Phylaktou, H., "Gas explosions in long closed vessels with obstacles. A turbulent combustion study applicable to industrial explosions," Ph.D. Thesis, University of Leeds, Leeds, UK, 1993.
12. Beer, J. M., and Chigier, N. A., *Combustion Aerodynamics,* Applied Science Publishers, Essex, UK, 1972.
13. Phylaktou, H., and Andrews, G. E., in *Fire and Explosion Hazards,* The Institute of Energy, London, 1991, p. 63.
14. Hjertager, B. H., Fuhre, K., and Bjorkhaug, M., *Combust. Sci. Technol.* 62:229 (1988).
15. Pu, Y. S. H., Ding, D. M. T., and Jarosinski, J., Paper presented at the 13th International Colloquium on the Dynamics of Explosions and Reactive Systems, Japan, 1991.
16. Harrison, A. J., and Eyre, J. A., *Combust. Sci. Technol.* 52:91 (1987).
17. Catlin, C. A., and Johnson, D. M., *Combust. Flame* 88:15 (1992).
18. Phylaktou, H., Andrews, G. E., Mounter, N., and Khamis, K. M., IChemE Symposium Series, No. 130, 1992.

COMMENTS

Calvin Chan, Atomic Energy of Canada, Ltd., Canada. The maximum turbulent intensity along the centerline of a hole (depending on the hole spacing) may not be the true maximum turbulent intensity attainable behind a grid plate.

Author's Reply. We agree that the maximum turbulence intensity may not be on the grid-hole centerline. It is more likely to be in the shear zone where the highest velocity gradients are present. However, the only experimental measurements of u'/U (in the near region downstream of the grid), against which Eq. (10) could be calibrated, were done on the centerline. The turbulence intensity along this line reached its maximum value at the end of the jet potential-core where the shear spread to the centre. It is argued in the paper that these measurements were (therefore) effectively in the shear region. It should be noted that the maximum turbulence measurements against which the predictive accuracy of the proposed relationship was tested were in the shear region. As shown in Figs. 5 and 6, good agreement was obtained. Nevertheless, it is evident that a more detailed characterisation of the turbulence behind grids is needed in both the axial and radial directions.

Twenty-Fifth Symposium (International) on Combustion/The Combustion Institute, 1994/pp. 111–124

INVITED TOPICAL REVIEW

STATE OF THE ART AND FUTURE NEEDS IN S.I. ENGINE COMBUSTION

R. R. MALY
Thermo- and Aerodynamik, F1M/T
Daimler-Benz AG, HPC G206
D-70546 Stuttgart, Germany

The paper reviews, in short, the state-of-the-art in SI engine combustion by addressing its main features: mixture formation, ignition, homogeneous combustion, pollutant formation, knock, and engine modeling. Necessary links between fundamental and practical work are clarified and discussed along with advanced diagnostics and simulation tools. The needs for further work are identified, the most important one being integration of all fundamental and practical resources to meet R&D requirements for future engines.

Introduction

Ever since the very birth of the internal combustion engine by Leonardo da Vinci in 1509 [1], the desire to improve its performance was the driving force both for experimental and theoretical work. Internal combustion turned out to be such a complicated phenomenon, however, that it kept both practical and academic researchers busy until the very day. Although, over the decades, much progress was made on both the practical and the theoretical side, virtually all technical advances were achieved by intuition or experimental trial and error methods rather than by rigid derivations and implementations based on fundamental laws. By now, the SI engine is highly developed, and traditional trial and error methods become unsuitable for meeting future goals. Fuel and engine properties form such a complex system of mutually interacting processes that integration of practical and theoretical work is mandatory. And it must be complemented with specific diagnostics and models for guiding and monitoring progress.

This paper attempts to review, in short, where we are today and to point out what we still need for the future in SI engine combustion. This requires bringing together knowledge both from practical engine work and from academic combustion studies. Since there is a wealth of information in both areas, it will be impossible to cover here all details explicitly. Therefore, emphasis is placed, rather, on main traits, and citations will be made preferably to the most recent work available. Recommended sources for additional review type informations are Heywood's text book [2]; the journal *Progress in Energy and Combustion Science;* the *Proceedings of the Symposium (International) on Combustion* and the *Transactions of the SAE.* The paper focuses on the fundamental aspects needed to cope with the practical problems in front of us.

Mixture Formation

External Mixture Formation:

The design details of intake manifolds determine to a large extent the volumetric efficiency and the transient characteristics of the SI engine. Easy to handle and fast semiempirical models are widely used for capturing the performance trends and the complex flow patterns even in variable geometry manifolds. They predict pressure distributions, pressure wave interactions, and mass flow rates quite reliably and may be complemented—if needed—by nonlinear models for higher accuracy [3]. They are extensively applied for practical design tasks, system analysis, and more recently, for providing reasonable initial conditions for running multidimensional computational fluid dynamics (CFD) codes. Usually, they are complemented by stationary flow-rig data and solve the majority of practical flow problems in the manifold, except mixture formation itself.

Due to valve overlap and valve timing, the manifold flow is complicated by a sequence of flow processes [4]: overlap back flow, forward induction flow, and displacement flow. Although the flow of residual gases is difficult to control, this flow pattern is quite effective in promoting mixture formation due to the repeated changes in flow direction; heating of fresh gases and walls by the burned gases; and forced, constricted flows through the orifice formed by valve and valve seat. About 80–90% of unburned hydrocarbons (UHC's) originate in the cold start and warm-up phase and constitute the major obstacle in meeting emission standards [5]. Liquid fuel enters the cylinder in large droplets and ligaments (Fig. 1), evaporates only partially, and causes abnormally high local incylinder UHC concentrations.

Substantial amounts of fuel injected during starting and warm-up do not even participate in combustion and are likely to end up in the lubrication system

FIG. 1. Ligament of gasoline spreading along the cylinder wall of an optical engine due to fuel film formation in the intake manifold in port injection. Chamber dimensions: Y: 25, X: 75 mm; intake valve at top in the center. Intake stroke: 60° (left) and 180° (right) ATDC, 1000 rpm, half load.

[6]. Aligning the fuel spray axis (impingement on the center of the valve) and heating the valve (up to 100°C to 200°C [7]) improves mixture formation but does not eliminate the underlying basic and unsolved boundary layer problems:

1. spray impingement;
2. droplet break-up and wall film formation;
3. film motion/evaporation in turbulent flows;
4. recondensation and fractional distillation; and
5. instationary mixing in two-phase flows.

There is an urgent need also for practical film sensors as well as for theoretical and numerical work. Simple correlation [7] and two-dimensional (2D) [8] models show encouraging results, but the real solution requires a three-dimensional (3D) CFD treatment with appropriate physical sub models capable of dealing with the complex flow processes and pressure wave interactions, including residual gases, sprays, and wall effects.

Internal Mixture Formation:

Due to the advent of 2D laser diagnostics (overviews are contained in Refs. 9 through 13), inflow and subsequent fate of fuel and residual gases inside the cylinder during intake and compression can be analyzed now with good accuracy. Thus, a far better insight into the detailed interactions between droplets and flow pattern is available.

Particle Image Velocimetry (PIV) flow field measurements in individual cycles around the intake valve revealed that the static flow shows a higher jet velocity than the dynamic flow [14,15]. There is also a noticeable cyclic variation in the details of the flow pattern, although the large structures are repeatable. Even cycle-resolved 2D velocity field measurements are possible in suitable optical engines, revealing the full history of the spatial and temporal development of flow structures, which may be followed up to ignition and into combustion [16]. During the intake stroke, large structures prevail, being dominated by the shape and direction of the incoming jet.

By suitable manifold design and chamber geometry, these structures may be used to control the degree of stratification quite effectively and to tailor mixture preparation to purpose. In the compression

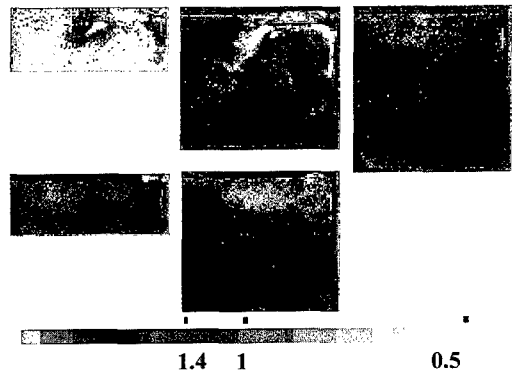

FIG. 2. Fuel distribution in an optical engine showing large- and small-scale mixing during the intake and compression stroke, respectively. Chamber dimensions: Y: 72, X: 75 mm; intake valve at top right-hand side. Measured by PLIF of Ethylmethylketone. Upper row, left to right: 60°, 120°, 180°; lower row, right to left: 240° and 300° ATDC, respectively. Bright yellow spots are fuel droplets. Scale: $\lambda = 1/\phi$. Residual variation in equivalence ratio at ignition timing: 0.8–1.2 [20].

stroke, the large structures are broken up into small ones, which partially survive until ignition timing. Modern four-valve engines with pent roof chambers deviate somewhat from this general pattern by developing a large tumbling flow, persisting well into the combustion phase. The tumble flow pattern has been shown to be very promising for controlling charge stratification and lean burn concepts [17,18]. PIV may also be used to measure the velocity of incoming droplets directly [16] so that consistent inflow conditions are accessible for practical work and model verification.

Although Rayleigh scattering may be used for measuring fuel concentrations in real engines [19], laser-induced fluorescence (LIF) is the more versatile and direct method. The fuel is seeded with appropriately selected tracer materials (e.g., Ketones, <5%) to match fuel properties. They are insensitive to oxygen in contrast to TMPD [20,21] and allow imaging of fuel vapor and droplets in engines (Fig. 2).

Measurements [20–23] reveal that

1. there is only large-scale mixing during the intake stroke;
2. small-scale mixing is accomplished mainly during the compression stroke;
3. at ignition timing, there is still an appreciable level of unmixedness (12–14% total standard variation of concentration across the charge or a variation of 0.8–1.2 in equivalence ratio);
4. small droplets (O: 20 μm) disappear during intake; large droplets (O: 200 μm) survive well into the

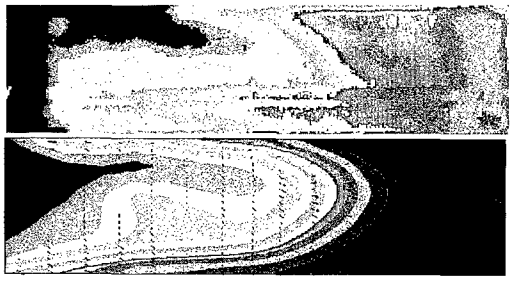

FIG. 3. Measured (at top, LIF of acetone tracer in stoichiometric propane-air) and calculated (at bottom, 3D STAR-CD) fuel concentration during the intake stroke in an optical engine at 45° ATDC and 1000 rpm. Chamber dimensions: Y: 18.8, X: 75 mm; intake valve at top left-hand side. Black: 0, red: 6% fuel.

compression stroke; they disappear abruptly, leaving rich pockets. At TDC no droplets exist;

5. small-scale mixing improves at higher engine speeds, although large-scale heterogeneities survive better due to reduced mixing times; and
6. the phasing of fuel injection and large-scale flow pattern have a significant influence on mixing quality and mixture distribution.

In direct-injection gasoline engines, the available mixing time is reduced significantly, requiring novel approaches for faster mixing. Air-assisted or very high-pressure injectors provide this and finer sprays [24,25]. A different approach uses a mixing chamber with a separate valve [26] filled with incylinder gases to spray into. This exemplifies that mixing processes may be efficiently shortened by intense flow fields. Although spray modeling is not satisfactory by far, flow fields and mixing processes can be calculated already by 3D CFD codes (KIVA, STAR-CD, FIRE). Even complex engine geometries with moving valves and pistons can be handled, although the ensemble-averaged formulations do not resolve the small-scale features seen by 2D imaging.

Model predictions agree remarkably well with ensemble-averaged images (50 cycles, Fig. 3) [27]. However, better turbulence models are needed to cope with compression effects as well as better spray, wall, and boundary models.

Spark Ignition and Flame Kernel Formation

In spite of the small mass fraction burned (0–2%), the flame development time is a sensible fraction ≅30%) of the total burn time. The early flame development contributes significantly to the cycle-to-cycle variation and engine performance [28]. The electrical and plasma physical aspects have been reviewed comprehensively, and the underlying fundamentals are known [29]. There are three basic discharge modes: breakdown, arc and glow discharge with characteristic properties and losses. The first one has the highest energy efficiency, and the last one has the lowest.

The electrically supplied energy is converted into a highly ionized plasma with high initial temperatures (60,000 K) and dissociated and ionized constituents in highly excited states. Therefore, chemical reactions are efficiently initiated by the high temperature and species concentrations at the plasma surface [30].

The plasma support fades away, however, over the spark time, and high-temperature chemistry approaches normal flame chemistry at about 300 μs. Although alternative spark ignition systems have been repeatedly proposed [31–33] for cost, reliability, and lifetime reasons, the glow discharge is still the dominating mode used in practice. Typical electrical characteristics are a 60-mA peak current, a 30-kV peak voltage, and a 2-ms discharge time. At most, 30% of the electrically supplied energy is actually utilized in ignition, requiring an optimum mean flow velocity of 12 m/s in the electrode gap [29,34].

The initial plasma channel (about 40 μm in diameter) develops into a hairpin-shaped flame kernel whose size depends on gas speed (Fig. 4). In combustible mixtures, this spark always initiates an active flame kernel whose fate, due to its small initial size, is susceptible to all kinds of external influences, which may even lead to the following propagation failures:

1. energy losses to electrodes or walls [35];
2. flow field effects [36];
3. mixture properties (air fuel ratio, dilution, mixedness [37], and fuel);
4. thermodynamic conditions [38,39], and
5. size/time dependence of turbulent scales [40].

There are numerous, mostly phenomenological, models in the literature [41–46] treating one or a few of these effects. The most complete verified one-dimensional (1D) model [47,48] includes all and predicts the full period from the supply of electrical spark energy to a fully developed flame in an engine. Three-dimensional modeling is in transition to applications accounting for heat losses and turbulence effects [49,50]. Very encouraging results have been obtained already [27,50,51], as shown in Fig. 5, regarding prediction of general shape, flame speed, thickness of the flame brush, the near wall behavior, and pressure traces.

These results indicate that incorporation of all influences into an ignition model and the use of appropriate (e.g., spectral) turbulence models are essential for correct treatment of flame kernel formation. The kernel needs a separate gridding to resolve geometrical details. Although the plasma effects may be simplified, there is a need for detailed

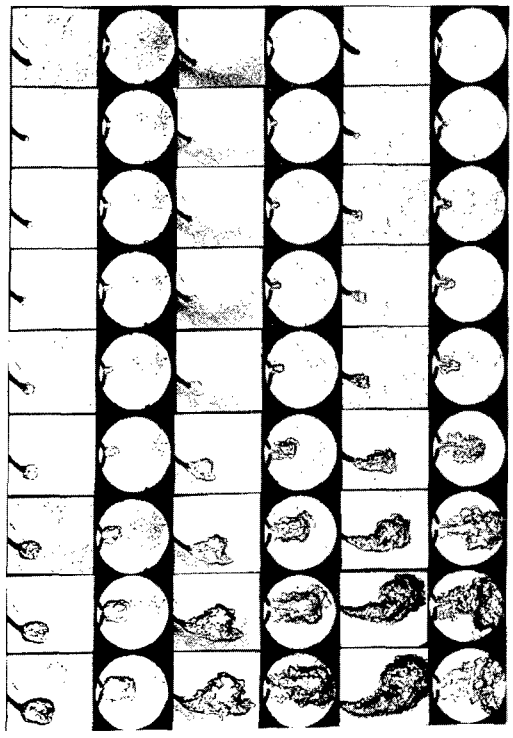

FIG. 4. Flame kernel development in a side chamber engine at different speeds. Propane air mixture, equivalence ratio 1, transistorized coil ignition (glow discharge: 60 mA, 30 kV peak values), thin electrodes. Simultaneous schlieren films from two orthogonal axes (left: axial; right: radial aspect). Speed: left pair, 300; center pair, 750; and right pair, 1250 L/min. Timing from top to bottom: 0.025, 0.05, 0.075, 0.1, 0.125, 0.25, 0.375, 0.5, and 0.625 ms after start of ignition [47,48].

submodels to treat the transition of plasma to flame chemistry and the fluid dynamics associated with spark-assisted flame kernel formation.

Homogeneous Combustion

Diagnostics:

Aside from conventional visualization by schlieren- or shadowgraphy and standard pressure transducers, nonintrusive laser-based imaging techniques [10–24] are now available for measuring flame structure, temperature, concentrations, radicals, flow, and turbulence in engines. Flame structures are most easily obtained by Mie scattering from seeding particles added to the intake air [52,53]. Even cycle-resolved measurements are possible, if copper vapor lasers are used [54,55]. Single images from subsequent cycles may be recorded by LIF of fluorescent HC molecules, which happen to be present in the fuel [56], or more reliably, by LIF of oxygen-insensitive dopants, e.g., ketones, added to the fuel [20]. Rayleigh measurements are also possible; they require, however, difficult to satisfy dust- and particle-free conditions. Flame thickness and integral scales of wrinkling are easily retrieved by image processing techniques [57,58]. Fractal analyses have frequently been tried but produce excessive scatter in the data and no physical insight. Neither the postulated inner and outer cutoff scales nor the slope can be extracted unambiguously [59].

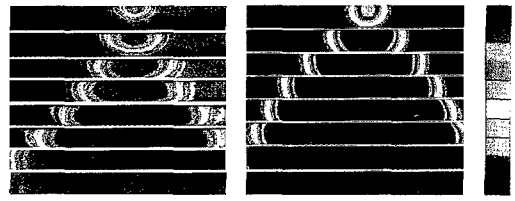

FIG. 5. Measured (left side: LIF of acetone tracer, 50 cycles averaged) and calculated (right side: 3D STAR-CD) flame propagation in an optical engine: propane air, ϕ = 1; compression ratio 10 : 1, 1000 rpm. Chamber dimension: X, 75 mm; top, cylinder head; bottom, piston surface; ignition timing, 14° BTDC. Sequence from above: 11°, 8°, 5°, 2° BTDC, 1°, 4°, 10°, 13° ATDC: red = burned, blue = unburned [27].

Direct temperature imaging in engines is still not possible. Work on two-line OH thermometry is in progress [60] but will not be generally applicable. The indirect means as Rayleigh scattering may be useful under special conditions. Single-shot coherent anti-Stokes Raman spectroscopy (CARS) is applicable for temperature and concentration measurements outside flame fronts, but the lack of resolution below 1000 K and being a point measurement limits its use severely.

Concentration of gases and fuel are easily imaged by LIF techniques (see above). If the laser is tuned to specific wavelengths, radicals as OH [60,61], NO [51], CH, or intermediates, e.g., HCOH (see Knock), can be readily measured qualitatively, sometimes quantitatively. The NO cannot be excited through the flame front at 193 nm because of strong absorption by reaction intermediates. However, work in progress shows promising results at 226 nm [62]. Although absolute data are difficult to obtain, relative LIF measurements are indispensable for model verification and analysis of spatial distributions. In combination with additional diagnostics or with models, they constitute a most powerful tool for practical and theoretical work. In Figs. 6 and 7, examples are shown of measured OH and NO distributions in engine flames.

Flow fields in fired engines are readily measured by laser Doppler velocimetry (LDV) or 2D PIV tech-

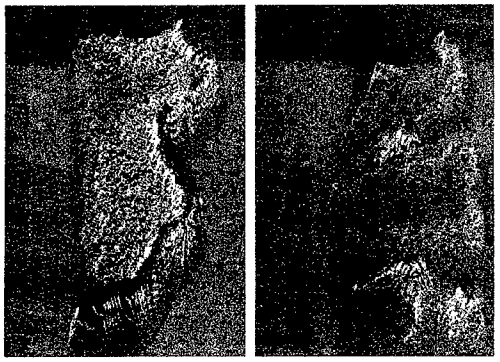

FIG. 6. LIF images of the OH distribution in a laser sheet through a propagating and quenched flame front in an engine simulator, respectively, 500 rpm, propane-air, equivalence ratio 1.5, quarter load [61].

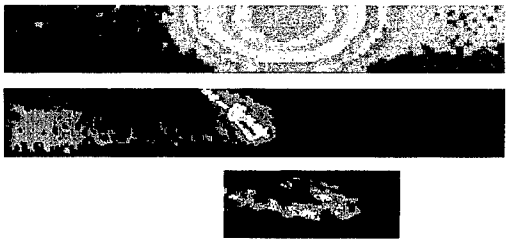

FIG. 7. Correlated LIF measurements of flame brush position by burned fraction (top), NO (center), and OH (bottom) distributions of propane-air combustion in an optical engine. Black: 0; red: maximum signal. Please note inhomogeneity in NO and OH distributions. Absorption by reaction products (193 nm) limits NO accessibility to incident side (left). Compression ratio 10:1, 1000 rpm, propane-air, equivalence ratio 1, ignition timing 20° BTDC, X-dimension: 75 mm [51].

niques either single shot [12,63], cycle resolved (using copper vapor lasers in a movie PIV [16]), or even 3D [13]. The cross-correlation technique with image shifting is to be preferred for its significantly higher accuracy and resolution. Thus, detailed informations on flow structure, time dependencies, and scales can be obtained under realistic conditions, even in single shots.

The needs required to obtain the information are well-characterized data on turbulent scales, quantitative and cycle-resolved LIF diagnostics, direct temperature measurements, and high-pressure NO diagnostics resolving thermal and prompt contributions. For access to production engines, adaptation to very small windows is a must that is not yet solved satisfactorily.

Reaction Kinetics:

Knowledge in this field and computing power have progressed to a point where even large detailed kinetics may be used for engine combustion [64–66] and reduced mechanisms with questionable accuracy can be avoided. Detailed reaction mechanisms can be automatically generated for large molecules so that realistic fuels become tractable [67]. To reduce computing times, detailed chemistry can be stored in libraries or tailored to demand by automatic reduction [68,69]. The applicability of current mechanisms to practical cases is as follows [70]:.

fuels—very well: paraffins, straight, branched, and NO_x chemistry; good: olefins and alcohols; fair: oxygenated hydrocarbons, ethers, and epoxides; bad: aromatics; and

processes—well theoretically: laminar flames, ignition in shock tubes, flow reactors, and static reactors; well practically: detonation; still difficult: pulsed combustion, turbulent flames, furnaces, burners, and combustion in engines.

Fundamental work is urgently needed on aromatics, multicomponent fuels, and detailed kinetics for real engines. Time-efficient and accurate models are needed for treating NO formation and reburn, post flame and exhaust pipe UHC oxidation, as well as kinetics of additives.

Turbulent Premixed Combustion:

Often apparent heat release rates derived from pressure signals are sufficient for practical applications. The turbulent burning velocity, however, is a function of the space and time-dependent thermodynamic, chemical and fluid dynamic conditions in the engine. Direct measurements are possible using visualization techniques in optically accessible engines. Simple, well-known correlation functions are available for the laminar burning velocity [71]—encompassing the thermodynamic and chemical effects—which work well and are extensively used in nondimensional engine codes.

The fluid dynamic effects, represented by the turbulent burning velocity, are harder to simplify due to widely different, possible regimes [72,73]. The bulk of available experimental data has been critically assessed, and correlation functions have been derived [40]. For thermodynamic purposes and heat release calculations, correlations of type

$$S_t/S_l = I_0\,[1 + A(u'/S_l)^n],$$

$$I_0 = \text{strain rate}, \quad A \approx 1, \ldots, 2.5, \quad n \approx 5/6, \ldots 1,$$

are widely used in phenomenological, fitted models handling practical combustion problems quite well.

For multidimensional and pollutant modeling, however, detailed effects of turbulence and chemistry must be captured. Various models are used, as-

suming a flamelet structure of the combustion zone. This is valid if the local reaction zone is much smaller than the integral turbulent length scale. Experiments in engines show [52,53] that this holds up to moderate engine speeds and even for very lean mixtures. Some flamelet models require precomputed strained flame libraries [74–76] to include detailed chemistry, available now for fuels up to C8. Others have closure methods derived from direct numerical simulation (DNS) [77], needing only unstrained flame speeds [50].

Engine tests indicate that strain, curvature, and dp/dt [78] must be included into libraries as well as local quenching in the flame front (Fig. 7). An extension to low turbulence ($u'/S_l = O: 1$) [48,74] is required. Numerical studies indicate also an important, still unaccounted time dependence in the reaction of a wrinkled flame front to a turbulent flow field [79]. For correct near-wall behavior, the burn time must not be equated to the turbulence time $t_t = k/\varepsilon$. Special flame-wall interaction models (spectral models [80] or the FIST model [81]) are required, accounting for the change in sensed scales during flame kernel formation and on approaching a wall.

Powder diffraction files (PDF) and presumed PDF (PPDF) models [82,83] can handle slow chemical reactions outside the flame front. In practice, the number of necessary scalars is so large that PDF transport equations must be solved by time-inefficient Monte Carlo methods. There is an urgent need to combine the advantages of flamelet and PDF models into a common, time-efficient multidimensional engine code so that processes in the burned region and in the exhaust can be included in reducing fuel consumption and pollutant emissions. Reasonable computing times will be possible if the detailed chemistry is reduced by multidimensional manifolds. [68,69].

Only the large scales in flows depend on geometrical details of the engine, whereas the small scales are intrinsically free of these effects. Thus, the large flow structures should be calculated directly without any turbulence model (DNS), and subgrid modeling should be used for treating effects of small scales (LES) only. Therefore, new types of models are emerging, being derived from DNS [50]. Although they are still under development, they are used already and form the basis for future submodels in LES codes. Calculations for a four-valve engine using LES [84,85] show an impressive agreement between calculated and measured flow and flame structures. Although the grid resolution required for LES is controversially discussed, these results clearly indicate the need to use as much DNS as possible and restrict modeling to the subgrid level, where conditions are better defined and submodels will work well.

Pollutants

Apart from the CO_2 emission, the most critical pollutants are NO_x and unburned hydrocarbons (UHC). Although engine-out emissions can be drastically reduced by the three-way catalyst (TWC), measures to reduce fuel consumption usually cause higher engine-out NO_x levels. The UHC's originate predominantly from the cold start–warm-up phase when the catalyst is still cold and inactive.

Nitric Oxides (NO_x):

Whereas NO formation (prompt and thermal) can be readily calculated for flames [86,87], direct measurements and calculations for engine conditions are still unsatisfactory. There is a strong need for a practical NO imaging technique for localizing in-cylinder NO sources throughout the combustion process and for verifying NO submodels and engine codes.

In modeling, it is accepted now that both thermal (extended Zeldovich) and prompt NO must be accounted for. Since it is difficult to obtain the OH concentration from simple mechanisms (required for the extended Zeldovich mechanism in the burned region), it is attractive to include combined flamelet and PDF submodels into multidimensional CFD codes. Available preliminary results [88,89] indicate that

1. prompt mechanisms play a significant role at the lower temperature end;
2. fuel chemistry affects NO production;
3. deposits may lead to higher NO levels due to higher charge temperatures; and
4. highly turbulence-enhanced combustion produces comparable NO levels as conventional turbulent combustion.

Unburned Hydrocarbons (UHC):

DNS [77,90,91] has opened up new insights into bulk and wall quenching. Heat losses, curvature, viscous dissipation and transient dynamics have significant effects, especially for small-scale turbulence. Simplified models have been derived for wall quenching [91], facilitating modeling of UHC from boundary layers in engine codes. There is a strong need for more theoretical and experimental work in this area to provide reliable, physically based submodels. Since most of the UHC emissions arise during cold start and warm-up of the engine. The total tailpipe UHC and the specific reactivity depend greatly on engine operating conditions, fuel composition, and type of catalyst. Results from engine tests [92–94] indicate for

Engine-out emissions:

1. It takes up to 6 s for the fuel-air mixture to reach the cylinder during cranking. During the first 30 s, about 75% of the UHC is unreacted fuel dropping to a steady-state value of 53% after about 60 s.

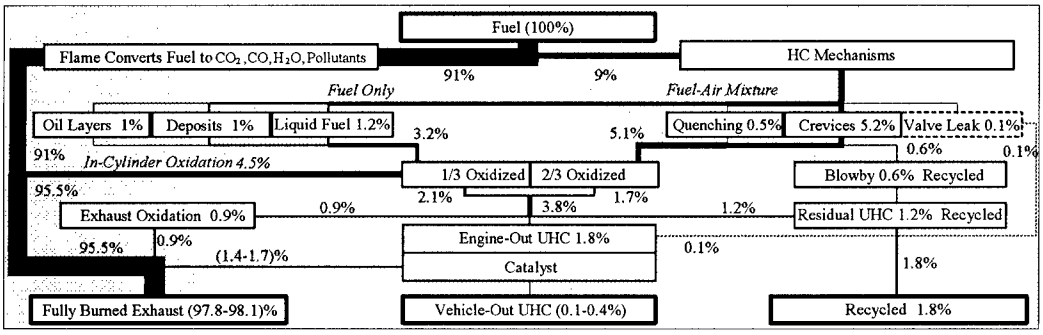

FIG. 8. Complete flow chart of normal combustion of gasoline fuel and UHC mechanisms. Numbers indicate the HC emission index in % fuel entering each engine cylinder, redrawn after Ref. 95.

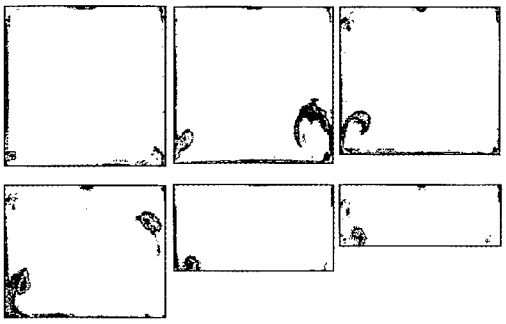

FIG. 9. Sequence of LIF images (acetone tracer in propane-air) from an optical engine showing in-cylinder UHC sources. Upper row: UHC flowing out of the topland crevice; sequence: BDC, 20° and ABDC, 40°. Lower row: wall-quenched UHC being scraped off oil-free walls forming roll-up vortices; sequence: 60°, 100°, and 120° ABDC. The outlet valve is at the top on the right-hand side.

2. The main components during warm-up are unburned fuel species and reaction products consisting of C2-C4 olefins, methane, and acetylene.
3. The specific reactivity right after cold start is due to unburned fuel.
4. The percentage of C2-C4 olefins with high reactivity and the specific reactivity increase as warm-up proceeds, although the total UHC's decrease drastically.

Catalyst-out emissions:

1. Before light-off, the C2-C4 olefins and, after light-off, the unburned fuel species dominate the specific reactivity.
2. Hydrocarbons with boiling points lower than the momentary catalyst temperature are hardly absorbed and hydrocarbons with higher boiling points are almost totally absorbed during catalyst warm-up.
3. After catalyst light-off, hydrocarbons with a higher reactivity are oxidized more readily. The ranking of the conversion efficiency is C2-C4 olefins > alkylbenzenes >> paraffins and benzenes.
4. The equivalence ratio has a significant influence on specific reactivity and mass of toxic air pollutants.

The current understanding of the mechanisms leading to UHC emissions from SI engines has recently been compiled into a complete flow chart [95]. In Fig. 12, the origins and subsequent processes are presented, causing UHC's from a warmed-up SI engine. Although most of the mechanisms are not rigidly known, the chart is an extremely useful guide for the needs both in practical and research work. The ranking of engine-out UHC sources is as follows:

crevices (38%), quenching (5%), oil layers (16%), deposits (16%), liquid fuel (20%), and exhaust valve leakage (5%).

It is noteworthy also that about 9% of the fuel escapes the normal combustion process and causes a loss of 6% in the indicated mean effective pressure (IMEP). Although these figures may vary for different engines and operating conditions, they are supported by recent engine work on

in-cylinder measurements of crevice flow and wall layers [96–98], which are corroborated by LIF images from an optical engine (Fig. 9);
fuel absorption-desorption in oil films [99]; and
effects by piston temperature [100] and exhaust valve leakage [101].

There are encouraging attempts to model UHC oxidation [102] and effects of engine design parameters on UHC emission [103]. If calibrated for a single operating condition, reasonably good results are obtained for other speeds, loads, air-fuel ratios, exhaust gas recirculation (EGR) rates, and spark timings. The model predicts that

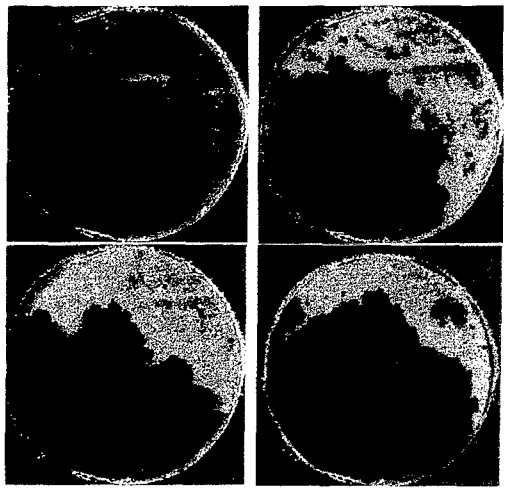

FIG. 10. Sequence of LIF images of formaldehyde formed in the endgas during transition from normal to knocking combustion exhibiting endgas inhomogeneity and formation of exothermic centers. Sequence (left to right, top to bottom, timing in degrees ATDC): 2°, random beginning of cool flame reactions; 4°, spot-wise formation of HCOH (inhomogeneity); 7°, apparently "homogeneous" HCOH-distribution in the NTC regime; and 9°, formation of hot flames at exothermic centers (burning up HCOH: large blue spot at 2 o'clock).

1. the bore-to-stroke ratio has a small effect;
2. a decrease in displacement per cylinder increases UHC; and
3. an increase in compression ratio or in crevice volume per displacement increases UHC.

These results agree well with the proposed mechanisms in Fig. 8.

Knock

Knock limits the maximum compression ratio and hence the efficiency of the engine. It is promoted by endgas temperature, fuel structures with long chains, and residuals carried over from previous cycles. Knock is a complex interaction of autoigniting exothermic centers and their mutual fluid dynamic responses in the inhomogeneous endgas.

The autoignition part is extensively treated and modeled in the literature and is well understood [67,104–106]. The low-temperature chemistry (<900 K) is started by the RO_2 isomeration processes producing OH radicals by QOOH decomposition consuming some fuel and liberating some heat at low rates. Slowly, a radical pool is built up, leading eventually to hot ignition as temperatures above 900 K are reached. This process may exhibit a distinct two-stage ignition behavior and a negative temperature coefficient region in the overall reaction. The effect of additives is by way of influencing the OH radical pool: additives, increasing the OH production, accelerate hot ignition, while additives, which remove OH, inhibit it. Antiknocks act either by retarding low-temperature oxidation and chain branching or by inhibiting the high-temperature HO_2-dominated hot ignition. Methyl-ter-butyl-ester (MTBE) and ethyl-ter-butyl-ester (ETBE) act in both regimes. In binary mixtures, the olefins act in the low-temperature region as radical scavengers and retard the activities of paraffins, whereas the paraffins act as radical scavengers in the negative temperature coefficient (NTC) region and retard the activity of olefins. Experimental high-pressure data of realistic fuels mixtures are becoming available [107–109].

This chemically based model does not explain strength or variability of the pressure waves in knocking combustion nor the material damage associated with it. The pressure signals correlate very poorly with endgas temperature—although this should be the prime controlling parameter—and even less so with the mass of unburned fuel at the onset of autoignition [110]. This is due to the fluid dynamic part following autoignition [111–113]: Contrary to general assumptions, autoignition occurs not uniformly throughout the endgas region but in localized spots imbedded in the inhomogeneous endgas (exothermic centers (ETC's)) with specific induction and excitation times [114–116].

These centers arise from incomplete mixing and constitute temperature and/or compositional heterogeneities. Transition from autoignition into knock is controlled by the properties of these exothermic centers: size, gradients, and spatial distribution in the endgas [112,113].

In Fig. 10, the transition of low-to high-temperature chemistry is shown by the formation and disappearance of formaldehyde in the endgas. The reactions start irregularly in the inhomogeneous endgas; cause an apparent "homogeneous" concentration (not temperature) distribution in the NTC region; and depending on local conditions, force some exothermic centers into the hot ignition regime, as visualized by the burn-out of the formaldehyde. In Fig. 11, data from simultaneous LIF and ultrahigh-speed schlieren reveal the spatial and temporal evolution of exothermic centers into a spectrum of slow and fast burning centers. In summary, there are three different modes of knocking combustion [112,113]:

Deflagration—The most common mode being characterized by small exothermic centers, steep gradients, and very weak pressure oscillations. After hot ignition, flame propagation is similar to normal flame propagation without causing any knock damage.

Thermal explosion—Is characterized by large centers with flat gradients. Pressure oscillations are

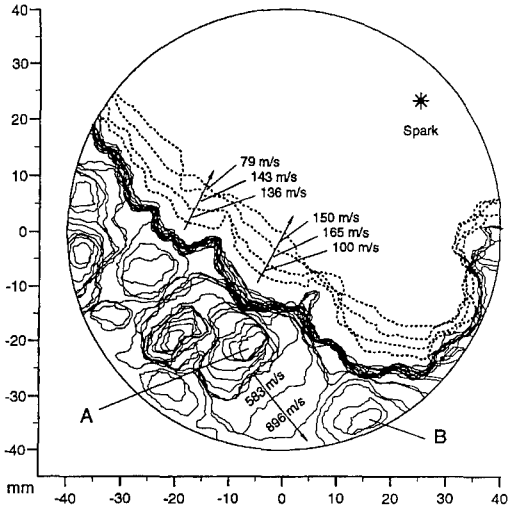

FIG. 11. Evaluated ultrahigh-speed schlieren movie (750,000 fps) showing spot-wise formation of exothermic centers (ETCs) in the endgas. Most centers (e.g., B) develop into deflagrations, whereas the lower right-hand side of A transits into a developing detonation. Note the random distribution of ETCs and the pushing back of the regular flame front by the fast pressure rise in the endgas.

moderate, and knock damage is very light if any at all.

Developing detonation—The most violent mode occurring rarely but causing intense pressure oscillations and rapid surface damage to materials is characterized by medium-sized centers having critical intermediate gradients, which support the gradual growth of strong pressure waves. This mode is detrimental to the engine.

In practice, all modes are present simultaneously. During the short excitation time, ETC's emit pressure waves that heat surrounding ETC's and shorten, thus, their induction time drastically. In consequence, local, initially mild knock modes may drive remote centers into a developing detonation mode directly or by an avalanche effect depending on the statistical temporal and spatial distribution of ETC's in the endgas. Although autoignition is controlled by temperature, engine knock with its intensity is controlled by the properties, distribution, and fluid dynamic interactions of ETC's resulting from preceding mixing processes. The developing detonation mode of knock is associated with very high rates of heat transfer to the walls causing thermoshock (>100 MW/m^2, $\Delta T_{\text{Surface}} > 150$ K), which is the prime cause for knock damage [112,117]. In crevices (topland region), pressure piling occurs, which may lead to excessive mechanical wall loadings causing knock damage in combination with high-heat transfer rates.

This combined autoignition and fluid dynamic description of knock explains consistently all known features in knocking combustion. All relevant processes are understood and can be modeled satisfactorily. There is a need, however, for reducing the submodels for detailed chemistry and shock/pressure wave interactions, so they can be incorporated time efficiently in 3D engine codes.

Modeling

Current engine design work still relies largely on phenomenological models because they can be calibrated to appreciable accuracy, and they are fast. These models generally lack, however, the detailed insight into the physical and chemical processes required for a truly predictive tool. This necessary insight is provided already to a fair amount by current (ensemble-averaged) multidimensional codes, although they are still under development and the computing times are long. Their accuracy is mainly determined by the quality of the submodels used. Therefore, many of them need to be improved considerably.

Even complicated engine flow fields can be calculated time and space dependent with good accuracy [118,119] and very recently also with moving valves and pistons [120]. Turbulence is generally modeled by the $k - \varepsilon$ model, which can be adjusted to give reasonable results, although it is unable to handle compressed turbulence and turbulent combustion at walls. Different submodels are used to compute engine combustion [27,121–123]. There are four general categories being valid for $\text{Re}_t = (L/\delta_l) \cdot (u'/S_l) \approx 100, \ldots, 500$ [124]:

1. Eddy Break Up (EBU) models: Valid if reaction rates are much faster than turbulent processes. In combination even with very simple turbulence models, they calculate thickness and speed of the turbulent flame front in any geometry. If adapted to one case, they do not necessarily work well for other cases, and they do breakdown at walls and cannot handle ignition.
2. Presumed PDF (PPDF) models: These modified EBU models calculate flow and temperature fields well but give only fair results for pressure traces. They are not truly predictive and require adjustment of model constants if the equivalence ratio is changed. Ignition cannot be handled either.
3. PDF models: They remove most deficiencies of the EBU model, account properly for reactive species and flow velocities, and work well for slow combustion and nongradient processes.
4. Flamlet models: They bring more physics into the EBU model and treat fast reactions in thin flame zones well. Detailed chemistry is introduced by strained flame libraries (Fig. 12 [125]). High num-

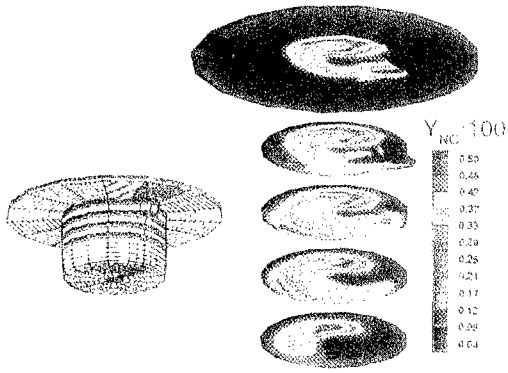

FIG. 12. Contour plots of NO-mass fractions calculated with detailed reaction kinetics at five cross sections (marked dark in the grid) computed for a direct injection stratified charge engine using KIVA II and a flamelet model [125].

bers of necessary dimensions (pressure, temperature, equivalence ratio, strain, curvature, *dp/dt*, etc.) cause excessive interpolation times and render detailed libraries inefficient.

Computations of engine combustion indicate that simple combustion models and/or reduced kinetic models can be used if parameters are adjusted to fit experimental data. A reasonable agreement of the cylinder pressure may be obtained for a limited database. Special models are required to account properly for flame kernel formation and near-wall behavior. A combination of the PDF and flamelet model is necessary for a complete description of pollutant formation in engines.

Conclusions

The demands of the future need a drastic reduction of fuel consumption and emissions as well as faster and efficient design and development of optimized engines and require practical solutions for complex interdependent processes that can be found only by integrating all available fundamental and practical resources. In engine combustion, the essential key elements are understood sufficiently well and fundamentally based support for practical applications is available. Specific diagnostic tools exist for direct optimization of engines and dedicated development of verified models, respectively. Engine modeling, including detailed pollutant chemistry, is on the verge to wide-spread use—replacing traditional trial and error methods. At the same time, the next generation codes, LES and DNS, should be developed, which on medium term will offer truly predictive power and advanced design tools to meet demands.

Acknowledgments

I want to thank all my colleagues and friends in the combustion community who kindly and generously provided me with papers, preprints, and valuable comments. I also want to thank all my coworkers, especially R. Herweg, G. König, and M. Zahn, whose research work contributed significantly to this paper. Part of the presented work was funded by the CEC.

REFERENCES

1. Hardenberg, H., SAE SP 977, 1993.
2. Heywood, J. B., *Internal Combustion Engine Fundamentals*, McGraw-Hill, New York, 1988.
3. Pearson, R. J., and Winterbone, D. E., SAE 900676, 1990.
4. Cheng, C. O., Cheng, W. K., and Heywood, J. B., SAE 912401, 1991.
5. Fraidl, G. K., Quissek, F., and Winklhofer, E., SAE 920416, 1992.
6. Fox, J. W., Min, K. D., Cheng, W. K., and Heywood, J. B., SAE 922170, 1992.
7. Almkvist, G., and Eriksson, S., SAE 932753, 1993.
8. Himmelbach, J., "Zweiphasenströmung mit schubspannungsgetrieben welligen Flüssigkeitsfilmen in turbulenter Heißluftströmung—Meßtechnische Erfassung und numerische Beschreibung," Ph.D. Thesis, University of Karlsruhe, Baden-Württemberg, West Germany, 1992.
9. Laurendeau, N. M., *Prog. Energy Combust. Sci.* 14:141–170 (1988).
10. Hanson, R. K., Seitzmann, J. M., and Paul, P. H., *Appl. Phys. B* 50:441–454 (1990).
11. Stepowski, D., *Prog. Energy Combust. Sci.* 18:463–491 (1992).
12. Reuss, D. L., *Proc. SPIE*, 2005:413–424 (1993).
13. Barnhart, D. H., Adrian, R. J., and Papen, G. C., *Appl. Optics* (1994), to appear.
14. Lee, J., and Farell, P. V., SAE 930480, 1993.
15. Valentino, G., Kaufman, D., and Farrell, P., SAE 932700, 1993.
16. Stolz, W., Köhler, J., Lawrenz, F., Meier, F., Bloss, W. H., Maly, R. R., Herweg, R., and Zahn, M., SAE 922354, 1992.
17. Kiyota, Y., Akishino, K., and Ando, H., SAE 920678, 1992.
18. Kuwahara, K., Watanabe, T., Takemura, J., Omori, S., Kume, T., and Ando, H., SAE 940986, 1994.
19. Zhao, F. Q., Taketomi, M., Nishida, K., and Hiroyasu, H., SAE 932641, 1993.
20. Lawrenz, F., Köhler, J., Meier, F., Stolz, W., Wirth, R., Bloss, W. H., Maly, R. R., Wagner, E., and Zahn, M., SAE 922320, 1992.
21. Felton, P. G., Bracco, F. V., and Bardsley, M. E. A., SAE 930870, 1993.
22. Baritaud, T. A., and Heinze, T. A., SAE 922355, 1992.

23. Shimizu, R., Matumoto, S., Furuno, S., Murayama, M., and Kojima, S., SAE 922356, 1992.
24. MacInnes, J. M., and Bracco, F. V., SAE 902079, 1990.
25. Abraham, J., Magi, V., MacInnes, J., and Bracco, F. V., SAE 940895, 1994.
26. Wojik, K., and Fraidl, G. K., *DMI—A Charge Stratification Concept for Future SI-Engines*, AVL Report, 1993.
27. Weller, H., Uslu, Gosman, A. D., Maly, R. R., Herweg, R., and Heel, B., *Commodia94*, 1994.
28. Bianco, Y., Cheng, W. K., and Heywood, J. B., SAE 912402, 1991.
29. Maly, R. R., in *Fuel Economy: Road Vehicles Powered by Spark Ignition Engines* (J. C. Hilliard and G. S. Springer, Eds.), Plenum Press, New York, 1983.
30. Xu, J., Behrendt, F., and Warnatz, J., *Commodia94*, 1994.
31. Ziegler, G. F. W., Wagner, E., Saggau, B., Maly, R. R., and Herden, W., SAE 840992, 1984.
32. Hensinger, D. M., Maxson, J. A., Holm, K., and Oppenheim, A. K., SAE 920414, 1992.
33. Cho, Y. S., Santavicca, D. A., and Sonntag, R. M., SAE 922168, 1992.
34. Ziegler, G. F. W., Schaudt, R., and Herweg, R., SAE Trans. 865031, 1986.
35. Pischinger, S., and Heywood, J. B., SAE 900021, 1990.
36. Herweg, R., Begleris, Ph., Zettlitz, P., and Ziegler, G. F. W., SAE 881639, 1988.
37. Cho, Y.-S., and Santacicca, D. A., SAE 932715, 1993.
38. Maly, R. R., Wagner, E., and Ziegler, G. F. W., SAE 830331, 1983.
39. Maly, R. R., Saggau, B., Wagner, E., and Ziegler, G. F. W., SAE 830 478, 1983.
40. Abdel-Gayed, R. G., Bradley, D., and Lawes, M., *Proc. R. Soc. London A414* 389–413 (1988).
41. Maly, R. R., and Vogel, M., *Seventeenth Symposium (International) on Combustion*, The Combustion Institute, Pittsburgh, 1978, pp. 821–831.
42. Maly, R. R., *Eighteenth Symposium (International) on Combustion*, The Combustion Institute, Pittsburgh, 1980, pp. 1747–1754.
43. Bradley, D., and Lung, F. K.-K., *Combust. Flame* 69:71–93 (1987).
44. Kono, M., Niu, K., Tsukamoto, T., and Ujiie, Y., *Twenty-Second Symposium (International) on Combustion*, The Combustion Institute, Pittsburgh, 1988, pp. 1643–1649.
45. Pischinger, S., and Heywood, J. B., *Twenty-Third Symposium (International) on Combustion*, The Combustion Institute, Pittsburgh, 1990, pp. 1033–1040.
46. Ko, Y., Arpaci, V. S., and Anderson, R. W., *Combust. Flame* 83:88–105 (1991).
47. Herweg, R., "Die Entflammung brennbarer turbulenter Gemische durch elektrische Zündanlagen-Bildung von Flammenkernen," Ph.D. Thesis, University of Stuttgart, Baden-Württemberg, West Germany, 1992.
48. Herweg, R., and Maly, R. R., SAE 922 243, 1992.
49. Mantel, T., SAE 920587, 1992.
50. Boudier, P., Henriot, S., Poinsot, T., and Baritaud, T., *Twenty-Fourth Symposium (International) on Combustion*, The Combustion Institute, Pittsburgh, 1992, pp. 503–510.
51. Krämer, M., Maly, R. R., and Breitling, T., *Fifteenth International Symposium on Wiener Motoren*, Wien, April 28–29, 1994.
52. zur Loye, A. O., and Bracco, F. V., SAE 870454, 1987.
53. Mantzaras, J., Felton, F. G., and Bracco, F. V., SAE 881633, 1988.
54. Ziegler, G. F. W., Herweg, R., Meinhardt, P., and Maly, R. R., *Proceedings on XXIII FISITA Congress 905001*, 1990.
55. Maly, R. R., Eberspach, G., and Pfister, W., *Proceedings on COMODIA 90*, 1990, pp. 399–404.
56. Winklhofer, E., Phillip, H., Fraidl, G., and Fuchs, H., SAE 930871, 1993.
57. Maly, R. R., Bray, K. N. C., and Chew, T. C., *Combust. Sci. Technol.* 66:139–147 (1989).
58. Bray, K. N. C., Chew, T. C., and Maly, R. R., *Proceedings on the 7th Symposium Turbine Shear Flow*, 1989.
59. Wirth, M., Keller, P., and Peters, N., SAE 932646, 1993.
60. Orth, A., Sick, V., Wolfrum, J., Maly, R. R., and Zahn, M., *Twenty-Fifth Symposium (International) on Combustion*, The Combustion Institute, Pittsburgh, 1994, submitted.
61. Becker, H., Monkhouse, P. B., Wolfrum, J., Cant, R. S., Bray, K. N. C., Maly, R. R., Pfister, W., Stahl, G., and Warnatz, R., *Twenty-Third Symposium (International) on Combustion*, The Combustion Institute, Pittsburgh, 1990, pp. 817–823.
62. Wolfrum, J., private communication, 1994.
63. Nino, E., Gajdeczko, B. F., and Felton, P. G., SAE 930872, 1993.
64. Keck, J. C., *Prog. Energy Combust. Sci.* 16:125–154 (1990).
65. Hochgreb, S., and Dryer, L. F., *Combust. Flame* 91:257–284 (1992).
66. Warnatz, J., *Twenty-Fourth Symposium (International) on Combustion*, The Combustion Institute, Pittsburgh, 1992, pp. 553–579.
67. Chevalier, C., Pitz, W. J., Warnatz, J., Westbrook, C. K., and Melenk, H., *Twenty-Fourth Symposium (International) on Combustion*, The Combustion Institute, Pittsburgh, 1992, pp. 93–101.
68. Maas, U., and Pope, S. B., *Twenty-Fourth Symposium (International) on Combustion*, The Combustion Institute, Pittsburgh, 1992, pp. 103–112.
69. Maas, U., and Pope, S. B., *Twenty-Fifth Symposium (International) on Combustion*, The Combustion Institute, Pittsburgh, 1994, submitted.
70. Westbrook, C. K., Engineering Foundation Confer-

ence on "Present and Future Engines for Automobiles." St. Barbara, CA, August 25–30, 1991.
71. Gülder, Ö. L., SAE 841000, 1984.
72. Warnatz, J., and Maas, U., *Technische Verbrennung*, Springer Verlag, Berlin, 1993.
73. Delamare, L., Borghi, R., and Gonzalez, M., SAE 910265, 1991.
74. Bray, K. N. C., *Proc. R. Soc. London A431*, 1990, pp. 315–335.
75. Fichot, F., Lacas, F., Veynante, D., and Candel, S., *Combust. Sci. Technol.* 90:35–60 (1993).
76. Said, R., and Borghi, R., *Twenty-Second Symposium (International) on Combustion*, The Combustion Institute, Pittsburgh, 1988, pp. 569–577.
77. Meneveau, C., and Poinsot, T., *Combust. Flame* 86:311–332 (1991).
78. Maly, R. R., *Improved Otto-Cycle by Enhancing the Final Phase of Combustion*, Final Report, CEC:EN3E-0056-D, 1989.
79. Cambray, P., and Joulin, G., *Combust. Sci. Technol.* submitted, 1993.
80. Weller, H. G., *The Development of a New Flame Area Combustion Model Using Conditional Averaging*, Thermo-Fluids Section Report TF/9307, Department of Mechanical Engineering, Imperial College, London, 1993.
81. Poinsot, T., Haworth, and Bruneaux, *Combust. Flame* 95:118 (1993).
82. Anand, M. S., and Pope, S. B., *Combust. Flame*, 67:127–142 (1988).
83. Borghi, R., Argueyrolles, B., Gauffie, S., and Souhaite, P., *Twenty-Third Symposium (International) on Combustion*, The Combustion Institute, Pittsburgh, 1990, pp. 1591–1599.
84. Naitoh, K., Tagaki, Y., Kuwahara, K., Krause, E., and Ishii, K., *Proceedings of AIAA 89-1886*, 1989.
85. Naitoh, K., Itoh, T., Tagaki, Y., and Kuwahara, K., SAE 920590, 1992.
86. Miller, J. A., and Bowman, C. T., *Energy Combust. Sci.* 15:287–338 (1989).
87. Bockhorn, H., Chevalier, C., Warnatz, J., and Weyrauch, V., "Experimental Investigation and Modeling pf Prompt NO Formation in Hydrocarbon Flames," *Heat Trans. Fire Combust.* HDT 166:11–17 (1991).
88. Studzinski, W. M., Liiva, P. M., Choate, P. J., Acker, W. P., Smooke, M., Brezinsky, K., Litzinger, T., and Bower, S., SAE 932815, 1993.
89. Cloutman, L. D., *Twenty-Fifth Symposium (International) on Combustion*, The Combustion Institute, Pittsburgh, 1994, submitted.
90. Poinsot, T., Veynante, D., and Candel, S., *J. Fluid Mech.* 228:561–606 (1991).
91. Poinsot, T., Baritaud, T., Henriot, S., Torres, A., and Trouvé, A., *Direct Numerical Simulation of Turbulent Combustion and Implications for Piston Engine Computations*. ECCOMAS, 2nd Computational Fluid Dynamics Conference, Stuttgart, 1994.
92. Brown, P. G., and Woods, W. A., SAE 922233, 1992.
93. Kubo, S., Yamamoto, M., Kizaki, Y., Yamazaki, S., Tanaka, T., and Nakanishi, K., SAE 932706, 1993.
94. Nitschke, R. G., SAE 932704, 1993.
95. Cheng, W. K., Hamrin, D., Heywood, J. B., Hochgreb, S., Min, K., and Norris, M., SAE 932708, 1993.
96. Peckham, M., and Collings, N., SAE 932643, 1993.
97. Peckham, M., and Collings, N., SAE 932643, 1993.
98. Peckham, M., and Collings, N., SAE 922237, 1992.
99. Gatellier, B., Trapy, J., Herrier, D., Quelin, J. M., and Galliot, F., SAE 920095, 1992.
100. Frank, R. M., and Heywood, J. B., SAE 910558, 1991.
101. Meernik, P. R., and Alkidas, A. C., SAE 932752, 1993.
102. Tamura, T., and Hochgreb, S., SAE 922235, 1992.
103. Trinker, F. H., Cheng, J., and Davis, G. C., SAE 932705, 1993.
104. Chevalier, C., Louessard, P., Müller, U. C., and Warnatz, J., "A Detailed Low-Temperature Reaction Mechanism of n-Heptane Auto-Ignition, JSAE," *Proceedings of the 2nd Symposium on Diagnostics and Modeling of Combustion in Reciprocating Engines*, 1990, pp. 93–97.
105. Pitz, W. J., Westbrook, C. K., and Leppard, W. R., SAE 912314, 1991.
106. Leppard, W. R., SAE 922325, 1992.
107. Filipe, D. J., Li, H. L., Miller, D. L., and Cernansky, N. P., SAE 920807, 1992.
108. Dagaut, P., Reuillon, M., and Cathonnet, M., *Combust. Sci. Technol.* accepted for publication, 1993.
109. Smith, J. R., Green, R. M., Westbrook, C. K., and Pitz, W. J., *Twentieth Symposium (International) on Combustion*, The Combustion Institute, Pittsburgh, 1984, pp. 91–100.
110. König, G., and Sheppard, C. G. W., SAE 902135, 1990.
111. Maly, R. R., Klein, R., Peters, N., and König, G., SAE 900025, 1990.
112. König, G., Maly, R. R., Bradley, D., Lau, A. K. C., and Sheppard, C. G. W., SAE 902136, 1990.
113. König, G., "Autoignition and Knock Aerodynamics in Engine Combustion," Ph.D. Thesis, Leeds University, Leeds, England, 1993.
114. Oppenheim, A. K., *Phil. Trans. R. Soc. London A* 315:471–508 (1985).
115. Lutz, A. E., "Numerical Study of Thermal Ignition," Sandia Report, SAND 88-8228 UC4, 1988.
116. Lutz, A. E., Kee, R. J., Miller, J. A., Dwyer, H. A., and Oppenheim, A. K., *Twenty-Second Symposium (International) on Combustion*, The Combustion Institute, Pittsburgh, 1988, pp. 1683–1693.
117. Schöffel, S., Hebeker, F.-K., and Maly, R. R., *Poster, 8th Symposium on Turbulent Shear Flow*, 1991.
118. McKinley, T. L., Primus, R. J., O'Rourke, P. J., and Butler, T. D., SAE 881612, 1988.
119. Lou, K. H., and Bray, K. N. C., SAE 920586, 1992.
120. Gosman, D., STAR-CD User Manual, Computational Dynamics, London, 1994.
121. Pinchon, I., SAE 890348, 1989.
122. Cheng, W. K., and Diringer, J. A., SAE 910268, 1991.

123. Kuo, T.-W., and Reitz, R. D., SAE 920425, 1992.
124. Borghi, R., Delamare, L., and Mantel, T., in *Unsteady Combustion* (F. E. C. Culic, M. V. Heitor, and J. Whitelaw, Eds.), Clover Academic Press, to appear, 1994.
125. Gill, A., Gutheil, E., and Warnatz, J., Third International Symposium on Diagnostics and Modeling of Combustion in Interval Combustion Engines, Comodia 94, Japan Society of Mechanical Engineers, 1994, pp. 583–588.

COMMENTS

A. K. Oppenheim, University of California, Berkeley, USA. Upon the plenary lecture of Bill Agnew [1], you had a hard act to follow—a task accomplished with flying colors. In effect, you brought up to date the menu of demands an engineer may have to clarify what is going on "at the piston top." He may have many reasons for them: economical, political, humanitarian, ecological, etc. The one I consider of utmost importance is the progress of technology. In this respect, your overlooking the significance of pressure measurement is quite auspicious. As brought up in our paper [2], pressure is the most informative measure of engine performance. It provides therefore the primary sensing element for prompt, microprocessor control for the execution of the exothermic process of combustion—a task referred to as "internal treatment" whereby fuel economy can be maximized in synergy with the minimization of pollutant emissions. After all, isn't the achievement of this goal the principal reason for your menu?

REFERENCES

1. Agnew, W. G., "Room at the Piston Top—Contributions of Combustion Science to Engine Design," *Twentieth Symposium (International) on Combustion,* The Combustion Institute, Pittsburgh, 1984, pp. 1–17.
2. Oppenheim, A. K., and Maxson, J. A., "A Thermochemical Phase Space for Combustion in Engines," Twenty-Fifth Symposium (International) on Combustion, 1994.

Author's Reply. There is no question about the goal, but there are many questions about how to achieve it. Engines have always been built to ensure an optimum pressure release for controlling fuel consumption and emissions either implicitly by appropriately designing it into the hardware or, more recently, by additional electronic control. However, by controlling the pressure release one can achieve only those limits that have been built into the hardware design. In order to really achieve minimum values of fuel consumption and emissions, it is necessary to know all relevant processes and interrelations in detail—as outlined in the paper—and to implement them in an optimum design. Only then the control of the pressure release gives useful results.

•

J. Chomiak, Chalmers University of Technology, Sweden. Your measurements show that the early burned portion of the charge produces most of the NO_x. Is this due to the temperature stratification (Mache effect) or due to other reasons? How general is this observation in terms of engine speed load and combustion chamber features?

Author's Reply. For any given net formation rate of NO production, as is the case in IC engines, the resulting NO concentration is its integral over time. Hence the regions having been burned earliest are the oldest ones and therefore exhibit the highest values. The measurements show just that. This is generally valid for all speeds, loads, and chamber features.

•

Lawrence A. Kennedy, Ohio State University, USA. For the CFD flow calculations, you indicated that quite good results were obtained for the intake and compression strokes. However, the initial conditions for the intake stroke (flow in through valves, etc.) are quite complex. How does one provide good detail initial conditions for such a complex situation which is influenced by geometry of values, lift, etc.

Author's Reply. The proper choice of inlet conditions is crucial to the accuracy of CFD calculations. The best results are obtained if the full geometry (air filter to exhaust) is included into the mesh that is used for calculations. Because of the high number of grid points required, this is expensive. Good results may be obtained with the following approach.

1. Precalculation of the mean air flow through the engine and the complete intake and exhaust manifolds using a 1D code (Promo, Wave, . . .)
2. Detailed meshing of the short (3–5 diameters) port sections inside the cylinder head, the valve seat region including the moving valves, and the combustion chamber including the moving piston.
3. Initial conditions:

— inflow conditions at 3D CFD boundaries set equal to the results of the 1D calculation (pressure, temperature, mean flow velocity, i.e., plug flow)

— inside the 3D calculation domain: mean flow velocity $\bar{U} = 0$, turbulence intensity 0.1 m/s $\leq u' \leq (0.1 - 0.3)\bar{U}$, integral length scale $L = (0.1 - 0.2)H$, where H is

the manifold diameter and piston head clearance, respectively.

After tens of time steps, the discontinuous initial conditions will equilibrate and a consistent flow field will result. This approach, however, will not account for residual flow structures and/or charge distributions due to valve overlap. Therefore, a more expensive detailed approach is to run 3D calculations for 2–3 consecutive full cycles, using the results from the preceding calculation as initial conditions for the next run. If stable flow patterns have been obtained, they can be used as reliable initial conditions for subsequent CFD calculations.

•

Rupert Klein, RWTH Aachen, ITM, Germany. It was pointed out in the lecture that strong shock waves and/or developing detonations, generated by sequential ignition of exothermal centers, lead to engine knock damage. The principal reason for the observed surface erosion—so it was argued—is the excessive thermal load that arises when the uppermost material layer is subject to large heat fluxes from the compressed combustion products. Pressures of ≈1000 bar would be required to produce similar damage through pure mechanical effects, and those would not be observed experimentally.

Comments:

1. The wave speeds of pressure pulses during the development of detonations are comparable to the elastic wave speeds of piston materials. Purely static estimates are insufficient in this regime. Resonant excitation of Rayleigh surface waves can generate maximum stresses in the material that exceed the maximum gas phase pressure by a factor of 3 and more.

2. During the development of a detonation, one finds pressure spikes that are up to 50 times larger than the pressure in the preshock unburnt gas. This corresponds to very localized pressure spikes of up to 2000 bar when a detonation forms in the precompressed end gas. As a result of the spatial and temporal localization, these phenomena are very difficult to measure.

Author's Reply. By careful experiments in a detonation chamber and in an optically accessible engine, using dedicated measuring techniques with highest spatial and temporal resolution for pressure and surface temperature/heat flux, the following facts were established for heavily knocking combustion under engine conditions (developing detonation mode):

1. The peak pressure did not exceed 400 bar for initial end gas pressures of 50 bar, corresponding to a measured pressure ratio of only 8 to 1. The corresponding mechanical stress was well below the maximum value permanently sustained by the piston material.

2. The associated rise in surface temperature (0.5-μm depth, time and space resolution 500 ns and 1 mm^2, respectively) is about 150 K, causing a thermally induced mechanical stress, exceeding the allowable limit by far (as a simple strain calculation shows).

3. A single knocking event of this strength caused a local crack in quartz windows. In all our experiments, the theoretical pressure spikes of 2000 bar or 50 times the initial pressure level were never observed. The detonation was never fully developed due to inadequate run-up time and space. In production engines, the knock levels are appreciably lower and still there is knock damage. Excessively high pressure spikes might occur only by positive interference/reflections of several pressure waves in very favorable geometries.

Twenty-Fifth Symposium (International) on Combustion/The Combustion Institute, 1994/pp. 125–133

CARS TEMPERATURE MEASUREMENTS AND THE CYCLIC DISPERSION OF KNOCK IN SPARK IGNITION ENGINES

D. BRADLEY,* G. T. KALGHATGI, C. MORLEY AND P. SNOWDON
Shell Research Limited
Thornton Research Centre
P.O. Box 1, Chester CH1 3SH, England

AND

JINKU YEO
Department of Mechanical Engineering
University of Leeds
Leeds, England

The use is described of the coherent anti-Stokes Raman spectroscopy (CARS) technique in a single-cylinder research engine to measure end-gas temperature in the regime that leads to the onset of knock. The investigations, under nominally the same running conditions, covered a large cyclic dispersion of knock, with knock occurring in about 80% of the cycles. In-cylinder pressures were measured with a transducer, and an ion gap signified flame arrival towards the end of the flame travel and just before autoignition. In general, the temperature increased by over 100 K, both with and without knock, as a result of exothermic preflame reactions. This measured elevation was supported by computations with a simple five-step model of autoignition, calibrated against measured autoignition times in a rapid compression machine. The temperatures measured just prior to knock increased with the severity of the knock. The observed severe cyclic dispersion of knock, under the conditions of the study, is attributed primarily to the cyclic dispersion of flame speeds. An increase in flame speed is associated with an increase in temperature and greater propensity to knock.

Introduction

The characteristic noise of knock is caused by acoustic excitation of the gas in the cylinder and of the engine block. It arises from pressure pulses generated by autoignition at one or more sites in the end gas. This comprises runaway exothermic chemistry with rapid temperature increases of more than 1000 K. Not all autoignitions, however, generate pressure pulses sufficiently strong to lead to knock, and these might be regarded as benign. With alkane-containing fuels, there is a possibility that so-called cool flame chemistry can cause reaction at earlier, lower-temperature, stages of the end-gas compression, with the resulting temperature rise (and possibly the accumulation of reactive products) influencing the subsequent explosive autoignition [1].

The paper discusses the end-gas temperatures measured prior to knock. Although a rapid burn rate might appear advantageous, in that burning might be completed before an autoignition delay time has elapsed, an increase in this rate increases the temperature of the end gas, which reduces the delay. Optimum balance between burn rate, autoignition chemistry, and spark timing, from cycle to cycle, is sought in engine management systems. The inevitable cyclic variations of burning velocity arising from turbulence make this difficult [2].

The study attributes the observed appreciable cyclic dispersion of knock to the cyclic dispersion of burn rate. Experiments were under nominally the same conditions of load, throttle, and equivalence ratio in a four-stroke engine, with a pancake-shaped combustion chamber and very little swirl. Pressure was measured by a pressure transducer, flame progress by an ion gap, and end-gas temperatures by coherent anti-Stokes Raman spectroscopy (CARS). The more rapid the burn rate, the greater was the tendency to engine knock. As the temperature increased due to exothermic, preknock reactions, statistically, so also did the severity of any subsequent knock.

This behaviour also is mimicked in a reduced, four-species, five-reaction model of autoignition. Both model and experiments focus on the regime leading up to autoignition and any subsequent onset of knock, rather than the factors that govern the

*Also Department of Mechanical Engineering, University of Leeds, Leeds, England.

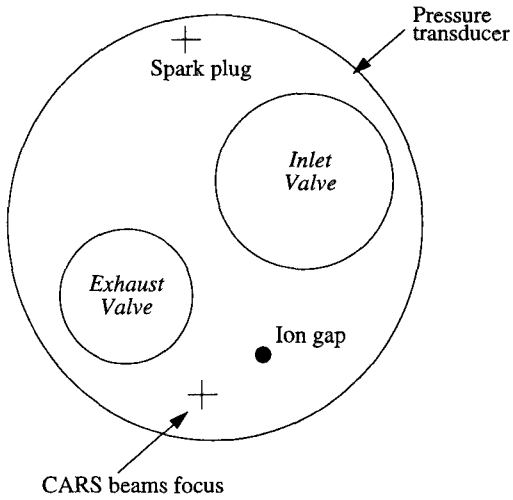

FIG. 1. Plan of measurement points.

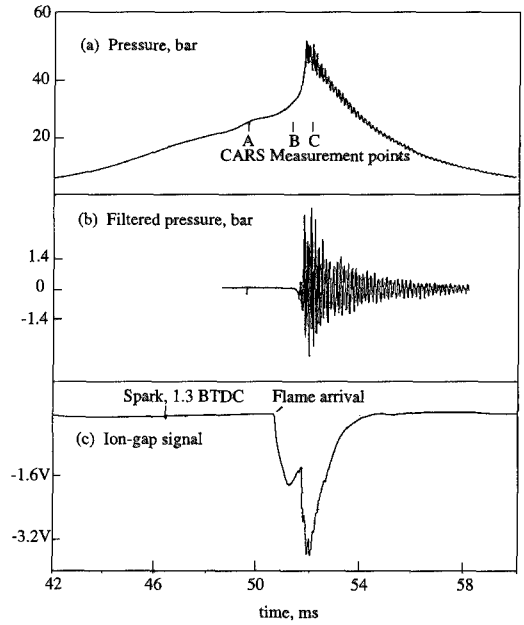

FIG. 2. Measured traces during a single cycle.

knock intensity. The latter are more complex, with three modes for the propagation of reaction from exothermic centres: deflagration, thermal explosion, and developing detonation, dependent upon the temperature gradient around the centre [3].

Experimental Details

The Engine and Signal Processing:

A single-cylinder Ricardo E6 engine was modified by inserting a plate with windows between the head and the block to allow optical access to the combustion chamber. The cylinder swept volume was 507 cm^3, with a compression ratio of 10.18 in all but the CARS calibration experiments, when it was 10.47. A Kistler Type 6001 transducer was wall mounted and water cooled. Ion-gap electrodes were mounted in the head close to the end gas, and measurements of the time interval between the spark and ion-gap currents gave the flame arrival time. The ion current pulses were characteristic of those associated with a propagating flame [4], and generally, the flame reached the probe before any knocking occurred. That flame arrival times were indicative of flame propagation was confirmed by the excellent correlation of such time with the pressure. Figure 1 shows the positions of the spark and ion gap, the pressure transducer, and the CARS measuring point. A crank-angle (CA) selector system generated timing pulses, as required. Data were recorded by a high-speed acquisition system (Biodata Microlink 4000) at a sampling rate of 500 kHz, and analysed with FAMOS software. The fuel was 90% iso-octane-10% heptane, equivalence ratio 1.13, and the engine ran at full throttle, at 1200 rpm. The spark passed at 13 crank-angle degrees, 1.8 ms before TDC (top dead centre). CARS lasers were triggered from a fixed crank-angle signal from each cycle. Figure 2 presents data acquired from a single engine cycle. Shown in Fig. 2(b) is the pressure signal digitally filtered between 5 and 25 kHz using FAMOS. Here knock is arbitrarily defined by a filtered pressure signal that exceeds 0.1 bar. Knock intensity (KI) is the difference between the maximum and minimum of this filtered signal. The conditions studied were for strong knock, with knock in about 80% of the cycles.

The CARS System:

CARS thermometry [5–7] now is established in engine research [1,8,9]. In the present work, a modeless laser of improved accuracy was developed [10]. Two laser beams were focused in the measurement volume, of about 1 mm^3, where excitations of nitrogen produced a signal beam. One of the incident beams was broadband over a range of wavelengths, and this led to the creation of a broadband signal beam. This was spatially filtered and dispersed by a spectrometer onto a photodiode array detector to generate the CARS spectrum.

As the temperature increases, the higher rotational levels of vibrational bands become more populated, to broaden the CARS spectrum. Temperatures were inferred by matching measured nitrogen spectra to those predicted by the Epsilon CARP PC code. Prior to this, CARS spectra were referenced using a non-resonant CARS spectrum from argon to account for

the spectral profile of the broadband laser beam. Instrument function parameters were derived to account for the contribution of the detection system to the spectral shape. This includes such effects as artificial broadening due to the finite width of the entrance slit to the spectrometer. Comparisons of an averaged, room-temperature, nitrogen spectrum with its computer code fit allowed the instrument function to be found.

The pump beam was formed by frequency doubling the output from a Nd:YAG laser, while the probe beam was the output from a broadband modeless dye laser. The Nd:YAG laser system produced two frequency-doubled outputs: one pumped the modeless dye laser system (80 mJ, 532 nm), and the other provided the CARS pump beam (90 mJ, 532 nm). The output from the modeless laser system (2 mJ, 1.0-nm bandwidth, centred on 607.5 nm) was combined with the green pump beam and transmitted via prisms to the engine test cell.

Validation of CARS Temperature Measurements:

The measurement technique was validated in three ways. In a high-temperature/high-pressure cell containing nitrogen, the measured (steady) temperatures exhibited a normal distribution, and as can be seen in Table 1(a), there is good agreement between the mean values of these and those measured by a thermocouple. The 95% confidence interval also is given and is tolerably small. Nonsteady calibrations were made at the centre of the engine combustion chamber at different crank angles, in both a motored engine and in one running on propane-air, but not knocking. About 80–85% of the spectra gave a sufficiently good spectral match. Measured mean temperatures and the 95% confidence intervals are given in Tables 1(b) and (c), which compare mean values with those calculated from the ideal gas law using the mean value of the measured pressure, known volume, and molar mass from the measured air consumption rate. It was assumed that no leakage of the charge occurred. There is, again, very good agreement between these temperatures and mean CARS temperatures.

Reduced Reaction Scheme for Autoignition

The delay time for autoignition must be greater than the time of arrival of the flame in the end gas to avoid autoignition. Because of the complexities of complete autoignition reaction schemes, there is a long tradition of reduced schemes, although more complete reaction schemes are now being treated [11]. Gray and Yang [12] employed a reduced scheme for the analysis of cool flame oscillations, whilst the seminal work of Halstead et al. [13] used a generic formulation to simplify the prediction of autoignition in engines. The regime of cool flames and negative temperature coefficients is entered towards the end of the compression stroke. There have been several other simplified descriptions of the chemistry [14–17]. The current, particularly simple, five-reaction scheme models the regime of negative temperature coefficient, which obtains towards the end of the compression stroke. It gives a good representation of this regime and of the autoignition delays in rapid compression machines [18]. The present rate data, in the form of Arrhenius "A" values and activation temperatures T_a, given in Table 2, were derived from experimental data from the rapid compression machine at Lille [19] for the same fuel, and kindly supplied by Professor L. R. Sochet and Dr. R. Minetti.

The five reactions of the scheme are as follows:

$$F + 12.35O_2 \xrightarrow{d} P \quad \text{direct reaction} \tag{1}$$

$$F + O_2 \xrightarrow{i} C \quad \text{chain initiation} \tag{2}$$

$$C \xrightarrow{b} 2C \quad \text{chain branching} \tag{3}$$

$$C + C \xrightarrow{q} P \quad \text{quadratic termination} \tag{4}$$

$$C \xrightarrow{l} P \quad \text{linear termination.} \tag{5}$$

Here F represents the fuel, C chain carriers, O_2 oxygen, and P the products of combustion. The 90% iso-octane-10% heptane fuel stoichiometry is taken to be

$$C_{7.9}H_{17.8} + 12.35O_2 \rightarrow 7.9CO_2 + 8.9H_2O. \tag{6}$$

The empirical form of the direct oxidation expression at high temperature follows that recommended by Westbrook and Dryer [20]:

$$\frac{d[F]}{dt} = -k_d[F]^a[O_2]^b \tag{7}$$

where [ ] indicates mole density. The constants a and b are assigned values of 0.25 and 1.5 and

$$\frac{d[O_2]}{dt} = -12.35k_d[F]^{0.25}[O_2]^{1.5}. \tag{8}$$

The total scheme comprises

$$\frac{d[F]}{dt} = -k_d[F]^{0.25}[O_2]^{1.5} - k_i[F][O_2] \tag{9}$$

TABLE 1
Calibration of CARS temperature measurements

(a) Using high-temperature/high-pressure cell

Pressure (bar)	Thermocouple temperature (K)	CARS temperature (K) mean	CARS temperature (K) 95% confidence interval
1.0	296	296	±15
6.4	296	298	±8
12.5	296	297	±10
21.6	296	297	±14
1.0	1205	1209	±29
5.53	693	694	±11
11.07	790	807	±21
15.15	596	594	±17

(b) Using motored engine

Crank angle (deg)	Motored Temperature (K)		
	Calculated	CARS mean	CARS 95% confidence interval
663	405	412	±10
683	497	504	±12
693	549	542	±22
703	593	609	±17

(c) Using engine fired with propane/air

Crank angle (deg)	Firing Temperature (K)		
	Calculated	CARS mean	CARS 95% confidence interval
663	451	458	±12
683	569	574	±21
713	706	719	±21

$$\frac{d[C]}{dt} = k_i[F][O_2] + (k_b - k_l)[C] - 2k_q[C]^2 \quad (10)$$

$$\frac{d[O_2]}{dt} = -12.35k_d[F]^{0.25}[O_2]^{1.5} - k_i[F][O_2] \quad (11)$$

and the energy equation, for a volumetric internal energy, E

$$\frac{dE}{dt} = k_d h_d[F]^{0.25}[O_2]^{1.5} + k_i h_i[F][O_2] + (k_b h_b + k_q h_q[C] + k_l h_l)[C] - Q. \quad (12)$$

Here h is the heat of reaction and Q is the volumetric

TABLE 2
Constants for the five (d–l) reaction autoignition model (Arrhenius "A" constant in mole m s units; activation temperature, T_a, in K; heat of reaction, h, kJ/mole)

	d	i	b	q	l
A	$7.0\ 10^5$	$2.0\ 10^7$	$5.2\ 10^{10}$	$2.5\ 10^2$	$1.0\ 10^{14}$
T_a	15,000	20,000	11,500	0	17,500
h	5,200	0	100	0	50

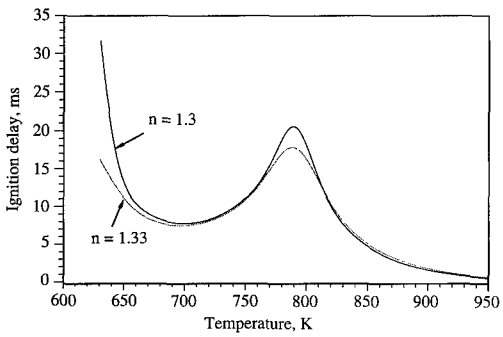

FIG. 3. Variation of computed autoignition delay time after instantaneous compression of stoichiometric mixture from 1 bar and 350 K.

heat loss rate, determined from the polytropic index of compression in the absence of reaction, and with variable ratio of specific heats. Optimisation of the various rate parameters was guided by Morley's correlation of the research octane number of alkanes with the rate of the branching reaction [21]. This correlation has been extended to include the termination rate [22], and the ratio of the rate constants, k_b/k_l, was chosen on this basis.

A simplified, but informative, application of the scheme is the computation of the variation of autoignition delay time with compression ratio. This is shown in Fig. 3 plotted against compression temperature. This assumes instantaneous polytropic compression of a stoichiometric mixture of the fuel, with indices, n, of 1.30 and 1.33, from a pressure of 1 bar and 350 K to the given temperature. The delay time is the total time to the onset of explosive autoignition. A cool flame may occur during this period. After the negative temperature coefficient regime, the delay time decreases substantially as a consequence of the modelled "high-temperature" direct reaction. It also is apparent that an increase in heat loss to the walls, associated with a decrease in the polytropic index, can increase the delay time.

When applied to the engine conditions, solutions to Eqs. (9) through (12) were obtained for the measured pressure-volume-time relationship, on the assumption that the composition and temperature in the end gas were spatially uniform. Up to the point of sparking, the computed chemical heat release was very small, and the polytropic index for the compression was found from the known pressure-volume relationship. Thereafter, the end gas was compressed by both the piston motion and the flame propagation, and as long as the heat release was negligible, the polytropic index was assumed to have the same value of 1.3. This enabled the end-gas temperature to be calculated from the measured pressure. However, in the later stages, the computations usually revealed some heat release and end-gas temperatures in excess of the polytropic values. This also was observed experimentally.

Experimental Results and Discussion

CARS temperatures were measured at three crank-angle timings, A, B, and C, as shown in Fig. 2(a). A range of knocking behaviour was observed, with extensive cyclic variations. For each timing, 250 spectra were collected. For the last set, C, at 28.8 CA degrees after TDC, a significant proportion of the measurements was after the onset of knock. However, only measurements before the onset were considered. Table 3 summarises the mean temperature and pressure at each crank angle, along with the respective 95% confidence intervals. Results are grouped according to whether there was knock during the cycle. The knocking cycles tended to be hotter in the later stages of compression than the non-knocking cycles, as shown by set C. This also is demonstrated in the CARS measurements of Nakada et al. [9].

The cyclic dispersion of the knock most probably arises from the stochastic nature of the turbulence, which influences the flame speed [2]. The temperature of residual gas from the previous cycle and its mixing also are important in governing the precompression, and hence end-gas, temperature [9]. Figure 4 shows how a shorter flame arrival time, the time for the flame to reach the ion gap after sparking, in turn correlates with a higher pressure. The mean temperature at the start of compression was esti-

TABLE 3
Summary of CARS temperatures
[mean temperatures (K) and pressures (bar); 95% confidence intervals in parentheses]

	Time after TDC		Nonknocking cycles		Knocking cycles	
Set	CA (deg)	(ms)	Temperature (K)	Pressure (bar)	Temperature (K)	Pressure (bar)
A	10.7	1.48	827 (30)	22.5 (0.16)	844 (20)	24.3 (0.21)
B	22.8	3.15	822 (57)	23.4 (0.22)	804 (33)	26.4 (0.27)
C	28.8	4.0	890 (43)	22.6 (0.3)	951 (41)	26.9 (0.64)

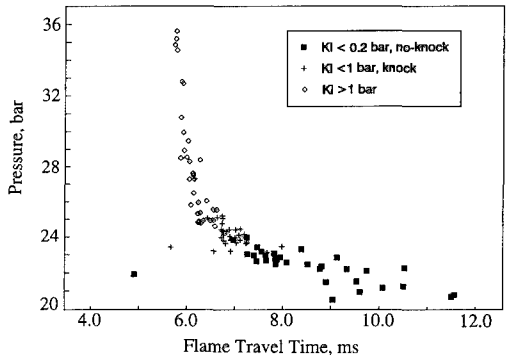

FIG. 4. Pressure at 28.8 CA degrees after TDC vs flame arrival time.

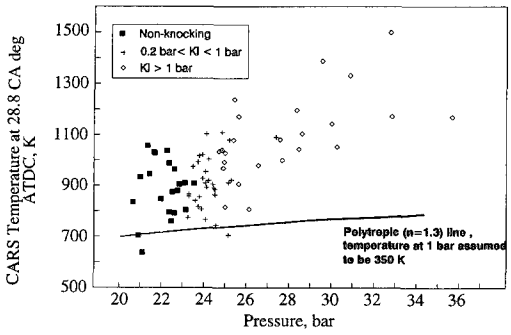

FIG. 5. Individual values of measured CARS temperatures, 28.8 CA degrees after TDC vs pressure.

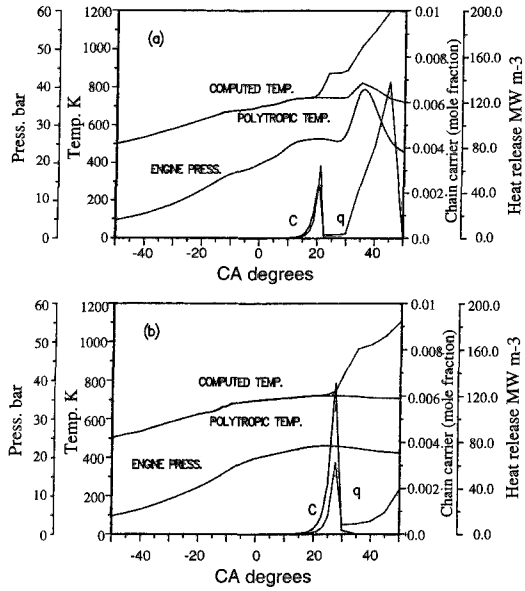

FIG. 6. Computed end-gas temperatures, mole fraction of chain carrier, C, and volumetric heat release rate, q, based upon measured pressure records; (a) knocking cycle, (b) nonknocking cycle.

mated from the calibration engine experiments to be 350 K, and with the measured polytropic index of 1.30, it was a simple matter to calculate the polytropic temperature associated with the pressure at which the measurement was made. The resulting temperatures are shown by the full line curve in Fig. 5. Also shown in this figure are individual CARS temperatures. These are elevated above the polytropic temperatures, even when knock did not occur. Lucht et al. [1] also have measured CARS temperatures that are higher than those estimated on the assumption of no heat release in the end gas. In addition, the high-speed engine photographs of Shiga et al. [23] suggest a cool flame in the end-gas region, prior to any knocking. Such temperature elevations arise from the early exothermic reactions, prior to autoignition.

The autoignition model provides a parametric confirmation of these phenomena. Shown in Fig. 6(a) is a measured pressure variation from a single knocking cycle. The curve above it gives the corresponding end-gas temperatures computed from this pressure, with a polytropic index of 1.30. The curve coincident

with, and above, this is the end-gas temperature computed with the model. It pulls away from the polytropic curve, with increasing temperature elevation, because of the developing exothermic reactions in the end gas. These give a volumetric heat release rate, q, shown by the lower curve. The curve C shows the mole fraction of the chain carrier C. Its peak marks the position of a cool flame, a transiently intense period of chemical reaction, with an associated temperature rise. After a further delay, in which the mole fraction of C decays, there are rapid increases in heat release and temperature, associated with pressure pulse generation. These occur at a computed time that approximates that observed in the measured pressure record. The simple model cannot be accurately predictive once autoignition is underway—nor does it include the eventual consumption of the end gas by the propagating flame. To model the onset of autoignition is easier than to model the details of knock.

Shown in Fig. 6(b) are the results of comparable computations for a nonknocking cycle. A cool flame is initiated later in the cycle, by which time, in practice, the end gas would have been consumed by the propagating flame. The end of this period, however, is not marked by the same appreciable increases in end-gas heat release and temperature that characterised the knock in Fig. 6(a). Despite the modelling limitations, the results indicate that the conditions in this region rapidly become much less favourable for pressure pulse generation, because of the piston-induced expansion.

The experiments and the application of the model both suggest that cyclic variations in knocking behaviour arise from cyclic variations in the burn rate, an increase in which, increases the end-gas pressure and temperature. This, in turn, increases the heat release from the reactions occurring there, and promotes the transition to a final phase in which the rate of heat release is sufficient to generate strong pressure pulses. This is in harmony with the finding of Lyon [24] that faster burn cycles start to knock earlier. As the onset of knock approaches, the temperature increases. Figure 5 demonstrates that, in general terms, the greater the resulting elevation in temperature at a fixed crank angle, the greater is the knock intensity. König and Sheppard [25] reached a similar conclusion, but attributed the considerable scatter they observed in this correlation, in part, to the varying temperature gradients within the end gas. The temperature gradient determines the mode of propagation of reaction from exothermic centres [3]. Sometimes severe knock was observed at quite a modest mean temperature. Interacting pressure pulses from different centres, and the triggering of one autoigniting centre by another, also influence the knock intensity.

Conclusions

1. The CARS technique of temperature measurement has been used successfully in an engine to determine end-gas temperatures in the regime prior to autoignition and knock.
2. There is severe cyclic dispersion of knocking cycles. An increase in flame speed was associated with an increase in end-gas temperature and a greater propensity to knock. This dispersion arises from the strong cyclic dispersion of flame speeds.
3. In experiments in which knock occurred in most cycles, there was usually an increase in temperature, of at least 100 K, due to exothermic autoignition reactions in the end gas. Larger temperature rises are associated with more severe knock.
4. A simple five-step chemical model can predict this temperature rise and, if the end-gas condition is known, the time to autoignition, but it cannot predict knock intensities.

Acknowledgments

The authors wish to acknowledge the contributions of Dr. C. R. McDonald and Mr. W. A. Clowes of Thornton Research Centre to the design and operation of the experiments.

REFERENCES

1. Lucht, R. P., Teets, R. E., Green, R. M., Palmer, R. E., and Ferguson, C. R., *Combust. Sci. Technol.* 55:41–61 (1987).
2. Al-Khishali, K. J., Boston, P. M., Bradley, D., Lawes, M., and Pegg, M. J., *Combustion in Engineering*, Institution of Mechanical Engineers, London, Vol. 1, pp. 175–180.
3. König, G., Maly, R., Bradley, D., Lau, A. K. C., and Sheppard, C. G. W., *SAE Trans.* 99:840–861 (1990).
4. Sheppard, C. G. W., and Ibrahim, E.-S. A. A., *Instrumentation for Combustion and Flow in Engines* (D. F. G. Durao, J. H. Whitelaw, and P. O. Witze, Eds.), Kluwer Academic Publishers, Dordrecht, The Netherlands, 1989, p. 355.
5. Eckbreth, A. C., *Laser Diagnostics for Combustion, Temperature and Species*, Abacus Press, Cambridge, MA, 1988.
6. Greenhalgh, D. A., "Quantitative CARS Spectroscopy," in *Advances in Nonlinear Spectroscopy* (R. H. Hester, Ed.), Wiley, New York, 1988.
7. Druet, S. A. J., and Taran, J.-P. E., *Prog. Quant. Electron.* 7:1 (1981).
8. Marie, J.-J., and Cotterau, M. J., SAE Paper No. 870458, 1987.
9. Nakada, T., Itoh, T., and Takagi, Y., SAE Paper No. 932644, 1993.
10. Skippon, S. M., Snowdon, P., and Ewart, P., *Appl. Opt.* 30:1008–1012 (1991).

11. Chevalier, C., Warnatz, J., Pitz, W. J., and Westbrook, C. K., *Twenty-Fourth Symposium (International) on Combustion,* The Combustion Institute, Pittsburgh, 1992, pp. 93–101.
12. Gray, B. F., and Yang, C. H., *J. Phys. Chem.* 73:3395 (1969).
13. Halstead, M. P., Kirsch, L. J., Prothero, A., and Quinn, C. P., *Proc. R. Soc. London A* 346:515 (1975).
14. Cox, R. A., and Cole, J. A., *Combust. Flame* 60:109–123 (1985).
15. Hu, H., and Keck, J., SAE Paper No. 872110, 1987.
16. Müller, U. C., Peters, N., and Liñán, A., *Twenty-Fourth Symposium (International) on Combustion,* The Combustion Institute, Pittsburgh, 1992, pp. 777–784.
17. Griffiths, J. F., Jiao, Q., Kordylewski, W., Schreiber, M., Meyer, J., and Knoche, K. F., *Combust. Flame* 93:303–315 (1993).
18. Bradley, D., and Yeo, J., *Proceedings of the Anglo-German Combustion Symposium,* British Section of the Combustion Institute, 1993, pp. 356–359.
19. Minetti, R., Ribaucour, M., Carlier, M., Fittschen, C., and Sochet, L. R., *Combust. Flame* 96:201–211 (1994).
20. Westbrook, C. K., and Dryer, F. L., *Prog. Energy Combust. Sci.* 10:1–57 (1984).
21. Morley, C., *Combust. Sci. Technol.* 55:115–123 (1987).
22. Morley, C., *Proceedings of the Anglo-German Combustion Symposium,* British Section of the Combustion Institute, 1993, p. 548.
23. Shiga, S., Kono, M., Iinuma, K., Karasawa, T., and Kurabayashi, T., *International Symposium on Diagnostics and Modeling of Combustion in Reciprocating Engines,* Tokyo, JSME, SAEJ, MESJ, 1985, p. 343.
24. Lyon, D., Institution of Mechanical Engineers, Paper No. C307/86, 1986.
25. König, G., and Sheppard, C. G. W., *SAE Trans.* 99:820–839 (1990).

COMMENTS

Alan Eckbreth, United Technologies Research Center, USA. In your CARS data reduction, did you account for the high nonresonant backgrounds introduced by the isooctane and *n*-heptane? How did you handle the varying nonresonant backgrounds that would result from mixture nonuniformities cycle to cycle? What values of the nonresonant susceptibilities did you use for the fuels used?

Dr. D. R. Snelling, National Research Council of Canada, Canada. Your pump beam energy is quite high (90 mJ) and depending on the pump beam diameter and the focal length of the lens used to generate the CARS signal, you could have very high focal intensities. Can you tell us the pump beam diameter, the lens focal length, and the phase-matching scheme, and would you comment on the possible effect of Stark broadening or stimulated Raman pumping on the nitrogen CARS spectrum. How did you account for the effect of varying nonresonant susceptibility on the CARS spectral signatures? The nonresonant susceptibility will vary from the nitrogen-filled high-pressure cell to the motored and fired propane/air fueled engine and to the end gas mixture. The nonresonant susceptibilities of heptane and octane are likely to be very high.

Reply to Comments of Eckbreth and Snelling. A 250-mm focal length lens focuses a beam of 25-mm diameter down to the measurement volume. Because of the age of the pump laser and the optical elements employed, it is estimated that <20 mJ of CARS pump energy and <0.5 mJ of Stokes energy enter the measurement volume. The computer code allows the nonresonant susceptibility (nrs) and/or the concentration of nitrogen to be varied. Variations of the nrs were found in separate studies to cause spectra changes similar to variations in nitrogen concentration at fixed nrs. Spectra were generated for various values of nrs at a fixed temperature. In the subsequent spectral fitting, the value of nrs was fixed at one that did not correspond to any values used to generate the spectra, and the start temperature was chosen to be different from that used for spectrum generation. These theoretical spectra were then fitted for temperature and nitrogen concentration simultaneously. A nitrogen concentration always was found that allowed the true temperature to be returned as that giving the best fit. In the engine experiments, an estimate of nrs was made from literature values and discussions with other practitioners, for each fuel. This was fixed and the temperature and nitrogen concentration were fitted simultaneously. Good spectral fits were always achieved. Thus, fitting nitrogen concentrations for fixed nrs allows for cyclic variations in the mixture.

•

Dieter Bruggemann, ITLR/University of Stuttgart, Germany. You have combined the laser beams in a collinear geometry. This arrangement can lead to a poor spatial resolution. Did you observe mixed spectra from different temperature regions, and if so, in which way did you evaluate them? By the way, some of your results are readily comparable to similar experiments published in Ref. 1.

REFERENCE

1. Bruggemann, D., Wies, B., Zhang, X. X., Heinze, T., and Knoche, K. F. "CARS Spectroscopy for Tempera-

ture and Concentration Measurements in a Spark Ignition Engine," in *Combusting Flow Diagnostics* (D. F. G. Durao et al., Eds.), Kluwer Academic Publishers, Dordrecht, The Netherlands, 1992.

Russel Lockett, Cranfield University, UK. You said that the spatial resolution of your colinear CARS system was 1.1 mm. What was the breadth of the lasers? Are you sure that the elevated temperatures that you claim are correlated with intense knocking cycles are not artificial, in the sense that the colinear CARS signal may have been contaminated by high-temperature signal originating from within the hot burnt gas region behind the higher speed flame fronts?

Reply to Comments of Lockett and Bruggeman. In contradiction to many CARS measurements in which the CARS beams propagate in the same direction as the flame front, in the present work the beams propagate across, in front of the flame front. Consequently, if the beams encounter the flame, they tend to be deflected, with resulting signal loss. Examination of the spectral fits of the generated CARS signals showed no signs of the distortions that might have been expected if there were contamination from higher temperature burnt gas.

•

O. L. Gulder, National Research Council of Canada, Canada. You conclude that an increased flame propagation speed is associated with an increase in the end gas temperature and a greater propensity to knock. One would think that there is a competition between the main flame front racing to consume the end gas and the reactions leading to autoignition in the end gas. A higher flame speed tilts the race in favor of the main flame front to consume the end gas before autoignition occurs. Within the framework of this conceptual picture, to state that the increased flame speed simply results in a greater propensity to knock could be misleading.

Douglas Greenhalgh, Cranfield University, UK. Some several years ago, Oscar Lee measured a correlation between flame propagation and flame speed in a low compression Sandia Disc engine at Howell. He clearly showed that, for low compression ratios, knock correlated to slow flame growth. This I believe is due to a competition between the development of end-gas or cool flame chemistry and the normal burnout of the mixture by the flame. At high compression ratios, perhaps the pressure and temperature accelerate the end-gas temperature so that the cool flame chemistry is faster than the flame growth. Can you comment?

Reply to Comments of Gulder and Greenhalgh. With the present combustion chamber, mixture, throttle setting, spark timing, and engine speed, a higher flame speed creates, through both piston and flame motions, higher temperatures and pressures in the end gas for a given crank angle. In general terms, the consequences of this on the time to autoignition are highly nonlinear. Figure 3 shows how an increase in temperature can decrease, increase, and decrease again the time to autoignition. For the present conditions, a decrease in this time more than offsets the increase in flame speed, and the mixture was more prone knock, contrary to the expectations of Dr. Gulder. On the other hand, we would agree with Professor Greenhalgh that there can be a contrary effect. Under different conditions, particularly those involving low compression ratios, where the end gas temperature is reduced, an increase in flame speed can be associated with an increase in the time to autoignition, in which case there would be less propensity to knock.

Twenty-Fifth Symposium (International) on Combustion/The Combustion Institute, 1994/pp. 135–141

DETECTION OF HOT SPOTS IN THE END GAS OF AN INTERNAL COMBUSTION ENGINE USING TWO-DIMENSIONAL LIF OF FORMALDEHYDE

B. BÄUERLE, F. HOFFMANN, F. BEHRENDT AND J. WARNATZ
Universität Stuttgart
Institut für Technische Verbrennung
Pfaffenwaldring 12, D-70569 Stuttgart, Germany

Over the last decade, a fundamental understanding of the chemical processes causing engine knock in internal combustion engines was achieved. It was shown numerically that inhomogeneities of the temperature distribution in the end gas of an engine as small as 20–30 K can influence the onset of engine knock drastically. This phenomenon is called induced ignition by a "hot spot." This paper reports on experiments to verify their existence and their predicted effect in a running spark ignition engine using realistic fuels. Due to the experimental error of available spectroscopic techniques, these small fluctuations in temperature cannot be detected directly. Using two-dimensional laser-induced fluorescence (2D-LIF) to monitor formaldehyde, which is formed early in an ignition process and is consumed before the combustion is completed, hot spots can be detected in the unburnt end gas.

The experimental set-up is based on a one-cylinder two-stroke engine in which quartz windows allow optical access to the combustion chamber. An excimer-pumped dye laser is used to excite formaldehyde, and the fluorescence signal is observed using an intensified charge-coupled device (CCD) camera.

From engine cycles under knocking conditions, a series of 2D-LIF frames is collected, showing the formation and consumption of formaldehyde in the end gas of the engine before the propagating regular flame front itself reaches this region. It is shown that engine knock starts with autoignition in small clearly bounded regions. The centres of autoignition are identified by the absence of formaldehyde within these regions due to its consumption during the ignition process.

Introduction

An increasing use of fossil fuels is followed by increasing pollutant emission. Saving fossil fuels, therefore, helps in improving the pollutant emission situation and, at the same time, saves the energy resources. Due to their high power-to-weight ratio and the high state of development, spark ignition engines are widely used in passenger cars. Optimizing combustion leads to higher efficiency that, in the case of spark ignition engines, is basically improved by increasing the compression ratio. This is followed by a higher temperature level at the end of the compression stroke, which, depending on the fuel, leads to engine knock. However, knock itself not only decreases the efficiency but also causes severe damage to the surfaces of the combustion chamber and, therefore, is one of the most interesting topics in engine combustion research.

Generally, knock is considered to be promoted by the ignition of exothermic centers (so-called "hot spots") in the end gas caused by inhomogeneities in temperature and/or in charge. Figure 1 shows schematically the formation of hot spots. After ignition (Fig. 1a), a flame front develops and travels across the combustion chamber (Fig. 1b). Both the compression by the moving piston and the expansion of the burnt gases lead to high pressures and fairly high temperatures in the end gas region, which promote autoignition in distinct zones (Fig. 1c) [1].

Ignition by hot spots is characterized mainly by three stages that occur more or less successively, namely, induction, ignition, and propagation. In some of these cases, when proper conditions are met, a deflagration can transform into a detonation that is mainly responsible for damages caused by engine knock [2,3].

The detailed chemical processes involved in the early phase of autoignition are fairly well understood. At temperatures typical for the end gas (approximately 650–800 K, i.e., cool flame conditions), the fuel consumption is initiated by two successive additions of oxygen molecules to initially formed fuel radicals. This is followed by various internal abstraction and isomerization reactions leading to chain branching and, finally, ignition [4,5]. Due to the formation of oxygen-containing ring structures during these steps, various partially oxidized species like peroxides, ketones, and aldehydes are formed as intermediates that, at higher temperatures, are finally ox-

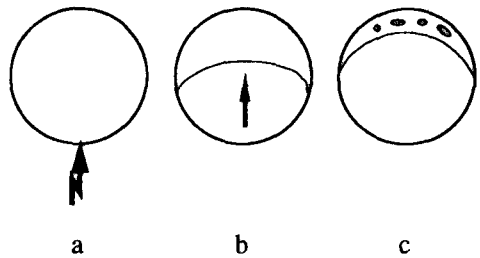

FIG. 1. Scheme of formation of hot spots.

idized to carbon dioxide. With respect to this experimental investigation, formaldehyde is the most interesting intermediate. In high-temperature regimes, formaldehyde is consumed very fast, whereas in low-temperature regimes of cool flames, the formation of formaldehyde is faster than its consumption. Several authors [6] propose mechanisms to describe the early formation of formaldehyde during ignition. Experimentally, formaldehyde was detected in the unburnt end gases under knocking conditions, see e.g., Rassweiler and Withrow [7].

Formaldehyde is a good natural tracer of knocking combustion, as it is not only consumed in normal flame fronts but also in later stages of homogeneous autoignition. Its abundance in the end gas region is used for detecting and studying the occurance of exothermic centres by using a two-dimensional laser-induced fluorescence (2D-LIF) technique. This technique [8] was successfully applied to an engine simulator to detect stable [9] and unstable [10] species and allows an excellent access to structural phenomena like hot spots, which cannot be analyzed using one-dimensional approaches.

Experimental

Investigations are carried out in an engine that has been especially adapted to the demands of 2D-LIF measurements. Figure 2 schematically shows the complete experimental setup. Basically, the complete setup consists of four main parts, i.e., the laser system including the light sheet optics, the research engine, the imaging system, and an engine data acquisition system. All components work together under the control of a delay generator (Spectroscopy Instruments SR 250) in order to establish exact timing.

The 4_0^1 transition of the $\tilde{A}^1A_2 \leftarrow \tilde{X}^1A_1$ of formaldehyde [11] is excited by an excimer-pumped dye laser (Lambda Physik LPX 205i, Lambda Physik FL 3002). The excimer laser works at a wavelength of 308 nm and produces pulses of a 28-ns duration (nominal) with maximum energies of 420 mJ. The dye laser using BMQ as dye is tunable from 335 to 375 nm. The conversion rate at the excitation wavelength of 353.2 nm is roughly 6%. The output beam of the dye laser is shaped into a two-dimensional plane of measurement (light sheet) of 50-mm width. The light sheet is obtained by a set of three quartz cylinder lenses, where the first two lenses form a Galileian telescope and the third lens focuses the light in the light sheet plane. The line of focus, in this case, has a thickness of less than 60 μm.

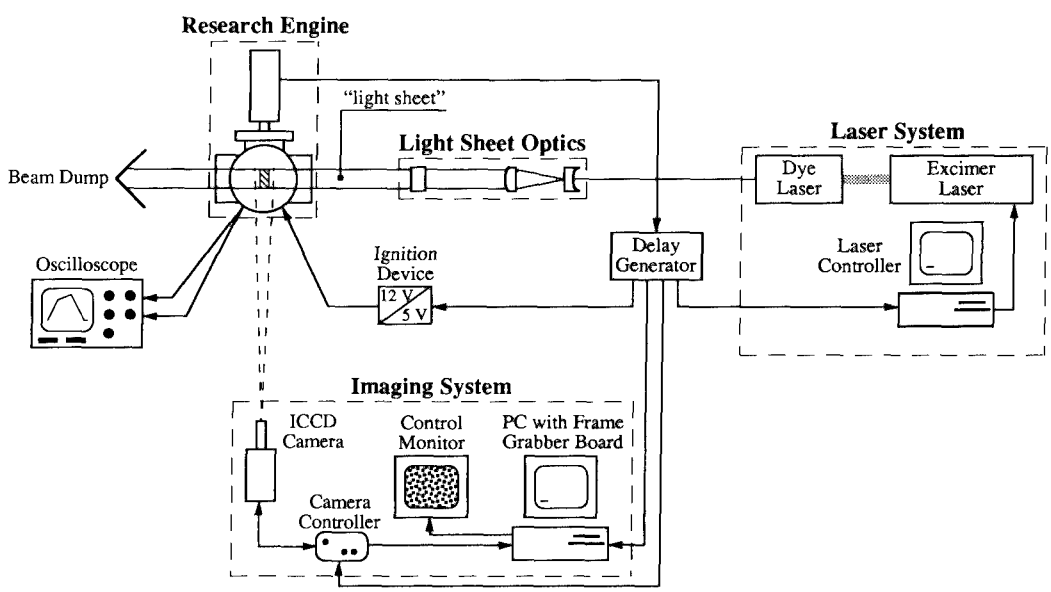

FIG. 2. Experimental setup.

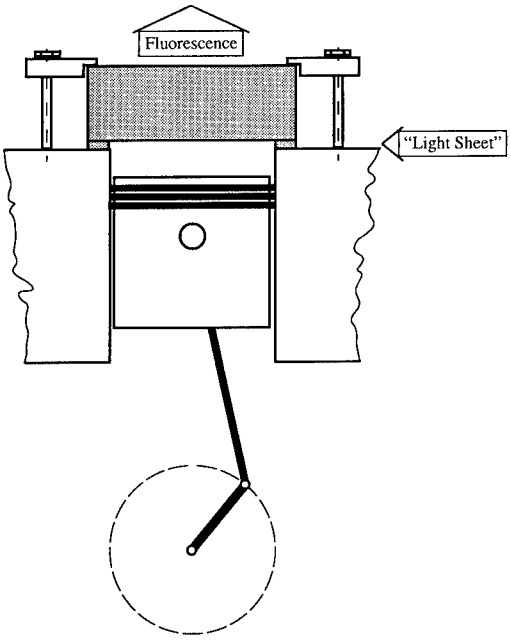

FIG. 3. Schematic cross section of the cylinder.

The research engine is a redesigned industrial two-stroke engine (ILO L372). Generally, two-stroke engines avoid the disadvantage of having valves in the cylinder head that would prevent full optical access to the combustion chamber. Major modifications have been made to the piston, the cylinder, and the cylinder head of the research engine. Figure 3 schematically shows a cross section of the modified engine; in addition, the directions of both the light sheet (excitation) and the fluorescence (signal) are shown. In particular, cylinder and cylinder head have been altered to allow oil instead of air cooling in order to obtain constant cylinder head temperatures. Optical access to the combustion chamber is realized by a quartz-ring window of a 4-mm height. A cylindrical quartz top window closes the combustion chamber. The originally crowned piston has been planed and fitted with an aluminum disk. Except for a pocket for the ignition electrode, the combustion chamber is disk shaped with a clearance height of slightly less than 4 mm. This ensures mainly two-dimensional flame propagation. The glass ring enables the light sheet to enter the combustion chamber from aside (in a plane perpendicular to the paper plane), and the full-size top window enables the fluorescence signal to leave perpendicular to the light sheet (Fig. 3). An electric dynamometer is coupled to the engine to brake and drive it. A large flywheel is fitted to the engine in order to stabilize its speed. The in-cylinder pressure is measured by a quartz pressure transducer (Kistler 6001) and stored in a digitizing oscilloscope (Tektronix 11201).

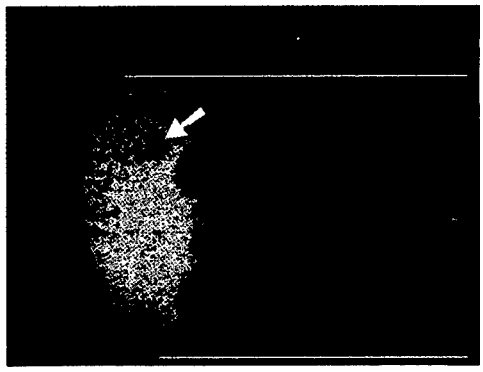

FIG. 4. 2D-LIF frame of formaldehyde at onset of autoignition.

The formaldehyde fluorescence signal is recorded with the imaging system, digitized, and stored for processing purposes. The images are taken with an intensified charge couple device (CCD) camera (Proxitronic Nanocam). Ultrashort exposure times ensure reduction of stray light caused by the flame. Since the fluorescence of formaldehyde is in the visible blue, a common camera lens (Nikon Makro *f*4/200 mm) can be used. The laser excitation wavelength as well as the stray light of long wavelength are blocked by a band pass filter (transmission 400–450 nm). The CCIR-video signal of the camera is digitized with a resolution of 8 bit by a frame grabber board (Matrox MVP-AT) in a personal computer. The software allows image recording, processing, and presentation.

Results and Discussion

Images of formaldehyde fluorescence are presented here. They are taken in different knocking cycles under equal conditions. The engine has been driven at a speed of 1000 rpm on fuel of 90 ON (90% *i*-octane, 10% *n*-heptane). Ignition has been set at 24° crank angle before top dead centre (CA BTDC) and only every fourth cycle has been fired (three skipped cycles). Skip firing has turned out to be necessary in order to ensure good cylinder filling.

Due to the repetition rate of the excimer laser, it is not possible to take more than one frame during one cycle of the engine. The effects observed here are typical for all knocking cycles allowing to use frames from different cycles to explain general features of autoignition in the unburnt end gas.

Figures 4 through 7 show 2D-LIF of formaldehyde in knocking cycles looking into the combustion chamber from above, via the full-size top window. The frames are taken with an exposure time of 100 ns, which fully encloses the laser pulse (28 ns). The grey values originally produced by the frame grabber

FIG. 5. 2D-LIF frame of formaldehyde early during autoignition.

FIG. 7. 2D-LIF frame of formaldehyde late during autoignition.

FIG. 6. 2D-LIF frame of formaldehyde during autoignition.

are transformed via a false colour code where 0 (no intensity) is denoted by black and 255 (maximum intensity) is denoted by red. The timing of all frames is 6° CA ATDC, i.e., 5 ms after ignition. Cycle-to-cycle variations of the combustion cause a shift of the onset of knock by up to a few degrees crank angle. Although the timing has been kept constant with respect to the engine crank shaft, the timing varies with respect to the corresponding pressure trace. Therefore, the frames show different stages of knocking combustion.

In the left part of the frames, the roughly crescent-shaped, coloured areas represent the unburnt end gas regions where fluorescence of formaldehyde is detected. The hazy tiny spots, distributed on a circular area, result from reflections of particles on the piston top and give an impression of the position of the combustion chamber (Fig. 7). The white flash at the cylinder wall in the lower right corner of the frame indicates the position of the spark electrode. In Fig. 4, the upper and lower white lines show the path of the light sheet and, with that, the detection area within the combustion chamber. The right-hand edges of the fluorescent regions show the leading edges of the flame fronts that started at the spark electrode. The black region to the right-hand side of the flame front represents the burnt gases, where no fluorescence of formaldehyde is detectable.

Figure 8 shows the pressure trace corresponding to the frame in Fig. 7. This pressure trace shows two peaks: a curved one resulting from the regular combustion and a peaked one, with a steep gradient, resulting from uncontrolled autoignition of the end gas. The two vertical bars indicate the timings of the frames in Fig. 4 (left) and Fig. 7 (right) relative to the pressure trace. The corresponding pressure traces of Figs. 4 through 6 are not presented here, but in order to give an idea of the timings of the frames relative to their pressure traces, the timing of Fig. 4 (left) has been fitted in Fig. 8. The trigger bars of Figs. 5 and 6 lie between the two.

The frame in Fig. 4 shows the situation at an early time of autoignition. This can be seen from the position of the trigger bar lying right at the onset of knock, i.e., at the beginning of the sharp pressure rise leading to the knock peak (Fig. 8, left bar). In that stage, a large end gas region with rather homogeneous distribution of fluorescence intensity can be seen as well as only one small hot spot in the upper region (see arrow) within the blue and green fluorescent area. Here, autoignition processes must have already started due to the absence of formaldehyde fluorescence in the hot spot. The right edge of the end gas represents the wrinkled flame front travelling through the combustion chamber.

The frame in Fig. 5 is taken right at the beginning of the sharp pressure rise, at a later stage than the one in Fig. 4. It shows a smaller end gas region. Again, on the right-hand edge of the fluorescing area, the edge of the regular flame front can be seen. Within the upper region of the end gas, there are two small hot spots next to each other, of about the size

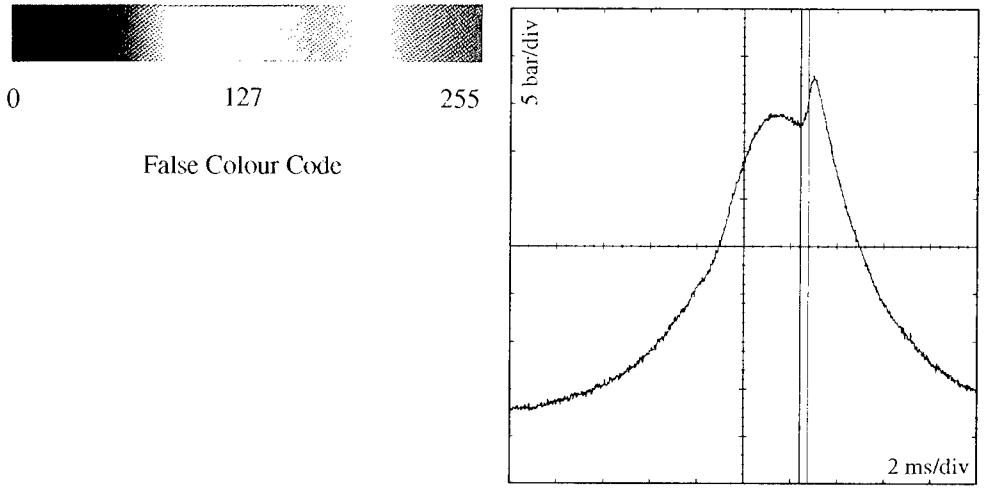

FIG. 8. Corresponding pressure trace to Fig. 7, including trigger bar for Fig. 4 (left bar).

of that one in Fig. 4, and a larger one at the cylinder wall in the middle. In the lower part, there is one large hot spot that might as well have been two small ones that already have ignited, grown, and merged to form the present shape. Generally, higher fluorescence intensities compared to Fig. 4 appear in a wider spread green area and more yellow spots.

Figure 6 shows the situation slightly later than in Fig. 5, at a time where the gradient of the sharp pressure rise is highest. In this case, the crescent shape of the end gas region can almost only be guessed. In the centre, there is high fluorescence intensity indicated by the red spots. Large areas are already caught by autoignition centres. In the upper part, right above the region with the very high fluorescence intensity, there are two hot spots that already have merged and grown so that they could merge with the largest structure just above it. This complete structure surely has ignited so that its edge towards the end gas can be considered to represent its flame front. That this structure is not produced by the regular flame front can be seen from the hazy fluorescence intensity stretching from the centre of highest fluorescence intensity to the upper end of the detection area. Besides, sequences of frames taken at various crank angles in knocking as well as in non-knocking cycles show that in neither case are there advancing, overlapping parts of the regular flame front producing hot-spot-like structures in the end gas region lying ahead. Another large structure can be seen in the middle right at the cylinder wall. This one has already merged with the hot spot above it, which for its part, is also connected with the very large structure described above. Here too, it can be said that autoignition already has taken place so that the edges towards the unburnt end gas represent a flame front. In the lower part of the end gas region, there is a further structure consisting of probably originally three hot spots that also have ignited, grown, and merged to form the observed structure. The regular flame front on the right-hand edge of the area has lost some of its wrinkles compared to Fig. 4.

The last frame, presented in Fig. 7, is taken at a late stage of autoignition. The corresponding pressure trace can be seen in Fig. 8 with the right vertical bar being the respective frame trigger. This is just before the peak pressure where the end gas is completely converted. Figure 7 shows very high fluorescence intensity in the middle of the unconverted fluorescing area of the end gas region. Next to it, a large ignited and grown autoignition centre can be seen near the cylinder wall. Some smaller hot spots can be seen in the lower and upper part of the detection area. The most remarkable detail in this frame is the completely smoothed regular flame front represented by the right-hand edge of the fluorescing area. In this case, it is straight and could be replaced by a line. This agrees with ultra-high-speed Schlieren frames (up to some 700,000 frames per second) taken by König et al. [12] and Bradley et al. [13] during a joint Commission of the European Communities (CEC) project using the same engine type.

Conclusions

The understanding of processes causing knock in spark ignition engines is essential to take measures against it. Detailed reaction mechanisms were developed to describe the underlying chemical processes. Most of the model calculations based on these

mechanisms assumed a homogeneous end gas, which is ignited more or less simultaneously when a certain temperature is reached. High-speed frames taken in engines demonstrated that this assumption is not perfectly valid. In numerical calculations, it was shown that local temperature fluctations as small as 20 to 30 K are sufficient to ignite parts of the end gas earlier than the surroundings.

Detection of the so-called hot spots using spectroscopic techniques for temperature measurements is limited due to the intrinsic measurement errors of these techniques. Due to the exponential dependence of the chemical rate of formation on temperature, a detection of intermediate species formed early in the autoignition process is more promising. Early papers, e.g. Ref. 7, on engine knock and cool flames pointed out that large amounts of formaldehyde are formed in these processes but are consumed during the following combustion phase. So, formaldehyde is a natural tracer to detect hot spots and to follow the early phases of engine knock.

The results presented here show frames taken in a running one-cylinder two-stroke engine using two-dimensional laser-induced fluorescence of formaldehyde. Its formation in the unburnt end gas is clearly shown. At several locations in the end gas, this formaldehyde is consumed before the regular flame front reaches these regions. This is interpreted as autoignition in these regions. Despite the fact that the frames reproduced in this paper result from different cycles, the correspondence of number and size of the hot spots visible in the end gas relates well with different temporal stages of autoignition. These stages are defined by the timing of the frames with respect to the evolution of the pressure peak caused by knock.

Acknowledgments

The financial support by the Commission of the European Communities within the JOULE programme is gratefully acknowledged.

The authors would like to thank the Physikalisch-Chemisches Institut of the Universität Heidelberg for supplying parts of the imaging software. The authors would also like to thank Dr. R. R. Maly and Dr. G. König, Daimler-Benz, for leaving the modification plots of the engine with us and for assisting us during the setup phase.

REFERENCES

1. König, G., Maly, R. R., Bradley, D., Lau, A. K. C., and Sheppard, C. G. W., *SAE Paper* 902136, 1990.
2. Maas, U., and Warnatz, J., in *AIAA Progress in Astronautics and Aeronautics* (A. L. Kuhl, J.-C. Leyer, A. A. Borisov, and W. A. Sirignano, Eds.), Vol. 131, AIAA, Washington, DC, 1990, pp. 3–18.
3. Goyal, G., Warnatz, J., and Maas, U., *Twenty-Third Symposium (International) on Combustion*, The Combustion Institute, Pittsburgh, 1990, pp. 1767–1773.
4. Warnatz, J., *Twenty-Fourth Symposium (International) on Combustion*, The Combustion Institute, Pittsburgh, 1992, pp. 553–579.
5. Chevalier, C., Pitz, W. J., Warnatz, J., Westbrook, C. K., and Melenk, H., *Twenty-Fourth Symposium (International) on Combustion*, The Combustion Institute, Pittsburgh, 1992, pp. 93–101.
6. Pollard, R. T., "Hydrocarbons," in *Chemical Kinetics*, Chap. 2 (C. H. Bamford and C. F. H. Tipper, Eds.), Elsevier, Amsterdam, 1977.
7. Rassweiler, G. M., and Withrow, L., *Indust. Eng. Chem.* 25:1359–1366 (1933).
8. Hanson, R. K., *Twenty-First Symposium (International) on Combustion*, The Combustion Institute, Pittsburgh, 1986, pp. 1677–1691.
9. Arnold, A., Becker, H., Suntz, R., Monkhouse, P., Wolfrum, J., Maly, R., and Pfister, W., *Opt. Lett.* 15:831–833 (1990).
10. Suntz, R., Becker, H., Monkhouse, P., and Wolfrum, J., *Appl. Phys.* B47:287–293 (1988).
11. Henri, V., and Schou, S. A., *Z. P.* 49:774 (1928).
12. König, G., Maly, R. R., Schöffel, S., and Blessing, G., "Gas/Surface Interactions and Damaging Mechanisms in Knocking Combustion—Effects of Engine Conditions," Sixth Periodic Report, CEC-Research Contract No. JOUE-0028-D-(MB), May, 1991.
13. Bradley, D., Pan, J., and Sheppard, C. G. W., "Gas/Surface Interactions and Damaging Mechanisms in Knocking Combustion—Turbulence and Flow Field Effects," Sixth Periodic Report, CEC-Research Contract No. JOUE-0028-D-(MB), May, 1991.

COMMENTS

H. Breitbach, RWTH-Aachen, Germany. 1. Has the sequence of LIF pictures you showed been taken from one cycle or assembled from different cycles?

2. Did you consider stronger knocking cycles with pressure amplitudes around 10–20 bar or more?

3. Do you have an explanation of why the hot spots in your configuration often seem to be very close to the wall although one would expect lower temperatures there due to heat transfer to the wall?

Author's Reply. 1. The LIF frames are taken from different cycles due to speed limitations in both the imaging and the laser systems.

2. No such cycles have been considered in the current

work. We are now able to run the engine under such conditions, so this will be investigated further.

3. There might be deposited particles deriving from grease or soot that have slightly higher temperatures. See also comment of John Griffiths.

•

J. F. Griffiths, University of Leeds, UK. Your observation that autoignition centers can originate close to the wall is interesting. This may result from the nature of the thermokinetic interactions that occur in the negative temperature-dependent region of reaction rate in alkane oxidation. This was described in the *Twenty-Fourth Symposium on Combustion* [1].

REFERENCE

1. Griffiths, J. F. et al., *Twenty-Fourth Symposium (International) on Combustion,* The Combustion Institute, Pittsburgh, 1992, p. 1809.

•

Dieter Bruggemann, ITLR/University of Stuttgart, Germany. Have you recorded LIF spectra to ensure that your light sheet images are really showing the distribution of formaldehyde and to exclude the possibility that other species are responsible for the signals?

Author's Reply. We have taken a fluorescence spectrum of the engine running under knocking conditions. The obtained spectrum shows slightly broadened peaks due to higher pressure levels (approximately 40 bar). Compared to a fluorescence spectrum taken from the literature (Möhlmann, 1985), the emission peaks of our "engine spectrum" are at the same positions. This ensures that we definitely obtain formaldehyde fluorescence.

•

Kermit C. Smyth, NIST, USA. Comment on the question of Nigel Tait, who asked about using the excimer output at 308 nm to image formaldehyde fluorescence directly. The absorption spectrum of formaldehyde extends to this wavelength region, but the excited vibrational levels of the upper electronic state are strongly predissociated. Thus, the quantum yield for fluorescence measurements is highest for the vibronic bands at longer wavelengths (which the authors used). Appropriate references are given in Harrington, J. E., and Smyth, K. C., *Chem. Phys. Lett.* 202:196 (1993).

Author's Reply. We do not think that formaldehyde can be excited with a broadband laser like the one we use.

•

H. May, University of Kaiserslautern, Germany. The results shown in this paper are of great interest for evaluating knocking behavior. A mixture of iso-octane and *n*-heptane corresponding to an octane number of 90 was used as fuel. Are there also results available for real gasolines?

Author's Reply. Because of the fact that higher hydrocarbons exhibit broadband UV absorption, the chosen fuel composition had to be of primary reference quality (pure iso-octane and pure *n*-heptane). Additionally, unknown fuel additives inhibit the use of realistic gasolines for LIF experiments. For these reasons, unfortunately, there are no results available for realistic gasolines.

•

J. Chomiat, Chalmers University of Technology, Sweden. You have shown distinctly that the hot spots are produced by decomposition of formaldehyde. Can you identify the reasons for the local appearance of the process? Is it due to mixture composition variations, bulk temperature nonuniformities, or boundary layer effects related to the negative temperature coefficient of the preflame reactions?

Author's Reply. In numerical simulations, it was shown that even small variations in temperature distribution, and to a lesser extent variations in species distributions, cause local bound, shorter ignition delay times leading to autoignition [3]. These conditions are always found in a running engine and therefore lead to knock if autoignition limits are exceeded.

In the present work, it has been shown that within the end gas region, where formaldehyde is present (and therefore detectable), hot spots can be observed due to rapid local formaldehyde consumption (no fluorescence detectable). Hot spots are *not produced* by the decomposition of formaldehyde!

So far, it is not known distinctly what the very origin of hot spots is—are they inhomogeneities in temperature or in species distribution?

Twenty-Fifth Symposium (International) on Combustion/The Combustion Institute, 1994/pp. 143–150

SIMULTANEOUS 2D SINGLE-SHOT IMAGING OF OH CONCENTRATIONS AND TEMPERATURE FIELDS IN AN SI ENGINE SIMULATOR

A. ORTH, V. SICK, AND J. WOLFRUM
Physikalisch-Chemisches Institut, Ruprecht-Karls-Universität Heidelberg
Im Neuenheimer Feld 253, 69120 Heidelberg Germany

AND

R. R. MALY AND M. ZAHN
Daimler-Benz AG, Aero- and Thermodynamics
Stuttgart, Germany

Two-dimensional (2D) temperature measurements in engines are required for the detailed understanding of the combustion process. Because of the unsteady and turbulent nature of engine combustion, these measurements must be performed on a single-shot basis to obtain cycle-resolved results. Details of the flame front structure are also important to know for the numerical modeling of internal combustion processes. Simultaneous measurements of temperature and hydroxyl radical distributions provide such data sets. The combustion of methane in a fully transparent square piston engine was studied with a combination of 2D laser-induced fluorescence of hydroxyl radicals and 2D Rayleigh scattering. A tunable KrF excimer laser at 248 nm was used for the measurements. The wavelength of the laser was tuned to excite the $P_2(8)$ transition in the OH (3,0) band of the A-X system. Spectral filtering of the resulting fluorescence to detect solely the fluorescence from the (3,2) band significantly reduces the effect of collisional quenching imposed to the fluorescence of the predissociating $v' = 3$ level by vibrational energy transfer (VET) to lower vibrational levels. Using a second camera, which only records the Rayleigh signals after appropriate filtering, allows the simultaneous measurement of temperature fields with a single laser. The analysis of corresponding OH and temperature images allowed the decision that the combustion conditions are in a regime where the flamelet approach for modeling is appropriate. Good agreement with model predictions has been achieved for the peak temperatures.

Introduction

While multidimensional laser sheet techniques gained increased popularity during the last years [1,2], there is still a challenge for further development of these techniques. One task will be to perform more quantitative measurements, while another one will be to apply the techniques to environments not yet studied. Additionally, there will be increased interest in combining different techniques in the sense of quantitative measurements and in correlating different quantities, like temperature and nitric oxide or flow and concentrations, etc. Especially, nonintrusive measurements in engines are important for an improved understanding of fuel/air mixing [3–6]. Whereas combined multidimensional measurements of different quantities in flames have been performed in a number of objects [7,8], the applications for engines are not well established. Measuring two different quantities usually requires two different wavelengths and, most of the time, two different lasers, e.g., for the simultaneous measurement of fuel and OH concentration distributions [6]. However, if the excitation wavelength is the same for different molecules or different processes, spectral filtering of the signals can achieve two or more results from a single laser pulse. Using exciplex formation and laser-induced fluorescence, liquid and vapor phases can be distinguished [9]. This is also possible with a combination of Mie scattering and laser-induced fluorescence [5]. Combining Rayleigh scattering and laser-induced fluorescence yields temperature and species concentrations [8]. This technique of simultaneous measurements of Rayleigh scattering and laser-induced fluorescence of hydroxyl radicals has now been applied to measurements in an engine simulator. Rayleigh measurements in engines were already used to measure mixture fractions [10], but no measurements during the combustion phase have been performed there. The combination of temperature and hydroxyl radical concentration measurements is very useful if details of the flame fronts have to be analyzed. For example, deviations from the assumptions of the flamelet model can be measured with this technique [8].

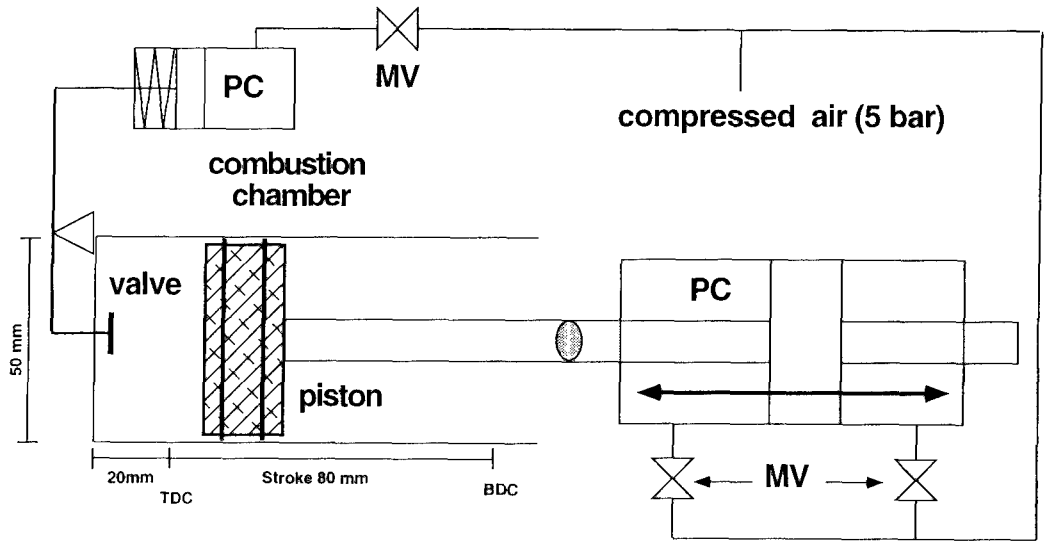

FIG. 1. Schematic setup of the pneumatic SI engine simulator. An electronic circuit controls the timing of the piston movement (PC: pneumatic control; MV: magnetic valve).

Experimental

We investigated the combustion process in a fully transparent SI engine simulator [11]. The cylinder of this engine is built entirely out of quartz plates. The square piston has a cross section of 50 × 50 mm. The piston movement was controlled by a pneumatic pressure system, which was used to simulate engine speeds of approximately 500 rpm. The compression ratio was adjusted to 1:5 with a stroke of 80 mm. Cycle-resolved pressure traces were measured with a pressure transducer (Kistler). Methane/air mixtures were stored in a cylinder and were injected through a single valve that was also used as an exhaust valve. As Fig. 1 shows, the engine was operated in a horizontal arrangement.

It is desirable to use short UV wavelengths for Rayleigh scattering since the Rayleigh signal increases with $1/\lambda^4$. For this reason, we used a tunable KrF excimer laser. The high pulse energy of this laser also allows the two-dimensional (2D) imaging of hydroxyl radicals. Because of the predissociation of the $v' = 3$ level, quenching has less influence on the signals, and the small Frank–Condon factor of the emission bands is partially compensated at elevated pressures as a result of less quenching losses but higher densities. If the (3,0) $P_2(8)$ transition of OH is excited at 248.456 nm, no temperature influence has to be taken into account to correct for changes in the population density given by the Boltzmann distribution. In the range 1300–3000 K, the fraction of molecules in $N'' = 8$ is constant within 10%. As has been pointed out several times [12–14], it is crucial to filter the fluorescence signals properly in order to avoid detection of fluorescence from $v' < 3$. These levels are populated via vibrational energy transfer (VET) and suffer from quenching. Thus, the measured signals would be sensitive to quenching. We used a bandpass filter with a center wavelength of 297 ± 6 nm. This filter transmits the fluorescence of the (3,2) vibrational band. Also important to obtain high signal levels is a camera lens with a large aperture. The achromatic lens systems we used had an f# = 2, thus increasing the signal strengths remarkably compared to the commonly used systems. Since we were interested in measuring the OH distribution and the temperature fields simultaneously, we used a second camera to record Rayleigh scattering. Figure 2 shows the experimental setup where the two cameras were mounted on the opposite sides of the engine. The Rayleigh signals had to be filtered from any fluorescence light. We found it appropriate to use a mirror coated for 248 nm and a color glass filter (Schott UG 5). Careful alignment of the two camera/lens/filter systems is necessary to make sure that the same plane is monitored by both cameras. As shown in Fig. 2, the laser illuminates a horizontal plane in the engine. The beam was rotated with a Dove prism and collimated to a light sheet of less than 300 μm in thickness. It is crucial to make sure that the sheet is not thicker because, otherwise, important details of the flame front, like superequilibrium concentrations of hydroxyl radicals [11], cannot be measured. The Bunsen burner shown in Fig. 2 was used to control the proper tuning of the laser to the $P_2(8)$ transition by maximizing the OH-LIF signal from this flame using camera 3. Special care

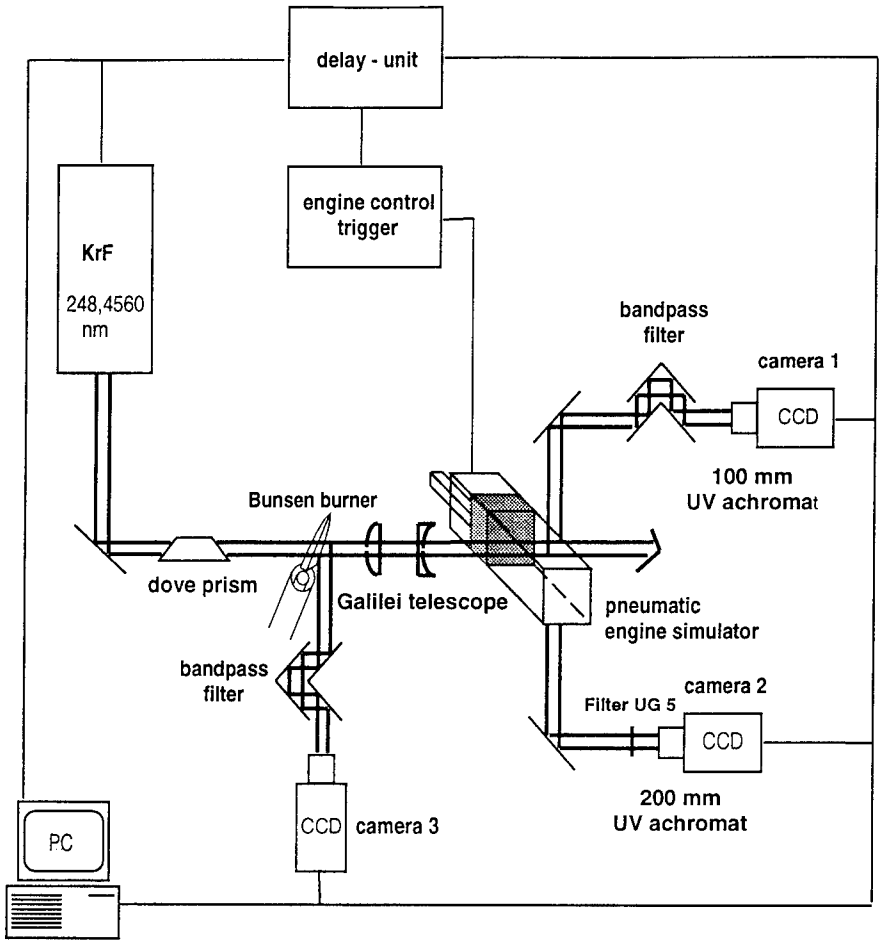

FIG. 2. Experimental setup for simultaneous Rayleigh and LIF measurements in an SI engine simulator. A tunable KrF excimer laser, tuned to the (3,0) $P_2(8)$ transition of hydroxyl radicals, was used for the measurements.

had to be taken to avoid scattering of the laser beam at any surface of the experiment. A certain distance from the walls had to be maintained for the Rayleigh measurements, whereas it was possible to follow the OH concentration up to the walls of the piston and the cylinder.

All signals were recorded with image-intensified charge-coupled device (CCD) cameras (Proxitronic Nanocam II) with gate times of 50 ns. Using frame grabber boards (Matrox MVP AT), the signals were digitized and processed, as will be described later in this paper. It is important to mention that cameras of the type we used have a fixed time for light detection given by the frame-transfer process. This frame transfer is set by the video frequency and cannot be altered. If signals are recorded at inappropriate times, the measured intensity is lower. For this reason, it is necessary to make sure either that images that are measured near frame transfers are rejected or that the experiment's timing is coupled to the frame-transfer frequency. Of course, this is not possible for many experiments in engines. But for the engine we used, we could set an external trigger for the engine operation and then couple cameras, lasers, and the engine to the frame-transfer process.

Whereas the interpretation of the laser-induced fluorescence (LIF) data is more straightforward to obtain information about thickness, curvature, and movement of the flame front, it is more complicated to analyze the Rayleigh images. The only corrections that have been made for the OH images are for irregular laser beam profiles and absolute energy fluctuations. For the Rayleigh images, a series of corrections and calibration procedures has to be used before temperature fields are obtained. Rayleigh scattering is proportional to the total particle number N. Thus, by using the ideal gas assumption, it is proportional to the pressure p and the cross section σ_s,

and is inversely proportional to the temperature [Eq. (1)]. It is also proportional to the laser energy I_0 and the probe volume V:

$$R_{\mathrm{Ray}} = VI_0pN\sigma_s/RT. \quad (1)$$

However, the cross section for Rayleigh scattering is different for different molecules, and the total cross section is the sum of the cross section for each type of molecule in a mixture weighted with its mole fraction [15]. This means that if the gas composition changes, the cross section changes and makes it impossible to obtain accurate temperature data without knowing the gas composition. Fortunately, for the methane/air mixtures investigated here, the variation in the total cross section between burnt and unburnt gases is smaller than 2% [8].

With this, the temperature at a point with coordinates (x,y) can be calculated from the measured Rayleigh intensity $R(x,y)$

$$T(x,y) = T_0cR_c(x,y)/R(x,y) \quad (2)$$

$$c = \sigma_{\mathrm{flame}}/\sigma_{\mathrm{fuel}}. \quad (3)$$

Here, T_0 is a reference temperature, where a calibration signal $R_c(x,y)$ is measured. If this signal is measured in ambient air, the calibration constant c takes into account that the cross section for air is different than that from the methane/air mixture. However, we chose another approach. We measured the reference signal with the methane/air in the engine at the crank angle where the measurements were taken, but without ignition. The temperature there can be calibrated against air/ambient pressure conditions, or it can be calculated adiabatically from thermodynamical data. This procedure has the advantage that the dynamic range of the signals and the camera match much better. Since heating increases the pressure during fired cycles, at corresponding crank angles, the pressure ratio has to be taken into account during data analysis. Equation (2) transforms to

$$T(x,y) = T_0cR_c(x,y)/R(x,y)(P/P_0)(I/I_0). \quad (4)$$

Additional processing of the data is necessary to obtain temperatures. Any residual light that is scattered from surfaces distorts the measurements. To take this into account, images were taken where the engine was flooded with helium. The Rayleigh cross section of helium is almost negligible, and therefore, the remaining measured intensity is scattered light. These images have to be subtracted from the measured Rayleigh images. Also, an image taken with the camera lens covered was taken and subtracted from all Rayleigh images. This background correction is necessary to exclude offsets of the digitizers and camera noise. Of course, all images with the exception of the latter one have to be normalized to the laser intensity profile. This profile is best determined by taking the reference image for normalization of all other images.

Results

Temperature and hydroxyl radical distributions have been measured simultaneously with a single laser pulse in a fully transparent SI engine simulator for different stoichiometries. All images shown here are taken in a plane parallel to the piston movement in the middle of the combustion chamber. The mixtures were ignited with a spark plug always located on the right side of the images. Since the cross sections imaged by the two cameras have different sizes, the OH images were rescaled to match the size of the temperature images. This was done by carefully comparing the image of a scale that was placed in the plane of the laser sheet. It is then possible to compare OH concentration fields with corresponding temperature fields. The image pairs of Fig. 3 nicely demonstrate how temperature and hydroxyl radical concentration are coupled. Even details of the temperature field also can be recognized in the OH images. We did not attempt to calibrate our LIF images to absolute values, but this could be done by comparing the measured signals from the engine simulator with signals obtained in a calibrated burner [16]. As was pointed out earlier [11], the laser sheet must be thinner than the flame front thickness to be able to resolve the flame front structure properly. Figure 4a shows one of the examples from Fig. 3 in an enlarged view, together with profiles along the white lines indicated in Fig. 4a. Entering the flame front from the unburnt gases, it is obvious that temperature is increasing before the OH concentration rises. From profiles like this, a (90–10%) flame front thickness was determined to be 300 ± 100 μm. This value represents the smallest flame front thicknesses found in the images, indicating that here the flame front was illuminated perpendicularly by the light sheet. The flamelet assumption is only valid if temperature and hydroxyl radical concentrations are correlated, as in laminar flames. The strong correlation found in our engine experiments confirms the validity of the flamelet approach for the conditions studied here. As expected, the spatial gap between temperature rise and OH concentration rise becomes less at higher pressures. Here, 300 μm were measured at P = 5.3 bar, compared to 500–700 μm at atmospheric pressure flames [8]. Although we did not attempt to measure absolute OH concentrations, the relative concentration profiles indicate superequilibrium values of hydroxyl radicals in the flame front, in agreement with previous measurements and modeling results [17]. This result is based on the fact that, in the exhaust gases, OH reaches equilibrium

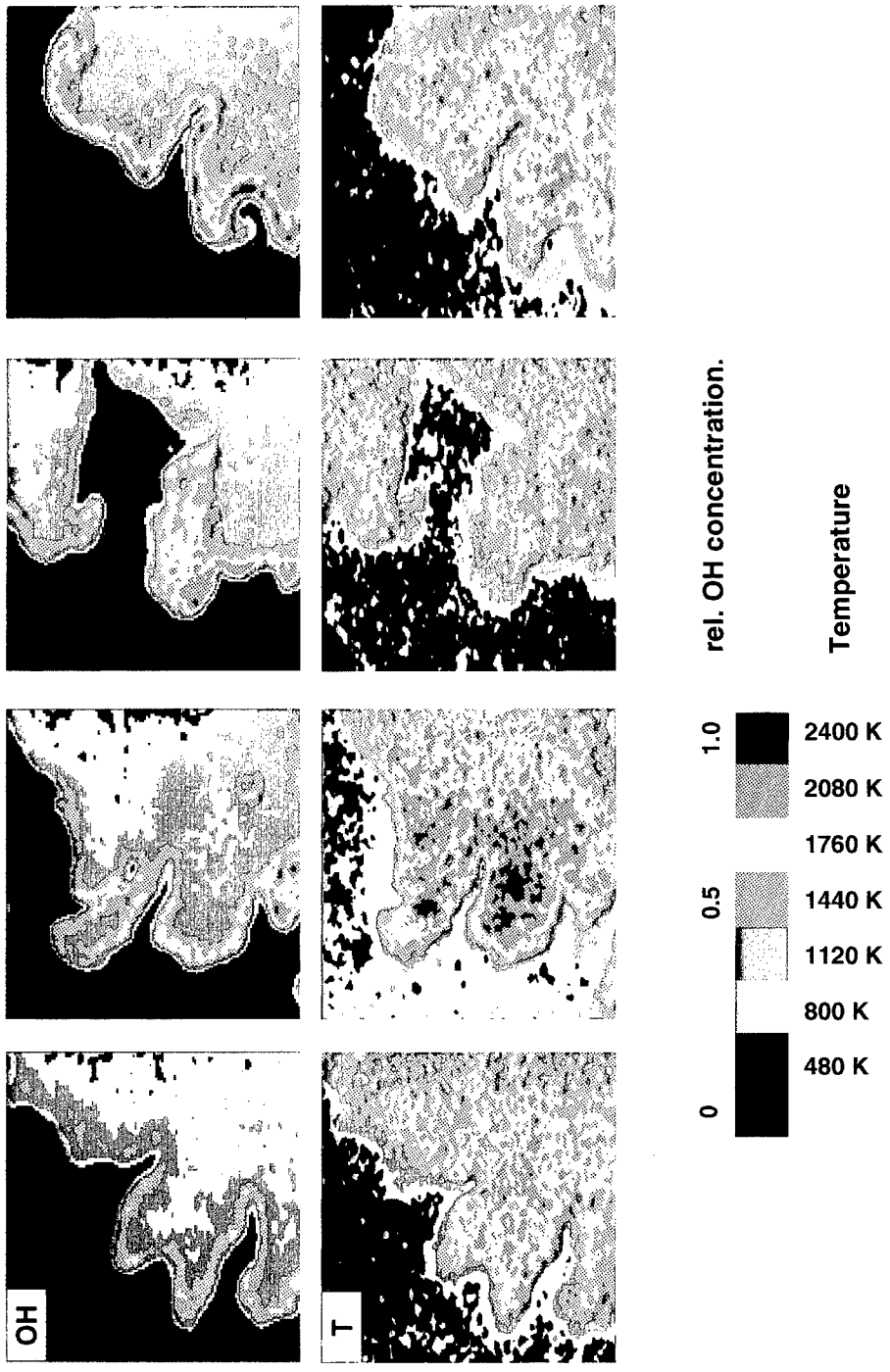

FIG. 3. Simultaneously measured single-pulse OH concentration and temperature distributions at $\varepsilon = 5$ and $\lambda = 1.1$. The imaged area is about 12×12 mm.

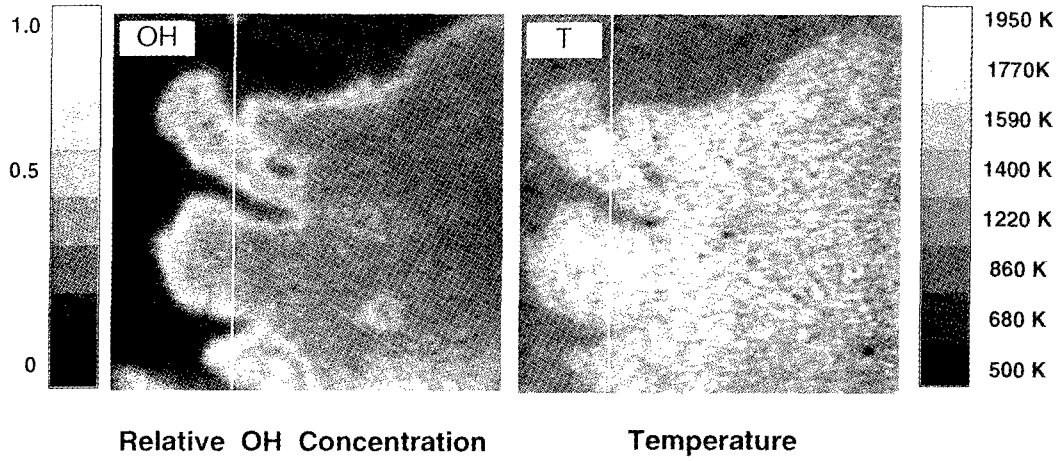

(a)

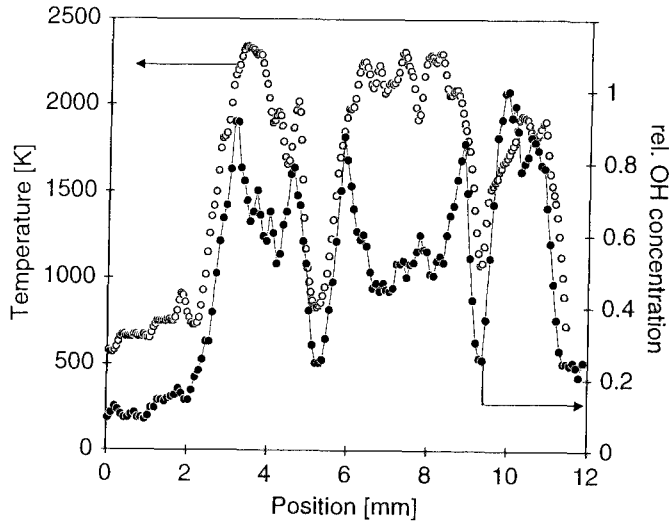

(b)

FIG. 4. (a) Enlarged example from Fig. 3. The positions for the vertical profiles of Fig. 4b are indicated as white bars. (b) Profiles of OH concentration and temperature at $\varepsilon = 5$ and $\lambda = 1.1$. There is a clear separation between temperature rise and increasing OH concentration on both sides of the profiles, where the image also shows unburnt areas in contrast to the two temperature drops in the middle of the profile.

values, so that the high concentrations in the flame front can be attributed to superequilibrium concentrations. The peak temperatures measured are in agreement with the predicted peak temperatures of 2300 K. If comparisons with modeling results are considered, not only single-pulse measurements are required for details of the combustion process, but also average temperature and concentration distributions are necessary. The presently used multidimensional codes for modeling combustion processes in engines always predict averaged data. To account for this demand, we calculated averaged temperature and hydroxyl radical concentrations. Figure 5a shows the averaged OH and temperature distribution for a lean mixture with $\lambda = 1.1$ and a compression ratio of 1:5. The engine simulator was operated at conditions corresponding to 500 rpm. The averaged peak temperature data were determined to be 1790 K with a statistical variance of ± 150 K. The estimated accuracy is 15% for our measurements. For a mixture with $\lambda = 1.2$, the averaged peak temperature is higher. Temperatures of 1990 K $\pm$ 120 K were measured for these conditions. The average was calculated from 15 single-shot images, with averaging

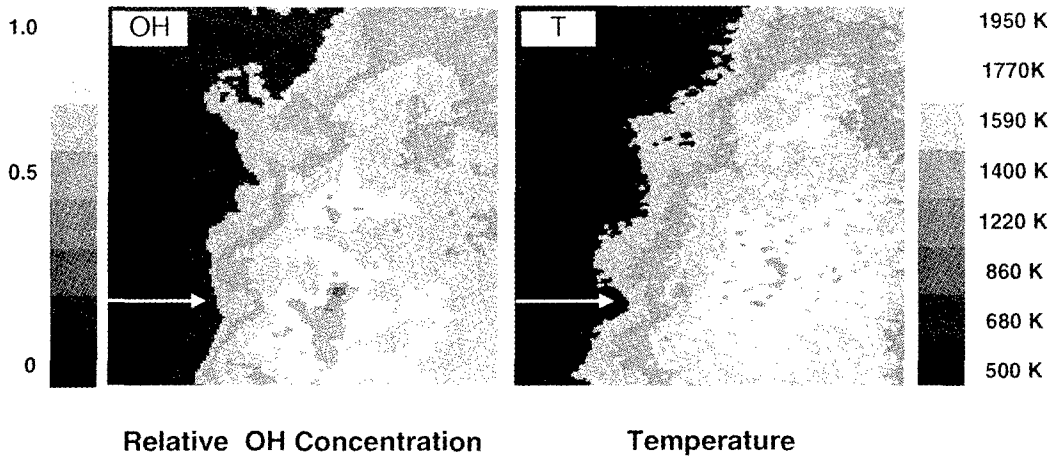

(a)

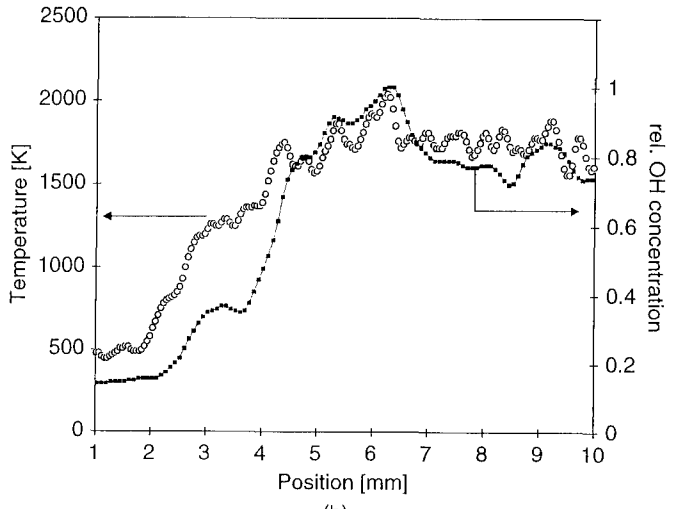

(b)

FIG. 5. (a) Averaged hydroxyl radical concentration and temperature distribution for $\varepsilon = 5$ and $\lambda = 1.1$. The image is the average of 25 single-pulse measurements. (b) Profiles from the averaged distributions of Fig. 5a.

over a 56 × 56 matrix in areas of the highest temperatures. The positions of the profiles shown in Fig. 5b are indicated in Fig. 5a. Major features of the flame front are given in both profiles. However, the spatial gap of the temperature and hydroxyl radical concentration rise in the flame front is larger than it is in the single-pulse measurements. If the coupling of both quantities has to be determined to decide about the validity of the flamelet concept for a given combustion process, single-pulse measurements are required. In the sense of obtaining ensemble average data for comparison with model predictions, it would be useful to acquire the data at fixed intervals for the, e.g., peak pressure. This procedure would reduce the influence of cyclic variability on the results.

Conclusions

We demonstrated that it is possible to use 2D Rayleigh scattering for temperature measurements in an SI engine simulator. Moreover, within a single laser pulse, the temperature and hydroxyl radical concentration distribution were measured using a tunable KrF excimer laser and two image-intensified CCD cameras. A significant dependence of the tempera-

ture on the mixture composition was measured, and from the analysis of OH and temperature profiles, the validity of the flamelet assumption for the conditions under study has been confirmed. Modeling results from previous studies [17] are confirmed by our measurements. Averaged data have been calculated to provide a data set for comparison with multidimensional models, which usually predict averaged data [18].

Acknowledgments

This work was sponsored by the Bundesministerium für Forschung und Technologie under Contract No. TECFLAM 03E6325L and Daimler-Benz AG, Stuttgart.

REFERENCES

1. Hanson, R. K., and Seitzman, J. M., in *Instrumentation for Flows with Combustion* (A. M. P. K. Taylor, Ed.), Academic Press, London, 1993.
2. Arnold, A., Bräumer, A., Buschmann, A., Decker, M., Dinkelacker, F., Heitzmann, T., Orth, A., Schäfer, M., Sick, V., and Wolfrum, J., *Ber. Bunsenges. Phys. Chem.* 97:1650–1661, 1993.
3. Baritaud, T. A., and Green, R. M., SAE Technical Paper Series 860025, Philadelphia, 1986.
4. Felton, P. G., Mantzaras, J., Bardsley, E. A., and Bracco, F. V., SAE Technical Paper Series 872074, Philadelphia, 1987.
5. Arnold, A., Dinkelacker, F., Heitzmann, T., Monkhouse, P., Schäfer, M., Sick, V., Wolfrum, J., Hentschel, W., and Schindler, K.-P., *Twenty-Fourth Symposium (International) on Combustion*, The Combustion Institute, Pittsburgh, 1992, pp. 1605–1612.
6. Arnold, A., Buschmann, A., Cousyn, B., Decker, M., Sick, V., Vannobel, F., and Wolfrum, J., SAE Technical Paper Series 9326966, Philadelphia, 1993.
7. Long, M. B., Levin, P. S., and Fourgette, D. C., *Opt. Lett.* 10:267–269 1985.
8. Dinkelacker, F., Buschmann, A., Schäfer, M., and Wolfrum, J., *Joint Meeting of the British and German Sections of the Combustion Institute*, British Section of the Combustion Institute, Cambridge, UK, 1993, pp. 295–298.
9. Melton, L. A., and Verdieck, J. F., *Twentieth Symposium (International) on Combustion*, The Combustion Institute, Pittsburgh, 1984, pp. 1283–1290.
10. Zhao, F. -Q., Taketomi, M., Nishida, K., and Hiroyasu, H., SAE Technical Paper Series 932641, Philadelphia, 1993.
11. Suntz, R., Becker, H., Monkhouse, P., and Wolfrum, J., *Appl. Phys. B* 47:287–293 1988.
12. Andresen, P., Bath, A., Gröger, W., Lülf, H. W., Meijer, G., and terMeulen, J. J., *Appl. Opt.* 27:365–378 1988.
13. Arnold, A., Lange, B., Bouché, T., Heitzmann, T., Schiff, G., Ketterle, W., Monkhouse, P., and Wolfrum, J., *Ber. Bunsenges. Phys. Chem.* 96:1388–1393 1992.
14. Steffens, K. L., Jeffries, J. B., and Crosley, D. R., *Opt. Lett.* 18:1355–1357 1993.
15. Dibble, R. W., and Hollenbach, R. E., *Eighteenth Symposium (International) on Combustion*, The Combustion Institute, Pittsburgh, 1981, pp. 1489–1499.
16. Sick, V., Arnold, A., Dießel, E., Dreier, T., Ketterle, W., Lange, B., Wolfrum, J., Thiele, K. -U., Behrendt, F., and Warnatz, J., *Twenty-Third Symposium (International) on Combustion*, The Combustion Institute, Pittsburgh, 1990, pp. 495–501.
17. Becker, H., Arnold, A., Suntz, R., Monkhouse, P., Maly, R. R., and Pfister, W., *Appl. Phys. B* 50:473–478 1990.
18. Herweg, R., and Maly, R. R., SAE Technical Paper Series 922243, Philadelphia, 1992.

Twenty-Fifth Symposium (International) on Combustion/The Combustion Institute, 1994/pp. 151–156

IN-CYLINDER CRANK-ANGLE-RESOLVED IMAGING OF FUEL CONCENTRATION IN A FIRING SPARK-IGNITION ENGINE USING PLANAR LASER-INDUCED FLUORESCENCE

MARTIN BERCKMÜLLER, NIGEL P. TAIT, RUSSEL D. LOCKETT, AND DOUGLAS A. GREENHALGH
School of Mechanical Engineering
Centre for Photonics and Optical Engineering
Cranfield University
Cranfield, England

AND

KIYOSHI ISHII, YASUHIRO URATA, HIDEZO UMIYAMA, AND KAZUO YOSHIDA
Honda R&D Co. Ltd.
Wako-shi, Japan

We present a quantitative planar laser-induced fluorescence (PLIF) method for imaging the in-cylinder fuel concentration in a spark-ignition engine. The method is based on fluorescence from a carbonyl compound added to the fuel and excited by an excimer laser at 308 nm. The method has been applied to the study of charge stratification in a lean burn engine equipped with a four-valve pent-roof cylinder head. In this engine, stratification is achieved by fuel injection through an inlet valve, the paths of rich fuel pockets from induction through compression to the point of ignition is shown by a series of crank-angle-resolved air-to-fuel ratio (AFR) images.

Introduction

Lean operation in spark-ignition engines can decrease the primary exhaust emissions and increase fuel economy. Lean combustion is substantially influenced by the mixture distribution inside the cylinder prior to ignition; if the mixture is too lean, then the initial flame kernel tends to be weak and the flame speed low. Charge stratification with a rich spot near the spark plug, at the time of ignition, in an otherwise close to homogeneous mixture, aids in the development of a strong early flame kernel and ensures a fast propagation through the charge that minimises misfire and partial burning. Knowledge of the mixture formation process during the inlet and compression stroke, the extent of stratification, and the level of fluctuation on a cycle-by-cycle basis would greatly aid in the design of lean burn engines.

Previous in-cylinder fuel concentration investigations have been made as point measurements, utilising Rayleigh [1] or Raman [2,3] scattering. Planar laser-induced fluorescence (PLIF) has been used to mark the flame front by imaging the OH radical [4,5] or marking the fuel with an acetaldehyde seed such that the unburned material is imaged [6]. Attempts to obtain fluorescence from iso-octane [7] have met with some success but have not produced quantitative results. Fuel concentration measurements have been made in nonfiring engines with PLIF by adding biacetyl to the fuel [8] or by burning pure ethylmethylketone in a square-piston engine [10].

In this paper, we present the development and application of a PLIF technique for the imaging of the fuel distribution in a slice through the cylinder of a firing internal combustion engine of modern pent-roof design. For these measurements, a single-cylinder engine incorporating a transparent cylinder liner and a transparent piston were used. The local fuel concentration was estimated from fluorescence of a low molecular weight ketone, in this case pentanone, which was added in known quantities to the fuel; the fluorescence was excited at 308 nm by a light sheet formed from a XeCl-excimer laser.

Fluorescence Tracers

For the investigation presented in this paper, iso-octane was chosen as the fuel. Although PLIF of iso-octane is possible with excitation at 248 nm [7], its use is limited to qualitative measurements because of its low quantum yield and because of a nonlinear relationship between its fluorescence yield and laser power. Excitation at 308 nm results in no discernible signal for sensible laser intensities. Moreover, the use of 248 nm may result in contamination of the fluorescence signal by polycyclic aromatic hydrocarbons formed during combustion. We have also observed

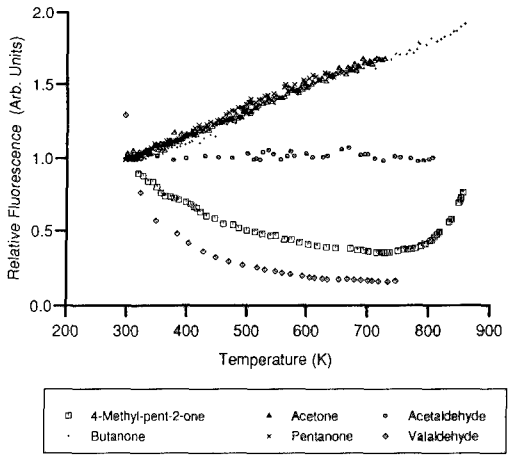

FIG. 1. Plots of relative quantum yield of fluorescence vs temperature for six different aldehydes and ketones.

that PLIF is possible, when excited at 308 nm, from commercial grade gasoline. At 1 bar, strong signals are possible; however, due to fluorescence quenching, the signal is very weak at typical compression pressures. We suspect that the latter signal is due to traces of aromatics in the fuel. Fluorescence from aromatic compounds is well known to be sensitive to quenching [9]. For these reasons, a fuel was chosen that was a blend of a seed species with a well-defined fluorescence behaviour, mixed into iso-octane.

The choice of a possible tracer is limited by the requirements that it should burn in a similar way to iso-octane, be soluble in iso-octane, and that its boiling point should closely match iso-octane to ensure representative vaporisation and mixing. Additionally, it should absorb at 308 nm and should be insensitive to quenching. It has been demonstrated that low molecular weight carbonyl compounds provide attractive fluorescent markers for hydrocarbon fuels in both combusting [4,11] and cold-flow situations [12]. In Fig. 1, the temperature dependence, at atmospheric pressure, of the relative fluorescence for six different fuel markers is shown. The fluorescence of acetaldehyde shows no temperature dependence at atmospheric pressure; however, it is highly volatile and therefore not suitable as a marker for iso-octane. The linear dependence of acetone, butanone, and pentanone indicates these species to be potential fuel markers. The pressure dependence of the fluorescence signal of various ketones has been shown to be reasonably linear [8]. Also, variations of oxygen partial pressure do not result in quenching variations at atmospheric pressure. The results of Baritaud [8] indicate that this quenching may not be a problem at elevated pressures.

To evaluate the influence of the boiling point of different fuel markers on fuel distribution, 20 fluorescence images were recorded for identical engine running conditions for both butanone and acetone as fuel markers. Nearly the same pattern was observed in the resulting mean images, with an overall difference of only approximately 6%. Some of the observed difference was due to cyclic variability, which was not entirely averaged due to the small number of instantaneous images. The repeatability of the measurements, determined from subsequent calibration images achieved by flooding the engine chamber with seed vapour at a known concentration, was about $\pm 2.5\%$. This uncertainty is composed of shot noise in the intensifier and camera, as well as spatial fluctuations in the laser intensity. Hence, the different volatilities of the seeds result in a small but measurable difference to the observed fuel distribution. Therefore, because the boiling point of pentanone (101.7 °C) more closely matches that of iso-octane (99.7 °C), it was chosen in preference to acetone (56.2 °C) and butanone (79.6 °C). Through experiment, a mixture of 3 parts iso-octane and 1 part pentanone by volume gave a good signal-to-noise ratio while remaining optically thin.

Experimental

Engine Design:

A single-cylinder engine with optical access was used. The engine was designed for lean burn combustion and to give good optical access, while retaining most of the engine characteristics of a typical production engine. The engine had a capacity of 0.36 litre and a compression ratio of 9.3:1. The four-valve pent-roof head was configured as in a production cylinder head and, as such, inducts nearly all the charge through only one inlet valve at the operation speed of 1500 rpm. The second inlet valve is simply opened fractionally and briefly at the end of induction to disperse an unwanted fuel buildup. The fuel was injected into the inlet port through a standard Honda fuel injector with an injection pressure of 2.5 bar gauge. The crankshaft was fitted with a 1° resolution encoder that provided data for an engine controller box, which generated signals to trigger the ignition and fuel injection timing and duration. In-cylinder pressures were recorded using a Kistler pressure transducer, which was fitted into the cylinder head. The overall air-to-fuel ratio (AFR) was monitored using an oxygen sensor built into the exhaust. The engine contained an elongated, hollow piston with a 45° mirror mounted on the crankcase inside the piston. This provided observation of images through a fused silica glass window located in the piston top. A fused silica cylinder was mounted in the block directly beneath the head and enabled a UV laser sheet to pass across the combustion chamber. The laser illuminated a plane approximately 13 mm below the spark

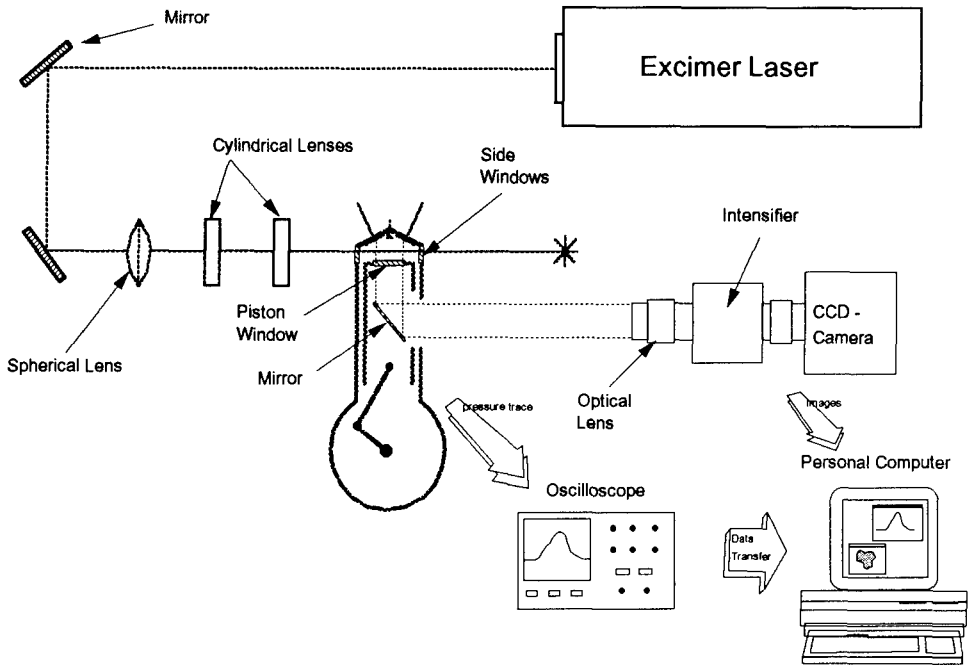

FIG. 2. Experimental setup.

plug parallel to the piston head and exiting the chamber at the opposite side of the cylinder (see Fig. 2).

Optical Setup and Considerations:

Measurements were made using a Lambda Physik 151 XeCl-excimer laser that produced about 150 mJ per 20-ns pulse at a specified crank angle. The beam was formed into a sheet approximately 0.25-mm thick for full field illumination of the accessible region. The images were acquired through the piston window using a 15-bit CCD-camera system, lens coupled with f1.2 optics to a gatable image intensifier (Princeton Instruments). An intensifier gate of 100 ns was used to discriminate against room light and combustion luminosity. The charge coupled device (CCD) camera has a framing rate of about 1 Hz, which means that it was not possible to image consecutive cycles. Each pixel on the CCD nominally collected light from a 0.25 × 0.25 × 0.25 mm volume. The true resolution will be less because of intensifier cross talk and distortions caused by viewing through the inhomogeneous charge when the engine was operating. For these reasons, 2 × 2 binning of the images resulted in no measurable loss of resolution. The true resolution was estimated to be better than 1 mm. Synchronisation of the laser and camera to the engine was achieved through a timing box connected to the crankshaft encoder. The timing of images could be set to a precision of 1° crank angle after top dead centre (ATDC).

Results and Discussion

To understand the mixing process during inlet and compression strokes, planar fuel concentration measurements for a range of different crank angles were made (Fig. 3). Because of the very short laser pulse duration (20 ns), each image provides data on the instantaneous fuel distribution at a particular crank angle for a single cycle. Twenty images were measured at a given crank angle for the same engine conditions, which were then combined to form an image of the cycle mean fuel concentration. Averaging over more than 20 cycles would improve accuracy of the measurement. It would, for example, smooth out single droplets visible in the mean image that originate only from one instantaneous image. However, 20 cycles were sufficient to obtain a reasonable picture of the mixing process and ensure that the data collection time was sensibly short and the data volume per measurement crank angle was less than 3 Mbytes.

The signal collected at each pixel of the camera is formed from several contributions. Part of which is proportional to the laser intensity and fuel concentration in the corresponding measurement volume, part arises from light scattered from the head, and part is from thermal noise in the CCD. Each of the data images presented in Fig. 3 was processed to remove the background contributions and then flat-fielded against an image obtained from a uniform concentration of the fuel marker. These corrections

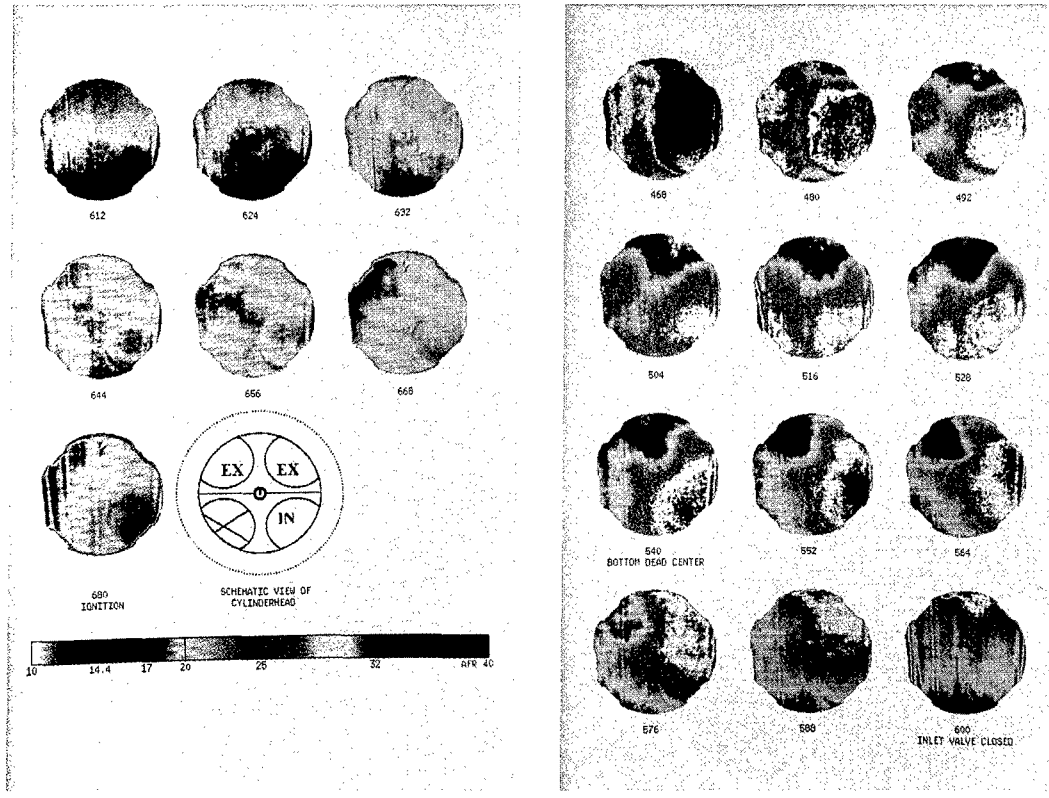

FIG. 3. In-cylinder crank-angle-resolved mean images of fuel concentration on an AFR scale. The numbers below images show the crank angle in degree after top dead centre (ATDC) at which the respective image was taken (0° is at combustion TDC). The images are oriented to the cylinder head as in the schematic view indicated. The dotted line in the schematic view indicates the cylinder bore proportional to the piston window diameter. The stoichometrie of the fuel used (3 parts iso-octane and 1 part pentanone) is 14.4 AFR.

were made on the basis of mean laser sheet characteristics. This introduced a small error because of pulse-to-pulse fluctuation in the laser sheet, which was responsible for introducing a slight linear modulation orthogonal to the laser propagation direction.

The laser-induced fluorescence (LIF) signal was also dependent on temperature and number density. To permit comparison between the images taken at different crank angles, signals were normalised to calibration conditions (atmospheric pressure and 331 K). The temperature dependence of the LIF signal from pentanone was linear (Fig. 1).

For images taken after the inlet valve was closed (600° ATDC), the in-cylinder temperature was calculated from the following expression:

$$p_1 T_1^{\gamma/1-\gamma} = p_2 T_2^{\gamma/1-\gamma} \tag{1}$$

which was derived from

$$p_1 v_1^{\gamma} = p_2 v_2^{\gamma} \tag{2}$$

and

$$pv = n\mathrm{RT}. \tag{3}$$

The politropic index $\gamma = 1.1$ was estimated by matching the results of Eq. (2) to the recorded pressure trace. We believe that the γ value of 1.1 in part reflects the enhanced heat transfer due to the large surface area of the elongated piston crevices.

The images were then corrected by multiplication with the factor f_1:

$$f_1 = \frac{v}{v_0} \cdot \frac{a + bT}{a + bT_0}. \tag{4}$$

For the images taken during the inlet stroke, the charge temperature was estimated from the engine temperature and ambient temperature to 313 K. The low in-cylinder pressure of 0.55 bar below atmospheric during the inlet stroke will lead to a temperature drop of the air entering the cylinder. This will be counter balanced by heat transfer from the cylinder walls (338 K water temperature) to the charge and mixing with hot residuals.

The images taken during the inlet stroke were then corrected by multiplication with the factor f_2:

$$f_2 = \frac{pT_0}{p_0T} \cdot \frac{a + bT}{a + bT_0} \tag{5}$$

where p was taken from the recorded pressure trace.

In Eqs. 4 and 5, the variables p_0, T_0, and V_0 represent pressure, temperature, and volume at calibration conditions; a and b are the coefficients for the temperature influence on LIF of the seed and are taken from Fig. 1.

This analysis results in relative maps of fuel concentration. Final images, shown in Figs. 3a and b, were converted to absolute AFRs. The composition of the calibration image was not defined well enough to use it as a direct calibration for AFR. The conversion was made on the basis that, since the overall equivalence ratio of the images near the combustion TDC was known and since the observed field was large enough, the mean value of the LIF in the laser sheet corresponded to the equivalence ratio as independently measured by the exhaust gas sensor. This rather crude estimation served the purpose of providing interpretable images. In principle, a better strategy would be to use an absolute calibration based on a calibration image taken with an accurate, known in-cylinder seed concentration. In practice, this is not trivial to achieve because of the need to ensure complete filling of the combustion chamber and ensuring that a gas with an accurately known partial pressure of seed is delivered to the chamber.

With our notation for combustion top dead centre at 0°, the intake valve opens at 340° ATDC and closes at 600° ATDC. Injection start is at 405° ATDC, and ignition is at 680° ATDC. The injection duration is approximately 30° crank angle, and the overall AFR is 20:1.

The images in Fig. 3a show that the first traces of the injected fuel reached the measurement plane at 468° ATDC or approximately 7 ms after the start of injection at the inlet side of the cylinder. The very lean and nearly homogeneous mixture observed in this image is believed to originate from unburned fuel remaining from the previous cycle. A small quantity of unburned gas is trapped in the crevices between the piston and the optical cylinder. The major part is probably from the inlet manifold and the valve. Fuel trapped on the upstream side of the valve will evaporate from the warm manifold walls during the whole cycle prior to induction and will then be scavenged into the cylinder with the air preceding the fresh injection of fuel. The bulk of the fresh fuel appeared at 480° ATDC at the exhaust side of the cylinder, with only a small trace visible at the inlet side. The fuel seems to follow two major paths within the cylinder. One is direct from the valve across the cylinder to the exhaust side, well above the measurement plane. The second track is close to the measurement plane originating from the fuel entering the cylinder at the inlet side. This track can be observed in the images 468°–504° ATDC. When the piston reaches bottom dead centre (540° ATDC), the charge with the highest velocity enters the measurement plane, and the effect of the anticlockwise swirl motion on the charge can be seen. The fuel appears again in the measurement plane during the compression stroke at the inlet side of the cylinder. In the subsequent images, the charge overall becomes richer because of compression. The fuel-rich area moves through the measurement plane in direction towards the cylinder head and appears again at the left-hand corner of the exhaust side. The fuel-rich stream observed in the images is apparently influenced both by tumble and swirl during the compression stroke. At the time of ignition, part of the fuel-rich track has already passed the spark plug and reappears in the measurement plane.

Conclusion and Future Work

We have successfully developed a PLIF method for measuring the fuel distribution within combustion chambers, which is based on fluorescence from low molecular weight carbonyl compounds added to the fuel. This method has been applied to a firing optical-accessed one-cylinder spark-ignition engine. Instantaneous planar fuel distributions at different crank angles in the inlet and compression stroke have been obtained. A series of such images provides a comprehensive picture of the overall fuel motion within the cylinder. The technique enables the detection of variations in fuel concentration of 2–3% at any given crank angle with a spatial resolution of better than 1 mm. Although an approximate method for obtaining AFR images was demonstrated, further work is needed to develop a rigorous quantitative method to convert relative fuel concentrations to absolute AFRs. Measurements at different measurement planes closer to the spark plug would also provide a more detailed picture of the in-cylinder fuel motion.

REFERENCES

1. Arcoumanis, C., and Enotiadis, A. C., *Exp. Fluids* 11:375–387 (1991).
2. Loyce, A., and Santavicca, D. A, *Am. Inst. Aeronautics Astronautics,* Paper No. AIAA-83–1551, 1983.
3. Smith, J. R., SAE Trans. 89:809–816 (1989).
4. Becker, H., Arnold, A., Suntz, R., Monkhouse, P., Wolfrum, J., Maly, R., and Pfister, W., *Appl. Phys.* B 50:473–478 (1990).
5. Suntz, R., Becker, H., Monkhouse, P., and Wolfrum, J., *Appl. Phys. B* 47:287–293 (1988).
6. Arnold, A., Becker, H., Suntz, R., Monkhouse, P., and

Wolfrum, J., *Optical Letters*, 1990, Vol. 15 (15), pp. 831–833.
7. Andresen, P., Meijer, G., Schluter, H., Voges, H., Koch, A., Hentschel, W., Oppermann, W., and Rothe, E., *Appl. Optics* 29:2392–2404 (1990).
8. Baritaud, T., and Heinze, T., SAE Paper No. 922355, 1992.
9. Birks, J. B., *Photophysics of Aromatic Molecules,* Wiley, London, 1970.
10. Lawrenz, W., Köhler, J., Meier, F., Stolz, W., Wirth, R., Bloss, W., Maly, R., Wagner, E., and Zahn, M., SAE Paper No. 922320, 1990.
11. Tait, N. P., and Greenhalgh, D. A., *Twenty-Fourth Symposium (International) on Combustion,* The Combustion Institute, 1992, pp. 1621–1628.
12. Tait, N. P., and Greenhalgh, D. A., *Ber. Bunsenges. Phys. Chem.* 1993, in press.

Twenty-Fifth Symposium (International) on Combustion/The Combustion Institute, 1994/pp. 157–165

A THERMOCHEMICAL PHASE SPACE FOR COMBUSTION IN ENGINES

A. K. OPPENHEIM AND J. A. MAXSON
University of California at Berkeley
Berkeley, CA 94720

The *phase space* introduced in this paper is based on the recognition that the combustion system is nonlinear, and takes advantage, therefore, of the classical concept of nonlinear mechanics: a space whose coordinates are all the dependent variables of the problem. In the case at hand, they consist of all the thermochemical parameters of the system. The dimension of this space is thus equal to the number of degrees of freedom. We name it the *Le Chatelier Space.* Its major asset lies in providing a map for the global effects of the thermochemical processes occurring in the *physical space* of the combustion chamber, expressed in terms of trajectories or manifolds. Obtained thereby is an analytical insight into the effective mechanism of the combustion system. Application of the method is illustrated by the evaluation of advantages one can accrue on this basis for a premixed charge engine. It is shown, in particular, that if, instead of a throttled homogeneous charge combustion, the exothermic process is executed in a *fireball mode* of a *direct injection stratified charge* system, the engine can be rendered the ability for part-load operation at wide-open throttle, with significant gains in fuel economy and concomitant reduction in pollutant emissions. Such a mode of combustion takes place within large-scale vortex structures generated and sustained by pulsed jets.

Method

Introduced here is a method of approach founded upon the recognition that the combustion system is intrinsically nonlinear. An insight into its essential processes occurring in the *physical space* should be based, therefore, on the classical concept of nonlinear mechanics: the *phase space,* i.e., one whose coordinates are the *dependent variables* of the problem. In the case of combustion, these are the thermochemical parameters. The dimension of this space is then equal to the number of degrees of freedom. We call it the *Le Chatelier Space.*

If the problem is formulated in terms of ordinary differential equations and the initial state is spatially and temporally uniform, the solution is expressed in terms of a trajectory in this multidimensional space. If the initial state is nonuniform, in space or in time, the trajectories form manifolds. All of them are strongly attracted by the end state (or states) of thermodynamic equilibrium. Thus, its coordinates play thus a commanding role in the analysis. We adopt, therefore, the mass fraction of products at equilibrium as the progress variable, while the equilibrium temperature is taken as the driving potential for thermochemical calculations. The latter take into account all the chemical species participating in chemical reaction, according to the so-called detailed kinetics model.

The computations are accordingly set up in three consecutive steps:

(A) Thermodynamics
(B) Thermochemistry
(C) Aerodynamics,

in contrast to the usual methods of computational fluid mechanics (CFM), where all of them are taken into account concurrently.

The first two pertain to the Le Chatelier Space. For design analysis, (A) provides an estimate of fuel economy, while (B) furnishes data on the formation of chemo-kinetically controlled pollutants, NO_x and CO. This is supplemented by (C) to provide information on the mechanism of processes occurring in the physical space, and, in particular, to refine the treatment of (B) and elucidate the cause of the unburnt hydrocarbon yield. Thereupon, if required, further progress in the analysis, to enhance its resolution, can be achieved by an iterative interplay between (B) and (C), whereby the calculations acquire more and more the usual character of CFM.

The concept of a thermochemical phase space is by no means new. One of its early versions in planar form was introduced some 20 years ago by Gray and Yang [1,2], exploited by the senior author and his associates a decade ago [3,4], and brought up recently in different connotations by Griffiths [5] and Maas and Pope [6,7], to mention just a few. Here, it is for the first time presented with particular relevance to combustion in engines, following its preliminary consideration in papers recently published [8–10].

Our studies stem from the observation made some

time ago [11] that pressure, recorded by an indicator diagram, is a particularly insensitive result of the conventional CFM solution. On the other hand, however, it is this diagram that represents the only useful product of the engine. It comprises, therefore, a valuable source of information on the performance of the combustion system and the design of ways and means for its amelioration. This paper is intended to provide a contribution towards this aim.

The method of approach adopted here is, in essence, addressed to the *inverse problem* with respect to that of the conventional CFM models. It should be regarded, therefore, as complementary to CFM rather than competitive. One should note in this connection that the solution obtained thereby is restricted per force to the provision of global data on the behavior of the reacting system, subject to an a priori assumed model. Introduced here, to start with, is the simplest one, founded upon the experimental studies reported at the last Symposium [12], according to which the combustion system in an engine cylinder consists of two major components: the reactants at frozen composition and the products at thermal equilibrium—the most one can identify in the inverse problem under study—with an interface where the exothermic process takes place that, in spite of its essential role as the intrinsic source of motive power, contains a practically negligible amount of mass and volume in the physical space.

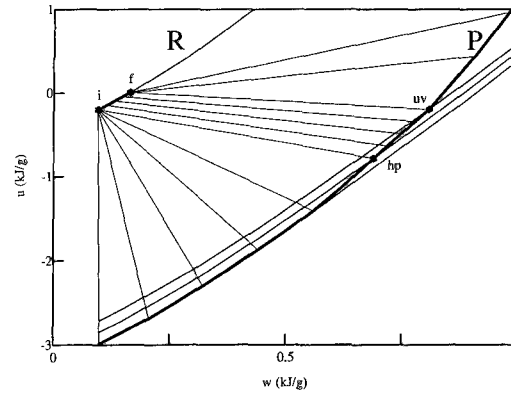

FIG. 1. Le Chatelier Diagram, for adiabatic combustion in an isochoric enclosure for a stoichiometric propane-air mixture initially at a pressure of 5 bars and a temperature of 65 °C *i-uv* and *f-hp*: initial and final states of combustion in an adiabatic and isochoric enclosure.

Formulation

Thermodynamics:

For the thermodynamic analysis of the two-component system specified above, the loci of states of reactants, R, and products, P, are expressed graphically in terms of internal energy, u, plotted as a function of the product of pressure and specific volume, w, as displayed in Fig. 1 [8]. This graph depicts a phase plane, which, upon the advice of Numa Manson, we call the *Le Chatelier Diagram.*

In an engine cylinder, at any instant of time, the pressure of the products is, in effect, equal to that of the reactants. From the conservation equations for mass, volume, and energy, it follows that constant pressure lines between corresponding points on R and P are straight, as delineated by the thin lines in Fig. 1 [8]. Thus, for the adiabatic process portrayed in this figure, it appears that the exothermic process is initiated at point i on R, leading to hp on P, and terminated at point f on R, culminating at uv on P.

Mechanical performance of an engine is expressed in terms of an indicator diagram obtained by the measurement of pressure $P(\Theta)$ and volume $V(\Theta)$ where, at constant speed (which is invariably the case at the relatively small time intervals pertaining to the execution of the combustion process in an engine), the crank angle, Θ, is a measure of time, t. Since $V(\Theta)$ is an algebraic function describing the kinematics of the crankshaft mechanism, $P(\Theta)$ can be considered formally as a time coordinate. This is, however, problematic, since it is a nonmonotonic function of time. On the other hand, in the course of combustion, the mass fraction of products at equilibrium, μ_P, is guaranteed to satisfy this condition and, consequently, it is adopted here as the principal progress variable. Its functional dependence on pressure and volume is greatly simplified by the observation that the two loci of states, P and R in Fig. 1, are remarkably straight in the domain of relevance between i and f, as well as between hp and uv—a feature that holds true for most practical circumstances. Thus, μ_P, referred to henceforth shortly as *mass fraction,* can be evaluated from the three conservation equations, to yield, in terms of pressure, P, and volume, V, normalized with respect to their initial values at i,*

$$\mu_P = \frac{\omega + \kappa + P^a + k(PV - P^a) - 1}{P + k(P_{uv} - P) - 1}. \quad (1)$$

The most problematic term here is the heat transfer to the walls. Its functional relationship, $\kappa = \kappa_f f(P,V)$, has been provided for this purpose by the results of an elaborate study of heat loss from combustion in enclosures reported in a companion paper [13], whereas, on the basis of Eq. (1),

$$\kappa_f = [P_f^a + k(P_{uv} - P_f^a) - 1]\mu_f - [P_f^a + k(P_f V_f - P_f^a) - 1] - \omega_f. \quad (2)$$

*Symbols are defined in the Nomenclature.

The normalized specific volume of products at equilibrium is then given by

$$v_P = [V - (1 - \mu_P)v_R]/\mu_P \tag{3}$$

while $v_R = P^{a-1}$.

Of particular importance to the analysis of the exothermic process of combustion is the determination of its initial, i, and final, f, states. This is done as follows.

1. The initial state is an essential singularity, for at $\mu_P = 0$, $v_P \equiv V_P/M_P = 0/0$; it can be evaluated, therefore, from Eq. (3) by L'Hospital's rule.
2. The final state, attained at $\mu_f = (\sigma\lambda_r + 1)/(\sigma\lambda_o + 1)$, where σ is the stoichiometric air-fuel ratio and λ is the reciprocal of the equivalence ratio, ϕ, the subscript r refers to reaction zones, and o denotes the overall value for the cylinder charge, must satisfy the condition $(d\mu_P/dP)_f = 0$, associated with a smooth decay so that $(d \ln V/d \ln P)_f = -1/n_e$, with subscript e denoting the polytropic process of expansion.

Thus, the thermodynamic analysis provides the basis for the evaluation of time (crank angle) resolved profiles of all the thermodynamic state parameters of the reactants and products.

Thermochemistry:

The exothermic reaction proceeds as a consequence of a *chemical source* and a *thermal source* [4].

The first is specified by kinetic rate expressions for the concentration growth rate of each chemical species participating in the reaction, expressed, in terms of conventional symbols, with the Newtonian dot notation for differentials with respect to time, as

$$\dot{C}_i = (a_j - a_i) \sum_{k=1}^{K} \cdot \left[a^{1-m_k} \prod_{i=1}^{I} C_i a_{ik} T^{n_k} \cdot \exp(-E_k/\mathcal{R}T) \right]. \tag{4}$$

The second expresses the rate of temperature rise as

$$\dot{T} = \dot{Q} + \dot{P} + \dot{S}. \tag{5}$$

Here, $\dot{Q} \equiv c_p^{-1} \Sigma \dot{C}_i, (-\Delta h)_i$, $\dot{P} \equiv v c_p^{-1}\, dP/dt$, while $c_p \equiv \Sigma\, C_i c_{pi}$, whereas

$$\dot{S} = (T_P - T)/\tau \tag{6}$$

where τ denotes the thermal relaxation time—an empirical constant [14].

Aerodynamics:

The inverse problem in aerodynamics is as follows: given an indicator diagram, derived from a pressure transducer measurement, with its interpretation on the thermochemical phase space for a two-component system, reveal the principal mechanism of the combustion field in the physical space—its place of origin. The resolution of this problem involves, of course, partial differential equations of turbulent flow [15]. In accordance with the thermodynamic model, the flow field is made up of two fluids: the reactants and the products. The interface between them involves a negligible amount of space and, especially at the initial stages of the process, can be disconnected.

Each of the two regimes of the flow field is governed by the Navier–Stokes equation

$$\frac{\partial \underline{u}}{\partial t} = -(\underline{u} \cdot \underline{\nabla})u - v\underline{\nabla}p + Re^{-1} \cdot [\Delta u + (\kappa\mu^{-1} + 3^{-1})\underline{\nabla}(\underline{\nabla} \cdot \underline{u})] \tag{7}$$

as well as by the corresponding vortex transport equation

$$\frac{\partial \underline{\xi}}{\partial t} = -(\underline{u} \cdot \underline{\nabla})\xi - \underline{\nabla}v \times \underline{\nabla}p + Re^{-1}\, \Delta\underline{\xi} + (\underline{\xi} \cdot \underline{\nabla})\underline{u} - (\underline{\nabla} \cdot \underline{u})\underline{\xi}. \tag{8}$$

According to the Helmholtz decomposition theorem, the velocity vector is split into rotational and irrotational components, i.e.,

$$\underline{u} = \underline{u}_\xi + \underline{u}_\varepsilon \tag{9}$$

where, by definition, $\underline{\nabla} \times \underline{u}_\xi = \underline{\xi}$ and $\underline{\nabla} \cdot u_\xi = 0$, while $\underline{\nabla} \cdot u_\varepsilon = 0$ whereas, by virtue of the continuity equation,

$$\underline{\nabla} \cdot \underline{u} = \underline{\nabla} \cdot \underline{u}_\varepsilon = \Delta\Phi = \frac{\partial}{\partial t} \ln v + (\underline{u} \cdot \underline{\nabla}) \ln v. \tag{10}$$

To comply with the basic premise of the thermodynamic model, specific volumes of each of the two fluids are taken to be spatially uniform. Within their fields, therefore, the second term in Eq. (10) is annihilated.

Thus, in terms of $K = P, R$ for each fluid, respectively, throughout their fields denoted by subscript f,

$$(\underline{\nabla} \cdot \underline{u}_K)_f = \frac{\partial}{\partial t} \ln v_K \tag{11}$$

while at any exothermic site, i.e., ignition or front marked by e,

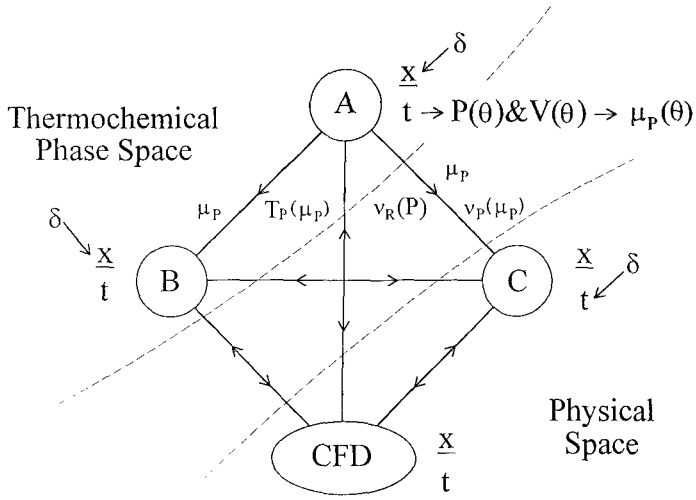

FIG. 2. Topological map.

$$(\underline{\nabla}\cdot\underline{u}_K)_e = \frac{\partial}{\partial t}\ln \nu_K \mp (\underline{S}_K\cdot\underline{\nabla})\ln \nu_K \qquad (12)$$

where $\underline{S}_K$ is the normal front velocity vector relative to the particle trajectory.

Since a source of products must coincide with a sink of reactants, noting that then $\underline{\nabla}\cdot\underline{u}_P > 0$, while $\underline{\nabla}\cdot\underline{u}_R < 0$,

$$\Delta\Phi_e = (\underline{\nabla}\cdot\underline{u}_P + \underline{\nabla}\cdot\underline{u}_R)_e = \frac{\partial}{\partial t}\ln(\nu_P/\nu_R) + (\underline{V}\cdot\underline{\nabla})\ln(\nu_P - \nu_R) \qquad (13)$$

the form of the last term resulting from the continuity and kinematic relations across the front whence

$$|\underline{V}| \equiv S_P - S_R = (a-1)S_R = U_R - U_P, \qquad (14)$$

where $a \equiv \nu_P/\nu_R$ and U_K is the normal component of the particle velocity at the front, whereas the normal front velocity is $W_F = S_R + U_R$. Equation (13) is a generalized version of a source blob [16], bringing to the forefront its aerodynamic significance.

Brought out thus, besides vorticity generation [17], is the essence of the dynamic role played by the exothermic process of combustion as an active participant of the flow field. This feature is of particular significance to turbulent fields where flame models are handicapped by their strictly local effects.

A solution of the inverse problem is, of course, subject to appropriate boundary and initial conditions. The first involve the usual demand for velocity vectors to vanish at the walls, as well to comply with front relations. The second are brought in by the process of ignition. For aerodynamics, their net effect are data on the coordinates t_i and $\underline{x}_i$ of the time and location of sites at which the exothermic process of combustion is initiated. Once this is known, a preliminary solution of Eqs. (7–13) can be obtained. The result has to comply with the thermodynamic conditions of constraint. This is implemented by a flux correction algorithm to satisfy the demand for the volume of the products to be $V_P(t) = \mu_R\nu_R$, wherefore the mass fraction of products, $\mu_R(t)$, and their specific volume, $\nu_R(t)$, are prescribed by Eqs. (1) and (3). The ignition sites are for this purpose established by a trial and error procedure on t_i and $\underline{x}_i$. To start with, these coordinates can be first identified in the turbulent field of reactants by interrogating, at a postulated t_i, over a prescribed domain, $\underline{x}_i$, where $|\underline{u}| < \varepsilon$—an arbitrarily small quantity—to pinpoint a reasonable number of stagnation cores within the large-scale vortex structures where, on account of the exceptionally small Damköhler, Reynolds, and Peclet numbers, thermal ignition is most likely to occur.

Logistics

The logistics of our method of approach are displayed in the topological map in Fig. 2.

Thermodynamics in (A) introduce mass fraction of products at equilibrium, μ_P, as the progress variable to serve as the primary reference coordinate for the evolution of the temperature of products at equilibrium, $T_P(\mu_P)$, and their specific volumes, $\nu_P(\mu_P)$.

Thermochemistry in (B) utilizes the equilibrium temperature as the potential for the term in the energy equation expressing the global effects of diffusion.

Aerodynamics in (C) are, in turn, controlled by the evolution of the mass fraction, $\mu_P(t)$, and of the spatially uniform specific volumes, $\nu_R(P)$ and $\nu_P(\mu_P)$, specified by the thermodynamic analysis, to reveal the essential mechanism of the two-component field

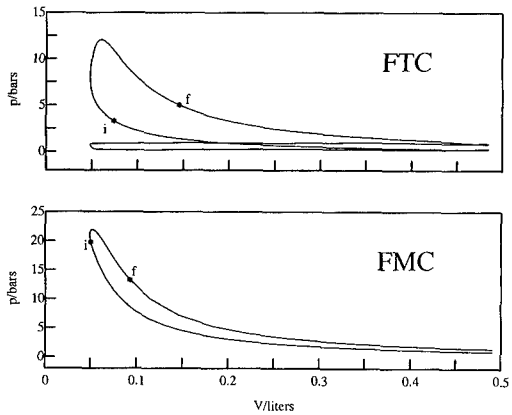

FIG. 3. Indicator diagrams for part-load operation of Renault F7P-700 engine at 2000 rpm. FTC—flame traversing the charge of the reference case 0 in Table 1. FMC—fireball mode of combustion in the ultimate case 6 in Table 1.

in the physical space where the process of combustion takes place.

All are in mutual relationship with computational fluid dynamics (CFD).

Implementation

Our method offers a fundamental background for the development and design of combustion in engines, thus furnishing an analogous service to engine technology as aerodynamics provided for aeronautics [9]. One starts with a *given* system and designs means for its improvement. We concentrate, in this connection, on the essential element of engine performance: the indicator diagram. Hence, the procedure we are introducing can be best described as *indicator diagram tailoring.*

Consider, for example, the four-stroke Renault F7P-700 we used for our initial studies of the Le Chatelier Space [14]. Its indicator diagram, at a representative part-load operation, is presented in the upper part of Fig. 3. The engine was run then in the conventional, throttled flame traversing the charge (FTC) mode of combustion. Displayed in the lower part of Fig. 3 is an indictor diagram yielding the same indicated mean effective pressure (IMEP) if the engine was operated in the ultimate unthrottled fireball mode of combustion (FMC) attainable by a direct injection stratified charge (DISC) engine system. Their operating conditions are specified in Table 1. In the parametric study we carried out [10], besides the reference case of FTC, denoted by 0, six cases of FMC were considered. As evident there, for cases 1–3 only, the effect of heat loss to the walls was varied, while Θ_i and Θ_f remained unchanged, whereas for cases 4–6, the crank angle interval between Θ_f and Θ_i was halved and Θ_i adjusted to yield maximum IMEP. Figure 3 refers in this respect to cases 0 and 6. Test data of the reference case also provided the calibration of the thermal relaxation time, yielding $\tau = 5\ \mu$s—a value we then employed for all our calculations.

A representative sample of the results we obtained is provided by Figs. 4 through 7. The figures depict the crank-angle resolved variation of the temperature, mass fraction, specific volumes, and NO and CO concentration profiles for cases 0 and 6, respectively. Performance parameters for all the seven cases under study are presented in Fig. 8, demonstrating clearly the advantages accruable by the stratified charge combustion in a fireball mode. They are, one should note, attained by executing the exothermic process of combustion at as low a temperature as possible—a goal achievable by significant dilution of the charge manifested by the low equivalence ratios. Their values, it should be pointed out, were carefully established by trial and error computations

TABLE 1
Operating conditions

	θ_i°	θ_f°	Q_W	ϕ_0	ϕ_c	Case
FTC	335	410	Q_H	1	1	0
FMC	335	410	Q_H	0.255	0.95	1
			$Q_H/2$	0.185	0.75	2
			0	0.110	0.50	3
	355	392.5	$Q_H/2$	0.185	0.60	4
			$Q_H/4$	0.145	0.50	5
			0	0.105	0.40	6

Note: Q_W—heat transfer to the walls, ϕ_0—effective overall equivalence ratio, and ϕ_c—effective equivalence ratio in the exothermic zone of a fireball.

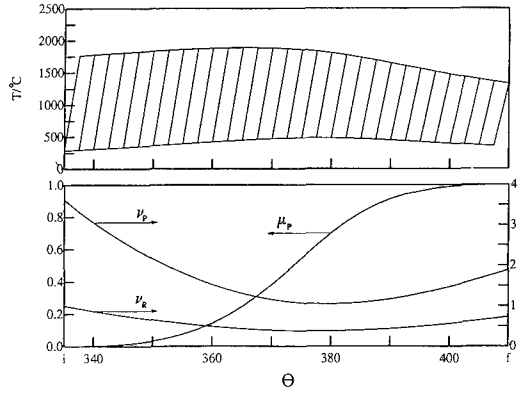

FIG. 4. Mass fraction, specific volumes, and temperature profiles for case 0, operating conditions of FTC in Table 1.

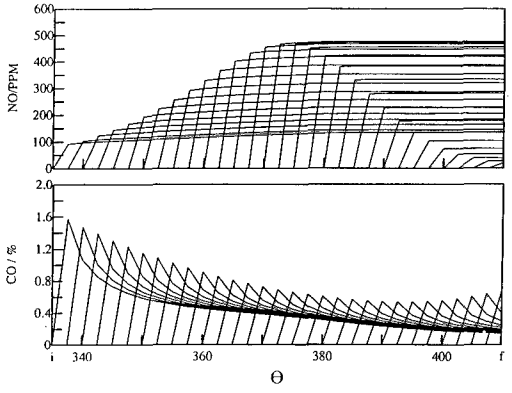

FIG. 5. Nitric oxide and carbon monoxide concentration profiles for case 0, operating conditions of FTC in Table 1.

using detailed kinetic reaction data obtained from Westbrook and Pitz in the updated version of their original publication [18], with mechanisms for both thermal and prompt NO formation (the latter being of particular significance at the relatively low temperatures under study), according to the compilation of Miller and Bowman [19]. In our calculations, as lower equivalence ratios in the fireball are attempted, sharp points of demarcation are reached, below which the oxidation mechanism ceases to proceed. This marks a typical threshold between ignition and extinction reached here as a consequence of dilution by excess air, reflected by ϕ_e, at a given temperature, rather than as the usual case of a low-temperature limit at a given ϕ_e [3,4]. In approaching this limit, one is confronted with a trade-off between the rap-

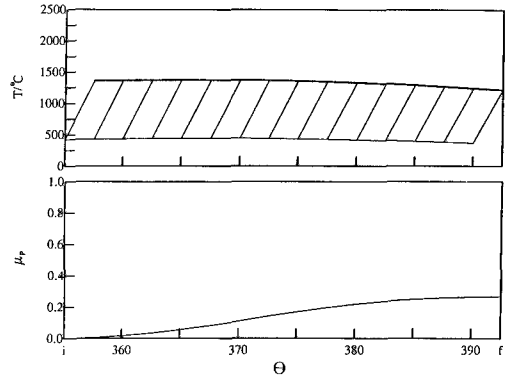

FIG. 6. Mass fraction, specific volumes, and temperature profiles for case 6, operating conditions of FMC at Θ_i = 355°, Θ_f = 392.5°, and Q_H = 0 in Table 1.

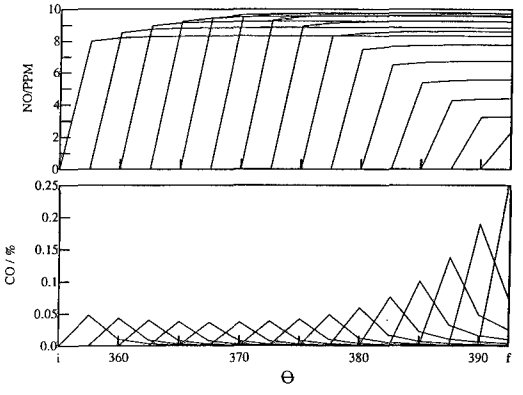

FIG. 7. Nitric oxide and carbon monoxide concentration profiles for case 6, operating conditions of FMC at Θ_i = 355°, Θ_f = 392.5°, and Q_H = 0 in Table 1.

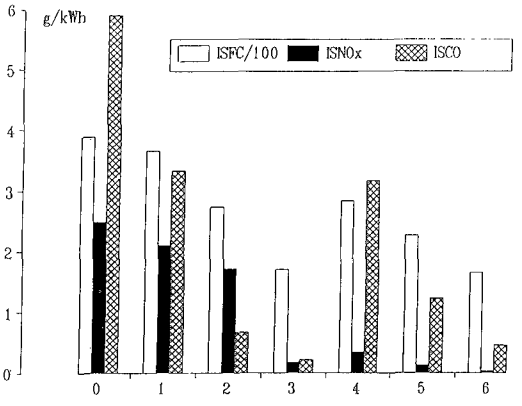

FIG. 8. Performance parameters, operating conditions specified in Table 1.

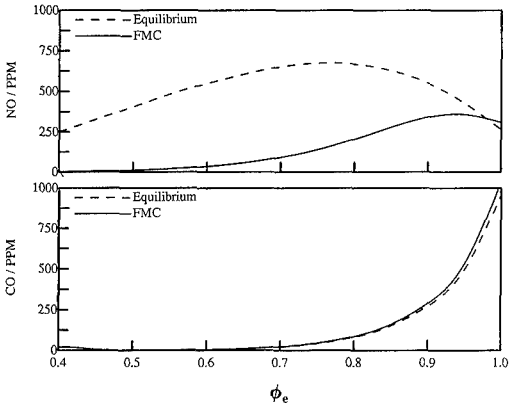

FIG. 9. FMC (fireball mode of combustion) and equilibrium concentrations of nitric oxide and carbon monoxide, in the whole charge of the working, substance at state f, with operating conditions specified in Table 1.

idly decreasing yield of NO and the concomitant augmentation of CO.

Figure 9 portrays a significant benefit of low-temperature combustion: the amount of NO produced by FMC becomes appreciably smaller than its equilibrium value at the same temperature and pressure. The chemo-kinetically generated CO is, however, quite close to its equilibrium value at all equivalence ratios.

Interpretation

1. This paper introduced the Le Chatelier Phase Space as incisive means for interpreting the mechanism of the thermochemical processes of combustion in engines.
2. Its concept stemmed from the recognition that engine combustion is intrinsically a nonlinear system where exothermic reactions occur in a turbulent flow field and progress from a nonequilibrium state towards thermodynamic equilibrium.
3. Thus, it ushered in a technology capable of both assessing the performance of a combustion system and providing guidance for engine development and design by an indicator diagram tailoring step-by-step procedure consisting of (A) thermodynamic, (B) thermochemical, and (C) aerodynamic analyses.

Nomenclature

a	stoichiometric coefficient
c	slope of the locus of states on the Le Chatelier Diagram; specific heat
C	species concentration
E	activation energy
h	specific enthalpy
k	c_P/c_R
M	mass
n	polytropic exponent
p	pressure
P	normalized pressure
Q	heat loss
$\mathfrak{R}$	universal gas constant
Re	Reynolds number
t	time
T	temperature
u	specific internal energy
$\underline{u}$	velocity vector
$\bar{v}$	normalized specific volume
V	normalized volume
$\underline{x}$	position vector
$\bar{a}$	$(n - 1)/n$
Θ	crank angle
κ	normalized heat loss to the walls, $Q_w/(c_R w_i)$; bulk viscosity
μ	mass fraction; shear viscosity
ξ	vorticity vector
τ	relaxation time
ϕ	equivalence ratio
Φ	velocity potential
ω	normalized work, $\int PdV/c_R$

Subscripts

c	compression
e	expansion; exothermic zone
f	final; field
hp	initial specific enthalpy and pressure
i	initial
I	interface
K	P, R
o	overall
p	constant pressure
P	products
r	relative to front
R	reactants
uv	initial specific internal energy and specific volume
w	walls
ε	irrotational
ξ	rotational

Acknowledgments

The authors wish to express their gratitude to Alexandre Chorin, Allen Kuhl, Bill Sirignano, and Forman Williams for the advice they provided on crucial aspects of the paper. Work on the paper was supported in part by PG&E, thanks to the auspice of Brian T. Stokes, for which the senior author is particularly thankful.

REFERENCES

1. Gray, B. F., and Yang, C. H., *J. Phys. Chem.* 69:2747–2750 (1965).
2. Yang, C. H., and Gray, B. F., *Eleventh Symposium (International) on Combustion,* The Combustion Institute, Pittsburgh, 1967, pp. 1099–1106.
3. Guirguis, R. H., Oppenheim, A. K., Karasalo, I., and Creighton, J. R., *Combustion in Reactive Systems, Progress in Astronautics and Aeronautics,* AIAA, New York, 1981, 134–153, Vol. 76.
4. Oppenheim, A. K., *Philos. Trans. R. Soc. London A* 315:471–508 (1985).
5. Griffiths, J. F., *Ann. Rev. Phys. Chem.* 36:77–104 (1985).
6. Maas, U., and Pope, S. B., *Combust. Flame,* 88:239–264 (1992).
7. Maas, U., and Pope, S. B., *Twenty-Fourth Symposium (International) on Combustion,* The Combustion Institute, Pittsburgh, 1992, pp. 103–112.
8. Oppenheim, A. K., and Maxson, J. A., *Progress of Astronautics and Aeronautics,* AIAA, Washington, DC, 1993, 365–382, Vol. 152.
9. Oppenheim, A. K., *ASME J. Fluids Eng.* 115:561–567 (1993).
10. Oppenheim, A. K., Maxson, J. A. and Shohad, S. M., SAE Paper 940479, 1994, 7 pp.
11. Oppenheim, A. K., and Rotman, D. A., ASME Paper 87-ICE-21, 1987, 18 pp.
12. Tamai, R., Maxson, J. A., Shepherd, I., Cheng, R. K., and Oppenheim, A. K., *Twenty-Fourth Symposium (International) on Combustion,* The Combustion Institute, Pittsburgh, 1992, pp. 1433–1439.
13. Oppenheim, A. K., *Combustion in Enclosures* in preparation.
14. Gavillet, G. G., Maxson, J. A., and Oppenheim, A. K., SAE Paper 930432, 1993, 20 pp.
15. Chorin, A. J., *Computational Fluid Mechanics,* Academic Press, Inc., Boston, 1989, xv + 223.
16. Ghoniem, A. F., Chorin, A. J., and Oppenheim, A. K., *Philos. Trans. R. Soc. London A* 304:303–325 (1982).
17. Rotman, D. A., Pindera, M. Z., and Oppenheim, A. K., *Progress in Astronautics and Aeronautics,* AIAA, New York, 1989, pp. 251–265, Vol. 113.
18. Westbrook, C. K., and Pitz, W. J., *Combust. Sci. Technol.* 37:117–152 (1984).
19. Miller, J. A., and Bowman, C. T., *Prog. Energy Combust. Sci.* 15:287–338 (1989).

COMMENTS

N. Peters, RWTH Aachen, Germany. You make great claims that are not substantiated in the paper. For instance, it is left to the reader to imagine how you evaluate Eq. (13) numerically. Are v_P and v_R continuous or do they jump at the flame front? Also, I believe that the limit $Ma \to 0$, $Re \to \infty$, $Da \to \infty$ is not a realistic one for premixed combustion in SI engines.

Author's Reply. Eq. (13) pertains to the evolution of the front, akin to what is popularly referred to as the *G Equation.* It should be treated, therefore, by a front tracking or capturing algorithm, based on the principles of analytic geometry. The start of the computations is described following Eq. (14). One should observe that the second term in Eq. (13) is nil at the points of ignition. Thereupon, one has a front between the field of products, **P**, and that of reactants, **R**, whose points are advanced at a local velocity $\mathbf{W}(\mathbf{u_P},\mathbf{u_R})$. At the next time step, the fields of **P** and **R** are updated by virtue of the Poisson equation expressed, in effect, by Eq. (13).

The terms v_P and v_R jump at the front. According to the algebra of Eq. (13), it is, in effect, a double jump expressing the demand of the continuity equation, according to which the birth of products must be concomitant with the death of reactants, so that v_P jumps up from zero, while v_R jumps down to zero.

It is true that the limit of $Ma \Rightarrow 0$, $Re \Rightarrow \infty$, $Da \Rightarrow \infty$ is not realistic for combustion in engines. But no model is entirely realistic. The author is, indeed, very grateful to Professor Peters for bringing this point up. Our major objective is not to develop a model to reconstruct everything that takes place in the course of combustion as faithfully as possible, but to bring out the essential features of the process as critically as is feasible, or, in other words, not to consider all the effects together at the same time, as is typical of CFD, but to *separate* them for scrutiny of their intrinsic nature, one by one, inasmuch as one can. From this point of view, assuming the perspective of the limit so succinctly identified by Professor Peters, may be just exactly "what the doctor ordered."

•

W.A. Sirignano, University of California, Irvine, USA. The use of the velocity divergence to treat discontinuities is very interesting and novel. Some interpretation of simple limiting cases would be helpful to the reader. For example, an explanation of the case of a propagating planar discontinuity would be useful. Perhaps the explanation of a case with cylindrical or spherical symmetry would also be helpful. In the piecewise uniform density case under consideration by the authors, isn't the last term in Eq. (12) zero?

Author's Reply. Dr. Sirignano provided the senior author with a good deal of pleasure and satisfaction by pointing out the essential feature of the aerodynamics of turbulent

combustion introduced in the paper. Providing the interpretation and examples as he recommends is unfortunately out of question in a Symposium paper because of the strict word limit. It is the deposition of exothermic energy ("heat release") that gives rise to the dilatation expressed by the velocity divergence, representing thus the intrinsic mechanism of this crucial event. Equation (12) codifies its fluid mechanical consequences: the unbalanced doublet modeling the source of products coupled with the sink of reactants that occurs at exothermic sites, i.e., at the points of ignition, expressed by the first term, and at the front, expressed by the second term. In the field, as presented by Eq. (11), the second term is, of course, nonexistent, according to his expectation.

Twenty-Fifth Symposium (International) on Combustion/The Combustion Institute, 1994/pp. 167–174

FUEL AND SOOT OXIDATION IN DIESEL-LIKE CONDITIONS

A. CAVALIERE
Dipartimento di Ingegneria Chimica
Università degli Studi di Napoli Federico II
Piazza Tecchio 80
80125 Napoli, Italy

AND

R. BARBELLA, A. CIAJOLO, A. D'ANNA AND R. RAGUCCI
Istituto di Ricerche sulla Combustione
CNR
Napoli, Italy

Diesel combustion has been studied under simplified experimental conditions in a nearly quiescent, high-temperature (900 K), high-pressure (4 MPa) environment by means of two-dimensional (2D) laser light scattering techniques and chemical analysis of gaseous and condensible material sampled by a fast-acting valve.

Two model fuels, constituted of a simple alkane hydrocarbon (tetradecane (TD)) and an aromatic/aliphatic mixture (α-methylnaphthalene/tetradecane), have been used in order to study the effect of the fuel specificity on the combustion process.

Temporal profiles of the scattering intensity and of the evolution of the oxidation progress evaluated by CO and CO_2 determinations, have shown the same behaviour independently on the fuel type and on the sampling location.

For both fuels, the combustion proceeds through the formation of CO and subsequent oxidation to CO_2, which is anticipated with respect to the appearance of a scattering signal due to soot formation and is almost completed in correspondence of the beginning of soot oxidation. The early phase of the latter process takes place in correspondence of the CO depletion when OH radicals become available. The importance of this result consists in the recognition that mechanisms of soot oxidation by an OH attack can realistically occur in diesel engine combustion and that this is the only pathway through which soot oxidation takes place in characteristic timescales comparable to those of its formation.

Introduction

The dependence of diesel spray combustion on the injected fuel quantity has been analyzed in a previous paper [1] in terms of structural features and pollutant generation under prototypical simplified conditions. It has been shown that the main combustion characteristics do not appreciably change in the range of fuel injection quantities typical of light duty diesel engines. The oxidation and pyrolysis take place, from the very early beginning after the ignition, in the whole spray on length scales smaller than the spray width so that the overall air-fuel mixing is relatively lean. Therefore, soot was very early formed also in the central part of the spray but with a carbon conversion lower than 3%.

For injection of higher fuel quantities, some authors [2,3] have reported that soot is distributed on the tip and on the periphery of the spray and that carbon conversion to soot is higher than 20%, whereas other researchers [4,5] have shown that soot clouds have been detected throughout the diesel plume, also in its central part, even though a higher soot concentration has been evaluated to be present in the head-vortex region of the combusting plume. Therefore, it has to be noted that discrepancy for the location of soot distribution is present in the literature for high quantities of injected fuel.

In this paper, the focus has been shifted from the analysis of spatial soot distribution, outlined above, to the study of the main pathways through which two fuels having different aromatic content are oxidized and pyrolyzed with particular regard to soot formation and destruction processes. Therefore, the influence of spatial soot distribution, also taking into account the aforementioned different features, can be discussed separately. The methodological approach of this paper is the same as that used in a previous one [1], i.e., all of the possible simplifications of the complex process occurring in the engines have been

adopted in order to separate the effect dependence on single external parameters. Simple model fuels (tetradecane and a tetradecane/*a*methyl naphthalene mixture) with the same atmospheric boiling point and similar critical temperature are injected in a nearly quiescent isobaric environment so that both the aerodynamics and the chemistry keep the minimum level of complexity of the diesel engine combustion.

Experimental Setup

Experimental tests were performed at 4 MPa and 900 K intake air temperature in a high-pressure flow reactor, with a rectangular test section, equipped with three quartz windows. A water-cooled five-hole 0.2-mm-i.d. diesel nozzle was mounted on a wall of the chamber. Six milligrams per hole of fuel was injected in 1.2 ms with a pressure opening of 20 MPa and a pressure peak of 40 MPa. The air flow (v_{air} = 1 m/s) was parallel to the walls and intersected perpendicularly to the spray on which both optical and chemical diagnostics were applied.

A Nd:YAG laser, tuned on the second harmonic (λ = 532 nm), was used. The laser beam was shaped either as a light sheet or as a uniform intensity beam, intersecting one of the five sprays at a 37° angle.

A microchannel plate-intensified charge coupled device (CCD) camera (512 × 512 pixels) was used to record light scattering images with different polarization states (at a 90° scattering angle). An interference filter was used for the rejection of the flame luminosity.

The luminous ignition delay time, defined as the time from the start of injection until the first luminosity has been detected, was measured using an ultraviolet enhanced photodiode placed in front of one of the windows and resulted to be 1.1 and 1.5 ms for tetradecane (TD) and tetradecane/*a*-methylnaphthalene (TD/*a*MN) mixture (60/40 vol.%), respectively.

Fast sampling of the combustion products was carried out by means of a high-speed (0.7-ms sampling time) valve located in place of one of the quartz windows. Measurements were performed at 20 and 30 mm from the nozzle on the axis of the spray.

Samples were withdrawn by a vacuum pump, passed through a fiberglass filter and through a cold trap to remove particulates. The gaseous products were analyzed by gas chromatography with thermal conductivity detection and with flame ionization detection.

The particulate was extracted by dichloromethane to separate the condensed species from soot. Quantitative analysis of the fuel components, i.e., tetradecane and *a*-methylnaphthalene contained in the condensed species, was performed by gas chromatography with flame ionization and mass spectrometry detection.

Further details on the experimental setup and analytical procedure have been reported elsewhere [1,6].

Results

Figure 1 reports two-dimensional (2D) laser light scattering patterns detected from a cross section of the plume at 20 mm from the nozzle outlet when both the incident and scattered light are vertically polarized. Each picture was obtained as an ensemble average of 100 images collected in 0.1 ms and is reported as a half pattern since it is nearly symmetric. The upper-half pictures are relative to the TD injection; meanwhile, the lower ones refer to the TD/*a*MN mixture. The left side refers to a temporal sequence of averaged images detected from 0.6 up to 1.8 ms from the injection beginning; the right side refers to times between 2.0 and 3.5 ms.

The four-level colour representation is indicative of a different scattering intensity, which increases along the sequence of blue, green, red, and white colors. The colour scale is an arbitrary logarithmic one. Therefore, the colours related to the lowest intensity level can be considered a limit of the background intensity, and consequently, single images with very different characteristics can also affect the intensity distribution. This means a random distribution of the blue colour, whereas the other colours are smoothly distributed, as it is expected for average images. Anyhow, the colour scale is the same for all the patterns and for both fuels so that a first qualitative behaviour can be inferred from the comparison of different patterns.

Following the upper-half patterns relative to tetradecane, it is clear that the high level of scattering intensity (white colour) extends on a wider region passing from t = 0.6 ms to t = 0.8 ms. Thereafter, this region shrinks, disappearing at t = 1.6 ms. From this time onwards, the red and green regions, relative to intermediate scattering intensity, enlarge and reach their maximum extension at t = 2.25 ms. Finally, they contract and completely disappear at t = 3.5 ms.

The lower-half patterns, relative to TD/*a*MN fuel, show the same qualitative behaviour with some peculiar differences. The white region (high scattering intensity) is present for a longer time, up to 1.8 ms, with a continuous decrease of its extension. The red regions (intermediate intensity) are distributed on the smallest region at t = 2 ms, whereas this occurred 0.5 ms earlier for tetradecane. This temporal shift is observed also for what concerns the maximum extension of the red region and of its final disappearance. It is of interest to stress that some differences between the two sequences of images appear in the early part of the injection time; therefore, some reasons for the differences in terms of liquid

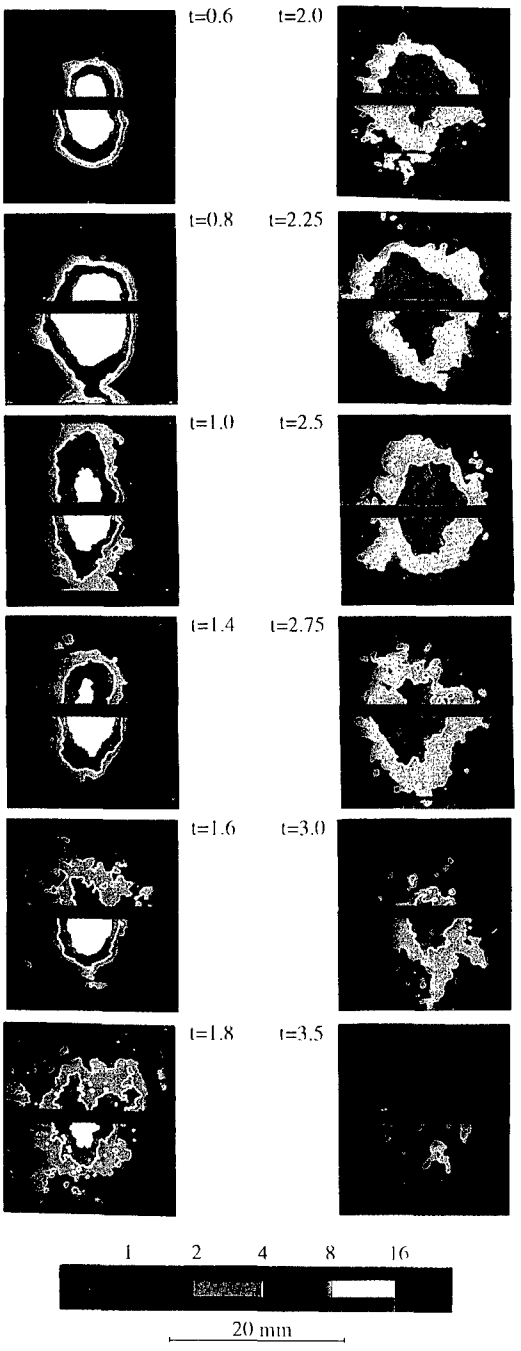

FIG. 1. Vertically polarized scattering patterns recorded at different times after the injection beginning from a cross section of burning spray at 20 mm from the nozzle outlet. The upper-half patterns are relative to tetradecane fuel. The lower half are relative to α-methylnaphthalene/tetradecane fuel.

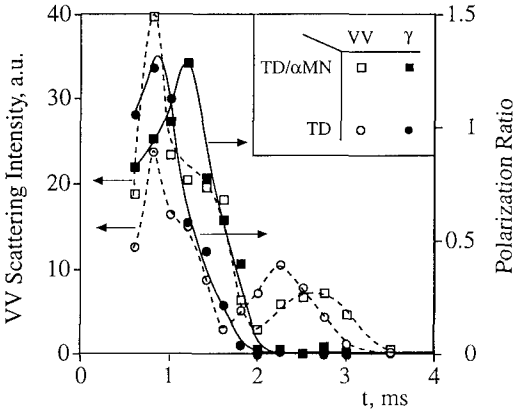

FIG. 2. Temporal profiles of spatial averages of (VV) vertically polarized scattering intensity and of (γ) polarization ratio for conditions reported in Fig. 1.

fuel distribution have to be taken into account. This can be attributed to the difference of the two fuels in terms of critical pressure, which may affect the rate of the evaporation process. This point (evaporation in supercritical conditions) is still not clear, and the literature is very poor in this field so that this is only a tentative explanation, and further study should be performed in order to clarify it.

The difference between the scattering patterns of the two fuels can be better described with the aid of Fig. 2. The dashed lines in the figure are the fitting of scattering values obtained by the spatial average of the intensity patterns reported in Fig. 1. The profiles show the presence of two maxima: the first one occurs at the same time for both fuels, and on the contrary, the second one is delayed of approximately 0.5 ms in the case of TD/αMN fuel with respect to TD injection.

In order to qualify the nature of the scatterers responsible for such behaviour, additional measurements of the polarization ratio (γ) were done and are represented in Fig. 2 by continuous lines. This measurement is obtained by deriving a ratio for the horizontally and vertically polarized scattered light, averaged according to the procedure described above. The polarization ratio profiles show only one maximum for each fuel centered at 1.0 and 1.2 ms, respectively. Thereafter, the polarization ratio continuously decreases down to a value around $3 \cdot 10^{-2}$, which keeps quite constant at a time longer than 2 ms. It is well known that such low values of the polarization ratio are due to scatterers with a size (D) smaller than the wavelength (λ_0) of the incident light ($D < 0.1\ \lambda_0$) [7,8], which will be named soot.

The average scattering intensities, reported in Fig. 3 for the four experimental conditions mentioned earlier, are representative of the temporal evolution of soot. The measurements are plotted as a function

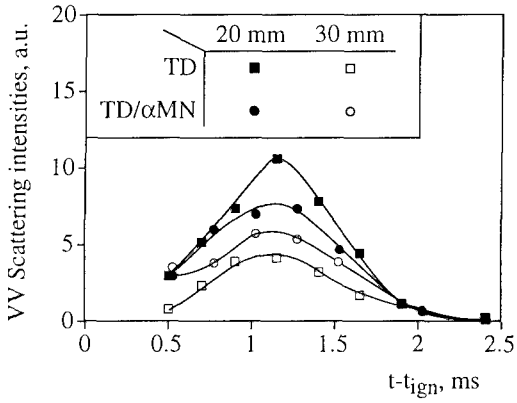

FIG. 3. Spatial averages of vertically polarized scattering intensity for two fuels and two cross sections of the burning spray vs time delay with respect to self-ignition time.

of the time delay Δt with respect to the ignition time ($\Delta t = t - t_{ign}$). They show common trends, since the four curves have one maximum, approximately located at $\Delta t = 1.1$ ms, and decrease in a nearly symmetric way on both sides in a temporal range of 1.5 ms.

Furthermore, the scattering intensity measurements in the soot region are lower at $z = 30$ mm with respect to those at $z = 20$ mm for both fuels and the measurements relative to the TD/αMN mixture are intermediate between those at $z = 20$ and 30 mm relative to TD.

Concentration profiles of the fuel and main combustion products were measured by sampling at 20 and 30 mm for the two fuels. Figure 4 reports, in the upper part, the mass fraction of the total carbon collected at 30 mm at different times from the fuel injection and, in the lower part, the development of the oxidation process expressed as the contribution of unburned fuel, CO and CO_2 to the total carbon.

The carbon mass fraction (Y_C) of the species collected at 30 mm for the two fuels increases at the beginning of the process, reflecting the arrival of the fuel spray in the sampling region. After 1 ms, a flat maximum of the Y_C is reached (Fig. 4a). In this phase, the total carbon remains constant, but unburned fuel, which is the main part of the sampled carbon, sharply decreases, leaving the place to CO, CO_2, and pyrolytic products. Thereafter, Y_C decreases for both fuels. CO is first formed and reaches a maximum value at 1.4 and 1.8 ms in TD and TD/αMN combustion, respectively. CO_2 is already formed at the ignition, but a complete oxidation degree is reached later on at 3.5 ms.

It is noteworthy that a smaller amount of CO and a larger formation of CO_2 have been detected in TD/αMN combustion. This effect is clearly shown in Fig. 5, where the ratio between the CO and CO_2

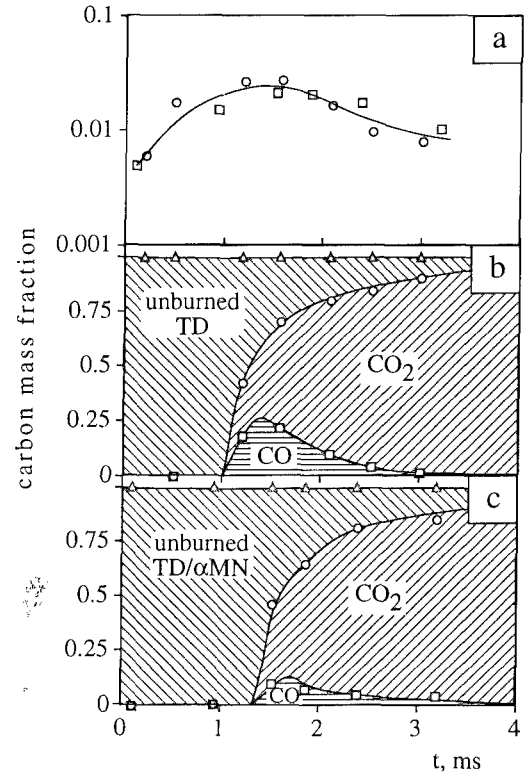

FIG. 4. Mass fractions at different times after the injection beginning for two fuels (tetradecane and α-methylnaphthalene/tetradecane): (a) total carbon mass fraction, Y_C (○: TD; □: TD/αMN); (b) and (c) □: CO mass fraction divided by the total mass fraction, Y_{CO}/Y_C; ○: CO + CO_2 mass fraction divided by the total carbon mass fraction, $(Y_{CO} + Y_{CO_2})/Y_C$; △: CO + CO_2 + fuel mass fraction divided by the total carbon mass fraction, $(Y_{CO} + Y_{CO_2} + Y_{fuel})/Y_C$.

concentrations measured at 20 and 30 mm for the two fuels are reported at different times from the fuel ignition. The CO/CO_2 ratio is higher for the aliphatic fuel with respect to the aromatic one and decreases at increasing times from the ignition, reaching very low values after about 1.5 ms for both fuels and distances from the nozzle.

Discussion

The use of two fuels that have similar boiling and critical temperatures is convenient in order to minimize physical aspects (atomization, dispersion, and evaporation) on the whole combustion process. Even though some differences in the fuel liquid distribution have been detected in the early part of the process, the evaluation of the possible chemical effects is significantly simplified.

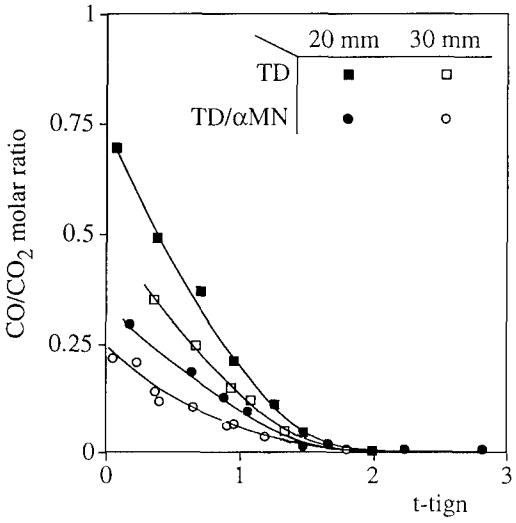

FIG. 5. CO/CO_2 molar ratio vs the time delay after ignition time for the two fuels and the two sampling locations.

Tetradecane has a cetane number of 93, and αMN has a cetane number of 0 so that aromatic mixture tested in this study has a cetane number of about 47, which is roughly half that of tetradecane. This results in a much longer ignition delay for the aromatic fuel [9,10]. The change of ignition delay greatly varies the fuel-air mixture and the jet penetration at the time of ignition since the fuel is mixing with air throughout the ignition delay time. Ideally, this study could be performed more systematically with two fuels with the same cetane number and different chemical composition and afterwards with two fuels with the same chemical composition and different cetane number. However, as a preliminary attempt to analyze soot oxidation in diesel-like conditions, it seems convenient to shorten the experimental work and to test whether some invariance of process timescales can be identified in order to draw the tentative conclusion of independence of these timescales on the fuel characteristics.

Furthermore, the relatively high ignition delay, typical of high-pressure flow reactor and bomb experiments, suggest to use test fuels with a very high cetane number in order to approach as much as possible to engine performance.

The self-ignition time of the TD/αMN mixture (t_{ign} = 1.5 ms) is longer than that of TD (t_{ign} = 1.1 ms) so that the whole chemical evolution is shifted of the same amount of time (0.4 ms). For this reason, the scattering intensity profiles attributed to soot (Fig. 3) and the CO/CO_2 ratio profiles (Fig. 5) have been reported starting from the ignition time so that the aforementioned effect can be disregarded in the data analysis. Both temporal profiles of the scattering intensity and the CO/CO_2 ratio show a common behaviour not dependent on the distance from the nozzle outlet and the fuel aromaticity. This means that similar parallel processes have to be envisaged. In particular, the independence of the maxima positions in Fig. 3 on the distance means that convection of the burning mixture along the spray axis is negligible. In fact, if this were the case, the maximum position at z = 20 mm should be shifted at z = 30 mm of a time $t^* = \Delta z/v_{mixture}$. The observed invariance of the maxima in Fig. 3 can be assessed with an accuracy of 0.1–0.2 ms so that an average mixture velocity in the order of 50–100 m/s has to be hypotized to explain the invariance itself. This average velocity was not observed even in the early injection time [1] when the momentum of the liquid phase ensures the greatest level of velocity during the whole injection time. Therefore, the temporal profiles of the scattering intensity in Fig. 3 have to be justified only on the ground of local transformation of the scatterers' characteristics or of their dilution due to the stirring process between soot-laden regions and unladen contiguous ones. The second possibility has to be considered only as secondary contribution. In fact, dilution is linearly proportional to any conservative variable. Figure 4a shows that the carbon mass fraction (a conservative variable) is only halved passing from the maximum to the final measured value (Δt = 2 ms); therefore, soot concentration (under the hypothesis that it does not undergo any transformation) should also be halved. This is not the case, since in Fig. 3, the scattering intensity reaches a very negligible value in the final part of the process; i.e., it decreases of more than one order of magnitude. Therefore, the only possible explanation for the temporal evolution of scattering intensity is the soot transformation. This is usually thought in terms of inception, growth, coagulation, and oxidation [11]. The first three stages are, of course, responsible for the increase of scattering intensity, whereas the only stage that justifies its decrease is the oxidation [12]. This statement is trivial for the inception, growth, and oxidation process, whereas it should be explicitly stated that the coagulation is a process that changes contemporaneously the soot size (D) and concentration (N). Therefore, the scattering signal that is proportional to ND^6 is affected in an opposite way by the simultaneous increase of D and the decrease of N. Anyway, since ND^6 can be considered as the product of soot volume fraction ($\Phi = ND^3$) and D^3, the scattering signal increases when only coagulation occurs (constant Φ and increasing D^3). This dependence of scattering intensity on D^6 can cause some problems in the analysis of single images, since small particles are scarcely detected due to the small dynamic range of the intensifier [4]. In the ensemble average of space-integrated measurements, reported here, this means only an underestimation of soot volume fraction in the early inception period where it

is likely to detect small soot particles. Therefore, this possible inaccuracy does not affect significantly the oxidation time, which is of primary interest in the following discussion. In summary, the temporal evolution of the scattering intensity of Fig. 3 can be interpreted as a soot formation and coagulation followed by a final soot oxidation phase.

The first stage before the inception takes 0.5 ms, the second one (i.e., formation, inception, growth, and coagulation) takes 0.5 ms again, and the final one (soot oxidation) develops in approximately 1 ms. All these characteristic times are nearly equal for both fuels, whereas the maximum scattering intensities are different according to ignition location and fuel type.

Another interesting feature deducible from the results in Fig. 4 is the difference between the two oxidative routes of the fuels. It consists in a more direct CO_2 conversion of the TD/*a*MN mixture passing through a lower concentration of CO. This difference could be attributed to the different ignition delays of the fuels, but this hypothesis has been excluded, analyzing fuels having the same ignition delays but different aromatic contents [13]. Thus, the difference has to be related to the different routes through which aliphatic and aromatic hydrocarbons are oxidized. The oxidation of aliphatic fuels proceeds, first of all, through the formation of small fragments of hydrocarbons, which further oxidize to CO by means of an OH radical attack. This reaction rate is about one order of magnitude higher than the reaction rate of CO oxidation to CO_2. This is deeply explained in the review of Westbrook [14] in which the comparison of the reaction rate, even at a lower temperature than that of the diesel-like condition, has been evaluated for both categories of reactions.

This means that the large production of light hydrocarbons in aliphatic hydrocarbon oxidation hinders the transformation of CO in CO_2. On the contrary, the oxidation of an aromatic hydrocarbon progresses through the direct formation of CO and cyclic unsaturated hydrocarbons. Thus, CO, in the presence of smaller quantities of hydrocarbons, can be suddenly oxidized to CO_2, and this justifies the increase of CO_2 concentration found in consequence of the increase of fuel aromaticity.

Finally, it is noteworthy that the ratio CO/CO_2 (Fig. 5) develops in a similar way for all the conditions independent of fuel type and sampling position when the values are reported against the time delayed with respect to the self-ignition time.

The CO/CO_2 ratio is lower for the TD/*a*MN injection, but for both fuels, CO is nearly negligible at $t - t_{ign} = 1.5$ ms. This time delay correlates with that one after which soot oxidation occurs. This is a noticeable correlation, since it is well known that both CO [14] and soot [12] are involved in oxidation reactions with the same species, i.e., OH radicals, and that it is reasonable to evaluate the reaction rate of the first reaction (CO + OH) [14] to be faster than the other one (soot + OH) [12]. Therefore, soot oxidation proceeds very efficiently only when CO is depleted.

It has to be stressed that the invariance of the characteristic times of soot formation and oxidation in terms of both chemical composition and ignitability is a posteriori confirmation of the very weak dependence of the pyrolysis process on both fuel characteristics (chemical composition and ignition delay). In fact, while it is possible that the different pyrolysis characteristic time can be attributed to only one fuel characteristic, it is very unlikely that the timescale invariance can be attributed to a so peculiar combination of opposite effects.

These considerations are specific of the combustion process studied in this paper in which the soot clouds are distributed throughout the combusting plume. In fact, it can be speculated that the soot presence also in the central part of the burning jet entails the proximity of the oxidation regions around relatively small clouds of soot [15].

This could also be the case of the final part of the combustion process of heavy duty diesel engines in which the injected fuel quantity is comparable to that used in our work. In this case, soot is clearly distributed also in the core of the diesel combustion process, or it is present in relatively small concentration behind the front of the burning jet [4,5].

It is doubtful whether the same arguments can be considered sound for diesel combustion conditions that yield the preferential location of both the self-ignition process [16] and the soot formation [2,3] within an extended pyrolysis region on the spray tip. However, it seems appropriate to refrain from further considerations, because it is possible that the detection of soot clouds only on the tip of the spray can be due to the Mie image [2], being bias to regions of large particles [4].

Conclusions

It has been shown that, for experimental conditions comparable to those occurring in the combustion process of direct-injection diesel engines, the characteristic times of soot inception, formation, and oxidation are in the order of 1 ms and that each of them is nearly independent on the fuel aromaticity, as expected in diffusion-controlled conditions.

Furthermore, it is important to stress that, when a suitable air-fuel mixing is allowed (as in the present experiment), not only the carbon conversion to soot is very low [1], but also soot oxidation is very efficient.

In respect to the last point, it is noteworthy that the soot oxidation time (~1 ms) measured in this work is shorter than that reported in the literature (~5 ms) for diesel engines [17]. This can be attributed to different diffusion times in the mixing process, as mentioned before.

A final conclusion concerns the observed correlation between the CO depletion and the beginning of soot oxidation. This is the first presumptive evidence that, in diesel combustion, the carbon particulate consumption proceeds through OH attack of soot rather than through the slower reaction with O_2 as oxidant [18]. It will be of great interest to confirm with other evidence this result because it shows that oxidation of fuel, as well as of soot, can progress along the same diffusive structure. Therefore, particular care should be devoted to enhancing turbulence only in the first part of the combustion process, when it controls the air-fuel mixing: otherwise, turbulence could quench the soot oxidation process in the final part of the diesel spray combustion.

It is mandatory to stress that this comment can be sound only in the case in which the soot clouds are distributed on relatively small length scales, as it supposed to occur in this diesel combustion process: therefore, it can be a practical suggestion only in this case. Otherwise, it is possible to obtain the opposite result. In fact, if the same diffusive structure (for oxidation of both fuel and soot) is quenched at the end of combustion, the only possible way of oxidizing soot is to increase the turbulent mixing before temperature decrease during the expansion period.

Acknowledgment

This work was funded by the Commission of the European Communities within the frame of the JOULE Programme within the contract JOU2-CT92-0055.

REFERENCES

1. Ragucci, R., Cavaliere, A., Ciajolo, A., D'Anna, A., and D'Alessio, A., *Twenty-Fourth Symposium (International) on Combustion*, The Combustion Institute, Pittsburgh, 1992, p. 1565.
2. Young-Ho, W., Kamimoto, T., and Kosaka, H., SAE Paper 920114, 1992.
3. Chang, Y. J., Kobayashi, H., Matsuzawa, K., and Kamimoto, T., *International Symposium on Diagnostics and Modeling of Combustion in Internal Engines*, COMODIA 85, Tokyo, The Japan Society of Mechanical Engineers, 1985, p. 149.
4. Dec, J. E., SAE Paper 920115, 1992.
5. Espey, C. E., and Dec, J. E., SAE Paper 930971, 1993.
6. Cavaliere, A., Ragucci, R., D'Alessio, A., and Noviello, C., *Combust. Sci. Technol.* 77:73 (1991).
7. D'Alessio, A., Beretta, F., and Cavaliere, A., *Combustion Measurements* (N. Chigier, Ed.), Hemisphere, New York, 1991, p. 301.
8. Beretta, F., Cavaliere, A., and D'Alessio, A., *Twentieth Symposium (International) on Combustion*, The Combustion Institute, Pittsburgh, 1984, p. 1249.
9. Westbrook, C. K., *International Symposium on Diagnostics and Modeling of Combustion in Internal Engines*, COMODIA 90, Kyoto, The Japan Society of Mechanical Engineers, 1990, p. 11.
10. Hoskin, D. H., Edwards, C. F., and Siebers, D. L., SAE Paper 920109, 1992.
11. Wagner, H. Gg., *Seventeenth Symposium (International) on Combustion*, The Combustion Institute, Pittsburgh, 1979, p. 3.
12. Neoh, K. G., Howard, J. B., and Sarofim, A. F., *Particulate Carbon Formation during Combustion* (D. C. Siegla and G. W. Smith, Eds.), Plenum Press, New York, 1989.
13. Cavaliere, A., Ciajolo, A., D'Anna, A., D'Alessio, A., and Ragucci, R., *Second International Conference on Fluidmechanics, Combustion, Emission and Reliability in Reciprocating Engines*, Capri, Italy, 1992, p. 167.
14. Westbrook, C. K., and Dryer, F. L., *Prog. Energy Combust. Sci.* 10:1 (1984).
15. Cavaliere, A., Ragucci, R., D'Alessio, A., and Noviello, C., "Analysis of Dense Sprays through Two-Dimensional Laser Light Scattering," paper presented at ILASS-EUROPE, Rouen, France, March 28–29, 1989.
16. Sato, J., Konishi, K., Okada, H., and Niioka, T., *Twenty-First Symposium (International) on Combustion*, The Combustion Institute, Pittsburgh, 1986, p. 695.
17. Kamimoto, T., Matsuoka, S., and Miyairi, Y., *I. Mech. E.* C103/82:259 (1982).
18. Neoh, K. G., Howard, J. B., and Sarofim, A. F., *Twentieth Symposium (International) on Combustion*, The Combustion Institute, Pittsburgh, 1984, p. 951.

COMMENTS

Christoph Espey, The Pennsylvania State University, USA. 1. The model fuels used in this study not only differ in the fraction of aromatics in the fuel, but also in the cetane number. In what way does the difference in the cetane numbers of both fuels affect your observations?

2. Did you consider using fuels with identical cetane numbers but different fractions of aromatics?

3. What causes the relatively long ignition delay in your work?

Author's Reply. Tetradecane has a cetane number of 93 and the aMN has a cetane number of 0, so the aromatic mixture, tested in this study, has a cetane number about 47, which is roughly half that of tetradecane. This results in a much longer ignition delay for the aromatic fuel [1,2]. The change of ignition delay greatly varies the fuel-air mixture and the jet penetration at the time of ignition since the fuel is mixing with air throughout the ignition delay time. Ideally, this study could be performed more syste-

matically with two fuels with the same cetane number and different chemical compositions and afterward, with two fuels with the same chemical composition and different cetane numbers. However, as a preliminary attempt to analyze soot oxidation in diesel-like conditions, it seems convenient to shorten the experimental work and to test whether some invariance of process time scales can be identified in order to draw the tentative conclusion of independence of these time scales on the fuel characteristics.

Furthermore, the relatively high ignition delay suggests keeping a very high cetane number fuel to approach engine performance as much as possible.

The longer ignition delay with respect to that measured in real diesel engines also has been measured in similar model experiments [2,3]. This difference can be attributed to physical factors, like lower temperature of fuel due to the cooling of the injector tip [2] and the lower mixing level in nearly quiescent conditions in respect to turbulent conditions of actual diesel engines.

REFERENCES

1. Westbrook, C. K., *International Symposium on Diagnostics and Modeling of Combustion in Internal Engines, COMODIA 90*, Kyoto, The Japan Society of Mechanical Engineers, 1990, p. 11.
2. Hoskin, D. H., Edwards, C. F., and Siebers, D. L., SAE Paper 920109, 1992.
3. Hiroyasu, H., *International Symposium COMODIA 85*, 1985, p. 53.

•

N. Peters, Institut fur Technische Mechanik, Germany. Your explanation of the beginning of soot oxidation after depletion of OH by CO appears questionable to me. I would think that the burnout of CO increases the temperature and thereby the radical level. This will increase surface oxidation reactions of all kinds.

Author's Reply. I would be cautious to give any conclusive explanation concerning this point because this is the first paper in which an experimental correlation between CO depletion and the beginning of soot oxidation is reported in diesel-like conditions. Therefore, we have referred to this correlation only as a "presumptive evidence" of soot oxidation by OH. I think we agree on this point, i.e., that OH radicals also are the main oxidants of soot in this peculiar diesel condition and that this is the main result related to the CO depletion. However, the explanation you give on why such depletion is an evidence of soot oxidation by OH is a further (if not the only) contribution to the clarification of this effect. Therefore, the coauthors and myself accept it as a significant explanation.

Twenty-Fifth Symposium (International) on Combustion/The Combustion Institute, 1994/pp. 175–181

THE DROPLET GROUP MICROEXPLOSIONS IN WATER-IN-OIL EMULSION SPRAYS AND THEIR EFFECTS ON DIESEL ENGINE COMBUSTION

H. Z. SHENG, L. CHEN,* Z. P. ZHANG* AND C. K. WU
Institute of Mechanics
Chinese Academy of Sciences
Beijing, China 100080

AND

C. AN AND C. Q. CHENG
Department of Vehicle Engineering
Beijing Institute of Technology
Beijing, China 100081

To clarify the combustion mechanism of water-in-diesel fuel emulsion sprays and to evaluate the possible benefit of emulsions in practical usage, combustion bomb experiments, dynamic engine tests, and computer simulation were carried out, and some useful conclusions have been reached.

The droplet group (lump-fashioned) microexplosions in water-in-diesel fuel emulsion sprays on an eddy-size scale during the atomization, evaporation, and combustion processes in a high-pressure, high-temperature bomb were observed with a multipulsed, off-axis, image-plane, ruby laser holocamera and a high-speed camera. The explosions eject droplet fragments from the spray region to several millimeters away, improving the fuel-air mixing process and speeding up the flame propagation. A no-water layer formed by a Hill vortex was also observed in emulsion droplets. The ambient temperature has the most important influence on the occurrence and violence of the microexplosion.

Road-load–simulation engine tests were carried out on a dynamic engine test bed. The experimental results show that emulsion fuels have no significant influence on fuel consumption and reduce engine torque if no adjustment is made for the injection system, but that smoke emission is much improved when emulsion fuel is used. The combustion characteristics and the rate of heat release are also analyzed to reveal the difference between emulsion and diesel fuel.

The relationships between the optimum water percentages and fuel consumption under various operating conditions were analyzed by numerical combustion modeling.

Introduction

Eighty years ago, water was first introduced into engine cylinders to increase engine output [1]. Since then, much attention has been paid to the preparation and use of water-in-oil (w/o) emulsified fuels with/without stabilizer, to improve the engine efficiency and exhaust emissions, or as safety fuels [2–7]. Microexplosion was first observed in 1965 [8]. Many questions cannot be well answered by the existing knowledge, since previous fundamental research on emulsions mainly emphasized droplet microexplosions at room pressure and the results from engine tests were often contradictory.

Do microexplosions take place in diesel engine cylinders? Which is the key factor controlling the emulsified fuel combustion, microexplosion or water-gas reaction? What are the detailed features of the explosion in spray combustion? Is the explosion strong enough to improve the combustion process? How can the microexplosion of emulsified fuels be effectively used in engines? Why have positive and negative energy saving been observed in engine tests? The interaction of droplets in sprays, the droplet size, the ambient pressure, and the heating history have significant effects on the combustion process, so the microexplosion in dense emulsified sprays under diesel engine combustion conditions needs further study for clarifying these issues.

In order to evaluate the potential energy saving by the use of emulsified fuels on a large scale, research was started several years ago to understand the mechanism of the microexplosion in sprays and its application in engines. In order to link the broken chain between droplet combustion and engine application for emulsions, experiments in a combustion bomb, dynamical engine tests, combustion

*Formerly Graduate Student at the Institute of Mechanics, Chinese Academy of Sciences.

modeling, and theoretical work were carried out [9,10,11].

The "lump-fashioned" droplet group microexplosion (in earlier publications, droplet group microexplosion was called "lump-fashion microexplosion") and a nowater layer in emulsion droplets were observed in the bomb by a multipulsed ruby laser holocamera [9]. The explosions were strong enough to expand the spray region and speed up flame propagation, which was verified by high-speed photography [10]. The road-load–simulation engine tests show no significant effects on energy saving by using emulsion, but the smoke can be reduced by 30%. The modeling reveals the combustion features and the optimum water percentage in emulsion for different operating conditions. The questions mentioned above are mainly answered by this series of work.

Microexplosion in Sprays under Diesel Engine Conditions

The early fundamental research was focused on the combustion of either isolated droplets or arrays of single droplets (h = 0.3–1.0 mm) suspended on quartz filaments or fine thermocouples under atmospheric pressure. Since the suspending filaments may be particularly detrimental to the study of combustion characteristics of evaporating emulsions, a droplet generator was employed to generate small droplets floating in an upward heated gas stream [12]. The internal phase size (the size of the dispersed phase in emulsion) may affect microexplosion [13]; the higher cylinder pressure may suppress the occurrence of microexplosion [14]. Emulsion sprays were macroscopically observed by high-speed schlieren photography in a combustion bomb (Zhejiang University, China). The theoretical work was also carried out based on the experimental results [15–17], even for a multicompound liquid [18].

Previous work on fuel spray research [19] emphasized the spray shape, penetration, and entrainment using hot-wire anemometer, particle tracing, high-speed photography, single-flash photography, instantaneous microphotography, schlieren photography, shadowgraph, Fraunhofer diffraction particle analyzers, and single-pulsed Gabor laser holography. However, these methods cannot measure the droplet velocity and trajectory and the microexplosion of the micron-sized moving particles in sprays, since the measurement needs very high resolution in a large field of view.

To observe the very weak diffraction from small moving droplets in a spray inside the high-pressure bomb, a multipulsed, off-axis, ruby laser holocamera was employed in this work. The holocamera can produce four single-mode laser pulses of 50 mJ at 30-ns pulse width. The pulse interval can be adjusted from 5 to 100 fs in 1-fs steps. The pressure drop in the injector was used as the synchronizing signal to trigger the laser beam after a 0.8–6.5-ms delay (controlled by a timer). The laser beam at first was split into an object wave and a reference wave by a splitter, and then the reference wave was expanded and collimated to 90 mm in diameter. The object wave was 50 mm. Two quartz windows of 48 mm in diameter with high optical quality were used as the optical path of the bomb. Passing through the bomb, the beam was premagnified up to 3.5 times with an h = 22 mm high-quality convex lens located between the bomb and the image plane, and recorded on a holographic plate located at the image plane. To avoid speckle noise and obtain homogeneous illumination in the field of view, a convergent white light beam was employed to reconstruct the 2D images by a 35-mm single lens reflex (SLR) camera. To verify the effects of the microexplosion, a series of high-speed photographic tests were made in the bomb under diesel engine combustion conditions with a 16-mm HYSPEED camera.

TABLE 1
Testing conditions in combustion bomb

Environment in bomb	
Pressure (MPa): 0.1, 2.4, 3.2, 4, 4.5, 5	
Temperature: 293, 723, 733, 753, 773, 823, 873, 923 K	
W/O emulsions	
Water fraction: 0, 10%, 12%	
Internal phase: 2 5 μm	
Viscosity: 5 centistoke at 293 K	
Holography (Nitrogen in bomb)	
Laser energy: 50 mJ/pulse	
Pulse width: <40 ns	
Pulse numbers: 1, 2, 3, 4	
Pulse interval: 50 μs, 100 μs	
High-speed photography (Fresh air in bomb)	
Focal length: 100 mm	
Aperture: f/2.3	
Film: black/white, ISO 400	
Camera speed: 3000 PPS	

The testing conditions simulate the cylinder pressure and temperature (Table 1, refer to Refs. 9 and 10). It is worth mentioning that a thermoisolating watercooling jacket covers the exposed part of the injector to keep the nozzle temperature under 353 K to prevent the evaporation of the water in emulsion before injection.

Droplet Group Microexplosions in Emulsion Sprays:

The droplet group microexplosions take place in eddy scale near the outer layer of the emulsion sprays (Fig. 1). The pictures taken at different moments show various strengths of the microexplosions.

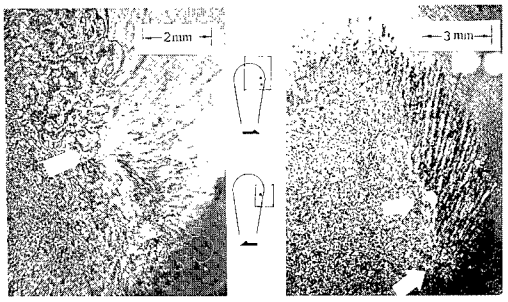

FIG. 1. Droplet group microexplosion of in w/o emulsion sprays; arrows point out the explosion centers (12% water, 773 K, 3.2 MPa, 3 × 100 fs, 2.3-ms delay).

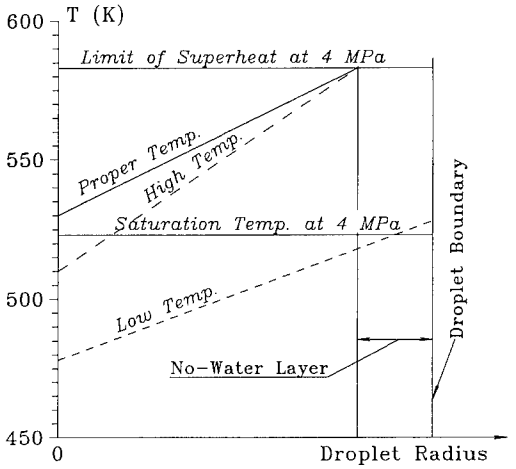

FIG. 2. The influence of different ambient temperature on droplet heating process and temperature gradient.

Lump-shaped flames were also observed by high-speed photography. The droplet group microexplosion is strong enough to eject fragments of torn droplets to a distance several millimeters away from the spray boundary at much higher speed, greatly expanding the spray head and spray angle, improving air-fuel mixing, and causing the flame edge to become unclear and irregular [10].

Perhaps the droplet group microexplosion occurs mainly in the turbulent eddy in which the droplets more or less have homogeneous size, similar heating history, and superheated state. If a droplet is exploding, the pressure wave may induce all the droplets in the same eddy to explode, an avalanche of microexplosions of droplet group. Different eddies have different sizes and different superheated states, so the explosions are also very different from one to another. The explosion region is near the spray head and outer layer, where the gas temperature is high enough and the droplets go through sufficient heating time to be superheated. Because of the explosion in the droplet group, the water fraction in the range of 8–12% has no significant influence on the violence of the explosion. No explosion was observed in the higher density, lower-temperature spray core.

If the ambient temperature is not high enough (733 K in the test), the water dots (internal phase of w/o emulsion) in the droplets will not be superheated and will evaporate and vanish before being heated into superheated state, and no microexplosion takes place (Fig. 2). If the ambient temperature is proper (773 K), all the water dots in droplets rapidly go over the saturation temperature (523.5 K at 4.0 MPa) and into a superheated state, a pseudo-stable state, and vaporize and explode at the same time when the outer water dots achieve the limit of superheat (583 K at 4.0 MPa). This tears up the droplet and greatly expands the spray region. If the temperature is too high (823 K), the heat transfer between gas and droplets is strong enough, some water dots near the outer layer are over the limit of superheat, but central water dots are not in superheated state in this case, the explosion occurs earlier and closer to the injector, and the violence of explosion is not very strong since all water dots do not explode at the same moment.

The torn droplets fly much faster in a lower gas density, causing a larger flame angle and stronger microexplosions. If the gas density is constant, gas pressure may have little effect on explosion violence. The injection pressures between 18 and 24 MPa have little effect on atomization and microexplosion of emulsions.

Droplet group microexplosion phenomena can be supported by high-speed photography[10], by which the bright diesel flame is more homogeneous, more yellow in color, and lasts a longer period than the emulsions flame; the ignition delay of emulsions is longer than diesel, but the flame propagation is much faster after ignition, and ignition occurs at multiple points simultaneously.

No-Water Layer in Emulsion Droplets:

When the gas in the bomb is heated up to 700 K, a comet-shaped vapor cloud surrounds the droplet, and water dots (1 fm) concentrate in the central part of the droplets. A no-water layer can also be recognized near the surface of the droplets from 10 times remagnified reconstructed holographs. The image is conceptually shown in Fig. 3.

The velocity difference between gas and droplets causes a uniaxially symmetrical shear stress, which reduces droplet speed, induces a Hill vortex (internal circulation) in the droplets, rotates the droplet, and then forms a rapidmixing layer. In this layer, the water dots will be moved onto the droplet surface and vanish before the water dots are heated up to the saturation temperature, favoring the no-water layer formation because of the low evaporation and dif-

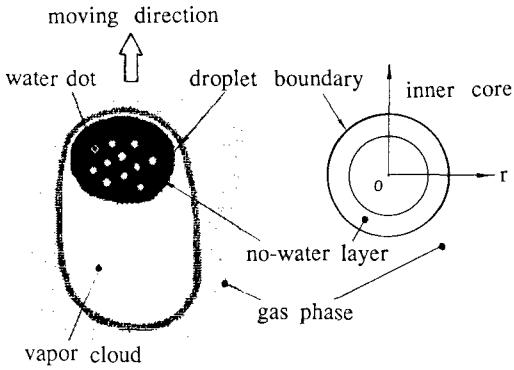

FIG. 3. The computer-treated image of evaporating w/o droplet and no-water layer model.

fusion rates of oil vapor. The circulation is not strong enough in the inner core to homogenize the temperature field and the water dot distributions in the whole droplet since new no-water layer still exists if the droplet is still moving. The water dots in the core are easily heated up to the superheat state if the ambient temperature is proper. When the water dots near the outer layer achieve the limit of superheat and evaporate, all the superheated water dots also evaporate and expand rapidly at the same moment, tearing up the fuel droplet—the microexplosion. The inhomogeneous situation is more easily kept and the microexplosion takes place more easily in big droplets than in small ones.

The no-water layer concept is very important in explaining the microexplosion of emulsion droplets. A no-water layer model [11] based on the Hill vortex analysis by Prakash and Sirignano [20] agrees very well with Aggarwal's work for hexane, decane, and hexadecane under the same operating conditions, and experimental data for emulsions. The system is treated as a sphere containing the inner core of the droplet as a homogeneous phase, with the no-water layer and gas phase around the droplet (Fig. 3). The model shows that the initial droplet diameter is another important factor in the microexplosion. If the initial droplet is too small, the residual water mass is too low or will even vanish before the droplet is heated up to the saturation point, and the explosion can hardly be observed in this condition. This result implies that the microexplosion effect may be helpful in the case of an old injection pump with lower injection pressure, where the atomization has deteriorated.

It may be conjectured that, the more the water in the emulsion, the larger the explosive energy will be. However, if the initial diameter of the emulsion droplet is held constant, the emulsion with larger water fraction will lose more water as a result of the existence of the vortex and no-water layer, thus lowering the surface temperature. The additional water gives the spray more initial momentum to improve the air-fuel mixing process. These factors may have opposite influences on the effects of the microexplosion on combustion. In our experiments, the water fraction has a weak influence on the occurrence of the microexplosion.

Engine Test under Simulated Road-Load Conditions

The effect of microexplosions on engine performance is fully dependent on the application. Many well-performed steady-state engine tests show that the energy saving is less than 5% for most diesel engines. The steady-state tests may be very different from road running: 20–30% benefits during road running were reported by many regional sources in China. To evaluate the potential benefits for emulsion applications, a large number of expensive road tests for different road conditions and different engines should be done because of the complicated influences. However, the results can hardly be repeatable and reliable. Therefore, a series of steady-state and road-load–simulation engine tests have been recently performed for this purpose on an AST-386 microcomputer-controlled dynamic engine test bed EDST-2 with a Siemens 200-kW DC electric dynamometer, which can run various road routines and measure engine parameters automatically.

The engine test bed very accurately controls engine torque (<1%) and speed (<10 rpm). To analyze the rate of heat release (ROHR), the cylinder pressures were recorded by AVL QC42D piezoelectric transducer, Kistler 5004 charge-voltage convertor, PEI encoder, and IBM microcomputer with PEI ECA911 software package. An improved compound band reject filtering (CBRF) filtering method [21] was employed to eliminate the effects of measurement passage on pressure curves for ROHR analysis. For evaluating the effects of emulsions on exhaust emission, both liquid and solid particles were measured in dynamic engine tests by a Hartridge MK3 Smokemeter, which has very fast response. For comparison, a Bosch Smokemeter was employed in the steady-state engine tests.

The microexplosion may have more effect on combustion in direct injection engines with a bowl combustion chamber, in which the mixing process occurs mainly in the bowl space, than on other types of diesel engine. The engine employed in this test is a V6 engine with cylinder bore/stroke of 150/150 mm, compression ratio 16.8, rated engine power 215 kW at 2600 rpm, and shallow bowl combustion chamber. The load characteristics of 1100–2100 rpm and the speed characteristics of 40 and 80% load were designed for steady-state engine tests.

The ECE-15, SAE J35 SEP88, free acceleration for smoke evaluation, 6-mode cycle (Chinese Stan-

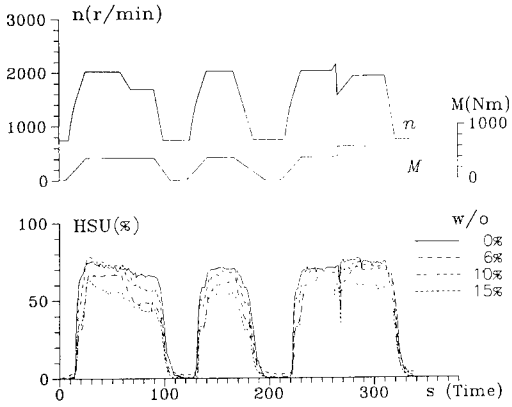

FIG. 4. Engine torque, speed, and smoke measurements under No. 1 Bus routine (Me-engine torque, HSU-Hartridge Smoke Unit).

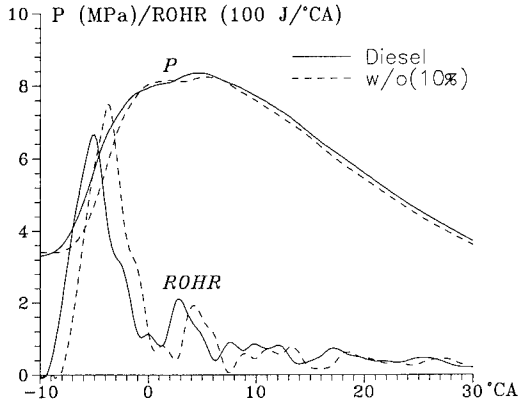

FIG. 5. The cylinder pressure and the rate of heat release (1500 rpm, 750 Nm).

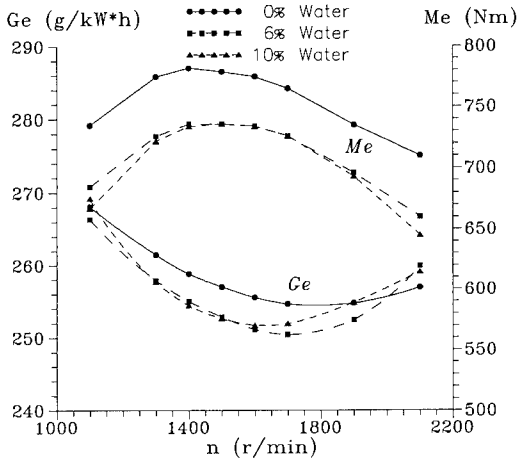

FIG. 6. Specific fuel consumption (water excluded) under engine speed characteristics test (Ge-break specific fuel consumption, Me-engine torque).

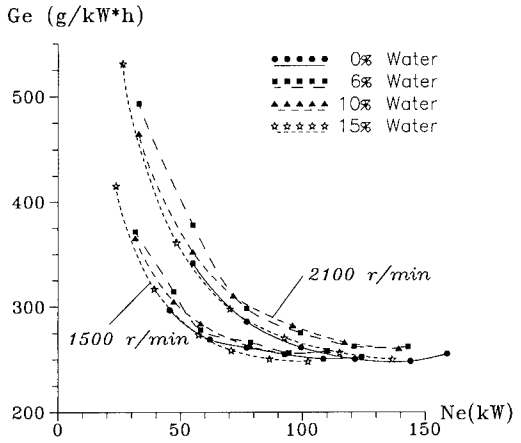

FIG. 7. Specific fuel consumption (water excluded) under engine load characteristics test (Ge-break specific fuel consumption, Me-engine torque).

dard), and Beijing No. 1 bus routines (Fig. 4) were all designed for engine dynamic tests. The No. 1 bus is the busiest bus running along the Chan'an Street across central Beijing, and the total mass of the bus is 19.2 tons with a typical 160-kW direct injection engine. The diesel fuel and emulsions with 6, 10, and 15% water in weight were chosen for all engine tests, since the optimum water percentage is about 10% according to our experiences. The results are summarized as follows.

The engine smoke is at least 30% HSU (Hartridge Smoke Unit) less than diesel fuel, and the water fraction (6–15%) has certain effects on HSU (Fig. 4 shows typical measurements). The water postpones the ignition about 0.2 ms, and the microexplosions change the combustion rate and ROHR (Fig. 5). Energy saving can be obtained under partial load conditions by emulsions, but negative effects may appear under high load conditions because of longer injection periods. The engine performances are a little bit better in the range of 1200–1800 rpm under 80% load (Fig. 6).

Figure 7 and Table 2 show that about 3–5% more energy was consumed by emulsion applications in both steady-state and dynamic engine tests without injection-timing adjustment. According to our previous work (unpublished), the injection timing should be adjusted 2 × CA (crank angle) in advance to obtain 3% average energy saving for emulsions. The exhaust temperature is reduced by the addition of water, especially for high load conditions, and engine torque is also lower since the maximum fueling volume rate is the same as the diesel. It is suggested that injection timing should be adjusted to optimize the engine performance and emissions.

TABLE 2
Fuel consumption in road-load test

	Emulsion/test (g)	Water content (%)	Energy saving (%)
6-Mode	970	0	0
	1065	6	−3.2
	1133	10	−5.1
	1178	15	−3.2
ECE-15	325	0	0
	360	6	−4.1
	370	10	−2.5
	385	15	−0.7
No. 1 Bus	1380	0	0
	1540	6	−4.9
	1570	10	−2.4
	1625	15	−0.1

The dynamic engine test shows that both fuel consumption and exhaust emissions have very good correlation with steady-state tests, which can qualitatively evaluate the emulsion applications if there is no dynamic test bed. For energy saving by emulsion applications, the positive effects are fully dependent upon the engine and operating conditions; 3–5% may be the maximum benefit according to our previous engine tests, this series of engine experiments, and other researchers' reports for well-performed engine tests. Sometimes the influence may be negative if no proper adjustment is made.

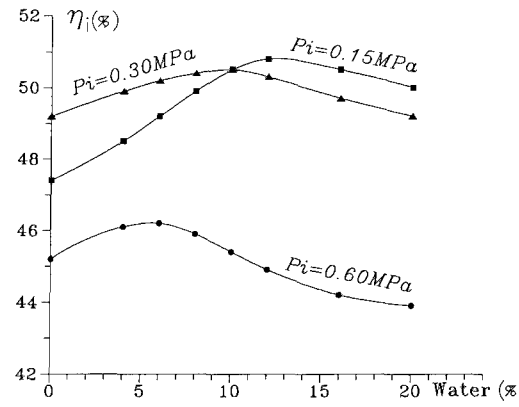

FIG. 8. The relation between water fractions and thermal efficiency (1500 rpm) (*i*-thermal efficiency, Pi-break mean effective pressure).

Computational Simulation of Engine Using Emulsions

A combustion model, which can predict the engine performance under low load conditions [22], was modified for emulsions. This model divides the injected fuel into 30 small packages. Air entrainment, droplet sizes, the evaporation process, and ignition delay in individual packages are calculated according to the transient injection pressure of the packages and then integrated by Duhamel Integral. The physical and chemical properties of the emulsions, ignition delay calculation, and the rates of air entrainment and evaporation were based on the water fraction to simulate the effect of the microexplosion. The simulated operating conditions are as follows: engine speed, 1500–2100 rpm BMEP, 0.13–0.6 MPa; water fraction, 0–20%. The combustion characteristics of emulsions are reasonable.

The higher initial momentum of emulsion sprays and the micro explosions raise the local air-fuel ratio. The combustion rate and engine efficiency, which are more significant under low load conditions where the initial momentum of diesel sprays is not sufficient, also increased. The fuel injection system is designed to match high load conditions, and under such conditions, the emulsion injection stops later. The combustion period is hardly shortened by the microexplosion because of the very large spray region already existing. For an engine at 1500 rpm, the optimum water fraction is 12–16% for idling and 6% for high load conditions (Fig. 8). The highest flame temperature appears later and is lowered by 200–300 K as a result of more abundant air and evaporation of the water in the flame region, which greatly improves the soot and No_x formation but slightly reduces the thermal efficiency. The ignition timing is 2 × CA later than diesel fuel, but combustion fin-

ished earlier. Postponing the injection has less effect on engine efficiency than for diesel fuel, since the microexplosion improves the combustion process.

Conclusions

Experiments using holography and high-speed photography in a high-pressure and high-temperature bomb, dynamic engine tests, and computer modeling were carried out to link the broken chain from the droplet combustion to engine application for emulsions.

Microexplosion is a phenomenon in which the microwater dots in the emulsion droplet are heated into an unstable superheated state and vaporize rapidly, tearing the droplet violently. A no-water layer (rapid-mixing layer) exists near the droplet surface because of the Hill vortex, and many microwater dots exist in the droplet inner core. A microexplosion occurs in a certain temperature range and becomes stronger at a proper ambient temperature. Raising chamber pressure has little effect on the occurrence of the explosion, but the penetration of the torn droplet will be much shorter as a result of higher gas density, which weakens the effect of the explosion.

Droplet group microexplosions in emulsion sprays occur on a turbulence eddy scale near the outer layer and the head of the spray. If the ambient temperature is proper, the explosion possesses enough energy to eject torn droplets to a distance several millimeters away from the spray boundary, improving atomization, evaporation, and air-fuel mixing processes and speeding up flame propagation. Since physical processes of liquid fuel combustion take a much longer time than chemical reaction, the microexplosion can speed up combustion rate and ROHR, raising engine thermal efficiency. Meanwhile, the injection timing must be adjusted, and the proper water fraction for different loads and the internal phase size of the emulsions must be carefully chosen. Emulsions may cause better efficiency under partial load conditions, especially for direct injection and old engines, but negative effects may occur for new engines under high load conditions. Much less soot is formed in emulsion spray combustion, and the engine smoke is at least 30% less than diesel fuel. The water fraction (6–15%) has no significant effects on engine smoke. No_x formation can be reduced because of the lower temperature by the addition of water.

In general, the road-load–simulation engine tests agree with the steadystate tests and the fundamental research for emulsions. The experimental results show that the microexplosion in emulsion sprays may occur under diesel engine combustion conditions. Engine efficiency can be slightly improved by emulsions under certain conditions through the microexplosions improving the mixing and combustion processes. The system efficiency is influenced by many complex factors, and improvements are not always present under all conditions.

Acknowledgements

This work was supported by the State Planning Commission of China. The authors are indebted to Prof. S. B. Yan, Institute of Acoustics, Chinese Academy of Sciences, for supplying the emulsion.

REFERENCES

1. Hopkinson, B., *Proc. Institution of Mechanical Engineers*, 679–715 (1913).
2. Dryer F. L., *Sixteenth Symposium (International) on Combustion,* The Combustion Institute, Pittsburgh, 1976, pp. 279–295.
3. Vichinievsky, R., Murat, M., Parois, A., and Dujen, M., *CIMAC Congress, I. Mech. E. Press, London, 1975,* pp. 615–652.
4. Callanhan, T. J., Ryan, I. T. W., O'Neal, G. B., and Waytulouis, R. W., SAE 830553, 1983.
5. Johnson, R. T., and Stoffer, J. O., SAE 830557, 1983.
6. Dryer, F. L., Rambach, G. D., and Glassman, I., paper presented at the 1976 Spring Meeting of the Central States Section of the Combustion Institute, 1976.
7. Jacques, M. T., *Combust. Flame* 29:77–85 (1977).
8. Ivanov, V. M., and Nefedov, P. I., NASA Technical Transal. TIF-258, 1965.
9. Sheng, H. Z., and Chen, L., *The 4th ICLASS,* The Fuel Society of Japan, Sendai, Japan, 1988, pp. 391–396.
10. Sheng, H. Z., Chen, L., and Zhang, Z. P., *The Seminar on Diesel Fuel Injection Systems,* Institution of Mechanical Engineers, London, 1989, pp. 49–56.
11. Sheng H.-Z., Zhang, Z.-P., and Wu, C.-K., *International Symposium COMODIA 90,* Kyoto, Japan, 1990, pp. 275–280.
12. Lasheras, J. C., Fernandez-Pello, A. C., and Dryer, F. L., *Combust. Sci. Technol.* 21:1–14 (1979).
13. Marrone, N. J., Kennedy, I. M., and Dryer, F. L., *Combust. Sci. Technol.* 33:299–307 (1983).
14. Wang, C. H., and Law, C. K., *Combust. Flame* 59:53–62(1985).
15. Law, C. K., Lee, C. H., and Srinvasan, N., *Combust. Flame* 37:125–143 (1980).
16. Birchley, J. C., and Riley, N., *Combust. Flame* 29:145–165 (1977).
17. Katsoulakos, P. S., *C84/83,* Institution of Mechanical Engineers, London, 1983, pp. 51–62.
18. Law, C. K., *Combust. Flame* 26:219–233 (1976).
19. Chigier, N., *Combust. Flame* 51:127–139 (1983).
20. Prakash, S., and Sirignano, W. A., *Int. J. Heat Mass Transfer* 253–288 (1980).
21. Shi, S.-X., and Sheng, H.-Z., *International Conference on Computers in Engine Technology,* Institution of Mechanical Engineers, London, 1989, pp. 325–332.
22. Sheng, H., *Trans. Chinese Soc. Intern. Combust. Engines* 3:243–256 (1985) (in Chinese).

Twenty-Fifth Symposium (International) on Combustion/The Combustion Institute, 1994/pp. 183–191

STRUCTURE OF A SPRAY FLAME STABILIZED ON A PRODUCTION ENGINE COMBUSTOR SWIRL CUP

FUMIAKI TAKAHASHI AND W. JOHN SCHMOLL
University of Dayton Research Institute
Dayton, OH 45469, USA

GARY L. SWITZER
Systems Research Laboratories, Inc., A Division of Arvin/Calspan
Dayton, OH 45440, USA

AND

DALE T. SHOUSE
Wright Laboratory, Aero Propulsion and Power Directorate
Wright-Patterson Air Force Base, OH 45433, USA

The near-field structure of a turbulent flame stabilized on a production gas-turbine engine combustor fuel injector/air swirler system (i.e., swirl cup) has been studied using phase-Doppler anemometry and coherent anti-Stokes Raman spectroscopy (CARS) at atmospheric pressure. A Jet-A fuel spray from a simplex atomizer impinges onto a coaxially located liquid filming surface between counterswirling air streams for secondary atomization using high shear forces. An inverted conical flame with a cone angle of ~90° was formed in the inner shear layer of the low-temperature droplet-laden hollow-cone air jet, which divides high-temperature internal and external recirculation zones. Small droplets disappeared in the inner and downstream spray regions by evaporation along the droplet trajectories at higher temperatures and longer residence times, thereby increasing arithmetic and Sauter mean diameters. No fuel droplets were found in the internal recirculation zone. Despite frequent laser-induced breakdown in the dense spray region, CARS thermometry successfully determined the gas temperature. The temperature histograms show a wide distribution inside the flame zone, indicating enhanced stirring of cold air, vaporized fuel, and hot combustion products. On the other hand, the fate of fuel droplets, which did not participate in the combustion process directly in the near field, must play an important role in determining the combustion efficiency and pollutant emission levels.

Introduction

In advanced combustion systems for aircraft gas-turbine engines, a large portion of combustion air is admitted into the primary zone through air swirlers in the dome in order to provide uniform fuel-air mixing and to reduce pollutant (NO_x) emissions [1]. Consequently, the development of a high-performance fuel injector/air swirler system plays a key role in achieving good fuel-lean stability at a low power operating condition, and thorough fuel-air mixing, efficient combustion, and low pollutant emissions at a high power condition. Despite the necessity of a fundamental understanding of spray-flame aerodynamics in the flow field generated by the swirler, quantitative measurements using nonintrusive laser diagnostic techniques have only begun in recent years. Thus, physical and chemical processes taking place simultaneously in such spray flames (i.e., the dynamic interactions between the swirling turbulent flow, fuel droplet vaporization, fuel vapor transport/mixing, and combustion) have not been fully understood.

Swirling flows have long been used in many practical combustion devices to control the stability and intensity of combustion and the size and shape of the flame region [2]. Early studies [3–8] on the characteristics of swirl combustion were mostly based on gaseous fuels. Characterization of swirl combustion has progressed with the development of various laser diagnostic techniques. Laser-Doppler velocimetry has long been a major tool in revealing the turbulent flow field in a combustor [5,7,8]. Recent studies [9–15] using phase-Doppler anemometry (PDA) have contributed greatly to the characterization of both swirling and nonswirling, combusting and noncombusting sprays. PDA provides spatially resolved information on the size and velocity of individual drop-

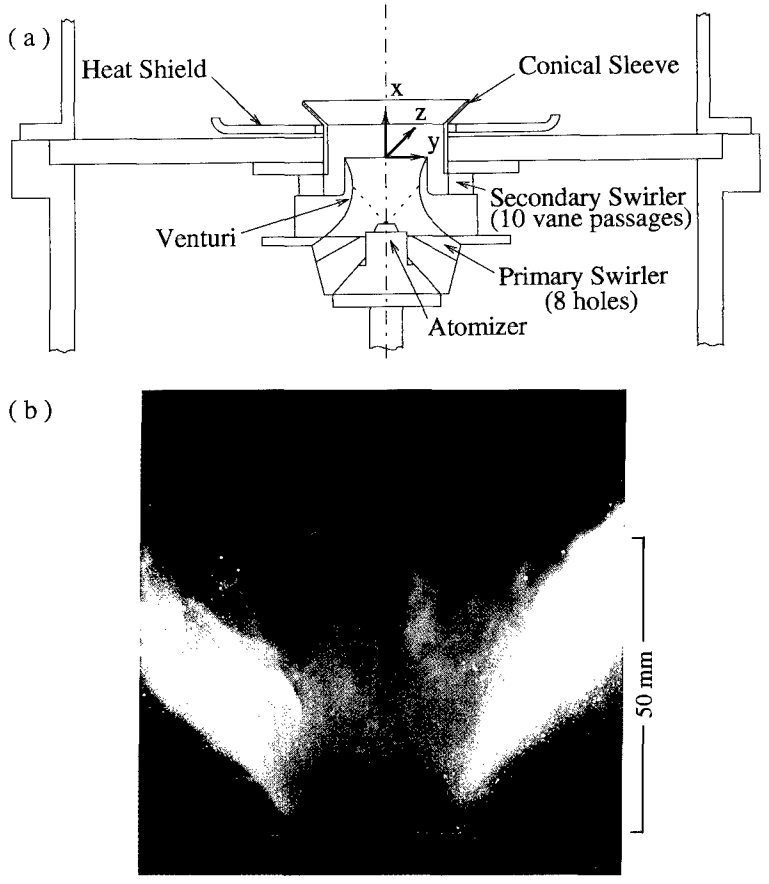

FIG. 1. (a) Schematic of the research combustor with a production gas-turbine engine combustor swirl cup. (b) A time-exposure (1/125 s) direct photograph of the Jet-A spray flame with instantaneous (10 ns) planar visualization of fuel droplets.

lets and gas velocity within the spray. More recently, attempts to measure scalars in the gas phase in spray flames have been made using various nonintrusive diagnostic techniques. A common difficulty in these measurements is the interference of liquid droplets. Species concentration has been measured with some success using exciplex fluorescence [16], laser-induced fluorescence [17], and absorption [15,18–20]. Comparable nonintrusive temperature measurements in spray flames have not been reported. Coherent anti-Stokes Raman spectroscopy (CARS) has been known to have significant advantages over other nonintrusive techniques [21]. The feasibility for CARS thermometry to provide reliable gas temperature measurements in practical combustion environments including the presence of liquid droplets has been examined [22–26].

In this study, droplet size, velocity components, and gas-phase scalar (temperature) have been measured using three-component PDA and CARS in a spray flame stabilized on a practical engine combustor swirl cup at atmospheric pressure. Although, in practical combustors, typical inlet air temperatures and pressures are substantially higher and multiple swirl cups are frequently used, the current single-cup research combustor must preserve some fundamental features of the spray combustion phenomena in real hardware. On the other hand, because slight changes in the hardware would result in significant differences in the combustion characteristics, it is meaningful to use actual combustor parts to avoid oversimplification. The purposes of this study are (1) to gain a better understanding of the coupled physical processes in a spray flame in a swirling flow generated by the swirl cup, and (2) to provide basic information useful for developmental and modeling efforts of the fuel atomizer/air swirler unit.

Experimental Techniques

In the research combustor used (Fig. 1a), a production engine (General Electric CFM56) combus-

tor dome swirl cup is attached on a mounting plate with small cooling holes placed in the inlet of a combustion chimney (150 × 150-mm rounded square cross section; 483-mm length) with quartz windows on three sides for laser diagnostics. The dome swirl-cup assembly consists of several separate parts: a 90°-spray-angle simplex atomizer, a primary swirler with eight holes (clockwise rotation if viewed from downstream), a venturi, a secondary swirler with 10 vane passages (counterclockwise rotation if viewed from downstream), and a 90°-cone-angle flare/sleeve. Jet-A fuel injects from the central simplex atomizer at a mass flow rate of 1.30 g/s (liquid pressure drop: 169 kPa), partially convecting downstream and partially impinging on the venturi inner surface to form a thin film for the secondary atomization by the counterrotating swirling air at room temperature. The total air mass flow rate through the swirl cup and the mounting plate cooling holes is 29.7 g/s (pressure drop: 508 mm H_2O, ~5% atmospheric pressure). Approximately 78% of the total air flows through the swirler. The calculated equivalence ratios based on the total and swirler air are approximately 0.67 and 0.86, respectively.

The three-component PDA (Dantec Measurement Technology) consists of an optic system and a covariance-type signal processor. An argon-ion laser (Coherent Innova 200) is used as a light source. The optic system includes a color separator/fiber-optic coupler unit with a Bragg cell, a two-dimensional (2D) fiber-optic transceiver probe with a velocity component separation based on color (514.5 nm: axial component; 488 nm: radial component), a one-dimensional (1D) transmitter probe (476.5 nm: tangential component), and a receiver. The Bragg cell is used to split the light from the laser (typical operating output: 5 W) into two beams with one beam frequency-shifted at 40 MHz to avoid directional ambiguity. The focal lengths of the 2D and 1D probe focusing lenses are 310 and 400 mm, respectively. The calculated fringe spacings of the 514.5-, 488-, and 476.5-nm beams are 4.1, 4.0, and 5.0 μm, respectively. The scattering light of 514 and 488 nm is detected by the receiver at a 70°-off-axis forward scattering mode, and that of 476.5 nm is detected by the 2D probe at a 90°-off-axis mode. The measuring volume is approximately 210-μm diameter × 100-μm length.

The construction and capabilities of the CARS system employed have been described in detail elsewhere [23]. The CARS system is based upon a frequency-doubled Nd:YAG laser (Quanta-Ray DCR-2) that provides 10-ns pulses of 532-nm radiation at a repetition rate of 10 Hz and a broadband (150 cm^{-1}) dye laser that is tuned to the Stokes vibrational frequency of the nitrogen molecule (607 nm). The system is configured with a folded-BOXCARS [21] optical geometry to produce a sampled spatial volume of ~1 mm^3, with the CARS information being generated within a path length of 2 mm. The accuracy of the CARS temperature determinations is estimated to range between 10% near room temperature and 5% near stoichiometric flame temperature, with the largest contribution to uncertainty resulting from shot-to-shot variation in the Stokes-laser spectral distribution.

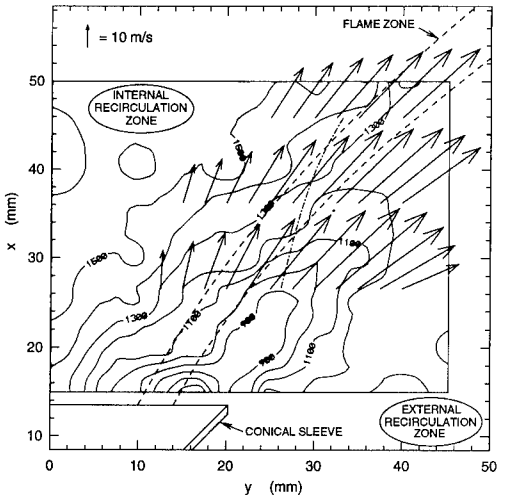

FIG. 2. Mean droplet velocity vector field and isotherms. –·–·–, maximum PDA data rate locus. Temperature in K.

Results and Discussion

Optical Observations:

Figure 1b shows a time-exposure direct photograph of the spray flame investigated with illumination by a sheet (~0.5-mm thickness) of Nd:YAG pulsed (10 ns) laser. The inverted conical flame (cone angle: ~90°) was stabilized inside the flared sleeve adjacent to its exit plane. The visible flame zone was blue near the swirl cup and deflected upward near the chimney windows. Yellow streaks caused by soot formation were seen downstream. The laser sheet illuminated the fuel droplets in the vertical plane containing the axis. A large number of droplets were seen along the flame zone, spreading out downstream. A densely populated droplet stream was observed, even outside the flame zone in the extension of the conical sleeve. A high-speed (5000 fps) color cinematography (not shown) revealed intense flame movement downstream, which made the flame zone in the time-exposure photographs appear thick.

PDA Measurements:

Figure 2 shows the mean droplet velocity vector field in the near-exit region. The PDA measurements

were made at three different heights from the exit plane of the venturi (x = 26.7, 36.4, 46.1 mm). The approximate location of the visible flame zone in the figure was measured by processing a scanned image of a time-exposure photograph. The isotherms from the CARS measurements and the locus of the maximum PDA data rate, also included in the figure, will be described in more detail later. The general direction of the droplet velocity vectors is in the extension of the 90°-cone-angle sleeve. The flame zone is located in the middle of the spray region nearly parallel to the droplet velocity vectors. This result represents a unique feature of the swirl-cup-stabilized spray flames, whereas simple pressure-atomizing spray flames are typically formed outside the entire spray (similar to gaseous diffusion flames) [13] or in the inner edge region of the spray (in case of swirl-stabilized flames [12]), where enough oxygen is available. Thus, the current result of the swirl-cup-stabilized flame shows enhanced oxygen penetration into the spray region as a result of turbulent stirring associated with the geometric configuration of the fuel atomizer and air swirler. Particularly, functional merits of the means for secondary atomization must be significant.

Figure 3 shows the total and size-classed data (droplet arrival) rates in the PDA measurements and the probability density functions (pdf's), or histograms, of the droplet diameter [P(d)] at selected locations. The total data rate was determined by dividing the number of attempted samples by the elapsed time, and the data rates for various droplet size classes were determined from the total data rate and the probability (the pdf times the bin width). The total data rate at x = 26.7 mm (Fig. 3a) reached a peak of 6000 Hz at y = 26 mm and decreased rapidly on both sides to ~10 Hz at y = 12.5 mm and 40 mm. No droplets were detected in the core region (y <12 mm). This is consistent with the laser-sheet visualization results (Fig. 1b). The histograms show a shift in the size distribution in the radial direction. In the outer region (y > 30 mm), a relatively sharp peak in a small diameter range (5–10 μm) is seen, whereas in the inner region (y < 25 mm), the probability of small droplets decreased and the distribution became wider. Consequently, the size-classed data rates show high number fluxes of small droplets in the outer region. As will be discussed in more detail later, the droplets in the outer region pass through a relatively low-temperature region, compared to those in the inner region. Apparently, disappearance of the droplets by evaporation started from smaller particles whose trajectories passed through a high-temperature region. The peak value of the total data rate decreased rapidly downstream [2400 Hz at z = 36.4 mm (Fig. 3b), 750 Hz at z = 46.1 mm (Fig. 3c)]. Because the droplet trajectories are inclined at ~45° with respect to the axis and expand downstream, dispersion of droplets is certainly a factor

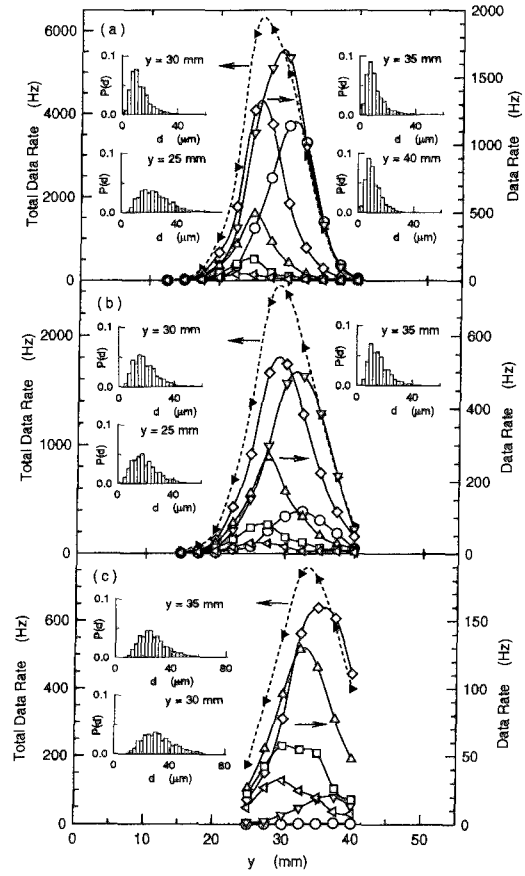

FIG. 3. PDA data rates and histograms of the droplet diameter. (a) x = 26.7 mm, (b) x = 36.4 mm, and (c) x = 46.1 mm. ---▶---, total; ○, 5 μm; ∇, 10 μm; ◇, 20 μm; Δ, 30 μm; □, 40 μm; ◁, 50μm.

contributing to the lowered data rate. Furthermore, disappearance of small droplets by evaporation occurred at longer residence times downstream.

In contrast to the present results on the reacting case, PDA measurements in an isothermal (water) spray from a similar swirl cup reported by Wang et al. [14] showed substantially high data rates of small droplets in the central region. The current results indicate that the engulfment of the droplets into the internal recirculation zone in the flame is prevented in two ways: (1) the droplets injected toward the recirculation zone are evaporated—the flux of droplets directly from the atomizer is low compared to that from secondary atomization, and (2) perhaps no droplets exist in the downstream stagnation region to come back into the recirculation zone.

Figure 4 shows the radial variations in the arithmetic (D_{10}) and Sauter (D_{32}) mean diameters at three different heights. The radial locations of the visible flame zone are also included in the figure. At

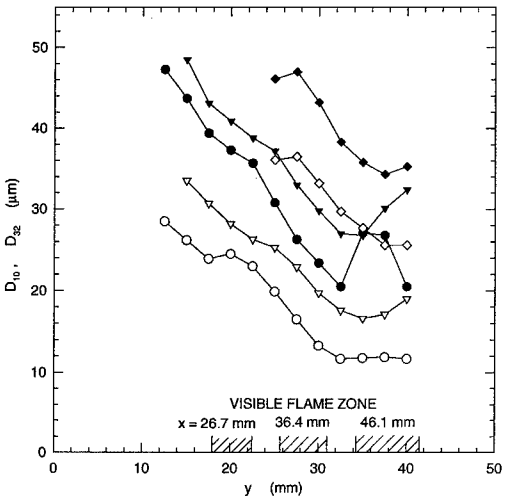

FIG. 4. Mean droplet diameters. ○ ●, x = 26.7 mm; ∇ ▼, x = 36.4 mm; ◇ ◆, x = 46.1 mm. Open: arithmetic mean (D_{10}); filled: Sauter mean (D_{32}).

x = 26.7 mm, D_{10} was small (~12 μm) in the outer spray region (y > 30 mm) and increased inwardly. As small droplets disappeared in the inner region, as described before, the mean diameter increased. In the downstream positions, the same trend was observed, and D_{10} increased because of evaporation at longer residence times. Here D_{32} was larger than D_{10}, as expected, because D_{32} reflects the volume of the droplets. Because D_{32} is influenced by the occasional arrival of droplets having large diameters (volumes), it exhibited more scatter than D_{10} in the outer spray region where the progress of evaporation was less than in the inner region.

Figure 5 shows the mean and root-mean-square (rms) fluctuations of the axial, radial, and tangential droplet velocity components for different size classes at z = 26.7 mm. The bin width used is 5 μm, and the diameter shown is the center value of each bin. For both axial and radial components, the mean velocity for a smaller size class showed a sharper peak than that of a larger size class. The mean tangential velocity component of a small size class was higher than that of a larger size class in the inner region and vice versa in the outer region. The rms's of a small size class for all three components were higher than those of a large size class. Small droplets follow the gas flow more closely because they possess lower inertia and drag forces. The mean axial and radial velocity components for the smallest size class (5 μm), which must be closest to the gas flow, peaked at y = 31 mm, indicating that the main airflow injected along the extension of the conical sleeve at 45°, creating the low-temperature zone outside the flame zone. Thus, the flame zone was formed in the inner shear layer of the air jet. As the flow diverged downstream, the maximum values of the velocity components decreased (not shown), but the trends were similar to those at x = 26.7 mm.

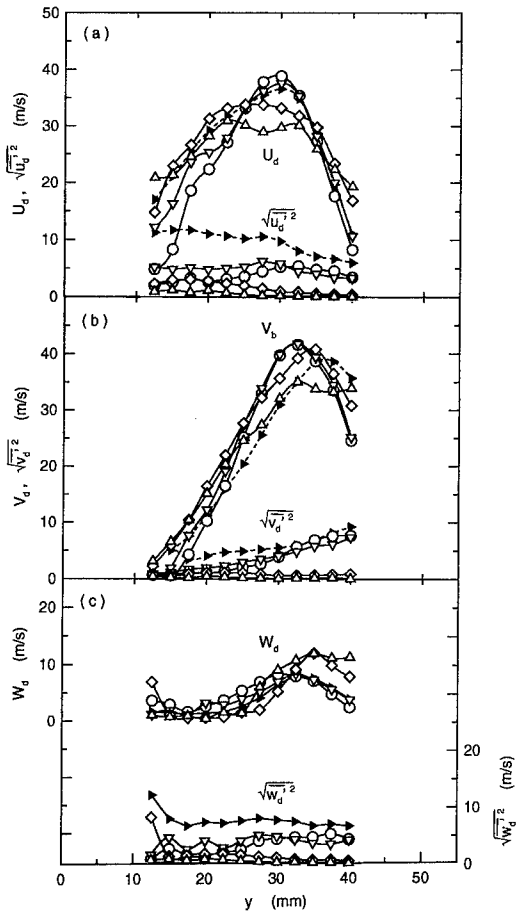

FIG. 5. Mean and root-mean-square fluctuation of (a) axial, (b) radial, and (c) tangential droplet velocity components. ---▶---, total; ○, 5 μm; ∇, 10 μm; ◇, 30 μm; Δ, 50 μm.

CARS Measurements:

The liquid fuel spray of this combustor presented a challenging environment for the CARS measurement technique. A high density of liquid droplets exhibited near the nozzle exit and at the edge of the visible flame contributed to several effects that complicated temperature measurements. Among these were beam steering, nonresonant CARS generation, and droplet-induced breakdown. Index of refraction gradients created by the high concentrations of droplets affected steering of the CARS pump and Stokes beams, thus prohibiting the necessary beam overlap and resulting in a loss of some temperature samples

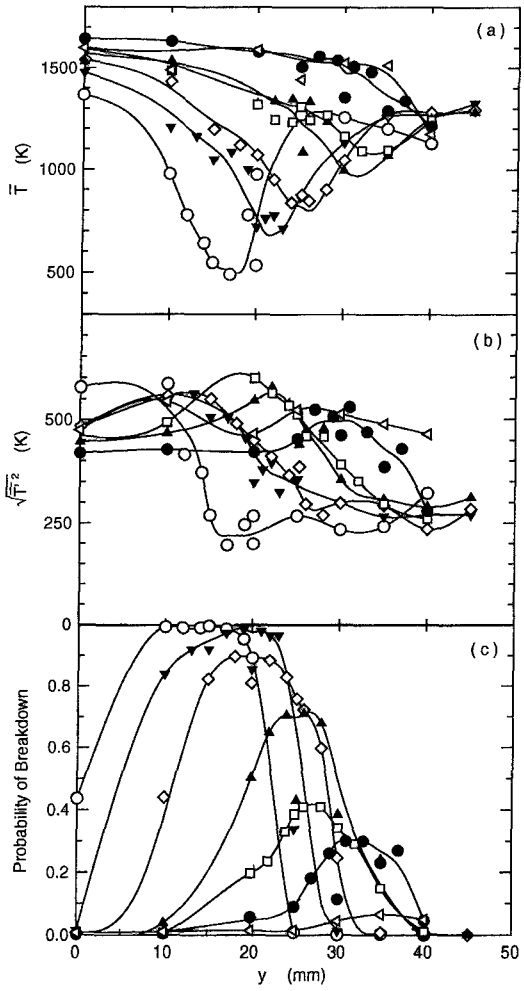

FIG. 6. (a) Mean and (b) root-mean-square fluctuation gas temperatures and (c) CARS droplet-induced breakdown rate. ○, x = 15 mm; ▼, x = 20 mm; ◇, x = 25 mm; ▲, x = 30 mm; □, x = 35 mm; ●, x = 40 mm; ◁, x = 50 mm.

at certain locations. The background contributions arising from nonresonant CARS and droplet-induced breakdown have been described [25] and were minimized for these measurements. Corrections for the nonresonant contribution were accommodated in the spectral fitting routines while background subtraction was employed to compensate for the background produced by droplet-induced breakdown.

Figure 6 shows the radial distributions of the mean and rms fluctuation temperatures and the probability of droplet-induced breakdown at various heights. The frequency of breakdown occurrence will be discussed later. The isotherms shown in Fig. 2 were derived from the results in Fig. 6a. The mean temperatures on the centerline in the internal recirculation zone were in the range of 1400–1650 K, and those in the outermost data points (y = 45 mm) in the edge of the external recirculation zone were ~1300 K. The low-temperature (500–1100 K) zone was formed along the direction of the cold droplet-laden air jet (see Fig. 2). The visible flame zone was formed just inside and along the low-temperature zone in the shear layer of the air jet. The low-temperature zone became less evident downstream ($x >$ 40 mm). The rms fluctuation temperature (Fig. 6b) was higher (400–600 K) in the internal recirculation zone with the maximum just inside the flame zone, compared to that outside (~300 K), indicating enhanced stirring of hot and cold fluid packets in the shear layer where the flame zone resided.

Figure 7 shows the temperature pdf's (histograms) with a bin width of 100 K at three different heights (x = 20, 30, and 40 mm). Four radial locations are selected: the centerline, a few millimeters inside the flame zone, the low-temperature zone, and y = 40 mm. In general, wide temperature distributions were observed in the central region inside the visible flame zone (Figs. 7a, 7b, 7e, 7f, 7i, and 7j), compared to the outer region including the low-temperature zone (Figs. 7c, 7g, and 7k) and the external recirculation zone (Figs. 7d, 7h, and 7l). The results show enhanced turbulent stirring between the high-temperature combustion products and the cold air near the flame zone. The minimum value in the temperature distribution decreased toward the nozzle along the centerline down to 300 K (Fig. 7a), indicating stirring between the cold air directly from the swirl cup and the combustion products recirculated. In the lower part of the low-temperature zone (Fig. 7c), a slight tendency of bimodal distribution was observed as a result of the occasional arrival of the hot gases (>2000 K) into the cold air. The narrower peaks of the temperature distribution in the external recirculation zone (Figs. 7d, 7h, and 7l) indicate that the hot combustion products and cold air are mixed well.

The probability of droplet-induced breakdown (Fig. 6c) was determined as the number of breakdown occurrences in the total attempted CARS samples at each location. The background subtraction scheme implemented into the spectral fitting routines made it possible to retrieve temperature information if the background shift was relatively small. Thus, the number of samples with breakdown includes both successful temperature measurements and discarded samples due to the disrupted signal. The breakdown probability reached ~0.99 in the near-exit dense spray region (x < 20 mm). The peak value greatly decreased downstream (~0.07 at x = 50 mm). Comparisons between the breakdown probability and the PDA data rate (Fig. 3) show both similarities and differences. Basically, both the breakdown probability and the PDA data rate depend on how dense the spray is at the point where the probe

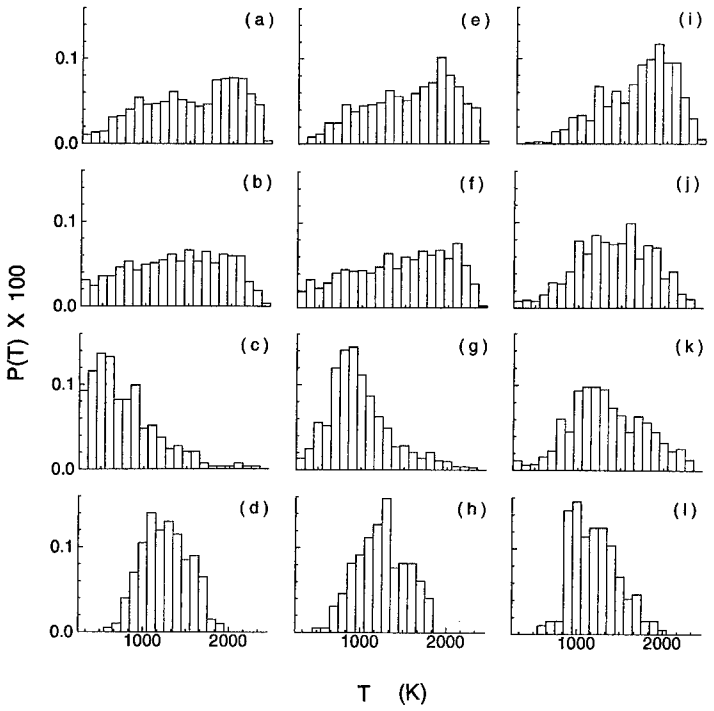

FIG. 7. Histograms of the gas temperature. x = 20 mm: (a) y = 0 mm, (b) y = 10 mm, (c) y = 22 mm, and (d) y = 40 mm. x = 30 mm: (e) y = 0 mm, (f) y = 20 mm, (g) y = 30 mm, and (h) y = 40 mm. x = 40 mm: (i) y = 0 mm, (j) y = 30 mm, (k) y = 37 mm, and (l) y = 40 mm.

volume is located; thus, in general, both peak in a dense region and decrease downstream. However, the breakdown curves show substantially broader distribution with tailing inwardly, and their peak locations, if interpolated for the heights for the PDA measurements, are closer to the centerline compared with the total PDA data rates. Major reasons for the differences must stem from the breakdown occurrence along the CARS laser beams. The energy flux of the focused beams of the CARS system is approximately 10^{11} W/cm^2, which is close to the breakdown threshold (order of 10^{12} W/cm^2) in a "clean" environment. Because the introduction of liquid droplets into these beams reduces the threshold by several orders of magnitude, breakdown occurs well before the beams attain their normal focus. The quality of measured variables and the size of each probe volume may contribute, to some extent, to the differences in the PDA data rate and the CARS breakdown probability measurements. The PDA data rate represents the number flux of the droplets times the cross-sectional area measured over the elapsed time, whereas the CARS breakdown is an instantaneous spatial quantity directly related to the number density of the droplets. The probe volume of CARS is three orders of magnitude larger than that of PDA, and the horizontal cross-sectional area is two orders of magnitude larger. Because of the large probe volume, the CARS breakdown data must have a significantly higher possibility of multiple droplets inside the probe volume in the dense spray region.

Near-Swirl-Cup Structure:

The combustion process in a combustor becomes evaporation-rate-controlled if the evaporation of droplets does not complete within a residence time in the system. A crude estimate for the critical mean droplet size above which evaporation starts to limit combustion efficiency can be made by considering a simple droplet evaporation process [2]. The residence time of the droplets from the swirl-cup exit to the height where the droplets would impinge on the chimney window, for example, determined by dividing the trajectory distance (~0.1 m) by the maximum velocity for large droplets (~30 m/s), is ~3 ms. The critical mean drop size at the residence time of 3 ms is estimated for kerosene (Jet-A) as ~60 μm [2]. Measured D_{32} is less than 60 μm in the whole measurement range (Fig. 2); thus, the evaporation rate must not be rate-controlling, in a global sense, if all droplets pass through the high-temperature region. However, a close examination of the structure of the spray flame revealed that a considerable portion of the fuel droplets outside the flame zone does not participate in the combustion process in the near-swirl-cup region. Some of these droplets must burn downstream, and others must enter into the external recirculation zone, evaporate, pyrolize, and mix with the cooling air. In a practical combustor, the external recirculation may be small or does not exist, depending on the shape of the dome. Furthermore, in a multiple-cup combustor, interaction between the ad-

jacent flames may occur. In any case, the fate of the droplets escaping from the flame in the near-exit region must be important in achieving a high combustion efficiency and reducing emissions of various pollutants.

Conclusions

The PDA and CARS measurements have provided useful information on the structure of a spray flame in a research combustor using actual engine combustor hardware. In spite of a high probability of laser-induced breakdown, CARS thermometry successfully determined the temperature field in the dense spray region of a simulated practical combustion system. An inverted conical flame zone is formed in the inner shear layer of the low-temperature droplet-laden hollow-cone jet, which divides the high-temperature internal and external recirculation zones. A large temperature fluctuation occurs inside the flame zone, as a result of intense stirring of packets of cold air, vaporized fuel, and hot combustion products. The droplet size distribution and, in turn, mean diameters are affected strongly by the level of evaporation, which depends on the temperature history and the residence time along the droplet trajectories. The mean and rms fluctuation velocity components depend on droplet size because of the difference in the traceability of a droplet to the turbulent flow. Although a crude estimate for the critical mean drop size shows that, in a global sense, the evaporation rate is not a rate-controlling factor, a significant portion of the droplets does not participate in the combustion process in the near field. The fate of these droplets is an important issue in terms of combustion efficiency and emission characteristics.

Acknowledgments

This work was supported by the U.S. Air Force, Wright Laboratory, Aero Propulsion and Power Directorate, Fuels and Lubrication Division, Wright-Patterson Air Force Base, OH, under Contract No. F33615-92-C-2207 (Technical Monitor: C. W. Frayne). Special thanks to GE Aircraft Engines for providing the swirl-cup hardware, Dantec Measurement Technology for loaning a PDA system, and Messrs. M.D. Vangsness, F. Timko, D. Sutkus, M. Burns, and M. Russell for assisting in the preparation of the experiments.

REFERENCES

1. Dodds, W. J., *Gas Turbine Industry Needs,* Gas Turbine Combustion Challenges and Laser Diagnostics Workshop, Ohio Aerospace Institute, April 1993.
2. Lefebvre, A. H., *Gas Turbine Combustion,* Hemisphere, New York, 1983, p. 127.
3. Beer, J. M., and Chigier, N. A., *Combustion Aerodynamics,* Applied Science, London, 1972.
4. Syred, N., and Beer, J. M., *Combust. Flame* 23:143–201 (1974).
5. Chigier, N. A., and Dvorak, K., *Fifteenth Symposium (International) on Combustion,* The Combustion Institute, Pittsburgh, 1975, pp. 573–585.
6. Lilley, D. G., *AIAA J.* 15:1063 (1977).
7. Gupta, A. K., Beer, J. M., and Swithenbank, J., *Sixteenth Symposium (International) on Combustion,* The Combustion Institute, Pittsburgh, 1977, pp. 79–91.
8. Gouldin, F. C., Depsky, J. S., and Lee, S. E., *AIAA J.* 23:95–102 (1985).
9. Mao, C.-P., Wang, G., and Chigier, N., *Twenty-First Symposium (International) on Combustion,* The Combustion Institute, Pittsburgh, 1988, pp. 665–673.
10. McDonell, V. G., Wood, C. P., and Samuelsen, G. S., *Twenty-First Symposium (International) on Combustion,* The Combustion Institute, Pittsburgh, 1988, pp. 685–694.
11. Cameron, C. D., Brouwer, J., and Samuelsen, G. S., *Fourth International Conference on Liquid Atomization and Spray Systems,* Sendai, Japan, August 1988, pp. 145–152.
12. Edwards, C. F., and Rudoff, R. C., *Twenty-Third Symposium (International) on Combustion,* The Combustion Institute, Pittsburgh, 1991, pp. 1353–1359.
13. Presser, C., Gupta, A. K., Avedisian, C. T., and Semerjian, H. G., *Twenty-Third Symposium (International) on Combustion,* The Combustion Institute, Pittsburgh, 1991, pp. 1361–1367.
14. Wang, H. Y., McDonell, V. G., and Samuelsen, G. S., *Twenty-Fourth Symposium (International) on Combustion,* The Combustion Institute, Pittsburgh, 1992, pp. 1457–1463.
15. McDonell, V. G., and Samuelsen, G. S., *Twenty-Fourth Symposium (International) on Combustion,* The Combustion Institute, Pittsburgh, 1992, pp. 1557–1564.
16. Melton, L. A., and Verdieck, J. F., *Twentieth Symposium (International) on Combustion,* The Combustion Institute, Pittsburgh, 1985, pp. 1283–1290.
17. Allen, M. G., and Hanson, R. K., *Twenty-First Symposium (International) on Combustion,* The Combustion Institute, 1988, pp. 1755–1762.
18. Chraplyvy, A. R., *Appl. Optics* 20:2620 (1981).
19. Adachi, M., McDonell, V. G., and Samuelsen, G. S., *Combust. Sci. Technol.* 75:179 (1991).
20. Drallmeier, J. A., and Peters, J. E., *Atomiz. Sprays* 1:63 (1991).
21. Eckbreath, A. C., *Laser Diagnostics for Combustion Temperature and Species,* Abacus Press, Cambridge, MA, 1988.
22. Switzer, G. L., Goss, L. P., Roquemore, W. M., Bradley, R. P., Schreiver, P. W., and Roh, W. B., *J. Energy* 4:209–215 (1980).
23. Switzer, G. L., and Goss, L. P., in *Temperature: Its Measurement and Control in Science and Industry* (J.

F. Schooley, Ed.), American Institute of Physics, New York, 1982, pp. 583–387.
24. Bedue, R., Gastebois, P., Bailly, P., Pealat, M., and Taran, J. P. E., *Combust. Flame* 57:141–153 (1984).
25. Dunn-Rankin, D., Switzer, G. L., Obringer, C. A., and Jackson, T. A., *Appl. Opt.* 29:3150–3159 (1990).
26. Zhu, J. Y., Tsuruda, T., Sowa, W. A., and Samuelsen, G. S., *J. Eng. Gas Turbine Power* 115:515–521 (1993).

COMMENTS

Ruey-Hung Chen, University of Central Florida, USA. The amount of fuel droplets not participating in the near-field combustion may depend on, and increases with, the ratio of the vaporization time scale (which is not a concern in gas phase combustion) to the near-field internal recirculation zone time scale (or velocity and length scales). In a previous study on gas-fueled swirl flames, the recirculation zone scales and flame length were shown to depend on the degree of recirculation and the ratio of fuel jet momentum to the recirculating flow momentum [1,2]. Would you please comment on how one should try to characterize the ratio of the two time scales, since it has implications for the completeness of combustion and pollutant emissions.

REFERENCES

1. Chen, R.-H., and Driscoll, J. F. *Twenty-Second Symposium (International) on Combustion,* The Combustion Institute, Pittsburgh, 1989.
2. Chen, R.-H. et al., *Combust. Sci. and Tech.* Pittsburgh, 71:197 (1990).

Author's Reply. The amount of fuel droplets not participating in the near-field combustion is independent of the *internal* recirculation zone time scale. Unlike many other initially unmixed flames, whether spray- or gas-fueled, in which the flame zone envelops the fuel jet, the structure of the present swirl-cup-stabilized spray flame is peculiar: The flame is formed radially inside the main fuel (spray) zone. This structure is due in part to, besides swirl, the unique air flow configuration and means of secondary atomization that define the boundary conditions at the swirl-cup exit. As a result, a substantial flux of fuel droplets is ejected outside the flame zone in the near field and partially engulfed in the *external* recirculation zone. The residence time and vaporization time scales can be determined using the regional characteristic velocity and temperature. However, since the characteristics of the external recirculation zone (and the subsequent downstream region) are highly system configuration dependent, the fate of the unburned fuel droplets should be assessed under more realistic conditions.

Twenty-Fifth Symposium (International) on Combustion/The Combustion Institute, 1994/pp. 193–199

DETERMINATION OF FLUE GAS ALKALI CONCENTRATIONS IN FLUIDIZED-BED COAL COMBUSTION BY EXCIMER-LASER–INDUCED FRAGMENTATION FLUORESCENCE

K. T. HARTINGER, P. B. MONKHOUSE AND J. WOLFRUM
Physikalisch-Chemisches Institut der Universität Heidelberg
Im Neuenheimer Feld 253, 69120 Heidelberg, Germany

AND

H. BAUMANN AND B. BONN
Institut für Kokserzeugung und Brennstofftechnik
DMT Gesellschaft für Forschung und Prüfung mbH
Franz-Fischer-Weg 61, 45307 Essen, Germany

Gas-phase sodium concentrations were measured for the first time in situ in the flue gas of a fluidized-bed reactor by the excimer-laser–induced fragmentation fluorescence (ELIF) technique. This method involves using ArF-excimer laser light at 193 nm to simultaneously photodissociate the alkali compounds of interest and excite electronically the alkali atoms formed. The resulting fluorescence from Na (3^2P) atoms can be readily detected at 589 nm. Measured signals were converted to absolute concentrations using a calibration system that monitors alkali compounds under known conditions of temperature, pressure, and composition and using the same optical setup as at the reactor. Several different coals were investigated under a specific set of reactor conditions at total pressures close to 1 bar. Sodium concentrations ranging from the sub-ppb region to 20 ppb were obtained, and a detection limit for sodium of 0.1 ppb under the present conditions was estimated. Over the course of the reactor programme, contrasting concentration histories were observed for the two lignites and the hard coal investigated. In particular, significantly higher sodium concentrations were found for the hard coal, consistent with both the higher chlorine and sodium contents determined in the corresponding coal analysis.

Introduction

Alkali metals and their compounds are unwanted trace constituents of coal combustion processes. Even at the ppb level, deposition of alkali vapours can lead to fouling and corrosion of reactor parts and downstream equipment in boilers and gas turbines [1]. Therefore, appropriate filter systems have to be Revised to remove the offending species. The effectiveness of such filters can only be assessed if alkali concentrations can be monitored quantitatively, continuously, and in situ at the appropriate temperatures and pressures. For monitoring and control work, online optical diagnostics offers the advantage over physical probes of nonintrusiveness and avoids sampling which (1) can lead to erroneous results due to sample changes prior to actual measurement and (2) is more time consuming. Sample times of up to an hour may be needed to obtain useful results, whereas in situ diagnostics with fast detection gives a result in seconds. The advantages of such an approach have been demonstrated for other industrial systems [2,3].

Alkali species occur in several forms in coal. Sodium is found as adsorbed NaCl or as organically bound material directly attached to the coal structure via carboxylic acid groups. Both these forms vaporize readily at the temperatures of fluidized-bed combustion (below ~1000 °C). Alkali species are also present in the mineral matter in the form of feldspars, etc., but these forms vaporize at much higher temperatures. Examples of sodium/sodium compound profiles as a function of temperature (thermodynamic equilibrium calculations) for pulverized coal combustion are given in Refs. 4 and 5. Under post-combustion conditions, sodium chloride (assuming the chlorine content of the coal is significant) and sodium hydroxide are expected to be the chief vapor phase species.

Various optical schemes have been employed for the measurement of alkali species. Although the atoms themselves can be detected very sensitively by fluorescence, their compounds cannot be detected directly this way, because their upper electronic states are repulsive. On the other hand, following UV photolysis, electronically excited fragments can form; the free alkali atoms can then be detected by fluorescence [6]. In the mid-1980s, the analytical potential of excimer-laser–induced fragmentation fluores-

cence (ELIF) for determining different alkali species using excimer lasers, either directly at 193 nm (ArF-excimer) or 248 nm (KrF-excimer) or with Raman shifting of excimer laser radiation, was demonstrated [7]. The excimer laser is to be favored for industrial applications because of its high spectral brightness compared to other UV light sources, as well as reliability, simplicity, and robustness.

Alternative excitation/detection strategies were examined recently using NaOH- and NaCl-seeded laboratory flames [8]; these schemes involved photolysis of the precursor compound by one laser wavelength or thermal dissociation followed by laser excitation of the atoms with another wavelength. The best sensitivity was obtained using the Na (3^2D-3^2P) transition at 818 nm. However, fluorescence detection at such long wavelengths in industrial systems with hot, glowing pipe material should be even more difficult than with the present detection wavelength at 589 nm. Furthermore, if two separate lasers are required for precursor dissociation and alkali atom excitation, overall cost and adjustment and operational effort will be increased considerably.

The quantitative application of fluorescence diagnostics in practical systems requires the accurate assessment of collisional quenching of the excited electronic states under investigation. The total quenching rate depends on the composition of the surrounding gas and on the efficiencies of quenching collisions with the individual constituents of the gas mixture. In industrial systems, nitrogen, carbon dioxide, and oxygen are among the main gaseous components and are known to quench alkali atom fluorescence strongly [9–11].

Flame emission following sampling procedures has frequently been used for alkali diagnostics, also in fluidized-bed systems (e.g., Ref. 12). A variant emission technique, laser-induced breakdown spectroscopy [13], was employed in situ in a coal gasifier and may be useful for some applications, especially with time-resolved detection.

Detection of alkali atoms by absorption is well established but is inherently much less sensitive than fluorescence. Conventional (nonlaser) absorption has been used for many years to monitor alkali atoms, e.g., for profiling volatilization from coal samples [14,15], for determining sodium and potassium release in the gasification of peat [16], and for alkali measurements following thermal dissociation of the compounds by an electric arc [17].

In this work, we employed photoinduced fragmentation/excitation with a commercial excimer laser as the basis of a method to determine absolute concentrations of alkali species in the flue gases of a pressurized fluidized-bed coal combustor down into the sub-ppb region. The system as a whole is straightforward in design and robust enough to withstand rough industrial conditions.

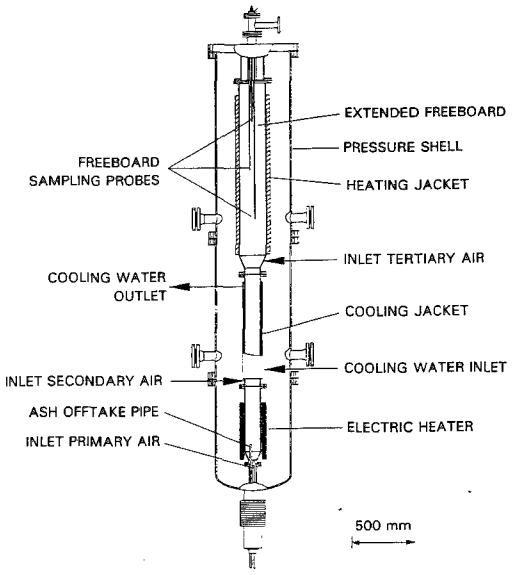

FIG. 1. Fluidized-bed reactor.

Experimental

The fluidized-bed reactor used for measurements of gas-phase alkalis is installed in the Institut für Kokserzeugung und Brennstofftechnik (Institute for Cokemaking and Fuel Technology) at DMT (Fig. 1) [18]. The actual reactor furnace is enclosed in a pressure shell designed to separate thermal and mechanical stresses, i.e., to keep the pressure forces away from the (hot) reactor walls. The shell can withstand pressures up to 20 bar, but will not be discussed further, because as a result of present limitations of materials at the optical access, diagnostics measurements reported here were made mainly at pressures close to 1 bar.

The reactor furnace has a rating of about 100 kW at 10 bar. It comprises a lower, fluidized-bed combustion zone and an upper, extended freeboard zone. In the lower part of the combustion zone, the bed material for startup can be electrically heated by a tubular oven. During the run, the heater was used for temperature control. The temperature measured on the reactor axis in the center of the fluidized-bed zone is the leading temperature for control of the combustion conditions.

The cross section of the extended freeboard is about three times that of the combustion tube. As a result, the residence time of the flue gas in the freeboard region was about 4.5 s at a fluidizing velocity of 1 m/s in the combustion section. To compensate for heat loss through the wall, the freeboard could be electrically heated. The maximum temperature at the surface of the heating jacket was 900 °C.

The outlet for the flue gas is located in the centre

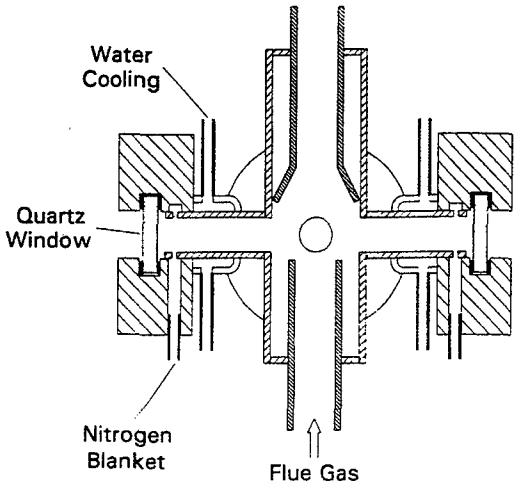

FIG. 2. Optical access to the flue gas.

of the top plate, which was the fix point of the entire reactor. The inner fluidized-bed reactor furnace was mounted to the top plate and could expand downwards under hot conditions. For disassembling and easy access to the top of the reactor, the outlet tubes were supplied with flanges.

The dust in the flue gas leaving the fluidized-bed combustor is, under conventional operating conditions (i.e., without ELIF-diagnostics facility), largely removed in a cooled cyclone. To prevent condensation of alkali compounds between the combustor and the measuring point, the flue gas duct had to be kept hot. Therefore, heat-resistant steel was selected for the flue pipe tubing, and the cooled cyclone was replaced by two cyclones in series to improve gas cleaning; both the tubing and the cyclones were equipped with electrical trace heating. Downstream, the flue gas was cooled in a heat exchanger and the remaining dust removed in a bag filter.

The four ports that provided optical access to the pipe were supplied with quartz windows. High-quality Suprasil windows were used in the path of the laser beam, while standard-quality quartz was found to be adequate for the detection ports. The optical access design is shown in Fig. 2. The conical element above the window part helped to keep dust away from the windows. Flushing with nitrogen further reduced dust load on the windows.

Setup for ELIF Measurements:

The setup for ELIF measurements is shown in Fig. 3. Measurements were made in the flue gas pipe after the second cyclone, at gas temperatures ~680 °C and pressures close to atmospheric. Alkali compounds were photolysed at 193 nm by a broadband

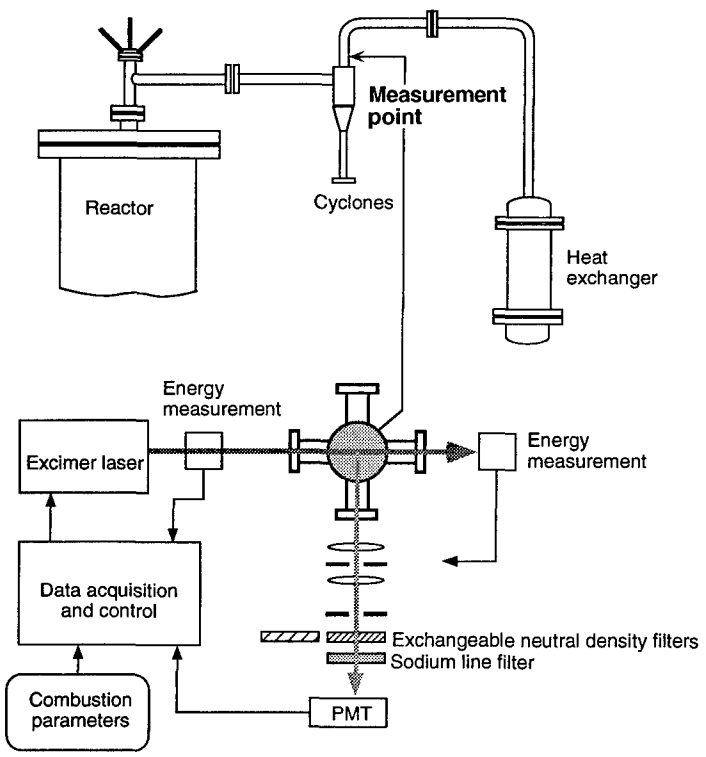

FIG. 3. Setup for ELIF measurements at the fluidized-bed reactor.

ArF-excimer laser using energy densities of several mJ/cm^2, well below the level where saturation effects are observed (~20 mJ/cm^2). The laser was operated at a repetition rate of 6.4 Hz; data were subsequently averaged computationally over 400 samples (corresponding to 1 min). The laser energy entering and leaving the pipe was monitored constantly and provided information, e.g., on the condition of the quartz windows. Fluorescence was detected perpendicular to the laser beam by a photomultiplier coupled to a boxcar system, using a time gate of 40 ns. To remove undesired radiation, a line filter (589 nm, full width at half maximum = 10 nm) was placed in front of the detector.

Calibration Procedure:

Calibration measurements were performed in a quartz cell, encased in a tubular oven (heatable to 1200 °C) with four ports for optical access. The optical setup and geometry were as for the reactor measurements. Alkali salt was filled into a reservoir, which was attached to the cell but heated separately, so that the vapour pressure of the salt could be varied independently [7,11]. To avoid salt condensation, the oven was constructed with effective insulation material, and the cell temperature was always maintained 50 °C higher than the reservoir temperature. Evacuated quartz tubes at the ports acted both as thermal insulators and minimised absorption of the laser beam in the hot oven atmosphere.

In the course of the calibrations, it was verified that the dependence of fluorescence signal on reservoir temperature corresponded to the vapour pressure dependence predicted by thermodynamic data [19]. Since the alkali number densities can be obtained from thermodynamic data, the calibration factor C_{det} can be determined using the following relations: The fluorescence signal S_{fl} from excited alkali atoms M^* can be expressed as

$$S_{\mathrm{fl}} = C_{\mathrm{det}} E_{\mathrm{laser}} n_{\mathrm{MX}} a_{\mathrm{abs}} q$$

where E_{laser} is the laser energy in the cell, n_{MX} the number density of the alkali salt MX, and a_{abs} its UV-absorption cross section for production of M^*, and q describes the quenching effect:

$$q = \frac{A}{A + Q} \quad \text{where } Q = \sum_i n_i v_i \sigma_i$$

and A is the inverse of the natural lifetime of M^*, Q the total quenching rate, n_i the number density of the quenching partner i, v_i the relative velocity of i and M^*, and σ_i the respective quenching cross section. Quenching effects were studied separately in the laboratory in Heidelberg and are reported elsewhere [11].

Results and Discussion

Data from the coal analysis (C, H, O, S, N, H_2O) and on-line data from the reactor (temperature, pressure, air flow rates, and CO_2 and O_2 content of the dried flue gas) were taken as input for calculating concentrations of N_2, CO_2, O_2, and H_2O in the flue gas using a set of linear equations. These major species data were used together with the available cross sections for collisional quenching of Na(3^2P) atoms [10,11] to compute the quenching factor q (0.04 for the present reactor conditions). Sufficient quenching data are now available for all major species, so that q can be reliably calculated. The q factor was then multiplied by the line filter transmission, photomultiplier response, and the appropriate UV-absorption cross section for NaCl to obtain an "efficiency" value for sodium. In principle, this efficiency has to be calculated for all sodium compounds present in the flue gas separately. In the present case, however, species other than NaCl can be neglected since (1) ELIF at 193 nm has the highest efficiency for NaCl [7], and (2) equilibrium calculations [4,5] have shown that NaCl is the dominant sodium species in the vapour phase. The concentration of the next most abundant species, NaOH, is a factor of 10 lower.

The measured signals were corrected for electronic offsets and normalized to the laser energy, taking into account the attenuation of the laser beam while passing through the windows and the flue gas. The difference between the total absorption as measured by the energy monitors and the absorption due to flue gas molecules (~10%), calculated using available data [20–22], and due to losses at the windows, is attributed to dust on the windows. The normalized fluorescence signals and the electronic settings (e.g., gain factor) were then combined with the calibration factor C_{det} and the efficiency value evaluated above to obtain absolute sodium concentrations.

Two lignites and a hard coal were investigated. Figure 4 shows typical results; the concentration of gas-phase sodium evaluated from the ELIF signals is plotted as a function of measurement time. Short, sharp peaks resulted from occasional tapping of the cyclone to remove ash. For all measurements, the reactor was programmed to run for 8 hours from 7 A.M.; program details are given in Fig. 4. A stable bed temperature was reached after 3–3-1/2 h. As can been seen in Figs. 4a through 4c, due to an increase in flue gas flow when the bed temperature was reduced, the temperature in the flue gas duct—and hence at the alkali measuring point—increased somewhat.

Experiments with the lignites were also performed using powdered limestone as sorbent for SO_2. The measured sodium concentrations were generally in the range 0.3–0.6 ppb for a bed temperature of 920 °C (note different y-axis scales for lignites I and II), both with and without limestone addition. On reduc-

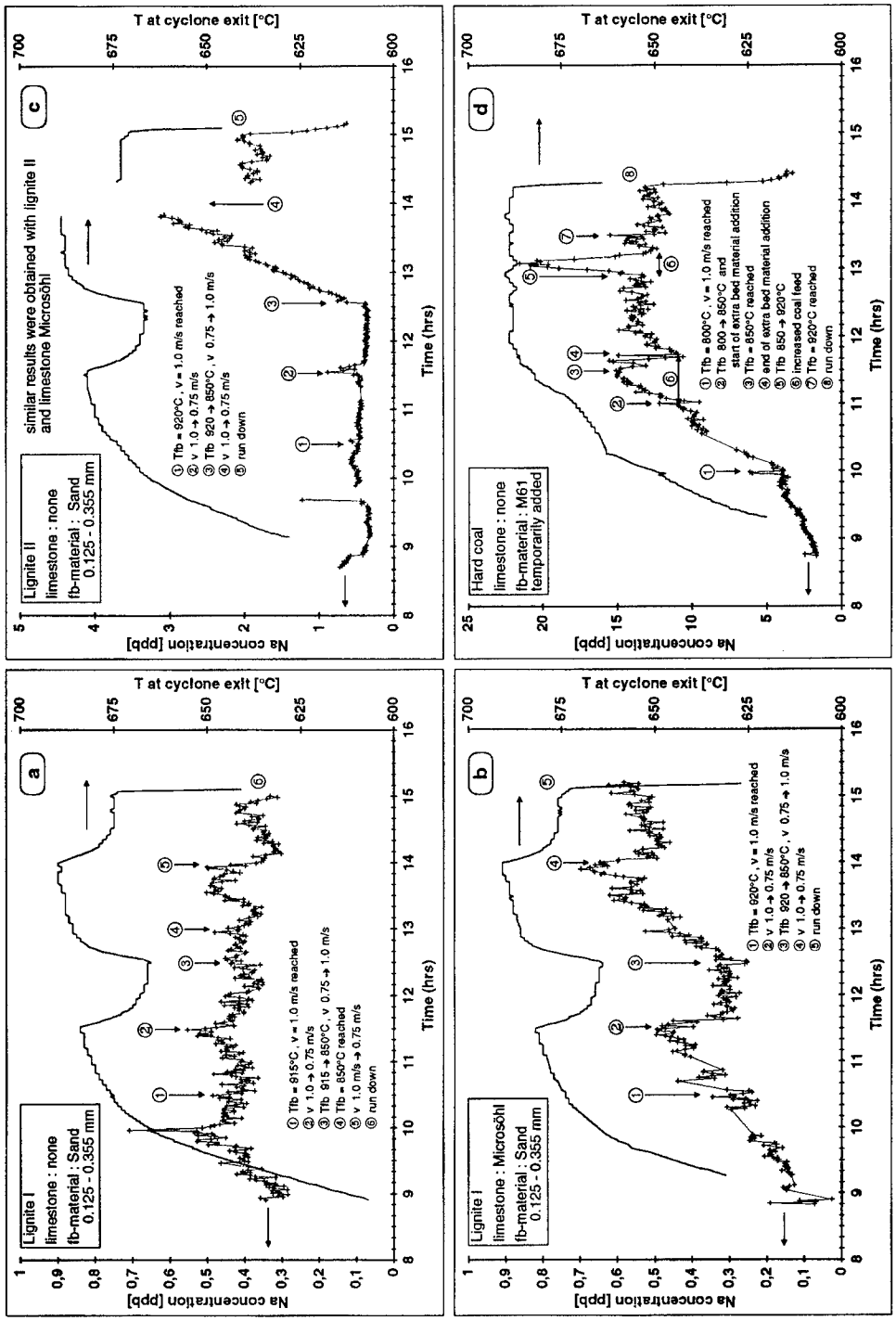

FIG. 4. Sodium concentration histories measured in the flue gas of the fluidized-bed reactor. Tfb = Temperature of the fluidized bed; v = fluidizing velocity. Temperatures immediately after the second cyclone (next to the measurement point) are also shown.

ing the bed temperature from 920 °C to 850 °C, a marked increase in signal (up to a factor of 10) was observed only for lignite II (Fig. 4c). Although the fluidized bed reached a stable temperature after ~30 min, the signal continued to rise. This phenomenon occurred in two independent runs on different days.

For the hard coal measurements, the run began at the lower bed temperature of 800 °C, but this was raised to 850 °C four hours and to 920 °C six hours after startup. Also, extra fluidizing material was added once and the coal feed increased (30–40%) twice, as shown in Fig. 4. The hard coal results show sodium concentrations up to 20 ppb, significantly higher than for the lignites. The two broad peaks (Fig. 4d) could be associated with the increases in coal feed.

The sodium content from the coal analyses and the CO_2 concentration in the flue gas were used to compute the maximum possible (i.e., assuming complete evaporation) sodium concentration in the flue gas. For the lignite I measurements, this was 1.8 ppm, for lignite II 0.5 ppm, and for the hard coal, 35–50 ppm. That the measured sodium concentrations are about three orders of magnitude below the maximum possible values is largely due to incomplete release of sodium from the coal minerals into the gas phase. Also, some loss of alkalis by heterogenous processes on the pipe walls or on ash particles in the flue gas flow may occur [23]. However, the measured Na concentrations do correlate approximately with the sodium coal content (as given by Na_2O in the ash) of 0.9 wt% for the hard coal and <0.1 wt% for the lignites. (It should also be noted that the ash content of the hard coal was 15.6%, as against 4.7 and 6.2% for lignites I and II.) The measured NaCl values also correlate with chlorine of the coal sample: Lignites I and II contain 0.04 and 0.03% of the air-dried material, respectively, whereas the hard coal contains 0.21% chlorine. Similar trends were found in previous studies [5,24], where signal intensities for sodium were found to increase with increasing total chlorine content. In Ref. 5, ELIF was used to obtain *relative* fluorescence signals for different coals in a drop tube furnace reactor, while Ref. 24 describes *absolute* sodium concentration measurements in a fluidized-bed reactor using probe sampling for flame emission spectroscopy. However, the results of Ref. 24 cannot be compared directly with our results since the reactor conditions were entirely different and the coals used were of different structure and composition.

For the measurements presented here, we estimate an overall factor of two uncertainty in the absolute measured concentrations. The main contributor was the calibration of the energy monitors during measurements, due to deposition of dust from the industrial environment on the detector optics. This problem has now been largely rectified by placing the optics and detector parts in a closed container, which will reduce this uncertainty to about 10–20% over a day. Other factors are (1) statistical errors of ~10% in the signal, (2) uncertainty in the quenching data (max. 10%), (3) uneven adherence of reactor dust to the windows, giving uncertainty in the laser energy in the flue gas, and (4) variations in absorption of the laser beam by the flue gas of about 10% over several seconds (this is mainly due to variations in the amount of ash in the flue gas, but fluctuations in gas composition, leading to variations in beam absorption, could also contribute slightly).

Finally, from equilibrium calculations [4,5], condensed NaCl is unlikely to be detected under the present conditions. Even if NaCl-coated ash particles were present in the flue gas flow, signals from such particles should be negligible, as shown by tests with 193-nm laser radiation on NaCl crystals [5].

Conclusions

These results from the DMT reactor are the first to be obtained from the flue gas of a fluidized-bed system using such an in-situ method. It was shown that usable fluorescence intensities can be obtained under realistic experimental conditions. Sodium concentrations were determined for a series of different coals, and distinct differences in concentration history with reactor conditions and coal type could be discerned. Based on the signal-to-noise ratios, a detection limit of 0.1 ppb is estimated for the present conditions.

Further measurements at the fluidized-bed reactor are in preparation, whereby necessary modifications to the optical access are being made so that the pressure can be raised to several bar and so that potassium concentrations also can be determined simultaneously. Test measurements on KCl performed in our laboratory cell suggest that a similar sensitivity could be achieved as for NaCl. Finally, measurements in collaboration with the University of Tampere/Finland are in preparation. Here, the atomic absorption/emission method of Ref. 17, in which the alkali compounds are dissociated by an electric arc, will be used simultaneously with the ELIF method to detect alkalis in the reactor flue gas. In this way, direct comparison of two different techniques will be feasible.

Acknowledgments

Support of this work by Deutsche Montan Technologie Gesellschaft für Forschung und Prüfung mbH, the Commission of the European Communities (Project No. JOUF-0052), and in the initial stages of the work, the Bundesministerium für Forschung und Technologie (Project No. 0326215B) is gratefully acknowledged. We thank U. Busch, B. Peters, M. Mayer, and L. Holl (DMT) for technical assistance. S. Nord is thanked for assistance with calibration measurements.

REFERENCES

1. Osborn, G. A., *Fuel* 71:131–142 (1992); Scandrett, L. A., and Clift, R., *J. Inst. Energy* 57:391–397 (1984).
2. Meienburg, W., Wolfrum, J., and Neckel, H., *Twenty-Second Symposium (International) on Combustion*, The Combustion Institute, Pittsburgh, 1990, pp. 231–236.
3. Arnold, A., Dinkelacker, F., Heitzmann, T., Hentschel, W., Monkhouse, P., Schäfer, M., Schindler, K. -P., Sick, V., and Wolfrum, J., *Twenty-Third Symposium (International) on Combustion*, The Combustion Institute, Pittsburgh, 1992, pp. 1605–1612.
4. Wibberley, L. J., and Wall, T. F., *Fuel* 61:87–92 (1982).
5. Helble, J. J., Srinivasachar, S., Ham, D. O., Boni, A. A., Charon, O., and Modestino, A., *Combust. Sci. Technol.* 81:193–205 (1992).
6. Davidovits, P., and Brodhead, D. C. *J. Chem. Phys.* 46:2968–2973 (1967); Silver, J. A., Worsnop, D. R., Freedman, A., and Kolb, C. E., *J. Chem. Phys.* 84:4378–4384 (1986).
7. Oldenburg, R. C., and Baughcum, S. L., *Anal. Chem.* 58:1430–1436 (1986).
8. Rensberger Weiland, K. J., Wise, M. L., and Smith, G. P., *Appl. Opt.* 32:4066–4073 (1993).
9. a) Takubo, Y., Okamoto, T., and Yamamoto, M., *Japan J. Appl. Phys.* 24:L263–L265 (1985); *Appl. Opt.* 25:740–743 (1986); Alfano, A., *Appl. Opt.* 28:5010–5015 (1989); b) Monkhouse, P., and Wolfrum, J., *Proceedings, Joint Meeting, Italian and Soviet Sections of the Combustion Institute*, Pisa, The Combustion Institute—Sezione Italiana, Naples, Italy, 1990.
10. Ham, N., and Hannaford, P., *J. Phys. B.* 12:L199–L203 (1979); Earl, B., Herm, R., *J. Chem. Phys.* 60:4568–4578 (1974); Barker, J. R., Weston, R. E., *J. Chem. Phys.* 65:1427–1442 (1976).
11. Hartinger, K. T., Nord, S., and Monkhouse, P., *Chem. Phys. Lett.* submitted.
12. Haase, W. J., Jr., Eckels, D. E., Kniseley, R. N., and Fassel, V. A., *Proceedings, Symposium on Instrumentation Control for Fossil Energy Progress*, Argonne Natl. Lab. Press, Argonne, Illinois, 1982, pp. 754–767.
13. Loree, T. R., and Radziemski, L. J., *Proceedings, 1981 Symposium on Instrumentation Control for Fossil Energy Progress*, Argonne National Laboratory Press, Argonne, Illinois, 1982, pp. 768–774.
14. Campisi, A., Report LO/88/003(1988), Research & Development Department, State Electricity Commission of Victoria/Australia.
15. Wen, C. S., Cowell, L. H., Smit, F. J., Boyd, J. D., and LeCren, R. T., *Fuel* 71:219–224 (1992).
16. Mojtahedi, W., Kurkela, E., and Nieminen, M., *J. Inst. Energy* 63:95–100 (1990).
17. Hernberg, R., Tampere University of Technology Publications 22, Finland, 1983.
18. Bonn, B., Baumann, H., Mayer, M., Internal VGB-Konferenz "Wirbelschichtsysteme," 1992, September 2–3, 1992, Essen Germany: Mayer, M., Bonn, B., and Baumann, H., *VDI-Ber.* 1090:83–90 (1993).
19. Chase, M. W., Davies, C. A., Downey, J. R., Jr., Frurip, R. A., McDonald, R. A., and Syverud, A. N., *J. Phys. Chem. Ref. Data* 14:(1) (1985).
20. Davidson, D. F., Chang, A. Y., Kohse-Höinghaus, K., and Hanson, R. K., *J. Quant. Spec. Radiat. Transfer* 42:267–278 (1989).
21. Lee, M. P., and Hanson, R. K., *J. Quant. Spectrosc. Radiat. Transfer* 36:425–440 (1986).
22. Hartinger, K. T., Nord, S., Monkhouse, P., to be published.
23. Lee, S. H. D., Myles, K. M., *Proceedings, International Conference on Fluidized-Bed Combustion*, Boston, 1987, Vol. 2, pp. 793–801.
24. Lee, S. H. D., Teats, F. G., Swift, W. M., and Banerjee, D. D., *Combust. Sci. Technol.* 86:327–336 (1992).

COMMENTS

Rolf Hernberg, Tampere University of Technology, Finland. In your method, the presence of ash particles in the flow could affect the intensity of the laser beam as well as the fluorescent light through absorption and scattering of the light. Do you have a way of accounting for such effects and their influence on the measured intensity?

Author's Reply. As can be seen from Fig. 3, energy monitors were used in front of and behind the measurement point to determine the total attenuation of the laser beam, which is due to (1) absorption by the window material, (2) ash on the windows, (3) ash immersed in the flue gas, and (4) gas-phase flue gas species in the measurement region (O_2,CO_2,H_2O). The absorption by the window material is well known, and the contribution by gas-phase species can be calculated from the flue gas composition and the temperature. The difference between these two contributions and the measured total attenuation is attributed, in the evaluation, to ash on the windows. Treating ash immersed in the flue gas as ash on the windows leads to only small errors in the normalized fluorescence signal, provided that the attenuation by the immersed ash is <90%, which was always the case.

Twenty-Fifth Symposium (International) on Combustion/The Combustion Institute, 1994/pp. 201–209

A FIELD STUDY ON THE TRACE METAL BEHAVIOUR IN ATMOSPHERIC CIRCULATING FLUIDIZED-BED COAL COMBUSTION

TERTTALIISA LIND, ESKO I. KAUPPINEN AND JORMA K. JOKINIEMI
VTT Aerosol Technology Group
P.O. Box 1401, FIN-02044 VTT, Finland

AND

WILLY MAENHAUT
University of Gent, Institute for Nuclear Sciences
Proeftuinstraat 86, B-9000 Gent, Belgium

Trace element behaviour in atmospheric circulating fluidized-bed combustion (CFBC) of Venezuelan bituminous coal was studied by determining particle size distributions in the CFBC flue gas. The size distributions of calcium, iron, aluminium, and 21 trace elements, Sc, V, Cr, Mn, Co, Ni, Zn, Ga, As, Se, Sr, Cd, Sb, Cs, Ba, La, Ce, Sm, Lu, Pb, and Th, in the size range 0.01–70 μm, were determined by collecting aerosols with a low-pressure impactor-cyclone sampling train from the flue gases of an 80-MW(th) CFBC boiler upstream of the electrostatic precipitator. The collected samples were analyzed gravimetrically and with instrumental neutron activation analysis (INAA), particle-induced x-ray emission analysis (PIXE), and inductively coupled plasma mass spectrometry (ICP-MS). The number size distributions of the aerosols were determined with a differential electrical mobility method in the size range 0.01–0.8 μm. In the ultrafine particle mode, i.e., $D_p < 0.1$ μm, the CFBC number concentrations varied strongly during the experiments, being one to two orders of magnitude lower than those observed in pulverized coal combustion. For all of the elements studied, 75% or more were found in particles larger than 5 μm. None of the studied elements showed significant vaporization and subsequent chemical surface reaction or condensation in the CFBC. The Sr, Sc, V, Zn, Ga, Cs, Ba, La, Sm, Lu, and Th size distributions resembled those of aluminium, suggesting their occurrence in aluminosilicate-rich particles in the fly ash. The association of the trace elements with aluminium in the fly ash particles may result from reactions of the trace elements with the aluminosilicate mineral particles inside the burning coal particles, or their initial occurrence in association with these minerals.

Introduction

Coal combustion is a major source of toxic species emitted to the atmosphere. During combustion, trace elements contained in the coal are transformed and either retained in the boiler bottom ash, captured by the gas cleaning devices, or released to the atmosphere as particles or gases. The total emission to the atmosphere depends on the transformations of the noncombustible matter in the coal during combustion, and on the gas cleaning equipment employed at the combustion unit.

The combustion behaviour of noncombustible matter in coal, including trace elements, is determined by their occurrence in the coal, the size and temperature history of the coal particle, the atmosphere the coal particle is exposed to, and the flow conditions in the combustion unit. The form of occurrence in the coal is important when connecting the combustion behaviour with the coal characteristics. Many studies on the occurrence of trace elements in the coal have revealed that they are found in various forms, as reviewed by Finkelman [1] and Swaine [2]. The trace elements are found in association with, e.g., pyrite and accessory sulphides, carbonates, clays, selenides, and organic matter. For many trace elements, the occurrence can only be determined speculatively, as most studies are based on indirect measurement, e.g., leaching behaviour or density determination (float and sink method) [2]. In a recent study, x-ray absorption fine structure spectroscopy (XAFS) method was used to study the occurrence of arsenic and chromium in several U.S. coals directly [3].

In many field and laboratory studies on pulverized coal combustion (PCC), the trace elements have been found to be enriched in the submicron particles [4–8]. The enrichment is believed to result from the vaporization of these species during the combustion, followed by condensation of the vaporized species on the surfaces of the pre-existing particles entrained in the flue gas [9]. During the pulverized coal combus-

tion, high number concentrations of fine particles are formed when the vaporized fraction of the refractory oxides (e.g., Fe, Mg, Si, Al, Ca) condenses homogeneously prior to the condensation of the trace metals. The condensation of the trace metals is proportional to the surface area of the particles, and hence occurs predominantly on the fine particle surfaces, resulting in their enrichment with condensed species [10]. Also, chemical reactions of trace element vapours at the fly ash particle surfaces would result in their enrichment in submicron ash particles [11]. This is particularly harmful to the environment, as particles in the size range 0.1–1.0 μm have been found to penetrate readily particle removal equipment [12]. Also, some of the condensed species on the emitted fly ash particles may be easily leached in dilute acids, enabling the transport of the trace elements into the surface water, soil, and finally into the groundwater. The trace elements that are not vaporized and thus retained in the residual ash particles during combustion are usually not easily removed from the ash particles by leaching in dilute acids. While in the ambient air, however, the fly ash particles may also be exposed to concentrated acids. This may occur either within accumulation mode ambient aerosol particles (0.1–1 μm in diameter, only submicron fly ash particles), within fog droplets (all emitted ash particles smaller than a few microns), or within cloud droplets (all emitted ash particles). As a result, the solubility of trace elements may increase prior to the dry and wet deposition.

Several elements have been found to partially vaporize in the pulverized coal combustion studies. Profound laboratory studies conducted by Quann et al. [7] showed large differences in the composition of the submicron particles for the coals with varying characteristics regarding rank and origin. The major components of the submicron fume were SiO_2 for bituminous coals, and MgO, CaO, and FeO for lower-rank coals. Enrichment in the fine particles was seen for, e.g., arsenic, antimony, cobalt, chromium, and manganese. Despite the enrichment of the trace elements, the major fraction of the total mass in the fine particles consisted of coal matrix elements. Also, major fractions of the trace elements were found in the supermicron fly ash particles, indicating that only minor fractions were released to the gas phase during combustion. In the field studies, vaporization and condensation behaviour has been observed for, e.g., arsenic, antimony, mercury, zinc, nickel, vanadium, copper, cadmium, strontium, barium, and selenium [4–6,13].

According to our recent studies on the submicron particle size distributions from the real-scale PCC [14], the submicron particles form two distinctive modes. Ultrafine mode was observed in the range 0.03–0.1 μm, being formed from the vaporized ash matrix species via nucleation. The intermediate mode was found between 0.3 and 0.7 μm, consisting mainly of coal matrix species. Accordingly, the assumption that all the submicron-sized particles have been formed from the gaseous ash species is not necessarily valid, and this has to be taken into account while interpreting the results of any previous studies on the ash matrix and trace element combustion behaviour.

Most of the studies on the trace element behaviour in coal combustion have concentrated on PCC. Fluidized-bed combustion (FBC) differs significantly from PCC. In FBC, the temperature history of the particles is different from that of a PCC because of large coal feed particle size and the dense bed the coal particles are fed to. The combustion times are longer [15], and the peak temperatures and heating rates lower than in the PCC, with gas temperatures of up to 1150 K and particle peak temperatures of up to 1700 K [16,17]. In FBCs, the gas atmosphere encountered by the coal particles varies with the position in the furnace [18]. In the circulating FBC (CFBC), the density of the bed decreases rapidly while going to the upper parts of the furnace, and there is more oxygen available for the combustion. All these parameters are expected to affect the behaviour of ash-forming constituents, including trace elements, during combustion.

Several studies have addressed the trace element partitioning in different sized particles in the fluidized bed combustion [e.g., 19,20,21]. However, no detailed data have been published on the submicron particle size distributions and composition. Consequently, the fraction of the trace metals released to the gas phase and later condensed during FBC is not known. In this study, we approached the problem by measuring, for the first time, detailed fly ash size distributions from a real-scale circulating fluidized-bed boiler flue gases upstream of the electrostatic precipitator using advanced aerosol measurement techniques. The particle characteristics, including physical (number and mass) as well as elemental size distributions, were determined in the particle size range 0.01–70 μm. The coal and limestone sorbent were also carefully characterized with regard to their mineral and trace metal contents. Size-classified fly ash particle samples were analyzed with instrumental neutron activation analysis (INAA), particle-induced x-ray emission analysis (PIXE) and inductively coupled plasma mass spectrometry (ICP-MS) methods for up to 50 elements. Detailed size distribution data for trace elements associated with both coal and limestone are compared with size distributions of elements abundant in coal and in limestone. The trace element vaporization and condensation as well as possible reactions inside the burning coal particles are discussed on the basis of experimental fly ash size distribution data. We have earlier reported data on the alkali metal behaviour in CFBC [22] and presented the analytical procedures used in INAA and PIXE analyses [26,27].

Process Description

The experiments were carried out at an 80-MW(th) steam-generating atmospheric circulating fluidized-bed combustion unit during two one-week periods in March and August 1990, hereby marked as 3/90 and 8/90, respectively [22]. Venezuelan bituminous coal was burned during the experiments, and limestone was used as a sulphur sorbent. In the experimental period 8/90, some English, higher-sulphur coal was accidentally mixed in the coal feed silo at the beginning of the experimental week. The process parameters are described in Ref. 22.

Methods

Aerosol Sampling:

The mass and elemental size distributions were determined by collecting size-classified coal combustion aerosol samples with an 11-stage multijet compressible flow Berner-type low-pressure impactor (BLPI) [4,23,24]. Because of high particle concentrations in the CFBC flue gas, double stages were used in the impactor in stages 7, 8, and 9 to prevent overloading of these stages during the latter experimental period, i.e., 8/90. Thin aluminium (Al) and polycarbonate (poreless Nuclepore, NP) films greased with Apiezon L vacuum grease were used as impaction substrates [24]. A cyclone with Stokes cut diameter of 5.4 μm was used as a precutter sampling device to prevent overloading of the upper BLPI stages. The cyclone-collected particles were size classified with the Bahco-sieve method. The BLPI and cyclone sampling system is described in more detail in Refs. 14 and 22.

The combustion aerosol number size distributions in the size range 0.01–0.8 μm were determined by sampling in-stack through a precyclone having a Stokes cut diameter of 2.5 μm, followed by dilution with a two-stage, ejector-based dilution system [25], and measuring the diluted aerosol with a differential mobility analyser (DMA, TSI model 3071) by using a condensation nucleus counter (CNC, TSI model 3020) as a number concentration sensor [14,22].

Analytical Techniques:

The BLPI samples were weighed carefully on a microbalance before and after the sampling. The cyclone-collected samples were weighed to determine the total mass of the samples and size classified with a Bahco-sieve method. The size fractions were weighed and stored for elemental analyses.

Up to about 50 elements were determined in the samples with INAA, ICP-MS, and PIXE. Only polycarbonate substrates were used for elemental analysis of the BLPI samples. Sample preparation, analysis procedures, and analytical errors are discussed in Refs. 26 and 27, respectively. For the inductively coupled plasma mass spectrometry (ICP-MS) analysis, the BLPI samples were digested in 1.5 mL of concentrated suprapure HNO_3 kept in an ultrasonic bath in a Teflon bomb for 4 h at 150 °C, and then diluted into 10 mL with 1% HNO_3. Cyclone-collected and size-classified samples were digested in 10 mL of concentrated suprapure HNO_3 and kept in an ultrasonic bath in a Teflon bomb for 8 h at 150 °C. After digestion, the solutions were filtered and analyzed with ICP-MS.

Coal and limestone sorbent were analyzed with INAA and ICP-MS, coal also with PIXE. For ICP-MS, the coal and limestone samples were prepared similarly as the cyclone-collected fly ash. Coal and limestone samples were analyzed for both experimental periods. The coal minerals were analyzed at the University of Kentucky using computer-controlled scanning electron microscopy (CCSEM).

Results and Discussion

Coal and Limestone Analysis:

The average concentrations for 21 trace elements, and Ca, Fe, and Al, in coal and limestone are presented in Table 1. The concentrations of Ni and Sr in the limestone and Cd in the coal were under the detection limit of INAA and PIXE. For these elements, the values given in Table 1 have to be considered as the highest concentration limit. The most abundant trace elements in this coal were Sr, Ba, and Mn (which was also abundant in limestone). For all the elements considered, the concentration in the coal was higher in the 8/90 sample than in the 3/90 sample. This can be explained by the addition of the English coal in the Venezuelan coal used during the 8/90 experimental period, but also, the composition of the same coal is not necessarily uniform. The chlorine content in the coal was 220 ppm.

During the experiments, the average limestone feed in the CFBC was 0.06 kg/s in 3/90 and 0.11 kg/s in 8/90. Coal feed was 2.60 kg/s during both experimental periods. Average feed particle sizes for coal and limestone were 2 mm and 200 μm, respectively. The higher limestone feed in the 8/90 experimental period was needed because of the high-sulphur English coal that was burned along with the Venezuelan coal. The ratio of the coal feed rate to the limestone feed rate was 43 and 27 for 3/90 and 8/90, respectively. Hence, considering the trace element concentrations in the coal and limestone from Table 1, we see that the trace elements are mostly fed to the CFBC in the coal. The amount of the trace elements that is fed in the limestone is typically few percent of the total trace element concentration. Limestone contributed more than 20% only for Mn and Ni.

TABLE 1
The trace element and calcium, iron, and aluminium concentrations in the Venezuelan coal and sorbent limestone.

Element	Coal (ppm)	Limestone (ppm)
Ca	2,720	346,000
Fe	2,060	3,240
Al	5,470	6,410
Sc	0.8	1.0
V	8.7	2.9
Cr	4.7	4.2
Mn	28	540
Co	1.0	0.7
Ni	3.7	<39
Zn	8.6	21
Ga	1.4	2.0
As	1.1	0.3
Se	7.9	0.3
Sr	23	<139
Cd	<0.5	1.1
Sb	0.3	0.1
Cs	0.2	0.5
Ba	35	41
La	1.6	3.7
Ce	2.8	7.4
Sm	0.3	0.6
Lu	0.03	0.1
Pb	1.1	4.4
Th	0.4	0.9

According to the CCSEM results, the mineral matter in the coal was mostly quartz (20% of the mineral matter), miscellaneous silicates (20%), and calcite (22%) [22]. Iron was found mainly as pyrite (8% of the mineral matter), as confirmed by Mössbauer spectroscopy [28].

Physical Size Distributions:

The submicron aerosol particle number size distributions showed two modes at about 0.02 and 0.3 μm [22]. The number concentrations below 0.1 μm varied strongly during the experiments, being one to two orders of magnitude lower than those reported for pulverized coal combustion [14].

The mass size distributions peaked at about 25 μm. Ninety-three percent of the particle mass was collected in the precutter cyclone, which had a cut diameter of 5.4 μm. Less than 0.1% of the mass was found in the particles smaller than 0.1 μm, and less than 1% in the particles between 0.1 and 1.0 μm. [22].

Differential Elemental Size Distributions:

We present the size distributions for Ca, Al, Mn, and Sr in Fig. 1. The major fraction of all these elements is found in the particles collected in the cyclone, i.e., with diameters larger than 5.4 μm. The relative amount of the particles in the cyclone vs BLPI is highest for Ca and Mn. Al and Sr show clear tendency towards finer particles. The largest particle mode peaks at 15–20 μm instead of 20–30 μm as in the case of Ca. No detectable amount of any of these elements was found in particles smaller than 0.1 μm, as can be seen from the small figure of Sr in the size 0.01–1 μm. No Sr is detected in particles <0.1 μm. Sr concentration increases at 0.1 μm, and detectable mass is observed in the size range 0.1–1μm, where a particle mode is seen in number size distributions [22].

The figure for Sr shows the effect of the double stages used in the BLPI during the experimental period 8/90. The concentrations from the period 3/90 are higher in the stages 5 and 6 because of the particle bounce and re-entrainment from the upper stages. In the measurements of 8/90, the particle bounce was minimized by using double stages in the stages 7, 8, and 9 to prevent overloading, and hence, the mass collected in the subsequent stages, i.e., 5 and 6, is smaller.

Elemental Mass Fraction Size Distributions:

Mass fraction size distributions present the mass of a certain element compared with the total mass of the particles in each particle size class. Mass fraction size distributions were determined for CFBC fly ash particles collected in the BLPI and cyclone. In Fig. 2, we present the mass fraction size distributions for Ca, Al, Mn, and Sr. The errors due to elemental and gravimetrical analyses were smaller than 20%.

None of the elemental concentrations presented in Fig. 2 show $(1/D_p)^n$ dependence on the particle size, indicative of vaporization followed by condensation or surface reaction [29,30]. The concentration is size independent only for very porous particles ($\varepsilon \approx 1$), which is not the case in the CFBC fly ash, as verified by SEM micrographs. In Fig. 2, we see small increase in the mass fraction size distributions with decreasing particle size for aluminium and strontium, but the increase starts in the supermicron particle size range, and no increase is seen in particles <1 μm. Hence, this increase is not due to the condensation or surface reaction process. The similar behaviour of aluminium and strontium mass fraction and differential size distributions suggests the same transformation mechanisms for these elements. Other elements that follow the size distribution of aluminium are Sc, V, Zn, Ga, Cs, Ba, La, Sm, Lu, and Th. This can result from the reactions of these elements with aluminosilicate particles, or these el-

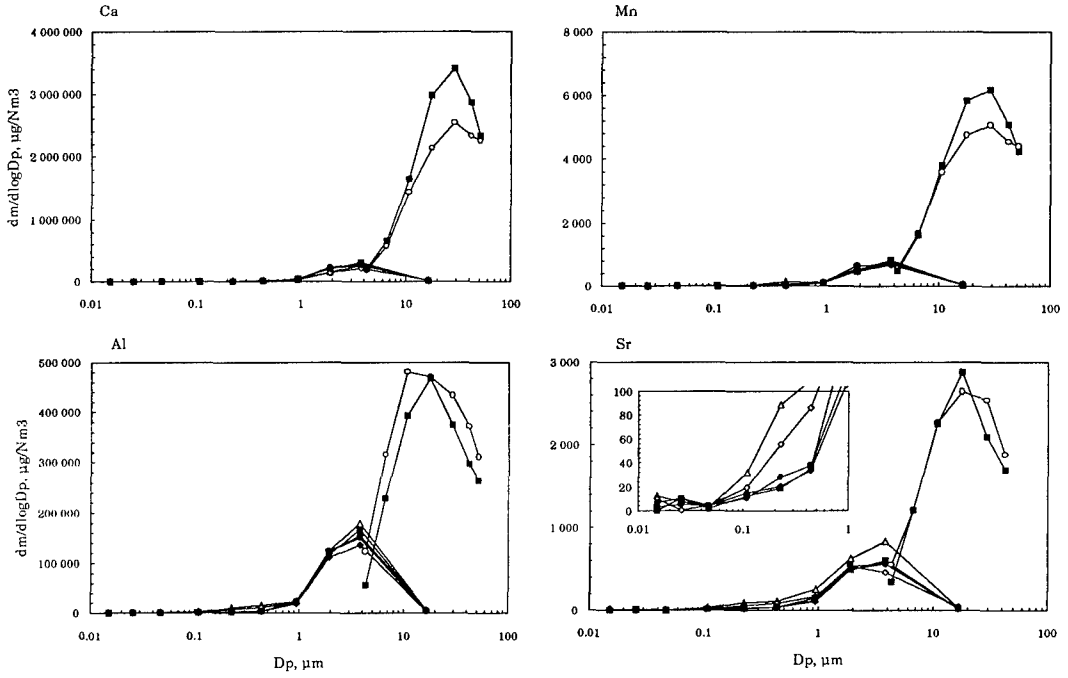

FIG. 1. The CFBC fly ash differential elemental size distributions for Ca, Al, Mn, and Sr determined with BLPI and precutter cyclone and analyzed with INAA and PIXE. Open markers denote the 3/90 and black markers the 8/90 experiments.

ements may be originally bound in the aluminosilicate minerals in the coal. Finkelman et al. [31] suggest the occurrence of strontium in the bituminous coals as partly organically bound and partly as celestite, but the leaching behaviour of strontium can also result from an association with the clays. Swaine [2] reports the occurrence of Sr in bituminous coals also in phosphate minerals and calcite. As phosphorus is low in this coal, the probable modes of Sr are the association with organic matter and calcite minerals. Sc, V, Zn, Ga, Cs, and rare earth elements (La, Sm, Lu) have been found in clay minerals [2]. The organically bound magnesium has been found to react with the aluminosilicate minerals inside or on the surface of the coal particles during PCC [14], so the size distributions of Sr may indicate reactions of the organically bound Sr, or Sr released from calcite, with the aluminosilicate minerals, even though, in FBC, the combustion conditions are different from PCC.

Calcium mass fraction size distributions show a clear increase when increasing particle size. In the largest size ranges, calcium constitutes almost 30% of the total particle mass. This is due to the large limestone feed particle size, with average particle size of 200 μm. Even though 33–42% of the manganese in the CFBC fly ash derives from the limestone, the manganese mass fraction size distribution is significantly different from the mass fraction size distribution of calcium. While calcium content in the fly ash particles increases with increasing particle size, there seems to be only slight increase in the fly ash size distributions of manganese in the largest particle sizes. Swaine [2] reports the occurrence of manganese in the bituminous coals predominantly in carbonate minerals and clays, minor amounts organically bound, and in pyrite. No clear conclusions can be made as to the occurrence of manganese in the CFBC fly ash, although the differential size distributions of calcium and manganese resemble each other.

The Distribution of the Trace Elements in Different Size Classes:

In Table 2, we show the distribution of the total particle mass, the trace elements, and calcium, iron, and aluminium in different size classes. The concentrations presented in Table 2 are average values for the two experimental periods. The concentration values for each size fraction from the two experimental periods were consistent (within 20%) for all the other elements but As. For arsenic, the 3/90 value was only

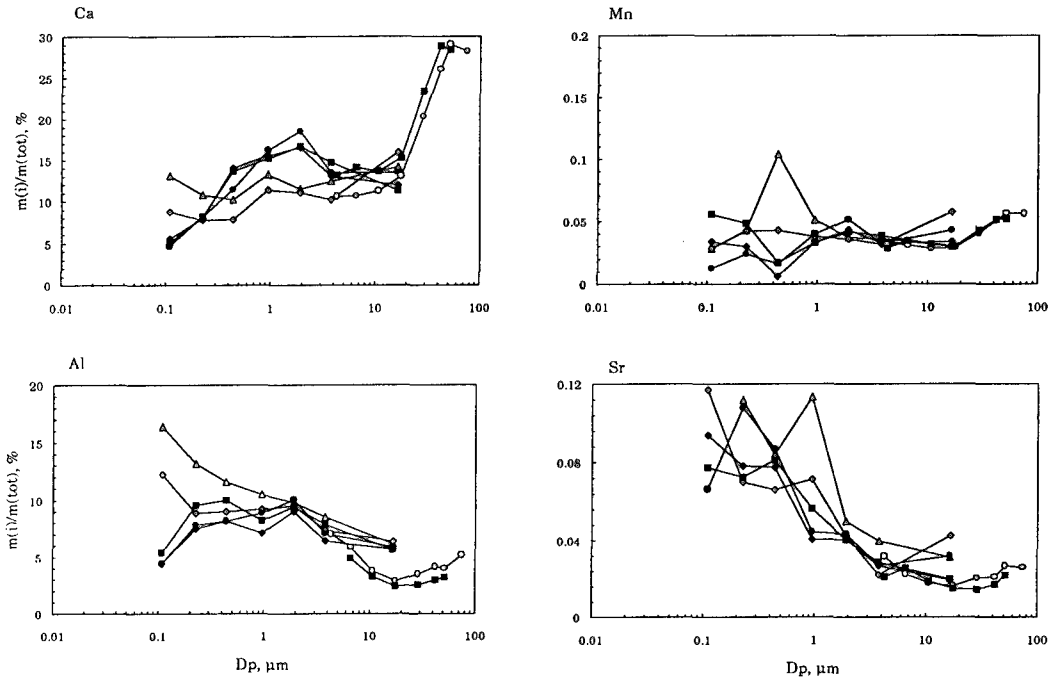

FIG. 2. The CFBC fly ash elemental mass fraction size distributions for Ca, Al, Mn, and Sr determined with BLPI and precutter cyclone and analyzed with INAA and PIXE. Open markers denote the 3/90 and filled markers the 8/90 experiments.

37% of the 8/90 value as a result of higher As concentration in the 8/90 coal.

The finest particle fraction consists of the particles with diameters 0.01–0.07 μm, corresponding to the ultrafine mode at number size distribution [22]. It contains less than 0.1% of the total particle mass collected in the BLPI and the cyclone. The trace element concentrations in this size range are low. For most elements, the concentration in Table 2 is expressed as the upper limit of the concentration (<), because the concentrations are too low to be detected with INAA, PIXE, and ICP-MS. The amount of the trace elements in this size fraction is less than 1% of the total amount of the given element collected.

The second particle size range is 0.07–1.4 μm, corresponding to the intermediate mode in the number size distribution at 0.3 μm. The particles in this size range contain 0.5–7.1% of the total concentration of the trace elements and 0.6% of the total mass of the particles collected. Three trace elements, Mn, Ni, and As, have less than 1% of the total concentration in this size range. A significant fraction of Mn and Ni (23–42%) enter the CFBC within the limestone feed, and in the distribution to the size classes, they seem to follow the behaviour of calcium.

The third size range is 1.4–5 μm and contains the rest of the particles collected in the BLPI. This size range consists mostly of the residual ash and limestone particles and contains 6.3% of the total particle mass collected. Here we can distinguish the depletion of the same elements as in the previous size class. Mn and Ni show very low percentages in this size range, following the behaviour of Ca. Sb and As show lower than average fractions in this size range. All the other trace elements have 11–18% of the total concentration in this size range.

The largest particle size range contains the particles that were collected in the precutter cyclone. The particles in this size range contain 93% of the total mass collected. They are abundant with Ca species, i.e, $CaSO_4$ and CaO. Twenty percent of the total particle mass in the cyclone-collected particles consists of Ca. A major fraction of all the trace elements was found in this large particle fraction, with more than 75% of the total concentration of each element in the cyclone-collected particles. When studied with a SEM, the particles in this size fraction were irregular in shape and consisted of large solid Ca-rich particles, and agglomerates containing several elements, e.g., Al, Si, Fe, and Ca.

Conclusions

In this study, we determined the distributions of 21 trace and three coal matrix elements in the fly ash

TABLE 2
The CFBC fly ash total mass, trace element, and calcium, iron, and aluminium concentrations in different size fractions determined according to the various particle modes

Element	Total (μm/Nm^3)	0.01–0.07 μm (%)	0.07–1.4 μm (%)	1.4–5 μm (%)	5–100 μm (%)
Mass	16,130,000	0.1	0.6	6.3	93
Ca	2,990,000	0.01	0.5	4.7	95
Fe	260,000	0.06	1.1	8.6	91
Al	598,000	0.05	2.0	14	85
Sc	94	0.2	4.1	16	80
V	785	0.1	3.8	17	79
Cr	441	<4.4	3.5	<8.9	83
Mn	6,259	<0.2	0.9	6.4	93
Co	122	0.8	3.2	17	79
Ni	2,112	<0.5	0.5	3.0	96
Zn	956	0.4	1.9	13	84
Ga	148	<0.1	2.6	11	87
As	152	<0.2	0.6	4.1	95
Se	1,076	<0.3	3.4	14	82
Sr	3,310	<0.3	3.0	11	85
Cd	56	<4.5	7.1	14	75
Sb	29	<0.2	1.8	8.9	89
Cs	20	<1.9	2.0	13	83
Ba	3,046	<1.9	<2.6	15	80
La	185	<0.1	3.4	16	81
Ce	387	<1.3	3.7	14	81
Sm	33	0.1	3.4	17	80
Lu	2.8	<2.3	2.5	12	83
Pb	256	<1.1	5.0	16	78
Th	56	<0.6	3.2	18	78

of an 80-MW(th) circulating fluidized-bed unit during the combustion of Venezuelan coal. The experiments were conducted upstream of the electrostatic precipitator. A limestone sorbent was used in the CFBC to capture SO_2 during the experiments. The trace elements in the CFBC originated mainly from coal. The detailed fly ash particle size distributions for the trace and matrix elements were determined from the flue gases in the size range 0.01–70 μm. None of the studied elements showed $(1/D_p)^n$ dependence on the particle size, indicative of significant vaporization followed by condensation or surface reaction in the CFBC. According to the data obtained in this study, only partial vaporization of the trace elements is possible. The Sr, Sc, V, Zn, Ga, Cs, Ba, La, Sm, Lu, and Th size distributions resembled those of aluminium, suggesting their occurrence in aluminosilicate-rich particles in the fly ash. The similar size distributions of the trace elements with aluminium may result from reactions of the trace elements with the mineral particles, or their initial occurrence in association with the minerals. More work is needed on the occurrence of the trace elements in the coal to connect the trace metal behaviour in combustion with the coal characteristics, and also on the determination of the trace metal reactions with the limestone sorbent particles.

Acknowledgments

The authors want to thank the Ministry of Trade and Industry of Finland and companies IVO, Ahlström, and Tampella for funding the study through the combustion research program LIEKKI. We are grateful to Professor Frank Huggins and Mr. Anup Shah from the University of Kentucky for CCSEM analyses. Willy Maenhaut is grateful to the Belgian "Nationaal Fonds voor Wetenschappelijk Onderzoek" and the "Interuniversitair Instituut voor Kernwetenschappen" for research support.

REFERENCES

1. Finkelman, R. B., "Modes of Occurrence of Potentially Hazardous Elements in Coal: Levels of Confidence," to be published.

2. Swaine, D. J., *Trace Elements in Coal,* Butterworth & Co. Ltd., Tiptree, UK, 1990.
3. Huggins, F. E., Shah, N., Zhao, J., Lu, F., and Huffman, G. P., *Energy Fuel* 7:482–489 (1993).
4. Kauppinen, E. I., and Pakkanen, T. A., *Environ. Sci. Technol.* 24:1811–1818 (1990).
5. Markowski, G. R., and Filby, R., *Environ. Sci. Technol.* 19:796–804 (1985).
6. McElroy, M. W., Carr, R. C., Ensor, D. S., and Markowski, G. R., *Science* 215:13–19 (1982).
7. Quann, R. J., Neville, M., and Sarofim, A. F., *Combust. Sci. Technol.* 74:245–265 (1990).
8. Quann, R. J., Neville, M., Janghorbani, M., Mims, C. A., and Sarofim, A. F., *Environ. Sci. Technol.* 16:776–781 (1982).
9. Flagan, R. C., and Seinfeld, J. H., *Fundamentals of Air Pollution Engineering,* Prentice-Hall, Englewood Cliffs, NJ, 1988, pp. 358–372.
10. Jokiniemi, J. K., Lazaridis, M., Lehtinen, K. E. J., and Kauppinen, E. I., "Numerical Simulation of Vapour-Aerosol Dynamics in Combustion Processes," *J. Aerosol Sci.* 25:429–446 (1994).
11. Linak, W. P., and Wendt, J. O. L., *Prog. Energy Combust. Sci.* 19:145–185 (1993).
12. Kauppinen, E. I., Ylätalo, S. I., Joutsensaari, J., and Jokiniemi, J. K., *Tenth Particulate Control Symposium and Fifth International Conference on Electrostatic Precipitation,* April 5–8, 1993, Washington, DC.
13. Davidson, R. L., Natusch, D. F. S., and Wallace, J. R., *Environ. Sci. Technol.* 8:1107–1113 (1974).
14. Joutsensaari, J., Kauppinen, E. I., Jokiniemi, J. K., and Helble, J. J., in *The Impact of Ash Deposition on Coal Fired Plants: Proceedings of the Engineering Foundation Conference* (J. Williamson and F. Wigley, Eds.), Taylor & Francis, 1994, pp. 613–624.
15. Sarofim, A. F., Beer, J. M., Baron, R. E., and Hodges, J. L., in *AFBC Technical Source Book* (S.-E. Tung and G. C. Williams, Eds.), Final Report, DOE/MC/14536–2544, 1987.
16. Tang, J. T., and Taylor, E. S., in *AFBC Technical Source Book* (S.-E. Tung and G. C. Williams, Eds.), Final Report, DOE/MC/14536–2544, 1987.
17. Hernberg, R., Stenberg, J., and Zethraeus, B., *Combust. Flame* 95:191–205 (1993).
18. Agarwal, P. K., and La Nauze, R. D., *Chem. Eng. Res. Des.* 67:457–480 (1989).
19. Weissman, S. H., Carpenter, R. L., and Newton, G. J., *Environ. Sci. Technol.* 17:65–71 (1983).
20. Clarke, L. B., *Fuel* 72:731–736 (1993).
21. Mojtahedi, W., Nieminen, M., Hulkkonen, S., and Jahkola, A., *Fuel Proc. Technol.* 26:83–97 (1990).
22. Lind, T. M., Kauppinen, E. I., Jokiniemi, J. K., Maenhaut, W., and Pakkanen, T. A., in *The Impact of Ash Deposition on Coal Fired Plants: Proceedings of the Engineering Foundation Conference* (J. Williamson and F. Wigley, Eds.), Taylor & Francis, 1994, pp. 77–88.
23. Kauppinen, E. I., *Aerosol Sci. Technol.* 16:171–197 (1992).
24. Hillamo, R. E., and Kauppinen, E. I., *Aerosol Sci. Technol.* 14:33–47 (1991).
25. Koch, W., Lödding, H., Mölter, W., and Munzinger, F., *Staub -Reinhaltung der Luft* 48:341–344 (1990).
26. Maenhaut, W., Kauppinen, E. I., and Lind, T. M., *J. Radioanalyt. Nucl. Chem.* 167:259–269 (1993).
27. Maenhaut, W., Royset, O, Vadset, M., Kauppinen, E. I., and Lind, T. L., *Nucl. Instrum. Meth. Phys. Res. B* 75:266–272 (1993).
28. Huggins, F. E., and Huffman, G. P., in *Mssbauer Analysis of the Iron-Bearing Phases in Coal, Coke and Ash, Analytical Methods for Coal and Coal Products* (C. Karr, Jr., Ed.), Academic Press, New York, 1979, Vol. III.
29. Flagan, R. C., and Friedlander, S. K., *Recent Developments in Aerosol Science* (D.T. Shaw, Ed.), Wiley, New York, 1978, pp. 25–59.
30. Hinds, W. C., *Aerosol Technology: Properties, Behaviour, and Measurement of Airborne Particles,* Wiley, New York, 1982, pp. 249–262.
31. Finkelman, R. B., Palmer, C. A., Krasnow, M. R., Aruscavage, P. J., Sellers, G. A., and Dulong, F. T., *Energy Fuels* 4:755–767 (1990).

COMMENTS

Dino Musmarra, CNR-Instituto di Ricerche Scilla Combustione, Italy. The mercury emissions from the combustion of coal are considered to be responsible for more than 50% of the total anthropogenic emissions. While your paper takes into account numerous metals, why is mercury not considered?

Author's Reply. In coal combustion, mercury has been found to be highly volatile, and a major fraction of it is expected to be found in the gas phase in the flue gas upstream of the particle removal equipment. In order to study the mercury behaviour in combustion, both gas phase and particulate phase mercury should be determined. In this study, however, we concentrated only on particulate phase in the flue gas, and no mercury was detected with any of the analysis methods used.

•

J. A. Kozinski, McGill University, Canada. 1. Do you have any idea how metals you have analyzed were distrib-

uted in the particle? Were they concentrated in the surface layers or inside ash particles?

2. What was the accuracy of metal concentration measurements in particles as small as 10 nm in diameter?

Author's Reply. We did not measure the distribution of the metals in individual fly ash particles. We collected the particles from the flue gas with a low-pressure impactor, which collects the particles according to their aerodynamic mobility. The elemental analyses were then carried out for these narrow, well-defined particle size-fractions collected in the impactor, not individual ash particles. From these analyses, no conclusions can be made on the distribution of the elements in individual ash particles.

Twenty-Fifth Symposium (International) on Combustion/The Combustion Institute, 1994/pp. 211–218

THE OXIDATION OF CALCIUM SULPHIDE AT THE TEMPERATURES OF FLUIDISED-BED COMBUSTORS

N. H. DAVIES AND K. M. LAUGHLIN
Coal Research Establishment
Stoke Orchard, Cheltenham
Gloucestershire GL52 4RZ, UK

AND

A. N. HAYHURST
Department of Chemical Engineering
University of Cambridge
Pembroke Street, Cambridge CB2 3RA, UK

Calcium sulphide is a major product from coal gasification processes that use limestone as a desulphurising agent; also, it may be formed in fuel-rich regions of fluidised-bed combustors. Complete conversion of CaS to $CaSO_4$ via the gas-solid reaction $CaS + 2O_2 \rightarrow CaSO_4$ is desirable to allow safe disposal of the bed ash material. This reaction has been investigated at temperatures from 650 °C to 1050 °C using thermogravimetric analysis. The results revealed, inter alia, a discontinuity in product formation with increasing temperature: Above 850 °C, CaO is also formed with the evolution of SO_2. This has been shown to be a result of the apparent solid-solid reaction $CaS + 3CaSO_4 \rightarrow 4CaO + 4SO_2$, which occurs above about 900 °C, when a liquid melt is probably produced. The observation of CaO production at 850 °C during CaS oxidation, however, is a consequence of the exothermicity of the reaction forming $CaSO_4$ raising the particle temperature above 900 °C, thereby initiating the solid-solid reaction between product $CaSO_4$ and reactant CaS. This rise in temperature, coupled to the change in porosity caused by both $CaSO_4$ and CaO formation, gives rise to slightly sigmoidal mass-time plots from the thermogravimetric experiments. A kinetic study of the oxidation of CaS to $CaSO_4$ has shown it to be first order in O_2, with a rate constant of $4.5 \pm 2.0 \times 0^{-4} \exp[-(5.7 \pm 1.5)10^3/T]$ m/s. The overall conclusion is that, although CaS is converted to $CaSO_4$ at the operating temperatures of fluidised-bed combustors, reaction between these two solids starts for particle temperatures between 850 °C and 900 °C, probably via a melt, and results in the undesirable evolution of SO_2.

Introduction

The use of limestone as a sulphur sorbent in coal combustion processes has resulted in a growing interest in the fate of CaS, which forms in fuel-rich regions of the combustor [1–3]. More recently, this interest has been heightened by the introduction of fluidised-bed coal gasification for use in power generation [4]. One such process is the British Coal Topping Cycle, which involves partial gasification of coal, producing a hot gas which, after cleaning, drives a gas turbine [5]. The residual char from the gasifier is burnt in a fluidised-bed combustor to raise steam, which drives another turbine. Limestone is added to the gasifier to remove the major sulphurous species, H_2S; it is important that the product CaS [6], on passing into the O_2-rich combustor, be oxidised to $CaSO_4$ to allow safe disposal of the ash, etc.

Experimental

A Stanton Redcroft STA 780 thermogravimetric analyser (TGA) was used to study the reaction

$$CaS + 2O_2 \rightarrow CaSO_4; \qquad \Delta H^\circ_{298} = -960.9 \text{ kJ/mol.} \quad (1)$$

It has been found [2,3] that, during CaS oxidation, SO_2 evolution may occur, depending on the temperature. Therefore, an infrared SO_2 analyser (from ADC), capable of measuring from 10 to 5000 ppm, was used to monitor the product gas stream continuously. This SO_2 analyser was calibrated before each test using a mixture of 2000 ppm SO_2 and N_2. The reactant gases were mixtures of O_2 and N_2. Pure (99.99%) CaS (supplied by Johnson Matthey), of mean particle size 45 μm, was used to eliminate the effect of impurities. BET (Brunauer, Emmett, and Teller) analysis of the CaS using Kr sorption gave the surface area of the CaS particles to be 0.92 m^2/g, and gave an average pore radius of about 5 nm.

A typical experiment involved heating CaS (approximately 10–20 mg) in the TGA to the required temperature in an atmosphere of N_2 flowing at a rate of 3.3×10^{-6} m^3/s. The particles were distributed over quartz wool to separate them and reduce any

effects of interparticle diffusion. On reaching the desired temperature, the gas atmosphere was changed to a mixture of O_2 and N_2. The sample's mass, the SO_2 concentration in the off-gases, and the reactor temperature were all recorded continuously; an experiment was stopped either when a constant sample mass was obtained or about 30 min reaction time had elapsed.

Any SO_2 evolved could be used in conjunction with the weight change to construct a simple mass balance over the system. This is because SO_2 can be assumed [3,7] to be produced by either

$$CaS + 3CaSO_4 \rightarrow 4CaO + 4SO_2; \qquad \Delta H^\circ_{298} = +1047.9 \text{ kJ/mol} \quad (2)$$

or

$$CaS + 3/2O_2 \rightarrow CaO + SO_2; \qquad \Delta H^\circ_{298} = -458.7 \text{ kJ/mol}. \quad (3)$$

In either case, CaO and SO_2 are formed in equimolar amounts. Therefore, assuming that $CaSO_4$ and CaO are the only solid products formed, the composition of the reacting solid at any time t can be calculated from

$$X_{CaO} = \frac{G}{M_0}\int_0^t y_{SO_2} dt \quad (4)$$

and

$$X_{CaSO_4} = \frac{1}{64M_0}[\Delta m + 16M_0X_{CaO}] \quad (5)$$

where X_i is the extent of conversion of CaS to species i, G the total molar flow rate of gas through the analyser, y_{SO_2} the mole fraction of SO_2 in the product gas, Δm the increase in the sample's mass, and M_0 the initial molar amount of CaS.

To verify that $CaSO_4$ and CaO were the only products formed, residues from experiments at 800 °C, 900 °C, and 950 °C were analysed using x-ray diffraction (XRD). Interestingly, at 800 °C, only $CaSO_4$ was formed, whereas at and above 900 °C, CaO was also produced. No evidence was found for $CaSO_3$, in agreement with other attempts [8] to identify it.

Results

Initially, experiments were performed between 850 °C and 1050 °C, using inlet O_2 concentrations of between 4 and 50 vol.% in N_2. An overall weight increase always occurred. The sample's mass and SO_2 profile are shown in Fig. 1 for a typical experiment at 950 °C and an O_2 concentration of 21 vol.%. The

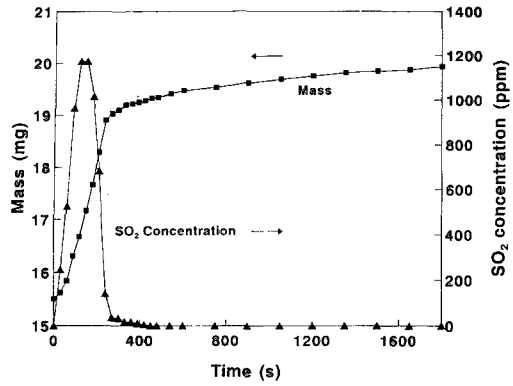

FIG. 1. Typical plots against time of the mass of the sample and concentration of SO_2 in the off-gases for the oxidation of CaS in a TGA at 950 °C, with an inlet O_2 concentration of 21 vol.% in N_2.

SO_2 readings shown have been deconvoluted assuming the sampling system behaves as a CSTR (continuously stirred tank reactor) with a measured mixing time constant of 5 s. Upon introducing O_2 to the sample, Fig. 1 shows a rapid initial weight increase for ≈5 min, the duration of which depends on the temperature and O_2 concentration. This weight increase is accompanied by the evolution of SO_2. This is followed by a longer period (>25 min) of slow weight gain and low concentrations of SO_2. The sample's weight continues to increase after SO_2 evolution has finished. An interesting feature of Fig. 1 is the slightly sigmoidal shape exhibited by the mass profile: There is a very short initial period (≈50 s) when the sample gains weight slowly, followed by a rapid rise and, finally, another period of slow weight increase. This was found to be a characteristic feature of these experiments; an explanation is presented later. Another observation worthy of note is the small overall increase in mass (about 4 mg) in Fig. 1, even after 30 min reaction time. Although the increase in sample weight varied depending on the conditions used, the final value was such that, if the sole product was $CaSO_4$, the conversion, X_{CaSO_4}, would be very small. This agrees with the presence of SO_2 in the off-gases, which suggests the formation of CaO and a corresponding reduction in sample weight.

Figures 2 and 3 show the effect of temperature on the conversion of CaS to CaO and $CaSO_4$, respectively, using an O_2 concentration of 4.2 vol.%. Very little oxide was formed at 850 °C (see Fig. 2), and this was the case for all O_2 concentrations. Also, the conversion to $CaSO_4$ at 850 °C was very low, reaching only 8% for 4.2 vol.% O_2. However, when the temperature was increased, more CaO and $CaSO_4$ were produced; also, they were formed more quickly. Again, the sigmoidal character of the curves in Figs 2 and 3 was evident in every experiment.

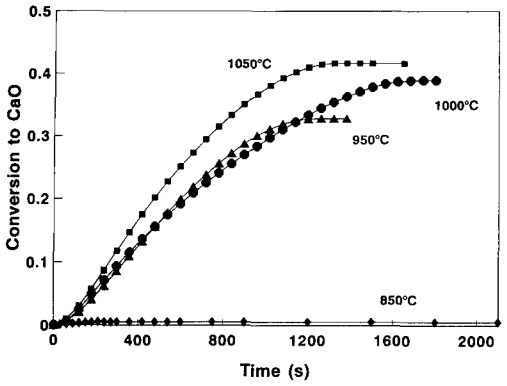

FIG. 2. The fractional conversion of CaS to CaO during CaS oxidation for an inlet O_2 concentration of 4.2 vol.% in N_2 and a variety of temperatures, as shown.

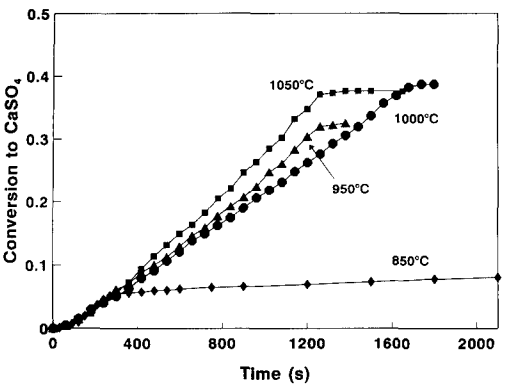

FIG. 3. Effect of temperature on the fractional conversion of CaS to $CaSO_4$ during CaS oxidation, using an inlet O_2 concentration of 4.2 vol.% in N_2.

Figure 4 shows how the ratio X_{CaO}/X_{CaSO_4} varies with time for each temperature and 21 vol.% O_2. The curves show a rapid initial increase to a maximum, followed by a gradual decay. The maximum and final values of X_{CaO}/X_{CaSO_4} increase with temperature. It appears that CaO production is greatest at the beginning of the reaction, and above 950 °C, X_{CaO}/X_{CaSO_4} has a maximum value greater than 1. Following this initial period, $CaSO_4$ formation increases relative to CaO, until a period is reached where X_{CaO}/X_{CaSO_4} becomes constant.

One difficulty in interpreting these results is that the reaction producing CaO is uncertain, being either the solid-solid reaction (2) in series with (1) or the solid-gas reaction (3) in parallel with (1). An idea of the mechanism may be gained from the SO_2 concentration profile in, e.g., Fig. 1. If reaction (3) occurs, the SO_2 concentration should have a maximum value at time $t = 0$ and decay gradually over a period of time. On the other hand, if there are only reactions

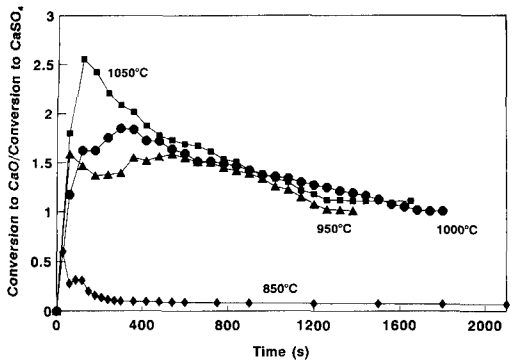

FIG. 4. Variation with time of the ratio of the fractional conversions to CaO and $CaSO_4$ for CaS oxidation at a range of temperatures and 21 vol.% O_2 in N_2.

(1) and (2) in series, the SO_2 concentration will be zero initially and then increase to a maximum before decaying. Figure 1 strongly suggests that the mechanism does involve reactions (1) and (2) in series. However, solid-solid reactions like (2) are improbable, being characteristically slow because of the slow diffusive processes associated with them.

Demonstration of the Reaction between CaS and $CaSO_4$

A mixture of CaS and analytical grade $CaSO_4$ (of mean particle size 20 μm) was prepared in the stoichiometric ratio 1:3. To ensure adequate contact between the two powders, they were mixed thoroughly in an automatic shaker for about 15 min. Before mixing, the $CaSO_4$ was dried in an oven overnight. Experiments were performed at 850 °C, 900 °C, 950 °C, 1000 °C, and 1050 °C in the TGA. The procedure involved heating the reactant mixture to 850 °C at a rate of 15 °C/min in an atmosphere of N_2. On reaching 850 °C, the temperature was ramped up at the highest heating rate of 25 °C/min to the final temperature, which was held for 30 min. Sample mass and SO_2 concentration in the off-gases were both monitored continuously throughout the experiment. The composition of the reacting solid was derived. For example, after 20 min at 950 °C, about 47% of the CaS and $CaSO_4$ had reacted to produce CaO and SO_2. At 1050 °C, 100% conversion to CaO was achieved. However, at 850 °C, no weight change or SO_2 was observed, and although a weight change was observed at 900 °C, no SO_2 was detected. A small conversion occurred during some tests throughout the initial heating-up period, and at 1050 °C, the reaction was complete even before 1050 °C was reached. Thus, the conversion to CaO increased with temperature above 900 °C. An important conclusion is that the solid-solid reaction (2) is indeed suffi-

ciently fast for it to be considered responsible for SO_2 release during CaS oxidation. However, the anomaly is that, if the reaction between CaS and $CaSO_4$ were truly a reaction between solids, such a fast rate would probably not be observed. This seems to suggest that the reaction may involve a gaseous intermediate, as suggested by Chen and Yang [9]. They proposed that $CaSO_4$ decomposes to give SO_3, which subsequently reacts with CaS, giving SO_2 and CaO as products. However, this was discounted here by performing another experiment in the TGA, in which a sample of pure $CaSO_4$ was heated from ambient to the high temperature of 1270 °C at a rate of 15 °C/min in a flow of N_2. No change in mass was observed until 1170 °C was reached. At 1210 °C, the overall mass had fallen by 15%. The temperature was held at 1270 °C, when the mass of the sample fell relatively rapidly. The indications are thus that $CaSO_4$ does not decompose until its temperature is above 1200 °C; this conclusion agrees with previous work [10]. The product gas from the TGA was continuously monitored for sulphur species using a mass spectrometer. Three masses were monitored: 48 (SO), 64 (SO_2), and 80 (SO_3). SO is a possible fragment of both SO_2 and SO_3. Only SO and SO_2 were detected, suggesting that the only sulphurous gas evolved during $CaSO_4$ decomposition at 1200 °C or above is SO_2; this supports the findings of Lau et al. [11]. The other possible way in which CaS and $CaSO_4$ interact is via a melt. Such a mechanism has been suggested before [8,12]. It has been postulated [12] that CaS and $CaSO_4$ are completely ionised during the formation of a liquid phase; the existence of a melt, however, could not be substantiated.

The formation of a melt was checked by taking again CaS and $CaSO_4$ in powder form and making a pellet (5-mm diameter) from the mixture. The pellet was then heated to 1000 °C in N_2, and the evolution of SO_2 was observed. Afterwards, the pellet was set in an epoxy resin, sectioned, and studied in an electron microscope. It then became clear that agglomeration of tiny particles had occurred as a result of them fusing together. Here then is visual evidence of CaS and $CaSO_4$ forming a liquid melt.

These TGA experiments clearly show that reaction (2) could be responsible for SO_2 evolution during CaS oxidation above 850 °C. There is still, however, a slight inconsistency between the results of the experiments in this section and those on the oxidation of CaS. In the latter, SO_2 was detected at 850 °C, whereas the solid-solid reaction in isolation appears to occur above this temperature (between 850 °C and 900 °C). One explanation may be that the oxidation reaction (1), being highly exothermic, causes the particle temperature to rise, thereby initiating the solid-solid reaction (2). The following section accordingly aims to discover if a CaS particle rises in temperature when reacting with O_2.

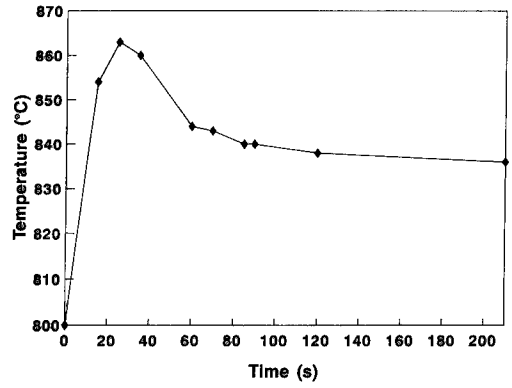

FIG. 5. Temperature history of a CaS particle (5-mm diameter) when reacting with O_2. The inlet concentration of O_2 is 21 vol.% in N_2.

Measurement of the Temperature Change of a CaS Particle during Oxidation

If CaS reacts with O_2 under adiabatic conditions to produce only m' moles of $CaSO_4$, the heat liberated is $Q = m'\Delta H$, where ΔH is the heat of reaction. Literature values [13] of ΔH give $Q = -902.5m'$ kJ at 1300 K. This heats up the m' moles of product from, say, 1300 K to T_{ad}, where $Q = m'C_p(T_{ad} - 1300)$ and C_p is the heat capacity of $CaSO_4$. Using an average value of $C_p = 179.9$ J/K mol, $T_{ad} = 6485$ K is obtained. It is highly unlikely, however, that such a rise will take place in practice, but it does suggest that a substantial temperature increase is possible.

To measure this temperature increase, a type K (2-mm diameter) thermocouple was inserted into a hole drilled in a 5-mm-diameter $CaCO_3$ particle. A small amount of high-temperature cement (Autostic) held the thermocouple in place. The particle was then placed into the hot zone of a horizontal, tubular, silicon carbide furnace. Firstly, the particle was heated to about 950 °C under a flow of N_2 and maintained at this temperature for about 2 h for calcination to finish. The N_2 was then replaced by a gaseous mixture containing 3500 ppm H_2S in N_2, which sulphided the particle. Sulphidation was continued for about 10 h to ensure an adequate buildup of CaS, after which the temperature was allowed to drop to 800 °C. The temperature of the particle was allowed to stabilise, whereupon the flow of H_2S was replaced with N_2. It is important to note that, at this point, there was no increase in temperature, which could have resulted as a consequence of a different gaseous flow rate over the particle. On replacing N_2 with air, the temperature of the particle began to increase sharply above 800 °C, reaching a maximum of 865 °C within 15 s. The temperature then fell over a period of about 180 s and stabilised at around 835 °C. The temperature profile is shown in Fig. 5. At 850

°C, the reaction between a mixture of CaS and $CaSO_4$ was found not to take place, but during CaS oxidation, it did. This may now be explained by the temperature increase [caused by reaction (1)] to somewhere between 850 °C and 900 °C, when the solid-solid reaction becomes feasible.

Discussion

It is now possible to interpret the results from the oxidation of CaS a little more fully. Reaction (2) between the product $CaSO_4$ and unreacted CaS appears to be responsible for the evolution of SO_2 at initial temperatures above about 850 °C. In this case, the oxidation of CaS can be broken down into its initial, intermediate, and final stages.

Initial Period:

Formation of $CaSO_4$ product will reduce the diffusivity of O_2 to the reaction front. However, $CaSO_4$ will be simultaneously consumed by the solid-solid reaction (2), giving CaO and SO_2. There will therefore be a gradual increase in the production of both $CaSO_4$ and CaO. Also, X_{CaO}/X_{CaSO_4} will increase, because $CaSO_4$ will be consumed faster than it is produced, as a result of the slow diffusion of O_2 to unreacted CaS. The magnitude of X_{CaO}/X_{CaSO_4} will depend on the temperature; it will increase with temperature, whilst reaction (2) becomes more prominent. These reactions, being restricted to the particle's surface, will result in a particle containing a core of CaS surrounded by a layer of $CaSO_4$, with CaO as the outermost layer.

Intermediate Period:

The rate of formation of both $CaSO_4$ and CaO is greatest during this period (see Figs 2 and 3). The outer layer of CaO has a greater porosity than $CaSO_4$, thereby increasing the diffusivity of O_2 into the particle. This in turn replenishes the supply of $CaSO_4$, which continues to react with CaS, producing more CaO and SO_2. As the reaction front moves further towards the centre of the particle, SO_2 from the solid-solid reaction (2) must pass through the outer layer of CaO en route to the bulk gas phase. In the presence of counter-diffusing O_2, $CaSO_4$ will form in the outer region of the particle via

$$CaO + SO_2 + 1/2O_2 \rightarrow CaSO_4; \qquad \Delta H^\circ_{298} = -502.2 \text{ kJ/mol.} \quad (6)$$

Therefore, X_{CaO}/X_{CaSO_4} becomes smaller.

Final Period:

Eventually, $CaSO_4$ formation around the particle again reduces access of O_2 to the reaction front, causing a reduction in further $CaSO_4$ production. Additionally, this will result in a lowering of the rate of CaO formation. Tucker [7] postulated that the SO_2 partial pressure at the CaS-$CaSO_4$ interface rises above the value for thermodynamic equilibrium of the solid-solid reaction (2), as SO_2 becomes trapped within the particle. The net result is that the solid-solid reaction (2) ceases.

Kinetics of $CaSO_4$ Formation

The experimental results obtained thus far have been difficult to interpret quantitatively because of the occurrence of the solid-solid reaction (2) at slightly above 850 °C during CaS oxidation. Therefore, to determine the kinetics of reaction (1) experiments were performed in the TGA in the temperature range 650 °C–800 °C, when reaction (2) does not occur, and only $CaSO_4$ forms in reaction (1). The rate of the initial stages of reaction (1) was obtained from the initial slope of plots of mass against time, as in Fig. 1.

The order of the reaction with respect to O_2 was examined at 800 °C and with O_2 concentrations of 4.2–80 vol.%. During the initial period, each mass plot was again slightly sigmoidal. Unlike in previous experiments, this cannot be attributed to changes in porosity of the particle caused by the formation of CaO, because no SO_2 was detected. A probable explanation may be that, because of the exothermicity of the reaction and the subsequent rise in particle temperature, the rate of reaction increases with time until the product $CaSO_4$ blocks access of O_2 to the CaS surface. The initial gradient of a plot of mass vs time was obtained by fitting a quadratic to the measurements using the software package SIGMAPLOT. Figure 6 shows the initial rate, normalised to the initial sample mass m_0, plotted against the O_2 concentration for tests at 800 °C. A straight line passing through the origin can be drawn through the points, demonstrating that reaction (1) is first order in O_2. The initial rate of reaction (in kg/s) of CaS may be expressed as

$$\frac{dm}{dt} = 64 m_0 \eta A_0 k_1 C_{O_2} \quad (7)$$

where A_0 is the BET surface area of the CaS particles (m^2/kg), k_1 the rate constant (m/s), C_{O_2} the O_2 concentration (kmol/m^3), and 64 kg/kmol the increase in mass when forming 1 kmol of $CaSO_4$ from 1 kmol of CaS. The effectiveness factor η gives the fraction of the total surface area of a particle which is available for reaction, and is characterised by the Thiele modulus ϕ [14] where

$$\phi = \frac{d}{6}\left(\frac{k_1 A_0 \rho_{CaS}}{D_e}\right)^{1/2} \quad (8)$$

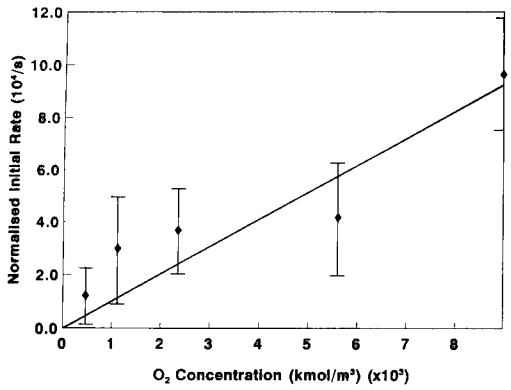

FIG. 6. Normalised initial rate of reaction (1) (from the initial gradient of a plot of normalised mass against time from a TGA experiment) against the corresponding inlet O_2 concentration for a temperature of 800 °C.

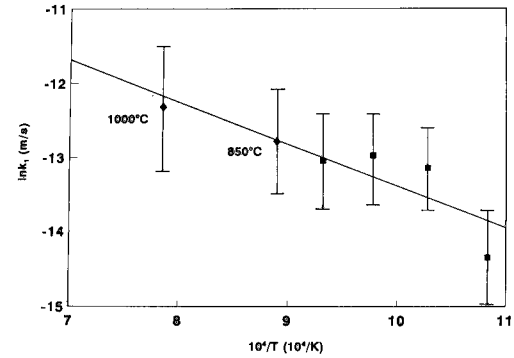

FIG. 7. Arrhenius plot (i.e., $\log_e k_1$ vs reciprocal temperature) for CaS oxidation in reaction (1). Values of k_1 were derived from the initial slope of a plot of normalised mass vs time using an inlet O_2 concentration of 21 vol.% and two temperature ranges: 650 °C–800 °C (■) and 850 °C–1000 °C (◆).

for a spherical particle of diameter d and density ρ_{CaS} and with D_e being the diffusivity of O_2 through the particle. The value of D_e was estimated using the expression $D_e = D_0\varepsilon_0^2$ [15], in which ε_0 is the initial porosity of the particle (6.5×10^{-3}). Here, D_0 is an overall diffusion coefficient given by $1/D_0 = 1/D_m + 1/D_k$, where D_m and D_k are the molecular and Knudsen diffusion coefficients, respectively [16]. The resulting values are $D_m = 5.5 \times 10^{-5}$ m²/s, $D_k = 1.5 \times 10^{-6}$ m²/s, and $D_0 = 1.5 \times 10^{-6}$ m²/s at a temperature of 800 °C. For a reacting spherical particle, η is given by [14]

$$\eta = \frac{3}{\phi}\left[\frac{1}{\tanh \phi} - \frac{1}{\phi}\right]. \quad (9)$$

The gradient of the plot in Fig. 6 equals $64A_0\eta k_1$; a least-squares fit gives the gradient as 0.101 m³/kmol s, from which $\eta k_1 = 1.7 \pm 1.0 \times 10^{-6}$ at 800 °C. Using this expression in conjunction with Eqs. (8) and (9), values of k_1, η, and ϕ were obtained iteratively. The resulting values of η and k_1 were 0.74 and $2.2 \pm 1.0 \times 10^{-6}$ m/s, respectively, at 800 °C. Further values of k_1 were derived in a similar manner at 650 °C, 700 °C, and 750 °C from the initial gradient of the mass-time plots. The resulting values of k_1 are presented in Fig. 7 as an Arrhenius plot, which is seen to be reasonably linear. Included in this plot are values of k_1 from the initial gradient of the mass-time plots at 850 °C and 1000 °C. The fact that they lie on the same line as the low-temperature values reinforces the view that, at high temperatures, CaS oxidation involves firstly reaction (1) forming $CaSO_4$, followed by CaO production in reaction (2). Values of η varied from 0.92 at 650 °C to 0.67 at 1000 °C. Figure 7 gave the activation energy of reaction (1) as 47 ± 12 kJ/mol. From the intercept of Fig. 7, a value for the pre-exponential factor of $4.5 \pm 2.0 \times 10^{-4}$ m/s was obtained. The rate constant for reaction (1) may therefore be represented by $k_1 = 4.5 \pm 2 \times 10^{-4} \exp[-(5.7 \pm 1.5)10^3/T]$ m/s. This makes reaction (1) a fairly fast process, with a relatively low activation energy, originating from the reaction being exothermic. The pre-exponential factor here should be compared with the theoretical maximum (from the kinetic theory of gases) of 200 m/s for the situation when *every* collision of a gaseous molecule with the solid surface results in reaction. Although this comparison makes the reaction in question appear to be relatively slow, its pre-exponential factor is actually higher than that for most gas-solid reactions.

It is also necessary to consider the influence of external mass transfer on the reaction. For reaction control, we require $1/k_1 >> 1/k_g$, where k_g is the external mass transfer coefficient and is characterised by the Sherwood number $Sh = k_g d/D_m$. If the gas surrounding the CaS particles is assumed to be stagnant, Sh = 2. Therefore, the above condition becomes $d << 2D_m/k_1$, and at 1000 °C, $D_m = 1.1 \times 10^{-4}$ m²/s, and $k_1 = 4.5 \times 10^{-6}$ m/s; thus, $d << 2(1.1 \times 10^{-4})/(4.5 \times 10^{-6}) << 49$ m, demonstrating that this criterion is satisfied and resistance to external mass transfer is negligible.

A value of k_1 may also be obtained from a heat balance on a CaS particle of mass m reacting with O_2:

$$\eta A_t k_1 C_{O_2}(-\Delta H_1) = \frac{m}{72} C_p \frac{dT_p}{dt} + A_e h(T_p - T_g) \quad (10)$$

in which A_t is the total (internal and external) surface area of one CaS particle, A_e is the external area, ΔH_1 the heat of reaction (1), C_p the specific heat capacity

of $CaSO_4$, 72 the molar mass of CaS, T_p the particle temperature, T_g the gas temperature, h the heat-transfer coefficient, and dT_p/dt the initial slope of the temperature profile in, e.g., Fig. 5. Initially, at $t = 0$, the second term on the right-hand side of the equation is zero because $T_p = T_g$. Hence, a value for k may be derived. Using the following values—$C_{O_2} = 2.2 \times 10^{-3}$ kmol/m^3, $\Delta H_1 = -9.5 \times 10^8$ J/kmol, $d = 45 \times 10^{-6}$ m, $C_p = 176.7 \times 10^3$ J/K kmol for $CaSO_4$ at 1100 K [13], and $dT_p/dt = 3.6$ K/s at $t = 0$—a value of $k_1 = 4.5 \pm 2 \times 10^{-6}$ m/s at 800 °C is obtained. This is in good agreement with the value obtained above of $2.2 \pm 1.0 \times 10^{-6}$ m/s from the TGA experiments.

By way of a final comment, it is worth noting that no evidence has appeared for reaction (3) between O_2 and CaS, yielding CaO. The real difficulty about favouring this reaction in preference to the solid-solid reaction (2) as a way of producing CaO and SO_2 is that, unlike (2), it lacks the property of functioning only above a threshold temperature, associated here with a phase change.

Conclusions

Oxidation of CaS at the operating temperatures of fluidised-bed combustors (900 °C) results in both $CaSO_4$ and CaO as products. The mechanism of the reaction initially involves the production of $CaSO_4$, which subsequently interacts with CaS, probably via a melt, forming CaO and SO_2. This reaction between the two solids CaS and $CaSO_4$ does not take place in isolation below a gas temperature of about 900 °C, but during CaS oxidation, the temperature of the reacting particle is raised because of the exothermicity of reaction (1) forming $CaSO_4$. This gives rise to SO_2 evolution, even at gas temperatures of 850 °C. Conversions to $CaSO_4$ are low as a result of the solid-solid reaction and/or the buildup of an impervious layer of $CaSO_4$ on the surface of the CaS particle. It proved possible to characterise fully the kinetics of reaction (1).

Acknowledgments

The authors wish to thank British Coal Corporation and the ECSC for their financial support. The views expressed are those of the authors and do not necessarily represent those of the supporting organisations.

REFERENCES

1. Anthony, E. J., Ross, G. G., Berry, E. E., Hemings, R. T., Kissel, R. K., and Doiron, C. C., *10th International Conference on Fluidised Bed Combustion*, 1989, pp. 131–139.
2. Pham, H. N., and Lawson, W. F., *AIChE J* 3:443 (1990).
3. Torres-Ordonez, R. J., Longwell, J. P., and Sarofim, A. F., *Energy Fuels* 3:506 (1989).
4. Abbasian, J., Hill, A. H., Wangerow, J. R., and Rehmat, A., presented at AIChE Annual Meeting, 1991.
5. Dawes, S. G., Arnold, M. STJ., Holmes, J., and Cross, P. J. I., *International Conference on Steam Plant for the 1990's*, Institution of Mechanical Engineers, London, 1990, pp. 125–137.
6. Davies, N. H., Hayhurst, A. N., and Laughlin, K. M., *Research Event*, Institution of Chemical Engineers, Rugby, England, 1993, p. 293.
7. Tucker, R. F., Ph.D. Thesis, University of Cambridge, Cambridge, UK, 1987.
8. Hayhurst, A. N., and Tucker, R. F., *J. Inst. Energy* 65:166–176 (1992).
9. Chen, J. M., and Yang, R. T., *Ind. Eng. Chem. Fund.* 18(2):134–138 (1979).
10. Grieveson, P., and Turkdogen, E. T., *Trans. Metall. Soc., AIME* 224:1086 (1962).
11. Lau, K. H., Cubiccioyo, D., and Hildenbrand, D. L., *J. Chem. Phys.* 66:4532–4539 (1977).
12. Kamphuis, B., Potma, A. W., Prins, W., and van Swaaij, W. P. M., *Chem. Eng. Sci.* 48:105–116 (1993).
13. Barin, I., *Thermochemical Data of Pure Substances*, V.C.H., Weinheim, Germany, 1989.
14. Aris, R., *The Mathematical Theory of Diffusion and Reaction in Permeable Catalysts the Theory of the Steady State*, Clarendon Press, Oxford, 1975, Vol. 1.
15. Wakao, N., and Smith, J. M., *Chem. Eng. Sci.* 17:825 (1962).
16. Perry, R. H., and Green, D., *Perry's Chemical Engineering Handbook* 6th ed., McGraw-Hill, 1984.

COMMENTS

Umberto Arena, Institute for Combustion Research, CNR, Italy. It is known that in CFBC loop there is an alternation of reducing and oxidizing zones. Do you believe that this alternation might affect the mechanism you proposed?

Author's Reply. Yes, there can be both reducing and oxidising zones in the same fluidised bed. We were concerned with the behaviour of CaS (from a fuel-rich gasifier) when admitted to an O_2-rich combustor, most probably burning char in, say, British Coal's Topping Cycle. CaS in a fuel-rich environment is most probably stable, but in an O_2-rich environment our proposed mechanism will operate.

The question relates to a CFBC with changes of overall stoichiometry. In a fuel-rich situation, sulfur usually exists as H_2S, which forms CaS on contact with CaO. On the

other hand, with excess O_2 present, most of the sulfur exists as SO_2 (of course, some SO_3 or COS might form), which in turn forms $CaSO_4$ in the presence of O_2. Of course, $CaSO_4$ in a fuel-rich region can react [1] in $CaSO_4 + H_2$ (or CO) $\rightarrow$ CaO + SO_2 + H_2O (or CO_2). Alternatively, CaS in an O_2-rich situation just reacts according to the mechanism described in the paper. Thus, the situation can become complex.

REFERENCE

1. Hayhurst, A. N., and Tucker, R. F., *J. Inst. Energy* 64:212 (1991) and 65:166 (1992).

•

Andrej Maček, National Institute of Standards and Technology, USA. Overall, it appears that your results indicate that oxidation of CaS to $CaSO_4$ is not very practical; if the temperature is high enough for efficient conversion of the sulfide to the sulfate (say 950 °C or higher), the latter will decompose to form the undesirable SO_2 (and CaO). Can you comment?

Author's Reply. Yes, at high temperatures calcium undergoes the sequence CaS $\rightarrow$ $CaSO_4$ $\rightarrow$ CaO. However, the paper does stress that not all the calcium is likely to end up as CaO, even at high temperatures. The evolution of SO_2 as a function of time shows that an isolated particle can be producing SO_2 (at a long reaction time) in the centre of a calcium particle and yet that SO_2 is taken up by the outer regions of the particle. Nevertheless, 100% conversion of CaS to $CaSO_4$ can only be achieved below a certain temperature.

•

Kristina Iisa, Oregon State University, USA. 1. Were external mass transfer limitations eliminated during the kinetic measurements of the CaS + O_2 reaction at temperatures below 850 °C?

2. The CaS + O_2 reaction is very exothermic and leads, as you demonstrated, to a temperature rise in the particle. Was this temperature rise taken into account when determining the kinetic constants of the CaS + O_2 reaction?

Author's Reply. 1. The sample (particle size 45 μm) was dispersed over quartz wool in the bucket of the TGA. In this way, the particles were separated from one another and offered no resistance to mass transfer. This is confirmed by calculations using the derived rate constants and also by experiments varying the particle size.

2. Only initial rates of reaction were analysed, so that this rate refers to the initial particle temperature, surface area, etc. Thus, there was no need to consider the temperature rise when deriving k_1.

•

Pradeep Agarwal, University of Wyoming, USA. 1. If a melt is required for reaction of CaS with $CaSO_4$, how does oxygen diffuse through the melt?

2. In the analysis, the BET surface area is assumed to be constant. If a melt forms, this is very unlikely.

3. The Arrhenius kinetics must be in terms of particle temperature.

Author's Reply. Only initial rates were handled quantitatively when measuring the rate constant for the oxidation of CaS in reaction (1). Thus, variations in *total* (internal and external) area were not considered.

Oxygen does diffuse through a liquid, but more slowly than in the gas phase. The likelihood is that there is always a sufficiently large gap (i.e., voidage) through which oxygen can diffuse.

Twenty-Fifth Symposium (International) on Combustion/The Combustion Institute, 1994/pp. 219–226

PRIMARY AND SECONDARY FRAGMENTATION OF COALS IN A CIRCULATING FLUIDIZED BED COMBUSTOR

UMBERTO ARENA,* ANTONIO CAMMAROTA AND RICCARDO CHIRONE

Istituto di Ricerche sulla Combustione
National Research Council (CNR)
Piazzale Tecchio 80,
80125 Napoli, Italy

Primary and secondary fragmentation of two Kentucky No. 9 coals, having similar proximate and ultimate analyses but different swelling indexes (2.5 and 9, respectively), were studied in a laboratory scale circulating fluidized bed combustor (CFBC). The apparatus, having a 41-mm i.d. and 1.92-m-high riser, was operated keeping fixed the gas velocity and the size of inert bed material at values of practical interest. Two experimental procedures were used to separately investigate primary and secondary fragmentation effects taking place during fluidized bed combustion of coals. Particle multiplication factor, i.e., the number of particles generated per one mother particle, was used to quantify these effects. Statistical functions of fragmentation (the probability of breakage by primary fragmentation, the probability density that a shrinking particle of a given size breaks into fragments, and the size distribution of subparticles produced by secondary fragmentation) were also determined and embodied into an available model for circulating fluidized bed combustion of coals. On the basis of this mathematical model, the relevance of primary fragmentation on some output variables chosen to characterize the performance of a circulating fluidized bed combustor was quantified.

Introduction

The modelling, design, and performances of circulating fluidized bed combustors (CFBC's) are affected by the comminution phenomena, which contribute to size reduction of coal and char particles [1–3]. Massimilla and his coworkers [4] recently reviewed phenomenology of comminution in fluidized bed combustion, pointing out that this can be seen as a result of at least four phenomena occurring in series parallel with each other and with combustion, namely, the primary fragmentation of coal, the secondary fragmentation of char, the fragmentation by percolation of relatively fine char, and the abrasive attrition among chars, bed inert solids, and combustor walls. Several papers [4–7] analyzed the role of comminution phenomena for what concerns operations of bubbling fluidized bed combustors (BFBC's). More recently, some studies [1,2] have been carried out to extend information to operative conditions typical of CFBC's, analyzing phenomenology and relevance of abrasive attrition and secondary fragmentation during combustion of a char particle.

These studies showed that when moving from bed captive regimes typical of BFBC's to bed transport regimes proper of CFBC's, the relevance of secondary fragmentation appears to increase [2]. Results indicated that the effect of the gas velocity and bed solids size was almost negligible within the range of these variables of practical interest. On the contrary, the extent of secondary fragmentation appeared strongly connected to char structure, whose mechanical properties are determined by the devolatilization process [8].

A scope of this paper is that of acquiring information about the correlation between initial size and structure of coal/char particles and phenomena of primary and secondary fragmentation. To this end, two coals having an almost similar chemical composition but a strongly different free-swelling index were tested. Experimental procedures were set up in order to isolate primary and secondary fragmentation effects from those of the other bed carbon comminution phenomena. Attention is focused on a coal particle from its sudden injection in a CFBC until its almost complete burnout. The relevance of primary fragmentation on the performance of a circulating fluidized bed (CFB) combustor continuously operated is estimated by means of an available mathematical model, evaluating carbon loading and size distribution of carbon particles in the riser.

Experimental

Apparatus:

The circulating fluidized bed combustor (Fig. 1) consists of a riser 41-mm i.d. and 1.92-m high, a solids collecting system, and a 41-mm i.d. recirculation

*Istituto di Energetica—Università di Perugia—Perugia, Italy

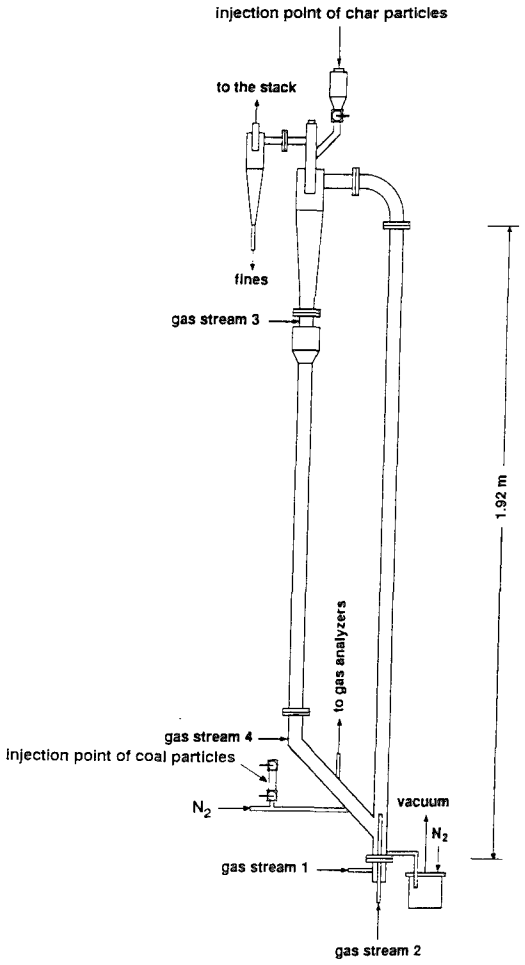

FIG. 1. Experimental apparatus.

column. The apparatus is not equipped with a device able to control solids circulation in the CFB loop. To avoid bypass through the recirculation column, fluidizing gas was divided into two streams: gas stream 1, consisting of nitrogen, maintained solids at the bottom of the riser in a state of bubbling fluidization; gas stream 2, preheated at a temperature of 700 °C, circulated solids in the loop. This latter stream consisted of nitrogen during primary fragmentation tests and of an oxygen-nitrogen mixture (4.5% O_2) during secondary fragmentation tests (such a low-oxygen concentration was used to expand the timescale of secondary fragmentation phenomena). Solids separated by a high-efficiency cyclone were conveyed to the recirculation column and transferred to the riser by means of a 41-mm-i.d. inclined pipe. Nitrogen (gas stream 3) was injected downstream the cyclone to wash out solids from any oxygen coming from the riser. During secondary fragmentation tests, a very small stream (less than 1% of the overall gas flow rate) of 4.5% O_2 oxygen-nitrogen mixture was injected immediately above the elbow connecting the recirculation column and inclined pipe (gas stream 4). An undervacuum vessel was connected to the bottom of the riser to collect solids at a given time. Solids were quenched by nitrogen to avoid further reaction between air and char. The riser was operated at 850 °C, while the rest of the loop was at about 700 °C. A probe placed in the middle of the inclined recirculation pipe was used for on-line gas analysis. Electronic transducers gave pressure profiles in each section of the loop. Solids concentrations along the riser were calculated using a pressure gradient technique [9].

Materials:

Properties of coals are reported in Table 1. Both are classified as Kentucky No. 9 coal, and their almost equal chemical compositions confirm this affinity. In the following, that having the low free-swelling index is indicated as Kentucky No. 9-L (or briefly, K9L); the other, having a high index, is indicated as Kentucky No. 9-H (K9H).

Both Kentucky No. 9 coals were used for primary fragmentation experiments, i.e., devolatilized by injection in the CFB combustor operated under inert atmosphere at 850 °C. The different swelling properties of parent coals strongly affected the generation of relative chars. Table 2 reports their chemical composition and physical properties, whereas micrographs of Figs. 2a and 2b give an idea of macroscopic differences in their mechanical structures. A comparative analysis of micrographs and of Table 2 data leads to the following considerations: (1) Char particles from K9H coal present several large pores: the structure appears kept together by thin bridges of carbonaceous material. (2) Several silica sand particles are visible in the structure of char obtained from K9H coal. These particles, which are probably captured at the plasticity stage during the devolatilization process and embodied by the char particle as it resolidificates at the end of devolatilization, are responsible for the higher ash content of K9H char particles compared to that of the parent coal.

Char particles obtained from both coals were sieved in order to obtain narrow cuts, which were then used to prepare batches of char particles of different initial sizes (Table 2).

Silica sand with a particle size distribution between 0.3 and 0.4 mm and a density of 2540 kg/m^3 was used as bed material.

Primary Fragmentation Test Procedure:

A batch of five coal particles, 9–10 mm as initial size, was injected at the middle of the inclined pipe by means of a pulse of nitrogen (Fig. 1) and fluidized

TABLE 1
Characteristics of coals used

Coal	Kentucky No. 9 L	Kentucky No. 9 H
Free-swelling index (ASTM D720)	2–2.5	8–9
Proximate analysis (%) (as received):		
Moisture	3.3	3.8
Ash	6.7	7.1
Volatile matter	41.5	38.2
Fixed carbon	48.5	50.9
Ultimate analysis (%) (dry basis):		
Carbon	70.9	71.6
Hydrogen	5.4	5.4
Nitrogen	1.6	2.0
Sulphur	3.4	3.2
Oxygen	11.8	10.4
Ash	6.9	7.4
Coal particle size (mm)	9–10	9–10

TABLE 2
Characteristics of chars used

Parent coal	Kentucky No. 9 L	Kentucky No. 9 H
Apparent particle density (kg/m^3)	815	436
Ultimate analysis (%) (dry basis)		
Carbon	76.9	57.2
Hydrogen	1.2	0.5
Nitrogen	0.3	0.2
Sulphur	0.5	0.3
Oxygen	2.2	1.3
Ash	18.9	40.5
Initial char particle size ranges (mm)	4–5; 5–6; 7–8	4–5; 5–6

at an overall gas velocity of 2.7 m/s by nitrogen streams 1 and 2. Devolatilizing coal particles mainly stayed in the dense zone of the riser because of their density and size; just occasionally, some of them ran along the loop. The experiment was stopped after a time interval (about 180 s) that was estimated by parallel investigation to correspond to the devolatilization time. At this point, all char and sand particles in the loop were collected in the undervacuum vessel and "gently" sieved. Fragments larger than 0.425 mm were analyzed to measure their size and number. Char particles collected from the bed were used for secondary fragmentation tests in successive runs.

Devolatilization time was evaluated by using the same apparatus and the same operating conditions of primary fragmentation tests. Batches of 9–10-mm coal particles were fluidized in the CFB combustor for a fixed time interval, then collected, sieved, and weighed to measure the losses due to volatile emissions. This procedure was reiterated with new batches, fluidizing for progressively longer time intervals, until the weight no longer diminished, thereby indicating the end of volatile release. The yield of volatile was estimated as being equal to about 43 and 43.5%, respectively, for K9L and K9H.

Secondary Fragmentation Tests Procedure:

A batch of ten char particles was injected into the loop at the top of the recirculation column. As particles reached the elbow upstream the inclined pipe, they contacted oxygen contained in gas stream 4. CO_2 detection made immediately downstream was used to determine when char particles were being recycled. They entered into the riser and reacted in the oxidizing atmosphere until they were entrained by the gas and conveyed to the cyclone. Particles were circulated in the CFB loop for a fixed time interval. Then combustion was stopped by switching the oxygen-nitrogen stream to nitrogen. All char and

sand particles in the loop were collected in the undervacuum vessel and sieved. The degree of carbon conversion was evaluated by weighing particles before and after the run and assuming carbon content of each char particle to be constant during burnoff. Chemical analyses validated this assumption, showing that carbon content varies less than 10% by weight. The particles of a batch that in a run did not undergo secondary fragmentation were those whose size was larger than or equal to the average size, corresponding to the assessed degree of conversion. Char particles collected from the bed were tested for further secondary fragmentation in successive runs. Particles smaller than 3 mm were not injected at the top of the recirculation column but in the receiver downstream the cyclone leg (Fig. 1) in order to avoid their entrainment by the outlet gas leaving the cyclone.

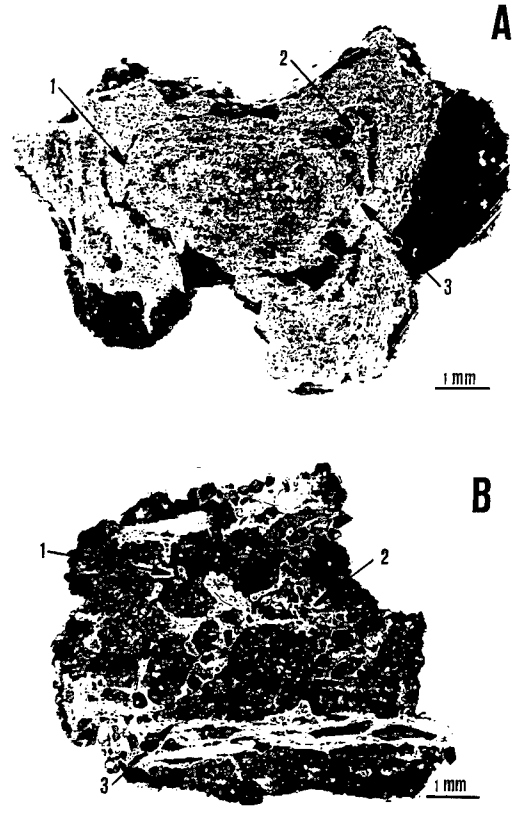

FIG. 2. Micrographs of char particles from (a) Kentucky No. 9 L coal and (b) Kentucky No. 9 H coal. 1, 2, and 3: tentative identification of carbon bridges connecting elements of the char particles.

Experimental Results and Discussion

Primary Fragmentation:

Primary fragmentation of coal occurred just after injection of particles into the fluidized bed as a consequence of internal stresses due to devolatilization and thermal shock. Volatile and moisture release, which is responsible for devolatilization stresses, takes place at rates influenced by coal properties and by rates of heat exchange between bed and coal particles [10].

It is expected that primary fragmentation in a CFB combustor occurs while coal particles are still in the dense zone at the bottom of the riser. In this so-called "primary zone," commercial boilers generally operate with values of gas velocity close to 2.7 m/s at which experiments in the present work were carried out.

Figure 3 reports particle size distribution on mass basis of fragments generated by primary fragmentation of K9L and K9H coal particles. The same figure also gives the probability of particle breakage S_f, i.e., the ratio between the number of particles that undergo fragmentation and that of particles injected into the bed; the particle multiplication factor N_{out}/N_{in}, i.e., the ratio between the number of particles collected at the end of devolatilization time and the number of injected particles; and the Sauter mean particle diameter of fragments d_p, evaluated on mass basis. High-swelling K9H coal produced a number of subparticles larger than that of K9L coal (N_{out}/N_{in} = 115 compared to N_{out}/N_{in} = 22) and characterized by a smaller average size (d_p = 3.1 mm compared to d_p = 3.6 mm).

Analysis of size distributions of Fig. 3 indicates that no particles larger than 6 mm were found in tests with K9H coal, whereas fragments up to 9 mm were collected using K9L coal. Moreover, in the case of K9L coal, there was only a negligible fraction (less than 1%) of fragments below 1 mm, while the presence of a large number of fragments (which represents, however, only the 4% on mass basis) was found in the size range 0.8–0.425 mm using K9H coal. These different contributions to the finest range, limited on mass basis but remarkable on numerical basis, mainly determined a so-much-larger value of N_{out}/N_{in} obtained when K9H coal was tested.

Relevance of Primary Fragmentation on CFBC Performance:

Relevance of primary fragmentation on the performance of a CFBC continuously operated was evaluated on the basis of a recently published mathematical model [11]. Output variables chosen to characterise the performance of the combustor are carbon loading and carbon particle size distribution in the riser. Model calculations were carried out assuming the following set of input variables: coal feed rate = 0.565 kg/h; solids mass flux = 40 kg/(sm^2);

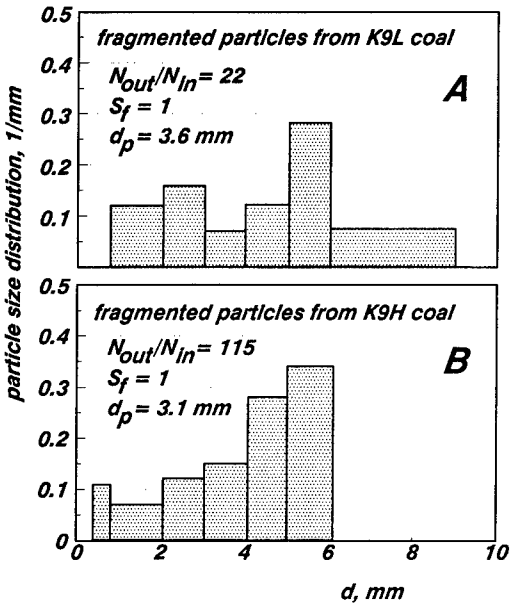

FIG. 3. Particle size distribution on mass basis of fragments generated by primary fragmentation.

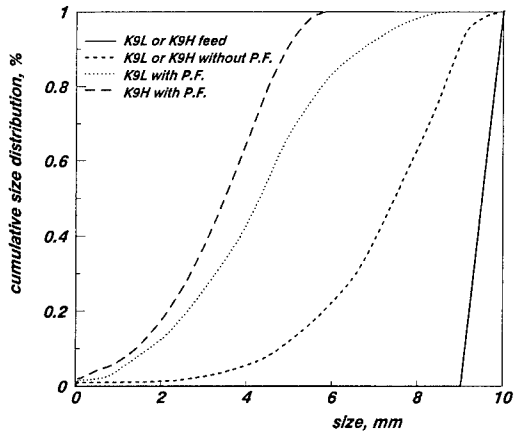

FIG. 4. Cumulative size distribution of carbon particles in the feed and in the riser of a CFBC combustor as evaluated by the mathematical model by Arena et al. [11].

and excess of air = 40%. The complete list of other design and operating variables is reported elsewhere [12]. Results of model calculations are reported in Table 3 for both coals, considering or not considering primary fragmentation. Figure 4 also gives cumulative distributions of carbon particles in the feed and in the riser. Comparative analysis of calculated data indicates that primary fragmentation should be taken into account in CFBC modelling. Neglecting this comminution phenomenon might lead to an error as high as 63% in some of the main output variables and to a misleading distribution of carbon particles in the riser.

Secondary Fragmentation:

Secondary fragmentation of char particles results from the weakening (by combustion) and breaking (by collisions) of bridges (indicated by arrows in Figs. 2a and 2b) connecting the various elements of a char particle [4]. According to this definition, the breakup occurs only when combustion has produced a sufficiently deep weakening of char structure, i.e., when carbon conversion of char particles is sufficiently greater than zero [2].

Data of Figs. 5a and 5b confirm the influence of the degree of conversion on the particle multiplication factor N_{out}/N_{in} (i.e., the number of particles generated per one char particle by secondary fragmentation), whatever the type and the initial particle size of char tested. N_{out}/N_{in} becomes greater than 1, i.e., secondary fragmentation occurs, only for a conversion larger than about 40%. Comparative analysis of Figs. 5a and 5b also indicates that particle multiplication factor relative to secondary fragmentation of K9H is about one order of magnitude larger than that of K9L. This indicates that char particles from K9H undergo a stronger secondary fragmentation phenomenon. The higher fragility of char mechanical structure (Fig. 2b), to some extent taken into account

TABLE 3
Results of model calculations

	Kentucky No. 9 L			Kentucky No. 9 H		
	Without primary fragmentation	With primary fragmentation	Relative difference (%)	Without primary fragmentation	With primary fragmentation	Relative difference (%)
Carbon loading in the riser (g)	46	20	−56	22	8	−63
Sauter mean carbon particle size, mm	2.2	1.2	−45	2.2	0.9	−59

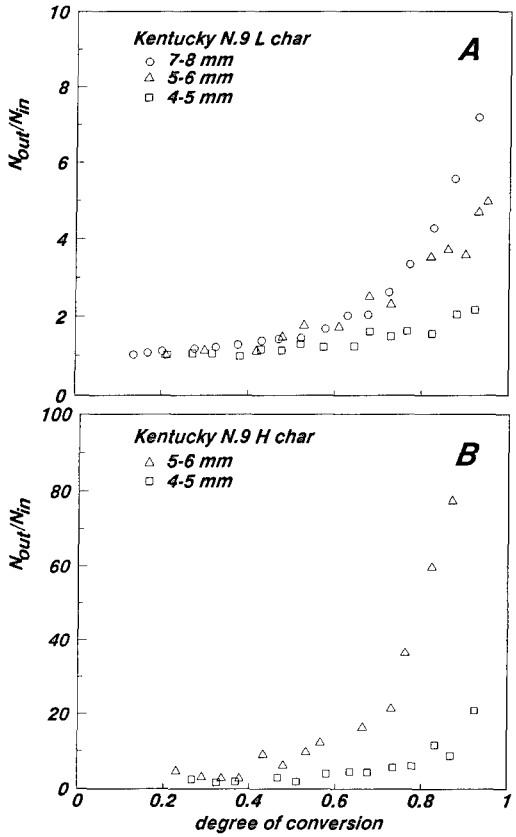

FIG. 5. The influence of the degree of conversion on the particle multiplication factor for different initial size of char particles from K9L and K9H.

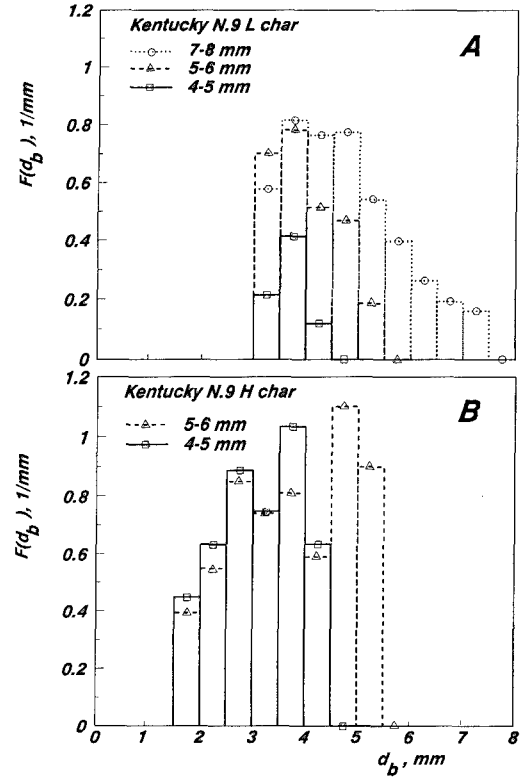

FIG. 6. The probability that a particle of size d_b is subjected to secondary fragmentation.

in the swelling index, might be considered as responsible of this different behaviour.

Data in Figs. 5a and 5b show that the initial char particle size, d_0, affects secondary fragmentation. N_{out}/N_{in} considerably increases when d_0 increases. This behaviour might be related to the increase of weak points in a nonhomogeneous structure when a larger char particle was tested [13].

Figures 6 and 7 give the statistical functions of secondary fragmentation to be embodied in particle size population balances involved in coal combustor modelling. These functions are the probability $F(d_b)$ that a shrinking particle breaks into fragments when its size crosses the size d_b, and the particle size distribution $f_w(d_f/d_b)$ of fragments of size d_f generated by the breaking of char particles of size d_b. The derivation of these functions from experimental data was described in previous works [2,7].

Figures 6a and 6b give the probability $F(d_b)$ obtained starting with several narrow cut batches of K9L and K9H chars of different initial sizes. The $F(d_b)$ curves present a maximum at a value of d_b ranging between 3.5 and 5 mm. For larger d_b, i.e., at a low degree of conversion, bridges connecting elements of a burning particle are not sufficiently weakened to break it into pieces. For smaller d_b, i.e., at a high degree of conversion, the particle becomes too small to react to collisions with fragmentation [2]. Experiments with $d_b < 3$ mm were carried out only for K9H char, because in this case, the amount of char particles that still underwent secondary fragmentation was not negligible. Data reported in Figs. 6a and 6b confirm that char particles of a larger initial size and those obtained from K9H coal have a larger probability of being subjected to secondary fragmentation.

The fragment size distributions on mass basis, $f_w(d_f/d_b)$, are reported in Figs. 7a and 7b. Each line in these figures is the best fitting curve among those that, for the fixed set of operating variables, satisfy the condition that $f_w(d_f/d_b)$ is equal to zero for $d_f/d_b = 0$ and $d_f/d_b = 1$. Generated fragments show a unimodal size distribution, whatever the values of initial char particle size and the type of parent coal. The most probable value of d_f/d_b varies, under the different operating conditions tested, in the relatively narrow interval between 0.85 and 0.95.

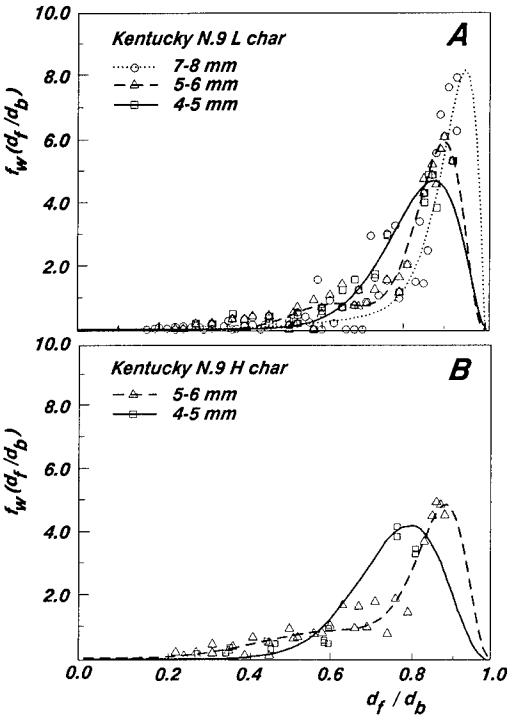

FIG. 7. Fragment size distribution $f_w(d_f/d_b)$, based on the mass of breaking particles.

Comparative analysis of curves relative to different initial char particle size indicates that, for both K9L and K9H chars, the similarity hypothesis, i.e., the possibility of expressing data relative to different initial sizes by means of a single $f_w(d_f/d_b)$ curve, is not strictly fulfilled. This finding greatly complicates char particle population balances involved in coal combustor modelling, where an integro-differential equation, embodying information on secondary fragmentation, has to be solved. A single relationship between fragment size distribution and the size of the breaking particles, whatever the size, cannot be used. Modelling work presently in progress is focused on the numerical solution of char particle population balances of the above-cited model [11], already modified to take into account different $f_w(d_f/d_b)$.

Conclusions

Primary fragmentation behaviour of 9–10 mm particles of a low- and a high-swelling coal was characterized by using a CFB combustor operated under the same experimental conditions. The high-swelling coal showed a sharper tendency to undergo primary fragmentation, with a production of a large number of relatively small fragments. Taking into account the similarity of chemical composition of the two coals, it should be permissible to refer the different primary fragmentation behaviour to properties of the mechanical structure of each coal and its char, to some extent taken into account by the swelling index.

Model calculations indicate that primary fragmentation should be taken into account in CFBC modelling. Neglecting this phenomenon might lead to an error as high as 63% in the evaluation of carbon loading and to a misleading size distribution of carbon particles in the riser.

Both the coals produced chars, which are candidates for undergoing secondary fragmentation. The high-swelling coal showed a value of particle multiplication factor of about one order of magnitude larger than that of low-swelling coal. The higher fragility of char mechanical structure obtained from high-swelling coal might be considered as responsible for this different behaviour.

Initial char particle size d_0 affects secondary fragmentation. The particle multiplication factor considerably increases when d_0 increases. This behaviour, which might be related to the increase of weak points in a nonhomogeneous structure, fails to strictly fulfil the similarity hypothesis, i.e., the possibility of expressing data relative to different initial size by means of a single $f_w(d_f/d_b)$ curve. This greatly complicates the solution of the char particle population balances involved in a coal combustor model.

Acknowledgments

Professor Leopoldo Massimilla gave an incomparable contribution to define the research program of this work and to analyze initial experimental results.

The authors are indebted to Dr. A. Malandrino (ENIRicerche–ENI Group) for his help in model calculations and to Mr. Giovanni D'Anna and Miss Olimpia De Robbio (FISIA–FIATIMPRESIT Group) for their help in performing experimental runs.

REFERENCES

1. Arena, U., Cammarota, A., Massimilla, L. Siciliano, L., and Basu, P., *Combust. Sci. Technol.* 73:383 (1990).
2. Arena, U., Cammarota, A., Chirone, R., and Massimilla, L., *Twenty-Fourth Symposium (International) on Combustion,* The Combustion Institute, Pittsburgh, 1992, pp. 1341–1348.
3. Engstrom, F., and Lee, Y. Y., *Circulating Fluidized Bed Technology III* (P. Basu, M. Horio, and M. Hasatani, Eds.), Pergamon Press, 1991, p. 15.
4. Chirone, R., Massimilla, L., and Salatino, P., *Prog. Energy Combust. Sci.* 17:297 (1991).
5. Sundback, C. A., Beér, J. M., and Sarofim, A. F., *Twentieth Symposium (International) on Combustion,* The Combustion Institute, Pittsburgh, 1984, p. 1495.
6. Stubington, J. F., and Linjewile, T. M., *Fuel* 68:155 (1989).

7. Chirone, R., Massimilla, L., and Salatino, P., *Combust. Flame* 77:79 (1989).
8. Street, P. J., Weight, R. P., Lightman, P., *Fuel* 48:343–365 (1969).
9. Arena, U., Marzocchella, A., Massimilla, L., and Malandrino, A., *Powder Technol.* 70:237; 71:116 (1992).
10. Pechana, R. P., and Gibbs, B. M., *Proceedings of 3rd International Fluidized Bed Combustion Conference*, London, DISC/9/65, 1984.
11. Arena, U., Malandrino, A., and Massimilla, L., *Can. J. Chem. Eng.* 69:860–868 (1991).
12. Malandrino, A., Arena, U., and Massimilla, L., in *Proceedings of the 11th International Conference on Fluidized Bed Combustion* (E. J. Anthony Ed.), ASME, 1991, pp. 841–848.
13. Chirone, R., and Massimilla, L., *Twenty-Second Symposium (International) on Combustion*, The Combustion Institute, Pittsburgh, 1988, pp. 267–277.

COMMENTS

Wei-Yin Chen, University of Mississippi, USA. In our study of primary fragmentation, we observed quite a lot of particles with the size of about 100 μm. Did you observe similar particles?

Author's Reply. The amount of fragments smaller than 425 μm resulting from primary fragmentation of the coals tested was negligible. It reached a maximum value of about 1% on a mass basis in the case of tests with Kentucky N_o9-H coal.

Twenty-Fifth Symposium (International) on Combustion/The Combustion Institute, 1994/pp. 227–234

COMPARISON OF MEASUREMENTS AND PREDICTIONS OF WALL HEAT FLUX AND GAS COMPOSITION IN AN OIL-FIRED UTILITY BOILER

M. G. CARVALHO, P. J. COELHO, A. L. N. MOREIRA, A. M. C. SILVA AND T. F. SILVA
Instituto Superior Técnico
Technical University of Lisbon
Department of Mechanical Engineering
Av. Rovisco Pais
1096 Lisboa Codex, Portugal

This paper reports a comparison of measurements and predictions of wall heat flux, temperature, and gas composition in a full-scale oil-fired utility boiler of 250 MWe. The numerical simulation of complex reactive flows in practical combustion systems is a very demanding problem as far as computational requirements are concerned. To decrease such requirements, a domain decomposition method is employed here. The domain is split into several subdomains, and an independent grid is employed in each one of them to solve the governing equations, visiting sequentially all the subdomains in an iterative fashion. Evaluation of mathematical models requires detailed and accurate experimental data. This question is also addressed in this paper, and measurements of mean temperatures, major gas species concentrations, and wall incident heat fluxes within the radiation chamber are reported here. From the analysis carried out, it is concluded that, on the whole, the predictions are in good agreement with the measurements. Because of the assumption of chemical equilibrium, the CO concentration is overestimated, and the CO_2 concentration is, consequently, underpredicted. Further measurements and predictions at partial load (100 MWe) demonstrate the predictive capability of the model.

Introduction

Comprehensive computer models have increasingly been used to predict the performance of boilers, including submodels for simulating the in-furnace processes, such as mixing, radiative heat transfer, or chemical kinetics [1–4]. However, assessment of these models is still limited because of the scarcity of available data. The present work gives a contribution to this evaluation task.

Utility boilers exhibit a very wide range of length scales; e.g., the height of the boiler is about four orders of magnitude larger than the diameter of the holes of a fuel-oil atomizer. Domain decomposition methods are a useful technique to deal with this problem since, otherwise, a very large number of grid notes is required, as shown in Ref. 5. Although domain decomposition methods have been widely used in the prediction of compressible flows in aeronautics, their application to incompressible flows has seldom been attempted [6,7], especially in the case of reactive flows. The application of a domain decomposition technique to the mathematical modeling of a utility boiler has recently been presented [8], but only the numerical issues were addressed. This paper concentrates on the comparison between the predictions and the measurements acquired in a boiler of the Portuguese Electricity Utility.

The development of the models mentioned above depends on the availability of accurate and appropriate experimental data for comparison. However, access for probing the furnace chamber of large-scale utility boilers is very restricted, and only a limited number of measurements have been made—almost exclusively at the furnace exit. Consequently, detailed in-furnace measurements are sparsely reported in the literature, and the understanding of most physical processes is inferred from measurements obtained in laboratory-scale models [9,10]. Measurements of the combustion and heat transfer characteristics are very expensive and limited by the geometry, time, and number of instruments and skills required, and the few detailed works reported in the literature are concerned essentially with plants typically below 80 MWe [1,2,11–13].

The preceding shows that comparison of current models with detailed benchmark data in full-scale combustion systems is important. In this context, the present paper reports the comparison of measurements and predictions of wall heat flux, temperature, and gas composition in a 250-MWe oil-fired utility boiler. Experimental data of spatially resolved temperatures and species concentrations of the combustion gases and wall incident heat fluxes in the radiation chamber were acquired for two different loads.

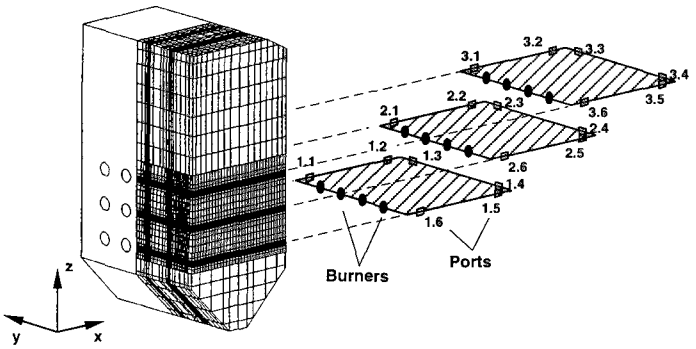

FIG. 1. Sketch of the boiler showing the grid, the burners, and the inspection ports.

The Utility Boiler and the Experimental Procedure

Boiler Geometry and Operating Conditions:

The data were taken in one of the boilers of the Power Plant of the Portuguese Company of Electricity. The boiler includes four units, each one with an installed capacity of 250 MWe.

The boiler dimensions are approximately 19.9-m high, 11-m wide, and 8.5-m deep. It is front fired by 12 atomized oil-burners arranged in an array of four burners disposed in three different levels. The burners are equipped with two-fluid atomizers of the turbulent chamber type [14]. Secondary air flows from the windbox through air registers and enters the furnace through an annulus formed between the oil nozzle and the burner throat (0.9-m diameter). At maximum capacity, residual fuel oil is supplied at a rate of 56 t/h with 5% excess air.

The boiler has several inspection ports, which have provided the necessary physical access to the probes used throughout the work. Figure 1 represents a schematic diagram to show the location of these ports. Each one is represented here by a two-digit figure: The first identifies the level from the bottom to the top and the second, the position ordered in the clockwise direction.

The boiler operating conditions considered in this paper include full and partial loads corresponding to 250 MWe and 100 MWe, respectively.

Experimental Method and Procedure:

The experimental techniques used throughout the work, as well as the arguments associated with assessments of accuracy, are based on previous experiments and are, therefore, presented here in a condensed form. Details will be published in Ref. 15.

Measurements of spatially resolved mean gas temperature and composition and incident wall heat fluxes were made in the radiation chamber by inserting purpose-designed probes through the inspection ports shown in Fig. 1. Gas temperatures were obtained with thermocouples manufactured from platinum and platinum-13% rhodium wires of 350-μm diameter. The thermocouple was supported on the tip of a 3.5-m-long water-cooled suction pyrometer and protected from radiation heat exchanges by a double shield. The gas velocity through the pyrometer could be varied by means of three compressed air pump ejectors up to 300 m/s, which was found to be large enough for the results to be independent of the suction velocity.

Major gas species concentrations (CO, CO_2, and O_2) were measured by gas sampling and subsequent analysis. The samples were withdrawn with a 3.5-m long, 50-mm outside diameter stainless-steel water-cooled probe with a tip orifice of 2 mm and analysed with infrared CO and CO_2 analysers and a paramagnetic analyser for O_2. The measurements were made on a dry basis, for which the sampling line comprised a water-cooled condenser, a calcium chloride drier, and cotton wool filters. Based on the analysis of Ref. 16, it is estimated that the results are close to density-weighted averages within 10% of the maximum measured value.

A specially designed total heat flux probe was used to measure the convective and radiative heat flux incident on the walls from a solid angle of 2π steradians up to a maximum of 500 kW/m^2, in the way suggested in Ref. 17. It consists of a water-cooled probe that houses a cylindrical block with a blackened front surface in order to give high radiation absorption. The probe was inserted through the inspection ports until the front face was leveled with the inside surface of the combustion chamber. The readings were obtained in millivolts and converted to heat flux (in kW/m^2) using a calibration curve provided by a black body furnace. The response time of the meter is of the order of 10 min, and based on the repeatability of the results, an accuracy of $\pm 5\%$ can be claimed for the measured values of heat flux.

The Mathematical Model

The mathematical model is based on the numerical solution of the density-weighted averaged con-

servation equations for mass, momentum, and energy, and transport equations for scalar quantities. Closure of the governing equations is accomplished using the k-ε eddy viscosity/diffusity turbulence model. The turbulent fluxes of scalar quantities are calculated via a gradient diffusion hypothesis.

The combustion model is based on the assumption that reaction rates are very fast compared with the mixing rates. Hence, combustion is controlled by diffusion rather than kinetic mechanisms. The fuel-oil droplets are assumed to vaporize instantaneously as soon as they leave the atomizer. It is also supposed that the mass diffusion coefficients of all the chemical species and the thermal diffusion coefficient are equal. If the heat released during combustion is significantly higher than the heat transferred to the surroundings, the instantaneous thermochemical state of the mixture may be related to a single, strictly conserved scalar variable. The mixture fraction was the scalar variable chosen for this purpose. The instantaneous thermochemical state of the mixture is calculated assuming chemical equilibrium and minimizing the free Gibbs energy. The turbulent fluctuations were taken into account by prescribing the mixture fraction probability density function as a clipped Gaussian.

The gas temperature may be calculated from the enthalpy using well-known thermodynamic concepts. However, the enthalpy does not change linearly with the mixture fraction because a significant part of the heat released during combustion is transferred by radiation to the walls. Hence, a piecewise linear relationship between instantaneous values of enthalpy and mixture fraction was used, as explained in Ref. [18].

The discrete transfer method was chosen to model the radiative heat transfer. Since the domain decomposition technique was not applied to the calculation of the radiative heat transfer, the discrete transfer method is applied as originally presented in Ref. 19. The absorption coefficient of the medium was calculated from the emissivity using the mixed gray and clear gas formulation extended to account for soot.

The Domain Decomposition Technique

The physical domain is divided into a given number of zones mapped using independent grids. Adjacent zones are overlapped in a small region containing one layer of control volumes of scalar variables from each one of the adjacent zones. The governing equations are discretized in each control volume using the finite volume/finite difference method. The standard discretization procedure is not affected by the domain decomposition technique. The interblock boundaries, i.e., boundaries between adjacent zones, just behave as a different kind of boundary that requires a particular treatment [8].

The solution of the governing equations for each zone requires previous knowledge of the fluxes across the overlapping regions of the zone considered. The treatment of the interblock boundaries, explained in detail in Ref. 8, ensures flux conservation across them. An integration procedure is used to transfer data from one zone to the other, and an interpolation method is employed to transfer data reversely.

In each iteration of the solution algorithm, each zone of the domain is treated sequentially. For each zone, the fluxes from the adjacent zones across the interblock boundaries are calculated first. Then, the governing equations are solved in a SIMPLE-like fashion, and the fluxes of each dependent variable at the interfaces of overlapping regions are stored before proceeding to the next zone.

Further details of the domain decomposition technique may be found elsewhere [8]. The analysis described there shows that the influence of the domain decomposition procedure on the convergence rate is negligible, but since fine grids may be confined to small regions, substantial reductions in CPU time are feasible. It is also shown that the accuracy of the numerical solution is not decreased as a result of the domain splitting and that there is continuity of the dependent variables across the interfaces. Here, attention is concentrated on the comparison between the predictions and the measurements, and the numerical issues mentioned above are not addressed.

Previous computations in a similar boiler using a single domain and three different grids with about 32,000, 65,000 and 85,000 grid nodes have shown that the differences between the numerical solutions are relatively small. Moreover, it was found that the influence of the grid refinement on the predictions is generally negligible compared with the differences between the numerical solution and the data. Based on these results, in the present work the utility boiler was divided into three zones or blocks, as sketched in Fig. 1. Zone 1 comprises the burners region and it was discretized using the finest grid with $32 \times 41 \times 44$ grid nodes. Coarser grids were employed in the ash hopper region (zone 2, $10 \times 18 \times 6$ grid nodes) and above the burners level (zone 3, $16 \times 18 \times 8$ grid nodes). This means that, on the whole, 61,112 grid nodes were employed. Domain decomposition does not extend to the calculation of the radiative heat transfer. In that case, an independent global grid with $10 \times 9 \times 20$ grid nodes was used. Earlier computations using a much finer grid ($16 \times 34 \times 60$ grid nodes) have shown that there is no need to use finer grids to solve the radiative heat transfer equation.

The CPU time required to achieve a converged solution is about 26 h using a VAX 9000-440. When a grid as fine as the one employed in the burners region is used everywhere, about 76,000 grid nodes and 40 h of CPU time are needed. This means that 35% of CPU time was saved by using the domain decomposition. A much more substantial reduction

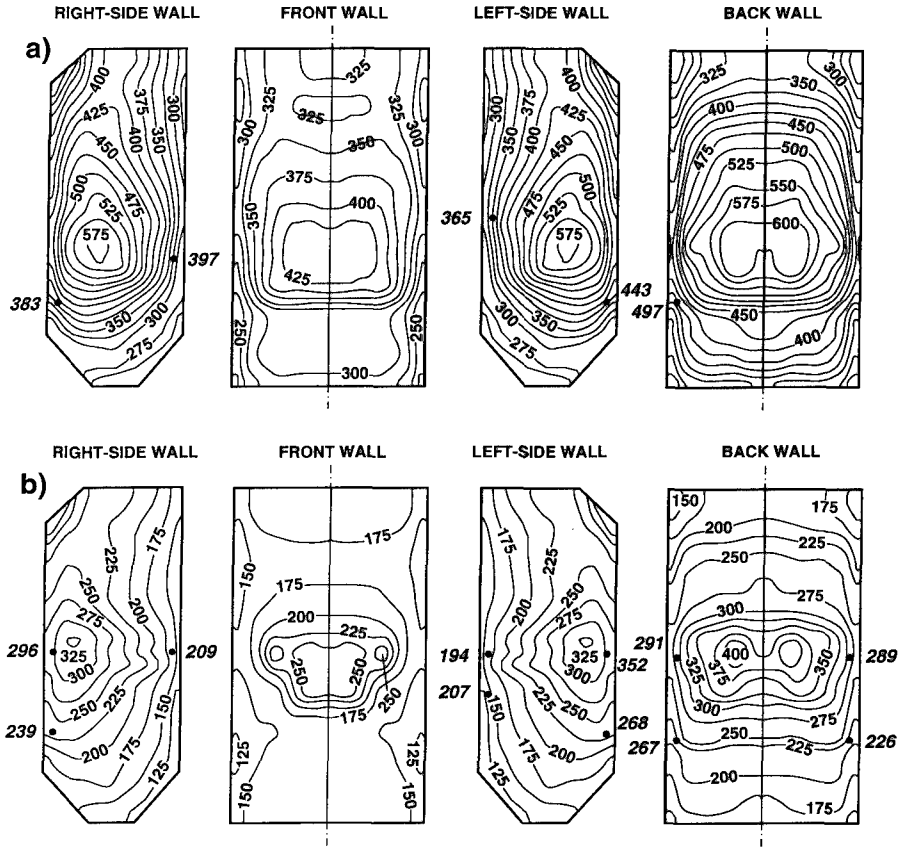

FIG. 2. Distributions of measured and predicted wall heat fluxes (kW/m²). (a) 250 MWe, (b) 100 MWe.

is expected by restricting grid refinement to the near burners region.

Results

The results are presented and discussed in this section under three headings. The first considers the measurements of local total heat fluxes for full and partial loads, which are then related to those of gas species concentrations and temperatures for full and partial loads in the second and third parts, respectively.

Total Heat Fluxes for Full and Partial Loads:

Figure 2 shows the predicted and measured wall incident heat fluxes in a folded-out view for full and reduced loads (250 and 100 MWe, respectively). The overall trend in the heat load is as expected from the visual observation of the flames, with higher predicted average values occurring at the centre of the rear and side walls, at the burners level. It is obvious that the extent of the analysis is limited by the existence of inspection ports only in the corners, which do not allow one to measure the expected peak on the axial distribution of the incident heat fluxes along the side walls [20]. However, the results are useful for the purposes of the discussion presented here.

A three-dimensional nature of the thermal radiation heat transfer in the boiler is also shown in Fig. 2 by the asymmetric distribution of the heat fluxes incident on the side walls, which exhibit average values on the left side about 15% larger than those on the right side. These asymmetries persist at reduced load, although less noticeable than those previously reported in a similar boiler but in slagged conditions [21]. These asymmetries can be attributed to differences between the fuel-air ratios in the various burners, as discussed by others [13,14] and cannot be predicted by the mathematical model, unless the actual fuel-air ratio in each burner were accurately known.

At the side walls, incident heat fluxes close to the front wall are consistently smaller than those predicted near the back wall. This trend is corroborated by the measurements. Regarding the asymmetry mentioned above, the predicted values at the ports

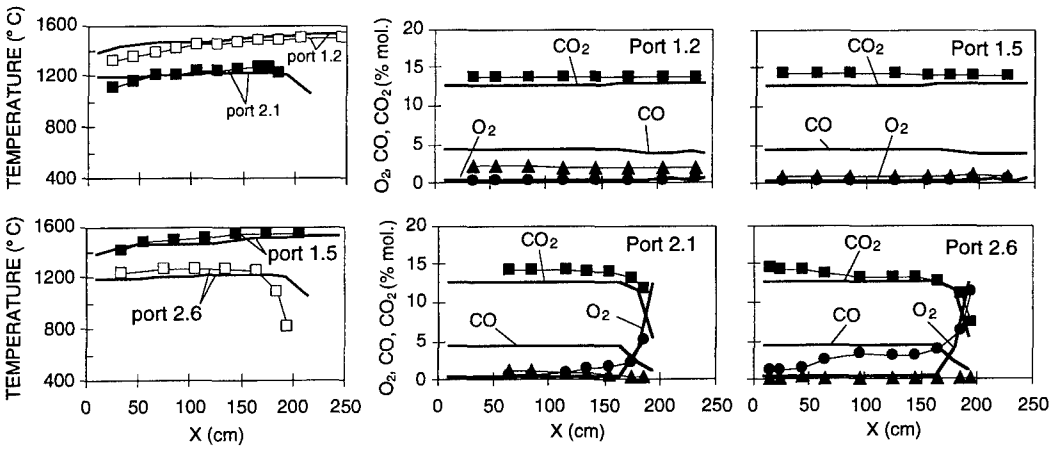

FIG. 3. Profiles of gas temperatures and gas species mole fractions at full load (solid lines—predictions; symbols—measurements).

where measurements are available are generally within the experimental uncertainty ($\pm 5\%$).

The measured values at full load vary between 370 and 500 kW/m^2 in the radiation chamber at the level of the burners. Predicted values go up to 600 kW/m^2 at the hottest spots where measurements are not available and decrease to 200–300 kW/m^2 in the ash hopper and to 250–400 kW/m^2 at the nose level. The predicted and measured distributions at reduced load are qualitatively similar but show an expected decrease of the incident heat fluxes of the order of 40–60%. Moreover, the highest fluxes are predicted to occur at a higher level. An explanation for this behaviour lies in the burners of the lower levels that do not operate at partial load, yielding a decrease of the heat release at the lower part of the boiler.

Gas Temperatures and Composition for Full Load:

A more detailed analysis of the previous results requires the knowledge of the thermochemical characteristics of the combustion gases within the radiation chamber. These are represented for full load in Fig. 3, which shows the profiles of mean temperature and gas species concentrations, along the distance measured from the interior furnace wall.

The model is able to predict the increase of gas temperatures from 1150 °C to 1200 °C in the vicinity of the front wall close to the burners up to 1400 °C 1600 °C in the vicinity of the rear wall. These variations of temperature are consistent with the imbalance between the energy released by combustion and the energy radiated by the flame to the boiler tubes, which is favorable to a larger parcel of the energy release along the depth of the boiler at the level of the burners and favorable to the energy radiated along the boiler height up to the nose level where chemical reactions are absent.

The temperature profiles measured on the side walls of the boiler and close to the burners (ports 2.1 and 2.6) show a flat distribution of temperature around 1200 °C within 1-1/2 m from the side wall, followed by a sharp decrease close to the burner axis, indicating that the probe is entering into the secondary air stream. This temperature decrease through port 2.6 is sharper than suggested by the predictions, but it should be noticed that this region is near the burner exit where the gradients of mean temperature are very high. The simplified burner geometry adopted and the lack of velocity data at the burner outlet make it difficult to draw conclusions about the performance of the mathematical model in this region.

The CO_2 and CO mole fraction profiles through ports 2.1 and 2.6 (see Fig. 3) also exhibit a sudden decrease, consistent with the temperature decrease, whereas the O_2 model fraction increases up to 16%. These evolutions are correctly predicted by the model. At larger distances from the wall, droplets of unburned liquid fuel block the probes and prevent measurements from being taken closer to the burner axis. The flat distributions of mean temperature and species concentrations within 1-1/2 m from the side wall suggest that combustion gases recirculate in that region. However, the presence of CO with levels around 1% suggests that combustion is not complete. The CO concentration is overpredicted in this region as expected from the use of the chemical equilibrium assumption. This is compensated by the underestimation of CO_2 concentration.

In the vicinity of the rear wall, gas temperatures are higher and show a flat distribution, as well as the gas species concentrations. Once again, the predictions are in good agreement with the measurements, except for the underestimation of CO_2 and the overestimation of CO concentrations.

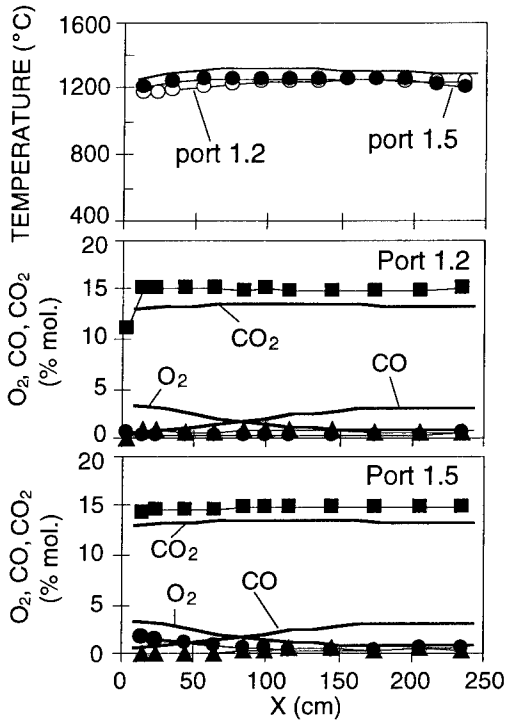

FIG. 4. Profiles of gas temperatures and gas species mole fractions at partial load (solid lines—predictions; symbols—measurements).

Gas Temperatures and Composition for Partial Load:

The effects of reducing the load to 100 MWe on gas temperatures and composition are shown in Fig. 4. The load is reduced by blocking the fuel flow rate in six burners (the outer burners of the second row and all of the first row), which results in increasing the overall excess air. As a consequence, gas temperatures decrease to around 1200 °C–1250 °C in the vicinity of the rear wall at the burners level. Here, the temperature is slightly overestimated. This may be attributed to an underestimation of the radiation loss, as supported by the underestimation of incident heat fluxes at ports 1.2 and 1.3.

Despite the higher excess air level of the present operating conditions, concentrations of CO up to 1% are still observed in the vicinity of the rear wall through ports 1.2 and 1.5. The predicted CO concentration is even higher, and conversely, the CO_2 mole fraction is underestimated, as also observed at full load. Close to the side wall, the oxygen mole fraction increases, and the CO mole fraction goes down to very low values.

From the energetic point of view, the main effect of decreasing the load is seen to be a decrease in gas temperatures within the radiation chamber with a consequent effect on the heat fluxes incident on the boiler tubes, as shown previously.

Conclusions

A full three-dimensional mathematical model of a 250-MWe utility boiler employing a domain decomposition technique was evaluated using spatial-resolved measurements of gas mean temperature and composition and wall incident heat fluxes within the radiation chamber. The measurements were performed with purpose-built probes inserted through the available inspection ports and included the use of a suction pyrometer, a suction sampling probe, and a total heat flux probe. The investigation encompassed the operation at full and partial loads (250 and 100 MWe).

Measured gas temperatures at full load reach maximum values around 1150 °C–1200 °C in the vicinity of the burners and of 1400 °C–1600 °C close to the rear wall. Concentrations of CO up to 1% were found within the combustion chamber above the ash pit, indicating an inadequate mixing and the existence of reducing atmospheres with the potential for localized corrosion. Total measured heat fluxes incident on the walls vary between 370 and 500 kW/m^2 at the level of the burners.

On the whole, the predictions of the model are in good agreement with the measurements. Random variations of the fuel-air ratio in the various burners yield an asymmetric distribution of the heat fluxes and, in minor extent, temperature and species concentrations. These variations cannot be predicted by the model and are responsible for discrepancies in the heat fluxes predictions. Moreover, CO concentration is overestimated because of the chemical equilibrium assumption whereas CO_2 concentration is correspondingly underestimated.

The effects of reducing load to 100 MWe are in accordance with the larger overall excess air due to the blockage of the fuel flow rate in six burners. However, and despite the increase of local concentrations of molecular oxygen, the CO levels remain nonzero in the vicinity of the left side wall. These trends are correctly predicted by the model.

Acknowledgments

The authors are indebted to EDP (Power Plant of Setúbal), where the measurements were taken under contract, and to the European Commission, which partially financed this work.

REFERENCES

1. Robinson, G. F., *J. Instit. Energy*, September:116–150 (1985).

2. Boyd, R. K., and Kent, J. H., *Twenty-First Symposium (International) on Combustion,* The Combustion Institute, Pittsburgh, 1986, pp. 265–274.
3. Lockwood, F. C., Papadopoulos, C., and Abbas, A. S., *Combust. Sci Technol.* 58:5–24 (1988).
4. Carvalho, M. G., and Coelho, P., *Eng. Comput.* 7:227–324 (1991).
5. Gillis, P. A., and Smith, P. J., *Twenty-Third Symposium (International) on Combustion,* The Combustion Institute, Pittsburgh, 1990, pp. 981–991.
6. Yung, C., Keith, T., and Witt, K., *Int. J. Numer. Methods Fluids* 9:167–183 (1989).
7. Wright, J. A., and Shyy, W., *J. Comput. Phys.*, 107:225–238 (1993).
8. Coelho, P. J., and Carvalho, M. G., *Int. J. Numer. Methods Eng.* 36:3401–3499 (1993).
9. Barlow, S. M., *Proceedings of International Symposium on Applied LDA to Fluid Mechanics* (Durão et al., Eds.) Lisboa, Portugal, July 1982, p. 8.4.
10. Costa, M., Costen, P., and Lockwood, F. C., *Combust. Sci. Technol.*, 75:129–154 (1991).
11. Wall, T. F., and Stewart, I. McC., *J. Inst. Fuel* May:235–240 (1975).
12. Bonin, M. P., and Queiroz, M., *Comb. Flame* 85:121–133 (1991).
13. Butler, B. W., and Webb, B. W., *Fuel* 70:1457–1464 (1991).
14. Lawn, C. J., *Principles of Combustion Engineering for Boilers*, Academic Press, London, 1987.
15. Cassiano, J., Heitor, M. V., Moreira A. L. N., and Silva, T. F., *Combust. Sci. Technol.* 98(1–3):199–216 (1994).
16. Heitor, M. V., and Moreira, A. L. N., *Prog. Energy Combust. Sci.* 19:259–278 (1993).
17. Chedaille, J., and Braud, Y., *Industrial Flows* S. J. Beer and M. V. Thring, Eds.), Edward Arnold Publishers, 1972, Vol. 1, "Measurements in Flames," IFRF London.
18. Abou-Ellail, M., Gousman, A., Lockwood, F. C., and Megahead, I., *J. Energy* 2:71–80 (1978).
19. Lockwood, F. C., and Shah, N., *Sixteenth Symposium (International) on Combustion*, The Combustion Institute, Pittsburgh, 1981, pp. 1405–1414.
20. Graf, R., and Payne, R., *Report on the C-17 Trials*, IFRF, Report No. F32/a/42, 1984.
21. Cassiano, J., Heitor, M. V., Moreira, A. L. N., and Silva, T. F., in *Energy Efficiency in Process Technology* (Pilovochi, Ed.), Elsevier, London, 1992, pp. 893–902.

COMMENTS

A. Sobiesiak, Queens University at Kingston, Canada. Our experience with the operation of and measurements on the large multiburner furnaces shows that it is extremely difficult to establish adequate input conditions (such as flow rates of fuel and air) for the steady-state simulation of the furnace. This is due to large variations in time and space (burner and furnace zones on/off operation) of the input condition of the industrial furnace. Such a mode of furnace operation will affect the measurements being taken (temperatures and heat fluxes) and requires caution when comparing measured and predicted values. Have you experienced similar problems in your work, and how did you deal with them?

In my second question I would like to ask, how is the sooting of the spray flames taken into account in your modelling?

Author's Reply. Yes, we experienced similar problems in our work. A strong and comprehensive cooperation of the people involved in the operation of the boiler is fundamental in order to keep the input conditions constant over large periods of time. However, the measurements reported here are part of a major collaborative work with the Portuguese Electricity Company (EDP) that has extended over several years. Therefore, the operation team was well aware of the requirements imposed by the nature of the experiments, namely in allowing the experimentalists to monitor and control the input conditions to the boiler. In this way, it was possible to overcome the adjustments made by the automatic control system and to decide when the measurements should be rejected.

A transport equation is solved for soot mass fraction that accounts for soot formation [1] and oxidation [2]. The absorption coefficient is calculated from the predicted soot volume fraction, and its contribution influences the total absorption coefficient and the radiative heat transfer.

REFERENCES

1. Khan, I., and Greeves, in *Heat Transfer in Flames*, Chap. 25 (N. Algan and J. Barr, Eds.), Scripta Book Co., 1974.
2. Magnussen, B., and Hjertager, *Sixteenth Symposium (International) on Combustion,* The Combustion Institute, Pittsburgh, 1977, pp. 719–728.

•

Scott A. Drennan, Coen Company, Inc., USA. Please discuss how parameters for spray drop size, velocity, evaporation, and combustion are handled in your model and how they may affect the results.

Author's Reply. It was assumed in the model that the spray droplets vaporize instantaneously as soon as they are introduced in the combustion chamber. The spray parameters might influence the results in the near-burner region,

but are expected to exhibit a marginal influence in the overall flow, combustion, and heat release patterns because of the dominant role played by radiation. The incorporation of a model for the spray is the subject of future research [1].

REFERENCE

1. Barreiros, A., Carvalho, M. G., Costa, M., and Lockwood, F. C., *Combust. Flame* 92:231–240 (1993).

•

C. F. M. Coimbra, Brigham Young University, USA. This work reports asymmetries in the experimental characterization of the boiler that were not predicted by the numerical calculations since a symmetry plane was assured. Given the furnace geometry, the reasons for these asymmetries can be attributed to either the different operating conditions of the burners (the aerothermal characteristics of each burner are highly affected by the downstream flow in the near-burner sections of the boiler) or to the improper consideration of swirling velocities. Would you please comment on the way the swirl was imposed to the wall burners? Were the velocities imposed as solid rotations oriented from the wall?

Author's Reply. The velocities are not imposed as solid rotations oriented from the wall. In fact, the direction of the swirl changes from burner to burner in a staggered pattern. Comparison between calculations performed for the whole combustion chamber and for only one half have shown that asymmetries in the predicted profiles along the inspection ports are negligible. Therefore, asymmetries cannot be explained by the swirling velocities.

•

Lixing Zhou, University of Beijing, China. Have you tried to combine your multiblock grid system with a multigrid algorithm, for example, using a coarse grid system for the whole furnace and a fine grid system for the near-burner region and then making iterations between the predictions in these two systems? I think that this kind of arrangement can also reduce the computational requirements.

Author's Reply. We did not use a multigrid algorithm in our code. As you point out, a multigrid algorithm could also save CPU time. However, the significant savings of computational requirements achieved by multigrid algorithms, reported mainly for isothermal flows, are greatly reduced for turbulent reactive flows.

•

Roman Weber, International Flame Research Foundation, The Netherlands. Your predictions of temperature in the vicinity of the burners are in very good agreement with the measured values. In order to achieve such good agreement, the near-burner zone fluid flow and mixing have to be accurately predicted. This requires a detailed representation of both the burner geometry and inlet flows. In your three-dimensional calculations, the burner geometry has been substantially simplified; consequently, details of the near-burner zone have been lost. Did you perform computations of a single burner prior to the boiler predictions in order to examine how the simplifications to the burner have affected the near-burner zone predictions, including temperature?

Author's Reply. The temperature predictions in the vicinity of burners reported in this paper correspond to the profiles through ports 2.1 and 2.6 at full load (Fig. 3). Because of access restrictions to the boiler, measurements could only be obtained from the side walls up to the axis of the burner closest to the wall. The temperature profile along those ports shows that the predictions and measurements are in good agreement near the wall, where combustion products are present, but they actually differ in the vicinity of the burners (see profile along port 2.6). Although each burner was discretized using 11 grid nodes in each direction, it is believed that a much finer grid would be needed to obtain an accurate solution in the near-burner zone. We did not perform any computations of a single burner prior to the boiler predictions. The usefulness of such calculations is questionable since they would not account for the interaction between the flames of neighbouring burners.

Twenty-Fifth Symposium (International) on Combustion/The Combustion Institute, 1994/pp. 235–242

EFFECT OF RADIATION ON NITROGEN OXIDE EMISSIONS FROM NONSOOTY SWIRLING FLAMES OF NATURAL GAS

A. SAYRE, N. LALLEMANT, J. DUGUÉ AND R. WEBER
International Flame Research Foundation
P.O. Box 10,000, 1970 CA IJMUIDEN, The Netherlands

The present study attempts to quantify the effect of radiation on nonpremixed, turbulent diffusion flame temperature and NO_x emissions for flames subjected to different overall heat extraction. Comprehensive in-flame data have been generated for two flames of similar strain field and luminosity in order to facilitate flame comparison. The flame produced in the refractory-lined furnace (flame 1) is shorter than that of the water-cooled confinement (flame 2) by around 30%, and the extent of combustion increases by 20% at a distance 27-mm downstream of the burner outlet. The density-averaged mean flame temperatures were 1850 and 1675 K, and furnace NO_x emissions were 49 and 33 ppm for flames 1 and 2, respectively.

The total radiative intensities calculated spectrally using the Exponential Wide Band model are in very good agreement with the measurements and indicate that the amount of radiant energy emitted directly by both flames is similar. Radiation plays a crucial role in extracting the energy from the postflame zone, and therefore, it affects the enthalpy of the products entrained from the external recirculation zone. Flame temperatures and NO_x emissions are strongly dependent on the energy of the flow entrained by the jets. It is concluded that the radiant fraction cannot be used as an exclusive NO_x scaling parameter to describe the effect of radiation on emissions of confined turbulent diffusion flames. Proper scaling parameters should incorporate the energy entrained (from external recirculation zone) into the flame, and therefore, these parameters have to take into account the amount of energy extracted from the postflame zone.

Introduction

It happens only too often that a low-NO_x burner, when installed in a furnace different from which it was originally tested, produces unacceptable NO_x emissions. This is predominantly due to unforeseen alterations to either in-furnace fluid flow or heat transfer. Therefore, the understanding of the effect of radiative heat transfer on the flame properties [1,2] and consequently NO_x emissions [3] becomes of considerable technical importance.

It is important to establish how the NO_x and CO emissions vary (scale) with burner inputs, burner size (thermal input), and thermal conditions in the furnace. For simple jet diffusion flames, there is a wealth of experimental information on how the emissions scale with Reynolds, Froude, and Damköhler numbers [4,5]. Recently, Turns and Myhr [3] provided some quantification of the effect of radiation on the flame temperature and NO emissions. They used four different fuels to generate nonswirling jet flames of different luminosity. It was demonstrated that the radiant fraction (defined as the amount of energy radiated directly from the flame normalized by the total thermal input) should be taken into account while scaling NO_x emissions of jet flames. In industrial situations, the scenario is often different. When the same burner is installed in furnaces of different heat extraction characteristics, the flame properties are altered mainly due to different overall heat transfer patterns in the furnace and not by alterations to the flame luminosity.

The primary objective of this study is to quantify the effect of radiation on flame temperature, NO_x and CO emissions under conditions of high and low heat extraction without altering flame luminosity.

Experimental

Natural Gas Burner:

A swirl-stabilized natural gas burner, shown in Fig. 1, has been used. The burner design incorporates a movable block swirler for easy and continuous variation in inlet swirl (from 0 to 1.2) and for the possibility of handling ambient and preheated combustion air. Options for fuel staging and flue gas recirculation, two of the most effective methods of NO_x reduction with natural gas firing, are provided. In Fig. 1, the dimensions of the burner elements are normalized to the diameter of the combustion air duct (D_0). The burner is available in 30 and 300 kW, 1.3, 4, and 12 MW versions and is being used in the SCALING 400 study [6]. For the experiments reported here, the 300-kW version (D_0 = 87 mm) is used. The central natural gas injector features

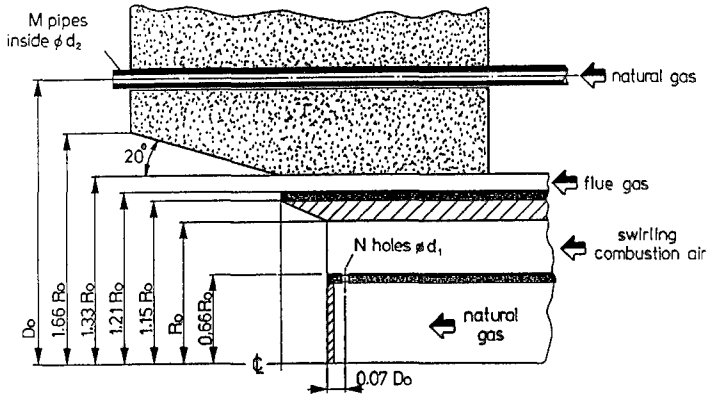

FIG. 1. Natural gas burner.

twenty-four 1.8-mm holes equally spaced on the circumference. The radial velocity of the natural gas is 140 m/s when all the fuel is supplied through the center injector at NTP. For the nominal 300 kW input and 15% excess ambient air, a Reynolds number of 52,000 is calculated on the basis of the equivalent diameter ($0.35 \cdot D_0$) of the combustion air annulus.

Experimental Furnace:

The experimental furnace used for the measurements is the vertically fired chamber of the Burner Engineering Research Laboratory. The confinement ratio, defined as the ratio of the furnace diameter to the burner quarl (tile) outlet diameter ($1.66 \cdot D_0$), is 7.5 and 8.9 for the refractory and bare-metal walls, respectively. For the in-flame measurements, panels were constructed with ports to allow access at five traverses located at AD/D_0 of 0.31, 1.25, 2.19, 3.94, and 4.96 (AD stands for axial distance measured from the quarl outlet).

Fuel Gas:

The volumetric composition of the natural gas used in the experiments is 0.965 CH_4, 0.017 C_2H_6, 0.01 C_3H_8, 0.01 C_{4+}, 0.03 CO_2, and 0.013 N_2. The following properties resulting from this composition are a density of 0.7 kg/Nm^3, stoichiometric air requirement of 16.58 kg_{dryair}/kg_{fuel}, and a lower calorific value of 46.7 MJ/kg.

Measurement Techniques:

Velocity measurements are performed nonintrusively by applying the laser Doppler anemometry technique on the combusting flow seeded with finely sized zirconia particles in the combustion air. Miniaturized versions of standard semi-industrial International Flame Research Foundation (IFRF) probes are used to intrusively sample gas composition and measure gas temperature by suction pyrometry. The permanent gases; CO, CO_2, H_2, O_2, NO_x, and total unburned hydrocarbons are measured using continuous gas analyzers. The flames were traversed with a narrow angle radiometer with a viewing angle of 1.42°, according to the technique described by Beér and Claus [7]. As described in the following sections, two flames are traversed at the first two measurement locations, $AD/D_0 = 0.31$ and 1.25 with the refractory-lined panel for the flame with hot wall conditions replaced with a cold target.

Experimental Results

Description of the Flames:

The experimental burner was used to generate stable and very symmetrical flames of 300-kW thermal input, two of which are described in this paper. The two flames differ only in furnace configuration with flame 1 being generated in the experimental furnace with refractory-line panels (hot wall condition), while flame 2 is generated in the same furnace assembled from water-cooled panels (cold wall condition). The two flames have identical burner input conditions, including inlet swirl (0.56), thermal input, and overall stoichiometry (15% excess air), as listed in Table 1. For both flames, all the fuel is supplied through the central gas injector (no fuel staging is applied). The flue NO_x emissions are 49 ppm (1.3 g_{NO_x}/kg_{fuel}) and 34 ppm (0.9 g_{NO_x}/kg_{fuel}) for flue gas temperatures of 1113 °C and 935 °C for flames 1 and 2, respectively. Around 29% of the total thermal input is extracted for flame 1, while for flame 2, a figure of 50% is applicable.

In-Flame Measurements:

The in-flame measurements include temperature, CO, CO_2, NO_x, O_2, and unburned hydrocarbons (UHC), as exemplified in Fig. 2. Time-mean axial velocities and root mean square (rms) values at the first traverse are shown in Fig. 3, demonstrating that an al-

TABLE 1
Parameters of flames 1 and 2

	Flame 1	Flame 2
Thermal input (kW)	316	312
Inlet swirl (–)	0.56	0.56
C.A. velocity (m/s)	28	28
C.A. temperature (°C)	39	42
N.G. flow-rate (kg/h)	22.7	22.4
N.G. injection temperature (°C)	35	42
N.G. injection pressure (kPa)	14	13
Heat extraction (kW)	93	144
Wall temperature (°C)	884	<100
Flue Gas Properties		
FEGT (°C)	1113	935
CO_2 (%)	10.1	9.9
O_2 (%)	3.0	3.0
NO_x (ppm)	49	34
NO_x (mg/Nm^3)	100	70
CO (ppm)	0	0

most identical strain field prevails in both flames. The same observation is valid for all the measured traverses (see Reference 8). In both flames, a small internal recirculation zone (IRZ) is formed in the burner vicinity. At the first measurement traverse, around 5.7 and 6.9% of the inlet flow is recirculated back to the flame root. The reverse flow energy, defined as the recirculated mass flow rate times the sensible heat, is 12.6 and 15.2 kW for flames 1 and 2, respectively. The measurements demonstrate that in flame 1, higher temperatures occur at the flame front (radial distance 0.8–1.0, see Fig. 3), than in flame 2.

Large external recirculation zones (ERZ) are formed in the furnace. In flame 1, the temperature of recirculating gases is around 1350 K (see Fig. 3), and the NO_x concentration is around 37 ppm. In flame 2, the ERZ contains combustion products of 920 K (see Fig. 3) and NO_x concentration of 25 ppm. An integration of the measured axial velocities shows that flame 1 entrains more than flame 2. At $AD/D_0 = 2.19$, the entrainment is 125% for flame 1, while only 75% for flame 2; at $AD/D_0 = 3.94$, the entrainment figures are 200 and 110% for flames 1 and 2, respectively.

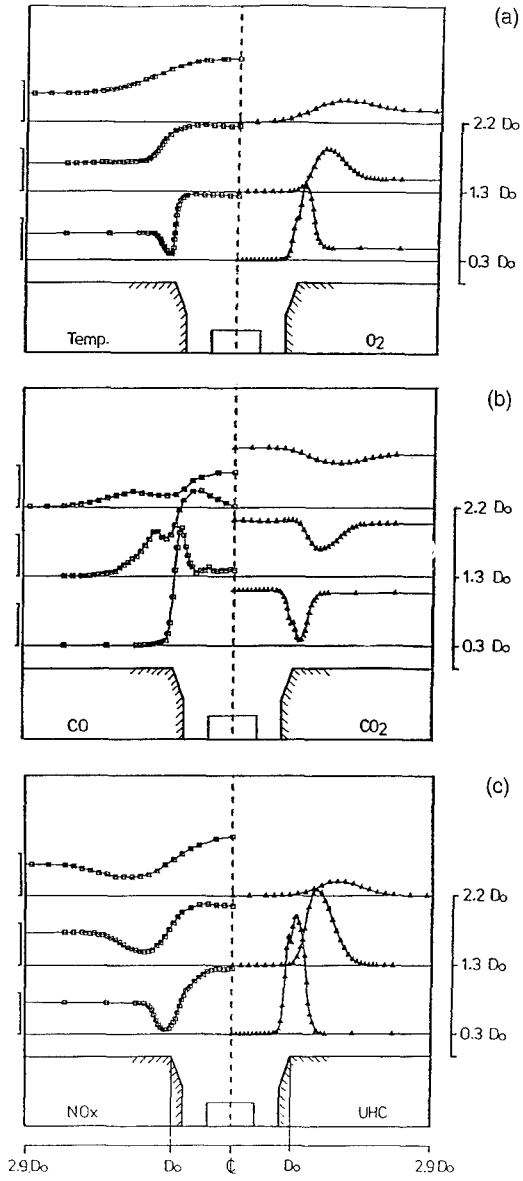

FIG. 2. In-flame measurements for flame 2. The values are scaled by the bars on the left-hand side, which represents (a) 1000 °C and 10% for temperatures and O_2; (b) 1 and 8% for CO and CO_2, respectively; (c) 40 ppm and 2% for NO_x and UHC.

Discussion

Rate of Combustion:

The conical flame shape derived using the in-flame measurements agrees very well with the visible flame boundaries taken from the photography. For both flames, a contour of 5000 ppm of carbon monoxide is found to match the qualitative description of the boundary from the photography. It is calculated that for flame 1 (hot walls), the flame length, volume, and surface area are 19.6 cm ($2.25 \cdot D_0$), 4185 cm^3, and 1332 cm^2, respectively. For flame 2 (cold walls), the figures of 25.6 cm ($2.95 \cdot D_0$), 5863 cm^3, and

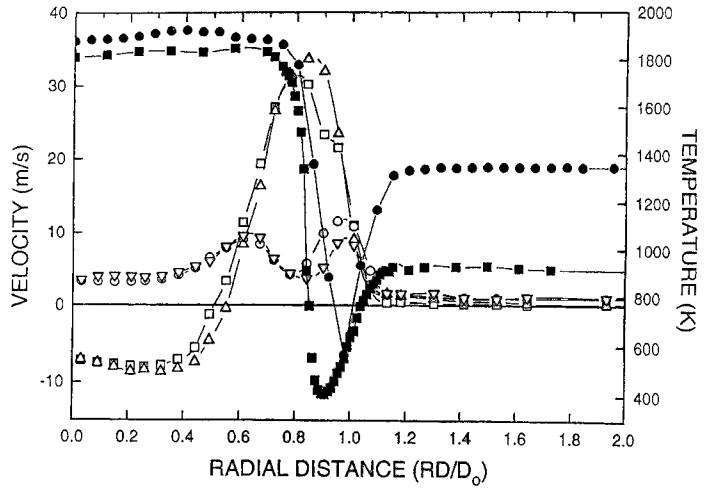

FIG. 3. Axial velocities and temperatures at AD/D_0 = 0.31. The ● designates flame 1 temperatures, and the ■ represents flame 2. The open symbols refer to the velocities with △ and □ representing flame 1 and flame 2 mean axial velocities and ○ and ▽ representing flame 1 and flame 2 rms axial velocities, respectively. RD stands for radial distance, D_0 = 87 mm.

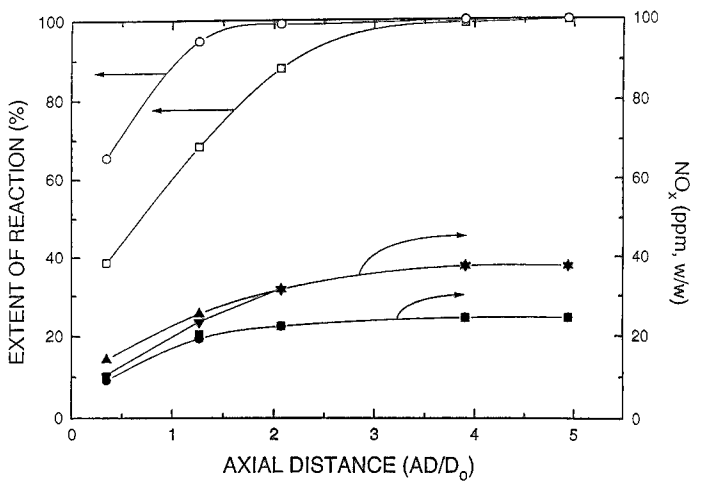

FIG. 4. Axial profile of extent of reaction and mass-averaged NO_x concentrations. The ○ signifies the extent of reaction for flame 1 and □ for flame 2; the ▼ signifies the NO_x value for flame 1 including the IRZ and ▲ excluding the IRZ; the ● signifies the NO_x value for flame 1 including the IRZ and ■ excluding the IRZ. AD stands for axial distance measured from the quarl outlet, D_0 = 87 mm.

1640 cm^2 are applicable. Another way of estimating the flame length is by calculating the extent of methane combustion (χ_{CH_4}) according to

$$\bar{m}_{CH_4} = 2\pi \int_{R_{min}}^{R_{max}} \bar{y}_{CH_4} \cdot \bar{\rho} \cdot \bar{U}(r) \cdot r \cdot dr \qquad (1)$$

$$\bar{\chi}_{CH_4} = \left(1 - \frac{\bar{m}_{CH_4}}{\bar{m}_{CH_4 inlet}}\right) \cdot 100 \qquad (2)$$

where $\bar{m}_{CH_4}$ is the methane mean-mass flow rate, $\bar{y}_{CH_4}$ is the mean-mass fraction of methane, $\bar{\rho}$ is the mean density, and $\bar{U}$ is the mean-axial velocity. The integration is performed from the flame center to the boundary of the jet (forward flow boundary). Figure 4 shows the extent of reaction confirming that at AD/D_0 = 2.25, methane combustion is completed for flame 1, while in flame 2, the combustion proceeds until a distance of AD/D_0 = 2.95. This is in agreement with the flame boundary determined visually.

The measured peak temperatures are 1945 and 1864 K, while the mass-mean-averaged values within the flame volumes defined above are 1850 and 1675 K for flames 1 and 2, respectively. It is estimated that the residence time is in the range 6–10 ms for flame 1 and around 40% longer for flame 2. For both flames, the NO_x concentrations increase with the distance from the burner tip until the end of the flame. The measurements show that NO_x concentrations remain practically unaltered in the postflame part of the furnace. In Fig. 4, the mass-averaged values of NO_x volume fraction within the forward flow

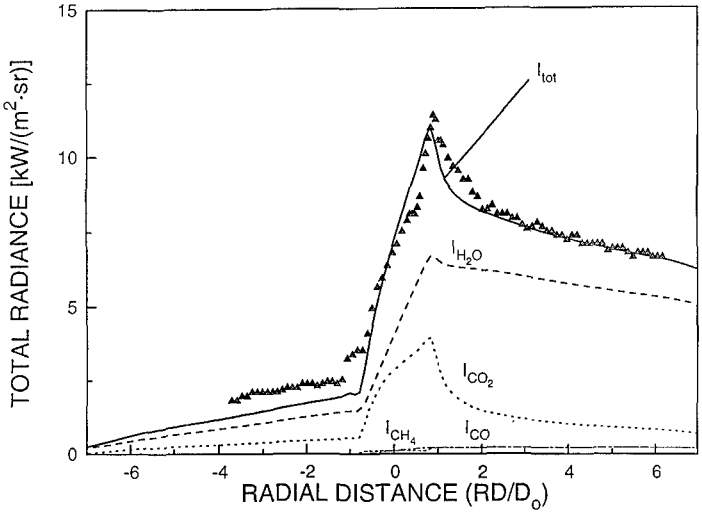

FIG. 5. Comparison between measured and predicted total radiance for flame 2 with the cold target at $AD/D_0 = 0.31$. The ▲ designates the measured total radiance. The solid line shows the spectral calculation using the exponential wide band model. The dotted lines represent the contributions of H_2O, CO_2, CO, and CH_4 to the predicted total radiance. $RD/D_0 = 0.0$ corresponds to the axis of the burner.

are plotted for both flames. The NO_x concentrations have been calculated with and without the internal recirculation zone included.

The measurements clearly indicate higher in-flame temperatures for flame 1 (hot refractory walls) than for flame 2 (water-cooled walls). It is important to establish whether the presence of the cold walls could have altered the radiative heat exchange between the flame and the surroundings to such a degree that the mean flame temperature dropped by 175 K. To this end, an analysis of the radiative transfer is performed. It will be shown later that the strongly cooled recirculating gases are responsible for the temperature difference and consequent lowering of NO_x emissions.

Radiative Heat Transfer:

The radiative transfer equation (RTE) reads as follows:

$$\frac{\partial I_\nu}{\partial s} = -k_a^r \cdot (I_\nu - I_\nu^0) \tag{3}$$

where the first term is the gradient of intensity and the second and third terms represent the absorption and emission of energy, respectively. The total intensity leaving a gas layer of length L can be obtained by integrating Eq. (3) over wave number ν in cm^{-1} and path length. This results in the following expression:

$$I(L) = \int_{\nu=0}^{\infty} I_\nu(0) \cdot \tau_\nu(0, L) \cdot d\nu + \int_{\nu=0}^{\infty} \left\{ \int_0^L \frac{\partial \tau_\nu(s', L)}{\partial s'} \cdot I_\nu^0(s') \cdot ds' \right\} d\nu \tag{4}$$

where $I(L)$ is the total intensity leaving the gas layer in $W/(m^2 \cdot sr)$, $I_\nu(0)$ is the spectral intensity incident upon the gas layer, I_ν^0 is the black-body spectral intensity in $W/(m^2 \cdot sr \cdot cm^{-1})$, and k_a^r is the spectral absorption coefficient of the gas in m^{-1}. The spectral transmissivity of the gas is given by

$$\tau_\nu(s', L) = e^{-\int_{s'}^{L} k_a^\nu(s'') \cdot ds''} \tag{5}$$

The intensity distributions shown in Fig. 5 are calculated spectrally using the exponential wide band model (EWBM) [9] along with the Chan and Tien scaling method [10,11]. The total pressure of the gas was taken as one atmosphere. The spectral calculations, which take into account the nonhomogeneity of the temperature and composition fields, are performed over wave number bands, assuming that the spectral overlap is not significant. In view of the temperature and concentrations prevailing in the flames, the following bands are included: 10–20 μm rotational; 6.3, 2.7, 1.87, and 1.38 μm for H_2O; 10.4, 9.4, and 4.3 μm for CO_2; 2.35 and 4.7 μm for CO; 7.66, 3.31, and 2.37 μm for CH_4. The 10–20 μm H_2O band is included in view of the fairly low temperatures in the ERZ (around 900–1350 K) and the high concentrations of water vapor [12]. The 15 μm CO_2 band, though of some importance at these temperatures, has been neglected since it requires special procedures to account for the overlapping. Moreover, it is expected that the band from water vapor in the 10–20 μm region is stronger since the H_2O/CO_2 partial pressure ratio is around 2. Following James and Edwards [1], the 2.7-μm band of CO_2 is neglected due to a maximum underprediction of total intensity by 8% when this band is excluded. The importance of the 2-μm band of CO_2 is estimated to be less than 2% of the total emissions [13] and, hence, is not included in the present calculations. All important

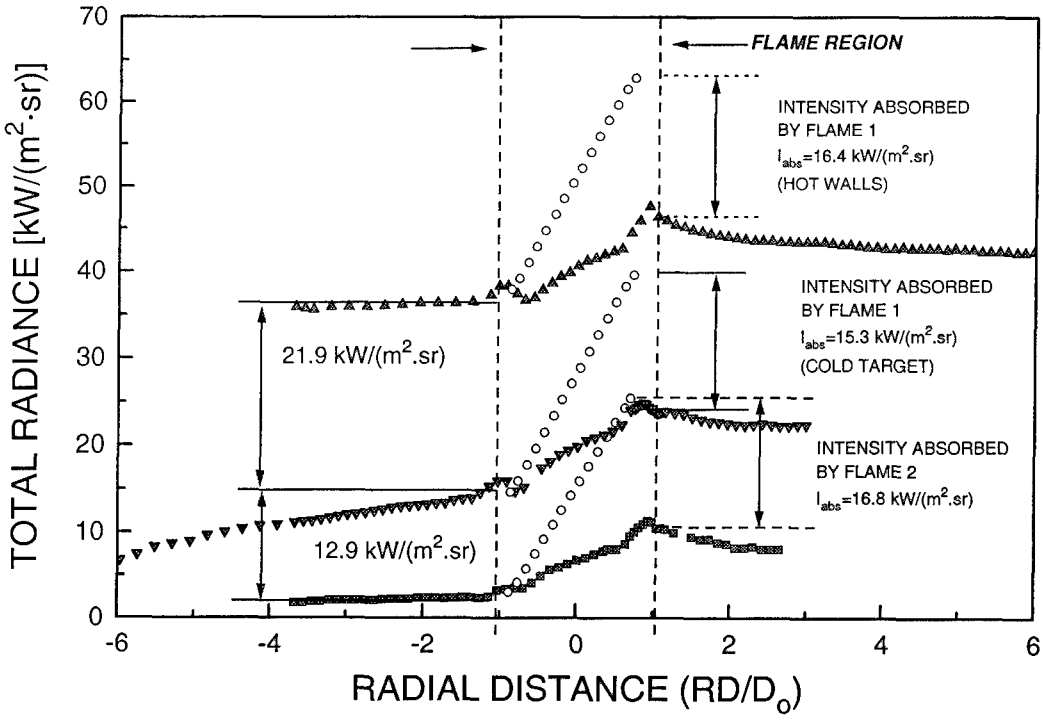

FIG. 6. Comparison of the radiative intensity absorbed for flames 1 and 2 at $AD/D_0 = 0.31$. The ▲ and ▼ designate the measured radiance for flame 1 with and without the contribution of the walls, respectively. The ■ designates the measured radiance for flame 2; ○ shows the calculated total intensity from Eqs. (6) and (7). $RD/D_0 = 0.0$ corresponds to the axis of the burner. 21.9 kW/(m^2·sr) is the contribution to the total radiance from the wall for flame 1; 12.9 kW/(m^2·sr) is the contribution due to the temperature difference in the ERZ of flames 1 and 2.

bands of CO [9] and CH_4 [9,14] are incorporated. As shown in Fig. 5, the calculated radiance agrees well with the measured values. The figure shows that the contribution from water vapor is about twice that of CO_2. The contribution of CO and CH_4 is seen to be unimportant. Since the total radiance calculations are uniquely based on the in-flame measurements, the good agreement between the measured and predicted total radiance provides a strong confidence in both the measurements and the calculation procedure.

Figure 6 shows the measured radiance of flames 1 and 2 with the cold target positioned on the other side of the furnace. For flame 1, the measured radiance with the cold target replaced with a refractory panel ($T = 1157$ K) is also shown. In all three cases, the difference between the radiance leaving the flame region ($RD/D_0 = +1$) and that entering ($RD/D_0 = -1$) is around 10 kW/(m^2·sr) [for flame 1 without the cold target, it is (47.6–37.3) kW/(m^2·sr); for flame 1 with the cold target, it equals (24.5–15.4) kW/(m^2·sr); and for flame 2 with bare metal walls, it is (11.4–2.5) kW/(m^2·sr)]. The total radiance incoming at the edge of the flame is certainly affected by both the wall emission and the net emission of the ERZ (see Fig. 6). However, the 10 kW/(m^2·sr) difference in the flame region is not affected by either.

Equation (3) can be used to estimate how much of the intensity has been absorbed within both flames. To this end, only the emission term of the right-hand side is considered, and the solution is as follows:

$$I(L) = I(0) + \int_0^L k_P(s) \cdot I^0[T(s)] \cdot ds. \qquad (6)$$

The Planck mean coefficient k_P in Eq. (6) is defined as

$$k_P \equiv \frac{\int_0^\infty k_a^\nu \cdot E_\nu^0 \cdot d\nu}{\sigma T^4(s)} \qquad (7)$$

where E_ν^0 is the spectral blackbody emissive power in W·m^{-1}. In Eq. (6), $I(0)$ stands for the incident intensity at the flame (left-hand side) boundary while $I(L)$ represents the intensity at the other (right-hand side) boundary. The results of the integration, using

as $I(0)$ the values measured at the flame boundaries, are shown in Fig. 6. All the bands of H_2O, CO_2, CO, and CH_4 were accounted for in the calculation of the Planck mean emission coefficient Eq. (7). For both flames, the absorbed intensity is about the same at 15 kW/(m^2·sr). Similarly, at the second measurement traverse, despite the differences in the flame temperatures and alterations to the gas composition, the absorption terms of Eq. (3) are very similar. Thus, the difference in the amount of energy absorbed by the two flames is proportional to the flame volume ratio (5863/4185 = 1.4), with more energy absorbed by flame 2 than flame 1.

The amount of energy emitted from both flames can be calculated as follows:

$$E_{\text{emitted}} = 4 \cdot \sigma \cdot \bar{T}^4 \cdot k_P(\overline{p_i}, \bar{T}) \cdot V_{\text{flame}} \qquad (8)$$

where V_{flame} is the flame volume; $\bar{T}$ and $\overline{p_i}$ are the mean flame temperature and partial pressures, calculated using density averaging; and σ is the Stefan–Boltzmann constant. The Planck mean coefficient has been calculated using the EWBM to be 0.85 m^{-1} (hot walls) and 1.0 m^{-1} (cold walls). The radiant emissions calculated using the mean flame temperature, concentrations, and volume, as specified above, are 9.4 and 10.5 kW, which corresponds to radiant fractions of 3.0 and 3.3% for flames 1 and 2, respectively. If the nonuniformity of the in-flame temperature and chemical composition are accounted for, the radiant flame emissions are 21.8 and 18.8 kW, using density-averaged properties to calculate the local coefficient.

Energy Balance of the Expanding Jets:

The considerations on radiative transfer indicate that the flames emit an almost identical amount of energy. Also, flame 2 may absorb around 40% more energy than flame 1. However, the analysis so far does not provide a reason for the substantially higher temperatures of flame 1. It is thus essential to compare the energy absorbed by the flames with that entrained from the ERZ into the jet flames.

Consider the expanding, combusting jets with the outer boundaries determined by the contour of zero axial velocity (where the jets interact with the ERZ). The first jet, corresponding to flame 1, should have the length of $2.25 \cdot D_0$, while the second jet (corresponding to flame 2) should be $2.95 \cdot D_0$ long. The flame volumes defined earlier are included within the expanding jets. The energy balance for the jets is as follows:

$$E_{\text{in}} + E_{\text{entr}} + E_{\text{abs}} = E_{\text{out}} + E_{\text{em}} \qquad (9)$$

where E_{in} is the thermal input, E_{entr} is the energy entrained into the expanding jet, E_{abs} and E_{em} are the radiant energy absorbed and emitted by the jets, and E_{out} is the energy contained in the jet at the end of the flame region. The first term is precisely known (see Table 1), while E_{out} and E_{entr} can be calculated using the in-flame measurements. For jet-flame 1, the calculated values are E_{out} = 517 kW and E_{entr} = 183 kW, while for jet-flame 2, values of E_{out} = 375 kW and E_{entr} = 118 kW are applicable. It is important to realize that the energy values cannot be calculated with an accuracy better than perhaps 10–20% due to the necessity of interpolating between the measurement traverses. However, the figures clearly demonstrate that the jet-flame 1 entrains twice as much energy as jet-flame 2 and, therefore, is "hotter." The amount of energy emitted (radiant fraction) and absorbed by both flames is substantially lower than the energy entrained from the ERZ. The latter is strongly dependent on the temperature of the combustion products of the ERZ and, therefore, related to the amount of energy extracted from the postflame zone by radiation (mainly) and convection.

Increase of the Methane Combustion Rate:

Figure 4 shows that just downstream of the burner quarl, the extent of methane combustion is about 65% for flame 1, while only 40% for flame 2. The combustion products entrained from the ERZ into the jets are at a higher temperature for flame 1 (1350 K) than for flame 2 (920 K). This results in a higher temperature of the gases recirculated via the IRZ back into the fuel injector (around 70 to 90 K hotter for flame 1) and, therefore, in the higher combustion rate inside the burner guard for flame 1.

Conclusions

Detailed in-flame measurements of velocity, turbulence, gas composition, temperature, and radiation were taken in two nonsooty, swirling flames of natural gas. The flames are of almost identical velocity (strain) fields with very rapid mixing prevailing. Flame 1 was positioned in a refractory-lined furnace with approximately 29% of the total thermal input extracted. Flame 2 was located in a furnace configured with water-cooled walls in which 50% of the thermal input was extracted. The NO_x flue emissions were 49 ppm (1.3 g_{NO_x}/kg_{fuel}) and 34 ppm (0.9 g_{NO_x}/kg_{fuel}) for flames 1 and 2, respectively, with almost all the NO_x formed within the flame volumes. It has been shown that the energy entrained from the ERZ into the swirling jets has strongly affected the flame temperatures. The lower NO_x emissions of flame 2 have been attributed to entraining the strongly cooled recirculating gases. The following has been concluded:

1. When the same burner is positioned in the refractory-lined rather than water-cooled furnace,

the flame has shortened from $2.95 \cdot D_0$ to $2.25 \cdot D_0$. The extent of (methane) combustion reaction increased from 45 to 65% at the first measurement traverse $0.31 \cdot D_0$ downstream of the burner quarl. A mechanism for the faster methane combustion rate inside the burner guard for flame 1 is proposed.

2. The amounts of radiant energy emitted and absorbed directly by both 300-kW flames (radiant fractions) are very similar. This implies that the radiant fraction cannot be used as an exclusive NO_x scaling parameter to describe the effect of radiation on emissions of confined turbulent diffusion flames. Radiation plays a crucial role in extracting the energy from the postflame zone and, therefore, controls the ERZ temperature (which corresponds to the furnace outlet temperature). The flame temperature and consequently NO_x emissions are strongly dependent on the latter through the jet entrainment. Proper NO_x scaling parameters should incorporate the energy entrained (from the ERZ) into the flame. Therefore, these parameters must account for the amount of energy extracted from the postflame zone.

Acknowledgments

We would like to thank N. Fornaciari, R. Sanford, and L. Clayton for their assistance during the measurements. The BERL is funded by the Gas Research Institute and the U.S. Department of Energy, Office of Industrial Processes, Advanced Industrial Concepts Division. The project was financed by the Gas Research Institute with the supervision of Dr. R. V. Gemmer.

REFERENCES

1. James, R. K., and Edwards, D. K., *J. Heat Trans.* 99:221 (1977).
2. Gore, J. P., and Faeth, G. M., *Twenty-First Symposium (International) on Combustion,* The Combustion Institute, Pittsburgh, 1986, p. 1521.
3. Turns, R. S., and Myhr, F. H., *Combust. Flame* 87:319, (1991).
4. Bilger, R. W., and Beck, R. E., *Fifteenth Symposium (International) on Combustion,* The Combustion Institute, Pittsburgh, 1975, p. 541.
5. Chen, R.-H., and Driscoll, J. F., *Twenty-Third Symposium (International) on Combustion,* 1990, p. 281.
6. Weber, R., Driscoll, J. F., Dahm, W. J. A., and Waibel, R. T., "Scaling Characteristics of the Aerodynamics and Low NO_x Properties of Industrial Natural Gas Burners," The SCALING 400 Study, GRI-93/0227, (1993); also avaiable as IFRF Doc No. F 40/y/9 (1993).
7. Beér, J. M., and Claus, J., "The Traversing Method of Radiation Measurement in Luminous Flames," IFRF Doc. C 72/a/6 (1967).
8. Sayre, A. N., Lallemant, N., Dugué, J., and Weber, R., "Scaling Characteristics of the Aerodynamics and Low NO_x Properties of Industrial Natural Gas Burners," The SCALING 400 Study, Part IV: The 300 kW BERL Test Results, Report submitted to the Gas Research Institute, 1994.
9. Edwards, D. K., in *Advances in Heat Transfer* (T. F. Irvine, Jr. and J. P. Harnett, eds.), Academic Press, New York, 1976, vol. 12, p. 115.
10. Chan, S. H., and Tien, C. L., *J. Quant. Spectrosc. Radiat. Trans.* 9:1291 (1969).
11. Tien, C. L., and Lee, S. C., *Prog. Energy Combust. Sci.* 8:41 (1982).
12. Leckner, B., *Combust. Flame* 19:33, (1972).
13. Leckner, B., *Combust. Flame* 17:37, (1971).
14. Brosmer, M. A., and Tien, C. L., *J. Quant. Spectrosc. Radiat. Trans.* 33:521 (1985).

COMMENTS

Ruey-Hung Chen, University of Central Florida, USA. As previously demonstrated in a smaller scale swirl burner, the internal recirculation zone properties, such as its residence time and the ratio of fuel jet momentum to recirculation zone velocity, determine the fuel-air mixing and flame behavior [1,2]. They should similarly determine NO_x (at least thermal NO_x) emission. Would you comment on the role of ERZ as it may affect the internal recirculation, as implied in your paper?

REFERENCES

1. Chen, R.-H., and Driscoll, J. F., *Twenty-Second Symposium (International) on Combustion,* The Combustion Institute, Pittsburgh, 1989, p. 535.
2. Chen, R.-H., et al., *Combust. Sci. Technol.* 71:197 (1990).

Author's Reply. The burner design utilizes both bluff-body and swirl stabilization in concert with radial injection of fuel into the combustion air stream to achieve stability over a wide range of operating conditions. The flames that are compared were produced under similar burner inlet conditions; hence, they possess a similar strain field and internal recirculation zone. The lower NO_x emissions for Flame 2 (cold walls) than for Flame 1 (hot walls) are therefore concluded to be solely a consequence of the lowering of the thermal NO_x production rate due to the entrainment of the colder combustion products into the reacting shear layer.

Twenty-Fifth Symposium (International) on Combustion/The Combustion Institute, 1994/pp. 243–250

ON THE EFFECTS OF FUEL LEAKAGE ON CO PRODUCTION FROM HOUSEHOLD BURNERS AS REVEALED BY LIF AND CARS

C. E. VAN DER MEIJ, A. V. MOKHOV,* R. A. A. M. JACOBS AND H. B. LEVINSKY
Gasunie Research
N.V. Nederlandse Gasunie
P.O. Box 19, 9700 MA Groningen, The Netherlands

Measurements of the distributions of CO, OH, and temperature in flames from two commonly used, commercially available household burners are presented. The local mole fractions of CO and relative distribution of OH have been obtained using laser-induced fluorescence, while the local temperatures have been determined by coherent anti-Stokes Raman scattering (CARS). For both burners, burning in the open air, CO formation outside the main flames has been observed and attributed to the leakage of fuel-air mixture at the edges of the flame, where the fuel is subsequently converted to CO in the boundary layer between the flame and the surroundings. For a rich-premixed, multiblade burner, which gives Bunsen-like flames, the CO produced by the leaking fuel appears to be oxidized by OH arising from the outer cones of adjacent flames, and burns out to low concentrations. In the case of a lean-premixed burner, the CO produced by fuel leakage remains in the cool boundary layer without adequate burnout. Possible consequences for appliance behavior are discussed.

Introduction

In the past, natural-gas appliances for household use have been approved for installation based upon their performance regarding flame stability, CO production, and soot formation. Over the years, burner manufacturers have developed rules of thumb for choosing combinations of design parameters, such as primary fuel-air ratio, port loading, and port spacing, to meet the approval specifications. The legislation of NO_x emission limits in many parts of the world has substantially complicated the process of burner design. Attempts at lowering NO_x emissions by reducing the flame temperature, for example by using flue-gas recirculation and lean-premixed combustion, often lead to reduced flame stability or increased CO emissions. In fact, the lowest NO_x emission obtainable in a given configuration is *always* limited by unacceptable stability problems or CO emissions. Burner design has thus become a trial-and-error, multiparameter optimization process, by which the designer is not sure whether the observed optimum is a coincidence of the chosen configuration or a fundamental physical limit.

One of the major drawbacks to this approach is that the measurements are global: Changes are made, for example, to the burner, and the emissions are measured in the exhaust of the appliance. This makes it difficult to separate "primary" effects (resulting from a change in the burner) from "secondary" influences (altered flow and heat-exchange characteristics within the combustion chamber due to the different burner). This is related to the practical observation of identical burners behaving very differently in different combustion chambers. Clearly, since the formation of pollutants in combustion systems is dependent upon the details of the combustion process itself (*local* concentrations of various chemical species, temperatures, etc.), insight into these details and the effect of parameter variations on them is required in order to properly evaluate origins of burner and appliance performance.

Whereas the paths to NO formation in natural gas flames and the primary factors influencing them are reasonably well understood [1], the origin of CO emissions in household appliances is not. Many appliances, such as cooking burners and hot-water heaters, utilize rich-premixed, Bunsen-type flames, where CO burnout depends on the admixing of ambient, or "secondary," air [2]. In this case, the absence of sufficient oxygen upon heat transfer (either in a heat exchanger or to the bottom of a pan) will clearly lead to excess CO emission. Another possibility is a combination of insufficient time for the burnout of CO, followed by "quenching" of CO oxidation during the heat-exchange process. In another context, Correa [3] has examined CO oxidation numerically in gases flowing along a cooled wall. For conditions characteristic for a gas-turbine combustor (wall temperature of 1100 K), he concluded that heat transfer to this wall was not fast enough to quench

*Permanent address: Institute for High Temperatures (IVTAN) Moscow, Russia

CO oxidation. However, he did suggest that the escape of unburned fuel from the primary combustion zone, converted to CO in a cooled boundary layer where CO oxidation is slow, could give rise to increased CO emissions.

In an effort to gain insight into the origin of unwanted CO emissions in practical systems, we have performed measurements of the spatial distributions of CO and OH, using laser-induced fluorescence (LIF), in laminar flames stabilized on several commonly used, commercially available household burners, burning in the open air. The type of burner varied from bar and blade burners, with rich-premixed, Bunsen-type flames, to lean-premixed burners. Since CO is primarily oxidized by OH [4], the distribution of this radical can assist in the analysis of the CO distributions. In order to convert the CO fluorescence to concentration, as well as for an additional interpretive diagnostic, spatially resolved temperature measurements have been performed using coherent anti-Stokes Raman scattering (CARS). In this paper, we report the results for two of these burners that show effects we ascribe to fuel leakage at the edges of the flame. To our knowledge, this is the first direct evidence of a contribution from fuel leakage to excess CO emissions.

Experimental Techniques

LIF:

Composite two-dimensional LIF images of the distributions of CO and OH were obtained using the experimental apparatus described previously [2,5]. The OH images were obtained by exciting the $Q_1(7)$ line in the $X^2\Pi(v'' = 0) \rightarrow A^2\Sigma^+(v' = 1)$ manifold at 283.2 nm and detected using a filter (centered at 360 nm, bandpass 56 nm) that passed most of the emission of the (0,1), (1,2), (2,2), and longer-wavelength bands while excluding emission from the (0,0). In this fashion, self-absorption of the fluorescence [2] was substantially reduced. With a beam diameter of 1 mm [5], 9-mJ pulses gave signals strong enough for our imaging configuration. Under these conditions, the absorption transition was partially saturated, but the broadband detection renders the signal sensitive to quenching. An additional complicating factor in the interpretation of the OH images is that vibrational relaxation, which would drain population to the undetected (0,0) and reshuffle the detected population, is dependent upon temperature and composition [2,6] in an as yet unknown manner. However, since the OH images are used here only as a qualitative diagnostic, they are uncorrected for these effects and deemed adequate for this purpose.

The CO images were made in the same focused-beam geometry reported earlier [2], since the use of the beam telescope [5] resulted in insufficient signal intensity. An improvement to the detection scheme was the addition of an interference filter (centered at 483.5 nm, bandpass 6 nm) to separate the CO fluorescence from possible hydrocarbon interference [7]. We estimate the total contribution from hydrocarbon emission in the flame front (where the effect is the most severe) under these conditions at 10% of the signal. Extra dynamic range was gained by the analog integration of the repeated LIF signals prior to readout, instead of adding the individually read signals in the computer. This improved the signal-to-noise ratio by a factor of 50 for 100-pulse averages. The CO fluorescence was calibrated by flowing 4000 ppm cold CO in N_2 through a cell, and converted to concentrations using the temperature dependence at 230.1 nm presented in Ref. 8 and the local temperature measured by CARS. The laser energy was monitored during the experiments, and the signals were corrected using the $I^{1.5}$ power dependence observed in our experiments. Inasmuch as this dependence is similar to that observed by Tjossem and Smyth [9], where they estimate photoionization as a major depopulation process, we neglect quenching effects here. We further mention that, in several fuel-rich flames where the postflame CO concentration is close to chemical equilibrium, the concentrations measured in this fashion differed from the calculated equilibrium concentrations generally by less than 20%, which we maintain as our high-temperature accuracy. This suggests that it is indeed possible to measure CO quantitatively using LIF.

Since the flames studied were stable and laminar, all LIF signals were averaged over 100 laser pulses. The scale of the LIF images corresponds to an area 4.3-cm wide and 10-cm high, unless otherwise indicated.

CARS:

Measurements of absolute temperature were performed using broadband planar BOXCARS for nitrogen thermometry, using a configuration very similar to that reported by Kröll et al. [10]. Briefly, 20% of the 532-nm light from a Nd:YAG laser (see Ref. 2 for details of the laser) was used to form the pump beams. The remaining 80% pumped a broadband dye laser (>90 cm^{-1} bandwidth at a peak wavelength of ~606.5 nm), which was used for the Stokes beam. The beams were focused using a f = 50-cm lens, yielding a focal volume of ~100-μm diameter and ~2-mm length. Typical pulse energies at the measurement volume were 50 mJ per 532-nm beam and 60 mJ in the Stokes beam. After separation from the 532-nm beam by a dichroic mirror, the CARS signal was focused on the slit of a 1-m spectrometer (Jobin-Yvon THR 1000). The broadband-CARS spectrum was recorded using a gated (100 ns) linear diode array (EG&G 1420HQ). The spectra were averaged over 100 laser pulses per point and divided by the

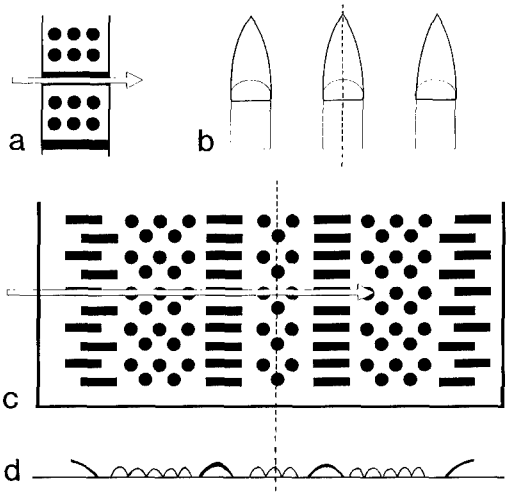

FIG. 1. (a) Perforation pattern for rich-premixed, multiblade burner; (b) side view of three blades from this burner, with flames; the dashed line indicates the middle of one of the elements, which corresponds to the positions of the black lines in Figs. 2 and 3; (c) perforation pattern for lean-premixed burner; (d) flame form from lean-premixed burner. The arrows in (a) and (c) indicate the path of the laser beam and, hence, the cross sections in which the two-dimensional images were made. The dashed lines in (c) and (d) correspond to the positions of the black lines in Figs. 6 and 7.

averaged dye spectrum (obtained by measuring the nonresonant CARS spectrum in a stream of methane) prior to analysis. Temperatures were extracted from the spectra using the CARP-PC [11] program. The reproducibility of the temperature determinations was on the order of 20 K, while the estimated accuracy is ± 30 K at flame temperatures.

In contrast to the LIF experiments, where the laser beam and the detector were positioned [2] to generate two-dimensional images, the temperature profiles were measured by moving the burner with precision positioners (25-μm accuracy, Daedal Corp.).

Burners:

A naturally aspirated, multiblade burner (14 elements) from an instantaneous hot-water heater was operated as obtained from the manufacturer. The perforation pattern is shown schematically in Fig. 1a. Each blade is 7-mm wide and 14-cm long; the slots are 0.5-mm wide, and the holes are 0.5 mm in diameter. Fired with Slochteren natural gas at 75% full load (18 kW), it produced rich-premixed, Bunsen-type flames (equivalence ratio, $\Phi = 1.33$) having an inner cone height of 4 mm and outer cones 6-cm high. A side view of three blades and their flames is illustrated in Fig. 1b.

The second burner was a lean-premixed burner from a condensing boiler, with the perforation pattern shown in Fig. 1c. The slots are 0.5-mm wide and 6-mm long; the holes have a diameter of 1.1 mm. Because of the normally high load of this burner and the limitations of our gas-handling system, a section (6.5 cm $\times$ 8.5 cm) of the burner deck was sawn off and placed in a smaller box used to mount radiant burners. The burner was operated using pure methane at $\Phi = 0.69$ (somewhat leaner than nominal), and at 550 kW/m^2, 45% of the nominal surface load. This gave the flame form shown in Fig. 1d.

Results and Discussion

Rich-Premixed Burner:

The composite two-dimensional fluorescence images of the distributions of CO and OH above two of the blades are presented in Figs. 2 and 3, respectively. The lowest point in these images is 1 mm above the burner surface. The false-color scale is in fluorescence "counts," and the images have been corrected for detector efficiency. The CO image is scaled logarithmically [2] to emphasize the lower signal levels. The regions of highest CO fluorescence intensity are between the inner and outer cones directly above the burner blades (the vertical black lines in Figs. 1b, 2, and 3 indicate the centerline of the flame above one of the blades). In addition, there appear to be "jets" of CO intensity *between* the blades of the burner. We remark here that, for other rich-premixed burners having nonlifted, Bunsen-like flames, we observe [12] only Bunsen-like CO images [2], which do not show these "jet" structures. In previous work [2] on two of the blades from this burner, although not strictly comparable (different load, primary aeration, and detection scheme), weak jets that were due, at least partially, to hydrocarbon fluorescence were observed. All observations taken together, we attribute these jets of CO as arising from fuel leakage at the edges of the burner. Since the inner cones of the flames are not visibly lifted, this is worrisome. Preliminary particle-tracking photographs indicate that some of the fuel-air mixture is skirting the primary flame front in the "overhang" region at the edges of the blades [13]. In this case, it is possible that the escaped fuel is converted to CO in the boundary layer between the cooler secondary air flowing between the burners and the outer cones of the flames, where there is still a substantial density of flame radicals.

The spatial relationship between the CO from the main flame, the jets, and the OH in the outer cone of the flames can be more readily visualized in Fig. 4, which is a horizontal cross section of Figs. 2 and

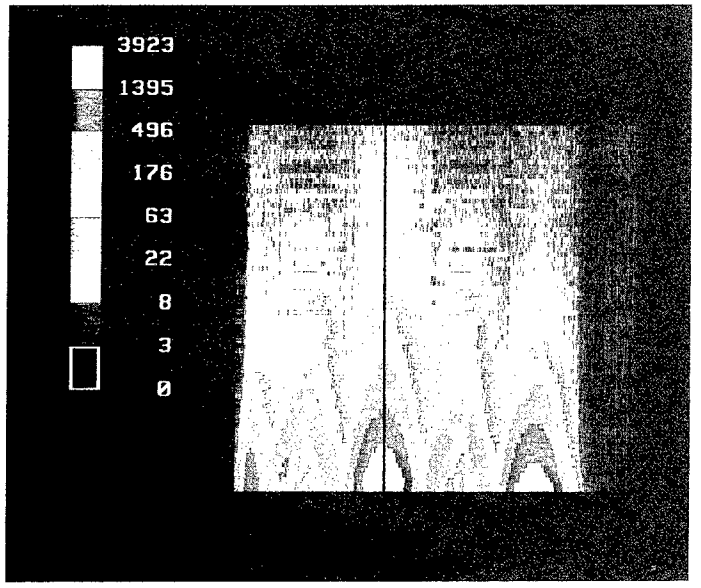

FIG. 2. Composite two-dimensional distribution of CO fluorescence intensity for rich-premixed burner. The scale is logarithmic and is in fluorescence "counts." Note that the imaged area in this figure is only 7.5-cm high, instead of 10 cm. The black line corresponds to the same position in Fig. 1b.

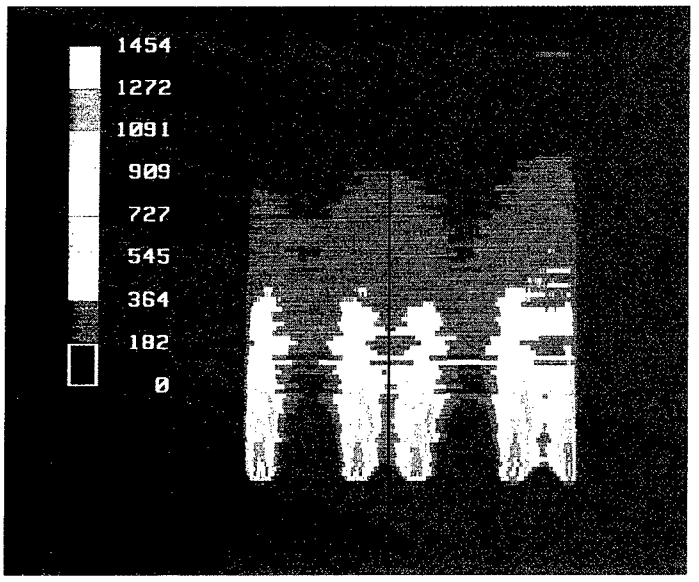

FIG. 3. Composite two-dimensional distribution of OH fluorescence for rich-premixed burner. The scale is in fluorescence "counts." The black line corresponds to the same position in Fig. 1b.

3 at 6 mm above one blade of the burner, together with the temperature measurements at this height. The temperature between the burners is still nearly room temperature, while it is above 2000 K across most of the surface of the blade. As was also observed in a Bunsen flame and in previous experiments with this type of burner [2], the majority of the CO from the inner cone is contained within the "arms" of the OH arising from the outer cone. Examining the cross section for CO fluorescence intensity, small peaks arising from the "jets" at +9 and −9 mm from the center of the blade are clearly visible. However, when converted to concentration, these peaks disappear completely on this scale (maximum 5% CO), as a result of the strong temperature dependence of the CO fluorescence at 230.1 nm [8] (for a constant mole fraction, the fluorescence intensity increases by a factor of ~20 upon going from flame temperatures to room temperature). Given that the measurements are calibrated at room temperature, we expect the accuracy of the CO concentrations at lower temperatures to be better than the accuracy of those derived

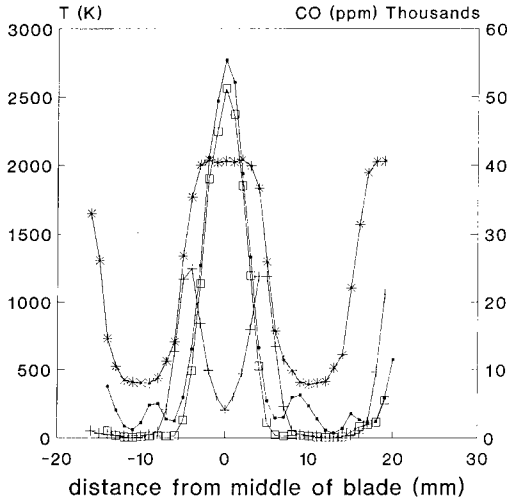

FIG. 4. Horizontal cross section of CO fluorescence intensity (small ■) and concentration (□), OH intensity (+), and temperature (°) at 6 mm above the burner. The right-hand axis is CO concentration in ppm; the left axis is absolute temperature and relative CO and OH fluorescence intensity (in arbitrary units).

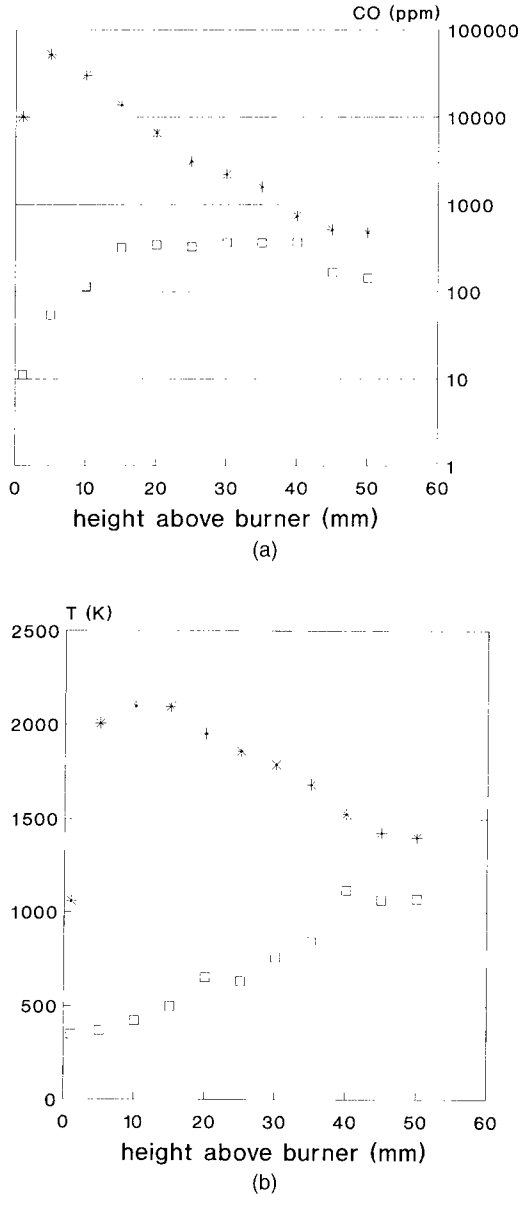

FIG. 5. (a) Vertical profiles of CO concentration measured above the middle of one of the blades, following the black lines in Figs. 1b and 2 (°), and between two blades (□); (b) vertical temperature profiles at the same two positions as in Fig. 5a (above blade, °; between blades, □).

at high temperature. In this regard, LIF detection of CO at this wavelength is an ideal tool for investigations involving fuel leakage. Also note that, at this height, the CO jets are just *outside* the arms of the OH distribution.

Having concluded that fuel leakage occurs from this burner, the question arises as to the consequences for possible CO emissions. The vertical profiles of CO concentration above one blade and between two blades are presented in Fig. 5a, and their respective temperature profiles in Fig. 5b. Whereas the main flame gases contain a maximum of nearly 6% CO, the concentration above the line between the burners never rises above ~350 ppm in the region where the jets from two blades merge. As the main flame mixes with the secondary air, the temperature decreases and with it the CO concentration, reaching ~450 ppm CO at a temperature of ~1400 K, 5 cm above the burner deck. Between the burners, the temperature rises through mixing with the flame gases to roughly 1100 K at 5 cm. The CO concentration remains nearly constant between 1.5 and 4 cm and then decreases to slightly more than 100 ppm. The reason that the CO between the burners can still burn out is shown by the merging of the OH in the outer cones shown in Fig. 3, also at a height of ~4 cm: The OH density indicates the presence of substantial concentrations of oxidizing species. We note that the visible outer cones in these flames always appear distinct. Clearly, the visible location of the outer cones is a poor indicator of chemical activity. These results seem to imply that this burner would emit *more* CO if the distance between the blades were increased substantially, an effect opposite to that expected for the main flames [2].

Above 5 cm, the highest point where temperature measurements were made, the CO concentration continues to decrease. Since we anticipate that the two temperature curves in Fig. 5b will eventually

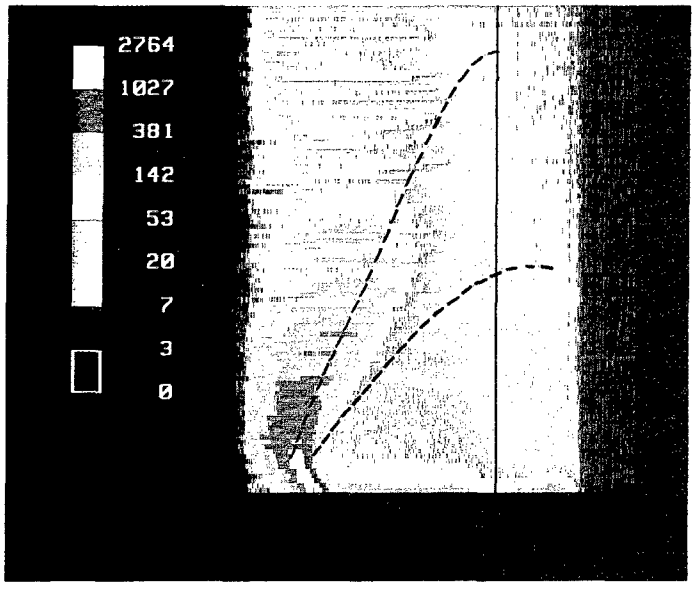

FIG. 6. Composite two-dimensional image of CO fluorescence intensity from lean-premixed burner, logarithmic scale. The dashed black lines are the two lowest contours of the OH distribution shown in Fig. 7. The solid black line corresponds to the same position as given in Figs. 1(c) and 1(d).

merge, we estimate the maximum CO concentration at 7.5 cm (the top of Fig. 2) at 100 ppm. Since practical appliances that utilize this type of burner generally place the heat exchanger at 15–20 cm above the burner, the CO still has time to oxidize even further. In an appliance, this particular burner produces very little CO under these conditions (<10 ppm).

Lean-Premixed Burner:

The two-dimensional images of the CO and OH distributions for this burner are shown in Figs. 6 and 7, respectively. Again, the CO image is scaled logarithmically. For convenience, the two lowest-intensity contours of the OH image are drawn in the CO image. The dominant feature of the CO image is the "plume" of high fluorescence intensity at the side of the burner, emanating from the outer edge of the lifted flame. Just above the burner, this plume contains 3% CO at 1500 K, while above the center of the burner the concentration is 2000 ppm at 1830 K. At 2 cm, the concentration of CO in both places is equal (500 ppm) at 370 K in the middle of the plume and 1800 K in the middle of the flame. At 5 cm above the burner, the plume has spread to nearly half the image at 100 ppm CO (350 K), while the hot CO in the middle of the burner has decreased to 370 ppm at 1715 K. With increasing distance above the burner, the surrounding air mixes further into the flame. While this dilutes the CO from the plume, it also reduces the temperature sufficiently to prevent the CO from oxidizing.

Although we cannot a priori rule out rapid quenching of CO oxidation through mixing with the surrounding air, we consider this to be unlikely. Since Correa's analysis [3] suggests that rapid, turbulent mixing of hot combustion gases with air is incapable of freezing in CO oxidation, it seems even more unlikely that the relatively slow laminar mixing in our case would be successful. Furthermore, measurements on other lean-premixed flames [12] under similar circumstances resolutely fail to show plumes unless the edges of the flame are lifted. The intimate association of the CO plume with a lifted flame seems to leave little room for an alternative explanation. Even though the edges of the flame are only slightly lifted (see Fig. 1c), it appears that copious quantities of CO can be formed.

In contrast with the rich-premixed burner described above, where OH from adjacent blades can oxidize the CO formed from fuel leakage, there is no "adjacent" flame in the lean-premixed burner. As can be seen in Fig. 6, the CO plume is *outside* the regions of lowest OH density, in the boundary layer between the flame and the surrounding cold air. Since hydrocarbons are effective radical scavengers [14], we expect fuel leakage to efficiently consume the OH and other radicals present as the fuel molecules are converted to CO. This itself will inhibit CO oxidation in the boundary layer. Although this was also true for the rich-premixed flame, the Bunsen-like flame structure can compensate for the loss of OH, since the outer cone (where the secondary air meets the hot combustion gases) generates high OH concentrations. The admixture of secondary air in the fuel-lean flame is expected only to cool the flame off and to quench the OH-producing reactions.

Appliances that utilize lean-premixed burners are

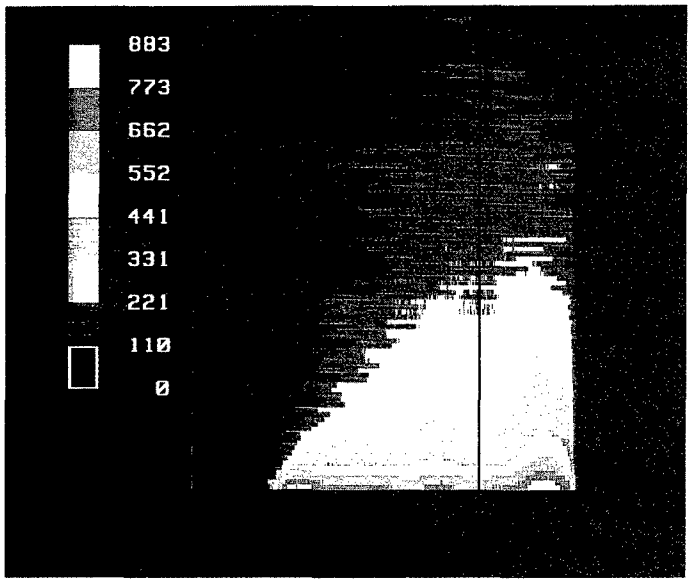

FIG. 7. Composite two-dimensional image of OH fluorescence intensity from lean-premixed burner. The solid black line corresponds to the same position as given in Figs. 1(c) and 1(d).

usually (but not always) "closed" in the sense that secondary air is excluded. In this case, the fuel leaks into a thermal boundary layer between the flame and the (water-cooled) wall of the combustion chamber. At this point, it is difficult to say whether the production of CO would follow the same course as described here. Future work will examine this issue in an optically accessible combustion chamber.

In an appliance, the water-cooled heat exchanger is normally at 5–6 cm above the surface of this burner. Under normal operating conditions, the appliance usually emits 100–150 ppm CO and several tens of ppm CH_4. (It is also clear that fuel leakage can give rise to residual methane emissions.) If the heat exchanger can quench CO oxidation completely (see Introduction), then the extant concentrations, 100 ppm cold and 370 ppm hot, will be frozen in. However, since the temperature in the middle of the burner is still high, and the reactions responsible for CO oxidation are still fast, it is possible that at least part of the 370 ppm will burn out during the heat-transfer process. (That such high CO concentrations are not generally seen in practice with this burner also seems to suggest this.) Independent of the fate of the hot CO, 100 ppm of cold CO will certainly survive the heat exchanger. In the absence of fuel leakage, the rate at which the hot gases are cooled will clearly determine the CO emission. The actual influence of a heat exchanger on CO formation in household appliances is as yet not known.

Whereas this discussion has centered on the influence of fuel leakage on CO emissions, the presence of hydrocarbons in combustion gases can also influence the formation of NO_2, which is an unwanted component in its own right. As shown by many workers (see, for example, Refs. 15 and 16), a few tens of ppm of hydrocarbons in the presence of sufficient oxygen can quantitatively convert NO to NO_2.

Summary and Conclusions

We have measured the absolute temperature and concentrations of CO and relative distributions of OH in two commercially available household burners, burning in the open air. In both cases, substantial local concentrations of CO *outside* the main flames have been observed and attributed to the leakage of fuel-air mixture around the edges of the flame, where the fuel is converted to CO in the boundary layer between the flame and the surroundings. The OH images have been seen to be useful in understanding the oxidation (or lack thereof) of the CO thus formed.

For the rich-premixed multiblade burner, the CO from leaking fuel appears to be oxidized by OH arising from the outer cones of adjacent flames, and burns out similarly to the CO from the main flames. In the case of the lean-premixed burner, the CO produced by fuel leakage appears to remain in the cool boundary layer without adequate burnout. The results for the fuel-lean flame also suggest that the oxidation of hot CO can continue through at least part of the heat-transfer process in a heat exchanger.

Future work will specifically address the role of the heat exchanger in CO oxidation, as well as the oxidation of CO in a closed combustion chamber. If it is ascertained that fuel leakage is the dominant

source of unwanted CO emissions, then the efforts to overcome the practical limitations to the development of low-NO_x techniques should shift their emphasis to flame stability, rather than focusing exclusively on CO oxidation.

Acknowledgments

We wish to thank W. van Dieren of EG&G Nederland for his assistance in enhancing the sensitivity of our detection system, and R. Dibble for helpful discussions concerning the effects of fuel leakage.

REFERENCES

1. Miller, J. A., and Bowman, C. T., *Prog. Energy Combust. Sci.* 15:287–338 (1989).
2. Van Oostendorp, D. L., Borghols, W. T. A., and Levinsky, H. B., *Combust. Sci. Technol.* 79:196–206 (1991).
3. Correa, S. M., *Fourteenth Annual Energy-Sources Technology Conference and Exhibition* (R. Ruiz, Ed.), ASME, New York, 1991, ASME/PD vol. 33.
4. Warnatz, J., *Ber. Bunsenges. Phys. Chem.* 83:950–957 (1979).
5. Van Oostendorp, D. L., Levinsky, H. B., Van der Meij, C. E., Jacobs, R. A. A. M., and Borghols, W. T. A., *Appl. Opt.* 32:4636–4640 (1993).
6. Smith, G. P., and Crosley, D. R., *Appl. Opt.* 22:1428–1430 (1983).
7. Aldén, M., Wallin, S., and Wendt, W., *Appl. Phys. B* 33:205–208 (1984).
8. Seitzman, J. M., Haumann, J., and Hanson, R. K., *Appl. Opt.* 26:2892–2899 (1987).
9. Tjossem, P. J. H., and Smyth, K. C., *J. Chem. Phys.* 91:2041–2048 (1989).
10. Kröll, S., Aldén, M., Bengtsson, P.-E., and Löfström, C., *Appl. Phys. B* 49:445–453 (1989).
11. CARP-PC is a commercially available computer code developed by AEA Technology, Harwell (UK), and supplied by Epsilon Research Ltd.
12. Van der Meij, C. E., and Levinsky, H. B., *Final Report "In-situ CO/NOx Formation"*, N.V. Nederlandse Gasunie Report TR/O 94.R.1501, 1993 (in Dutch).
13. Lewis, B., and Von Elbe, G., *J. Chem. Phys.* 11:75–97 (1943).
14. Westbrook, C. K., and Dryer, F. L., *Prog. Energy Combust. Sci.* 10:1–57 (1984).
15. Hori, M., Matsunaga, N., Malte, P. C., and Marinov, N. M., *Twenty-Fourth Symposium (International) on Combustion*, The Combustion Institute, Pittsburgh, 1992, pp. 909–916.
16. Barnes, F. J., Bromly, J. H., Edwards, T. J., and Mandyczewsky, R., *1989 International Gas Research Conference*, Government Institutes, Inc., Rockville, MD, 1989, pp. 1363–1372.

COMMENTS

Michael Haug, Lehrstuhl fur Technische, Germany. Your assumption that unburnt CH_4 is converted in the boundary layer to CO can be clarified by direct CH_4-LIF experiments or by seeding the CH_4 flow with a fluorescent dopant. Do you intend to focus on that problem?

Author's Reply. Whereas we are not aware of a LIF-detection scheme that is specific for methane, the suggestion of using a suitable seed molecule with which one can discriminate burned from unburned gases (NO_2, for example) is certainly worth further consideration. We shall return to the problem of fuel leakage in the near future.

Twenty-Fifth Symposium (International) on Combustion/The Combustion Institute, 1994/pp. 251–259

ON THE AERO-THERMAL CHARACTERISTICS OF GASIFIER-FUELLED GAS TURBINE COMBUSTORS WITH COMPLEX GEOMETRIES

N. H. KANDAMBY AND F. C. LOCKWOOD
Department of Mechanical Engineering
Thermofluids Section
Imperial College of Science, Technology and Medicine
London SW7 2BX, UK

This paper describes the application of a mathematical model to predict the aerodynamics, combustion, and NO emission performances of a gas turbine combustor. The numerical basis of the model is a specially constructed code that uses a generalised nonorthogonal and boundary conforming coordinate system. The gas turbine is a component of the British Coal "Topping Cycle," a coal-fired fluidised-bed–based combined-cycle technology. A distinctive feature of this study is therefore that the fuel for the gas turbine is produced from the partial gasification of coal. Since this fuel contains nitrogenous species derived from the fuel-bound nitrogen of the parent coal, there is concern that these species might give rise to high NO emissions from the combustor. In addition to the fuel NO, the prompt and thermal NO are modelled. The aerodynamic and combustion performances of the combustor, a Frame-9 unit, for this rather unusual fuel are found to be generally good, with no indication of flame stabilisation difficulties and only a relatively small temperature nonuniformity over the exit plane. This nonuniformity can be traced to products that manage to "skirt round" the dilution jet flows. The predicted level of NO emission corresponds remarkably well with that measured. Most importantly, a significant reduction of NO to N_2 by NH_3 occurs within the primary zone, with the result that the NO emission from the gas turbine component of the Topping Cycle is considerably diminished.

Introduction

This paper describes the application of a mathematical model to predict the combustion performance of and NO emissions from a gas turbine fuelled with coal-derived fuel gas. The gas turbine forms a part of the "Topping Cycle," a fluidised-bed–based combined-cycle technology being developed by British Coal's Coal Research Establishment (CRE) for the high-efficiency (circa 47%) generation of electric power. The raw coal is first partially gasified in an air-blown spouted fluidised bed to provide the fuel for the gas turbine. The residual char is transferred to a circulating fluidised-bed combustor (CFBC) to produce the heat required to generate steam. The efficiency of the Topping Cycle is expected to exceed that of typical oxygen-blown Integrated Gasification Combined Cycle (IGCC) technology because of the following: a high overall conversion efficiency is achieved; the need for an energy-consuming air separation unit is obviated; hot gas cleaning is employed; and because high-grade heat is produced by the CFBC, enabling a high-efficiency steam cycle. A complete description of the British Coal Topping Cycle may be found in Refs. 1 and 2. The gas turbine combustion system of the Topping Cycle consists of a tubo-annular type combustor assembly, which will be used to power a General Electric Frame-9 machine. The combustor design is being tested by CRE, using a single-flame tube, in order to evaluate the combustor performance for the coal gas combustion.

Mathematical modelling has now been used to assist the design of gas turbines burning conventional fuel for some two decades [3–8], and this work has highlighted the combined importance of accurate geometrical and physical modelling for performance predictions of combustors. However, most of the existing prediction procedures use either simplified models of combustors or focus attention only on some of the physical processes. A complete three-dimensional (3D) mathematical procedure to address both these aspects is mainly limited by the required numerical and computational effort. The mathematical model presented here constitutes a 3D modelling methodology, including the subprocesses such as thermal radiation, fuel, prompt and thermal nitric oxide formation, while retaining the geometrical accuracy. In conventional gas turbines, the main mode of nitric oxide formation is by the thermal mechanism, and Refs. 9 and 10 demonstrate the importance of the incorporation of a radiation model on nitric oxide formation in gas turbine combustors. The use of the products of coal gasification as a fuel presents special problems, in part because of its mod-

est calorific value, but more particularly because this fuel contains significant quantities of nitrogenous species derived from the fuel-bound nitrogen of the parent coal. While the typical NO emissions from well-designed and operated fluidised beds are small, the possibility of increased levels of NO emissions from the gas turbine component of the Topping Cycle is a cause for concern.

In general, the front and exit portions of conventional gas turbine cans are comprised of opposing boundaries of largely differing curvature. The application of a step-wise castellated cartesian approximation of the curved boundaries in such cases results in an uneconomic grid density when attempting to obtain adequate numerical resolution. Within the constraints of a cartesian framework, the only remedy is to simplify one of the curved boundaries in a manner that departs significantly from the exact geometrical shape. In order to circumvent this difficulty, a mathematical model is constructed on a generalised coordinate system of boundary-conforming mesh, based on the existing cartesian CINAR code developed by this group for three-dimensional combustors.

The Mathematical Model

The mathematical model is formulated for steady incompressible high Reynolds number flows. The governing equations for the mean flow, the continuity, and the conservation laws may be expressed in a generalised coordinate frame as

$$\frac{1}{|J^{-1}|}\frac{\partial}{\partial \bar{x}^j}\{\rho U^j\} = S_m \tag{1}$$

$$\frac{1}{|J^{-1}|}\frac{\partial}{\partial \bar{x}^j}\left\{\rho U^j v_i + \rho\langle U''^j v_i''\rangle \beta^j_m + p\beta^j_i - \frac{\mu\beta^j_m}{|J^{-1}|}\left[\beta^a_m \frac{\partial v_i}{\partial \bar{x}^a} + \beta^a_i \frac{\partial v_m}{\partial \bar{x}^a}\right]\right\} = S^i_v \tag{2}$$

$$\frac{1}{|J^{-1}|}\frac{\partial}{\partial \bar{x}^j}\left\{\rho U^j \phi + \rho\langle U''^j \phi''\rangle \beta^j_m \beta^a_m \frac{\Gamma_\phi}{|J^{-1}|}\frac{\partial \phi}{\partial \bar{x}^a}\right\} = S_\phi \tag{3}$$

where $U^j = \beta^j_m v_m$ denotes the contravariant velocity components, while β denotes the adjoint matrix of the inverse Jacobian in the mapping from curvilinear coordinate system $\{\bar{x}^i;\ i = 1, 3\}$ to a reference Cartesian frame $\{x^i;\ i = 1, 3\}$, and $\rho\ \langle U''^j{}_\circ''\rangle$ represents the turbulent transport terms. To avoid Christoffel symbols in the momentum equations that result from the local gradients of base vectors, and to obtain a strong conservative form, the momentum conservation is considered with respect to Cartesian velocity components. The scalar transport equation stands for the balance equations of the submodels for turbulence transport, combustion, radiation, and for the pollutant formation chemistry.

The Numerical Technique

For the numerical solution of the governing equations, the flow domain is discretised by hexahedral, nonoverlapping control volumes using a composite-block transfinite interpolation technique [11,12]. A nonstaggered variable arrangement is implemented, with the variables stored at the geometric centres of the control volumes. The discrete equations are then obtained by the conventional method of finite volume integration. The coefficients of the resulting algebraic equations are assembled with respect to the convection and principle diffusion face fluxes, using the hybrid differencing method [13]. For numerical stability, the cross-diffusion face fluxes are accumulated in the source term, since the geometrical factors contained within them (the off-diagonal elements of $\beta\beta^t$) can be of either sign depending on the discrete mesh. The convective face fluxes are computed according to a pressure smoothing technique [14], in order to circumvent the pressure velocity decoupling of the collocated variable arrangement. The set of discretised equations is then solved using the Strong Implicit Procedure [15] for matrix inversion, along with the SIMPLE algorithm [16] to correct the pressure and convective face fluxes. The correction for the face fluxes is estimated only with respect to the principle pressure gradients across the cell faces, which leads to a stable pressure correction equation.

The Physical Models

Turbulence Model:

The two equation k-ε eddy viscosity closure [17] is used to model the turbulence transport terms, where the turbulent viscosity and the eddy diffusivity are obtained in terms of the turbulence kinetic energy and its dissipation rate determined from their modelled transport equations. The turbulent stresses and the flux vectors may be expressed as

$$\rho\langle U^{j''} v_1''\rangle = \frac{\mu_t}{|J^{-1}|}\left[\beta^a_m \frac{\partial v_i}{\partial \bar{x}^a} + \beta^a_i \frac{\partial v_m}{\partial \bar{x}^a}\right] - \frac{2\mu_t}{3}\frac{1}{|J^{-1}|}\frac{\partial}{\partial \bar{x}^a}\{U^a\}\,\delta^i_m - \frac{2}{3}\rho k \delta^i_m \tag{4}$$

$$\rho\langle U^{j''}\phi''\rangle = \Gamma_{t,\phi}\frac{\beta^a_m}{|J^{-1}|}\frac{\partial \phi_i}{\partial \bar{x}^a}. \tag{5}$$

Combustion Model:

The conserved scalar approach is used to model the combustion [18,19], of which the chemical reactions between the element species admitted from initially segregated streams are considered to be governed by the mixing pattern of the streams. The thermochemical state of the flow is then related to a strictly conserved scalar f, the mixture fraction, in the form of state relations: the chemical state equations of the combustion model, the state equations for static enthalpy, and the perfect gas law. The chemical state relations are estimated assuming a binary single-step fast reaction for the fuel element disappearance, which results in a set of piecewise linear functions in mixture fraction space. The mean thermochemical properties are then obtained using the single-point presumed-shape scalar probability density function (pdf) approach, which accounts for the fluctuations of the scalar field [18,19]. In the computations, a β distribution is assumed for the probability density function. Its distribution characteristics are obtained by the mean and the variance field of the mixture fraction determined from their modelled transport equations.

Radiation Model:

To account for the radiative heat transfer within the flow domain, additional balance equations are solved for the enthalpy and radiation fields. In gas turbine combustors, although it can be considered that the ratio of radiative temperature loss to the adiabatic flame temperature (which is roughly proportional to the ratio of combustor volume to the total mass flux) is small compared with conventional combustors, its influence on the temperature field and, therefore, on nitric oxide formation is considered significant [9,10]. In the computational scheme, the thermal radiation transfer is determined by the non-equilibrium diffusion radiation model of Arscott et al. [20], which gives a good compromise between accuracy and computational effort when used on a generalised nonorthogonal frame. The radiation transfer equations, determined from the P_2 projection of the general P_n equations [21], may be expressed as

$$\frac{1}{|J^{-1}|}\frac{\partial}{\partial \bar{x}^j}\{|J^{-1}|q_i^j\} = 4\kappa(T^4 - T_r^4);$$

$$q_i^j = -\frac{4}{3\kappa}\frac{\beta_{in}^j\beta_{in}^a}{|J^{-1}|^2}\frac{\partial T_r^4}{\partial \bar{x}^a} \qquad (6)$$

where q, T_r, and κ respectively denote the radiation flux vector, radiation temperature, and the gas absorption coefficient. Assuming that the background medium consists of a mixture of grey gases, the absorption coefficient is then computed by

$$\varepsilon(L) = 1 - \exp(-\kappa L) = \sum_n a_n(T)\,[1 - \exp(-k_n(p_w + p_c)L)] \qquad (7)$$

based on the "two clear gas plus grey gas model" of Truelove [22].

Pollutant Model for Nitric Oxide:

Unlike gas turbine combustors burning conventional fuels, the major source of NO formation in the combustor of the Topping cycle is by NH_3, which is formed from the fuel-bound nitrogen of the coal in the gasification process [23]. The coal gas consists of CO, H_2, and N_2 as the major compounds, having an adiabatic flame temperature of about 1800 K, and NH_3 and CH_n as minor compounds. Accordingly, transport equations for NH_3, NO, and N_2 are solved for the NO chemistry, which includes the global NO formation reactions by fuel, thermal (Zeldovich), and prompt mechanisms, and the reduction reactions by NH_3 and O_2 as illustrated below. The reaction source terms are assembled based on the kinetic parameters given by de Soete [24,25].

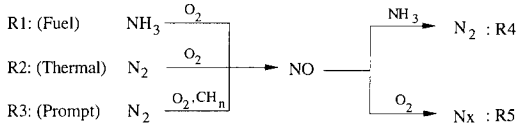

Simulation Details

The combustor geometry and the mesh generated are shown in Figs. 1 and 2. The fuel injector is placed within double concentric counter swirlers, the inner feeding the fuel and the outer feeding the primary air. The peripheral ports on the flame tube are the secondary, intermediate, and dilution holes, corresponding to a conventional air distribution system. The effects of the flame-tube cooling have been considered to be of secondary importance in determining parameters of interest in this phase of the programme, and therefore, the splash cooling skirts and the discharge duct sweat cooling holes have been neglected in the computations. The results presented are for a combustor operating pressure of 8 bar. The remaining operational details are summarised in Table 1. Experimental results are being obtained by CRE as part of a development programme. At this stage, only the combustor exit temperatures and nitric oxide emission values are available for a series of test compositions of the fuel. The prediction results are reported here for a synthesis fuel (CO 14%, H_2 11%, N_2 72.5% by volume) doped with 660 ppmv NH_3 and 2.5% CH_4.

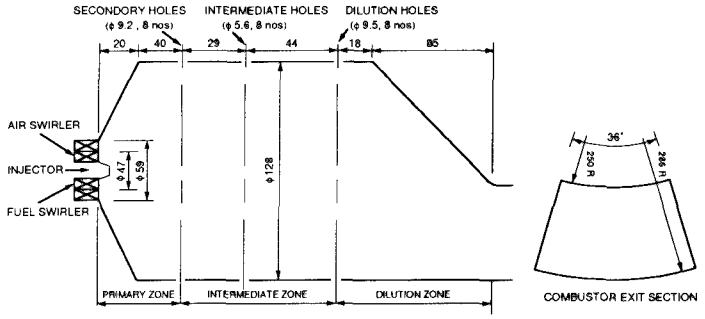

FIG. 1. Schematic diagram of the gas turbine combustor (dimensions in mm).

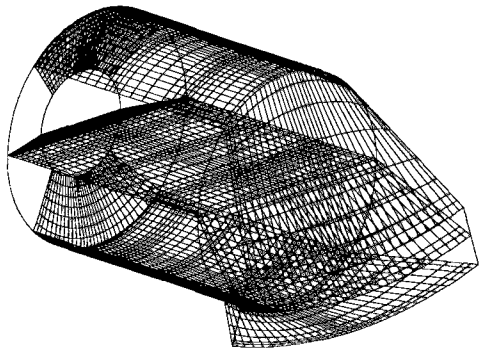

FIG. 2. The computational mesh (31 × 31 × 44). Surfaces are indicated for the top, centre, and bottom nodal layers.

TABLE 1
Combustor operating conditions

Fuel mass flow:	0.162 kg/s	
Air fuel ratio:	2.0	
Fuel distribution:	37.0% injector,	63.0% fuel swirler
Air distribution:	18.4% primary air swirler,	36.9% secondary jets,
	15.2% intermediate jets,	29.5% dilution jets
Temperature:	220 °C fuel,	350 °C air
Swirl numbers:	−1.15 fuel swirler,	0.95 air swirler

Results and Discussion

Aerodynamics and Combustion:

The predicted flow field in the combustor axial plane of symmetry and in the transverse planes passing through the secondary and the dilution jets, superimposed with a colour-coded mixing pattern, is shown in Fig. 3. The secondary air jets penetrate to the centre of the combustor, and a certain proportion of this air is entrained into the recirculation zone created by the axial inlet flow swirlers. Because of the symmetric condition at the centre of the combustor and also the mass transferred from the jet columns, the radial momentum of the jets is rapidly reduced from about 15 mm away from the combustor centre, where the jets become strongly deflected in the azimuthal direction by the swirling axial flow (see Fig. 3b). The swirling motion of the axial flow augments the mass transfer from the secondary air jets to the reverse flow regime near the centre of the combustor and also enhances the mixing within the flow recirculation zones, where these are clearly observed from the mixing pattern indicated in Figs. 3a and 3b. The enhanced mixing in the reverse flow near the centre of the combustor is also in part the result of the toroidal vortex motion of the entrained secondary air streams caused by the tangential momentum transferred to the secondary air jets.

Rapid mixing of fuel and air is also observed in the shear layer between the counter-swirling flows that envelope the recirculating flow. The combustion of fuel is, therefore, initiated in the shear-layer envelope with the aid of primary air admitted through the air swirler and is completed in the reverse flow regime at the centre of the combustor with the aid of air entrained from the secondary jets. It is also observed that the composition of the flow is near stoichiometric at the outer edge of the shear-layer envelope and in the neighbourhood of the flow stagnation point (z = 75 mm) at the centre of the combustor. Combustion products at peak temperatures emerge from these zones and are convected downstream, resulting in high-temperature regions as indicated in Fig. 4c. The hot products generated at the centre of the combustor pass axially into the intermediate zone, while the products from the outer edge of the shear-layer envelope pass around the secondary jets and into the intermediate zone. A small proportion of this flow travels along the combustor wall, with the remainder being transferred towards the centre of the combustor. Although the combustion of fuel is nearly complete at the end of the pri-

mary zone, weak fuel streams (~3% mass fraction) pass around the secondary jet columns and into the intermediate zone, and are completely consumed by the introduction of the intermediate air. The radial momentum of the intermediate air jets, although completely destroyed after penetrating only about one third of the combustor radius, is nonetheless sufficient to prevent unburnt fuel from passing further downstream towards the dilution zone. This is an important design requirement of gas turbine combustors, enabling effective cooling of the combustion products in the dilution zone. If unburnt fuel were to reach the dilution zone, high-temperature streams would extend more towards the combustor exit. Further, if pockets of unburnt fuel pass into the dilution zone, their combustion would be suppressed by the quenching effect in the dilution zone, resulting in unburnt fuel emission and reducing the combustion efficiency.

Noting the low oxygen concentration in the primary zone (Fig. 4b) along with the fact that near complete combustion of fuel is achieved there, it can be inferred that the rate of air entrainment into the primary zone matches closely the stoichiometric air requirement for the combustion of the coal gas. This indicates that the air flow pattern produced according to the rates of primary and secondary air admission provides a suitable mixing and volume fraction for combustion of this fuel. As a result, combustion stability of the fuel and also, as will be discussed below, minimised nitric oxide formation are ensured. This is of course provided that sufficient mixing takes place in the primary zone for fuel combustion, which is indeed observed. Downstream of the primary zone the oxygen concentration gradually increases, consequent of the mass transferred from radial air jets. However, the increased oxygen concentration at the centre of the combustor, in the intermediate zone, is marginal. This is due to the proportionally larger quantity of combustion products passing into this region, compared with the rate of air entrained from the secondary jets. The combustion products that pass into this region are those formed near the secondary jet stagnation point augmented by the products generated by the combustion of unburnt fuel in the intermediate zone and, as mentioned earlier, a certain proportion of the products formed at the outer edge of the shear-layer envelope. The consequence of this distribution of combustion products is that the temperature at the centre of the combustor in the intermediate zone remains at a high level, only about 100 K below the adiabatic flame temperature. The major mixing of combustion products with air occurs across the plane of the dilution jets, downstream of which the flow properties gradually tend to be uniform.

The velocity plot (Fig. 3a) also shows that the penetration of the dilution jets is similar to that of the primary jets. However, the dilution jets are axially deflected prior to reaching the combustor centre and a certain proportion of the hot combustion products pass through the deflected columns. This proportion of products is then rapidly mixed with the large amount of dilution air released to the main flow just downstream of the jet deflection point, a fact that is clearly reflected in the temperature and the oxygen contour plots (Figs. 4a and 4c). The combustion products that pass around the dilution jets appear to mix at a slower rate with the air entrained from the dilution jets. Plots at the exit plane (Figs. 4b and 4d) reveal that four lean-mixed streams of products with dilution air extend up to the exit of the combustor, two towards the turbine blade tip side and two towards the blade root side. The inclusion of discharge duct sweat cooling holes in the calculations would shift these streams towards the centre of the exit section, but would not eliminate them. This must be considered as a design weakness. Apart from these localised lean-mixed streams, however, the variation of flow properties is observed to be small over the majority of the exit plane. The average oxygen concentration and temperature variation in this region are 8–9% and 1000–1575 K, respectively. The predicted outlet temperature distribution factor (OTDF) of the combustor is 11.3%, whereas the measured value is 8.7%. Because the combustor is essentially adiabatic and the exit profiles are quite uniform, conformity between the measured and predicted exit temperatures must be expected. It should be noted that the small asymmetry of the properties at the exit plane is due to the effect of the inlet flow swirl (which extends towards the combustor exit) becoming progressively distorted by the complex asymmetrical geometry of the exit nozzle section.

Nitric Oxide Predictions:

In the computations, the NO model constants have been held at the recommended values, with the exception of the pre-exponential factor of the fuel NO and associated reactions (R1, R4, and R5) that were optimised to ensure, quite reasonably, that the locations of peak temperature and NO concentrations coincide. This optimisation was carried out in a numerical test case for a hypothetical axisymmetric combustor and for a base fuel containing CO, H_2, and N_2 having the same calorific value and stoichiometry as that of the fuel reported here. The optimisation is justified because the effects of temperature and concentration fluctuations on the reaction rates are necessarily ignored. The parameters so optimised were then held constant for all the subsequent NO calculations, which includes a range of fuel compositions being tested. In the present calculations for the fuel that also contains CH_4, and which incorporate the thermal and prompt NO formation, the predicted NO emission value of 204 ppmv compares remarkably well with the measured value of 200 ppmv.

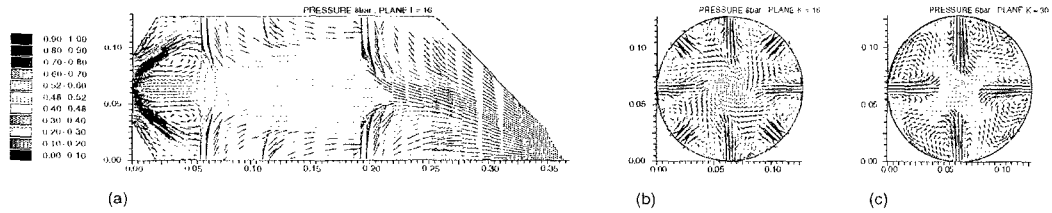

FIG. 3. The combustor velocity field (a) on the combustor symmetry plane, (b) on a transverse plane passing through secondary jets, and (c) on a transverse plane passing through the dilution jets. The colour code indicates the fuel and air mixing pattern by the mixture fraction. The stoichiometric mixture fraction for the fuel, $f_{st} = 0.515$.

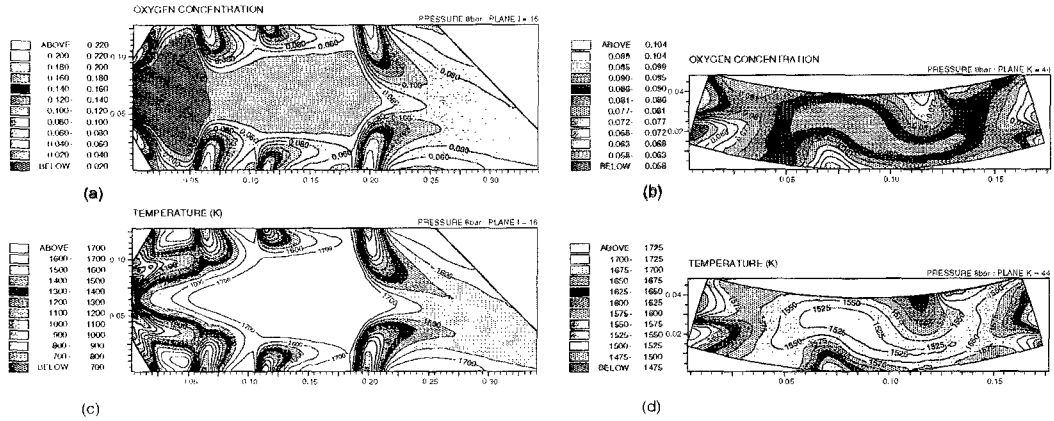

FIG. 4. The oxygen and temperature distribution. Figures (a) and (c) indicate the distributions in the combustor symmetry plane. Figures (b) and (d) indicate the variations in the combustor exit plane.

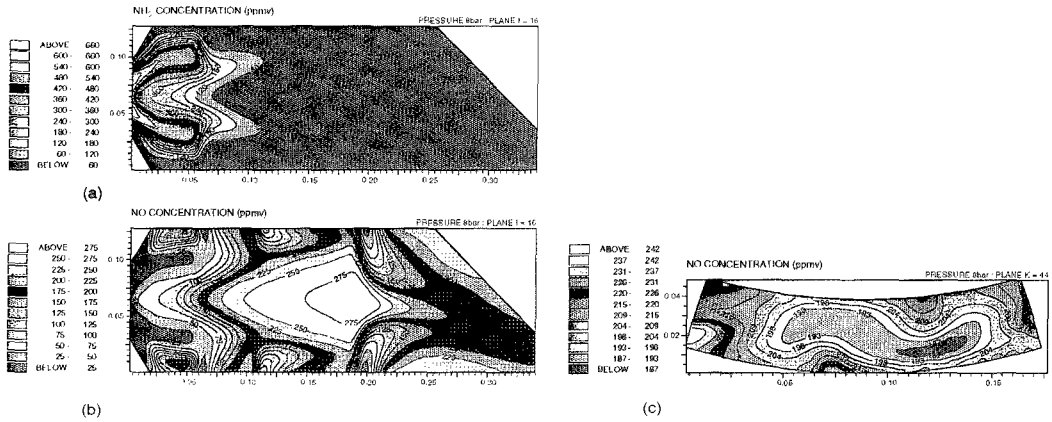

FIG. 5. The NH_3 and NO concentrations on the symmetry and exit planes.

Figures 5a through 5c show the results of the NO predictions. The NH_3 reactions extend almost to the intermediate jets (Fig. 5a) because of the oxygen-lean condition in the primary zone. Although a substantial reduction of NH_3 appears to occur across the shear layer between the counter-swirling flows (~480–300 ppmv), and within the primary zone flow vortex towards its outer edge (~660–480 ppmv), a corresponding rise in the NO production is not observed in this region (Fig. 5b). It was observed from a test calculation that the reduction of NH_3 concentration from 660 to about 500 ppmv occurs within these two zones as a result of mixing alone (that is with reactions suppressed). It should also be noted that, in this region, the temperature is generally below 1300 K, so that the generation of thermal and prompt NO is low. Therefore, it can be postulated that NO is in fact generated by NH_3 with the available oxygen in that region (reaction R1), and is subsequently depleted in the presence of large NH_3 concentrations (reaction R4), the end product of which is N_2. This latter reaction, named as the "Thermal DeNox" [26], corresponds to the NO reduction method in commercial combustors by NH_3 injection. From the calculations, some 65% of the NH_3, which would otherwise generate NO within and near to the shear-layer envelope, is observed to be reduced, with a strong proportion of the reduction occurring in the shear layer. This two-step reduction of NH_3 to N_2 in the gas turbine unit is, therefore, an important feature for the development of the Topping Cycle, since a substantial amount of fuel NO emissions would otherwise result by the use of coal.

The major source of NO generation in this combustor is due to the NH_3 reactions in the presence of oxygen in the secondary air and occurs in the neighbourhood of the secondary jets and near to the stagnation point at the centre of the combustor. Also, high concentrations of NO are observed at the outer edge of shear-layer envelope, corresponding to the high-temperature zones, and a gradual increase of NO is observed towards the end of the intermediate zone. It can be reasonably argued that the increase near to the outer edge of the shear layer is by the thermal and prompt NO formation due to the high temperatures prevailing in this zone. The high NO concentration near the end of the intermediate zone is in part the result of NO transfer to the centre of the combustor in a similar manner to that of the combustion products explained earlier, augmented by an increase of NO due to the thermal mechanism. Towards the exit of the combustor, the NO concentration is gradually reduced as a result of the mixing with the dilution air and by the reduction reactions with oxygen. In the context of the global kinetic mechanisms considered in these computations, the end products of the NO reduction pathway with oxygen is not traced. The possible compounds would be other nitrogen oxides stable at the combustor exhaust temperature and perhaps, according to de Soete [27], a small quantity of N_2. Quantification of these species fractions would necessitate calculations using complete, or suitably reduced, NO kinetic schemes [28]. The NO contours at the exit plane (Fig. 5c) show a reasonable uniformity in the mid section, in agreement with that of temperature and oxygen concentration. The relatively high NO concentration at the edges of the exit section corresponds to the NO transported along with the lean-mixed streams, which was explained earlier.

Concluding Remarks

Predictions for the aerodynamics, combustion, and NO emissions have been obtained for a gasifier-fuelled gas turbine using a three-dimensional mathematical model constructed on a generalized coordinate system. It is believed that gas turbine performance computations for such fuels have not previously been performed. The experimental data available at this stage limit the model validation work that so far has been possible to perform. Nonetheless, the indications of this work, as well as those from the experimental researchers who have consulted our predictions, suggest that the simulation is sound.

The combustor of this study, a tubo-annular can, generally performs well when fuelled with a coal-derived gas for the conditions considered. For example, the fuel is all consumed well upstream of the dilution zone and the rate of air entrainment into the primary zone is consistent with that required to achieve stoichiometry. High temperatures persist near the combustor centre well downstream, but this nonuniformity is largely eliminated by mixing in the dilution zone. However, a small portion of the combustion products manage to "skirt round" the dilution jets in the form of four streams at somewhat higher temperatures than the mean value. The implication of the severity of this would require a further investigation of the flow mixing in the passage within the combustor exit and the turbine inlet.

The NH_3 content of the fuel gas is responsible for NO production in the primary zone. However, and very importantly, a significant amount of the NH_3 is reduced to N_2 in the presence of the NO with the result that the amount of NO emerging from the zone is small. Because of this reduction, the level of NO finally emitted by the combustor is much lower than would otherwise be the case. The majority of the combustor NO is produced by the fuel NO mechanism in the transition region from the primary to intermediate zones. High NO concentrations also occur at the outer edge of the primary zone shear-layer envelope, where the temperatures are high as a result of the thermal and prompt mechanisms.

Nomenclature

a	weighting coefficients of the radiation absorption model
$\lvert J^{-1}\rvert$	determinant of the inverse Jacobian matrix of coordinate transformation
k	kinetic energy of turbulence, coefficients of the model for radiation absorptivity
L	mean path length of radiation rays at a spatial point
OTDF	outlet temperature distribution factor, OTDF $= (T_{max} - T_{ex})/(T_{ex} - T_{inl})$, where "max" and "ex" indicate the maximum and mean exhaust temperatures, and "inl" indicates the average fuel and air inlet temperature
p_w, p_c	partial pressure of water vapour and CO_2
P	total pressure
q	radiation flux vector
T	temperature
U	velocity vector expressed as a contravariant tensor
v	velocity vector expressed with respect to a cartesian base
$x, \bar{x}$	cartesian coordinate space, generalized coordinate space

Greek Symbols

β	adjoint matrix of the inverse jacobian in the mapping from curvilinear to cartesian frame
ε	emissivity
Γ	diffusion coefficient
μ	viscosity
ρ	density

Superscripts and Subscripts

j, m, a	dummy indices that correspond to Einstein summation convention
i	cartesian coordinate directions $i = 1, 2, 3$

Acknowledgments

The authors gratefully acknowledge the Coal Research Establishment for the financial support. Particular thanks are owed to Mr. G. Kelsall of the CRE for his instructive technical collaboration.

REFERENCES

1. Kelsall, G. J., Smith, M. A., Todd, H., and Burrows, M. J., ASME 91-GT-384, 1991.
2. Kelsall, G. J., Smith, M. A., and Cannon, M. F., ASME 93-GT-413, 1993.
3. Coupland, J., and Priddin, C., in *Turbulent Shear Flow* (L. Bradbury, F. Durst, B. E. Launder, J. L. Lomley, F. N. Schmidt, and J. H. Whitelaw, eds.), Springer-Verlag, New York, 1986, Vol. 5, pp. 310–323.
4. Witting, S., Bauer, H. J., and Noll, B., AGARD CP-422:28, 1987.
5. McGuirk, J. J., AGARD CP-422:31, 1987.
6. Boyson, F., Ayers, W. H., Swithenbank, J., and Pan, Z., *J. Energy* 6:368–375 (1982).
7. Alizadeh, S. and Moss, J. B., AGARD CP-536:7 (1993).
8. McGuirk, J. J., and Palma, M. L. M., *Comput. Methods Appl. Mech. Eng.* 96:65–92 (1992).
9. Maidhof, S., and Janicka, J., AGARD CP-536:10, 1993.
10. Lefebvre, A. H., *Int. J. Heat Mass Transfer* 27:1493–1510 (1984).
11. Rizzi, A., and Erikson, L. E., AIAA 81-0999, 1981.
12. Gordon, W. J., and Hall, C. A., *Int. J. Numerical Methods Eng.* 7:461–477 (1973).
13. Spalding, D. B., *Int. J. Numerical Methods Eng.* 4:551 (1972).
14. Rhi, C. M., and Chow, W. L., *AIAA* 21:1525–1532 (1983).
15. Stone, H. L., *SIAM J. Num. Anal.* 5:530–558 (1969).
16. Patankar, S. V., *Numerical Heat Transfer and Fluid Flow*, Hemisphere Publishing Corporation, New York, 1980.
17. Jones, W. P., and Launder, B. E., *Int. J. Heat Mass Transfer* 15:301–314 (1973).
18. Bilger, R. W., *Turbulent Reacting Flows* (P. A. Libby and F. A. Williams, Eds.), Springer-Verlag, New York, 1980, pp. 66–113.
19. Jones, W. P., and Whitelaw, J. H., *Combust. Flame* 48:1–26 (1982).
20. Arscott, J. A., Gibb, J., and Jenner, R., *European Symposium*, The Combustion Institute, Sheffield, 1973, p. 674.
21. Duderstatd, J. J., and Martin, W. R., *Transport Theory*, John Wiley & Sons Inc., New York, 1979.
22. Truelove, J. S., "A Mixed Grey Gas Model for Flame Radiation," AERE HARWELL R-8494, 1976.
23. Anna-Karin Hjalmarsson, "NO_x Control Technologies for Coal Combustion," IEA Coal Research IEACR/24, 1990.
24. de Soete, G. G., *European Symposium on Combustion*, The Combustion Institute, Sheffield, 1973, pp. 439–444.
25. de Soete, G. G., *Fifteenth Symposium (International) on Combustion*, The Combustion Institute, Tokyo, 1975, pp. 1093–1102.
26. Lyon, R. K., "Method for the Reduction of the Concentration NO in Combustion Effluents Using Ammonia," U.S. Patent 3900, p. 554, 1975.
27. de Soete, G. G., *The Role of NO and N_2O Formation/Destruction Chemistry in Coal Combustion Control Technologies*, Coal Forum, 1993.
28. Lindstedt, R. P., Lockwood, F. C., and Selim, M. A., "Reduced Mechanisms for Ammonia Oxidation in Premixed Laminar Flames," *Combust. Sci. Technol.*, to appear, 1994.

COMMENTS

Philip C. Malte, University of Washington, USA. Your results show that the modeled maximum temperature (of approximately 1700 K) is located well downstream of the primary zone of the liner, in the intermediate zone. Because of this, is there significant premixing prior to the onset of chemical energy release? If this is true, and also because of the modest combustion temperatures occurring, it is likely that NO_x forms by all three kinetic pathways, which are Zeldovich, nitrous oxide, and prompt. It appears that your modeling only includes thermal NO_x (i.e., Zeldovich kinetics under the influence of equilibrium O atom) and prompt NO_x.

Author's Reply. The modelled maximum temperature in the combustor occurs downstream of the primary zone mainly because of the increased concentration of high-temperature combustion products convected into this region from the near-stoichiometric combustion zones. This has been explained in the paper. The combustion model used in this prediction does not allow for premixing without combustion, and the fuel combustion mainly occurs within the stoichiometric mixture fraction surface, except in the immediate vicinity outside of the surface.

Although the NO formation in the combustor can result according to the fuel, thermal, and prompt mechanisms, it was observed that the major contribution is from the fuel NO mechanism. When only the thermal and prompt NO are simulated (the fuel NO pathway being suppressed), the NO emission was observed to be less than 25% of the NO emissions with only the fuel NO pathway activated. Apparently, the maximum concentration of thermal and prompt NO closely matches the maximum temperature, and also because of the convection of fuel NO products (formed from NH_3 oxidation) into the high-temperature zone (which is similar to the transport of combustion products), the maximum NO concentration by all three mechanisms occurs in the maximum temperature region. It should also be noted that the thermal and prompt NO formations in gasifier fuelled gas turbine combustors are less significant than in conventional fuel burnt gas turbine combustors, because of the modest calorific value of the fuel burnt, which results in comparatively low maximum temperatures.

•

E. Djavdan, Air Liquide, France. 1. Are the assumptions of the diffusive radiation model that you use in your calculations valid for your configuration?

2. Are your NO concentration results sensitive to the radiation model? Have you quantified this sensitivity?

Author's Reply. 1. The average absorption coefficient and also the average optical thickness in gas turbine combustors are usually high because of the high operating pressures (see Refs. 1 and 2 below). This means that the penetration depth of radiation rays is small in gas turbine combustors, which enables, reasonably, the assumption that the radiation intensity is only weakly coupled to the angular position in respect to the radiation energy transfer between spatial points separated over large distances. The nonequilibrium diffusion radiation model, which is a P_2 projection, or a truncation of the general P_n equations, is formulated mainly based on this assumption, and so its use in gas turbine applications is justified.

2. The sensitivity of the NO concentrations to the radiation model has not been evaluated in the present mathematical model for this application. However, it is felt that under the condition of high gas absorption coefficients, the results based on the present radiation model should closely match those of using a more complete, but computationally expensive, higher-order P_n or discrete transfer radiation model.

REFERENCES

1. Siegel, R., and Howell, J. R., *Thermal Radiation Heat Transfer,* Hemisphere Publishing Corp., Washington, DC, 1981.
2. Lockwood, F. C., McGuirk, J. J., and Shah, N. G., AIAA-83-1506, AIAA 18th Thermophysics Conference, Montreal, Canada, 1983.

Twenty-Fifth Symposium (International) on Combustion/The Combustion Institute, 1994/pp. 261–268

A MODEL FOR FLAME KERNEL GROWTH AT AIRCRAFT RELIGHT CONDITIONS

DERYUH LIOU
Combustion Technology Division
Industrial Technology Research Institute
Chutung, Taiwan, ROC

DOMENIC A. SANTAVICCA
Turbulent Combustion Laboratory
The Pennsylvania State University
University Park, PA, USA

A one-dimensional (1D), comprehensive numerical model for the prediction of flame kernel development at high altitude relight conditions in aircraft gas turbines is proposed and tested. The main purpose of this study is to develop a new methodology to numerically solve the very complicated governing equations involved in the flame kernel initiation and propagation in turbulent flow fields. Generally speaking, the surface area of a wrinkled flame cannot be directly described by one-dimensional approaches. However, this problem is overcome by incorporating a fractal model into the one-dimensional governing equations. Meanwhile, the concept of high-activation-energy asymptotic analysis is also applied to provide the relationships between the average turbulent transport coefficients and reaction rate and their laminar counterparts.

An artificial thermal conductivity submodel is used to reflect the fact that rapid mixing always exists inside spark kernels in the early stages of kernel development. The effect of flame stretch, which plays an important role in flame propagation, is also included in the model. Numerically, the governing equations are first discretized by the power-law scheme and then solved by the PISO algorithm. In general, the numerical predictions are in good agreement with the experimental results. With minor modification, this numerical approach may be applied to spark ignition problems in SI engines as well.

Introduction

Flameout in aircraft gas turbines poses a potential threat to pilots and passengers. In-flight flameout is more apt to occur at high altitudes [1,2] where the inlet pressure and temperature are much lower than those on the ground. Whenever flameout occurs, combustion has to be re-established in the combustors. Capacitor-type surface discharge igniters have been widely adopted to deliver the necessary heat sources for relight. During sparking, the electric energy is locally converted to thermal energy to raise the temperature of a combustible mixture to a level at which the reaction is rapid and self-sustaining. One of the requirements for successful ignition in a combustor is that the kernel must grow fast enough to reach the recirculation region in the primary zone before it is swept away. Therefore, flame kernel development is an important factor to the relight performance of gas turbines [2].

In this study, a one-dimensional (1D) comprehensive model is developed to predict flame kernel propagation at relight conditions. Although many numerical models have been proposed for the prediction of kernel development, only a few of them [3,4] have been exclusively developed for spark ignition in turbulent flows, e.g., Akindele et al. [3] studied flame kernel growth in turbulent fuel-air mixtures and Herweg and Maly [4] developed a one-dimensional model to predict flame kernel growth inside SI engines.

The model in this paper incorporates the concept of high-activation-energy asymptotic analysis and the fractal description for wrinkled flame surfaces. Theoretically, two- or three-dimensional models are superior to one-dimensional approaches in terms of providing a detailed description of the flame surface. However, due to the extremely small characteristic scales involved in the spark ignition process, these models may be computationally inefficient at present. In our one-dimensional model, the description of the wrinkled flame surface area is obtained from the well-known fractal models, and the equivalent turbulent transport properties are derived from the concept of high-activation-energy asymptotic analysis.

Formulation and Modeling

Mathematical Formulation:

Spark ignition can be mathematically described by the conservation equations of mass, species, momentum, and energy. To simplify the approach, two as-

sumptions are made. First, it is assumed that the diffusion of species is governed by Fick's law, namely, $Y_iV_i = D_i\nabla Y_i$, where V_i, Y_i, and D_i are the diffusion velocity, mass fraction, and mass diffusivity of species i, respectively. Second, it is assumed that viscous dissipation and heat radiation are negligible. Consequently, the mass-weighted, 1D conservation equations in spherical coordinates are [5]

$$\frac{\partial\bar{\rho}}{\partial t} + \frac{1}{r^2}\frac{\partial(\bar{\rho}r^2\tilde{u})}{\partial r} = 0 \tag{1}$$

$$\frac{\partial(\bar{\rho}\tilde{Y}_i)}{\partial t} + \frac{1}{r^2}\frac{\partial(\bar{\rho}r^2u\tilde{Y}_i)}{\partial r} = \frac{1}{r^2}\frac{\partial(\bar{\rho}r^2D_{i0}\partial\tilde{Y}_i/\partial r)}{\partial r} + (\overline{\dot{\omega}_i})_T \tag{2}$$

$$\frac{\partial(\bar{\rho}\tilde{u})}{\partial t} + \frac{1}{r^2}\frac{\partial(\bar{\rho}r^2\tilde{u}^2)}{\partial r} = -\frac{\partial\bar{P}}{\partial r}\frac{1}{r^2}\cdot\frac{\partial(\mu_0r^2\partial\tilde{u}/\partial r)}{\partial r} \tag{3}$$

$$C_p\frac{\partial(\bar{\rho}\tilde{T})}{\partial t} + \frac{C_p}{r^2}\frac{\partial(\bar{\rho}r^2\tilde{u}\tilde{T})}{\partial r} = \frac{D\bar{P}}{Dt} + \frac{1}{r^2}\frac{\partial(r^2k_0\partial\tilde{T}/\partial r)}{\partial r} + \sum\left(\bar{\rho}D_{i0}\frac{\partial\tilde{Y}_i}{\partial r}C_{p,i}\frac{\partial\tilde{T}}{\partial r}\right) + Q_F(\overline{\dot{\omega}})_T - Q_{\text{loss}} + S \tag{4}$$

where

$$Q = -\sum_{i=1}^{m}\left[\frac{W_i(v_i'' - v_i')}{W_F(v_F'' - v_F')}\cdot\left(\Delta h_{i,f}^{\circ} + \int_{T_0}^{T}C_{p,i}\,d\tilde{T}\right)\right] \tag{5}$$

$$C_p = \sum\tilde{Y}_iC_{p,i}. \tag{6}$$

In arriving at Eqs. (2) through (4), mixing length models have been proposed for the turbulent flux terms to solve the problems of closure. Thus, a general form is employed for the turbulent flux terms:

$$\overline{\rho\psi_i''u''} = -\bar{\rho}\Gamma_T(\partial\tilde{\psi}_i/\partial r) \tag{7}$$

where Γ_T is a turbulent transport coefficient, Ψ represents any physical quantity, and Ψ'' is any mass-weighted fluctuating quantity, the tilde represents Favre average, and the overbar denotes mean average. Meanwhile, $\bar{\dot{\omega}}_i$ is the chemical production rate of species i; S is the energy deposition rate of an external heat source, and Q_{loss} denotes energy loss through walls or electrodes; $D_{i,0}$, μ_0, and k_0 denote the overall mass, momentum, and heat transport coefficients, respectively. Each overall transport coefficient consists of the molecular and turbulent transport coefficients. The terms Q_F, W_i, and $\Delta h_{i,f}^{\circ}$ denote heat of combustion per unit mass of fuel consumption, molecular weight of species i, and heat of formation of species i, respectively. Due to the relatively small value of the summation term in Eq. (4), the molecular mass diffusion coefficient is directly replaced by an overall diffusion coefficient to make the energy equation applicable to both laminar and turbulent flows. Numerical evidence shows that this replacement does not significantly affect the solution. Moreover, if the mixture is assumed to be ideal, the following equation of state for ideal gas is used:

$$\bar{P} = \bar{\rho}(R_u/\bar{M})\tilde{T} \tag{8}$$

where R_u is the universal gas constant and M denotes the mean molecular weight of the mixture.

Modeling:

The surface area of a wrinkled flame cannot be directly described by one-dimensional approaches. To overcome this problem, an equivalent planar flame model is suggested. For a wrinkled flame in the flamelet regime, an equivalent planar flame, which has the same preheat volume as the wrinkled flame but a different flame propagation speed at any point on the flame surface, is proposed. Thus,

$$A_T/A_L = (\delta_p)_T/(\delta_p)_L \tag{9}$$

where A is surface area and δ_p represents the thickness of the preheat zone. This equivalent planar flame is schematically shown in Fig. 1. Meanwhile, as suggested by Damköhler [6], the ratio of the turbulent flame speed to the laminar flame speed is equal to the ratio of the wrinkled flame area to the planar flame area. However, neither the turbulent flame speed nor the wrinkled flame area is known.

In recent years, Gouldin [7] has proposed that turbulent flame fronts could be treated as constant property surfaces embedded in turbulent flows. As a result, turbulent flame surfaces may be characterized by the mathematics of fractals. In their proposal, the fractal behavior of turbulent flames are limited by an upper bound and a lower bound, which are also referred to as the outer cutoff (ε_0) and inner cutoff (ε_i), respectively. Based on Damköhler's and Gouldin's hypotheses, the relationship between the flame surface area, the flame speed, and the fractal cutoffs is given as [8,9]

$$S_T^0/S_L^0 = A_T/A_L = (\varepsilon_0/\varepsilon_i)^{\Re-2} \approx (L/\eta)^{\Re-2} \tag{10}$$

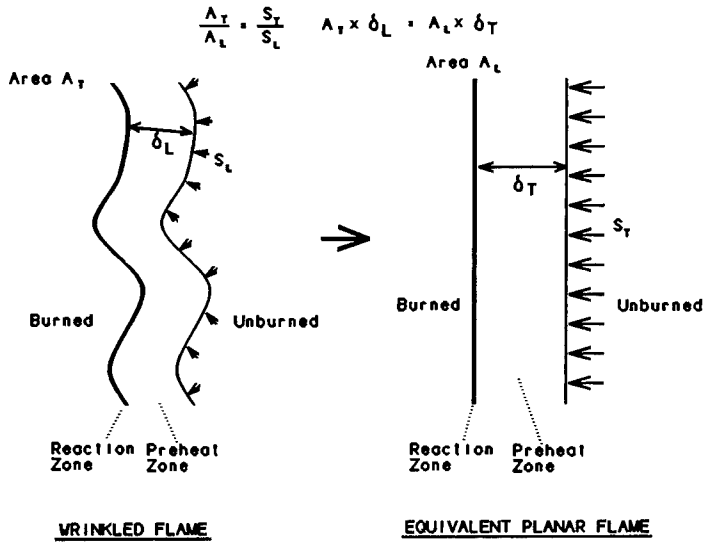

FIG. 1. Schematic illustration of the equivalent planar flame model for a wrinkled flame in laminar flamelet regime.

where $\mathcal{R}$ is the fractal dimension that is a measure of surface roughness, L is the integral scale, η is the Komolgorov scale, and superscript 0 denotes the unstretched state. Since the kernel size measured in our experiments is always greater than integral scale, a fixed value, integral scale L, is used to replace outer cutoff (ε_0).

From asymptotic analysis, a laminar flame of high activation energy can be divided into two zones: a relatively thick preheat zone followed by a very thin reaction zone. The analysis shows that convection and diffusion are dominant in the preheat zone, while reaction balances diffusion in the reaction zone. By applying these results to the equivalent flame, the values of the turbulent transport coefficients can be found.

Due to the convection-diffusion balance in the preheat zone, integrating Eq. (4) over the preheat zone, 0^+ to $0^+ + (\delta_p)_T$, yields

$$C_p \rho_u S_T^0 (\tilde{T}_{0+} - \tilde{T}_u) \approx k_0 (\tilde{T}_b - \tilde{T}_u)/(\delta_p)_T \qquad (11)$$

where linear approximation is used for the temperature gradient, and continuity, $\rho\tilde{u} = \rho_u S_T =$ constant, is applied. Subscripts b and u represent the burned and the unburned states, and $\tilde{T}_{0+}$ is approximately equal to $\tilde{T}_b$. As a result, Eq. (11) can be further simplified as

$$k_0/(\delta_p)_T \approx C_p \rho_u S_T^0. \qquad (12)$$

Similarly, integration of the species Eq. (2) over the mass diffusion zone, 0^+ to $0^+ + (\delta_m)_T$, yields

$$\overline{\rho_b} (D_{i0})_b/(\delta_m)_T \approx \rho_u S_T^0 \qquad (13)$$

where $(\delta_m)_T$ is the thickness of mass diffusion zone.

From the diffusion-reaction balance in the reaction zone, the heat conduction term in Eq. (4) is equal to the rate of chemical heat release. After integration, Eq. (4) becomes

$$k_0(\tilde{T}_b - \tilde{T}_{0+})/(\delta_R)_T \approx \langle \overline{\dot{\omega}_F} \rangle_T \cdot Q_F \qquad (14)$$

where $\langle \dot{\omega}_F \rangle_T$ and $(\delta_R)_T$ are the integrated reaction rate of fuel over the reaction zone and the thickness of the reaction zone, respectively.

Similar integrations for a laminar unstretched flame yields

$$k_L/(\delta_p)_L \approx C_p \rho_u S_L^0 \qquad (15)$$

$$\rho_b (D_{iL})_b/(\delta_m)_L \approx \rho_u S_L^0 \qquad (16)$$

$$k_L (T_b^0 - T_{0+}^0)/(\delta_R^0)_L \approx \langle \overline{\dot{\omega}_F} \rangle_L \cdot Q_F \qquad (17)$$

where subscript L represents laminar state.

Dividing Eq. (12) by Eq. (15) gives

$$\begin{aligned} k_0/k_L &\approx [(\delta_p)_T/(\delta_p)_L] \cdot [S_T^0/S_L^0] \\ &\approx [(\varepsilon_0/\varepsilon_i)^{\mathcal{R}-2}]^2. \end{aligned} \qquad (18)$$

In order to obtain Eq. (18), Eqs. (9) and (10) are employed. Meanwhile, from Eqs. (13) and (16), the ratio of the turbulent and the laminar mass diffusivity is given by

$$\begin{aligned} D_{i0}/D_{iL} &\approx (\delta_m)_T/(\delta_m)_L \cdot [S_T^0/S_L^0] \\ &\approx (\delta_m)_T/(\delta_m)_L \cdot (\varepsilon_0/\varepsilon_i)^{\mathcal{R}-2} \end{aligned} \qquad (19)$$

where the ratio of ρ_b to ρ_b is assumed to be close to unity. The two diffusion-zone thicknesses, $(\delta_m)_L$ and

$(\delta_m)_T$, may be related to the preheat zone thicknesses, $(\delta_p)_L$ and $(\delta_p)_T$. As derived by Chung and Law [10], the flame thickness ratio of $(\delta_m)_L$ to $(\delta_p)_L$ in laminar flows is equal to the inverse of the Lewis number. However, in well-stirred combustion, diffusion processes in the flame are expected to be controlled by turbulence rather than molecular diffusion. Thus, all of the turbulent transport coefficients are expected to have the same value at a very high Reynolds numbers. Hence, the ratio of $(\delta_m)_T$ to $(\delta_p)_T$ approaches unity as the strength of turbulence increases. Between these two extremes, turbulence and molecular motion contribute to the transport process; however, the degree of contribution from each mechanism is not clear so far. Therefore, a relationship between the thickness of the mass diffusion zone, δ_m, and the thickness of the preheat zone, δ_p, at different turbulence levels must be given. In this study, the ratio of δ_m to δ_p, which is assumed to be a function of turbulence intensity, laminar flame speed, and the Lewis number, is given as

$$\delta_m/\delta_p = 1/f(u'/S_L, \mathrm{Le}) \tag{20}$$

where

$$f(u'/S_L^0, \mathrm{Le}) = 1 - [(1 - \mathrm{Le})/(1 + u'/S_L^0)^{1/2}]. \tag{21}$$

Equation (20) is a heuristic model [5] that considers the contribution from the laminar and the turbulent parts. In Eq. (21), the function f increases or decreases monotonically to unity when the turbulence intensity increases from 0 to an extremely high level. Thus, the ratio δ_m/δ_p is correctly described by Eqs. (20) and (21) for flames in laminar and very turbulent flows. Therefore, the ratio of the turbulent mass diffusivity to the laminar mass diffusivity is

$$D_{i_0}/D_{i_L} = [\mathrm{Le}/f(u'/S_L, \mathrm{Le})] \cdot [(\varepsilon_0/\varepsilon_i)^{\mathfrak{R}-2}]^2. \tag{22}$$

From Eqs. (14) and (17), the ratio of the two reaction rates is expressed as

$$\langle\overline{\dot{\omega}_F}\rangle_T/\langle\overline{\dot{\omega}_F}\rangle_L = (k_0/k_L) \cdot [(\delta_R^0)_L/\langle\delta_R\rangle_T] \tag{23}$$

where the assumption of $(\tilde{T}_b - \tilde{T}_{0+}) \sim (T_b^0 - T_{0+}^0)$ is made. However, the ratio of the two reaction zone thicknesses, $(\delta_R^0)_L/\langle\delta_R\rangle_T$, is unknown. It is reasonable to expect that this reaction rate ratio is dependent on large and small length scales of the turbulent field [11]. If we further assume that the dependency can be represented by a simple function, the ratio is expressed as

$$\langle\overline{\dot{\omega}_F}\rangle_T/\langle\overline{\dot{\omega}_F}\rangle_L \approx [(\varepsilon_0/\varepsilon_i)^{\mathfrak{R}-2}]^{2+y} = [(\varepsilon_0/\varepsilon_i)^{\mathfrak{R}-2}]^z \tag{24}$$

where $z = 2 + y$ and is determined by using an imaginary planar flame with a speed about four times greater than the laminar speed in the laminar flame calculation at this stage. The momentum equation is usually not used for spark ignition simulation in a homogeneous and electrode-free and wall-free flow field after the breakdown phase. In arriving at Eqs. (18), (22), and (24), the flame is totally unstretched. For a stretched flame, a stretch factor I_0 [12] is used to take account of the effect of flame stretch. For a stretched flame, when the stretch factor is not strongly related to the wrinkled surface area to volume ratio, Eqs. (18), (22), and (24), may be expressed as

$$k_0/k_L = [I_0 \cdot (\varepsilon_0/\varepsilon_i)^{\mathfrak{R}-2}]^2 \tag{25}$$

$$D_{i_0}/D_{i_L} = [\mathrm{Le}/f(u'/S_L, \mathrm{Le})] \cdot [I_0 \cdot (\varepsilon_0/\varepsilon_i)^{\mathfrak{R}-2}]^2 \tag{26}$$

$$\bar{\omega}_{i_T} = \bar{\omega}_{i_L} \cdot I_0^2 \cdot [(\varepsilon_0/\varepsilon_i)^{\mathfrak{R}-2}]^z \tag{27}$$

Solution Procedure

Discretization:

The governing equations of the model are integrated over control volumes first and then discretized into finite-difference equations by using the power-law scheme [13]. The discretized equations are then solved by the PISO algorithm [14]. The computation domain is a cone-shaped region that extends outward from the origin of the coordinates with a solid angle $\delta\xi$. All physical quantities in a control volume are calculated and stored at the corresponding nodal points. In this study, the minimum grid spacing is 0.02 mm, and the time increment is 5 μs.

Linearization of Reaction Rate:

The production rate of any species i may be expressed in an Arrhenius form

$$(\overline{\dot{\omega}_i})_L = [W_i(\nu_i'' - \nu_i')/W_F(\nu_F'' - \nu_F'')]B \cdot \rho^{a+b} \cdot T^n \cdot \exp(-E/\mathrm{R}_u T) \cdot Y_F^a \cdot Y_0^b \tag{28}$$

where B is the pre-exponent frequency factor, E is the activation energy, and ν_i'' and ν_i' are the stoichiometric coefficients of species i on the production and reaction sides, respectively. For spark ignition in C_3H_8-air mixtures, five species, C_3H_8, O_2, H_2O, CO_2, and N_2, are considered. The reaction orders, a and b, are 0.65 and 1.15 [15], respectively. The pre-exponent factor is obtained from a laminar flame calculation by correctly reproducing the laminar flame speed [16].

Meanwhile, due to mass conservation, species i at time steps $l + 1$ and l are satisfied by

$$(Y_i^{l+1} - Y_i^l)/\dot{m}_i = \text{Constant} \tag{29}$$

where m_i is the mass of species i created in the reaction. By performing a Taylor expansion of Eq. (28) and substituting Eq. (29) into the expanded equation, a linear form for the reaction rate of species i is derived.

Initial Size of Spark:

The size of a spark channel is not a constant value during sparking. However, Sloane has shown [17] that the numerical results obtained with a fixed channel size differ only a few percent or less from those obtained with a variable channel size. Therefore, constant channel radius assumption is employed to simplify the numerical approach. The equivalent radius of a semispherical spark is given by

$$r_0 = (3/8 \cdot I_m \cdot V_m)^{1/3} \tag{30}$$

where I_m and V_m are the measured current (in A) and voltage (in V) of an arc-type cylindrical spark channel [18]. Meanwhile, the energy discharge rate per unit volume as a function of radius is given by [17]

$$Pw(r) = Pw_0/(1 + \exp[(r - r_0)/\delta r]) \tag{31}$$

where Pw_0 is the maximum power density during sparking, and δr is a steepness parameter. The parameter δr indicates the degree of the edge of a square waveform being smoothed [16], and a value of 0.5 mm is used in this study.

Artificial Thermal Conductivity:

It has been shown [19] that the spark energy discharged in the first few microseconds produces violent turbulence inside a flame kernel. Apparently, the spark-induced turbulence can efficiently distribute spark energy inside the kernel and may cause different kernel growth. A model with artificial thermal conductivity inside a flame kernel is introduced as

$$k_{\text{art}} = k \cdot (T - T_{ad})^5 \cdot 10^{-3} \tag{32}$$

where k_{art} is the artificial thermal conductivity. The molecular-level thermal conductivity, and other transport properties like mass diffusivity, viscosity, and specific heat at constant pressure can be calculated from formulas in the literature [20,21].

Stretch Factor:

The stretch factor is mathematically derived as [4]

$$\begin{aligned} I_0 \approx 1 &- (\delta_l/S_L) \\ &\cdot [K_T + (1 + \rho_u/\rho_b)/r_f] \\ &\cdot [1/\text{Le} - (\text{Le} - 1/\text{Le}) \cdot T_a/2T_{ad}] \end{aligned} \tag{33}$$

where T_a and T_{ad} are the activation temperature and adiabatic flame temperature, respectively, δ_l is the laminar flame thickness, and K_T is the turbulent strain rate and can be evaluated using the formula shown by Abdel-Gayed et al. [22]. However, Eq. (33) can only be used when the Lewis number is greater or less than unity. When the Lewis number is very close to unity, the stretch factor should be approximately equal to 1.

Results and Discussion

In order to provide data for comparison, spark ignition experiments were conducted in a turbulent flow reactor [5]. The turbulent flow reactor can generate homogeneous turbulence and uniform velocity in the test section. A high-speed schlieren photographic system was used to record the images of the flame kernels. The equivalent kernel radius, which is defined as a semi-circle with the projected area the same as that of the kernel, can be calculated. In this experiment, a surface discharge ignition system typical of those used in aircraft is employed to initiate combustion. The spark energy is 1.8 J, and the discharge duration is about 100 μs. The tip of the igniter is flush with the wall of the test section. The test conditions and turbulent characteristics are listed in Table 1.

To solve the discretized equations, the exponent z in Eq. (27) has to be known first. From planar flame calculations, the values of z vary slightly over the test pressures. It is 1.44 for $p = 0.6$ atm and 1.45 for $p = 1.0$ atm. These values are reasonable because the thickness of the reaction zone of the equivalent flame should not increase linearly as that of the preheat zone or diffusion zone does. The exponent of almost constant value means that the ratio of reaction rates is controlled by the characteristic scales of turbulent field only.

Since no dissociation or ionization process is considered in the spark ignition model, the thermal conductivity directly obtained from the JANAF table [19] are usually underestimated. An artificial conductivity model, Eq. (32), is used in our calculation. To examine the validity of the proposed artificial thermal conductivity model, test calculations have been performed for a 30 mJ arc-discharge spark in a stoichiometric propane-air mixture. Heat loss through the electrode or the wall is not considered, and a 50% energy-transfer efficiency is assumed in these calculations. Figure 2 shows the temperature profiles of two flame kernels with and without artificial thermal conductivity. For spark ignition with artificial thermal conductivity, the temperature inside the flame kernel is evenly spread within a short period of time. However, without artificial thermal conductivity, the temperature profile still does not reach a uniform state at 1 ms after spark initiation.

TABLE 1
Summary of the test conditions, turbulence characteristics, and discharge characteristics

Parameters	Pressure (atm) 1.0		0.6
Mixture		C_3H_8-Air	
Equivalence ratio Φ	0.8, 1.0, 1.4		0.8, 1.0, 1.4
Turbulence intensity u' (m/s)	0.17, 1.60		0.17, 1.60
Temperature T (K)	300		300
Integral length scale L (mm)	~5		~5
Discharge type		Arc	
Spark energy		1.8 J	

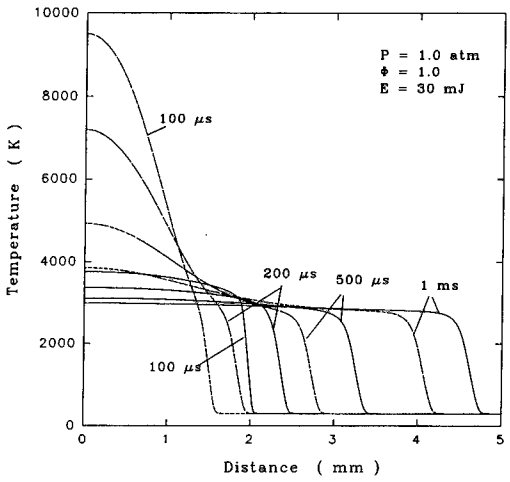

FIG. 2. The predicted temperature profiles for flame kernels initiated by a 30-mJ spark in atmospheric, stoichiometric C_3H_8-air mixture. Dash lines: no artificial conductivity; solid lines: with artificial conductivity.

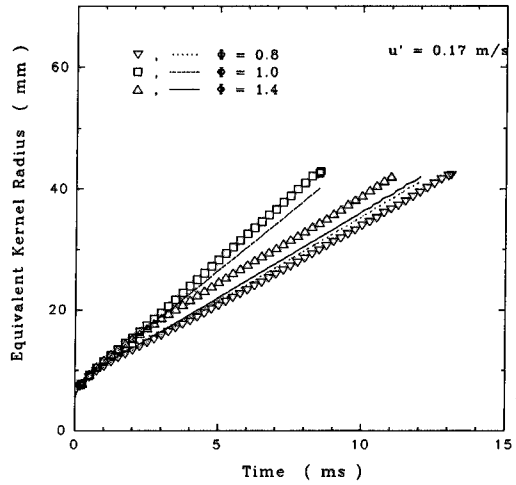

FIG. 3. Comparison between the predicted and the measured kernel radii at $P = 1.0$ atm and $u' = 0.17$ m/s, where u' is turbulence intensity, Φ is equivalence ratio, symbols represent measurements, and lines denote predictions.

Compared with Maly's results [23], the temperature profiles obtained with the artificial thermal conductivity model are more reasonable. Moreover, the flame kernel propagation rate is also different. Thus, at a given time, the kernel front spreads to a farther distance when the artificial thermal conductivity model is applied.

Numerical simulations of spark ignition in propane-air mixtures were carried out at various test conditions. The comparison between the predicted and the measured kernel radii at $p = 1.0$ and 0.6 atm are presented in Figs. 3 through 6. Turbulence is not included in the computation scheme in the first 0.9 ms since the spark-induced turbulence is usually strong in this period. The numerical predictions are, in fact, in very good agreement with the experimental results. Although, for certain cases, the difference between the prediction and the measurement is about 15%, this deviation is, however, relatively small and usually acceptable in turbulent combustion simulations. It is also interesting to note that, for the ignition at fuel-rich and low turbulence intensity conditions, most of the prediction inaccuracy appears in the first 3 μs. This may be due to the exclusion of spark-generated radicals in our calculation. In Fig. 6, the predictions and measurements show that the kernel growth curves for $\Phi = 1.0$ and 1.4 are almost identical, while kernel growth in the $\Phi = 0.8$ mixture is the slowest, although the laminar flame speed at $\Phi = 1.4$ (Le = 0.98) is about 30% slower than that at $\Phi = 1.0$ (Le = 1.34) and is approximately equal to that at $\Phi = 0.8$ (Le = 1.67). Thus, for a mixture with nonunity Le, flame kernel behavior is not only controlled by the laminar flame speed but is also affected by flame stretch. However, for unity Le flow,

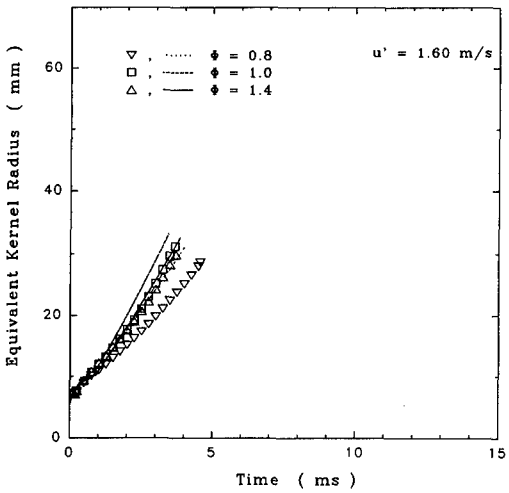

FIG. 4. Comparison between the predicted and the measured kernel radii at $P = 1.0$ atm and $u' = 1.60$ m/s, where u' is turbulence intensity, Φ is equivalence ratio, symbols represent measurements, and lines denote predictions.

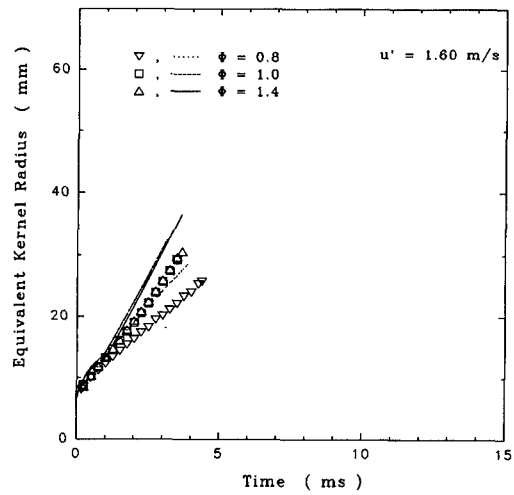

FIG. 6. Comparison between the predicted and the measured kernel radii at $P = 0.6$ atm and $u' = 1.60$ m/s, where u' is turbulence intensity, Φ is equivalence ratio, symbols represent measurements, and lines denote predictions.

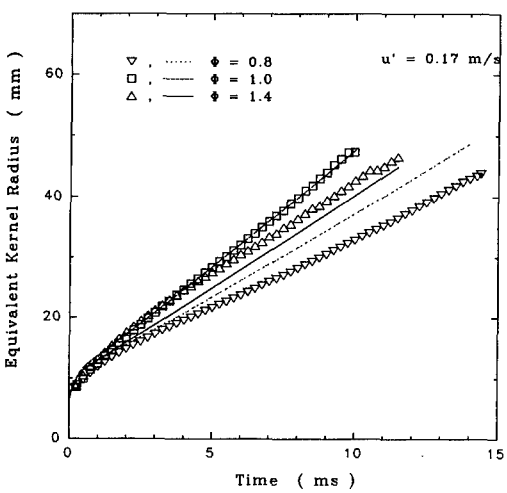

FIG. 5. Comparison between the predicted and the measured kernel radii at $P = 0.6$ atm and $u' = 0.17$ m/s, where u' is turbulence intensity, Φ is equivalence ratio, symbols represent measurements, and lines denote predictions.

as for the $\Phi = 1.4$ case, stretch has no effect on flame propagation.

Conclusions

A one-dimensional comprehensive model that incorporates a fractal description and asymptotic analysis is developed to predict flame kernel growth in turbulent flow fields. With the use of an artificial thermal conductivity inside the flame kernel, the model successfully predicted flame kernel development at various operating conditions. Although this model has been initially designed for the prediction of kernel behavior at in-flight flameout conditions, it is expected that this model can be applied to spark ignition in SI engines, if the effect of electrode geometry is properly dealt with in the early stages. The model may also provide a means to estimate the average turbulent transport properties. In order to improve this model, future extensive study of flame stretch and surface area of a wrinkled flame must be conducted experimentally and theoretically, and more advanced modeling approaches [24] should be considered.

Acknowledgment

This work was supported by Garrett Engine Division, Allied-Signal Aerospace Company, USA.

REFERENCES

1. Lefebvre, A. H., *Gas Turbine Combustion,* McGraw-Hill, New York 1983.
2. Low, H. C., Wilson, C. W., Abdel-Gayed, R. G., and Bradley, D., *Evaluation of Novel Igniters in a Turbulent Bomb Facility and a Tubo-Annular Gas Turbine Combustor,* AIAA/ASME/SAE/ASEE 25th Joint Propulsion Conference, July 10–12, 1989.

3. Akindele, O. O., Bradley, D., Mak, P. W., and McMahon, M., *Combust. Flame* 47:129–155 (1982).
4. Herweg, R., and Maly, R. R., SAE Technical Paper 922243.
5. Liou, D., "Flame Kernel Development in Atmospheric and Subatmospheric Turbulent Flows," Ph.D. Thesis, Pennsylvania State University, University Park, PA, 1994.
6. Damköhler, G., *Z. Electrochem.* 46:601 (1940).
7. Gouldin, F. C., *Combust. Flame* 39:249–266 (1987).
8. Santavicca, D. A., Liou, D., and North, G. L., SAE Technical Paper 900024.
9. Matthews, R. D., and Chin, Y.-W., SAE Technical Paper 910079.
10. Chung, S. H., and Law, C. K., *Combust. Flame* 72:325–336 (1988).
11. Spalding, D. B., *Thirteenth Symposium (International) on Combustion,* 649–657.
12. Bray, K. N. C., *Proc. R. Soc. London A* The Combustion Institute, Pittsburgh, 1970, pp. 431:315–335 (1990).
13. Patankar, S. V., *Numerical Heat Transfer and Fluid Flow,* Hemisphere, New York, 1980.
14. Issa, R. I., Ahmadi-Befrui, B., Beshay, K. R., and Gosman, A. D., *J. Comput. Phys.* 93:388–410 (1991).
15. Westbrook, C. K., and Dryer, F. L., *Prog. Energy Combust. Sci.* 10:1–57 (1984).
16. Law, C. K., Zhu, D. L., and Yu, G., *Twenty-First Symposium (International) on Combustion,* 1988, pp. 1381–1402.
17. Sloane, T. M., *Combust. Sci. Technol.* 73:367–381 (1990).
18. Raizer, Y. R., *Gas Discharge Physics,* Springer-Verlag, New York, 1991.
19. Au, S., Haley, R., and Smy, P. R., *Combust. Flame* 88:50–60 (1992).
20. Chase, M. W., et. al., *JANAF Thermochemical Tables,* 3rd ed., *J. Phys. Chem. Ref. Data* 14(1) (1985).
21. Kee, R. J., et. al., Sandia Report SAND86-8246, UC-401, reprint 1990.
22. Abdel-Gayed, R. G., Bradley, D., and Lawes, M., *Proc. R. Soc. London A* 414:389–413 (1987).
23. Maly, R., in *Fuel Economy in Road Vehicles Powers by Spark Ignition Engines,* (J. C. Hillard and G. S. Springer, Eds.), Plenum Press, 1984, pp. 91–148.
24. Pope, S. B., *Prog. Energy Combust. Sci.* 11:119–192 London (1985).

COMMENTS

C. T. Avedisian, Cornell University, USA. This is an interesting and potentially useful study concerning the influence of a spark on ignition. I have several questions for clarification.

1. How important is the term dP/dt in the energy equation for the conditions of your calculation (was pressure assumed to be constant)?

2. You mentioned that the spark created "violent turbulence." Did you calculate the "decay" of the turbulence created?

3. How long was the spark kept on in the experiments, and did you vary the spark duration in the calculation?

Author's Reply. 1. In a constant-pressure environment, dp/dt significantly affects flame kernel development in the blast-wave phase. Since the electric discharge system used in our study was an arc discharge, the pressure was assumed to be constant.

2. The turbulence of flow field would dominate the kernel growth process within a few hundred microseconds after spark onset. Therefore, we did not consider the effect of the decay of spark-generated turbulence in the report.

3. Because the spark duration and energy (90 μs and 1.8 J) were very typical to the discharge systems used in aircraft gas turbines nowadays, we did not vary the discharge duration, energy, and/or power profiles in our experiment or calculation.

•

I. P. Nikolova, Bureau of Mines, USA. If the round shape is the sole one, which shape is expected to be obtained by this model? I was pleased to hear that kernel hemispherical at origin distorts. I have had experience in modeling a kernel evolution, originally spherical, that distorts due to convection during the time of evolution.

Author's Reply. Based on experimental observation, kernel shape could be spherical for surface discharge igniters or cylindrical for electrode-type igniters at the initial stage. However, those initially cylindrical kernels would transform to be spherical ones in ~100 μs. In our study, since the igniter tip was flush with the wall of the test chamber, the initially spherical kernels would become semispherical kernels within 200 μs. Meanwhile, kernels were also slightly distorted along the flow direction. To simplify the numerical approach, a semispherical-kernel assumption was employed in our calculation.

•

N. Shah, Sundstrand Power Systems, USA. The abstract implied a high-altitude relight study; however, the temperature and pressure studies, which are the critical two parameters, were not reported.

Author's Reply. Only operating conditions at 0.6 and 1.0 atm were reported in this paper at this time; however, other conditions (e.g., 0.3 atm) can be found in Liou's Ph.D. thesis [5]. Meanwhile, although the study was conducted at room temperature, the effect of low mixture temperature will be investigated in our future study.

Twenty-Fifth Symposium (International) on Combustion/The Combustion Institute, 1994/pp. 269-275

FUEL SAVING BY HEAT-RECIRCULATING COMBUSTION USING FIBRE MATS

SUNAO NAKAMURA* AND FELIX WEINBERG
Imperial College
London SW7, England

Radiant fibre mat burners are redesigned so as to incorporate a high degree of heat recirculation from burnt products to cold reactants into the combustion process, with the object of making them substantially more efficient and also to extend the range of flame stability to poorer fuels and leaner mixtures. The performance of a variety of burner systems is studied, including, in particular, designs in which an assembly of the fibre mats themselves is used as heat exchanger. Burners in which the radiant surface is heated by flame products rather than, as has been conventional, by the upstream flame boundary allow a much greater range of reactant flows. A theory based on the highly stirred reactor concept as ultimate limitation to flame stability is developed to estimate absolute maxima to preheat and blow-out. Extensive series of flow, temperature, and composition measurements, mostly for methane/air mixtures, demonstrate substantial improvements in heating efficiencies and ranges of flame stability; thus, radiant efficiency has been increased more than fourfold, while mixtures of heat content corresponding to two-thirds of the normal limit of flammability can be burnt stably. Theory implies that further improvements are possible. It is shown that stacked mats provide a compact and adequate heat exchanger that lends itself readily to multi-burner industrial designs suitable for use with fuels such as blast furnace gas.

Introduction and Aims

Burners that are designed to transfer heat principally by radiation from a flame-heated refractory mat, or matrix, offer a number of advantages, including reduced emission of pollutants, uniform heating, and the potential for using low grade fuels [1–3]. In these devices, a flame fed by a gaseous fuel/air mixture stabilises on the downstream surface of the radiating mat. NKK mats made of layers of ceramic and sintered fine metal fibres [4] have been used because they are able to withstand high temperatures (up to 1300–1400 K), are highly permeable to gas flow, and have a very high thermal conductivity in a plane parallel to their surface but not at right angles thereto. It was shown [2,4] that, with a premixed methane/air flame stabilised immediately downstream of a stainless steel fibre mat, radiation fluxes in excess of 100 $kW \cdot m^{-2}$ could be realised. Such mats need not be planar but may be bent into various shapes, e.g., cylinders designed to surround pipes to be heated.

The burners, however, also suffer from particular disadvantages: notably the escape of much of the heat of combustion with the outflowing products—over 75% in the original work—and a very limited flow range for stable combustion. Flame stability is limited by quenching at low velocities (at high mat temperatures, ignition of the reactants by the upstream surface of the mat is also possible) and, at the other extreme, by lift-off of the flame from the downstream surface (see Fig. 1a), which occurs as soon as the linear flow velocity reaches the burning velocity. Thus, the absolute flow rates as well as their range were rather limited. The basic problem with the original design is that the minimum product temperature at which a flame can be stabilised over practically useful flow ranges is substantially higher than the maximum temperature the mat can withstand. That is why the product gases had to carry away such a large proportion of the energy released, giving the burner a low radiant efficiency.

The object of the present research was to overcome these shortcomings by using the particular properties of the mat to extract heat from the burned products and recycle it to the reactants. The principle of recirculating heat from hot products to cold reactants by heat exchange without intermixing of the gases has been the subject of a great many studies, particularly in the UK and in Japan (for a review, see Ref. 5). Such burners can be used to achieve substantial fuel savings at constant flame temperature, or, by raising the temperature in the reaction zone on borrowed heat, they allow increases in combustion rate and thermodynamic efficiency for energy conversion and heat transfer. The increased reaction rate then makes it possible to burn very lean mixtures and poor fuels, substantially below the normal burn-

*Permanent address: NKK Corporation, Kawasaki, Japan.

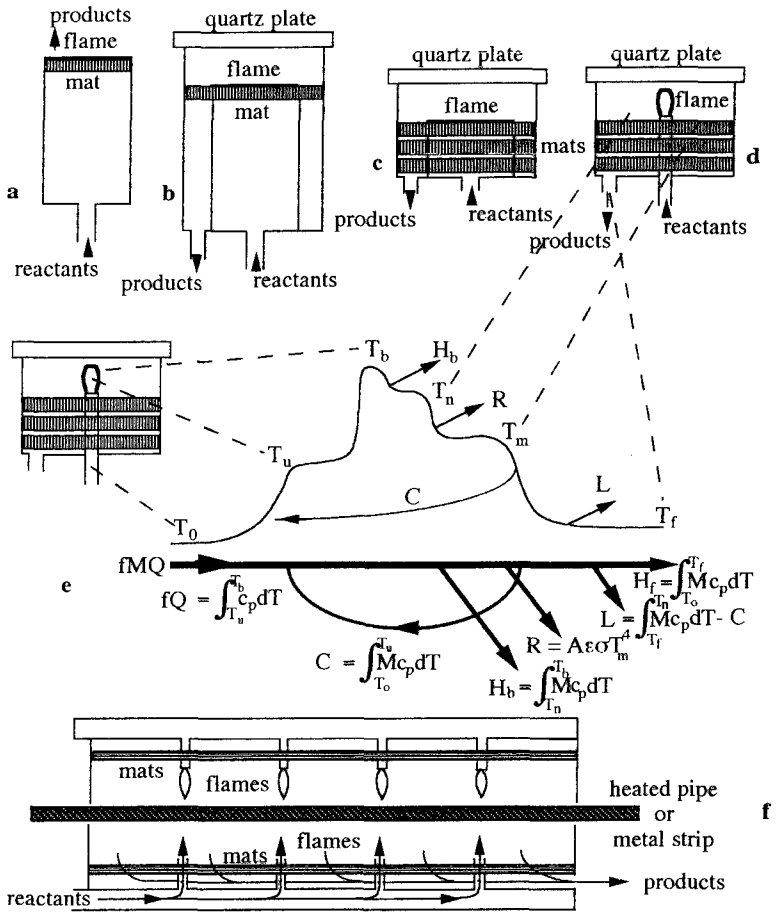

Symbols

A = area
T = temperature
f = fraction of stoichiometric
M = mass flow rate
Q = heat of combustion of stoichiometric mixture
C = heat recirculated/time
R = heat radiated/time
H = heat convected/time
L = heat loss from burner body/time

c_p = specific heat at constant pressure
ε = emissivity
σ = Stefan's constant

Suffices:
o = ambient
u = unburnt (just upstream of flame)
b = burnt (just downstream of flame)
m = from or by mat
1,2, ...n = at location so marked
f = final (at burner exit)

FIG. 1. (a) through (d) Laboratory burner systems described in text, (e) illustration of temperature distribution and energy flow calculation using system (d) as example, and (f) industrial burner.

ing limit. This can greatly increase the radiant efficiency of the burners and, additionally, widens the range of potential fuels, e.g., to blast furnace gas and other industrial waste gases.

Burner Systems

A variety of systems were designed for investigation, based on the anisotropic thermal conductivity of the mat with its large value lying in the plane of the metal fibres parallel to its surface. In order to compress the extensive series of measurements into the permissible length of a symposium paper, the principal designs, nomenclature, heat flows, and temperature distributions have all been summarised schematically in Fig. 1.

Figure 1a illustrates the basic radiant mat burner [1–4]. It is shown in an upright position so that ra-

diation and hot products flow in the same direction, though in practice it is frequently not used in that orientation. Its radiant efficiency is seen to be (R/fMQ). The maximum value of the numerator is fixed by the highest temperature the mat will withstand and the lowest value of the denominator by the above-mentioned flame stability limitations. The object of all the subsequent designs is to increase this quantity by raising the reaction temperature (and hence flame stability) on "borrowed" enthalpy. Figure 1b illustrates a simple scheme, based on conduction within the mat and a counterflow heat exchanger; the flow channels may be folded.

The burners were variously constructed of thin-walled steel (where required to hold mats) and quartz tubing and could be insulated externally with blankets of Kaowool. Thin thermocouples were placed in the centres of reactant inlets and product outlets and upstream and downstream of the flames and of the mats. Together with the metering of fuel and air flows, these measurements allowed the convected gas enthalpies and any changes in their flows to be monitored at every stage throughout the apparatus, as illustrated in Fig. 1e. A fused silica top plate was used, because of its transparency to radiation in the infra red. The gases also lose heat to it by convection, and this is available output if the top cover is used as a hot plate. In addition to monitoring the corresponding heat loss from the gas, the total heat available from the plate was determined calorimetrically, by timing the temperature rise of water placed in a container that rested on its surface. Thus, in addition to the radiant efficiency, we also record the total heating efficiency $= (R + H_b)/fMQ$. The emissivity, ε, in $R = A\varepsilon\sigma T^4$, was obtained from previous [2] experimental measurements. (In the systems of Figs. 1b and 1c, R is the sum of radiation from the inner and outer mat areas at their different temperatures.)

The design of Fig. 1c dispenses with the counterflow heat exchanger section of Fig. 1b by adding to the number of mats so as to make it superfluous. This offers a number of practical advantages, since it allows the burner system to be greatly shortened. It minimises heat losses to the surroundings, and the principle is particularly useful for industrial designs (see below and Fig. 1f) in which the radiant mat is wrapped around the object to be heated. Because of their substantial thermal conductivity, quite a small number of mats stacked on top of one another proved sufficient to replace the convective section of the counter-flow heat exchanger.

Figure 1d shows a more radical modification of the basic principle, which is made possible by the aforegoing modifications. The basic concept of heating the mat by the cold, reactant, side of the flame constitutes a major limitation on all the previous designs. It restricts the inlet flow velocity to values smaller than the burning velocity and hence limits the power throughput, especially for lean mixtures and poor fuels. It also confines the mat's temperature to a value much below the final flame temperature and the mat area to that of the flat flame. The design of Fig. 1d, by aiming to use instead the products to heat the mat, avoids these limitations. The exact shape and position of the flame becomes immaterial, so that the ranges of flame stability are greatly extended, higher flow velocities become permissible, inlet tubes of small diameters may be used, and the radiating area of the mat may be increased. The freedom to decrease the diameter of the inner tube, as well as the resultant increase in efficiency, is again particularly useful for industrial practice (see below and Fig. 1f).

The measurements carried out on these systems allowed detailed energy flow audits, as illustrated in Fig. 1e, to be carried out for each modification. Most of the work was carried out with natural gas as the fuel. Stability loci for flames of various configurations were obtained as functions of fuel-air ratio and flow velocity. Gas analyses were carried out ahead of the flame (to check on any pre-reaction in the preheating section) and at the burner exit (to monitor completeness of reaction).

Results

The work was carried out in 15 phases, comprising several burner designs, varying numbers of mats, reactant compositions, and flow rates, yielding a large body of results, of which only an illustrative selection can be included within the permissible length. Gas analyses for hydrocarbons, carbon monoxide, and carbon dioxide after the preheating stage and in the exit showed no prereaction even at our maximum preheat and confirmed that chemical reactions always go to completion in the flame even when the reactant mixture is very lean and in rapid flow (maximum CO concentration 0.003).

Figure 2a illustrates the profound effect that even quite inelaborate methods of heat recirculation have on the minimum fuel content for flame stability. Curves (i) and (iii) refer to systems a and b of Fig. 1, while curve (ii) obtains its heat recirculation by counterflow alone; i.e., the mat in Fig. 1b does not extend beyond the central tube. Thus, the leanest flame stabilisable at an initial flow velocity of 0.15 m/s decreases from 5.6 to 3.6% methane by volume, while the leanest mixture at which the mat radiates substantially extends from 8.8 to 6.5%. Fig. 2b illustrates corresponding effects on efficiencies for the same burner configurations, for a 0.75 stoichiometric methane/air mixture, flowing at 0.1 m/s. It will be seen that the radiant efficiency more than doubles, while the total heating efficiency (radiation + convection to the top plate) rises from less than 15 to over 70%. As discussed above, the efficiencies are highest at the lowest flow velocities and energy throughputs.

The effect of number of mats, flow velocity, and

methane content on the percentage of heat recirculated for novel systems of the kind shown in Fig. 1d is illustrated in Fig. 3a. It will be seen that a stack of four mats can recycle over 60% of the total throughput for the leanest of mixtures in slow flow, making additional heat exchange superfluous. The radiant efficiency can reach 65% and the total heating efficiency 90% (see Fig. 3b which summarises the major heat flows in energy audits as percentages of the input). However, for a constant number of mats, the heat loss carried away by the products increases, as may be expected, at higher flow rates. Should such flows be required for particular applications, it is anticipated that increasing the length and rearranging the geometry of the metallic fibres in the mats will yield further improvements in thermal conductivity, providing a simple alternative to increasing the number of mats in the stack.

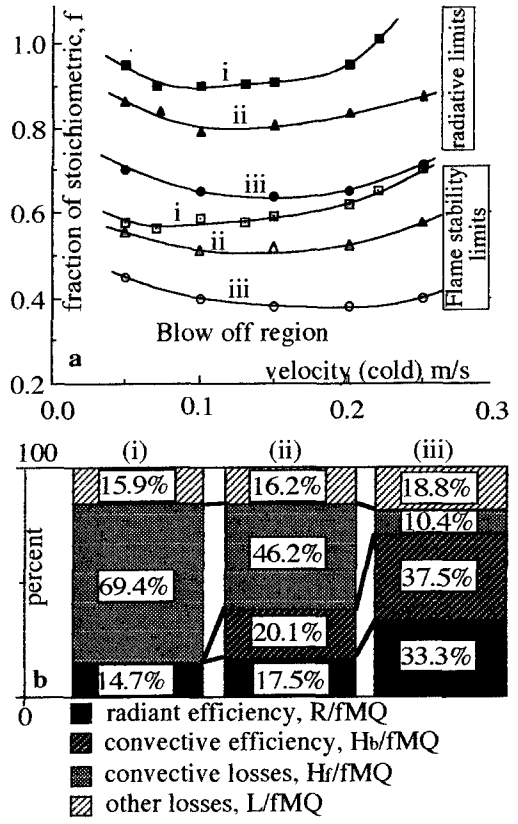

FIG. 2. Effect of heat recirculation on (a) limits and (b) energy audit. See text for experimental conditions and description of burner systems (i), (ii), and (iii).

Ultimate Theoretical Limitations

Since the maximum radiation flux is fixed by the properties of the mat (its emissivity and the highest temperature it will withstand), maximising efficiency may be regarded as minimising (fMQ) in such a way as to maintain the maximum mat temperature. Reducing Q and f implies the use of low calorific value fuels and lean mixtures, respectively, but the consequent reduction in reaction temperature requires further increases in heat recirculation so as to raise flame stability to a practical value.

For a constant rate of heat recirculation, increasing the flow rate lowers pre-flame temperature. This factor, together with the dominance of heat losses as flow rate tends to zero, has been used [6] to explain the shape of stability curves for heat recirculating burners in general. However, if we regard the number of mats (or their effective thermal conductivity) as an independent variable, the complementary idealisation is equality of gas temperatures of the reactant and product streams emerging from each mat. Thus, the ultimate limitations are kinetic: at the high preheat, long residence time, end it is pre-reaction in the reactants; at the other extreme, it is blow-out. In order to reach desired power levels with lean mixtures and poor fuels, high gas velocities are required. For systems such as that illustrated in Fig. 1d, decreasing the inlet tube diameter at constant mass flow rate increases flow velocity, ultimately approaching a highly stirred reactor system.

It has previously been suggested [5] that blow-out in heat-recirculating combustors may be regarded in terms of well-stirred reactor theory. This is because the system operates at very high flow velocities and levels of turbulence, and the leanest mixture for which a flame can be stabilised is likely to represent a reaction rate limitation. The observation that graphs of limiting mass flow rate at blow-out, plotted against percentage fuel, become almost vertical has been accounted for in terms of an activation energy such that a very large increase in reaction rate is occasioned by a very tiny increase in final flame temperature. The latter was indeed found to be virtually constant at the limit [6,7]. The volume relevant to blow-out may be less than the entire chamber volume [8], but we shall, in any case, only be considering reaction rates as ratios.

The theory is generalised for all reactants in terms of effective global kinetics. Similar methods can then be applied to particular cases, using particular reaction mechanisms with detailed kinetics. We represent the rate of reaction, w, as

$$w = K[r]^n \exp(-E'/T) \qquad (1)$$

where K is a constant, $[r]$ is the concentration of reactants (there may be more than one), n is the reaction order, and E' is the activation energy divided by the universal gas constant—these symbols are in addition to those listed in Fig. 1. We can express $[r]$

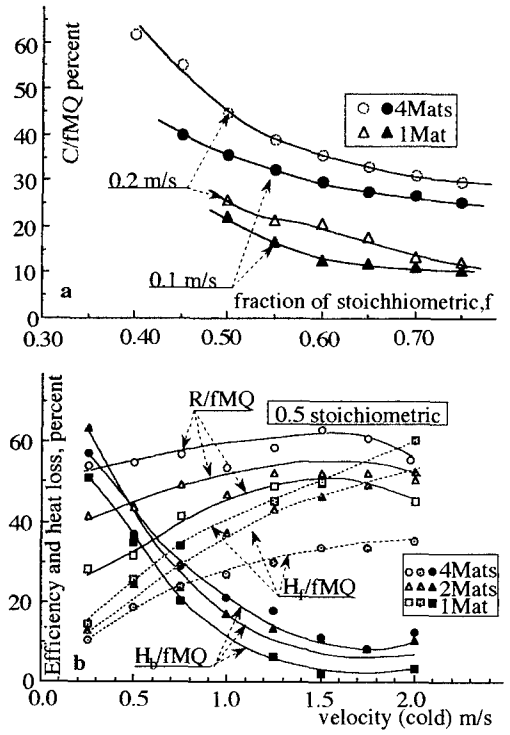

FIG. 3. Multiple mats in burner system of Fig. 1d variable flow velocity and fuel content: (a) fraction of heat recirculated, (b) energy audit at $f = 0.5$.

as a function of T, as the reaction proceeds and/or as products are intermixed with reactants, making the usual assumptions of a single overall reaction and constant physical properties of the gas (here largely air), so that

$$[r] = [r_u]\left(\frac{T_u}{T}\right)\left(\frac{T_b - T}{T_b - T_u}\right). \tag{2}$$

We now calculate the peak reaction rate by substituting Eq. (2) into Eq. (1), differentiating and equating to zero to find the temperature, T_p , at which it occurs. Differentiation yields

$$(1/T_p) = (1/T_b) + (n/E') \tag{3}$$

(in addition to two uninteresting solutions at $T = T_b$ and $T = 0$ K).

Changing the variable to $x = (E'/T) - (E'/T_b)$ gives the peak reaction rate, w_p, and normalising by dividing by the initial reaction rate in the unburned state gives

$$(w_p/w_u) = (n/x_u)^n \exp(x_u - n). \tag{4}$$

The lower absolute limit to preheating is set by prereaction of the reactants in the heat exchanger. In practice, this generally necessitates an increase in flow velocity. The preheating reaction rate usually does not follow the same rate law as that which applies in the flame, because of the absence of flame-generated radicals. The fact that, for ignition, the required radicals have to be generated ab initio and in situ provides a safety margin for the calculation employing the flame rate law, which follows. Let us set the condition for maximum permissible prereaction arbitrarily at $(w_p/w_u) = 100$. A further generous safety margin is provided by the volume of the combustion chamber, the corresponding gas residence time being much greater than the corresponding quantities for the hot mat heat exchanger; the above criterion should be multiplied by the appropriate ratio of these residence times. Taking natural logarithms in Eq. (4) for the above ratio of 100,

$$n \cdot \log_e(n/x_u) + x_u = 4.6 + n. \tag{5}$$

This equation can be solved numerically; for the limited range of n, which represents reasonable values of reaction orders, the solution is

$$x = 5.51 + 2.14n. \tag{6}$$

Thus, the limiting preheat temperature, $T_{u,\max}$, is given by

$$T_{u,\max} = \left[\frac{1}{T_b} + \frac{1}{E'}(5.51 + 2.14\,n)\right]^{-1}. \tag{7}$$

For the case of methane, much previous data is available: taking $E' = 24{,}000$, $n = 1$ [9] and the constant value at the upper stability limit of $T_b = 1500$ K (a compromise between Refs. 6 and 7); $T_{u,\max} = 1{,}015$ K. In heat-recirculating burners with adequate residence time in the reaction zone, the stability limit has been found [6] to be governed by a relationship very similar to that representing the variation of the limit of flammability with initial temperature. If we approximate by writing

$$\text{limiting vol.\% } CH_4 = (1500 - T_u)/228 \tag{8}$$

or

$$f_{\text{limiting}} = 0.69 - T_u/2166 \tag{8a}$$

the leanest attainable methane content is 2.1%, or the minimum $f = 0.22$. Although leaner mixtures have previously been burned in the most efficient heat-recirculating burners, apparently without prereaction, confirming the generous margin allowed by the above assumptions, this prediction is substantially below values attained in the present work. It provides

a target for further improvements in flame stability and theoretically attainable radiant efficiencies.

We can also use the above theoretical model to estimate the maximum preheat-induced increase in blow-out rate for each fixed reactant concentration. The ratio (w_p/w_u) used to calculate the maximum prereaction condition relates solely to the temperature rise across the flame. However, w_u itself changes rapidly with the variable preheat temperature, T_u. To calculate the increase in reaction rate and, hence, the blow-out velocity that preheating by heat recirculation makes possible, we need to refer the maximum reaction rate to a constant value—here, taken as the initial reaction rate w_0 at room temperature T_0. The ratio of the initial reaction rates at preheat temperature T_u to that at T_0 is

$$\frac{w_u}{w_0} = \left(\frac{T_0}{T_u}\right)^n \exp\left[\frac{E}{R}\left(\frac{1}{T_0} - \frac{1}{T_u}\right)\right]. \tag{9}$$

Multiplying $(w_{p,u}/w_u)$ by Eq. (9) and assuming that, for these dilute mixtures, the temperature rise due to reaction is independent of preheat gives

$$\frac{w_{p,u}}{w_{p,0}} = \left(\frac{T_{b,0} - T_0}{T_{b,u} - T_u} \cdot \frac{T_{b,u}}{T_{b,0}}\right)^n \exp\left[E'\left(\frac{1}{T_{b,0}} - \frac{1}{T_{b,u}}\right)\right]$$

$$= \left(\frac{T_{b,u}}{T_{b,0}}\right)^n \exp\left[E'\left(\frac{1}{T_{b,0}} - \frac{1}{T_{b,u}}\right)\right] \tag{10}$$

where the second suffix stands for the prereaction state (u for preheated, 0 for unpreheated). The final flame temperature corresponding to the maximum preheat temperature without prereaction (Eq. (7)) is 795 K. Substitution into Eq. (10) gives this absolute maximum ratio as 2.74×10^6. This is a measure of the benefit that heat recirculation confers on flame stability. The actual numbers are somewhat academic because one consequence of these large ratios is that, without preheat, no flame would be stabilisable in this mixture (the composition corresponds to substantially less than half the flammability limit).

Industrial Systems

Figure 1f shows a representative example of multi burner industrial designs based on the principle illustrated in Fig. 1d. Depending on whether the object to be heated is a pipe or a strip of plate, for example, the system may be either axisymmetric or two-dimensional. A load to be heat treated may traverse through the furnace, in which case leakage of products or ambient gas at the points of entry and exit must be minimised. This can be achieved by avoiding a pressure differential across these partitions by balancing compression at the reactant inlet against suction at the product exit. In the case of the axisymmetrical systems, the convective component of heat transfer to the load and hence the proportion of heat left for recirculation can be varied, to some extent, by introducing swirl around the axis. In addition to natural gas, burners have been operated with blast furnace and coke oven gas.

Conclusions

1. By recirculating heat from products to reactants and, particularly, by using for this purpose the high thermal conductivity of the radiating mats themselves, very substantial improvements in radiant and useful output efficiencies have been obtained. Radiant efficiency could be improved from under 15 to 65% and overall heating efficiency (including convective transfer to the top plate) to 90%.
2. It is possible to burn much poorer fuels and/or leaner mixtures by this means. The lean stability limit has been lowered from 5.6 to 3.6% methane by volume in mixture with air, for example.
3. A theory based on the highly stirred reactor concept has been developed, applied to estimate the ultimate limitations due to prereaction and blow-out, and compared with experimentally achieved enhancements. It implies that further improvements are possible, in principle.
4. The method of heat recirculation developed, based on conduction within multiple mats, lends itself to achieving the required heat transfer in very short flow paths. This has led to developments of practical burners for specific purposes. The use of blast furnace gas as fuel has been demonstrated.

Acknowledgments

We thank the NKK Corporation for support of this study and Dr. F. B. Carleton for experimental help.

REFERENCES

1. Tidball, R. K., Kendall, R. M., and Kennedy, J. M., *Twelfth Annual Energy Sources Technology*, ASME PD, 1989, Vol. 25, p. 85.
2. Kawaguchi, O., Otoh, T, Nakamura, S. A., Todoroki, A., and Y. Murayama, Y., *Twenty-Third Symposium (International) on Combustion,* The Combustion Institute, Pittsburgh, 1990, p. 1019.
3. Zabielski, M. F., Freihaut, J. D., and Egolf, C. J., *ASME Publication: Fossil Fuel Combustion,* PD—Vol. 33:41 (1991).
4. Nakamura, S., Murayama, Y., and Todoroki, A., *De-*

velopment of High Radiant Fibre Mat Burner, NKK Technical Review, Paper No. 60, 1990, Vol. 45.
5. Weinberg, F. J., *Advanced Combustion Methods,* Academic Press, London and New York, 1986.
6. Jones, A. R., Lloyd, S. A., and Weinberg, F. J., *Proc. R. Soc.* A360:97 (1978).
7. Gover, M., Kermani, N., and Weinberg, F. J., *Combust. Sci. Technol.,* 72:1, (1992).
8. Barat, R. B., *Combust. Sci. Technol.,* 84:187 (1992).
9. Westbrook, and Dryer, *Combust. Sci. Technol.,* 27:31 (1981).

COMMENTS

Lawrence Kennedy, The Ohio State University, USA. A series of papers on using porous materials to recirculate energy to the incoming gases has been published by Echigo. These date to 1983, and the latest 1994 [*Int. J. Heat Mass Transfer* 36 (1994)]. While his work employs an alternating flow configuration, it has many similarities in its applications.

Author's Reply. No response required.

Twenty-Fifth Symposium (International) on Combustion/The Combustion Institute, 1994/pp. 277–289

INVITED LECTURE

COMBUSTION SCIENCE FOR INCINERATION TECHNOLOGY

JOST O. L. WENDT
Department of Chemical Engineering
University of Arizona
Tucson, AZ 85718

The major impediments to public acceptance of incineration as a waste disposal technology are emissions of organic compounds, dioxins, and toxic metals. Combustion science provides insight into mechanisms governing each of these three issues. It accomplishes two things: It identifies potential problems before they occur in the field, and it proposes solutions to known problems after they have occurred. In this paper, the practical relevance of combustion science to incineration technology issues is reviewed, and important gaps and needs are identified.

Turbulent mixing plays a most important role in the destruction of organic wastes in practical units. Emissions of products of incomplete combustion are also more often governed by the effects of physical combustion processes on kinetics, rather than by chemical kinetics alone. For example, incinerator failure modes can arise through wayward trajectories of rogue droplets after atomization, or, in rotary kilns, through the formation of puffs, caused by the transient release of waste from containerized sorbents and subsequent incomplete mixing. Prediction of these phenomena requires a detailed knowledge of the fundamentals of turbulent reactive flows.

Toxic metals are transformed in the incinerator environment, and the high temperatures can be exploited to allow these metals to be managed. Metal/sorbent chemistry at high temperature is not known, but it is important, since it can control the ultimate impact of these metals upon the environment.

Introduction

The impact of hazardous chemicals on the environment has become a major issue of public concern. Since the invited review on waste combustion by Seeker [1], incineration has become an even more unloved orphan technology for the disposal of hazardous waste [2]. This has not diminished interest within the combustion community, however; thus, it is appropriate to revisit the issue and to determine whether combustion science can find solutions for existing problems or merely find problems for existing solutions. The focus of this paper will be on hazardous waste incineration, rather than on municipal waste combustion, although important aspects of the latter relating directly to hazardous waste problems will also be treated.

The three major impediments to public acceptance of hazardous waste incineration are (1) air emissions of organic compounds; (2) releases of dioxins and furans (also organic, but treated separately here, for reasons described below) into the environment; and (3) the ultimate environmental impact of toxic and heavy metals, which are often present in wastes. It is therefore useful to review the potential impact of combustion science on each of these three issues.

All waste transformations occur through chemistry, and the chemical rate at which waste is destroyed will, in some way, affect how much of it remains to enter the total environment. However, chemistry may not be the only issue: Physical processes may play an equal or even more dominant role. Figure 1 depicts how both the type of waste and the method in which the waste is introduced into the system can impact the air and land environments, even in the presence of sophisticated pollution control equipment downstream of the combustion chamber. Some waste can be injected as a liquid, either into the main combustion chamber or into the afterburner. Misdirected, "rogue" waste droplets may bypass the main flame and fail to be consumed [3]. Other waste, either as solid or as liquid-soaked sorbents, is initially contained in barrels or similar containers. The containers drop into the combustion chamber, one at a time, and waste is released to form a "puff," which may or may not be consumed in the afterburner [4,5]. An emergency safety valve can release toxic products into the air, in order to protect pollution control equipment downstream during system upsets [6]. The thesis proposed here is that combustion science, which yields engineering insight into how these failure modes arise, can suggest methods either to mitigate their effects or to suggest alternative procedures that minimize risk to the public.

Emission of organic compounds may result from unreacted compounds initially in the waste or, more importantly, from by-products of incomplete com-

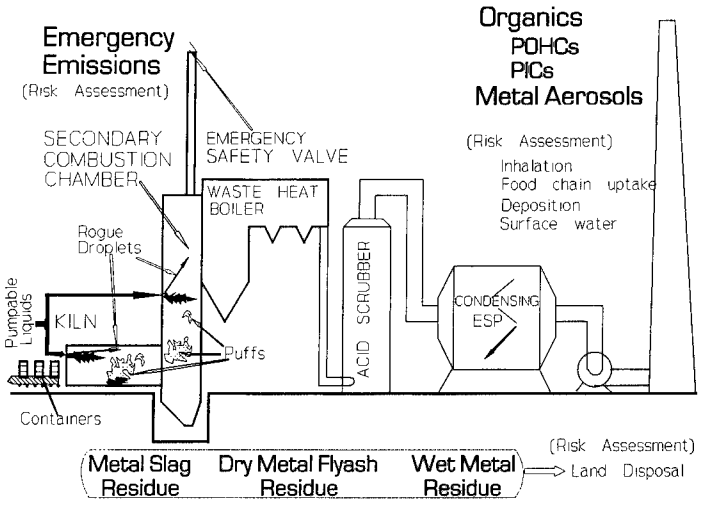

FIG. 1. Environmental impact of hazardous waste incineration.

bustion. In the United States, emission limitations are interwoven among regulations relating to both air quality [7] and hazardous waste management [8]. When total air emissions of all hazardous air pollutants from a single source fail to exceed 25 tons/year, the only specific organic compounds, whose emissions are currently regulated, are those species contained in the initial waste. This is, in part, because the list of potentially harmful organic species to be measured might be endless, while many other organic compounds, such as methane or propane, are associated with minimal health risk. It is likely, however, that the current strict European limitations on emissions of dioxins and furans, comprising an especially insidious class of organic by-products, will soon be followed across the Atlantic.

Toxic metals are transformed into various species in the combustion chamber, and conditions there may exert either a benign or a malignant influence on the impact of the metal on the total environment. Combustion conditions affect the size-segregated composition of the metal aerosol leaving the combustor and will determine the ease with which the metals may be collected. Metal speciation, with associated water leachability considerations, distributed among the slag residue and the collected fly ash will impact humans through the land and/or water environment, while the size-segregated metal speciation of the emitted aerosol impacts humans both through inhalation and through uptake via surface water and the food chain. Combustion conditions will influence the route taken, and this suggests a fruitful area for combustion science to address a problem.

Emissions of Organic Compounds

Organic compounds in the original waste are designated as "principal organic hazardous constituents (POHC's)." Emissions of these are regulated in the United States to ensure 99.99% destruction, at least during test burns. Polychlorobiphenyls (PCB's) and dioxins require 99.9999% destruction removal efficiency (DRE).

It is appropriate to revisit the field data of Trenholm et al. [9], in which the fraction of the original waste compound escaping out of the stack, after all the various air pollution control devices, is plotted against the concentration of the waste in the feed (Fig. 2). Data were from eight different full-scale incinerators, operated at various conditions. The field data (open symbols) show that the overall waste destruction process is not first order, but rather second order, with respect to waste concentration, and this is in contrast to what one would expect from kinetic considerations when free radical concentrations are largely determined by combustion of the primary (waste-free) fuel. Lyon [10] has shown that free radical branching is diminished at low concentrations of combustibles, but the low waste concentrations here do not correspond to low concentrations of combustibles because of the primary fuel. Using a detailed kinetic mechanism developed by Ho and Bozelli [11], Barat has explored the role of chemical kinetics on the effect of initial waste concentration (in a premixed mixture of CH_2Cl_2, CH_4, and air) in perfectly stirred/plug flow reactor configurations [12]. Figure 2 shows results both for the effluent from a perfectly well-stirred reactor (dashed line) and for the effluent from a subsequent plug flow reactor with heat loss (dotted line). Although *macromixing* considerations do influence the waste destruction behavior, the (pseudo) second-order behavior in the field data is not apparent from the *premixed* detailed gas-phase kinetic calculations, which do not consider *micromixing* complications. It does, however, appear in the prototype, *turbulent diffusion* flame data of Kramlich

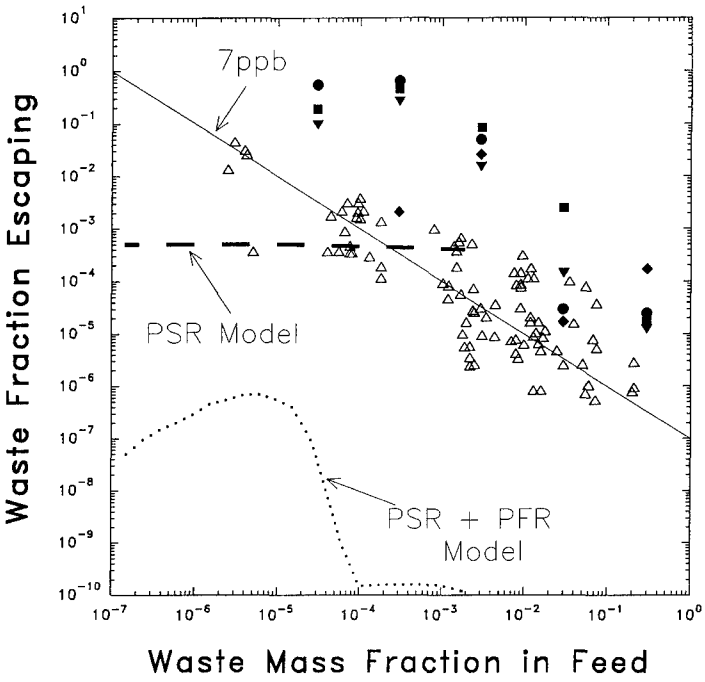

FIG. 2. Organic emissions. Destruction of original waste compound. Open symbols, △, denote field data from eight full-scale incinerators [9]. Dashed and dotted lines denote kinetic modeling results of perfectly stirred reactor (PSR Model) and PSR plus plug flow reactor (PSR + PFR model) configurations, respectively [12]. Shaded symbols, ●, ■, ▼, and ◆, denote laboratory data describing destruction of four different wastes in a prototype turbulent diffusion flame [13].

[13], also shown on Fig. 2 (shaded symbols, with each symbol representing a different waste compound). The implications here are quite profound, since the data indicate a concentration floor (about 7 ppb for the field data [13], but somewhat higher for the lower-temperature laboratory data) below which emissions cannot be lowered. Is this limit a *fundamental* constraint in turbulent mixing processes? What are the factors that affect its value? Kramlich [13] has proposed a qualitative hypothesis involving local equilibria in a heterogeneous mixture, but recent modeling approaches to turbulent mixing [14] might allow this to be quantified and, therefore, should be performed.

The major problem regarding organic emissions from incinerators is not the lack of destruction of the original waste compound, but, rather, the formation of a plethora of organic, possibly toxic or mutagenic, by-products, otherwise known as products of incomplete combustion (PIC's). The perception is that these by-products may be more harmful than the original waste, yet it is not practical to attempt to isolate and measure each organic species known to be harmful. One useful approach to address this issue is to merge combustion science with toxicology, with a view to determining how waste composition and combustion conditions influence the mutagenicity of compounds contained in the emissions. Thus, the way the incinerator or combustor is operated can (hopefully) be directly tied to the human health risk, including that of cancer. This approach requires an inexpensive, rapid test that can be related to mutagenic risk to humans. Such a test is the Ames Test. In this test, the "detector" consists of mutated salmonella bacteria (*salmonella typhimurium* TA98 (+S9)). Upon contact with the organic chemical, the number of these that revert back to their original form can be correlated with potential mutagenic risk of that chemical to humans. Figure 3 shows data [15] relating mutagenic activity (per unit of fuel burned) to combustor/incinerator size. Clearly, the larger-sized equipment has more complete combustion and, hence, fewer pyrolysis compounds, which are

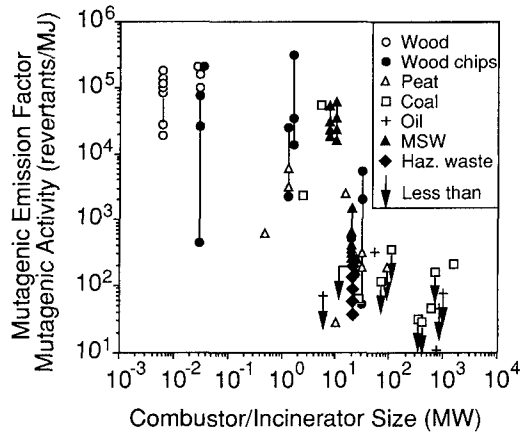

FIG. 3. Organic emissions. Products of incomplete combustion. Mutagenic emission factors [15].

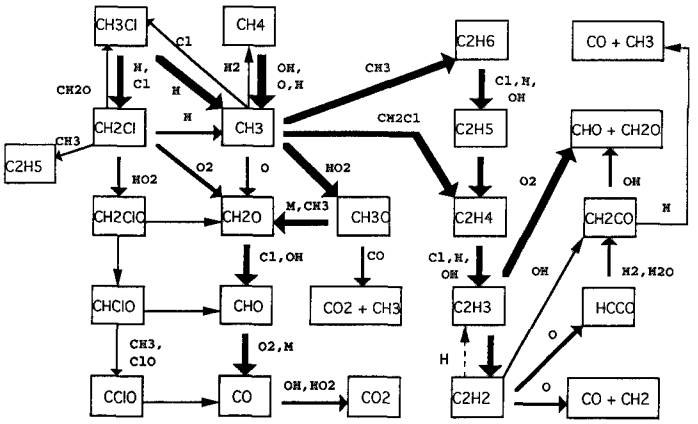

FIG. 4. Reaction chemistry. Kinetic paths in the destruction of chlorinated hydrocarbons [12,18].

expected to be high in mutagenic activity. Note the relative roles of biomass combustion (wood and wood chips) at 5×10^4 revertants/MJ compared to hazardous waste incinerators at 1×10^2 revertants/MJ. Recent combustion research by Mulholland et al. [16] has shed light on the role of chlorine on the mutagenicity of combustion by-products. At high pyrolysis temperatures, chlorine enhances the formation of nonchlorinated aromatic mutagenic compounds. At low pyrolysis temperatures, however, chlorinated hydrocarbons appear to form a new class of chlorinated organic mutagens. Other research [17], conducted in the course of a fruitful collaboration between both engineering and health risk assessment laboratories of EPA, has classified the mutagenic emissions from rotary kiln puffs (with no afterburner); from pesticide incineration, with and without NO_x abatement technology; from residential heating, industrial and utility boilers burning oil, coal, and wood; from municipal waste combustors; and from the field burning of agricultural plastic. Agricultural plastic formed 2.5×10^5 revertants/MJ of heat, similar to residential wood stoves. Puffs from polyethylene and toluene/sorbent wastes formed 1.9×10^4, and 14×10^4 revertants/MJ, respectively. The other sources were substantially lower in mutagenic emissions.

Kinetic Limitations

Recent years have seen very significant advances in the development of validated, detailed chemical reaction sets governing the fate of chlorinated hydrocarbons [11,18–25]. Senkan [20] has compiled a survey of rate constants in the C/H/Cl/O system. A prototype set for the combustion of methyl chloride with methane [11,18] is found on Fig. 4. In this reaction scheme, which was also used for the kinetic modeling results shown in Fig. 2, the more dominant reaction paths are denoted by the thicker arrows. The presence of a chlorinated hydrocarbon has two important effects. First, it enhances and accelerates CH_4 conversion to higher hydrocarbons (C_2H_y), the subsequent oxidation of which constitutes an important route to CO. Second, it leads to significant concentrations of HCl, which scavenges OH, and thus effectively retards CO burnout. The first effect is consistent both with the high-temperature pyrolysis data of Mulholland et al. [16], showing enhanced production of mutagens, and with the observed enhancement of soot formation [25], due to the presence of chlorine. Incinerator failure modes through kinetically controlled limitations also can arise through wall quenching of reactions and through the low combustible concentration limit identified by Lyon [10]. Under well-mixed conditions, the latter limitation can be overcome through the addition of clean fuels to re-establish radical chain branching.

Physical Mixing Limitations

Physical mixing limitations have already been discussed with respect to the Trenholm field data in Fig. 2. Here, two quite different, but insightful, examples of mixing-limited failure modes are presented, namely, the examples of rogue droplets and transient puffs. There are doubtless other examples, but these two are chosen here because they serve to demonstrate how facets of combustion science are able to contribute to incineration technology.

Rogue Droplets:

Atomization is not ideal and produces a distribution of droplet sizes. Larger droplets (300 μm or greater) tend to gather at the edge of atomizer sprays, and those droplets also contain appreciable momentum. Droplets become rogue when they bypass the very hot flame zones (see Fig. 1) frequented by the rest of the "herd" and proceed to the cooler regions

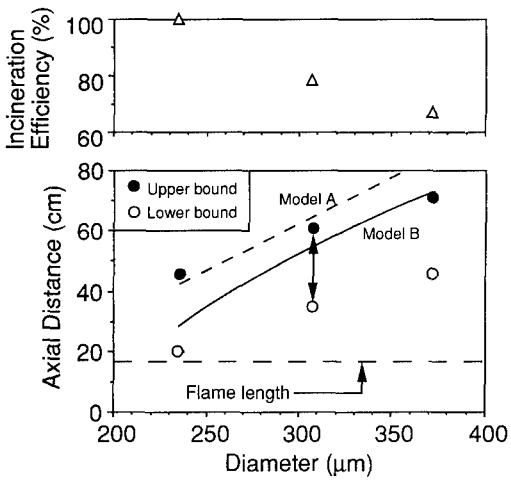

FIG. 5. Rogue droplets. Measured burnout (△) and upper (●) and lower (○) bounds of droplet trajectory endpoints in an IFRF Type II (high swirl) turbulent diffusion flame. Dashed line (Model A) denotes predictions of droplet trajectory axial endpoints, using measured mean velocity field, but otherwise no adjustable parameters. Solid line (Model B) represents model predictions with different droplet burning rate parameter, obtained from a companion experiment [3].

where they may be incompletely consumed and, thus, are more likely to cause harm to humans. One would like to be able to predict the trajectory of potential rogue droplets so that the probability of incomplete droplet burnout and subsequent PIC formation can be ascertained. One might hypothesize that with the ready availability of computational fluid dynamic models to predict the mean velocity flow field, it should be a simple matter to superimpose the equations of droplet motion in order to calculate droplet trajectories and burnout points. Unfortunately, Mulholland et al. [3] have shown that the problem is not that simple, and turbulent fluctuations must also be predicted and taken into account. Results shown in Fig. 5 depict droplet endpoints when a uniform, monosized stream of droplets was injected, at uniform velocity and angle, into a 100-kW laboratory combustor to just pass by a turbulent diffusion flame. The significant point is that there exists a large spread between maximum and minimum values of droplet penetration. A model, based on mean gas velocities, is not adequate, and what is needed is a more direct simulation of turbulent fluctuations so that risk of droplet bypassing can be properly calculated. Fig. 5 also shows that average burnout decreases as rogue droplet penetration increases.

Transient Puffs:

When contained liquid wastes bound on sorbents are introduced one container at a time into a rotary kiln environment, the liquid is rapidly released and forms a "puff," which can travel through the afterburner and cause a transient failure mode. The issue here is to relate the amount of waste, waste properties, sorbent properties, and container design to puff intensity (instantaneous combustible exhaust concentration) and puff magnitude (integrated "unsatisfied oxygen demand"). Research on rotary kiln phenomena at the University of Utah has focussed on the release of hydrocarbons from contaminated soils [26] and on scale-up of the heat-transfer aspects [27]. Analysis of full-scale rotary kiln behavior was completed by a group from Louisiana State University [28], who showed that severe stratification throughout the kiln length was a severe problem. For the convenience of this author, the focus of discussion here will be the work conducted at the Environmental Protection Agency (EPA) [4,5,29–31]. The EPA work first consisted of parametric studies on a 73-kW rotary kiln incinerator simulator. It was found that puff could be very easily formed by even the smallest amounts of waste (Fig. 6) and that puff magnitude increased with increasing temperature and kiln rotation speed (Fig. 7) [5,29,30].

A prototype model of the release of liquid waste from sorbent clumps [29–31] was able to describe the overall puff features observed (overall timescales of minutes, containing multiple peaks of puff intensity, see Fig. 6). The model consisted of two parts: heat transfer to and mass transfer from a sorbent clump, followed by discrete surface renewal events that depended on kiln rotation speed. This model was able to support and rationalize the data (see Fig. 7), which indicated, for example, that puff magnitude increased with temperature and with kiln rotation speed. Both phenomena are due to enhanced waste release rates: increased temperature increases the driving force for mass transfer of waste out of the sorbent; increased kiln revolutions per minute (rpm) exposes more fresh, waste-saturated sorbent to the surface and, thus, lowers the effective resistance to mass transfer. The research helped rank wastes in terms of boiling point and oxygen demand and allowed extrapolation to other sorbents and other containers. One practical application of this experimental and theoretical research has been the development of low puff-generating containers [31], which modulate the rate at which new surface in the sorbent clumps is exposed to the kiln. Another application has been to devise more appropriate (with less risk to the public) emergency safety vent procedures [6]. Both applications to incineration technology were possible because of engineering insight gained through combustion science, i.e, through looking at the complicated problem, not in all its detail, but rather, in terms of a fundamental prototype that replicated its key features.

A key issue, only now being addressed, is how to scale-up results from the 73-kW EPA simulator to

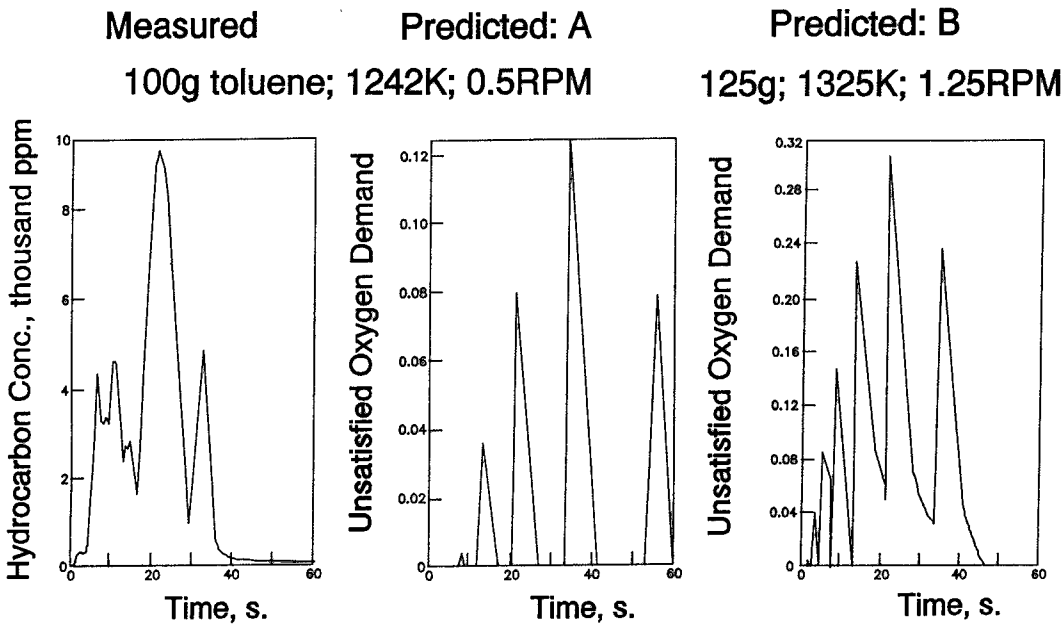

FIG. 6. Transient puffs. Measured and predicted toluene puff shapes. Measured hydrocarbon trace and predicted trace, A, are for 100 g toluene on sorbent, with kiln at 1242 K and 0.5 RPM. Predicted trace, B, is for 125 g toluene with kiln at 1325 K and 1.25 RPM [29].

full-scale units. This requires a method to quantify mixedness in the gas phase and current work, using a cold flow physical model, and an application of Kerstein's linear eddy model [14] shows promise in being able to predict intensity of segregation, I, defined by Danckwerts [32]

$$I = \frac{(c')^2}{C(1 - C)}$$

as a function of space, time, and kiln-operating parameters [33]. The quantity c' represents a concentration (mole fraction) fluctuation, and C represents the mean mole fraction of, say, gaseous toluene waste in the main flow. During generation of a puff, values of $I = 0.01$ are typical [33], which (with assumptions of a Gaussian probability density function and instantaneous chemical reaction rates) corresponds to an unburned fraction of toluene of 10%, even at 50% overall excess air (SR = 1.5). Full-scale kilns have significant stratification [28], and this must also be considered in attempting any scale-up methodology for gas-phase mixing.

A conclusion to be drawn from both these examples of rogue droplets and transient puffs is that there is an urgent need to develop models that quantify, predict, and scale-up the turbulent mixing process in the gas phase. This is a challenging undertaking, addressing, as it does, that one of the most complex unsolved problems is combustion science, namely, that of unmixed turbulent combustion. Recent work [34] from the EPA-funded Northeast Hazardous Substance Research Center uses linear eddy modelling together with detailed chemical kinetics and suggests that the organic speciation measured in the exhaust can be related to the (kinetic or mixing) failure mode that occurred in the combustor. If successful, this approach could have profound implications and points to yet another application of combustion science to incineration technology.

Dioxins

No discussion of incineration issues would be complete without some acknowledgment of the importance of emissions of polychlorinated dibenzo-*p*-dioxins (PCDD) and polychlorinated dibenzofurans (PCDF). These compounds have been considered extremely toxic and somewhat mutagenic, and most significantly, they have been linked to suppression of the immune system in humans. Their appearance in Lake Huron core samples correlates very well with the temporal data on production of chloroaromatics, starting in 1940 [35]. Critical reviews of the role of dioxins in hazardous waste incineration and in cement kilns cofired with hazardous wastes have been compiled by Helble [35] and Dellinger et al. [36], respectively.

All dioxins are not alike. There are 75 dioxin con-

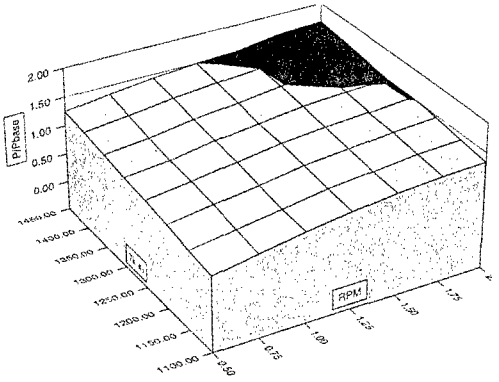

Predicted

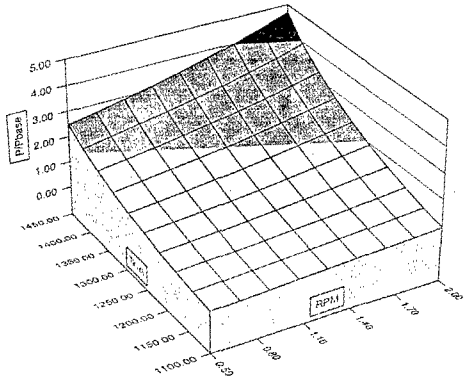

Measured

FIG. 7. Transient puffs. Predicted (upper) and measured (lower) effects of kiln temperature and kiln rotation speed on relative puff magnitude, P/P_{base} [31].

geners and 135 furan congeners. By far, the most toxic is 2,3,7,8 Tetra Chlorinated Dibenzo-p-Dioxin (TCDD). Emissions may be regulated in two ways: in toxic equivalent (TEQ) ng/dscm and in total dioxins/furans. Data from municipal waste incinerators, medical waste incinerators, cement plants, and hazardous waste incinerators show a ratio of TEQ/total equal to approximately 0.02 (i.e., 30 ng/dscm total dioxin/furan = approximately 0.6 ng/dscm TEQ), although this ratio depends on the mix of dioxin species created, and this varies slightly from unit to unit. Total PCDD/PCDF in the exhaust correlate poorly with ash in the feed and somewhat better with the chlorine feed rate. They correlate very well with temperature at the inlet of the particulate control device, suggesting that formation occurs there [35].

The primary, but possibly not the only, route to dioxin formation appears to be through catalysis in the air-pollution control device. There are homogeneous routes as well [4], but these require fuel-rich zones, as in transient puffs. The most likely route, in practice, appears to be through catalysis, especially on copper chloride ($CuCl_2$), although it is probable that other copper-based catalysts also play a role. The catalyst allows the formation of Cl_2 (from HCl via the Deacon reaction), which is a critical intermediate in the process. The catalytic process is strongly inhibited by sulfur [37] or rather high ratios of S/Cl. The low values of copper and of carbon in the fly ash and the high values of sulfur (relative to Cl) in coal combustion flue gases all serve to explain why dioxin formation is less of a problem in utility boilers than in incinerators. The catalytic formation of PCCD competes with its oxidation, suggesting an optimum temperature window, at 300 °C. Combustion conditions in the combustor play important roles in forming most probable precursors, such as 2,4,5 trichlorophenol. *De-novo* synthesis from a carbonaceous compound as simple as CO_2 and/or carbon residue in the ash is also possible but less likely. Indeed, a list from the most likely to the least likely catalytic precursors would be as follows: (1) 2,4,5 trichlorophenols; (2) halogenated aliphatics; (3) benzene + $AlCl_3$; (4) alkanes + HC; (5) carbon residue + HCl; (6) CO_2 + HCl. Data [35,36] show that many cement kilns and commercial incinerators operate with very low dioxin emission levels, and so current research is directed toward quantification of these mechanisms. From a combustion science point of view, current research is also directed toward determination of a suitable, more easily measurable, surrogate hydrocarbon compound in order to replace the slow and expensive analyses of collected samples for PCCD.

Toxic and Heavy Metals

Metal emissions from hazardous waste incinerators are regulated in the United States by both Title III of the Clean Air Act Amendments [7] and by a human risk-based analysis. Table 1 [38] lists those metals that are controlled and provides calculated, hypothetical, emission limits, based on the risk-based assumptions listed. Note that carcinogens are more tightly regulated than noncarcinogens. However, speciation of the metal is of critical importance, since that determines the ease with which they will ultimately enter the air, water and soil environments. Toxic metal air emissions from cement kilns cofired with hazardous wastes have been evaluated by Dellinger et al. [36], while Linak and Wendt [38] provide a review of mechanisms underlying toxic metal emissions from incinerators.

Metal Volatility:

The fact that many toxic metals will vaporize during combustion has been reported elsewhere

TABLE 1
Proposed RCRA metal emission limits for a hypothetical 8.8 MW rotary kiln incinerator corresponding to a Tier II analysis[a]

Carcinogenic metal[b]	Emission rate (g/h)	Concentration[c] (mg/Nm^3)	Concentration[d] dry, 11% O_2 (mg/Nm^3)
As	0.82	0.051	0.056
Be	1.5	0.093	0.103
Cd	2.0	0.12	0.14
Cr[e]	0.30	0.019	0.021

Noncarcinogenic metal	Emission rate (g/h)	Concentration[c] (mg/Nm^3)	Concentration[d] dry, 11% O_2 (mg/Nm^3)
Sb	110	6.8	7.5
Ba	18,000	1,110	1,230
Pb	32	2.0	3.6
Hg	29	1.8	2.2
Ni	7,300	450	500
Se	1,500	93	103
Ag	1,100	68	75
Tl	111	6.8	7.5

[a]Based on 8.8 MW, 16,200 Nm^3/h flow rate (100 % excess air), rural location, noncomplex terrain, no impinging structures, 15.25-m stack height, 355 K stack gas temperature.

[b]Carcinogenic metal emissions resulting in 1 unit risk. Note that the *sum* of carcinogenic metals risk may not exceed 1 unit risk.

[c]Emission rate divided by volumetric flow (wet), not corrected to dry, standard oxygen conditions. Calculated stack gas contains 10% water and 11% oxygen.

[d]Corrected to dry, 11% oxygen conditions (EC convention).

[e]RSD refers to Cr^{+6} compounds only. Cr^{+3} compounds are not included. However, all chromium is considered Cr^{+6} unless site-specific speciation is performed.

[1,36,38]. The ensuing metal vapors will then either nucleate at the lower temperatures downstream, to form tiny particles less than 0.1 μm in diameter, or condense around existing larger particles. Mercury usually fails to condense at all, but its emission is of greater importance in both coal and municipal waste combustion [38] than in hazardous waste incineration. The presence of chlorine has a great influence on metal speciation and metal volatility [38–42]. The practical result of this is that chlorine will lower the dewpoint of the metal, maintain it in the vapor form for longer times until cooler parts of the combustor are reached, and lead to a less mature aerosol containing more submicron particles in the exhaust. The data of Linak et al. [39] are significant, since they suggest that nickel, normally present as a refractory solid metal oxide even under combustion conditions, is vaporized in the presence of chlorine. Eddings and Lighty [43] have shown, on the other hand, that metal release from heated soils does not follow simple equilibrium calculations that fail to consider aluminosilicate compounds. Dellinger et al. [36] present data that show that very much less cadmium, a volatile metal, was emitted into the air than that added to the input of a cement kiln, and this suggests that high combustion temperatures can also serve to combine metals with other substances.

Metal Scavenging by Sorbents:

Metal vapors and larger sorbent particles can interact in various ways. At temperatures below the metal dewpoint, the metal will physically condense around existing particles to form a $1/d_p^2$ dependence of metal concentration in the continuum regime, when particles are much larger than the gas mean free path, or a $1/d_p$ dependence in the Knudsen free molecular regime, when they are not. This is shown

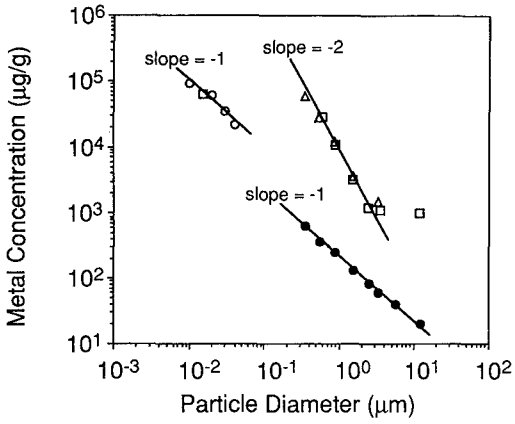

FIG. 8. Metal emissions. Concentration/particle size consequences of film condensation and surface reaction of metal vapors. Open symbols: sodium [44, 45]; shaded symbols: arsenic [45].

for sodium on coal fly ash in Fig. 8 [44]. If the metal speciation in the gas phase is water soluble, i.e., as for sodium, the condensed film will most likely also be water soluble. Calculations have shown [38] that coagulation between a nucleated metal vapor and a dispersed sorbent is slow, does not serve to scavenge the metal, and is not important.

At temperatures well above the dewpoint, metal vapors can chemically react with the surfaces of particles in the disperse phase. This yields a $1/d_p$ dependence for metal concentration in sampled particles for both exterior surface-controlled and interior pore diffusion-controlled reactions, where reaction occurs close to the exterior surface. The data of Haynes et al. [45] are especially significant, for they indicate that small quantities of arsenic, present in coal, can be reactively scavenged above the dew point by coal fly ash to yield a $1/d_p$ dependence (in the continuum regime), as shown in Fig. 8. Arsenic is known to react with calcium to form $Ca_3(AsO_4)_2(s)$. A weak, or zero, particle size dependence, as found by Scotto et al. [41] for the lead/kaolinite system in combustor postflame gases, suggests no pore diffusion limitations.

Uberoi and Shadman [46,47] have shown in bench-scale thermogravimetric reactors that lead reacted with aluminosilicates in kaolinite to form $PbO.Al_2O_3.SiO_2$ and that this process is enhanced when melting of the surface layer occurs. Cadmium also reacted with bauxite to form crystalline $CdO.Al_2O_3$, with no melting. In the absence of melting, uptake of cadmium on kaolinite was low, because of pore plugging. Scotto et al. [41,42] showed that lead uptake by kaolinite in a downflow combustor was diminished by chlorine. Chlorine serves to lower the concentration of the (likely) reactive metal species, which are the oxides or hydroxides. In the presence of

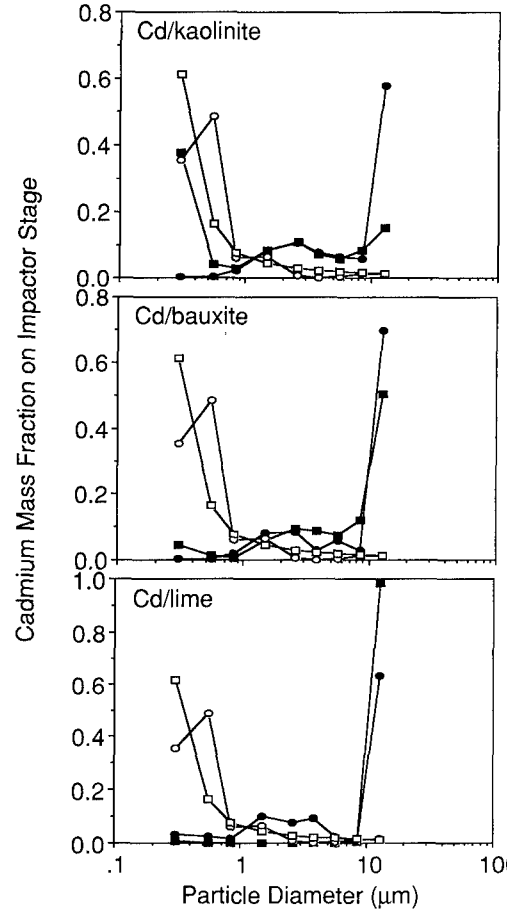

FIG. 9. Metal emissions. Interactions between cadmium and various sorbents in a semi-industrial scale, 82 kW, swirl flame incinerator [48]. Impactor mass fraction distribution for (top) Cd/kaolinite/Cl system; (center) Cd/bauxite/Cl system; and (bottom) Cd/hydrated lime/Cl system. ○ Cd baseline; □ Cd/Cl; ● Cd/sorbent; ■ Cd/sorbent/Cl.

a small amount of chlorine, lead that did not react with the substrate was water soluble, while lead that did react was water insoluble [41]. Thus, the high combustor temperatures can be exploited to help isolate the metal from both air and water environments.

Recent data obtained at the EPA, to be presented at this symposium [48], have shown that toxic metal scavenging at high incinerator temperatures is more efficient than bench-scale reactor studies suggested. Figure 9 shows that at combustor temperatures, cadmium not only is very effectively captured by bauxite but also by kaolinite (in contrast to Ref. 47) and also by lime, where no obvious reaction product exists. Figure 9 also shows how chlorine enhances small particle formation without sorbent present, but it can diminish scavenging effectiveness, at least for the Cd/

A: Mechanism I

Bauxite/Cd/Cl
Reaction/Crystal

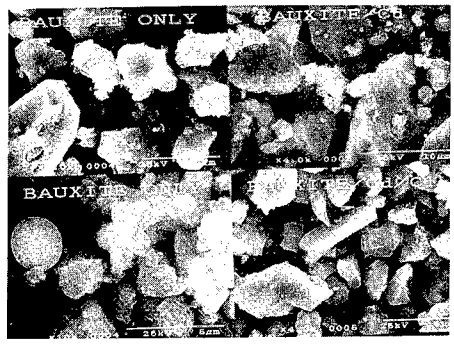

B: Mechanism II

Kaolinite/Cd/Cl
Kaolinite/Pb/Cl
Reaction/melt

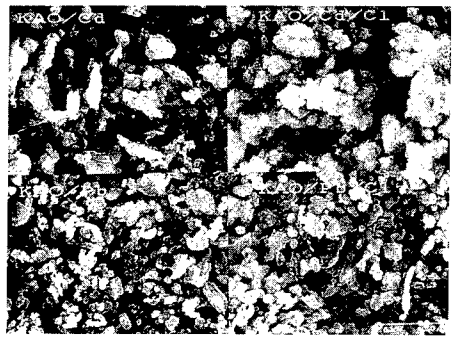

C: Mechanism II

Lime/Cd/Cl
Solution/melt

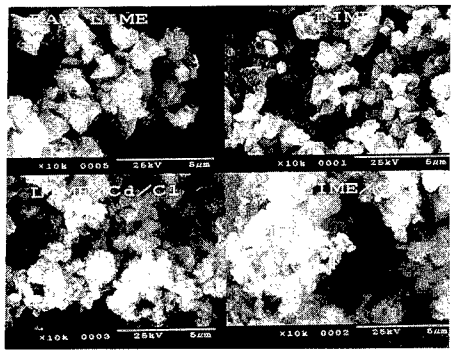

FIG. 10. Metal emissions. Scanning electron micrographs of captured metals, shown (in part) in Fig. 9.

bauxite and Cd/kaolinite systems. There appear to be two fundamentally different mechanisms for cadmium capture, as shown on the scanning electron micrographs in Fig. 10. Those labeled as "bauxite only" or "lime" show morphology of the sorbent alone after passing through the combustor with neither metal nor chlorine present. The other labels are self-explanatory. Mechanism I forms a crystalline product of reaction (say, $CdO.Al_2O_3.SiO_2$ or $CdO.Al_2O_3$), and this process is effective in the absence of pore plugging, i.e., for the Cd/bauxite system. Mechanism II comes into play at high temperature when pore plugging is an issue, as in the Cd/kaolinite system at moderate temperatures [47]. At high incinerator temperatures, melting at the surface overcomes this resistance, and a reaction/melt process takes place. With the Cd/Lime system, the melt is formed by the act of dissolution of the metal into a eutectic. Thus, mechanism II has the potential to allow reactive scavenging of multiple metals and does not require crystalline reactive sites. The high temperatures are benign, since they serve to isolate the toxic metal from the environment, rather than allow it to be dispersed into the air.

Conclusions

The major issues regarding incinerator technology are emissions of organics, dioxin, and toxic metals. Combustion science provides useful engineering insight that can be used to resolve these issues. Bioassay analyses of collected emissions provide insight relating health risk to waste composition and combustion conditions. Organic emissions from incinerators are largely determined by physical processes (coupled with kinetics) rather than chemical kinetics alone. Prediction of (possible) failure modes will require (direct) simulation of turbulent fluctuations rather than that of turbulent mean flows alone. Likewise, prediction and assurance of complete and safe destruction of wastes by incineration requires solution of one of the more challenging problems in combustion science, namely that of turbulent reactive flows and mixing.

Dioxin emission is primarily a postflame catalytic phenomenon, although flame conditions may influence likely precursors. Sulfur is an effective poison to this catalytic activity. There is need to identify an easily measurable surrogate for dioxin, and combustion science directed toward elucidation of kinetics of formation of dioxins and their precursors may help fill that need.

The total environmental impact of toxic metals is greatly influenced by metal chemical kinetic mechanisms occurring inside the combustion chamber and beyond. Toxic metals can be managed, and it is possible to exploit the high temperatures of incineration to allow toxic metals to be reactively scavenged, on collectable and disposable commercial sorbents. At high temperatures, there are two types of toxic metal-scavenging mechanisms: (1) formation of crystalline product and (2) formation of a eutectic or reaction product melt. Combustion science can help in determining appropriate mechanisms and in developing multifunctional sorbents for many metals.

Acknowledgements

This paper would not have been possible without the long standing collaboration of William P. Linak of the Combustion Research Branch of the EPA. Many of the research results presented here originated in that laboratory, with whom the author has enjoyed an association for over a decade. Special acknowledgments are also due to Paul M. Lemieux, Brian K. Gullett, and David M. DeMarini of the EPA; James A. Mullholland of the Georgia Institute of Technology; Hubert W. Schenck of the University of Arizona; Adel F. Sarofim and G. Sacchi of MIT; Randall W. Seeker and Richard K. Lyon of Energy and Environmental Research Company; John C. Kramlich of the University of Washington; JoAnn Lighty and David W. Pershing of the University of Utah; Micheal P. Heap of Reaction Engineering International; Joseph W. Bozzelli and Robert B. Barat of the New Jersey Institute of Technology; and Joseph J. Helble of PSI Technology Inc.

REFERENCES

1. Seeker, W. R., *Twenty-Third Symposium (International) on Combustion*, The Combustion Institute, Pittsburgh, 1990, p. 867.
2. Costner, P., and Thornton, J., *Playing with Fire: Hazardous Waste Incineration*, A Greenpeace Report, Greenpeace U.S.A., Washington, DC, 1990.
3. Mulholland, J. A., Srivastava, R. K., Wendt, J. O. L., Robinson, S. B., and Lanier, W. S., *Combust. Flame* 86:297–310 (1991).
4. Linak, W. P., Kilgroe, J. D., McSorley, J. A., Wendt, J. O. L., and Dunn, J. E., *J. Air Pollution Control Assoc.* 37:54 (1987).
5. Linak, W. P., McSorley, J. A., Wendt, J. O. L., and Dunn, J. E., *J. Air Pollution Control Assoc.* 37:935 (1987).
6. Lemieux, P. M., Linak, W. P., DeBenedictis, C., Ryan, J. V., and Wendt, J. O. L., *Haz. Waste Haz. Mater.*, in press.
7. Clean Air Act Amendments, Public Law 101-549, 104 Stat. 2399-2712, Nov. 15, 1990.
8. Resource Conservation and Recovery Act, Subtitle C, Sections 3001–3013, 42 N.S.C., Sections 6921–6934 (1976) and Supplement IV (1980), Amended (1986).
9. Trenholm, A., Gorman, P., and Jungclaus, G., *Performance Evaluation of Full-Scale Hazardous Waste Incinerators*, EPA Report EPA-600/2–84–181e, available through NTIS Report No. PB 85 129542.
10. Lyon, R. K., *Twenty-Third Symposium (International) on Combustion*, The Combustion Institute, Pittsburgh, 1990, p. 903.
11. Ho, W., and Bozzelli, J. W., *Twenty-Fourth Symposium (International) on Combustion*, The Combustion Institute, Pittsburgh, 1992, p. 743.
12. Barat, R. B., personal communication, 1994.
13. Kramlich, J. C., *Combust. Sci. Technol.* 74:17 (1990).
14. Kerstein, A. R., *Combust. Sci. Technol.* 60:391 (1988).
15. Ahlborg, U. G., and Victorin, K., *Waste Manag. Res.* 5:203 (1987).
16. Mulholland, J. A., Sarofim, A. F., Longwell, J. P., Lafleur, A.L., and Thilly, W. G., *Environ. Health Perpectives Suppl.* 102 (suppl. 1):283 (1994).
17. DeMarini, D. M., Williams, R. W., Perry, E., Lemieux, P. M., and Linak, W. P., *Combust. Sci. Technol.* (1991).
18. Barat, R. B., and Bozelli, J. W., *Combust. Sci. Technol.* 1993, in press.
19. Ho, W. P., Barat, R. B., and Bozzelli, J. W., *Combust. Flame* 88:265 (1992).
20. Senkan, S. M., in "Survey of Rate Constants in the C/H/Cl/O System" (W. C. Gardiner, Jr.), *Combustion Chemistry*, 2nd ed., 1993.
21. Senkan, S. M., Yilirim, R., and Gutman, D., *Twenty-Fourth Symposium (International) on Combustion*, The Combustion Institute, Pittsburgh, 1992, p. 749.
22. Fisher, E. M., Koshland, C. P., Hall, M. J., and Lucas, D., *Twenty-Third Symposium (International) on Com-*

bustion, The Combustion Institute, Pittsburgh, 1990, p. 895.
23. Lee, K. Y., and Puri, I. K., *Combust. Flame* 94:191 (1993).
24. Tsang, W., *Combust. Sci. Technol.* 74:99 (1990).
25. Frenklach, M., *Combust. Sci. Technol.* 74:283 (1990).
26. Lighty, J. S., Eddings, E. G., Lingren, E. R., Deng, X. X., Pershing, D. W., Winter R. M., and McClennen, W. H., *Combust. Sci. Technol.* 74:31 (1990).
27. Owens, W. D., Silcox, G. D., Lightly, J. S., Deng, X. X., Pershing, D. W., Cundy, V. A., Leger, C. B., and Jakway, A. L., *Combust. Flame* 86:101 (1991).
28. Lester, T. W., Cundy, V. A., Montestruc, A. N., Leger, C. B., Acharya, S., and Sterling, A. M., *Combust. Sci. Technol.* 74:67 (1990).
29. Wendt, J. O. L., and Linak, W.P., *Combust. Sci. Technol.* 61:169 (1988).
30. Wendt, J. O. L., Linak, W. P., and Lemieux, P. M., *Haz. Waste Haz. Mater.* 7:41 (1990).
31. Lemieux, P. M., Linak, W. P., McSorley, J. A., and Wendt, J. O. L., *Combust. Sci. Technol.* 85 (1–6):203 (1992).
32. Danckwerts, P. V., *Appl. Sci. Res. A* 3:279 (1952).
33. Schenck, H., "Mixing Characterization of Transient Puffs in a Rotary Kiln Incinerator," Ph.D. Dissertation, University of Arizona, Tucson, AZ, 1994.
34. Brouwer, J., Sacchi, G., Longwell, J. P., Sarofim, A. F., "Mixing and Chemical Constraints on PIC Production during Chlorocarbon Combustion," paper presented at *Twenty-Fifth Symposium (International) on Combustion*, to be published in Combust. Flame.
35. Helble, J., *Analysis of Dioxin Emissions from the Incineration of Hazardous Waste*, Report of work performed as AAAS/EPA Fellow in the Office of Solid Waste, Permits and State Programs Division, U.S. EPA, Washington DC, Sept., 1993.
36. Dellinger, H. B., Pershing, D. W., Sarofim, A. F., *Evaluation of the Origin, Emissions and Control of Organic and Metal Compounds from Cement kilns Co-Fired with Hazardous Wastes*, Report of the Scientific Advisory Board on Cement Kiln Recycling, June, 1993.
37. Gullett, B. K., Bruce, K. R., and Beach, L. O., *Chemosphere* 20 (10–12):1945–1952 (1990).
38. Linak W. P., and Wendt, J. O. L., *Prog. Energy Combust. Sci.* 19:145–185 (1993).
39. Linak, W. P., Srivastava, R. K., and Wendt, J. O. L., *Combust. Sci. Technol.*, in press.
40. Linak, W. P., and Wendt, J. O. L., *Fuel Proc. Technol.*, in press.
41. Scotto, M. V., Uberoi, M., Peterson, T. W., Shadman, F., and Wendt, J. O. L., *Fuel Proc. Technol.*, in press.
42. Scotto, M., Peterson, T. W., and Wendt, J. O. L., *Twenty-Fourth Symposium International) on Combustion*, The Combustion Institute, Pittsburgh, 1992, p. 1109.
43. Eddings, E. G., and Lighty, J. S., *Combust. Sci. Technol.* 85:375 (1992).
44. Neville, M., and Sarofim, A. F., *Fuel* 64:384–390 (1985).
45. Haynes, B. S., Neville, M., Quann, R. J., and Sarofim, A. F., *J. Colloid Interface Sci.* 87 (1):266–278 (1982).
46. Uberoi, M., and Shadman, F., *AIChE J.* 36 (2):307–309 (1990).
47. Uberoi, M., and Shadman, F., *Environ. Sci. Technol.* 25 (7):1285–1289 (1991).
48. Linak, W. P., Srivastava, R. K., and Wendt, J. O. L., "Sorbent Capture of Nickel, Lead and Cadmium in a Laboratory Swril Flame Incinerator," paper presented at *Twenty-Fifth Symposium (International) on Combustion*, 1994, to be published in Combust. Flame.

COMMENTS

Loo Yap, BOC Group Tech. Ctr., USA. The turbulent diffusion flame data of Kramlich cited imply a mixing-limited concentration floor beyond which emissions may not be lowered. Some recent observations by us on chlorinated-hydrocarbon flames which have been submitted for publication may present an even more fundamental constraint. In these observations, mixing limitations have been completely removed by studying premixed strained laminar flames. At moderate Cl/H ratios, double-flame structures were generated; a waste decomposition flame followed by a retarded CO oxidation flame. By applying only moderate strain, the second flame can be extinguished, resulting in a large emission of partially oxidized chlorocarbons. Extending these results, using high turbulence levels to promote mixing may result in regions of high strain limiting combustion/destruction of even well premixed pockets. The required strain increased with oxygen concentrations, implying fundamental benefits to judicious use of oxygen-enriched or oxygen-based incineration.

Author's Reply. This is a most interesting comment, and I look forward to the appearance of your paper. Indeed, the effect noted may be due to turbulence phenomena related to flame stretch in both premixed systems and diffusion systems. Your results and those of Kramlich (Ref. 13) suggest that combustion conditions can influence the magnitude of this lower bound of POHC emission. This would appear to be an area in which combustion science can help answer an important practical, yet fundamental, question, namely, what exactly is the origin of the residual POHC emission from field units, and what is the lowest possible limit of this emission?

●

J. A. Kozinski, McGill University, Canada. 1. Would you please comment on the perspectives for toxic metals capture in fluidized beds and rotary kiln incineration systems.

2. Do you think that combustion process modifications rather than postcombustion treatment will play a major role as an "environmental protection tool" in the future?

Author's Reply. Toxic metals can be captured in fluidized bed systems, as has been shown by Ho et al. [1]. In rotary kiln systems, toxic metals can be captured in the slag as well as in the disperse phase. In both systems, high temperatures are exploited to render the resulting metal-containing compound to be water unleachable, and thus more benign to the overall environment. In my view, combustion process modifications will play a major role, not only in the minimization of toxic emissions from the combustion chamber, but also in ensuring that the necessary postcombustion contaminant removal equipment can never be overloaded.

REFERENCE

1. Ho, T. C., Chen, C., Hopper, J. R., and Oberacker, D. A., *Combust. Sci. Technol.* 85:101–116 (1992).

•

Lawrence A. Kennedy, The Ohio State University, USA. You discussed the problem of "puffs" in incineration technology that result from the batch loading of waste material. Can such waste be injected under a more controlled manner to reduce the "puffs"?

Author's Reply. One method is to use the special containers of Ref. 31. Even better would be to introduce liquid wastes as a constant atomized stream. However, batch introduction is often the only practical method for small quantities of liquid wastes, especially if handling is to be kept to a minimum.

•

L. Douglas Smoot, Brigham Young University, USA. In your presentation, you discussed only environmental issues relating to incineration technology. Is not the use of incineration also challenged by other technologies that are perceived to be more acceptable? For example, in order of preference, does not incineration follow recycling, conversion (e.g., gasification) and combustion (e.g., power or steam generation)? What is the appropriate role for incineration, assuming the emissions can be managed?

Author's Reply. There is no doubt that waste minimization and recycling are much preferable to waste generation and disposal. However, I believe that, although there is room for substantially decreasing the amount of waste being generated in industrial societies, there will always be a need for the disposal of some wastes. I believe that the proper incineration of toxic wastes is preferable to both land disposal and to long-term storage (as has been suggested by some). I am not convinced that other technologies, such as gasification, entail less risk to the public than does incineration. We know a lot about incineration; enough, in fact, to be able clearly to identify potential problems with it. The same can generally not be said of the other waste disposal technologies that are currently under consideration. I think that, for some time to come, there will have to be a place for incineration as a waste disposal option.

•

Horst-Henning Grotheer, DLR, Germany. Could you please comment on the possibility of burning control by using on-line analysis of selected species. To what extent could such head-end techniques be able to replace the more expensive end-of-the-pipe techniques currently in use?

Author's Reply. In my view, development of instrumentation for on-line analyses of appropriate selected species in incinerator exhaust gases is one of the most important combustion science activities currently underway. Success in this area is essential in order to gain public acceptance of incineration as an appropriate waste management technology. In-line analysis of selected species in the combustor chamber would be useful to allow combustion controls to track and mitigate transient effects caused by waste variations. Combustion science already has led to development of front-end methods that diminish the magnitude of transient puffs in rotary kilns, as described in Ref. 31.

•

John Veranth, Aptus, Inc., USA. The following should be considered critical combustion science issues:

1. Better measures of "combustion performance." Current measurements such as CO/CO_2 ratio and DRE are not representative of the fine details of the process.

2. Most research is, of necessity, done on simple systems with few components. Incineration always involves complex multicomponent mixtures. Otherwise, the material would be recycled. Techniques for dealing with the interactions in complex mixtures are needed to realistically extrapolate research results to full-scale systems.

Author's Reply. This is a good comment with which I agree.

Twenty-Fifth Symposium (International) on Combustion/The Combustion Institute, 1994/pp. 291–297

BURNING RATE ENHANCEMENT AND SOOT REDUCTION THROUGH BLENDING IN CHLORINATED WASTE INCINERATION

T. X. LI AND C. K. LAW
Department of Mechanical and Aerospace Engineering
Princeton University
Princeton, NJ 08544, USA

An experimental investigation has been conducted on the droplet combustion of mixtures of chlorinated hydrocarbons in a hot, oxidizing environment, with emphasis on binary mixtures consisting of a lightly chlorinated hydrocarbon and a heavily chlorinated hydrocarbon. The rationale is that, by using a lightly chlorinated combustible waste instead of regular fuel oils to assist in the destruction of an incineration-resistant heavily chlorinated waste, both wastes can be simultaneously destroyed without the cost expenditure for the fuel oil feed stock. Results indeed demonstrate that the heavily chlorinated tetrachloroethane (TECA) can be made to burn vigorously with the addition of only about 20–25% of the lightly chlorinated, equally volatile chloroheptane or dichlorobutane. It is further shown that this result can be approximately correlated by the mixture chlorine-to-hydrogen ratio, Cl/H, in that in the lightly to moderately chlorinated regime of Cl/H < 1, the flame temperature and hence the burning rate are only moderately reduced with increasing chlorination, and decreasing heat release, because of the reduced stoichiometric need for air. However, for the massively chlorinated regime of Cl/H > 1, the flame temperature and burning rate decrease quite rapidly with increasing chlorination because now reduction in heat release dominates. The results also show that while the lightly chlorinated hydrocarbon promotes burning of the heavily chlorinated hydrocarbon, the latter tends to substantially reduce the extent of soot formation from the former. The mutual benefit associated with the blending approach studied herein is emphasized.

Introduction

A large class of liquid hazardous wastes is halogenated hydrocarbons, of which a great many are incineration resistant [1,2]. The presence of the halogen not only lowers the heat of combustion from that of the nonhalogenated hydrocarbon, but it also tends to retard the overall oxidation rate because of scavenging of the hydrogen radicals. Thus, a viable approach toward enhancing the destruction efficiency of hazardous waste incinerators is to mix liquid fuels with the normally incineration-resistant halogenated wastes so that the resultant mixture is rendered to burn well. As such, it is of inherent practical interest to develop a rational blending strategy toward optimizing the combustion characteristics and minimizing the cost of the feed stock [3].

In response to the above interests, Sorbo et al. [4] and Sorbo and Chang [5] investigated the gasification and burning characteristics of droplets of pure chlorinated hydrocarbons (CHCs), as well as their mixtures with regular hydrocarbon fuels as represented by the normal alkanes. These studies yield the interesting results that the lightly chlorinated monochloroalkanes burn almost as well as the normal alkanes, and that the heavily chlorinated alkanes, such as 1,1,2,2-tetrachloroethane (TECA) and tetrachloroethene (PERC), basically do not burn. However, they can be rendered to burn quite vigorously by adding only a small quantity, say 20–25% by volume, of an equally volatile alkane. The burning is further enhanced when the alkane additive is less volatile than the heavily chlorinated wastes. These blending concepts recently have also been explored for spray combustion systems [6].

While the positive results of Refs. 4 and 5 are interesting and encouraging, the adoption of this blending strategy still requires a net expenditure of regular fuels with the associated cost. Recognizing that a lightly chlorinated hydrocarbon (LCHC) can burn almost as well as the regular hydrocarbons, it is attractive to explore the possibility of mixing an LCHC that burns well with a heavily chlorinated hydrocarbon (HCHC) that does not burn well such that the mixture itself can be rendered to burn well. Since both CHCs are hazardous wastes that not only have no intrinsic value, but actually need to be disposed of, their simultaneous destruction through proper mixing appears to offer a rational strategy for blending. Thus, the first objective of this investigation is to explore if robust burning can be achieved for such mixtures. We shall demonstrate that this is indeed possible, and that such burning rate enhancements can also be approximately assessed based on the

chlorine-to-hydrogen ratio (Cl/H) of the mixture as suggested previously for mixtures with alkanes [4,5,7].

Our second objective is to further manipulate the flexibility offered by mixing to reduce soot formation in CHC incineration, recognizing that soot emission can be significantly higher for CHCs because of the scavenging of hydrogen by chlorine. We shall subsequently show that the blending approach for enhanced burning mentioned above has the additional benefit of reducing soot formation in that, while the LCHC helps the HCHC to burn, addition of the HCHC to the LCHC also reduces the extent of soot formation of the mixture.

The experimental specifications are given in the next section, which is then followed by presentation and discussion of results on burning rate enhancement and soot reduction.

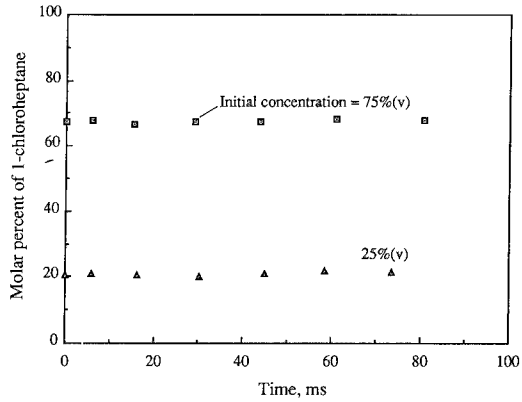

FIG. 1. Temporal variation of the molar fraction of 1-chloroheptane in binary mixtures of TECA/1-chloroheptane with initial concentrations of 25 and 75 vol%. Results demonstrate that the mixture composition basically remains constant during the droplet lifetime.

Experimental Methodology

A schematic of the experimental apparatus can be found in Ref. 4. The experiment basically involves generating a stream of monodisperse droplets with controlled size and spacing by using the ink-jet printing technique, downward injecting it into the postcombustion flow of a flat-flame burner, and subsequently igniting and burning it in an environment of controlled temperature and oxygen concentration. The data taken include the instantaneous droplet size recorded by stroboscopically back-lighted microphotography, the instantaneous flame size from the local width of the flame streak, and the instantaneous droplet composition as well as the amount of the soot present in the gas phase by using a phase-discriminating sampling probe. Operation of the sampling probe is based on inertia separation [8,9]. As the droplet stream flows downward, a gentle suction is applied to it in the lateral direction at the sampling location. The intensity of suction is controlled such that only components in the gas phase are sucked in and subsequently filtered for soot, leaving the extinguished droplet by the suction port to be separately collected in a chilled vial for further analysis on a gas chromatograph.

All data to be reported were obtained in a 21-mol% oxygen environment. Active droplet gasification and burning were confined to the chamber segment within which the gas temperature increased from 980 to 1040 K and then decreased back to 950 K. The initial droplet diameters ranged from 280 to 290 μm.

Experiments were conducted with binary mixtures of TECA with n-nonane, 1-chloroheptane, and 1,4-dichlorobutane. Since the normal boiling points of TECA, nonane, chloroheptane, and dichlorobutane are, respectively, 420, 424, 433, and 435 K, preferential gasification of the individual constituents is not expected to be significant, provided that the mixtures behave as ideal mixtures. We have established the ideality of these mixtures by determining that the droplet composition remains basically constant during the droplet lifetime. Figure 1 shows representative results on the molar fractions of chloroheptane in TECA/chloroheptane mixture droplets experimentally determined through sampling and subsequently GC/MS analysis. These results allow us to interpret the droplet combustion characteristics as those arising from the combustion of mixtures of constant composition during the droplet lifetime.

Results and Discussion

We first describe the visual appearance of the flame streaks of the droplet streams of various mixtures. For pure nonane, the flame streak is blue, indicating that there is practically no soot formation. For pure chloroheptane, the flame streak consists of a long, bright yellow sooting segment lasting about 80% of the droplet lifetime, preceded by a short blue flame segment, which lasts about 2% of the lifetime. The streak ends in a narrow blue flame. The first blue segment represents the period of droplet heating, during which the flame size is small and the flame temperature is low, both of which are not favorable for soot formation. The middle yellow sooting segment is itself embedded within and adjacent to a blue flame; this structure is anticipated in that the soot layer in diffusion flames lies on the fuel side of the flame. Elimination of the sooting segment as the flame regresses toward the end of the droplet lifetime is also well explained in previous work [8]. The flame streak for dichlorobutane is qualitatively similar to that of chloroheptane, except its yellow lumi-

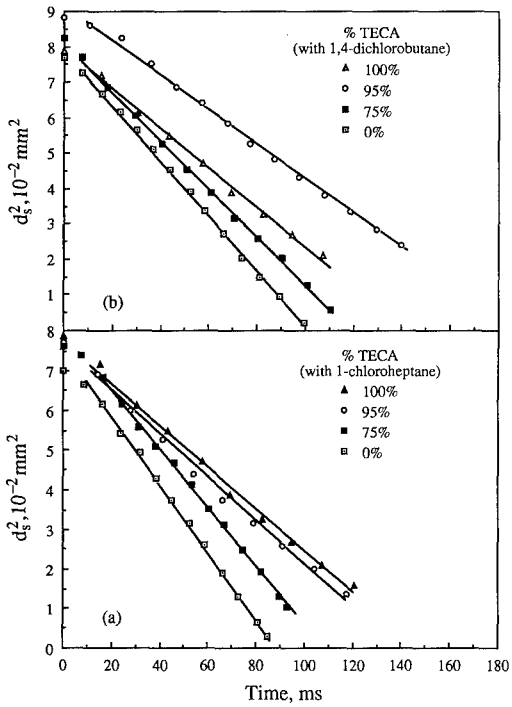

FIG. 2. d^2-law plots for droplets of (a) TECA/1-chloroheptane and (b) TECA/1,4-dichlorobutane mixtures.

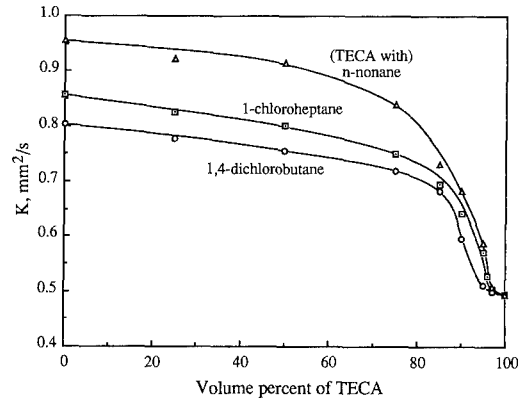

FIG. 3. Burning rate constants of mixtures of TECA with n-nonane, 1-chloroheptane, and 1,4-dichlorobutane as functions of volume percent of TECA.

nosity is much stronger. TECA gasification is characterized by a very faint bluish green luminous streak that is only visible in a darkened room. In our previous study [4], we have demonstrated that the gasification rate of the TECA droplet is the same in either oxidizing or nonoxidizing environments. Thus, this "luminous flame" does not represent chemistry with active oxidative heat release. For the mixtures, when small quantities of chloroheptane or dichlorobutane are added to TECA, droplet gasification assumes the intense burning mode. The yellow luminous flame segment, however, is visually less intense than that of the pure chloroheptane or dichlorobutane, indicating the possibility of soot reduction through the addition of TECA. However, when TECA is added to the normally nonsooting nonane, the mixture burns with a yellow luminous flame. We shall return to these points later.

Based on the classical d^2-law of droplet combustion, Figs. 2a and 2b plot the temporal variation of the square of the droplet diameter, d_s, for mixtures of chloroheptane and dichlorobutane with TECA. The nearly linear variations clearly show that the d^2-law holds, and further substantiate the results of Fig. 1 that the droplet composition basically does not change during the droplet lifetime. From the d^2-t plot of Fig. 2, the gasification rate constant, defined as $K = -d(d_s^2)/dt$, can be determined. Figure 3 shows K as a function of the TECA concentration for the three mixtures. It is seen that the nonane mixture has the highest burning rate, followed by the chloroheptane mixture and then the dichlorobutane mixture. This is reasonable because of the progressively increased amount of chlorination. Furthermore, with increasing TECA addition, the burning rate continuously decreases, which is also reasonable. The decrease, however, exhibits two regimes of distinctively different behavior. It is seen that, for TECA less than 75–80%, the burning is strong, and the decrease is rather gradual and minimal. However, for higher TECA concentrations, the burning is significantly weakened, and the burning rate decreases rapidly to approach the limiting value of pure TECA gasification. The results of Fig. 3 on mixtures of chlorinated hydrocarbons are similar to previous observations on mixtures of alkanes with either TECA or PERC [4,5], and clearly demonstrate the potential of inducing rapid burning of an HCHC by the addition of a small amount of an LCHC.

In order to identify the cause for the observed behavior, we have plotted in Figs. 4 and 5 for the chloroheptane and dichlorobutane mixtures the calculated adiabatic flame temperature (T_{ad}) for the stoichiometric reaction between the fuel mixture and the experimental oxidizing environment, the heat release per unit mass of the "fuel" mixture (q), and the stoichiometric oxidizer-to-fuel mass ratio (σ). It is seen that q decreases steadily and significantly with increasing TECA addition and therefore cannot explain the abrupt change in behavior of K. The calculated adiabatic flame temperature, however, does resemble the behavior of the gasification rate constant in that it decreases only gradually until TECA addition reaches Cl/H $\approx$ 1. Then it decreases rapidly. These two results show that, even if the heat release q is significantly reduced in the regime of vigorous burning when Cl/H $<$ 1, the flame temperature is

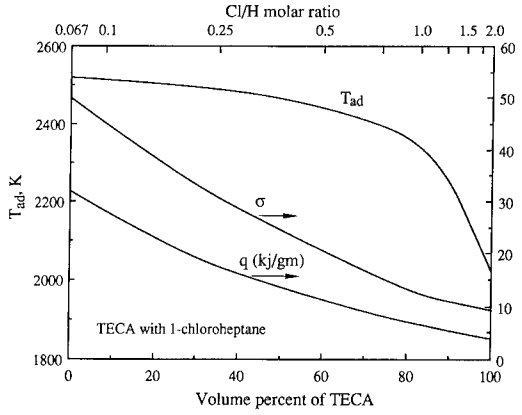

FIG. 4. Variations of the adiabatic flame temperature (T_{ad}), the heat release per unit mass of fuel (q), and the stoichiometric oxidizer-to-fuel mass ratio (σ) as functions of volume percent of TECA for mixtures of TECA with 1-chloroheptane.

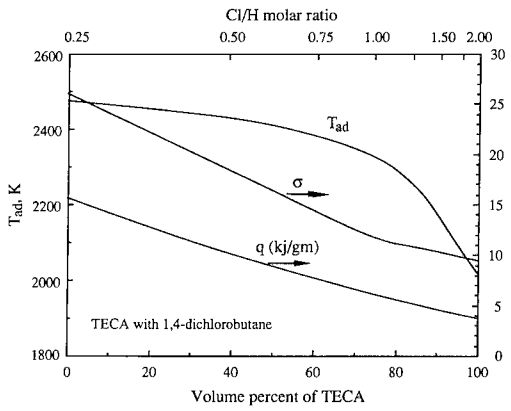

FIG. 5. Variations of the adiabatic flame temperature (T_{ad}), the heat release per unit mass of fuel (q), and the stoichiometric oxidizer-to-fuel mass ratio (σ) as functions of volume percent of TECA for mixtures of TECA with 1,4-dichlorobutane.

not proportionally reduced. This behavior can be largely explained by noting that, since the mixture is partially oxidized by chlorine leading to the formation of HCl, the stoichiometric requirement for oxygen from the ambient gas, which consists of a large amount of nitrogen, is reduced. Consequently the amount of heat needed to heat up the ambient gas to T_{ad} is also reduced. Thus, it is reasonable that T_{ad} decreases gradually even though q is significantly reduced with increasing chlorination. When Cl/H exceeds unity, however, all the hydrogen has been oxidized by chlorine, and the continuous reduction in the stoichiometric oxidizer requirement is expected

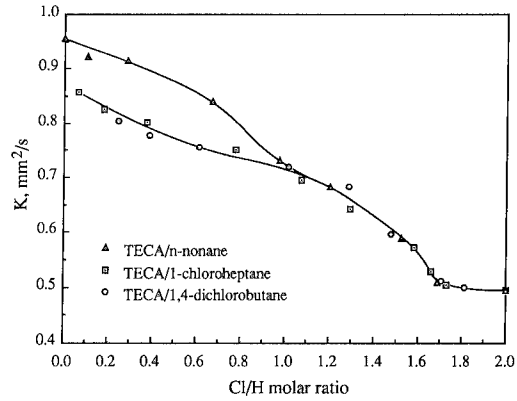

FIG. 6. Burning rate constants as functions of Cl/H molar ratio for mixtures of TECA with n-nonane, 1-chloroheptane, and 1,4-dichlorobutane.

to be greatly slowed down. Then, with the continuous reduction in the heat release q, the flame temperature will decrease rapidly. The above reasoning is substantiated by the behavior of the stoichiometric oxidizer-to-fuel mass ratio, σ, which shows a fairly rapid decrease with increasing chlorination until the Cl/H is close to unity. The subsequent decrease becomes milder. Indeed, given the behavior of σ and q shown in Figs. 4 and 5, the responses of T_{ad} and K are simply consequences of the d^2-law description of droplet combustion. It may also be noted that there are secondary factors for the behavior of K, such as the decrease in the specific heat with increasing chlorination, which increases the flame temperature in the Cl/H < 1 regime, and the further reduction in the heat release in the Cl/H > 1 regime due to chlorine dissociation as well as chlorine-inhibited oxidation of CO to CO_2 [10].

The significance of the Cl/H ratio in determining the burning intensity is further demonstrated in Fig. 6, in which K is plotted vs Cl/H for the three mixtures. It is seen that K starts to decrease fairly rapidly beyond Cl/H $= 1$, and that the data for the three mixtures correlate fairly well in terms of the Cl/H ratio for the Cl/H > 1 regime, while the LCHC mixtures correlate well for all the mixture concentrations.

We next study the effect of blending on soot formation. As mentioned earlier, when chloroheptane or dichlorobutane is added to TECA, not only is the gasification rate of the mixture greatly increased compared to that of pure TECA, but the yellow luminosity of the flame normally associated with the burning of LCHCs is also reduced, indicating the corresponding reduction in soot formation for these LCHCs. To quantify this behavior, in Fig. 7 we have plotted for TECA/dichlorobutane mixtures the temporal variation of the soot content, S, defined as the instantaneous amount of soot associated with

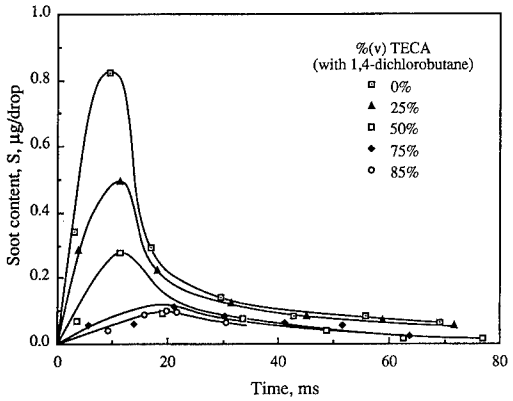

FIG. 7. Temporal variations of the soot content for mixtures of TECA/1,4-dichlorobutane of various concentrations.

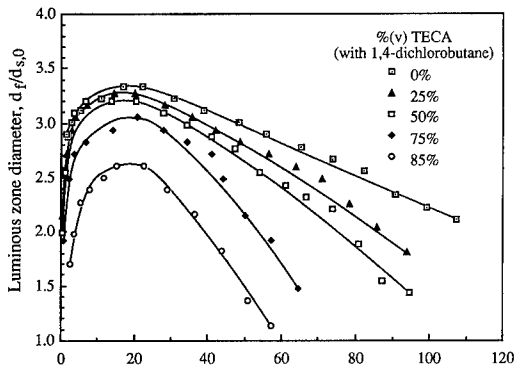

FIG. 8. Temporal variations of the luminous zone diameter for mixtures of TECA/1,4-dichlorobutane of various concentrations.

a burning droplet. Soot formation from the TECA/chloroheptane droplet is not large enough for accurate experimental determination.

Figure 7 then shows that, subsequent to ignition, the soot content first increases and then decreases, and that it decreases with increasing TECA addition. The former result is characteristic of soot formation in droplet burning [8] and corresponds closely with the behavior of the flame size. In Fig. 8, we have therefore plotted the measured diameter of the luminous zone as burning progresses, recognizing that the luminous zone not only represents the soot layer, but its dimension also approximates well the flame size. It is seen that the luminous zone size indeed increases and then decreases with time. The increase is due to fuel vapor accumulation effect [11], and the eventual decrease is caused by the continuously decreasing droplet size. Comparing Figs. 7 and 8, and noting that there is a slight time delay in abstracting

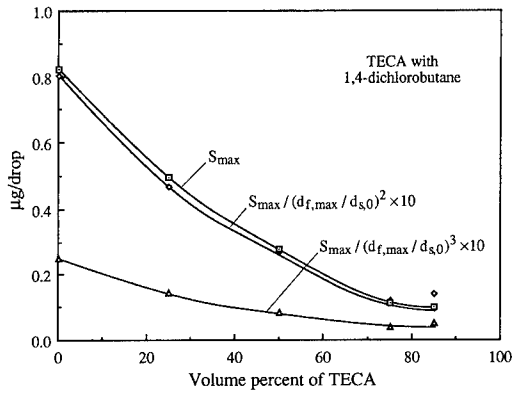

FIG. 9. Maximum soot content and the corresponding soot densities as functions of the volume percent of TECA for TECA/1,4-dichlorobutane mixtures.

the soot samples from the burning droplet, it is seen that S peaks at about the same state at which the luminous zone size peaks, indicating that the instantaneous amount of soot present is proportional to the instantaneous flame size. This is an important point in assessing the effect of TECA addition on soot formation in that, while Fig. 7 shows that S decreases with increasing TECA addition, Fig. 8 shows that the luminous zone size also decreases with increasing TECA addition. The smaller flame size for higher TECA concentrations is anticipated on the basis of the correspondingly reduced stoichiometric oxidizer requirement, σ. Indeed, the expression for the flame size as given by the d^2-law explicitly shows that it decreases with decreasing σ, provided the mass burning rate remains approximately the same, as in the case of the Cl/H < 1 situations. It is therefore necessary to first separate out this physical, volume, effect associated with the luminous zone size before assessment can be made regarding any possible chemical effect in the observed soot reduction with increasing TECA addition.

Thus, in Fig. 9 we have plotted the maximum soot content, S_{max}, as a function of TECA addition, as well as the soot "densities" at S_{max}, obtained by dividing S_{max} by the second and third powers of the nondimensional maximum luminous zone diameter, $(d_{f,max}/d_{s,0})$. Since $d_{s,0}$ is approximately the same for all runs, it is inserted only for the sake of nondimensionalization. Scaling of S_{max} by $(d_{f,max}/d_{s,0})^2$ is meaningful if the thickness of the soot shell is approximately constant for all situations, while scaling by $(d_{f,max}/d_{s,0})^3$ implies that the thickness of the soot shell is proportional to the flame diameter. The results show conclusively that, after appropriate scaling, the resulting soot densities still decrease significantly with increasing chlorination, regardless of the specific scaling used. This indicates that the observed soot reduction is caused both by the physical effect

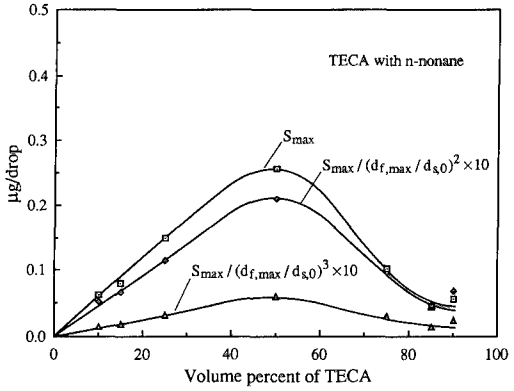

FIG. 10. Maximum soot content and the corresponding soot densities as functions of the volume percent of TECA for TECA/*n*-nonane mixtures.

of flame size reduction and by intrinsic chemical effects. The specific chemical factor(s) that could have caused the reduction are, however, not clear. In this regard, we note that, while flame temperature has been identified as a key parameter in influencing soot formation in diffusion flames [12], the calculated adiabatic flame temperatures for the present mixtures actually do not change too much in the Cl/H < 1 regime. A greater extent of flame temperature reduction with increasing TECA addition can be obtained by allowing for the slower diffusion rate of TECA, although a quantitative assessment would require a detailed computational simulation of the combustion process. Another possible factor is that, since TECA is readily converted to trichloroethylene, which is very chemically stable, including the tendency for soot formation [13,14], the sooting propensity of TECA in the present flame environment is low. In this sense, TECA can be regarded as a chemical diluent in the concentration of soot formation species.

We have also performed experiments with toluene droplets under the same experimental conditions so as to provide a reference on the sooting intensities of the mixtures studied. Results show $S_{max} = 0.209\ \mu g$/drop and $(d_{f,max}/d_{s,0}) = 3.20$, yielding $S_{max}/(d_{f,max}/d_{s,0})^2 = 0.0205\ \mu g$/drop and $S_{max}/(d_{f,max}/d_{s,0})^3 = 0.0064\ \mu g$/drop. Compared with the values shown in Fig. 9, it is clear that 1,4-dichlorobutane has a much stronger propensity to soot than toluene, which is normally considered to be a sooty fuel.

Finally, in Fig. 10 we have plotted the maximum soot content and soot densities for mixtures of TECA and the normally non-sooty nonane. Here the addition of TECA increases the amount of soot formation such that the soot content peaks around 50% of TECA addition. This result demonstrates that a different blending approach is needed when either an LCHC or a regular non-sooting hydrocarbon oil is added to an HCHC. In the former case, the extent of soot reduction monotonically decreases with increasing HCHC addition, while in the latter case, the soot content has a maximum at a certain mixture concentration.

Concluding Remarks

In the present study, we have demonstrated the viability of mixing lightly chlorinated wastes with heavily chlorinated wastes so that both wastes can be destroyed without the cost expenditure normally associated with using regular fuel oil to promote burning of incineration-resistant wastes. We have further found that such a blending approach carries the additional benefit of reducing the amount of soot formation, and have identified that the cause of this reduction is both physical and chemical in nature. Although the study was conducted for chlorinated hydrocarbons and for droplet burning, the fundamental concepts responsible for the observed beneficial effects are of such a general nature that it is reasonable to expect that they are also applicable to other halogenated wastes and to general diffusion combustion situations.

Only mixtures with equally volatile components have been studied. In Ref. 4, we have also explored the potential of enhancing the combustibility of the mixture by manipulating the volatility differential of the components. Specifically, it was suggested that the burning can be further enhanced if the more combustible fuel component is also the less volatile one. Transferring this concept to the present waste mixtures, we should then require that the HCHC be more volatile than the LCHC. Thus, most but not all of the HCHC will be preferentially gasified early in the droplet lifetime, so that it will have a longer residence time to react. In terms of reduced soot formation, we note from Fig. 9 that soot formation is reduced as long as there is a reasonable amount of the heavily chlorinated hydrocarbon present in the droplet. Since liquid-phase diffusional resistance will always retain some of the less volatile component in the droplet interior, we expect that reduced soot formation can again be realized because it is always present in the gasified mixture. Detailed studies, however, are needed to identify the compositional range and the volatility differential of these mixtures such that these beneficial effects can be maximized.

Acknowledgments

It is a pleasure to acknowledge C. J. Sung and D. L. Zhu for their technical contributions during the course of this research, and the National Science Foundation and the Office of Naval Research for their support of this program. We also thank Dr. Win Tsang and a reviewer for useful suggestions.

REFERENCES

1. Dempsey, C. R., and Oppelt, E. T., *Air Waste* 43:25–73 (1993).
2. Kramlich, J. C., Heap, M. P., Seeker, W. R., and Samuelsen, G. S., *Twentieth Symposium (International) on Combustion*, The Combustion Institute, Pittsburgh, 1985, pp. 1991–1999.
3. Law, C . K., *Combust. Sci. Technol.* 74:1–15 (1990).
4. Sorbo, N. W., Law, C. K., Chang, D. P. Y., and Steeper, R. R., *Twenty-Second Symposium (International) on Combustion*, The Combustion Institute, Pittsburgh, 1989, pp. 2019–2025.
5. Sorbo, N. W., and Chang, D. P. Y., *Combust. Sci. Technol.* 85:419–435 (1992).
6. Thomson, M., Lucas, D., Koshland, C. P., and Sawyer, R. F., Paper No. 93–098, Fall Technical Meeting of the Western State Section, The Combustion Institute, Menlo Park, CA, October 18–19, 1993.
7. Chelliah, H. K., Law, C. K., and Sorbo, N. W., ASME Publications, HTD-Vol. 176, 1991, pp. 49–56.
8. Randolph, A. L., and Law, C. K., *Combust. Flame* 64:267–284 (1986).
9. Randolph, A. L., and Law, C. K., *Twenty-First Symposium (International) on Combustion*, The Combustion Institute, Pittsburgh, 1988, pp. 1125–1130.
10. Bose, D., and Senkan, S. M., *Combust. Sci. Technol.* 35: 187–202 (1983).
11. Law, C. K., *Prog. Energy Combust. Sci.* 8:171–201 (1982).
12. Glassman, I., *Twenty-Second Symposium (International) on Combustion*, The Combustion Institute, Pittsburgh, 1988, pp. 295–311.
13. Molholland, J. A., Sarofim, A. F., and Beér, J. M., *Combust. Sci. Technol.* 85:405–417 (1992).
14. Mulholland, J. A., Sarofim, A. F., Sosothikul, P., Monchamp, P. A., Plummer, E. F., and Lafleur, A. L., *Combust. Flame* 89:103–115 (1992).

COMMENTS

Andrej Maček, National Institute of Standards and Technology, USA. Your results include instantaneous soot measurements around the droplet by means of a gas-sampling probe. One might expect that soot concentrations will depend on detailed positioning of the probe relative to the droplet and perhaps its size. Have you observed such variations?

Author's Reply. Yes, there is a slight time delay in abstracting the soot sample, as mentioned in the text. The extent of delay can be assessed from, say, shifts in the maxima between the plots for soot content and the luminous zone diameter in Figs. 7 and 8.

•

Wolfgang Wiese, Technische Hochschule, Darmstadt, Germany. What is the reason for the decrease in burning rate at a Cl/H ratio of 1? Is it that HCl cannot be formed from all forms of Cl?

Author's Reply. The dominant cause for the reduction in the flame temperature and hence droplet burning rate is the slowdown in the decrease of σ for Cl/H > 1, as discussed in the text. The incomplete conversion of Cl to HCl is part of the phenomenon, but not the primary explanation.

•

Kalyan Annamalai, Texas A&M University, USA. Adiabatic flame temperatures under complete combustion can be shown to be proportional to q/v_{O_2} where q is the heating value per kilogram of fuel and v_{O_2} is the stoichiometric O_2 in kilograms per kilogram of fuel. A plot of (q/v_{O_2}) vs blend percent may explain the drop in $T_{\text{adiabatic}}$ vs blend percent.

Author's Reply. Instead of q/σ, we have separately plotted q and σ, which is more illuminating. Of course, a plot of q/σ would show a rapid decrease for Cl/H > 1 in the same manner as the adiabatic flame temperature. This point is referred to in the text.

Twenty-Fifth Symposium (International) on Combustion/The Combustion Institute, 1994/pp. 299–306

MODELING HETEROGENEOUS/HOMOGENEOUS REACTIONS AND TRANSPORT COUPLING FOR CATALYTIC COMBUSTION OF METHYL CHLORIDE OVER A Mn-BASED CATALYST

HASAN KARIM AND LISA D. PFEFFERLE
Department of Chemical Engineering
Yale University
New Haven, CT 06520, USA

PENELOPE MARKATOU
Automated Analysis Corporation
Peoria, IL, USA

AND

MITCHELL SMOOKE
Department of Mechanical Engineering
Yale University
New Haven, CT 06520, USA

The effect of boundary-layer flow and heterogeneous/homogeneous reaction chemistry in determining product selectivity for catalytically promoted oxidation of ultralean CH_3Cl over a Mn-based catalyst was investigated numerically. This work has relevance to modeling of more general catalytic combustion systems in defining the importance of transport and chemistry interactions. In this study, we find that the presence of Mn-based catalyst can significantly decrease the temperature necessary to achieve a given conversion of CH_3Cl. The numerical study of the experiment used plug-flow, lumped-parameter transport, and laminar-flow models with detailed gas-phase chemistry. These flow models coupled with gas-phase reaction mechanisms from the literature and an experimentally determined surface reaction rate were used to illustrate heterogeneous/homogeneous reaction coupling and how it is influenced by transport. Kinetic modeling shows that the heterogeneous and homogeneous interaction occurs through CH_3Cl decomposition on the surface that initiates gas-phase reaction. For the slower velocity, there is small difference in plug-flow model and detailed laminar boundary-layer model predictions. The difference in prediction between flow models becomes larger at the high velocity, with shorter residence time, where the higher surface temperature needed for equivalent conversion causes surface reaction products to be converted before they can be transported to the bulk. The important parameter for modeling heterogeneous/homogeneous interactions is the Damköhler number with respect to gas-phase consumption of species produced by surface reaction.

Introduction

Previous work in our laboratory [1] has shown that an adiabatic catalytically stabilized thermal (CST) combustor can stabilize combustion of even heavily chlorinated mixtures, achieving high destruction levels (beyond detection limits: 99.994% +) of methyl chloride and methylene chloride with short residence times (5–20 ms) and improved flame stability. Subsequent flow reactor studies showed that, compared to an equivalent noncatalytic "hot wall" reactor, the catalyst can provide *more* than wall heating, significantly lowering temperature requirements for destruction and altering gas-phase chemistry.

Our previous work on oxidation of CH_3Cl over a Mn-based catalyst [1,2] showed that the Mn-based catalyst initiated reaction in the gas phase through dehalogenation of the CH_3Cl. Several recent studies have provided a good basis for the homogeneous chemistry models for methyl chloride oxidation for rich [3a], near stoichiometric [3b,4], and lean conditions [5]. The current work examines this reaction system numerically and investigates the coupling between both homogeneous and heterogeneous chemistry and transport in the boundary layer over the catalyst, which can affect both conversion and intermediate product selectivity [6].

Description of the Experiment

The experiments on gas-phase oxidation of CH_3Cl/air mixtures modeled in this study were carried out

previously using an isothermal flow reactor [1,2,5]. The measurement technique and catalyst are described in these references. Using an isothermal reaction length of 13.5 cm and an inlet fuel concentration of 4600 ppm in air ($\phi = 0.033$), runs were made with inlet reference velocities of 170, 340, and 510 cm/s (298 K).

Although the Mn-based catalyst is active for decomposition of CH_3Cl, it is not active for CH_4 oxidation under similar operating conditions. Thus, it was hypothesized that the catalyst promoted CH_3Cl oxidation through activation of the C—Cl bond. Low conversion surface reaction studies were carried out both under oxidative and nonoxidative conditions. This work [1,2] determined that the function of the Mn catalyst is consistent with an overall reaction that breaks the C—Cl, bond-producing C_2H_6, and 2Cl given by reaction (S1):

$$2CH_3Cl \rightarrow C_2H_6 + 2Cl. \qquad \text{(S1)}$$

Since only stable products were measured and since further reaction of surface products in the gas phase is likely at the test conditions, the rate of progress and sensitivity analyses of the detailed kinetic model were used to evaluate possible direct surface products. The overall CH_3Cl destruction rate was determined through directly checking the carbon product material balance. It was concluded that (1) the surface reaction involves only the decomposition of CH_3Cl to mainly C_2H_6 and Cl (C_2H_3Cl and HCl as minor surface products), (2) the overall rate shows a first-order dependence on CH_3Cl, and (3) O_2 does not play a role in the surface reaction. Assuming an Arrhenius rate expression for the overall surface reaction rate for CH_3Cl consumption, a pre-exponential factor of $4.8 \times 10^{+9}$ moles/cm^2 s and an activation energy of 52 kcal/mol were calculated. These values were used for the surface reaction in all model calculations reported without adjustment. The pre-exponential constant is based on geometric surface area. The fully sintered Mn-based catalyst performed similarly when prepared with impregnation solutions, varying precursor concentration by two orders of magnitude and maintaining nearly constant activity over long-term testing.

Models

Description of the Laminar Boundary-Layer Model:

For catalytic combustion inside the tubular reactor ($R_e \approx 200$–600), the following equations describe the conservation of momentum, total energy, and chemical species for a steady process applying the normal boundary-layer approximations:

Continuity Equation:

$$\frac{\partial(r\rho v)}{\partial r} + \frac{\partial(r\rho u)}{\partial x} = 0. \qquad (1)$$

Axial Momentum:

$$\rho v \frac{\partial u}{\partial r} + \rho u \frac{\partial u}{\partial x} + \frac{\partial p}{\partial x} - \rho g - \frac{1}{r}\frac{\partial}{\partial r}\left(\mu r \frac{\partial u}{\partial r}\right) = 0. \qquad (2)$$

Radial Momentum:

$$\frac{\partial p}{\partial r} = 0. \qquad (3)$$

Species Equation:

$$\rho v \frac{\partial y_i}{\partial r} + \rho u \frac{\partial y_i}{\partial x} + \frac{1}{r}\frac{\partial}{\partial r}(r\rho y_i V_{ir}) = w_i W_i \qquad i = 1, 2, \ldots n. \qquad (4)$$

Energy Equation:

$$\rho u c_p \frac{\partial T}{\partial x} + \rho v c_p \frac{\partial T}{\partial r} - \frac{1}{r}\frac{\partial}{\partial r}\left(r\lambda \frac{\partial T}{\partial r}\right) + \sum_{i=1}^{n} \rho y_i V_{ir} c_{p_i} \frac{\partial T}{\partial r} + \sum_{i=1}^{n} w_i W_i h_i = 0. \qquad (5)$$

Equation of State:

$$\rho = \frac{PW}{RT} \quad \text{where } \frac{1}{W} = \sum \frac{y_i}{W_i}. \qquad (6)$$

In the energy equation, the compressive and viscous dissipation terms were neglected. In all equations, r refers to the coordinate direction perpendicular to the flow, and x refers to the direction of flow; u and v are the velocities of gas mixture in the axial and radial direction; ρ is the density of gas mixture; λ is the thermal conductivity of the mixture; μ is the viscosity of the mixture; c_p is the specific heat of the mixture; W is the molecular weight of the mixture; y_i is the mass fraction of species i; c_{pi} is the specific heat capacity of species i; h_i is the specific enthalpy of species i; V_{ir} is the ith component of the diffusion velocity in the r direction; W_i is the molecular weight of ith species i; w_i is the molar production rate per unit volume of the ith species and is given by

$$w_i = \sum v_{ki} q_k \qquad (7)$$

where v_k is the stoichiometric coefficient of species

i in the kth reaction and q_k is the progress variable for the kth reaction.

Initial Conditions ($x = 0$):

For axial velocity,

$$u = U_{\max}\left[1. - \left(\frac{r}{\text{radius}}\right)^2\right]. \tag{8}$$

For temperature, $T = T_{\text{inlet}}$ is specified. The species $y_i = y_{i,\text{inlet}}$ is specified where $y_{i,\text{inlet}}$ are the mass fractions of reactant chemical species, as given by the inlet equivalence ratio for the mixture.

Boundary Conditions at the Center of the Tube ($r = 0$):

$$\frac{\partial u}{\partial r} = 0, \quad \frac{\partial T}{\partial r} = 0, \quad \frac{\partial y_i}{\partial r} = 0, \qquad \text{at } r = 0. \tag{9}$$

Boundary Conditions at Wall ($r = r_{\text{wall}}$):

For temperature, $T = T_{\text{wall}}$ is specified throughout the length of the wall, except for a small length near the inlet where the temperature is made to linearly increase from inlet temperature to wall temperature. Axial velocity of $u = 0$ is specified. For species taking part in the surface reaction (either reactant or product), the condition specified is $\rho_i y_i V_{ir} + w_{is} = 0$; and for the nonreacting species, $V_{ir} = 0$ is specified. The measured surface reaction rate is used to calculate w_{is}.

Method of Solution:

The conservation equations (Eqs. (2) through (5)), initial conditions, and boundary conditions are transformed by introducing stream function φ (von Mises transformation [7]) as an independent variable, defined as $\partial\varphi/\partial x = -\rho r v$, and $\partial\varphi/\partial r = \rho r u$. This facilitates the solution procedure by eliminating the convective derivative in the radial direction and also satisfying the continuity equation automatically. The solution strategy including the discretization technique, modified Newton method, adaptive gridding, and adaptive x stepping are discussed in detail by Markatou and coworkers [8,9]. It takes approximately 11 h on an HP-735 to obtain the numerical solution for a tube 13.5-cm long and a cold inlet velocity of 170 cm/s.

Plug-Flow and Lumped-Parameter Models:

In the plug-flow model, there are no gradients in the r direction and isothermal, isobaric conditions are assumed. In this case, the species equation is given below:

TABLE 1
Nusselt number for fully developed laminar flow, uniform wall cooling (j_h'') and uniform generation (G)

The Nusselt number for no generation

$$Nu_h = \frac{2j_h''a}{\lambda(T_m - T_w)} = 48/11$$

The Nusselt number for uniform volumetric generation

$$\frac{\lambda}{r}\left(\frac{\partial}{\partial r} r \frac{\partial T}{\partial r}\right) + G = u\rho c_p \frac{\partial T}{\partial x} \tag{1}$$

$$\frac{u}{u_m} = 2\left(1 - \frac{r^2}{r_w^2}\right) \tag{2}$$

$$\left(\frac{\partial T}{\partial r}\right)_{r=r_w} = \frac{-j_h''}{\lambda} \tag{3}$$

From 1, 2, and 3

$$T - T_w = \frac{Gr_w^2}{8\lambda}\left(1 - \frac{r^2}{r_w^2}\right)^2 + \frac{r_w j_h''}{4\lambda}\left(3 - 4\frac{r^2}{r_w^2} + \frac{r^4}{r_w^4}\right)$$

$$T_m - T_w = \int_0^1 \frac{u}{u_m}(T - T_w)d(r/r_w)^2 = \frac{Gr_w^2}{16\lambda} + \frac{11}{24}\frac{r_w j_h''}{\lambda}$$

$$Nu \propto \frac{1}{G}$$

$$\frac{dy_i}{d\tau} = \frac{w_i W_i}{\rho} \tag{10}$$

where τ denotes a residence time, x/u. For the plug-flow model, the catalytic reaction products are mixed uniformly over each differential volume. In the lumped-parameter formulation, radial convection is neglected, and radial diffusion in the heat and mass equations (Eqs. (3) and (4)) are represented by a flux at the wall, ($j_{i,w}''$, in the case of species), as estimated by the product of a transfer coefficient (h_m or h_T) and driving force between the bulk and wall. These transfer coefficients are obtained either by correlation from experimental data or derived by solution of uncoupled energy and species equation with appropriate assumptions and boundary conditions. This approach is illustrated in Table 1 through derivation of the dimensionless heat transfer coefficient ($Nu_h = h_T\ell/\lambda$, ℓ is the length scale defining the linear gradient) for fully developed laminar flow in a tube with or without uniform heat generation in the bulk assuming a constant wall flux.

The dimensionless mass transport parameter is called the Nusselt number for mass transport ($Nu_{m,o} = h_m\ell/D_i$) or the Sherwood number (Sh). From heat/mass transfer analogy, the correlation developed for Nu_h can be used for $Nu_{m,o}$ for equivalent boundary conditions (e.g., constant T or y_i at the wall) pro-

vided the concentration of species is dilute and no reaction occurs in the gas phase. In the case of fully developed laminar flow in a tube with no generation in the bulk, for constant wall temperature/concentration, $Nu_{m,o} = Nu_h = 3.657$, and for constant wall flux, $Nu_{m,o} = Nu_h = 4.36$. When homogeneous reactions of the diffusing species occur in the gas phase, the y_i profile will be distorted, thereby increasing/decreasing the diffusional flux at the wall. For this case, assuming a single reaction that is not highly exoergic, a correction factor F (reaction) can be introduced such that

$$Sh = Nu_m = F\,(\text{reaction})Nu_{m,o}. \tag{11}$$

The function F (reaction) depends primarily on the Damköhler number (Dam), which is the ratio of predominant transport and reaction timescales for reactive species [10]. For a first-order homogeneous reaction with rate constant k'''

$$F\,(\text{reaction}) = \frac{Dam^{1/2}}{\sinh(Dam)} \tag{12}$$

where $Dam = k'''\delta_m^2/D_i$. This Damköhler number with respect to consumption of the diffusing species in the boundary layer is a function of the surface reaction rate because the surface reaction products significantly accelerate methyl chloride conversion in the gas phase. Researchers often use experimental data of $j''_{i,w}/A_w$ to obtain Nu_m from the following expression:

$$Sh = Nu_m = \frac{j''_{i,w}}{A_w \rho D_i\left[\dfrac{(y_{i,w} - y_{i,\infty})}{\delta_m}\right]} = \frac{h_m \delta_m}{D_i} \tag{13}$$

where A_w and δ_m, are the area and thickness of mass transfer boundary layer, respectively, across which mass flux $j''_{i,w}$ diffuses; D_i is the diffusivity; $y_{i,w}$ and $y_{i,\infty}$ are wall and bulk mass fraction of species i, respectively. Care must be exercised while using correlations for calculating transport correlations, as the scaling often does not hold far from the conditions (boundary conditions and bulk source/sink mechanisms) where the correlation was originally obtained. In many combustion problems where reaction and transport are strongly coupled, lumped-parameter models cannot be used. Note in the example in Table 1, the Nu_h derived depends strongly on the generation term.

Discussion of Results

The detailed gas-phase reaction mechanism used in this study was taken from our previous study of noncatalytic oxidation of fuel lean CH_3Cl [5]. Recent thermodynamic and transport data were used from the literature [4]. The gas-phase mechanism consists of 47 species and 240 homogeneous reactions. The overall heterogeneous reaction was used as a wall boundary condition in the parabolic model and products were assumed to be uniformly mixed across each differential volume in the plug-flow model.

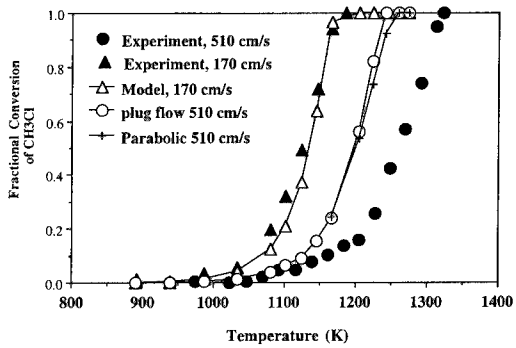

FIG. 1. Comparison of model prediction and experimental data for CH_3Cl conversion as a function of temperature for cold velocity of 170 and 510 cm/s.

Figure 1 shows model predictions for conversion of CH_3Cl fuel in the catalytic reactor at velocities of 170 and 510 cm/s, along with experimental values obtained from the work of Hung et al. [1]. At the slower velocity of 170 cm/s, there is no observable difference in prediction of species profile by the plug or parabolic model, and as such, the "model" curve in Figs. 1, 3, 4, and 5 represents prediction by both models. At the lower velocity, the predictions of both models compare well with the experimental data for CH_3Cl conversion, slightly underpredicting at low conversions. The models and experiment show significant (1%) CH_3Cl conversion occurring at 950 K with complete conversion achieved around 1200 K. At the higher flow velocity, a difference in prediction between the plug-flow and laminar-flow models is observed especially at the higher temperatures. This was expected because the higher flow velocity yields a shorter gas-phase residence time increasing the surface temperature required for gas-phase CH_3Cl conversion. This increases the Damköhler number for the consumption of CH_3Cl in the boundary layer because the reaction rate constant increases faster with temperature than the transport rate is increased due to a thinner boundary layer. At high Damköhler numbers due to transport limitations, both CH_3Cl and surface reaction products exhibit steep radial gradients, which are affected by reaction in the gas boundary layer. As a result, solution of the coupled equations for momentum, species, and energy involving detailed transport mechanisms is required for predictions of conversion and product selectivity in the overall reactor.

At the faster velocity, both models predict a faster decay than observed experimentally at higher temperatures. At a temperature where most of the predicted CH_3Cl decomposition occurs through surface reaction, predictions of conversion and intermediate species are good for both flow velocities. The correct low-temperature predictions at both flow velocities confirm that the surface decomposition reaction rate used is accurate. The coupling between surface reaction products and ignition in the gas phase, however, is not completely described, as evidenced by too fast of an initiation of gas-phase reaction for the 510 cm/s case. The model and experiment both show a region where the surface reaction rate is mass transfer limited, but gas-phase oxidation of the CH_3Cl is not yet significant. Rate of progress analysis shows that during the initiation, for both velocities, most of the CH_3Cl is decomposed through the hydrogen abstraction from CH_3Cl by Cl atom. The uncertainty in the rate constant used for this reaction at high temperature and the sensitivity of the rate on the Cl concentration may be a reason for faster initiation. A recently published paper by Huh et al. [11] also reports predictions of significantly early consumption of CH_3Cl, and CH_3Cl + Cl was the major route for CH_3Cl consumption. They suggest increasing the rate of $H_2 + Cl \rightleftarrows HCl + H$, which also would improve our predictions. These authors used the mechanism of Senkan and coworkers [3a], which is substantially similar to the one used in this study with the exception of the rates for the $CH_2Cl + CH_2Cl$ and $CH_2Cl + CH_3$. These differences do not significantly affect predicted initiation of the gas-phase CH_3Cl consumption. Another possibility is that the surface reaction products vary with reaction conditions. Model cases were run using Cl_2 as the chlorine-containing surface reaction product. This assumption delays initiation of gas-phase combustion for both velocities. In addition, C_2H_3Cl peak is underpredicted by approximately one order of magnitude at lower temperatures, and as a result, the Cl_2 as a major product is unlikely. Inclusion of C_2H_3Cl as a second carbon-bearing surface reaction product is possible, but the surface formation mechanism and relative energetics would imply C_2H_5Cl desorption as well, which was not observed experimentally at low temperatures. Using C_2H_3Cl as a surface reaction product along with C_2H_6 as a model boundary condition also lowers the C_2H_6 prediction (refer to C_2H_6 section), which is already underpredicted.

A model consisting of two annular plug-flow reactors linked using the lumped-parameter mass transfer coefficient h_m (Eq. (13)) was used to examine the effect of transport on conversion and product selectivity for this reaction system. Figure 2 shows calculated CH_3Cl conversion for a range of surface temperatures as a function of mass transfer boundary-layer thickness $\delta_m = D/Nu_m$. As shown, the flow/transport can significantly affect the calculated conversion. It should be emphasized that apriori estimation of the mass transfer coefficient for these conditions is only qualitatively possible because the appropriate Damköhler number to be used in Eq. (12) changes with the contribution from the surface reaction (a function of both surface temperature and flow). For cases where the reaction is slow enough so that surface reaction products can be transported to the bulk prior to significant consumption, lumped-parameter models can be used reliably. Unfortunately, this is not the case in many combustion applications.

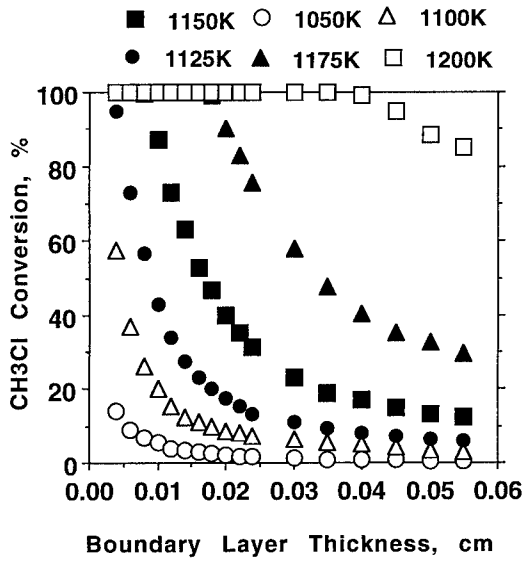

FIG. 2. CH_3Cl conversion for a mean residence of 25 ms as predicted by the lumped-parameter model as a function of boundary-layer thickness δ_m; tube diameter = 0.158 cm.

A key feature of the modeled system is the coupling between surface and gas-phase chemistry, which makes the gas-phase Damköhler number dependent on surface reactivity. Figure 3 shows predicted CH_3Cl conversion for gas-phase chemistry only, surface reaction only, and with both chemistries included in the model. Surface reaction products are observed to significantly accelerate the gas-phase destruction of CH_3Cl. This coupling produces a test of the gas-phase model under conditions where C_2 chemistry is very important because of the high fraction of carbon that goes through CH_2Cl; thus, C_2 intermediates before oxidizing. The following section discusses a rate of progress analysis for stable products and compares experimental and model predictions, highlighting areas requiring further study.

CO and CO_2:

Figure 4 shows experimentally measured CO and CO_2 concentrations and model predictions. A peak

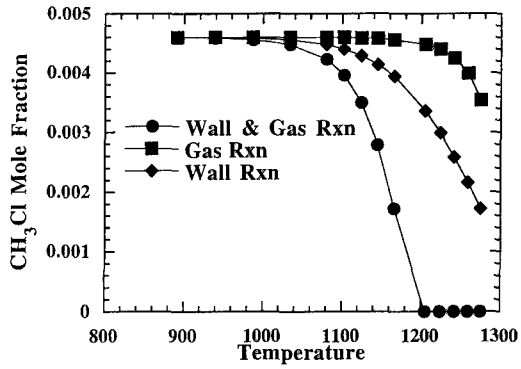

FIG. 3. Comparison of predicted CH_3Cl profile as function of temperature for gas chemistry only, surface reaction only, and with both chemistries for the cold velocity of 170 cm/s.

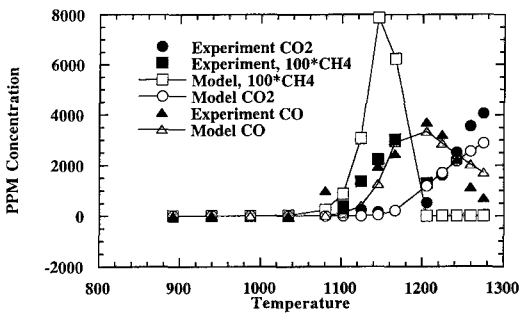

FIG. 4. Comparison of model prediction and experimental data for C_1 compounds as function of temperature for the cold velocity 170 cm/s.

CO concentration of ≈4000 ppm was measured from the Mn-coated tube, which represents nearly 90% of the carbon in the system (inlet CH_3Cl concentration of 4600 ppm). CO persisted at temperatures well above that required to achieve complete conversion of CH_3Cl, and the measured concentration of CO_2 increased significantly (above 10%) only after complete conversion of CH_3Cl at temperatures above 1200 K. These trends are predicted well by the kinetic mechanism used in the model and is in contrast to the rapid formation of CO_2 well before complete combustion of fuel CH_3Cl in a noncatalytic alumina tube used in our earlier study [5]. This contrast can be explained in terms of the slower oxidation rate of CO by reactions (R1) and (R2) (below) at the lower temperature of reaction in the catalytic case. Progress variable analysis shows that CO is primarily converted to CO_2 through the following two reactions:

$$CO + OH = CO_2 + H \qquad (R1)$$

$$CO + OCl = CO_2 + Cl. \qquad (R2)$$

This observation is consistent with earlier studies [4,5]. At low temperature, CO is created mostly by the following reaction:

$$HCO + O_2 = CO + HO_2. \qquad (R3)$$

The model prediction of peak CO concentration is in agreement with the experimental data, but the slower decay of CO and consequent increase in CO_2 predicted may be due to oxidation of CO by the Mn-based catalyst, which is not accounted for in the kinetic mechanism.

Methane (CH_4):

As illustrated in Fig. 4, the model overpredicts CH_4 concentration by a factor of 2.5, and the peak predicted concentration occurs earlier in temperature than experimentally observed. Lower yields of CH_4 were measured in the Mn reactor than in the noncatalytic alumina reactor [5]. The concentration profile for CH_4 over the Mn-based catalyst has a broad maximum (of ≈30 ppm), while the CH_4 concentration profile measured in the noncatalytic alumina reactor has a sharper peak at ≈1300 K (maximum of 70–80 ppm). Progress variable analysis shows that CH_4 is mostly created by the following two reactions:

$$CH_3 + HCl = CH_4 + Cl \qquad (R4)$$

$$CH_3Cl + CH_3 = CH_2Cl + CH_4. \qquad (R5)$$

At lower temperatures, reactions (R4) and (R5) contribute equivalently toward CH_4 formation. At temperatures above 1200 K, however, CH_4 formation mostly takes place through reaction (R4). Decomposition of methane mainly takes place through the following two abstraction reactions:

$$CH_4 + O = CH_3 + OH \qquad (R6)$$

$$CH_4 + OH = CH_3 + HO_2. \qquad (R7)$$

This explains the broad maximum in the lower-temperature catalytic reactor where O and OH concentrations are relatively low.

Vinyl chloride (C_2H_3Cl):

Experimental and predicted vinyl chloride (C_2H_3Cl) concentration profiles are plotted in Fig. 5. C_2H_3Cl is the first reaction intermediate measured as temperature is increased. Only the assumption that Cl is produced from a surface reaction correctly

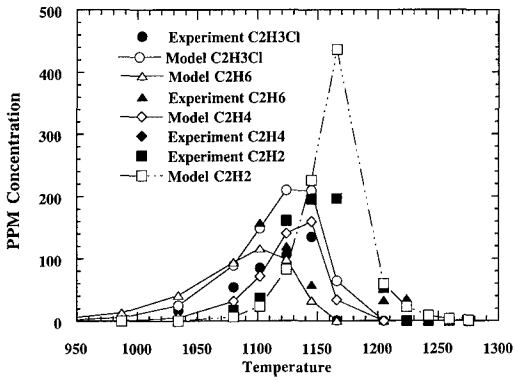

FIG. 5. Comparison of model prediction and experimental data for C_2 compounds as function of temperature for the cold velocity 170 cm/s.

predicts the trend of C_2H_3Cl formation at lower temperature and the magnitude of the peak concentration. Assumption of C_2H_3Cl and HCl as surface reaction products both overpredicts C_2H_3Cl and seriously underpredicts C_2H_6 (refer to C_2H_6 section). Model predictions of the C_2H_3Cl concentration profile are in satisfactory agreement with experimental measurements. A higher peak concentration of C_2H_3Cl (220 ppm vs 140 ppm experimentally observed from Fig. 5) was predicted with a peak concentration at slightly lower temperatures than experimentally observed. Sensitivity and rate of progress analyses show that vinyl chloride is mainly produced by the activated pathway of methylene chloride recombination reaction (R8) and unimolecular decomposition of 1,2-$C_2H_4Cl_2$ (R9).

$$CH_2Cl + CH_2Cl = C_2H_3Cl + HCl \quad (R8)$$

$$1,2\text{-}C_2H_4Cl_2 = C_2H_3Cl + HCl. \quad (R9)$$

Acetylene (C_2H_2):

A peak C_2H_2 concentration of slightly over 200 ppm (Fig. 5) was measured in the Mn tube as compared to the model prediction of 310 ppm (Fig. 5). The model correctly predicts the persistence of C_2H_2 after most of the other intermediate species (except CO and C_2H_6) decreased below detectable limits at 1225 K. This is explained by the formation of C_2H_2 late in the reaction pathway through decomposition of C_2H_3Cl combined with reaction of $C_2H_3 + O_2 = C_2H_2 + HO_2$ (reaction (R10)). Rate of progress calculations from the model confirmed this and also showed that the major reactions for destruction of C_2H_2 are activated reactions.

Ethane (C_2H_6):

The most dramatic difference in the C_2 concentration profiles between the Mn catalytic reactor and the alumina noncatalytic reactor [5] is the significantly higher C_2H_6 production observed over the Mn-based catalyst. Figure 5 shows the experimentally determined ethane profile and the model prediction. The model predicts a peak concentration of 125 vs 150 ppm, observed experimentally. The C_2H_6 concentration does not reach detectable concentrations in the noncatalytic reactor. The high concentration of C_2H_6 produced in the Mn reactor is consistent with the low conversion studies, which demonstrated that the role of the Mn-based catalyst is to break the C—Cl bond in CH_3Cl, resulting in surface production of ethane and Cl radicals. Alternate assumptions that CH_3 and Cl or C_2H_3Cl and HCl are produced by surface reaction instead of C_2H_6 fail to predict the C_2H_6 profile experimentally observed by over an order of magnitude.

Ethylene (C_2H_4):

Peak C_2H_4 concentrations of ≈70 ppm (Fig. 5) were measured from the Mn reactor. The model profile shown in Fig. 5 overpredicts the C_2H_4 concentration by a factor of nearly 3. Since in the noncatalytic case [5] all of the kinetic models used overpredicted the magnitude of C_2H_4 as well, the difference between model and experimental measurements is due to uncertainty in the rate constants for C_2 compounds in the presence of chlorine. It should also be noted that C_2 selectivities are greatly affected by the recombination steps of CH_2Cl with itself and with CH_3 and that the relative concentration of these species is affected by the chlorine radical concentration. The problem in the overprediction of C_2H_4 is more pronounced in the catalytic case than in the noncatalytic case (and for ultralean conditions vs rich conditions) because a larger fraction of the carbon goes through the CH_2Cl intermediate, which is destroyed predominantly through C_2 channels. Other models for CH_3Cl oxidation in the literature [3,4] result in significantly greater overprediction of ethylene for both in our catalytic and noncatalytic experiments. The main difference in these models that affects C_2H_4 predictions is in the parameters used for the QRRK/RRKM analysis of the recombination steps of CH_2Cl with itself and with CH_3. The greater overprediction of C_2H_4 in the catalytic case may be a result of a surface oxidation step. Although this catalyst is not active for C_2H_6 or CH_4 oxidation (consistent with C_2H_6 desorption) it shows some activity for oxidation of C_2H_4 and higher alkanes.

Conclusions

The results of this study help identify mechanisms for the initiation and promotion of the gas-phase combustion of CH_3Cl through the use of a Mn catalyst. A Mn-based catalyst was shown to stabilize gas-phase combustion of CH_3Cl at lower temperatures than achievable, thermally by heterogeneous/homogeneous chemical interactions. Although intermediate species distributions were relatively well predicted using a detailed gas-phase kinetic scheme for CH_3Cl oxidation coupled with an experimentally measured surface decomposition rate for CH_3Cl, other surface reactions such as oxidation of CO and higher hydrocarbons may explain some of the noted differences. For the lower flow condition studied (170 cm/s), the plug-flow and laminar boundary-layer model predicted approximately the same CH_3Cl conversions. However, for higher velocity (510 cm/s) studied, the laminar boundary-layer model predicted better CH_3Cl conversion. A mixing-layer model shows that for this reaction system, because of the fast reaction of surface-generated products in the gas phase, both C_1 and C_2 profiles can vary significantly as a function of transport rates.

Acknowledgments

We acknowledge the financial support of the Physical Sciences Department of the Gas Research Institute, Contract No. 5086-260-1249, and the State of Connecticut, Department of Higher Education and the many useful discussions with Dr. Stephen Hung (GE, Schenectady) whose experimental work guided the development of the model.

REFERENCES

1. Hung, S. L., Barressi, A., and Pfefferle, L. D., *Twenty-Third Symposium (International) on Combustion,* The Combustion Institute, Pittsburgh, 1992, pp. 91–107.
2. Hung, S. L., "Catalytically Stabilized Thermal Combustion of Methyl Chloride," Ph.D. Thesis, Yale University, New Haven, CT, 1991.
3. a) Karra, S. B., Gutman, D., and Senkan, A. M., *Combust. Sci. Technol.* 60:45 (1988); Karra, S. B., and Senkan, S. M., *Ind. Eng. Chem. Res.* 27:1163–1168 (1988). b) Senkan, S., "Survey of Rate Constants in the C/H/Cl/O System," in *Combustion Chemistry* (W. C. Gardiner, Ed.), 2nd ed. Springer-Verlag, New York, 1993.
4. Ho, Wenpin, and Bozzelli, J., *Combust. Sci. Technol.* 85:23–63 (1992).
5. Hung, S. L., Wand Pfefferle, L. D., *Combust. Flame* 87:91–107 (1992).
6. Hickman, D. A., and Schmidt, L. D., *J. Catalysis* 136:300 (1992).
7. Schlichting, H., *Boundary Layer Theory,* 4th ed., McGraw Hill, New York, 1960.
8. Markatou, Penelope, Pfefferle, Lisa D., and Smooke, Mitchell D., *Combust. Flame* 93:185–201 (1993).
9. Markatou, Penelope, "A Computational Study of Methane/Air and Hydrogen/Air Combustion above a Heated Catalytic Surface," Ph.D. Thesis, Yale University, New Haven, CT, 1991.
10. Rosner, Daniel E., *Transport Processes in Chemically Reacting Flow Systems,* Butterworths, Stoneham, MA, 1986.

Twenty-Fifth Symposium (International) on Combustion/The Combustion Institute, 1994/pp. 307–316

ACTIVE, OPTIMAL CONTROL OF A MODEL INDUSTRIAL, NATURAL GAS–FIRED BURNER

D. ST. JOHN AND G. S. SAMUELSEN
UCI Combustion Laboratory
University of California, Irvine
Irvine, CA 92717–3550, USA

Optimal, active control of a model industrial, swirl-stabilized, natural gas–fired burner is considered as a strategy to attain and maintain low flue-gas NO_x concentration ($[NO_x]$) and high combustion efficiency (η_c), simultaneously. A performance index, J, has been defined such that the maximization of J correlates to optimal burner performance, with respect to $[NO_x]$ and η_c. Two parameters, swirl intensity (S') and excess air (EA), known to affect the value of J, are made amenable to control and incorporated as variable burner inputs. The two measurable burner outputs, $[NO_x]$ and η_c, are continuously monitored via a bank of extractive probe emission analyzers, similar to those proposed for industry as continuous emission monitoring systems (CEMS). The settings of EA and S' are automatically adjusted by a specialized search algorithm in order to maximize the performance index, thereby optimizing η_c and $[NO_x]$. Two fundamentally differing search algorithms are explored. The first is a variation of Powell's direction-set method and incorporates a simple hill-climbing, line-maximization technique. The second technique uses the genetic algorithm analogy, which works in parallel from a population (set) of burner inputs and associated fitness (performance index) values in order to generate more highly fit (better performing) populations. The control scheme is shown, in both cases, to increase overall burner performance. Advantages and disadvantages to each of these algorithms are identified and discussed. While promising, a robust practical application of optimal, active control will benefit from a refined and more mature search technique, possibly including a hybridized combination of one or more methods.

Introduction

In the combustion of natural gas for heat generation in industrial and commercial applications, a major consideration is the flue-gas minimization of nitric oxide (NO) and nitrogen dioxide (NO_2), collectively referred to as NO_x. The current driving force in the United States is the Clean Air Act of 1990, which limits the amount of NO_x allowed to be released into the atmosphere annually [1]. The concern with these pollutants is their role as precursors in urban photochemical oxidant ("smog") formation [2]. Indeed, in the Los Angeles Air Basin (where geography and a remarkable population of both people and automobiles make air quality a special concern), local regulations are even more strict than the national standard [3].

In addition to the reduction of NO_x emissions, another goal in commercial and industrial heat generation is the maximization of combustion efficiency. The driving force in this case is the association of higher combustion efficiency with overall thermal efficiency and, therefore, lower operating costs. Even a fraction of a percent in overall thermal efficiency can equate to substantial savings in fuel costs.

Optimally, then, a natural gas burner would operate at conditions that produce the lowest NO_x emission and yield the highest combustion efficiency. Typically, however, conditions for which the highest efficiency is obtained are not the same conditions where low NO_x emission can be found, and vice versa [4]. Also, the control of a practical burner is usually in the hands of an expert, human operator who adjusts the burner according to his or her notion of how a "good" reaction should look. Further, optimal burner operating conditions can be subject to both changes initiated by an operator or process control system (e.g., modifications in fuel load, fuel type, or burner geometry), as well as subtler changes in fuel composition or changes caused by degradation of equipment. Even assuming an expert operator *could* find the optimum operating conditions for any *sensed* change in boundary conditions, it is conceivable that there could be changes *unsensed* by the operator (thereby shifting the optimum operating condition) for which no action would be taken.

A continuous, active, optimal control scheme would, in principle, address this issue. The objectives of the present work explore the application of such a scheme to minimize NO_x formation with the concomitant attainment and maintenance of high combustion efficiency in a model, industrial, natural gas–fired burner. The first objective is to identify

parameters that (1) are amenable to control, and (2) affect NO_x formation and combustion efficiency. The second objective is to develop a methodology, including a strategy for measuring combustion efficiency and NO_x concentration in the exhaust gases and the ability to actively articulate the parameters identified as control inputs. The final objective is the integration and comparison of appropriate search and optimization techniques.

Approach

Methods for the control of NO_x emission can be separated into two groups according to whether they are performed during or after the combustion process. Technologies in the first group aim to prevent the formation of NO_x, while postcombustion controls seek to destroy or remove oxides of nitrogen from the exhaust gases [5]. The definition of "control," in this context, is simply the reduction or prevention of NO_x emission into the atmosphere. In the context of the present investigation, "control" is expanded to include the slightly broader notion of manipulating burner inlet parameters in order to optimize overall performance of a burner, with respect to NO_x emission and combustion efficiency.

Currently, practical control of NO_x in natural gas–fired burners is limited to either modifying equipment (e.g., retrofit with low-NO_x burners, flue-gas recirculation, overfire air, staged combustion) or modifying operating conditions (e.g., low excess air, off-stoichiometric combustion, burners-out-of-service, biased burner firing). While each of these techniques has been shown to be effective in reducing the emission of nitrogen oxides, none is designed to react to changes in combustion operating conditions [6]. In other words, these methods are passive.

The present approach involves modification of combustion operating conditions and is of an active nature. The controller responds to a set of input variables (i.e., NO_x concentration in the flue gas and combustion efficiency) by adjusting a set of some output variables (i.e., parameters known to affect the input variables) in order to optimize the input set.

Active control of combustion processes is only recently beginning to be explored. In combustion-based propulsion systems, studies are addressing the control of pressure oscillation (an indication of instability and performance degradation) [7]. An optimizing, active control strategy has been performed with some success using pressure oscillations and volumetric heat release of a dump combustor as controller inputs [8]. In the area of active control of natural gas burners, very little has been done, especially with respect to optimizing pollutant emission. Closed-loop control of the fuel-to-air ratio has been performed on a natural gas–fired boiler using an infrared-radiation–based sensor [9], and an effort has been made to maximize combustion efficiency of a model gas turbine combustor with an active control approach [10], but never has the optimization of both efficiency and pollutant emission been attempted with anything but passive control strategies.

Parametric studies were performed on the model, industrial burner [4]. NO_x concentration corrected to 3% O_2 by volume in the flue gas (hereafter noted as "$[NO_x]$") and combustion efficiency (η_c) were determined across a range of stable excess air (EA) and swirl intensity (S') values, for several different nozzle geometries. Swirl intensity is given by

$$S' = \frac{2 \cdot S_g \cdot A_t}{\pi \cdot r_0 \cdot d_a \cdot R} = \left(\frac{\dot{m}_\phi}{\dot{m}_\phi + \dot{m}_a}\right)^2 \qquad (1)$$

where $\dot{m}$ is mass flow rate. The subscripts ϕ and a refer to the swirl air stream and the axial air stream, respectively. The term S_g is the geometric swirl number, as defined by Feikema et al. [11], where A_t is the total area of the tangential (swirl) inlets, r_0 is the radius to the tangential inlets, and d_a is the throat diameter. Both EA and S' are calculated from knowledge of the inlet air and fuel flow rates.

A database of burner performance was established for a variety of nozzle geometries across the range of lean excess air and swirl intensity values, where each nozzle could be operated with a stable reaction. Figure 1 is a plot of selected $[NO_x]$ and η_c results as a function of excess air and swirl intensity for a typical nozzle geometry. As this figure shows, NO_x concentration tends to increase along with combustion efficiency. Conditions do exist, however, where $[NO_x]$ is relatively low and η_c remains relatively high [4].

The qualitative idea of "peak" burner performance must be defined in quantitative terms, based on a tradeoff between $[NO_x]$ and η_c, in the form of a performance index, J. This performance index then becomes the variable that is maximized by the controller, indirectly optimizing NO_x concentration and combustion efficiency.

The shape of a particular performance index is a design decision and is defined based on the relative importance assigned to each measured parameter. In the case of the present experiment, performance is defined in terms of combustion efficiency and NO_x concentration and is assigned the following form:

$$J = w_{\eta_c} g(\eta_c) + w_{[NO_x]} f([NO_x]) \qquad (2a)$$

$$f([NO_x]) = \begin{cases} 1 - 0.75 \cdot \left(\dfrac{[NO_x]}{[NO_x]_{limit}}\right)^4; & [NO_x] \le [NO_x]_{limit} \\ (1 - 0.75) \cdot \dfrac{[NO_x]_{max} - [NO_x]}{[NO_x]_{max} - [NO_x]_{limit}}; & [NO_x] > [NO_x]_{limit} \end{cases} \qquad (2b)$$

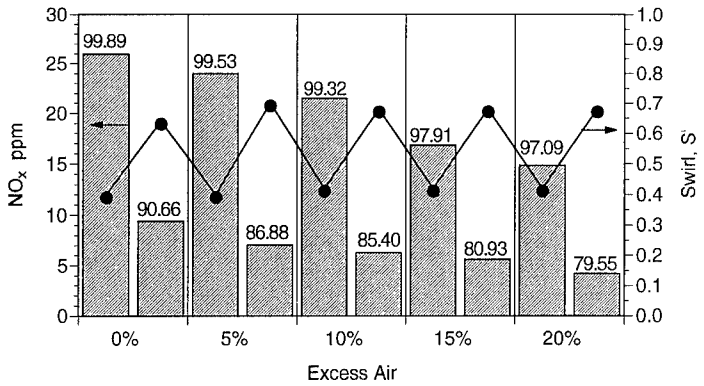

FIG. 1. NO_x concentration and combustion efficiency for a co-swirl nozzle at low and high swirl values for various excess air conditions. Combustion efficiency is listed above each bar [4].

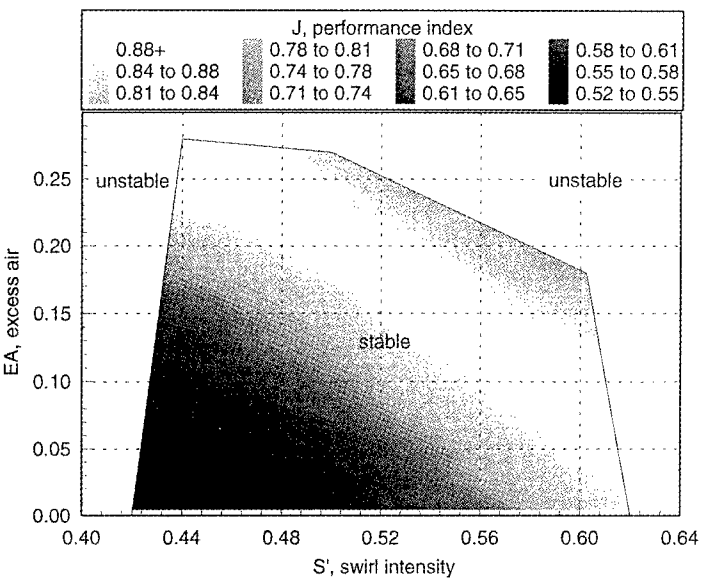

FIG. 2. Performance index, J, as a function of excess air, EA, and swirl intensity, S', for indicated stability range. Shaded area is interpolated from a grid of 93 points. White area is band of "good" performance.

$$g(\eta_c) = \left(\frac{\eta_c - \eta_{c,\min}}{100\% - \eta_{c,\min}}\right)^{1/2} \tag{2c}$$

where $w_{\eta c}$ and $w_{[NO_x]}$ are positive weighting factors that sum to one. The terms $[NO_x]_{\max}$ and $\eta_{c,\min}$ are set according to the ranges expected for a particular burner geometry. The definition of the efficiency function term is such that an increasing reward (i.e., an increase in J) is applied as combustion efficiency increases. The $[NO_x]$ function is slightly more complex, with the performance index decreasing until $[NO_x]$ surpasses a user-defined limit, $[NO_x]_{\text{limit}}$, beyond which J decreases linearly to $[NO_x]_{\max}$. The purpose of this piecewise definition of $f([NO_x])$ is to impose a high penalty on J above $[NO_x]_{\text{limit}}$ and a rapidly decreasing penalty for measurements below this limit. In other words, the contribution from $f([NO_x])$ to J is high as long as the measured NO_x concentration is below the specified limit. The value of $[NO_x]_{\text{limit}}$ can have practical significance, such as the permitted NO_x emission limit for a particular burner application.

The performance index, thus defined, is shown graphically in Fig. 2 for one of the nozzles across the range of stable excess air and swirl intensity values. Note from Eq. (2) that the performance index, J, is bound between 0 and 1 and increases monotonically with both a decrease in NO_x concentration and an increase in combustion efficiency. Optimal performance of the burner would correspond to $J = 1$, where η_c is 100% (1.00) and $[NO_x]$ is zero. As combustion efficiency approaches $\eta_{c,\min}$ and NO_x concentration approaches $[NO_x]_{\max}$, J approaches 0. Hence, the responsibility of the controller (which has no knowledge regarding the shape of the performance index surface) is to evaluate J at the current EA and S' setpoint, compare this value with past performance, and determine a new setpoint such that the performance index, J, approaches a maximum. This region of maximum J is indicated on Fig. 2 in a clear band and

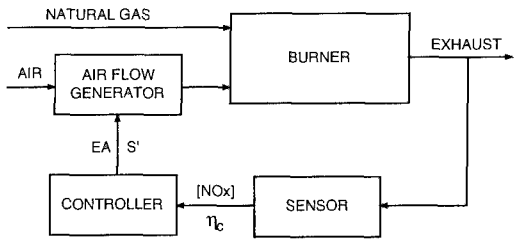

FIG. 3. Figurative representation of components in the active control loop. Fuel and air mix and react in the *burner*, the object under control. The *sensor* samples species concentrations in the exhaust and calculates combustion efficiency (η_c), and NO_x concentration corrected to 3% O_2 ([NO_x]). These values are sent to the *controller*, which evaluates burner performance, *J*, and determines the excess air (*EA*) and swirl intensity (S') setpoint, which are then sent to the *air flow generator*.

is defined as the region of desired, or "good," performance.

Using excess air and swirl intensity as the two input parameters, a control scheme having four distinct components was developed, as figuratively depicted in Fig. 3. The *burner* component is the object under control, the performance of which is the subject of this study. The *sensor* must convert information in the exhaust gases into [NO_x] and η_c signals for input to the controller. The *air flow generator* is responsible for reading *EA* and S' signals output by the controller and adjusting the axial and swirl air mass flow rates accordingly. The final, and most important, component in the current approach is the *controller*, which consists of an algorithm having the general responsibility of continuously searching the space of *EA* and S' in order to optimize the output variables, [NO_x] and η_c.

Experiment

This study makes use of facilities already in place at the UCI Combustion Laboratory [4], as well as additional equipment incorporated into the test stand specifically for the present work on active control. The experiment performed is best described with respect to the four components introduced in the previous section and figuratively represented in Fig. 3.

Burner:

Figure 4 provides a cutaway view of the model, natural gas–fired burner. The reaction is up fired and swirl stabilized, and the nominal fuel load rating is 30 kW (100,000 Btu/h). Features making this burner valuable as a research tool include a variable quarl

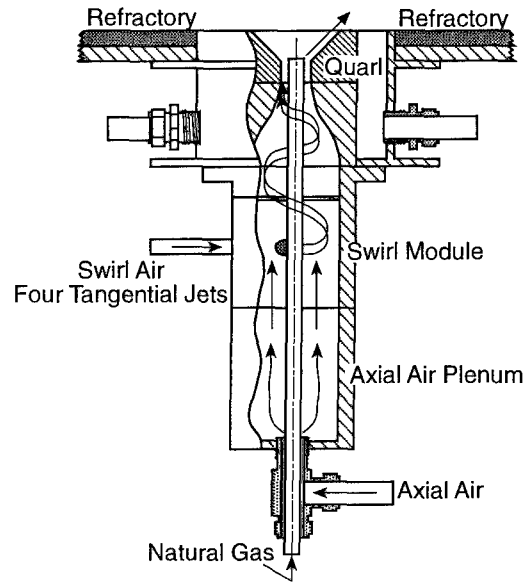

FIG. 4. Model industrial burner.

angle and fuel nozzle, and the ability to alter the aerodynamic characteristics by varying the amounts of axial air, swirl air, and secondary (dilution) air.

The burner exhausts into an octagonal furnace enclosure, the walls of which may be configured to impose variable exit boundary conditions including heat loading and downstream flow-field geometry. These walls may also be replaced with transparent windows to facilitate laser diagnostic techniques being performed in parallel with the experiment presented in this paper.

For the current experiment, the nozzle geometry, furnace geometry, fuel load, quarl angle, and secondary air flow rate are held constant. The only parameters varied for the purpose of active control are axial air flow rate and swirl air flow rate.

Sensor:

In the present study, an extractive probe technique, similar to the type used as continuous emission monitoring systems (CEMS) in the burner industry, is employed to measure the concentrations of carbon monoxide ([CO]), carbon dioxide ([CO_2]), hydrocarbon species ([HC]), oxygen ([O_2]), and nitrogen oxides (the uncorrected sum of [NO] and [NO_2], [NO_x]$_{measured}$) in the flue gas. A fraction of the exhaust gas is continuously removed from a well-mixed portion of the stack. The sample stream is then divided and fed to each of five species concentration analyzers. One hundred samples are taken over a period of 20 s at each setpoint. The average absolute NO_x signal, [NO_x]$_{measured}$, is converted to a value that

is corrected to 3% oxygen by volume in the exhaust gases, $[NO_x]$. Combustion efficiency is calculated as well, using the heat and carbon contents of the fuel, along with averaged [CO], $[CO_2]$, and [HC] values. Care is taken to preserve the integrity of the sample between extraction and analysis points.

$[NO_x]$ and η_c are measured by the sensor and sent to the controller. The controller, in turn, uses these values, along with previous performance index values and its specific search algorithm, to determine changes in EA and S' values, which are then sent to the air flow generator.

Air Flow Generator:

The heart of the air flow generator involves a magnetic actuator valve and a mass flow sensor in each of the two combustion air paths (swirl and axial). Each valve and sensor package is referred to collectively as a mass flow controller (MFC). Each MFC reads a setpoint in the form of a DC voltage, linearly proportional to the desired mass flow. Internal to each MFC is a closed-loop controller that adjusts the valve such that the sensor output voltage agrees with the setpoint voltage.

The software aspect of the air flow generator consists of a simple conversion from excess air and swirl intensity values (received from the controller) to voltage setpoints. The total air flow required, $\dot{m}_{tot}$, is determined using the theoretical fuel to air ratio of natural gas, the fuel load, and the desired excess air value (EA). Given m_{tot} and swirl intensity (S'), the swirl air flow ($\dot{m}_\phi$) and axial air flow ($\dot{m}_a$) values are extracted and converted to voltage setpoints.

Controller:

In general, the controller is designed to continuously receive inputs in the form of $[NO_x]$ and η_c, and determine new EA and S' outputs, improving performance of the burner over time.

NO_x concentration and combustion efficiency values are time-averaged at steady-state conditions for a given excess air and swirl intensity setpoint. The steady-state values of $[NO_x]$ and η_c are used by the controller to evaluate performance at the present EA and S' setpoint based on the value of the performance index, defined above, which defines a trade-off between the real values of concern.

An important note is that the controller component in this experiment does not perform *control* in the classical sense. Classical control presupposes some form of analytical or numerical model of the process under control. The failure of classical control techniques to be applied to the control and optimization of practical combustion processes lies in the lack of any sort of practical, computationally simple model defining a relationship between inputs and outputs.

In this study, the controller is more aptly described as a specialized search and optimization algorithm, the description of which has thus far been kept intentionally general. The purpose of this generality is to allow flexibility in implementation of a search algorithm, of which there are many to choose. In this way, different optimization algorithms can be incorporated into the controller, and the efficiency of one can be compared with the performance of another.

Several techniques have been identified as holding promise in this approach, two of which are explored in this work: a direction-set algorithm and a genetic algorithm [12,13,14]. Search techniques were selected based on their satisfaction of several requirements for application to a combustion system. These include the following: (1) applicability in multiple dimensions; (2) lack of dependency on an underlying model describing the process; (3) concern for performance values at a given point (or set of points) only, without requiring a database or look-up table of performance index values; and (4) the ability to function within a constrained search domain. Specifically, the search domain is constrained by the line $EA = 0$ (fuel-rich operation is not permitted) and by empirically determined stability limits.

Direction-set method

The first technique implemented in this study, and the simpler of the two, is a direction-set method. The algorithm is based on and adapted from Powell's method in two dimensions [13]. The basic procedure is described as follows: Given an initial starting point (S_i', EA_i, $i = 0$), maximize J along some initial direction, a_i. Call that point (S_{i+1}', EA_{i+1}). From there, search along a direction perpendicular to the initial direction ($a_{i+1} = a_i + \pi/2$) for the maximum J. Call that point (S_{i+2}', EA_{i+2}). Now, maximize J along the line passing through the two points (S_i', EA_i) and (S_{i+2}', EA_{i+2}). Call the new point (S_{i+3}', EA_{i+3}), let $a_{i+3} = a_i + \pi/6$, increment i by 3 and repeat.

In this way, the third line search is always in the direction of the greatest increase in J achieved by the first two line searches. The reinitialization of the search direction every three iterations ensures that convergence to a single path does not occur. Each time J is maximized along a particular direction, a separate, line-maximization routine is followed. This subalgorithm uses a simple *hill-climbing* search, where the search variables, S' and EA, step along the search direction until the performance index, J, ceases to increase. A hill-climbing technique is employed in this initial approach for one reason: By examining the character of the J surface (Fig. 2), it appears to be essentially unimodal with respect to swirl intensity and excess air, therefore ensuring that the first maximum along any line is the global maximum on that line. However, this technique has a drawback in that it will always converge to the first

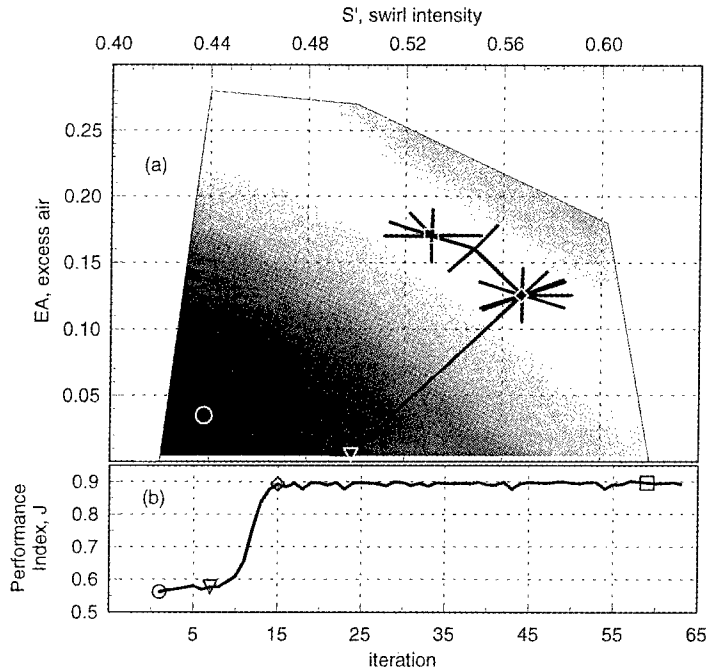

FIG. 5. Direction-set search results. Symbols along search path (a) correspond with symbols on plot of performance history (b).

maximum encountered and therefore will most likely not reach the global maximum in a multimodal response surface.

Genetic algorithm

The genetic analogy can be a powerful search technique [14]. Based on natural selection mechanics, the description of this method requires language borrowed from that field of study. The algorithm starts with a population of individuals. An individual consists of a binary string coded so as to represent a single point in EA and S' space. The fitness of each individual (its scaled performance index value) is evaluated, and a new population is produced based on the previous generation's fitness. Individuals are selected for reproduction according to each one's fitness: Individuals with higher fitness have a better chance of reproduction. Each binary string individual selected for reproduction functions as a chromosome and may undergo crossover with its mate based on a finite probability that crossover will occur. In addition, each allele, or character in the binary string, has a small probability of mutating (changing from a 1 to a 0 or vice versa).

The particular coding utilized, the number of individuals per population, and the probabilities selected for crossover and mutation all can have an effect on the efficiency of this algorithm. Selection of these parameters was based on engineering judgment and rules of thumb developed in the field of genetic algorithm research [14]. Excess air and swirl intensity are coded as 10-bit binary strings, with the first five bits representing swirl intensity, and the last five bits representing excess air. Population size is limited by the time required to measure performance for a single individual, and is set to 12 in this study. A crossover probability of 50% was chosen to ensure vigorous reproduction, and the mutation probability was set at 10%.

Results

Figure 5 illustrates a representative performance history from the direction-set method. Beginning at 3.0% excess air and a swirl intensity of 0.44, J is maximized along the initial direction, $a_0 = 11\pi/6$. Search continues along $a_1 = \pi/3\ (a_0 + \pi/2)$, where J is maximized in the region of "good" performance. At this point, after 15 iterations, J reaches a value of 0.893. The search proceeds and converges around $S' = 0.53$, $EA = 17\%$.

Figure 6 displays a typical performance history generated by the genetic algorithm technique. The distribution of the individuals in the first generation is initialized uniformly across the search domain. Following fitness (performance) evaluation of the first generation, reproduction and crossover produce the second generation, which is more fit than its predecessor. Indeed, as Fig. 6 shows, both the minimum and the average performance index values increase with each successive generation. By the fourth generation, most of the individuals lie clustered about the point $S' = 0.53$, $EA = 17\%$.

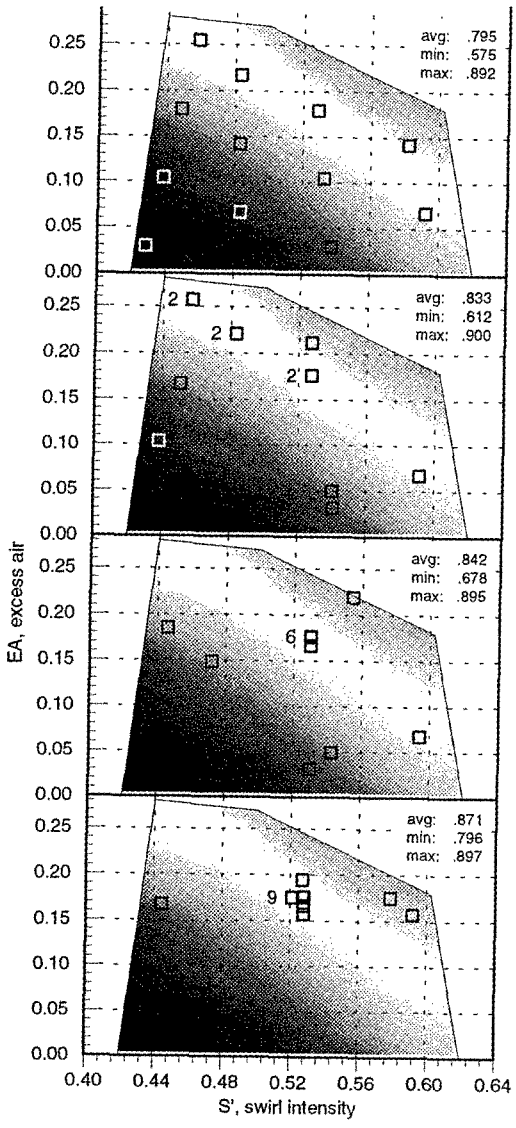

FIG. 6. Representative genetic algorithm search results. Each graph represents a single population of 12 individuals (points). Successive generations converge to the region defined as "good" performance. Number of individuals in a cluster is indicated where markers overlap. Average, minimum, and maximum performance index values are listed as well.

Several interesting observations may be drawn from these results. First, they demonstrate that an active, optimal control scheme can lead to improvement in overall burner performance with respect to combustion efficiency and NO_x emission. The time between performance evaluations is essentially the same for both techniques, so that a comparison of the two techniques is appropriate, pointing out the strengths and weaknesses inherent to each.

The direction-set method attains operation in the region of "good" performance in 15 iterations. Once a peak is reached, the controller does not deviate from this location, and performance flattens out. The algorithm is shown to maintain operation in a region of "good" performance. However, there is no guarantee that the peak reached is the global peak. This region happens to be the only peak across the surface, but every system is not guaranteed to be as unimodal.

The genetic algorithm, by virtue of its initialization across the entire stable region, visits areas of "good" performance relatively early, but does not converge significantly until the fourth generation, which is relatively late compared to the direction-set results. However, confidence that this final point is a global maximum is higher, because the algorithm effectively searches the entire surface, while the direction-set technique only searches along a narrow line. A primary drawback to the genetic algorithm method of search is in the area of maintenance. Even after the fourth generation, excursions far from the region of "good" performance occur, as individuals continue to mutate.

In this particular demonstration, the direction-set algorithm seems to be a better method of optimizing performance. However, for a general system, where multiple extrema may exist, the genetic algorithm would seem to have a clear advantage. An even better solution may lie in the hybridization of these two techniques, where, for instance, a genetic algorithm locates the area of the global maximum, and hands over control to the direction-set method, which seeks out and maintains operation on the local peak.

The time between performance evaluation iterations is limited, in the present case, by the time required to obtain a stable extractive probe measurement. While the controller has a response time on the order of milliseconds, the extractive probe sensor has a response on the order of 1 min. The extractive probe would be suitable for boiler and furnace applications where (1) load changes occur on the order of hours, and (2) continuous emission monitoring systems (CEMS) are installed by regulatory mandate. However, a more rapid response sensor technology, if available (e.g., laser-based detection of CO and NO), would reduce the time between iterations by two orders of magnitude.

Conclusions

Industrial sources of air pollutants in urban areas will be required in the future (1) to attain and maintain low NO_x emission, and (2) to do so without sacrificing high combustion efficiency. The present study addresses these needs with an optimal, active

control approach. The investigation of active control leads to several conclusions:

1. Optimal, active control is a viable method for attaining and maintaining low-emission, high-efficiency performance of a natural gas–fired burner.
2. Active control methods have the advantage of adapting to changing load, particular burner idiosyncrasies, and changes in system performance over time.
3. A trade-off can be defined between combustion efficiency and NO_x concentration in the form of a performance index. This index can then be used as a viable search criterion.
4. The two search techniques explored in this study have advantages and disadvantages, and a generically applicable, robust approach will likely involve a combination of two or more optimization methods.
5. The sensor technology adopted for the present application is readily adaptable to the CEMS requirements evolving for impacted urban areas. The control inputs are also easily implemented.

Acknowledgments

This program is supported by the California Institute of Energy Efficiency (CIEE) and the Southern California Gas Company (SoCalGas). We are grateful for the continued guidance and interest provided by Dr. Diane Fisher, the Program Monitor at CIEE, and Mr. Cherif Youssef, the Program Monitor at SoCalGas. Also, special thanks go to Mr. Matt Miyasato, without whom this effort would not have been possible, and to Mr. Kevin Trout and Mr. Stephen Dunn for their assistance.

REFERENCES

1. Zahodiakin, P., *An Introduction to the Clean Air Act of 1990,* Business Publishers, Inc., Silver Springs, Maryland, 1990.
2. Samuelsen, G. S., in *Environmental Impact and Assessment Handbook* (J. Rau and D. Wooten, Eds.), McGraw-Hill, New York, 1979, pp. 3-1–3-165.
3. Rule 1146.1, *Emissions of Oxides of Nitrogen from Small Industrial, Institutional, and Commercial Boilers, Steam Generators, and Process Heaters,* South Coast Air Quality Management District, amended July 10, 1992.
4. Miyasato, M. M., and Samuelsen, G. S., *Combust. Sci. Technol.,* submitted.
5. Sarofim, A. F., and Flagan, R. C., *Prog. Energy Combust. Sci.* 2:1–25 (1976).
6. *Summary of NO_x Control Technologies and Their Availability and Extent of Application,* U.S. Environmental Protection Agency, Research Triangle Park, NC, Publication No. EPA-450/3–92–004, February 1992.
7. McManus, K. R., Poinsot, T., and Candel, S. M., *Prog. Energy Combust. Sci.* 19:1–29 (1993).
8. Padmanabhan, K. T., Bowman, C. T., and Powell, J. D., *Western States Section of the Combustion Institue, Fall Technical Meeting,* Paper 93–092, Menlo Park, CA, 1993.
9. Zabielski, M. F., and Daigle, L. J. L., *Proceedings of Symposium on Industrial Combustion Technologies,* The American Society for Metals, International, Metals Park, OH, 1986, pp. 199–203.
10. Brouwer, J., Ault, B. A., Bobrow, J. E., and Samuelsen, G. S., *Twenty-Third Symposium (International) on Combustion,* The Combustion Institute, Pittsburgh, 1990, pp. 1087–1092.
11. Feikema, D., Chen, R.-H., and Driscoll, J. F., *Combust. Flame* 80:183–195 (1990).
12. Vanderplatts, G. N., *Numerical Optimization Techniques for Engineering Design: with Applications,* McGraw-Hill, New York, 1984, pp. 71–101.
13. Press, W. H., Flannery, B. P., Teukolsky, S. A., and Vetterling, W. T., *Numerical Recipes: the Art of Scientific Computing,* Cambridge University Press, New York, 1986, pp. 274–334.
14. Goldberg, D. E., *Genetic Algorithms in Search, Optimization and Machine Learning,* Addison-Wesley Publishing Company, Inc., Reading, MA, 1989.

COMMENTS

Roman Weber, International Flame Research Foundation, The Netherlands. Your experimental burner incorporates both inlet swirl and excess air ratio as two variables to control NO_x emissions. In the industry, NO_x emissions are controlled by either air or fuel staging, recirculation of flue gas from the furnace exhaust back to the burner, or by enhancing on entrainment of combustion products into the flame. Do you have plans to develop and test NO_x control strategies for these techniques?

Author's Reply. We recognize that swirl intensity and excess air may not always be practical as inputs to a combustion control scheme. Likewise, $[NO_x]$ and η_c may not always be the output parameters of concern in all systems. However, we feel the approach presented in this paper can be applied to any system, simply by changing the performance index to reflect the output quantities that *are* of interest and by incorporating inputs that *can* be controlled in a particular system. The key is that the input parameters

on which a control algorithm searches must have some effect on the output parameters that are under control.

As an example, consider a scheme to control NO_x emissions and overall thermal efficiency, η_{th}, on a system that incorporates flue gas recirculation. The same approach to control as that presented in the paper could be taken. In this case, the performance index would be a function of $[NO_x]$ and η_{th} and the search variables would be related to recirculation of the flue gas (percentage recirculated, etc.). The point is that this optimization scheme may be applied to any system where there are system variables that can stand some adjustment, as long as those system variables have an effect on the performance index (output variables).

We are currently investigating the incorporation of other burner parameters (inputs and outputs) into the control strategy introduced in this paper.

•

R. T. Waibel, John Zink Co., USA. It is important to include the effect of excess air when considering efficiency. This could be done by minimizing excess oxygen as well as NO_x, CO, and unburned hydrocarbons. In addition, the measurement and control might be simplified by eliminating the measurement of unburned hydrocarbons. Practical experience shows that minimizing CO also minimizes unburned hydrocarbon emissions.

Author's Reply. We agree that the effect of excess air is important. Excess air affects many output parameters in a combustion system. In this paper, the effect of excess air on NO_x concentration ($[NO_x]$) and combustion efficiency (η_c) has been shown. Excess air certainly has an effect on other output parameters, including volumetric heat loading (which may be measured as the spatial temperature distribution of a reaction). This will be directly related to the thermal efficiency of a system. For a given system, measurement of excess oxygen can be an indirect measurement of the system's thermal efficiency. In a system where a compact, high-temperature reaction is desired, it may then be desirable to minimize excess oxygen. In such a system, this would be equivalent to optimizing thermal efficiency.

In the experiment presented in this paper, two parameters have been optimized, $[NO_x]$ and η_c. The thermal efficiency, η_{th}, of our system could be defined, and this parameter could be included in the definition of the performance index. In this way, thermal efficiency could be optimized as well. If low excess oxygen correlated with high thermal efficiency in our definition, then an excess air term would effectively be incorporated into the performance index.

Our experience also agrees with the statement that "minimizing CO also minimizes UHC emissions." During our testing, UHC emissions are monitored routinely to ensure that the furnace is free of fuel just prior to lighting the burner. We include a measurement of unburned hydrocarbons in our calculation of combustion efficiency simply because the measurement is readily available and it gives us a more accurate reflection of the percent to which combustion is complete. In a practical system, however, it might be more reasonable to simply monitor CO emissions, as an indirect measurement of combustion efficiency. Indeed, it is [CO] in the exhaust that typically falls under government regulation, as opposed to combustion efficiency. Again, the control scheme presented here could incorporate any parameters that were deemed important into the performance index.

•

Anthony Hamins, National Institute of Standards and Technology, USA. The careful measurements that were presented showed that the combustion efficiency (η_c) has values ranging from near unity to approximately 80%. Determination of η_c requires independent measurements of CO, CO_2, hydrocarbons, and O_2. What was the total uncertainty in the η_c measurement? Were the measurements normalized to obtain near unity η_c? Did the calibration scheme somehow insure a near unity η_c value under certain conditions?

Author's Reply. Combustion efficiency, η_c, was calculated based on the concentrations of CO, CO_2, and hydrocarbons in the stack, and with knowledge of the composition of the fuel (carbon content, higher heating value). The actual equation used is adapted from an equation presented by Goodger [1]:

$$\eta_c = 1 - \frac{C_f}{C_m}\left[\frac{[CO]\cdot \Delta h}{HHV} - [HC]\right]$$

where C_f is the fraction of fuel-bound carbon, C_m is the total measured fraction of carbon in the exhaust products, and [CO] and [HC] are the measured fractions of carbon monoxide and hydrocarbon species, respectively. The Δh term is the difference in the enthalpies of converting C to CO_2 and C to CO (the energy lost due to the incomplete conversion of CO to CO_2). Finally, the term HHV is the measured higher heating value of the natural gas.

The total uncertainty in the calculation of η_c is a function of the uncertainty in each term's measurement. This ranged from 0.40 to 0.66%. The calculated values of η_c are absolute values (i.e., the measurements were not normalized). A value of unity was not insured under any conditions, and combustion efficiency was simply a function of the actual measurements taken at a given condition.

REFERENCE

1. Goodger, E. M., *Combustion Calculations*, MacMillan Press, Ltd., 1977, pp. 74–75.

•

R. V. Serauskas, Gas Research Institute, USA. In considering applying this strategy to a practical control system,

say via microprocessor-actuated feedback, would you recommend a system based on algorithms (such as direction sets or genetic algorithms) which appear either to take long times to converge or show erratic values along their trajectory to convergence?

Author's Reply. In any practical system, three options are available for application to a control scheme: (1) classical feedforward or feedback control, (2) some sort of look-up table or empirical fit of the data to a function, and (3) some kind of search and optimization algorithm.

The first option requires the knowledge of a mathematical relationship between burner outputs and inputs. For the case of practical, turbulent combustion processes, this option must be eliminated since a simple, reliable model does not yet exist. The second option requires an empirical mapping of burner inputs to outputs. While not entirely impractical, a control scheme based on this idea will be neither robust nor adaptable. That is, the look-up table must be updated as changes in the system occur (due to changing fuel compositions, degradation of equipment, etc.).

With the above information, and for reasons stated in the paper (lack of a need for a priori information, etc.), in applying a control strategy to a practical combustion system we recommend a scheme based on algorithms.

Twenty-Fifth Symposium (International) on Combustion/The Combustion Institute, 1994/pp. 317–323

COLD-FLOW SIMULATION OF MUNICIPAL WASTE INCINERATORS

SANGMIN CHOI, JONG SUK LEE, SOONG KEE KIM AND DONG HOON SHIN
Department of Mechanical Engineering
Korea Advanced Institute of Science and Technology
Taejon, 305-701, Korea

Configurations of combustion chamber and air distribution are major parameters that influence the performance of incinerators. Cold-flow simulations have been performed experimentally and numerically for selected designs of grate-type municipal waste incinerators. Counterflow and parallel-flow arrangements are considered for the combustion chamber configuration. Two-dimensional water table models of 1/20 scale were made for cold-flow tests, and numerical models have been developed. Flow visualizations using water table flow models and computational results using the numerical model are in good agreement. Velocity vector fields and concentrations of tracer gases are evaluated, and the effects of combustion chamber geometry, amount of overfire air, and jet direction have been investigated. Mixing characteristics in the combustion chamber are examined by adopting a newly defined mixing parameter, which has value of zero when gases are mixed completely and whose departure from zero indicates the degree of nonmixing. In representing the degree of mixing over the entire chamber, probability density function of this mixing parameter is more adequate. It is useful in comparative assessments of incinerator chambers and flow designs. Interpretation of flow field predictions in terms of residence time of combustion gases and velocity uniformity is also presented. It is suggested that understanding of local flow characteristics should be preceded in assessing the incinerator performance.

Introduction

Assured treatment for pollution minimization has recently attracted attention in addition to the more traditional viewpoint of volumetric reduction and thermal energy recovery from the municipal solid waste incineration. These considerations are effectively reflected in the governmental regulations or guidelines by Germany [1], the United States [2], Japan [3], and other countries.

The technical background for low-pollution incineration processes is customarily summarized by the importance of the 3T's (time, temperature, and turbulence); thorough mixing of the combustion gases with air, adequate residence time, and even temperature distribution inside the furnace chamber are prerequisites for successful performance of incinerators. One can easily find reasonings for the 3T concept, but more careful definitions are necessary. In the usual incinerator environment, the flow mixing time must be emphasized because chemical reaction is not considered to be rate limiting. One must carefully design mixing devices to promote turbulence, which enhances mixing. It is necessary to maintain the combustion gas temperature above a certain level, and localized low-temperature pockets must be minimized [4].

Incinerator designers frequently rely on cold-flow simulations, in much the same manner as boiler and furnace engineers. Reduced-scale water flow models [5,6] and wind tunnel models [7] are employed for visualization and measurements of flow inside the combustion chambers. Numerical flow simulations are also extensively utilized [8–10,12,13], mainly because the flow parameters can be easily manipulated.

The present study focuses on comparative evaluation of combustion chamber configuration alternatives. Since the geometric shape of chambers and combustion air distribution pattern can significantly influence the flow characteristics, several alternative schemes are suggested and optimal flow parameters are predicted both by water table tests and numerical simulations. Examinations of the flow fields that would lead to good incinerator performance are attempted.

Model Geometry and Flow Cases

The object of modeling in this study is the combustion chamber of municipal waste incinerators. The flow field inside the combustion chamber is highly turbulent and three-dimensional. In this study, however, combustion chamber modeling is simplified and limited to two-dimensional geometry. Two-dimensional models allow a much simpler treatment, while maintaining a good deal of the physical significance. For example, Nasserzadeh et al. [9] showed a strong two-dimensionality of flow field from their three-dimensional computation of a grate-

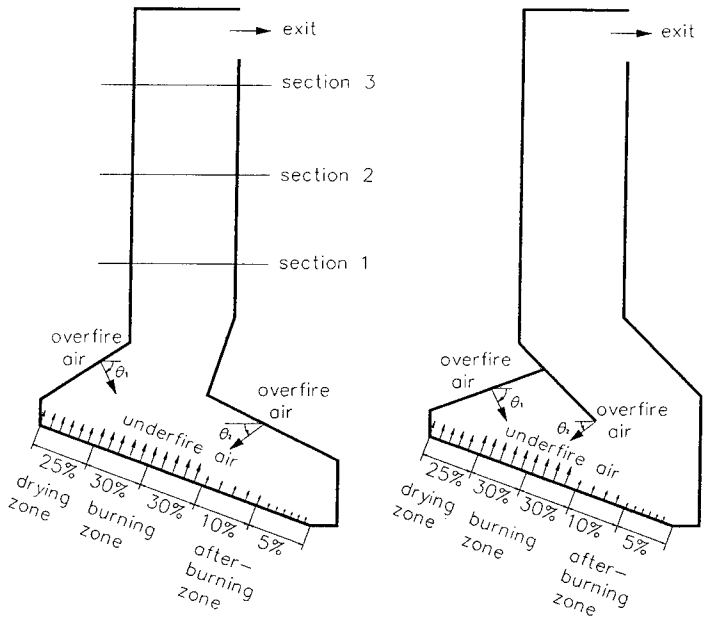

(a) Counter flow type (b) Parallel flow type

FIG. 1. Two types of model geometry for visualization experiments and numerical simulations: (a) counterflow type, (b) parallel-flow type.

type incinerator. Moreover, the cross flow pattern, which is seen in the region where overfire air jet mixes with combustion gas flow, can be characterized as two-dimensional for $s/d < 10$, where d and s are the diameter and distance of two nozzles, respectively [11]. The present study is limited to the cold flow inside the combustion chamber. This is not because heat transfer and combustion reaction are not important in the incinerator performance, but investigation of the simplified cold flows provides adequate understanding especially in terms of mixing characteristics and overall flow pattern in the combustion furnaces [8].

Two combustion chamber types, classified according to the relative movement of waste and combustion gas, are considered: a counter flow type (gas flows in the reverse direction to the waste movement) and a parallel flow type (gas flows in parallel direction to the waste), as sketched in Figs. 1(a) and 1(b), respectively. The passage of underfire (primary) air for combustion is divided into five sections of the grate: one drying zone, two burning zones, and two afterburning zones. The typical distribution of underfire air is shown in Fig. 1. The overfire (secondary) air is supplied at the front and/or rear walls of combustion chamber. Exit gas leaves the combustion chamber at the upper right corner, and it then passes through heat exchangers and gas-cleaning devices.

In order to observe the flow field inside the combustion chamber, reduced-scale models are commonly used for flow visualization and direct measurement of velocities. Two-dimensional water table models (1/20 scale) were constructed for the cold-flow test in this study. The overall flow circulation is driven by a supply pump, and the flow rates at the injection ports are controlled by flow-regulating devices. The underfire air velocity is uniformly set at each injection port, invoking the assumption that the flow will become uniform through the wastes on the grate. Overfire air is injected at high speed through a slit at various angles. For visualization, neutrally buoyant particles are injected into the combustion chamber at the injection ports, and the flow field is recorded by an overhead camera.

Flow simulation experiments using the water table model have difficulty in changing the chamber shape or flow conditions as well as limitation in flow simulation such that thermal and chemical reactions cannot be incorporated. In order to overcome these shortcomings, a numerical model has been developed to cope with parametric variations of chamber design and to generate information on the flow field within the combustion chamber. In this study, a commercial code, FLUENT, has been secured. This employs the finite difference method using control volume, and it solves the conservation equations of mass, momentum, energy, and chemical species [14]. The governing equations are differenced on the curvilinear grid for complex geometry, and a staggered grid is exploited for the storage of velocities and pressures. Numerical calculation is carried out for a real size combustion chamber, and air is the working

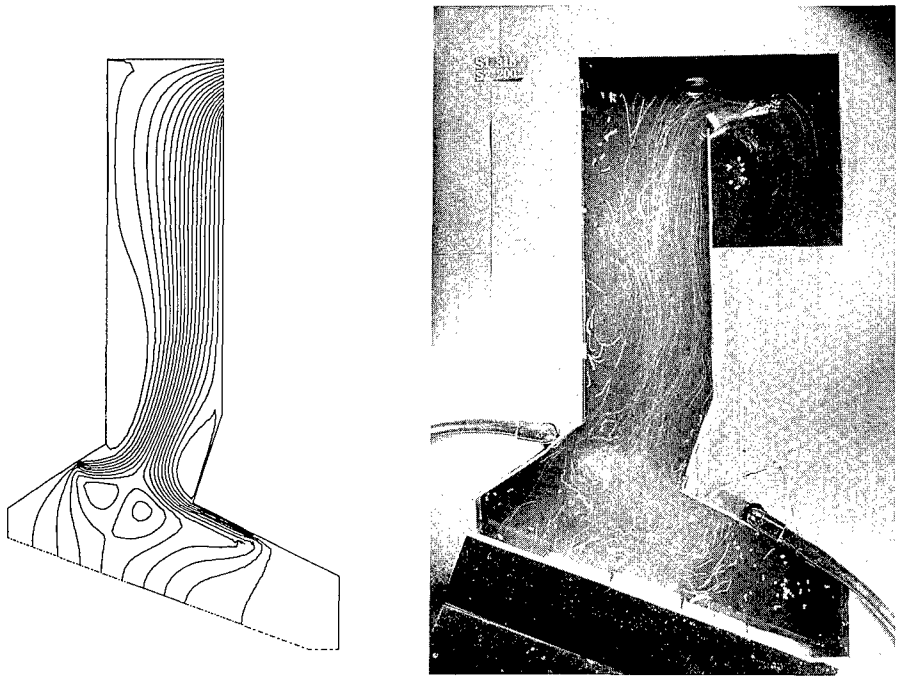

(a) Computational streamlines (b) Experimental streamlines

FIG. 2. Comparison of computational and experimental streamlines for case C2: (a) computational streamlines, (b) experimental streamlines.

fluid. Computational mesh is formed by 60 × 70 nodes, which are clustered near the walls and overfire air injection jets where the velocity gradients are high. Uniform flow conditions are specified as the boundary conditions for underfire air inlet zones, and jets of 50 m/s are prescribed as the overfire air inlet boundary conditions. A free boundary condition is enforced at the exit of the combustion chamber.

The effects of overfire air are studied by supplying 30% of total air as overfire air, and the effects of overfire air injection angle are also examined. The results are presented in this paper for the following flow parameters:

case C1: counter flow, no overfire air;

case C2: counter flow, 30% overfire air ($\theta_1 = 45°$, $\theta_2 = 20°$);

case C3: counter flow, 30% overfire air ($\theta_1 = 0°$, $\theta_2 = 0°$);

case P1: parallel flow, no overfire air;

case P2: parallel flow, 30% overfire air ($\theta_1 = 45°$, $\theta_2 = 45°$); and

case P3: parallel flow, 30% overfire air ($\theta_1 = 0°$, $\theta_2 = 0°$).

Results and Discussion

The roles of combustion chamber configuration and overfire air injection method have been investigated by means of cold-flow simulations, experimentally and numerically. Flow fields are visualized using water table flow models and compared with numerical simulation results. Typical results of numerical calculations can be represented by a velocity vector plot, as displayed in Fig. 2(a) for case C2. The effects of overfire air injection and the gas-flow distribution from the bed are easily discernible by comparing velocity vector plots for different cases. Results for different chamber configurations also demonstrate the effect of flow path geometry.

Comparison between Experimental and Computational Results:

In order to validate the numerical computations, observations from the water table model experiments were cross-checked. Figure 2(b) shows the stream lines observed for case C2. From the comparison of Figs. 2(a) and 2(b), similarity in flow patterns is apparent, except for the size of recirculation zone near the wall. It is believed that the currently available turbulence models fail to predict the recirculation region accurately, because of the strong curvature effect [15]. On the other hand, insufficient two-dimensionality, stemming from the effects of surface tension at the channel side walls of the water table

model, can also affect the strength of the recirculation. It is expected that a more elaborate turbulence model and an improvement of the water table apparatus produce improved comparison. However, the present results provide useful data to assess the flow and mixing phenomena.

Mixing:

Importance of mixing in mass burn incinerators cannot be overexaggerated. Underfire air is delivered to the waste bed over the grate, and it produces combustion gas, with variable composition and temperature. In most cases, gas from the drying region is high in moisture content, low in temperature, and contains incomplete combustion products (possibly organic pollutants and their precursors). Combustion gas from the main burning zone of the bed contains partially burned substances. Overfire air is intended to mix these combustion gases with fresh air, which will generate adequate temperature and oxygen conditions to enhance subsequent oxidation (organic pollutants such as dioxins can be destroyed at elevated temperatures [4]). Turbulence plays an important role, but resultant mixing is of major concern.

Ravichandran and Gouldin [8] investigated the degree of mixing by numerically calculating the concentration of tracer gases. Overfire air is treated as a different species compared to the combustion gases produced by the underfire air. One can construct an equiconcentration contour plot from the results, but comparative evaluation of computational results cannot be quantified. If one wants to check the mixing of several different species originating from different regions of the bed, the situation becomes even more complicated.

In an effort to quantify the degree of mixing, a mixing parameter is defined as the sum of deviations, i.e.,

$$a = \sqrt{\frac{\sum_{i=1}^{N} (X_i - X_{i0})^2}{2}} \qquad (1)$$

where X_i is the local mass fraction ($m_i/\sum_{i=1}^{N} m_i$) of ith tracer and X_{i0} is the mass fraction at the completely mixed condition. Complete mixing of gases is denoted by $a = 0$, and the degree of nonmixing is presented by the departure of a from zero. It is noted that the value of a is dependent on the number of trace gases, initial mole fractions, and injection positions. However, comparative evaluation is warranted when the conditions are properly selected. Typical contour plots of the mixing parameter a for case P2 is depicted in Fig. 3. In this case, the gases are identified as six different species: five from the bed and one from the overfire air injector. The inlet

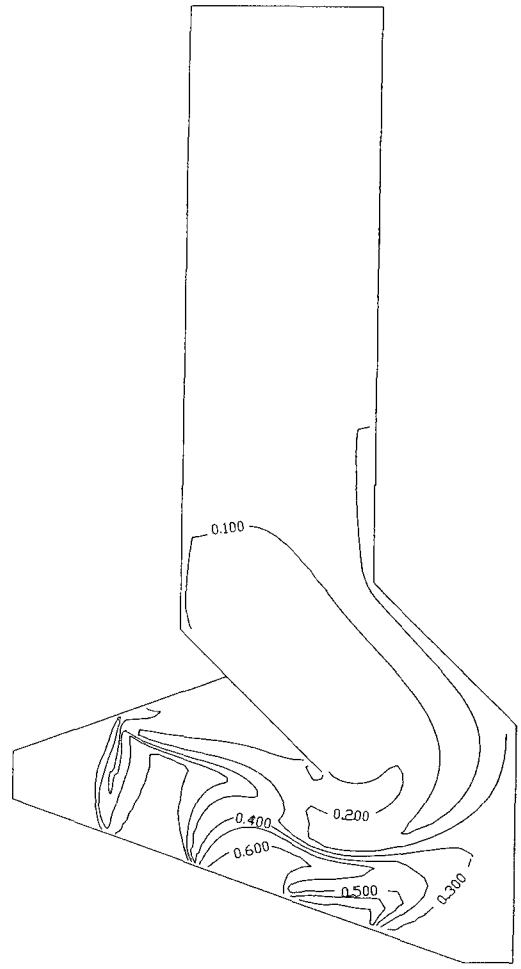

FIG. 3. Typical contour plot of mixing parameter for case P2.

regions are seen to be low in mixing, but mixing improves as the gas flows downstream. Mixing is very active in the primary combustion chamber (approximately from the bed to the so-called fully mixed height where the straight portion of the chamber starts) and the overfire air jet region, and mixing is more or less complete when the gas reaches the secondary combustion chamber. This is consistent with the definition of the fully mixed height [2] in the furnace: the point beyond the final air addition location where complete mixing should have occurred. Also observed in this plot is that mixing does not improve in the recirculation zones: under and above the radiation panel of the parallel flow design.

In order to compare the degree of mixing for different combustion chamber designs and overfire air injection schemes, the local mixing parameter a is presented by way of the probability density function

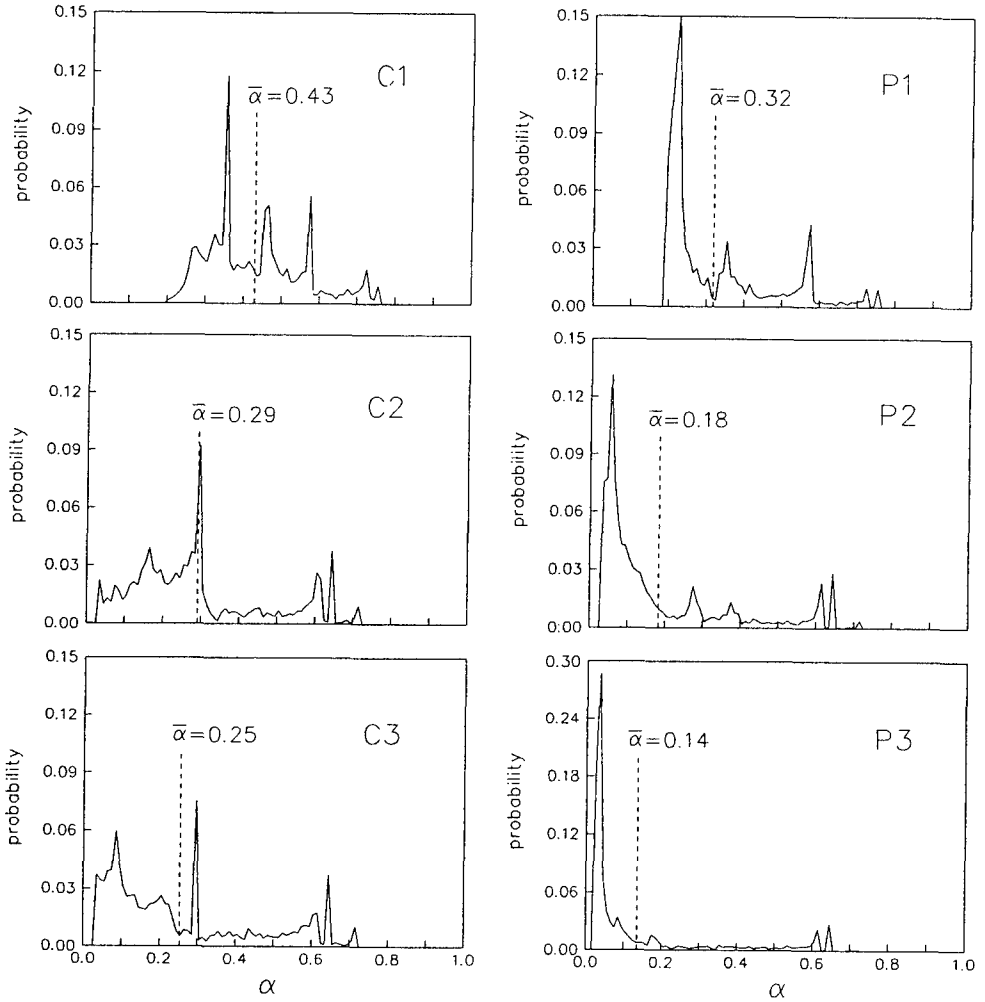

FIG. 4. Probability density functions of mixing parameters α (note that the scale for case P3 is different from others).

(PDF). This PDF indicates the degree of mixing over the entire combustion chamber. If one can oversimplify the situation, incinerator design is considered to be good in mixing when PDF of α is shifted toward 0. Furthermore, an averaged mixing parameter $\bar{\alpha}$ may be understood to be a single quantitative expression for the degree of mixing. Probability density functions of mixing parameter for six cases illustrated in Fig. 4 demonstrate the effects of overfire air and its injection angle. It is clear that overfire air enhances mixing significantly (compare cases C1 to C2 and C3, and P1 to P2 and P3, respectively). The injection angle of the overfire air has a significant impact on mixing characteristics.

Residence Time of Combustion Gas:

The residence time of combustion gas is defined as the duration of stay in the combustion chamber before the gas exits out of it. The local residence time is calculated by integrating the instantaneous velocity along the path line [8]. Figures 5(a) and 5(b) show the residence times at the corresponding source locations. For the cases of no overfire air injection (cases C1 and P1), cross-sectional variations in residence times are noticeable. Combustion gases from the main burning region escape faster than gases from the drying and after-burning zones. Injection of overfire air improves mixing, and residence times from the various bed locations become more or less evenly distributed. Also shown in the figures are the mass-averaged residence times ($\bar{\tau}$). However, mean values do not adequately represent the local flow behavior. One may recall that the residence time of combustion gas from the drying zone of the bed needs to be long enough for organic pollutants to be destroyed. In this case, a detailed understanding of

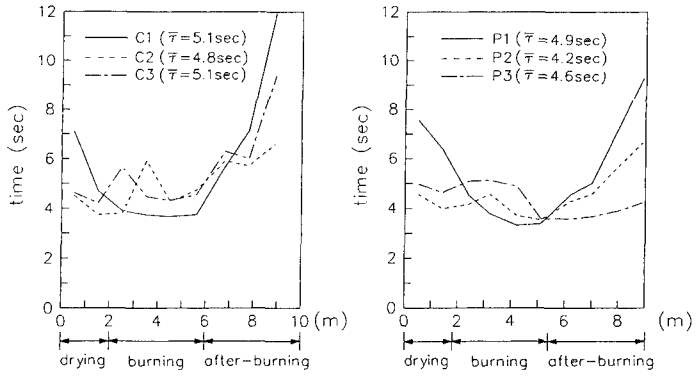

(a) Counter flow type (b) Parallel flow type

FIG. 5. Residence time of combustion gas originating from the bed (bed location is indicated as a distance from the feeder inlet and averaged-time $\bar{\tau}$ is also shown here): (a) counterflow type, (b) parallel-flow type.

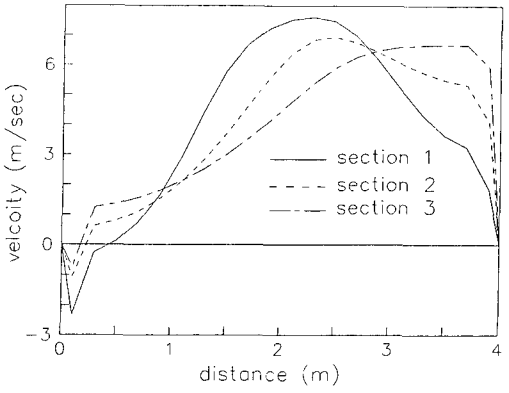

FIG. 6. Typical velocity profiles at selected cross sections of the chamber—case C2 (section numbers 1, 2, and 3 represent the corresponding locations in Fig. 1).

local flow characteristics will be useful in assessing the incinerator performance. It is also worth noting that the minimum required residence time in the secondary chamber is sometimes explicitly specified [1]. In such cases, the residence time for the primary combustion chamber and the secondary chamber must be separately evaluated.

Flow Uniformity:

Consider the velocity distribution in the secondary combustion chamber shown in Fig. 2(a). A characteristic feature of this region is the presence of recirculation zones. Cross-sectional velocity distributions shown in Fig. 6 for case C2 clearly portray the nonuniformity of flow field. The recirculating or near-zero velocity region is virtually a dead zone when viewed as a gas flow passage. Since the degree of mixing is also poor around the recirculating region, an increase of local residence time is not beneficial. When the flow recirculates, flow speed of the remaining region increases sharply in order to maintain the total flow rate. This locally high-speed gas flow can lead to an increase of particle carryover. Therefore, one must carefully avoid the presence of recirculation or severely nonuniform flow field.

Boiler designers sometimes install flow-straightening vanes or bull noses near the sharp turns to minimize these recirculation problems. Similar modifications of incinerator chambers have been attempted: addition of bull nose type turns [2] or baffles [10]. However, an abrupt change of flow direction (for example, near the radiation panel or the bull nose corner, etc.) may cause the deposition of particulate matters.

Injection of overfire air appears to increase the strength of recirculation while it is effective in mixing of gases. Therefore, in assessing the effect of overfire air injection, one must carefully examine these competing objectives.

Conclusions

Cold-flow simulations have been performed experimentally and numerically for selected designs of municipal waste incinerator, and the effects of combustion chamber geometry, amount of overfire air, and jet direction have been examined. Flow visualizations by the water table flow model are in good agreement with the calculated velocity vector field, except for the strength of recirculation. The computational model adequately predicts the characteristic flow fields for chamber configurations of counter flow type and parallel flow type, with and without an overfire air injection.

The degree of mixing inside the combustion chamber can be suitably evaluated by using a newly defined mixing parameter a. The probability density function of a, reduced from the local mixing parameters at all computational nodes, is effective for a

comparative assessment of incinerator chamber and flow designs.

The residence time of combustion gases must be evaluated for individual volumetric elements, because the averaged residence time may be misleading. Complex geometry of combustion chamber and injection of overfire air can result in a detrimental effect of increasing the strength of recirculation, whereas they, in general, enhance mixing of gases inside the combustion chamber. Therefore, overall effects of design parameters should be evaluated carefully. Finally, it is suggested that the understanding of local flow characteristics should be preceded in assessing the incinerator performance.

Acknowledgments

The authors are grateful for the financial support by Korea Ministry of Environment, Samsung Heavy Industries, Daewoo Corporation, and Daewoo Shipbuilding and Heavy Machinery.

REFERENCES

1. Technische Anleitung zur Reinhaltung der Luft (TA-Luft, 1986), 17. Bundes-Immissionsschutzgesetz (17. BImSchG, 1990), Germany.
2. Schindler, P. J., and Nelson, L. P., "Municipal waste combustion assessment: Technical Basis for Good Combustion Practice," EPA-600/8-89-063, 1989.
3. *Guidelines for Prevention and Removal of Dioxins*, Ministry of Health and Welfare, Japan, 1990.
4. Seeker, W. R., and Lanier, W. S., "Municipal waste combustion assessment: Combustion control of organic emission," EPA/530-SW-87-02, 1987.
5. Cohan, L. J., in *Incinerator and Solid Waste Technology* (R. K. Hampton, Ed.), ASME, New York, 1975, pp. 75–83.
6. Fehr, M., and Vaclavinek, J., *Int. J. Energy Res.* 16:277–283 (1992).
7. Bohn, T. J., *Strömungsuntersuchungen am Modell der MVA-Hamm nach Vorgabe von MAB-LENTJES am 15.05.1991*, Essen University, 26.6.1991, Germany, 1991.
8. Ravichandran, M., and Gouldin, F. C., *Combust. Sci. Technol.* 85:165–185 (1992).
9. Nasserzadeh, V., Swithenbank, J., and Jones, B., *J. Inst. Energy* 64:166–175 (1991).
10. Nasserzadeh, V., Swithenbank, J., Scott, D., and Jones, B., *Waste Management* 11:249–261 (1991).
11. Nissen, W. R., *Combustion and Incineration Processes*, Marcel Dekker, Inc., New York, 1978.
12. Kitamura, R., et al. *R&D Kobe Steel Eng. Rep.* 43:79–82 (1993).
13. Ide, Y., et al., *Kawasaki Heavy Industries Rep.* 117:79–85 (1993).
14. *FLUENT User's Guide*, v.4.0, 1991, Fluent Inc.
15. Lakshminarayana, B., *AIAA J.* 24:1890–1917 (1986).

Twenty-Fifth Symposium (International) on Combustion/The Combustion Institute, 1994/pp. 325–331

IN SITU DETECTION OF HAZARDOUS WASTE

CHARLES S. McENALLY AND ROBERT F. SAWYER
Department of Mechanical Engineering
University of California at Berkeley
Berkeley, CA 94720, USA

CATHERINE P. KOSHLAND
Department of Environmental Health Sciences
University of California at Berkeley
Berkeley, CA 94720, USA

AND

DONALD LUCAS
Energy and Environment Division
Lawrence Berkeley Laboratory
Berkeley, CA 94720, USA

Chlorinated hydrocarbon (CHC) concentrations have been successfully measured in situ in nonreacting gas mixtures and in flames. These measurements were made by fragmenting the CHCs with a 193-nm excimer laser and detecting the CCl fragment with a second laser via laser-induced fluorescence. Since fragmentation produces vibrationally excited CCl molecules, we can efficiently detect them by exciting the $1 \rightarrow 0$ band of the $X^2\Pi \rightarrow A^2\Delta$ transition at 284.7 nm, and observing the resulting fluorescence in the $\Delta v = 0$ bands at 278 nm. This detection strategy minimizes potential interferences from Raman scattering and fluorescence from other species. The O_2 concentration strongly affects the sensitivity since O_2 reacts rapidly with the CCl fragment before vibrational relaxation is complete. For our partially optimized apparatus and a 5-s measurement time, the detection limit for C_2H_5Cl mixed with 5% O_2, 15% CO_2, and N_2 is 100 ppb. The only interference found in flames was due to CCl produced by chemical reactions; however, its concentration is negligible except at the flame front. Interferences from flame emission were negligible, and no interfering fluorescence from other species was detected. These results indicate that our technique is capable of monitoring sub-ppm total CHC emissions from incinerators.

Introduction

Hazardous waste incineration benefits society by destroying toxic substances that would otherwise accumulate in landfills or be released to the environment; however, emissions of unburned or incompletely burned wastes from improperly operating incinerators can pose health risks to nearby populations. Currently, waste emissions are not directly measured during normal operation, and toxic byproduct emissions are never measured. The public has strongly and successfully opposed incineration during the last few years; less than 20% of incinerable wastes are actually incinerated [1]. Direct, continuous monitoring of emissions would protect public health more effectively than current practice and would allow society to fully utilize the proven benefits of hazardous waste incineration.

Chlorinated hydrocarbons (CHCs) are an important waste category, since almost 40% of incinerated waste contains some chlorine and highly toxic CHCs are often found in incinerator emissions [1]. We have proposed measuring CHC emissions with the technique of excimer-laser fragmentation-fluorescence (ELFF), wherein the CHCs are photofragmented with a pulsed 193-nm excimer laser, and then the concentration of the CCl fragment is measured via laser-induced fluorescence (LIF) [2]. ELFF possesses many of the desirable characteristics of LIF: high sensitivity, good spatial resolution, rapid temporal response, and the ability to perform in situ measurements. Fragmentation extends LIF to larger molecules, such as CHCs, which are insufficiently fluorescent to be detected directly [3].

The primary advantage of CCl-based ELFF relative to other techniques suitable for measuring CHCs, such as resonantly enhanced multiphoton ionization (REMPI) spectroscopy [4,5], is that it responds to all CHCs simultaneously, and consequently does not rely upon assumptions about which

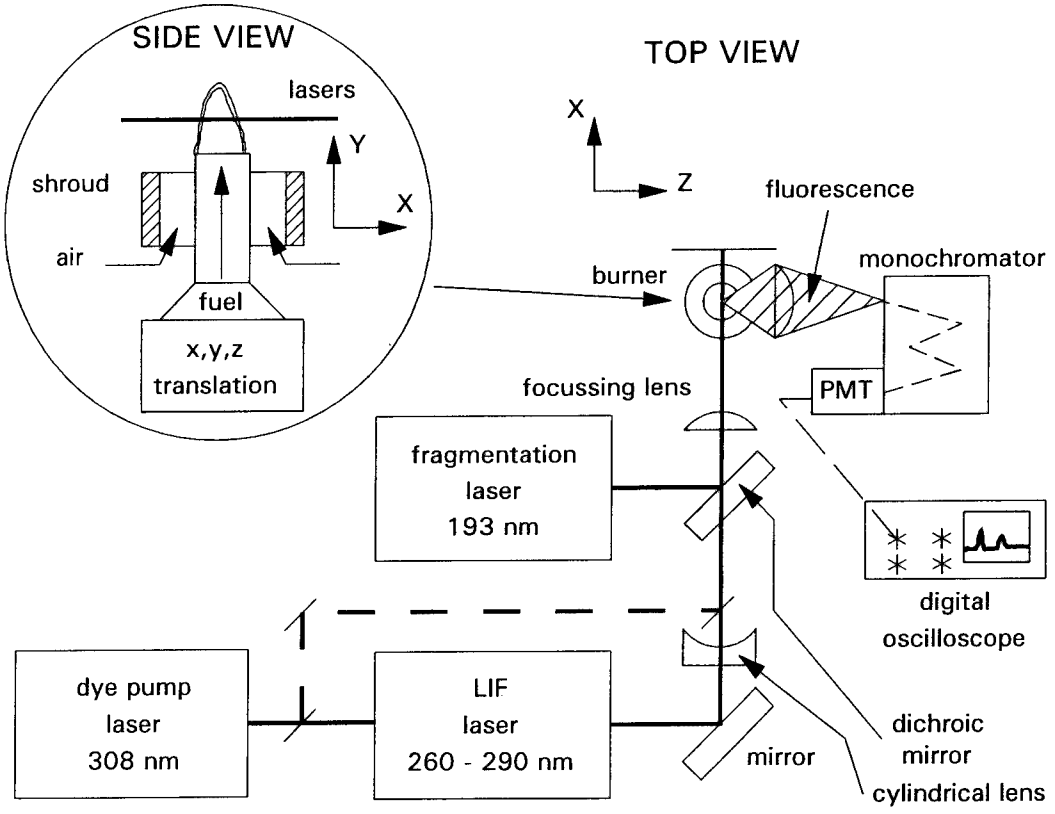

FIG. 1. Schematic of our ELFF apparatus.

species are most likely to be emitted. In our previous work, CCl-based ELFF successfully detected every tested CHC (chloromethane, several chloroethylenes and chloroethanes, and chlorobenzene), yet was immune to interferences from inorganic chlorine compounds (HCl and Cl_2) and regular hydrocarbons [6]. The detection limits for all compounds were 10 ppb or better, for a 5-s response time. While this detection limit may not be sufficient for extremely toxic species such as PCBs, large emissions of any CHC reflect off-design operation of a practical incinerator that requires corrective action. Jeffries et al. [7] have also applied ELFF to CHC detection but with the Cl atom as the detected fragment; although they obtain very good detection limits, HCl generates an unacceptable interference.

In this paper, we examine the impact of incinerator conditions on ELFF detection. First, we have measured the effects of added O_2 and CO_2 on the ELFF signal from C_2H_5Cl/N_2 mixtures, since they will comprise two of the main bath gases in incinerator exhausts. Second, we have measured CHCs in several C_2H_5Cl jet flames to identify any interferences with the ELFF measurements; the flames probably pose any interferences that might be present in an incinerator exhaust. The jet flame configuration was chosen because it allows us to make uninterrupted measurements from reactants to products.

Experimental Apparatus

Our apparatus for performing ELFF measurements is shown schematically in Fig. 1. A 193-nm Lambda-Physik EMG 102MSC pulsed excimer laser (the "fragmentation laser") photolyzes the CHCs, and an excimer-pumped Lambda-Physik FL3002 dye laser (the "LIF laser") excites fluorescence from the CCl fragments. The LIF laser uses coumarin 153 laser dye and a BBO frequency-doubling crystal to produce tunable-wavelength light between 260 and 290 nm, which overlaps several vibrational bands of the CCl $X^2\Pi \rightarrow A^2\Delta$ electronic transition: $0 \rightarrow 0$ (277.80 nm), $0 \rightarrow 1$ (271.45 nm), and $1 \rightarrow 0$ (284.69 nm) [8]. We excite the Q_{11} heads of these transitions, where many rotational transitions overlap, to obtain the strongest fluorescence intensities and to minimize the importance of the rotational population distribution, and then detect the entire $0 \rightarrow 0$ and $1 \rightarrow$

1 fluorescence bands at 278 nm, where the strongest fluorescence occurs since the CCl $\Delta v = 0$ transition probabilities are much greater than those for $\Delta v \neq 0$ [8].

The paths of the laser beams are shown by heavy lines in Fig. 1. Since only multiphoton photodissociation can create CCl, we focus the fragmentation light with a 250-mm–focal-length quartz lens; detection occurs at the focal point where the beam cross section is 2 × 0.5 mm. The intensity is sufficient to drive multiphoton absorption, but not to cause sparks or plasma formation from air. A dichroic mirror reflects the fragmentation beam toward the focussing lens; the LIF beam passes through this mirror, so that the two beams become collinear. A cylindrical lens modifies the LIF light so that both beams have the same size and shape at the focal point. The 308-nm light that pumps the dye laser can be re-directed by several mirrors to pass through the dichroic mirror and focussing lens, as shown by the heavy dotted lines in Fig. 1. The beams are superimposed by maximizing their transmission through a pinhole. Pulse energies are measured with a Gentec ED 500 joulemeter (excimer lasers) and with a Molectron J9LP joulemeter (LIF laser). Typical pulse energies at the focal point are 80 μJ (193 nm), 200–400 μJ (260–290 nm), and 70 mJ (308 nm).

A function generator/pulse generator combination triggers the fragmentation and LIF lasers with an adjustable time interval between them, denoted Δt. The variation in the actual firing point of the lasers limits the shortest reproducible Δt to 100 ns; the pulses from all three lasers are roughly 20-ns wide. The maximum repetition rate of the system is 10 Hz, limited by the 308-nm laser. A photodiode in the vicinity of the lens and mirror sees reflections from both lasers; its output gives a measurement of Δt and provides a synchronization signal for the detection system.

A 50-mm-diameter, 75-mm–focal-length lens collects emission at a 90° angle to the beam paths and focuses it onto the entrance aperture of a 0.3-m MacPherson scanning monochromator. The intersection of the laser beams with the image of the aperture defines a measurement volume 1 (X) by 2 (Z) by 0.2 (Y) mm. The monochromator transmits light at a selectable wavelength to a Hamamatsu R928 photomultiplier tube, whose output is digitized by a LeCroy 9410 digital oscilloscope. The ELFF signal, denoted S_f, is the height of the emission pulse that accompanies the LIF laser. Because of aliasing and laser pulse energy fluctuations, S_f varies by roughly 10% from shot to shot.

For room-temperature experiments, measurements are made in the core of a jet of nonreacting gases flowing out of an 8-mm-diameter tube into ambient air. C_2H_5Cl/N_2 mixtures are prepared manometrically in stainless steel sample cylinders and then combined with a coflow of N_2 and other gases. All gases flow directly from commercially supplied cylinders and are metered with rotameters. The final concentration of C_2H_5Cl is estimated to be accurate to within 20%. We find flow rates that prevent significant mixing of room air with the jet at the measurement volume by increasing the flow rate of a constant C_2H_5Cl concentration mixture until S_f is constant. The flow rates are sufficient to ensure that each laser shot photolyzes a fresh mixture.

We also performed measurements in flames generated by a double-lipped, 15-mm-diameter Bunsen burner, which is shown in the inset to Fig. 1. Fuel mixtures composed of C_2H_5Cl, N_2, He, CH_4, and/or air flow through the burner and react with room air. The Reynolds numbers are less than 100, so the flow is laminar. The flames are generally 10–20-mm tall and flicker noticeably. The burner is mounted on manual translation stages that are adjusted so that the measurement point is centered on the flame in the Z direction and is 5 mm above the burner surface. A motorized stage can scan the burner in the X direction relative to the measurement point, allowing X profiles of emission to be collected. A 40-mm-diameter cylindrical plexiglass shroud around the burner promotes flame stability; its upper lip is below the lip of the burner so that the lasers do not pass through it.

Although the fragmentation laser is insufficiently focussed to cause laser-induced breakdown in air or in CH_4 flames, it can produce breakdown in C_2H_5Cl-seeded fuel mixtures, causing the flame to jump to several times its initial height. We believe this is due to rapid expansion of the ionized gases, which can absorb most of the energy from the laser pulse. The flames quickly return to their initial state, and no long-term effects have been observed.

To assist interpretation of the CHC profiles, we measure OH profiles by exciting the OH $X^2\Pi \rightarrow A^2\Sigma^+$ ($0 \rightarrow 0$) absorption band with the 308-nm light and monitoring fluorescence in the $0 \rightarrow 1$ emission band at 347 nm [9]. Since we are not interested in quantitative OH measurements, we do not attempt to correct the measured OH profiles for changes in rotational distributions, quenching, etc., at different locations in the flame.

Results and Discussion

Most of the results presented in this paper were obtained by exciting the CCl $1 \rightarrow 0$ transition (284.7 nm) and observing the $0 \rightarrow 0$ emission band (278.4). Figure 2 shows the emission at different wavelengths that results when this strategy is applied to 15 ppm of C_2H_5Cl mixed with N_2 flowing out of the tube. The detection strategy is shown on a partial CCl energy-level diagram in the upper left-hand corner of the figure. The CCl fluorescence is clearly separated from the scattered laser light; furthermore, the flu-

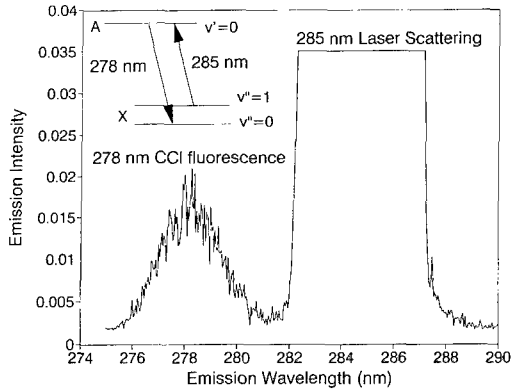

FIG. 2. Emission scan showing the spectral separation of CCl emission and laser scattering that occurs when the 1 → 0 band is excited, for 15 ppm C_2H_5Cl and N_2 flowing out of the tube.

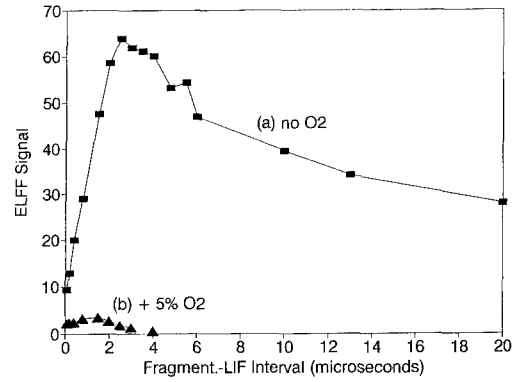

FIG. 4. CCl emission, with and without O_2, as a function of Δt for 15 ppm C_2H_5Cl and N_2 flowing out of the tube. The LIF laser is tuned to the CCl 1 → 0 transition.

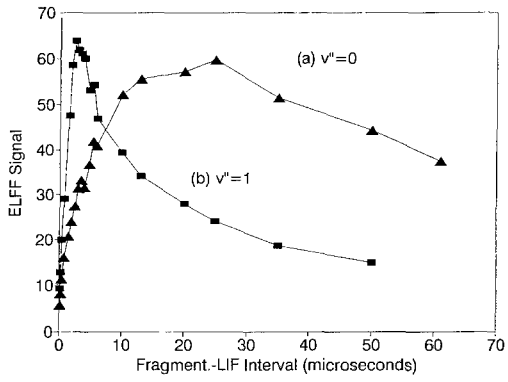

FIG. 3. CCl emission as a function of Δt for 15 ppm C_2H_5Cl and N_2 flowing out of the tube, and two different detection strategies.

orescence is on the blue side of the LIF laser wavelength, which has important implications for suppressing interferences. Since other species in the exhaust will predominantly be in $v = 0$, any Raman and fluorescence interferences will be stronger on the red side of the LIF laser wavelength. For normal LIF, this strategy would have poor detection limits, since the fractional population of $v = 1$ is usually small at thermal equilibrium. However, photofragments are usually formed in high vibrational levels and must relax to $v = 0$, so the fractional population of intermediate levels can be large; the flexibility this allows in choosing a detection strategy is one of the advantages of ELFF detection [3].

Vibrational relaxation of the CCl fragments is demonstrated by Fig. 3, which compares the dependence of S_f on Δt for two detection strategies. The data have not been corrected for differences in the pulse energy of the LIF laser at the two excitation wavelengths [70% more at 284.7 nm; curve (b)]. Each curve is proportional to the concentration of CCl in the vibrational level that was excited, since the other parameters governing the fluorescence signal are independent of Δt. Therefore, curve (a) shows the time evolution of the $v = 0$ population and curve (b) that of the $v = 1$ population. Both populations are very small at small Δt, implying that most of the CCl molecules are initially formed in $v > 1$ levels. They then relax to $v = 0$ through collisional energy transfer, passing through the intermediate levels along the way. As they pass through $v = 1$, its population peaks at $\Delta t = 2.5$ μs. As further relaxation occurs, the $v = 1$ population decreases, while that of $v = 0$ continues to rise until $\Delta t = 25$ μs, when removal of fragments due to reactions becomes important. The maximum S_f for the two detection strategies in Fig. 3 differ by less than 10%, so the detection limit of 5 ppb for C_2H_5Cl/N_2 mixtures obtained previously for 0 → 1 excitation also applies to the 1 → 0 strategy.

However, reactions remove CCl at a much faster rate when O_2 is added, so the shorter optimum Δt for 1 → 0 excitation becomes a great advantage. Figure 4 compares the dependence of S_f on Δt with and without addition of O_2. The addition of 5% O_2 shifts the maximum S_f to shorter Δt and reduces it by a factor of 20. Since the vibrational frequencies of O_2 (1580 cm^{-1}) and N_2 (2360 cm^{-1}) are both far removed from that of ground-state CCl (867 cm^{-1}) [10], addition of O_2 should not change the vibrational relaxation rates significantly. The fluorescence quenching rate due to the added O_2 is independent of Δt, so it can only affect the magnitude of the maximum S_f and cannot cause the observed shift to shorter Δt. Therefore, the observed changes in shape between curves (a) and (b) must be due to fast reaction between CCl and O_2. In fact, measurements

of CCl + O_2 reaction rates by other researchers indicate that the characteristic time for this reaction under our conditions is 0.1 μs [11,12]. The peak in S_f occurs later at 1.5 μs as a result of the competing effects of vibrational relaxation into $v = 1$ and reactive removal; $\Delta t = 1.5$ μs is used for the flame experiments presented in the following sections. We have also examined CO_2 addition; the maximum of S_f is unchanged until CO_2 comprises more than 25% of the mixture. Consequently, the net effect of the O_2 and CO_2 background in actual incinerator exhausts will be to reduce the detection limit to 100 ppb.

This detection limit is specific to our apparatus and can be improved. For example, excimer lasers that generate five times the pulse energies at 193 nm of our laser are commercially available. In experiments where the fragmentation pulse energies were varied by inserting wire screens into the beam path, S_f depended linearly on the fragmentation energy, indicating that a fivefold improvement in the detection limits is possible. Also, the detection limit is limited by scattered LIF laser light that leaks through the monochromator [6]; therefore, any improvement in the spectral discrimination of the detection system would translate into an improvement in the detection limits.

The remainder of the results concern flame studies; they indicate that scattered laser light will also be the primary limitation to CHC detection in more hostile environments. One potential source of interference with ELFF measurements in flames is emission from the flame itself. Our nonpremixed C_2H_5Cl flames are green at their base and turn yellow partway to the tip. In the green zone, the emission is dominated by molecular bands due to OH (280–320 nm), CH (390 and 430 nm), and C_2 (465, 515, 540, and 610 nm) [9]. The C_2 bands are responsible for the green color. Pure CH_4 flames generate similar emission, except that the C_2 bands are weaker, so that the blue CH emission at 430 nm dominates the spectrum. In the yellow part of the flame, broadband soot emission in the visible dominates the spectrum, although the molecular bands are still evident. The emission band at 690 nm is unidentified. CCl emission at 278 nm has been observed in other CHC-doped flames [13]; the resolution of our detection system is insufficient to distinguish it from the OH $A^2\Sigma^+ \rightarrow X^2\Pi$ $(1 \rightarrow 0)$ band at 283 nm.

The flame emission consists of discrete photons that arrive at the detector at random times. At 278 nm, the rate is about one flame emission photon every 20 μs. The ELFF signal occurs within the 20-ns pulse width of the LIF laser. Therefore, the flame emission will produce one interfering photon every 1000 laser shots on average, so this source of interference is insignificant. Since the soot emission is confined to wavelengths greater than 300 nm, the interference will not be any greater from much sootier flames.

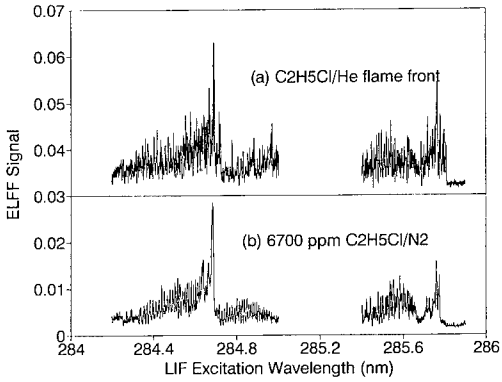

FIG. 5. Excitation scans at the flame front of a 40% C_2H_5Cl/He nonpremixed flame and for 6700 ppm C_2H_5Cl and N_2 flowing out of the tube. Emission is measured at 278 nm.

A second potential interference is fluorescence excited by the LIF laser from species other than CCl. To test this possibility, 278-nm emission excited by the LIF laser without the fragmentation laser was measured in the flames. The only fluorescence observed was due to CCl generated by chemical reactions at the flame front.

Figure 5 compares an excitation scan of 278-nm emission excited by the LIF laser alone at the flame front of a nonpremixed 40% C_2H_5Cl/He flame [curve (a)], with the same scan excited by both lasers from a 6700-ppm C_2H_5Cl/N_2 mixture [curve (b)]. Curve (b) shows the $1 \rightarrow 0$ absorption bands of CCl; clearly, most of the fluorescence observed in the flame scan is from the same bands of CCl. Since the fragmentation laser was not present, the CCl observed in the flame must have been generated by thermal reactions. The slight differences in the two scans are probably only noise in the flame scan, caused by flame flicker and weaker signal.

Figure 6 shows translation scans measured in the same nonpremixed C_2H_5Cl/He flame, again without fragmentation pulses. In curve (a), the LIF laser was tuned to the CCl $0 \rightarrow 1$ Q_{11} bandhead at 284.69 nm, and in curve (b), it was tuned to 285.85 nm, away from any CCl transitions (compare with Fig. 5). When the laser was tuned to the CCl transition, fluorescence was seen at the flame front, but when it was de-tuned, no fluorescence was excited anywhere in the flame. The most likely molecular interferences would be from species with broad absorption bands, such as polycyclic aromatic hydrocarbons (PAHs). However, any PAH species that strongly absorbed at 284.69 nm would also absorb at 285.85 nm, so the absence of fluorescence in the de-tuned scan at the sooting flame front, where PAH should exist, indi-

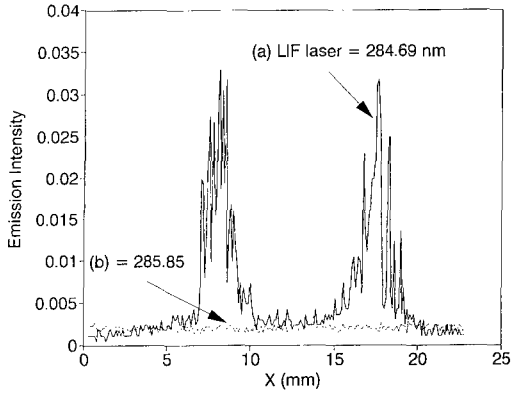

FIG. 6. Horizontal profiles taken with the LIF laser tuned to 284.69 and 285.85 nm in a nonpremixed flame with 40% C_2H_5Cl/He as fuel. Curve (a) is offset from the x axis by 0.03.

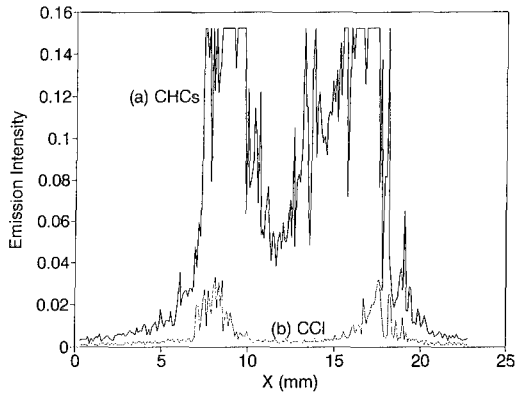

FIG. 8. Horizontal profiles of total CHCs and of flame-generated CCl measured in a nonpremixed flame with a fuel composition of 40% C_2H_5Cl/He.

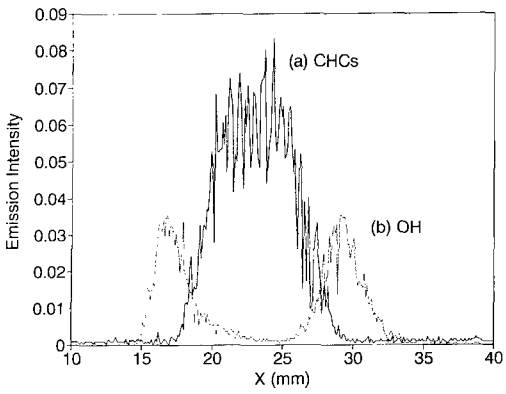

FIG. 7. Horizontal profiles of CHCs and OH measured in a partially premixed flame with a fuel composition of 1% C_2H_5Cl/26% CH_4/73% air.

cates that PAH fluorescence is unlikely to interfere with ELFF measurements of CHCs. The profiles in Fig. 6 show that the flame-generated CCl drops off rapidly on either side of the flame front, so interferences from flame-generated CCl will not affect measurements in most parts of flame systems, or in incinerator exhausts.

Figure 7 shows OH and total CHC profiles measured through a partially premixed CH_4/air flame seeded with 1% C_2H_5Cl. The CHC profile was measured with the LIF laser tuned to the CCl $0 \rightarrow 0$ transition. The observed emission shows all of the proper characteristics of CCl generated from photolysis of CHCs; i.e., it disappears if either laser is not present, if the fragmentation-LIF interval is made very large, if the detector is tuned off of 278 nm, or if the LIF laser is tuned off of the CCl absorption transition. The profiles themselves make intuitive sense; OH is observed at the edges of the flame, but not elsewhere, and CHCs are observed in the fuel cone and disappear at the flame front. Both profiles are noisy because of flame unsteadiness.

Figure 8 shows profiles of total CHCs and of flame-generated CCl for a 40% C_2H_5Cl/He nonpremixed flame. Both profiles were obtained with the LIF laser tuned to the CCl $1 \rightarrow 0$ band; the only difference is that the fragmentation laser was not present for curve (b). The digitizer was saturated at a value of 0.15 in several places in the total CHCs profile. The curve is somewhat different from that of Fig. 7 in that the signal drops within the fuel cone. We believe this is a consequence of self-absorption of CCl fluorescence and of breakdown within the fuel cone. Neither of these phenomena is likely to be occurring in the flame of Fig. 7, where the C_2H_5Cl concentration is 40 times smaller. The signal from the CHCs is greater than that from the flame-generated CCl at every point in the profiles in Fig. 8, so the flame-generated CCl is not a prohibitive interference. The CHCs profile shows tails at each edge of the flame front, when X is between 2–7 and 18–23 mm. Measurements of emission from a mercury lamp through a pinhole at the focal point indicate that these tails are caused by the finite sharpness of the detection volume: Although the emission drops by 1/2 over 1 mm, it only drops by 1/50 over 10 mm. Since the edges of the laser beams drop off more sharply, the tails can be removed by translating the burner in the Z direction, which is perpendicular to them.

Implications for Incineration

Two main results have emerged from these experiments: The sensitivity of our ELFF technique is reduced under combustion conditions by a factor of 20,

and the sooting hydrocarbon flame environment does not present any significant interferences that would preclude ELFF monitoring of CHC concentrations in incinerator exhausts. Thus, with our apparatus, the detection limit for C_2H_5Cl is 100 ppb for spatially resolved, in situ measurements with a detection time of 5 s.

The detection limits necessary for emissions monitoring are not well defined, since they ultimately depend on assessment of health risks posed by specific incinerators. However, some risk assessments have concluded that the risks from organic emissions allowed by current regulations are acceptable [1]. These regulations require that toxic compounds present in the waste at concentrations of 100–10,000 ppm be destroyed by at least 99.99%. Thus, if we assume a dilution factor from waste to exhaust of 10, the maximum emission currently allowed is 100 ppb. Since that is for an individual waste compound, the total concentration of CHCs emitted may be somewhat higher. Therefore, the detection limit achieved by our current apparatus appears to be adequate for continuous monitoring.

Acknowledgments

The National Institutes of Environmental Health Sciences funded this research through the Superfund Basic Research Program, Contract No. P42 ES047050–01. D. Lucas was also supported in part by a grant from the U.S. E.P.A. We thank A. K. Oppenheim and N. J. Brown for loaning us equipment.

REFERENCES

1. Dempsey, C. R., and Oppelt, E. T., *J. Air Waste Manage. Assoc.* 3:558 (1993).
2. Lucas, D., Koshland, C. P., McEnally, C. S., and Sawyer, R. F., *Combust. Sci. Technol.* 85:271 (1992).
3. Rodgers, M. O., Asai, K., and Davis, D. D., *Appl. Opt.* 19:3597 (1980).
4. Rohlfing, E. A., *Twenty-Second Symposium (International) on Combustion,* The Combustion Institute, Pittsburgh, 1988, p. 1843.
5. Cool, T. A., and Williams, B. A., *Combust. Sci. Technol.* 82:67 (1992).
6. McEnally, C. S., Sawyer, R. F., Koshland, C. P., and Lucas, D., *Appl. Opt.* 33:3977 (1994).
7. Jeffries, J. B., Raiche, G. A., and Jusinski, L. E., *Appl. Phys. B* 55:76 (1992).
8. Mélen, F., Houbrechts, Y., Dubois, I., and Bredohl, H., *J. Phys. B,* 16:2523 (1983).
9. Pearse, R. W. B., and Gaydon, A. G., *The Identification of Molecular Spectra,* Chapman and Hall, London, UK, 1965.
10. Huber, K. P., and Herzberg, G., *Molecular Spectra and Molecular Structure, IV: Constants of Diatomic Molecules,* Van Nostrand Reinhold Company, Princeton, NJ, 1979.
11. Tyerman, W. J. R., *Trans. Faraday Soc.* 65:2948 (1969).
12. Tiee, J. J., Wampler, F. B., and Rice, W. W., Jr., *Chem. Phys. Lett.* 73:519 (1980).
13. Dagnall, R. M., Smith, D. J., Thompson, K. C., and West, T. S., *Analyst* 94:871 (1969).

COMMENTS

Kermit C. Smyth, National Institute of Standards and Technology, USA. For hydrocarbon diffusion flames, strong broadband molecular fluorescence is observed upon irradiation with UV light, and laser-induced incandescence from soot particles occurs for sufficiently high laser fluences. I'm surprised that you did not observe one or both of these interferences when irradiating rich flame regions at 284.7 nm.

Author's Reply. We believe several factors prevent PAH fluorescence or laser-induced soot incandescence from interfering with our CHC measurements. First, we are not concerned with emission during the intense 193-nm fragmentation pulse, and the probe laser has only a modest intensity of roughly 10^6 W/cm^2. Second, both PAH fluorescence and soot incandescence are broadband signals that are strongly suppressed by the 2-nm bandpass of our monochromator. Finally, the horizontal scans shown in Fig. 6 of the paper were made roughly halfway between the visible flame tip and the lip of the burner, whereas maximum soot concentrations occur nearer to the tip of the flame. Assuming that the soot concentrations in our flames were at least as great as those of non-premixed C_2H_4/air flames studied by Santoro et al. [1], soot densities greater than 1000 mg/m^3 would have been encountered during the horizontal scans. This exceeds the average exhaust stack particulate concentrations for all incinerator types [2]. Therefore, we are confident that the conditions we studied are more likely to produce interferences than those of actual incinerator exhausts, and the failure to observe such interferences means they will not be a problem for application of our technique to incineration monitoring.

REFERENCES

1. Santoro, R. J., Yoh, T. T., Horvath, J. J., and Semerjian, H. G., *Combust. Sci. Technol.* 53:89 (1987).
2. Dempsey, C. R., and Oppelt, E. T., *Air Waste Manage. Assoc.* 3:558 (1993).

Twenty-Fifth Symposium (International) on Combustion/The Combustion Institute, 1994/pp. 333–344

INVITED TOPICAL REVIEW

INJECTION, DISPERSION, AND COMBUSTION OF LIQUID FUELS

W. D. BACHALO
Aerometrics, Inc.
Sunnyvale, CA 94086, USA

A review of the research in fuel spray combustion is offered with emphasis on experimentation in spray dynamics. Atomization and fuel-air mixing have been identified as areas in which advancements in the combustion technology are still possible. The development of optical diagnostics has enabled the detailed characterization of fuel spray injection, and subsequent turbulent mixing, in model combustors. Difficulties in making measurements in nonreacting and reacting spray environments, including high drop number densities, drop deformations, nonuniform drop temperatures, refractive index variations, and particle concentration gradients, are discussed. A brief review of experiments in both nonreacting and reacting sprays is provided. Improvements realized in the measurement techniques for drop number density and volume flux are also described. Other areas needing further investigation have been identified. Methods for simultaneously measuring the drop temperature and fuel vapor concentration are under development and some key characteristics of these methods have been outlined. Since the spray drop interaction with turbulent flows in the combustion chamber has a considerable impact on the combustor performance, the parameters and correlations affecting the drop response are reviewed.

Introduction

A considerable percentage of our energy resources is derived from the combustion of liquid fuels in the form of sprays. For this reason, spray formation and liquid atomization have been investigated in order to unravel the mechanisms involved in the liquid breakup [1–7], atomization, and spray drop dynamics [8–14], especially with respect to requirements for combustion. The conditions of the introduction of the spray injection, dispersion, vaporization, and burning of the fuel with stoichiometric proportions of air in a well-mixed environment affect the combustion stability, efficiency, and pollutant formation. In particular, aerodynamic efficiency of redistribution and mixing of the fuel and air in the combustion chamber, and the dilution of the combustion products to the desired temperature level and proper temperature profile, determine the quality of the combustion and the levels of emissions generated. Of particular concern are the formation of the oxides of nitrogen, carbon dioxide, carbon monoxide, soot, and unburned hydrocarbons.

It is not yet completely clear what the most favorable spray conditions should be for optimum combustor performance, and thus, research is needed to define the effects of all parameters that influence the combustion process. These parameters are the mean drop size and drop size distribution at each location within the spray plume, drop velocity distribution, drop velocity relative to the air velocity, drop number density (spatial and temporal), and drop temperature. The spray interaction with the turbulent environment and its effect upon evaporation affect the mixing and dispersion of the fuel. Aerodynamic mixing of the fuel spray and combustion all transpire under highly turbulent flow conditions, with the drops undergoing heat and mass transfer with the local fuel-air ratios extensively controlled by the aerodynamics.

New trends in combustor development have focused upon the necessity to reduce soot and NO_x emissions [14–19]. Sturgess et al. [14] have concluded that, for gas turbine combustors in the near term, the only feasible approaches that can be used to meet the emission standards are changes in the fuel injectors and in the combustor liner dilution air hole patterns used to further promote mixing. The predicament encountered in the design of combustors is that schemes implemented to reduce soot lead to an augmentation in NO_x and vice versa. For example, raising the combustion temperature by increasing the combustion zone equivalence ratio reduced CO formation and excess smoke. This was achieved by using airblast fuel injectors to accomplish finer atomization and improved fuel-air mixing. Unfortunately, the resulting higher combustion temperatures at all operating conditions increased the formation of NO_x. Strategies proposed to overcome this dilemma include the use of staged combustion using a rich-burn, quick-quench, lean-burn (RQL) approach. A critical requirement of the approach is the rapid and efficient mixing of the fuel spray with the air, which depends upon the size and shape of the recirculation zone, the drop size distribution, and

the design of the air dilution jets, among other factors.

The development of laser-based diagnostics to reliably characterize the spray size distributions, the drop dynamics, and the turbulent mixing in nonreacting and reacting environments has been timely in terms of the development of advanced combustion technology. The phase-Doppler method [20–22] provides a means for achieving the simultaneous measurements of the spray drop size, velocity, number density, and volume flux in practical sprays [23–25]. More recently, the method has been combined with rainbow refractometry to enable the simultaneous measurement of the drop temperature. Once deployed, this added capability should serve to provide greater insight into the dynamics and the evaporation and combustion of liquid fuels.

A comprehensive review of spray combustion research is not possible in the limited space available. Several excellent reviews have been written on this subject by Chigier [26], Faeth [27], Law [28], Sirignano [29], and Williams [30]. This review is focused on the injection of the atomized fuel, the fuel-air mixing, and the characterization of the subsequent interactions of the fuel spray drops with the complex turbulent air flow in the combustion chamber. The primary emphasis will be upon the experimental observations that have been conducted, and some of the potential measurement problems encountered in spray combustion environments will be addressed. Advances in the spray diagnostics have significantly improved the reliability and detail of the data that may now be obtained.

Spray Characterization Methods

The evolution of spray characterization methods has made an exceptional contribution to our ability to research and understand spray combustion phenomena. The Fraunhofer diffraction method described by Swithenbank et al. [31] and others [32–33] gained acceptance as an efficient and reliable means to obtain Sauter mean diameter (D_{32}) measurements in practical sprays. The method provided a simple line-of-sight measurement of the concentration-based mean diameter. Unfortunately, the method does not provide information on the drop dynamics and is very sensitive to beam steering resulting from refractive index gradients, and hence fails in combustion environments. Interest in measuring the drop size and velocity, as well as the spatially and temporally resolved number density and volume flux, led to the development of methods incorporating the laser-Doppler velocimeter. As a consequence of these efforts, the phase-Doppler particle analyzer was developed for spray measurements [20–22], and it has become a very useful instrument for spray characterization in nonreacting and reacting sprays. Since the phase-Doppler method has been described in great detail in numerous papers, what will be discussed are the measurement characteristics, problems associated with spray combustion characterizations, and the developments in the technology to deal with the problems identified. Of primary concern is the measurement reliability of not only the drop size distributions, but also of the drop number density.

Number Density Limitations:

Operation of the phase-Doppler method, or any other single particle counting method, in high drop number density environments may lead to coincident particle occurrences in the measurement volume. Although the sample volume can be made very small to ensure a low probability that there is no more than one drop in the sample volume at one time, in the dense spray region, coincident occurrences may give rise to errors. A detailed analysis for estimating the probability of coincident occurrences is given by Edwards and Marx [34]. The authors assumed an ideal system in this analysis for which all coincident occurrences were rejected by the instrument logic. Two Poisson filters were employed, one for the spatial distribution of the particles

$$P_x = e^{-NV} \tag{1}$$

and a second

$$P_t = e^{-\lambda t} \tag{2}$$

for the temporal or arrival time statistics. Since the size of the sample volume will be different for different particle sizes, the analysis also accounted for this change in the sample volume. The particles were assumed to be distributed randomly and homogeneously in space and to have a number density N. The analysis of Edwards and Marx indicated that, for an ideal system, the mean drop size, and particularly D_{32}, would be reported without significant error even with a low probability for acceptance of the measurements. Only the particle number density and volume flux would have significant error.

In reality, the instrument is imperfect because it may not reject all coincident occurrences. Logic systems including redundant phase measurements, signal-to-noise ratio checks, and signal amplitude measurements have been incorporated into the instruments to prevent erroneous measurements from being made. The performance of the phase-Doppler particle analyzer (PDPA) under conditions of two particles passing the sample volume at one time is described in Sankar et al. [35].

Drop Deformations:

When dealing with high-pressure, high-velocity sprays, or sprays in reacting environments in which the high temperatures reduce the surface tension, particular attention must be devoted to the forces on the drop that produce incremental drop deformation, thus causing the drop to deviate from its spherical shape. It is possible to assess the deformation of the drop with the use of the measured mean relative velocity, v, and an estimate of the ambient gas density. The analysis of small deformations and oscillations of a drop in a moving gas by Hinze [36] indicates that the drop deformation will vary as a function of the Weber number given as

$$\frac{\delta}{d} = -0.047We \tag{3}$$

where δ is the radial displacement of each fluid element from its undeformed state. For the drop oscillations resulting from a sudden introduction of a drop into the air stream with very small or very large viscosity, the deformation is

$$\frac{\delta}{d} = -0.085We \tag{4}$$

which is almost twice that of the steady-state case. In a recent study by Hsiang and Faeth [3], the correlation for a steady disturbance was proposed as

$$\frac{d_{\max}}{d_{\min}} = (1 + 0.07We^{0.5})^3. \tag{5}$$

Measurement errors of the phase-Doppler instrument resulting from asphericity of the drops can be estimated by assuming that the sphere is deformed aerodynamically into an oblate or prolate spheroid (when the deformations are not extreme). Using simple geometry, the local radius of curvature can be calculated. The local radius of curvature for a drop deformed by a flow in the direction of the measurement beam pair is described by the calculations of Bachalo and Sankar [37]. These results and the data of Alexander et al. [38] show that the measured size will either be larger or smaller than the equivalent sphere, depending on the measurement orientation relative to the axes of the deformed drop. Researchers have also used drop size measurements simultaneously from two orthogonal beam pair orientations from a two-component system to estimate the deformation of large drops [39]. The drop deformation information is also needed in the correction of the C_D for modeling these sprays [18], so such measurements are of value.

Mass Flux and Number Density Measurements:

Measurements of the local mass flux and number density are important capabilities of the phase-Doppler instrument. Several reports have indicated successful measurements of these quantities [22,23,25,40]. However, there also have been reports indicating large variances in the measurements. There are several explanations for these discrepancies, including nonuniformities in the spray patterns, large variations in the drop trajectories as a function of drop size, measurements of only a single velocity component, drop deformation, and excessive drop number densities. A problem has been the possible inability of the instrument to detect and process signals from small drops that produce signals with low signal-to-noise ratio (SNR). A signal processor based on the discrete Fourier transform (DFT) that provides the optimum method for signal frequency and phase measurement has been developed [41] to overcome this problem. The reliable detection of the smallest particles in the size distribution that also possess the lowest SNR has been enhanced with the invention and development of the Fourier transform burst detector (FTBD) (Ibrahim and Bachalo, 1994, U.S. Patent 5,289,391). Signal detection is now based upon the relative coherence or SNR of the signal and serves to detect and process signals with SNR as low as -6 dB or lower. The relevance of the signal processor development is that the dependence of the measurements on the instrument setup parameters has been minimized [42].

The method used for determining the number density has also been improved. Use of the transit time, or time required for the drop to pass through the sample volume, has reduced the error due to random drop trajectories and false triggers of the burst detector. The number density is obtained as

$$N = \frac{1}{T_t} \sum_i \frac{\sum_j t_g(i,j)}{V_i}. \tag{6}$$

A critical factor is the in situ determination of the sample volume when measuring sprays in complex swirling flows in cases where only two simultaneous velocity components are being measured. In these environments, the light-scattering intensity approach [43] appears to offer promise for resolving this problem. Recent comparisons of the measured number densities with beam extinction measurements have shown good agreement [42]. Incorporation of the signal intensity validation and a better understanding of the trajectory-dependent light scattering [44] have allowed more reliable measurements of the largest drops in the distributions and, consequently, the volume flux.

Nonuniform Drop Heating:

In combustion environments, the effect of nonuniform temperature within the drop on the drop size measurements may be another potential source of error. The liquid heating time, τ_H, which is defined as the penetration time of a drop by a thermal diffusion wave from the surface to its center, is discussed by Sirignano [29]. The estimation of the drop heating time for spherically symmetric heating was estimated as

$$\tau_H = \rho_l c_l d_0^2 / 4\lambda_l \tag{7}$$

and the drop lifetime was presented as

$$\tau_L = \rho_d d_0^2 / 8\rho D \log(1 + B) \tag{8}$$

and the ratio is

$$\frac{\tau_H}{\tau_L} = 2 \frac{\lambda}{\lambda_l} \frac{c_l}{c_p} \log(1 + B). \tag{9}$$

Note that the ratio is independent of the drop diameter, indicating that the problem of nonuniform temperature may occur over all initial drop sizes. Depending on the conductivity, specific heats, and transfer number, the drops may be at nearly uniform temperature or show large temperature gradients. Law and Sirignano [45] provide information on the drop radial temperature distributions for spherically symmetric drop vaporization. Schneider and Hirleman [46] investigated the influence of spherically symmetric refractive index gradients on the size measurements of spherical particles larger than the light wavelength. The resulting error in the size measurement is approximately ±5% for 30° forward scatter detection in the severest condition.

Drop Temperature Measurements:

Accurate drop temperature in a reacting spray is an important parameter that needs to be measured and that will allow further insight into drop heating, vaporization, and heat and mass transfer during the combustion of fuel sprays. Although various spectroscopic and nonspectroscopic techniques have been considered for drop temperature measurements [47,48], the successful measurement of individual drop temperatures in complex reactive environments has not been possible, to date. The use of exciplex fluorescence has been demonstrated [47], but unfortunately, the fluorescence is quenched in an oxygen environment. Furthermore, liquid fuels may contain aromatic hydrocarbons, which can produce fluorescence emissions that will mask the fluorescence spectrum of the dopants. Currently, a method is under development to allow the nonintrusive, in situ, simultaneous measurements of the drop size, velocity, and temperature in a turbulent swirling and recirculating flow field [49]. The method is based on the measurement of the rainbow angle [50], which depends upon the drop index of refraction. For single-component fuels, the dependence of the refractive index as a function of temperature is known. This method is also affected by the nonuniform heating of the drop [51], which may cause errors in the measurements. The problem is currently under investigation.

Massoli et al. [52] suggested a second approach for measuring the drop index of refraction, which involves measuring the light-scattering intensity ratio of the horizontally polarized light (incident and scattered) at two scattering angles, $I_{HH}(33)/I_{HH}(60)$. Their results were in excellent agreement with the rainbow method. With the index of refraction variation resulting from temperature changes $(\delta m/\delta T)_p$ known, the drop temperature can be derived. For uniformly heated drops and a single-component fuel, an accuracy of ±5 °C was claimed. The simultaneous measurement of the refractive index also provides information for correcting the drop sizing for index of refraction effects.

Mixing and Evaporation:

Experiments designed to study the mixing of the air streams in a swirling flow have utilized the approach of tagging the seed particles in the flow in one region with a fluorescent dye [53]. Particle tagging allowed the separation of fluid arriving from the outer part of the flow from the air flowing through the swirler. A method for the measurement of the path-averaged hydrocarbon vapor concentration in fuel sprays has been described by Billings and Drallmeier [54] and Drallmeier and Peters [55]. Detection of the light extinction simultaneously at two wavelengths allowed the measurement of the vapor in transient sprays.

Fuel Injection

Numerous practical means for supplying the necessary energy to the liquid to break the liquid into small drops have been considered for the atomization of fuels. Pressure swirl atomizers have found a wide range of acceptance for use in gas turbine, industrial, and domestic combustors, as well as in other combustors, because of their simplicity and low cost. These atomizers are being superseded by various airblast and air-assist atomizers [56]. Other approaches receiving attention are electrostatic atomizers [57], ultrasonic atomizers, and hybrid pressure swirl atomizers using piezoelectric crystals to excite the instability modes [58]. To improve the atomization for gas turbine and industrial combustors, which would then reduce the smoke and soot formation, prefilm-

ing airblast atomizers were developed [59]. Variations of this design that include fuel swirl are commonly used in high-compression-ratio gas turbojet engines. An extensive discussion of the design parameters affecting airblast atomizer performance is given by Lefebvre [56]. With pressure swirl atomizers, the high liquid injection pressure leads to liquid velocities that greatly exceed the velocity of the surrounding air velocity. The liquid kinetic energy, turbulence, and shear forces dominate the breakup [60,61], with the air flow playing a more passive role. Alternatively, with airblast and air-assist atomizers, the high relative velocity between the liquid sheet and the air is now furnished by the air, with the liquid injected at low velocity. These atomizers produce better spray uniformity, higher combustion efficiency, lower smoke production, and a lower pattern factor [14], although there are some differences of opinion on this observation.

The radial distribution of the axial velocity of the spray produced by airblast atomizers is quite different from that of the pressure swirl atomizer [62,63]. For an airblast atomizer, the large drops have the lowest velocity, whereas the small drops ($D_{10} \sim 10$ μm) at the center of the distribution have the highest velocity. For this reason, the airblast atomizer appears to produce a more favorable condition for combustion since the large drops that require a greater residence time for evaporation are moving at a velocity that is approximately 10 times slower, which also allows more time for interaction with the swirling recirculating flow. The atomization air in the airblast atomizer also contributes to the mixing and supplies additional air for combustion. With the pressure swirl atomizer, it is the large drops that are typically moving at velocities an order of magnitude or more faster than the small drops. Thus, the relative difference in the drop velocities in the two types of atomizers may be the factor leading to the reduction of the soot formation and improved performance. Odgers et al. [64] report finding no measurable effect of drop size on combustion efficiency. The authors claim that, in almost all previous studies, some other parameter was changed as well as the drop size.

Drop Collisions and Coalescence:

Drop collisions and coalescence in the dense spray region, as well as in the dilute spray, have been described as a reason for the development and evolution of drop size distributions with downstream distance in the spray. The probability for drop collisions can be estimated from a knowledge of the drop speed relative to other target drops and the drop number density. For example, the swept volume, Ω_i, for a drop of diameter d_i to collide with a drop of mean diameter D_{10}, moving at a mean relative velocity, v_i, is

$$\Omega_i = \frac{\pi(d_i^2 + D_{10})^2}{4} v_i t_i. \tag{10}$$

This approximation indicates the dependence of the swept volume on the relative velocity and the possible interaction time, t_i. Assuming a spatial Poisson distribution of particles of number density N particles per cm^3, then

$$P_{ci} = N\Omega_i e^{-N\Omega_i} \tag{11}$$

where P_{ci} is the probability of a collision for the particle of diameter d_i with another particle of mean diameter D_{10} within time t_i, based on the probability of another particle existing in the swept volume, Ω_i. The description is complicated by the facts that drops of different size may be traveling at velocities (magnitude and direction) that are a function of their size and location in the developing spray and that drops will decrease in size and velocity because of evaporation.

Particle collisions may lead to coalescence, breakup, or a rebound depending on several parameters, including the Weber and Ohnesorge numbers [65,66]. In a recent paper, Qian and Law [67] suggest there are five distinct collision regimes: bouncing, coalescence with minor deformation, coalescence with substantial deformation, coalescence followed by separation for near head-on collisions, and coalescence followed by separation for off-center collisions. Numerical simulations of drop collisions by Nobari and Tryggvason [68] considered off-center collisions.

Transient Fuel Injection

Diesel Injection:

Transient spray injection such as that used in diesel and spark ignition (SI) engines shows some unique atomization characteristics. Diesel injection may take place into a relatively quiescent environment at pressures of approximately 15 atm and at injection pressures of between 50 and 180 MPa [69]. The important combustion parameters are the fuel penetration, mixing, and vaporization. These parameters depend upon the spray drop velocity and trajectory, the drop size distribution, and the turbulent gaseous flow field. Tsao et al. [70] note that injection rate and duration are also important parameters since they influence the pressure rise in the cylinder after ignition. It was recognized that just fine atomization was not sufficient for achieving efficient combustion, since the spray must be able to penetrate into the chamber under a range of chamber conditions. If the drops are too small, rapid evaporation will occur, and the fuel vapor and flame will not penetrate far enough into the combustion chamber. Injector parameters such as the number of orifices in

the injector, hole size and length of the orifice hole, and the hole angle all affect the performance [69]. Interaction of the spray with the air swirl in the chamber and the squish serve as effective mechanisms in the mixing and vaporization of the fuel spray.

The increasing restrictions on NO_x and particulate emissions from diesel engines have led to some innovative approaches in reaching these goals. Konno et al. [71] attempted to augment turbulent mixing during injection with the use of an auxiliary chamber. A high-pressure air-fuel jet was injected into the main combustion chamber after the start of the main injection. This was reported to result in a factor of 3 reduction in particulate production. Golding [72] observed a similar improvement when injecting a methane-air jet to enhance the turbulent mixing late in the injection cycle. Tow et al. [73] showed promising results in terms of NO_x and particulate reductions when using staged or split injections. A variety of multiple injection strategies were examined in addition to ramped injections in which the rate of change of the fuel injection was varied. This work followed the earlier work of Bower and Foster [74], who indicated that the fuel-air mixing could be enhanced by the augmented fuel spray penetration achieved with the split injection. Predictions using the modified KIVA code made by Patterson et al. [18] indicated that fuel injection at lower pressure resulted in increased soot emissions, but an increase to very high pressures has a limited usefulness in reducing soot and NO_x emissions.

Detailed measurements of the drop size and velocity of transient diesel injection were obtained by Koo and Martin [75,76]. They observed that the factors affecting the drop size and velocity were the fuel properties, pump speed, fuel quantity delivered, the needle lift, and the combustion chamber geometry.

Spark Ignition Engines:

Spark ignition (SI) engines using port fuel injection (PFI) also show a strong dependence of the emissions and performance on the atomization quality and fuel-air mixing [77–80]. As with diesel applications, the atomization is highly transient and must be accomplished over a wide range of operating parameters. Dementhon and Vannobel [80] investigated the injection of fuel into the manifold of a SI engine operating with gasoline. Their interest was in the effect of the manifold and combustion chamber aerodynamics on the fuel-air mixing. Depending on the angle of injection and the air flow, fuel films also formed on the valve and valve seat. Fuel injection into a manifold with similar flow conditions was investigated by Nemecek et al. [77].

Turbulent Dispersion

Information on the spray characteristics produced by the various atomizers operating in a quiescent environment is useful for the basic development of these systems. However, one might ask whether such studies are relevant for spray combustion applications since the injection generally takes place in highly turbulent swirling flows with recirculation and reaction. The drop size distributions and even the spray formation mechanisms may be significantly altered by the interaction with the ambient turbulent flow. Furthermore, the high-temperature combustion environment reduces the surface tension of the liquid and rapidly evaporates drops smaller than 10 μm in times on the order of milliseconds.

Turbulence Coupling:

Sprays are generally injected into the flow with sufficient momentum to significantly alter the continuous-phase flow field, at least locally. Thus, turbulence coupling between the dispersed phase and the continuous phase needs to be considered. Near the injector, the dispersed phase generally dominates the gas-phase turbulence in the host environment. A degree of turbulence is generated by the liquid during the spray formation and by the wakes of the drops in the dense spray region. Further downstream, two-way coupling exists between the dispersed phase and the gas. The drop number density is still high, and relatively large velocities still exist between the drops and the gas phase. Simultaneously, the gas-phase turbulence of the surrounding swirling flow and the turbulence that was induced by the injection velocity upstream begin to have a greater influence on the redistribution of the smaller drops within the spray. However, the spray number density and the drop slip velocities are still high enough to produce a significant effect upon gas-phase turbulence. Further downstream, the drops are dispersed by a combination of the spray axial and radial momentum and the interaction with the turbulent flow field, so the number density and slip velocities decrease substantially. The coupling is one way again in this region, but from the gas-phase turbulence to the dispersed phase. The dispersed phase now has an insignificant effect upon the gas phase.

Spray Interactions with Turbulent Flows:

In recent years, there has been a considerable interest in the study of the interaction of the spray drops and the air flow swirl as a result of the need to develop smaller clean-burning engines while maintaining performance. Recirculation, generated by augmenting the swirl, which reduces the axial momentum of the flow and, combined with the positive streamwise pressure gradient, results in a reversed-

flow region, is also used to increase the residence time and enhance mixing. When contemplating such concepts as the rich-burn, quick-quench, lean-burn method for NO_x reduction, it is imperative that rapid mixing in the initial fuel-rich zone is achieved without formation of pockets of near-stoichiometric burning. The mixing time depends on the size of the recirculation zone, the drop size distribution, and the degree of turbulence. A combination of the injector air, the swirler air, wall-cooling air, and the dome-cooling air all contribute to the supply of active air that also drives the fuel-air mixing [14,81]. The shear flows created by the swirl, which in some cases have counter-rotating components, and the wall jets, will produce large-scale eddies with which the spray drops must interact and, consequently, enhance the large-scale turbulent mixing.

The smallest turbulent length scales will be on the order of the drop diameters. It is known that the restoring force or drag needed to change the particle velocity to the velocity of the gas in the new surroundings is generated by the relative or slip velocity, so the fuel droplets will essentially always lag the flow. The degree of the velocity lag depends upon the flow acceleration, turbulence intensity, and mass of the drops. No matter how small the drops, they will be buffeted by the flow with random velocities having large variations in magnitude and direction. It may therefore be misleading to estimate evaporation rates and heat and mass transfer based on the studies of drops in a quiescent environment or as drops moving in a quasi-laminar environment.

Drop Response to Turbulence:

Several studies have been conducted to elucidate the interaction of particles with highly turbulent flows [82–87]. The drop drag correlation of Torobin and Gauvin [88] was validated experimentally for a polydisperse collection of drops in a turbulent air flow by Rudoff et al. [89]. The drop response to the large-scale eddies is assumed to be most important to the dispersion of the spray drops in the flow since it is the large-scale turbulent motion that is most effective in transporting the range of drop sizes over distances on the scale of the flow field. The analysis of Hinze [82] led to the expression that approximates the drop response as

$$\frac{d_m}{\Lambda} \leq \left[\frac{u'\Lambda}{\nu}\left(\frac{\rho_d}{\rho} + \beta\right)\right]^{-1/2} \tag{12}$$

where Λ is the macroscale of the turbulence, u' is the root-mean-square (rms) of the velocity fluctuations, and β is given by

$$\beta = 1 + \frac{\rho}{2\rho_d} \tag{13}$$

which is approximately equal to 1 for a large density ratio between the drop and the gas. For the basic case of a subsonic jet of exit diameter D emanating into still air at an exit velocity U, the expression reduces to

$$\frac{d_m}{D} = \left[\frac{C}{\frac{u'}{U} Re_D \left(\frac{\rho_d}{\rho} + 1\right)}\right]^{1/2} \tag{14}$$

where C is an empirical constant, u'/U is the actual turbulence intensity, and Re_D is the jet exit Reynolds number. As an example, for an axisymmetric jet with $C = 0.4$ at a jet Reynolds number of approximately 16,000, the largest drops that will respond well to the turbulence fluctuations are 5.0 μm. Thus, for sprays within a highly turbulent flow, a preponderance of the drops will significantly lag the large-scale turbulent fluctuations. As stated earlier, the implication is that the evaporation and heat transfer for drops in a quiescent environment will not be representative of the actual situation.

The response of the drops to large-scale eddies also has been described in terms of the Stokes number [90] as

$$St = \frac{1}{\tau}\frac{\Lambda}{v} \tag{15}$$

where v is the relative velocity between the particle and the eddy convection velocity. For a transit Stokes number greater than 1, the drop is likely to respond to the turbulent eddy. Dring and Suo [90] suggested that, for a drop within a large-scale eddy, the magnitude of the centrifugal forces relative to the Stokes drag forces may be estimated by the centrifugal Stokes number given as

$$St_\psi = \frac{18\nu}{\psi d^2}\frac{\rho}{\rho_d} \tag{16}$$

where ψ is the angular velocity.

The largest drop that will adequately respond to the motion of the small-scale eddies was derived from the Stokes law particle relaxation and the Kolmogorov time scales $\tau_k = (\nu/\varepsilon)^{0.5}$ as [82]

$$\frac{\tau}{\tau_k} = 0.38 Re\, D^{1.5}\left(\frac{x}{D}\right)\left(\frac{d}{D}\right)^2\left(\frac{\rho_d}{\rho}\right) \tag{17}$$

where ε is the local turbulence dissipation rate, x is the distance from the jet exit, and D is the exit diameter of the jet. For a first approximation, $\tau/\tau_k = 1$ was taken as a reasonable choice to provide a lower bound to determine whether the drop size, or more accurately the drop mass, is small enough to respond to the smallest turbulent scales in the flow. At a jet

Reynolds number of 16,000 (jet mean velocity of 50 m/s), the diameter of a water drop meeting the above criteria is 0.3 μm. Therefore, none of the drops in a typical spray can be expected to respond to the Kolmogorov time scales in a turbulent jet. Hence, the drops will always experience a relative velocity that is random in trajectory and magnitude relative to the drop moving at the mean flow velocity, or the local velocity of the large-scale motion.

Drop Interaction with Large-Scale Eddies:

Experiments have been conducted to aid in the understanding of the particle interaction with the turbulence [9,91–95]. The initial studies [9] focused on the redistribution of the spray when interacting with turbulent swirling flows with recirculation and the time-averaged spray drop dynamics. Time-resolved measurements were then applied in the measurements of a spray flame. These results showed possible evidence of clustering of the drops at a period that correlated with the shedding frequency of the dilution air flow [95]. The formation of clusters due to the interaction with turbulence has been the subject of several studies [94–96].

An illustrative example of the basic mechanisms of the cluster formation was given by Hancock et al. [94] using a novel flow visualization technique. The method involved the injection of water drops into a $TiCl_4$-laden gaseous flow, which then forms TiO_2 particles of approximately 1 μm in diameter. The visualization method clearly showed how small drops with a mass that can respond to the vortex will tend to accumulate in the core of the vortex. It is easy to anticipate that spray drops in the size range between the 1-μm particles and the 70-μm drops will have a continuum of responses from being entrained in the vortex to only showing a small deflection in the trajectory. An experimental investigation of the interaction of a spray with large-scale eddies was conducted by Bachalo et al. [86,91] in an effort to quantify the drop response to the eddies at various flow Reynolds numbers and the fundamental mechanisms in drop dispersion and cluster formation.

Spray Evaporation and Combustion

Drop evaporation has been the subject of extensive studies with the focus being on single drops, as well as on sprays. Unfortunately, most of these studies have considered isolated drops in quiescent or very low turbulence environments, as discussed in the review by Beer and Chigier [97]. The drop evaporation is described as [64]

$$\tau_e = \frac{d_0^2}{\beta} \tag{18}$$

where

$$\beta = \frac{8\dfrac{\lambda}{c_p}\ln(1 + B)}{\rho_d} \tag{19}$$

with the symbols described in the nomenclature. The values of β for heptane, for example, were $\beta = 0.96$ for a single drop and $\beta = 0.47$ for a uniform spray. For a monodispersed drop stream combustion of kerosene, the total combustion time t_c was approximated as

$$\tau_c = 2.5 \times 10^{-6}\, d_0^2 \tag{20}$$

where d_0 is the initial drop diameter in micrometers. Typical drop combustion times are 0.25 ms for a 10-μm drop and 25 ms for 100-μm drops. Note that, at a mean velocity of 20 m/s, a 10-μm drop will travel approximately 2 mm, and 100-μm drops will travel 200 mm during this time, which may be well beyond the flame zone.

Researchers have assumed that the drops will rapidly acquire the velocity of the air stream, so the drop Reynolds number and the enhancement of the heat and mass transfer from the drop by the relative motion disappear [64]. However, the basic analysis on the drop response to the turbulence indicates that this is not the case, as the drops do not equilibrate with the turbulent flow velocity fluctuations. Because the drops are more likely to lag the smaller scale turbulent fluctuations, it may be concluded that these smaller scale fluctuations will be more effective in increasing the local convection and, hence, the drop mass transfer rates. Chin and Mongia [98,99] have studied the effects of temperature on the drop breakup, and convection on drop evaporation. They show that, at Re_d greater than 50, the evaporation time with forced convection is approximately one-half that of the stagnant case [98]. Gokalp et al. [100] have also investigated the influence of turbulence on the global transfer rates from heptane and decane drops.

Spray Combustion Measurements

The development of the phase-Doppler particle analyzer has enabled the detailed measurement of drop size and velocity and the number density and volume flux in realistic spray combustion environments [63,95,101–105]. Bachalo et al. [95] obtained drop size and velocity measurements in an unconfined fuel spray combustion and observed the apparent formation of drop clusters that had a periodicity that correlated with the shedding frequency of the coannular dilution air flow. Edwards and Rudoff [105] obtained measurements of the drop size and velocity in a research furnace of 0.57 m in diameter and 0.93 m in height. The size-classified mean velocity of the spray drops showed a maximum velocity

difference between the 2-μm drops and the 40-μm drops of approximately 10 m/s. Williams [106] suggests that drops of 100 μm in diameter with relative velocities on the order of 10 cm/s will be extinguished. Thus, the penetration of these drops beyond the flame zone may be expected, resulting in excess unburned hydrocarbon (UHC) emissions. The fact that the large drops escape the combustion is clearly visible in the flame photographs of Presser et al. [103].

Gas-phase and spray drop size and velocities were measured by Bulzan [107] for a simplex air-assist atomizer operating in a swirl coflow air stream used to stabilize the flame. Anisotropic turbulence was observed, with the axial and radial velocity fluctuations being much larger than the angular velocity fluctuations. Measurements of the flow velocity and turbulence parameters, as well as the drop size and velocity, for an airblast atomizer operating on methanol were reported by McDonell and Samuelsen [62]. Both nonreacting and reacting conditions were also considered. They found that the effect of the reaction had only a minor effect on the mean velocity and turbulence intensity at an axial station of 50 mm (the beginning of the reaction zone). Anisotropy of the turbulence was observed to increase with reaction.

Chehroudi and Ghaffarpour [108] investigated the effects of swirl and dilution air flow rates on the shape and stability of a kerosene flame on a model combustor, with comparisons made of the noncombusting and combusting cases. Their flow visualization showed nonuniformly distributed separated fingerlike regions of visible flames wrapped around the spray sheath. These structures were possibly due to large-scale eddies formed by the swirling flow. Investigations by Li et al. [109,110] explored the combustion and flame extinction of methanol sprays conveyed by nitrogen into a counterflowing oxygen stream. Detailed measurements showed the expected slight increase in D_{32} as the flame was encountered. The number density showed a dramatic decrease within the flame and was approximately three orders of magnitude less than in the nonburning case.

Summary and Conclusions

Improvements in the combustion performance and reduction of pollutant emissions, including NO_x and soot, are primary objectives of combustion research and development. It has been recognized that improvements in combustion may be realized through a better understanding of the fuel atomization, injection, and aerodynamic mixing in the combustor. Spray formation and atomization have received a good deal of attention both through the research on the detailed studies of spray formation mechanisms and the development of advanced atomization techniques. There is a need for further research on the impact of the spray quality on the combustion efficiency and pollutant formation. Several parameters, such as the drop penetration, evaporation rate, drop reaction to the mean swirling flow and to the large-scale turbulent fluctuations, need to be quantified in terms of their influence on the combustor performance.

Developments in the instrumentation have provided the means to obtain reliable experimental data on the sprays, and spray interactions with the turbulent flow in nonreacting and reacting environments. Reliable measurements in these difficult environments require the most sophisticated methods, such as real-time Fourier analysis signal detection and processing, and logic systems to prevent or at least minimize errors. Measurement methods continue to be developed to provide better accuracy and reliability in the spray combustion environments, which are characterized as highly three-dimensional turbulent two-phase flows with recirculation. Measurements of the gas-phase turbulence in the presence of the dispersed phase require the adoption of careful seeding procedures. Simultaneous in situ drop temperature measurements are being attempted in an effort to add another dimension to the information needed to understand the drop dynamics and vaporization.

Drop response to the turbulent flow has a significant effect on the mixing and distribution of fuel in the combustor. Basic analyses show that even the smallest drops will not follow the small-scale turbulent fluctuations. Drop vaporization and mass transfer rates are dependent upon the relative velocity between the drops and the gas phase. Thus, studies of interactions between sprays and turbulence continue to be an important area of research. It also appears that turbulence modeling efforts have not reached the point of predicting the spray behavior in highly turbulent flows. Future experimental research must focus on the fundamental mechanisms associated with the spray interaction with the turbulence and the formation of localized voids and regions of high spray concentration (clusters), as this phenomenon produces fuel-rich and fuel-lean pockets leading to soot and NO_x formation. Careful experimental studies need to be conducted on the evaporation of sprays in a controlled environment, with parameters such as the turbulence levels and drop concentrations being varied and measured.

Nomenclature

B	transfer number
C_D	drag coefficient
c_l	liquid specific heat
c_p	gas specific heat at constant pressure
D	jet exit diameter
D_{10}	linear mean diameter

D_{32}	Sauter mean diameter
d	drop diameter
d_m	largest drop to respond adequately to large-scale turbulence
$d_{\min}$	minor axis of deformed sphere
$d_{\max}$	major axis of deformed sphere
d_1	axis parallel to the measurement axis
d_2	axis perpendicular to the measurement axis
d_0	initial drop diameter
N	drop number density
P	joint Poisson probability
P_{ci}	probability of a drop collision
P_t	temporal Poisson probability
P_x	spatial Poisson probability
Re_d	drop Reynolds number
Re_D	jet Reynolds number
St	Stokes number
St_c	centrifugal Stokes number
T_t	total time for the sample
t_i	drop interaction or observation time
t_g	period of the drop passage of the probe volume
U	jet exit velocity
u'	rms turbulent velocity fluctuations
V	probe sample volume
V_i	sample volume for the particles in size class i
v_i	mean relative velocity of drop size class, d_i
v	relative velocity, drop to gas
We	Weber number, $We = \rho v^2 d/\sigma$
x	distance from the jet exit

Greek Symbols

δ	radial displacement of fluid element, drop deformation
ε	local turbulence dissipation rate
γ	particle rate in size class d_i
λ_l	liquid thermal conductivity
λ	gas thermal conductivity
Λ	macroscale of turbulence
μ	dynamic viscosity
ν	kinematic viscosity
ρ	gas density
ρ_d	drop liquid density
σ	surface tension
τ	characteristic drop response time
τ_H	liquid heating time
τ_L	drop lifetime
τ_k	Kolmogorov time scales
τ_e	evaporation time
τ_c	combustion time
Ω_i	swept volume by the drop
ψ	angular velocity

REFERENCES

1. Pilcher, J. M., and Miesse, C. C., WADC Technical Report 56–344, ASTIA Document No. AD 118142, March, 1957.
2. Eroglu, H., and Chigier, N., *J. Fluids Eng.* 113(Sept.):453–459 (1991).
3. Hsiang, L.-P., and Faeth, G. M., AIAA Paper 94–0560, 32nd Aerospace Sciences Meeting, January, 1994.
4. Faeth, G. M., *Twenty-Third Symposium (International) on Combustion,* The Combustion Institute, Pittsburgh, 1990, pp. 1345–1352.
5. Wu, P.-K., Ruff, G. A., and Faeth, G. M., *Atomiza. Sprays* 1:421–440 (1991).
6. Mao, Chien-Pei, Chuech, S. G., and Przekwas, A. J., *Atomiza. Sprays,* 1(2):215–235 (1991).
7. Farago, Z., and Chigier, N., *Atomiza. Sprays,* 2(2):137–153 (1992).
8. Brena de la Rosa, A., Sankar, S. V., Wang, G., and Bachalo, W. D., *J. Eng. Gas Turbines Power* 114(July):72–81 (1992).
9. Brena de la Rosa, A., Sankar, S. V., Wang, G., and Bachalo, W. D., *J. Eng. Gas Turbines Power* 115(July):499–506 (1993).
10. Bachalo, W. D., Houser, M. J., and Smith, J. N., *Atomiza. Spray Technol.* 3:53–72 (1987).
11. Wang, H., Sowa, W., McDonell, and Samuelsen, G. S., AIAA-91-2353, 27th Joint Propulsion Conference, Sacramento, June, 1991.
12. Chang, K.-C., Wang, M.-R., Wu, W.-J., and Hong, C.-H., *J. Propul. Power* 9(1):28–34 (1993).
13. Lavergne, G., Trichet, P., Hebrard, P, and Biscos, Y., *J. Eng. Gas Turbines Power* 115(July):461–466 (1993).
14. Sturgess, G. J., McKinney, R. G., and Morford, S. A., *J. Eng. Gas Turbines Power* 115(July):570–580 (1993).
15. Rizk, N. K., and Mongia, H. C., *J. Eng. Gas Turbines Power* 115(July):603–611 (1993).
16. Rizk, N. K., and Mongia, H. C., *J. Eng. Gas Turbines Power* 115(July):612–619 (1993).
17. Peters, J. E., *J. Propul.* 4(3):193–206 (1988).
18. Patterson, M. A., Kong, S.-C., Hampson, G. J., and Reitz, R. D. SAE Technical Paper 940523, 1994.
19. Gupta, A. K., AIAA Paper 91–1964, 27th Joint Propulsion Conference, Sacramento, June, 1991.
20. Bachalo, W. D., *Appl. Opt.* 19:363–370 (1980).
21. Bachalo, W. D., and Houser, M. J., *Opt. Eng.* 23:583–590 (1984).
22. Bachalo, W. D., Rudoff, R. C., and Brena de la Rosa, A., AIAA Paper 88–0236, 26th Aerospace Sciences Meeting, January 1988.
23. Dodge, L. G., and Schwalb, J. A., Paper No. 88-GT-27, ASME Gas Turbine and Aeroengine Congress and Exposition, Amsterdam, 1988.
24. McDonell, V. G., Wood, C. P., and Samuelsen, G. S., *Twenty-First Symposium (International) on Combustion,* The Combustion Institute, Pittsburgh, 1986.
25. McDonell, V. G., and Samuelsen, G. S., *Twenty-Second Symposium (International) on Combustion,* The Combustion Institute, Pittsburgh, 1988.
26. Chigier, N., *Fluid Mechanics and Heat Transfer in Sprays,* ASME, 1993, FED-Vol. 178/HTD-Vol. 270.

27. Faeth, G. M., *Prog. Energy Combust. Sci.* 13:293–345 (1987).
28. Law, C. K., *Combust. Flame* 26:605–617 (1976).
29. Sirignano, W. A., *J. Fluids Eng.* 115:(Sept.), 345–378 (1993).
30. Williams, F. A., *Combustion Theory, The Fundamental Theory of Chemically Reacting Flow Systems,* 2nd ed., Benjamin Cummings, Menlo Park, CA, 1985.
31. Swithenbank, J., Beer, J. M., Taylor, D. S., Abbot, D. and McCreath, G. C., *Experimental Diagnostics in Gas Phase Systems,* (B. T. Zinn, Ed.), Progress in Astronautics and Aeronautics, AIAA Inc., New York, 1977, Vol. 53, pp. 421–447.
32. Felton, P. G., Hamidi, A. A., and Aigal, A. K., ICLASS-85, Paper No. IVA/4, 1985.
33. Dodge L. G., Rhodes, D. J., and Reitz, R. D., *Appl. Opt.* 26(11):2144–2154 (1987).
34. Edwards, C. F., and Marx, K. D., *Atomiza. Sprays* 2:319–366 (1992).
35. Sankar, S. V., Ibrahim, K. M., and Bachalo, W. D., *Particle Particle Syst. Char.* 11:35–42 (1994).
36. Hinze, J. O., *Appl. Sci. Res A* 1:263–272 (1947–48).
37. Bachalo, W. D., and Sankar, S. V., 2nd International Conference on Fluid Measurements and Its Application, Beijing, China, October 1994.
38. Alexander, D. R., Wiles, J. J., Schaub, S. A., and Seeman, M. P., *SPIE Particle Sizing Spray Anal.* 573:67–72 (1985).
39. Brena de la Rosa, A., and Bachalo, W. D., NSF Report ISI-8960434, 1992.
40. Zhu, J. Y., Rudoff, R. C., Bachalo, E. J., and Bachalo, W. D., AIAA Paper 93-0361, 31st Aerospace Sciences Meeting, January 1993.
41. Ibrahim, K. M., Werthimer, G. D., and Bachalo, W. D., *Proceedings of the 5th International Symposium on the Applications of Laser Techniques to Fluid Mechanics,* Lisbon, Portugal, July 1990.
42. Zhu, J. Y., Bachalo, E. J., Rudoff, R. C., and Bachalo, W. D., *Atomiza. Sprays,* submitted.
43. Qui, H.-H., and Sommerfeld, M., *J. Exp. Fluids* 13:393–404 (1992).
44. Sankar, S. V., Inenaga, A., and Bachalo, W. D., paper presented at the Sixth International Symposium on the Application of Laser Techniques to Fluid Mechanics, Lisbon, Portugal, July 1992.
45. Law, C. K., and Sirignano, W. A., *Combust. Flame* 28:175–186 (1977).
46. Schneider, M., and Hirleman, E. D., *Appl. Opt.* 33(12) (1994).
47. Murray, A. M., and Melton, L. A., *Appl. Opt.* 24:2783–2787 (1985).
48. Welles, M. R., and Melton, L. A., *J. Heat Transfer* 112:1008–1013 (1990).
49. Sankar, S. V., Ibrahim, K. M., Buermann, D. H., Fidrich, M. J., and Bachalo, W. D., 3rd International Congress on Optical Particle Sizing, Yoohama, Japan, August 23–26, 1994.
50. Roth, N., and Anders, K., *Proceedings of the 6th International Symposium on the Application of Laser Techniques to Fluid Mechanics,* Lisbon, Portugal, 1992.
51. Schneider, M., Hirleman, E. D., Saleheen, H., Chowdhury, D. Q., and Hill, S. C., *Third International Congress on Optical Particle Sizing,* Yokohama, Japan, August 1993, pp. 323–326.
52. Massoli, P., Berreta, F., D'Alessio, A., and Lazzaro, M., *Appl. Opt.*, 32(18):3295–3301 (1993).
53. Sankar, S. V., Brena de la Rosa, A., Isakovic, A., and Bachalo, W. D., *Proceedings of the 5th International Symposium on the Application of Laser Techniques to Fluid Mechanics,* Lisbon, Portugal, July 1990.
54. Billings, T. P., and Drallmeier, J. A., AIAA 93-2033, 29th Joint Propulsion Conference, Monterey, June 1993.
55. Drallmeier, J. A., and Peters, J. E., *Atomiza. Sprays* 1:(1):63–68 (1991).
56. Lefebvre, A. H., *J. Eng. Gas Turbines Power* 114(January):89–96 (1992).
57. Kelly, A. J., *Aerosol Sci. Technol.* 12:526–537 (1990).
58. Dressler, John, L., Contract Report Wright Laboratory, Wp, AFB. WL-Tr-93-2049, March 1993.
59. Lefebvre, A. H., and Miller, D., College of Aeronautics Report Aero No. 193, 1966.
60. Wu, P. K., Tseng, L.-K., and Faeth, G. M., AIAA 92-0462, 30th Aerospace Sciences Meeting, January 1992.
61. Zhou, Z. W., and Lin, S. P., AIAA 92–0459, January, 1992.
62. McDonell, V. G., and Samuelsen, G. S., *J. Propul. Power* 7(5):684–691, (1991).
63. Presser, C., Gupta, A. K., Avedisian, C. T., and Semerjian, H. G., *Twenty-Third Symposium (International) on Combustion,* The Combustion Institute, Pittsburgh, 1990, pp. 1361–1367.
64. Odgers, J., Kretschmer, D., and Pearce, G. F., *J. Eng. Gas Turbines Power* 115(July):523–532 (1993).
65. Ashgriz, N., and Poo, J. Y., *J. Fluid Mech* 221:183–204 (1990).
66. Jiang, Y. J., Umemura, A., and Law, C. K., *J. Fluid Mech.* 234:171 (1992).
67. Qian, J., and Law, C. K., AIAA 94–0681, 32nd Aerospace Sciences Meeting, January 1994.
68. Nobari, M. R. H., and Tryggvason, T., AIAA 94–0835, 32nd Aerospace Sciences Meeting, January 1994.
69. Carabell, K. D., and Farrel, P. V., *Fluid Mechanics and Heat Transfer in Sprays,* ASME, 1993, FED-Vol. 178/HTD Vol. 270, pp. 81–86.
70. Tsao, K. C., Dong, Y., and Xu, Y., *Proceedings of the Fifth International Conference on Liquid Atomization and Spray Systems,* Gaithersburg, July 1991, pp. 299–306.
71. Konno, M., Chikahisa, T., and Murayama, T., SAE Paper 920467, 1992.
72. Golding, L. H., Master's Thesis, University of Wisconsin, 1992.
73. Tow, T. C., Pierpont, D. A., and Reitz, R. D., SAE Technical Paper 940897, 1994.

74. Bower, G. R., and Foster, D. E., SAE Paper 930864, 1993.
75. Koo, J-Y., and Martin, J. K., SAE Paper 900397, March 1990.
76. Koo, J-Y., and Martin, J. K., SAE Paper 910179, March 1991.
77. Nemecek, L. M., Wagner, R. M., and Drallmeier, J. A., ILASS Americas, 7th Conference, Bellevue, Washington, June 1994.
78. Vannobel, F., Dementhon, J. B., and Robart, D., *Proceedings of the 6th International Symposium on the Applications of Laser Techniques to Fluid Mechanics,* Lisbon, Portugal, July 1992.
79. Yang, J., Kaiser, E. W., Siegl, W. O., and Anderson, R. W., SAE Paper 930711, 1993.
80. Dementhon, J. B., and Vannobel, F., *Sprays and Aerosol 91,* 91-ILASS, Guilford, NC, September 1991.
81. Rizk, N. K., and Mongia, H. C., *J. Eng. Gas Turbines Power* 115(July):603–611 (1993).
82. Hinze, J. O., *Progress in Heat and Mass Transfer,* Pergammon Press, New York, 1972, Vol. 6.
83. Brown, D. J., and Hutchinson, P., *J. Fluids Eng.* 101(June):265–269 (1979).
84. Simo, J. A., and Lienhard, J. H., 27th National Heat Transfer Conference, Transport Phenomena Associated with Aerosol, Minneapolis, MN, July 1991.
85. Kamalu, N., Tang, L., Troutt, T. R., Chung, J. N., and Crowe, C. T., *International Conference on Mechanics of Two-Phase Flows,* Taiwan, June 1989, pp. 199–202.
86. Bachalo, W. D., Bachalo, E. J., and Sankar, S. V., Invited Paper, *Proceedings of the Second International Conference on Fluid Mechanics,* Beijing, 1993, pp. 1130–1141.
87. Kresta, S. M., Ph.D. Thesis, McMaster University, Ontario, Canada, October 1991.
88. Torobin, L. B., and Gauvin, W. H., *Can. J. Chem. Eng.* 37(4):129–141 (1959).
89. Rudoff, R. C., Kamemoto, D. Y., and Bachalo, W. D., AIAA 91-0074, 29th AIAA Aerospace Sciences Meeting, Reno, NV, 1991.
90. Dring, R. P., and Suo, M., *J. Energy* 2:232–237 (1978).
91. Bachalo, W. D., Bachalo, E. J., and Sankar, S. V., AIAA 93-0697, 31st Aerospace Sciences Meeting, January 1993.
92. Hardalupas, Y., Taylor, A. M. K. P., and Whitelaw, J. H., *Phil, Trans. R. Soc. Lond. A* 341:411–442 (1992).
93. Chang, K.-C., Wang, M.-R., Wu, W.-J., and Hong, C.-H., *J. Propul. Power* 31(1):68–74 (1993).
94. Hancock, R. D., Jackson, T. A., and Nejad, A. S., *Appl. Opt.,* 31(9):1163–1166 (1992).
95. Bachalo, W. D., Rudoff, R. C., and Sankar, S. V., ASTM STP 1083, 1990, pp. 209–224.
96. Bellan, J., and Harstad, K., *Int. J. Heat Mass Transfer* 31:1655–1668 (1988).
97. Beer, J. M., and Chigier, N. A., *Combustion Aerodynamics,* Chap. 6 (J. M. Beer, Ed.), Applied Science, London, 1972, Fuel and Energy Science Monographs.
98. Chin, J. S., and Mongia, H. C., *Atomiza. Sprays,* submitted.
99. Chin, J. S., and Mongia, H. C., 39th ASME International Gas Turbine and Aero Engine Conference, submitted.
100. Gokalp, I., Chauveau, C., Simon, O., and Chesneau, X., *Combust. Flame* 89:286–298 (1992).
101. Edwards, C. F., Rudoff, R. C., and Bachalo, W. D. *Proceedings of the 5th International Symposium on the Application of Laser Techniques to Fluid Mechanics,* Lisbon, Portugal, July 1990.
102. Reitz, R. D., ASTM STP 1083 (E. D. Hirleman, W. D. Bachalo, and and P. G. Felton, Eds.), 1990, pp. 225–237.
103. Presser, C., Gupta, A. K., and Semerjian, H. G., *Combust. Flame* 92:25–44 (1993).
104. Presser, C., and Gupta, A. K., *Heat Transfer in Fire and Combustion Systems,* 1993, ASME HTD-Vol. 250.
105. Edwards, C. F., and Rudoff, R. C., *Twenty-Third Symposium (International) on Combustion,* The Combustion Institute, Pittsburgh, 1990, pp. 1353–1359.
106. Williams, A., *Prog. Energy Combust,* 2:167–179 (1976).
107. Bulzan, D. L., NASA Technical Memorandum 106130, January 1993.
108. Chehroudi, B., and Ghaffarpour, M., Paper 92-GT-124, ASME International Gas Turbine and Aeroengine Congress, Cologne, Germany, June 1992.
109. Li, S. C., Libby, P. A., and Williams, F. A., Fluid Mechanics and Heat Transfer in Sprays, 1993, ASME FED-Vol. 178/HTD.
110. Li, S. C., Libby, P. A., and Williams, F. A., 14th International Colloquium on Dynamics of Explosions and Reactive Systems, University of Coimbra, Coimbra, Portugal, August 1993.

Twenty-Fifth Symposium (International) on Combustion/The Combustion Institute, 1994/pp. 345–352

INFLUENCE OF AMBIENT PRESSURE ON DROP-SIZE AND VELOCITY DISTRIBUTIONS IN DENSE SPRAYS

ARVIND K. JASUJA AND ARTHUR H. LEFEBVRE*
School of Mechanical Engineering
Cranfield University
Cranfield
Bedford MK43 OAL, England

The primary aim of the research is to determine the capabilities of modern noninvasive diagnostics for characterising the sprays produced by a practical gas turbine atomizer when operating at realistic engine conditions of pressure, fuel type, and fuel-air throughput. A single-velocity-component Phase Doppler Particle Analyzer is used to measure local variations of drop-size distributions and drop velocities along three spray radii at downstream distances from the atomizer of 50 and 70 mm. In the 50-mm plane, excessive signal rejection rates limit measurements to a maximum air pressure of 9 bar and a maximum kerosine flow rate of 18.6 g/s. At the 70-mm measurement plane, satisfactory results are obtained at air pressures up to 12 bar and fuel-flow rates up to 24.8 g/s. The results show that increases in ambient air pressure lead to larger mean drop sizes and lower mean drop velocities in the spray. This is attributed to the fact that the beneficial effect of an increase in air pressure in raising Weber number is more than offset by several adverse factors, all of which are related to the increase in fuel-flow rate that accompanies an increase in air pressure at constant fuel/air ratio.

Introduction

Prefilming airblast atomizers are widely used in both aircraft and industrial gas turbine combustors. Satisfactory fuel-air mixture preparation is widely accepted as being crucial to optimum gas turbine combustion performance. Most of the previous researches on prefilming airblast atomization have employed specially designed atomizers featuring nonswirling atomizing air. The use of nonswirling air facilitates experimental research, but the results obtained have only limited practical interest because most of the airblast atomizers used in modern gas turbines employ swirling air streams to atomize and disperse the fuel.

Previous studies on practical airblast atomizers featuring swirling air streams (Refs. 1 and 2, for example) have provided useful insights into drop-size distributions and spray/flow field interactions, but in all cases, either the ambient air pressure or the liquid flow rate have been appreciably lower than the values associated with engine operation at high power conditions. The objective of the present work is to remedy this deficiency by attempting spatially resolved droplet size and velocity measurements in the dense sprays produced by swirling air streams at high pressures and high fuel throughputs.

*Visiting Professor.

Experimental

The main component of the spray facility is a large cylindrical test vessel designed to operate at high internal pressures. A flexible optical window arrangement permits the use of a variety of laser-based diagnostics. A multistage screw compressor is used to supply the high-pressure air needed to pressurise the test vessel and also to deliver air to the fuel injector, which is located at one end of the pressure vessel and is arranged to spray horizontally along its major axis, as shown schematically in Fig. 1. A rotameter/turbine flowmeter combination is used to measure the fuel-flow rates delivered to the fuel injector. The rotameter handles flow rates up to 68 kg/h, while the pelton wheel flowmeter covers flow rates between 45 and 408 kg/h.

Atomizer:

The fuel injector is essentially a prefilming airblast atomizer, designed by SNECMA and shown schematically in Fig. 2. Low-velocity fuel is first spread into a thin, circumferentially uniform sheet on an annular surface and is then sandwiched between two high-velocity swirling air streams. This configuration promotes a high shearing action between the fuel and the atomizing air and also ensures that the resulting spray is well matched to the combustor airflow pattern. The cone angle of the fuel spray is determined by a complex interaction between the swirling

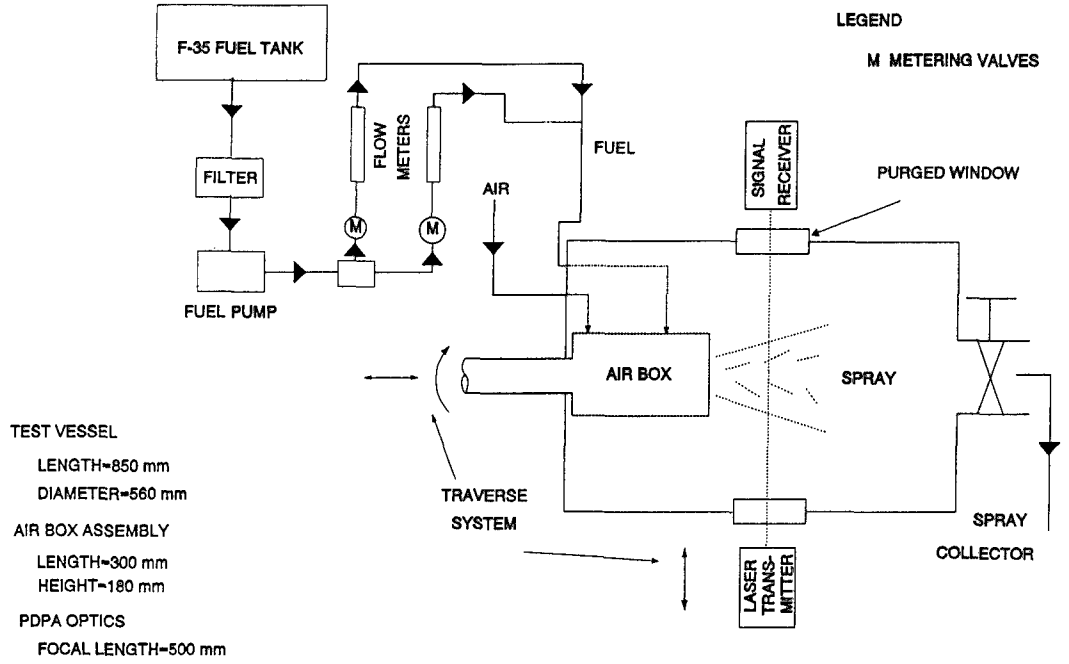

FIG. 1. High-pressure spray facility.

atomizing air streams and the air flow through the liner cup holes shown in Fig. 2. The fuel injector is fitted into a high-pressure airbox that is located inside the test vessel, as shown in Fig. 1.

Two separate and independent traverse systems for the high-pressure spray rig are provided. The traverse system for the laser diagnostics is a mechanical one providing three degrees of freedom. Normally, the optical system moves along the horizontal diameter of the pressure vessel. The repeatability of positioning in this direction is within 0.25 mm. The second traverse system provides two degrees of freedom for the airbox relative to the diagnostics line of sight. The first one is a linear movement along the longitudinal axis of the pressure vessel, while the second is a rotational movement around the axis of the airbox. As both of these movements are controlled by a computer-operated stepper motor, very precise and repeatable injector positioning and repeatability of position can be achieved.

Spray Diagnostics:

Four optical-quality quartz windows provide the desired optical access into the pressure vessel. Each of these large windows has a multipoint purge feed of high-velocity air to prevent the deposition of fuel on the windows. A single-component Phase Doppler Particle Analyzer (PDPA) featuring a 10-mW He-Ne laser, manufactured by Aerometrics Inc., was used in this study. It is described as a single-component system because it measures just one component of particle velocity, in this case the velocity component along the main axis of the cylindrical test vessel, which also coincides with the main axis of the conical spray. The theoretical principles on which the PDPA is based have been described by Bachalo and Houser [3]. The instrument was operated in the forward-scatter mode, this being the most favourable orientation for dense spray measurements. During the course of the investigation, special attention was paid to the setting up and operation of the PDPA. The voltage supplied to the photomultiplier tube (PMT) can have a significant effect on the measurements. If the voltage is set too high, signals from the large drops will saturate the PMTs, resulting in a rejection of those signals; thus, the measurement will be biased in favour of the smaller drops in the spray. On the other hand, if the voltage is set too low, signals from small drops will not be detected at all, and the measurements will then be biased in favour of larger drops. Thus, the operator must try several voltage settings in order to identify a range over which the mean drop sizes change only slightly with changing PMT voltage. For these experiments, the PMT voltage was chosen for a given data set to give the lowest overall rejection rate but was then kept constant for all the measurements along the radius. The actual PMT voltage settings employed were 320 V at 1 bar, 380 V at 4 bar, and 420 V at 9 and 12 bar.

The probe volume dimensions were kept fairly

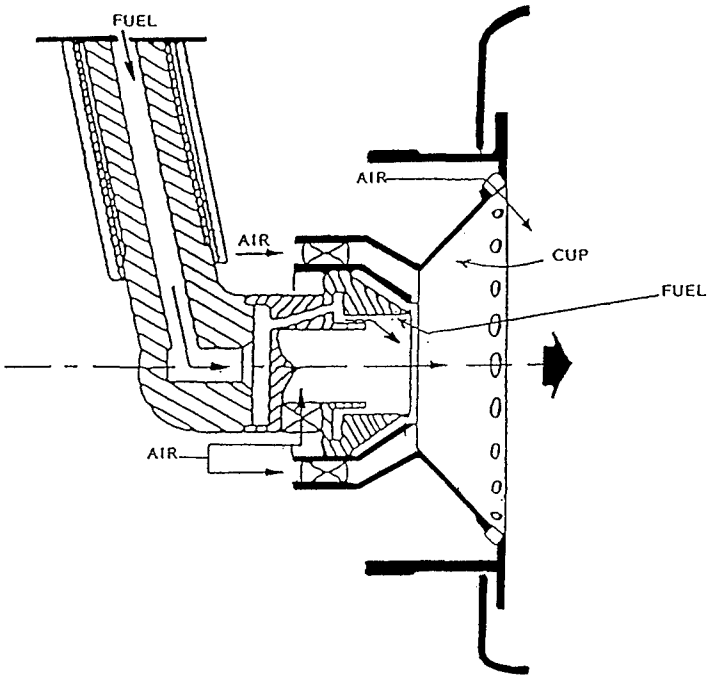

FIG. 2. Fuel injector.

constant by operating on the most favourable track setting with due regard to the problem of particle coincidence in dense droplet regions. In a few instances, this resulted in somewhat higher droplet rejection rates. For a given track setting, the maximum permissible diameter range was used to avoid artificially biasing the data. In contrast, the velocity offset settings were changed as necessitated by observations such as, for example, the presence of negative or near-negative droplet velocities.

Over the entire range of air pressures from 1 to 12 bar, the degree of laser-beam steering encountered as a result of refractive index gradients was judged to be insignificant. The realignment of optics at high pressures was found to be only of marginal benefit to the signal quality, which is consistent with the findings of Drennan et al. [2]. Attenuation of the laser beams was observed to increase with increases in fuel throughput and with decreases in the downstream distance of the measurement plane. This deterioration in electrical signal-to-background noise ratio can be observed on the oscilloscope and leads to high data rejection rates. As the characteristics of the scattered light reaching the receiver are very dependent on the ratio of beam intensity to spray density, clearly a more powerful laser would enhance the dense spray measurement capability of the PDPA.

Test Conditions:

The test conditions were selected to simulate those encountered in gas turbines. The measurements were taken with a pressure drop across the atomizer, $\Delta P/P$, of 5%, at fuel/air ratios of 0.1 and 0.2. The ambient air pressures employed were 1, 4, 9, and 12 bar. Aviation kerosine (μ = 0.0013 kg/ms, σ = 0.0277 kg/s^2, ρ = 784 kg/m^3—all at 15 °C) was used throughout the test programme. Data were taken at downstream distances from the atomizer face of 50 and 70 mm along radii perpendicular to the spray axis for angular positions of 0°, +90°, and −90° relative to a vertical line drawn through the spray axis. Detailed measurements were made at radial increments of 2 mm for spray radii between 12 and 30 mm, but increments of 4 mm were used for radial positions between 0 and 12 mm, and 30 to 38 mm. Because of the long run times incurred, the radial increment was kept constant at 4 mm for tests at 12 bar. Five thousand droplet samples were taken at each measurement point for all test conditions, except for a few selected positions at 12 bar where the sample size was restricted to around 2000 drops to avoid long run times.

Results

A typical output from the Aerometrics instrument comprises droplet-size and velocity histograms together with the size-velocity correlation. From such curves can be extracted information on variations in drop-size distributions and drop velocities with changes in atomizer operating conditions. Figures 3 and 4 illustrate the results of detailed spray measure-

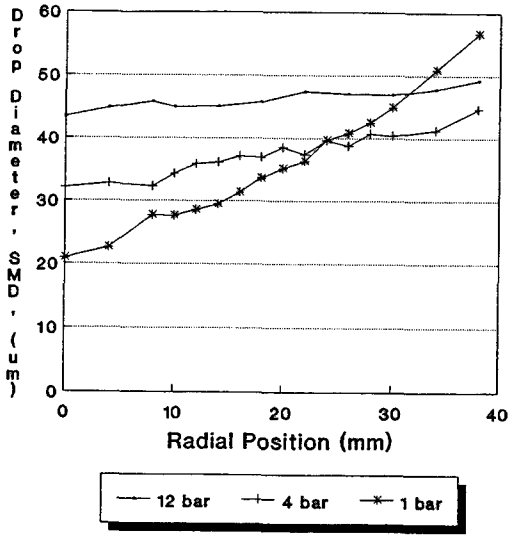

FIG. 3. Variation in SMD with radial position in spray. Fuel/air ratio (FAR) = 0.1.

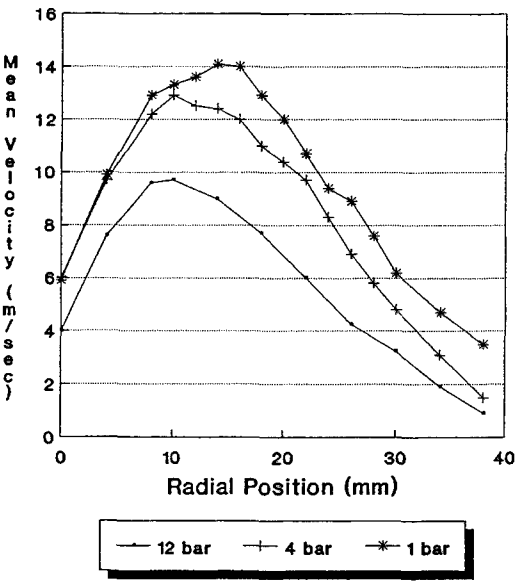

FIG. 4. Drop mean velocity distributions for FAR = 0.1.

ments carried out at air pressures, P_A, of 1, 4, and 12 bar. The atomizer pressure drop, $\Delta P/P$, is 0.05, and the fuel/air ratio is 0.1, corresponding to an actual fuel flow of 24.8 g/s at the highest air pressure. The axial distance of the measurement plane downstream of the atomizer, z, is 70 mm. Radial positions of 0 and 38 mm correspond to the axis and outer edge of the spray, respectively. Figure 3 indicates an increase in Sauter mean diameter (SMD) along the spray radius at a given air pressure. This increase in SMD diminishes with increase in P_A. For example, the variation in SMD along the spray radius at 1, 4, and 12 bar is 35, 12 and 5 μm, respectively. These data show that the distribution of drop sizes within the spray becomes more uniform with increase in P_A. The effect of variation in P_A on SMD shows no clear trend, but in most regions of the spray, the SMD increases with increase in P_A. Figure 4 shows droplet mean velocity data for the same conditions. As the instrument used was a single-component type, only axial velocity information was obtained. In this figure, the mean velocity is observed to diminish with increase in air pressure. Both the centre and the outer edge of the spray are characterised by relatively low mean droplet velocities.

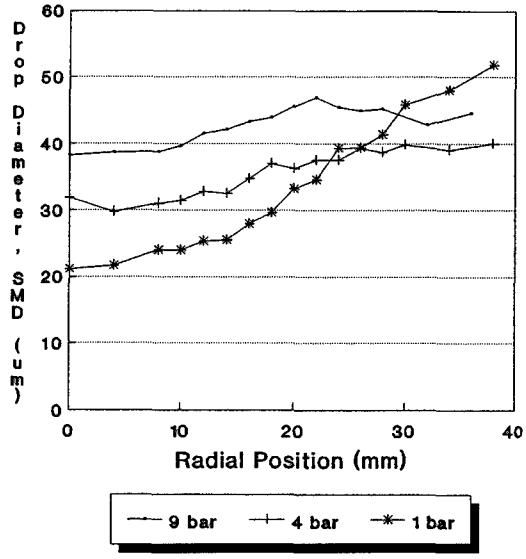

FIG. 5. Variation in SMD with radial position in spray. FAR = 0.1.

Figure 5 shows similar data to Fig. 3 for a downstream distance of 50 mm. In these experiments, the air pressure was limited to 9 bar and the fuel flow rate to 18.6 g/s. Comparison between the two figures reveals little effect of downstream distance on SMD, which suggests that atomization is complete within 50 mm of the fuel injector. The corresponding velocity data (not shown) follow exactly the same trends as the data shown in Fig. 4 for the longer downstream distance, except that the mean velocities measured at the spray axis are lower at the highest levels of P_A. A negative velocity was recorded at the spray axis for an air pressure of 9 bar, which suggests the existence of a recirculatory droplet pattern in the inner regions of the spray.

Spray measurements at higher fuel-flow rates, corresponding to a fuel/air ratio of 0.2, were confined to 1- and 4-bar air pressures because the signal quality

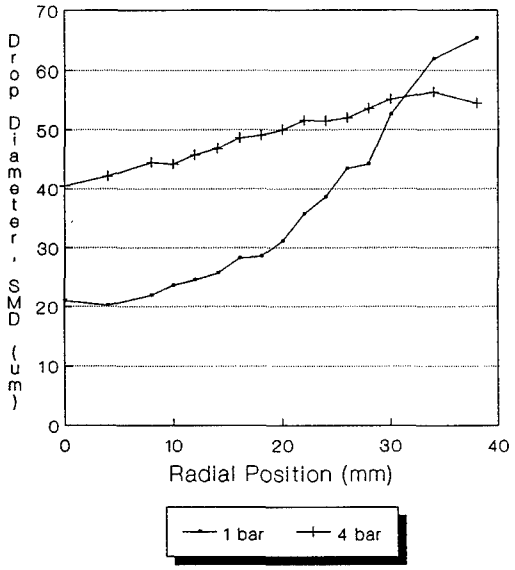

FIG. 6. Variation in SMD with radial position in spray. FAR = 0.2.

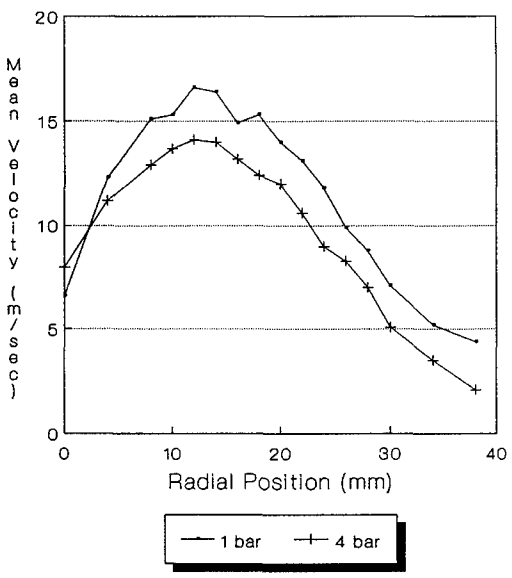

FIG. 7. Drop mean velocity distributions for FAR = 0.2.

deteriorated at higher levels of P_A. The data obtained for z = 70 mm are presented in Figs. 6 and 7. If Fig. 6 is examined alongside Fig. 3, there appears to be little difference in SMD at 1 bar, but SMD values are appreciably higher at 4 bar for the higher fuel-flow rates shown in Fig. 6. The droplet mean velocity distributions shown in Figs. 4 and 7 for the two different fuel throughputs exhibit only small differences in absolute values at any given level of air pressure.

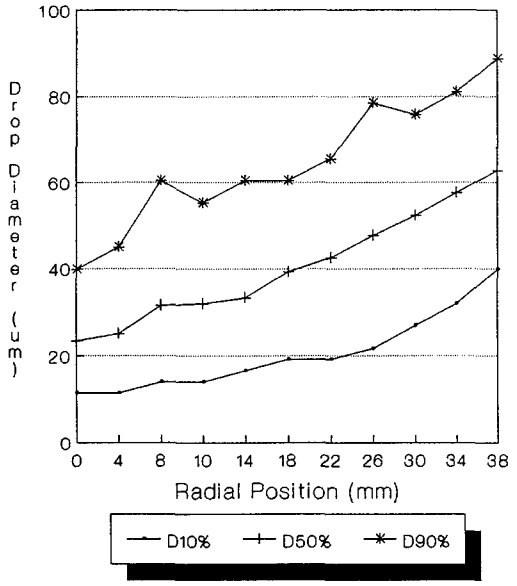

FIG. 8. Drop size distributions for P_A = 1 bar and FAR = 0.1.

Examination of the data presented in Figs. 3, 5, and 6 reveals some interesting and unexpected results. Throughout most of the spray region, an increase in pressure leads to an increase in mean drop size. This contradicts what one might anticipate intuitively since an increase in air density would be expected to intensify the aerodynamic shear forces causing liquid disintegration. Only in the outer, more dilute regions of the spray does the spray exhibit the customary decline in SMD with increase in air pressure. Unfortunately, there are no comparable studies available in the open literature that feature PDPA measurements at high air pressures on the type of atomizer employed in this investigation. Moreover, no information is available on the manner and extent to which changes in air pressure affect the cone angle of the spray.

In an attempt to shed more light on this issue, it was decided to examine the behaviour of different drop-size classes in addition to SMD. Three drop-size classes corresponding to 10, 50, and 90% cumulative volume points, i.e., D_{10}, D_{50}, and D_{90}, were selected. Not surprisingly, the D_{50} data conform closely to the SMD [4]. As illustrated in Figs. 8 and 9 for air pressures of 1 and 12 bar, respectively, the different diameter classes exhibit fairly similar behaviour across the spray radius. The mean axial velocities corresponding to the three different size classes are plotted in Figs. 10 and 11 for the two extreme levels of pressure. These figures show that, at the higher air pressure, the three drop-size classes possess practically the same mean axial velocity, while, at the lower pressure, there is a noticeable difference

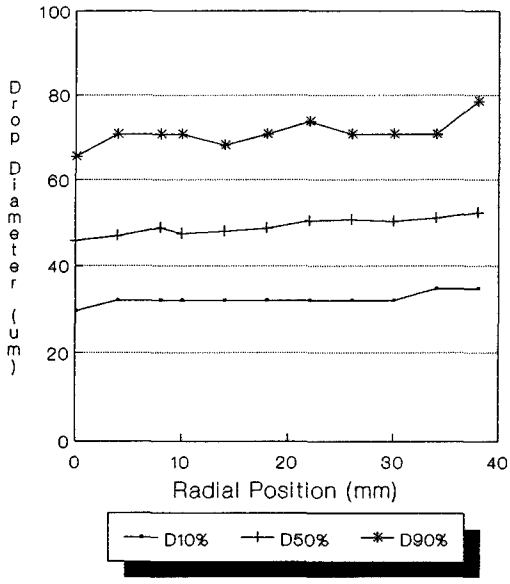

FIG. 9. Drop size distributions for P_A = 12 bar and FAR = 0.1.

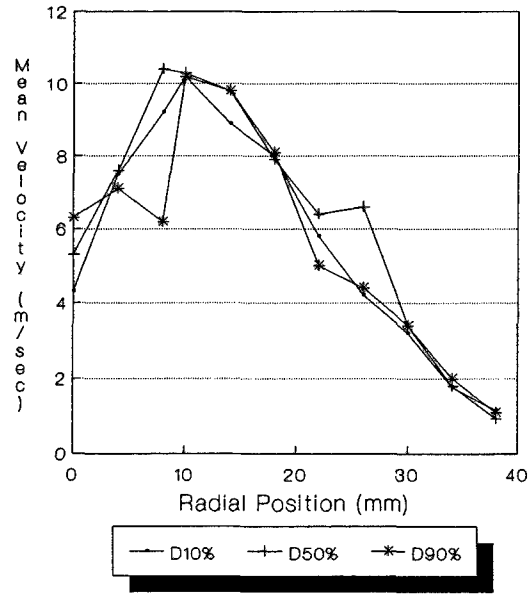

FIG. 11. Drop mean velocity distributions for P_A = 12 bar and FAR = 0.1.

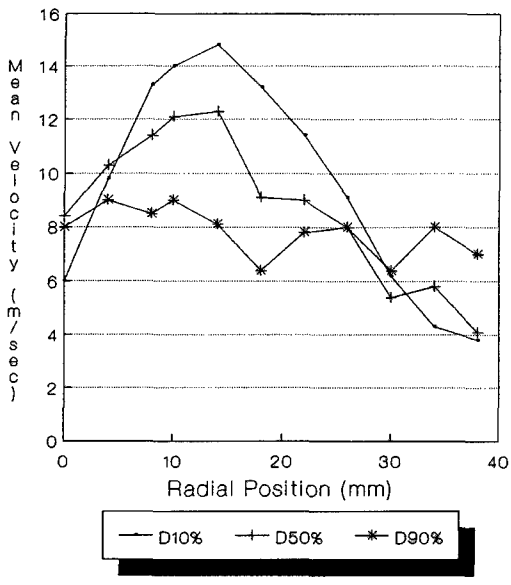

FIG. 10. Drop mean velocity distributions for P_A = 1 bar and FAR = 0.1.

in the mean velocities in the inner spray regions. This difference in droplet velocity at low air pressures is attributed to the influence of air pressure on the aerodynamic force ($0.5\,\rho_A U_A^2$) experienced by a droplet in a flowing air stream. At high pressures, this force is large enough to accelerate all the droplets up to a common velocity, regardless of size. At low pressures, however, where aerodynamic forces are appreciably lower, only the smallest droplets in the spray can attain a velocity close to that of the atomizing air stream. The larger drops lag behind the smaller drops to an extent that depends on their size, as shown in Fig. 10.

Figure 12 shows the effect of air pressure on the radial distribution of D_{90} within the spray. At all pressures, D_{90} is seen to increase with increase in spray radius. This same effect was also observed for the other drop-size classes, D_{10} and D_{50}. Measurements on the effect of air pressure on the mean axial velocities corresponding to a given size class revealed low mean velocities (1–2 m/s) near the outer edge of the spray at high pressures. Experiments carried out at 9 bar revealed negative velocities, which implies the existence of a recirculatory airflow pattern. It is conceivable, therefore, that the existence in close proximity of low-velocity negative and positive flows could give rise to droplet coalescence, which could account for the observed large drop sizes at higher air pressures. It is also possible that, at high pressures, some of the smallest droplets are passing by undetected, the light scattered by them being lost in the general background noise, which increases with pressure. However, a large number of small droplets would have to be missed out for the effect to be significant since SMD is more strongly influenced by the larger drops in the spray.

Another possible explanation for the observed increase in droplet diameter with air pressure is the reduction in relative velocity between the fuel and

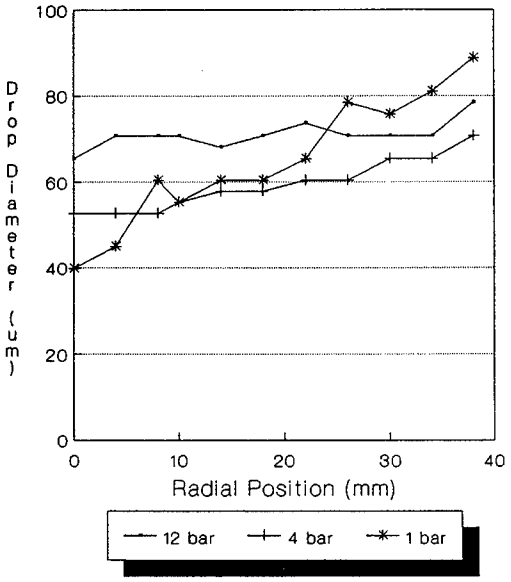

FIG. 12. Variation of D_{90} with radial position in spray. FAR = 0.1.

the atomizing air that accompanies an increase in P_A. The atomizing air velocity remains constant regardless of variations in P_A because the atomizer operates at a constant value of $\Delta P/P$. However, for a constant fuel/air ratio, and assuming the fuel-film thickness at the atomizing edge remains constant, the fuel velocity is directly proportional to the fuel-flow rate which, in turn, is proportional to P_A. Thus, an increase in air pressure must inevitably be accompanied by a reduction in relative velocity. It is recognized that the fuel-film thickness may not be independent of fuel-flow rate and, in fact, is likely to increase with increase in fuel-flow rate. This would diminish the force of the relative velocity argument, but if the fuel-film thickness does increase with fuel-flow rate, this would also impair atomization since it has been established both theoretically and experimentally that mean drop size is proportional to the square root of the initial fuel-film thickness [5,6]. Thus, regardless of whether the influence of an increase in air pressure on atomization quality is manifested via a reduction in relative velocity or an increase in fuel-film thickness or, as is likely, a combination of both these effects, the end result is always to impede atomization and raise the SMD.

Droplet coalescence has been mentioned already as a possible cause of larger drop sizes at high pressures. In these experiments, the fuel/air *mass* ratio was kept constant regardless of variations in air pressure. Thus, the *volumetric* fuel/air ratio increased in direct proportion to P_A. This has little practical significance for the spray as a whole, which is always fairly dilute, but in the initial dense breakup region, an increase in volumetric fuel concentration has two adverse effects on atomization: (1) it provides a greater opportunity for droplet coalescence to occur, and (2) it restricts the interaction between the atomizing air and the fuel. Because, with increase in P_A, a larger proportion of the breakup region is occupied by fuel and, in consequence, a smaller proportion by air, not only is there more fuel to atomize, but the "accessibility" of the fuel to the atomizing air is diminished. By the time the atomizing air has achieved complete access to the fuel, the conditions for sheet and ligament breakup are less favourable. This is believed to be the main reason why drop sizes tend to increase with increase in P_A, despite the higher Weber number.

For this hypothesis to have any substance, an increase in fuel throughput at a constant air pressure should result in a higher SMD. Although the data available for such an assessment are sparse, some confirmation may be obtained by comparing the results presented in Figs. 3 and 6. These data correspond to exactly the same test conditions, except that, in one case (Fig. 6), the fuel-flow rate is twice that of the other (Fig. 3). Examination of these two figures shows that, at 1 bar, the SMD values are largely independent of fuel-flow rate. This is perhaps hardly surprising since, at this low pressure, the fuel-flow rate is always relatively low. However, at a pressure of 4 bar, where the effect of doubling the fuel-flow rate is appreciably higher, comparison of Figs. 3 and 6 shows significantly higher values of SMD for the higher fuel-flow rate.

It is concluded, therefore, that the observed increase in SMD with increase in air pressure is due not to the effect of pressure per se but is caused by the higher fuel-flow rates associated with atomizer operation at high pressures.

Conclusions

From detailed measurements of drop sizes and drop velocities carried out over wide ranges of air/fuel ratio and ambient air pressure on a practical airblast atomizer featuring swirling air flows the following conclusions are drawn.

1. The feasibility of obtaining detailed spray droplet data at an operating pressure of 12 bar and a fuel throughput of 24.8 g/s has been demonstrated using a single-component Phase Doppler Particle Analyzer.
2. Higher fuel throughputs and reductions in measurement plane distance from the atomizer below 70 mm resulted in excessive attenuation of the laser beams before and after the measurement probe volume. This extinction resulted in high data rejection rates. Clearly, a more powerful laser

would alleviate this problem and extend the measurement capability of the PDPA.

3. All the experimental data obtained on the influence of ambient air pressure on mean drop size show that an increase in air pressure above the normal atmospheric value causes the SMD to increase. Although the basic effect of an increase in air pressure is to raise the Weber number and thereby improve atomization, this beneficial effect is more than offset by several adverse effects, all of which are related to the increase in fuel-flow rate that accompanies an increase in air pressure at constant fuel/air ratio. These include increase in initial fuel-film thickness, reduction in relative velocity between fuel and atomizing air, increased droplet coalescence, and lower accessibility of the fuel to the atomizing air.
4. The mean axial velocities of the droplets in the spray diminish with increase in air pressure, which also tends to make droplet velocities more uniform and less dependent on individual drop size. Both these effects are attributed to the influence of air pressure on the aerodynamic forces experienced by droplets in a flowing air stream.

Acknowledgments

The financial support provided for this work by the CEC as part of its "Low Emissions Combustor Technology" BRITE/EURAM programme is gratefully acknowledged. Special thanks are also due to Mr. C. K. Tam of Cranfield University for his painstaking efforts in acquiring the experimental data contained in this paper.

REFERENCES

1. Hebrard, P., Trichet, P., and Bardey, X., *Proceedings of 5th International Conference on Liquid Atomization and Spray Systems*, NIST Special Publication 813, Gaithersburg, MD, 1991, pp. 669–678.
2. Drennan, S. A., Sowa, W. A., and Samuelson, G. S., ASME Paper 90-GT-393, 1990.
3. Bachalo, W. D., and Houser, M. J., *Optics Eng.* 23(5):583–590 (1984).
4. Jasuja, A. K., and Tam, C. K., AIAA Paper No. 92-3232, 1992.
5. Squire, H. B., *Br. J. Appl. Phys.* 4:167–169 (1953).
6. Rizk, N. K., and Lefebvre, A. H., *ASME J. Eng. Power* 102:706–710 (1980).

COMMENTS

A. K. Gupta, University of Maryland, USA. I have a clarification, a comment, and a question. Were the tests carried out at 12-atm fuel supply pressure or chamber pressure? Providing SMD data in the spray yields little information on the size and number density distributions of the spray. What are the accuracy and precision of your reported data?

Author's Reply. The droplet measurements were undertaken at chamber air pressures of up to 12 bar. The authors agree with the comment that providing SMD data alone gives little insight with respect to size distributions. For this as well as other reasons outlined in the paper, analysis included D10, D50, and D90 diameters. Number density data were not presented in the paper partly because of to paper length restrictions, but more importantly because the data quality was believed to be unreliable. This was because of the use of a single-velocity component system in a spray field featuring recirculating flow. The level of precision regarding the drop size-velocity measurements using phase Doppler systems has been covered adequately in the published literature.

•

Scott A. Drennan, Coen Company, Inc., USA. In your experiment, the flow rates of liquid and atomizing air increase as ambient pressure is increased, causing an increase in the spray density and possibly an increase in the data rejection rate. Please discuss how you feel this increased data rejection rate at higher pressures affects your spray statistics. It is also interesting to note the decreased radial variation in drop size and velocity as the ambient pressure is increased. Do you believe that a collapsing effect on the spray at elevated pressure is causing this decreased radial variation? Were data acquired at axial locations closer to the spray tip to determine how the spray evolves axially? Perhaps the spray at high pressure indicates a size-velocity correlation closer to the spray tip, as seen in the low-pressure spray data, which decays rapidly because of increased ambient air drag forces at high pressure.

Author's Reply. For the entire set of data outlined in the paper, the maximum rejection rates encountered were below 10%. Under these circumstances, we believe the spray statistics did not change significantly with increasing air pressure. We do not have any spray images at high air pressures to identify the change or lack of change in spray cone angle placement. Consequently, we are unable to say whether this may be an influencing factor in the decreased radial variation in drop size and velocity. Spray measurements were made at two axial locations only: 50 and 70 mm from the injector tip. Evolution of the spray at shorter axial distances could not be ascertained due to excessive laser beam attenuation and data rejection rate.

Twenty-Fifth Symposium (International) on Combustion/The Combustion Institute, 1994/pp. 353–361

ANALYSIS OF DROPLET ARRIVAL STATISTICS IN A PRESSURE-ATOMIZED SPRAY FLAME

J. T. HODGES AND C. PRESSER
Chemical Science and Technology Laboratory
National Institute of Standards and Technology
Gaithersburg, MD 20899, USA
A. K. GUPTA
Department of Mechanical Engineering
University of Maryland
College Park, MD 20742, USA
AND
C. T. AVEDISIAN
Sibley School of Mechanical and Aerospace Engineering
Cornell University
Ithaca, NY 14853, USA

The statistical behavior of droplets in a kerosene pressure-atomized spray was investigated under swirling and burning conditions. This case was studied in order to better understand individual droplet transport processes downstream of the fuel spray flame. A two-component phase-Doppler particle sizing system was employed to provide information on the droplet size and velocity distributions as well as interarrival-time statistics. Time-resolved information is presented on the instantaneous values of diameter, and the respective axial and radial velocity components. The results provide some evidence of nonsteady interarrival-time statistics (associated with droplet clustering) immediately downstream of the fuel nozzle and at radial coordinates near the center of the spray. This unsteady statistical behavior was most prominent within the shear layer formed near the inner spray boundary. Decomposition of the results into size classes indicated that clustering (attributed to entrainment by recirculating gases) occurred only for the smallest droplets, 0–20 μm in diameter. For larger droplets, analysis on the random nature of the spray process revealed that droplet transport generally follows steady Poisson statistics. Furthermore, the information provided here shows that size-class decomposition is important in the analysis of spray behavior.

Introduction

Improved understanding of spray combustion phenomena requires a detailed knowledge of the interaction between the droplets and the surrounding chemically reacting flow field. Therefore, novel strategies that address optimization of fuel/air mixing processes can lead to increased combustion efficiency and reduced emission of unburnt fuel into the surrounding environment. The importance of matching the fuel spray pattern with the associated aerodynamic flow field has been recognized through the direct application of laser sheet photography. Studies have shown that droplets pass through the flame sheet relatively unburnt when using commercially available atomizers [1]. Information dealing with the effect of the gas flow field (both mean and fluctuating quantities) on the trajectory of individual droplets of various sizes is critical to determine the dispersion of droplets within the surrounding air stream.

Recent developments with phase-Doppler interferometry (PDI) have allowed simultaneous measurement of both size and velocity distributions, and time-resolved information [2]. The effect of aerodynamic turbulence on droplet dispersion can be obtained with PDI in different environments, including swirling and burning droplet-laden streams. Reitz [3] found that droplet mean and fluctuating velocities were close to that of the gas stream for situations where the droplet-size–velocity correlation coefficient was low. This occurred in regions of the spray where the relative velocity between the droplets and gas stream was small, for example, in downstream regions and in the center of the spray. Edwards and Rudoff [4] found that groups of droplets of specified size range have different velocities, and that mean velocity decreases with smaller droplet size class. The droplet velocities associated with the smaller-sized droplets were found to merge smoothly into the gas-phase velocity. The velocity of the gas remained be-

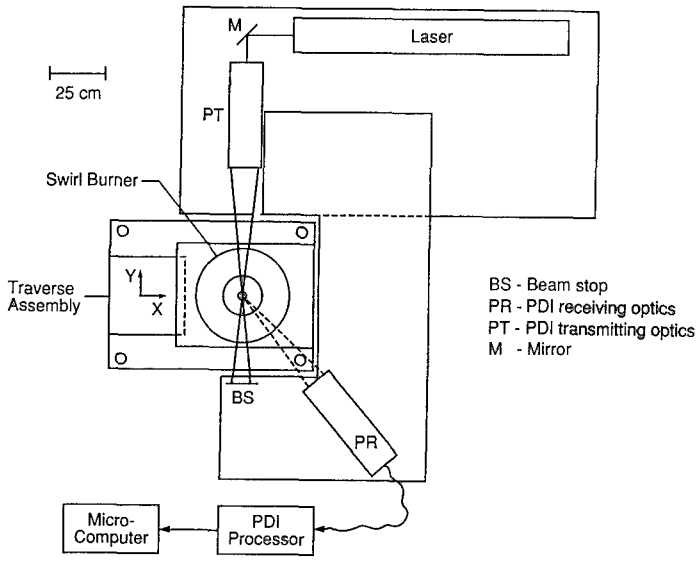

FIG. 1. Schematic of the experimental droplet velocity/sizing apparatus.

low that of the smallest droplet size class throughout each radial profile except near the dense spray boundary (in the near-injector region) where sensitivity to the smallest droplet sizes was lost. Bulzan et al. [5] have found both experimentally and numerically that the fluctuating radial gas-phase velocity is significantly lower than the axial component in a downward-facing air-assisted water spray. The magnitude of the radial fluctuations remains smaller than the axial component with increasing axial position, although the flow becomes more isotropic.

The focus of this investigation was to provide time-resolved information on the instantaneous droplet velocities and interarrival-time statistics as correlated with droplet size and spray position. Data are presented for a swirling kerosene spray flame, as opposed to earlier studies under nonburning conditions [6,7]. This study provides further insights pertinent to a better understanding of droplet interaction with the surrounding air stream.

Experimental Arrangement

Spray Combustor Facility:

Experiments carried out in the spray combustion facility (SCF) simulate operating conditions found in practical combustion systems (see Fig. 1). The swirl burner includes a moveable-vane swirl generator with a 12-vane cascade; the vanes rotate simultaneously in order to impart the desired degree of swirl intensity (both positive and negative) to the combustion air flow [8]. The pressure-jet nozzle used in the present study was nominally operated at a fuel flow rate of 3.2 kg/h (line pressure at about 6.89 kPa). The combustion air, supplied to the burner via a 101-mm-diameter pipe surrounding the fuel nozzle, was nominally set at 64.3 kg/h. This provided good flame stability at an overall input fuel/air equivalence ratio of 0.75. Further details of the experimental facility are presented in Ref. 8.

The unconfined spray is injected vertically upward from the nozzle exit, located at the burner exit. A stepper-motor–controlled spray assembly traversing system allows movement in both the vertical and horizontal planes so that highly resolved spatial profiles can be obtained within the spray flame. The optical setup is fixed while the burner spray assembly is moved. In this fashion, radial profiles of the spray properties are obtained at different axial positions.

Measurement of Droplet Size, Velocity, and Time of Arrival

A two-channel phase-Doppler interferometer (PDI) is used to obtain droplet time of arrival, droplet size, and velocity data. By "time of arrival" is meant the time relative to the start of data acquisition at which a given droplet is detected. Measurements were repeated at several selected positions to ensure a repeatability that was generally better than 5% near the spray boundary.

Results and Discussion

Size/Velocity Distributions and Time of Arrival:

Two positions were selected to illustrate the behavior of the individual droplets, one at the centerline and the second near the spray boundary (i.e., the

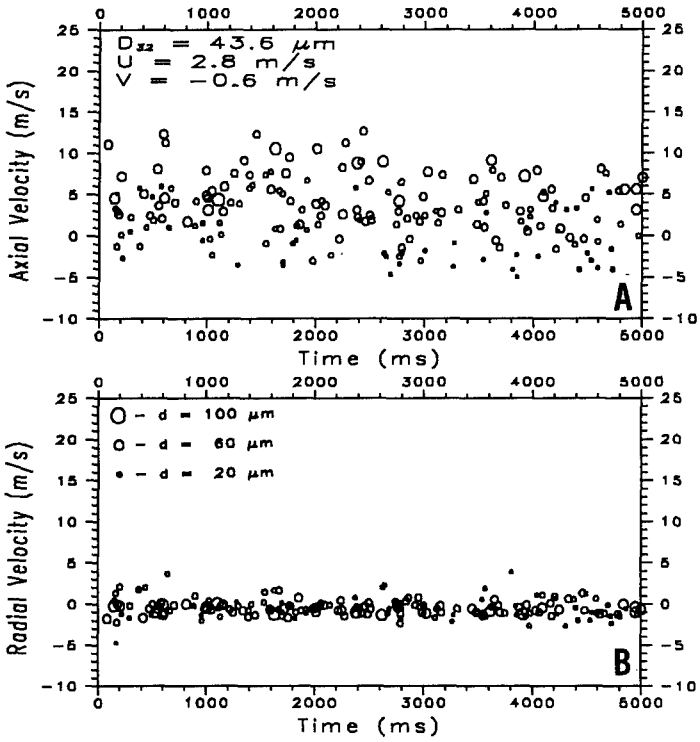

FIG. 2. Time history of droplet (a) axial and (b) radial velocity at $r = 0$ and $z = 10$ mm. Velocity time histories are coded to represent change in droplet diameter.

position radially outward near the outer edge of the spray where droplet size is maximized). Results are presented in Figs. 2 and 3 at an axial position, z, of 10.0 mm and for radial positions, r, of 0 and 10.2 mm, respectively. Each figure includes the droplet axial and radial velocity time of arrival (note the difference in scales for time in Figs. 2 and 3). The data points in each figure are also coded to represent the droplet diameter (for $1 \leq D \leq 100\ \mu$m, see scale in frame B of each figure). At $r = 0$ (see Fig. 2a), the presence of both negative and positive droplet axial velocities is attributed to recirculated droplets and to droplets injected directly from the nozzle, respectively. Near the spray boundary (at $r = 10.2$ mm), the results indicate the presence of droplets originating solely from the nozzle exit (i.e., only positive axial velocities are revealed in Fig. 3a). In a previous study [9], it was shown that a bimodal size distribution is detected near the spray centerline and is attributed to the formation of a recirculation zone (consisting of mostly smaller-sized droplets) downstream of the nozzle. These results are of interest to burning studies since smaller droplets found under these conditions are captured by the gaseous recirculation pattern and transported upstream toward the nozzle. Under nonburning conditions [7], the strength of the central toroidal recirculation zone is much larger and stronger than that which develops for burning conditions. Although the recirculation zone in the burning spray is relatively weak, smaller droplets are transported upstream along the spray centerline and subsequently swept into the droplet mainstream along the spray boundary. At downstream positions, data were not obtained near the spray centerline because of the low data rates that were associated with the dramatically reduced droplet concentrations. Near the spray boundary, the size and velocity distributions were essentially the same as those at $z = 10$ mm because of the lack of axial droplet deceleration [10]. This lack of deceleration is attributed to the increased gas-phase volumetric flow rate that is induced by the combustion process.

The diameter of individual droplets corresponding to each droplet arrival time is shown in Figs. 2 and 3. The figures indicate that the droplets (i.e., both large and small) randomly enter the measurement volume. Spectral density analysis carried out with time-of-arrival data obtained during a previous investigation [11] did not indicate the presence of any dominant frequencies in the spray at $z \geq 10$ mm. High-speed cinematography has shown the presence of a high-frequency pulsation (at approximately 1 kHz) in the spray jet and apparent clustering of droplets immediately downstream of the nozzle ($z < 10$ mm), which is attributed to liquid sheet breakup [8]. This pulsation appears to decay rapidly within a few millimeters of the nozzle exit.

At the spray centerline, the data rate is much lower than detected near the spray boundary (see Figs. 2 and 3). Both swirl and combustion act to reduce the

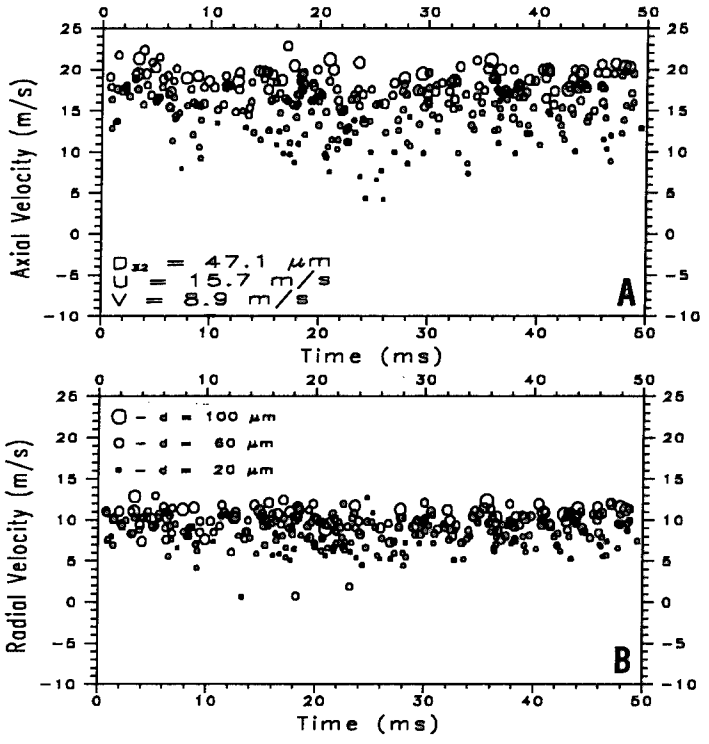

FIG. 3. Time history of droplet (a) axial and (b) radial velocity at r = 10.2 mm and z = 10 mm. Velocity time histories are coded to represent change in droplet diameter.

droplet concentration and therefore the data rate. The larger droplets that are fewer in number often pass with less frequency through the measurement volume at high velocity. At both radial positions, there is an obvious trend for the axial velocity sequence; viz., transport of the smaller droplets is at lower axial velocities while the larger droplets move at higher velocities. The radial velocity sequences presented in Figs. 2b and 3b indicate less correlation between size and velocity as compared with the axial velocity results.

Droplet Interarrival Statistics:

The time-of-arrival PDI data shown in Figs. 2 and 3 indicate that droplets pass through the probe volume in a random fashion (the term *random* is used in the sense that, at any instant, the detection of a droplet cannot be predicted a priori). A quantitative interpretation of single-point, time-resolved spray data can be carried out based on the recently developed ideal spray theory of Edwards and Marx [12,13]. In this theory, the ideal spray, which is defined as a discrete stochastic process, is comprised of droplets (treated as noninteracting point particles) randomly passing through a given point in space. The droplet flux within an ideal spray, in general, follows either homogeneous (steady in time) or inhomogeneous Poisson statistics. In a statistical sense, the ideal spray is defined completely by knowledge of the time-dependent process intensity function, $\lambda(t)$, where t represents time and for which the intensity function is equivalent to the particle arrival rate. Consequently, the probability of realizing a given set of droplet interarrival times depends solely on the intensity function. Note that a time-of-arrival sequence of $M + 1$ droplets constitutes a realization of M interarrival times, where the interarrival time is the difference in arrival time between successive droplets.

The functional form of $\lambda(t)$ can be used to classify the spray into three basic types [13]: (1) steady, (2) unsteady-deterministic, or (3) unsteady-random, corresponding to situations for which the intensity function is (1) independent of time, (2) time-dependent and deterministic, or (3) time-dependent and random, respectively. If the intensity function is time invariant, i.e., steady, then the spray follows homogeneous Poisson statistics.

Any ordering of the spray will influence the intensity function and therefore affect the droplet interarrival (or occurrence) statistics. In an actual spray, unsteady statistics can exist because of ordering and clustering of droplets as, for example, a result of aerodynamic effects or by periodicity generated by system pulsations. Statistical analysis of the occurrence events can therefore provide information regarding the nature of randomness of the spray field.

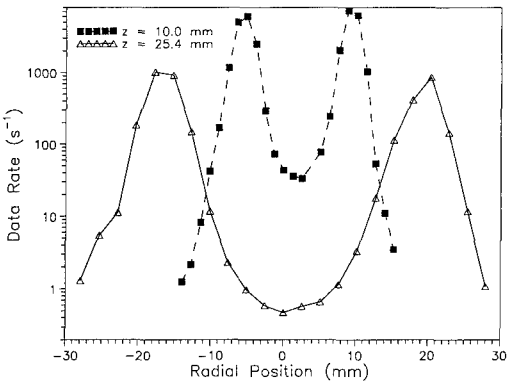

FIG. 4. Variation of phase-Doppler data rate with radial position at $z = 10$ mm and $z = 25.4$ mm.

The intensity, which represents the droplet arrival rate at a given point within the spray, is equivalent to the droplet flux (units, s^{-1}) passing through the measurement volume. Its magnitude is proportional to the local droplet concentration and velocity distribution integrated over the projected area of the probe volume. The actual measured intensity, $\lambda_m(t)$, also known as the data rate, is proportional to the fraction of droplet arrival events, β, which yield a validated response by the measurement apparatus, i.e., $\lambda_m(t) = \beta\lambda(t)$. At very high system gain, the validation fraction will tend to decrease as a consequence of increased detector signal noise. In this study, the gain was varied with radial position in order to accommodate changes in droplet mean diameter. At coordinates corresponding to relatively high gain and small mean droplet diameter, the validation fraction, as indicated by the PDI, was low, with $\beta \sim (0.2\text{–}0.4)$. Conversely, within the spray boundary, where the droplet mean diameter was large, system gain was reduced, and validation fraction was of the order $\beta \sim (0.6\text{–}0.8)$. It is important to note that, although the validation fraction alters the magnitude of the data rate, the shape of the interarrival-time distribution function is unaffected.

The expected value of the intensity, $\langle\lambda\rangle$, is equivalent to the average particle arrival rate and can be determined by dividing the number of interparticle events, M, by a sufficiently long time interval over which the particle events are observed to occur. Two radial profiles of the data rate, $\lambda_m = \beta\langle\lambda\rangle$, corresponding to $z = 10$ and 25.4 mm, are presented in Fig. 4. The profiles are nearly symmetric about the spray centerline, with somewhat increased asymmetry for $z = 10$ mm. Near the spray centerline, both profiles exhibit pronounced minima resulting from the relatively low droplet concentration. Conversely, the measured peak intensity of both profiles occurs near the spray boundary, with a maximum arrival rate at $z = 10$ mm of approximately 8×10^3 s^{-1}. At $z = 25.4$ mm, the radial spread of the spray is more than twice that of the $z = 10$ mm profile. Along the spray axis, the depleted droplet concentration yields a centerline data rate that is over three orders of magnitude less than the peak value of 10^3 s^{-1} near the spray boundary. One notes that the radial profile of the intensity, $\langle\lambda(r)\rangle$, differs in magnitude, and slightly in form, from the data rate, $\lambda_m(r)$, because of the spatial variation of the validation fraction, $\beta(r)$. With regard to $\langle\lambda(r)\rangle$, the reduction in the validation fraction at the spray centerline (relative to the peak value near the spray boundary) increases the magnitudes of the central minima of Fig. 4 by a factor of approximately 3.

In order to justify the dilute spray assumption (explicitly assumed in the model of an ideal spray), the ratio of droplet diameter, D, to interparticle separation, Λ, is estimated using values based on measured spray properties. For characteristic ratios, $D/\Lambda << 1$, it is expected that the average interparticle separation may be considered large enough so that the dilute spray approximation can be justified. The interparticle separation can be approximated by the cube root of the reciprocal of droplet number density, i.e., $\Lambda \sim N^{-1/3}$. The smallest interparticle separation was found to occur near the nozzle exit and spray boundary, where the maximum droplet number density and diameter were approximately 3500 particles cm^{-3} and 80 μm, respectively. Based on these values, it was estimated that this characteristic ratio was small, $D/\Lambda \sim 0.12$. This result shows that, on the average, the most dense region of the spray was relatively dilute although it is recognized that, at any given time, the ratio D/Λ can be much higher as a result of the occurrence of random fluctuations in interparticle spacing.

The occurrence statistics of the spray were quantified via the normalized interarrival-time-distribution histogram, $H(\tau_j,\Delta\tau_j)$, which was obtained from the phase-Doppler data. This histogram can be generated by counting the number of interparticle arrival times occurring within the jth time bin τ_j of width $\Delta\tau_j$, as:

$$H(\tau_j,\Delta\tau_j) = \frac{1}{M\Delta\tau_j} \cdot \text{count}[\tau_j - \Delta\tau_j/2 \le \tau < \tau_j + \Delta\tau_j/2] \tag{1}$$

where τ represents a measured arrival time and M is the total number of interarrival events. The interarrival probability density function, $h(\tau)$, which is a continuous function describing a process of infinite duration, is defined in terms of $H(\tau_j,\Delta\tau_j)$. In the limit of infinite sample population, M, and infinitesimal bin width, $\Delta\tau_j$, namely ($\lim \Delta\tau_j \to 0$, $M \to \infty$), then $H(\tau_j,\Delta\tau_j) \to h(\tau)$. Therefore, given a finite

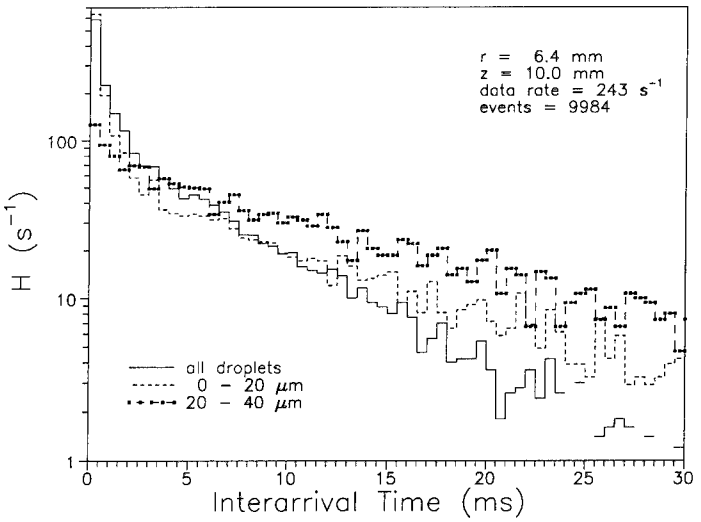

FIG. 5. Probability distribution of interarrival times for different diameter-based size classes at $z = 10$ mm and $r = 6.4$ mm.

sample population, $H(\tau_j, \Delta\tau_j)$ is an approximation to $h(\tau)$.

For a steady Poisson process, the interarrival probability density function, $h(\tau)$, is well known and is given in terms of the interarrival time, τ, and intensity, λ, as [14]

$$h(\tau) = \lambda e^{-\lambda\tau} \tag{2}$$

so that, for a steady spray, a plot of $\ln[h(\tau)]$ vs τ will have a constant slope equal to λ and intercept equal to $\ln(\lambda)$.

Given a sufficiently large sample size and exponential distribution characteristic of a steady spray, the relationship between $\ln[H]$ and τ will approach linearity. With this idea in mind, several representative normalized interarrival-time histograms, $H(\tau_j, \Delta\tau_j)$, were calculated from the time-series data (obtained at selected positions in the spray flame) and compared with the theoretical behavior of a statistically steady spray. For example, this statistical analysis was carried out for data obtained at $z = 10$ mm and $r = 6.4$ mm (see Fig. 5). At this position, recirculated droplets begin to interact with the droplets that are transported downstream directly from the nozzle. Three interarrival-time histograms were constructed from the following three diameter classes: (a) all sizes, (b) 0–20 μm , and (c) 20–40 μm. Nearly 10^4 particles were sampled over class (a), with about 6000 in class (b) and 3000 in class (c). At this position, the average measured intensity (over all size classes) was 243 s^{-1}, and the droplet number density was 250 particles cm^{-3}.

For the pair of curves corresponding to classes (a) and (b) in Fig. 5, there is a statistically significant departure from linearity at short interarrival times. Note that, since class (b) comprises nearly 60% of the entire population, the histogram for class (a) is heavily weighted by that class. This accounts for the similarity of the histograms for classes (a) and (b). For class (b), there is a relatively abrupt change in the magnitude of the histogram slope (intensity) that occurs at an interarrival time of approximately 3.5 ms. This result indicates an unsteadiness in the arrival-time statistics for the 0–20-μm-diameter size class at the coordinates $z = 10$ mm and $r = 6.4$ mm. This behavior persists as one moves toward the spray centerline where there is an abundance of smaller droplets. In contrast, the histogram for class (c) shown in Fig. 5 conforms more closely to the exponential distribution given by Eq. (2), thus revealing that the largest droplets exhibit nearly steady interarrival-time statistics. Near the spray boundary at $z = 10$ mm and $r = 10.2$ mm, the histogram (over all size classes) is consistent with steady Poisson statistics. At this location, the spray is relatively dense and is comprised mainly of larger droplets ($N \sim 2700$ particles cm^{-3} and $\lambda_m = 6198\ s^{-1}$).

In a droplet cluster, there exists a locally high droplet number density (above the mean value), which results in relatively short interarrival times. Although droplet clustering occurs even in steady sprays as a consequence of the random character of the droplet flux, in this discussion, the term "clustering" applies to those situations for which the interarrival times differ in a *statistically significant* fashion from steady Poisson statistics. Furthermore, since these statistics are derived from temporally resolved single point observations, clustering is used in the temporal sense. As an example of such clustering, it is apparent in the histogram of Fig. 5 class (b) that the probability density of the short interarrival times is increased (relative to that which would exist given steady Poisson statistics at the same mean intensity) with a concomitant reduction in the occurrence rate of the longer time scales. Without further analysis, a

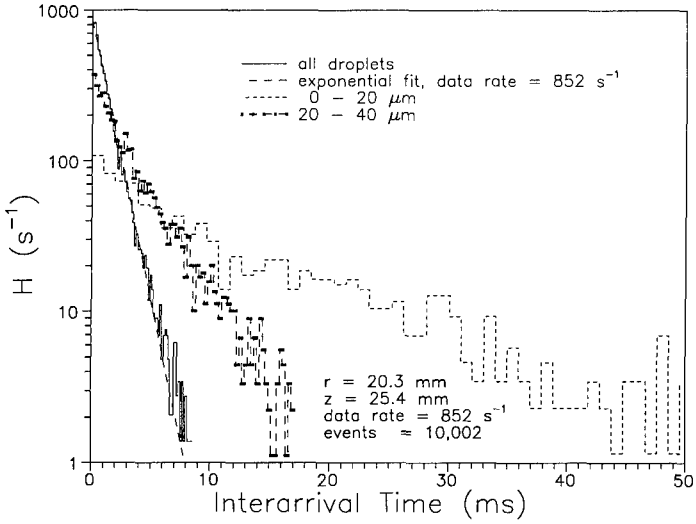

FIG. 6. Probability distribution of interarrival times for different diameter-based size classes at $z = 25.4$ mm and $r = 20.3$ mm.

distinction cannot be made between clustering that is associated with (1) closely spaced droplets traveling nominally at the same velocity and (2) droplets traveling at different velocities yet passing through the measurement volume at short time intervals (in this case, the droplets do not remain in close proximity over a significant time interval).

At the axial location $z = 10$ mm [corresponding to the class (b) data of Fig. 5], the maximum degree of unsteadiness, as measured by the departure from linearity of the $\ln H(\tau)$ data, occurred at a radial position located roughly midway between the spray centerline and spray boundary, whereas, for the class (c) results, all the interarrival-time histograms exhibited steady behavior throughout the entire range of radial positions. Thus, droplet clustering was most intense near the shear layer (in the region that lies between the spray boundary and recirculating gases toward the center of the spray) and was limited to the smaller droplets. It is expected that only the smallest droplets, having relatively small Stokes (St) numbers, follow the gas-phase turbulence, and the larger droplets with high momentum and large St tend to be unaffected by the gas-phase flow. This correlation with St is consistent therefore with a clustering mechanism for which only the smallest of droplets are swept by recirculating eddies formed in the shear layer. Such droplet-laden eddies interact with the main part of the spray to produce a fluctuating and hence unsteady occurrence of smaller droplets, which interact with the droplets coming directly from the nozzle. The existence of a bimodal size distribution (attributed to the recirculation of smaller droplets into the main droplet stream coming directly from the nozzle) further supports the assertion that unsteady interarrival-time statistics occur in the shearing region as a result of eddy transport of smaller droplets.

The interarrival-time histograms for the three size classes [(a), (b), and (c)] are presented in Fig. 6 for data obtained downstream near the spray boundary at the coordinates $z = 25.4$ mm, $r = 20.3$ mm. At this position, the droplet number density was 430 particles cm^{-3}, with droplets ranging in size from 10 to 90 μm in diameter. Also presented is the exponential distribution based on the measured average intensity of 852 s^{-1} (straight dashed line). The histogram corresponding to case (b) of Fig. 6 indicates some unsteadiness for the 0–20-μm-diameter droplets, although the departure from linearity of this histogram is less than the case (b) result of Fig. 5 taken at $z = 10$ mm and $r = 6.4$ mm. This result provides additional evidence of spatial inhomogeneity in the droplet arrival-time statistics. Inspection of Fig. 6 reveals also that the histograms corresponding to cases (a) and (c) are nearly linear and conform with steady Poisson statistics. Furthermore, the measured distribution of case (a) is accurately reproduced [with Eq. (2)] using the measured average intensity. The linearity of the case (a) data indicates that the nonsteady behavior associated with the smaller droplets was masked by the relatively abundant larger droplets.

Summary

The transport of fuel droplets in a kerosene pressure-atomized spray flame was investigated using phase-Doppler interferometry to measure droplet size, velocity, and arrival time at selected axial and radial positions within the spray. Along the spray centerline and near the spray boundary, the droplet axial velocities were found to correlate with droplet diameter; i.e., higher velocities were associated with the largest droplets. Negative axial velocities (con-

sisting mostly of smaller recirculated droplets) were observed near the centerline and attributed to recirculation patterns induced by the swirling air.

Analysis of the time-series data indicated that droplet arrival is random and consistent with Poisson statistics. Steady interarrival-time statistics were obtained for the larger droplets within and external to the spray boundary. Toward the internal shear layer separating the spray and recirculated air, significant nonsteady statistical behavior was observed for the smaller droplets. The results suggest the occurrence of a clustering mechanism resulting from droplet entrainment by eddy structures formed in the shear layer. In general, these findings illustrate that it is very important to segregate the spray into size classes because of the strong dependence of such transport mechanisms on droplet diameter.

Acknowledgments

The authors acknowledge the partial support of this work by the U.S. Department of Energy, Conservation and Renewable Energy, Office of Industrial Processes, Advanced Industrial Concepts Division. Messrs. Neil Rossmeissl and Marvin Gunn are the project monitors. The work of CTA was supported by the New York State Center for Hazardous Waste Management (Dr. Ralph R. Rumer, Director). The technical assistance of Messrs. Michael J. Carrier and James D. Allen is greatly appreciated.

REFERENCES

1. Presser, C., Gupta, A. K., Avedisian, C. T., and Semerjian, H. G., *Twenty-Third Symposium (International) on Combustion*, The Combustion Institute, Pittsburgh, 1991, pp. 1361–1367.
2. Bachalo, W. D., and Rudoff, R. C., in *Liquid Particle Size Measurement Techniques*, ASTM STP 1083 (E. D. Hirleman, W. D. Bachalo, and P. G. Felton, Eds.), American Society for Testing and Materials, Philadelphia, 1990, Vol. 2, pp. 209–224.
3. Reitz, R. D., in *Liquid Particle Size Measurement Techniques*, ASTM STP 1083 (E. D. Hirleman, W. D. Bachalo, and P. G. Felton, Eds.), ASTM, Philadelphia, 1990, Vol. 2, pp. 225–237.
4. Edwards, C. F., and Rudoff, R. C., *Twenty-Third Symposium (International) on Combustion*, The Combustion Institute, Pittsburgh, 1990, pp. 1353–1359.
5. Bulzan, D. L., Levy, Y., Aggarwal, S. K., and Chitre, S., *Atomiza. Sprays* 2(4):445–462 (1992).
6. Presser, C., and Gupta, A. K., AIAA 93–0132, *31st AIAA Aerospace Sciences Meeting*, Reno, NV, 1993.
7. Presser, C., and Gupta, A. K., in *Heat Transfer in Fire and Combustion Systems* (B. Farouk, M.P. Menguc, R. Viskanta, C. Presser, and S. Chellaiah, Eds.), ASME, New York, 1993, HTD-Vol. 250, pp. 79–92.
8. Presser, C., Gupta, A. K., and Semerjian, H. G., *Combust. Flame* 92:25–44 (1993).
9. Presser, C., Gupta, A. K., Semerjian, H. G., and Avedisian, C. T., *J. Propul. Power* 10:631 (1994).
10. Gupta, A. K., Presser, C., Hodges, J. T., and Avedisian, C. T., AIAA 94-0115, *32nd Aerospace Sciences Meeting*, Reno, NV, 1994.
11. Zurlo, J. R., Presser, C., and Gupta, A. K., *Atomiza. Sprays*, in review.
12. Edwards, C. F., and Marx, K. D., *6th Annual Conference on Liquid Atomization and Spray Systems (ILASS Americas '93)*, Worcester, MA, 1993, pp. 245–259.
13. Edwards, C. F., and Marx, K. D., Paper No. 93-082, Western States Section—Combustion Institute, 1993 Fall Meeting, Menlo Park, CA.
14. Snyder, D. L., *Random Point Processes*, John Wiley, New York, 1975.

COMMENTS

J. A. Bossard, Arizona State University, USA. What are some of the implications of your work in addressing the discrepancies that exist between temporal measurements (i.e., the PDPA) and spatial measurements (i.e., PIV), particularly with regard to differences in measured number density and volume flux?

Author's Reply. For temporal-based measurements of droplet number density and volume flux, the functional form of the interarrival time distribution function must be known in order to account properly for statistical biases in the raw data. Specifically, with knowledge of the interarrival statistics and effective probe volume dimensions, droplet number density and volume flux can be determined from droplet velocity and diameter measurements. Yet the results of this work demonstrate that in real sprays, droplet interarrival times (especially for the smallest droplets) do not always follow steady Poisson statistics. Consequently, given a situation for which the arrival time statistics are unsteady, a priori assumption of statistically steady behavior is not justified and will lead to erroneous estimates of measured number density and volume flux. It is thus possible that some discrepancies between temporal and spatial measurements may be attributed to the failure to account properly for unsteadiness in the interarrival time statistics of droplets or tracer particles. In an analogous fashion, one must know the interparticle distance distribution function when determining number density and volume flux from

spatial measurements. The occurrence of statistically significant *spatial* clustering would need to be accounted for in the determination of droplet number density and volume flux from such data.

•

Joseph J. Sangiovanni, United Technologies Research Center, USA. Does your data analysis properly account for droplet coalescence? For example, when small, faster moving droplets collide with larger, slower moving droplets. If droplet coalescence is accounted for, can you then quantify coalescences by analysis of droplet arrival time statistics as functions of droplet size, number density, and position?

Author's Reply. Droplet coalescence does not explain the unsteadiness in the measured interarrival time statistics. As discussed in the text, the minimum mean interdroplet spacing is relatively large so that droplet collision is a rare event. Furthermore, even in the densest region of the spray (where the likelihood of droplet collision is highest), the arrival time statistics remained steady. Unsteadiness in the statistics was observed only in the relatively dilute spray interior. Finally, the unsteady behavior was associated with only the smaller-sized droplets. However, as suggested in your question, collisions would tend to occur between smaller- and larger-sized droplets. Consequently, a collision-induced departure from steady statistics would be expected for small and large droplets. Since only the smallest droplets exhibited unsteady behavior, droplet coalescence does not then explain satisfactorily the occurrence of statistical unsteadiness.

Coalescence would influence the occurrence rate within any size class of droplets that are undergoing collisions. One could model the probability of droplet coalescence to quantify its effect on the form of the interarrival time distribution. For example, with no correlation between droplet arrival time and the collision probability (for droplets within a sufficiently narrow size class), coalescence events would be randomly distributed among these droplets. As a result, the form of the interarrival time distribution for such a size class would remain unaffected by collisions. Consequently, droplet coalescence may not necessarily result in unsteady interarrival time statistics. Nevertheless, droplet coalescence would tend to increase the number of larger droplets and concurrently deplete the relative abundance of smaller-sized droplets. An increase in the occurrence rate of larger droplets proceeding in the downstream direction might provide some evidence of droplet coalescence since droplet evaporation and deceleration tend to reduce the droplet occurrence rate.

Twenty-Fifth Symposium (International) on Combustion/The Combustion Institute, 1994/pp. 363–370

2D LASER DIAGNOSTICS OF LIQUID METHANOL FOR INVESTIGATION OF ATOMIZATION AND VAPORIZATION DYNAMICS IN A BURNING SPRAY JET

R. BAZILE AND D. STEPOWSKI
CORIA, URA CNRS 230, University of Rouen
76821 Mont Saint Aignan Cedex, France

Single-shot planar imaging of Raman scattering of liquid methanol, as well as laser-induced fluorescence of dissolved dye, has been used to investigate atomization and vaporization dynamics in the early stages of a burning spray jet. Within the limited dynamic range of the camera, these linear techniques provide signal levels that are locally proportional to the mass of liquid intercepted by the laser sheet, whereas the techniques based on elastic interactions with the spray could not provide quantifiable data in this region of large size dispersion.

High-speed 2D maps of the condensed mass field of the initial jet display the dynamic behaviour of the structures induced by different regimes of air-blast atomization. The technique has enabled us to obtain planar instantaneous pictures of the liquid phase velocity field in the early development of the burning spray.

When a droplet vaporizes, the signal level on its (blue) Raman image scales as its actual volume d^3, whereas the signal level on its (red) dye fluorescence image scales as its initial volume d_0^3, since the mass of dissolved dye does not vaporize. The comparison of the simultaneous images provides useful information on the vaporization dynamics in the burning spray. The data have been obtained in terms of evaporation constant from size reduction of single droplets or in terms of vaporized mass fraction of injected fuel from integrated measurements.

Introduction

Knowledge of the state and dynamics of the fuel droplet size distribution in the early development stages of a burning spray jet is useful for investigating the different combustion regimes that may be involved in flame stabilization. Because of the broadness of the size distribution and the limited dynamic range of the detectors, quantifiable time- and space-resolved information are very difficult to obtain.

Laser diagnostics based on elastic interactions are practically inapplicable, as the scattered intensities range over several orders of magnitude from the Rayleigh size regime to the upper Mie regime. This broad dynamic range can be apparently reduced by the time or space integrations that are involved in the imaging techniques (shadowscopies, diffractoscopies, stroboscopies . . .), but such artifacts may induce deleterious bias in the data interpretation.

The laser techniques based on spontaneous Raman and fluorescence interactions provide emissions at specific shifted wavelengths with intensities that are proportional to the number of molecules in the probe volume. However, these frequency shifts are practically insensitive to the phase in which the probed molecules are found, and it is impossible to discriminate between liquid and vaporized contributions of a given species. Very promising results have been obtained by the exciplex fluorescence technique [1], in which a laser-assisted reaction between organic additives occurs predominantly in the condensed phase. Unfortunately, this technique is very difficult to apply in a flame because the excited monomer in the vapor phase is strongly quenched by oxygen.

In the exciplex fluorescence method, the liquid additives that have been doped into the fuel are assumed to be coevaporative with it. Alternatively, the present paper reports on development and application of different methods in which only the condensed molecules are laser probed by Raman or fluorescence techniques. In the latter case, the liquid fuel has been doped with a very low concentration of an organic fluorescent dye that does not vaporize. In the former case, as a result of the much greater molecular density in liquid phase compared with the vapor phase, the Raman-scattered intensity from the vaporized fuel is always below the instantaneous detection threshold of the detector. Thus, in both cases, the measurement is insensitive to the thermochemical environment (collisional quenching), as the dissolved dye or fuel molecules are laser probed in the same condensed phase.

These techniques may be used to provide single-

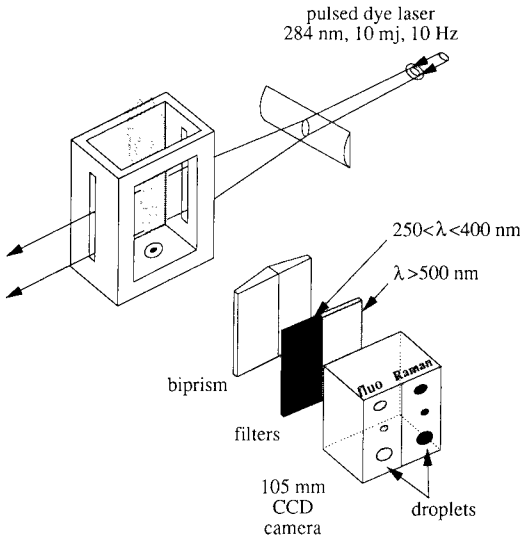

FIG. 1. Apparatus. The biprism and associated filters are only used in vaporization dynamics studies for obtaining simultaneous Raman and dye fluorescence images. A copper vapor laser was used for high-speed experiments.

shot 2D maps of the atomized liquid core on which the signal level scales as the local mass fraction of intercepted liquid fuel. Such a dynamic behaviour allows for further image processing with particle image velocimetry (PIV).

Furthermore, while the (blue) Raman signal level from an individual droplet scales as its actual volume ($\approx d^3$), the simultaneous (red) fluorescence signal level from that droplet scales as its initial volume ($\approx d_0^3$) since the dissolved dye does not vaporize. The comparison provides useful information on the local vaporization dynamics in the burning spray. This information can be obtained in terms of evaporation constant from individual droplet size reductions or in terms of vaporized mass fraction of injected fuel from integrated measurements.

Experimental Setup

The experimental apparatus is shown in Fig. 1. The laser diagnostics have been performed in the near development field of a burning spray, of which the initial zone is pictured in Figs. 2 and 3. The spray is produced by a coaxial air-blast injector in which liquid methanol issues at low velocity (0.35 ms^{-1}) from a central tube (2-mm diameter) and is atomized by a parallel air flow issuing at high velocity (60–110 ms^{-1}) from an annular duct. This injector is located at the bottom of a water-cooled chamber (8 × 8 cm) equipped with large quartz windows. Details have been described in previous papers [2,3], which report on phase-Doppler and OH fluorescence mapping in this spray jet.

The pulsed radiation (λ_0 = 284 nm, Δt = 10 ns, ε = 10 mJ, f = 10 Hz) provided by the second harmonic of a dye laser pumped by a YAG laser is focused into a vertical light sheet (20-mm height, 300-μm thick) passing through the axis of the spray. The laser-induced emissions are imaged at 90° onto a

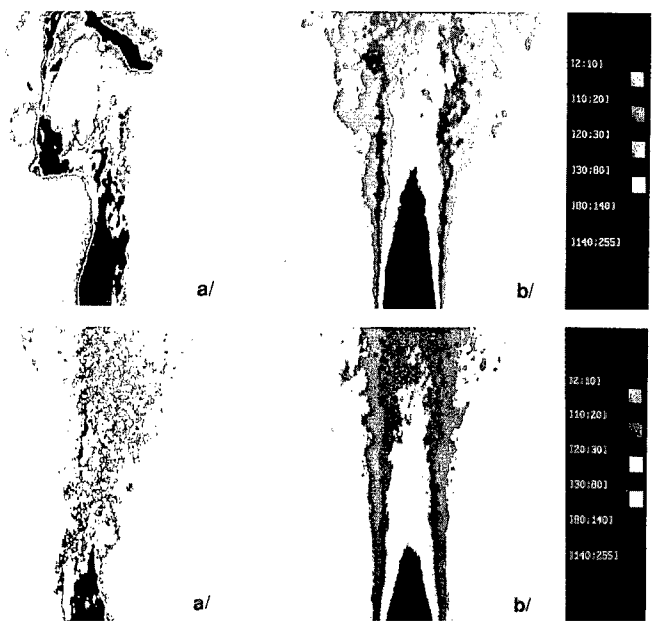

FIG. 2 and 3. Planar Raman imaging of liquid methanol just above the coaxial air-blast injector. The marked signal levels are proportional to the mass fraction of liquid fuel in the laser field. Fig. 2 (top): ΔU = 50 ms^{-1}, χ = 66; Fig. 3 (bottom): ΔU = 110 ms^{-1}, χ = 30. (a) Single-shot image; (b) ensemble average picture from over 200 laser shots.

gated intensified charge-coupled device (CCD) camera (Proxitronix, Δt_{gate} = 50 ns) with a 105 mm-F/4.5 objective lens equipped with a high-pass filter ($\lambda > 300$ nm). With the camera located 300 mm from the laser sheet, the magnification is about 0.5. The video signal is digitized by a frame grabber board (Matrox MVP-AT, 512 × 512, 8 bits) connected to a PC. The specific signal processings are described in the different sections and figures of this article.

Atomization Mapping

Single-Shot Maps of the Liquid Methanol Raman Scattering:

As methanol is linearly excited by a UV laser, the molecules scatter Raman-shifted radiations (λ_1 = 308.9 nm, λ_2 = 309.9 nm, λ_3 = 292.5 nm) that are mainly due to the stretching vibration modes of CH and CO. With caution that no absorption or optical breakdown occur, the signal intensity is proportional to the number of condensed molecules in the probed volume. Figures 2 and 3 show examples of planar imaging of liquid methanol just above the air-blast injector. The height of the laser sheet has been limited with a diaphragm to 20 mm to ensure a constant laser irradiance (within 10%) over the incident field. Neither laser nor Raman radiations are absorbed by methanol. A nonlinear color scaling has been used to visualize the strong gradients, but the marked signal levels that are proportional to the energy onto the CCD are a direct measure of the local mass fraction of liquid fuel in the laser field. However, unavoidable uncertainties on the spatial resolution remain as both the laser and Raman radiations may be refracted in the high gradient zones.

It is worth noting that the contribution of the small droplets that are detected (Figs. 2a, 3a) on the single-shot images is no longer visible on the ensemble average picture (Figs. 2b, 3b) that has been postprocessed. This dynamic limitation, which can never be overcome when either space or time integrations are basically involved in a diagnostic, underscores the requirement of statistical analyses based on instantaneous space-resolved measurements. This requirement is still more evident when comparing Figs. 2 and 3: The resolved pictures (Figs. 2a and 3a) show the very strong influence of the atomization velocity (through the Weber number) on the instantaneous liquid jet structures (which has drastic consequences on the combustion regimes [3]), whereas the average pictures (Figs. 2b and 3b) are still quite similar. The minimum droplet diameter that can be estimated from the signal level on its Raman image is about 50 μm, which corresponds to two resolved elements on the laser plane.

High-Speed 2D Maps by Dye Fluorescence:

When a small amount ($C_0 \approx 2$ ppm) of Rhodamin 6G is dissolved in liquid methanol, the laser pulse induces a yellow fluorescence emission over a broad spectral range (525–610 nm) that is determined by the spectroscopic structure of the dissolved dye molecule. Since the dye population is so low that laser absorption and fluorescence trapping are negligible, the fluorescence intensity is proportional to the mass of dissolved dye in the probed volume, since the fluorescence yield is fixed by the constant rate of quenching collisions with solvent methanol molecules. For this particular experiment, the laser beam from a copper vapor laser (ε = 4 mJ, Δt = 70 ns, f = 5 kHz, λ = 510 nm) was focused into a vertical light sheet (500-μm thick) passing through the axis of the jet just above the injector.

A 30-mm-height view field of the fluorescence emission was imaged through a high-pass filter ($\lambda >$ 550 nm) onto the photographic film (Kodak 400 ISO) of a high-speed roller camera. A series of 30 successive pictures has been obtained and digitized (1500 × 2000) for different atomization velocities that have been shown [2] to induce different regimes of flame stabilization in the spray. A morphological classification of the atomization liquid jets can be set as a function of a nondimensional number, $\chi = Re/We^{0.5}$, that compares the liquid Reynolds number to the atomization Weber number [4,5]. This composite number accounts for the dynamic structure of the initial liquid jet which can modify the air-blast atomization. The successive examples shown in Figs. 4a through 4f (ΔU_0 = 70 m/s, $\chi \approx 50$) correspond to a transition between two atomization regimes: the "membrane type ligament" ($\chi >> 50$) and the "fiber type" ($\chi << 50$).

2D Instantaneous Velocity Field of the Liquid Jet:

The particle image velocimetry (PIV) has been applied to a pair of successive fluorescence images from the previous series with ΔU_0 = 70 m/s. In this particular experiment, the velocity field is tracked by the liquid phase itself (in terms of mass fraction) with strong gradients and large size dispersion, whereas continuous seeding with calibrated particles is usually required for PIV application. However, a shift of the first image by the mean axial velocity ($\Delta h = \bar{v}\Delta t$) has made it possible to obtain the instantaneous map of the liquid velocity field in the earliest stage of the burning spray. The correlations were investigated for overlapping cells containing 256 × 256 pixels. The velocity field shown in Fig. 5 is consistent with the phase-Doppler data that have been obtained [2] in the near field of that spray jet. This promising result shows that it would be possible to obtain the instantaneous size-classified field of the Weber number in the atomized jet.

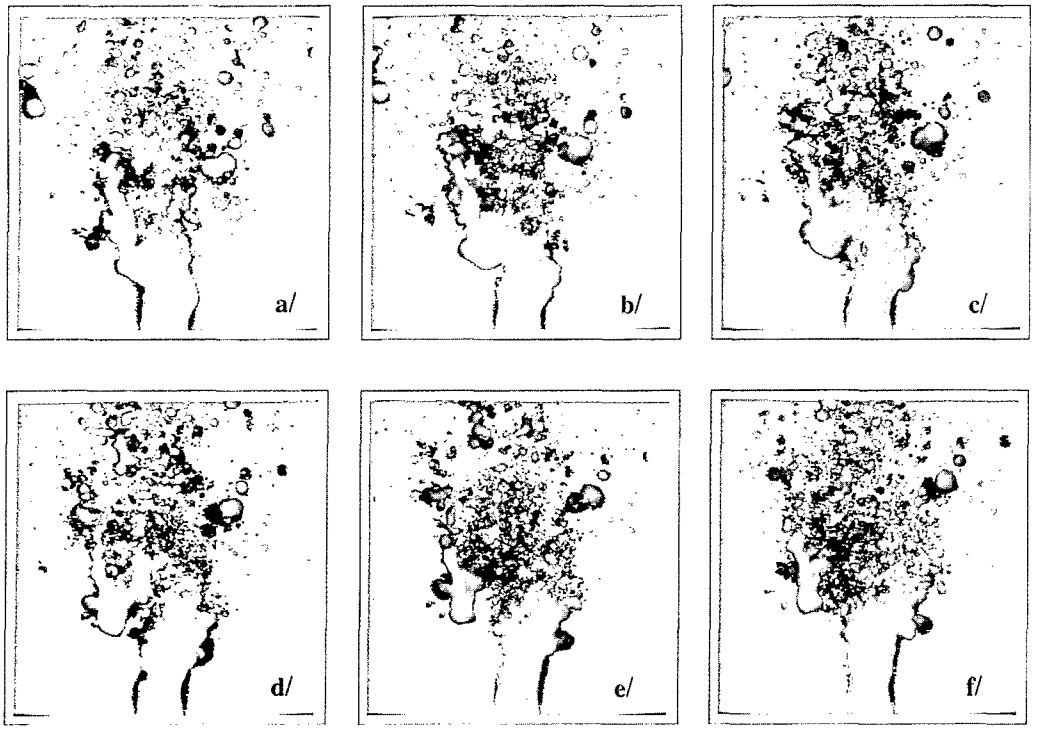

FIG. 4. Series of successive (Δt = 200 μs) images (750 × 750) of dissolved dye fluorescence in the early development of the atomized jet under burning conditions. Each picture images a field of 12-mm width × 12-mm height immediately upon the coaxial air-blast injector (ΔU = 70 ms^{-1}, χ = 47).

Vaporization Dynamics

The Raman scattering and the dissolved dye fluorescence induced by the single-shot UV excitation can be simultaneously and selectively detected using different pass-band filters. Calibration experiments in a stream of monosized droplets [6] have shown that both signals are proportional to the droplet volume under our linear excitation conditions and over the tested size range (120–450 μm). The very small amount ($C_0 \approx 0.02$ ppm) of Rhodamin did not modify the Raman yield of liquid solvent. However, when a droplet vaporizes, the integrated signal level on its Raman image scales as its actual volume d^3, whereas the signal level on its fluorescence image scales as its initial volume d_0^3 before any vaporization has occurred, since the mass of dissolved dye does not vaporize. The two signals were initially equalized in the liquid core of the cold jet, then, at downstream distances, any intensity difference between fluorescence and Raman signal can be related to vaporization effects irrespective of spray dispersion.

A biprism equipped with two filters was interposed before the camera (see Fig. 1) so as to provide two parallel images of the same field of view (13 × 20 mm) at each laser shot (one for the Raman scattering, the other for the fluorescence). Real-time processing (4 Hz) is performed in two selected windows that correspond to the same imaged field of view (5 × 2 mm) (Fig. 6a). Optical aberrations may induce spatial uncertainty when comparing two images, but the shift (±1 pixel) is smaller than the minimum size of the droplet that can be detected ($d_{min} \approx 50\,\mu$m). The signals in the observed window can be integrated and interpreted in terms of mass fraction, or they can be analyzed in terms of area under individual peaks, which are proportional to d^3 and d_0^3 on the Raman and fluorescence profiles, respectively (Fig. 6b). However, in the latter case, one must make sure that the probed droplets are completely immersed in the laser sheet. A criterion for this is provided by the ratio $a = I_r/(\Delta x)^3$, which compares the integrated intensity on the Raman image of a single droplet to the third power of its apparent diameter estimated on that Raman image. Calibration experiments [6] have shown that a holds a constant value a_0 when spherical droplets completely inside the laser sheet are linearly excited and detected.

Mass Flux of Vaporization along the Spray Axis:

The integrated signals of Raman scattering I_r and fluorescence I_f in the window have been averaged

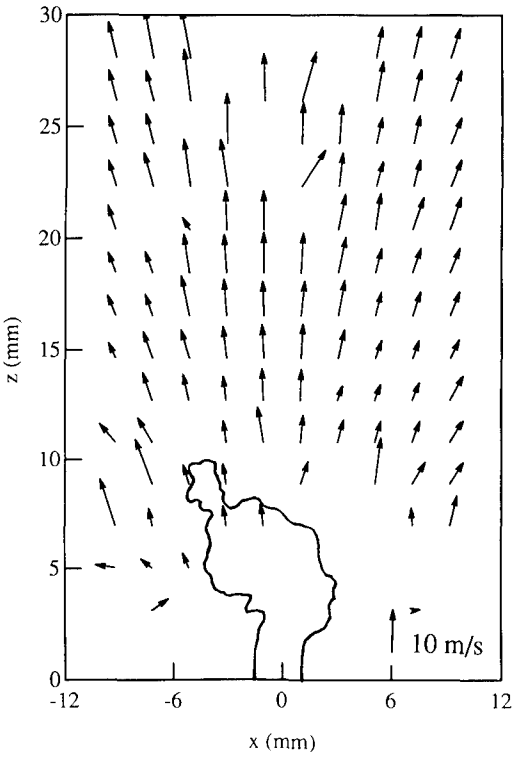

FIG. 5. Example of instantaneous velocity field (PIV) of the liquid phase in the burning spray derived from single-shot 2D images of dissolved dye fluorescence. The field covered by this velocity picture is broader than the field shown in Fig. 4.

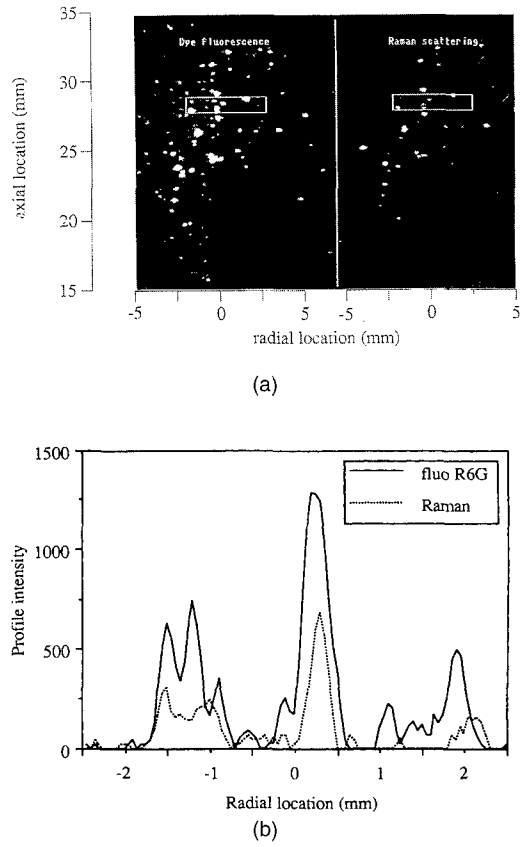

FIG. 6. Processing of the two parallel images. (a) Example of two parallel images (dye fluorescence on the left, Raman scattering on the right) simultaneously induced by a single laser shot in the burning spray. (b) Pair of radial profiles in the two selected windows shown in (a).

over 200 laser shots. Thus, the relative difference $\phi(h) = 1 - \bar{I}_r/\bar{I}_f$ which is plotted in Fig. 7 as a function of the probing height measures the mass fraction of injected methanol that has been vaporized in the stream tube up to the probed volume. This relative measurement technique is independent of the dispersion of the spray. However, when the evaporation of a droplet reaches completion, the fluorescence yield of the dissolved dye drops abruptly to zero according to Perrin's law [6]. With $C_0 = 0.02$ ppm, this cutoff occurs for $d_0^3/d^3 \approx 10^3$, which is higher than the dynamic range of the imaging system ($\approx$200). Thus, the droplets that have completely vaporized before reaching the probing window are not accounted for in the measurement. Let $\bar{I}_f' = \bar{I}_f/\beta$ be the ideal fluorescence intensity as if the fluorescence yield were still constant when d/d_0 reaches zero (i.e., the solid dye phase). Then, the actual mass fraction ϕ' can be extrapolated by using $\phi'(h) = 1 - \beta(h) + \beta(h)\phi(h)$ (see Fig. 7). [The procedure for estimating $\beta(h)$ is described in the next section.] This corrected mass fraction $\phi'(h)$ continues to increase on the axis toward completion. The derivative $\partial\phi'/\partial h$ of that cumulative mass fraction of vaporized fuel provides a reduced rate of vaporization per length unit. The dashed curve in Fig. 7 shows that most of the fuel vapor production on the axis of the burning spray takes place between 12 and 30 mm above the injector, which is the range of liftoff heights where the flame is stabilized [2].

Size Reduction of the Droplets, Evaporation Constant:

In a quiet homogeneous environment, the diameter of a spherical droplet decays [7] according to $d^2 = d_0^2 - kt$. The simultaneous fluorescence and Raman signal in the observed window have been analyzed in terms of area under the corresponding peaks, I_f and I_r, which are proportional to d_0^3 and d^3, respectively. Along with the area, the Raman peak width Δx was measured, and the data for which $|I_r/(\Delta x)^3 - a_0| > 30\%$ were rejected. This validation

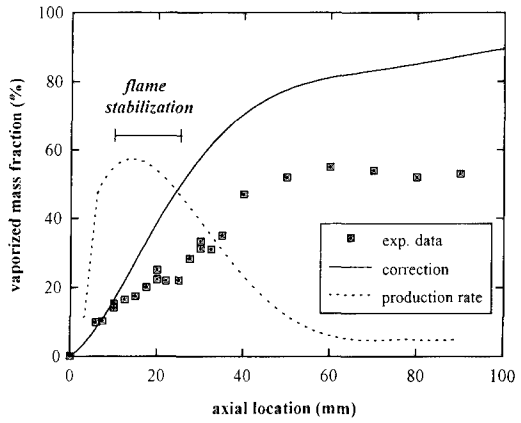

FIG. 7. Mass fraction of vaporized fuel along axis of burning spray ($\Delta U = 110$ ms^{-1}, $\chi = 30$). ⊡ ⊡ ⊡: Relative difference between fluorescence and Raman intensities. (———): Cumulative mass fraction of vaporized fuel; this corrected curve accounts for the contribution of the droplets that have completely vaporized before the probing event. (--------): Reduced rate of vaporization per length unit along the spray axis.

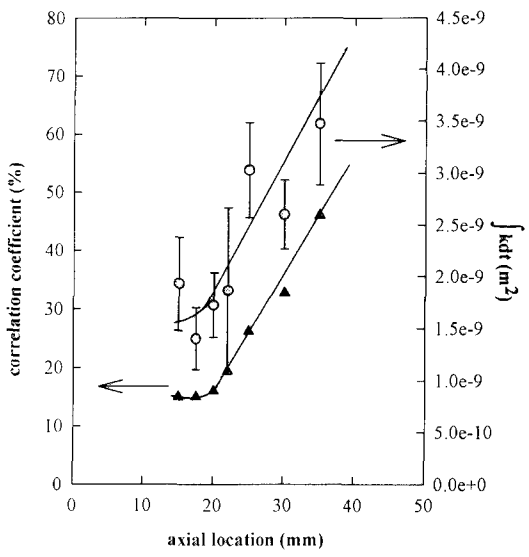

FIG. 8. Cumulative evolution of vaporization constant along axis of the burning spray ($\chi = 30$). The coefficient of correlation with respect to the d^2 law is also provided.

procedure has appeared to be crucial. Then, for each pair of peaks, $A = a_0^{-2/3}(I_f^{2/3} - I_r^{2/3})$ is a direct measure of $\int k dt$ where the evaporation constant is integrated over the time of flight of the droplets through the burning spray up to the laser-probing event.

In Fig. 8, $A(h)$ is plotted as a function of the height above the injector along with the correlation of the

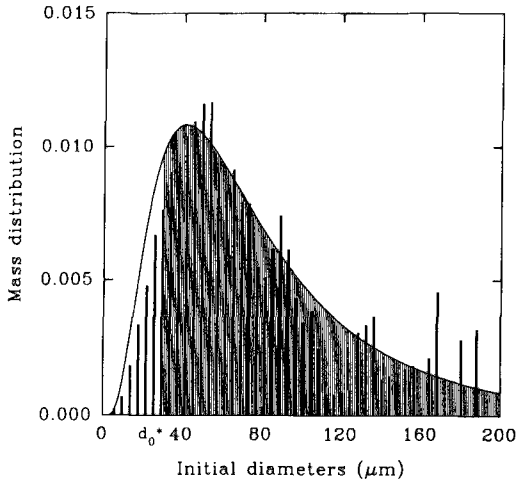

FIG. 9. Earliest available mass distribution on the axis of the burning spray ($\chi = 30$). Full line is the lognormal function fitted to the distribution (vertical bars) derived from phase-Doppler measurements. Dashed area from the cut-off at d_0^* represents the global fluorescence intensity where vaporized droplets are no longer accounted for.

data with the d^2 decay law: Although the temperature is low in the early stages, both the convection-induced enhancement of k and the long residence time of the inertial droplets in that environment lead to noticeable levels of A as soon as it can be measured. Beyond a transition zone (15 mm $< h <$ 20 mm) where both the validation rate and the correlation are low, A increases regularly along with the correlation to the d^2 law. As phase-Doppler data [2] show that the velocity of the droplets that we consider ($d > 50$ μm) is nearly constant in this region, the increase of A can be credited to the thermal enhancement of k in the combustion zone. The derived evaporation constant, $k \approx 2.10^{-6}$ m^2 s^{-1}, is somewhat higher than the expected value for a quiet passive environment at the flame temperature [8]. This can be due to the forced convection experienced by the inertial droplets that are laser probed.

The droplet size distribution from phase-Doppler measurements (5–200 μm) in the early stage ($h =$ 10 mm, $r = 0$) of the spray development [2] has been fitted to the lognormal distribution function [9] and then weighted by d_0^3, so that the area $\Gamma_0 = \int_0^\infty d_0^3 p(d_0) dd_0 = [\gamma]_0^\infty$ shown in Fig. 9 represents the global fluorescence intensity at the injector exit. For higher location in the flow, the ideal fluorescence intensity decay would be solely due to the dispersion of the spray, $F(h)$, according to $I_f'(h) = \Gamma_0 F(h)$ (if the dye fluorescence yield were constant). As evaporation takes place, the droplets with initial diameter smaller than $d_0^* = [\int_0^h (k/v) dh]^{1/2}$ that have completely vaporized before reaching elevation h are no

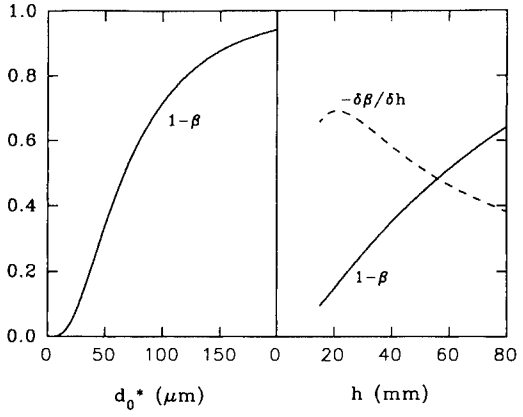

FIG. 10. (a) Contribution (to the ideal fluorescence signal) of vaporized droplets (with $d_0 < d_0^*$) that are not accounted for. (b) Growth of the probability, $1 - \beta$, that the droplets have completely vaporized before reaching elevation h on the axis. The dashed curve represents the density of probability that vaporization of the droplets occurs at elevation h.

longer detected. The actual fluorescence intensity is reduced, $I_f(h) = \Gamma(h)\, F(h) = [\gamma]_{d_0}^{\infty} F(h) = \beta I_f'(h)$, as is the dashed area in Fig. 9. The growth of $1 - \beta(d_0^*) \equiv [\gamma]_0^{d_0^*}/[\gamma]_0^{\infty}$ is plotted in Fig. 10a. Using the experimental dependence of $\int_0^h (k/v)dh$ on h, the growth of $1 - \beta$ as a function of the height above the injector is plotted in Fig. 10b. The expression $1 - \beta(h)$ can be interpreted as the probability, in terms of mass, that the droplets have completely vaporized before reaching elevation h on the axis. Therefore, $-(\partial\beta/\partial h)$ (the dashed curve in Fig. 10b) represents the density of probability that full consumption of the droplets occurs at elevation h. The range of height where fuel consumption is most probable fits with the zone where combustion takes place on the spray axis [2].

Concluding Remarks

Single-shot 2D laser diagnostics based on spontaneous Raman and dye fluorescence in the liquid phase have been shown to provide quantifiable information on atomization and vaporization dynamics in the early stages of a burning spray jet. Under our conditions, no lasing or stimulated Raman radiations have been detected, and calibration experiments have ascertained that the induced signal levels scale as the mass of intercepted liquids within the dynamic range of the detector. A test has been implemented to select the data corresponding to spherical droplets completely immersed in the laser sheet and linearly detected by the CCD. The evaporation constant has been estimated from the size reduction of the droplet falling in the dynamic range of the imaging system (50–300 μm). The droplets that have completely vaporized before reaching the probe volume were not directly accounted for in the mass measurement of the vaporization rate, but a satisfactory correction for this bias and statistical data on the mass rate of droplet consumption have been obtained by using the size distributions from phase-Doppler measurements.

Acknowledgments

This work was supported by the PRC "moteur fusée" (CNES-CNRS-SEP). The authors thank B. Lecordier and E. Rouland for their assistance in the PIV processing.

REFERENCES

1. Melton, L. A., and Verdieck, J. F., *Combust. Sci. Technol.* 42:217–222 (1985).
2. Goix, P. J., Edwards, C. F., Cessou, A., Dunsky, C. M., and Stepowski, D., *Combust. Flame* 98:205–219 (1994).
3. Stepowski, D., Cessou, A., and Goix, P., *Twenty-Fifth International Symposium on Combustion*, The Combustion Institute, Pittsburgh, 1994, to be published in *Combust. Flame*.
4. Farago, Z., and Chigier, N., *Atomiz. Sprays* 2:137–153 (1992).
5. Kennedy, J. B., and Roberts, J., ILASS-Americas, Fourth Annual Conference, Hartford, CT, 1990.
6. Bazile, R., and Stepowski, D., *Exp. Fluids* 16:171–181 (1994).
7. Spalding, D. B., *Fourth Symposium (International) on Combustion*, The Combustion Institute, Pittsburgh, 1953, pp. 847–864.
8. Chigier, N. A., and McCreath, C. G., *Acta Astronaut.* 1:687–710 (1974).
9. Lefebvre, A. H., in *Atomization and Spray*, Hemisphere Publishing Corporation, New York, 1989, pp. 79–103.

COMMENTS

J. Bellan, Jet Propulsion Laboratory, USA. As your drops evaporate, the concentration of the dye increases within each drop. Although you started with a negligible concentration of 0.02 ppm, this concentration might increase to the point where you no longer have a single component, but a two-component drop. If this were so, would the internal drop dynamics of the dye influence methanol evaporation to the extent that you could no longer compare your

experimental results with the theoretical predictions for an isolated drop of methanol?

Author's Reply. This effect would have to be accounted for if we were able to detect and measure the droplets over a wide size range. In the present experiment, because of the limited range of the camera dynamics ($\simeq 200$), the maximum dye concentration within the investigated droplets is about 8 ppm. For such a dilution, it is hoped that methanol evaporation is not significantly influenced by the dye additive.

Twenty-Fifth Symposium (International) on Combustion/The Combustion Institute, 1994/pp. 371–379

THE STRUCTURE OF THE DENSE CORE REGION IN TRANSIENT DIESEL SPRAYS

GREGORY J. SMALLWOOD, ÖMER L. GÜLDER AND DAVID R. SNELLING
National Research Council Canada
IERT/Combustion Technology
Ottawa, Ontario K1A 0R6, Canada

Intermittent and highly transient dense diesel sprays were investigated using two-dimensional laser light scattering and transmission techniques to decipher the internal spray structure. The experiments were conducted at maximum injection pressures ranging from 19 to 32 MPa using an electronic diesel injector with a single-hole nozzle. The experiments involved the imaging of the unperturbed structure of the dense core region of a full-cone intermittent diesel spray on photographic film at high resolution and the simultaneous measurement of laser sheet transmission along the centerline of the spray by an array consisting of 2048 diodes. At all injection pressures, line-of-sight laser sheet transmission measurements showed that the dense core region is fragmented very near to the nozzle exit, about 25–30 nozzle diameters downstream, and perhaps much closer. Further downstream from this location, the transmission measurements and simultaneous 90° scattering images revealed that the structure has an intermittent appearance with pockets of dense spray separated by relatively void regions. Two-dimensional images displayed a highly atomized spray structure beyond 50 nozzle diameters downstream, with no indication of an intact liquid core for the range of injection pressures studied. After eliminating the secondary scattering present by applying a low-pass filter and subtracting the filtered image from the original image, it was demonstrated for enlarged views of the spray that the scattering is from randomly spaced point sources, which were interpreted as droplets, rather than liquid columns, ligaments, or large blobs of fuel. It seems that pressure-atomized and fully pulsed round liquid sprays have a significantly different near-field structure than their steady counterparts. These findings, along with the recent work of others, are inconsistent with the existence of a long (on the order of 100 nozzle diameters or more) intact liquid core in unsteady diesel sprays.

Introduction and Background

Ignition and combustion in diesel engines is controlled by temporal and spatial variations in the fuel/air mixing process. This turbulent mixing is in turn dependent upon the atomization and vaporization characteristics of the intermittent fuel spray. Therefore, an understanding of the transient diesel spray structure is required to achieve a reasonably detailed description of the diesel combustion process [1,2]. However, there is a lack of knowledge regarding the mechanics of transient spray formation and the influence of the operating and design parameters [3–5]. As a result, optimizing diesel engine performance and reducing pollutant emissions is achieved by using lengthy iterative testing and development procedures. To reduce this development effort, multidimensional numerical codes are being used as a design tool to simulate different aspects of diesel engine operation. Although modeling efforts to understand the dynamics of the dense clusters of droplets are progressing rapidly [6], the lack of experimental data that describes the internal structure of unsteady sprays limits the development of physically sound spray submodels required for numerical codes [7].

A recent review summarizes the current understanding of the dense spray structure in steady liquid sprays [8]. There exist a large number of unsteady spray studies devoted to describing the external features and peripheral structures of the spray, many of which have been reviewed recently [2,5]. A less studied area is the internal structure of full-cone transient diesel sprays. Due to the very high optical density of these sprays, the internal features have been considered in the past to be nonvisible [9]. Thus, efforts to determine the internal structure of diesel sprays experimentally have been confronted with difficult challenges.

The interest in the internal structure in general, and the nature of an intact liquid core in particular, has several causes. The geometry and the dynamics of the core is a result of the jet breakup process, which controls the initial droplet size and velocity [9]. Also, the existence of a very dense or intact liquid core region may favor higher soot formation rates

due to rich mixtures and minimal air penetration. Although the presence of an intact liquid core in unperturbed intermittent diesel sprays has never been visualized directly, correlations describing the intact core length or breakup length, using data obtained by conductivity probes, have been reported [5,10], indicating distances comparable to diesel engine combustion chamber dimensions.

The presence of an intact liquid core has also been inferred from data representing spray-tip penetration as a function of time [11]. This data indicated that the jet is divided into two regions: a developing region from the nozzle orifice to transition and a fully developed region beyond the transition point. By applying jet disintegration theory developed for continuous liquid jets, expressions were derived for the data showing that the tip of the fuel plume moves at an almost constant velocity during the initial portion of the injection period, followed by a sharp transition to decelerating motion. The transition was interpreted to be that from an intact liquid core to an atomized spray.

Other reports on the nature of the intact core are based on observations made with direct photography and shadowgraphy, which produce line-of-sight images [12,13]. Due to the high obscuration by these sprays, it is difficult to obtain sufficient information related to the internal structure of full-cone transient diesel sprays from the line-of-sight-averaged photographs. Even by slicing the spray with a slit as small as 1-mm wide, it was impossible [12] to distinguish between tightly packed droplets, ligaments, and an intact liquid core in a dense spray due to high obscuration. A valid approach is to observe Mie scattering from laser sheet illumination, which has shown results that are inconsistent with the presence of a long intact liquid core in intermittent diesel sprays [14–16].

Cavaliere *et al.* [15] performed two-dimensional laser light scattering measurements to investigate the atomization and dispersion processes of unsteady diesel sprays. In this seminal paper [15], it was demonstrated that the fuel jet is already fragmented at the nozzle exit during the needle lift. One of the major conclusions was that the main part of the liquid, including the inner region of the jet, is fragmented at a distance from the nozzle notably shorter than that measured in similar but steady sprays [15]. Similar observations regarding the length of the intact core have been reported in Refs. 14 and 16.

Here, we report experimental data obtained on an intermittent diesel spray produced by an electronic diesel injector. Measurements were carried out using Mie scattering from laser sheet illumination, to determine the velocity, and combined with the sheet transmission, to observe the structure in the dense core region of a transient diesel spray.

Experimental Methodology

Optical Apparatus:

Laser sheet illumination has been applied to provide detailed structural information at planar cross sections parallel to the spray centerline at different time delays after the start of injection. The factors affecting image quality appeared in a recent review of experimental considerations regarding the use of photography in imaging of sprays [17]; thus, only the unique aspects of the experimental layout shown in Fig. 1 are described here.

The dense core visualization imagery was achieved using the output of a flashlamp-pumped dye laser, which was shortened by external Pockels cells to create a pulse of a 50-ns duration. This was done to eliminate blurring in the image due to high velocities present in the spray. The laser beam was geometrically filtered through 50-μm slits to reduce the divergence, resulting in a maximum sheet width of 165 μm fwhm (as measured by a beam profiler) over the field of view of the camera. The laser sheet intersected the spray centerline axis, and a camera recorded Mie scattering from the spray normal to the laser sheet. To reduce secondary scattering (multiple scattering) from spray outside of the laser sheet, the energy was attenuated to 0.08 mJ for these photographs. The spray was imaged on Kodak Gold 100 photographic film, using a Nikon F-801 camera with a Micro-Nikkor 105-mm lens and an extension ring to achieve a magnification of 1.14. The field of view of the camera was 31 mm in the spray axis direction, and the laser sheet extended 41 mm in this direction.

For the laser sheet transmission measurements, a Princeton Instruments PDA-2048 unintensified linear photodiode array was placed 120 mm past the spray axis on the path of the laser sheet. The laser sheet was 1.5-mm thick at this position and was centered on the 2.5-mm length of the photodiodes. The array consisted of 2048 diodes, each 25-μm wide, extending for 50.8 mm parallel to the spray axis direction. The magnification from the spray axis to the diode array was 1.22, so that each diode represented a 20-μm region of the spray axis. The signal on the photodiode array was digitized at 16 bits to give sufficient dynamic range for the measurement of transmission.

For the spray-tip velocity measurements, the same optical apparatus was used, except that a second laser was added producing two-color double exposures on the film. The two colors were blue (λ = 454 nm) and green (λ = 545 nm). The lasers were triggered sequentially, with the delay between the laser pulses in the range of 10–50 μs. The energy after the slits was 1.05 mJ for the blue laser and 0.65 mJ for the green laser.

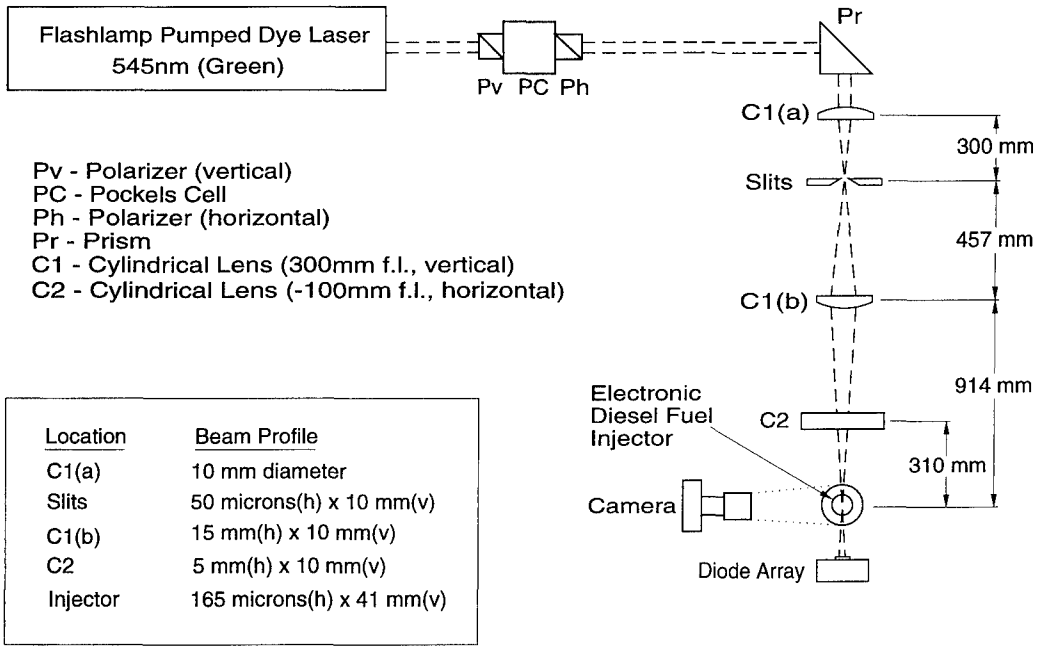

FIG. 1. Top-view schematic showing optical layout for Mie scattering and transmission measurement of the dense core region in diesel sprays.

Injection Apparatus:

Measurements were made on a transient spray produced by an electronically controlled, single-hole, accumulator-type diesel injector manufactured by BKM, Inc. A nozzle tip with a hole diameter and length of 0.34 and 0.9 mm, respectively, was used with the electronic injector. The measurements were made at maximum injection pressures of 19, 27, and 32 MPa, with fuel delivery of 11, 23, and 34 mg/injection, respectively. All measurements were made at atmospheric backpressure and room temperature. The liquid used for these experiments was No. 2-D diesel fuel. The injector was fitted with pressure transducers to measure both the rail and accumulator pressures. The illumination of a helium-neon laser, which was directed past the tip of the nozzle onto a photodiode, was scattered by the fuel during injection. This caused a decrease in the diode signal, which was used to determine the injection duration of 3.5 ms. The injection characteristics for a pulse at 27 MPa are shown in Fig. 2.

To put the operating regime of this injector into perspective with respect to previous work dealing with breakup length, the breakup length was estimated from published information [5] for the experimental conditions listed above. The estimated breakup length was several hundred hole diameters. At higher backpressures and temperatures, such as those found in an operating diesel engine, the effects of fluid mechanics and vaporization should be accelerated, causing the atomization process to occur more quickly, and over a shorter distance.

Results

Spray-Tip Velocity Measurements:

The spray-tip velocity was measured using two-color, double-pulse, laser sheet–illuminated double-exposure photography. For these photographs, excessive laser energy was used to deliberately induce enough secondary scattering so that all the liquid present was imaged onto the film. Thus, even if the spray tip was not in the plane of the laser sheet, it would appear due to the secondary scattering, resulting in an effect similar to using a thicker laser sheet. The velocity was determined by measuring the distance between the tips of the blue and green images and dividing this by the time separation between the two laser pulses. Measurements were made for maximum injection pressures of 19, 27, and 32 MPa. The delay from the beginning of the injection varied from 10 to 700 μs, and the resulting tip penetrations were from 1 to 100 mm (3–300 hole diameters). The results shown in Fig. 3 clearly indicate that the spray-

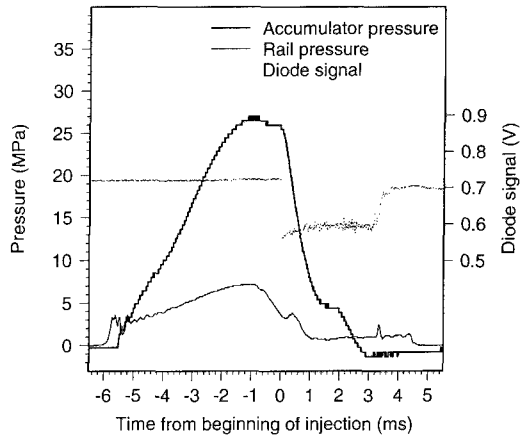

FIG. 2. Injection pressure signals for 27 MPa pulse. Drop in diode signal indicates presence of spray.

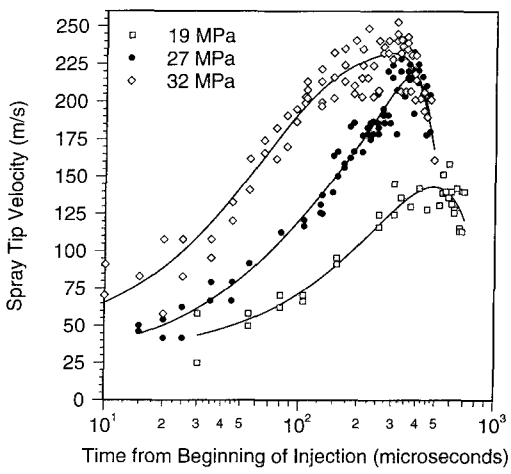

FIG. 3. Spray-tip velocity as a function of time from beginning of injection at typical diesel maximum injection pressures. The solid lines indicate best-fit curves to the experimental data for each of the three maximum injection pressures.

tip velocity varied during injection. There was strong acceleration of the spray tip for the first 200 μs, with the peak velocity reached at 300–500 μs, followed by deceleration to lower velocities. As the maximum injection pressure increased, the peak velocity also increased, and the time to reach the peak velocity was reduced. There was no constant velocity region in any of these sprays. Inspection of Fig. 3 does not reveal behavior that would indicate a sharp transition from an intact liquid core to an atomized spray.

Direct Visualization:

Photographic direct visualization of the dense spray region has been considered difficult, because the primary scatterers were obscured by a contiguous field of relatively uniform illumination produced by secondary scattering [12]. For the experiments discussed here, the technique applied, outlined below, was developed by Gülder *et al.* [16]. All spray components intersected by the laser sheet, defined as primary scatterers, were in focus. This was because the sheet width of 165 μm was less than the depth of focus of the camera lens, which ranged from 250 μm at $f/2.8$ to 3 mm at $f/16$. There was a dense spray field between these primary scatterers and the camera lens. This spray, not intersected by the laser sheet and mostly outside of the in-focus region of the camera lens, caused secondary (or multiple) scattering. Since the secondary scattering was from out-of-focus spray, the blurring caused the image of the scattered radiation to spread over a larger area and to have a more uniform, less intense distribution of energy than an in-focus image would have.

The effects of secondary scattering were reduced by closing the aperture on the camera lens by 2–3 stops. The reason that this was effective was that the secondary scattering was less intense than the primary scattering, since the secondary scattering results from primary scattering radiation being rescattered by liquid outside of the light sheet. Most of the secondary scattering was from out-of-focus sources, thus, enlarging the image area and reducing the energy density striking the film. Thus, by closing the aperture, the energy density from the secondary scattering was reduced below the gross fog level of the film, while the primary scattering was still able to produce an exposure. This could also have been achieved by reducing the laser intensity proportionately. It should be noted that in bracketing these exposures, one f-stop more exposure did result in visible secondary scattering on the film, while one f-stop less exposure resulted in nothing appearing on the film, not even the illumination from primary scatterers.

The results (Fig. 4) displayed a high level of atomization in the probed region of 50–140 hole diameters from the injector tip, with no indication of an intact liquid core. This held true over a range of peak injection pressures from 19 to 32 MPa, as observed in Figs. 4a through 4c. Images were recorded at delays ranging between 50 μs and 3.5 ms from the beginning of injection. The detail was observed more clearly in an enlarged view of a portion of Fig. 4b, centered 70 hole diameters downstream, reproduced as Fig. 5a. The photographic image in Fig. 5a was digitized and processed to eliminate the secondary scattering present by applying a low-pass filter and then subtracting this filtered image from the original image. The result of this image processing (Fig. 5b)

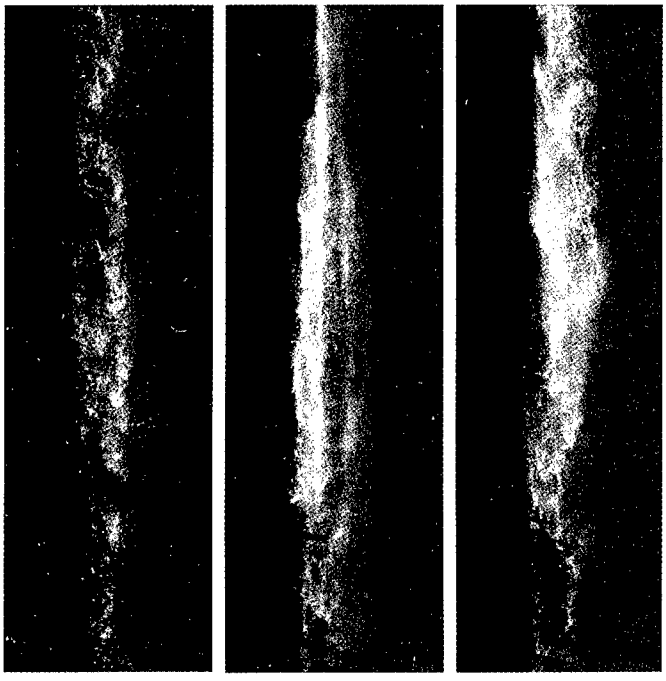

(A) (B) (C)

FIG. 4. Dense core region of diesel spray showing complete atomization and no evidence of an intact liquid core. Experimental conditions: $f/16$; 0.08-mJ laser energy; magnification 1.14; hole diameter, 0.34 mm; delay time, 1 ms; 17–48 mm (50–140 hole diameters) from the injector tip. Maximum injection pressure is (a) 19 MPa, (b) 27 MPa, and (c) 32 MPa.

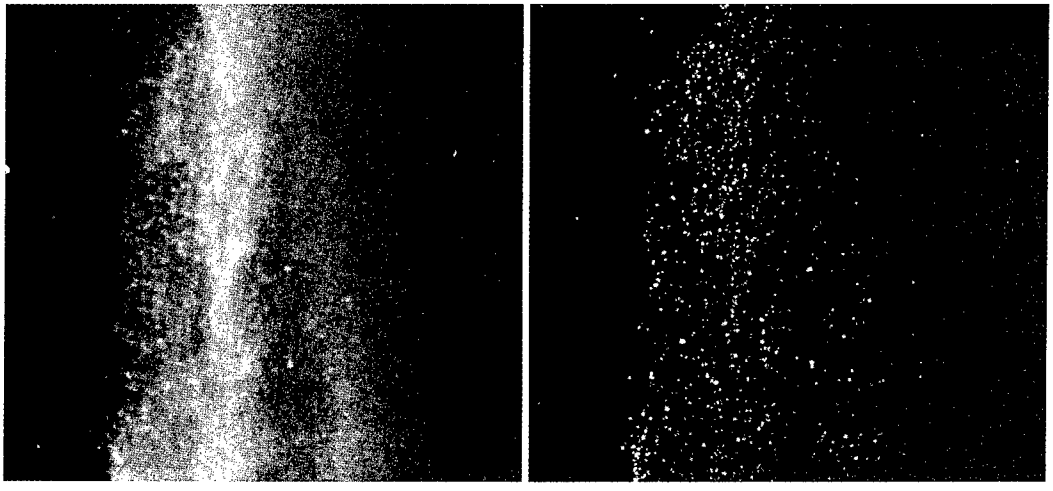

(a) (b)

Scale (mm) 0 1 2 3

FIG. 5. (a) Enlargement from Fig. 4b centered 24 mm (70 hole diameters) from the nozzle. (b) Result of image processing (a), showing that scattering emanates from point sources, with no evidence of connected structures.

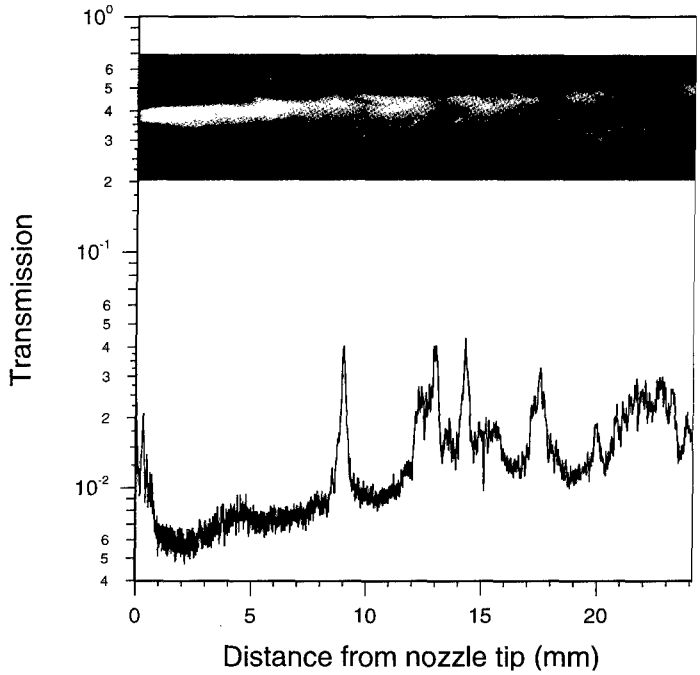

FIG. 6. Transmission of laser sheet energy as a function of distance from the injector. The photograph shows the Mie scattering simultaneously recorded. Note the transmission peaks at 9, 13, 14.5, 17.5, and 22 mm from the nozzle and the corresponding lack of scattered illumination at these locations. Experimental conditions: $f/2.8$; 0.002-mJ laser energy; magnification 1.14; maximum injection pressure, 27 MPa; hole diameter, 0.34 mm; delay time, 1 ms; 0–70 hole diameters from the injector tip.

illustrated that the illumination emanated from randomly spaced point sources, which were interpreted as droplets. There was no evidence of extended sources that would have indicated an intact core, ligaments, or large blobs of fuel. The number density distribution of droplets did not seem to be homogeneous since the point sources of illumination were unequally distributed, with dark regions indicating the absence of droplets. It should be noted that the sheet thickness was equal to only a few droplet diameters, and thus, the presence of regions without droplets was reasonable, even for a dense spray. The result of the image processing was relatively insensitive to the filter characteristics.

Transmission Measurements:

The transmission of the laser sheet through the centerline of the spray was measured relative to the laser sheet intensity in the absence of spray, as a function of distance downstream of the nozzle tip. Direct visualization photographs were taken simultaneously. A typical example, at 1 ms from the beginning of injection and 27 MPa maximum injection pressure, is shown in Fig. 6. The spray in the region from the nozzle exit to 24 mm (70 hole diameters) downstream is shown in the photograph. The scattering intensity was too great to resolve detail in the dense core region, from near the tip to 9 mm (25 hole diameters) downstream, where the intensity had decreased to a level at which individual droplets were observed. Further downstream from this location, the structure appeared intermittent, with pockets of dense spray separated by relatively void regions. There was less than 1% transmission of the laser sheet from 0.7 to 8.5 mm, followed by oscillations in the transmission from 1 to 5% at locations further downstream.

As observed in Fig. 6, the line-of-sight transmission was inversely correlated with the degree of scattering observed normal to the laser sheet. For repeated experiments, the line-of-sight transmission continued to show correlated behavior, although there was pulse-to-pulse variation in the distance to the first void and the subsequent intermittent structure. The high level of attenuation combined with the high scattering intensity observed in the dense core region before the first void indicates that there were a large number of air/liquid interfaces. This implies that the liquid is fragmented, entraining a substantial air fraction, in this region. The radius of curvature of these interfaces was presumably small (i.e., droplets or fine wrinkles) since large radii interfaces scatter predominately in the forward direction and would have contributed to the transmission.

Five sets of transmission data were averaged and smoothed at each time interval (from 50 μs to 3 ms) to produce the results displayed in Fig. 7, which show the variation of the transmission behavior as a function of time as well as the downstream location. For the data at 50, 100, and 250 μs, the spray tip was within the field of view, indicated by the regions of 100% transmission. From 1 to 3 ms, the transmission is increasing at all locations, rising to well above 10% for most of the spray beyond 10 mm at 3 ms. The region of maximum

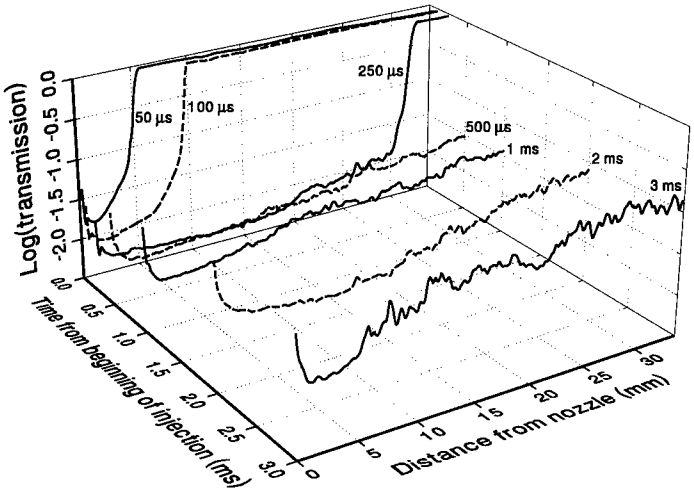

FIG. 7. Transmission of laser sheet energy as a function of both time from beginning of injection and distance from the injector. The solid and dashed lines were used to improve the definition of results at adjacent time intervals. Experimental conditions: delay times of 50, 100, 250, and 500 μs and 1, 2, and 3 ms; 0–100 hole diameters from the injector tip; maximum injection pressure, 27 MPa; hole diameter, 0.34 mm.

attenuation extends the furthest at 250 μs, where it extends almost 15 mm. This region becomes continually shorter in length at all later time intervals.

Discussion

In steady pressure-atomized sprays, the dense spray region consists of an intact liquid core (similar to the potential core of a single-phase turbulent jet) surrounded by a dispersed flow region that begins at the injector exit [8,18]. The atomization progresses by primary breakup forming droplets through stripping from boundary layers on the rippled liquid core surface, followed by a secondary breakup of ligaments and large drops. In analogy with this picture of the steady spray atomization mechanism, the highly transient and intermittent diesel sprays were thought to have a similar structure.

An unsteady diesel spray is a fully pulsed jet (i.e., no mass flow between pulses). Previous studies of single-phase fully pulsed jets showed significant differences between steady and pulsed jets. The entrainment in fully pulsed jets was much higher than the steady or partially pulsed jets [19]. Also, the velocity profile spreading and volume flow rate were increased in pulsed jets in the near field [20,21]. These studies indicate that steady jet characteristics are recovered only when a certain downstream location is reached, and the near field is greatly altered [22].

Recent measurements reported by Cavaliere *et al.* [15] and Yule and Filipovic [10] support the view that unsteady diesel sprays do not behave like steady ones. The unsteady fluid dynamics of the liquid jet plays an important role in the atomization. The fuel injected when the injector needle is fully lifted is fragmented some millimeters downstream of the nozzle exit. In contrast, the breakup length for steady diesel sprays is evaluated to occur much later (some centimeters downstream) [15]. By using an improved conductivity probe, it was inferred that the intact core or breakup zone in unsteady diesel sprays is not a simple liquid column but probably consists of a distributed chaotic assembly of sheets and ligaments disintegrating into droplets, with a very high void fraction (about 99%) within it [23,24].

The results presented herein indicate that if there is an intact liquid core in diesel sprays, its length is of the order of 30 nozzle diameters or less. Beyond that position, the spray displays a highly atomized flow field. The description by Yule of the breakup length, consisting of disintegrating sheets and ligaments with a very significant void fraction [23], also implies that an intact core is not present in diesel sprays. Since the transient behavior of conventional diesel injectors is more severe than that of the injector studied here, the unsteady fluid dynamics are more pronounced, and the breakup should occur more rapidly.

Conclusions

Intermittent and highly transient dense diesel sprays were investigated using two-dimensional laser light scattering and transmission techniques to decipher the internal spray structure. The following remarks summarize the findings.

1. The presence of secondary scattering and high obscuration have hampered previous attempts to view the structure of the dense core region of a full-cone transient diesel spray. Through careful experimental design, using laser sheet illumination, and careful control of exposure, this region has been observed. As a recommendation, the maximum aperture available should be used in or-

der to minimize the depth of field, and the exposure should be controlled by filtering the energy in the laser beams.

2. Two-dimensional images displayed a highly atomized spray structure beyond 50 nozzle diameters downstream, with no indication of an intact liquid core for the range of injection pressures studied. After eliminating the secondary scattering present by applying a low-pass filter and subtracting the filtered image from the original image, it was demonstrated for enlarged views of the spray that the scattering is from randomly spaced point sources, which were interpreted as droplets, rather than liquid columns, ligaments, or large blobs of fuel.
3. At all injection pressures, line-of-sight laser sheet transmission measurements showed that the dense core region was fragmented very near to the nozzle exit, about 25–30 nozzle diameters downstream and perhaps much closer. Further downstream from this location, the transmission measurements and simultaneous 90° scattering images revealed that the structure has an intermittent appearance with pockets of dense spray separated by relatively void regions.
4. It is apparent that pressure-atomized and fully pulsed round liquid sprays have a significantly different near-field structure than their steady counterparts. These findings, along with the recent work of others, are inconsistent with the existence of a long (on the order of 100 nozzle diameters or more) intact liquid core in unsteady diesel sprays.

Acknowledgments

We thank Y. Coté, M. F. Baksh, D. Gareau, and S. M. Aval who helped to set up the experimental rigs. The work reported herein has been supported by the internal research funds of the National Research Council (Sub-Project No. CSS02) and by the PERD program of the Canadian Government (Project No. 15114).

REFERENCES

1. Henein, N. A., *Prog. Energy Combust. Sci.* 1:165–207 (1976).
2. Kamimoto, T., and Kobayashi, H., *Prog. Energy Combust. Sci.* 17:163–189 (1991).
3. Bracco, F. V., in *Recent Advances in the Aerospace Sciences* (C. Casci, Ed.), Plenum Press, New York, 1985, p. 189.
4. Chigier, N. A., *Fifth International Conference on Liquid Atomization and Spray Systems (ICLASS-91)*, NIST Special Publication 813, Washington, 1991, pp. 1–15.
5. Hiroyasu, H., *Fifth International Conference on Liquid Atomization and Spray Systems (ICLASS-91)*, NIST Special Publication 813, Washington, 1991, pp. 17–31.
6. Bellan, J., and Harstad, K., *Twenty-Third Symposium (International) on Combustion*, The Combustion Institute, Pittsburgh, 1990, pp. 1375–1381.
7. Takagi, T., Fang, C. Y., Kamimoto, T., and Okamoto, T., *Combust. Sci. Technol.* 75:1–12 (1991).
8. Faeth, G. M., *Twenty-Third Symposium (International) on Combustion*, The Combustion Institute, Pittsburgh, 1990, pp. 1345–1352.
9. Chehroudi, B., Chen, S.-H., Bracco, F. V., and Onuma, Y., SAE Paper No. 850126, 1985.
10. Yule, A. J., and Filipovic, I., *Int. J. Heat Fluid Flow* 13:197–206 (1992).
11. Hiroyasu, H., Kadota, T., and Arai, M., in *Combustion Modelling in Reciprocating Engines* (J. N. Mattavi and C. A. Amann, Eds.), Plenum Press, New York, 1980, p. 369.
12. Ishikawa, M. and Murakami, T., *Second International Conference on Liquid Atomization and Spray Systems (ICLASS-82)*, University of Wisconsin, Madison, 1982, pp. 85–92.
13. Balles, E. N., and Heywood, J. B., *J. Eng. Gas Turbine Power* 111:451–457 (1989).
14. Bower, G. R., and Foster, D. E., SAE Paper No. 892101, 1989.
15. Cavaliere, A., Ragucci, R., D'Alessio, A., and Noviello, C., *Twenty-Second Symposium (International) on Combustion*, The Combustion Institute, Pittsburgh, 1989, pp. 1973–1981.
16. Gülder, Ö. L., Smallwood, G. J., and Snelling, D. R., SAE Paper No. 920577, 1992.
17. Chigier, N., *Prog. Energy Combust. Sci.* 17:211–262, (1991).
18. Wu, P.-K., and Faeth, G. M., *Atomization Sprays* 3:265–289 (1993).
19. Bremhorst, K., and Hollis, P. G., *AIAA J.* 28:2043–2049 (1990).
20. Favre-Marinet, M., and Binder, G., *J. Mech.* 18:355–394 (1979).
21. Crow, S. C., and Champagne, F. H., *J. Fluid Mech.* 48:547–591 (1971).
22. Kouros, H., Medina, R., and Johari, H., *AIAA J.* 31:1524–1526 (1993).
23. Yule, A. J., and Salters, D. G., *An Improved Technique for Measuring the Break-Up of Diesel Sprays*, Proc. ILASS-Europe 92, Amsterdam, Sept. 1992.
24. Yule, A. J., and Salters, D. G., *Atomization Sprays* 4:41–63 (1994).

COMMENTS

Michael Haug, Lehrstuhl fur Technische/RWTH Aachen, Germany. 1. Did you evaluate the velocities of the structures inside the spray? Your experimental equipment, using the two-color technique, can be modified to obtain two time-delayed, color-separated laser sheets.

2. Did you investigate the area right below the nozzle at high resolution? Did you find the spray already broken up? We are making a similar investigation, and have observed interesting phenomena caused by cavitation effects inside the nozzle.

Author's Reply. 1. The two-colour technique for measurement of spray-tip velocity could be applied, unmodified, to determine the velocities of the dense clusters within the spray, although this has not yet been performed.

2. The region from the nozzle tip to 25 nozzle diameters downstream is the most dense part of the spray. This is confirmed by the combined transmission/direct visualization results, which illustrate this region as having the lowest transmission and highest scattering. With the current experiment, it was not possible to view the internal structure of the spray in this region. However, as stated in the paper, scattering emanates from gas/liquid boundaries, indicating that the liquid must be highly fragmented in this region to produce the high levels of scattering and attenuation observed. This fragmentation could be due to vapor produced by cavitation inside the nozzle and/or air entrainment.

•

R. Ragucci, Istituto di Ricerche sulla Combustione—CNR, Italy. Would the authors give a physical explanation of the image enhancement technique they have used to support the early atomization of the spray. The authors claim that by subtracting an average image they were able to obtain evidence for the absence of sheets and ligaments and the presence of nonatomized structures. Does this procedure have a physical justification? Have the authors performed systematic measurements on a significant ensemble of images?

Author's Reply. Despite our best efforts to suppress secondary scattering through the use of new, enhanced tomographic technique, some haze was still evident in the images. In an attempt to further improve the identification of the sources of illumination in the images, well-established image-processing techniques were applied to eliminate the haze. In essence, haze is a low spatial frequency component in the image. Sheets and ligaments would appear as extended sources of illumination, whereas droplets would appear as point sources. In either case, the source would have a much higher spatial frequency than the haze. For extended sources, the high spatial frequency would be normal to the predominant axis of the source. Instead of using a high-pass filter to remove the haze, a low-pass finite impulse response filter [1] was applied to a digitized image of Fig. 5a and the resulting image subtracted from the original image. This permitted visual inspection of the low-pass filtered image, which showed only the low spatial frequency haze, with no evidence of an intact core, ligaments, or large blobs of fuel. This was performed to assess the application of digital image-processing techniques to tomographic images and to support the conclusions previously derived from interpretation of the photographic images.

REFERENCE

1. Pratt, W. K., *Digital Image Processing,* John Wiley and Sons, New York, 1991, pp. 241–258.

Twenty-Fifth Symposium (International) on Combustion/The Combustion Institute, 1994/pp. 381–388

SIMILARITY ANALYSIS OF SPRAY DIFFUSION FLAMES IN A UNIDIRECTIONAL SHEAR-LAYER FLOW

Y. TAMBOUR* AND D. KATOSHEVSKI**

*Department of Aerospace Engineering, **Department of Applied Mathematics
Technion-Israel Institute of Technology
Haifa 32000, Israel

A spray diffusion flame that results from an evaporating multisize (polydisperse) spray of fuel droplets suspended in one of the streams of a unidirectional shear-layer flow is analyzed. The droplets and their vapors spread into a coflowing stream, in which the oxidizer is contained, and feed the flame. Similarity solutions are presented for the evolution in droplet-size distributions across the shear layer, and the effects of various drop-size distributions on the fuel-vapor concentrations and on flame geometry and temperature are examined. The lateral location of the flame is obtained here via the solution of Schvab–Zeldovich type equations. The present results indicate that (1) sprays that contain mainly large droplets produce smaller amounts of vapor and thus result in a cooler flame that is located closer to the spray stream, and (2) sprays of different initial drop-size histograms, but of similar Sauter mean diameter (SMD) values may (under certain operating conditions) form flames of similar shapes.

Introduction

Fuel sprays produced by industrial atomizers usually contain drops of a wide range of sizes. Thus, such sprays are termed "multisize" or "polydisperse" sprays. When a spray of fuel droplets is injected into a quiescent environment, or into a coflowing air flow, a shear layer will develop at the edges of the spray flow between the two adjacent streams. In spray combustion research, it is important to analyze the evaporation of fuel droplets across the shear layer and their effect on the spread of fuel vapors into the coflowing air stream since the fuel-vapor local concentrations, together with other governing parameters, eventually determine the location and structure of the spray diffusion flame that will result upon ignition.

Theoretical studies of evaporating drops in vortices were presented by Bellan and Harstad [1] and by Yang and Sichel [2]. These studies are related to the unidirectional shear flows to be studied in the present paper, although they do not deal with multisize (polydisperse) sprays as will be considered here. Such multisize evaporating sprays were recently studied experimentally (in 1988, 1989, and 1992) by Lazaro and Lasheras [3–6]. They measured the longitudinal evolution in the total mass distribution of the liquid phase across a shear-layer flow formed by two unidirectional streams. The velocity of the stream containing the spray was about 10 m s^{-1} while the other stream was at rest. Experimental data for the Sauter mean diameter (SMD) distribution of the spray across the shear layer were also reported by Lazaro and Lasheras [3–6]. The above experimental data served for a qualitative comparison with theoretical results by Katoshevski and Tambour [7], who analyzed the behavior of multisize evaporating liquid sprays in a shear-layer flow.

The qualitative comparison between the results of Katoshevski and Tambour for typical computed total mass distributions of the liquid phase and experimental data reported by Lazaro and Lasheras [3–5] shows strong similarity between the two sets of profiles. This supports the assumptions and boundary conditions employed in Katoshevski and Tambour's theoretical study. The general behavior of the theoretical SMD distribution of the spray across the shear layer also compared well with the reported experimental results of Lazaro and Lasheras.

The aforementioned theoretical study was carried out for evaporating sprays without the presence of a flame. Thus, the purpose of the present study is to utilize the mathematical procedure presented by the authors [7] and analyze here the effect of various drop-size distributions on fuel-vapor concentrations across the shear layer and on the geometry and temperature of the spray diffusion flame.

Governing Equations

A steady, incompressible laminar shear layer that is formed by two adjacent parallel streams of different velocities is considered here. A polydisperse

*Professor.
**Doctoral Student.

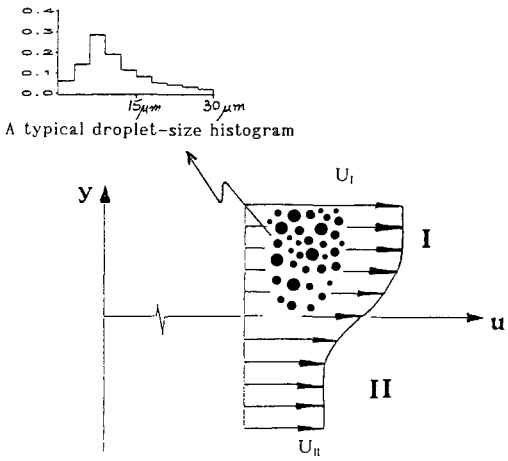

FIG. 1. Schematic description of the problem.

spray of droplets is suspended in one of the gas streams (see Fig. 1). In handling the gas-phase velocity field, we basically follow the treatment presented by Katoshevski et al. [8], which will not be repeated here. The spray is represented here by 10 sectional balance equations (see Refs. 9 through 14 for detailed derivation).

The spray sectional balance equations are given by

$$u_j \frac{\partial \tilde{Q}_j}{\partial x} + v_j \frac{\partial \tilde{Q}_j}{\partial y} + \tilde{Q}_j \left[\frac{\partial u_j}{\partial x} + \frac{\partial v_j}{\partial y}\right]$$

$$= \frac{D_j}{\mu/\rho} \frac{\partial^2 \tilde{Q}_j}{\partial y^2} + \frac{\hat{x}_c}{\hat{U}} (-C_j \tilde{Q}_j + B_{j,j+1} \tilde{Q}_{j+1});$$

$$j = 1, 2, \ldots, N_s \tag{1}$$

where x and y are nondimensional longitudinal and lateral coordinates, respectively, N_s is the total number of droplet-size sections, and $\tilde{Q}_j$ is the mass fraction of size section j. The coefficients C_j and $B_{j,j+1}$ are sectional evaporation coefficients (see Refs. 9 through 14). The terms $\hat{x}_c$ and $\hat{U}$ are characteristic longitudinal distance and velocity, respectively.

The spray sectional momentum equations are as follows:

$$u_j \frac{\partial u_j}{\partial x} + v_j \frac{\partial u_j}{\partial y} = a_j(u - u_j) + \frac{\hat{x}_c}{U} \frac{1}{\tilde{Q}_j} (S_{j,x}^{L,M} - u_j S_j) \tag{2a}$$

$$u_j \frac{\partial v_j}{\partial x} + v_j \frac{\partial v_j}{\partial y} = a_j(v - v_j) + \frac{\hat{x}_c}{U} \frac{1}{\tilde{Q}_j} (S_{j,y}^{L,M} - v_j S_j) \tag{2b}$$

where the last term on the right-hand side of Eqs. (2) represents loss of linear momentum due to evaporation of droplets in section j ($u_j S_j$), and the linear momentum added to section j due to droplets from higher sections ($S_j^{L,M}$) (see Ref. 11). In the above equations, a_j is given by

$$a_j = 18 \frac{1}{Re} \frac{\rho}{\rho_d} \frac{\hat{x}_c^2}{\hat{d}_j^2} = \frac{\text{const}}{\hat{d}_j^2}. \tag{3}$$

Next, for the shear-layer setup, we follow the similarity transformation presented in Ref. 7 by which all governing equations are presented in terms of a similarity coordinate η,

$$\eta = \left[\frac{1}{2}(a + 1)\right]^{1/2} x^{(a-1)/2} y \tag{4}$$

and in terms of a stream function Ψ,

$$\Psi = \left[\frac{1}{2}(a + 1)\right]^{-1/2} x^{(a+1)/2} f(\eta). \tag{5}$$

Here a is a negative power of x that represents the deceleration of the free flow velocities U_I and U_{II} (see Fig. 1). For nondecelerating flows, a equals zero. Since in Eq. (4) the coordinate y is nondimensional, one can employ the following relation,

$$y^* = \hat{x}_c y (\sqrt{Re})^{-1} \tag{6}$$

for obtaining a dimensional lateral coordinate y^*. As shown above, the dimensional distance y^* is a function of the flow Reynolds number Re and the characteristic distance $\hat{x}_c$.

Rewriting the above conservation equations in terms of η and $f(\eta)$, one obtains the following sectional spray balance equations:

$$\frac{D_j}{\mu/\rho} Q_j'' + f Q_j' = -(2 - \beta)\Delta_o \cdot (-\bar{C}_j Q_j + \bar{B}_{j,j+1} Q_{j+1})(1 - f') + (1 - q_j)(1 - \beta)\eta[f' Q_j' + f'' Q_j] \tag{7}$$

where the primes denote differentiation with respect to η and β is a parameter related to the power a via

$$\beta = \frac{2a}{1 + a}. \tag{8}$$

In the near field, *outside the shear layer* (i.e., far from the interface between the two streams), the velocity lag of the droplets depends on their size and is represented here by an approximate mathematical relation

$$U_j = q_j(x)U_I \tag{9}$$

where the governing equation for $q_j(x)$ outside the shear layer is obtained via Eq. (2a) after dropping the second term on the left-hand side, which vanishes outside the shear layer, and the last term on the right-hand side, which is negligible (see Ref. 7 for details). Hence, the governing equation for $q_j(x)$ is given by

$$\frac{dq_j}{dx} = \frac{a_j(1 - q_j)}{x^a q_j} - \frac{a}{x} q_j. \tag{10}$$

Within the shear layer, we assume that the velocity lag of droplets in the longitudinal direction can be described in a similar way to that of the velocity lag of droplets *far* from the shear-layer interface. That is,

$$u_j = q_j(x)u. \tag{11}$$

In the lateral direction, on the other hand, we do not wish to describe v_j as a product of $q_j(x)$ and v, since this will simply mean that the droplets in the shear layer follow the streamlines of the host gas. To circumvent this, we write

$$v_j = v \tag{12}$$

and in the droplet-diffusion coefficient D_j [which appears in Eqs. (1) and (7)], we incorporate the transport of droplets in the lateral direction across the shear layer due to drag forces and vortices.

Sprays in unidirectional shear-layer flows were studied by Lazaro and Lasheras [3–6]. They indicated that vortices that develop in the mixing layer between two streams play an important role as a transfer mechanism for droplets that move from the spray stream to the adjacent stream. Although in the present study we do not present hydrodynamic solutions for such vortices, we account for this transfer mechanism via the coefficient D_j.

The remaining governing equations are as follows.

Fuel-vapor diffusion equation:

$$\frac{m_f''}{Sc_f} + fm_f' = (2 - \beta)\Delta_v \sum_{j=1}^{N_s} (-\bar{C}_j Q_j + \bar{B}_{j,j+1} Q_{j+1}) \cdot (1 - f') + (2 - \beta)\Delta_R \nu_f M_f \cdot \frac{\bar{M}}{M_o M_f} m_o m_f \hat{Q}_{t,c} \exp(-E/RT) \tag{13}$$

Oxidizer diffusion equation:

$$\frac{m_o''}{Sc_o} + fm_o' = (2 - \beta)\Delta_R \nu_o M_o \cdot \frac{\bar{M}}{M_o M_f} m_o m_f \hat{Q}_{t,c} \exp(-E/RT) \tag{14}$$

Energy equation in terms of temperature:

$$\frac{\bar{T}''}{Pr} + f\bar{T}' = -(2 - \beta)\hat{Q}_{t,c} \frac{h_v}{c_p \hat{T}_c} x^{\delta-\lambda} \Delta_v \sum_{j=1}^{N_s} \cdot (-\bar{C}_j Q_j + \bar{B}_{j,j+1} Q_{j+1})(1 - f') + \hat{Q}_{t,c} x^{\delta} \frac{1}{Pr} \sum_i (Le_i m_i')\bar{T}' - (2 - \beta) \cdot \frac{1}{c_p \hat{T}_c} \Delta_R x^{\delta-\lambda} \frac{\bar{M}}{M_o M_f} m_o m_f \hat{Q}_{t,c}^2 \cdot \exp(-E/RT) \sum_i h_i \nu_i M_i. \tag{15}$$

The term Q_j is the normalized mass fraction of section j. The coefficients $\bar{B}_{j,j+1}$ and $\bar{C}_j$ [in Eqs. (7), (13), and (15)] are normalized sectional evaporation coefficients (see Ref. 7), m_i is the normalized mass fraction of chemical species i, and $\bar{T}$ is the normalized temperature.

In the above equations, additional source terms that do not appear in Ref. 7 are present because of the combustion reaction. These are the last term on the right-hand side of Eqs. (13) through (15), which is an Arrhenius type of reaction term, and the second term on the right-hand side of Eq. (15), which represents transport of heat due to mass diffusion fluxes. Here ν_i and M_i are the stochiometric molar number and molecular weight of chemical species i, respectively, R is the universal gas constant, E is the activation energy, and T is the temperature.

The global reaction is described by

$$\nu_f M_f + \nu_o M_o \xrightarrow{k} \nu_p M_p \tag{16}$$

where k is the reaction constant and the index p is for the reaction products. The Damköhler numbers for evaporation (Δ_v) and for chemical reaction (Δ_R) are defined respectively as

$$\Delta_v = \hat{A} \frac{\hat{x}_c}{\hat{U}} \tag{17}$$

and

$$\Delta_R = \frac{\hat{x}_c}{\hat{U}} \frac{k\rho}{\bar{M}} x^{\delta-a+1} \tag{18}$$

where $\hat{A}$ represents a characteristic evaporation rate and $\bar{M}$ is an average molecular weight defined as

$$\bar{M} = \sum_i (\nu_i M_i) \Big/ \sum_i \nu_i. \tag{19}$$

In deriving Eqs. (7) and (13) through (15), we have assumed that the total mass of the droplets at the upper edge of the shear layer decays as x^δ ($\delta < 0$), and we have also assumed that

$$T_{-\infty} - T_{+\infty} = \hat{T}_c x^\lambda \quad (\lambda \leq 0) \tag{20}$$

where $\hat{T}_c$ is a characteristic temperature differential. As to the change of the total mass of the droplets in the longitudinal direction (x^δ), it is interesting to note that, in a spray jet flow, experimental results by Yule et al. [16] show that, *along the centerline* of the jet, the total droplet mass fraction decreases with the longitudinal distance as x raised to the power of -1. This value was used in Tambour's [9] theoretical simulation of the downstream evolution in spray mass radial distributions, which agreed well with the above-mentioned experimental data. The power λ represents the decrease in temperature differential with the longitudinal distance between the "upper" and "lower" free flows outside the shear layer. For obtaining similarity solutions, we assume that both powers, δ and λ, have the same numerical value. In Eq. (15), Pr is the host-gas Prandtl number, and Le_i is the Lewis number of chemical species i. The term c_p is the specific heat at constant pressure of the gas mixture, and h_v is the droplets' latent heat of vaporization. The summation in the second term on the right-hand side of Eq. (15) over the mass diffusion fluxes ($Le_i m_i'$) vanishes when assuming the same value for the specific heat capacities of all chemical species.

Schvab–Zeldovich Formulation

In order to obtain a solution for the geometry of the flame, it is convenient to transform the above governing equations [Eqs. (7) and (12) through (15)] into the well-known Schvab–Zeldovich form of equations. This is carried out as follows. First, we present the following abbreviated notations for some of the terms which appear in Eqs. (7) and (12) through (15):

$$S_R = (2 - \beta)\Delta_R \frac{\bar{M}}{M_o M_f} m_o m_f \hat{Q}_{t,c} \exp(-E/RT) \tag{21}$$

$$E_j = (2 - \beta)\Delta_v \cdot(-\bar{C}_j Q_j + \bar{B}_{j,j+1} Q_{j+1})(1 - f') \tag{22}$$

$$\zeta_j = (1 - q_j)(1 - \beta)\eta[f' Q_j' + f'' Q_j] \tag{23}$$

$$Sc_j = \frac{\mu/\rho}{D_j} \tag{24}$$

where the latter is a sectional Schmidt number for droplets.

Then, Eqs. (7) and (12) through (15) can be rewritten as follows:

$$\frac{Q_j''}{Sc_j} + \frac{fQ_j'}{Sc_j} + fQ_j'\left(1 - \frac{1}{Sc_j}\right) = -E_j + \zeta_j \tag{25}$$

$$\frac{m_f''}{Sc_f} + \frac{fm_f'}{Sc_f} + fm_f'\left(1 - \frac{1}{Sc_f}\right) = \nu_f M_f S_R + \sum_{j=1}^{N_s} E_j \tag{26}$$

$$\frac{m_o''}{Sc_o} + \frac{fm_o'}{Sc_o} + fm_o'\left(1 - \frac{1}{Sc_o}\right) = \nu_o M_o S_R \tag{27}$$

$$\frac{\bar{T}''}{Pr} + \frac{f\bar{T}'}{Pr} + f\bar{T}'\left(1 - \frac{1}{Pr}\right) = -\left(\frac{1}{c_p \hat{T}_c}\hat{Q}_{t,c}\sum_i h_i \nu_i M_i\right)S_R - \hat{Q}_{t,c}\frac{h_v}{c_p \hat{T}_c}\sum_{j=1}^{N_s} E_j. \tag{28}$$

Now, summing the droplets' sectional equations [Eq. (25)] over all j ($j = 1, 2, 3, \ldots N_s$),

$$\sum_{j=1}^{N_s}\frac{Q_j''}{Sc_j} + \sum_{j=1}^{N_s}\frac{fQ_j'}{Sc_j} + \sum_{j=1}^{N_s} fQ_j'\left(1 - \frac{1}{Sc_j}\right) = -\sum_{j=1}^{N_s} E_j + \sum_{j=1}^{N_s}\zeta_j \tag{29}$$

and adding this summation to the fuel-vapor conservation equation [Eq. (26)] results in

$$\left(\frac{m_f}{Sc_f} + \sum_{j=1}^{N_s}\frac{Q_j}{Sc_j}\right)'' + f\left(\frac{m_f}{Sc_f} + \sum_{j=1}^{N_s}\frac{Q_j}{Sc_j}\right)' + fm_f'\left(1 - \frac{1}{Sc_f}\right) + \sum_{j=1}^{N_s} fQ_j'\left(1 - \frac{1}{Sc_j}\right) = \nu_f M_f S_R + \sum_{j=1}^{N_s}\zeta_j. \tag{30}$$

Next, dividing the oxidizer diffusion equation [Eq. (27)] by $\hat{\nu}$, where $\hat{\nu}$ is defined by

$$\hat{\nu} = \frac{\nu_o M_o}{\nu_f M_f} \tag{31}$$

and subtracting the resulting equation from Eq. (29), one obtains

$$\left(\frac{m_f}{Sc_f} - \frac{m_o}{\hat{\nu}Sc_o} + \sum_{j=1}^{N_s}\frac{Q_j}{Sc_j}\right)''$$
$$+ f\left(\frac{m_f}{Sc_f} - \frac{m_o}{\hat{\nu}Sc_o} + \sum_{j=1}^{N_s}\frac{Q_j}{Sc_j}\right)' + fm_f'\left(1 - \frac{1}{Sc_f}\right)$$
$$- \frac{1}{\hat{\nu}} fm_o'\left(1 - \frac{1}{Sc_o}\right) + \sum_{j=1}^{N_s} fQ_j'\left(1 - \frac{1}{Sc_j}\right)$$
$$= \sum_{j=1}^{N_s}\zeta_j. \tag{32}$$

Then, using a new function S which is defined as

$$S = \frac{m_f}{Sc_f} - \frac{m_o}{\hat{\nu}Sc_o} + \sum_{j=1}^{N_s}\frac{Q_j}{Sc_j} \tag{33}$$

one finally obtains

$$S'' + fS' = -\sum_{j=1}^{N_s} fQ_j'\left(1 - \frac{1}{Sc_j}\right) + \sum_{j=1}^{N_s}\zeta_j \tag{34}$$

which is a Schvab–Zeldovich type equation.

The last term on the right-hand side of Eq. (34) vanishes for the far field since q_j approaches unity [see Eq. (23)]. Thus, Eq. (34) is integrated numerically in the absence of this last term to obtain far-field solutions. Then, approximate near-field solutions can be obtained via substituting near-field values of q_j into Eq. (34).

Note that, according to Eq. (33), the flame is located at the locus for which

$$S - \sum_{j=1}^{N_s}\frac{Q_j}{Sc_j} = 0 \tag{35}$$

and therefore, after obtaining solutions for Q_j, one substitutes these solutions into Eq. (35) to obtain the lateral flame location in the similarity plane (η).

The boundary conditions for Q_j are

$$\eta \to +\infty; \qquad Q_j(+\infty) = Q_{j,\infty} \tag{36a}$$

$$\eta \to -\infty; \qquad Q_j(-\infty) = 0 \tag{36b}$$

where $Q_{j,\infty}$ is a polydisperse drop-size histogram that is given far from the shear layer in the lateral direction (i.e., at $\eta \to \infty$). Far from the interface at the edge of the "lower" stream (i.e., at $\eta \to -\infty$), no droplets are present, and thus, Q_j equals zero for all droplet-size sections.

The boundary conditions for the vapors are

$$\eta \to +\infty; \qquad m_f(+\infty) = m_{f,\infty} \tag{37a}$$

$$\eta \to -\infty; \qquad m_f(-\infty) = 0. \tag{37b}$$

The boundary conditions for the oxidizer are given by

$$\eta \to +\infty; \qquad m_o(+\infty) = 0 \tag{38a}$$

$$\eta \to -\infty; \qquad m_o(-\infty) = m_{o,-\infty}. \tag{38b}$$

and the boundary conditions for S are as follows:

$$\eta \to +\infty; \qquad S_\infty = \frac{m_{f,\infty}}{Sc_f} + \sum_{j=1}^{N_s}\frac{Q_{j,\infty}}{Sc_j} \tag{39a}$$

$$\eta \to -\infty; \qquad S_{-\infty} = -\frac{m_{o,-\infty}}{\hat{\nu}Sc_o}. \tag{39b}$$

Results and Discussion

Since the fuel-vapor local concentrations, together with other governing parameters, eventually determine the location and structure of the spray diffusion flame that will result upon ignition, we begin by analyzing the lateral distribution of fuel vapors across the shear layer. The profiles of fuel-vapor concentrations that are produced by evaporation of various initial droplet-size distributions *before ignition* are presented in Fig. 2. We compare four types of initial droplet-size histograms, which are listed in Table 1 and shown on the left-hand side of Fig. 2. As indicated by the results that are presented in Fig. 2, the lateral distributions of vapor strongly depend on the initial drop-size histograms. It is evident that histogram A, which is comprised mainly of small droplets, produces larger amounts of vapor than the spray represented by histogram D, in which larger droplets are present.

Next, we present lateral distributions of the fuel vapor and oxygen in the presence of the flame (see Fig. 3) and compare our results with the above-described solutions for the nonburning case. As one marches "downward," there is a buildup of fuel vapor as a result of the evaporation process, and then vapor is consumed by the flame. The flame location is indicated by the lateral point at which the fuel-vapor concentration becomes zero. At this location, the oxygen concentration reduces to zero as well.

The effect of the initial drop-size histogram on the flame geometry is shown in Fig. 4 for two cases, (i) and (ii), for which the total liquid fuel mass fractions are 8 and 5%, respectively. For the same total fuel mass fraction, initial drop-size histograms that produce smaller amounts of fuel vapor will result in cooler flames (see Table 2), which are located closer to the spray stream (see flame D in Fig. 4). Reducing

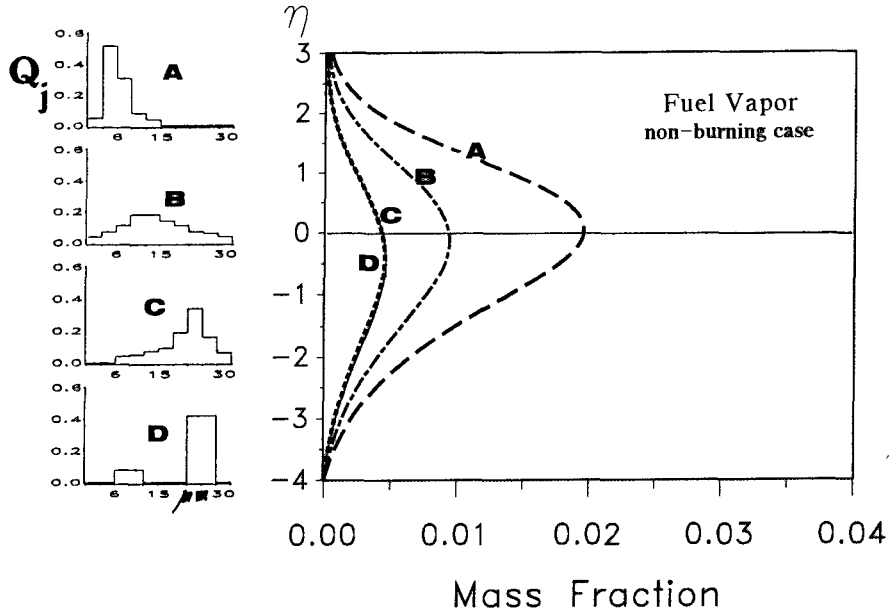

FIG. 2. Effect of various initial droplet-size distributions (given by drop-size histograms A, B, C, D) on vapor distribution across the shear layer for the nonburning case.

TABLE 1
Sectional droplet properties

Section no. (j)	1	2	3	4	5	6	7	8	9	10
d_l–d_u (μm)[a]	0–3	3–6	6–9	9–12	12–15	15–18	18–21	21–24	24–27	27–30
$\Delta\bar{C}_j$	15.00	2.86	1.32	0.81	0.57	0.44	0.35	0.30	0.25	0.22
$\Delta\bar{B}_{j,j+1}$	0.71	0.53	0.41	0.33	0.28	0.24	0.21	0.18	0.17	—
a_j	444.4	49.38	17.78	9.10	5.49	3.67	2.63	1.98	1.54	1.23
$Q_{j,\infty}$ (A in Fig. 3)	0.05	0.52	0.31	0.08	0.04	0.00	0.00	0.00	0.00	0.00
$Q_{j,\infty}$ (B in Fig. 3)	0.04	0.07	0.11	0.18	0.18	0.14	0.11	0.07	0.06	0.04
$Q_{j,\infty}$ (C in Fig. 3)	0.00	0.00	0.04	0.05	0.07	0.09	0.19	0.34	0.16	0.06
$Q_{j,\infty}$ (D in Fig. 3)	0.00	0.00	0.08	0.08	0.00	0.00	0.00	0.42	0.42	0.00
$Sc_j = 1.8$ for all j.		Host-gas properties: $a = 0$; $\beta = 0$; $Sc_i = Pr = 1$								

[a]The terms d_l and d_u are the lower and upper limits of section j, respectively, in terms of droplet diameter.

the total amount of liquid fuel from 8 to 5% for the same drop-size histogram will shift the flame from the oxygen stream (i.e., negative η values) toward the spray stream (i.e., positive η values).

It is interesting to note that, before ignition, the evaporation of the bimodal droplet distribution D results in a fuel-vapor profile that is almost identical to the one resulting from the general polydisperse distribution C (see Fig. 2). This is due to the fact that both distributions have approximately the same initial SMD (18.5 μm for C and 18.7 μm for D). It is therefore not surprising that the flames resulting from both sprays are almost identical in geometry (see flames C and D in Fig. 4). One can also conclude from the preburning vapor distributions shown in Fig. 2 that sprays that contain mainly small droplets produce a larger amount of fuel vapor, and hence, stoichiometric conditions (at which the flames settle) are reached at a "lower" location (see, for example, flame A in Fig. 4). Similar trends were obtained by Allison and Clarke [16], albeit for a gaseous flame in a shear-layer flow.

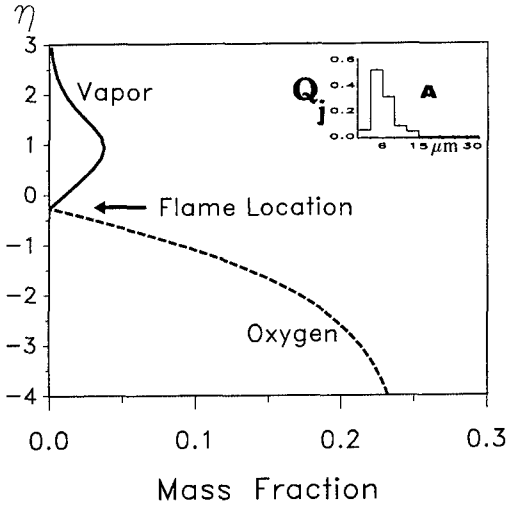

FIG. 3. Effect of initial drop-size distribution, given in terms of drop-size histogram A (see upper right-hand-side corner) on vapor and oxygen mass fraction distributions across the shear layer, for 8% total mass fraction of the liquid fuel.

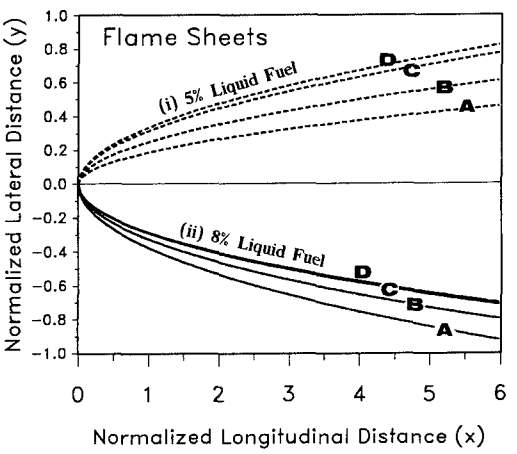

FIG. 4. Effect of various initial droplet-size distributions (given in terms of drop-size histograms A, B, C, D) on the flame-sheet geometry (x and y are nondimensional coordinates) for two cases of the liquid fuel total mass fractions: (i) 5 and (ii) 8%.

In conclusion, new similarity solutions have been presented for evaporating multisize sprays that burn in a shear-layer setup. It has been shown how various initial drop-size histograms affect the flame geometry and its temperature. In this regard, it has been illustrated how sprays of different size histograms, but of similar SMD values, may (under certain operating conditions) form flames of similar shapes.

TABLE 2
Flame temperatures (in Kelvin) for various initial drop-size distributions

%Fuel/histogram	A	B	C	D
5%	1902	1848	1793	1777
8%	2381	2337	2309	2305

Nomenclature

a_j	defined by Eq. (3)
$\hat{A}$	characteristic evaporation rate
$\bar{B}_{j,j+1}$	sectional vaporization coefficient
$\bar{C}_j$	sectional vaporization coefficient
c_p	heat capacity at constant pressure
$\hat{d}_j$	average drop diameter of section j
D_j	droplet-diffusion coefficient, represents lateral transport of droplets due to drag forces and vortices
E	activation energy
f	function of η [see Eq. (5)]
h	enthalpy
j	section number
k	reaction rate constant
m_i	normalized mass fraction of the species i
M	molecular weight
$\bar{M}$	average molecular weight [Eq. (19)]
N_s	total number of droplet-size sections
Q_j	normalized mass fraction of size section j
$\hat{Q}_{t,c}$	characteristic total mass fraction of the liquid phase
Pr	Prandtl number
$q_j(x)$	ratio of the velocity of droplets from section j and the host-gas velocity
Re	Reynolds number
S	Schvab–Zeldovich function
Sc	Schmidt number
S_R	reaction source term
T	temperature
$\bar{T}(\eta)$	normalized temperature
$\hat{U}$	characteristic longitudinal velocity
u	longitudinal velocity of the gas flow
x	normalized longitudinal coordinate
$\hat{x}_c$	characteristic longitudinal distance
y	normalized lateral coordinates
y^*	dimensional lateral coordinate
Greek	
α	power of x in the expression for U_I
β	parameter related to the power α
δ	a power, representing the decrease of liquid mass with x

λ	a power, representing the decrease of temperature differential with x
Δ_v	Damköhler-like number for evaporation
Δ_R	Damköhler number for reaction
μ	host-gas viscosity
ν	stoichiometric coefficient
$\hat{\nu}$	defined in Eq. (31)
Ψ	stream function
ρ	host-gas density
η	similarity variable

Subscripts

d	droplet
f	fuel
o	oxidizer
I	denotes the spray stream
II	denotes the "lower" stream
$+\infty$	"upper" free flow
$-\infty$	"lower" free flow

REFERENCES

1. Bellan, J. and Harstad, K., *Twenty-Third Symposium (International) on Combustion*, The Combustion Institute, Pittsburgh, 1990, pp. 1375–1381.
2. Yang, M.-H., and Sichel, M., 1987 Proceedings of the Fall Meeting of the Eastern States Section of the Combustion Institute, 1987.
3. Lazaro, B. J., and Lasheras, J. C., *Twenty-Second Symposium (International) on Combustion*, The Combustion Institute, Pittsburgh, 1988, pp. 1991–1998.
4. Lazaro, B. J., and Lasheras, J. C., *Phys. Fluids A* 1(6):1035–1043 (1989).
5. Lazaro, B. J., and Lasheras, J. C., *J. Fluid Mech.* 235:143–178 (1992).
6. Lazaro, B. J., and Lasheras, J. C., *J. Fluid Mech.* 235:179–221 (1992).
7. Katoshevski, D., and Tambour, Y., *Phys. Fluids A* 5(12):1–13 (1993).
8. Katoshevski, D., Frankel, I., and Weihs, D., *Fluid Dyn. Res.* 12:153–161 (1993).
9. Tambour, Y., *Combust. Flame* 60:15–28 (1985).
10. Tambour, Y., *Combust. Flame* 58:103–114 (1984).
11. Tambour, Y., and Zehavi, S., *Combust. Flame* 95:383–409 (1993).
12. Greenberg, J. B., Silverman, I., and Tambour, Y., *Combust. Flame* 93:90–96 (1993).
13. Silverman, I., Greenberg, J. B., and Tambour, Y., *Atomiza. Sprays* 2:193–224 (1992).
14. Silverman, I., Greenberg, J. B., and Tambour, Y., *Combust. Flame* 93:97–118 (1993).
15. Allison, R. A., and Clarke, J. F., *Combust. Sci. Technol.* 23:113–123 (1980).
16. Yule, A. J., Seng, C. A. H., Felton, P. G., Ungut, A., and Chigier, N., *Combust. Flame* 44:71–84 (1982).

Twenty-Fifth Symposium (International) on Combustion/The Combustion Institute, 1994/pp. 389–395

HEAT, MASS, AND MOMENTUM TRANSFER ABOUT ARBITRARY GROUPS OF PARTICLES

HARRY A. DWYER
Department of Mechanical and Aeronautical Engineering
University of California, Davis
Davis, CA 95616-5294, USA

AND

H. NIRSCHL, P. KERSCHL, AND V. DENK
Technical University of Munich
Freising, Germany

The flow over groups of particles with heat and mass transfer has been numerically simulated at intermediate Reynolds numbers, and the flow characteristics have been studied and documented. The method of approach consisted of using a new overset mesh technique and a numerical solution of the Navier–Stokes equations. Group behavior has been observed for all the particle configurations studied, and significant changes in drag and heat transfer have been documented for particles within a group. The influence of surface mass transfer has been analyzed with the changes in skin friction and heat transfer, as in single particle flows. The methods used in this paper are new to particle dynamics, and they can be extended to arbitrary-shaped particles in arbitrary configurations. The methods developed in this paper can be extended to reacting spray flows to offer detailed knowledge in the near future.

Introduction

The three-dimensional flow over groups of particles has been an important problem in fluid mechanics, heat transfer, and combustion since the foundation of these subjects, and there has been considerable progress made at low Reynolds numbers [1]. Until recently, there has been only a limited amount of theoretical information available for single or two particles in three-dimensional flows at finite or intermediate Reynolds numbers [2,3], and it has been known that a breakthrough in numerical technique and/or computer capability would be necessary to treat more complex configurations of particles. The view of the present authors is that a good numerical technique is available, and the recent developments in computer hardware will allow for hundreds and even thousands of particles to be treated in the coming years. These new capabilities will allow for moving particles and chemical reactions. The relatively new numerical method is the overset mesh approach named "Chimera," and this approach allows for each particle to be meshed and solved independent of the other particles in the group [4–7]. The price to be paid for the mesh independence is interpolation between meshes and the appearance of invalid points in the computational region. These new problems have been addressed in recent studies [7], and progress is proceeding at a rapid pace.

Methods of Approach

The problem addressed in this paper consists of groups of three-dimensional particles at temperature T_w held fixed in a uniform flow at temperature T_∞ (Fig. (1)). The fixed particles are spherical with diameter D and rigid with no slip at the surface, and we further assume that the fluid is incompressible with a constant density ρ and dynamic viscosity μ. The Reynolds number Re for this flow is defined as $\mathrm{Re} = (\rho V D/\mu)$. The flow equations solved are the Navier–Stokes, continuity, and the thermal energy equations in control volume form. The equations are nondimensionalized using the diameter D of a particle as a characteristic length, V_∞ as a characteristic velocity, $T_\infty - T_w$ as a characteristic temperature difference, and ρV_∞^2 as the pressure scale. The dimensionless form of the governing equations are

$$\frac{\partial}{\partial t}\int\int_V\int \mathbf{V}\,d\mathcal{V} + \int\int_S \mathbf{V}\cdot\mathbf{n}\,dA = 0$$

$$\frac{\partial}{\partial t}\int\int_V\int \mathbf{V}\,d\mathcal{V} + \int\int_V\int \mathbf{V}\cdot\nabla\mathbf{V}\,dV = -\int\int_S p\mathbf{n}\,dA + \frac{1}{\mathrm{Re}}\int\int_S \mathbf{n}\cdot\tau\,dA$$

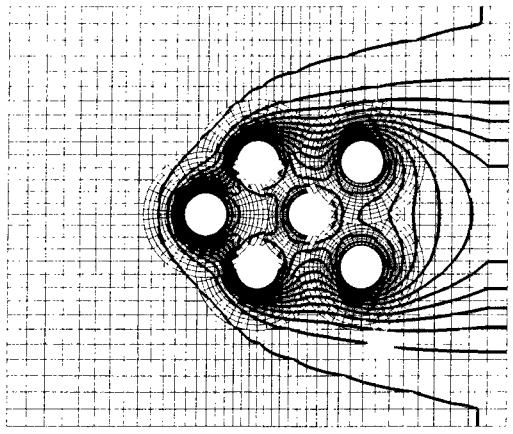

FIG. 1. Temperature contours for six-particle configuration: Re = 10; mass transfer; dimensionless contour range: $T'(\max) = 1$; $T'(\min) = 0$.

$$\frac{\partial}{\partial t}\int\int_V\int T d\mathcal{V} + \int\int_V\int \mathbf{V}\cdot\nabla T dV = \frac{1}{\mathrm{Re}\,\mathrm{Pr}}\int\int_S (\nabla T)\cdot n dA$$

where the velocity vector is $\mathbf{V} = u\hat{i} + v\hat{j} + w\hat{k}$, corresponding to the Cartesian coordinate components, p is the dynamic flow pressure, $\bar{\bar{\tau}}$ is the viscous stress tensor, and T is temperature. The Prandtl number is $\mathrm{Pr} = \nu/a$, where ν is the kinematic viscosity and a the thermal conductivity. The Nusselt number for the particle is defined as

$$\mathrm{Nu} = \frac{1}{A_s(T_x - T_w)}\int\int_S \nabla T\cdot\mathbf{n} dA$$

and the drag and lift coefficients

$$c_d = \frac{F_d}{0.5\rho U_\infty^2 \pi D^2/4} \qquad c_l = \frac{F_l}{0.5\rho U_\infty^2 \pi D^2/4}.$$

We have also studied the distribution of the pressure, viscous normal, and shear stress as well as the rate of heat transfer over the surface of the sphere.

The solution algorithm for the equations is described in detail in Refs. 2 and 8, and it will only be briefly outlined here. The three velocity components and the temperature are marched in time using an implicit, predictor/corrector, alternating direction scheme. The pressure change or correction algorithm consists of solving a Poisson equation derived from the continuity equation. In general, it can be said that the stability and convergence properties of the numerical method used with multiple Chimera meshes have been similar to single-mesh calculations. However, there has been an approximate 30–50% increase in the number of iterations needed for convergence, and this is due to the transfer of information between meshes. In the present paper, we have used second-order central differences everywhere in the flow, and an artificial viscosity has not been introduced into the numerical method. The methods used in this paper have been very efficient, since all of the flows have been calculated on an Intel 486DX2 processor in less than 10 h of computational time.

The Chimera or Overset Grid Scheme Approach:

In the overset grid approach, the grid generation is simplified in that individual grids are handled independently and superimposed over the main mesh. All grids are structured in the computational space, and structured grids lend themselves to implicit algorithms that have good convergence properties with the full Navier–Stokes equations. For the main grid, we take a simple rectangular grid, and the minor grid is body fitted. The grids can also be stretched in all three directions of the coordinate system to improve resolution near boundaries or interesting flow features.

Figure 1 shows a typical Chimera grid configuration and solution in the symmetry plane of the flow over six spherical particles. (Note: The figure will be explained in detail in the Results section of the paper.) The main mesh is slightly stretched near the particle group, and for the identical particles, we have chosen a spherical mesh. Other geometries are not excluded, and it is also possible to study more complex particle geometries with the use of hyperbolic or elliptic grid generators. The spherical grid is stretched in the radial direction to resolve the flow near the surface of the particle.

The Chimera scheme can be divided into two major parts, as given below (the detailed procedure is described elsewhere [7]).

Part A: Determination of the holes and fringe points

The holes are the points in the major mesh where the rigid body is located, and these points must be excluded from the solution procedure. In Fig. 2, the holes are marked with the hollow squares, and the solution solver skips these points with the use of an integer flag set to zero for holes. The holes also can exist in the minor mesh, and this occurs when points in the minor mesh are located outside of the main grid region or inside another minor mesh hole region.

Part B: The interpolation scheme

An important feature of the Chimera grid method is its ability to accurately interpolate the solution from one mesh to another at the fringe points. This has been accomplished with the use of trilinear interpolation in the generalized *cubical and logical*

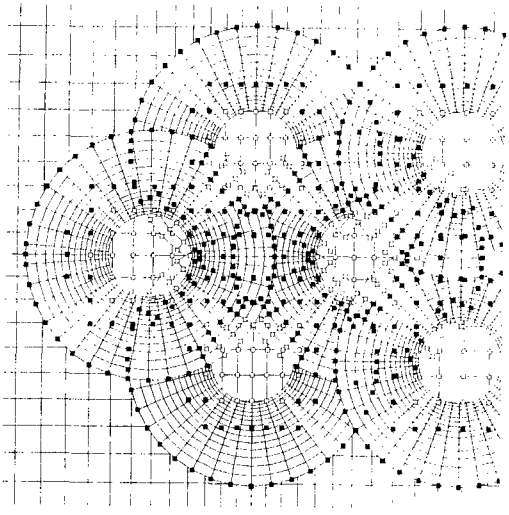

FIG. 2. Grid topology for six-particle configuration, fringe points as solid squares, and holes as hollow squares.

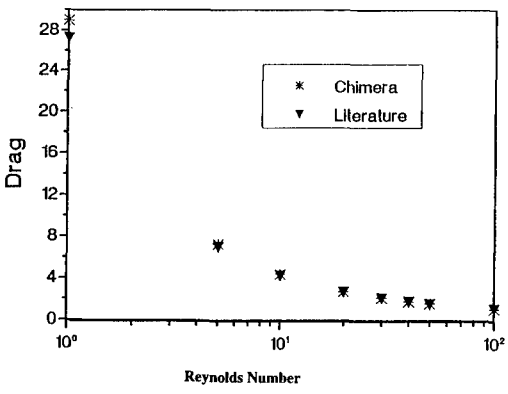

FIG. 3. Comparison of Chimera or overset mesh results with experimental values from the literature.

space of the body-fitted coordinate system. A difficult part of this procedure is to find the logical integer space location of the fringe point in the other corresponding mesh. The location has been found with the use of Newton's method to solve the defining nonlinear simultaneous equations. With the location known, it is then a simple procedure to interpolate between grid points without the solution of simultaneous equations.

The Chimera grid scheme and the numerical method were tested in two and three dimensions against solutions that are well known, and the agreement is excellent [7]. An example of this agreement is presented in Fig. 3, where the drag curve for a single particle has been calculated with the present overset method and compared with experimental results from the standard literature sources [1]. The overset mesh results were calculated with a full three-dimensional code and without the use of symmetry planes. The mesh size for the main mesh was $31 \times 31 \times 31$ and the minor mesh $21 \times 21 \times 15$, which is the same mesh size as the multiparticle results given in the present paper.

Results

Four-Particle Configuration:

This paper is built around two configurations of particles, and for both of these configurations, we have considered flows with and without wall mass transfer. The mass transfer only consists of wall blowing, and a diffusion equation for species is not solved. The configurations studied are four and six particles, and the numerical labeling of the particles is shown in Fig. 4. (For the four-particle case particles, five and six were deleted.) The basic philosophy of the research program is to systematically build our knowledge of the flow around groups of particles. We begin this process with the four and six groups of particles in a plane, and this will be extended to hundreds of particles in future years. With the particles

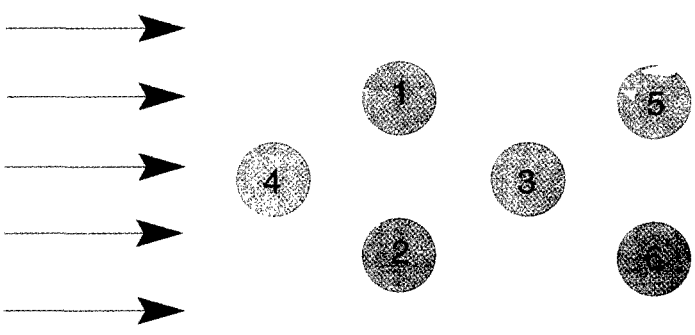

FIG. 4. Particle numbers for Tables 1 and 2 and text discussion.

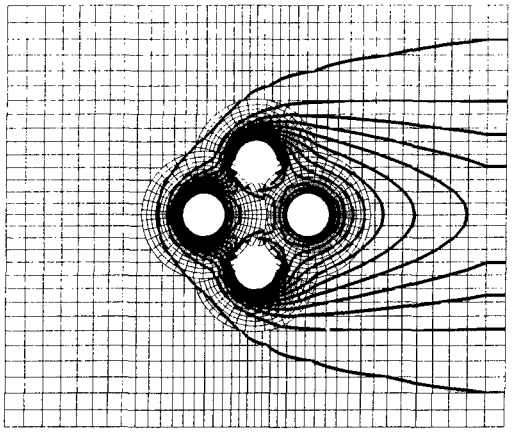

FIG. 5. Temperature contours for four-particle configuration: Re = 10; no mass transfer; dimensionless contour range: $T'(\max) = 1$; $T'(\min) = 0$.

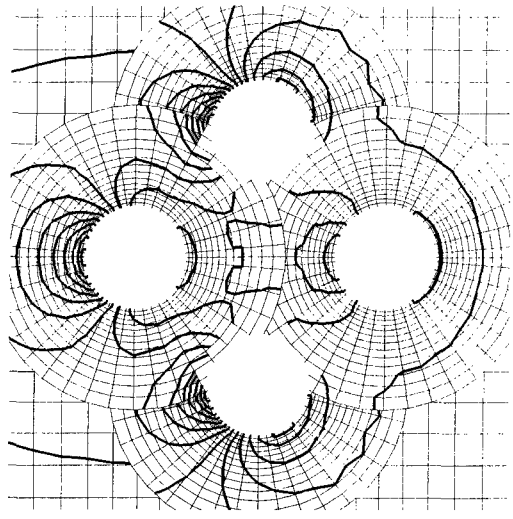

FIG. 6. Pressure contours for four-particle configuration: Re = 10; no mass transfer; dimensionless contour range: $p'(\max) = 1.885$; $p'(\min) = -0.877$.

all contained in a plane, the maximum interference or blockage will occur, and this feature is an important one in defining the group behavior of the particles.

We begin the discussion with the four-particle group, and the results are shown in Figs. 5 through 7 and Table 1. Figure 5 presents the dimensionless isotherms about the particles, which are defined as $T' = (T - T_w)/(T_\infty - T_w)$, and there are 14 uniformly spaced isotherms about the particles. The spacing between particle centers is 1.75 diameters; the Reynolds number based on a single particle is 10, and it is clear that a group type of behavior is observed. A study of the isotherms reveals that the maximum dimensionless temperature in the interior of the four particles is $T' = 0.285$, and this represents a relatively cold region of the flow.

The dimensionless pressure isobars are shown in Fig. 6, $P' = (p - p_\infty)/(\rho V_\infty^2/2)$, and the maximum

TABLE 1
Drag and heat transfer for four particle configuration

Particle	Case	Pressure drag	Friction drag	Pressure lift	Friction lift	Nusselt number
1	Re = 10 $Vw = 0$	1.525	2.587	−0.1957	−0.1714	2.774
1	Re = 10 $Vw = 0.1$	1.512	2.336	−0.2339	−0.2291	2.330
2	Re = 10 $Vw = 0$	1.524	2.586	0.1957	0.1714	2.775
2	Re = 10 $Vw = 0.1$	1.512	2.336	0.2339	0.2290	2.330
3	Re = 10 $Vw = 0$	0.639	1.347	0	0	1.658
3	Re = 10 $Vw = 0.1$	0.639	1.191	0	0	1.282
4	Re = 10 $Vw = 0$	1.48	2.599	0	0	3.207
4	Re = 10 $Vw = 0.1$	1.42	2.301	0	0	2.766

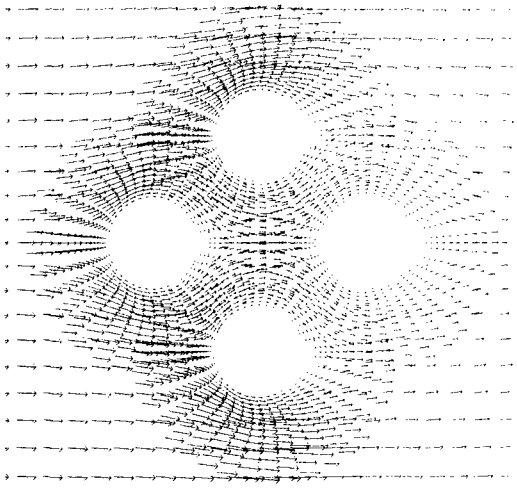

FIG. 7. Velocity vectors for four-particle configuration: Re = 10; no mass transfer.

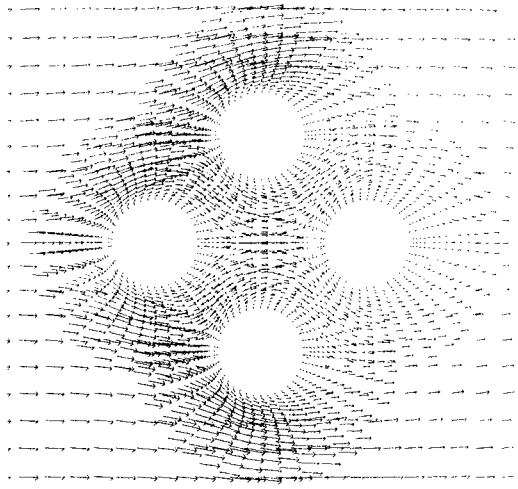

FIG. 8. Velocity vectors for four-particle configuration: Re = 10; mass transfer.

pressure occurs on the stagnation point of forward particle 4, and the minimum pressures on side particles 1 and 2 (the minimums occur approximately 45° from the side outer shoulders). The values for the maximums and minimums are $p_{max} = 1.885$ and $p_{min} = -0.8774$, and these values are similar to a single particle in a Reynolds number of 10 flow [1]. In the central region between the particles, the pressure is close to the free stream value and there are relatively weak gradients. It should be noted at this point that the use of overset meshes presents a challenge to graphics presentations, and it has been necessary to not plot "hole" values in some of the meshes since these points are not valid in the computation. Also, the plotting routines will place contours in different locations in cells of different sizes on different meshes, and these minor plotting problems can be seen in many of the graphs in this paper. This problem is particularly evident for the pressure contours, since the pressure field is calculated at cell area locations and shifted to cell centers for plotting.

The flow vectors in the symmetry plane of the particles are shown in Fig. 7, and it is seen that the flow inside the particles is lower than that outside and around the particles. The influences of the flow and pressure on the individual drag, lift, and heat transfer on the particles are substantial and are presented in Table 1. This table also includes results with wall mass transfer, and the nonblowing case can be identified as $V_w = 0$. The lead particle in the configuration, 4, has the maximum heat transfer or Nusselt number, but not the maximum drag, and this is a direct result of the increased pressure behind particle 4. The heat transfer is less for the particles behind due to the cooling created by the first particle. The values of drag for particles, 1, 2, and 4 are very close to single-particle results [1]; however, the heat transfer over particles 1 and 2 has been reduced.

The most significant change in surface characteristics has occurred for the trailing particle, 3, and Table 1 shows that the drag has been reduced by more than one-half and that the heat transfer has been by reduced by almost that amount. Particles 1 and 2 experience a small amount of lift, which would tend to pull the group configuration apart. The lift is caused by the low pressures on the outside of the configuration, as well as the larger fluid velocities and shear on the outer part of the group.

The next phase of the study involves the introduction of mass transfer at the surface of the particles. The mass transfer amount we have used is 10% of the free stream velocity, $V_w = V_w/V_\infty = 0.1$, and this represents 40% of the mass flow into the particle-projected area in the free stream. The velocity vectors with mass transfer present are shown in Fig. 8, and the increased flow in the central region of the particles can be seen. In general, it can be said that the drag components and Nusselt number decrease, and the slight decrease in the pressure drag for particle 4 has been caused by the increased pressure in the central region between the particles, and this is directly caused by the mass addition. The side particles 1 and 2 exhibit behavior very similar to single particles, where the friction drag and heat transfer are reduced by the mass transfer; however, the pressure drag remains almost the same.

Another feature of the mass addition has been an increase in the lift forces on the side particles 1 and 2, and this is due to both the pressure and shear components of the lift. The pressure isobars for this flow are presented in Fig. 9, and the general features are similar to Fig. 6 without mass transfer. The most

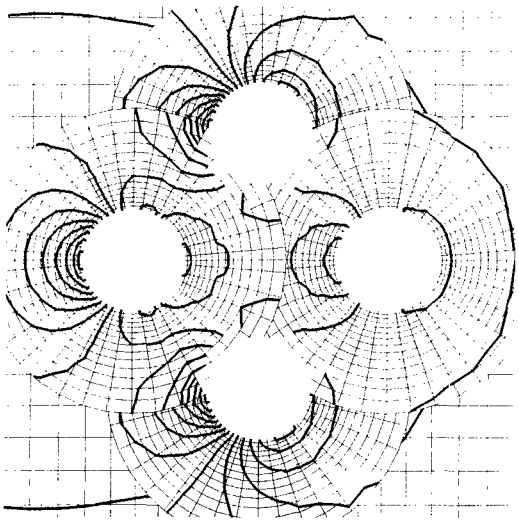

FIG. 9. Pressure contours for four-particle configuration: Re = 10; mass transfer; dimensionless contour range: $p'(\max) = 0.867$.

significant feature is the slight pressure increase in the central region and a slight decrease in pressure gradients throughout the flow.

Six Particle Configuration:

The next phase of this paper is the extension to six particles, and a solution with temperature isotherms is presented in Fig. 1 with the two additional particles placed behind particle 3. When Fig. 1 is compared to that of flow over four particles in Fig. 5, it is clear that the group behavior has increased. This group behavior is most obvious in the broadening of the outer isotherm and the decrease of isotherms in the inner region of the particle group. The minimum temperature in this central region is similar to the four-particle group; however, the size of this region has increased. Another interesting behavior is the increase of the size of the cooled group wake.

We will begin the detailed analysis of the flow with the drag, lift, and Nusselt number results shown in Table 2, where again, results are given with and without surface mass transfer. In general, it is seen that

TABLE 2
Drag and heat transfer for six-particle configuration

Particle	Case	Pressure drag	Friction drag	Pressure lift	Friction lift	Nusselt number
1	Re = 10 $Vw = 0$	1.392	2.403	−0.1917	−0.1755	2.711
1	Re = 10 $Vw = 0.1$	1.351	2.139	−0.2250	−0.2326	2.261
2	Re = 10 $Vw = 0$	1.397	2.408	0.1917	0.1770	2.712
2	Re = 10 $Vw = 0.1$	1.356	2.145	0.2263	0.2339	2.263
3	Re = 10 $Vw = 0$	0.6282	1.210	0	0	1.492
3	Re = 10 $Vw = 0.1$	0.5981	1.038	0	0	1.100
4	Re = 10 $Vw = 0$	1.468	2.561	0	0	3.194
4	Re = 10 $Vw = 0.1$	1.394	2.252	0	0	2.748
5	Re = 10 $Vw = 0$	0.884	1.637	−0.0586	−0.1173	1.920
5	Re = 10 $Vw = 0.1$	0.8387	1.417	−0.0456	−0.0698	1.486
6	Re = 10 $Vw = 0$	0.893	1.640	0.0554	0.1131	1.918
6	Re = 10 $Vw = 0.1$	0.8422	1.419	0.0429	0.0673	1.486

particles 1 through 4 exhibit a slight decrease in drag and heat transfer, and this is attributed to the increased blockage by the larger group of particles. Particles 5 and 6 have been added to the rear of the group, and they exhibit substantially reduced values of drag and heat transfer; however, since they are near the edge of the group, their drag and heat transfer values are not as low as particle 3, which is totally inside the group. Surface mass transfer causes changes similar to the four-particle group, and most aspects of the flow seem to be similar between the two configurations.

A study of the velocity vectors and pressure contours for the mass transfer case show that the velocities have already begun to show a repetitive pattern between particles 1–2 and 5–6. The pressure contours show that the pressure becomes more uniform in the group central region, and the level of pressure in this region also increases on the average. It has also been observed that there is a slight increase in the pressure on all of the particles, and this appears to be a result of the group behavior. It appears from these limited results that a repetitive pattern sets up quickly at this Reynolds number regime, however it should be mentioned again that the particles are in a plane. Therefore, it is clear that the results must be extended to larger and more general groups of particles at a higher Reynolds number, and this work will be carried out in the coming years.

Conclusions

The major conclusions of this paper are as follows:

1. The Navier–Stokes equations around groups of particles have been solved with heat and mass transfer at an intermediate Reynolds number.
2. All the particle configurations studied showed particle group behavior with and without mass transfer. Particles at the front and edge of the group exhibited single-particle behavior; however, interior particles had significant changes in flow and heat transfer coefficients. The introduction of surface mass transfer reduced skin friction and heat transfer, as has been documented in single-particle flows.
3. The overset grid approach has shown itself efficient, flexible, and accurate. The authors also plan to extend the present results to unsteady groups of large particles with chemical reactions.

REFERENCES

1. Clift, R., Grace, J. R., and Weber, M. E., *Bubbles, Drops and Particles*, Academic Press, New York, 1978.
2. Dandy, D. S., and Dwyer, H. A., *J. Fluid Mech.* Vol. 216, pp. 381–410.
3. Kim, I., Elghobashi, S., and Sirignano, W., *J. Fluid Mech.* Vol. 246, pp. 465–488.
4. Benek, J. A., Steger, J. L., Dougherty, F. C., and Buning, P. G., *AEDC-TR-85-64*, Arnold Air Force Station, TN, 1986.
5. Dougherty, F. C., "Development of a Chimera Grid Scheme with Applications to Unsteady Problems," Ph.D. Thesis, Stanford University, Stanford, CA, 1985.
6. Buning, P. G., Chiu, I. T., Obayashi, S., Rizk, Y. M., and Steger, J. L., "AIAA Atmospheric Flight Mechanics Conference," Minneapolis, MN, AIAA Paper-88-4359-CP, 1988.
7. Nirschl, H., Dwyer, H. A., and Denk, V., *J. Comp. Phys.*, 1993, submitted.
8. Dwyer, H. A., *Prog. Energy Combust. Sci.* 15:131–158 (1989).

Twenty-Fifth Symposium (International) on Combustion/The Combustion Institute, 1994/pp. 397–405

ENTRAINMENT AND EVAPORATION OF DROPS IN THE LAMINAR PART OF A TWO-DIMENSIONAL DEVELOPING MIXING LAYER

F. FICHOT, J. BELLAN AND K. HARSTAD
Jet Propulsion Laboratory
California Institute of Technology
Pasadena, CA 91109, USA

A formulation has been developed that combines the simplicity of an experimentally derived well-established correlation for describing the development of a mixing layer, and a rigorous approach for the description of the dynamics and evaporation of dense or dilute clusters of drops in large coherent vortices.

An extensive parametric study has been performed by varying the radius of the drops in the drop-laden stream both for high and low air/fuel mass ratio, as well as for constant initial drop number density, but at varying air/fuel mass ratio. The air/fuel mass ratio has also been varied at fixed drop radius in the drop-laden stream. Additional parameters independently varied were the temperature of the hot air stream, its velocity, and the velocity ratio between the two streams.

The results show that it is possible to optimize the relative number of drops (with respect to the initial value) entrained into the coherent vortices of the mixing layer by using the velocity ratio as control parameter. The eventual liquid mass entrained in the cluster is an increasing function of the drop radius in the drop-carrying stream for typical drop number densities in sprays. The mass fraction of the evaporated fuel in the clusters can be optimized by using the velocity of the hot air stream as a control parameter.

It is also shown that, in agreement with existing observations, the average drop radius may increase with axial distance from the mixing layer inception point, and the reasons for this are explained.

Introduction

Mixing layers are an inherent feature of many particle-laden flows. They occur whenever a particle-laden flow travels with a velocity different from that of the flow around it. In fuel sprays injected into combustion chambers, the mixing layer at the edge of the spray has the important function of transferring heat from the ambient to the spray. During this process, momentum transfer and mass transfer occur as well.

Hernan and Jimenez [1] showed that most of the momentum transfer in a mixing layer occurs before paring of the large-scale coherent vortices that are instrumental in both momentum transfer and drop dispersion. Drop dispersion in shear layers, mixing layers, wakes, and jets has been extensively studied for small particle loading by mass [2–6], for small particle loading by volume [2–6], or for large particle loading by mass in the case of particles made of a heavy material such as glass [7]. In these situations, the interaction between flow and particles is limited to the flow influencing the dynamics of the particles. The effect of the particles on the flow is minimal (except when the particle loading is very large by mass), and the interaction between the particles is negligible. No equivalent studies exist in situations when the particle-number density is very large to the point that the particles affect the dynamics of the flow, and that there is substantial particle thermodynamic interaction affecting the heating and evaporation of particles. The reason for the lack of investigations in these more complicated situations is the difficulty of performing experimental measurements in the high–particle-number-density regime, and the difficulty of modeling the two-way coupling between particles and flow as well as the multiparticle thermodynamic interactions.

The modeling approach described in this paper shows that it is possible to achieve a qualitative understanding of high–number-density particle-laden mixing layers by using a combination of rigorous analysis and well-established experimental correlations.

Physical Configuration and Formulation

Figure 1 shows the physical configuration modeled here. A two-dimensional (2D) mixing layer is established between two streams separated by a splitter plate: a hot air stream characterized by temperature T_1 density ρ_1, and velocity U_1, and a drop-laden stream at a lower temperature and higher velocity. The drop number density, temperature, density, and velocity of the drops are n_2, T_{2d}, ρ_l, and U_{2d}, and the equivalent quantities for the carrying flow are T_{2g}, ρ_{2g}, and U_{2g}. According to the results of Brown and

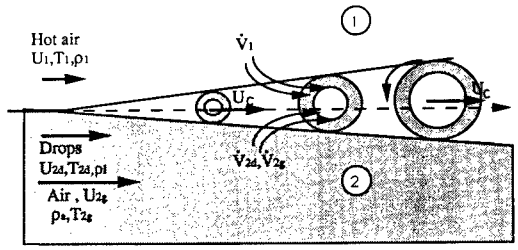

FIG. 1. Sketch of the two-dimensional mixing layer.

Roshko [8] and Roshko [9], the mixing layer is characterized by large coherent vortices convecting downstream. Ho and his coworkers [10,11] have observed that a particle-free mixing layer remains laminar for an extended length before the appearance of small-scale turbulent structures and that their inception point is determined from the initial Strouhal number, Str^0, and the initial vorticity thickness, δ^0. The present model pertains to the laminar part of the mixing layer.

The large coherent vortices of the mixing layer convect at velocity U_c with respect to the splitter plate trailing edge, and it is assumed that, according to observations, they can be portrayed in 2D by circles [1] whose diameter grows linearly with the abscissa [12]. The entrainment rate from the hot air stream is $\dot{V}_1$, whereas the gas and drop entrainment rate from the second stream are $\dot{V}_{2g}$ and $\dot{V}_{2d}$, respectively. For particle-free, 2D, fully developed, spatially growing, subsonic shear layers, the entrainment rates from the two streams have been correlated [12] from an extensive number of experiments to be

$$E_v = \dot{V}_2/\dot{V}_1 = f^{1/2}[1 + 0.33(1 - s)(1 + f^{1/2})/(1 + sf^{1/2}] \tag{1}$$

where $s = U_2/U_1$ and $f = \rho_2/\rho_1$. The same correlation is assumed to be valid in the present situation except that $s = \bar{U}_2/U_1$ and $f = \bar{\rho}_2/\rho_1$, where $(\bar{\ })$ represents an average over gas and drops.

It is additionally assumed that the drops form a cluster similar to those observed in jets and sprays [7,13–15], that the cluster is monodisperse (the averaging is based upon liquid mass conservation and evaporation-rate continuity), and that the outer boundary of the cluster and vortex coincide, being located the at radial position R_{ou} ("*ou*" stands for outer) from the center of the vortex. The vortex boundary is defined as the boundary of the volume containing the gas entrained into the vortex, so that if r is the radial coordinate from the cluster center, $U_{ou} = U_{gr,ou}$. Other assumptions are as follows: the vortex has a constant outer tangential velocity; the radial and azimuthal velocity of drops and gas can be expressed as sums of irrotational and solid-body motion [16]; the entrained gas angular momentum is distributed throughout the vortex, and it is modeled as the sum of an irrotational motion and a solid-body motion; and the angular momentum of the entrained drops is neglected. The number of drops entrained in the vortex per second and unit vortex length is $a_d\dot{V}_{2g}n_2$, where a_d depends upon the Stokes number, $St = \rho_1(2R_d^0)^2|U_{2d} - U_c|/(18\mu R_{ou})$, where R_d^0 is the initial drop radius and μ is the gas viscosity. Consistent with observations [5,6], $a_d = 1$ if $St < 10^{-1}$ and $a_d = 0$ if $St > 10$. For $10^{-1} < St < 10$, here $a_d, = 0.5\ (1 - \log_{10} St)$, so that a continuous function $a_d(St)$ is obtained.

Averaging processes for the drop-carrying stream yield $\bar{\rho}_2 = (1 + \Phi^0)n_2m_d^0$, where Φ^0 is the initial air/fuel mass ratio in the stream and m_d^0 is the initial mass of a drop. If one defines $\bar{U}_2$ from $\bar{\rho}_2(U_c) - \bar{U}_2)^2 \equiv \rho_1(U_1 - U_c)^2$ consistent with Ref. [12], then $\rho_1\ (U_1 - U_c)^2 \equiv \bar{\rho}_2(U_c - U_{2g})^2 + n_2m_d^0(2U_c - U_{2g} - U_{2d})(U_{2g} - U_{2d})$. Finally, an average outer tangential velocity of the gas is defined as $U_{g\theta,ou} = [\rho_1\dot{V}_1(U_1 - U_c) + (\rho_{2g}\dot{V}_{2g}(U_{2g} - U_c)]/(\rho_1\dot{V}_1 + \rho_{2g}\dot{V}_{2g})$.

The conservation equations are as follows:

1. continuity of the evaporation rate

$$dN_c/dt + (d\bar{R}_d/dt)N_c/\bar{R}_d = a_d\dot{V}_{2g}n_2R_d^0/\bar{R}_d - 2\pi R_{ou}n_c \max(0; u_{d,ou} - u_{ou}) - N_c\dot{m}_{ev}/(3m_d) \tag{2}$$

where N_c is the number of drops and n_c is the drop number density in the cluster, $n_c = N_c/[\pi(R_{ou}^2 - R_{in}^2)]$ where "*in*" identifies the inner cluster radius, $\bar{R}_d$ is the averaged drop radius in the cluster, and the drop evaporation rate, $\dot{m}_{ev}$, is taken proportional to $\bar{R}_d$. The second term on the right-hand side (RHS) accounts for drops lost from the cluster through centrifugation.

2. conservation of liquid mass

$$dN_c/dt + (d\bar{R}_d/dt)3N_c/\bar{R}_d = a_d\dot{V}_{2g}n_2(R_d^0/\bar{R}_d)^3 - 2\pi R_{ou}n_c \max(0; u_{d,ou} - u_{ou}) - N_c\dot{m}_{ev}/m_d \tag{3}$$

3. conservation of gas mass, m_g

$$dm_g/dt = -(dN_c/dt)(m_g + m_d)/N_c + \rho_1\dot{V}_1(1 + C_{TM})/N_c - 2\pi R_{in}\rho_g(u_{d,in} - u_{g,in})/N_c + \dot{m}_{ev} - 2\pi n_c m_d \max(0; u_{d,ou} - u_{ou})/N_c + n_2m_d^0E_v\dot{V}_1/N_c \tag{4}$$

where $C_{TM} = E_v(T_1/T_{2g})/[\Phi^0/(\Phi^0 + \rho_{2g}/\rho_1)]$.

4. conservation of the air mass, m_a

$$N_c dm_a/dt = -(dN_c/dt)m_a + \rho_1\dot{V}_1 [1 + C_{TM}(1 - Y^0_{FV})] - 2\pi R_{in}\rho_g(u_{d,in} - u_{g,in})Y_{a,i} + D_{a,ou}N_c \quad (5)$$

where Y^0_{FV} is the initial mass fraction of vapor fuel, $Y_{a,i}$ is the mass fraction of air in the interstitial cluster region defined by the space between the spheres of influence around each drop, and $D_{a,ou}$ accounts for air mass diffusion at the vortex boundary [16]. The sphere of influence for each drop is defined [16] as centered at the drop center and having for radius the half distance between the centers of two adjacent drops.

5. conservation of gas angular momentum

$$\rho_g[\partial u_{g\theta}/\partial t + u_{g\theta}(\partial u_{g\theta}/\partial r) + u_{gr}u_{g\theta}/r] = F_{g\theta} + \frac{\gamma_1}{r} + \gamma_2 r \quad (6)$$

where

$$F_{g\theta} = n_c(\dot{m}_{ev} + 0.5\rho_g A_d C_D|\mathbf{U}_s|)(U_{d\theta} - U_{g\theta}) \quad (7)$$

$$\int_0^{R_{ou}} (\gamma_1/r + \gamma_2 r)2\pi r dr = \rho_1\dot{V}_1(1 + C_{TM})U_{g\theta,ou} \quad (8)$$

$$\partial U_{g\theta,ou}/\partial t = 0. \quad (9)$$

In Eqs. (6) through (9), $F_{g\theta}$ is the drag force, $\mathbf{U}_s$ is the slip velocity, A_d is the drop surface area, C_D is the drag coefficient, γ_1 is the irrotational motion of the gas, and γ_2 is the solid-body rotation of the gas.

6. conservation of mass in the inner vortex core devoid of drops

$$R_{in}u_{gr,in} = -0.5R^2_{in}(d \ln \rho_g/dt) + \rho_1\dot{V}_1(1 + C_{TM})R^2_{in}/(2\pi R^2_{ou}\rho_g) \quad (10)$$

7. global conservation of total enthalpy

$$dH_g/dt = (H_g + 0.5m_d\langle u^2_d\rangle_i + H_d)(dN_c/dt)/N_c + \dot{m}_{ev}\{C_{pfv}T_{gs} - C_p(T_{gi} - T_{gs}) \div [\exp[\beta(Z_s - Z_i)] - 1]\} + 2\pi R_{in}\rho_g C_{pg}T_{gi}(u_{d,in} - u_{g,in})/N_c + \rho_1\dot{V}_1T_1(C_{p1} + C_{p2}C_{TM})/N_c - 0.5d[m_d\langle u^2_d\rangle_r]/dt + n_2m^0_dC_{p1}T_{2_d}E_v\dot{V}_1N_c - 2\pi R_{ou}n_cH_d \max(0; u_{d,ou} - u_{g,ou}) + D_{H_{g,ou}}. \quad (11)$$

In Eq. (11), the terms on the RHS represent, respectively, the changes due to the number of drops variation; a source due to evaporation; a sink due to gas lost to the vortex core; a source due to gas entrainment from both streams; a sink due to the time change in the drops' kinetic energy; source due to drop entrainment from the drop-laden stream; a sink due to loss of drops that are centrifuged out from the cluster; and diffusion of heat from the outer gas phase at the vortex boundary [16]. H_g is the gas enthalpy whereas H_d is the enthalpy of a drop, $H_d = m_dC_{pl}4\pi \int_0^{R_d} T_d(r)r^2dr$, and C_p is the heat capacity at constant pressure. The averaging symbol $\langle\ \rangle$ is over all drops either in the interstitial space (subscript i), or in the radial direction (subscript r). Quantities β and $Z(r_d)$ have been calculated previously [17,18] together with the solution of the diffusion equations inside the sphere of influence of each drop. The radial coordinate inside the sphere of influence is r_d, and Z_s and Z_i are the values at the drop surface and at the edge of the sphere of influence, respectively. Here $\beta = -\dot{m}_{ev}/(4\pi R^0_d)$ and $Z(r_d) = (\theta^{ou}_g)^{0.65} \int_0^{R_i} dr_d/(r^2_d\theta^{ou}_g)^{0.65}$, where $\theta_g = C_{pg}T_g/L_{bn}$ with L_{bn} being the latent heat of evaporation and R_i being the radius of the sphere of influence.

The radial gas momentum equations and the momentum equations for the drops have been derived previously [16].

Initial Conditions

It is assumed that the cluster is initially a small ring defined by R^0_{ou} and R^0_{in}, and thus, the initial Lagrangian coordinate defining the cluster position, X^0_c, is non null. An extrapolation of the linear growth rate [12] is used to find the time, $\hat{t}$, at which R^0_{ou} is reached, and thus, $X^0_c = u_c\hat{t}$ is found.

Initial dependent variables in the cluster have the same value as those in the drop-carrying stream so that $\Phi^0_c = \Phi^0_2$, $T^0_{gi} = T_{2g}$, $Y^0_{ji} = Y_{2j}$, where "j" denotes a species.

The calculations are stopped at the onset of small-

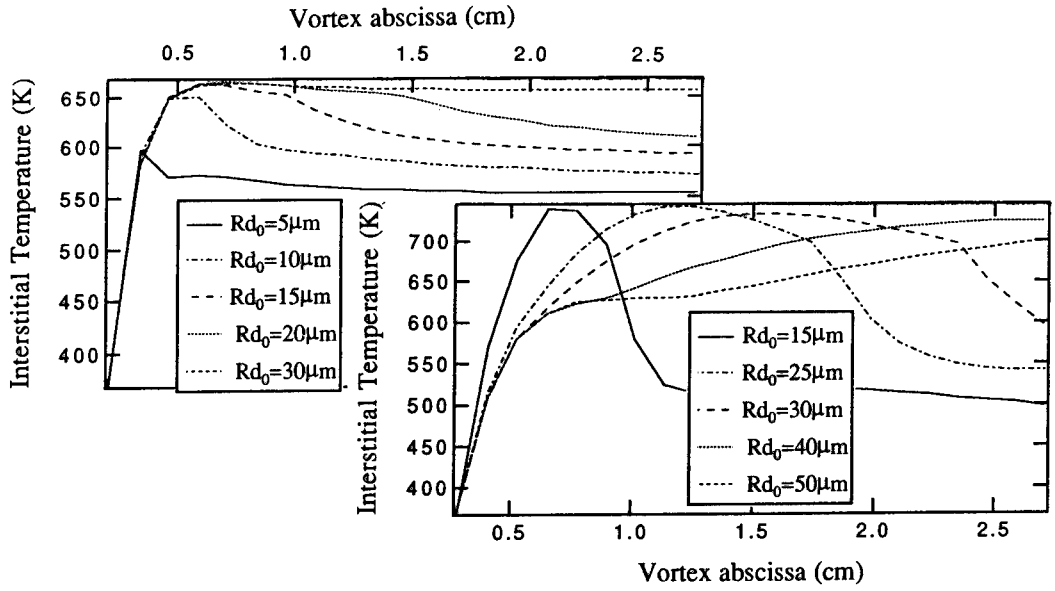

FIG. 2. Interstitial cluster gas temperature vs the vortex abscissa for $\Phi^0 = 5$ (top) and for $\Phi^0 = 0.5$ (bottom). Other parameters are $U_1 = 1$ m/s, $U_{2l} = U_{2g} = 10$ m/s, $T_1 = 1000$ K, $T_{2g} = 370$ K, $T_{2l} = 350$ K.

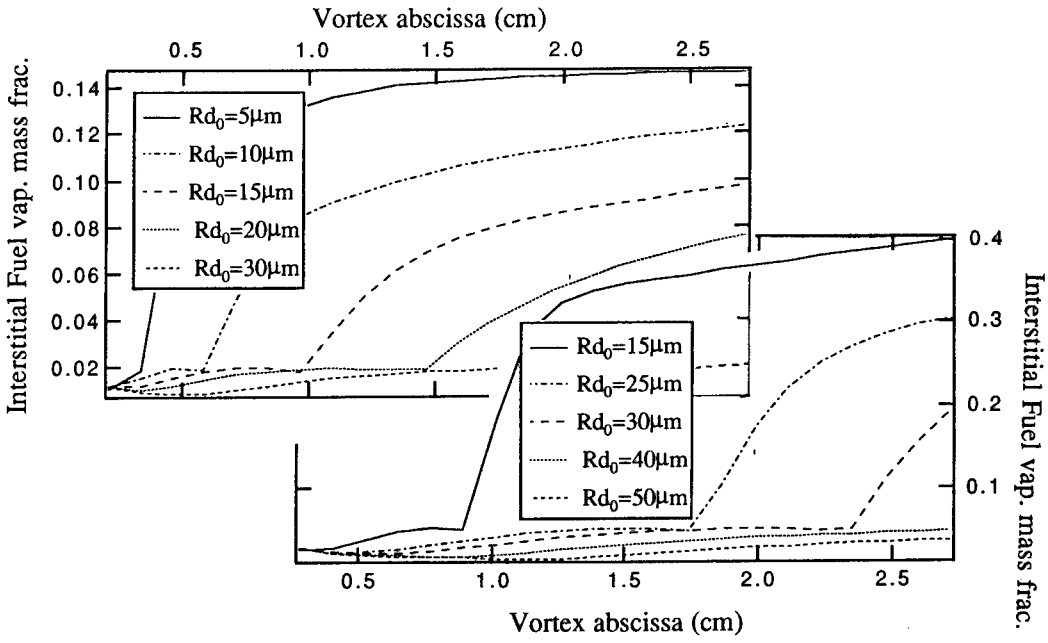

FIG. 3. Interstitial fuel vapor mass fraction ($Y_{FV,i}$) versus the vortex abscissa for $\Phi^0 = 5$ (top) and for $\Phi^0 = 0.5$ (bottom). Other parameters are $U_1 = 1$ m/s, $U_{2l} = U_{2g} = 10$ m/s, $T_1 = 1000$ K, $T_{2g} = 370$ K, $T_{2l} = 350$ K.

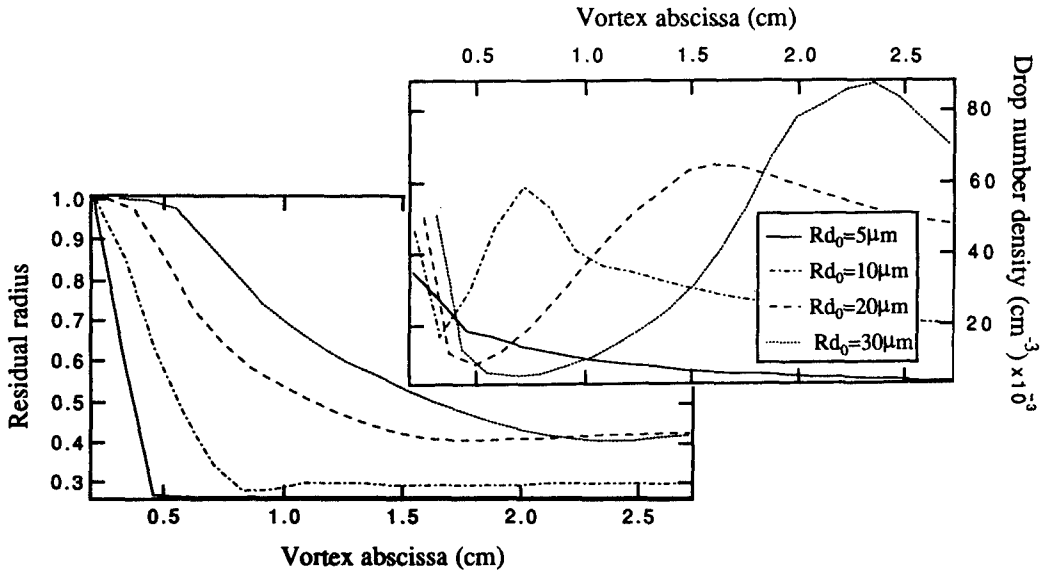

FIG. 4. Residual drop radius ($\bar{R}_d/R_d^0$) and drop number density (n_c) vs the vortex abscissa for fixed n_2 and varying R_d^0 (and thus E_v). Other initial conditions are listed in Fig. 2 caption.

scale turbulence defined by $X_T = 4(s + 1)L^0/(s - 1)$, where L^0 is the initial instability wavelength and $Str^0 = \delta^0/L^0$.

Discussion of Results

All calculations were performed for n-decane, for which $\Phi^0_{\text{stoich}} = 15.7$. Nominal properties for n-decane were listed elsewhere [19]. Physical intuition indicates that competition between $\mathcal{R}_1$ = (evaporation rate/entrainment rate) and $\mathcal{R}_2$ = (drop ejection rate/entrainment rate) determines the drop size in the cluster. Simple but tedious manipulations show that the residual drop radius decreases with time if $\mathcal{R}_1 > 1$ and increases with time if $\mathcal{R}_1 < 1$, independently of $\mathcal{R}_2$. However, if $\mathcal{R}_2 > 1$, the liquid mass in the cluster decreases, and since $\bar{R}_d/R_d^0 < 1$, N_c decreases, whereas if $\mathcal{R}_2 < 1$ the liquid mass in the cluster increases. For most situations analyzed here $\mathcal{R}_1 > 1$ and $\mathcal{R}_2 < 1$, initially.

A baseline calculation was performed for $U_1 = 1$ m/s, $U_{2d} = U_{2g} = 10$ m/s, $R_d^0 = 15\,\mu$, $\Phi^0 = 1.5$, T_1 1000 K, $T_{2d} = 350$ K, and $T_{2g} = 370$ K. The results show that three stages can be observed in the transient behavior of the mixing layer, but that these three stages are not necessarily separated. First, entrainment of hot air produces a decrease in the liquid/gas mass ratio, an increase in T_{gi}, and a decrease in n_c due to gas expansion. Evaporation becomes important when T_{gi} and N_c increase, resulting in an approximately constant liquid/gas mass ratio and a decrease in n_c. Finally, $\bar{R}_d$, T_{gi}, and $Y_{FV,i}$ reach asymptotic values.

Parametric studies performed by varying R_d^0 showed that quantitative behavior is different when $\Phi^0 = 5$ and $\Phi^0 = 0.5$. It should be realized that $E_v = 1.25$ when $\Phi^0 = 5$ and $E_v = 2$ when $\Phi^0 = 0.5$ because E_v depends upon Φ^0 through $\bar{\rho}_2$. Figures 2 and 3 show, respectively, T_{gi} and $Y_{FV,i}$ vs the Lagrangian coordinate for various R_d^0's for the two values of Φ^0. For initially higher mass and volume loading (and a larger E_v), evaporation is greatly delayed because of the higher drop number density. This explains the larger T_{gi} during the initial phase and the much smaller T_{gi} during the latter phase, after the drops have heated up and removed a substantial amount of heat from the gas (since n_c is larger). Once the drops are hot, evaporation becomes important, and the decrease in T_{gi} corresponds to a simultaneous increase in $Y_{FV,i}$. Smaller drops heat faster because of their smaller size. At fixed Φ^0, as R_d^0 is smaller and thus n_2 (and n_c) is larger, the heat sink represented by the drops is larger, and thus the reduction in T_{gi} is larger.

A similar study was performed by varying R_d^0, but now n_2 was kept constant while Φ^0 varied, and E_v increased from 1.14 for $R_d^0 = 5\mu$ to 2.49 for $R_d^0 = 30\,\mu$. When R_d^0 is smaller and n_2 is kept constant, the liquid mass is smaller, and thus, the drop-carrying stream (and the cluster) is more dilute. These more dilute clusters heat up faster, and their $\bar{R}_d/R_d^0$ decreases faster as the relative number of drops (with respect to N_c^0) entrained is smaller. As a result, for these dilute clusters, $Y_{FV,i}$ is at most 10^{-2}. Figure 4

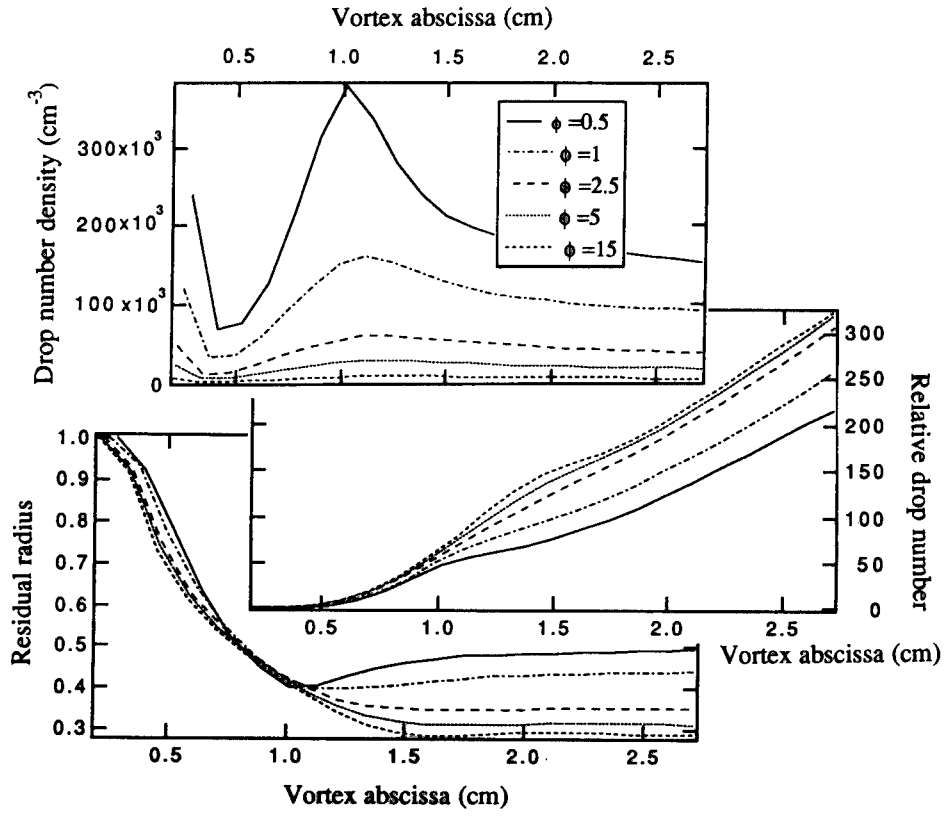

FIG. 5. Drop number density in the cluster (n_c), relative drop number (with respect to N_c^0) and drop residual radius ($\bar{R}_d/R_d^0$) vs the vortex abscissa for various values of Φ^0. Other initial conditions are listed in Fig. 2 caption.

shows both that $\bar{R}_d/R_d^0$ stays larger with increasing R_d^0 and that the drop number density peaks higher with increasing R_d^0. Thus, the eventual maximum liquid mass in the cluster is an increasing function of R_d^0 at fixed n_2, U_1, and velocity ratio. The result is not necessarily obvious since larger drops are heavier and thus more difficult to entrain. Mathematically, this is shown by the fact, that for $s > 1$, E_v is a nonmonotonic function of Φ^0 through Eq. (1) and the definition of $\bar{\rho}_2$. In the range of Φ^0 (and thus R_d^0 since n_2 is fixed) investigated here, E_v is an increasing function of Φ^0, thus explaining the results. It is expected that, for larger drops and thus smaller Φ^0's, a maximum will be reached for the liquid mass entrained. Calculations proving this point are not shown because, for these very large values of R_d^0, the eventual value of n_c is unrealistically large compared to spray observations.

Parametric studies performed by varying T_1 from 400 to 1300 K (and accordingly, E_v from 0.9 to 1.72) show that the relative number of drops entrained is insensitive to T_1 above 800 K, whereas the value is much smaller for 400 K. Since $p = 1$ atm, a low T_1 implies a large ρ_1 and thus a smaller s, which hinders entrainment of particles. Since the results show that the residual drop radius is a decreasing function of T_1, whereas the drop number density is an increasing function of T_1, the liquid mass entrained seems to be constant, except perhaps for $T_1 = 400$ K, in agreement with the indications from the relative number of drops.

Figures 5 and 6 document in detail the influence of Φ^0 upon the cluster behavior. Heating and evaporation dominate the initial regime, whereas drop entrainment dominates the final regime. The initial regime is itself composed of two distinct subregimes. The first subregime is characterized by entrainment of hot air, thus increasing T_{gi}, by drop centrifugation inside the vortex and cluster volume increase, thereby decreasing n_c, and by drop evaporation, thereby decreasing $\bar{R}_d$. For smaller Φ^0's, drop heating is slower, and thus T_{gi} stays larger longer. The second subregime, starting around $X_c = 0.5$ cm, is characterized by an increase in drop entrainment from the drop-laden stream, as evidenced by the increase in the liquid-gas mass ratio, the relative num-

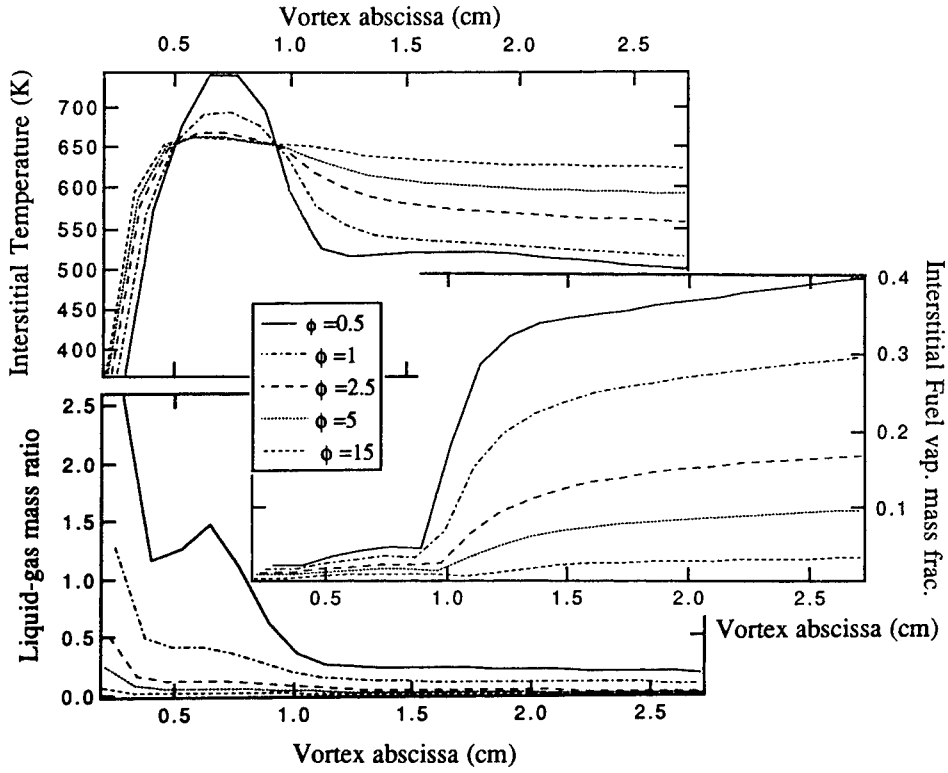

FIG. 6. Interstitial cluster gas temperature (T_{gi}), fuel vapor mass fraction ($Y_{FV,i}$), and liquid-gas mass ratio in the cluster vs the vortex abscissa for various values of Φ^0. Other initial conditions are listed in Fig. 2 caption.

ber of drops, and n_c; the result is a slower T_{gi} increase for small Φ^0's and the formation of a plateau for larger Φ^0's corresponding to cooling of the gas phase due to drop heating. During this initial regime, $\bar{R}_d$ decreases, resulting in only a moderate increase in $Y_{FV,i}$ because N_c is still relatively low. The final regime initiates around $X_c = 1$ cm and is characterized by a large increase in N_c, resulting in an increase in the liquid-gas mass ratio and n_c (since the cluster volume increases only moderately). Heat transfer to a larger number of drops reduces T_{gi} substantially, and $Y_{FV,i}$ increases considerably. For smaller Φ^0's (i.e., larger n_2), there is a larger reduction in T_{gi} and increase in $Y_{FV,i}$. Despite evaporation, $\bar{R}_d$ increases because $\mathfrak{R}_1 < 1$. Lund and Sojka [20] have indeed observed that the Sauter mean diameter can increase with axial position in a spray. The present results show the reasons for this observation. Consistent with this explanation, $\bar{R}_d$ increases most and the relative drop number increases least for the smaller Φ^0. As Φ^0 is large and the drop-laden stream is dilute, entrainment of drops is not sufficient to increase $\bar{R}_d$, and instead $\bar{R}_d$ continues to decrease. For large Φ^0 it is also easier to entrain the drops (at fixed s), so that the relative drop number is maximum.

Results obtained by varying s parametrically are illustrated in Figs. 7 and 8. The initial and final regimes discussed above are present here as well, although they are not so clearly separated. Of special interest is the fact that, past the very initial part of the calculation ($X_c > 0.25$ cm), T_{gi} and $Y_{FV,i}$ are, respectively, an increasing and a decreasing function of s. An exception is found for T_{gi} at very large values of s because of the optimization of the relative number of drops entrained as explained below. The relative number of drops entrained is a nonmonotonic function of s, just as it was shown to be a nonmonotonic function of R_d^0 at fixed s. The maximum relative number of drops occurs at $s = 20$, resulting in a reduction in T_{gi} since heat is removed by the drops from the gas phase. These results thus suggest that it is possible to optimize entrainment of drops from the mixing layer into the large coherent vortices by using the velocity ratio as a control parameter. These findings agree with the observations of Crowe et al. [5,6] and complement existing results showing that drop dispersion in large coherent eddies is optimized at $St = 1$, a phenomenon which was called "the focusing effect" [6]. The present results show that, ad-

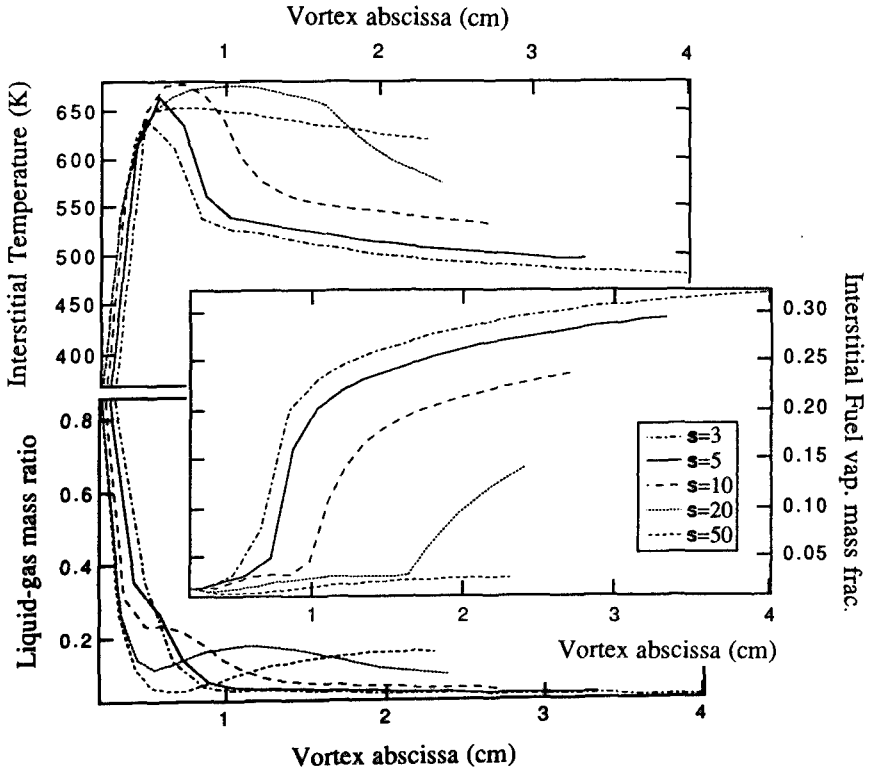

FIG. 7. Interstitial cluster gas temperature (T_{gi}), fuel vapor mass fraction ($Y_{FV,i}$), and liquid-gas mass ratio in the cluster vs the vortex abscissa for various values of s. Other initial conditions are listed in Fig. 2 caption.

ditionally, drop entrainment can be optimized by changing s when Φ^0, T_1, T_{2g}, T_{2d}, and f are fixed.

Calculations were also performed by varying U_1 to be 1, 5, 15, 25, and 50 m/s. The results show that the relative drop number is an increasing function of U_1 (in agreement with the fact that E_v is a decreasing function of s), but that $Y_{FV,i}$ is a nonmonotonic function of U_1, attaining a maximum at intermediate values (U_1 = 15 m/s).

The value of $Y_{FV,i}$ is determined by competition between evaporation, entrainment, and volume expansion of the cluster. As U_1 increases, s decreases and E_v increases. As N_c becomes larger, $\bar{R}_d$ increases to the point that $\dot{m}_{ev}$ decreases because of the larger time necessary to heat the drops. Plots of $\bar{R}_d$ and T_{gi} show the largest increase in $\bar{R}_d$ and the largest reduction in T_{gi} for U_1 = 25m/s, thereby supporting this interpretation.

Summary and Conclusions

A model of drop entrainment in a mixing layer has been developed by combining a simplified formulation of the mixing layer based upon experimental correlations and a more rigorous formulation describing the dynamics and evaporation of dense or dilute clusters of drops in cylindrical, axisymmetric vortices.

Calculations were performed by varying an extended number of parameters. The results show, in agreement with observations, that the average drop radius may increase with the distance from the inception of the mixing layer, and that the velocity ratio between the two streams controls drop entrainment into the mixing layer. Additionally, it is shown that, in the range of drop-number-density values typical of sprays, it is possible to maximize the liquid mass entrained by using the drop radius as a parameter, and that it is possible to optimize the relative number of drops (with respect to the initial value) entrained into the large coherent vortices by using the velocity ratio between streams as parameter. The velocity of the hot air stream has been shown to be a parameter controlling the interstitial fuel vapor mass fraction.

Acknowledgments

This work has been performed at the Jet Propulsion Laboratory under the sponsorship of the Société Européene de Propulsion (F.F.), and the U.S. Air Force Wright Patterson Laboratory (J.B. and K.H.) through an agreement with the National Aeronautics and Space Administration.

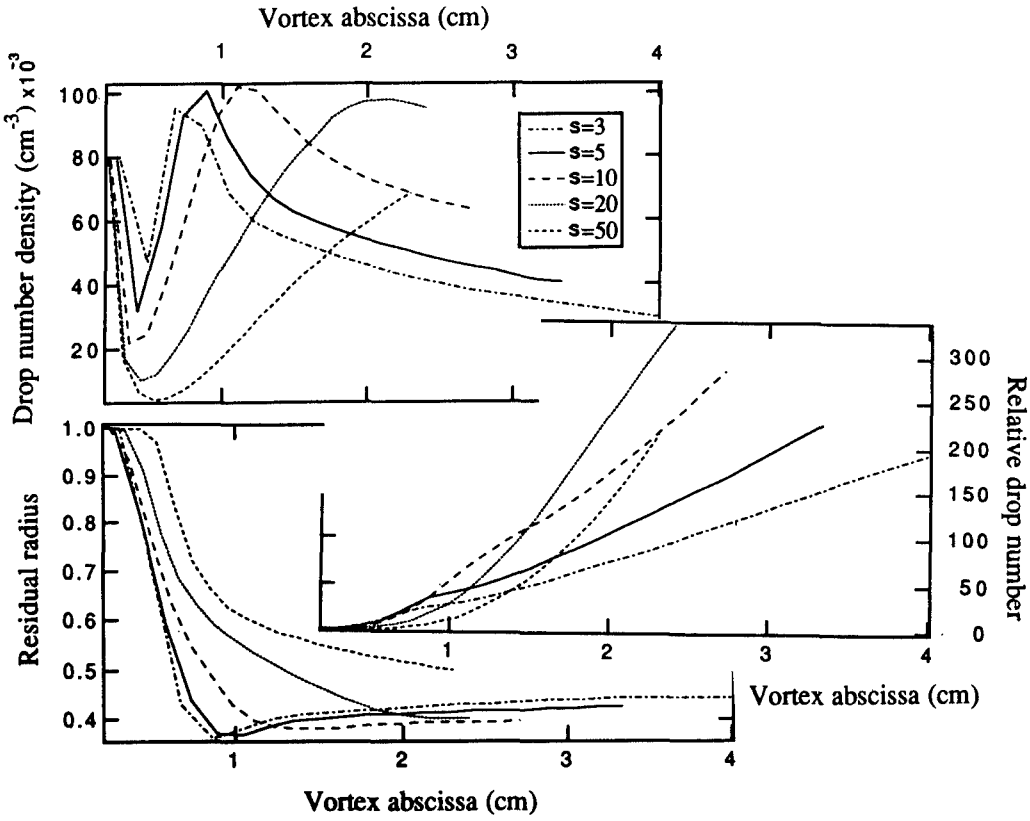

FIG. 8. Drop number density in the cluster (n_c), relative drop number (with respect to N_c^0), and drop residual radius ($\bar{R}_d/R_d^0$) vs the vortex abscissa for various values of s. Other initial conditions are listed in Fig. 2 caption.

REFERENCES

1. Hernan, M. A., and Jimenez, J., *J. Fluid Mech.* 119:323–345 (1982).
2. Lazaro, B. J., and Lasheras, J. C., *J. Fluid Mech.* 235:143–178 (1992).
3. Lazaro, B. J., and Lasheras, J. C., *J. Fluid Mech.* 235:179–221 (1992).
4. Lazaro, B. J., and Lasheras, J. C., *Phys. Fluids A.* 1 (6):1035–1044 (1989).
5. Crowe, C. T., Chung, J. N., and Troutt, T. R., *Prog. Energy Combust. Sci.* 14:171–194 (1988).
6. Crowe, C. T., Chung, J. N., and Troutt, T. R., *Particulate Two Phase Flow*, Chap. 18, (M. Roco, Ed.), Butterworth-Heinemann, Boston, 1993.
7. Longmire, F. K., and Eaton, J. K., *J. Fluid Mech.* 236:217–257 (1992).
8. Brown, G. L., and Roshko, A., *J. Fluid Mech.* 64(4):775–816 (1974).
9. Roshko, A., *AIAA J.* 14(10):1349–1357 (1976).
10. Huang, L.-S., and Ho, C.-M., *J. Fluid Mech.* 210:475–500 (1990).
11. Zohar, Y., and Ho, C.-M., "Dissipation Scale and the Control of Fine Scale Turbulence in a Mixing Layer," *J. Fluid Mech.*, submitted.
12. Dimotakis, P., *AIAA J.* 24(11):1791–1796 (1986).
13. Mizutani, Y., Nakabe, K., Fuchihata, M., Akamatsu, F., Zaizen, M., and El-Emam, S. M., *Atomization Sprays* 3:125–135 (1993).
14. McDonnel, V., Adachi, M., and Samuelsen, G. S., *Combust. Sci. Technol.* 82:225–248 (1992).
15. Rudoff, R. C., Brena de la Rosa, A., Sankar, S. V., and Bachalo, W. D., Paper AIAA-89-0052.
16. Bellan, J., and Harstad, K., *Twenty-Third Symposium (International) on Combustion*, The Combustion Institute, Pittsburgh, 1990, pp. 1375–1381.
17. Bellan, J., and Harstad, K., *Int. J. Heat Mass Transfer* 31(8):1655–1668 (1988).
18. Bellan, J., and Harstad, K., *Combust. Flame* 79:272–286 (1990).
19. Bellan, J., and Harstad, K., *Int. J. Heat Mass Transfer* 30(1):125–136 (1987).
20. Lund, M. T., and Sojka, P. E., *ILASS'93 Proceedings* Worcester, MA, pp. 14–18.

Twenty-Fifth Symposium (International) on Combustion/The Combustion Institute, 1994/pp. 407–412

VORTEX PAIRING AND DROPLET DISPERSION IN A TURBULENT, FREE SHEAR LAYER

K. T. KIGER AND J. C. LASHERAS
Department of Applied Mechanics and Engineering Sciences
University of California, San Diego
9500 Gilman Drive, Mail Code 0411
La Jolla, CA 92093-0411, USA

An experimental characterization of the entrainment and transport of small droplets in a turbulent, plane mixing layer is presented. Specifically, this study addresses the contribution of vortex pairing to the dispersion process. The experimental data were obtained using optical measurements that allowed for the characterization of mean, root mean square (rms), and conditional-averaged profiles of attenuation, in addition to the conditional-averaged evolution of the dispersed-phase number frequency and velocity for the various-sized particulate. It is shown that the pairing process resulting from the combination of harmonic and subharmonic forcing contributes to an increased rate of homogenization of the droplet concentration across the mixing layer when compared to the case of single-frequency forcing. The amount of homogenization depends strongly on the history of the flow and the size of the particulate.

Introduction

The characterization of droplet-turbulence interaction is fundamental to the development of spray models related to numerous physical applications. The theoretical formulations for the conservation equations of multiphase flows often require closure terms relating the transfer between the phases. Although these terms have been successfully modeled with empirical laws in several specific applications, they do not usually allow for a full understanding of the physical mechanisms involved. Thus, the complete experimental characterization of the evolution of the two phases in a prototypical, turbulent flow is critical to the general formulation of spray models. For this purpose, in this paper we present instantaneous, particle-turbulence measurements of a polydispersed droplet spray mixing in a plane, turbulent, free shear layer.

Extensive research of the past two decades has determined that over a wide range of Reynolds numbers, turbulent, free shear flows contain a large-scale, coherent vortical structure with a superimposed, small-scale random motion [1,2]. From the perspective of two-phase flow applications, it is important to determine how these large eddies affect the mixing of the dispersed phase. Recent experimental studies [3,4], as well as numerical simulations [5,6], have shown that the large coherent eddies play a central role in the entrainment and mixing of the particles in the developing region of natural and forced mixing layers. Specifically, it was found that these structures selectively entrain particles based upon their size and create strong instantaneous gradients in concentration across the vortex. It was also shown that the ratio of the particle's viscous relaxation time to the flow timescale (Stokes number) is a dominant parameter controlling the extent of the mixing.

Since the work of Winant and Browand [2], it has been known that the growth of a plane mixing layer is dominated by the amalgamation of the coherent structures, often referred to as vortex pairing. Thus, as the pairing process is predominantly responsible for the growth of the mixing region, the next logical extension for study is the role of the vortex pairing upon particulate dispersion. Limited experiments in the initial region of jets [7] and numerical simulations of planar free shear layers [8,9] indicate the possibility of enhanced dispersion during the pairing process. However, there remains a lack of a complete characterization of how the pairing process contributes to the dynamics of the particulate in the general case of a polydispersed spray. The intent of this research is to experimentally determine the fundamental mechanism of particle dispersion during pairing through the characterization of the particulate concentration and conditional-averaged number frequency. Also of interest to multiphase flow is particle-turbulence interaction, as characterized by the exchange of momentum and energy between the phases. The authors have measured the kinetic energy transferred between the phases for this flow, but have published them elsewhere due to space limitations [14].

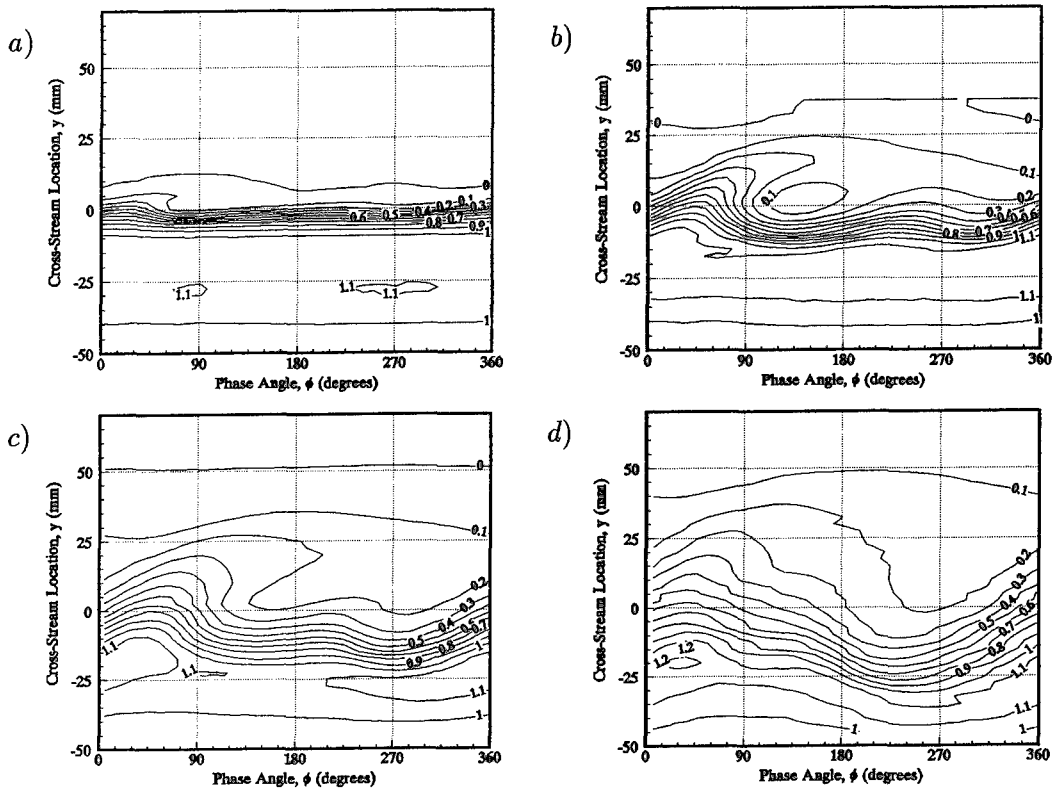

FIG. 1. Phase-averaged attenuation contours for (a) x = 20 mm, (b) x = 100 mm, (c) x = 180 mm, and (d) x = 260 mm. Phase angle ϕ corresponds to subharmonic component of forcing signal; ϕ = 360° is equivalent to t = 1/70 = 0.0143 s.

Experimental Facility and Measurements

The experimental facility consists of a horizontal wind tunnel exiting into a stagnant test section, where a shear layer is formed at the end of a splitter plate. A uniform, polydispersed spray of water droplets is created within the wind tunnel, using an array of air blast atomizers. The spray then flows past the splitter plate, where it mixes with the ambient air. Further details of the experimental facility can be found elsewhere [3].

The measurements were made utilizing two optical techniques: laser attenuation measurements and phase Doppler anemometry (PDA). For the laser attenuation, a photodiode was used to measure the intensity of a 5 mW He-Ne laser passed through the test section. Provided the droplets are spherical, form a dilute suspension, and there are no multiple scatterings, it can be shown from Mie theory [10] that the attenuation of the beam's intensity, I/I_0 will be given by

$$\xi = -\ln\left(\frac{I}{I_0}\right) = 3L\bar{a}\int_0^\infty \frac{\bar{f}(D)}{D}\,dD$$

where L is the length of the beam passing through the spray, $\bar{f}(D)$ is the average volume probability distribution function (PDF) along the beam, and D is the droplet diameter. Even though the attenuation measurements do not isolate the effects of size from concentration, it has been observed that the shape of the attenuation and concentration profiles exhibit similar trends [10]. In contrast with the attenuation results, the PDA uses the interference pattern created at the intersection of two crossed laser beams to simultaneously measure the velocity and size of individual particles. Thus, the spray is described by the statistical information collected from individual particles passing through a very small region.

The flow conditions at the exit of the wind tunnel produces turbulent air flow with an average velocity of 18 m/s and a 2% free stream turbulence level, while the initial momentum thickness is approximately 2 mm with a 15% turbulence level. The water droplets are observed to have a relatively uniform number PDF in the cross-stream (y) direction, with a range extending from 5 to 100 μm, and a Sauter mean diameter of approximately 30 μm. In order to force the mixing layer, a vertical velocity perturbation

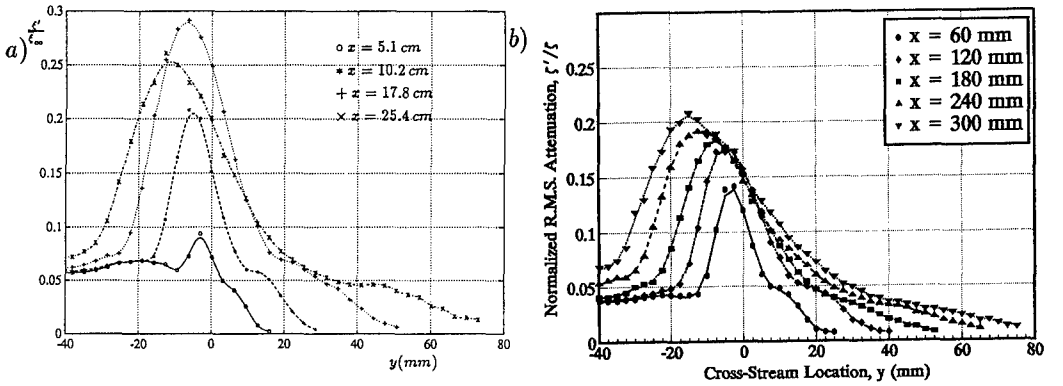

FIG. 2. Evolution of rms attenuation profiles for (a) single-frequency forcing (from Ref. 4), and (b) pairing mode forcing.

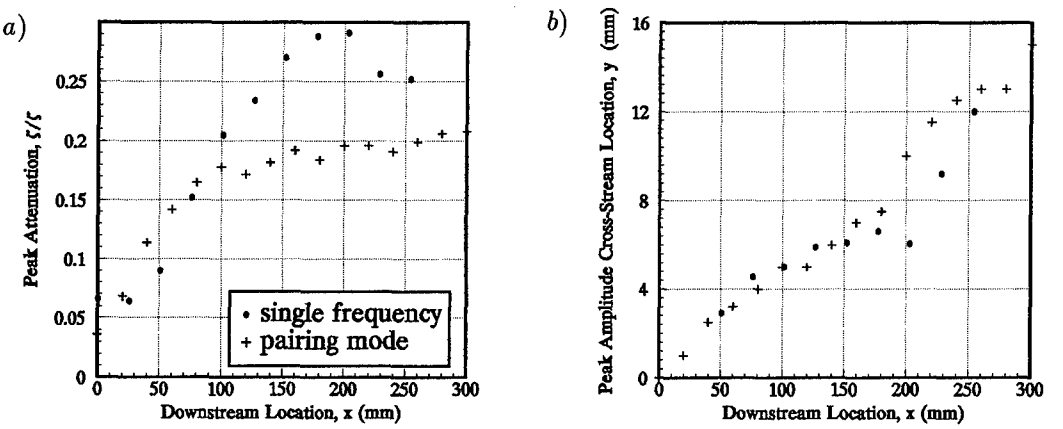

FIG. 3. Downstream evolution of the rms peak (a) amplitude and (b) cross-stream location (absolute value) for single-frequency forcing (from Ref. 4) and pairing mode forcing.

is introduced at the end of the splitter plate, using a speaker and a manifold chamber [11]. To obtain a consistent pairing sequence within the test section, the shear layer is forced with the sum of the harmonic and first subharmonic frequencies of the most unstable wavelength measured in the naturally evolving shear layer (140 and 70 Hz, respectively).

Results and Discussion

Isocontour levels of the phase-averaged attenuation surfaces are shown in Fig. 1. The measurements were obtained by simultaneously recording the forcing signal and the attenuation signal measured by the photodiode. The concentration timeseries was then discretized and averaged into 36 different bins based upon the phase of the subharmonic component of the forcing signal, resulting in an ensemble-averaged surface over 450 individual subharmonic wavelengths.

The measurements show the early response of the droplets to the formation of two equally spaced, but unequal strength, vortex structures (Fig. 1, x = 20 and 100 mm). This corresponds to a rapid growth of the initially most amplified frequency of 140 Hz. Individually, these structures marked by the droplet concentration gradients qualitatively resemble similar flow features found in single-frequency forcing results [4]. Namely, for each period of the harmonic forcing, there is the formation of a "streak" with decaying attenuation entrained from the free stream of the spray. This streak is drawn longitudinally over what is found to be the core of the vortex, forming a large depletion "hole" (prominently visible in the strong vortex, but shown only as a slight dip in the weaker one). As one moves downstream (x = 180 and 260 mm), the phase-averaged surfaces show a

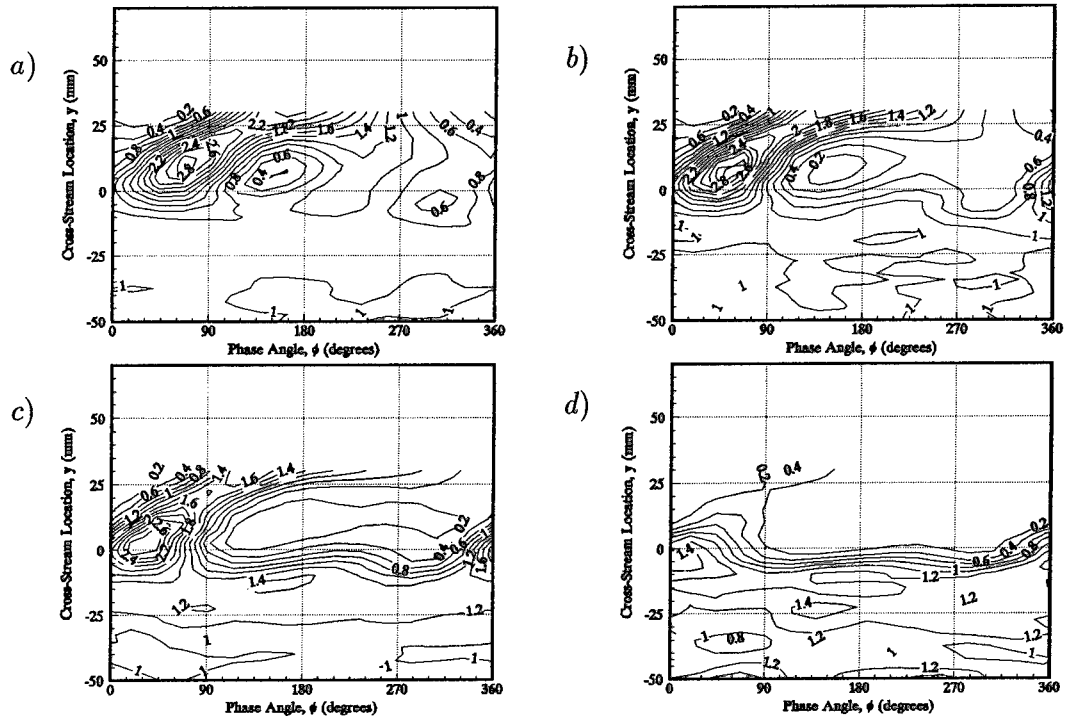

FIG. 4. Nomalized number frequency contours at $x = 100$ mm for (a) $D < 10\ \mu$m, (b) $10 < D < 20\ \mu$m, (c) $20 < D < 40\ \mu$m, and (d) $D > 40\ \mu$m.

clear development of the particle dispersion as the pairing is completed. During the initial stages of the pairing, the streak produced by the smaller vortex is observed to move into the effective core of the merging pair and to be dispersed by the comingling vortices. This is highlighted at $x = 260$ mm by the disappearance of the strong depletion hole that had previously formed. At $x = 260$ and 300 mm, what remains of the smaller streak merges with the root of the larger streak, and larger-sized particles begin to be entrained inside the core. Thus, the merging process provides a homogenization mechanism to bring large- and small-sized particulate within the core of the vortex. Excluding the small-scale effects due to the three-dimensional instabilities [12,13] and the mixing transition, which in our experiments occur at later stages of the shear layer, there is no physical mechanism by which this can be accomplished in the single-frequency forcing case.

Figures 2a and 2b show the normalized development of the attenuation root mean square (rms) profiles, for the single frequency (from Ref. 4) and pairing case. In Fig. 2a, it is observed that the peak value of the rms undergoes a strong growth and then a decay, accompanied by a broadening of the peak base. For the pairing case, Fig. 2b shows a similar profile shape with a slightly different evolution. Here, the peak undergoes a monotonic increase throughout the development, while the "plateau" in the external region is eroded through the last half of the test section. The details of this comparative evolution can be observed in Figs. 3a and 3b, where the peak rms amplitude and cross-stream location are plotted as a function of the streamwise coordinate. For the single-frequency case, the amplitude and location exhibit an abrupt change at $x = 200$ mm. Lázaro and Lasheras [4] attributed this behavior to the large external streak impacting upon its upstream neighbor. Prior to streak reconnection, the maximum fluctuation occurs as the structure transitions between the streak and the core. When streak reconnection occurs, it increases the attenuation near the external braid region and causes the peak fluctuation level to shift toward the inner side of the mixing layer. In contrast to this, for the pairing case, the peak rms grows steadily, and its cross-stream location varies almost linearly with no sharp discontinuities (Fig. 3b). Since the final vortex size is similar for both cases (the fundamental frequency in the single forcing case was the same and the subharmonic frequency used in the pairing case, namely, 70 Hz), these results indicate that streak reconnection is not taking place in the paired structure due to a less-developed external streak. This is consistent with the fact that the vorticity was initially distributed into two vortices per wavelength, each developing their own smaller

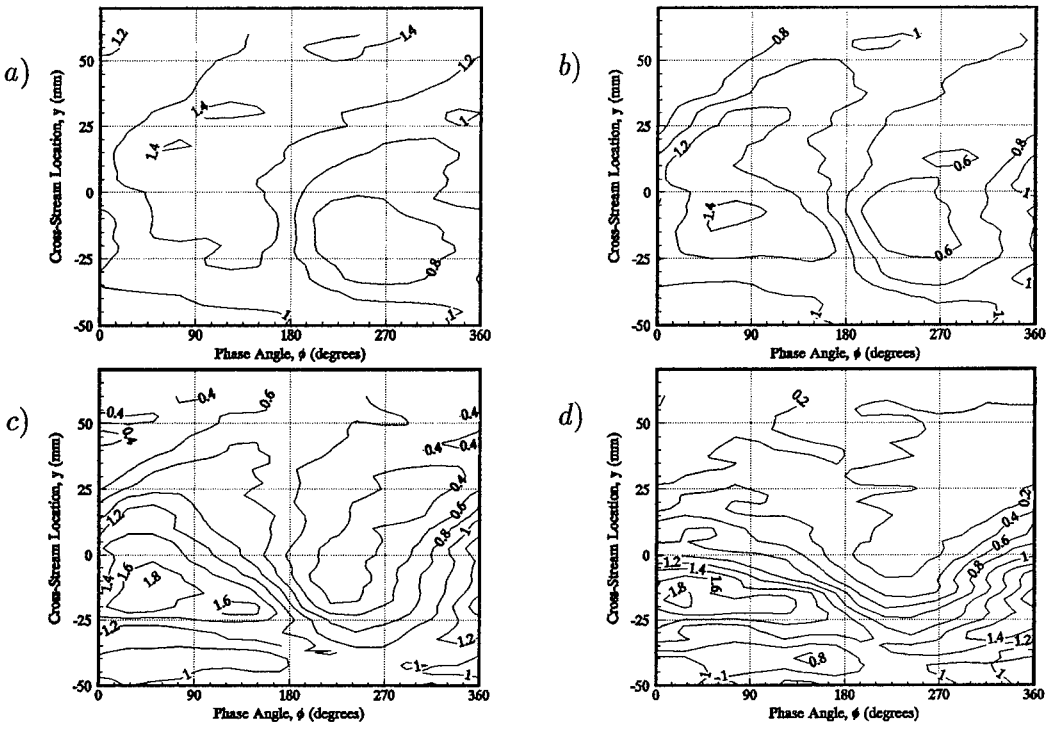

FIG. 5. Nomalized number frequency contours at $x = 260$ mm for (a) $D < 10\ \mu$m, (b) $10 < D < 20\ \mu$m, (c) $20 < D < 40\ \mu$m, and (d) $D > 40\ \mu$m.

streaks until the pairing disrupted the growth and scattered one of the streak's particles throughout the lower inside region of the merged core. These observations are in agreement with the phase-averaged attenuation results shown previously in Fig. 1.

Along with the observation of the evolution of the attenuation, it is useful to consider how the size of the droplets affects the dispersion process. The size information measured by the PDA was discretized into four bins: 2–10 μm, 10–20 μm, 20–40 μm, and 40–100 μm. From these measurements, the conditionally averaged number frequency was then defined to be the percentage of particles of the total sample that were within the given size range at a given phase angle. If this quantity is normalized by the average freestream value, it would describe the change in probability of finding a particle within a given size range at the specified phase. Smoothed contour plots of the normalized number frequency are shown for the four size ranges at two downstream locations in Figs. 4 and 5. The first location, $x = 100$ mm, corresponds to a point where the harmonic component is dominant and shows the effects found in the initial developing region of the shear layer. From these results, there are some obvious differences and similarities in how the different-sized particles are dispersed. As one moves from the relatively uniform freestream through the mixing region, the strong inhomogeneities caused by the vortex structures become evident. For the smallest sized particulate ($D < 10\ \mu$m) at $x = 100$ mm, observe how there is a sharp increase in probability in the external portion of the largest streak region ($\phi \sim 70$ deg, $y \sim +10$ mm). There is also a decrease in the number frequency in the core region of the largest vortex. This indicates that the smallest size class has been entrained strongly through the mixing layer by the external streak. The strong increase in number frequency (200–300%) in the external region shows that most of the particulate present in this region is of the smallest size. There is also a similar structure produced by the smaller vortex ($\phi \sim 270$ deg, $y \sim 0$ mm), but with a much weaker influence. As the size of the droplets is increased, the same trends can be seen, but they happen at a different scale. Specifically, the high probability "ridge" and its maximum peak (corresponding to the streak structure in the attenuation measurements) shift further away from the core of the vortex and closer to the particle-laden free stream. There is also a decrease in the response of the particulate to the flow in general and, in particular, to the smaller vortex. These differences can be explained by considering the response times of the different sizes in relation to the flow timescales.

The smallest sizes, with the least inertia, will have the smallest response times and tend to follow the flow's fluctuations. In this particular example, the response of the drops depends on three different flow timescales: the harmonic disturbance timescale, $1/f$ (~7 ms); the subharmonic disturbance timescale, $2/f$ (~14 ms); and the exposure time to the flow, t_e (~16 ms). The larger droplets are not dispersed as far as the smaller ones due to the fact that their response time is the same order of magnitude as the exposure time. Additionally, they tend to filter out the higher-frequency harmonic disturbances, in preference to the subharmonic. In contrast to this, Fig. 5 (x = 260 mm) presents how the pairing has changed the evolution. For the smallest size, the most dramatic effect is the increased amount of homogenization and the lack of a well-defined streak structure. Here, the peak probabilities fluctuate within 50% of the free stream value. This is consistent with the fact that the smallest sizes will follow the flow closely and hence receive the greatest benefit from the strong mixing that occurs during the pairing. As the size increases, the inhomogeneous streaks caused by the coherent structures begins to re-emerge. For the intermediate and large sizes, this is manifested by the increased probability streak, and the decreased probability hole, which are now occurring on a scale corresponding to the subharmonic disturbance. It is thus shown that the pairing does increase the amount of homogenization, but the effectiveness of this mixing will vary strongly with the droplet size due to their varying response times to the flow evolution.

Conclusions

Qualitative experimental results have been presented to characterize turbulent, two-dimensional shear flow mixing of a dilute, polydispersed spray under the effect of vortex merging. A comparison with droplet dispersion caused by a single harmonic perturbation shows that the pairing process produces an increased homogenization in concentration, but the effectiveness of the mixing is greater for the smallest sizes and decays with increasing size. The observed enhancement of the particle density in the internal region of the mixing layer is attributed to the fact that as the pairing occurs, most of the droplets that had been entrained by the streak of the weaker vortex are brought toward the core of the pairing structure. The current data suggests that the droplet concentration and size distribution resulting from the subharmonic structure will be qualitatively different from the one evolving from single-frequency forcing.

REFERENCES

1. Brown, G. L., and Roshko, A., On density effects and large structure on turbulent mixing layers. *J. Fluid Mech.* 64:775–816 (1974).
2. Winant, C. D., and Browand, F. K., Vortex pairing: The mechanism of turbulent mixing-layer growth at moderate Reynolds number. *J. Fluid Mech.* 63:237 (1974).
3. Lázaro, B. J., and Lasheras, J. C., Particle dispersion in the developing free shear layer. Part 1. Unforced flow. *J. Fluid Mech.* 235:143–178 (1992).
4. Lázaro, B. J., and Lasheras, J. C., Particle dispersion in the developing free shear layer. Part 2. Forced flow. *J. Fluid Mech.* 235:179–221 (1992).
5. Tang, L., Wen, F., Yang, Y., Crowe, C. T., Chung, J. N., and Troutt, T. R., Self-organizing particle dispersion mechanism in a plane wake. *Phys. Fluids A* 4(10):2244–2251 (1992).
6. Chein, R., and Chung, J. N., Simulation of particle dispersion in a two-dimensional mixing layer. *AIChE J.* 34(6):946–954 (1988).
7. Longmire, E. K., and Eaton, J. K., Structure of a particle-laden round jet. *J. Fluid Mech.* 236:217–257 (1992).
8. Chein, R., and Chung, J. N., Effects of vortex pairing on particle dispersion in turbulent shear flows. *Int. J. Multiphase Flow* 13(6):785–802 (1987).
9. Martin, J. E., Meiburg, E., and Narayanan, R., The dispersion and focusing of heavy particles in a two-dimensional mixing layer. *Bull. Am. Phys. Soc. Div. Fluid Mech.* 37(8):1777 (1992).
10. Lázaro, B. J., "Particle dispersion in turbulent free shear flows" Ph. D. Dissertation, University of Southern California, Los Angeles, CA, 1989.
11. Fiedler, H. E., and Mensing, P., 1985 The plane turbulent shear layer with periodic excitation. *J. Fluid Mech.* 150:281–309 (1985).
12. Bernal, L. P., "The coherent structure of turbulent mixing layers." Ph. D. Dissertation, California Institute of Technology, Pasadena, CA, 1981.
13. Lasheras, J. C., and Choi, H., Three-dimensional instability of a plane free shear layer: An experimental study of the formation and evolution of streamwise vortices. *J. Fluid Mech.* 189:53–86 (1988).
14. Kiger, K. T., and Lasheras, J. C., Effect of vortex pairing on particle dispersion and kinetic energy transfer in a two-phase turbulent shear layer. *J. Fluid Mech.*, submitted (1994).

Twenty-Fifth Symposium (International) on Combustion/The Combustion Institute, 1994/pp. 413–421

APPLICATION OF AN INTEGRATED PHASE DOPPLER INTERFEROMETER/ RAINBOW THERMOMETER/POINT-DIFFRACTION INTERFEROMETER FOR CHARACTERIZING BURNING DROPLETS

SUBRAMANIAN V. SANKAR, DALE H. BUERMANN, KHALID M. IBRAHIM AND WILLIAM D. BACHALO
Aerometrics, Inc.
550 Del Rey Avenue, Sunnyvale, CA 94086, USA

A laser-based, nonintrusive diagnostic instrument has been developed for simultaneously measuring the velocity, size, temperature (refractive index) of burning droplets, and the gas-phase temperature field surrounding the burning droplet. The developed diagnostic is suitable for experimental studies involving single droplet/droplet array combustion. The size and velocity of the droplets are measured using the well-established phase Doppler interferometric technique. The temperature/refractive index of the droplets are determined by measuring the primary rainbow location with a linear charge coupled device (CCD) array. The gas-phase temperature distribution is inferred from interferograms obtained with point-diffraction interferometry (PDI). The three diagnostic techniques have been completely integrated to yield a single diagnostic instrument. New algorithms have been developed for extracting and normalizing the interferograms from noisy digital images. Methods for unambiguous phase unwrapping were also identified. The integrated diagnostic was tested by applying it to the case of isolated burning *n*-heptane droplets in motion. Using a combined experimental/theoretical approach, it was possible to extract the radial temperature profile of the gas phase surrounding the droplet in addition to the droplet velocity, size, and temperature. The integrated diagnostic tool has significant potential for studying fundamental droplet combustion processes and for validating state-of-the-art droplet/spray combustion models.

Introduction

Over the years, the burning/evaporation characteristics of isolated droplets have been studied extensively with the purpose of elucidating fundamental phenomena important to the overall spray combustion process. Detailed reviews of the current state-of-the-art in the area of single droplet combustion are provided in Refs. 1 through 3. With recent advances in computational capabilities, numerical treatment of the problem of single droplet combustion has been undertaken by different researchers [4–6].

However, because of the small spatial scales involved in the combustion of droplets, detailed experimental characterization of the droplet combustion zone is not a trivial task, and therefore, experimental validation of theoretical models is very difficult. Optical, nonintrusive techniques appear to be the most suited for probing the droplet combustion zone. Although coherent anti-Stokes Raman scattering (CARS) has been successfully applied to a combusting droplet stream [7], many issues associated with CARS in spray combustion remain to be resolved. Laser interferometric techniques provide a relatively easy and inexpensive alternative to spectroscopic techniques such as CARS. Gupta and Rossi [8] have used a laser schlieren holographic interferometry system to measure the relative gas-phase temperature field surrounding burning droplets.

In this paper, we discuss the development and application of an integrated phase Doppler interferometer/rainbow thermometer/point-diffraction interferometer for simultaneously measuring the droplet velocity, size, temperature, and the gas-phase temperature field surrounding a burning droplet in motion.

Laser Diagnostics

Phase Doppler Interferometer:

Phase Doppler interferometry [9] is a well-established optical, nonintrusive diagnostic technique for simultaneously measuring the velocity and size of individual droplets in complex spray environments. The theoretical principles of phase Doppler interferometry is well known [9] and, therefore, will not be discussed here.

Rainbow Thermometer:

Rainbow thermometry [10] takes advantage of the fact that the rainbow angle is a function of the refractive index of the droplet. Therefore, by measur-

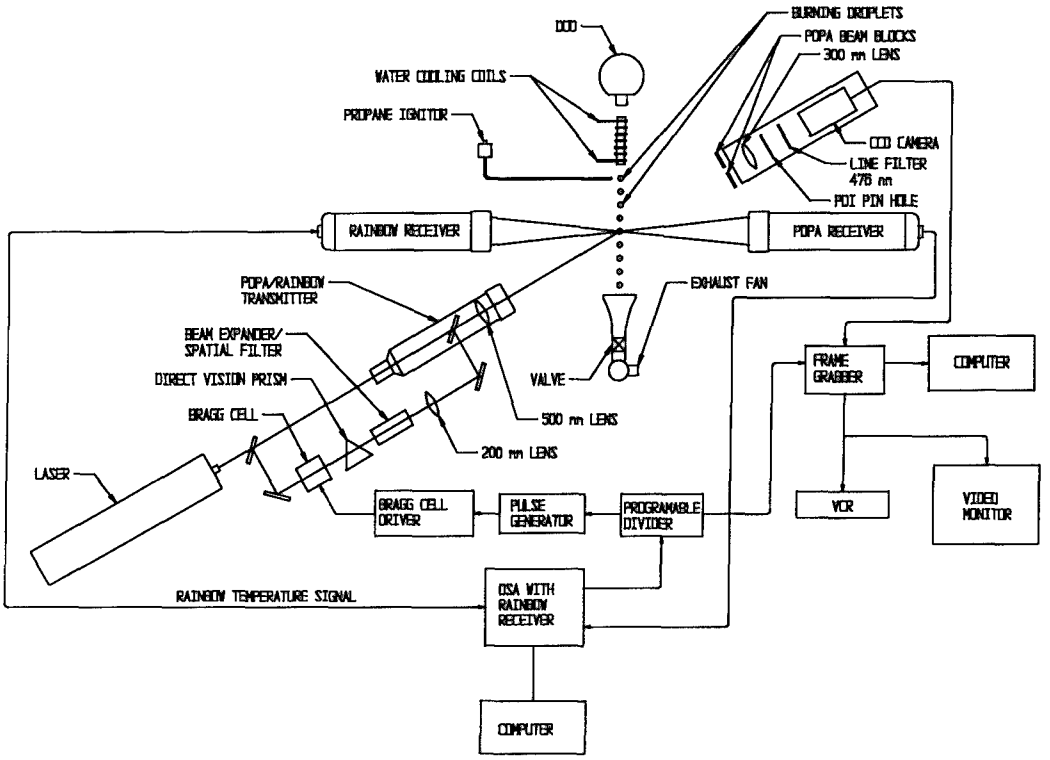

FIG. 1. Schematic of the integrated phase Doppler interferometer/rainbow thermometer/point-diffraction interferometer.

ing the rainbow location with the help of a linear array detector, such as a charge coupled device (CCD), the refractive index of the droplet can be determined. Since refractive index varies with temperature, the droplet temperature can also be inferred if the relationship between the refractive index and temperature is known a priori. Sankar et al. [11] have developed a rainbow thermometer for homogeneous droplet temperature measurement in reactive sprays. However, it is important to recognize that in situations where the droplet transient heating time is of the same order of magnitude as the droplet lifetime, the presence of temporally varying radial temperature gradients are possible. This could lead to erroneous temperature measurements [12].

Point-Diffraction Interferometer:

The point-diffraction interferometer (PDI) is a very simple interferometer in which a small aperture located at the Fourier transform plane of an imaging lens is used to diffract a small portion of the incident light into a spherical reference wave front [13]. The remaining portion of the propagating object wave front is uniformly attenuated by some means. The attenuated object wavefront subsequently interferes with the reference wavefront to form an interferogram.

Integrated System:

An Aerometrics' phase Doppler particle analyzer (PDPA), a rainbow thermometer [11], and a point-diffraction interferometer were integrated to yield a single diagnostic tool. A schematic of the developed integrated PDPA/rainbow thermometer/PDI system is shown in Fig. 1. It basically consists of an optical transmitter, a PDPA optical receiver, a rainbow optical receiver, a PDI optical receiver, a Doppler signal analyzer (DSA) with an additional module for droplet temperature measurement, a frame grabber for recording the interferograms, and two data acquisition computers synchronized with each other.

Optical transmitter

The optical transmitter of the integrated diagnostic system provides the necessary laser beams for simultaneously conducting phase Doppler interferometry, rainbow thermometry, and point-diffraction interferometry. The phase Doppler part of the integrated system was configured to measure only one component of velocity and droplet diameter. The

green (514.5 nm) beam from a 5-W argon-ion laser was split into two and used for phase Doppler interferometry, whereas a single blue beam (488.0 nm) was used for rainbow refractometry. Because rainbow rays exhibit an inherent tendency to be strongly polarized perpendicular to the scattering plane, the blue rainbow "pump" beam was polarized perpendicular to the plane containing the optical transmitter and receiver. Also, the horizontally polarized blue beam (488.0 nm) from the argon-ion laser was used for the PDI. The optical transmitter of a standard PDPA was slightly modified to accommodate the two additional blue beams (the rainbow "pump" beam and the PDI beam) along the same optical axis of the transmitter. A single 500-mm f.l. transmitter lens was used to focus the two green beams and the rainbow "pump" beam at the measurement probe volume. On the other hand, the pulsed PDI beam was first focused by means of a 200-mm f.l. lens before being collimated by the 500-mm f.l. transmitter lens, see Fig. 1. The collimated PDI beam had a diameter of approximately 1.5 cm and the rainbow "pump" beam diameter was larger than the green PDPA laser beam diameter by a factor of about 2.

In order to be able to "freeze" the droplet motion, provision was made to pulse the PDI beam for a short duration after the entry of the droplet into the measurement probe volume. An acousto-optic Bragg cell was used for this purpose. The horizontally polarized blue beam was first diffracted into higher-order beams by means of a Bragg cell operating at 40 MHz. The first-order diffracted beam was chosen for recording the interferogram. The Bragg-cell driver was initially adjusted such that the diffracted energy of the chosen first-order beam was minimal. The leading edge of the PDPA gate signal, signifying the entry of the droplet into the measurement probe volume, was then used to trigger a pulse generator, which provided a pulse with an adjustable pulse width ranging from about 1 to 100 μs. For the current application, the pulse width was chosen to be 3 μs. This pulse was subsequently used to modulate the *rf* signal provided by the Bragg-cell driver, thus momentarily causing significant energy to be diffracted into the interferogram beam and, thereby, freezing the droplet motion.

Optical receivers

The optical receiving system of the integrated diagnostics includes three separate receivers: one each for phase Doppler interferometry, rainbow thermometry, and point-diffraction interferometry. The PDPA receiver consisting of a 1000-mm f.l., *f*/9.5 front lens was placed in the forward scatter direction at a scattering angle of 30°. The rainbow receiver consisting of a 500-mm f.l., *f*/4.8 front lens was placed diametrically opposite to the PDPA receiver at a scattering angle of 150°. The PDI receiver was placed directly in the path of the blue PDI beam.

The details of the configuration of the PDPA receiver is available in Ref. 9 and is therefore not described here. The rainbow receiver consists of a 500-mm focal length, *f*/4.8 spherical triplet as its front lens for collecting and collimating the scattered light in the backscatter direction. A 238-mm focal length, *f*/2.3 spherical triplet focuses the collimated light on to a 400-μm slit, which acts a spatial filter. A 50-mm focal length spherical triplet placed behind the spatial filter collimates the collected light, which is then focused onto a linear CCD array (1024 active pixels) by means of a fast cylindrical lens.

The details of the PDI optical receiver is shown schematically in Fig. 1. A system of beam block, polarizer, and optical line filter is used in the PDI receiver to eliminate interference by the green PDPA beams and the blue rainbow "pump" beam. A 300-mm f.l. lens is placed in the PDI laser beam path, and a polarization filter with a small aperture is placed at its focal plane. The aperture in the polarization filter is created by increasing the laser power, in the absence of burning droplets, till the focused PDI beam is able to burn the emulsion off the filter. The presence of a burning droplet induces phase shift in the transmitted wavefront. The object wavefront, after passing through the filter, interferes with the spherical reference wavefronts created by the aperture to form an interferogram. The visibility of the interferogram depends upon the relative intensities of the object and reference beam, and this can be balanced by rotating the polarizer in its plane. The droplet and the resulting interferogram are imaged onto a CCD TV camera by the 300-mm f.l. imaging lens.

Data acquisition/signal processing system

The data acquisition system for the integrated diagnostics includes two computers: one for controlling the DSA and the other for controlling the frame grabber. The DSA is a frequency domain signal processor that is capable of extracting the velocity and size of the droplets from the phase Doppler signals. For droplet temperature measurement, the linear CCD output is sampled and digitized at 10 MHz by a dedicated rainbow signal processor, which is an add-on/plug-in module to the DSA. The rainbow signal processor has a digital peak detector for detecting the rainbow location. The rainbow peak location and intensity are tagged along with the DSA data packet that contains the standard phase Doppler information. This data packet is then transferred to the DSA data acquisition computer for further analysis and postprocessing.

A second dedicated computer is used to control the frame grabber. The video output of the TV camera is continuously digitized by means of an Imaging Technology VS-100 frame grabber and displayed on an Electrohome high-resolution monitor. The two

independent data acquisition systems are synchronized to sample on the same droplet by using the PDPA gate as an external trigger for the frame grabber. The external trigger signifies the presence of a droplet within the PDPA/rainbow thermometer measurement probe volume and causes the frame grabber to freeze an image of the interferogram in its memory. For every valid PDPA gate, a new interferogram is captured and stored in the frame grabber memory. If desired, the data rate can also be slowed down by means of a programmable divider circuit. Between two external triggers, the frame grabber provides a video output of the contents of its memory at the standard NTSC rate of 30 frames per second. This video output is displayed on a high-resolution video monitor and is simultaneously videotaped by means of a Panasonic AG 7300 S-VHS video recorder. This enables playback and processing of the captured interferograms at a later time.

Measurement Uncertainty:

The sizing uncertainty with phase Doppler interferometry is a function of various parameters, including the optical configuration, the signal processing scheme employed, and the refractive index of the droplet. For the current application, the sizing uncertainty is estimated to be about $+/-3$ μm. Two main sources of errors were identified for droplet temperature measurement with rainbow thermometry. This includes the inherent presence of high-frequency oscillations in the rainbow signal and the shift of the rainbow signal due to translatory motion of the droplets. If uncorrected, these errors can give rise to measurement uncertainties as high as $+/-5$ °C. The main source of error in the gas-phase temperature estimation using point-diffraction interferometry arises due to the difficulty in accurately specifing the gas-phase composition. A 20% error in estimating the molar refractivity gives rise to approximately a 10% error in temperature estimation. On the other hand, an error in the measurement of the droplet temperature translates to an almost identical absolute error in the measurement of the gas-phase temperature.

Experimental Setup

The integrated diagnostic system was applied to the case of burning *n*-heptane droplets in a drop-combustion facility. The basic components of the drop-combustion facility are a drop-on-demand droplet generator for creating fuel droplets at different rates, an ignition system for initiating the combustion process, and an air suction system to move the gas phase surrounding the droplets at approximately the same velocity as the moving droplet. The latter helps to minimize forced convection effects. A water recirculating system is used to protect the tip of the drop-on-demand generator from the heat generated by the burning droplets and also to prevent the flame from propagating all the way up to the tip of the generator. The droplets were ignited by allowing them to pass through a very small propane flame. The flame extinguishes itself at about 5.5 cm below the ignition source.

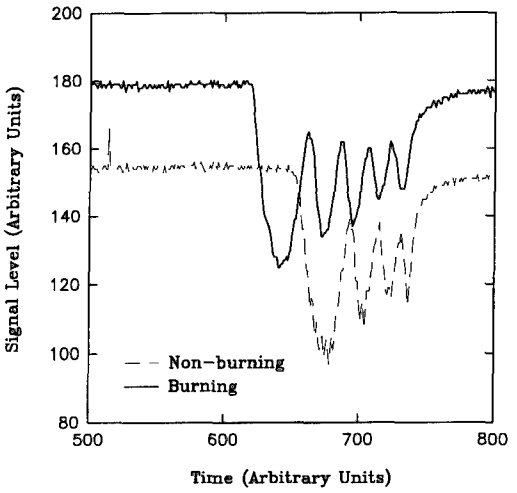

FIG. 2. Digital oscilloscope traces of typical rainbow signals obtained for burning and nonburning *n*-heptane droplets. A vertical offset has deliberately been introduced between the two traces for improved clarity. The diameter of the nonburning droplet (dash-dotted line) is 300 μm, and the diameter of the burning droplet (solid line) is 270 μm.

Results and Discussion

The integrated droplet diagnostic system was tested by applying it to the case of burning *n*-heptane droplets. For this study, the droplets were generated at a rate of about 20/s. The measurement point was chosen to be 4.5 cm below the ignition source. At this point, the velocity of the falling droplet was measured to be 1.0 m/s. This implies that the inter-droplet spacing was approximately 5 cm, practically a case of moving droplets burning in isolation with the ambient air temperature being approximately 297 K. The instantaneous diameter of the burning droplet measured (after correcting for the higher droplet temperature) by the PDPA at this location was 270 μm. For nonburning droplets, the diameter at the same location was measured to be 300 μm.

Figure 2 shows typical rainbow signals (digital oscilloscope traces) obtained by the rainbow thermometer for nonburning and burning heptane droplets. The shift in the rainbow peak corresponds to 105 pixels of the CCD, which implies a change in droplet

FIG. 3. Raw, unprocessed digital interferogram obtained for a burning n-heptane droplet in motion. The dark spot at the center of the interferogram represents the burning droplet, which is moving from top to bottom. The droplet size is 270 μm.

FIG. 4. Digitally filtered, normalized, and scaled interferogram.

temperature of 21 °C. This, in turn, corresponds to an absolute droplet temperature of 318 K. This temperature is well below the boiling point of 371 K for n-heptane. The relatively low droplet temperature coupled with a fairly large change in the droplet diameter (about 30 μm) suggests that the bulk of the heat transferred from the flame, during the approximately 0.04 s of burning, was used to vaporize the liquid with only a small portion going toward the heating up of the droplet itself.

A typical photograph of the recorded point-diffraction interferogram is shown in Fig. 3, where the dark spot at the center of the interferogram represents the burning droplet. Only the coordinates of the center of the droplet were obtained from the interferogram. Inferring the droplet surface from the interferogram proved to be difficult. Therefore, the droplet surface was located based on the PDPA measured size. If x and z denote the horizontal and vertical axes, respectively, of the interferogram, then the frame grabber memory coordinates corresponding to the center of the burning droplet are determined to be $x = 221$ and $z = 250$. The x-coordinate of the frame grabber memory ranges from 0 to 479, and the z-coordinate ranges from 0 to 511. In Fig. 3, the direction of motion of the burning droplet is from top to bottom.

The raw, unprocessed digital interferogram presented in Fig. 3 shows the presence of high-frequency noise caused by diffraction from dust particles on the optical surfaces and interference from the optical line filter that is placed directly in front of the CCD camera. Furthermore, the visibility of the fringes can be seen to vary across the interferogram. For improved visualization of the fringes in the interferogram and for quantitative extraction of gas-phase temperature profiles, the high-frequency noise has to be filtered out, and the interferogram has to be properly normalized and scaled so that the visibility of the fringes remains close to 1 across the interferogram. The description of an algorithm that was developed to automatically filter, normalize, and scale the recorded digital interferogram will be published at a later time. Figure 4 presents the normalized/scaled interferogram that was obtained by applying the newly developed algorithm to the interferogram shown in Fig. 3. The normalized interferogram can then be mathematically expressed as follows:

$$I_n(x,z) = \cos[\Delta\phi(x,z)]. \tag{1}$$

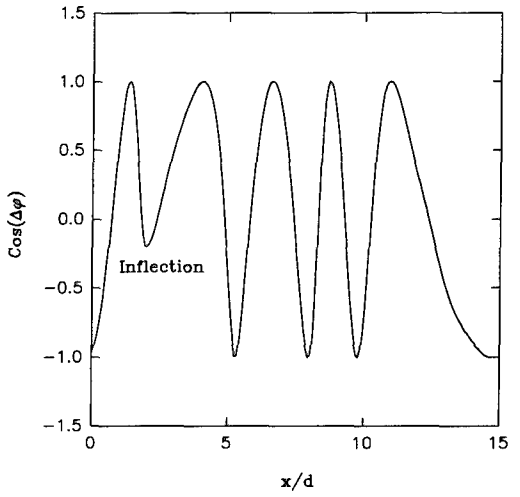

FIG. 5. Experimentally obtained (from the normalized interferogram) variation of $\cos(\Delta\phi)$ with x at $z = 250$.

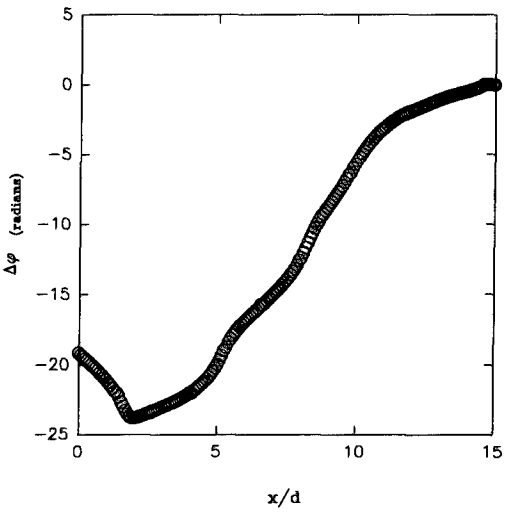

FIG. 6. Unwrapped phase ($\Delta\phi$) variation.

The mean temperature field surrounding the falling burning droplet can be ideally expected to be axisymmetric. However, the extraction of the three-dimensional (3D) axisymmetric temperature field from the interferogram involves several steps. In this paper, we shall only discuss the extraction of the radial (from the droplet surface at $z = 250$) temperature profile. The first step toward this has already been discussed and is the filtering/normalization of the acquired digital interferogram. The next step is to perform the phase unwrapping from the normalized interferogram, as described by Eq. (1). However, taking the inverse cosine of the left-hand side of Eq. (1) will not directly yield $\Delta\phi$. On the other hand, it will yield $\Delta\phi_\pi$, which varies only between 0 and π. The phase unwrapping process then involves a transformation of $\Delta\phi_\pi$ to $\Delta\phi$. This unwrapping process is complicated by the ambiguity in determining whether the phase is increasing or decreasing. However, it was correctly recognized that maxima and minima locations in the $\Delta\phi$ distribution will cause inflections in the $\cos(\Delta\phi)$ profile and in the corresponding $\Delta\phi_\pi$ profile. The experimentally obtained $\cos(\Delta\phi)$ profile showing the presence of an inflection near the vicinity of the droplet surface is presented in Fig. 5. As discussed earlier, the data presented in this figure correspond to the horizontal line defined by $z = 250$ in Fig. 3. Furthermore, because of radial symmetry, only one-half of the $\cos(\Delta\phi)$ variation has been shown. The inflection shown in Fig. 5 could either represent a minimum or a maximum in the $\Delta\phi$ variation. This issue was clarified using a theoretical simulation to compute $\Delta\phi$ and $\Delta\phi_\pi$ variations for an assumed radial temperature distribution. The theoretical simulations clearly demonstrated the existence of an inflection in the $\Delta\phi_\pi$ variation corresponding to a minimum in the $\Delta\phi$ variation. Based on this information, the experimentally obtained $\cos(\Delta\phi)$ variation presented in Fig. 5 was unwrapped to obtain the experimental $\Delta\phi$ variation, which is presented in Fig. 6.

Assuming refraction effects to be negligible, the $\Delta\phi$ variation presented in Fig. 6 can be mathematically represented as follows:

$$\Delta\phi(x) = \frac{2\pi}{\lambda}\int_{y_1}^{y_2} [n(x,y) - n_{\text{ref}}]\, dy \tag{2}$$

where λ is the wavelength of light, $n(x,y)$ is the refractive index of the gas phase, n_{ref} is the ambient refractive index of the gas phase, and y is the path of object beam through the axisymmetric density field. Assuming radial symmetry, Eq. (2) can be expressed as

$$\Delta\phi(x) = \frac{4\pi}{\lambda}\int_{r=x}^{r=R} \frac{[n(r) - n_{\text{ref}}]r\, dr}{\sqrt{r^2 - x^2}} \tag{3}$$

where R is the radius at which point the temperature reaches the ambient temperature. Furthermore, the Abel transformation can be used to obtain the following expression for describing the radial variation of the refractive index, $n(r)$:

$$n(r) = n_{\text{ref}} - \frac{\lambda}{2\pi^2}\int_{x=r}^{x=R} \frac{\Delta\phi'(x)dx}{\sqrt{x^2 - r^2}}. \tag{4}$$

The radial variation of the gas-phase density $\rho(r)$ can then be expressed as

$$\rho(r) = \frac{m}{N}\left[\frac{n^2(r) - 1}{n^2(r) + 1}\right] \tag{5}$$

where m is the molecular mass of the gas phase and N is the Lorentz–Lorenz molar refractivity of the medium. Both these quantities are of course dependent upon the composition of the gas phase. Since the spatial variation of the gas composition is not immediately available for the case of the burning droplet, as a first approximation, the assumption of constant gas composition was made. Having determined the gas-phase density variation, the radial temperature variation can be determined from the gas law

$$T(r) = \frac{pm}{R_u \rho(r)} \tag{6}$$

where p is the pressure and R_u is the universal gas constant.

For increased spatial resolution, the size of the interferogram imaged on the TV camera was restricted to an area approximately $15 \times 15\ d$, where d is the droplet diameter. However, earlier studies [7] show that it is reasonable to expect that the gas-phase temperature will reach the ambient temperature at only about 40 d from the droplet surface. Because of the possibility that only part of the temperature field surrounding the droplet might have been recorded in the interferogram, it was not possible to directly integrate Eq. (4) to obtain the refractive index variation. Hence, a combined experimental/theoretical approach was undertaken to extract the radial temperature distribution of the gas phase surrounding the burning heptane droplet.

The approach undertaken basically involves representing the gas-phase temperature variation by means of the following, rather arbitrarily chosen, five-parameter equation:

$$T(r) = A\left(\frac{r + C}{d}\right) \exp\left[-B\left(\frac{r + C}{d}\right)^E\right] + D. \tag{7}$$

The five parameters can be varied to obtain an assumed temperature distribution. The gas-phase density variation corresponding to this assumed temperature distribution can be obtained from Eq. (6), and Eq. (5) yields the corresponding refractive index variation. Finally, Eq. (3) can be used to compute the theoretical $\Delta\phi$ variation, namely, $\Delta\phi_{\text{theor}}$. Using a trial and error approach, the various parameters in Eq. (7) can be varied till a set of parameters is obtained that yields a droplet surface temperature equal to the measured droplet temperature and very good agreement between $\Delta\phi_{\text{exp}}$ and $\Delta\phi_{\text{theor}}$. Figure 7 presents an assumed radial temperature variation ($A = 47$; $B = 0.0147$; $C = 80$; $D = 305$; $E = 2.22$) that was found to yield good agreement between $\Delta\phi_{\text{exp}}$ and $\Delta\phi_{\text{theor}}$, see Fig. 8.

The radial temperature profile presented in Fig. 7 shows that the maximum temperature is achieved at a radial distance of about 5 d from the surface of the burning n-heptane droplet. The maximum gas-phase temperature is about 450 K (cool-flame) with the measured droplet temperature being 318 K. This temperature is comparable to that measured for a single burning raw Paraho shale oil (433 K) by Gupta and Rossi [8].

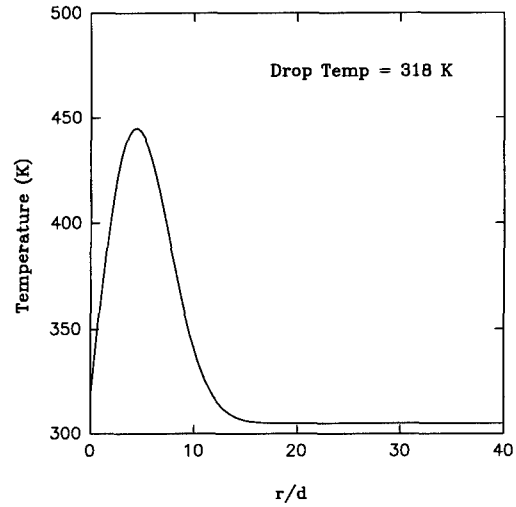

FIG. 7. Assumed radial variation of the gas-phase temperature surrounding the burning n-heptane droplet.

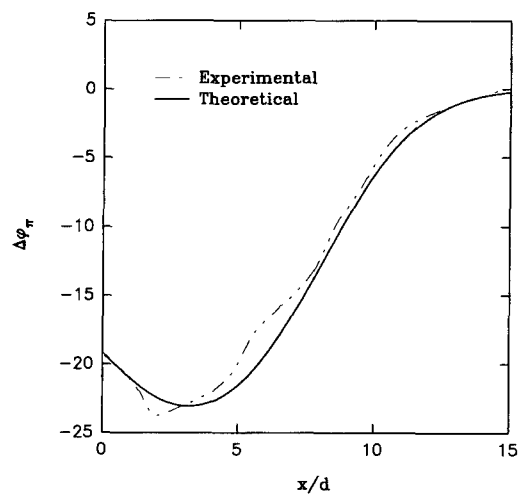

FIG. 8. A comparison of the agreement between the theoretical and experimental phase ($\Delta\phi$) profiles.

Conclusions

The newly integrated diagnostics appears to be an excellent tool for characterizing burning droplets in controlled single droplet/droplet array combustion

experiments. The ability to simultaneously measure the instantaneous droplet velocity, droplet size, droplet temperature, and the gas-phase temperature field will allow for the experimental study of droplet heating, droplet vaporization, and heat transfer to the droplets. As such, the integrated diagnostics can be used to validate state-of-the-art droplet combustion models. Though only the radial temperature profile from the droplet surface was extracted in this study, the procedure discussed herein can be used to completely extract the 3D axisymmetric temperature field surrounding the burning droplet. In situations where the flow field is not axisymmetric, it is possible to validate the theoretical models by using the temperature profiles predicted by the model to compute a theoretical interferogram and then comparing it with an experimentally obtained interferogram.

Acknowledgment

The authors are grateful to the National Science Foundation for supporting this work under Grant No. III-9261296.

REFERENCES

1. Law, C. K., *Prog. Energy Combust. Sci.* 8:171–201 (1982).
2. Faeth, G. M., *Prog. Energy Combust. Sci.* 9:1–76 (1983).
3. Sirignano, W. A., *Prog. Energy Combust. Sci.* 9:291–322 (1983).
4. Haywood, R. J., Nafziger, R., and Renksizbulut, M., *J. Heat Trans.* 111:495–502 (1989).
5. Megaridis, C. M., and Sirignano, W. A., *Twenty-Third Symposium (International) on Combustion,* The Combustion Institute, Pittsburgh, 1990, pp. 1413–1421.
6. Chiang, C. H., Raju, M. S., and Sirignano, W. A., *Twenty-Seventh Aerospace Sciences Meeting,* Reno, Nevada, AIAA-89–0834, 1989.
7. Zhu, J. Y., Dunn-Rankin, D., *Appl. Optics* 30:2672–2674 (1991).
8. Gupta, A. K., and Rossi, I., *Eighteenth Aerospace Sciences Meeting,* Reno, Nevada, AIAA-80-0349, 1980.
9. Bachalo, W. D., Brena de la Rosa, A., and Sankar, S. V., in *Combustion Measurements* (N. Chigier, Ed.), Hemisphere Publishing Co., New York, 1991, p. 229.
10. Roth, N., Anders, K., and Frohn, A., *J. Laser Applications* Jan./Feb.:37–42 (1990).
11. Sankar, S. V., Ibrahim, K. M., Buermann, D. H., Fidrich, M. J., and Bachalo, W. D., *3rd Intl. Congress on Optical Particle Sizing,* Yokohama, Japan, 1993.
12. Schneider M., Hirleman, E. D., Saleheen, H., Chowdhury, D. Q., and Hill, S. C., *3rd Intl. Congress on Optical Particle Sizing,* Yokohama, Japan, 1993.
13. Smartt, R. N., and Steel, W. H., *J. Appl. Phys.* 14 (Suppl. 14-1):351–356 (1975).

COMMENTS

Rudolf Maly, Daimler-Benz AG, Germany. Could you please comment on the applicability of the rainbow technique to practical sprays with droplet distributions centered around 20 μm. Did you apply your technique to such sprays, and what are the results for turbulent sprays where the droplets may be nonspherical and/or have oscillating surfaces?

Author's Reply. Rainbow refractometry/thermometry is applicable to sprays. However, for such applications, it is essential that we simultaneously measure the size of the droplet as the rainbow location is also a function of droplet size for droplets less than about 150 μm in diameter. At present, we estimate the minimum droplet diameter for which rainbow refractometry can be applied to be about 20 μm. With some improvements to the optics and signal processing scheme, this may be lowered to about 10 μm. Beyond this size limit, the technique is inherently limited by the physics of light scattering. We have fully integrated a rainbow thermometer with a phase-Doppler interferometer and have applied this integrated diagnostics for successfully measuring the size, velocity, and temperature of individual fuel droplets in a swirl-stabilized spray flame where the mean droplet diameters were about 40 μm. The rainbow pattern appears to be very sensitive to particle shape, and therefore, nonspherical particles may not give rise to a distinct rainbow pattern. We have studied this effect using controlled experiments but are unable to comment on the presence of nonspherical and/or oscillating droplets in the spray flame that we have studied.

•

V. A. Bossard, Arizona State University, USA. Have you made measurements of the rainbow angle from nonhomogeneous droplet temperature profiles (and hence index of refraction profiles)? And is the temperature profile a unique function of the rainbow angle?

Author's Reply. We have performed measurements with burning droplets generated by a drop-on-demand generator. At points very close to the ignition source, we have observed a rainbow behavior that is very similar to theoretical predictions for droplets exhibiting inhomogeneous temperature profiles. We are currently addressing the reverse problem, namely extracting temperature profiles from the rainbow characteristics, and at this time are unable to comment on the uniqueness of this solution.

•

Dieter Bruggemann, ITLR/University of Stuttgart, Germany. Your instrument is certainly very interesting. Concerning droplet thermometry, have you thought about a direct comparison of the rainbow method and the exciplex fluorescence thermometry?

Author's Reply. Yes, in the future we would like to compare the results of rainbow thermometry with those available in the literature for exciplex thermometry and CARS thermometry.

Twenty-Fifth Symposium (International) on Combustion/The Combustion Institute, 1994/pp. 423–430

THE EFFECT OF INITIAL DIAMETER ON FREE DROPLET COMBUSTION WITH SPHERICAL FLAME

H. HARA AND S. KUMAGAI
Research Laboratory
Noritz Corporation
728–8, Ishikawa-cho, Hachioji, Tokyo 192, Japan

Two kinds of experiment have been conducted to study the effect of the initial droplet diameter on the burning behavior of a single free droplet with a spherical flame. One is performed under microgravity, which is realized in a freely falling chamber to establish a spherical flame around a large droplet of about 400-μm initial diameter. The other is to investigate the combustion of small droplet under normal gravity, whose initial diameter is about 70 μm. The small droplet is injected up vertically and ignited by an electric spark after passing through the apex of its trajectory. Even under normal gravity, for such a small droplet, a spherical flame can be observed through the image intensifier. In this study, the fuel used is *n*-heptane as sooting fuel.

The time dependence of the squared droplet diameter is categorized into two types with the initial droplet diameter. (1) The so-called d^2 law is established for the entire period of burning, except for the initial period, where the droplet diameter is not changed markedly. This type can be observed for large droplets in the microgravity experiment. (2) The evaporation constant decreases at the later period of burning after the d^2 law is held. This type can be observed for small droplets in the experiment under normal gravity. It is recognized that extinction occurs around the time when the evaporation constant begins to decrease.

Soot formation tends to be enhanced as the initial droplet diameter is increased, and the no-soot formation can be observed for a small droplet of about 70-μm initial diameter.

Introduction

Combustion of a single fuel droplet has been investigated for about 4 decades to obtain fundamental information on the fuel spray combustion. To approach the real configuration of a droplet that is encountered in the spray combustion, the first experiment [1] for free droplet combustion was conducted under microgravity about 25 years ago, and a series of studies [2–7] on the theme has been continued by some researchers of different nations. Currently, the behavior of droplet combustion has been explored for the entire period of burning, and some new fundamental features on droplet combustion have been verified.

However, it was not sufficient to simulate the real droplet combustion, because there still remained a difference between sizes of droplets; i.e., the initial droplet diameter used in the previous experiments is about 1 mm, which is 10–100 times larger than that in a spray. It is reasonable to expect that the droplet size affects the behavior of droplet combustion; namely, there exists the dependence of droplet combustion on its initial diameter. From the theoretical aspect, extinction of a burning droplet is predicted on the basis of the reduced Damköhler number, which is affected by the droplet diameter [8]. The burning behavior of droplets smaller than about 400 μm in initial diameter has not yet been elucidated, probably by reason of experimental difficulty. Thus, the combustion of a smaller droplet should be examined to elaborate the burning characteristics of the real-sized droplet in a spray combustion, including the effect of initial droplet diameter on its burning behavior.

In the present study, to investigate the burning behavior of a free droplet, about 70 and 400 μm in initial diameter with spherical flame, two kinds of experiment have been conducted. One is performed under microgravity using large droplets of about 400-μm initial diameter. The other is to investigate the combustion of small droplets under normal gravity, whose initial diameter is about 70 μm. In the latter, different values of spark energy are used to examine its effect on the burning behavior.

Experimental Apparatus and Procedure

All experiments are conducted with *n*-heptane at room temperature (298 K) and atmospheric pressure (0.101 MPa). The explanations about two kinds of

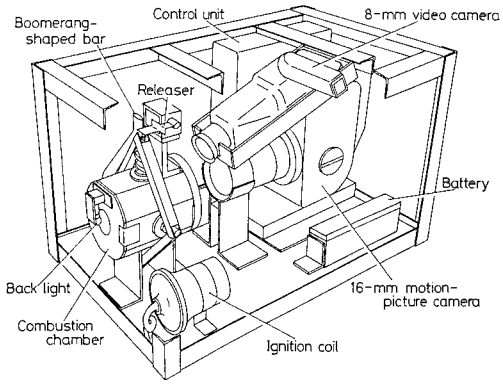

FIG. 1. Falling assembly.

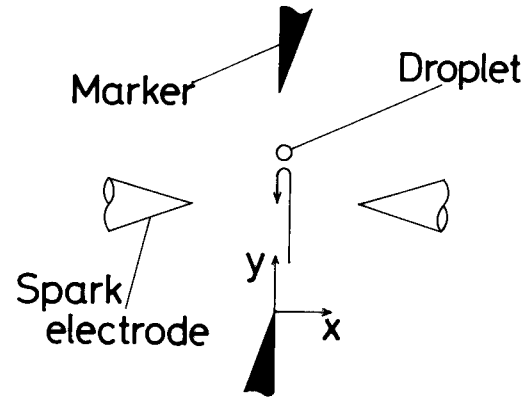

FIG. 2. Schematic diagram of droplet trajectory.

experiment mentioned above are described separately.

Experiment under Microgravity for Large Droplet Combustion:

Details of experimental apparatus and procedures have been described in the previous paper [5]. The microgravity condition is realized in a freely falling chamber. The falling assembly, 370 × 560 × 340 mm and 25 kg, contains a combustion chamber, an 8-mm video camera, a 16-mm motion-picture camera, and a control unit, as shown in Fig. 1. The video camera is slanted down at an angle of 20° for monitoring and adjustment. By adjusting the backlight lamp, photographs of both droplet and flame can be taken simultaneously.

Experiment under Normal Gravity for Small Droplet Combustion:

A method to produce a small droplet (less than 100 μm in diameter) is originated by using a technique developed for the jet printer. A droplet is injected from the tip of a convergent nozzle located at the top of a fuel tank when the pressure inside the nozzle is elevated instantaneously. This is performed by applying an electric pulse to a piezoelectric transducer, which is installed at the bottom of the fuel tank. By using this apparatus, it is possible to produce a droplet at an optional position and time.

The small droplet is injected up vertically and ignited by an electric spark after passing through the apex of its trajectory. Ignition timing is controlled so as to balance the downward momentum of droplet with the spark disturbance. The trajectory of a small droplet is shown schematically in Fig. 2. Because the droplet trajectory is very sensitive to the wet condition on the nozzle tip, an arbitrary injection makes the trajectory changed from the appropriate one. Therefore, the droplet is injected at a frequency of 1 Hz to maintain almost the same wet condition on the nozzle tip. Any one droplet seems to be influenced considerably by neither the preceding nor the following, since the burning duration is as short as about 10 ms.

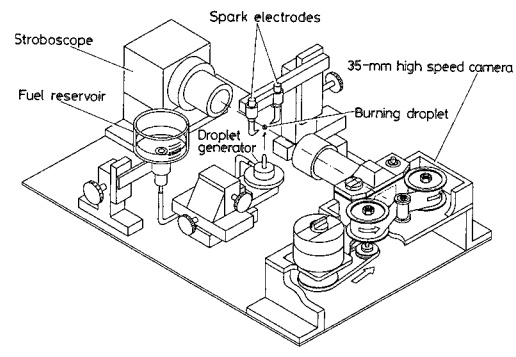

FIG. 3. Experimental setup for small droplet combustion.

By using a 35-mm high-speed camera (1000 frames/s), silhouette images of droplets and their positions are taken with a stroboscopic backlight.

The experimental setup is shown in Fig. 3. Generation of the droplet, initiation of the spark, and opening of the camera shutter are adjustable at intervals of 1 ms with a sequence controller.

Results and Discussion

Sequential photographs of burning droplets are shown in Fig. 4 for the data on microgravity experiments and in Fig. 5 for the data on normal gravity experiments, respectively. In Fig. 4 (d_0 = 380 μm), it cannot be observed that any soot shell [5] is formed. In this case, the light emission due to hot soot particles can be observed only at the early and

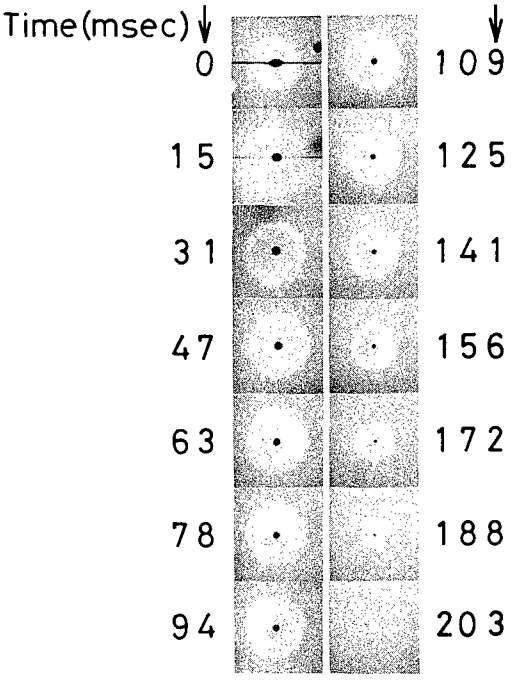

FIG. 4. Sequential photographs of burning droplet (d_0 = 380 μm).

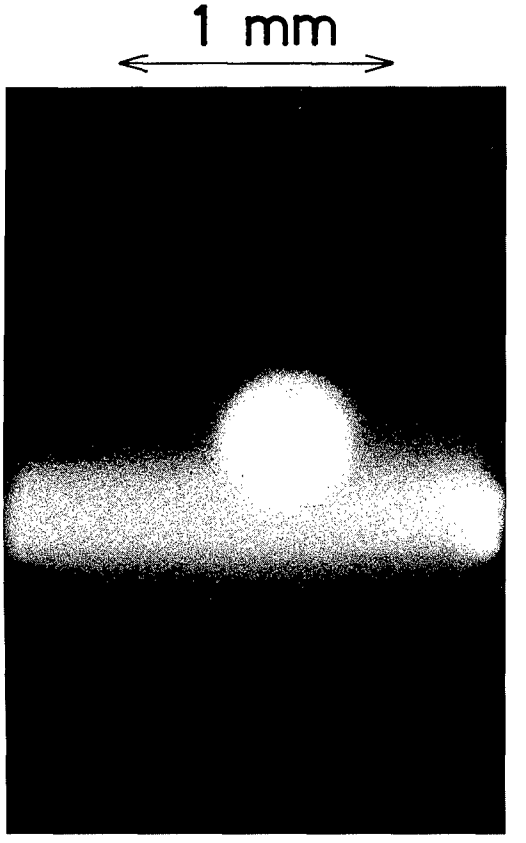

FIG. 6. Photograph of spherical flame for small droplet burning.

middle period of burning, and at the final period of burning, the visible flame is a blue and not a bright yellow flame, corresponding to soot formation. This result is ascertained from observation by the 8-mm video camera. Jackson and coworkers [11,12] have shown the results on the formation of soot shell with a free droplet, whose initial diameter is 440 μm at least. As mentioned above, in this experiment, the formation of soot shell cannot be observed with the initial droplet diameters (370, 380, and 400 μm), which are a little less than those used in Refs. 11 and 12. In Fig. 5, on small droplet combustion, there is no soot formation, and consequently, a blue flame of weak emission is established. The backlight, which is enough to expose for a burning droplet, obscures the image of its flame. Thus, the droplet image alone is observed in this experiment. In this picture, a pair of vertical dark objects shows the tips of camera markers, and the dark circle indicates the droplet. The image of the flame, as taken through an image intensifier, is shown in Fig. 6. In this picture, the bright circle and the horizontal column indicate the flame

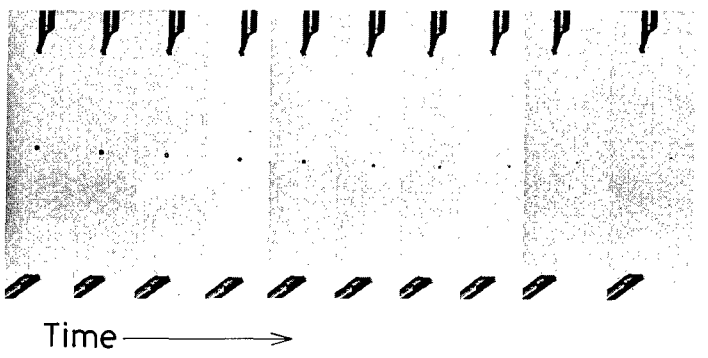

FIG. 5. Sequential photographs of burning droplet (d_0 = 70.4 μm, time interval = 1 ms).

and the ignition spark, respectively. Consequently, for such a small droplet, the flame shape is almost spherical, even under normal gravity and even at the instance of ignition when it is expected that the droplet experiences a strong disturbance from the spark. This fact leads to expectation that the spherical flame can be maintained throughout the burning time, and natural- and forced-convection effects are too small to distort the flame shape from spherical.

The initial droplet diameter d_0 is defined as that measured in the frame just before a droplet begins to decrease in diameter.

Burn-Out and Extinction:

Values of the square of droplet diameter d^2, flame diameter D, and flame/droplet diameter ratio D/d against time, t, are plotted in Fig. 7 for the large droplet in the microgravity experiment. Observed values of $d^2(t)$, the droplet trajectory $[x(t),y(t)]$, and the droplet velocity $[v_x(t),v_y(t),v(t)]$ in laboratory coordinates are shown in Figs. 8 and 9 for the small droplet in the normal gravity experiment.

From the results, the time dependence of d^2 is categorized into two types with the initial droplet diameter d_0. (1) The so-called d^2 law is established for the entire period of burning, except for the initial period where the droplet diameter is not changed markedly, as shown in Fig. 7. This type can be observed as burnout for large droplets that are examined in the microgravity experiment. (2) The evaporation constant decreases at the later period of burning after the d^2 law is retained, as shown in Figs. 8 and 9. It is recognized that extinction occurs around the time when the value of the evaporation constant decreases. In this study, the extinction diameter d_e is defined as the droplet diameter just after deviation from the $d^2 - t$ linear relationship. This type can be observed for small droplets in the normal gravity experiment. In Figs. 8 and 9, it can be recognized that the droplet diameter continues to decrease gradually with a low evaporation constant after extinction. This fact suggests that postevaporation occurs in the hot ambience, which is caused by the heat liberation from a burning droplet before extinction.

For the large droplet, the value of D/d increases at the early period of burning, and then, after passing through an inflection point, it continues to increase toward infinity. This tendency is inconsistent with the result derived from the quasisteady theory, which shows that the value of D/d keeps constant for the entire period of burning.

Extinction in the droplet burning is expected theoretically [8,9] and numerically on the basis of the reduced Damköhler number and can be experimentally observed at the later stage of burning for the small droplets in the normal gravity experiment.

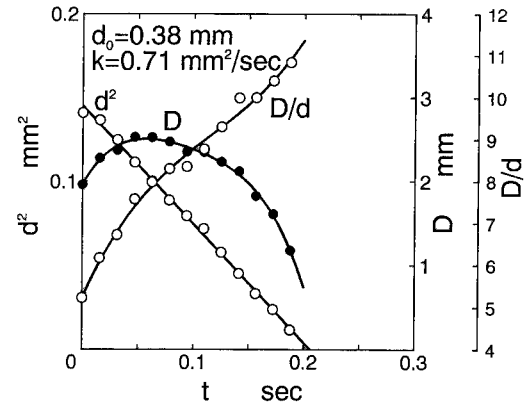

FIG. 7. Flame diameter D, squared droplet diameter d^2, and flame/droplet diameter ratio D/d vs time t.

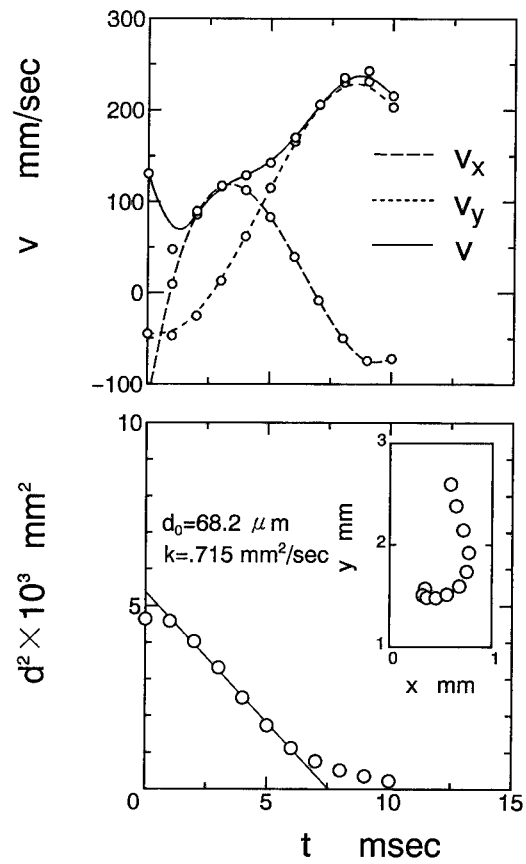

FIG. 8. Trajectory of a burning droplet, squared droplet diameter d^2, and droplet velocity in laboratory coordinates (v_x,v_y,v) vs time t (spark energy = 3 μJ).

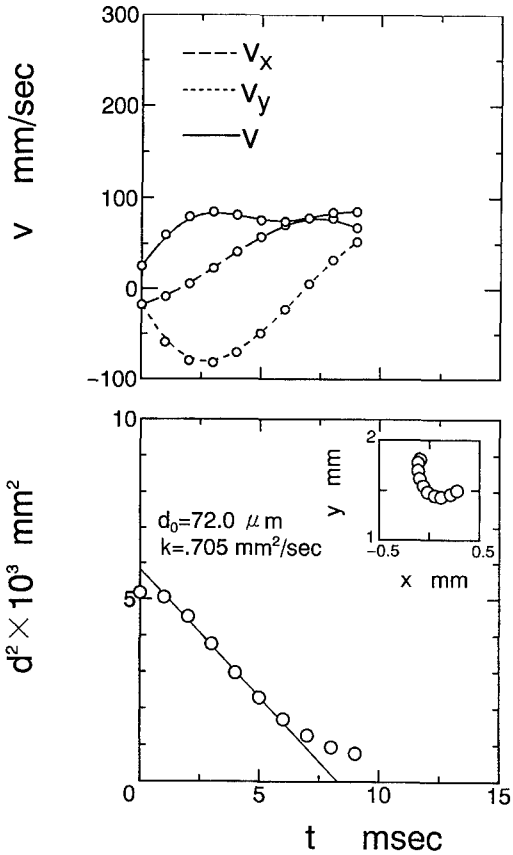

FIG. 9. Trajectory of a burning droplet, squared droplet diameter d^2, and droplet velocity in laboratory coordinates (v_x, v_y, v) vs time t (spark energy = 1.9 μJ).

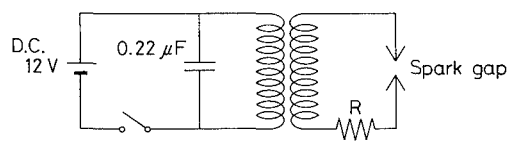

FIG. 10. Electrical circuit to produce composite spark.

Effect of Spark Energy on Small Droplet Combustion:

Figure 10 shows the simple electrical circuit to produce the composite spark. The spark energy is varied by using the resistance R of 100 and 150 $k\Omega$, and measured values (for the inductance component) are only 3.0 and 1.9 μJ, respectively. The fraction of the spark energy to the total enthalpy of the droplet (d_0 = 70 μm) is about 0.1%, so the effect of the spark energy heating up the ambience is expected to be negligible, as compared with the heat liberation from a burning droplet. Although one would wonder whether a droplet can be ignited by a spark energy

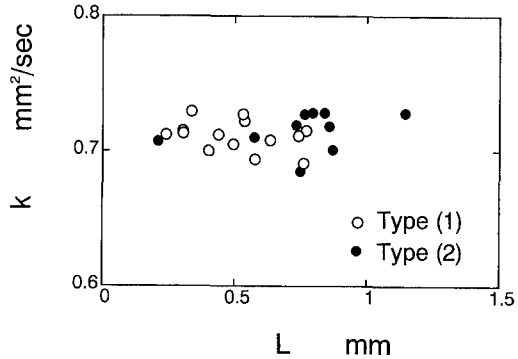

FIG. 11. Evaporation constant k vs mean distance L between droplet and spark column.

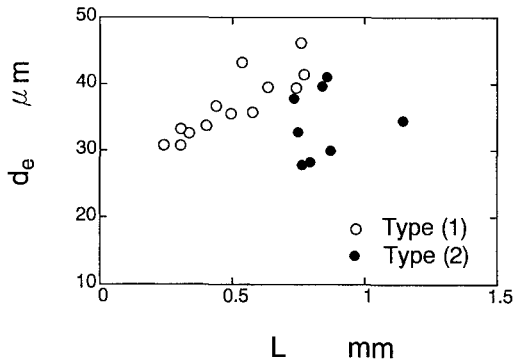

FIG. 12. Extinction diameter d_e vs mean distance L between droplet and spark column.

much smaller than the minimum ignition energy of a gas mixture, it is an experimental fact that ignition is possible for such a small droplet. In this study, the ignition behavior is different from that in the case of obtaining the minimum ignition energy of a gas mixture, which can establish the flame propagation after the flame kernel is created.

Figure 11 shows the evaporation constant k against L, which is the mean distance from the spark column to the droplet center during burning, and types 1 and 2 express data with the spark energy of about 1.9 and 3 μJ, respectively. From this figure, it can be recognized that there is no correlation between k and L for both energies, and therefore, there is not a significant effect of the ambience heating on the evaporation constant. However, d_e is increased with increasing L and smaller with larger spark energy at a constant L, as shown in Fig. 12. From the droplet trajectories in Figs. 8 and 9, it can be expected that there is some air flow induced by the spark [10], which is enhanced with increasing spark energy, and that the relative motion of ambient air to the droplet is increased with decreasing L. This fact suggests that

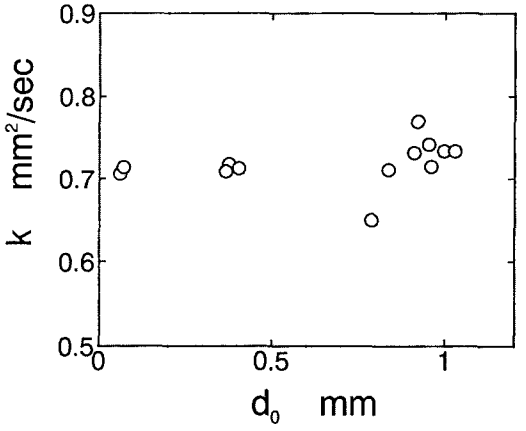

FIG. 13. Evaporation constant k vs initial droplet diameter d_0.

forced convection affects the extinction diameter; namely, it makes the burning time until extinction longer, even though it is small enough not to influence k considerably. As mentioned above, in this experiment, the droplet velocity in laboratory coordinates is not equivalent to the real relative velocity to ambient air, because the air flow is created by the ignition spark with the capacitance component. Unfortunately, it is difficult to measure the relative velocity of ambient air directly, so its estimation is limited to the qualitative consideration. The quantitative measurement of relative air velocity and observation of sequential flame images are future problems to investigate.

Evaporation Constant:

Figure 13 shows the dependence of evaporation constant k on initial droplet diameter d_0 together with data for droplets around 1 mm in initial diameter from the previous work [5]. Each point for d_0 from 60 to 70 μm corresponds to an averaged value for each 10-μm interval. From Fig. 13, it seems that k tends to increase slightly, if at all, with increasing d_0, in contrast with the recent data by Jackson and coworkers [11,12], which show a decreasing tendency of evaporation constant with increasing initial diameter. This fact is also inconsistent with the result from the simplest quasi-steady theory and indicates a possibility that some unsteady nature plays an important role in the droplet combustion.

Conclusions

To elucidate the effect of the initial diameter on the burning behavior of n-heptane droplet, two kinds of experiments were conducted at room temperature and atmospheric pressure. The main results are summarized below.

1. The time dependence of d^2 is categorized into two types, which depends on the initial droplet diameter: (a) the $d^2 - t$ linear relationship is established for the entire period of burning for the large droplet; (b) the value of k decreases after the d^2 law is retained for the small droplet, i.e., extinction occurs.
2. Burnout can be observed for the large droplet examined in the microgravity experiment, and extinction can be observed for the small droplet examined in the normal gravity experiment.
3. With decreasing d_0, the value of k decreases slightly, if at all.
4. Soot formation tends to be enhanced as the initial droplet diameter is increased, and no soot formation can be observed for a small droplet of about 70 μm in initial diameter.
5. Some unsteady nature plays an important role for the droplet combustion of n-heptane.

REFERENCES

1. Kumagai, S., Sakai, T., and Okajima, S., *Thirteenth Symposium (International) on Combustion,* The Combustion Institute, Pittsburgh, 1971, pp. 779–785.
2. Okajima, S., and Kumagai, S., *Fifteenth Symposium (International) on Combustion,* The Combustion Institute, Pittsburgh, 1975, pp. 401–407.
3. Shaw, B. D., Dryer, F. L., Williams, F. A., and Haggard, J. B., *Acta Astronaut.,* 17:1195–1202 (1988).
4. Hara, H., and Kumagai, S., *Progress in Astronautics and Aeronautics,* AIAA, Inc., New York, 1989, Vol. 132, pp. 139–149.
5. Hara, H., and Kumagai, S., *Twenty-Third Symposium (International) on Combustion,* The Combustion Institute, Pittsburgh, 1990, pp. 1605–1610.
6. Yang, J. C., Jackson, G. S., and Avedisian, C. T., *Twenty-Third Symposium (International) on Combustion,* The Combustion Institute, Pittsburgh, 1990, pp. 1619–1625.
7. Cho, M. Y., and Dryer, F. L., *Twenty-Third Symposium (International) on Combustion,* The Combustion Institute, Pittsburgh, 1990, pp. 1597–1604.
8. Law, C. K., *Combust. Flame* 24:89–98 (1975).
9. Niioka, T., Hasegawa, S., Tsukamoto, T., and Sato, J., *Combust. Flame* 86:171–178 (1991).
10. Shaw, B. D., Dryer, F. L., and Williams, F. A., and Gat, N., *Combust. Flame* 74:233–254 (1988).
11. Jackson, G. S., Avedisian, C. T., and Yang, J. C., *Int. J. Heat Mass Trans.* 35:2017–2033 (1992).
12. Jackson, G. S., and Avedisian, C. T., Paper AIAA-93–013, 31st Aerospace Sciences Meeting, Reno, NV, Jan. 1993.

COMMENTS

C. T. Avedisian, Cornell University, USA. 1. What spark duration did you use to ignite the heptane droplets and how did it compare with the droplet burning time? In Ref. 12 cited in your paper [1], the spark duration was less than 0.1% of the total burning time for the heptane droplet sizes studied, and ignition was by two sparks generated across (radially) retractable electrodes that were placed on opposite sides of the droplet to reduce effects of initial conditions [2,3] on burning.

2. You note differences in sooting on d_0, and Fig. 13 shows no definite trend of K with d_0. Previous work suggests that soot formation may affect droplet burning rates for near spherically symmetric burning conditions [1]. Are there any aspects of your experimental design and procedures that could neutralize the effects of soot, or influence soot formation and the development of a soot shell, on the droplet burning process?

3. Could you comment on the accuracy and repeatability of the data you report (extinction, soot shell and flame diameters, and burning rates)? Flame diameters, in particular, can be difficult to measure accurately because the flame boundary is usually not as well defined as the droplet boundary. Burning rates require differentiating the variation of droplet diameter (squared) with time, which can further magnify uncertainties in K values.

REFERENCES

1. Jackson, G. S., and Avedisian, C. T., *Proc. R. Soc. London A* 446:257 (1994).
2. Choi, M. Y., Dryer, F. L., and Haggard, J. B., *Twenty-Third Symposium (International) on Combustion,* The Combustion Institute, Pittsburgh, 1990, p. 1597.
3. Williams, F. A., *Acta Astronaut.* 12:547 (1985).

Author's Reply. 1. In the experiments of small droplet combustion, the spark durations until 50 and 90% of the total energy released are about 0.7 and 2.0 ms, respectively. These durations cannot be ignored to compare with the droplet lifetime, and such long spark durations may affect the burning behavior. However, the spark energy itself can be considered as a more important factor than its duration to influence the droplet burning, especially the burning constant. The spark energies used in the present study are about 3.0 and 1.9 μJ, and therefore such weak energies do not seem to affect the droplet burning significantly although their durations are not sufficiently short.

2. We consider that there are not any particular aspects as questioned. In our previous study on ethanol as nonsooting fuel, there is the same trend of k with d_0 as n-heptane. This fact suggests that soot formation cannot influence the evaporation constant significantly although ethanol has the character to absorb water vapor. In addition, the factor affecting the droplet burning, especially the evaporation constant, is not only the soot formation but also the unsteadiness of gas phase around the droplet.

3. All measurements of the droplet and flame were made manually with a vernier after their film images were projected onto the screen and magnified about 10–30 times larger than the real sizes. If the droplet images can be taken clearly on the film, even this measuring method can supply accurate values. We consider that the measured values do not have significant errors or problems, because only clear image data were employed for the measurements. The flame diameter was measured on the basis of the outer edge of bright flame for sooting flame and the maximum luminosity for nonsooting flame.

•

Kevin Davis, Sandia National Laboratories, USA. Past work has shown that sooting tendency of a fuel decreases from single droplet experiments [diameter typically ~O(100's μ)] to spray experiments [diameter typically ~O(10's μ)]. Do your results (decreased sooting at smaller diameters) suggest that droplet size plays a minor role in the sooting tendencies of a fuel in practical devices?

Author's Reply. Results of the present study show the tendency of decreasing soot formation with decreasing initial droplet diameter and no soot formation in small droplet burning whose diameter is less than about 70 μm. However, it can not be simply expected that droplet diameter plays a minor role in soot formation in the spray combustion of practical devices, since the present experiments were conducted in the idealized condition. In practical combustion devices, there are many other factors affecting soot formation, namely number density of droplets, aerodynamic influences, local fuel-air ratio, temperature distribution, and so on. These factors related to soot formation in the practical devices seem to play more a important role than the droplet diameter, provided that the droplets used are small enough.

•

Benjamin D. Shaw, University of California, Davis, USA. 1. Your data for small droplets indicate that in addition to buoyant flows, forced convection for nonzero droplet-gas velocities was present. Do you think that these flows may have influenced your results on flame extinction?

2. In your small-droplet experiments, you injected a stream of droplets at a frequency of 1 Hz. Do you expect that the vapor trail associated with this droplet stream affected the ignition, combustion, or extinction of droplets in an appreciable manner?

Author's Reply. 1. From Figs. 6, 11, and 12 in our paper, it can be recognized that, to some degree, forced convection affects the extinction diameter. Convection makes the burning time until extinction longer even though it is small enough not to influence the evaporation constant and the sphericity of the flame configuration. Thus, if the convec-

tive motion is nonexistent, it is reasonable to expect that the extinction diameter is larger than that under the influence of the forced convection. However, we can not discuss the effect of the convection on the extinction quantitatively, since the real relative ambient air velocity to the droplet cannot be measured.

2. Ignitability of a fuel droplet is so sensitive to the vapor condition around it that the vaporized fuel associated with the droplet stream can advance ignition, while a considerable amount of vapor accumulation may be necessary to influence the combustion of droplets. If there remains considerable vapor associated with the droplet stream, it may influence establishment of the spherical flame. However, as shown in Fig. 6, the spherical flame can be observed at the moment of ignition, and its sequential images were also shown in our presentation. These facts suggest that there is not enough vapor accumulation around the droplet before ignition to affect the droplet burning itself.

Twenty-Fifth Symposium (International) on Combustion/The Combustion Institute, 1994/pp. 431–438

INTERACTIVE COMBUSTION OF TWO DROPLETS IN MICROGRAVITY

M. MIKAMI AND H. KATO
The University of Tokyo
Hongo, Bunkyo-ku
Tokyo 113, Japan

J. SATO
Ishikawajima-Harima Heavy Industries Co., Ltd.
Toyosu, Koto-ku
Tokyo 135, Japan

AND

M. KONO
The University of Tokyo
Hongo, Bunkyo-ku
Tokyo 113, Japan

Interaction between two burning fuel droplets have been studied experimentally for a wide range of initial separation distance between two droplets. Experiments were performed in microgravity. Results show that for an initial separation distance within a certain range, the transition from two separated flames to a merged flame occurs initially, and then the contrary mode transition occurs due to the gas-phase unsteadiness. The burning lifetime has a minimum for a certain initial separation distance. In order to explore instantaneous interaction effects, the instantaneous burning rate correction parameter is introduced. The correction parameter includes effects of the liquid-phase unsteadiness on $d^2 - t$ curves, both of the droplet in array and the single droplet, and is a function of the normalized droplet diameter. When the instantaneous burning rate correction parameter is positive, positive interaction occurs, which causes the burning rate larger than that of the single droplet. When the initial separation distance is larger than a certain value, in the earlier stage of combustion, the positive interaction occurs due to radiative heat transferred from the other flame, and in the later stage, the negative interaction occurs due to oxygen starvation between the flames. When the initial separation distance is smaller than the value, the negative interaction occurs for an entire period of combustion. The initial separation distance at which the burning lifetime has a minimum is almost consistent with that at which the positive interaction is a maximum in the earlier stage.

Introduction

In spray combustion, droplets burn interactively, and the combustion mechanism is different from that of the single droplet due to interaction between the droplets. Droplet array combustion has been studied experimentally [1–6] and theoretically [7–10] to understand the interaction from a microscopic viewpoint. It is important to use the basic and the simplest configuration, that is, two droplets, in order to improve understanding of the multiple-droplet combustion mechanism.

Theoretically, there are some methods for solving the problem based on the quasi-steady analysis [7–10]. They extend the quasi-steady analysis for the single-droplet combustion [11] to that for two-droplet combustion. This is applicable to microgravity combustion better than normal gravity combustion because gravity effects are not considered in the analysis. In order to compare experimental results with the predictions, experiments in microgravity are required.

Experimentally, there exist some experiments on two-droplet combustion. However, they have been performed in normal gravity, except for the experiment by Brzustowski et al. [7]. In the microgravity experiment by Brzustowski et al., the burning behavior was not examined in detail. Rex et al. [1] and Konishi et al. [6] obtained burning rate constant of two droplets from the $d^2 - t$ plot and showed the dependence of the burning rate constant on the initial droplet configuration in normal gravity. Since the burning rate is not actually constant, Miyasaka and Law [4] introduced the burning rate correction parameter:

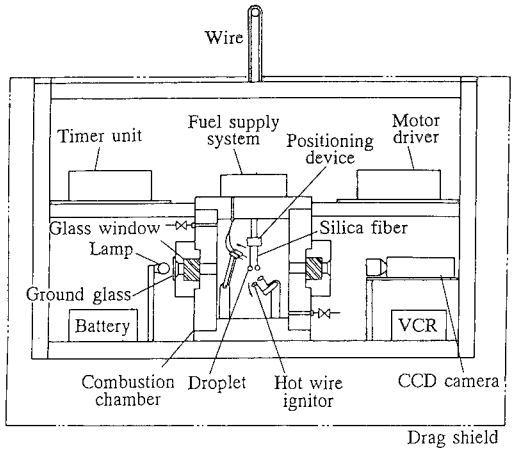

FIG. 1. Schematic diagram of the experimental apparatus.

$$\eta(t) = K(t)/K_{S0} \tag{1}$$

where $K(t)$ is the instantaneous burning rate of the droplets in array and K_{S0} is the burning rate constant of the single droplet. Miyasaka and Law [4] and Xiong et al. [5] examined the dependence of $K(t)$ and $\eta(t)$ in low pressures and normal gravity on the instantaneous separation distance. They concluded that the droplet heating was retarded due to the interaction. However, the burning rate of the single droplet is not constant [12]. The above approach in which the burning rate of the single droplet was treated as a constant is not appropriate for estimating the real interaction effects, which includes the liquid-phase unsteady effects on $d^2 - t$ curves, both of the droplet in array and of the single droplet.

In order to include the liquid-phase unsteady effects on $d^2 - t$ curves in the burning rate correction parameter, we introduce an instantaneous burning rate correction parameter:

$$\varepsilon(d/d_0) = K(d/d_0)/K_S(d/d_0) - 1 \tag{2}$$

where $K(d/d_0)$ is the instantaneous burning rate of the droplet in array and $K_S(d/d_0)$ is the instantaneous burning rate of the single droplet for the same normalized droplet diameter (d/d_0). If $\varepsilon(d/d_0)$ is given, $K(d/d_0)$ is easily inferred from Eq. (2).

In the present study, experiments in microgravity have been performed on the burning of two suspended droplets of equal size and of the same fuel in atmospheric pressure air for a wide range of the initial separation distance. Normal gravity experiments have also been performed to compare with the microgravity experiment. Results are compared with the quasi-steady theory. The instantaneous burning rate correction parameter is introduced and interaction effects on the instantaneous burning rate are discussed.

Experimental Apparatus and Procedure

Figure 1 schematically shows the experimental apparatus. The combustion chamber is a closed aluminum cylinder with a capacity of 2×10^6 mm^3. Fuel (n-heptane) is automatically fed on to the tips of two silica fibers in the chamber through two hypodermic needles from a stepping motor-driven syringe. Almost identical, two droplets aligned horizontally were dispensed in air at atmospheric pressure and initially 295 ± 1 K at the same time (the ratio of the diameter of the smaller droplet to that of the larger one was within the range from 0.97 to 1.0). Then they were ignited by two hot wires at the same time. Each hot wire, formed into a loop, surrounded each droplet and was removed from the droplet immediately after ignition. For the case of microgravity combustion experiments, the droplets were ignited in microgravity about 2 s after dispensing them in normal gravity. Two seconds are very short in comparison with the evaporation lifetime of the n-heptane droplet at room temperature. So, prevaporization before ignition would be negligible in these experiments. Microgravity conditions were attained by dropping the apparatus with a drag shield in the drop tower at the University of Tokyo, which provides about 1.4-s microgravity conditions (less than 10^{-4} times that of normal gravity).

Two orthogonal views of the combustion process were taken by two charge coupled device (CCD) cameras, respectively, through the windows of the chamber. One view is a back illumination to visualize the droplet and the other view shows a direct photograph of the flame. The video images were taken into a computer memory, and then characteristic lengths of the digitized images were measured on the screen.

The well-known suspended droplet technique was adopted so that the distance between the droplet centers (l) could be kept constant for the entire period of combustion. The constant l was required in order to compare experimental results with existing theory. If we adopted a free droplet technique, the distance (l) would no longer be constant because it is rare to realize a burning free droplet without drift velocity [12], and the velocity varies with time [13]. The distance (l) was varied from 3.2 to 14.0 mm. Single droplet combustion experiments were also performed to compare with the results of two droplets. The suspending fiber diameter and its tip sphere diameter were 0.125 and 0.22 mm, respectively. The initial droplet diameter (d_0) was 0.81 ± 0.03 mm for microgravity experiments and 0.9 ± 0.1 mm for normal gravity experiments. The droplet was nearly elliptical in shape due to the existence of the fiber in-

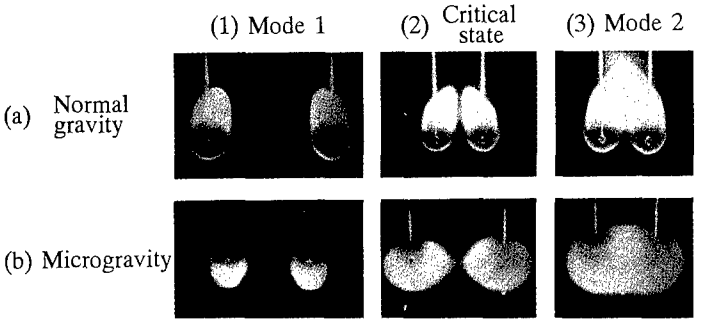

FIG. 2. Direct photographs of the flame for different flame shape modes.

side, and thus, an equivalent spherical droplet diameter was used as the droplet diameter. The equivalent diameter was calculated as the cubic root of the product of the major diameter with the squared minor diameter [14].

Results

Flame Shape Mode:

Flames surrounding two droplets were observed from the direction perpendicular to the droplet centerline by a color CCD camera. The blue flame was observed initially, but for almost the entire period, the yellow luminous flame was observed, because the luminosity from the yellow luminous flame prevented the blue flame from being visualized. The word "flame" represents the yellow luminous flame in the present paper. The flame shapes are classified roughly into two modes (Fig. 2): individual flames surrounding each droplet (Mode 1) and one merged flame surrounding two droplets (Mode 2) [7–9]. Figure 2 (column 2) shows the critical state in which two flames touch each other. The flame shapes in microgravity (Fig. 2 (row b)) are qualitatively in good agreement with the theoretical predictions by quasi-steady analysis [7–9].

Figure 3 shows temporal variations of the flame dimensions in microgravity for an initial separation distance (l/d_0) of 10.7, where l/d_0 is the ratio of the distance between the droplets to the initial droplet diameter. Symbols are defined in the figure. Here, S denotes the degree of the flame separation and C the degree of the flame mergedness. When S is positive ($C = 0$), the flame shape is in Mode 1. When S is equal to 0 ($C > 0$), the flame shape is in Mode 2. As the flame diameter (D_v and D_h) increases, two flames approach each other, and then the transition occurs from Mode 1 to Mode 2. As the flame diameter (D_v) decreases, the contrary transition occurs from Mode 2 to Mode 1.

The dependence of the flame modes on time (t) and on the initial separation distance (l/d_0) in microgravity is shown in Fig. 4. Time is normalized by the

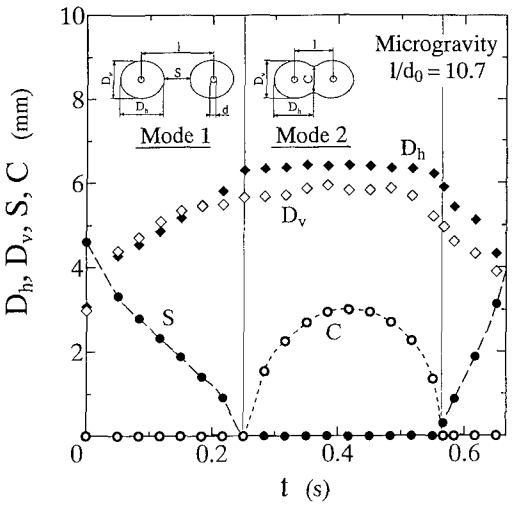

FIG. 3. Temporal variations of the flame dimensions in microgravity.

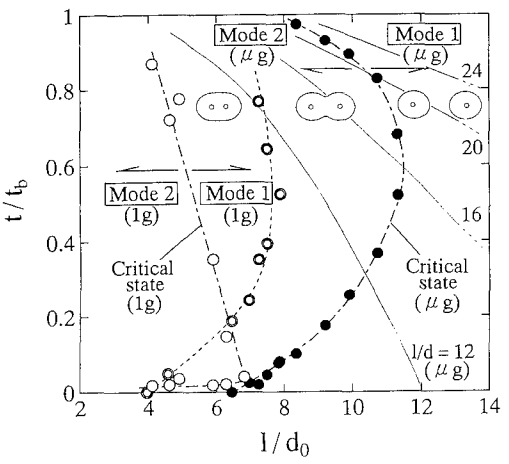

FIG. 4. Dependence of the flame shape mode on time (t/t_b) and on the initial separation distance (l/d_0).

burning lifetime (t_b). The chain line with solid circles is the locus of the time in the critical state (Fig. 2). The time at which C is equal to D_v in Mode 2 is also shown as the dotted line with the double circle. When l/d_0 is larger than a certain value ($(l/d_0)_{C1}$), the flame shape is in Mode 1 for the entire period of combustion. When l/d_0 is smaller than a certain value ($(l/d_0)_{C2}$), the flame shape is in Mode 2 for the entire period of combustion. When l/d_0 is between $(l/d_0)_{C1}$ and $(l/d_0)_{C2}$, flame mode changes from Mode 1 into Mode 2 and then from Mode 2 into Mode 1 with time, or only the transition from Mode 1 to Mode 2, occurs. According to the quasi-steady analysis, the flame shape depends only on a instantaneous separation distance (l/d). The flame diameter is the largest at ignition and decreases with decreasing droplet diameter. Therefore, only the transition from Mode 2 to Mode 1 should occur for relatively small l/d_0 in the quasi-steady state. The existence of the transition from Mode 1 to Mode 2 seen in Fig. 3 suggests that the gas-phase unsteadiness, which is due to the fuel vapor accumulation effect [15], affects the flame shape mode and, therefore, its criticality.

The locus of the time in the critical state in normal gravity is also shown as the chain line with open circles. The shape of the locus is different from that in microgravity. Though the transition from Mode 1 to Mode 2 exists, it occurs immediately after ignition. Then, combustion proceeds almost in quasi-steady state in normal gravity.

Temporal Variation of Squared Droplet Diameter:

Results obtained from microgravity experiments can be compared with existing theoretical predictions by the quasi-steady analysis [8,9]. Theoretical $d^2 - t$ curves were calculated by using the interaction coefficient obtained analytically by Umemura et al. [9]. The interaction coefficient is the ratio of the burning rate of the droplets in array to the burning rate constant of the single droplet (K_{S0}) so that K_{S0} is required to calculate the $d^2 - t$ curves. Actually, the instantaneous burning rate of the single droplet increases with time (Fig. 5). We used the maximum burning rate of the single droplet obtained from the present experiment as K_{S0}.

Temporal variations of the squared droplet diameter in microgravity and the theoretical curves are shown for a different initial separation distance (l/d_0) in Fig. 5. Here, $d^2 - t$ curves are normalized by the squared initial droplet diameter (d_0^2). For the single-droplet case ($l/d_0 = \infty$), the instantaneous burning rate increases with time and reaches K_{S0}. The difference between the experimental results and the theoretical results are mainly caused by the droplet heating, which is neglected in the theory. As l/d_0 decreases, the heating period decreases until $l/d_0 = 9.9$. But further decrease in l/d_0 causes the heating period longer. This is the same dependence of the heating period on l/d_0 as that in the experiment by Miyasaka and Law [4]. They focused on the combustion with small $l/d_0 \leq 5$.

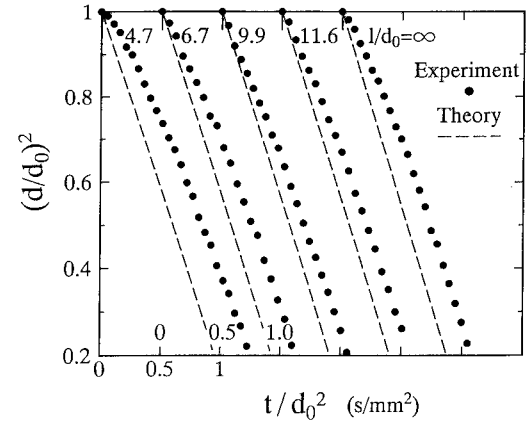

FIG. 5. Temporal variations of the squared droplet diameter ($(d/d_0)^2$) in microgravity for different initial separation distance (l/d_0).

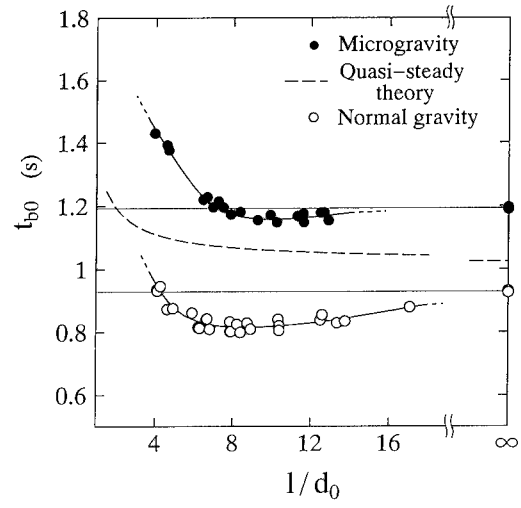

FIG. 6. Dependence of the burning lifetime (t_{b0}) on the initial separation distance (l/d_0).

Burning Lifetime:

The dependence of the burning lifetime (t_{b0}) on the initial separation distance (l/d_0) is shown in Fig. 6. Here, t_{b0} is the burning lifetime of the droplet with $d_0 = 1$ mm, to which all the burning lifetimes (t_b) were corrected by assuming $d^2 -$ law for t_b. The infinite l/d_0 denotes the single-droplet combustion.

In normal gravity, t_{b0} has a minimum at a certain

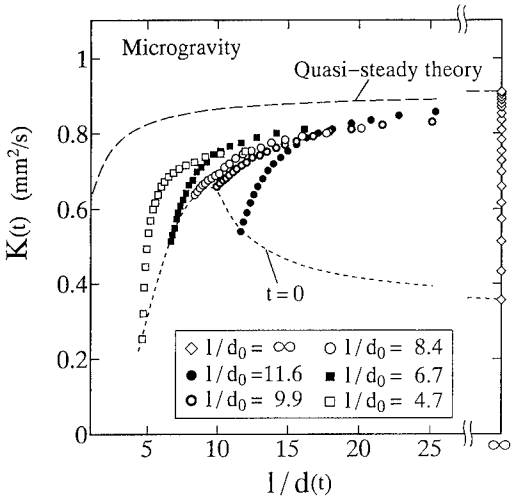

FIG. 7. Dependence of the instantaneous burning rate ($K(t)$) in microgravity on the instantaneous separation distance ($l/d(t)$) for different initial separation distance (l/d_0).

l/d_0. As l/d_0 decreases, natural convection around each droplet is enhanced. This increases oxygen supply to the flame. Further decrease in l/d_0 causes oxygen starvation between two flames. For the merged flame, the flame surface area of the lower part decreases as a decreasing separation distance. Competition of these factors changes with l/d_0 and with time and causes the dependence of t_{b0} on l/d_0.

The dependence of t_{b0} in microgravity on l/d_0 has never been examined by other researchers. As seen in Fig. 6, t_{b0} in microgravity decreases slightly with decreasing l/d_0 until it reaches the minimum around $l/d_0 = 10$ and then increases sharply. Two droplets can exist side by side if $l/d_0 > 1$. Otherwise, they will touch and merge into one droplet of twice volume. In this case, the burning behavior must be the same as that for $l/d_0 = \infty$, and t_{b0} is estimated to be $2^{2/3}$ times t_{b0} for $l/d_0 = \infty$ (about 1.9 s in microgravity); t_{b0} seems to approach $2^{2/3}$ times t_{b0} for $l/d_0 = \infty$ with decreasing l/d_0.

The present data obtained in microgravity can be compared with theoretical predictions [8,9]. The theoretical t_{b0} based on the quasi-steady assumption was calculated by using the above-mentioned interaction coefficient [9]. In the calculation, the initial droplet diameter (d_0) was 0.81 mm, and the final diameter was 0.22 mm, which are the same as the average droplet diameter and the tip sphere diameter of the fiber in the experiment, respectively. The theoretical burning lifetime (t_b) was also corrected to that of the droplet with $d_0 = 1$ mm. The prediction shows that the instantaneous burning rate decreases monotonically with decreasing instantaneous separation distance (l/d), and therefore, t_{b0} increases monotonically with decreasing initial separation distance (l/d_0). Contrary to the prediction, t_{b0} has a minimum for a certain l/d_0 and is larger than the theoretical value for any l/d_0.

The difference between the experimental results and the theoretical prediction (Fig. 5) is mainly caused by the difference of the droplet heating, which is neglected in the theory, because the temporal change in the instantaneous burning rate is not large in the later period of combustion. In Fig. 5, the heating period has a minimum for $l/d_0 = 9.9$. This l/d_0 is close to the l/d_0 at which t_{b0} has a minimum. According to the quasi-steady theory, t_{b0} increases with decreasing l/d_0 due to the increase in the oxygen starvation between the flames. The decrease in t_{b0} with decreasing l/d_0 for large l/d_0 is possibly caused by the increase in radiative heat transferred from the other flame to the droplet [3]. The effects of the interaction on droplet heating are discussed later.

Discussion

Interaction Effects on Instantaneous Burning Rate:

In order to investigate detail interaction effects, Miyasaka and Law [4] introduced the burning rate correction parameter ($\eta(t)$) (Eq. (1)) in which the burning rate of the single droplet was treated as a constant. The present results (Fig. 5), however, show that the squared droplet diameter is not a linear function of time, even for the single-droplet case ($l/d_0 = \infty$). The above approach in which the burning rate of the single-droplet was treated as a constant is not appropriate for estimating the real effects of the interaction.

Even if both $d^2 - t$ curves of the single droplet and the droplet in array are not linear, both instantaneous burning rates can be compared for the same normalized diameter (d/d_0). In order to include the liquid-phase unsteady effects on $d^2 - t$ curves in the burning rate correction parameter, we introduce an instantaneous burning rate correction parameter (ε) that is defined in Eq. 2. Both the instantaneous burning rate of the droplet in array ($K(d/d_0)$) and the instantaneous burning rate of the droplet ($K_S(d/d_0)$) are functions of the normalized diameter (d/d_0). Also, $\varepsilon(d/d_0)$ is a function of d/d_0. If $\varepsilon(d/d_0)$ is given, $K(d/d_0)$ is estimated through Eq. (3). When $\varepsilon(d/d_0)$ is positive, $K(d/d_0)$ is larger than $K_S(d/d_0)$ for the same d/d_0. We call this "positive interaction." When $\varepsilon(d/d_0)$ is negative, "negative interaction" occurs.

The instantaneous burning rate ($K(t)$) was derived from a polynomial fit of the $d^2 - t$ curve [4,5]. The values of $K(t)$ for different l/d_0 are plotted every 0.05 t/t_b vs the instantaneous separation distance ($l/d(t)$) in Fig. 7. According to the quasi-steady theory, $K(t)$ is only a function of l/d. Experimental results show that $K(t)$ is a function of $l/d(t)$ and l/d_0; $K(t)$ for different l/d_0 increase and approach an asymptote with

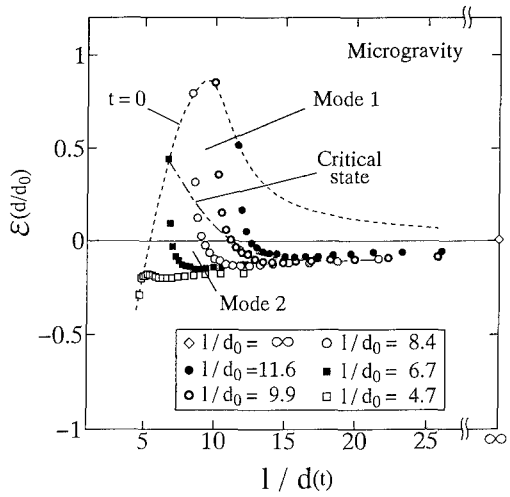

FIG. 8. Dependence of the instantaneous burning rate correction parameter ($\varepsilon(d/d_0)$) on the instantaneous separation distance ($l/d(t)$) for different initial separation distance (l/d_0).

increasing $l/d(t)$. The deviation of $K(t)$ from the asymptote is due to the slow evaporation during the heating period. If the instantaneous burning rate of the single droplet ($K_s(t)$) is constant, dependence of $\eta(t)$ on $l/d(t)$ is the same as that of $K(t)$ on $l/d(t)$. However, $K_s(t)$ changes largely with time during combustion. As mentioned above, the instantaneous burning rate correction parameter ($\varepsilon(d/d_0)$) (Eq. (2)) should be introduced to include the liquid-phase unsteady effects on the $d^2 - t$ curve of the single droplet.

The instantaneous burning rate correction parameters ($\varepsilon(d/d_0)$) were derived and are plotted vs $l/d(t)$ every 0.05 $(d/d_0)^2$ in Fig. 8. For $l/d_0 > 5.4$, the positive interaction occurs in the earlier stage. The correction parameter $\varepsilon(d/d_0)$ decreases with $l/d(t)$ (or with time) and then the positive interaction transfers to the negative one. As $l/d(t)$ increases, $\varepsilon(d/d_0)$ approaches an asymptote. The existence of this positive interaction causes the minimum in the burning lifetime (t_{b0}) (Fig. 6). For $l/d_0 < 5.4$, $\varepsilon(d/d_0)$ is negative for the entire period of combustion and to be smaller for smaller l/d_0 when l/d is the same. This is consistent with the conclusion derived from the experiments with small $l/d_0 \leqslant 5$ by Miyasaka and Law [4] that the droplet heating is retarded due to the interaction.

Radiation heat transferred from the other flame to the droplet may affect the droplet array combustion. The radiative heat transferred from the other flame promotes droplet heating. On the other hand, the oxygen starvation between the flames suppresses combustion. We suppose two extreme cases to reveal both effects.

First, we suppose that the oxygen starvation does not occur between the flames, but radiative heat transfer is considered in Mode 1 (Fig. 2). The droplet heating is enhanced by the radiative heat from the other flame. The instantaneous burning rate ($K(d/d_0)$) is larger than and its temporal change is smaller than those of the single droplet because the droplet in array is heated faster than the single droplet. Therefore, $\varepsilon(d/d_0)$ decreases and approaches 0 as the droplet heating proceeds and the droplet surface decreases with time. During combustion, $\varepsilon(d/d_0)$ is positive and is larger at smaller l/d_0 for the same d/d_0 because the radiative heat is larger at smaller l/d_0. When l/d_0 becomes small enough, the radiative heating effect becomes small because the relative flame surface for one droplet becomes small.

Second, we suppose that the oxygen starvation occurs between the flames but the radiative heat transfer is not considered. As the separated flames approach each other, the oxygen starvation becomes more severe in the earlier stage of combustion. In the later stage, the oxygen starvation effect decreases as the distance between the flames (S) increases with time (Fig. 3). In this case, $\varepsilon(d/d_0)$ is negative during combustion. It decreases until S becomes the smallest and then increases with time. In the later stage, $\varepsilon(d/d_0)$ approaches the oxygen diffusion limit. This oxygen starvation effect is larger at smaller l/d_0.

The overlapping effect of the radiative heating and the oxygen starvation causes the dependence of $\varepsilon(d/d_0)$ on $l/d(t)$ for different l/d_0.

Burning Behavior at a Constant Separation Distance:

In this experiment, the distance between the droplets (l) is fixed during combustion. As the droplet diameter (d) decreases, the instantaneous separation distance (l/d) increases. However, we can predict the burning behavior of two droplets at a constant l/d. As seen in Fig. 4, the time when the line at a constant l/d intersects the line at a constant l/d_0, which is not shown in Fig. 4, increases with decreasing l/d_0. Therefore, temporal variation of the burning characteristics at a constant l/d is understood as the variation of the burning characteristics observed in the present experiments with decreasing l/d_0 at a constant l/d.

As seen in Fig. 4, when l/d is less than 22, the lines at a constant l/d intersect the critical state line at one point. Therefore, only the transition from Mode 1 to Mode 2 occurs during combustion at a constant l/d. When l/d is larger than 22, the combustion proceeds in Mode 1.

According to Fig. 7, $K(t)$ increases until it has a maximum and then decreases with time at a constant l/d. This decrease in $K(t)$ is caused by the increased oxygen starvation after the droplet heating. Therefore, the flame diameter continues to increase to get

more oxygen or approaches the steady-state value at a constant l/d. According to the quasi-steady analysis, the flame shape depends only on l/d. The combustion phenomena, however, is unsteady in practice even if l/d is constant.

According to Fig. 8, $\varepsilon(d/d_0)$ continues to decrease with time at a constant l/d. Due to the radiative heating, $\varepsilon(d/d_0)$ is positive in the earlier stage and decreases as the droplet is heated up at $l/d > 5.4$. Even when the droplet heating is over, $\varepsilon(d/d_0)$ continues to decrease due to the oxygen starvation effect. If the steady state exists, $\varepsilon(d/d_0)$ approaches the steady-state value.

Conclusions

Experiments on interactive combustion of two droplets were performed in microgravity. Dependence of burning lifetime and instantaneous burning rate on initial separation distance was examined by introducing an instantaneous burning rate correction parameter. The main conclusions are as follows:

1. The gas-phase unsteadiness, which is due to the fuel-vapor accumulation effect, affects the transition of the flame shape mode and, therefore, its criticality. As the droplets burn within a certain range of the initial separation distance, the transition from two separated flames to a merged flame occurs initially, and then the contrary transition occurs.
2. When the initial separation distance is larger than a certain value, in the earlier stage of combustion, the existence of the other flame causes positive interaction, which increases the burning rate due to radiative heat transferred from the other flame, and in the later stage, negative interaction occurs due to oxygen starvation between the flames.
3. The burning lifetime has a minimum at a certain initial separation distance. This minimum is almost consistent with the maximum of the positive interaction in the earlier stage.

Acknowledgment

This work was supported by the Special Coordination Fund for Promoting Science and Technology through the Science and Technology Agency of the Japanese Government.

REFERENCES

1. Rex, J. F., Fuhs, A. E., and Penner, S. S., *Jet Propul.* 26:179–187 (1956).
2. Kanevsky, J., *Jet Propul.* 26:788 (1956).
3. Fedoseeva, N. V., *Adv. Aerosol Phys.* 2:110–118 (1972).
4. Miyasaka, K., and Law, C. K., *Eighteenth Symposium (International) on Combustion*, The Combustion Institute, Pittsburgh, 1981, pp. 283–292.
5. Xiong, T. Y., Law C. K. and Miyasaka, K., *Twentieth Symposium (International) on Combustion*, The Combustion Institute, Pittsburgh, 1985, pp. 1781–1787.
6. Konishi, K., Kono, M., and Iinuma, K., *Trans. Jpn. Soc. Mech. Eng.* 51:2218–2224 (1985).
7. Brzustowski, T. A., Twardus, E. M., Wojcicki, S., and Sobiesiak, A., *AIAA J.* 17:1234–1242 (1979).
8. Labowsky, M., *Combust. Sci. Technol.*, Vol. 22:217–226 (1980).
9. Umemura, A., Ogawa, S., and Oshima, N., *Combust. Flame* 41:45–55 (1981).
10. Umemura, A., *Eighteenth Symposium (International) on Combustion*, The Combustion Institute, Pittsburgh, 1981, pp. 1355–1363.
11. Williams, F. A., *Combustion Theory* 2nd ed., Benjamin/Cummings, Menlo Park, CA, 1985.
12. Choi, M. Y., Dryer, F. L., and Haggard, J. B., *Twenty-Third Symposium (International) on Combustion*, The Combustion Institute, Pittsburgh, 1991, pp. 1597–1604.
13. Avedisian, C. T., Yang, J. C., and Wang, C. H., *Proc. R. Soc. London A* 420:183–200 (1988).
14. Kobayashi, K., *Fifth Symposium (International) on Combustion*, Reinhold, 1955, pp. 141–148.
15. Law, C. K., Chung, S. H., and Srinivasan, N., *Combust. Flame* 38:173–198 (1980).

COMMENTS

C. T. Avedisian, Cornell University, USA. 1. You showed a calculated burning rate that your data seemed to approach in the limit of large spacing between the droplets. Since heptane produces soot, was soot formation included in this calculation?

2. Were properties assumed to be constant in your model, and if so how were their values selected?

3. Soot particles produced during combustion of isolated and near-stationary droplets burning in a buoyancy-free environment often are trapped in a region between the flame and droplet, and sometimes form a shell-like structure [1–4]. Were soot shells visible using your photographic arrangement, and if so, did they experience the same interactive effects as the flames did when the droplet spacing was varied?

REFERENCES

1. Shaw, B. D., Dryer, F. L., Williams, F. A., and Haggard, J. B., *Acta Astronaut.* 17:1195 (1988).

2. Avedisian, C. T., Yang, J. C., and Wang, C. H., *Proc. R. Soc. Lond. A* 420:183 (1988).
3. Hara, H., and Kumagai, S., *Twenty-Third Symposium (International) on Combustion,* The Combustion Institute, Pittsburgh, 1990, p. 1605.
4. Jackson, G. S., Avedisian, C. T., and Yang, J. C., *Int. J. Heat Mass. Transfer* 35(8):2017 (1992).

Author's Reply. A calculated burning rate is obtained through the equation, $K = \eta K_{s0}$, where η is the burning rate correction parameter (Refs. 8 and 9 in the paper) and K_{s0} the burning rate constant of the single droplet. In the present paper, K_{s0} is the maximum value of the instantaneous burning rate of the single droplet obtained in the present experiment. The term η is a function only of instantaneous separation distance (l/d). Properties need not be estimated.

As for soot formation, the information about it is included in K_{s0} since the authors use the experimental value. The effect of soot formation, however, is not considered in η. In the present experiments, soot shells were observed. At a small initial separation distance (l/d_0), a soot shell surrounds two droplets. The soot shells experience interactive effects similar to the flames. However, we did not focus upon the soot shell structure in the present paper. The interactive effects of the soot shell and the flame are still unknown.

•

A. Kowalemicz, Radom Technical University, Poland. What was the ratio of flame diameter to droplet diameter under microgravity conditions during droplet burning? (According to prior literature, it is typically about 9.)

Author's Reply. Under the condition shown in Fig. 3, the ratio of the flame diameter (D_v) to the droplet diameter (d) is 3.6 at ignition and increases with time during burning. This is qualitatively the same as the single droplet combustion of n-heptane in microgravity [1]. The authors guess that you are talking about the ratio of the maximum flame diameter (D_{vm}) to the initial droplet diameter (d_0). Here D_{vm} denotes the maximum value of D_v (Fig. 3) during burning. D_{vm}/d_0 is 7.2 in Fig. 3. D_{vm}/d_0 is larger at a smaller initial separation distance (l/d_0).

REFERENCE

1. Hara, H., and Kumagal, S., *Twenty-Third Symposium (International) on Combustion,* The Combustion Institute, Pittsburgh, 1991, pp. 1605–1610.

Twenty-Fifth Symposium (International) on Combustion/The Combustion Institute, 1994/pp. 439–446

CLARIFICATION OF THE FLAME STRUCTURE OF DROPLET BURNING BASED ON TEMPERATURE MEASUREMENT IN MICROGRAVITY

M. MIKAMI, M. NIWA AND H. KATO
The University of Tokyo
Hongo, Bunkyo-ku, Tokyo 113, Japan

J. SATO
Ishikawajima-Harima Heavy Industries Co., Ltd.
Toyosu, Koto-ku, Tokyo 135, Japan

AND

M. KONO
The University of Tokyo
Hongo, Bunkyo-ku, Tokyo 113, Japan

In microgravity, soot accumulates inside the flame in droplet combustion. The yellow luminosity prevents the inner structure of the flame from being revealed. No experimental work has been conducted on the flame structure of the droplet burning in microgravity. Microgravity experiments on the droplet burning were performed for the purpose of clarifying the flame structure of spherically symmetrical burning of the droplet by using the drop tower. Gas temperature was measured by thermocouples with tip parts that are concentric with the spherical flame. This configuration reduces heat loss from the contact point of the thermocouple to the supporting wires. The gas-temperature distributions and temporal variations of the flame temperature were obtained and were examined for an ambient pressure ranging from 0.1 to 1.1 MPa. As results, it was found that the maximum temperature zone, that is, the primary reaction zone, exists about 0.8 mm outside the outer edge of the yellow luminous zone at 0.1 MPa for *n*-heptane droplets. The distance between the reaction zone and the outer edge of the yellow luminous zone decreases with increasing ambient pressure. The flame temperature is almost constant at the normalized time ranging from 0.3 to 0.6 and less dependent on the ambient pressure than on oxygen concentration of the ambient gas. In the later period of combustion, the flame temperature decreases with time because of the increase in the soot accumulation.

Introduction

For the last few decades, studies on the spherically symmetrical burning of single fuel droplets have been conducted experimentally and theoretically in view of their usefulness for improving the understanding of droplet combustion mechanism and for providing information relevant to practical combustors [1–4]. The spherically symmetrical burning of the droplet is well understood through one-dimensional quasi-steady analysis [5]. Recently, Shuen et al. [6] conducted a numerical calculation in which variable properties, finite-rate chemical kinetics, and a full treatment of phase equilibrium at the droplet surface are accommodated. However, almost no experimental work has been conducted on the flame structure of the spherical flame in microgravity.

The flame structure around the burning droplet has been studied in normal gravity [7–9]. Aldred et al. [7] measured gas temperature around the burning suspended droplets and burning porous spheres. Kadota and Hiroyasu [8] measured flame temperature of the droplet around the stagnation point. Subramanyam et al. [9] measured temperature of a wake flame and an envelope flame. The results show that the flame temperature decreases with increasing ambient pressure. However, the numerical calculation by Shuen et al. [6] shows that the flame temperature increases with ambient pressure.

In microgravity, soot accumulates inside the flame. The yellow luminosity prevents us from deriving information on the inner structure of the flame. It also prevents the blue flame from being visualized. As for microgravity experiments by the free fall method, the dimension of the experimental setup is limited. It is not easy to develop an optical measurement system for microgravity experiments.

Based on the above-mentioned, the present mi-

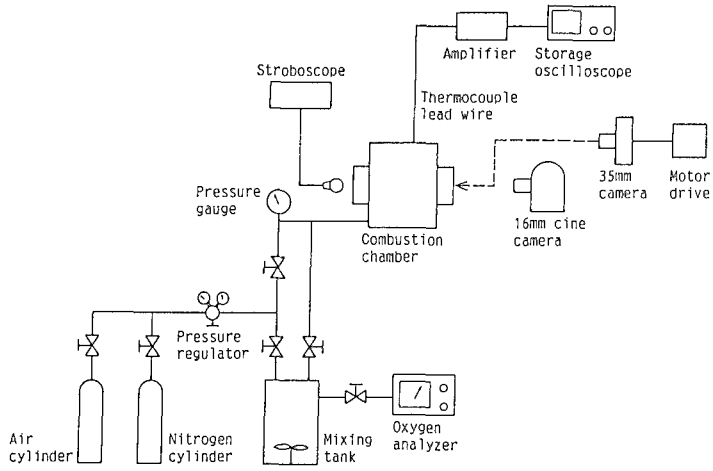

FIG. 1. Schematic diagram of the experimental apparatus.

crogravity experiments on droplet burning were conducted for the purpose of clarifying the flame structure of spherically symmetrical burning of the droplet. Gas temperature was measured by thermocouples with tip parts that are concentric with the spherical flame. The temperature distributions around the droplet and temporal variations of the flame temperature were obtained and were examined. Air and nitrogen-diluted air were used as the ambient gases in the pressure range from 0.1 to 1.1 MPa.

Experimental Apparatus and Procedure

General Description:

Microgravity conditions of 1.4-s duration were attained by using the drop tower (KONSTUM H-2), 10 m in height, in the Department of Aeronautics and Astronautics, University of Tokyo. The experimental apparatus (Fig. 1) and procedure used in the present work are basically the same as those used in the previous works [10], and thus, only a brief explanation is provided here.

An n-heptane droplet was suspended at the tip end of a silica fiber. The tip end of the 0.125-mm-diameter silica fiber was rounded to facilitate the suspension of the droplet. The initial diameter of the droplet is 0.8 ± 0.1 mm throughout the experiment. The initial temperatures of the droplet and the surrounding gas were about 298 K. The droplet was nearly elliptical in shape, and thus, an equivalent diameter d was used as the droplet diameter; $d = (a^2b)^{1/3}$, where a and b are the maximum diameters of the droplet, in the directions perpendicular and parallel to the longitudinal axis of the silica fiber, respectively. A hot wire was used to ignite the droplet. Electric power was applied to the wire simultaneously with the start of drop of experimental apparatus. Just after the ignition, the power was switched off, and the wire was removed from the vicinity of the droplet. A 16-mm cine camera of 60 frames per second was used to photograph the initial and the burning droplet and to measure their diameters. To obtain shadow photographs, a stroboscope was used for the background light source. The stroboscope flashed at 15 Hz. Therefore, in this case, sequential frames of direct photographs are approximately replaced by those of shadow photographs every fourth frame because of the overwhelmingly high intensity of the background light as compared with the direct light of the flame region.

Ambient gas pressure was in the range from 0.1 to 1.1 MPa. The effect of the pressure was examined mainly by use of pure air as the ambient gas. To vary the oxygen concentration of the ambient gas, nitrogen-diluted air was used.

In the present work, ignition was defined in the photograph as the instant of appearance of any luminosity that surrounds the droplet, and the burnout as the instant when the luminosity became invisible.

Temperature Measurement:

In microgravity, the temperature field around the burning droplet becomes spherically symmetric. Fine thermocouples located around the droplet were used to measure gas-temperature distributions and the temporal variations of the gas temperature. The configuration of the thermocouples is shown in Fig. 2. To reduce the heat loss by conduction from the contact point to the supporting part, the tip part of the thermocouple was formed into a concentric shape with the spherical yellow luminous flame. It is well known that the heat loss by conduction from the

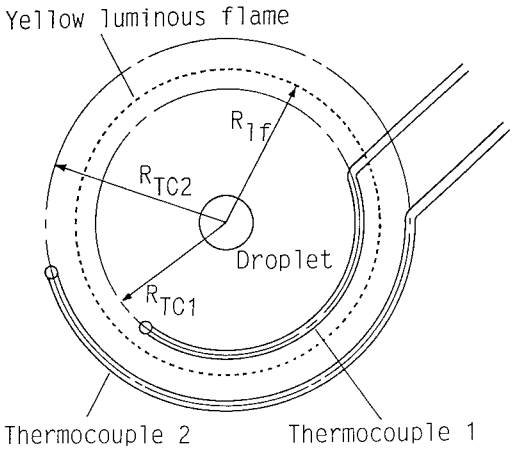

FIG. 2. Arrangement of the concentric thermocouples with the spherical yellow luminous flame.

contact point to the supporting part is small, for practical purposes, as long as the gas temperature is constant within an area with a radius at least 50 times as large as the bead radius at the contact point [11]. In this experiment, the length of the tip part, along which there is no temperature gradient, is at least 200 times as large as the bead radius. The distances between the droplet and thermocouples 1 (R_{TC1}) and 2 (R_{TC2}) were measured from photographs.

The thermocouples are made of Pt/Pt-13%Rd and are 20 μm in diameter. The tip bead diameter is about 50 μm. Catalysis, which occurs on the platinum wire surface, may affect the reaction in the gas phase. To suppress the catalytic effect, the surface of the thermocouple is coated with silica [12]. Two thermocouple outputs were amplified and were stored in a oscilloscope. The outputs from the oscilloscope were converted into the gas temperatures.

Results and Discussion

Figure 3 shows direct photographs of the yellow luminous flames and the thermocouples at different times for different ambient pressures. The yellow luminous flames are spherical for the entire period of combustion for all ambient pressures tested in the present research. As the yellow luminous flame diameter increases, the outer edge of the yellow luminous flame passes the thermocouples one after the other. Then, as the yellow luminous flame diameter decreases, the outer edge of the yellow luminous flame passes the thermocouples again. In these photographs, the yellow luminous flame passes the thermocouples twice for 0.4 and 0.6 MPa and once for 0.8 and 1.1 MPa. The number of times of the yellow luminous flame passing the thermocouples depends on the distance between the droplet and the thermocouples (R_{TC1} and R_{TC2}) and on the ambient pressure.

Figure 4 shows a typical example of the temporal

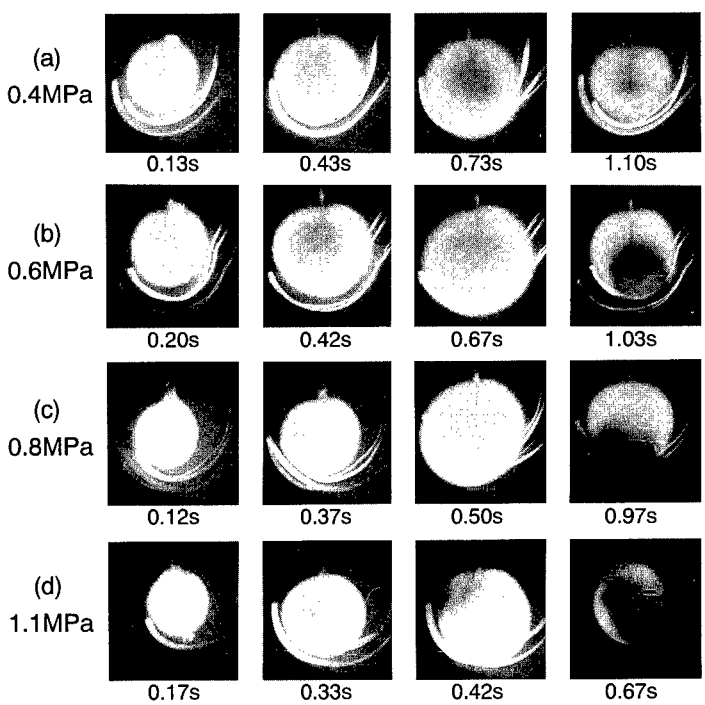

FIG. 3. Direct photographs of the burning droplet and the thermocouples at different sequences for different ambient pressures.

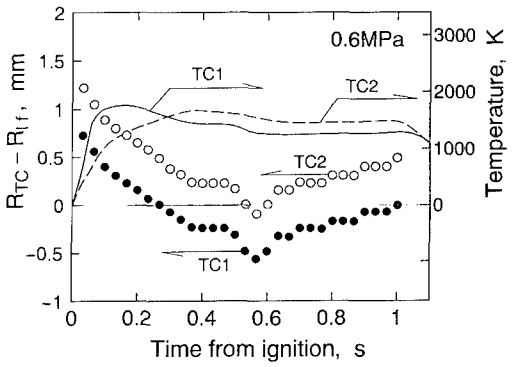

FIG. 4. Temporal variations of the relative position of the thermocouples to the outer edge of the yellow luminous zone and temporal variations of the gas temperature.

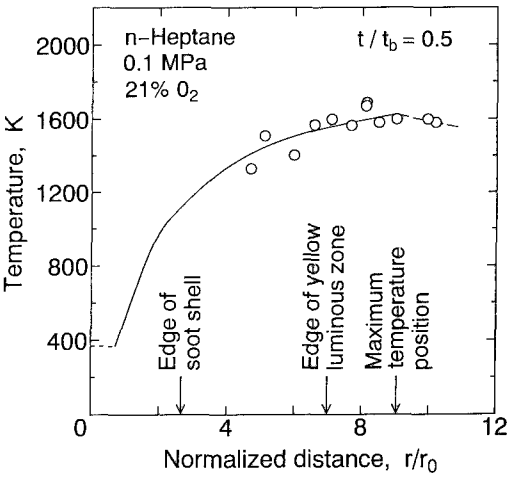

FIG. 5. Typical temperature distribution and locations of the outer edge of the soot shell, the outer edge of the yellow luminous zone, and the maximum temperature position at 0.1 MPa.

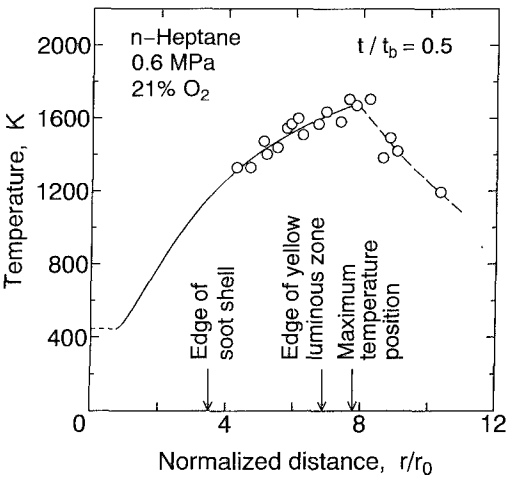

FIG. 6. Typical temperature distribution and locations of the outer edge of the soot shell, the outer edge of the yellow luminous zone, and the maximum temperature position at 0.6 MPa.

variations of the gas temperature and the relative position of the thermocouples to the outer edge of the yellow luminous flame. Here, R_{TC} is the distance between the thermocouple and the droplet (Fig. 2), and R_{lf} is the yellow luminous flame diameter. As the yellow luminous flame diameter increases, $R_{TC} - R_{lf}$ decreases. When $R_{TC} - R_{lf}$ becomes 0, the outer edge of the yellow luminous flame just passes a thermocouple. From this figure, one temperature datum at each thermocouple position is obtained for each time. If such experiments are performed repeatedly for different thermocouple positions, temperature distribution for each time are obtained. When the reaction zone in the flame just passes the thermocouple, the gas temperature at the thermocouple position becomes maximum. Because the maximum temperature zone in the flame is considered to be primary reaction zone, the flame temperature, that is, the reaction zone temperature, is obtained from the gas-temperature variation with time. If this experiment is performed for different thermocouple positions repeatedly, temporal variation of the flame temperature is obtained.

Temperature Distribution:

Figures 5 and 6 show typical temperature distributions at 0.1 and 0.6 MPa, respectively. In order to extrapolate the temperature distribution from the measured temperature values, the data inside the flame are fitted as a function based on the quasi-steady analysis with the flame sheet model [5],

$$T = T_1 - C_0 + C_0 \cdot \exp[C_1 \cdot m \cdot \{1/(r_1/r_0) - 1/(r/r_0)\}/(4\pi r_0)]$$

where T_1 is droplet temperature, m is mass evaporation rate, r_1 is droplet radius, and r_0 is the initial droplet radius. Here, T is a function of normalized distance (r/r_0), and C_0 and C_1 are the ratio of the heat of vaporization to the heat capacity and the ratio of the heat capacity to the thermal conductivity, respectively. Though the combustion proceeds unsteadily in practice because of the fuel vapor accumulation, gas-phase quasi steadiness can be assumed inside the flame so long as the normalized flame radius is $r_f/r_1 < O[(\rho_l/\rho_g)^{0.5}]$, and the above equation can be used [13]. The normalized flame size is smaller than $O[(\rho_l/\rho_g)^{0.5}]$ under the conditions shown

in Figs. 5 and 6. We used C_0 and C_1 as fitting parameter because it is not easy to estimate C_0 and C_1 due to the existence of soot inside the flame. Here, T_1 is estimated as the boiling temperature of the fuel, and r_1 and m are estimated through the equations

$$r_1^2 = r_0^2 - K \cdot t/4$$

and

$$m = \pi \rho_l \cdot r_1 \cdot K/2$$

where ρ_l is the density in the liquid phase and K is the burning rate constant, which is approximated as

$$K = 4r_0^2/t_b$$

where t_b is the burning time. The locations of the outer edge of the yellow luminous zone are shown in Figs. 5 and 6. These locations were determined from photographs. The figures show that the outer edge of the yellow luminous zone exists inside the maximum temperature position. This is the reason why the gas temperature in Fig. 4 reaches a maximum in the earlier stage before the outer edge of the yellow luminous flame passes the thermocouple. These figures also show that temperature gradient near the maximum temperature position inside the flame at 0.1 MPa is smaller than that at 0.6 MPa. This smaller temperature gradient suggests broader reaction zone. Reaction rate is smaller at lower pressure. The temperature gradient at the droplet surface at 0.1 MPa is larger than that at 0.6 MPa, perhaps as a result of the forced fitting of the data with the smaller temperature gradient near the maximum temperature position at 0.1 MPa. The outer edge of the soot shell [14] is also shown in Figs. 5 and 6. The soot shell diameter at 0.1 MPa is larger than that at 0.6 MPa. The temperature of the soot shell at 0.1 MPa does not change with time very much, which is about 1100 K. On the other hand, the temperature of the soot shell at 0.6 MPa changes with time approximately from 1300 to 1000 K.

The temperature distributions at 0.1 MPa for different time (t/t_b) are shown in Fig. 7 and those at 0.6 MPa in Fig. 8. At 0.1 MPa, the temperature distribution does not change with time very much. The temperature gradient at the droplet surface decreases slightly with time. At 0.6 MPa, the maximum temperature position moves away from the droplet and then approaches the droplet with time. The temperature gradient at the droplet surface decreases substantially with time, and the maximum temperature also decreases with time.

As mentioned above, the maximum temperature position exists outside the yellow luminous zone. The maximum temperature position is consistent with the blue flame position. It is difficult to observe the blue flame because of the luminosity from the yellow luminous zone for hydrocarbon fuel. Therefore, flame diameter data in microgravity obtained experimentally from photographs are mostly the yellow luminous flame diameter data. On the other hand, the flame diameter obtained theoretically is more nearly represented by the blue flame diameter. It is important to know the difference between the blue flame diameter and the yellow luminous flame diameter. Figure 9 shows the dependence of the distance between the maximum temperature position and the outer edge of the yellow luminous zone on the ambient pressure. This is an averaged distance of the values obtained for t/t_b from 0.2 to 0.7. The distance decreases with increasing ambient pressure.

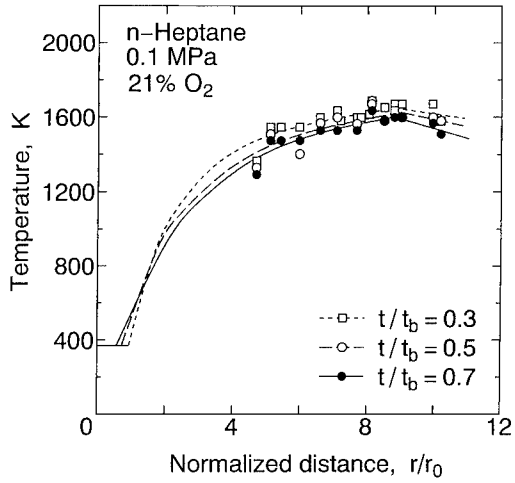

FIG. 7. Temperature distributions in the gas phase at 0.1 MPa for different times.

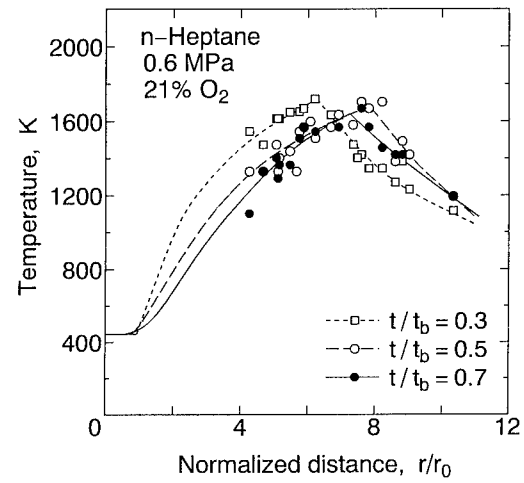

FIG. 8. Temperature distributions in the gas phase at 0.6 MPa for different times.

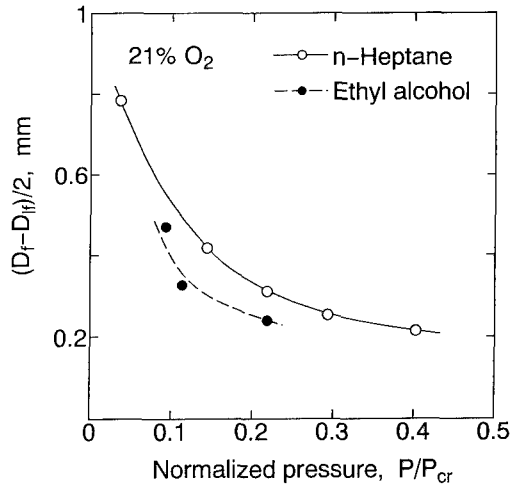

FIG. 9. Dependence of the distance between the flame and the outer edge of the yellow luminous zone on the ambient pressure for different fuels.

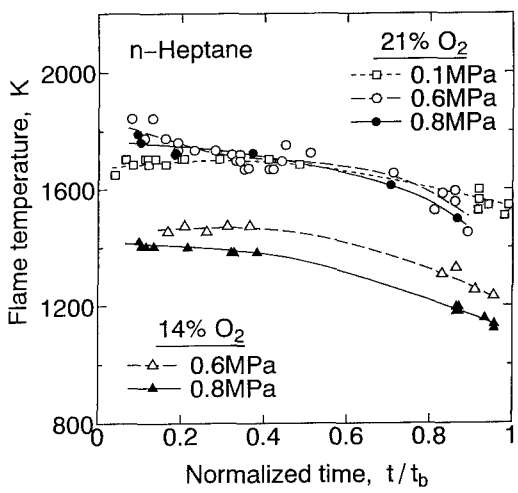

FIG. 10. Temporal variations of the flame temperature for different ambient pressures and for different oxygen concentrations of the gas.

Temporal Variation of the Flame Temperature:

Figure 10 shows temporal variations of the flame temperature for different ambient pressures and different ambient gases. Here, time (t) is normalized by the burning time (t_b). When the ambient gas is air (21% O_2) at 0.1 MPa, the flame temperature increases slightly in the earlier stage, then becomes constant, and decreases with time in the later stage. At 0.6 and 0.8 MPa, it decreases with time initially, then becomes almost constant, and decreases again in the later stage. At the time from 0.3 to 0.6, the

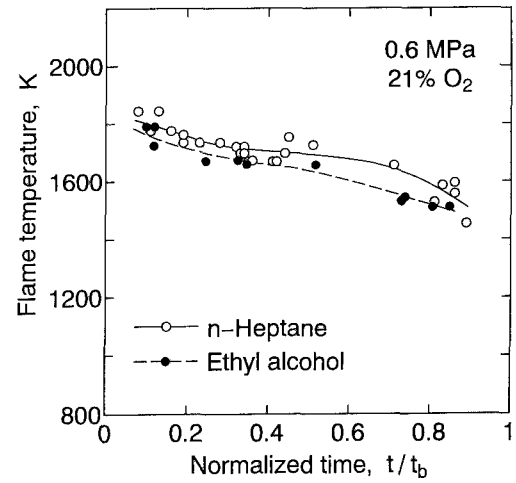

FIG. 11. Temporal variations of the flame temperature for different fuels.

flame temperatures at different ambient pressures have almost the same value 1700 K. It is corrected to 1782 K by considering the radiative heat loss from the thermocouple [12]. This value is about 440 K lower than the adiabatic flame temperature of the stoichiometric n-heptane–air mixture. According to numerical calculation results [6], the flame temperature increases with ambient pressure. However, Subramanyam et al. [9] measured the temperature of flame surrounding a porous sphere and the results show that the flame temperature decreases with increasing ambient pressure. In the current experiments, there is no pressure dependence of the flame temperature at the normalized time between 0.3 and 0.6. When the ambient gas was diluted, the flame temperature is smaller than that for air and is smaller at the higher ambient pressure. As for temporal variation of the flame temperature, the temperature decreases with time in most cases. However, the numerical calculation results [6] show that the flame temperature increases with time. Temporal variations of the flame temperatures of n-heptane and ethyl alcohol are shown in Fig. 11. The flame temperature of the ethanol droplet is slightly lower than that of heptane. Its dependence on time is the same as that for heptane.

The flame temperature decreases with time, and at the normalized time from 0.3 to 0.6, it is independent of the ambient pressure. The heat capacity of soot inside the flame may affect the flame temperature dependence. The amount of soot increases with time and ambient pressure, which decreases the flame temperature. Without the heat capacity increase with time and ambient pressure, the flame temperature dependence on time and ambient pressure will become the same dependence as that shown in the numerical calculation by Shuen et al. [6], in

which variable properties, finite-rate chemical kinetics, and a full treatment of phase equilibrium at the droplet surface are accommodated, but the effects of soot are not included. The numerical calculation by Saitoh et al. [15] shows that the flame temperature with radiative heat loss becomes 25% lower than that without radiative heat loss. The decrease in the flame temperature with time may also be affected by this radiative heat loss.

The presence of soot affects the temperature field as a result of the large heat capacity and the radiation. The development of a droplet combustion theory including the soot formation, accumulation, and radiation is required.

Conclusions

Microgravity experiments on droplet burning were conducted for the purpose of clarifying the flame structure of spherically symmetrical burning of the droplet. Gas temperature was measured by a thermocouple with a tip part that is concentric with the spherical flame. The temperature distributions around the flame and temporal variations of the flame temperature were obtained and were examined for an ambient pressure ranging from 0.1 to 1.1 MPa. The main conclusions are as follows:

1. At lower ambient pressure, the maximum temperature zone exists farther from the droplet, and the temperature gradient around the maximum temperature zone is smaller. This suggests broader reaction zone at lower ambient pressure.
2. The maximum temperature zone, that is, the reaction zone, exists outside the outer edge of the yellow luminous zone. The distance between the reaction zone and the yellow luminous zone is about 0.8 mm at 0.1 MPa for *n*-heptane droplets. It decreases with increasing ambient pressure.
3. The flame temperature is almost constant at the normalized time ranging from 0.3 to 0.6. In the later period, the flame temperature decreases with time.
4. The presence of soot affects the temperature field because of the large heat capacity and radiation. The development of theory including the soot formation, accumulation, and radiation is required.

REFERENCES

1. Williams, A., *Combust. Flame* 21:1–31 (1973).
2. Faeth, G. M., *Prog. Energy Combust. Sci.* 3:191–224 (1977).
3. Sirignano, W. A., *Prog. Energy Combust. Sci.* 9:291–322 (1983).
4. Law, C. K., *Third International Colloquium on Drops and Bubbles*, Monterey, CA, 1988, pp. 321–337.
5. Williams, F. A., *Combustion Theory*, 2nd ed., Benjamin/Cummings, Menlo Park, CA, 1985.
6. Shuen, J. S., Yang, V., and Hsiao, C. C., *Combust. Flame* 89:299–319 (1992).
7. Aldred, J. W., Patel, J. C., and Williams, A., *Combust. Flame* 17:139–148 (1971).
8. Kadota, T., and Hiroyasu, H., *Combust. Flame* 55:195–201 (1984).
9. Subramanyam, R., Gollahalli, S. R., and Brzustowski, T. A., *Fourteenth Symposium (International) on Combustion*, The Combustion Institute, Pittsburgh, 1975, pp. 409–417.
10. Sato, J., Tsue, M., Niwa, M., and Kono, M., *Combust. Flame* 82:142–150 (1990).
11. Mashima, M., and Isobe, T., *Theory of Measurement Technique*, Press of Tokyo University, Tokyo, 1977, (in Japanese).
12. Kaskan, W. E., *Sixth Symposium (International) on Combustion*, The Combustion Institute, Pittsburgh, 1957, pp. 134–143.
13. Law, C. K., Chung, S. H., and Srinivasan, N., *Combust. Flame* 38:173–198 (1980).
14. Shaw, B. D., Dryer, F. L., Williams, F. A., and Haggard, J. B., Jr., *Acta Astronaut.* 17(11/12):1195–1202 (1988).
15. Saitoh, T., Yamazaki, K., and Viskanta, R., *Trans. Japan Soc. Mech. Eng.* 57:1485–1490 (1991).

COMMENTS

C. T. Avedisian, Cornell University, USA. 1. A fiber support is known to influence several aspects of the burning of droplets, such as the droplet shape and heat transfer between the droplet and flame. How were these extraneous effects accounted for in your experimental results?

2. Did you correct for heat losses through the thermocouple and radiation effects?

Author's Reply. There exist some effects of the fiber on droplet burning.

The droplet shape is nearly elliptical during burning. The temperature field close to the droplet is not expected to be spherically symmetric. However, the asymmetry in the temperature field should be smaller at locations further from the droplet. At the outer edge of the yellow luminous flame, this effect is negligible because the yellow luminous flame was spherical in the present experiments. The authors measured the gas temperature outside the soot shell. The temperature field measured in the present experiments would be mostly spherical. The flame quenching oc-

curs locally near the fiber in the initial stage. This would also be a negligible effect because the quenched area is small compared to the area of the entire flame.

Heat transfer from the flame to the droplet through the fiber may make an effect on the droplet burning, especially in the later stage. However, a comparison between suspended droplet combustion and free droplet combustion [1] shows that they are qualitatively the same though there are quantitative differences, such as larger burning rate of the suspended droplet compared with that of the free droplet. The authors think that the heat through the fiber does not affect the temperature field qualitatively.

In order to surpress the heat loss through the thermocouple, the thermocouple was formed into the concentric shape with the spherical yellow luminous flame (Fig. 2) as mentioned in the present paper. This kind of temperature correction was not required and was not made. The radiation correction was also not made because the results in the present paper won't change qualitatively in spite of the correction.

REFERENCE

1. Mikami, M., Niwa, M., Sato, J., and Kono, M., *Nensho no Kagaku to Gijutsu* (translation Combustion Science and Technology) 1(4):255–264 (1994) (Japanese Combustion Journal, abstract to appear in *Combust. Sci. Technol.*).

•

Anthony Hamins, National Institute of Standards & Technology, USA. Temperature measurements were made with very delicate, small thermocouples in a cantilever beamlike configuration. Did the passage of the flame affect the thermocouple bead location? Were the thermocouples coated by soot as the flame developed? If yes, how large was the effective bead diameter? Is it possible to estimate the time-dependent radiation correction to the thermocouple measurements?

Author's Reply. Sequential photographs show that the thermocouple bead position was not affected by the flame passage. The speed of the flow around the droplet (Stefan flow) decreases rapidly with increasing distance from the droplet. We did not measure gas temperature near the droplet surface but outside the soot shell. The flow speed at the thermocouple position would not be large enough to affect the bead position.

As you pointed out, if soot shell passes the thermocouple, the thermocouple is then coated with soot. This causes a nonnegligible error in measuring the gas temperature. Therefore, the authors focussed upon the temperature field outside the soot shell as mentioned above and then extrapolated it to the droplet surface.

Twenty-Fifth Symposium (International) on Combustion/The Combustion Institute, 1994/pp. 447–453

IGNITION EXPERIMENT OF A FUEL DROPLET IN HIGH-PRESSURE HIGH-TEMPERATURE AMBIENT

RYOTA NAKANISHI, HIDEAKI KOBAYASHI, SHINICHIRO KATO AND TAKASHI NIIOKA
Institute of Fluid Science
Tohoku University
Katahira, Sendai 980-77, Japan

In order to obtain the ignition behavior at supercritical pressures, ignition times of a single fuel droplet were measured in high-pressure high-temperature ambient. A suspended droplet of *n*-hexadecane or *n*-heptane with a diameter of 0.35–1.4 mm was quickly immersed in an electric furnace with a temperature up to 950 K. Attachment of the droplet, movement of the furnace, and ignition measurement were carried out in an air vessel with pressures up to 3 MPa.

At low pressures, ignition times of both fuels decreased with the initial droplet diameter and then increased. Therefore, the ignition time variation with the initial droplet diameter has a minimum. This phenomenon, however, disappeared at high pressures. Also, the ignitable limit of droplet diameter, below which the droplet vaporized completely before ignition, decreased as pressure increased.

In the case of a droplet burning at high pressures, the preceding experiment showed that the burning rate constant increased and had a maximum around the critical pressure of fuel. This is significantly caused by variable properties around the critical point such as thermal conductivity and diffusion coefficient; and therefore, the present ignition time was expected to show similar characteristics due to the same reason. Ignition time, however, decreased monotonously with pressure, and even at supercritical pressures, the ignition time behavior did not change much. Being different from the case of combustion, it is suggested that drastic changes of properties did not take place in ignition processes.

Introduction

Most practical combustors are operated at high pressures, and combustion pressure has continued to increase year by year. However, knowledge of ignition and combustion mechanisms at high pressures is limited, and new approaches to research are especially needed to elucidate their behaviors at supercritical pressures.

Pioneer work on high-pressure combustion was conducted by Faeth and coworkers [1,2] who found that the lifetime of a single burning droplet decreased with pressure and then slightly increased at supercritical pressure. Gollahalli and Brzustowski [3] measured the extinction velocity of a flame established forward of a model droplet, showing that it increased with pressure. Kadota and Hiroyasu [4] also showed that the droplet lifetime decreased with pressure. Recently, one of the present authors and his group [5–7] reported the interesting fact that the burning rate constant has a maximum point around the critical pressure. This was confirmed by the measurement of the droplet lifetime in a microgravity field and the estimation of the burning rate constant based on a microgravity experiment [8].

Tsukamoto and Niioka [7] made a numerical simulation of a single-fuel droplet burning in a high-pressure oxidant environment and showed that the maximum burning rate constant resulted from significantly variable properties around the critical pressure. A diffusion flame on the liquid fuel surface exposed to an oxidant stagnation-point flow was also investigated under high pressures [9], because this counterflow diffusion flame is similar to the diffusion flame surrounding the fuel droplet [6]. The flame extinction experiments showed that a diffusion flame might be controlled by chemical kinetics, which changes with pressure, but that kinetics itself did not affect the maximum burning rate constant phenomenon.

Numerical simulations were also conducted on evaporation [10] and ignition of a droplet [10,11], and some characteristics due to variable properties under critical to supercritical pressures were obtained. Ignition experiments, however, have not been carried out, mostly due to the difficulty of conducting high-pressure experiments. Only one ignition experiment [12] at high pressures over the critical point for some fuels has been reported, but the droplet size was quite large, i.e., over 1.6 mm. Therefore, the characteristic ignition phenomena [13–17] appearing in small droplets are not dealt with in Ref. 12.

In the present experiment, ignition times of a fuel droplet with a diameter of 0.35–1.4 mm, suddenly

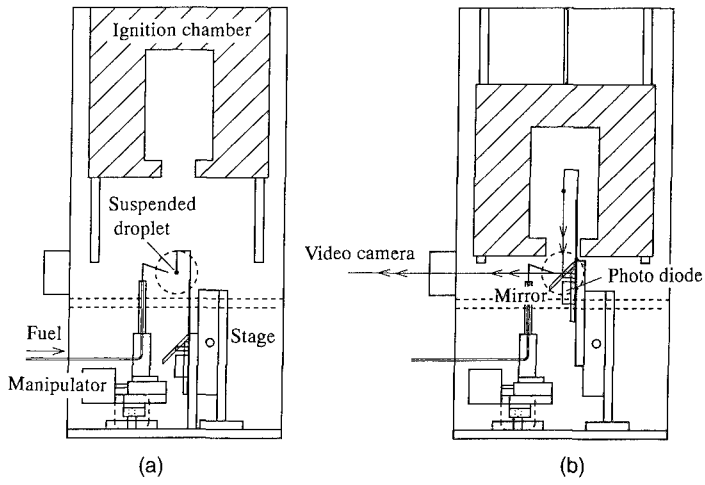

FIG. 1. Schematic explanation of the experimental setup inside the high-pressure vessel.

exposed to a hot oxidant atmosphere, were measured under high pressures of up to 3 MPa; their behaviors in a high-pressure ambient are discussed here. As was the case in previous studies [13–17], the ignition time increased with an increase in the droplet diameter, but when the diameter became smaller, the ignition time again increased. The variation of ignition time with the droplet diameter, therefore, had a minimum at a certain diameter. When the droplet diameter was further decreased, ignition time went to infinity and ignition did not take place. This is because the evaporation mass flux increases in smaller droplets, and the chemical reaction rate is insufficient to cause consumption. Finally, there is a limiting diameter below which ignition is impossible. This interaction of or competition among phenomena of mass transfer and chemical kinetics is similar to the ignitable limit in the counterflow system of fuel flow and airflow [6,9]. The objective of the present experiment was to examine the high-pressure behavior of these interacting phenomena in droplet ignition, with special attention to the ignition characteristics in high pressure over the critical point.

Experimental Apparatus and Method

The present experimental apparatus and techniques are similar to those previously used [12,14–18]; namely, a suspended fuel droplet is quickly inserted into an electric furnace and suddenly exposed to a hot air environment. The point which is most difficult and also different from the preceding experiment is that the whole experimental sequence must proceed in a high-pressure vessel with a pressure of up to 3 MPa.

Figure 1 is a schematic representation of only the inside of the high-pressure vessel. The state before a droplet enters the furnace is shown in Fig. 1a, and that after the droplet enters the furnace is shown in Fig. 1b. As seen in Fig. 1a, liquid fuel is supplied from a high-pressure micropump into the high-pressure vessel and a small amount of it spills from the point of a fine stainless steel tube, which is adjusted by a manipulator. A droplet with a diameter of 0.35–1.4 mm is put onto a fine silica fiber with a diameter of 100 μm. In order to attach the droplet easily, the end of the silica fiber is spherical with a diameter of about 250 μm.

The stage at which the mirror is installed and the silica fiber with a droplet shifts upward about 10 cm, followed by lowering of the ignition chamber, which is heated electrically in advance, is shown in Fig. 1b. The droplet is surrounded by heated walls with a temperature of up to 950 K, and therefore, its temperature is increased mainly by radiative heating. The droplet is observed by means of a mirror and a pyrex glass window, with simultaneous detection of ignition moment by a photodiode, whose response time is about 1.8 μs. Time zero is defined as the moment when a droplet passes through the entrance of the electric furnace and its moment is detected by a photointerrupter.

The size of the experimental high-pressure vessel is 424 (width) $\times$ 424 (depth) $\times$ 700 (height) mm^3, and its interior is cylindrical with a diameter of 250 mm and a height of 500 mm. The above-mentioned experimental setup, shown in Fig. 1, is installed in this cylindrical part of the high-pressure vessel, having a diameter of 50 mm, with three windows.

Fuels used are *n*-heptane as a volatile fuel and *n*-hexadecane as a less volatile one. The initial temperature of a droplet is room temperature, and the ambient pressure is 0.1–3 MPa.

A droplet is suddenly immersed in a hot air environment. However, as shown by an alumel-chromel thermocouple with a diameter of 12.7 μm placed at the droplet position instead of the droplet, 70 ms is

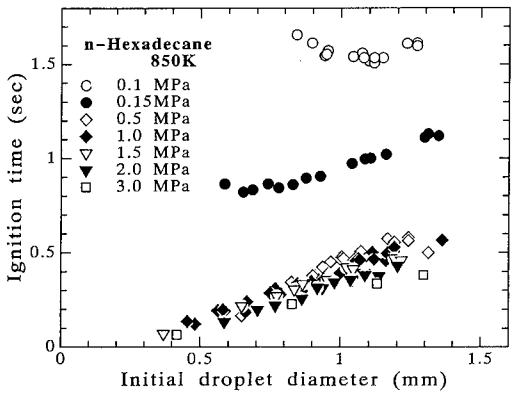

FIG. 2. The variation of ignition time with the initial droplet diameter at 850 K and at various pressures for n-hexadecane.

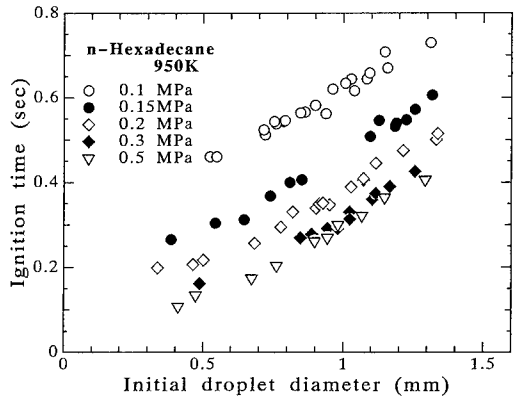

FIG. 3. The variation of ignition time with the initial droplet diameter at 950 K and at low various pressures for n-hexadecane.

required until the temperature attains the furnace temperature from the initial temperature. The actual time for this rise in temperature must be shorter since the thermocouple has a time constant for heat conduction. Because of this elapse of time, short ignition times less than about 100 ms cannot be considered exactly as the ignition time of a droplet suddenly exposed to a specified high temperature.

Here, we must look at the effect of natural convection. An OH band emission image recorded by an intensified charge coupled device (CCD) camera was first emitted in a region below the droplet and then began to surround the droplet, because the evaporated fuel gas descended due to natural convection. However, the time from the emission to ignition was less than 30 ms, which can be neglected in the present ignition time range. Also, it is evident by microgravity experiments [19] that ignition time differences are quite small between the normal gravity and the microgravity, and therefore, the effect of natural convection on ignition of a droplet is small.

Results and Discussion

Figure 2 shows the variation of ignition time with initial droplet diameter for hexadecane at an ambient temperature 850 K. As the ambient pressure increased, ignition time decreased, but the tendencies of ignition times were various. A region of negative slope of the experimental data existed at atmospheric pressure (0.1 MPa), that is, the ignition time of droplets with a small initial diameter decreased as the diameter increased. On the other hand, at elevated pressures, the ignition time increased as the droplet diameter increased.

The above-mentioned ignition time characteristics are due to the competition between the mass transfer and the chemical reaction. Large droplets have a large heat capacity and need a comparatively long time for the surface temperature to increase up to around the boiling point. This is because the general tendency of ignition time showed a positive slope in Fig. 2. However, as demonstrated in previous reports [13–17], since a droplet with a small diameter (d) produces a large mass flux ($\dot{m}$) of fuel gas ($\dot{m} \sim 1/d$), a longer chemical reaction time is needed, and as a result, the slope of experimental data might become negative in $P = 0.1$ MPa.

The reason why this tendency was reversed at high pressures is as follows. The mass transfer time (t_m) is proportional to d^2/D, where D is the diffusion coefficient, and therefore, t_m is roughly proportional to P, where P denotes pressure. On the other hand, the chemical reaction time (t_c) is in proportion to $\rho/\dot{\omega}$, where ρ and $\dot{\omega}$ denote density and chemical reaction rate, respectively, which is proportional to the square of density in the reaction of two molecular reactions, and therefore, t_c is proportional to P^{-1}. This implies that the second Damköhler number, $D_2 = t_m/t_c \sim P^2$, increases with pressure and that the contribution of the reaction time to ignition time does not play a dominant role in high pressure.

Ignition times are plotted at a high ambient temperature of 950 K in Fig. 3. The datum points on the left side in Figs. 2 and 3 correspond to ignitable limit diameters, below which a droplet had vaporized before ignition and ignition was impossible because of the long reaction time. These limit diameters shifted to smaller diameters at higher pressures, which also means that the Damköhler number increases at high pressures. If the ambient temperature increases, the reaction time becomes shorter, and it is difficult for the minus slope to appear. Therefore, Fig. 3 shows only the positive slope even at atmospheric pressure.

Figures 4 and 5 show ignition times for n-heptane. The boiling point of n-heptane is lower than that of n-hexadecane. Therefore, n-heptane easily vaporizes

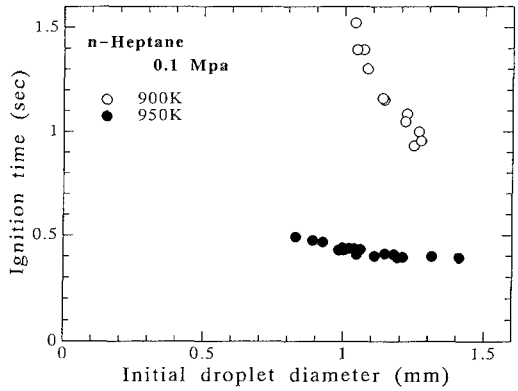

FIG. 4. The variation of ignition time with the initial droplet diameter at 900 K and at low various pressures for n-heptane.

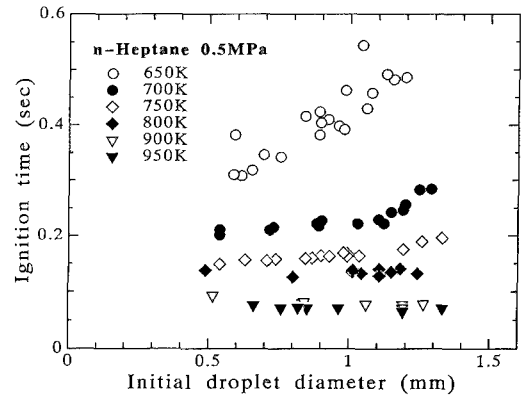

FIG. 6. The variation of ignition time with the initial droplet diameter at various ambient temperature and at 0.5 MPa for n-heptane.

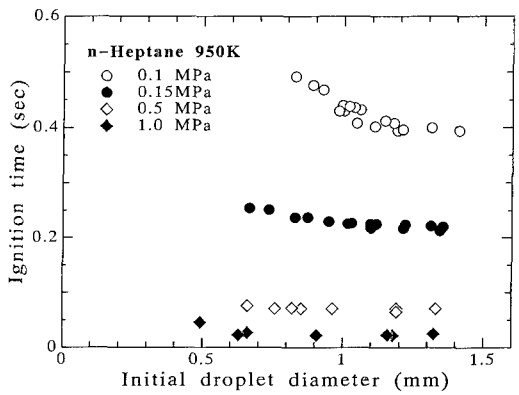

FIG. 5. The variation of ignition time with the initial droplet diameter at 950 K and at low various pressures for n-heptane.

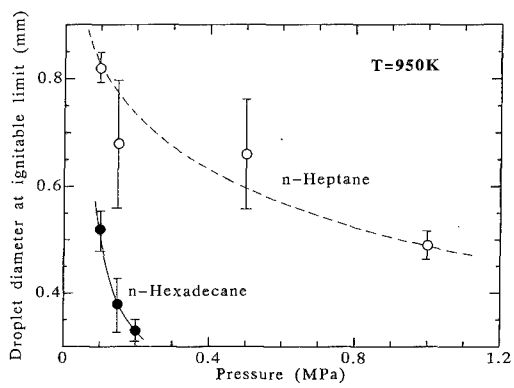

FIG. 7. Droplet diameter at ignitable limit plotted as a function of pressure at 950 K.

and the vaporization time becomes quite short. This phenomenon is more significant in smaller droplets. As a result, since a large mass flux of vaporized fuel gas leads to a long reaction time, a steeper negative slope is obtained at 0.1 MPa in Fig. 4. With an increase in initial droplet diameter, there must be a minimum ignition time such as shown in Fig. 2. As we increased pressure or ambient temperature, as seen in Figs. 4 and 5, however, ignition time curves with gentle slopes gradually resulted.

We confirmed this ignition time behavior in detail. Figure 6 shows the case of a pressure of 0.5 MPa for various ambient temperatures. The datum points on the left side in Fig. 6 correspond approximately to the ignitable limits as in the preceding figures. It can be noticed that the negative slopes obtained in Figs. 4 and 5 were no longer observed at a pressure of 0.5 MPa, even at various low ambient temperatures.

Noticeable errors appear easily in very short ignition times less than approximately 0.1 s at high pressures due to the time needed for a droplet to be inserted into the furnace. Experimental errors also exist in the ignitable limit of diameter below which a droplet has completely vaporized before ignition. However, the general tendency of the ignitable limit of diameter to decrease as pressure increases was consistent with the case of n-hexadecane. Figure 7 shows the droplet diameter at the ignitable limit at an ambient temperature of 950 K. The upper sides of the curves in Fig. 7 correspond to the ignitable region and the lower sides to the nonignitable region. It is natural that the minimum droplet diameter for n-heptane is larger than that for n-hexadecane, because the mass flux for n-heptane is too large to react quickly. In addition to this, the temperature of evolved fuel gas also affects the minimum droplet diameter. A droplet of n-hexadecane releases hot fuel gas since the surface temperature close to the boiling point is quite high, but n-heptane evolves a large

mass flux of cold fuel gas. Therefore, it follows that a long reaction time is needed, and as a necessary consequence, the ignitable limit diameter is larger than in the case of n-hexadecane.

Compared with the same ignition problem solved numerically, experimental data of ignitable limit are one order greater than numerical data, but qualitatively, a good consistency was obtained [11]. As the most possible reasons for this discrepancy, internal flow in a droplet and cooling by the quartz fiber used for suspension, which were neglected in the numerical calculation, should be considered. Since a droplet is suspended in a small sphere with a diameter of 250 μm at the end of a silica fiber, the ignitable limit diameters may not be measured accurately. In the case of higher ambient temperature, for example, the ignitable limit of diameter should decrease, and so this effect may be significant. As mentioned earlier, the smaller a droplet is during vaporization, the larger the mass flux of fuel gas becomes. Therefore, in the present range of the ambient temperature, the condition for ignition should become stricter, and it is quite logical to consider that ignition no longer occurs if a droplet continues only to vaporize up to around 250 μm. The other plausible reason for the discrepancy between the preceding theory and the present experiment may be the chemical parameters. Except for the region of the ignitable limit, however, the discrepancy is not so large. Therefore, it is considered that the most probable reasons must be the physical effects mentioned above.

The variation of ignition time with pressure for various ambient temperatures is shown in Figs. 8 and 9. As explained above, ignition time of a droplet with a diameter of 1 or 0.8 mm decreased monotonically with pressure, showing a strong dependence of ignition time in lower pressures. (The longitudinal axis in Figs. 8 and 9 is a logarithmic scale.) Furthermore, it should be noted that a smooth variation of ignition time was observed even at pressures above the critical pressure of n-hexadecane (P_c = 1.53 MPa). Previous reports [5–7] showed that the burning rate constant of a droplet had a maximum around the critical pressure, both experimentally and theoretically. The characteristic feature around the critical pressure originates from the drastic variation of properties concerned with heat and mass transfer. This curious change around the critical pressure did not occur in the present ignition time experiments. This tendency is consistent with the theoretical results [11].

The complicated critical condition may not be attained even at an ambient pressure equal to the critical pressure of a fuel, unless the temperature of a droplet is close to the critical temperature. The present case deals with ignition, and so, the whole ignition event must take place in the field of temperature below the critical temperature around a droplet. Moreover, the present case is a mixture of fuel and air. In the vicinity of the droplet surface,

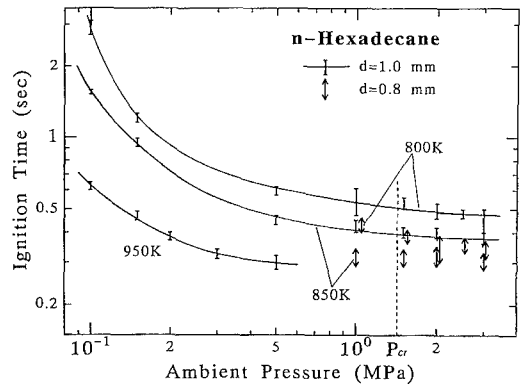

FIG. 8. The variation of ignition time with pressure for n-hexadecane.

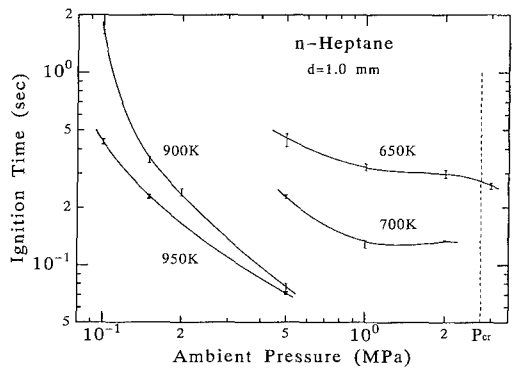

FIG. 9. The variation of ignition time with pressure for n-heptane.

therefore, a condition close to the critical condition must not be formed since the fuel concentration is not very high, being different from the case of combustion.

A large thermal conductivity around the critical pressure was expected to enhance the heat transfer to a droplet, resulting in rapid ignition at high ambient temperatures. Conditions close to the complex critical conditions may be difficult in the case of n-hexadecane in Fig. 8, because the critical temperature of n-hexadecane is high (722 K). Since the critical temperature of n-heptane is 540 K, one datum point in Fig. 9 might give the characteristic feature mentioned above. However, in order to further elucidate this ignition behavior around the critical pressure, further difficult experiments, as well as further numerical simulations, must be carried out.

Concluding Remarks

High-pressure experiments in which a single fuel droplet was suddenly placed in a high-temperature ambient resulted in the following findings:

1. Ignition time of a droplet decreased monotonically with pressure, and a significant variation of ignition time was not observed around the critical pressure, unlike the case of a burning droplet.
2. Ignition time near the ignitable limit decreased with the initial droplet diameter at low pressures, but this phenomenon disappeared at high pressures.
3. The initial droplet diameter at the ignitable limit decreased as pressure increased.

The main difficulty of the experiment was to attach a droplet to a fine silica fiber at supercritical pressures because of the very small value of the surface tension force. More precise experiments under a microgravity field and using a free droplet will be conducted in the future.

Acknowledgment

The authors express their thanks to Mr. S. Hasegawa for his technical assistance on this experiment.

REFERENCES

1. Faeth, G. M., Dominicis, D. P., Tulpinsky, J. F., and Olson, D. R., *Twelfth Symposium (International) on Combustion,* The Combustion Institute, Pittsburgh, 1969, pp. 9–18.
2. Canada, G. S., and Faeth, G. M., *Fourteenth Symposium (International) on Combustion,* The Combustion Institute, Pittsburgh, 1973, pp. 1345–1354.
3. Gollahalli, S. R., and Brzustowski, T. A., *Fifteenth Symposium (International) on Combustion,* The Combustion Institute, Pittsburgh, 1975, pp. 409–417.
4. Kadota, T., and Hiroyasu, H., *Eighteenth Symposium (International) on Combustion,* The Combustion Institute, Pittsburgh, 1981, pp. 275–282.
5. Takahashi, M., Niioka, T., Sato, J., and Yamakawa, M., *Burning Rate Constant of Fuel Droplet under High Pressure,* Technical Report of National Aerospace Laboratory TR-1001, (in Japanese) 1988.
6. Niioka, T., Hasegawa, S., Tsukamoto, T., and Sato, J., *Combust. Flame* 86:171–178 (1991).
7. Tsukamoto, T., and Niioka, T., *Microgravity Sci. Technol.* 4:219–222 (1993).
8. Sato, J., Tsue, M., Niwa, M., and Kono, M., *Combust. Flame* 82:142–148 (1990).
9. Hiraiwa, T., Ono, N., and Niioka, T., *Twenty-Fourth Symposium (International) on Combustion,* The Combustion Institute, Pittsburgh, 1993, pp. 239–245.
10. Tsukamoto, T., and Niioka, T., in *Dynamics of Heterogeneous Combustion and Reacting Systems* (A. L. Kuhl, et al., Eds.), Progress in Astronautics and Aeronautics, AIAA Inc., New York, 1993, Vol. 152, pp. 263–279.
11. Tsukamoto, T., Okada, H., and Niioka, T., *Trans. Jpn. Soc. Aero. Space Sci.* 35:165–176 (1993).
12. Kadota, T., Hiroyasu, H., and Oya, H., *Trans. Jpn. Soc. Mech. Eng.* 41:2475–2485 (1975) (in Japanese).
13. Niioka, T., Saitoh, T., and Ishiguro, S., *A Numerical Approach to Fuel Droplet Ignition,* Technical Report of National Aerospace Laboratory TR-628T, 1980.
14. Saitoh, T., Ishiguro, S., and Niioka, T., *Combust. Flame* 48:27–32 (1982).
15. Takei, M., Tsukamoto, T., and Niioka, T., *Combust. Flame* 93:149–156 (1993).
16. Mawid, M., and Aggarwal, S. K., *Combust. Sci. Technol.* 65:137–146 (1989).
17. Faeth, G. M., and Olson, D. R., *SAE Trans.* 77:1793–1802 (1968).
18. Bergeron, C. A., and Hallett, W. L. H., *Combust. Sci. Technol.* 65:181–194 (1989).
19. Takei, M., Kobayashi, H., and Niioka, T., *Microgravity Sci. Technol.* 3:184–187 (1993).

COMMENTS

I. Gökalp, CNRS-LCSR, France. Could you comment on the buoyancy effects on your results, especially under high pressure conditions?

Author's Reply. Generally, the buoyancy effect is large at high pressure, but it is expected that the effect on ignition time is not significant, because ignition time becomes short at high pressure. Actually, ignition point is located close to the droplet at high pressure, although ignition occurs beneath the droplet at low pressure.

•

C. T. Avedisian, Cornell University, USA. 1. How were the 0.5 mm equivalent diameter droplets placed on the 100 μm diameter fibers?

2. Could you state how droplet dimensions were extracted from the movie films and approximately how many data sets (d,t) figured into determining a given burning rate?

Author's Reply. 1. A very small amount of liquid fuel supplied from a micropump spills from the point of a fine stainless-steel tube and is put onto a fine fiber. It was very hard work, but by trial and error droplets with a diameter up to 0.35 mm were possible.

2. The burning rate constant is not the present subject, but it was published in Refs. 5 and 6. The burning rate

constants at very high pressures were determined by several data points at least, except the initial transient region.

•

Michael Winter, United Technologies Research Center, USA. When the conditions exceed the critical pressure and temperature, do the droplets remain suspended on the fiber, or do they fall off due to loss of surface tension?

Author's Reply. If the critical condition is attained, the droplet cannot remain suspended. In the present case, however, the droplet temperature must be lower than the critical temperature. Before the temperature rises to the critical temperature, ignition must take place. Sometimes after ignition, droplet slides down a silica fiber.

•

Alon Gany, Princeton University, USA. Did you measure the temperature inside the droplet during the ignition process?

Author's Reply. No, we did not measure the temperature inside the droplet. A fine silica fiber has a bead at the end, and so the temperature measurement does not have a significant meaning in this experiment.

Twenty-Fifth Symposium (International) on Combustion/The Combustion Institute, 1994/pp. 455–461

EFFECTS OF NATURAL CONVECTION ON TWO STAGE IGNITION OF AN *n*-DODECANE DROPLET

MITSUAKI TANABE MICHIKATA KONO
Department of Aeronautics and Astronautics
University of Tokyo
Hongo, Bunkyo-ku, Tokyo 113, Japan

JUN'ICHI SATO
Research Institute
Ishikawajima-Harima Heavy Industries Co., Ltd.
Koto-ku, Tokyo 135, Japan

AND

JENS KOENIG, CHRISTIAN EIGENBROD AND HANS J. RATH
ZARM (Center of Applied Space Technology and Microgravity)
Bremen University
Am Fallturm, D-28359 Bremen, Germany

The effects of natural convection on two-stage spontaneous ignition of a fuel droplet were studied experimentally. A suspended *n*-dodecane droplet of 0.7 mm in its initial diameter was employed. Ignition phenomena were observed by a fine thermocouple (0.025 mm) and by an interferometer so as to detect an invisible cool flame. A direct photographic method with a back light was also used to measure the droplet diameter. Ambient temperature was limited within the range where the cool flame can be observed (500 to around 800 K) and ambient pressure ranged between 0.1 and 1.0 MPa. Experiments were carried out under normal and microgravity conditions, and results were compared.

Investigations were done mainly on the induction times at 0.2 and 1.0 MPa. Experiments showed longer first induction times (time to appearance of cool flame) under normal gravity than under microgravity in certain ambient conditions. Significant differences between critical temperatures, below which cool flame or hot flame does not appear, were also observed between the two gravity conditions. The induction times differed up to a factor of 3, and the critical temperature differed about 60 K. For the second stage, slightly increased induction times were observed under normal gravity conditions at 0.2 MPa. Differences observed between both gravity conditions can be explained by the effects of natural convection driven by the downward force due to the dense fuel vapor and by the buoyancy due to the cool flame.

Introduction

Knowledge of spontaneous ignition characteristics of a fuel droplet is indispensable to understand spray combustion and to design practical combustors.

The models of the ignition process had been well developed, and it is now possible to simulate ignition characteristics of the isolated single droplet by numerical approaches [1–4]. These theoretical models usually neglect natural convection to simplify the formulation and to save computation time. On the other hand, most of the experimental works have been done under normal gravity, using large droplets of more than 0.5 mm in diameter, where natural convection is inevitable. Hence, almost no experimental data are available for the validation of the theoretical models. To obtain the required experimental data, microgravity experiments are desirable, as natural convection is negligibly weak.

As well as the availability of the microgravity data, understanding of the effects of natural convection is necessary because it provides a useful insight when the models are required to be calibrated or validated by the existing experimental data. Microgravity experiments have often been performed in the field of droplet evaporation and combustion, and effects of natural convection have been well documented by comparing normal and microgravity data [5–7]. However, only a few studies have been done by using microgravity on the spontaneous ignition of the single fuel droplet [8–10]. Faeth and coworkers [8,10] found slight differences between ignition times un-

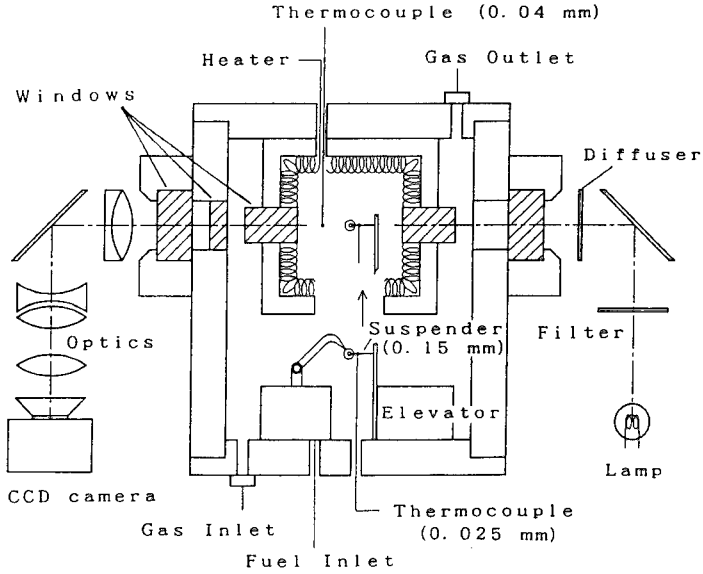

FIG. 1. Schematic of the experimental apparatus.

der both gravity conditions. Since the differences in their results were not significant, the role of natural convection has not been recognized as important and is usually neglected. Their experiments were conducted at atmospheric pressure with about 1 s of microgravity. Natural convection is stronger at high pressure, and it develops with time. Thus, investigations at higher pressures with longer periods of microgravity are necessary to clarify the effects of natural convection.

In the field of premixed combustion, two-stage ignition phenomena due to the different chemical reaction mechanisms for low and high temperatures is well known [11–14]. It has been well recognized that the low-temperature mechanism of the first stage is of great importance because it dominates characteristics of unwanted self-ignition like engine knock. The low-temperature mechanism can also play an important role in the ignition process of droplets over a wide range of ambient conditions. Indeed, even if the ambient temperature is too high for this mechanism, there is always a certain region around the droplet where the gas temperature is sufficiently low so that the mechanism works. This point, however, has not been well recognized so far, and no systematic research on the two-stage ignition of single droplets has been done. Ignition phenomena were often observed by light emission from flames, and it was impossible to detect the first stage of a cool flame in which light emission is very weak. As a result, studies had been restricted to the second stage.

Recently, the authors succeeded in observing the first stage by using a fine thermocouple and a double-exposure-type interferometer, both of which can detect ignition through a sudden temperature change. Through application of this technique and by using microgravity conditions, the present work clarifies the two-stage ignition of a fuel droplet under the absence of natural convection.

Experimental Apparatus

Spontaneous ignition experiments were carried out with the apparatus shown in Fig. 1.

This apparatus simulates the situation of a single droplet that is suddenly injected into a combustor. A fuel droplet, which is formed at the lower section of the high-pressure chamber, is quickly inserted into the electric furnace situated in the upper section. The time required to move the suspended droplet was 120 ms. This yields an almost stepwised gas-phase temperature rise around the droplet.

The electric furnace produces an ambient temperature up to 850 K. The lower section, where the droplet is produced, was kept at room temperature so that the initial droplet temperature can be defined as room temperature. The inner wall of the electric furnace is covered with a material of high-heat conductivity to achieve an almost uniform temperature at its surface. This results in a small temperature gradient in the ambient gas.

n-Dodecane was used since it is one of the typical components of practical fuels. The initial droplet diameter (D_0) was controlled within a narrow range around 0.7 mm, and the droplet was suspended on a 0.15-mm quartz glass filament. This suspender was placed horizontally.

Air was used as the ambient gas. Ambient temperature (Ta) ranged from 500 to around 800 K and ambient pressure (Pa) from 0.1 to 1.0 MPa.

Two thermocouples were used. One (type *K*, 0.04

mm in diameter) was attached to the furnace to measure the ambient temperature. The other (type S, 0.025 mm) was attached to the suspender about 3.5 mm away from the droplet center. This was used to detect ignition by measuring the gas temperature in the vicinity of the droplet.

A charge coupled device (CCD) camera was used to take direct photographs of the igniting droplet with a very dim backlight. These pictures were recorded on an 8-mm video tape with a frame speed of 50 s^{-1}. The droplet diameters were measured from these pictures. Since the droplet takes an ellipsoidal shape, the diameter was defined as that of a sphere that has the same volume as the ellipsoid. Instead of these optics shown in the figure, a Michelson interferometer was employed in some of the normal gravity experiments. Interferograms were used to observe the density field around the droplet and to determine the place where ignition starts.

Microgravity experiments were conducted with the same apparatus as normal gravity experiments using the 5- and 110-m droptowers (ZARM, Germany) and the parabolic flights (Caravell, France). Each of these enables about 1, 4.7, and 20 s of microgravity, respectively.

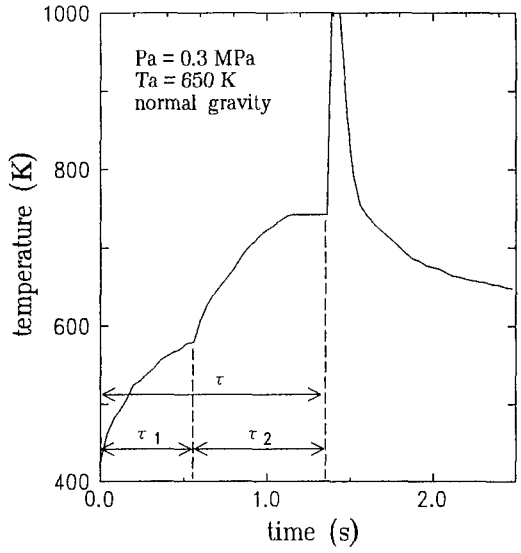

FIG. 2. Gas-phase temperature history in the vicinity of droplet in the case of two-stage ignition.

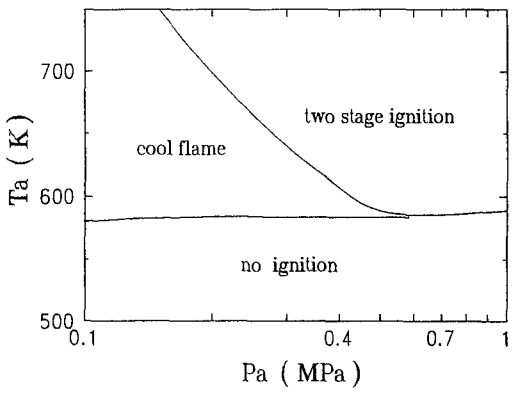

FIG. 3. Ignition regions of 0.7-mm *n*-dodecane droplets at normal gravity.

Results and Discussions

Ignition Criteria and Ignition Regions

In the present work, ignition was determined as a sudden inflection of the gas-phase temperature in the vicinity of the droplet, which is measured by the thermocouple.

A typical temperature history in the vicinity of the droplet in the case of two-stage ignition is shown in Fig. 2. The origin of abscissa is when the droplet reaches a specific position in the furnace. At this instant, the thermocouple shows a temperature lower than the ambient temperature of 650 K. This is due to the cooling effect caused by the suspender, which was initially room temperature.

Two inflections of the gas-phase temperature can be seen in this figure. The period between the time 0.0 and the first inflection is defined as "τ_1" (first induction time), as shown in the figure. In a similar manner, the period between the first inflection and the second one is defined as "τ_2" (second induction time), and that between time 0.0 and the second inflection is defined as "τ" (total induction time).

After the first inflection, the measured temperature rises beyond the ambient temperature and reaches a plateau of about 740 K. This temperature is related to the temperature of a cool flame. Experiments at other ambient temperatures show that the level of the plateau has a week dependence on ambient temperature. These facts agree with the result from the temperature measurements of cool flames that were stabilized by a premixed burner [13]. Though their measurements were done using heptane fuel, the important mechanisms of the cool flame of the *n*-dodecane droplet are believed to be the same. This plateau seems to exist as a result of an overall negative temperature dependence of the reaction rate around 800 K [14,15]. After the second inflection, the temperature rises to more than 1000 K, and a bright yellow flame appears. The first inflection is due to the onset of cool flame, and the second one is due to the ignition of the hot flame.

Ignition regions under normal gravity are shown in Fig. 3. In the cool flame region, where a relatively low temperature exists, only the first stage occurs, but

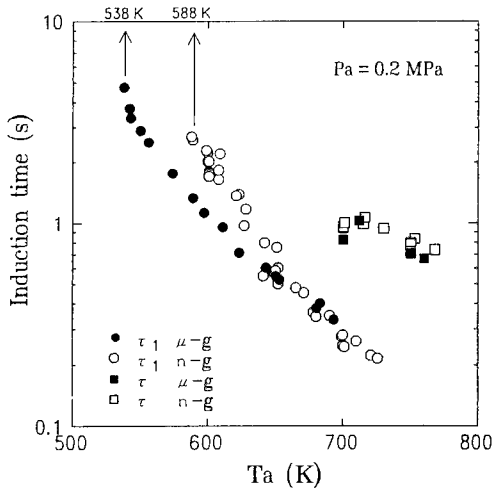

FIG. 4. Comparison of induction times under normal and microgravity conditions at 0.2 MPa.

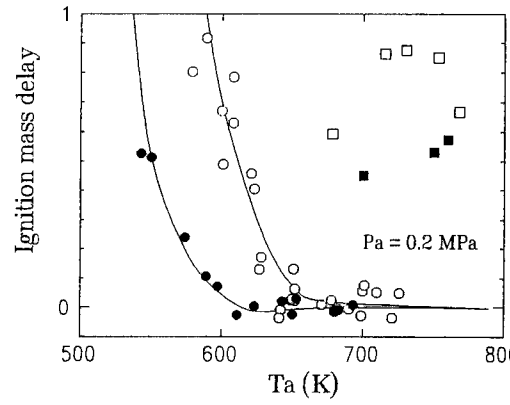

FIG. 5. Comparison of ignition mass delays under normal and microgravity conditions at 0.2 MPa (circles: first stage; squares: second stage).

second step, hot flame, does not follow it. The droplet disappears before ignition. Two-stage ignition was observed at higher pressures. As pressure increases, the second induction time decreases very quickly. Namely, τ_2 becomes almost zero and τ becomes τ_1 at high pressures. As the second induction time became very short and it was impossible to distinguish the first inflection from the second one, phenomena observed by the thermocouple appeared as if it is one stage at pressures of more than 0.5 MPa. However, a two-step temperature rise could be confirmed even at 1.0 MPa by the interferometry.

At ambient temperatures higher than 750 K, though it is not included in this figure, two-step temperature rise around the droplet can also be observed from the interferograms. That is, even the ambient temperature is higher than the temperature of the cool flame, the low-temperature reactions can cause sudden temperature rise in the vicinity of the droplet where gas temperature is lower. Even if this temperature rise cannot reach the ambient temperature, it must have influence on the ignition phenomena by yielding a rapid evaporation of the droplet since the gas-phase temperature gradient near the droplet surface increases, and heat inflow to the droplet is promoted.

Effects of Natural Convection on Ignition at 0.2 MPa:

Figure 4 shows ambient temperature dependance of the induction times. In this, as well as the following figures, solid symbols show microgravity data, and open symbols show normal gravity data. In these figures, cool flame limits are also shown by means of arrows. Here, the cool flame limit was determined as a critical ambient temperature below which the first stage of cool flame does not appear. Under microgravity conditions, there were a few cases in which the cool flame appeared after it had evaporated completely. However, these cases are excluded here.

The first induction times τ_1 at 0.2 MPa under normal gravity diverge from the microgravity data at a certain point. The ambient temperature at the divergent point is 670 K. In the region where the ambient temperatures are higher than this point, there is no remarkable difference between normal and microgravity. On the other hand, normal gravity data show greatly increased values at temperatures below the point of divergence. They increase to about twice that of microgravity near the cool flame limit. Elongated induction times yield the higher value of the limit under the normal gravity condition. Since the induction time should be shorter than the droplet life time, a longer induction time works negatively to achieve the occurrence of cool flame during the droplet life time, and it narrows down the cool flame region.

The total induction times τ at 0.2 MPa under normal gravity are lengthened slightly for all conditions.

For the purpose of estimating the amount of vapor formation preceding the onset of the first stage, the ignition mass delay [2] is plotted against ambient temperature in Fig. 5. This ignition mass delay was calculated using

$$1 - (D_i/D_0)^3$$

where D_0 is the initial droplet diameter and D_i is the diameter at the onset of the first stage, both of which are measured from the video pictures. This definition was chosen because one can estimate the fractional mass loss of the droplet by simple volume measurement. In some cases, the ignition mass delays were

slightly negative, which simply means an expansion of the droplet through density decrease in the liquid phase due to temperature increase.

Below a certain temperature, the ignition mass delays of the first stage differ for the two gravity conditions. This temperature is almost the same value as that of the diverging point, which could be found in Fig. 4. Above this temperature, the ignition mass delays take almost the same value for the two gravity conditions, which is approximately zero. This indicates that the droplet is still in its heat-up period and that it has produced only a small amount of vapor before the onset of the first stage. Thus, the different induction times between both gravity conditions happened in cases where the cool flame appears after the heat-up period. On the contrary, there is no significant difference if it appears during the heat-up period.

The reason why the induction times differ only in the cases where the cool flame appears after the heat-up period can be explained considering the strength of natural convection. Natural convection is driven by two kinds of density differences between the gas in the vicinity of the droplet and the surrounding ambient gas. One is due to the reduced gas-phase temperature around the droplet because the droplet has a lower temperature than ambient gas and acts as a heat sink. The other is due to n-Dodecane vapor, which is denser than air even at an identical temperature, due to its larger molecular weight. During the heat-up period, there is little vaporization, and natural convection is driven only by the density difference induced by the reduced temperature. After the heat-up period, a quantity of n-Dodecane evaporates from the droplet, and this causes strong convection. Thus, natural convection suddenly becomes stronger after the heat-up period.

The reason why the first induction times under normal gravity are lengthened can be explained as follows: Whether the induction times under normal gravity are lengthened or shortened is determined by two competing effects. On one hand, the period needed to heat up the droplet and let it evaporate is shorter under normal gravity compared with microgravity. This is because natural convection promotes the heat inflow to the droplet [16] and contributes to a quick temperature rise on the droplet surface. This effect helps to shorten the induction time. Hence, if the induction time is vapor-formation predominated, it will be shortened by natural convection. On the other hand, the temperature rise due to chemical reactions is slower under normal gravity since the convectional flow around the droplet removes heat and chemical intermediates that are produced by chemical reactions in the gas phase. This effect lengthens the induction time under normal gravity. That is, under normal gravity, the Damkohler number is small, due to a short characteristic residence time caused by natural convection, and the ignitability decreases. Thus, if the induction time is predominated by the chemical reaction, it must be elongated by natural convection. At higher temperatures, the chemical reaction rates are very high, and they cause cool flame soon after vapor formation. The largest part of the induction time is the time that is necessary to start producing fuel vapor. This is true especially in the temperature region where the cool flame starts during the above-mentioned heat-up period. At lower temperatures, however, chemical reaction rates are very low, and the cool flame appears after the mixture of fuel and air is well developed. Thus, the induction time is predominated by the chemical heat release.

There is almost no effect of natural convection on τ_1 in the high-temperature region because convection itself is not well developed. On the contrary, natural convection lengthens the induction times in the low-temperature region because convection is strong enough, and the time is controlled through the chemical heat release.

As temperature decreases, the effect of convection appears stronger because of the following two facts: First, the natural convection can be stronger at low temperatures because the induction time is longer and the convection can develop with time. Second, at lower temperatures, the heat and species loss due to the convection becomes more significant relative to the production of them by chemical reaction because reaction becomes slower very rapidly as temperature decreases but the loss does not.

To observe the density distribution around the droplet, a Michelson interferometer was used. In Fig. 6, fringes that are extracted from digitized interference images are shown. The numbering of each fringe is a measure of the density averaged through the optical path; that is, as the number increases, density increases. Positive values express higher density than the one of the ambient gas, and negative values express lower density.

A development of downward natural convection can be seen in pictures 1 to 2 of Fig. 6. The dense vapor drives strong downward natural convection that develops over time. In picture 3, the place where a certain temperature increase (density decrease) first occurred was detected successfully. The first stage starts below the droplet under the ambient conditions where the induction periods are elongated through natural convection. In this figure, the first stage started near the edge of the vapor layer. There is enough fuel vapor, the residence time is relatively long, and the temperature is high at the boundary of the convective flow and the quiescent ambient gas. Thus, the probability to start the first stage seems to be highest at this region.

After the onset of the first stage, a weak upward natural convection appears (picture 4). This convective flow is not so strong that it can deform the vapor layer around the droplet. As seen from this picture, the density field around the droplet seems to be

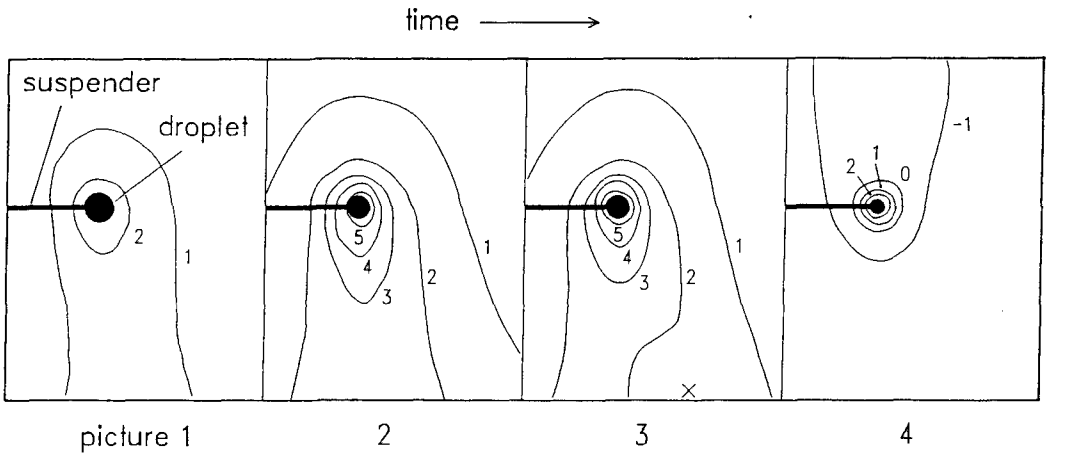

FIG. 6. Density field around droplet by interferometric fringes: $Pa = 0.2$ MPa and $Ta = 590$ K, normal gravity. (1) At 580 ms, convection starts; (2) at 2580 ms, development of convection; (3) at 2600 ms, ignition, ignition point is marked by "X"; (4) at 2640 ms, during combustion of cool flame.

spherical. The convection is weak because the temperature of this cool flame is very close to the ambient temperature and also because the downstream of fuel vapor compensates for it.

The difference of total induction times under both gravity conditions in Fig. 4 can be determined as the difference of the second induction times, as the first induction times do not differ for either gravity conditions at high ambient temperatures. During the second induction times, a cool flame exists. The slight difference of total induction times for both gravities is caused by natural convection due to both cool flame and fuel vapor. Since the buoyancy due to cool flame and the downward force of fuel vapor compensate with each other, realizing very weak convection, the difference of induction times is slight. Since the ignition mass delays are not around zero, as seen from Fig. 5, indicating that the induction times are dominated by chemical reactions, natural convection lengthens them.

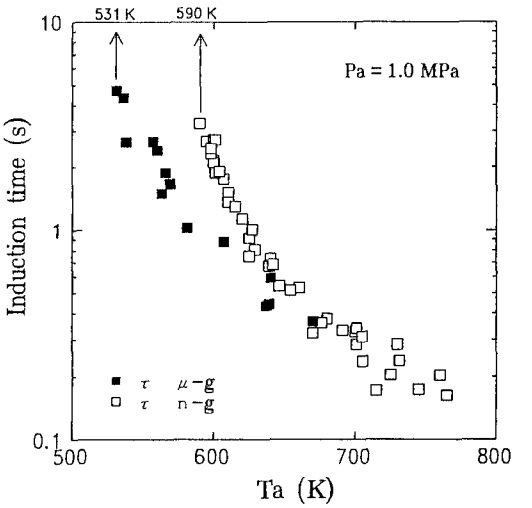

FIG. 7. Comparison of induction times under normal and microgravity conditions at 1.0 MPa.

Effects on Ignition at 1.0 MPa:

Total induction times τ at 1.0 MPa are plotted in Fig. 7. A similar tendency as τ_1 in Fig. 4 can be seen. The ambient temperature is 640 K at the divergent point. Even at temperatures higher than this divergent point, the normal gravity data show slightly increased values, but this difference was determined to be within an acceptable range of deviation. At lower temperatures, the total induction times under normal gravity are elongated and they are three times that of microgravity near the ignitable limit (a critical temperature below which the droplet does not ignite). The ignitable limits differ by about 60 K.

At 1.0 MPa, second induction times are approximately zero. Thus, the total induction time under normal gravity should not be affected by the cool flame. The difference of the total induction times between both gravities is the difference of the first induction times. The difference can be explained in the same way as the case of τ_1 at 0.2 MPa. Namely, strong convection due to dense fuel vapor lengthens the first induction time, and it yields the elongated total induction time. In Fig. 8, the ignition mass delays of 1.0 MPa are shown. The temperature of the diverging point in this figure is the same as in Fig. 7, supporting the above explanation.

Since natural convection is expected to be stronger at higher pressures, the difference between normal

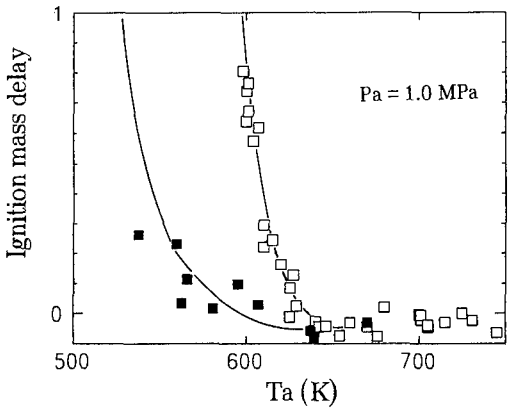

FIG. 8. Comparison of ignition mass delays under normal and microgravity conditions at 1.0 MPa.

and microgravity is more apparent at 1.0 than 0.2 MPa.

Conclusions

From the precise observation of the gas-phase temperature and the density field in the vicinity of the droplet and through comparisons of normal and microgravity data, the following conclusions were reached.

Spontaneous ignition of an *n*-dodecane droplet takes place in two stages. The first induction times at 0.2 and 1.0 MPa are lengthened under normal gravity compared with the microgravity case. This difference occurred at relatively low ambient temperatures, where the first stage of cool flame starts after the heat-up period. It is attributed to the reduced residence time due to the strong convection caused by dense fuel vapor. In such cases, cool flame starts below the droplet.

Total induction times at 0.2 MPa are slightly elongated under normal gravity conditions. The convection caused by a cool flame and fuel vapor elongates them by yielding reduced residence time. It is slightly because this convection is weak, for the buoyancy of the cool flame compensates for the downward force of fuel vapor.

The different induction times yield a significant difference between the cool flame limits or ignitable limits under microgravity and those under normal gravity. Under normal gravity, this temperature is much higher than that under microgravity at both 0.2 and 1.0 MPa.

Acknowledgments

This work is supported by the Special Coordination Fund for Promoting Science and Technology through the Science and Technology Agency of the Japanese Government and by a grant from the German Space Agency (DARA), Funding No. 50QV89633. Special thanks to Dr. H. Nomura and the Nikki Co. for offering a great opportunity of parabolic flights.

REFERENCES

1. Niioka, T., Ishigro, S., and Saitoh, T., Technical Report of National Aerospace Laboratory, TR-628T (1980).
2. Law, C. K., *Combust. Flame* 31:285 (1978).
3. Ruszalo, R., and Hallett W. L. H., *Combust. Sci. Technol.* 86:183 (1992).
4. Mun Y. Choi, Seog Y. Cho, Frederik L. Dryer and John B. Haggard, Jr. "Computational/Experimental Basis for Conducting Alkane Droplet Combustion Experiments on Space-Based-Platforms," *Microgravity Fluid Mechanics, IUTAM Symposium,* Bremen, 1991, Springer-Verlag, New York, p. 337, 1992.
5. Hiroshi Nomura, Michikata Kono, M., Jun'ichi Sato, Günther Marks, Heinrich Iglseder and Hans J. Rath "Effects of the Natural Convection on Fuel Droplet Evaporation," *Microgravity Fluid Mechanics, IUTAM Symposium,* Bremen, 1991, Springer-Verlag, New York, p. 245, 1992.
6. Knight, B., and Williams, F. A., *Combust. Flame* 38:111 (1980).
7. Sato, J., Tsue, M., Niwa, M., and Kono, M., *Combust. Flame* 82:142 (1990).
8. Faeth, G. M., and Olson, D. R., *SAE Trans.* 77:1793 (1968).
9. Takei, M., Kobayashi, H., and Niioka, T., *Microgravity Sci. Technol.* VI/3 (1993).
10. Faeth, G. M., Karhan, B. L., and Yanyecic, G. A., *AIAA J.* 6 (4):684 (1967).
11. Westbrook, C. K., Warnatz, J., and Pitz, W. J., *Twenty-Second Symposium (International) on Combustion,* The Combustion Institute, Pittsburgh, 1988, p. 893.
12. Benson, S. W., *Twenty-First Symposium (International) on Combustion,* The Combustion Institute, Pittsburgh, 1986, p. 703.
13. Morley, C., *Twenty-Second Symposium (International) on Combustion,* The Combustion Institute, Pittsburgh, 1988, p. 911.
14. Ciezki, H. K., and Adomeit, G., *Combust. Flame* 93:421 (1993).
15. Griffiths, J. F., *Combust. Flame* 93:202 (1993).
16. Ranz, W. E., and Marshall, W. R., Jr., *Chem. Eng. Progr.* 8 (4):141,173 (1952).

Twenty-Fifth Symposium (International) on Combustion/The Combustion Institute, 1994/pp. 463–474

INVITED TOPICAL REVIEW

IMPACT OF COAL PYROLYSIS ON COMBUSTION

PETER R. SOLOMON
Advanced Fuel Research, Inc.
87 Church Street, East Hartford, CT 06108, USA

AND

THOMAS H. FLETCHER
Department of Chemical Engineering
Brigham Young University
350 CB, Provo, Utah 84602, USA

The pyrolysis process has impacts throughout coal combustion. The roles of pyrolysis in various aspects of the coal combustion process are described, including the devolatilization yield, nitrogen release, softening and swelling, soot formation, and char reactivity. These processes can be understood and quantitatively predicted using recently developed network pyrolysis models that describe the transformation of the coal's chemical structure. The models are described and examples of their predictive ability for important coal combustion phenomena are presented.

Introduction

It has been said that, other than the volatile yield, the details of coal pyrolysis are unimportant in combustion. The argument is that pyrolysis occurs rapidly, whereas char oxidation occurs slowly, and thus, it is the latter that controls the overall process. But a closer examination suggests that pyrolysis exerts its influence throughout the life of the solid particle from injection to burnout.

When coal enters a hot furnace and is heated, it may soften and swell. These processes are a function of the coal's fluidity, which is mostly determined by pyrolysis. The fluidity of the coal is controlled by the way bond breaking and cross-linking reactions affect the coal's organic matrix. These reactions can be drastically influenced by chemical changes in the coal induced by weathering. The swelling of the coal particle is caused by expanding bubbles of gaseous volatiles produced by pyrolysis in the viscous liquid. Depending on the heating rate, temperature, and particle size, either a particle may swell or the bubbles may rupture. Coal softening affects the porosity and internal surface area of the resulting char. Softening, therefore, affects the ignition, particle trajectory in the furnace, reactivity, and eventual fragmentation.

The ignition of the coal may be due to heterogeneous oxidation of the particle or to homogeneous combustion of the pyrolysis volatiles. The relative rates of solid oxidation and volatile evolution determine which type of ignition occurs first.

The pyrolysis process controls the product distribution of tar, char, and gases. The tar is the primary source of soot, which dominates radiative heat transfer in the volatile flame region. The rates and forms of sulfur and nitrogen evolution are initially controlled by pyrolysis. Char burnout is dependent on the amount of char after devolatilization, particle morphology (after possible melting and swelling) and intrinsic reactivity. The intrinsic reactivity is modified as pyrolysis reactions condense the organic network.

Finally, the chemistry and size distribution of the ash (important to slagging and fouling) are influenced by char temperature and morphology during oxidation. Particle temperature, which impacts the melting, vaporization, and chemical reactions of the minerals, is related to a variety of factors, including char intrinsic reactivity and morphology. Both of these are controlled by pyrolysis. Particle morphology affects the char fragmentation, which influences the size of ash particles.

Any attempt to quantitatively predict how pyrolysis affects these combustion events requires a detailed pyrolysis model; a single global devolatilization rate is not sufficient. The detailed model must describe (1) the thermal decomposition of the coal's organic matrix, (2) the release of network fragments as tar, (3) the release of light gas species from decomposition of functional groups attached to the condensed ring structures, and (4) the condensation or cross-linking of the organic matrix and the accompanying formation of gas species.

Several recent detailed pyrolysis models based on statistical decomposition of networks or chains that represent the coal's organic matrix have been pro-

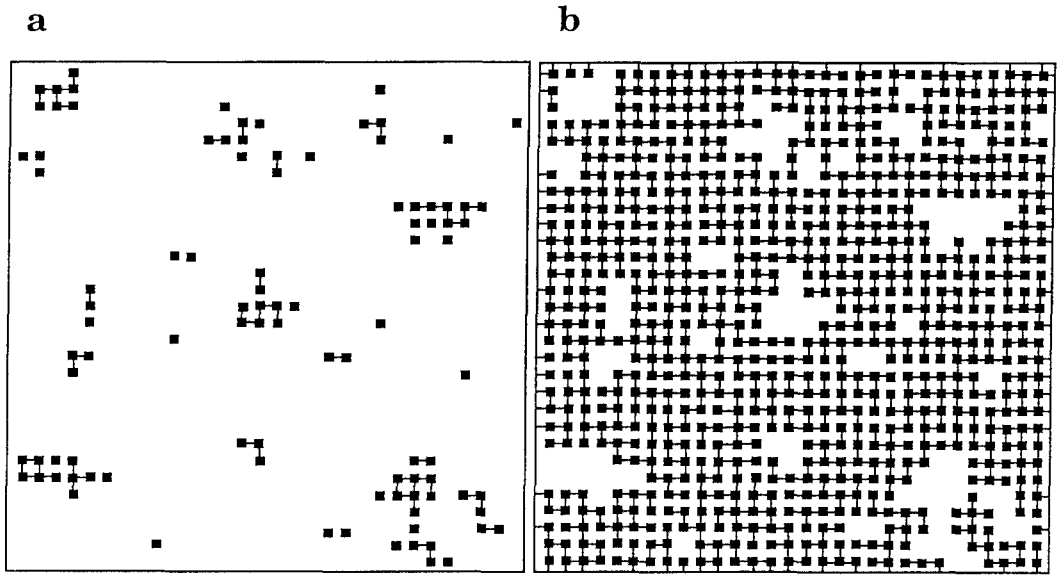

FIG. 1. Monte Carlo simulations of a square lattice with coordination number of 4 and 55% of the bridges intact, showing (a) the 11% of the clusters that are detached from the lattice and (b) the clusters still attached to the matrix [12].

posed to describe these processes [1–21]. This paper presents the general concepts of these models and describes the relationship between pyrolysis events and the predictions of the models. The relationship between pyrolysis and char reactivity is not reviewed in detail due to space limitations.

Network Models of Pyrolysis

Pyrolysis models have progressed from empirical relationships to models that are based on the chemical structure of the parent coal. There have been numerous reviews of the empirical models that employ single reaction rate decomposition, parallel reaction decompositions, and distributed activation energy rate decomposition. In this paper, we consider only the recent detailed chemical models. Additional comparisons of these network models are available [13,22]. Three network models of coal pyrolysis that approximate the breakdown of the macromolecular coal structure are the functional group, depolymerization, vaporization, and cross-linking (FG-DVC) model [10,21]; the FLASHCHAIN model [16–18]; and the chemical percolation devolatilization (CPD) model [12,14,19].

The basic approach of the network pyrolysis models is to treat the coal macromolecular structure as a lattice of aromatic clusters (monomers) connected by aliphatic bridges. The geometry, or degree of branching of the network, is expressed by the number of possible attachments per cluster, often called the coordination number ($\sigma + 1$). A coordination number of 2.0 represents a linear chain polymer, while higher coordination numbers represent more complex cross-linked structures. Network models assign molecular weights to the monomers and use statistics to determine the rate of breaking of interconnecting bridges based on some distribution of activation energies. Oligomers that are disconnected from the coal lattice by bridge breaking become metaplast and tar.

The importance of lattice statistics in the breakup of the coal macromolecule is illustrated in Fig. 1 for a square lattice (coordination number of 4). After 55% of the connecting bridges are broken at random, only 11% of the clusters are detached from the original lattice. The fraction of liberated fragments from a lattice is a nonlinear function of the fraction of ruptured bridges. The molecular weight distribution of the fragments depends on the coordination number. Both Monte Carlo methods and percolation statistics have been used to calculate the relationship between the number of ruptured bridges and the distribution of fragments. Monte Carlo methods give maximum flexibility in specifying the initial lattice structure, but percolation lattice statistics permit a closed-form solution, which reduces computational time. Approaches using percolation statistics assume that coal can be represented as either a linear chain [3–5,16–18] or a loopless tree structure, called a Bethe lattice [6–9,12,13,19,21]. Since the coal macromolecule is large, the Bethe lattice approximation does not introduce significant error [12]. A model using one

bridge network with a coordination number for the initial bridges and a separate interconnected network with a second coordination number for cross-linking, referred to as a 2-σ model, was developed to increase the flexibility and match both initial extract yields and final tar yields [13,21].

As shown in Fig. 1, the lattice statistics determine a distribution of oligomers (monomers, dimers, etc.). The fragment molecular weight is calculated from the oligomer number and the weight of the interconnecting bridges and side attachments. Generalized vapor pressure expressions have been developed for coal tar [23,24] based on molecular weight and temperature. The vapor pressure of the detached material determines the partition between the vapor (tar) and the liquid (metaplast). Tar vapor is convected from the particle along with other light gases, while the metaplast remains in the char until (a) higher temperatures are achieved to vaporize more metaplast or (b) subsequent cross-linking reactions occur to reattach the metaplast to the char. Since the light gases within the particle will be at the ambient pressure and the heavy species will be at their vapor pressure (to first order, independent of the ambient pressure), the molar ratio of tar to light gases will decrease with increasing pressure in agreement with the observed effect of pressure on tar yields.

Recent measurements of the chemical structure of coals and chars by ^{13}C NMR solid-state spectroscopy [25,26] provide input parameters for the network models. These measurements determine the following: the total number of attachments per cluster ($\sigma + 1$), the fraction (p) of attachments that are bridges rather than side chains, the average molecular weight per monomer cluster, and the average molecular weight per side chain. Solvent swelling characteristics and pyridine extract yields have also been used to determine input parameters [10,21].

The three network models use several similar assumptions: (1) a network that decomposes to form fragments when bridges between aromatic clusters are randomly broken, (2) a vapor-liquid equilibrium model to determine the molecular weight and amount of the cluster released as tar, and (3) a cross-linking model that reattaches the clusters. Differences between the models are related to how the network is described. The essential features of the network is the coordination number. A coordination number of 2 is assumed in FLASHCHAIN. The coordination number in FG-DVC is based on the initial extract yield and pyrolysis tar yield. This number is near 2 (i.e., chainlike). However, during pyrolysis, new bridges may form so that the cross-linked char can have a higher coordination number. This variable coordination number was implemented both with a Monte Carlo simulation and with the 2-σ percolation theory. This feature of FG-DVC allows it to fit extract yields and char viscosity.

The coordination number in CPD is from NMR data. The NMR data indicate an average of 2.5–3 bridges and 1.5–2 side chains per aromatic cluster or a coordination number between 4 and 5. However, some of the bridges indicated by the NMR analysis may actually be loops or substituted rings (such as aniline). Such a high coordination number does not permit accurate prediction of pyridine extracts, meaning either that the NMR data include a significant number of loops or that the interpretation of pyridine extracts as coming from the lattice is erroneous. Alternatively, it is possible that in coal the initial distribution of bridges and side chains is not random, as described by the Bethe lattice. The formation of coal may favor clusters that have two bridges and two side chains. If this is the case, the appropriate coordination number for network decomposition is the number of possible bridges, not the sum of bridges and side chains.

The FG-DVC model specifies yields of all light gas species, with yields determined from thermogravimetric Fourier transform infrared (TG-FTIR) experiments [21,27]. This model also correlates cross-linking reactions with evolution of certain light gases [10,15]. Other models describe light gas evolution as part of the network by specifying the number of side chains per cluster in addition to the number of connecting bridges per cluster. This latter approach has been used successfully to determine total light gas yields as a function of coal type [12,14,16–19], but it has not been used to calculate individual species.

Devolatilization

The most dramatic effect of coal pyrolysis on coal combustion is the rapid release of volatile matter. Since many coals may release more than 50% of their mass as volatile matter, gas-phase volatile combustion significantly increases temperatures in a relatively short time. In certain burner geometries for pulverized coal, the mass released during devolatilization creates a local volume expansion that is large enough to influence near-burner fluid dynamics. The volatile yield also affects the amount of char that must be burned heterogeneously.

The total volatile yield is a function of coal type, temperature, heating rate, pressure, and particle size. Particle size effects become small at diameters below 200 μm and are usually ignored in pulverized coal applications. Particles larger than 1 mm, such as those used in fluidized bed applications, exhibit significant internal mass transfer limitations that can lead to tar secondary reactions and deposition inside the particle [28].

Although early data indicated no significant effect of heating rate on total volatile yield [29], recent experiments show a small increase in yield with increasing heating rate [30]. Heating rate effects can be explained by the competition between tar formation

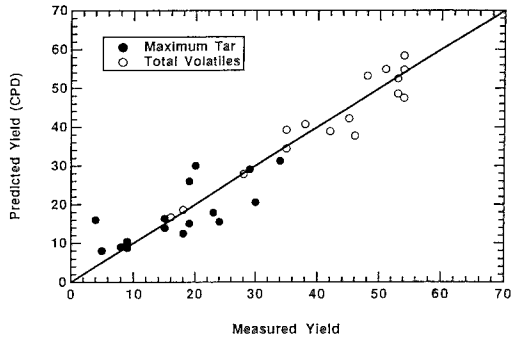

FIG. 2. Comparison of predicted and measured tar and total volatile yields using the CPD model with coal-dependent input coefficients directly from solid-state ^{13}C NMR data for 16 coals for a range of heating rates (0.5–10^4 K/s) and temperatures (1000–1300 K) [19].

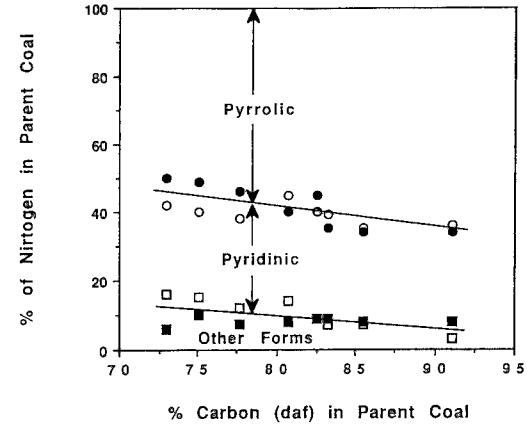

FIG. 3. Comparison of forms of nitrogen in the Argonne Premium coals as analyzed by XPS [43] (open symbols) and by XANES [44] (solid symbols).

(bridge breaking), tar destruction (cross-linking), and tar evolution (mass transfer), all of which depend differently on temperature [10]. At high heating rates, depending on particle size, internal heat transfer limitations become important, and particles may exhibit large internal temperature gradients [31].

The rate of devolatilization is sometimes thought to have little impact on comprehensive pulverized coal combustion models, since it happens so rapidly. However, it has been shown that using an unrealistic rate can affect the prediction of the flame zone near the burner, particularly in swirling flows [32,33]. Determination of devolatilization rates is hampered by the fact that mass release occurs during particle heat-up, and reported rates at a given heating rate vary by three orders of magnitude [34]. The large range in reported rates is due to the lack of temperature measurements during devolatilization [34,35]. Measurements of particle temperature during devolatilization, using FTIR emission/transmission particle cloud measurements [36] and single-particle two-color infrared pyrometry measurements [37,38], have substantially reduced the uncertainty in rates.

The network models have been successful in relating chemical features of parent coals to the pyrolysis behavior. For example, ^{13}C NMR measurements of four key chemical features of 16 coals were used directly (i.e., no adjustable coal-dependent parameters) in the CPD model to predict tar and total volatile yields for a wide range of pyrolysis temperatures and heating rates [19], as shown in Fig. 2. Methods have been developed for both the FLASHCHAIN and FG-DVC models for predicting input coefficients from elemental composition. These show reasonable success in predicting tar and total volatile yields [39–41]. A more detailed scheme is required to deduce input coefficients for models that predict light gas species as well as tar yields [21,40]. Network models of coal pyrolysis have successfully been used to calculate coal-dependent rates and yields of light gas and tar as a function of temperature, heating rate, and pressure.

Nitrogen Release

The amount of nitrogen released from the coal during devolatilization, along with the form of the nitrogen species and transformation to NO_x precursors such as HCN and NH_3, is important to pollutant control strategies. For example, low-NO_x burners work on the principle that the devolatilized nitrogen species will form N_2 rather than NO_x under locally fuel-rich conditions. The form of nitrogen in the coal, particularly if it is entirely contained in aromatic groups or in peripheral side chains, determines the nitrogen species released during devolatilization. Coal nitrogen is thought to occur mainly in five-member (pyrrolic) or six-member (pyridinic) aromatic ring structures [42–44]. Both x-ray photoelectron spectroscopy (XPS) and x-ray absorption near-edge structure (XANES) spectroscopy indicate the presence of additional species that may include quaternary nitrogen or aromatic amines. Figure 3 shows the quantitative agreement between XPS and XANES analyses of the major forms of nitrogen in the Argonne Premium coals. Pyrrolic nitrogen is the most common form, followed by pyridinic for all coal ranks; other forms are relatively small. Davidson [45] provides a more detailed review of the forms of nitrogen in coal.

Nitrogen release during devolatilization is a function of final temperature [46,47], even though the total devolatilization yield may increase only slightly after a certain temperature, as shown in Fig. 4. The high-temperature nitrogen release is due to graphitization-type reactions, where the char becomes

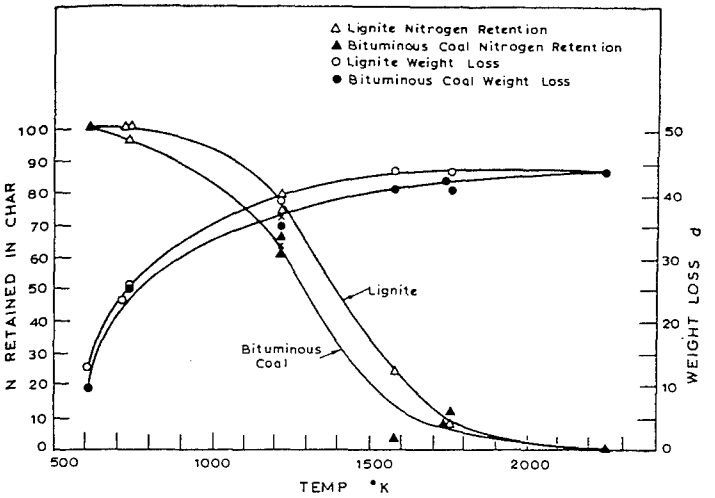

FIG. 4. Nitrogen retention in char and weight loss (dry) for coal heated in crucibles as a function of temperature [45].

more aromatic and releases heteroatoms preferentially to carbon. Nitrogen release increases with increasing heating rate and decreases with increasing pressure [48].

Two questions arise regarding nitrogen release: (a) what are the primary devolatilization products and (b) what are the products after secondary pyrolysis. Of interest is the amount of HCN and NH_3 formed, since detailed models exist to describe the reaction chemistry of HCN and NH_3 to form NO_x [49]. Since nitrogen in the parent coal exists mainly in aromatic ring structures, it is logical to assume that the nitrogen release occurs mainly in tar molecules during tar release and then as light gases during high-temperature graphitization reactions [50,51].

At rapid heating rates (>1000 K/s) and temperatures lower than 700 °C, HCN is not a primary product [50–53]. Even at rapid heating rates, tar release generally occurs before any HCN is released. No NH_3 is generally seen during rapid pyrolysis in heated grid experiments [51] or entrained flow experiments [52,53]. However, Kambara et al. [54] recently measured NH_3 yields during devolatilization at 1000 K/s and correlated these yields with quaternary nitrogen content. Nelson et al. [42] also reported NH_3 yields from devolatilization in a fluidized bed reactor with estimated initial heating rates of 10^4 K/s.

At low heating rates, such as in thermogravimetric analysis (TGA) devolatilization experiments at 30 °C/s, both HCN and NH_3 are measured, with a dominance of NH_3 rather than HCN [53]. Low rank coals release a larger fraction of nitrogen as HCN and NH_3 than high rank coals at these low heating rates. Bassilakis and coworkers [53] rationalize that the NH_3 evolution observed at low heating rates is due to the conversion of HCN to NH_3 in the pores of the char, with hydrogen donation from the solid char. A model was developed to describe the conversion of HCN to NH_3 inside the coal particle, based on the residence time of light gas inside the particle [53]. This model was used to explain the NH_3 yields observed in TGA experiments and in Nelson's fluidized bed coal pyrolysis experiments [42]. In Nelson's lower-temperature experiments, the NH_3 is formed when the coal particle is at or near the bed temperature and the heating rate has slowed down considerably.

Secondary pyrolysis of coal tar and light gases results in the formation of HCN and soot. Chen and Niksa [52] showed that the soot can initially contain a significant amount of nitrogen, since it is formed from vaporized tar that often contains most of the devolatilized nitrogen. At increased temperatures, the fraction of nitrogen contained in the soot decreases as heteroatoms are expelled due to graphitization reactions. Secondary pyrolysis of tar and soot are, therefore, important to understanding nitrogen species evolution during volatile combustion.

The amount of nitrogen evolved at a given temperature and heating rate is a function of coal rank but is not proportional to the tar yield. Figure 5 shows total nitrogen release as a function of carbon content of the parent coal in flat flame methane burner experiments [55]. Heating rates in this experiment were approximately 5×10^4 K/s, and particle temperatures reached approximately 1400 K. Tar yields from lignites (<70% carbon) are significantly lower than from high volatile bituminous coals (75–80% carbon), yet the two coals release comparable fractions of nitrogen during pyrolysis. This is consistent with the observations that low rank coals (which have low tar yields) release a larger fraction of nitrogen as light gas than do medium rank coals (which have high tar yields). Only the low volatile bituminous coals (85–90% carbon) exhibit low amounts of nitrogen release.

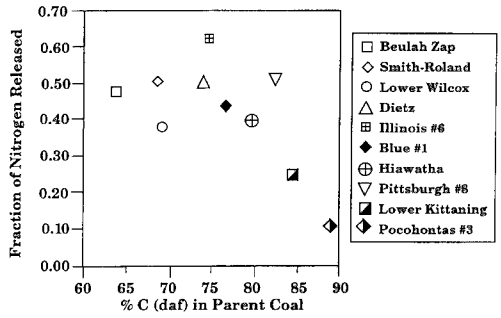

FIG. 5. Fraction of nitrogen released during devolatilization as a function of coal rank (i.e., carbon content) in flat flame methane burner experiments in 6 mole% post-flame oxygen [55]. Residence times were 47 ms, and the heating rate was approximately 5×10^4 K/s. Samples were taken prior to significant char oxidation.

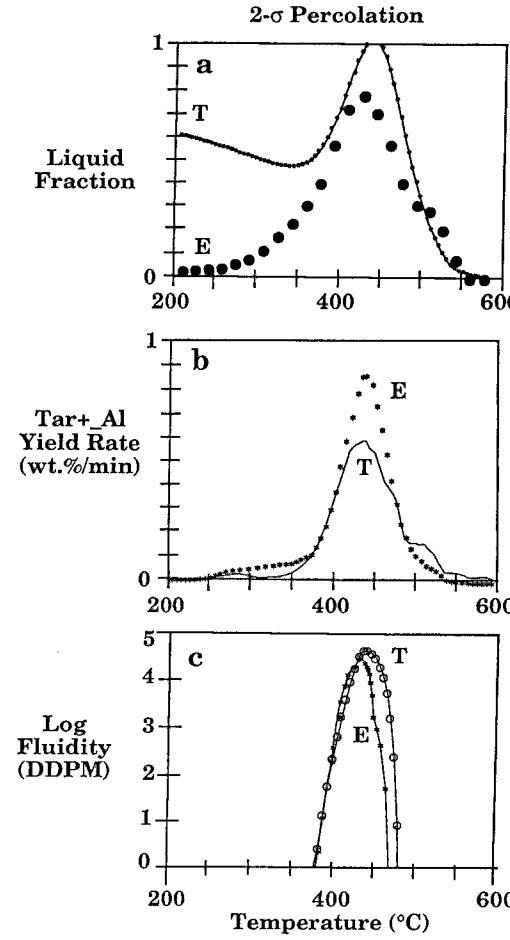

FIG. 6. Comparison of 2-σ percolation theory for liquid fraction, tar yield rate, and Gieseler fluidity for Pittsburgh No. 8 bituminous coal pyrolyzed at 3 K/min^{-1}. T = theory; E = experimental data [21].

Softening and Swelling

The swelling of coal is important in combustion because it affects the char particle's size and porosity and, hence, its trajectory, ignition, reactivity, fragmentation, and ash size distribution. Swelling occurs during pyrolysis in coals, which soften, and is caused by the evolution of gases, which form bubbles that expand within the softened particles. For fluidized or fixed beds, in which large coal particles heat relatively slowly, particle diameters can increase. For PC firing, particle sizes may not increase due to the high heating rates, but significant changes occur in the char morphology due to bubble formation. The most complete description of bubble formation is the multi-bubble model of Oh et al. [56], which includes the effect of bubble growth, bubble transport to the surface, and diffusion of gases through the liquid. The following discussion considers softening first and then bubble formation.

Softening:

The softening of coal is most often measured at low heating rates with a Giessler Plastometer [57]. Data at higher temperatures have been obtained by Fong et al. [58] in a device designed for rapid heating. Both the slow and fast heating rate results exhibit an increase in fluidity as the coal melts and pyrolyzes, followed by a decrease as the char solidifies (see Fig. 6c). As demonstrated by Fong et al. [58] and Oh et al. [56], the maximum in fluidity is associated with a maximum in extractable molecules. Proton magnetic resonance thermal analysis (PMRTA) experiments of Lynch et al. [59,60], which measure the fraction of mobile molecules in the coal, show a corresponding maximum in the "mobile fraction" in the coal (Fig. 6a). In the language of the network models, the increase in fluidity is associated with the thermal decomposition of the network, while the subsequent decrease is associated with the network recondensation or cross-linking.

There are a number of factors that contribute to the softening of coal. van Krevelen and coworkers [61,62] and Neavel [63] relate the fluidity of coal to the detached molecular fraction called "metaplast." The factors that control the particle's fluidity include (1) the fraction of metaplast formed; (2) the fluidity of the metaplast fraction; (3) the dependence of this fluidity on temperature; (4) the contributions of suspended solids in the metaplast, both "chunks" of char and mineral particles; and (5) the formation of bubbles due to trapped gases.

Several models for coal viscosity have been proposed, which consider all of the influences except the bubbles. The models were based on the two-step

process described by Van Krevelen and coworkers [61,62], which assumes the following reactions to occur on heating:

$$\text{coal} \xrightarrow{k_1} \text{metaplast} \xrightarrow{k_2} \text{coke}.$$

Models for fluidity in which the rate of formation and destruction of metaplast is described by global rates k_1 and k_2 employ empirical expressions for viscosity as a function of the metaplast fraction [53,58,64].

Solomon et al. [20] also employ an empirical model for viscosity based on the metaplast fraction, but a network model [10,21] is used to predict the metaplast fraction. The metaplast is defined as the fraction of molecules that are not attached to the network. The increase in metaplast is associated with bond-breaking reactions, while the solidification is due to cross-linking. Low rank coals generally do not exhibit fluidity because the cross-linking reactions occur at lower temperatures than the bond-breaking reactions [15,65].

A comparison of theory and experiment for Giessler fluidity, tar yield, and the PMRTA liquid fraction is presented in Fig. 6 from Ref. 21. The data are compared to the FG-DVC 2-σ percolation model. For a single coal, these network models allow all of these events to be predicted at arbitrary heating rate and pressure with a single pair of kinetic rates for bond breaking and cross-linking. In Fig. 6a, the lack of agreement at low temperature is due to the fact that the model does not include the effect of temperature on the molecule's mobility.

The use of network models also makes it possible to understand why weathering (oxidation) is so effective in reducing fluidity [21]. The apparent reason is that oxidation leads to low-temperature cross-linking. Such cross-linking in a two-dimensional network increases the coordination number and is thus extremely effective in reducing metaplast fraction.

Swelling:

Swelling models have been developed by several investigators [56,66–68]. The basic physics is contained in the single bubble model of Chiou and Levine [66], who considered the swelling rate of a pulverized coal particle of external radius r_2 with a single void of radius r_1 with spherical symmetry. The swelling they depict is due to the pressure of trapped evolved gases, doing work against viscous forces. The pressure within a bubble can be determined from the rate of gas evolution predicted by a pyrolysis model and an assumed diffusion rate of gases through the liquid. In the work of Zhao and Best [68], the viscosity was predicted as in Ref. 20. Two additional parameters were also required to describe the effect of bubble bursting that limits swelling at high heating rates: a critical bubble wall stress and the wall surface tension.

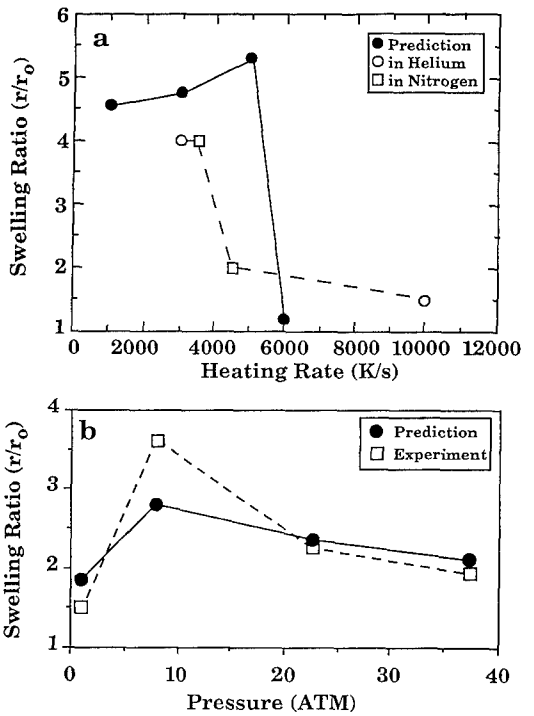

FIG. 7. (a) Comparison of experimental data (open symbols) and predicted (closed symbols) particle swelling ratios as a function of heating rate and (b) comparison of model prediction (closed symbols) and experiment (open symbols) [71] for swelling ratio vs ambiant pressure, for Illinois No. 6 coal (nominal rad = 31 μm), at a heating rate between 1000 and 1150 K/s.

According to the above model [68], a bubble grows until the rate of gas filling the bubble equals the rate of diffusion through the wall or else until the pressure difference across the wall exceeds the critical wall stress and the bubble ruptures. Experimental observations for the swelling ratio (r/r_0) of final radius r to initial radius r_0 and predictions are presented in Fig. 7a. For a heating rate of 5000 °C/s and below, cenospheres are formed, and the swelling ratio can be as high as 4. The model of Oh et al. [56] predicts a similar swelling ratio. At heating rates above 5000 °C/s, the evolution of gas is too fast and the bubbles rupture, reducing the swelling. This rupture phenomenon, which has been observed experimentally [67,69,70], is not included in Oh's model [56].

Figure 7b compares the theory and experiment [71] for the swelling ratio of an Illinois no. 6 coal as a function of pressure. With increasing pressure, the more volatile components of tar are held in the particles for longer times, decreasing viscosity at the critical time of gas evolution and increasing (r/r_0). With a further increase in pressure, the compressive external envi-

ronment results in a reduction in swelling. Similar results at high pressure were predicted by Oh et al. [56].

Secondary Pyrolysis and Soot Formation

Secondary pyrolysis of coal devolatilization products in fuel-rich regions of coal flames produce significant amounts of soot. The soot in the flame region thermally radiates heat to cooler regions of the furnace and therefore cools the flame. Since furnace walls are generally cooler than the flame temperature, the presence of soot may cool the flame by several hundred degrees. Predictions of the flame temperatures resulting from volatile combustion must, therefore, account for soot radiation.

While soot from combustion of pure hydrocarbons has been studied extensively, relatively little is known about coal-derived soot. Coal tar contains aromatic compounds with average molecular weights in the range of 350 amu, and therefore, the mechanism for soot formation from coal tar differs from combustion of fuels such as butane and acetylene, which require the formation of aromatic rings. Contrails of soot were visualized in single-particle combustion experiments by McLean et al. [72] and by Seeker et al. [73]. A single-particle model, including a local soot cloud, was developed by Lau and Niksa [74]. A model for secondary reactions of coal tar was developed based on homogeneous cracking of tar produced in a packed bed reactor [75].

Pyrolysis-induced soot formation experiments have shown the beginnings of chemical structure changes leading to soot formation [76–79]. Wornat and coworkers [78] defined soot yield as the devolatilization products that were not soluble in dichloromethane. Their results for a Pittsburgh no. 8 coal indicated that soot yields increased with both residence time and temperature, while the soluble fraction of the coal tars decreased proportionally. Related experiments by Chen et al., [79], using tetrahydrofuran (THF) as the solvent, showed similar results for a Pittsburgh no. 8 coal and a Dietz subbituminous coal. Both Wornat's and Chen's data indicate that while soot yields increase with temperature, the total yield of soot plus tar remains constant, as shown in Fig. 8.

Important radiative properties for modeling soot radiation are the soot volume fraction and the soot particle size. A thermophoretic sampling probe was used to sample soot and tar samples from a high-temperature pyrolysis experiment as a function of residence time [80]. Preliminary results indicate that initial soot particles formed are approximately 25 nm in diameter, while agglomerates reach sizes of 200–800 nm in 130 ms. This is different behavior than observed in the single-particle combustion experiments [72,73], where the flame around individual particles causes soot particles to form in contrails. When the tar is free to expand in a cloud away from the particle, such as in a pyrolysis experiment or in a fuel-rich cloud, the soot does not form such contrails.

A study employed an FTIR to study soot concentrations in flames [81,82]. A comparison of the soot concentration (proportional to the attenuation of infrared radiation across the flame) for three samples is shown in Fig. 9a. The demineralized Rosebud (which has twice the tar yield of the raw Rosebud) produces about twice the maximum soot yield compared to the raw sample. The char (which has no tar) produces almost none. As shown in Fig. 9b, the soot production increases with the yield of tar as determined in pyrolysis experiments [81]. This relationship between tar and soot is consistent with other results [78,79,83].

Char Reactivity

This section is concerned with the effect of coal pyrolysis on char reactivity. Space limitations allow for only a brief qualitative discussion. There are two important effects: physical and chemical.

The physical effects determine the char morphology. The plastic properties of the coal affect the size of the char particle and its pore distribution. The pore distribution determines the diffusion of reactants within the particle, which is often a rate-limiting step for char oxidation.

The chemical effects of pyrolysis determine the char's intrinsic reactivity. The intrinsic reactivity controls the char burning rate in zone I (the kinetic region) and affects zone II (the pore diffusion region). Theoretically, the condensation of the coal's macromolecular network at the latter stages of pyrolysis leads to a reduction in the active site density, which reduces the intrinsic char reactivity. Experimentally, intrinsic reactivities are observed to decrease with the increasing extent of pyrolysis [85–88] and seem to correlate with the aromatic hydrogen concentration of the char [84]. In low rank coals (oxygen concentration greater than 13%), several studies [84,89,90] show that organically bound alkali and alkaline earth metals (especially calcium) control the intrinsic oxidation when measured at low temperature.

Conclusion

The pyrolysis process has impacts throughout coal combustion. The devolatilization yield affects the initial amount of char that must be oxidized. The rate of devolatilization can affect the near-burner structure of the flame. The nitrogen release during devolatilization is important to low-NO_x burner strategies. The pyrolysis product distribution, particularly the amount of tar, affects the amount of soot pro-

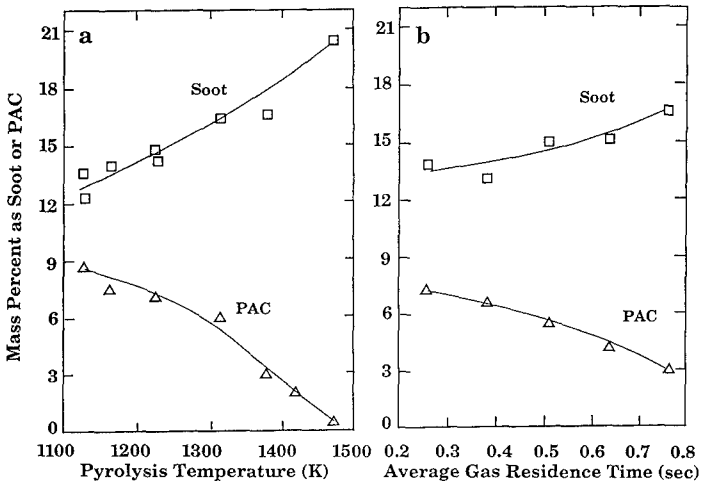

FIG. 8. Soot and soluble polyaromatic compound (PAC) yields under various pyrolysis conditions: (a) experiment set 1, residence time = 0.75 s; (b) experiment set 2, temperature = 1375 K [78].

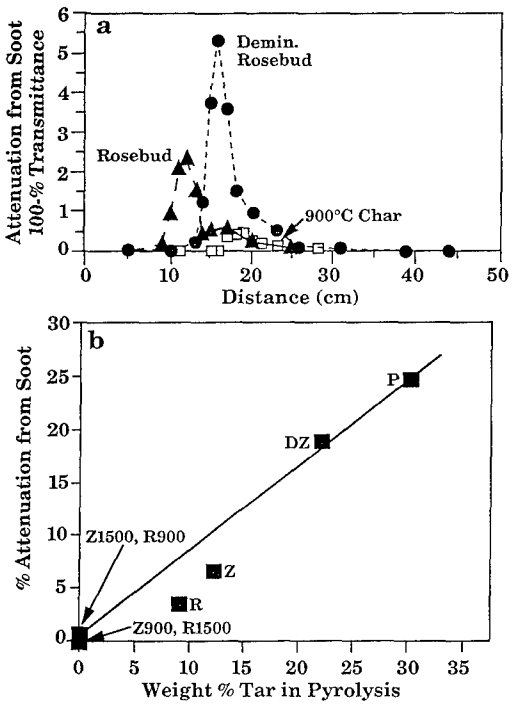

FIG. 9. Correlation of soot production with tar yield. (a) Comparison of soot attenuation for three samples burned in a flame stabilized by preheated air and (b) correlation of the maximum soot attenuation with tar yield in pyrolysis in an entrained flow reactor. P = Pittsburgh; DZ = demineralized zap; Z = zap; R = Rosebud; numbers are pyrolysis temperature for char [81].

duced, which in turn affects the temperature in the flame zone due to radiative loss. The softening behavior of the coal during pyrolysis affects the size, porosity, and internal surface area of the char, which affect the high-temperature reactivity. Detailed pyrolysis models have been developed based on the chemical structure of coal. The network pyrolysis models have shown the ability to quantitatively predict many of these major pyrolysis phenomena.

Acknowledgments

Work done at Advanced Fuel Research, Inc. was sponsored under Contract No. DE-AC21-86MC23075 with the U.S. Department of Energy Morgantown Energy Technology Center. The work at Brigham Young University was sponsored in part by the Advanced Combustion Engineering Research Center, funded by the National Science Foundation, the State of Utah, 31 industrial participants, and the U.S. Department of Energy. The authors would like to thank Dr. M. A. Serio, Dr. Y. Zhao, Ms. S. Charpenay, and Mr. M. L. Tanner for their help on the manuscript.

REFERENCES

1. Gavalas, G. R., *Coal Pyrolysis*, Elsevier, Amsterdam, 1982, p. 51.
2. Gavalas, G. R., Cheong, P. H., and Jain, R., *Ind. Eng. Chem. Fundam.* 20:122 (1981).
3. Solomon, P. R., and King, H. H., *Fuel* 63:1302 (1984).
4. Solomon, P. R., Squire, K. R., and Carangelo, R. M., *Proceedings of the International Conference on Coal Sciences*, Peragom, Sydney, Australia, 1985, p. 945.

5. Squire, K. R., Carangelo, R. M., DiTaranto, M. B., and Solomon, P. R., *Fuel* 65:833 (1986).
6. Niksa, S., and Kerstein, A. R., *Combust. Flame* 66:95 (1986).
7. Niksa, S., *Combust. Flame* 66:111 (1986).
8. Niksa, S., and Kerstein, A. R., *Fuel* 66:1389 (1987).
9. Niksa, S., Kerstein, A. R., and Fletcher, T. H., *Combust. Flame* 69:221–228 (1987).
10. Solomon, P. R., Hamblen, D. G., Carangelo, R. M., Serio, M. A., and Deshpande, G. V., *Energy Fuels* 2:405 (1988).
11. Niksa, S., *AIChE J.* 34:790 (1988).
12. Grant, D. M., Pugmire, R. J., Fletcher, T. H., and Kerstein, A. R., *Energy Fuels* 3:175 (1989).
13. Solomon, P. R., Hamblen, D. G., Yu, Z. Z., and Serio, M. A., *Fuel* 69:754 (1990).
14. Fletcher, T. H., Kerstein, A. R., Pugmire, R. J., and Grant, D. M., *Energy Fuels* 4:54 (1990).
15. Solomon, P. R., Serio, M. A., Desphande, G. V., and Kroo, E., *Energy Fuels* 4:42 (1990).
16. Niksa, S., and Kerstein, A. R., *Energy Fuels* 6:647–665 (1991).
17. Niksa, S., *Energy Fuels* 5:665–673 (1991).
18. Niksa, S., *Energy Fuels* 5:673–683 (1991).
19. Fletcher, T. H., Kerstein, A. R., Pugmire, R. J., Solum, M. S., and Grant, D. M., *Energy Fuels* 6:414–431 (1992).
20. Solomon, P. R., Best, P. E., Yu, Z. Z., and Charpenay, S., *Energy Fuels* 6:143–154 (1992).
21. Solomon, P. R., Hamblen, D. G., Serio, M. A., Yu, Z. Z., and Charpenay, S., *Fuel* 72 (4):469–488 (1993).
22. Smith, K. L., Smoot, L. D., Fletcher, T. H., and Pugmire, R. J., *The Structure and Reaction Processes of Coal,* Plenum, New York, 1994, pp. 273–323.
23. Suuberg, E. M., Unger, P. E., and Lilly, W. D., *Fuel* 64:956 (1985).
24. Fletcher, T. H., Grant, D. M., and Pugmire, R. J., *ACS Div. Fuel Chem. Preprints* 36 (1):250–257 (1991).
25. Solum, M. S., Pugmire, R. J., and Grant, D. M., *Energy Fuels* 3:187 (1989).
26. Orendt, A. M., Solum, M. S., Sethi, N. K., Pugmire, R. J., and Grant, D. M., *Advances in Coal Spectroscopy* (H. L. C. Meuzelaar, Ed.), Plenum Press, New York, 1992, pp. 215–254.
27. Solomon, P. R., Serio, M. A., Carangelo, R. M., Bassilakis, R., Gravel, D., Baillargeon, M., Baudais, F., and Vail, G., *Energy Fuels* 4:319–333 (1990).
28. Saxena, S. C., *PECS* 16:55–94 (1990).
29. Anthony, D. B., Howard, J. B., Hottel, H. C., and Meissner, H. P., *Fifteenth Symposium (International) on Combustion,* The Combustion Institute, Pittsburgh, 1974, pp. 1303–1317.
30. Gibbins-Matham, J., and Kandiyoti, R., *Energy Fuels* 2:505–511 (1988).
31. Hertzberg, M., Zlochower, I. A., and Edwards, J. C., "Coal Particle Pyrolysis Mechanisms and Temperatures," Bureau of Mines Report 9169, 1988.
32. Smith, J. D., Smith, P. J., and Hill, S. C., *AIChE J.* 39:1668–1679 (1993).
33. Fletcher, T. H., "Sensitivity of Combustion Calculations to Devolatilization Rate Expressions" presented at the AFRC Fall Meeting, Sandia National Laboratories, Livermore, CA, Sandia Report No. SAND85-8854, available NTIS, 1985.
34. Solomon, P. R., Fletcher, T. H., and Pugmire, R. J., *Fuel* 72:587–597 (1993).
35. Freihaut, J. D., and Proscia, W. M., *Energy Fuels* 3:625 (1989).
36. Solomon, P. R., Serio, M. A., Carangelo, R. M., and Markham, J. R., *Fuel* 65:182–194 (1986).
37. Fletcher, T. H., *Combust. Sci. Technol.* 63:89–105 (1989).
38. Fletcher, T. H., *Combust. Flame* 78:223–236 (1989).
39. Niksa, S., and Kerstein, A. R., *Proceedings of the International Conference on Coal Science,* Banff, Canada, 1993, Vol. 2, pp. 397–400.
40. Zhao, Y., Serio, M. A., and Solomon, P. R., *ACS Div. Fuel Chem. Preprints* 39:(1994); see also Zhao, Y., Serio, M. A., and Solomon, P. R., "A Method of Predicting Coal Devolatilization Behavior Based on Coal Elemental Compositions," submitted to the *Twenty-Fifth Symposium (International) on Combustion,* The Combustion Institute, Pittsburgh, (1994).
41. Niksa S., *Energy Fuels* 8:659–670 (1994); see also Niksa, S., "Predicting the Devolatilization Behavior of any Coal from its Ultimate Analysis," *Twenty-Fifth Symposium (International) on Combustion,* The Combustion Institute, Pittsburgh, 1994.
42. Nelson, P. F., Buckley, A. N., and Kelly, M. D., *Twenty-Fourth Symposium (International) on Combustion,* The Combustion Institute, Pittsburgh, 1992, pp. 1259–1267.
43. Kelemen, S. R., Gorbaty, M. L., Vaughn, S. N., and Kwiatek, P. J., *ACS Div. Fuel Chem. Preprints* 38 (2):384–392 (1993).
44. Mitra-Kirtley, S., Mullins, O. C., Branthaver, J., van Elp, J., and Cramer, S. P., *ACS Div. Fuel Chem. Preprints* 39 (2):762–768 (1993).
45. Davidson, R. U., "Nitrogen in Coal," IEA Report No. IEAPER/08 1994.
46. Pohl, J. H., and Sarofim, A. F., *Sixteenth Symposium (International) on Combustion,* The Combustion Institute, Pittsburgh, 1976, pp. 491–501.
47. Blair, D. W., Wendt, J. O. L., and Bartok, W., *Sixteenth Symposium (International) on Combustion,* The Combustion Institute, Pittsburgh, 1976, pp. 475–489.
48. Cai, H. Y., Guell, A. J., Dugwell, D. R., and Kandiyoti, R., *Fuel* 72:321–327 (1993).
49. Miller, J. A., and Bowman, C. T., *PECS* 15:287–338 (1989).
50. Solomon, P. R., and Colket, M. B., *Fuel* 57:749–755 (1978).
51. Freihaut, J. D., Proscia, W. M., and Mackie, J. C., *Combust. Sci. Technol.* 93:323–347 (1993).
52. Chen, J. C., and Niksa, S., *Energy Fuels* 6:254–264 (1992).
53. Bassilakis, R., Zhao, Y., Solomon, P. R., and Serio, M. A., *Energy Fuels* 7:710–720 (1993).

54. Kambara, S., Takarada, T., Yamamoto, Y., and Kato, K., *Energy Fuels* 7:1013–1020 (1993).
55. Mitchell, R. E., Hurt, R. H., Baxter, L. L., and Hardesty, D. R., "Compilation of Sandia Coal Char Combustion Data and Kinetic Analysis," Sandia Report SAND92-8208, available NTIS (1992).
56. Oh, M. S., Peters, W. A., and Howard, J. B., *AIChE J.* 35:5 775–792 (1989).
57. ASTM D 2639-74 (reapproved 1980).
58. Fong, W. S., Khalil, Y. F., Peters, W. A., and Howard, J. B., *Fuel* 65:195 (1986).
59. Lynch, L. J., Sakurovs, R., Webster, D. S., and Redlich, P. J., *Fuel* 67:1036 (1988).
60. Lynch, L. J., Webster, D. S., Sakurovs, R., Barton, W. A., and Maher, T. P., *Fuel* 67:579 (1988).
61. van Krevelen, D. W., *Coal*, Elsevier, Amsterdam, 1961.
62. Chermin, H. A. G., and van Krevelen, D. W., *Fuel* 36:85 (1957).
63. Neavel, R. C., in "Coal Plasticity Mechanism: Inferences from Liquefaction Studies" (M. L. Gorbaty, J. W. Larsen, and I. Wender, Eds.), *Coal Science 1*, Academic Press, New York, 1982.
64. Franked, N. A., and Acrivos, A., *Chem. Eng. Sci.* 22:847 (1976).
65. Suuberg, E. M., Lee, D., and Larsen, J. W., *Fuel* 64:1668 (1985).
66. Chiou, M. J., and Levine, H. B., "Investigation of Structure Deformation of Coal Particles in Pyrolysis" Report from Jaycor.
67. Solomon, P. R., and Hamblen, D. G., *Chemistry of Coal Conversion* (R. H. Schlosberg, Ed.), Plenum Publishing, New York, 1985, pp. 121–151.
68. Zhao, Y., and Best, P. E., "Measurement and Modeling of Advanced Coal Conversion Processes," Final Report, U.S. DoE/METC Contract No. DE-AC21-86MC23075, 1993.
69. Pohl, J. M., Kobayashi, H., and Sarofim, A. F., "The Effects of Temperature and Time on the Swelling of Pulverized Coal Particles", Industrial Liason Program, Symposium Paper, MIT, Oct. 2, 1979.
70. Gale, T. K., Bartholomew, C. H., and Fletcher, T. H., "Decreases in the Swelling and Porosity of Bituminous Coals During Devolatilization at High Heating Rates," *Combust. Flame* (1994), accepted.
71. Lee, C. W., Scaroni, A. W., and Jenkins, R. G., *Fuel* 70:957 (1991).
72. McLean, W. J., Hardesty, D. R., and Pohl, J. H., *Eighteenth Symposium (International) on Combustion*, The Combustion Institute, Pittsburgh, 1980, p. 1239.
73. Seeker, W. R., Samuelson, G. S., Heap, M. P., and Trolinger, J. D., *Eighteenth Symposium (International) on Combustion*, The Combustion Institute, Pittsburgh, 1980, p. 1213.
74. Lau, C. W., and Niksa, S., *Combust. Flame* 95:1–21 (1993).
75. Serio, M. A., Peters, W. A., and Howard, J. B., *Industr. Eng. Chem. Res.* 26:1831–1838 (1987).
76. Fletcher, T. H., Solum, M. S., Grant, D. M., Critchfield, S., and Pugmire, R. J., *Twenty-Third Symposium (International) on Combustion*, The Combustion Institute, Pittsburgh, 1990, p. 123.
77. Pugmire, R. J., Solum, M. S., Grant, D. M., Critchfield, S., and Fletcher, T. H., *Fuel* 70:414–423 (1991).
78. Wornat, M. J., Sarofim, A. F., and Longwell, J. P., *Energy Fuels* 1:431 (1987).
79. Chen, J. C., Castagnoli, C., and Niksa, S., *Energy Fuels* 6:264–271 (1992).
80. Ma, J., Dean, M., Rossman, J., Sastrawinata, T., Webb, B., and Fletcher, T. H., "Properties of Soot from Coal," presented at the Fall 1993 WSS/CI Meeting, SRI, Menlo Park, CA, Oct. 18–19, 1993.
81. Solomon, P. R., Chien, P. L., Carangelo, R. M., Best, P. E., and Markham, J. R., *Twenty-Second Symposium (International) on Combustion*, The Combustion Institute, Pittsburgh, 1988, pp. 211–221.
82. Brewster, B. S., Smoot, L. D., Solomon, P. R., and Markham, J. R., *Energy Fuels* 7:884–890 (1993).
83. Nenniger, R. D., Howard, J. B., and Sarofim, A. F., *Proceedings of the 1983 International Conference on Coal Science*, Pittsburgh, PA, Aug. 15–19, 1983, p. 521.
84. Charpenay, S., Serio, M. A., and Solomon, P. R., *Twenty-Fourth Symposium (International) on Combustion*, The Combustion Institute, Pittsburgh, 1992, pp. 1189–1197.
85. Best, P. E., Solomon, P. R., Serio, M. A., Suuberg, E. M., Mott, W. R., Jr., and Bassilakis, R., *ACS Div. Fuel Chem. Preprints* 32 (4):138 (1987).
86. Khan, R., *Fuel* 66:1626 (1987).
87. Radovic, L. R., Walker, P. L., and Jenkins, R. G., *Fuel* 62:1209 (1983).
88. Radovic, L. R., Walker, P. L., and Jenkins, R. G., *Fuel* 62:849 (1983).
89. Floess, J. K., Longwell, J. P., and Sarofim, A. F., *Energy Fuels* 2:756–764 (1988).
90. Solomon, P. R., Serio, M. A., and Henninger, S. G., *ACS Div. Fuel Chem. Preprints* 31 (3):200 (1986).

COMMENTS

Stephen Niksa, SRI International, USA. I appreciate your even-handed coverage of the futures that our models have in common. However, nominal rates of devolatilization based on a single first-order chemical reaction that you report for your BYU and AFR data have magnitudes and activation energies that are much higher than those that have been reported during the past three decades. Now that FLASHCHAIN predictions explain the lower rates without resorting to heat or mass transport resistances [1], there is an enormous body of experimental and modeling

results that contradict your values. Your values do not reconcile any discrepancies because there is so much information that disagrees with them.

REFERENCE

1. Niksa, S., *Energy Fuels* 8:670 (1994).

Author's Reply. During the past three decades, most kinetic rates reported in the literature for coal pyrolysis reactions have been measured in experiments where the coal particle temperatures were estimated, not measured. In most cases, rates were reported only for a narrow range of heating rates. This resulted in wide discrepancies in reported rates and activation energies even for similar coals under nominally the same heating rates and temperatures. Investigation of the discrepancies leads to the conclusion that particle temperatures were inaccurately estimated in many cases [1–3]. When particle temperatures were measured, the rates are at the high end of the range that is in the literature [4–7]. When a distributed activation energy model (DAEM) is used to fit data over a range of heating rates, the frequency factors are in the range of 10^{13}–10^{15} s^{-1} and the activation energies are in the range of 45–60 kcal. DAEM models of this kind do fit data over a wide range of heating rates.

Niksa's FLASHCHAIN predictions [8] do not explain the lower rates, they simply show that a chemical reaction with a distribution of rates will yield a low apparent activation energy when fit with a single rate model over a narrow range of heating rates. This fact is well known and has been discussed in many previous publications by others. We agree with Niksa that there is a large body of results that contradict the values that were presented in our presentation, but none of the contradicting results were obtained with coal particle measurements.

REFERENCES

1. Freihaut, J. D., and Proscia, W. M., *Energy Fuels* 3:625 (1989).
2. Solomon, P. R., Serio, M. A., and Suuberg, E. M., *Prog. Energy Combust. Sci.* 18:133–220 (1992).
3. Solomon, P. R., Fletcher, T. H., and Pugmire, R. J., *Fuel* 72:587–597 (1993).
4. Solomon, P. R., Serio, M. A., Carangelo, R. M., and Markham, J. R., *Fuel* 65:182 (1986).
5. Serio, M. A., Hamblen, D. G., Markham, J. R., and Solomon, P. R., *Energy Fuels* 1:138 (1987).
6. Fletcher, T. H., *Combust. Sci. Technol.* 63:89–105 (1989).
7. Fletcher, T. H., *Combust. Flame* 78:223–236 (1989).
8. Niksa, S., *Energy Fuels* 8:670 (1994).

•

Larry Baxter, Sandia National Laboratories, USA. Are there relationships between the parameters used in the network devolatilization models (C^{13} nmr, FTIR, extra four yields, etc.) and traditional descriptions of coal in terms of maceral groups?

Author's Reply. The relationships between the parameters used in network devolatilization models and measurements of the heterogeneity of coal, such as maceral groups and microlithotypes, have not been explored in great detail. Maceral concentrates have, however, been analyzed by ^{13}C NMR, FTIR, and other techniques. For example, carbon aromaticity in maceral groups follows in the order: inertinite > vitrinite > exinite. Parameters used in current network models represent only average properties of the coal.

Twenty-Fifth Symposium (International) on Combustion/The Combustion Institute, 1994/pp. 475–483

AN EXPERIMENTAL STUDY OF HIGH-TEMPERATURE, OXIDATIVE PULVERIZED COAL DEVOLATILIZATION

LASSE HOLST SØRENSEN
Department of Combustion Research
Risø National Laboratory
DK-4000 Roskilde, Denmark

OLE BIEDE
Laboratory of Heating and Air Conditioning
Technical University of Denmark
DK-2800 Lyngby, Denmark

ROBERT E. PECK
Department of Mechanical and Aerospace Engineering
Arizona State University
Tempe, Arizona 85287, USA

Flat-flame coal-dust burner and entrained-flow reactor experiments were performed to study the devolatilization of size-graded Pittsburgh #8 coal samples under rapid heating, oxidizing conditions. The flat-flame burner characterized by high heating rates, high temperatures, and short residence times was used on three different particle-size cuts and two proximate volatiles-to-oxygen equivalence ratios. The entrained-flow reactor characterized by high heating rates, lower temperatures, and longer residence times was used at two different ambient temperatures. Solid samples were collected at different positions and thereby different residence times in the flames and subjected to ultimate and TGA proximate analysis. The results indicate that, in rapid heating systems (10^5 K/s), release of primary volatiles occurred within 5–10 ms. The 10–20- and 30–40-μm fractions gave approximately the same total volatile yield of 50% and peak temperatures of 1550 K, while the conversion for a 0–75-μm fraction was 5% higher with measured peak temperatures 100 K higher, indicating in situ combustion of small particles and devolatilization of large particles. Increasing equivalence ratio lowered the temperatures around 100 K, and volatiles yield decreased 5%. Devolatilization kinetics for flat-flame burner (FFB) and entrained-flow reactor (EFR) were fit by the distributed activation energy parallel reaction model using literature data combined with a total volatile yield estimate of 52% and ultimate analysis data from the flame experiments. Thermogravimetric analyzer (TGA) devolatilization profiles of the collected samples and comparisons of characteristic temperature and time of devolatilization to time of diffusion were found to be very useful tools in the analyzing process of the experimental results.

Introduction

Knowledge of coal devolatilization kinetics and pyrolyzate composition and yields is important in order to determine the energy released by oxidation of volatiles in combustion and gasification environments. This information also facilitates the development of computational models to predict the performance of coal-fired furnaces and boilers [1]. Because of the difficulty in obtaining well-defined flame data for model validation, most prior work [2,3] has attempted to determine release kinetics of individual species by methods such as thermogravimetric analysis with Fourier-transformed infrared gas analysis. The results have been used to devise a variety of theoretical models for coal devolatilization.

The purpose of this study is to obtain some basic experimental data on coal devolatilization for conditions encountered in practical pulverized-coal combustor gasifiers. Coal particle devolatilization is observed under a wide range of temperatures, heating rates, and oxidizing conditions. Solid samples collected at various residence times are subjected to elemental and thermogravimetric analyzer (TGA) analysis to determine changes in composition and characteristic devolatilization profiles. This information is used to explain the occurrence of various devolatilization events as a function of the experimental conditions. Further, an efficient data reduction scheme is developed to determine rate constants suitable for use in comprehensive coal combustion models.

Experimental

In the present study, experiments were performed using a flat-flame coal-dust burner and an entrained-flow reactor to provide a wide range of particle temperatures and heating rates up to 10^5 K/s. Flat-flame burners [4] and entrained-flow reactors [5] have proven useful in previous coal devolatilization studies. Particulate samples collected at various residence times were analyzed by TGA to characterize the solid-phase evolution during devolatilization.

Flat-Flame Burner:

The 6.35-cm diameter Meker-type flat-flame burner (FFB) [4] used is designed to stabilize premixed, laminar coal-dust/oxidizer flames. Pulverized coal supplied from a fluidized-bed feeder is mixed with oxidizer at the burner inlet. The reactants are passed upward through three stainless-steel screens, which provide appropriate pressure drop and heat loss to anchor the flame: the cold-gas velocity is 10.3 cm/s and the hot-gas velocity is 51.5 cm/s at a temperature of 1500 K. A typical maximum residence time is 100 ms. A multiwavelength infrared pyrometer technique [6] is used to measure thermal radiation intensity from the pulverized coal flame. Emission and transmission measurements at three wavelengths (1.6, 2.3, 3.8 μm) are used to determine the solid-phase temperature. Additional measurements at 4.4 μm, which is within the fundamental CO_2 vibration band, and local CO_2 concentrations are used with the former to estimate the gas temperature. Temperature measurement methods and error analysis are discussed fully in Ref. 6. Experimental methods and uncertainties are discussed in Ref. 4. Sample collection and temperature measurements were performed in separate runs. By using a water-quench probe at various heights in the flame, solid samples were collected, trapped, filtered, and subsequently dried in a convection oven. Gas composition was measured at all collection points [1,7]. Details of the instrumentation and data reduction may be found elsewhere [7].

Entrained-Flow Reactor:

A 62-mm-i.d. × 1-m-long electrically heated entrained-flow reactor (EFR) [8] was used to study devolatilization at longer residence time of 200–700 ms. A numerical flow code [9] was calibrated by laser-Doppler anemometry measurements and used to calculate particle residence times in the reactor as well as gas velocities at the probe inlet in order to collect samples isokinetically. Particles were collected with a 25-mm-diameter, water-cooled, stainless-steel probe, quenched with nitrogen at the probe inlet, and collected in a micro cyclone. The reactor data compared favourably with four other Nordic reactors in a Nordic intercalibration project [5,10]. The gas and wall temperatures are isothermal: hence, the particle temperature and conversion may be estimated using a heat balance and a mass balance equation. A recent thorough review on the use of entrained-flow reactors is given in the literature [11].

Thermogravimetric Analyzer:

The solid samples from FFB and EFR were subject to proximate and ultimate analysis. A Dupont 951 TGA was used for the proximate analysis following the method proposed by Elder [12]. As the sample is progressively heated and weighed in the TGA, the effluent products are carried away in a He-gas flow. To determine mass conversion of the char samples from EFR and FFB, the ash tracer technique was used. Ash tracer technique only gives a quantitative mass conversion that is prone to error. TGA mass-conversion curves obtained under inert conditions are used to characterize the solid-phase evolution during devolatilization. By registering how the sample devolatilization profiles change, it can be determined if, e.g., missing mass conversion is connected with changes in devolatilization characteristics.

Test Conditions:

For the FFB experiments cases 1, 2, and 3, a PSOC 1549 Pittsburgh #8 coal with elemental composition [wt% dry ash free (daf)] (C,H,N,S,O) = (84.07, 5.18, 1.26, 1.25, 8.24) was used in fuel-lean conditions with respect to ASTM volatiles (275 mg coal particles per liter air) for three different particle size ranges: 30–40, 10–20, and 0–75 μm. An additional case 1_2 was run under fuel-rich conditions (475 mg coal particles per liter air). Entrained-flow reactor experiments (case 4) were performed on a PSOC 1451 Pittsburgh #8 with the elemental composition (wt% daf) (C,H,N,S,O) = (83.14, 5.81, 1.65, 2.49, 6.91) in 0.5% O_2 in N_2 at 810 and 995 K. Table 1 summarizes the flame conditions.

Results:

Measured gas and solid temperatures and mass losses are plotted as a function of residence time for the three FFB cases in Figs. 1 through 3. Residence time is calculated from $t = \int(dx/v)$, where v is the local gas velocity from the continuity equation taking $v = v_0[T(x)/T_0]$. The term v_0 is the cold-gas inlet velocity of 10.3 cm/s. Calculated particle slip velocities were less than 0.1 m/s for 75-μm particles and less than 0.02 m/s for 30–40-μm particles. In all FFB cases, measured solid and gas temperatures peak adjacent to the burner screen and decrease downstream as a result of particle radiation heat loss. All significant mass loss occurs within 5–10 ms. Figure

TABLE 1
Conditions for experiments by flat-flame burner (cases 1 through 3) and entrained-flow reactor (case 4)[a]

Case No./ Fig. No.	PSOC No.	d_p (μm)	ϑ	$V_{prox,daf}$ (%)	Ash_{dry} (%)
FFB-1_1/1	1549	30–40	0.8	37.6	8.5
FFB-1_2/n	1549	30–40	1.4	37.6	8.5
FFB-2/3	1549	10–20	0.8	37.9	11.6
FFB-3/4	1549	0–75	0.8	37.5	9.7
EFR-4_1/4	1451	25–45	0.	38.9	17.8
EFR-4_2/4	1451	25–45	0.	38.9	17.8

[a]PSOC No.: sample identification: d_p: particle-size cut used in experiment: ϑ: equivalence ratio: proximate volatiles to oxygen; $V_{prox,daf}$: TGA-proximate volatile yield: Ash_{dry}: dry ash content in sample: n: not shown.

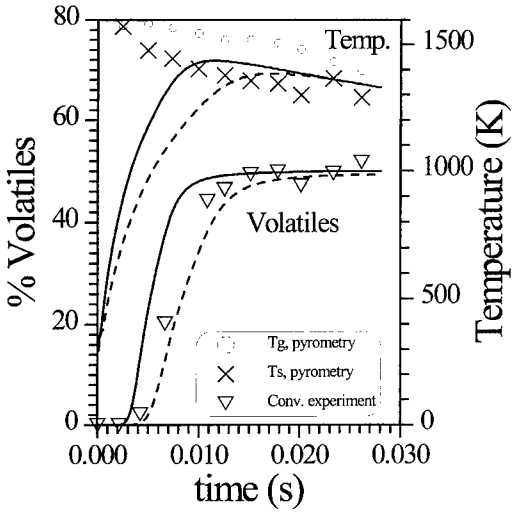

FIG. 1. Temperature and mass conversion profiles for FFB case 1_1, 30–40 μm particles. Calculated lines: solid, 35 μm and dashed, 45 μm.

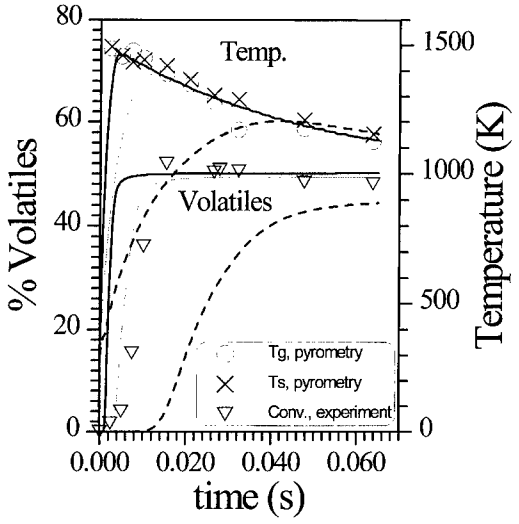

FIG. 2. Temperature and mass conversion profiles for FFB case 2, 10–20-μm particles. Calculated lines: solid, 20 μm: short dashed, 35 μm: long dashed, 75 μm.

4 shows measured and calculated mass conversions for two EFR cases, one at an ambient temperature of 810 K and one at an ambient temperature of 995 K.

Each particulate sample was subject to TGA proximate analysis. Besides quantifying proximate components, i.e., water, volatiles, ash, and fixed carbons, the technique provides a detailed characterization of coal devolatilization characteristics. Representative TGA devolatilization profiles for FFB-processed coal samples for case 1_1 are shown in Fig. 5. It can be seen that negligible weight loss occurs before 5-ms residence time (samples A, B, C) but that devolatilization is nearly complete by 10 ms (sample E). Even though no further mass loss occurs at long residence times in the flame, these samples will decompose under TGA conditions. Samples (E and F) taken late in the flame exhibit a devolatilization tail almost identical to the unburned coal. This finding suggests that TGA low-temperature volatiles are released early in a high-temperature flame, while heavier fractions of the coal containing a relatively large amount of oxygen and hydrogen remain almost unaffected.

The measured oxygen concentration in the flame dropped to below 1.5% within 10 ms. Gas-species concentrations were rather stable from 10–60 ms. Typical major gas-species composition was as follows: O_2 = 1.5%, CO_2 = 14%, CO = 5%, H_2 = 2%, N_2 = 75%. n-Paraffin hydrocarbon concentrations were in ppm: $CH_4 = 5 \cdot 10^3$, $C_2H_6 = 2 \cdot 10^2$, $C_3H_8 = 10$, $C_4H_{10} = 10$, $C_5H_{12} = 2$–10, $C_6H_x = 2 \cdot 10^2$. A more detailed product distribution and flame structure data may be found in Refs. 1 and 7.

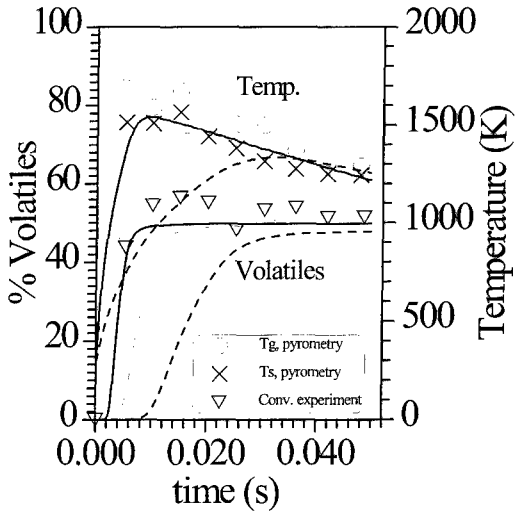

FIG. 3. Temperature and mass conversion profiles for FFB case 3, 0–75-μm particles. Calculated lines: solid, 35 μm: long dashed, 50 μm: short dashed, 75 μm.

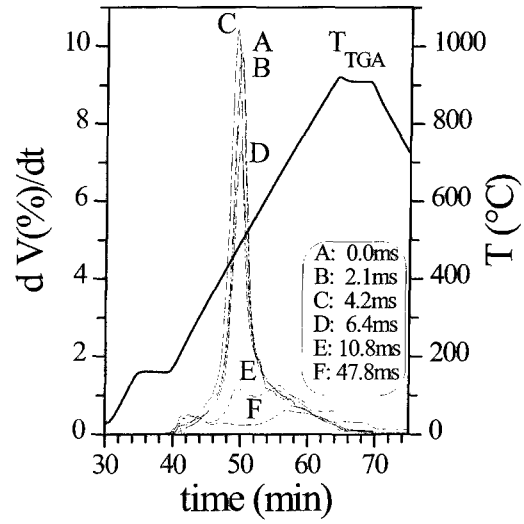

FIG. 5. DTG graphs for FFB-processed chars, case 1. A, feed coal: B through F, chars with residence time 2.1–47.8 ms in FFB flame: T_{TGA}, temperature/time progress.

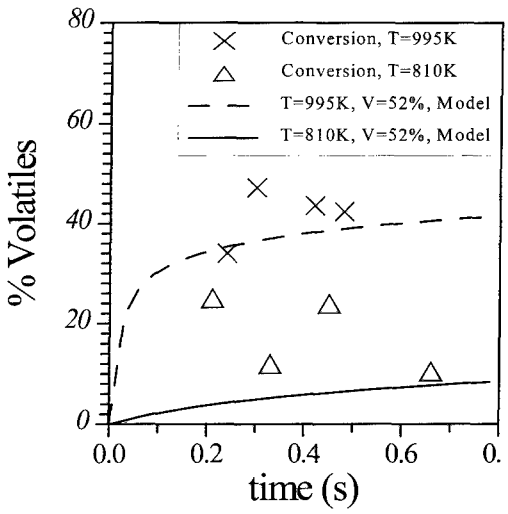

FIG. 4. Mass conversion profiles at 810 and 995 K for EFR case 4, 25–45-μm particles.

Theoretical

In this section, a theoretical model for predicting coal devolatilization during combustion is developed and later compared with the experimental results. The model incorporates species-specific rate constants taken from the literature along with a new FFB-based calibration procedure. The model complexity is consistent with its intended use in more comprehensive coal combustor performance codes.

Mass Conversion:

Devolatilization is described by a number of independent, parallel, first-order reactions, one for each gas species, using a distributed activation energy parallel reaction model (DAEP model):

$$\frac{dV_i}{dt} = k_{0,i} \exp\left(\frac{-E_i \pm \sigma_{E,i}}{RT_p}\right)(V_{0,i} - V_i). \quad (1)$$

The activation energy of each reaction is described by a statistical distribution. Frequency factor, $k_{0,i}$, activation energy, E_i, and standard deviation on activation energy, $\sigma_{E,i}$, must be known for each species. These are taken from Serio et al. [3] and listed in Table 2.

The initial potential amount of each species, $V_{0,i}$, must also be known. Merrick [13] proposed that the potential yield of individual volatile species should be predicted from a set of linear equations by the least-squares solution technique, closing the mass balance by using 10 equations to find the 10 unknowns: char, CH_4, C_2H_6, CO, CO_2, tar, H_2, H_2O, NH_3, and H_2S.

The observation equation is written as follows:

$$\mathbf{A}[n,m] \cdot \mathbf{b}[m] = \mathbf{c}[n] \quad (2)$$

$\mathbf{A}[n,m]$ matrix of known or estimated coefficients representing the correlations between gas yields and corresponding elements in the coal, char, and volatiles and total-volatile/char ratio

$\mathbf{b}[m]$ solution vector, containing the found gas yields

TABLE 2
Input parameters for the distributed activation energy parallel reaction model: predicted component fractions, kinetic parameters, and characteristic devolatilization peak temperatures[a]

Predicted component	Serio [3] fraction	FFB fraction	(KJ/mole) E_i	σ_i	$\log(k_{0,i})$	FFB/EFR $T_{max,i}$ (K)	FFB/EFR $t_{(1/2),i}$ (ms)	TGA $T_{max,i}$ (K)	TGA $t_{(1/2),i}$ (s)
Char	0.40	0.48							
CH_4 (tight)	0.020	0.018	249.4	16.6	11.5	1517	0.53	965	43.0
CH_4 (loose)	0.015	0.014	249.4	16.6	13.2	1284	0.38	863	34.4
CH_4 (extra loose)	0.015	0.014	249.4	12.5	13.9	1209	0.34	827	31.6
C_nH_{2n} (aliphatic)	0.19	0.1756	249.4	12.5	14.2	1179	0.32	813	30.5
CO (loose)	0.050	0.05	332.6	49.9	18.1	1170	0.24	873	26.4
CO (tight)	0.022	0.0225	336.7	12.5	15.2	1456	0.36	1030	36.3
CO (extra tight)	0.020	0.0	378.3	12.5	13.3	1908	0.56	1290	50.7
CO_2 (loose)	0.006	0.006	281.4	12.5	16.8	1087	0.24	793	25.7
CO_2 (tight)	0.005	0.005	318.6	16.6	15.0	1399	0.35	985	35.1
Tar	0.43	0.21	230.0	12.5	14.9	1029	0.27	720	26.0
TGA[1]	0.11								
H_2 (aromatic)	0.012	0.0080	336.7	49.9	14.0	1596	0.44	1099	41.4
H_2O (loose)	0.011	−0.0165	249.4	12.5	13.2	1286	0.38	864	34.5
H_2O (tight)	0.011		271.9	12.5	12.8	1451	0.45	964	39.4
HCN (loose)	0.009	0.0020	249.4	12.5	13.2	1286	0.38	864	34.5
HCN (tight)	0.022	0.0050	353.4	39.5	12.8	1859	0.56	1241	50.2
H_2S	0.024	0.0064	230.0	12.5	14.9	1029	0.27	720	26.0

[a]FFB/EFR heating rate of 10^5 K/s and TGA heating rate of 0.5 K/s. H_2S is in FFB fraction assumed to follow the tar fraction, since no kinetics for H_2S were given by Serio et al. CO (extra tight) is in FFB fraction assumed to stay in the char or with tar.

c[n] ultimate composition of the coal (daf mass basis) and estimated correlations between elemental composition and specific gas yields.

To improve the accuracy of the mass balance, two more constraints are applied, giving 12 equations to find 10 unknowns [14]. The unknown components ($b[m]$) are described by their fractional elemental *mass* contributions of C, H, O, N, and S. One representative elemental char composition for all cases is estimated from the composition of the samples after devolatilization has been completed. The tar composition is a complex function of the release rates of all individual species and, thus, the heating rate and particle condition during a dynamical process. Since measurement of primary tar composition from tars collected in an under-stoichiometrical flame is not possible, the tar composition is here chosen identical to the composition of the coal particle. If better knowledge of tar composition exists from any particular experiments, e.g., enrichments in hydrogen, these values should be used.

Also, total volatile yields and correlations between specific gas yields and coal composition should be prescribed. Correlations between the elemental composition of the coal and individual gas yields are taken from the work of Serio et al. [3] that used a Pittsburgh #8 coal with daf mass-basis composition (wt%): (C,H,O,N,S) = (0.821, 0.056, 0.082, 0.017, 0.024). The gas fractions found by Serio et al. are listed in Table 2.

Assuming that the ratios of yields of methane, aliphatic, and H_2 to coal hydrogen and the ratio of CO and CO_2 to oxygen are constant from one Pittsburgh #8 sample to another under rapid heating experiments, these species are estimated from the species found by Serio et al. [3]. Since, in the ultimate analysis, oxygen is measured "by difference," the oxygen-to-carbon ratio can be regarded as an adjusting parameter connected to the calculated water yield that may be allowed negative (if small). Total volatile yield is estimated from the FFB and EFR experiments, giving a total volatile yield of 52–60% daf, which is supported by other studies on Pittsburgh #8 [3,4,5,9]. In the following (see Figs. 1 through 4), all calculated devolatilization yields are based on an assumption of a total volatile yield of 52% daf. The found species yields are shown in Table 2 as FFB fractions. Species rate constants and characteristic times of devolatilization given a heating rate are evaluated at the temperature of maximum devolatilization rate $T_{max,i}$, defining a threshold for devolatilization, and used to

qualitatively discuss experimental and modelled results.

Particle Temperature:

In order to evaluate rate constants and characteristic times of devolatilization, the particle thermal history must be known. The time coordinate for mass loss in Figs. 1 through 3 is referenced to the first measurement point rather than the start of particle heatup during the sampling experiments, in accordance with measured solid and gas temperatures. Indeed, the first reported temperatures exceed the threshold for devolatilization, whereas no significant mass loss occurs until a few milliseconds later. The samples collected early in the flame (samples B and C) show almost no effect on overall TGA-volatile kinetics, showing that the actual particle temperatures near the burner during sampling are in general lower than the optically measured values because of the influence of multiple emitters and/or probe cooling effects. In the absence of complete thermal histories, the mean particle temperature used in the kinetic model was calculated from an energy balance equation [14] as follows:

$$m_p C_p \frac{dT_p}{dt} = hA_p(T_a - T_p) + \varepsilon\sigma A_p(T_w^4 - T_p^4) + Q_{\text{vap}} + Q_{\text{vol}} + Q_c \quad (3)$$

where the thermal inertia is expressed in terms of convective heat transfer, thermal radiative heat transfer, heat losses due to vaporization and devolatilization, and heat generated at the particle by heterogeneous reaction. The particle specific heat was calculated using the Merrick equation [13]. Since, for each experiment, the interpretations of measured transmission/emission intensities of gas and solids are mutually interdependent [6], a mean temperature of the measured solid and gas temperatures is used to define the ambient gas temperature. Wall temperatures are taken to be 25 °C since the flame is optically thin. The calculated particle temperatures are referenced to the devolatilization time scale in Figs. 1 through 3.

Characteristic temperature and time of devolatilization

For a given heating rate, β, the characteristic temperature of maximum devolatilization rate for a specific gas, $T_{\max,i}$, is reached within a time

$$\tau_{q,i} = (T_{\max,i} - T_0)/\beta. \quad (4)$$

For a reaction characterized by an activation energy set (E_i, $\sigma_{E,i}$) and frequency factor $k_{0,i(\sigma_{E,i} \neq 0)}$, $T_{\max,i}$ is found by

$$T_{\max,i} = \frac{1}{\frac{R}{E_i} \ln \frac{k_{0,i} R T_{\max,i}^2}{\beta E_i}} \quad (5)$$

where $k_{0,i} = k_{0,i}(\sigma_{E,i} \neq 0)/\{1 - 0.4\{1 - \exp(-\sigma_{E,i}/2.5)\}$ [15]. The half-time of devolatilization at $T_{\max,i}$, $t_{(1/2),i}$ is then approximately given by [14]

$$t_{(1/2),i}\,(T_{\max,i}) = \frac{\ln 2}{k_{0,i} \exp\left(-\frac{E_i}{RT_{\max,i}}\right)}. \quad (6)$$

In Table 2, the characteristic temperature, $T_{\max,i}$ and the half-time of devolatilization, $t_{(1/2),i}$ are listed for FFB and EFR heating rates at 10^5 K/s and for TGA heating rates at 0.5 K/s.

For larger molecules like tar, $t_{(1/2),i}(T_{\max,i})$ is a measure of the time of decomposition and hence may indicate whether the molecules react further before leaving the parent particle as a "primary" product. To predict the importance of secondary reactions, $t_{(1/2),i}$, $(T_{\max,i})$ should be compared to characteristic times of diffusion, τ_{diff}, and convection, τ_{conv}, as proposed by Russel et al. [16]. For pore sizes at around 0.1–1 μm, typical residence times for small molecules (<100 amu) are about 1 ms, while, for larger molecules (100–500 amu) in 100-μm nonsoftening particles, the typical residence times are 1–10 ms or even longer. Since $t_{1/2,i}(T_{\max,i}) < 0.6$ ms for all components in Table 2 at heating rates of 10^5 K/s, secondary effects may be of importance in flames for heating rates $>10^5$ K/s, in particular for tar molecules, according to the DAEP model. In general, $t_{(1/2),i}$, $(T_{\max,i})$ is of the order of seconds for heating rates of 0.5 K/s in a TGA: hence, only slight secondary reactivity is expected. In the DAEP model, the increasing mass conversion with heating rate obtained comparing a flame with the TGA is mainly reflected in increased tar release, as found from calibration of the DAEP model to flame experiments. The large tar fraction reported by Serio et al. [3] and shown in Table 2 implies that, in the Functional Group model used by Serio et al., tar and gases are released in competition from the same pool.

Discussion

The calculated particle temperatures using the heat-balance equation are shown in Figs. 1 through 3, assuming different particle sizes. Using the mean particle size for each of the cases, it is observed that, within 10 ms, the calculated particle temperatures reach the measured ambient temperatures. For all particle-size ranges used here, the devolatilization is nearly completed within 5–10 ms.

The predicted coal conversion is compared to

measured mass loss in Figs. 1 through 3 for the FFB (cases 1 through 3) and in Fig. 4 for the EFR (case 4). Temperature profiles calculated from Eq. (3) for different particle sizes indicate heating rates of 10^5 K/s. The corresponding reaction time scale confirms that devolatilization of the mean particle size in each case is within 5–10 ms. The overall mass conversion yield in cases 1 through 3 is well predicted assuming a total volatiles yield of 52 w/w%. Case 1_1 (30–40 μm) and case 2 (10–20 μm) show an almost identical mass conversion of 50% daf and peak temperature of 1550 K. The results in Fig. 3 for the 0–75 μm particles show a 5% higher total mass loss and 100 K higher peak temperature than in the size-graded experiments (Figs. 1 and 2). This result stems from the abundance of smaller particles (<10 μm), which may even burn heterogeneously before the large particles begin to devolatilize. For 35-μm particles, a maximum char conversion of 5–6% daf during the first 20 ms is calculated using char reactivity parameters proposed by Mitchell [17].

In cases 2 and 3, a small decrease in measured weight loss is observed at longer residence times. This is probably attributed to larger quantities of soot that are collected together with the char. This effect may influence the result so that a total volatile yield of 52 w/w% seems to be a minimum for the Pittsburgh #8 under rapid heating conditions.

In case 2, for the 10–20-μm particles, the mass conversion is predicted to occur earlier than experimentally observed. The calculated particle temperature used in the model reaches maximum temperature within less than 2 ms. The experimentally observed devolatilization delay in this case may indicate some mass transfer limitations not accounted for in our calculations. If the dominant pore size is much smaller than the particle grain size, Knudsen or structural diffusion becomes important and slows down diffusion rate. Another explanation for the devolatilization delay may be particle clustering or internal heat transfer effects not considered here. Finally, and most likely, nonisokinetic sampling or the cooling effect from the water-cooled probe with an observed backmixing zone of 1–5 mm is significant very near the inlet position in this case. More experimental evidence is needed to define the upper heating rate limit for thermal and mass transfer resistance determining pyrolysis rate.

Increasing the equivalence ratio from 0.8 to 1.4 for the 30–40-μm fraction in case 1_2, the peak temperature decreased around 100 K relative to case 1_1, and volatiles yield decreased 5% [14].

In case 4 (EFR experiment), the volatile yield of 42–47 w/w% at 995 K for residence times of 200–500 ms is well predicted by the DAEP model with an assumption of a total pool of 52 w/w%. These experimental values compare well with data obtained with wire mesh [18]. As seen from Fig. 4, the calculations significantly underpredict the early volatile yield at 810 K. This indicates the presence of reactions with faster reaction rates at low temperatures than provided in Table 2, for example, reactions characterized by lower activation energies and frequency factors, i.e., molecules that are adsorbed or weakly bound to the coal structure. A large scatter is observed at 810 K, indicating a large sensitivity of experimental conditions at this temperature, i.e., temperature, collection efficiency (20–30%). Below 1000 °C the flow in the EFR is not laminar: hence, particles dispersed right after injection. However, all data points represent rather high devolatilization yields, in agreement with literature data [18,19]. At these low temperatures, major parts of tars and molecules released will be mainly primary since $t_{(1/2),i}$ $(T_{\max,i}) >> \tau_{\text{diff}}$, and the release of these gases will not strongly affect char production through secondary reactions.

For each individual gas, e.g. tar, for a certain high heating rate, the release of tars is kinetically limited well below the temperature of maximum devolatilization rate, $T_{\max,i}$. Above $T_{\max,i}$, diffusion limitations are important when $t_{(1/2),i}$ $(T_{\max,i})$ and τ_{diff} are comparable.

Conclusions

Published kinetic parameters and correlations for volatiles partitioning were used together with standard coal characterization data, TGA observations, and total yields from flat-flame burner experiments to predict devolatilization by a distributed activation energy parallel reaction model. Predicted devolatilization behaviour compared favourably with results from experiments performed in a flat-flame burner for three different size ranges on a Pittsburgh #8 coal at heating rates of 10^5 K/s in oxidizing conditions. Primary volatiles release occurred in the flat flame within 5–10 ms. With an equivalence ratio of 0.8, the 10–20- and 30–40-μm fractions gave approximately the same volatiles yield (50%) and peak temperatures (1550 K), while conversions for a 0–75-μm fraction were 5% higher, with measured peak temperatures 100 K higher. Increasing equivalence ratio lowered the temperatures around 100 K, and volatiles yield decreased 5%.

Using the same TGA-derived kinetic parameters and gas-species yields to predict devolatilization rates in an entrained-flow reactor that is characterised by heating rates as high as for the flat-flame burner but lower temperatures showed that the model was unable to predict the early release of volatiles at the lowest temperature of 810 K. At this low temperature, the volatile release was higher than expected from the TGA-derived devolatilization kinetics. This shows that the effect of high heating rates on the devolatilization process already is significant at low temperatures, indicating that, at these temperatures,

the half-time of tar release is low. At 995 K, the devolatilization is well estimated by the model.

Using thermogravimetry on char samples was found to be useful in the interpretation of flame data since TGA-proximate analysis adds additional information to the standard proximate analysis. While a standard proximate analysis only gives the volatility of the samples, which could be a result of several processes, the differential TGA profiles showed that, not only was no mass conversion observed early in the flame, but also no significant phase changes, since the total differential TGA profiles of samples taken early in the flame showed almost no changes from the differential TGA profile of the feed sample. The differential TGA profiles also showed that volatiles released in the TGA from samples taken late in the flame were released mainly as a high-temperature tail, almost identical to the tail from the feed sample. This indicates that TGA low-temperature volatiles are released early in a high-temperature flame, while the heavier retained fractions of the coal remain almost unaffected.

Nomenclature

A	external area
C	specific heat
d	diameter
E	apparent activation energy
h	convective heat transfer coefficient
k	frequency factor
m	mass
Q	heat generated or consumed
R	gas constant
t	time
T	temperature
V	volatile yield
β	heating rate
ε	emissivity, $\varepsilon = 0.8$
σ	Stefan–Boltzmann constant $= 5.67 \cdot 10^{-8}$ $W/m^2\ K^4$
σ	standard deviation on activation energy
τ	characteristic time
ϑ	volatiles-to-oxygen ratio

Subscripts

a	ambient gas
c	heterogeneous char combustion
conv	convection
diff	diffusion
E	apparent activation energy
g	gas
i	specific gas
max	maximum
P	particle
s	solid
vap	vaporization
vol	devolatilization
w	wall
0	initial condition
1/2	half time of devolatilization

Acknowledgments

The research was supported by the Danish Ministry of Energy, and the Danish power companies ELSAM I/S and ELKRAFT A.m.b.A., Coal samples were provided by the U.S. DOE-PETC.

REFERENCES

1. Biede, O., Sørensen, L. H., and Peck, R., *Pyrolysis and Ignition of Coal at Pulverized-Coal Combustion*, Laboratory of Heating and Air Conditioning, Technical University of Denmark, EFP-88 jr. No. 1323/88-23, 1992 (mostly in Danish).
2. Solomon, P. R., Serio, M. A., Carangelo, R. M., Bassilakis, R., Gravel, D., Baillargeon, M., Baudais, F., and Vail, G., *Energy Fuels* 4:319 (1990).
3. Serio, M. A., Hamplen, D. G., Markham, J. R., and Solomon, P. R., *Energy Fuels* 1:138 (1987).
4. Peck, R. E., Altenkirch, R. A., and Midkiff, K. C., *Combust. Flame* 55:331 (1984).
5. Hustad, J. E., Aho, M. J., Hupa, M., Noopila, T., Sørensen, L. H., Clausen, S., Kiørboe, L., Gromulski, J., Bengtsson, M., and Leckner, B., *Riv. Combustibili* 44:257 (1990).
6. Mackowski, D. W., Altenkirch, R. A., Peck, R. E., and Tong, T. W., *Combust. Sci. Technol.* 31:139 (1983).
7. Behring, K. A., "Flat-Flame Burner Studies of Pulverized-Coal Devolatilization," Master's Thesis, Arizona State University, Tempe, Arizona, 1991.
8. Sørensen, L. H., Clausen, S., Astrup, P., Jensen, P. A., Porsdal, H., and Olsen, A., *Fundamentals in Combustion*, Risø National Laboratories, Denmark, Em jr.nr. 1323/85-4, 1991.
9. Gosman, A. D., and Ideriah, F. J. K., *Teach-2E: A General Computer Program for Two-Dimensional, Turbulent, Recirculating Flows*, Imperial College, London S.W.7, 1976.
10. Sørensen, L. H., Saatamoinen, J., and Hustad, J. E., "Comparison of Char Reactivity Results by Using Different Theoretical Models," in *Nordic Seminar On Combustion and Gasification Reactivities of Solid Fuels*, Jyväskylä, 1993.
11. Carpenter, A. M., and Skorupska, N. M., *Coal Combustion—Analysis and Testing*, IEA Coal Research, London, 1993.
12. Elder, J. P., *Fuel* 62:580 (1983).
13. Merrick, D., "Thermal Decomposition of Coal: Mathematical Models of the Chemical and Physical Changes," in *Coal Science and Chemistry* (A. Volborth, Ed.) Elsevier, Amsterdam, 1987, p. 307.
14. Sørensen, L. H., Biede, O., and Peck, R. E., *Using the DAE-Model to Interpret Oxidative Coal Pyrolysis Experiments Performed by Flat-Flame Burner, Entrained-Flow Reactor and Thermogravimetric Analyzer*, Risø National Laboratories, Denmark, Risø-R-669(EN), 1993.
15. Braun, R. L., and Burnham, A. K., *Energy Fuels* 1:153 (1989).

16. Russel, W. B., Saville, D. A., and Greene, M. I., *AICHE J.* 65:25 (1979).
17. Mitchell, R. E., *On the Products of the Heterogeneous Oxidation Reaction at the Surface of Burning Coal Char Particles*, Sandia National Laboratories, 1988.
18. Gibbins, J. R., "Investigations of Primary Coal Pyrolysis Processes using a Variable Heating Rate Wiremesh Apparatus," Ph.D. Thesis, Imperial College, London, 1988.
19. Seery, D. J., Freihaut, J. D., Proscia, W. M., Howard, J. B., Peters, W., Hsu, J., Hajaligol, M., Sarofim, A., Jenkins, R., Mallin, J., Espindola-Merin, B., Essenheigh, R., and Misra, M. K., *Kinetics of Coal Pyrolysis, Final Report*, United Technical Research Center, Report 956966-F, 1989.

Twenty-Fifth Symposium (International) on Combustion/The Combustion Institute, 1994/pp. 485–491

VOLATILE MATTER RELEASE, PARTICLE/CLOUD IGNITION, AND COMBUSTION OF NEAR-STOICHIOMETRIC SUSPENSIONS OF PULVERISED COAL

J. A. LUCAS AND T. F. WALL
Department of Chemical Engineering
University of Newcastle
Newcastle 2308, Australia

The ignition characteristics of a cloud of pulverised coal flowing in a drop-tube furnace are examined. Cloud ignition is defined at the minimum gas temperature at which significant oxygen consumption occurs. This is accompanied by the generation of carbon dioxide and oxides of nitrogen, and the formation of a visual flame. Cloud ignition occurs at several hundred degrees above that for the ignition of some single coal particles. For three coals the cloud ignition temperature decreased with oxygen partial pressure, but was not sensitive to fuel equivalence ratio or particle size (as has been observed for single particles).

For the three coals examined, pyrolysis measurements show the existence of a tar/light hydrocarbon/oxygen mixture at the cloud ignition temperature. On combustion, the accompanying temperature increase results in coal burnoffs from 35 to 65% even though the combustible volatile matter prior to the ignition event corresponds to less than 6.5% burnoff. Different trends of tar and methane combustion and soot formation are observed in the experiments as gas temperature and oxygen levels were changed; however, significant tar combustion was always observed at cloud ignition. A mechanistic model is proposed to explain the observations.

Ignition Measurements

Previous measurements [1,2] have characterised the ignition behaviour of pulverised coal fed to a furnace as a pulse with a mass of 2–10 mg or continuously with air in near-stoichiometric proportions. In the latter—continuous measurements—the temperature of the drop-tube furnace was increased at a slow rate (10 °C/min) to establish a continuous steady state. A visual record (by video camera) and gas composition measurements of O_2, CO_2, CO, and NO monitored the associated combustion. A schematic of the apparatus used for the continuous experiments is shown in Fig. 1.

Events identified at several gas temperatures are defined as follows [1,2]:

1. T_g—the minimum gas temperature to observe an ignition "flash" associated with particle ignition in the pulse experiment.
2. T_f—the minimum temperature to observe a "flash" from particle ignition in the continuous experiment.
3. T_c—the "cloud ignition" temperature at which the visual record shows that the coal plume ignites with a significant reduction in the measured O_2 levels (noted T_{O2}) and the generation of several hundred ppm of NO.

Figure 2 gives these temperatures for a number of size fractions (63–90, 90–125, 125–150, 150–180 μm) of the three coals of Table 1. The lower ignition temperatures (T_g and T_f) have previously been taken to characterise coal ignition [3], but are associated [1,2] with the ignition of a small proportion of the coal fed, in that a single flash is observed for several thousand particles fed and no oxygen consumption is measured. At the cloud ignition temperature, observed at gas temperatures some 200 °C higher, all particles are observed to ignite in an explosion-like event with significant combustion, and therefore with energy generation. The present paper is concerned with these events, their association with volatile matter, and their potential influence on ignition in pulverised coal flames.

The cloud ignition measurements were made with excess air levels of about 40%. As the coal is fed centrally with about 20% of the air with the balance mixed radially in this flow, no exact estimate of the dust concentration at the location of ignition is obtained. Rather, conditions reported here are those calculated for the resultant mixtures.

Coal Pyrolysis and Combustion Experiments

In pyrolysis measurements, size-graded pulverised coal was fed with high-purity nitrogen to a drop-tube furnace, to achieve similar temperatures, heating

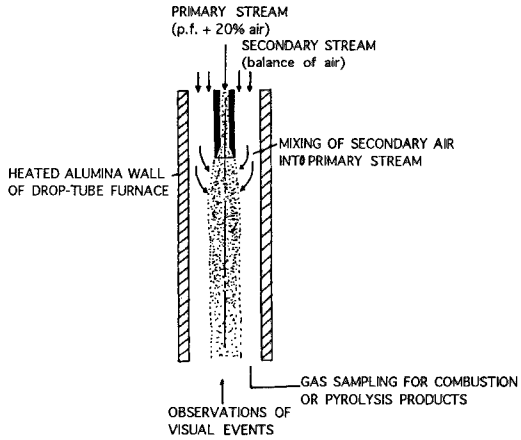

FIG. 1. Diagram of the experimental apparatus used for the continuous ignition experiments.

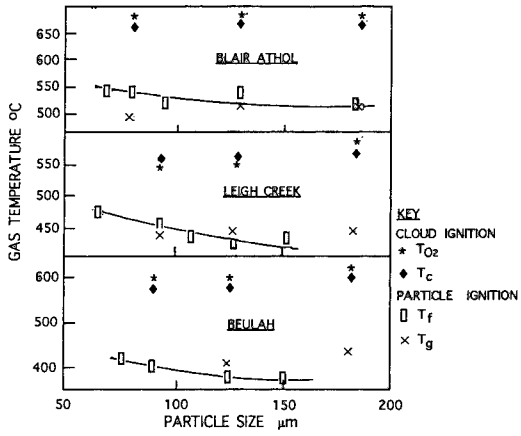

FIG. 2. Particle and cloud ignition temperatures (T_{O_2}, T_c—cloud ignition; T_f, T_g—particle ignition).

rates, and holding times as for the continuous ignition measurements. Typically, for a 150-μm particle heated to 700 K, the heating rate is estimated to be 4000 K/s (100 ms to reach 700 K), the holding time at this temperature was 300 ms, and the residence time within the furnace was 400 ms. After passing through the furnace the char was separated from the gas, with the gas, passing through a cell (heated to a fixed temperature of 200 °C) located in a Fourier transform infrared (FTIR) spectrometer, for identification of H_2O, CO_2, CH_4, C_2H_4, CO, and tars and then to a gas chromotograph for analysis of CH_4. The sampled char was mounted with KBr for FTIR analysis. Experiments were also carried out with O_2/N_2 mixtures to examine the extent of combustion of the pyrolysis products.

The temperatures reported here are the gas temperatures that are measured in the furnace, with inert gas flowing through but without combustion. The particles have adequate residence time in the furnace to heat to this temperature (<100 ms) in both the pyrolysis and combustion experiments. As the ignition experiments were undertaken as the furnace is heated slowly, the ignition temperatures correspond to the minimum temperatures necessary for ignition.

Results

Pyrolysis:

The FTIR spectra at intervals of 50 °C in gas temperature, given in Figs. 3 through 5, indicate that the pyrolysis products are progressively evolved as temperature increases in the following sequence: CO_2 (2300 cm^{-1}) and H_2O (3400–4000, 1200–2000 cm^{-1}), then the aliphatic tars (~2940 cm^{-1}), then CO (~2140 cm^{-1}), and then CH_4 (3025 cm^{-1}). For Beulah lignite, this sequence and the temperatures for initial detection correspond to those found for Montana lignite [4]. The spectra for Blair Athol and Leigh Creek coals also show ethene peaks. No peaks

TABLE 1
Coal Analysis (As Fired)

	Proximate analysis (db)				Ultimate analysis (db)				
	H_2O (ad)	Ash	VM	FC	C	H	N	S	O
Beulah lignite	13.5	9.9	51.1	39.0	63.8	4.3	0.84	0.6	20.7
Leigh Creek brown coal	7.9	22.3	34.9	42.8	54.2	3.06	1.26	0.83	15.3
Blair Athol subbituminous coal	6.4	8.6	32.1	59.4	75.8	4.23	1.65	0.32	9.31

Note: db, dry basis; ad, air dried; VM, volatile matter; FC, fixed carbon.

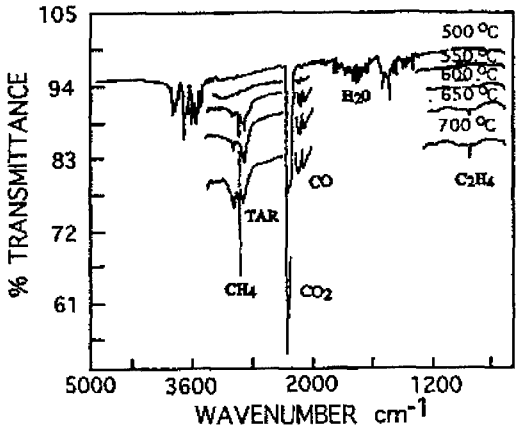

FIG. 3. FTIR gas spectra of the pyrolysis products (released at the indicated temperature) from Leigh Creek coal (T_c = 660 °C).

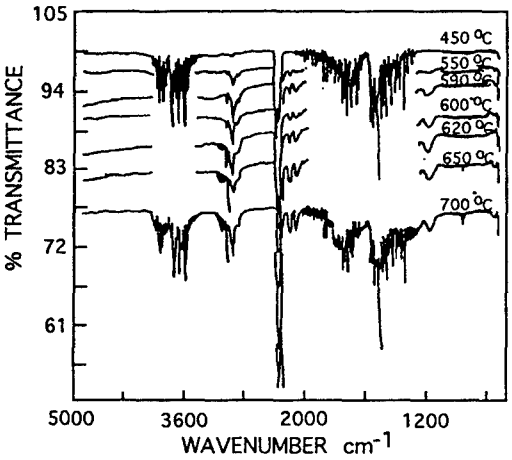

FIG. 4. FTIR gas spectra of the pyrolysis products (released at the indicated temperature) from Beulah lignite (T_c = 600 °C).

are evident for aromatic tars (expected at ~3000 cm^{-1}). The development of a sloping baseline evident in Fig. 5 for Blair Athol coal, which is quite marked at 700 °C, is consistent with the presence of soot in the gas sample.

Also shown in Fig. 5 are theoretical curves for soot transmission based on the known spectral transmissivity of a soot cloud, for comparison with the sloping baseline. These curves are based on the following equation [5] for transmittance (T) as a function of wavelength [2]: $T = \exp(-C_0 C_s L/\rho_s \lambda^d)$, where the empirical constant C_0 is taken as 7 [5], ρ_s as 2×10^3 kg/m^3, d as unity, L as the path length of the gas cell (0.16 m), and C_s as the mass conversion of the coal to soot. The curves shown in Fig. 5 are for different

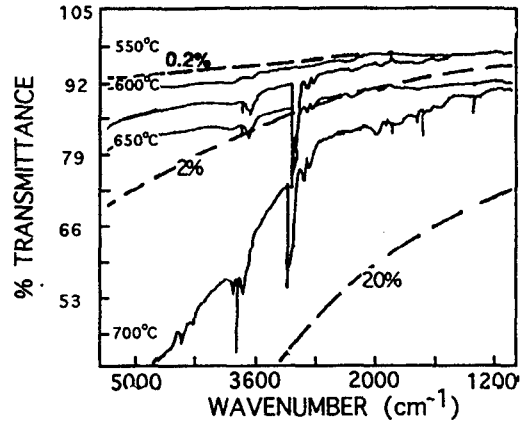

FIG. 5. FTIR gas spectra of the pyrolysis products (released at the indicated temperature) from Blair Athol coal (T_c = 660 °C). Also shown are the theoretical curves for soot transmission, at various mass % conversions of coal (daf) to soot.

values of C_s. The results indicate that at the cloud ignition temperature for Blair Athol (680 °C), in excess of 2% of the coal has been converted to soot.

The FTIR spectra for the chars of the three coals (collected during the pyrolysis experiments) showed no significant change in the peak at 800 cm^{-1}, typical of aromatic structures, with increasing temperature, indicating little release of aromatic tars during pyrolysis. This is consistent with the findings of others [6], that low-temperature tar may have a highly aliphatic nature.

In the FTIR spectra of the pyrolysis gases, the area of the aliphatic hydrocarbon peak at 2940 cm^{-1} was taken as a qualitative measure of the tar evolution from the three coals. By comparing the ratio of tar to methane yields reported for Montana lignite [4] with those found for Beulah lignites, at various temperatures, a quantitative measure of the tar released during pyrolysis could be obtained for this particular fuel.

Combustion:

Figures 6a through 6c give the estimated yields of tar and the measured CH_4, being the major hydrocarbon gas, for pyrolysis (0% O_2) and during combustion, with a summary of the reactions observed given in Table 2. The figures show a general increase in both tar and methane yields with increasing temperature. There were significant differences found in the combustion behaviour of the three fuels.

Beulah lignite (Fig. 6a), in the presence of oxygen, showed no tar reaction (depletion) at temperatures below its cloud ignition temperature and no tar cracking. In fact, tar reaction commenced at a temperature in excess of the cloud ignition temperature

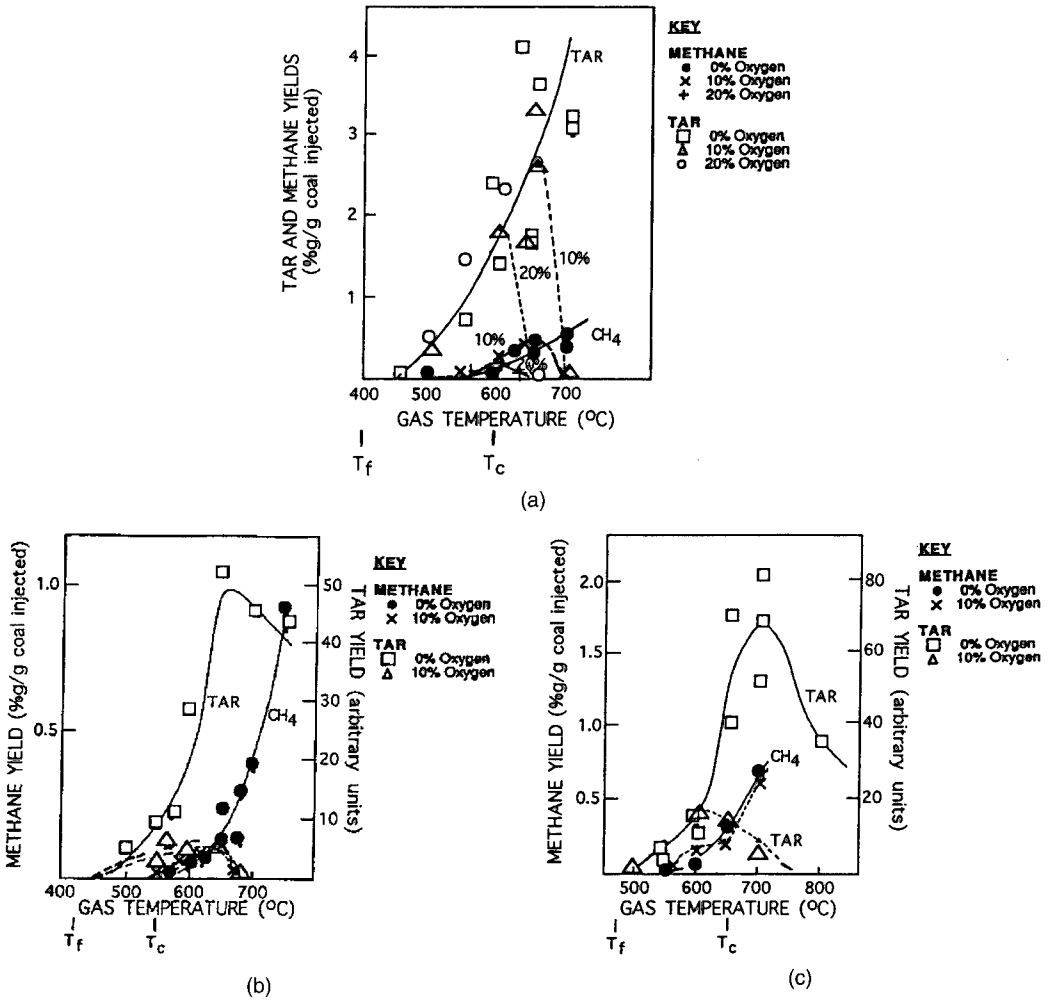

FIG. 6. (a) Methane and tar yields for Beulah lignite under pyrolysis; 10% O_2 and 20% O_2 combustion conditions. (b) Methane and tar yields for Leigh Creek coal under pyrolysis, and 10% O_2 combustion conditions. (c) Methane and tar yields for Blair Athol coal under pyrolysis, and 10% O_2 combustion conditions.

TABLE 2
Combustion Characteristics of the Three Fuels

Fuel	Tar reaction	Tar cracking	Soot formation	Methane reaction
Beulah lignite	at T_c	no	no	at T_c
Leigh Creek	below T_c	yes	no	above T_c
Blair Athol	below T_c	yes	yes	none

(~600 °C) for the lower oxygen (10%) containing environment. The tar yields at a temperature just below that where tar reaction is observed, together with the known air/fuel ratio, may be used to calculate the tar mass concentrations existing within the furnace. These mass concentrations indicate that Buelah lignite tar has a flammability limit (i.e., it does not react at lower concentrations) of 0.08% v/v in air and

0.13% v/v in 10% O_2/N_2 (based on an estimated tar molecular weight of 200). A similar reduction was also observed for methane combustion.

Leigh Creek tar (Fig. 6b) reacted at temperatures below the cloud ignition temperature, with the proportion combusting increasing significantly with temperature. This behaviour was very different to that of Beulah lignite tar. The flammability limit for Leigh Creek tar was apparently reached at temperatures below that of cloud ignition. Tar cracking was observed for this fuel. Methane combustion commenced at temperatures in excess of the cloud ignition temperature.

Blair Athol (Fig. 6c) showed similar behaviour to Leigh Creek in terms of the tar reaction; however, there was no significant consumption of methane at the temperatures of the experiment. In addition, significant tar cracking was observed at higher temperatures, with the formation of soot. Soot was not detected in the presence of oxygen for this fuel.

Combustion at the Gas Temperature Where Single Particle Ignition and Cloud Ignition Are Observed

At the temperatures for single particle ignition (T_g), little or no evolution of combustible volatile matter is observed for any of the three coals. There is, therefore, little oxygen (less than 2% of that available) consumption at these temperatures. Together with visual observations, this indicates that ignition at these temperatures is isolated, involving only single particles and only a minute proportion of the total particle population (estimated as 1 in 10,000 to 100,000).

Cloud ignition appears to be an entirely different event, wherein the entire coal plume ignites in an explosion-like phenomenon with significant heat release (as indicated by a related high visible radiation emission) and oxygen consumption. Although the reaction behaviour of the released volatiles is different for the three fuels, at varying gas temperatures there are several common features. During the pyrolysis experiments, as the temperature increased, the first combustible volatile species to be released was found to be tar, being first detected at temperatures 100 °C–150 °C below that at which cloud ignition is observed (T_c). At the cloud ignition temperature, significant tar has been released (tar being the dominant combustible species) with, perhaps, some hydrocarbon gases. For the three fuels, the combustion of the tars was always observed at T_c (in some cases it occurred at lower temperatures), and rapid consumption was observed at higher temperatures. Significant methane combustion was not always observed at the cloud ignition temperatures. Complete methane combustion was generally associated with complete tar combustion. Tar was always associated with the cloud ignition of all three fuels.

Characteristics of Cloud Ignition

A series of experiments was undertaken to determine the sensitivity of the cloud ignition temperature to adjustable experimental variables—coal particle size (from 70 to 180 μm), inlet O_2 partial pressure, and fuel equivalence ration (from 0.7 to 3.5) (by varying the coal feed rate at fixed air flows). The reproducibility of the observed cloud ignition temperature was ± 20 °C at fixed conditions. For the three coals, only the O_2 partial pressure was significant, with typically a 150 °C reduction in T_c being noted for inlet O_2 increasing from 10 to 50%. This trend has been predicted previously for heterogeneous ignition, but the sensitivity of particle size is also expected for this ignition mechanism [3] but was not observed for the cloud ignition of the three fuels. Experiments with pulverised petroleum coke (of 9% volatile matter content) did reveal a 50 °C increase in the cloud ignition temperature with particle size, indicating the possibility of heterogeneous ignition for this fuel [7].

At low temperatures, prior to cloud ignition in the combustion experiments, the extent of combustion is quantified by the oxygen consumption of the continuous ignition measurements. For the three coals, this was less than 2%, even though combustible matter was present. The pyrolysis measurements quantify the proportion of coal released as volatile matter and its composition. At cloud ignition, as given in Table 3, this proportion corresponds to a coal mass loss from 0.9 to 5.5% for the three coals, which would give an adiabatic gas temperature rise from 60 °C to 390 °C. The burnoff (as estimated by oxygen consumption) observed in the combustion experiments ranged from 35 to 65%, greatly exceeding the mass loss due to the volatile matter released at the cloud ignition temperature. This is apparently due to the increased gas temperature and particle temperatures following ignition, resulting in further volatile release and char combustion. (The relative contributions of these forms of mass loss are, however, undetermined.)

To understand the mechanism of cloud ignition, the cloud must be clearly defined. As pulverised coal particles are fed into a hot gas stream (the "ambient gas"), they are heated, and some particles ignite. During the heating process, each particle evolves its own volatile matter. These gases easily mix to result in a cloud containing coal particles and their combined evolved volatiles. The "cloud," a volume containing particles and volatiles, is heated by the ambient gas and may be considered in the same way as an individual particle is in the analysis of ignition in terms of the rates of energy release and generation. A treatment along these lines has been undertaken

TABLE 3
Characteristics Estimated at the Temperatures of Cloud Ignition (T_c)

	Pyrolysis						Combustion
		% of coal released as volatiles					
Coal	T_c °C	Tar	CH_4	Other HC's	Volatile burnoff %[a]	Adiabatic temp. rise[b] °C	Burnoff at T_c %[c]
Leigh Creek	545	0.9 ± 0.1	0.005	0.2	0.9	60	65 ± 15
Beulah lignite	580	2.5 ± 0.5	0.2	0.2	3	180	65 ± 15
Blair Athol	680	5.5 ± 0.5[a]	0.3	0.7	6.5	390	35 ± 15

[a]Estimated from pyrolysis volatile yield.
[b]Calculated assuming combustion of the released volatiles.
[c]Estimated from the O_2 consumption at T_c (combustion experiments).
[d]With an additional, estimated, 2.0% of coal converted to soot (Fig. 4).

in the development of a mathematical model of the cloud ignition process [7]. The model incorporates the effects of transient heating. Such a model reproduces the sensitivity trends outlined earlier for particle size, oxygen partial pressure, and stoichiometry, which differ from the sensitivity reported for single particle ignition [3]. The cloud here is represented in the model as a spherical volume, initially containing coal particles and air, which is heated by the surrounding ambient hot gas. As the cloud heats, the particles may release combustible volatile matter or combust heterogeneously, and the temperature of the cloud gas therefore increases, often slightly above that of the ambient gas. If the rate of energy loss to the ambient is in balance with the rate of combustion energy release, no ignition is deemed to occur. A slight further increase in the ambient temperature results in a rapid increase in the combustion within the cloud volume and therefore its temperature (for the cloud, energy release rate > energy loss rate). This ambient temperature is then the cloud ignition temperature. Subsequent to this event, the experimentally determined burnoff of the coals range from 35 to 65%. Experimentally, at the cloud ignition temperature, there is also an observed change from individual particle ignition to an instantaneous ignition of the entire coal particle population. Both the model and the pyrolysis experiments indicate that tar is the dominant combustible gas species at ignition. The model also predicts that tar release (and combustion) is associated with the ignition event. The results are consistent with the following mechanism: heated particles release tar. Individual particles ignite, but there is insufficient combustion, and therefore energy release, prior to cloud ignition. When the rate of cloud energy release exceeds the rate of cloud energy loss it ignites. This may be initiated by the tar reaction when two criteria are simultaneously satisfied:

1. Sufficient tar is required to produce a flammable gas mixture. (This appears as the limiting factor for Beulah lignite, Fig. 6a.)
2. The energy release rate from the tar reaction must exceed the energy loss rate from the cloud volume. (This appears to be the limiting factor for Blair Athol and Leigh Creek, Figs. 6b and 6c.)

The coals give different cloud ignition temperatures, an observation that may be explained by differences in tar type and reactivity.

This conclusion is the same as that of Hertzberg [8] for experiments in which the autoignition temperature of a cloud in a spherical "bomb" was found to be controlled by the coal pyrolysis.

Conclusions

An experimental study has identified the ignition characteristics of a flowing cloud of pulverised coal particles in a drop-tube furnace, defined as the minimum gas temperature for significant oxygen consumption, CO_2 and NO_x generation, and the formation of a visual flame.

The formation of a flammable mixture of tar and oxygen is shown to be associated with ignition. For three coals, at the gas temperatures for cloud ignition, pyrolysis experiments indicate a coal mass loss of from 0.9 to 6.5% as a result of the measured volatiles that have been released. Following ignition at this condition, the oxygen consumption corresponds to coal burnoffs from 35 to 65% because of the increased temperatures established during the ignition process. The study did not identify the extent of volatile or char combustion comprising these burnoff levels.

For the three coals examined, different sequences

of tar combustion and/or cracking to form soot were observed prior to or at cloud ignition. It is speculated that the character and reactivity of the evolved tar are responsible for the differences in cloud ignition temperatures for the three fuels investigated.

REFERENCES

1. Wall, T. F., Phong-anant, D., Gururajan, V. S., Lucas, J., and Tate, A., *Combust. Flame* 72:111–118 (1988).
2. Wall, T. F., Gupta, R. P., Gururajan, V. S., and Zhang, D. K., *Fuel* 70:1011–1016 (1991).
3. Essenhigh, R. H., Mistra, M. K., and Shaw, D. W., *Combust. Flame* 77:3 (1989).
4. Suuberg, E. M., Peters, W. A., and Howard, J. B., *I&EC Process Design Development* 17:37 (January 1978).
5. Viskanta, R., and Menguc, M. P., *Handbook of Heat and Mass Transfer* Chap. 22, (N. P. Cheremisinoff, Ed.), Gulf Publishing, Houston, Texas, 1990, Vol. 4.
6. Saxena, S. C., *Prog. Energy Combust. Sci.* 16:55–94 (1990).
7. Lucas, J. A., "Volatile Matter and the Ignition of Clouds of Pulverised Coal," Ph.D. Thesis, Newcastle University, Newcastle, Australia 1993.
8. Hertzberg, M., "Autoignition Temperature for Coal Particles Dispersed in Air," *Fuel* 70:1115–1123 (1991).

COMMENT

Larry Baxter, Sandia National Laboratories, USA. The material you refer to as tar is reported to be highly aliphatic and is measured by the strength of the 2940-cm^{-1} C-H stretch in the FTIR spectrum. This would include many of the light gases other than methane (C_2H_4, C_3H_8, C_4H_{10}, . . .) that do not condense at room temperature. Could the events leading to cloud ignition, i.e., consumption of what you call tar, be equally well described as ignition of C_2–C_4 aliphatic gases? If so, can the early reaction of these gases relative to methane be a reflection of their lower flammability limits? Does this bear on the somewhat counterintuitive interpretation of tars (in the traditional sense) initiating ignition?

Author's Reply. GC analysis of the pyrolysis gases showed that methane was the dominant light hydrocarbon gas, some 10 times greater than other light gases (C_2–C_5). It was therefore assumed that the C-H stretch at 2940 cm^{-1} in the FTIR spectrum was due primarily to long-chain (C_{15}–C_{30}) aliphatic hydrocarbons rather than light gases. This hypothesis is being tested in present work.

Twenty-Fifth Symposium (International) on Combustion/The Combustion Institute, 1994/pp. 493–501

THE EFFECT OF PULVERIZED COAL INJECTION AND VOLATILE MATTER CONTENT OF COAL ON COMBUSTION CHARACTERISTICS AROUND THE RACEWAY ZONE IN THE BLAST FURNACE

HIDEO TSUGE, TAKAO YOSHIDA, HIDEYUKI AOKI AND TAKATOSHI MIURA
Department of Biochemistry and Engineering
Tohoku University
Aoba, Aramaki, Aoba-ku, Sendai, 980 Japan

A two-dimensional mathematical model is developed to describe transport phenomena in a packed bed of coke in front of a blast furnace tuyere with and without pulverized coal injection (PCI). The model consists of two submodels: one is a pulverized coal (PC) combustion model in the blowpipe and the other is a combustion model in the packed bed of coke where the thermal radiation is considered. In this model, coke particles in the raceway are treated as a continuous phase, and both phases of gas and coke particles are calculated by using the Eulerian approach.

This model is applied to practical operating conditions in the blast furnace. As the residence time of PC particles in the blowpipe is quite short, its burn-off in the blowpipe is very small, and the PC particles mainly burn in the raceway cavity. While the burn-off of PC particle increases with the volatile matter content, some particles reach the inner wall of tuyere when high-volatile coal is used. When PC is injected into tuyere, more oxygen is consumed, and a higher temperature rise appears at the region closer to the tuyere tip in the raceway than those of all coke operation. The temperature profiles in the raceway with PCI and without PCI are different from each other due to the difference of flow regime.

Introduction

The operation with pulverized coal injection (PCI) into a blast furnace tuyere is employed for reducing the coke feed rate. It is known that operating conditions such as kinds of coal, pulverized coal (PC) diameter, and the injection method of PC influence the combustion behavior in the raceway zone. When the feed rate of PC increases, the unburned char accumulated in the furnace causes the permeability through the coke bed to decrease. It follows that the stable state of operation cannot be achieved. Few experimental attempts such as in recent literature [1] are made to examine the PCI method and the limit of the PCI rate in the blast furnace. In order to predict the unburned char production at PCI operation and to clarify the limit of the PCI rate, it is important to analyze the heat and mass transfer phenomena around the raceway zone. It is, however, too difficult to obtain the accurate information in the blast furnace especially in the raceway zone.

A mathematical model provides a useful and powerful tool for investigating the effect of uncertain factors on the combustion characteristics of pulverized coal. Concerning the mathematical models, several studies are carried out on the one-dimensional analysis of coke combustion [2] and PC combustion [3], and all models analyze the phenomena of gas flow, reaction, and heat transfer [4–6]. Drastic simplifying assumptions are used in the previous models, especially near the raceway zone. An accurate mathematical model is furthermore required to evaluate the effect of a large amount of PC and the use of rich oxygen on the blast furnace operation.

In this study, we develop the simulation model to predict the transport phenomena near the raceway zone, where the effects of the volatile matter content in coal on combustion behavior and the operating condition with and without PCI on the shape of the raceway and distributions of temperature and gas species concentration are examined.

Model Formulation

This model consists of two submodels: one is a PC combustion model in the blowpipe and the other is a combustion model in the packed bed of coke. The blowpipe model calculation is carried out on an axisymmetrical coordinate system, and the coke bed model is on a rectangular two-dimensional coordinate system, where the calculated results of the blowpipe model are used as inlet conditions. The motion of PC particles in both submodels is solved by the Lagrangian approach, coke particles in the raceway are treated as a kind of fluid, and the flow field of the coke bed is calculated by using a two-phase flow approach.

Governing Equations:

The general form of conservation equations of mass, momentum, and energy for gas and the packed bed of coke is

$$\frac{\partial}{\partial x}(a_i \rho_i U_i \phi_i) + \frac{1}{\zeta}\frac{\partial}{\partial y}(\zeta a_i \rho_i V_i \phi_i) = \frac{\partial}{\partial x}\left(\Gamma_{\phi i}\frac{\partial \phi_i}{\partial x}\right) + \frac{1}{\zeta}\frac{\partial}{\partial y}\left(\zeta \Gamma_{\phi i}\frac{\partial \phi_i}{\partial y}\right) + S_{\phi i} + S_{d\phi} \quad (1)$$

where the general variable $\phi_i (i$ = gas, bed) is unity for the continuity equation and otherwise represents one of the dependent variables as follows: the gas velocity components (U_g,V_g), the velocity components of coke particles (U_b,V_b), turbulent energy (k_t), eddy dissipation rate (ε_t), enthalpy (h_g, h_b), and mass fraction of chemical species (m_j:j = volatile matter, O_2, N_2, CO_2, H_2O, CO, and H_2). The term ζ is taken to be y on the axisymmetrical coordinate and 1 on the two-dimensional one; $\Gamma_{\phi i}$ is the exchange coefficient; $S_{\phi i}$ is the source term in the gas and solid phases, and $S_{d\phi}$ is the source term between PC particle and the gas phase whose coupling is estimated using the PSI-cell method [16]. Values of $\Gamma_{\phi i}$ and $S_{\phi i}$ for the coke bed model are shown in Table 1. The solution method for the blowpipe model is the same as our previous work [7]. The partial differential equations (1) are calculated simultaneously with the method of Patankar [8].

Pulverized Coal Combustion Model in the Blowpipe:

The combustion of PC is a complicated process because of involving turbulent flow, chemical reaction, and heat and mass transfer. Simplification of the governing equations is achieved by adopting the following assumptions:

1. The particle is spherical.
2. There is no breakup or coalescence of the particle.
3. The particle is initially composed of raw coal, char, and ash.
4. Raw coal is composed of volatile matter and char; char is considered to be pure carbon.
5. Particle temperature is uniform within the sphere.

Using the above assumptions, we have carried out the prediction of the combustion characteristics in the one-dimensional laminar-flow furnace [9] and the two-dimensional turbulent-flow furnace [10] and have confirmed the performance of the model.

Chemical reactions

A PC particle injected into the blowpipe is heated by the radiation from surrounding gas and wall and the convective heat transfer; then it releases the volatile matter. Coal devolatilization is modeled by parallel, first-order reactions [10], where the rate constants have Arrhenius form, the kinetic parameters are taken from Ubhayakar et al. [11], and the mass-stoichiometric factors are taken from Burgess et al. [12].

Concerning the heterogeneous reactions of char, both in the blowpipe and in the raceway of the coke bed, the overall rate for char-oxygen reaction at the external surface area depends on a combination of chemical reaction and diffusion of oxygen to the particle surface. The rate coefficients are taken from Field's [13] experimental data.

Particle heating

The heat convection, radiation, heat release by chemical reaction and latent heat of devolatilization are considered in the particle heating process. Although the fraction of the combustion heat transferred to the particle from volatile matter and char depends on practical operating conditions such as temperatures of particle and surrounding gas, these are assumed to be 0.3 and 0.5, respectively, for simplification of calculation based on the analysis of the laminar-flow furnace [9]. The latent heat of devolatilization is assumed to be 626.2 kJ/kg determined from the experimental data of Baum and Street [14].

Particle motion

The particle velocity in the blowpipe and the raceway can be calculated from the equation of motion. Instantaneous gas velocity in each direction is obtained by adding the mean velocity and turbulent velocity fluctuation, which is chosen randomly from an isotropic Gaussian distribution with standard deviation of $(2k_t/3)^{0.5}$. The drag coefficient of particle is a function of particle Reynolds number and taken from Clift et al. [15].

Combustion behavior of pulverized coal

Particles are divided into 10 classes in the initial injection point and 10 classes in the initial particle diameter by 10 μm based on measured particle diameter distribution (from 10 to 100 μm), and trajectory is calculated for three representative particles for each class. The particle interacts with gas flow field producing source terms $S_{d\phi}$ of mass, momentum, and enthalpy in Eq. (1) [16].

Combustion Model in the Coke Bed:

Chemical reactions

In the coke bed model, the following seven reactions are considered (VM means volatile matter):

1. VM + a O_2 → Products.
2. CO + 1/2 O_2 → CO_2.
3. H_2 + 1/2 O_2 → H_2O.

TABLE 1
Source terms in the coke bed model

i	ϕ_i	$\Gamma_{\phi i}$	$S_{\phi i}$
Gas	1 (mass)	0	0
	U_g	μ_{eff}	$\frac{\partial}{\partial x}\left(\mu_{\text{eff}}\frac{\partial U_g}{\partial x}\right) + \frac{\partial}{\partial y}\left(\mu_{\text{eff}}\frac{\partial V_g}{\partial x}\right) - \alpha_g\frac{\partial P}{\partial x} - S_{bu}$
	V_g	μ_{eff}	$\frac{\partial}{\partial x}\left(\mu_{\text{eff}}\frac{\partial U_g}{\partial y}\right) + \frac{\partial}{\partial y}\left(\mu_{\text{eff}}\frac{\partial V_g}{\partial y}\right) - \alpha_g\frac{\partial P}{\partial y} - S_{bv}$
	m_j	$\rho_g D_e$	R_j
	h_g	$\frac{\lambda_g}{C_{pg}}$	$Q_h + \Sigma R_j Q_{rj} - \nabla\cdot\mathbf{q}_g$
	k_t	$\frac{\mu_{\text{eff}}}{\sigma_k}$	$G - \rho_g\varepsilon_t$
	ε_t	$\frac{\mu_{\text{eff}}}{\sigma_\varepsilon}$	$\frac{\varepsilon_t}{k_t}(C_1 G - C_2\rho_g\varepsilon_t)$
Bed	1 (mass)	0	0
	U_b	μ_b	$\frac{\partial}{\partial x}\left(\mu_b\frac{\partial U_b}{\partial x}\right) + \frac{\partial}{\partial y}\left(\mu_b\frac{\partial V_g}{\partial x}\right) - \alpha_b\frac{\partial P}{\partial x} + S_{bu} + S_{pu}$
	V_b	μ_b	$\frac{\partial}{\partial x}\left(\mu_b\frac{\partial U_b}{\partial y}\right) + \frac{\partial}{\partial y}\left(\mu_b\frac{\partial V_b}{\partial y}\right) - \alpha_b\frac{\partial P}{\partial y} + S_{bv} - S_{pv}$
	h_b	$\frac{\lambda_{eb}}{C_{Pb}}$	$-Q_h + \Sigma R_j Q_{rj} - \nabla\cdot\mathbf{q}_b$

C_1	C_2	σ_k	σ_ε
1.44	1.92	0.90	1.22

$$G = \mu_{\text{eff}}\left\{2\left[\left(\frac{\partial U_g}{\partial x}\right)^2 + \left(\frac{\partial V_g}{\partial y}\right)^2\right] + \left(\frac{\partial U_g}{\partial y} + \frac{\partial V_g}{\partial x}\right)^2\right\}$$

4. $C + 1/2\ O_2 \rightarrow CO$.
5. $C + O_2 \rightarrow CO_2$.
6. $C + CO_2 \rightarrow 2CO$.
7. $C + H_2O \rightarrow CO + H_2$.

Combustion of volatiles (reaction 1)

The single-step overall reaction is assumed in the combustion process of volatiles. The chemical reaction is considered to occur rapidly, and thus, the overall rate is controlled by a turbulent diffusion process where the eddy-dissipation model [17] is utilized.

CO oxidation (reaction 2)

The reaction rate of CO oxidation is taken to be a smaller value between that estimated by the eddy-dissipation model and the chemical reaction rate measured by Howard [18].

Hydrogen oxidation (reaction 3)

It is reported by He et al. [3] that hydrogen is not found at the atmosphere of oxygen concentration less than 5 mol.%. For the region of the local oxygen concentration greater than 5 mol.%, the rate is determined from the eddy-dissipation model, while no oxidation reaction on hydrogen occurs for that less than 5 mol.%.

Char heterogeneous (reactions 4 through 7)

Char heterogeneous reactions are assumed to be first-order irreversible with respect to the gas concentration to react and controlled by a combination of chemical reaction and diffusion of reacting gas within the micropore and to the boundary layer of a particle surface. Especially for the coke oxidation reactions, (4 and 5), the experimental data are reported

by Field et al. [19] for the overall carbon consumption, i.e., the sum of reactions 4 and 5. The ratio CO/CO_2 at the coke surface is then given by Arthur's data [21]. The rate constant of reaction 6 is adopted from Heynert et al. [20] and that of reaction 7 from Kuwabara et al. [2].

Mass transfer rate estimation

The effective diffusion coefficient of gas phase is evaluated from De Ligny's correlation [22] in terms of Peclet, Reynolds, and Schmidt numbers as follows:

$$\frac{1}{\mathrm{Pe}} = \frac{C_{d1}}{\mathrm{Re}\cdot\mathrm{Sc}} + \frac{C_{d2}}{1 + C_{d3}/(\mathrm{Re}\cdot\mathrm{Sc})} \tag{2}$$

where the magnitudes of C_{d1}, C_{d2}, and C_{d3} are given by fitting the measured data of Gunn and Pryce [23] to the above equation.

Heat transfer rate estimation

The effective thermal conductivity of the packed bed of coke is estimated using Kunii–Smith's equation [24]. The convective heat transfer coefficient is obtained from Ranz's equation [25]:

$$\frac{d_b h_{cb}}{\lambda_g} = 2.0 + 0.6(9\ \mathrm{Re})^{0.5}\ \mathrm{Pr}^{0.33}. \tag{3}$$

The rate of convective heat transfer is thus calculated from

$$Q_h = A_b h_{cb}(T_g - T_b). \tag{4}$$

The effective thermal conductivity of gas phase passing through the packed bed of coke is given by analogy between heat transfer and mass transfer. All of the heat of homogeneous reactions is given to the gas phase, while all of the heat of heterogeneous reactions at the coke particle surface is given to the solid phase.

Radiative heat transfer in the raceway zone

The S4 discrete-ordinates method is used in this analysis. The S4 approximation could be sufficient to estimate the radiative field in the raceway zone. The following assumptions are employed:

1. Only CO_2 and H_2O are considered as the radiative gas species, where the gray-gas formulation is assumed and the emissivity of gas is represented as the weighted sum of gray gases.
2. Coke particles and PC are also gray, and those temperatures are different from gas temperature, respectively.
3. The scattering by coke particles and PC is ignored because of the uncertainty of scattering properties of coke and PC particles.
4. The boundary surface surrounding the raceway zone is formed with coke particles and emits and reflects the radiant energy.

Radiative transport equation

The radiative intensity transport including PC is governed by the radiative transport equation (RTE) [26]. Based on the above assumptions, the RTE also including the coke particles can be written as

$$\begin{aligned}(\Omega\cdot\nabla)I(r,\Omega) = &-\left(\kappa_g + \kappa_c + \sum_i \kappa_{\mathrm{PC},i}\right)I(r,\Omega)\\ &+ \kappa_g I_{b,g}(r) + \kappa_c I_{b,c}(r)\\ &+ \sum_i \kappa_{\mathrm{PC},i} I_{b,\mathrm{PC},i}(r)\end{aligned} \tag{5}$$

where $I(r,\Omega)$ is the radiation intensity, which is a function of the position r and the direction Ω; $I_{b,g}(r)$, $I_{b,c}(r)$, and $I_{b,\mathrm{PC},i}(r)$ are the intensity of the blackbody radiation at each temperature of gas, coke particles, and PC in the ith size group, respectively; κ_g, κ_c, and $\kappa_{\mathrm{PC},i}$ are the local absorption coefficient of gas, coke particles, and PC in the ith size group, respectively, whose calculations are modeled as shown below.

The boundary condition for Eq. (5) is given by [27]:

$$\begin{aligned}I(r,\Omega) = &\ \varepsilon_c I_{b,c}(r)\\ &+ \frac{\rho_c}{\pi}\int_{\mathbf{n}\cdot\Omega<0} |\mathbf{n}\cdot\Omega| I(r,\Omega')d\Omega'\end{aligned} \tag{6}$$

where $I(r,\Omega)$ and $I(r,\Omega')$ are the outgoing and incoming intensities of radiation at the boundary surface, respectively; ε_c and ρ_c $(= 1 - \varepsilon_c)$ are the emissivity and reflectivity of coke particles; $\mathbf{n}$ is the unit normal vector along the raceway boundary surface.

Radiative properties

It is necessary to determine the radiative properties, i.e., the absorption coefficients of gas, coke particles, and PC. The absorption coefficient of the gas mixture of CO_2 and H_2O is obtained using the effective emissivity ε_g as

$$\kappa_g = -\frac{\ln(1 - \varepsilon_g)}{L_{op}} \tag{7}$$

where L_{op} is the optical length at each direction in each computational cell and ε_g is calculated by the mixed gray gas assumption of Hottel [28]. The absorption coefficient of PC is as follows [26]:

$$\kappa_{\mathrm{PC},i} = \frac{\varepsilon_{\mathrm{PC}}\pi D_{\mathrm{PC},i}^2 N_{\mathrm{PC},i}}{4} \tag{8}$$

where ε_{PC} is the emissivity of PC and $D_{PC,i}$ and $N_{PC,i}$ are the diameter and the number density of PC in the ith size group, respectively. The local number density, the temperature, and the diameter distribution of PC in the raceway are determined when the particle trajectories are calculated with the Lagrangian method. On the other hand, the absorption coefficient of coke particles can be written in the same manner as that of PC, as shown in Eq. (9), where ε_c is the emissivity of the coke particles. The number density of coke particles N_c is determined from the particle diameter of coke D_c and bed voidage a_g, as shown in Eq. (10).

$$\kappa_c = \frac{\varepsilon_c \pi D_c^2 N_c}{4} \tag{9}$$

$$N_c = \frac{6(1 - a_g)}{\pi D_c^3}. \tag{10}$$

Both ε_{PC} and ε_c are assumed to be 0.9.

Discrete-ordinates equation

Equation (5) is replaced with a set of equations for a finite number of M ordinate directions in the two-dimensional coordinate system [27]. The detailed description of the solution procedure is found in many literatures [27,29]. After the convergence is achieved, the divergence of radiative heat flux, which is expressed as the source term in steady-state conservation equation of enthalpy, is calculated.

Raceway Boundary:

It is necessary for obtaining the combustion characteristics in the raceway to evaluate the particle-moving region in the coke bed. The following conditions are assumed for the particle-moving region:

1. The vertical powder pressure of coke is negative.
2. The horizontal interaction force between the gas and solid is larger than the critical value of static friction force between the coke particles.
3. The voidage within CV is larger than that at the minimum fluidization condition.

The critical value of static friction force between the coke particles in condition 2 is the product of vertical powder pressure in CV and the internal friction coefficient (tangent to the internal friction angle).

Source term arising from interaction between gas and solid phase

The momentum exchange rate between gas and solid phase is calculated by the source terms S_{bu} and S_{bv}. When the voidage is less than 0.8 in CV, S_{bu} is evaluated as the pressure drop due to the friction between gas and coke particles described by Ergun's equation [30] as

$$S_{bu} = \left(150 \frac{(1 - a_g)^2 \mu_g}{a_g \psi_c^2 d_b^2} + 1.75 \frac{|U_g - U_b|(1 - a_g)\rho_g}{\psi_c d_b}\right) a_g (U_g - U_b). \tag{11}$$

On the other hand, when the voidage is greater than 0.8, the expression of S_{bu} is based on the drag force of fluid acting on a single particle as

$$S_{bu} = \frac{3}{4} C_D \frac{|U_g - U_b| a_g \rho_g (1 - a_g)}{d_b} \cdot f(a_g) a_g (U_g - U_b) \tag{12}$$

where

$$C_D = \frac{24}{\mathrm{Re}_p}[1 + 0.15(\mathrm{Re}_p)^{0.687}] \quad \mathrm{Re}_p < 1000$$

$$C_D = 0.44 \quad \mathrm{Re}_p \geq 1000$$

$$f(a_g) = a_g^{-2.65} \tag{13}$$

where $f(a_g)$ evaluates the effect of the presence of other particles investigated by Wen and Yu [31] and acts as a correction to the usual Stokes law for free fall of a single particle. The expression for the source term in the vertical direction S_{bv} is the same as that in the horizontal direction.

Source term arising from gravitational force

The powder pressure in a coke bed is needed for determining the raceway boundary and the momentum generation caused by the gravitational force. The powder pressure affected by the gas flow is estimated by integrating a modified Janssen's equation [32] including the term F due to gas-solid interaction force from the bed surface to the depth of CV.

$$\frac{dP_v}{dh_d} = \rho_b g - F - \frac{4}{D_T} \mu_w K_a P_v \tag{14}$$

where K_a is a ratio of the horizontal powder pressure to the vertical one at dynamic state and evaluated from Rankine's equation as

$$K_a = \frac{1 - \sin\theta_i}{1 + \sin\theta_i}. \tag{15}$$

At the region of voidage greater than that of minimum fluidization, the powder pressure, which is not transported downward, is a deduction of the inter-

TABLE 2
Analysis of the coal samples

Coal	Proximate analysis (wt.%-db) VM	Ash	Ultimate analysis (wt.%-daf) C	H	N	S	Calorific value (MJ/kg)
Saraji	19.5	9.0	89.2	4.7	2.0	0.7	32.9
Witbank	34.3	7.2	83.6	5.1	2.2	0.7	31.4
Taiheiyo	44.6	15.6	77.5	6.5	1.0	0.2	26.4

daf = dry ash free.

TABLE 3
Calculation conditions

Blowpipe				
Blast	Feed rate		4.241	kg/s
	Inlet velocity		188	m/s
	Temperature		1450	K
	Pressure		386	kPa
	Composition	Oxygen	24.7	wt.%
		Moisture	3.1	wt.%
PC	Feed rate		0.165	kg/s
	Temperature		300	K
PC air	Feed rate		0.0186	kg/s
	Temperature		300	K
	Pressure		386	kPa
	Composition	Oxygen	23.3	wt.%
		Moisture	0	wt.%
Coke bed without PCI				
Blast	Feed rate		4.5	kg/s
	Velocity at tuyere		288	m/s
	Temperature		1318	K
	Pressure		384	kPa
	Composition	Oxygen	23.5	wt.%
		Moisture	3.6	wt.%

action force between gas and solid from particles weight within the volume.

Results and Discussion

Calculated Results of PC Combustion Model in the Blowpipe:

The blowpipe is attached to the blast furnace tuyere and the lance tip from which PC is injected into the blowpipe is at 670-mm upstream of tuyere along the center axis. The calculated domain of the blowpipe is 800 mm in length from the tuyere. The three kinds of coal used in this study are Saraji, Witbank, and Taiheiyo, having different volatile matter content from one another. The proximate and ultimate analyses of the coal samples are given in Table 2, and the calculation conditions are given in Table 3.

The particle trajectories of Saraji coal is shown in Figs. 1a through 1c, where 10 representative particle trajectories are drawn for each diameter. The small particles cannot disperse toward the radial direction, while some particles over 60 μm disperse in close to

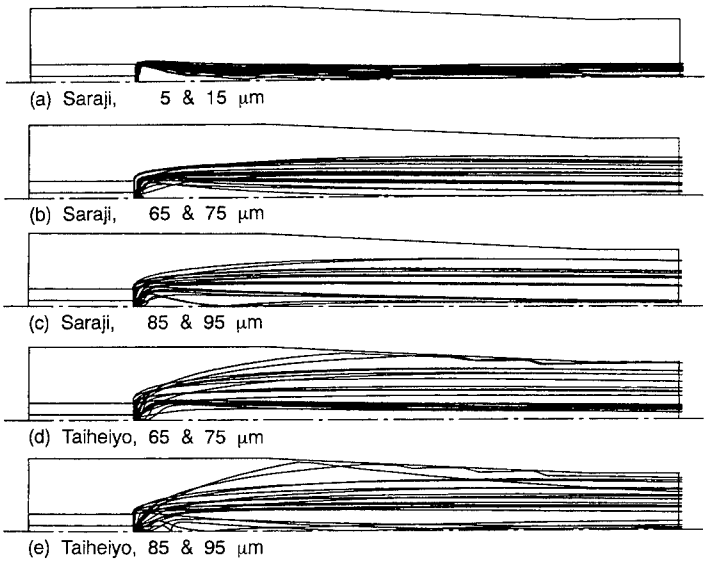

FIG. 1. Predicted particle trajectories of (a through c) Saraji and (d and e) Taiheiyo coal in the blowpipe.

the inner wall of the blowpipe. This is because the large particle has a large initial momentum in the radial direction.

Particle trajectories of Taiheiyo coal in diameters of 65, 75, 85, and 95 μm are shown in Figs. 1d and 1e. The radial dispersion of a high-volatile PC is more significant than that of low-volatile one. It is caused by the release and combustion of a large amount of volatile matter in front of a lance tip. In addition, this greater dispersion would cause the collision of PC against the tuyere wall and the wear of tuyere. The mean residence time of PC is about 5 ms for any kind of coal. The burn-off of PC in the blowpipe is the arithmetic mean, which is based on the initial amount of combustible content of coal and 5.8% for Saraji, 8.1% for Witbank, and 16.4% for Taiheiyo coal, respectively, and appears to increase as the volatile matter content is high.

Calculated Results of Combustion Model in the Coke Bed:

The estimation is carried out on the practical blast furnace having 14.8 m in bed diameter and 38 tuyere, which is modeled as having the same horizontal cross-sectional area per one tuyere in the two-dimensional calculation. The analytical region is then 7.4 m in width, 0.61 m in depth, and 6.0 m in height with coke particles of 20 mm in diameter. The tuyere having a 25-mm opening width is located at 1 m from the bottom of the furnace, corresponding to the blowpipe outlet area. The inlet condition at the tuyere without PCI is also shown in Table 3 and is the same practical operating condition of productivity (iron formation rate per unit volume of blast furnace in a day) as with PCI. The calculations are carried

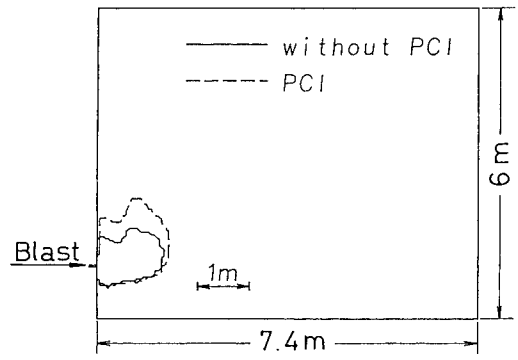

FIG. 2. Comparison of predicted raceway shape with and without PCI.

out in the case of condition with PCI (Witbank coal) and without PCI (all coke operation). In the case of operation with PCI, averaging values that are obtained from calculated results in the blowpipe combustion model are used for the gas-phase inlet condition. The particle trajectory calculation in the coke bed is restarted from the final calculated result in the blowpipe combustion model.

Figure 2 shows the comparison of predicted raceway shape with and without PCI. It is apparent that the coke particle–moving region is large in the case with PCI compared with the case without PCI. This is because the rapid release of volatile matter from PC and gas-phase combustion of volatiles and char combustion inside the raceway zone may cause the gas volume expansion, which excludes the coke particles from the raceway zone.

Figure 3 shows the predicted distribution of concentration of CO, CO_2, and O_2 and of the tempera-

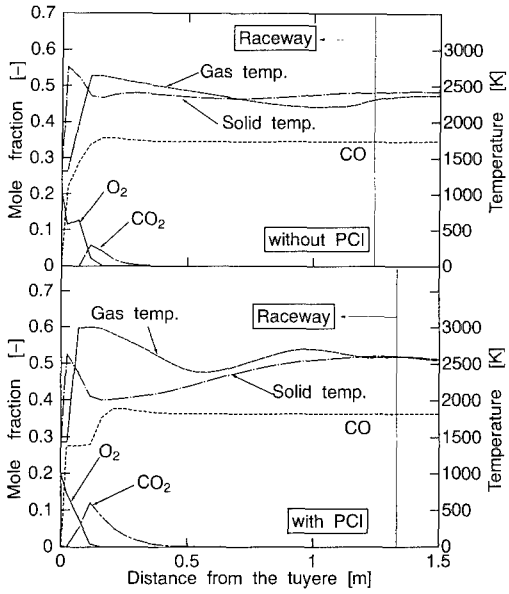

FIG. 3. Comparison of predicted gas composition and temperature of gas and solid phases with and without PCI.

ture of gas and solid phases along the tuyere axis in the case with and without PCI. In both cases, the oxygen supplied from tuyere is rapidly consumed by reaction with coke and PC, and simultaneously, CO_2 concentration once increases. The distributions with PCI move toward the tuyere because PC is burning near the tuyere. In the case of PCI, it is observed that the maximum gas temperature increases due to the PC combustion, and the minimum solid temperature decreases near the tuyere tip where the solution loss reaction is dominant. The temperature distributions with and without PCI are different from each other due to the change of flow regime of the gas and solid phases.

Conclusions

The mathematical model proposed in this study can predict the raceway shape, the flow pattern of the gas and coke particles inside the raceway, the PC combustion, the heat and mass transfer, and the reactions in the coke bed simultaneously. This work is summarized as follows:

1. Predicted results of the blowpipe model show that the residence time of PC in the blowpipe is quite short, and the burn-off of PC is very small, especially in the use of the low-volatile coal. On the other hand, in the use of the high-volatile coal, the dispersion of PC toward the radial direction increases and would cause the wear of tuyere.
2. The comparison for the practical operation with and without PCI is carried out in the coke bed model. When PC is injected into tuyere, more oxygen is consumed and higher rise of temperature appears at the region closer to the tuyere tip in the raceway. The temperature distributions with and without PCI are different from each other due to the change of flow regime of the gas and solid phases.

Nomenclature

A_b	specific surface area of coke bed (m^{-1})
C_p	drag coefficient (−)
C_P	specific heat (J/kg K)
d_b	particle diameter of bed (m)
D_e	effective diffusivity (kg/m s)
D_T	equivalent diameter of packed bed (m)
g	gravitational acceleration (m/s^2)
h_c	convective heat transfer coefficient (W/m^2 s)
h_d	bed depth (m)
P	pressure (Pa)
P_v	vertical powder pressure (Pa)
$\mathbf{q}$	vector of radiative heat flux
Q_h	convective heat transfer rate (W)
Q_r	reaction heat transfer rate (W)
R	reaction rate (kg/s)
T	temperature (K)

Greek Symbols:

α	volume fraction of i phase (−)
λ_g	thermal conductivity of gas (W/m K)
μ	viscosity (Pa s)
μ_w	dynamic friction factor between wall and particle (−)
ρ	density (kg/m^3)
ψ_c	shape factor (−)
θ_i	internal friction angle (rad)

Subscripts:

b	bed
c	coke particle
e, eff	effective
g	gas
i	gas or bed
j	chemical species
PC	PC particle

REFERENCES

1. Matsuura, M., Mitsufuji, H., Furukawa, T., and Ohno, Y., *Zairyo-to-Process* 3:82 (1990).
2. Kuwabara, M., Hsieh, Y., and Muchi, I., *Tetsu-to-Hagané* 66:1918–1927 (1980).

3. He, J., Kuwabara, M., and Muchi, I., *Tetsu-to-Hagané* 72:1847–1854 (1986).
4. Yagi, J., Takeda, K., and Ohmori, Y., *Trans. Iron Steel Inst. Jpn.* 22:884–892 (1982).
5. Sugiyama, T., and Sugata, M., *Seitetsu-Kenkyuu* 325:34–43 (1987).
6. Kuwabara, M., Takane, S., Sekido, K., and Muchi, I., *Tetsu-to-Hagané* 77:1593–1600 (1991).
7. Nogami, H., Miura, T., and Ohtani, S., *Twenty-Sixth Symposium on Combustion (Japan)*, Tokyo, 1988, pp. 221–222.
8. Patankar, S. V., *Numerical Heat Transfer and Fluid Flow*, McGraw-Hill, New York, 1980.
9. Sato, M., Fukai, J., Miura, T., and Ohtani, S., in *Coal Combustion* (J. Feng, Ed.), Hemisphere, New York, 1988, pp. 215–222.
10. Kobayashi, H., Howard, J. B., and Sarofim, A. F., *Sixteenth Symposium (International) on Combustion*, The Combustion Institute, Pittsburgh, 1976, pp. 411–425.
11. Ubhayakar, S. K., Stickler, D. B., von Rosenberg, C. W., Jr., and Gannon, R. E., *Sixteenth Symposium (International) on Combustion*, The Combustion Institute, Pittsburgh, 1976, pp. 427–436.
12. Burgess, J. M., Jamaluddin, A. S., McCarthy, M. J., Mathieson, J. G., Nomura, S., Truelove, J. S., and Wall, T. F., *Joint Symposium of ISIJ and AIMM*, 1983, pp. 129–141.
13. Field, M. A., *Combust. Flame* 13:237–252 (1982).
14. Baum, M. M., and Street, P. J., *Combust. Sci. Technol.* 3:231–243 (1971).
15. Clift, R. M., Grace, J. R., and Weber, M. E., *Bubble, Drop and Particles*, Academic Press, New York, 1978, p. 97.
16. Crowe, C. T., Sharma, M. P., and Stock, D. E., *J. Fluid Eng.* 99:325–332 (1977).
17. Magnussen, B. F., Hjertager, B. H., Olsen, J. G., and Bhaduri, D., *Seventeenth Symposium (International) on Combustion*, The Combustion Institute, Pittsburgh, 1979, pp. 1383–1393.
18. Howard, J. B., Williams, G. C., and Fine, D. H., *Fourteenth Symposium (International) on Combustion*, The Combustion Institute, Pittsburgh, 1970, pp. 975–986.
19. Field, M. A., Gill, D. W., Morgan, B. B., and Hawksley, P. G. W., *Combustion of Pulverized Coal*, Chenery and Sons Ltd, Banbury, 1967 pp. 186–200.
20. Heynert, G., and Williams, J., *Stahl Eisen* 79:1545–1554 (1959).
21. Arthur, J. R., *Combustion of Pulverized Coal*, Chenery and Sons Ltd, Banbury, 1967, pp. 201–205.
22. De Ligny, C. L., *Chem. Eng. Sci.* 25:1177–1181 (1970).
23. Gunn, D. J., and Pryce, C., *Trans. Inst. Chem. Eng.* 47:T341–T350 (1969).
24. Kunii, D., and Smith, M., *AIChE J.* 6:71–77 (1960).
25. Ranz, W. E., *Chem. Eng. Prog.* 48:247–253 (1952).
26. Denison, M. K., and Webb, B. W., *Sixth Symposium (International) on Transport Phenomena in Thermal Engineering*, Seoul, Korea, 1993, pp. 187–192.
27. Fiveland, W. A., *Trans, ASME J. Heat Trans.* 106:699–706 (1984).
28. Hottel, H. C., *Section in Heat Transmission*, McGraw-Hill, New York, 1954.
29. Kim, T. K., and Lee, H., *Int. J. Heat Mass Transfer* 30:1711–1721 (1988).
30. Ergun, S., *Chem. Eng. Prog.* 48:89–94 (1952).
31. Wen, C. Y., and Yu, Y. H., *Chem. Eng. Prog. Symp. Ser.* 67:100–111 (1966).
32. Janssen, H. A., *V.D.I.-Zeit.* 39:1045–1049 (1895).

COMMENT

Robert Hurt, Sandia National Laboratories, USA. Your model predicts that the extent of reaction, or burnout, in the raceway zone varies greatly with parent coal, increasing with increasing volatile matter. Could you provide a breakdown of the total burnout into high-temperature volatile loss and char oxidation/gasification on a dry, ash-free basis? Could you then identify the mechanism responsible for the overall trend—is it an effect of temperature, gas composition, char yield, char reactivity, etc.?

Author's Reply. The burn-off of pulverized coal in the blowpipe is Saraji: 5.8%, Witbank: 8.1%, Taiheiyo: 16.4%, respectively, and increases proportionally with volatile matter content. The total burn-off through the blowpipe and raceway is Saraji: 44.3%, Witbank: 74.2%, Taiheiyo: 96.5%, respectively, as the residence time of pulverized coal is about 30 ms for any kind of coal. The reason is as follows: We use the two-competing reaction model for coal devolatilization and assume that 30% of combustion heat of volatile matter is transferred to the coal particle, following the rapid temperature rise in the use of high-volatile coal and further volatile matter release.

Twenty-Fifth Symposium (International) on Combustion/The Combustion Institute, 1994/pp. 503–509

PERFORMANCE PREDICTIONS OF PULVERISED-COAL FLAMES OF POWER STATION FURNACE AND CEMENT KILN TYPES

F. C. LOCKWOOD AND B. SHEN
Department of Mechanical Engineering
Imperial College of Science, Technology and Medicine
London SW7 2BX, UK

This paper describes the numerical simulation of two types of engineering pulverised-coal (PF) flames: that emanating from a nonswirling high-velocity cement kiln burner and that formed by power station swirl-stabilised burners. The mathematical model is distinguished by the incorporation of a second-moment Reynolds stress closure to model the turbulence. Such a model has not been previously applied to two-phase PF flames. Predictions given by two forms of the Reynolds stress model along with those given by the conventional k-ε turbulence model are compared with test combustor data for the two flame types. The Reynolds stress models do not demonstrate any consistent advantage over the simple k-ε model in either case. In particular, the persistent and important difficulty of predicting well the ignition location for centrally fired swirl burners is not corrected by the more advanced turbulence models. Moreover, the Reynolds stress models suffer severe numerical stability limitations when applied to practical flames. The evidence suggests that the second-moment closure should be extended to the scalar equations if improved predictions are to be secured. However, for the present PF combustion modelling, this requires the solution of an additional 12 transport equations, which is not practical for engineering purposes. We conclude that it will not be possible to isolate the turbulence model failings from the combustion ones until reliable two-phase velocity data become available for turbulent-combusting PF flames. Against this background, simple rather than complex NO models are all that can be justifiably used. Even so, the NO emissions from the cement kiln and power station furnace type flames of this study are predicted with useful precision.

Introduction

The existing literature on the mathematical modelling of pulverised-coal (PF) flames in engineering equipment is now fairly extensive [1–5]. While it generally appears possible to simulate fairly well some downstream performance quantities, such as the local wall heat-transfer rates, difficulties have been experienced in predicting various features of the near burner region (NBR) for particular burner types. For instance, when the fuel is centrally injected, the predicted particle ignition locations are typically shifted upstream with respect to the experimental observations resulting in a premature depletion of the oxygen [3]. This engenders the mediocre prediction of important quantities crucially dependent on the NBR such as flame stability, NO emissions, and to a lesser extent, the degree of char burnout ultimately attained.

The search for the cause of the predictive shortcomings is seriously encumbered by the difficulty of obtaining a complete range of data in PF flames within the NBR. There is in particular a degree of scarcity of reliable velocity data for the two phases that borders on nonexistence, although recent LDA work at the International Flame Research Foundation (IFRF), in which the laser beams are shielded to minimise obscuration problems, deserves mention [4]. In this virtual total absence of velocity data, it is almost impossible to know whether the predictive difficulties are ascribable to defects of the turbulence model, the relatively simple k-ε one being almost exclusively deployed, or to some defect of the PF combustion modelling; for example, the fact that the time scale of the secondary cracking of the primary products of pyrolysis has been universally ignored [3].

In an effort to distinguish turbulence model failings from combustion model ones, it is reasonable to consider the substitution of the overworked k-ε turbulence model by a more advanced Reynolds stress model. Confidence in the k-ε workhorse would then be reinforced or undermined, depending on the compatibility of its predictions with those of the Reynolds stress model. Now, although second-moment Reynolds stress models have been an active subject of research for a not inconsiderable period of time, see Refs. 6 through 8 for example, documentation of their application to engineering combustors, as opposed to more simple laboratory flows, has been remarkably meagre. To our knowledge, no previous application of such models to pulverised-coal combustion has been described in the archived literature.

The present paper is concerned with the prediction of PF combustor flows using second-moment turbulence models. The data used are new, and they have been collected in two test combustors: one in the authors' laboratory at Imperial College (ICSTM) and the other at the IFRF. In both cases, the flames are large enough to be usefully representative of industry conditions. In the former case, two swirl burners typical of power station practice were used, whereas the latter trial was designed to simulate the unswirled long flame typical of cement kilns.

The Mathematical Model

The mathematical model is based on the FAFNIR code developed in and extensively tested by the authors' group [9]. It is applicable to two-dimensional axisymmetric two-phase combusting flows and embodies: an Eulerian solution treatment for the gas phase, a Lagrangian one for the particulate phase, and a nonequilibrium diffusion procedure for the thermal radiation. The current version of FAFNIR includes: a single reaction model of devolatilisation, turbulence decay rate control of the volatiles combustion, and combined diffusion/chemical kinetics control of the char combustion. Many variants of the devolatilisation and combustion modelling that have appeared in the literature over the years have been tried, and complete studies of the effects of acceptable variations of the model parameters have been effected [3,5]. The basic FAFNIR code is well described in numerous preceding papers, e.g., Ref. 5, and only the newly incorporated features need to be related here.

Second-Moment Turbulence Closures

In second-moment turbulence closures, Reynolds stresses are calculated from their own modelled transport equations. A general Reynolds stress transport equation for steady flows can be written as [8]

$$\frac{\partial(\bar{\rho}\tilde{U}_k\widetilde{u_i''u_j''})}{\partial x_k} = P_{ij} + \Phi_{ij} - \frac{2}{3}\varepsilon\delta_{ij} + D_{ij} + G_{ij} \quad (1)$$

where the overbar designates the conventional mean, the tildes imply the density-weighted mean, and the double primes indicate the fluctuating part of the density-weighted average. The terms on the right-hand side may be specified as follows:

The production term:

$$P_{ij} = -\left(\bar{\rho}\widetilde{u_k''u_j''}\frac{\partial\tilde{U}_i}{\partial x_k} + \bar{\rho}\widetilde{u_k''u_i''}\frac{\partial\tilde{U}_j}{\partial x_k}\right). \quad (2)$$

The redistribution term Φ_{ij} is split into two parts, modelled by

$$\Phi_{ij,1} = -c_1\bar{\rho}(\varepsilon/k)(\widetilde{u_i''u_j''} - (2/3)\delta_{ij}k) \quad \text{and}$$
$$\Phi_{ij,2} = -c_2\bar{\rho}(P_{ij} - (1/3)\delta_{ij}P_{ii}). \quad (3)$$

The diffusion term:

$$D_{ij} = \frac{\partial}{\partial x_k}\left(\mu_1\frac{\partial\widetilde{u_i''u_j''}}{\partial x_k} + c_s\bar{\rho}\frac{k}{\varepsilon}\widetilde{u_k''u_1''}\frac{\partial\widetilde{u_i''u_j''}}{\partial x_k}\right). \quad (4)$$

The velocity-pressure correlation term:

$$G_{ij} = -\overline{u_i''}\frac{\partial\bar{p}}{\partial x_j} - \overline{u_j''}\frac{\partial\bar{p}}{\partial x_i}. \quad (5)$$

This term arises from the density-weighted formulation, appearing only in the density-varying situations. Its effect on the flow field appears to be small [9], and it is not considered in the present study.

The dissipation rate of the turbulence energy is calculated from the following transport equation:

$$\frac{\partial(\bar{\rho}\tilde{U}_k\varepsilon)}{\partial x_k} = \frac{\partial}{\partial x_k}\left(c_\varepsilon\bar{\rho}\frac{k}{\varepsilon}\widetilde{u_i''u_j''}\frac{\partial\varepsilon}{\partial x_k}\right) + c_{\varepsilon 1}\bar{\rho}\frac{\varepsilon}{k}\left(\frac{1}{2}P_{ii}\right) - c_{\varepsilon 2}\bar{\rho}\frac{\varepsilon^2}{k}. \quad (6)$$

The modelling of the redistribution term in Eq. (1) is the subject of much debate [6], and as such, two sets of constants in Eq. (3) were investigated. The first of these is attributed to Gibson and Launder [10], who set $c_1 = 1.8$ and $c_2 = 0.6$, and referred to herein as the RST-A model; and the second is attributed to Gibson and Younis [11], where $c_1 = 3.0$ and $c_2 = 0.3$, termed the RST-B model. Other constants take the following values: (c_s, c_ε, $c_{\varepsilon 1}$, and $c_{\varepsilon 2}$) = (0.22, 0.18, 1.45, and 1.90), respectively, as recommended by Ref. 11.

For a consistent second-moment closure, the scalar flux analogue of Eq. (1) would be solved. However, experience of scalar flux transport equations is to date limited. More importantly, for complete consistency in the present two-phase reacting formulation, no less than 12 additional equations would have to be resolved for scalar fluxes, and the very considerable computational effort could not be acceptable. We solve instead the following transport equation for a scalar property:

$$\frac{\partial(\bar{\rho}\tilde{\phi})}{\partial x_k} = \frac{\partial}{\partial x_k}\left(\frac{\mu_e}{\sigma_\phi}\frac{\partial\tilde{\phi}}{\partial x_k}\right) + \tilde{S}_{g,\phi} + \tilde{S}_{p,\phi} \quad (7)$$

where $\tilde{S}_{g,\phi}$ is the gas-phase source term and $\tilde{S}_{p,\phi}$ is

the particulate-phase source term. We retain the eddy-viscosity concept, embodied in the first two terms on the right-hand side of the equation, to account for the diffusive fluxes. This corresponds to the conventional k-ε model treatment, excepting that here the turbulent viscosity is calculated using k obtained from Eq. (1) for the normal stresses and ε obtained from Eq. (6).

Numerical Treatment

The computations were performed on a staggered grid to enhance the numerical stability. The grid was optimised to be computationally efficient and to ensure grid independence of the calculations. Due to the inevitable lack of measured information at the flow entrance, much of the inlet boundary condition information had to be assumed. The axial velocities were specified as uniform based on mass flow rates, whereas the radial velocities were set to zero. The normal stresses at inlet were assigned to be 2/3 of the local turbulence kinetic energy and the shear stresses to zero.

An important, but insufficiently stated, difficulty is that the use of Reynolds stress turbulence models generally results in very much reduced numerical stability due to the absence of explicit and stabilising turbulent diffusion terms in the momentum equations compared with conventional turbulent viscosity based models such as the k-ε one. This has proved to be particularly disadvantageous when applications to complex engineering combustors are attempted, and this has certainly been the experience here.

The Post-Processor of NO Simulations

The aerodynamics and combustion are unaffected by the nitrogen chemistry, and therefore, an efficient and computationally economical calculation of NO emissions is achieved through postprocessing the converged solutions of the primary variables. Both fuel NO and thermal NO are simulated in the present study, whereas prompt NO is neglected. The fuel NO was simulated by De Soete simplified models [12–14]. Thermal NO was modelled by the "extended Zeldovich" mechanism using the reaction rate proposed by Ref. 15.

Experimental Conditions

The ICSTM furnace is a vertically oriented cylinder, 0.6 m in diameter and 3.0 m in length, downfired along its axis by a double-concentric swirl burner having a refractory quarl. A full description of this furnace and its instrumentation can be found in Refs. 3 and 16. The experiments referred to herein were conducted using two distinct types of burners: one with a central bluff body in the primary nozzle

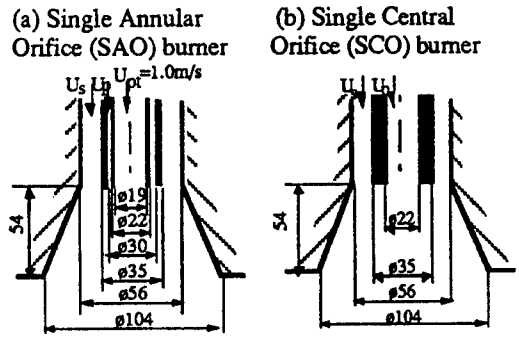

FIG. 1. The power station type burner geometries of the ICSTM furnace (length in millimeters).

and the other without, referred to as the single annular orifice (SAO) burner and the single central orifice (SCO) burner, respectively. Their geometries are shown in Fig. 1, where U_p represents the primary air velocity, U_s represents the secondary air velocity, and U_{pt} represents the primary air through the central tube for the SAO burner.

The IFRF cement kiln is larger than the ICSTM combustor, having a diameter of 0.78 m and a length of 9.75 m. The flame considered in the present study was produced by a nonswirling monochannel burner for a primary air flow amounting to 20% of the total air supplied. Details of this combustor and the associated instrumentation can be found in Ref. 17, where the flame presented herein is designated 89.

The operating conditions for both the ICSTM and IFRF burners are listed in Table 1. The test fuels were a medium volatile UK bituminous coal (Gedling) for the ICSTM furnace and a medium volatile USA bituminous coal (Raven) for the IFRF cement kiln. The conventional specifications of these two fuels are also given in Table 1.

Results and Discussion

Cement Kiln Type Flame

The IFRF flame was typical of cement kiln practice with the primary jet emerging at high velocity, resulting in high gradients at inlet. In consequence, the predictions were performed on a 100 × 50 grid with high refinement near the burner. The axial distributions of the oxygen concentration, temperature, and NO concentration are shown in Fig. 2. The axial distance is normalised by the cement kiln diameter of 0.78 m.

In Fig. 2a, the onset of the ignition is indicated by the sudden drop of the oxygen concentration. Due to the absence of a swirl-generated reverse flow zone, the cement kiln flames are normally lifted with ignition occurring due to the irradiation of the char

TABLE 1
Operating conditions of and coal properties used in the IFRF experimental cement kiln and the ICSTM experimental power station furnace

	IFRF burner	ICSTM burners SAO	ICSTM burners SCO
Coal feed rate (kg/h)	280	14	14
Primary air flow rate (kg/h)	604	31.8 + 1.0[a]	32.8
Secondary air flow rate (kg/h)	2654	120.4	120.4
Primary air temperature (°C)	20	80	80
Secondary air temperature (°C)	810	300	300
Swirl number	0	1.03	1.03
Excess air (%)	9	15	15

Proximate analysis (%)	Raven coal, USA	Gedling coal, UK	Ultimate analysis (%)	Raven coal, USA	Gedling coal, UK
Volatile	24.0	35.8	C	82.2	72.6
Fixed	69.9	53.7	H	4.6	5.05
Carbon ash	6.0	4.2	N	1.4	1.29
Moisture		6.3	S	0.8	1.55
			O	4.8	15.31

[a]The mass flow rate of primary air through the central tube for SAO burner is 1 kg/h, and the total mass flow rate of primary air is still 32.8 kg/h, same as that of the SCO burner.

particles by the hot walls. Predictions of the liftoff or ignition distance represent a rather severe test for the mathematical model. The axial distributions of the oxygen concentration along the axis of the cement kiln show that the predicted onsets of ignition are in good agreement with the measurements. The predicted oxygen concentrations on the axis in the downstream region are, however, lower than the measured data. In order to identify the source of the discrepancy, the particle burnout along the axis was calculated. This is defined as the sum of the mass released from the particulate phase to the gas phase, integrated over the radius and divided by the input mass flow rate of carbon on a dry ash-free basis. The predicted exit burnout value for the k-ε model was 97.5%, higher than the corresponding measured value 96%. The underpredicted downstream oxygen concentration is a consequence of the overprediction of char combustion. It is noted [2,5] that char kinetics constants are usually determined for temperatures more representative of the NBR than the far field and that the use of these constants throughout the combustor may lead to overestimated char burnout.

The radial profiles of the oxygen concentration obtained with the k-ε model are closer to the measurements, as seen in Fig. 3. The large discrepancies of the RST-A model at the station $x/D = 2.7$ are the

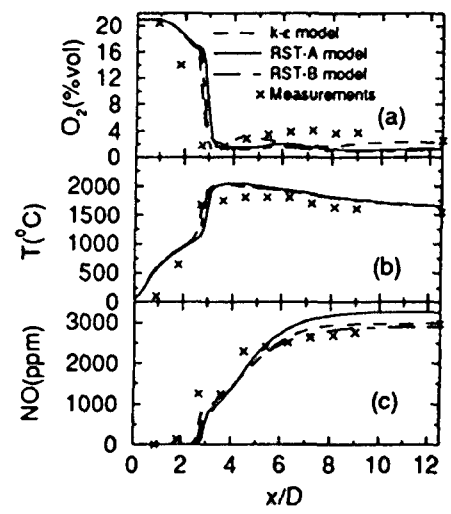

FIG. 2. On-axis distributions of the oxygen concentration, temperature, and nitric oxide concentration for the IFRF cement kiln.

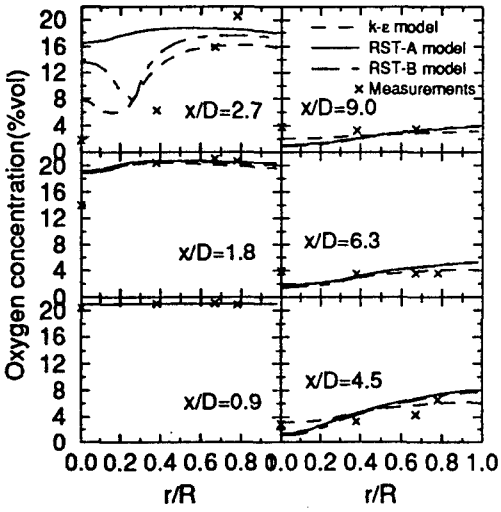

FIG. 3. Radial distributions of oxygen concentration for the IFRF cement kiln.

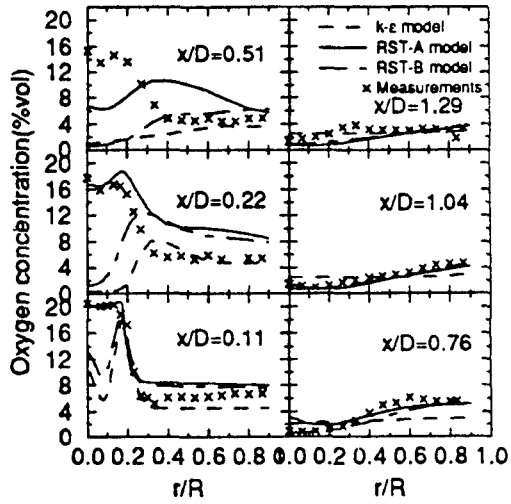

FIG. 5. Radial distributions of oxygen concentration for the ICSTM furnace, SCO burner.

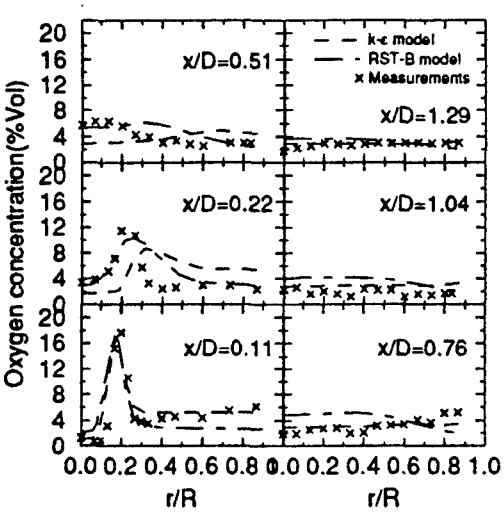

FIG. 4. Radial distributions of oxygen concentration for the ICSTM furnace, SAO burner.

result of excessive predicted ignition delay. At locations further downstream, the radial gradients predicted by both RST models are somewhat exaggerated. This suggests an underestimation of the scalar diffusion with the RST models. It was found that the turbulent viscosity μ_t, which is based on the assumption for turbulence isotropy, obtained from the anisotropic RST models was smaller in the downstream region than that given by the isotropic k-ε model. Although reducing the Schmidt number in Eq. (7) would improve the distribution of the oxygen concentration in the downstream region, such tampering is hard to justify. These observations suggest that the consistent use of second-moment closure for the turbulence flux in the scalar equation may be desirable. This has been done with some success in a reported study of the mixing of two fluids of very different densities [8]. For the present PF flames, this remedy, as mentioned above, incurs an unacceptably expensive computational penalty.

The predicted temperatures are generally higher than the measured ones, as shown in Fig. 2b, a not unexpected discrepancy in the downstream region where the oxygen concentrations are underpredicted. Measured temperatures are in any case usually a little lower than the true values due to radiation and conduction losses.

Figure 2c shows that NO concentrations are generally better predicted. It was found that thermal NO constituted more than two-thirds of the total NO emissions, this is the main NO formation mechanism at the high temperatures that characterises cement kiln operation.

Power Station Type Flames

Convergence difficulties were experienced for the SAO burner due to the large velocity gradients near the centre line. This compounded the already delicate stability of RST-based methods, and convergence could not be procured for the RST-A model. The predictions presented for this burner are therefore restricted to those of the k-ε model and the RST-B model. Comparisons with experimental data for both the SAO and the SCO burners were made at a station very near the quarl exit to about one furnace diameter (0.6 m) downstream, where the composition of species and the temperature are already uniform. The results are shown in Figs. 4 through 8.

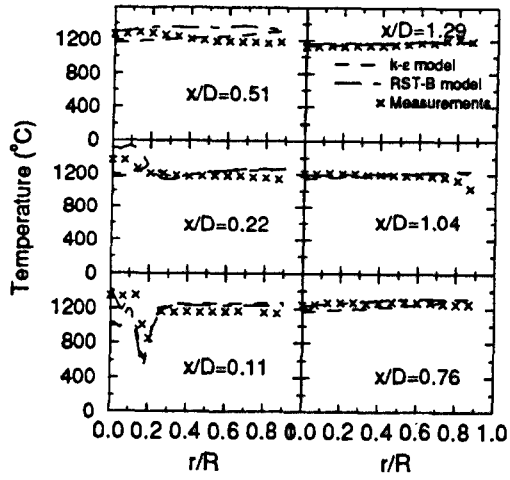

FIG. 6. Radial distributions of temperature for the ICSTM furnace, SAO burner.

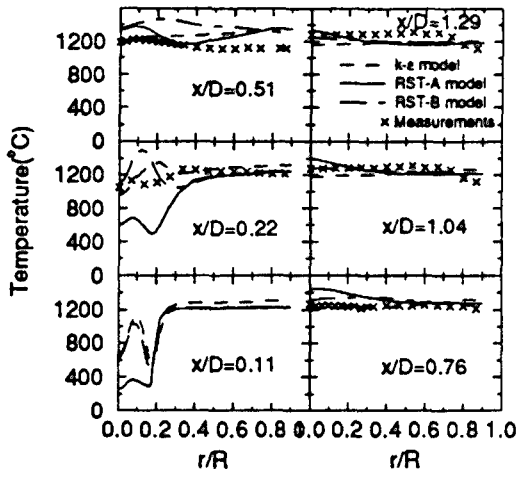

FIG. 7. Radial distributions of temperature for the ICSTM furnace, SCO burner.

The predicted radial distributions of the oxygen concentration are compared with the measurements in Figs. 4 and 5 for the SAO and the SCO burners. The axial location is normalised by the furnace diameter of 0.6 m. In Fig. 4, for the SAO burner at the first and very near burner station of $x/D = 0.11$, there is little to choose between the k-ε and RST models. For stations $x/D = 0.22$ and 0.51, the oxygen concentrations with the RST-B model are somewhat better predicted than for the k-ε model. The main predictive difficulty for the SCO burner, Fig. 5, and the one mentioned in the Introduction, has been that the predicted ignition location is too near the burner. The RST-A model corrects this, at the expense of poorer predictions downstream. At the last station, $x/D = 1.29$, the results of the k-ε model agree well with the experimental data for both the SAO and SCO burners, whereas the gradients predicted by the anisotropic RST models are overestimated. Both RST models predict slower rates of return of anisotropy to isotropy in the downstream region.

The predictions of the gas temperatures are shown in Figs. 6 and 7. The temperature field for the SAO burner, Fig. 6, is generally well estimated. Not unexpectedly, in view of the difficulty of predicting the oxygen field for the SCO burner, the temperature field is also less well predicted for this burner, Fig. 7., Particularly disappointing is the fact that at the upstream station of $x/D = 0.22$, where the oxygen concentration predictions were fairly good for the RST-A model, the corresponding temperature predictions are poor.

As would be expected for this type of furnace [16], the thermal NO was found to be extremely small for both burners due to the low temperatures. In Fig. 8, the predicted NO concentrations in the upstream region for the SAO burner are generally lower than the experimental data. Increasing the reaction rate of the gas-phase fuel NO formation would improve the predictions, but the exit value would then be higher than measured. This may imply that a NO reduction mechanism occurs. For example, significant reduction of NO by the char would correct the prediction. The char reduction scheme proposed by Levy et al. [18] was tried in the present study, but its influence was discovered to be negligible. In view of the less satisfactory prediction of the oxygen and temperature fields for the SCO burner, the corresponding predicted NO concentrations are not presented.

Concluding Remarks

The application of Reynolds stress closures to complex engineering flows, such as the present pulverised coal flames, is rendered especially difficult due to the absence of explicit turbulent diffusion terms in the mean momentum equations. For the nonswirling cement kiln type flame, the second-moment closures offer little advantage over the traditional k-ε model; indeed, the RST predictions are generally poorer for the variables considered, which exclude velocity due to the lack of reliable measurements. For the power station type swirl burners, the RST models again do not demonstrate definite and clear-cut superiority over the k-ε approach. The perennial problem of early predicted ignition for burners of the single central orifice (SCO) kind is corrected by the RST-A model, but at the expense of poorer prediction elsewhere.

Since it is unacceptable that the more advanced closure should not exhibit predictive advantage and because of inconsistencies in the k-ε and RST values of μ_t, it is concluded that a consistent treatment ex-

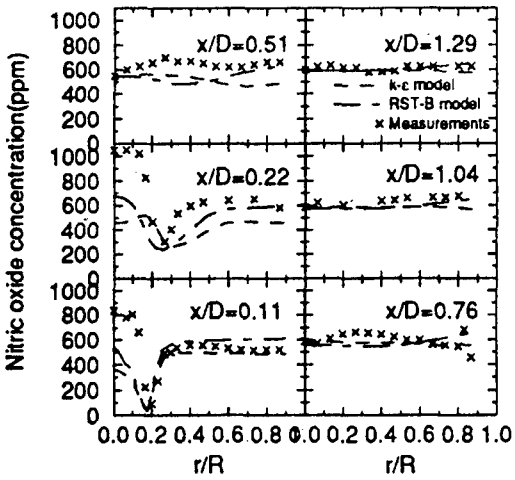

FIG. 8. Radial distributions of nitric oxide concentration for the ICSTM furnace, SAO burner.

tended to include the solution of second-moment scalar flux equations is required. Since for pulverised-coal flames modelled in the present manner, a further 12 equations would require to be solved, this is not a practicable remedy. In addition, as pointed out in the study of isothermal flows in [9,19], predictions of the RST model are more sensitive to the boundary conditions than those of the k-ε model. On the basis of the collected evidence of this study, one is unfortunately led to the important conclusion that in the absence of a decent quantity of reliable two-phase flow data, which are extremely difficult to procure for PF flames, it will not be possible to make much further progress in isolating combustion model defects from turbulence model ones. Nonetheless, the overall predictive capability that already exists is sufficient to assist an accomplished design engineer to a useful extent.

The NO predictions are totally dependent on the quality of the flow and combustion variable simulations; thus, it is not possible to distinguish reliably among proposed fuel NO kinetic schemes. The present simple scheme demonstrates fair agreement with the measurements, and it is, therefore, recommended. The majority of the NO produced in cement kilns is thermally derived, whereas fuel-derived NO predominates in power station circumstances.

Acknowledgment

The authors wish to acknowledge the Commission of the European Communities (CEC) for the financial support of this study under Contract No. JOUE-0051-C. They also wish to acknowledge Drs. T. M. Lowes (Blue Circle Cement) and J. P. Smart (IFRF) for their assistance in interpreting the cement kiln experiments, and Dr. W. P. Jones (ICSTM) for his invaluable advice on Reynolds stress modelling.

REFERENCES

1. Smoot, L. D., Hedman, P. O., and Smith, P. J., *Prog. Energy Combust. Sci.* 10:359–441 (1984).
2. Truelove, J. S., and Holcombe, D., *Twenty-Third Symposium (International) on Combustion*, The Combustion Institute, Orleans, MA, 1990, pp. 963–971.
3. Costa, M., Costen, P., Lockwood, F. C., and Mahmud, T., *Twenty-Third Symposium (International) on Combustion*, The Combustion Institute, Orleans, MA, 1990, pp. 973–980.
4. Weber, R., Dugue, J., Sayre, A., and Visser, B. M., *Twenty-Fourth Symposium (International) on Combustion*, The Combustion Institute, Sydney, 1992, pp. 1373–1380.
5. Lockwood, F. C., and Mahmud, T., *Twenty-Second Symposium (International) on Combustion*, The Combustion Institute, Seattle, 1988, pp. 165–173.
6. Launder, B. E., *Int. J. Heat Fluid Flow* 10:282–300 (1989).
7. Weber, R., Visser, B. M., and Boyan, F., *Int. J. Heat Fluid Flow* 11:225–235 (1990).
8. Hogg, S., and Leschziner, M. A., *Int. J. Heat Fluid Flow* 10:16–27 (1989).
9. Shen, B., "The Application of Second-Moment Turbulence Closures to 2-D Pulverised-Coal Flames," Ph.D. Thesis in preparation, Imperial College, University of London, London.
10. Gibson, M. M., and Launder, B. E., *J. Fluid Mech.* 86:491–511 (1978).
11. Gibson, M. M., and Younis, B. A., *Phys. Fluids* 29:28–48 (1986).
12. De Soete, G. G., *Fifteenth Symposium (International) on Combustion*, The Combustion Institute, Tokyo, 1975, pp. 1093–1102.
13. De Soete, G. G., *Twenty-Third Symposium (International) on Combustion*, The Combustion Institute, Orleans, MA, 1990, pp. 1257–1264.
14. Lockwood, F. C., and Romo-Millares, C. A., *J. Inst. Energy* 65:144–152 (1992).
15. Sawyer, R. F., *Eighteenth Symposium (International) on Combustion*, The Combustion Institute, Waterloo, 1981, pp. 1–22.
16. Abbas, T., Costen, P., and Lockwood, F. C., *Combust. Flame* 91:346–363 (1992).
17. Van de Kamp, W. L., and Smart, J. P., "The effect of burner design and operation and fuel type on the properties of cement kiln flames," IFRF Doc NO F 97/y/1, 1992.
18. Levy, J. M., Chan, L. K., Sarofim, A. F., and Beer, J. M., *Eighteenth Symposium (International) on Combustion*, The Combustion Institute, Waterloo, 1981, pp. 111–120.
19. Lockwood, F. C., and B. Shen, *The First Asian Computational Fluid Dynamics Conference*, Hong Kong, 1995, submitted.

Twenty-Fifth Symposium (International) on Combustion/The Combustion Institute, 1994/pp. 511–518

RADIATIVE HEAT TRANSFER IN PULVERIZED-COAL-FIRED BOILERS—DEVELOPMENT OF THE ABSORPTIVE/REFLECTIVE CHARACTER OF INITIAL ASH DEPOSITS

G. H. RICHARDS AND J. N. HARB
Department of Chemical Engineering
Brigham Young University
Provo, UT 84602, USA

L. L. BAXTER
Combustion Research Facility
Sandia National Laboratories
Livermore, CA 94550, USA

AND

S. BHATTACHARYA, R. P. GUPTA AND T. F. WALL
Department of Chemical Engineering
The University of Newcastle
Australia

Emission Fourier transform infrared (FTIR) spectroscopy data provide in situ, time-resolved, spectral emissivity measurements for ash deposits generated from two U.S. Powder River Basin coals. The first 3 h of deposit growth on a tube in cross flow in a pilot-scale furnace detail the development of surface emissivity with time. Measured emissivities vary significantly with wavelength, indicating the influence of the physical properties and chemical composition of the deposit. At long wavelengths ($>7\ \mu$m), emission features exhibit characteristics of silica, sulfates, and silicates. The spectral emissivity measured in this region approaches a steady value due to an increase in deposit thickness and the size of particles in the deposit. In contrast, deposits are not opaque at shorter wavelengths where the measured emissivity is influenced by the properties of the underlying metal surface. Theoretical predictions of the emissivity of a particulate layer were performed, and results are compared to the measured values. The theory adequately predicts the general features of spectral variation of the emissivity. The predicted trends in emissivity with particle size and deposit composition are also consistent with experimental observations. Total (Planck-weighted) emissivities are calculated from the measured spectral values for the deposits at the tube temperatures. They increase with time from the clean tube value (0.2–0.3) to values typical of deposits formed from western U.S. coals (0.45–0.55). Calculated total absorptivities are found to be lower than the corresponding emissivities.

Introduction

Radiative transfer is the dominant heat transfer mechanism in the furnace region of pulverized-coal-fired boilers. It accounts for about 80% of the total heat transfer in the furnace region of a clean boiler, and significantly less ($\approx$10%) in the convective pass. Typical deposits from western U.S. coals consist of fine particles that reflect up to 70% of incident radiation [1]. The reflective/absorptive properties of ash deposits are an important part of engineering calculations of heat transfer in a utility boiler. For example, reducing the wall emissivity from 0.8 to 0.4 in a computer simulation of a utility boiler can cause an increase of 110 °C in the calculated furnace exit gas temperature [1]. Field experience with western U.S. coals confirms both the formation of low emissivity deposits and the corresponding increases in furnace exit gas temperature [2]. This paper presents theoretical predictions of the spectral emissivity of coal ash deposits as a function of particle size and composition. These predictions are compared with in situ, time-resolved measurements of spectral emissivities from ash deposits formed in a pilot-scale combustor, among the first data of this type to be collected under simulated boiler conditions.

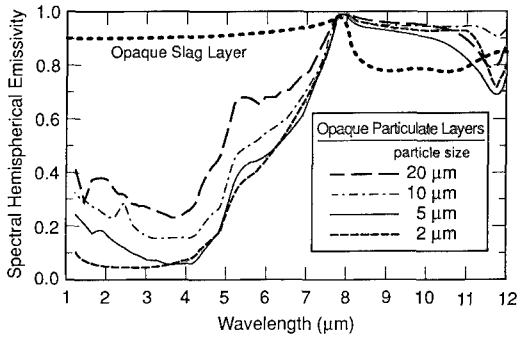

FIG. 1. Predictions of spectral hemispherical emissivity (ε_λ) for opaque particulate deposits as a function of particle size. The uniform ash composition is that of a calcium aluminosilicate with 4.65% Fe_2O_3 [3].

Theory

Radiative Properties of Deposits:

The radiative properties of coal ash deposits are a function of both the chemical composition and the physical nature of the deposit. Fine condensable salts or particulate (<10 μm) often contribute to initial layers of ash deposits and may be highly reflective [1]. As larger particles accumulate, the deposit emissivity tends to increase. The temperature gradient through the deposit may cause the outer layer to sinter, at which point it may absorb over 90% of the incident radiation, depending on its composition [3]. Although the term emissivity strictly applies to a smooth surface of a pure material, it has been used to characterize emission from irregular particulate and other participating layers in the present study, as done previously by others. [4,5].

Deposit emissivities vary with wavelength from a low of approximately 0.2 to greater than 0.9, as will be shown later in this investigation. A Planck-weighted average is used to obtain a total emissivity appropriate for many engineering calculations. This total emissivity (ε_t) depends on both the spectral emissivity and the Planck function (P) evaluated at the deposit surface temperature and is given by

$$\varepsilon_t(T_s) = \frac{1}{\sigma T_s^4} \int_{\lambda=0}^{\infty} \varepsilon_\lambda(\lambda,T_s) P(\lambda,T_s)\, d\lambda \qquad (1)$$

where ε is emissivity, T is absolute temperature, λ is wavelength, and σ is the Stefan–Boltzmann constant. Subscripts t, s, and λ represent total, surface, and spectral, respectively.

In general, the spectral emissivity, ε_λ, and spectral absorptivity, a_λ, are equal according to Kirchoff's law under the assumption of diffuse radiation. Therefore, the Planck-weighted total absorptivity can be determined as follows:

$$\begin{aligned} a_t(T_s,T_f) &= \frac{1}{\sigma T_f^4} \int_{\lambda=0}^{\infty} a_\lambda(\lambda,T_s) P(\lambda,T_f)\, d\lambda \\ &= \frac{1}{\sigma T_f^4} \int_{\lambda=0}^{\infty} \varepsilon_\lambda(\lambda,T_s) P(\lambda,T_f)\, d\lambda. \end{aligned} \qquad (2)$$

In contrast to the total emissivity, the total absorptivity depends on both the surface temperature and the flame temperature. Planck-weighted radiative properties are used in this investigation to approximate total radiative properties applicable to furnace calculations. For a large variety of materials relevant to combustion problems, the Planck-weighted properties decrease with increasing temperature [1,3,6].

Prediction of Radiative Properties for Particle Layers and Slags:

Deposit radiative properties vary significantly with wavelength, indicating the influence of the chemical composition and physical properties of the deposit. However, many engineering applications do not account for the spectral nature of radiative heat transfer and assume an average surface emissivity. The approach used here is to obtain first-order predictions of the spectral emissivity as a function of the chemical composition and physical properties of the deposit. These predictions are qualitatively compared with measured results for ash deposits. The Planck-weighted averages can then be used in engineering applications.

In predicting the emissivity of ash deposits, the deposits are treated as an optically thick layer of monosized, isothermal, spherical particles of known optical properties [1,7]. While none of these assumptions is completely accurate, the first-order effects of scattering are derivable from such a model. Scattering is important since particle layers tend to backscatter (reflect) a significant fraction of the incident flame radiation. A 16-flux discrete ordinates method was used to solve the radiative transport equation through the simulated particulate layer [1]. Particle size and complex refractive index are provided as input. The model accounts for multiple scattering of radiation, which significantly influences the calculated radiative properties. Scattering was assumed to be independent according to Brewster [8]. These calculations are applied to the porous, particulate-based deposits found in the initial layers of ash deposits. In addition, the emissivity of a layer of molten slag (which was approximated as an optically smooth surface) was estimated from the complex refractive index of the slag [3,9].

Spectral emissivity predictions are illustrated in Figs. 1 and 2 for opaque particle layers based on the spectral optical properties of two ash types. Figure 1

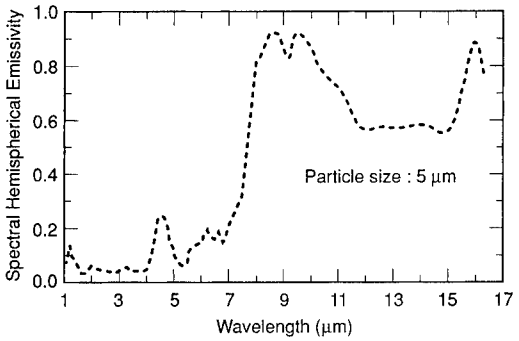

FIG. 2. Spectral emissivity predictions for an opaque layer of $CaSO_4$ particles [11]. (Optical data at wavelengths longer than 7.5 μm are for ammonium sulfate crystals [10] as calcium sulfate data were not available for this region.)

is based on data for slags ($SiO_2/Al_2O_3 \approx 2$, $CaO/Al_2O_3 \approx 0.6$, $Fe_2O_3 \approx 5\%$) [3] and shows a region of low emissivity at wavelengths < 5 μm, where particle size influences the predicted results. The features indicated between 4 and 6 μm may be associated with gas-phase carbon dioxide (4–5 μm) and water (5–6 μm) absorption that was not completely eliminated from the literature values used for the optical constants. There are no known absorption bands for this type of material in this region. These residual gas emission features tend to exaggerate the particle size effect. The true particle size effect, as indicated in the data from 3 to 4 μm, is largely a result of particle scattering, as small particles tend to backscatter more radiation (leading to lower emissivities and higher reflectivities) than larger particles. By contrast, ε_λ generally exceeds 0.9 for a smooth, iron-containing slag layer. The spectral emissivity predicted for $CaSO_4$ particles (Fig. 2) also shows a region of low emissivity at wavelengths < 7.5 μm, followed by a region of high emission at 8–10 μm. The $CaSO_4$ data were used at the short wavelengths; however, data at wavelengths greater than 7.5 μm are for $(NH_4)_2SO_4$ crystals as calcium sulfate data were not available [10,11].

The results in Figs. 1 and 2 illustrate some important qualitative trends that may be expected in real systems. First, the spectral nature of the emissivity is clearly evident. In particular, the spectral emissivity is quite low at the short wavelengths, the spectral region where much of the radiation in a commercial furnace is exchanged. Second, the particulate nature of the deposit has a measurable influence on its radiative properties. This, again, is especially evident at shorter wavelengths where the ash is relatively transparent and most of the radiation is backscattered by multiple interactions with particles in the deposit. In contrast, no scattering occurs for a smooth opaque slag layer, and any incident radiation is either reflected or absorbed. However, because of the approximate nature of these predictions, it is important to compare them to measured values in order to assess the validity of the trends and the magnitude of the predicted results.

Experimental Apparatus and Procedure

Emission FTIR Spectroscopy:

A diagnostic tool based on emission Fourier transform infrared (FTIR) spectroscopy has been developed to measure in situ properties of ash deposits in real time [12,13]. In this investigation, this tool was used to monitor deposits generated on a stainless steel probe in Sandia's Multifuel Combustor (MFC). The MFC is a 0.1-MBtu/h, down-fired facility with an open test section at the furnace exit to allow optical and probe access to the flow of combustion products [14,15]. The ceramic walls of the combustor are electrically heated to provide the desired temperature profile. Deposits were formed on an air-cooled cylindrical probe (1.6-cm O.D.) in cross flow. The probe was rotated continuously about its axis during each 3-h test to form a nominally uniform deposit around the tube circumference.

The radiative emission from a region approximately 5 mm in diameter on the bottom half of the probe was collected by a set of off-axis paraboloidal mirrors (effective f# = 4.3) and focused into the aperture of the FTIR spectrometer. A commercial, rapid-scanning interferometer (Biorad FTS-40/60) was used with a liquid nitrogen-cooled, broadband mercury-cadmium-telluride (MCT) detector and a germanium-based beam splitter. The MCT detector is sensitive over the wavelength range of 2.8–22 μm. Emitted radiation from the bottom of the probe was collected to minimize the contribution of reflected furnace radiation to the total signal. The radiative emission from the probe was compared to that of a blackbody calibration source to determine the spectral emissivity of the probe or deposit surface. The surface temperature of the probe was held constant, typically between 450 °C and 600 °C, whereas the deposit surface temperature varied with time as the deposit grew.

Emission spectra were collected at a resolution of 2 cm^{-1}. Typically, 64 individual interferograms were coadded and deconvolved to obtain a single emission spectrum, requiring about 1 min. Significant interference from infrared active gases (CO_2 and H_2O) in the optical path was also observed. At a resolution of 2 cm^{-1}, some of the gas-phase emission and absorption bands are isolated in the spectrum and appear as narrow peaks, while others are unresolved and appear as broad features. In all cases, the deposit and probe surface emission appear as broad features. The deposit emissivity can be obtained from the spectral

TABLE 1
Proximate, ultimate, heating value, and ash analyses of the coals used in this study (proximate and heating values are given on a dry, ash-free basis)

	Coal A	Coal B	Ash oxide	Coal A	Coal B
Moisture (%)	22.9	21.3	SiO_2	25.03	30.31
Ash (% dry)	5.51	6.46	Al_2O_3	11.36	16.27
Proximate [% dry ash free (daf)]			Fe_2O_3	8.18	5.04
FC	54.2	42.0	TiO_2	0.66	1.27
VM	45.8	58.0	CaO	28.88	21.07
Ultimate (% daf)			MgO	5.60	4.74
C	72.4	74.8	Na_2O	1.57	1.41
H	5.2	5.4	K_2O	0.25	0.35
O	20.9	18.3	P_2O_5	0.81	0.91
N	1.1	1.0	SO_3	17.65	17.46
S	0.4	0.5	undetermined	0.01	1.17
Heating value (Btu/lb)	13,562	13,119			

regions where gas-phase species do not dominate the signal. A more detailed description of the data reduction procedure is available elsewhere [16].

An accuracy of ±5% was estimated by comparison of measurements of radiation from the blackbody calibration source with expected values. Perhaps more significant is the potential error from uncertainties in the deposit temperature and the presence of a temperature gradient through the deposit. The deposition probe temperature was measured to ±20 °C, resulting in an uncertainty of ±5–10% in the spectral emissivity, depending on the wavelength. The effect of the temperature gradient is more difficult to quantify, although the magnitude of the gradient was greatly reduced as the probe cooled during rotation from the top (exposed to furnace radiation) to the bottom where the measurement was taken.

Experimental Conditions:

Deposits were generated at combustor wall temperatures of both 1300 °C and 900 °C, resulting in gas temperatures at the deposition probe of approximately 900 °C and 700 °C, respectively. The probe surface temperature was maintained at 600 ± 20 °C when operating at the higher wall temperature and at 475 ± 20 °C for the experiments performed at the lower wall temperature. At these probe temperatures, over 90% of the total radiative flux from a blackbody is within the spectral region measured by the interferometer (2.8–22 μm). The surface of the probe was cleaned and polished prior to each experiment.

Two U.S. subbituminous coals from the Wyodak-Anderson seam of the Powder River Basin were used in this investigation. The properties of the two coals, Coal A and Coal B, are listed in Table 1. The coal feed rate was approximately 1.8 kg/h for all experiments.

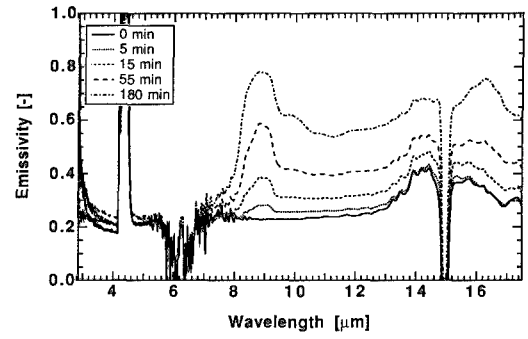

FIG. 3. Spectral emissivity measurements for ash deposits generated from Coal A as a function of time during the first 3 h of deposition. Furnace wall temperature = 900 °C. The spectral regions at 4.2–4.7, 5.5–7.5, and 14.4–15.2 μm are influenced by gas interference and are therefore not characteristic of the deposit.

Experimental Results and Discussion

Figure 3 illustrates the time-resolved spectral emissivity from the in situ FTIR measurements for Coal A. These spectra were obtained at a bulk gas temperature of 900 °C and have been digitally filtered to remove some of the narrow peaks attributed to the gas-phase interference of infrared active components in the vitiated flow. Residual interference appears as features at 4.2–4.7 μm and 14.4–15.2 μm (CO_2 interference) and at 2.9–3.0 μm and 5.5–7.5 μm (H_2O

interference). These infrared-active gases are opaque over the path length of this experiment in these regions. Their temperatures differ from that of the surface by large amounts. The gases in the combustor effluent are at 900 °C–1300 °C, depending on the experiment, whereas those in the laboratory air are at room temperature. By contrast, the deposit surface temperature varied from 300 °C–600 °C, depending on the experiment. Hot band emission from the hot gases produced emissivities greater than one when normalized by the Planck function evaluated at the probe temperature. However, gas interference does not always increase the computed emissivity. Radiative absorption by room-temperature gases in the laboratory environment prevented probe (or gas) radiation from reaching the detector, producing very low values of computed emissivities. For these reasons, gas interferences in the regions cited above produced emissivities that are artifacts that can be either much too high or much too low. The data in the remaining regions do not suffer from gas-phase interferences.

The initial emissivity shown in Fig. 3 is that of the clean stainless steel probe taken at temperature prior to the initiation of coal flow. The emissivity appears relatively constant across the spectrum at approximately 0.2, except for the regions of gas-phase interference. An emissivity less than 0.3 is consistent with literature values for polished stainless steel [17]. There is little change in the spectra with time at wavelengths less than 7 μm as ash is deposited on the probe. Ash deposits from western coals rarely contain chemical species with strong absorption features in this region. Therefore, the measured emissivity of initial deposits from these coals will be influenced significantly by the emissivity of the deposition probe and the scattering of small particles. The influence of the deposition probe was seen in a similar experiment performed with a heavily oxidized mild steel deposition probe that had an emissivity of 0.8 at wavelengths less than 7 μm. In that experiment, the measured emissivity (<7 μm) was approximately 0.75, significantly higher than the measured values shown in Fig. 3, as a result of the higher tube emissivity. Calculations indicate that a deposit of 5-μm ash particles ($Fe_2O_3 \approx 5\%$ as in Fig. 1) must be approximately 50-μm thick to be opaque at a wavelength of 4 μm.

Changes in emissivities with time are larger at wavelengths greater than 7 μm as chemical species with strong absorption features in this region are deposited on the probe surface. The spectral structure derives from the presence of sulfate, silica, and silicate species in the deposit, as discussed elsewhere [12,13].

After the combustion tests, the deposition probe (including the deposit) was cast in epoxy, cross-sectioned, and polished for examination using scanning electron microscopy (SEM) with x-ray analysis. The

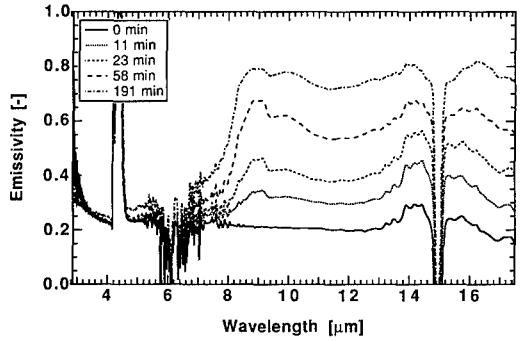

FIG. 4. Spectral emissivity measurements for ash deposits generated from Coal B as a function of time during the first 3 h of deposition. Furnace wall temperature = 900 °C. The spectral regions at 4.2–4.7, 5.5–7.5, and 14.4–15.2 μm are influenced by gas interference and are therefore not characteristic of the deposit.

SEM analysis of the Coal A deposit showed an average deposit thickness of approximately 25 μm with very few ash particles larger than 10 μm in the deposit. The deposit consisted of an inner layer ($\approx$15-μm thick) of very small particles (<5 μm), mainly quartz, calcium silicate, calcium aluminosilicate, and calcium-rich particles. A thin film of sodium sulfate appeared to have condensed on the surface of the probe, while a thin coating of calcium sulfate appeared on the surface of the calcium-rich particles. A few larger silicate and calcium-rich particles were attached to the outside of this layer.

The presence of sulfate in the deposit from Coal A is evident by comparing the predicted sulfate emissivities (Fig. 2) with the data (Fig. 3) at wavelengths greater than 7 μm (Fig. 2). SEM observations confirm the presence of sulfates on calcium-rich particle surfaces. In addition to sulfates, the spectra of Fig. 3 indicate the presence of silica and silicates at wavelengths greater than 7 μm. The combined contributions of silica and sulfates give rise to the prominent feature at about 9 μm, with silicates contributing primarily at wavelengths greater than 10 μm.

Figure 4 presents the measured spectral emissivity values of the deposit from Coal B as a function of time. At wavelengths less than 4 μm, the emissivity is similar to that of the deposit from Coal A and the clean stainless steel probe. The spectra from the Coal B deposit also show evidence of the presence of sulfate, silica, and silicate material. However, the spectral emissivities as a function of time are significantly different at the longer wavelengths (7–14 μm) than those of the Coal A deposit, indicative of the different chemical composition of the deposit. Specifically, elemental analysis of the two deposits showed the Coal B deposit to have more silicon and aluminum than the Coal A deposit.

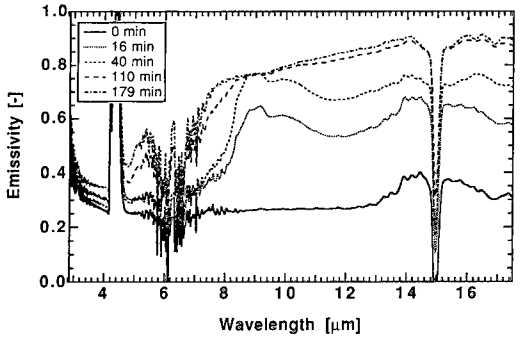

FIG. 5. Spectral emissivity measurements for ash deposits generated from Coal B as a function of time during the first 3 h of deposition. Furnace wall temperature = 1300 °C. The spectral regions at 4.2–4.7, 5.5–7.5, and 14.4–15.2 μm are influenced by gas interference and are therefore not characteristic of the deposit.

SEM analysis showed the Coal B deposit to be approximately 35-μm thick (measurements ranged from 10 to 60 μm), with an inner layer similar to that of the Coal A deposit. The Coal B deposit contained significantly more particles larger than 5 μm in diameter, many of which were calcium aluminosilicate and quartz. The largest particles observed in the deposit were 30 μm in diameter.

Figure 5 presents the on-line emissivity results for the Coal B deposit at the high wall temperature (1300 °C). The measured spectral emissivity of the clean probe is slightly greater ($\approx$0.3) than that at the lower temperature, as a result of increased oxidation of the stainless steel surface. Emissivities measured during the first 40 min of deposition are similar to those measured at the lower probe and furnace temperature (Fig. 4). However, the emissivity at 110 min shows no distinct sulfate and silicate features, and the emission over the wavelength range of 5–17.5 μm is increased. No significant difference in the spectral emissivity at 110 min and 179 min is observed at wavelengths greater than 8 μm. These observations indicate that species emissions in these regions are saturated, and further addition of deposit will not change the spectral emissivity.

The SEM analysis of the high-temperature deposit revealed a 15-μm inner layer similar in composition to the deposits described previously. The outer layer of the deposit contained significantly more large particles (up to 60 μm) than the low-temperature deposits described previously. The average deposit thickness was approximately 150 μm, although the thickness ranged from 30 to 175 μm. The larger particles were mainly quartz, calcium silicate, and calcium aluminosilicate. Many calcium-rich particles containing a thin layer of calcium sulfate were also present in the deposit. Larger particles and thicker deposits both led to saturated emission bands in the spectra, as observed in Fig. 3, consistent with the predictions discussed earlier.

In general, the measured spectral emissivity increased with time as ash accumulated on the tube surface. The magnitude of the change was small at short wavelengths ($\approx$4 μm) because of the low absorptivity of the ash in this region. In fact, most of the measured emissivities at short wavelengths corresponded to deposits of insufficient thickness to be considered opaque. By contrast, the increase of the spectral emissivity at long wavelengths (>7 μm) is significant. This increase is due to the accumulation of a particulate layer whose emissivity was higher than that of the tube substrate. The high values of the spectral emissivity at the long wavelengths are consistent with values calculated for opaque deposits (see Fig. 1).

Emission features characteristic of deposit composition were also evident at long wavelengths. The inner layer of the deposit showed distinct sulfate (8.8–9.3 μm) and silica (9.1–9.4 μm) emission, with an increased contribution from both species as the deposit continued to grow. By contrast, most aluminosilicates emit in the wavelength regions from 9.5 to 11 μm. The relative contributions of silicates compared with sulfates and silica are significantly different for the two coals, with Coal B indicating greater amounts of aluminosilicates than Coal A. This implies higher aluminosilicate content in Coal B than Coal A, as is consistent with the measured aluminum composition of the deposits. The species-dependent features in the spectral emissivity became less pronounced with time, especially for the high-temperature deposits from Coal B (Fig. 5). As particle size and deposit thickness increase, emission bands saturate first near their centers. As deposit thickness or particle size continues to increase, the emission of the saturated regions does not change, but that of the nonsaturated wings continues to increase until it, too, is saturated. The combined effects of larger particles and thicker deposits cause the spectral variation of the emissivity to decrease, and the magnitude of the emissivity to increase.

Total Emissivities and Absorptivities:

Figure 6 illustrates the total (Planck-weighted) emissivity as a function of time for the two Coal B deposits. In both cases, the total emissivity increased with time as the ash deposit formed on the probe surface. The two deposits differ in composition, structure, and temperature. The dependence of deposit emissivity on temperature alone (independent of composition and structure) cannot be determined by direct comparison of the two lines in Fig. 6. The emissivity of the high-temperature deposit is greater than that from the low-temperature deposit. The deposits formed at high temperature are thicker at any

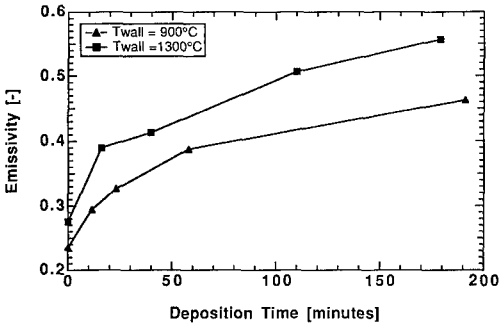

FIG. 6. Calculated total emissivity as a function of time for deposits generated from Coal B at wall temperatures of 900 °C and 1300 °C. Calculated using Eq. (1) with constant surface temperatures of 500 °C and 600 °C, respectively.

given time and contain a larger fraction of large particles, leading to higher emissivities. As is clear from Figs. 3 through 5, Planck-weighted emissivities of both deposits decrease with increasing temperature, all else being equal, because of the shift of radiative exchange to lower wavelengths with increasing temperature.

Total deposit absorptivities were estimated for the most mature deposits of Fig. 6, assuming the spectral incident flux to be a blackbody distribution at a flame temperature of 1800 K. At this temperature, approximately two-thirds of the energy in the blackbody spectrum occurs at wavelengths less than 3.5 μm. Experimental data were not available at these wavelengths as a result of the limited response of the MCT detector. Integration of Eq. (2) over the wavelength range of 3.5–22 μm results in total absorptivity values of 0.39 and 0.51 for the low and high wall temperature deposits, respectively. These absorptivity values are lower than the corresponding total emissivity values (0.46 and 0.56), an effect due to the shift of the most intense spectral regions of radiative exchange to shorter wavelength as temperature increases.

Conclusions

In situ, time-resolved measurements of the spectral emissivity of ash deposits are reported for two U.S. Powder River Basin coals using emission FTIR spectroscopy. Trends in observed deposit emissivity with composition, thickness, and temperature are consistent with SEM/EDS measurements and predicted results. At long wavelengths (>7 μm), features in the emission spectra are observed as a result of the chemical composition of the deposit. At shorter wavelengths (<4 μm), the ash particles are relatively transparent and the measured emissivity is influenced by the probe surface and somewhat by particle size. As the deposits thicken and mature, the spectral and total emissivities approach a constant value, indicating the effect of increased deposit thickness and the incorporation of large particles (>20 μm) into the deposit. Large particles and thick deposits also decrease the spectral variation of the emissivity. Total emissivities, calculated from the measured spectral values for each deposit, increase with time from the clean probe value (0.2–0.3) to values of 0.45–0.55. Calculated total absorptivities are found to be lower than the corresponding emissivities.

Acknowledgments

Support for this study was received from the Australian Research Council, the U.S. Department of Energy through the Pittsburgh Energy Technology Center's Direct Utilization Advanced Research and Technology Development Program, and the Advanced Combustion Engineering Research Center (ACERC) at Brigham Young University. Funds for ACERC are received from the National Science Foundation, the State of Utah, 29 industrial participants, and the U.S. Department of Energy. We also wish to acknowledge the contribution of Don Hardesty, manager of Sandia's Combustion Research Department. The contributions of Gian Sclippa and Al Salmi, who assisted in operation and maintenance of the MFC, are also appreciated.

REFERENCES

1. Wall, T. F., Bhattacharya, S. P., Zhang, D. K., Gupta, R. P., and He, X., *Prog. Energy Combust. Sci.* 19:489–504 (1993).
2. Baxter, L. L., and DeSollar, R. W., *Fuel* 72(10):1411–1418 (1993).
3. Goodwin, D. G., "Infrared Optical Constants of Coal Slags," Ph.D. Thesis, Stanford University, Stanford, CA, 1986.
4. Hottel, H. C., and Sarofim, A. F., *Radiative Transfer*, McGraw-Hill, New York, 1967.
5. Modest, M. F., *Radiative Heat Transfer*, McGraw-Hill, New York, 1993.
6. Baxter, L. L., Fletcher, T. H., and Ottesen, D. K., *Energy Fuels* 2:423–430 (1988).
7. Bohren, C. F., and Huffman, D. R., *Absorption and Scattering of Light by Small Particles*, John Wiley & Sons, New York, 1983.
8. Brewster, M. Q., *Thermal Radiative Transfer & Properties*, John Wiley & Sons, Inc., New York, 1992.
9. Siegel, R., and Howell, J. R., *Thermal Radiation Heat Transfer*, McGraw-Hill, New York, 1992.
10. Toon, O. B., Pollack, J. B., and Khare, B. N., *J. Geophys. Res.* 81(33):5733–5748 (1976).
11. Touloukian, Y. S., and Ho, C. J., (Eds.), *Thermal Ra-*

diative Properties of Nonmetallic Solids, Thermophysical Properties of Materials, Plenum Press, New York, 1989, Vol. 8.

12. Baxter, L. L., Richards, G. H., Ottesen, D. K., and Harb, J. N., *Energy Fuels* 7:755–760 (1993).
13. Baxter, L. L., in *Engineering Foundation Conference on the Impact of Ash Deposition on Coal Fired Plants*, Engineering Foundation Press, Solihull, England, 1993.
14. Baxter, L. L., and Dorra, L., ASME Paper No. 92-JPGC-FACT-14, 1992.
15. Baxter, L. L., Hencken, K. R., and Harding, N. S., in *Twenty-Third Symposium (International) on Combustion*, The Combustion Institute, Orleans, France, 1990, pp. 993–999.
16. Baxter, L. L., and Hardesty, D. R., *The Fate of Mineral Matter During Pulverized Coal Combustion: Quarterly Report for January–March 1993*, SAND94–8215, 1994.
17. Incropera, F. P., and DeWitt, D. P., *Fundamentals of Heat and Mass Transfer*, 2nd ed., John Wiley & Sons, New York, 1985.

Twenty-Fifth Symposium (International) on Combustion/The Combustion Institute, 1994/pp. 519–525

EVOLUTION OF POROSITY AND THERMAL CONDUCTIVITY DURING CHAR OXIDATION

YONY WEISS, YOSSI BENARI, ISAAC I. KANTOROVICH, AND EZRA BAR-ZIV°
Department of Mechanical Engineering
Ben-Gurion University of the Negev
Beer-Sheva, Israel

AND

GERNOT KRAMMER,°° ANTHONY MODESTINO, AND ADEL F. SAROFIM
Department of Chemical Engineering
Massachusetts Institute of Technology
Cambridge, MA 01239, USA

Measurements of the natural convection drag and the photophoretic force have been conducted for Spherocarb char particles as a function of carbon conversion. These forces were obtained by measuring the balancing voltage with and without laser heating during the reaction of single particles in an electrodynamic balance. The photophoretic force was determined by subtraction of the calculated natural convection force, after an initial transient corresponding to about 5% carbon conversion during which the natural convection force was dominant. The particle conductivity inferred from the photophoretic force was found to decrease by more than one order of magnitude as the reaction progressed, qualitatively in agreement with models of the dependence of conductivity on porosity. Confirmation of the temperature gradient across the particle was provided by the development of asphericity in the particles when heated from below, but not when heated uniformly. The simultaneous measurements of the mass, diameter, and particle conductivity as a function of carbon conversion provide a critical test of pore evolution models since the reaction rate is dependent on the accessibility of the internal surface area to the reactant gas through the open pore structure and the thermal conductivity is dependent on the connectivity of the solid structure. Induction periods were observed before the reaction rate accelerated and the particle conductivity declined, confirming the influence of pore structure on both. Particles could be reacted to a high conversion of greater than 95% without any evidence of fragmentation, providing further insight on the connectivity of the solid surfaces.

Introduction

The effect of pore structure on the reactivity and fragmentation of char, although extensively studied, is still poorly understood. One incompletely resolved problem area is the accessibility of the interior of the porous volumes within the char to the reacting gas external to a particle, which is one of the many factors determining reactivity. Another is the continuity of the connectivity of the char, which determines fragmentation. The dependence of combustion properties of chars on the nature of the pore structure is evident from the calculated values of the critical porosity for fragmentation for chars, which can vary, for simple assumed pore shapes and pore network structures [1], from 0.26 to 0.968. The problem is further complicated by the recent observations that the carbon structure undergoes rearrangement during reaction, which results in a shrinkage of particles under chemically controlled reaction conditions [2] and a decrease in the intrinsic rate of reactivity at high carbon conversions [3].

The present study is directed at examining the size, shape, density, and fragmentation of char over its entire oxidation history using an electrodynamic balance (EDB). In the EDB, a single particle is levitated by electrodynamic forces, and a DC voltage is applied across the top and bottom electrodes to balance the forces—gravitational, natural convection, photophoretic—acting on a particle. The particle can be heated and the changes in reaction rate and particle morphology followed over a wide range of conversions. The advantage of the EDB over conventional thermogravimetric analyzers is the ability to study the reaction of individual particles 50–200 μm in size, providing a measure of interparticle variability and overcoming interparticle interactions [4]. An addi-

°Nuclear Research Center, Negev, Israel.
°°University of Technology, Graz, Austria.

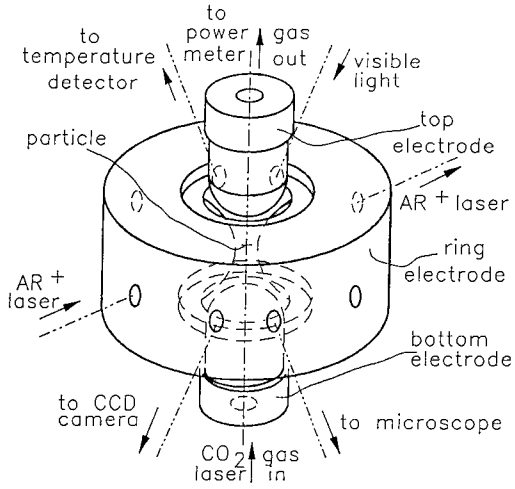

FIG. 1. Schematic of the electrodynamic balance with CO_2 laser heating force from the bottom.

tional advantage introduced in this paper is that of measuring the changes in thermal conductivity of the particle by measurement of the photophoretic force when the particle is heated from below. The conductivity can be measured continuously by interrupting the laser heating periodically during a run and determining the difference in balancing voltage, at a given weight, due to natural convection and photophoresis. After subtraction of the natural convection force, the thermal conductivity can be inferred from the photophoretic force. It is therefore possible to follow the connectivity of the solid portions of a char, as inferred from its thermal conductivity, as well as the rate of reaction, as a function of conversion. These simultaneous measurements provide new insights on the evolution of the pore structure.

Experiments have been performed on synthetic char particles, Spherocarb, which have been extensively studied because they provide a reproducible material that can approximate a high surface area coal char. The Spherocarb particles have the further advantage of being spherical and being fairly uniform in size.

Experimental

The char oxidation studies were carried out in an EDB laser heated from below and a thermogravimetric analyzer (TGA). A schematic representation of the EDB is provided in Fig. 1. The electrodynamic field used to levitate the particle is produced by an AC voltage applied between the ring electrode and the top and bottom electrodes. Vertical forces on the particle are balanced by a DC voltage applied across the top and bottom electrodes. The particle position is maintained in the center of the balance with a vertical stability of better than 0.5% of the particle diameter by projecting an image on a photodiode array detector, which is used both to provide a signal to the feedback controller and a measure of the particle vertical diameter [4]. In addition, a particle image is focused on a charge-coupled device (CCD) camera and recorded at 24 frames per second. The particle is heated by a CO_2 laser operated in the TEM*01 mode to provide a doughnut intensity profile that enhances the particle stability. The beam can be interrupted on command using a laser shutter controller. The temperature of the particle is measured by a two-color infrared pyrometer [5]. During an experiment, the size, shape, and radiation signals are collected continuously.

The initial particle diameters ranged from 165 to 200 μm, the initial particle density from 447 to 617 kg/m^3, and the initial temperatures from 785 to 800 K. For this range of conditions, the oxidation of the Spherocarb particles is in the chemically controlled regime since previous studies [4] have shown that the reaction rate is still given by the Arrhenius rate expression obtained at lower temperatures with an activation energy of 36 kcal/mol consistent with regime I kinetics. For the experiments in the thermogravimetric analyzer, the particles were in the size range of 160–220 μm, the particle density was 400–900 kg/m^3, and the surface area in the range of 950 to 1020 m^2/g. The composition of the Spherocarb is 96.9% carbon, 2.4% hydrogen, and 0.7% oxygen.

Measurement of Particle Charge and Density:

The EDB provides a measure of the mass to charge ratio for a particle. The charge, q, can be obtained by imposing a flow of known velocity u across the particle and measuring the change in the balancing voltage. For a known gas flow through the bottom of the chamber, the balance between the particle weight and the sum of the drag force and the balancing electrical voltage, for a particle of mass m and diameter d, is given by

$$mg = 3\pi d\mu u + \frac{qc}{z_0} V \qquad (1)$$

where c is the instrument constant with a value of about 0.5, z_0 is the distance between electrodes, V is the balancing voltage, and μ the gas viscosity. The charge on particle may be obtained from the change in voltage with changes in velocity [i.e., $q = -(3\pi d\mu z_0/c)/(dV/du)$]. This permits the determination of the particle mass m and, given the diameter d, the particle density ρ_p.

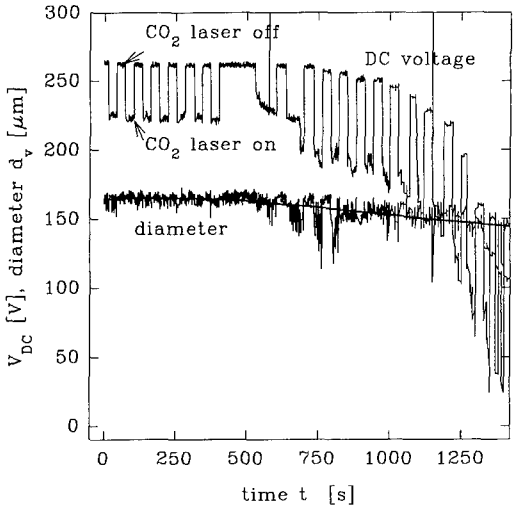

FIG. 2. Spherocarb particle oxidation in an electrodynamic balance with CO_2 laser heating from the bottom. DC balancing voltage and vertical particle diameter vs time.

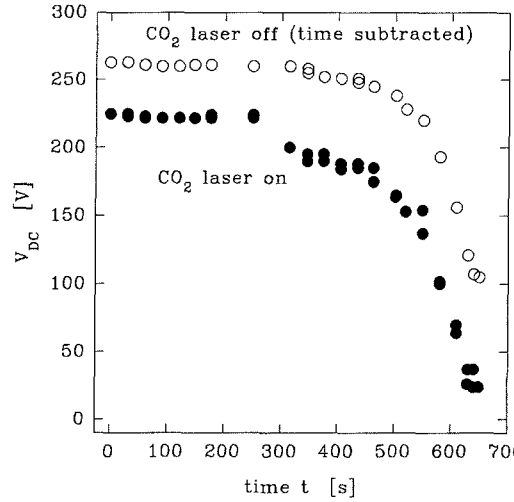

FIG. 3. Spherocarb particle oxidation in an electrodynamic balance with CO_2 laser heating. DC balancing voltage vs actual reaction (laser heated) time.

Measurement of Natural Convection and Photophoresis:

The force balance on a particle that is suspended at the center of the EDB and is irradiated from the bottom is given by

$$mg = \frac{qc}{z_0} V + F_c + F_p \qquad (2)$$

where the weight of the particle is balanced by a combination of the force generated by the DC voltage, the natural convection F_c, and the photophoresis F_p. The method of operation was to interrupt the laser heating at periodic intervals using the laser shutter. It had been previously determined that the time constant for cooling of particles was of the order of tens of milliseconds [4]. The voltage V_0, once the particle is at ambient temperature, provides a measure of particle mass, $mg = qV_0c/z_0$. Additional information is provided by the change in voltage $V_0 - V$ with and without laser heating. This difference provides a measure of the combined natural convection and photophoretic forces: $F_c + F_p = (V - V_0)mg/V_0$.

Results

The balancing voltages V_0 and V with and without laser irradiation are shown in Fig. 2 for the case of heating from below. The temperature to which the particle is heated is 790 K. When the laser heating is interrupted at the start of a run, the balancing voltage is seen to drop by about 50 V, or a little less than 20% of the voltage needed to balance a particle. For a period of about 1000 s, the voltage is seen to change little with time. After this induction period, the balancing voltage is seen to drop and the difference in voltage with and without heating to increase to about 100 V, or about 80% of the voltage needed to balance a particle. Since the time of interest is that in which the particles are reacting, the data are replotted in Fig. 3 as a function of only the time during which the particles were heated or reacted. The induction time before the reaction rate begins to accelerate corresponds to a period during which the particles were heated for 350 s. During this initial period, little seems to occur to the diameter, the particle shape, or the difference $V - V_0$ in balancing voltage.

From here on out, the results will be presented as a function of carbon conversion rather than time. The changes in density and diameter are shown in Fig. 4. The shrinkage in the particle diameter is consistent with the results obtained earlier for chemically induced ordering of the carbon structure [3]. The slight decrease in density shows that the shrinkage in particle volume does not quite compensate for the loss in mass. An additional observation made was that the particles heated from below developed into oblate ellipsoids over time. Examination of the progressive reaction frame by frame showed that the particles were consumed preferentially from the bottom but as they became top-heavy would flip over so that the preferential carbon consumption, although always occurring on the bottom heated surface, was evened over the top and bottom of the particle as a result of the periodic flipping over of the particle. In order to confirm that the distortion of the particles

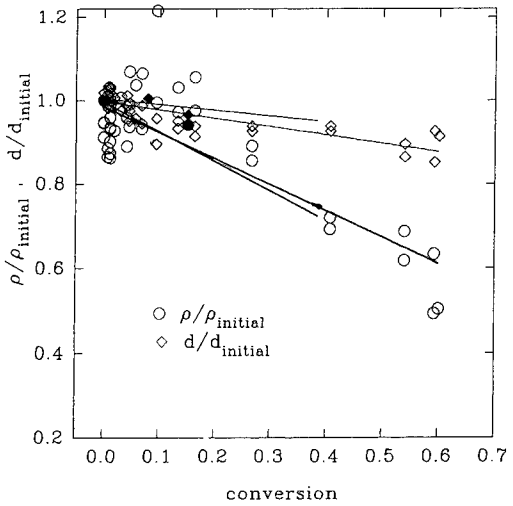

FIG. 4. Spherocarb particle oxidation in an electrodynamic balance with CO_2 laser heating. Dimensionless particle diameter and particle density vs conversion.

was due to uneven heating, the Spherocarb particles were reacted on a pan in a thermogravimetric analyzer, periodically extracted, and examined under a microscope. Under these conditions, no departure from symmetrical carbon consumption was observed. Silhouettes of particles reacted in the EDB heated from below, which showed the major change in shape, and from the TGA are shown in Fig. 5 for selected carbon conversions.

Discussion

The major difference in this study from that of previous studies is the difference in balancing voltage with and without laser heating. This difference provides interesting new insights on the evolution of pore structure during reaction. The sum of the forces normalized by the *actual* (not initial) weight of the particle is shown as a function of carbon conversion in Fig. 6. The large number of points up to 0.05 conversion reflects the long induction time before the

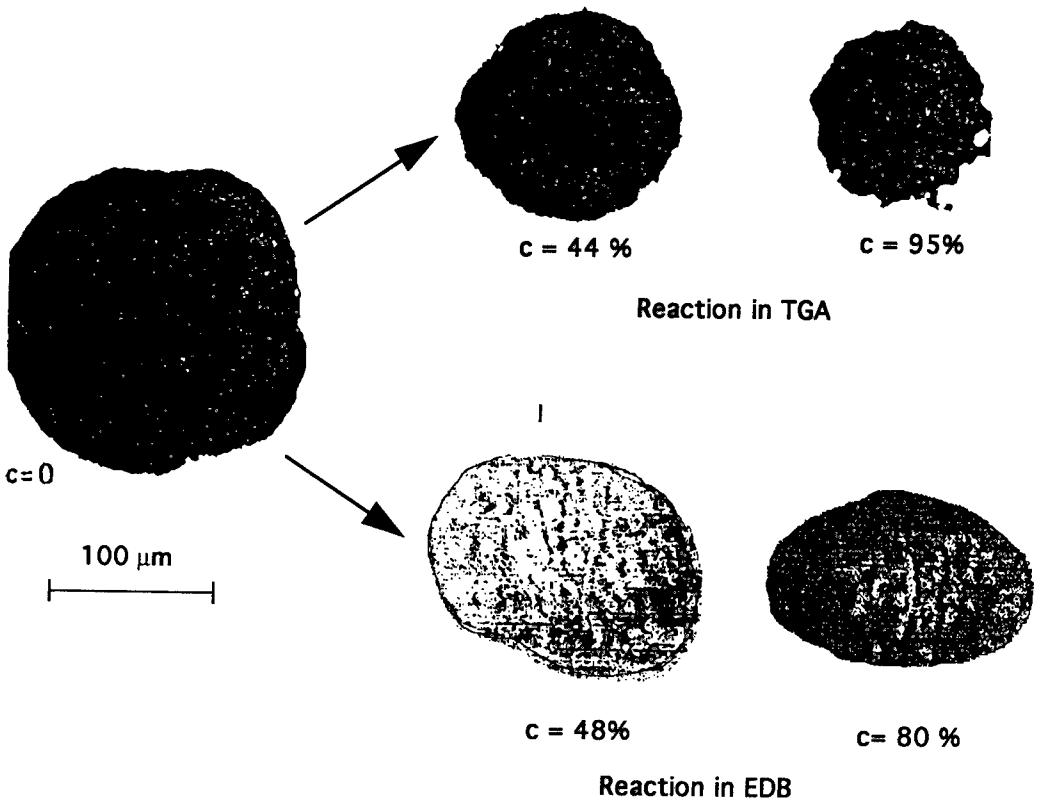

FIG. 5. Images of single Spherocarb particles at different conversions: zero conversion; 48% conversion, CO_2 laser heating from below in an EDB; 80% conversion, CO_2 laser heating from below in an EDB; 45% conversion, TGA experiment; 95% conversion, TGA experiment.

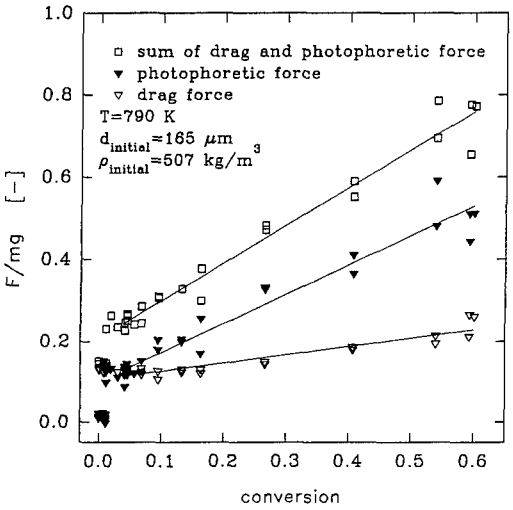

FIG. 6. Spherocarb oxidation in an EDB. 1. Sum of the photophoretic force and the drag force, 2. drag force, 3. photophoretic force, all divided by the actual particle weight plotted vs conversion. The error bars give an estimated maximum contribution of the nonsphericity on the drag force and the photophoretic force.

reaction accelerated. It can be seen that the sum of forces acting on the particle increases from about 0.15 times the weight near zero conversion (not visible because of overlap of data), rising rapidly up to 0.25 near 0.03 conversion, and increasing approximately linearly with conversion up to 0.8 at a carbon conversion of 0.6. In order to evaluate the photophoretic force, it is necessary to first separate the drag force F_c due to natural convection, using the previous experimental and computational study of natural convection from spheres at low Grashoff numbers by Dudek et al. [6]. The drag force using the measured particle diameter and temperature is plotted in Fig. 6. The natural convection accounts for most of the observed imposed force at zero conversion. The calculated natural convection force over the weight of the particle is approximately constant since the decrease in diameter just about compensates for the change in mass of the particle.

Photophoresis:

The photophoretic force is determined from the difference of the total force measured by the interrupted heating and the calculated natural convection. The photophoretic force increases up to a value equal to 0.6 times the weight of the particle at 60% carbon conversion.

The photophoretic force F_p on a particle of diameter d much greater than the gas mean free path and a particle density ρ_p, irradiated from one side with a flux density I [with units of energy/(area)(time)], is given by [7]

$$F_p = \frac{3\pi\mu^2 d[-dT/dz]}{2T_p\rho_g} \tag{3}$$

for the case of a particle conductivity much greater than the gas conductivity, where μ is the gas viscosity, ρ_g is the gas density evaluated at the particle temperature T_p, and $(-dT/dz)$ is the temperature gradient across the particle and can be approximated by

$$-\frac{dT}{dz} \cong \frac{I}{k_p} \tag{4}$$

where k_p is the particle conductivity. In the analysis, the particle is assumed to be black and opaque, although, if needed, the photophoresis may be calculated for any particle optical constants [8].

Particle Conductivity:

The photophoretic force can be used to obtain thermal conductivity. First, an energy balance on the particle can be used to relate the temperature of the particle to the incident flux density, to give [4]

$$I = \frac{8k_g(T_p - T_g)}{d}. \tag{5}$$

Equations (3) through (5) can be combined to obtain the following relation between the photophoretic force and the ratio of gas to particle conductivities:

$$\frac{F_p}{mg} = \frac{72\mu^2(T_p - T_g)}{gT_p\rho_g\rho_p d^3}\frac{k_g}{k_p}. \tag{6}$$

The ratio of thermal conductivity to particle conductivity obtained using Eq. (6) is shown in Fig. 7. It is difficult to obtain a value of the solid conductivity close to 0% conversion since the natural convection dominates. But the thermal conductivity falls rapidly and can be already estimated at 5% carbon conversion. Furthermore, the conductivity decreases by more than an order of magnitude as the fractional carbon conversion increases from 0.05 to 0.5.

The thermal conductivity provides an interesting measure of the interconnectivity of the solid space in the char. The Spherocarb particles have much of their porosity in included bubbles. It is therefore instructive to compare the changes in conductivity obtained here with the models presented in the literature. One of the first is due to Maxwell. This model treated the conductance of regularly spaced spheres of one conductivity in a continuous matrix of a second conductivity [9], but it is inadequate for handling high-porosity solids where the voids are overlapping.

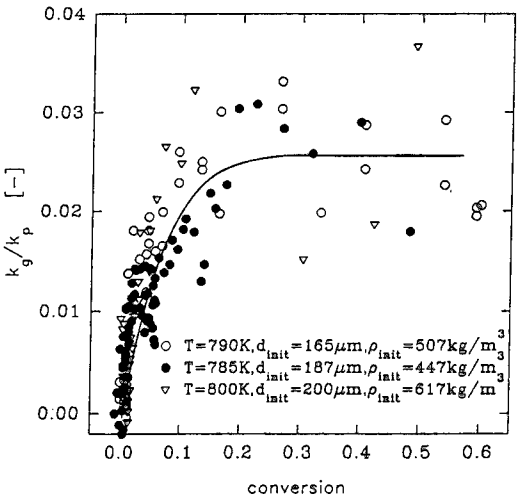

FIG. 7. Spherocarb oxidation in an EDB. The ratio of the gas conductivity to the particle conductivity estimated from the photophoretic force vs conversion.

The case of random overlapping spherical spheres has been handled by Kim and Torquato [10]. For gaseous voids that are not conducting, this model provides the ratio of the effective particle conductivity to the solid conductivity as a function of the void volume fraction ϕ. The Spherocarb particles are on average 70% void prior to reaction. Since the density decreases by a factor of up to 0.5 (at a conversion of 0.6), the void fraction ϕ will increase up to a value of 0.85. For this carbon conversion, the present study shows k_g/k_p to have values of about 0.025, corresponding to k_p values of 2.29 W/(m)(K). The analyis of Kim and Torquato gives values of 0.05 for the ratio of the effective to solid conductivity at $\phi = 0.85$. The conductivity of the solid matrix would therefore be 46.4 W/(m)(K). This value can be compared to those of extruded polycrystalline graphitic carbon, which mostly lie, at 790 K, in the range of 20–100 W/(m)(K) [11]. The extraction of conductivity at different conversions gives slightly different values of the conductivity of the continuous matrix, showing that the overlapping void model gives a reasonable but imperfect approximation of the porosity in Spherocarb at different stages of conversion. This illustration, however, demonstrates how the ability to measure the thermal conductivity of individual particles provides an additional test of the models for pore evolution during oxidation.

Particle Asphericity:

The development of oblate ellipsoids provides a confirmation of the temperature gradient across a particle when heated from below. From Eqs. (4) and (5), it may be shown that the maximum temperature difference across a particle is about $8(T_p - T_g)(k_g/k_s)$. For the bottom heating experiments, this can yield temperature differentials across a particle of greater than 50 °C after 10% conversion. Since the activation energy for the reaction of Spherocarb is about 36 kcal/mol, this temperature differential would provide a factor of 3 difference in the rate of reaction between the top and bottom of the particle, sufficient to explain the preferential consumption of carbon at the bottom of a particle. The temperature differential will increase as the particle conductivity decreases with increasing conversion, which explains the evolution of disk-shaped particles [12]

Induction Time:

The induction for the chemical reaction has been observed previously in thermogravimetric studies of Spherocarb oxidation and is in part due to the transient buildup of surface oxide complexes [13]. Clearly, the induction time for conduction is coupled to that in reaction, but it is not clear at this time why there is such a strong dependence of conductivity on conversion at the low conversions. The 5% of the carbon consumed must have been distributed in critical conduction paths, as the difference in porosity between 0 and 5% conversion is not large.

Fragmentation:

A further check of porosity models is provided by the fragmentation behavior of particles. As particles approach complete conversion, it is difficult to stabilize them in an EDB. Complementary experiments were therefore carried out in a conventional thermogravimetric analyzer. The particles were reacted to 95% conversion, and the decrease in diameter was measured using an optical microscope. The mean and standard deviation of the diameter for a sample size of 10 particles are shown in Fig. 8. The results show evidence of particle shrinkage, as had been observed previously [3]. However, the particles showed no evidence of fragmentation even at the highest conversions. Since the particle volume decreased by a factor of 0.32, for a particle with initial porosity of 0.7 the final porosity is 0.955. These results are supportive of the models such as the random spherical void model [14] that predict that percolation occurs only at high porosities (0.97).

Concluding Comments

The use of interrupted heating in the EDB provides a means of measuring the sum of the natural convection and photophoretic forces acting on a particle. For an unreacted char, the thermal conductivity is high enough that the natural convective drag force overwhelms the photophoretic force. However,

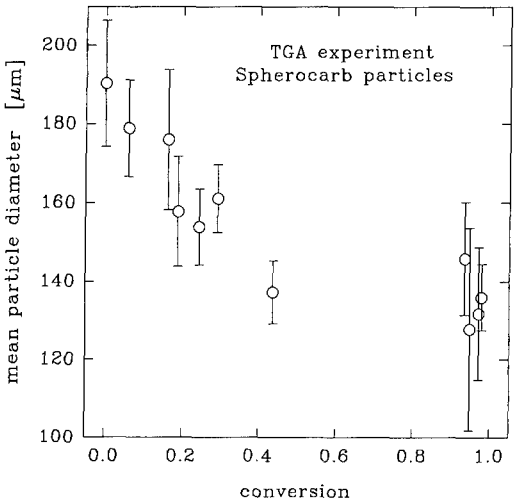

FIG. 8. Diameter of Spherocarb particles oxidized in a thermogravimetric analyzer in pure oxygen vs conversion (one point corresponds to the mean diameter of 10 measurements, and the error bars represent the standard deviation).

as the porosity of a particle increases, the thermal conductivity decreases to the point that the photophoresis can be measured and used to calculate the thermal conductivity. The values of the thermal conductivity, providing a measure of the connectivity of the solid portions of the carbon, provide an additional test for models on the evolution of pore structure during oxidation. The results on the Spherocarb are qualitatively consistent with the predictions of models that treat the char as a matrix containing randomly distributed voids.

Acknowledgments

The authors are grateful to the following for partial support of the study: the United States-Israel Binational Science Foundation (Grant No. 88-157), the Israel Ministries of Science and Technology and Absorption in Science, the U.S. DOE (Grant No. DE-FG22-91PC91294), and the Austrian Science Foundation. They are grateful to Dr. Alan Kerstein for discussions on models of conduction of porous solids.

REFERENCES

1. Kerstein, A. R., and Niksa, S., *Twentieth Symposium (International) on Combustion*, The Combustion Institute, Pittsburgh, 1984, pp. 941–949.
2. Hurt, R. M., Dudek, D. R., Longwell, J. P., and Sarofim, A. F., *Energy Fuels* 26:443–449 (1988).
3. Hurt, R. M., "Reactivity Distributions and Extinction Phenomena in Coal Char Combustion," Paper WSS/CI3–019, Western States Meeting of Combustion Institute, Salt Lake City, UT, March 1993.
4. Bar-Ziv, E., and Sarofim, A. F., *Prog. Energy Combust. Sci.* 17:1–65 (1991).
5. Bar-Ziv, E., and de Botton, G., *Aerosol Sci. Technol.* 15:1–7 (1991).
6. Dudek, D. R., Fletcher, T. H., Longwell, J. P., and Sarofim, A. F., *Int. J. Heat Mass Transfer* 31:863–873 (1988).
7. Fuchs, N. A., *Mechanics of Aerosols*, Pergamon, Oxford, U.K., 1964.
8. Pluchino, A. B., *Appl. Opt.* 22:103–106 (1983).
9. Maxwell, J. C., cited in Carslaw, H. S., and Jaeger, J. C., *Conduction of Heat in Solids*, Oxford University Press, Oxford, U.K., 1959, p. 428.
10. Kim, I. C., and Torquato, S., *J. Appl. Phys.* 71:2727–2735 (1992).
11. Purdue University Thermophysical Properties Research Center, *Thermophysical Properties* (Touloukian, Y. S., Ed.), Plenum, New York, 1970, Vol. 2.
12. Weiss, Y., and Bar-Ziv, E., "Further Development of the Electrodynamic Chamber and Non Uniform Shrinkage during Oxidation of Char Particles," *Combust. Flame* 95:362–373 (1993).
13. Floess, J. K., Ph.D. Thesis, Chemical Engineering Department, Massachusetts Institute of Technology, Cambridge, MA, 1985.
14. Elam, W. T., Kerstein, A. R., and Rehr, J. J., *Phys. Rev. Lett.* 52:1516–1519 (1984).

Twenty-Fifth Symposium (International) on Combustion/The Combustion Institute, 1994/pp. 527–535

A TRANSIENT KINETICS STUDY OF THE COMBUSTION REACTIVITY OF A COAL CHAR

P. SALATINO, F. ZIMBARDI AND M. PAULICELLI
Dipartimento di Ingegneria Chimica
Universita' "Federico II"
Istituto di Ricerche sulla Combustione—C.N.R.
P.le V. Tecchio, 80125 Napoli, Italy

Transient kinetics experiments have been used to characterize the combustion reactivity and the reactive surface area of char obtained from a bituminous coal. They consisted of isothermal-pulsed combustion of char samples with reiterated combustion and desorption stages. Experiments showed that the combustion rate passed through a sharp maximum at the beginning of each combustion stage, to decline afterwards as the carbon conversion degree increased. Combustion rate and reactive surface area have been determined as functions of the carbon conversion degree and of the oxygen partial pressure during the combustion stage. Direct correlation between combustion rate and reactive surface area is satisfactory at low-oxygen partial pressure; it becomes poorer when data at higher pressure are included in the comparison.

A descriptive model based on a Monte Carlo simulation technique has been developed to shed light on some features of transient and steady behaviour observed in experiments. In particular, the relevance of nonuniform reactivity of the exposed surface to the combustion behaviour and to overall char reactivity is assessed on the basis of qualitative comparison between model calculations and experimental results. Simulation results suggest that a pronounced "screening effect" of more stable surface oxides with respect to more reactive ones takes place. It should be responsible for the sharp maxima observed in the combustion rate vs time experimental relationship at the beginning of the combustion stages. The model predicts the steady combustion rate to be lower than that obtained by averaging the intrinsic reactivity of different classes of active sites on the basis of their concentrations in the unconverted solid.

Introduction

One of the challenging issues in combustion science is the problem of defining some "intrinsic" reactivity index of carbons towards oxygen, by correcting the observed burning rates for the effects of intraparticle diffusion and of the chemical and morphological heterogeneity of the solid. The first level approach to this problem is that of relating apparent combustion rates measured under conditions of chemical kinetic control (commonly indicated as regime I conditions) to the total surface area (TSA) of the carbon. This approach, although simple, presents significant drawbacks:

1. The TSA is measured by physical adsorption of gases different from oxygen at temperatures far below those at which combustion takes place; it is questionable whether the same surface is "seen" by oxygen molecules at temperatures of practical interest in combustion. This point has been addressed by several authors [1–5]; and
2. reference to TSA *tout court* hides the heterogeneous character of the carbon surface, which is actually made up of regions of different reactivity depending on the local concentration and chemical reactivity of active sites. The subject is extensively surveyed in review articles by Laurendeau [6], Essenhigh [7], and more recently, by Walker [8].

The substantial inadequacy of this procedure is confirmed by the analysis of a body of data carried out by Smith [9], who observed large discrepancies between "intrinsic" reactivities (i.e., combustion rates normalized with respect to TSA) of carbons of various nature at the same temperature and oxygen partial pressure.

In the attempt to overcome these drawbacks, some authors [10–13] have devised transient kinetics (TK) experimental techniques. These are based on the analysis of the dynamic response of a batch of carbon burning in an environment containing a time-dependent oxygen concentration, typically according to step or square pulse profiles. The amount of carbon desorbed as CO or CO_2 after oxygen feed is suddenly interrupted can be related to the amount of surface oxide formed during combustion and unstable at the reaction temperature. This value is eventually worked out to yield the reactive surface area (RSA) of the carbon; RSA, unlike TSA, is a function of temperature and oxygen partial pressure in addition to

TABLE 1
Properties of the South African coal

Net calorific value (kJ kg^{-1})	26,300
Proximate analysis (%)	
Moisture	2.3
Volatile matter	22.6
Fixed carbon	59.8
Ash	15.3
Ultimate analysis (%)	
on dry basis	
Carbon	68.0
Hydrogen	3.8
Sulfur	0.6
Nitrogen	1.2
Oxygen	10.9
Ash	15.5
Free-swelling index	
(ASTM D 720–67)	1–2
Random vitrinite reflectance	
(%)	0.72

the properties of the carbon. The importance of RSA as a normalizing surface for obtaining intrinsic combustion rates is widely discussed by Radovic and coworkers [10–12].

A study of the combustion reactivity of a coal char based on isothermal TK experiments is presented in the following. Experiments have been designed to investigate the influence of oxygen partial pressure and of carbon burnoff on the combustion rate and on the RSA. A descriptive model, based on a simple representation of the solid as a two-dimensional (2D) square lattice made up of cells of different reactivity, is used to simulate the observed behaviour and to shed light on the influence of the existence of sites of different reactivity on the overall combustion rate.

Experimental

Materials:

The carbon used in the experiments is char obtained from quick devolatilization of particles of South African bituminous coal. The properties of the coal are reported in Table 1. Coal devolatilization was carried out by feeding particles about 2–3 mm in size into a bed of silica sand (300–400 μm in diameter) fluidized with nitrogen at a temperature of 1123 K for about 5 min. Particles were then retrieved, ground, and sieved to obtain samples in the size range of 75–125 μm. Ash content of the char is 20% by mass.

Gases used in TK experiments were oxygen-nitrogen mixtures of technical grade during the combustion stages and helium of chromatographic grade during the desorption stages.

Apparatus and Technique:

The experimental apparatus consisted of a 15-mm i.d. vertical tubular quartz reactor. The lower section of the reactor, filled with quartz powder, served as a gas preheater. In the upper section, about 50 mg of char sample were introduced, sandwiched between two quartz wool plugs. The char sample was thoroughly mixed with about 1 g of quartz powder 100 μm in size in order to minimize the possible occurrence of hot spots under combustion conditions. The reactor was electrically heated in a tubular furnace equipped with a proportional-integral-differential (PID) temperature controller. The sample temperature was monitored by means of a type K shielded thermocouple 1 mm in diameter placed inside the bed.

Samples were dried at 380 K overnight prior to the TK experiments. They were outgassed by rapid heating to the temperature of 1123 K for about 2 min under nitrogen atmosphere, followed by rapid cooling to the test temperature. The TK experiments were carried out isothermally at 693 K. Each run consisted of the iteration of a cycle of a combustion (C) and a desorption (D) stage pursued until complete conversion of the sample was achieved. During the C stage, oxygen-nitrogen mixture at the desired oxygen concentration was fed to the reactor at the flow rate of 60 NL/h. During the D stage, helium was fed at the same flow rate. The C stages lasted from a few minutes to about 1 h, depending on the oxygen partial pressure. The D stages lasted 20 min under all the experimental conditions. On the whole, each TK run consisted of 5–7 complete C + D cycles. During the run, gases leaving the bed were continuously drawn through a probe and analyzed by means of a Hartmann Braun Uras 3E NDIR gas analyzer to monitor CO and CO_2 molar fractions at the outlet, X_{CO}, and X_{CO_2}, respectively.

The residence time distribution (RTD) of the transfer line and of the gas analyzer has been evaluated by means of separate pulse experiments using CO_2 as a tracer. The RTD could be approximated satisfactorily by that of a sequence of three continuously stirred tank reactors (CSTR) with an overall space time of 2.5 s and a variance of 2.2 s^2. Although very limited, the influence of the transfer line and of the analyzer on the dynamic response was accounted for by deconvolution of the measured concentration signal.

Rates of carbon removal were obtained as $F(X_{CO} + X_{CO2})$, where F is the total molar flow rate of gas through the bed. Results have been expressed in terms of the carbon conversion degree $f = (m_0 - m)/m_0$, where m_0 and m are, respectively, the initial

and the actual mass of carbon in the reactor and of the rate of change of f, $df/dt = (-1/m_0)(dm/dt)$.

Theory

The TK experiments have been simulated by means of a descriptive model based on a Monte Carlo technique. In view of the descriptive character of the model, a number of simplifying assumptions have been made, which are not believed to significantly affect the qualitative comparison between experimental results and model calculations.

The solid is represented by means of a 2D square lattice (Fig. 1). Only the upper side of the lattice is exposed to the gaseous atmosphere. Periodic boundary conditions are imposed on its lateral sides. Each cell of the lattice represents a reactive site. It is assumed that two types of reactive sites are present, denoted with C_1 and C_2. Prior to starting the simulation, each cell of the lattice is marked at random as either C_1 or C_2 according to a fixed value of site concentration $a = C_1/(C_1 + C_2)$.

Many different combustion mechanisms have been proposed in the literature, either for noncatalytic [6,14] or for catalytic [15] oxidation of carbon. For the sake of simplicity, the simple combustion mechanism based on two steps, first-order nondissociative oxygen adsorption and zero-order desorption, is assumed [16]. Oxygen chemisorbs irreversibly onto reactive sites, according to

$$C_i + \frac{1}{2} O_2 \rightarrow C_i(O); \qquad r_a = k_a \cdot p; \qquad i = 1,2 \quad (1)$$

where r_a expresses the frequency at which sites undergo adsorption, p is oxygen partial pressure, and k_a is the adsorption constant. A single adsorption constant k_a is assumed regardless of the type i of the site. This simplifying assumption is consistent with the observation that activation energies for oxygen chemisorption are much less dependent on the type of site than are desorption activation energies [17]. Desorption occurs according to the following parallel paths:

$$C_1(O) \rightarrow CO, CO_2 \qquad r_{d,1} = k_{d,1} \quad (2)$$

$$C_2(O) \rightarrow CO, CO_2 \qquad r_{d,2} = k_{d,2} \quad (3)$$

with $k_{d,1} > k_{d,2}$, where $r_{d,i} = k_{d,i}$ represents the turnover frequency of sites i and $t_i = 1/k_{d,i}$ is the time after which a complex formed by oxygen chemisorption on an i site vanishes as either CO or CO_2. Surface migration of chemisorbed oxygen is not considered.

The TK experiment is simulated by sequences of combustion and desorption stages.

Combustion stage

The combustion stage consists of N_c discrete time steps. At each step, sites belonging to the frontier of the lattice, i.e., those which can be reached by oxygen, are flagged. Then N_a frontier sites are marked at random as chemisorbed, with N_a given by

$$N_a = k_a \cdot p \, N_{fr} \quad (4)$$

subject to the constraint $k_a \cdot p \leq 1$, where N_{fr} is the number of frontier sites. Chemisorption on a site already chemisorbed is ineffective. The time at which a site undergoes chemisorption designates the beginning of the site turnover interval: a counter associated with each chemisorbed site is updated at each step, and after t_i time iterations, the site is depleted. N_c is large enough to provide for steady combustion rate to be reached at the end of the combustion stage, before moving on to the desorption stage.

Desorption stage

No oxygen chemisorption occurs during this stage, and only desorption of previously chemisorbed sites takes place. At each time step, the counter associated with chemisorbed sites is updated, and sites are depleted when their turnover time t_i expires. Desorption is carried on until all chemisorbed sites have vanished.

Variables evaluated during the simulation procedure are the rate of site consumption, the total number of sites vanishing during the desorption stage (related to RSA), and the fraction of frontier sites of types 1 and 2. Input variables are the initial fraction a of sites of type 1, the product $k_a \cdot p$, and the desorption constants $k_{d,i}$, where $i = 1,2$. Computations have been performed using a CONVEX C210 vector computer.

Results and Discussion

Experimental Results:

Typical results of TK experiments are exemplified in Fig. 2, showing mole fractions of CO and CO_2 at the reactor outlet as a function of time during iterated combustion and desorption cycles. In the same figure, the CO_2/CO ratio is plotted as a function of time. Data in Fig. 2 were obtained at 0.21 atm oxygen partial pressure during the combustion stage. Experiments carried out at oxygen partial pressures of 0.1 and 1 atm yielded results qualitatively similar to those in Fig. 2. Apart from the initial spike at the beginning of each C stage, the CO_2/CO molar ratio in the exit gases was relatively constant during burnoff at the values of 2.9, 3.1, and 3.2 for 0.1, 0.21, and 1 atm oxygen partial pressure, respectively. The very limited change of the CO_2/CO ratio over a 10-fold

A

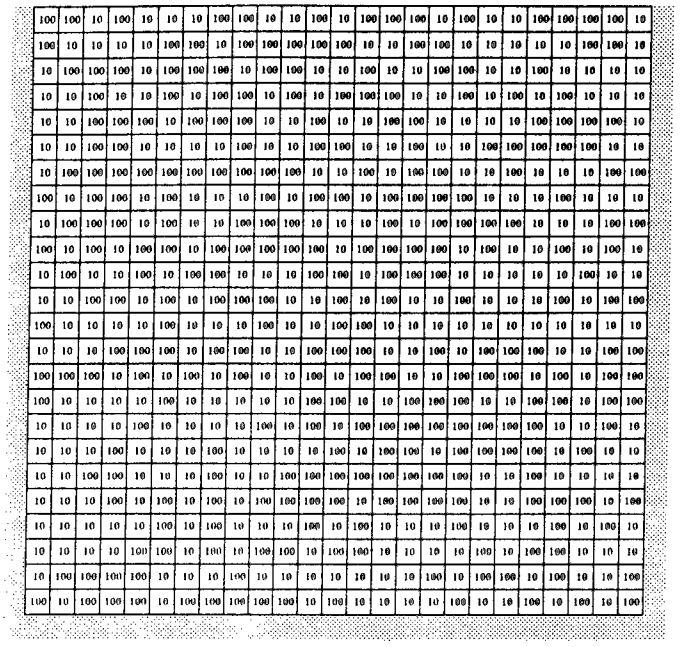

B

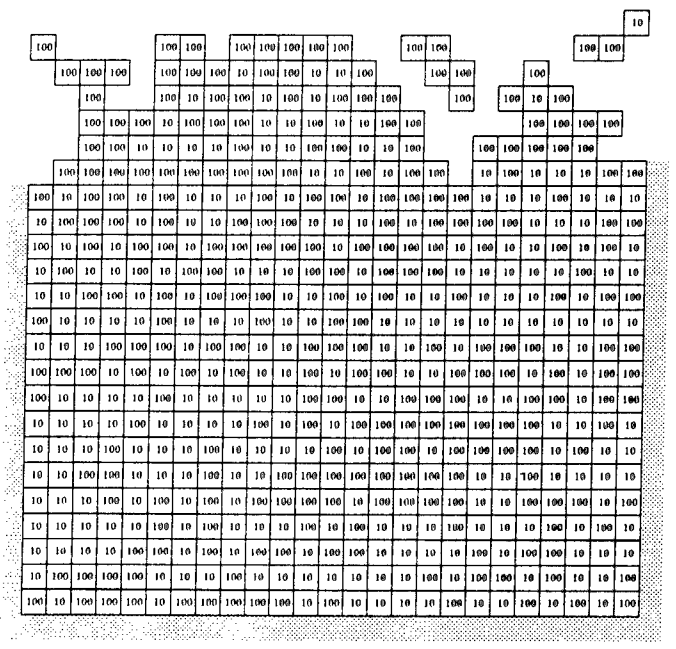

FIG. 1. 2D square lattice (24 × 25) representing the solid. Numbers in the cells are turnover times $t_i = 1/k_{d,i}$ associated with each site: (A) the lattice at the beginning of the computation ($a = 0.5$), (B) the lattice after 100 iteration steps in the combustion stage ($k_a \cdot p = 1$; $k_{d,1} = 0.1$; $k_{d,2} = 0.01$).

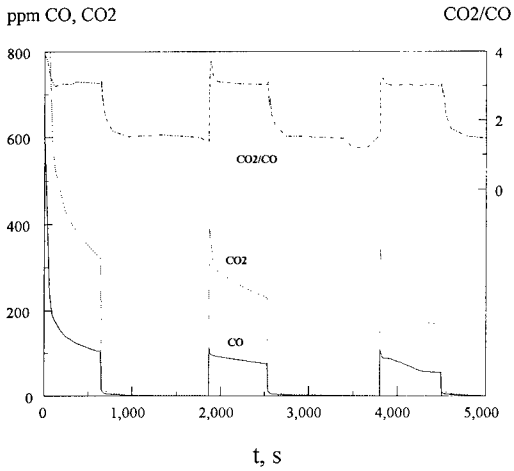

FIG. 2. Typical result of a TK experiment. Three cycles of C and D stages are represented: p = 0.21 atm during the combustion stage; T = 693 K; gas flow rate = 60 Nl/h.

change of O_2 concentration suggests that homogeneous CO oxidation was negligible. Values of CO_2/CO during combustion are larger than predicted by Tognotti et al. [18] and should be related to extensive catalytic effects of the inorganic constituents of the char.

The overall transient behaviour in the combustion stages appears to be the result of two combined effects: (1) a fast transient phenomenon occurring very early in the combustion stage and consisting of a sudden increase followed by rapid decay of the combustion rate as well as of the CO_2/CO ratio and (2) a slower decline of combustion rate with an almost constant CO_2/CO ratio as the carbon conversion degree increases. Notably, the maximum reaction rate at the beginning of each combustion stage is larger than that observed at the end of the previous combustion stage. Similar phenomena have been reported by Brown et al. [13] (in both oxygen and steam gasification of carbon) and previously by Tucker and Mulcahy [19], Bonnetain et al. [20], and Laine et al. [21]. Two mechanisms should be at work to explain the pulse of combustion rate at the beginning of the C stage. Tucker and Mulcahy suggested that the observed decay of reaction rate is the result of the desorption of unstable surface oxides followed by the building up of stable surface complexes, which limits further progress of reaction. In this respect, the desorption stage between two successive combustion stages would have a regenerating effect on the surface, providing enough time for more stable surface oxides to be desorbed and restoring a higher level of surface reactivity. Another factor to explain pulses of combustion rate might be possible: the heating up of carbon particles due to oxygen chemisorption at the beginning of the C stage. Oxygen chemisorption has proved to be largely exothermic, integral heats of adsorption as large as 60 kcal/mol being reported in the literature [22,23]. Thermal effects during early oxygen chemisorption of coal chars in a DTA have also been reported by Brown et al. [13]. With reference to the present experiments, it can be evaluated that particle temperature might increase by as much as 15 K if chemisorption of an amount of oxygen equal to that desorbed during the D stages would occur adiabatically. It must be noted, however, that in the present experiments the char sample was thoroughly dispersed in a bed of quartz powder. The characteristic thermal diffusion time under unsteady heat generation conditions can be conservatively estimated as $\tau_h = d_p^2/a_h \sim 0.05$ s, where a_h is the relevant thermal diffusivity ($a_h \sim 10^{-4}$ m^2/s for air, $\sim 10^{-7}$ m^2/s for quartz or char). It follows that transient combustion rate associated with nonisothermal behaviour, if any, should take place over a timescale much shorter than the decay time observed in experiments. In addition, the slight, though appreciable, increase of the CO_2/CO ratio at the beginning of the C stage (observed also by Brown et al. [13]) further reinforces the idea that fast depletion of reactive sites (yielding preferentially CO_2) and building up of less reactive surface oxides is relevant to the observed transient behaviour.

Values of CO and CO_2 concentration measured after the fast decay at the beginning of the combustion stage have been worked out to obtain "steady" combustion rates df/dt as a function of carbon burnoff f and of oxygen partial pressure p. The ratio df/dt has been found to vary almost linearly with oxygen partial pressure, as is apparent from Fig. 3, where $(df/dt)/p$ is reported as a function of carbon burnoff. The question regarding the reaction regime associated with combustion of the same char at temperatures around 690 K has been addressed in Refs. 1 and 2, where it was concluded that combustion essentially occurs on the surface of meso- and macropores, whereas microporous domains are negligibly penetrated by oxygen. The persistence of diffusional resistances within micropores, in spite of the low temperature at which combustion is carried out, might partly explain the reaction order close to unity.

The CO_2 and CO concentrations rapidly drop at the beginning of the D stage, and so does the CO_2/CO ratio, consistently with a mechanism that associates larger CO_2/CO ratios to the desorption of more reactive sites. Data obtained in the desorption stage are worked out to yield the value of RSA, according to the following equation:

$$\mathrm{RSA} = \frac{1}{m_0}\int_0^{t_d} F(X_{\mathrm{CO}} + 2X_{\mathrm{CO_2}})\,dt \qquad (5)$$

where t_d is the duration of the desorption stage. In

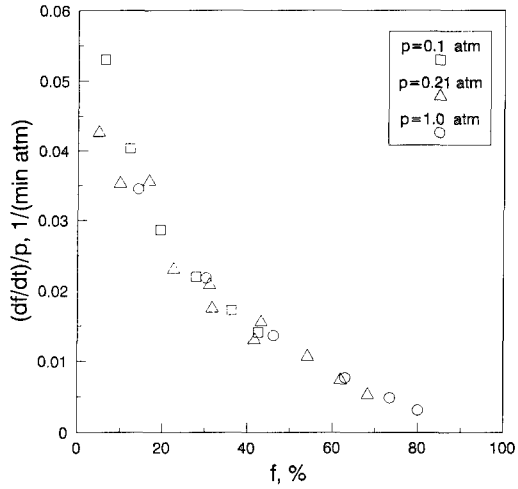

FIG. 3. Rate of change of carbon conversion degree per unit oxygen partial pressure $(df/dt)/p$ vs f for different oxygen partial pressures in the combustion stage.

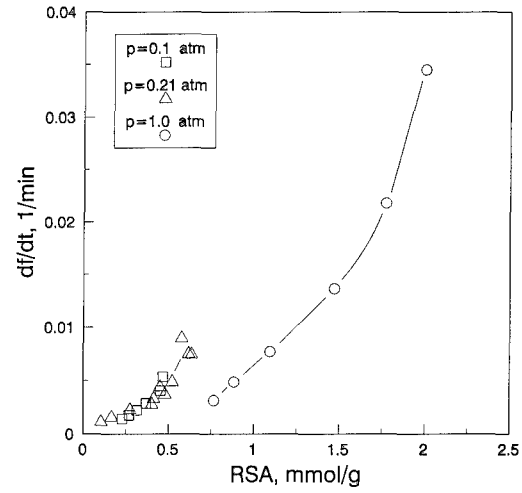

FIG. 5. Correlation between df/dt and RSA.

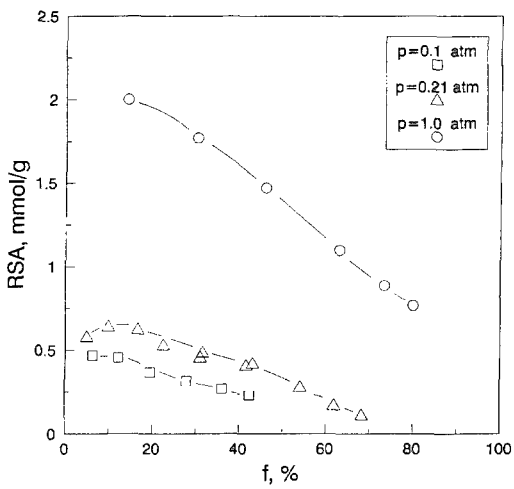

FIG. 4. RSA vs f for different oxygen partial pressure during the combustion stage.

view of the difficulty of assigning a precise value to the surface occupied by a surface oxide, RSA has been expressed as mmoles of atomic oxygen desorbed per gram of carbon initially charged into the reactor. Carbon removal during the desorption stage contributed negligibly to burnoff. Values of RSA measured at different carbon conversion degrees and oxygen partial pressures are given in Fig. 4.

Figure 5 represents a cross plot of Figs. 3 and 4 with the purpose of directly correlating combustion rate df/dt to RSA at any burnoff and oxygen partial pressure. Correlation is rather good at the lower oxygen partial pressures but deteriorates when data at $p = 1$ atm are compared with those for the lower pressures. This implies that the goal to obtain, through RSA, a simple index to express the intrinsic reactivity of the char is only partially reached: the same value of df/dt (0.007) is observed, for instance, at $p = 0.21$ atm, $f = 0.1$ and at $p = 1$ atm, $f = 0.6$, whereas values of RSA corresponding to the two conditions differ, being 0.6 mmol/g and 1.2 mmol/g, respectively.

Model Calculations:

A 100×1000 lattice made up of an equal number of C_1 and C_2 sites ($a = 0.5$) has been used to represent microporous domains of the char not penetrated by oxygen [1,2].

Values of the product $k_a \cdot p$ and of $k_{d,1}$ and $k_{d,2}$ have been changed so as to compare results corresponding to the three cases:

$$k_a \cdot p > k_{d,1} > k_{d,2}$$

$$(k_a \cdot p = 1; \quad k_{d,1} = 0.1; \quad k_{d,2} = 0.01) \quad \text{(a)}$$

$$k_{d,1} > k_a \cdot p > k_{d,2}$$

$$(k_a \cdot p = 0.1; \quad k_{d,1} = 1; \quad k_{d,2} = 0.01) \quad \text{(b)}$$

$$k_{d,1} > k_{d,2} > k_a \cdot p$$

$$(k_a \cdot p = 0.01; \quad k_{d,1} = 1; \quad k_{d,2} = 0.1) \quad \text{(c)}$$

The values of $k_a \cdot p$ and $k_{d,i}$, as well as of a, used in the computations have no direct relation with the

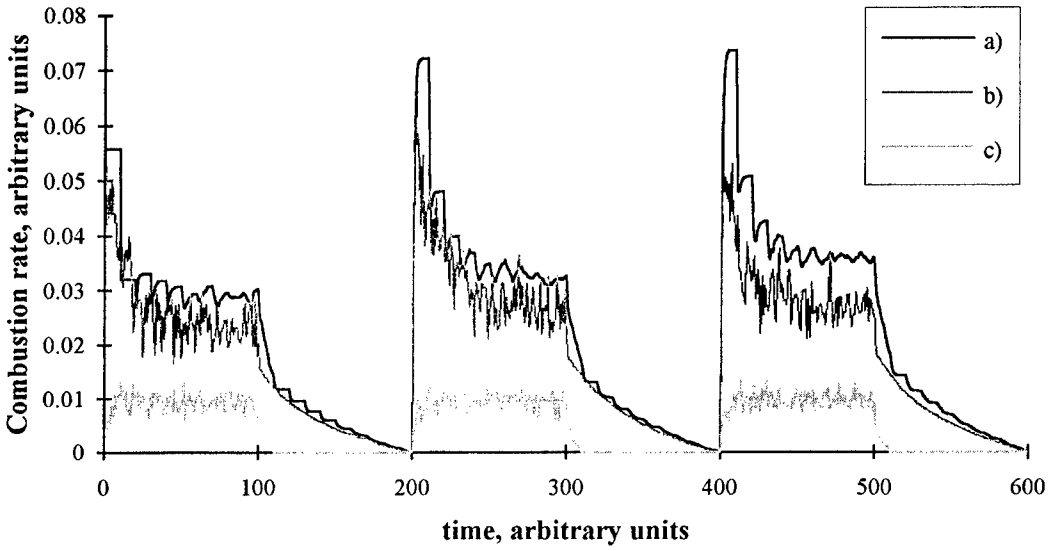

FIG. 6. Combustion rate vs time relationship from the Monte Carlo simulation model. Case (a): $k_a \cdot p = 1$; $k_{d,1} = 0.1$; $k_{d,2} = 0.01$. Case (b): $k_a \cdot p = 0.1$; $k_{d,1} = 1$; $k_{d,2} = 0.01$. Case (c): $k_a \cdot p = 0.01$; $k_{d,1} = 1$; $k_{d,2} = 0.1$.

real experiment. They have been arbitrarily chosen with the only purpose of shedding light on the qualitative aspects of transient kinetics experiments. Results are shown in Fig. 6 as profiles of the carbon combustion rate per unit char surface area vs time. Close similarity between curves for cases (a) and (b) and those obtained in experiments (Fig. 2) is observed. A sudden increase followed by a fast decay of the combustion rate occurs at the beginning of the combustion stage when combustion is fully or partially controlled by the rate of desorption. This is due to preferential consumption of the more reactive C_1 sites and to the building up of the slowly reacting C_2 sites on the exposed carbon surface. The latter act as a screen towards further combustion of C_1 sites. This "screening effect" is expected to be markedly dependent on the topology of the spatial distribution of sites, expressed, among others, by the site coordination number and by the lattice dimensionality. During the desorption stage, enough time is allowed for complete desorption of both C_1 and C_2 sites. This regenerates the initial status of the surface ($a = 0.5$) and increases the average surface reactivity for the subsequent combustion stage.

The transient behaviour is different when the adsorption rate $k_a \cdot p$ is smaller than the desorption rate of any site (case (c)). At the beginning of each combustion stage, there is an induction interval during which the reaction rate increases, as the surface coverage of sites by chemisorbed oxygen, wiped out during the previous desorption stage, is regenerated by the slow adsorption process. The relative abundance of surface sites of the two types (C_1 and C_2) stays nearly constant and equal to the bulk value of $a = 0.5$.

Steady combustion rates r_s per unit surface area of carbon are 0.036, 0.026, and 0.0092 for cases (a), (b), and (c), respectively (Fig. 6). If r_s is calculated according to the Langmuir–Hinshelwood (LH) kinetic model applied to series-parallel paths (1), (2), and (3) and assuming additive contributions to the reaction rate of sites C_1 and C_2 weighed by their concentrations a and $(1 - a)$, respectively, then the following expression is obtained:

$$r_{s,\mathrm{LH}} = k_a \cdot p \left(\frac{a}{\dfrac{k_a \cdot p}{k_{d,1}} + 1} + \frac{1 - a}{\dfrac{k_a \cdot p}{k_{d,2}} + 1} \right). \quad (6)$$

Equation (6) leads to $r_{s,\mathrm{LH}} = 0.0504$, $r_{s,\mathrm{LH}} = 0.050$, and $r_{s,\mathrm{LH}} = 0.0095$ in the cases (a), (b), and (c), respectively. The finding that $r_{s,\mathrm{LH}} > r_s$ in any case should warn about the assumption of additive contributions of sites having different desorption rates when evaluating carbon combustion rates from temperature programmed desorption (TPD) spectra [17]. The screening effect might increase the importance of the more stable active sites far beyond the level that would be expected on the basis of their concentration in the unconverted char. This is particularly so under desorption-controlled combustion conditions.

Conclusions

Transient kinetics (TK) experiments with iterated sequences of combustion and desorption have been directed to obtaining combustion rates and reactive surface areas (RSA) of char of a bituminous coal as a function of oxygen partial pressure and of the degree of carbon conversion. Attempts to correlate combustion rate directly to RSA at different oxygen partial pressures and carbon burnoff are not in every case satisfactory. The difference between reactivities of sites of different nature is the starting point to explain the sharp maximum combustion rate observed within the present work, and by previous authors, at the beginning of combustion stages during TK experiments.

A descriptive model assumes that the solid is made up of two types of reactive sites having different desorption rates, and it predicts sharp extremes in the reaction rate vs the time relationship when reaction is even partially controlled by the surface oxide desorption rate. The "screening effect" of less reactive sites with respect to more reactive ones is responsible for this behaviour and brings into the problem the effect of the topology of the spatial distribution of reactive sites in the solid matrix. No maximum in the combustion rate vs time relationship, but rather a smooth increase at the beginning of the combustion stage is predicted in the fully adsorption-controlled combustion of carbon. Because of the screening effect, steady combustion rates are smaller than those predicted according to the LH kinetic model with the assumption of additive contributions of sites having different reactivity.

Acknowledgments

The relentless guide of Professor Leopoldo Massimilla, who passed away during the preparation of this paper, is gratefully acknowledged. The authors are indebted to Mr. Sabato Masi for the precious assistance in the experimental work.

Notation

d_p	char particle diameter
df/dt	rate of change of carbon conversion degree
f	carbon conversion degree
F	total gas molar flow rate in the reactor
k_a	adsorption rate constant
$k_{d,i}$	desorption rate constant for sites of type i
m_0, m	initial and actual mass of carbon in the reactor
N_a	number of sites undergoing chemisorption per iteration step
N_c	number of time steps in the combustion stage
N_{fr}	number of sites belonging to the lattice frontier
p	oxygen partial pressure
r_a	adsorption frequency
$r_{d,i}$	i-site turnover frequency
r_s	steady combustion rate
$r_{s,\mathrm{LH}}$	steady combustion rate according to the LH kinetic model
RSA	reactive surface area
t	time
t_d	duration of the desorption stage
t_i	i-site turnover time
TSA	total surface area
$X_{\mathrm{CO}}, X_{\mathrm{CO_2}}$	molar fractions of CO and CO_2 in outlet gases
a	concentration of sites C_1 in the lattice
a_h	thermal diffusivity
τ_h	characteristic thermal diffusion time

REFERENCES

1. Salatino, P., Zimbardi, F., and Masi, S. *Carbon* 31:501 (1993).
2. Salatino, P., and Zimbardi, F., *Carbon* 32:51 (1994).
3. Floess, J. K., Longwell, J. P., and Sarofim, A. F., *Energy Fuels* 2:18 (1988).
4. Hurt, R. H., Sarofim A. F., and Longwell, J. P., *Energy Fuels* 5:290 (1991).
5. Hurt, R. H., Sarofim A. F., and Longwell, J. P., *Fuel* 70:1079 (1991).
6. Laurendeau, N. M., *Prog. Energy Combust. Sci.* 4:221 (1978).
7. Essenhigh, R. H., in *Chemistry of Coal Utilization,* Chap. 19 (M. A. Elliott, Ed.), 2nd Supp., Wiley, New York, 1981.
8. Walker, P. L., Jr., *Carbon* 28:261 (1990).
9. Smith, I. W., *Nineteenth Symposium (International) on Combustion,* The Combustion Institute, Pittsburgh, 1982, p. 1045.
10. Lizzio, A. A., Jiang, H., and Radovic, L. R., *Carbon* 28:7 (1990).
11. Radovic, L. R., Jiang H., and Lizzio, A. A., *Energy Fuels* 5:68 (1991).
12. Radovic, L. R., Lizzio A. A., and Jiang, H., in *Fundamental Issues in Control of Carbon Gasification Reactivity* (J. Lahaye and P. Ehrburger, Eds.), Kluwer Academic, Dordrecht, 1991, p. 235.
13. Brown, T. C., Lear, A. E., Ma, C., and Haynes, B. S., in *Fundamental Issues in Control of Carbon Gasification Reactivity* (J. Lahaye and P. Ehrburger, Eds.), Kluwer Academic, Dordrecht, 1991, p. 307.
14. Ahmed, S., and Back, M. H., *Carbon* 23:513 (1985).
15. Radovic, L. R., Walker, P. L., Jr. and Jenkins, R. G., *J. Catal.* 82:382 (1983).
16. Essenhigh, R. H., *Energy Fuels* 5:41 (1991).

17. Du, Z., Sarofim, A. F., Longwell J. P., and Mims, C. A., *Energy Fuels* 5:214 (1991).
18. Tognotti, L., Longwell, J. P., and Sarofim, A. F., *Twenty-Third Symposium (International) on Combustion,* The Combustion Institute, Pittsburgh, 1990, p. 1207.
19. Tucker, B. G., and Mulcahy, M. F. R., *Trans. Faraday Soc.* 65:274 (1969).
20. Bonnetain, L., Duval, X., and Letort, M., *Proceedings 4th Conference on Carbon,* Pergamon Press, Oxford, 1960, p. 107.
21. Laine, N. R., Vastola, F. J., and Walker, P. L., Jr., *J. Phys. Chem.* 67:2030 (1963).
22. O'Neil, M., and Phillips, J., *J. Phys. Chem.* 91:2867 (1987).
23. Essenhigh, R. H., *Twenty-Second Symposium (International) on Combustion,* The Combustion Institute, Pittsburgh, 1988, p. 89.

Twenty-Fifth Symposium (International) on Combustion/The Combustion Institute, 1994/pp. 537–544

PREDICTING THE EVOLUTION OF FUEL NITROGEN FROM VARIOUS COALS

STEPHEN NIKSA
Molecular Physics Laboratory
SRI International
333 Ravenswood Avenue, Menlo Park, CA 94025, USA

Nitrogen release from most coal types occurs by three mechanisms: tar shuttling, HCN production from char-N, and combustion of char-N. This modeling study extends FLASHCHAIN to characterize the first two N-release mechanisms for heating rates from 5 to 10^4 K/s, temperatures to 1550 K, pressures from vacuum to several atmospheres, and 13 coals of rank from sub-bituminous through low volatile bituminous. Based primarily on the accuracy of predicted tar yields, the agreement among predicted and observed evolution histories of tar-N, HCN, and char-N and the nitrogen contents of tar is within experimental uncertainty throughout this domain.

Under conditions of rapid heating, tar shuttling is the only mechanism for nitrogen release as long as tar is being expelled, but for slower heating conditions, it is overlapped by HCN production from char-N. The predictions correctly depict the rank dependence of nitrogen evolution, exhibiting a broad maximum for *hv* bituminous coals before falling off for low volatility coals. Tar shuttling is almost entirely responsible for this trend. Also, the predicted nitrogen contents of tar increase throughout primary devolatilization as cumulative tar yields grow, in accord with measured values. HCN production from char-N has an extremely broad thermal response that is well represented with a very broad distribution of activation energies. Predicted char-N and HCN evolution histories for numerous coals based on the same energy distribution are within experimental uncertainty of observed levels for several coal types, although indications that HCN production becomes slower for coals of progressively higher rank are also considered.

Introduction

Pulverized coal flames in utility boilers generate NO_x, primarily by converting nitrogen incorporated into the coal's organic components, because production by thermal mechanisms is effectively inhibited by regulating flame temperatures. The mechanisms for fuel nitrogen conversion with coal remain to be established, although they are already known to be far more complicated than the direct production of HCN that initiates fuel nitrogen conversion with most liquid and gaseous fossil fuels.

Fuel nitrogen is expelled in three stages during pulverized fuel firing. It is first liberated during primary devolatilization as a structural element in heavy, aromatic compounds collectively called tar [1]. Among succeeding stages, this one is the most sensitive to specific properties of different coal types. In the second stage, additional fuel nitrogen is expelled from char as HCN (and occasionally NH_3) on time scales that are considerably longer than those for tar evolution. At the same time, the volatiles undergo secondary and oxidative pyrolysis in hot, fuel-rich gases that convert some of the nitrogen in tar into HCN [2,3]. The remainder is incorporated into soot along with the aromatic components of tar molecules [4,5], counteracting the devolatilization of fuel nitrogen in the primary devolatilization stage. Eventually, in the third stage, oxygen contacts the char and soot, liberating additional nitrogen either by direct chemical conversion to NO or by thermal dissociations induced by the higher particle temperatures associated with char combustion.

Even though this phenomenology is reasonably well established by laboratory studies, it has never before been implemented in modeling because it has not been possible to predict the yields and evolution rates of tar within useful tolerances until very recently. Indeed, this paper demonstrates that, for the most part, reliable predictions of fuel nitrogen evolution rest upon accurate models for tar evolution, simply because tar is the main shuttle for fuel nitrogen during primary devolatilization and also because tar evolution depends on the coal properties more than any other aspect of devolatilization behavior.

In this modeling study, FLASHCHAIN, one of the newer depolymerization models for primary de-

*This paper is a Numerical Modeling Study (B) in the areas of (6.2) Coal and Organic Solids Combustion (7.1) Pyrolysis, Devolatilization, and Gasification (10.4) NO_x, SO_x, and Dioxins.

volatilization, is supplemented with concise mechanisms to account for nitrogen release via tar evolution and via HCN production from char nitrogen to simulate nitrogen evolution from diverse coal types. FLASHCHAIN is an ideal foundation for models of nitrogen evolution because the ultimate analysis is the only sample-specific information it requires to simulate any coal's devolatilization behavior at any operating conditions. This unique capability enables detailed comparisons among the predictions and a comprehensive database compiled from the results of several reported laboratory studies. The database represents heating rates from 5 to 10^4 K/s, pressures from vacuum to several atmospheres, and temperatures from 800 to 1500 K. It also features nitrogen species distributions and tar nitrogen contents from 13 different coal samples that represent ranks from subbituminous to low volatile bituminous.

Overview of the Theory

Only qualitative aspects of the devolatilization model are presented here because extensive formulations [6,7] and performance evaluations [8–10] are already available. In FLASHCHAIN, the coal's cross-linked macromolecular structure is modeled as a mixture of chain fragments ranging in size from a monomer to the nominally infinite chain. The diverse assortment of structural components in real coals is rendered coarsely with four generic structural components: aromatic nuclei, labile bridges, char links, and peripheral groups. Aromatic nuclei are refractory units having the characteristics of the hypothetical aromatic cluster based on ^{13}C nuclear magnetic resonance (NMR) analysis. They also contain all the nitrogen in the coal, consistent with x-ray photoelectron spectroscopy (XPS) characterizations that indicate a predominance of pyrrolic and pyridinic nitrogen in all coal types, with appreciable quaternary nitrogen only in low rank coals [3,11,12]. Except for HCN production from their nitrogen, nuclei are immutable. Nuclei are interconnected by two types of linkages: labile bridges or char links. Labile bridges represent groups of aliphatic, alicyclic, and heteroatomic functionalities, not distinct chemical bonds. They contain all the oxygen, sulfur, and aliphatic carbon, but no aromatic components. Being refractory, char links are completely aromatic with no heteroatoms.

In the model's four-step reaction mechanism, labile bridges are the key reaction centers because bridge conversion governs both tar and gas formation. Conversion of a bridge initiates two distinct reaction pathways, either to generate smaller fragments including precursors to tar or to form a new refractory char link accompanied by the immediate release of noncondensible gases. The pathway to char links depletes the bridge population without inducing fragmentation, thereby suppressing the production of tar precursors. For both processes, oxygen plays a distinctive role, accelerating the bridge conversion rate and shifting the selectivity between scission and spontaneous char condensation toward the production of char links. Of course, the oxygen concentration in bridges is a strong function of rank. Tar formation proceeds by the flash distillation analogy [13], in which a phase equilibrium relates the instantaneous mole fractions of like fragments in the tar vapor and condensed phase.

This framework for primary devolatilization is adapted to describe fuel nitrogen evolution by accounting for two additional processes: the release of nitrogen as a structural element in the aromatic nuclei in tar molecules and production of HCN from the nitrogen in aromatic nuclei throughout the condensed phase, collectively called char-N. Both processes are monitored in terms of the average moles of nitrogen per mole of nuclei in the condensed phase at any instant, denoted by η, assuming that the nitrogen in coal is randomly distributed among nuclei of different size and constitution. The conservation law for η relates the time rate of change of the total moles of nitrogen in the condensed phase to the production rates of HCN and tar-N. It can be shown that this relation reduces to a simple first-order process:

$$\frac{d\eta}{dt} = -k_{\mathrm{HCN}}\eta \qquad \eta(0) = \eta_0 \tag{1}$$

where

$$k_{\mathrm{HCN}} = -\frac{d}{dt}\left\{\ln\left[\int_0^\infty \exp\left(-\int_0^t Ae^{-E/RT(t')}dt'\right) \cdot f(E)\,dE\right]\right\}$$

$$f(E) = \frac{1}{\sqrt{2\pi}\,\sigma}\exp[-(E - E_{\mathrm{HCN}})^2/2\sigma^2]$$

η_0 = the initial moles of nitrogen per mole of aromatic nuclei, which is proportional to the weight fraction of nitrogen in the coal initially.

Instantaneous values for η appear in the production rate of HCN from char-N according to

$$\frac{dY_{\mathrm{HCN}}}{dt} = k_{\mathrm{HCN}}\left[\sum_{j=1}^{\infty} jx_j\right]\eta \quad Y_{\mathrm{HCN}}(0) = 0 \tag{2}$$

where Y_{HCN} is the molar yield of HCN. Once Y_{HCN} is evaluated, the HCN yields can be expressed as fractions of the coal's original mass or nitrogen content. The x_j are the moles of fragments with degree of polymerization j in the condensed phase. The summation, therefore, compiles the fraction of the original aromatic nuclei present in the condensed phase at any instant. The product of the instantane-

ous value of η and this summation also specifies the nitrogen content in char. The molecular weight of nuclei is also continuously updated to account for HCN release, based on the instantaneous value of η/η_0.

The nitrogen expelled with tar molecules is evaluated as the fraction of the original nitrogen in the cumulative tar mixture, f^{N}_{tar}, which is governed by

$$\frac{df^{N}_{tar}}{dt} = \frac{\eta}{\eta_0}\sum_{j=1}^{J^*} j\Gamma_j \qquad f^{N}_{tar}(0) = 0 \qquad (3)$$

where Γ_j is the evolution rate of tar molecules of degree of polymerization j, up to the maximum value J^*. The mass fraction of nitrogen in tar can be determined from f^{N}_{tar}.

Model Parameters

FLASHCHAIN's extended submodel for coal constitution [7] drastically reduces the input requirements by incorporating regressions among a sample's elemental composition and all other input data. The ultimate analysis now specifies initial values for all structural parameters in the submodel for coal constitution. Whereas most of the reactivity parameters are the same for all coal types, the handful that change for every sample are correlated with the elemental compositions of labile bridges, which are also evaluated from the ultimate analysis of the whole coal. These relationships have been used in evaluations with more than 90 different coals. And in 4 of 5 cases, the predicted and observed values are within experimental uncertainty. None of the relations for either the structural or the reactivity parameters have been adjusted to simulate nitrogen evolution, so the tar yields, tar N, and weight loss in this paper are predictions in the most literal sense.

The only parameters assigned to predict nitrogen evolution are those in k_{HCN}. This rate was assigned by matching the predictions to data in Fig. 1 reported by Cai et al. [14] on nitrogen evolution from an Ill. No. 6 coal for heating rates from 5 to 5000 K/s at atmospheric pressure. As explained more fully below, this comparison also revealed that the thermal response of HCN production from char-N can only be represented by a distributed activation energy model (DAEM), for which the mean and standard deviation were assigned as 209 and 66.9 kJ/mole, respectively. The pseudofrequency factor is $2 \times 10^5\ s^{-1}$.

General Guidelines for the Data Evaluations

The three laboratory studies selected for this model evaluation monitored the fractional evolution of fuel nitrogen among tar, HCN, and char for coals across the rank spectrum. This group contains the

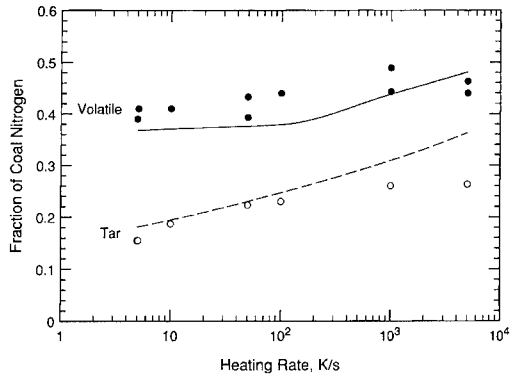

FIG. 1. Comparison between predicted and observed volatile-N (solid curve and ●) and tar-N (dashed curve and ○) from an Ill. No. 6 coal for various heating rates to 1225 K with a 5-s hold period at 0.1 MPa reported by Cai et al. [14].

only two experimental studies that assigned closures on the nitrogen balances for individual runs [1,4], as well as the most recent laboratory study of nitrogen evolution during primary devolatilization [14]. A fourth study provides the data on nitrogen mass fractions in tar [15]. Data reported for heating rates from 5 to 5000 K/s were acquired with wire-grid heaters in which the sample was dispersed in a layer only a few particles deep. Thermometry for the system used by Cai et al. [14] has been subjected to detailed characterization and is thought to be among the most reliable in the literature. The reported time-temperature histories and pressures were used directly in the simulations.

The much earlier studies of vacuum pyrolysis by Freihaut et al. [1] imposed nonuniform heating rates, variable reaction periods at intermediate temperatures, then slow approaches to extended soaking at higher ultimate temperatures. Only the total reaction time was uniform at about 10 s in all cases. Fortunately, thermocouple records of several operating conditions were reported for the stainless steel mesh used for temperatures to 1300 K (but not for the tungsten screens used at hotter temperatures). Close fits for the simulations were developed with uniform heating rates and variable isothermal reaction periods to intermediate temperatures so that uncertainties associated with the thermal histories are not inordinate. The simulations are based on a pressure of 0.015 MPa. Only the data that closes the nitrogen balances to within 10% are included.

Chen and Niksa used their new radiant coal flow reactor operated in its mode that eliminates secondary pyrolysis of the volatiles [4,16]. This entrained flow furnace heats coal suspensions with radiant fluxes as large as 60 W/cm^2 at atmospheric pressure for which calculated particle heating rates exceed 10^4 K/s. Simulations of these data are based on uniform

heating at 1.5×10^4 K/s to 1550 K with no isothermal reaction period and quenching at 13,300 K/s. The simulations for the entrained flow reactor used by Freihaut et al. [15] are based on uniform heating at rates from 2000 to 6000 K/s, depending on the ultimate temperature, followed by a 0.1-s isothermal reaction period.

In the forthcoming FLASHCHAIN predictions, the operating conditions of temperature, heating rate, time, and/or pressure were varied to match those in the experiments, whereas the sample's ultimate analysis was used to specify initial values for all structural and reactivity parameters. A simulation of each thermal history requires less than 3 min on a 20-MHz, 386-type personal microcomputer. Coal properties are given in the primary references for the experimental work. Whereas carbon content is a satisfactory rank variable, the nitrogen contents show no trend whatsoever across the rank spectrum. The initial values of η_0 show no trend with rank either. Initially, there is, on average, one nitrogen atom for every 2.5–4 aromatic nuclei, and each nucleus typically has between two and four 6-membered rings.

Results

Provided that the pressure is below about 10 MPa, predicted tar and total yields for all coals at all operating conditions are within experimental uncertainty for all cases considered in this paper, as demonstrated separately [10,17]. The case used to specify the value for k_{HCN} for all coal types appears in Fig. 1. Total fractional nitrogen evolution appears along with the fractional tar N for heating at 5 to 5000 K/s to 1225 K with a 5-s isothermal reaction period. The predicted volatile-N and tar-N are within experimental uncertainty at all heating rates except the fastest. However, this may not be a flaw in the predictions because 5000 K/s is probably faster than the time it takes for coal particles to actually be heated in wire mesh heaters. Note that the equally observed values for 1000 and 5000 K/s are consistent with this rationale. Both of the predictions correctly grow for faster heating rates, especially for tar-N. Tar-N increases in proportion to the tar yields, which increase for faster heating rates; in fact, the predicted tar and total yields are within experimental uncertainty throughout, as reported separately [17]. The growth in volatile-N for faster heating rates is actually more revealing. It is impossible to represent this tendency with an ordinary rate constant in a single first-order reaction regardless of the parameter values. Volatile-N is predicted to diminish slightly with any single first-order reaction simply because there are more precursors to HCN in the char whenever tar evolution is suppressed, as it is for slower heating rates. In contrast, with a DAEM for HCN production, asymptotic yields of HCN are achieved at any sustained

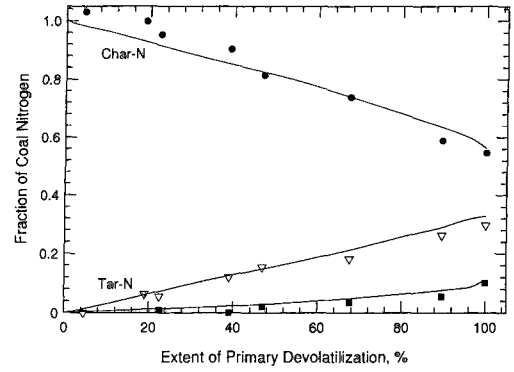

FIG. 2. Comparison between predicted and observed char-N (solid curve and ●), tar-N (∇ and dotted curve), and HCN (dashed curve and ■) from an Ill. No. 6 coal for devolatilization during heatup at more than 10^4 K/s. The abscissa indicates the percentage of the ultimate weight loss of 55.9 daf wt. pct for each of the residence times examined by Chen and Niksa [16].

ultimate temperature, irrespective of heating rate. Being the sum of tar-N and HCN, the volatile-N increases for faster heating rates only because the tar-N does. Consequently, the data in Fig. 1 conclusively demonstrate that HCN production from char exhibits an extremely broad thermal response that requires a DAEM.

Cai et al. [14] evaluated the impact of pressures to 70 MPa on nitrogen release by heating the same coal at 1000 K/s to 975 K then holding for 10 s. The observed and predicted values at atmospheric pressure agree closely, being 0.37 vs 0.38 for volatile-N and 0.22 vs 0.29 for tar-N. At 1 MPa, the comparisons are also favorable, being 0.29 vs 0.25 for volatile-N and 0.19 vs 0.15 for tar N. However, at higher pressures, the model underpredicts the tar yields and tar N, although it correctly predicts that yields of HCN increase only very slightly for elevated pressures up to 70 MPa at this thermal history. This discrepancy is due to underpredicted tar yields for this coal, although FLASHCHAIN predictions for several other coals at elevated pressures are accurate [8].

Once the parameters in k_{HCN} were assigned with Fig. 1, no parameters were adjusted for any of the succeeding evaluations with data. The comparison with the data from Chen and Niksa for very rapid heating conditions appears in Fig. 2. The fractional nitrogen evolution data is plotted against the extent of primary devolatilization, evaluated as observed weight loss for progressively longer reaction times expressed as a fraction of the observed ultimate yield (of 55.9 daf wt.%) for this heating rate and pressure. This abscissa circumvents the need to relate the measured residence times to thermal histories, which were not measured. For this case of transient devolatilization during heatup at a rate exceeding 10^4 K/s,

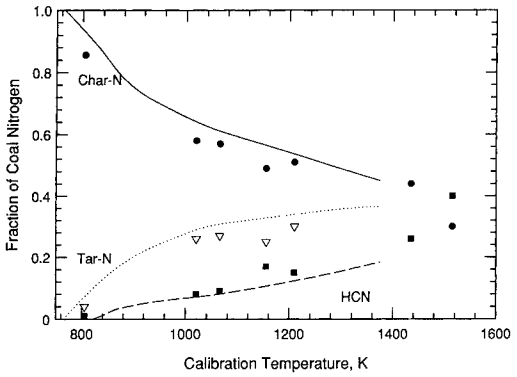

FIG. 3. Comparison between predicted and observed char-N (solid curve and ●), tar-N (∇ and dotted curve), and HCN (dashed curve and ■) from a Utah *hv* bituminous coal for the vacuum pyrolysis experiments of Freihaut et al. [1] at heating rates from 60 to 550 K/s, depending on the ultimate temperature, during a total reaction time of about 10 s. The abscissa indicates the ultimate temperatures in calibration trials, which are substantially higher than values with coal.

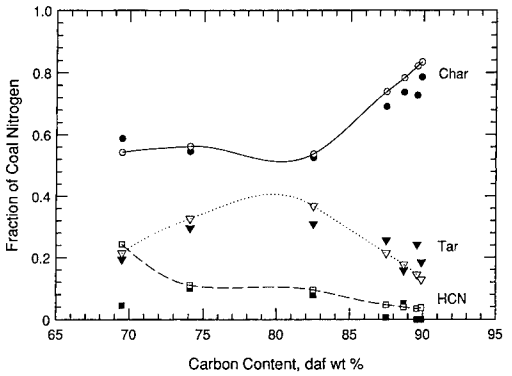

FIG. 4. Comparison between predicted and observed char-N (solid curve and ○ vs ●), tar-N (dotted curve and ∇ vs ▼), and HCN (dashed curve and □ vs ■) from several coals for devolatilization during heatup at more than 10^4 K/s vs the daf carbon content of the samples.

the predicted evolution of char-N is within experimental uncertainty throughout. The predicted release of tar-N and HCN are also within experimental uncertainty.

The evaluation in Fig. 3 is for nitrogen evolution on much longer time scales from a western bituminous coal under vacuum. Nominal heating rates were varied from 60 to 550 K/s, depending on the ultimate temperature, although total reaction time is fixed at 10 s for all cases. Predictions appear only to 1300 K because the thermal histories for the runs at higher temperatures were not characterized in the published reports. Again, the predicted evolution of char-N is within experimental uncertainty throughout, as is the growing contribution from HCN at hotter temperatures. It also appears that the values for temperatures above 1300 K lie along the trajectories of the predictions. The predicted tar-N values are reliable, except for an overprediction by 3 to 4% at higher temperatures. This case conveys the mistaken impression that HCN and tar-N are generated simultaneously; in fact, the extended soaking periods at each temperature in these experiments provides time for substantial HCN production after the tar-N has reached its asymptotic value.

Coals from across the rank spectrum are considered in the evaluation in Fig. 4, based on the ultimate nitrogen evolution data reported by Chen and Niksa. Each case is for primary devolatilization during heatup at rates in excess of 10^4 K/s to the point where asymptotic weight loss was achieved; thus there were no isothermal reaction periods. Predicted char-N levels correctly exhibit the minimum nitrogen retention observed for *hvA* bituminous coals and are within experimental uncertainty for all coal types. Predicted HCN levels are insensitive to coal rank for the short contact times in these experiments and within experimental uncertainty for all but the subbituminous sample. The predicted levels of tar-N are within experimental uncertainty across the rank spectrum. They correctly exhibit a maximum above 0.4 for *hv* bituminous coals, then fall below 0.2 for the low volatility and subbituminous samples. The discrepancy in the evaluation of the HCN yield from the subbituminous coal is not incriminating because the measured values indicate a sizable breach of closure in the nitrogen balance, which is probably due to NH_3 production [5].

The cases considered to this point generally validate the predicted char-N and HCN evolution histories for diverse coal types and operating conditions, and predicted tar-N levels are also reliable in most cases. But two aspects of primary nitrogen evolution remain ambiguous: (1) whether fractional tar-N is proportional to the fractional tar yield and (2) whether HCN production rates depend on coal rank.

This model assumes that nitrogen is randomly distributed among nuclei and monitors only average nitrogen loadings and nuclei concentrations. Consequently, predicted tar-N levels are proportional to the fractional tar yield because all nuclei are equally likely to appear in tar precursors during devolatilization. This premise is supported by most of the pertinent data, as seen in Fig. 5. This parity plot compares tar yields vs tar-nitrogen fractions for nine coals used in recent experiments [14,16]. The trapezoid defined by the dotted lines contains almost 85% of the 44 points for four coal types from the vacuum pyrolysis study of Freihaut et al. [15]. It lies below the diagonal for direct equivalence, presumably because tar yields are on the dry, not daf, basis. (Daf tar yields are greater than dry tar yields, but tar-N is

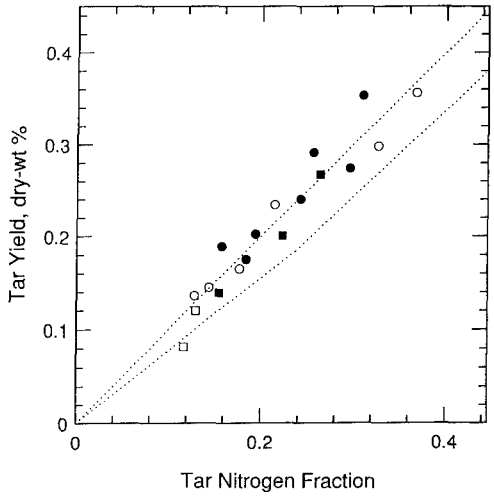

FIG. 5. Parity plot of tar yields on the dry basis vs tar nitrogen fraction for the observed (●) and predicted (○) ultimate nitrogen evolution for Chen and Niksa's conditions and for the observed (■) nitrogen evolution at different heating rates for an Ill. No. 6 coal reported by Cai et al. [14]. The trapezoid defined by the dotted lines contains 85% of 44 points from the Freihaut et al. vacuum pyrolysis study with four coals [1].

TABLE 1
Tar-N contents (daf wt.%)

Coal sample	T_r(K)	Observed [15]	Predicted
F1520	980	0.68	1.14
	1100	0.80	1.17
	1335	0.92	1.21
	1515	0.98	1.26
F1451	980	1.67	1.51
	1100	1.72	1.54
	1215	1.69	1.58
	1335	1.73	1.61
	1435	1.74	1.68
	1515	1.73	1.70
F1516	980	1.39	1.27
	1100	1.29	1.33
	1215	1.45	1.38
	1335	1.48	1.42

the same on either basis.) This region also contains all the points from Cai et al.'s [14] study. But about half of the points for Chen and Niksa's [16] data are above the region, indicating mass loss via tar evolution over and above the tar-N levels. In contrast, the predicted points for Chen and Niksa's experiments are within the trapezoid, except for a low volatility sample.

Chen and Niksa's [16] data are exceptional in indicating preferential mass loss as tar vs fractional tar-N because their tar yields also include the yields of oils, whereas the others do not. Values calculated for their conditions in Fig. 5 do not include oils and, therefore, illustrate the magnitude of this effect. Oils are single-ring aromatic compounds; thus, we would expect them to be generated by the same mechanism as tar. But the discrepancies for Chen and Niksa's data in Fig. 5 could be an indication that oils do not contain any nitrogen. If that is so, then oils may be generated as tar decomposition products with a simultaneous release of HCN.

Another, more direct, perspective on tar-N is seen in the comparison between predicted and observed nitrogen mass percentages in Table 1. The data are from the entrained flow, atmospheric pyrolysis studies of Friehaut et al. [15] The predicted tar-N contents are highest for the *hvA* bituminous and lowest for the subbituminous coal and also increase as the cumulative tar yields grow for progressively hotter reactor temperatures, in accord with the data. Predicted values are fairly accurate for the *hvA* and medium volatile bituminous coals but too large by 25 to 50% for the subbituminous coal. Although, here too, the database is very limited, it seems that preferential nitrogen incorporation in tar may depend on rank. Perhaps under these conditions, the abundance of oxygen in low-rank coals promotes NH_3 production via OH and HCN [18] on a time scale even shorter than that for tar evolution during primary devolatilization, depleting the low-rank tars of their nitrogen before they are released from the coal matrix.

The second ambiguous aspect pertains to a rank dependence for HCN production from char-N. The predicted char-N evolution histories in this paper based on the same k_{HCN} are remarkably accurate for coals across the rank spectrum. However, the dataset with the greatest representation of coal types, Chen and Niksa's, represents nitrogen evolution only up to the point where HCN evolution commences. Data for longer reaction times are more meaningful although, unfortunately, this database is sparse and contradictory. Freihaut et al.'s vacuum pyrolysis study is the most comprehensive. Figure 6 shows the fractional HCN yields attributable solely to char-N for four coal types. Unfortunately, temperatures along the abscissa do not even indicate the maximum achieved in each of these cases. At least the thermal histories are the same for all coals, so the relative differences are meaningful. In so far as HCN production at all temperatures above 1000 K in Fig. 6 increases monotonically for coals of lower rank, this data clearly supports lower values of k_{HCN} for coals of higher rank. However, Cai et al. subjected a medium volatile bituminous to the heating rate and pressure studies described in connection with Fig. 1. For this coal, the predicted tar and total yields and tar-N levels are within experimental uncertainty for

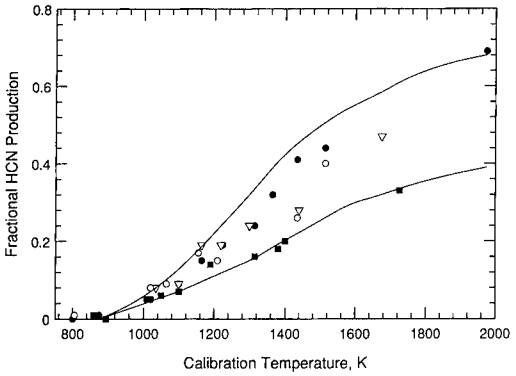

FIG. 6. Fractional HCN yields attributable solely to char N vs calibration temperature in vacuum pyrolysis experiments reported by Freihaut et al. [1] for a subbituminous (●), Utah bituminous (∇), Colorado bituminous (○), and Pittsburgh bituminous (■).

all thermal histories examined at atmospheric pressure. But the volatile-N levels can only be reproduced with faster values of k_{HCN}, in direct contradiction to the rank dependence evident in the data in Fig. 6.

Discussion

On a molar basis, nitrogen is a sparse element in coal, being present in fewer than half of all aromatic nuclei and in only about 1 in 10 ring structures, on average. Thus, nitrogen decomposition chemistry does not play any discernible role in the bridge conversion chemistry responsible for the formation of tar precursors. As long as tar is being expelled during the initial stage of primary devolatilization, fuel nitrogen is simply shuttled into the vapor phase as a structural element in tar molecules. Although simple in the sense that nitrogen chemistry need not be resolved to explain nitrogen evolution, this insight is hard to implement because tar evolution is strongly rank dependent and, until very recently, impossible to predict even for similar coal types.

FLASHCHAIN reliably predicts tar yields and evolution rates from coals across the rank spectrum at most operating conditions, based only on the sample's ultimate analyses. As demonstrated by the close evaluations against nitrogen evolution data in this paper, this unique capability enables reliable predictions for fuel-nitrogen evolution from virtually any coal type and thermal history at low-to-moderate pressures. Nitrogen release from all bituminous coal ranks can be accurately modeled with only two processes: tar shuttling and HCN production from char-N. Under conditions of rapid heating, tar shuttling is the only mechanism for nitrogen release as long as tar is being expelled, but for slower heating rates, it is overlapped by HCN production from char-N. Most important, tar shuttling is almost entirely responsible for the observed rank dependence of nitrogen release that, in general, mimics tar yields by exhibiting a broad maximum for *hv* bituminous coals before falling off for low volatility coals.

Virtually all data on tar N evolution indicate that fractional tar yields are directly proportional to fractional tar-N levels, corroborating the random dispersion of nitrogen among average aromatic nuclei in this model. With low rank coal tars, however, fuel nitrogen conversion may be accelerated by OH to the point where it decomposes before tar is expelled at even the fastest heating rates of interest. More data is needed to clarify this aspect and to validate the apparent proportionality between tar yields and tar-N levels at the highest heating rates.

The activation energy distribution assigned to k_{HCN} is broader than any assigned for bridge conversion in even the lowest rank coals, where bridge compositions are extremely heterogeneous because of the abundance of oxygen. Qualitatively, this indicates an extremely broad thermal response for HCN production that is due, in all likelihood, to multiple precursors for HCN in char-N. Although speculative, it is reasonable to expect that these precursors become more stable as their surrounding domains of condensed aromatic rings become more extensive, as occurs throughout the devolatilization of any coal type. Aromatic nuclei are also more massive in coals of higher rank, thus, the HCN precursors in higher rank coals should be relatively more stable than those in lower rank coals. Indeed, this tendency is evident in the HCN yields attributed to char-N for the older data reported by Freihaut et al. But this trend has been contradicted recently under very closely controlled conditions; therefore, more data is needed to launch any definitive conclusion.

In the meantime, a single value of k_{HCN} can be recommended for HCN production from char N, especially for simulated pulverized fuel-firing conditions. The resolution of tar shuttling and HCN production in this model is already an improvement over the simple proportionality between HCN yields and weight loss invoked in all current applications simulators. Such rudimentary approaches have no prospects whatsoever to describe nitrogen evolution from different coal types because tar shuttling is responsible for this rank dependence. The release of tar-N is also worth resolving from HCN production during primary devolatilization because of its subsequent fate, especially since a substantial fraction of tar-N can be incorporated into soot during secondary and oxidative pyrolysis of volatiles. Once it has been reincorporated into a carbonaceous matrix, this nitrogen is more prone to NO_x conversion, like the nitrogen in burning char particles. This potentially important aspect of aerodynamic NO_x abatement has not yet

been evaluated, although the model developed here is the first step in that direction.

REFERENCES

1. Freihaut, J. D., Zabielski, M. F., and Seery, D. J., *Nineteenth Symposium (International) on Combustion*, The Combustion Institute, Pittsburgh, 1983, p. 1159.
2. Bruinsma, O. S. L., Geertsma, R. S., Bank, P., and Moulijn, J. A., *Fuel* 67:334 (1988).
3. Nelson, P. F., Buckley, A. N., and Kelley, M. D., *Twenty-Fourth Symposium (International) on Combustion*, The Combustion Institute, 1992, p. 1259.
4. Chen, J. C., and Niksa, S., *Twenty-Fourth Symposium (International) on Combustion*, The Combustion Institute, Pittsburgh, 1992, p. 1269.
5. Chen, J. C., Castagnoli, C., and Niksa, S., *Energy Fuels* 6:264 (1992).
6. Niksa, S., and Kerstein, A. R., *Energy Fuels* 5:647 (1991).
7. Niksa, S., *Energy Fuels* 8:659 (1994).
8. Niksa, S., *Energy Fuels* 5:665 (1991).
9. Niksa, S., *Energy Fuels* 5:673 (1991).
10. Niksa, S., *Energy Fuels* 8:671 (1994).
11. Burchill, P., and Welch, L. S., *Fuel* 68:100 (1989).
12. Wallace, S., Bartle, K. D., and Perry, D. L., *Fuel* 68:1450 (1989).
13. Niksa, S., *AIChE J.* 34:790 (1988).
14. Cai, H.-Y., Guell, A. J., Dugwell, D. R., and Kandiyoti, R., *Fuel* 72:321 (1993).
15. Freihaut, J. D., Proscia, W. M., and Seery, D. J., *Energy Fuels* 3:692 (1989).
16. Chen, J. C., and Niksa, S., *Energy Fuels* 6:254 (1992).
17. Niksa, S., *Twenty-Fifth Symposium (International) on Combustion*, The Combustion Institute, Pittsburgh, 1994 (in press).
18. Aho, M. J., Hamalainen, J. P., and Tommavouri, J. L., *Combust. Flame* 95:22–30 (1993).

Twenty-Fifth Symposium (International) on Combustion/The Combustion Institute, 1994/pp. 545–552

GAS EXCHANGE BETWEEN THE BUBBLE AND EMULSION PHASES DURING BUBBLING FLUIDIZED BED COAL COMBUSTION ELUCIDATED BY CONDITIONAL GAS SAMPLING

ICHIRO NARUSE AND KAZUTOMO OHTAKE
Department of Ecological Engineering
Toyohashi University of Technology
Tempaku-cho, Toyohashi 441, Japan

KAZUHIRO KOIZUMI, KOJI KURAMOTO AND GUO-QING LU
Department of Energy Engineering
Toyohashi University of Technology
Tempaku-cho, Toyohashi 441, Japan

A method for gas composition measurements in bubble and emulsion phases has been developed and applied to bubbling fluidized bed coal combustion. Resolution of the bubbles from the emulsion phase is based on detection of the time change of the pressure difference between two points along the path of bubbles.

Cold model experiments confirm that the conditional sampling performs as expected. The probe is demonstrated to resolve bubbles from the emulsion phase correctly. In addition, with single CO_2 bubbles formed in the fluidized bed under the minimum fluidization condition by air, gas exchange between the bubble and emulsion phases is characterized by using this sampling system. Gas in a bubble tends to remain in the bubble provided that the ratio of bubble rising velocity to gas velocity in the emulsion phase exceeds a certain value.

This sampling method is also applied to coal combustion conditions in order to elucidate the roles of bubble and emulsion phase in the combustion process. For fluidizing material of smaller particle diameter, the combustion of volatile matter mainly takes place in the bubble phase. NO concentration in the bubble phase becomes lower than that in the emulsion phase, while N_2O shows the opposite tendency. This might be caused by homogeneous reactions of NO to form N_2O in the bubble phase.

Introduction

Generally, during bubbling fluidized bed coal combustion (BFBC), bubble and emulsion phases are present in dense beds. It is important to characterize the combustion in each phase to attain the ultimately high combustion efficiencies and low concentrations of environmental pollutants such as NO, N_2O, NO_2, and SO_2. The authors believe that this approach can contribute to the design of more sophisticated fluidized bed boilers.

From this viewpoint, a method for separate measurements of gas compositions in the bubble and emulsion phases is needed for BFBC. Other researchers have evaluated several different approaches, but none is satisfactory. Monitoring the electrostatic capacitance [1] or optical transmissivity [2] are the typical ways to detect the bubble and emulsion phases. Under coal combustion conditions, however, capacitance probes may promote ionic chemical reactions on their charged surface. And optical probe signals may be distorted by the luminosities of bed materials and burning coal. Zirconia oxygen sensors [3,4] and X-rays transmission [5,6] have also been tried, but these methods also show their peculiar problems at combustion conditions.

In this study, the time variation of the pressure difference between two points along the path of bubbles is monitored to resolve the bubble and emulsion phases, following the Davidson model [7]. A calibration from a cold model confirms that this method can resolve the two phases, as expected. The pressure difference was compared with the image of bubble movement on the pictures simultaneously taken by a high-speed video camera, in which a wave inserter was mounted. A single CO_2 bubble was formed under the minimum fluidization condition driven by air; characteristics of gas exchange between the bubble and emulsion phases were studied by using the developed conditional sampling. Finally, this sampling system was applied to the coal combustion condition. The particle diameter of fluidizing materials was changed to control both the bubble size and its rising velocity in the bed. The roles of bubble and emulsion

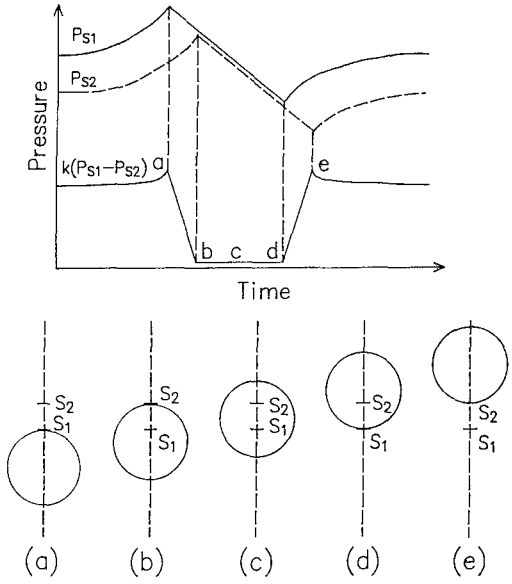

FIG. 1. Pressure difference across two probes when a bubble passes by.

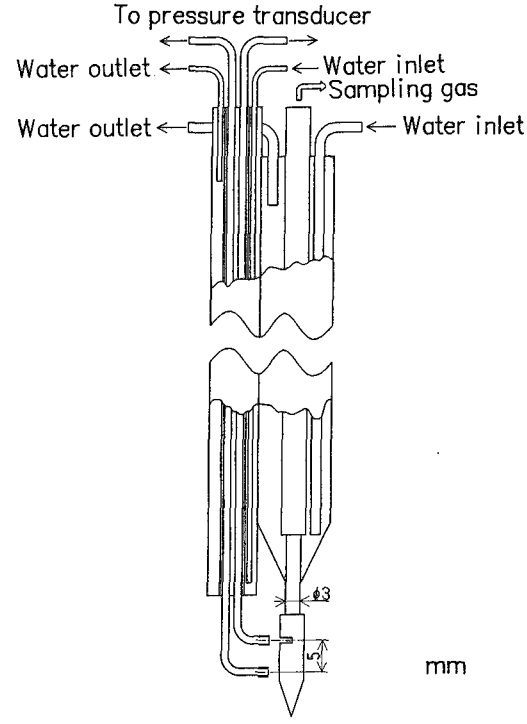

FIG. 2. Schematic of the conditional sampling probe.

phase on coal combustion could be explained from the results.

Experiments

Principle of Measurement to Separate Bubble from Emulsion Phase:

The principle of resolving the bubble and emulsion phases is to measure the time change of the pressure difference between two points along the path of bubbles. Figure 1 shows the expected pressure difference across two probes (P_{S1} and P_{S2}), based on the Davidson model [7] when a bubble passes across the probes. In this figure, $k(P_{S1} - P_{S2})$ indicates a signal that is proportional to the pressure difference between two probes. When a bubble approaches one pressure probe, the pressure gradually increases. Once the probe is within the bubble, the pressure decreases. When the bubble breaks free of the probe, the pressure increases again. Note also that when both probes are immersed in one bubble, the pressure difference almost vanishes. These characteristics were used to distinguish bubbles from the emulsion phase.

Conditional Sampling Probe and Sampling System:

The above-mentioned principles are implemented with the sampling probe shown in Fig. 2. The right part consists of a water-cooled sampling probe, and the left part contains the water-cooled pressure detectors. The distance between the two pressure probe tips was 5 mm, which set the minimum detectable bubble size. Fine stainless steel mesh was attached to each probe tip to prevent plugging from particles. The sampling port into the sampling probe tip was located opposite to the upper pressure probe. In the cold model experiments, the water-cooled part was removed.

Figure 3 shows the conditional sampling system. The signal of pressure difference was measured with a solid-state pressure transducer. This voltage signal was introduced into a Schmidt trigger circuit that controlled two solenoid valves in the gas sampling line. In the Schmidt trigger circuit, the threshold value that distinguishes bubbles from the emulsion phase was selected according to the expected pressure difference for a single bubble from the Davidson model [7], accounting for the response time of the solenoid valves.

Calibration by Cold Model Experiments:

Figure 4 shows a schematic diagram of the two-dimensional cold model calibration experiment. Individual CO_2 bubbles were injected into the fluidized bed operated at the minimum fluidization velocity.

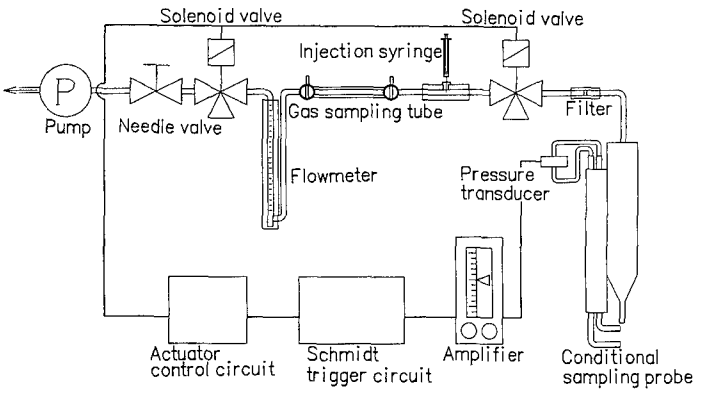

FIG. 3. Conditional sampling system.

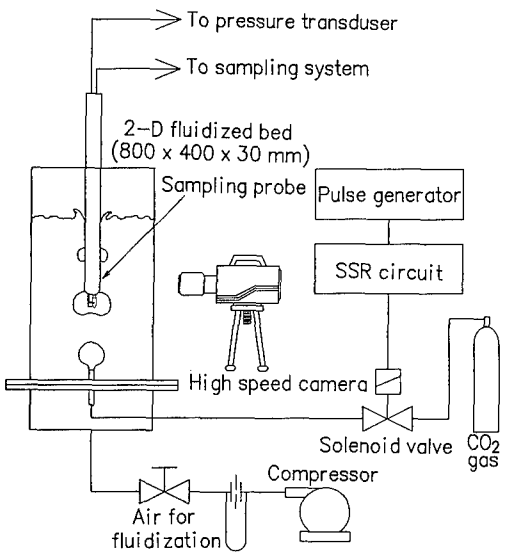

FIG. 4. Two-dimensional cold model for calibration tests.

The pressure difference signal was recorded by a wave inserter and compared with the displacement of a bubble, which was simultaneously recorded with a high-speed video camera. Gas exchange between the bubble and emulsion phases was characterized in both two- and three-dimensional cold models. Three different sizes of silica sand (d_p = 0.59–0.84, 0.29–0.59, and 0.15–0.42 mm) were used as the bed material.

Bubbling Fluidized Bed Coal Combustion Experiments:

A laboratory-scale bubbling fluidized bed coal combustor [8] of 0.1-m diameter and 0.7-m high, shown in Fig. 5, was used. Coal (particle diameter: d_p = 1.19–1.68 mm) was fed into just above the air distributor. Silica sand was used as the bed material. The bed temperature and the combustion stoichiometry were fixed at 1073 K and 1.2, respectively. The superficial gas velocity was 1.2 times the minimum fluidization velocity. NL coal, the properties of which are shown in Table 1, was used. O_2, CO_2, CO, and N_2O were detected by TCD and ECD gas chromatography, and NO was analyzed by a NO_x meter.

Results and Discussion

Test of Conditional Sampling in the Cold Model:

In Fig. 6, the measured pressure difference in the cold model is compared to that calculated from the Davidson model [7]. The time when a single bubble reaches the first pressure detector (S1) is defined as "zero." The observed results are in good agreement with the calculated values. Figure 7 shows the relationship between the bubble location recorded on high-speed video pictures and the pressure difference signal. The left part indicates the pressure difference. The position of both pressure probes is also indicated. As observed from these photos, when both probes are immersed in one bubble, the pressure difference nearly reaches zero, demonstrating that the probe can correctly resolve the bubble from emulsion phases. No disturbance is induced by the probe when a bubble passes through the probe tip. In some cases, however, the bubble may be divided by the probe.

Based on such histories of the pressure difference, the timing of the solenoid valves was selected, as shown in Fig. 8, to accommodate the different response times to open and close the valves so that gas was sampled only from bubbles. Under these control cycles, this conditional probe samples only about 10% of the volume in a single bubble.

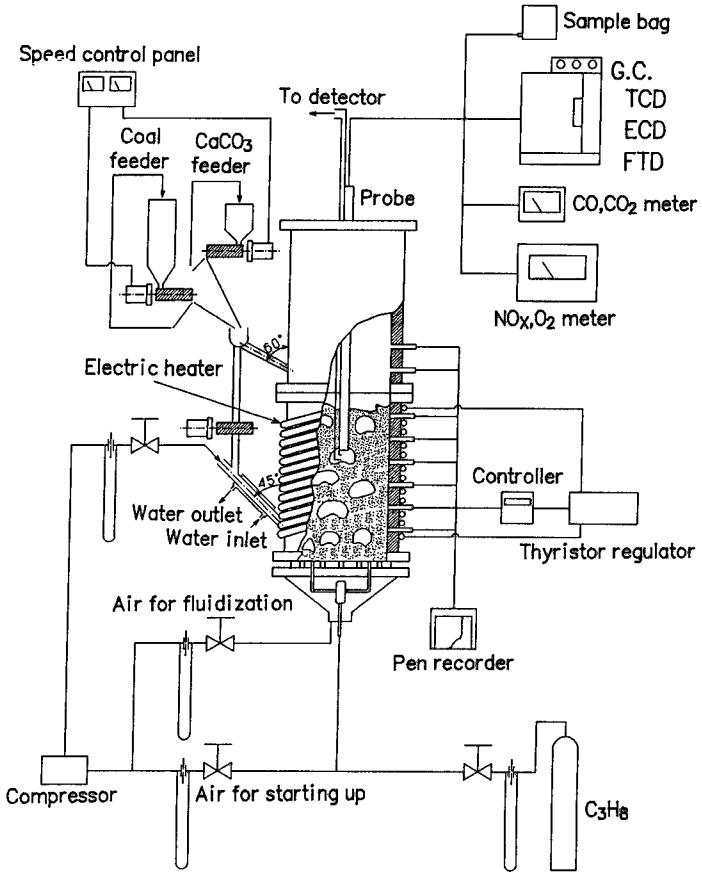

FIG. 5. Schematic diagram of lab-scale fluidized bed coal combustor.

Characteristics of Gas Exchange between the Bubble and Emulsion Phases:

Figure 9 compares the change of CO_2 concentrations along the axis of the dense cold model obtained by conditional sampling and by ordinary continuous sampling. Continuous sampling indicates that all the gas in both bubble and emulsion phases is sampled. In these experiments, u_b/u_f (u_b: bubble rising velocity; u_f: estimated mean gas velocity in the emulsion phase) was varied as one of the fluidization parameters. The u_b/u_f ratio was increased for sample particle diameters of bed material. In other words, with fine particles, the bubble rising velocity was faster than the gas velocity in the emulsion phase.

From Fig. 9, CO_2 concentrations just above the CO_2 injection nozzle from conditional sampling are higher than those from continuous sampling for all values of u_b/u_f. For $u_b/u_f = 3.39$, the result obtained by conditional sampling exceeds that by continuous sampling for all regions of the dense bed. For $u_b/u_f = 0.78$, in contrast, both results fall on the same line for heights above 125 mm. Similar results were observed with the three-dimensional cold model experiments.

These results are caused by the change in bubble rising velocity for different u_b/u_f caused by variations in the stream lines of gas around a bubble, as shown in Fig. 10 [9]. This figure suggests that the fluidizing gas flows through a bubble when u_b/u_f is less than unity, transporting CO_2 from a bubble into the emulsion phase. In the case of u_b/u_f being larger than unity, on the other hand, the gas circulation around a bubble is steady because the rise velocity of the bubble is slower than the gas velocity in the emulsion phase. CO_2 remains in the bubble under such conditions.

Measurement to Resolve the Bubble and Emulsion Phases during Combustion:

Once it was confirmed that the newly developed probe could sample only the gas in a bubble without contaminations from the emulsion phase, this probe was applied to BFBC. Under coal combustion con-

TABLE 1
Coal properties

Coal	Proximate analysis			Ultimate analysis		
	Volatile matter	Fixed carbon (mass%, dry)	Ash	H	C (mass%, daf)	N
NL coal	28.1	60.3	11.6	5.02	81.31	1.67

daf = dry ash free.

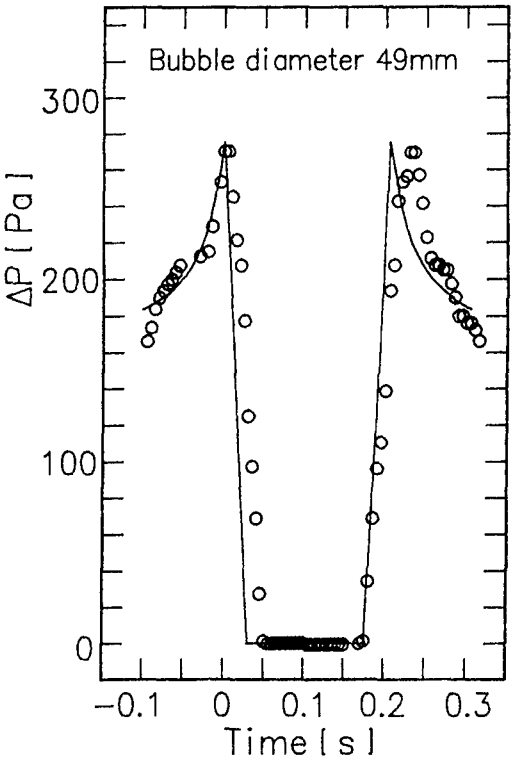

FIG. 6. Comparison between the measured pressure difference and that calculated by the Davidson model.

ditions, however, many bubbles are formed in the dense bed. Therefore, the pattern of fluidization under the combustion condition differs from that under the above-mentioned cold flow conditions that have individual bubbles. Figure 11 indicates the time change of the pressure difference during coal combustion with silica sand of d_p = 0.59–0.84 mm. The pressure probe was located at 150 mm above the distributor at the center of the combustor. Under this experimental condition, bubbles pass across the sampling probe at about 4 Hz, and the average bubble size is 25 mm. The signal shape in one period under combustion conditions is similar to that obtained in the cold flow experiments of Fig. 6. This suggests that our sampling system can be applied to combustion conditions.

Figures 12 and 13 show profiles of gas species concentrations along the central axis of the combustor for cases of different diameters of bed material in the ranges of d_p = 0.59–0.84 mm and 0.15–0.42 mm, respectively. The former case (Fig. 12) shows that the result of conditional sampling does not differ so much from that of continuous sampling. On the other hand, for the smaller particles (Fig. 13), both results differ appreciably. In particular, O_2 concentrations from conditional sampling near the distributor are much higher than those from continuous sampling. With conditional sampling, the gradient of O_2 concentration also becomes steeper. This result indicates that the combustion of volatile matter evolved from the coal in the emulsion phase and near the bubble boundary mainly takes place in the bubbles. The volatile matter evolved from coal particles in the emulsion phase will be carried into bubbles, because the vertical pressure drop in the emulsion is higher than that in the bubbles with smaller particles.

With smaller particles, NO concentrations in the bubble phase become lower than that in the emulsion phase, while N_2O follows the opposite tendency. This might be caused by such homogeneous decomposition reactions for NO [10,11] in the bubble phase as $NO + NCO \rightarrow N_2O + CO$, $NO + NH \rightarrow N_2O + H$, $NO + CO \rightarrow 1/2N_2 + CO_2$ and $NO + NH \rightarrow N_2 + OH$. In these reactions, NCO is produced by the oxidation reaction of HCN. Thereafter, the gas-phase reactions involving evolved fragments of volatile N (i.e., NH_i and HCN species) play a role in NO destruction. Heterogeneous char reactions contribute little to NO destruction since the char concentration in the dense bed is only about 2 vol.%.

Conclusions

A method to resolve gas compositions in the bubble and emulsion phases was developed and applied to fluidized bed coal combustion conditions by mea-

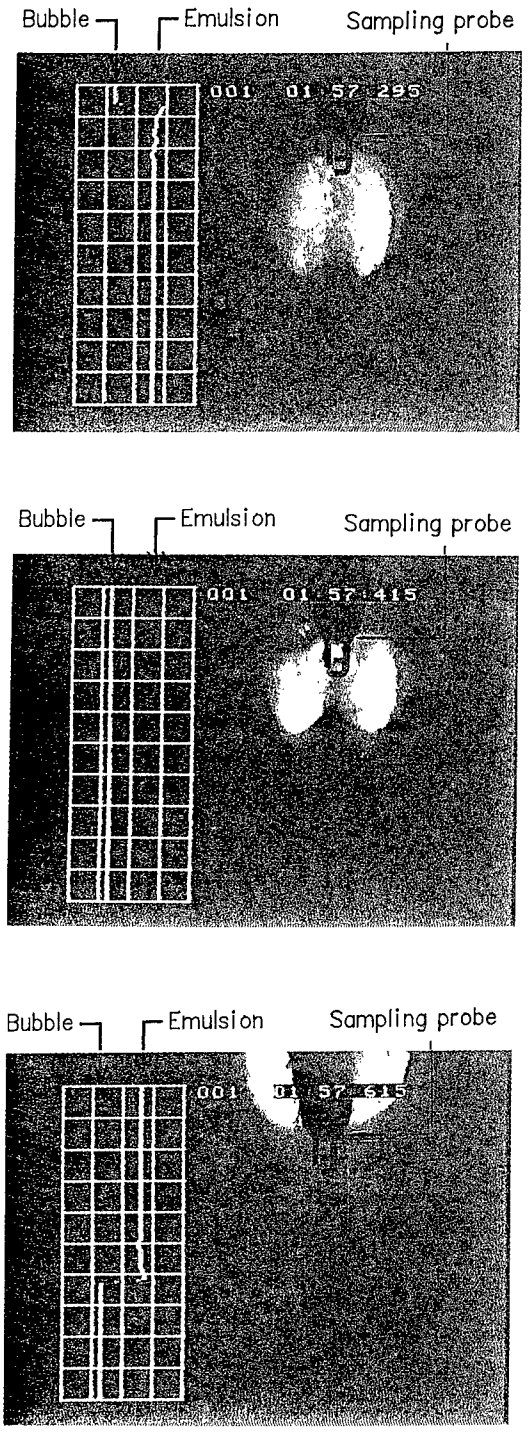

FIG. 7. Simultaneous record of bubble images and pressure difference signals.

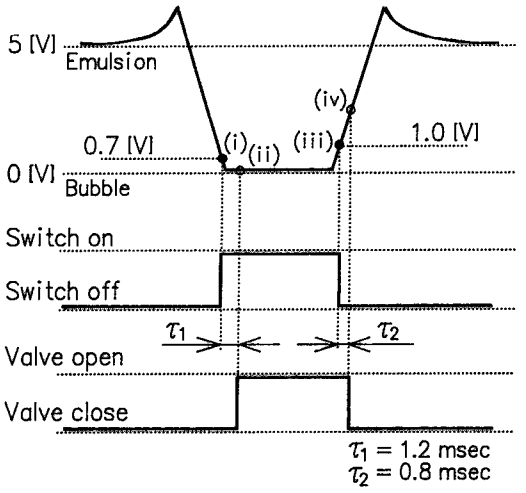

FIG. 8. Timing of opening/closing of the solenoid valve to sample only the gas in a bubble.

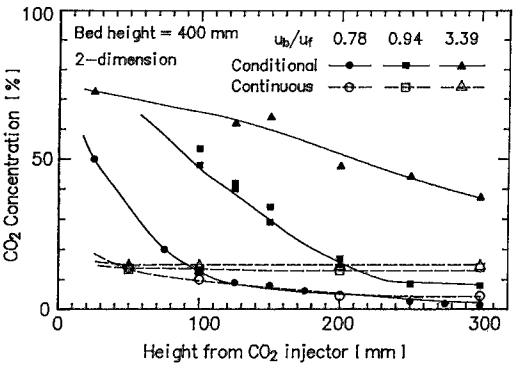

FIG. 9. Variation of CO_2 concentrations along the axis of the two-dimensional cold model (solid line: conditional sampling; broken line: continuous sampling).

suring the time change of the pressure difference between two points along the path of bubbles.

Cold flow calibration confirmed that the probe could separate the bubble and emulsion phases. Characteristics of gas exchange between the bubble and emulsion phases were characterized for single CO_2 bubbles formed under the minimum fluidization conditions with air. The concentration of CO_2 in a bubble is especially sensitive to the change of flow pattern around bubbles, which is a function of the ratio of the bubble-rising velocity to the gas velocity in the emulsion phase. This ratio was varied for different particle sizes.

The conditional sampling was applied to coal combustion conditions in order to characterize the roles

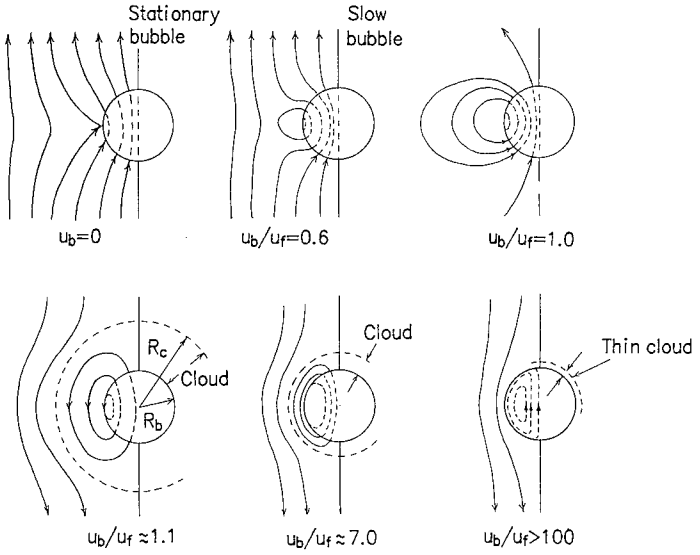

FIG. 10. Stream lines of gas around a bubble.

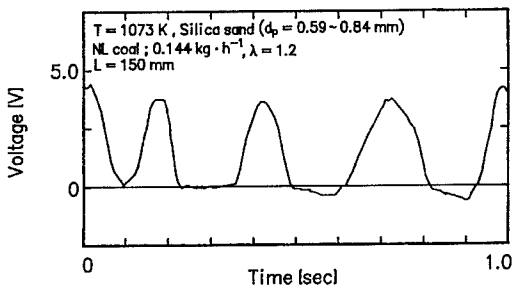

FIG. 11. Time change of pressure difference under the combustion condition in the bubbling fluidized bed.

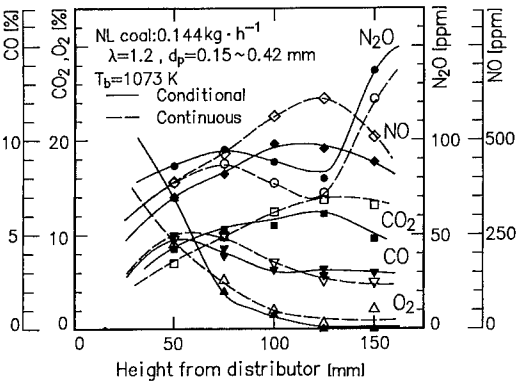

FIG. 13. Change of gas species concentrations along the central axis of the combustor (d_p = 0.15–0.42 mm).

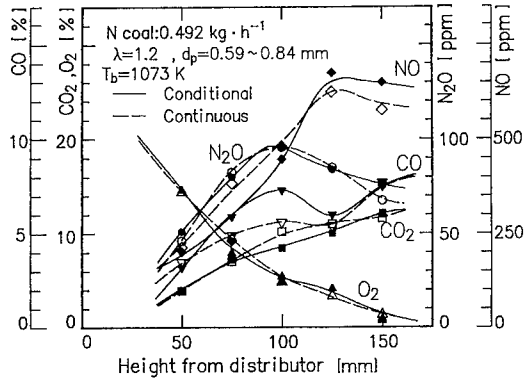

FIG. 12. Change of gas species concentrations along the central axis of the combustor (d_p = 0.59–0.84 mm).

of bubble and emulsion phases during fluidized bed coal combustion. For smaller fluidizing particles, the volatile matter evolved from coal mainly burnt in the bubble phase. NO concentration in the bubble phase became lower than that in the emulsion phase, while N_2O indicated the opposite tendency. This might be due to homogeneous reactions relating to NO and N_2O in the bubble phase.

Acknowledgment

This work was partly supported as Grant in Aid of Scientific Research [Encouragement Research (A)], by The Ministry of Education, Science and Culture, Japan, under Contact No. 05750672.

REFERENCES

1. Werther, J., and Molerus, O., *Int. J. Multiphase Flow* 1:103 (1973).
2. Yasui, G., and Johanson, L. N., *AIChE J.* 4:445 (1958).
3. Ljungstroem, E., and Langer, V., *J. Inst. Energy* 62:34 (1989).
4. Stubington, J. F., and Chan, S. W., *Twenty-Second Symposium (International) on Combustion*, The Combustion Institute, Seattle, 1988, pp. 287–294.
5. Rowe, P. N., and Partridge, B. A., *Trans. Inst. Chem. Eng.* 43:157 (1965).
6. Grohse, E. W., *AIChE J.* 1:358 (1955).
7. Davidson, J. F., *Trans. Inst. Chem. Eng.* 39:230 (1961).
8. Naruse, I., Imanari, M., Koizumi, K., Yuan, J.-W., and Ohtake, K., *Second International Symposium on Coal Combustion*, The Institute of Thermal Science and Engineering, Tsinghua University, Beijing, 1991, pp. 523–530.
9. Davidson, J. F., and Harrison, D., *Fluidized Particles*, Cambridge University Press, Cambridge, 1963.
10. Yamamoto, Y., Itoh, H., Yuan, J.-W., Naruse, I., and Ohtake, K., *Trans. Jpn. Soc. Mech. Eng. Ser. B*, 59, 564:2560 (1993).
11. Naruse, I., Yamamoto, Y., Imanari, M., Yuan, J.-W., and Ohtake, K., *Twenty-Fourth Symposium (International) on Combustion*, The Combustion Institute, Sydney, 1992, pp. 1415–1422.

Twenty-Fifth Symposium (International) on Combustion/The Combustion Institute, 1994/pp. 553–560

A METHOD OF PREDICTING COAL DEVOLATILIZATION BEHAVIOR BASED ON THE ELEMENTAL COMPOSITION

YUXIN ZHAO, MICHAEL A. SERIO, ROSEMARY BASSILAKIS AND PETER R. SOLOMON
Advanced Fuel Research, Inc.
87 Church Street, East Hartford, CT 06108, USA

An interpolation method was proposed to correlate the input parameters of a coal devolatilization model [functional group–depolymerization, vaporization, cross-linking (FG–DVC)] to coals of a wide range of ranks, and is conceptually applicable to other devolatilization models. This method uses a set of well-defined coals (library coals) to form a triangular mesh in the van Krevelen diagram. If an unknown coal is within a triangle formed by three library coals, the model input parameters for this unknown coal can be interpolated from those of the three library coals based solely on the elemental composition. This method extends the FG–DVC model to be able to model any coal that can be interpolated, without the requirement for any additional characterization of the coal. It is also easy to accommodate more library coals so that a wider range of coal types can be covered. The validity of this method was demonstrated by comparing the tar yield measurements and the predictions for 27 coals over a wide range of pressures and heating rates. For most of the coals, the predictions compare very well with the data. For selected coals, data were available on the variation of the yield of total volatiles with pressure and heating rate, and again, good agreement was obtained. The model could be improved by using additional parameters to describe the exchangeable cation content, sulfur content, and/or the maceral composition.

Introduction

Coals come in various ranks and from different geological origins. Substantially different characteristics are commonly observed for coals of different ranks. Coal samples from the same seam could exhibit large variations in their devolatilization and related thermal and combustion behavior. Such variations have a significant impact on the design and operating conditions of coal combustion systems. It is imperative that coals are well characterized before their utilization. This normally requires sophisticated instrumentation and special expertise, which are not likely to be available in a single laboratory. Robust methods of predicting coal devolatilization behavior before invoking expensive experiments can be of practical importance.

Recently, there have been developments of several coal devolatilization models [1–6], which have various capabilities for predicting coal thermal decomposition under practical conditions. A common shortcoming of these models is that they require a large set of data inputs, including kinetic parameters, gas precursor compositions, and additional parameters describing the coal polymer structure. These input data must be generated based on a series of experimental measurements for each coal of interest. Predictions are limited to coals that have already been studied. This limitation has long been criticized, although it originates from the complicated nature of the coal structure. On the other hand, some investigators have tried to correlate the devolatilization properties to the coal types. For example, Ko et al. [7] and Neavel et al. [8] have developed methods of predicting the upper bound of tar yields, X_{tar}, from the coal elemental composition. The predicted X_{tar} can be used as an input parameter for general tar kinetic models such as those developed by Serio et al. [9] and Suuberg et al. [10]. Niksa and coworkers [6,11,12] have also proposed a correlation method for the FLASHCHAIN coal devolatilization model that predicts the tar and the total volatile yields in pyrolysis based on ultimate analysis.

This paper presents a general method that provides a direct correlation between coal elemental compositions and the input parameters of a general coal devolatilization model, FG–DVC [1–3], which can predict, in addition to the tar and total volatile yields, the yields of individual gas species, the tar molecular weight distribution, and the char fluidity. This model was validated for the eight Argonne Premium coals based on measurements of pyrolysis kinetics from thermogravimetric–Fourier transform infrared spectrophotometry (TG–FTIR) analysis, solvent extraction, and solvent swelling to measure extractables and initial cross-link density, respectively, Gieseler plastometer experiments to measure fluidity, pyrolysis-FIMS to measure the tar molecular weight distribution, and ultimate analysis to determine the elemental compositions (C, H, O, N, S) [3].

The large number of experimental inputs allowed the development of a model that can make detailed predictions of coal devolatilization, as indicated above. However, this feature presented a difficulty when applying the model to unknown coals. The correlation method presented in this paper allows the application of the FG–DVC model to coals of a wide range of types without prior knowledge of them, except the elemental analysis, and supports our contention that the FG–DVC model is a general model that can perform expeditious evaluations of coal thermal decomposition under many heating rate and pressure regimes. This correlation approach, in its preliminary form, has been implemented into a two-dimensional coal combustion model, PCGC-2 [13]. After a description of the method, the model predictions are compared with tar yield data collected at rapid heating rates and various pressures from the literature [7,14–21], and with tar yields at slow heating rates measured with TG–FTIR analysis in our laboratory.

FG–DVC Model and Its Input Parameters

The FG–DVC (functional group–depolymerization, vaporization, cross-linking) model is a general coal devolatilization model that predicts coal thermal decomposition into light gases, tar, and char [1–3]. It also predicts other related thermal property changes, i.e., coal fluidity and swelling, during pyrolysis. Recent improvements of this model have given it the ability to predict the evolution of gaseous sulfur and nitrogen species [22]. The following is just a brief description of this model, as the details have been published elsewhere [1–3,22,23].

Coal has a very complicated structure that is essentially a mixture of an aromatic matrix, the side chain components and some loose fragments. The thermal decomposition of the coal structure involves many parallel and competitive processes. In modeling these processes, FG–DVC uses two submodels. The FG model simulates the thermal evolution of various functional groups, and the DVC model predicts the depolymerization, vaporization, and cross-linking processes occurring in the coal polymer network. In the FG submodel, the gas evolution from functional group precursors is modeled with parallel first-order differential equations, and a distributed activation energy formulation is used to reflect the diversity of coal structures. The thermal evolution of the coal polymer matrix is modeled with a network model [2], which consists of nodes and the connections between them. The nodes represent the polymer clusters, and there are two types of connections between them, i.e., bonds and crosslinks. At elevated temperatures, there is a competition between bond breaking and cross-linking. The properties of the network are fully determined by these two competing processes through percolation theory [24]. The most important property of the network is the molecular weight distribution of the clusters. The heavy molecules remain in the condensed phase to become char, while the light ones evaporate to become tar. The vaporization is calculated based on a mechanism given by Fletcher et al. [25]. The tar rate is further limited by internal transport, which is assumed to be controlled by the total rate of gas species evolution plus the light tar [1]. This mechanism enables the model to predict the pressure variation of tar yields.

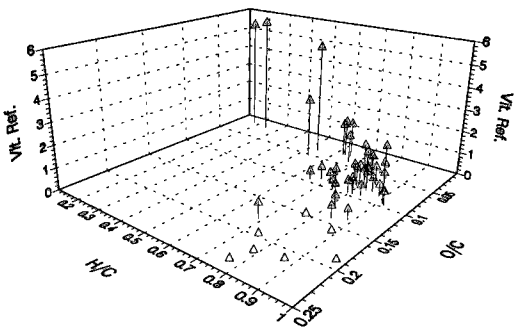

FIG. 1. Variation of vitrinite reflectance of coals from the PSOC DOE Sample Bank as a function of H/C and O/C ratios in the van Krevelen diagram.

Input parameters are required to describe the coal structure and its evolution kinetics. Sets of parameters have been developed for the eight coals provided by the Argonne Premium Coal Sample Program [26], employing various analytical methods, including TG–FTIR, solvent swelling and extraction, fluidity, nuclear magnetic resonance (NMR), and FIMS [1,3].

Correlation Approach

The behavior of coal when subjected to a physical and chemical analysis or treatment exhibits rank dependence in most instances. For example, Solomon et al. [3] have shown a consistent variation of coal functional group compositions with rank. The basis of the correlation formulation presented here relies on the well-known van Krevelen diagram [27], which indicates that the progress of coalification in terms of the coal's hydrogen to carbon (H/C) and oxygen to carbon (O/C) atomic ratios forms a distinctive band in the H/C and O/C two-dimensional plane. Each coal has a coordinate (O/C, H/C) in the van Krevelen diagram. Figure 1 illustrates the variation of the vitrinite reflectance index (v.r.i.), as a function of H/C and O/C, for 45 coals from the Penn. State Coal Sample Bank (PSOC). As the v.r.i. is commonly accepted as a rank indicator, it is reasonable to assume that there exists a correlation between rank and elemental composition. Therefore, a parameter for an unknown coal can be interpolated from those for

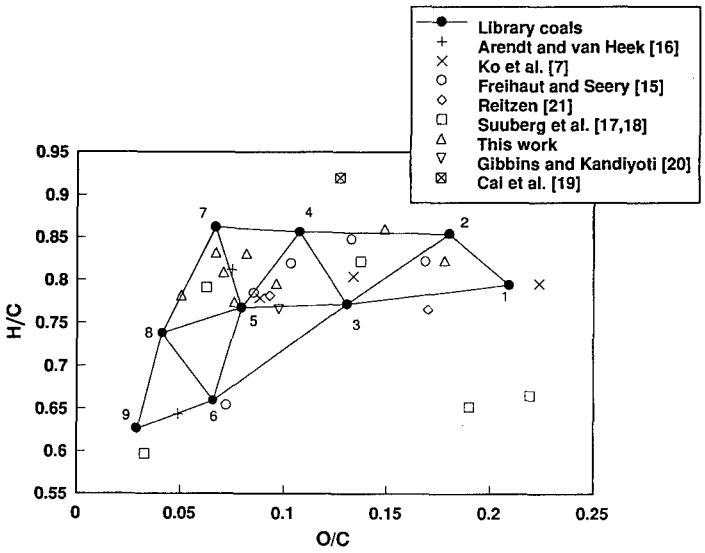

FIG. 2. The interpolation mesh in the van Krevelen diagram and coals used for tar yield comparisons. Coals in the interpolation mesh are 1. Beulah-Zap, 2. Wyodak, 3. Illinois #6, 4. Blind Canyon, 5. Pittsburgh #8, 6. Upper Freeport, 7. PSOC 1448, 8. PSOC 1474, and 9. PSOC 1521.

a set of coals that are well studied based on a comparison of the elemental compositions. These well-defined coals are called library coals, a term used by Williams et al. [28].

It is proposed to use a two-dimensional linear interpolation method commonly used in finite-element analyses, with O/C and H/C as two rank indicators. Let x be a parameter of an unknown coal, and $x^0(i)$ $(i = 1,N)$ are the corresponding parameters of the N library coals. The N library coals form a two-dimensional triangular element mesh in the van Krevelen diagram, as displayed in Fig. 2, where N is 9 and each node represents a coal. The mesh nodes are plotted as filled circles, and other symbols in the plot are the coals to be interpolated. Each triangular element contains three nodes (coals). If an unknown coal is inside the element J, whose three nodal numbers are $i_J^{(1)}$, $i_J^{(2)}$, and $i_J^{(3)}$, the unknown parameter, x, is interpolated as

$$x = (1 - r - s)\cdot x^0(i_J^{(1)}) + r\cdot x^0(i_J^{(2)}) + s\cdot x^0(i_J^{(3)}) \tag{1}$$

where r and s $(0 \leq r, s \leq 1)$ are the local coordinates of the unknown coal in element J and are determined from the positions of the unknown coal and the three interpolating coals in the van Krevelen diagram. Let U denote the point of the unknown coal in the van Krevelen diagram. Here $\Delta(i_J^{(1)}, i_J^{(2)}, i_J^{(3)})$, $\Delta(i_J^{(1)}, U, i_J^{(3)})$, and $\Delta(i_J^{(1)}, i_J^{(2)}, U)$ are the areas of the triangles formed by nodes $(i_J^{(1)}, i_J^{(2)}, i_J^{(3)})$, $(i_J^{(1)}, U, i_J^{(3)})$, and $(i_J^{(1)}, i_J^{(2)}, U)$, respectively. The terms r and s are calculated as follows

$$r = \frac{\Delta(i_J^{(1)}, U, i_J^{(3)})}{\Delta(i_J^{(1)}, i_J^{(2)}, i_J^{(3)})} \qquad s = \frac{\Delta(i_J^{(1)}, i_J^{(2)}, U)}{\Delta(i_J^{(1)}, i_J^{(2)}, i_J^{(3)})}. \tag{2}$$

The interpolation mesh is composed of nine coals, six of which come from the Argonne Premium Coal Sample Program and three of which are PSOC coals (PSOC 1474, PSOC 1448, and PSOC 1521). Extensive experimental studies have been carried out on the Argonne Premium Coals, and model input parameters are well established [3]. Predictions of the pyrolysis yields of these coals under various conditions are in very good agreement with the data collected in several types of reactors [29]. The Lewiston–Stockton coal was not used as a library coal because it has a very similar elemental composition to the Pittsburgh Seam Coal. The Pocahontas #3 coal was not selected since it has a very high rank and is far away from the rest of the coals. The three PSOC coals were added to this mesh recently, so that a larger area is covered. The functional group compositions and the pyrolysis kinetic parameters of these three coals were obtained based on data from TG–FTIR analysis and solvent extraction experiments performed in our own laboratory and fluidity data from the PSOC coal database.

With this scheme, any of the parameters for the FG–DVC model can be interpolated for an unknown coal when its elemental composition is identified. The interpolation of the functional group compositions of the oxygen, sulfur, and nitrogen gases requires special care in order to maintain a proper mass closure. For example, the total amount of the oxygen

containing functional groups is limited by the oxygen content. Therefore, instead of interpolating the amounts of oxygen gas precursors directly, only the fraction of oxygen in a functional group is calculated and is used to compute the amount of this functional group from the oxygen content. The same procedure is followed for the sulfur and nitrogen gases.

Prediction of Tar and Total Volatile Yields

Tar comprises up to about 50% of the total volatiles during coal combustion for most coals. The secondary reactions of tar produce soot, PAH, and light gases that affect ignition, flame stability, and the radiative properties of the flame. Tar yields vary with coal type and are affected by reactor conditions such as pressure and heating rate. The interpolation scheme presented above enables the FG–DVC model to predict the tar yield of a coal under various pressure and heating-rate conditions from its elemental analysis. To verify this capability, tar yield data were assembled from the literature and were compared with the model predictions. These data were measured with heated grid systems under fast devolatilization conditions (heating rates from 100 °C/s to 1000 °C/s) for various coals and pressures (10^{-4}–7 MPa). In addition to these data, tar yields from eight PSOC coals were measured with a TG-FTIR system at a heating rate of 30 °C/min and atmospheric pressure. The details of the TG–FTIR system have been presented elsewhere [30]. The data used for model verification were selected to span a wide range of coal types (from lignite to low-volatile bituminous) and pyrolysis conditions. Part of the data set was taken from the tabulation given by Ko et al. [7].

For each of these coals, the FG–DVC input parameters were interpolated with the scheme proposed above, and the tar yields from these coals were predicted with the pressures and the heating rates specified in these references. Eleven coals from the references and the eight PSOC coals are inside the mesh, and the standard interpolations were performed. The Pocahontas, Illinois #6, and North Dakota lignite studied by Suuberg et al. [17] are outside the mesh and were predicted with the input parameters of the corresponding Argonne coals. The Alabama bituminous coal studied by Freihaut and Seery [15], the Beulah Zap coal studied by Ko et al. [7], and the Illinois #6 coal studied by Cai et al. [19] were modeled based on input files used for the Upper Freeport coal, Zap lignite, and Illinois #6 coal of the Argonne Premium Coal Sample Program, respectively. The Colstrip lignite studied by Reitzen [21] is close to the edge of the triangle formed by the Zap lignite, Wyodak, and Illinois #6 coals and was modeled with an elemental composition inside this triangle and closest to Colstrip.

The predictions and the data are compared in Fig. 3. The standard error of the estimate, σ, is calculated as follows:

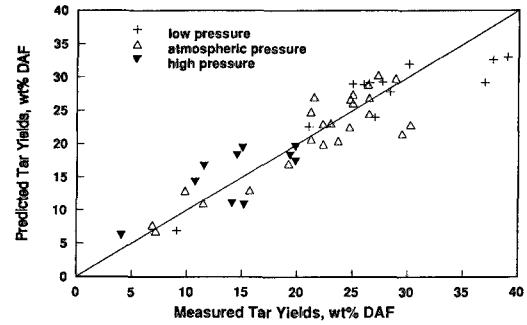

FIG. 3. Comparison of the measured and the predicted tar yields for coals given in Fig. 2.

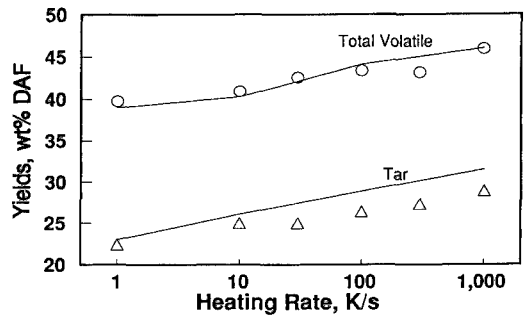

FIG. 4. Variations of tar (△) and total volatile (○) yields as a function of heating rate for a Linby coal studied by Gibbins and Kandiyoti [20]. The lines are the predictions, and the symbols are the data.

$$\sigma = \left[\sum_{i}^{N} \frac{(Y_i^m - Y_i^p)^2}{N} \right]^{1/2} \tag{3}$$

where Y_i^m and Y_i^p are the measured and predicted tar yields [in wt.%, dry ash free (daf)], and N is the number of data points compared. The standard errors of the estimates are 3.8, 3.1, and 3.4% for data collected at vacuum, atmospheric, and high pressures, respectively. The overall standard error of the estimate is 3.4%. This is in the same range as the experimental scatter commonly encountered in tar measurements.

Figure 4 compares the predicted and the measured variations of tar and total volatile yields as a function of heating rate for a Linby coal studied by Gibbins and Kandiyoti [20]. For an Illinois #6 coal studied by Cai et al. [19], the variations of tar and total volatile yields as a function of heating rate and pressure were predicted and are compared with the data in Fig. 5. These plots show that the predictions

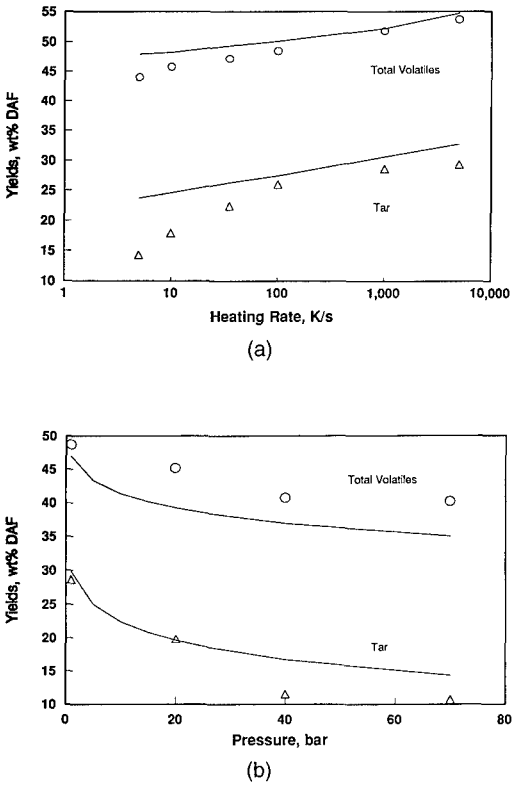

FIG. 5. (a) Variations of tar (△) and total volatile (○) yields as a function of heating rate at atmospheric pressure for an Illinois #6 coal studied by Cai et al. [19]. The lines are the predictions and the symbols are the data. (b) Variations of tar (△) and total volatile (○) yields as a function of pressure at 1000 K/s for an Illinois #6 coal studied by Cai et al. [19]. The lines are the predictions, and the symbols are the data.

are in reasonably good agreement with the data. It should be noted that this is achieved based only on the elemental compositions, without further prior knowledge of these coals.

Discussion

The success of this interpolation scheme depends on a thorough understanding of the library coals. Selection of these library coals must be performed with care so that none of these coals has unusual behavior and deviates from coals of the same rank. Although the current mesh contains only nine coals, it is one advantage of this method that it can be easily extended to include more coals. Adding more coals in the interpolation mesh will certainly increase the reliability of the predictions and will allow coverage of a wider range of coal types.

A few large discrepancies were observed for some coals, indicating the need for further improvements in the correlation method and/or the FG–DVC model. Underpredictions of tar yields in vacuum were observed for a group of Pittsburgh seam coals, for which the measured tar yields (in wt.%, daf) are 39.0 [15], 37.0 [10], and 37.7% [18] and the predicted tar yields are 33.0, 29.2, and 32.6%, respectively. However, good agreement was obtained at atmospheric pressure for these coals (26.5 [10] vs 24.5% and 26.5 [17] vs 26.9%). Since the pressure variations are correctly predicted for most other coals, the high-vacuum tar yields for the Pittsburgh seam coals appear to be caused by a mechanism particular to these coals. The model also underpredicts tar yields for the PSOC 1519 and 1492 coals. The Sesser subbituminous coal studied by Ko et al. [14] is the only coal that has a large overpredicted atmospheric pressure tar yield (21.5 [14] vs 27.0%). This coal seems to be an unusual coal, as a relatively low tar yield was also reported by Reitzen [21] (11%). For most of the coals, the predictions are within ±3% of the data, and the standard error of the estimate calculated without the above large discrepancies is 2.5%.

The basis of this interpolation method is the assumption that coals within the same rank classification behave similarly. Predictions based on this method are targeted at the normal or mean behavior of coals within the same rank. Deviations from normal, however, should be expected. If the deviation is large and cannot be identified with an existing mechanism, the behavior of that coal becomes unpredictable with the current method. The comparisons presented in Figs. 3 through 5 indicate that, for most of the coals tested, the deviations are small enough that the tar yields are well predicted. The use of a van Krevelen diagram to represent coal rank is well accepted, so there is a sound basis for using the O/C and H/C ratios as interpolation coordinates. However, this assumption requires the accurate determination of the coal elemental composition. The fact that the oxygen content is usually determined by difference is the major reason for the inaccuracy of the coal elemental compositions, especially for high-rank coals which have low oxygen contents. Coals having a high sulfur content can cause a difficulty in measuring the oxygen content by difference, and the true hydrogen content can be obscured by moisture present during the analysis. An inaccurate elemental composition of a coal results in a displacement from its "true" position in the van Krevelen diagram, which will cause a deviation in the predictions.

Tar formation is the result of many processes: bond breaking, cross-linking, internal transport of metaplast, and vaporization. Particularly rank dependent are the bond-breaking and cross-linking

processes. There exists evidence that the tar yield is affected by various cations in coals [31–34]. Serio et al. [34] recently studied the effects of demineralization and ion exchange of three cations (K^+, Ba^{2+}, Ca^{2+}) on the pyrolysis tar yields of Zap lignite and Wyodak subbituminous coals and found that the tar yields are reduced for coals exchanged with all three cations. It was suggested that cations may act as initial cross-links and influence retrogressive reactions. Since the coal cation content is not directly linked to rank, this effect is not accounted for in our model and may contribute to the difference between the predictions and data. The cation content will be considered as an additional parameter in determining tar yields in future studies. Other parameters that will be considered for improving the model capabilities include the proximate volatile matter content, the total and/or organic sulfur content, and the maceral composition. While parameters based on more sophisticated analytical techniques, such as Fourier transform–infrared (FT-IR) or NMR could be considered, this type of information is not readily available for most coals.

Correlation relations between elemental compositions and maximum yields have previously been developed by Ko et al. [7] and Neavel et al. [8]. Their correlation expressions were able to effectively model the tar data that were used in developing the correlations. However, it is not clear how well these correlations can be applied to coals that are outside the respective data sets. This paper demonstrates that a correlation method based on nine coals is able to make good predictions for a set of 27 untested coals. This advantage of a wider range of applicability will be further confirmed by comparing the predictions with the pyrolysis data from additional untested coals.

Niksa and coworkers [6,11,12] have also used a correlation method for their coal devolatilization model. Their approach is similar to ours in that it is based on the correlation of model input parameters to coal elemental composition. However, each input parameter has a separate correlation with rank. In addition, the FLASHCHAIN model on which these correlations are based involves very different assumptions about coal structure, pyrolysis chemistry, and pyrolysis kinetics when compared with FG–DVC.

The approach outlined in this paper also differs from those of Ko et al. [7] and Neavel et al. [8] in that, in addition to correlating the maximum tar yields with coal rank, the whole set of the basic input parameters of the FG–DVC model is interpolated, which allows for much more extensive predictions of coal devolatilization than these simple correlations. Such capabilities are due to the high level of development of the FG–DVC model, whose basic theoretical features can be found in previous publications [1–3].

Our correlation scheme appears to provide adequate descriptions of the total volatile and tar yields as well as their variations with heating rates for the Linby coal studied by Gibbins and Kandiyoti [20] (Fig. 4). For the Illinois #6 coal studied by Cai et al. [19] (Fig. 5), a reasonable comparison is obtained at high heating rates and pressures up to 20 bar. The relatively large discrepancies at pressures higher than 20 bar and at low heating rates (for tar yield only) probably indicate the need for further improvement of the description of tar transport in the FG–DVC model.

The yields and the compositions of the volatile gases are also important. The capability of FG–DVC in predicting the total volatile yields has been demonstrated in Figs. 4 and 5. The amounts of individual gas species are also predicted by FG–DVC along with the tar yields, and this is one of the chief advantages of this model when compared to the FLASHCHAIN [6,11,12] model. However, comparisons are more difficult because of the relatively small amount of available data. This will be a subject of further studies.

Conclusions

An interpolation method was proposed to correlate the input parameters of a coal devolatilization model, FG–DVC, for untested coals, and is conceptually applicable to other devolatilization models. This method uses a set of well-defined coals (library coals) to form a triangular mesh in the van Krevelen diagram. If an unknown coal is within a triangle formed by three library coals, the model input parameters for this unknown coal can be interpolated from those of the three library coals based solely on a knowledge of the elemental composition. This method allows the FG–DVC model to be used for any coal that can be interpolated. It is also easy to accommodate more library coals, so that a wider range of coal types can be covered. The validity of this method was demonstrated by comparing the tar yield measurements and predictions for 27 coals over a wide range of pressures and heating rates. For most of the coals, the predictions compare very well with the data.

Acknowledgments

This work was supported by the Morgantown Energy Technology Center of the U.S. Department of Energy, through Contracts Nos. DE-AC21-86MC23075 and DE-AC21-93MC30040. The authors wish to acknowledge helpful comments from Professor Eric M. Suuberg of Brown University. They also thank the Energy and Fuels Research Center of the Pennsylvania State University for the supply of the PSOC coal samples and data.

REFERENCES

1. Solomon, P. R., Hamblen, D. G., Carangelo, R. M., Serio, M. A., and Deshpande, G. V., *Energy Fuels* 2:405 (1988).
2. Solomon, P. R., Hamblen, D. G., Yu, Z.-Z., and Serio, M. A., *Fuel* 69:754 (1990).
3. Solomon, P. R., Hamblen, D. G., Serio, M. A., Yu, Z.-Z., and Charpenay, S. C., *Fuel* 72:469 (1993).
4. Grant, D. M., Pugmire, R. J., Fletcher, T. H., and Kerstein, A. R., *Energy Fuels* 3:175 (1989).
5. Niksa, S., and Kerstein, A. R., *Energy Fuels* 5:647 (1991).
6. Niksa, S., *Energy Fuels* 5:673 (1991).
7. Ko, G. H., Sanchez, D. M., Peters, W. A. and Howard, J. B., *Twenty-Second Symposium (International) on Combustion,* The Combustion Institute, Pittsburgh, (1988) p. 115.
8. Neavel, R. C., Smith, S. E., Hippo, E. J., and Miller, R. N., *Proceedings of International Conference on Coal Science,* Dusseldorf, Germany, 1981, p. 1.
9. Serio, M. A., Peters, W. A., and Howard, J. B., *Ind. Eng. Chem. Res.,* 26:1831 (1987).
10. Suuberg, E. M., Peters, W. A., and Howard, J. B., *Seventeenth Symposium (International) on Combustion,* The Combustion Institute, Pittsburgh, 1979, p. 117.
11. Niksa, S., and Kerstein, A. R., *Am. Chem. Soc. Div. Fuel Chem. Preprints* 38(4):1346 (1993).
12. Niksa, S., and Kerstein, A. R., *Proceedings of International Conference on Coal Science,* Banff, Alberta, 1993, Vol. II, p. 397.
13. 93-PCGC-2, Users Manual, Brigham Young University and Advanced Fuel Research, Inc., 1993.
14. Ko, G. H., Peters, W. A., and Howard, J. B., *Fuel* 66:1118 (1987).
15. Freihaut, J. D., and Seery, D. J., *Am. Chem. Soc. Div. Fuel Chem. Preprints* 26(2):133 (1981).
16. Arendt, P., and van Heek, K.-H., *Fuel* 60:779 (1980).
17. Suuberg, E. M., Unger, P. E., and Larsen, J. W., *Energy Fuels* 1:305 (1987).
18. Suuberg, E. M., Lee, D., and Larsen, J. W., *Fuel* 64:1668 (1985).
19. Cai, H.-Y., Güell, A. J., Dugwell, D. R., and Kandiyoti, R., *Fuel* 72:322 (1993).
20. Gibbins, J. R., and Kandiyoti, R., *Fuel* 68:895 (1989).
21. Reitzen, T. R., "Effects of Pyrolysis Conditions on Products of Interests in Formed Coke Production," Master's Thesis, Massachusetts Institute of Technology, Cambridge, MA, 1978.
22. Bassilakis, R., Zhao, Y., Solomon, P. R., and Serio, M. A., *Energy Fuels* 6:710 (1993).
23. Hamblen, D. G., Yu, Z. Z., Charpenay, S., and Serio, M. A., *Proceedings of International Conference on Coal Science,* Banff, Alberta, 1993, Vol. II, p. 401.
24. Stauffer, D., and Aharony, A., *Introduction to Percolation Theory,* 2nd ed., Taylor & Francis, London, UK, 1991.
25. Fletcher, T. H., Kerstein, A. R., Pugmire, R. J., Solum, M. S., and Grant, D. M., *Energy Fuels* 6:414 (1992).
26. Vorres, K. S., *Energy Fuels* 4(5):420 (1990).
27. van Krevelen, D. W., *Coal,* 3rd ed., Elsevier Publishing Company, Amsterdam, 1993.
28. Williams, A., Pourkashanian, M., Bysh, P. and Norman, J., Keynote address to the Coal Utilization and the Environment Conference, May 18–20, 1993, Orlando, FL.
29. Serio, M. A., Solomon, P. R., Yu, Z.-Z., Deshpande, G. V., and Hamblen, D. G., *Am. Chem. Soc. Div. Fuel Chem. Preprints* 33(3):91 (1988).
30. Solomon, P. R., Serio, M. A., Carangelo, R. M., Bassilakis, R., Gravel, D., Baillargeon, M., Baudais, F., and Vail, G., *Energy Fuels* 4:319 (1990).
31. Tyler, R. J., and Schafer, H. N. S., *Fuel* 65:757 (1986).
32. Morgan, M. E., and Jenkins, R. G., *Fuel* 65:764 (1986).
33. Wornat, M. J., and Nelson, P. F., *Energy Fuel* 6:136 (1992).
34. Serio, M. A., Kroo, E., Teng, H., and Solomon, P. R., *Am. Chem. Soc. Div. Fuel Chem. Preprints* 38(2):577 (1993).

COMMENTS

Patrick Gilot, Laboratoire G.R.E., France. In the case of nonsoftening coals, calculations show that depending on size, diffusive flow (Fickian diffusion) can become the most important way of tar transport inside the particle, especially around 1 atm of external pressure. This mechanism of transport can overcome the convective flow. Thus, it is difficult to assume that there are not mass transfer limitations inside the particle. Could you comment on that point?

Author's Reply. The presence or absence of internal mass transport limitations for tar has been the subject of considerable debate in the literature [1,2,3]. While calculations sometimes indicate these limitations are present, they are often based on estimates of the tar diffusivity which may be off by orders of magnitude. Most pyrolysis experiments cannot confirm or deny the existence of these limitations since the tar yield is usually not measured in real time, but only after quenching the experiment. The absence of a particle size effect on yields does not necessarily mean that no internal transport limitations occurred, but that those that may have occurred did not lead to secondary reactions. There is direct experimental evidence that demonstrates the existence of some type of mass transfer effect, namely the well-known effect of applied inert

gas pressure on coal pyrolysis product yields [2,3]. Most early attempts to model this phenomenon assumed that external mass transport of tar was the primary limitation. However, as discussed in Ref. 1, most recent modeling efforts, including our own, have utilized the flash distillation assumption that requires equilibrium of the heavy tars in the light gas species. This has been applied to both softening and nonsoftening coals and is consistent with what has been historically described as an internal mass transport limitation.

REFERENCES

1. Solomon, P. R., Serio, M. A., and Suuberg, E. M., *Prog. Energy Combust. Sci.* 18:133–220 (1992).
2. Howard, J. B., in *Chemistry of Coal Utilization,* Chap. 12 (M. Elliott, Ed.), Wiley, New York, Second Supplementary Vol., 1981.
3. Suuberg, E. M., in *Chemistry of Coal Conversion,* Chap. 4, (R. H. Schlosberg, Ed.), Plenum, New York, 1985.

•

Jerzy Tomeczek, Silesian Technical University, Poland. What definition of tar do you use in your presentation?

Author's Reply. The definition of the tar yield is an operational definition that varies from one experiment to the next depending on the collection devices and solvents used for the tar fraction. Tar is defined by most investigators as the material that is vaporized during pyrolysis but is condensible at room temperature. A discussion of some of the methods used to define tar is included in a recent review article [1]. The differences in these methods can account for some of the variability between the model predictions and data and could contribute as much as $\pm 10\%$ on a relative basis.

The main difficulty is collecting all of the tar from the numerous surfaces that it may encounter in the collection system. For this reason, most of the missing material from a pyrolysis experiment is usually from the tar fraction, and the tar yields are usually underreported. However, since some tar can redeposit onto the char surfaces (e.g., in an entrained flow reactor experiment) one must be careful to extract only this material and not additional material (called extractables) that did not vaporize during the course of the experiment.

REFERENCE

1. Solomon, P. R., Serio, M. A., and Suuberg, E. M., *Prog. Energy Combust. Sci.* 18:133–220 (1992).

•

A. E. Jacob Akanetuk, Stanford University, USA. Most of the presented work has concentrated on the chemical decomposition kinetics of devolatilization. Have there been experiments to show that the rate of the devolatilization process is controlled by intrinsic chemical kinetics and not internal mass transport or external heat transfer?

Author's Reply. The effect of mass transport on tar yields has been discussed above. As indicated above, there are relatively few experiments that are able to definitively establish the effect of internal mass transfer on devolatilization rates since the yields are not usually measured in real time. One exception is the work of Arendt and van Heek [4] where a thermobalance coupled with an on-line mass spectrometer allowed for real-time measurements of volatile product yields including tar (by difference). Although the total yields of volatile products declined with increasing pressure from 1.1 MPa N_2 to 10 MPa N_2, the shapes of the evolution curves for tar and gas evolution were largely unchanged.

As discussed in Ref. 1, there are many examples of experiments where external heat transfer controls the devolatilization rate. This is not necessarily a problem, as long as the temperature of the pyrolyzing particles is well known. There are many pitfalls involved in calculation of the particle temperature in high heating rate experiments because of uncertainties in the thermal and optical properties along with the local heat transfer coefficients. Consequently, under these conditions, only experiments where particle temperatures have been measured by an optical technique are reliable for kinetic determinations. At low heating rates, thermogravimetric analysis (TGA) experiments over a range of heating rates can be used to reliably establish pyrolysis kinetic rates since the experiments can be designed to allow a thermocouple to record the thermal history of the pyrolyzing particles. The kinetic parameters obtained from TGA experiments can also be used to test the consistency of kinetic rates determined at high heating rates.

REFERENCE

1. Arendt, P., and van Heek, K. H., *Fuel* 60:779 (1981).

Twenty-Fifth Symposium (International) on Combustion/The Combustion Institute, 1994/pp. 561–568

NEAR-EXTINCTION AND FINAL BURNOUT IN COAL COMBUSTION

ROBERT H. HURT AND KEVIN A. DAVIS
Combustion Research Facility
Sandia National Laboratories, Livermore, CA 94550, USA

The late stages of char combustion have a special technological significance, as carbon conversions of 99% or greater are typically required for the economic operation of pulverized coal-fired boilers. In the present article, two independent optical techniques are used to investigate near-extinction and final burnout phenomena for Illinois #6 and Pittsburgh #8 bituminous coals. Captive-particle image sequences, combined with in situ optical measurements on entrained particles, provide dramatic illustration of the asymptotic nature of the char burnout process. Single-particle combustion to complete burnout is seen to comprise two distinct stages: (1) a rapid high-temperature combustion stage, consuming about 70% of the char carbon and ending with near-extinction of the heterogeneous reactions due to a loss of global particle reactivity, and (2) a final burnout stage occurring slowly and at lower temperatures. For particles containing mineral matter, the second stage can be further subdivided into (2a) late char combustion, which begins after the near-extinction event and converts carbon-rich particles to mixed particle types at a lower temperature and a slower rate, and (2b) decarburization of ash—the removal of residual carbon inclusions from inorganic (ash) frameworks in the very late stages of combustion. This latter process can be extremely slow, requiring over an order of magnitude more time than the primary rapid combustion stage. For particles with very little ash, the loss of global reactivity leading to early near-extinction is believed to be related to changes in the carbonaceous char matrix, which evolves over the course of combustion as a result of simultaneous oxidation and heat treatment. More realistic models are needed to predict the asymptotic nature of char combustion and to make accurate predictions in the range of industrial interest.

Introduction

The late stages of char combustion have a special technological significance, as carbon conversions of 99% or greater are typically required for the economic operation of commercial-scale boilers. Achieving such high conversions is difficult in certain cases, especially in connection with boilers retrofitted with combustion zone modifications for NO_x abatement [1]. While there is an extensive literature on ignition [2] and char combustion [3–5], little attention has been paid to extinction in the important late stages of combustion, in part due to the difficulty of making scientifically meaningful measurements on highly reacted samples in which inorganic material (ash) is the majority constituent.

In the present article, two independent optical techniques are used to make kinetic measurements on complex highly reacted samples with high inorganic content. The first technique uses *in situ* optical measurements on entrained char particles burning in a laminar flow reactor, coupled with a recently proposed criterion [6] for distinguishing inorganic from carbon-rich particles by measurement of their spectral emissive factors* in the near-infrared. After eliminating inorganic particles (which could otherwise masquerade as low-reactivity carbon-rich particles), conversion-dependent kinetic parameters are determined for the carbon-rich particles alone. The second technique uses a new captive-particle imaging apparatus equipped for simultaneous near-infrared thermography. This system is specifically designed for qualitative and quantitative investigation of the late stages of char combustion. The combination of these two techniques is used to investigate near-extinction and final burnout phenomena for Illinois #6 and Pittsburgh #8 bituminous coals. A goal of this work is to ascertain whether existing char combustion

*The spectral emissive factor at 800 nm, ε_{800} for an irregularly shaped, emitting particle, with a diameter along the flow axis of d_p, is defined as the average spectral radiance (W/cm^2 sr^{-1} μm^{-1}) of the particle at a given wavelength (here 800 nm) divided by the spectral radiance of a spherical black body with diameter d_p. The spectral emissive factor is, in essence, the particle spectral emissivity multiplied by a shape factor, $A_p/(\pi d_p^2/4)$, where A_p is the projected area of the particle as viewed from the optical axis.

kinetics models can be extrapolated to high conversion, or whether more detailed models of carbon burnout are needed that deal specifically with the chemical and physical phenomena unique to this region.

Previous Work:

A number of previous investigations of pulverized coal combustion have used single-particle imaging techniques, based on high-speed photography of entrained particles [7,8], holographic techniques [9], and charged-coupled device (CCD) array detection [10]. Captive-particle techniques have been used by various groups [11–13] for the study of coal devolatilization and combustion, with emphasis on swelling, morphological changes, and burnout times. These techniques have generated important insights, but none is designed specifically for quantitative investigation of the kinetics of extinction and final burnout for particles in the pulverized size range (<200 μm). There is little information on extinction in coal combustion. Essenhigh [5] reports one study on flame extinction, Ubhayakar et al. [14] have examined the thermal extinction of single graphite particles heated by a laser in cold surroundings, and Mulcahy [15] has analyzed the graphite data of Ubhayakar et al. [14].

Although numerous papers report on the characterization of commercial or pilot-scale residues [16–18], few studies have focused on the late stages of char combustion under carefully controlled conditions. Among those, Vleeskins and Nandi [19] have investigated the fuel-related factors determining the degree of coal burnout in a drop tube furnace. Mitchell [20] observed numerous particles with low temperatures at high conversion and has identified them as highly reacted, high-inorganic-content char particles. A recent paper examined the low-temperature particles in more detail [6], using an optical diagnostic to distinguish inorganic from carbon-rich particles by in situ measurement of their spectral emissive factors, ε_{800}, at a wavelength of 800 nm. It was found that a threshold value of 0.3 for the emissive factor could be used to statistically classify particles as carbon-rich ($\varepsilon_{800} > 0.3$) or inorganic ($\varepsilon_{800} < 0.3$) with an error rate or frequency of incorrect assignment of 4% or less. Application of the diagnostic indicates that most particles still contain substantial amounts of carbon at the point of abrupt temperature decrease, and that this residual carbon is oxidized slowly in a second, low-temperature combustion stage. In that work, near-extinction was defined as a large and abrupt, but mathematically continuous, decrease in particle temperature in the late stages of char combustion due to loss of global, or apparent, reactivity. This phenomenon is distinguished from true extinction, as defined by Mulcahy [15], which has a mathematically discontinuous nature, as discussed in the earlier work. The present paper continues the investigation of the late stages of combustion by acquiring data at longer residence times, by determining conversion-dependent kinetics, and by applying a new captive-particle imaging technique specifically designed to probe near-extinction and final burnout.

Materials and Experimental Procedures

Illinois #6 (PSOC-1493D) and Pittsburgh #8 (PSOC-1451D) high-volatile bituminous coals were chosen for this investigation. The two independent combustion experiments, involving entrained and captive particles, respectively, are described separately below. Figure 1 depicts the captive-particle imaging (CPI) apparatus. Char particles of 50–300 μm in diameter are placed on a low-density particle support and inserted into the flow reactor through a open test section in the quartz wall (see Fig. 1). The support is surrounded by a small conical cooling coil that maintains the particle at 200 °C–300 °C, while it is brought into the focal volume of a modified long-focal-length microscope. The cooling coil is then retracted, the particle is rapidly heated by the surrounding gases, and its ignition, combustion, and burnout behavior is imaged at high resolution using both reflected visible light and emitted light in the near infrared. Char samples for CPI experiments were prepared by injection of raw coal into a 1600 K gas stream containing 6 mole% oxygen in the laminar flow reactor and extraction of samples after 47 ms residence time, at the approximate end of primary devolatilization. The young char samples at this point have lost approximately half their total mass but still contain significant hydrogen (1–3 wt. %) and will release residual volatile matter in the early phases of the CPI experiments. Most but not all of the particles from these softening coals have fully solidified by 47 ms.

Because transport processes for particles in the pulverized size range are dominated by diffusion, conduction, and radiation, and not by convection [3], a mechanical suspension technique, if properly designed, will accurately simulate char combustion in entrained flows. (Note that convection does play a role in the combustion of larger particles and in other combustion subprocesses such as devolatilization.) For pulverized char combustion studies, the suspension device can be allowed to perturb the flow field, and thus the convective processes, if it does not present a significant barrier to diffusion, conduction, or radiation to and from the particle. The particle support used consists of a platinum ring, spanned in several places by 75-μm-diameter platinum wires that provide support for a thin layer of fine (5-μm-diameter) Al_2O_3 fibers (99% pure). Quantitative estimates [21] indicate that the low-solid-volume fraction of the fiber bed provides an environment in which the gas-to-particle mass and heat transfer coefficients are

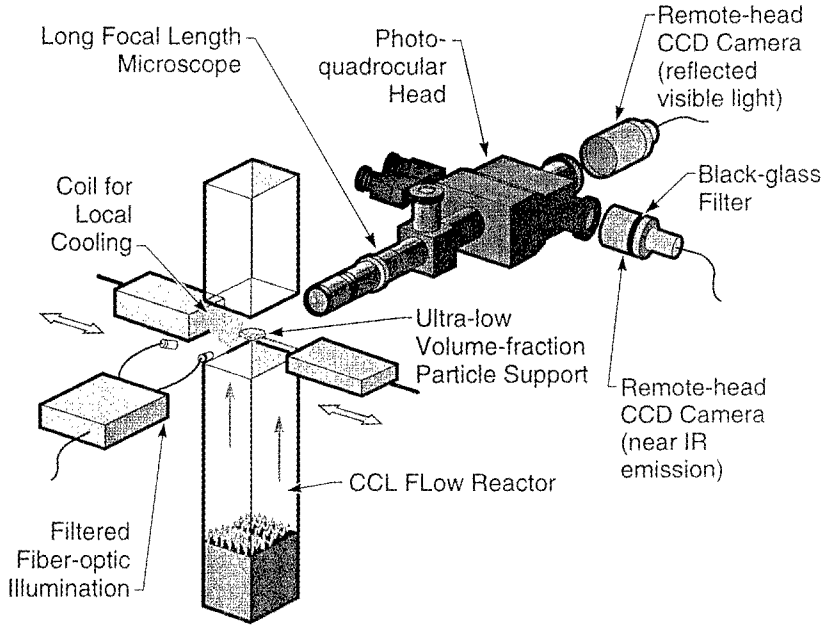

FIG. 1. Schematic of the captive-particle imaging apparatus. Analog and digital image acquisition, storage, and processing hardware are not shown.

very similar to those for entrained particles. The flow field and the temperature transients at the beginning of the experiment have been characterized and are discussed in detail elsewhere [21]. Maximum heating rates are approximately $2 \cdot 10^3$ K/s with good shot-to-shot reproducibility. The rapid and reproducible temperature transients combined with the avoidance of transients in gas composition make this flow configuration useful for investigating char combustion and burnout phenomena.

The optical system comprises a long-focal-length microscope (model K2 of Infinity Photo-Optical) modified by addition of an internal beam splitter to allow simultaneous dual video imaging of the same field of view. Two CCD cameras record one image formed by reflected visible light (supplied by fiber-optic illumination) and a second formed by near-infrared emission from the particle surfaces. The near-infrared emission (700–1000 μm in wavelength) is selectively imaged by incorporating an optical filter in the quadrocular head, while reflected radiation in the same wavelength band is rejected by placement of an infrared filter within the fiber-optic illuminator. The fiber-optic illumination is rejected so successfully that this second optical channel records no image whatsoever until the particles reach approximately 900 K and begin to emit significantly in the near-infrared. The near-infrared channel has been calibrated with a high-temperature black-body source, and the thermographic images are digitized and quantitatively analyzed to determine particle radiance temperatures.

In the second independent experiment, optical measurements were made of particle size, temperature, and emissive factor during combustion of dilute streams of entrained particles in a laminar flow reactor described elsewhere [20]. Residence times greater than 117 ms were obtained by rapid quenching and collection of solid samples followed by reinjection and further combustion. The collection and reinjection process has been shown to have no effect on the subsequent kinetics for single particles, although it may change the size distribution of the bulk sample by inducing fragmentation and/or reagglomeration of fines during collection and handling [22]. Because particle sizes are measured in situ, single-particle kinetics can be determined from the optical data with no errors introduced by the reinjection procedure. Total ash was used as a tracer to determine carbon conversions for the bulk samples, and the weight loss at 47 ms residence time (where the visible volatiles flame disappears) was used to put the conversions on a volatile-matter-free, or char, basis.

Results

Captive-Particle Imaging:

Image sequences were obtained for approximately 100 particles of Illinois #6 and Pittsburgh #8 coal chars, which exhibit statistical particle-to-particle

variations in size, morphology, and ash content. Figure 2 is a single-camera sequence illustrating the typical combustion behavior of particles of high mineral content. Shortly after retraction of the cooling coil, a bright red optical emission from the solid surfaces becomes evident (see image at 0.12 s in Fig. 2), indicating an elevated particle temperature. The bright incandescence lasts for about 1/2 s before it fades, indicating a significant decrease in particle temperature. Note that the temperature decrease occurs under nearly isothermal conditions in the gas phase (the local gas temperature is actually *increasing* slightly), and while the char particle still contains much visible dark material, typically elemental carbon.*

After the temperature decrease, combustion continues, slowly converting the carbon-rich particles to mixed particle types containing elemental carbon in their cores, or as islands within a coherent inorganic matrix. The final stage of the combustion process consists of the removal of these elemental carbon inclusions from a predominately inorganic matrix. This process, which we refer to here as "ash decarburization," can be extremely slow, requiring 10–30 s for the particle represented in Fig. 2. Another unique characteristic of high-mineral-content particles is that their combustion and burnout generally occur without dramatic changes in the particle morphology or size. The mineral matter provides a cohesive framework from which elemental carbon is removed while preserving much of the original particle shape. No fragmentation or structural rearrangement of the particles is typically observed. The ash frameworks, however, are often observed to slowly consolidate and densify after most of the carbon disappears, due perhaps to sintering mechanisms.

The low-mineral-content, low-density particles, in contrast, undergo profound morphological changes during combustion. Consumption of carbon from these particles often results in loosely connected, fragile structures at moderate to high conversion. Such particles are much more likely to dissociate during combustion, but instead of producing distinct fragments as often observed for entrained particles [23], they are typically observed to contract or reagglomerate to yield a single ash particle. Further work is needed to understand the contraction process and its implications for fragmentation. It is particularly noteworthy that particles of very low mineral content also exhibit a brief period of bright incandescence followed by a distinct decrease in emission before the particle size and morphology change dramatically.

To explore the near-extinction phenomenon in greater detail, dual images of reflected visible light and near-infrared emission were obtained for selected particles. An example dual-image sequence is shown in Fig. 3, along with time-resolved radiance temperatures* determined from digitization of the near-infrared images. The combined data and images show a period of bright incandescence from 0.8 to 1.2 s, followed by a relatively abrupt drop in temperature of 125 K and a long, slow, nearly isothermal, final burnout to a carbon-free ash particle. The gradual decrease in radiance temperature at long times is in part due to decreases in emissivity, but the initial rapid decrease reflects a decrease in actual temperature, since it is large, and occurs abruptly while the particles are still optically black. These data are particularly useful for defining the point of near-extinction—it occurs (1) when the local gas temperature is nearly constant or increasing slightly, (2) when the particle diameter is 85% of the initial diameter, (3) while the particle is still dark under visible illumination, before the appearance of visible surface ash. This near-extinction is observed even for particles containing very small amounts of mineral matter (as inferred from the size of the final ash particle). For these low-ash particles, the near-extinction is clearly not caused by the formation of an ash-film diffusion barrier.

In Situ Optical Measurements on Entrained Particles:

The second independent experiment produced a set of single-particle size, temperature, and emissive factor measurements for Illinois #6 coal char at various residence times. These data indicate a gradual transition from a population of fully ignited char particles at 72 ms to a predominance of low-temperature particles at 117 ms and, finally, to a predominance of inorganic-rich particles (with emissive factors < 0.3) at 306 ms. Figure 4 shows the time evolution of the particle temperatures and sizes for a subset of this raw data with emissive factors greater than 0.3 (representing the carbon-rich particles and mixed particle types [6]). The temperatures in Fig. 4 have been

*Most, but not all, of the black material observed in these highly reacted samples is elemental carbon, the remainder being primarily iron-bearing phases, as determined by laser spark spectroscopy. The phrase "elemental carbon" is used here to refer to organic carbon (which is impure and contains small amounts of nitrogen, sulfur, oxygen, etc.) as distinct from inorganic carbon (e.g, in carbonates).

*Radiance temperature is defined as the temperature of a hypothetical black body emitting the same radiative power as the real object (particle) in the wavelength range of interest (here 700–1000 nm). For carbon-rich particles such as those found up to about 2 s in Fig. 4, whose emissivities are approximately 0.8 [24], true particle temperatures will be approximately 20 K greater than the reported radiance temperatures. The true temperatures of inorganic-rich and mixed particles are difficult to estimate because of the unknown and variable optical properties of ash on a particle-by-particle basis.

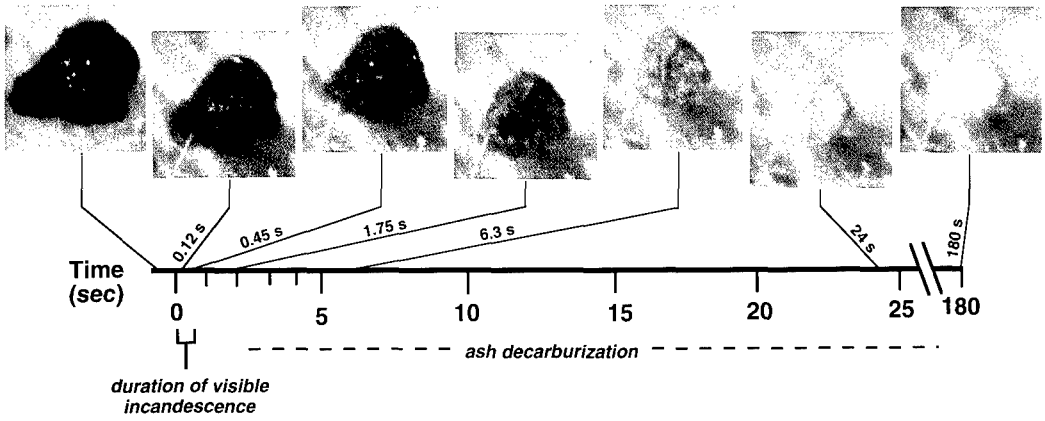

FIG. 2. Single-camera captive-particle image sequence for a typical Illinois #6 coal char particle. Combustion of ≈150-μm particle in 6 mole% oxygen at a steady-state local gas temperature of 1360 K. Images formed by reflected visible light. Images and time line show the duration of the rapid, incandescent combustion phase and the lower-temperature final burnout phase.

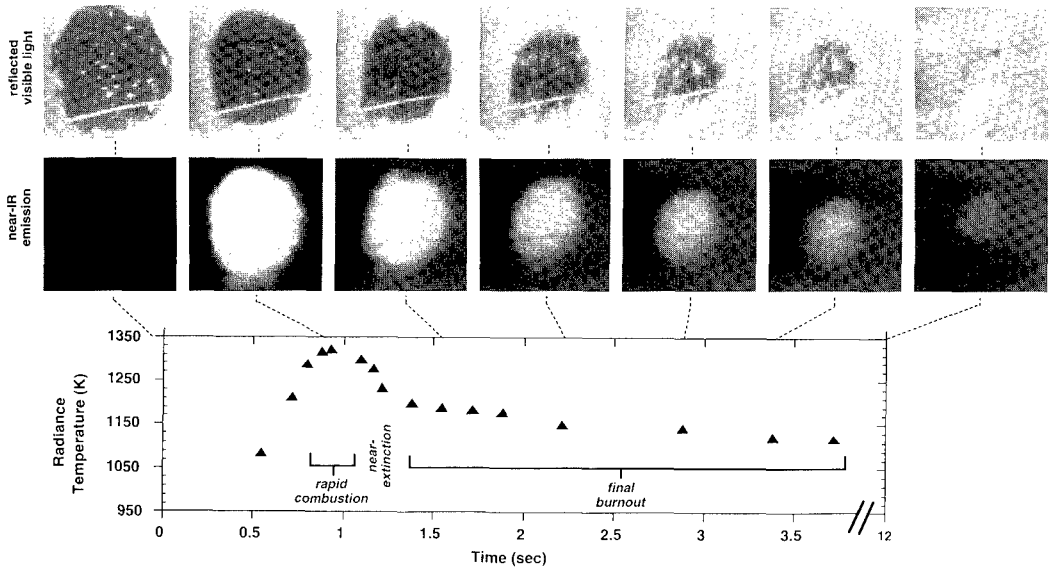

FIG. 3. Dual-camera captive-particle image sequence for typical Illinois #6 coal char particle. Combustion of ≈200-μm particle in 6 mole% oxygen at a steady-state local gas temperature of 1250 K. Zero time is defined as the point of first visible incandescence, which corresponds to a particle temperature of approximately 900 K.

normalized by subtracting the local gas temperature, which changes slightly along the reactor length, to facilitate comparison among data at different residence times. The temperature *difference*, as plotted in Fig. 4, is a convenient indicator of the reaction rate at any point. Also shown in Fig. 4 are the theoretical temperature limits for diffusion-limited burning and for inert particles, calculated for various assumptions (see Fig. 4 caption).

Figure 4 clearly shows a large temperature drop or near-extinction occurring between 72 ms (69% bulk conversion) and 117 ms (75% bulk conversion). At 117 ms and beyond, a large group of particles is observed at or near the gas temperature, with a smaller but significant group having temperatures from 50 to 300 K above that of the gas. A small number of particles (approximately 10 of 184, or 6%) are still seen at the high temperatures associated with the rapid combustion phase. Different particles undergo near-extinction and final burnout at different times

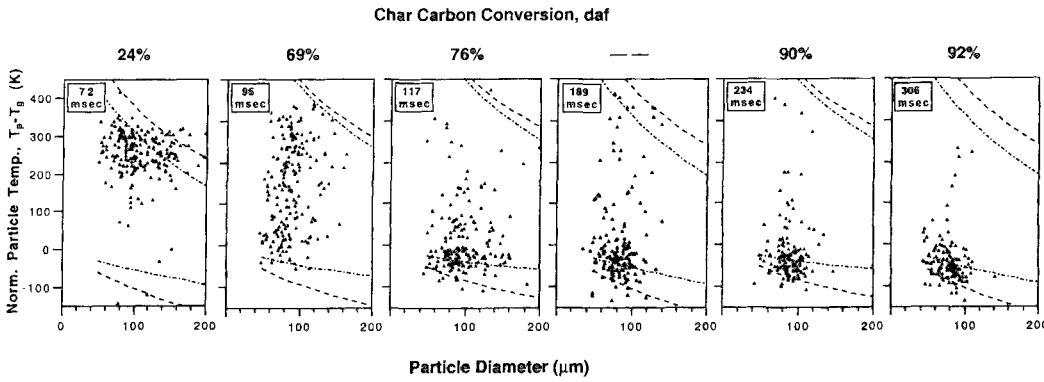

FIG. 4. Optical measurements of particle size and normalized particle temperature for combustion of Illinois #6 coal in 12 mole% oxygen. Points represent carbon-rich particles with emissive factors greater than 0.3. The number of low-emissive-factor particles excluded from Fig. 4 increases from 8 of 184 (4% of the total) at 117 ms to 151 of 241 (63% of the total) at 309 ms. Curves at high temperature represent diffusion limits for two assumptions regarding the product ratio: dashed line for CO/CO_2 molar ratio given by $3 \times 10^8 E^{(-60/RT_p)}$ with RT_p in kcal/mol [25]; dot and dash pattern for CO as sole reaction product. Curves at low temperature are temperature limits for inert particles with varying total emissivities: dashed line for $\varepsilon = 0.8$, dot and dash pattern for $\varepsilon = 0.4$.

as a result of differences in particle density, reactivity [6], and initial ash content [20].

Conversion-Dependent Reactivities:

Figure 5 presents global char reactivities at various conversions in the form of pre-exponential factors, A, extracted from the optical data using a model of gas-particle transport processes [25]. For this calculation, global kinetic parameters° previously determined for Illinois #6 coal in the early-to-intermediate stages of combustion [25] were adopted and the pre-exponential factor adjusted with conversion to match the mean measured particle temperature for the mean particle size. The reactivity in Fig. 5 decreases monotonically during combustion, dropping by a factor of 5 at 90% conversion. Conversion-dependent char reactivities have been previously observed under other conditions—see for example, Hecker et al. [26]. The dashed line in Fig. 5 represents the assumption on which global kinetic models are typically based—a constant, conversion-independent global reactivity. An exception is the recent model of Charpenay et al. [27], which bases char reactivity on instantaneous char hydrogen content and thus has the potential to describe some conversion dependence. The global kinetic model assumption does not lead to large errors below 50% conversion, but by 70% conversion, the reactivity has decreased by a factor of about 2, and numerous near-extinction events are observed (see Fig. 4).

Discussion and Conclusions

The combination of in situ optical measurements and independent captive-particle image sequences provides dramatic illustration of the asymptotic nature of the char burnout process. Single-particle combustion to complete burnout comprises two distinct stages: (1) a rapid high-temperature combustion stage, consuming approximately 70% of the char carbon and ending with near-extinction of the heterogeneous reactions as a result of loss of global particle reactivity, and (2) a final burnout stage occurring slowly and at lower temperatures. For particles containing mineral matter, the second stage can be further subdivided into (2a) late char combustion, which begins after a near-extinction event and converts carbon-rich particles to mixed particle types at a lower temperature and a slower rate, and (2b) decarburization of ash—the removal of residual carbon inclusions from inorganic (ash) frameworks in the very late stages of combustion. This latter process can be extremely slow, requiring over an order of magnitude more time than the primary rapid combustion stage.

To understand the origin of the low reactivities, consider the classical Thiele theory of gas-solid reactions, where the overall particle burning rate, q, in

°The global parameters are a reaction order of 0.5 and activation energy of 22.5 kcal/mole, and a CO/CO_2 ratio given by $CO/CO_2 = 3.10^8 e^{(60/RT_p)}$ with R in kcal/mol-K and T_p in K. Varying the assumed values of the reaction order, activation energy, and CO/CO_2 ratio was observed to have some effect on the reactivities, but not the basic downward trend in Fig. 5. The loss of reactivity with conversion is a gross effect for this system that is related to changes in the solid fuel properties and not to the form or details of the rate expression.

zone II scales with char properties as $q \sim (\rho_c)^{1/2} (S)^{1/2} (k_i)^{1/2} (D_{eff})^{1/2}$. Here ρ_c is the mass of carbon per unit particle volume, S is the internal surface per gram of carbon, k_i is the intrinsic reactivity of that surface, and D_{eff} is the effective diffusion coefficient in the porous particle. In general, the combustion process, which consists of oxidative carbon removal and simultaneous high-temperature heat treatment [28], can alter each of these parameters: ρ_c [5], k_i [26], A [29], and D_{eff} [30]. The low global reactivities (expressed per unit external particle area) during ash decarburization are not surprising, as the inorganic matter displaces carbon, leading to a low value of ρ_c and can also act as a diffusion barrier (low D_{eff}). This carbon depletion effect alone will produce low global reactivities at very high burnout for ash-containing particles.

A more significant observation is the initial temperature drop, which we refer to as a near-extinction event, which is exhibited by most of the particles investigated. The near-extinction is caused by a loss of global reactivity* and occurs for both high- and very low-ash-content particles, often before ash becomes visible on the particle surfaces. For particles with very little ash, the loss of global reactivity is clearly related to changes in the carbonaceous phase, rather than interactions with the bulk mineral matter.** Because coal chars are microporous carbons, k_i, A, and D_{eff} are all strongly influenced by the crystallinity and ultrafine structure of the carbonaceous matrix. In a concurrent paper, Davis et al. [31] demonstrate that the carbon crystalline structure evolves dramatically over the course of the combustion process under the conditions of interest here.

The asymptotic nature of the char combustion process has important implications for the modeling of carbon burnout in furnaces. Current global models typically used assume a reactivity that is independent of conversion and consequently predict high particle temperatures and rapid heterogeneous combustion rates until the solid fuel is completely consumed. This simplified approach leads to a systematic error—carbon persists well beyond the point at which global kinetic models predict complete burnout. More realistic conversion-dependent models are needed to make accurate predictions in the range of industrial interest.

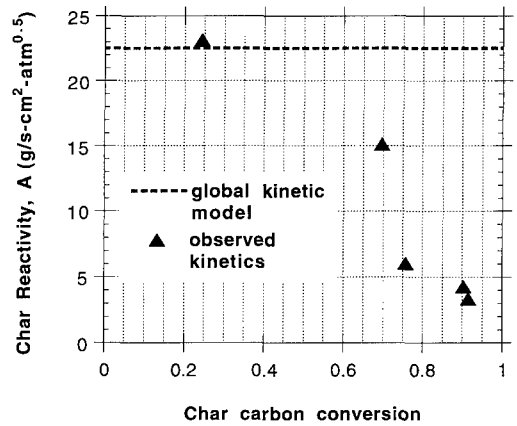

FIG. 5. Effect of carbon conversion on the reactivity of carbon-rich particles of Illinois #6 coal char. Combustion in 12 mole% oxygen for residence times from 72 to 306 ms. Particles with emissive factors less than 0.3 (inorganic-rich particles) were excluded prior to analysis. Triangles—measured reactivities; solid line—fitted curve; dashed line—global kinetic model of Hurt and Mitchell [25], presented for comparison.

Nomenclature

A	global reactivity, g-carbon cm^{-2} s^{-1} atm^{-n} (cm^{-2} of external area)
A_p	projected area of a char particle along the optical axis
D_{eff}	effective diffusivity, cm^2 s^{-1}
d_p	particle diameter, cm
k_i	intrinsic reactivity, g-carbon cm^{-2} s atm (cm^{-2} of total area)
R	gas constant, kcal mole^{-1} K^{-1}
q	overall particle burning rate, g-carbon cm^{-2} s^{-1} (cm^{-2} of external area)
t	time, s
S	total surface area, m^2 g^{-1}
T_g	gas temperature, K
T_p	particle temperature, K
X	char carbon conversion, volatile-matter-free basis

Greek symbols

ε	total emissivity, or emissivity
ε_{800}	spectral emissive factor at 800 nm, or "emissive factor"

*Particle temperature depends upon particle size through equations describing mass and energy transport, and spontaneous thermal extinction has been observed under some conditions [14] as particle size decreases during combustion at constant reactivity. This is not the mechanism involved in the present study, however. Calculations performed for both sets of conditions (in the CPI and entrained flow experiments) indicate that decreases in particle size at constant reactivity cannot explain the observed near-extinction events. The magnitude of the temperature drop (and burning rate decrease) during near-extinction is a function of its surroundings; it is larger at high oxygen levels and low gas temperatures, but the underlying cause is the same—a loss of global reactivity.

**Note that the carbonaceous phase is defined here to include small quantities of finally dispersed mineral matter, if any, which may increase the intrinsic reactivity of carbon surfaces through catalysis.

λ radiation wavelength, nm
ρc mass of carbon per unit particle volume, g cm^{-3}

Acknowledgments

Financial support for this work is provided by the U.S. Department of Energy Pittsburgh Energy Technology Center's Direct Utilization Advanced Research and Technology Development Program. The technical contributions of James Ross, Richard Yee, C. Scott Kelley, Carlos Gethers, and F. William Kent are gratefully acknowledged.

REFERENCES

1. Fiveland, W. A., and Jamaluddin, A. S., *Combust. Sci. and Technol.*, 81:147–167 (1992).
2. Essenhigh, R. H., Misra, M. K., and Shaw, D. W., *Comb. Flame* 77:3–30 (1989).
3. Field, M. A., *Combustion Flame* 14:237–252 (1970).
4. Smith I. W., *Nineteenth Symposium (International) on Combustion*, The Combustion Institute, Pittsburgh, 1982, pp. 1045–1065.
5. Essenhigh, R. H., in *Chemistry of Coal Utilization, Second Supplementary Volume* (M.A. Elliot, Ed.) John Wiley and Sons, New York, 1981, p. 1153.
6. Hurt, R. H., *Energy Fuels* 7:721 (1993).
7. McLean, W. J., Hardesty, D. R., and Pohl, J. H., *Eighteenth Symposium (International) on Combustion*, The Combustion Institute, Pittsburgh, 1981, pp. 1239–1248.
8. Timothy L. D., Froelich, D., Sarofim, A. F., and Beer, J. M., *Twenty-First Symposium (International) on Combustion*, The Combustion Institute, Pittsburgh, 1986, p. 1141.
9. Seeker, W. R., Samuelsen, G. S., Heap, M. P., and Trolinger, J. D., *Eighteenth Symposium (International) on Combustion*, The Combustion Institute, Pittsburgh, 1981, p. 1213.
10. Schroeder, A. R., Thompson, D. M., Daves, G. G., Buckius, R. O., Krier, H., and Peters, J. E., *Twenty-Fourth Symposium (International) on Combustion*, The Combustion Institute, Pittsburgh, 1992, p. 1161.
11. Essenhigh, R. H., and Yorke, G. C., *Fuel* 44:177 (1965).
12. Shibaoka, M., *J. Inst. Fuel* 42:59 (1969).
13. Thomas, C. G., Shibaoka, M., Gawronski, E., Gosnell, M. E., Brunckhorst, L. F., and Phong-anant, D., *Fuel* 72(7):907 (1993).
14. Ubhayakar, S. K., and Williams, F. A., *J. Electrochemical Soc.* 123:747 (1976).
15. Mulcahy, M.F.R., "The Combustion of Carbon," in *Oxygen in the Metal and Gaseous Fuel Industries*, The Chemical Society, London, 1977, p. 175.
16. Walsh, P. M., Xie, J., Douglas, R. E., Battista, J. J., and Zawadzki, E. A., "Unburned Carbon Loss from Pulverized Coal Combustion," *Fuel*, submitted.
17. Nandi, B. N., Brown, T. D., and Lee, G. K., *Fuel* 56:125 (1977).
18. Shibaoka, M., *Fuel* 64:263 (1985).
19. Vleeskens, J. M., and Nandi, B. N., *Fuel* 65:797 (1986).
20. Mitchell, R. E., *Twenty-Third Symposium (International) on Combustion*, The Combustion Institute, Pittsburgh, 1990, pp. 1297.
21. Hurt, R. H., Davis, K. A., and Hardesty, D. R., in *Coal Combustion Science—Quarterly Progress Report*, Sandia Technical Report, July–September, 1993.
22. Hurt, R. H., Davis, K. A., and Hardesty, D. R., in *Coal Combustion Science—Quarterly Progress Report*, Sandia Technical Report, SAND94–8215, January–March, 1993.
23. Baxter, L. L., *Comb. Flame* 90:174 (1992).
24. Baxter, L. L., Fletcher, T. H., and Ottesen, D. K., *Energy Fuels* 2:423 (1988).
25. Hurt, R. H., and Mitchell, R. E., *Twenty-Fourth Symposium (International) on Combustion*, The Combustion Institute, Pittsburgh, 1992, p. 1243.
26. Hecker, W. C., McDonald, K. M., Reade, W., Swensen, M. R., and Cope, R. F., *Twenty-Fourth Symposium (International) on Combustion*, The Combustion Institute, Pittsburgh, 1992, pp. 1225.
27. Charpenay, S., Serio, M. A., and Solomon, P. R., *Twenty-Fourth Symposium (International) on Combustion*, The Combustion Institute, Pittsburgh, 1992, p. 1189.
28. Suuberg, E. M., in *Fundamental Issues in Control of Carbon Gasification Reactivity*, Kluwer Academic Publishers, Norwell, MA, 1991, pp. 269.
29. Smith, I. W., and Tyler, R. J., *Fuel* 51:312 (1972).
30. Mitchell, R. E., and Tsai, N. K., *International Conference on Coal Science Proceedings*, 1993, Vol. 1, p. 19.
31. Davis, K. A., Hurt, R. H., Yang, N. Y. C., and Headley, T. J., *Twenty-Fifth Symposium (International) on Combustion*, The Combustion Institute, Pittsburgh, 1994.

Twenty-Fifth Symposium (International) on Combustion/The Combustion Institute, 1994/pp. 569–576

ON THE COMBUSTION OF WOOD-CHAR SPHERES IN O_2/N_2 MIXTURES—EXPERIMENTS AND ANALYSIS

S. DASAPPA AND H. V. SRIDHAR
ASTRA
Indian Institute of Science
Bangalore 560 012, India

P. J. PAUL AND H. S. MUKUNDA
Department of Aerospace-Engineering
Indian Institute of Science
Bangalore 560 012, India

U. SHRINIVASA
Department of Mechanical Engineering
Indian Institute of Science
Bangalore 560 012, India

This paper discusses the results from experiments and analyses of the combustion of wood-char spheres for varying O_2 in an O_2-N_2 mixture. The experiments show that for particle diameters (d_0) in the range 2–15 mm, the char burn time (t_b) in air is given by $t_b \sim d_0^{1.57}$ at 300 K. At higher ambient temperatures, the exponent on d_0 goes up to 2.0. The results at reduced oxygen fraction show extinction at partial conversion and zero conversion at oxygen mass fractions less than 0.14 at an ambient temperature of 300 K. Regarding flow effects, for Reynolds number (Re) more than 500, conversion is only partially complete for runs at 300 K. The mathematical model consists of a spherically symmetric porous body undergoing heterogeneous conversion with finite-rate chemistry and associated diffusion into the pores. Free and forced convective heat and mass transfer effects outside the sphere are approximately modeled. The results show a near complete agreement on most aspects. The extinction at low ambient oxygen fraction and the extinction after partial conversion at low oxygen fractions or in presence of forced convection are argued to be due to the process of becoming statically unstable. The results of lower ambient oxygen limit, also observed in some sparsely conducted experiments, apparently have implications in planetary evolution studies.

Introduction

Wood-char combustion with O_2/N_2 mixtures is of importance in several industrial processes, more particularly in wood gasifiers, where one of the active processes is the oxidation of carbon at reduced oxygen fractions. A review on gasification of coal char is given by Laureandeau [1]. Earlier, Mukunda et al. [2] studied single wood-sphere combustion, including that of the char. The model included diffusion and reaction in the pores and char conversion times slightly under those predicted from experiments. The predicted core temperatures ranged between 1600 and 1650 K. The experiments of Kuwata et al. [3] and experiments conducted here have shown temperatures with a maximum of 1000 K. The model used in Ref. 2 contained a C-O_2 reaction alone, and the reaction of C-CO_2, likely to be important at high temperatures, was neglected. Also, in a gasifier operation, the possibility of reactions of char at reduced oxygen concentrations exists. The number of explorations into such effects in the literature seems limited [4,5].

The present work has been undertaken to obtain more detailed experimental data on the weight loss, the core and surface temperatures with time, extinction, and related features at reduced oxygen fraction; and the flow effects on wood-char spheres between 2- and 25-mm diameter, a range of interest in wood gasifiers. A computational analysis of the process is also made, to understand the physics of char combustion and to bring out the controlling processes at various regimes of combustion.

The Experiments

The experimental setup consists of a quartz reactor 40-mm in diameter placed in a temperature-controlled furnace [6]. For high-temperature runs, the reactant gas is preheated to the furnace temperature by letting the gas pass through a helical quartz tube

wound around the reactor. The flow rate of the gas is measured using a capillary flowmeter. Air or a mixture of oxygen and nitrogen is used depending upon the requirements. In the latter case, flow rates of O_2 and N_2 are measured before mixing and being led into the reactor. The oxygen fraction is further checked by a gas analysis of the mixture.

The char samples of size 2.0–15 mm are prepared either by burning dried wood spheres (*Ficus*) in air and quenching them at the end of flaming combustion or by heating them slowly in an inert environment. The density of char obtained by the former method is 180 ± 20 kg/m^3, and the latter method is 400 ± 30 kg/m^3. Density of the char is calculated from the weight of the char sphere and the volume obtained by measuring the diameter. The diameter is averaged over measurements on many locations on the sphere. The charcoal spheres obtained are repeatedly dried in an oven at 373 K and cooled in a desiccator a few times before use. In some cases, the char samples obtained at the end of the pyrolysis process are nonspherical and are shaped by filing to true spheres.

Porosity is obtained from the apparent density of the porous char and the solid char by the relation $\varepsilon = (1 - \bar{\rho}/\rho_c)$. This value is verified in a few cases by the water absorption technique. A dried sample is dipped in water and allowed to soak for a few hours. After removal, the sample is weighed. The difference in the initial weight before soaking and the final weight after soaking gives the amount of water absorbed. This would give the void fraction in the porous char, which is the porosity of the given char sample.

The sample was suspended, using a fine wire basket, from a balance and heated using a spirit lamp flame enclosing the entire sphere so that oxidation of char is prevented and the temperature of the char is increased to 900 K. The sample was then placed inside the reactor maintained at the required temperature, and the reactant gas was passed through the reactor. The total conversion time and the flow rate of the reactant were noted. During the experiments at low Re (<50), it was observed that the diameter of the char sphere was gradually decreasing with the ash layer covering the sphere. However, the carbon core was visible through the ash layer till the end of the burn time. For runs with air at 300 K, conversion could not be initiated below a diameter of 2 mm. With varying O_2 fraction, ($Y_{O_2,\infty}$) below 0.14, the char particle quenched after introduction into the reactor. This phenomenon was found similar for different diameters in the range of 4–14 mm. The conversion was found incomplete for $Y_{O_2,\infty} < 0.21$. In these experiments, it was ensured that flow effects did not influence the results by keeping Re < 30. Experiments on the effect of flow velocity were conducted by varying the flow rate of air into the reactor, thus changing Re. It was found that for Re > 500, the conversion was incomplete, with a weight loss of about 60–95% depending upon the mass fraction of oxygen. Also, it was noticed that the ash was getting blown off from the surface in most such cases. Experiments were also conducted to determine the core temperature by inserting a 100-μm Pt-Pt 13% Rh thermocouple at the center of a wood sphere undergoing combustion. During this period, the temperature was monitored, and it never exceeded 950 K.

The Model

The processes taking place during the combustion or gasification of porous carbon spheres are the diffusion and convection of the species and energy in the porous medium and the heterogeneous reaction between the gaseous species and the char. These are modeled in the present analysis using the unsteady spherically symmetric one-dimensional conservation equations. The conservation equations are

$$\frac{\partial}{\partial t}(\rho\varepsilon Y_i) = \frac{1}{r^2}\frac{\partial}{\partial r}\cdot\left(-\rho v r^2 Y_i + r^2 \bar{D}\rho \frac{\partial}{\partial r} Y_i\right) + \dot{\omega}_i''' \tag{1}$$

$$\frac{\partial \varepsilon}{\partial t} = \frac{-\dot{\omega}_c'''}{\rho_c} \tag{2}$$

$$\frac{\partial}{\partial t}(\bar{\rho} c_p T) = \frac{1}{r^2}\frac{\partial}{\partial r}\cdot\left(-\rho v r^2 c_p T + r^2 k \frac{\partial T}{\partial r}\right) - H_c \dot{\omega}_c''' \tag{3}$$

where $\bar{\rho} = \rho_c(1 - \varepsilon) + \rho\varepsilon$ is the average density of porous char, ρ_c is nonporous char density, ε is the porosity of the char, and $\dot{\omega}_c'''$ is the volumetric reaction rate of char with O_2 and CO_2, including the contribution due to growing of pores.

$$\dot{\omega}_c''' = \dot{\omega}_{c_{O_2}}''' + \dot{\omega}_{c_{CO_2}}'''. \tag{4}$$

The subscripts i = 1, 2, and 3 refer to species CO, CO_2, and N_2, respectively.

The volumetric reaction rate is related to the heterogeneous reaction rate per unit surface area by

$$\dot{\omega}_c''' = \dot{\omega}_c'' S_g \rho_{ap} \tag{5}$$

where ρ_{ap} is the apparent density of the char and S_g

is the surface area per unit volume of the char, which is given by Howard [7], as $S_g \rho_{ap} = 2\varepsilon/r_p$.

The surface reaction rate of carbon with oxygen is given by Howard:

$$\dot{\omega}''_{CO_2} = -\frac{M_c S_1 S_2 X_{OS}}{(S_1 X_{Os} + S_2)} \tag{6}$$

where X_{Os} is the mole fraction of oxygen at the surface and S_1 and S_2 are the rate constants for absorption and desorption, respectively, given by

$$S_1 = A_c P \exp\left(\frac{-E_1}{RT}\right) \Big/ (\sqrt{2\pi M_{O_2} RT}) \tag{7}$$

$$S_2 = A_f \exp\left(\frac{-E_2}{RT}\right). \tag{8}$$

Smith and Tyler [8] use a single rate expression as $R_s = 1.34 \exp(-32{,}600/RT)$ (g/cm^2 s) for coal-char particles of 22–89 μm in size, for a temperature range of 630–1812 K. The rates calculated match with that of Eq. (8), implying that the desorption process is rate limiting in their experiments.

The reaction rate of carbon with CO_2, suggested by Semechkova and Frank-Kamenetskii and referred to in Blackwood and Ingeme [9], is given by

$$\dot{\omega}'''_{CCO_2} = -\frac{k_1 p_{CO_2} - k_2 p_{CO}^2}{1 + k_3 p_{CO} + k_4 p_{CO_2}}. \tag{9}$$

No gas-phase reactions are considered. The oxidation of CO is neglected because the mass fraction of CO inside the sphere during the reaction process is too low to contribute toward any heat release.

The diffusion process are modeled after Howard [7] and discussed in our earlier work [2,6]. The reaction rate per unit area $\dot{\omega}''_c$ is related to $\dot{\omega}'''_c$ by $\dot{\omega}'''_c = \dot{\omega}''_c 2\varepsilon/r_p$.

The details of pore treatment are the same as in Ref. 6 and are not repeated here.

Initial, Interface, and Boundary Conditions

At $t = 0$, the temperature in the sphere is set at 900 K. The precise nature of the concentration profile does not matter, as the transients die down in a small fraction of the conversion time. The interface conditions at $r = r_s$ are the continuity of heat and mass fluxes. These are as [2]

$$D_g \rho \left.\frac{\partial Y_i}{\partial r}\right|_{rs} = Q(Y_{i\infty} - Y_{iS});$$

$$k \left.\frac{\partial T}{\partial r}\right|_{rs} = c_p Q(T_\infty - T_S) - \dot{R}'' \tag{10}$$

where $\dot{R}''$ is the radiative heat flux from the surface of the sphere and

$$Q = \frac{(\rho v)_S \exp(-B_0)}{[1 - \exp(-B_0)]}, \qquad B_0 = \frac{(\rho v)_S c_p}{k\mathrm{Nu}}. \tag{11}$$

Equation (10) is obtained from the solution of spherically symmetric one-dimensional conservation equations for the gas phase [2], and the effect of free and/or forced convection is accounted for by choosing the appropriate value of the Nusselt number (Nu). Nu = 2 in the absence of either free or forced convection but increases in the presence of convection. In earlier work [2], the char sphere encountered only free convection. In the present case, with flow velocities, both will be present.

Method of Solution:

The solution calls for integration of the parabolic system of partial differential equations with the initial and boundary conditions noted above. The independent variable r is transformed into a V, defined as $V = (4/3)\,\pi r^3$, making the system of equations fully conservative and removing the singularity at $r = 0$. The integration of the transformed equations is carried out in the same way as in Ref. 6.

Choice of Parameters:

The choice of physical, thermodynamic, and transport properties is based on the mean char properties presented as follows:

$$\rho_c = 1900 \text{ kg/m}^3 \quad r_p(t = 0) = 50\ \mu\text{m}$$

$$c_p = 1.25 \text{ kJ/kg K}$$

$$H_c = 32.60 \text{ MJ/kg} \quad k_c = 1.85 \text{ W/m K}.$$

Rate parameters for the C + O_2 reaction are

$$A_c = 1/150 \quad E_1/R = 1700 \text{ K}$$

$$E_2/R = 20{,}000 \text{ K}\ A_f = 0.0875 \text{ moles/m}^2 \text{ s}.$$

Rate parameters for the C + CO_2 reaction are as in Ref. 6. The term k_c is the conductivity of the solid phase at temperatures of 900–1200 K. This value of k_c leads to porous char conductivity of 0.4–0.5 W/m K, which is the same as in Refs. 10,11 and accounts for conduction and radiation inside the char. The thermal conductivity of the gas phase, k_g, is calculated locally. The rate parameters used in the present study for the C + O_2 and the C + CO_2 reactions are from Howard [7] and Blackwood and Ingeme [9], respectively. The initial porosity of the wood char considered is in the range of 0.75–0.85, consistent with the present measurements as well as of

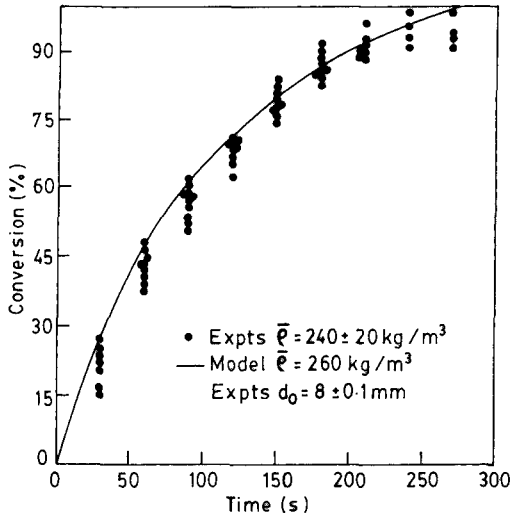

FIG. 1. The conversion with time—experiments and predictions for particle diameter of 8 mm; ambient temperature = 300 K.

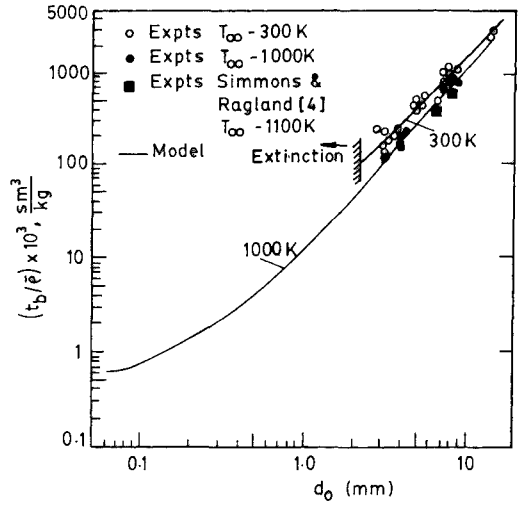

FIG. 2. Burn time for different particle diameters along with the predictions for ambient temperature of 300 and 1000 K (experimental data of Simmons and Ragland [5]).

Groeneveld and van Swaaij [12]. The initial radius of the pore is obtained from Groeneveld [13], where wood char was used for measurements. The parameters in the kinetic expression used presently are obtained from Blackwood and Ingeme. The rate of the backward reaction k_2 is obtained from the appropriate equilibrium constants. The emissivity in the expression for radiant heat loss is taken at 0.95.

Results and Discussion

Figure 1 shows the results of char conversion (x_c) with time for an 8-mm-diameter char particle at ambient condition. Char conversion is the ratio of the difference between the initial weight and the weight at any time t to the initial weight. Both experimental data and predictions from the model are presented here. The predictions compare well with the experimental data within the range of experimental error. This result would justify the choice of kinetic and transport parameters chosen for the model.

Figure 2 shows the experimental data and the prediction of burn time normalized with respect to density of char with initial char diameter for combustion in air on a log-log plot. A curve fit to these data leads to $t_b \sim d_0^{1.87}$, indicating the diffusion-dominated combustion; the departure from the $t_b \sim d_0^2$ law is due to the presence of free convection. Also shown are the experimental results for 4- and 8-mm particles in air for an ambient temperature of 1000 K. The results follow the d^2 law up to a particle size of about 1 mm. It is clear that the rise in the ambient temperature from 300 to 1000 K has raised the exponent from 1.87 to 2, because the free convection effects are very small in the latter case. Predictions in both cases seem excellent. The experiments at 300 K show extinction at a 2-mm particle size. At 1000 K, the transition from the diffusion to kinetic regime takes place in the range downward of 1 mm. Experimental results from Simmons and Ragland [5] on the combustion of char cubes are also plotted in Fig. 2, based on volume and estimated density from the available data. The burn time results of Simmons and Ragland at 1100 K are slightly lower than from the present experiments, and the predictions at 1000 K are within the experimental errors.

Predictions on the ratios of mass fraction of O_2 and CO_2 at the core to the surface are plotted with time normalized with respect to the time for full conversion at an oxidizer temperature of 1000 K in Fig. 3. In the case of the 100-μm particle, the ratio for O_2 is about 0.8, indicating that the oxygen mass fraction available at the core and the surface is nearly the same in contrast to the 400-μm particle where the ratio is about 0.3, thus switching from the kinetic to the diffusion limit. Due to the availability of O_2 throughout the particle, the ratio of CO_2 at the core to the surface is higher in the 100-μm particle compared with the 400-μm particle diameter during the burn time.

As mentioned earlier, in Ref. 2, the predicted peak core temperature was 1600–1650 K and is different from the earlier experimental data. This aspect is analyzed now. Figure 4 shows the plot of core temperature history found in the experiments and various models. The measured temperature data from this work and from Kuwata et al. [3] show clearly the peak temperature to be about 900–950 K. In earlier work

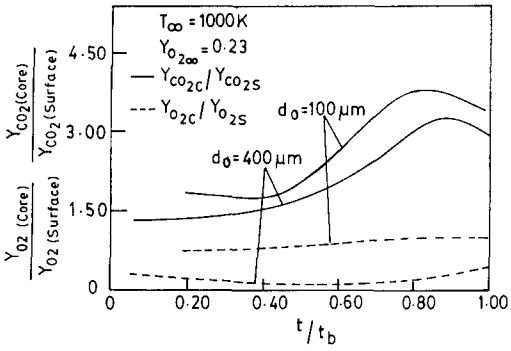

FIG. 3. Variation of the ratio of mass fractions of O_2 and CO_2 between the core and the surface for oxidizer temperature of 1000 K for an 8-mm-diameter char sphere burning in air with normalized time.

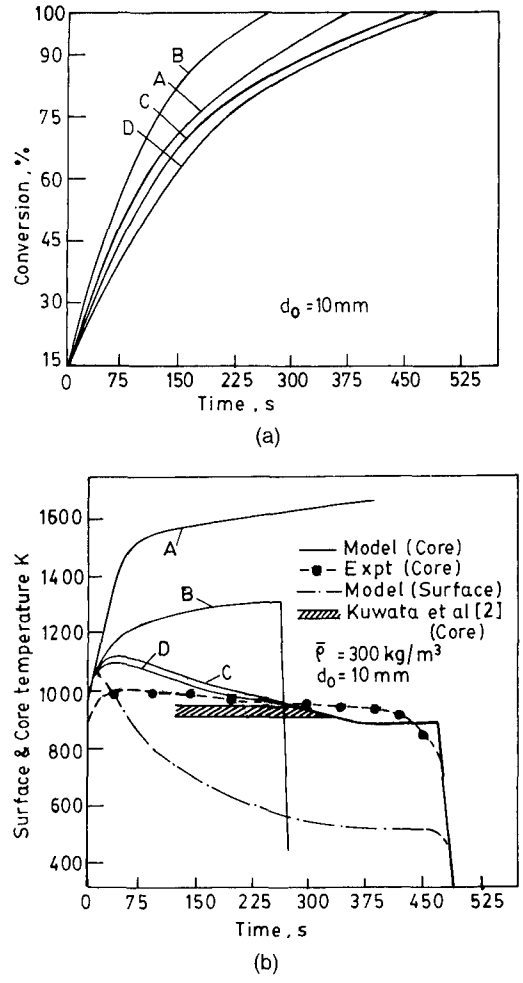

FIG. 4. Effect of the C + CO_2 reaction and thermal conduction of char on (a) conversion and (b) temperature profiles for a 10-mm-diameter char sphere burning in air. (case A: No C + CO_2 reaction and conductivity at 300 K; case B: similar to case A with addition of the C + CO_2 reaction; case C: similar to case A with thermal conductivity for high temperature; case D: similar to case C with addition of the C + CO_2 reaction).

[2] in which only the C + O_2 reaction was treated along with an equilibrium of CO and CO_2, the results showed an increase of the core temperature from 1000 K to about 1650 K toward the end (Fig. 4, curve A). As the fraction of CO_2 present inside the sphere is not small, it was argued that the endothermic CO_2-C reaction was necessary to be included. Also, the data on conductivity for red hot char showed different values [10,11]. Hence, the influence of the conductivity also is examined. The results with various options are presented as curves B, C, and D in Fig. 4. Case B indicates the results with the inclusion of the C + CO_2 reaction mechanism along with C + O_2. The effect of endothermicity is found to be significant in reducing the peak core temperature to about 1250 K. Case C concerns the effect of enhanced conductivity due to high temperature. It is seen that the conductivity plays an important role in reducing the peak core temperature to about 1150 K. Case D indicates the results with the addition of the C + CO_2 reaction to case C. The difference between cases C and D with regard to the core temperature and the conversion profile is not appreciable. It is clear that the contribution toward the reduction of core temperature is due to the conductivity of char; inclusion of the C + CO_2 reaction mechanism is not essential for a good prediction of the peak temperature in the present case.

Another aspect that needs consideration is the burn time of the particle. In case A, the burn time predicted was slightly lower than the range of the experimental results obtained, whereas in case B, where the CO_2 reaction is introduced, the burn time is reduced by about 25%, indicating the contribution from the C + CO_2 reaction. Enhanced thermal conductivity, as in case C, has increased the burn time of the particle compared to that of case B, with more heat loss from the reaction zone of the char particle to the ambient and reduction in the peak core temperature. Inclusion of the CO_2 reaction to case C has not altered the reaction time, indicating lower importance of this reaction. This result should be contrasted with case B, where the reaction time was reduced by 25% with CO_2. It is clear from these results that the contribution from the CO_2 reaction would be significant at elevated temperatures and, thus, should not be neglected. Thus, for the other cases, like the one studied by Ubhayakar and Williams [14], the effect of endothermicity, due to the high activation energy reaction C—CO_2, could be significant.

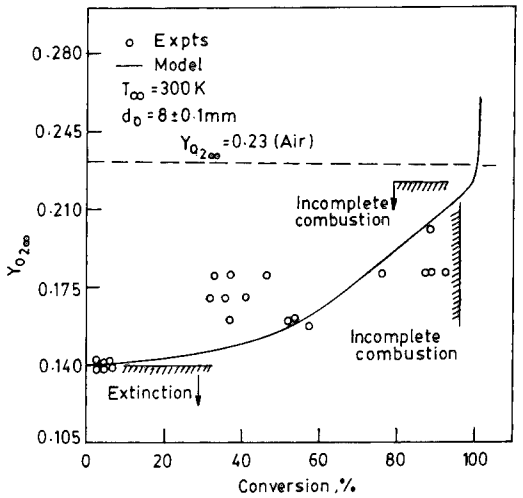

FIG. 5. Effect of ambient oxygen fraction on conversion at ambient temperature of 300 K.

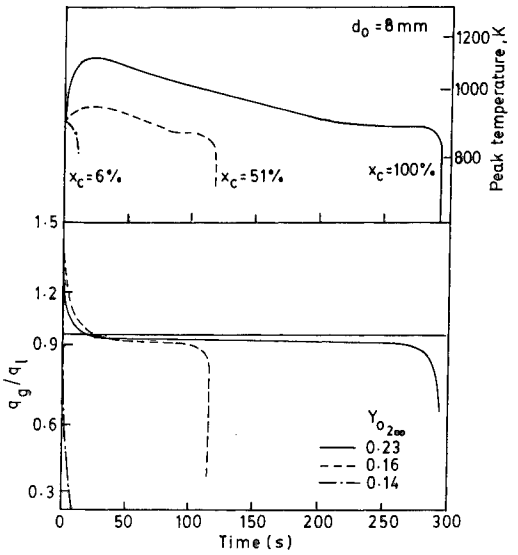

FIG. 6. Peak temperature and the ratio of the heat generation to the heat loss rate with conversion for different $Y_{O_2\infty}$.

Figure 5 shows the effect of ambient oxygen concentration on the conversion for an 8-mm-diameter char particle. In the experimental results mentioned earlier, it was found that below $Y_{O_2\infty} = 0.21$ with N_2 being the diluent, the conversion was incomplete. It is seen from Fig. 5 that there is a gradual decrease in the percentage conversion with a reduction in $Y_{O_2\infty}$. For ambient mass fractions of O_2 below 0.14, the conversion is less than 6%, thus indicating that the reactions are not self-sustaining below this oxygen fraction. This is interpreted as extinction. Similar results were obtained from the mathematical analysis for varying particle diameter, with extinction occurring at $Y_{O_2\infty} = 0.14$. These results are consistent with those obtained by Rashbash and Langford [4] and Watson et al. [15] where combustion of wood and paper spheres were considered, respectively. It has been suggested that the planetary atmosphere should have a changing oxygen fraction during evolution and fire or its impossibility could be a strong agent of natural selection [16]. In this connection, the lower limit of oxygen fraction to sustain combustion ($Y_{O_2\infty} = 0.14$) would be of interest.

Extinction is being caused by reduction in the particle diameter and by reduction in the ambient oxygen mass fraction. To understand the causes for extinction, an analysis of the heat generation and heat loss terms was carried out. The heat generation in the present context is the heat released due to char combustion, and the heat loss is the convective and radiative heat loss from the particle surface. With reduction in the initial particle diameter (d_0), toward the kinetic limit, the heat generation rate is proportional to the volume (d_0^3) and decreases faster than the heat loss rate, which is proportional to the surface area (d_0^2). This causes the extinction. Figure 6 shows the plot of peak temperature and the ratio of the heat generation to the heat loss rate with time for different cases of oxygen fraction. In all these cases, the initial temperature was set at 900 K. The peak temperature increases up to 1200 K before coming down somewhat linearly in time. An interesting feature of the plot is the sudden dip in temperature profile at 880 ± 20 K for all three cases considered. This temperature corresponds to the extinction condition. Calculations over a wider range of parameters confirmed the same temperature for extinction. For instance, in one numerical experiment, the initial temperature was set at 1000 K instead of 900 K for $Y_{O_2\infty} = 0.14$. In this case, the temperature dropped sharply at 890 K after a 23% conversion, instead of a 6% conversion at 900 K. In all of the cases, the ratio of the heat generation to the heat loss rate is more than unity in the temperature rise region and below unity as conversion proceeds. It must be noted that during this period, the sphere is also decreasing in size. This extinction limit is similar to the stability limit obtained for the stirred reactor and discussed extensively in the combustion literature (chapters 6 and 16 of Refs. 17 and 18, respectively).

Results of the effect of flow velocities in the reactor chamber at 300 K of ambient temperature are presented in terms of $t_b/\rho d^{1.8}$ vs Re in Fig. 7. The results of conversion are also presented. The observed conversion is largely in excess of 90–93% in most cases. The predictions for the effect of velocity are carried out by augmenting the free convention with the forced convective heat and mass transfer. Two models for the presence of ash layer were in-

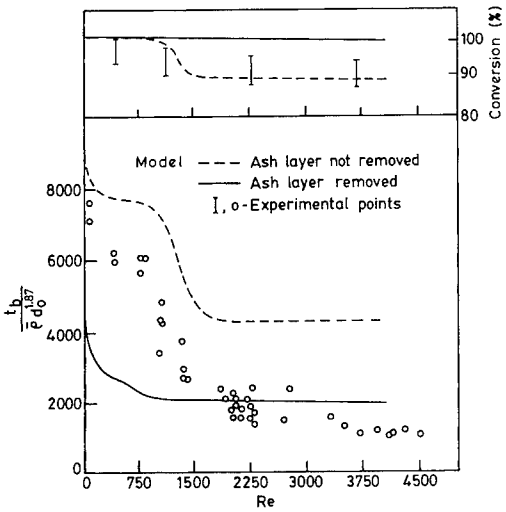

FIG. 7. The effect of Reynolds number on the conversion time of char spheres.

voked: (a) the ash layer is not removed, (b) the ash layer is continuously stripped away by the flowing gas. It was observed experimentally that beyond Re of 500, the ash layer was being blown away. (The predictions from these two models are described as (a) and (b).) Simulation of case (a) is performed by setting the sphere diameter at the initial value, and as reaction proceeds, more and more of the outer layer will become inert. Case (b) is simulated by taking the sphere diameter as reducing with time, since the material in the outer part gets consumed by reaction. The experimental results fall between the limits of cases (a) and (b). They are more close to limit (a) at lower Re and close to limit (b) at higher Re. Even so, the conversion results are close to model (a); model (b) predicts conversion close to 100%. This is possibly because of the additional heat loss to the wire basket, which becomes important only toward the end of conversion. Perhaps with increasing Re, the amount of ash being removed due to flow effects is also increasing, reaching a limit at around Re = 2000. The reduction in burn time around Re = 500, both in the experiments and the model, is consistent with the results obtained by Kuwata et al. [3] on the paper spheres. The increase in burn time beyond Re of 500 observed in Kuwata et al. has not been observed here either experimentally or from the model.

Conclusions

The experimental and modeling aspects related to the combustion of char in an ambient atmosphere with varying oxygen concentration has been discussed in this paper. The conversion time dependence for the char oxidation was shown to be $t_b \sim d_0^n$, where $n = 1.9$ and 2.0 for combustion at $T \sim 300$ and 1000 K, respectively, for particle diameters above 1 mm. The importance of conductivity of char and the C + CO_2 reaction during char combustion was brought out. For the range of the present study, the C + CO_2 reaction was not essential to explain the observed peak temperatures and burn times. Extinction of particle during combustion occurred at an ambient oxygen mass fraction of 0.14 for $T \sim 300$ K. The extinction of the char particle and incomplete combustion were shown to be due to the heat loss rate dominating the heat generation.

Nomenclature

d_0	initial diameter (m)
D	diffusion coefficient (m^2/s)
$\bar{D}$	effective diffusivity (m^2/s)
ε	porosity
$E_{1,2}$	activation energy (Eqs. (8) and (9)) (kJ/mol)
H_C	heat of combustion of carbon (MJ/kg)
$k, k_c, \bar{k}$	thermal conductivity of gas, carbon, and porous char (W/m K)
M_i	molecular weight of species i (kg/mol)
Nu	Nusselt number
p	pressure (Pa)
q_g, q_l	heat generation and heat loss rates (W)
r	radial coordinate (m)
r_p	pore radius in char (m)
R	universal gas constant (J/kg mol K)
S_g	surface area per unit mass of the char (m^2/kg)
t	time (s)
$\dot{R}''$	radiation flux (W/m^2)
$S_{1,2}$	rate constants of Eq. (7)
T	temperature (K)
Y_i	mass fraction of species i
k_1–k_4	rate constants of Eq. (10)
x_c	conversion
X_{OS}	mole fraction of oxygen at surface
ρ	density of gas (kg/m^3)
$\dot{\omega}_i'''$	volumetric reaction rate of Eq. (4) (kg/m^3 s)

REFERENCES

1. Laurendeau, N. M., *Prog. Energy Combust. Sci.* 4:221 (1978).
2. Mukunda, H. S., Paul, P. J., Shrinivasa, U., and Rajan, N. K. S., *Twentieth Symposium (International) on Combustion*, The Combustion Institute, Pittsburgh, 1984, pp. 1619–1628.
3. Kuwata, M., Stumbar, E., and Essenhigh, R., *Twelfth Symposium (International) on Combustion*, The Combustion Institute, Pittsburgh, 1969, pp. 663–674.

4. Rashbash, D. J., and Langford, B., *Combust. Flame* 12:33–40 (1968).
5. Simmons, W., and Ragland, K., *Combust. Sci. Technol.* 46:1–15 (1986).
6. Dasappa, S., Paul, P. J., Mukunda, H. S., and Shrinivasa, U., *Chem. Eng. Sci.* 49 (2):223–232 (1994).
7. Howard, J. B., *Combustion of Carbon with Oxygen*, Technical Report, MIT, 1967.
8. Smith, I., and Tyler, R., *Combust. Sci. Technol.* 9:87–94 (1974).
9. Blackwood, J. D., and Ingeme, A. J., *Aust. J. Chem.*, 13:194–209 (1960).
10. Anon. *Gas Engineers' Handbook*, McGraw Hill Book Co. Inc., New York, 1934.
11. Goldman, J., Xieu, D., Oko, A., Milne, R., and Essenhigh, R. H., *Twentieth Symposium (International) on Combustion*, The Combustion Institute, Pittsburgh, 1984, pp. 1365–1372.
12. Groeneveld, M. J., and van Swaaij, W. P. M., *Chem. Eng. Sci.* 35:307–313 (1980).
13. Groeneveld, M. J., *The Co-Current Moving Bed Gasifier*, Ph.D. Thesis, Twente University of Technology, Netherlands, 1980.
14. Ubhayakar, S. K., and Williams, F. A., *J. Electrochem. Soc. (Solid State Sci. Technol.)* 123(5):747–756, (1976).
15. Watson, A. J., Lovelock, J. E., and Margulis, L., *Biosystems* 10:293–298 (1978).
16. Robinson, J., *Paleogeogr. Paleoclimatol., Paleoccol. (Global Planet. Change Sect.* 75:223–240 (1989).
17. Vulis, L. A., *Thermal Regimes of Combustion*, McGraw Hill, New York (1961).
18. Spalding, D. P., *Combustion and Heat Transfer*, Oxford Pergamon Press, New York, 1979.

COMMENT

Reginald E. Mitchell, Stanford University, USA. You found that your wood-char spheres burned with decreases in diameter, diameter changing with burnoff to the 1.87 power. One would expect that for diffusion-limited burning, diameter would vary with burnoff to the second power (i.e., the d^2 power law dependence). Since mass equals density times volume, if the d^2 power law dependence is not observed, then density must decrease with mass loss. In your calculations of burning times, you assumed that density was constant. Constant-density diffusion-limited burning requires a d^2 dependence of diameter with mass loss, otherwise mass is not conserved. Would you comment on this apparent discrepancy? Might it be possible that your wood-char spheres burned along grains and that particle shape was changing during mass loss, the particles becoming more like prolate spheroids? Such behavior would support a power dependency less than 2.

Author's Reply. It is true that the theory for a constant-density diffusion-limited situation produces a d^2 dependence on burning time. However, our theory assumes neither constant density nor diffusion limitedness. The heat and mass flux in the gas phase are modified by free convection, which is also taken into account in the theory. The exponent of 1.87 is obtained as a net effect of all these factors. From the result obtained on the burning time for varying diameters, we concluded that the situation is close to diffusion-limited conditions.

The exponents are 1.87 and 2.0 for ambient temperatures of 300 and 1000 K respectively. The difference is explained due to differences in mass transfer caused by free convection for the low ambient temperature. The result is further substantiated by the observation (not presented in the paper) that the reaction rate is limited to one cell close to the surface, and hence combustion proceeds virtually by the shrinking core mechanism.

Partially burnt char was examined and no significant ovality was found. Since the initial porosity was large, the resistance offered by pores to diffusion was small in all cases studied. Hence the diffusivities along and across the grains are almost the same.

Twenty-Fifth Symposium (International) on Combustion/The Combustion Institute, 1994/pp. 577–584

SOOT MASS GROWTH AND COAGULATION OF SOOT PARTICLES IN C_2H_4/AIR-FLAMES AT 15 BAR

S. HANISCH, H. JANDER, Th. PAPE AND H. Gg. WAGNER
Institut für Physikalische-Chemie der Universität
Tammannstraße 6, 37077 Göttingen, Germany

The growth of soot particles has been studied in flat C_2H_4/air flames burning at 15 bar. Laser extinction and scattering were measured simultaneously as a function of distance from the burner, together with temperature and concentration profiles of aliphatic and polycyclic hydrocarbons.

In 15 bar C_2H_4/air flames with surplus carbon densities $\rho_c > 10^{18}$ C atoms/cm^3, final particle numbers N_∞ are found that are higher than at lower pressures. The growth of $f_{v\infty}$, the final soot mass, proceeds via increasing particle number density and not as at normal pressure via larger particles. The particle coagulation rate decays quite rapidly with time leading to larger final particle number density. The apparent active lifetime of soot particles (k_f^{-1}) at 15 bar depends on temperature and, in addition, on the surplus carbon density ρ_c. The quantity k_f/ρ_c is a function of temperature. The polycyclic aromatic hydrocarbons (PAH) appear very early in the C_2H_4/air flame, but they are also consumed very rapidly to very low final mole fraction $x_{PAH} \approx 10^{-9}$. The carbon density of C_2H_2 decreases strongly in the phase of soot growth. The final value $[C_2H_2]_\infty$ of about 10^{-6} g/cm^3 is high enough for further soot growth, so that the ceasing of coagulation and soot mass growth at 15 bar cannot be explained by a lack of C_2H_2. It rather seems to be the decreasing activity of soot particles.

Introduction

Premixed laminar flames have often been used in studies of soot formation processes, and many of these studies have been performed at low pressure [1–11]. In technical systems, high pressures are often applied, which may exceed 100 bar. At this high pressure, measurements in shock tubes can be performed relatively easily, while studies of high-pressure flames are difficult, as the spatial extension decreases with increasing pressure.

Previous measurements of soot formation in C_2H_4/air flames have been extended to pressures up to 70 bar and temperatures from 1400 to 2100 K [12,13,15]. For the high-pressure flames, however, conclusions could only be drawn from measurements in the burned gases. Investigations of the pressure dependence of final soot volume fraction $f_{v,\infty}$ in C_2H_4/air flames have shown that, up to several bar, $f_{v,\infty}$ increases proportional to p^2. Towards higher pressures (>7 bar), $f_{v,\infty}$ growth is approximately proportional to p [14,15]. Measurements in sooting C_2H_4/air flames burning at $p \approx 1$ bar have shown that particle growth in these flames ceases, although the concentration of C_2H_2 as a representative growth species was quite high in the burned gases [25]. This is attributed to a decrease in soot particle activity [22,23]. Measurements in high-pressure C_2H_4/air flames indicated that the particle growth process stops as a result of a lack of C_2H_2 in the burned gases [14]. Shock-tube experiments point to still other reasons for the final decrease of soot particle growth rate. It seems necessary, therefore, to investigate particle growth and coagulation in premixed flames burning at elevated pressure. In this paper, measurements are reported that have been performed at 15 bar. This seems to be the highest possible pressure where some quantitative information about the soot growth process in the main reaction zone and the soot forming zone of premixed flames can be obtained. Measured were time-resolved profiles of soot volume fraction f_v, particle number density N, and particle diameter d at flame temperatures between 1500 and 2000 K in weakly and richly sooting flames by optical methods. In addition, profile measurements of temperatures and of the major stable aliphatic and aromatic (PAH) compounds, together with the water gas components, were performed.

Experimental Arrangement

The burner consists of a central burner that was surrounded by a second flat flame-shielding burner. Both burners were protected against convection of the surrounding gas by a special burner housing. In order to stabilise a laminar premixed flame that does not show polyhedral structure with many thin luminous soot streaks over a wide range of pressure and gas flow, a high-pressure central burner had to be developed It consisted of a parcel of aluminium foils

with a thickness of 0.015 mm. Every second aluminium foil had a corrugated profile, so that small vertical channels with a diameter of 0.03 mm resulted. The parcel of aluminium foils was carefully fitted into a cooling block of copper. The central and the shielding burner were cooled separately by two cooling systems. The burner housing consisted of a water-cooled steel tube with a ceramic lining on the inside. This gave a nearly vortex-free gas flow.

The optical setup for the laser extinction and scattering measurements is described in detail elsewhere [16,17,32]. The absorption measurements were performed at $\lambda = 633$ nm and the scattering measurements at $\lambda = 488$ nm. The complex refractive index given in Ref. 18 was used for the data evaluation. The mean error of the extinction coefficient k_{ext} and scattering factor Q_{vv} is $\Delta k_{ext}/k_{ext} \approx 10\%$ and $\Delta Q_{vv}/Q_{vv} \approx 18\%$.

The flame-temperature profiles were measured by the Kurlbaum Method [19]. Often, flames here are characterised by their measured temperatures at 10-mm height above the burner. Gas samples were taken by a fine quartz probe thermostated at 250 °C. The flame gases were analysed using gas chromatography. The PAH were condensed into two cooling traps connected in series. After sample preparation the liquid samples were analysed qualitatively and quantitatively by high-performance liquid chromatography (HPLC) and identified by comparison with standards. Soot particles have also been investigated by electron microscopy.

Experimental Results

Soot Particles in the Post Flame Gases at 15 Bar:

The time-resolved profiles of the extinction and scattering measurements at different C/O ratios and unburned gas velocities in the high-pressure C_2H_4/air flames were used to calculate soot volume fraction f_v, particle number density N, and particle diameter d, applying the known equations derived from Mie theory [20] with $f_v = N * \bar{v}$ and $\bar{v} = 1/6 * \pi * d^3$. The variation of particle number density and particle diameter with time at different flame conditions determines the soot volume fraction f_v. Some typical profiles of particle number density N and particle diameter d at two C/O ratios and different unburned gas velocities, together with the flame temperatures for three flames, are given in Fig. 1. The beginning of soot particle growth in the first 10 ms of these flames is difficult to resolve because the main oxidation and particle forming zone is very narrow, and the density gradient (Schlieren effect) is very steep, especially for the 6- and 9-cm/s flames. The resolution in the low-speed C_2H_4/air flame with $v = 3$ cm/s is better. The lowest clearly measurable signals in these flames can be obtained at about 4-

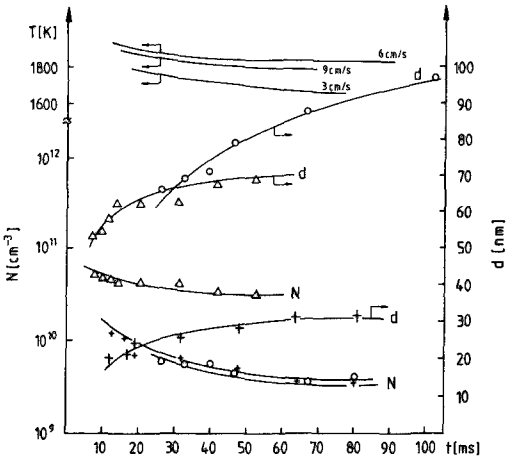

FIG. 1. Profiles of particle number density N, particle diameter d, and flame temperatures for two C/O ratios: 0.61 and 0.73 and different unburned gas velocities in a C_2H_4/air flame at $p = 15$ bar. O: C/O = 0.61, v = 3 cm/s; + C/O = 0.61, v = 6 cm/s; Δ: C/O = 0.73, v = 9 cm/s.

mm height above the burner. To follow the anisotropy of the particle shape the depolarisation ratios δ_v were measured in all flames. Here, δ_v was found between 0.1 and 0.4%, values that show that the particles do not differ much from spherical particles and that no fluorescence is found. In the early phase of the combustion process, soot particles grow very fast, especially in flames with $T \geqslant 1840$ K, and the growth ceases very early.

Figure 1 shows that two quantities influence particle diameters, namely (1) the flame temperature, and (2) the C/O ratio. In the flame with the lowest flame temperature and rather high C/O ratio, the largest spherical particle diameters are observed (100 nm). With an increase in flame temperature of about 200 K and the same C/O ratio, particle growth stops quite early in the flame, and smaller final diameters of $d_\infty = 30$ nm are reached. With increasing C/O ratio at the same flame temperature, the final particle diameter increases. The decrease of particle number density N with time is due to a rapid coagulation of the soot particles, which cannot be resolved quantitatively in the first part of the sooting zone. Compared to atmospheric hydrocarbon flames, the profiles of N at 15 bar show a typical effect: For certain flame conditions, coagulation of the soot particles ceases early in the flame, and high particle number densities in the postflame gases result. The highest final particle number density N_∞ is found in the flame with the highest C/O ratio. The influence of temperature on N_∞ seems to be small.

In Fig. 2, the d_∞ and N_∞ are plotted as a function of $[C/O - (C/O)_{crit}]$. For three different flow veloc-

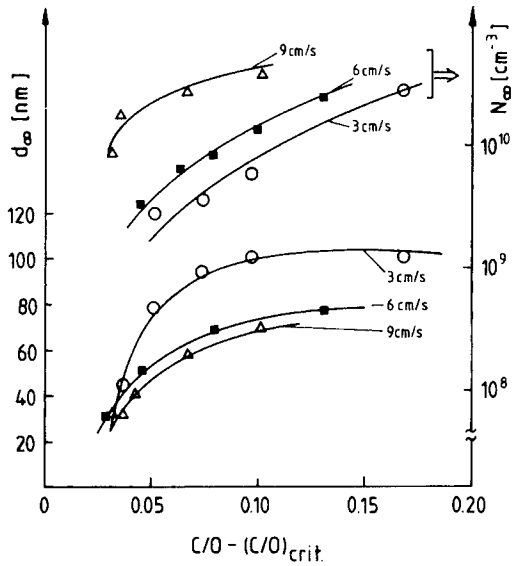

FIG. 2. Final particle diameter d_∞ and particle number density N_∞ as a function of [C/O − (C/O)$_{crit}$] at three unburned gas velocities and a burning pressure of p = 15 bar. [C/O − (C/O)$_{crit}$]: carbon content above the threshold of soot formation; (C/O)$_{crit}$: the threshold of soot formation. $v_{unb.gas}$: O: 3 cm/s; ■: 6 cm/s; ▲: 9 cm/s.

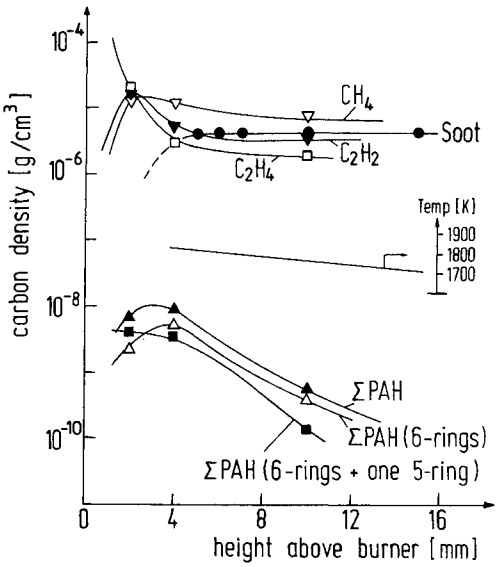

FIG. 3. Carbon densities (g/cm^3) of stable carbonaceous compounds in the postflame gases of a C_2H_4/air flame; p = 15 bar; C/O = 0.68; $v_{unb.gas}$ = 6 (cm/s); T (h = 10 mm) = 1750 K.

ities, the expression in the bracket represents the carbon content above the threshold of soot formation. The graphs indicate the influence of flow speed, which means temperature, and C/O ratio on N_∞ and d_∞.

The final particle number density in flames at normal pressure is practically always the same. In the postflame gases of the 15 bar C_2H_4/air flames, N_∞ depends on surplus carbon: The higher the surplus carbon content, the higher N_∞, and it depends on temperature: N_∞ increases with increasing flame temperature.

The influence of flame temperature on d_∞ is well known from C_2H_4/air flames burning at 1 and 5 bar [21]. There N_∞ remains practically constant, and $f_{v\infty}$ increases nearly exclusively by the growth of d_∞. In the 15 bar flames, particle diameters become larger with decreasing flame temperature (lower flow velocity), but for [C/O − (C/O)$_{crit}$] > 0.1, which corresponds to a surplus carbon density of ρ_c = 2.4 * 10^{18} C atoms/cm^3, d_∞ seems to reach a final "end value" of about 100 nm. Obviously, the particle size does not increase further in these flames.

Stable Hydrocarbons in the Postflame Gases at 15 bar:

The concentrations of the water gas components and of aliphatic and aromatic hydrocarbons in the flame gases behind the main flame zone are important for the description of soot particle growth. Therefore, the burned gas was analysed using gas chromatography and HPLC. The experimental results showed that the water gas equilibrium is established. Some resulting carbon-density time profiles are given in Fig. 3. The major hydrocarbon in the burned gases is CH_4. This is similar to C_2H_4/air flames burning at a pressure of 10 bar [15].

The maxima of CH_4 and C_2H_2 concentrations are found at similar heights above the burner, but the C_2H_2 concentration decreases faster in the phase of soot growth to a value similar to that of soot. Besides the major aliphatic compounds, CH_4, C_2H_2, C_2H_4, and C_2H_6, several different PAH were detected: The product spectrum of the measured PAH is similar to that in 1-bar flames. It shows two main types of PAH:

(1) pericondensed PAH with only six-membered rings, e.g., phenanthrene, $C_{14}H_{10}$; anthracene, $C_{14}H_{10}$; pyrene, $C_{16}H_{10}$; benz(*a*)anthracene, $C_{18}H_{10}$; benz(*k*)fluoranthene, $C_{20}H_{12}$; benz(*a*)-pyrene, $C_{20}H_{12}$; and
(2) pericondensed PAH with six-membered rings and mostly one five-membered ring, e.g., fluoranthene, $C_{16}H_{10}$; acephenantrylene, $C_{16}H_{12}$; crysene, $C_{18}H_{12}$; benz(*b*)fluoranthene, $C_{20}H_{12}$.

PAH with side chains were not found; their concentrations are therefore below the detection limit, which amounts to a mole fraction of $x_i < 5 * 10^{-10}$.

In Fig. 3, the two characteristic classes of PAH are

shown. The PAH with only six-membered rings have a maximum at 4-mm height above the burner, while the maximum of the PAH with one five-membered ring lies closer to the burner. Towards longer reaction times, their carbon density decreases faster than the carbon density of the PAH that contain only six-membered rings. The summation of carbon densities of PAH, Σ_{PAH}, has a maximum at 4-mm height above the burner and decreases towards 10-mm height above the burner to a value that is more than one order of magnitude lower. This takes place in the phase where soot volume fraction has nearly reached its final value.

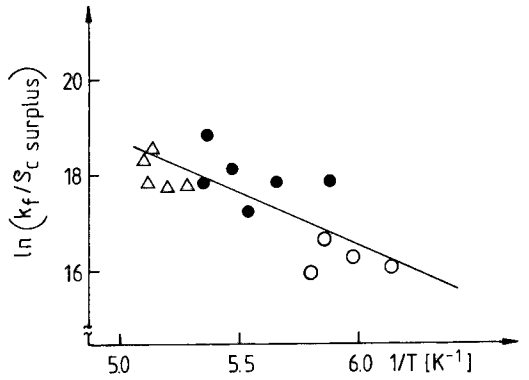

FIG. 4. Arrhenius diagram of the normalised first-order rate constant k_f/ρ_c; $v_{unb,gas}$: O: 3 cm/s; ●: 6 cm/s; Δ: 9 cm/s. C/O ratios: 0.58–0.73; k_f/ρ_c in [cm³/mol · s].

Discussion

In a previous paper, the influence of pressure on soot formation, derived from measurements of f_v, N, and d in the burned gases of ethylene/air flames for pressures up to 70 bar, has been described [14]. These measurements pointed to a change in soot formation mechanism towards higher pressures with respect to higher carbon atom densities: the final particle number density increases towards higher pressure, and the soot mass growth seems to decay at high pressures, as a result of a lack of addable substances as C_2H_2.

In this paper, experiments are described that have been performed in order to follow quantitatively the time dependence of soot volume fraction, of particle number density, and of the surrounding atmosphere. As mentioned above, the highest pressure where such measurements can be reasonably well performed with the usual laser techniques at the moment is about 15 bar. From these measurements, information is obtained about soot mass growth and coagulation. The measurements of the concentrations of the gaseous species clearly show that, at 15 bar and at higher pressure, part of the remaining carbon is stored in CH_4. The concentration of the remaining C_2H_2 is, compared to 1-bar flames, high enough so that it cannot be the limiting factor for further soot growth, as indicated in Ref. 14 on the basis of data obtained at 70 bar.

The mass growth of soot can often be quite well described by the simple formula [13,21,24].

$$\frac{df_v}{dt} = k_f * (f_{v\infty} - f_v) \qquad (1)$$

with $f_{v\infty}$ being the final soot volume fraction.

Up to about 5 bar in premixed flames, k_f seems to depend only on temperature [15,21,25,26], with an apparent activation energy around 200 kJ/mol. The surplus carbon density ρ_c in these flames was $\rho_c < 5 * 10^{17}$ C atoms/cm³, where ρ_c was estimated by the following equation: $\rho_c = \rho_{c,total} * [(C/O) - (C/O)_{crit}]/$ (C/O). Measurements in C_2H_4/air flames burning at pressures higher than 10 bar have indicated that k_f may depend on the C/O ratio [16]. The k_f values obtained here at 15 bar confirm this observation. They do not lie on a single curve. In Fig. 4, values of k_f divided by ρ_c for the 15-bar C_2H_4/air flames are plotted as a function of $1/T$. They can be reasonably well approximated by a straight line, with an "activation energy" of about 200 kJ/mol. This is in agreement with results obtained from pyrolysis experiments in shock waves at similar or higher carbon atom densities [27].

The soot mass growth process is driven by the activity of the soot particles, by flame temperature, and by the concentration of gas-phase growth species (see Fig. 2). Here, the decay of soot growth rate must be attributed to decreasing "particle activity" because the C_2H_2 concentration in the later phase of the combustion process $[C_2H_2]_\infty$ (see Fig. 3) already is sufficiently high for further soot growth.

Soot particles grow by soot mass growth and by coagulation. During coagulation, the particles collide and stick together (meet and stick model), forming new soot particles. The dynamics of an aerocolloidal system like soot particles can be described by Brownian coagulation. The Smoluchowski equation describes the decay of the total particle number density with time [29–31]:

$$\frac{dN}{dt} = -k_c * N^2. \qquad (2)$$

The coagulation rate constant (cm³/s) for spherical particles, k_c, depends weakly on temperature. It also depends on pressure, particle size, gas viscosity, and external fields. From Eq. (2), the coagulation rate constant k_c can be obtained by a plot of $1/N$ vs reaction time. The data of $1/N$ vs reaction time in the 15-bar flame are no longer linear in the whole meas-

TABLE 1
Coagulation rate constants for the first and second (rapid and slow) part of coagulation at different C/O ratios and flame temperatures, expressed as unburned gas velocity v (cm/s)

v cm/s	C/O	$k_{c1} * 10^{10}$ (cm³/s)	$k_{c2} * 10^{10}$ (cm³/s)
3	0.568	—	—
	0.582	56	34
	0.605	36	16
	0.628	10	5
	0.699	2.6	1.6
6	0.610	126	31
	0.626	89	24
	0.645	58	5
	0.660	17	10
	0.681	—	1.3
	0.712	—	1
9	0.662	47	10
	0.667	10	5
	0.673	6	1.5
	0.698	5	1.4
	0.733	9	2.6

ured regime. In the first phase of coagulation, the particles coagulate fast. With progressing reaction time, coagulation of the particles seems to become slower. The resulting curves of $1/N$ vs time are bent. Similar effects were already found in C_2H_4/air flames burning at 10 bar [17]. For a simplified evaluation of the nonlinear curves, the experimental data were approximated by two linear curves. In Table 1, the formal coagulation rate constants k_{c1} (cm³/s) (first part of coagulation) and k_{c2} (second part of coagulation) are listed for the different C_2H_4/air flames at $p = 15$ bar.

Obviously, the coagulation rate is influenced by (1) flame temperature, and (2) surplus carbon density, as can be seen in Table 1. The influence of the C/O ratio on the coagulation rate constant in C_2H_4/air flames burning with $T = 1800$ K at pressures from 10 to 15 bar is shown in Fig. 5. The plot shows the different phases of coagulation in the postflame gases, given by β_1 and β_2. Here, β is the normalised coagulation rate constant $k_c/k_{c,\mathrm{cont}}$, ($k_{c,\mathrm{cont}}$ = the reduced coagulation rate constant in the continuum regime); β_1 represents coagulation of the particles in the early phase of the coagulation process, β_2 in the later phase. For the two regions of coagulation, a similar dependence of β_1 and β_2 on C/O is found. For C/O ratios less than 0.60, values of β_1 and β_2 are constant. With increasing C/O ratios, both decrease,

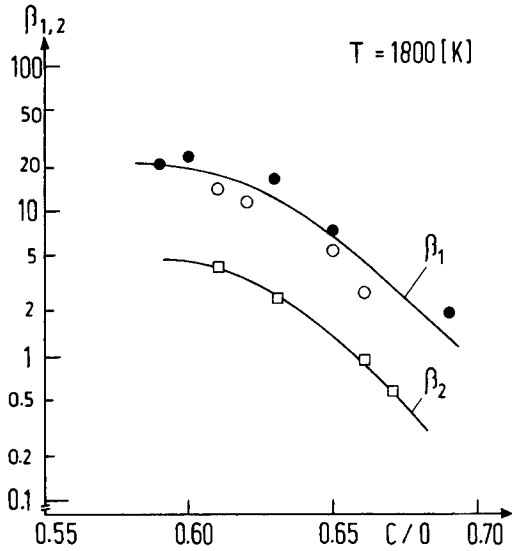

FIG. 5. Normalised coagulation rate constants β_1 and β_2 as a function of C/O ratios. β_1: early phase of coagulation; β_2: later phase of coagulation. $\beta \equiv k_c k_{c,\mathrm{cont}}$; $k_{c,\mathrm{cont}}$: coagulation rate in the continuum regime.

and β_2 reaches for C/O > 0.65 values which are even lower than 1.

The measured C_2H_4/air flames at 15 bar are in the regime of Knudsen numbers between $1 < K_n < 4$, the transition region between the free molecular flow regime ($K_n > 10$) and the continuum regime with $K_n < 1$ [16,17]. The theoretical calculation of β, assuming monodisperse, spherical particles at a flame temperature of 1800 K and a pressure of 15 bar, gives values of $\beta = 1$–3 [17]. A size distribution of the particles, in our case a lognormal size distribution with a geometric standard deviation of $\sigma_g = 2$ at $T = 1800$ K and $p = 15$ bar, gives $\beta = 10$–20 [17]. The experimental data for β_1 and β_2 are mostly found in the range between the regime of monodisperse spherical particles and that of particles with a standard deviation of $\sigma_g = 2$ (effectively, $\sigma_g < 2$). Towards higher C/O ratio, the β values tend towards those of the monodisperse particles. Investigations of the coagulation of soot particles in 10-bar flames showed that, for Knudsen numbers of about 1 and ρ_c values higher than 10^{18} C atoms/cm³, the β values are also lower than 1 [16,17]. This seems to be a typical result for C_2H_4/air flames at elevated pressures. The decrease of β_1 and β_2 may be attributed to (1) the width of the size distribution, and (2) the "activity of the particles," which ceases with reaction time. Therefore, the sticking probability of particles decreases and tends to zero. The consequence is a diminishing coagulation of particles, resulting in a high particle number density. For high-pressure C_2H_4 flames with $\rho_c > 10^{18}$ C atoms/cm³, the final

soot volume fraction $f_{v\infty}$ increases mainly via final particle number density N_∞ (see Figs. 1 and 2) and not by growth of the size of the particles (see Fig. 2), as in flames burning around 1 bar.

A further result of C_2H_4 flames burning at pressures $p > 10$ bar is that the channelling of the fuel carbon into postflame products leads to fewer substances than, e.g., in an atmospheric C_2H_4/air flame. Besides the water gas components, only CH_4, C_2H_2, C_2H_4, and soot are available in higher concentrations. The PAH, which either have only six-membered rings or have six-membered rings plus one five-membered ring, disappear already at very short reaction times where strong soot growth takes place.

Conclusions

From the laser extinction and scattering measurements in a C_2H_4/air flame burning at 15 bar, time-dependent profiles of soot volume fraction f_v, particle number density N, and particle diameter d at different C/O ratios (0.59–0.73) and different flame temperatures (1600–2000 K) were obtained. Additional profile measurements of aliphatic and aromatic hydrocarbons, PAH, have been performed.

The profile measurements of soot particles showed that the particle diameters increase very strongly at the beginning of soot formation and reach constant values early in the postflame gases. Coagulation of the particles also ceases relatively early in the postflame gases of the 15-bar flame, so that high final particle number densities N_∞ can result. With increasing surplus carbon content, N_∞ reaches more than 10 times higher values at $p = 15$ bar than at $p = 1$ bar while d_∞ tends towards constant values. At this pressure, $f_{v\infty}$ is proportional to ρ_c^3, so that $f_{v\infty}$ is mostly due to an increase of N_∞. The methane and acetylene profiles are different compared to the corresponding profiles in the 1-bar C_2H_4/air flames. The maxima of both compounds are similar. However, C_2H_2 decreases strongly in the phase of soot growth. Its final value $[C_2H_2]_\infty$ is similar to the final soot volume $f_{v\infty}$, which implies that the carbon density of C_2H_2 would be sufficiently high for further soot mass growth. Methane does not behave like C_2H_2, so that CH_4 becomes the major component of all analysed hydrocarbons, including soot.

The density of PAH analysed in the burned gas is more than three orders of magnitude lower than the carbon density of soot. Pericondensed PAH with only six-membered rings or with six-membered rings and one five-membered ring could be analysed. The concentrations of PAH with side chains are below the detection limit ($x_i < 5 * 10^{-10}$). The PAH are formed very early in or before the phase of strong soot growth, but they are consumed rapidly to very low mole fractions that are not higher than $x_{PAH} \approx 10^{-9}$.

For higher surplus carbon densities ρ_c (about $\geqslant 10^{18}$ C atoms/cm^3), the data about soot mass growth can be described by a normalised first-order rate constant k_f/ρ_c (ρ_c = surplus carbon density). This is in agreement with the results of pyrolysis experiments in shock waves [27]. The activity of the growing soot particles decays as a result of flame temperature but apparently also decays after they have reached a certain size, probably by organising inactive surface lattice planes (like the C-axis direction of graphite). In the regime of surplus carbon density with $\rho_c > 10^{18}$ C atoms/cm^3, the coagulation rate constant β reaches values below 1. The particles still collide but do not stick together anymore.

Acknowledgments

Financial support by the commission of the European Communities within the frame of the JOULE Program, by the National Swedish Board for Industrial and Technical Development (NUTEK), and by the Joint Research Committee of European Automobile Manufacturers (Fiat, Peugeot SA, Renault, Volkswagen, and Volvo) within the IDEA Program is gratefully acknowledged.

REFERENCES

1. Tompkins, E. E., and Long, R., *Twelfth Symposium (International) on Combustion,* The Combustion Institute, Pittsburgh, 1965, p. 625.
2. Bockhorn, H., Fetting, F., Wannemacher, G., and Wenz, H. W., *Nineteenth Symposium (International) on Combustion,* The Combustion Institute, Pittsburgh, 1982, p. 1413.
3. Bockhorn, H., Fetting, F., and Wenz, H. W., *Ber. Bunsenges. Phys. Chem.* 87:1067 (1983).
4. Bockhorn, H., Fetting, F., and Heddrich, A., *Twenty-First Symposium (International) on Combustion,* The Combustion Institute, Pittsburgh, 1986, p. 1001.
5. Bockhorn, H., Fetting, F., and Wieschnowsky, U., *Twenty-Second Symposium (International) on Combustion,* The Combustion Institute, Pittsburgh, 1988, p. 343.
6. Homann, K. H., and Wagner, H. Gg., *Eleventh Symposium (International) on Combustion,* The Combustion Institute, Pittsburgh, 1967, p. 371.
7. Homann, K. H., *Comb. Flame* 11:265 (1967).
8. Homann, K. H., *Twentieth Symposium (International) on Combustion,* The Combustion Institute, Pittsburgh, 1984, p. 857.
9. Loeffler, S., and Homann, K. H., *Twenty-Third Symposium (International) on Combustion,* The Combustion Institute, Pittsburgh, 1990, p. 355.
10. Howard, J. B., Bittner, J. D., and Palmer, H. B., "Chemistry of Intermediate Species in the Rich Combustion of Benzene," in *Soot in Combustion Systems and its Toxic Properties* (J. Lahaye and G. Prado, Eds.), Plenum Press, New York, 1983, NATO Conference Series VI, Vol. 7, p. 95.

11. Lam, F. W., Howard, J. B., and Longwell, J. P., *Twenty-Second Symposium (International) on Combustion,* The Combustion Institute, Pittsburgh, 1988, p. 323.
12. Boehm, H., Hesse, D., Jander, H., Luers, B., Pietscher, J., Wagner, H. Gg., and Weiss, M., *Twenty-Second Symposium (International) on Combustion,* The Combustion Institute, Pittsburgh, 1988, p. 403.
13. Luers, B., Jander, H., and Rudolph, G., VDI-Berichte No. 922, VDI-Verlag, Düsseldorf, Germany, 1991, p. 191.
14. Boehm, H., Feldermann, Chr., Heidermann, Th., Jander, H., Luers, B., and Wagner, H. Gg., *Twenty-Fourth Symposium (International) on Combustion,* The Combustion Institute, Pittsburgh, 1992, p. 991.
15. Boenig, M., Feldermann, Chr., Jander, H., Luers, B., Rudolph, G., and Wagner, H. Gg., *Twenty-Third (International) Symposium on Combustion,* The Combustion Institute, Pittsburgh, 1990, p. 1581.
16. Feldermann, Chr., Ph.D. Thesis, University of Goettingen, Germany, 1992.
17. Feldermann, Chr., Jander, H., and Wagner, H. Gg., *Z. Phys. Chem.* in press.
18. Dalzell, W. H., and Sarofim, A. F., *Trans. ASME., J. Heat Transfer* 91:100 (1969); see also Lee, S. C., and Tien, C. L., *Eighteenth Symposium (International) on Combustion,* The Combustion Institute, Pittsburgh, 1980, p. 1159.
19. Gaydon, A. G., *The Spectroscopy of Flames,* 2nd ed., Chapman and Hall, London, 1974.
20. Mie, G., *Ann. Physik* 25:377 (1908).
21. Maetzing, H., and Wagner, H. Gg., *Twenty-First Symposium (International) on Combustion,* The Combustion Institute, Pittsburgh, 1986, p. 1047.
22. Frenklach, M., and Clary, D. W., *Twenty-First Symposium (International) on Combustion,* The Combustion Institute, Pittsburgh, 1986, p. 1067.
23. Woods, L. T., and Haynes, B. S., *Comb. Flame* 85:523 (1991).
24. Haynes, B. S., and Wagner, H. Gg., *Z. Phys. Chem. N.F.* 133, 201 (1982).
25. Baumgaertner, L., Hesse, D., Jander, H., and Wagner, H. Gg., *Twentieth Symposium (International) on Combustion,* The Combustion Institute, Pittsburgh, 1984, p. 959.
26. Baumgaertner, L., Jander, H., and Wagner, H. Gg., *Ber. Bunsenges. Phys. Chem.* 87:107 (1983).
27. Bauerle, St., Karasevich, Y., Slavov, St., Tanke, D., Tappe, M., Thienel, Th., and Wagner, H. Gg., submitted to the *Twenty-Fifth Symposium (International) on Combustion.*
28. Geck, C., Diplom Thesis, University of Goettingen, 1975.
29. Friedlander, S. K., *J. Colloid Interface Sci.* 67:387 (1978).
30. Fuchs, N. A., *The Mechanics of Aerosols,* Pergamon Press, New York, 1964.
31. Hidy, G. M., *J. Colloid Sci.* 20:123 (1965).
32. D' Alessio, A., Di Lorenzo, A., Borghese, A., Beretta, F., and Masi, S., *Sixteenth Symposium (International) on Combustion,* The Combustion Institute, Pittsburgh, (1977), p. 695.

COMMENTS

K. H. Homann, TH Darmstadt, Germany. In the 1-bar flames, deactivation of the soot particles seems to be mainly an internal, "unimolecular" process. At 15 bar it looks like a "bimolecular" process, the surrounding gas phase apparently influencing the rate. Do you think that the preferential formation of CH_4 and the reduced formation of C_2H_2 have something to do with this change in the deactivation mechanism?

Author's Reply. As far as we can say from profile measurements up to 15 bar and from calculations, the maximum C_2H_2 as well as the CH_4 concentrations are essentially determined in the main reaction zone. What varies is the consumption of both species in the flame (soot formation and slow oxidation). We cannot yet answer the question of how much CH_4 is coming from the soot particles.

•

Peter B. Sunderland, University of Michigan, USA. Your conclusions depend strongly upon your measurements via scattering of soot particle diameter, *d*, a parameter you do not define. If your diameters represent primary particle sizes, your measurements of up to 100 nm are a factor of 3 greater than those widely observed using transmission electron microscopy (TEM). If, on the other hand, your diameters represent equivalent diameters of soot aggregates, this is an inadequate description of the chainlike structure of soot. Such problems may be circumvented by the use of TEM in measuring soot particle sizes.

Author's Reply. The possible presence of soot particle chains in flames is indeed a problem that has been discussed in the literature in great detail. It is also well known that the chainlike structures seen by microscope (TEM and REM) need not be representative for soot particles present in the flame. The values reported here are formal particle diameters obtained optically as described [1–3]. The diameters of the primary particles for the same flames measured by TEM and REM are smaller (~30–35 nm) than the optical ones. This indicates the important point that the optical particle number density reported is probably a lower limit (but rather close to the real value).

REFERENCES

1. D'Alessio, A., in *Particulate Carbon,* Plenum Press, New York-London, 1981, pp. 207–256.
2. Jones, A. R., *Combustion Institute European Symposium* (F. J. Weinberg, Ed.), Academic Press, London, 1973, p. 376.
3. Jones A. R., *Proc. R. Soc. Lond. A* 366:111–127 (1979). Prado, G., Jagoda, J., Neoh, K., and Lahaye, J., *Eighteenth Symposium (International) on Combustion,* Pittsburgh, 1981, p. 1127.

•

Jorma Jokiniemi, VTT Energy, Finland. Why is the sticking coefficient of soot particles decreasing as a function of pressure? Experimental results of Wagner (University of Vienna) and Flagan (CalTech) show that inert metal particles coagulate at room temperature with a high sticking coefficient.

Author's Reply. Coagulation of growing soot particles in flames is different from coagulation of metal particles. The sticking of soot particles in the early phase is partly due to chemical bonds; later on, when mass growth decays van der Waals forces become important. For "old soot particles," the stability of the soot aggregates in flames decreases with increasing temperature [1,2].

REFERENCES

1. Graham S. C., and Homer, J. B., *Faraday Symp. Chem. Soc.* 7:85 (1973).
2. Friedlander, S. K., in *Smoke, Dust and Haze,* John Wiley & Sons, New York, 1977.

Twenty-Fifth Symposium (International) on Combustion/The Combustion Institute, 1994/pp. 585–592

SUPPRESSION OF SOOT FORMATION IN ETHENE LAMINAR DIFFUSION FLAMES BY CHEMICAL ADDITIVES

T. NI, S. B. GUPTA AND R. J. SANTORO
Department of Mechanical Engineering
The Pennsylvania State University
University Park, PA 16802, USA

The effects of methane, methanol, ethanol, 1-propanol, 2-propanol, carbon dioxide, and carbon disulfide addition on soot formation in ethene laminar diffusion flames were examined. In this study, one-dimensional (1D) laser-induced incandescence (LII) and fluorescence measurements were used to determine soot volume fraction and relative soot precursor concentration, respectively, in the ethene and (ethene + additive) flames. Up to 60% reductions in soot volume fraction were found with the addition of 25% methanol to an ethene diffusion flame. More significant soot reductions were observed with the addition of carbon disulfide. It has been shown that a more than 50% reduction in soot volume fraction was achieved by adding 9.5% CS_2. Experimental results strongly suggest suppression of soot formation by methanol and carbon disulfide to be mainly a chemical effect.

Introduction

The ramifications of soot formation on the environment, public health, and hardware performance in practical combustion systems have long been identified. The current need for understanding and control of soot formation stems from the future increase in the aromatic content of commercial fuels, as well as the prospect of stricter environmental standards. One of the practical approaches to soot reduction is to blend additives into the fuel, so as to alter the soot nucleation and growth processes or to enhance soot oxidation.

Although the effects of various additives on soot formation have been observed by numerous researchers, relatively little is known about the mechanisms involved in soot suppression. Phenomenological theories have been suggested to explain the influence of additives on the formation of soot particles. For example, modest reductions in soot loading in diffusion flames by addition of inert species, such as Ar and N_2, have largely been attributed to lower flame temperatures and decreased fuel concentrations (dilution) [1–3]. Such effects are believed to significantly decrease the reaction rates of processes leading to soot formation. However, large reductions in soot formation by additives have been explained by chemical mechanisms. Soot suppression by alcohol addition has been observed both in shock tubes [4,5] and in flames [6]. Frenklach and Yuan [4], in studies of the effects of methanol and ethanol addition to benzene on soot formation, have attributed the suppression effect to enhanced oxidation of soot and soot precursors by OH generated from alcohol pyrolysis and removal of hydrogen atoms. The most effective gaseous soot suppression additives appear to be sulfur compounds, such as H_2S [7], SF_6 [8], and SO_2 [7,9]. It has been suggested that SO_2 promotes the oxidation of soot precursors and soot particles, probably due to increased OH concentration [10]. Gulder [11], however, reports that for mole fractions less than 40%, SO_2 has no direct chemical influence on soot formation, and the soot reduction observed is purely due to lower flame temperature and fuel concentration. Randolph and Law [12], based on studies involving the addition of propanol and hexanol to hydrocarbon droplet studies, question the role of the hydroxyl group of alcohol in soot suppression. They have reported that the addition of alcohol reduces soot by the same amount as other soot-controlling additives, indicating the dilution of the fuel concentration to be the dominant factor in soot reduction with no observable chemical effect [12].

The present study was undertaken to examine the importance of chemical effects when soot-suppressant additives, such as methanol and carbon disulfide, are introduced into ethene diffusion flames. A series of controlled experiments were performed to isolate such effects.

Experimental Approach

In these experiments, a laminar diffusion flame was established using a coannular burner, which consists of a 1.1-cm-diameter fuel tube surrounded by a 10.2-cm-diameter air tube [13]. A 40.5-cm-long brass cylinder was used as a chimney to shield the flame from laboratory air currents. Two holes diametrically

TABLE 1
Flow conditions and calculated adiabatic temperatures[a] (T_{AD}) of ethene-additive mixture diffusion flames

Flame No.	Fuel (cm^3/s)	Additive (cm^3/s)[b]	Mole% of additive	C% of additive	T_{AD} (K)
1	C_2H_4 (3.85)				2370
2	C_2H_4 (3.30)	CH_4 (1.10)	25.0	14.2	2345
3	C_2H_4 (3.30)	CH_3OH (1.10)	25.0	14.2	2347
4	C_2H_4 (3.08)	CH_4 (1.54)	33.3	20.0	2336
5	C_2H_4 (3.08)	CH_3OH (1.54)	33.3	20.0	2338
6	C_2H_4 (3.08)	C_2H_5OH (0.77)	20.0	20.0	2343
7	C_2H_4 (3.30)	1-C_3H_7OH (0.37)	10.1	14.2	2353
8	C_2H_4 (3.30)	2-C_3H_7OH (0.37)	10.1	14.2	2352
9	C_2H_4 (3.66)	CS_2 (0.38)	9.5	5.0	2361
10	C_2H_4 (3.30)	CS_2 (1.10)	25.0	14.2	2346
11	C_2H_4 (3.30)	CO_2 (1.10)	25.0	14.2	2328

[a]Calculated using NASA Chemical Equilibrium Code.
[b]Vapor flow rate.

opposite and 0.8 cm in diameter were used for passing the laser beam through the flame. Another 5 × 5 cm slot covered with a quartz plate provided optical access for the emitted light. The air and gaseous fuel flows to the burner were metered with calibrated rotameters. Liquid additives, which were supplied by a precision syringe pump, were vaporized and mixed with the fuel in a vaporizer. The temperature of the vaporizer was maintained to within 5 °C of the boiling point of the liquid additives. To prevent any condensation of the liquid additives, the fuel line and fuel tube were heated with a heating wire. By varying the electric voltage applied to the heating wire, the temperature of the fuel flow at the lip of the burner was maintained at 60 °C for all fuel mixtures regardless of whether a liquid additive was introduced. This approach ensures that all the flames were established at the same ambient condition.

Flames burning ethene (CP grade, 99.5%) mixed with methane (CP grade, 99%), methanol (HPLC grade, 99.5%), ethanol (CP grade, 99%), 1-propanol (HPLC grade, 99.5%), 2-propanol (HPLC grade, 99.5%), carbon dioxide (bone dry grade, 99.8%), and carbon disulfide (HPLC grade, 99.5%) were studied. When an additive was introduced into the fuel line, the ethene flow rate was reduced in appropriate proportion in order to keep the total carbon flow rate constant. This ensures similar flame sizes and shapes. The air flow rate was maintained at 1060 cm^3/s for all flames. Table 1 summarizes the flow conditions and calculated adiabatic flame temperatures for the flames studied.

Laser-induced incandescence (LII) was applied to obtain spatial distribution of soot volume fraction (f_v) in the flames. The one-dimensional (1D) LII technique employed here is a modification of the technique followed by Quay et al. [14], where these authors have made point measurements while using a calibration scheme to measure local soot volume fraction quantitatively.

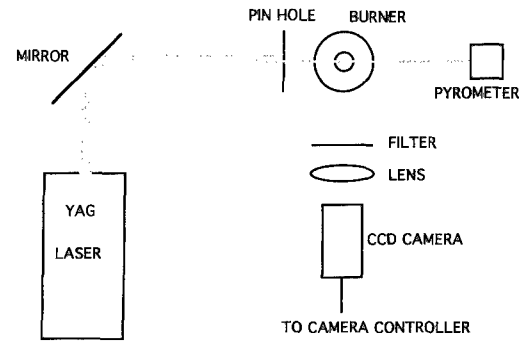

FIG. 1. Schematic diagram of 1D laser-induced incandescence experimental setup.

The optical setup for these measurements is given in Fig. 1. A Nd:YAG pulsed laser (Surelite, Continuum) operating at 10 Hz was used as an intense light source. A 1-mm-diameter pinhole was placed in front of the burner, which allowed only the center portion of the 6-mm-diameter laser beam to heat the soot particles. Diffraction effects were minimized by placing the pinhole as close as possible to the flame. In such a practice, the center portion of the near Gaussian beam is virtually uniform and intense enough to heat the soot particles to their vaporization temperature without additional focusing. Since the beam is unfocussed, the beam size across the flame is virtually constant, thus, eliminating the error associated with the change in the probe volume across the beam in

a 1D measurement. Both the 1064 nm and frequency-doubled 532-nm beams were used in this experiment. Comparison of 1064 and 532 nm excitation showed no significant difference on 1D LII profiles obtained for the ethene flames, although the use of 1064-nm beam showed certain advantages in penetrating heavily sooting flames. The laser beam behind the pinhole was monitored and maintained at 1.5 mJ/pulse, which corresponds to an average light fluence of 2.5×10^7 W/cm^2 for 8-ns full width at half-maximum (FWHM) laser pulse. The induced incandescence at a 90° angle was imaged with a 105-mm UV camera lens (Nikon, *f*/4.5) onto an intensified charge coupled device (CCD) camera (Princeton Instruments, Model ICCD-576S/RB). The camera was gated-on immediately after the laser pulse for 18 ns. A narrow band interference filter (transmittance centered at 460 nm) was placed in front of the camera to prevent light scattering from soot particles by the laser beam from reaching the detector and to reject most background luminosity and laser-induced fluorescence. Laser-induced incandescence images were acquired by averaging over 40 laser pulses. A calibration factor was used to obtain absolute local soot volume fraction. Measurements made using a light extinction/scattering technique on a well-established ethene laminar diffusion flame provided the calibration factor [13]. The uncertainties in the soot volume fractions derived from the 1D LII measurements were less than 5%.

The effect of the additives on soot precursor formation was assessed using laser-induced fluorescence measurements attributed to polycyclic aromatic hydrocarbon (PAH) species formed in the flames. The association of similar broadband laser-induced fluorescence, observed in both premixed and diffusion flames, with PAH species has been reported in the past [15–19]. Some controversy remains regarding the correspondence between this broadband fluorescence and PAH species since the direct association of the observed fluorescence with specific PAH species has not been unambiguously established. Thus, there is the possibility that other large hydrocarbon species such as polyenes and polyynes can contribute to the observed fluorescence. Nonetheless, we argue that variations in the concentrations of these species would also reflect the overall hydrocarbon kinetics that characterize the soot precursor evolution. Furthermore, it should be noted that the PAH species responsible for the fluorescence signals may not be soot precursors themselves, but rather they could be byproducts formed along the reaction route to soot particles. Again, in this work their concentration is argued to follow proportionally the soot precursor formation process. With these assumptions stated, the observed fluorescence variations are used in the present study to infer effects on soot precursors in the flames caused by the introduction of additives.

The optical setup for 1D PAH fluorescence imaging is very similar to that used for LII measurements, except that the excitation energy is much lower (<50 μJ/pulse). Since the spectra of both LII [14] and PAH [18] fluorescence are broadband in nature, it is difficult to isolate the fluorescence signal from LII emission. In this experiment, the excitation laser energy was kept below the LII threshold so that only the fluorescence, which is linear with laser fluence, was observed. The excitation sources are a Nd:YAG laser operated at 532 nm for the detection of large PAH and a Nd:YAG pumped dye laser with frequency doubling to 290 nm for the detection of small PAH. The laser, when operated at the 532-nm wavelength, excites only PAH molecules that contain roughly more than 5 aromatic rings [20], whose emission at 650 ± 10 nm was measured. The UV beam of 290 nm excites both large and small PAH molecules. By placing a combination of a 305-nm cutoff filter (WG305) and a UV-pass filter (UG11) in the front of the camera, only the emission ranging from 305 to 380 nm, which corresponds to small PAH molecules (approximately less than 5 rings), was captured. The camera was gated-on for 5 ns during the laser pulse. Fluorescence from 200 laser pulses were accumulated to generate a 1D fluorescence intensity profile.

The fluorescence lifetime for the PAH species was measured in the flame and observed to be approximately 30 ns in duration. The fluorescence lifetime for these species in the absence of collisional quenching is expected to be about 200 ns [20]. Thus, collisional quenching reduces the fluorescence lifetime by only an order of magnitude. Then, for the present conditions, quenching reduces the fluorescence lifetime rather than reducing the number of excited molecules. Thus, the effects of collisional quenching can be minimized by detecting the fluorescence during the laser pulse using an appropriately short gate width as was the procedure in the present experiments. The fluorescence intensity, therefore, was not corrected for collisional quenching, and the fluorescence is argued to be linearly proportional to the PAH concentration at approximately equivalent locations in the flame. From the measurements of the fluorescence lifetime for these species, we estimate that a change in the collisional quenching of a factor of 2 would only change the measured fluorescence by ±10% or less.

The temperature distribution measurements were made using the rapid insertion thermocouple technique similar to that described by Kent and Wagner [21]. In this technique, the soot deposited on the thermocouple surface is burned off in the oxidation zone of the flame prior to making a measurement at a new location. The uncoated Pt/Pt-10% Rh thermocouple was made from 127-μm-diameter fine wires. The temperature measurements were not corrected for radiation effects. Nonetheless, this tech-

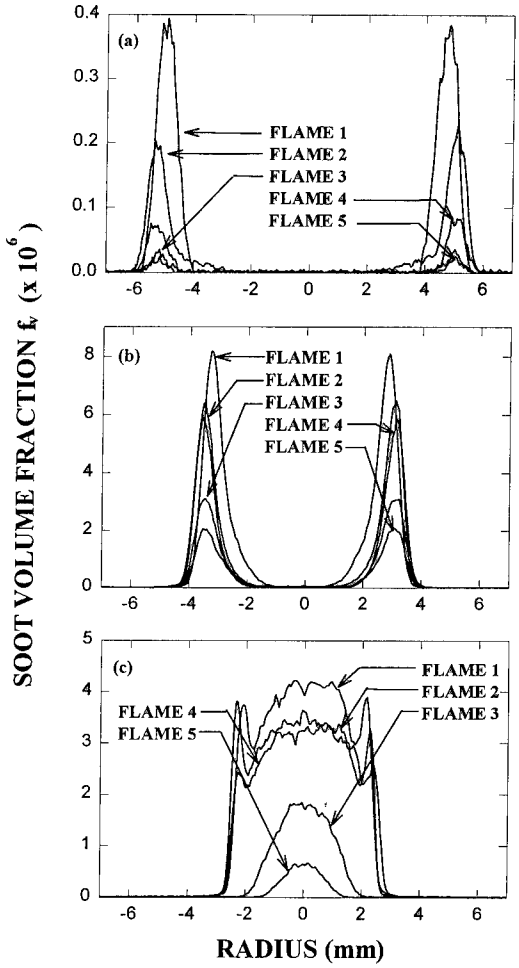

FIG. 2. Soot volume fraction profiles in the pure ethene diffusion flame (flame 1) and the flames mixed with 14.2 C% methane (flame 2), 20 C% methane (flame 4), 14.2 C% methanol (flame 3), and 20 C% methanol (flame 5): (a) 7-mm height; (b) 30-mm height; (c) 60-mm height.

nique provides accurate measurement of relative temperature changes.

Results and Discussion

Alcohol Addition:

Figure 2 shows the radial soot volume fraction profiles at three heights in the flames. The addition of 25% methanol (14.2 C%, flame 3) reduces the soot concentration by 60%, at least for all axial locations. Such strong reductions in soot loading suggest that chemical effects may be involved in the suppression of soot formation by methanol. In order to differentiate the chemical effects from dilution and temperature effects resulting from methanol addition, an ethene/methane mixture (which does not have an OH group, flame 2) was used for comparison. The comparison of the effect of methanol addition with methane addition on soot volume fraction f_v, as shown in Fig. 2, reveals that methanol addition reduces f_v substantially, as compared to methane addition. The difference between methanol addition and methane addition cannot be attributed to additional soot formed from methane because the soot concentration in a pure methane diffusion flame [2] is less than a twentieth of that in the ethene flame. Previous studies of laminar diffusion flames indicate that lowering flame temperature can significantly reduce soot formation [1–3]. However, this thermal effect was ruled out, since the calculated adiabatic temperature of ethene/methanol flames closely matches that of the ethene/methane flames (see Table 1). In fact, the ethene/methanol flame temperature in the soot inception zone, as measured by a thermocouple, is 10 °C higher than in the ethene/methane flame due to less radiative heat loss. These observations strongly suggest that a chemical interaction is the dominant effect in soot suppression by methanol addition.

In order to gain further insight into the chemical processes leading to soot reduction, measurements of PAH fluorescence were obtained in ethene, ethene/methanol, and ethene/methane flames. Polycyclic aromatic hydrocarbon species are often viewed as precursors to soot particles [22] and are a possible source of mass for soot growth [23]. As it is difficult to quantify the quenching effect and thermal effect on fluorescence intensity, absolute PAH concentration measurements were not obtained. However, in diffusion flames, the concentration of oxygen, which strongly quenches the fluorescence of most organic compounds, is negligible in the PAH formation zone, and the temperature profiles of the ethene/methanol and ethene/methane flames are very close to each other. Thus, PAH fluorescence measurements can provide information about the relative change of PAH concentration. Figure 3 shows radial profiles of PAH fluorescence intensity taken at a height of 10 mm above the fuel tube exit for ethene, ethene/methanol, and ethene/methane flames. It is interesting to note that the fluorescence intensities of larger PAH species excited by the 532-nm-wavelength laser beam achieve their maximum slightly further away from the centerline as compared to the profiles of smaller PAH species. A similar result has been previously reported by Smyth et al. [24] for Wolfhard–Parker slot burner studies of methane diffusion flames. Comparison of fluorescence profiles in ethene/methanol and ethene/methane flames indicates that the fluorescence intensities of both large and small PAH species are lower in the ethene/methanol flame. These results support an argument that the addition of methanol reduces the formation of soot

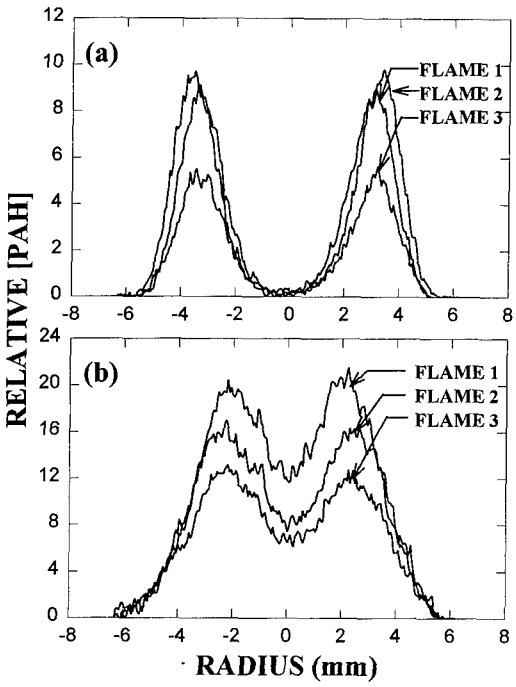

FIG. 3. Comparison of PAH fluorescence intensities of the pure ethene flame (flame 1) and the flames mixed with 14.2 C% methane (flame 2) and 14.2 C% methanol (flame 3) at the 10-mm height: (a) excited at a wavelength of 532 nm, (b) excited at a wavelength of 290 nm.

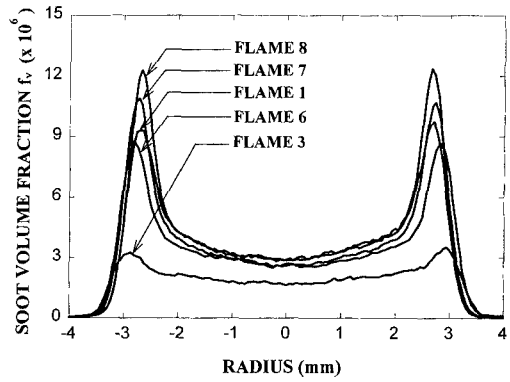

FIG. 4. Comparison of soot volume fraction profiles of the pure ethene flame (flame 1) and the flames mixed with 14.2 C% methanol (flame 3), 20 C% ethanol (flame 6), 14.2 C% 1-propanol (flame 7), and 14.2 C% 2-propanol (flame 8) at the 40-mm height.

particles by retarding the formation of the key soot precursors or oxidizing them through OH attack.

In order to further understand the role of the hydroxyl group in alcohols, three other alcohols (ethanol, 1-propanol, and 2-propanol) have been added to an ethene laminar diffusion flame. Figure 4 shows the radial soot volume fraction (f_v) profiles at the 40-mm axial location of the flames. Comparison with the pure ethene flame illustrates that not all alcohols are equally effective in soot suppression. Methanol was observed to reduce soot significantly, while ethanol and propanol have much less of an effect on the soot concentration. Indeed, 1-propanol and 2-propanol were found to slightly increase soot concentration. Since ethanol is a nonsooting fuel, this result reveals that the dilution effect, i.e., the reduction of soot concentration by diluting a sooting fuel with a nonsooting fuel species, is not significant in reducing f_v in the present studies. It should be noted that these results are consistent with the fact that the pyrolysis of methanol [25] generates OH radicals, which can oxidize soot particles or soot precursors, while the main pyrolysis product of ethanol [26] is ethene and water. In droplet flame studies, Randolph and Law found that the hydroxyl group in hexanol has no effect on soot concentration [12]. A possible explanation is that hexanol, like ethanol, does not produce a significant amount of OH radicals during pyrolysis.

Frenklach and Yuan [4] suggested a hydrogen removal mechanism to explain the effect of alcohol addition on soot formation. In their mechanism, hydrogen atoms were removed through the following reactions:

$$H + ROH \rightarrow H_2 + RO \quad (1)$$

$$H + ROH \rightarrow H_2 + R'OH \quad (2)$$

$$H + ROH \rightarrow OH + RH. \quad (3)$$

Hydrogen atoms are believed to play a key role in the production of reactive radical species in the formation of soot precursors [27]. Removal of hydrogen atoms should slow down the reactions toward soot formation. However, the lack of soot reduction by 1-propanol and 2-propanol addition does not support this mechanism as a general explanation for the effects of all alcohols.

Carbon Disulfide Addition:

During the combustion of fuel with carbon disulfide as an additive, Sye and Hwang observed a marked decrease in the formation of polycyclic aromatic hydrocarbons [28], the intermediates for soot particle formation. In the pyrolysis processes of hydrocarbons, carbon disulfide has been used to minimize the formation of coke [29]. In present work, CS_2 was added to ethene diffusion flames to study the chemical influence of CS_2 on soot formation. Figure 5 shows LII measurements at three heights above the burner for ethene, ethene/CS_2 and ethene/CO_2 flames. These profiles reveal that at lower

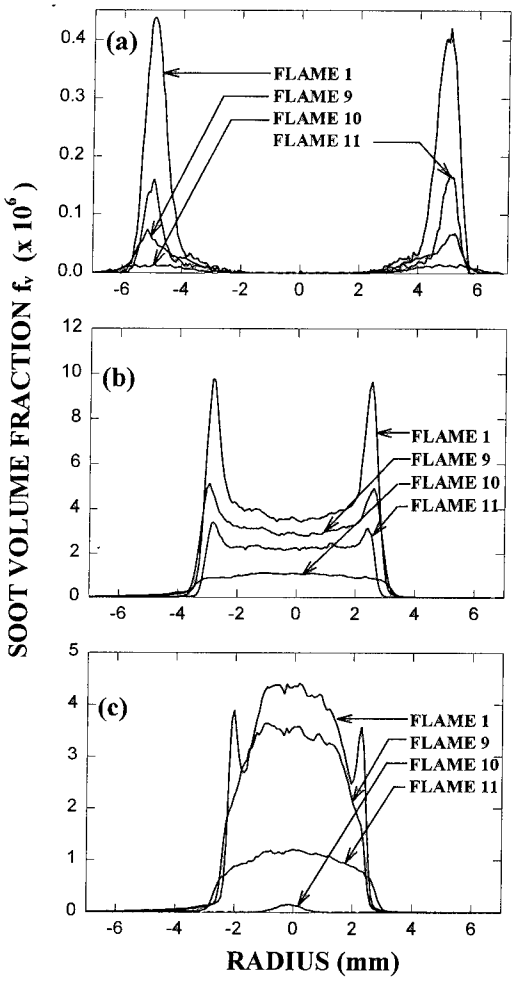

FIG. 5. Soot volume fraction profiles of the pure ethene flame (flame 1) and the flames mixed with 5.0 C% carbon disulfide (flame 9), 14.2 C% carbon disulfide (flame 10), and 14.2 C% carbon dioxide (flame 11): (a) 7-mm height, (b) 40-mm height, (c) 60-mm height.

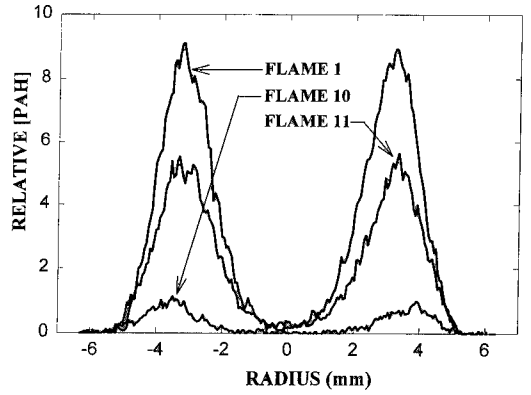

FIG. 6. PAH fluorescence intensity profiles of the pure ethene flame (flame 1) and the flames mixed with 14.2 C% carbon dioxide (flame 11) and 14.2 C% carbon disulfide (flame 10) at 10-mm height excited at a wavelength of 532 nm.

heights in the flame, the addition of 9.5 and 25% CS_2 (5.0 and 14.2 C%, respectively) substantially reduces the formation of soot. For the purpose of comparison, carbon dioxide was introduced into the ethene diffusion flame and a considerable reduction of soot was observed. This reduction may be due to lower adiabatic flame temperature (listed in Table 1), dilution, and chemical effects [30,31]. Although the adiabatic temperatures of ethene/CS_2 flames are higher than ethene/CO_2 flames with the same fuel-to-additive ratio, the soot volume fraction in ethene/CS_2 flames was substantially lower than that in the ethene/CO_2 flame at low heights. These results lead to the conclusion that a chemical effect due to the addition of CS_2 is important in soot suppression observed, and this chemical effect in the lower part of the flame is stronger than the effects due to CO_2 addition.

However, higher in the flames, the influence on soot concentration by CS_2 addition becomes less effective. At 60 mm above the burner, the soot volume fraction in the ethene +25% CS_2 (14.2 C%) flame is observed to be higher than in the ethene +25% CO_2 (14.2 C%) flame. A possible explanation for this observation is that the addition of CS_2 retards the formation and growth of soot particles rather than enhancing soot burnout. Recently, Gulder reported that the addition of less than 40% SO_2 does not have a chemical influence on soot concentration in diffusion flames [11]. Considering CS_2 oxidation to SO_2 in the oxidation zone of the diffusion flame and the lack of burnout enhancement, our results are consistent with Gulder's observation.

The measurements of PAH fluorescence further confirm the conclusion that the chemical interaction of CS_2 is significant. As shown in Fig. 6, the addition of 25% CS_2 (14.2 C%) reduces the fluorescence intensity of large PAH species by more than 90%. As a comparison, the same amount of CO_2 reduces fluorescence intensity by 40%. The mechanism involving the chemical interaction is not known yet. But it is expected that sulfur atom, an oxidizing species, is generated during the pyrolysis of CS_2 and may participate in the destruction of aromatic hydrocarbons similar to OH radical. The absorption of sulfur on soot particle surface may also slow down the rate of soot growth. It has been reported that sulfur and carbon disulfide can chemically bond to active sites on the carbon surface [32]. The resulting carbon-sulfur surface compound is extremely stable at 700 °C [33] and still exists at temperatures up to 927 °C [34,35]. It might be possible that the formation of such sur-

face compounds reduces the number of active carbon sites on soot surface, thus, preventing continuous growth of the soot particles. However, to date, no experimental evidence is available to support the existence of such a surface compound in the soot growth regions where temperatures as high as 1200 °C exist. Further investigation is needed to confirm this hypothesis.

Conclusions

1. It was demonstrated that the addition of methanol and CS_2 into ethene diffusion flames can significantly reduce the formation of soot particles.
2. Chemical interaction was found to play an important role in the suppression of soot formation by methanol and carbon disulfide addition.
3. Measurements of fluorescence from polycyclic aromatic hydrocarbons in ethene diffusion flames indicate that these species are reduced significantly by methanol and CS_2 addition.

Acknowledgment

Funding for this work from the Office of Naval Research under Grant No. N00014-93-0185 with Dr. Gabriel D. Roy as contract monitor is gratefully acknowledged.

REFERENCES

1. Schug, K. P., Manheimer-Timnat, Y., Yaccarino, P., and Glassman, I., *Combust. Sci. Technol.* 22:235–250 (1980).
2. Santoro, R. J. and Semerjian, H. G., *Twentieth Symposium (International) on Combustion*, The Combustion Institute, Pittsburgh, 1984, pp. 997–1006.
3. Axelbaum, R. L., Flower, W. L., and Law, C. K., *Combust. Sci. Technol.* 61:51–73 (1988).
4. Frenklach, M., and Yuan, T., *Sixteenth International Symposium on Shock Tubes and Waves*, Aachen, West Germany, 1987, pp. 487–493.
5. Alexiou, A., Williams, A., and Abdalla, A. Y., *Prepr. Am. Chem. Soc. Div. Fuel Chem.* 36:1547–1554 (1991).
6. Kadota, T., and Hiroyasu, H., *Combust. Flame* 55:195–201 (1984).
7. Haynes, B. S., Jander, H., Matzing, H., and Wagner, H. Gg., *Nineteenth Symposium (International) on Combustion*, The Combustion Institute, Pittsburgh, 1982, pp. 1379–1385.
8. Mitchell, J. B. A., and Miller, D. J. M., *Combust. Flame* 75:45–55 (1989).
9. Lawton, S. A., *Combust. Flame* 75:175–181 (1989).
10. Cotton, D. H., Friswell, N. J., and Jenkins, D. R., *Combust. Flame* 17:87–98 (1971).
11. Gulder, O. L., *Combust. Flame* 92:410–418 (1993).
12. Randolph, A. L., and Law, C. K., *Twenty-First Symposium (International) on Combustion*, The Combustion Institute, Pittsburgh, 1986, pp. 1125–1131.
13. Santoro, R. J., Semerjian, H. G., and Dobbins, R. A., *Combust. Flame* 51:203–218 (1983).
14. Quay, B., Lee, T.-W., Ni, T., and Santoro, R. J., *Combust. Flame* 97:384–392 (1994).
15. Coe, D. S., Haynes, B. S., and Steinfeld, J. L., *Combust. Flame* 43:211–214 (1981).
16. Miller, J. H., Mallard, W. G., and Smith, K. C., *Combust. Flame* 47:205–214 (1982).
17. Prado, G., Garo, A., Ko, A., and Sarofim, A., *Twentieth Symposium (International) on Combustion*, The Combustion Institute, Pittsburgh, 1985, pp. 989–996.
18. Beretta, F., Cincotti, V., D'Alessio, A., and Menna, P., *Combust. Flame* 61:211–218 (1985).
19. Petarca, L., and Marconi, F., *Combust. Flame* 78:308–325 (1989).
20. Berlman, I. B., *Handbook of Fluorescence of Aromatic Molecules*, Academic Press, New York, 1971.
21. Kent, J. H., and Wagner, H. Gg., *Combust. Sci. Technol.* 41:245–269 (1984).
22. Haynes, B. S., and Wagner, H. Gg., *Prog. Energy Combust. Sci.* 7:229–273 (1981).
23. McKinnon, J. T., and Howard, J. B., *Twenty-Fourth Symposium (International) on Combustion*, The Combustion Institute, Pittsburgh, 1992, pp. 965–971.
24. Smyth, K. C., Miller, J. H., Dorfman, R. C., Mallard, W. G., and Santoro, R. J., *Combust. Flame* 62:157–181 (1985).
25. Cribb, P. H., Dove, J. E., and Yamazaki, S., *Twentieth Symposium (International) on Combustion*, The Combustion Institute, Pittsburgh, 1985, pp. 779–787.
26. Rotzoll, G., *J. Anal. Appl. Pyrolysis* 9:43–52 (1985).
27. Frenklach, M., Clary, D. W., Gardiner, W. C., Jr., and Stein, S. E., *Twentieth Symposium (International) on Combustion*, The Combustion Institute, Pittsburgh, 1985, pp. 887–901.
28. Sye, W. F., and Hwang, S. S., *J. Chin. Chem. Soc.* 36:235–240 (1989).
29. Bajus, M., and Baxa, J., *Collect. Czech. Chem. Commun.* 50:2903–2909 (1985).
30. Du, D. X., Axelbaum, R. L., and Law, C. K., *Twenty-Third Symposium (International) on Combustion*, The Combustion Institute, Pittsburgh, 1991, p. 1509.
31. Zhang, C., Atreya, A., and Lee, K., *Twenty-Fourth Symposium (International) on Combustion*, The Combustion Institute, Pittsburgh, 1992, pp. 1049–1057.
32. Blayden, H. E., and Patrick, J. W., *Carbon* 5:533–544 (1967).
33. Chang, C. H., *Carbon* 19:175–186 (1981).
34. Sykes, K. W., and White, P., *Trans. Faraday Soc.* 52:660–671 (1956).
35. Owen, A. J., Sykes, K. W., Thomas, D. J. D., and White, P., *Trans. Faraday Soc.* 49:1198–1206 (1953).

COMMENTS

Omer L. Gülder, National Research Council, Canada. I have two comments and a question. The first comment is that in our experiments with liquid hydrocarbon fuels (mixtures of isooctane and toluene), the addition of methanol has not caused as much suppression as you observed in ethene flames. The behavior of ethene may not be typical of higher hydrocarbons. The second comment is related to the chemical influence of methanol addition on the soot formation process. In the pyrolysis of methanol, acetylene concentrations are very small as compared with those observed in methane pyrolysis. This could be one of the possible reasons that methanol addition suppresses soot formation more than methane does.

My question is whether you observed any changes in the visible flame height when you introduced the additives to the fuel side. If you did, then the comparison of the soot concentrations at the same downstream flame location would not be meaningful.

Author's Reply. Regarding your first comment, the difference between your results with liquid hydrocarbon fuels and our gas phase studies may be due to fuel volatility effects [1]. In our experiments, the added concentration of methanol was controlled directly, whereas in liquid fuel studies, the relative volatility of the fuel mixture components will determine how much methanol is vaporized and when the vaporization occurs during the combustion process [1]. Thus, our two studies may not be directly comparable as to the effectiveness of methanol addition on soot reduction.

As to your second comment, we would agree that acetylene is an important intermediate species in soot formation. The specifics of the chemical mechanism by which soot formation is reduced in this study have not been specifically identified.

The flame height in these studies varied from 87 mm for the pure C_2H_4 flame to 67 mm for C_2H_4/20% CH_3OH flame. However, the residence time to reach a specific height in the flame does not change in these buoyancy-dominated laminar diffusion flames, particularly under the conditions used in this study of maintaining a constant carbon atom volume flow rate. Thus, comparisons at similar heights represent comparable residence times, which we believe is an appropriate basis from which to compare the effects of the additives.

REFERENCE

1. Randolph, A. L., and Law, C. K., *Combust. Flame* 64:267–284 (1986).

•

Rudolf R. Maly, Daimler Benz, Germany. Your results suggest that addition of sulfur compounds to fuels reduces soot. In diesel engines it is well known that minute quantities of sulfur compounds increase soot emission. Would you please elaborate on these controversial results? Or do your results have no relation to soot in practical combustion systems?

Author's Reply. The reduction of particulate emissions from diesel engines as sulfur content of the fuel decreases is well known, as you point out. However, tail pipe particulate emissions from diesel engines include soot particles and species that condense on the soot particles. The reduction in fuel-bound sulfur appears to affect the condensable species fraction of the particulate emissions from diesel engines (e.g., H_2SO_4) strongly [1]. Thus, it is not clear that soot particle concentrations are reduced directly as fuel-bound sulfur is reduced.

Regarding your question as to the practical implications of our finding with regard to carbon disulfide addition, we are not proposing the addition of sulfur to fuels to reduce soot. As our study shows, the chemical pathway by which the additive affects the soot formation chemistry is important, whether that is by an alcohol or a sulfur-containing species. As we observed, some alcohol additives increased soot formation. Thus, the key to a reduction in soot formation via a chemical route lies in the formulation of the additive. It is hoped that our work lends insight into that process under diffusion flame conditions.

REFERENCE

1. *Diesel Particulate Emissions: Measurement Techniques, Fuel Effects, Control Technology,* (J. H. Johnson, T. M. Baines, and J. C. Clerc, Eds.), SAE, Inc., Warrendale, PA, 1992.

Twenty-Fifth Symposium (International) on Combustion/The Combustion Institute, 1994/pp. 593–600

IRON/SOOT INTERACTION IN A LAMINAR ETHYLENE NONPREMIXED FLAME

JIE ZHANG AND CONSTANTINE M. MEGARIDIS
Department of Mechanical Engineering
University of Illinois at Chicago
Chicago, IL 60607–7022, USA

A laminar, coannular, ethylene/air nonpremixed flame doped with ferrocene additive is employed to address the fundamental question of how iron becomes incorporated into the carbonaceous soot phase, thus interfering with the soot formation processes. The structure and chemical composition of individual aggregates are characterized with respect to flame coordinates via a combination of thermophoretic sampling, transmission electron microscopy, and energy dispersive spectrometry.

Soot aggregate microstructure clearly reveals iron occlusion, as well as stratification of soot layers over the occluded phase. The study provides physical evidence that the soot and iron compounds combine in the flame to form a hybrid (inhomogeneous) particulate phase. The reported observations are consistent with the hypothesis that ferrocene decomposes early in the combustion process and before the onset of soot particle inception, thus forming a fine aerosol for the subsequent deposition of carbonaceous substances. Examination of a series of inhomogeneous soot aggregates shows that the flame aerosol composition varies with flame coordinates. In particular, aggregates transported in the soot annulus near the luminous flame front are primarily composed of carbon and oxygen, with traces of iron finely dispersed through the aggregate matrix. On the other hand, carbonaceous soot transported at low heights and near the flame axis contains iron in its elemental form. Finally, soot aggregates in all other areas of the flame contain both iron and oxygen, thus implying the possible presence of iron oxides within the carbonaceous matrix.

Introduction

Use of fuel additives is an effective way of improving control over soot formation mechanisms within combustion systems. Even though the employment of certain additives has been shown to cause substantial reduction in soot emissions under specific conditions, their widespread implementation as soot suppressors is seriously impeded by their unknown mechanisms of operation [1]. Certain metallic additives appear to be of particular importance; iron compounds, for example, pose little threat to the environment and have long been known [2] to be soot inhibitors.

Ferrocene or dicyclopentadienyl iron [$(C_5H_5)_2$ Fe] is a well-known organometallic soot suppressor in gaseous- and liquid-fuel combustion media. It has a crystal structure, is readily synthesized, and is air stable, nontoxic, and soluble in most practical fuels. Its boiling point is 249 °C, it undergoes intense sublimation at temperatures below 100 °C and retains its chemical structure up to 500 °C. These favorable properties of ferrocene, along with its high vapor pressure even at modest temperatures, contribute to its widespread use in combustion technologies. It should be noted, however, that previous laboratory investigations involving ferrocene have shown both pro- [3,4] and antisoot [5,6] action, depending on flame conditions.

Several iron-additive studies have addressed the fundamental question of how the iron becomes incorporated into the carbonaceous phase, thus interfering with the soot processes. In those studies, withdrawal of bulk particulate samples for further chemical analysis provided some insight on the chemical character of inhomogeneous soot in iron-seeded flames. The primary objective of the laboratory work described herein was to provide high–spatial-resolution information on individual particulate microstructure and composition within laminar, coannular, ethylene/air nonpremixed flames seeded with trace amounts of ferrocene. An important aspect of the study was to characterize the distribution of iron in soot at a single aggregate scale, and elucidate the modes of interaction between iron combustion products and carbonaceous soot within laminar nonpremixed flames. The structure and chemical composition of individual aggregates were characterized as functions of flame coordinates via a combination of thermophoretic sampling [7], transmission electron microscopy, and a high-resolution microanalysis technique (energy-dispersive spectrometry).

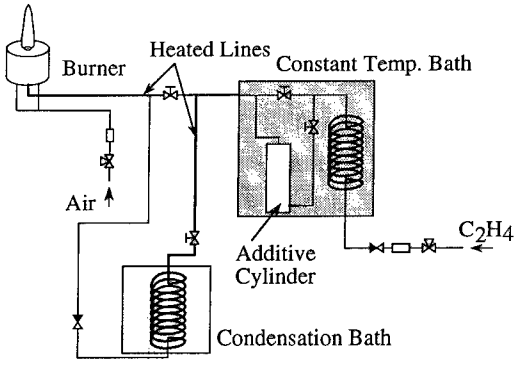

FIG. 1. Experimental setup and fuel additive system.

Experimental Apparatus and Related Measurements

Burner:

The current study employs an atmospheric, laminar, ethylene/air nonpremixed flame, which is based on a coannular burner consisting of two concentric tubes of 11.1- and 101.6-mm i.d., respectively. CP grade (99.5%) ethylene fuel flows freely through the inner tube, while the ventilating dry air flow passes through the annulus between the two tubes. A detailed description of the burner is given elsewhere [8]. Ethylene and air-flow rates of 3.85 cm^3/s and 713 cm^3/s, respectively, produce a soot-laden flame that displays a very stable shape and a height of 88 mm. The flame is shielded by a transparent cylindrical chimney to prevent interference with laboratory air currents. Even though the flame displays a very bright yellow luminosity that indicates the presence of microscopic soot particles, it does not release any soot to the environment. The soot and velocity fields in the above flame have been extensively analyzed using light-scattering and transmission measurements [8–10], as well as a thermophoretic sampling technique, which, in conjunction with electron microscopy, provided information on the morphological character of soot particles as a function of flame coordinates [11–13].

Apparatus:

The setup used in this study was identical to the one employed in the unseeded fuel work [11–13], with appropriate modifications needed for the incorporation of the iron additive in the fuel stream. These modifications mainly include fuel-line preheat and continuous-temperature monitoring, both required to prevent condensation of ferrocene vapor on the fuel-supply tube walls. Figure 1 displays the experimental configuration implemented for the dispersion of ferrocene vapor in the fuel stream. The system features a ferrocene sublimation cylinder that was designed to supply a known amount of ferrocene vapor into the ethylene stream prior to issuance into the burner. This stainless-steel cylinder contained a number of ferrocene powder layers (99.5% purity) interchanged with compartments of 2.38-mm-diameter stainless-steel beads. The seeded flow was filtered before exiting from the cylinder, in order to ensure that only gas vapors were carried into the burner. The pure ethylene flow was monitored before passage from the ferrocene cylinder with a thermal-type digital mass flowmeter rated for an accuracy of $\pm 2\%$ of full scale. Since the fuel-flow rate was kept stable, the additive loading of the fuel stream depended only on the temperature of the sublimation cylinder, which was controlled using a constant-temperature bath capable of maintaining temperatures up to 120 °C with a ± 1 °C accuracy. At steady-state flow conditions, the temperature of the seeded gas at the exit of the sublimation cylinder equilibrated slightly below the bath temperature (70 °C vs 75 °C). Theoretical calculations based on the known dependence of ferrocene vapor pressure on temperature [14], showed that a fuel temperature of 70 °C results in ferrocene concentration of 0.35% by weight of ethylene (525 ppm on a mole basis). The actual seeding rates of the fuel stream were measured by a ferrocene condensation bypass loop, as shown in Fig. 1. This procedure has been used by other investigators [15], and is based on complete condensation of the ferrocene additive carried by the fuel stream during its passage through a glass coil submerged within a NaCl/ice bath (-20 °C), and subsequently weighing the condensed mass. Two separate tests were performed for a steady-state fuel temperature of 70 °C, which showed that the fuel stream was indeed saturated by ferrocene vapor. The fuel lines downstream of the ferrocene cylinder were maintained at a slightly higher temperature than that of the fuel by a set of tape heaters and digital temperature controllers. This was necessary to ensure delivery of the entire amount of ferrocene vapor to the inner tube of the burner. It should be noted that the ferrocene loading of the carrier stream is comparable to the gaseous impurities carried with the ethylene gas (0.5% mole). A detailed chemical analysis determined that these impurities consisted of carbon, hydrogen, oxygen, and nitrogen; therefore, they should have no effect on the flame aerosol.

Soot Sampling:

The soot field in the flame under investigation was examined using a thermophoretic sampling technique that has been shown [7,16] to provide an accurate representation of the morphological character of flame-borne aerosols. This method is based on the phenomenon of thermophoresis, which drives the flame-borne soot to the cold surface of a precisely

positioned probe, where it is ultimately captured. The thermophoretic probe supports a 200-Å-thick elemental carbon substrate that provides a fine background for high-resolution observations using transmission electron microscopy. In summary, thermophoretic sampling provides soot microsamples from well-defined flame coordinates and allows subsequent morphological and chemical characterization using electron microscopy techniques.

Chemical Characterization of Soot:

The elemental content of the dispersed soot aerosol phase in the flame was investigated through energy-dispersive spectrometry (EDS), an x-ray technique providing information on the chemical character of thin specimens with resolution of the order of a few nanometers. Energy-dispersive spectrometry is based on the phenomenon during which electrons of appropriate energy impinge on a thin sample, causing the emission of x-rays whose energies and relative abundance depend upon the composition of the sample. The character of the emitted x-rays is used to analyze the elemental content of microvolumes using the appropriate instrumentation. In general, EDS microanalysis is easy to implement, is sensitive to low concentrations with minimum detection limits of the order of 0.1%, and has a relative precision of 1–5%. In addition, the technique is practically nondestructive and requires minimal sample preparation. The soot microsamples collected using thermophoretic sampling were analyzed by an EDS apparatus installed on a JEOL Model JEM-100CX scanning/transmission electron microscope equipped with a Noran Instruments Model Z-MAX Si(Li) light-element detector. This instrument is capable of detecting all elements heavier than beryllium (atomic number of 4) and was first calibrated with a graphite specimen sample. The detection capabilities of the EDS apparatus include all elements in the soot matrix, with the sole exception of hydrogen, which is known to be present in young soot (low heights) in relatively low concentrations.

Results

When the ethylene fuel stream was seeded with 0.35 wt.% ferrocene vapor, a noticeable decrease of the flame height was observed. Flame appearance measurements were conducted by means of a charge-coupled device camera/image acquisition and analysis setup used to capture and measure flame images. It was found that the ferrocene-seeded flame height was 83 mm, compared to 88 mm of the unseeded flame. However, since flame seeding required fuel preheat to 70 °C, the flame height variation could not be solely attributed to the presence of ferrocene. An additional flame—burning pure ethylene fuel preheated to 70 °C—also displayed a height of 88 mm, thus suggesting that the shorter height of the seeded flame is entirely due to the presence of ferrocene.

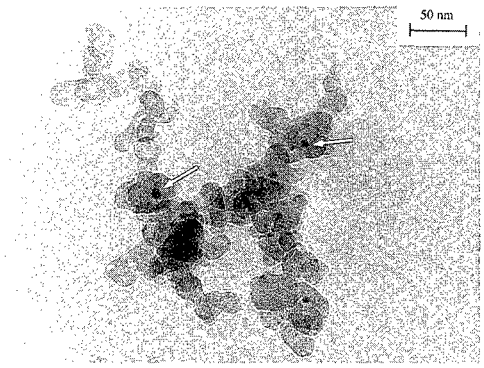

FIG. 2. Electron photomicrograph of a mature soot aggregate collected from the ferrocene-seeded flame. This particular aggregate was collected from the flame axis at a height z = 50 mm above the burner mouth. The arrows point to the iron occluded phase distributed randomly over the aggregate matrix.

The uniform texture of unseeded-flame aggregates, as observed through transmission electron microscopy [11–13], emphasizes their homogeneous carbonaceous nature. The morphological character of soot aggregates collected thermophoretically from the ferrocene-seeded flame was examined by electron microscopy. Figure 2 shows an electron photomicrograph of a mature soot aggregate collected from the ferrocene-seeded flame. This aggregate displays the familiar chainlike structure of flame soot but also exhibits a striking difference from the soot formed in unseeded flames [11–13]; a finer dispersed phase (see arrows) is distributed randomly over the aggregate matrix. This phase, which is almost opaque to the electron beam—in contrast to the carbonaceous matrix, which appears partially translucent to the incident beam—will be shown in the following to be related to the presence of the additive vapor in the fuel stream and the iron compounds generated by chemical reactions involving ferrocene in the fuel-rich zone of the flame. The aggregate structure displayed in Fig. 2 is typical of all mature aggregates collected from the vicinity of the flame axis. However, aggregates collected from the annular region [8] (annulus of maximum soot volume fraction) at intermediate and higher portions of the flame did not appear to contain any inclusions. Aggregates collected from the annular region low in the flame did show sparse inclusions. These observations provide physical evidence that the soot and iron-additive phases combine in certain regions of the seeded flame to form a hybrid (inhomogeneous) particulate phase.

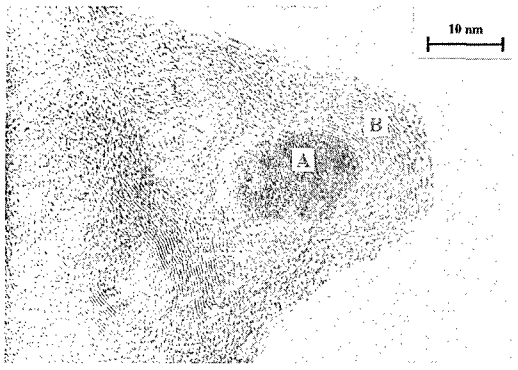

FIG. 3. Atomic-resolution electron photomicrograph detailing typical soot aggregate microstructure in the vicinity of an additive occlusion (A). Concentric layers of carbonaceous soot (B) around the iron occlusion are apparent. The displayed detail belongs to an aggregate collected from an off-axis location at a height z = 40 mm above the burner mouth.

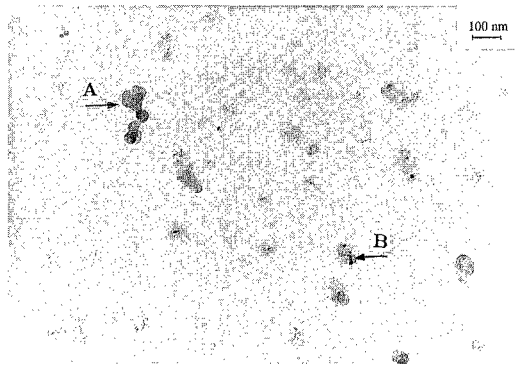

FIG. 4. Electron photomicrograph of soot nascent particles collected from the axis of the seeded flame at a height z = 30 mm. The isolated aggregate shown by arrow A was collected during the probe passage through the soot annulus. The finer phase (arrow B) is related to the ferrocene additive.

Atomic-resolution electron microscopy was employed to examine the heterogeneous nature of soot aggregates collected from the ferrocene seeded flame. Figure 3 displays an atomic-resolution electron photomicrograph detailing typical soot aggregate microstructure in the vicinity of an additive occlusion (A). The finely dispersed additive fragments within the soot matrix were found to be consistently smaller than 15 nm. The concentric layers (shells) of carbonaceous soot (B) around the additive occlusion are also apparent, thus suggesting that the iron combustion products precipitate early in the combustion process to provide nuclei for surface deposition of incipient soot and subsequent graphitization. Electron microscope specimen tilting techniques were implemented to determine the relative position of the metallic inclusions with respect to the soot surface. It was found that, in all instances, the additive phase was entirely encapsulated in the carbonaceous matrix. It is worth noting that the inhomogeneous aggregate section shown in Fig. 3 resembles those reported in a recent study of the catalytic effects of several compounds on carbonization reactions [17].

The hypothesis that iron compounds homogeneously nucleate in a flame before the onset of soot particle inception has been proposed by Ritrievi et al. [3] to explain the detectable optical signals obtained at low heights of their ferrocene-doped premixed flames. Evidence in support of this hypothesis has also been provided by Bonczyk [5]. This scheme was investigated in the current study by means of a simple line-of-sight light extinction measurement. A He-Ne laser beam passing through the flame axis was employed, and the light transmission was measured by a detector positioned at the path of the beam. In contrast to the undoped flame, measurable extinction was obtained below z = 10 mm from the burner mouth of the seeded flame, thus suggesting that particle inception appears at an earlier residence time when the fuel stream contains ferrocene. This evidence is consistent with the mature aggregate microstructure shown in Fig. 3, which depicts stratification of soot layers over the occluded additive phase.

The morphology of particulate samples collected from the lowest section of the ferrocene-doped flame was found to be fundamentally different than the mature soot aggregates shown in Fig. 2. Even though well-defined soot aggregates were detected as low as z = 10 mm on the soot annular region, their appearance on the flame axis was delayed up to an axial location above z = 30 mm. This is consistent with the optical measurements of Santoro et al. [8], who reported that soot particles were first detected on the axis of the unseeded flame at a height z = 25 mm. Figure 4 presents a sample collected from the axis of the seeded flame at a height z = 30 mm above the burner mouth. A large population of solitary, ill-defined, seemingly stable particles is shown, along with isolated aggregates (arrow A) that were probably collected during the probe passage through the soot annulus. Specimen tilting was employed to examine the three-dimensional structure of the nascent particles depicted in Fig. 4. This procedure revealed that the particles were deposited in a "stretched" fashion over the carbon substrate. As a result, some of the particles shown in Fig. 4 are substantially larger than the soot primary sizes. The above suggests the earlier presence of a fluid substance (possibly associated with soot precursors) that partially evaporated after capture by the thermophoretic probe. It is therefore believed that the appearance of the nascent particles, as shown in Fig. 4, has been affected by the collection

process. However, most of the nascent particles contained a finer phase (arrow B) that was found through chemical microanalysis to be related to the ferrocene additive. This fine-metal phase, which was characteristic of all samples collected from the vicinity of the flame axis between the heights of $z = 15$ and 30 mm, was highly polydisperse and showed an aggregated character with primary particles of the order of a few nanometers. The presence of the fragmented phase in the interior of the nascent particles suggests that the additive combustion products precipitate early in the combustion process, to provide nuclei for the subsequent onset of carbonaceous soot inception mechanisms. It is worth noting that the solitary nascent particles observed in our ferrocene-seeded flame, although substantially larger, resembled the carbonaceous precursor microparticles present in similar unseeded ethylene flames [18].

The chemical content of soot aggregates and incipient particles collected from several locations of the ferrocene-seeded flame was investigated through EDS microanalysis. The spatial resolution of this technique is relatively high, being typically around 5 nm. As a result, several spectra were obtained over the entire span of each aggregate. It should be emphasized that the absence of an element from an x-ray spectrum does not necessarily imply its absence. It is possible that an element may be present at quantities below the detectability threshold of the spectrometer. Figure 5 displays three typical x-ray spectra obtained when the microanalysis probe was directed at different sections of individual aggregates collected from various locations of the ferrocene-seeded flame. It should be noted that the electron probe used in the analysis is designed to examine the elemental character of microvolumes, typically from 1 to 100 μm^3. However, since a typical sample examined in the current study is very thin, the probe electron column penetrates the sample, therefore, some interference was observed from the excitation of the copper grids supporting the carbon substrate. This interference portrayed itself in the form of one or more copper peaks in the energy spectrum. The x-ray spectrum shown in Fig. 5a corresponds to a carbonaceous aggregate section. The two main elements detected are carbon and copper. Obviously, the carbon peak results from the presence of this element in both the soot matrix and the substrate phase, while the copper peak indicates the excitation of the grid material by the electron probe transmitted through the thin substrate. This qualitative chemical analysis is characteristic of carbonaceous aggregate sections that do not contain additive occlusions. However, when the x-ray microprobe was directed at an occlusion similar to those displayed in Fig. 3, a different x-ray spectral pattern was obtained (see Fig. 5b). The presence of carbon and copper was accompanied by a detectable amount of iron, indicating the incorporation of this element within the inhomogeneous particulate phase. The multiple peaks for iron reaffirm the notion that chemical elements emit x-rays at different energy levels. The finding that no oxygen traces were detected in that analysis suggests very low or no presence of iron oxides in that section of the aggregate matrix. This observation excludes oxidation of the occluded iron phase during the time period between sample collection and electron

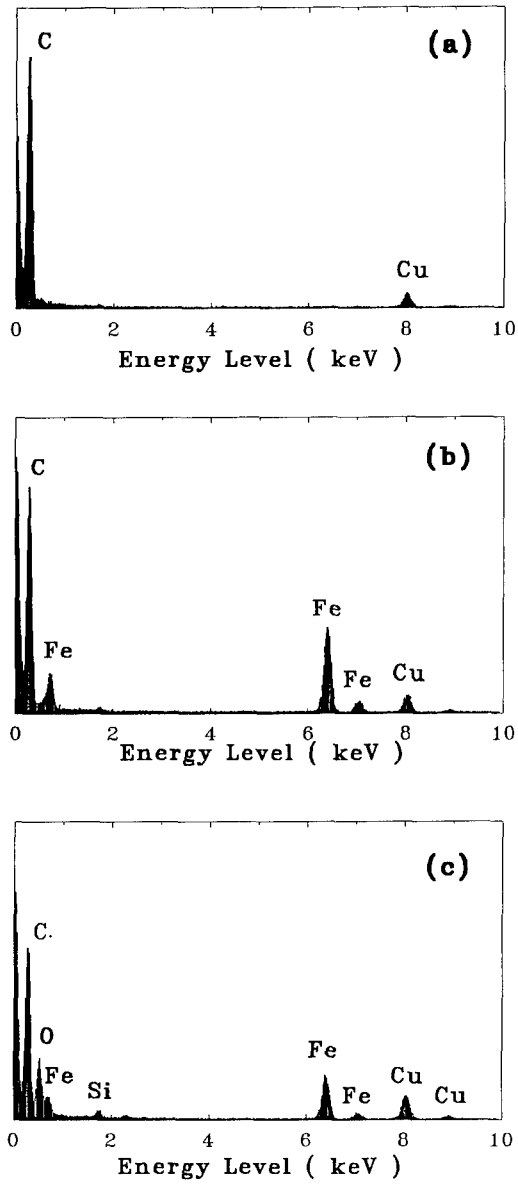

FIG. 5 Three typical x-ray spectra obtained when the EDS microanalysis probe was directed at different sections of individual soot aggregates collected from various locations of the ferrocene-seeded flame.

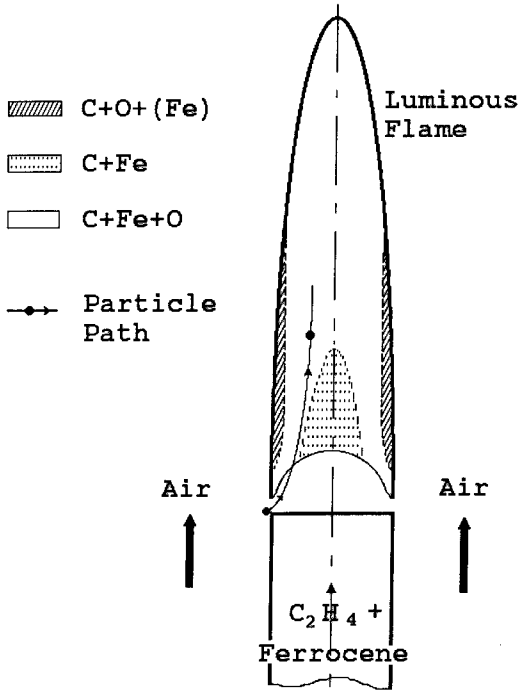

FIG. 6 Schematic of carbonaceous-soot/iron map of the ferrocene-seeded flame, as determined by microchemical characterization of individual aggregates collected from the flame. Note that iron was only sparsely detected in the carbonaceous phase of aggregates collected from the soot annulus [C + O + (Fe)].

microscope analysis (typically a few hours). Finally, Fig. 5c shows a typical x-ray spectrum for soot aggregates collected from the higher portions of the seeded flame, which are richer in oxygen. The simultaneous presence of iron and oxygen at that specific aggregate location suggests that the chemical state of iron might be in the form of an oxide. The small peak of silicon seen in Fig. 5c is attributed to the involvement of this element in the commercial production of the carbon substrates used to capture the soot. Finally, it should be noted that soot aggregates also contain unknown quantities of hydrogen which cannot be identified because of the inability of our x-ray analysis instrumentation to detect very light elements ($Z < 4$).

The additive intervention was evaluated with spatial precision throughout the flame zone. Microchemical examination of aggregates collected from various heights of the ferrocene-seeded flame (ranging from 10 to 70 mm) revealed the carbonaceous-soot/iron map that is schematically depicted in Fig. 6. A pattern code has been utilized in that figure to identify three distinct flame regimes whose approximate boundaries are depicted by dashed lines. A single particle path has also been drawn in that figure to denote the strong entrainment of air at low heights [10]. Soot aggregates transported in the flame annular region near the luminous front are primarily composed of carbon and oxygen, with occasional traces of iron. On the other hand, soot collected from low heights and near the flame axis contains elemental iron occlusions. Finally, soot aggregates sampled from all other areas of the flame contain both iron and oxygen, thus suggesting the possible presence of iron oxides within the carbonaceous matrix (C + Fe + O).

Discussion

Our flame aggregate observations, both in terms of morphology and elemental composition, are consistent with the hypothesis that ferrocene decomposes early in the combustion process before the onset of soot particle inception, thus forming a fine aerosol for the subsequent deposition of the carbonaceous phase. Since the effect of trace amounts of iron on flame temperature has been found to be negligible [5,15], the occlusion of iron compounds within the soot phase has been a primary suspect for the soot-suppressing role of iron additives. However, the controversy around the specific chemical character of these compounds within the carbonaceous matrix remains unresolved.

Ritrievi et al. [3] isokinetically extracted soot samples from their premixed flames and used Auger electron spectroscopy to determine the relative stratification between iron and carbon in the soot particles. They reported that the iron was concentrated in the cores of the particles and was distributed radially outward in progressively smaller concentrations. The chemical state of iron in the soot matrix, as determined via Mössbauer spectroscopy, was iron metal in a highly dispersed phase within the carbon matrix. It should be noted, however, that the particles examined by Ritrievi et al. were collected in the postflame zone. Bonczyk [5] collected soot on a water-cooled disk positioned above a ferrocene-seeded isooctane/air diffusion flame. The condensate was analyzed vs depth using electron spectroscopy for chemical analysis (ESCA), which provided no evidence for or against particulate heterogeneity. It was reported, however, that the postflame particles were composed of Fe_2O_3, with little or no trace of carbon present. Mitchell [6] employed EDS to examine if iron was present in soot samples collected on a molybdenum foil placed above a crude oil crucible flame. Even though iron was clearly present in the postflame soot samples, the spectrometer used in Ref. 6 was incapable of detecting the presence of either carbon or oxygen. Scanning Auger microscopy was used by Mitchell [6] to determine the elemental stratification of the soot samples. Carbon and oxygen

were detected on the surface of the sample, while oxygen and iron were detected in the particle core. X-ray photoelectron spectroscopy (XPS) showed [6] that some percentage of the iron found in the sample was in the form of iron oxide and some in the form of elemental iron. Finally, Hahn and Charalampopoulos [19] used a stainless-steel probe to sample soot particles from several heights of flat, premixed, propane/oxygen/nitrogen flames seeded with iron pentacarbonyl. Subsequent analysis by XPS found Fe_2O_3 to be the dominant iron species in the soot matrix.

As shown in Fig. 6, soot collected at low heights and near the axis of the seeded flame contained iron in its metal form, which was concentrated in clearly defined occlusions. The encapsulation of iron fragments by soot layers averted oxidation after capture on the thermophoretic probes. On the other hand, soot aggregates collected from the rest of the flame contained both iron and oxygen, although the samples extracted from the annular region did not appear to contain well-defined fragments. Finer dispersion of iron within the soot matrix may have allowed postcapture sample oxidation. However, this possibility could not be verified or ruled out by means of the techniques employed in this study.

The soot aerosol component segregation shown in Fig. 6 was attributed to the transport mechanisms of ferrocene combustion products within the flame field. In particular, the rapid rise in gas temperature above the burner mouth (flame axis already at 500 °C at a height $z = 3$ mm [10]) causes the thermal decomposition of ferrocene. Because of the absence of oxygen from the core of the flame at low heights, the iron naturally exists in its free metal form. The absence of macroscopic iron occlusions from the soot transported in the annular region is attributed to the combined effects of the strong radial velocity component low in the flame (see particle path in Fig. 6), as well as the intense thermophoretic forces that strongly oppose the diffusion of precipitated compounds toward the flame sheet (high-temperature zone).

Finally, it should be noted that information regarding the spatial distribution of chemical elements within the inhomogeneous aggregate phase is especially valuable during the implementation of optical diagnostic techniques in processes involving multicomponent combustion aerosols [15]. Two simplified configurations have been suggested by Charalampopoulos et al. [15] regarding the segregation of components within the soot aggregate matrix: (1) a coated-sphere model, where typical particles are composed of an inorganic core coated by carbonaceous soot, and (2) a dispersed-phase model, where the inorganic compounds are finely (randomly) dispersed throughout the soot matrix. Our morphological observations in the laminar flame studied herein present evidence in support of the coated-sphere model at flame regions near the flame axis. The dispersed-phase model appears to be more appropriate for all other aggregates, and especially those transported in the soot annular region.

Conclusions

A laminar, coannular, ethylene/air nonpremixed flame seeded with ferrocene additive has been employed to address the fundamental question of how iron becomes incorporated into the carbonaceous soot phase, thus interfering with the soot formation processes. The structure and chemical composition of individual aggregates were characterized as functions of flame coordinates via a combination of thermophoretic sampling, transmission electron microscopy, and energy-dispersive spectrometry.

Mature soot aggregate microstructure revealed stratification of soot layers over the occluded iron phase, thus providing physical evidence that the soot and iron compounds combine in the flame to form inhomogeneous particulates. At all instances where the occluded phase was identifiable, it was entirely encapsulated in the carbonaceous matrix. These observations are consistent with the hypothesis that ferrocene decomposes early in the combustion process and before the onset of soot particle inception, thus forming a fine aerosol for the subsequent deposition of carbonaceous substances. Examination of a series of inhomogeneous soot aggregates showed that the flame aerosol composition greatly varies with flame coordinates. In particular, aggregates transported in the soot annulus near the luminous flame front are primarily composed of carbon and oxygen, with traces of iron finely dispersed through the aggregate matrix. On the other hand, carbonaceous soot collected from low heights and near the flame axis contained elemental iron occlusions. Finally, soot aggregates sampled from all other areas of the flame contained both iron and oxygen, thus implying the possible presence of iron oxides within the carbonaceous matrix.

Acknowledgment

This work was supported by the National Science Foundation under Grant No. CTS-9109166. The use of the electron microscopy facilities at UIC and Northwestern University is acknowledged with appreciation.

REFERENCES

1. Howard, J. B., and Kausch, W. J., Jr., *Prog. Energy Comb. Sci.* 6:263–276 (1980).
2. Frazee, J. D., and Anderson, R. C., *Fuel* 38:329–331 (1959).

3. Ritrievi, K. E., Longwell, J. P., and Sarofim, A. F., *Combust. Flame* 70:17–31 (1987).
4. Feitelberg, A. S., Longwell, J. P., and Sarofim, A. F., *Combust. Flame* 92:241–253 (1993).
5. Bonczyk, P. A., *Combust. Flame* 87:233–244 (1991).
6. Mitchell, J. B. A., *Combust. Flame* 86:179–184 (1991).
7. Dobbins, R. A., and Megaridis, C. M., *Langmuir* 3:254–259 (1987).
8. Santoro, R. J. , Semerjian, H. G., and Dobbins, R. A., *Combust. Flame* 51:203–218 (1983).
9. Santoro, R. J., and Semerjian, H. G., *Twentieth Symposium (International) on Combustion*, The Combustion Institute, Pittsburgh, 1984, p. 997.
10. Santoro, R. J., Yeh, T. T., Horvath, J. J., and Semerjian, H. G., *Combust. Sci. Technol.* 53:89–115 (1987).
11. Megaridis, C. M., and Dobbins, R. A., *Twenty-Second Symposium (International) on Combustion*, The Combustion Institute, Pittsburgh, 1988, p. 353.
12. Megaridis, C. M., and Dobbins, R. A., *Combust. Sci. Technol.* 66:1–16 (1989).
13. Megaridis, C. M., and Dobbins, R. A., *Combust. Sci. Technol.* 71:95–109 (1990).
14. Jacobs, M. H. G., Van Ekeren, P. J., and De Kruif, C. G., *J. Chem. Thermodynamics* 15:619–623 (1983).
15. Charalampopoulos, T. T., Hahn, D. W., and Chang, H., *Appl. Opt.* 31:6519–6528 (1992).
16. Rosner, D. E., Mackowski, D. W., and Garcia-Ybarra, P., *Combust. Sci. Technol.* 80:87–101 (1991).
17. Oberlin, A., in *Chemistry and Physics of Carbon* (P. A. Thrower, Ed.), Marcel Dekker, New York, 1989, Vol. 22, p. 1.
18. Dobbins, R. A., and Subramaniasivam, H., in Mechanisms and Models of Soot Formation, *Lecture Notes in Physics*, Springer-Verlag, New York, to appear.
19. Hahn, D. W., and Charalampopoulos, T. T., *Twenty-Fourth Symposium (International) on Combustion*, The Combustion Institute, Pittsburgh, 1992, p. 1007.

COMMENT

R. L. Axelbaum, Washington University, USA. Your results indicate that the Fe is acting as a nucleation site for soot and thus is coated with soot early in the flame. Recognizing that particle diffusivities are small, one would expect that most of the Fe in the annular region is covered with soot and that enhanced oxidation would not occur until sufficient soot oxidation occurs to expose the Fe particles. Your results do not indicate such a delay. Could you please comment on this?

Author's Reply. The coating of inorganic fragments by soot has been consistently observed in the vicinity of the flame axis but not at the annular region. In fact, a continuous reduction of the size of the Fe occlusions was observed with radial location from the flame axis to the soot annulus. As stated in the paper, aggregates collected from the soot annulus did not contain well-defined occlusions, although they did contain some iron. This observation is consistent with the hypothesis that iron is finely dispersed through the carbonaceous particles transported in the vicinity of the annular region. The fine dispersion of Fe throughout the aggregate phase implies that some Fe molecules reside on the soot surface or close to it. Therefore, soot oxidation in the presence of iron can occur on the particle surface, as soon as sufficient oxidant concentrations and appropriate temperatures are present. Fe dispersion may also allow transport of the inorganic molecules from underneath to the soot surface, where they can catalytically enhance carbon oxidation reactions [1,2]. Regarding the soot particles transported in the vicinity of the flame axis, the encapsulation of Fe crystals within the soot phase does not preclude the simultaneous presence of dispersed Fe in the carbonaceous matrix surrounding these fragments. Finally, it is relevant to mention that diffusion of elemental iron through 25-nm-thick carbon layers (characteristic of the primary particle sizes observed in the flame examined) requires only a few milliseconds [3]. This suggests that there is adequate time for the iron to penetrate the surrounding soot matrix and emerge to the particle surface within the residence time constraints of the flame considered.

REFERENCES

1. Walker, P. L., Jr., Shelef, M., and Anderson, R. A., in *Chemistry and Physics of Carbon* (P. L. Walker, Jr., Ed.), Marcel Dekker, New York, 1968, Vol. 4, p. 287.
2. McKee, D. W., *Carbon* 23:707–713 (1985).
3. Ritrievi, K. E., Longwell, J. P., and Sarofim, A. F., *Combust. Flame* 70:17–31 (1987).

Twenty-Fifth Symposium (International) on Combustion/The Combustion Institute, 1994/pp. 601–608

NONLUMINOUS DIFFUSION FLAME OF DILUTED ACETYLENE IN OXYGEN-ENRICHED AIR

GEN SUGIYAMA

Japan Automobile Research Institute, Inc.
2530 Karima, Tsukuba-shi, Ibaraki, 305, Japan

A soot-reducing mechanism of fuel dilution and oxygen enrichment in laminar diffusion flames is suggested. Analysis using the Burke–Schumann theory for the shape of overventilated diffusion flames has shown that there is a critical ratio of stoichiometric coefficients of the fuel and the oxidizer under which the gas flows from the fuel side to the oxidizer side throughout the flame. When this condition is satisfied, the soot growth region vanishes. A similar result is also found in a numerical simulation for diffusion flames that do not satisfy the Burke–Schumann assumption of uniform flow field. KIVA code is used for that purpose. The theoretically predicted direction of gas-flow across the flame sheet is verified in an experiment in a coaxial-flow diffusion flame. Soot cloud and velocity fields are visualized through a laser sheet method in the experiment. The fuel is a mixture of acetylene and nitrogen. The oxidizer is a mixture of oxygen and nitrogen. The compositions of the reactants are controlled so that the adiabatic flame temperature is kept constant to avoid the effect of temperature change. Experimental results show substantial reduction of scattered light intensity by fuel dilution and oxygen enrichment. When a sufficient amount of nitrogen is added to the fuel, nonluminous blue flames are obtained. At higher oxygen concentrations, blue flames are obtained at higher flame temperature region. When oxygen concentration in the oxidizer is 70 vol.%, blue flames are obtained up to 2250 K. The critical condition of the reactants for nonluminous flames agrees with the theoretical prediction when the oxidizer is ordinary air. In oxygen-enriched conditions, the fuel must be diluted more than theoretically predicted.

Introduction

This paper explains a soot-reducing mechanism of fuel dilution and oxygen enrichment in hydrocarbon-air diffusion flames. The major effect of fuel dilution on soot formation in diffusion flames has been considered to be temperature change. Glassman and Yaccarino have studied the effect of flame temperature on soot formation for several types of hydrocarbon by adding nitrogen to the fuel [1]. They also compared the result of adding nitrogen and argon and concluded that the change of fuel partial pressure has little effect in the range they used. Other authors also have reported the effect of fuel dilution [2–4]. Kent and Wagner concluded that nitrogen addition to the fuel lowered the soot produced per unit fuel volume more than can be explained by lowered measured temperatures [2]. So far, however, the mechanism of soot reduction by fuel dilution besides the temperature effect mechanism has not been fully clarified.

This paper shows that the Burke–Schumann theory provides a candidate for the soot-reduction mechanism in laminar diffusion flames of diluted fuel and oxygen-enriched air. An experiment in a coaxial-flow diffusion flame was conducted to verify the mechanism. A numerical simulation of laminar diffusion flames was also conducted for flames that do not satisfy the Burke–Schumann assumption of uniform velocity field.

Theoretical Background

The soot-formation process can generally be considered to be a function of the species concentration, temperature distribution, soot particle trajectories, and residence times [5]. In this paper, the author especially emphasizes the point that the soot-formation process in laminar diffusion flames depends on soot particle trajectories and residence times and that there is a method to control them without change in flame temperature.

In some regions, gas flows across the flame sheet from the oxidizer side to the fuel side of the diffusion flame. In coaxial-flow diffusion flames, these regions lie near nozzle ports. Soot particle trajectories are determined by the gas flow field and thermophoretic effect [6]. Near nozzle ports of ordinary diffusion flames, gas flow across the flame sheet forces soot particles to travel in fuel-containing regions and surface growth occurs. In this paper, the author shows that an appropriate combination of fuel dilution and oxygen enrichment changes the gas velocity near the nozzle port so that the soot growth region vanishes.

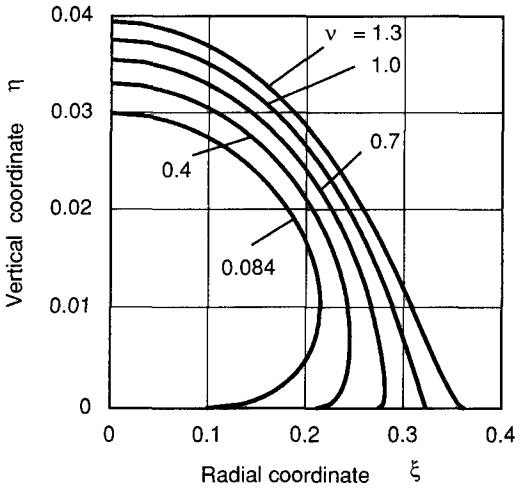

FIG. 1. Shapes of diffusion flames predicted in the Burke–Schumann theory.

The mechanism is explained using the Burke–Schumann theory. Although the Burke–Schumann theory has several restrictions (such as the uniform velocity assumption), the author thinks that the theory is useful for understanding the essential effect of fuel dilution and oxygen enrichment on the shape of the diffusion flame and soot formation. To consider the effect on soot formation qualitatively, the author used the following very simple model for soot formation. In the model, soot inception occurs at the flame sheet predicted in the Burke–Schumann theory, and soot-particle velocity coincides with gas velocity, which is assumed to be uniform. Soot-particle growth was assumed to occur when soot particles travel in a fuel-containing region in the flame. Under these assumptions, it depends only on the flame shape whether soot growth occurs or not.

The discussion was restricted to only overventilated conditions. In the following discussion, the overall oxygen excess ratio is 8.6 and is kept constant. Figure 1 shows shapes of several diffusion flames. In Fig. 1, only half of the flame is shown, and the scale is nondimensional. The parameters ξ and η are defined as

$$\xi = r/B \tag{1}$$

$$\eta = zD/VB^2 \tag{2}$$

where r is the radial distance, z is the vertical distance, B is the diameter of the outer tube, D is the diffusion coefficient, and V is the velocity of gas. The parameter ν in Fig. 1 is defined as

$$\nu = (\nu_f/X_{f0})/(\nu_O/X_{O0}) \tag{3}$$

where ν_f and ν_O are stoichiometric coefficients of acetylene and oxygen, X_{f0} is the mole fraction of acetylene in fuel, and X_{O0} is the mole fraction of oxygen in oxidizer. Decreasing the acetylene concentration in the fuel or increasing the oxygen concentration in the oxidizer increases parameter ν. When needed, flame temperature can be kept constant. If so, Eq. (4) must be satisfied:

$$\nu_f(1 - X_{f0})/X_{f0} + \nu_O(1 - X_{O0})/X_{O0} = \text{constant}. \tag{4}$$

The ratio of tube diameters normally required in Burke–Schumann theory discussions is determined from the overall oxygen excess ratio and Eq. (4) for each value of ν. The diameter of the inner tube is given in Fig. 1 as an intercept on the ξ coordinate axis.

Since overventilation is assumed, the flame sheet always closes at the center axis. The curve in Fig. 1 with ν of 0.084 gives the shape of an ordinary acetylene-air diffusion flame. In this condition, the flame sheet diverges into the oxidizer side near the nozzle, and the diameter of the widest flame region exceeds the diameter of the nozzle. In this flame, if a soot particle is formed at the flame sheet near the nozzle exit where η is less than 0.01, it then travels into a fuel-rich region after inception and soot-growth will occur. If ν increases, the flame sheet tends to change its shape, and the diverging region reduces. The critical condition lies at ν equal to 1. When ν exceeds 1, the flame sheet uniformly converges to the center axis with no diverging region. For suppressing soot formation, the conditions where ν exceeds 1 is interesting. If ν exceeds 1, the velocity direction at the flame sheet is toward the oxygen-containing region throughout the flame and soot growth will not occur. The reason the critical value of ν is 1 seems apparent from its physical meaning. However, it should be noted that when diffusion-coefficient values of relevant gases differ, the critical ν will not become 1.

The parameter ν is also controllable by adding oxygen to the fuel or fuel to the oxidizer. In such partially premixed conditions, the discussion here also applies, though the physical meaning of Eq. (3) must be expanded. Naturally, conditions causing premixed combustion must be treated quite differently. Partially premixed diffusion flames are, therefore, not included in the following discussion.

Thus, there are fuel and oxidizer compositions in laminar diffusion flames in which the soot growth region vanishes and nonluminous flames will be obtained.

Experimental Apparatus

In the present study, the soot cloud in diffusion flames was visualized through a laser sheet method.

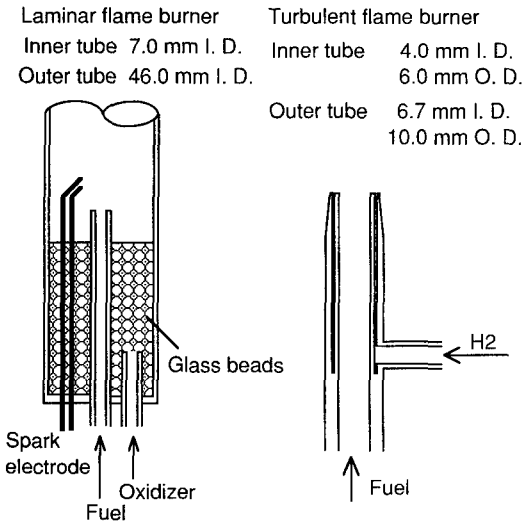

FIG. 2. Diffusion flame burners.

For two extreme conditions of v, the velocity fields of the gas were visualized by a particle trace method.

The diffusion flame burner consists of two coaxial glass tubes, as shown in Fig. 2. The outer tube is used as the duct of oxidizer flow. Fuel emerges from the inner tube, and a diffusion flame is stabilized at the port of the inner tube. The inner diameter of the outer tube is 46 mm. The inner diameter and the thickness of the inner tube are 7 and 1 mm, respectively. Glass beads fill the outer tube upstream to make a uniform flow field.

The oxidizer is a mixture of oxygen and nitrogen. The mass flowrate of oxygen is 57.9 mg/s and kept constant while that of nitrogen in the oxidizer varies from 21.7 to 190 mg/s. Thus, oxygen concentration of the oxidizer is varied from 21 to 70%. The fuel is a mixture of acetylene and nitrogen. The mass flowrate of acetylene is 2.2 mg/s and is kept constant. The amount of nitrogen added to the fuel is varied from 0 to 48.5 mg/s. As the mass flowrate of oxygen and acetylene is constant, the overall oxygen excess ratio is constant at 8.6. In this range of flowrate conditions, the flame is laminar. The Reynolds number defined from the flowrate and the diameter of the inner tube is from 23 to 532.

The burner used for turbulent flames is shown in Fig. 2. The aim of the turbulent diffusion flame experiment is to check the validity of the concept under different flow speed conditions. The inner diameters of the inner and outer tubes are 4.0 and 6.7 mm, respectively. The thickness of the inner tube is 1.0 mm. The port of the outer tube is sharpened. The fuel is a mixture of acetylene and nitrogen. Hydrogen, used to stabilize the flame, emerges from the clearance between inner and outer tubes. Surrounding air is used as an oxidizer. Mass flowrate of acetylene is 109 mg/s. When the flowrate exceeds 77 mg/s, the flame height becomes independent of the flowrate. The mass flowrate of hydrogen is 3.1 mg/s. The hydrogen flow heat of combustion is 6% of the total. From 0 to 780 mg/s of nitrogen is added to the acetylene. In the experiment for turbulent flames, only the amount of nitrogen added to the acetylene was varied, and the critical flowrate of nitrogen at which the flame became blue was measured.

An Ar-ion laser (Spectra-Physics type 604, 514.5-nm wavelength, 1.3-W operating power) was used as a light source for the laser sheet method. The laser beam was modified to a plane shape by two cylindrical lenses. The laser sheet was set to include the center axis of the nozzle. A monodisperse polystyrene latex (PSL) was used to correct the distribution of the light intensity of the laser sheet and optical constants of the optics. The diameter of the PSL is 88 nm, and the number density is 1.27×10^{15} m^{-3}. The scattered light image from the soot cloud in the flame was observed by a charge coupled device (CCD) camera system (Hamamatsu photonics, C3640-50) with an interference filter. The image data was corrected for spontaneous emission from the flame. Scattering intensity was converted nominally to the number density of the corresponding monodisperse soot particle, which has a diameter of 100 nm and refractive index of 1.99–0.55i [7]. Due to the limited dynamic range of the CCD camera, regions with scattering intensity less than 1% of the maximum value cannot be detected in one picture.

Small glass balls (Sumitomo 3M, Scotchlight Glass-bubbles C15/250; nominal density is 0.15 g/cc, and the residual fraction on U.S. 80 mesh is less than 5 wt.%) were added to the gas flow as tracers to visualize the velocity field. In addition, a 1-kHz optical chopper was used.

Experimental Results

Figure 3 shows the effect of oxygen enrichment in air and fuel dilution. The conditions used in Fig. 3 satisfy Eq. (4) so that the adiabatic flame temperature is kept constant at 2540 K. When oxygen concentration in the oxidizer increases from 21 to 60%, the scattered light level reduces to 10^{-5} times the original level.

With further dilution, the CCD camera system is unable to detect scattered light and a nonluminous flame is obtained. The flame then becomes blue. Figure 4 shows the nitrogen concentration in fuel at which a nonluminous flame is obtained. The concentration of nitrogen in fuel required to obtain a nonluminous flame is almost independent of oxygen concentration in the oxidizer. Figure 4 also shows the theoretical adiabatic flame temperature. At higher oxygen concentrations, blue flames are obtained in higher flame temperature regions. When the oxygen

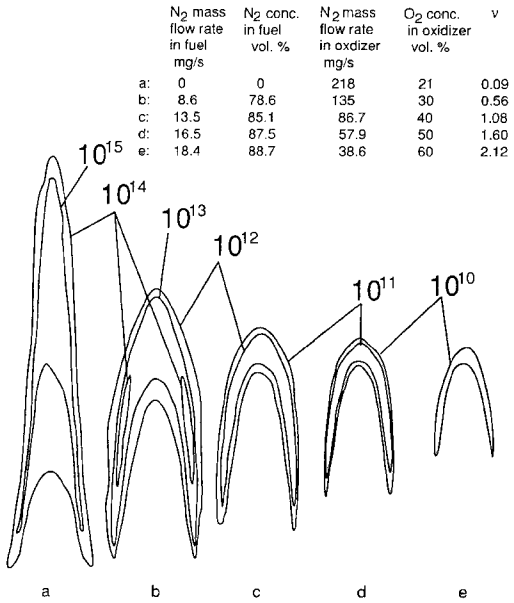

FIG. 3. Scattering light intensity contour of diffusion flames. Oxygen concentration is varied from 21 to 60 vol.%. Adiabatic flame temperature is 2540 K. C_2H_2 mass flowrate in the fuel is kept constant at 2.2 mg/s. O_2 mass flowrate in the oxidizer is kept constant at 57.9 mg/s.

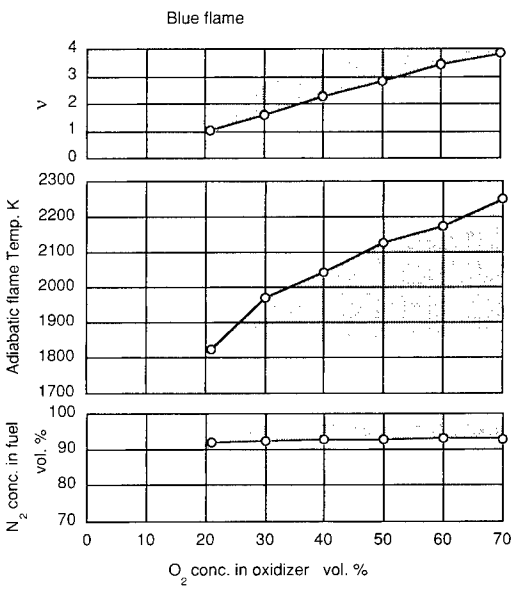

FIG. 4. Conditions for blue flames. C_2H_2 mass flowrate in the fuel is kept constant at 2.2 mg/s. O_2 mass flowrate in the oxidizer is kept constant at 57.9 mg/s.

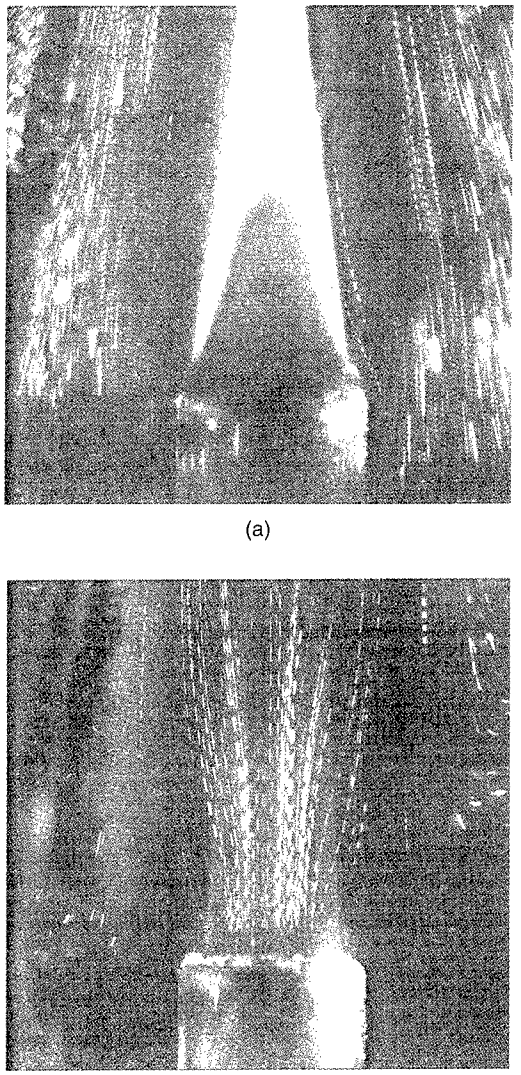

FIG. 5. Particle trace image. (a) Oxygen concentration in the oxidizer is 21 vol.%. The fuel is acetylene. The parameter v is 0.084. (b) Oxygen concentration in the oxidizer is 70 vol.%. Nitrogen concentration in the fuel is 89 vol.%. The parameter v is 2.64.

concentration in the oxidizer is 70 vol.%, blue flames are obtained up to 2250 K. When the oxygen concentration in the oxidizer is 21 vol.%, blue flames are obtained up to 1850 K. The critical condition of the reactants for nonluminous flames agree with the theoretical prediction when the oxidizer is ordinary air. Although the theoretical value of v for the critical condition is 1, the actual value in an oxygen-enriched condition exceeds that. However, considering the ac-

curacy of the assumption in the theoretical discussion, this discrepancy is not surprising. Possibly, the assumption that soot-particle velocity coincides with gas velocity does not hold at higher temperatures due to the increased relative importance of thermophoresis on the soot velocity.

Velocity fields of two extreme conditions are shown in Fig. 5. It is obvious that when v exceeds 1, gas flows across the flame sheet from the fuel to the oxidizer throughout the flame. On the contrary, when v is 0.084, gas flows from the oxidizer to the fuel near the nozzle. These relations between v and the flow direction through the flame sheet agree with the theoretical prediction.

In the turbulent flame in air, when nitrogen mass flowrate in the fuel exceeds 640 mg/s (nitrogen concentration in the fuel exceeds 83 vol.%), a nonluminous flame is obtained. The critical condition of v for nonluminous flame is 0.51. This is about half that observed in laminar flames and lower than the theoretical value. In turbulent flows, there will be other effects such as increased air entrainment or partial premixing due to the air flow through the quenching zone near the nozzle port. However, the difference in the critical condition of v between laminar and turbulent flames is not so large compared to the difference in speed of the gas jets. This observation suggests that in the experiment for laminar flames, the change of gas speed has little effect on the critical value of v.

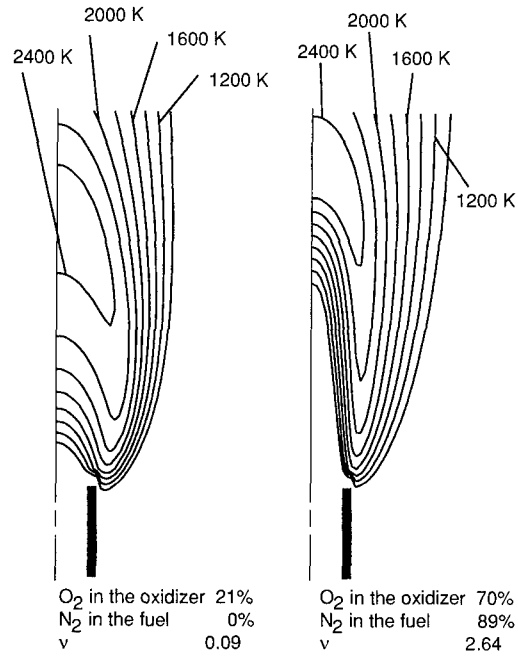

FIG. 6. Temperature profiles predicted in a numerical simulation.

Numerical Simulation

One problem in applying the Burke–Schumann theory to practical flames is that uniform velocity is assumed. In the present study, a numerical simulation was performed to predict profiles of temperature and species and velocity field in diffusion flames; KIVA [8,9] code was used for that purpose. The flow was treated as laminar. The Prandtl number and Schmidt number were assumed to be 0.74 and 0.95, respectively. The chemical reaction was treated as a one-step reaction in which reactants are oxygen and acetylene. The products were assumed to be carbon dioxide and water. The chemical reaction was assumed to occur instantly whenever oxygen encounters acetylene in the same computational cell. The effect of buoyancy was simply neglected. The wall surfaces of the tubes were assumed to be no-slip and adiabatic. An axial symmetry was assumed, and the calculation was performed in two-dimensional cylindrical coordinates. The computational cells are 0.5 mm in the radial direction and 2 mm in the axial direction.

The simulated temperature profiles of the diffusion flames are shown in Fig. 6. The result of the simulation indicates that the maximum temperature of the flame is near the adiabatic flame temperature of the stoichiometric mixture. This result supports the validity of the use of the adiabatic flame temperature as a characteristic flame temperature.

Concentration of acetylene is another important factor. Simulation results show that there is some difference in concentration of acetylene in the same temperature regions for different v conditions. The simulated species concentrations are shown in Fig. 7. The concentration of acetylene is shown in Fig. 7 as a coupling function defined as follows:

$$\beta = X_f/v_f - X_O/v_O. \tag{5}$$

For example, the maximum coupling function in the region of temperature range from 2000 to 2200 K is about 0.005 in an ordinary air-acetylene flame. However, that value becomes about 0.0013 when the oxygen concentration is 70%. This temperature range corresponds to that found in the shock tube experiments [10,11] where the soot formation rate reaches maximum. These changes in local temperature and concentration will reduce the soot formation rate. However, it is difficult to explain the cause of blue flame in terms of concentration and temperature only.

The flame shape and velocity profile are shown in Fig. 8. Direction of flow through the flame sheet changes substantially with changes in the parameter v. When the parameter v is less than 1, the direction

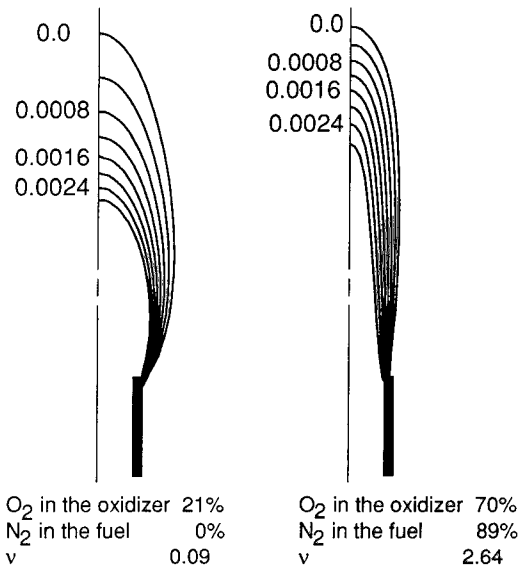

FIG. 7. Coupling functions predicted in a numerical simulation.

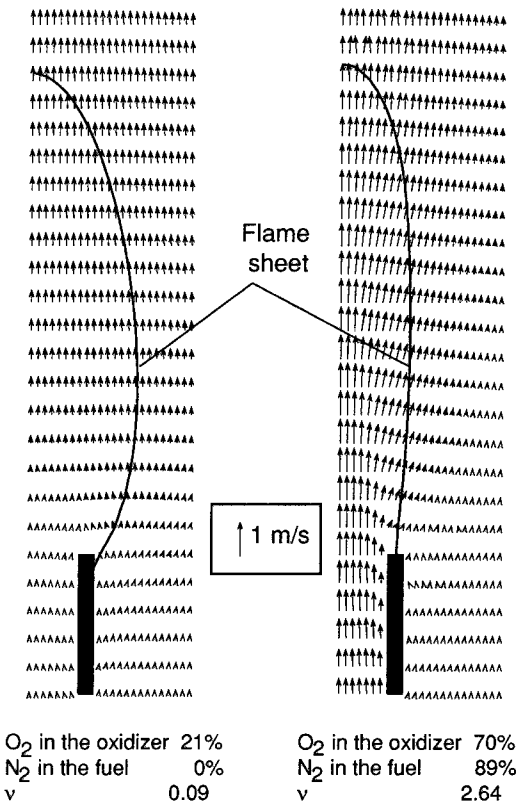

FIG. 8. Profiles of velocity and flame sheets predicted in a numerical simulation. The length of the arrows means flow velocity. The arrow in the center gives the scale.

of the gas velocity across the flame sheet near the nozzle exit is from the oxidizer to the fuel. Soot growth will occur in this condition. When the parameter ν exceeds 1, the radial velocity of gas increases, and gas flows across the flame sheet from the fuel to the oxidizer side throughout the flame, and soot growth will not occur. Similar results for the relation of the velocity and ν were also shown in the discussion of the Burke–Schumann theory, as well as in the experiment. In addition, the axial velocity of fuel increases with increases in ν, while flame height remains unchanged. These changes in velocity field will decrease the residence time of soot in the growth region.

Conclusions

A soot-reducing mechanism of fuel dilution and oxygen enrichment was newly suggested. The mechanism was explained by a change of the velocity field and the flame shape of laminar diffusion flames. The parameter ν, which is determined from the ratio of the stoichiometric coefficients and concentrations, essentially affects the relation of gas velocity and flame sheet in laminar diffusion flames. The parameter ν can be controlled by fuel dilution and oxygen enrichment in oxidizer without changing the maximum flame temperature. There is a critical condition of ν for obtaining nonluminous flames.

REFERENCES

1. Glassman, I., and Yaccarino, P., *Eighteenth Symposium (International) on Combustion*, The Combustion Institute, Pittsburgh, 1981, pp. 1175–1183.
2. Kent, J. H., and Wagner, H. Gg., *Twentieth Symposium (International) on Combustion*, The Combustion Institute, Pittsburgh, 1984, pp. 1007–1015.
3. Axelbaum, R. L., Flower, W. L., and Law, C. K., *Combust. Sci. Technol.*, 61:51–73 (1988).
4. Gülder, Ö. L., and Snelling, D. R., *Combust. Flame* 92:115–124 (1993).
5. Villasenor, R., and Kennedy, I. M., *Twenty-Fourth Symposium (International) on Combustion*, The Combustion Institute, Pittsburgh, 1992, pp. 1023–1030.
6. Haynes, B. S., and Wagner, H. Gg., *Ber. Bunsenges. Phys. Chem.* 84:499–506 (1980).
7. Lee, S. C., and Tien, C. L., *Eighteenth Symposium (International) on Combustion*, The Combustion Institute, Pittsburgh, 1981, pp. 1159–1166.
8. Amsden, A. A., Ramshaw, L. D., O'Rourke, P. J., and Dukowicz, J. K., *KIVA: A Computer Program for Two- and Three-Dimensional Fluid Flows with Chemical*

Reactions and Fuel Sprays, Los Alamos National Laboratory Report, LA-10245-MS, 1985.
9. Amsden, A. A., O'Rourke, P. J., and Butler, T. D., *KIVA-II: A Computer Program for Chemically Reactive Flows with Sprays*, Los Alamos National Laboratory Report, LA-11560-MS, 1989.
10. Yoshizawa, Y., Kawada, H., and Kurosawa, M., *Seventeenth Symposium (International) on Combustion*, The Combustion Institute, Pittsburgh, 1978, pp. 1375–1381.
11. Frenklach, M., Ramachandra, M. K., and Matula, R. A., *Twentieth Symposium (International) on Combustion*, The Combustion Institute, Pittsburgh, 1984, pp. 871–878.

COMMENTS

R. H. Essenhigh, Ohio State University, USA. You mentioned that you had studied the flow field in your diffusion flames by use of tracers, and I believe you computed the flow field as well.

1. Is that so, and how did they compare?
2. Have you examined, measured, or calculated the path trajectories of the different species? This can be calculated in principle using the species stream function [1].
3. Do you think that the history of the species along this trajectory path is likely to be significant in soot formation?

REFERENCE

1. Essenhigh and Wu, *Combust. Flame* 65:227, 241 (1986).

Author's Reply. The velocity of gas relative to the flame sheet changes when oxygen concentration of the oxidizer is increased and fuel is diluted with inert species. This is shown in the experiment, numerical simulation, and analytical discussion in the Burke–Schumann theory in the present study. The effect of fuel dilution and oxygen enrichment on the relation between flow velocity and flame sheet was well predicted qualitatively as described in the paper. Quantitatively, however, experimentally obtained flow field and flame shape differ from the prediction because natural convection was simply neglected in the simulation. Sunderland et al. describe the soot paths in buoyant and nonbuoyant jet diffusion flames [1].

The author thinks the trajectories of each species affect the soot formation process in luminous diffusion flames, because the species trajectories determine the concentration of the relevant species. The trajectories of each species were not calculated in the present study because the present study discusses the mechanism of blue flame caused by a change of soot velocity.

REFERENCE

1. Sunderland, P. B., Mortazavi, S., Faeth, G. M., and Urban, D. L., *Combust. Flame* 96:97–103 (1994).

•

R. L. Axelbaum, Washington University, USA. This paper postulates that the soot growth region vanishes when the convective flow across the flame is from the fuel to the oxidizer. Based on this, a criterion is put forward that states that flames will be nonluminous when gas flow is from fuel to oxidizer. This criterion might be valid if the inception zone were infinitesmally thin; however, inception occurs over a finite region and particles can be produced throughout this region. Surface growth can also occur in this region, but even if it does not, soot growth is possible by inception alone.

Evidence of luminous flames when the flow is from fuel to oxidizer is available in the literature. For example, Atreya et al. [1] measured soot volume fraction in a diluted methane/enriched oxygen counterflow diffusion flame. For this flame, the soot region occurs 5 mm on the fuel side of the stagnation plane, and convection is from the fuel to the oxidizer. Based on the criterion of the present paper, this flame should be nonluminous. On the contrary, this flame is clearly luminous and has a peak soot volume fraction of nearly 3×10^{-7}. Thus, a criterion based on flow direction alone cannot account for nonluminous flames.

The experimental evidence in the present paper does not demonstrate that flow direction is responsible for producing nonluminous flames. Rather, the results show that for the observed nonluminous flames, the flow is from the fuel to the oxidizer.

REFERENCE

1. Atreya, A., Wichman, I., Guenther, M., Ray, A., and Agrawal, S., "An Experimental and Theoretical Study of Radiation Extinction of Diffusion Flames," Second International Microgravity Combustion Workshop, NASA Lewis Research Center, Cleveland, Ohio, Sept. 15–17, 1992.

Author's Reply. Actually, soot inception occurs in a finite region. In this point, the author agrees with you. In the analytical discussion of the present study, soot inception was assumed to occur at thin flame sheet for simplification. However, the author thinks that the soot formation does not occur if the residence time of soot precursor in the fuel-containing region is much shorter than the time scale of soot formation. The point is not the width of the soot

formation area itself, but the time scale. When a suitable combination of fuel dilution and oxygen enrichment is applied, residence time becomes much shorter than the time scale of soot formation without change in the flame temperature. It is a widely accepted idea that the large part of soot mass is formed through surface growth. So, the discussion in the present study concentrates on suppression of soot surface growth. There is a possibility of soot formation by inception alone, as you point out. To answer your point, the author thinks that we should know the limitation of the diameter and number density of soot particles in the soot cloud that can emit visible radiation, and whether such soot cloud can be formed through the soot inception process alone. These subjects are open problems.

The effect of thermophoresis on the soot velocity is the problem when quantitative prediction is required. The effect is important when flame temperature is high. Figure 4 in the paper shows the experimentally obtained condition of nonluminous flame. There is a difference in parameter ν between theoretical value ($\nu = 1$) and experimental value ($\nu > 1$ at high-temperature conditions). The mechanism of the soot suppression caused by the change of the flow field is described in the discussion using Burke-Schumann theory in the paper. The author thinks that the analytical discussion in the paper is useful to understand the physical mechanism. The author did not try to demonstrate the mechanism of blue flame from the experimental evidence only.

Twenty-Fifth Symposium (International) on Combustion/The Combustion Institute, 1994/pp. 609–617

SOOT FORMATION IN TURBULENT NONPREMIXED KEROSINE-AIR FLAMES BURNING AT ELEVATED PRESSURE: EXPERIMENTAL MEASUREMENT

K. J. YOUNG, C. D. STEWART AND J. B. MOSS
School of Mechanical Engineering
Cranfield Institute of Technology
Bedford, England

Detailed scalar property maps have been constructed for turbulent jet flames of prevaporised kerosine, burning in a coflowing air stream and confined within an optically accessed cylindrical chamber, which permits operation at elevated pressure. Time-averaged measurements of spatially resolved soot volume fraction by path-integrated laser absorption and tomographic inversion, temperature by fine wire thermocouple, and mixture fraction by microprobe sampling and mass spectrometric analysis are reported at chamber pressures from 1 to 6.4 bar.

Whilst the principal objective of the study has been to develop a database for modelling and computational prediction, the centreline data admit presentation in a standardised form, based on the centreline flame length to the maximum soot concentration, which permits analysis of the pressure dependence from turbulent flames of differing sizes. In this form, the peak soot volume fractions and soot formation rates appear linearly dependent on pressure, exhibiting a peak mass fraction of soot carbon of 7%, substantially independent of pressure. The peak soot loading, at the highest pressure investigated, approaches 120 gm^{-3} before complete laser extinction renders the flame inaccessible to further measurement. The high carbon loading and enhanced radiative loss lead to reduced mean temperatures throughout the flame by comparison with more widely studied gaseous fuels such as ethylene. Measured temperatures do not exceed 1438 K anywhere on the centreline of the flame at 1 bar, for example.

Introduction

Concerns for the environmental impact of particulate emissions from diesel engines and gas turbines have recently added fresh impetus to research into the mechanisms of soot formation in nonpremixed flames and smoke production in practical combustion systems. An important additional component of recent studies has been an increased awareness of the role of computational prediction in the analysis and evaluation of advanced combustion chamber designs. This has placed further burdens on the supporting experiments undertaken in relation to both the range of properties measured and their detailed resolution.

Experimental studies of sooting processes to date have focused primarily on laminar flames, seeking to identify—in the absence of a detailed understanding of the chemical kinetic mechanisms—the key global features of soot growth and oxidation (cf. Refs. 1 and 2). Whilst mechanisms inferred from such experiments play an important part in model development, their suitability for turbulent flame prediction subsequently can only be evaluated by comparison with more representative experiments.

The available measurement base is particularly sparse in respect to engine applications that employ blended fuels and that are characterised by nonpremixed turbulent burning at elevated operating pressures. In addition, however, engine combustion typically encompasses the complex physical processes of multicomponent fuel droplet evaporation and mixing in a highly turbulent flow, confined within irregular geometrical boundaries. Somewhat simpler configurations are clearly better suited to the primary tasks of developing and evaluating computationally tractable models of sooting processes in turbulent flames. In the programme of experimental measurements reported here—and in a companion paper that will describe their computational prediction—the two-phase flow and complex geometrical features have been omitted in order to focus on soot production, free from the additional uncertainties introduced by droplet processes and ill-defined boundary conditions. These uncertainties apply equally to theoretical models and to a wide range of measurement techniques.

The measurement campaign reported here therefore explores the influence of pressure on soot production during the confined turbulent jet-flame burning of prevaporised aviation kerosine. In so doing, it generates detailed property maps for the three key scalar variables—the soot volume fraction, the

TABLE 1
Experimental conditions

	Flame					
	A	B	C	D	E	F
Absolute pressure (bar)	1.0	2.03	2.70	3.72	4.81	6.44
Fuel flow rate (g/min)	8.0	9.5	12.5	12.5	18.5	28.0
Fuel exit velocity (m/s)	22.3	13.8	13.0	9.7	11.2	13.2
Fuel exit temperature (K)	598	633	623	626	630	658
Air exit velocity (m/s)	0.23	0.36	0.25	0.24	0.20	0.14
Exit Reynolds number	9,500	11,300	14,400	14,800	21,900	32,800

temperature, and the mixture fraction—throughout a range of confined coflowing flames.

Experimental Programme

The cornerstone of theoretical models of turbulent nonpremixed flames is the conserved scalar approach [3]. In the fast chemistry limit, turbulent mixing is rate controlling, and this may be characterised by the distribution of a conserved scalar, the mixture fraction, free from the complexities of chemical reaction. The computation of mixture fraction statistics, typically the Favre mean and variance, $\tilde{\xi}$ and $\widetilde{\xi''^2}$, is therefore central to turbulent flame prediction. Even in circumstances where slower rate processes may prevail, such as those of soot formation and oxidation, the mixture fraction approach still admits important simplifications, most notably in relation to combustion models based on laminar flamelets [4].

In identifying flame properties for measurement, the mixture fraction should evidently feature prominently. Whilst some success has been reported in multispecies measurements by Raman spectroscopy, which then permits the determination of mixture fraction by summation [5], the technique is inapplicable in heavily sooting, and strongly radiating, flames. In the absence of a suitable optical technique, measurements of mean mixture fraction have been undertaken more intrusively in the present study by microprobe sampling and mass spectrometric analysis.

By choosing an axisymmetric jet-flame configuration, the local time-averaged soot volume fraction can be inferred comparatively simply from integral line-of-sight laser absorption measurements by tomographic inversion.

These data are here complemented by fine wire thermocouple measurements of mean temperature.

Detailed mean property maps have been constructed for coflowing jet flames of prevaporised kerosine, confined within a cylindrical pressure vessel and operated at pressures ranging from 1 to 6.4 bar. This pressure upper bound was set by the soot yield, in that total extinction of the incident laser beam occurred during the soot volume fraction measurements, and the flame structure became quite inaccessible.

The selection of other key experimental flame characteristics, in particular the fuel-jet exit diameter, D_0, and velocity, V_0, reflect the complex interplay between flame length and its containment, exit Reynolds number and turbulence level, and flame liftoff stability. The lower bound exit Reynolds number was set at 10^4, whilst rim stabilisation, even employing an annular pilot flame, became difficult for the prevaporised kerosine jet at exit velocities $\geq 20\ \mathrm{ms}^{-1}$. The measurement conditions actually investigated are identified in Table 1 and reflect a compromise between these competing factors.

Experimental Detail

The experimental rig has been designed to combine ready access for detailed probe and optical property measurement with a basic flow field that can be accurately computed. The confined coflowing jet-flame configuration selected is illustrated in Fig. 1. The turbulent flame is contained within a borosilicate glass tube of 155-mm diameter, mounted in a pressure casing that has been designed to withstand a working pressure of 17.5 bar.

Access for measurement, both by probes and laser-based instrumentation, is achieved through a spe-

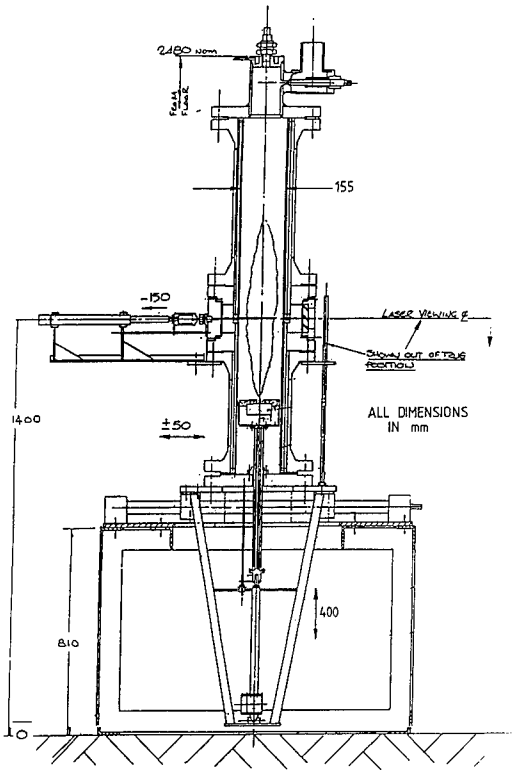

FIG. 1. Experimental configuration.

cially designed module fitted with four diametrically opposed schlieren-quality fused silica windows, each of 75-mm diameter, and four symmetrically distributed instrument ports. A machined spacer then links two borosilicate tube sections and provides uninterrupted access to the flame through an 8-mm-high slot.

The burner comprises a 1.5-mm-diameter cylindrical nozzle, surrounded by a coaxial annular slot, 0.25-mm wide, on which is burnt a rich ethylene-oxygen laminar premixed flame to rim-stabilise the turbulent kerosine jet flame. The kerosine is a standard aviation grade (Avtur) having a C/H ratio of the form $C_{12.5}H_{24.4}$, encompassing 14% H by mass and 20% aromatic content by volume. The mass flow through the pilot flame is typically 2% of that through the primary jet. The kerosine is prevaporised in a resistively heated brass prechamber, situated immediately upstream, into which the liquid fuel is sprayed through a water-cooled nozzle of 0.5-mm diameter. The prechamber is maintained at a temperature of ~800 K, and the flash-evaporated kerosine vapour is discharged at a temperature of ~600 K. This prechamber did not show any evidence of significant lacquering throughout the measurement campaign.

The burner jet can be traversed vertically within the pressure vessel, permitting access to approximately 450 mm of the flame height. The complete casing assembly can also be traversed horizontally—relative to a laboratory-fixed optical system—providing optical access across the 75-mm diameter of the pressure vessel windows. All positions across the complete diameter of the borosilicate glass tube are accessible to the gas sampling probe and fine wire thermocouple.

Radial profiles of time-averaged soot volume fraction have been measured by He-Ne laser absorption. Local values of Beer–Lambert turbidity, τ,

$$\ln(I/I_0) = \int_0^L \tau(s)\, ds$$

were retrieved by Fourier deconvolution from multiple path-integrated measurements of transmitted beam intensity, I [6]. The latter were obtained by traversing the flame at right angles to the stationary incident laser beam across the complete flame width. The local soot volume fraction is then inferred from the turbidity by invoking the small-particle Rayleigh limit and specifying the complex soot refractive index ($m = 1.92 - 0.45i$) for 632.8 nm [7]. In view of the uncertain nature of kerosine soot, this value was chosen in part for consistency with our earlier studies [8,9].

One further modification introduced in transposing the laser absorption technique from laminar to turbulent sooting flames lies in the interpretation of the logarithmic relative intensity ratio in the Beer–Lambert law. Depending upon the level of fluctuation, the more appropriate $[\ln(I/I_0)]_{\text{mean}}$ may differ significantly from the more accessible $\ln[I/I_0]_{\text{mean}}$ and must be accommodated in the data-logging software.

The range of conditions accessible to absorption measurement is bounded by the increasing probability of total laser light extinction with increasing working pressure. The path-integrated transmitted intensity was digitally sampled and the mean value determined at each position from of order 10^3 samples. Low levels of sampled transmitted intensity falling within the mean system background noise (typically $I/I_0 < 10^{-3}$) were routinely counted and logged as a fraction of the total sample. From the data reported here, in the worst case, this fraction reached 60% at a height of $X = 150$ mm in the 6.4-bar flame. For the majority of conditions investigated however, and including all the data at 3.7 bar and below, this fraction did not exceed 10%.

Distributions of mean mixture fraction were determined by quartz microprobe sampling and mass spectrometric analysis. Samples of the local mixture, both gaseous and particulate, were withdrawn from the flame through a 0.5-mm orifice into a quartz tube, where they were mixed with additional oxygen and reacted over a heated platinum catalyst. All the carbon in the ingested sample was oxidised to CO_2

and the mean mixture fraction inferred from the mass ratio of CO_2 to N_2, measured in a small quadrupole mass spectrometer. Under increasingly heavy sooting conditions, accompanying increases in pressure, this proved the most difficult of the measurement techniques to apply. Solid carbon deposition on the exterior of the probe, leading eventually to blocking of the sampling orifice, was unavoidable. Both probe scouring, by withdrawing the probe into its guide, and oxidation in a second "pilot" flame, located on the opposite side of the pressure vessel, were employed during traverses. Additionally, it proved particularly difficult to establish satisfactory levels of O_2 addition, given the large variations in mixture composition across the flame, and to balance the accompanying chemical heat release with the electrical heating supplied. The mixture fraction data are accordingly restricted to pressures below 3 bar.

Mean temperature was measured by fine wire thermocouple (wire diameter 50 μm, platinum/platinum 10% rhodium), incorporating a mean radiation correction based on exchange with the borosilicate tube at an assumed wall temperature of 600 K. In heavily sooting turbulent flames, it might be argued that such a correction exaggerates the radiative loss, since the flame is no longer optically thin and exchange with higher temperature soot surfaces within the flame must also occur. This correction is typically of the order of 50 K in the sooting regions, however, but might be considered to be offset by the less quantifiable uncertainty in thermocouple emissivity, here taken to be 0.2, but in the absence of surface deposits of soot. The correction applied scales approximately linearly with the assumed emissivity.

Further detail of these experimental techniques in the present application is provided in Ref. 10.

Results

Radial distributions of the following mean properties—soot volume fraction, $\bar{f}_v$, mixture fraction, $\bar{\xi}$, and temperature, $\bar{T}$—were measured at a number of discrete axial positions in the flame. Figures 2a and 2b present representative data from confined flames at pressures of 1 and 2.7 bar. Individual data points are plotted with respect to the probe measurements, whilst the soot volume fraction is presented after curve fitting and tomographic Fourier inversion. The probe data are typically taken from a complete radial traverse and imaged about the flame centreline.

At the lowest height measured, $x = 100$ mm, the mixture fraction data do evidence some asymmetry, notably towards the edge of the flame. This is believed to be aerodynamic disturbance at small flame widths when the probe must completely span the flame in gaining access to the opposite extreme of the diameter. The obstruction created by the thermocouple in similar circumstances, by its design, is much smaller, and the influence on the data is greatly reduced. At the higher heights displayed here, the disturbance is generally minimal.

As anticipated from laminar diffusion flame studies [1], the peak mean soot volume fraction lies typically to the rich side of the peak mean temperature. The radial spreading rate is correspondingly reduced for soot, relative to the other scalars, temperature, and mixture fraction, and the peak value has migrated to the flame centreline by a height of 300 mm. Broadly similar trends are evident at higher operating pressures. Substantially increased levels of peak soot volume fraction are measured on the flame centreline, accompanying increasing pressure: 9.4×10^{-6} at 1 bar; 30.6×10^{-6} at 2.7 bar; and 62.9×10^{-6} at 4.8 bar. However, differences in fuel flow rate, and hence flame size, must be incorporated into any systematic comparisons. These will be described in the following section.

By comparison with the soot levels reported in ethylene jet flames [11,8], the present kerosine data at atmospheric pressure represent an approximately fourfold increase. The associated temperature levels are significantly reduced—peak values in the presence of centreline soot are typically ~1500 K in the case of ethylene, but ~1350 K with prevaporised kerosine. Whilst increased soot loading may have a direct impact on thermocouple temperature measurement, as described earlier, the principal influence is expected to be that of enhanced radiative loss.

Discussion and Interpretation

The dependence of soot formation rate on working pressure is of particular concern in engine applications. In both the aircraft gas turbine and the diesel engine, the fuel is injected into the combustion chamber as a liquid in the form of a fine spray. Inferences regarding the pressure dependence of sooting processes from engine measurements are therefore complicated by additional physical effects such as those of combustion chamber pressure on droplet penetration and fuel-air mixture preparation. Gross variations in sooting behaviour may then accompany increases in pressure whilst providing only limited insight into the underlying processes.

Whilst our primary objective here is to develop property maps for purposes of computational prediction, these data do permit a more generalised interpretation of the pressure dependence of soot formation for a practically relevant fuel, burning in a turbulent nonpremixed flame. By prevaporising the kerosine fuel, the underlying turbulent mixing field is in principle less sensitive to changes in chamber pressure.

Figures 3 and 4 illustrate the evolution of soot volume fraction and temperature along the flame cen-

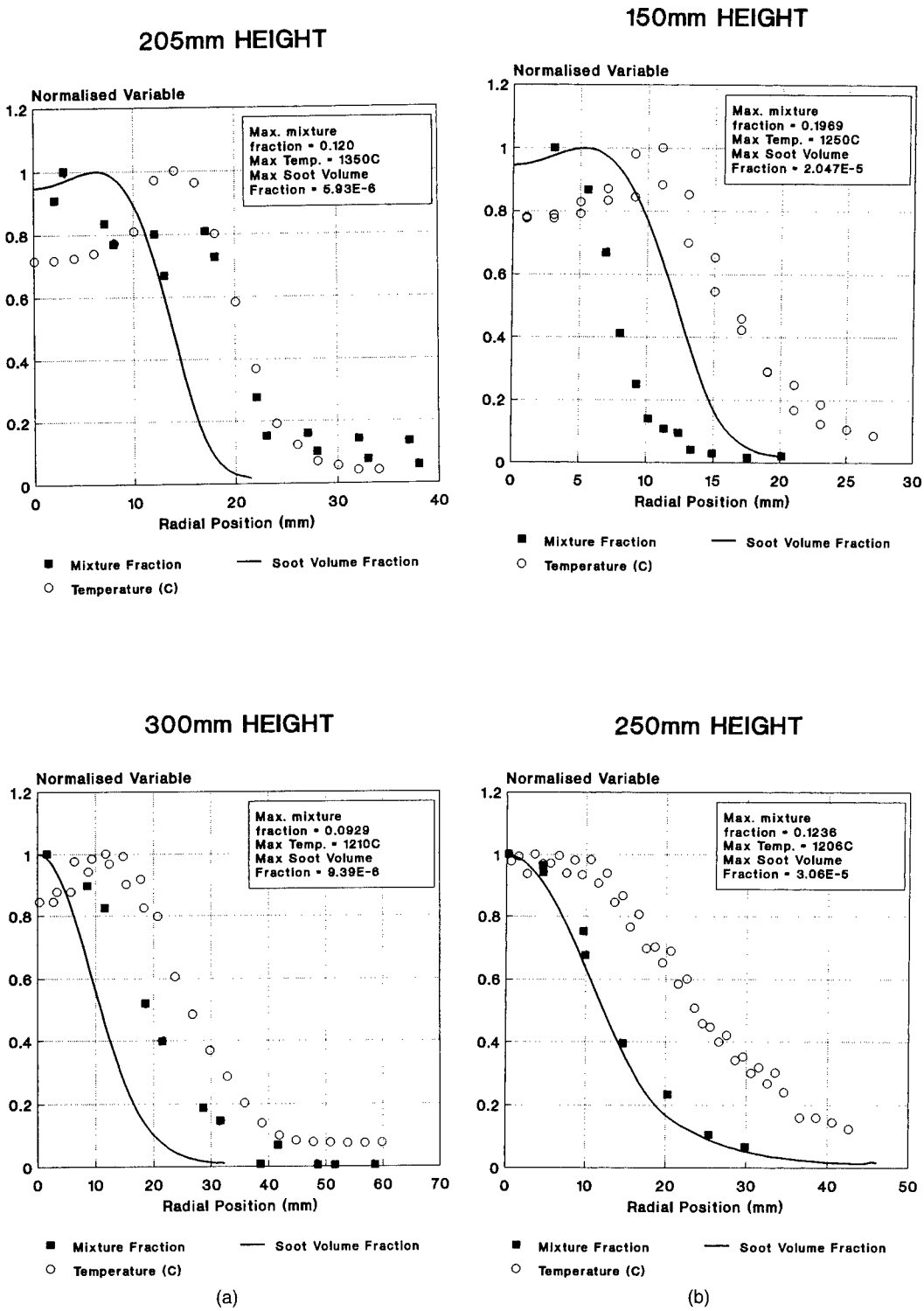

FIG. 2. Variation with flame height of radial profiles for mean mixture fraction, temperature, and soot volume fraction at (a) 1 bar (X = 205, 300 mm), (b) 2.7 bar (X = 150, 250 mm).

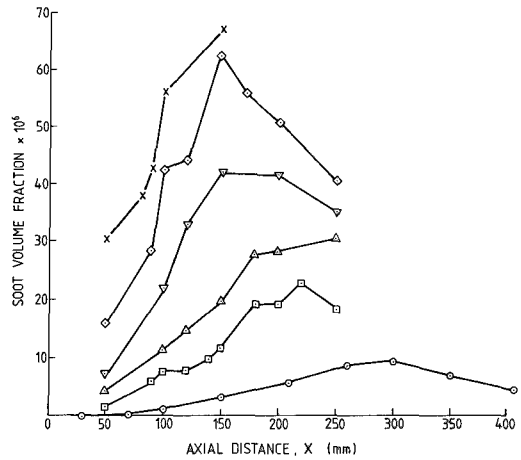

FIG. 3. Axial variation of centreline soot volume fraction with operating pressure, ○ 1 bar, □ 2 bar, Δ 2.7 bar, ∇ 3.7 bar, ◇ 4.8 bar, × 6.4 bar.

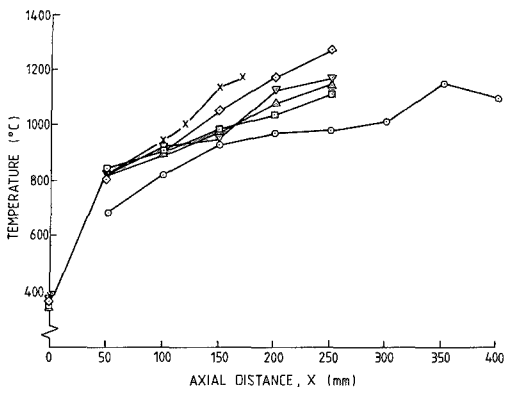

FIG. 4. Axial variation of centreline mean temperature with operating pressure, ○ 1 bar, □ 2 bar, Δ 2.7 bar, ∇ 3.7 bar, ◇ 4.8 bar, × 6.4 bar.

treline with increasing pressure. The peak condition, $\bar{f}_v = 6.7 \times 10^{-5}$ at 6.4 bar, corresponds to a mass concentration ($\rho_s \bar{f}_v$) of 120 gm^{-3}, at which approximately 75% of the local carbon is bound in particulate soot [estimated from $(\rho_s \bar{f}_v / \bar{\rho}\bar{\xi})$].

Distinguishing the effects of pressure from those of other scalars is particularly difficult in nonpremixed flames where the temperature and composition of a typical fluid element vary significantly throughout the flame. In the present experiments, the variation in fuel flow rate with increasing chamber pressure—broadly maintaining a balance between fuel exit Reynolds number and velocity—does produce flames of different size. Figure 4 suggests that very different temperature-time histories prevail in the six flames. They have therefore been standardised relative to flame length, here chosen to be the

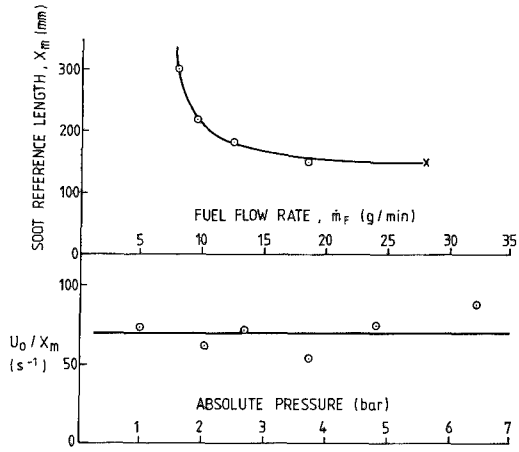

FIG. 5. Variation of flame length (centreline maximum soot volume fraction) with fuel flow rate, and reciprocal timescale (fuel exit velocity/soot reference length) with operating pressure.

axial position, x_m, at which the mean soot volume fraction attains its maximum value. The variation of x_m with the flow rate of prevaporised kerosine is illustrated in Fig. 5. At the highest pressure, 6.4 bar, a discernible maximum has not been reached within the measured range, and x_m has been simply set to the largest measurement height. The asymptotic character of Fig. 5 with increasing flow rate (and exit Reynolds number, cf. Table 1) suggests that the resulting uncertainty is modest.

A systematic reduction of the data to a broadly common form is possible in terms of average properties of jets.

In particular, for $x > x_c$ (approximately 6–8 exit diameters), the centreline velocity of a jet discharging from a nozzle decreases hyperbolically with downstream distance, x, in the form [12]

$$\frac{\bar{u}_{CL}}{u_j - u_\infty} = \frac{x_c}{x}$$

where u_j and u_∞ denote the jet exit and coflow velocities, respectively. A measure of similitude therefore prevails relative to centreline velocity provided $\{u_j - u_\infty\}/x_m$ is constant (cf. Fig. 5), since

$$\bar{u}_{CL}(x/x_m) = \frac{x_c[(u_j - u_\infty)/x_m]}{x/x_m}.$$

Centreline soot fluxes, $\rho_s \bar{f}_v \bar{u}_{CL}$, at specific fractions of the flame length x_m then simply scale according to the local soot volume fraction, $\bar{f}_v$.

Figure 6 presents the centreline temperature data from Fig. 4 in a standardised form, relative to x/x_m. Whilst the data collapse across all six flames is not

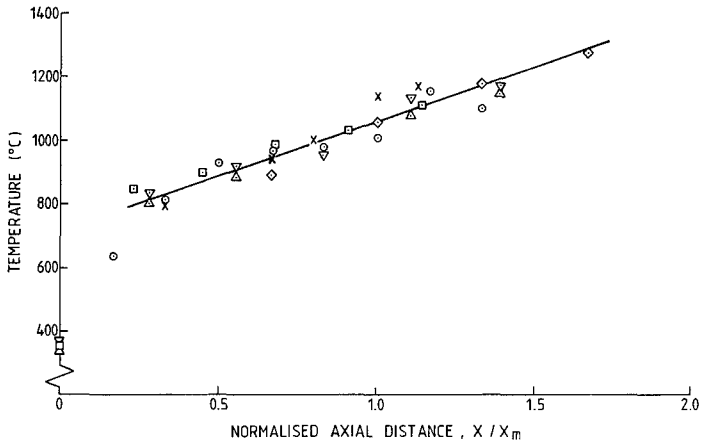

FIG. 6. Variation of centreline temperature with normalised axial distance for all the flames investigated (data as in Fig. 4).

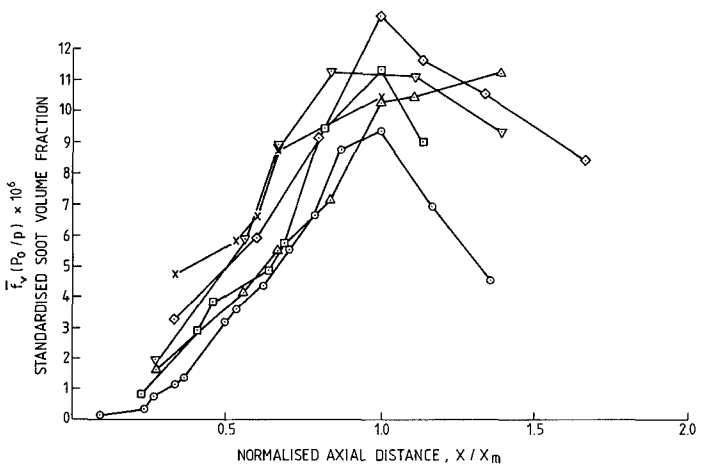

FIG. 7. Variation of centreline standardised soot volume fraction ($\bar{f}_v\{p_0/p\}$) with normalised axial distance (data as in Fig. 3).

perfect, it encourages the view, together with the distribution of centreline velocity, that a common basis exists for the analysis of axial variations of soot volume fraction with pressure. It is noteworthy that, whilst peak off-axis flame temperatures decrease with increasing pressure (cf. Fig. 2), these centreline values do not indicate any significantly enhanced radiative loss with the increasing soot volume fraction. The maximum centreline soot volume fraction at a particular height (as illustrated in Fig. 3) is typically accompanied by a peak temperature that has not yet reached the centreline, and the local source of peak radiative emissions is also off-axis.

In circumstances of fixed soot mass fraction, $(\rho_s f_v/\rho)$, we would expect the soot volume fraction to increase linearly with working pressure. Alternatively, we might choose to compare values of f_v, measured at different pressures, by standardising to a reference pressure, p_0, and introducing the modified variable $f_v(p_0/p)$. Figure 7 illustrates the variation of this standardised soot volume fraction with normalised distance, x/x_m, for the centreline data from all the flames investigated here.

Whilst Fig. 7 exhibits some scatter, the soot formation region $x/x_m < 1$ is plausibly characterised by a peak value of $(p_0/p)\bar{f}_v \simeq 10^{-5}$ and a spatial gradient of

$$\frac{d}{d(x/x_m)}\{f_v(p_0/p)\} \simeq 1.4 \times 10^{-5}$$

over the complete range of operating pressures. These representative values correspond to a peak soot mass fraction, $\rho_s \bar{f}_v/\bar{\rho} = 0.07$ and an average formation rate at 1 bar of $d(\rho_s \bar{f}_v)/dt = 0.1$ kg m^{-3} s^{-1}, scaling linearly with pressure. Data in the burnout regime $x > x_m$ are comparatively sparse, but further significant variation with pressure is evident. In particular, the linear variation with pressure incorporated in Fig. 7 appears to overestimate its influence on soot burnout.

There are very few studies of turbulent sooting

nonpremixed flames, burning at elevated pressure, against which to compare the present findings. Flower [13] has, however, reported integral measurements of soot yield in turbulent jet flames of ethylene-air at pressures from 1 to 8 bar. In the absence there of temperature measurements, detailed comparisons between flames on the basis of temperature-time history is not possible: however, the peak integrated soot volume fraction was reported to increase as $p^{1.4}$.

Similar measurements in ethylene-air laminar diffusion flames by Flower and Bowman [14] suggested a pressure dependence of $p^{1.2}$, whilst a p^2 relationship was inferred by Moss et al. [4] from their extinction measurements on a Wolfhard–Parker burner for pressures up to 3 bar.

These pressure dependencies are generally smaller than those inferred from premixed flame studies. Over comparable ranges of pressure, for example, McFarlane et al. [15] suggested increases in soot formation rate for C_5 and C_6 hydrocarbon-air flames approaching p^3. Similar levels have been reported more recently by Wagner and coworkers [16,17] in premixed ethylene-air flames, although they observed a weaker pressure dependence ($\sim p$) at pressures >10 bar. The interpretation of this diminished sensitivity at high pressure in terms of the reduced concentrations of C_2H_2 fragments available for continued mass growth would not, however, appear applicable to nonpremixed flames burning at lower pressure.

The identification of a peak soot mass fraction in Fig. 7, common to all the flames, suggests that mass growth is eventually limited by the available carbon, but that growth to that point is largely determined by temperature. There appears to be little further pressure dependence beyond the linearly increasing carbon content per unit volume that accompanies increasing working pressure.

Conclusions

Detailed measurements of soot volume fraction, temperature, and mixture fraction are reported in a confined turbulent jet flame of prevaporised kerosine in a coflowing airstream, burning at pressures in the range 1–6.4 bar. Illustrative radial profiles are presented at discrete axial heights with a view to computational prediction.

The evolution of properties along the flame centreline are analysed to identify the underlying pressure dependence of the soot formation process. These data are amenable to presentation in a standardised form that suggests an essentially linear dependence of peak soot volume fraction and rate of formation on pressure. The peak mass fraction of soot carbon in all these flames is approximately 7%, attained at a mean temperature of 1340 K and mixture fraction of 0.12. The peak soot loading, measured in the 6.4-bar flame, reached 120 gm^{-3}.

Acknowledgments

The authors are pleased to acknowledge the support and interest of the Defence Research Agency (Pyestock), Rolls Royce plc., and the Science and Engineering Research Council in the research reported here.

REFERENCES

1. Haynes, B. S., and Wagner, H. Gg., *Prog. Energy Combust. Sci.* 1:229 (1981).
2. Glassman, I., *Twenty-Second Symposium (International) on Combustion*, The Combustion Institute, Pittsburgh, 1989, p. 295.
3. Bilger, R. W., *Prog. Energy Combust. Sci.* 1:87 (1976).
4. Moss, J. B., Stewart, C. D., and Syed, K. J., *Twenty-Second Symposium (International) on Combustion*, The Combustion Institute, Pittsburgh, 1989, p. 413.
5. Starner, S. H., Bilger, R. W., Dibble, R. W., and Barlow, R. S., *Combust: Flame* 83:63 (1991).
6. Shepp, L. A., and Logan, B. F., *IEEE Trans. Nucl. Sci.* NS-21(June):21 (1974).
7. Mullins, J., and Williams, A., Fuel 66:277 (1987).
8. Young, K. J., Stewart, C. D., Syed, K. J., and Moss, J. B., *Tenth International Symposium on Air Breathing Engines*, AIAA, New York, 1991, p. 239.
9. Stewart, C. D., Syed, K. J., and Moss J. B., *Combust. Sci. Technol.* 75:211 (1991).
10. Young, K. J., "Soot Formation in Turbulent Vaporised Kerosine-Air Jet Flames at Elevated Pressure," Ph.D. Thesis, Cranfield Institute of Technology, Bedford, England, 1993.
11. Kent, J. H., and Honnery, D. R., *Combust. Sci. Technol.* 54:383 (1987).
12. Hinze, J. O., *Turbulence*, McGraw-Hill, New York, 1959.
13. Flower, W. L., *Twenty-Second Symposium (International) on Combustion*, The Combustion Institute, Pittsburgh, 1989, p. 425.
14. Flower, W. L., and Bowman, C. T., *Twentieth Symposium (International) on Combustion*, The Combustion Institute, Pittsburgh, 1985, p. 1035.
15. McFarlane, J. J., Holderness, F. H., and Whitcher, F. S. E., *Combust. Flame* 8:215 (1964).
16. Mätzing, H., and Wagner, H. Cg., *Twenty-First Symposium (International) on Combustion*, The Combustion Institute, Pittsburgh, 1986, p. 1047.
17. Bohm, H., Felderman, Chr., Heiderman, Th., Jander, H., Luers, B., and Wagner, H. Gg., *Twenty-Fourth Symposium (International) on Combustion*, The Combustion Institute, Pittsburgh, 1992, p. 991.

COMMENTS

M. Pinar Menginc, University of Kentucky, USA. 1. With increasing pressure, it is natural to expect agglomeration of soot particles. If this agglomeration process is not accounted for in the tomographic deconvolution, f_v for soot particles may be significantly different. Would you please comment?

2. Does the radiation loss correction required on thermocouple readings remain the same for different pressures (which correspond to different soot volume fractions in the flame)?

Author's Reply. The extinction data have all been interpreted in the small particle Rayleigh limit in order to provide a consistent basis for comparison. Turbulent flame experiments such as these are perhaps an unsuitable vehicle for assessing the influence of pressure on optical cross sections resulting from differences in agglomeration.

The radiation corrections applied to the thermocouple measurements consider the flame to be optically thin under all conditions and therefore do not depend on the level of soot volume fraction.

•

Ian Kennedy, University of California, Davis, USA. The flame appears to be large in comparison with the confining duct. A significant axial pressure gradient may be induced. This pressure gradient may have an impact on turbulent flame mixing and, hence, on soot formation. Was the axial pressure gradient measured and is it important for modeling of the flame?

Author's Reply. Confinement of the flame within the borosilicate liner does induce an axial pressure gradient. The gradient is quite small, however, since the maximum flame diameter only occupies some 60% of the complete liner (cf. Fig. 2) and the initial coflow air velocities do not exceed 0.5 ms^{-1} (cf. Table 1). The modest influence on turbulent mixing can be readily incorporated in subsequent jet flame computations [cf. Young (1993)], and the differences relative to unconfined flames appear small [cf. Young et al. (1991)].

Twenty-Fifth Symposium (International) on Combustion/The Combustion Institute, 1994/pp. 619–626

EXPERIMENTAL AND THEORETICAL STUDY OF DIESEL SOOT REACTIVITY

F. MARCUCCILLI, P. GILOT, B. STANMORE* AND G. PRADO
Laboratoire Gestion des Risques et Environnement Université de Haute Alsace
25 Rue de Chemnitz
68200 Mulhouse, France

In order to provide data for modelling the performance of a regenerative soot filter, a study of the oxidation kinetics of diesel soot in the temperature range from 600 °C to 800 °C was undertaken. Isothermal burning rates at a number of temperatures were measured in rectangular soot beds within a thermobalance. The technique was easy to use, but the combustion rate was found to depend on bed mass. The oxidation process was thus limited by mass transfer effects.

A two-dimensional mathematical model of oxygen transfer was developed to extract the true kinetic rates from experimental data. The two-dimensional approach was required because significant oxygen depletion occurred along both axes. Using assumed kinetic rates, oxygen concentration profiles in the gas phase above the bed and within the bed were calculated. The true kinetics at a number of temperatures were then established by matching predicted oxygen consumption with measured consumption.

Application of the model required values of the effective diffusion coefficient for oxygen within the bed. Accordingly, the structure and properties of the soot aggregates were determined. A supplementary study was carried out to identify the appropriate primary reaction products. The measured kinetic rates were then used in a simpler, monodimensional model to evaluate the mean oxygen mass transfer coefficients to the surface of the bed.

The results show that burning below about 730 °C is in regime 1 and can be described by

$$K = 6.9 \times 10^{12} \exp(-207{,}000/RT) \quad (\mathrm{s}^{-1})$$

with $R = 8.314$ J mol^{-1} K^{-1}. Above 730 °C, there is a decrease in apparent activation energy, probably due to thermal "annealing," which changes the microstructure of the carbon. As a result, the inherent reactivity declines and/or the bed becomes less accessible to oxygen.

Introduction

The soot particles emitted by automotive diesel engines present an environmental hazard if inhaled. They irritate the bronchi and lungs, and the PAH materials adsorbed onto their surface are known to be carcinogenic. Accordingly, the emission limits set by legislation have been progressively lowered; for example, in California, they now stand [1] at 0.05 g km^{-1} for light vehicles. In Europe, where the diesel is more popular, the limits are presently higher at 0.14 g km^{-1} for light vehicles and 0.36 g (kWh)$^{-1}$ for large trucks. More stringent requirements will be in place for new models produced after 1996.

One means of lowering emissions is a particulate trap mounted in the exhaust line. This is a ceramic filter (often impregnated with a catalyst) that captures the particles and burns them off when the exhaust gas temperature is high enough. The exhaust gas temperature of an idling diesel is only 150 °C but rises to 700 °C at full load. The latter temperature is high enough to burn a reactive carbon like soot.

There have been a number of studies of the oxidation of diesel soot (see for example Refs. 2–4). Soot characteristics vary, depending on the fuel and the operating conditions in the engine. However, the activation energies reported have ranged from 11 to 221 kJ mol^{-1}, which suggests that in some cases, the experimental conditions or the analysis of the results have been inadequate. The most recent values lie in the vicinity of 200 kJ mol^{-1}, which indicates regime 1 conditions.

A consortium of European motor manufacturers, which has been supporting a program to develop this technique, has funded work in five laboratories. The work described here is part of that collaborative program and was directed towards supplying kinetic data for a mathematical model of regeneration in a particulate trap. It concerns the combustion phase, examining the oxidation kinetics of a diesel soot at typical trap temperatures. It also examines the kinetics

*Present address: Department of Chemical Engineering, University of Queensland, 4072 Australia.

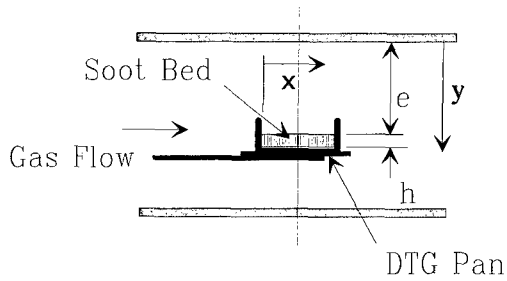

FIG. 1. Arrangement of crucible and soot bed.

of the gas-phase oxidation of carbon monoxide in the same temperature range. Most of the work was carried out by thermogravimetric analysis (TGA) with soot beds contained in a crucible (Fig. 1). Some supplementary studies were performed in a fixed bed to better simulate combustion of a deposit in a trap.

The soot examined was collected through a sample line from a small diesel engine running at moderate load. A cordierite filter operating at 300 °C was used to remove the solids from the gas stream.

Experimental

The sample of soot was characterised both physically and chemically by a number of techniques, including scanning electron microscopy (SEM), x-ray diffraction, Brunauer-Emmet-Teller (BET), and laser diffraction particle sizing. The bulk density was measured directly. Soot composition was investigated by elemental analysis, x-ray fluorescence, and an Fourier transform infrared (FTIR) scan.

Combustion studies were performed in two different apparatuses: a thermobalance and a fixed bed. The thermobalance was a Linseis Model L81, which was operated with the gas-flow horizontal. The initial sample mass was varied from 10 to 30 mg. Because of the low bulk density of the soot, large bed volumes were necessary to give the required masses. A rectangular quartz crucible 26-mm long, 12-mm wide, and 6-mm deep was used to contain the sample.

The combustion tests were carried out isothermally by preheating the samples at 10 °C per minute to operating temperature under a flow of nitrogen and then introducing the oxidant gas mixture. Most of the tests were carried out in a 10% mixture by volume of oxygen in nitrogen, which is a typical oxygen concentration for diesel exhaust gases. The operating temperatures ranged from 600 °C to 800 °C.

In order to derive the oxygen consumption rate from the rate of mass loss in the crucible, the composition of the product gas must be known. The literature suggests that carbon dioxide is the preferred product at low temperatures and that the CO_2/CO ratio ($=r$) decreases with temperature. The composition of the primary gas product was, therefore, examined by means of a gas analyser fitted to the gas outlet. Blank runs using a premixed $CO/O_2/N_2$ feed in the absence of soot were necessary in order to evaluate the gas-phase oxidation of CO to CO_2 over the temperature range involved.

The initial surface area was measured by BET methods using nitrogen at 77 K, as well as samples partly burned isothermally at 600 °C and 800 °C.

The fixed bed tests were supplementary studies carried out to confirm the kinetic values under conditions that better simulate bed regeneration. Their accuracy was poor because of rapid burnout, especially at the higher temperatures, in relation to the response time of the gas analysers. A 2-mm bed of soot was laid onto a quartz frit in a 28-mm-diameter quartz tube maintained at constant temperature. The gas passed downwards through it, and the oxidation rate was measured by means of CO/CO_2 analysers located immediately downstream.

Results

The soot sample appeared under the electron microscope as spherules clustered together into clumps and chains. A size distribution performed with a Zeiss image analyser showed that most of the spherules lay in a diameter range between 7 and 45 nm, with the mean around 19 nm at a standard deviation of 9 nm. Since the aggregates displayed no particular morphology, ascribing a diameter to them was difficult. They showed a wide variation in characteristic dimension, but a crude estimate of diameter was 0.1 μm.

When sized by laser diffraction, soot suspensions slurried by hand in methanol returned a size distribution with a mean of 147 μm, indicating the presence of large agglomerates. After ultrasound treatment, the distribution resolved into trimodal form with the number frequency dominated by a peak at 160 nm, which was taken as the mean size of the aggregates for diffusion calculations.

The bulk density was very low, only 25 kg m^{-3}. The total porosity ϕ_1 ($=0.976$) and the porosity within the aggregates ϕ_2 ($=0.480$) were calculated from this and an assumed particle (spherule) density of 2000 kg m^{-3}. The BET surface area was 227 m^2 g^{-1}. When compared with the calculated external surface area for 19-nm spheres of 157 m^2 g^{-1}, it suggests that some internal pore area is present.

The TGA tests returned an ash content of around 12% unburned material. The composition of the mineral matter found by x-ray diffraction and x-ray fluorescence suggests that the ash components were cordierite from the sample filter and calcium sulphate from oil additives. Ultimate analyses were carried out on the original sample and also on a sample

TABLE 1
Ultimate analyses of diesel Soot*

Element	C	H	N	O	S
Virgin soot	83.5	1.04	0.24	10.5	1.13
Degassed soot	83.8	0.85	0.22	10.7	0.10

*Mass %, dry basis, oxygen values determined by analysis.

degassed at 13 mPa and 150 °C for 5 h. The results are shown in Table 1.

Only 83.5% of the soot is actually carbon. The sulphur was apparently present as compounds adsorbed on the particle surface, whereas the oxygen was strongly bonded. Since the fall in hydrogen content during degassing was slight, few adsorbed hydrocarbons are present. Between 3.5 and 4.5% of the total mass is unaccounted for, probably in the form of silicon, aluminium, and metals.

On raising the temperature of a sample at 10 °C per minute, there was a negligible loss of mass up to 450 °C, even in 10% oxygen, which emphasises the strength of the oxygen bonding. The FTIR analysis revealed the presence of C=O, C—O—C, and C—O—H bonds, and some aromatic structures. When heated to 900 °C under nitrogen, a mass loss of 12% was sustained.

The initial BET surface area of 227 $m^2\ g^{-1}$ increased with burnout, as shown in Fig. 2. The area increases more rapidly with burnout at 600 °C than at 800 °C, and both areas are greater than if the shrinking core model is applied to the spherules.

The CO_2/CO ratio in the gaseous product from soot oxidation at 600 °C and 700 °C was in the range 1.0–1.1 in accordance with Ref. 5, but it was very high at 800 °C. Blank runs in the form of gas-phase oxidations of CO to CO_2 in premixed CO/10% O_2/N_2 mixtures without soot present in the thermobalance were performed. At 600 °C, no oxidation was detected, while at 700 °C, CO conversion was slightly less than 10%. At 800 °C, it had risen to over 90%. As a result, it was impossible to identify the primary product during soot oxidation tests at 800 °C. For the analysis of the experimental results, the value of r was taken as unity under all conditions, i.e., $f = 2.0$.

In every case, the thermograms for isothermal soot burning in the thermobalance gave constant rates of mass loss over the initial stages. Accordingly, this rate could be used to give K from Eq. (1). However, the rate was a function of initial sample mass, as shown in Fig. 3, with the effect becoming more pronounced at higher temperatures. This indicated that mass transfer limitations were operating and, therefore, needed to be accounted for.

Analysis of Results

The reaction was regarded as first order, based on the literature [6] and a preliminary study carried out at three different oxygen concentrations. For a first-order reaction, the rate constant K (s^{-1}) can be related to the instantaneous volumetric rates of oxygen consumption and mass loss in the thermobalance by

$$r_{O_2} = K\rho_g C = f r_C \quad (\text{kg m}^{-3}\ \text{s}^{-1}) \qquad (1)$$

where f is a stoichiometric coefficient (kg of oxygen per kg of carbon).

$$f = \frac{4}{3}\left(\frac{1 + 2r}{1 + r}\right).$$

In our apparatus, it was apparent that diffusion processes were limiting the oxidation reaction. One- and two-dimensional, steady-state mathematical models [7,8] of the system were developed. With the mass transfer processes specified, the reaction rate K could then be estimated. The flow enclosure in the thermobalance and the rectangular soot bed are depicted in Fig. 1 with the coordinate system as shown.

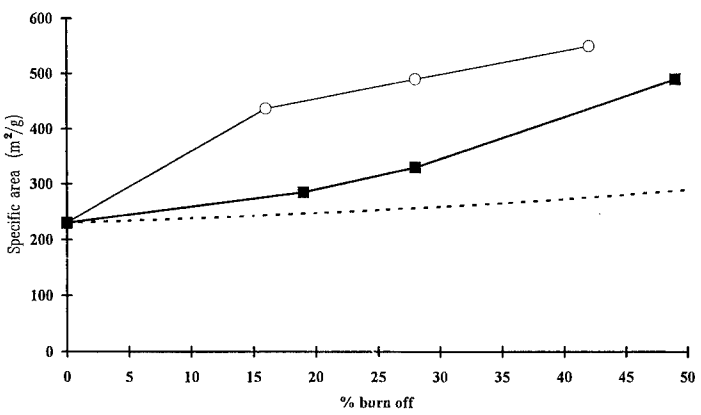

FIG. 2. Effect of burnoff on BET surface areas: ○ 600 °C; ■ 800 °C; --- shrinking core model.

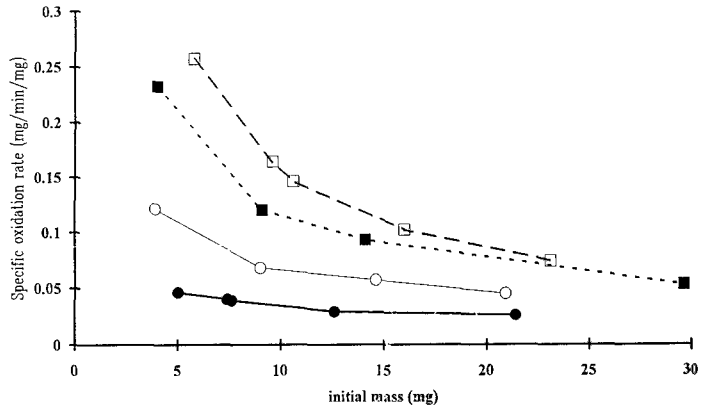

FIG. 3. Effect of sample mass on combustion rate: ● 600 °C; ○ 650 °C; ■ 700 °C; □ 800 °C.

The monodimensional model [7] uses a mean transfer coefficient for oxygen to the surface of the bed. In the present case, the oxygen concentration boundary layer could not fully develop above the bed (its thickness was greater than e), and a two-dimensional approach was better [8]. From the continuity equation and an oxygen balance, the oxygen mass fraction C in the freeboard ($0 < y < e$) is given by

$$\frac{\partial C}{\partial x} - \frac{\rho_g D}{G_T}\left[\frac{\partial^2 C}{\partial x^2} + \frac{\partial^2 C}{\partial y^2}\right] = 0 \qquad (2)$$

with boundary conditions

$$C_{(0,y)} = C_0; \qquad \left[\frac{\partial C}{\partial y}\right]_{(x,0)} = 0.$$

The length-to-depth ratio of the gas volume below the crucible lip was always greater than 5:1 so that end effects were neglected.

Within the soot bed ($e < y < e + h$), where D_e is the effective oxygen diffusion coefficient, the equivalent expression is

$$\frac{\partial}{\partial x}\left[\frac{1}{1 - C}\frac{\partial C}{\partial x}\right] + \frac{\partial^2 C}{\partial y^2} - \frac{K}{D_e}C = 0 \qquad (3)$$

subject to the boundary conditions

$$\left[\frac{\partial C}{\partial x}\right]_{(0,y)} = \left[\frac{\partial C}{\partial x}\right]_{(L,y)} = 0; \qquad \left[\frac{\partial C}{\partial y}\right]_{(x,e+h)} = 0.$$

The simultaneous solution of Eqs. (2) and (3) gave the oxygen concentrations within the system.

The magnitude of the diffusion coefficient D_e is important for the solution. As indicated in the morphology results, the soot structure is comprised of primary spherules (19-nm mean diameter) agglomerated into 160-nm-diameter aggregates. There are three levels of porosity present:

1. porosity between the aggregates;
2. porosity between the spherules within an aggregate; and
3. porosity within the spherules.

The first two will influence the value of D_e, whereas the third will come into play only during internal burning, when it will influence the burning regime. By considering the interstices between particles to be equivalent to parallel-sided cylindrical pores, oxygen diffusion was found to lie in the Knudsen regime. The equivalent pore diameters for each porosity were calculated as $d_1 = 40$ nm and $d_2 = 8.7$ nm by using the appropriate solid density (bulk or aggregate) in

$$d_i = 4\phi_i/A_i\rho_s \quad \text{(m)}. \qquad (4)$$

The effective diffusion coefficient was found from a series model in which D_{e1} and D_{e2} are the coefficients for the two levels of pore volume:

$$D_e = \frac{2}{(1/D_{e1}) + (1/D_{e2})} \quad (\text{m}^2\ \text{s}^{-1}). \qquad (5)$$

The individual coefficients for oxygen in a cylindrical pore were evaluated from

$$D_i = 2d_i(2RT/M\pi)^{1/2}/3 \quad (\text{m}^2\ \text{s}^{-1}). \qquad (6)$$

To convert the diffusivity in a cylindrical pore to that in an actual solid matrix, Satterfield [9] suggests $D_{ei} = \phi_i D_i/\tau_i$, where the tortuosity is an adjustable parameter. If τ is taken as 4, it leads to a final expression for the overall bed:

$$D_e = 1.6 \times 10^{-8}\, T^{1/2} \quad (\text{m}^2\ \text{s}^{-1}). \qquad (7)$$

Equations (1) and (2) were solved numerically by finite difference with an initial arbitrary value supplied for K at each temperature. The value of G_T was regarded as independent of y and x because of the com-

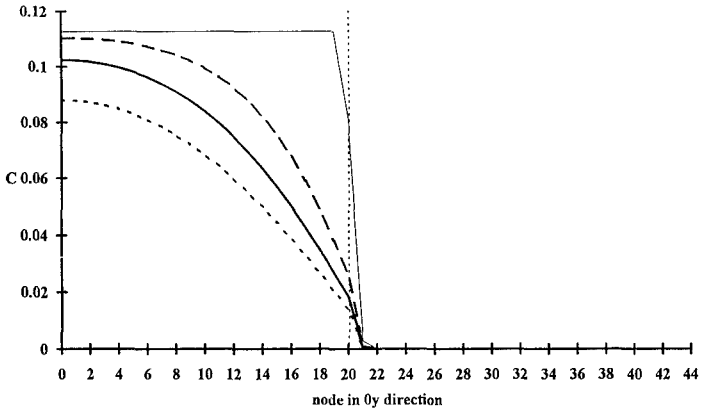

FIG. 4. Oxygen concentration profiles at 800 °C: ---- bed surface; —— concentration at node 0 in the x direction: —— node $x = 3$; — node $x = 6$; --- node $x = 10$.

paratively low oxidation rates. From the solution, the rate of solid consumption in a bed of width Z was found from

$$R_c = -\frac{dm}{dt} = Z \int_e^{e+h} \int_0^L r_c \, dx \, dy \quad (\text{kg s}^{-1}). \quad (8)$$

With the oxygen concentrations known throughout the bed, the integration of Eq. (8) was performed numerically. The error difference between the experimentally determined value of R_c and the model-derived value of soot consumption was determined for a number of values of K. The value that gave the minimum difference was accepted as the result for that temperature.

The two-dimensional model was applied to the experimental system. When solving Eq. (1) and (2) with assumed values for K, distinct minima in the error differences appeared. During the solution process, two simplifications were found to be possible. Above the bed, the diffusive flux in the x direction was negligibly small in relation to the convective. Inside the bed, the fraction $1/(1 - C)$ could be taken as unity. Above a mesh size of 484 nodes ($x = 11$, $y = 44$), the solutions were found to be mesh independent.

The calculated distributions of oxygen concentration above and within the bed show that in all cases (even at 600 °C), there is only partial penetration of oxygen into the bed. This is predicted [7] from the magnitude of the bed Thiele modulus $\theta_{1-2} = h(K/D_e)^{1/2}$, for which the porosities 1 and 2 control bed diffusion. At the extreme temperature of 800 °C depicted in Fig. 4, in which the vertical dashed line at the node point $y = 20$ represents the bed surface, the thickness of the active burning layer is less than 1/10th of a millimetre. The thin active layer was observed in practice in the form of grains of ash present only on the bed surface.

There was a thick mass transfer boundary layer in the gas flow, extending to the wall of the furnace (Fig. 4). There was also initial depletion of oxygen in the direction of gas flow. The monodimensional model [7] requires that oxygen concentrations in the x direction within the bed are constant. This was valid at the lower temperatures and approximately true for the higher (see Fig. 4 for the 800 °C bed), where the oxygen concentrations for 8 of the 11 x-nodes lie together. Accordingly, mean mass transfer coefficients were calculated from the experimentally determined Damkohler numbers for all bed thicknesses [7]. The mass transfer coefficients are defined from the oxygen flux to the bed surface by $\omega = h_m \rho_g (C_b - C_{y=0})$.

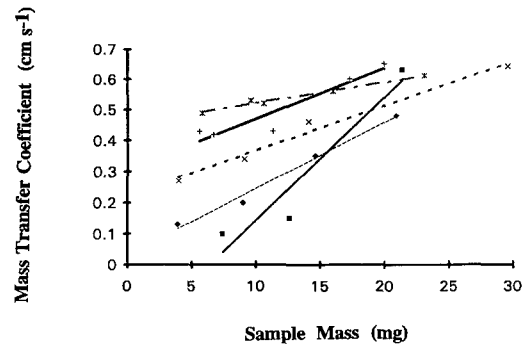

FIG. 5. Mean mass transfer coefficients, monodimensional model: ■ 600 °C; ♦ 650 °C; × 700 °C; + 750 °C ✳ 800 °C.

The calculated values of h_m are plotted against bed mass in Fig. 5. The results for 30-mg beds were around 0.6 cm s^{-1}, which is similar in magnitude to the value predicted from the boundary-layer theory [10]. It is apparent that access of oxygen to the bed surface is better for the larger beds, in which the surface is closer to the top of the crucible. The values increase with temperature, as predicted by the boundary-layer theory. Natural convection currents generated by the heat release at the higher reaction rates may also assist the mass transfer process.

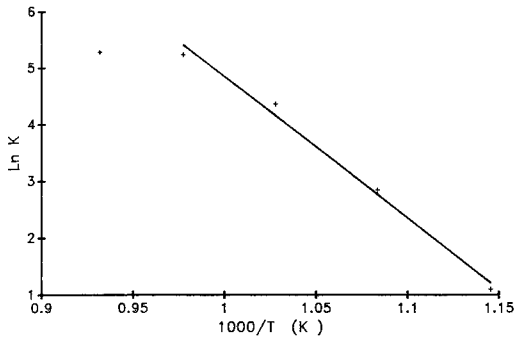

FIG. 6. Arrhenius plot of reactivity.

The kinetic rates evaluated from the model are presented in Arrhenius form in Fig. 6. The activation energy derived by considering only the four lower temperatures is 207 kJ mol^{-1}, which is consistent with the literature for this regime. The values reported by other authors are 191 [11], 221 [3], and 178 [4] kJ mol^{-1}. The rates of reaction are also similar.

Discussion

An apparent change in regime is seen around 730 °C, where the activation energy begins to fall. Similar behaviour was observed with carbon black at the same temperature [10]. It could represent a genuine decrease in the kinetic rate and/or could be the result of a variation in the diffusion coefficient used in the derivation of K. The effect responsible occurs within the aggregates in the former case and within the bed structure in the latter.

In view of simultaneous changes to apparent activation energy and rate of generation of surface area, the most obvious explanation is that combustion within the spherules has moved from regime 1 to regime 2. To check this hypothesis, the particle (spherule) Thiele modulus $\theta_3 = 0.5\, d_p (K/4D_e)^{1/2}$ was calculated using the measured reactivities, and with Eq. (9) giving the diffusion coefficient [9].

$$D_e = 48.5 \frac{\phi_3^2 T^{0.5}}{\tau S_v} \quad (\mathrm{m^2\, s^{-1}}). \qquad (9)$$

The surface area S_v was taken as the difference between the BET and geometric external areas (70 m^2 g^{-1}). An initial porosity of $\phi_3 = 0.05$ was assumed, but the final result was insensitive to this parameter because of the small spherule diameter.

The results calculated for θ_3 are less than 0.01 for all temperatures and indicate that regime 1 burning should apply over the whole temperature range studied. Similarly, predictions by Neoh et al. [12] of effectiveness factors for 20-nm soot particles burning in oxygen at 1775 K range from 0.74 in 0.5-nm pores to 0.99 in 4-nm pores.

Ishighuro et al. report [13] that spherules of carbon black when partly burned at 600 °C appeared hollow, by transmission electron microscopy, but appeared to be solid when partly burned at 800 °C. Diesel soot burned at 500 °C developed porosity and rearranged to give larger, more ordered crystallites. As burnout proceeded, the outer crystallite shells peeled off, leading to a slow decrease in diameter. It is probable that competing effects were at work—the crystallite growth was a result of the elevated temperature, and the increase in porosity was a result of oxidation.

The behaviour of carbon black mentioned above has been noted in our own laboratories. In contrast, with the soot, there were no differences detectable by electron microscopy in the structures of samples burned at 600 °C and 800 °C. The surface area remained unchanged after heating to 800 °C in nitrogen, and there was very little change in surface area with burnout in 10% oxygen at 600 °C and 800 °C (Fig. 2). The measured increases in area in Fig. 2 are both higher than that calculated from the shrinking core model, which indicates internal burning in both cases.

In summary, it is unlikely that there has been a change in the access of oxygen to the spherules as the temperature rose from 600 °C to 800 °C. There remains, however, the contradictory evidence of a slower growth in surface area accompanying an apparent decrease in activation energy.

Suuberg [14] has summarised the thermal "annealing" of carbons and concluded that the principal factors are structural ordering and loss of catalytic impurities (which is relevant only at very high temperatures). Changes in the structure of carbons, i.e., a tendency for crystallites to grow, is likely even at 800 °C. A genuine change in reactivity of the soot could occur if the carbon structure had been modified. It is likely that the annealing processes referred to have produced greater order in the crystallites and that fewer active sites (edge atoms) are available for reaction. The process would be assisted by the greater extent of heteroatom removal occurring at 800 °C.

If a change in carbon reactivity is not responsible, a change in bed structure could account for the apparent change in regime, even though the inherrent reactivity was retained. Lahaye and Prado have pointed out [15] that spherules have no individual existence and that aggregates constitute the real entity. The outer crystallite sheets are common between adjacent spherules and suffer preferential attack by oxygen. When this occurs, it will be one location where new surface area is generated.

A possible explanation for our anomalous results

is that at 800 °C, the structural ordering caused during heatup made the aggregates less porous. As shown in Fig. 4, oxygen hardly penetrated into the bed so that crystallite growth could proceed unimpeded by oxidation. In fact, a change was experimentally observed when our soot was heated to 800 °C under nitrogen, as the particles began to cohere.

Since the resistance to diffusion is predominantly within the aggregates, any diminution in their porosity would lower the effective diffusion coefficient of the bed. The model indicates that if the diffusion coefficient at 800 °C was 0.0018×10^{-4}, rather than 0.0052×10^{-4} m^2 s^{-1} as used in obtaining the K value, then the observed burnout results would be obtained. Such a modification would produce the change in apparent activation energy observed in Fig. 6 and would also account for the slow appearance of surface area with burnout.

Conclusions

Thermogravimetric analysis is a suitable technique for measuring soot reactivity, providing mass transfer effects are accounted for. When beds of diesel soot are burned in the temperature range from 600 °C to 800 °C, oxygen transfer limits reaction rates even at the lowest temperature. A two-dimensional model was required to extract the true kinetics from measured burning rate data. A simpler monodimensional model gave values of the mean oxygen mass transfer coefficients to the bed surface. Below 730 °C, the soot burns in regime 1 conditions at a kinetic rate given by

$$K = 6.9 \times 10^{12} \exp(-207{,}000/RT) \quad (\mathrm{s}^{-1})$$

with $R = 8.314$ J mol^{-1} K^{-1}. Above 730 °C, there is a fall in apparent activation energy, probably the result of thermal annealing of the soot. This may lower inherent reactivity and/or increase resistance to mass transfer, following a change in the structure in the bed.

Nomenclature

A_i	specific surface area	(m^2 kg^{-1})
C	mass fraction of oxygen	(−)
d_i	equivalent pore diameter	(m)
d_p	spherule diameter	(m)
D	bulk diffusion coefficient of oxygen	(m^2 s^{-1})
D_e	effective diffusion coefficient of oxygen	(m^2 s^{-1})
e	clearance above bed surface, Fig. 1	(m)
f	stoichiometric coefficient	(−)
G_T	total mass flux of oxidant gas	(kg m^{-2} s^{-1})
h	depth of soot bed, Fig. 1	(m)
h_m	mean mass transfer coefficient, oxygen	(m s^{-1})
K	kinetic oxidation rate	(s^{-1})
L	length of soot bed, Fig. 1	(m)
M	molecular mass of oxygen	(kg mol^{-1})
m	mass of bed	(kg)
r	mole ratio, carbon dioxide/carbon monoxide	(−)
r_C, r_{O_2}	carbon, oxygen consumption rates	(kg m^{-3} s^{-1})
R_c	rate of solid combustion	(kg s^{-1})
S_v	particle surface area, volume basis	(m^2 m^{-3})
T	temperature	(K)
x, y	coordinate system	(m)
Z	bed width	(m)

Greek characters

θ_i	Thiele modulus	(−)
ϕ_i	porosity	(−)
τ_i	tortuosity	(−)
ρ_g	gas density	(kg m^{-3})
ρ_s	density of solid	(kg m^{-3})
ω	mass flux of oxygen	(kg m^{-2} s^{-1})

Subscript

b	in the bulk
i	relating to level of porosity

REFERENCES

1. Walsh, M. P., and Bradow, R., "Diesel Particulate Control Around the World," SAE Paper 910130, 1991.
2. Otto, K., Sieg, M. H., Zinbo, M., and Bartosiewics, L., "The Oxidation of Soot Deposits from a Diesel Engine," SAE Paper 800336, 1980.
3. Frohne, J. Ch., Reisig, H., and Schadlich, H. K., *Erdol und Kohle-Erdgas-Petrochemie* 43:152 (1989).
4. Ciambelli, P., Corbo, P., Parella, P., Scialo, M., and Vaccaro, S., *Thermochim. Acta* 162:83 (1990).
5. Du, Z., Sarofim, A. Z., Longwell, J. P., and Tognotti, L. in *Fundamental Issues in Control of Carbon Gasification Reactivity* (J. Lahaye and P. Ehrburger, Eds.), Kluwer Academic Publishers, Dortrecht, 1991, p. 91.
6. Walker, P. L., Jr., Rusinkof, J. R., and Austin, L. G., *Adv. Catalysis*, 11:133 (1959).

7. Stanmore, B. R., Gilot, P., and Prado, G., *Thermochim. Acta* 240:79 (1994).
8. Marcuccilli, F., Ph.D. Thesis, Université de Haute Alsace, Mulhouse, France, 1993.
9. Satterfield, C. N., *Mass Transfer in Heterogeneous Catalysis*, MIT Press, Cambridge, MA, 1970, p. 59.
10. Gilot, P., Bonnefoy F., Marcuccilli, F., and Prado, G., *Combust. Flame* 95:87 (1993).
11. Miyamoto, N., Hou, Z., and Ogawa, H., "Catalytic Effects of Metallic Fuel Additives on Oxidation Characteristics of Trapped Diesel Soot," SAE Paper 881224, 1988.
12. Neoh, K. G., Howard, J. B., and Sarofim, A. F., *Twentieth Symposium (International) on Combustion*, The Combustion Institute, Pittsburgh, 1984, p. 951.
13. Ishiguro, T., Suzuki, N., Fujitani, Y., and Morimoto, H., *Combust. Flame* 85:1 (1991).
14. Suuberg, E. M. in *Fundamental Issues in Control of Carbon Gasification Reactivity* (J. Lahaye and P. Ehrburger, Eds.), Kluwer Academic Publishers, Dortrecht, 1991, p. 284.
15. Lahaye, J., and Prado, G., in *Particulate Carbon Formation During Combustion* (D. C. Siegla and G. W. Smith, Eds.), Plenum Publishing, New York, 1981, p. 33.

COMMENT

Kalyan Annamalai, Texas A&M University, USA. You have shown that CO oxidation is considerably increased in the presence of soot. This presumably is due to increased surface area offered by soot rather than due to direct CO_2 production. So if soot is oxidizing to CO, can this CO oxidize in gas phase providing heat release in gas phase? Is CO oxidation accounted for in your model? What is the product of oxidation of soot? Is it possible that you are oxidizing more CO at high temperature and reducing O_2 concentration in bed? Can the leveling off of rate with T be due to CO oxidation? Can there be recirculating flow in the corner of the crucible due to abrupt change in area of flow?

Author's Reply. We are sure that, in our experimental conditions and without any soot, there is no CO oxidation in the gas phase below 700 °C. At 800 °C, almost all the CO is oxidized.

In the presence of soot:

1. Below 700 °C, the CO_2/CO ratio is found to be unity during the entire oxidation process. As no CO gas phase oxidation is possible, CO and CO_2 are both considered as primary products of soot oxidation. Even if CO is oxidized on the surface of the soot particles, CO_2 is still considered as a primary product of soot oxidation.

2. Above 700 °C, there is no way to know, with our experimental setup, what the primary products of soot oxidation are, due to a possible gas phase oxidation. For that reason, the ratio has been arbitrarily kept at unity up to 800 °C.

The gas phase oxidation of CO is not accounted for in the model. The heat released by this oxidation does not seem to be significant since no temperature rise is detected by the thermocouple located above the soot surface during an isothermal oxidation at 800 °C when the oxidant mixture is introduced.

The gas phase oxidation of CO above 700 °C, over the soot bed, reduces the oxygen concentration available for soot oxidation. However, from estimations (See ref. 8 of the paper), the mean residence time of CO in the convective flow *over the soot* is small so that most of the CO oxidation occurs between the end of the crucible and the outlet section of the reactor. Then soot combustion is probably not significantly affected.

The oxygen mass transfer coupled to the real hydrodynamic flow around the crucible has been recently computed. The presence of the lips of the crucible, not accounted for in the present model, can affect the oxygen flux at the soot surface by roughly 15%. The complete modelling is proposed in Ref. 1.

REFERENCE

1. Gilot, P., Brillard, A., and Stanmore, B. R., "Geometric Effects on Mass Transfer during Thermogravimetric Analysis. Application to Diesel Soot Reactivity," *Combust. Flame,* submitted.

Twenty-Fifth Symposium (International) on Combustion/The Combustion Institute, 1994/pp. 627–634

SOOT FORMATION AT ELEVATED PRESSURES AND CARBON CONCENTRATIONS IN HYDROCARBON PYROLYSIS

ST. BAUERLE, Y. KARASEVICH, ST. SLAVOV, D. TANKE, M. TAPPE, TH. THIENEL AND H. GG. WAGNER
University of Göttingen
Tammannstrasse 6, Göttingen 37077, Germany

For the formation of soot in mixtures of ethylene, *n*-hexane, and benzene in argon behind reflected shock-wave induction periods, soot growth rate constants and soot yields were measured at various temperatures, pressures, and C-atom concentrations using light extinction techniques.

As expected, the three substances investigated behave differently regarding soot formation, the strongest difference being between aromatic and nonaromatic fuels. Induction times and soot growth rate constants do not show any significant pressure effect within the accuracy of the experiment under the conditions employed. The data for ethylene and *n*-hexane agree quantitatively fairly well, whereas benzene shows induction times that are shorter and rate constants that are larger by about an order of magnitude than those of the nonaromatics for equal C-atom concentrations.

The previously observed general shape and behaviour of the soot yield curves could be confirmed, with maximum soot yields, at temperatures between 1800 and 1950 K. For similar experimental conditions of temperature, pressure, and carbon concentration, the sooting propensity increases from *n*-hexane to ethylene to benzene. The large pressure range covered in this study revealed different pressure dependencies of soot formation for the three hydrocarbons investigated. For *n*-hexane, the influence of pressure on soot yield in pyrolysis is very small. For ethylene, soot yield scales with pressure, whereas for benzene, a different behaviour was found, resulting in lower soot yields at higher pressures at otherwise equal conditions. Soot yields are also depending on C-atom concentration. Particle diameters of soot from pyrolysis determined by electron microscopy can be described by a narrow log-normal size distribution, with $\sigma_g \approx 0.2$. The average particle diameters are 20–30 nm for all conditions of temperature, pressure, and C-atom concentration employed in this study. Assuming spherical particles, this leads to final number densities of 10^{11} to $10^{13}/cm^3$.

Introduction

In practical combustion devices, soot formation and oxidation depend on fuel type, mixture composition, pressure, and temperature (for reviews, see e.g. Refs. 1 through 5). One of the important technical parameters is the pressure at which combustion takes place. While stationary burners mostly operate close to atmospheric pressure, values above 100 bar may be reached in modern diesel engines. The shock-tube technique allows one to study soot formation under controlled conditions, at temperatures, pressures, and carbon concentrations similar to those in practical applications.

For a number of unsaturated hydrocarbons pyrolysis experiments in shock tubes have been performed below 10 bar [6–9]. These experiments show a rather typical dependence of soot formation on temperature, carbon density, and fuel structure. At higher pressures up to 250 bar, rates of soot formation in shock tubes have been measured at temperatures between 1700 and 2800 K for ethylene [10]. High-pressure shock-tube experiments on the pyrolysis of *n*-hexane have been performed by Hwang et al. [11].

Here, experiments are described about soot formation under similar pyrolytic conditions with ethylene, *n*-hexane, and benzene, performed behind reflected shock waves at temperatures between 1700 and 2300 K for pressures up to 100 bar and C-atom concentrations between $2 \cdot 10^{17}$ and $2 \cdot 10^{19}$ C atoms/cm^3. The measurements were especially performed in order to determine the influence of pressure on soot formation and seperate it from that of C-atom density.

Three different techniques have been used: (1) extinction measurements of a HeNe laser beam at 632.8 nm, (2) gas chromatography (GC) analysis of gaseous end products, and (3) analysis of soot samples by electron microscopy.

Quantities to characterize soot formation are the induction period of soot formation τ, the soot yield SY, the formal soot growth rate k_f, final particle diameters and number densities as functions of temperature, C-atom concentration, fuel structure, and especially pressure.

Experimental

The experimental setup has been described previously [11]; therefore, only a few details are given.

The experiments were performed behind reflected shock waves in a 70-mm i.d. steel shock tube with a 4.5-m-long driven section, a 3.5-m-long driver section, and a 28-mm-thick tube wall. Shock speed was measured with Kistler piezoelectric pressure transducers. Reflected shock parameters were calculated [12,13] using the measured incident shock speed. The typical shock wave attenuation was always less than 2%/m.

The conversion of hydrocarbon to soot was measured via the attenuation of the light beam from a 15-mW HeNe laser operated at $\lambda = 632.8$ nm. The light extinction profiles $I(t)$ were converted into soot volume fraction profiles $f_v(t)$ using Beer's law [6] and the refractive index given by Lee and Tien [14]. A sampling flask [15] allowed the taking of gas and soot samples simultaneously. The valve opened at about 5 ms after the reflected shock wave passed for about 10 ms. Directly afterwards, the gas samples were gas chromatographically analyzed on a GC (Packard Model 419) with 5-ft 60/80 mesh Carbosieve and 2-m 5 Å molecularsieve columns. The following substances were quantitatively determined: H_2, CH_4, C_2H_2, C_2H_4, and C_2H_6. Soot was collected on carbon film grids (mesh size 400) and on Al surfaces. Soot particle diameters were determined with transmission electron microscope (TEM) and raster electron microscope (REM).

The hydrocarbon/argon test gas mixtures were prepared manometrically and mixed by convection in stainless steel cylinders at least 48 h before use. The gases ethylene (>99.8% Linde) and Ar (>99.998% Messer-Griesheim) were used without further purification. Benzene (>99.7% Riedel-De Haen) and *n*-hexane (>97% Merck) were purified by distillation. Total densities behind reflected shock waves were varied from $3 \cdot 10^{-5}$ to $70 \cdot 10^{-5}$ mol/cm^3; C-atom concentrations were varied from $2 \cdot 10^{17}$ to $2 \cdot 10^{19}$ atoms/cm^3 in the temperature range 1700–2300 K.

Experimental Results

Figure 1 shows a typical soot concentration time profile for benzene pyrolysis together with the measured pressure. Clearly visible are the passage of the incident and reflected shock front. After a short induction period, the soot concentration increases strongly and tends towards a constant value that determines soot yield *SY*.

The absolute value of the induction period τ depends somewhat on the experimental technique used. However, the order of magnitude and the dependence on parameters like pressure, temperature, and C-atom concentration should be similar for different experimental techniques. Here, the induction time τ is defined as the intersection of the inflectional tangent with the time axis, as indicated in Fig. 1.

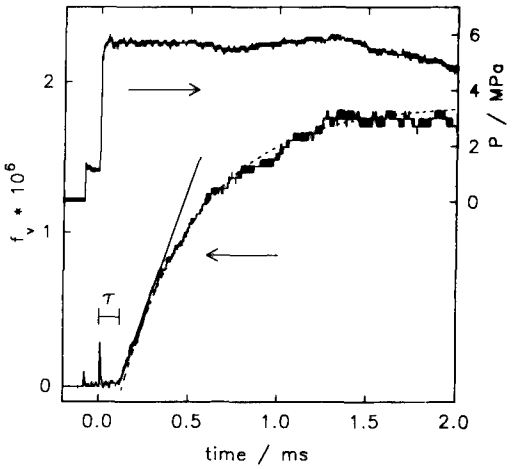

FIG. 1. Converted soot concentration profile and experimental pressure record for benzene pyrolysis: $T = 1890$ K, $P = 50$ bar, [C] $= 5 \cdot 10^{17}$/cm^3. Upper line: Pressure time profil; lower line: soot concentration time profil; dashed line: first-order fit ($k_f = 2200\ s^{-1}, f_{v\infty} = 1.85 \cdot 10^{-6}$). In both signals, the incident and reflected waves are clearly visible. The expansion wave arrives after about 1.7 ms. The induction time τ is defined as the intersection of the inflectional tangent with the time axis.

The plot shows the "smooth" start of soot formation that passes over into a fast growth region and slows down later on to reach a constant value of f_v, the final soot volume fraction $f_{v\infty}$.

The upper parts of the f_v profiles are approximated by an empirically obtained first-order rate law [10,16], where k_f is used as a measure for the rate of soot formation:

$$\frac{df_v}{dt} = k_f \cdot (f_{v\infty} - f_v). \tag{1}$$

The dashed line in Fig. 1 shows how the apparent first-order rate constant of soot mass growth k_f and the final soot volume fraction $f_{v\infty}$ were derived by a numerical fitting procedure. From the latter, soot yields were computed.

In general, the three substances investigated behave differently regarding soot formation under pyrolytic conditions. This will be discussed in the following for τ, k_f, average particle diameters d_∞, and *SY*.

Induction Time:

The influence of temperature, pressure, and C-atom concentration on the induction period τ was investigated. Figure 2 shows the influence of temperature for a fixed carbon density in an Arrhenius-type diagram. Plotted is log $(1/\tau)$ vs $1/T$ for benzene

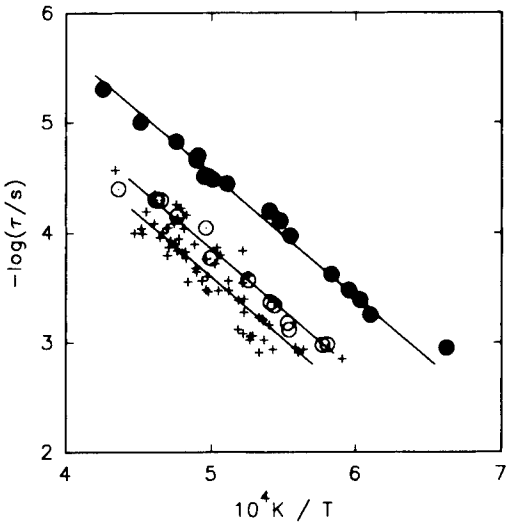

FIG. 2. Arrhenius-type plot of $\log(1/\tau)$ vs $1/T$ for the three hydocarbons investigated. ●: benzene, P = 50 bar, [C] = $2.5 \cdot 10^{18}/cm^3$; ○: ethylene, P = 50 bar, [C] = $2.5 \cdot 10^{18}/cm^3$; +: n-hexane, P = 20–100 bar, [C] = $3.2 \cdot 10^{18}/cm^3$; solid lines: best fits.

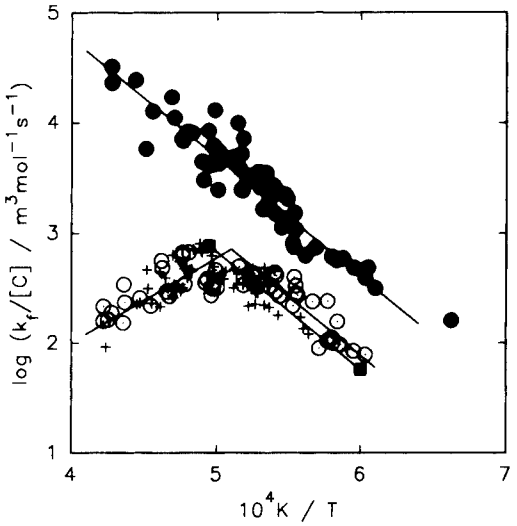

FIG. 3. Temperature dependence of the first-order rate k_f, normalized by the carbon concentration for the three hydrocarbons investigated. ●: benzene, P = 5–50 bar, [C] = 2.5 to $25 \cdot 10^{17}/cm^3$; ○: ethylene, P = 6–100 bar, [C] = 2.0 to $6 \cdot 10^{18}/cm^3$; +: n-hexane, P = 25–100 bar, [C] = $3.2 \cdot 10^{18}/cm^3$; ■: 10 bar C_2H_4/air flame [21].

(p = 50 bar, [C] = $2.5 \cdot 10^{18}/cm^3$), ethylene (p = 50 bar, [C] = $2.5 \cdot 10^{18}/cm^3$), and n-hexane (p = 25–100 bar, [C] = $3.2 \cdot 10^{18}/cm^3$). For the three hydrocarbons investigated, linear curves with similar activation energies of about 215 kJ/mol but different pre-exponential factors are obtained. As the curve for hexane shows, under the conditions employed, practically no pressure dependence of the induction period is observed, in agreement with earlier experiments [11]. The same holds for ethylene and benzene. Figure 2 shows that as temperature increases, τ decreases. For a given temperature and C-atom concentration, the beginning of soot formation for benzene pyrolysis is about an order of magnitude faster than for ethylene and hexane pyrolysis.

In general, as the C-atom concentration increases, the induction period decreases. For benzene, the C-atom concentration has been varied by two orders of magnitude, between 2 and $250 \cdot 10^{17}$ C atoms/cm^3, and a strong dependence on carbon concentration is observed. The data fall onto one curve if normalized by C-atom concentration. The curve can be expressed by

$$1/\tau = [C]^n \cdot A \cdot \exp(-E_{Ind}/RT). \qquad (2)$$

For benzene, the following parameters are obtained for carbon densities between 0.4 and $40 \cdot 10^{-6}$ mol/cm^3: $n = 0.75$, $A = 3.2 \cdot 10^{15}$ (cm^3/mol)$^{0.75}$ s^{-1}, and E_{Ind} = 260 kJ/mol. Induction times from the benzene experiments of Graham [6] fit fairly well in this representation.

For ethylene C-atom concentrations of $3–14 \cdot 10^{-6}$ mol/cm^3 were employed, and only a weak dependence is observed. For hexane, carbon densities were varied between 5 and $40 \cdot 10^{-6}$ mol/cm^3, and hardly any dependence of τ on C-atom concentration was found.

First-Order Rate Constant:

As described above, apparent first-order rate constants k_f were derived from the latter part of the experimental f_v curves by a fitting procedure. In this context, k_f has been interpreted [16,18–20] as an effective measure of the "active lifetime" of soot particles, assuming that they are loosing their reactivity. The influence of temperature on k_f is shown in Fig. 3 in the form of an Arrhenius diagram. The rate constants can be rather well represented when they are normalized by the carbon concentrations. The pressure was varied between 5 and 100 bar, and no influence of pressure was observed on k_f/[C] for the three hydrocarbons investigated for the temperatures and carbon-atom concentrations employed in this study. For ethylene and n-hexane, the data can be represented by a single curve showing a maximum at a temperature of about 2000 K. For benzene, no maximum is observed in the temperature range covered. For a given temperature ≤2000 K and C-atom concentration, benzene has an up to 10 times higher rate constant k_f than ethylene and n-hexane. The apparent activation energies for the three hydrocarbons for

the temperature range 1600–2000 K again are very similar, with a value for E_{kf} of about 200 kJ/mol. Data from 10-bar ethylene/air premixed flames [21], normalized by an "effective" carbon concentration (discussed below), are also shown for this temperature range, and they are very similar to the ethylene/*n*-hexane shock-tube pyrolysis data.

Particle Size REM/TEM:

Soot samples were obtained from *n*-hexane and benzene pyrolysis. Samples were taken under all conditions employed in the optical measurements, at temperatures between 1700 and 2300 K, pressures between 25 and 100 bar, and C-atom concentrations in the range from 2 to $200 \cdot 10^{17}/cm^3$. The soot probes collected were examined by means of REM and TEM. The primary particles, approximated as spheres, are arranged in agglomerates. Only the diameters of clearly identifiable particles are determined. The results from REM (where the gold coating has to be taken into account) and TEM electron microscopy agree fairly well. The visual impression of the micrographs obtained from different experiments is identical. The diameters of primary spherical particles can be described by a log-normal size distribution with a geometric standard deviation σ_g of approximately 0.2. The way the soot samples were taken may slightly influence the size distribution present in the shock tube. The evaluations show that average soot particle diameters are in the range of 20–30 nm. These data indicate that in shock-tube pyrolysis, under the conditions applied here, C-atom concentration and pressure do not exhibit a marked influence on particle diameters.

Soot Yield:

Soot yield is defined as carbon present as soot referred to total carbon content. Carbon present as soot was calculated using the soot volume fraction $f_{v\infty}$ [see Eq. (1)] and a soot density of $\rho_{soot} = 1.86$ g/cm^3. In Fig. 4a, soot yield curves for ethylene, *n*-hexane, and benzene as a function of temperature for similar C-atom concentration and a pressure of $P \approx 50$ bar are given. Additionally for *n*-hexane, the soot yield curves obtained at 25 and 100 bar coincides with the 50-bar soot yield curve. So, a single curve fits all *n*-hexane soot yield data. The soot yield curves show the bell shape observed by Graham et al. [6] and Frenklach et al. [8] for near-atmospheric pressure and by Hwang et al. [11] for high pressures. There is a pronounced maximum of soot yield with temperature, for ethylene near 1850 K, for *n*-hexane around 1950 K, and for benzene at about 1800 K. For a given C-atom concentration, benzene shows a much higher propensity to soot than ethylene and *n*-hexane. Only a slight dependence of the maximum temperature $T_{SY,max}$ on C-atom concentration is observed.

Gaseous end products of shock-tube pyrolysis were sampled and analyzed by GC. Measurements were made for various temperatures at a pressure of 50 bar for concentrations of 7.5 and $200 \cdot 10^{17}$ C atoms/cm^3 for benzene, and for ethylene and *n*-hexane at concentrations of $35 \cdot 10^{17}$ C atoms/cm^3. Quantitatively analyzed were H_2, CH_4, C_2H_2, C_2H_4, and C_2H_6. By the use of a reference substance in the shocked gas, concentrations could be determined with an accuracy of about 10%. Concentrations were measured absolutely, and yields were referred to the total carbon concentrations employed. The GC and optical measurements were independent of each other, but the mass balances for C and H atoms for the different experiments fit fairly well, confirming the refractive index used [14]. The main hydrocarbons found were C_2H_2 and CH_4.

Quantitative yields of these gas products for a temperature of 1900 K and C-atom concentration of $\approx 3 \cdot 10^{18}/cm^3$ were calculated. The final acetylene (methan) yield found was 45% (3%) for *n*-hexane pyrolysis, 40% (1%) for ethylene pyrolysis, and 30% (less than 1%) for benzene pyrolysis.

For the three hydrocarbons investigated, the C_2H_2 concentrations show a pronounced minimum at the temperature where the soot yields exhibit a maximum. For benzene, e.g., at the maximum temperature $T_{SY,max} = 1800$ K, about 20% of carbon was converted to gaseous end products. This is consistent with a soot yield of 80% found for this condition. In general, for the temperature region 1800–2300 K, the amount of carbon found in the gas phase as percentage of total carbon concentration is complementary to the soot yield curves, for all conditions employed.

The influence of pressure on soot yield is different for the three hydrocarbons investigated. Hardly any pressure dependence is observed for *n*-hexane at pressures between 20 and 100 bar. Only a slight shift of the curve towards higher temperatures for lower pressures can be noticed [11]. For ethylene, the soot yield data as a function of pressure and temperature for similar C-atom concentrations are plotted in Fig. 4b. There is an increase in soot yield from about 45% at 25 bar to 90% at 100 bar. The data show that ethylene soot yield *SY* is proportional to P_{tot}; this trend holds down to pressures of about 6 bar [15]. Tanke [15] also reports a strong dependence of soot yield on C-atom concentration.

For benzene, data for pressures of 5 and 50 bar and different C-atom concentrations are shown in Fig. 4c. The curves represent best fits, and practically the same curve is found for the data symbolized by × and △. Data below 1700 K are not shown as induction periods become too long. The × and ◇ denote soot yields for similar C-atom concentrations at pressures of 5 and 50 bar. The 5 bar data are taken

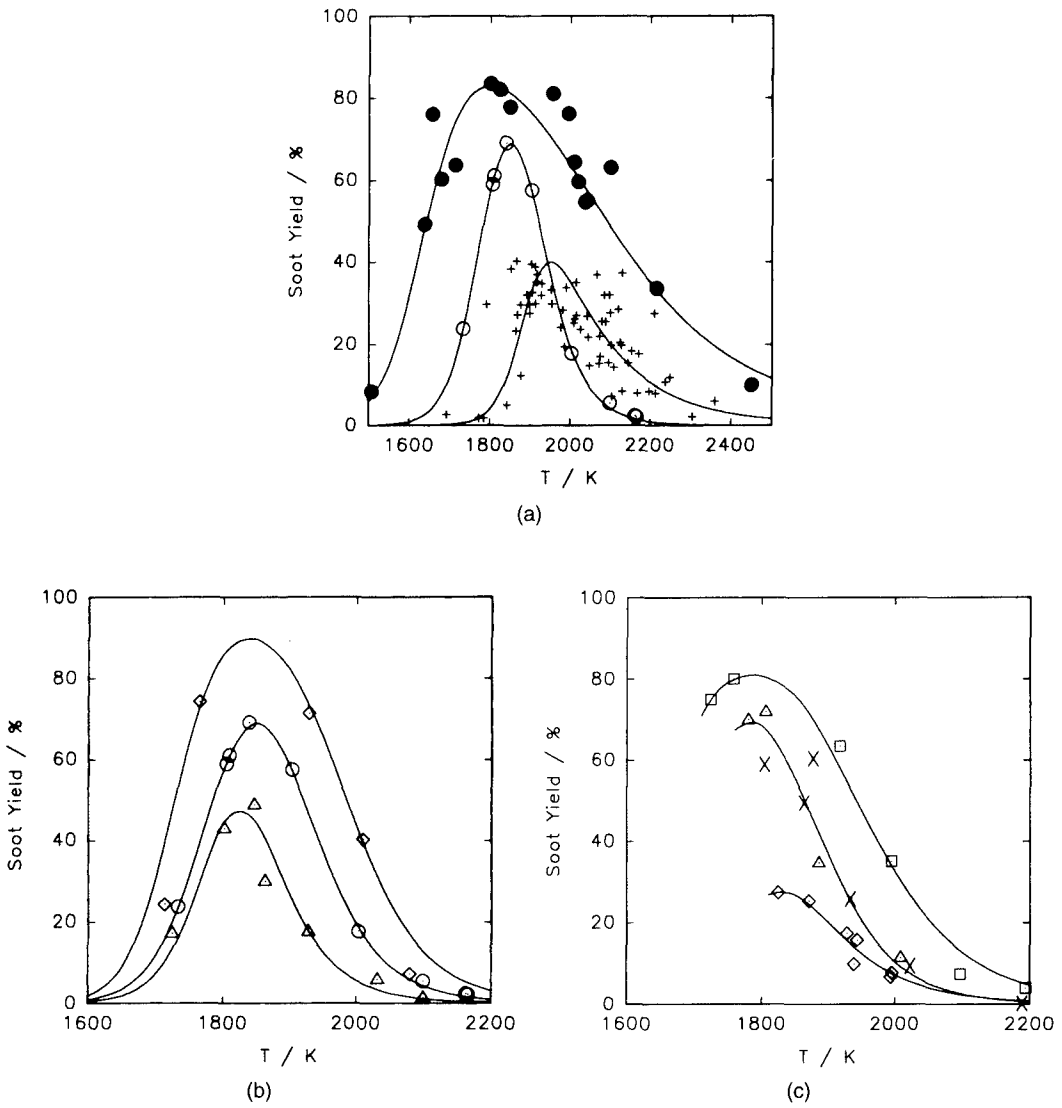

FIG. 4. (a) Plot of soot yield SY vs T for the three hydrocarbons investigated. ●: benzene, $P = 50$ bar, $[C] = 2.5 \cdot 10^{18}/cm^3$; ○: ethylene, $P = 50$ bar, $[C] = 2.5 \cdot 10^{18}/cm^3$; +: n-hexane, $P = 20$–100 bar, $[C] = 3.2 \cdot 10^{18}/cm^3$; solid lines: best fits. (b) Plot of soot yield SY vs T for ethylene pyrolysis at three different pressures, for a constant carbon concentration $[C] = 2.5 \cdot 10^{18}/cm^3$. △ triangle up: $P = 25$ bar; ○: $P = 50$ bar; ◇: $P = 100$ bar; solid lines: best fits. (c) Plot of soot yield SY vs T for benzene pyrolysis at different pressures and carbon concentrations. ◇: $P = 50$ bar, $[C] = 2.5 \cdot 10^{17}/cm^3$; △: $P = 50$ bar, $[C] = 5.0 \cdot 10^{17}/cm^3$; □: $P = 50$ bar, $[C] = 7.5 \cdot 10^{17}/cm^3$; ×: $P = 5$ bar, $[C] = 2.5 \cdot 10^{17}/cm^3$; solid lines: best fits.

under similar conditions as those of Graham et al. [6], and the observed dependence of soot yield with temperature is in accordance with his results. Furthermore, Fig. 4c shows a decrease in soot yield from low pressure (5 bar) to high pressure (50 bar) at equal carbon concentrations. This differs from the pressure dependence observed for ethylene.

The data represented by open symbols shows the influence of carbon concentration. Soot yield curves for benzene pyrolysis at a pressure of 50 bar for benzene fractions of 200, 400, and 600 ppm are plotted, showing an increase in soot yield with increasing carbon concentration for a given temperature and pressure.

Combining all the data demonstrates the dependence of soot yield on pressure and C-atom concen-

tration. The soot yield indicated by the middle curve can be achieved either by a pressure of 5 bar and a carbon concentration of $2.5 \cdot 10^{17}$ atoms/cm^3 ($\times$) or by a pressure of 50 bar and a carbon concentration of 5.0×10^{17} atoms/cm^3 ($\triangle$). For a given carbon concentration ($2.5 \cdot 10^{17}$ atoms/cm^3), an increase in pressure by an order of magnitude, from 5 to 50 bar ($\times$ and $\diamond$), results in only half the soot yield.

Discussion

For the three hydrocarbons, ethylene, *n*-hexane, and benzene, soot formation behind refleceted shock waves has been investigated in order to check the influence of pressure on soot formation in pyrolysis. Optical measurements have been performed to determine soot yields, and gas samples have been analyzed to obtain information about gaseous growth species. Soot samples were examined by electron microscopy to measure average particle diameters.

In general, the three substances investigated behave differently regarding soot formation, the strongest difference being between aromatic and nonaromatic fuels. No pressure dependence of the induction times and of the formal rates of soot growth, normalized by carbon concentration, was found. The data for ethylene and *n*-hexane agree quantitatively fairly well, whereas benzene shows induction times that are shorter and rate constants that are larger by about an order of magnitude than those of the nonaromatics for equal C-atom concentrations.

A main part of that difference is due to processes in the pyrolysis of the different hydrocarbons. For *n*-hexane, very early in the reaction methane is formed, which is not readily available for the formation of higher hydrocarbons. For soot formation from alkanes and alkenes, first acetylene has to be formed from which later polycyclic aromatics result. That works more readily from ethylene than from *n*-hexane so that also the formation of polycyclic aromatics, especially towards higher pressures, is favoured, as can be seen from the increase of the soot yield of ethylene with pressure. It is to be expected that the number density of initially formed soot particles is higher for ethylene than for *n*-hexane and still higher for benzene. During benzene pyrolysis, acetylenes and polycyclic aromatics are formed, which favours soot growth in any phase.

As described above, the results of the gas analysis show a complementary behaviour of the gaseous end product curves to the soot yield curves. The main hydrocarbons found are CH_4 and C_2H_2, and the concentrations of the latter are much higher than in comparable high-pressure flat flames. The argument made for high-pressure flat flames that soot growth stops because of lack of gaseous growth species seems, therefore, not to be valid for shock-tube conditions.

For *n*-hexane, the derived soot yield curves are very similar at different pressures, and soot yields are low compared to benzene. If one compares the soot yields of hexane and ethylene, the experiments with ethylene at 25 bar gives similar amounts of soot as hexane at all pressures used here. The soot yield in experiments with ethylene is pressure dependent, and at higher pressures, it is higher than that in hexane pyrolysis. The ethylene pyrolysis at 100 bar results in similar soot yields as benzene pyrolysis at 50 bar.

Frenklach et al. [8] reported a pressure effect in toluene pyrolysis. The maximum of the soot yield curve is shifted 300 K in temperature and without changing the value of this maximum. Our results for benzene pyrolysis show a decrease in soot yield with increasing pressure in the range of 5 bar to 50 bar at lower C-atom concentration ($[C] \approx 2 \cdot 10^{17}$/cm^3), but no temperature shift of the soot yield curve has been observed.

The term k_f depends on total carbon concentration, as can be seen in Fig. 3. In premixed flames, most of the initial carbon is oxidized to CO and CO_2. An estimation of carbon still available for soot formation behind the oxidation zone can be made from gas analysis results. Here, too, the main hydrocarbons found are C_2H_2 and CH_4 [21]. The latter is mainly formed in the oxidation zone and is known to play only a minor role in soot formation. An "effective" carbon concentration can, therefore, be calculated as $[C]_{eff} = [C]_{tot} - [CO_2] - [CO] - [CH_4]$, with values of $2 \cdot 10^{17}$ to $8 \cdot 10^{17}$ C atoms/cm^3, about the same order of magnitude as in shock-tube pyrolysis. In Fig. 3, the soot growth rate constants k_f, normalized by carbon density, for soot formation from ethylene under shock-tube and flat-flame conditions are plotted. For the shock-tube data, the total C-atom concentration has been used; for the flat-flame data, an "effective" carbon concentration was calculated in the manner described above. The data for pyrolysis and the flat flame are very similar, indicating that the different chemical environments have little influence on k_f.

Using the optically determined final soot volume fraction and the here-obtained average particle diameters of 20–30 nm, final particle number densities can be calculated, assuming $N = f_v/\bar{v}$ ($\bar{v}$ = mean particle volume) and spherical particles. For an average diameter of 25 nm, $\bar{v}$ is approximately 10^{-17} cm^3. For the 50-bar benzene experiments with a carbon density of $2 \cdot 10^{17}$/cm^3, an $f_{v\infty}$ value of $5 \cdot 10^{-7}$ was found, which gives an N_∞ of $5 \cdot 10^{10}$/cm^3. For the experiments with a carbon density larger by two orders of magnitude, similar diameters, but larger soot volume fractions of about $f_{v\infty} \approx 10^{-4}$, were determined, giving an N_∞ of 10^{13}/cm^3. For atmospheric pressure premixed flames, number densities of 10^9 to 10^{10}/cm^3 are typically found [2], whereas for 70-

bar premixed ethylene-air flames, a number density of $10^{12}/cm^3$ was obtained [22].

The primary particles are formed by surface growth and coagulation. The latter process can be described by the Smoluchowski equation:

$$\frac{dN}{dt} = -k_{coag} \cdot [N]^2 \qquad (3)$$
$$\tau_{coag} = (k_{coag,theo} \cdot N_\infty)^{-1}$$

which leads to a characteristic half-life of coagulation τ_{coag} of the particles. Using the particle diameters determined by electron microscopy, Knudsen numbers can been calculated for the investigated temperatures and pressures. They are of the order of 0.1 to 1, and therefore, our experimental conditions are in the transition region from the slip flow regime to continuum [23]. In this region, calculated theoretical values of the coagulation rate constant are of the order of $5 \cdot 10^{-10}$ cm^3/s. For the benzene experiments with low-carbon densities, a final particle number density, $N_\infty = 5 \cdot 10^{10}/cm^3$, results in a half-life of 40 ms. This is too long to see coagulation in our experiments. For the high-carbon densities employed, $N_\infty = 10^{13}/cm^3$, giving coagulation half-lifes of only 0.2 ms, well within the observation timescale of the shock-tube measurements. Therefore, one would expect different final particle diameters, depending on the characteristic times for coagulation, or rather stable agglomerates.

Conclusion

The difference in behaviour regarding soot formation between aromatic and nonaromatic fuels could be confirmed in this study for high pressures and carbon concentrations. *n*-hexane shows only low soot yields, even at high pressure, with small k_f values and long induction times. Benzene shows the highest propensity to soot, with short induction times, large k_f values, and a slight decrease in soot yield from low to medium pressure. Ethylene behaves basically like a nonaromatic fuel, with values for τ and k_f similar to hexane. But with increasing pressure, increasing soot yields are found, indicating a change in behaviour towards aromatic fuels. Despite these differences between the fuels, average particle diameters, obtained by electron microscopy of soot samples, are very similar under all experimental conditions employed. The data can be described by a narrow lognormal size distribution, with average diameters of 20–30 nm. The different amounts of soot are, therefore, essentially determined by number densities. Furthermore, the results show that at higher pressures, the "meet and stick" coagulation model cannot be applied any more. The gas analysis shows that a lack of acetylene cannot be responsible for the end of coagulation and soot growth, as observed in high-pressure ethylene-air flames.

REFERENCES

1. Wagner, H. Gg., *Seventeenth Symposium (International) on Combustion,* The Combustion Institute, Pittsburgh, 1979, p. 3.
2. Haynes, B. S., and Wagner, H. Gg., *Prog. Energy Combust. Sci.* 7:229 (1981).
3. Lahaye, J., and Prado, G., *Soot in Combustion Systems and its Toxic Properties,* Plenum Press, New York, 1983.
4. Wagner, H. Gg., AGARD Report No. 422, Nato, 1988, p. 24–1.
5. Glassman, I., *Twenty-Second Symposium (International) on Combustion,* The Combustion Institute, Pittsburgh, 1988, p. 295.
6. Graham, S. C., Homer, J. B., and Rosenfeld, J. L., *Proc. R. Soc. London* A 344:259 (1975).
7. Wang, T. S., Matula, R. A., and Farmer, R. C., *Eighteenth Symposium (International) on Combustion,* The Combustion Institute, Pittsburgh, 1981, p. 1149.
8. Frenklach, M., Taki, S., and Matula, R. A., *Combust. Flame* 49:275 (1983); Frenklach, M., Taki, S., Durgaprasad, M. B., and Matula, R. A., *ibid.* 54:81 (1983); Frenklach, M., Ramachandra, M. K., and Matula, R. A., *Twentieth Symposium (International) on Combustion,* The Combustion Institute, Pittsburgh, 1984, p. 871.
9. Simmons, B., and Williams, A., *Combust. Flame* 71:219 (1988).
10. Geck, C. C., Diploma Thesis, Universität Göttingen, Göttingen, Germany, 1975.
11. Hwang, S. M., Vlasov, P., Wagner, H. Gg., and Wolff, Th., *Z. Phys. Chem. Neue Folge* 137:129 (1991).
12. Greene, E. F., and Toennies, J.P., *Chemische Reaktionen in Stoßwellen* (Translated by H. Gg. Wagner), Dr. Dietrich Steinkopff Verlag, Darmstadt, 1959.
13. Gardiner, W. C., Jr., Walker, B. F., and Wakefield, C. B., in *Shock Waves in Chemistry* (A. Lifshitz, Ed.), Marcel Dekker, New York, 1981.
14. Lee, S. C., and Tien, C. L., *Eighteenth Symposium (International) on Combustion,* The Combustion Institute, Pittsburgh, 1981, p. 1159.
15. Tanke, D., Ph.D. Thesis, Universität Göttingen, Göttingen, Germany, 1994.
16. Haynes, B. S., and Wagner, H. Gg., *Z. Phys. Chem. Neue Folge* 133:201 (1983).
17. Wagner, H. Gg., "Mass Growth of Soot," in *Soot in Combustion Systems and its Toxic Properties* (J. Lahaye, and G. Prado, Eds.), Plenum Press, New York, 1983.
18. Mätzing, H., and Wagner, H. Gg., *Twenty-First Symposium (International) on Combustion,* The Combustion Institute, Pittsburgh, 1986, p. 1047.

19. Böhm, H., Hesse, D., Jander, H., Lüers, B., Pietscher, J., Wagner, H. Gg., and Weiss, M., *Twenty-Second Symposium (International) on Combustion*, The Combustion Institute, Pittsburgh, 1988, p. 403.
20. Bönig, M., Feldermann, Chr., Jander, H., Lers, B., Rudolph, G., and Wagner, H. Gg., *Twenty-Third Symposium (International) on Combustion*, The Combustion Institute, Pittsburgh, 1990, p. 1581.
21. Feldermann, Ch. J., Ph.D. Thesis, Universität Göttingen, Göttingen, Germany, 1992.
22. Böhm, H., Feldermann, Chr., Heidermann, Th., Jander, H., Lüers, B., and Wagner, H. Gg., *Twenty-Fourth Symposium (International) on Combustion*, The Combustion Institute, Pittsburgh, 1992, p. 991.
23. Hidy, G. M., and Brock, J. R., *The Dynamics of Aerocolloidal Systems*, Pergamon Press, New York,1979.

COMMENTS

Esko I. Kauppinen, VTT Aerosol Technology Group, Finland. I did not get in detail how you sampled particles from the shock tube for analysis in the TEM. How much could you change the structure of agglomerates during the sampling when you reduce the pressure to ambient conditions? It is known that loose agglomerates may break up by flow-induced shear forces. This relates to the conclusion that the sticking coefficient approaches zero at high carbon concentrations.

Author's Reply. The EM samples have been obtained from the shock tube end plate, collected on TEM grids, respectively aluminum plates mounted at the wall of the sampling valve, in the sampling flow and in the sampling flask. The diameters of the spherical particles analyzed by TEM and SEM did not differ markedly for the different collecting methods. The agglomerate sizes were different but did not change towards longer residence times anymore (small effective sticking coefficient).

•

Ömer L. Gülder, National Research Council of Canada, Canada. Your benzene pyrolysis results show a decrease in soot yield with increasing pressure, from 5 to 50 bar, at a given C-atom concentration, in contrast to the behaviour of ethylene and *n*-hexane. Do you have any explanation for the observed behaviour of benzene, and do you expect similar results for other aromatic hydrocarbons?

V. Knorre, Moscow Automobile and Road Construction, Technical University, Russia. 1. Will you comment on the mechanism of soot formation suppression in the case of *n*-hexane and why this mechanism does not work in the case for example of ethylene?

2. What is the mechanism of the decrease in sticking coefficient?

3. Please comment on the minimum in the curve for benzene.

Author's Reply. At present, we relate the different soot yields of benzene, ethylene, and *n*-hexane for different pressures mainly to the different concentrations of PAH and acetylenes at the very beginning of soot particle formation. The formation of acetylenes and PAH is more complicated for *n*-hexane than for C_2H_4. Towards high pressures, the C_2H_4 and the C_6H_6 soot yields become similar, and it could be that the yield for *n*-hexane will also rise towards high pressures. At low pressure, soot formation in benzene proceeds in a way different from that in C_2H_4 as a result of the "early availability of bigger building bricks." Towards elevated pressure, the concentration of small radicals, which are necessary for the formation of acetylenes and higher PAH and initial soot particles, decreases thus reducing benzene soot yield in a certain pressure range for low carbon atom densities. For carbon atom densities near and above 10^{18} cm^{-3}, the effect disappears. Measurements that should help to clarify the situation are underway.

The decrease of the sticking coefficients for larger particles seems to be due to the formation of carbon layers at the particle surface similar to carbon planes in graphite. The particles do not merge any more, and the "glue between the particles"—due to surface growth—becomes much less active so that the sticking is based on van-der-Waals forces.

•

P. A. Tesner, All Russian Scientific Research Institute, Russia. The interesting experimental results you obtained during shock tube pyrolysis are different from our results obtained from atmospheric pressure pyrolysis. Meanwhile, our experimental results are in good agreement with those obtained during flat flame combustion conducted at different pressures.

Twenty-Fifth Symposium (International) on Combustion/The Combustion Institute, 1994/pp. 635–643

THERMAL AND CHEMICAL INFLUENCES ON THE SOOT MASS GROWTH

M. BACHMANN, W. WIESE AND K. H. HOMANN
Institut für Physikalische Chemie
Technische Hochschule Darmstadt
Petersenstr. 20, D-64287 Darmstadt, Germany

Charged soot particles in the mass range between $2 \cdot 10^3$ and $3 \cdot 10^4$ u were analyzed by a Wien filter mass spectrometer. Several gases were injected into sooting premixed low-pressure flames. The results show that molecular oxygen does not oxidize young soot particles of the mass range studied. High intensities of the injection gas flow cause a high amount of PAH-ions. Under these conditions, more PAHs are formed than in undisturbed flames. Two flames could be stabilized simultaneously on a burner consisting of two sintered plates. The particle mass growth in these flames is due to surface growth. From the mass distributions at different distances from the burner, the mass growth rate constants could be estimated. These constants are proportional to the particles' surface area. Lean flames next to a sooting flame cause a lower amount of soot in the sooting flame. Flames with low temperatures decrease the mass growth rate. The changes in the growth rate constants can be explained by the different temperatures in the flames. Hydrogen/oxygen flames beside sooting flames cause a slower mass growth. The results show that high concentrations of H atoms do not increase the surface growth rate.

Introduction

Soot formation is sensitive to external influences. Such interactions are caused, for example, by a stream of gas into the flame, cooling by a solid body, seeding, etc., in contrast to intrinsic properties of premixed flames such as fuel, C/O, flow velocity, or burning pressure. The former effects have been described mostly qualitatively or through the change of the amount of soot [1–3]. In this paper, such an influence on the growth of the smallest soot particles is studied. In particular, the effect of a second flame, directly neighboring the sooting flame, is investigated. This has a certain bearing on turbulent diffusion flames, where sooting and nonsooting regions are temporarily close to each other. In the case of two adjacent flames, the interdiffusion of H atoms is of interest, since the models of the mechanism of soot formation stress the important role of H [4,5].

It is only for electrically charged species that the transition from molecular precursors to soot particles and their initial growth can be studied [6,7]. Therefore, the influences were examined for the charged species. The mass distributions of soot particles were analyzed using a Wien filter mass spectrometer [8]. Large precursor molecules, also in their ionized form, could be detected with a time-of-flight mass spectrometer (TOF-MS). Previous experiments with charged soot particles and comparison of charged and uncharged polycyclic aromatic hydrocarbons [9] show that there is no principal difference in the chemical behavior of large charged and neutral species.

We used flames that have already been characterized by previous workers to a certain degree, but we have to accept some undefined conditions caused by the injection and the neighboring flame. The purpose of this work is to study the response of the initial soot formation in its environment that cannot be evoked by changing the normal flame parameters and, thereby, to learn more about soot formation in general.

Experimental

Flame System:

Two different flame arrangements were used:

1. Different gases were injected into a standard premixed ethyne/oxygen flame stabilized on a vertically movable flat flame burner (75-mm diameter). The C/O ratio of this slightly sooting flame was 1.06, the velocity of the unburned gas v_u = 0.42 m/s, and the pressure p = 27 mbar.

   The gases were added perpendicularly to the flow direction through a quartz capillary with 1-mm inner diameter and a 2.5-mm outer diameter. The capillary was movable in vertical and horizontal directions. The flame was always probed along the burner axis.
2. Two flames could be stabilized simultaneously on a burner consisting of two sintered plates (70 × 50 mm) side by side, divided by a 2-mm strip. This two-flame burner is shown in Fig. 1. It enables

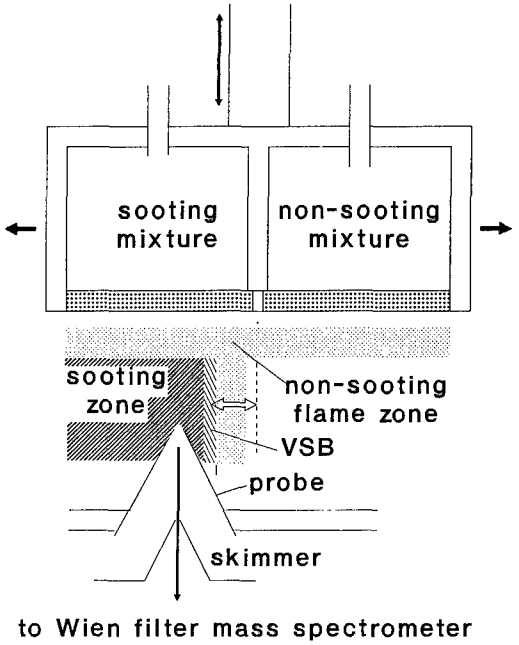

FIG. 1. The two-flame burner, which is vertically and horizontally movable to the probe. VSB: Vertical soot border area (**see later**).

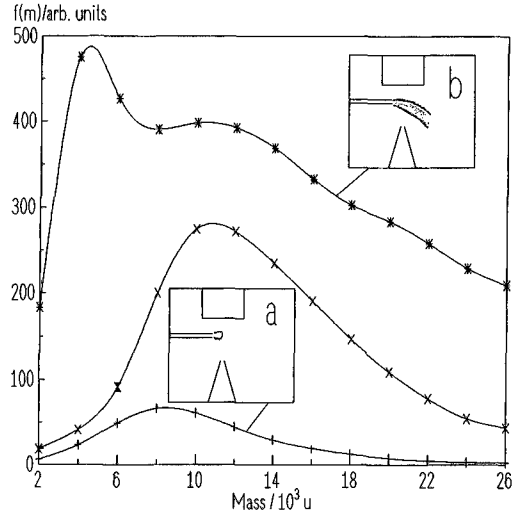

FIG. 2. Soot particle mass distributions at $h = 20$ mm. Injection of N_2 at $h = 9$ mm into a sooting ethyne/oxygen flame. Distance from the burner axis is 10 mm. ×: with capillary, no injection; +: $\dot{V}(N_2) = 0.25$ mL/s; *: $\dot{V}(N_2) = 0.5$ mL/s. Pictogram a: shape of the observed cloud at low-injection gas flows. Pictogram b: shape of the observed soot beam at high-injection gas flows.

the examination of the mutual influence of two different flat flames under low pressure, which was varied between 15 and 40 mbar. The burner was vertically and horizontally movable with respect to the position of the probe.

Analytical System:

The flames were probed by a conical quartz probe and the charged soot particles in the molecular beam were mass selected with a Wien filter mass spectrometer, which was described previously [8]. This instrument was developed for the determination of the mass distribution in the range from $2 \cdot 10^3$ to $3 \cdot 10^4$ u. Only results from positively charged particles will be reported.

Results and Discussion

Injection of Gases into the Sooting Flame:

Figure 2 shows the effect on the particle mass distribution, if nitrogen is injected sideways into the oxidation zone of the sooting flame. Low-injection flows up to about 0.25 mL/s (NTP) (normal temperature and pressure) cause lower mass distribution intensities and smaller mean masses. Around the point of injection, a small darker cloud is observed (pictogram a). From heat-transfer calculations, the temperature difference between the quartz capillary and the exiting gas flow was estimated to be only about 15 K for a flow of 0.25 mL/s. Therefore, the change in the mass distribution is attributed mainly to dilution, which lowers the concentration of ethyne in the soot formation zone.

The gas temperature at a larger injection gas flow (0.5 mL/s) is about 100 K lower than the temperature of the capillary. A yellow shining beam of soot can be seen along the injection flow (pictogram b), which means that the soot concentration becomes larger. In fact, the charged particle number density increases by more than a factor of 2, the mean mass is shifted toward larger values, and the half width of the distribution widens. The number density of the particles in the upper mass range increases more than that of the smaller particles. This higher amount of soot through this limited temperature decrease is in accordance with the results of Wagner and coworkers [3,10] who showed that the number density of soot particles increases with decreasing temperature.

At low masses ($4 \cdot 10^3$ u), a new maximum appears. Since these particles occupy the transition regime between molecules and solid particles, the sample beam was also analyzed with a reflectron TOF-MS of higher resolution [7]. The TOF mass spectrum without injection (Fig. 3a) shows that the particles up to a mass of about $3 \cdot 10^3$ u are not soot particles

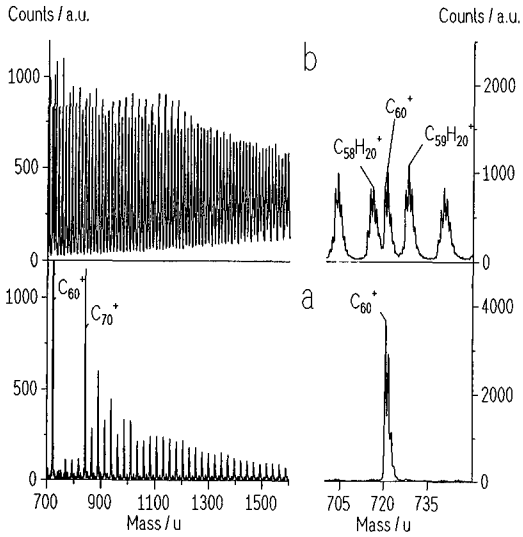

FIG. 3. Time-of-flight mass spectra of positively charged flame ions. The spectra are truncated at 1600 u for reasons of representation. Same conditions as in Fig. 2: (a) no injection flow and (b) at an injection flow of 0.5 mL/s N_2.

but fullerenes. However, with an injection flow of 0.5 mL/s (Fig. 3b), this mass range is occupied almost totally by large PAH ions. This can clearly be seen when the sprectrum is displayed with maximum resolution (Fig. 3, right-hand side). To discuss the difference in the mass distribution, the behavior of large PAH and soot in the undisturbed flame must be regarded [7]. Heavy PAH reach maximum concentration at about 10 mm. They grow to a mass of about $2.5 \cdot 10^3$ u and disappear rapidly through the formation of the first soot particles of about twice that mass. The further growth of the soot particles at low pressure mainly takes place by heterogeneous decomposition of hydrocarbons such as ethyne and butadiyne [8]. Of the PAH with masses up to about 400 u, only a small fraction survives the combined attack of oxidation, thermal decomposition, and addition reactions at the end of the oxidation zone. Their growth and increase in concentration in the burned gas (20 mm) is much slower than in the presoot zone.

The influence of a moderately cooling gas jet on the PAH reactions is that it inhibits thermal decomposition and oxidation, thereby causing a general increase in PAH concentration. The PAH are transported into the soot formation zone convectively with the jet. These larger PAH concentrations first provide higher number densities of very large PAH from which soot particles are formed. Second, they make possible PAH surface reactions to come into concurrence with those of ethyne and butadiyne, the concentrations of which are lowered by cooling [3]. This explains the strong increase both in large PAH and incipient soot particles as well as the increased soot particle mass growth, which should be diminished by cooling if only ethyne and polyynes decomposed at the soot surface [8].

In Figs. 4a and 4b the changes in the number density and most probable mass are compared if nitrogen, oxygen, or helium are injected at the beginning of the soot formation zone. The principal shape of the curves is similar for all three gases: At low-injection flows the number density and mean mass decrease, whereas both increase at larger flows. These general dependencies and the specific differences with the three gases confirm that dilution and cooling, having opposite effects, are important. Comparing the chemically inert nitrogen and helium, one notices that the latter dilutes and cools less, since it diffuses more rapidly and has the lower molar heat capacity.

In the case of oxygen injection, the minimum in the most probable mass is shifted slightly to higher flows in comparison to nitrogen. Since oxygen supports the combustion, the cooling effect is weaker. At a flow of 0.2 mL/s, the most probable mass is larger for oxygen injection, while the number density is the same as in the case of nitrogen. This means that the total amount of soot is higher if oxygen is injected. A possible reason is the weaker cooling effect of oxygen. From this observation, it must also be concluded that molecular oxygen is not an important oxidizing species for small soot particles. This result is in agreement with the behavior of larger soot particles, which are mainly oxidized by OH radicals [11,12].

The Two-Flame Burner:

The vertical soot border

On the two-flame burner, a sooting flame was stabilized beside a nonsooting flame. The soot-containing region is limited in two directions, as shown in Fig. 1: (1) perpendicular to the flow direction in a certain distance from the burner and (2) parallel to the flow direction toward the lean flame. This limiting line is called vertical soot border (VSB), which is the 1–2-mm thin region where the yellow luminosity decays to zero. The term l_{VSB} gives the distance between the plane of the strip that divides the sintered plate and the VSB (open arrow in Fig. 1).

The VSB is mostly located on the side of the sooting flame. In only two cases it was found on the side of the nonsooting flame. Table 1 gives the l_{VSB} values for several flames at 15, 27, and 40 mbar. For the 27 and 40 mbar sooting flames, the C/O (1.06) and v_u (42 cm/s) were kept constant. At 15 mbar, slightly different values (1.20 and 46 cm/s) were chosen for reasons of flame stability and for a comparable amount of soot.

With increasing pressure, the VSBs were shifted

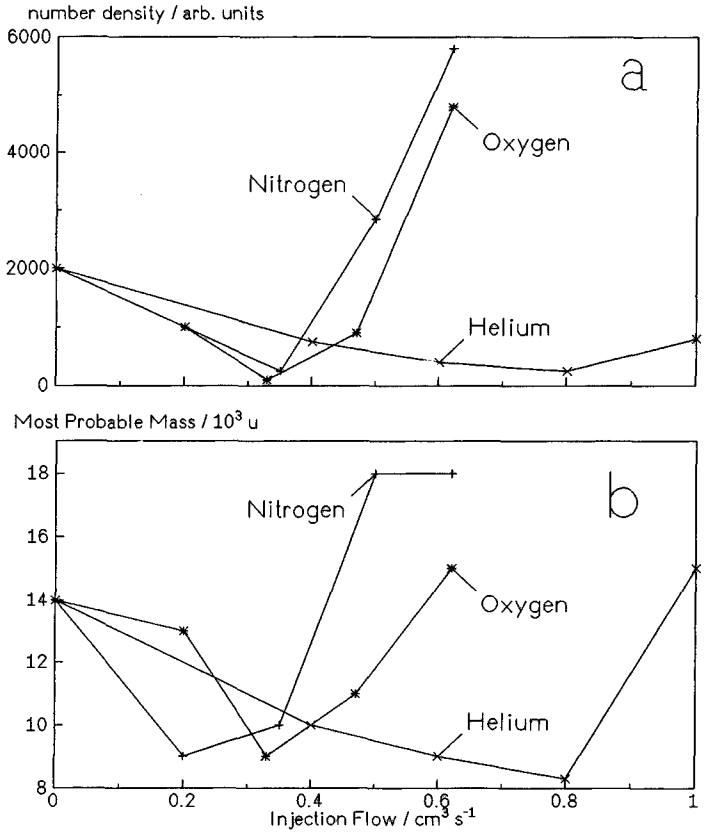

FIG. 4. Injection of gases at h = 13 mm. Values measured at h = 20 mm: (a) change of the number density with the injection flow and (b) Change of the most probable mass with the injection flow.

toward the middle of the two-flame burner. This is due to the decrease of diffusion, which causes a net transport of hydrocarbons from the fuel rich into the leaner flame and of oxidizing species in the opposite direction.

At all pressures, it is observed that raising the C/O in the nonsooting flame side leads to a shift of the VSB toward the right-hand side (Fig. 1). This is not unexpected because of the larger overall hydrocarbon concentration with increasing C/O.

An increase in the unburned gas velocity, which leads to a higher temperature on the leaner side, moves the VSB to the sooting side. This behavior is due to the larger extension of the leaner flame and the lower sooting tendency at higher temperatures.

Hydrogen/oxygen mixtures were also burned as nonsooting flames. At 27 and 40 mbar, a change from a stoichiometric to a 3:1 hydrogen/oxygen ratio does not lead to a shift in l_{VSB}. This is reasonable, because there is no change in the overall carbon concentration and the temperature. The influence of H atoms is discussed below.

Mass distributions were determined at different distances from the burner at the VSB and for comparison at a 10-mm distance from it toward the center of the sooting flame. At the VSB, the influence of the nonsooting flame is maximum; here, the total number density of charged soot particles decreases sharply. The measurements were carried out at the smallest distance from the nonsooting flame, where charged soot particles could be detected and the mass distribution could be properly determined. Measurements at 10 mm off the VSB show how the influence of the nonsooting flame decreases with the distance.

Figure 5 gives mass distributions at the VSB and at a 10-mm distance from it. At the VSB, the most probable mass increases from about $7.5 \cdot 10^3$ u at a 12-mm distance from the burner to $16 \cdot 10^3$ u at 16 mm (Fig. 5b). Nearer to the center of the sooting flame, the mass growth is faster and starts at lower distances from the burner (Fig. 5a). Here, the charged particle number density is roughly larger by a factor of 2 (see the different scalings).

Modelling of the particle surface growth

The mass growth of young soot particles in flat low-pressure flames up to a mass of about $3 \cdot 10^4$ u is dominated by surface growth, since the total number density is low [8,13]. For a very simple model, the reaction can be written as

$$P(m_i) + C_2H_2 \rightarrow P(m_{i+1}) + x\ H_2$$

TABLE 1
Results from the two-flame burner

	Flame conditions					Results		
No.	p (mbar)	C/O sooting	v_u/m s^{-1} sooting	C/O nonsooting	v_u/m s^{-1} nonsooting	l_{VSB}/mm	$\kappa \cdot$[A](VSB) arbitrary units	$\kappa \cdot$[A] (VSB + 10 mm) arbitrary units
1	15	1.2	46	0.4	25	20		
2				0.4	46	30		
3				0.8	46	10		
4	27	1.06	42	0.4	25	15	12	14
5				0.4	42	20	12	14
6				0.8	25	10[a]	2	2.5
7				0.8	42	5	9	12
8				H/O:2/1	42	20		
9				H/O:3/1	42	20		
10	40	1.06	42	0.4	25	8	11	13
11				0.4	42	10		
12				0.8	25	5[a]	3	3
13				0.8	42	0	12	13
14				H/O:2/1	42	10	7	13
15				H/O:3/1	42	10	4	10

[a]On the nonsooting side of the burner. The values $\kappa \cdot$[A] were obtained by modeling (see text).

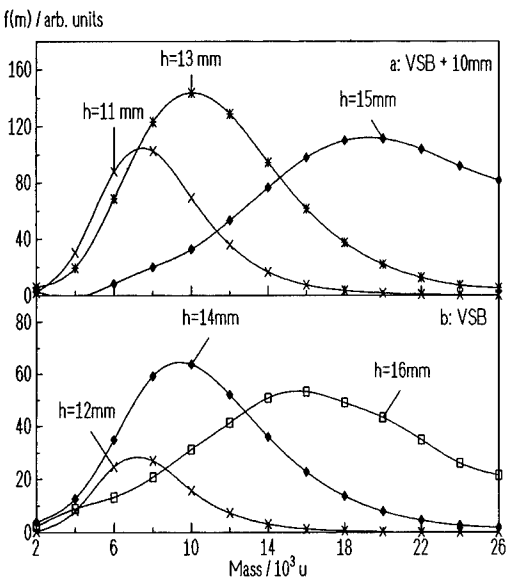

FIG. 5. Experimental mass distributions from the two-flame burner at different distances h from the burner, flame conditions: p = 40 mbar; sooting flame: C/O = 1.06, v_u = 0.42 m s^{-1}; nonsooting flame: C/O = 0.40, v_u = 0.25 m s^{-1}. (a) measured at a distance of 10 mm from the VSB in the sooting zone. (b) measured at the VSB.

A particle of the mass m_i reacts with ethyne to form a particle of the mass m_{i+1}. This is not meant as an elementary reaction, the loss of hydrogen is taken as an independent process. The growth rate is proportional to the surface area; that means, it is proportional to $m^{2/3}$, if the particles are spherical. In this case, the change of the mass distribution can be described by the following rate law [8]:

$$\begin{aligned} d(f(m_i))/dt &= -k_i \cdot [A] \cdot f(m_i) \\ &\quad + k_{i-1} \cdot [A] \cdot f(m_{i-1}) \\ &= -\kappa \cdot m_i^{2/3} \cdot [A] \cdot f(m_i) \\ &\quad + \kappa \cdot m_{i-1}^{2/3} \cdot [A] \cdot f(m_{i-1}) \end{aligned}$$

where $f(m_i)$ is the mass distribution function and k_i is the rate coefficient for a particle of the mass m_i. Here, i is chosen in a way that $m_i - m_{i-1}$ equals the mass of a C_2-unit (24 u); [A] is the concentration of ethyne; κ is a mass-independent growth rate constant. For $f(m)$ at $t = 0$, the first measured mass distribution is taken and its change is calculated by numerical solution of the rate law. The soot particles in this mass range only exist in a small range of distances from the burner (4–5 mm) in the soot formation zone where the temperature hardly changes. Therefore, the temperature was assumed to be con-

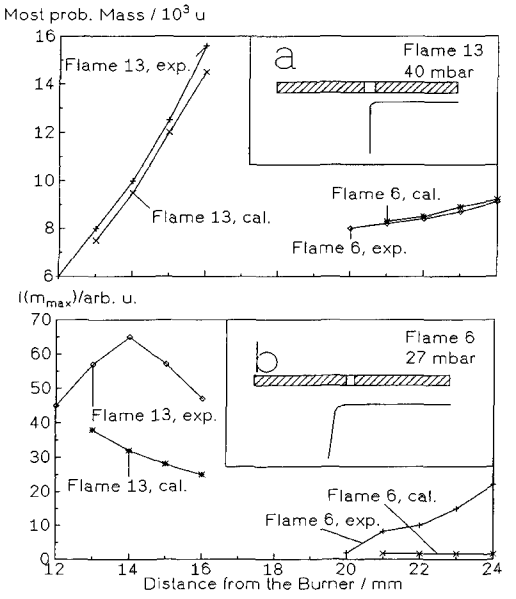

FIG. 6. Comparison of calculated and measured values in flames 6 and 13 at the VSB. (a) The most probable mass. The pictogram shows the shape of the VSB in flame 13. (b) The intensity of the most probable mass. The pictogram shows the shape of the VSB in flame 6.

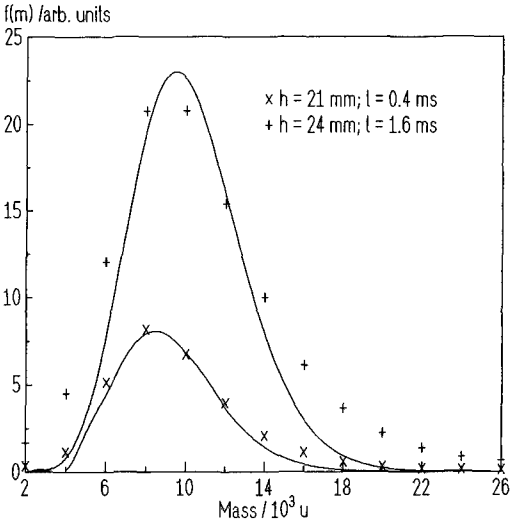

FIG. 7. Comparison of calculated and measured mass distributions from flame 6 at the VSB. The measured distributions are plotted with symbols, the calculated ones by lines.

stant. These calculated distributions were compared with the experimental distributions at the respective times. The model does not include a change of $f(m)$ by spontaneous ionization. Therefore, only the shape of the distributions and not its absolute height can be calculated. In the case of almost constant number densities, as in butadiene flames [8], the particle growth is well described by this model. The values of $\kappa \cdot [A]$ are listed in Table 1 together with l_{VSB} values. They are given for the VSB and for 10 mm in the sooting zone.

Figs. 6a and 6b compare the measured and the computed values of the most probable mass and the intensity of the most probable mass at the VSB for two different flame combinations. It can be seen that the increase of the most probable mass is described very well (Fig. 6a). In the flames on the two-flame burner, the number density changes strongly with the distance from the burner, particularly in flame No. 6. The pictograms show the shapes of the two VSBs. In flame No. 13, at a pressure of 40 mbar, the VSB is nearly perpendicular to the burner surface, so that the intensity hardly changes. The VSB in flame No. 6 is not completely perpendicular to the burner surface. Therefore, the place of measurement moves into the sooting region with increasing distance from the burner, which causes the increase of the measured number density.

Figure 7 shows the measured distributions together with the calculated distributions for flame No. 6 at the VSB. In this case, there is the greatest difference between the measured and the calculated intensity of the most probable mass. For comparison, the distributions were normalized to the measured ones. The distributions at $t = 0.4$ ms are in very good accordance. The differences in the shape of the distribution increase with time. But it can be seen that the model describes well the change of the most probable mass, although the change in the number density is neglected.

From $\kappa \cdot [A]$, a rate constant for the reaction of a soot particle of a specific mass with ethyne can be calculated. For a soot particle with a mass of $1 \cdot 10^4$ u and a mole fraction $x(C_2H_2) = 0.08$ [3], at a flame temperature of 2000 K, a rate constant of $k = 1.4 \cdot 10^{13}$ cm^3 mol^{-1} s^{-1} is calculated for $\kappa \cdot [A] = 10$. These values lead to a reaction probability of $2 \cdot 10^{-3}$. The rate constant for the surface growth in low-pressure butadiene flames was determined to $2 \cdot 10^{12}$ cm^3 mol^{-1} s^{-1} [8]. This value is lower by a factor of about 5 in comparison to the value in ethyne flames, although the temperature in butadiene flames is higher. This result shows that k is not only dependent on the temperature, but also on the surface properties of the soot particles formed from different fuels.

The values for the surface growth rate given by Roth and Hospital [6] who analyzed small charged soot particles under very similar conditions are in good accordance to the values found in this work.

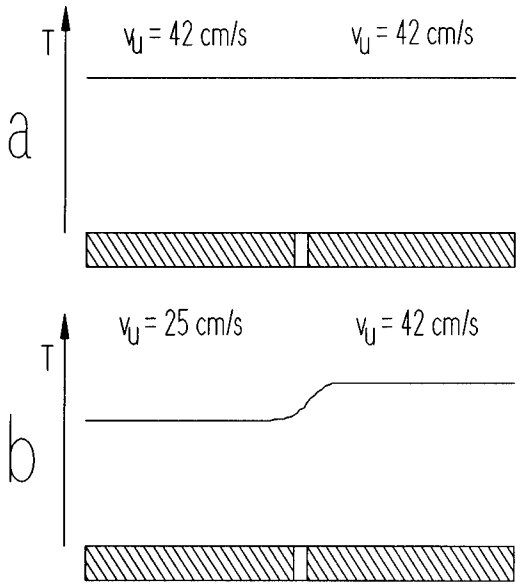

FIG. 8. Schematic temperature profiles on the two-flame burner. (a) Both flames have the same v_u. (b) The flames have a different v_u.

Sooting and leaner ethyne/oxygen flames on the two-flame burner

Since the simple model is suitable to describe the increase of the most probable mass with distance from the burner, the quantity $\kappa \cdot [A]$ is taken as a measure of the influence of the second flame on the soot mass growth. In the neighboring flame, two values of the C/O (0.4 = stoichiometric mixture; 0.8 = fuel rich but nonsooting) and of the unburned gas velocity v_u (25 and 42 cm/s) were applied (see Table 1). Flames with a larger v_u have a higher maximum temperature, while an increase in C/O means larger concentrations of unsaturated hydrocarbons such as C_2H_2 and C_4H_2 in the burned gas.

If v_u is varied in the stoichiometric flame, there is no effect on $\kappa \cdot [A]$ in the sooting flame. An increase in the C/O to 0.80 leads to a substantial decrease (factor of 6) in the soot particle growth rate, if the v_u of the nonsooting flame is 25 cm/s. Simultaneously, the VSB moves by as much as 25 mm toward the leaner flame. However, if v_u is now raised to 42 cm/s, there is a strong increase in $\kappa \cdot [A]$, almost to the value with the stoichiometric flame. This causes the VSB to move back toward the sooting flame. The $\kappa \cdot [A]$ values show a similar change when the pressure is increased from 27 to 40 mbar. This behavior can be explained by the temperatures at the VSB.

Figure 8a shows schematically the temperature profiles for the case of identical v_u in both flames. The temperature difference between the two flames is rather low, but it increases if v_u of the leaner flame is lower (Fig. 8b). At the VSB, first soot particles are observed. Therefore, it can be assumed that here the local C/O ratio is nearly the same in all flames. In the three flames that show similar values of $\kappa \cdot [A]$, the VSB is always in the middle of the sooting side of the burner, where the temperature is always nearly the same. In the C/O = 0.8, v_u = 25 cm/s flame, the VSB is on the side of the cool, nonsooting flame, where the temperature is rather low. This leads to the slow mass growth in this flame.

Influence of H atoms

An interesting observation can be made in the case of hydrogen flames as nonsooting flames. In these flames, the green chemiluminescence of C_2^s can only be observed on the hydrogen/oxygen side, if the ethyne flame is sooting. A reason why this diffusion only takes place beside sooting flames may be that the concentrations of diffusing hydrocarbons are too low in nonsooting flames.

The results from the flames with a hydrogen/oxygen flame as a nonsooting flame demonstrate the influence of H atoms on the soot mass growth. The mole fraction of H atoms in the burned gas of the 3:1 hydrogen/oxygen flame is about 0.25 [14]. From other experimental results [4], one would expect that the high concentration would lead to a fast mass growth. But the values of $\kappa \cdot [A]$ show very low values. This could be explained by the low temperatures in these flames. Eberius and coworkers [14] investigated a hydrogen/oxygen flame at 13 mbar and found a maximal flame temperature of 1100 K. The temperature hardly differs between the two investigated hydrogen/oxygen flames. The concentration of H atoms is higher in the 3:1 hydrogen/oxygen flame, but the value of $\kappa \cdot [A]$ decreases. This shows that H atoms do not increase the mass growth rate under these conditions.

Acknowledgment

We gratefully acknowledge the financial support extended by the "Fonds der Chemischen Industrie" and the "Deutsche Forschungsgemeinschaft" for this research.

REFERENCES

1. Haynes, B. S., Jander, H., and Wagner, H. Gg., *Seventeenth Symposium (International) on Combustion*, The Combustion Institute, Pittsburgh 1979, p. 1365.
2. Wright, F. J., *Combust. Flame* 15: 217 (1970).
3. Homann, K. H., and Wagner, H. Gg., *Ber. Bunsenges. Phys. Chem.* 69:20 (1965).
4. Frenklach, M., and Wang, H., *Twenty-Third Symposium (International) on Combustion*, The Combustion Institute, Pittsburgh, 1990, p. 1559.
5. Mauss, F., Peters, N., and Bockhorn, H., *Proceedings of the Anglo-German Combustion Symposium 1993*,

British Section of the Combustion Institute, Cambridge, 1993, p. 470.
6. Roth, P., and Hospital, A., *Twenty-Fourth Symposium (International) on Combustion*, The Combustion Institute, Pittsburgh, 1992, p. 981.
7. Baum, Th., Löffler, S., Löffler, Ph., Weilmünster, P., and Homann, K. H., *Ber. Bunsenges. Phys. Chem.* 96:841 (1992).
8. Wegert, R., Wiese, W., and Homann, K. H., *Combust. Flame* 95:61 (1993).
9. Homann, K. H., and Wolf, H., *Twenty-First Symposium (International) on Combustion*, The Combustion Institute, Pittsburgh, 1986, p. 1013.
10. Bonne, U., and Wagner, H. Gg., *Ber. Bunsenges. Phys. Chem.* 69:35 (1965).
11. Fenimore, C. P., and Jones, G. W., *J. Phys. Chem.* 71:593 (1967).
12. Neoh, K. G., Howard, J. B., and Sarofim, A. F., *Twentieth Symposium (International) on Combustion*, The Combustion Institute, Pittsburgh, 1984, p. 951.
13. Wegert, R., *Dissertation*, Technische Hochschule Darmstadt, Darmstadt, Germany D17, 1993.
14. Eberius, K. H., Hoyermann, K., and Wagner, H. Gg., *Thirteenth Symposium (International) on Combustion*, The Combustion Institute, Pittsburgh, 1970, p. 713.

COMMENTS

M. Frenklach, Penn State University, USA. In support of Professor Bockhorn's comment on the more likely effect of H_2 on the reduction in soot formation rather than by H atoms as suggested by the authors, there are additional considerations. Shock-tube experiments [1] showed that addition of relatively small amounts of H_2 to acetylene pyrolysis suppresses dramatically the formation of soot. Furthermore, soot formation in fuel blends was interpreted as the effect of H_2 and not H [1]. Also, the value of 10^{-3} determined in the present study for the overall probability of acetylene reacting with soot particle surface is consistent with the surface-growth model we suggested [2]. The essential elements of this model are

$$C_{soot}-H + H \xrightarrow{k_1} C^{\bullet}_{soot} + H_2$$

$$C^{\bullet}_{soot} + H \xrightarrow{k_2} C_{soot}-H$$

$$C^{\bullet}_{soot} + C_2H_2 \xrightarrow{k_3} \text{Growth.}$$

Assuming that $[C^{\bullet}_{soot}]$ is determined primarily by the first two reactions [3], we obtain the following for the rate of surface growth: $(k_1/k_2)k_3[C_2H_2]$. Under combustion conditions, $k_2/k_2 \sim 10^{-2}$ and $k_3 \sim 10^{12}$ [mol/cm^{3}s], consistent with the overall reaction probability of 10^{-3}.

REFERENCES

1. Frenklach, M., Yuan, T., and Ramaschandra, M. K., *Energy Fuel* 2:462 (1988).
2. Frenklach, M., and Wang, H., *Twenty-third Symposium (International) on Combustion*, The Combustion Institute, Pittsburgh, 1991, p. 1559.
3. Frenklach, M., and Wang, H., *Phys. Rev. B* 43:1520 (1991).

Author's Reply. According to the comment, the mass growth rate is not dependent on the H-atom concentration. In our experiments, we increased the H/H_2 ratio in the ethyne flame by the adjacent hydrogen flame. This increase did not lead to faster mass growth. The inhibition by hydrogen atoms is not considered in the model. Thus, our results showing that H atoms do not increase the mass growth rate are not in disagreement with the mentioned model.

•

H. Bockhorn, University of Kaiserslautern, Germany. When increasing the hydrogen/oxygen ratio in hydrogen-oxygen flames from 2 to 3—as you did in your experiments—you increase the partial pressure of molecular hydrogen considerably more than the partial pressure of hydrogen atoms. Considering that the essential step of the HACA sequence applied to surface growth as proposed by Frenklach, viz.:

$$\text{(surface)-CH} + H \rightleftarrows \text{(surface)-C}^{\bullet} + H_2,$$

is reversible, an increase of the partial pressure of molecular hydrogen would decrease the surface growth rate. From this, I do not see any contradiction between your experiments and the surface growth mechanism suggested by Frenklach.

Author's Reply. The mole fraction of molecular hydrogen in an undisturbed ethyne/oxygen flame at the beginning of the soot formation is about 15–20%, while the concentration of H atoms is very low. Therefore, the increase in the concentration of H atoms is stronger than in the concentration of hydrogen, if the hydrogen/oxygen ratio is raised in the adjacent hydrogen/oxygen flame. Another point that should be considered is the high value of the diffusion coefficient of H atoms. On the other hand, under the conditions of our experiment with rather low temperatures, the deactivation reaction proposed by Frenklach

$$\text{(surface)-C}^{\bullet} + H \rightarrow \text{(surface)-CH}$$

becomes more important, because of its presumably low activation energy.

•

Andreas Hornung, Universitaet Kaiserslautern, Germany. Did you try to exclude the temperature-decreasing effect during the injection of O_2, N_2, or He by using preheated gases to get information about the changes in chemical processes caused by gas injection and not by decreasing the temperature?

Author's Reply. Heating of the injected gas was not necessary. The gas flows were very low, so that the gas was heated by the flame. This could be shown by our heat transfer calculations.

Twenty-Fifth Symposium (International) on Combustion/The Combustion Institute, 1994/pp. 645–651

OPTICAL CHARACTERIZATION OF RICH PREMIXED CH_4/O_2 FLAMES ACROSS THE SOOT FORMATION THRESHOLD

A. D'ALESSIO, G. GAMBI, P. MINUTOLO AND S. RUSSO
Dipartimento Ingegneria Chimica
Università degli Studi di Napoli
Federico II, Napoli, Italy

AND

A. D'ANNA
Istituto di Ricerche sulla Combustione, C.N.R.
Napoli, Italy

Light scattering, fluorescence, and C_2 emission induced by an ultraviolet laser source and uv-visible absorption have been used to study the phenomenological aspects of formation, destruction, and chemical transformation of high molecular mass structures formed in rich premixed methane flames at atmospheric pressure.

High molecular mass structures are formed in CH_4/O_2 flames with C/O ratios down to 0.35. This value, corresponding to their formation threshold, is noticeably lower than the soot threshold limit (C/O = 0.45).

Different flames have been analyzed across the soot threshold limit, varying the C/O ratio and the maximum flame temperature, and no dramatic changes in the properties of the high molecular mass structures have been found in the passage from nonsooting to sooting conditions. Their role as soot precursors seems to be connected to a kinetically controlled passage from aromatic functionalities with one or two rings to higher polycondensed aromatic functionalities more than to a carbonization process of these structures.

High molecular mass structures are easily photofragmented by an ultraviolet laser source with high-energy pulses, and the consequent C_2 emission has been attributed to these structures more than to soot particles. From a practical point of view, the spatial distribution of these potential pollutants, whose toxic properties are largely unknown, can be easily followed in practical diffusion flames by monitoring the 2D fluorescence due to C_2 photofragments employing an ultraviolet laser source.

Introduction

Polycyclic aromatic hydrocarbons (PAH) with molecular mass up to 300 u and soot are the species more commonly identified in rich combustion [1–3]. The presence of structures with intermediate molecular masses was detected a long time ago in low-pressure premixed flames by Homann and Wagner [1] employing mass spectrometric analysis of the gases withdrawn with molecular beam sampling and by Tompkins and Long [4] through a chemical characterization of the sampled material. Additional characterization has been made by Wersborg et al. [5] by mass spectrometry, electron microscopy, and optical absorption measurements and by Howard and Bittner [6] through a mass spectrometric analysis of the neutral species. Recently, Homann [7] has reported the mass distribution function of the ionic species detected at the soot inception and in the growth stages. These ions showed a continuous mass distribution function with a first maximum at 200 u due to PAH and a second one at 6000 u due to soot particles. More recently, evidence of the formation of high molecular mass structures in premixed flames has been obtained by absorption measurements at different wavelengths carried out by Haynes et al. [8] and Harris and Weiner [9] and by sampling measurements by Howard and coworkers [10–12] and D'Alessio et al. [13].

In the last few years, we have proposed an optical method for the characterization of high molecular mass structures based on the measurements of light scattering, absorption, and fluorescence both in the ultraviolet and in the visible regions [13–15]. This approach has been used, together with a chemical characterization of the sampled material, to study the soot inception in premixed ethylene flames [13] and for a preliminary analysis of rich nonsooting methane flames [16].

In the present work, light scattering, fluorescence, and C_2 emission induced by an ultraviolet laser source and uv-visible absorption were employed to

analyze formation, destruction, and chemical transformation of high molecular mass structures in the transition from nonsooting to sooting flames by changing both the C/O ratio and the maximum flame temperature. The C_2 emission measurements allowed us to give an interpretation of which species are easily photofragmented, producing C_2 radicals in nonsooting conditions.

Experimental Apparatus

Laser light scattering, extinction, and laser-induced fluorescence measurements were performed in rich premixed flat methane/oxygen flames stabilized at atmospheric pressure on a McKenna porous plate burner employing the fourth harmonic of a Nd:YAG laser (λ_0 = 266 nm). The fuel and oxidant were fed to the center of the burner with the C/O ratio ranging from 0.35 to 0.5 and the gas velocity from 3.3 to 6.2 cm/s (STP).

In order to suppress the interference from C_2 emission and soot incandescence, the energy of the light pulses was attenuated below 50 μJ, employing a variable attenuator. The beam was then focused by a 300-mm cylindrical lens on the burner.

The laser was also operated at high energy (4 mJ) and focused into the flame by a 300-mm spherical lens. In such conditions, fluorescence measurements have been performed in order to follow laser-induced C_2 emission profiles.

The light scattered at 90° to the direction of the incident laser beam was focused on the entrance slit of an f/8.8 spectrometer with focal length of 500 mm; a polarization analyzer was placed in front of the monochromator. The pulsed signal from the photomultiplier, on the exit slit of the monochromator, was processed by a boxcar averager.

Extinction and temperature measurements were made using a calibrated strip film tungsten lamp. For the extinction measurements, the chopped image of the lamp was focused at the centre of the flame and then at the entrance slit of the monochromator. The signals were processed and digitized by a lock-in system to avoid emission from the flame. In the sooting region of the flames, temperature was determined by the Kurlbaum technique, and, in the nonsooting flames, by the Na-line reversal method.

Results

A broadband emission peaked around 330 nm is the most prominent feature of the fluorescence excited by low-energy laser pulses at λ_0 = 266 nm either in nonsooting flames or in the preinception region of sooting flames [13]. At higher pulse energy, the intensity of ultraviolet emission increases without changing the spectral shape, and the typical emission

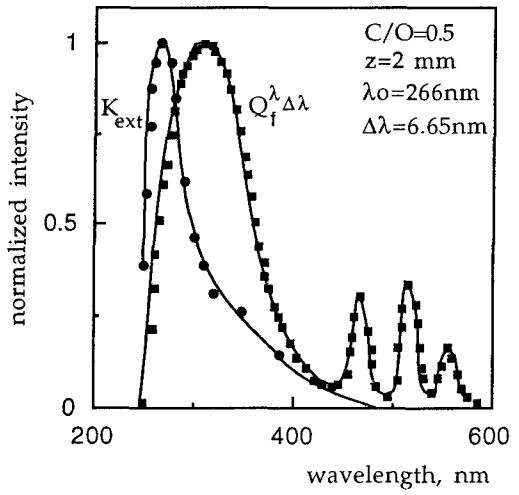

FIG. 1. uv-Visible absorption and laser-induced emission normalized spectra, excited in the ultraviolet at 266 nm, in the soot preinception zone (z = 2 mm) of a slightly sooting (C/O = 0.5) premixed methane/oxygen flame.

due to the Swan bands of the C_2 radical emerges in the visible. This effect is clearly shown in Fig. 1, where fluorescence and laser-induced C_2 emissions are reported together with the absorption spectrum obtained in the preinception region of a sooting flame. When the flames are in a soot-forming regime, a broadband structure is also present in the visible, and C_2 emission emerges over this background at high pulse energy [17].

Absorption and fluorescence in the near-uv–visible region of the spectrum of rich hydrocarbon flames come mainly from delocalized π electrons in structures with double bonds such as polyenes and aromatic molecules. Generally, larger structures with delocalized π electrons have a smaller energy difference between the fundamental and the first excited electronic state so that they can absorb and fluoresce at longer wavelengths. The radiative channel is just one of the deactivation processes; the more flexible the molecules are, the more relevant nonradiative decay channels are [18]. For this reason, polyenes do not usually fluoresce. Following this scheme, we attribute the ultraviolet component of the fluorescence spectra to aromatic functionalities with one or two rings and fluorescence in the visible to the aromatic functionalities with three or more rings, without trying to attribute the spectroscopic behaviour to specific compounds.

A systematic series of measurements was undertaken in flames with C/O ratio ranging from 0.35 to 0.5 at different heights above the burner, in order to investigate the relationship between the ultraviolet fluorescence, the C_2 emission, and the absorption at λ_0 = 266 nm. Some of these results are reported in

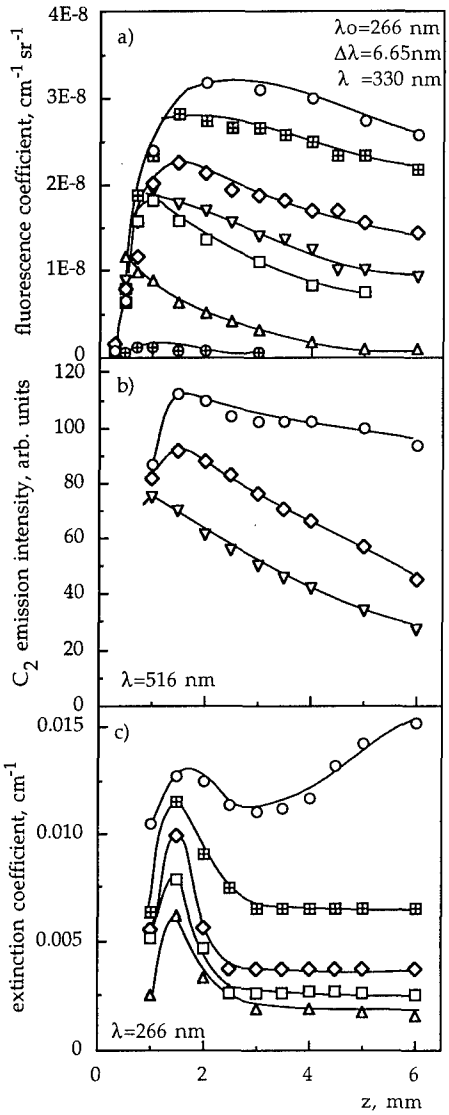

FIG. 2. (a) Monochromatic fluorescence coefficient profiles, in the uv at 330 nm, (b) C_2 fluorescence intensity profiles, and (c) extinction coefficient profiles for flames with C/O ranging from 0.5 to 0.35. λ_0 = 266 nm. ○ C/O = 0.5; ⊞ 0.48; ◇ 0.45; ▽ 0.41; □ 0.4; △ 0.38; ⊕ 0.35.

Fig. 2. The monochromatic fluorescence coefficient at λ = 330 nm rises very sharply at approximately 0.3–0.5 mm above the burner, corresponding to a residence time below 1 ms. Then it passes through a maximum that shifts from 0.5 to 2 mm at increasing C/O ratios (Fig. 2a). The subsequent behaviour in the burned gas region is very different depending on the C/O ratio: For the leanest investigated flame, ultraviolet fluorescence decays to zero, while, in the soot-forming conditions (C/O > 0.45), it decreases

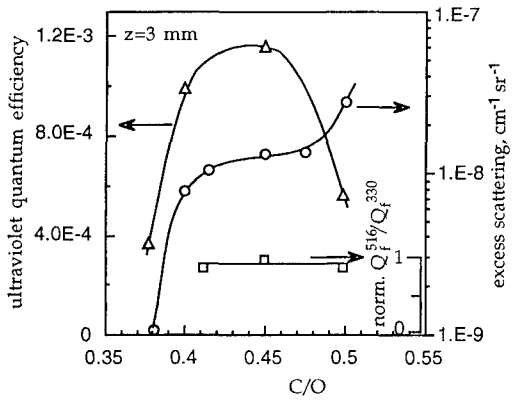

FIG. 3. Ultraviolet quantum efficiency, normalized ratio between C_2 fluorescence at λ = 516 nm and ultraviolet fluorescence at λ = 330 nm coefficients and excess elastic scattering coefficient as a function of the C/O ratio.

slowly along the flame. The C_2 emission shows the same behaviour as the monochromatic fluorescence coefficient at λ = 330 nm (Fig. 2b), whereas the absorption coefficient at λ = 266 nm exhibits a very rapid rise and a maximum roughly at the same position as the ultraviolet fluorescence one. Afterwards, the absorption coefficient steeply decays in both nonsooting and sooting flames (Fig. 2c). In the burned gas region, while ultraviolet fluorescence and C_2 emission both decrease, absorption increases in soot-forming conditions and remains quite constant in the nonsooting ones.

Further understanding of these features comes from the analysis of the ratio between the energy emitted from the ultraviolet band and that absorbed at the fluorescence excitation wavelength λ_0 = 266 nm, i.e., the quantum efficiency of the ultraviolet fluorescence process η_{uv}. The quantum efficiency is an indicator of the relative importance of the radiative channel to nonradiative channels. As a general rule, greater flexibility of the structure gives a lower quantum efficiency, whereas rigid cyclic structures, such as that of aromatic molecules, have high quantum efficiency [18].

Figure 3 shows η_{uv}, and the ratio between the C_2 emission at 516 nm and fluorescence emission at 330 nm detected at 3 mm above the burner reported as a function of the C/O ratio. In the same diagram, the "excess scattering," i.e., the difference between the measured elastic Rayleigh scattering and that due to the major gaseous compounds present in flame, is also illustrated. Elastic light scattering is roughly proportional to the sum of the polarizability of the individual bonds inside the structure, and therefore, it increases with the molecular mass. The detection of light scattering in excess with respect to that due to gaseous compounds is an unambiguous indicator of the presence of high molecular mass structures

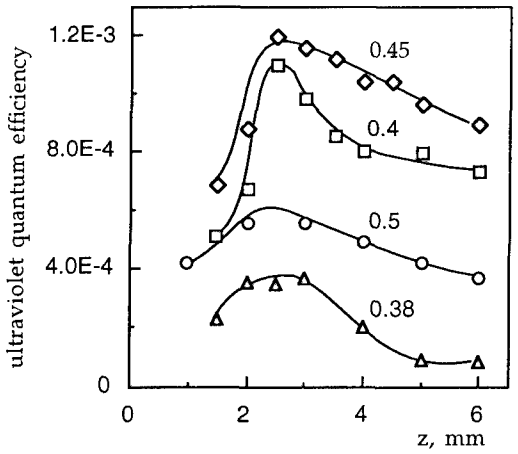

FIG. 4. Ultraviolet quantum efficiency profiles for flames with C/O ranging from 0.5 to 0.38.

and/or particles in the flame. The excess scattering profile, reported in Fig. 3, shows that it starts to be detected in blue flames with C/O around 0.35. Increasing C/O, this profile has a plateau up to the soot formation threshold (C/O = 0.45), and then it steeply rises. Furthermore, the quantum efficiency exhibits a maximum that takes place at a C/O ratio slightly lower than that where the strong increase in the scattering due to soot inception occurs.

Flames with C/O ratio below the soot threshold limit (C/O < 0.45) exhibit noticeable absorption and fluorescence in the ultraviolet but not in the visible; furthermore, excess scattering is detectable down to a C/O ratio around 0.35. It follows that, in rich nonsooting flames, high molecular mass structures that do not absorb and consequently do not emit in the visible are formed. The absence of the visible features indicates that they are not aggregates of condensed benzenoid structures, as soot is. Furthermore, the measured quantum efficiency is very low, and since it can be related to the degree of aromatization of the structures, it follows that its increase indicates an enrichment in the relative amount of one or two ring aromatic functionalities inside the structure.

The same effect can be observed in Fig. 4, which reports η_{uv} as a function of the height above the burner for different C/O ratios. For a fixed C/O ratio, η_{uv} starts from very low values in the preheating region, then goes through a maximum just downstream of the region of the maximum of fluorescence and extinction. As the C/O ratio increases, fluorescence, quantum efficiency, and excess scattering increase continuously up to the soot threshold limit at C/O = 0.45. Beyond this C/O threshold, when excess scattering strongly increases, large polybenzenoid structures are rapidly formed and absorb both in the ultraviolet and visible but do not fluoresce in the ultraviolet around 330 nm since they consist of more than two rings; thus, the quantum efficiency of this band decreases. The same interpretation can be given for the decrease of the η_{uv} in near-sooting flames at increasing height above the burner.

The ratio between C_2 emission and ultraviolet fluorescence remains constant across the soot formation threshold. This behaviour, together with the results reported in Figs. 2a and 2b, shows that the C_2 emission at high uv laser-pulse energy is always proportional to the ultraviolet fluorescence intensity below and above the soot threshold limit. Our results agree with those found by Bengtsson and Aldén [19] and furthermore qualify them. C_2 emission is produced by the photolysis of the high molecular mass structures and not by soot particles. Their photolytic efficiency is so high that this process is more relevant than the C_2 emission from condensed polybenzenoid structures, i.e., soot particles, even in soot-forming flames.

The variation of the optical properties of the flames across the soot formation threshold was also studied by comparing, at a fixed C/O ratio, the behaviour of flames with different maximum temperatures. Another series of experiments was undertaken in rich flames with C/O = 0.5 at different flow rates. Figure 5 reports the results obtained for three flames with maximum temperature of 1700, 1760, and 1800 K measured around 2.5 mm. The flame with maximum temperature of 1760 K is the previously examined one. These experiments allow characterization of the role of high molecular mass structures and their aromaticity, going from nonsooting to sooting conditions, varying only the maximum flame temperature. The monochromatic fluorescence coefficients at λ = 330 nm follow the same trends of Fig. 2a: a very rapid onset around 0.3 mm above the burner, a peak in the oxidation zone, and a further relatively slow decay, which is more pronounced for the higher temperature flames. Conversely, strong differences are exhibited by the visible fluorescence at λ = 480 nm, also reported in Fig. 5a: The onset of this feature is clearly retarded with respect to the ultraviolet fluorescence one, and it increases very sharply for the coldest flame, whereas it is barely detectable for the hottest one. Monochromatic extinction coefficients at λ = 266 nm and λ = 532 nm are also reported in Fig. 5 for the same flames together with the profiles of the excess scattering coefficient. The ultraviolet extinction rises very early and passes through a maximum around 1.5 mm for all the flames; later on, it has another very strong increase only for the coldest flame. Extinction in the visible is below the detection limit for the hottest flame. For the other flames, it is very low up to 3 mm; afterwards, it increases more rapidly for the coldest one. Excess scattering starts to be detectable at 1 mm, because the strong gradient of temperature and concentration of gaseous compounds limit the accuracy

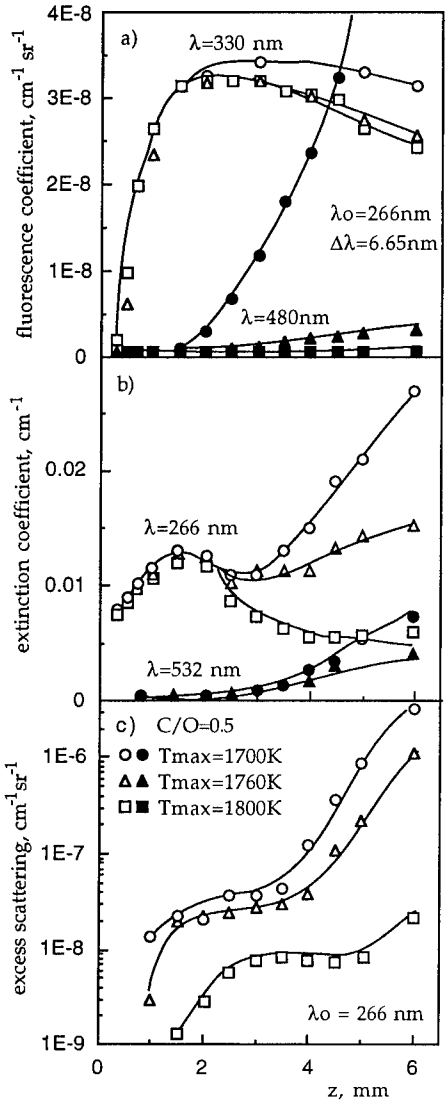

FIG. 5. (a) Monochromatic fluorescence coefficient, in the uv at 330 nm and in the visible at 480 nm, (b) monochromatic extinction coefficient, in the uv at 266 nm and in the visible at 532 nm, and (c) excess elastic scattering coefficient profiles for three flames with C/O = 0.5 and maximum temperature, respectively, of 1700, 1760, and 1800 K. λ_0 = 266 nm.

of the measurement up to the reaction zone. After that, excess scattering rises and reaches an almost constant value beyond 2 mm. This quantity increases by two orders of magnitude for the sooting colder flames, while it slowly increases for the hottest one. All these results show that the formation process of high molecular mass structures takes place very early in the flame and is not noticeably different for sooting

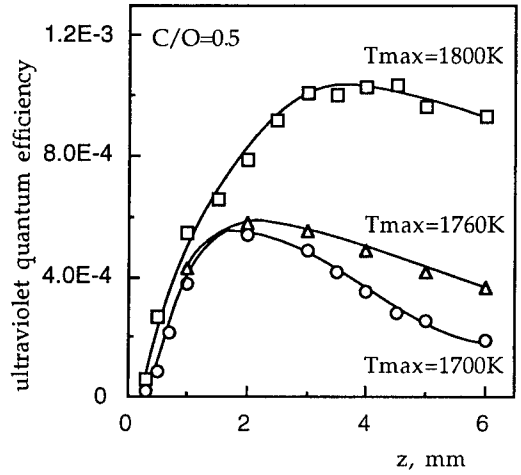

FIG. 6. Quantum efficiency profiles for three flames with C/O = 0.5 and maximum temperature, respectively, of 1700, 1760, and 1800 K.

and nonsooting flames. On the contrary, the onset of visible fluorescence and absorption at 2 mm shows that the formation of condensed polybenzenoid structures is retarded.

Figure 6 reports η_{uv} for the three flames. It increases with the height above the burner for all the flames, then reaches a maximum that is higher for the hottest flame. The decrease of η_{uv} is more relevant for the coldest flame and is just appreciable for the hottest one. The stronger increase of η_{uv} for the nonsooting hottest flame indicates a larger and more persisting contribution of the one or two ring aromatic functionalities inside the high molecular mass structure than in the sooting case.

Discussion

High molecular mass structures containing aromatic functionalities not larger than two rings are formed very early in the preheating region of rich flames with C/O ratios higher than C/O = 0.35. The initial concentration of these structures increases with the C/O ratio, but it is not very sensitive to the maximum flame temperature. Their average molecular mass, as evaluated by ultraviolet scattering/absorption ratio, ranges between 2000 and 8000 u [13]. The early formation of the high molecular mass structures suggests that they are a product of a fast polymerization of aliphatic radicals, which are just formed in the fuel preheating region.

Benzene is also detectable very early in the fuel preheating region [20,21], so that it is not surprising that small aromatic functionalities are inserted in these structures. These aromatic functionalities do not have a direct correlation with the low mass aro-

matic hydrocarbons detected by mass spectrometry or chromatography because their profiles along the flames are quite different. Benzene decays rapidly after the first formation zone [3], while the ultraviolet fluorescence persists also in the burned gas region.

In flames above the soot threshold limit at the end of the oxidation zone, extinction goes through a maximum and then exhibits a slight decay that can quite well justify the onset of soot formation [13]. However, this behaviour is shown also by nonsooting flames and may be attributed also to oxidation, which is almost surely the case for the leaner flames investigated. Since all the radicals H, OH, and O peak in the same region, it is quite difficult to give a clear-cut answer to this problem with the available data.

The presence of a critical barrier between the formation of one or two structures, observed by varying the C/O ratio, the residence time, and the maximum flame temperature, and the formation of structures with a larger number of condensed rings can be explained assuming that, if the local concentration of critical radicals and small aromatics has a proper value, then the buildup of benzenoid structures is quite fast. This point of view is similar to that of Markatou et al. [22], who have recently modelled the soot limits of laminar premixed flames. However, it is worthwhile to point out that the approach of those authors is largely different from ours since they assume that the formation of the polybenzenoid structures takes place from aromatic compounds in the gas phase and not from aromatization of a macromolecular structure.

Finally, the analysis of C_2 emission has shown that these structures are much more easily fragmented than soot particles by ultraviolet radiation. The correspondence between C_2 emission induced by ultraviolet laser and broadband ultraviolet fluorescence has an interesting diagnostic application because it can be used, eventually for 2D detection, to monitor in practical combustion systems the time and spatial evolution of particles that are not soot particles, but rather large molecular mass structures.

Conclusions

The present work gives a characterization of the high molecular mass structures formed in rich premixed flames employing absorption, fluorescence, light scattering, and C_2 emission induced by uv laser.

High molecular mass structures are formed for C/O ratios down to 0.35, noticeably lower than the soot threshold limit. Their formation onset takes place in the preheating zone of the flame well before the soot nuclei formation. It shows that they come from an early polymerization of aliphatic radicals.

This material does not show dramatic changes in properties passing from nonsooting to sooting flames changing either the C/O ratio or the maximum flame temperature. Their role as soot precursors seems to be connected to a kinetically controlled passage from aromatic functionalities with one or two rings to higher polycondensed aromatic functionalities.

C_2 emission induced by an ultraviolet laser with high energy pulse is due to these structures, which are much more easily photofragmented than soot particles. From a practical point of view, the spatial distribution of these potential pollutants, whose toxic properties are largely unknown, can be followed in practical flames by monitoring the fluorescence due to C_2 molecules employing a high-energy ultraviolet laser source.

REFERENCES

1. Homann, K. H., and Wagner, Gg., *Eleventh Symposium (International) on Combustion*, The Combustion Institute, Pittsburgh, 1966, p. 371.
2. D'Alessio, A., Di Lorenzo, A., Sarofim, A. F., Beretta, F., Masi, S., and Venitozzi, C., *Fifteenth Symposium (International) on Combustion*, The Combustion Institute, Pittsburgh, 1975, p. 1427.
3. Bockhorn, H., Fetting, F., and Wenz, H. W., *Ber. Bunsenges. Phys. Chem.* 87:1067 (1983).
4. Tompkins, E. E., and Long, R., *Twelfth Symposium (International) on Combustion*, The Combustion Institute, Pittsburgh, 1969, p. 625.
5. Wersborg, B. L., Fox, L. K., and Howard, J. B., *Combust. Flame* 24:1 (1975).
6. Howard, J. B., and Bittner, J. D., "Structure of Sooting Flames," presented to N.A.T.O. Workshop on "Soot in Combustion Systems and its Toxic Properties," Le-Bischenberg, France, 1981.
7. Homann, K. H., "Precursor Formation," in *Soot Formation in Combustion, an International Round Table Discussion* (H. Jander and H. G. Wagner, Eds.), Vandenhoech & Ruprecht, Gottingen, 1989, p. 101.
8. Haynes, B. S., Jander, H., and Wagner, H. Gg., *Ber. Bunsenges. Phys. Chem.* 84:585 (1980).
9. Harris, S. J., and Weiner, A. M., *Twenty-Second Symposium (International) on Combustion*, The Combustion Institute, Pittsburgh, 1988, p. 333.
10. Lam, F. W., Howard, J. B., and Longwell, J. P., *Twenty-Second Symposium (International) on Combustion*, The Combustion Institute, Pittsburgh, 1989, p. 323.
11. Lam, F. W., Howard, J. B., and Longwell, J. P., *Twenty-Third Symposium (International) on Combustion*, The Combustion Institute, Pittsburgh, 1990, p. 1477.
12. McKinnon, J. T., and Howard, J. B., *Twenty-Fourth Symposium (International) on Combustion*, The Combustion Institute, Pittsburgh, 1992, p. 965.
13. D'Alessio, A., D'Anna, A., D'Orsi, A., Minutolo, P., Barbella, R., and Ciajolo, A., *Twenty-Fourth Sympo-*

sium (International) on Combustion, The Combustion Institute, Pittsburgh, 1992, p. 973.

14. D'Anna, A., D'Alessio, A., and Minutolo, P., in *Soot Formation in Combustion: Mechanisms and Models* (H. Bockhorn, Ed.), Springer-Verlag, 1994, Springer Series in Chemical Physics, Vol. 59.
15. D'Alessio, A., Minutolo, P., Gambi, G., and D'Anna, A., *Ber. Bunsenges. Phys. Chem.* 97:1574 (1993).
16. Minutolo, P., Gambi, G., D'Alessio, A., and D'Anna, A., *Combust. Sci. Technol.*, in press.
17. Beretta, F., D'Alessio, A., D'Orsi, A., and Minutolo, P., *Combust. Sci. Technol.* 85:455–470 (1992).
18. Jaffé, H. H., and Orchin, M., *Theory and Applications of Ultraviolet Spectroscopy*, John Wiley and Sons Inc., New York, 1962.
19. Bengtsson, P. E., and Aldén, M., *Combust. Flame* 80:322–328 (1990).
20. Harris, S. J., Weiner, A. M., Blint, R. J., and Goldsmith, J. E. M., *Twenty-First Symposium (International) on Combustion*, The Combustion Institute, Pittsburgh, 1988, p. 1033.
21. Harris, S. J., Weiner, A. M., and Blint, R. J., *Combust. Flame* 72:91 (1988).
22. Markatou, P., Wang, H., and Frenklach, M., *Combust. Flame* 93:467 (1993).

Twenty-Fifth Symposium (International) on Combustion/The Combustion Institute, 1994/pp. 653–659

SOME PHYSICO-CHEMICAL PARAMETERS OF SOOT FORMATION DURING PYROLYSIS OF METHANE AND METHANE-ACETYLENE AND METHANE-BENZENE MIXTURES

P. A. TESNER AND S. V. SHURUPOV
All-Russian Institute of Natural Gas
142717, Moscow obl., p/o Razvilka, VNIIGAS, Russia

Under isothermal conditions, pyrolysis of methane and its mixtures with acetylene and benzene was investigated at temperatures 1200 °C–1400 °C and methane concentrations 20–80%. Particle number density was shown to depend linearly on methane concentration, as was earlier demonstrated for acetylene. The equation of particle number density (N) was determined for methane as follows:

$$N = 9.4 \cdot 10^{20}[CH_4] \exp(-39{,}400/T).$$

The activation energy of soot aerosol formation during methane pyrolysis was 328 kJ/mol. For both methane-acetylene and methane-benzene mixtures, inhibition of the soot particles formation from methane was obtained. Soot particles were formed only from benzene or acetylene, whereas methane was consumed for particle growth. Promotion of heterogeneous methane decomposition on the surface of soot particles formed from acetylene or benzene was found.

Introduction

Abundant literature is devoted to the soot formation process, and several detailed reviews are available [1–5]. However, the kinetics of soot formation under pyrolysis of hydrocarbons is not sufficiently investigated. The nonisothermal technique was employed in earlier work [6,7], so reliable kinetic parameters could not be obtained.

We have developed an isothermal technique [8] to investigate the soot formation kinetics during pyrolysis of hydrocarbons, and simple kinetic parameters for acetylene pyrolysis have been obtained [9]. The present work deals with the investigation of the soot formation kinetics during pyrolysis of methane and of methane-acetylene and methane-benzene mixtures.

Experimental Technique

The experimental technique used did not differ from that described in detail elsewhere [8].

The pyrolysis of hydrocarbons was carried out in a quartz tube 20 mm in diameter heated in an electric oven (Fig. 1). Isothermality of measurements was provided by heating a mixture of gases in channels 1 mm in diameter at gas flow velocity 90–100 m/s. The mixture of gases containing methane was fed along two channels of an alumina pipe 20-cm long, whose end was in the beginning of the constant-temperature zone. The flow rate of gas in each channel was 800 cm^3/min. Additionally, 400 cm^3/min of helium were fed to the inlet of the reactor to blow off the soot formed. Measurements made with wire thermocouples 0.2 mm in diameter have shown that the temperature of the gas in the channel 1 mm in diameter 5–7 mm from the end of the channel differs from that in the reaction space by no more than 10°.

The soot carried out of the reactor by the gas stream was trapped in a bag filter. The soot deposited on the reactor walls at temperatures below 600 °C did not differ in its surface area from the soot collected in the filter. Therefore, it was withdrawn and studied together with the soot from the filter. The soot deposited at higher temperatures was covered with pyrolytic carbon, and its surface area was smaller than that of the soot from the filter. This soot was withdrawn and investigated separately. Soot was weighed by analytical balance. The accuracy of soot yield measurements was ±5%.

The yield of pyrolytic carbon deposited on the reactor walls was obtained by burning it in the air flow, followed by carbon dioxide reaction with alkali.

The surface area of the soot was measured by nitrogen adsorption at the temperature of liquid nitrogen. For each soot sample, the measurements of the surface area were performed twice, and the average value of the surface area was taken. The accuracy of the surface area measurements was ±5%.

Four sets of experiments have been performed under the following conditions.

1. At temperatures 1300 °C and 1400 °C and methane concentrations from 20 to 80%.

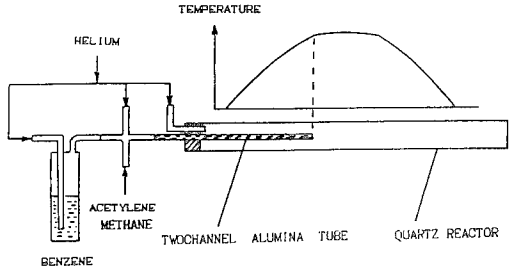

FIG. 1. Diagram of the apparatus for conducting pyrolysis under isothermal conditions.

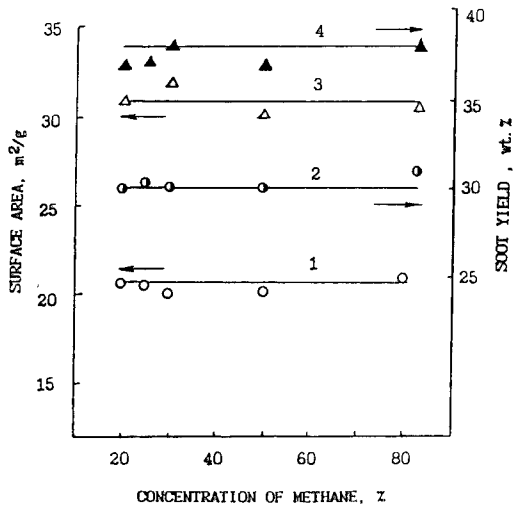

FIG. 2. Surface area and soot yield vs methane concentration. 1, 2—temperature 1300 °C; 3, 4—temperature 1400 °C.

2. At constant methane concentration 20% and temperatures from 1200 °C to 1400 °C.
3. Pyrolysis of a methane-acetylene-helium mixture at constant concentration of helium 20% and at temperature 1300 °C.
4. Pyrolysis of a methane-benzene-helium mixture at constant concentration of methane 20% and at temperature 1300 °C.

Results

The results of the first set of experiments, namely the values of the surface areas and the yield of the soot trapped by the bag filter and deposited in the cold part of the reactor tube are given in Fig. 2. The results obtained reveal that the surface area is independent of the methane concentration. It can be mentioned that, at methane concentrations less than 20%, the soot yield increases, whereas the surface area decreases.

The results obtained (Fig. 2) were processed as follows. For each experiment, the soot particle number density (N) was calculated on the basis of soot yield (a) and surface area (A). Simple geometrical considerations were used for this purpose.

The surface (F, cm^2) and the weight (G, g) of a soot particle of diameter d (cm) equal

$$F = \pi d^2 \qquad G = \pi d^3 \gamma/6 = \pi d^3/3$$

where γ is specific density of soot particles, $\gamma = 2.0$ g/cm^3. Therefore, the surface area (A, cm^2/g) of the soot particle is

$$A = F/G = 3/d.$$

The number of particles in 1 g of soot (N_0, g^{-1}) is

$$N_0 = 1/G = 3/\pi d^3.$$

Hence,

$$N_0 = 3A^3/3^3\pi = A^3/9\pi. \tag{1}$$

If the surface area (A) is in m^2/g, then

$$N_0 = 10^{12}A^3/9\pi. \tag{2}$$

The flux of soot particles (Q, min^{-1}) was calculated according to the following equation:

$$Q = N_0 \cdot a \cdot c \tag{3}$$

where c is the flux of the hydrocarbon's carbon (g/min) and a is the yield of soot trapped by the filter and deposited in the cold part of the reactor.

Soot particle number density was calculated according to the next equation, supposing that coagulation between soot particles does not change the surface area (see Discussion).

$$N = K \cdot Q/P \tag{4}$$

where N is soot particle number density (cm^{-3}), K is a fitting coefficient taking into account the soot deposited in the hot zone of the reactor and equal to 1.5, and P is the gas flow rate at the temperature of the experiment (cm^3/min).

A peculiarity of the experimental technique for investigation of soot formation under pyrolysis of hydrocarbons in the reactor tubes consists of the formation of diverse carbon forms. Their approximate balance at maximum soot yield was as follows (wt.%).

1. The soot carried out into the bag filter and deposited in the cold part of the reactor at temperatures below 600 °C, representing 40%.
2. The soot deposited on the walls of the reactor hot zone, representing 23%.
3. Pyrolytic carbon film on the reactor walls, representing 18%.

Thus, at the highest degree of methane decomposition, nearly 80% of the carbon from methane is converted to soot and pyrolytic carbon, and 20% remains in the pyrolysis gas.

The ratio of the surface area of soot trapped by the filter and deposited in the cold part of the reactor

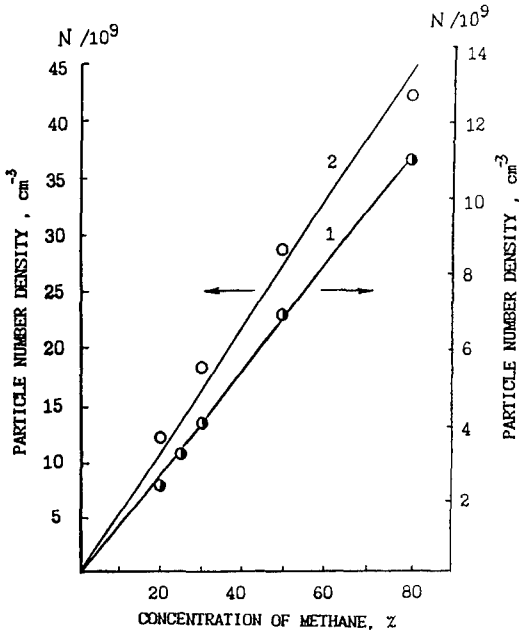

FIG. 3. Particle number density vs methane concentration. 1—temperature 1300 °C; 2—temperature 1400 °C.

to the surface area of soot deposited in the hot zone of the reactor is 1.05. So the ratio of soot coated with pyrolytic carbon to that deposited in the hot zone is $(1.05)^3 = 1.16$. Therefore, the real yield of soot deposited in the hot zone amounts to 23/1.16 = 20 wt.%. Thus, the fitting coefficient taking into account the fraction of soot particles deposited on the hot walls of the reactor can be estimated for the first approximation as follows: $K = (40 + 20)/40 = 1.5$.

The results of the calculation are given in Fig. 3. The results obtained clearly certify that the particle number density N is of first order in methane concentration. A similar dependency was also observed for acetylene [9] and lately demonstrated for benzene. It should be mentioned that the linear dependence obtained for particle number density on hydrocarbon concentration is not influenced by inaccurate estimation of the fitting coefficient K.

The results obtained for the second set of experiments are summarized in Table 1 and in Fig. 4. Dependence of the soot particle number density on temperature and methane concentration is approximated by the following equation:

$$N = 9.4 \cdot 10^{20}[CH_4] \exp(-39{,}400/T) \quad (5)$$

where $[CH_4]$ is concentration of methane, mole fraction, and T is temperature, K.

The methane-acetylene and methane-benzene mixtures (the third and fourth sets of experiments) were investigated using the technique described in

TABLE 1
Calculation of the particle number density at different temperatures

Temperature (K)	Surface area, A (m²/g)	Soot yield, a (wt.%)	Particle number density [calculated by Eq. (4)], N (cm⁻³)
1473	14.0	15.0	$0.45 \cdot 10^9$
1523	16.5	24.0	$1.20 \cdot 10^9$
1573	20.5	30.0	$2.70 \cdot 10^9$
1623	25.0	34.5	$5.70 \cdot 10^9$
1673	31.0	38.0	$1.20 \cdot 10^{10}$

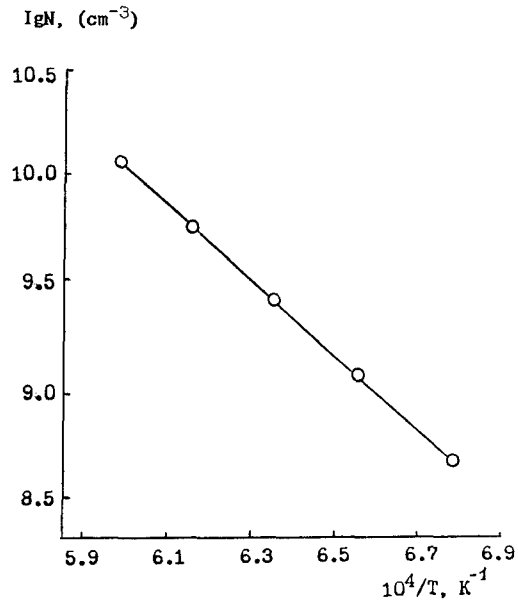

FIG. 4. Particle number density. Concentration of methane is 20%.

Ref. 8. All the experiments were performed at temperature 1300 °C. The results were processed in the same way as in the work of Ref. 8. Fluxes of soot particles (Q, s^{-1}) were obtained for both the individual hydrocarbons and their mixtures. The ratios of additive soot fluxes to experimental ones as well as to the soot fluxes of benzene or acetylene were calculated (Tables 2 and 3).

In addition, the surface areas were calculated supposing that only acetylene or benzene can form soot particles, whereas methane is consumed only for the particle growth according to Eq. (3) of Ref. 8:

$$A_m = A_n/(1 + H)^{1/3} \quad (6)$$

where A_m is the surface area of soot formed during

TABLE 2
Fluxes of soot particles ($Q/10^{12}$, s^{-1}) for benzene-helium-methane (20%) mixture

Experiment (E) Additive calculation (A)	Benzene concentration (%)					
	0.4	1.0	1.7	3.8	4.5	8.0
E (mixture)	0.19	0.60	1.02	2.10	2.65	4.80
E (benzene)	0.25	0.62	1.06	3.36	2.80	5.00
A	0.46	0.83	1.26	2.56	3.00	5.16
A/E (mixture)	2.42	1.38	1.23	1.22	1.13	1.07
E/E (benzene)	0.76	0.97	0.96	0.90	0.95	0.96

TABLE 3
Fluxes of soot particles ($Q/10^{12}$, s^{-1}) for methane-acetylene-helium (20%) mixture

Experiment (E) Additive calculation (A)	Acetylene concentration, %					
	2.0	4.0	7.0	10.0	13.0	20.0
E (mixture)	0.50	0.89	1.45	2.30	2.93	3.55
E (acetylene)	0.22	0.54	1.06	1.24	1.61	2.49
A	1.49	1.78	1.95	2.38	2.70	3.47
A/E (mixture)	2.98	2.00	1.34	1.03	0.92	0.98
E/E (acetylene)	2.27	1.64	1.37	1.85	1.81	1.42

pyrolysis of the hydrocarbon mixture (m^2/g), A_n is the surface area of soot formed during pyrolysis of acetylene or benzene (m^2/g), and H is the increase in the mass of soot particles from acetylene or benzene due to decomposition of methane molecules.

When calculating the weight of the soot particles formed from methane molecules of methane-acetylene and methane-benzene mixtures, it was observed that degree of methane decomposition in the presence of hydrocarbons exceeded that from the methane-helium mixture. Taking this fact into consideration, the soot fluxes (q, g/s) for hydrocarbon mixtures and individual hydrocarbons, the additive soot fluxes, and the experimental values of the surface areas of hydrocarbon mixtures are given in Figs. 5 and 6. The curves obtained by Eq. (6) are also presented in these figures. The difference between the ordinates of the soot flux curves for the hydrocarbon mixtures and the additive calculation (the shaded area in Figs. 5 and 6) reveals the observed soot yield increase. For the methane-benzene mixture, a soot flux increase equal to 100 and 35% was observed at benzene concentrations 1 and 8%, respectively. For the methane-acetylene mixture, the soot flux increase was 6 and 13% for acetylene concentrations 4 and 16%, respectively.

The higher promotion effect observed for the methane-benzene mixture compared with methane-acetylene and acetylene-benzene mixtures [8] can be explained as follows. First, the surface area of the soot formed from acetylene and benzene (34.0 and

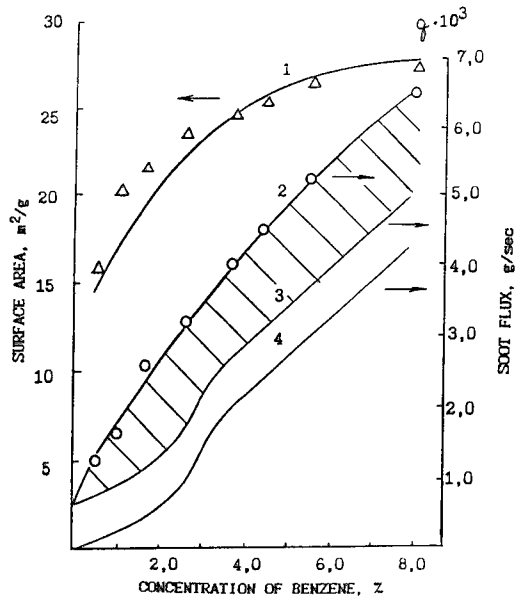

FIG. 5. Surface area and soot flux vs benzene concentration. 1, 2, 3—benzene-helium-methane (20%) mixture; 4—benzene-helium mixture; 2, 4—experimental soot flux; 3—additive soot flux.

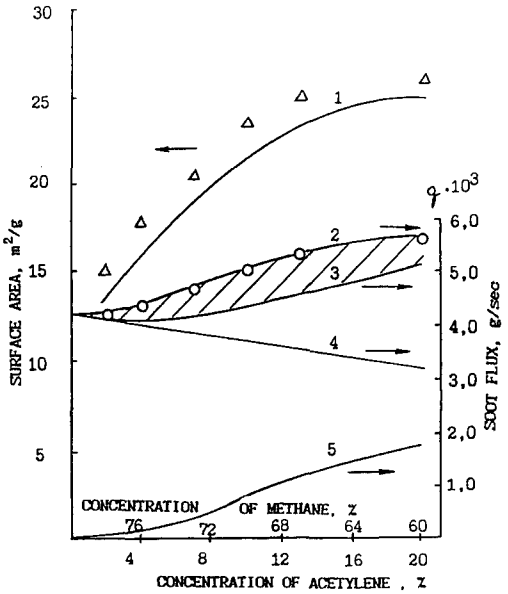

FIG. 6. Surface area and soot flux vs acetylene concentration. 1, 2, 3—acetylene-methane-helium (20%) mixture; 4—methane-helium mixture; 5—acetylene-helium mixture; 2, 4, 5—experimental soot flux; 3—additive soot flux.

32.0 m^2/g, respectively, at 1300 °C) is higher than that of soot formed from methane (20.5 m^2/g). Second, during the pyrolysis of the acetylene-benzene mixture [8], the mass of the acetylene molecules from which soot particles were formed was three times less than the mass of the benzene molecules consumed for only the growth of soot particles. In the experiments with methane mixtures, the ratio of the masses of soot particles formed from acetylene or benzene was two or six times higher than the mass of methane consumed in soot particle growth. Therefore, the total soot particle surface on which particles grow was higher, thus permitting the observation of the promotion effect. For these reasons, the promotion effect for the methane-benzene mixture was higher than for the methane-acetylene mixture.

We have not observed the promotion effect in the work of Ref. 8 for this reason. So the soot yield was taken as additive.

Because of the observed weight increase in the carbon formed from methane, the particle weight gain [H in Eq. (6)] caused by particle growth from methane was calculated from the experimental data obtained.

Coincidence of the curves obtained by calculation according to Eq. (6) with the experimental curves for both mixtures can be considered satisfactory. But careful analysis reveals an essential difference.

The results presented in Table 2 for the methane-benzene mixture show the same tendency as for the acetylene-benzene mixture [8]. The ratio of the additive soot flux to the experimental mixture flux exceeds 1. The fact that this ratio approaches 1 with increasing benzene concentration is attributed to decreasing soot flux from methane to additive soot flux. The ratio of the experimental soot flux to that from benzene approaches 1 for all benzene concentrations (except benzene concentration 0.4%). This fact permits us to draw the conclusion that benzene fully inhibits soot particle inception from methane, and the latter is consumed for only soot particle growth.

Another result was observed for the methane-acetylene mixture (Table 3). The calculation by Eq. (6) satisfactorily coincides with the experimental data, and the ratio of the additive soot flux to the experimental mixture flux exceeds 1 at a low acetylene concentration. It should be mentioned that the ratio of the experimental soot flux to that for acetylene exceeds 1 for all experiments. The experimental results obtained reveal that, in spite of the acetylene inhibition of the soot particle inception from methane, the inhibition does not result in complete cessation of the particle inception from methane. This point is considered in the discussion.

The observed inhibition of the soot particle formation from methane in the presence of acetylene and benzene can be attributed to a longer induction period for methane compared with both acetylene and benzene as was explained in Ref. 8.

Discussion

The linear dependence of particle number density upon methane concentration obtained during pyrolysis of methane is also confirmed for acetylene [9] and lately for benzene.

The soot particle number densities from both methane and acetylene are expressed by similar equations:

$$\underline{\text{methane}}$$
$$N = 9.4\ 10^{20}\ [CH_4]\ \exp(-39{,}400/T)$$

$$\underline{\text{acetylene}}$$
$$N = 3.0\ 10^{22}\ [C_2H_2]\ \exp(-41{,}000/T)$$

Some remarks were presented in works 10 and 11 that throw a shadow of doubt upon the results obtained from the investigation of soot formation during hydrocarbon pyrolysis by the calculation used in the present work, as the coagulation of soot particles was not taken into consideration.

Coagulation certainly occurs during the process of soot particle formation. The optical measurements made during hydrocarbon pyrolysis in shock tubes and at flat-flame combustion show the maximum soot particle number density. The descending part of the

curve on this maximum is interpreted as a coagulation.

Unfortunately, the optical measurements do not make it possible to answer the question as to what particles are responsible for the decrease in particle number density at the initial stage of soot formation. Assuming that there occurs a coagulation of the spherical soot particles formed, one has to use the term "coalescence" [12], i.e., a concept of liquid drops. It is very difficult to agree upon this concept. There are no experimental data available confirming that soot particles made of carbon atoms might be liquid at 2000 K.

It may be supposed that a decrease of soot particle number density is connected with a molecular process of heterogeneous decomposition of the long-chain polyyne molecules, as well as of soot particle nuclei on the surface. Krestinin [13] supposes and proves by calculation that the soot particle nuclei are made up of long-chain polyyne molecules. These particles contain up to 25–30 carbon atoms, so the optical systems can register them along with soot particles and tar.

The chain structure of soot is an outcome of the particle coagulation. But this coagulation being accompanied by a decrease in soot particle number does not result in the decrease of the soot surface area. This is a well-known result, and it was proved by coincidence of the data obtained by measuring the soot surface area by the use of both adsorption and electron microscopy [1, p. 113]. The particle number density being measured in our work is the soot particles leaving the zone of soot formation. Certainly, we know little about the processes occurring in this zone, but the spherical soot particles leaving this zone have some concrete physical meaning. They are the elementary particles that determine the soot dispersion properties.

The experimental results for the pyrolysis of methane-acetylene and methane-benzene mixtures allow us to conclude that acetylene is the main intermediate product on the pathway methane → soot. Actually, it is a well-known fact that acetylene is the first compound formed at methane pyrolysis. Benzene is also formed at methane pyrolysis, but later. But in our work [8], it was shown that benzene cannot form soot particles in the presence of acetylene.

Soot formation from methane via a stage of acetylene generation explains the observed difference in soot formation from methane-benzene and methane-acetylene mixtures. Obviously, the soot particles formed from acetylene inhibit the soot inception from methane as well as during pyrolysis of a methane-benzene mixture. But acetylene does not influence additional generation of acetylene molecules from methane. Acetylene formed additionally from methane molecules increases the concentration of acetylene and results in a surplus of soot particles, thus giving an impression of formation of the soot particles from methane.

Soot formation during pyrolysis of a methane-benzene mixture has been investigated in other work [7] at the same concentrations of the compounds and the same temperatures as in this work. The authors also observed the absence of additivity in particle number density. But they did not reveal the likeness of the soot fluxes from mixtures with the benzene ones. This can be attributed to nonisothermality of the experimental technique used.

Conclusions

1. During methane pyrolysis under isothermal conditions, the particle number density of soot depends linearly on methane concentration. The particle number density is described by the following equation:

$$N = 9.4 \cdot 10^{20}[CH_4] \exp(-39{,}400/T).$$

2. During pyrolysis of methane-benzene mixtures, soot particles are formed only from benzene, and methane is consumed only for particle growth.
3. Promotion of soot formation from methane is observed at pyrolysis of both methane-acetylene and methane-benzene mixtures.

Acknowledgment

The research described in this publication was made possible in part by Grant N RNA000 from the International Science Foundation.

REFERENCES

1. *Carbon Black* (J.-B. Donnet, R. C. Bansal, and M.-J. Wang, Eds.), Marcel Dekker, New York, 1993.
2. Glassman, I., *Twenty-Second Symposium (International) on Combustion,* The Combustion Institute, Pittsburgh, 1988, p. 295.
3. Haynes, B. S., and Wagner, H. Gg., *Prog. Energy Combust. Sci.* 7:229 (1981).
4. *Particulate Carbon. Formation during Combustion* (D. C. Siegla and G. W. Smith, Eds.), New York, Plenum Press, 1981.
5. Lahaye, J., and Prado, G., in *Chemistry and Physics of Carbon* (P. L. Walker and P. A. Thrower, Eds.), Marcel Dekker, New York, 1978, Vol. 14, p. 167.
6. Tesner, P. A., *Formation of Solid Carbon from Hydrocarbons in Gas Phase,* Moscow, Khimiya, 1972.
7. Prado, G., and Lahaye, J., in *Particulate Carbon* (D. C. Siegla and W. G. Smith, Eds.), New York, Plenum Press, 1981, p. 143.
8. Tesner, P. A., and Shurupov, S. V., *Combust. Sci. Technol.* 92:61 (1993).

9. Krestinin, A. V., Tesner, P. A., and Shurupov, S. V., in *Extended Abstracts of the Second International Conference on Carbon Black*, Centre National Recherche Scientifique, Mulhouse, France, 1993, p. 23.
10. Wersborg, B. L., Howard, J. B., and Williams, G. C., *Fourteenth Symposium (International) on Combustion*. The Combustion Institute, Pittsburgh, 1973, p. 929.
11. Harris, S. J., Weiner, A. M., and Ashcraft, C. C., *Combust. Flame* 64:65 (1986).
12. Harris, S. J., and Weiner, A. M., *Annu. Rev. Phys. Chem.* 36:31 (1985).
13. Krestinin, A. V., *Khim. Fiz.* 13:121 (1994).

Twenty-Fifth Symposium (International) on Combustion/The Combustion Institute, 1994/pp. 661–669

HIGH-TEMPERATURE PYROLYSIS AND OXIDATION OF FULLERENE C_{60} BEHIND SHOCK WAVES

S. VON GERSUM AND P. ROTH
Institut für Verbrennung und Gasdynamik Universität Duisburg
47048 Duisburg, Germany

Submicron fullerene C_{60} particles dispersed in a carrier gas and shock-heated to temperatures of about 2000 K evaporate in a few microseconds to form C_{60} vapour. In a first group of experiments, the high-temperature pyrolysis of C_{60}/Ar mixtures behind reflected shock waves was studied at temperatures 2370 K $\leq T \leq$ 3500 K. Spectral- and time-resolved emission in the wavelengths range 280 nm $\leq \lambda \leq$ 580 nm was detected by an intensified charge coupled device (CCD) camera. From the time-dependent emission at specified wavelengths, the decomposition rate of C_{60} was determined, which seems to obey an Arrhenius law. At temperatures above 2600 K, spectral band structures appear, which could be identified to result from C_2 emission. In the second group of experiments, the high-temperature oxidation of fullerene in C_{60}/O_2/Ar mixtures was studied at temperatures 1655 K $\leq T \leq$ 2705 K and pressures between 1.5 and 2.6 bar. The progress in the oxidation was measured by tunable IR-diode laser absorption of CO and CO_2. Additionally, the spectral and time-resolved emission during the fullerene oxidation was recorded by the CCD camera. From the time-dependent increase of CO concentration and the time-dependent decrease of the spectral emission, apparent rate coefficients for the formation of CO and the disappearance of C_{60} were determined.

Introduction

The existence of fullerenes as a new carbon morphology has been established during the last few years. The C_{60} molecule discovered to be stable by Kroto et al. in 1985 [1] was proposed to be a soccer-ball-shaped cage where the carbon atoms are placed at the edges of 12 pentagons and 20 hexagons. The proposed structure was confirmed in an immense number of studies, see for example Refs. 2 through 6. A comparison of measured optical spectra of C_{60} with calculated energy states was one method that provided proof for the spherical hollow structure of C_{60}. For this purpose, C_{60} was either deposited as a thin film or was present in a solution. Gas-phase spectra of free C_{60} molecules were detected only in the infrared region [2]. Fullerenes were found in premixed low-pressure flames by Löffler and Homann [7] by applying mass spectroscopy. Howard [8] detected several fullerene structures in various optimized flames.

At room temperature, fullerene C_{60} is a brown-black powder, which is meanwhile commercially available. We have combined our experiences on particle evaporation, soot oxidation, and shock-wave kinetics to study fullerene pyrolysis and oxidation at high temperatures. Because of the very rapid evaporation of the submicron fullerene particles, the high-temperature reactions proceed in the gas phase. The aim of this study is to present kinetic data for the thermal and oxidation stability of C_{60}.

Experimental

The experimental setup used to study fullerene pyrolysis and oxidation at high temperatures is shown schematically in Fig. 1. It consists of an aerosol generator for dispersing fullerene powder, the main shock tube for heating the C_{60}-containing aerosol to high temperatures, a spectrograph with intensified charge coupled device (CCD) camera for emission measurements, and a tunable IR-diode laser that was used simultaneously for absorption measurements of oxidation products CO and CO_2.

The C_{60} powder was dispersed in Ar by an expansion-wave-driven aerosol generator, see Rajathurai et al. [9]. It consists of a glass vessel of $V = 3 \cdot 10^4$ cm^3 volume connected to a glass tube of 5-cm inner diameter, which is separated by a thin diaphragm from a high-pressure tube of the same diameter. A thin dispersion plate is positioned near the diaphragm, which carries for every experiment about 100 mg of the fullerene powder. Before starting the powder dispersion, the whole apparatus was evacuated to a pressure of about 10^{-4} mbar. Subsequently, the high-pressure tube was filled with Ar. After bursting of the diaphragm, the high-pressure gas Ar expands in the form of a supersonic expansion wave into the evacuated vessel, thus dispersing the fullerene powder and bringing it into aerosol form. The size of the fullerene particles in the generated aerosol is between 100 and 600 nm. In case of oxidation experi-

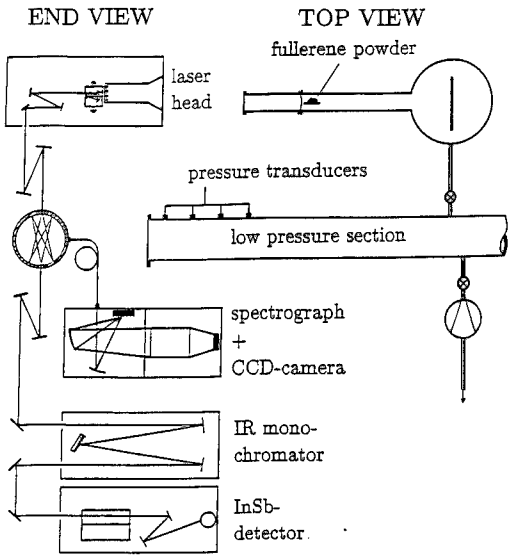

FIG. 1. Aerosol generator and low-pressure section of the shock tube with IR-diode laser system and intensified CCD camera.

ments, a certain amount of O_2 was added to the aerosol. The fullerene C_{60} powder used during the present experiments was supplied by Hoechst AG, Germany. It contains about 1% C_{70}. The generated aerosols were subsequently transported into the running section of a shock tube. During the aerosol generation and the subsequent transfer procedure into the shock tube, an unknown amount of particles were lost. Therefore, it was not possible to determine the initial C_{60} concentration precisely.

The stainless steel shock tube has an internal diameter of 8 cm, a total length of 11 m, and a running section of 7.2 m in length. The initial pressure of the aerosol measured by calibrated diaphragm-type pressure transducers was in the range from 25 to 50 mbar. The shock velocity was measured by piezoelectric pressure transducers positioned at known distances along the shock-tube axis. The post-shock temperature and pressure were calculated from the incident shock speed by applying one-dimensional conservation equations.

The light emitted from the shock-heated C_{60}-containing aerosol was focussed via a light fiber on the entrance slit of a 1/8-m spectrograph, which has a spectral range of $\Delta\lambda = 250$ nm and a resolution of 1.3 nm. The spectrally resolved light was detected by an intensified CCD camera (LA VISION, Germany), allowing a fast time shift of the optical information. For this purpose, only a few lines at the top of the CCD sensor chip were illuminated for a certain time interval. The stored spectral emission was stepwise transferred line by line into the dark zone of the CCD chip, which served as a memory. In this way, the spectral as well as the temporal behaviour of the emitted light could be recorded. Spectral effects of the quantum efficiency of the intensifier were taken into account. The time resolution of the CCD camera system, which depends on the number of illuminated chip lines times the data transfer rate per line, is in the present case about 30 μs.

The optical setup for measuring CO and CO_2 consists of a tunable IR-diode laser, a specially designed multipass cell (Fraunhofer Institut, Germany), a 0.5-m monochromator, and an infrared detector. The laser beam was focussed on the entrance window and traverses the shock tube 16 times, thus enlarging the optical absorption path length. The vertical and horizontal distance between the external focal points was 12 mm each. The out-coming laser radiation enters the monochromator, which served as a filter for laser modes and for spectral emission, and was subsequently focussed on the detector. For calibration purposes, a gas cell or an etalon was inserted into the laser beam. The laser was pulsed with a frequency of 55 kHz and was tuned over the 0-1 P5 absorption line of CO at $\nu = 2123.70$ cm^{-1}. Absorption measurements of CO_2 were performed at the 00°0-00°1 R 28 transition at $\nu = 2369.09$ cm^{-1}. Both IR-diode laser measurements and emission measurements were performed in the same optical plane. For more details of the tunable IR-diode laser system, see Refs. 10 through 12.

Results

Emission Measurements in C_{60}/Ar Mixtures:

The emission measurements of C_{60}/Ar mixtures were conducted behind reflected shock waves in the temperature range of 2370 K $\leq T \leq$ 3500 K at pressures between 1.3 and 2.2 bar. For every shock-tube experiment, the spectral- and time-resolved emission was recorded by the CCD camera.

Typical examples of spectral- and time-resolved C_{60}/Ar emission are illustrated in Fig. 2. Below 280 nm, a measurable emission could not be recorded. In the upper part of Fig. 2, two spectra obtained at $t = 50$ μs and $t = 900$ μs for a post-shock temperature of $T = 3000$ K are shown. The intensity signals are composed of two parts: a continuously increasing quasi-black-body background radiation (illustrated by the baselines) and relatively broad line structures appearing at $\lambda \approx 435$ nm and $\lambda = 473$ nm followed by a sharp peak at $\lambda = 517$ nm. The 50-μs emission curve is higher by a factor of 2 in the absolute intensity.

Similar spectra were obtained from all other experiments performed at conditions $T > 2600$ K. In the temperature range 2370 K $\leq T \leq$ 2600 K, the measured spectral emission did not show any band structure. It increased with increasing wavelength

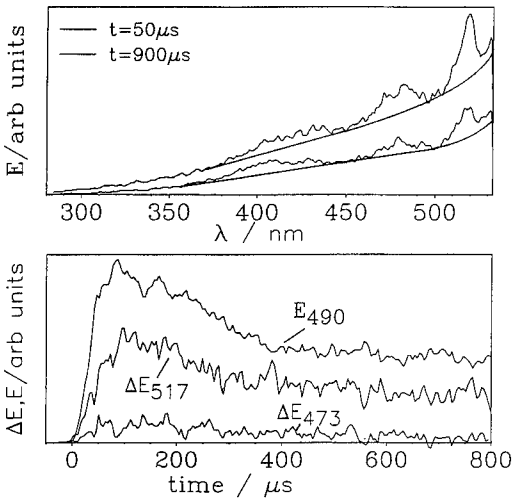

FIG. 2. C_{60}/Ar emission at T = 3000 K; upper part: spectral-resolved emission; lower part: time-resolved intensity (E_{490}) and intensity differences (ΔE_{473} and ΔE_{517}).

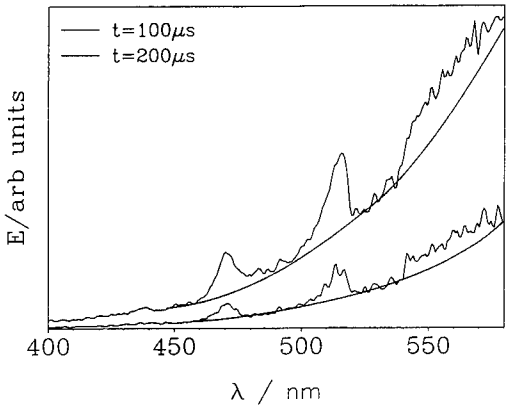

FIG. 3. Spectral-resolved emission in C_{60}/O_2/Ar mixture. T = 2590 K; [O_2] = 13%.

similar to the baselines in the upper part of Fig. 2 and with very weak changes in time. An example of the time evolution of the spectral emission at three different wavelengths is shown in the lower part of Fig. 2. The absolute emission intensity at λ = 490 nm (between the band structures) characterizes the time-dependent behaviour of the baseline curve. To the contrary, the emissions at λ = 473 nm and λ = 517 nm are the intensity differences between the respective peak band intensities and the baseline. All three emission curves increase rapidly after shock arrival, show maxima at about 100 μs, and decrease again to nearly constant levels. Similar results were obtained from all other experiments.

Emission and Concentration Measurements in C_{60}/O_2/Ar Mixtures:

The oxidation experiments in C_{60}/O_2/Ar mixtures were performed in the temperature range of 1655 K $\leq T \leq$ 2705 K at post-shock pressures between 1.5 and 2.6 bar. The C_{60} powder was dispersed in gas mixtures containing 9–15% O_2 in Ar. The progress in the fullerene oxidation was simultaneously monitored by spectral emission measurements and by CO or CO_2 absorption measurements.

A typical example of spectral emission measured in the wavelength range 400 nm $\leq \lambda \leq$ 580 nm is shown in Fig. 3. The C_{60} was in this case dispersed in a gas mixture containing 13% O_2 and shock-heated to a temperature of T = 2590 K. Contrary to the experiments without O_2, band structures appear at λ = 473 nm and λ = 517 nm even at this relatively low temperature, and also, the intensity decreases with increasing time very fast. A broad intensity bulge can be observed between λ = 540 and 565 nm. Similar intensity distributions were obtained at conditions T > 2150 K.

An example of tunable IR-diode laser absorption at the CO wavelength in a reacting C_{60}/O_2/Ar mixture is shown in Fig. 4. The sequence of 14 laser scans was recorded from a mixture containing 13% O_2, which was shock-heated to a temperature of 2550 K. The time of shock arrival is within the second scan. The shock causes vibrations of the multipass cell indicated by the periodical changes in the transmitted laser intensity, but the vibrations do not affect the absorption measurements. In the lower part of Fig. 4, selected scans are shown in more detail with an enlarged time or frequency scale. Scan A was recorded before shock arrival and shows the undisturbed laser light distribution. Beginning with the first post-shock scan B, absorption lines of CO appear, showing increasing absorption in scans C-D, which indicates increasing CO concentration in the high-temperature reaction system. Similar results were obtained from other CO and CO_2 absorption measurements.

The evaluation of the measured spectral absorption of CO and CO_2 in terms of partial pressure or concentration was made by applying the Lambert-Beer law:

$$p_a = -\ln[I(\nu)/I_0(\nu)]/lS\,\Phi_\nu \qquad (1)$$

where $I_0(\nu)$ and $I(\nu)$ are the incident and the transmitted laser intensity at frequency ν and l is the absorption path length. The line strengths S of the observed CO and CO_2 vibrational-rotational lines are well known [10,11]. The term Φ_ν is the line shape function, which can in the present case well be described by Voigt profiles [11,12]. Concentrations of CO or CO_2 were obtained by fitting calculated Voigt profiles to the measured spectral intensity distribu-

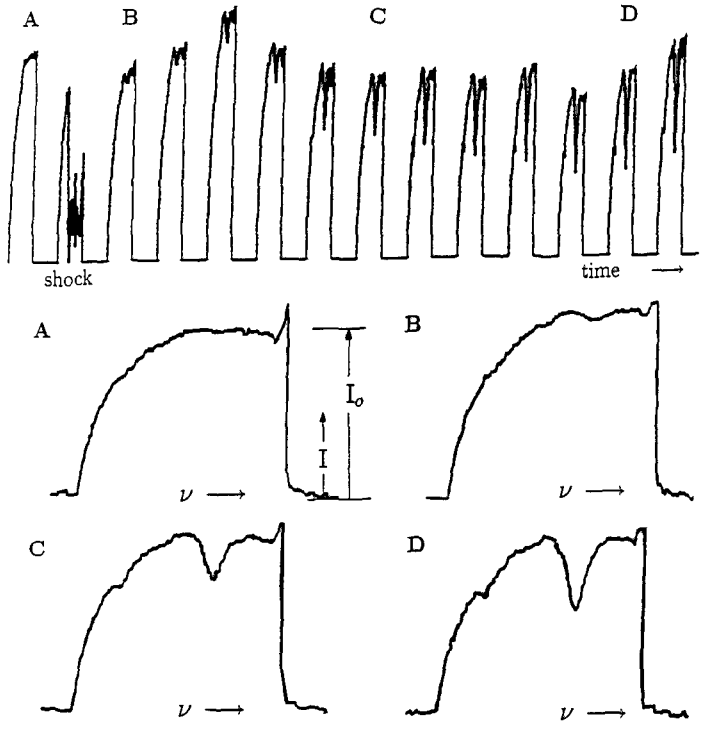

FIG. 4. IR-diode laser scans with CO absorption lines obtained from a shock-tube experiment of a reacting $C_{60}/O_2/Ar$ mixture. T = 2590 K; O_2 = 13%.

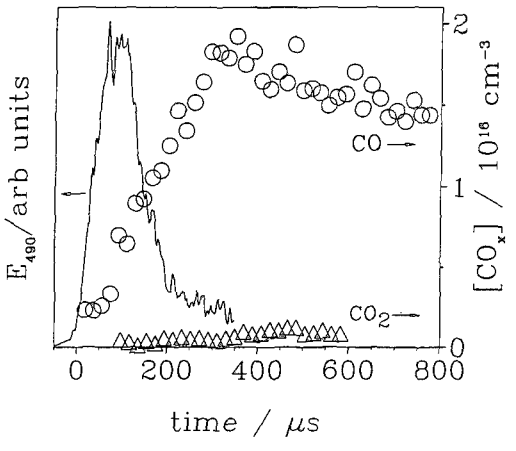

FIG. 5. Time-dependent CO concentration and E_{490} emission (T = 2350 K; $[O_2]$ = 12.5%) and CO_2 concentration measured at slightly different conditions (T = 2330 K; $[O_2]$ = 10.7%) in reacting $C_{60}/O_2/Ar$ mixtures.

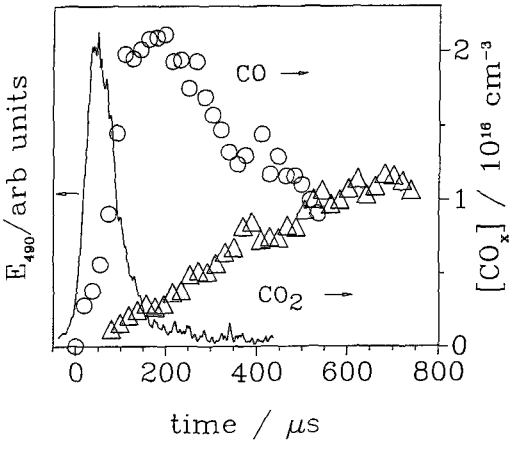

FIG. 6. Time-dependent CO concentration and E_{490} emission (T = 2550 K; $[O_2]$ = 13.0%) and CO_2 concentration (T = 2590 K; $[O_2]$ = 13.4%) in reacting $C_{60}/O_2/Ar$ mixtures.

tion of each laser scan. Typical time-dependent concentrations of CO and CO_2 obtained from four different $C_{60}/O_2/Ar$ experiments are shown in Figs. 5 and 6. Although the temperatures are almost identical for the two examples in Fig. 5, significant differences in the time evolution of the two reaction products are obvious. CO increases nearly linearly with time, reaches a maximum at about 300 μs, and decreases again. The concentration of CO_2 is under similar reaction conditions more than a factor of 15 lower. The additional solid line in Fig. 5 represents the time behaviour of light emitted at λ = 490 nm.

TABLE 1
Experimental conditions, measured CO and CO_2 formation rates, and emission characteristics k_{490} in $C_{60}/O_2/Ar$ mixtures

T (K)	p (bar)	$[O_2]$ (%)	$d[CO]/dt$ ($cm^{-3}\,s^{-1}$)	$d[CO_2]/dt$ ($cm^{-3}\,s^{-1}$)	k_{490} (s^{-1})	$[CO]_{max}$ (cm^{-3})
1655	1.63	15.1	$0.3 \cdot 10^{19}$			$0.2 \cdot 10^{16}$
1760	1.58	9.4	$0.3 \cdot 10^{19}$			$0.2 \cdot 10^{16}$
2130	2.62	14.5	$4.0 \cdot 10^{19}$		$3.3 \cdot 10^{3}$	$1.4 \cdot 10^{16}$
2140	1.68	9.9	$1.6 \cdot 10^{19}$		$7.1 \cdot 10^{3}$	$1.2 \cdot 10^{16}$
2250	2.46	12.0	$1.9 \cdot 10^{19}$			$0.4 \cdot 10^{16}$
2280	2.24	13.8	$3.8 \cdot 10^{19}$		$4.7 \cdot 10^{3}$	$1.4 \cdot 10^{16}$
2330	2.52	10.7		$0.2 \cdot 10^{19}$	$7.7 \cdot 10^{3}$	
2350	2.30	12.5	$5.5 \cdot 10^{19}$		$8.3 \cdot 10^{3}$	$1.9 \cdot 10^{16}$
2500	2.53	12.8		$1.8 \cdot 10^{19}$	$10.0 \cdot 10^{3}$	
2550	2.58	13.0	$12.0 \cdot 10^{19}$			$2.2 \cdot 10^{16}$
2590	2.28	13.4		$1.9 \cdot 10^{19}$	$12.0 \cdot 10^{3}$	
2700	2.38	12.4	$11.0 \cdot 10^{19}$		$19.0 \cdot 10^{3}$	$1.6 \cdot 10^{16}$

The emission reaches a maximum at about 100 μs and disappears completely within 400 μs. The examples in Fig. 6 were obtained under temperature conditions that were approximately 200 K higher than the previous ones. CO increases within 150 μs to a maximum value of about 2×10^{16} cm^{-3} and decreases during the whole measurement time of about 800 μs. The solid line in Fig. 6 again represents the emission at $\lambda = 490$ nm. The emission reaches a maximum within 50 μs and disappears completely after 300 μs. It is remarkable that for the experiments in both Figs. 5 and 6, the maximum value of the sum of CO and CO_2 is about 2 to 2.5×10^{16} cm^{-3}. It is reached at a time where the corresponding emission signals E_{490} are approximately zero. The experimental conditions of all $C_{60}/O_2/Ar$ experiments together with the resulting formation rates of CO and CO_2 at $t \approx 0$ and the maximum CO concentrations are listed in Table 1. The formation rates of both CO and CO_2 clearly increase with temperature, whereas the maximum CO concentrations do not show a clear temperature dependence.

Discussion

The C_{60}/Ar Reaction System:

It can be assumed that several subsequent processes occur in the shock-heated C_{60}/Ar aerosol. Because of the relatively high vapour pressure of C_{60}, the solid agglomerated carbonaceous particles evaporate rapidly at high temperatures. Calculations based on thermodynamic data for fullerene C_{60} given by Mathews et al. [13] and by Matsuo and Suga [14] indicate a complete evaporation of the particles within about 30 μs. This value was also experimentally confirmed by some laser light-scattering measurements behind shock waves, which cannot be presented here. This means for all our experiments that the initial reactant C_{60} is a gas-phase compound for most of the observation time.

The emission signals obtained for temperatures $T < 2600$ K are quasi-continuous spectra and were assumed to be typical for C_{60} vapour. This assumption is further supported by the fact that no significant changes in time were observed. The spectral distributions are self-similar; i.e., for every experiment, the intensity ratio at two fixed wavelengths is approximately the same.

For conditions $T > 2600$ K, the measured emission shows both a continuous and a band structure. The different bands at 517, 473, and 438 nm can be related to the 0-0, 1-0, and 2-0 $d^3\Pi_g \leftarrow a^3\Pi_u$ transitions of C_2. The relatively broad, weak band at 405 nm was identified to be the $A^1\Pi_u \leftarrow X^1\Sigma_g^+$ transition of C_3. The observed emission at $T > 2600$ K must, therefore, be a superposition of at least C_{60}, C_2, and C_3 radiation. We therefore identify the following emissions:

$$E_{490} \text{ with } C_{60}$$
$$\Delta E_{517}, \Delta E_{473}, \Delta E_{438} \text{ with } C_2$$
$$\Delta E_{405} \text{ with } C_3.$$

The intensity profiles shown in the lower part of Fig. 2 can therefore be associated with the respective species concentrations. It is remarkable that all traces in the lower part of Fig. 2 very rapidly increase after shock arrival. The fast rate of appearance of the C_2 emission is particularly surprising, indicating that the thermal decomposition of C_{60} is not a simple C_2 abstraction process under our reaction conditions. The

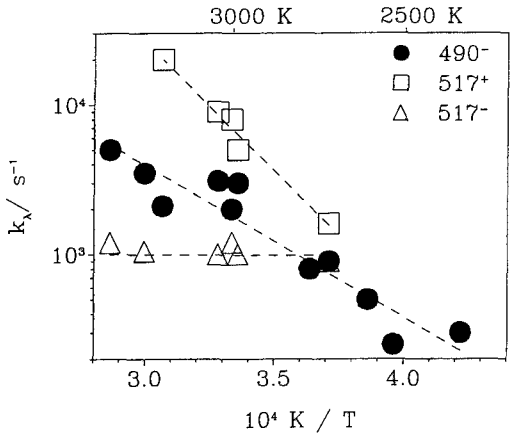

FIG. 7. Apparent rate coefficients based on emission measurements for C_{60} disappearance k_{490}, C_2 disappearance k_{517}^-, and C_2 appearance k_{517}^+ in C_{60}/Ar systems.

time profiles of the emissions ΔE_{517} and ΔE_{473} were in all cases exactly the same with proportionality factors between 2.6 and 4.0. It was not possible to separate the C_3 emission ΔE_{405} clearly from the C_{60} baseline, so a further evaluation was not made. Emission of other carbon fragments like C_4 and C_6 could not be identified. The intensity ratios $\Delta E_{473}/\Delta E_{490}$ and $\Delta E_{517}/\Delta E_{490}$ taken at a fixed time increased with temperature, indicating an increasing amount of C_2 compared to C_{60}.

The measured time-dependent emission intensity profiles of Fig. 2 (lower part), of Figs. 5 and 6, and of other experiments not shown in this article can further be evaluated in terms of kinetic parameters. We define rate coefficients k_λ for the disappearance rate or appearance rate of the various emission signals by the respective slopes normalized with the maximum emission:

$$k_\lambda = \left| \frac{1}{E_{\lambda,\max}} \left(\frac{dE_\lambda}{dt} \right) \right|_t . \qquad (2)$$

The application of Eq. (2) to the $\lambda = 490$ nm emission (C_{60}) just behind the intensity maximum results in rate coefficients k_{490} for the disappearance rate of C_{60}. All values obtained are summarized in the Arrhenius diagram of Fig. 7, see closed circles. The dashed line represents a least-square fit to the data points, where the apparent activation energy is about 195 kcal/mol.

The emission at $\lambda = 517$ nm (C_2) is characterized both by the signal increase at $t \approx 0$ and by the signal decrease at $t = t_m$, which is the time of maximum emission. We have applied Eq. (2) to both parts of all measured emission signals. The sets of apparent rate coefficients k_{517}^+ (squares) and k_{517}^- (triangles) are also shown in Fig. 7. The formation rate of C_2 (k_{517}^+) is obviously much higher than the disappearance rate (k_{517}^-). It is a factor of 3–10 higher than the disappearance rate of E_{490} radiation (C_{60}) and has an apparent activation energy of about 330 kJ/mol. This means that neither the reaction $C_{60} \rightarrow C_{58} + C_2$ nor the complete conversion reaction $C_{60} \rightarrow 30\ C_2$ can be used to explain the time behaviour of the emission signals. It seems that after the breakup of the C_{60} molecules, secondary reactions of C_2, C_3, and other fragments must be considered under our high-temperature conditions. This statement presumes that the measured respective emissions are representative for the species concentrations.

The C_{60}/O_2/Ar Reaction System:

As in the previous case, the spectra measured in the high-temperature C_{60}/O_2/Ar system are a superposition of a continuous C_{60} emission and a band-structured C_2 emission, which appeared in the present case for conditions $T > 2100$ K. Each continuous emission spectrum could be well described by black-body radiation calculated for the experimental temperature. The spectral bands at $\lambda = 473$ nm and $\lambda = 517$ nm were again identified to be C_2 transitions. The procedure to evaluate the time-dependent emission signals is the same as described before. The application of Eq. (2) to the disappearance rate of all E_{490} emission (C_{60}) measurements results in apparent rate coefficients k_{490} listed in Table 1. At comparable temperatures, the k_{490} values of Table 1 are more than a factor of 20 higher than the corresponding value obtained from the C_{60}/Ar experiments. The very high scattering of the emission signals at $\lambda = 473$ nm and $\lambda = 517$ nm made a further evaluation of the data impossible. Emission maxima were detected within the first 100–200 μs at temperatures below 2250 K. At higher temperatures, a much faster rate of appearance of the respective emissions was observed, which could not be correctly resolved by the camera system. The C_2 emissions decayed to zero at the same time as the emission E_{490} (C_{60}).

The evaluation of the measured time-dependent concentrations of CO and CO_2 during oxidation of fullerene C_{60} is aggravated by the fact that the concentration of the quasi-gas-phase initial reactant C_{60} is not known. All oxidation experiments were performed with a significant excess of O_2. The sum of CO and CO_2 concentrations measured at later reaction times was in nearly all experiments equal to 2×10^{16} cm^{-3}. From the assumption of a complete oxidation of the fullerene carbon to CO or CO_2, we end up with an initial C_{60} concentration of $[C_{60}]_0 = 3.5 \times 10^{14}$ cm^{-3}. From the initial slopes of the mea-

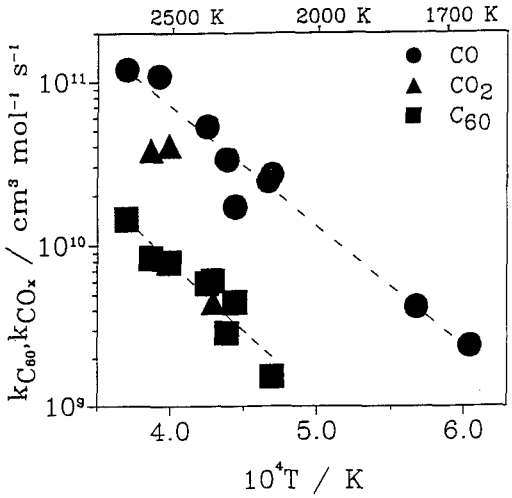

FIG. 8. Apparent rate coefficients for CO formation k_{CO} and C_{60} consumption $k_{C_{60}}$.

sured CO and CO_2 concentrations, apparent rate coefficients

$$k_{CO_x} = \left(\frac{d[CO_x]}{dt}\right)_{t=0} \frac{x}{[C_{60}]_0 \cdot [O_2]_0 \cdot 2} \quad x = 1\ CO \quad x = 2\ CO_2 \tag{3}$$

were determined. Results obtained are summarized in Fig. 8. The k_{CO} clearly show Arrhenius behaviour. The three CO_2 measurements (triangles) are factors of 3–12 below the k_{CO} values and indicate (if reasonable at all) a stronger temperature dependence. An apparent rate coefficient for the disappearance of C_{60} can be obtained from the emission measurements at $\lambda = 490$ nm by

$$k_{C_{60}} = k_{490}/[O_2]_0. \tag{4}$$

Values of $k_{C_{60}}$ obtained are also included in Fig. 8 (squares). They also show Arrhenius behaviour. Least-square fits to the CO and C_{60} data in Fig. 8 are indicated as dashed lines and lead to the following expressions:

$$k_{CO} = 6.2 \times 10^{13} \exp(-140\ kJ\ mol^{-1}/RT)\ cm^3\ mol^{-1}\ s^{-1}$$

$$k_{C_{60}} = 1.0 \times 10^{14} \exp(-187\ kJ\ mol^{-1}/RT)\ cm^3\ mol^{-1}\ s^{-1}.$$

The overall uncertainties of k_{CO} and $k_{C_{60}}$ due to scattering and possible experimental errors are estimated to be about 50 and 80%, respectively. Both rate coefficients have comparable apparent activation energies. The absolute values differ by about an order of magnitude. A comparison with literature values is not possible because no other data are available. It is at the moment too early to evaluate the fullerene oxidation experiments further. An accepted oxidation mechanism is not available, so computer simulations or computer fittings of the measured CO and CO_2 concentration profiles are premature.

Summary

The high-temperature pyrolysis and oxidation of fullerene was studied in C_{60}/Ar and C_{60}/O_2/Ar mixtures. The progress in the chemical rate processes was recorded both by spectral- and time-resolved emission spectroscopy and by tunable IR-laser spectroscopy of CO and CO_2. The following conclusions were drawn:

1. C_{60} vapour is stable up to 2100 K in an inert atmosphere within 1 ms.
2. At temperatures $T > 2600$ K, C_{60} decomposed, and C_2 and C_3 were identified as decomposition products.
3. Oxidation of C_{60} by O_2 was observed at temperatures $T > 1500$ K with CO being the main oxidation product.
4. Time profiles of CO and spectral emission at $\lambda = 490$ nm were interpreted as apparent rate coefficients for CO formation and C_{60} consumption.

A detailed interpretation of the present data based on a kinetic model is at the moment not possible.

Acknowledgments

The authors wish to thank Fa. Hoechst AG, Germany, for the supply of fullerene powder. The financial support of the Deutsche Forschungsgemeinschaft is gratefully acknowledged.

REFERENCES

1. Kroto, H. W., Heath, J. R., O'Brien, S. C., Curl, R. F., and Smalley, R. E., *Nature* 318:162–163 (1985).
2. Frum, C. I., Engleman, R., Jr., Hedderich, H. G., Bernath, P. F., Lamb, L. D., and Huffman, D. R., *Chem. Phys. Lett.* 176:504–508 (1991).
3. O'Brien, S. C., Heath, J. R., Curl, R. F., and Smalley, R. E., *J. Chem. Phys.* 88:220–230 (1988).
4. Radi, P. P., Hsu, M. T., Brodbelt-Lustig, J., Rincon, M., and Bowers T., *J. Chem. Phys.* 92:4817–4822 (1990).
5. Lykke, K. R., and Wurz, P., *J. Phys. Chem.* 96:3191–3193 (1992).

6. Sandler, P., Lifshitz, C., and Klots, C. E., *Chem. Phys. Lett.* 200 5:445–450 (1992).
7. Löffler, S., and Homann, K. H., *Twenty-Fourth Symposium (International) on Combustion*, The Combustion Institute, Pittsburgh, 1992, pp. 355–362.
8. Howard, J. B., *Twenty-Fourth Symposium (International) on Combustion*, The Combustion Institute, Pittsburgh, 1992, pp. 933–946.
9. Rajathurai, A. M., Roth, P., and Fißan, H., *Aerosol Sci. Technol.* 12:613–619 (1990).
10. Brandt, O., and Roth, P., *Combust. Flame* 77:69–78 (1989).
11. Roth, P., Brandt, O., and von Gersum, S., *Twenty-Third Symposium (International) on Combustion*, The Combustion Institute, Pittsburgh, 1990, pp. 1485–1491.
12. von Gersum, S., and Roth, P., *Twenty-Fourth Symposium (International) on Combustion*, The Combustion Institute, Pittsburgh, 1992, pp. 999–1006.
13. Mathews, C. K., Sai Baba, M., Lakshmi Narasimhan, T. S., Balasubramanian, R., Sivaraman, N., Srinivasan, T. G., and Vasudeva Rao, P. R., *J. Phys. Chem.*, 96:3566–3568 (1992).
14. Matsuo, T., and Suga, H., *Solid State Comm.* 83 (9):711–715 (1992).

COMMENTS

K. H. Homann, Inst. Fuer Physik. Chemie, Germany. You found that the apparent activation energy for oxidation of C_{60} was larger than that of thermal decomposition, although C_{60} is thermally very stable. Do you have an explanation for that?

Author's Reply. The activation energies for the disappearance rates of the $\lambda = 490$ nm emission are comparable for thermal decomposition and oxidation of fullerene C_{60}. We have related this emission to the C_{60} concentration. This is an assumption, which can be incorrect because the emission at this wavelength can be influenced by broadband emission of other C clusters like C_{58}, C_{56}, etc., which are present in the system. The C_2-formation rates evaluated from the pyrolysis experiments and the CO-formation rates during C_{60} oxidation are both above the corresponding $\lambda = 490$ nm disappearance rates and show a stronger temperature dependence.

•

I. S. Zaslonko, Semenov Institute of Chemical Physics, Moscow. Did you compare your results on fullerene thermal decomposition with observable rate constants for black soot thermal decomposition? Is there the specific impact of fullerene structure or not?

Author's Reply. At the moment we have no rate coefficient data for the thermal decomposition of carbon black available, so that we cannot compare it to our C_{60} measurements.

•

Assa Lifshitz, The Hebrew University of Jerusalem, Israel. 1. How can you account for such a low activation energy for the ejection of C_2 from C_{60}? The value that you obtained is far below the thermochemical value (heat of reaction).

2. Since the ionization energy of C_{60} is very similar to (or even smaller than) that of C_2 ejection, is it possible that the first step is ionization followed by decomposition of the ion?

Author's Reply. 1. We know that our activation energy for the C_2 formation is below the thermochemical value, but we have no explanation for this discrepancy.

2. Yes, it is possible that C_{60} is ionized before it decomposes under our experimental conditions.

•

Adel F. Sarofim, MIT, USA. Although your reactions are with vaporized fullerenes, it would still be interesting to compare your data with those obtained on soots at elevated temperatures or fullerenes at lower temperature. How does the efficiency of O or O_2 attack compare with those obtained on soots? It is interesting to note that Ciombelli and coworkers at the University of Salerno find that, at much lower temperatures (300 °C–500 °C), fullerenes are more reactive than soots. Could you also comment on the possibility that the CO_2 that you observe might be produced from the gas-phase oxidation of CO?

Author's Reply. 1. It is not so easy to compare rate coefficients for homogeneous and heterogeneous reactions. If we assume C_{60} to be a solid particle and apply the formalism for heterogeneous reactions to it, then the reaction probability for C_{60} oxidation by O_2 is about a factor of 10 lower than the comparable value for soot at conditions $T > 1700$ K.

2. We believe that CO_2 is produced both from gas-phase oxidation of CO as well as from reactions of O_2 with fullerene or its fragments.

•

Christopher Pope, MIT, USA. I would like to say how encouraging it is to see kinetic studies of fullerenes under conditions relevant to combustion. Of special interest would be the C_{60} + OH reaction, which I expect to be much slower than oxidation by O_2 [1].

The possible mechanism of the C_{60} + O_2 reaction might

be that of excitation of the C_{60} to the first excited singlet state, which undergoes an intersystem crossing to $^3C_{60}$ [2]. Your activation energy is roughly the same as the energy gap between the ground state and the first singlet excited state for C_{60} (46.1 kcal/mol).

My question is on the basis of using $\lambda = 490$ nm as the signature for C_{60}. How uniquely does it define the C_{60} concentration, or might other species expected to be found in your system also emit at this wavelength? My concern is that other large clusters (probably decomposition products of C_{60}) might have sufficiently broadbanded emissions to obscure the signal; if so, your measured rate might be a composite of the rates for, e.g., $C_{60} + O_2$, $C_{58} + O_2$, $C_{56} + O_2$, etc.

REFERENCES

1. Pope, C. J., Ph.D. Thesis, Massachusetts Institute of Technology, Cambridge, MA, 1993.
2. Arbogast, J. W., et al., *J. Phys. Chem.* 95:11 (1991).

Author's Reply. The use of the $\lambda = 490$ nm emission as a measure for C_{60} is an assumption. We expect that other larger C clusters also contribute to the emission at this wavelength. A kinetic interpretation of the formation rates of CO and CO_2 as well as the disappearance rate of the $\lambda = 490$ nm emission during fullerene oxidation is at the moment not possible. In so far, your suggested sequence of reactions is one approach to interpret the apparent rate data.

Twenty-Fifth Symposium (International) on Combustion/The Combustion Institute, 1994/pp. 671–678

FURTHER TESTING OF THE FULLERENE FORMATION MECHANISM WITH PREDICTIONS OF TEMPERATURE AND PRESSURE TRENDS

CHRISTOPHER J. POPE AND JACK B. HOWARD
Department of Chemical Engineering
Massachusetts Institute of Technology
Cambridge, MA 02139, USA

A previously published detailed kinetic mechanism for C_{60} and C_{70} formation in flames is explored beyond the previously performed preliminary test of kinetic plausibility. Consideration of the sensitivity of model predictions to rate coefficients for the specific reaction types shows that the only remaining area of uncertainty is in how the forward rates of the individual C_2H_2 addition/ring-formation reactions are affected by the varying amounts of curvature-induced strain introduced. An overall test of the mechanism's sensitivity to the thermochemical properties of the species reinforces the kinetic plausibility of the mechanism by confirming that none of the reactions in the mechanism has an insuperable thermodynamic barrier.

The mechanism's ability to predict trends with temperature and pressure is limited by the simplified modeling approach used. Existing data are consistent with maxima in fullerene formation with respect to both temperature and pressure. The mechanism predicts a maximum fullerene formation rate near 2100 K, reflecting competition between processes accelerated by higher temperatures (H abstraction and intramolecular rearrangements) and processes thermodynamically disfavored by higher temperatures (C_2H_2-addition/ring-formation and intramolecular rearrangements). Predictions of a monotonic increase in fullerene formation rate with increasing pressure are explained in terms of the chemical processes not yet included in the fullerene formation mechanism, most notably reactive coagulation of PAH with each other and with soot.

Introduction

The molecular weight processes leading to polycyclic aromatic hydrocarbons (PAH) formation in flames have been extensively studied [1–4]. These studies emphasize planar PAH formation, since such species are predominant. The chemistry of soot particle formation and surface growth [4–15] has also been a topic of research for a long time. In 1985, fullerenes, spheroidal pure-carbon molecules were discovered [16]. Of these, C_{60} was found to be most prevalent, having a truncated icosahedral structure (like a soccer ball). Early speculations on the existence of fullerenes in flames were linked with the concept of the possible role of fullerenes or related curved structures as soot nuclei [16–18]. Frenklach and Ebert [19] argued against fullerenes as soot nuclei but did entertain fullerene formation in flames, suggesting benzo[ghi]fluoranthene as a suitable place of departure from planar PAH growth.

Ionic forms of fullerenes were found in flames [20,21]. The ability to produce macroscopic quantities of fullerenes [22] led to a flurry of analytical chemistry studies on C_{60} and the next most prevalent fullerene, C_{70} [23]. The results of the analytical chemists led the way for confirmation of the existence of fullerenes C_{60} and C_{70} in flames [24], confirming earlier inconclusive evidence [25,26].

The question of the mechanism of fullerene formation remained. These approaches have been reviewed previously [23,27–29]. The mechanisms fall in three general classes: (1) growth of curved aromatic shells leading to cage closing [30,31]; (2) fullerene formation inside of young soot particles [32]; and (3) planar carbon rings coalescing and rearranging to yield fullerenes [33–36]. None of these discussions gives a detailed description of intermediates or subjects the proposed mechanisms to critical testing.

A detailed kinetic mechanism for C_{60} and C_{70} formation in flames has been presented, with a preliminary test of kinetic plausibility performed via detailed modeling [29,37]. The mechanism was developed on the premise that fullerenes are a novel form of polycyclic aromatic compound and that their precursors in flames are curved PAH. The mechanism therefore blends into the backdrop of decades of combustion research in molecular weight growth processes, since only reactions known to occur in PAH chemistry are used in construction of the mechanism.

In summary, the fullerene formation mechanism starts with fluoranthene ($C_{16}H_{10}$), with growth proceeding by successive H abstraction and acetylene addition [1–4]. Additional processes necessary for

H elimination and cage closing are included, such as intramolecular rearrangement [38], to ensure proper placement of 5- and 6-membered rings. Key intermediates in the mechanism are PAH of C_{5v} symmetry, including corannulene (dibenzo[ghi,mno] fluoranthene, $C_{20}H_{10}$), which recently was confirmed to exist in flames [39].

The fullerene formation mechanism is further assessed and tested in this paper by determining the sensitivity to rate coefficients and thermochemical properties and the ability to predict trends in the effects of temperature and pressure on fullerene formation in flames.

Sensitivities to Input Parameters

Theoretical studies of flame chemistry can be supported by detailed kinetic modeling of the complete flame chemistry when the reactions being studied are sufficiently well known [40]. This approach was deemed unsuitable for the preliminary test of kinetic plausibility. The composition profiles resulting from coupled convection, diffusion, and reaction of all flame species are computed in such simulations, so the chemical mechanism used as input must be sufficiently detailed to include all the important types of reactions. Whereas approximate mechanisms exist for the formation of small PAH in combustion [1–4], formation of the initial fullerene precursors (such as fluoranthene, benzo[ghi]fluoranthene, and corannulene) is not included. Also, due to limited understanding of aromatics oxidation and growth chemistry, prediction of concentrations of smaller species important to fullerene formation (e.g., C_2H_2, H atom, and H_2) are sufficiently inaccurate to obscure testing of the fullerene formation mechanism.

Therefore, the kinetic testing focuses on only the fullerene formation mechanism. To that end, input conditions and concentrations of the reactants supporting the fullerene-forming chemistry are taken from experimental measurements in a fullerene-producing flame, thereby avoiding the need to compute them as part of the modeling. When the necessary supporting chemistry is sufficiently complete and reliable, testing the fullerene formation mechanism via simulation of the complete flame chemistry will be desirable. Simulations were done using the CHEMKIN-II subroutine packages [41] and the plug-flow simulator SENKIN [42]. Each calculation took approximately 30 CPU seconds on the MIT Cray X-MP.

Input conditions for testing are for an experimentally studied premixed benzene/oxygen/10% argon fullerene-producing flame: combustion chamber pressure, 40 torr (5.34 kPa); ϕ, 2.2; and inlet gas velocity (298 K, 40 torr), 25 cm/s. Mole fraction profiles for C_{60} and C_{70} [43,44] and major stable flame species [26] in this flame have been reported. Peak fullerene mole fractions are approximately 4×10^{-6} for C_{60} and 6×10^{-6} for C_{70}.

Species whose concentrations are needed as inputs are H, H_2, C_2H_2, and the initial fullerene precursor (fluoranthene). Base case values for temperature (2050 K) and the mole fractions of H_2 (0.12) and C_2H_2 (0.06) are representative of flame values in the region of interest. The base case H atom mole fraction is 0.025—five times the global equilibrium value (obtained via the CHEMKIN-II compatible version of STANJAN [45]) for the flame conditions (ϕ, pressure) at 2050 K. A factor of 5 is representative of the ratios of measured H atom concentrations to global equilibrium predictions for a near-sooting ($\phi = 1.8$) benzene flame [46]. Since the results of the simulation give fractional conversion of fullerene precursor with time, the input mole fraction of fluoranthene was only important in ruling out a proposed fullerene formation pathway of dimerization of C_{5v} species [29].

The mechanism has already been found to give substantial (>~50%) conversion of fluoranthene to fullerenes C_{60} and C_{70} in a time representative of the time available for their production in the flame (~5 ms) [29]. One of the more surprising features was that the detailed 124-elementary-reaction mechanism yielded results consistent with an overall first-order reaction (rate coefficient k^*) preceded by an induction time (τ^*). Where $x \equiv$ conversion of fluoranthene to $C_{60} + C_{70}$, except for low (<~20%) conversions, the results fit the form

$$x = 1 - e^{[-k^*(t-\tau^*)]}$$

where $k^* \approx 363\ s^{-1}$ and $\tau^* \approx 2.26$ ms. A third parameter was the predicted C_{70}/C_{60} ratio at $t = \infty$ (R_∞), which was 1.5, in excellent agreement with flame data [44]. Comparisons between model predictions can be simply expressed in terms of k^*, τ^*, and R_∞.

The effect of input mole fractions of H, H_2, and C_2H_2 on the predictions has been discussed previously [29]. Briefly, increased C_2H_2 or decreased H_2 mole fractions dramatically accelerates predicted fullerene formation, while increased H-atom mole fraction moderately enhances fullerene formation.

Forward rate coefficients used for the four types of reactions found to be important in the fullerene formation mechanism are taken from analogous reactions of planar PAH (Table 1). Examples of reactions for these four reaction types are shown in Fig. 1. Reverse rate coefficients are calculated from microscopic reversibility, with thermodynamic properties estimated from a group additivity method developed for curved PAH containing hexagons and pentagons, with properties of aryl radicals derived from the stable parent via bond-dissociation energies [37].

Exploration of the specific effects of each rate

TABLE 1.
Base case rate coefficients for important types of reactions used in the fullerene formation mechanism, in the Arrhenius form $k = A \exp(-E/RT)$. A has units of cm^3/mol-s, except for reaction types 5-3 and 6, for which the units are s^{-1}, and E is in kcal/mol.

Reaction type		A	E	Reference
1	(H abstraction)	2.50E + 14	15.99	47
23	(C_2H_2 addition/ ring closing)	4.00E + 13	10.11	47
5-3	(H elimination/ ring closing)	1.00E + 13	0.0	1
6	(rearrangement)	8.51E + 12	62.86	48

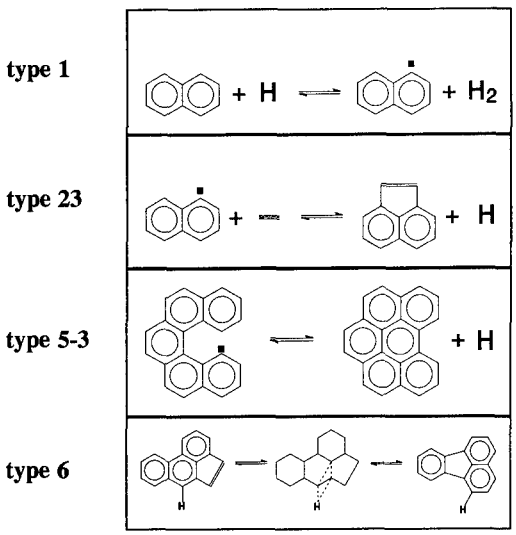

FIG. 1. Examples of reactions representative of types 1, 23, 5-3, and 6 of the fullerene formation mechanism [29].

coefficient used on fullerene formation predictions was done for the four reaction types found to be important: 1; 23; 5-3; and 6. Each rate coefficient was varied separately, keeping all the other rate coefficients the same as the base case. The results are presented in Table 2. Reaction types 1 and 23 both appear to be almost equally rate-limiting. There are 40 type 1 reactions and 31 type 23 reactions in the mechanism, as compared to 10 of type 5-3 and two of type 6, so the results reflect the importance of the reaction types 1 and 23, especially since most of the growth sequence is composed exclusively of these reaction types. Reaction type 5-3 is nowhere near rate limiting, which is encouraging since the rate coefficient of 10^{13} s^{-1} is probably artificially high. The rate coefficient would have to be smaller than that for the

TABLE 2.
Effect of rate coefficients on global parameters for fullerene modeling

Reaction type	Adjustment to rate coefficient	k° (1/s)	τ°(ms)	R_∞
[Base case]	[None]	363	2.26	1.55
1	10× larger	905	1.18	1.05
1	10× smaller	51.4	13.1	6.36
23	10× larger	513	1.31	6.38
23	10× smaller	90.8	11.9	1.05
53	10× larger	363	2.26	1.55
53	10^7 smaller	363	2.33	1.61
53	10^8 smaller	361	2.90	2.29
6	10× larger	364	2.27	1.55
6	82× smaller	362	2.32	1.67

rearrangement (type 6), which is quite unlikely, to affect the predictions.

The predictions are not strongly sensitive to the rearrangement rate coefficient. A value of the rearrangement rate coefficient derived from the data of Scott and Roelofs [38] is roughly 82 times smaller than the Brouwer and Troe [48] high-pressure limit rate coefficient at 2050 K. The only noticeable effect is on R_∞, which has been explained previously [49]. The insensitivity of k° and τ° to the rearrangement rate is encouraging since it was later found that the azulene $\rightleftarrows$ naphthalene rearrangement is in the falloff region at 40 torr and 2050 K. A quantum RRK falloff calculation based on the vibrational frequencies of azulene [50] showed that $k/k_\infty \cong 0.011$ at the base case temperature and pressure. (Coincidentally, the falloff k for the Brouwer and Troe rate is only 10% larger than that derived from the Scott and Roelofs data.) The kinetic plausibility of the mechanism is not strongly dependent upon the type 6 rate coefficient.

The rate of H abstraction (type 1) from curved PAH is unlikely to be different from that from planar PAH. Therefore, the most important class of reactions for which reliable rate coefficients are needed is for strained ring formation (type 23). Consideration of reverse reaction rates shows the ring-forming steps between benzo[ghi]fluoranthene ($C_{18}H_{10}$) and the C_{5v}-$C_{30}H_{10}$ to have very strong reverse reactions, possibly due to the amount of strain introduced into the molecule. Since the above testing varied *all* type 23 reactions' rates, instead of those of specific reactions, the sensitivity is probably overstated. In short, further work on strained ring-formation rates would be needed to disprove the current mechanism.

Calculation of reverse rate coefficients is dependent upon the set of thermodynamic (thermo.) properties used for the intermediate species. Exploration

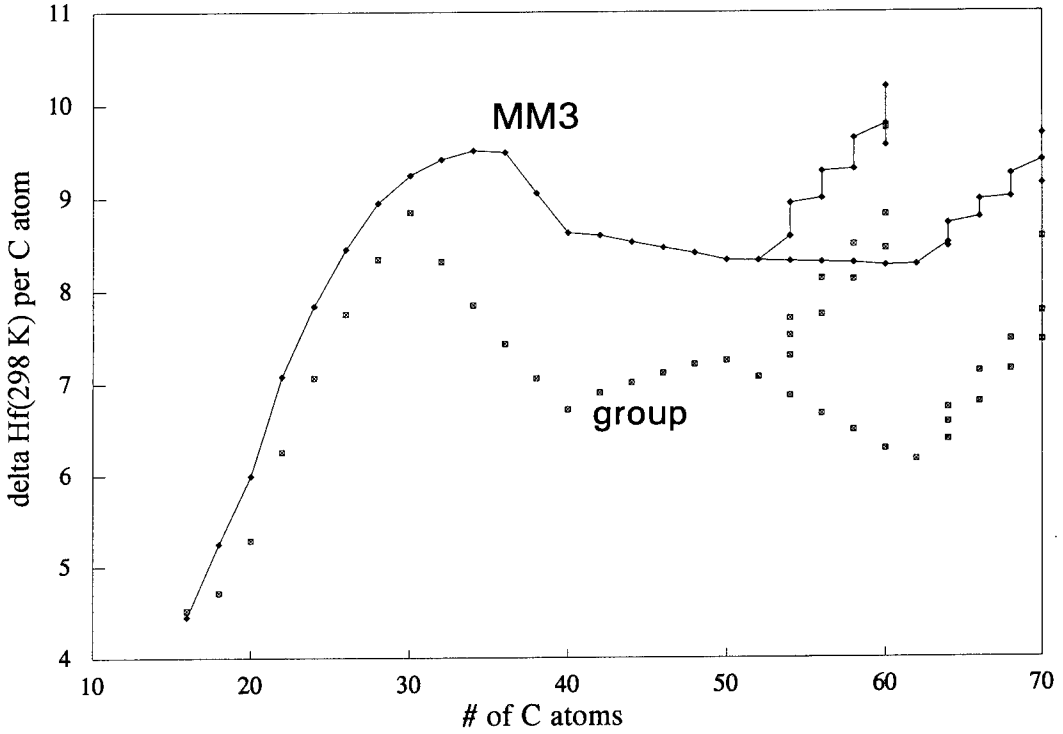

FIG. 2. ΔH_f° per carbon atom for the stable species in which all the carbon atoms are in rings in the fullerene formation mechanism—comparison of group additivity (symbols) and MM3 values (symbols and lines).

of the validity of the results derived from the group additivity approach is ongoing, but an overall test of the sensitivity to the thermo. properties is accessible. A set of thermo. properties for the stable species in the mechanism has been calculated via the 1992 version of MM3, a molecular mechanics package [51]. MM3 is used to obtain standard heats of formation, since it has been found to most reliably reproduce experimental results for both planar PAH [52] and for the fullerene C_{60} [53], which can be seen as an extreme case of structures with strain-inducing five-membered rings. The resulting thermo. properties are noticeably different for many of the species in the mechanism (Fig. 2), yet the resulting predictions of fullerene formation are not strongly affected (Fig. 3). The times for 50% conversion to fullerenes are ~4.2 ms for the group additivity thermo. and ~5.5 ms for the MM3 thermo. Thus, the plausibility of the mechanism is not likely to be disproved by any further improvements in thermochemical properties of the proposed intermediates.

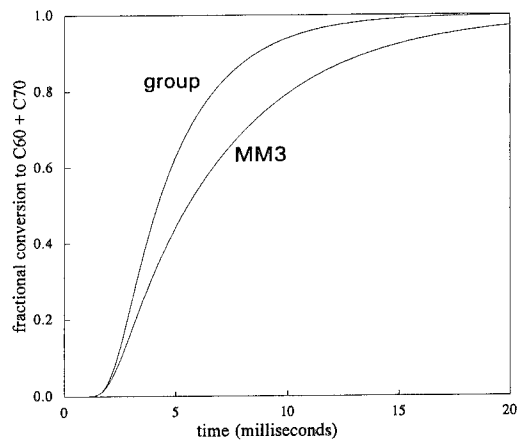

FIG. 3. Predicted fractional conversion of fluoranthene to C_{60} + C_{70} for two different sets of thermochemical properties—MM3 and group additivity.

Effects of Temperature and Pressure

An additional test of the mechanism's validity is its ability to predict observed trends in C_{60} and C_{70} formation with respect to temperature and pressure. Fullerene formation in flames has been observed to increase monotonically [24,43] or to exhibit a maximum [32] with increasing temperature. While the trend with increasing pressure is mixed, subatmo-

spheric pressures favor fullerene formation [24,43]. The mechanism's predictive capabilities are discussed below in terms of overall features of the mechanism that could be expected to contribute to temperature and pressure dependence, followed by the results of model predictions.

H abstraction reactions (type 1) can be expected to be accelerated by increasing temperature, largely through the strong temperature dependence of the concentrations of abstracting radicals, especially H atom. Pyrolysis of C—H bonds, which also leads to radical sites for hydrocarbon addition, would also accelerate with increased temperature, due to the high activation energy of the process. Thermodynamic equilibrium also favors aryl radical formation, even to the point of allowing multiple σ-radical sites on a given PAH [12]. (All molecular-weight growth processes would be favored by increased aryl radical formation, not just fullerene precursor formation.) Cyclization processes that form strained ring structures (types 23 and 5-3) are expected to have a higher activation energy than those for flat 6-ring or 5-ring formation and, as such, contribute to the temperature dependence. Intermolecular rearrangements (type 6) have high activation energies and would also be favored by increasing temperature.

Global equilibrium, however, only favors PAH and fullerenes up to a certain temperature (~2000–2600 K, depending on conditions), beyond which C_2H_2 and polyacetylenes are favored [37,54]. Viewing the fullerene formation mechanism in terms of ΔG for different reaction types, H abstraction (type 1) and H elimination/ring closing (type 5-3) become more favored (ΔG decreases) as T increases, but C_2H_2 addition/ring closing (type 23) and intramolecular rearrangements (type 6) become less favored (ΔG increases) as T increases.

The main feature of fullerene formation chemistry that could lead to pressure dependence is the need for removal of hydrogen, leading to a net increase in the number of moles. While H-abstraction (type 1), C_2H_2 addition/ring-closing (type 23), and rearrangement (type 6) reactions have no net mole change, the dehydrogenation/ring-closing (type 5–3) reactions lead to a net increase in the number of moles, which is in contrast with flat PAH formation. While many PAH6 ring-formation sequences (e.g., 4-phenanthrenyl + $C_2H_2 \rightleftarrows$ pyrene + H) are comparable to those of the present fullerene formation mechanism (or perhaps the converse is more accurate), PAH6 growth includes ring formations requiring two C_2H_2 additions (e.g., phenyl + 2 $C_2H_2 \rightleftarrows$ naphthalene + H; 1-coronenyl + 2 $C_2H_2 \rightleftarrows$ benzo[a]coronene + H) that lead to a net decrease in the number of moles and that would, therefore, be favored by higher pressures. Although reactive coagulations of two aryl radicals also decrease the number of moles, the relation of coagulation reactions to the pressure dependence of fullerene formation is complex and is discussed at length below. Pressure-dependent rate processes, involving chemical activation, might be faster at lower pressures. Unimolecular processes (types 5-3 and 6) can show falloff behavior, but this is expected to be less important as the size of the molecule increases.

Predictions were made for the base case species concentrations, varying only temperatures between 1800 and 2200 K. In terms of the global first-order formation rate and induction time, though τ^* decreases monotonically from 1800 to 2200 K by roughly one-third, this is more than offset by a ninefold monotonic decrease in k^* over the same temperature range, the net effect being a monotonically decreasing rate of fullerene formation as temperature increases.

Some limitations of the current method for simulating the flame are apparent here. One way to compensate for not simulating the entire flame chemistry is to obtain trends for the input species (H, H_2, and C_2H_2) concentrations from global equilibrium calculations. Summarizing the results [37], the predicted equilibrium H atom mole fraction follows a van't Hoff relation corresponding to the ΔH of $1/2H_2 \rightleftarrows$ H (~54 kcal/mol); H_2 changes very little with temperature, and C_2H_2 is orders of magnitude above equilibrium values, making predicted equilibrium trends irrelevant, so only the H atom can be compensated for in this way. Predictions using the H atom mole fractions modified to reflect equilibrium trends show a more complex T dependence. The variable τ^* decreases monotonically by a factor of 14 between 1800 and 2200 K. Fitted values of k^* range over less than a factor of 2, showing a maximum near 2000 K. The overall prediction indicates a maximum in fullerene formation rate with a temperature near 2100 K (Fig. 4).

Recent work [32] shows maxima in peak fullerene ion concentrations with temperature, although the maxima occur at a higher temperature (~2200 K). The predicted maximum in fullerene formation rate might reflect physical reality: comparison with the data of Howard et al. [43], which reflects a monotonic increase in fullerene formation with increasing temperature, is limited by not knowing the actual temperatures of the flames studied; the data may have been taken in a temperature range below any maximum in fullerene formation rate, so the two data sets [32,43] might not be inconsistent. In short, temperature trends predicted by the mechanism are not demonstrably inconsistent with data.

The mechanism's predictive capacity for trends with respect to pressure were tested similarly, fixing all other input parameters at the base case while varying pressure from 0.01–1.0 atm, which more than covers the range of pressures of known fullerene-producing flames. The predicted rate of fullerene formation was found to increase linearly with pressure, i.e., $k^* \propto p$ and $\tau^* \propto p^{-1}$, which can be explained in terms of the types of reactions found in the mech-

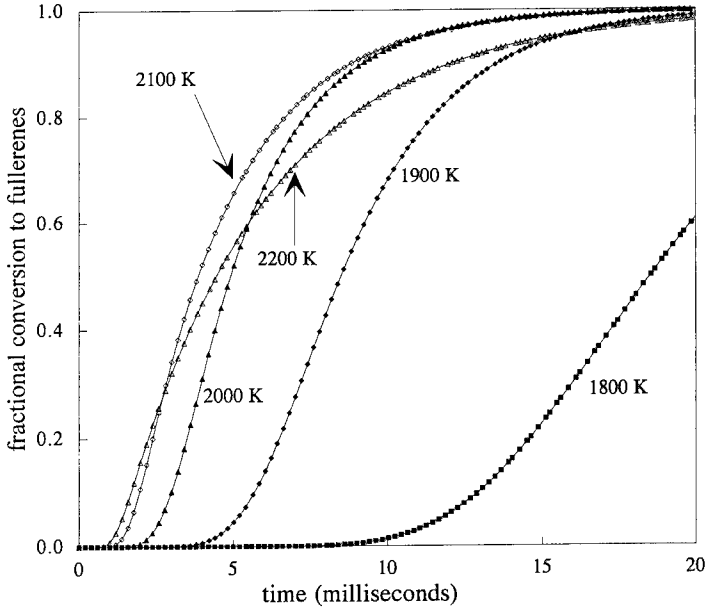

FIG. 4. Predicted fractional conversion of fluoranthene to C_{60} + C_{70} for temperatures from 1800–2200 K.

anism. Reactions of type 1 have their forward rates proportional to [H] and their reverse rates proportional to $[H_2]$; similarly, the forward and reverse rates for type 23 reactions are proportional to $[C_2H_2]$ and [H], respectively. Since the mole fractions of H, H_2, and C_2H_2 are effectively constant during the simulations, the concentrations of these species are proportional to pressure. Therefore, the forward and reverse rates of most of the reactions in the mechanism increase linearly with pressure. Accordingly, type 5-3 reactions are not rate limiting since their reverse rates would increase linearly with pressure while their forward rates remain constant. Type 6 rates are not directly affected by pressure and are also not rate limiting. Since the mechanism as tested proceeds in a forward direction from the initial fullerene precursor to C_{60} and C_{70}, the predicted rate of fullerene formation increases linearly with increasing pressure due to the concentration effect.

The effect of pressure on the input mole fractions of H, H_2, and C_2H_2 was next considered, via global equilibrium. Again, the equilibrium mole fraction of H_2 is largely insensitive to pressure, that of C_2H_2 is orders of magnitude below the experimentally based input value. The equilibrium H atom mole fraction is proportional to $p^{-1/2}$; this pressure dependence can also be derived from considering the reaction $1/2H_2 \rightleftarrows H$. Use of this pressure dependence for the H atom mole fraction still gives a predicted monotonic increase, but to a lesser extent ($k^* \propto p^{0.6}$, $\tau^* \propto p^{-0.6}$), in rate of formation with increasing pressure. This prediction still qualitatively disagrees with known trends, but additional effects of pressure on flame chemistry must be considered.

Two limitations of this study with respect to the prediction of pressure effects are not accounting for the pressure dependence of the C_2H_2 mole fraction, which is unknown, and are not including molecular weight growth pathways leading to flat PAH and soot formation. The same arguments used to explain the predictions for fullerene-formation also indicate that flat PAH formation would be enhanced by increasing pressure. However, as explained above, the pressure dependence is expected to be stronger for the flat PAH. The extent of soot formation in fullerene forming flames is known to increase strongly with increasing pressure [55], probably reflecting the p^2 dependence of the formation of new particles and, hence, new substrate for mass deposition, by reactive coagulation of large PAH. Therefore, as pressure is increased, the competition between fullerene formation and flat PAH and soot formation would be assumed to shift strongly toward soot formation, consistent with observations that fullerenes formation decreases as pressure is increased toward atmospheric.

Discussion

Testing of the previously published fullerene formation mechanism [29] has gone beyond the initial preliminary test of kinetic plausibility and has not disproved the mechanism. Predictions change little within reasonable ranges for values of the types 5-3 and 6 rate coefficients. Fullerene formation rates are strongly affected by the choice of rate coefficient for reaction types 1 and 23. Use of one rate coefficient

for all the type 23 reactions does not reflect the varying degrees of strain introduced by these ring-forming reactions; refining the rate coefficients accordingly will appreciably improve the reliability of predictions.

Predicted fullerene formation rates are relatively insensitive to the thermochemical properties used. The MM3 calculated properties are likely to be close enough to the actual properties to preclude dramatic changes in the model predictions due to more accurate thermo. properties. This finding is quite important in confirming that no single step in the mechanism has a prohibitively large thermodynamic barrier [49].

The ability of the mechanism to predict observed trends in fullerene formation with respect to temperature and pressure are limited by the simplified modeling approach used. However, the level of qualitative consistency with the data is encouraging, as is the ability to reconcile inconsistencies with explanations based on known concepts of molecular weight growth processes.

Additional progress in predicting fullerene formation in flames will be promoted by progress in areas such as prediction profiles of species like H, H_2, and C_2H_2; aromatics oxidation chemistry and kinetics, especially since oxidation can be a vehicle for 5-membered-ring formation; and modeling of coagulation of PAH with each other and with soot. These topics are already active areas of research, showing that fullerene formation in flames can be constructively viewed as a subset of already-considered molecular weight growth processes.

Fullerene formation studies have also contributed to existing knowledge of molecular-weight growth processes. Consideration of intramolecular rearrangements is not only pertinent to fullerene formation but also the chemistry of smaller PAH. The need for thermochemical properties of curved PAH containing both 5- and 6-membered rings is leading to improved group additivity approaches as well as greater insight into the applicability of computational chemistry techniques. Finally, consideration of the possible inter-relation of fullerenes and soot is leading to enhanced interest in the structure and properties of soot.

In conclusion, the vast experience of the combustion community in addressing the behavior of carbon in high-temperature environments is showing itself to be of considerable value in approaching related topics of interest in understanding fullerenes, the new members of the carbon family.

Acknowledgments

We are grateful to the Division of Chemical Sciences, Office of Basic Energy Sciences, Office of Energy Research, U.S. Department of Energy, under Grant No. DE-FG02-84ER13282 for financial support of the research.

REFERENCES

1. Frenklach, M., Clary, D. W., Gardiner, W. C., Jr., and Stein, S. E., *Twentieth Symposium (International) on Combustion*, The Combustion Institute, Pittsburgh, 1984, p. 887.
2. Frenklach, M., and Warnatz, J., *Combust. Sci. Technol.* 51:265 (1987).
3. Bauer, S. H., and Jeffers, P. M., *Energy Fuels* 2:446 (1988).
4. Harris, S. J., and Weiner, A. M., *Twenty-Second Symposium (International) on Combustion*, The Combustion Institute, Pittsburgh, 1988, p. 333.
5. Howard, J. B., Wersborg, B. L., and Williams, G. C., *Faraday Symp. Chem. Soc.* 7:109 (1973).
6. Wersborg, B. L., Howard, J. B., and Williams, G. C., *Fourteenth Symposium (International) on Combustion*, The Combustion Institute, Pittsburgh, 1973, p. 929.
7. Wersborg, B. L., Yeung, A. C., and Howard, J. B., *Fifteenth Symposium (International) on Combustion*, The Combustion Institute, Pittsburgh, 1975, p. 1439.
8. Harris, S. J., and Weiner, A. M., *Comb. Sci. Technol.* 31:155 (1983).
9. Colket, M. B., Hall, R. J., Sangiovanni, J. J., and Seery, D. J., *The Determination of Rate-Limiting Steps during Soot Formation*, Report No. UTRC89-13, United Technologies Research Center, East Hartford, CT 06108, 1989.
10. Lam, F. W., Howard, J. B., and Longwell, J. P., *Twenty-Second Symposium (International) on Combustion*, The Combustion Institute, Pittsburgh, 1989, p. 323.
11. Frenklach, M., and Wang, H. *Twenty-Third Symposium (International) on Combustion*, The Combustion Institute, Pittsburgh, 1990, p. 1559.
12. Howard, J. B., *Twenty-Third Symposium (International) on Combustion*, The Combustion Institute, Pittsburgh, 1990, p. 1107.
13. McKinnon, J. T., and Howard, J. B., *Combust. Sci. Technol.* 74:175 (1990).
14. McKinnon, J. T., and Howard, J. B., *Twenty-Fourth Symposium (International) on Combustion*, The Combustion Institute, Pittsburgh, 1992, p. 965.
15. Dobbins, R. A., and Subramaniasivam, H., in *Mechanisms and Models of Soot Formation—Lecture Notes in Physics* (H. Bockhorn, Ed.), Springer-Verlag, in press.
16. Kroto, H. W., Heath, J. R., O'Brien, S. C., Curl, R. F., and Smalley, R. E., *Nature* 318:162 (1985).
17. Kroto, H. W. *Nature* 329:529 (1987).
18. Kroto, H. W., and McKay, K., *Nature* 331:328 (1988).
19. Frenklach, M., and Ebert, L. B., *J. Phys. Chem.* 92:561 (1988).
20. Gerhardt, Ph., Löffler, S., and Homann, K. H., *Chem. Phys. Lett.* 137:306 (1987).
21. Gerhardt, Ph., Löffler, S., and Homann, K. H., *Twenty-Second Symposium (International) on Com-*

bustion, The Combustion Institute, Pittsburgh, 1989, p. 395.
22. Kraetschmer, W., Lamb, L. D., Fostiropoulos, K., and Huffman, D. R., *Nature* 347:354 (1990).
23. Kroto, H. W., Allaf, A. W., and Balm, S. P., *Chem. Rev.* 91:1213 (1991); Wilson, M. A., Pang, L. S. K., Willett, G. D., Fisher, K. J., and Dance, I. G., *Carbon*, 30:675 (1992).
24. Howard, J. B., McKinnon, J. T., Makarovsky, Y., Lafleur, A., and Johnson, M. E., *Nature* 352:139 (1991).
25. Pope, C. J., Master's Thesis, Massachusetts Institute of Technology, Cambridge, MA, 1988.
26. McKinnon, J. T., Ph.D. Thesis, Massachusetts Institute of Technology, Cambridge, MA, 1989.
27. Haufler, R. E., Chai, Y., Chibante, L. P. F., Conceicao, J., Jin, C., Wang, L.-S., Maruyama, S., and Smalley, R. E., *Mater. Res. Soc. Symp. Proc.* 206:627 (1991).
28. Curl, R. F., *Nature* 363:14 (1993).
29. Pope, C. J., Marr, J. A., and Howard, J. B., *J. Phys. Chem.* 97:11001 (1993).
30. Goeres, A., and Sedlmayr, E., *Chem. Phys. Lett.* 184:310 (1991).
31. Smalley, R. E., *Acc. Chem. Res.* 25:92 (1992).
32. Baum, Th., Löffler, S., Löffler, Ph., Weilmünster, P., and Homann, K.-H., *Ber. Bunsenges. Phys. Chem.* 96:841 (1992).
33. Wakabayshi, T., and Achiba, Y., *Chem. Phys. Lett.* 190:465 (1992).
34. Heath, J. R., in *Fullerenes—Synthesis, Properties, and Chemistry of Large Carbon Clusters* (Hammond, G. S., and Kuck, V. J., Eds.), ACS Symposium Series 481, American Chemical Society, Washington, DC, 1992, Ch. 1, pp. 1-21.
35. von Helden, G., Gotts, N. G., and Bowers, M. T., *Nature* 363:60 (1993).
36. Hunter, J., Fye, J., and Jarrold, M. F., *Science* 260:784 (1993); *J. Phys. Chem.* 97:3460 (1993).
37. Pope, C. J., Ph.D. Thesis, Massachusetts Institute of Technology, Cambridge, MA, 1993.
38. Scott, L. T., and Roelofs, N. H., *J. Am. Chem. Soc.* 109:5461 (1987).
39. Lafleur, A. L., Howard, J. B., Marr, J. A., and Yadav, T., *J. Phys. Chem.* 97:13539 (1993).
40. Warnatz, J., *Twenty-Fourth Symposium (International) on Combustion*, The Combustion Institute, Pittsburgh, 1992, p. 553.
41. Kee, R. J., Rupley, F. M., and Miller, J. A. *Chemkin-II: A Fortran Chemical Kinetics Package for the Analysis of Gas-Phase Chemical Kinetics*, Sandia Report, SAND89-8009, Sandia National Laboratory, Livermore, CA, 1989.
42. Lutz, A. E., Kee, R. J., and Miller, J. A., *SENKIN: A Fortran Program for Predicting Homogeneous Gas Phase Chemical Kinetics with Sensitivity Analysis*, Sandia Report, SAND87-8248, Sandia National Laboratory, Livermore, CA, 1988.
43. Howard, J. B., Lafleur, A. L., Makarovsky, Y., Mitra, S., Pope, C. J., and Yadav, T. K., *Carbon* 30:1183 (1992).
44. Mitra. S., Pope, C. J., Gleason, K. K., Makarovsky, Y., Lafleur, A. L., and Howard, J. B., *Mater. Res. Soc. Symp. Proc.* 270:149 (1992).
45. Reynolds, W. C., *STANJAN Multicomponent Equilibrium Program* v.3.60, available on disk, 1986.
46. Bittner, J. D., and Howard, J. B., *Eighteenth Symposium (International) on Combustion*, The Combustion Institute, Pittsburgh, 1981, p. 1105.
47. Frenklach, M., and Wang, H., in *Mechanisms and Models of Soot Formation—Lecture Notes in Physics* (H. Bockhorn, Ed.), Springer-Verlag, in press.
48. Brouwer, L., and Troe, J., *Int. J. Chem. Kin.* 20:379 (1988).
49. Pope, C. J., and Howard, J. B., *Eastern Section of the Combustion Institute*, Fall Technical Meeting, 1993, p. 303.
50. Chao, R. S., and Khanna, R. K., *Spectrochim. Acta* 33:53 (1977).
51. Allinger, N. L., Li, F., Yan, L., and Tai, J. C., *J. Computational Chem.* 11:868 (1990).
52. Wang, H., and Frenklach, M., *J. Phys. Chem.* 97:3867 (1993).
53. Beckhaus, V. H. -D., Rüchardt, M. K., Diederich, F., Kao, M., and Foote, C. S., *Angew. Chem.* 104:69 (1992).
54. McKinnon, J. T., *J. Phys. Chem.* 95:8941 (1991).
55. Howard, J. B., McKinnon, J. T., Johnson, M. E., Makarovsky, Y., and Lafleur, A. L., *J. Phys. Chem.* 96:6657 (1992).

Twenty-Fifth Symposium (International) on Combustion/The Combustion Institute, 1994/pp. 679–685

THE FORMATION OF AROMATIC CARBON IN SOOTING ETHYLENE FLAMES

A. CIAJOLO, A. D'ANNA, R. BARBELLA AND A. TREGROSSI
CNR, Istituto Ricerche Combustione
P. le V. Tecchio, 1-80125 Napoli, Italy

The concentration profiles of soot, acetylene, diacetylene, benzene and condensed species were measured inside a slightly sooting (C/O = 0.64) and a sooting (C/O = 0.78) premixed ethylene flame at atmospheric pressure.

Condensed species (CS) were analyzed by gas chromatography and mass spectrometry, identifying and quantifying polycyclic aromatic hydrocarbons (PAH) with molecular mass up to 400 u. PAH species with masses in the range between 400 and 1000 u were not detected, even when isolating the heaviest fractions of the condensed species by solvent solubility and liquid chromatography techniques. The sum of PAH quantified by gas chromatography and mass spectrometry did not totally justify the CS weight, and a spectroscopic characterization of the CS (uv-visible, fluorescence, and infrared spectroscopy) was attempted. The spectroscopic behaviour of the CS shows that a low degree of ring condensation and/or a certain degree of aliphatic functionality has to be supposed in the unidentified high molecular mass fraction of the condensed species.

The aromatic carbon, mostly represented by benzene and CS, showed the maximum concentration early in both the flames, at the onset of soot formation but, differently from the slightly sooting flame, a fast reincrease of CS and benzene was found in the burned gas region of the sooting flame. Moreover, the consumption of CS in the region of soot inception was faster in the sooting flame where oxygen is less available for their oxidation, thus the decrease in their concentration was not only due to oxidation, but also to the participation of these species in soot inception.

Introduction

In search for the routes through which soot is formed, the history of the fuel carbon atoms has been followed by optical and sampling techniques along premixed flames. Polyacetylenes before [1], polycyclic aromatic hydrocarbons after [2], and finally fullerenes [3,4] have been detected as high-molecular-weight species in rich premixed flames, which are the preferred experimental apparatus for soot formation studies.

It has usually been found that the higher the molecular weight of these compounds the lower their concentration [5] and the more difficult the determination of their profiles. Most of the work has been devoted to the identification of high-molecular-weight species in ionic form [3,6] and few data are available on neutral species even in a range of molecular masses that are "gas chromatographable," i.e., up to 300 u [2,7]. Furthermore, in previous work, it has been found that the contribution of PAH of up to 300 u (coronene) to the species condensed along premixed ethylene flames [8] and in low-pressure benzene flames [9] is relatively small and the largest part of the heavy material remained unidentified.

A deeper characterization of these species is desirable in order to cover the large "world" of carbon-containing species formed inside rich flames, also considering that the decrease of their concentration in correspondence of soot formation [8,9] suggests their possible role in soot inception.

In the present study, the concentration profiles of the aromatic carbon condensed along a slightly sooting and a sooting premixed ethylene flame at atmospheric pressure were obtained. The composition and the chemical nature of these species were analyzed by applying an array of chemical (gas chromatography, liquid chromatography, and mass spectrometry) and spectroscopic techniques (uv-visible, fluorescence, and infrared spectroscopy) in order to extend the identification range to higher masses.

Experimental Apparatus and Analytical Procedure

Soot, condensed species, and gaseous combustion products were sampled by means of a stainless steel water-cooled probe (i.d. = 2 mm) on a slightly sooting (C/O = 0.64) and on a sooting (C/O = 0.78) premixed ethylene/oxygen flame at atmospheric pressure. The flames were stabilized on a water-cooled stainless steel porous plate burner (d = 60

mm) and surrounded by a shroud of nitrogen (i.d. = 62.4 mm, o.d. = 74 mm). The fuel and oxidant were fed to the center of the burner and the fresh gas velocity was kept constant at 50 mm/s. The burner was enclosed in a quartz housing to keep the flame protected against convection of the surrounding gases. Temperature measurements were performed by means of a fast response Pt-Pt/10% Rh thermocouple and the maximum values that resulted were 1670 K and 1630 K at 2 mm for the slightly sooting and sooting flame, respectively. Downstream of the flame, temperature decreases reached, at 6 mm, values of 1600 K and 1500 K for the two flames.

On-line gas chromatography with a flame ionization detector was used for the analysis of the light hydrocarbons.

The particulate (soot and condensed species) was collected on a teflon filter and in a cold trap placed before the filter. The particulate was extracted with dichloromethane (DCM) in order to separate the condensed species (CS) soluble in DCM from the insoluble carbonaceous material defined as soot. The amount of CS was determined by evaporating the solvent and weighing the CS sample on an analytical balance but, before the evaporation, the condensed species, dissolved in a known volume of DCM, were first analyzed by gas chromatography and mass spectrometry to allow the identification and quantification of volatile components (e.g., naphthalene) usually lost during the evaporation procedure.

Polycyclic aromatic hydrocarbons with molecular masses up to 202 u were analyzed in the condensed species by gas chromatography with mass spectrometry detection (GC-MS) and with flame ionization detection (GC-FID).

Mass spectrometry of the CS in the range from 200 to 1000 u, which is beyond the capability of GC-MS techniques, was done by direct introduction of the samples into a HP 5989A mass spectrometer through a Particle Beam HP 59890B generator. The particle beam is commonly used as interface in the liquid chromatography–mass spectrometry analysis (particle beam LC-MS), but in this work the sample was injected into the flow of the mobile phase (methanol) through a Rheodyne loop valve without passing through the chromatographic column. The sample, transported by the mobile phase, flows directly in the particle beam generator, which nebulizes and vaporizes the flow separating the volatile mobile phase from the sample which, in this way, is introduced in the mass spectrometer source. In the vaporization phase, the volatile components of the sample are lost along with the mobile phase hindering the detection of components with molecular mass below 200 u. This technique was tested with a mixture of standard PAH and calibration factors that were obtained for the quantitative analysis.

The condensed species, dried and weighed, were separated by solvent solubility into hexane soluble and insoluble fractions. The hexane solubles were fractionated by normal phase high-pressure liquid chromatography (HPLC) on a silica-bonded column using hexane as eluent. This technique allows the isolation of a low-mass PAH fraction that contains alkyl-substituted and alkyl-unsubstituted PAH from two (naphthalene) to seven rings (coronene). Polycyclic aromatic compounds with more than seven rings and heavier organic compounds were strongly retained on the top of the column so that their elution was accomplished after the elution of low-mass PAH by backflushing the column with a hexane-dichloromethane mixture. This class of compounds will be referred to as the high-mass aromatic fraction.

GC-MS analysis confirmed the presence of PAH from two (naphthalene) to seven rings (coronene) in the low-mass PAH fraction, whereas high-mass aromatics and hexane insolubles were not analyzable by gas chromatographic techniques. Particle beam–mass spectrometry (PB-MS) used for the analysis of CS was also used as an analytical technique for the qualitative analysis of the high-mass aromatics and hexane insolubles.

Ultraviolet-visible spectroscopy of the low-mass aromatics, high-mass aromatics, and hexane insolubles was performed on a Hewlet-Packard 8452A spectrophotometer with the use of standard 1 cm path-length quartz cells.

Fluorescence emission spectroscopy was done on a Perkin-Elmer LS50B spectrofluorimeter. Emission spectra were recorded at two excitation wavelengths: 266 and 355 nm.

FT-IR spectra of the samples dissolved in DCM and dried on KBr disks were obtained using a Perkin-Elmer 1600 FTIR spectrometer.

Results

Figures 1 and 2 show the concentration profiles of C_2H_4, C_2H_2, C_4H_2, and C_6H_6 for a sooting (C/O = 0.78) and a slightly sooting (C/O = 0.64) ethylene flame, respectively.

In the sooting flame, C_2H_4 shows a fast consumption throughout the first oxidation region, whereas C_2H_2 and C_4H_2 are rapidly formed, showing a maximum at the end of the oxidation zone, and then their concentration decreases, approaching the final values downstream of the flame (Fig. 1). The same behaviour is shown in the slightly sooting flame (Fig. 2), but in this case C_2H_2 is formed in lower amounts and C_4H_2 was below the detection limit.

The concentration profiles of C_6H_6 in the two flames show a remarkable difference in the burned gas region. In fact, benzene profiles exhibit a first maximum early in both flames, after which benzene concentration rapidly reincreases in the burned gases of the sooting flame (Fig. 1), whereas it decreases in

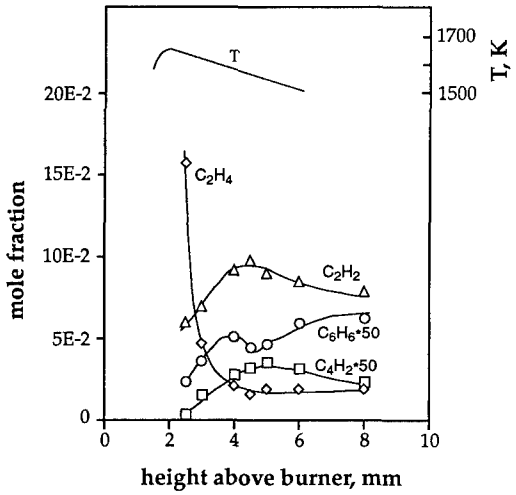

FIG. 1. Mole fraction profiles of ethylene, acetylene, diacetylene, and benzene in a sooting ethylene/oxygen flame (C/0 = 0.78).

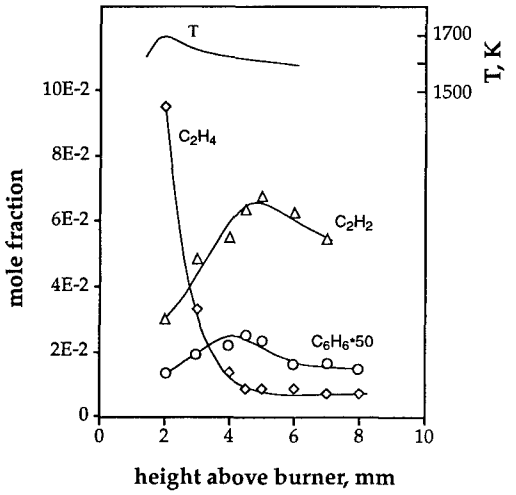

FIG. 2. Mole fraction profiles of ethylene, acetylene, and benzene in a slightly sooting ethylene/oxygen flame (C/0 = 0.64).

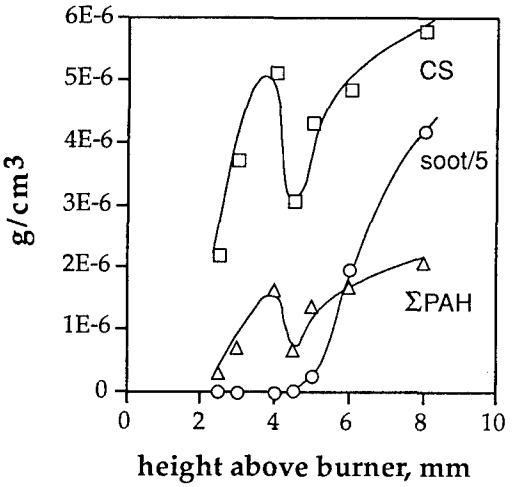

FIG. 3. Concentration profiles of condensed species (CS), soot, and total PAH (ΣPAH) in a sooting ethylene/oxygen flame (C/0 = 0.78).

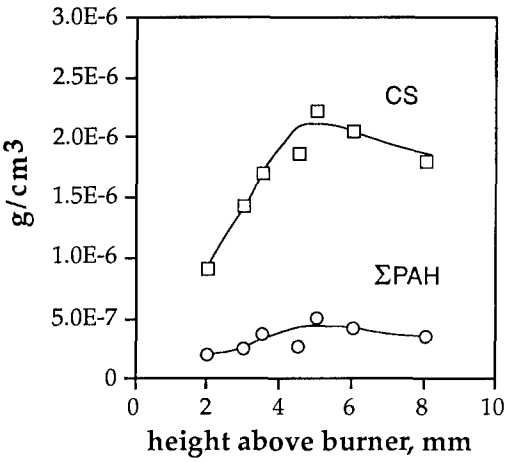

FIG. 4. Concentration profiles of condensed species (CS) and total PAH (ΣPAH) in a slightly sooting ethylene/oxygen flame (C/0 = 0.64).

the burned gases of the slightly sooting flame without going through any further maxima (Fig. 2).

The condensed species (CS) follow trends very similar to benzene, as shown by their profiles reported in Figs. 3 and 4 for the 0.78 and 0.64 flames, respectively. Soot concentration was determined only in the sooting flame and its profile is also reported in Fig. 3.

Condensed species are formed in larger amounts in the sooting flame and present a first maximum within the main oxidation zone, and then their concentration decreases, reaching a minimum in correspondence of the formation of the first soot particles. Thereafter, the concentration of CS reincreases but is rapidly outweighed by soot concentration (Fig. 3). In the oxidation zone of the slightly sooting flame, CS concentration has a first maximum, as in the sooting flame, but does not reincrease in the burned gas region, and soot is below the detection limit of the experimental procedure (Fig. 4).

The qualification of the molecular masses belonging to the CS was done by using gas chromatography and mass spectrometry techniques, which cover together the mass range up to 1000 u. Gas chromatog-

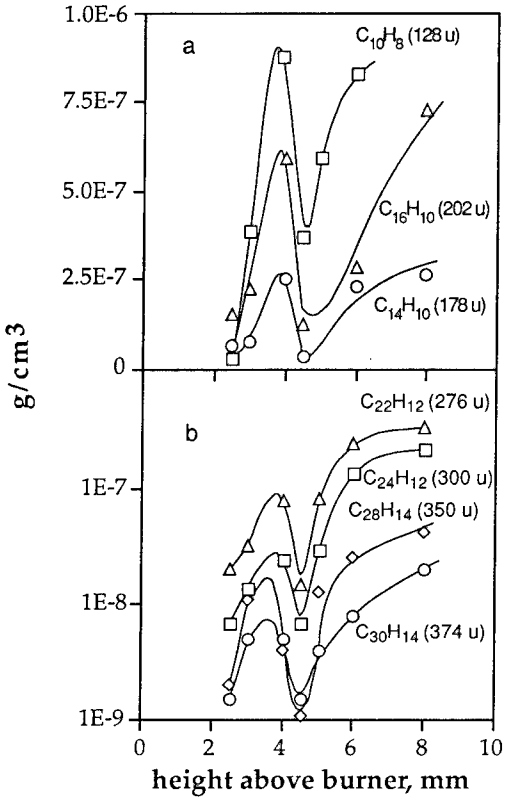

FIG. 5. Concentration profiles of (a) $C_{10}H_8$, $C_{16}H_{10}$, $C_{14}H_{10}$ and (b) $C_{22}H_{12}$, $C_{24}H_{12}$, $C_{28}H_{14}$, $C_{30}H_{14}$ in a sooting ethylene/oxygen flame (C/0 = 0.78).

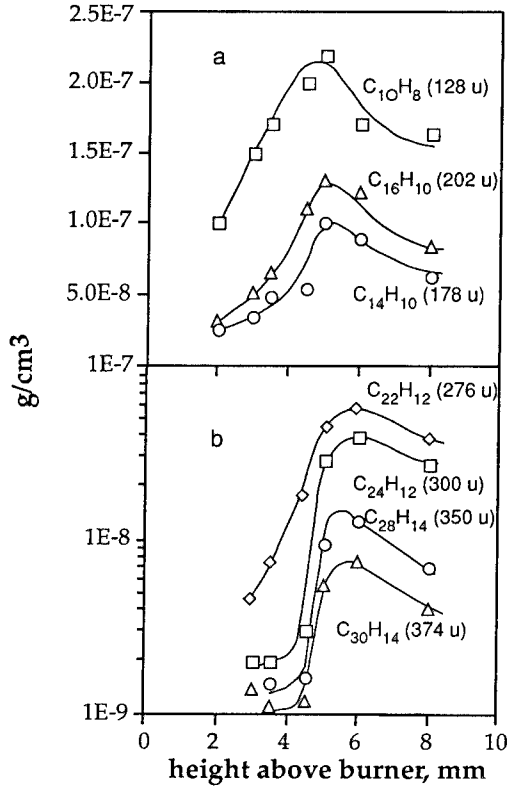

FIG. 6. Concentration profiles of (a) $C_{10}H_8$, $C_{16}H_{10}$, $C_{14}H_{10}$ and (b) $C_{22}H_{12}$, $C_{24}H_{12}$, $C_{28}H_{14}$, $C_{30}H_{14}$ in a slightly sooting ethylene/oxygen flame (C/0 = 0.64).

raphy with flame ionization detection (GC-FID) is able to analyze PAH from naphthalene to coronene, but this technique is not useful above 202 u and total PAH identified by GC-FID were no more than 20 wt.% of the CS [8].

Mass spectrometry of the CS dissolved in DCM and transferred to the mass spectrometer through a particle-beam interface (PB-MS) was able to identify high masses above 202 u in the bulk of the CS sample (volatile compounds with molecular mass <202 u are lost by this technique). The peaks relative to the molecular PAH ions were quantified in the mass spectrum by comparison with PAH standards, but it is worth emphasizing that on each peak of the mass spectrum there is the superimposition of different PAH having the same molecular mass and different structures (e.g., 202 u corresponds to fluoranthene, pyrene, acephenanthrylene, and aceanthrylene), and the larger the molecular weight the larger the number of the possible isomers. By PB-MS analysis, molecular ions of PAH up to 400 u were detected and quantified; the mass signals were too low above this mass value.

The sum of PAH quantified by both GC-FID and PB-MS contributes to the CS in a larger measure in the sooting flame (35 wt.%) than in the slightly sooting one (25 wt.%) and their profiles run below the CS profiles, following a parallel trend as shown in Figs. 3 and 4 where PAH profiles are also reported.

The profiles of the most abundant molecular masses of PAH are reported in Figs. 5 and 6 for the two flames. They show the decay of the PAH concentration with increasing molecular mass going from the smallest identified PAH ($C_{10}H_8$, MW = 128 u) toward the largest one ($C_{30}H_{14}$, MW = 874 u). A slight shift between the maxima of the masses up to 202 u and the masses above 202 u is observed along the axis of the slightly sooting flame (Fig. 6).

By analogy with the characterization procedure of heavy fuel oils, a bulk analysis of the aromatic fractions contained in the CS was undertaken through the separation of the condensed species by solvent solubility into two fractions: hexane solubles and hexane insolubles. The hexane solubles were further separated by HPLC in two classes of compounds. The first class of compounds was totally constituted of low-mass PAH up to coronene (300 u), and accounted for the 60 wt.% of the hexane solubles as

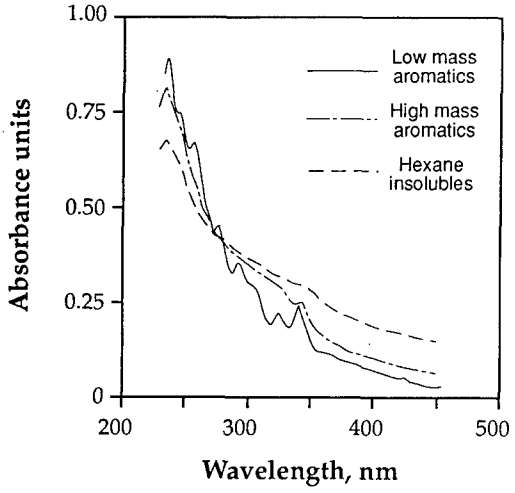

FIG. 7. Ultraviolet-visible spectra of low-mass aromatic, high-mass aromatic, and hexane insoluble fractions collected at 5 mm in a sooting ethylene/oxygen flame (C/0 = 0.78).

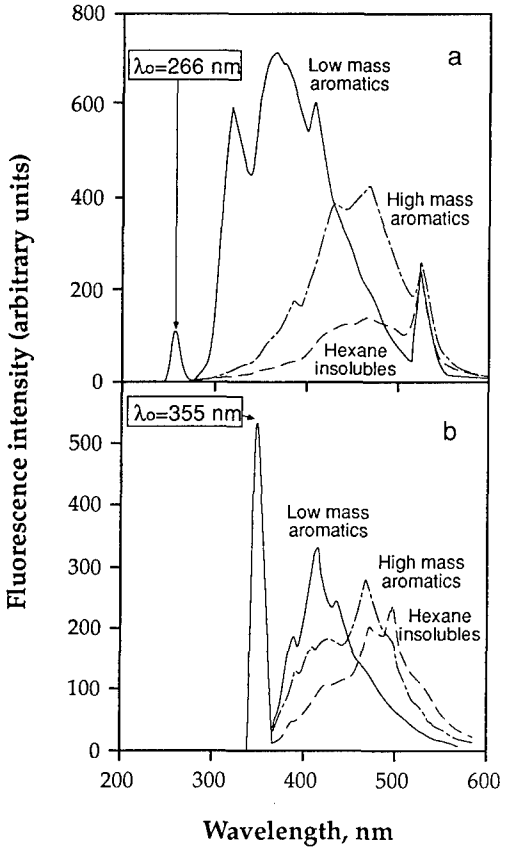

FIG. 8. Fluorescence spectra at different excitation wavelengths of (a) λ_0 = 266 nm and (b) at λ_0 = 355 nm of low-mass aromatic, high-mass aromatic, and hexane insoluble fractions collected at 5 mm in a sooting ethylene/oxygen flame (C/0 = 0.78).

evaluated by the quantitative GC-FID and PB-MS analysis of this fraction. The second class, named high-mass PAH, was constituted of heavier PAH from 300 to 400 u, which account for the 10 wt.% of this class. PAH from 300 to 400 u were also found in the hexane insolubles, but their contribution to this fraction is even negligible.

The obvious advantage of the solubility separation and liquid chromatography procedure is the possibility of a subsequent analysis of the three CS fractions: low-mass PAH, high-mass PAH, and hexane insolubles by other analytical techniques. Moreover, the heavier components of the CS are in this way separated from the lighter, usually more abundant compounds, enhancing the sensitivity of the procedures regarding the determination of large masses.

Further spectroscopic analyses of some selected samples, reported in the following paragraphs, were undertaken in order to attempt a deeper characterization of the unidentified species while at the same time characterizing their optical behaviour with the perspective of a possible comparison with in-situ optical measurements.

Ultraviolet-visible absorption and fluorescence emission are signatures of the aromatic character of the sample. Figure 7 reports the uv-visible absorption spectra of the low-mass aromatics, high-mass aromatics, and hexane insolubles collected in the sooting flame at 5 mm. The shapes of the uv-visible spectra exhibit a large absorption peak in the uv region that extends up to the visible region. The intensity of the absorption decreases in the uv and rises in the visible going from low-mass to high-mass aromatics and hexane insolubles. The structureless shape of the uv-visible spectra hinders the discrimination among different aromatic systems contained inside each fraction, and some peaks, attributable to single PAH, are evident just in the spectrum of low-mass aromatics.

Fluorescence spectra are more structured than uv-visible spectra, showing peaks characteristic of different aromatic rings. Fluorescence spectra of the low-mass aromatics, high-mass aromatics, and hexane insolubles sampled at 5 mm in the sooting flame are reported in Figs. 8a and 8b. These spectra were obtained by exciting with two different excitation wavelengths: 266 and 355 nm.

The fluorescence spectrum of the low-mass PAH excited in the uv shows a first maximum at 320 nm, typical of two-ring PAH, and two peaks at 390 and 405 nm, mainly due to three- and four-ring PAH [10]. Fluorescence spectra of high-mass aromatics and hexane insolubles develop more toward the vis-

ible, showing a broader shape with not-well-resolved peaks and a lower fluorescence emission (Fig. 8a).

Fluorescence emission of low-mass aromatics is depressed by exciting to a longer wavelength (355 nm) (Fig. 8b), whereas the enhancement of the fluorescence emission of high-mass aromatics and hexane insolubles is achieved. In this case, the emission maxima of the three classes are better discriminated and these maxima are shifted toward the visible going from low- to high-mass aromatics and hexane insolubles.

Infrared analysis of the low-mass PAH showed a strong absorption signal at 3050 cm^{-1} because of C-H aromatic stretching and a low signal at 2850–2980 cm^{-1} because of C-H aliphatic absorption. Conversely, in the heavier CS fractions (high-mass aromatics and hexane insolubles), the C-H aromatic absorption at 3050 cm^{-1} was less evident and C-H aliphatic absorption at 2850–2980 cm^{-1} prevailed.

Discussion

The structures of the two flames are described by the distributions of the most abundant hydrocarbon products: acetylene, diacetylene, and benzene, mostly formed at the end of the main oxidation zone when the fuel is almost completely consumed (Figs. 1 and 2).

The pyrolytic routes through which the fuel is transformed in unsaturated and aromatic compounds is preferred in higher C/O ratio conditions where acetylene, diacetylene, and benzene are formed in larger amounts (Fig. 1). Acetylene does not show significant differences between the two flames, increasing at the end of the oxidation zone and decreasing in the burned gas region of the flame. On the contrary, the formation of the first aromatic, benzene, presents peculiar differences between the two flames. In the sooting flame, benzene concentration increases up to a maximum located at the end of the oxidation zone, then reincreases in the postoxidation zone of the flame (Fig. 1), whereas benzene concentration shows the usual rise-decay profile in the slightly sooting flame, similar to the acetylene profile (Fig. 2).

Aromatic species from 128 to 400 u are contained in the condensed species and also their profiles follow the same peculiar trend of benzene in both the flames (Figs. 3 through 6). These compounds can be considered representative of all the heavy aromatic carbon formed in the flame.

The different sooting tendency in the two flames can be related just to the different behaviour of the total aromatic carbon (benzene and condensed species). In the slightly sooting flame, soot is below the detection limit and the slow depletion of aromatic carbon at the end of the main oxidation zone (Fig. 4) has to be due to oxidation and thermal decomposition, which causes the destruction of the aromatic building bricks necessary for soot inception.

Condensed species are formed in larger amounts in the sooting flame and their depletion is decisively steeper in correspondence with soot inception. The aromatic carbon depletion has to be due to molecular growth leading to soot inception more than to oxidation and thermal decomposition, which occur to a lower extent in higher C/O conditions where the oxygen is less available and the temperature is lower. The peculiar trend of the aromatic carbon has already been found in other works [1,2,5,7] and attributed to a temperature effect [5]. However, it can be supposed that this reincrease can derive from PAH released from the soot structure with a mechanism similar to that already postulated to justify the formation of fullerene in sooting flames [3].

Only PAH up to 400 u were identified in the condensed species even extending the mass range of identification up to 1000 u (limit of the mass spectrometer system). The sum of PAH quantified by gas chromatography and mass spectrometry partially contributes to the CS weight (Figs. 3 and 4) and a spectroscopic characterization of the CS (uv-visible, fluorescence, and infrared spectroscopy) was attempted to give further insights on the unidentified species. To this end, the heavier components of the CS were separated from the low-mass PAH by solvent solubility and liquid chromatography procedure.

PB-MS of heavier components of the CS (high-mass aromatics and hexane insolubles) confirmed the presence of PAH in the range between 300 and 400 u, but these compounds account for no more than 10 wt.% of these fractions. On the other hand, the spectroscopic behaviour of these heavier aromatic species indicated that these compounds are more absorbing and fluorescing in the visible than low-mass PAH (Figs. 7 and 8), and this behaviour is typical of high-molecular-weight species. The presence of both aromatic and aliphatic C-H functionalities suggests that mixed aromatic-aliphatic structures with a low degree of ring condensation and a high molecular weight have to be contained in the unidentified heavy species collected in flames.

REFERENCES

1. Homann, K. H., and Wagner, H. Gg., *Eleventh Symposium (International) on Combustion*, The Combustion Institute, Pittsburgh, 1968, p. 371.
2. Bockhorn, H., Fetting F., and Wenz H. W., *Ber. Bunsenges. Phys. Chem.* 87:1067 (1983).
3. Baum, Th., Loffler, S., Loffler, Ph., Weilmunster, P., and Homann, K. H., *Ber. Bunsenges. Phys. Chem.* 96 (74):841 (1992).
4. Howard, J. B., *Twenty-Fourth Symposium (Interna-*

tional) on Combustion, The Combustion Institute, Pittsburgh, 1992, p. 933.
5. Homann, K. H., *Twentieth Symposium (International) on Combustion*, The Combustion Institute, Pittsburgh, 1984, p. 857.
6. Homann, K. H., in *Soot Formation in Combustion, An International Round Table Discussion* (Jander and Wagner, Eds.), Vandenhoeck & Ruprecht, Goettingen, Germany, 1990.
7. Kovacs, R., Loffler, S., and Homann, K. H., "Detection of Large Aromatics in Flames by REMPI-MS," in *Soot Formation in Combustion—Mechanisms and Models* (H. Bockhorn, Ed.), Springer-Verlag, Berlin, in press.
8. D'Alessio, A., D'Anna, A., D'Orsi, A., Minutolo, P., Barbella, R., and Ciajolo, A., *Twenty-Fourth Symposium (International) on Combustion*, The Combustion Institute, Pittsburgh, 1992, p. 973.
9. McKinnon, J. T., and Howard, J. B., *Twenty-Fourth Symposium (International) on Combustion*, The Combustion Institute, Pittsburgh, 1992, p. 965.
10. Berlman, I. B., *Handbook of Fluorescence Spectra of Aromatic Molecules*, Academic Press, New York, 1971.

COMMENTS

Christine Kubitza, Technische Hochschule Darmstadt, Germany. Can you distinguish between certain C_4H_x-hydrocarbons by using a GC/FID? Only the profile of C_4H_2 is shown, so is the formation of C_4H_4 and C_4H_6 negligible?

Author's Reply. The gaschromatographic analysis was able to distinguish between the various C_4H_X hydrocarbons present in the flame gases, and the presence of C_4H_2 (diacetylene) was much more relevant than the other C_4H_X hydrocarbons, which were almost negligible. Thus, only the profile of diacetylene is reported in the work also because this species is significant in polyacetylene formation.

Twenty-Fifth Symposium (International) on Combustion/The Combustion Institute, 1994/pp. 687–704

INVITED LECTURE

MULTICHANNEL REACTIONS IN COMBUSTION

TH. JUST
Institute of Physical Chemistry of Combustion
DLR, Stuttgart, Germany

A survey is given on two theoretical treatments of multichannel reactions: (1) a strong collision model and (2) solutions of the master equation based upon an exponential energy gap model for the energy transfer by collisions. Theoretical results for a three-channel model reaction, obtained by (1) and (2), are compared. Deficits of the strong collision model are discussed. Rotational effects and their different influences on channel exits are qualitatively treated. Recent experimental results on channels of important reactions in combustion chemistry, such as CH_3 + OH, CO + OH, C_2H_2 + OH, C_2H_5 + O_2, and phenyl + O_2, are presented.

Introduction

Concentrations of pollutants in the burnt gases, as well as effects on flame stability, the local laminar flame speeds, ignition, knocking phenomena, etc., are a result of the interaction between chemistry and flow field. It appears as a fascinating idea to exploit today's enormously increasing computing power for the purposes of practically useful flame modelling. In the future, such models may gain a hitherto unimagined importance in industry. Still, there is a bottleneck in doing such modelling for realistic three-dimensional configurations; this is the coupling of—necessarily large—chemical submodels to models describing the turbulent flow field. Even with the largest computers, unreasonable computing times are needed to realistically simulate turbulent combustion with complete chemistry. However, there are interesting developments under way to remove this difficulty. These developments concern efficient ways for the systematic reduction of large chemical systems such that important features of the reacting system do not disappear. Mathematical reduction techniques will be applied locally, determined by the local conditions of T, p, and mixture ratio [1,2].

If this concept of reducing large chemical systems and coupling the reduced systems to turbulence proves successful, we can predict that mathematical models for the reliable simulation of combustion processes will become a tool for engineers in the near future. This in turn will give chemical kinetics a new and increasing importance.

The success of these anticipated new simulation models depends on carefully designed submodels. Besides a model for simulating turbulent flow, we need reliable large chemical kinetic models. The latter provide the basis for the mathematical reduction strategy. When setting up chemical submodels, we have to make use of interpolation or extrapolation methods for rate coefficients in large ranges of pressures and temperatures, because it appears impossible to measure all relevant elementary rate coefficients in combustion chemistry in the range of p and T that are of industrial interest. In contrast to practical needs, the majority of rate coefficients determined experimentally are obtained at normal or lower pressures and often at temperatures below 1000 K. For the simulation of, e.g., combustion in gas turbines or in piston engines, we need information on rate coefficients up to about 30 bar and temperatures between approximately 500 and 3000 K. Consequently, we need well-developed methods to predict the change of rate coefficients and, equally important, methods to predict the change of branching ratios of relevant multichannel reactions with T and p. Particularly, the change of branching ratios may have drastic effects on modelled parameters, as flame speeds or pollutant concentrations. The most prominent and classical example is the reaction of H + O_2 either to HO_2 or to OH + O. With increasing pressure, we observe at certain temperatures an increasing preference of the system to react into the rather inactive HO_2 channel instead of into the channel OH + O. The latter results in two highly reactive radicals. Preferential branching into HO_2 may stop almost completely all flame reactions.

Experimental facts obtained on product channels over the last decade demonstrate that the more we investigate reactions in detail, the more we realize that many "bimolecular reactions" in hydrocarbon oxidation are anything but one-channel processes.

Numerous publications have appeared on the subject of complex reactions in the past. For textbooks on this subject, see Ref. 3. Models based on simple steady-state analysis have been developed [4–9,62]. The obvious advantage of these models is that important basic physical effects can easily be made transparent. But most models circumvent the difficult prob-

lem of satisfactorily treating the energy transfer processes. Nevertheless, with some restrictions and caution, they may be used for interpolating purposes.

Discussions based on analytical or numerical solutions of the master equation [10,11] allowed a much more satisfying inclusion of energy transfer processes. In the case of unimolecular one-channel processes, the obtained results led to useful interpolation recipes [10], which allow an easy and, as far as comparisons with experimental data could be made, rather accurate prediction of falloff curves. These procedures considerably improve chemical kinetic models for combustion simulation. Extensions of the discussion of the master equation to treat multichannel systems have been sparse up to now.

In the following sections, a short and somewhat specialized survey is given: first, on some mathematical tools aimed at numerical solution procedures of the master equation for complex reactions; included also is a discussion of the progress made in an increasingly realistic modelling of energy-specific rate coefficients $k(E,J)$; and second, on some recent, mainly experimental results for multichannel reactions of combustion relevance.

Multichannel Reactions

Strong Collision Model:

We start with a two-channel model, as it is depicted in the following scheme:

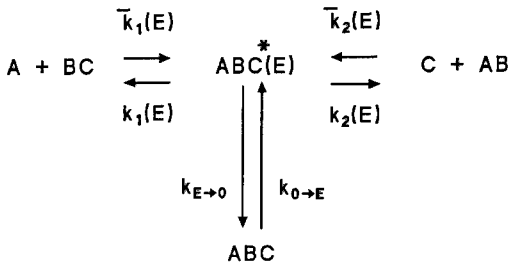

The scheme shows all processes related to the dissociation of ABC and to the complex bimolecular reaction from either $A + BC$ or $C + AB$. To make the formulae not too complicated, we first neglect rotational effects.

The differential equation for the change of ABC is

$$\frac{dABC}{dt} = -ABC \cdot \sum_{E_1} k_{0\to E} + \sum_{E_1} k_{E\to 0} \cdot ABC^*(E).$$

Here, $k_{0\to E}$ is the one-step exciting rate coefficient from the ground state, the stable molecule ABC, to the metastable states $ABC^*(E)$, where E is considered for energies above the lowest exit; $k_{E\to 0}$ is the deexcitation coefficient. Both coefficients are connected by the Boltzmann function $f_v(E)$: $k_{0\to E}/k_{E\to 0} = f_v(E)$.

Similar equations for $[dABC^*(E)]/dt$ can be written down, but they are not given here. For $[dABC^*(E)]/dt$, we use the steady-state approximation:

$$\frac{dABC^*(E)}{dt} \approx 0.$$

The coefficient $k_{E\to 0}$ is set equal to Z in the frame of the strong collision assumption, where Z is the number of collisions under experimental conditions: $Z = Z_{LJ} \cdot M$. After some algebraic manipulations, we get a set of kinetic differential equations containing complex rate coefficients, which may be compared to measurable global rate coefficients.

$$\begin{aligned}\frac{dA}{dt} \approx{}& ABC \cdot \sum_{E_1} k_1(E) \cdot f_v(E) \\ &\cdot \frac{Z}{Z + k_1(E) + k_2(E)} - A \cdot BC \cdot K_{c1} \\ &\cdot \sum_{E_1} k_1(E) \cdot f_v(E) \cdot \frac{(Z + k_2(E))}{Z + k_1(E) + k_2(E)} \\ &+ C \cdot AB \cdot K_{c2} \cdot \sum_{E_2} k_1(E) \cdot f_v(E) \\ &\cdot \frac{k_2(E)}{Z + k_1(E) + k_2(E)} \end{aligned} \tag{1}$$

$$\begin{aligned}\frac{dC}{dt} \approx{}& ABC \cdot \sum_{E_2} k_2(E) \cdot f_v(E) \cdot \frac{Z}{Z + k_1(E) + k_2(E)} \\ &+ A \cdot BC \cdot K_{c1} \cdot \sum_{E_2} k_2(E) \cdot f_v(E) \\ &\cdot \frac{k_1(E)}{Z + k_1(E) + k_2(E)} - C \cdot AB \cdot K_{c2} \\ &\cdot \sum_{E_2} k_2(E) \cdot f_v(E) \cdot \frac{(Z + k_1(E))}{Z + k_1(E) + k_2(E)} \end{aligned} \tag{2}$$

$$\begin{aligned}\frac{dABC}{dt} \approx{}& -ABC \cdot \sum_{E_1} (k_1(E) + k_2(E)) \\ &\cdot f_v(E) \cdot \frac{Z}{Z + k_1(E) + k_2(E)} \\ &+ A \cdot BC \cdot K_{c1} \cdot \sum_{E_1} k_1(E) \cdot f_v(E) \\ &\cdot \frac{Z}{Z + k_1(E) + k_2(E)} \\ &+ C \cdot AB \cdot K_{c2} \cdot \sum_{E_2} k_2(E) \cdot f_v(E) \\ &\cdot \frac{Z}{Z + k_1(E) + k_2(E)} . \end{aligned} \tag{3}$$

In these formulae, the terms $k_i(E)$ are the energy-specific rate coefficients. The normalized Boltzmann distribution is $f_v(E)$; the equilibrium constant connecting products to the stable molecule ABC is K_{ci}.

$K_{c1} = ABC/(A \cdot BC)$, etc. Deriving the formulae (1) through (3), we used that $\bar{k}_1(E)/k_1(E) = K_{c1}(E)$. This can be based upon the assumption of microscopic reversibility. For a more detailed discussion of this matter, see e.g. Ref. 3.

Limiting cases for large and low Z can be easily extracted from Eqs. (1) through (3). For the sake of clarity, in Eqs. (1) through (3), rotations were neglected. If we take rotational effects into account, we assume that the rotational populations are very quickly equilibrated. This is mainly based on experimental evidence of energy transfer at low levels of v and J. See, e.g., recent experiments on CH_3O [66]. The assumption of fast rotational equilibration is used in practically all chemical-kinetic calculations published up to now. Modelling of rate coefficients using this assumption produces plausible results, thereby giving justification a posteriori. We set $ABC^*(E,J) \approx ABC_J^*(E) \cdot f_J$.

The barriers E_i become dependent on J: $E_i(J)$. Now the terms $k_i(E)$ are $k_i(E,J)$; the terms K_{ci} transform into $K_{ci} \cdot f_J$ and ABC into $ABC_J \cdot f_J$. $(dA)/(dt)$ gets the label J: $(dA_J)/(dt)$, etc. Including rotation in the framework of our assumption $ABC^*(E,J) \approx ABC_J^*(E) \cdot f_J$, we obtain e.g. for the $\bar{k}_1(E,J)$,

$$\bar{k}_1(E,J) = K_{c1}(E,J) \cdot k_1(E,J)$$

$$\bar{k}_1(E,J) = K_{c1} \cdot f_J \cdot f_v(E) \cdot k_1(E,J).$$

The essence is that in this model, we consider individual molecules ABC_J, whereby the energy E is taken relative to the vibrational ground state of ABC_J. In order to compare with global rate coefficients, the J-dependent expressions constructed analogously to the formulae (1) through (3) have to be summed over all allowed J. The Boltzmann factor f_J becomes simply a weight factor in a final summation of all ABC_J.

A global description of the changes of A, C, and ABC with time is as follows:

$$\frac{dA}{dt} = ABC \cdot k_A(T,M) - A \cdot BC \cdot K_{c1} \cdot k_{AA}(T,M) + C \cdot AB \cdot K_{c2} \cdot k_{CA}(T,M) \quad (1a)$$

$$\frac{dC}{dt} = ABC \cdot k_C(T,M) + A \cdot BC \cdot K_{c1} \cdot k_{CA}(T,M) - C \cdot AB \cdot K_{c2} \cdot k_{CC}(T,M) \quad (2a)$$

$$\frac{dABC}{dt} = -ABC \cdot k_{tot}(T,M) + A \cdot BC \cdot K_{c1} \cdot k_A(T,M) + C \cdot AB \cdot K_{c2} \cdot k_C(T,M). \quad (3a)$$

Here, $k_{tot} = k_A + k_C$. The equations are written analogously to the set (1) through (3). The coefficient $K_{c1} \cdot k_{AA}$ refers to the reaction of $A + BC$ into ABC and $C + AB$; $K_{c1} \cdot k_{CA}$ refers to the route from $A + BC$ into $C + AB$, etc.

This model is very simple with respect to the energy transfer processes. We have assumed that excited states $ABC_J^*(E)$ connect with the stabilized, energetically unstructured molecule ABC by only one rate coefficient $Z = Z_{LJ} \cdot M$. In the "modified strong collision model," we may approximately regard energy transfer in a global way. For this purpose, Z may be multiplied by a weak collision factor β_c. In reality, we have a much more complicated process of energy transfer within the large number of quantum states of the molecule. The full system of coupled differential equations for the states $ABC(E)$ has to be treated. For a one-channel decay, the appropriately defined β_c multiplied with the pertinent rate coefficient for the strong collision assumption results in the numerical value of the low-pressure rate coefficient obtained by treating the master equation (see below). In multichannel systems, the simple multiplication of $Z = Z_{LJ} \cdot M$ with β_c is indeed, for some of the rate coefficients of Eqs. (1) through (3), a rather poor way to take energy transfer into account. The results, calculated from using Eqs. (1) through (3), may differ considerably in the falloff regime, as it will be demonstrated below.

The three equations for A, C, and ABC are of general validity. Starting with the molecule ABC, we describe a two-channel decay. The corresponding coefficients are found in the first parts of the formulae. When back reactions are important, we can take from the formulae the corresponding coefficients for them. Beginning with $A + BC$ on the other hand, we have the system for chemical activation, which reacts over excited $ABC^*(E)$ states either to stabilized ABC or into the product channel $C + AB$.

The yield of C starting from $A + BC$ may be of interest. In an experimental situation with negligible back reactions, we easily derive $[C(t)]/[A(t = 0)] = [(k_{CA})/(k_{AA})] \cdot [1 - A(t)/A(t = 0)]$. With increasing pressure, k_{CA} starts to decrease when $Z \geq k_1(E) + k_2(E)$.

The dependence of the global rate coefficients in Eqs. (1a) through (3a) on T and M and their mutual ratios may be complicated. The behaviour strongly depends on the relative energy differences of the exit channels and the specific properties of the $k_n(E)$. Exit channels may be characterized by "loose" or "tight" transition states. This is of course reflected in the $k_n(E)$'s (see "Rotational Effects").

Based upon a steady-state analysis, Miller and coworkers [13,14] treated multichannel reactions proceeding along the reaction path with several intermediate bound states (isomers) until reaching the exits. This model neglects energy transfer by colli-

sions and is applicable in the published form only to situations where stabilization is not important.

The main deficit of the strong collision model is that it describes weak collision effects rather poorly, even when Z is multiplied by β_c. Results generated by this model are useful for combustion modelling close to the high-pressure limit or, when considering yields in multichannel reactions, for conditions where little stabilization takes place. We expect the strongest deviations from solutions of the master equation in all terms of Eqs. (1) through (3) where Z appears as a product term in the nominator. It was shown by Just and Troe [15] that at the low-pressure limit, the solutions of the master equation for the dissociation coefficients of the channels above the lowest one differ by large factors when compared with the results obtained by the strong collision model. The deviations from the solutions of the master equation are smaller, however, if we compare those terms in Eqs. (1) through (3) where Z appears only in the denominator.

The Weak Collision Model. The Master Equation:

A much better, but more complex, description of the multichannel reactions can be obtained by discussing solutions of the pertinent set of master equations. This is in general a large set of coupled, linear differential equations. Methods to solve such large systems, typical for chemical kinetics, have been improved further in the last 10 years. The basic mathematics for the solution of systems of linear differential equations with constant coefficients are rather simple. Problems are confined in the handling of the huge number of coupled differential equations. For medium-sized molecules, the number of coupled equations may be on the order of 10^{10} in an energy interval of about 100 kcal/mol.

Near the low-pressure limit, one can try to treat the problem analytically by solving an integral equation, assuming plausible models for the probabilities P_{ij} of the energy transfer by collisions [16]. At pressures in the falloff regime and higher, the best way is approximately to solve numerically the system of coupled linear differential equations. To this end, one divides the energy interval in which calculations are to be made into suitable subintervals to reduce the number of coupled equations. In the following, we will assume a finite number N of equations corresponding to N equally spaced energy intervals ΔE.

The differential equations have the following general structure:

$$\frac{dABC_i}{dt} = S_i - Z\cdot ABC_i\cdot\sum_j P_{ij} + Z\cdot\sum_j ABC_j \cdot P_{ji} - ABC_i\cdot(k_{1i} + k_{2i}\ldots). \quad (4)$$

The indices i and j denote level numbers and correspond to energies E_i or E_j above the vibrational ground state of $ABC_J(0)$. Again, in order to make the equations more easily read, the label J is omitted. All coefficients, level populations, etc. in the framework of our basic assumption

$$ABC(J,E) \approx ABC_J(E)\cdot f_J$$

refer to groups of molecules that have J in common. The $k_n(E,J)$ for the different channels n are abbreviated by $k_{n,i}$.

The source term S_i describes the flux into the level i (or energy range i) of the molecule $ABC_J(i)$ from back reactions $A + BC$ and $C + AB$.

In the present two-channel example, $S_i = \bar{k}_{1i}\cdot A\cdot BC + \bar{k}_{2i}\cdot C\cdot AB$. Based upon microscopic reversibility, the source term can be written as a function of the energy-specific rate coefficients k_{1i}:$\bar{k}_{1i} = K_{c1}\cdot f_J\cdot f_i\cdot k_{1i}$. The energy transfer probabilities P_{ij} in Eq. (4) are normalized: $1 = \Sigma_{j=0}^{N} P_{ij}$. If we apply for the P_{ij} an exponential model that is widely in use for numerical and analytical calculations, we can write for the P_{ij}

$$P_{ji} = K_i\cdot\exp[-(E_j - E_i)/a]$$

$$P_{ij}\cdot f_i = P_{ji}\cdot f_j$$

$$P_{ij} = K_i\cdot\frac{\rho_j}{\rho_i}\cdot\exp[-(E_j - E_i)\cdot(1/a + 1/RT)].$$

In the formulae, a is the energy transfer parameter. The normalized Boltzmann factor is $f_i = \rho_i/Q_V\cdot\exp(-E_i/RT)$, with $\rho_i \equiv \rho_V(E_i)$ as density of states (number of states i per energy interval). Here, Q_v is the partition function, which for numerical calculations may be defined as $Q_V = \Sigma_0^N \rho_i \cdot\exp(-E_i/RT)$.

The determination of the normalizing coefficients K_i for the P_{ij} is straight forward; the K_i can be determined successively [12].

Method for the solution of the system of coupled differential equations:

We start with a matrix formulation of the system

$$\frac{d\mathbf{b}}{dt} = (A)\cdot\mathbf{b} + \mathbf{S}(t). \quad (5)$$

The vector $\mathbf{b}$ comprises the time-dependent level populations of $ABC_J(E_i)$. $ABC_J(E_i)$ is abbreviated further by b_i. (A) is the matrix of the coefficients, as they are shown in Eq. (4). The vector $\mathbf{S}(t)$ contains the elements of the source term: $(K_{c1}\cdot f_J \cdot A\cdot BC\cdot k_{1l}\cdot f_l + K_{c2}\cdot f_J\cdot C\cdot AB\cdot k_{2l}\cdot f_l)$.

Beneath the lowest exit level $l < i_1$, all elements are 0. For convenience, we abbreviate the terms $K_{c1}\cdot f_J\cdot A\cdot BC$ by $F_A(t)$. We define $F_C(t)$ analogously.

The source term may then be conveniently written as

$$\mathbf{S}(t) = F_A(t)\cdot\mathbf{FK}_A + F_C(t)\cdot\mathbf{FK}_C.$$

The vector $\mathbf{FK}_A$ contains the elements $(k_{1l}\cdot f_l)$; $\mathbf{FK}_C$ contains $(k_{2l}\cdot f_l)$.

The appropriate discussion of Eq. (5), that is, the adequate inclusion of weak collision effects in the falloff regime, is rather lengthy and complex. The reader may find a mathematical discussion in Smith et al. [17] (see also Ref. 3c).

As the final result, slightly different expressions compared to Refs. 17 and 18 are given:

$$k_A(T,M) = \sum_{J=0}^{J_{\text{end}}} f_J\cdot k_A(J)$$

$$k_C(T,M) = \sum_{J=0}^{J_{\text{end}}} f_J\cdot k_C(J).$$

The term $\lambda_0(J)$ is the smallest (negative) eigenvalue of $(A(J))$. The reader is reminded that $-\lambda_0(J)$ must equal the sum of all decay coefficients. In the two-channel case, we have $k_A(J) + k_C(J) = -\lambda_0(J)$. For $k_A(J)$, it can be shown [17] that $k_A(J) = \Sigma_{i1(J)}^{N} k_{1i}(J)\cdot g_i^0(J)$, where the terms $g_i^0(J)$ are the elements of the normalized eigenvector of $(A(J))$. A similar relation holds for $k_C(J)$.

$$k_{AA}(T,M) = \sum_{J=0}^{J_{\text{end}}} f_J\cdot\left[k_A(J) + k_C(J)\cdot\sum_{i=0}^{N} U_{Ai}(J) - \sum_{i=i2(J)}^{N} k_{2i}(J)\cdot U_{Ai}(J)\right]$$

$$k_{CA}(T,M) = \sum_{J=0}^{J_{\text{end}}} f_J\cdot\left[k_C(J)\cdot\sum_{i=0}^{N} U_{Ai}(J) - \sum_{i=i2(J)}^{N} k_{2i}(J)\cdot U_{Ai}(J)\right].$$

The coefficients $U_{Ai}(J)$ are the solutions of a system of linear equations with right-hand sides given by the elements of the respective source terms [17]:

$$(A(J))\cdot\mathbf{U}_A(J) = \mathbf{FK}_A(J). \tag{6}$$

A similar relation holds for $U_{Ci}(J)$. The term J_{end} is determined by the disappearance of the potential minimum. It can be shown [18] that for $k_{AA}(T,M)$ and $k_{CA}(T,M)$, the terms in the square brackets are almost the same as those that have been derived by Smith et al. [17]. The solution presented here was derived with lesser approximations.

Unfortunately, the coefficient $k_{CA}(T,M)$, which also appearing in $k_{AA}(T,M)$, is the difference of two larger numbers, which makes necessary calculations with higher numerical precision.

The determination of the smallest eigenvalue λ_0:

The smallest (negative) eigenvalue $\lambda_0(J)$ of $(A(J))$ multiplied by -1 represents the sum of all decay coefficients into the various channels. With simple, but plausible models for P_{ij}, the eigenvalues $\lambda_0(J)$ for the low-pressure limit can be determined by solving approximately an integral equation [16]. The case of a two-channel decay was analytically treated by Just and Troe [15].

For practical purposes, where we need the rate coefficients in the falloff regime, it is convenient to determine $\lambda_0(J)$ by an iteration process. Again, the integration interval is divided into N subdivisions: ΔE (Gilbert et al. [19,12]).

The Low-Pressure Limits of Multichannel Reactions:

Just and Troe [15] analytically solved the integral equation, neglecting rotational effects. An exponential model for the energy transfer was assumed. With the definition $h(E)$ for the rotationless case, $h(E) \equiv ABC(E)/(f_v(E)\cdot ABC)$, it was obtained [16,20] that

$$h(E) \simeq \frac{Z\cdot\sqrt{\beta_c}}{k_1(E) + k_2(E)}\cdot\exp\left(-\frac{E - E_1}{a}\right)$$

$$\text{for } E \geq E_1$$

$$\beta_c \equiv \left[\frac{a}{a + F_E(T)\cdot RT}\right]^2$$

$$F_E(T) \equiv \int_{E_1}^{\infty}\frac{f_v(E)}{f_v(E_1)}\cdot dE.$$

The corresponding rate coefficients for a two-channel decay including rotational effects are as follows:

$$k_{\text{tot}} = \sum_{J=0}^{J_{\text{end}}} f_J\cdot\int_{E_1(J)}^{\infty} h(E,J)\cdot f(E)\cdot[k_1(E,J) + k_2(E,J)]\cdot dE$$

$$k_1 = \sum_{J=0}^{J_{\text{end}}} f_J\cdot\int_{E_{1(J)}}^{\infty} h(E,J)\cdot f(E)\cdot k_1(E,J)\cdot dE$$

$$k_2 = \sum_{J=0}^{J_{\text{end}}} f_J\cdot\int_{E_{2(J)}}^{\infty} h(E,J)\cdot f(E)\cdot k_2(E,J)\cdot dE.$$

Here, J_{end} is determined by the disappearance of the potential minimum; $h(E,J)$ is obtained from the formula above by replacing $k_i(E)$ by $k_i(E,J)$ and E_1 by $E_1(J)$. Presently, as mentioned already, a discussion

of rotational effects is only possible in the case of rotational decoupling $ABC(E,J) \approx ABC_J(E) \cdot f_J$.

All rate coefficients for channels above the lowest exit E_1 contain a particular factor reflecting the energy transfer from the lowest exit energy E_1 up to the channel under consideration. In the two-channel example, we find the following for $J = 0$:

$$\frac{k_2}{k_{\text{tot}}} \propto \exp\left[-\frac{(E_2(0) - E_1(0))}{a}\right].$$

With a typical a of about 0.5 to 1 kcal/mol, the exponential factor may cause a large reduction of the numerical values of the pertinent decay coefficients for these channels. This effect does not appear in the strong collision theories. Since a may depend on the nature of the collision partner, we expect a measurable influence on the rate coefficients for the higher channels. Experimental evidence for this particular effect has not appeared yet.

Rotational Effects

There are two types of rotational influence on the rate coefficients: first, the change of the heights of the exit barriers, and second, the change of the $k(E,J)$ with J.

Effects on the Barrier Heights:

The barrier height is counted in relation to the vibrational ground state $ABC_J(v_i = 0)$. In a two-channel system, we may either have the two exits characterized each by a Morse-type potential or by one Morse and one non-Morse (the latter with an intrinsic "bump" at the exit) or have two non-Morse-type exits. For the "bump" of the non-Morse potential, which is practically fixed at some set of reaction coordinates, it is rather easy to calculate the change of the barrier height with J, since we have a fixed ratio of the moments of inertia of the reference state $ABC_J(0)$ to the transition state.

The effective barrier $E_1(J)$ may be given by

$$E_1(J) = E_1(J = 0) + (B_{\text{TS}} - B) \cdot J(J + 1).$$

Since B_{TS} in practical cases is slightly smaller than B, we observe only a small reduction of the effective barrier height with J.

In a first and, for practical purposes, useful approximation, we may characterize the change of the barrier height for Morse-type potentials as

$$E_1(J) \approx E_1(J = 0) + C_\nu \cdot [B \cdot J(J + 1)]^\nu - B \cdot J(J + 1)$$

where C_ν and ν are semiempirical coefficients. Their values depend on how the change of I_{TS} with changing distance of the fragments is modelled. Empirically, one finds $C_\nu \propto [I/I_{\text{TS}}]^{2\nu/3}$ and $\nu \approx 1$ for most nonlinear molecules.

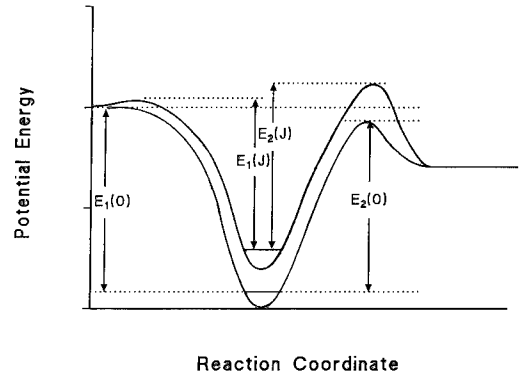

FIG. 1. Loose and tight exits. Change of the barrier heights with J.

Since in practical cases C_ν is considerably smaller than 1, we observe a rather strong decrease of the effective barrier height with increasing J. For details, see Ref. 20.

In Fig. 1, barrier effects for a loose and a tight exit are depicted. It is assumed that for $J = 0$, the tight exit is lower than the loose one. If the difference of the barrier heights for $J = 0$ is not too large, we can have a situation where for some $J > J_{\text{crit}}$, the tight exit becomes even higher than the loose one. For increasing J, the tight exit appears more and more blocked. Summing over the rotational states, including the weight factor f_J, we anticipate a "switching" of the rate coefficients for the two-channel decay of ABC with increasing temperatures. Dissociation through the loose exit becomes dominant. Examples that have to be interpreted by considering these effects are, e.g., the two-channel decays of C_2H_4 and of H_2CO.

When treating a bimolecular reaction starting from the loose entrance, Fig. 1, we anticipate by the same arguments a negative activation energy for the rate coefficient associated to the product channel. On the basis of a RRKM model, these effects together with properties of the $k_i(E,J)$ were discussed by Golden and coworkers [4,5] and by Benson and coworkers [7,8].

Effects on $k_i(E,J)$:

The properties of the transition states (TS states) directly influence the numerical values of the pertinent energy-specific rate coefficients:

$$k(E,J) = W(E - E_1(J))/(h \cdot \rho_\nu(E,J)).$$

In the case of a Morse-type potential, numerical

evaluation of $k(E,J)$ may become difficult. Realistic potential functions would not strictly follow a Morse function. However, as long as quantum chemical calculations do not provide us with better potential functions, Morse-type potentials serve as an acceptable approximation.

For low J, we have locations of the transition state at rather large distances between the molecular moieties that are separating (or recombining). The properties of the transition states may change considerably with J. With increasing J, the separation between the two fragments is decreasing. The pertinent moments of inertia for the TS states vary considerably. It is rather complicated to adequately regard the properties of the TS states for the numerical evaluation of the energy-specific rate coefficients $k(E,J)$. Above the barrier $E_1(J)$, the number of states $W(E - E_1(J))$ may strongly depend on the separation Δq of the two fragments. Those bending modes, and particularly those hindered internal rotations of the unexcited molecule that are affected by the dissociation, become transitional modes. Bending modes are converted into hindered rotations, whereby the potential function for the hindered rotors depends on the location $q(J)$ on the reaction coordinate.

Quite recently, the problem was reconsidered by Smith [21] who presented a new mathematical discussion in the frame of phase space theory.

For nonlinear molecules, as symmetric prolate tops, it is assumed that the rotational states of the external K rotor, associated with the smaller moment of inertia, may be treated as belonging to degenerate vibrational modes. They couple by Coriolis interaction with bending vibrations. The number of K states is restricted by $|K| \leq J$. K states as degenerate vibrations have to be accounted for in the respective expressions for $W(E - E(J))$, $\rho_v(E,J)$, and Q_v [26,27].

Generally, the coupling constraints for the appropriate conservation conditions for the angular moments involved make the treatment difficult. The reader will find in Ref. 21 numerous references to the present methods of treating external rotors as well as internal hindered rotors.

For the discussion of recombination coefficients that are measured generally at low temperatures, the approximate treatment of loosened bending modes as free rotations seems to work quite well, and the mathematical description does not give expressions that are too complex [21,26].

Up to the present, it is still one of the greatest difficulties in reaction rate theories to locate (and to characterize) loose TS states along the reaction coordinate q with a higher degree of accuracy, since potential curves as functions of (E,J,q) would have to come from rather accurate quantum-chemical calculations. Wardlaw and Marcus [22] presented a study on the effects of varying the potential function between the separating fragments. The numerical values for the $k(E,J)$ are preferentially dependent on the assumed potential functions for the bending modes transforming gradually into hindered rotations. They are less dependent on the potential function for the bond fission.

More recent work on this topic, assuming rather realistic interaction potentials that can be used for larger separation distances, was presented by Maergoiz et al. [23]. Results from phase space theory are compared with direct counting by a statistical adiabatic channel model (SACM) [24,25].

Discussing reactions at higher temperatures, we see an increasing influence of those *TS* states that are located closer to the mass centre of the system. With increasing J, the almost free rotors at small J gradually change into hindered rotors and eventually transform into the pertinent bending modes. The accuracy of the $k(E,J)$ to be calculated is somewhat limited, partly because the interaction potential between the separating molecules at varying separation distances can only be guessed at present. This is particularly true for smaller separations of the mass centres of the fragments. Approximate methods to interpolate between the limiting cases of low and high J on the basis of Morse-type potentials have been developed, e.g., by Troe [26]. Smith, within the framework of phase space theory, gives formulae valid for all J [21]. Simplified interaction potentials for the hindered rotation of the fragments are discussed in Refs. 21 and 22.

For a "loose" exit, the effective barrier height considerably decreases with increasing J. The $k(E - E(J))$ may change when comparing the same height over the barrier $E(J)$ for different J. For a "tight" exit, the barrier height decreases much more slowly and the $k(E - E(J))$ stay rather similar when compared at the same difference $E - E(J)$ for increasing J. An instructive example, the $k(E,J)$'s for the two exits of the H_2CO decay into $H_2 + CO$ (tight) and $H + HCO$ (loose), respectively, was calculated by Troe [27] (Fig. 2).

In many multichannel reactions, we may have structural changes of the intermediate bound states during the process. An example would be $NO + NH_2 \rightarrow N_2 + H_2O$. The entrance configuration $ONNH_2$ changes to HONNH (*cis*, *trans*) and from there to the probable end products $N_2 + H_2O$. We have hydrogen shifts that proceed stepwise over isomers of $ONNH_2$. The presumption is that in the density of states $\rho(E)$, but more prominently in $W(E - E_i(J))$, changes of coupled bending and stretching frequencies associated with the quasi-rotating H atom at larger energies may occur. The numerical values of the $k(E)$'s may change considerably when compared with simple calculation neglecting these effects [28]. Quantum chemical calculations, such as performed by the Melius group for systems with internal isomerization [13,29,30], contribute valuable data with respect to barrier heights and associated

vibrational frequencies of the intermediate as well as of the entrance and exit transition states.

A very interesting and illustrative example, applying a physically plausible, sophisticated model of internal two-dimensional (2D) rotation of H, was recently presented by Wagner et al. [31]. These authors discussed the dissociation of HCN. Isomerization from HCN to CNH was accounted for. There are contributions to the density of states from molecular states at larger energies, where the H atom behaves as a hindered two-dimensional rotor. Associated with the 2D rotation, stretching vibrations become distorted. This consequently results in considerable anharmonicity for these vibrations. The calculated effect on the state density ρ of HCN was in the order of a factor of 8 when compared with ρ obtained in the standard way. Because HCN is a small molecule, these contributions of anharmonic vibrations and 2D rotation to ρ are more prominent than one would expect it to be for a larger molecule. The agreement of the calculated low-pressure value k_0 with experimental results is satisfactory. The associated β_c for the HCN decay attains a reasonable value [31].

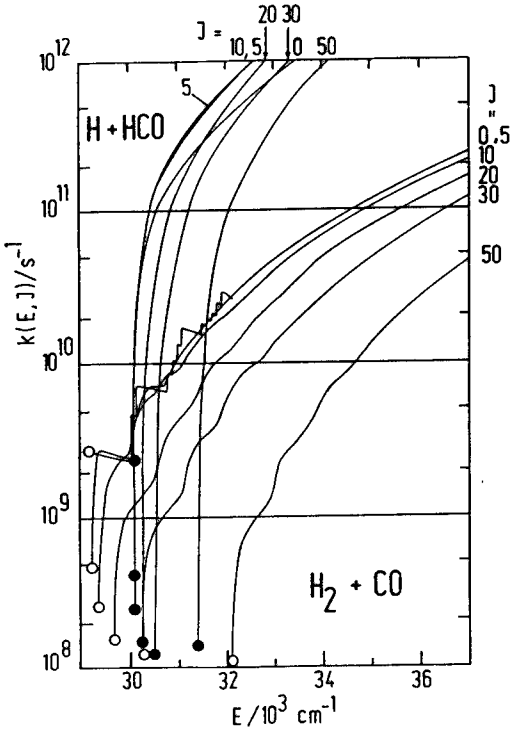

FIG. 2. Calculated $k(E,J)$ for a loose and a tight exit. Decay of H_2CO [27].

Falloff Effects of Rate Coefficients of Multichannel Reactions at a Given J

Some numerical examples will be presented for simple $k(E)$. Since the change of the barrier heights with J depends on finer details of the particular system under consideration, no calculations summing over all allowed J states are given here. Nevertheless, the order of magnitude of effects caused by energy transfer, comparing master equation solutions with results from a strong collision model for a given J, e.g., $J = 0$, will become apparent.

The $k(E)$'s are modelled as

$$k_i(E - E_i(J)) = k_{0i}(E_i(J)) \cdot \frac{(E - E_i(J) + E_{i,Z})^{s_R+s_L-1}}{(E + E_Z)^{s-1}}.$$

The $k_{0i}(E_i(J))$ in a small energy interval just above the barrier contain in the "loose" case factors that model the contribution of transitional states. We may assume that in typical situations, the $k_0(E)$ for a loose exit are about 10–50 times larger than the $k_0(E)$ for a tight exit. For an illustrative example, see again Fig. 2. The term s_R is the number of "rigid" vibrational frequencies; s_L represents, in the case of a loose exit, an effective number that approximately takes into account the contributions of the transitional modes [20,26].

The energy transfer parameter a is 0.5 kcal/mol. The size of the energy interval ΔE was taken as 0.5 kcal/mol, $N = 180$. The assumed "graining" of the total energy interval is sufficient for the present purpose. Numerical results did not depend strongly on changing ΔE. The calculated examples serve to demonstrate typical differences between the strong collision model and the master equation treatments. Numerical values of the normalization coefficients K_i for the P_{ij} were calculated as described above. The λ_0 and the normalized populations $ABC_i/\Sigma_{i=0}^{N} ABC_i$ were obtained by iteration [12], and finally, solutions by Gaussian elimination for the coefficients U_i from Eq. (6) were generated. Most interesting are cases where we have exits with different properties.

Model Example for a Three-Channel Decay, Fixed J:

$A + BCD$ reacts either to an adduct $ABCD$ or into two channels: $C + ABD$ or $D + ABC$, respectively. Example 1, Fig. 3, resembles a situation where we have in the order of increasing barriers E_A(tight), E_C(tight), and E_D(loose) TS states at the exits. A practical example, at least with a similar ordering of the E_i's and associated properties of the TS states, is the decay of vinylacetylene, C_4H_4, investigated experimentally by Braun-Unkhoff et al. [32] (see below).

In the model example, the exit barriers increase by 2 kcal/mol each. The lowest exit was assumed to be 70 kcal/mol; the next two are at 72 and 74

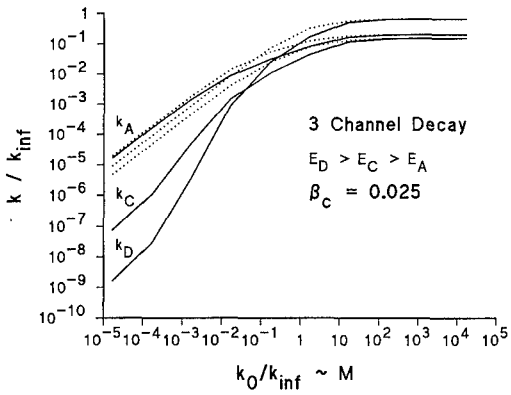

FIG. 3. Example calculation for tight, tight, loose exits (see text). Dotted lines: strong collision model with $\beta_c = 0.025$. Close to the barriers, the $k_{i,0}$ are assumed: $k_{A,0} = 1$; $k_{C,0} = 1$; $k_{D,0} = 10$. The units for the $k_{i,0}$ are in μs^{-1}.

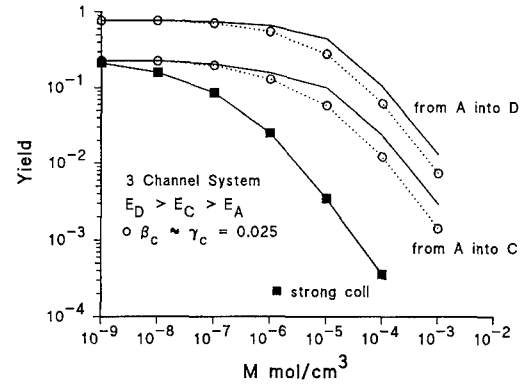

FIG. 4. Yields of C and D, starting from the loose entrance A. Circles: strong collision model with $\beta_c = 0.025$; Squares: strong collision model with $\beta_c = 1$.

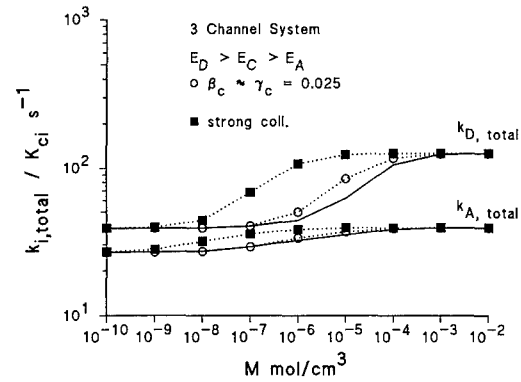

FIG. 5. Density dependence of the total rate coefficient associated with the consumption of either A or D (see text). Circles: strong collision model with $\beta_c = 0.025$; squares: strong collision model with $\beta_c = 1$.

kcal/mol, respectively. The numerically calculated reduced falloff curves for $J = 0$ clearly show the dramatic decrease of the coefficients for the two upper exits at low pressures. A strong collision model cannot reproduce these effects at all. Even the succession of the rate coefficients at low pressures is incorrect. At higher pressures, we observe a "channel switching" for the highest exit that has a loose configuration. At the high-pressure limit, k_D becomes larger than k_A:

$$k_D = \sum_{i_3}^{N} k_3(E_i) \cdot f(E_i) > k_A = \sum_{i_1}^{N} k_1(E_i) \cdot f(E_i).$$

The model was constructed such that at energies E_i slightly above the third exit we have $k_3(E_i) > k_1(E_i)$. For comparison, Fig. 3 also shows the results of the strong collision model. It is interesting to note that in the falloff range for the two channels above the entrance, the k_i may be proportional to M^n, where $n > 1$. In the one-channel case, we always have $n \leq 1$.

Model Example for a Complex Bimolecular Reaction with Two Exits:

If we are interested in a complex reaction starting with $A + BCD$ and then reacting either to the stabilized $ABCD$ or into the two channels $C + ABD$ and $D + ABC$, we can construct the yields as defined above for $A(t)/A(0) < 1$. The yields were calculated for $J = 0$ only. No summing over J was performed (see Fig. 4). At increasing densities, the deviation of the master equation result from the simplified treatment, according to Eqs. (1) through (3), is noticeable for this model. A factor of about 2 at higher densities does occur. This may be important for critical reactions in a kinetic system for combustion modelling, when data are extrapolated by using a too simple model. Further systematic investigations on this problem are needed.

As a next example, we consider the reaction starting from either the lowest or the highest entrance. Figure 5 shows the total rate coefficients $k_{i,\text{total}}$ (normalized with the associated K_{ci}) as a function of M.

The differences for certain M between the master equation and the strong collision model treatment appear dependent on which channel we start.

Analogously to the terms in Eqs. (1) through (3), the coefficient, e.g., for $k_{D\text{total}}$, is proportional to

$$\sum_{E_3} k_3(E) \cdot f_v(E) \cdot \frac{Z + k_1(E) + k_2(E)}{Z + k_1(E) + k_2(E) + k_3(E)}.$$

Here, Z appears in the nominator and in the denominator as a sum term. First of all, this limits possible

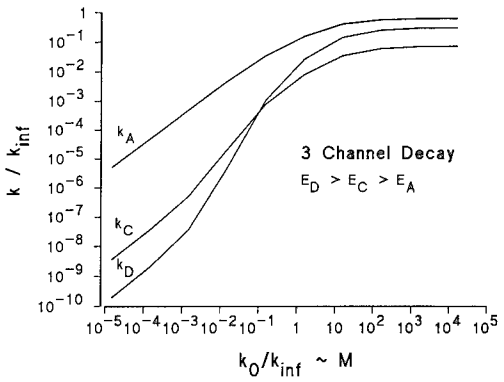

FIG. 6. Example calculation for loose, tight, loose exits (see text). Close to the barriers, the $k_{i,0}$ are assumed: $k_{A,0} = 10$; $k_{C,0} = 1$; $k_{D,0} = 10$. The units for the $k_{i,0}$ are in μs^{-1}.

differences. In this specific example, the strong collision model deviates by a factor of 1.5 or less. Finer details, as the different behaviour of $k_{A,\text{total}}$ and $k_{D,\text{total}}$, depend on the relative magnitudes of Z and the $k_i(E)$ in the respective terms for $k_{A,\text{total}}$ and $k_{D,\text{total}}$, which are not discussed further here.

If in this case we want to make corrections for weak collision effects, we cannot take the factor β_c. This factor was developed for the strong collision model to take globally into account energy transfer for dissociation. In the dissociation case, far from chemical equilibrium, but in the quasi-steady state, we have an underpopulation of the states ABC_i relative to f_i near the barrier. This is the typical situation where measurements are made and compared with theoretical models. In the case of chemical activation, again far from chemical equilibrium, we would observe an overpopulation relative to f_i in the vicinity of the barrier.

The energy transfer in the situation of chemical activation, or in particular for photochemical activation of molecular states far above the dissociation barriers of the ground state molecule, may be approximately regarded by defining a second global correction factor γ_c. For a discussion, see Ref. 33.

On the other hand, for thermal reactions, one should work with a consistent set of Equations (Eqs. (1) through (3)); the global correction factor has to be the same in all terms of the formulae. Otherwise, we would violate the thermodynamic equilibrium conditions for the ratio of the rate coefficients. In the presented numerical example, perhaps by chance, the two correction factors are very similar in numerical value. If it is not so, one has to decide on an average global correction factor in order to stay consistent. Solutions of the master equation will be, of course, intrinsically consistent.

Fig. 6 depicts an example of E_A(loose), E_C(tight), and E_D(loose) TS states at the exits. This resembles a situation of the lower CH_3OH channels (see below). Because of the loose exit of the lowest channel, the associated k_A dominates at all pressures. However, at higher pressures, the relative contributions of the other two channels are reversed compared with the situation at low pressures.

Contributions of Parallel Reactions

So far, we have neglected parallel reactions that do not proceed via a complex-forming intermediate. Experiments in limited T and particularly limited p ranges do not always provide clear evidence whether a direct route, e.g., an abstraction route, is participating, and if so, to which degree. For practical modelling, this question is important when extrapolations to higher pressures have to be made. In the case of $C_2H_5 + O_2$, it seems established that a direct abstraction route to $HO_2 + C_2H_4$ is not prevailing for $T < 700$ K [52] (see below). Theory may help to clear doubtful cases. Harding and Wagner [63] investigated H + HCO that reacts either to H_2 + CO directly or to the same products by an intermediate excited H_2CO with the chance of adduct stabilization. The theoretical result is that for pressures up to 1 bar, the abstraction is more prominent than the route via the intermediate complex. Another important reaction in combustion modelling, $C_2H_3 + O_2$, may be best described by a complex-forming and a direct abstraction route. In this case, the two reaction paths result in different products (see below). A detailed theoretical analysis of this system, considering both paths, has not appeared yet to the knowledge of the author.

Experimental Results on Some Multichannel Reactions

A systematic sensitivity analysis applied to large chemical kinetic systems was recently performed by Warnatz [1]. Important reactions were identified for the modelling of laminar flame speeds and of ignition. Mainly chainlike hydrocarbons were considered. In the following text, results on some of these selected reactions are shortly discussed. The importance of a reaction within a large system depends on the answers we want to obtain from the combustion simulation. Modelling of pollutant formations, as e.g PAH's, soot, aldehydes, or NO, shows that more reactions than selected in Ref. 1 have to be carefully considered. A systematic investigation of this point has not been performed, but for practical purposes, it has to be done in future.

Bimolecular Reactions with Bound Intermediates:

It is rather difficult to determine experimentally accurate branching ratios in larger T and p ranges.

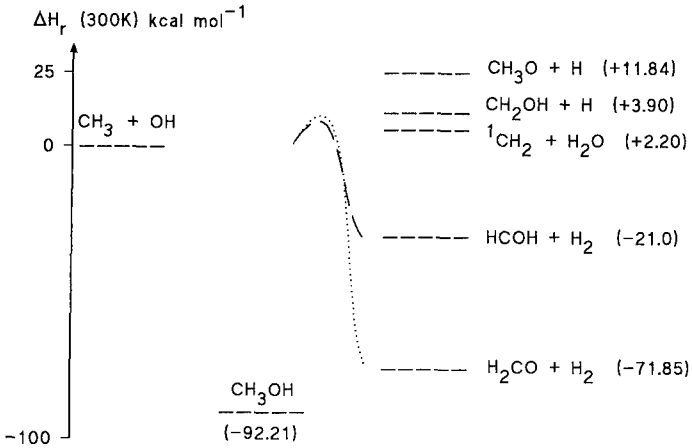

FIG. 7. Lower barriers for the multichannel system CH_3 + OH (see text).

Nevertheless, there are now appearing more and more quantitative experimental data on multichannel reactions relevant to combustion chemistry. Rate coefficients for the different channels are preferably measured under conditions where stabilization to the bound state(s) can be suppressed. In cases of possible contributions of stabilization channels under combustion conditions, additional investigations are needed. Some of the more recent results will be addressed here. The reader may find a rather extensive compilation of rate coefficients for combustion modelling in Ref. 34, which has been recently published.

$H + O_2$, $CO + OH$:

For the modelling of hydrocarbon combustion, the two well-known reactions

$$\begin{array}{ccc} H + O_2 & \rightleftarrows & OH + O \\ & \downarrow\uparrow & \\ & HO_2 & \end{array} \qquad \text{(R1)}$$

and

$$\begin{array}{ccc} CO + OH & \rightleftarrows & CO_2 + H \\ & \downarrow\uparrow & \\ & HOCO & \end{array} \qquad \text{(R2)}$$

are particularly important. Flame speeds, ignition limits, etc. depend critically on reaction (R1). The eventually formed CO_2 in hydrocarbon oxidation is mainly produced by the route in reaction (R2) (see Warnatz [35]).

Recent measurements by Masten and coworkers [36] on $H + O_2 \rightarrow O + OH$ have established that for $k = A \cdot T^n \cdot \exp(-E/RT)$, the exponent n equals 0, in contrast to older measurements that were best interpolated with $n = -0.9$ [34]. The older but widely used rate coefficient for $H + O_2$ is systematically too low for $T > 1800$ K. Since reaction (R1) is so important in hydrocarbon combustion modelling, we need a rather high accuracy for this rate coefficient over a large T range. Recent experimental determinations of reaction (R1) agree within $\pm 25\%$ [34,36]. Theoretical calculations using plausible potential curves at the two exits (seen from HO_2) by Troe [37] are well in accord with these new experimental results. More recent theoretical calculations are referred to in Ref. 36.

Concerning reaction (R2), $OH + CO \rightarrow CO_2 + H$, a new theoretical study by Kudla and Schatz [38] has demonstrated that despite great efforts, the strongly curved $k(T)$ in the temperature range between 500 and about 1200 K is still not well modelled at the lower temperature end. The discrepancies arise from the fact that the entrance potential OH + CO experimentally shows a small maximum which is up to now not reproduced by ab initio calculations [38]. Recent experimental studies of Hippler et al. [39] determining the recombination of OH + CO up to 200 bar in the T range from 250 to 700 K clearly resulted in a positive temperature dependence of the high-pressure recombination coefficient with T. This may be interpreted best by a small potential hill at the entrance channel.

CH_3 + OH:

Methyl reactions play important roles in combustion modelling. In particular, information on $CH_3 + OH \rightarrow$ products is needed.

Measurements in a flow reactor at temperatures between 300 and 700 K resulted in the determination of bimolecular rate coefficients for the channels in the range of about 4 kcal/mol above the entrance channel CH_3 + OH [40,41].

Figure 7 depicts a preliminary picture of the likely potential barriers as they were extracted from the measurements. There are two important new features:

1. The exit to $^1CH_2 + H_2O$ is relative to the entrance higher by 2.2 kcal/mol. Together with recent measurements from the $^1CH_2 + H_2O$ side by Carstensen and Wagner [42], it appears most plausible to increase the heat of formation of $^3CH_2$ [43] by about 1 kcal/mol to get a consistent interpretation of the experiments. This correction is within the error limits of the heat of formation for $^3CH_2$.
2. The channels forming mainly $HCOH + H_2$ and to a lesser extent $H_2CO + H_2$ were recently found experimentally [40,41]. The experimental barrier lies about 2.0–3.0 kcal/mol above the entrance.

Walch [44] predicted the barrier for $HCOH + H_2$ to be lower by 5.2 kcal/mol relative to the entrance. This is in conflict with the experimental findings that point strongly to a higher barrier. For a more detailed interpretation of the experimental results in the future, one should consider that the tight exit barrier in relation to the loose entrance becomes higher with increasing J. This will cause increasing blocking of the channel exit. Because of the rather small energy differences between the exit channels, it is to be expected that successful prediction of yields needs rather exact data for the $k_i(E,J)$ in this case. The next higher channel is a loose one leading to H_2COH + H. This exit is located relative to the entrance about 4 kcal/mol higher [41]. For $T \leq 700$ K, there was no experimental indication of contributions of this channel. One may predict that as soon as this channel opens at a certain temperature above 700 K, it will become dominant in relation to the lower channels with tight exits.

At temperatures $\leq$700 K, the H_2COH + H channel exit is likely determined by $k(E,J)$'s that, for energies E at and slightly above the exit, might not be much larger or even lower than the $k(E,J)$'s associated with the lower exits. Such a typical behaviour of $k(E,J)$'s for a loose TS state with J is represented in Ref. [27] (Fig. 2). The $k(E,J)$'s just at the barrier decrease with increasing J, because the contributing states of the K rotor ($|K| \leq J$) increase the density of states $\rho(E,J)$ (Fig. 2). The system CH_3 + OH was modelled by Dean and Westmoreland [45]. They used a rather simple QRRK approach. The stabilization channel at 1 bar below 1400 K was predicted to be the most important one. Mainly by using barrier heights different from the experimental ones [41], they predicted among the complex bimolecular reactions CH_2OH + H to be the dominant channel at all temperatures, which is in conflict with the experimental findings between room temperature and 700 K.

C_2H_2 + OH → Products:

The main exit channels are likely H + ketene or H + HCCOH and perhaps $C_2H + H_2O$. Barriers and intermediate bound states for these and additional channels have been investigated by Miller and Melius [13]. At low temperatures, the system forms an adduct characterized by a small potential hill at the entrance. Experimental results for this complicated system are compiled in Ref. 34. A theoretical analysis based upon several levels of RRKM theory was performed [13]. Recently, Fulle et al. [65] determined the limiting high-pressure rate coefficient for the channel leading to the adduct C_2H_2OH; T ranged from 300 to 600 K. The obtained activation energy E_a of 1.7 kcal/mol for k_{inf} should be close to the barrier height of the entrance channel. Miller and Melius have calculated 1.5 kcal/mol for the entrance barrier [13].

Although C_2H_2 + OH is important in combustion modelling [55], no conclusive experimental results on the nature of the products for the high-temperature range are available [34].

$CH_3 + O_2$ → Products:

Ignition of methane/O_2 or methane/air mixtures sensitively depends on this reaction. Two channels are discussed in the literature: one leading to H_2CO + OH, the other to CH_3O + O (see Refs. 46 and 34). For combustion modelling, the branching ratio may be quite important, since at typical combustion temperatures CH_3O is not stable and decays quickly into H_2CO and H. The net effect is the production of two reactive radicals.

Quite recently, Walch [47] presented a calculation of the potential energy surface for these products. These calculations are very helpful for the interpretation of the measurements that show an unusual behaviour of the OH channel. The electronic surface $^2A''$ connects the entrance $CH_3 + O_2$ with the channel exit CH_3O + O, whereas the exit to H_2CO + OH belongs to a $^2A'$ surface and is not directly coupled to the entrance (Fig. 8). The product channel H_2CO + OH can only be reached by an "electron hopping" from one surface to the other close to the crossing point of both curves (Fig. 8). Therefore, we expect a low A factor for the rate coefficient of the H_2CO + OH channel in this case. Preliminary results of Fraatz et al. [48], Naumann et al. [49], Braun-Unkhoff et al. [50a], and Hessler [50b] support this. The A factor was found to be in the range of $2 \cdot 10^{11}$ $cm^3\ mol^{-1}\ s^{-1}$ [48–50a] to $2 \cdot 10^{12}$ $cm^3\ mol^{-1}\ s^{-1}$ [50b]. Although the barrier for the H_2CO + OH exit is only 13.7 kcal/mol in relation to the 24 kcal/mol barrier for CH_3O + O, the low A factor brings down the rate coefficient. The temperature below which the H_2CO + OH channel dominates cannot be given presently.

$C_2H_5 + O_2$ → Products:

Alkyl + O_2 → products plays an important role in low-temperature oxidation. Ignition delay is influ-

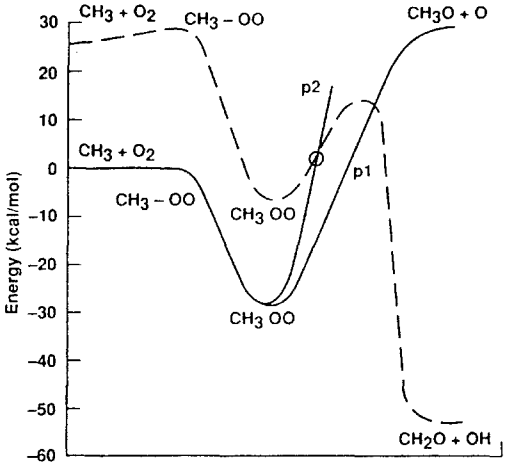

FIG. 8. Potential energies for the two reaction channels of $CH_3 + O_2$ [47] (see text). The circle marks the crossing of the lower $^2A''$ with the higher $^2A'$ surface.

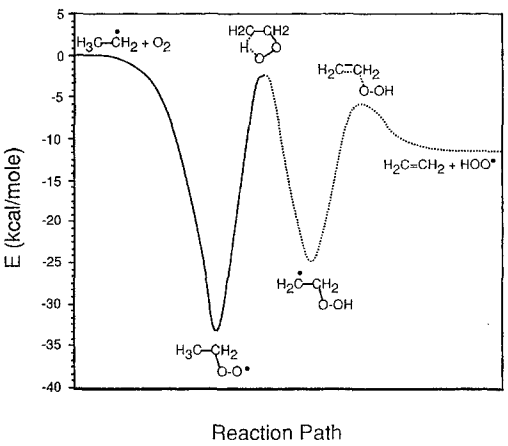

FIG. 9. Loose entrance, tight exit for $C_2H_5 + O_2$ [52].

enced at high pressures and temperatures around 700 K by the stabilization of RO_2 radicals and their further rearrangement that may lead via a complex mechanism either to HO_2 or, in part, eventually to OH radicals (see e.g., Chevalier et al. [51]). Wagner et al. [52] experimentally studied some Alkyl + O_2 reactions, the stabilization reaction, and the production of HO_2. Wagner presented in Ref. 52 a theoretical discussion of $C_2H_5 + O_2 \rightarrow C_2H_5O_2 \rightarrow HO_2 + C_2H_4$. This is a reaction of the loose → tight type, the exit channel lying lower than the entrance channel (Fig. 9). The analysis was based upon a modified ($Z \cdot \beta_c$) strong collision RRKM theory. Rotational effects were considered approximately by effective J's, based upon thermal averages of the rotational energy. Variational TS states for the entrance channel

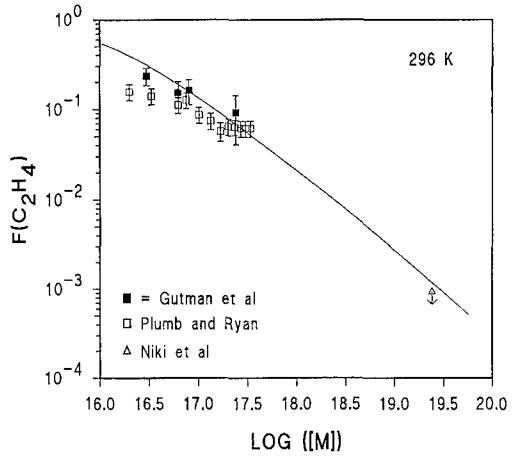

FIG. 10. Yield of C_2H_4, calculated with a modified strong collision model [52] (see text; Plumb and Ryan [67]; Niki et al. [68]).

were used. The full set of kinetic equations (1) through (3) was applied, since the experimental T range was such that back reactions and dissociation of $C_2H_5O_2$ had to be considered. Weak collision effects other than $Z \cdot \beta_c$ were not taken into consideration. With some adjusted parameters for the TS states, the experimental results could be described quite well. Particularly, the yields at different pressures and temperatures were predicted better than within a factor of 2 (Fig. 10). The interesting question remains whether the inclusion of true falloff effects by applying a master equation treatment could have changed conclusions, particularly concerning the accuracy of the interpolation between different experimental results on the rate coefficients $k_i(T,M)$. This reaction system, because of reliable experimental data in a larger p and T range, may perhaps serve as a future test case for studying differences obtained by either strong collision RRKM or master equation treatments.

$C_2H_3 + O_2 \rightarrow$ *Products:*

Slagle et al. [53] observed as sole reaction products $H_2CO + HCO$ at temperatures below 600 K. The yield was found independent of pressure in the investigated pressure range. The system $C_2H_3 + O_2$ is rather complicated. It is of the type loose entrance → tight exit channels. Westmoreland [54] discussed 10 possible reaction channels. A simple strong collision RRKM treatment was applied. The isomerizations along the reaction path were treated by sequences of two-channel reactions with stabilization to the respective isomer. Parameters were adjusted to fit Slagle's experiments [53]. The prediction is that around $T \approx 2000$ K and 1 bar, the channel $C_2H_2 + HO_2$ becomes dominant over $HCO + H_2CO$. This

channel switching may occur at different (perhaps lower) temperatures, if more accurate barrier heights as well as better properties of the TS states at the respective barriers will become available. The possibility of a direct abstraction reaction was not considered.

In a modelling study trying to establish a uniform set of reactions for nonaromatic hydrocarbons, Chevalier [55] found better agreement between measured and predicted laminar flame speeds for acetylene and ethylene flames if the channel C_2H_2 + HO_2 is open above 1500 K.

Phenyl + O_2 → Products:

Presently, there is not much known about high-temperature oxidation reactions of aromatic radicals. Recent attempts to model laminar flame velocities of benzene flames [1,55] demonstrated that phenyl + O_2 likely plays a key role in the reaction scheme for benzene oxidation. It is also probable that this reaction together with phenyl + C_2H_2 is important in the reaction scheme for the generation of soot precursors. In a study on phenyl + O_2 above 1200 K, it was revealed that the experimental results can be best interpreted assuming a three-channel reaction. The type is loose → tight → tight (Fig. 11). The main channel leads to phenoxy and O; however an unexpected immediate H-atom production was observed. This is presently explained by a second tight exit leading to *p*- or *o*-quinone + H (see Frank et al. [56]).

The ratio between the dominant and the second channel is about 3 to 1 in the investigated T range. There is a certain similarity to C_2H_3 + O_2, because the dominating TS state in this system is a four-membered ring: O_2 bridges the two C atoms in C_2H_3 [54]. Here, we assume for the quinone exit a complex where O_2 likely bridges opposite C atoms in the phenyl radical [56]. More detailed research to justify this hypothesis is needed.

Multichannel Decays:

At higher temperatures, the decay of hydrocarbons, even of small ones, proceeds as a multichannel process in almost all recently investigated cases. These reactions can play important roles when ignition phenomena have to be modelled. Moreover, detailed knowledge of such reactions is mandatory when, e.g., by shock tube methods, bimolecular radical-radical reactions at high temperatures are to be investigated. In shock tube techniques, the primary decay of some selected precursor often serves as the radical source for the particular investigation. Decay channels of the precursor have to be known, otherwise the interpretation of shock tube data may become ambiguous.

CH_3 → Products:

The two channels for CH_2 decay into CH to H (dominant) and CH + H_2 were recently studied by Markus et al. [57] and Dean and Hanson [58]. The tight exit to CH + H_2 lies about 2.5 kcal/mol below the H-atom exit. Nevertheless, the H-atom channel is dominating in the investigated T range from 2100 to 3500 K. A theoretical analysis of the decay coefficients is missing in the literature.

The observed experimental facts point to a combination of rotational effects and tight properties of the TS state for the CH exit relative to those of the loose H exit. At high temperatures, the tight exit may become more and more blocked for relevant J's (see the discussion above). Ab initio calculations of the surface near the exits were recently performed by Aoyagi et al. [58]. They also calculated the high-pressure limit of the association reaction CH_2 + H → CH_3.

Vinylacetylene → Products:

This system was recently studied by several groups [59]. The most complete study stems from Braun-Unkhoff [32]. A three-channel decay was observed.

$$\begin{aligned} C_4H_4 &\rightarrow C_2H_2 + C_2H_2 \\ &\rightarrow C_4H_2 + H_2 \\ &\rightarrow C_4H_4 + H. \end{aligned}$$

The system has tight, tight, loose exits in the order as written.

The dominant channel is the formation of two acetylene molecules. It is interesting to note that in the investigated T and p range, the two molecular channels are practically independent of M, whereas the data for the H-producing channel approximately show a behaviour proportional to M. Figure 3 depicts for the system tight, tight, loose a relatively larger deviation of the highest exit from the high-pressure limit than for the two other lower channels. This is true for a certain range of M. Qualitatively, this effect may be understood. The population above the highest exit is considerably depleted by the reaction through the highest exit associated with a rather large $k_3(E)$ in relation to the two lower channels. A theoretical analysis of the expected structures of the TS states including the calculation of the barrier heights was recently presented by Melius et al. [30]. An attempt to predict the $k(T,M)$'s for this system has not been undertaken yet.

Toluene → Products:

There are two exit channels open at combustion temperatures. The lower one leads to benzyl and H, the higher one to phenyl + CH_3. In shock tube ex-

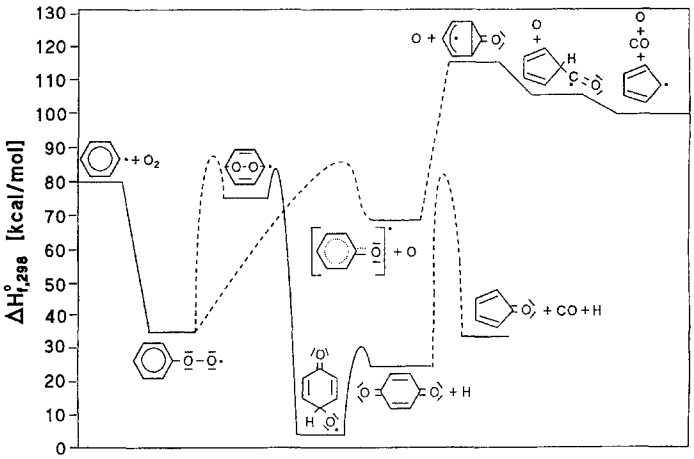

FIG. 11. Barriers for the reaction of phenyl with O_2. Loose, tight, tight (see text). The dotted lines refer to barriers that were experimentally determined by Frank et al. [56].

periments performed up to 2000 K, the dominating channel is benzyl + H [60,34]. Even toluene with two loose exits does not exhibit an orderly behaviour. Because of the different moments of inertia $I^{\#}$ at the respective TS states, one for H···benzyl, the other for H_3C···phenyl, we obtain two markedly different C_v's (see Section 3.1). The smaller one is associated with the larger $I^{\#}$ and belongs to the CH_3 exit. This causes for the higher J a stronger reduction of the barrier height for the CH_3 channel compared with the H channel, thus forcing the system more and more to the direction of dissociation into CH_3 + phenyl at higher temperatures. A detailed analysis based on the different $k_i(E,J)$ obtained by a SACM treatment was given by Luther et al. [61].

Conclusions

It was the purpose of the author to give a short survey on selected aspects of modelling multichannel reactions as well as on recent experimental results of some of these reactions relevant in the combustion of hydrocarbons.

How accurately do we have to interpolate or extrapolate rate coefficients stemming usually from a rather limited experimental basis? The answer to this question can be obtained by performing a sensitivity analysis of the system under consideration. The needed accuracy for the rate coefficients in the p and T domain may be different for different systems. Sensitivity analysis helps to determine the degree of sophistication needed for modelling selected rate coefficients in the given p and T range.

Numerical mathematical methods for treating master equations are available in the case of multichannel reactions. These methods can be applied on workstations or even on personal computers.

Up to now, practically all models applied to simulate complex reactions for combustion kinetics were developed under the assumption of rotational equilibration of the molecular states. How strongly this assumption affects numerical results cannot be precisely answered today. However, since these processes are very fast in the time scale of combustion chemistry, researchers agree that neglect of rotational relaxation appears tolerable with respect to other uncertainties in the models.

The satisfying treatment of a selected multichannel system depends on appropriate models for the involved $k(E,J)$.

But, as we would say in Germany, "The devil's in the details."

Until today, some of these "details," particularly the difficulties in modelling satisfactorily the $k(E,J)$, have prevented broader application of strong collision models or master equation treatments for combustion applications.

For practical purposes of combustion simulation, we need more detailed investigations on selected model systems that enable us to test various degrees of simplification of the modelled energy-specific rate coefficients against experimental results. This also comprises tests of strong collision models including global corrections as β_c vs master equation treatments.

Further, we need more data on barrier heights and on the frequency patterns of the associated TS states to replace too simple models for $k(E,J)$. Fortunately, quantum chemical methods now deliver data with improved accuracy so that they become more and more useful in advanced kinetic modelling.

For one-channel reactions, empirical relations have been proposed to correct for energy transfer effects in the falloff range down to the low-pressure limit. Presently, it is not clear whether similar procedures can be developed for multichannel systems. There is perhaps a good chance to do this for the

total rate coefficient of a complex bimolecular reaction. The situation for dissociation reactions is less favourable. Except for the main channel, there is likely only a little chance to do this in a simple manner for the other channels in multichannel decays.

Investigation of multichannel reactions has considerable practical importance, and it appears as an interesting and challenging field for both theorists and experimentalists.

Acknowledgment

The author would like to thank J. Troe, A. F. Wagner, and H. H. Grotheer for a critical and helpful discussion of the manuscript.

REFERENCES

1. Warnatz, J., *Twenty-Fourth Symposium (International) on Combustion,* The Combustion Institute, 1992, p. 553.
2. Maas, U., and Pope, S. B., *Twenty-Fourth Symposium (International) on Combustion,* The Combustion Institute, 1992, p. 103.
3. a) Robinson, P. J., and Holbrook, K. A., *Unimolecular Reactions,* Wiley-Interscience, London, 1972. b) Forst, W., Theory of Unimolecular Reactions, Academic Press, New York, 1973. c) Gilbert, R. G., and Smith, S. C., Theory of Unimolecular and Recombination Reactions, Blackwell Scientific Publications, Oxford, 1990.
4. Golden, D. M., *J. Phys. Chem.* 83 (1):109 (1979).
5. Golden, D. M., and Larson, C. W., *Twentieth Symposium (International) on Combustion,* The Combustion Institute, 1984, p. 595.
6. Smith, J. W., *J. Chem. Soc. Faraday Trans.* 87 (15):2271 (1991).
7. Mozurkewich, M., and Benson, S. W., *J. Phys. Chem.* 88:6429 (1984).
8. Mozurkewich, M., Lamb, J. J., and Benson, S. W., *J. Phys. Chem.* 88:6435 (1984).
9. Lamb, J. J., Mozurkewich, M., and Benson, S. W., *J. Phys. Chem.* 88:6441 (1984).
10. Troe, J., *Ber. Bunsenges. Phys. Chem.* 87:161 (1983).
11. Tardy, D. C., and Rabinovitch, B. S., *J. Chem. Phys.* 45:3720 (1966); *J. Chem. Phys.* 48:1282 (1967).
12. Gilbert, R. G., Luther, K., and Troe, J., *Ber. Bunsenges. Phys. Chem.* 87:169 (1983).
13. Miller, J. A., and Melius, C. F., *Twenty-Second Symposium (International) on Combustion,* The Combustion Institute, 1988, p. 1031.
14. Miller, J. A., Parrish, C., and Brown, N. J., *J. Phys. Chem.* 90:3339 (1986).
15. Just, Th., and Troe, J., *J. Phys. Chem.* 84:3068 (1980).
16. Troe, J., *J. Chem. Phys.* 66:4745 (1977).
17. Smith, S. C., McEwan, M. J., and Gilbert, R. G., *J. Chem. Phys.* 90:4265 (1989).
18. Just, Th., to be published.
19. Gilbert, R. G., Luther, K., and Troe, J., *Ber. Bunsenges. Phys. Chem.* 87:169 (1983).
20. Troe, J., *J. Phys. Chem.* 83:114 (1979).
21. a) Smith, S. C., *J. Phys. Chem.* 97:7034 (1993). b) Smith, S. C., *J. Phys. Chem.* 97 (4):2406 (1992). c) Smith, S. C., *J. Phys. Chem.* 95 (5):3404 (1991).
22. Wardlaw, D. M., and Marcus, R. M., *J. Chem. Phys.* 83:3462 (1984).
23. a) Maergoiz, A. I., Nikitin, E. E., and Troe, J., *Z. Phys. Chem.* 172:129 (1991). b) Maergoiz, A. I., Nikitin, E. E., and Troe, J., *J. Phys. Chem.* 95:5117 (1991).
24. Quack, M., and Troe, J., *Ber. Bunsenges. Phys. Chem.* 78:240 (1974).
25. Troe, J., *J. Chem. Soc. Faraday Trans.* 87:2299 (1991).
26. Troe, J., *J. Chem. Phys.* 79:6017 (1983).
27. Troe, J., *J. Phys. Chem.* 88:4375 (1984).
28. Gilbert, R. G., Whyte, A. R., and Phillips, L. F., *Int. J. Chem. Kinet.* 18:721 (1986).
29. Melius, C. F., and Binkley, J. S., *Twentieth Symposium (International) on Combustion,* The Combustion Institute, 1984, p. 575.
30. Melius, C. F., Miller, J. A., and Evleth, E. M., *Twenty-Fourth Symposium (International) on Combustion,* The Combustion Institute, 1992, p. 621.
31. Wagner, A. F., Kiefer, J. H., and Kumaran, S. S., *Twenty-Fourth Symposium (International) on Combustion,* The Combustion Institute, 1992, p. 613.
32. Braun-Unkhoff, M., Kurz, A., and Frank, P., *Seventeenth International Symposium on Shock Waves and Shock Tubes,* AIP American Institute of Physics, 1990, p. 493.
33. Troe, J., *J. Phys. Chem.* 87:1800 (1983).
34. Baulch, D. L., Cobos, C. J., Cox, R. A., Esser, C., Frank, P., Just, Th., Kerr, J. A., Pilling, M. J., Troe, J., Walker, R. W., and Warnatz, J., *J. Phys. Chem. Ref. Data* 21:411 (1992).
35. Warnatz, J., in Combustion Chemistry (W. C. Gardiner, Ed.), Springer, New York, 1984, p. 197.
36. a) Masten, D. A., Hanson, R. K., and Bowman, C. T., *J. Phys. Chem.* 94:7119 (1990). b) Yu, C. L., Frenklach, M., Masten, D. A., Hanson, R. K., and Bowman, C. T., *J. Phys. Chem.* 98:4770 (1994). c) Du, H., and Hessler, J. P., *J. Chem. Phys.* 96:1077 (1992).
37. Troe, J., *Twenty-Second Symposium (International) on Combustion,* The Combustion Institute, 1988, p. 843.
38. Kudla, K., and Schatz, G. C., *J. Chem. Phys.* 95 (3):1635 (1991).
39. Hippler, H., *et al.,* to be published.
40. Humpfer, R., Oser, H., Grotheer, H. H., and Just, Th.: *Twenty-Fifth Symposium (International) on Combustion,* The Combustion Institute, Pittsburgh, 1994, pp. 721–731.
41. Humpfer, R., Oser, H., and Grotheer, H. H., *Int. J. Chem. Kinet.* (1994), in press.
42. Carstensen, H. H., and Wagner, H. Gg., Max-Planck-Institut für Strömungsforschung, Research Report 9/1993, ISSN 0436-1199.
43. Kee, R. J., Rupley, F. M., and Miller, J. A., Sandia

Report, SAND87–8215, UC4 (1987) and update (1991).
44. Walch, S. P., *J. Chem. Phys.* 98:3163 (1993).
45. Dean, A. M., and Westmoreland, P. R., *Int. J. Chem. Kinet.* 19:207 (1987).
46. Klatt, M., Röhrig, M., and Wagner, H. Gg., *Ber. Bunsenges. Phys. Chem.* 95:1163 (1991).
47. Walch, S. P., *Chem. Phys. Lett.* 215:81 (1993).
48. Fraatz, W., et al., Doctoral Thesis, University of Göttingen, Institut für Physikalische Chemie, 1990.
49. Naumann, C., Horn, Chr., Braun-Unkhoff, M., and Frank, P., to be published.
50. a) Braun-Unkhoff, M., Naumann, C., Wintergerst, K., and Frank, P., *VDI-Berichte* 1090:287 (1993). b) Hessler, J. P., to be published.
51. Chevalier, C., Pitz, W. J., Warnatz, J., Westbrook, C. K., and Melenk, H., *Twenty-Fourth Symposium (International) on Combustion,* The Combustion Institute, 1992, p. 93.
52. Wagner, A. F., Slagle, I. R., Sarzynski, D., and Gutman, D., *J. Phys. Chem.* 94:1853 (1990).
53. Slagle, I. R., Park, J.-Y., Heaven, M. C., and Gutman, D., *J. Am. Chem. Soc.* 106:4356 (1984).
54. Westmoreland, Ph. R., *Combust. Sci. Technol.* 82:151 (1992).
55. Chevalier, Ch., Doctoral Thesis, University of Stuttgart, Institut für Technische Verbrennung, 1993.
56. Frank, P., Herzler, J., Just, Th., and Wahl, C., *Twenty-Fifth Symposium (International) on Combustion,* The Combustion Institute, Pittsburgh, 1994, pp. 833–840.
57. Markus, M. W., Woiki, D., and Roth, P., *Twenty-Fourth Symposium (International) on Combustion,* The Combustion Institute, 1992, p. 581.
58. a) Dean, A. J., and Hanson, R. K., *Int. J. Chem. Kinet.* 24:517 (1992). b) Aoygai, M., Shepard, R., Wagner, A. F., Dunning, Th.H., Jr., and Brown, F. B., *J. Phys. Chem.* 94:3236 (1990).
59. a) Colket, M. B., *Twenty-First Symposium (International) on Combustion,* The Combustion Institute, 1986, p. 851. b) Hidaka, Y., Tanaka, K., and Suga, M., *Chem. Phys. Lett.* 130:195 (1986). c) Kiefer, J. H., Mitchell, K. I., Kern, R. D., and Yong, J. N., *J. Phys. Chem.* 92:677 (1988).
60. Braun-Unkhoff, M., Frank, P., and Just, Th., *Twenty-Second Symposium (International) on Combustion,* The Combustion Institute, 1988, p. 1053.
61. Luther, K., Troe, J., and Weitzel, M. K., *J. Phys. Chem.* 94:6316 (1990).
62. Dean, A. M., *J. Phys. Chem.* 89:4600 (1985).
63. Harding, L. B., and Wagner, A. F., *Twenty-First Symposium (International) on Combustion,* The Combustion Institute, 1986, p. 721.
64. Troe, J., *J. Chem. Soc. Faraday Trans. II* 90:2303 (1994).
65. Fulle, D., Hamann, H., Hippler, H., and Jäntsch, C., to be published.
66. Geers, A., Kappert, J., Temps, F., and Wiebrecht, W., *Chem Phys. Lett.* 179:191 (1991).
67. Plumb, I. C., and Ryan, K. R., *Int. J. Chem. Kinet.* 13:1011 (1981).
68. Niki, H., Maker, P. D., Savage, C. M., and Breitbach, L. P., *J. Phys. Chem.* 86:3825 (1982).

COMMENTS

Joseph W. Bozzelli, Chemistry and Chemical Engineering, New Jersey Institute of Technology, USA. Early in your lecture, you showed that at high temperature, a loose transition state with a higher barrier could lead to a higher reaction rate (dominate the products) over that of a somewhat lower energy channel, with a tight or stiff transition state. Is it possible that a stiff transition state in the formation of HCOH + H_2 from chemically activated CH_3OH is responsible for the apparent activation energy you had on the potential energy diagram for the CH_3 + OH combination?

Author's Reply. The system CH_3 + OH has not been fully analysed yet. This would, e.g., mean thoroughly to take into account rotational effects at the respective barriers. This task will be done in the future. My prediction is that at and below the highest temperature applied in our experiments so far, the stiff transition state is dominating our experimental results on HCOH + H_2. At higher temperatures, an increasing influence of the higher exists belonging to loose transition states may take over. The pressure and temperature behaviour of the coupled reaction coefficients may turn out quite complicated.

•

Phillip R. Westmoreland, University of Massachusetts, Amherst, USA. Your analysis, especially as emphasized by Hippler's data on the rate constant for CO + OH, shows that many important combustion reactions are associations that produce thermalized adducts only at high enough pressures. For the chemically activated decomposition channels, the pressure or density dependence is an inverse falloff, pressure independent at low pressures. For rate-constant measurements at low pressures with no product detection, it is thus important to recognize that pressure-independent rate constants may be associated reactions.

Author's Reply. At very low pressures at a given temperature, I would expect pressure-independent rate coefficients reflecting reactions with no association. At increasing pressures, contributions of association reactions may start to appear in the global rate coefficient.

•

Bruce W. Gerhold, Phillips Petroleum Co., USA. The calculations for the reaction $CO + OH = CO_2 + H$ provide a unified interpretation of many observations. The prediction of high-pressure quenching of HOCO suggests an additional mechanism leading to CO emissions from high-pressure practical devices (for example, gas turbines). Since HOCO is not commonly measured in atmospheric pressure systems, I assume HOCO will dissociate if high-pressure gas containing HOCO expands through a turbine. Can you comment on the likely dissociation products following a rapid expansion? What mole fraction HOCO is calculated for a 100-atm gas turbine combustion gas, and what exhaust atm/mole fraction CO may be generated through this mechanism? Finally, high-pressure flow reactor kinetic studies may suffer from a similar problem.

Author's Reply. Under gas turbine conditions, there is in my opinion not much of a chance of forming relevant amounts of HOCO. However, I have to admit that I didn't do any calculations in this direction.

Twenty-Fifth Symposium (International) on Combustion/The Combustion Institute, 1994/pp. 705–712

THERMAL DECOMPOSITION OF CH_2 VERIFIED BY PRODUCT CONCENTRATION MEASUREMENTS OF C, H, AND CH

M. W. MARKUS AND P. ROTH
Institut für Verbrennung und Gasdynamik
Universität Duisburg
47048 Duisburg, Germany

AND

A. M. TEREZA
Semenov Institute
Academy of Sciences
Moscow, Russia

At temperatures $T \geq 2200$ K, ketene (CH_2CO) is known as a convenient, reproducible and well-defined CH_2 source. In experiments performed behind reflected shock waves, the subsequent reactions of CH_2 were monitored by concentration measurements of various product species, including C, H, and CH, using atomic resonance absorption and ring dye laser absorption spectroscopy. The time histories of these species were investigated in various initial ketene (5–75 ppm)/argon mixtures in the temperature range 2200–3400 K at pressures $0.7 \leq p \leq 2.4$ bar. From the concentration slopes at $t \approx 0$, apparent rate coefficients for C, H, and CH formation were determined, but only the C concentration profiles at early reaction times have direct kinetic significance. From these data, the rate coefficient of the thermal decomposition reaction

$$CH_2 + M \overset{k_2}{\rightleftharpoons} C + H_2 + M$$

$$k_2 = 1.60 \times 10^{14} \exp(-32{,}200\ K/T)\ cm^3\ mol^{-1}\ s^{-1} \qquad (R2)$$

could directly be determined. The second possible, but energetically unfavourable, CH_2 decomposition channel forming CH + H was found to have no influence on the observed product concentrations in the given experimental region. The full time-resolved concentration profiles obtained were further analysed by comparing them with computer simulations based on a reaction mechanism containing 20 elementary reactions. From the temporal structure of the profiles, rate coefficients for the most important reactions could be derived. In the given temperature range, the mechanism used is able to predict the concentration profiles of all observed species in the highly diluted ketene/argon mixtures.

Introduction

Methylene is one of the simplest hydrocarbon compounds. Since CH_2 is a very reactive intermediate, its reactions are important in almost every high-temperature hydrocarbon reaction system. Although being of great kinetic interest, the knowledge of many CH_2 reactions is only at a qualitative stage. Since UV–laser-pulse photolysis of ketene has been established as a convenient CH_2 source, several reactions were investigated at low pressures and moderate temperatures [1–4]. Wagner and Zabel [5] studied the thermal decomposition of ketene at temperatures above 1300 K. They found CH_2 and CO to be the only decomposition products that let ketene appear to be a suitable thermal methylene source. Frank et al. [10] studied the thermal decomposition of CH_2CO highly diluted in argon at temperatures up to 2800 K behind reflected shock waves and measured H and CO by VUV absorption. They confirmed the results of Wagner and Zabel [5] and gave first insights into bimolecular reactions of CH_2 with ketene and H atoms.

In the present study, the reaction conditions of ketene/argon systems were extended to temperatures where CH_2 thermal decomposition occurs. The aim was to get a better understanding of the chemical processes involved by measuring time-dependent concentration profiles of all important products H, C, and CH. Dean and Hanson [6] discussed the C and CH concentration profiles obtained from methane or ethane pyrolysis systems by introducing a two-channel scheme for the CH_2 thermal decomposition. The time histories of the measured species could be well predicted by using nearly equal rate coefficients for the two possible CH_2 decomposition channels,

giving C + H_2 or CH + H, respectively. The authors of the present study also achieved good results in comparing their CH profiles from ethane/methane thermal decomposition systems with calculations based on a quite similar mechanism [7,8]. But Kiefer and Kumaran [9] demonstrated that Dean's and our experiments also could be reproduced by a totally different scheme, mostly based on fast bimolecular reactions. In their mechanism, the CH_2 decomposition channel forming CH appeared with only minor importance for the entire reaction system.

The modern optical diagnostic techniques RDLS (ring dye laser spectroscopy) and ARAS (atomic resonance absorption spectroscopy) allow the detection of the most important intermediate species with high sensitivity and accuracy in highly diluted systems. The use of ketene as a reliable and direct CH_2 source overcomes the influences introduced by secondary reactions of more complex radical sources like ethane or methane. The present data base, together with computer modelling, should lead to a more complete picture of CH_2 reactions based on elementary reaction steps.

Experimental

Ketene was synthesized in a flow reactor made of quartz glass by pyrolysis of acetic anhydride vapour at t = 500 °C and $p \approx 20$ mbar. Under these conditions, acetic anhydride is known to decompose nearly exclusively to ketene and acetic acid with a very low level of impurities, mostly residual acetic anhydride [11]. Ketene was separated from by-products by passing the gas through a condensor and a cold trap, both held at −50 °C, and was afterwards condensed in a cold trap at −196 °C. The crude ketene was further purified by trap-to-trap distillation at reduced pressure. Gas samples were analysed by a quadrupole mass spectrometer. At high detection sensitivity, no significant impurities were found, so the ketene can be estimated to have a purity level of better than 99%. The ketene/argon mixtures were prepared in an ultrahigh vacuum (UHV) mixing vessel made of stainless steel. Only argon of highest commercially available purity (99.9999%) was used for dilution. The CH_2CO was synthesized and analysed right before preparing and using the gas mixture.

The UHV shock tube used for this study has an inner diameter of 79 mm and a running section 6.0 m in length [12]. It is equipped with two optical absorption diagnostics arranged in the same plane but perpendicular to each other. One observation path is part of an ARAS spectrometer consisting of a microwave discharge lamp, the shock tube absorption path, and a 1-m focal length VUV monochromator equipped with a solar blind photomultiplier. All H atom measurements were performed at the 121.6-nm H_a line. For the C atom measurements, the CI absorption at 156.1 nm was used. For details of the ARAS technique and calibration, see Ref. 13 (H atoms) and Ref. 14 (C atoms).

Because of the relatively high absorption cross section of CO in the vacuum UV spectral region, it was possible to apply the VUV spectrometer for CO measurements. The $A^1\Pi - X^1\Sigma^+$ (1,0) vibronic transition of CO was excited in the microwave lamp and the emitted light at 151 nm was passed through the shock tube absorption path. To get the required relation between spectral absorption and CO concentration, calibration experiments were performed behind reflected shock waves using mixtures of known CO concentrations in the temperature range between 1800 and 3700 K. The CO absorption during the CH_2CO pyrolysis was measured to verify the initial ketene concentrations. Within the uncertainty limit of the CO calibration of about 25%, plateaus equal to the initial CH_2CO concentration were obtained. Because of the better signal-to-noise ratio, the higher sensitivity, and the lower calibration uncertainties, we also used C atom measurements at very high temperatures, around 4000 K (complete CH_2 dissociation), to control the concentration of the initial reactant. The mixtures of 5 to 75 ppm CH_2CO in argon were found to be stable within the two days of operation. The effect of ketene adsorption at the shock tube walls was reduced by flushing the tube with the mixture before every experiment.

The ring dye laser technique used to measure CH concentrations has been described in detail in Ref. 15. The resonance absorption in the Q branch of the $A - X(0,0)$ band at 431.1131 nm is known to be most efficient for quantitative measurements at temperatures around 3000 K [16]. The absorption signals were converted into concentration profiles using a spectroscopic model for the CH line absorption [16]. Efforts to measure $^1CH_2$ concentrations by ring dye laser absorption in the $\tilde{b}\,^1B_1 - \tilde{a}^1A_1$ (0,14,0 − 0,0,0) band at $\lambda \approx 590$ nm at single rotational line frequencies given by Herzberg and Johns [17] failed even in mixtures containing up to 1000 ppm CH_2CO in argon. Therefore, kinetic information on CH_2 pyrolysis was only obtained from product species measurements given below. The ring laser was mounted on an optical table in a separate room and was connected to the shock tube via an optical fiber 60 m in length. Si photodetectors were used to monitor the incident and the absorbed laser light. The time resolution of the ring dye laser spectrometer was about 3 μs. The time-dependent absorption signals caused by the formation of atomic or molecular species were stored in transient recorders and were then transmitted to a personal computer for storage and further processing.

Results

The experiments on CH_2 thermal decomposition were conducted behind reflected shock waves in the

temperature range 2200 K $\leq T \leq$ 3400 K at pressures 0.7 bar $\leq p \leq$ 2.4 bar. The initial concentration of CH_2CO diluted in argon was varied between 5 and 75 ppm. Because of the comparable detection sensitivities for C atoms and CH radicals, the ARAS and the RDLS diagnostics could be applied simultaneously; i.e., CH and C time histories were both measured in the same experiment. To get an experimental overlap with the very sensitive H atom measurements, C and H atoms were measured alternately in a mixture of 10 ppm CH_2CO/argon.

In 45 individual experiments, absorption signals of H, C, and CH were recorded during CH_2 pyrolysis. They were directly transformed into concentrations by applying calibration curves (H, C) or the known line center absorption cross section (CH). Typical individual examples of measured time histories are shown in Figs. 1a through 1d. In the case of H atoms, the signal increases after shock arrival, reaching a quasi-stationary value after some hundred microseconds. The same behaviour was found in all other H atom experiments. It is a remarkable fact that the early part of the profiles was always curved.

The C and CH concentration profiles in Figs. 1a through 1d show sharp maxima. For low-temperature experiments, the C atom concentrations increased linearly with time within 10 to 100 μs and decreased again quite rapidly to a constant value. The height of the plateau was shifted to higher concentrations with increasing temperature. For temperatures above 3000 K, no significant maximum was observed. Here, the C atom concentrations increased rapidly and remained constant for some hundred microseconds.

In the case of CH, all signals increased immediately after shock arrival, reached a maximum value, and decreased again to a low level. The half width of the profiles was always smaller than that of the C atoms. Immediately after shock arrival, the slope of the concentration profiles was found to be nearly linear. The yield of CH from the CH_2CO pyrolysis,

$$Y_{CH} = [CH]_{max}/[CH_2CO]_0$$

increased linearly with temperature to a maximum value of about 6% near 2600 K. For higher temperatures, the CH yield decreased again slightly. At temperatures above 3200 K, the CH concentrations were below the detection limit of the ring laser diagnostic for the present experimental conditions. Table 1 summarizes the experimental conditions and some characteristics of the measured H, C, and CH concentration profiles.

Discussion

The influence of temperature and pressure on the formation of the observed species was studied in a wide range of postshock conditions. It is not an easy task to analyze the more than 69 measured concentration profiles in a simple analytical way or to reduce the data to simple kinetic expressions. Although computer modelling seems to be necessary for the complete discussion, we started the data evaluation with a quantity that only takes the gradients of the different profiles at $t \approx 0$ into account. Similar to the procedure discussed in the case of methyl decomposition [8,18], apparent formation rate coefficients for the early species formation were determined:

$$k_{X,\mathrm{app}} = (d[X]/dt)_{t\approx 0}/[CH_2CO]_0\,[Ar];$$
$$X = \mathrm{H, C, CH.}$$

The apparent rate coefficients for the different species are summarized in the Arrhenius plots of Figs. 2 and 3. The k_{app} values of H and CH differ significantly from each other and do not show a systematic temperature dependence; see Fig. 2. Unlike the results of the CH_3 thermal decomposition [18], no significant pressure dependence was observed for the CH formation. On the other hand, the apparent rate coefficients for the C atom formation given in Fig. 3 show Arrhenius behaviour, although a grouping of the experimental points with respect to the initial concentrations of ketene is quite obvious. From the different behaviour of the three apparent rate coefficients, it seems reasonable to conclude that mainly C and not CH and H must be regarded as the primary decomposition product of CH_2:

$$CH_2 + M \overset{k_2}{\leftrightharpoons} C + H_2 + M;$$
$$\Delta H_{298} = 79 \text{ kcal/mol}$$
$$\overset{k}{\leftrightharpoons} CH + H + M;$$
$$\Delta H_{298} = 102 \text{ kcal/mol.} \qquad \text{(R2)}$$

The second reaction channel has a much higher heat of formation and seems not to contribute significantly to the CH formation in the observed experimental range. The observation that the CH formation occurs very rapidly after shock-front arrival, even at low temperatures, leads to the conclusion that CH is obviously produced mainly by fast bimolecular reactions of CH_2. A further energetic argument also supports the above hypothesis. If the reaction channel CH + H were the predominant formation path for H atoms, an activation energy close to 102 kcal/mol could be expected for H atom abstraction. But the apparent rate coefficient for H formation shows only a little temperature dependence, which additionally exhibits an unclear tendency. Therefore, bimolecular reactions of CH_2 and its products are again more probable sources of H atoms at early reaction times, even at high temperatures.

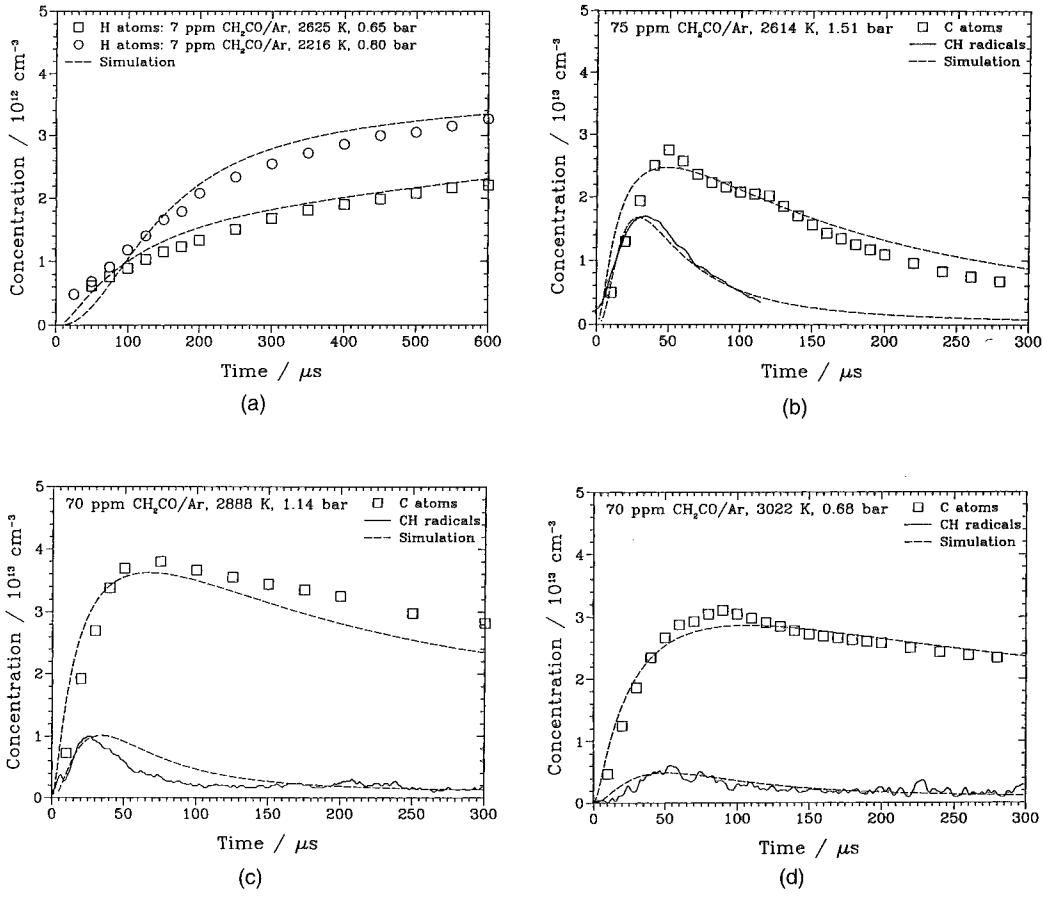

FIG. 1. (a) through (d) Examples of the concentration profiles measured during the pyrolysis of ketene (open symbols and solid line, respectively) in comparison with calculated profiles (dashed lines) based on the mechanism given in Table 2.

The apparent rate coefficients for the formation of C atoms summarized in Fig. 3 clearly show Arrhenius behaviour. For experiments performed in ketene/argon mixtures with low initial concentrations (10 and 60 ppm) and for those performed at low postshock pressures (70 ppm ketene, $p \leq 1$ bar), the individual apparent rate coefficients show a linear temperature dependence with a reasonable slope compared to the heat of formation of reaction (R2). A good fit to the experimental points by an Arrhenius expression was found to be

$$k_2 = 1.60 \times 10^{14} \cdot \exp(-32200\ \mathrm{K}/T)\ \mathrm{cm^3\ mol^{-1}\ s^{-1}}.$$

For the group of experiments described above, reaction (R2) can be assumed to be the most important formation path of C atoms in the observed temperature range. Systematic deviations from the mean value given above, illustrated by the dashed line in Fig. 3, were found for those data points of k_{app} that were obtained at lower temperatures and higher initial concentrations. This can be explained by the influences of additional bimolecular reactions contributing to the CH_2 consumption at very early reaction times, resulting in a decrease of the apparent C atom formation rates with increasing initial concentrations. For comparison, rate coefficients given in earlier studies [6,8,9,19] are also included in Fig. 3. These values were estimated to fit experimental data obtained from ethane or methane pyrolysis systems using a complicated kinetic mechanism. To our knowledge, the present study is the first direct result of C atom abstraction during the thermal decomposition of methylene.

The further evaluations of the measured full time-dependent concentration profiles of H, C, and CH were performed based on a kinetic model. The mechanism of Frank et al. [10] was used as a basis. It was extended by additional reactions found in the

TABLE 1
Experimental Conditions and Results Obtained from H, C, and CH Measurements in Ketene Pyrolysis Systems

T K	p bar	$[CH_2CO]_0$ ppm	$(d[C]/dt)_0$ mol cm^{-3} s^{-1}	$[C]_{max}$ mol cm^{-3}	$[C]_{300\mu s}$ mol cm^{-3}	$(d[CH]/dt)_0$ mol cm^{-3} s^{-1}	$[CH]_{max}$ mol cm^{-3}
3278	1.04	10	0.61×10^{-6}	3.57×10^{-11}	3.50×10^{-11}	—	—
3309	0.99		1.00	2.56	2.56	—	—
3430	1.01		1.19	2.69	2.64	—	—
2455	1.26	60	0.71	3.35	0.28	1.29×10^{-6}	1.49×10^{-11}
2554	1.28		0.91	4.53	1.56	1.56	2.08
2501	1.06		0.70	4.01	1.55	1.04	1.76
2991	1.19		1.43	6.59	4.68	0.79	1.13
2888	1.14	70	1.51	6.38	6.38	1.15	1.66
3103	1.18		1.79	6.92	5.85	0.80	1.20
2165	1.21		0.61	2.67	0.19	1.06	2.41
2462	1.38		0.95	3.67	0.56	1.69	2.71
2410	1.29		0.48	2.71	0.31	1.52	2.71
3022	0.68		1.19	5.16	3.84	0.29	0.88
2586	0.73		0.66	2.56	1.07	0.64	1.24
2344	0.77		0.30	1.58	0.37	0.44	1.54
2599	0.66		0.48	2.79	1.38	0.42	1.15
2616	2.39		1.42	5.10	0.88	5.25	3.89
2781	2.30		1.97	6.18	2.41	4.20	3.34
2459	2.41		1.07	3.37	0.31	5.47	4.63
2936	2.42		2.31	6.92	5.06	2.96	2.66
2457	1.38	75	0.65	3.12	0.13	1.82	2.79
2348	1.29		0.42	1.57	0.17	1.43	2.32
2441	1.33		0.67	2.80	0.40	1.51	2.34
2390	1.32		0.79	3.82	0.40	1.53	2.64
2710	1.11		0.88	4.67	1.86	1.26	1.73
3071	1.24		—	—	—	0.99	1.43
2614	1.51		1.12	4.15	1.01	2.28	2.83
2272	1.33		0.47	2.26	0.19	1.18	1.71

T K	p bar	$[CH_2CO]_0$ ppm	$(d[H]/dt)_0$ mol cm^{-3} s^{-1}	$[H]_{100\mu s}$ mol cm^{-3}	$[H]_{200\mu s}$ mol cm^{-3}	$[H]_{400\mu s}$ mol cm^{-3}	$[H]_{600\mu s}$ mol cm^{-3}
3349	1.30	5	2.32×10^{-8}	3.24×10^{-12}	5.48×10^{-12}	7.21×10^{-12}	8.35×10^{-12}
2718	1.40		3.19	2.52	3.79	4.85	5.48
2641	1.46		3.00	2.86	4.12	5.11	5.80
3132	1.43		1.90	2.27	4.04	6.33	7.72
2436	1.46		3.05	4.05	4.95	5.98	6.54
3208	1.15	7	5.13	4.47	6.43	8.45	9.73
3485	1.07		5.35	4.38	6.46	8.62	9.73
2203	1.36		4.80	5.75	7.31	8.12	8.57
2952	2.27		9.56	7.22	9.98	11.49	12.11
2625	0.65		1.42	1.48	2.21	3.16	3.67
2344	0.75		2.29	2.04	3.32	4.78	5.41
2216	0.80		1.45	1.96	3.45	4.75	5.41
3440	2.09		8.45	8.87	11.16	13.20	14.85
2936	1.09	10	13.5	4.04	6.14	8.85	10.59
3397	1.09		5.19	4.81	7.75	10.59	11.33
3237	1.12		3.85	4.30	6.33	8.63	9.23
3184	1.15		4.12	4.48	6.87	8.85	10.59

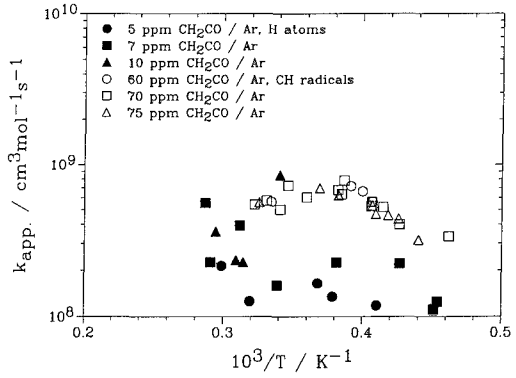

FIG. 2. Arrhenius plot of the measured apparent rate coefficients for the H and CH formation during ketene pyrolysis.

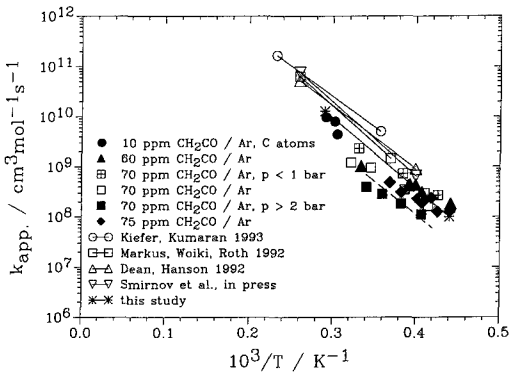

FIG. 3. Arrhenius plot of the measured apparent formation rate coefficient for C formation during ketene pyrolysis. For comparison, estimated rate coefficients for the reaction $CH_2 + M \leftrightharpoons C + H_2$ obtained from literature are also included.

literature [4,8,6,19,21] and by other reasonable reactions with estimated rate coefficients. The kinetic scheme was initially composed of 58 elementary reactions. The number of reactions could be reduced to 20 by a detailed sensitivity analysis using the SENKIN program code from SANDIA [22]; see Table 2. The reaction scheme starts with the thermal decomposition of ketene, giving the products CH_2 and CO. Other possible decomposition product paths that were included in the full scheme showed negligible sensitivity with respect to the observed species. In the present mechanism, we did not distinguish between $^3CH_2$ and $^1CH_2$. The latter is widely believed to be the initial product of the ketene decomposition. For the given experimental conditions, thermal equilibrium between these electronic states should be established very fast. All rate coefficients for CH_2 reactions given in Table 2 are therefore mean effective values for both energetic states of methylene.

Besides the methylene thermal decay via reaction (R2), the simplified mechanism of Table 2 is dominated by bimolecular reactions of CH_2 with methylene itself and with the observed product species

$$CH_2 + CH_2 \leftrightharpoons \text{products} \qquad \text{(R3)–(R6)}$$

$$CH_2 + X \leftrightharpoons \text{products;}$$

$$X = \text{H, C, CH.} \qquad \text{(R7)–(R11)}$$

The disproportionation reactions (R3)–(R6) contribute to the formation of all three measured species especially at low temperatures. The rate coefficients given in Table 2 are derived from fittings of the calculated concentration profiles to the measured ones. As can be seen from Table 2, the rate coefficients k_3 and k_4 were found to be higher than k_5 and k_6. Our k_3 value is slightly higher than the value reported by Glarborg et al. [20]. On the other hand, k_4 was found to be a factor of 3 lower than the value estimated by Frank et al. [10]. The rate coefficients k_5 and k_6 were estimated from our experiments at temperatures $T \leq 2500$ K.

Reactions (R7)–(R10) were found to be especially sensitive to the formation and removal of C and CH. Starting with the rate coefficients estimated in the literature [10,6,19,21], an optimized set of rate coefficients k_7 to k_{10} (see Table 2) was obtained from our fitting procedure. Reaction (R11) is known to be very important in hydrocarbon pyrolysis:

$$CH_2 + H \leftrightharpoons CH + H_2. \qquad \text{(R11)}$$

Rate coefficients reported in the literature [10,23–25] range between $k_{11} = 8 \times 10^{12}$ and 2×10^{14} $cm^3\ mol^{-1}\ s^{-1}$. Our H and CH profiles were found to be very sensitive to reaction (R11). Best fits to our experimental profiles were obtained with

$$k_{11} = 1.3 \times 10^{14}\ cm^3\ mol^{-1}\ s^{-1}$$

which is in good agreement with the values reported by Kiefer and Kumaran [9], Boullart and Peeters [23], Böhland et al. [24], and Zabarnick et al. [25]. The rate coefficient estimated in Ref. 10 is lower by about one order of magnitude. Reaction (R12), together with reactions (R13) and (R14) (see Table 2), was found to be important for the removal of CH, especially at temperatures above 3000 K. Good fits were obtained with the value given in Table 2, which is close to those given in [8,6,19]. Reactions (R15)–(R20) make only a minor contribution to the formation and removal of the species measured in this work.

A sensitivity analysis of the simplified reaction mechanism of Table 2 applied to various measured

TABLE 2
Simplified Kinetic Mechanism to Describe the Measured Concentration Profiles in CH_2CO/Argon Pyrolysis Systems

	Reaction	A $cm^3\ mol^{-1}\ s^{-1}$	E_a kcal/mol	ΔH_{298} kcal/mol	Ref.
1	$CH_2CO + Ar \rightleftharpoons CH_2 + CO + Ar$	2.30×10^{15}	57.6	78	6
2	$CH_2 + Ar \rightleftharpoons C + H_2 + Ar$	1.60×10^{14}	64.0	79	see text
3	$CH_2 + CH_2 \rightleftharpoons C_2H_2 + H_2$	3.00×10^{13}	0	−131	est., see text
4	$CH_2 + CH_2 \rightleftharpoons C_2H_3 + H$	3.20×10^{13}	0	−64	est., see text
5	$CH_2 + CH_2 \rightleftharpoons CH_3 + CH$	5.00×10^{12}	0	−8	est., see text
6	$CH_2 + CH_2 \rightleftharpoons CH_4 + C$	1.00×10^{13}	0	−32	est., see text
7	$CH_2 + CH \rightleftharpoons C_2H_2 + H$	4.00×10^{13}	0	−128	est., see text
8	$CH_2 + CH \rightleftharpoons C_2H + H_2$	8.00×10^{13}	0	−100	est., see text
9	$CH_2 + C \rightleftharpoons C_2 + H_2$	6.00×10^{13}	0	−64	est., see text
10	$CH_2 + C \rightleftharpoons C_2H + H$	2.00×10^{13}	0	−11	est., see text
11	$CH_2 + H \rightleftharpoons CH + H_2$	1.30×10^{14}	0	−78	see text, 21
12	$CH + Ar \rightleftharpoons C + H + Ar$	3.00×10^{14}	67.0	81	17
13	$CH + C \rightleftharpoons C_2 + H$	1.50×10^{14}	0	−61	est.
14	$CH + H \rightleftharpoons C + H_2$	1.58×10^{14}	0	−23	16
15	$CH + C_2H_2 \rightleftharpoons C_3H_2 + H$	1.26×10^{14}	0	−38	16
16	$CH_4 + Ar \rightleftharpoons CH_3 + H + Ar$	3.39×10^{17}	90.8	105	4
17	$C_2H_2 + C \rightleftharpoons C_3 + H_2$	1.00×10^{14}	0	−28	est.
18	$C_2H_3 + Ar \rightleftharpoons C_2H_2 + H + Ar$	3.00×10^{15}	32.0	38	4
19	$H_2 + Ar \rightleftharpoons H + H + Ar$	2.24×10^{14}	96.0	104	4
20	$C_2H_2 + Ar \rightleftharpoons C_2H + H + Ar$	3.00×10^{16}	108.0	132	4

concentration profiles obtained in a wide range of experimental conditions yielded a rather complex picture. The sensitivities of the bimolecular reactions (R3)–(R11) with respect to the measured species are in most cases of the same order of magnitude. In a single experiment, the sensitivities also changed with reaction time from one reaction to another. The contribution of individual elementary reactions to the formation and removal of the measured H, C, and CH profiles depends on the nature of the species, as well as on the experimental conditions. A clear preference to only one or two individual reactions did not exist. All these circumstances aggravated the evaluation of the more than 69 experimental profiles and made it a real kinetic puzzle. On the other hand, the large data base, the wide range of experimental conditions, and the satisfactory prediction of the experimental profiles by the reaction mechanism of Table 2 make the rate coefficients given there a reliable data set. The present scheme appeared to be, in principle, a cutout of the complex methane pyrolysis mechanism of Kiefer and Kumaran [9], containing 76 elementary reactions. Most of the estimated rate coefficients in Table 2 can be found there, with comparable orders of magnitude. Compared to their model, the present experimental results lead to a further reduction of the influence of the CH_2 decomposition channel forming CH + H. In the present experimental region, the contribution of this reaction path on the measured H and CH concentrations could be neglected. Some typical results obtained from simulations based on the reaction scheme of Table 2 are shown in Figs. 1a through 1d. In the given range of experimental conditions and for all species observed, the measured concentration time histories could be well reproduced; see the dashed lines in Figs. 1a through 1d.

Conclusions

The CH_2 thermal decay was investigated in shock-heated ketene/argon mixtures at temperatures above 2200 K. The time histories of the most prominent product species H, C, and CH were recorded using ARAS and RDLS. From the analysis of the measured concentration profiles, rate coefficients for the CH_2 thermal decomposition and some important bimolecular reactions including CH_2, CH, C, and H could be derived. The CH_2 pyrolysis system was found to be dominated by the CH_2 thermal decomposition reaction, forming C atoms and molecular hydrogen, as well as by fast CH_2 bimolecular reactions, forming H, C, and CH. No significance was found for the need of a two-channel model for the methylene thermal decomposition. A proposed simplified kinetic mechanism containing 20 elementary reactions is able to predict the measured concentration profiles within their experimental uncertainties.

Acknowledgments

The authors would like to thank Ms. N. Schlösser and Ms. C. Kmiecik for their help in conducting the experiments. The financial support of the Deutsche Forschungsgemeinschaft is gratefully acknowledged.

REFERENCES

1. Koch, M., Temps, F., Wagener, R., and Wagner, H. Gg., *Ber. Bunsenges. Phys. Chem.* 94:645–650 (1990).
2. Böhland, T., Temps, F., and Wagner, H. Gg., *Ber. Bunsenges. Phys. Chem.* 90:468–475 (1986).
3. Laufer, A. H., *Rev. Chem. Intermed.* 4:225 (1981).
4. Mallard, W. G., Westley, F., Herron, J. T., and Hampson, R. F., *NIST Chemical Kinetics Database—Ver. 4.0*, NIST Standard Reference Data, Gaithersburg, MD, 1992, and papers referred there.
5. Wagner, H. Gg., and Zabel, F., *Ber. Bunsenges. Phys. Chem.* 75:114–118 (1971).
6. Dean, A. J., and Hanson, R. K., *Int. J. Chem. Kinet.* 24:517–532 (1992).
7. Markus, M. W., and Roth, P., *Int. J. Chem. Kinet.* 24:433–445 (1992).
8. Markus, M. W., Woiki, D., and Roth, P., *Twenty-Fourth Symposium (International) on Combustion*, The Combustion Institute, Pittsburgh, 1993, pp. 581–588.
9. Kiefer, J. H., and Kumaran, S. S., *J. Phys. Chem.* 97:414–420 (1993).
10. Frank, P., Bhaskaran, K. A., and Just, T. H., *J. Phys. Chem.* 90:2226–2231 (1986).
11. Fisher, G. J., McLean, A. F., and Schnizer, A. W., *J. Org. Chem.* 18:1055–1057 (1953).
12. Roth, P., Barner U., and Löhr, R., *Ber. Bunsenges. Phys. Chem.* 83:577–583 (1979).
13. Thielen, K., and Roth, P., *Ber. Bunsenges. Phys. Chem.* 87:920–925 (1983).
14. Lindackers, D., Burmeister, M., and Roth, P., *Twenty-Third Symposium (International) on Combustion*, The Combustion Institute, Pittsburgh, 1991, p. 251.
15. Markus, M. W., and Roth, P., *Proceedings of the 18th International Symposium on Shock Waves*, Springer Verlag, Berlin, 1992, Vol. 2, pp. 1011–1018.
16. Dean, A. J., and Hanson, R. K., *J. Quant. Spectrosc. Radiat. Transfer* 42:5, 375–384 (1989).
17. Herzberg, G., and Johns, J. W. C., *Proc. R. Soc. A* 295:107–128 (1966).
18. Markus, M. W., and Roth, P., *Proceedings of the 19th International Symposium on Shock Waves*, in press.
19. Smirnov, V. N., Tereza, A. M., and Zaslonko, I. S., *Kinet. Catal.* 35(1):1 (1994).
20. Glarborg, P., Miller, J. A., and Kee, R. J., *Combust. Flame* 66:177 (1986).
21. Roth, P., and Just, Th., *Proceedings of the 14th International Symposium on Shock Waves*, New South Wales University Press, Kensington, N.S.W., Australia, 1983, p. 705.
22. Lutz, A. E., Kee, R. J., and Miller, J. A., Sandia National Laboratories Report, SAND87-8248, 1988.
23. Boullart, W., and Peeters, J., *J. Phys. Chem.* 96:9810 (1992).
24. Böhland, T., Temps, F., and Wagner, H. Gg., *Ber. Bunsenges. Phys. Chem.* 91:1205 (1987).
25. Zabarnick, S., Fleming, J. W., and Lin, M. C., *J. Chem. Phys.* 85:4373 (1986).

COMMENTS

Thomas Just, DLR, Germany. Going down to very low initial concentrations of CH_2, you might have a chance to distinguish better the two channels:

$$CH_2 \rightarrow C + H_2$$
$$\rightarrow CH + H$$

Author's Reply. This should be possible, but we have to consider the limits in the detection sensitivities for the product species, particularly for C and CH.

•

Phillip R. Westmoreland, University of Massachusetts, Amherst, USA. Ketene will produce singlet CH_2, which will quickly relax at your conditions to maintain an equilibrium population with the ground-state triplet CH_2. Do you expect that singlet and triplet methylene will have the same rate for decomposition to $C + H_2$?

Author's Reply. In our measurements, we cannot distinguish between the two electronic states of CH_2 and were only able to measure the decomposition products. In the temperature range of the present study, $^1CH_2$ contributes to a maximum of about 20% of the total methylene concentration. We therefore regard the present results as a good approximation for the ground state $^3CH_2$ thermal decomposition. From the significant difference in the geometrical structures of the two electronic CH_2 states and because of the spin conservation rule, a different decomposition behaviour of $^1CH_2$ and $^3CH_2$ can be expected. It would be interesting to study in the future the thermal decomposition of methylene by direct observation of both electronic states at high temperatures.

Twenty-Fifth Symposium (International) on Combustion/The Combustion Institute, 1994/pp. 713–719

THE THERMAL REACTIONS OF CH_3

K. P. LIM AND J. V. MICHAEL*
Chemistry Division, Argonne National Laboratory, Argonne, IL 60439, USA

The thermal reactions of CH_3 radicals have been investigated in reflected shock waves experiments at temperatures between 1224 and 2520 K. The fast dissociation of CH_3I served as the source of CH_3. Experiments were performed at three loading pressures with variations in $[CH_3I]_0$. H atoms formed in the reaction, $2CH_3 \rightarrow C_2H_5 + H$, were measured by the atomic resonance absorption spectrometric (ARAS) technique. The product ethyl radicals subsequently decompose to give a second H atom and ethylene. A reaction mechanism was used to fit the data, and the resulting value for the rate constant was $5.25 \times 10^{-11} \exp(-7384\ K/T)$ cm^3 molecule^{-1} s^{-1}. This value is compared to earlier determinations. At higher temperatures, 2150–2520 K, the H-atom formation rate was dominated by CH_3 thermal dissociation. With simulations, the rate constant for $CH_3 + Kr \rightarrow CH_2 + H + Kr$ could be determined. The rate constant for this process is $k = 4.68 \times 10^{-9} \exp(-42506\ K/T)$ cm^3 molecule^{-1} s^{-1}. This result is compared to earlier experimental determinations and also to theoretical calculations using the semiempirical Troe formalism.

Introduction

The thermal reactions of methyl radicals in the gas phase have been the subject of countless studies during the past 40 years. Since the pioneering work of Gomer and Kistiakowsky [1], there have been over 60 publications on the CH_3 self-reactions, as noted in the NIST database [2]. Most have been concerned with the low temperature–high pressure process, $2CH_3 + M \rightarrow C_2H_6 + M$. However, there are several high-temperature shock tube studies, where rate constants for the molecular and atom elimination processes, i.e., $2CH_3 \rightarrow C_2H_4 + H_2$ and $2CH_3 \rightarrow C_2H_5 + H$, respectively, [3–12] have been measured.

Warnatz reviewed this earlier work [13] and concluded that $k = 1.66 \times 10^{-8} \exp(-16{,}117\ K/T)$ cm^3 molecule^{-1} s^{-1} (1500–2500 K) for $2CH_3 \rightarrow C_2H_4 + H_2$. Following earlier H-atom atomic resonance absorption spectrometric (ARAS) results of Roth and Just [11] and Roth [12], Warnatz [13] preferred $k = 1.33 \times 10^{-9} \exp(-13350\ K/T)$ cm^3 molecule^{-1} s^{-1} (1500–3000 K) for $2CH_3 \rightarrow C_2H_5 + H$; however, this has been superseded by a more recent ARAS investigation by Frank and Braun-Unkhoff [14] who report $k = 4.65 \times 10^{-11} \exp(-6840\ K/T)$ cm^3 molecule^{-1} s^{-1} (1320–2300 K). This latter value is theoretically more reasonable because this A factor is consistent with that for the back reaction when it is divided by K_{eq}. In our recent work on the thermal decomposition of CH_3Cl [15], a high value for $2CH_3 \rightarrow C_2H_5 + H$ was obtained for 1550–1900 K. The branching ratio between dissociation and elimination continues to be a subject of research. We note that molecular elimination has not been directly observed but only inferred from observations of both precursor (e.g., C_2H_6) and CH_3.

The confusion as to what values to use for the respective processes still persists, as seen in recent investigations. Davidson et al. in their C_2H_6 [16] pyrolysis study used an earlier value for $2CH_3 \rightarrow C_2H_4 + H_2$ from Just [17]. For $2CH_3 \rightarrow C_2H_5 + H$, they used the Frank and Braun-Unkhoff [14] value. Kiefer and Kumaran [18] have, however, used only the Braun-Unkhoff value, thereby assuming that $k = 0$ for $2CH_3 \rightarrow C_2H_4 + H_2$. Even though $\Delta H°$ (0 K) for molecular elimination is only 30.9 kcal mole^{-1}, their assumption may still be sound. If either the 1,2 or 1,1 [19] elimination processes occur through symmetrical transition states, then they violate Woodward-Hoffman rules. The transition states would be tight and both might then have quite high barriers. If these barriers are near to or higher than that for $2CH_3 \rightarrow C_2H_5 + H$, then, using Rice–Ramsperger–Kassel (RRK) theory, molecular elimination would be improbable because these transition states are tighter than that for atomic elimination. Hence, C_2H_4 would result from C_2H_5 dissociation, and only $2CH_3 \rightarrow C_2H_5 + H$ should be considered in modeling the high-temperature data.

Here, we have used the H-atom ARAS technique to observe CH_3 reactions after initial formation from the fast dissociation of CH_3I. The experiment is,

*The submitted manuscript has been authored by a contractor of the U.S. Government under Contract No. W-31-109-ENG-38. Accordingly, the U.S. Government retains a nonexclusive, royalty-free license to publish or reproduce the published form of this contribution, or allow others to do so, for U.S. Government purposes.

therefore, similar to that of Frank and Braun-Unkhoff [14]. It is not, however, a repeat of their study because the presently used photometer system is substantially more sensitive. Thus, data can be obtained with much less source concentration, at both higher and lower temperatures, thereby diminishing the effects of secondary reactions. Hence, the present results can be viewed as an extension of the Frank and Braun-Unkhoff [14], Roth and Just [11], and Roth [12] data.

Experimental

Apparatus:

The present experiments were performed with a shock tube, previously described [20], operating in the reflected mode. Incident shock velocities were measured with eight pressure transducers (PCB Piezotronics, Inc., Model 1132A). Final temperature and density for each experiment were determined from loading pressure and temperature and the incident shock velocity. Corrections for nonidealities due to boundary layer formation were applied [20,21]. The photometer system was radially located 6 cm from the end plate and had an optical path length of 9.94 cm. Transmittances and the differentiated signals from the pressure transducers were recorded with a dual-channel (Nicolet 4094C) digital oscilloscope. Since the pressures of condensable gases were well below saturation, all pressure measurements with an MKS Baratron capacitance manometer in an all glass vacuum line were stable, and mixture preparation by the partial pressure method was routine. Reactant pressures were likewise measured with an MKS Baratron capacitance manometer shortly before shock firing. The time between reactant introduction into the shock tube and firing was 30 seconds.

H-Atom Detection:

The ARAS technique was used to monitor $[H]_t$. As in earlier H-atom ARAS studies [22–27], the lamp was operated at 40 watts microwave power and 2 torr of prepurified He. An atomic filter section was used to establish the fraction of non-$Ly_{\alpha-H}$ light. Enough H_2 and CH_4 impurities are present in the He to give an easily measured H-atom signal through an O_2 (1 atm of dry air) gas filter. Under these conditions, the lamp is not reversed, and a Doppler-broadened calculation at an equivalent lamp temperature of 480 K with the known oscillator strength for $Ly_{\alpha-H}$ will give an exact relationship between absorbance, $ABS = -\ln T_r$, and [H], and this relationship is nearly linear above ~700 K for $T_r = I/I_0 \geq 0.1$ [22,23].

We have carried out experiments to show that this procedure is accurate. Steady-state levels of [H]

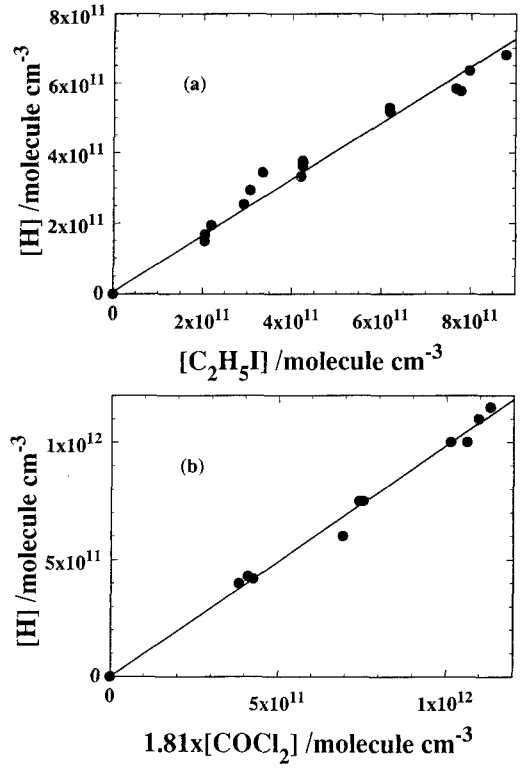

FIG. 1. The plots are the steady-state yields of [H] as determined from the line absorption calculations vs the initial reactant concentrations in the (a) $C_2H_5 + M \rightarrow C_2H_4 + H + M$ and (b) $Cl + H_2 \rightarrow H + HCl$ studies (see text).

formed from two reactions have been measured and used for calibration. Herzler and Frank [28] previously used $C_2H_5 + M \rightarrow C_2H_4 + H + M$ (C_2H_5 formed from the thermal decomposition of C_2H_5I) as an H-atom source and have shown, from concurrent I-atom ARAS observations, that secondary chemistry is unimportant at low $[C_2H_5I]_0$. They also indicated that $C_2H_5I \rightarrow C_2H_4 + HI$ should be <0.2 of the total decomposition; otherwise, the H + HI reaction would affect their measured profiles. The present results (1481–2020 K) with C_2H_5I are shown in Fig. 1a. The ordinate values are determined from line absorption calculations [23] at the temperatures of the experiments. Assuming that $k = 0$ for $C_2H_5I \rightarrow C_2H_4 + HI$, the slope of the line in the figure should be one, whereas the actual value is (0.80 ± 0.03). Hence, our most pessimistic conclusion is that the line absorption calculational method can at most be in error by ~+20%; however, if HI elimination occurs, then this error is less. In the other calibration experiments, we used the $Cl + H_2 \rightarrow H + HCl$ reaction. The Cl-atom source was $COCl_2$. We showed earlier that 1.81 Cl atoms were formed for every molecule dissociated (i.e., 9.5% $COCl_2 \rightarrow CO$

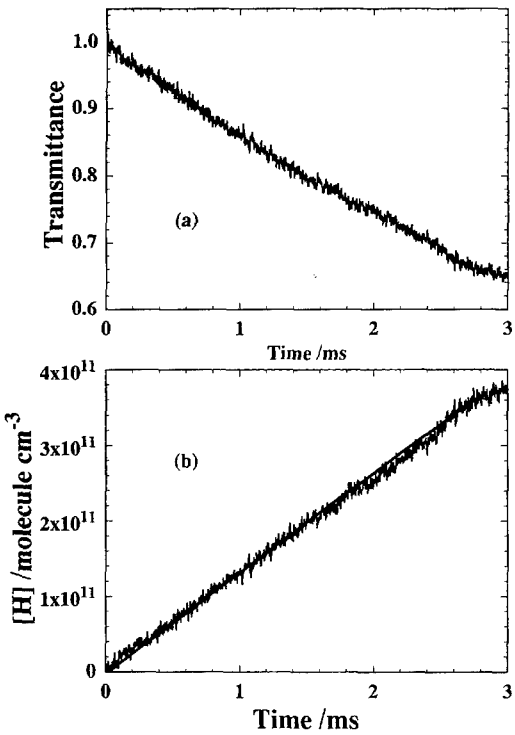

FIG. 2. The top panel displays a typical experimental record showing decreasing ARAS signal as H atoms are produced from the thermal reactions of CH_3 radicals. The experimental conditions are T = 1903 K, P = 244 torr, ρ = 1.240 × 10^{18} cm^{-3}, and X_{CH_3I} = 6.120 × 10^{-6}. The signal is converted to absolute [H] using a specifically calculated curve-of-growth from a line absorption calculation at 1903 K. The H-atom profile is displayed in the bottom panel. The solid line is the [H] yield determined from the full reaction mechanism simulation shown in Table 1.

+ Cl_2) [29]. Figure 1b shows results of between 1784 and 2381 K. The ordinate values are again determined from line absorption calculations [23]. The slope of the line is (0.99 ± 0.03). These two calibrations show that accurate absolute [H] can be determined from line absorption calculations (probably better than from these two chemical methods), simply because the oscillator strength for $Ly_{\alpha-H}$ is theoretically better known than those for any other transition in the entire field of spectroscopy.

Kinetics Experiments:

Thirty-four experiments have been performed between 1224 and 2520 K with CH_3I as the CH_3 source. Figure 2a shows a typical raw data signal from which $[H]_t$ against time, Fig. 2b, can be constructed by converting (ABS) to [H] through a line absorption calculation at the temperature of the experiment. Use of a Doppler source gives much more sensitivity than used in earlier ARAS studies on the present reaction [11,12,14]. Since the method is sensitive, blank experiments with Kr were performed since even research grade Kr contains small amounts of H_2 and CH_4. For $T \leq 2520$ K, the measured rate, $\Delta H/\Delta t$, from H_2 or CH_4 was <15% of that when CH_3I was present. This observation did place an upper limit on the T range of the present study.

Gases:

High-purity He (99.995%), used as the driver gas, was from Air Products and Chemicals, Inc. Scientific grade Kr (99.997%), the diluent gas in reactant mixtures, was from MG Industries. Ultrahigh-purity grade He (99.999%) for the resonance lamp and high-purity H_2 (99.995%) for the atomic filter were from Airco. Analytical grade CH_3I (99%) and C_2H_5I (99%) were from Aldrich Chemical Co. Inc. Both were purified by bulb-to-bulb distillation, retaining only the middle thirds.

Results and Discussion

These experiments were carried out with low $[CH_3I]_0$ (between 0.74 and 3.69 × 10^{13} molecules cm^{-3}) and low density (1.24 to 3.21 × 10^{18} molecules cm^{-3}). In order to fit the measured $[H]_t$, the importance of secondary chemistry had to be assessed. A numerical simulation with the known decomposition rate for CH_3I [30] coupled with the chemical mechanisms used by Roth and Just [11] or Frank and Braun-Unkhoff [14] was carried out for the experiment shown in Fig. 2, giving the simulation in Fig. 3. Under most conditions, similar simulations showed (1) that CH_3 was almost instantaneously produced, (2) that $[H]_t$ vs t was nearly linear, (3) that $[CH_3]$ decreased by only 10–20%, and (4) that almost no C_2H_6 was formed, over the experimental times. Including the fast process, $C_2H_5 \rightarrow C_2H_4 + H$, k for $2CH_3 \rightarrow C_2H_5 + H$ could then be calculated to within ~±15%, as $k = 0.5\ (\Delta[H]/\Delta t)\ (1/0.9[CH_3I]_0)^2$. In numerical integrations with the mechanism shown above the dashed line in Table 1, k for $2CH_3 \rightarrow C_2H_5 + H$ (k_5 in the table) was then parametrically refined by more extensive data fitting. This mechanism uses fewer reactions than earlier [11,12,14] because many reactions are unimportant due to the lower $[CH_3I]_0$ used here. Also, $2CH_3 \rightarrow C_2H_4 + H_2$ is excluded for reasons given in the introduction. With only the partial mechanism of Table 1, the values for k_5 from the 34 experiments were determined and are plotted in Fig. 4. Roth and Just's [11] and Frank and Braun-Unkhoff's [14] results are also shown for comparison. The present results are almost the same as those of Roth and Just and are only ~20% lower than those of Frank and Braun-

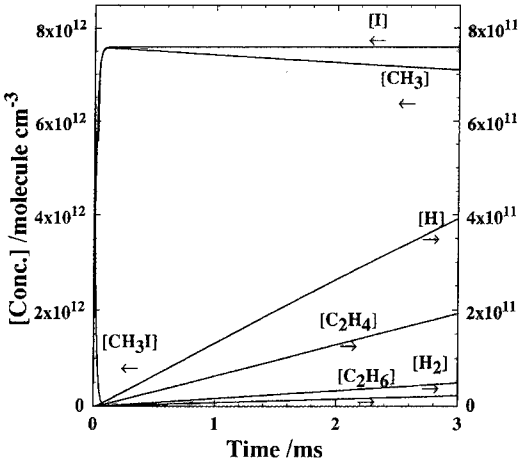

FIG. 3. A plot of reactant and product profiles from a simulation of the self-reaction of CH_3 radicals based on the mechanism in Table 1. The conditions are the same as in the actual experiment of Fig. 2.

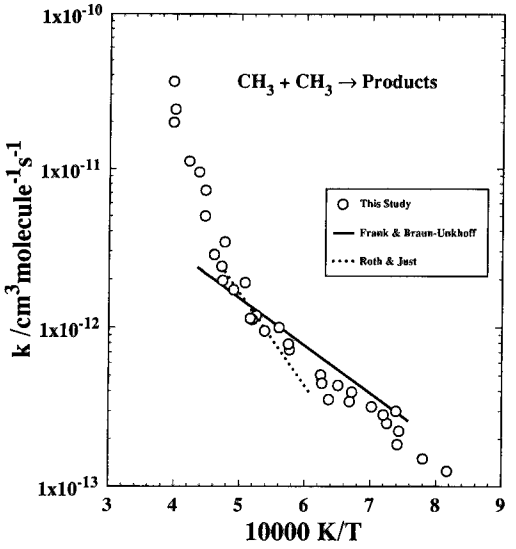

FIG. 4. An Arrhenius plot of the experimentally determined second-order rate constants for the CH_3 self-reaction on the assumption that the [H] yield comes from only reaction (5) of Table 1. Published results from other studies are also plotted for comparison.

Unkhoff. However, the derived k_5 at high T becomes strongly non-Arrhenius. This strong curvature is unreasonable because the back reaction would have to have a rate constant many times faster than the H + C_2H_5 collision rate. Clearly, other H-producing reactions become important above ~2000 K, and Roth et al. [8] and Frank and Braun-Unkhoff [14] have identified the source as being due to CH_3 dissociation.

Dean and Hanson [36] and Markus et al. [37] have recently reported results in which CH-radical [36,37], C-atom [36], and H-atom [37] concentration profiles were measured in hydrocarbon pyrolyses. The respective T ranges were 2500–3800 and 2100–3000 K. The profiles could be explained by including the pyrolyses of CH_3, CH_2, and CH, i.e., reactions

TABLE 1
The mechanism for the thermal reactions of CH_3[a]

1.	$CH_3I \rightarrow CH_3 + I$	$k_1 = \rho \times 4.17 \times 10^{-9} \exp(-21419\ K/T)$[b]
2.	$I + CH_3 \rightarrow CH_3I$	$k_2 = k_1/(2.897 \times 10^{25} \exp(-26203\ K/T))$ [31]
3.	$I + CH_3I \rightarrow HI + CH_2I$	$k_3 = 8.32 \times 10^{-10} \exp(-17162\ K/T)$ [32]
4.	$CH_3 + CH_3 \rightarrow C_2H_6$	$k_4(T, \rho)$ = from [33,34,16]
5.	$CH_3 + CH_3 \rightarrow C_2H_5 + H$	k_5 = to be fitted
6.	$CH_3 + CH_3 \rightarrow CH_2 + CH_4$	$k_6 = 1.32 \times 10^{-12} \exp(-7165\ K/T)$ [35]
7.	$C_2H_5 \rightarrow C_2H_4 + H$	$k_7 = \infty$
8.	$CH_4 \rightarrow CH_3 + H$	$k_8 = \rho \times 3.16 \times 10^{23}\ T^{-8.11} \exp(-58854\ K/T)$ [18]
9.	$CH_3 \rightarrow CH_2 + H$	k_9 = to be fitted
10.	$CH_3 \rightarrow CH + H_2$	$k_{10} = k_9 \times 0.886 \exp(1718\ K/T)$[c]
11.	$CH_2 + CH_3 \rightarrow C_2H_4 + H$	$k_{11} = 1 \times 10^{-10}$[d]
12.	$CH_2 \rightarrow CH + H$	$k_{12} = \rho \times 3.39 \times 10^{-9} \exp(-46100\ K/T)$[c]
13.	$CH_2 \rightarrow C + H_2$	$k_{13} = k_{12} \times 0.413 \exp(12489\ K/T)$[c]
14.	$CH \rightarrow C + H$	$k_{14} = \rho \times 1.66 \times 10^{-10} \exp(-32209\ K/T)$ [18]

[a]All rate constants are in molecular units.
[b]From Ref. 30, ρ is the total density in molecules cm^{-3}.
[c]See text.
[d]Estimated.

(9), (10), and (12) through (14) of Table 1. In our simulations, either set of rate constants were acceptable but seemed to underestimate the importance of molecular elimination (reactions (10) and (13)). Kiefer and coworkers [18,38] have on the basis of thermochemistry questioned the relative branching ratios between atomic and molecular elimination in both CH_3 and CH_2. Use of the Kiefer and Kumaran [18] rate constants gave $[H]_t$ predictions that were high, and we therefore carried out our own theoretical estimates.

Clearly, both decompositions, CH_3 and CH_2, will be in their low-pressure limits above 2000 K. It is then only necessary to evaluate the limiting low-pressure rate constants. We made theoretical estimates of k_{sc}^0 with the semiempirical Troe method [39–41] using JANAF thermochemical parameters [42]. We can agree with Kiefer and Kumaran's CH_3 cracking rate constants to within <20% if the energy transfer parameter $\Delta E_{down} = 625\ cm^{-1}$ (i.e., $-\Delta E_{all} \cong 112\ cm^{-1}$) instead of their value of $-\Delta E_{all} = 150\ cm^{-1}$. Our predicted branching ratio, reaction (10) divided by reaction (9), is 0.886 exp(1718 K/T) for 2000–2500 K and is about the same as Kiefer and Kumaran's estimate, 0.87 exp(1334 K/T), for a somewhat higher T range. Our value is also similar to that of Wagner [43] who has fitted the lower temperature results for the back reactions, $CH_2 + H$ and $CH + H_2$, with $-\Delta E_{all} = 50\ cm^{-1}$ [44]. At 2000 and 2500 K, this prediction gives ratios, 3.3 and 2.0, respectively, compared to the present, 2.1 and 1.8. None of these theoretical values, which are dependent on the differences in the endothermicities for the two channels, agrees with reported experimental values [36,37], however, Kiefer and Kumaran [18] used their ratio and absolute rate constants to successfully fit some of the Dean and Hanson [36] profiles. We also carried out theoretical calculations for CH_2 cracking, reactions (12) and (13) of Table 1. Our calculations can again agree with Kiefer and Kumaran to within <30%; however, we have to use an energy transfer parameter of $\Delta E_{down} = 542\ cm^{-1}$ (i.e., $-\Delta E_{all} \cong 100\ cm^{-1}$) in contrast to their reported value of $-\Delta E_{all} = 43\ cm^{-1}$. The predicted branching ratio $k_{13}/k_{12} = 0.413$ exp(12489 K/T), showing that molecular elimination is the only important process at high T, and this agrees with Kiefer's [18,38] conclusions.

In our final analysis, we again fitted all of the $[H]_t$ results using the entire set of rate constants shown in Table 1. Reaction (11) is estimated from the isoelectronic process, $O + CH_3$, and reaction (14) is from Kiefer and Kumaran. We use our own theoretical estimates for CH_2 cracking, which are consistent with Kiefer and Kumaran as noted above. In agreement with Frank and Braun-Unkhoff [14], we also conclude that H production by radical pyrolysis predominates over bimolecular production, reaction (5), above ~2100 K, and therefore, most of the excess H production (see Fig. 4) is from these pyrolyses. On the other hand, they are of negligible importance below ~1950 K, giving <10% of the H-atom yield. We have, therefore, used only those results between 1224–1938 K to determine the rate constants for reaction (5) of Table 1. Figure 5 shows the resulting Arrhenius plot with the linear least-squares line,

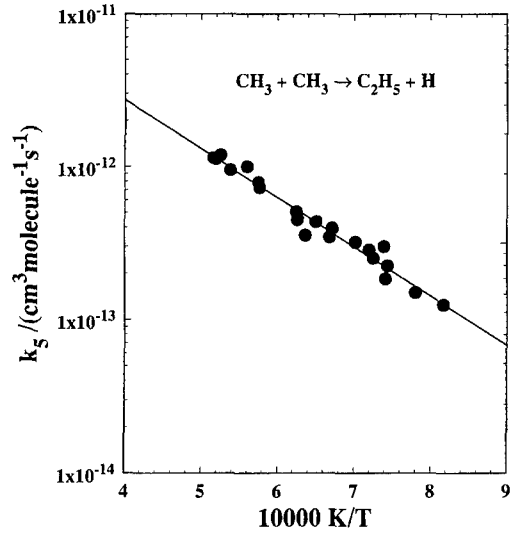

FIG. 5. An Arrhenius plot of the rate constants for the CH_3 self-reaction to give $H + C_2H_5$. The reaction (5) values are determined from fits to the data below 1938 K with the full mechanism of Table 1.

$$k_5 = (5.25 \pm 1.19) \times 10^{-11} \exp(-7384 \pm 312\ K/T)\ cm^3\ molecule^{-1}\ s^{-1}. \quad (1)$$

Equation (1) is only 15–25% lower than Frank and Braun-Unkhoff's [14] result (1320–2300 K) and is therefore in excellent agreement.

The fitting procedure for CH_3 cracking was then applied to those experiments >2098 K, where the effects of reaction (5), fixed by Eq. (1), gave <50% $[H]_t$. We set k_{10}/k_9 at our theoretical value. The derived results for $CH_3 + Kr \rightarrow CH_2 + H + Kr$ are shown in Fig. 6 along with those from Dean and Hanson [36] and Markus et al. [37]. The theoretical results from Kiefer and Kumaran [18] and Wagner [43] are also shown for comparison. Our experimental results give

$$k_9 = 4.68 \times 10^{-9} \cdot \exp(-42506\ K/T)\ cm^3\ molecule^{-1}\ s^{-1} \quad (2)$$

for $2098 \leq T \leq 2520$ K. The points deviate from Eq. (2) by ±67% at the 1σ level. Values for k_{10} can be calculated from this equation and the branching ra-

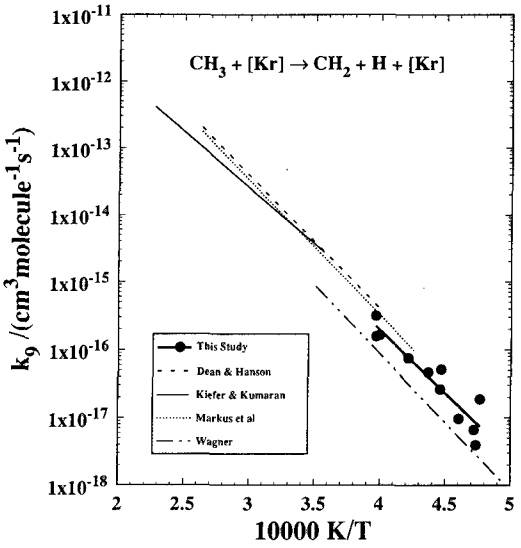

FIG. 6. An Arrhenius plot of the rate constants for the decomposition of CH_3 to give H + CH_2. The reaction (9) values are determined from fits to the data in the temperature range, 2098–2520 K, using the full mechanism of Table 1. Also shown for comparison are earlier experimental [36,37] and theoretical results. [18,43].

tio. Comparing Eq. (2) to our theoretical calculation, the collisional deactivation parameter, ΔE_{down}, has to be modified downward. Equation (2) can be recovered to within $\pm 14\%$ if $\Delta E_{down} = 437$ cm^{-1} (i.e., $-\Delta E_{all} \cong 84$ cm^{-1}). Theoretical extrapolation with the adjusted ΔE_{down} to 3000–4000 K then gives values that are exactly one-half of Kiefer and Kumaran's. We therefore agree with them that the apparent activation energy should decrease due to falloff effects. Inspection of Fig. 6 shows that the present values agree within experimental error to those of Dean and Hanson [36] and, particularly, Markus et al. [37]. Finally, the theoretical results of Wagner and coworkers [43,44] are 0.30–0.45 of Eq. (2). The point to this latter theoretical study was to explain the lower T data on the back reactions. Using only a single energy transfer parameter, $-\Delta E_{all} = 50$ cm^{-1}, their success was impressive. Hence, if $-\Delta E_{all}$ can be allowed to slightly increase with increasing T (e.g., from 50–84 cm^{-1}), then their work demonstrates that all existing data on both forward and back reactions for this system can now be reconciled with theory.

In summary, the present results reinforce the explanation of earlier results on the thermal reactions of CH_3; namely, rate constants based on H-atom formation contain contributions not only from $2CH_3 \rightarrow C_2H_5$ + H but also from the thermal cracking of CH_3. With the low $[CH_3I]_0$ used here, CH_3 reactions can be partitioned into three relatively separate regimes. At low temperature and high pressure, recombination to form C_2H_6 is the only important pathway. Because this process involves stabilization, with a decreasing efficiency factor as temperature increases, its importance at pressures of ~1 atm diminishes as temperature increases above ~1250 K. The $2CH_3 \rightarrow C_2H_5$ + H process then accounts for nearly all of the reactivity up to ~1950 K at which point the pyrolysis of CH_3 then becomes the most important H-atom-producing process. The implications of these results on the oxidative modeling of hydrocarbons are complicated because there may be regions, depending on pressure, temperature, and absolute $[CH_3]$, where two or more of these three destruction mechanisms contribute. Detailed modeling then becomes absolutely essential for explaining the experimental results.

There is an important theoretical implication from Eq. (1). In a Rice–Ramsperger–Kassel theory (RRK) formulation for CH_3 recombination, rate, constants based on C_2H_6 formation have the form

$$k_{\text{recombination}} = k_{\text{add}} \int_{\varepsilon_0}^{\infty} \frac{\beta\omega f(\varepsilon)d\varepsilon}{(k_{f\varepsilon} + k_{b\varepsilon} + \beta\omega)} \quad (3)$$

where k_{add}, $k_{f\varepsilon}$, $k_{b\varepsilon}$, β, ω, and $f(\varepsilon)$ refer to (1) the high-pressure rate constant for CH_3 self-reaction; (2) the specific RRK (or RRK–Marcus theory (RRKM)) rate constant for forward dissociation; (3) the specific RRK (or RRKM) rate constant for backward dissociation at the threshold energy, ε_0; (4) the collisional deactivation efficiency; (5) the collision rate constant; and (6) the RRK (or RRKM) normalized distribution function for a given temperature, respectively. This equation shows that the limiting high-pressure rate constant should be k_{add}. However, rate constants based on $2CH_3 \rightarrow C_2H_5$ + H have the form

$$k^{bi} = k_{\text{add}} \int_{\varepsilon_0}^{\infty} \frac{k_{f\varepsilon} f(\varepsilon)d\varepsilon}{(k_{f\varepsilon} + k_{b\varepsilon} + \beta\omega)} \quad (4)$$

implying that at high temperature and low pressure (the present conditions), $k^{bi}_{\lim P\to 0} \leq k_{\text{add}}$; i.e., k_{add} is the upper limit. We note that the A factor from Eq. (1) is 5.25×10^{-11} cm^3 molecule^{-1} s^{-1}, which is already the collision rate constant corrected for the electronic degeneracy ratio [15]. In contrast, recent estimates based on Eq. (3) experiments and analysis from Walter et al. [33] suggest decreasing k_{add} values with increasing temperature. Their extrapolated estimate at 2000 K would be 1.7×10^{-11} cm^3 molecule^{-1} s^{-1}. This disagreement requires a continuing theoretical assessment on this important combustion reaction.

Acknowledgments

The authors wish to thank Drs. A. F. Wagner, L. B. Harding, and J. P. Hessler for a thorough reading of the manuscript and helpful suggestions. This work was sup-

ported by the U.S. Department of Energy, Office of Basic Energy Sciences, Division of Chemical Sciences, under Contract No. W-31-109-Eng-38.

REFERENCES

1. Gomer, R., and Kistiakowsky, G. B., *J. Chem. Phys.* 19:85–91 (1951).
2. Mallard, W. G., Westley, F., Herron, J. T., Cvetanovic, R. J., and Hampson, R. J., *NIST Chemical Kinetics Database—ver 3.0*, NIST Standard Reference Data, Gaithersburg, MD, 1991.
3. Tsuboi, T., *Jpn. J. Appl. Phys.* 17:709–716 (1978).
4. Gardiner, W. C. Jr., Owen, J. H., Clark, T. C., Dove, J. E., Bauer, S. H., Miller, J. A., and McLean, W. J., *Fifteenth Symposium (International) on Combustion*, The Combustion Institute, Pittsburgh, 1975, pp. 857–868.
5. Kern, R. D., Singh, H. J., and Wu, C. H., *Int. J. Chem. Kinet.* 20:731–747 (1988).
6. Hidaka, Y., Nakamura, T., Tanaka, H., Inami, K., and Kawano, H., *Int. J. Chem. Kinet.* 22:701–709 (1990).
7. Chiang, C. C., and Skinner, G. B., *J. Phys. Chem.* 85:3126–3129 (1981).
8. Roth, P., Barner, U., and Loehr, R., *Int. Symp. Shock Tubes Waves Proc.* 12:621–628 (1980).
9. Kiefer, J. H., and Budach, K. A., *Int. J. Chem. Kinet.* 16:679–695 (1984).
10. Roth, P., and Just, Th., *Material Research Symp. Proc.* NBS Special Publication 561, 1979, Vol. 10, p. 91.
11. Roth, P., and Just, Th., *Ber. Bunsenges. Phys. Chem.* 83:577–583 (1979).
12. Roth, P., *Forsch. Ingenieurwes.* 46:93 (1980).
13. Warnatz, J., in *Combustion Chemistry* (W. C. Gardiner, Jr., Ed.), Springer-Verlag, New York, 1984, pp. 197–509.
14. Frank, P., and Braun-Unkhoff, M., *Proceedings of the Sixteenth Symposium on Shock Tubes and Waves*, VCH, Weinheim, 1988, pp. 379–385.
15. Lim, K. P., and Michael, J. V., *J. Chem. Phys.* 98:3919–3928 (1993).
16. Davidson, D. F., Di Rosa, M. D., Hanson, R. K., and Bowman, C. T., *Int. J. Chem. Kinet.* 25:969–982 (1993).
17. Just, Th., *Proceedings of the Thirteenth International Symposium on Shock Tubes and Waves*, SUNY, Albany, 1982, pp. 54–67.
18. Kiefer, J. H., and Kumaran, S. S., *J. Phys. Chem.* 97:414–420 (1993).
19. Raghavachari, K., Frisch, M. J., Pople, J. A., and Schleyer, P. v. R., *Chem. Phys. Lett.* 85:145–149 (1982).
20. Michael, J. V., *Prog. Energy Combust. Sci.* 18:327–347 (1992), and references cited therein.
21. Michael, J. V., and Sutherland, J. W., *Int. J. Chem. Kinet.* 18:409–436 (1986).
22. Lynch, K. P., Schwab, T. C., and Michael, J. V., *Int. J. Chem. Kinet.* 8:651–671 (1976).
23. Maki, R. G., Michael, J. V., and Sutherland, J. W., *J. Phys. Chem.* 89:4815–4821 (1985).
24. Michael, J. V., and Wagner, A. F., *J. Phys. Chem.* 94:2453–2464 (1990).
25. Michael, J. V., *J. Chem. Phys.* 92:3394–3402 (1990).
26. Shin, K. S., and Michael, J. V., *J. Phys. Chem.* 95:5864–5869 (1991).
27. Shin, K. S., and Michael, J. V., *J. Chem. Phys.* 95:262–273 (1991).
28. Herzler, J., and Frank, P., *Ber. Bunsenges. Phys. Chem.* 96:1333–1338 (1992).
29. Lim, K. P., and Michael, J. V., *J. Phys. Chem.* 98:211–215 (1994).
30. Saito, K., Tahara, H., Kondo, O., Yokubo, T., Higashihara, T., and Murakami, I., *Bull. Chem. Soc. Jpn.* 53:1335–1339 (1980).
31. Equilibrium constant calculated from the molecular parameters given in: Herzberg, G., *Molecular Spectra and Molecular Structure*, Van Nostrand Reinhold, New York, 1966, p. 621.
32. Based on I + CH_4: Golden, D. M., Walsh, R., and Benson, S. W., *J. Am. Chem. Soc.* 87:4053–4057 (1965).
33. Walter, D., Grotheer, H.-H., Davies, J. W., Pilling, M. J., and Wagner, A. F., *Twenty-Third Symposium (International) on Combustion*, The Combustion Institute, Pittsburgh, 1990, pp. 107–114.
34. Hwang, S. M., Rabinowitch, M. J., and Gardiner, W. C., Jr., *Chem. Phys. Lett.* 205:157–162 (1993).
35. Calculated from backward rates with results by: Böhland, T., Dobé, S., Temps, F., and Wagner, H. Gg., *Ber. Bunsenges. Phys. Chem.* 89:1110–1116 (1985), and equilibrium constants.
36. Dean, A. J., and Hanson, R. K., *Int. J. Chem. Kinet.* 24:517–532 (1992).
37. Markus, M. W., Woiki, D., and Roth, P., *Twenty-Fourth Symposium (International) on Combustion*, The Combustion Institute, Pittsburgh, 1992, pp. 581–588.
38. Kiefer, J. H., *Twenty-Fourth Symposium (International) on Combustion*, The Combustion Institute, Pittsburgh, 1992, p. 588.
39. Troe, J., *J. Chem. Phys.* 65:4745–4757 (1977); ibid. 4758–4775 (1977).
40. Troe, J., *J. Phys. Chem.* 83:114–126 (1979).
41. Troe, J., *Ber. Bunsenges. Phys. Chem.* 87:161–169 (1983); Gilbert, R. G., Luther, K., and Troe, J., ibid. 169–177 (1983).
42. Chase, M. W., Jr., Davies, C. A., Downey, J. R., Jr., Frurip, D. J., McDonald, R. A., and Syverud, A. N., *J. Phys. Chem. Ref. Data* 14:(1) (1985).
43. Wagner, A. F., unpublished results.
44. Wagner, A. F., and Harding, L. B., in *Isotope Effects in Gas-Phase Chemistry* (J. A. Kaye, Ed.), American Chemical Society, Washington, 1992, ACS Symposium Series 502, pp. 48–63.

Twenty-Fifth Symposium (International) on Combustion/The Combustion Institute, 1994/pp. 721–731

THE REACTION SYSTEM CH_3 + OH AT INTERMEDIATE TEMPERATURES. APPEARANCE OF A NEW PRODUCT CHANNEL

ROBERT HUMPFER, HARRY OSER, HORST-HENNING GROTHEER AND THOMAS JUST
Institut für Physikalische Chemie der Verbrennung, DLR
Pfaffenwaldring 38, 70503 Stuttgart, FRG

In an extension of our work at lower temperatures, the title reaction was measured directly in a flow reactor at temperatures up to 700 K and at pressures of 0.65 and 3.25 mbar. OH was used in an excess over CH_3. Both reactants along with the reaction products were monitored by mass spectrometry. CH_3 profiles served as the major observable quantity for the extraction of rate data by using computer simulation.

The fitted total rate coefficients were divided into individual channel rate coefficients by the mass spectrometric measurement of the reaction products. For CH_3 + OH, this led to a rate coefficient, k_{1a}, into the stabilization channel, and another one, k_{1e+f}, referring to the sum of two H_2-eliminating channels yielding the biradical HCOH, and CH_2O. These latter channels have not been measured before. In order to distinguish between them, we switched from OH to OD to get

$$CH_3 + OD \rightarrow HCOD + H_2 \qquad (1'e)$$

$$\rightarrow H_2CO + HD \qquad (1'f)$$

so that these channels could be determined by their byproducts, H_2 and HD, respectively. The use of OD makes it also possible to measure the channel

$$CH_3 + OD \rightarrow {}^1CH_2 + HDO \qquad (1'd)$$

through its byproduct, HDO.

A comparison of the rate coefficients for both systems, i.e., CH_3 + OH and CH_3 + OD, indicates that, within our error limits, no significant isotope effect takes place. By including our previous measurements along with additional ones at 600 K, to be published elsewhere, we arrive at the following recommendations for the channel rate coefficients in units of cm^3 molec s:

$$k^0_{1a} = 3.7 * 10^{-29} \exp(1280/T), \qquad k^\infty_{1a} = 1.7 * 10^{-10}$$

$$k_{1d} = 4.4 * 10^{-11} \exp(-1100/T)$$

$$k_{1e} = 9.1 * 10^{-11} \exp(-1500/T)$$

$$k_{1f}(700\ K) = 1.7 * 10^{-12}.$$

Since simulation is needed for the deduction of the rate coefficients, an uncertainty factor of 2 has to be attributed to these numbers.

The reaction channels to CH_3O + H (1b) and to CH_2OH + H (1c) could not be detected.

Introduction

According to its significance for virtually all hydrocarbon flames, the title reaction has attracted a lot of attention during recent years, both from an experimental [1–7] as well as a theoretical point of view [8–12]. Its fascination arises from its occurrence via a bound intermediate, chemically excited methanol, which can react into a variety of product channels. The six most important ones are as follows [12]:

$$CH_3 + OH + (M) \rightarrow CH_3OH + (M)$$
$$-92.21\ kcal\ mol^{-1} \qquad (1a)$$
$$\rightarrow CH_2OH + H$$
$$+3.90\ kcal\ mol^{-1} \qquad (1b)$$
$$\rightarrow CH_3O + H$$
$$+11.84\ kcal\ mol^{-1} \qquad (1c)$$
$$\rightarrow {}^1CH_2 + H_2O$$

$$+2.2 \text{ kcal mol}^{-1} \quad (1d)$$

$$\rightarrow HCOH + H_2$$

$$-21.0 \text{ kcal mol}^{-1} \quad (1e)$$

$$\rightarrow CH_2O + H_2$$

$$-71.85 \text{ kcal mol}^{-1} \quad (1f)$$

The reaction enthalpies (at 300 K) are mostly calculated from the Sandia compilation [13]. For the $^1CH_2$ channel, we use a value as derived from our earlier kinetic measurements [5], and for the HCOH channel, we quote a value of Melius [14] obtained by BAC-MP4 calculations.

In modern chemical kinetic data compilations [15–17], at best the first four of these product channels are considered. In fact, most experimental studies are carried out at a single temperature (mostly ambient), and in most cases, the interest is focused on the determination of the total rate coefficient, k_{1tot}. Only very recently, a systematic study of the individual product channels was started in our laboratory [4,5]. By covering the low-temperature portion (300–500 K) of the Arrhenius plot, we were able to determine k_{1a} and k_{1d} and their temperature dependence. In the present study, the temperature range is extended to 700 K.

Following a suggestion of Wagner [18], we paid particular attention on the occurrence of channels (1e) and (1f), in which the complex $[CH_3OH]^*$ eliminates a H_2 molecule to yield the biradical HCOH or formaldehyde. These channels have been considered in the early theoretical work of Harding et al. [19]. Very recently, Walch [12] has again postulated the HCOH channel to occur with a barrier below CH_3 + OH, so that it should be accessible even at ambient temperature. In fact, we failed to detect any signals of H_2 and/or $HCOH/H_2CO$ between 300 and 500 K and consequently neglected these channels in our low-temperature studies [4,5]. In the present study, however, carried out at 700 K, we clearly observed a primary formation of molecular hydrogen along with 30-amu signals from HCOH and/or H_2CO. By the use of OD instead of OH, we could show that the detected hydrocarbon species is predominantly the carbenelike species HCOH (HCOD in this case), rather than formaldehyde. To our knowledge, this is the first measurement of this reaction channel. Further measurements of CH_3 + OD at 600 K [20] revealed a strong temperature dependence of the biradical channel, so it is plausible that this channel escaped our detection at temperatures below 500 K. At the same time, by extrapolation, it underscores the potential importance of this channel around 1000 K.

Experimental

Flow Reactor Technique:

A diagram of our reactor assembly is shown in an earlier publication [21], and a more detailed description of its operation may be found in a paper to be published elsewhere [20], so only a very brief outline will be given here. A resistance-heated copper block surrounded by a radiation shield was suspended from the reactor top flange. It provided a sufficiently flat temperature profile (700 ± 5 K within the zone covered by the movable injector, i.e., between x = 5 cm and x = 40 cm). For the reactor, we used a quartz tube of 55-cm length and 25.5-mm diameter. Its walls and the walls of the movable injector were coated with B_2O_3 (see Ref. 20), resulting in wall coefficients of 6–8 s^{-1} for CH_3 and about 6 s^{-1} for OH, as measured in this study.

The reactor was coupled by a conventional nozzle and skimmer system to a quadrupole mass spectrometer that was operated at sufficiently low electron energies (between 11 and 20 eV; 12.1 eV for our main observable, CH_3) to reduce undesired fragmentation.

Generation and Calibration of Radicals:

In the case of radical-radical reactions, it is almost impossible, because of the interference of self-reactions and other side reactions, to ensure pseudo–first-order kinetics. Thus, computer modeling is required for the deduction of the rate coefficients, with the prerequisite that the concentration of the minor component must also be known absolutely. In addition, the profile of the excess component in the absence of the other reactant is generally time-dependent because of self-reaction or wall loss. The need to calibrate both reactants and to measure both types of profiles contrasts with the more commonly studied radical/atom + inert molecule systems.

OH source

OH was used as excess component since it is less prone to self-reaction and has a lower mass spectrometric sensitivity than CH_3. As described in Ref. 20, it was prepared in the fixed radical source through $H_2O + F \rightarrow OH + HF$, the F atoms being generated in a microwave discharge of F_2 diluted in He. The OH concentration profiles along the flow tube were monitored by scavenging OH with an excess of C_4H_{10} fed through the movable injector. Close to the OH source, the obtained concentrations approached the ones as determined from the consumption of F_2 in the microwave.

CH_3 source

CH_3 was prepared in initial concentrations of 2.2 × 10^{11} molec cm^{-3} through pyrolysis of azomethane:

$$CH_3NNCH_3 \rightarrow 2CH_3 + N_2.$$

The source is a part of the movable injector, and its design is described in detail in Ref. 20. Under typical conditions, 80% of the azomethane was decomposed to yield nearly the corresponding amount of CH_3 as determined by scavenging CH_3 with F_2. A small fraction of the CH_3 was lost through the reaction

$$CH_3NNCH_3 + CH_3 \rightarrow CH_3NNCH_2 + CH_4$$

to form CH_4, which was measured to amount to roughly 2% of the initial azomethane. This renders a negligible kinetic contribution of the CH_3NNCH_2 radicals. The potential reaction of excess OH with CH_3NNCH_3 surviving the pyrolytic zone was checked for experimentally. With the pyrolytic coil switched off, it was found that about 20% of the CH_3NNCH_3 decayed in a 20-fold excess of OH, so that the contribution of the much smaller amount of CH_3NNCH_3 surviving pyrolysis could be neglected. We also established that distortions of the flat reactor temperature profile through the pyrolytic oven could be neglected because of its special design (see Ref. 20). At 700 K, we thus have a very suitable CH_3 source. Unfortunately, this good performance is only achieved in a narrow temperature window between 600 and 800 K since at lower temperatures the perturbation of the reactor temperature profile is no longer negligible, whereas at higher temperatures a considerable azomethane fraction dissociates upstream of the pyrolitic oven, leading to undesired subsequent reactions.

Purity of gases and preparation of precursors

Gas purity grades were as follows: helium 99.999%, F_2 99% (4.96% mixture in helium 99.996%). H_2O was bidistilled. Azomethane was prepared from a CuCl- containing complex following a procedure from the literature [22]. After distillation, it was cooled and stored as a liquid from which gaseous samples were drawn periodically. The purity was determined by GCMS to be better than 99%.

Results of Experiments and Modeling

Measurement of the Total Rate Coefficient for CH_3 + OH:

As mentioned, the usual scheme for the evaluation of pseudo–first-order reactions was not used. Instead, rate coefficients were deduced by systematically refining the simulations of the measured decay curves. The usual kinetic procedure could only be taken to provide raw values for the simulations. The reason is seen in Fig. 1. Here, an OH profile is shown as determined by the scavenger butane. Obviously, a fairly strong decay is observed, resulting from the fast reaction sequence

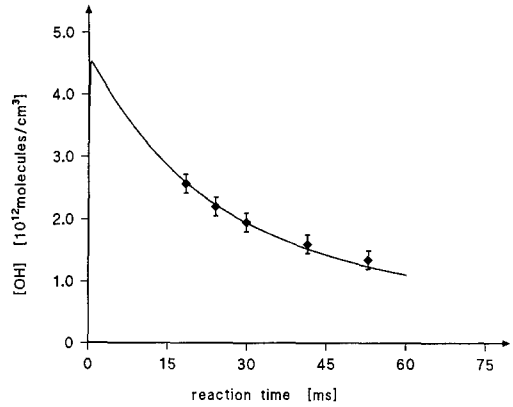

FIG. 1. OH profile as determined by scavenging with butane (symbols). The solid line is simulated. Conditions: $[OH]_0 = 4.7 \times 10^{12}$ molec cm^{-3}, $p = 3.0$ mbar, $v = 10$ m/s.

$$(6) \quad OH + OH \rightarrow H_2O + O$$

$$(7) \quad O + OH \rightarrow O_2 + H.$$

For CH_3 + OH measurements, we used a larger flow velocity, and therefore, the OH loss was less pronounced than in Fig. 1. Nevertheless, the increased OH concentration toward the source region results in an apparently increased reaction rate of CH_3 + OH for high positions of the CH_3 injector, which are translated into large reaction times. Consequently, our log[CH_3] curves were no longer straight lines; rather, their slopes increased with reaction time. This effect and its computational assessment are discussed in detail in Refs. 4 and 5. The experimental conditions of our decay measurements are displayed in Table 1. The $[F]_0$ concentrations correspond to OH concentrations at the top end of the reactor. The initial OH concentrations as experienced by the CH_3 radicals at the start of the reaction, i.e., for the lowest injector position, are lower by roughly a factor of 2. In the quoted $[F]_0$ range, usually 10 decay profiles of CH_3 were measured, each for a different $[F]_0$ value. In principle, from each profile an individual rate coefficient could be extracted. We chose rather to match the complete ensemble with a common simulation. For this simulation, the rate coefficients of Table 2 were taken from only one source [16]* whenever possible. Results of

*On the basis of the CEC value [16] for k_6, i.e., k_6 (700 K) = $4.1 * 10^{-12}$ cm^3 molec^{-1} s^{-1}, no good match between experiment and simulation could be achieved. The curve shown in Fig. 2 was obtained for k_6 (700 K) = $3.0 * 10^{-12}$ cm^3 molec^{-1} s^{-1}, and this is the extrapolated value of another recent recommendation [23]. For the wall loss, the simulation yielded $k_9 = 6$ s^{-1}.

TABLE 1
Summary of experimental conditions and results
(Concentration units: 10^{11} cm^{-3}, k in 10^{-11} cm^3 molec^{-1} s^{-1})

CH_3 + OH measurements

p mbar	v m/s	t_{max} ms	$[H_2O]$	$[F]_0$	$[CH_3]_0$	k_{1tot}
3.25	30.6	10.8	1300	23–163	2.2	2.1
0.65	15.4	23.4	650	24–178	2.2	1.5

CH_3 + OD measurements

p mbar	v m/s	t_{max}	$[D_2O]$	$[F]_0$	$[CH_3]_0$	k'_{1tot}
0.65	16.4	23.2	650	22–170	2.2	2.4

the simulations, along with some of the measured profiles, are shown in Fig. 2. The resulting rate coefficients are

$$k_{1tot}(700\text{ K}, 3.25\text{ mbar}) = 2.1 * 10^{-11}\text{ cm}^3\text{ molec}^{-1}\text{ s}^{-1}$$

and

$$k_{1tot}(700\text{ K}, 0.65\text{ mbar}) = 1.5 * 10^{-11}\text{ cm}^3\text{ molec}^{-1}\text{ s}^{-1}.$$

As to be pointed out in the next section, these numbers do not include the contribution of the $^1CH_2$ channel.

Product Measurements and Channel Rate Coefficients:

The aim of this study is to provide rate coefficients into the individual product channels at 700 K. At this temperature, we did not find CH_2OH/CH_3O signals,** so we have to deal with a simplified system:

$$CH_3 + OH + (M) \rightarrow CH_3OH + (M) \quad (1a)$$
$$\rightarrow {}^1CH_2 + H_2O \quad (1d)$$
$$\rightarrow HCOH + H_2 \quad (1e)$$
$$\rightarrow CH_2O + H_2 \quad (1f)$$

Because of the presence of a large excess of H_2O as needed for the OH production, channel (1d) is in an early steady state; i.e., any CH_3 radical entering this channel will be re-formed under the assumption that the reverse channel is unbranched. In this case, one gets

$$k_{1tot} = k_{1a} + k_{1e} + k_{1f}.$$

The channel rate coefficients may be written as

$$k_{1i} = \Gamma_i * k_{1tot}$$

and the branching ratio Γ_i is the amount of the product (i) per reactant consumed, e.g.,

$$\Gamma_a = CH_3OH/\Delta CH_3.$$

Reaction products were measured absolutely at a reaction time corresponding to a CH_3 consumption of 90%.

For the pressure-dependent stabilization channel, a full falloff curve would be desirable. Given the pressure limitations of the flow reactor technique, only the lower portion of the falloff curve of (1a) is accessible at 700 K. Relative CH_3OH yields are $CH_3OH/\Delta CH_3 = 0.35$ at 3.25 mbar. and $CH_3OH/\Delta CH_3 = 0.09$ at 0.65 mbar. The resulting rate coefficients for the stabilization channel fit rather well into a falloff analysis (see below).

For the channels (1e) and (1f), we measured a product at mass 30, corresponding to both HCOH and H_2CO and with an unknown sensitivity for HCOH. On the other hand, H_2 eliminated through both channels could be measured absolutely. For the relative H_2 abundance we got $H_2/\Delta CH_3 = 0.65$.

The contribution of other H_2 sources such as heterogeneous H_2 formation at the walls could be shown to amount to 20%, so that 80% of the measured H_2 abundance may be attributed to channels (1e) and/or (1f). This leads to

**H atoms were detected, but we attributed them mostly to reactions (7) and (12).

TABLE 2
Reaction scheme and rate coefficients (rate coefficients refer to 700 K and 0.65 mbar; units of k are molec cm^{-3} s^{-1})

1a	$CH_3 + OH + (M) \rightarrow CH_3OH + (M)$	2.0×10^{-12} this work
1b	$CH_3 + OH \rightarrow CH_2OH + H$	negligible
1c	$CH_3 + OH \rightarrow CH_3O + H$	negligible
1d	$CH_3 + OH \rightarrow {}^1CH_2 + H_2O$	9×10^{-12} this work
1e	$CH_3 + OH \rightarrow HCOH + H_2$	1.1×10^{-11} this work
1f	$CH_3 + OH \rightarrow CH_2O + H_2$	1.7×10^{-12} this work
5	$H_2O + F \rightarrow OH + HF$	2.5×10^{-11} [24]
6	$OH + OH \rightarrow H_2O + O$	3.0×10^{-12} [23]
7	$O + OH \rightarrow O_2 + H$	2.4×10^{-11} [16]
8	$OH + F \rightarrow O + HF$	5.8×10^{-11} [24]
9	OH (wall) → products	6 this work
10	O (wall) → 1/2 O_2	6 estimated, this work
11	H (wall) → 1/2 H_2	10 this work
12	$CH_3 + O \rightarrow CH_2O + H$	1.4×10^{-10} [16]
13	$CH_3 + H + (M) \rightarrow CH_4 + (M)$	5×10^{-13} [16]
14	$CH_3 + CH_3 + (M) \rightarrow C_2H_6 + (M)$	1×10^{-12} [16]
15	CH_3 (wall) → products	6–8 this work
16	${}^1CH_2 + H_2O \rightarrow CH_3 + OH$	8×10^{-11} [25]
17	${}^1CH_2 + OH \rightarrow CH_2O + H$	3×10^{-11} [15]
18	$OH + H_2 \rightarrow H_2O + H$	6×10^{-13} [16]
19	$OH + CH_3OH \rightarrow H_2O + CH_2OH$	3.4×10^{-12} [16]
20	$OH + CH_2O \rightarrow H_2O + CHO$	1.8×10^{-11} [16]
21	$OH + HCOH \rightarrow CO_2 + H_2 + H$	1.8×10^{-11} estimated

$$k_{1e+f}(700\ K) = 1.3 * 10^{-11}\ cm^3\ molec^{-1}\ s^{-1}.$$

The important point of this section is the occurrence of H_2-eliminating channels at intermediate temperature (700 K).

Total Rate Coefficient for CH_3 + OD:

The use of OD instead of OH allows the mass spectrometric distinction between channels (1e) and (1f):

$$CH_3 + OD \rightarrow HCOD + H_2 \quad (1'e)^{\dagger}$$
$$\rightarrow H_2CO + HD \quad (1'f)$$

In addition, in this case using OD, channel (1d) is no longer in an early steady state because ${}^1CH_2$ reacts mainly with the excess D_2O as used for the OD production, to yield CH_2D:

$$CH_3 + OD \rightarrow {}^1CH_2 + HDO \quad (1'd)$$
$${}^1CH_2 + D_2O \rightarrow CH_2D + OD. \quad (16')$$

The total rate coefficient is therefore given by

$$k'_{1tot} = k'_{1a} + k'_{1d} + k'_{1e} + k'_{1f}.$$

The corresponding decay curves are steeper in comparison to those for CH_3 + OH, yet otherwise very similar, so that they need not be shown here. For the experimental conditions, see Table 1. The decay curves could be matched by using the modified mechanism according to Table 4, and the result is

$$k'_{1tot}(700\ K, 0.65\ mbar) = 2.4 * 10^{-11}\ cm^3\ molec^{-1}\ s^{-1}.$$

Product Measurements and Channel Rate Coefficients for CH_3 + OD:

In order to provide more insight into the channels eliminating molecular hydrogen, we measured their complete product profiles [20]. The profiles show that the product pair HCOD + H_2 is primarily formed and is at this temperature strongly favored over H_2CO + HD. It must be borne in mind, however, that H_2CO at 30 amu is not only caused by channel (1'f). The reaction CH_3 + O yields a much larger contribution. By the same token, our 31-amu signals include a minor contribution from

$$CH_2D + O \rightarrow CHDO + H \quad (12')$$

in addition to the main contribution from

† For the notation, see footnote to Table 4.

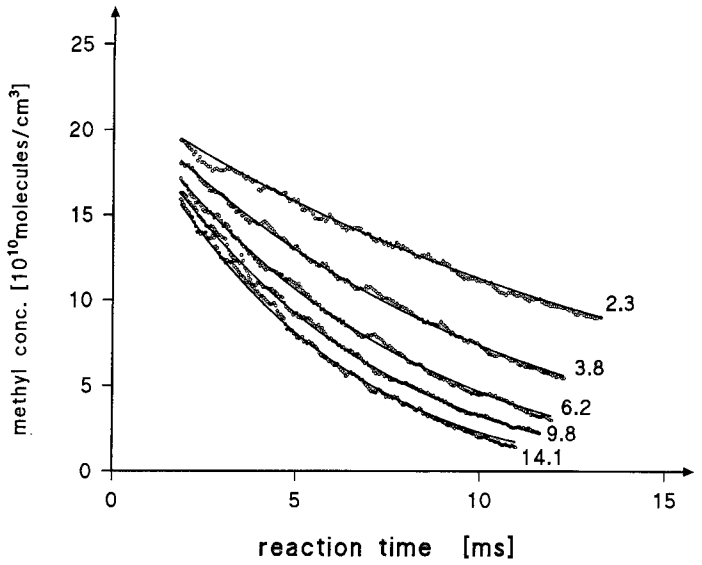

(a)

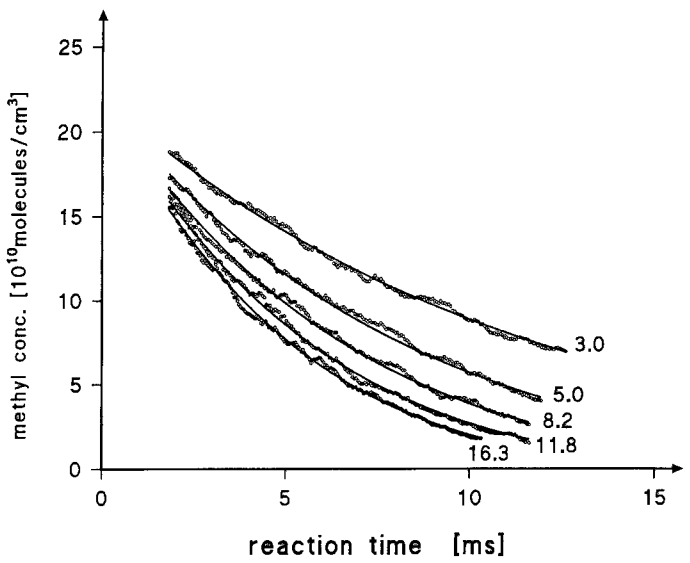

(b)

FIG. 2. (a) and (b) Measured and simulated CH_3 decay curves for CH_3 + OH. The number at each curve denotes the respective [OH] concentration in units of 10^{12} molec cm^{-3} at the top end of the reactor as obtained from $[F]_0$. The OH concentration at the start of the reaction is lower. For further conditions, see Table 1, 3.25 mb.

$$CH_3 + OD \rightarrow HCOD + H_2 \quad (1'e)^{\dagger}$$

This is shown in Table 3. Its first line displays the product signals as measured at 90% CH_3 consumption and referring to CH_3OD, HCOD, CH_2O, HDO, HD, and H_2. The HCOD/H_2CO data are in parentheses since both species were not calibrated. Rather, their concentrations were derived by the simulation of the complete system and by comparison to the calibrated H_2/HD signals. Contributions of reactions other than channels (1′e) and (1′f) were calculated and are shown in the second line (for a more detailed discussion, see Ref. 20). Subtraction leads to the corrected product concentrations. For the determination of the channel rate coefficients, the calibrated H_2/HD yields were used. Fortunately, these are

† The contribution from $CH_2D + OD \rightarrow CHDO + HD$ (1″f) is very small and is omitted in Table 4.

TABLE 3
Stable reaction products of CH_3 + OD (concentrations are in units of 10^{10} cm^{-3} and refer to 90% consumption of $[CH_3]_0 = 2.2 * 10^{11}$ cm^{-3}; $T = 700$ K, $p = 0.65$ mbar)

	H_2	HD	(CH_2O)	(HCOH)	HDO	CH_3OD
measured yield	7	1	6	6.0	8	1.5
yield of side reactions	0.5	0	5	0.5	3	0.0
primary yield	6.5	1	1	5.5	5	1.5

fairly unperturbed. The result is as follows (for the error bars see below):

$$k'_{1a} = 2.0 * 10^{-12} \text{ cm}^3 \text{ molec}^{-1} \text{ s}^{-1}$$

$$k'_{1d} = 9 * 10^{-12} \text{ cm}^3 \text{ molec}^{-1} \text{ s}^{-1}$$

$$k'_{1e} = 1.1 * 10^{-11} \text{ cm}^3 \text{ molec}^{-1} \text{ s}^{-1}$$

$$k'_{1f} = 1.7 * 10^{-12} \text{ cm}^3 \text{ molec}^{-1} \text{ s}^{-1}.$$

Discussion

Sensitivity Analysis for k_{1tot}:

A sensitivity analysis was performed for a methyl decay as our main observable under the conditions of our 0.65-mbar measurements. To this end, the rate coefficient of each reaction of the mechanism shown in Table 2 was either increased by 50% or decreased by 50%, and the resulting simulated decays were compared with the standard decay corresponding to the set of rate coefficients given in Table 2. The effect of the five most sensitive reactions is displayed in Fig. 3. Other reactions, such as the heterogeneous losses of CH_3 or OH, exhibit much smaller sensitivities, and those of the remaining reactions may be neglected.

The mechanism underlying Fig. 3 is simple: CH_3 radicals are consumed to a large extent by the title reaction, CH_3 + OH (1). OH radicals, however, recombine upstream and downstream of the CH_3 injector to form O atoms [reaction (6)], for which a competition exists between the reactions O + OH (7) and CH_3 + O (12). Consequently, the sensitivities of these latter reactions show different signs. With the error limits taken from Ref. 16 of ± 0.15 for reaction (6) and ± 0.2 for reaction (12), our sensitivity analysis shows that the extracted k_{1tot} values may in the worst case vary by roughly a factor of 2 if k_6 and k_{12} are varied within the given limits. If, on the other hand, the values of k_6 and k_{12} may be taken as fixed, only the experimental error bar of about 25% has to be attributed to our k_{1tot} results.

To work in an excess of CH_3 rather than OH would decrease the uncertainty caused by the model by reducing the undesired O atom generation, yet it would do so at the expense of the experimental error bar because of the smaller mass spectrometric sensitivity for OH radicals.

For a sensitivity analysis of the HCOH channel see Ref. 20.

Summary for the Individual Channels of CH_3 + OH:

For an overview, we present here the results of our earlier studies [4,5] along with those of the present one and of a paper to be published elsewhere [20].

Stabilization channel

Our earlier measurements for the stabilization channel [4,5] could be fitted by a Troe expression (see Ref. 26) using a temperature-independent high-pressure limiting rate coefficient of $k_{1a}^{\infty} = 1.7 * 10^{-10}$ cm^3 $molec^{-1}$ s^{-1}.

The low-pressure limiting rate coefficient, k_{1a}^0, was determined from

$$k_{(-1a)}^0 = \beta_c * k_{(-1a)}^{0,sc}$$

using the Troe model along with $\beta_c = [a/(a + F_e k_B T)]$, $a = a_0(T/1000)^n$, $a_0 = 1.5$ kcal/mol, $n = 1.07$, and F_e ranging from 1.052 at 300 K to 1.193 at 1000 K. This procedure led us [27] to the curves as shown in Fig. 4 for 300 and 480 K. By using these same parameters, we obtained the 700 K curve. Obviously, by some fine tuning the match could be improved, but on the basis of only two new measurements, this does not seem worthwhile. Our calculation yields approximate values for k_{1a}^0, which can be fitted by $k_{1a}^0 = 3.7 * 10^{-29} \exp(1280/T)$ cm^6 $molec^{-2}$ s^{-1} for temperatures between 300 and 700 K.

Nonfinding of CH_3O/CH_2OH

These two routes may be assumed to have no barriers. The CH_3O channel lies energetically too high for any significant contribution at 700 K. However, for the CH_2OH channel with the enthalpies based

TABLE 4
Modified reaction mechanism for the CH_3 + OD system[a] (rate coefficients refer to 700 K and 0.65 mbar; units of k are molec cm^{-3} s^{-1})

1′a	$CH_3 + OD + (M) \rightarrow CH_3OD + (M)$	2.0×10^{-12} this work
1′d	$CH_3 + OD \rightarrow {}^1CH_2 + HDO$	9×10^{-12} this work
$1''d_H$	$CH_2D + OD \rightarrow {}^1CHD + HDO$	6×10^{-12} this work
1′e	$CH_3 + OD \rightarrow HCOD + H_2$	1.1×10^{-11} this work
$1''e_H$	$CH_2D + OD \rightarrow DCOD + H_2$	4.4×10^{-12} this work
$1''e_D$	$CH_2D + OD \rightarrow HCOD + HD$	6.6×10^{-12} this work
1′f	$CH_3 + OD \rightarrow CH_2O + HD$	1.7×10^{-12} this work
5′	$D_2O + F \rightarrow OD + DF$	2.5×10^{-11}
6′	$OD + OD \rightarrow D_2O + O$	3.0×10^{-12}
7′	$O + OD \rightarrow O_2 + D$	2.4×10^{-11}
8′	$OD + F \rightarrow O + DF$	5.8×10^{-11}
9′	OD (wall) → products	6 this work
10	O (wall) → 1/2 O_2	6 estimated, this work
11	H (wall) → 1/2 H_2	10 estimated, this work
11′	D (wall) → 1/2 D_2	10 estimated, this work
12	$CH_3 + O \rightarrow CH_2O + H$	1.4×10^{-10}
$12'_H$	$CH_2D + O \rightarrow CHDO + H$	1.1×10^{-10}
$12'_D$	$CH_2D + O \rightarrow CH_2O + D$	3×10^{-11}
14	$CH_3 + CH_3 + (M) \rightarrow C_2H_6 + (M)$	1×10^{-12}
15	CH_3 (wall) → products	6–8 this work
15′	CH_2D (wall) → products	6–8 this work
16′	${}^1CH_2 + D_2O \rightarrow CH_2D + OD$	3.4×10^{-11} [25]
17′	${}^1CH_2 + OD \rightarrow CH_2O + D$	3×10^{-11}
18′	$OD + H_2 \rightarrow HDO + H$	6×10^{-13}
20′	$OD + CH_2O \rightarrow HDO + CHO$	1.8×10^{-11}
21″	OD + HCOD → products	1.8×10^{-11}

[a]In order to facilitate the comparison with Table 2, the same numbering is maintained. Reactions where an H atom is replaced by D in one of the reactants are denoted by a prime. Double prime means that, in both reactants, H is substituted. In the case of CH_2D reactions, a subscript H or D denotes whether H or D is affected by the reaction. Many more reactions are possible but are not included since they play only minor roles. For this same reason, reactions (13) and (19) from Table 2 are omitted, which is certainly justified under our conditions of low initial methyl concentrations.

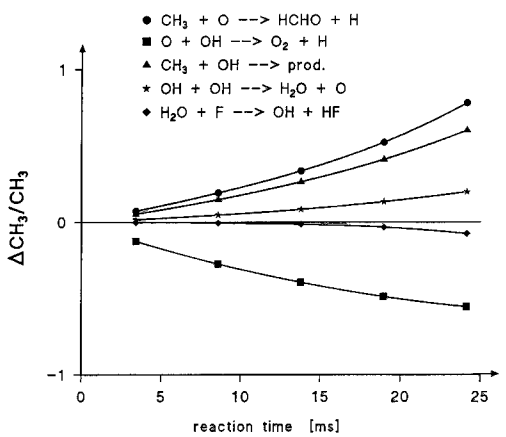

FIG. 3. Sensitivity analysis for k_{1tot}.

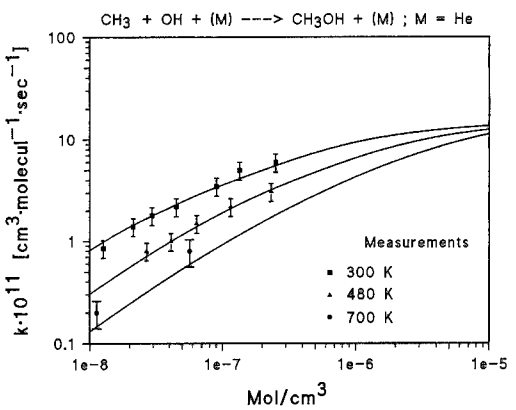

FIG. 4. Falloff curves for the stabilization channel between 300 and 700 K.

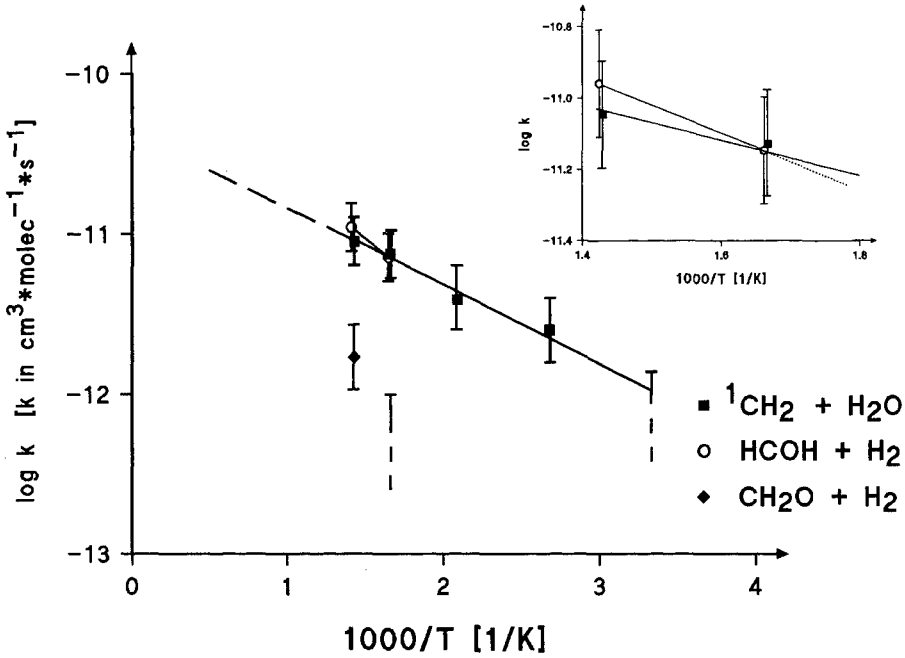

FIG. 5. Arrhenius diagram for the $^1CH_2$ channel and for those eliminating H_2. The open bars denote that here only an upper limit can be given. The inset shows the new results for the $^1CH_2$ channel and the HCOH channel in an expanded display.

on the Sandia compilation [13], one would expect a reaction enthalpy of 3.90 kcal/mol, and this is very close to the barrier found for the HCOH channel (see below). Therefore, the nonfinding of CH_2OH means either that this route has a very low A factor, which is unlikely in view of its loose transition state (TS), or that the assumed reaction enthalpy is incorrect. In fact, Seetula and Gutman [28] have reported new measurements for the heat of formation of CH_2OH resulting in -2.13 kcal/mol at 300 K, which is nearly 2 kcal/mol higher than the Sandia value. Seetula and Gutman's finding has been questioned by some workers [29] and has been supported by others (see Ref. 25 for references). Incorporating the Seetula Gutman value, we recently [30] estimated as a preliminary expression

$$k_{1b} = 2.3 \times 10^{-10} * \exp(-4120/T/\mathrm{K})\ \mathrm{cm^3\ molec^{-1}\ s^{-1}}$$

leading at 700 K to a rate coefficient of only 7×10^{-13} $\mathrm{cm^3\ molec^{-1}\ s^{-1}}$, so that indeed we would not see this channel.

$^1CH_2$ channel

The new measurements for this channel extend our earlier results, as shown in Fig. 5. Because of fragmentation, our HDO measurements are not very accurate, as reflected by the error bars of k'_{1d} (shown in Fig. 5), yet they allow a further conclusion. The difference, $k'_{1tot} - k'_{1d} = k'_{1a} + k'_{1e} + k'_{1f} = 1.5 * 10^{-11}$ $\mathrm{cm^3\ molec^{-1}\ s^{-1}}$ at 0.65 mbar, is in full accord with our result for $k_{1tot} = k_{1a} + k_{1e} + k_{1f}$ at the same pressure, suggesting that the reaction into the individual channels takes place without strong isotopic effects. Therefore, the primes in our notation may be omitted.

H_2-eliminating channels

In our temperature range, the HCOH channel dominates. The results of this study, along with some further measurements at 600 K [20], are also displayed in Fig. 5. For k_{1e} (HCOH channel), a preliminary rate expression can be provided as follows:

$$k_{1e} = 9.1 * 10^{-11} \exp(-1500/T)\ \mathrm{cm^3\ molec^{-1}\ s^{-1}}.$$

One has to bear in mind that our activation energy of $E_a(1e) = 3.0$ kcal/mol is only approximate.

For the H_2CO channel, at present only a rate coefficient at 700 K may be given:

$$k_{1f}(700\ \mathrm{K}) = 1.7 * 10^{-12}\ \mathrm{cm^3\ molec^{-1}\ s^{-1}}.$$

It is in particular for these two channels that measurements at higher temperatures are urgently needed.

Meaning of the HCOH Channel for Flame Models:

At flame temperatures, the exit channel into H + CH_2OH is probably the predominant one [31–33]. This suggests that the HCOH channel may be significant in the intermediate-temperature regime where it may have an effect on ignition or quenching phenomena. At these temperatures, competition with the stabilization channel is possible even at pressures relevant for a practical flame. Therefore, the question arises as to what subsequent reactions the HCOH biradical might undergo. At present, virtually nothing seems to be known experimentally about its gas phase kinetics. At moderate temperatures, H atom migration to transform HCOH into H_2CO will be strongly hindered by a relatively large barrier of about 32 kcal/mol, recently predicted by Melius [14].

Acknowledgments

We gratefully acknowledge financial support from the German ministry for research and technology (BMFT) through the project TECFLAM II. We are grateful to Dr. C. Wahl and Mr. M. Kapernaum for preparing the azomethane samples. The careful reading of the manuscript by our reviewers is gratefully acknowledged.

REFERENCES

1. Hochanadel, C. J., Ogren, P. J., and Sworski, T. J., *J. Phys. Chem.* 84:129 (1980).
2. Anastasi, C., Beverton, S., Ellermann, T., and Pagsberg, P., *J. Chem. Soc. Faraday Trans.* 87:2325 (1991).
3. Bott, J. F., and Cohen, N., *Int. J. Chem. Kinet.* 23:1017 (1991).
4. Oser, H., Stothard, N. D., Humpfer, R., and Grotheer, H. H., *J. Phys. Chem.* 96:5359 (1992).
5. Oser, H., Stothard, N. D., Humpfer, R., Grotheer, H. H., and Just, Th., *Twenty-Fourth Symposium (International) on Combustion,* The Combustion Institute, Pittsburgh, 1992, pp. 597–604.
6. Hughes, K. J., Pereira, A. R., and Pilling, M. J., *Ber. Bunsenges. Phys. Chem.* 96:1352 (1992).
7. Fagerström, K., Lund, A., Mahmoud, G., Jodkowski, J. T., and Ratajczak, E., *Chem. Phys. Lett.* 204:226 (1993).
8. Dean, A. M., and Westmoreland, P. R., *Int. J. Chem. Kinet.* 19:207 (1987).
9. Green, N. J., Pereira, A. R., Pilling, M. J., and Robertson, S. H., *Twenty-Third Symposium (International) on Combustion* 1990, poster.
10. Jordan, M. J. T., Smith, S. C., and Gilbert, R. G., *J. Phys. Chem.* 95:8685 (1991).
11. Dean, A. M., Bozelli, J. W., and Ritter, E. R., *Combust. Sci. Technol.* 80:63 (1991).
12. Walch, S. P., *J. Chem. Phys.* 98:3163 (1993).
13. Kee, R. J., Rupley, F. M., and Miller, J. A., Sandia Report, 1987, and update, 1991.
14. Melius, C., private communication, 1993.
15. Tsang W., and Hampson, R. F., *J. Phys. Chem. Ref. Data* 15:1087 (1986).
16. Baulch, D. L., Cobos, C. J., Cox, R. A., Frank, P., Just, Th., Kerr, J. A., Pilling, M. J., Troe, J., Walker, R. W., and Warnatz, J., *J. Phys. Chem. Ref. Data* 21:411 (1992). Cited as "CEC data."
17. Westley F., Frizzell, D. H., Herron, J. T., Hampson R. F., and Mallard, W. J., NIST Chemical Kinetics Database, Gaithersburg, MD, 1993.
18. Wagner, A., private communication, 1992.
19. Harding, L. B., Schlegel, H. B., Krishnan, R., and Pople, J. A., *J. Phys. Chem.* 84:3394 (1980). L. B. Harding, H. B. Schlegel, R. Krishnan, and J. A. Pople, in *Potential Energy Surfaces and Dynamics Calculations* (D. G. Truhlar, Ed.), Plenum, New York, 1981, pp. 169–183.
20. Humpfer, R., Oser, H., and Grotheer, H. H., *Int. J. Chem. Kinet.*, in press.
21. Grotheer, H. H., Riekert, G., Walter, D., and Just, Th., *Chem. Phys. Lett.* 148:530 (1988).
22. Jahn, F. P., *J. Am. Chem. Soc.* 59:1761 (1937).
23. Atkinson, R., Baulch, D. L., Cox, R. A., Hampson, R. F., Kerr, J. A., and Troe, J., *J. Phys. Chem. Ref. Data* 21:1125 (1992).
24. Walther, C. D., and Wagner, H. Gg., *Ber. Bunsenges. Phys. Chem.* 87:403 (1983).
25. Carstensen, H. H., and Wagner, H. Gg., "Untersuchung der Reaktionen von $^1CH_2$ mit H_2O und D_2O," MPI für Strömungsforschung, Diploma-thesis, Göttingen, Bericht 9/1993, June 1993.
26. Troe, J., *Ber. Bunsenges. Phys. Chem.* 87:161 (1983).
27. Oser, H., Dissertation Thesis, Dr. rer. nat., University of Stuttgart, Stuttgart, Germany, 1993.
28. Seetula, J. A., and Gutman, D., *J. Phys. Chem.* 96:5401 (1992).
29. Ruscic, B., and Berkowitz, J., *J. Phys. Chem.* 97:11451 (1993).
30. Grotheer, H. H., Kelm, S., Driver, H. S. T., Hutcheon, R. J., Lockett, R. D., and Robertson, G. N., *Ber. Bunsenges. Phys. Chem.* 96:1360 (1992).
31. Roth, P., and Just, Th., *Twentieth Symposium (International) on Combustion,* The Combustion Institute, Pittsburgh, 1985, p. 807.
32. Dombrowsky, Ch., Hoffmann, A., Klatt, M., and Wagner, H. Gg., *Ber. Bunsenges. Phys. Chem.* 95:1685 (1991).
33. Grotheer, H. H., and Just, Th., *Combust. Sci. Technol.* 91:15 (1993).

COMMENTS

Joseph W. Bozzelli, New Jersey Institute of Technology, USA. Can you put an upper limit or estimate on the dissociation rate constant of ^{1}HCOH (unimolecular isomerization to CH_2O) from your experimental data? This will likely be in or near the low-pressure limit under your conditions.

Author's Reply. In our mass spectrometer, we are unable to see isomerization. It should, however, not play a significant role at our moderate temperatures, because of an isomerization barrier of about 32 kcal/mol, counted from the HCOH side [1].

We do see a decline of our HCOD yields at reaction times much larger than those of the paper, and we attribute it to a reaction with excess OH (OD in this case). In this regard, HCOH seems to be more reactive than its counterpart, H_2CO, yet much less reactive than the other important biradical in our system, $^1CH_2$.

REFERENCE

1. Melius, C., *BAC-MP4 Heats of Formation and Free Energies,* Sandia National Laboratories, April 1993.

Twenty-Fifth Symposium (International) on Combustion/The Combustion Institute, 1994/pp. 733–739

BIFURCATION ANALYSIS OF METHYL RADICAL OXIDATION IN OPEN SYSTEMS. THE LOW-PRESSURE REGIME

M. A. GRELA AND A. J. COLUSSI
Department of Chemistry
University of Mar del Plata
7600 Mar del Plata, Argentina

Domains of bistability and hysteresis in the isothermal oxidation of methyl radicals by O_2 in low-pressure flow reactors are identified by means of continuation algorithms using a mechanism based on experimental results. Control (unfold) parameters comprise the reactants' inflows, F, residence time τ, and the probabilities, γ, of chain carrier losses per collision with reactor walls. The effect of methane addition is also investigated. In the spanned ranges, the singular points detected correspond to single folds of stable into unstable branches, marking the onset of narrow hysteresis loops. Orbits of bistability were found by tracing out the folds in two parameters: (F,τ) or (F_i,F_j). This analysis discloses the rich kinetic behavior expected for this system, in which the "branching" reaction ($H + O_2 \rightarrow OH + O$) produces an inert radical toward the reactant. It also predicts the existence of high- and low-oxidation regimes under certain conditions and provides the basis for process optimization, i.e., for minimizing methyl losses, or for maximizing methyl yields in the sensitized oxidation of added methane.

Introduction

Increasingly stringent economical and environmental constraints require more efficient approaches to the optimization of chemical processes. If nonlinear features are involved, model analysis may be the only viable route to the detection of singular, and perhaps desirable, behavior. In such cases, empirical correlations, rules-of-thumb, and trial-and-error experimentation must be complemented, or replaced, by computer-aided design based on realistic models [1,2].

The oxidative dimerization of methane catalyzed by metal oxides is one of the most intensively investigated processes for converting natural gas into more valuable products [3]. A well-established aspect of its mechanism of reaction is the fact that methyl radicals, formed by heterogeneous oxidation of methane, desorb into the gas phase where they undergo dimerization or further oxidation into CO_x [4]. A recent report on the inertness of the catalyst oxides toward CH_3(g) [5] suggests that the improvement of selectivity, i.e., the suppression of carbon oxides, partially rests with the control of gas-phase oxidation reactions [3,6].

However, despite exhaustive testing of many catalytic materials and reaction conditions, the goals of high methane conversion and selectivity remain elusive [3,7]. As the limits to performance are approached, it appears that mixing control or catalyst selection and preparation do not hold the key to further improvements. Some time ago, we decided to investigate the chemistry of this system in a systematic manner by experimentally disengaging the purely heterogeneous processes from those occurring in the gas phase [8,9]. Thus, while probing into the details of gas-solid interactions, such as O_2 chemisorption and methane heterogeneous oxidation on catalytically active metal oxides, we also focused our attention on the kinetics and mechanism of methyl radical oxidation in flow reactors [10,11]. A very recent report describing high-temperature, low-pressure experiments led to rate parameters for the key elementary reaction

$$CH_3 + O_2 \rightarrow CH_2O + OH \qquad (1)$$

which have been since confirmed [11]. In the course of such experiments, we met with nonlinear kinetic behavior usually associated with ignition and extinction phenomena, which was rationalized in terms of a branched chain mechanism.

In this context, the possibility that, by careful process control, one could steer the system into a steady state of low oxidation, and thereby improve selectivity, seems to deserve further consideration. In this paper, we report a bifurcation analysis of the low-pressure oxidation of methyl radicals in flow reactors bearing on such issues, which reveals complex dependences of conversion on accessible parameters.

The Mechanism

Throughout, reference is made to the mechanism presented in Table 1. Rate constants are given in

TABLE 1
Mechanism of oxidation of methyl radicals at low pressures

Reaction	Rate constants[a,b]
(1) $CH_3 + O_2 \rightarrow CH_2O + OH$	1.49×10^5
(2) $CH_3 + O_2 \rightarrow CH_3O + O$	6.86×10^3
(3) $O_2 + H \rightarrow OH + O$	6.49×10^7
(4) $CH_2O + OH \rightarrow HCO + H_2O$	1.53×10^{10}
(5) $HCO + O_2 \rightarrow CO + HO_2$	2.23×10^{10}
(6) $CH_3 + HO_2 \rightarrow CH_3O + OH$	1.99×10^{10}
(7) $CH_3O \rightarrow CH_2O + H$	7.87
(8) $OH + OH \rightarrow H_2O + O$	4.21×10^9
(9) $CH_3 + O \rightarrow CH_2O + H$	7.83×10^{10}
(10) $CH_2O + O \rightarrow HCO + OH$	1.37×10^{10}
(11) $CH_2O + H \rightarrow HCO + H_2$	1.07×10^{10}
(12) $CH_3O + O_2 \rightarrow CH_2O + HO_2$	1.84×10^7
(13) $HCO \rightarrow CO + H$	21.9
(14) $HO_2 + H \rightarrow OH + OH$	1.10×10^{11}
(15) $HO_2 + OH \rightarrow O_2 + H_2O$	1.41×10^{10}
(16) $CH_3O + OH \rightarrow CH_2O + H_2O$	1.81×10^{10}
(17) $CH_3 + HO_2 \rightarrow CH_4 + O_2$	3.61×10^9
(18) $CH_3O + H \rightarrow CH_2O + H_2$	1.99×10^{10}
(19) $OH + O \rightarrow O_2 + H$	1.35×10^{10}
(20) $CH_3O + O \rightarrow CH_2O + OH$	6.03×10^9
(21) $CH_3O + O \rightarrow CH_3 + O_2$	2.06×10^9
(22) $OH + H \rightarrow H_2 + O$	1.98×10^8
(23) $HO_2 + H \rightarrow O_2 + H_2$	2.33×10^{10}
(24) $HO_2 + O \rightarrow OH + O_2$	2.12×10^{10}
(25) $HO_2 + HO_2 \rightarrow H_2O_2 + O_2$	1.81×10^9

[a]Rate constants in mole/dm^3, s units, at 1025 K.

[b]All rate constants, except for reactions (3) and (10), taken from Refs. 21 and 22; rate constants for reactions (7) and (9) were calculated assuming identical molecule-N_2 and molecule-wall energy transfer collision efficiencies. The rate constant for reaction (3) is from Ref. 23, and for reaction (10) from Ref. 24. Although reactions (18) through (25) have small sensitivity coefficients under the investigated conditions, they were included in all calculations.

dm^3/(mole s) at 1025 K. This mechanism simulates the experiments described in Ref. 11, which involve measurements of methyl radical decay in a low-pressure, well-stirred flow tank reactor in the presence of O_2(g), at temperatures above 1000 K. Methyl radicals were generated in situ by fast decomposition of azomethane, and detected by on-line molecular beam mass spectrometry with electron impact ionization at 20 eV.

The inflow of reactants and effusive escape of all species, processes that do not appear explicitly in Table 1, were included in the differential equations for each species X_i. Thus, under steady flow, the latter consist of chemical terms, corresponding to the reactions in Table 1, plus a flow term, $k_{ei}([X_i]_0 - [X_i])$, where k_{ei} stands for the escape rate constant (the reciprocal of residence time) of species i, and the subscript 0 refers to the steady-state concentration of the same species that would be attained in the absence of reaction. If F_i is the flow rate of reactant i in M/s, then $F_i = k_{ei}\,[X_i]_0$. At low pressures, one must also consider radical losses on reactor walls. We deal jointly with variable residence times, $\tau = 1/k_e$, and with first-order losses by means of Eq. (I) [11,12]:

$$k_{ei} = k_0\,(T/M_i)^{1/2}\lambda \qquad \text{(I)}$$

where k_0 only depends on reactor geometry, and $\lambda \geq 1$ is a parameter reflecting the efficiency of radical destruction on reactor walls. The term λ is related to the reaction probability per collision γ, $\gamma = (\lambda - 1)k_{ei}/\omega_i$, where ω_i is the frequency of collisions made

by species i with reactor walls; $\lambda = 1$ corresponds to the case of inert walls [11].

Under such experimental conditions, energy transfer is so slow that all radical association reactions are deep in their falloff regions; their initial adducts (such as $C_2H_6^\circ$ and $CH_3O_2^\circ$) cannot be stabilized and are therefore ignored [11]. This does not detract from generality because several bimolecular radical terminations still occur via disproportionation reactions, which are not pressure limited. Simulations based on the mechanism of Table 1 using k_1 and γ, the collective efficiency of heterogeneous radical carrier losses, as adjustable parameters led to

$$\log k_1 = 8.92 - 3840/T \qquad \text{(II)}$$

and to $\gamma \approx 7 \times 10^{-4}$ above 1000 K. Very recent measurements of k_1, carried out by Yu et al. [13] and by Hessler [14] are in excellent agreement with Eq. (II) and validate the mechanism of Table 1 as a reliable basis for the ensuing kinetic analysis. About 1000 K, the alternative initiation, reaction (2), is about 25 times slower than reaction (1), although its importance increases with temperature.

It should be realized that in this case reactions (2) and (3)

$$CH_3 + O_2 \rightarrow CH_3O + O \qquad (2)$$

$$H + O_2 \rightarrow OH + O \qquad (3)$$

which would be formally classified as branching, actually produce two species, CH_3O and OH, which do not react directly with methyl radicals. Chain loops can only be closed through OH attack on formaldehyde, reaction (4), followed by the sequence (5-6-7), which slowly regenerates H. An alternative path reaches step 3 via reactions (8) and (9). Thus, *CH_2O is intimately involved in the development of branching in the oxidation of methyl radicals.*

On closer inspection, one realizes that the sequence (1 + 8 + 9 + 3) corresponds to the stoichiometry $2CH_3 + 2O_2 = 2CH_2O + H_2O + O$, i.e., to a nonbranching pathway. In contrast, the cycle comprising steps (1 + 4 + 5 + 6 + 7 + 3) amounts to $2CH_3 + 3O_2 = 2OH + O + CH_2O + H_2O$, i.e., generates two radical centers per methyl radical.

Such complexity exceeds that of cubic autocatalysis, and even that of the well-investigated $H_2 + O_2$ reaction [15]. Actually, the mechanism of Table 1 resembles the Shell model, a generalized kinetic scheme simulating autoignition in diesel engines, in the sense that both involve formaldehyde as the degenerate branching agent [16]. Clearly, the so-called net branching factor, $\phi_b = 2k_3\,[O_2] - k_{eH}$, which plays such an important role in the analysis of conventional oxidations, does not represent a useful criterion for autocatalysis in this case [16–18].

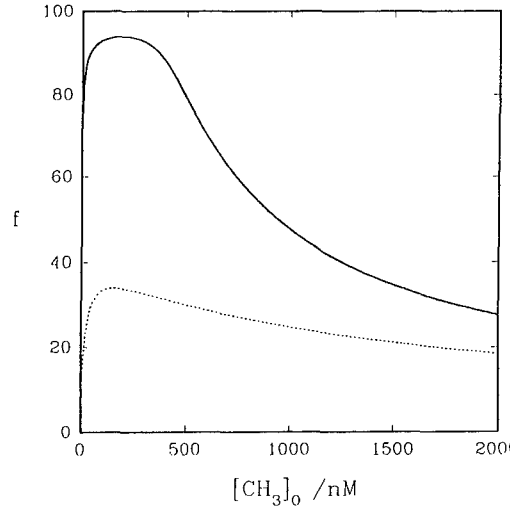

FIG. 1. f vs $[CH_3]_0$, at $[O_2]_0 = 1000$ nM, $k_0 = 0.185$ $K^{-1/2}\,s^{-1}$, 1025 K. Solid curve: $\lambda = 1$; broken curve: $\lambda = 19.5$.

Sensitivity Analysis near Operating Conditions in Ref. 11

Given the mechanism of Table 1, and initial steady-state values for the nine concentration variables (found by means of the FACSIMILE package) [19], AUTO programs are able to map the evolution of such a state upon variation of a defined control parameter $P(1)$ [20]. They also calculate the determinant and eigenvalues of the Jacobian $\{\partial^2 X_i/\partial t \partial X_j\}$, i.e., the stability of the solutions, identifying limit points and bifurcation points along the trajectory $\{X_i\} = G\{X_i, P(1)\}$. In addition, they can also perform continuation analysis from critical points as a function of a second, the unfolding, parameter $P(2)$.

The experimental studies of Ref. 11, with $\lambda \simeq 20$ for all radicals, revealed a dominance of first-order over second-order carrier terminations. Starting with $[CH_3]_0 = 6.5$ nM (nM $= 10^{-9}$ M), $[O_2]_i = 1000$ nM, $k_0 = 0.185\,K^{-1/2}\,s^{-1}$, $T = 1025$ K, the complete mechanism leads to 14% conversion, i.e., $f = 100 \times \{1 - ([CH_3]/[CH_3]_0)\} = 14$. Using AUTO, we found no critical points by varying the following parameters one at a time, within the ranges $1.0 \times 10^{-3} < [CH_3]_0 < 4.0 \times 10^3$ nM, $2.0 \times 10^{-3} < [O_2]_0 < 5.0 \times 10^3$ nM, and $1.85 \times 10^{-4} < k_0 < 5.09\,K^{-1/2}\,s^{-1}$, while keeping the remaining ones fixed at their starting values, for either $\lambda = 1$ or 19.5 (Figs. 1, 2, and 3).

The dependence of f on λ is shown in Fig. 4. Individual variation of escape rate constants for OH, H, O, and HO_2 radicals, from $\lambda = 19.5$ down to 1.4, merely increases f from the experimental value of 14% to 26.5, 20.0, 14.4, and 15.8%, respectively. However, f increases to 50% if the λ's for H and OH are simultaneously relaxed. As we will see in the fol-

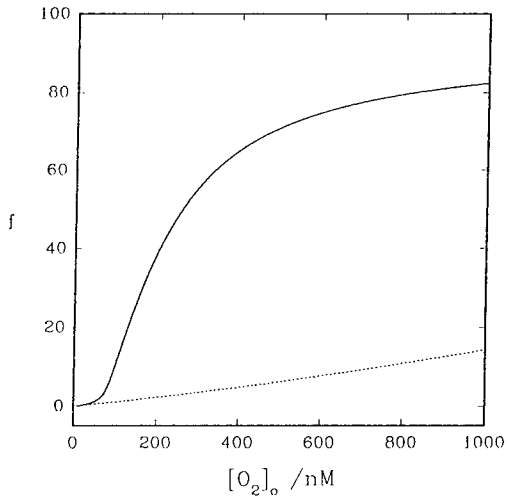

FIG. 2. f vs $[O_2]_0$, at $[CH_3]_0$ = 6.5 nM, k_0 = 0.185 $K^{-1/2}$ s^{-1}, 1025 K. Solid curve: λ = 1; broken curve: λ = 19.5.

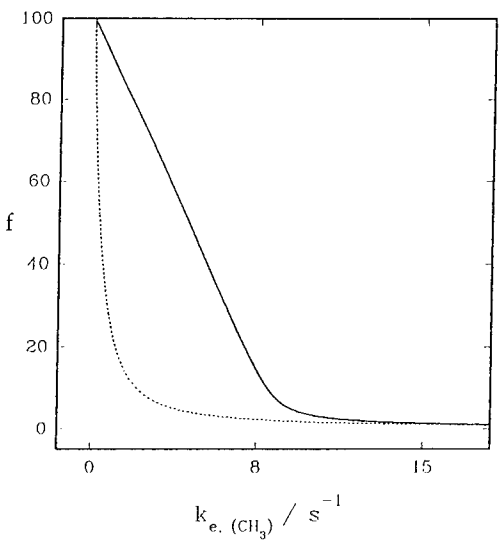

FIG. 3. f vs k_{eCH3}, at $[O_2]_0$ = 1000 nM, $[CH_3]_0$ = 6.5 nM, 1025 K. Solid curve: λ = 1; broken curve: λ = 19.5.

lowing section, limit ignition and extinction points are only possible for $[O_2]_0$ values smaller than those employed in Ref. 11, the precise values depending on residence times.

Bifurcation Analysis of the Isothermal Oxidation of Methyl Radicals

Since we were primarily interested in identifying experimental parameters whose variations within specified ranges might induce nonmonotonous responses on methyl radical concentration, we began by mapping f at λ = 1 and fixed $[CH_3]_0$ for different values of $[O_2]_0$ using k_0 as control parameter. We also exchanged the roles of $[O_2]_0$ and k_0 to possibly detect disjoint critical regions, such as isolas.

Typical results of our calculations are shown in Fig. 5. Curve *a* corresponds to $[CH_3]_0 = [O_2]_0$ = 0.16 nM. In this case we found no critical points, but an abrupt variation of f with k_{eMe}. For $[O_2]_0$ = 20 nM, one already finds two critical, or turning, points 1 and 2, in which one of the Jacobian eigenvalues vanishes, marking the onset of an unstable branch (curve *b*). In this scale, it is not possible to discern the unstable branch connecting both turning points. The narrow hysteresis loop is blown up in Fig. 6. A "memory" effect is still apparent in curve *c*, an otherwise stable branch. Figure 7 displays the results of the complementary analysis, using $[O_2]_0$ as control parameter. The existence of "threshold" concentrations, or flow rates, of dioxygen at longer resident times is readily apparent (curves *c* and *d*).

The results of a two-parameter continuation of critical points appear as loops in Figs. 5 and 7. In Fig. 5, points 3 and 4 correspond to the minimum (6.22 nM) and maximum (33.89 nM) concentrations of O_2, below and above which bistability ceases to exist under given constraints, respectively. Alternatively, one can continue the conjugate points 1 and 2 in Fig. 5, employing $[CH_3]_0$ as bifurcation parameter at fixed $[O_2]_0$. Again, one obtains an orbit defining the hysteresis region (Fig. 8), with points 3 and 4 marking the convergence of ignition and extinction.

The Addition of Methane

We also explored the kinetic effect of methane additions. This scenario is realized by gas-phase processes taking place at low concentrations of dioxygen, following the partial heterogeneous oxidation of methane into methyl radicals over metal oxides. The analysis is now based on the mechanism of Table 1, expanded with reactions (26) through (29):

$$CH_4 + H \rightarrow CH_3 + H_2 \quad (26)$$

$$CH_4 + OH \rightarrow CH_3 + H_2O \quad (27)$$

$$CH_4 + O \rightarrow CH_3 + OH \quad (28)$$

$$CH_4 + HO_2 \rightarrow CH_3 + H_2O_2 \quad (29)$$

with $k_{26} = 3.29 \times 10^8$, $k_{27} = 1.15 \times 10^9$, $k_{28} = 4.92 \times 10^8$, and $k_{29} = 1.97 \times 10^4$ M^{-1} s^{-1} at 1025 K [21,22].

In Fig. 9, we show the results of calculations for mixtures of $[CH_3]_0 = [CH_4]_0$ = 0.16 nM, using $[O_2]_0$ as control parameter. In this case, we display

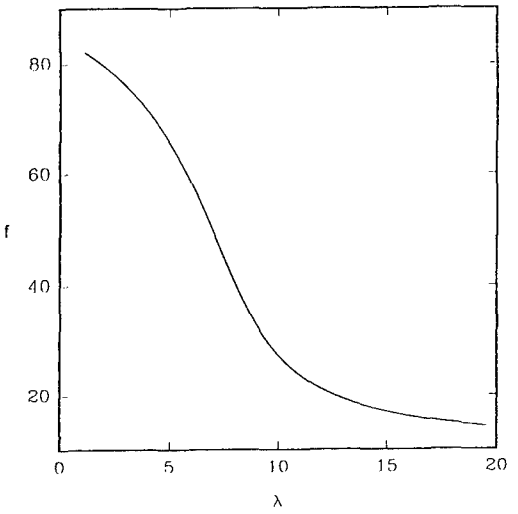

FIG. 4. f vs λ, at $[O_2]_0$ = 1000 nM, $[CH_3]_0$ = 6.5 nM, k_0 = 0.185 $K^{-1/2}$ s^{-1}, 1025 K.

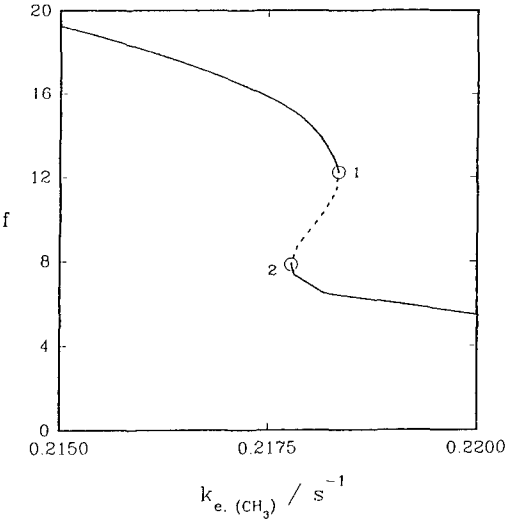

FIG. 6. Zoomed view of the section of curve b within the loop in Fig. 5.

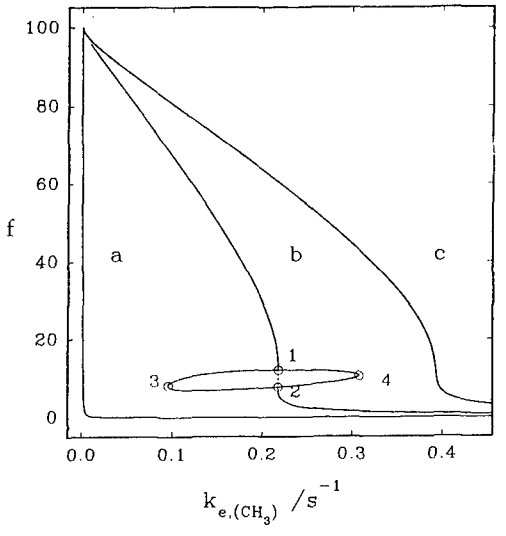

FIG. 5. f vs k_{eCH3}, at $[CH_3]$ = 0.16 nM. Curves a, b, and d correspond to $[O_2]_0$ = 0.16, 20, and 50 nM, respectively. The loop is the orbit of limit points, i.e., the loci of steady states for which the Jacobian and one of its eigenvalues vanish, enclosing the hysteresis region. Points 3 and 4 are defined by $[O_2]_0$ = 6.22 and 33.9 nM, and their abscissas, respectively.

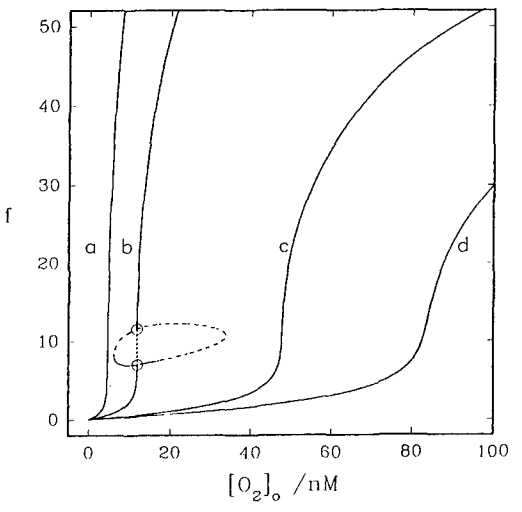

FIG. 7. f vs $[O_2]_0$, at $[CH_3]_0$ = 0.16 nM, 1025 K. Curves a, b, c, and d correspond to k_{eCH3} = 0.0765, 0.153, 0.382, and 0.534 s^{-1}, respectively. The broken loop is a projection of the loop in Fig. 5.

the limit orbits f vs $[O_2]_0$ for methyl radicals and methane, with k_0 (proportional to the reciprocal of residence time) as the unfolding parameter. It is worth comparing the methyl limit orbit with that of Fig. 7, which corresponds to the case $[CH_4]_0$ = 0; now the upper convergence point extends up to $[O_2]_0$ ≈ 60 nM. Notice that, since the oxidation of methane produces methyl radicals, their limit orbits are anticorrelated.

A more dramatic display of nonlinearity is presented in Fig. 10, in which the residence time is kept constant, k_{eCH3} = 0.153 s^{-1}, and $[CH_4]_0$ is used as the unfolding parameter. In this case, the orbit of limit points corresponding to the oxidation of methyl radicals extends into the negative quadrant, reflecting net production. However, particularly at large

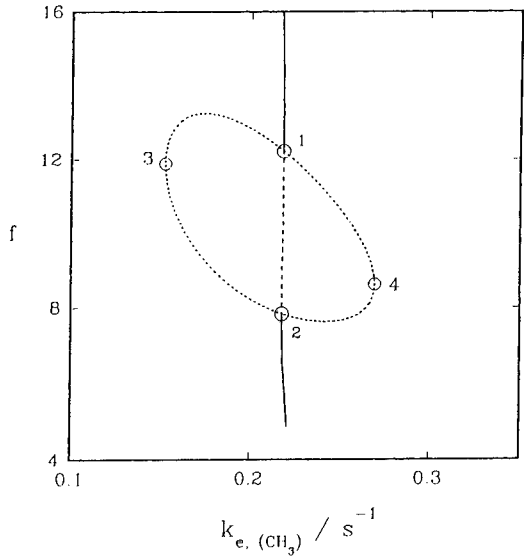

FIG. 8. f vs k_{eCH3}, at $[O_2]_0$ = 20 nM, 1025 K. Points 1 and 2 in this figure and in Fig. 5 are the same. The limit orbit in this case has been calculated using $[CH_3]_0$ as second bifurcation parameter. Points 3 and 4, where ignition and extinction converge, are defined by $[CH_3]_0 = 5.6 \times 10^{-3}$, 0.32 nM, and their abscissas, respectively.

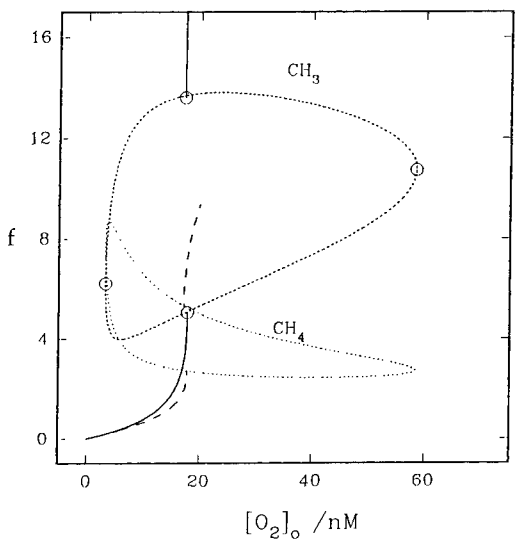

FIG. 9. f vs $[O_2]_0$, at $[CH_3]_0 = [CH_4]_0$ = 0.16 nM. Solid curve is the steady-state branch for methyl radicals at k_{eCH3} = 0.153 s^{-1}; long-dashed curve, the steady-state branch for methane at k_{eCH3} = 0.153 s^{-1}. The short-dashed loop corresponds to methyl radical, and the dotted one to methane.

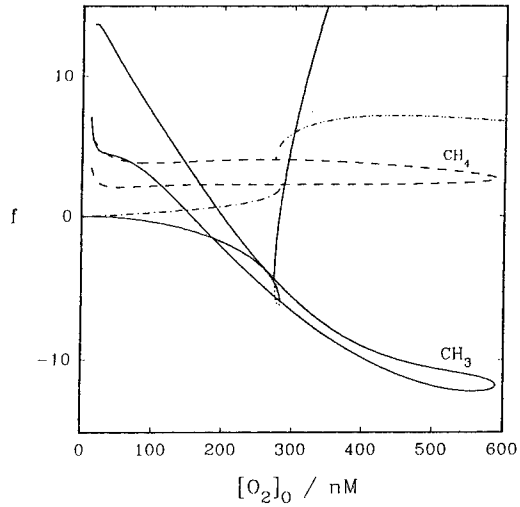

FIG. 10. f vs $[O_2]_0$, at k_{eCH3} = 0.153 s^{-1}. The loops correspond to the limit orbits for methyl and methane obtained using $[CH_4]_0$ as second bifurcation parameter. Solid curve and dash-dotted curve are the steady-state branches for methyl radicals and methane, respectively, calculated for $[CH_3]_0$ = 0.16 nM and $[CH_4]_0$ = 8 nM.

values of $[O_2]_0$, mass balance reveals that a large fraction of reacted methane oxidizes to carbon monoxide and water rather than to methyl radicals. The stationary state loci for methane and methyl, beginning at $[O_2]_0$ = 0, $[CH_3]_0$ = 0.16 nM, $[CH_4]_0$ = 8 nM, are also shown. Particularly striking is the fact that the methyl steady-state curve crosses its limit orbit as a stable branch. However, it should be realized that, at such intersection, although both curves share the same values of f, $[O_2]_0$ and k_e, *they have different values of* $[CH_4]_0$. In other words, one can have two different mixtures possessing the same steady concentration of methyl radicals, one corresponding to a stable steady state and the other to a limit point. On the other hand, at the second crossing, ca. $[O_2]_0 \approx 280$ nM, the curve folds into an unstable branch, marking the point where the extent of oxidation of methyl radicals suddenly reverses its trend, tracking the abrupt onset of methane ignition. Here, in contradistinction with the first crossing, a given mixture has two accessible stationary levels of methyl radicals. This behavior contrasts with the one found in a similar calculation for $[CH_3]_0 = [CH_4]_0$ = 0.16 nM (not shown in Fig. 10), in which the conversions of both species are positive for all values of $[O_2]_0$. It is clear that such diversity precludes obvious generalizations, and underscores the irreplaceable role of this type of analysis in assessing the actual behavior of branched chain oxidations in flow reactors.

Process optimization, i.e., maximizing the yield of methyl radicals that may be produced by gas-phase oxidation of methane, amounts to locating the ex-

trema of the objective functional, $g = ([CH_3] - [CH_3]_0)/[CH_4]_0$ (the product of conversion times selectivity), on the steady-state manifold of the mechanism of Table 1, a ready option of AUTO [20]. An extension of these ideas to pressures at and above atmospheric, with and without simultaneous heterogeneous oxidation of CH_4, is underway [25, 26].

Nomenclature

Symbol	Meaning	SI unit
f	conversion or extent of reaction	—
F	mass flow rate	mole dm^{-3} s^{-1}
k_e	escape rate constant	s^{-1}
k_i	reaction rate constant	s^{-1} or dm^3/(mole s)
k_0	geometric factor	$K^{-1/2}$ s^{-1}
Greek symbols		
γ	heterogeneous reaction probability per collision	—
λ	efficiency of heterogeneous radical losses	—
τ	residence time	s
ϕ_b	branching factor	s^{-1}
ω	frequency of gas-wall collisions	s^{-1}

REFERENCES

1. Frenklach, M., in *Chemical Reactions in Complex Mixtures,* Chap. 11, (A. V. Sapre and F. J. Krambeck, Eds.), Van Nostrand, Reinhold, New York, 1991.
2. a) Villermaux, J., *Chem. Eng. Sci.* 48:2525 (1993); b) Miller, J. A., Kee, R. J., and Westbrook, C. K., *Annu. Rev. Phys. Chem.* 41:345 (1990).
3. a) Amenomiya, Y., Birss, V. R., Goledzinowski, M., Galuszka, J., and Sanger, A. R., *Catal. Rev.—Sci. Eng.* 32:163 (1990), and references therein; b) Fox, J. M., *Catal. Rev.—Sci. Eng.* 35:169 (1993).
4. Lunsford, J. H., Cisneros, M. D., Hinson, P. G., Tong, T., and Zhang, H., *Faraday Discuss. Chem. Soc.* 87:13 (1989), and references therein.
5. Tong, Y., and Lunsford, J. H., *J. Am. Chem. Soc.* 113:4741 (1991).
6. Mackie, J. C., *Catal. Rev.—Sci. Eng.* 33:169 (1991).
7. Tonkovich, A. L., Carr, R. W., and Aris, R., *Science* 262:5131 (1993).
8. Amorebieta, V. T., and Colussi, A. J., *J. Phys. Chem.* 92:4576 (1988).
9. Amorebieta, V. T., and Colussi, A. J., *J. Phys. Chem.* 93:5155 (1989).
10. Colussi, A. J., and Amorebieta, V. T., "Reactive vs. Adsorbed Oxygen in the Heterogeneous Oxidation of Methane over Li/MgO," paper presented at the ACS Symposium on Methane and Alkane Conversion, 207th ACS National Meeting, San Diego, CA, March 1994.
11. Grela, M. A., Amorebieta, V. T., and Colussi, A. J., *J. Phys. Chem.* 96:7013 (1992).
12. Grela, M. A., and Colussi, A. J., *J. Phys. Chem.* 88:5995 (1984).
13. Yu, C.-L., Wang, C., and Frenklach, M., "Shock Tube Determination of the Rate Coefficient for the Reaction of CH_3 with O_2," paper presented at the Third International Conference on Chemical Kinetics, NIST, Gaithersburg, MD, July 1993.
14. Hessler, J. P., "High Temperature Study of $CH_3 + O_2 \rightarrow OH + H_2CO$," paper presented at the Third International Conference on Chemical Kinetics, NIST, Gaithersburg, MD, July 1993.
15. Gray, P., and Scott, S. K., *Chemical Oscillations and Instabilities,* Oxford University Press, Oxford, UK, 1990.
16. Cox, R. A., in *Modern Gas Kinetics,* Chap. C2 (M. J. Pilling, and I. W. M. Smith, Eds.), Blackwell, Oxford, UK, 1987.
17. Gray, P., *Twenty-Third Symposium (International) on Combustion,* The Combustion Institute, Pittsburgh, 1990, pp. 1–19.
18. Johnson, B. R., Scott, S. K., and Tomlin, A. S., *J. Chem. Soc. Faraday Trans.,* 87:2539 (1991).
19. Curtis, A. R., and Sweetenham, W. P., *FACSIMILE: a Computer Program for Flow and Chemistry Simulation, and General Initial Value Problems,* Harwell, UK, 1987.
20. a) Doedel, E., Keller, H. B., and Kernevez, J. P., *Int. J. Bifurcation Chaos* 1:493 (1991); b) ibid, 1:745 (1991); c) Doedel, E., and Kernevez, J. P., AUTO: Software for Continuation and Bifurcation Problems in Ordinary Differential Equations, California Institute of Technology, Pasadena, CA, 1986.
21. Tsang, W., and Hampson, R. F., *J. Phys. Chem. Ref. Data* 15:1087 (1986).
22. Westley, R., Herron, J. T., Cvetanovic, R. J., Hampson, R. F., and Mallard, W. G., NIST Chemical Kinetics Database, Version 2.01, National Institute of Science and Technology, Gaithersburg, MD, 1990.
23. Yuan, T., Wang, C., Yu, C.-L., Frenklach, M., and Rabinowitz, M. J., *J. Phys. Chem.* 95:1258 (1991).
24. Herron, J. T., *J. Phys. Chem. Ref. Data,* 17:967 (1988).
25. Shi, C., Xu, M., Rosynek, M. P., and Lunsford, J. H., *J. Phys. Chem.* 97:216 (1993).
26. Grela, M. A., and Colussi, A. J., to be submitted.

Twenty-Fifth Symposium (International) on Combustion/The Combustion Institute, 1994/pp. 741–748

A SHOCK TUBE STUDY OF THE CO + OH → CO_2 + H REACTION

MARGARET S. WOOLDRIDGE, RONALD K. HANSON AND CRAIG T. BOWMAN
High Temperature Gasdynamics Laboratory
Department of Mechanical Engineering
Stanford University
Stanford, CA 94305, USA

The rate coefficient for the reaction

$$CO + OH \rightarrow CO_2 + H \qquad (1)$$

has been determined using mixtures of nitric acid (HNO_3), carbon monoxide (CO), and argon in incident shock wave experiments. Upon shock heating, the nitric acid rapidly decomposes into OH and NO_2. The OH subsequently reacts predominantly via reaction (1). Quantitative OH time histories were obtained by continuous-wave (cw) narrow-linewidth UV laser absorption of the $R_1(5)$ line of the $A^2\Sigma^+ \leftarrow X^2\Pi_i$ (0,0) transition at 32,606.56 cm^{-1} (vacuum). In some experiments, helium was added to the reactant mixture to examine CO vibrational excitation effects on the rate coefficient determination. It was found that the rate of excited CO ($v = 1$) with OH is less than the rate of ground-state CO ($v = 0$) with OH, which is in agreement with previous state-dependent work. The experiments were conducted over the temperature range 1090–2370 K and the pressure range 0.19–0.82 atm. The second-order rate coefficient was determined to be

$$k_1(T) = 2.12 \times 10^{12} \exp[-2630/T\ (K)]\ (cm^3\ mol^{-1}\ s^{-1})$$

with overall uncertainties of +16, −12% at high temperatures and +19, −22% at low temperatures. These results are in good agreement with recent studies of reaction (1) and are well fit by a chemically activated intermediate model. The current work also provides a link to previous low-temperature data.

Introduction

The reaction

$$CO + OH \rightarrow CO_2 + H \qquad (1)$$

is important in both combustion processes and pollutant formation [1,2]. This reaction is the principal heat-releasing reaction in hydrocarbon combustion and is the primary channel for conversion of CO into CO_2. Warnatz [2] has identified CO + OH as a reaction "with both considerable sensitivity and uncertainty" with respect to gas-phase combustion. His investigation concludes that NO formation in propane-air flames and flame velocities in methane-, propane-, and benzene-air flames all show significant sensitivity to reaction (1).

The CO + OH reaction has been studied extensively through both experimental and theoretical investigations. The rate coefficient displays significant non-Arrhenius behavior over the temperature regime of 298–3000 K. Although room-temperature evaluations appear to be in agreement [3], there is a significant degree of scatter in the data at higher temperatures.

The present investigation was conducted for several important reasons. First, the OH radical generation technique employed allows for a direct determination of the rate coefficient for reaction (1) at high temperatures. Second, the technique results in a reduction in the scatter of the high-temperature data, which improves the accuracy of the rate coefficient determination. Finally, this work provides a link to the flow reactor results that exist at lower and intermediate temperatures.

Nitric acid (HNO_3) is used as a source of hydroxyl radicals. The nitric acid decomposes virtually instantaneously (<1.5 μs at 1500 K) into OH and NO_2. When mixtures of nitric acid dilute in carbon monoxide are used, the OH radical reacts predominantly with CO via reaction (1). Consequently, absorption profiles of the OH radical can be used to directly determine the rate coefficient for reaction (1).

Experimental Details

All experiments were conducted behind incident shock waves using either of two stainless steel, pressure-driven shock tube facilities. The first shock tube consists of a 2.3-m-long driver section and a 10.5-m-long driven section, with a 15.24-cm continuous in-

ternal diameter. The second shock tube consists of a 6-m-long driven section (14.3-cm internal diameter) and a 2.4-m driver section (5-cm internal diameter). Prior to each experiment, the driven section was evacuated to approximately 5×10^{-6} torr; the subsequent leak-plus-outgassing rate was approximately 20×10^{-6} torr/min. Shock speeds were measured using four platinum thin-film gauges equipped with amplifiers that triggered three time-interval counters. Shock wave attenuation was typically 0.5–2% per meter. All postshock conditions were calculated using one-dimensional shock wave relations, assuming a chemically and vibrationally frozen test gas. The calculation inputs were the initial test gas temperature, pressure, and composition, and the shock speed at the measurement position. Helium was used as the driver gas for all experiments.

The gases employed for reactant mixtures were Matheson Purity argon (99.9995%), Liquid Carbonic CP grade carbon monoxide (99.5%), and Liquid Carbonic ultrahigh purity (99.999%) helium. The nitric acid was purchased in 90% aqueous solution and subsequently dehydrated using the technique described by Wooldridge et al. [4]. All test gas mixtures were prepared using a partial pressure technique in a 2.3-L Teflon-coated mixing tank with a magnetic stirrer. A passivation process, also described in Ref. 4, was used to control wall-adsorption effects in the shock tube.

The diagnostic system consisted of a Spectra-Physics 380A continuous-wave (cw) ring dye laser operated on Rhodamine 590 laser dye and pumped by a Spectra-Physics 164 argon ion laser (4 W, all lines visible). The visible wavelength output of the ring dye laser cavity was monitored by a Burleigh WA-10 wave meter, and the laser mode quality was monitored by a Spectra-Physics 470 scanning interferometer (2-GHz free spectral range). The fundamental laser frequency was intracavity doubled to the UV by a temperature-controlled AD*A crystal, and the laser was operated with the galvo tuning rhomb assembly in place. Wavelength control was improved by conducting a manual scan across the absorption line shape in a reference flame of methane and air. The wavelength was centered at the peak absorption of the $R_1(5)$ line prior to each experiment. The UV beam (approximately 1.0-mm diameter) passed through the shock tube perpendicular to the shock tube axis through calcium fluoride windows. The beam intensity was measured before and after passing through the shock tube via fast UV photodiode detectors (EG&G UV100BQ, electronic 3-dB bandwidth of 350 kHz) with 2.5-mm-diameter active surface areas. The incident (I_o) and differenced ($I_o - I$) laser intensities were recorded on a Nicolet 2090 digital oscilloscope using a 0.2-μs sampling rate. The noise on the differenced signal was typically 0.1% of the incident signal, corresponding to a detectivity limit of approximately 1 ppm at $T = 1400$ K, $P = 0.3$ atm, and a path length of 15.24 cm.

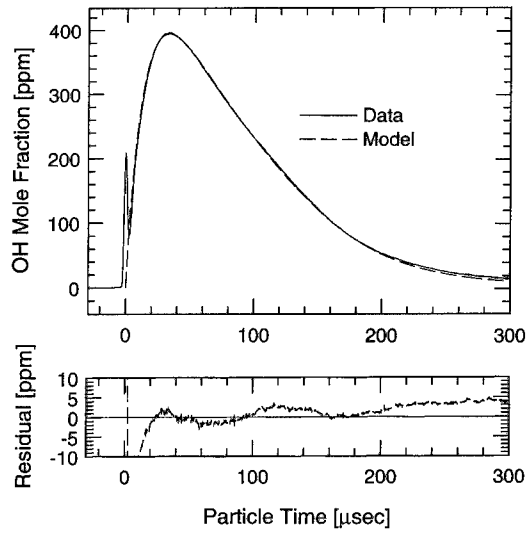

FIG. 1. Comparison of experimental and calculated Chemkin II OH profiles using best-fit $k_1 = 2.41 \times 10^{11}$ cm^3 mol^{-1} s^{-1}, CO = 1.41%, and HNO_3^o = 607 ppm (incident shock, $T = 1273$ K, $P = 0.486$ atm). The spike in the absorption trace at $t = 0$ is due to beam steering of the laser beam by the incident shock wave.

Results

Figure 1 shows a typical low-temperature OH mole fraction profile. The experimental conditions of this trace are $T = 1273$ K, $P = 0.486$ atm, CO = 1.41%, and HNO_3^o = 607 ppm, where HNO_3^o is the initial concentration of nitric acid in the shock tube at the time of the experiment. The absorption data were converted to mole fraction data by applying Beer's law for a narrow-line radiation source, as follows:

$$I/I_o = \exp(-k_\nu P \chi_{OH} L).$$

Here, I and I_o are the transmitted and incident radiation intensities, respectively, k_ν is the spectral absorption coefficient (cm^{-1} atm^{-1}), P is the total pressure (atm), χ_{OH} is the mole fraction of OH, and L is the path length through the absorbing medium (cm). The absorption coefficient was calculated using the technique described in Wooldridge et al. [4]. The uncertainty in k_ν for the conditions of this investigation is $\pm 5\%$, set primarily by uncertainty in the oscillator strength for this transition.

The mole fraction data were converted from laboratory time (t_l) to particle time (t_p) using the relation $t_p = (\rho_2/\rho_1)\, t_l$, where ρ_1 is the initial density of the

TABLE 1
Reaction mechanism: rate coefficients in the form $k = AT^{\beta} \exp(-\theta/T)$ (units are mol, cc, s, and K)

Reaction	A	β	θ	Ref.
⇒ 1. $CO + OH = CO_2 + H$	2.12×10^{12}	0.0	2630.	[a]
⇒ 2. $HNO_3 + M = OH + NO_2 + M$	1.01×10^{16}	0.0	17280.	8
⇒ 3. $OH + OH = H_2O + O$	9.40×10^{-5}	4.77	−4570.	4
⇒ 4. $NO_2 + H = NO + OH$	1.00×10^{14}	0.0	0.	[b]
5. $H + HO_2 = OH + OH$	1.40×10^{14}	0.0	540.	18
6. $HO_2 + NO = NO_2 + OH$	2.11×10^{12}	0.0	−241.	18
7. $H_2 + O = OH + H$	5.06×10^{4}	2.67	3166.	18
8. $OH + H_2 = H_2O + H$	1.17×10^{9}	1.3	1825.	18
9. $NO_2 + M = NO + O + M$	1.10×10^{16}	0.0	33000.	19
10. $NO_2 + O = NO + O_2$	1.00×10^{13}	0.0	300.	19
11. $O + HO_2 = O_2 + OH$	1.40×10^{13}	0.0	540.	18
12. $OH + HO_2 = H_2O + O_2$	7.50×10^{12}	0.0	0.	18
13. $H + O_2 = OH + O$	9.33×10^{13}	0.0	7448.	20
14. $H_2 + O_2 = H + HO_2$	3.30×10^{13}	0.0	27126.	21
15. $H + H + M = H_2 + M$	1.00×10^{18}	−1.0	0.	18
16. $H + O_2 + M = HO_2 + M$	3.61×10^{17}	−0.72	0.	18
Enhanced efficiency for $H_2O \times 18.6$, $CO_2 \times 4.2$, $H_2 \times 2.9$, $CO \times 2.1$				
17. $CO(v = 0) + Ar = CO(v = 1) + Ar$	5.13×10^{12}	1.0	−213	[c]
18. $CO(v = 0) + He = CO(v = 1) + He$	6.25×10^{10}	1.0	−99	[c]
19. $CO(v = 0) + CO(v = 1) = CO(v = 1) + CO(v = 1)$	1.32×10^{12}	1.0	−175	[c]
20. $CO(v = 0) + CO(v = 0) = CO(v = 1) + CO(v = 0)$	1.32×10^{12}	1.0	−175	[c]

⇒, reactions important in this study.
[a]This work.
[b]Estimate from NIST Chemical Kinetics Data Base, 1993.
[c]Rate coefficients of the form $k = AT^{\beta} \exp(+\theta/T^{1/3})$, used only for high-temperature data reduction. See text for details.

test gas mixture and ρ_2 is the density of the test gas mixture behind the incident shock wave.

The data were analyzed using the Chemkin-II [5] chemical kinetics simulation package, the Chemkin thermodynamic database [6], the Senkin [7] modeling package, and the reaction mechanism shown in Table 1. This 20-reaction mechanism was developed from a more comprehensive 117-reaction model using sensitivity analysis to eliminate reactions that were unimportant for the conditions of the present study.

The low-temperature OH profiles ($T < 1500$ K) were analyzed as follows. First, the peak of the data trace was fit by adjusting the initial amount of HNO_3 present. If necessary, the rate of the HNO_3 decomposition reaction, (2), was then adjusted to fit the initial rise in the OH profile (but never outside the uncertainty limits quoted in Wooldridge et al. [8]). The latter portion of the profile was then fit by adjusting the rate coefficient of reaction (1). The determination of the best fit to the experimental profile was aided by the sensitivity analysis shown in Fig. 2 for the conditions of Fig. 1, and by the residual trace shown at the bottom of Fig. 1. The residual was generated by subtracting the calculated profile from the experimental data trace. The sensitivity analysis was used to determine the region of the OH profile where the influence of reaction (1) was dominant. The optimum fit parameters were determined by matching the slope of the decaying OH profile and minimizing the residuals in this region. Equal weighting was given to each of these characteristics. Figure 2 shows that the CO + OH reaction is dominant for times after approximately 100 μs.

For the high-temperature data ($T > 1500$ K), it was necessary to account for the vibrational relaxation of the carbon monoxide in the data analysis. These data were reduced using the additional relaxation reactions [9] shown at the bottom of Table 1, which are expressed in a Landau–Teller format. In addition, reaction (1) is modeled as a pair of vibration-level-dependent reactions

$$CO(v = 0) + OH \rightarrow CO_2 + H \qquad (1a)$$

$$CO(v = 1) + OH \rightarrow CO_2 + H. \qquad (1b)$$

The thermal rate coefficient for reaction (1) was de-

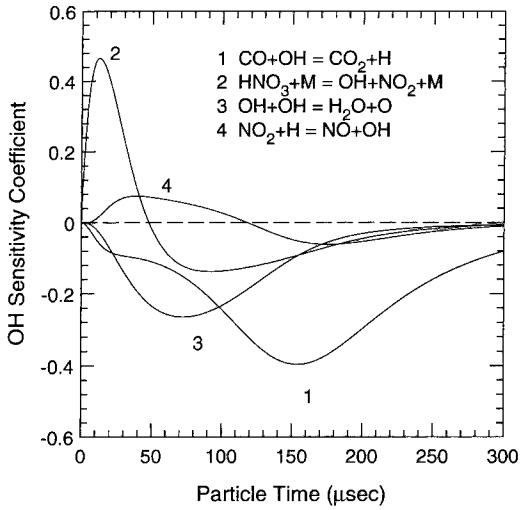

FIG. 2. OH sensitivity plot for conditions of Fig. 1. The sensitivity coefficient α_{ij} is defined as the partial derivative of the species mole fraction χ_j with respect to the rate constant parameter A_i, normalized by the maximum species mole fraction χ_j^{max} and the rate constant parameter A_i: $\alpha_{ij} = (A_i/\chi_j^{max})(\partial\chi_j/\partial A_i)$.

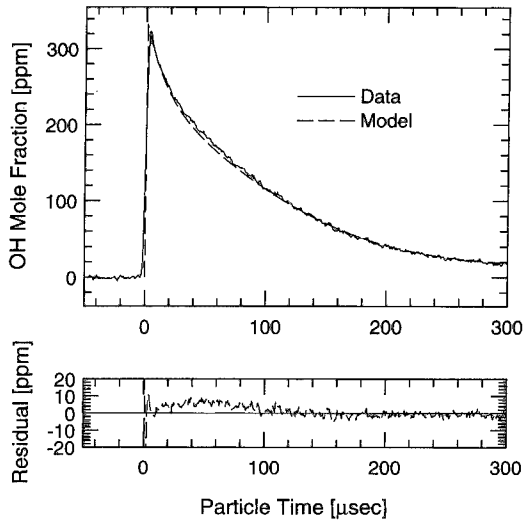

FIG. 3. Comparison of experimental and calculated Chemkin II OH profiles using best-fit $k_1 = 6.53 \times 10^{11}$ cm^3 mol^{-1} s^{-1}, CO = 2.01%, He = 5.02%, and HNO_3^o = 338 ppm (incident shock, T = 2262 K, P = 0.199 atm).

termined using the Boltzmann-weighted sum of the rate coefficients:

$$k_1(T) = f_{v=0}\, k_{1a}(T) + f_{v=1}\, k_{1b}(T)$$

where

$$f_{v=i} = \exp(-E_{v=i}/RT))/Q_{vib}$$

is the fractional population of the ith state, Q_{vib} is the vibrational partition function, $E_{v=i}$ is the energy of the ith vibrational level, and $T = T_{vibrational} = T_{equilibrium}$. During the time frame of a high-temperature experiment, the CO was not vibrationally equilibrated, and the populations of the vibrational states were changing. We define the effective rate coefficient as follows:

$$k_1^{eff}(T) = f_{v=0}(t)k_{1a}(T) + f_{v=1}(t)k_{1b}(T)$$

where the population fractions are approaching the thermal distribution as defined above.

The rate coefficient for reaction (1b) was set as 0.5 times that of reaction (1a), in accordance with the investigation by Dreier and Wolfrum [10], although this parameter was varied to determine its effect on $k_1(T)$ (see below).

Accounting for vibrational relaxation of CO is not necessary for temperatures below 1500 K, as at these temperatures, the equilibrium population of CO in the ground vibrational level is greater than 87%. For the low-temperature data, $k_1(T) \cong k_{1a}(T)$.

Vibrational relaxation of OH is less than 2 μs throughout the temperature range of this study (Zuhrt et al. [11]). In addition, less than 10% of the OH is in the excited state (v = 1) even at the highest temperatures investigated. Consequently, the OH was treated as vibrationally equilibrated in the data analysis.

Figure 3 shows a typical high-temperature OH mole fraction profile. The OH is formed nearly instantaneously (<0.5 μs) and subsequently decays as the hydroxyl radical reacts primarily via reactions (1a) and (1b). The experimental conditions corresponding to Fig. 3 are T = 2262 K, P = 0.199 atm, He = 5.02%, CO = 2.01%, and HNO_3^o = 338 ppm. The best fit of the high-temperature data was determined by adjusting the rate coefficient of reaction (1a), with $k_{1b}(T)/k_{1a}(T) = 0.5$, and the initial amount of HNO_3 present in the model. As with the low-temperature data, the sensitivity analysis and the residual were used to determine the optimum fit parameters. Figure 4 shows the OH sensitivity analysis for the conditions of Fig. 3 and indicates that reaction (1a) is the dominant reaction affecting the OH profile after approximately 100 μs.

Figure 5 shows the evolution of the calculated $k_1^{eff}(T)$ over time for the conditions of Figure 3. The CO is modeled as starting entirely in the ground vibrational level (v = 0); hence, $k_1^{eff}(T)$ starts at $k_{1a}(T)$. As the v = 1 state is populated, $k_1^{eff}(T)$ approaches the thermal rate coefficient $k_1(T)$. Only the thermal rate coefficient is reported for the high-temperature data.

Additional experiments were conducted with he-

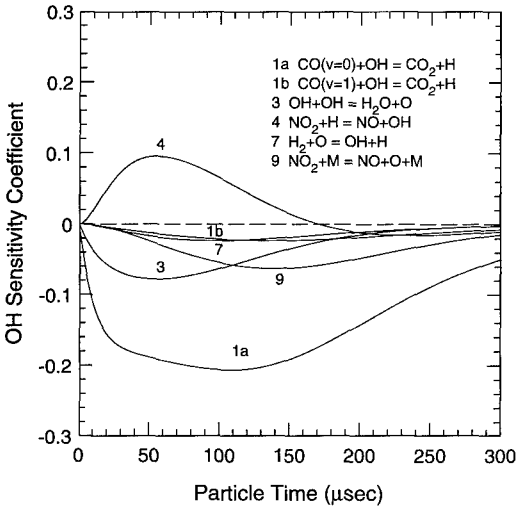

FIG. 4. OH sensitivity plot for conditions of Fig. 3. Reactions (1a) and (1b) are described in greater detail in the text.

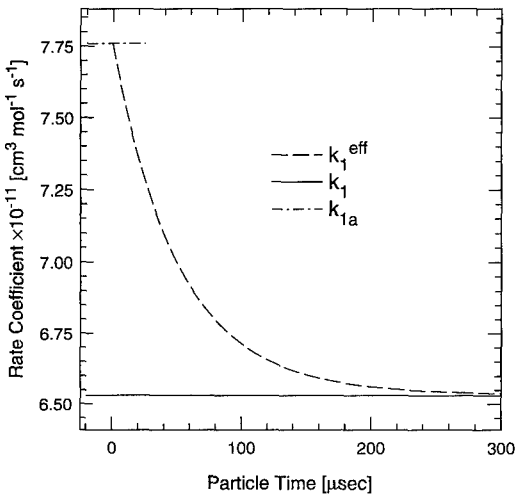

FIG. 5. The evolution of the calculated k_1^{eff} over time, approaching the equilibrium value of k_1 (for the conditions of Fig. 3).

lium included in the test gas mixture, in order to further establish the role of CO vibrational relaxation in reaction (1). When these experiments were analyzed without considering vibrational relaxation, the results were systematically about 15% lower than the rate coefficients determined from the experiments that did not include helium. This observation is consistent with the results of Dreier and Wolfrum that the rate of excited CO with OH is less than the rate of ground state CO with OH. The helium data were subsequently analyzed in the manner described above, incorporating the relaxation model for CO. The experiments did not show sufficient sensitivity to $k_{1b}(T)/k_{1a}(T)$ to enable a more accurate determination of this ratio.

Table 2 summarizes the shock conditions and the resulting values determined for k_1. The data span a temperature range of 1090–2370 K and a pressure range of 0.19–0.82 atm. There is no measurable pressure dependence within the statistical scatter of the data. The data are plotted in Fig. 6 and fit by the following expression [of the form $A \exp(-\theta/T)$] for the rate coefficient of the bimolecular reaction:

$$k_1(T) = 2.12 \times 10^{12} \cdot \exp[-2630/T(\mathrm{K})](\mathrm{cm}^3\ \mathrm{mol}^{-1}\ \mathrm{s}^{-1}).$$

The standard deviation for this expression is 9%.

The total uncertainty in the rate coefficient of reaction (1) for the temperature extremes is determined by combining the effects of each of the independent sources of uncertainty through the relation

$$\text{total uncertainty} = [\Sigma(\text{uncertainty})^2]^{1/2}.$$

Table 3 summarizes the results of the uncertainty analysis for k_1.

At high temperatures, the dominant sources of uncertainty are the ratio k_{1b}/k_{1a} and the combined effect of the uncertainties in the rate coefficients for reactions (2) through (4), leading to an overall uncertainty of +16%, −12%. At temperatures greater than ~2000 K, the uncertainty in the decomposition rate of NO_2, reaction (9), does affect the CO + OH rate determination. A ± 25% uncertainty in the rate coefficient for reaction (9) leads to a ±5% uncertainty in k_1. The effect of uncertainty in the vibrational relaxation rate coefficients, reactions (17) through (20), on the k_1 determination was also investigated and found to be negligible. At low temperatures, the dominant source of uncertainty is the combined effect of the uncertainties in rate coefficients for reactions (2) through (4), leading to an overall uncertainty of +19%, −22%. The uncertainty in shock speed measurement, boundary layer effects, and uncertainty in other rate coefficients were found to have negligible impact on the determination for $k_1(T)$ throughout the temperature range.

Discussion

Figure 6 shows the rate coefficients determined in the present work and from other high-temperature studies of k_1. The current data are in good agreement with the recent shock tube study of Yu et al. [12] and with the high-temperature flame data of Vandooren

TABLE 2
Experimental conditions and results

T (K)	P (atm)	k_1 ($cm^3\ mol^{-1}\ s^{-1}$)	HNO_3^o (ppm)	CO (%)	He (%)
1086	0.248	1.76×10^{11}	659	1.98	
1136	0.310	1.91×10^{11}	838	2.00	
1147	0.421	2.17×10^{11}	666	1.95	
1157	0.428	2.06×10^{11}	750	2.52	
1184	0.434	1.94×10^{11}	900	2.00	
1245	0.467	3.05×10^{11}	187	2.00	
1259	0.364	2.62×10^{11}	220	2.00	
1265	0.478	2.60×10^{11}	945	2.00	
1273	0.486	2.41×10^{11}	607	1.41	
1278	0.192	2.92×10^{11}	393	2.19	
1282	0.185	2.50×10^{11}	503	2.05	
1292	0.425	2.84×10^{11}	29	1.95	
1318	0.436	3.48×10^{11}	185	2.00	
1319	0.473	3.34×10^{11}	250	2.00	
1320	0.506	2.61×10^{11}	867	2.00	5.11
1324	0.428	3.23×10^{11}	146	2.12	
1352	0.410	3.12×10^{11}	51	1.94	
1357	0.196	2.82×10^{11}	990	2.13	
1370	0.200	2.96×10^{11}	174	2.16	
1382	0.309	3.26×10^{11}	410	2.35	
1476	0.462	3.18×10^{11}	198	2.00	
1479	0.434	3.42×10^{11}	183	1.99	9.98
1490	0.435	3.89×10^{11}	90	2.00	
1504	0.370	4.31×10^{11}	169	2.00	
1611	0.338	4.59×10^{11}	212	1.04	
1714	0.308	5.03×10^{11}	209	1.00	
1748	0.382	4.09×10^{11}	192	2.00	
1783	0.239	5.21×10^{11}	260	1.00	
1812	0.287	5.36×10^{11}	214	1.00	
1816	0.292	5.29×10^{11}	720	1.97	
1875	0.763	4.85×10^{11}	493	2.31	
1929	0.307	5.10×10^{11}	857	1.90	
1957	0.815	5.26×10^{11}	325	1.09	
1988	0.256	6.20×10^{11}	276	1.00	
2124	0.230	6.38×10^{11}	315	2.01	
2144	0.262	5.82×10^{11}	524	1.99	5.08
2227	0.221	6.23×10^{11}	335	2.00	
2236	0.239	6.76×10^{11}	404	2.00	4.99
2262	0.199	6.53×10^{11}	338	2.01	5.02
2292	0.217	6.70×10^{11}	273	2.26	10.0
2318	0.205	6.86×10^{11}	792	2.09	10.0
2319	0.248	6.38×10^{11}	218	2.00	4.99
2343	0.200	6.96×10^{11}	285	2.02	
2365	0.245	6.28×10^{11}	260	2.02	

et al. [13]. The data of Ravishankara and Thompson [14] end just below the lowest-temperature data from this investigation, but the two works agree within their respective uncertainties. Figure 6 also includes for comparison the recommended rate expression for reaction (1) given by Baulch et al. [3], which lies above the data for temperatures in the range 400–1400 K.

Figure 7 is an Arrhenius diagram over an extended temperature regime, showing the current work along with some other investigations of k_1. It is well known that reaction (1) exhibits a pressure dependence be-

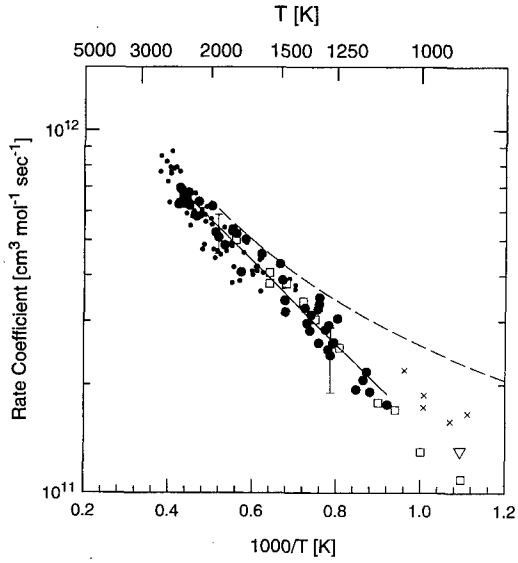

FIG. 6. Arrhenius plot of rate coefficients for reaction (1), CO + OH → CO_2 + H, determined from the present experiments. Also shown are results from other recent determinations of k_1. The solid line is a fit to the present work, where $k_1 = 2.12 \times 10^{12} \exp(-2630/T\ [\mathrm{K}])$ ($cm^3\ mol^{-1}\ s^{-1}$). The dashed line is the recommendation by Baulch et al. [3]. The vertical error bars are the overall uncertainties determined for the present work (see Table 3). The symbols denote the following works: ●, current work; •, Yu et al. [12]; □, Vandooren et al. [13]; △, Westenberg and deHaas [17]; ×, Ravishankara and Thompson [14].

low temperatures of approximately 1000 K [15]. Larson et al. [15] used a chemically activated intermediate model to describe reaction (1). They concluded that CO + OH → CO_2 + H can be modeled using the following system of elementary reactions:

$$\mathrm{CO + OH \Leftrightarrow HOCO}$$
$$\mathrm{HOCO \Leftrightarrow H + CO_2}$$
$$\mathrm{CO + OH \Rightarrow H + CO_2.}$$

Their results for $P = 100$ torr are shown in Fig. 7 as the dot-dashed line. The calculated rate coefficient falls below the results from the present study and the results from Yu et al. for temperatures above 1200 K.

Frenklach and Gardiner [16] used this same approach for their theoretical study of reaction (1). Their findings for $P = 100$ torr are shown in Fig. 7 as the solid line. The results by Frenklach and Gardiner are in good agreement with the current work and with the results of Ravishankara and Thompson.

Conclusions

The rate coefficient for CO + OH → CO_2 + H has been measured via narrow-linewidth UV laser absorption of OH. A fit to the data yields the following expression valid in the temperature range 1090–2370 K:

TABLE 3
Uncertainty analysis for reaction (1): CO + OH → CO_2 + H

Parameter	Uncertainty	Effect on k_1	
Dominant sources of uncertainty at high temperatures ($T > 1500$ K):			
OH abs. coeff. (%)	+5	+4.3	
	−5		−1.8
k_2, k_3, and k_4 (%)	+20, +11, + 40		−9.8
	−20, −16, −40	+9.6	
k_{1b}/k_{1a} (%)	1	+11	
	0.25		−3.0
k_9 (%)	+25	+5	
	−25		−5.0
Total uncertainty = $[\Sigma(\text{uncert.})^2]^{0.5}$ (%):		+16	−12
Dominant sources of uncertainty at low temperatures ($T < 1500$ K):			
OH abs. coeff. (%)	+5	+1	
	−5		−5
k_2, k_3, and k_4 (%)	+20, +25, +40		−21
	−20, −23, −40	+19	
Total uncertainty = $[\Sigma(\text{uncert.})^2]^{0.5}$ (%):		+19	−22

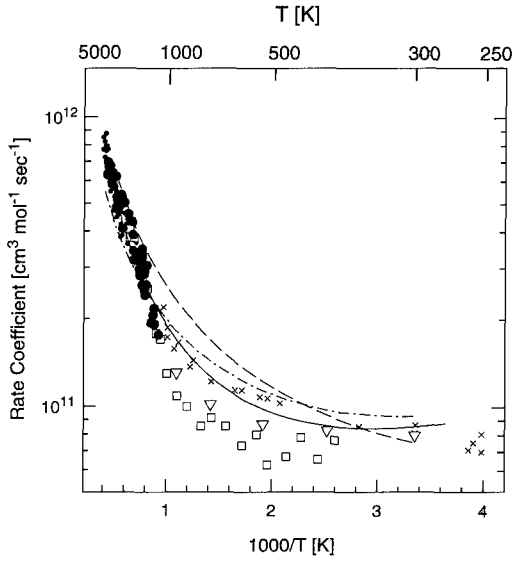

FIG. 7. Arrhenius plot of rate coefficients for reaction (1), CO + OH → CO_2 + H, over an extended temperature range. Also shown are results from other recent determinations of k_1. The dashed line is the recommendation by Baulch et al. [3]. The solid line is the theoretical prediction by Frenklach and Gardiner [16] for a pressure of 100 torr. The dot-dashed line is the theoretical prediction by Larson et al. [15] for a pressure of 100 torr. The symbols denote the following works: ●, current work; •, Yu et al. [12]; □, Vandooren et al. [13]; △, Westenberg and deHaas [17]; ×, Ravishankara and Thompson [14].

$$k_1(T) = 2.12 \times 10^{12} \cdot \exp[-2630/T\ (\mathrm{K})](\mathrm{cm}^3\ \mathrm{mol}^{-1}\ \mathrm{s}^{-1})$$

with an overall uncertainty ranging from +16%, −12% at high temperatures to +19%, −22% at low temperatures.

This study agrees well with the high-temperature investigation by Yu et al. and also provides a link to intermediate-temperature studies. In addition, this investigation confirms the conclusion of Dreier and Wolfrum that vibrational excitation of CO reduces the rate of reaction (1).

Acknowledgments

This work was supported by the U.S. Department of Energy, Office of Basic Energy Sciences. We would like to thank Sam Rea, Steven T. Wooldridge, and David F. Davidson for helpful comments and their assistance in the laboratory.

REFERENCES

1. Berry, R. S., and Lehman, P. A., *Annu. Rev. Phys. Chem.* 22:47–84 (1971).
2. Warnatz, J., *Twenty-Fourth Symposium (International) on Combustion,* The Combustion Institute, Pittsburgh, 1992, pp. 553–579.
3. Baulch, D. L., Cobos, C. J., Cox, R. A., Esser, C., Frank, P., Just, Th., Kerr, J. A., Pilling, M. J., Troe, J., Walker, R. W., and Warnatz, J., *J. Phys. Chem. Ref. Data* 21:566–569 (1992).
4. Wooldridge, M. S., Hanson, R. K., and Bowman, C. T., *Int. J. Chem. Kinet.* 26:389–401 (1994).
5. Kee, R. J., Rupley, F. M., and Miller, J. A., *Chemkin-II: A FORTRAN Chemical Kinetics Package for the Analysis of Gas-Phase Chemical Kinetics,* Sandia National Laboratories Report No. SAND89–8009, 1989.
6. Kee, R. J., Rupley, F. M., and Miller, J. A., *The Chemkin Thermodynamic Data Base,* Sandia National Laboratories Report No. SAND87-8215B, 1990.
7. Lutz, A. E., Kee, R. J., and Miller, J. A., *SENKIN: A FORTRAN Program for Predicting Homogeneous Gas Phase Chemical Kinetics with Sensitivity Analysis,* Sandia National Laboratories Report No. SAND87-8248, 1988.
8. Wooldridge, M. S., Hanson, R. K., and Bowman, C. T., *Nineteenth International Symposium on Shock Waves,* Springer-Verlag, Heidelberg, 1994, in press.
9. Millikan, R. C., and White, D. R., *J. Chem. Phys.* 39:3209–3213 (1963).
10. Dreier, T., and Wolfrum, J., *Eighteenth Symposium (International) on Combustion,* The Combustion Institute, Pittsburgh, 1981, pp. 801–809.
11. Zuhrt, Ch., Zülicke, L., and Umansky, S. Ya., *Chem. Phys.* 105:15–26 (1986).
12. Yu, C. L., Wang, C., and Frenklach, M., Eastern States Section/Combustion Institute Meeting, 1990.
13. Vandooren, J., Peeters, J., and Van Tiggelen, P. J., *Fifteenth Symposium (International) on Combustion,* The Combustion Institute, Pittsburgh, 1974, pp. 745–753.
14. Ravishankara, A. R., and Thompson, R. L., *Chem. Phys. Lett.* 99:377–381 (1983).
15. Larson, C. W., Stewart, P. H., and Golden, D. M., *Int. J. Chem. Kinet.* 20:27–40 (1988).
16. Frenklach, M., and Gardiner, W. C., Jr., *Basic Research on Natural Gas Combustion Phenomena,* GRI Report No. GRI-93/0351, 1993.
17. Westenberg, A. A., and deHaas, N., *J. Chem. Phys.* 58:4061–4065 (1973).
18. Miller, J. A., and Bowman, C. T., *Prog. Energy Combust. Sci.* 15:287–338 (1989).
19. Hanson, R. K., and Salimian, S., in *Combustion Chemistry* (W. C. Gardiner, Jr., Ed.) Springer-Verlag, New York, 1984, pp. 361–421.
20. Masten, D. A., Hanson R. K., and Bowman, C. T., *J. Phys. Chem.* 94:7119–7128 (1990).
21. Masten, D. A., *A Shock Tube Study of Reactions in the H_2/O_2 Mechanism,* Stanford University HTGL Report No. T-269, 1990.

Twenty-Fifth Symposium (International) on Combustion/The Combustion Institute, 1994/pp. 749–757

THE USE OF CARBON MONOXIDE/HYDROGEN BURNING VELOCITIES TO EXAMINE THE RATE OF THE CO + OH REACTION

IAN C. MCLEAN, DAVID B. SMITH AND SIMON C. TAYLOR
British Gas plc
Gas Research Centre
Ashby Road, Loughborough LE11 3QU, UK

New measurements of burning velocity are reported for selected CO/H_2 mixtures in air, to provide data for examining the rate of the CO + OH reaction. Burning velocities were obtained from measurements on constant-pressure expanding spherical flames. Flame speeds over the first 35 mm of travel were measured by high-speed schlieren cine photography and extrapolated to infinite radius, using a simple phenomenological model, to yield one-dimensional (1D) values. Extensive computational testing shows that the burning velocities obtained are accurate to within 3%. Experimental burning velocities were then compared with 1D computed values, obtained using full kinetics.

Fuel mixtures of 95% CO + 5% H_2 and 50% CO + 50% H_2 with air were studied across the stoichiometric range, along with stoichiometric mixtures with varying H_2/CO ratio. The 95 + 5% mixture was the prime object of study, since computation revealed that burning velocities for this mixture had the greatest sensitivity to the CO + OH reaction. For the 95 + 5% mixture, the maximum burning velocity was 0.65 $\pm$ 0.02 m s^{-1} at 51.7% fuel; the stoichiometric value was 0.34 m s^{-1}. For the 50 + 50% mixture, the corresponding velocities were 1.82 $\pm$ 0.06 (at 47.2% fuel) and 1.20 m s^{-1}.

Computed 1D burning velocities agreed well with experiment when the 1976 recommendation of Baulch et al. for the rate of the CO + OH reaction was used. A more recent recommendation gave values more than 20% too high. Further computation revealed that the reaction exerts its influence on the burning velocity of these flames at low temperatures, in a relatively narrow region around 1165 K. Use of different (artificially derived) rate expressions, but having a common value at 1165 K, produced essentially the same burning velocities. Implications of this for flame chemistry are explored.

Introduction

Laminar burning velocities are widely used for validating kinetic models of flames. Although by no means a complete test, they do, nevertheless, constitute a rigorous partial test of any model. For most fuels, burning velocity is sensitive to relatively few reactions [1]; the validation will then focus on this subset of reactions.

Clearly, for such validation exercises to have merit, the experimental data on which they are based must be accurate. Unfortunately, this requirement has not always been met; burning velocity is notoriously hard to measure accurately. Recently, we introduced a new method for measuring burning velocities with greater accuracy [2] and demonstrated its application to hydrogen/air mixtures. The method measures the speeds of expanding spherical flames and extrapolates the data to infinite radius to remove stretch effects, thus recovering the one-dimensional (1D) burning velocity. A particular advantage of the method is the fact that the reliability of the underlying methodology can be tested by computer modelling.

In this paper, we extend the measurements to some carbon monoxide/hydrogen mixtures burning in air, with the prime aim of examining the crucial reaction $CO + OH \rightarrow CO_2 + H$. Despite the endeavours of many kineticists, uncertainty in the rate of the reaction remains large, especially at high temperatures. The recent evaluation [3] by a European panel of experts funded by the European Community (hereafter referred to as the CEC evaluation) concluded that the uncertainty was 60% at room temperature, rising to a factor of 3 at 2000 K. The evaluators' commentary is particularly pertinent: "The large scatter of the high temperature measurements does not allow exact assignment of a rate constant. Thus, a relatively high rate has been chosen *compatible with flame simulations* which are very sensitive to the rate of this reaction" (emphasis added). Since that evaluation, Warnatz [4] has suggested that the rate needs to be raised by a further 25%, again based largely on the needs of flame simulations.

In view of this uncertainty, and since carbon monoxide/hydrogen burning velocities are particularly sensitive to the rate of the CO + OH reaction, the provision of more reliable burning velocities for this

system seems highly desirable. The paper presents new experimental data and investigates their simulation by flame modelling. As described later, care was taken to select experiments that would provide the most sensitive test of this reaction.

Experimental

Flames were burned in a spherical bomb of 600-mm diameter, fitted with windows allowing visible access over the central 70-mm diameter of flame travel where the pressure rise is negligible. Flame propagation was recorded by high-speed (4000 frames per second) cine-photography of the schlieren image, with the camera speed calibrated by a 1-kHz timing signal. Mixtures were ignited by spark from centrally located electrodes with a spark gap of about 0.7 mm. The spark energy was adjusted to the minimum needed for ignition.

Gas mixtures were made up in the bomb by partial pressures, stirred for 20 min to ensure thorough mixing, then left for a further 10 min to allow them to come to rest. All mixtures were made up to atmospheric pressure (101.3 kPa) and 298.0 ± 0.5 K. Gases used (with purity shown in parentheses) were carbon monoxide (99.5%) with impurities O_2 (1000 ppm), N_2 (3000 ppm), CO_2 (800 ppm), and hydrocarbons (100 ppm); hydrogen (99.95%); and cleaned, filtered, compressed air.

Measurements were repeated at least once as standard practice. Practical limits on operation at both lean and rich mixtures were caused by the flames becoming buoyant. Close to these extremes, flame records, although marginally distorted by buoyancy, were deemed usable, but the resulting burning velocities will have slightly reduced accuracy.

The analysis of the film records yields flame speeds. In traditional constant-pressure bomb experiments, flame speed is assumed to be constant. A simple phenomenological analysis, details of which have been given previously [2], shows that there are two reasons why this is not strictly correct: flame stretch and density variation due to finite flame thickness. The analysis shows that the flame speed dr/dt varies with flame radius r according to

$$dr/dt = S_b^\circ/(1 + b/r) \qquad (1)$$

with dr/dt tending to the planar 1D value S_b° as r tends to infinity. The relaxation parameter b equals $k + l$, where k is the "density correction" term and l contains the Markstein length, representing the influence of stretch on burning velocity. Integrating Eq. (1) gives the final equation

$$r + b \ln r = S_b^\circ t + \text{constant}. \qquad (2)$$

This expression was fitted to the experimental data to derive values for b (used for determining Markstein lengths, and to be reported in a later paper) and S_b°. Finally, the conventional burning velocity S_u° is obtained by multiplying S_b° by the calculated density ratio ρ_b°/ρ_u where subscripts u and b refer to unburnt and burnt gas, respectively. This is a valid procedure since S_b° is a 1D value.

Modelling

Flame modelling was used for two purposes: to test the validity of the experimental method and to calculate burning velocities for comparison with experimental results.

For testing the experimental methodology, both planar 1D and expanding spherical flame computations were performed. The planar computations used the Sandia Laboratories' PREMIX program [5], slightly modified to ensure strict conservation of mass and energy. Expanding flames were modelled using a program developed at British Gas but derived from PREMIX and retaining its CHEMKIN and transport property routines [6,7]. For these computationally intensive tasks, mixture-averaged transport properties were used. The computations were initiated from a high-temperature (5000 K) central core, given by a Gaussian profile with a width of 1 mm or less. A very simple model of thermal radiation, based on that of Chen et al. [8] and including contributions from CO_2, H_2O, and CO, was incorporated into the model.

The planar flame computations used for calculating burning velocities for comparison with experiment were performed using the full multicomponent transport formulation. This usually led to higher burning velocities than when using mixture-averaged transport, though the differences never exceeded 5%.

The base kinetic scheme used in the computations is shown in Table 1. Rate data are taken from the recent CEC evaluation [3,9] where possible and from the earlier Warnatz review [10] otherwise. The rate of the CO + OH reaction was adjusted, as described later, to improve the performance of the model.

Results and Discussion

Targeting the Experiments:

In order to concentrate on the rate of the CO + OH reaction in the most effective manner, 1D flame computations were performed to determine those mixtures where the burning velocity was most sensitive to this reaction. The optimum fuel mixture was found to be 95% CO + 5% H_2. The pattern of major sensitivity coefficients for this mixture over the stoichiometric range is shown in Fig. 1. Although these data depend on the validity of the whole mechanism, the dependence is so weak that it would need a major

TABLE 1
Base reaction mechanism. Rate coefficients in form $k = AT^n \exp(-E/RT)$
(units of dm, mol, s, kJ)

No.	Reaction	A	n	E	Ref.
1.	$H + O_2 = OH + O$	3.49E + 13	−0.70	7.13E + 01	9a
2.	$O + H_2 = OH + H$	5.12E + 01	2.67	2.63E + 01	3
3.	$OH + H_2 = H_2O + H$	1.02E + 05	1.60	1.38E + 01	3
4.	$OH + OH = H_2O + O$	1.51E + 06	1.14	4.16E − 01	3
5.	$H + OH + M = H_2O + M$	2.21E + 16	−2.00	0.00E + 00	3
	Collision efficiencies:				
	N_2/1/ H_2O/6.4/				3
6.	$H + H + M = H_2 + M$	9.79E + 10	−0.60	0.00E + 00	3
	Collision efficiencies:				
	H_2/1/ O_2/0.4/ H_2O/6.5/ N_2/0.4/ Ar/0.35/ CO/0.75/ CO_2/1.5/				10
7.	$H + O_2 + M = HO_2 + M$	1.41E + 12	−0.80	0.00E + 00	3
	Collision efficiencies:				
	N_2/1/ H_2O/1.1/ H_2/1.5/				3
8.	$H_2O_2 + M = OH + OH + M$	1.20E + 14	0.00	1.90E + 02	3
9.	$H + H_2O_2 = H_2 + HO_2$	1.69E + 09	0.00	1.57E + 01	3
10.	$H + H_2O_2 = H_2O + OH$	1.02E + 10	0.00	1.50E + 01	3
11.	$O + H_2O_2 = OH + HO_2$	6.62E + 08	0.00	1.66E + 01	3
12.	$OH + H_2O_2 = H_2O + HO_2$	7.83E + 09	0.00	5.57E + 00	3
13.	$HO_2 + HO_2 = H_2O_2 + O_2$	4.22E + 11	0.00	5.01E + 01	9
14.	$H + HO_2 = OH + OH$	1.69E + 11	0.00	3.66E + 00	3
15.	$H + HO_2 = H_2 + O_2$	4.28E + 10	0.00	5.90E + 00	3
16.	$H + HO_2 = H_2O + O$	3.01E + 10	0.00	7.20E + 00	3
17.	$O + HO_2 = OH + O_2$	3.19E + 10	0.00	0.00E + 00	3
18.	$OH + HO_2 = H_2O + O_2$	2.89E + 10	0.00	−2.08E + 00	3
19.	$CO + OH = H + CO_2$	6.32E + 03	1.50	−2.08E + 00	3
20.	$CO + O + M = CO_2 + M$	5.30E + 10	0.00	−1.90E + 01	10
21.	$CO + O_2 = CO_2 + O$	2.53E + 09	0.00	2.00E + 02	10
22.	$CO + HO_2 = CO_2 + OH$	1.50E + 11	0.00	9.90E + 01	10
23.	$HCO + M = H + CO + M$	1.57E + 11	0.00	6.59E + 01	9
	Collision efficiencies:				
	Ar/1/ H_2/2.9/ O_2/1.1/ H_2O/18.6/ N_2/1.1/ CO/2.1/ CO_2/4.3/				10
24.	$HCO + O_2 = CO + HO_2$	3.01E + 09	0.00	0.00E + 00	3
25.	$HCO + H = CO + H_2$	9.03E + 10	0.00	0.00E + 00	3
26.	$HCO + OH = CO + H_2O$	1.02E + 11	0.00	0.00E + 00	3
27.	$HCO + O = CO + OH$	3.01E + 10	0.00	0.00E + 00	3
28.	$HCO + O = CO_2 + H$	3.01E + 10	0.00	0.00E + 00	3

departure from our current scheme to produce a significant change in the results. Except in very rich mixtures, the CO + OH coefficient is by far the largest. This mixture, therefore, formed the main thrust of the present experiments, but to augment the experimental database, further measurements were made on a 50% CO + 50% H_2 mixture across the stoichiometric range and on stoichiometric mixtures with varying H_2/CO ratio.

Test of Methodology:

As stated in the Introduction, the experimental methodology can be verified by computation. The first step is to check the applicability of the phenomenological model. From the expanding flame code, computed values of flame speed vs radius were obtained, as shown in Fig. 2. These computed data were then treated as if they were experimental by applying Eq. (2) to derive optimum values of b and S_b°. But in these computational cases, the true 1D burning velocities can be calculated from the 1D flame code, using the same kinetic scheme and transport properties. The two sets of S_b° values are compared in Table 2. Differences are within 5% and generally less than 3%, with the largest difference occurring in near-stoichiometric mixtures.

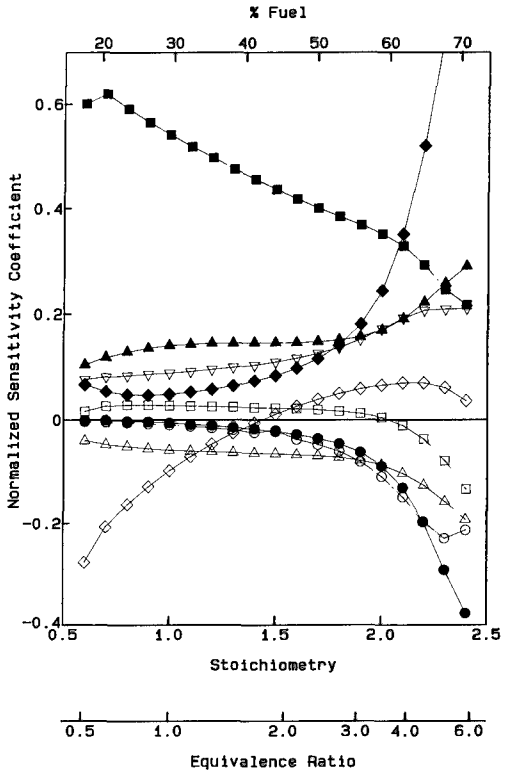

FIG. 1. Sensitivity coefficients vs stoichiometry for 95% CO + 5% H_2 mixture burning in air. ■ CO + OH; ◆ H + O_2; □ CO + O + M; △ H + HO_2 = H_2 + O_2; ▽ O + H_2; ◇ H + O_2 + M; ○ HCO + M; ● HCO + H; and ▲ H + HO_2 = OH + OH.

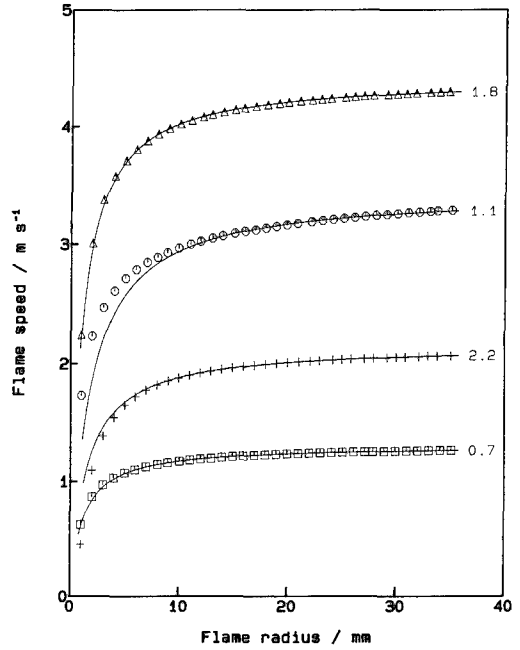

FIG. 2. Computed flame speeds vs radius for 95% CO + 5% H_2 mixture. Stoichiometry of fuel/air mixture listed by each curve. Symbols: detailed model. Lines: Eq. (1) using best fit to computed data.

These computations were performed on adiabatic flames. However, in practice, heat loss occurs by radiation from burnt gases behind the flame, reducing the flame speed. Therefore, the second step in validating the methodology is an assessment of the magnitude of this effect on the 1D flame speeds S_b^o derived by the application of Eq. (2). The results in Table 2 show that the effect was small in the fastest-burning flames but increased towards the lean and rich limits. The largest difference found was 5% in a lean mixture. We expect experimental data to be affected in a similar way.

By these computational checks, the methodology has been subjected to more rigorous testing than is possible for other methods of burning velocity measurement. The various components in the overall uncertainty of the experimental burning velocities have been estimated as follows: First, there is random uncertainty arising in the experimental runs, estimated to be ±1% over most of the stoichiometric range, and slightly higher near the extremes. Second, errors of −4.1 to +1.1% arise in the application of the phenomenological model. These appear to form a trend and, therefore, probably have a systematic basis. But since we do not yet understand them well enough to be confident of using them to correct the experimental data, we have treated them as random. We estimate the overall uncertainty (one standard deviation) in the reported burning velocities arising from these two effects to be ±3%.

Radiative losses are systematic, always causing an underestimate of burning velocity. The experimental burning velocities could be corrected for this error using the values shown in Table 2. But since these were derived using an approximate radiation model, we consider that this procedure is not warranted.

Measured Burning Velocities:

Burning velocities for the 95% CO + 5% H_2 and 50% CO + 50% H_2 mixtures are plotted in Fig. 3 as a function of stoichiometry, defined as mole fraction of fuel divided by mole fraction of fuel in a stoichiometric mixture. Equivalence ratio is also indicated. For the 95 + 5% mixtures, the maximum velocity is 0.65 ± 0.02 m s^{-1} at a stoichiometry of 1.75 (51.7% fuel); the stoichiometric value is 0.34 m s^{-1}. For the 50 + 50% mixture, the maximum is 1.82 ± 0.06 m s^{-1} at a stoichiometry of 1.6 (47.2% fuel), with a stoichiometric value of 1.20 ms^{-1}. Results for stoichio-

TABLE 2
Comparison of derived 1D flame speeds S_b° (m s^{-1}) with true planar values for modelled[a] flames using 95% CO + 5% H_2 as fuel

Stoichiometry	S_b° from planar 1D calc. (Col. A)	S_b° derived from expanding flame (Col. B)	% Difference (Col. B − Col. A)	S_b° derived from expanding flame with radiation (Col. C)	% Difference (Col. C − Col. B)
0.7	1.298	1.305	+0.5	1.243	−5.0
1.1	3.584	3.437	−4.1	3.295	−4.3
1.4	4.572	4.476	−2.1	4.325	−3.5
1.8	4.433	4.413	−0.4	4.412	−0.02
2.2	2.125	2.150	+1.1	2.097	−2.5

[a]All computations used base mechanism.

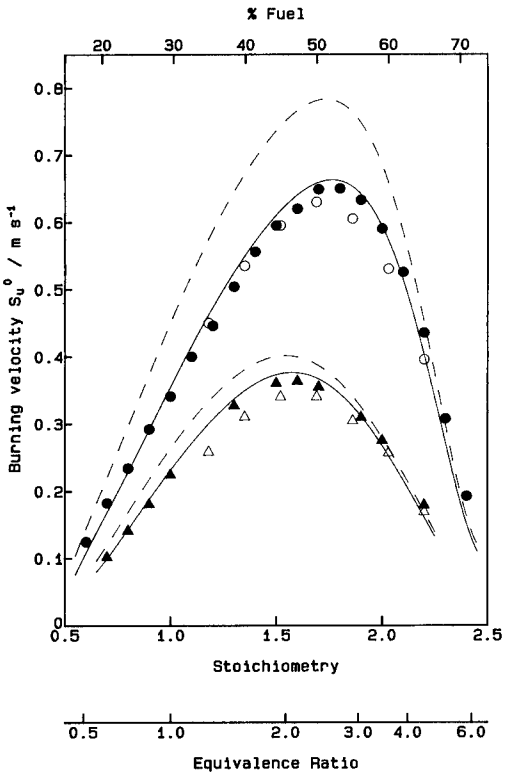

FIG. 3. Burning velocity of CO/H_2/air mixtures as a function of stoichiometry for two fuel compositions. Note that burning velocities for 50% CO + 50% H_2 mixtures are plotted at 1/5 scale (so burning velocity = 5× scale reading) in order to emphasize the more important 95% CO + 5% H_2 results. ● 95% CO + 5% H_2 mixtures, present experiments; ○ 95% CO + 5% H_2 mixtures, Scholte and Vaags data [11]; ▲ 50% CO + 50% H_2 mixtures, present experiments; △ 50% CO + 50% H_2 mixtures, Scholte and Vaags data [11]; ----- model, base mechanism; and —— model, Baulch rate for CO + OH.

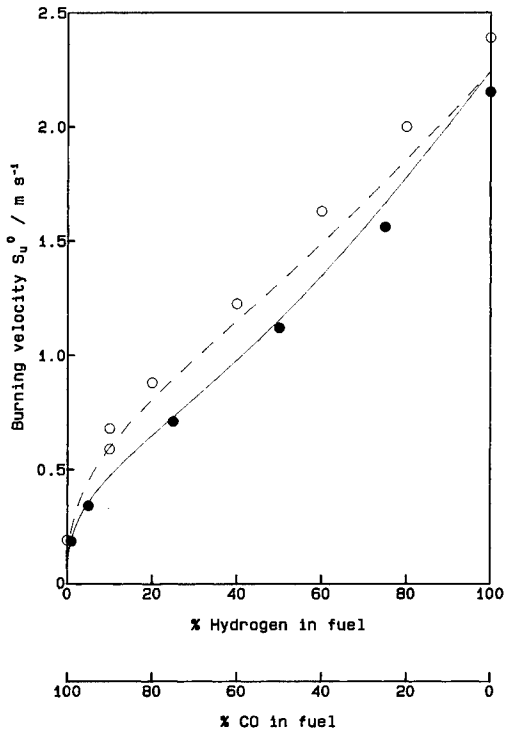

FIG. 4. Burning velocity as a function of CO/H_2 fuel composition for stoichiometric CO/H_2/air mixtures. ● Present experiments; ○ Günther and Janisch data [12]; ----- model, base mechanism; ——— model, Baulch rate for CO + OH.

metric mixtures with varying H_2/CO ratio are shown in Fig. 4.

The most widely quoted sets of data available in the literature are provided by the work of Scholte and Vaags [11] and Günther and Janisch [12]. Comparisons between the data of Scholte and Vaags and

our results are shown in Fig. 3. To make this comparison possible, velocities for the two mixtures were obtained by interpolation of the original Scholte and Vaags data; this leads to uncertainties of up to 0.02 m s^{-1} in the derived values. For the 95 + 5% case, the Scholte and Vaags values are in close agreement with our data up to the maximum velocity, but fall below ours in richer mixtures. For the 50 + 50% mixture, the agreement is not so good; Scholte and Vaags' data are consistently lower, with agreement worse in the leaner mixtures. We had previously found [2] fairly good agreement with Scholte and Vaags' data for hydrogen/air mixtures.

The data by Günther and Janisch [12] cover the case of stoichiometric mixtures with varying H_2/CO ratio. Figure 4 shows that their values are significantly higher than ours. The differences vary from ca. 10% in high-H_2 mixtures to almost 40% in low H_2. It is noteworthy that the Günther and Janisch data are also well above those of Scholte and Vaags for mixtures with varying H_2/CO ratio giving maximum burning velocities.

In broad terms, the above agreements and disagreements may be explained as follows. Günther and Janisch used a Mach–Hebra nozzle burner to obtain flat-sided conical flames. Burning velocity was derived from flow velocity into the flame (measured by particle tracking) and the cone angle (obtained by schlieren photography). Their burning velocities were referenced to the unburned gas temperature. But if, following Fristrom [13] and Dixon-Lewis and Islam [14], the proper reference surface is in the hot part of the flame—as we have previously argued for hydrogen flames [2]—then divergence effects will cause the Günther and Janisch values to be too high. Although the size of their nozzle is not stated explicitly, a diameter of 10 mm is implied. Following Dixon-Lewis [15], this means burning velocity overestimates of ca. 20%.

Scholte and Vaags used essentially the same method for their measurements but determined the inlet velocity from the gas flow rate divided by burner area. For this to be accurate, the velocity profile from the nozzle must be entirely uniform. But this cannot be so, as there will always be a boundary layer. Its magnitude will depend on burner diameter and flow rate, but one estimate [16] suggests that it is about 20% of their burner area. The effect of this misdetermination of flow velocity is to render the measured burning velocities too low by the same amount. But, in addition to this effect, the Scholte and Vaags data need correcting for divergence in precisely the same way as do those of Günther and Janisch. By coincidence, the errors in divergence and flow velocity largely cancel out, thus explaining the broad agreement between Scholte and Vaags' data and our own.

In addition to these principal sets of data, Yumlu [17] has reported some burning velocities for lean CO/H_2 mixtures at a stoichiometry of 0.68. His values are higher than our 95 + 5% and 50 + 50% results by 5–10%, but the trend is similar to ours. His measurements were made by stabilizing flat flames on a porous matrix burner, at different flow rates and corresponding varying degrees of heat loss. By extrapolation to zero heat loss, the critical flow rate and, hence, burning velocity was determined. Although such flames are flat, they are not strictly 1D since the flow diverges through the flame, as revealed in particle track photographs [18]. This will again lead to overestimates of burning velocity that, although difficult to quantify, are expected to fall in the range of 10–20%.

Jahn [19] produced an early and fairly comprehensive set of measurements, but as his CO contained some water, no detailed comparison with the present results is possible. Comparison of Jahn's values for hydrogen and methane with some of our other data suggests that his values are low by 7–8%.

In summary, it seems likely that none of these previous measurements are entirely acceptable. Those by Scholte and Vaags are probably the best, though largely because of a fortuitous cancellation of errors. Because of the validation tests performed on the present measurements, we believe our data provide a more reliable basis for validating chemical models.

Computed Burning Velocities:

Results of 1D computations using the base kinetic scheme are compared with experimental burning velocities for the 95% CO + 5% H_2 mixture in Fig. 3. While this mechanism very adequately reproduces our experimental burning velocities for hydrogen/air [2], this is not so when CO is added. Now over almost the whole stoichiometric range, the computed values are much too high, by more than 20%. The sensitivity coefficient information (Fig. 1) leads to the strong suspicion that the CO + OH reaction is the culprit. Further computations were, therefore, performed using various lower rate expressions.

Simple sensitivity coefficient considerations suggested the base rate needed to be lower by 35%, providing the first trial expression. Agreement with experiment was now better than 4% over most of the stoichiometric range. The earlier recommendation of Baulch et al. [20] produced very similar results, giving the excellent agreement shown in Fig. 3. If one allows for radiation, the experimental values are raised slightly, further improving the agreement.

The sensitivity coefficient information shown in Fig. 1 suggests that the only other practical means of improving the computations would be a significant lowering of the rate of the reaction $H + HO_2 \rightarrow OH + OH$. But the large change needed (a threefold reduction) is well outside the uncertainty factor [3] and has a deleterious effect on H_2/air flame simulations. Thus, we conclude that there is no realistic

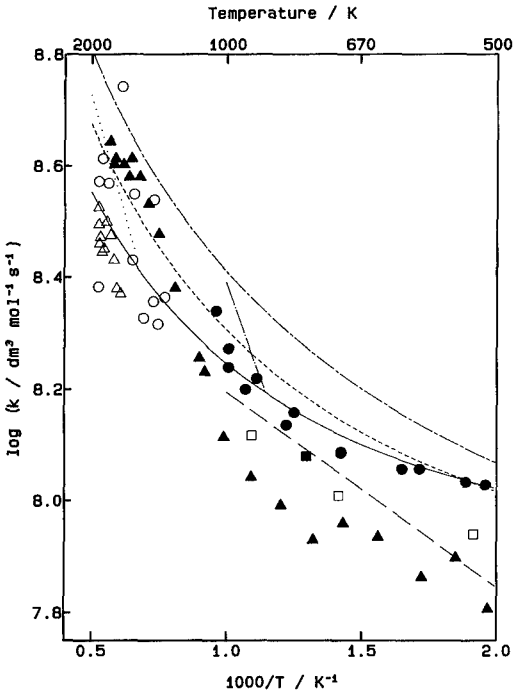

FIG. 5. Compilation of available rate data for reaction $CO + OH \rightarrow CO_2 + H$. —·—· CEC [3]; ——— Baulch et al. [20]; ------ Warnatz [10]; ——— Bonne and Wilson; ····· Gardiner et al.; ·—·— Kijewski and Troe; ■ Atri et al.; ○ Brabbs et al.; ▲ Vandooren et al.; △ Peeters and Mahnen; □ Westenberg and de Haas; ● Ravishankara and Thompson [21]. Full list of references taken from [3].

alternative to adjusting the CO + OH reaction, in which case the earlier value of Baulch et al. [20] is strongly preferred to the more recent, higher, CEC recommendation.

The available rate data for the reaction are presented in Fig. 5. The lack of real evidence in favour of the high recommendation of the CEC panel is particularly noticeable. The Baulch expression [20], on the other hand, provides a reasonable fit to the available data, including those of Ravishankara and Thompson [21], which are probably the most reliable. Recalling the evaluators' assessment, quoted in the Introduction, it would appear that they were misled by the apparent needs of flame simulations. Insofar as burning velocities formed part of the database used for such simulations, the likely explanation is that incorrect burning velocity data were used in these previous attempts at validating models. This provides further evidence for the general point that basing rate evaluations on data other than direct kinetic experiments is usually unsatisfactory.

The fact that the two alternative rate expressions for CO + OH indicated above (i.e., CEC rate × 0.65 and Baulch et al.) gave very similar burning velocities has interesting implications, which are now explored. The two rates have rather different temperature dependences but become equal at a temperature of 1165 K, suggesting that this region of the flame may be significant in determining burning velocity. To test this hypothesis, further computations were performed using artificially derived rate expressions. The first was a simple Arrhenius expression tangential at 1165 K to that of Baulch et al. Two others were derived from this by doubling and halving the activation energy, with corresponding adjustments to the *A* factors to maintain the same rate constant at 1165 K.

The startling finding was that, despite the large sensitivity of this reaction, use of these artificial rates led to only small changes in burning velocity—usually less than 3%. Thus, very different rate expressions for CO + OH yield essentially the same burning velocities, as long as they have the same value at 1165 K. It seems that the burning rate of these flames is overwhelmingly governed by the chemistry occurring in a narrow region of the flame around 1165 K. In contrast, the CO + OH reaction rate profiles are broad; they start at temperatures of 500 ± 100 K (depending on stoichiometry), peak around 1300–1400 K, and extend up to the final flame temperature. They have no special features around 1165 K. It is interesting to speculate on whether this pattern of behaviour is peculiar to this system or has wider significance. We plan to pursue this point further.

One immediate consequence of this is that the use of burning velocities to test the rate of the CO + OH reaction only provides a sensitive test at this one temperature; no direct inference can be made about the rate at other temperatures.

Although lowering the rate of the CO + OH reaction significantly improves the agreement between experiment and modelling at most stoichiometries, for the leanest (stoichiometry <0.7) and the richest mixtures (stoichiometry >2.1), computed burning velocities fall below experimental. The onset of buoyancy in slower burning mixtures can explain the discrepancy on the lean side, but on the rich side, the larger differences suggest a kinetic explanation. Figure 1 indicates the options available. Reactions 1 and 23 were found to have insufficient variation of sensitivity coefficient with stoichiometry to influence only the richest mixtures, and, furthermore, any changes adversely affected H_2 or CH_4 flame simulations. On the other hand, reaction 25 (HCO + H) does possess the desired features: a drop of 25% in its rate (well within the uncertainty factor [3]) gives a very reasonable fit across the whole stoichiometric range. However, the evidence for such a change is not strong, and any conclusion must, therefore, be tentative.

Finally, computed burning velocities for the 50 + 50% mixture and for stoichiometric mixtures with increasing H_2 are shown in Figs. 3 and 4, respectively,

revealing a pattern broadly the same as for the 95 + 5% case. That is, using the CEC rate for CO + OH produced burning velocities that were too high, but the position was again remedied by using the Baulch value.

Conclusions

1. Previous burning velocities for CO/H_2 provide an inadequate basis for the accurate validation of kinetic models. New measurements are reported that significantly improve the database.
2. Computed burning velocities are inconsistent with these new data, if a high rate is used for the CO + OH reaction. The 1976 recommendation of Baulch et al. yields much better results.
3. Dropping the rate of the HCO + H reaction further improves the simulations in very rich mixtures, though this conclusion should be regarded as tentative.

Acknowledgments

The authors are grateful to British Gas plc for permission to publish this paper. They also acknowledge with thanks contributions from Drs. J. K. Worrell, C. Robinson and M. J. Brown.

Note Added in Proof

The rate coefficient used for Reaction (1) ($H + O_2 = OH + O$) was taken from an interim report of the CEC panel [9a]. The final report [9b] contains a slightly different recommendation. Additional computations show that the effect of this change on modelled burning velocities is negligible in most cases. Where there is a difference, it is always small (less than 2.5%) and marginally improves the agreement with experiment. All of the conclusions in the paper apply to the updated mechanism.

REFERENCES

1. Warnatz, J., *Twentieth Symposium (International) on Combustion,* The Combustion Institute, Pittsburgh, 1985, pp. 845–856.
2. Dowdy, D. R., Smith, D. B., Taylor, S. C., and Williams, A., *Twenty-Third Symposium (International) on Combustion,* The Combustion Institute, Pittsburgh, 1990, pp. 325–332.
3. Baulch, D. L., Cobos, C. J., Cox, R. A., Esser, C., Frank, P., Just, Th., Kerr, J. A., Pilling, M. J., Troe, J., Walker, R. W., and Warnatz, J., *J. Phys. Chem. Ref. Data* 21:411–734 (1992).
4. Warnatz, J., *Twenty-Fourth Symposium (International) on Combustion,* The Combustion Institute, Pittsburgh, 1992, pp. 553–579.
5. Kee, R. J., Grcar, J. F., Smooke, M. D., and Miller J. A., *A Fortran Program for Modeling Steady Laminar One-Dimensional Premixed Flames,* Sandia Report SAND85-8240, 1985.
6. Kee, R. J., Rupley, F. M., and Miller J. A., *Chemkin-II: A Fortran Chemical Kinetics Package for the Analysis of Gas-Phase Chemical Kinetics,* Sandia Report SAND89–8009, 1989.
7. Kee, R. J., Dixon-Lewis, G., Coltrin, M. E., and Miller J. A., *A Fortran Computer Code Package for Evaluation of Gas-Phase Multicomponent Transport Properties,* Sandia Report SAND86-8246, 1986.
8. Chen, J.-Y., Liu, Y., and Rogg, B., in *Reduced Kinetic Mechanisms for Applications in Combustion Systems,* Chap. 12 (N. Peters and B. Rogg, Eds.), Springer-Verlag, Berlin, 1993.
9. Baulch, D. L., Cobos, C. J., Cox, R. A., Frank, P., Hayman, G., Just, Th., Kerr, J. A., Murrells, T., Pilling, M. J., Troe, J., Walker, R. W., and Warnatz, J., a) private communication: *Summary Table of Kinetic and Mechanistic Parameters Recommended by the CEC Chemical Kinetics Data Evaluation Panel,* Appendix 1 of Chemical Kinetics for Combustion (Chemcom) Fifth Periodic Report, March 1993. b) *Combust. Flame* 98:59–79 (1994).
10. Warnatz, J., in *Combustion Chemistry,* Chap. 5 (W. C. Gardiner, Jr., Ed.), Springer-Verlag, New York, 1984.
11. Scholte, T. G., and Vaags, P. B., *Combust. Flame* 3:511–524 (1959).
12. Günther, R., and Janisch, G., *Chem. Ing. Technol.* 43:975–978 (1971).
13. Fristrom, R. M., *Phys. Fluids* 8:273–280 (1965).
14. Dixon-Lewis, G., and Islam, S. M., *Nineteenth Symposium (International) on Combustion,* The Combustion Institute, Pittsburgh, 1982, pp. 283–291.
15. Dixon-Lewis, G., *Phil. Trans. R. Soc. London A* 292:45–99 (1979).
16. Garner, F. H., Long, R., and Thorley, B., *Fuel* 33:398–408 (1954).
17. Yumlu, V. S., *Combust. Flame* 11:190–194 (1967).
18. Levy, A., and Weinberg, F. J., *Seventh Symposium (International) on Combustion,* Butterworths, London, 1959, pp. 296–303.
19. Jahn, G., reproduced in Lewis, B., and von Elbe, G., *Combustion, Flame and Explosions of Gases,* Academic Press, New York, 1961, pp. 384–386.
20. Baulch, D. L., Drysdale, D. D., Duxbury, J., and Grant, S., *Evaluated Kinetic Data for High Temperature Reactions,* Butterworths, London, 1976, Vol 3, pp. 203–251.
21. Ravishankara, A. R., and Thompson, R. L., *Chem. Phys. Lett.* 99:377–381 (1983).

COMMENTS

G. Dixon-Lewis, University of Leeds, UK. The comparisons between theory and experiment, as described in the paper, are based on entirely objective measurements of the velocities of outward movement of spherically expanding premixed flames during the early pre-pressure period in a constant-volume bomb. Similar comparisons were carried out some years ago by Dixon-Lewis on H_2/air flames [1], and later for three further H_2/air flames and two H_2/CO/air flames [2] (the latter based on otherwise unpublished spherical flame speed measurements by Dixon-Lewis, Smith, and Taylor). It is particularly noteworthy to find that, after several years of additional refinements of the reaction rate expressions other than that for the OH + CO reaction, the more extensive comparison described in the present paper confirms earlier conclusions [2] and favours the Baulch and Drysdale recommendation [3] for the OH + CO rate expression over higher valued, more recent recommendations.

REFERENCES

1. Dixon-Lewis, G., *Combust. Sci. Technol.* 34:1 (1983).
2. Dixon-Lewis, G., *Complex Chemical Reaction Systems* (J. Warnatz and W. Jager, Eds.), Springer Series in Chemical Physics, Springer-Verlag, Heidelberg, 1987, Vol. 47, p. 265.
3. Baulch, D. L., and Drysdale, D. D., *Combust. Flame* 23:215 (1974).

Author's Reply. It was an oversight on our part not to refer to Dixon-Lewis's contributions [1] to our understanding of CO/H_2 flames. This is particularly so since, as he notes, two of the present authors (DBS and SCT) played a small part in that earlier study.

We are of course gratified that our conclusions agree with those of Dixon-Lewis. However, we would stress that CO/H_2 flames (at least as far as burning velocity is concerned) seem sensitive to the rate of the CO + OH reaction only at relatively low temperatures (around 1165 K). Thus, burning velocities by themselves allow no conclusions to be drawn about the rate at other (particularly higher) temperatures. We are therefore perfectly prepared to accept the new measurements of Wooldridge et al. [2]. These data, taken together with the lower temperature rates and our conclusions about the rate around 1100 K, present an interesting challenge for the theoreticians.

REFERENCE

1. Dixon-Lewis, G., *Combust. Sci. Technol.* 34:1 (1983).
2. Wooldridge, M. S., Hanson, R. K., and Bowman, C. T. *Twenty-Fifth Symposium (International) on Combustion*, The Combustion Institute, Pittsburgh, 1994, pp. 741–748.

Twenty-Fifth Symposium (International) on Combustion/The Combustion Institute, 1994/pp. 759–766

NEW RESULTS ON MOIST CO OXIDATION: HIGH PRESSURE, HIGH TEMPERATURE EXPERIMENTS AND COMPREHENSIVE KINETIC MODELING

TAE J. KIM, RICHARD A. YETTER AND FREDERICK L. DRYER
Department of Mechanical and Aerospace Engineering
Princeton University
Princeton, New Jersey 08544, USA

The kinetics of moist carbon monoxide oxidation have been studied experimentally for pressures from 1 to 9.6 atm, temperatures from 960 to 1200 K, and equivalence ratios from 0.33 to 2.1. New data were used in combination with prior flow reactor, shock tube, and static reactor data to develop a revised comprehensive reaction mechanism for the $CO/H_2O/O_2$ system. In particular, the new data span the explosion limit behavior of the system and place significantly increased emphasis on the kinetics involving the hydroperoxyl radical. Revisions of the rates recommended in an earlier comprehensive mechanism are needed in order to reproduce experimental observations. While six reaction recommendations were modified, the most important were the kinetic parameters for $H_2O + O = OH + OH$ and $HO_2 + OH = H_2O + O_2$.

Experimentally, the second limit for this reaction system was determined at much higher pressures than previously studied. Near the limit, an increase in pressure results in a two order of magnitude decrease in the oxidation rate. Away from the limit, the pressure dependence of the rate is similar in both the nonexplosive and explosive regimes. In the nonexplosive regime, the kinetics are straight chain in nature and governed by the reactions $H + O_2 + M = HO_2 + M$, $CO + HO_2 = CO_2 + OH$, and $CO + OH = CO_2 + H$. The overall temperature dependence of the oxidation is very large (77 kcal/mol). In the explosive regime, chain-branching phenomena dominate and are controlled by the reactions $H + O_2 = OH + O$, $CO + OH = CO_2 + H$, and $O + H_2O = OH + OH$. The overall temperature dependence of the oxidation is significantly lower (40 kcal/mol). The sensitivity of the reaction rate to moisture saturates at much lower moisture concentration in the nonexplosive regime. At high pressures (>25 atm), the oxidation of CO through $CO + OH = CO_2 + H$ and $CO + HO_2 = CO_2 + OH$ is numerically predicted to approach a limiting ratio of one-half.

Introduction

Characterization of moist carbon monoxide oxidation, in particular, its hydroperoxyl reaction chemistry, has typically involved studies in static reactors at subatmospheric pressure and below 800 K. In earlier work in which we developed and validated a comprehensive reaction mechanism for CO oxidation, we stated that the reactions involving HO_2 and H_2O_2 were most likely going to require further consideration. Many of the reactions involving these species involve an association complex at low temperatures and a direct abstraction reaction at high temperatures. These competing channels result in an overall rate constant behavior with a negative activation energy at low temperatures and a positive activation energy at high temperatures. For example, this type of behavior has been recently observed for reactions of $HO_2 + HO_2 = H_2O_2 + O_2$ [1] and $H_2O_2 + OH = H_2O + HO_2$ [2,3]. Testing reaction mechanisms against static reactor experimental results is necessarily insensitive to the high-temperature characterization of such reactions, and these reactions are essential for modeling conventional high-pressure combustion environments. This paper presents new experimental data on the moist carbon monoxide reaction at appropriate pressures and temperatures to increase the sensitivity of observations to the abstraction channels for some of these reactions. The experimental data are then utilized to revise and extend the comprehensive reaction mechanism published earlier [4].

Parametric studies of the $CO/H_2O/O_2$ system are performed in a flow reactor for pressures from 1 to 9.6 atm, temperatures from 960 to 1200 K, and for equivalence ratios from 0.33 to 2.1. The present data span both the explosive and nonexplosive kinetic regimes as well as the boundary between them. Figure 1 displays prior data on the moist CO explosion limits [5–8] in comparison to the conditions reported here.

Experiment

Experiments have been conducted in a variable temperature ($600 < T < 1200$ K), variable pressure

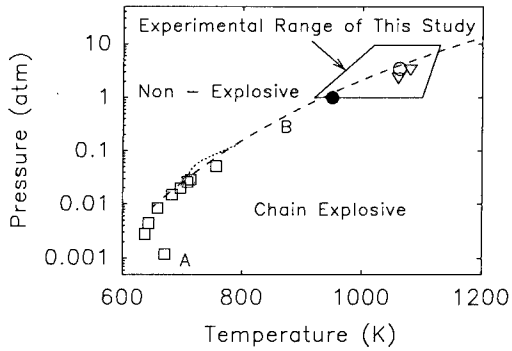

FIG. 1. The moist CO/O_2 explosion limits that separate explosive from nonexplosive chemistry. The first and second limits are given by A and B, respectively. Previous explosion limits data [6–8] are also shown. The third body, M, is N_2. The figure key is as follows: ○ 0.65% H_2O, φ = 1, this study; ∇ 0.65% H_2O, φ = 0.33, this study; ● 1.04% H_2O, φ = 1 [8]; □ 1.0% H_2, φ = 1 [6]; ····· 20% H_2, φ = 1 [7]; ---- [M] = $2k_1/k_9$.

($1 < P < 20$ atm) flow reactor [9–13] with residence times ranging from 10 ms to 2 s. A schematic diagram of the variable pressure flow reactor is given in Fig. 2. Carbon monoxide and water vapor, along with about 10% of the total nitrogen flow, are injected into the carrier and oxidizer stream at the mixer, located just prior to a conical silica foam diffuser. The mixer is jet stirred and has a nominal turnover time of about 0.5% of the total test time. A combined ferrous alloy/tungsten electrical resistance heater is used to heat the carrier gas upstream of the test section. The flow reactor is operated as a steady, isobaric flow device, and the time from mixing to sample position is varied by moving the mixer/diffuser assembly along the quartz test tube.

The pressure vessel is designed to enclose not only the reactor section (the reactor duct heaters and insulation) but also the positioning mechanism and fuel/water vapor injection probe, which axially locates the fuel/carrier mixing section relative to the sampling location. The reaction duct itself is quartz, 173-cm long with a 10.16-cm inside diameter. The entire quartz tube is surrounded by electric heaters, which maintain the walls at the initial gas temperature. This creates a nearly adiabatic system since chemical energy release in this highly dilute mixture results in small gas/wall temperature gradients.

In order to translate flow reactor position into reaction time, the mean velocity distribution along the centerline is measured under cold flow conditions using pitot-static probe techniques. These measurements are related to experimental conditions through Reynolds number correlations.

A hot water-cooled, stainless steel sample probe is mounted in the reactor end flange and is used to continuously extract and convectively quench a small portion of the reacting gases. From the probe, the gas sample flow is sent to a Fourier transform infrared (FTIR), a continuous electrochemical analyzer for O_2, and continuous nondispersive infrared (NDIR) analyzers for CO and CO_2. The sample temperature is measured with a silica-coated Pt/Pt-13% Rh thermocouple. Further details concerning these experiments can be found in Ref. 11.

Reaction Mechanism

The reaction mechanism resulting from this study is given in Table 1. Reverse rate constants are derived from the listed forward rates and equilibrium constants calculated from the thermochemical data presented in Table 2 [14,15]. The present reaction mechanism is a revision of the comprehensive reaction mechanism of Yetter et al. [4]. In another recent paper [12], mixtures of hydrogen/oxygen were studied for pressures of $1 < P < 15.7$ atm and temperatures of $850 < T < 1010$ K. The HO_2/H_2O_2 rate expressions utilized earlier [4] had been critically evaluated for temperatures below 800 K. For encompassing these new experiments [12] and the ones reported here, reactions involving adducts and pressure dependencies of recombination reactions

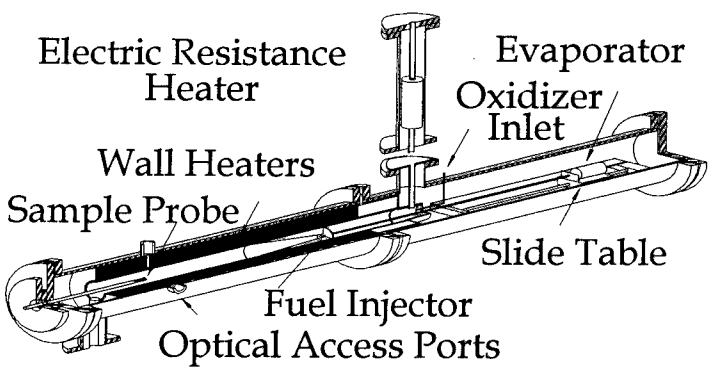

FIG. 2. A cutaway view of the variable pressure flow reactor.

TABLE 1
$CO/H_2/O_2$ reaction mechanism
(units are cm^3 mol s kcal K; $k = AT^n \exp(-E_a/RT)$ unless specified)

	$\log(A_f)$	n_f	$E_{a,f}$	UF[b]	T[a]	Ref.
H_2-O_2 chain reactions						
1. $H + O_2 = O + OH$	14.28	0.0	16.44	2	962–2,577	37
2. $O + H_2 = H + OH$	4.71	2.67	6.29	1.5	297–2,495	38
3. $OH + H_2 = H + H_2O$	8.33	1.51	3.43	1.5	250–2,581	39
4. $O + H_2O = OH + OH$	6.47	2.02	13.40	2.5	250–2,000	19
H_2-O_2 dissociation/recombination reactions						
5. $H_2 + M = H + H + M$	19.66	−1.40	104.38	3	600–2,000	18[c]
$H_2 + Ar = H + H + Ar$	18.77	−1.10	104.38	2	600–5,000	18
6. $O + O + M = O_2 + M$	15.79	−0.50	0.00	1.3	2,000–10,000	18
$O + O + Ar = O_2 + Ar$	13.28	0.0	−1.79	1.3	2,000–4,000	18
7. $O + H + M = OH + M$	18.67	−1.0	0.00	10		18
8. $H + OH + M = H_2O + M$	22.35	−2.0	0.00	2	1,000–3,000	18
$H + OH + Ar = H_2O + Ar$	21.92	−2.0	0.00	2	1,000–3,000	18
Formation and Consumption of HO_2						
9. $H + O_2 + M = HO_2 + M$	19.79	−1.42	0.00	3	200–2,000	21[d]
$H + O_2 + Ar = HO_2 + Ar$	15.18	0.0	−1.00	2	300–2,000	40
$H + O_2 = HO_2$	13.65	0.0	0.00	1.3	298	22
10. $HO_2 + H = H_2 + O_2$	13.82	0.0	2.13	2	298–773	18
11. $HO_2 + H = OH + OH$	14.23	0.0	0.87	2	298–773	18
12. $HO_2 + O = OH + O_2$	13.24	0.0	−0.40	1.2	200–400	18
13. $HO_2 + OH = H_2O + O_2$	16.28	−1.00	0.00	2	254–1,050	see text
Formation and consumption of H_2O_2						
14. $HO_2 + HO_2 = H_2O_2 + O_2$	14.62	0.0	11.98			
	11.11	0.0	−1.629	3	650–800	1[e]
15. $H_2O_2 + M = OH + OH + M$	17.08	0.0	45.50	2	700–1,500	41[d]
$H_2O_2 + Ar = OH + OH + Ar$	16.28	0.0	43.00	2	700–1,500	23
$H_2O_2 = OH + OH$	14.47	0.0	48.40	2	1,000–1,500	23
16. $H_2O_2 + H = H_2O + OH$	13.00	0.0	3.59	3	283–800	41
17. $H_2O_2 + H = H_2 + HO_2$	13.68	0.0	7.95	5	283–800	18
18. $H_2O_2 + O = OH + HO_2$	6.98	2.0	3.97	3	250–800	18
19. $H_2O_2 + OH = H_2O + HO_2$	12.00	0.0	0.00			
	14.76	0.0	9.56	2	250–1,250	3[e]
Oxidation of CO						
20. $CO + O + M = CO_2 + M$	13.40	0.0	−4.54	4	1,000–3,000	41
$CO + O + Ar = CO_2 + Ar$	13.34	0.0	−4.54	4	1,000–3,000	41
21. $CO + O_2 = CO_2 + O$	12.40	0.0	47.69	2	1,500–3,000	18
22. $CO + OH = CO_2 + H$	7.176	1.3	−0.765	1.5	250–2,500	42
23. $CO + HO_2 = CO_2 + OH$	13.78	0.0	22.95	3	700–1,000	43
Formation and consumption of HCO						
24. $HCO + M = H + CO + M$	17.27	−1.0	17.00	5	637–832	44
$HCO + Ar = H + CO + Ar$	17.27	−1.0	17.00	5	637–832	44
25. $HCO + O_2 = CO + HO_2$	12.88	0.0	0.41	5	295–713	45
26. $HCO + H = CO + H_2$	13.86	0.0	0.00	2	296–418	46
27. $HCO + O = CO + OH$	13.48	0.0	0.00	3		18
28. $HCO + OH = CO + H_2O$	13.48	0.0	0.00	3		18

[a] T is the temperature range over which the rate constant parameters are evaluated.
[b] UF is an estimated uncertainty factor for the specified T range; $+\Delta k/k = UF - 1$ and $-\Delta k/k = UF^{-1} - 1$.
[c] Efficiency factors for pressure-dependent reactions with an unspecified collision partner are $\varepsilon_{N_2} = 1.0$, $\varepsilon_{H_2} = 2.5$; $\varepsilon_{H_2O} = 12$, $\varepsilon_{CO} = 1.9$; $\varepsilon_{CO_2} = 3.8$. All other species have efficiencies equal to unity.
[d] k_{uni} is given for reaction 15 as a Troe fit [20] with $F_c = 0.5$ [23] and for reaction 9 as a Lindemann fit [20].
[e] k for reactions 14 and 19 are the sums of two rate constant expressions.

TABLE 2
Thermochemical constants at 298.15 K (units are cal mol^{-1} deg^{-1} for C_p and S and kcal mol^{-1} for ΔH_f

Species	ΔH_f	S	C_p
H	52.101 ± 0.001	27.416 ± 0.004	4.97[a]
O	59.55 ± 0.024	38.492 ± 0.005	5.24
OH	9.318 ± 0.29	43.905 ± 0.01	7.17
H_2	0	31.232 ± 0.008	6.89
O_2	0	49.106 ± 0.008	7.02
H_2O	−57.795 ± 0.01	45.13 ± 0.01	8.03
HO_2	3.0 ± 2.0	54.76 ± 0.02	8.34[b]
H_2O_2	−32.53	55.68	10.30
CO	−26.42 ± 0.04	47.24 ± 0.01	6.96
CO_2	−94.05 ± 0.012	51.10 ± 0.03	8.87
HCO	10.40 ± 1.9	53.69 ± 0.01	8.27
N_2	0	45.793 ± 0.005	6.97
Ar	0	37.007 ± 0.001	4.97

[a]All data are from Ref. 14 except $\Delta H_f(HO_2)$. Polynominal fit coefficients from Ref. 16.

[b]$\Delta H_f(HO_2)$, from Ref. 15. For HO_2, polynominal fit coefficients are derived from Ref.17.

needed to be reconsidered. The rate constant expressions for reactions (4), (9), (13) through (15), and (19) in Table 1 have been modified in response to recently reported elementary kinetic data and the present mechanistic studies.

The change in k_4 is predicated on the recent measurements of Sutherland et al. [19]. Falloff for reaction (9) is expressed in terms of a Lindemann fit [20] using the Slack [21] low-pressure expression and the Cobos et al. high-pressure data [22]. Falloff for reaction (15) is expressed in a Troe fit [20] using the data of Brouwer et al. [23]. The rate constants, k_{14} and k_{19}, are from Hippler and coworkers [1,3] and are expressed as the sum of two exponentials.

The rate constant k_{13} is based on the low-temperature data ($254 < T < 382$ K) of Keyser [24] and recent high-temperature data (1050 K) of Hippler and Troe [3,25]. Figure 3 is an Arrhenius plot of these data and other kinetic studies. The data of Keyser [24] is the favored low-temperature rate recommended by two recent critical reviews [20,26]. The high-temperature data exhibit considerably more scatter. In the original mechanism, reaction (13) was from the critical review of Tsang and Hampson [18], which was based upon the low-temperature data of Sridharan et al. [31]. Roesler et al. [33] have shown that for fuel lean $CO/H_2O/O_2$ mixtures at 1000 K and 1 atm, where reaction (13) is among the most sensitive but with the largest uncertainty, the Tsang and Hampson expression [18] underpredicted the necessary amount of termination. The measurements of

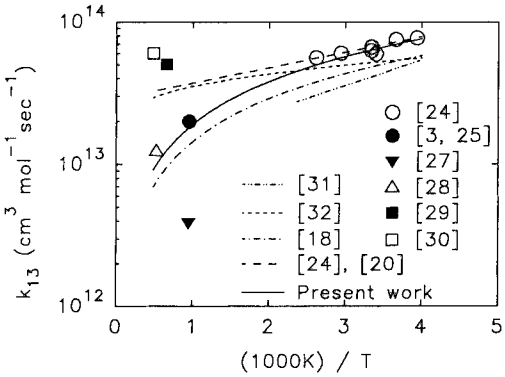

FIG. 3. An Arrhenius plot for the $HO_2 + OH = H_2O + O_2$ reaction. Recent data acquired by Keyser [24] and Hippler and Troe [3,25] were used to generate the curve fit of this recommendation given by $k_{13} = 1.9 \times 10^{16} T^{-1}$. Also shown are the recommended fits of Tsang and Hampson [18], Keyser [24], Sridharan et al. [31], and Gonzalez et al. [32].

Hippler and Troe [3,25] are in agreement with the observations of Roesler et al. [33]. Using the data of Keyser [24] and Hippler and Troe [3,25], a new rate constant expression for k_{13} between 298 and 1050 K is reported here (Table 1).

Finally, Chaperon efficiencies for recombination/dissociation reactions were treated in the same manner as in our earlier work [4]. The reaction parameters for CO + O + M remain ill-defined, and additional elementary studies are needed for this reaction [4].

After conversion of the spatial flow reactor data into reaction time using velocity data, the kinetic data were modeled assuming a zero-dimensional, isobaric, adiabatic, homogenous system. The kinetic and associated sensitivity equations were solved using SENKIN [47]. For modeling and data comparisons, model predictions were time shifted to match the point of 50% fuel consumption [8].

Results and Discussion

In Fig. 4, experimental and calculated profiles of the CO mole fraction X(CO), as a function of residence time, are presented for 1 and 3.46 atm at 1040 K ($\phi = 1$). The symbols are the experimental data, and the lines are model predictions using the refined (solid line) and original (dashed line) mechanisms. At 1 atm, the initial condition of the mixture is within the explosive region, which is below the second limit (see Fig. 1). Here, the predictions of the two mechanisms are virtually identical. As the dilute mixture begins to react at constant pressure, the temperature of the gas rises to a final temperature of 1110 K. At

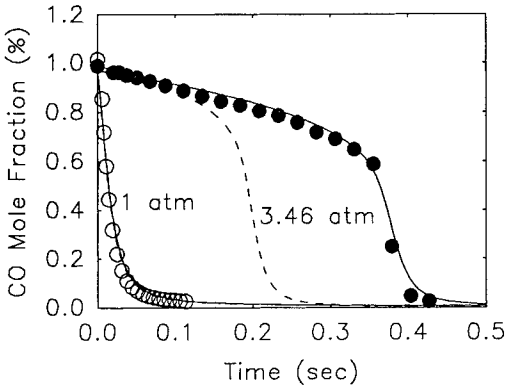

FIG. 4. A comparison of 1 and 3.46 atm data with model predictions using the original mechanism of Yetter et al. [4] ------and the present mechanism————. Initial conditions are an initial temperature of 1040 K, 1.0% CO, 0.5% O_2, 0.65% H_2O, balance N_2. For the 1 atm case, the two model predictions are essentially identical.

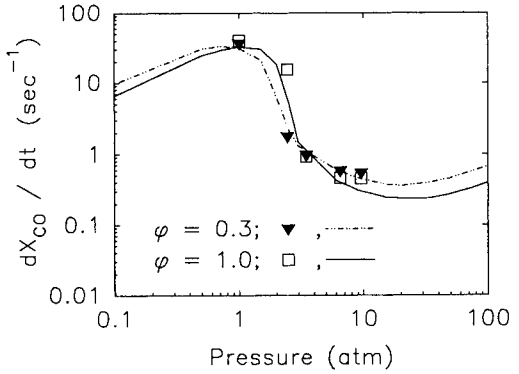

FIG. 5. The effect of pressure on the rate of CO oxidation at 1040 K for equivalence ratios of 1 and 0.333. The oxidation rate is given by the mean slope of dX_{co}/dt between 15 and 65% fuel consumption. Initial mole fractions are 1.0% CO and 0.65% H_2O, balance N_2. Symbols are the experimental data, and lines are the model calculations.

3.46 atm, the initial condition is in the nonexplosive regime, just above the second limit. The CO data exhibit an initial period of slow decay followed by a sudden transition to fast decay. This transition occurs at the temperature of the second limit. Calculations based on the original mechanism cross the second limit at a lower temperature/higher X(CO) than the data, with the resulting reaction times differing by a factor of 2. Predictions using the refined mechanism compare well with the higher-pressure data.

The second explosion limit data for stoichiometric moist CO/O_2 mixtures are shown in Fig. 1 to correlate with $[M] = 2k_1/k_9$, the classical second explosion limit result for stoichiometric H_2/O_2 mixtures. The effect of varying the H_2O concentration at the CO/O_2 second limit has been investigated numerically for a 1.0% CO, 0.5% O_2 mixture at 3.46 atm [11]. As the $X(H_2O)$ approaches zero, the explosion temperature asymptotically increases. For $X(H_2O)$ exceeding 0.0065, increasing $X(H_2O)$ has little effect on the explosion temperature. Thus, the H_2/O_2 submechanism controls the explosion condition in the present experiments and those of Yetter et al. [8]. This result is consistent with earlier theory [34,35].

At the second limit, the effect of varying the equivalence ratio was also studied. As the O_2/CO ratio increases, the explosion condition is shifted to higher temperatures/lower pressures (Fig. 1). This effect results from a change in HO_2 consumption paths from a suppression of H-atom concentrations relative to O and OH [33]. This trend agrees with other data [6] and is also numerically predicted by the revised reaction mechanism [11].

Figure 5 shows how the overall oxidation rate responds to pressure, for a fixed temperature of 1040 K and initial mole fraction of 1% CO and two equivalence ratios (ϕ = 1 and 0.33). As the second explosion limit is crossed, the oxidation rate decreases by approximately two orders of magnitude. However, the dependence of the oxidation rate with respect to pressure is nearly the same in both the explosive and nonexplosive regimes. The oxygen dependence of this reaction at atmospheric pressure has been shown to be a complex function of temperature [33]. At 1040 K (Fig. 5), there is no oxygen dependence. At lower temperatures, oxygen addition inhibits the reaction, while at higher temperatures, oxygen addition accelerates the reaction. Here, we note similar complexities in oxygen dependence due solely to changes in reaction pressure.

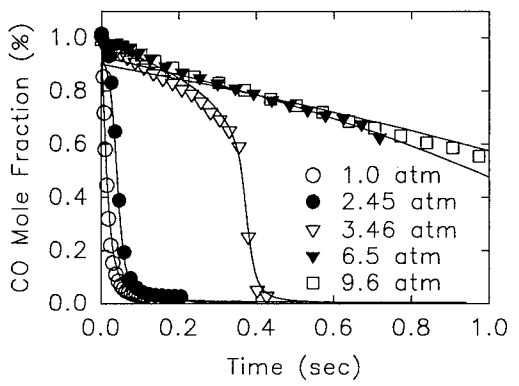

FIG. 6. Detailed comparisons of experimental CO decay profiles (symbols) with modeling predictions based on the refined mechanism (lines). For pressures from 1 to 9.6 atm, the initial mole fractions are 1.0% CO, 0.5% O_2, and 0.65% H_2O, balance N_2. The initial temperature was 1040 K.

Figure 6 presents detailed comparisons of the ex-

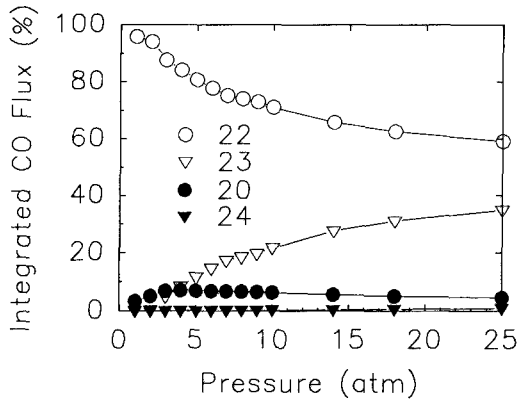

FIG. 7. Numerical calculations of the time-integrated CO flux at 1 atm (open bars) and 9 atm (solid bars) as a function of pressure. Initial conditions are the same as for the previous figure. Reaction numbers correspond to those listed in Table 1.

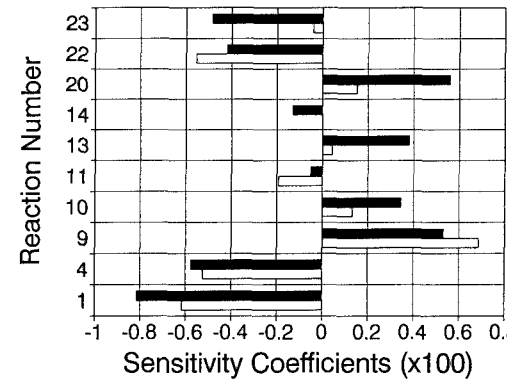

FIG. 8. Sensitivity coefficients given by $(\partial Y_{CO}/\partial \ln k_j)$ at the point of 50% CO consumption for 1 and 9 atm. Y_{CO} is the CO mass fraction and k_j is the jth rate constant. The mixture is the same as in Fig. 6. Reaction numbers correspond to those listed in Table 1.

perimental data with model comparisons for pressures from 1 to 9.6 atm and $\phi = 1$. The inhibiting effect of pressure is clearly seen on the reaction profiles. As pressure is increased, the mechanism changes from explosive chemistry, to transition chemistry, and then to nonexplosive chemistry. Similar agreement between experiment and model is obtained for $\phi = 0.33$ [11].

As the pressure is increased, different reaction sets in the mechanism become important. Numerical calculations showing the effects of increasing pressure on the various CO fluxes are presented in Fig. 7. At atmospheric pressure, the system is explosive and reaction (22) consumes about 95% of the CO. As the pressure is increased, the amount of termination resulting from reaction (9) increases relative to the branching from reaction (2). As a result, the H, O, and OH levels are suppressed relative to the HO_2 levels, and reaction (23) becomes important as a means of converting CO. At 25 atm, reaction (23) consumes over 35% of the CO, while reaction (22) consumes less than 60%. Note that the fluxes of reactions (22) and (23) asymptotically approach one another.

Sensitivity and reaction flux analyses were utilized to identify changes in the reaction mechanism due to pressure (Fig. 8). At atmospheric pressure, the sensitivity coefficients are dominated by those for reactions (2), (9), (22), and (4). The sensitivity coefficients for the other reactions including (10), (11), (20), (23), and (13) are relatively small. In contrast, the sensitivity coefficients for many of these reactions are of comparable magnitude at 9 atm. While the mechanism remains very sensitive to reactions (2) and (9), the system is more sensitive to reactions (23) and (20) than to (22). Furthermore, the sensitivity of the system to reactions (13), (4), and (14) are larger

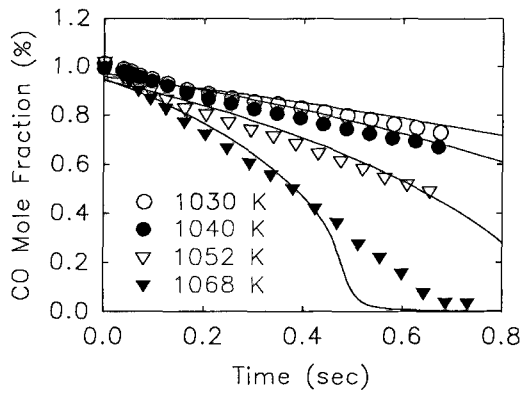

FIG. 9. Comparisons of experimental CO profiles with modeling predictions for initial temperatures from 1030 to 1068 K at 6.5 atm. The mixture is the same as in Fig. 6.

than at atmospheric pressure. From reaction flux analysis, the overall reaction is branched chain in nature at atmospheric pressure and driven by reactions (2), (22), and (4). As pressure is increased, this branched chain sequence is heavily suppressed, and the overall reaction becomes straight chain, driven by reactions (9), (22), and (23). Increasing pressure also slows the oxidation rate because of the increased importance of terminating reactions such as (9), (13), and (20).

Of particular interest is that the experimental system is highly temperature sensitive in the nonexplosive regime. In Fig. 9, the lowest and highest initial temperatures differ by only 38 K, less than a 4% change in initial temperature. However, the reaction rate increases by more than a factor of 5. Model predictions are again in good agreement with data, and

an Arrhenius plot yields an activation energy for the overall rate of 77.2 kcal/mol for the range of conditions studied here. This activation energy is much larger than the 40 kcal/mol [36] found in the explosive regime over a similar temperature range but at atmospheric pressure. The noted disparity of experimental and numerical results at 1068 K at large extents of reaction points to a small remaining uncertainty in the ratio for k_1/k_9 (which strongly affects the transition to explosive kinetics).

The effects of varying the equivalence ratio on the overall oxidation rate were studied at 1040 K (Fig. 5). At pressures of 1 and 3.46 atm, oxygen addition had no effect on the initial oxidation rate. The independence of oxygen concentration at 1 atm was also recently reported by Yetter et al. [8]. At 2.45 atm, oxygen addition shifts the explosive condition to lower pressures so that the oxidation rate is reduced. Experiments varying the equivalence ratio from 0.33 to 2.1 (P = 6.5 atm, T_{in} = 1040 K, initial CO of 1.0%) indicate that O_2 accelerates the oxidation in the nonexplosive regime according to $[O_2]^{1/4}$. This oxygen dependency is consistent with global kinetic studies of Dryer and Glassman [36] in the explosive regime at 1 atm and at temperatures above 1040 K. Thus, the effect of oxygen addition as a function of pressure can be complex and nonintuitive. However, the current reaction mechanism accurately predicts these trends.

The effect of varying $X(H_2O)$ on the initial oxidation rate was also studied in the nonexplosive regime (P = 6.5 atm, T_{in} = 1040 K, ϕ = 1, initial CO of 1.0%). As in the explosive regime, the rate was found to be sensitive to small quantities of H_2O. However, the accelerating effect of H_2O on the initial rate saturates at much lower water mole fractions, approximately 0.3%, in comparison to 3% in the explosive regime [4,8], in part because of increased pressure efforts on the competition of reactions (1) and (9).

Conclusions

The kinetics of moist CO oxidation have been experimentally investigated in a variable pressure flow reactor at pressures ranging from 1 to 9.6 atm, temperatures from 960 to 1200 K, and equivalence ratios from 2.1 to 0.33. Over this temperature range, the reaction dynamics of HO_2 and H_2O_2 have considerable uncertainty, and the elementary rates can exhibit significant non-Arrhenius behavior. There are no prior kinetics systems observations in the literature against which to validate HO_2/H_2O_2 mechanistic behavior over this range of conditions. By increasing the pressure above the second explosion limit in this temperature range, we have obtained such mechanistic data by studying moist CO oxidation. Similar conditions are of direct relevance to combustion and emissions chemistry of energy conversion systems. These data were used in combination with prior flow reactor, shock tube, and static reactor data to revise our previously published comprehensive mechanism. Updates of the rate constants for several HO_2/H_2O_2 reactions based on new elementary kinetic rate data were necessary to achieve agreement between high-pressure experimental measurements and model predictions. The existing literature rates for reactions (22) and (23) predict that at high pressures, CO_2 formation occurs through both channels. In separate studies of high-pressure hydrogen/oxygen kinetics, the present hydrogen/oxygen submechanism produces predictions in agreement with experimental results. Thus, both the present work and recent pure hydrogen/oxygen kinetic studies [12] are self-consistent. The significant point is that literature data for the direct oxidation of CO are self-consistent at our conditions.

Acknowledgments

The support of the U.S. Department of Energy, Office of Basic Energy Sciences through Grant No. DE-FG02-86ER-13503, is gratefully acknowledged. The authors thank Dr. J. F. Roesler for helpful discussions and Dr. J. Troe for his personal communication on HO_2 rate constant measurements. Mr. P. Michniewicz and Mrs. Y. S. Stein are acknowledged for assistance in performing the experiments.

REFERENCES

1. Hippler, J., Troe, J., and Willner, J., *J. Chem. Phys.* 93:1755 (1990).
2. Lightfoot, P. D., Vegret, B., and Lesclauz, R., *Chem. Phys. Lett.* 1:120 (1988).
3. Hippler, J., and Troe, J., *Chem. Phys. Lett.* 192:333 (1992).
4. Yetter, R. A., Dryer, F. L., and Rabitz, H., *Combust. Sci. Technol.* 79:97 (1991).
5. Dixon-Lewis, G., and Williams, D. J., in *Comprehensive Chemical Kinetics* (C. H. Bamford and C. F. Tipper, Eds.), Elsevier, Amsterdam, 1991, Vol. 17, pp. 1–248.
6. Hoare, D. E., and Walsh, A. D., *Trans. Faraday Soc.* 50:37 (1953).
7. Griffiths, J. F., and Sykes, A. F., *J. Chem. Soc. Faraday Trans. I.* 85:3059 (1989).
8. Yetter, R. A., Dryer, F. L., and Rabitz, H., *Combust. Sci. Technol.* 79:129 (1991).
9. Yetter, R. A., Ilincic, N., Dryer, F. L., Allen, M., and Gatto, J., *29th JANNAF Combustion Meeting,* NASA Langley Research Center, Hampton, VA, Oct., 1992.
10. Vermeersch, M. L., Held, T. J., Stein, Y., and Dryer, F. L., *SAE Trans.* 100:162 (1991).
11. Kim, T. J., M.S.E. Thesis, Princeton University, Princeton, NJ, 1994.
12. Kim, T. J., Yetter, R. A., and Dryer, F. L., "H_2/O_2

Kinetics: High Pressure Experimental Studies and Comprehensive Mechanism Development," *Combust. Sci. Technol.*, submitted.
13. Held, T. J., Ph.D. Thesis, Princeton University, Princeton, NJ, 1993.
14. Chase, M. W., Jr., Davies, C. A., Downey, J. R., Jr., Fulrip, D. J., McDonald, R. A., and Syverud, A. N., *J. Phys. Chem. Ref. Data.*, Vol. 14, Suppl. 1 (1985).
15. Hills, A. J., and Howard, C. J. *J. Chem. Phys.* 81:4458 (1984).
16. Kee, R. J., Ripley, F. M., and Miller, J. A., *The CHEMKIN Thermodynamic Data Base,* Sandia National Laboratories, Report No. SAND 80–8003, 1987.
17. Ritter, E. R., and Bozzelli, J. W., *THERM: Thermodynamic Property Estimation for Radicals and Molecules,* New Jersey Institute of Technology, Newark, NJ, 1987.
18. Tsang, W., and Hampson, R. F., *J. Phys. Chem. Ref. Data* 15:1087 (1986).
19. Sutherland, J. W., Patterson, P. M., and Klemm, R. B., *Twenty-Third Symposium (International) on Combustion,* The Combustion Institute, Pittsburgh, 1990, p. 51.
20. Baulch, D. L., Cobos, C. J., Cox, R. A., Esser, C., Frank, P., Just, T., Kerr, J. A., Pilling, M. J., Troe, J., Walker, R. W., and Warnatz, J., *J. Phys. Chem.* 21:411 (1992).
21. Slack, M. W., *Combust. Flame* 28:357 (1973).
22. Cobos, C. J., Hippler, H., and Troe, J., *J. Phys. Chem.* 89:342 (1985).
23. Brouwer, L., Cobos, C. J., and Troe, J., *J. Chem. Phys.* 86:6171 (1987).
24. Keyser, L. F., *J. Phys. Chem.* 92:1193 (1988).
25. Troe, J., personal communication, 1993.
26. Atkinson, R., Baulch, D. L., Cox, R. A., Hampson, R. F., Jr., Kerr, J. A., and Troe, J., *J. Phys. Chem. Ref. Data* 18 (Suppl. III):881 (1989).
27. Day, M. J., Thompson, K., and Dixon-Lewis, G., *Fourteenth Symposium (International) on Combustion,* The Combustion Institute, Pittsburgh, 1973, p. 133.
28. Friswell, N. J., and Sutton, M. M., *Chem. Phys. Lett.* 15:108 (1972).
29. Peeters, J., and Mahnen, G., *Fourteenth Syposium (International) on Combustion,* The Combustion Institute, Pittsburgh, 1973, p. 133.
30. Goodings, D. M., and Hayhurst, A. N., *J. Chem. Soc. Faraday Trans. II* 84:745 (1988).
31. Sridharan, U. C., Qiu, L. X., and Kaufman, F., *J. Phys. Chem.* 88:1281 (1984).
32. Gonzalez, C., Theisen, J., Schlegel, H. B., Hase, W. L., and Kaiser, E. W., *J. Phys. Chem.* 96:1767 (1992).
33. Roesler, J. F., Yetter, R. A., and Dryer, F. L., *Combust. Sci. Technol.* 95:161 (1994).
34. Brokaw, R. S., *Eleventh Symposium (International) on Combustion,* The Combustion Institute, Pittsburgh, 1967, p. 1063.
35. Yetter, R. A., and Dryer, F. L., *Twenty-Fourth Symposium (International) on Combustion,* The Combustion Institute, Pittsburgh, 1992, p. 757.
36. Dryer, F. L., and Glassman, I., *Fourteenth Symposium (International) on Combustion,* The Combustion Institute, Pittsburgh, 1973, p. 987.
37. Pirraglia, A. N., Michael, J. V., Sutherland, J. W., and Klemm, R. B., *J. Phys. Chem.* 93:282 (1989).
38. Sutherland, J. W., Michael, J. V., Pirraglia, A. N., Nesbitt, F. L., and Klemm, R. B., *Twenty-First Symposium (International) on Combustion,* The Combustion Institute, Pittsburgh, 1986, p. 929.
39. Michael, J. V., and Sutherland, J. W., *J. Phys. Chem.* 92:3853 (1988).
40. Baulch, D. L., Drysdale, D. D., Horne, D. G., and LLoyd, A. C., *Evaluated Kinetic Data for High Temperature Reactions,* Butterworths, London, 1976, Vols. 1 and 2.
41. Warnatz, J., in *Combustion Chemistry* (W. C. Gardiner, Jr., Ed.), Springer-Verlag, New York, NY, 1985.
42. Baulch, D. L., Drysdale, D. D., Duxbury, J., and Grant, S. J., *Evaluated Kinetic Data for High Temperature Reactions,* Butterworths, London, 1973, Vol. 3.
43. Atri, G. M., Baldwin, R. R., Jackson, K., and Walker, R. W., *Combust. Flame* 30:1 (1977).
44. Timonen, R. S., Ratajczak, E., Gutman, D., and Wagner, A. F., *J. Phys. Chem.* 91:5325 (1987).
45. Timonen, R. S., Ratajczak, E., and Gutman, D., *J. Phys. Chem.* 92:651 (1988).
46. Timonen, R. S., Ratajczak, E., and Gutman, D., *J. Phys. Chem.* 91:692 (1987).
47. Lutz, A. E., Kee, R. J., and Miller, J. A., *SENKIN: A Fortran Program for Predicting Homogeneous Gas Phase Kinetics with Sensitivity Analysis,* Sandia National Laboratories Report No. SAND87-8248, 1990.

Twenty-Fifth Symposium (International) on Combustion/The Combustion Institute, 1994/pp. 767–774

KINETIC PARAMETERS FOR THE INITIATION REACTION $RH + O_2 \rightarrow R + HO_2$

T. INGHAM, R. W. WALKER, AND R. E. WOOLFORD
School of Chemistry
Hull University
Hull, North Humberside HU6 7RX, UK

Results from studies of the oxidation of isobutene between 400 °C and 520 °C have been used to determine Arrhenius parameters for an important chain initiation reaction (5).

$$(CH_3)_2C = CH_2 + O_2 \rightarrow CH_2C(CH_3)CH_2 + HO_2. \quad (5)$$

Product analysis reveals that 2,5-dimethylhexa-1,5-diene (DMHDE) is a major product, formed in reaction (7) which is the *major* termination process. With minor corrections to the relationship, $k_5[\text{i-}C_4H_8][O_2]$ = initial rate of formation of DMHDE, accurate values of k_5 are determined and used to obtain $\log(A_5/\text{dm}^3\ \text{mol}^{-1}\ \text{s}^{-1}) = 9.68 \pm 0.44$ and $E_5 = 161.2 \pm 6.4$ kJ mol^{-1}. These parameters are in excellent agreement with those for the analogous reactions $HCHO + O_2$ and $C_3H_6 + O_2$. No other reliable data are available.

$$2CH_2C(CH_3)CH_2 \rightarrow \text{DMHDE}. \quad (7)$$

Novel experiments involving the addition of small amounts of hydrocarbons (mostly alkenes) to $C_3H_6 + O_2$ mixtures have been used to determine k_c for a number of primary initiation reactions. The approach is extremely simple and involves only the measurement of the initial rates of formation of hexa-1,5-diene and of propene oxide.

$$RH + O_2 \rightarrow R + HO_2. \quad (C)$$

A database is recommended for the Arrhenius parameters of (C) for general use in modelling.

Although good data now exist [1] for many of the faster exothermic elementary reactions of type A, where

$$X + RH \rightarrow XH + R \quad (A)$$

X = OH, O, CH_3, for example, relatively few rate constants have been obtained for slower, endothermic processes where $X = HO_2$, RO_2, and O_2, many of which, for example (B) [2], play a key rate-determining role in the autoignition region 600–1200 K.

$$HO_2 + C_4H_{10} \rightarrow H_2O_2 + C_4H_9 \quad (B)$$

$$RH + O_2 \rightarrow R + HO_2. \quad (C)$$

Reaction (C) is a key step in determining the onset of second-stage ignition [3], and recently, Emdee et al. [4] modelled the oxidation of toluene at about 1000 K and claimed that the rate was most sensitive to the value of k_{ct}.

$$C_6H_5CH_3 + O_2 \rightarrow C_6H_5CH_2 + HO_2. \quad (Ct)$$

Reaction (C) is highly endothermic, with ΔH = +190 kJ mol^{-1} when RH contains a tertiary C—H bond, and about +165 when RH = toluene. Many factors have contributed to the difficulty of determining k_c

(i) Generally, chain processes dominate RH consumption and product formation.

(ii) Surface initiation, with a much lower activation energy, often occurs at a rate many orders of magnitude higher than (C).

(iii) (C) may be totally masked by secondary initiation very early in reaction [5].

(iv) Radical branching often occurs, such as $H + O_2 \rightarrow OH + O$, and separation of the two processes may be extremely difficult.

Studies [6] of C_3H_6 oxidation under carefully controlled conditions have shown that the difficulties (i)–(iv) can be reduced to a minor role, essentially because the allyl radical, produced in reaction (1), is stabilised by electron delocalisation and is very unreactive towards O_2. The allyl radicals are removed mainly by recombination to form hexa-1,5-diene (HDE). As a consequence, k_1 can be determined with only a minor (ca. 20%) correction to the simple basic principle that, at the steady state, the rate of initiation equals the rate of termination, so that

$$k_1[C_3H_6][O_2] = R_{HDE} \quad \text{(i)}$$

where R_{HDE} is the initial rate of formation of HDE. Over the range 400–520 °C, $A_1 = 10^{9.29\pm0.41}$ dm^3 mol^{-1} s^{-1}, and $E_1 = 163.5 \pm 6$ kJ mol^{-1}

$$C_3H_6 + O_2 \rightarrow CH_2CHCH_2 + HO_2. \quad (1)$$

These parameters may be compared [7] with $A_2 = 10^{10.31}$ dm^3 mol^{-1} s^{-1} and $E_2 = 163 \pm 6$, bearing in mind that $\Delta H_1 = \Delta H_2 = 164 \pm 5$ kJ mol^{-1} and that $E_{-1} \approx E_{-2} \approx 0$. The value of $A_2/A_1 \approx 10$ is consistent with the loss of entropy of activation in the transition state of reaction (1) due to electron delocalisation in the emerging allyl radical.

$$HCHO + O_2 \rightarrow HCO + HO_2. \quad (2)$$

Studies [8] of butene-1 and *trans*-butene-2 oxidation under the same conditions as used for propene oxidation show no product evidence of an octadiene, which would be formed by recombination of butenyl radicals. However, with both butenes, buta-1,3-diene is a major initial product and is formed in reaction (3).

$$CH_3CHCHCH_2 + O_2 \rightarrow CH_2{=}CH{-}CH{=}CH_2 + HO_2. \quad (3)$$

Reaction (3) is fast and leads to high concentrations of HO_2 and H_2O_2, and as a result, factors (i), (iii), and (iv) interfere with the determination of k_c.

In contrast, studies of the oxidation of isobutene between 400 °C and 520 °C reveal that 2,5-dimethylhexa-1,5-diene (DMHDE) is a major initial product and indicate that the methylallyl radicals formed by H-atom abstraction from isobutene are unreactive towards O_2, and hence undergo radical-radical reactions such as (4). Determination of k_5 should be possible, and the study provides a very important test of the validity of the data obtained for k_1 and of the approach used.

$$2CH_2C(CH_3)CH_2 \rightarrow CH_2{=}\underset{\underset{CH_3}{|}}{C}{-}CH_2CH_2{-}\underset{\underset{CH_3}{|}}{C}{=}CH_2 \quad (4)$$

$$(CH_3)_2C{=}CH_2 + O_2 \rightarrow CH_2C(CH_3)CH_2 + HO_2. \quad (5)$$

Experimental

Reactions were carried out in aged boric-acid-coated Pyrex vessels. Gas chromatography was used to determine product concentrations. Particular attention was paid to initial yields. Further particulars are given elsewhere [6].

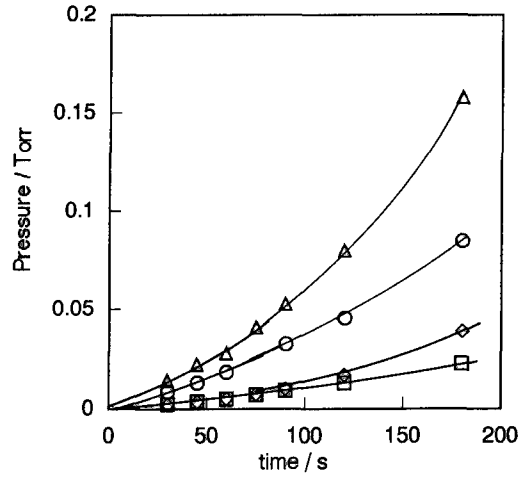

FIG. 1. Product vs time profiles at 470 °C. i-C_4H_8 = 4, O_2 = 30, N_2 = 26 torr. □, DMHDE; ◇, methacrolein; ○, isobutene oxide; △, acetone.

Results and Discussion

Figure 1 shows [product]-time profiles for the mixture containing 4, 30, and 26 torr of isobutene, O_2, and N_2, respectively, at 470 °C. The main products are acetone, methacrolein, isobutene oxide, 2,5-dimethylhexa-1,5-diene (DMHDE), and HCHO. All are formed autocatalytically and as primary products. A number of other mixtures were studied in the same detail at 470 °C and at 400 °C, 440 °C, 500 °C, and 520 °C. Only those components of the mechanism that are essential for the determination of k_5 will be discussed here.

Addition of HO_2 radicals to isobutene gives isobutene oxide in reaction (10). The key reactions for the determination of k_5 are reactions (9) and (10) and the reactions below involving the formation and removal of methylallyl radicals (MA).

$$(CH_3)_2C{=}CH_2 + O_2 \rightarrow MA + HO_2 \quad (5)$$

$$OH/HO_2 + (CH_3)_2C{=}CH_2 \rightarrow MA + H_2O/H_2O_2 \quad (6)$$

$$2MA \rightarrow DMHDE \quad (7)$$

$$MA + HO_2 \rightarrow (CH_3)_2C{=}CH_2 + O_2 \quad (8)$$

$$HO_2 + HO_2 \rightarrow H_2O_2 + O_2 \quad (9)$$

$$HO_2 + (CH_3)_2C{=}CH_2 \rightarrow (CH_3)_2\underset{\underset{O}{\backslash\,/}}{C{-}CH_2} + OH. \quad (10)$$

The essential features are:

(i) (7)–(9) are termination reactions.

(ii) MA is unreactive towards O_2 and undergoes mainly radical-radical reactions.

(iii) OH chemistry involves only propagation steps in the early stages of reaction.

Determination of k_5:

On reaching the steady state (ca. 10^{-3} s), the rate of generation of radicals and their rate of removal may be equated as in Eq. (ii), where R_p, R_s, R_b, and R_t are the initial (after 10^{-3} s) rates of primary initiation, secondary initiation, radical branching, and radical termination, respectively.

$$R_p + R_s + R_b = R_t. \quad \text{(ii)}$$

As $[H_2O_2]$ is low and initial rates are used, R_s is effectively zero (confirmed by computer analysis). Assuming $R_b = 0$ (see later) and that, with DMHDE a major product, reaction (7) is the sole termination process, then (ii) may be simplified to give (iii), where $(R_{DMHDE})_0$ is the *initial* rate of formation of DMHDE.

$$k_5[C_4H_8][O_2] = k_7[MA]^2 = (R_{DMHDE})_0. \quad \text{(iii)}$$

The values are obtained very carefully by a "chord method," whereby mean rates of formation at each time are calculated and then extrapolated back to zero time to obtain $(R_{DHMDE})_0$. Figure 2 shows a typical plot used to obtain the values at 470 °C. The values of $(R_{DMHDE})_0$ obtained in this way are summarised in Table 1 for all mixtures and temperatures used. Use of Eq. (iii) then gives the values of $(k_5)_{obs}$ listed in column 8 of Table 1. Over relatively wide ranges of mixture composition, the values at each temperature vary by no more than about 50%. They tend to rise as $[O_2]$ increases, as observed when the $C_3H_6 + O_2$ system was interpreted in a similar manner [6]. When compared with values from $C_3H_6 + O_2$ studies, $k_5/k_1 = 5 \pm 2$ at all temperatures, which is consistent with a difference of 2 in path degeneracy and a slightly weaker C—H bond dissociation energy (ca. 5 kJ mol^{-1}) in the β position in isobutene.

Refinement of the Interpretation:

The treatment of the results may be refined by allowing for termination through reactions (8) and (9). Equation (ii) is now written as in Eq. (iv), and the additional contributions are then calculated.

$$(k_5)_{obs}[C_4H_8][O_2] = k_7[MA]^2 + k_8[MA][HO_2] + k_9[HO_2]^2. \quad \text{(iv)}$$

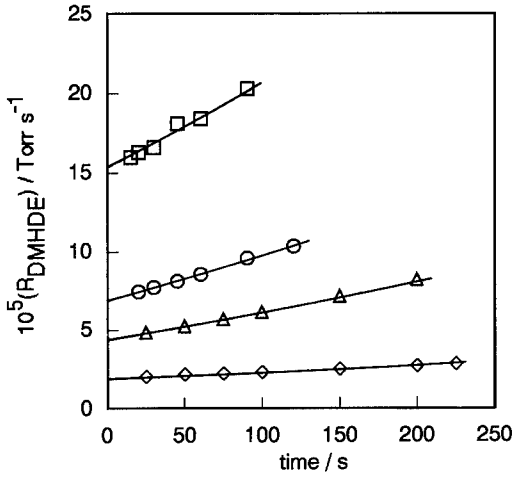

FIG. 2. "Chord" plots to obtain $(R_{DMHDE})_0$ at 470 °C.

	i-C_4H_8	O_2	N_2/torr
□	4	56	0
○	4	30	26
△	4	20	16
◇	4	10	46

The value of $k_9 = 1.87 \times 10^9 \exp(-775/T)$ dm^3 mol^{-1} s^{-1} is known accurately [1], but no value is available for k_8. However, for the analogous reaction of allyl radicals, $k_{11} = 1.6 \times 10^9$ dm^3 mol^{-1} s^{-1} over the temperature range 380 °C–520 °C from studies [9] of the decomposition of 4,4-dimethylpent-1-ene in the presence of O_2 and $k_8 = k_{11}$ will be assumed.

$$CH_2CHCH_2 + HO_2 \rightarrow C_3H_6 + O_2. \quad (11)$$

Further, although k_7 for the recombination of MA radicals is not known, it is likely to be very similar to $k_{12} = 3.0 \times 10^9$ dm^3 mol^{-1} for the recombination of allyl radicals [10].

$$2CH_2CHCH_2 \rightarrow CH_2{=}CHCH_2CH_2CH{=}CH_2. \quad (12)$$

As [MA] is then calculated from $[(R_{DMHDE})_0/k_7]^{1/2}$, little error in [MA] is likely. $[HO_2]$ can be calculated from the initial rate of formation of isobutene oxide $(R_{BO})_0$, since $k_{10} = 10^{8.85} \exp(-6390/T)$ dm^3 mol^{-1} s^{-1} is known very accurately from independent studies [11]. As will become clear later, only significant errors in the values of k_7, [MA], and $[HO_2]$ will be important in the determination of k_5 because its value is mainly influenced by results at low $[O_2]$, where the additional termination processes (8) and (9) are relatively minor.

Table 1 gives the values of $(R_{DMHDE})_0$ and $(R_{BO})_0$, from which the values of [MA] and $[HO_2]$ are cal-

TABLE 1
Summary of results for the calculation of k_5 and k_{13}

1	2	3	4	5	6	7	8[a]	9[b]
Mixture/torr								
C_4H_8	O_2	N_2	$10^5(R_{DMHDE})_0$/ torr s^{-1}	$10^5(R_{BO})_0$/ torr s^{-1}	$10^5k_8[MA][HO_2]$/ torr s^{-1}	$10^5k_9[HO_2]^2$/ torr s^{-1}	$(k_5)_{obs}$/ $dm^3\ mol^{-1}\ s^{-1}$	$Corr(k_5)_{obs}$/ $dm^3\ mol^{-1}\ s^{-1}$
	520 °C							
4	30	26	37.5	85.5	13.4	4.0	0.153	0.228
4	20	36	23.6	51.0	6.3	1.41	0.146	0.197
4	15	41	18.0	37.0	4.0	0.74	0.148	0.188
4	10	46	11.3	20.9	1.76	0.24	0.140	0.165
4	5	51	5.5	8.9	0.55	0.043	0.136	0.150
	500 °C							
4	56	0	32.0	132	24	14.5	0.069	0.151
4	30	26	16.9	49.2	6.5	2.0	0.068	0.102
4	20	36	13.7	29.1	3.4	0.70	0.082	0.107
4	10	46	5.9	11.1	0.86	0.10	0.071	0.082
4	5	51	2.9	5.9	0.32	0.028	0.069	0.077
10	30	20	32.5	88.5	6.4	1.05	0.052	0.070
	470 °C							
4	56	0	15.3	75.5	12.4	7.5	0.032	0.073
4	30	26	6.9	25.7	2.85	0.87	0.027	0.041
4	20	36	4.5	12.8	1.12	0.21	0.026	0.0335
4	10	46	2.03	4.50	0.27	0.026	0.0235	0.027
4	5	51	1.04	2.15	0.093	0.006	0.024	0.0265
10	30	20	15.6	44.0	2.9	0.41	0.024	0.029
	440 °C							
4	56	0	8.8	56.4	10.1	8.5	0.0174	0.054
4	30	26	3.2	15.9	1.70	0.68	0.0118	0.0205
4	20	36	1.85	8.4	0.69	0.185	0.0103	0.0152
4	10	46	0.86	2.8	0.155	0.021	0.0095	0.0116
10	30	20	7.8	32	2.10	0.42	0.0116	0.0155
	400 °C							
4	56	0	4.2	37.5	7.6	9.6	0.0078	0.040
4	30	26	1.20	10.5	1.14	0.75	0.0042	0.0108
4	20	36	0.71	4.5	0.39	0.135	0.0037	0.0067
10	30	20	3.9	1.85	1.45	0.37	0.0055	0.0080

[a]Column 8, use of Eq. (iii).
[b]Column 9, use of Eq. (iv).

culated, together with the initial rates of the two additional termination processes (8) and (9). Use of Eq. (iv) then gives the corrected values of $(k_5)_{obs}$ shown in column 9 of Table 1. As seen, the correction is significant at high $[O_2]$, but relatively small at low $[O_2]$ and high [DMHDE]. However, as a consequence, the corrected values of $(k_5)_{obs}$ are now more markedly dependent on O_2. Reliable values of k_5 could be obtained by a simple extrapolation to zero $[O_2]$, but following computer modelling of the system, there is strong evidence for a radical branching process, which may be expressed kinetically as reaction (13).

$$MA + HO_2 \rightarrow \text{branching.} \qquad (13)$$

Since [MA] and $[HO_2]$ are both known, then an allowance for the effect of reaction (13) on the value of k_5 can be made very simply in an analytical treatment. Equation (ii) is now modified to (v),

$$k_5[C_4H_8][O_2] + k_{13}[MA][HO_2] = (R_{DMHDE})_0 + k_8[MA][HO_2] + k_9[HO_2]^2 \qquad (v)$$

and the left-hand side can be equated to $(k_5)_{obs}[C_4H_8][O_2]$, where $(k_5)_{obs}$ is the corrected value in column 9 of Table 1. Rearrangement of this equality then gives Eq. (vi).

$$(k_5)_{obs} = k_5 + \frac{k_{13}[MA][HO_2]}{[C_4H_8][O_2]}. \qquad (vi)$$

TABLE 2
Values of k_5 and k_{13}

T/°C	k_5/dm^3 mol^{-1} s^{-1}	k_{13}/dm^3 mol^{-1} s^{-1}
400	0.0017 ± 0.0010	4.0 × 10^9
440	0.0077 ± 0.0009	3.7 × 10^9
470	0.0225 ± 0.0018	3.2 × 10^9
500	0.065 ± 0.006	2.9 × 10^9
520	0.125 ± 0.005	3.6 × 10^9

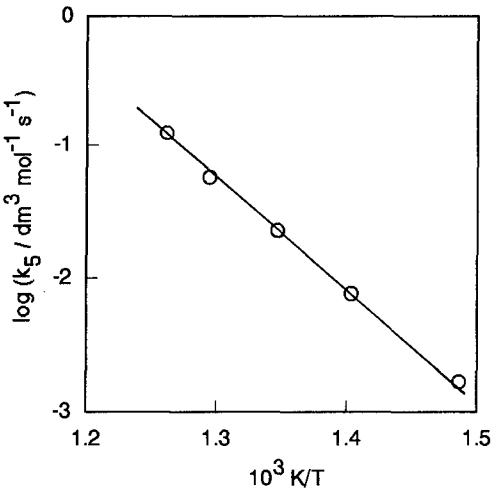

FIG. 3. Arrhenius plot for k_5.

Plots of $(k_5)_{obs}$ (corrected) against [MA][HO_2]/[C_4H_8][O_2] give very good straight lines at each temperature, from which the intercepts give k_5 and gradients give k_{13}. At all temperatures, other than 400 °C, the values of k_5 can be obtained accurately, and they are summarised in Table 2, together with the values of k_{13}. Figure 3 shows the good line obtained from the Arrhenius plot for k_5, and values of A_5 = $10^{9.68\pm0.44}$ dm^3 mol^{-1} s^{-1} and E_5 = 161.2 ± 6.4 kJ mol^{-1} are obtained.

Importantly, virtually the same value of k_5 at each temperature is obtained from the simple interpretation using Eq. (iii), providing the results for [O_2] < 30 torr are used. An Arrhenius plot of the k_{13} values gives A_{13} = $10^{8.82\pm0.35}$ dm^3 mol^{-1} s^{-1} and E_{13} = −10.0 ± 10 kJ mol^{-1}. Alternatively, between 400 °C and 520 °C, k_{13} = (3.5 ± 1) × 10^9 dm^3 mol^{-1} s^{-1}.

Table 3 summarises all the data obtained for the primary initiation reaction. The excellent agreement of the activation energies for RH = HCHO, C_3H_6, and i-C_4H_8 confirms the validity of the data and of the method used.

Use of the C_3H_6 + O_2 Reaction for the Determination of k_c:

The success in determining *directly* values of rate constants for the primary initiation process, previously virtually unobtainable by experiment, has led to novel studies involving the addition of suitable hydrocarbons and related compounds to C_3H_6 + O_2 mixtures in order to determine other values of k_c.

When *small* amounts of compound RH containing C—H bonds of dissociation energy comparable to that in the allyl C—H bonds in C_3H_6 are added to C_3H_6 + O_2 mixtures, then additional primary initiation occurs through reaction (C).

$$RH + O_2 \rightarrow R + HO_2. \qquad (C)$$

Providing R has a facile reaction, as in all cases studied here, then [allyl] >> [R], and the recombination of allyl radicals (12) remains the major termination step. With the simple case where (12) is the only termination step and low O_2 pressures are used, so that any radical branching reactions are negligible, then the ratio k_c/k_1 can be obtained from Eq. (vii).

$$\frac{R_{HDE}}{(R_{HDE})_0} = 1 + \frac{k_c[RH]}{k_1[C_3H_6]} \qquad (vii)$$

where R_{HDE} and $(R_{HDE})_0$ are the initial rates of formation of HDE in the presence and absence of RH. Figure 4 shows typical plots for the initial yields of HDE and propene oxide for the mixture containing 12, 18, and 30 torr of C_3H_6, N_2, and O_2, respectively, at 470 °C in the presence and absence of 1 torr of penta-1,4-diene (PDE). The yields of both products rise significantly when PDE is added. Initial values of $R_{HDE}/(R_{HDE})_0$ can be obtained accurately, and by the use of Eq. (vii), values of k_c/k_1 can be deter-

TABLE 3
Arrhenius Parameters for RH + $O_2 \rightarrow$ R + HO_2

RH	log(A/dm^3 mol^{-1} s^{-1})	E/kJ mol^{-1}	T/°C	Ref.
HCHO	10.31	163 ± 6	400–540	7
C_3H_6	9.29 ± 0.41	163.5 ± 5	400–520	6
i-C_4H_8	9.68 ± 0.44	161.2 ± 6.4	400–520	present work

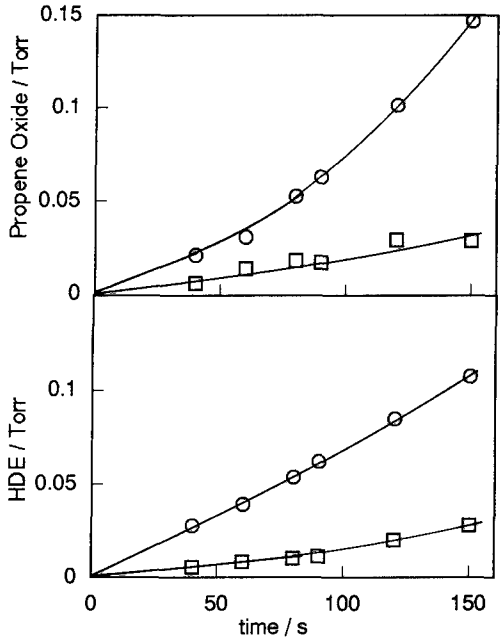

FIG. 4. Formation of HDE and propene oxide in addition studies. C_3H_6 = 12; O_2 = 30; N_2 = 18 torr. □, PDE = 0; ○, PDE = 0.4 torr.

TABLE 4
Kinetic data for PDE + $O_2 \rightarrow CH_2CHCHCHCH_2$ + HO_2 at 470 °C

Mixture/torr				k_c/k_1	k_c/k_1
PDE	C_3H_6	N_2	O_2	[Eq. (vii)]	(corrected)
1.0	12	18	30	39	52
0.4	12	38	10	45.5	50
0.4	12	18	30	46.5	55.5

mined, which are summarised in Table 4 for three mixtures. An allowance can be made for radical branching through reaction (14) [6] and for additional radical termination via (9) and (11).

$$CH_2CHCH_2 + O_2 \rightarrow 2 \text{ radicals} + \text{products} \quad (14)$$

$$CH_2CHCH_2 + HO_2 \rightarrow C_3H_6 + O_2. \quad (11)$$

$[CH_2CHCH_2]$ is calculated from R_{HDE} and k_{12}, and $[HO_2]$ from the initial rate of formation of propene oxide (15) and k_{15}. Details of the correction are given elsewhere [6].

$$HO_2 + C_3H_6 \rightarrow C_3H_6O + OH. \quad (15)$$

The magnitude of the correction (Table 4) rises with $[O_2]$, as found [6] in the determination of both k_1 and k_5, but does not exceed about 30%. From $A_1 = 10^{9.29}$ dm^3 mol^{-1} s^{-1} and E_1 = 163.5 kJ mol^{-1}, and the mean value of k_c/k_1 = 52.5, then k_c = 0.27 dm^3 mol^{-1} s^{-1} at 470 °C (with an accuracy of about 20%).

Relatively reliable Arrhenius parameters for k_c(PDE) can be calculated. Allowing for the path degeneracy difference of 1.5 and the extra loss (ca. 19 J mol^{-1} K^{-1}) of entropy of activation in the formation of the pentadienyl radical (where electron delocalisation occurs across the full carbon chain) compared with that in the formation of the allyl radical, then A_1/A_c = 15, and from k_c/k_1 = 52.5, then $E_1 - E_c$ = 41.2 kJ mol^{-1}. In consequence, A_c(PDE) = $10^{8.0}$ dm^3 mol^{-1} s^{-1}, and with E_1 = 163.5, E_c(PDE) = 122 kJ mol^{-1}. The activation energy may be validated independently. With $E_{-c} \approx 0$, so that ΔH_c (PDE) = 122 kJ mol^{-1}, then with ΔH_c for a normal secondary C—H bond in an alkane equal to 201 kJ mol^{-1}, the resonance energy of stabilisation in the pentadienyl radical is 79 kJ mol^{-1}, in exact agreement with the value suggested by McMillen and Golden [12]. Table 5 summarises values of k_c/k_1 and k_c, determined for several additives RH. The increase in the values from propene to isobutene/*trans*-but-2-ene to 2-methylbut-2-ene to 2,3-dimethylbut-2-ene is consistent, after allowance for the different path degeneracies, with a systematic reduction in the allyl C—H bond dissociation energy of 8 kJ mol^{-1} for each additional CH_3 group in the alkene structure. Similar values of k_c for but-1-ene and pent-1-ene are expected, as each alkene contains one allyl CH_2 group. Similar values are also expected for isobutene and *trans*-but-2-ene, and the value of k_c(isobutene)/k_1 is in excellent agreement with the value obtained for k_5/k_1 = 3.8 from the two independent sets of Arrhenius parameters given earlier.

When k_c/k_1 falls below 5, the increase in R_{HDE} is too small for precise measurement unless $[RH]/[C_3H_6]$ exceeds 0.1, which is undesirable. When toluene at a pressure of 1 torr is added to the mixture used above, the increase in R_{HDE} is barely perceptible, and only a maximum value of $k_c/k_1 <$ 0.03 at 500 °C can be determined. Recently, Emdee et al. [4] have modelled the oxidation of toluene at about 930 °C and claim that the rate is most sensitive to the value of k_{ct}. From their analysis, $A_{Ct} = 3.0 \times 10^{11}$ dm^3 mol^{-1} s^{-1} and E_{ct} = 173 kJ mol^{-1}, which give k_{ct} = 0.61 dm^3 mol^{-1} s^{-1} at 500 °C, which is a factor of 20 higher than the *maximum* value possible in the present studies. The value of A_{ct} obtained by Emdee et al. is a factor of 100 too high, and $A_{ct} \approx A_1 = 2.0 \times 10^9$ dm^3 mol^{-1} s^{-1} and $E_{ct} \approx E_1$ = 163.5 kJ mol^{-1} are more likely Arrhenius parameters. As $\Delta S_{ct} \approx 0$, then $A_{ct} \approx A_{-ct}$, so that $A_{ct} \approx 2 \times 10^9$ dm^3 mol^{-1} s^{-1}, in close agreement with $A_{-1} = 1.6 \times 10^9$ dm^3 mol^{-1} s^{-1} at 500 °C [6].

$$C_6H_5CH_3 + O_2 \rightarrow C_6H_5CH_2 + HO_2. \quad (Ct)$$

TABLE 5
Kinetic data[a] for RH + $O_2 \rightarrow$ R + HO_2

RH	k_c/k_1	k_c/dm^3 mol^{-1} s^{-1}	T/°C	log(A_c/dm^3 mol^{-3} s^{-1})	E_c/kJ mol^{-1}
$(CH_3)_2C=CHCH_3$	30.5	0.0282	420	9.8	151
$(CH_3)_2C=C(CH_3)_2$	145	0.134	420	9.9	143
t-$CH_3CH=CHCH_3$	4.3	0.075	500	9.6	158
	4.9	0.0045	420	9.6	158
$(CH_3)_2C=CH_2$	5.5	0.0051	420	9.68[b]	161.2[b]
$CH_3CH_2CH=CH_2$	12	0.011	420	9.1	146
$CH_3CH_2CH_2CH=CH_2$	15	0.014	420	9.1	145
$CH_2=CHCH_2CH=CH_2$	52.5	0.327	470	8.0	122
$C_6H_5CH_3$	<2	<0.03	500	9.3[c]	164[c]

[a]Corrected as described in the text.
[b]Values obtained from direct study.
[c]Recommended values, see text.

Database for RH + $O_2 \rightarrow$ R + HO_2:

Although the data are limited, there is an urgent need for a database for the primary initiation reaction which is a key elementary step in combustion mechanisms. Data for RH = alkane will be extremely difficult to determine experimentally, and given the high level of consistency in the present results, the following parameters are suggested.

	A/dm^3 mol^{-1} s^{-1} (per C—H bond)	E/kJ mol^{-1}
I	7.0×10^9	ΔH
II	7.0×10^8	ΔH
III	7.0×10^7	ΔH

I localised electron in free radical R (e.g., alkanes, simple oxygenates).
II Delocalised electron involving loss of one rotation, (e.g., alkenes, alkylbenzenes).
III Delocalised electron involving loss of two rotations, (e.g., $CH_2=CH\underline{CH_2}CH=CH_2$).

The database is reliable up to about 1200 K (factor of 2) unless there is a marked degree of non-Arrhenius behaviour in reaction (C).

Acknowledgments

We are grateful to Shell Research Ltd. for continued support.

REFERENCES

1. Baulch, D. L., Cobos, C. J., Cox, R. A., Frank, P., Just, Th., Kerr, J. A., Pilling, M. J., Troe, J., Walker, R. W., and Warnatz, J., *J. Phys. Chem. Ref. Data* 21:411 (1992).
2. Pitz, W. J., and Westbrook, C. K., *Combust. Flame* 63:113 (1986).
3. Warnatz, J., Paper presented at the 12th International Symposium on Gas Kinetics, Nottingham, UK, September, 1992.
4. Emdee, J. L., Brezinsky, K., and Glassman, I., *J. Phys. Chem.* 96:2151 (1992).
5. Walker, R. W., *Reaction Kinetics*, Specialist Periodical Reports, Chemical Society, London, 1974, Vol. 1, p. 161.
6. Stothard, N. D., and Walker, R. W., *J. Chem. Soc. Faraday Trans.* 87:241 (1991).
7. Baldwin, R. R., Fuller, A. R., Longthorn, D., and Walker, R. W., *J. Chem. Soc. Faraday Trans. I* 70:1257 (1974).
8. Stothard, N. D., and Walker, R. W., unpublished work.
9. Lodhi, Z. H., and Walker, R. W., *J. Chem. Soc. Faraday Trans.* 87:681 (1991).
10. Baulch, D. L., Cox, R. A., Frank, P., Just, Th., Kerr, J. A., Pilling, M. J., Troe, J., Walker, R. W., and Warnatz, J., *Combust. Flame* 98:59 (1994).
11. Stothard, N. D., and Walker, R. W., *J. Chem. Soc. Faraday Trans.* 86:2115 (1990).
12. McMillan, D. F., and Golden, D. M., *Annu. Rev. Phys. Chem.* 33:493 (1982).

COMMENT

Joseph W. Bozzelli, New Jersey Institute of Technology, USA. Figure 1 in your paper shows that acetone is the major product in the isobutene + O_2 reaction system. It is clearly higher in concentration than isobutene oxide, methacrolein, and DMHDE—listed in order of decreasing concentration.

Is it likely that the acetone results from the following reaction scheme?

	HO_2 Addition	Unimolecular Isomerization (H-atom shift)	Dissociation
	$C_2C{=}C + HO_2 \rightarrow C_2C(OOH)C. \rightarrow$	$C_3COO.$	$\rightarrow C_3C. + O_2$

$C^3C.$ will rapidly react with HO^2 to exothermic, and more active, products:

$$C_3CO. + OH \quad \text{and then } C_3CO. \rightarrow C_2C{=}O \text{ (acetone)} + CH_3.$$

The high (acetone) then shows the above reaction scheme occurs much faster than isobutene oxide formation. This would explain results of some other researchers failing to observe cyclic ethers from reactions of R. + O_2, i.e., dissociation of the adduct(s) to HO_2 + olefin is faster than the cyclic ether formation.

Fast propagation of R. + HO_2 to RO + OH is further supported via the methacrolein product yields from reaction of MA with HO_2.

Author's Reply. Acetone is undoubtedly the major product and is formed via OH addition in the so-called Waddington mechanism:

$$OH + (CH_3)_2C{=}CH_2 \rightarrow (CH_3)_2\underset{\underset{OH}{|}}{C}{-}CH_2 \xrightarrow{O_2} (CH_3)_2\underset{\underset{\underset{H}{|}}{O}}{C}{-}\underset{\underset{\underset{O}{|}}{O}}{CH_2} \rightarrow CH_3COCH_3 + OH + HCHO.$$

When $(CH_3)_3C$ radicals are formed under essentially the same conditions from isobutane (by H abstraction) and from tetramethylbutane (by homolysis), acetone is *not* observed in the initial products, but is formed in a secondary process from isobutene (as above) [1,2].

The reaction of $(CH_3)_3C$ radicals with O_2 gives isobutene in a yield of 99%, the remaining 1% being isobutene oxide. Further, the reaction $(CH_3)_3C + HO_2 \rightarrow (CH_3)_3CO + OH$ would be of negligible importance because $(CH_3)_3C + O_2$ is very fast ($k = 10^8$ dm^3 s^{-1}) and $[HO_2]/[O_2] \approx 10^{-6}$. The situation with methylallyl (MA) + HO_2 is completely different. MA has no easy reaction with O_2 (or any other molecular species), so that [MA] is relatively high and the radical is consumed mainly through radical-radical processes:

$$MA + MA \rightarrow CH_2{=}C(CH_3)CH_2CH_2C(CH_3){=}CH_2$$

$$MA + HO_2 \rightarrow (CH_3)_2C{=}CH_2 + O_2$$

$$MA + HO_2 \rightarrow CH_2C(CH_3)CH_2OOH \xrightarrow{O_2}$$

$$CH_2 = C(CH_3)CHO + OH + HO_2.$$

In summary, the acetone formation cannot be used to provide additional evidence for the R + O_2 mechanism, which remains far from clear.

REFERENCES

1. Baker, R. R., Baldwin, R. R., and Walker, R. W., *J. Chem. Soc. Faraday Trans. I* 75:140 (1979).
2. Baldwin, R. R., Hisham, J. W. M., Keen, A., and Walker, R. W., *J. Chem. Soc. Faraday Trans. I* 78:1165 (1982).

Twenty-Fifth Symposium (International) on Combustion/The Combustion Institute, 1994/pp. 775–781

FORMATION OF METHOXY AND HYDROXYMETHYL FREE RADICALS IN SELECTED ELEMENTARY REACTIONS

S. DÓBÉ AND T. BÉRCES
Central Research Institute for Chemistry
Hungarian Academy of Sciences
Pusztaszeri u. 59-67, H-1025 Budapest, Hungary

AND

F. TEMPS, H. Gg. WAGNER AND H. ZIEMER
Max-Planck-Institut für Strömungsforschung
Bunsenstrasse 10, D-3703 Göttingen, Germany

The fast flow technique combined with laser-induced fluorescence (LIF) and laser magnetic resonance (LMR) detections have been used to obtain branching ratios for CH_3O and CH_2OH formation, respectively, in various reactions. A detailed study of the product yields showed that reaction $F + CH_3ONO \rightarrow FNO + CH_3O$ is a clean methoxy radical source at low temperature that gives CH_3O with practically 100% efficiency. The branching ratios for CH_3O and CH_2OH formation in the reaction of F with CH_3OH are $k_{1a}/(k_{1a} + k_{1b}) = 0.57 \pm 0.05$ and $k_{1b}/(k_{1a} + k_{1b}) = 0.41 \pm 0.05$, respectively, between 300 and 600 K independent of temperature; $F + CH_3OH \rightarrow HF + CH_3O$ (1a), $F + CH_3OH \rightarrow HF + CH_2OH$ (1b).

The branching ratios for product radical formation in reactions $X + CH_3OH \rightarrow HX + CH_3O$ and $X + CH_3OH \rightarrow HX + CH_2OH$ (where X = F, OH, and Cl) were studied between 298 and 612 K. The considerable decrease of exothermicity in the order of F, OH, and Cl reactions is expected to go with a decrease in reactivity and a simultaneous increase in selectivity, which is indeed experienced for reactions $F + CH_3OH$ and $OH + CH_3OH$. However, the reaction $Cl + CH_3OH$ was found to be a "high reactivity high selectivity" process yielding CH_2OH radicals with practically 100% yield up to about 500 K. The fast reaction and the relatively small temperature dependences of the branching ratios indicate that some specific effects govern the kinetics of this reaction.

Combustion implications and utilization of the results in kinetic experiments are discussed.

Introduction

Hydrogen atom abstraction reactions are frequently used in flow systems to obtain free radicals. However, in such reactions, more than one reactive species are often formed in competing reaction channels, as demonstrated below by the reaction of the F atom with methanol:

$$F + CH_3OH \rightarrow HF + CH_3O \qquad (1a)$$

$$F + CH_3OH \rightarrow HF + CH_2OH \qquad (1b)$$

The yield of product formation can be characterized by the branching ratio, which is given for the formation of product i as $\Gamma_i = k_i/\Sigma k_i$, where k_i is the rate constant for the formation of product i and Σk_i stands for the sum of the rate constants of all parallel reaction channels. Determination of product branching ratios is of primary importance for the identification of relatively clean, efficient radical sources and for revealing side reactions that may interfere in the application of such reactions.

Competing reaction channels may yield species of very different reactivity and with different subsequent reactions. Therefore, the values of the branching ratios and their temperature dependences, used as inputs in combustion and atmospheric modeling studies, can have a fundamental influence on the outputs of model calculations. A good example for this is provided by the hydrogen atom abstraction reactions by OH radicals from methanol:

$$OH + CH_3OH \rightarrow H_2O + CH_3O \qquad (2a)$$

$$OH + CH_3OH \rightarrow H_2O + CH_2OH \qquad (2b)$$

These are the major CH_3OH-consuming reactions in methanol combustion and flame [1], which yield CH_3O and CH_2OH radicals. The interest in the formation and reactions of CH_3O and CH_2OH has considerably increased since the recognition of methanol as an environmentally more acceptable alternative fuel.

In this work, product branching ratios were deter-

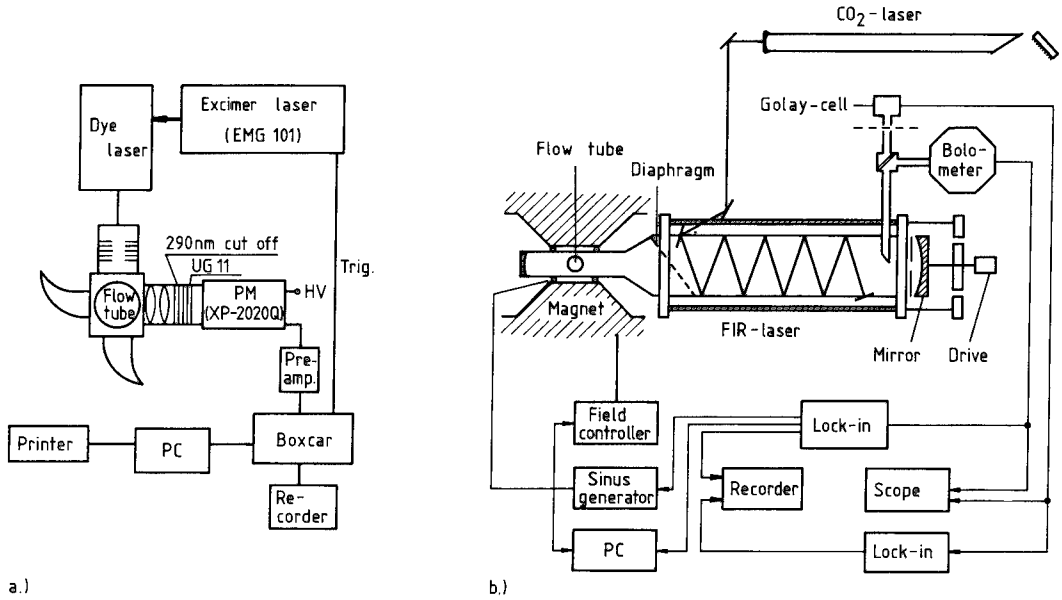

FIG. 1. Detection devices of the fast flow systems used for monitoring (a) CH_3O by LIF and (b) CH_2OH by LMR.

mined, in the temperature range of 298–612 K, for reactions (1) through (4).

$$Cl + CH_3OH \rightarrow HCl + CH_3O \quad (3a)$$

$$Cl + CH_3OH \rightarrow HCl + CH_2OH \quad (3b)$$

$$F + CH_3ONO \rightarrow FNO + CH_3O \quad (4)$$

The implications of the results in combustion models and in the application of experimental kinetic techniques are discussed.

Experimental

Methoxy and hydroxymethyl branching ratios were determined in fast flow systems operated in laboratories at Budapest and Göttingen, respectively. The detection techniques employed in the investigations are presented schematically in Fig. 1.

Methoxy radicals were detected by laser-induced fluorescence (LIF) using an excimer laser-pumped frequency doubled dye laser at 292.8 nm excitation wavelength [2] (Fig. 1a). The fluorescence induced by the laser pulse was collected through glass filters onto the cathode of a photomultiplier and was processed by a gated boxcar integrator. Wood's horns and baffles served to reduce the scattered light. The sensitivity of CH_3O detection was 1×10^9 cm^{-3} (S/N = 1).

Hydroxymethyl radicals were monitored with a far infrared laser magnetic resonance (LMR) spectrometer (Fig. 1b). The absorption volume was located intracavity; the absorption signal was detected by a liquid helium-cooled Ge bolometer and was processed by a lock-in amplifier. CH_2OH radicals were detected in the form of HO_2, which were formed in the laser tube by the reaction $CH_2OH + O_2 \rightarrow CH_2O + HO_2$. Detection in the form of HO_2 provided better sensitivity compared to CH_2OH and allowed the use of the fast and quantitative gas titration reactions $F + H_2O_2$ and $CHO + O_2$ in hydroxymethyl yield determinations. The LMR parameters of the HO_2 detection were $\lambda = 163$ μm and $B_0 = 0.25$ Tesla [3]. The detection limit for CH_2OH was 5×10^8 cm^{-3} (S/N = 1). Signals were found proportional to concentrations.

Electrically heated quartz flow tubes of 4.0-cm internal diameter were used in all experiments. In room-temperature investigations, the reactors were coated with thin films of Teflon. No coatings were used above 298 K. The temperature was kept constant over the 35-cm reactor length within $\Delta T = \pm 4$ K.

The reactors were equipped with coaxial moveable injectors for introducing atomic and radical reactants. Fluorine atoms were generated by flowing dilute F_2/He mixtures through Al_2O_3-lined microwave discharges. The F atoms were introduced directly in the reactors or were converted into other species inside the injector by fast reactions. Thus, the radical reactants Cl and OH were produced by the reactions $F + HCl$ and $F + H_2O$, respectively. Reactions of methoxy and hydroxymethyl formation were carried out in the reactors at a fixed position of the inlets

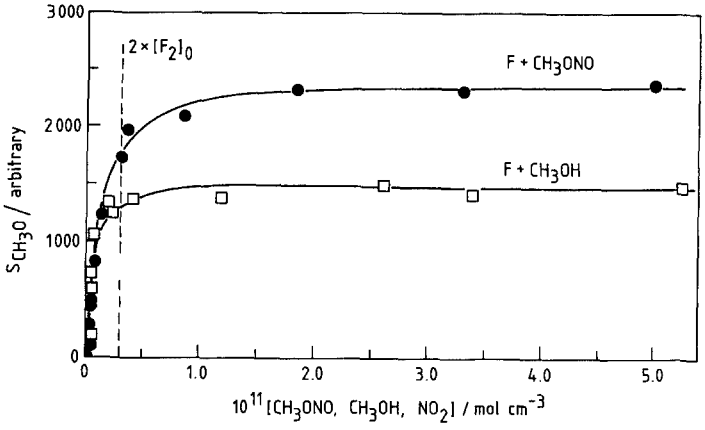

FIG. 2. Profiles of methoxy LIF signals vs stable reactant concentrations at t = 4.5 ms reaction time.

(i.e., at constant reaction time) by reacting the transient species with the stable reactants. Mixtures of the stable reactants with helium entered the reactors at the top through side arms.

Helium (Messer–Griesheim, 99.9999%) was the carrier gas. Other gases used in the experiments were of the highest purity commercially available. Methanol (≥97%) was obtained from Merck. CH_2O was prepared by pyrolyzing paraformaldehyde, while CH_3ONO was synthesized from methanol with nitrous acid.

The gas flows were regulated by mass flow controllers and needle valves. Linear flow rates varied in the range v = 6–40 m/s. Typical overall pressure in the reactors was P = 2.8 mbar. Concentrations of CH_3O and CH_2OH radicals were in the range of 1×10^{-13}–4×10^{-12} mol/cm^3. More details of the experimental techniques can be found in Refs. 4 and 5.

Results and Discussion

The principle of the comparative method developed and used in this work for the determination of the branching ratios of product formation in radical + molecule → radical + molecule type reactions is to compare, at a given reaction time t, the concentration of the product radical (CH_3O and CH_2OH, respectively) formed in the investigated reaction with the concentration of the same radical produced in a reference reaction under comparable experimental conditions. The latter requirement was met if the concentrations of the free radical reactants were the same in both the studied and the reference experiments and if the stable reactant was in excess large enough to assure complete conversion of the radical reactants into products. The reference reactions were

$$F + CH_3ONO \rightarrow FNO + CH_3O \qquad (4)$$

and

$$F + CH_2O \rightarrow HF + CHO \xrightarrow{+\,O_2} HO_2 + CO \qquad (5)$$

in the determinations of the branching ratios for CH_3O and CH_2OH formation, respectively. In the selection of these reference reactions, it was taken into account that the yield of product radical formation in reactions (4) and (5) was 100%, within the limits of experimental errors, as shown by calibrations (see below). In a few experiments, carried out above 400 K, reaction (1a) served as reference reaction.

The branching ratio for the formation of radical R, Γ_R, was obtained from the ratio of the radical-concentration-proportional signals, S_R, measured in the studied reaction and in the reference process: $\Gamma_R = (S_R/S_R^{ref})\,\Gamma_R^{ref}$, where Γ_R^{ref} is the branching ratio for R formation in the reference reaction. The advantage of this method (as well as of all comparative methods) is that a comparison of two values of the same experimental observable is made, and therefore, the effect of systematic errors is either eliminated or minimized.

Room-Temperature CH_3O and CH_2OH Branching Ratios in Reactions (1) and (4):

Reactions F + CH_3OH and F + CH_3ONO selected for detailed kinetic studies may serve as reference reactions in other investigations.

The formation of methoxy radical was studied in a series of experiments in which the fluorine atom concentration was kept at a constant value, and the concentration of the stable reactants was varied. Representative methoxy LIF profiles are presented in Fig. 2. In the case of both reactions, the LIF signals increased first rapidly with increasing concentration of the stable reactant and then attained a limiting high concentration value.

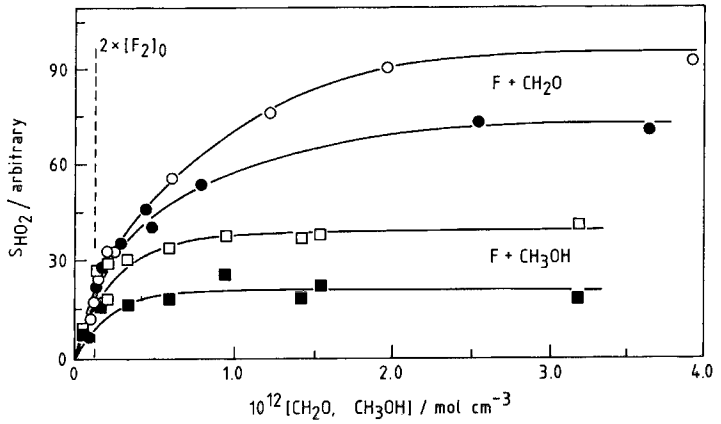

FIG. 3. Profiles of hydroperoxyl LMR signals vs CH_2O and CH_3OH concentrations. Open and full symbols refer to t = 4.4 ms and t = 8.4 ms reaction times, respectively.

The CH_3O LIF signals were transformed into methoxy concentrations by a calibration procedure based on the complete conversion of CH_3 by NO_2 into CH_3O in the presence of a large excess of methyl radicals [6]. (The CH_3 radicals were generated inside the inlet by reaction F + CH_4.) A plot of S_{CH_3O} vs NO_2 concentration gave a good straight line at low nitrogen dioxide concentrations. Using the initial slope as the methoxy calibration factor and assuming 100% dissociation of F_2 in the discharge [7], one obtains from the limiting value of the methoxy LIF signals the branching ratios given in the first and fourth row of Table 1 (T = 298 K). The error limits appearing in the table and throughout the paper are 1 standard deviation and indicate precision only. (The estimated systematic errors are 15–30 %.) The Γ values have been corrected for the different wall consumption rates of the transients.

Similar studies to those of CH_3O radicals were carried out to obtain the yield of CH_2OH formation in reaction F + CH_3OH. Typical plots of the HO_2 LMR signals as a function of methanol concentration are shown in Fig. 3. Included in the figure are also the S_{HO_2} vs $[CH_2O]$ plots for the reference reaction F + CH_2O. This reaction yields CHO radicals, which are then converted by the fast reaction with O_2 quantitatively into HO_2 [7]. A calibration of the HO_2 LMR signal with reaction F + $H_2O_2 \rightarrow$ HF + HO_2 [7] showed indeed that reaction of the F atom with formaldehyde is a single-channel process forming HF and formyl radical (which reacts with O_2 to give HO_2). Using $\Gamma_{HO_2} = 1$ for the reference reaction (5), a branching ratio of $k_{1b}/(k_{1a} + k_{1b}) = 0.41 \pm 0.04$ is obtained for CH_2OH formation.

There is no published branching ratio for CH_3O formation in reaction F + CH_3ONO. Our results indicate that the yield of CH_3O formation is unity, which makes this reaction a promising new methoxy radical source. Since reaction (3) is both fast and quantitative, it is well suited also for gas titrations in discharge flow studies.

There are a number of published data available on the methoxy radical yield in the F + CH_3OH reaction. Our $\Gamma_{CH_3O} = 0.57 \pm 0.05$ value is in excellent agreement with most other direct measurements, thus, with the infrared chemiluminescence results (0.53 ± 0.36 [8]) and the mass spectrometric data (0.59 ± 0.06 [9], 0.60 [10], and 0.58 ± 0.23 [11]), whereas it is higher than the CH_3O branching ratio reported in a recent LIF study (0.4 ± 0.1 [12]). Our $\Gamma_{CH_2OH} = 0.41 \pm 0.04$ value is about 30% lower than the ratio obtained by Pagsberg et al. (0.56 [13]). The present work appears to be the first one that obtains in the same study branching ratios for both CH_3O and CH_2OH radical formation in the reaction of F atoms with CH_3OH. The sum of the two branching ratios is unity within the limits of experimental errors: $\Gamma_{CH_3O} + \Gamma_{CH_2OH} = 0.98 \pm 0.07$.

The branching ratios determined for CH_3O and CH_2OH formation in reaction F + CH_3OH do not fit in with the expectations based on thermochemical and statistical considerations, which are in favor of H-atom abstraction from the CH_3 rather than the OH group. There is probably no barrier or very small barrier for the reaction; thus, the value of the branching ratio is determined by the difference in the activation entropies rather than the activation energies of the CH_3O- and CH_2OH-forming channels.

The concentration plots presented in Figs. 2 and 3 can be used to obtain estimates for the rate constants of some of the investigated reactions. The ratios of the initial slopes supply $k_4/k_{1a} \approx 0.8$ and $k_5/k_{1b} \approx 1.4$. Taking $k_1 = 7.7 \times 10^{13}$ cm^3 mol^{-1} s^{-1} from the literature [10] and using the branching ratios determined for reaction (1) in this work, $k_4 \approx 3.6 \times 10^{13}$ cm^3 mol^{-1} s^{-1} and $k_5 \approx 4.3 \times 10^{13}$ cm^3 mol^{-1} s^{-1} are estimated.

Branching Ratios for CH_3O and CH_2OH Formation in Reactions of X + CH_3OH:

Free radicals CH_3O and CH_2OH can be produced most obviously by H-atom abstraction from metha-

TABLE 1
Branching ratios for methoxy and hydroxymethyl radical formation

Reaction	Γ_{CH_3O} and Γ_{CH_2OH}			
	298 K	390 K	482 K	612 K
$F + CH_3OH \rightarrow HF + CH_3O$ (1a)	0.57 ± 0.05		0.62 ± 0.05	
$F + CH_3OH \rightarrow HF + CH_2OH$ (1b)	0.41 ± 0.04	0.37 ± 0.15		0.45
$OH + CH_3OH \rightarrow H_2O + CH_3O$ (2a)	≈0.1[a]		0.15 ± 0.05	0.23 ± 0.07
$OH + CH_3OH \rightarrow H_2O + CH_2OH$ (2b)				0.71
$F + CH_3ONO \rightarrow FNO + CH_3O$ (4)	1.02 ± 0.10			
$Cl + CH_3OH \rightarrow HCl + CH_3O$ (3a)	0.01 ± 0.01		0.04 ± 0.02	
$Cl + CH_3OH \rightarrow HCl + CH_2OH$ (3b)	0.93 ± 0.05	0.88 ± 0.15		

[a]Estimated value (see text).

TABLE 2
Thermochemistry and overall rate constants for H-atom abstraction reactions $X + CH_3OH$

Reaction	ΔH°_{298} (kJ mol^{-1})	k^{ov}_{298} (cm^3 mol^{-1} s^{-1})	Reference
$F + CH_3OH \rightarrow HF + CH_3O$ (1a)	−125.9	7.7×10^{13}	10
$F + CH_3OH \rightarrow HF + CH_2OH$ (1b)	−159.8		
$OH + CH_3OH \rightarrow H_2O + CH_3O$ (2a)	−54.8	5.5×10^{11}	21
$OH + CH_3OH \rightarrow H_2O + CH_2OH$ (2b)	−88.7		
$Cl + CH_3OH \rightarrow HCl + CH_3O$ (3a)	12.6	3.2×10^{13}	21
$Cl + CH_3OH \rightarrow HCl + CH_2OH$ (3b)	−21.3		
$H + CH_3OH \rightarrow H_2 + CH_3O$ (6a)	8.4	9.0×10^{8}	22
$H + CH_3OH \rightarrow H_2 + CH_2OH$ (6b)	−25.5		
$Br + CH_3OH \rightarrow HBr + CH_3O$ (7a)	78.2	6.1×10^{6}	20[a]
$Br + CH_3OH \rightarrow HBr + CH_2OH$ (7b)	44.3		

[a]Calculated from k_{-7b} and K_{7b}.

nol. In a series of investigations, the reactions of F, OH, and Cl with methanol (reactions (1), (2), and (3)) were studied. Branching ratios were determined with the comparative method, using constant concentrations of the free radical reactants and methanol in excess, which assured complete consumption of the radical reactants at the selected reaction time. Branching ratios obtained in the 298–612 K temperature range are given in Table 1.

The room-temperature branching ratios show significant changes when the free radical reactant changes from F through OH to Cl. At room temperature, practically all chlorine atoms are converted into hydroxymethyl radicals in the reaction of Cl + CH_3OH, while the methoxy radical yield is higher than 50% in the F + CH_3OH reaction. Reaction OH + CH_3OH appears to be an intermediate case.

The room-temperature branching ratios determined for reaction F + CH_3OH in this work have been compared already with literature data. Our branching ratios obtained for reaction Cl + CH_3OH at 298 K are in accordance with previous findings [9,14–16] that indicate that the methoxy radical concentration produced in the reaction did not exceed the detection limits of the applied analytical techniques. Reaction OH + CH_3OH was too slow at room temperature to be studied in our flow systems, and the reported branching ratios show disparity. In a laser photolysis/resonance fluorescence study $k_{2a}/(k_{2a} + k_{2b}) = 0.11 \pm 0.03$ was obtained for the branching ratio of CH_3O formation [17] in reasonable agreement with the value of 0.15 ± 0.08 derived from the analysis of kinetic isotope effect measurements [18] and with the mass spectrometric result of 0.17 ± 0.13 [9]. On the contrary, Hess and Tully [19] concluded from their laser photolysis/LIF data that hydrogen abstraction from the hydroxy site is nearly inactive at room temperature. Extrapolation of our 482 and 612 K data to 298 K results in a few hundredths for the CH_3O yield. Taking into account all these values, a branching ratio of $k_{2a}/(k_{2a} + k_{2b}) \approx 0.1$ may be given as an estimate for the yield of

CH_3O formation at 298 K in reaction OH + CH_3OH.

In case of the F + CH_3OH reaction, no temperature dependence exceeding the error limits can be seen, and we suggest $k_{1a}/(k_{1a} + k_{1b}) = 0.59$ and $k_{1b}/(k_{1a} + k_{1b}) = 0.41$ for the whole 300–600 K temperature range. For reaction OH + CH_3OH, a definite methoxy yield increase occurs from a room-temperature value of about 0.1 up to a ratio of 0.2–0.3 at 600 K. Hägele et al. [17] reported an even more significant increase, i.e., $\Gamma_{CH_3O} = 0.11 \pm 0.03$ and $\Gamma_{CH_3O} = 0.22 \pm 0.07$ at 298 and 393 K, respectively. From these results, one can predict that formation of CH_3O becomes dominant above 1000 K. Finally, little is known of the temperature dependence of the branching ratios in the reaction of Cl with methanol. Although the error limits in our CH_3O and CH_2OH yield determinations above room temperature are quite large, nevertheless, one can expect that the branching ratio for CH_2OH formation is still around or above 0.9 at 500 K.

The temperature dependences of the branching ratios may be examined in terms of the thermochemistry of the CH_3O and CH_2OH-forming reactions. Recent kinetic studies suggest a heat of formation for the CH_2OH radical that is higher by 17 kJ mol^{-1} than the value in common use; i.e., $\Delta H^\circ_{f,298}(CH_2OH) = -9 \pm 6$ kJ mol^{-1} [5,20]. With this value and a reasonable difference for the CH_3O and CH_2OH heats of formation, $\Delta H^\circ_{f,298}(CH_3O) = 25$ kJ mol^{-1} is obtained [5]. Using the new heats of formation for CH_3O and CH_2OH, together with other thermochemical data taken from Ref. 21, the reaction heats presented in Table 2 are calculated. Literature rate constants for the overall reactions are also included in the table. In order to extend the reaction series toward endothermic processes, data for reactions H + CH_3OH (6) and Br + CH_3OH (7) are also given.

A significant change in the reaction heats is seen in the reaction series. For all members of the series except reaction (3), the increase of exothermicities is accompanied by an increase in the reaction rates (obviously as a result of the decrease of the activation energies). The increasing reactivity goes with a similarly significant decrease in selectivities (i.e., a decrease of the differences between Γ_{CH_3O} and Γ_{CH_2OH}) and a small decrease of the temperature dependence of the branching ratios. These tendencies seem to be governed by the reaction energetics, as shown in Fig. 4, where the energy diagrams of reactions X + CH_3OH are presented. The barrier heights (given in parentheses) were calculated by the semiempirical "bond strength–bond length" (BSBL) method [23], which provides predictions based mainly on the properties (energies) of the breaking and forming bonds. Although the calculated barrier heights are probably overestimated, however, the tendencies appear to be reliable and are in agreement with the observations.

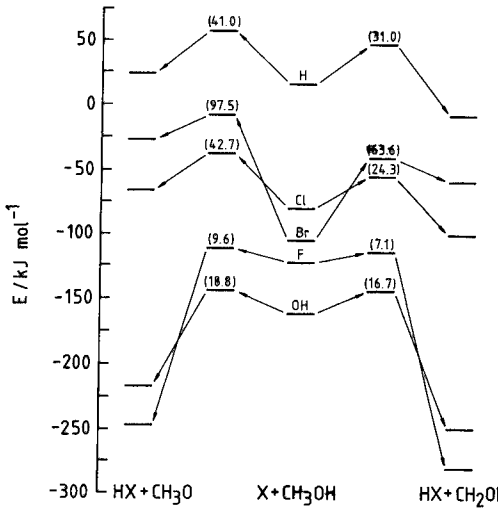

FIG. 4. Energy diagram for the reactions X + CH_3OH (X = H, F, Cl, Br, and OH). The barrier heights given in parentheses are calculated values (obtained by the BSBL method) and are relative to the energies of the initial states.

There is one striking exception among the reactions studied. This is reaction Cl + CH_3OH, which does not fit into the reaction series. The reaction rate is much higher and the temperature dependence of the branching ratios appears to be smaller for reaction Cl + CH_3OH than for the more exothermic OH + CH_3OH reaction. Note that this is the opposite of what is expected from the results of BSBL calculations. Moreover, it may be mentioned that no apparent correlation was found between the reactivities of Cl atoms and OH radicals toward oxygenated organic species including alcohols [24], whereas an essentially linear correlation was established in the case of reactions toward alkanes. Either an anomalous reaction mechanism (different from simple H-atom abstraction) or a specific effect, as for instance a polar effect, prevails in case of reaction Cl + CH_3OH.

Implication in Combustion-Related Kinetic Studies:

Rate parameters for CH_3O and CH_2OH reactions are required in models of methanol combustion and combustion models of other organic compounds. This work provides information on potential free radical sources that can be utilized in the experimental determinations of such type of kinetic data: (1) Reaction F + CH_3ONO is an ideal source of methoxy radicals in fast flow studies at low temperatures, since it yields CH_3O in a fast and quantitative reaction. Decomposition and H-atom abstraction from CH_3ONO may cause complications above 400 K. (2) Reaction Cl + CH_3OH is a clean source of CH_2OH radical below 600 K both in flow discharge and in

flash photolytic systems. The use of Cl-atom sources other than Cl_2 decomposition is recommended in order to avoid chain reactions. (3) The temperature independence of the kinetics of radical formation in reaction F + CH_3OH makes this reaction a feasible source of both CH_3O and CH_2OH in the whole temperature range, where these radicals are thermally stable. Use of this source may give rise to problems in product formation studies since reactions of CH_3O and CH_2OH often lead to the same products.

The branching ratios of CH_3O and CH_2OH formation in reaction OH + CH_3OH at typical combustion temperatures is of primary importance, since the two radicals may enter into different reactions and react with different rates. The present results imply that CH_3O formation is a minor channel at room temperature, but a definite increase in the rate of formation occurs with increasing temperature. Although the branching ratios, and especially the values for higher temperatures, are known with relatively large uncertainties, we estimate on the basis of all available data that the rate of CH_3O formation in reaction OH + CH_3OH becomes similar to that of CH_2OH at combustion relevant temperatures.

Acknowledgment

The research described in this work was supported in part by the Hungarian Science Foundation (OTKA Project No. 1803). The technical assistance of Mr. M. Otting in the experiments is acknowledged.

REFERENCES

1. Grotheer, H. H., Kelm, S., Driver, H. S. T., Hutcheon, R. J., Locket, R. D., and Robertson, G. N., *Ber. Bunsenges. Phys. Chem.* 96:1360–1376 (1992).
2. Inoue, G., Atkimoto, H., and Okuda, M., *J. Chem. Phys.* 72:1769–1775 (1980); Kappert, J., and Temps, F., *Chem. Phys.* 132:197–208 (1989).
3. Stimpfle, R. M., Perry, R. A., and Howard, C. J., *J. Chem. Phys.* 71:5183–5190 (1979).
4. Dóbé, S., Bérces, T., and Szilágyi, I., *J. Chem. Soc. Faraday Trans.* 87:2331–2336 (1991).
5. Dóbé, S., Otting, M., Temps, F., Wagner, H. Gg., and Ziemer, H., *Ber. Bunsenges. Phys. Chem.* 97:877–884 (1993).
6. Slagle, I. R., and Gutman, D., *J. Am. Chem. Soc.* 104:4741–4748 (1982).
7. Temps, F., and Wagner, H. Gg., *Ber. Bunsenges. Phys. Chem.* 88:410–414 (1984); Walther, C. D., and Wagner, H. Gg., *Ber. Bunsenges. Phys. Chem.* 87:403–409 (1983); Temps, F., Ph.D. Thesis, Max-Planck-Institut für Stromungsforschung, Göttingen, 1983.
8. Wickramaaratchi, M. A., Setser, D. W., Hildebrand, H., Koerbitzer, B., and Heydtmann, H., *Chem. Phys.* 94:109–129 (1985).
9. Meier, U., Grotheer, H. H., and Just, Th., *Chem. Phys. Lett.* 106:97–101 (1984).
10. Khatoon, T., and Hoyermann, K., *Ber. Bunsenges. Phys. Chem.* 92:669–673 (1988).
11. Durant, Jr., J. L., *J. Phys. Chem.* 95:10701–10704 (1991).
12. Bogan, D. J., Kaufman, M., Hand, C. W., Sanders, W. A., and Brauer, B. E., *J. Phys. Chem.* 94:8128–8134 (1990).
13. Pagsberg, P., Munk, J., Sillensen, A., and Anastasi, C., *Chem. Phys. Lett.* 146:375–381 (1988).
14. Sander, S. P., Peterson, M., Watson, R. T., and Patrick, R., *J. Phys. Chem.* 86:1236–1240 (1982).
15. Michael, J. V., Nava, D. F., Payne, W. A., and Stief, L. J., *J. Chem. Phys.* 70:3652–3656 (1979).
16. Payne, W. A., Brunning, J., Mitchell, M. B., and Stief, L. J., *Int. J. Chem. Kinet.* 20:63–74 (1988).
17. Hägele, J., Lorenz, K., Rhäsa, D., and Zellner, R., *Ber. Bunsenges. Phys. Chem.* 87:1023–1026 (1983).
18. McCaulley, J. A., Kelly, N., Golde, M. F., and Kaufman, F., *J. Phys. Chem.* 93:1014–1018 (1989).
19. Hess, W. P., and Tully, F. P., *J. Phys. Chem.* 93:1944–1947 (1989).
20. Seetula, J. A., and Gutman, D., *J. Phys. Chem.* 96:5401–5405 (1992).
21. Atkinson, R., Baulch, D. L., Cox, R. A., Hampson, Jr., R. F., Kerr, J. A., and Troe, J., *J. Phys. Chem. Ref. Data* 21:1125–1568 (1992).
22. Tsang, W., *J. Phys. Chem. Ref. Data* 16:471–508 (1987).
23. Bérces, T., and Dombi, J., *Int. J. Chem. Kinet.* 12:123–139 (1980).
24. Wallington, T. J., Skewes, L. M., Siegel, W. O., Wu, C.-H., and Japar, S. M., *Int. J. Chem. Kinet.* 20:867–875 (1988).

Twenty-Fifth Symposium (International) on Combustion/The Combustion Institute, 1994/pp. 783–791

THE REACTION OF HYDROPEROXY-PROPYL RADICALS WITH MOLECULAR OXYGEN

JOSEPH W. BOZZELLI
Chemistry and Chemical Engineering Department
New Jersey Institute of Technology
Newark, NJ 07102, USA

AND

WILLIAM J. PITZ
Lawrence Livermore National Laboratory
Livermore, CA 94551, USA

The addition of hydroperoxy-alkyl radicals to molecular oxygen is an important process leading to chain branching at conditions related to autoignition and engine knock, as well as in the low-temperature oxidation of paraffins. Rate constants and product channels for the reaction of hydroperoxy-propyl radicals with O_2 are estimated using thermodynamic properties, bimolecular quantum Kassel analysis, and transition state theory. Thermochemistry of the relevant molecules and radicals is estimated using group additivity and bond dissociation groups for radicals. Results show that the rates of the hydroperoxy-propyl radical addition to O_2 are near their high-pressure limits for pressures of 1 atm and above. The main products at 0.1–15 atm are stabilization, reverse reaction to hydroperoxy-propyl + O_2, and alkyl-carbonyl-hydroperoxide + OH. Dissociation rates and product channels of the stabilized adducts are estimated using unimolecular quantum Kassel analysis because stabilization is the most important hydroperoxy-propyl radical + O_2 product channel. At low temperatures, below about 700 K, the stabilized peroxy adducts react primarily to alkyl-carbonyl-hydroperoxide + OH, products that lead to chain branching. At higher temperatures, above about 700 K, the stabilized peroxy adducts react primarily to hydroperoxy-propyl radical + O_2, initial reactants, which inhibits the overall oxidation. The switch in decomposition product channels, from low to high temperature, correlates well with the experimentally observed negative temperature coefficient behavior for propane oxidation. Rate expressions for reaction of each of the three hydroperoxy-alkyl isomers with O_2 and for dissociation of the stabilized adducts are calculated for a series of pressures over a temperature range of 300–2100 K. Accurate rate expressions for alkylperoxy and hydroperoxy-alkyl reactions are essential to predict the negative temperature coefficient behavior for alkanes.

Introduction

The reaction of hydroperoxy-alkyl radicals with molecular oxygen is an important process in the low-temperature (typically below 900 K) chemistry of hydrocarbon oxidation. In reduced mechanisms [1–3] that retain only the essential features of the low-temperature chemistry related to autoignition and engine knock, this is the principal reaction leading to the formation of OH radicals and chain branching. The reaction of molecular oxygen with hydroperoxy-alkyl radicals is also an essential part of fully detailed chemical kinetic mechanisms used to simulate the chemistry leading to autoignition and knock [4,5].

The addition of molecular oxygen to hydroperoxy-alkyl radicals is illustrated in the following reactive sequence:

$$\mathrm{CCC} + \mathrm{OH} \rightleftarrows \mathrm{CC.C} + \mathrm{H_2O} \quad (1)$$

(alkyl radical formation)

$$\mathrm{CC.C} + \mathrm{O_2} \rightleftarrows \mathrm{CC(OO.)C} \rightleftarrows \mathrm{CC(OOH)C.} \quad (2)$$

(addition/isomerization)

$$\mathrm{CC(OOH)C.} + \mathrm{O_2} \rightleftarrows \mathrm{CC(OOH)COO.} \quad (3)$$

(second addition of O_2)

$$\mathrm{CC(OOH)COO.} \rightleftarrows \mathrm{CC(=O)COOH} + \mathrm{OH} \quad (4)$$

(isomerization/reaction)

$$\mathrm{CC(=O)COOH} \rightleftarrows \mathrm{CC(=O)CO.} + \mathrm{OH} \quad (5)$$

(chain branching).

(In the above notation, each carbon atom is saturated, except where a radical site is noted.) The key feature of this reaction sequence is that two OH radicals plus an alkoxy radical are generated (reactions 4 and 5) for each OH consumed; thus, the sequence is chain branching. Alkyl-carbonyl-hydroperoxides, as produced by reaction 4, have been measured in a motored CFR engine running on *n*-octane, *n*-heptane, and *n*-pentane [6]. Rates to various product channels of hydroperoxyl-alkyl + O_2 have not been experimentally measured or theoretically calculated. We estimate thermodynamic parameters, rate constants, and product channels for O_2 addition to the three isomers of hydroperoxy-propyl radicals using transition state theory [7] for isomerization, bimolecular QRRK theory [8], and accurate thermochemical estimations [9]. Unimolecular QRRK [10] is used to calculate the pressure and temperature dependencies of the rates of the stabilized adduct decomposition channels. These computational tools allow a thermochemical kinetics-based estimation [11] of the rates and product paths that evolve from the addition of hydroperoxy-alkyl radicals to molecular oxygen. The rate constants can then be input to a detailed chemical kinetic mechanism to elucidate the dominant reaction paths at conditions relevant to automotive engine knock.

High-Pressure Rate Constants

The reactions of O_2 with the three isomers of hydroperoxy-propyl radicals were examined: CC.COOH, C.CCOOH, and CC(OOH)C. Reaction paths considered for all three cases are given in Table 1. The thermodynamic properties for the relevant radicals and stable parents were obtained by group additivity using THERM [9] (Table 2) with updated H/C/O groups and bond dissociation groups [17]. The thermochemical data allow calculation of reverse reaction rate constants by microscopic reversibility.

Several types of reactions need to be considered for each of the hydroperoxy-alkyl radicals. Details on these k_∞ rate constants are also in Table 1.

Addition to O_2 (e.g., CC.COOH + O_2 → CC(OO.)COOH):

The forward rate constant was based on CH_2OH + O_2 times a factor of 1/2 for steric effects [12]. The reverse rate constant was obtained by microscopic reversibility.

Hydrogen Transfer (e.g., CC(OO.)COOH → C.C(OOH)COOH):

This reaction represents the intramolecular transfer of an H atom. The activation energy (E_a) for the forward rate of this reaction was estimated by

$$E_a = \text{ring strain} + E_{\text{abst}} \left\langle \begin{matrix} \text{primary} \\ \text{secondary} \\ \text{tertiary} \end{matrix} \right\rangle + \Delta H_{\text{rxn}}$$

where ΔH_{rxn} is the enthalpy of reaction (only included if reaction is endothermic). The ring strains are 6.0, 0.1, and 6.0 kcal/mole for rings containing five, six, and seven members, respectively [18]. The ring strains were validated with comparisons of modeling and experimental results on the ethyl + O_2 reaction system [15,19]. The activation energy for abstraction (E_{abst}) was estimated from the reverse reaction (exothermic direction). The reverse reaction is assumed to have an E_{abst}, which is the same as an alkyl radical abstracting an H-atom from a propyl-hydroperoxide,

$$\text{CCCOOH} + \text{R.} = \text{CCCOO.} + \text{RH}$$

where R is an alkyl radical. The activation energy of this reaction was estimated from an Evans–Polanyi plot (E_{abst} vs ΔH_{rxn}) [20] of the similar H-atom abstraction reaction, RH + R.′ = R. + R′H. A reduction of 0.3 kcal/mole in E_{abst} for each kcal/mole of exothermicity was obtained.

Pre-exponential factors for the RO_2 isomerization were obtained using RADICALC [7], a computer code that implements transition state theory. RADICALC calculates the change in entropy of the radical to the transition state due to loss or gain of internal rotors, of specific vibrations, and of optical isomers. Table 3 gives the output from the RADICALC code, which describes these changes in entropy from the CC(OOH)COO. radical to the transition state for subsequent isomerization:

```
CC(OOH)C = CC(OOH)C
 |    |     ¦    |
 H   .OO    H ---- OO
```

Results of the calculations show that the loss of internal rotors is the major contribution to the loss of entropy and, thus, the reduction in Arrhenius pre-exponential factor for these H-atom transfer reactions. The pre-exponential factors show a decrease with increasing size of the molecule in this mass range due to the increase in moments of inertia of the rotors that are tied up in the transition state.

HO_2 Elimination (e.g., C.C(OOH)COOH → C=CCOOH + HO_2):

The reverse rate constants for HO_2 addition to the propene hydroperoxides ($C_3H_6O_2$) species (three isomers) were estimated, and the forward rates calculated by microscopic reversibility. The pre-exponential factor for HO_2 addition was assumed similar to that for addition of HO_2 to ethylene [15,29]. The

TABLE 1
High pressure rate constants for reaction paths considered.

Reaction	A (s^{-1} or cm^3/mole-s)	E_a (kcal/mole)
CC(OOH)C. + O_2 → products		
CC(OOH)C. + O_2 → CC(OOH)COO.	3.0×10^{12}	0.0[a]
CC(OOH)COO. → CC(OOH)C. + O_2	2.95×10^{14}	30.62[b]
CC(OOH)COO. → CC.(OOH)COOH	2.02×10^{11}	20.10[c]
CC.(OOH)COOH → CC(OOH)COO.	4.14×10^{10}	15.45[b]
CC.(OOH)COOH → CC(=O)COOH + OH	4.53×10^{13}	3.00[d]
CC.(OOH)COOH → C=C(OOH)C + HO_2	1.42×10^{13}	24.53[e]
CC(OOH)COO. → C.C(OOH)COOH	4.86×10^{10}	20.84[f]
C.C(OOH)COOH → CC(OOH)COO.	8.89×10^{6}	7.66[b]
C.C(OOH)COOH → C=CCOOH + HO_2	1.41×10^{12}	17.22[g]
C.C(OOH)COOH → C=COOH + CH_2O + OH	1.64×10^{13}	37.04[h]
CC.COOH + O_2 → products		
CC.COOH + O_2 → CC(OO.)COOH	3.0×10^{12}	0.0[a]
CC(OO.)COOH → CC.COOH + O_2	8.2×10^{14}	31.40[b]
CC(OO.)COOH → CC(OOH)C.OOH	1.45×10^{12}	22.80[i]
CC(OOH)C.OOH → CC(OO.)COOH	2.97×10^{11}	14.71[b]
CC(OOH)C.OOH → CC(OOH)C=O + OH	5.07×10^{13}	3.00[d]
CC(OOH)C.OOH → CC=COOH + HO_2	1.41×10^{13}	22.05[c]
CC(OO.)COOH → C.C(OOH)COOH	2.17×10^{12}	26.70[j]
C.C(OOH)COOH → CC(OO.)COOH	3.96×10^{10}	13.55[b]
C.C(OOH)COOH → C=CCOOH + HO_2	1.42×10^{12}	17.23[g]
C.C(OOH)COOH → C=COOH + CH_2O + OH	1.64×10^{13}	37.00[h]
C.CCOOH + O_2 → products		
C.CCOOH + O_2 → .OOCCCOOH	3.0×10^{12}	0.0[a]
.OOCCCOOH → C.CCOOH + O_2	2.91×10^{14}	30.60[b]
.OOCCCOOH → HOOCCC.OOH	1.14×10^{10}	16.80[k]
HOOCCC.OOH → .OOCCCOOH	2.38×10^{9}	8.72[b]
HOOCCC.OOH → HOOCCC=O + OH	8.06×10^{13}	3.00[d]
HOOCCC.OOH → C=COOH + CH_2O + OH	9.75×10^{13}	38.14[h]
.OOCCCOOH → HOOCC.COOH	4.57×10^{11}	24.37[l]
HOOCC.COOH → .OOCCCOOH	1.29×10^{10}	14.55[b]
HOOCC.COOH → C=CCOOH + HO_2	1.14×10^{12}	16.58[g]

[a]1/2 (for steric effects) of CH_2OH + O_2 (high-pressure limit) [12].

[b]From microscopic reversibility (MR).

[c]$A = 10^{13.66}10^{\Delta S/4.6}$ degeneracy (1), $\Delta S = -10.83$ cal/mole-K (loss of two rotors). E = ring strain + ΔH + $E_{abstraction}$ = 6 + 4.21 + 9.9 = 20.1 kcal/mole.

[d]A from A_- = 1/2 of C_2H_4 + OH (addition) = $0.5 \times 5.4 \times 10^{12}$ [13] and MR. E = 3.0 kcal [14].

[e]A from MR and A_- = C_2H_4 + HO_2 (addition) = $10^{11.5}$. $E = \Delta U$ + 10.0 kcal/mole [15].

[f]$A = 10^{13.66}10^{\Delta S/4.6}$ degeneracy (3), $\Delta S = -15.87$ (loss of three rotors). E = ring strain + ΔH + $E_{abstraction}$ = 0.1 + 13.18 + 7.5 = 20.84 kcal/mole.

[g]A from MR and A_- = C_2H_4 + HO_2 (addition) = $10^{11.5}$. $E = \Delta U$ + 10.0 kcal/mole [15].

[h]A and E from MR. k_- is 1/2 of C_2H_4 + CH_3 (addition) where $A_- = 0.5 \times 1.26 \times 10^{11}$ and E_- = 7.7 kcal/mole [16].

[i]$A = 10^{13.66}10^{\Delta S/4.6}$ degeneracy (2), $\Delta S = -8.27$ cal/mole K (loss of two rotors). E = ring strain + ΔH + $E_{abstraction}$ = 6 + 7.64 + 9.2 = 22.8 kcal/mole.

[j]$A = 10^{13.66}10^{\Delta S/4.6}$ degeneracy (3), $\Delta S = -8.29$ cal/mole K (loss of two rotors). E = ring strain + ΔH + $E_{abstraction}$ = 6.0 + 13.18 + 7.5 = 26.7 kcal/mole.

[k]$A = 10^{13.66}10^{\Delta S/4.6}$ degeneracy (2), $\Delta S = -17.96$ cal/mole K (loss of three rotors). E = ring strain + ΔH + $E_{abstraction}$ = 0.1 + 7.5 + 9.2 = 16.8 kcal/mole.

[l]$A = 10^{13.66}10^{\Delta S/4.6}$ degeneracy (2), $\Delta S = -10.58$ cal/mole-K (loss of two rotors). E = ring strain + ΔH + $E_{abstraction}$ = 6.0 + 9.82 + 8.55 = 24.37 kcal/mole.

TABLE 2
Thermodynamic data at 298 K

Species	ΔH_f°	S°
OH	9.32	43.89
HO_2	3.80	54.73
CH_3	35.12	46.38
CH_2O	−26.02	52.26
C=COOH	−6.37	75.63
C.CCOOH	3.44	88.60
CC.COOH	0.79	90.51
CCC.OOH	−1.66	85.19
C.C(OOH)C	−0.93	86.61
CC.(OOH)C	−8.43	85.14
C=CCOOH	−14.24	84.00
C=C(OOH)C	−15.57	83.54
HOOCCC=O	−67.63	92.83
CC(=O)COOH	−70.31	91.46
CC(OOH)C=O	−67.63	90.65
CC(OO.)COOH	−34.06	100.88
CC(OOH)COO.	−34.06	100.88
C.C(OOH)COOH	−21.16	108.18
CC.(OOH)COOH	−28.66	105.34
CC(OOH)C.OOH	−26.26	103.39
HOOCC.COOH	−19.44	110.70
.OOCCCOOH	−29.69	102.87
HOOCCCOO.	−29.69	102.87
HOOCCC.OOH	−21.89	105.38

Units: ΔH_f° in kcal/mole; S° in cal/(mole K).

activation energy was assumed to be ΔU + 10.0 kcal/mole, where ΔU is the change in internal energy in the reaction [15]. The enthalpies of formation are given in Table 2.

OH Elimination (e.g., HOOC.CCOOH → O=CCCOOH + OH):

The reverse rate constant, OH addition, was estimated and the forward rate calculated by microscopic reversibility. The reverse reaction is considered analogous to the addition of an OH radical to one carbon of the double bond in ethylene.

Alkyl Group Elimination (e.g., C.C(OOH)COOH → C=COOH + .COOH):

The reverse rate constant was estimated and the forward rate was calculated by microscopic reversibility. The reverse reaction is the addition of the alkyl radical .COOH to a double bond. This is considered to be analogous to the addition of a propyl radical to one carbon of the double bond in ethylene.

TABLE 3
RADICALC transition state theory calculation

CCQCOO. → CC.QCQ (transition state)
= −IR/CCQC—OO/ − IR/CCQ—COO/ − V/C—H/
−2V/H—C—C/ − V/H—C—O/ + V/C.H/
+2V/H.C—C/ + V/H.C—O/ + V/5 mem ring/

Entropy increments (cal/mol K)

Temperature (K)	298	1500
−1 * IR/CCQC—OO/	−6.200	−8.462
−1 * IR/CCQ—COO/	−5.949	−8.675
−1 * V/C—H/	0.000	−0.455
−2 * V/H—C—C/	−0.101	−3.777
−1 * V/H—C—O/	−0.076	−2.053
V/C.H/	0.001	0.834
2 * V/H.C—C/	0.414	5.120
V/H.C—O/	0.207	2.560
V/5 mem ring/	0.252	2.682

Net entropy increments applied:

Temperature (K)	Entropy (cal/mol K)
298.1500	−11.4530
500.0000	−11.8756
600.0000	−12.0056
800.0000	−12.1664
1500.0000	−12.2271

A factor = 1.516×10^9/s
TEXP = 7.3741×10^{-1}

Notation: IR denotes internal rotor; V denotes bending or stretching vibration; TEXP is the temperature exponent of the modified Arrhenius form rate constant; Q denotes "OOH."

Calculations

Energized-complex/QRRK theory, as described by Dean [10], was used to model the addition of hydroperoxy-propyl radicals to O_2. Details of the CHEMACT code used for the calculations are given in Ref. 8. The geometric mean frequencies required for the calculations were obtained from the heat capacity data in Table 2, using the method described in Ref. 21. Lennard-Jones parameters were obtained from tabulations [22] and from a calculation method based on group additivity where groups representing transport properties were developed [23]. Data were also taken from estimations based on molar volumes and compressibility [24]. The bath gas was assumed to be nitrogen. Important modifications to the code include use of the Ω integral [22] for calculation of

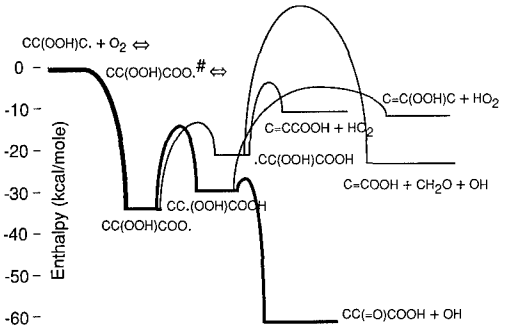

FIG. 1. Potential energy level diagram for CC(OOH)C. + O_2. The line thickness gives an indication of the relative importance for a particular reaction channel.

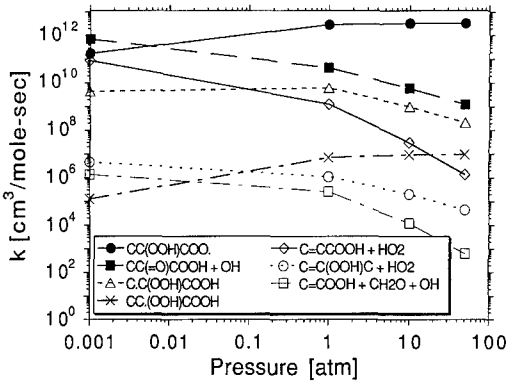

FIG. 2. Rate constants of the various channels of CC(OOH)C. + O_2 at 800 K as a function of pressure.

the collision frequency and the calculation of the collision efficiency, β, as a function of temperature using the method of Gilbert et al. (Eq. (4.7) of Ref. 25) and an exact calculation of $f(E)$. Energy transferred per collision was taken from Gardiner and Troe [26]. Detailed comparisons of other QRRK calculations with this modified code and RRKM analysis show excellent agreement for the major reaction channels [19].

Results and Discussion

Chemical Activation Reactions:

CC(OOH)C. + O_2

The energy level diagram and input parameters are shown in Fig. 1 and Table 1, respectively. The reaction channels for CC(OOH)COO.‡ include dissociation back to reactants, stabilization to CC(OOH)COO., and isomerization via hydrogen shifts with subsequent β-scission/stabilization. The barriers to isomerization are about 12 kcal/mole lower than dissociation back to reactants (Fig. 1) so that there is sufficient energy in the adduct CC(OOH)COO.‡ to isomerize before it is stabilized. The dominant product channel above 0.1 atm is stabilization. The next important product channel is CC(=O)COOH + OH (carbonyl formation), which is the only channel considered in the literature [27]. The channel to .CC(OOH)COOH also has some significance (Fig. 1).

Figure 2 shows the apparent rate constants for the product channels of CC(OOH)C. + O_2 with pressure. Results are shown at 800 K because hydroperoxy-alkyl + O_2 reactions are most important in the temperature range of 600–900 K where low- and intermediate-temperature chemistry controls the oxidation of hydrocarbons [4]. At temperatures above 900 K, alkyl radicals decompose by β-scission more rapidly than they add with molecular oxygen. Figure 2 (filled circles) shows that the dominant channel for CC(OOH)C. + O_2 is stabilization (CC(OOH)CCO.), except at very low pressure. This is the case for oxygen addition to all three isomers of hydroperoxy-propyl. A fraction (approximately 1% at 1 atm) of the chemically activated CC(OOH)COO.‡ reacts over the barrier to other products. The dominant path to other products involves an intramolecular abstraction of the H atom that is attached to the same carbon as the hydroperoxide group (filled squares in Fig. 2):

$$\text{CC(OOH)COO.}^{\ddagger} \rightarrow \text{C}\dot{\text{C}}\text{(OOH)COOH}^{\ddagger}$$

$$\text{C}\dot{\text{C}}\text{(OOH)COOH}^{\ddagger} \rightarrow \text{CC(=O)COOH} + \text{OH}.$$

This C—H bond is somewhat weakened (ca. 4 kcal/mole) from the usual secondary H because of the presence of the C—OO bond. The next most important reaction is an intramolecular abstraction of the H atom that is attached to the *terminal* carbon atom:

$$\text{CC(OOH)COO.}^{\ddagger} = \text{C.C(OOH)COOH}$$

This path is about a factor of 6 slower than carbonyl formation at all pressures above 1 atm and 800 K (triangles in Fig. 2). The rates for reaction to other products shown in Fig. 2 are considerably less important, except at very low pressures (0.01 atm) where the product channel C=CCOOH + HO_2 becomes significant. This channel results from decomposition of C.C(OOH)COOH‡ to C=CCOOH + HO_2 before stabilization.

Figure 3 illustrates rates vs temperature at 15 atm because hydroperoxy-alkyl + O_2 reactions are most relevant under conditions of high pressures related to engine knock. The dominant channels are the same as in Fig. 2 with product paths competing more

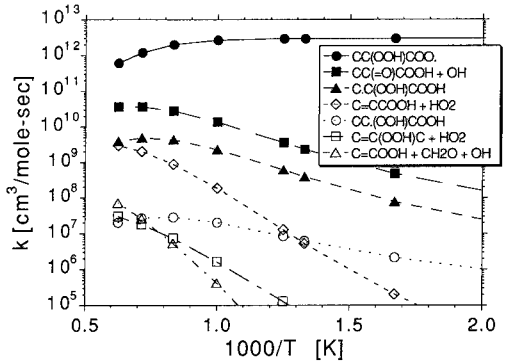

FIG. 3. Rate constants of the various channels of CC(OOH)C. + O_2 at 15 atm as a function of temperature.

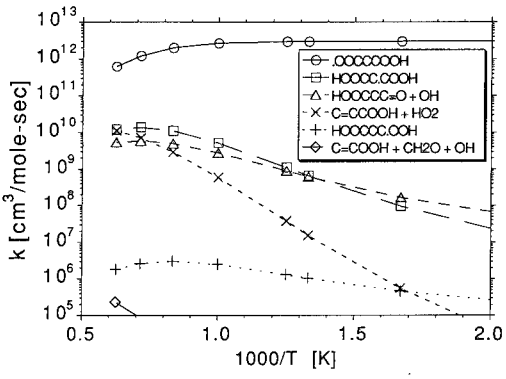

FIG. 4. Rate constants of the various channels of C.CCOOH + O_2 at 15 atm as a function of temperature.

effectively with stabilization as the temperature increases.

CC.COOH + O_2

The important product channels are similar to those of CC(OOH)C. + O_2 at 15 atm. Stabilization of the peroxy adduct is the most important. The channel with the second highest rate at 15 atm is carbonyl formation (CC(OOH)C=O + OH). The third most significant path involves an intramolecular abstraction of the H atom that is attached to the terminal carbon atom to give C.C(OOH)COOH. This adduct will decompose to C=CCOOH + HO_2. Its rate at 15 atm is about a factor of 4 below the rate to CC(OOH)C=O + OH. The rates of the remaining three products are more than two orders of magnitude lower over the temperature range of interest (600–900 K) at 15 atm.

C.CCOOH + O_2

The apparent rate constants for six product channels at 15 atm are illustrated in Fig. 4. Again, stabilization of the peroxy adduct is most important. After

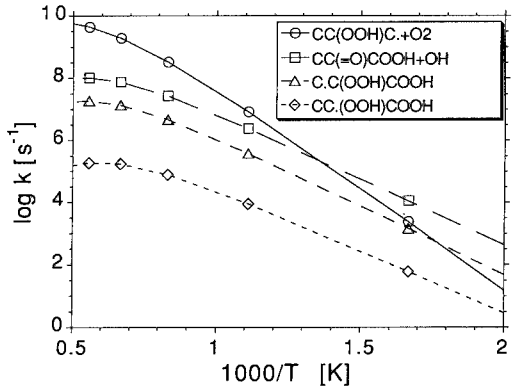

FIG. 5. Rate constants for the decomposition of CC(OOH)COO. at 15 atm as a function of temperature.

stabilization and reverse reaction, two product channels are competitive. For temperatures below about 730 K, carbonyl formation (HOOCCC=O + OH) exceeds HOOCC.COOH formation. For temperatures above about 730 K, HOOCC.COOH formation exceeds carbonyl formation. HOOCC.COOH formation involves an intramolecular abstraction of the secondary H atom and has not been considered previously in the literature. The HOOCC.COOH adduct will decompose to C=CCOOH + HO_2, which is a less reactive product set than HOOCCC=O + OH.

Dissociation Reactions—Fate of Stabilized Adducts:

The computed results for the rate of O_2 addition to hydroperoxy-propyl radicals show that the main product path is stabilization for pressures of 0.1 atm and higher (Fig. 2). It is, therefore, important to determine the fate of the stabilized peroxy adducts as a function of temperature at pressures relevant to combustion applications.

CC(OOH)COO. → products:

The computed rate vs $1/T$ for important product channels is shown in Fig. 5 at 15 atm. These results have important implications with respect to negative temperature coefficient behavior for propane oxidation. At 600 K, the dominant products are CC(=O)COOH + OH, which lead to chain branching because a second OH radical is produced via

$$CC(=O)COOH \rightarrow CC(=O)CO. + OH.$$

As the temperature is raised to 900 K, the dominant path is dissociation back to molecular oxygen and CC(OOH)C., an alkyl radical that mainly dissociates to propene + HO_2. Again, HO_2 is relatively unreactive compared to OH. Therefore, as the tem-

TABLE 4
Rate expressions for hydroperoxy-propyl + O_2 and for decomposition of adducts

	Log A	n	E_a	P
		CC.COOH + O_2 →		
1	40.98	−9.21	7.83	1
1	31.86	−6.17	5.70	15
2	33.16	−6.42	12.10	1
2	26.18	−4.31	11.38	15
3	17.79	−2.46	14.05	1
3	14.58	−1.44	14.79	15
4	43.17	−9.79	16.24	1
4	29.23	−5.35	13.86	15[a]
5	40.79	−8.53	21.77	1
5	30.28	−5.39	21.31	15
		C.CCOOH + O_2 →		
6	37.59	−8.04	7.18	1
6	27.42	−4.72	4.52	15
7	33.85	−6.98	11.35	1
7	23.96	−4.04	9.40	15
8	41.10	−9.22	15.21	1
8	25.78	−4.39	12.24	15
5	39.94	−8.31	20.55	1
5	27.26	−4.55	19.22	15
		CC(OOH)C. + O_2 →		
9	37.73	−8.11	7.12	1
9	27.90	−4.88	4.62	15
10	32.68	−6.34	11.73	1
10	23.81	−3.70	10.22	15
4	43.57	−10.05	15.31	1
4	26.70	−4.83	11.55	15[a]
5	39.84	−8.46	20.53	1
5	25.10	−4.13	18.28	15
		CC(OO.)COOH →		
2	39.62	−8.81	30.18	1
2	29.02	−5.37	27.32	15
4	49.30	−11.88	36.75	1[a]
4	33.12	−6.63	32.36	15
		C.C(OOH)COOH →		
2	44.87	−10.73	30.41	1
2	28.46	−5.61	26.93	15[a]
5	26.60	−4.70	20.78	1
5	17.68	−1.79	18.42	15
11	23.60	−3.62	38.66	1
11	19.49	−2.07	38.30	15
10	41.02	−9.97	25.27	1[a]
10	22.83	−4.43	20.74	15[a]
		.OOCCCOOH →		
7	31.69	−6.88	22.76	1[a]
7	21.10	−3.51	19.67	15.
8	45.02	−10.66	33.72	1[a]

TABLE 4 (*continued*)
Rate expressions for hydroperoxy-propyl + O_2 and for decomposition of adducts

	Log A	n	E_a	P
8	28.37	−5.30	29.07	15
5	46.42	−10.60	41.89	1
5	29.05	−5.24	37.90	15.
		HOOCC.COOH →		
5	25.72	−4.47	19.75	1
5	16.86	−1.57	17.42	15
		CC(OOH)COO. →		
10	34.40	−7.38	26.37	1
10	23.72	−3.96	23.35	15
4	41.24	−9.73	29.46	1[a]
4	25.66	−4.75	24.95	15

Products:
1 CC(OO.)COOH
2 CC(OOH)C=O + OH
3 CC=COOH + HO_2
4 C.C(OOH)COOH
5 C=CCOOH + HO_2
6 C(OO.)CCOOH
7 C(OOH)CC=O + OH
8 C(OOH)C.COOH
9 CC(OOH)COO.
10 CC(=O)COOH + OH
11 C=COOH + CH_2O + OH

Units: cm^3 mole s kcal.
$k = AT^n \exp(-E_a/RT)$. $300 < T < 2100$ K.
Maximum error in fit ranges from 7–35%, except as noted. Reverse rates can be obtained using thermodynamic data (Table 2) and microscopic reversibility. P is pressure in atm. "=" denotes a double bond.
[a]Maximum error, 41–56%.

perature is raised from 600 to 900 K, the dominant path changes from chain branching and the production of highly reactive OH to one of chain propagation with production of relatively unreactive HO_2. This switch contributes to the negative temperature coefficient behavior observed over this temperature range at 15 atm [28].

CC(OO.)COOH → products and .OOCCCOOH → products:

The trends at 15 atm are similar to CC(OOH)-COO. decomposition (Fig. 5), with OH production and chain branching dominating below 650 K and reverse reaction back to O_2 dominating above 650 K. Again, this contributes to the negative temperature

coefficient behavior experimentally observed over this temperature regime at 15 atm.

Reaction Rate Parameters:

The modified Arrhenius expressions for all significant product channels (> 1%) are given in Table 4. These rate constants are useful for inclusion in a chemical kinetic mechanism to treat propane oxidation over the low- to intermediate-temperature regime (600–900 K). For temperatures above about 900 K, the decompositions of alkyl and alkylperoxy radicals are rapid, so hydroperoxy-propyl + O_2 no longer plays a significant role. Experimental measurements of these rate constants are needed to validate the present calculations. Thermodynamic property and kinetic data may be obtained by Internet electronic mail (bozzelli@tesla.njit.edu or pitz@llnl.gov) or on disk by writing to the authors.

Summary

Kinetic and thermodynamic properties for reaction of hydroperoxyl-propyl radicals with molecular oxygen were analyzed. The dominant channels ranked by order of importance are stabilization, followed by reverse reaction to hydroperoxyl-propyl + O_2, and reaction to alkyl-carbonyl-hydroperoxide + OH. The radical addition to O_2 rates are near the high-pressure limits for pressures of 1 atm and above. Several reaction channels were found to be important that had not been identified previously in the literature. These paths involved the intramolecular abstraction of an H atom that was bonded to an alkyl carbon that had no attached O atom. The resulting products are olefinic hydroperoxide + HO_2. Reaction rates from the QRRK analysis were fit to modified Arrhenius expressions for use in chemical kinetic mechanisms. Rate constants for dissociation of the stabilized adducts are also presented. Product channels for reaction of the stabilized adducts switch from chain propagation to dissociation back to alkyl-hydroperoxide radical + O_2 with increasing temperature. This switch in decomposition products results in a decrease in hydrocarbon conversion that corresponds to the observed negative temperature coefficient regime.

Acknowledgment

The authors wish to thank A. M. Dean for many useful discussions.

REFERENCES

1. Hu, H., and Keck, J., SAE Paper No. 872110, 1987.
2. Morley, C., *Combust. Sci. Technol.* 55:115 (1987).
3. Griffiths, J. F., *Combust. Flame* 93:202–206 (1993).
4. Westbrook, C. K., Pitz, W. J., and Leppard, W. M., SAE Trans. SAE-912314 (1991).
5. Chevalier, C., Pitz, W. J., Warnatz, J. and Westbrook, C. K., *Twenty-Fourth (International) Symposium on Combustion*, The Combustion Institute, Pittsburgh, PA, 1992, pp. 93–101.
6. Blin-Simiand, N., Rigny, R., Viossat, V., Circan, S., and Sahetchian, K. A., *Combust. Sci. Technol.* 88:329 (1993).
7. Bozzelli, J. W., and Ritter, E. R., *Chemical and Physical Processes in Combustion*, The Combustion Institute, Pittsburgh, PA, 1993, Vol. 103, p. 459.
8. Dean, A. M., Bozzelli, J. W., and Ritter, J. W., *Combust. Sci. Technol.* 80:63–85 (1991).
9. Ritter, E. R., and Bozzelli, J. W., *Int. J. Chem. Kinet.* 23:767 (1991).
10. Dean, A. M., *J. Phys. Chem.* 89:4600 (1985).
11. Golden, D., in *Fossil Fuel Combustion* (A. F. Sarofim and W. Bartok, Eds.), 1993, chap. 2, p. 111.
12. Benson, S. W., *Can. J. Chem.* 61:881 (1983).
13. Atkinson, R., Baulch, D. L., Cox, R. A., Hampson, R. F., Jr., Kerr, J. A., Troe, J., *J. Phys. Chem. Ref. Data* 18:881 (1989).
14. Bozzelli, J. W., and Dean, A. M., *J. Phys. Chem.* 97:4427–4441 (1993).
15. Bozzelli, J. W., and Dean, A. M. *J. Phys. Chem.* 94:3313 (1990).
16. Tsang, W., and Hampson, R. F., *J. Phys. Chem. Ref. Data* 15:1087–1279 (1986).
17. Lay, T., and Bozzelli, J. W., *Chemical and Physical Processes in Combustion*, The Eastern States Section Meeting of the Combustion Institute, Paper No. 100 (1–4), 1993.
18. Dorofeeva, O. V., Gurvich, L. V., and Jorish, V. S., *J. Phys. Chem. Ref. Data* 15:437–464 (1986).
19. Chang, A. Y., and Dean, A. M., "Exxon Research and Engineering," personal communication, Annandale, NJ, 1993.
20. Evans, M. G., and Polanyi, M., *Trans. Faraday Soc.* 34:11 (1938).
21. Ritter, E. R., Ph.D. Thesis, New Jersey Institute of Technology, Newark, NJ, May, 1989.
22. Reid, R. C., Prausnitz, J. M., and Poling, B. E., *Properties of Gases and Liquids*, 4th ed., McGraw-Hill, New York, 1987.
23. Bozzelli, J. W., Transcal Code, personal communication, 1993.
24. Ben-Amotz, D., and Herschbach, D., *J. Phys. Chem.* 94:3393 (1990).
25. Gilbert, R. G., Luther, K., and Troe, J., *Ber. Bunsenges. Phys. Chem.* 87:164 (1983).
26. Gardiner, W. C., Jr., and Troe, J., in *Combustion Chemistry* (W. C. Gardner, Jr., Ed.), Springer-Verlag, New York, 1984, pp. 114–126.
27. Benson, S. W., *Prog. Energy Combust. Sci.* 7:125–134 (1981).
28. Koert, D. N., Miller, D. L., and Cernansky, N. P., *Combust. Flame* 96:34–49 (1994).
29. Wagner, A. F., Slagle, I. R., Sarzynski, D., and Gutman, D., *J. Phys. Chem.* 94:1853–1868 (1990).

COMMENTS

R. W. Walker, Hull University, England. You estimate the activation energy for $RO_2 \rightarrow QOOH$. May I ask how reliable you think the estimate is? Both Pilling and I have good experimental data that the barrier is considerably higher than you suggest. Also is it not inevitable that Pilling's data on the neopentylperoxy system can be successfully modelled if the lower barrier is adopted?

Author's Reply. The estimates of activation energy for the hydrogen transfer reactions of peroxy radicals to hydroperoxy-alkyl radicals, ROO. → R′.COOH, have been shown to accurately model the experimental data on a number of alkyl radical R. + O_2 reactions. The R. + O_2 reactions include ethyl [15], allyl, HCO, and vinyl [14]. Additional, nonpublished calculations on R. + O_2 reaction systems, where our analysis shows agreement with experimental data in the literature, include propyl, tert-butyl, and neopentyl radical systems. We continue to model and analyze these reaction systems in order to incorporate them correctly in our mechanisms and to understand them more fully.

Our analysis and match of data on the neopentyl system incorporate falloff effects using a quantum RRK chemical activation analysis, a high-pressure limit *A* factor for R. + O_2, thermodynamics, and microscopic reversibility for the reverse dissociation. We use transition state theory and a lower (ca. 6 kcal/mole) barrier than reported in Hughes et al. [1] (below) for the hydrogen transfer isomerization, with a subsequent barrier and tight transition state for epoxide (C_2C_yCCOC) plus OH formation. There is also a significant contribution to OH formation from $C_3CC.OOH$ via a chemical activated path.

An important aspect of our interpretation on these reaction systems is that both forward and reverse reactions R. + $O_2 \leftrightarrow$ olefin + HO_2, where R is ethyl, propyl, *t*-butyl, or a similar alkyl radical, are rapid at temperatures 500–600 K and above. This component of the R + O_2 reaction system is in pseudoequilibrium, with a small amount of bleed reaction to the epoxide and other channels that produce OH. Reactive OH radicals and chain branching are also produced by the reaction hydroperoxy-alkyl radicals (R′.COOH) with O_2 which is present in combustion environments at high levels. A number of publications are referred to in this article, where the observed negative temperature regimes cannot be explained without inclusion of these hydroperoxy-alkyl + O_2 reactions.

REFERENCE

1. Hughes, K. J., Halford-Maw, P. A., Lightfoot, P. D., Turanyi, T., and Pilling, M. J., *Twenty-Fourth Symposium (International) on Combustion,* The Combustion Institute, Pittsburgh, 1992, p. 645.

•

W. Tsang, National Institute of Standards and Technology, USA. QRRK is a method for calculating specific rate constants. In chemical activation or falloff calculations, another key parameter refers to energy transfer effects. The value used whether they be β or a step size down or all should always be reported. Only through this can we determine transferable information. In many cases, chemical activation results are insensitive to this parameter. This should be noted. Information presented regarding these issues would be very valuable for users of the information in this paper.

Author's Reply. We thank you for noting this omission and agree it should be included in this type of calculation results. We used a $\Delta E_{average}$ of 830 cal, which yielded a ΔE_{down} for the first well (peroxy radical adduct) of 1.393 kcal. ΔE's were not changed with temperature. There is some change in the results with different ΔE's. Use of a $\Delta E_{average}$ of 350 cal yielded a calculated ΔE_{down} of 776 cal for the peroxy adduct. Example differences in $\log_{10} k$ at 1 atm and 900 K for the average ΔE's of 830 and 350 cal are as follows: stabilization into the first well equals 12.03 and 11.82, reaction of the peroxy adduct back to R + O_2 equals 12.19 and 12.28, reaction to major product CC(=O)COOH + OH equals 11.28 and 11.39 respectively, CC(OOH)C. + O_2 system.

Quantum RRK theory is used to calculate $k(E)$, and the beta collision factors (modified strong collision approach of Gilbert, Luther, and Troe [25]) are used to calculate falloff effects. A geometric mean set of vibrational frequencies with one external rotation included was used to calculate densities of states for the adducts. The adducts have a relatively large number of vibrations and a number of hindered internal rotors with relatively large moments of inertia; use of more complete vibrational sets yielded similar results.

Twenty-Fifth Symposium (International) on Combustion/The Combustion Institute, 1994/pp. 793-800

REACTION OF HYDROPEROXY *t*-BUTYL RADICALS AND *t*-BUTYL PEROXY *t*-BUTYL RADICALS IN RELATION TO CHAIN PROPAGATION IN COMBUSTION

L. BATT
Department of Chemistry
University of Aberdeen
Aberdeen AB9 2UE, UK

M. A. KHAN
Ministry of Defence
Desto Laboratories
Chaklala Rawaepindi, Pakistan

AND

T. J. MITCHELL
Loker Hydrocarbon Research Institute
University of Southern California
Los Angeles, CA 90007, USA

Hydroperoxyl *t*-butyl radicals (I) or *t*-butyl peroxy *t*-butyl radicals (II) were generated in an oxygen-free system. This allowed an unequivocal measure of the ratio of olefin to epoxide formation to be made.

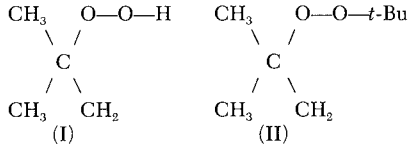

For hydroperoxy alkyl radicals, the two paths are competitive over the temperature range 413–473 K with olefin production becoming more dominant as the temperature is raised.

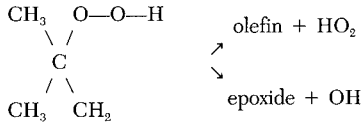

Some controversy surrounds the primary mechanism for the oxidation of alkyl radicals at temperatures up to 900 K. Strong arguments have been put forward for both exclusive olefin and exclusive epoxide formation. By comparing our results with this work, we conclude that the primary path is indeed exclusive olefin formation. The controversy may be reconciled by proposing that epoxide formation arises as the result of secondary reactions involving the addition of HO_2 or RO_2 to the primary olefin product. Pressure-dependent processes complicate the issue. However, it is difficult to see how any collisional stabilisation process would lead to increased epoxide formation in view of the present evidence available. This work shows that the addition of RO_2 to olefins results in the almost exclusive production of epoxide, at least at lower temperatures. For *t*-butyl peroxy *t*-butyl radicals over the temperature range 363–403 K, the path involving the production of epoxide is ≥98%.

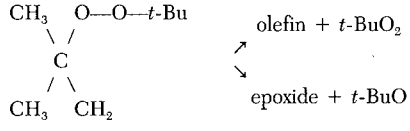

Further evidence is required on the reaction of hydroperoxy and alkylperoxy alkyl radicals.

Introduction

In relation to the mechanism of hydrocarbon oxidation at temperatures less than about 900 K, the chemistry of alkyl and alkyl peroxy radicals plays a central role [1]. The reaction of alkyl radicals R with O_2 can lead either to RO_2, the isomersiation of which can lead to propagation and branching reactions, or to an alkene + HO_2, which can constitute a termination reaction under many conditions because of the relative inertness of HO_2. (HO_2

$$\begin{array}{lll} R + O_2 \rightleftarrows RO_2 \longrightarrow R_{-H}O_2H & \nearrow & \text{olefin} + HO_2 \\ \quad\quad\quad\quad\quad\quad\quad\quad\quad\quad & \searrow & \text{epoxide or} \\ \text{olefin} + HO_2 & & \text{oxirane} + OH \end{array}$$

may take part in a propagation reaction with the hydrocarbon fuel (RH), but this process has a high activation energy and is, therefore, slow. In addition, the pressure-dependent

$$HO_2 + RH \rightarrow H_2O_2 + R$$

decomposition of H_2O_2 is also slow under these conditions. The balance between the two

$$H_2O_2 + M \rightarrow 2OH + M$$

paths in the global scheme above governs the rate and products of the reaction. The chemical mechanisms involved are, however, controversial, which adds considerable uncertainty to hydrocarbon oxidation models.

Wagner et al. [2] have published a careful experimental and theoretical description of the C_2H_5 + O_2 reaction, which concludes that both the peroxy radical and $C_2H_4O_2H$ (referred to as QOOH by McAdam and coworkers [3,4]) are on the reaction path to C_2H_4 + HO_2

$$C_2H_5 + O_2 \rightleftarrows C_2H_5O_2 \rightleftarrows \underset{\text{(QOOH)}}{C_2H_4OOH} \rightarrow C_2H_4 + HO_2$$

$$C_2H_4OOH \downarrow \begin{array}{c} O \\ / \quad \backslash \\ CH_2—CH_2 \end{array} + OH$$

McAdam and coworkers [3,4] consider QOOH an unacceptable intermediate

1. because their self-consistent set of rates for various alkyl peroxy to QOOH isomerisations suggest that the barrier between RO_2 and QOOH is too high; and
2. because of their measurements of the formation of oxiranes from alkanes + HO_2.

They consider the rate-limiting step to be the addition to form QOOH, which implies that the formation of oxirane from the QOOH is much faster than the decomposition back to alkene + HO_2. This is contrary to Gutman et al.'s [2] mechanism, which considers alkene + HO_2 as the sole product from QOOH. This last result is supported by the recent results of Dobis and Benson over the temperature range 243–368 K, using the very low pressure reactor (VLPR) technique [5] by definition at low pressure, and by the results of Kaiser et al. [10] over a much wider pressure range at ambient temperatures. Direct production of alkene + HO_2 has to be ruled out because of well-documented evidence for the observed negative temperature dependence of the oxidation of C_2H_5.

$$C_2H_5 + O_2 \longrightarrow C_2H_4 + HO_2$$

Wagner et al. propose that oxirane production from the HO_2 + C_2H_4 reaction must involve multiple steps. Accordingly, this work seeks to provide information on hydroperoxy and alkyl peroxy alkyl reactions related to butyl radicals in an O_2-free system. Two systems have been used to examine the relative ease of formation of alkene and oxirane from these types of radicals. One system generates the hydroperoxy *t*-butyl radical (I), and the other system generates the *t*-butyl peroxy *t*-butyl radical (II).

$$\begin{array}{c} CH_3 \quad O—O—H \\ \backslash \quad / \\ C \\ / \quad \backslash \\ CH_3 \quad CH_2 \\ \text{(I)} \end{array} \qquad \begin{array}{c} CH_3 \quad O—O—t\text{-Bu} \\ \backslash \quad / \\ C \\ / \quad \backslash \\ CH_3 \quad CH_2 \\ \text{(II)} \end{array}$$

These reactions have an important bearing on an unresolved question in combustion chemistry in terms of primary product formation.

HCl Catalysed Decomposition of Ditertiary Butyl Peroxide

The HCl catalysed decomposition of ditertiary butyl peroxide (dtBP) was carried out in a static system over the temperature range 363–403 K in an apparatus used described previously [6]. The method was to admit the peroxide (1–3 torr) and HCl (1–2.5 torr) plus CF_4 (50 torr) from a mixing vessel to the reaction vessel. CF_4 was present mainly to allow a known

amount of dtBP/HCl to be transferred rapidly and efficiently to the reaction vessel. At the end of the run (200–3600 s), the contents of the reaction vessel were passed through a U-tube containing auramine–which efficiently removed the HCl—and condensed at 77 K in two traps. Most of the CF_4 was removed at 90 K, and the contents of the traps were transferred to a U-tube and allowed to warm to room temperature. Products and remaining peroxide were analysed using on-line gas-liquid chromatography (GLC) analysis in an all glass system. Extents of reaction amounted to no more than 10% of the peroxide decomposed. The products can be accounted for by the following reaction scheme:

$$\text{dtBP} \longrightarrow 2\ t\text{-BuO} \tag{1}$$

$$t\text{-BuO} + \text{HCl} \longrightarrow t\text{-BuOH} + \text{Cl} \tag{2}$$

$$\text{Cl} + \text{dtBP} \longrightarrow \text{dtBP}_{-\text{H}} + \text{HCl} \tag{3}$$

$$\text{dtBP}_{-\text{H}} \begin{array}{l} \xrightarrow{a} \text{isobutene} + t\text{-BuO}_2 \\ \xrightarrow{b} \text{isobutene oxide} + t\text{-BuO} \end{array} \tag{4}$$

$$\text{Cl} + \text{Product} \longrightarrow \text{Product}_{-\text{H}} + \text{HCl}. \tag{5}$$

The most likely product in step (5) is concluded to be acetone produced as a result of the decomposition of t-BuO:

$$t\text{-BuO} \xrightarrow{\text{M}} \text{acetone} + \text{CH}_3 \tag{6}$$

Analysis of this mechanism leads to the following rate law:

$$-\frac{d[\text{dtBP}]}{dt} = \frac{2k_1k_3}{k_5}\frac{[\text{dtBP}]^2}{[\text{Product}]}.$$

This result is consistent with the results of Flowers et al. [7] who also studied the HCl catalysed decomposition of dtBP over the temperature range 363–393 K and at 50 torr. The data show that the reaction rate is second order with respect to peroxide (2.0 ± 0.2, Fig. 1) and inversely proportional to product concentration and independent of HCl concentration (Table 1). An Arrhenius plot (Fig. 2) gives the following parameters:

$$\log(k_{\text{obs}})/\text{s}^{-1}) = 18.0 \pm 1.4 - (169.5 \pm 10.5\ \text{kJ}/2.303\ \text{RT}).$$

By substituting the Arrhenius parameters for step (1) into the above expression [8],

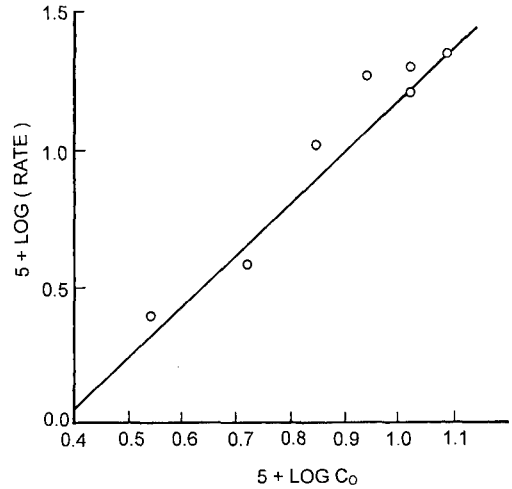

FIG. 1. dtBP rate law in the HCl catalysed decomposition of dtBP.

TABLE 1
dtBP + HCl: Variation of k_{obs} with HCl concentration at 383 K

[HCl]/M × 10–5	$k_{\text{obs}}/10^{-5}\ \text{s}^{-1}$
3.45	1.92
5.20	2.06
6.88	2.21
8.62	2.07
10.3	1.89
	Average 2.03 ± 0.10

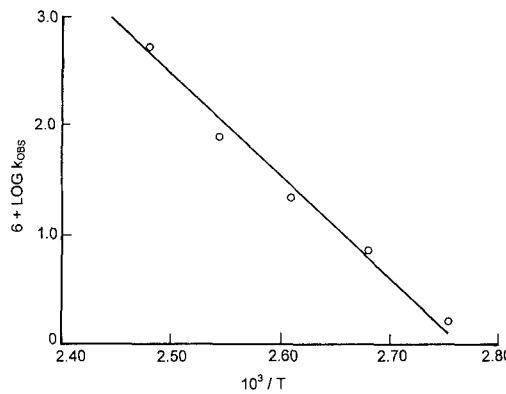

FIG. 2. Arrhenius plot for the HCl catalysed decomposition of dtBP.

$$\log (k_1/s^{-1}) = 15.5 \pm 0.5 - (156.9 \pm 2.1 \text{ kJ}/2.303 \text{ RT})$$

it may be concluded that the temperature dependence of the ratio k_3/k_5 is given by

$$\log (k_3/k_5) = 2.5 \pm 1.5 - (12.6 \pm 10.7 \text{ kJ})/2.303 \text{ RT}.$$

Any further interpretation of the Arrhenius parameters is not warranted in view of the relatively large errors involved. The radical $dtBP_{-H}$ constitutes an alkyl peroxy alkyl radical, as noted in the introduction as Structure II. Compared to the oxidation system exemplified by C_2H_5/O_2, this radical cannot revert to a peroxy radical structure. It can only react to form olefin or oxiraine. One point is clear: Both stable products are observed for reactions (4a) and (4b). This is contrary to the results of Flowers et al. [7] who found no evidence for olefin formation. This is not a major criticism of their results because the oxirane accounts for ≥98% of the product via reaction (4b) as opposed to reaction (4a). This implies that the addition of alkyl peroxy radicals to olefins result in the almost exclusive formation of oxirane. This conclusion has been reached at temperatures that are much lower than those used in the work of Walker and coworkers [3,4]. Higher temperatures in our system result in the unimolecular decomposition of dtBP taking over as the main path for production formation. Any quantitative extrapolation of our results to the temperatures of Walker and coworkers is unwarranted in view of the small yields of olefin.

Decomposition of *t*-Butyl Hydroperoxide

Although the above study shows that two paths are open for the decomposition of the alkyl peroxy alkyl radical (II), the situation is not exactly the same as the hydroperoxy alkyl radical (I). The reason for this is if the parent alkyl hydroperoxide and dialkyl peroxides are considered—using the same number notation—the RO—OH bond strength is some 20 kJ mol^{-1} stronger than that in RO—OR [6]. There is no reason for this situation to change upon the

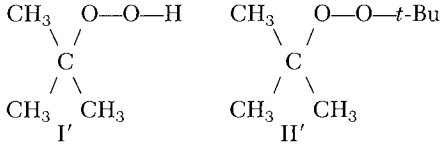

production of the two radicals involved. The subtle weakening of the O—O bond in the radical (II), as opposed to the radical (I), probably explains the dominance of oxirane formation. It was realised that the hydroperoxyl alkyl radical could be generated by allowing neat *t*-butyl hydroperoxide to decompose over the temperature range 413–473 K. The method was to admit the peroxide (1 torr) plus CF_4 (50 torr) from a mixing vessel to the reaction vessel. CF_4 was present mainly to allow a known amount of peroxide to be transferred rapidly and efficiently to the reaction vessel. Preliminary experiments soon revealed that conventional GLC analysis with any metal present prior to analysis led to spurious results as a result of heterogeneous decomposition of the peroxide. By using different-shaped reaction vessels and thus altering the surface-to-volume ratio, it was easy to show that the decomposition process was affected by the surface. Heterogeneous effects were minimised by using a spherical reaction vessel coated with boric oxide, although this remains the greatest uncertainty. However, no surface effects were observed when studying the unimolecular decomposition of *t*-butyl hydroperoxide in the same system [6]. Subsequent to the initiation process, it is clear that there are two types of abstractable hydrogen atoms

$$t\text{-BuO}_2\text{H} \longrightarrow t\text{-BuO} + \text{OH} \quad (7)$$

$$t\text{-BuO} \xrightarrow{\text{M}} \text{acetone} + \text{CH}_3. \quad (6)$$

Any of these radicals (say R′) may take part in the abstraction process:

$$\text{R}' + t\text{-BuO}_2\text{H} \longrightarrow \text{R}'\text{H} + t\text{-BuO}_2 \quad (8)$$

$$\text{R}' + t\text{-BuO}_2\text{H} \longrightarrow \text{CH}_2\text{C(CH}_3)_2\text{O}_2\text{H} + \text{R}'\text{H}. \quad (9)$$

Thus, *t*-butanol, acetone, methane, and ethane were observed as products. Also detected at the lowest temperatures were small amounts of ditertiary butyl peroxide. Two studies [12,13] indicate that $t\text{-BuO}_2$ will isomerise under these conditions. Unfortunately, there is a conflict between these two studies in that one [12] finds no evidence for oxirane formation from the

$$t\text{-BuO}_2 \longrightarrow \text{CH}_2\text{C(CH}_3)_2\text{O}_2\text{H} \quad (10)$$

decomposition of $\text{CH}_2\text{C(CH}_3)_2\text{O}_2\text{H}$, whereas the other [13] assumes exclusive formation of oxirane from the same radical. The Arrhenius parameters also differ from one another:

$$\log (k_{10}/s^{-1}) = (13.7 \pm 0.5) - (120 \text{ kJ}/2.303 \text{ RT}) \quad [13]$$

$$\log (k_{10}/s^{-1}) = 13.9 - (145 \text{ kJ}/2.303 \text{ RT}). \quad [12]$$

TABLE 2
Experimental results for the decomposition of t-butyl hydroperoxide (1 Torr)
(Reaction time 3600 s)

T (K)	t-BuOOH/10^{-5} M Initial	Final	Isobutene (10^{-6} M)	Isobutene oxide (10^{-6} M)	k_{11a}/k_{11b}
413	3.30	3.14	0.40	0.45	0.90 ± 0.02
423	3.22	2.99	0.69	0.71	0.97 ± 0.07
433	3.14	2.24	4.31	3.78	1.14 ± 0.2
453	3.00	2.12	4.55	3.24	1.40 ± 0.1
463	2.94	0.95	9.44	6.18	1.53 ± 0.1

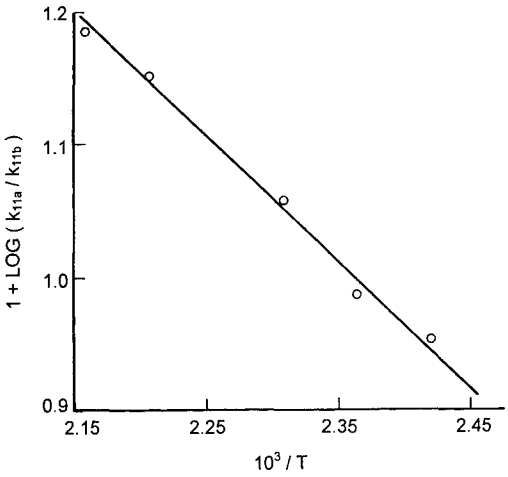

FIG. 3. Arrhenius plot for the decomposition of the hydroperoxy t-butyl radical.

In fact, at 473 K, the rate constants differ by a factor of 3 × 10–3. However, it is clear from both studies that extensive isomerisation of t-BuO_2 occurs under our conditions. It appears that our system is an even better source of $CH_2C(CH_3)_2O_2H$ than we had originally believed. Process (8) and (9) will lead to several products, but we maintain that isobutene oxide and isobutene may only arise as a result of the radical produced in reaction (9):

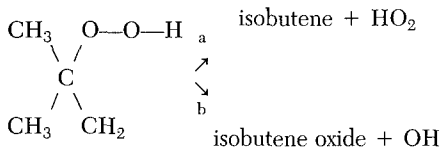

(11)

What is immediately striking about the results is that unlike the previous study, the two routes in process (11) are competitive (Table 2). As a result of carrying out several runs (usually six) at each temperature, one may determine the ratio of the rate constants k_{11a}/k_{11b} with suitable reproducibility (Table 2). An Arrhenius plot (Fig. 3) leads to the following result:

$$\log (k_{11a}/k_{11b}) = 2.3 \pm 0.4 - (18.2 \pm 2.9 \text{ kJ}/2.303 \text{ RT}).$$

Discussion

This work shows that both alkene and oxirane are formed near 430 K from the decomposition of hydroperoxy alkyl radicals. In addition, we may conclude from the Arrhenius parameters that the pre-exponential factor favours olefin formation by a magnitude of 100, whereas the activation energy term favours oxirane formation. In other words, the large pre-exponential factor in favour of the alkene is consistent with Wagner et al.'s [2] failure to observe the oxirane route, since in the R + O_2 system, they postulate that the QOOH is produced (by isomerisation of RO_2) with plenty of energy to surmount the barriers to either set of products so that the activation energy terms are not important. This would remove the objections by Walker and coworkers [3,4] referred to as (1) in the introduction.

Extrapolation of our result to the temperature range (675–793 K) of the Hull group's experiments at similar pressures on oxirane formation [3] gives k_{11a}/k_{11b} = 11 ± 4. Despite the uncertainties that this extrapolation may involve, it is clear that the two paths remain competitive. This is contrary to their assumption [3] that all QOOH formed by addition of HO_2 to alkene forms oxirane rather than reverting to reactants and would invalidate their rate constants. However, the correlation demonstrated between the rate and the alkene ionisation potential is not consistent with other steps in the mechanism being rate determining.

An estimate of the ratio from the work of the Hull group can be obtained in the following way. They have published rate data for the addition of HO_2 to isobutene [4]. The

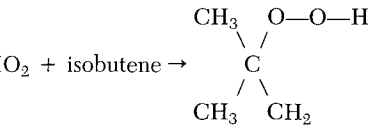

(−11a)

Arrhenius parameters for this reaction are given by:

$$\log (k_{-11a}/M^{-1}\,s^{-1}) = 8.61 - (50 \pm 5\ \text{kJ}/2.303\ RT).$$

By using group additivity rules [9], one may estimate that $\Delta H^{\circ}_{-11a} = -43.7\ \text{kJ mol}^{-1}$ and $\Delta S^{\circ}_{-11a} = -121\ \text{J mol}^{-1}\ \text{K}^{-1}$. This gives

$$\log (k_{11a}/s^{-1}) = 13.1 - (93.7\ \text{kJ}/2.303\ RT).$$

The rate constant for reaction (11*b*) can be taken from their estimate for several similar reactions [3] to be given by

$$\log (k_{11b}/s^{-1}) = 12.0\ (69 \pm 5\ \text{kJ}/2.303\ RT).$$

Hence, their ratio for the rate constants k_{11a}/k_{11b} is given by

$$\log (k_{11a}/k_{11b}) = 1.1 \pm 0.5 - (24.7 \pm 7\ \text{kJ}/2.303\ RT).$$

The difference from our result is largely in the pre-exponential factor.

The inconsistencies remain, and we can offer no complete explanation except to note that the QOOH is formed in different ways in the three experiments, H abstraction, HO_2 addition, and RO_2 isomerisation, and there is a possibility that more than one form of QOOH species is involved. For instance, the addition process will result in an initial energy-rich adduct. In the HCl/dtBP system, the only radical that can be produced from the Cl sensitised decomposition of dtBP is that depicted as II. This is unequivocal. Over the temperature range 363–403 K, the dominant product from the decomposition of the radical II is the oxirane. Higher temperatures result in the unimolecular decomposition of dtBP taking over as the dominant path for product formation, which limits our temperature range. Our results imply that oxirane formation will still be the dominating decomposition path for the radical II at higher temperatures than those used in this study. Oxirane formation could be more important than olefin formation up to temperatures as high as 900 K. We find this both interesting and very relevant to combustion. In the *t*-BuO_2H system, two types of radicals are produced from the radical-sensitised decomposition of the peroxide—the radical of interest (reaction 9) and *t*-BuO_2 (reaction 8). Two studies [12,13] report on the isomerisation of *t*-BuO_2. Although there is conflict between these two studies, their results imply rapid isomerisation of *t*-BuO_2 under our conditions of 413–473 K. (Using higher temperatures than these would result in complications associated with the breaking of the *t*-Bu-O_2 bond.) This provides strong evidence that the radical I is uniquely produced in our system. Extrapolation of our results to higher temperatures introduce uncertainties, but these results imply that the two routes for the decomposition of the radical I remain competitive up to temperatures of 900 K. We find this result very relevant to combustion.

Although the picture is not completely clear, as noted above, certain conclusions may come to be in respect of the mechanism for the oxidation of radicals, such as C_2H_5. A generally accepted mechanism would be that given in the introduction with the absence of direct olefin production from the alkyl radical and oxygen such that the RO_2 adduct either redissociates back to R and O_2 or isomerises. This isomer (QOOH) then either forms olefin + HO_2 or oxirane + OH. There is considerable evidence for the isomerisation of RO_2 to a stable QOOH species, especially for larger alkyl groups (i.e., longer chain), and this is thought to play a significant role in hydrocarbon combustion processes [11]. However, in the case of the C_2H_5 radical, the weight of evidence [2,5,10] favours the unique formation of C_2H_4 as the primary product. This product arises as a result of the addition of C_2H_5 to O_2 rather than a direct abstraction process. The adduct either rearranges to form C_2H_4 and HO_2 or becomes deactivated and redissociates to form C_2H_5 and O_2. The discrepancy between the work of Wagner et al. [2] and Walker and coworkers [3,4] can be resolved in terms of secondary formation of oxirane as a result of the addition of RO_2 to olefins would result in almost exclusive formation of oxirane. The work of Wagner et al. and, in particular, Dobis and Benson refers to very low pressures that favour the uncollisionised reaction of RO_2^{**}. Higher pressures could result in the formation of different products. It is possible that the uncollisioned reaction of RO_2^{**} results in exclusive olefin formation, whereas partial deactivation opens up the possibility of epoxide formation. RO_2^{*}, as opposed to RO_2^{**}, represents a partially collisionally deactivated alkyl peroxy radical.

$$RO_2^{**} \longrightarrow \text{olefin} + HO_2$$

$$RO_2^{**} + M \longrightarrow RO_2^{*} + M$$

$$RO_2^{*} \longrightarrow \text{epoxide} + OH.$$

However, this conclusion is not supported by the results of Wallington et al. [10] from studies at higher pressures where no evidence for epoxide formation was found. Further information would be obtained by studying the following:

1. The addition of HO_2 to olefins using a time-resolved technique.
2. The decomposition of $C_2H_4O_2H$ generated via the decomposition of ethyl hydroperoxide.
3. The addition of C_2H_5 to O_2 over a wide temperature and pressure range.

Conclusions

Over the temperature range 363–403 K, the decomposition of the *t*-butyl peroxy *t*-butyl radical leads to predominantly isobutene oxide formation

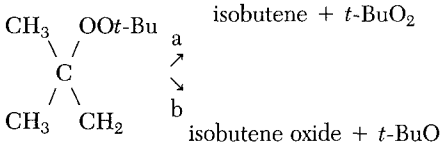

(4)

In contrast, over the temperature range 413–473 K, for the decomposition of the hydroperoxy *t*-butyl radical the two similar paths are competitive

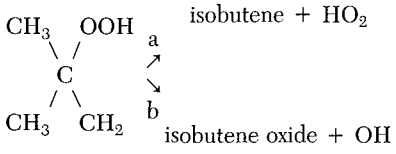

(11)

Acknowledgments

Support is acknowledged from Shell Research Ltd., S.E.R.C., The Pakistani Government, and the University of Aberdeen. The discussion with C. Morley (Shell Research Ltd.) is also acknowledged, whose comments are both refreshing and incisive. Travel grants from the Combustion Institute (British Section), The Royal Society, and Aberdeen University are acknowledged. The very constructive comments of the referees are much appreciated. This paper is dedicated to David Gutman in view of his unique contribution to the field of combustion kinetics. His death in November 1993 is both premature and tragic.

REFERENCES

1. Westbrook, C. K., Pitz, W. J., and Leppard, W. R., SAE 912314, Society of Automotive Engineers, 1991.
2. Wagner, A. F., Slagle, I. R., Sarzyniski, D., and Gutman, D., *J. Phys. Chem.* 94:1853–1868 (1990).
3. McAdam, K. G., and Walker, R. W., *J. Chem. Soc. Faraday Trans.* 2 83:1509–1517 (1987); Baldwin, R. R., Dean, C. E., and Walker, R. W., ibid., 82:1445–1455 (1986).
4. Slothard, N. D., and Walker, R. W., *J. Chem. Soc. Faraday Trans. I* 86:2115–2119 (1990).
5. Dobis, O., and Benson, S. W., *J. Am. Chem. Soc.* 115:8798–8809 (1993).
6. Sahetchian, K. A., Rigny, R., Tardieu de Maleissye, J., Batt, L., Khan, M. A., and Mathews, S., *Twenty-Fourth Symposium (International) on Combustion,* The Combustion Institute, Pittsburgh, 1992, pp. 115–121.
7. Flowers, M., Batt, L., and Benson, S. W., *J. Chem. Phys.* 37:2662–2668 (1962).
8. Batt, L., and Benson, S. W., *J. Chem. Phys.* 36:895–901 (1962).
9. Benson, S. W., *Thermochemical Kinetics,* 2nd ed., Wiley, New York, 1976.
10. Kaiser, E. W., Wallington, T. J., and Andino, J. M., *Chem. Phys. Lett.* 168:309–313 (1990).
11. Benson, S. W., *Oxidation Commun.* 2:169–188 (1982).
12. Sawerysyn, J.-P., Sochet, L.-R., Carlier, M., and Lucquin, M., *Bull. Soc. Chim. France* 3–4:199–206 (1977).
13. Baldwin, R. R., Hisham, M. W. M., and Walker, R. W., *J. Chem. Soc. Faraday Trans. I* 78:1615–1627 (1982).

COMMENTS

R. W. Walker, Hull University, England. 1. Were you able to check that the product ratio (isobutene/oxirane) did not vary with reaction time? If a fixed reaction time was used, was there considerable consumption of reactant at the higher temperatures used? If so, how would this affect the product ratios?

2. I also ask whether $t\text{-BuO}_2 \rightarrow t\text{-Bu} + O_2$ can compete with $t\text{-BuO}_2 \rightarrow$ QOOH and so provide an alternative source of isobutene?

Author's Reply. 1. Professor Walker raises an important issue concerning the product ratios in reactions (4) and (11). For reaction (4), only very small amounts of isobutene were produced. Comparable amounts of product species in particular isobutene were added to the reaction mixture without discernable loss. Similar experiments were carried out for reaction (11) with the same conclusions, but product ratios could be affected at the highest temperatures employed.

2. Professor Walker also raises the important question of whether reaction (12) can provide an alternative source of isobutene compared to isomerisation.

$$t\text{-BuO}_2 \rightarrow t\text{-Bu} + O^2. \qquad (12)$$

As pointed out in the paper, it was precisely this contri-

bution that restricted the temperature range in our study of reaction (11). Slagle *et al.* have shown that D(t-Bu-O_2) = 153 ± 2 kJ mol^{-1} [14]. A reasonable assumption is that the pre-exponential factor $A_{12} = 1.0 \times 10^{14}\ s^{-1}$. In terms of Baldwin *et al.*'s Arrhenius parameters for the isomerisation of t-BuO_2 [13], the ratio of isomerisation compared to bond breaking is 1000 at 473 K, i.e., reaction (12) makes no contribution to the yield of isobutene. Alternatively, if the Arrhenius parameters of Sawerysyn *et al.* are taken [12] (see text) the ratio is much smaller. These workers carried out their experiments over the temperature range 413–553 K. It is clear that at the higher temperatures employed by these workers, the bond breaking process (12) complicates a study of the isomerisation process (10). It therefore makes their Arrhenius parameters for the isomerisation process suspect.

The implications for the mechnism of the oxidation of t-butyl and for that matter ethyl radicals remain the same. Both the epoxide (oxirane) and olefin should be primary products depending upon the temperature and the pressure.

REFERENCE

14. Slagle, I. R., Ratajczak, E., and Gutman, D., *J. Phys. Chem.* 90:402–407 (1986).

Twenty-Fifth Symposium (International) on Combustion/The Combustion Institute, 1994/pp. 801–808

EXPERIMENTAL STUDIES OF Cl-ATOM REACTIONS AT HIGH TEMPERATURES: $Cl + H_2 \rightarrow HCl + H$ FROM 291 TO 1283 K

GEORGE YAW ADUSEI AND ARTHUR FONTIJN
High-Temperature Reaction Kinetics Laboratory
The Isermann Department of Chemical Engineering
Rensselaer Polytechnic Institute
Troy, New York 12180-3590, USA

A method is presented for producing Cl atoms for kinetic experiments above 750 K. Combined with a low temperature Cl-atom production technique, rate coefficients for the title reaction have been obtained over a wide temperature range. The Cl atoms were generated by flash photolysis of CCl_4 for the low-temperature measurements and by pulsed laser photolysis of NaCl for the high-temperature measurements. The relative Cl-atom concentrations were monitored by time-resolved resonance fluorescence. The data are well fitted by the expression $k_1(291\text{–}1283\ K) = 4.4 \times 10^{-11} \exp(-2568\ K/T)$ cm^3 molecule^{-1} s^{-1}, with 2σ precision limits of ± 9 to $\pm 16\%$, depending on temperature, and corresponding 2σ accuracy limits of about $\pm 26\%$. There is good agreement between the rate coefficients measured here and those from previous low-temperature studies, leading to the recommendation $k_1(200\text{–}1283\ K) = 2.3 \times 10^{-16} (T/K)^{1.63} \exp(-1592\ K/T)$ cm^3 molecule^{-1} s^{-1}, with a suggested 2σ accuracy limit of $\pm 28\%$ for the combined data. A transition state theory calculation based on a semiempirical London–Eyring–Polanyi–Sato (LEPS) potential energy surface gives excellent agreement with the combined experimental results. Extension of our previous recommendation for the reverse reaction to lower temperatures leads to $k_2(200\text{–}1200\ K) = 6.6 \times 10^{-16} (T/K)^{1.44} \exp(-1241\ K/T)$ cm^3 molecule^{-1} s^{-1}, with 2σ accuracy limits within $\pm 25\%$. There is excellent agreement between the present data and the predicted expression from that reaction and equilibrium data.

Introduction

The reactions involving Cl atoms are of major interest to combustion-generated pollution and flame inhibition problems [1,2]. Yet, no direct measurements above about 700 K had apparently been made. Previously, we have reported on direct measurements on reactions of O and H atoms at elevated temperatures using high-temperature photochemistry (HTP) reactors [3–8]. Because of their essentially wall-less environment, these reactors are ideal for observations on such combustion intermediates, which recombine readily on walls, a problem especially severe for halogen atoms [9]. To apply this technique to Cl atoms, one faces the problem that common low-temperature photolytic techniques for their production are unsuitable for higher temperatures, as they involve precursors that are thermally unstable and/or react very fast with Cl atoms. However, we have also studied reactions of metal atoms in a slightly modified form of the reactors [10–13], in which metal halides are vaporized and photodissociated. As halogen atoms are produced in this process, it appears well suited for studies of their reactions. In this, the first application of this approach, it has been employed to extend the temperature range of the rate coefficient measurements of

$$Cl + H_2 \rightarrow HCl + H \qquad (1)$$

which is about 4 kJ mol^{-1} endothermic [14]. This reaction is particularly well suited for such a study, as a consistency check is available from our recent study of the reverse reaction [6]:

$$HCl + H \rightarrow Cl + H_2. \qquad (2)$$

Based on it and equilibrium data [14], we recommended

$$k_1(300\text{–}1200\ K) = 4.9 \times 10^{-11} \cdot \exp(-2567\ K/T)\ \text{cm}^3\ \text{molecule}^{-1}\ \text{s}^{-1} \qquad (3)$$

an extension to which is given in the Appendix of this paper.

Reaction (1) is a major source of HCl, an undesirable product of combustion. Baulch et al. [15] recommended $k_1(200\text{–}650\ K) = 2.40 \times 10^{-11} \exp(-2200\ K/T)$ cm^3 molecule^{-1} s^{-1} based on four sets of direct measurements. Of these, Westenberg and deHaas [16] employed a discharge flow system with electron spin resonance detection of the Cl atoms to investigate the reaction between 251 and 456 K. The other three studies used the flash photolysis-

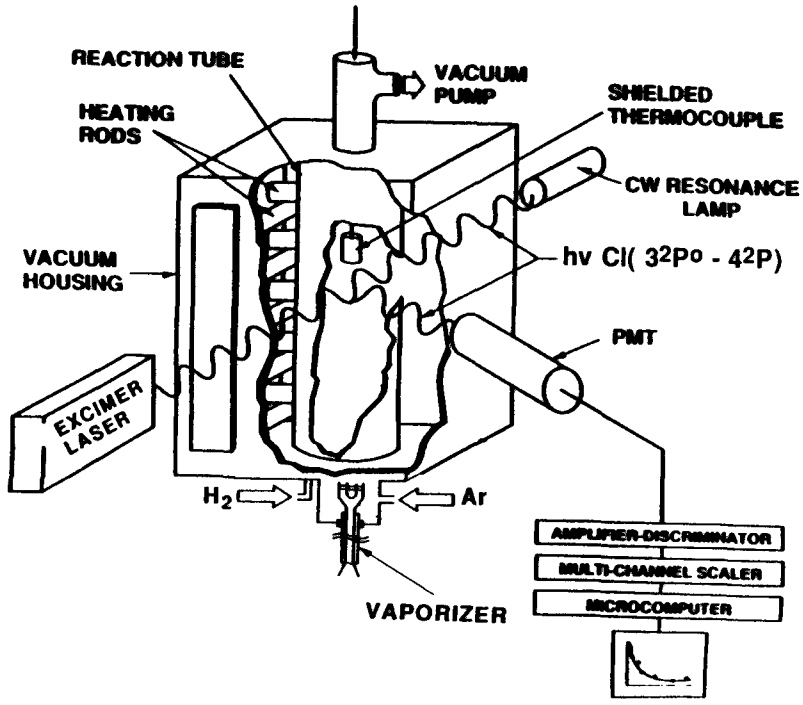

FIG. 1. The HTP reactor.

resonance fluorescence technique (FP-RF), of which the HTP is a higher temperature variant. Davis et al. [17] worked only at 298 K, whereas rate coefficient measurements by Lee et al. [18] covered the 200–500 K range. Lee et al. also reported a similar study for the 213–350 K range by Watson et al., which has not been published independently. Since then, Miller and Gordon [9] have employed FP-RF for a study between 200 and 500 K.

Experimental

Two experimental arrangements were used. For experiments in the 291–800 K range, an HTP reactor shown as reactor B by Mahmud et al. [5] was used. That reactor was also used for the H + HCl study, [6] where essentially the same operating and data analysis procedures were used [3,7,8,10]. Briefly, CCl_4/Ar mixtures flowed through a moveable cooled inlet (to prevent thermal decomposition) and mixed with the Ar bath gas and H_2 introduced at the upstream end of the reactor. The gases flowed toward the reaction zone where Cl atoms were generated by flash photolysis of CCl_4 through a MgF_2 window.

For temperatures between 750 and 1283 K, the reactor was modified, as shown in Fig. 1, by replacing the cooled-inlet with a vaporizer that consisted of an alumina crucible (1.0-cm i.d. and 1.0-cm long) fitted into a helical tungsten coil. To produce Cl atoms, the crucible was filled with NaCl and heated by passing current through the tungsten coil. The NaCl vapor was mixed with the Ar bath gas and H_2, and Cl atoms were produced by single-photon KrF laser photolysis at 248 nm through a Suprasil window ($\lambda > 161$ nm). Knowledge of NaCl concentrations is not needed, but rough estimates can be made. The number of molecules of NaCl vaporized per unit time; N_{NaCl} can be approximated by dividing the power generated in the coil-crucible assembly by the latent heat of vaporization [19]. N_{NaCl} is converted to a volumetric flow rate and combined with the total gas flow to obtain [NaCl]. Variations in [NaCl] from 4×10^{14} to 3×10^{15} molecules cm^{-3} were obtained by changing the current passing through the tungsten coil and/or the total gas flow rate.

In both reactor modes, relative Cl concentrations were monitored in real time, using atomic resonance fluorescence lines between 134 and 140 nm [20]. The source of resonance radiation was a microwave discharge flow lamp through which a 0.1% mixture of Cl_2 in He flowed at 3.2 mbar. The fluorescence intensity, proportional to [Cl], was measured using a photomultiplier tube, situated behind a BaF_2 window ($\lambda \gtrsim 134$ nm) [21] and a dry N_2 filter.

The materials used were Ar (99.998%), from the liquid, and pure H_2 (99.999%) (Linde); CCl_4 (99.99%) and NaCl (Aldrich); 1.09% H_2 (99.9995%)

in Ar (99.999%) (Matheson); and 0.1% Cl_2 (99.9%) in He (99.999% U.H.P.) (MG industries). The CCl_4/Ar mixtures were prepared by controlling partial pressures of the components in a bulb, and the compositions thus obtained were verified by gas chromatography.

Rate coefficients were obtained from fluorescence intensity decays with time, as described in detail elsewhere [3,7,8,10]. All the experiments were carried out under pseudo-first-order conditions, [Cl] << [H_2], for which the fluorescence intensity I decay with time can be represented by

$$I = I_0 \exp(-k_{ps1}t) + B. \quad (4)$$

Here, $I_0 + B$ is the intensity at time $t = 0$, k_{ps1} the pseudo-first-order rate coefficient, and B is the background due to scattered light. The values of k_{ps1} are obtained by fitting [22] observed I vs t profiles to Eq. (4). The exponentiality of these plots is verified by a two-stage residual analysis procedure [3]. The rate coefficients, k_i, at given temperatures, pressures, and photolysis conditions, are subsequently determined from a least-squares fit to typically five or six pairs of k_{ps1} vs [H_2] observations.

Results

The 68 measurements of k_1 and the conditions under which they were obtained are summarized in Table 1. A plot of the data is shown in Fig. 2. We observed significant signal deterioration above about 1283 K; therefore, no measurements were made above that temperature. Plots of $[k_1(T) - k_i]/k_1(T)$, where $k_1(T)$ at the given T is obtained from the expression given below and k_i are the measured rate coefficients, show the independence of the results of the variations in total pressure P, corresponding to total gas concentration [M], average gas velocity $\bar{v}$, flash/laser energy F, and cooled inlet-to-reaction zone distance z. In addition, results from two different H_2 cylinders from two different sources agreed, thus errors arising from interference from reaction products, photofragments, or impurities in the gases were negligible. The good agreement between the data from the two Cl-atom production techniques shows the independence of the results of the Cl source used. The combined data are well fitted by an expression of the form $k(T) = a \exp(-e\ K/T)$ to yield

$$k_1(291\text{–}1283\ \text{K}) = 4.4 \times 10^{-11} \cdot \exp(-2568\ K/T)\ \text{cm}^3\ \text{molecule}^{-1}\ \text{s}^{-1} \quad (5)$$

with covariance matrix elements, $\sigma_a^2 = 8.81 \times 10^{-3}a^2$, $\sigma_{ae} = 4.12 \times 10^{-11}a$, and $\sigma_e^2 = 2237$. These are combined [23] to yield 2σ precision levels of the fit between a minimum of $\pm 9\%$ at 562 K and a maximum of $\pm 17\%$ at 291 K. Allowing for possible systematic errors of $\pm 20\%$, probably excessive, the 2σ accuracy limits are estimated to range from ± 21 to $\pm 26\%$.

In Fig. 3, the present data and the best fit are compared with results from earlier studies of reaction (1). It can also be seen that though each data set can be approximated by an Arrhenius expression, the combined results show some curvature and can be best fitted by a three-parameter expression of the form $k(T) = A(T/K)^n \exp(-E\ K/T)$. A nonlinear least-squares fit of the individual data weighted according to their associated uncertainties to that expression yields

$$k_1(200\text{–}1283\ \text{K}) = 2.26 \times 10^{-16}\ (T/K)^{1.63} \cdot \exp(-1592\ K/T)\ \text{cm}^3\ \text{molecule}^{-1}\ \text{s}^{-1}. \quad (6)$$

The associated statistical data are $\sigma_A^2 = 2.04 \times 10^{-1}\ A^2$, $\sigma_{An} = -2.54 \times 10^{-2}\ A$, $\sigma_{AE} = 13.058\ A$, $\sigma_n^2 = 3.27 \times 10^{-3}$, $\sigma_{nE} = -1.377$, and $\sigma_E^2 = 1.59 \times 10^3$. The 2σ precision levels vary from $\pm 6\%$ at 340 K to $\pm 19\%$ at 200 K. Allowing again for $\pm 20\%$ for possible systematic errors for the combined data leads to a recommended 2σ accuracy limits within $\pm 28\%$. A two-parameter fit to the combined data yielded somewhat larger 2σ precision limits, i.e., ± 7 to $\pm 21\%$.

Discussion

The temperature dependence of the rate coefficients for the reverse reaction were shown to be in accord with semiempirical transition state theory (TST) calculations [6]. The same treatment can be applied here. Following the general recommendation of Glasstone et al. [24], a linear transition state is assumed. The London–Eyring–Polanyi–Sato (LEPS) [25–27] approach is used to calculate the potential energy surface in the region of the saddle point based on the following equations:

$$Q_i = 1/4D_e\ \{(3 + \Delta) \exp(-2\beta(R_i - R_e)) - (2 + 6\Delta) \exp(-2\beta(R_i - R_e))\} \quad (7)$$

$$J_i = 1/4D_e\{(1 + 3\Delta) \exp(-2\beta(R_i - R_e)) - (6 + 2\Delta) \exp(-2\beta(R_i - R_e))\} \quad (8)$$

$$V_1 = Q_1 + Q_2 + Q_3 + \{1/2[(J_1 - J_2)^2 + (J_2 - J_3)^2 + (J_3 - J_1)^2]\}^{1/2} \quad (9)$$

$$V_s = V_1/(1 + \Delta) \quad (10)$$

Here, Q and J are coulombic and exchange energies,

TABLE 1
Summary of Rate Coefficient Measurements on the Cl + H_2 Reaction

T[a] (K)	P (mbar)	[M] (10^{18} cm^{-3})	[Photolyte] (10^{15} cm^{-3})	[H_2] (10^{14} cm^{-3})	z (cm)	$\bar{v}$ (cm s^{-1})	$F.E.$, (J)	$k \pm \sigma_k$ (cm^3 molecule^{-1} s^{-1})
291	467	11.7	6.5[b]	0.0–65.4[d]	28[f]	6	25	0.81 ± 0.07(−14)[h]
291	333	8.3	4.5[b]	0.0–64.7[d]	28	6	25	0.71 ± 0.05(−14)
292	200	5.0	2.7[b]	0.0–84.0[d]	28	4	25	0.91 ± 0.03(−14)
303	467	11.2	1.5[b]	0.0–64.5[d]	28	6	12	1.30 ± 0.05(−14)
303	333	8.0	2.4[b]	0.0–64.2[d]	28	6	12	1.44 ± 0.04(−14)
304	333	8.0	3.2[b]	0.0–32.3[d]	28	12	12	1.24 ± 0.05(−14)
306	200	4.7	4.2[b]	3.7–36.9[d]	28	9	21	0.91 ± 0.37(−14)
309	200	4.7	2.5[b]	0.0–70.0[d]	28	5	21	1.08 ± 0.14(−14)
309	200	4.7	2.5[b]	0.0–69.0[d]	28	5	29	1.01 ± 0.38(−14)
318	467	10.6	6.5[b]	0.0–64.4[d]	28	6	25	1.38 ± 0.95(−14)
319	267	6.1	3.3[b]	0.0–32.4[d]	28	12	25	1.26 ± 0.52(−14)
321	267	6.0	4.3[b]	3.84–26.6[d]	28	9	18	1.36 ± 0.03(−14)
324	267	6.0	4.4[b]	0.0–26.7[d]	28	9	25	1.57 ± 0.27(−14)
336	533	11.5	3.9[b]	6.5–37.5[d]	28	10	18	2.08 ± 0.21(−14)
336	533	11.5	1.8[b]	13.1–75.0[d]	28	5	18	1.81 ± 0.09(−14)
336	467	10.1	3.9[b]	0.0–22.7[d]	28	10	12	1.85 ± 0.04(−14)
346	470	9.9	2.0[b]	16.4–93.5[d]	28	17	21	2.41 ± 0.14(−14)
347	250	5.2	4.8[b]	0.0–46.7[d]	28	8	21	2.36 ± 0.06(−14)
347	250	5.2	1.9[b]	0.0–46.9[d]	28	17	21	2.92 ± 0.08(−14)
360	267	5.4	2.6[b]	0.0–47.8[d]	28	8	12	2.83 ± 0.09(−14)
360	533	10.7	2.8[b]	0.0–46.9[d]	28	8	12	3.46 ± 0.05(−14)
360	267	5.4	2.4[b]	0.0–23.4[d]	28	16	12	3.03 ± 0.09(−14)
378	260	5.1	4.8[b]	0.0–48.5[d]	28	8	15	3.54 ± 0.18(−14)
379	533	10.2	1.6[b]	0.0–48.3[d]	28	8	15	4.23 ± 0.11(−14)
397	267	4.9	1.9[b]	0.0–48.7[d]	28	9	25	6.16 ± 0.31(−14)
398	533	9.7	2.9[b]	0.0–43.7[d]	28	8	25	5.82 ± 0.21(−14)
400	560	10.2	4.3[b]	0.0–14.8[d]	28	8	15	5.11 ± 0.17(−14)
404	267	4.8	4.9[b]	0.0–13.3[d]	28	10	15	5.88 ± 0.59(−14)
406	533	9.5	4.1[b]	0.0–15.9[d]	28	10	10	7.04 ± 0.47(−14)
407	267	4.7	2.6[b]	0.0–17.3[d]	28	8	10	7.30 ± 0.21(−14)
408	600	10.7	1.0[b]	0.0–28.7[d]	28	9	21	7.28 ± 0.49(−14)
415	260	4.7	1.9[b]	0.0–91.0[d]	28	20	18	6.90 ± 0.37(−14)
420	550	9.5	3.8[b]	0.0–12.3[d]	28	10	10	8.06 ± 0.19(−14)
422	267	4.6	1.6[b]	0.0–10.5[d]	28	20	10	7.15 ± 0.21(−14)
424	267	4.6	1.7[b]	0.0–12.9[d]	28	10	10	9.39 ± 0.36(−14)
434	683	11.4	1.6[b]	0.0–4.40[e]	28	8	15	1.34 ± 0.04(−13)
440	267	4.4	3.7[b]	3.84–21.9[d]	28	9	15	1.13 ± 0.17(−13)
440	267	4.4	2.1[b]	1.92–9.35[d]	28	18	15	9.00 ± 0.16(−14)
441	683	11.2	1.5[b]	0.63–4.30[e]	28	10	18	1.36 ± 0.05(−13)
480	766	11.6	1.3[b]	0.64–4.10[e]	28	10	18	1.83 ± 0.11(−13)
480	686	10.4	1.4[b]	0.08–4.17[e]	28	9	18	2.13 ± 0.03(−13)
489	326	4.8	2.8[b]	0.57–3.37[e]	28	11	18	2.37 ± 0.05(−13)
503	245	3.8	2.1[b]	1.84–10.5[d]	17	18	18	2.76 ± 0.21(−13)
518	245	3.5	2.4[b]	0.0–11.8[d]	28	16	18	2.67 ± 0.22(−13)
538	467	6.0	2.4[b]	0.0–11.8[d]	28	16	12	6.86 ± 0.29(−13)
562	326	4.2	1.6[b]	2.7–15.8[d]	22	24	21	4.66 ± 0.20(−13)
562	530	6.8	1.6[b]	1.6–17.0[d]	22	12	21	3.31 ± 0.13(−13)
572	328	4.2	3.3[b]	0.5–2.9[e]	28	12	21	4.63 ± 0.32(−13)
673	136	1.5	1.6[b]	0.0–1.05[e]	25	25	15	1.16 ± 1.94(−12)
674	267	2.9	2.6[b]	0.0–1.53[e]	15	15	15	1.09 ± 0.52(−12)
682	268	2.8	2.6[b]	0.42–1.85[e]	25	15	18	1.28 ± 0.52(−12)
739	400	3.9	2.4[c]	0.19–0.74[e]	[g]	27	230	1.12 ± 0.09(−12)
741	400	3.9	1.5[b]	0.19–0.88[e]	20	27	10	1.14 ± 0.06(−12)

TABLE 1
(*continued*)

T^a (K)	P (mbar)	[M] (10^{18} cm^{-3})	[Photolyte] (10^{15} cm^{-3})	[H_2] (10^{14} cm^{-3})	z (cm)	$\bar{v}$ (cm s^{-1})	F.E., (J)	$k \pm \sigma_k$ (cm^3 molecule^{-1} s^{-1})
746	400	3.9	0.9[c]	0.38–1.83[c]	—	13	125	1.15 ± 0.13(−12)
775	134	1.3	1.4[b]	0.06–0.67[c]	20	29	10	1.87 ± 0.13(−12)
795	135	1.2	0.4[c]	0.08–0.54[d]	—	29	225	2.01 ± 0.33(−12)
857	290	2.4	0.4[c]	0.0–0.68[d]	—	28	106	2.05 ± 1.05(−12)
857	290	2.4	2.7[c]	0.0–0.73[e]	—	28	118	1.97 ± 0.06(−12)
1009	150	1.1	0.9[c]	0.0–0.07[d]	—	13	113	3.85 ± 0.27(−12)
1033	213	1.5	1.3[c]	0z.0–0.32[e]	—	15	113	3.37 ± 0.20(−12)
1038	137	1.0	1.8[c]	0.0–0.04[d]	—	21	135	3.49 ± 0.19(−12)
1102	133	0.9	0.5[c]	0.07–0.27[d]	—	27	58	5.07 ± 0.15(−12)
1103	250	1.7	1.6[c]	0.0–0.33[e]	—	27	245	4.85 ± 0.14(−12)
1128	149	1.0	1.2[c]	0.0–0.08[d]	—	23	236	5.82 ± 0.64(−12)
1138	150	1.0	0.5[c]	0.0–0.21[d]	—	21	225	6.05 ± 0.34(−12)
1257	167	1.0	0.6[c]	0.0–0.16[d]	—	25	69	5.76 ± 0.72(−12)
1263	172	1.0	0.6[c]	0.04–0.18[e]	—	29	135	7.15 ± 0.47(−12)
1283	419	2.4	0.4[c]	0.02–0.17[d]	—	28	113	7.46 ± 1.53(−12)

[a]σ_T/T = 2%.
[b]Used CCl_4 as photolyte with flash photolysis.
[c]Used NaCl as photolyte with laser photolysis; concentrations estimated as discussed.
[d]Used pure H_2.
[e]Used 1.09% H_2 in Ar.
[f]z = 28 cm corresponds to premixing of reactant and bath gases.
[g]Used vaporizer in place of the cooled inlet.
[h]Read as (0.81 ± 0.07) × 10^{-14}.

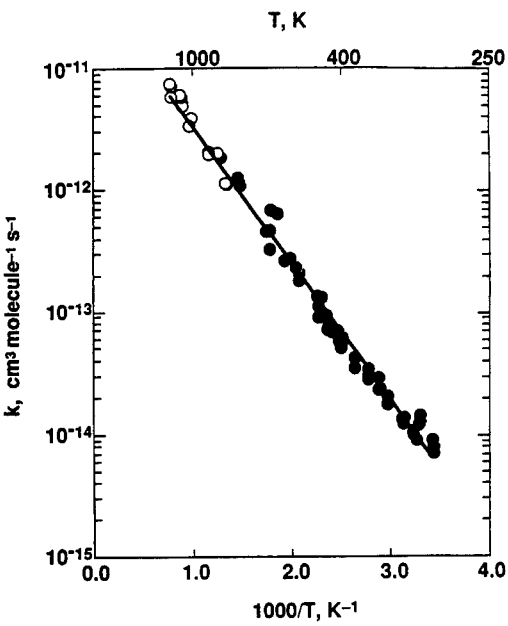

FIG. 2. Summary of the present measurements for the Cl + H_2 reaction: (○) NaCl photolysis; (●) CCl_4 photolysis; and (———) best-fit, Eq. (5).

V_I is the London potential, Δ is the Sato parameter, and V_s is the Sato potential. The subscript i takes the values 1, 2, and 3; R_1 is the H-H distance, R_2 is the H-Cl distance, and $R_3 = R_1 + R_2$. The Morse parameters [28] for H-H are equilibrium distance R_{e1} = 7.41 nm, classical dissociation energy D_{e1} = 458.39 kJ mol^{-1}, and molecular constant β = 12.75. For H-Cl, the corresponding parameters are R_{e2} = 19.44 nm^{-1}, D_{e2} = 445.66 kJ mol^{-1}, and β = 18.68 nm^{-1}. The transition state is located by adjusting the value of Δ to obtain approximately the experimental activation energy at 300 K. That process locates the transition state to be approximately at H-H° = 0.977 nm and H-Cl° = 1.045 nm with Δ = 0.184. The symmetric and bending frequencies for the transition state are calculated to be 1312 and 728 cm^{-1}, respectively. At this transition state, the classical activation energy, E_c of 28.9 kJ mol^{-1} is obtained, which is corrected [27] to give E_0 = 19.1 kJ mol^{-1}. This E_0 is combined with a theoretical A factor, obtained from the symmetric and bending frequencies, to yield

$$k_{\mathrm{Icalc}}(T) = 4.44 \times 10^{-10}\, T^{-0.5} \cdot [1 - \exp(-6324\ \mathrm{K}/T)] \exp(-2300\ \mathrm{K}/T) \div [1 - \exp(-1888\ \mathrm{K}/T)]$$

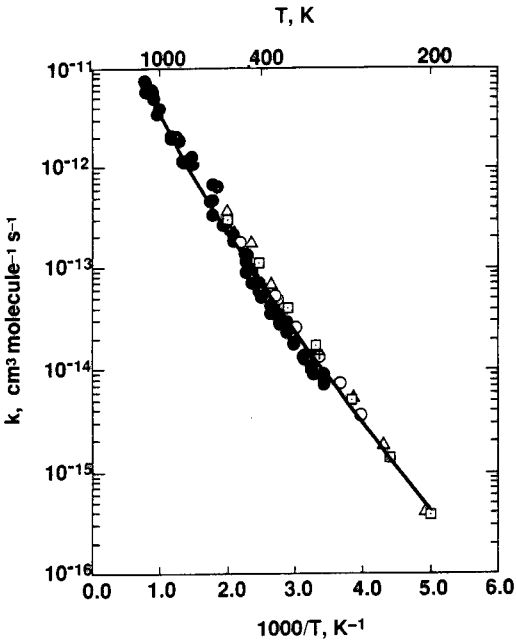

FIG. 3. Combined rate coefficient measurements for the Cl + H_2 reaction: (●) present data; (⊡) Miller and Gordon [9]; (○) Westenberg and de Haas [16]; (+) Davis et al. [17]; (△) Lee et al. [18]; and (———) best-fit to combined data, Eq. (6).

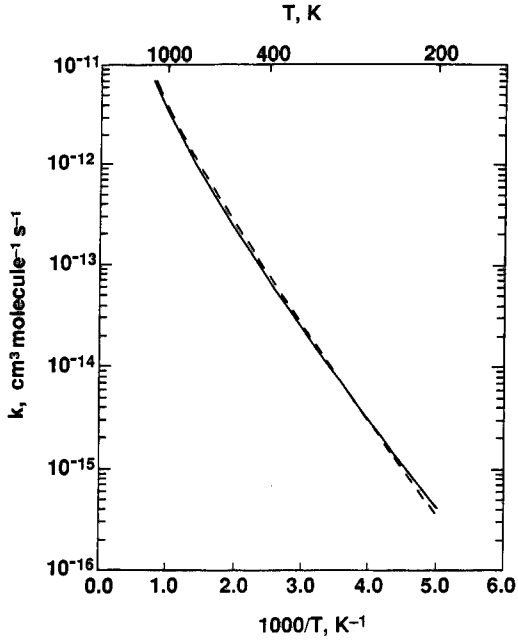

FIG. 4. Comparison of calculated rate coefficients with experimental results: (———) best-fit to combined data, Eq. (6); (– – –) $k_{1calc}(T)$, Eq. (11).

$$[1 - \exp(-1048\ \mathrm{K}/T)]^2\ \mathrm{cm}^3\ \mathrm{molecule}^{-1}\ \mathrm{s}^{-1}. \quad (11)$$

Equation (11) predicts an increase in the apparent activation energy from 18 to 32 kJ mol^{-1} over the 200–1283 K temperature range. This increase can be attributed mostly to the temperature dependence of the vibrational partition function of the bending motion of the transition state. In Fig. 4, the TST expression Eq. (11) is compared with the best fit to all experimental data and is seen to confirm the slight curvature depicted by the experimental best fit, Eq. (6).

Equation (6) can also be compared to the $k_1(T)$ expression calculated from $k_2(T)$ for the reverse reaction, Appendix A, and equilibrium data. Using current thermochemical data [14], we obtain for the equilibrium coefficients $K(T) = k_2(T)/k_1(T) = 0.57 \exp(485\ \mathrm{K}/T)$, which yields

$$k_1(200\text{–}1200\ \mathrm{K}) = 1.12 \times 10^{-15}\ (T/\mathrm{K})^{1.44} \cdot \exp(-1725\ \mathrm{K}/T)\ \mathrm{cm}^3\ \mathrm{molecule}^{-1}\ \mathrm{s}^{-1}. \quad (12)$$

In Fig. 5, Eq. (12) is compared to Eq. (6) and seen to be in excellent agreement. From the present data and those of the reverse reaction, the heat of reaction (1) is estimated, from $E_1 - E_2 = \Delta H$, to be 4.1 kJ

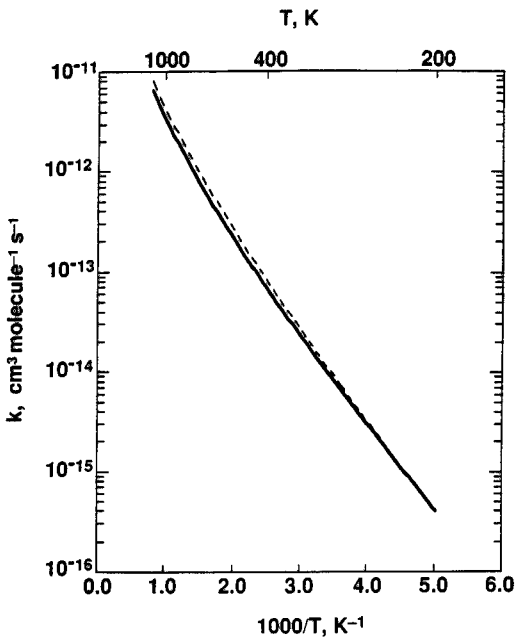

FIG. 5. Comparison of the predicted and experimental results for the Cl + H_2 reaction: (———) best-fit to combined data, Eq. (6); (– – –) predicted $k(T)$, Eq. (12).

mol^{-1}. This value is in full accord with the 4 kJ mol^{-1} heat of reaction calculated from thermochemical data [14].

Conclusions

A photolytic method for the study of Cl-atom reactions at high temperatures has been developed. Combined with a low-temperature Cl-atom production technique, direct rate coefficients for reaction (1) have been obtained from 291 to 1283 K and have been combined with literature data to lead to a recommendation for the 200 to 1283 K temperature range. The combined results are in excellent agreement with transition state theory calculations and with those predicted from the reverse reaction. The technique can now be applied to other Cl reactions, such as those with hydrocarbons. It should be applicable to other halogen atoms as well, of interest for instance to halon combustion problems. As the reactor can be operated at temperatures up to 1800 K, the upper limit of the present study can likely be surpassed by other combinations of metal halides and photolysis wavelengths.

Appendix

We previously reported [6] for the HCl + H → Cl + H_2 reaction

$$k_2(300\text{–}1200\ \text{K}) = 2.8 \times 10^{-11} \cdot \exp(-2082\ \text{K}/T)\ \text{cm}^3\ \text{molecule}^{-1}\ \text{s}^{-1}. \quad (A1)$$

In the region of temperature overlap, this expression was shown to be in good agreement with earlier measurements [9,29,30]. However, there was no attempt to combine these results with the lower temperature data of Miller and Gordon [9], which is needed for comparison to the present study. The combined k_2 data are compared in Fig. 6 and show some curvature. They are well fitted by a three-parameter expression of the same form as that used for $k_1(T)$:

$$k_2(200\text{–}1200\ \text{K}) = 6.6 \times 10^{-16}\ (T/\text{K})^{1.44} \cdot \exp(-1241\ \text{K}/T)\ \text{cm}^3\ \text{molecule}^{-1}\ \text{s}^{-1} \quad (A2)$$

with covariance matrix elements, $\sigma_A^2 = 5.98 \times 10^{-2}\ A^2$, $\sigma_{An} = -8.89 \times 10^{-3}\ A$, $\sigma_{AE} = 4.219\ A$, $\sigma_n^2 = 1.37 \times 10^{-3}$, $\sigma_{nE} = -0.502$, and $\sigma_E^2 = 6.75 \times 10^2$. The 2σ precision levels vary from ±6% at 491 K to ±14% at 200 K. Again, allowing for ±20% systematic errors leads to 2σ accuracy limits within ±25%.

In the derivation of Eq. (A2), no use has been made of the recommendation of Baulch et al. [15], as it was derived from the then available data on reaction (1).

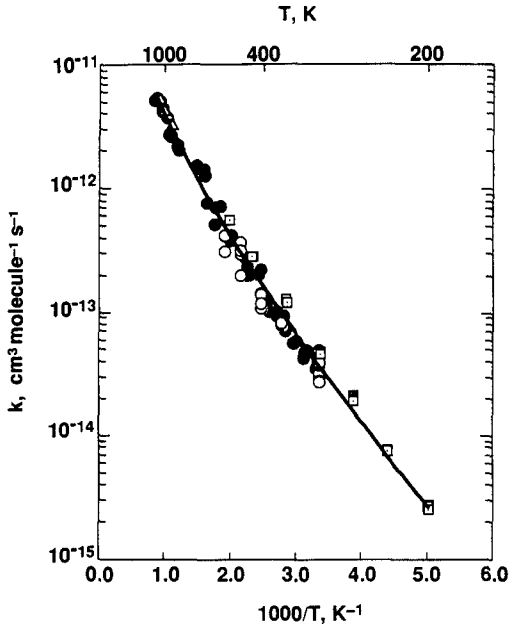

FIG. 6. Comparison of rate coefficient measurements for the HCl + H reaction: (●) Adusei and Fontijn [6]; (⊡) Miller and Gordon [9]; (○) Ambidge et al. [29]; (△) Benson et al. [30]; and (———) best-fit to combined data, Eq. (A2).

Acknowledgments

This work has been supported by the Department of Energy, Office of Basic Energy Science, under Grant No. DE-FG02-84ER1332. We thank W. F. Flaherty and G. Dalakos for assistance with the experiments.

REFERENCES

1. Tsang, W., *Combust. Sci. Technol.* 74:99 (1990).
2. Karra, S. B., Gutman, D., and Senkan, S. M., *Combust. Sci. Technol.* 60:45 (1988).
3. Ko, T., Adusei, G. Y., and Fontijn, A., *J. Phys. Chem.* 95:8745 (1991).
4. Ko, T., Fontijn, A., Lim, K. P., and Michael, J. V., *Twenty-Fourth Symposium (International) on Combustion*, The Combustion Institute, Pittsburgh, 1992, p. 735.
5. Mahmud, K., Kim, J.-S., and Fontijn, A., *J. Phys. Chem.* 94:2994 (1990).
6. Adusei, G. Y., and Fontijn, A., *J. Phys. Chem.* 97:1409 (1993).
7. Marshall, P., Ko, T., and Fontijn, A., *J. Phys. Chem.* 93:1922 (1989).

8. Ko, T., Marshall, P., and Fontijn, A., *J. Phys. Chem.* 94:1401 (1990).
9. Miller, J. C., and Gordon, R. J., *J. Chem. Phys.* 75:5305 (1981).
10. Fontijn, A., and Futerko, P. M., in *Gas-Phase Metal Reactions* (A. Fontijn, Ed.), North Holland, Amsterdam, 1992, Ch. 6.
11. Marshall, P., Narayan, A. S., and Fontijn, A., *J. Phys. Chem.* 94:2998 (1990).
12. Narayan, A. S., Slavejkov, A. G., and Fontijn, A., *Twenty-fourth Symposium (International) on Combustion*. The Combustion Institute, Pittsburgh, 1992, p. 727.
13. Fontijn, A., Blue, A. S., Narayan, A. S., and Bajaj, P. N. *Combust. Sci. Technol.*, in press.
14. Chase, Jr., M. W., Davies, C. A., Downey, Jr., J. R., Frurip, D. J. McDonald, R. A., and Syverud, A. N., *JANAF Thermochemical Tables*, 3rd ed., *J. Phys. Chem. Ref. Data* 14 (1):743 (1985).
15. Baulch, D. L., Duxbury, J., Grant, S. J., and Montague, D. L., *J. Phys. Chem. Ref. Data* 10:(1), 122 ff. (1981).
16. Westenberg, A. A., and deHaas, N., *J. Chem. Phys.* 48:4405 (1968).
17. Davis, D. D., Braun, W., and Bass, A. M., *Int. J. Chem. Kinet.* 2:101 (1970).
18. Lee, J. H., Michael, J. V., Payne, W. A. Stief, L. J., and Whytock, D. A., *J. Chem. Soc. Faraday Trans. 1* 73:1530 (1977).
19. *Chemical Engineers' Handbook*, 5th ed., (Perry, R. H., and Chilton, C. H., Eds.), McGraw-Hill, New York, 1973, p. 3–112.
20. Davis, D., and Braun, W., *Appl. Opt.* 7:2071 (1968).
21. Okabe, H., *Photochemistry of Small Molecules*, John Wiley, New York, 1978, p. 120.
22. Marshall, P., *Comput. Chem.* 11:219 (1987).
23. Wentworth, W. E., *J. Chem. Educ.* 42:96 (1965).
24. Glasstone, S., Laidler, K. J., and Eyring, H., *The Theory of Rate Processes*, McGraw-Hill Book Co., New York, 1941, p. 87.
25. Laidler, K. J., *Chemical Kinetics*, 3rd ed., Harper Collins Publishers, 1987, p. 68 ff.
26. Smith, I. W. M., in *Modern Gas Kinetics Theory, Experiments and Application* (M. J. Pilling, and I. W. M. Smith, Eds.), Blackwell Scientific Publications, London, 1978 p. 55 ff.
27. Johnston, H. S., *Gas Phase Reaction Rate Theory*. The Ronald Press Company, New York, 1966, pp. 169 ff, 333 ff.
28. Huber, K. P., and Herzberg, G., *Constants of Diatomic Molecules*, Van Nostrand Reinhold, New York, 1979, pp. 250, 286.
29. Ambidge, P. F., Bradley, J. N., and Whytock, D. A., *J. Chem. Soc. Faraday Trans. 1* 72:2143 (1976).
30. Benson, S. W., Cruickshank, F. R., and Shaw, R., *Int. J. Chem. Kin.* 1:29 (1969)

Twenty-Fifth Symposium (International) on Combustion/The Combustion Institute, 1994/pp. 809–816

THERMAL DECOMPOSITION OF CH_2Cl_2

K. P. LIM AND J. V. MICHAEL
Chemistry Division
Argonne National Laboratory
Argonne, IL 60439, USA

The thermal decomposition of CH_2Cl_2 has been investigated in reflected shock wave experiments at temperatures between 1400 and 2300 K and at three different loading pressures with various initial CH_2Cl_2 concentrations. The resulting product Cl atoms are monitored by the atomic resonance absorption spectrometric (ARAS) technique. A reaction mechanism is used to numerically simulate the measured Cl-atom profiles in order to obtain rate constants for the two primary dissociation reactions: (1) $CH_2Cl_2 \rightarrow CHCl + HCl$, and (2) $CH_2Cl_2 \rightarrow CH_2Cl + Cl$. The experimental second-order Arrhenius expressions for the two reactions are $k_1/[Kr] = 2.26 \times 10^{-8} \exp(-29{,}007\ K/T)$ cm^3 molecule^{-1} s^{-1} and $k_2/[Kr] = 6.64 \times 10^{-9} \exp(-28{,}404\ K/T)$ cm^3 molecule^{-1} s^{-1}, with standard deviations of ± 43 and 40%, respectively. The results are compared to theoretical calculations using the semiempirical Troe formalism. The best fits to the experimental data are obtained with threshold energy and collisional energy transfer parameters of $E_1^\circ = 73.0$ kcal mole^{-1} and $\Delta E_{1\mathrm{down}} = 630$ cm^{-1}. Similar values for reaction (2) are $E_2^\circ = \Delta H_2^\circ$ (0 K) = 78.25 kcal mole^{-1} and $\Delta E_{2\mathrm{down}} = 394$ cm^{-1}.

Introduction

Because of needs in incineration strategies for the destruction of chlorocarbon molecules [1–4], we have studied the thermal decompositions of CH_3Cl, CCl_4, and $COCl_2$ in prior investigations from this laboratory [5–7]. The analytical method used in these studies has been Cl-atom atomic resonance absorption spectrometry (ARAS). The present work on the thermal decomposition of CH_2Cl_2 is a continuation investigation on the chloromethane class of molecules.

The thermal decomposition of CH_2Cl_2 has previously been studied using tubular flow reactors with 1 atm Ar as bath gas by Bozzelli and coworkers [8,9]. Because the initial reactant densities were high in comparison to the present work, a fairly extensive chemical modeling effort with sensitivity analysis was required in this work to explain both the thermal decomposition and subsequent experiments on the oxidation by O_2. The oxidation proceeds after thermal initiation through two possible reactions,

$$CH_2Cl_2 \xrightarrow{k_1} CHCl + HCl \qquad (1)$$

$$\xrightarrow{k_2} CH_2Cl + Cl. \qquad (2)$$

Because there are relatively few prior studies on this and related reactions, Bozzelli and coworkers used best estimates for the thermochemistry of the various species and subsequently applied Rice–Ramsperger–Kassel (RRK) theory [10,11] to calculate some unknown rate constants for use in the chemical model. The obvious question arises as to whether the predictions from theory are in accord with experiment. Because the relative importance of reactions (1) and (2) can be directly assessed by observing both the rate and yields of Cl-atom formation in a dilute system using the ARAS technique, the present study is designed to answer this question.

Measurements of the thermal decomposition of CH_2Cl_2 have been made with three loading pressures in reflected shock wave experiments at low dilution. The measured Cl-atom profiles are explained by considering reactions (1) and (2), and the experimental results for both processes are discussed in terms of Troe type theoretical fits to the data.

Experimental

Apparatus

All experiments were carried out in the reflected shock mode with a shock-tube apparatus that has been previously described [12]. Briefly, the shock-tube apparatus consisted of two sections: a 7-m 304 stainless steel tube (i.d. 9.74 cm) and a driver chamber. A thin aluminum diaphragm (4 mil, unscored 1100-H18) separated the two sections. The tube was

*The submitted manuscript has been authored by a contractor of the U.S. Government under Contract No. W-31-109-ENG-38. Accordingly, the U.S. Government retains a nonexclusive, royalty-free license to publish or reproduce the published form of this contribution, or allow others to do so, for U.S. Government purposes.

routinely pumped to $<10^{-8}$ Torr between experiments by an Edwards Vacuum Products, Model CR100P, packaged pumping system. The incident shock velocity was determined from eight pressure transducers (PCB Piezotronics, Inc., Model 1132A) placed at fixed intervals toward the end of the tube. Final temperature and density for each experiment were determined from the incident velocity of the shock front and the initial thermodynamic conditions. Corrections for nonidealities due to boundary layer formation were subsequently applied [12,13]. The photometer system was radially located 6 cm from the endplate and had an optical-path length of 9.94 cm. An EMR G14 solar blind photomultiplier tube was used to measured transmittances from the resonance lamp. Transmittances and the differentiated signals from the pressure transducers were recorded with a dual-channel (Nicolet 4094C) digital oscilloscope. Since the pressures of condensable gases were well below saturation, all pressure measurements with an MKS Baratron capacitance manometer in an all-glass vacuum line were stable, and mixture preparation by the partial-pressure method was routine. Reactant pressures were likewise measured with an MKS Baratron capacitance manometer shortly before shock firing. The time between reactant introduction into the shock tube and firing was 30 s.

Cl-Atom Detection

The Cl-atom resonance lamp used in the experiments has been described in previous works [5–7] and is similar to that discussed by Whytock et al. [14] and Clyne and Nip [15]. The lamp was operated at 50 watts microwave power in a mixture containing 1×10^{-3} of Cl_2 in helium. The flowing pressure in the lamp was 2.0 torr. It is important to control these conditions in order to eliminate fluctuations in the day-to-day photometer operation. This configuration gives a multiplet (133.6–139.6 nm) structure that is somewhat reversed. Resonance radiation was observed through a BaF_2 crystal window filter without wavelength resolution. A typical experimental record is shown in Fig. 1, where a decreasing ARAS signal results after the CH_2Cl_2 sample has been shock-heated. The fraction of light that is Cl-atom resonance radiation was determined earlier in CCl_4 experiments [5,6]. These indicated that $86(\pm 2)\%$ of the light is resonance radiation. Since this fraction is known, absorbance by Cl atoms can be determined from the expression $(ABS)_t \equiv -\ln I_t/I_0$.

In earlier work from this laboratory, the curve of growth for Cl atoms has been established from the measurements of long-time steady-state absorptions of Cl atoms from the thermal decomposition of CH_3Cl [5]. The result of these experiments can be expressed in a modified form of Beer's law, $T_\infty = I_\infty/I_0 = \exp(-\kappa[Cl]^a)$. When [Cl] is expressed in units of atoms cm^{-3}, the values of κ and a were deduced, giving

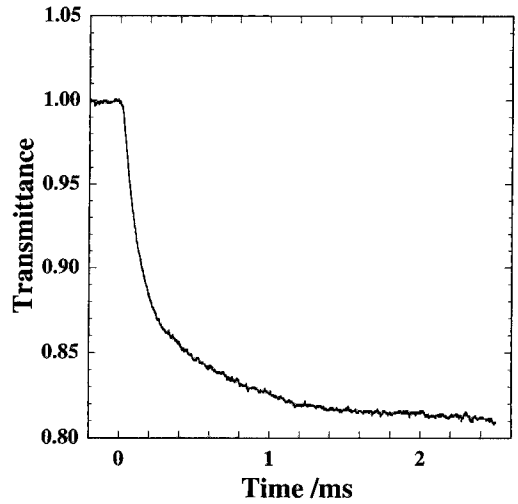

FIG. 1. A typical experimental record showing decreasing ARAS signal as Cl atoms are produced from the thermal decomposition of CH_2Cl_2. [Cl] rapidly attains a near-steady-state value. The experimental conditions are as follows: $T = 1804$ K, $P = 227$ torr, $\rho = 1.214 \times 10^{18}$ cm^{-3}, and $X_{CH_2Cl_2} = 2.885 \times 10^{-5}$.

$$(ABS)_\infty = 4.41 \times 10^{-9}[Cl]^{0.581}. \quad (3)$$

This result has been corroborated by subsequent experiments using CF_3Cl as the source of Cl atoms [16]. Since secondary reactions of Cl with the substrate are no longer possible, the Cl-atom absorption signal unambiguously points to the complete dissociation of the CF_3Cl molecules. These independent experiments yielded results that were in complete agreement with Eq. (3), thus confirming the conclusions from the CH_3Cl study. Using the expression from Eq. (3), the measured Cl-atom absorbance profiles, $(ABS)_t$, can be easily converted to Cl-atom concentrations, $[Cl]_t$.

Gases

The high-purity He (99.995%), used as the driver gas, was obtained from Air Products and Chemicals, Inc. Scientific-grade Kr (99.997%), used as the diluent gas in reactant mixtures, was obtained from MG Industries. Airco Industrial Gases supplied the ultra–high-purity-grade He (99.999%) used in the resonance lamp. Research-grade Cl_2 (99.999%) was obtained from MG Industries and was used as received. Analytical-grade CH_2Cl_2 was obtained from Mallinckrodt Specialty Chemicals Co. and was purified by bulb-to-bulb distillation, retaining only the middle

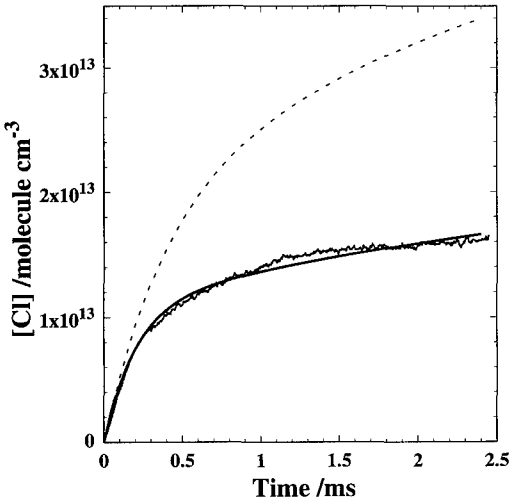

FIG. 2. The experimental profile of [Cl], derived from Fig.1. The solid line is a simulated fit that is based on the mechanism in Table 1. The dashed line shows the [Cl] that would have been observed if molecular elimination, reaction (1), did not occur, i.e., if an equivalent experiment with CF_3Cl were performed. The solid-line fit required k_1 = 2975 s^{-1}, k_2 = 1700 s^{-1}, and k_5 = 300 s^{-1}.

third, before use. The sample was further subjected to mass spectrometric analysis to verify its purity.

Results

Fifty-two experiments were performed at three different loading pressures and at temperatures between 1400 and 2300 K. The data are not shown because of space limitations; however, a table is available on request from J. V. Michael. Using Eq. (3), the measured absorption signals were converted to $[Cl]_t$. A typical result is shown in Fig. 2. We found that [Cl] always increased rapidly to a near steady-state value; however, depending on temperature, there was a subsequent small increase in concentration that could extend over ~1 ms after the initial rapid rise. Unlike all earlier studies from this laboratory [5–7,16], the maximum [Cl] never came close to equaling the initial reactant concentration; i.e., if the experiment shown in Fig. 2 had been carried out with the same rate of formation using CF_3Cl instead of CH_2Cl_2, then the dashed line in the figure would have been observed. This depressed yield of [Cl] immediately means that some reaction or reactions serve to perturb the reaction away from unit stoichiometry.

In order to understand the possible reaction perturbations that might explain the depressed yields, the mechanism shown in Table 1 was numerically integrated. With the small $[CH_2Cl_2]_0$ (7–16 ppm) used in the experiments, reactions (3), (4), and (7) of Table 1 contribute negligibly to the [Cl] profile under all conditions. If these reaction-rate constants are set to zero, the resulting predictions of $[Cl]_t$ change at most by a few percent under all conditions. Apparently, the major process that perturbs the reaction from unit stoichiometry is reaction (1), the molecular elimination channel. The long-time slow buildup of [Cl] is formally attributed to the chloromethyl-radical decompositions, reactions (5) and (6) in Table 1; however, it should be noted that, if reaction (3) is negligible, then reaction (6) is likewise unimportant. We also investigated the possible contributions from both self- and cross-recombination and disproportionation reactions of these chloromethyl radicals. There are a total of nine such reactions, and Bozzelli and coworkers [8] have theoretically determined rate constants for these processes. With their estimates, our conclusion is that these reactions are also negligible under the low concentration conditions of the present study. Hence, all of the present experiments can be explained by fitting the observed profiles to three rate constants, (1), (2), and (5); however, even though the contributions of reactions (3), (4), (6), and

TABLE 1
The mechanism for the decomposition of CH_2Cl_2

(1)	$CH_2Cl_2 \rightarrow CHCl + HCl$	k_1 = to be fitted
(2)	$CH_2Cl_2 \rightarrow CH_2Cl + Cl$	k_2 = to be fitted
(3)	$Cl + CH_2Cl_2 \rightarrow CHCl_2 + HCl$	$k_3 = 6 \times 10^{-11} \exp(-1615\ K/T)$[a]
(4)	$CHCl + CH_2Cl_2 \rightarrow C_2H_3Cl_3$	$k_4 = 2.5 \times 10^{-11}$[b]
(5)	$CH_2Cl \rightarrow CH_2 + Cl$	k_5 = to be fitted[c]
(6)	$CHCl_2 \rightarrow CHCl + Cl$	k_6 = to be fitted[c]
(7)	$HCl + Kr \rightarrow H + Cl + Kr$	$k_7 = 6.97 \times 10^{-11} \exp(-40{,}765\ K/T)$[d]

[a]Value based on Ref. 17. Units are cm^3 $molecule^{-1}$ s^{-1}.
[b]Estimated. Units are cm^3 $molecule^{-1}$ s^{-1}.
[c]k_5 and k_6 are taken to be equal.
[d]Ref. 18.

(7) are negligible, they are included in the final simulations.

In order to determine rate constants, the Table 1 mechanism was numerically integrated with various values for k_1, k_2, and k_5. The predicted Cl-atom profiles were then compared to experiment. Since the values for k_5 were generally less than $0.2(k_1 + k_2)$, the long-time buildup is effectively weakly coupled to the rates for (1) and (2). Hence, the values for k_1 and k_2 could be easily determined by mutual adjustment until the short-time rapid buildup matched the experiment. The solid line in Fig. 2 shows a typical fit for the first-order values given in the figure caption. Anticipating that the reactions will be nearly second-order, we determined second-order rate constants for the entire range of experimental conditions. The results for $k_1/[\mathrm{Kr}]$ and $k_2/[\mathrm{Kr}]$ are plotted in Arrhenius form in Figs. 3 and 4, respectively. Linear-least-squares analysis gives

$$k_1/[\mathrm{Kr}] = 2.26 \times 10^{-8} \exp(-29{,}007\ K/T)\ \mathrm{cm^3\ molecule^{-1}\ s^{-1}}, \tag{4}$$

and

$$k_2/[\mathrm{Kr}] = 6.64 \times 10^{-9} \exp(-28{,}404\ K/T)\ \mathrm{cm^3\ molecule^{-1}\ s^{-1}}. \tag{5}$$

The points shown in the two figures deviate by ±43 and ±40% from Eqs. (4) and (5), respectively, at the one standard deviation level. The expression for the atomic elimination reaction (5) is identical within experimental error to that for CH_3Cl decomposition, $1.09 \times 10^{-8}\exp(-29{,}325\ K/T)$ $\mathrm{cm^3\ molecule^{-1}\ s^{-1}}$ (1600–2100 K), over the common range of temperature overlap [5].

Discussion

In earlier studies from this laboratory on CH_3Cl [5] and CF_3Cl [16], molecular elimination in competition with atomic elimination was not observed. In the $COCl_2$ decomposition study [7], molecular elimination was observed; however, it amounted to only about 10% of the total decomposition. These results could be easily rationalized in terms of thermochemistry because the molecular processes were more endothermic than atomic elimination in all cases except $COCl_2$, where the threshold energy was substantially higher than the $\Delta H°$ (0 K), making molecular elimination less likely than simple atomic dissociation. In the present case, it is obvious by inspection of Eqs. (4) and (5) that molecular elimination is dominating over atomic elimination. This may mean that the two processes occur at roughly the same threshold energy, indicating the need for a careful assessment of the thermochemistry for the two channels.

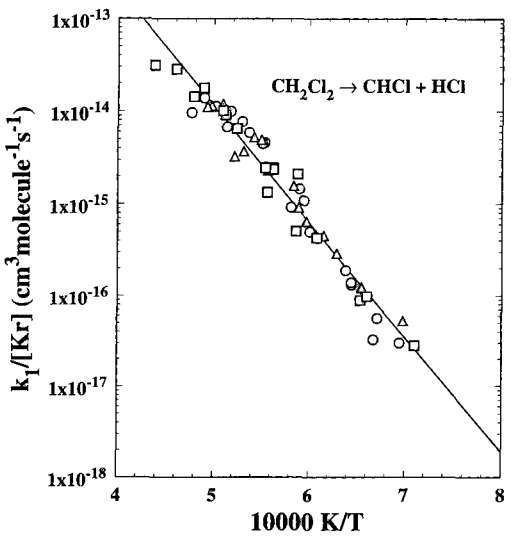

FIG. 3. The Arrhenius plot of the second-order rate constants for reaction (1) at three loading pressures: (○) 16 torr, (△) 11 torr, and (□) 6 torr. The solid line [Eq. (4)] is the linear-least-squares fit to the data.

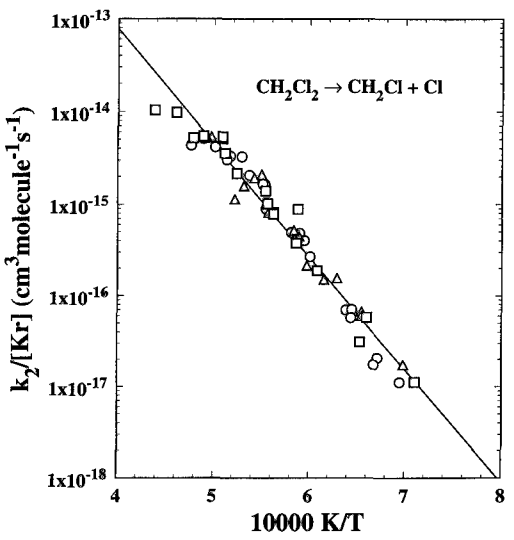

FIG. 4. The Arrhenius plot of the second-order rate constants for reaction (2) at three loading pressures: (○) 16 torr, (△) 11 torr, and (□) 6 torr. The solid line [Eq. (5)] is the linear-least-squares fit to the data.

TABLE 2
Parameters for the theoretical evaluation of $CH_2Cl_2 \rightarrow CHCl + HCl$[a]

Temperature (K)	F_{anh}	F_{rot}	F_E	$(k_{10}^{sc}/[Kr])/cm^3$ molecule^{-1} s^{-1}	S_K	B_K	β_c	$F(k_0/k_\infty)$[b]
1400	1.47	1.811	1.312	8.42×10^{-16}	5.40	12.4	0.109	0.283
1500	1.47	1.783	1.340	3.83×10^{-15}	5.56	12.3	0.096	0.296
1600	1.47	1.754	1.370	1.40×10^{-14}	5.70	12.1	0.086	0.314
1700	1.47	1.726	1.400	4.31×10^{-14}	5.84	11.9	0.076	0.336
1800	1.47	1.698	1.432	1.15×10^{-13}	5.97	11.7	0.068	0.360
1900	1.47	1.669	1.464	2.70×10^{-13}	6.08	11.6	0.060	0.385
2000	1.47	1.642	1.498	5.76×10^{-13}	6.19	11.4	0.054	0.411
2100	1.47	1.614	1.533	1.12×10^{-12}	6.29	11.1	0.048	0.436
2200	1.47	1.586	1.570	2.03×10^{-12}	6.39	10.9	0.043	0.461
2300	1.47	1.559	1.607	3.45×10^{-12}	6.48	10.7	0.039	0.484

[a]E_1° = 73.0 kcal mole^{-1} and ΔE_{1down} = 630 cm^{-1}. The JANAF molecular parameter values for CH_2Cl_2 give $\rho(E_0)$ = 3143 states/cal mole^{-1} at the threshold energy.
[b]Evaluated at 11 torr loading pressure.

There are three critical evaluations of thermochemical data for the species involved in reactions (1) and (2). The JANAF tables [19] give thermodynamic functions for CH_2Cl_2, CHCl, and HCl, whereas values for CHCl and CH_2Cl are listed by Manion and Rodgers [20]. Lias et al. [21] have reported $\Delta_f H^\circ$ (0 K) values from appearance potential measurements for all species. There is a $\Delta_f H^\circ$ (0 K) discrepancy for CHCl between JANAF (79.8 kcal mole^{-1}) and the other two compilations (70.9 kcal mole^{-1}). Hence, ΔH_1° ranges between 79.0 (JANAF) and 70.1 kcal mole^{-1} (Manion and Rodgers; Lias et al.). For CH_2Cl, Manion and Rodgers give $\Delta_f H^\circ$ (0 K) = 29.25 kcal mole^{-1}; however, this value is probably only accurate to $\pm$1–2 kcal mole^{-1}. Using this value, ΔH_2° (0 K) = 79.04 kcal mole^{-1}, indicating that the molecular elimination channel may be lower lying than atomic elimination, depending on the barrier height for the reverse reaction (-1).

Reactions (1) and (2) have been theoretically analyzed by using the semi-empirical Troe theoretical formalism [22–24]. As in earlier studies [7,25], we fitted the experimental data by allowing variations in both E° and ΔE_{down}. The latter quantity specifies the collisional deactivation efficiency factor, β_c.

To our knowledge, the barrier height for reaction (1) has never been estimated from electronic structure calculations. It has therefore been necessary to construct a fairly rigid transition state for this process by empirical methods. The limiting high-pressure rate constant, $k_{1\infty}$, which is dependent on E_1°, can then be calculated by conventional transition-state methods. The calculation of k_{10}^{sc}/Z_{LJ} is unambiguous [22–24] and follows procedures described earlier [5,7,25]. The term Z_{LJ} for CH_2Cl_2 + Kr collisions is evaluated from Lennard–Jones parameters as determined from polarizabilities estimated from procedures described by Hirschfelder, Curtiss, and Bird [26] along with the method of Cambi et al. [27] for obtaining σ_{12} and ε_{12}/k. With molecular parameters for CH_2Cl_2 taken from JANAF, several theoretical calculations were performed as functions of both E_1° and ΔE_{1down}. The best fit was obtained with values (73.0 kcal mole^{-1}, 630 cm^{-1}); however, (75.0, 874) and (71.0, 394) also gave acceptable fits. The Troe fit parameters are shown in Table 2 for (73.0, 630), and the predicted bimolecular rate constants are plotted in Fig. 5 in comparison with the data at the three loading pressures.

If the back reaction (−1) is assumed to have a zero barrier height, then E_1° would be equal to ΔH_1^0 (0 K). Use of the previously mentioned JANAF value, ΔH_1^0 (0 K) = 79.0 kcal mole^{-1}, requires an unreasonably high value for ΔE_{1down} and gives fits that are much too steep and not a good representation of the data. Acceptance of the value implied by Manion and Rodgers, ΔH_1^0 (0 K) = 70.1 kcal mole^{-1}, would be compatible with the present results but would imply a barrier height for the reverse process of 2.9 kcal mole^{-1}. Also, with E_1° = 73.0 kcal mole^{-1}, the values for K_{1eq} and the high-pressure rate constant for reaction (1) are respectively calculated as

$$K_{1eq} = 1.135 \times 10^{26} \exp \cdot (-33{,}694\ K/T) \text{ molecules cm}^{-3} \quad (\pm 3\% \text{ at } 1\sigma) \tag{6}$$

and

$$k_{1\infty} = 3.10 \times 10^{14} \exp(-38{,}053\ K/T) \text{ s}^{-1} \quad (\pm 1\% \text{ at } 1\sigma) \tag{7}$$

for the temperature range 1400–2300 K. Equation

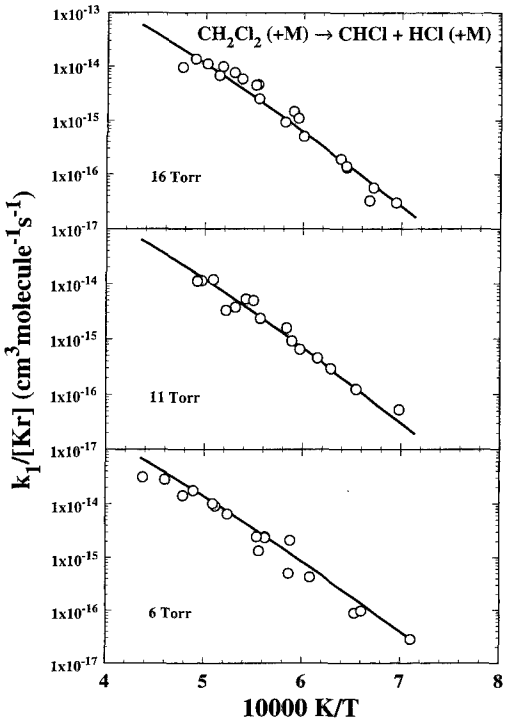

FIG. 5. A comparison of the experimental data for k_1/[Kr] to the theoretical calculations. The solid lines are calculated from the Troe's semiempirical theory using E_1° = 73.0 kcal mole^{-1} and $\Delta E_{1\text{down}}$ = 630 cm^{-1}.

(7) divided by Eq. (6) gives an apparent high-pressure activation energy for the back reaction of about 8.7 kcal mole^{-1}, but Eq. (6) can also be divided into the calculated values for k_1/[Kr] to predict values for k_{-1}/[Kr]. For 11 torr loading pressure, between 1400 and 2300 K,

$$k_{-1}/[\text{Kr}] = 9.12 \times 10^{-25} T^{-2.62}\ \text{cm}^6\ \text{molecule}^{-2}\ \text{s}^{-1}. \quad (8)$$

Since theory fits experiment (Fig. 5), similar values can be obtained by dividing Eq. (6) into the experimental result, Eq. (4).

$$k_{-1}/[\text{Kr}] = 1.99 \times 10^{-34} \cdot \exp(4687\ \text{K/T})\ \text{cm}^6\ \text{molecule}^{-2}\ \text{s}^{-1}. \quad (9)$$

At this pressure, either expression, (8) or (9), shows a negative T-dependence, whereas the high-pressure analysis yields a positive activation energy of 8.7 kcal mole^{-1}. This indicates that, at 11 torr loading pressure, the reaction is nearer to the third- than the second-order limit and also that much of the T-dependence is carried in the β_c factor. This point is corroborated by comparing theoretical k_1/[Kr] to β_c k_{10}^{∞}/[Kr]. The former varies from 21 to 48% of the latter over the temperature range, showing that reaction (1) is nearer to the second- than the first-order limit.

Troe calculations have also been performed to understand reaction (2). Though earlier values of molecular parameters for CH_2Cl have been reported and have been used for thermodynamic function evaluation [20], here we have elected to use recent electronic structure results from Harding [28] with the vibrations slightly scaled to reflect certain observed frequencies. These calculations show that the structure is slightly bent from a planar configuration. We have calculated the absolute entropy for CH_2Cl and find that the new calculation is only ~1.2% higher at all temperatures than that of Manion and Rodgers. Harding's estimation for $\Delta_f H^\circ$ (0 K) is only approximate, and therefore, we have again performed calculations with both E_2° and $\Delta E_{2\text{down}}$ as parameters. As before [5,7], $k_{-2\text{LJ}}$ was calculated with a Lennard–Jones collision model from estimated CH_2Cl polarizabilities [26] using the method of Cambi et al. [27] The result between 1400 and 2300 K is $k_{-2\text{LJ}} = (5.44 \pm 0.15) \times 10^{-11}$ cm^3 molecule^{-1} s^{-1}. The experimental rate constants were then compared to Troe calculations at mutual values of E_2° and $\Delta E_{2\text{down}}$ ranging from 81.25 kcal mole^{-1} and 560 cm^{-1}, respectively, to 75.25 and 268. All fits were acceptable, with the one at 78.25 and 394 being only slightly superior at all pressures. This latter calculation is shown in Table 3 and is plotted with the data in Fig. 6. Between 1400 and 2300 K, the calculated equilibrium constant can be expressed to within ±2% by

$$K_{2\text{eq}} = 2.203 \times 10^{26} \exp \cdot (-38{,}822\ K/T)\ \text{molecules cm}^{-3}. \quad (10)$$

The value for the high-pressure limiting-rate constant is

$$k_{2\infty} = 1.33 \times 10^{16} \exp \cdot (-39{,}017\ K/T)\ \text{s}^{-1}\ (\pm 2\%\ \text{at}\ 1\sigma). \quad (11)$$

Reaction (2) is also predicted to be near the low-pressure limit, as shown by comparing theoretical k_2/[Kr] to β_c k_{20}^{∞}/[Kr]. In this case, the former ranges from 65 to 74% of the latter over the temperature range.

Lastly, theoretical calculations have been carried out to see whether the values for k_5 that are specified from the experimental fits are reasonable. This reaction will undoubtedly be in the low-pressure limit, and therefore, we have estimated β_c k_{50}^{∞}/[Kr] using $E_5^\circ = \Delta H_5^\circ$ (0 K) = 92.6 kcal mole^{-1}. The predicted T-dependence is generally too steep; however, the

TABLE 3
Parameters for the theoretical evaluation of $CH_2Cl_2 \rightarrow CH_2Cl + Cl$[a]

Temperature (K)	F_{anh}	F_{rot}	F_E	$(k_{20}^{sc}/[Kr])$/cm^3 molecule^{-1} s^{-1}	S_K	B_K	β_c	$F(k_0/k_\infty)$[b]
1400	1.47	1.832	1.291	2.02×10^{-16}	5.32	12.8	0.057	0.652
1500	1.47	1.806	1.317	1.04×10^{-15}	5.45	12.5	0.050	0.662
1600	1.47	1.779	1.344	4.24×10^{-15}	5.56	12.2	0.043	0.671
1700	1.47	1.752	1.371	1.44×10^{-14}	5.67	11.9	0.038	0.681
1800	1.47	1.726	1.400	4.17×10^{-14}	5.77	11.7	0.033	0.691
1900	1.47	1.699	1.430	1.06×10^{-13}	5.87	11.4	0.030	0.700
2000	1.47	1.672	1.461	2.42×10^{-13}	5.96	11.2	0.026	0.710
2100	1.47	1.646	1.493	5.02×10^{-13}	6.04	10.9	0.023	0.719
2200	1.47	1.620	1.525	9.60×10^{-13}	6.12	10.7	0.021	0.728
2300	1.47	1.594	1.559	1.72×10^{-12}	6.19	10.5	0.019	0.737

[a]$E_2^\circ = \Delta H_2^\circ$ (0 K) = 78.25 kcal mole^{-1} and ΔE_{2down} = 394 cm^{-1}. The JANAF molecular parameter values for CH_2Cl_2 give $\rho(E_0)$ = 4958 states/cal mole^{-1} at the threshold energy.
[b]Evaluated at 11 torr loading pressure.

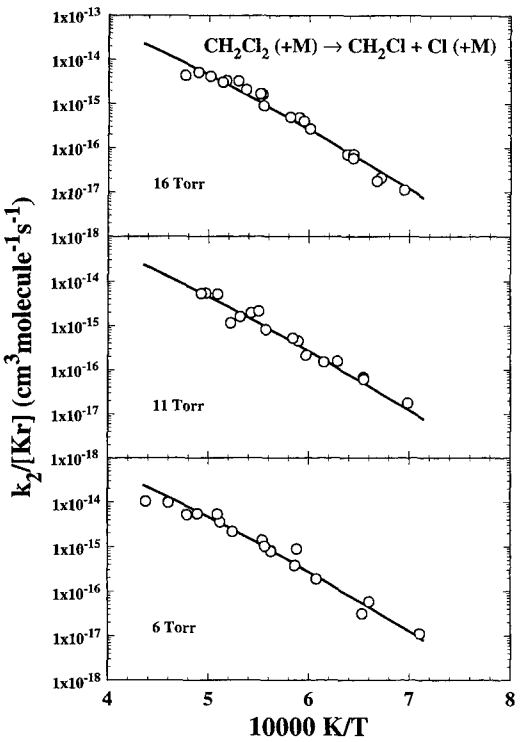

FIG. 6. A comparison of the experimental data for $k_2/[Kr]$ to the theoretical calculations. The solid lines are calculated from the Troe's semiempirical theory using $E_2^\circ = \Delta H_{20}^\circ$ = 78.25 kcal mole^{-1} and ΔE_{2down} = 394 cm^{-1}.

magnitudes for k_5 in the middle range of temperature can be justified with values of β_c between 0.55 and 0.72.

In conclusion, the main finding from this study is that the molecular elimination process in the thermal decomposition of CH_2Cl_2 predominates over the atomic process. This conclusion suggests that the JANAF value for the heat of formation for CHCl is overestimated, but the value given by Manion and Rodgers is compatible with the present result. The heat of formation for CH_2Cl from Manion and Rodgers might be high by ~0.8 kcal mole^{-1}; however, the present conclusion is clearly only accurate to ~ ±3 kcal mole^{-1}, and this is higher than the uncertainty in their estimate. Second, we find relatively large values for ΔE_{down} in both reactions (1) and (2). For best fits, it has been necessary to use different values for the two reactions, and this may suggest that energy transfer from the activated molecule may be dependent on total energy. Lastly, since both reactions are near to the second-order limit, the values for k_∞ [Eqs. (7) and (11)] used in the calculation are not firm but are simply implied by the theoretical formalism presented.

Acknowledgments

The authors wish to thank Drs. A. F. Wagner, L. B. Harding, and J. P. Hessler for a thorough reading of the manuscript and helpful suggestions. We also thank Professor M.-C. Su from Butler University for help with some of the experiments. This work was supported by the U.S. De-

partment of Energy, Office of Basic Energy Sciences, Division of Chemical Sciences, under Contract No. W-31-109-Eng-38.

REFERENCES

1. Graham, J. L., Hall, D. L., and Dellinger, B., *Environ. Sci. Tech.* 20:703–710 (1986).
2. Oppelt, E. T., *J. Air Poll. Contr. Assoc.* 37:558–586 (1987).
3. Senkan, S. M., *Environ. Sci. Tech.* 22:368–370 (1988).
4. Hart, J. R., and Franco, G., *Proceedings of the Third Symposium on the Incineration of Hazardous Wastes*, San Diego, CA, 1989, Paper 15.
5. Lim, K. P., and Michael, J. V., *J. Chem. Phys.* 98:3919–3928 (1993).
6. Michael, J. V., Lim, K. P., Kumaran, S. S., and Kiefer, J. H., *J. Phys. Chem.* 97:1914–1919 (1993).
7. Lim, K. P., and Michael, J. V., *J. Phys. Chem.* 98:211–215 (1994).
8. Ho, W., Barat, R. B., and Bozzelli, J. W., *Combust. Flame* 88:265–295 (1992).
9. Ho, W., and Bozzelli, J. W., *Twenty-Fourth Symposium (International) on Combustion*, The Combustion Institute, Pittsburgh, 1992, pp. 743–748.
10. Dean, A. M., *J. Phys. Chem.* 89:4600–4608 (1985).
11. Westmoreland, P. R., and Dean, A. M., *AIChE J.* 32:1971–1979 (1986).
12. Michael, J. V., *Prog. Energy Combust. Sci.* 18:327–347 (1992), and references cited therein.
13. Michael, J. V., and Sutherland, J. W., *Int. J. Chem. Kinet.* 18:409–436 (1986).
14. Whytock, D. A., Lee, J. H., Michael, J. V., Payne, W. A., and Stief, L. J., *J. Chem. Phys.* 66:2690–2695 (1977).
15. Clyne, M. A. A., and Nip, W. S., *J. Chem. Soc. Faraday II* 72:838–847 (1976).
16. Kiefer, J. H., Sathyanarayana, R., Lim, K. P., and Michael, J. V., *J. Phys. Chem.*, in press.
17. Based on, DeMore, W. B., Sander, S. P., Golden, D. M., Hampson, R. F., Kurylo, M. J., Howard, C. J., Ravishankara, A. R., Kolb, C. E., and Molina, M. J., *Chemical Kinetic and Photochemical Data for Use in Stratospheric Modeling*, Evaluation No. 10, JPL Publication 92–20, August 15, 1992.
18. Seery, D. J., and Bowman, C. T., *J. Chem. Phys.* 48:4314–4317 (1968).
19. Chase, M. W., Jr., Davies, C. A., Downey, J. R., Jr., Frurip, D. J., McDonald, R. A., and Syverud, A. N., *J. Phys. Chem. Ref. Data* 14(1) (1985).
20. Manion, J. A., and Rodgers, A. S., *Thermodynamic Tables, Non-Hydrocarbons*, Thermodynamics Research Center, Texas A & M University Press, College Station, TX, June 30, 1993, pp. r-7250–r-ref-7251.
21. Lias, S. G., Bartmess, J. E., Liebman, J. F., Holmes, J. L., Levin, R. D., and Mallard, W. G., *J. Phys. Chem. Ref. Data* 17(1) (1988).
22. Troe, J., *J. Chem. Phys.* 65:4745–4757 (1977); ibid. 4758–4775 (1977).
23. Troe, J., *J. Phys. Chem.* 83:114–126 (1979).
24. Troe, J., *Ber. Bunsenges. Phys. Chem.* 87:161–169 (1983); Gilbert, R. G., Luther, K., and Troe, J., ibid. 169–177 (1983).
25. Lim, K. P., and Michael, J. V., *Preprint, 207th American Chemical Society Symposium on Combustion Chemistry and Soot Formation, Fuel Chemistry Division* 39:131–135 (1994).
26. Hirschfelder, J. O., Curtiss, C. F., and Bird, R. B., *Molecular Theory of Gases and Liquids*, Wiley, New York, 1966, p. 951.
27. Cambi, R., Cappelletti, D., Liuti, G., and Pirani, F., *J. Chem. Phys.* 95:1852–1861 (1991).
28. Harding, L. B., private communication, September, 1993.

Twenty-Fifth Symposium (International) on Combustion/The Combustion Institute, 1994/pp. 817–824

THE UNIMOLECULAR DECOMPOSITION OF 1-CHLOROETHYL RADICAL

V. D. KNYAZEV, Á. BENCSURA, I. A. DUBINSKY, AND D. GUTMAN*
Department of Chemistry
The Catholic University of America
Washington, DC 20064, USA

AND

S. M. SENKAN
Department of Chemical Engineering
University of California
Los Angeles, CA 90024, USA

The kinetics of the unimolecular decomposition of the 1-chloroethyl radical have been studied. The reaction was isolated for quantitative study in a heated tubular flow reactor coupled to a photoionization mass spectrometer. Rate constants for the decomposition were obtained in time-resolved experiments as a function of temperature (848–980 K) and bath gas density (3–22 $\times$ 10^{16} molecule cm^{-3}) in He, Ar, and N_2. The rate constants are in the falloff under the conditions of the experiments.

The falloff behavior was analyzed using a Master Equation analysis. A transition state model was created to obtain values of the microcanonical rate constants, $k(E)$, needed to solve the Master Equation. The transition state model provides the high-pressure limit rate constants for the decomposition reaction (k_1^∞ ($CH_3CHCl \rightarrow CH_2CHCl + H$) = $1.94 \times 10^9\ T^{1.22} \exp(-19{,}510\ K/T)\ s^{-1}$) and the reverse reaction (k_{-1}^∞ ($H + CH_2CHCl \rightarrow CH_3CHCl$) = $3.35 \times 10^{-14}\ T^{0.86} \exp(-75.3\ K/T)\ cm^3\ molecule^{-1}\ s^{-1}$). Values of $\langle \Delta E \rangle_{down}$ for the energy loss probability were obtained for each experiment using the exponential-down model. The values of $\langle \Delta E \rangle_{down}$ display a pronounced positive temperature dependence with average values of 255 (He), 360 (Ar), and 261 (N_2) cm^{-1}. Parametrization of the temperature and pressure dependence of the unimolecular rate constant for the temperature range 298–1500 K and pressures 0.001–10 atmospheres is provided using the modified Lindemann–Hinshelwood expression.

Introduction

The development of a better understanding of the rates and mechanisms of the high-temperature reactions of chlorinated hydrocarbons (CHCs) is of considerable importance to the combustion community because of the increasing role that incineration plays in the treatment of hazardous chemical wastes that frequently contain these compounds [1]. In addition, the reactions of CHCs are also important in the production of useful chemicals from natural gas via chlorination followed by the pyrolysis [2] or oxidative pyrolysis [3] of the chlorinated components of the natural gas.

To date, detailed chemical kinetic mechanisms of oxidation and pyrolysis of several CHCs have been developed and tested to predict species concentration profiles measured in laboratory flames [4,5] and in flow reactors [6,7].

However, an examination of these mechanisms reveals that the proposed rate parameters of many of the reactions were estimated using a variety of approaches [8], clearly indicating the need for more experimental measurements.

Recent modeling work also reveals the need to quantitatively describe kinetics of isomer-specific reactions of CHCs to account for product distributions observed in experiments [9,10]. This is crucial because the rates and mechanisms of reactions of specific isomers can be substantially different, as in the case of the chloroethyl radicals, CH_3CHCl and CH_2ClCH_2, which are important in the combustion of virtually all chlorinated C_1 and C_2 hydrocarbons. These radicals can form as a consequence of hydrogen abstraction from C_2H_5Cl by OH, Cl, O, and H attack. It is significant, however, to note that CH_3CHCl radicals are preferentially produced due to the weaker α—C—H bond dissociation energies in C_2H_5Cl [10,11]. Under pyrolytic conditions, the major reaction pathway for the CH_3CHCl radical is its unimolecular decomposition:

$$CH_3CHCl + M \rightarrow C_2H_3Cl + H + M \qquad (\Delta H^\circ_{298} = 39.3\ \text{kcal/mole}). \quad (1)$$

*Deceased.

However, in the presence of O_2, the following reaction effectively competes with reaction (1):

$$CH_3CHCl + O_2 \rightarrow C_2H_3Cl + HO_2 \quad (\Delta H^\circ_{298} = -10.3 \text{ kcal/mole}). \quad (2)$$

Since reaction (1) is in the falloff regime under the conditions of interest to combustion, the determination of its rate as a function of both temperature and density is important for the development of detailed reaction mechanisms. In this paper, we report the results of an experimental investigation of reaction (1) in the presence of three different bath gases and over a temperature range of 848–980 K. The experimental data were analyzed using a Master Equation/RRKM approach. Parametrization of the temperature and pressure dependence of the unimolecular rate constant for the temperature range of 298–1500 K and pressures of 0.001–10 atmospheres is provided using the modified Lindemann–Hinshelwood expression.

Experimental Study

1-chloroethyl radicals were produced at elevated temperatures by pulsed laser photolysis, and their unimolecular decay was subsequently monitored in time-resolved experiments using photoionization mass spectrometry. Details of the experimental apparatus [12] and procedures [13] used have been described before and so are only briefly reviewed here.

1-chloroethyl radicals were produced by the pulsed, 193 nm laser photolysis of 1,1-dichloroethane

$$CH_3CHCl_2 \xrightarrow{193\text{ nm}} CH_3CHCl + Cl$$
$$\longrightarrow \text{other products} \quad (3)$$

or 3-chloro-2-butanone

$$CH_3C(O)CHClCH_3 \xrightarrow{193\text{ nm}} CH_3CHCl + \text{products}$$
$$\longrightarrow \text{other products} \quad (4)$$

or by the 248-nm laser photolysis of 1-bromo-1-chloroethane

$$CH_3CHClBr \xrightarrow{248\text{ nm}} CH_3CHCl + Br$$
$$\longrightarrow \text{other products.} \quad (5)$$

Neither the photolysis wavelength nor the nature of the radical precursor had any observable influence on the kinetics of 1-chloroethyl radical decomposition. Initial conditions (precursor concentration and laser intensity) were selected to provide low radical concentrations (less than 10^{11} molecule cm^{-3}) such that reactions between radical products had negligible rates compared to that of the unimolecular decomposition of 1-chloroethyl radicals.

Pulsed unfocused 248 or 193 nm radiation ($\approx$5 Hz) from a Lambda Physic EMG 201MSC excimer laser was directed along the axis of a heatable uncoated quartz reactor (1.05 cm i.d.). Gas flowing through the tube at $\approx$4 m s^{-1} contained the radical precursor (<0.5%) and an inert carrier gas (He, Ar, or N_2) in large excess. The flowing gas was completely replaced between laser pulses.

Gas was sampled through a hole (0.043 cm diameter) in the side of the reactor and formed into a beam by a conical skimmer before the gas entered the vacuum chamber containing the photoionization mass spectrometer. As the gas beam traversed the ion source, a portion was photoionized and mass selected. 1-chloroethyl radicals were ionized using the light from a chlorine resonance lamp (8.8–8.9 eV). Temporal ion signal profiles were recorded on a multichannel scaler from a short time before each laser pulse up to 20 ms following the pulse. Data from 3,000 to 60,000 repetitions of the experiment were accumulated before the data were analyzed.

The 1-chloroethyl ion signal profiles were fit to an exponential function ($[CH_3CHCl]_t = [CH_3CHCl]_0 e^{-k't}$) by using a non-linear least-squares procedure. Experiments were performed to establish that the decay constants did not depend on the initial CH_3CHCl concentration (provided that the concentration was kept low enough to ensure that radical-radical reactions had negligible rates in comparison to the unimolecular reaction), the nature or concentration of radical precursor, or the laser wavelength (193 or 248 nm) and its intensity. The exponential decay constants depended only on temperature and bath gas density.

Below 750 K, the CH_3CHCl decay constants (k') were low (typically 20–50 s^{-1}) and independent of temperature for any given gas density. This temperature-independent loss is attributed to heterogeneous processes.

$$CH_3CHCl \longrightarrow \text{heterogeneous loss.} \quad (6)$$

Above 850 K, the decay constant increased rapidly with rising temperature due to the increasing importance of the thermal decomposition of the 1-chloroethyl radical, reaction (1). The CH_3CHCl decay constants were analyzed, assuming that the 1-chloroethyl radicals were consumed only by two elementary reactions (1) and (6). At low temperatures, only the heterogeneous loss (reaction (6)) is observed. Above 850 K, the sum of the two loss processes is observed with the CH_3CHCl exponential decay constants equal to $k' = k_1 + k_6$.

Sets of experiments at five different fixed helium densities (3–23 $\times$ 10^{16} molecule cm^{-3}) and four

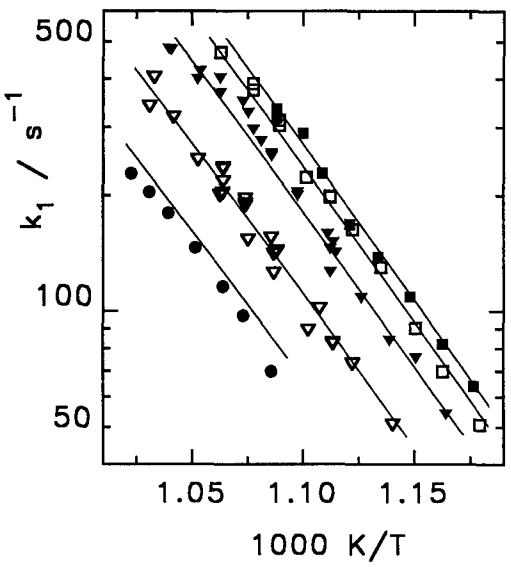

FIG. 1. Plot of CH_3CHCl unimolecular rate constants (k_1 vs $1000/T$) for different He densities. Units are atom cm^{-3}. Densities of He are ●: 3×10^{16}; ▽: 6×10^{16}; ▼: 12×10^{16}; □: 18×10^{16}; ■: 22×10^{16}.

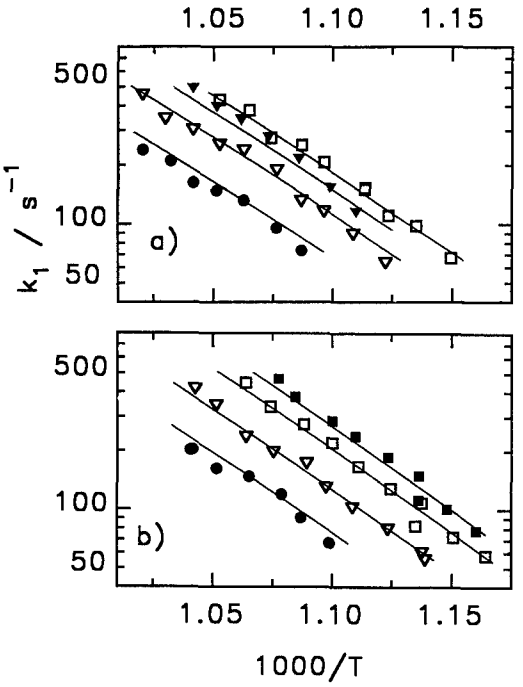

FIG. 2. Plot of CH_3CHCl unimolecular rate constants (k_1 vs $1000/T$) for different densities of (a) Ar and (b) N_2. Units are molecule cm^{-3}. Densities of bath gas are ●: 3×10^{16}; ▽: 6×10^{16}; ▼: 9×10^{16}; □: 12×10^{16}; ■: 18×10^{16}.

densities of argon (3–12 $\times$ 10^{16} molecule cm^{-3}) and nitrogen (3–18 $\times$ 10^{16} molecule cm^{-3}) were performed to determine k_1 as a function of temperature. The CH_3CHCl exponential decay constant, k', was measured as a function of temperature keeping the concentration of all gases constant. Calculations of k_1 from measurements of k' require knowledge of k_6 above 750 K. Whereas k_6 was directly determined below 750 K, it could not be measured above this temperature due to the additional loss of radicals by unimolecular decomposition. Below 750 K, k_6 was directly determined, and it was found to be essentially temperature independent. Values of k_6 above 750 K needed for the data analysis were obtained by a relatively small extrapolation, assuming that k_6 retains this temperature independence up to the highest temperature of this study, 980 K. To minimize possible errors in the determination of k_1 caused by the assumed continued temperature independence of k_6 above 750 K, experiments to obtain k_1 were conducted at temperatures sufficiently high to assure that $k' > 3k_6$. It was this criterion that established the lowest temperature used to determine k_1 in each set of experiments. The highest temperature used at each total gas density was determined by the fact that decay constants above 500 s^{-1} could not be measured accurately.

A potentially complicating factor in these experiments is the possible isomerization of 1-chloroethyl radicals to 2-chloroethyl radicals during the photolysis process. However, the 2-chloroethyl radical is expected to decompose at significantly lower temperatures than those used in the present experiments due to a much lower C—Cl bond energy in comparison with the C—H bond energy. No signs of a possible contribution of this effect were detected at temperatures lower than 750 K.

The unimolecular rate constants for reaction (1) obtained from these sets of experiments are shown in Figs. 1 and 2. Estimated uncertainties in the k_1 determinations vary from $\pm 10\%$ in the middle of the temperature range to $\pm 15\%$ at the extreme temperatures used.

The only polyatomic product of reaction (1) observed in the present study was CH_2CHCl. The relative sensitivity of CH_2CHCl and C_2H_4 was determined by adding calibrated flows of these compounds into the reactor. An upper limit for the possible formation of ethylene was experimentally estimated to be <10% of the CH_2CHCl formed at [He] = 6.0×10^{16} molecule cm^{-3} and T = 920 K, and <5% of the CH_2CHCl formed at [He] = 6.0×10^{16} molecule cm^{-3} and T = 970 K. The temporal behavior of the rising vinyl chloride product signal

mirrored that of the decaying 1-chloroethyl radical signal.

Data Analysis and Discussion

The unimolecular rate constants $k_1(T,[M])$ were analyzed to obtain information on weak collision effects for the bath gases used and to provide expressions for evaluating $k_1(T,[M])$ values over a wide range of temperatures and pressures.

The parameters of the potential energy surface for the reaction

$$H + CH_2CHCl \rightleftarrows CH_3CHCl \qquad (-1,1)$$

were proposed by Barat and Bozzelli [14] based on thermochemical estimation. Their mechanism for reaction (−1.1) begins with the addition of an H atom to the double bond of vinyl chloride, forming an excited CH_3CHCl radical. The excited CH_3CHCl can either decompose back to H + CH_2CHCl (route A) or isomerize via 2,1 H-atom migration forming a CH_2CH_2Cl radical, which subsequently decomposes to Cl + C_2H_4 (route B):

$$H + CH_2CHCl \underset{A}{\rightleftarrows} CH_3CHCl \underset{B}{\rightarrow} CH_2CH_2Cl \rightarrow$$

$$Cl + C_2H_4.$$

QRRK analysis by Barat and Bozzelli [14] indicated that route B was the favored route. The values of barrier heights for route A (43.2 kcal mol^{-1}) and route B (38.0 kcal mol^{-1}) suggested by them would imply that the thermal decomposition of CH_3CHCl should also proceed via route B, i.e., the main products of reaction (1) should be Cl + C_2H_4.

This conclusion was not supported by our experimental results, which indicate that the main channel of CH_3CHCl thermal decomposition is that of H-atom elimination with the formation of vinyl chloride. The process is similar to the H-atom elimination in the reaction

$$C_2H_5 \rightarrow C_2H_4 + H. \qquad (7)$$

Since no experimental information is available on the temperature dependence of the high-pressure limit rate constant of reaction (−1,1), we chose to create a transition state model of this reaction by analogy with reaction (7), the high-pressure limit of which is known in the temperature range 200–1100 K [15,16]. This analogy is based on the fact that both reactions involve an H-atom elimination from the CH_3 group with the simultaneous formation of a double bond. Hence, one can expect the parts of the potential energy surfaces of both systems corresponding to this reactive motion to be similar. Frequencies of the transition state were selected to ensure the same temperature dependence of the function

$$A_{vib}(T) = Q_{vib}^{\ddagger}(T)/Q_{vib}(T)$$

for both reactions (1) and (7). Here, $Q_{vib}^{\ddagger}(T)$ and $Q_{vib}(T)$ are the partition functions of the vibrational degrees of freedom of the transition state and parent molecule, and $A_{vib}(T)$ represents the "vibrational component" of the pre-exponential factor. The transition state for reaction (7) was taken from Feng et al. [15]. The geometry and frequencies of the CH_3CHCl radical were taken from Chen and Tschuikow-Roux [17]. There exists an addition barrier in reaction (−1). Hence, the transition state is tight, and the moments of inertia of the transition state and CH_3CHCl radical do not differ significantly. They were taken to be equal in the model. Frequencies and rotational constants of CH_2CHCl were taken from Gullikson and Nielsen [18] and Hayashi and Inagusa [19]. Molecular parameters of the 1-chloroethyl radical, the transition state, and vinyl chloride used in the current study are given in Table 1. CH_3CHCl, CH_2CHCl, and the transition state have no overall rotational symmetry. The hindered internal CH_3 rotor in CH_3CHCl has symmetry number 3, and the transition state has two optical isomers. Hence, the decomposition reaction has a reaction path degeneracy of 6 [21].

The heat of formation of vinyl chloride was taken as equal to 5.5 kcal mol^{-1} [22–24]. The heat of formation of the 1-chloroethyl radical was determined recently [17,25] based on a competitive bromination study and the known value of the heat of formation of ethyl radical. The value of the heat of formation of CH_3CHCl calculated by Chen and Tschuikow-Roux [17] is ΔH°_{f298} = 18.1 ± 1.0 kcal mol^{-1}. After adjustment for the most recent value of the heat of formation of ethyl radical [17], the 1-chloroethyl radical heat of formation becomes ΔH°_{f298} = 18.3 ± 1.0 kcal mol^{-1}, which coincides with the value calculated [17] from known heats of formation of the species involved in the reaction

$$CH_3CH_2Cl + CCl_3 \rightarrow CH_3CHCl + CCl_3H \qquad (8)$$

and the heat of reaction (8) calculated by the *ab initio* (U)HF/6-31G* method. The resulting enthalpy of reaction (1) is ΔH°_{298} = 39.3 kcal mol^{-1}, and the corresponding zero level energy change ΔE_0 = 38.3 kcal mol^{-1}.

Based on *ab initio* calculations, Schlegel and Sosa [26] estimated that the barrier for addition of hydrogen atom to the unsubstituted carbon of vinyl chloride (E_{-1}) is 1.2 kcal mol^{-1} lower than for the addition to ethylene. With the corresponding barrier for ethylene equal to 2.2 kcal mol^{-1} [15,16], E_{-1} = 1.0 kcal mol^{-1}, and the barrier for decomposition is

TABLE 1
Molecular Parameters of CH_3CHCl, CH_2CHCl, and Transition State ($CH_3CHCl^{\ddagger}$)

Vibrational frequencies (cm^{-1})
CH_3CHCl [17]
3059, 2958, 2928, 2866, 1466, 1455, 1407, 1280, 1075, 1008, 996, 693, 463, 378
CH_2CHCl [18]
3130, 3080, 3030, 1610, 1370, 1280, 1030, 943, 896, 724, 620, 395
$CH_3CHCl^{\ddagger}$
3000 (3), 1350 (2), 1300, 1200, 1100, 1000, 900, 850, 700, 600, 310

Overall rotations: rotational constants (cm^{-1}) and symmetry numbers
CH_3CHCl [17], $CH_3CHCl^{\ddagger}$
A = 1.401 (active); B = 0.1831 (inactive); C = 0.1674 (inactive); $\sigma = 1$
CH_2CHCl [19]
$(ABC)^{1/3} = 0.4103$; $\sigma = 1$

Methyl group internal rotation in CH_3CHCl [17]:
Rotational constants $a = 6.569$ cm^{-1}; $\sigma = 3$.
Rotational barrier $V_0 = 0.77$ kJ mol^{-1}.
Lennard–Jones parameters [20]

Gas	ε/k (K)	σ (Å)
He	10.22	2.551
Ar	93.3	3.542
N_2	71.4	3.798
CH_3CHCl^{a}	300.0	4.898

[a]Taken to be the same as for C_2H_5Cl.

equal to $E_1 = 39.5$ kcal mol^{-1}. Since hindered internal rotation in CH_3CHCl is treated classically, the energy here is calculated relative to the minimum of the potential energy of this torsional motion. We have accepted this value for the model used in fitting the experimental data. The effect of variation of the decomposition energy barrier E_1 by ± 1 kcal mol^{-1} (corresponding to the error limits of ΔH°_{f298} (CH_3CHCl)) and by ± 2 kcal mol^{-1} (corresponding to the combined uncertainty of ΔE_0 and E_{-1}) on the results of fitting is discussed below.

The barrier height for internal rotation in the 1-chloroethyl radical is equal to 0.77 kcal mol^{-1} [17]. The density of states function of this hindered internal rotation required for the modeling of unimolecular decomposition was calculated using the formulas obtained by the Inverse Laplace Transform of the classical partition function [27]. The deviation of the classical partition function from the exact values [28] was not higher than 5% at all temperatures above 298 K.

The model of reaction (−1,1) described above results in the following expressions for high-pressure limit rate constants of reaction (−1,1) at 298 K < T < 1500 K:

$$k_1^{\infty} = 1.94 \times 10^9\, T^{1.22} \exp(-19{,}510\ K/T)\ s^{-1} \quad (9)$$

$$k_{-1}^{\infty} = 3.35 \times 10^{-14}\, T^{0.86} \cdot \exp(-75.3\ K/T)\ cm^3\ molecule^{-1}\ s^{-1} \quad (10)$$

The measured rate constants of reaction (1) were reproduced using Master Equation simulations. The "exponential down" model [21,29] of collisional energy transfer was adopted to characterize the probability of deactivation of a CH_3CHCl molecule with a total initial internal energy E in active degrees of freedom to a final energy E' by collision with a molecule of bath gas:

$$P(E',E) = A \exp(-[E - E']/\langle \Delta E \rangle_{down}); E' < E \quad (11)$$

where $\langle \Delta E \rangle_{down}$ is the average energy lost in deactivating collisions and A is a normalization constant.

The method of Gilbert and coworkers [21,30] of solving the Master Equation was employed. The energy bin size used was 20–40 cm^{-1}. The independence of the calculated rate constants on the energy bin size in the interval 10–40 cm^{-1} and on the initial population distribution was separately shown for values of $\langle \Delta E \rangle_{down}$ from 100 cm^{-1} to 700 cm^{-1} at temperatures and pressures corresponding to the conditions of the experiments. By comparing exact values of the partition functions and high-pressure limit rate constants with those obtained by numerical integration, it was found that errors resulting from numerical convolution of density of states and sum of states functions, as well as from numerical integration, are not more than 2% of the exact values at the temperatures of the experiments.

Falloff from the high-pressure limit was reproduced for each value of $k_1([M],T)$ by the solution of the Master Equation using only $\langle \Delta E \rangle_{down}$ as an adjustable parameter. The fitted values of $\langle \Delta E \rangle_{down}$ with $E_1 = 39.5 \pm 1$ kcal mol^{-1} indicate a positive temperature dependence for all three bath gases used (Fig. 3). They can be fitted to linear dependencies:

$$\langle \Delta E \rangle_{down} = (0.66 \pm 0.07)\, T - (350 \pm 64)\ cm^{-1} \text{ for He;}$$

$$\langle \Delta E \rangle_{down} = (0.93 \pm 0.19)\, T - (509 \pm 175)\ cm^{-1} \text{ for Ar; and}$$

$$\langle \Delta E \rangle_{down} = (1.33 \pm 0.18)\, T - (867 \pm 162)\ cm^{-1} \text{ for } N_2.$$

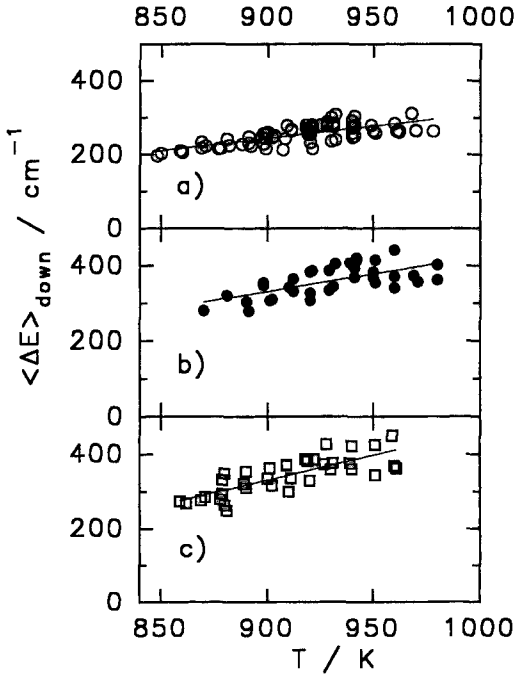

FIG. 3. Plot of values of $\langle \Delta E \rangle_{down}$ vs temperature derived from the values of k_1 for (a) He, (b) Ar, and (c) N_2 as the bath gas. The lines through the data are from the fits of the temperature dependencies of $\langle \Delta E \rangle_{down}$.

The average values of $\langle \Delta E \rangle_{down}$ in the temperature range used are 255 (He), 360 (Ar), and 344 (N_2) cm^{-1}.

The values of $\langle \Delta E \rangle_{down}$ resulting from the fitting procedure with the accepted barrier height for decomposition (E_1 = 39.5 kcal mol^{-1}) are independent of pressure, showing the good quality of fit. The variation of E_1 by ± 1 kcal mol^{-1} resulted in significant changes of the fitted values of $\langle \Delta E \rangle_{down}$: 373/185 cm^{-1} (He), 521/263 cm^{-1} (Ar), and 518/245 cm^{-1} (N_2) with the lower values corresponding to the lower value of the energy barrier. A ± 2 kcal mol^{-1} variation of E_1 resulted in an even higher change of $\langle \Delta E \rangle_{down}$: 604/140 cm^{-1} (He), 843/200 cm^{-1} (Ar), and 903/183 cm^{-1} (N_2).

The results of fitting with the barrier height E_1 equal to 37.5, 38.5, or 40.5 kcal mol^{-1} exhibited no pressure dependence within the range of scatter of individual points. However, a change of E_1 by + 2 kcal mol^{-1} (E_1 = 41.5 kcal mol^{-1}) resulted in fitted values of $\langle \Delta E \rangle_{down}$ that exhibited visible pressure dependence, indicating that this value of the barrier height for decomposition results in a poor fit of experimental data and is unrealistic. This result supports our choice of the value of ΔH°_{f298} (C_2H_3Cl) used in the current study, 5.5 kcal mol^{-1}, rather than the higher value that can be found in the literature, 8.4 kcal mol^{-1} [31]. Usage of the latter value would suggest a too high value of E_1 = 42.4 kcal mol^{-1}, which will result in an even worse quality of fit. This conclusion is not absolute, however, since the sum of uncertainties in all the thermochemical parameters involved, ΔH°_{f298} (CH_3CHCl), E_{-1}, and E_1 (± 3 kcal mol^{-1}), approximately equals the difference between these two values of ΔH°_{f298} (C_2H_3Cl). The positive temperature dependence of $\langle \Delta E \rangle_{down}$ was preserved for all three bath gases in the cases of the barrier height E_1 equal to 37.5, 38.5, or 40.5 kcal mol^{-1}.

Almost no data are available in literature about either the decomposition of 1-chloroethyl radical or the reverse reaction (−1). The only two experimental measurements of Ahmed and Jones [32] and Jones and Ma [33] of the rate constant of the reaction of H atoms with C_2H_3Cl did not distinguish between the different routes forming 1-chloroethyl and 2-chloroethyl radical. According to estimations by Barat and Bozzelli [14], the barrier height for H-atom addition to the chlorinated site should be approximately 3 kcal mol^{-1} higher than to the $-CH_2$ group. At room temperature, this results in more than two orders of magnitude difference between the rate constants for these two routes, allowing us to neglect addition to the −CHCl group of vinyl chloride.

Fitting of the results of Ahmed and Jones [32] and Jones and Ma [33] (which are in the falloff region) using the Master Equation approach gives a value of $\langle \Delta E \rangle_{down}$ that is probably too low: 27 cm^{-1}. Increasing the barrier height for the association reaction (−1) by 1 kcal mol^{-1} (thus obtaining E_{-1} = 2.0 kcal mol^{-1}, close to the barrier for the H + C_2H_4 reaction, and E_1 = 40.9 kcal mol^{-1}) gives a higher value of $\langle \Delta E \rangle_{down}$ = 108 cm^{-1}. However, the quality of fit in this case is poorer.

Although these two studies [32,33] agree reasonably well on the rate constant values of reaction (−1), they strongly disagree on the rate constants of the similar reactions of H atoms with C_2H_3Br and C_2H_3F, with discrepancies up to a factor of 2. Consequently, the experimental uncertainty of these studies is at least a factor of 2, and it is impossible to use these data to adjust the model of reaction (−1,1).

Discussion

The current study provides the first direct determination of the rate constant of the unimolecular decomposition of the 1-chloroethyl radical. Under the conditions of these experiments, the reaction is essentially in its falloff region. Therefore, it was possible to quantitatively characterize the weak collision effects responsible for the falloff behavior of this reaction.

The values of $\langle \Delta E \rangle_{down}$ determined in the current study for three bath gases (He, Ar, and N_2) at tem-

peratures 848–980 K are in the range 200–300 cm^{-1} for He and 250–450 cm^{-1} for Ar and N_2. The average value for He as bath gas (255 cm^{-1}) is close to those found, using similar methods, in studies of the unimolecular decomposition of C_2H_5 (250 cm^{-1}) [15], n-C_3H_7 (220 cm^{-1}) [34], CH_3CO (140–280 cm^{-1}) [35], *i*-C_3H_7 (136–210 cm^{-1}) [36], neo-C_5H_{11} (300 cm^{-1}) [37], and *t*-C_4H_9 (230 cm^{-1}) [28].

The fitted values of $\langle \Delta E \rangle_{down}$ exhibit an increase with temperature for all three bath gases used in the current study. However, the scatter of individual data points does not allow us to draw any conclusion about the exact analytical form of this temperature dependence.

Our analysis of the $C_2H_5 \rightleftarrows H + C_2H_4$ system demonstrated a strong dependence of $\langle \Delta E \rangle_{down}$ on temperature, increasing from 70–100 cm^{-1} at 300 K to 280 cm^{-1} at 1100 K. This dependence was best fit with the directly proportional dependence $\langle \Delta E \rangle_{down} = 0.255\ T\ cm^{-1}$. The analysis of the *i*-$C_3H_7 \rightleftarrows H + C_3H_6$ system [36] also supports a strong temperature dependence of $\langle \Delta E \rangle_{down}$ for He as bath gas. Therefore, we recommend using the linear directly proportional dependencies for evaluating the rate constant values of reaction (1) outside the range of our experimental conditions:

$$\langle \Delta E \rangle_{down} = 0.279\ T\ cm^{-1} \text{ for He as bath gas} \tag{12}$$

$$\langle \Delta E \rangle_{down} = 0.387\ T\ cm^{-1} \text{ for Ar as bath gas} \tag{13}$$

$$\langle \Delta E \rangle_{down} = 0.379\ T\ cm^{-1} \text{ for } N_2 \text{ as bath gas.} \tag{14}$$

The coefficients in formulas 12 through 14 are obtained from the fitting of the data on $\langle \Delta E \rangle_{down}$ vs T.

Parametrization of Rate Constants

We use these recommended dependencies in a parametrization of k_1 in helium, argon, and nitrogen, which provides rate constant values throughout the temperature range of 298–1500 K and pressures of 0.001–10 atm. The modified Lindemann–Hinshelwood expression [38] was used:

$$\frac{k_1}{k_1^\infty} = \frac{k_1^0[M]/k_1^\infty}{1 + k_1^0[M]/k_1^\infty} F(F_{cent}, [M]). \tag{15}$$

The values of the rate constant in the above temperature and pressure intervals were calculated by the Master Equation/RRKM method using the model of reaction (1) described above and assuming the directly proportional (Eqs. (12) through (14)) temperature dependence of $\langle \Delta E \rangle_{down}$ for helium, argon, and nitrogen as bath gas.

The calculated values of k_1 at different temperatures and pressures were fitted with the modified Lindemann–Hinshelwood expression (15), and the resulting parameters are (298 K $\leqslant T \leqslant$ 1500 K):

$$k_1^\infty = 1.935 \times 10^9\ T^{1.222} \exp(-19{,}510\ K/T)\ s^{-1}$$

and

$$k_1^0 = 7.586 \times 10^{16}\ T^{-6.976} \cdot \exp(-22{,}090\ K/T)\ cm^3\ molecule^{-1}\ s^{-1}$$

$$F_{cent} = 0.6559 \times \exp(-T/1219\ K) + 0.3441 \times \exp(-T/279.1\ K)$$

for helium as bath gas;

$$k_1^0 = 2.138 \times 10^{16}\ T^{-6.810} \cdot \exp(-21{,}970\ K/T)\ cm^3\ molecule^{-1}\ s^{-1}$$

$$F_{cent} = 0.6762 \times \exp(-T/1212\ K) + 0.3238 \times \exp(-T/304.2\ K)$$

for argon as bath gas;

$$k_1^0 = 2.630 \times 10^{16}\ T^{-6.821} \cdot \exp(-21{,}980\ K/T)\ cm^3\ molecule^{-1}\ s^{-1}$$

$$F_{cent} = 0.6702 \times \exp(-T/1222\ K) + 0.3298 \times \exp(-T/299.0\ K)$$

for nitrogen as bath gas.

The average deviation of the parametrized values of k_1 from the Master Equation rate constants over this large range of conditions is 6%, with a maximum deviation of 38% at 900–1000 K at the lowest pressures considered.

Due to the uncertainty in the temperature dependence of $\langle \Delta E \rangle_{down}$ discussed earlier, caution is advised in using the results of this extrapolation outside the temperature range of the current study.

Summary

The unimolecular decomposition of 1-chloroethyl radical in helium, argon, and nitrogen has been studied in the falloff region. A transition state model of reaction (1) was developed, which provides the high-pressure limit rate constants. The model was used to provide the values of energy-specific rate constants ($k(E)$) for the Master Equation analysis.

The experimental values of k_1 were reproduced by Master Equation/RRKM modeling, and the temper-

ature dependence of $\langle \Delta E \rangle_{down}$ was addressed. Finally, parametrized expressions are presented, which provide values of k_1 over a wide range of pressures and temperatures.

Acknowledgment

This research was supported by the National Science Foundation, Division of Chemical, Biochemical, and Thermal Engineering under Grant No. CTS-9311848.

REFERENCES

1. Senkan, S. M., *Environ. Sci. Technol.* 22:368 (1988).
2. Weissman, M. and Benson, S. W., *Int. J. Chem. Kinet.* 16:307 (1984).
3. Senkan, S. M., *Chem. Eng. Prog.* 12:58 (1987).
4. Chang, W. D., and Senkan, S. M., *Environ. Sci. Technol.* 23:442 (1989).
5. Qun, M., and Senkan, S. M., *Combust. Sci. Technol.* in press.
6. Fisher, E. M., Koshland, C. P., Hall, D., Sawyer, R., and Lucas, D., *Twenty-Third Symposium (International) on Combustion,* The Combustion Institute, Pittsburgh, 1990, p. 1273.
7. Ho, W., Yu, Q.-R., and Bozzelli, J. W., *Combust. Sci. Technol.*, 85:23 (1992).
8. Senkan, S. M., *Adv. Chem. Eng.* 18:95 (1992).
9. Shi, Y., and Senkan, S. M., *J. Phys. Chem.* 95:5181 (1991).
10. Senkan, S. M., Yildirim, R., and Gutman, D., *Twenty-Fourth Symposium (International) on Combustion,* The Combustion Institute, Pittsburgh, 1992, p. 749.
11. Niedzielski, J., Tschuikow-Roux, E., and Yano, T., *Int. J. Chem. Kinet.* 16:621 (1984).
12. Slagle, I. R., and Gutman, D., *J. Am. Chem. Soc.* 107:5342 (1985).
13. Slagle, I. R., Batt, L., Gmurczyk, G., Gutman, D., and Tsang, W., *J. Phys. Chem.* 95:7732 (1991).
14. Barat, R. B., and Bozzelli, J. W., *J. Phys. Chem.* 96:2494 (1992).
15. Feng, Y., Niiranen, J. T., Bencsura, A., Knyazev, V. D., Gutman, D., and Tsang, W., *J. Phys. Chem.* 97:871 (1993).
16. Hanning-Lee, M. A., Green, N. J. B., Pilling, M. J., and Robertson, S. H., *J. Phys. Chem.* 97:860 (1993).
17. Chen, Y., and Tschuikow-Roux, E., *J. Phys. Chem.* 96:7266 (1992).
18. Gullikson, C. W., and Nielsen, J. R., *J. Mol. Spectrosc.* 1:158 (1957).
19. Hayashi, M., and Inagusa, T., *J. Mol. Struct.* 220:103 (1990).
20. Reid., R. C., Prausnitz, J. M., and Sherwood, T. K., *The Properties of Gases and Liquids*, 3rd. ed., McGraw-Hill, New York, 1977.
21. Gilbert, R. G., and Smith, S. C., *Theory of Unimolecular and Recombination Reactions,* Blackwell, Oxford, 1990.
22. Kolesov, V. P., and Papina, T. S., *Russian Chem. Rev.* 52:425 (1983).
23. *Thermodynamic Properties of Individual Substances* (Gurvich, L. V., Veyts, I. V., and Alcock, C. B., Eds.), Hemisphere, New York, 1992, Vol. 2 (1).
24. Seasholtz, M. B., Thompson, T. B., Rondan, N. G., Ruiz, J. M., and Colegrove, B. T., manuscript in preparation. Oral presentation at *Midwest Thermodynamics Symposium,* 1993.
25. Miyokawa, K., and Tschuikow-Roux, E., *J. Phys. Chem.* 94:715 (1990).
26. Schlegel, H. B., and Sosa, C., *J. Phys. Chem.* 88:1141 (1984).
27. Knyazev, V. D., Dubinsky, I. A., Slagle, I. R., Gutman, D., *J. Phys. Chem.* 98:5279 (1994).
28. Pitzer, K. S., and Gwinn, W. D. *J. Chem. Phys.* 10:428 (1942).
29. Rabinovich, B. S., and Tardy, D. C., *J. Chem. Phys.* 45:3720 (1966).
30. Gaynor, B. J., Gilbert, R. G., and King, K. D., *Chem. Phys. Lett.* 55:40 (1978).
31. Stull, D. R., Westrum, E. F., Jr., and Sinke, G. C. *The Chemical Thermodynamics of Organic Compounds,* Wiley, New York, 1969.
32. Ahmed, M. G., and Jones, W. E., *Can. J. Chem.* 63:2127 (1985).
33. Jones, W. E., and Ma, J. L., *Can. J. Chem.* 64:2192 (1986).
34. Bencsura, A., Knyazev, V. D., Xing, S.-B., Slagle, I. R., and Gutman, D., *Twenty-Fourth Symposium (International) on Combustion,* The Combustion Institute, Pittsburgh, 1992, p. 629.
35. Bencsura, A., Knyazev, V. D., Slagle, I. R., Gutman, D., and Tsang, W., *Ber. Bunsenges. Phys. Chem.*, 99:1338 (1992).
36. Seakins, P. W., Robertson, S. H., Pilling, M. J., Slagle, I. R., Gmurczyk, G. W., Bencsura, A., Gutman, D., and Tsang, W. *J. Phys. Chem.* 97:163 (1993).
37. Recalculated from the results of Ref. 13 using the Master Equation.
38. Gilbert, R. G., Luther, K., and Troe, J. *Ber. Bunsenges. Phys. Chem.* 87:169 (1983).

Twenty-Fifth Symposium (International) on Combustion/The Combustion Institute, 1994/pp. 825–831

DECAY MECHANISM OF CF_3H OR CF_2HCl IN $H_2/O_2/Ar$ FLAMES

H. RICHTER, J. VANDOOREN AND P. J. VAN TIGGELEN
Laboratoire de Physico-Chimie de la Combustion
Université Catholique de Louvain, B-1348 Louvain-la-Neuve, Belgium

The aim of this work has been the establishment of a combustion mechanism of CF_3H and CF_2HCl in $H_2/O_2/Ar$ flames. The structures of a lean flame seeded with 3% of CF_3H and of two stoichiometric flames seeded respectively with 3% CF_3H or 1% CF_2HCl have been investigated at low pressure (4.6 kPa) by using the molecular beam-sampling technique coupled with a mass spectrometer (MBMS). The data reduction of the experimental results has allowed development of a decay mechanism for CF_3H and CF_2HCl in flames. Those mechanisms have been applied to model the investigated flames by means of the PREMIX code using the experimental temperature profiles. The comparison of computed mole fraction profiles with experimental ones allows estimation of some rate coefficients not available in the literature. A good agreement between experimental and computed profiles is observed. From the burning velocities of $CO/H_2/O_2/Ar$ flames seeded with variable quantities of CF_3H or CF_2HCl, the small inhibition efficiency of CF_2HCl has been established. It is related to the elementary process $CF_2H + O \rightarrow CF_2O + H$.

Introduction

For some years, chlorofluorocarbons (CFC) and other halocarbons have been of great public concern because of their probable contribution to the stratospheric ozone depletion [1]. After the regulation of most of these compounds in the Montreal Protocol, the replacement of CF_3Br and CF_2ClBr as fire extinguishers is required. A systematic research of alternative compounds necessitates the detailed knowledge of their action in flames. The decrease of the burning velocity indicates a macroscopic inhibiting effect [2], while more detailed information about the chemical burning mechanism can be obtained by the investigation of the flame structure. So, Biordi et al. [3] have investigated the structures of flames with CF_3Br added to $CH_4/O_2/Ar$ flames, and the structure of a $CO/H_2/O_2/CF_3Br$ flame has been measured by Safieh et al. [4]. These authors ascribe the inhibiting effect of CF_3Br to the following reactions:

$$(1)\quad CF_3Br + H \rightarrow CF_3 + HBr$$

$$(2)\quad CF_3 + OH \rightarrow CF_2O + HF$$

$$(3)\quad HBr + H \rightarrow H_2 + Br$$

$$(4)\quad HBr + OH \rightarrow H_2O + Br$$

They explain the inhibition efficiency by competition of the branching process (5) $H + O_2 \rightarrow OH + O$ with Reactions (1) and (3). Furthermore, Reactions (2) and (4) compete with the usual chain propagation steps (6) $H_2 + OH \rightarrow H_2O + H$ and (7) $CO + OH \rightarrow CO_2 + H$. To test an eventual inhibiting effect of the CF_3 fragment, Vandooren et al. [5] have added 3% CF_3H to a stoichiometric $CO/H_2/O_2/Ar$ flame. The inhibiting effect of CF_3H has been explained by the competition of Reaction (8) $CF_3H + H \rightarrow CF_3 + H_2$ with the branching step (5) and by the consumption of OH during process (2) competing with the propagating steps (6) and (7). The much less important inhibiting effect of CF_3H compared with CF_3Br was explained by the formation of HBr in Reaction (1) instead of H_2 in Reaction (8). Moreover, HBr acts also as an inhibitor by means of Reactions (3) and (4) while H_2 is a fuel.

There also have been several numerical attempts to model inhibition in flames. Day et al. [6] have examined numerically the impact of HBr on the burning velocity of $H_2/O_2/N_2$ flames. From their comparison of calculated with experimental values, a simplified inhibition mechanism has been suggested. Dixon-Lewis and Simpson [7] have extended such an approach to H_2/air mixtures seeded with HBr or HCl. In 1983, Westbrook [8,9] suggested a detailed mechanism for the CF_3Br consumption in hydrocarbon/air flames using mainly the mechanism of Biordi et al. [3], but adding some reactions. Unfortunately, Westbrook's mechanism has never been validated against experimental concentration profiles available in the literature [3,4] for low-pressure flames. Only the structure of freely propagating flames had been simulated at atmospheric pressure, but without any comparison with experimental data. Of course, inhibited flames with CH_4 as the fuel are already complicated systems to model the impact of fluorocarbon additives.

TABLE 1
Initial composition of the investigated flames

Flame	H_2 (%)	O_2 (%)	Ar (%)	Halocarbon (%)	v_0 (cm s^{-1})
FP1	18.6	76.5	4.9	none	59.8
FP2	17.1	76.5	3.4	CF_3H = 3	59.8
FS1	25.4	12.7	61.9	none	65.4
FS2	23.9	12.7	60.4	CF_3H = 3	65.4
FS3	24.9	12.7	61.4	CF_2HCl = 1	65.4

Having these complexities in mind, we have selected in this work the H_2/O_2 system as reference flames because of their well-documented burning mechanism and the relatively low number of species that can interact with the added compounds. We have studied the influence of 3% CF_3H on the structure of lean and stoichiometric $H_2/O_2/Ar$ flames. The structure of a stoichiometric $H_2/O_2/Ar$ flame seeded with 1% CF_2HCl has been measured, too. A chemical mechanism for the CF_3H or CF_2HCl decay has been developed and tested by numerical modeling. The macroscopic inhibition effect of CF_3H and CF_2HCl has been investigated by measuring burning velocities of $CO/H_2/O_2/Ar$ flames seeded by CF_3H or CF_2HCl mixtures.

Experimental Methods and Data Reduction

Five premixed $H_2/O_2/Ar$ flames have been stabilized on a Spalding–Botha burner of 5-cm diameter. There were two reference flames FP1 and FS1, a lean one and a stoichiometric one, as well as three flames seeded with either 3% CF_3H or 1% CF_2HCl. The composition of the fresh gas mixtures of the investigated flames is summarized in Table 1, as well as the initial flow velocities at 298 K. The pressure in the combustion chamber was 4.6 kPa for all flames. The flame structures have been established by using a molecular beam-sampling technique coupled with a mass spectrometer (MBMS) described previously by Peeters and Mahnen [10]. The following species, H, H_2, O, OH, H_2O, O_2, and Ar have been monitored throughout all flames; HF, CO, CO_2, and CF_2O have been measured in flames FP2, FS2, and FS3; CF_3H in flames FP2 and FS2; CF_2HCl and HCl have been monitored in the flame FS3. The structures of the lean flames FP1 and FP2 have been described previously [11]. The signals measured in burned gases at 18 mm from the burner surface were compared with those of a calibration mixture containing H_2, O_2, Ar, CO, CO_2, and CF_2O. For H, O, OH, and H_2O species, the occurrence of the partial equilibrium confirmed experimentally in burned gases allows the conversion of relative signal intensities to absolute mole fractions. The equilibrium constants were derived from the JANAF tables [12] at the flame temperature occurring at 18 mm from the burner surface. The temperature profiles have been measured by using a Y_2O_3-BeO–coated Pt-Rh6%/Pt-Rh30% thermocouple. The measuring junction was located 0.2 mm from the cone tip corresponding to the location where the sampling process begins. The heat losses by radiation have been corrected by using the electric compensation method [13]. Then, the signal intensity profiles can be converted to the corresponding mole fraction profiles. For each intermediate distance, the individual mole fractions have been corrected by the same factor, which takes into account the change of the molecular beam density with temperature [11]. That factor has been calculated in order to keep the sum of the mole fractions equal to one.

The deduction of rate coefficients requires the knowledge of the individual mole fluxes and the net reaction rates of at least one reactant or product of the investigated reaction. For the calculation of the mole fluxes we took into account physical processes such as convection and thermal and molecular diffusions:

$$F_i = AN_i(v + V_i) \tag{1}$$

where F_i is mole flux of species i (mol cm^{-2} s^{-1}); A is expansion area ratio; N_i is concentration of species i (mol cm^{-3}); v is local convection velocity (cm s^{-1}); and V_i is local diffusion velocity of species i (cm s^{-1}).

The net reaction rate R_i of the individual species i is the gradient of the mole flux F_i:

$$R_i = \frac{1}{A}\frac{dF_i}{dz}. \tag{2}$$

From the net reaction rates R_{CF_3H}, R_{CF_2HCl}, and R_{CF_2O} in flames FP2, FS2 and FS3, the rate coefficients of the following elementary steps

$$(8) \quad CF_3H + H \rightarrow \text{products}$$

$$(9) \quad CF_3H + O \rightarrow CF_3 + OH$$

TABLE 2
Decay mechanism of CF_3H [rate coefficients k_i ($cm^3\ mol^{-1}\ s^{-1}$) = $AT^n \exp(-E_a/RT)$]

No.	Reaction	A	n	E_a (cal mol^{-1})	Ref.
(7)	$CO + OH \rightarrow CO_2 + H$	1.29×10^{07}	1.3	−770	8, 9
(−7)	$CO_2 + H \rightarrow CO + OH$	1.41×10^{09}	1.3	21,580	8, 9
(8)	$CF_3H + H \rightarrow CF_3 + H_2$	1.16×10^{14}	0	17,470	14
(9)	$CF_3H + O \rightarrow CF_3 + OH$	1.10×10^{12}	0	3,187	14
(11)	$CF_2O + H \rightarrow CFO + HF$	4.51×10^{13}	0	22,864	14
(12)	$CF_3H + OH \rightarrow CF_3 + H_2O$	2.65×10^{04}	2.45	3,088	14
(13)	$CF_3 + H \rightarrow CF_2 + HF$	5.48×10^{13}	0	0	20a
(2)	$CF_3 + OH \rightarrow CF_2O + HF$	3.00×10^{14}	0	0	this work
(14)	$CF_2 + OH \rightarrow CFO + HF$	1.00×10^{13}	0	0	8, 9
(15)	$CFO + H \rightarrow CO + HF$	2.50×10^{13}	0	0	this work
(16)	$CFO + OH \rightarrow CO_2 + HF$	1.00×10^{14}	0	0	8, 9

TABLE 3
Decay mecanism of CF_2HCl [rate coefficients k_i ($cm^3\ mol^{-1}\ s^{-1}$) = $AT^n \exp(-E_a/RT)$]

No.	Reaction	A	n	E_a (cal mol^{-1})	Ref.
(7)	$CO + OH \rightarrow CO_2 + H$	1.29×10^{07}	1.3	−770	8, 9
(−7)	$CO_2 + H \rightarrow CO + OH$	1.41×10^{09}	1.3	21,580	8, 9
(10)	$CF_2HCl + H \rightarrow CF_2H + HCl$	4.65×10^{14}	0	15,361	14
(11)	$CF_2O + H \rightarrow CFO + HF$	4.51×10^{13}	0	22,864	14
(14)	$CF_2 + OH \rightarrow CFO + HF$	1.00×10^{13}	0	0	8, 9
(15)	$CFO + H \rightarrow CO + HF$	2.50×10^{13}	0	0	this work
(16)	$CFO + OH \rightarrow CO_2 + HF$	1.00×10^{14}	0	0	8, 9
(17)	$CF_2HCl + OH \rightarrow CF_2Cl + H_2O$	1.28×10^{12}	0	3,320	21
(18)	$CF_2H + H \rightarrow CF_2 + H_2$	2.00×10^{13}	0	0	this work
(19)	$CF_2H + O \rightarrow CF_2O + H$	1.00×10^{13}	0	0	this work
(20)	$CF_2Cl + H \rightarrow CF_2 + HCl$	2.00×10^{13}	0	0	19
(21)	$CF_2Cl + OH \rightarrow CF_2O + HCl$	3.00×10^{13}	0	0	19
(22)	$HCl + OH \rightarrow H_2O + Cl$	2.25×10^{12}	0	1,021	22
(23)	$H + HCl \rightarrow H_2 + Cl$	2.29×10^{13}	0	3,500	8, 9
(−23)	$H_2 + Cl \rightarrow HCl + H$	2.24×10^{13}	0	4,260	8, 9
(24)	$H + Cl_2 \rightarrow HCl + Cl$	3.72×10^{14}	0	1,800	8, 9
(−24)	$HCl + Cl \rightarrow H + Cl_2$	1.62×10^{14}	0	48,180	8, 9
(25)	$Cl + Cl + M \rightarrow Cl_2 + M$	2.00×10^{14}	0	−1,790	8, 9
(−25)	$Cl_2 + M \rightarrow Cl + Cl + M$	1.00×10^{14}	0	48,480	8, 9
(26)	$H + Cl + M \rightarrow HCl + M$	6.03×10^{08}	1.0	−36,520	8, 9
(−26)	$HCl + M \rightarrow H + Cl + M$	6.61×10^{12}	0	70,000	8, 9

$$(10)\quad CF_2HCl + H \rightarrow CF_2H + HCl$$

$$(11)\quad CF_2O + H \rightarrow CFO + HF$$

have been deduced previously [14]. They will not be discussed further and are reported in Tables 2 and 3.

Mechanism Development and Numerical Modeling

All computations have been performed with the PREMIX code [15] and the corresponding CHEMKIN thermodynamic database [16] which has been supplemented for some halogenated species with Burcat and McBride's values [17]. Thermal and

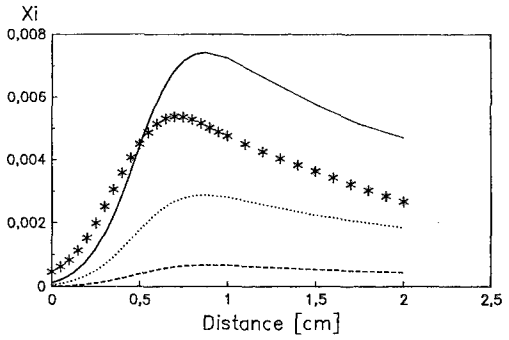

FIG. 1. Profile of CF_2O in the stoichiometric flame (FS2): exp.: *; $k_2 = 2\ 10^{13}$ (WB+): -----; $k_2 = 1\ 10^{14}$ (WB+): ·····; $k_2 = 3\ 10^{14}$ (WB+): ———.

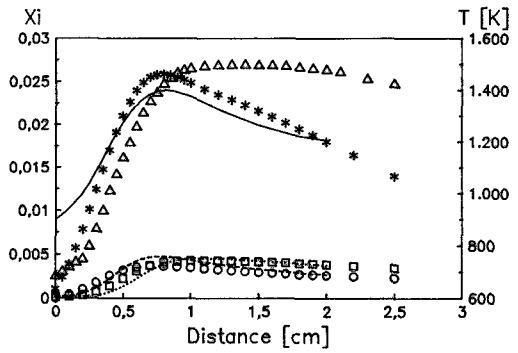

FIG. 2. Profiles of H, O, OH and of the experimental temperature in the stoichiometric flame (FS2): H (experimental): *; H (WB+): ———; O (experimental): ○, O (WB+): - - - - - -; OH (experimental): □; OH (WB+): ·····; experimental temperature [K]: Δ (right scale).

molecular diffusion are included in the code. Experimental temperature profiles have been used. As a first step, the structures of the reference flames FP1 and FS1 have been calculated by means of the H_2/O_2 mechanisms proposed by Miller et al. [18] and Westbrook [9]. The computation confirms very well the experimental results for both H_2/O_2 mechanisms. Now, those mechanisms could be completed by the reactions responsible for the decay of either CF_3H (FP2, FS2) or CF_2HCl (FS3). The actual reaction mechanism includes a minimum of reactions involving radical intermediates that have not been detected in order to avoid the use of poorly known rate coefficients. The reaction mechanisms of both additives will be discussed separately.

Mechanism of CF_3H Decay:

For the modeling of the CF_3H decay, the mechanism is listed in Table 2. The rate coefficients of Reactions (2) and (15) have been determined in this work. To the best of our knowledge, there are no experimental values available in the literature for Reactions (2), (14), (15), and (16), though Westbrook [8,9] has produced a mechanism involving these reactions by assuming rate coefficients analogous to those of CH_i species. We have considered Westbrook's values for rate coefficients k_{14} and k_{16} as reasonable; they are therefore kept unchanged in the actual mechanism. In addition, we have used the experimental value for k_{13} measured by Tsai and McFadden [20a]. Rate coefficient k_2 is deduced by fitting the CF_2O profile with the experimental data. Figure 1 compares the experimental CF_2O profile in flame FS2 with those calculated by using Westbrook's mechanism [9] for H_2/O_2 supplemented by the data in Table 2 and by varying the rate coefficient k_2. A satisfactory agreement is obtained for k_2 equal to 3×10^{14} cm^3 mol^{-1} s^{-1}. This value differs greatly from Westbrook's estimated data (4×10^{12} cm^3 mol^{-1} s^{-1}) [8,9]. The reason for the discrepancy comes from the fact that Westbrook assumes an analogy between Reaction (2) $CF_3 + OH \rightarrow CF_2O + HF$ and $CH_3 + OH \rightarrow CH_2 + H_2O$. But the processes are basically different: in the case of Reaction (2), there is F abstraction with O insertion, while, in the methyl reaction, only H abstraction occurs. Reaction $CF_3 + O \rightarrow CF_2O + F$ has been neglected since, when the rate coefficient measured by Tsai et al. [20b] is used, this reaction contributes only 5% of the total CF_2O produced in flame FS2. Similarly, the rate coefficient of reaction $CF_3 + O_2 \rightarrow$ products is so small that such a process would contribute at the most 1/1000 of the actual CF_2O production. In a similar way as for k_2, the rate coefficient $k_{15} = 2.5 \times 10^{13}$ cm^3 mol^{-1} s^{-1} has been selected so that the computed CO profile fits the experimental one. The mechanism for H_2/O_2 combustion suggested by Miller et al. [18] or the one suggested by Westbrook [9] induces really minute differences for the profiles of all species. To a first approximation, they can be considered to be equally good. For the sake of legibility of the figures, we show only the results based on Westbrook's mechanism supplemented with the rate coefficients of Table 2. This mechanism is called (WB+). The comparison between the experimental results relative to the stoichiometric flame FS2 and the modeling with the (WB+) mechanism is exhibited in Figs. 2, 3, and 4. Figure 2 indicates a good agreement for H, O, and OH. The computed H mole fraction near the burner remains too high since the mechanism (WB+) does not take into account eventual catalytic recombination of H radicals on the burner surface. In Fig. 3, we notice a slight shift of the computed profiles toward the burned gases region, but the agreement is good for all carbon-containing species (Fig. 4). The calculated profiles for the stable species containing carbon have been com-

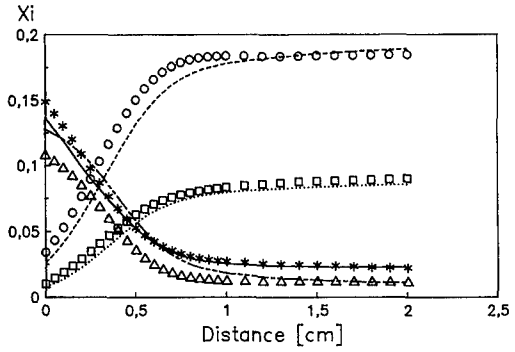

FIG. 3. Profiles of H_2, H_2O, HF, and O_2 in the stoichiometric flame (FS2): H_2 (experimental): °; H_2 (WB+): ———; H_2O (experimental): ○; H_2O (WB+): ------; HF (experimental): □; HF (WB+): ·····; O_2 (experimental): Δ; O_2 (WB+): — - - —.

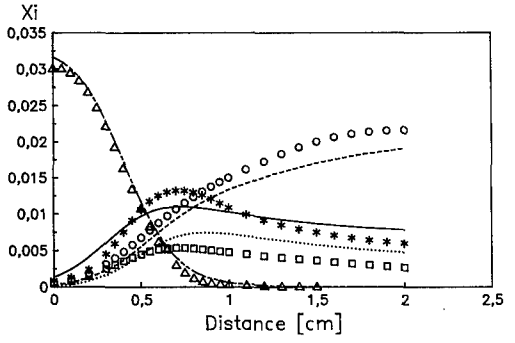

FIG. 4. Profiles of CO, CO_2, CF_2O, and CF_3H in the stoichiometric flame (FS2): CO (experimental): °; CO (WB+): ———; CO_2 (experimental): ○; CO_2 (WB+): ------; CF_2O (experimental): □; CF_2O (WB+): ·····; CF_3H (experimental): Δ; CF_3H (WB+): — - - —

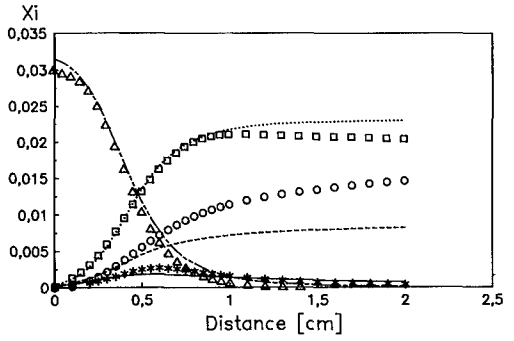

FIG. 5. Profiles of CO, CO_2, CF_2O, and CF_3H in the lean flame (FP2): CO (experimental): °; CO (WB+): ———; CO_2 (experimental): ○; CO_2 (WB+): ------; CF_2O (experimental): □; CF_2O (WB+): ·····; CF_3H (experimental): Δ; CF_3H (WB+): — - - —

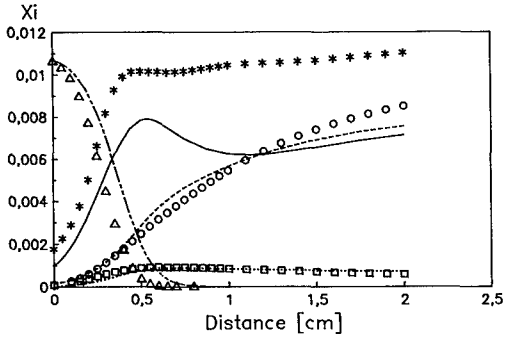

FIG. 6. Profiles of HCl, CO_2, CF_2O and CF_2HCl in the stoichiometric flame (FS3): HCl (experimental): °; HCl (WB++): ———; CO_2 (experimental): ○; CO_2 (WB++): CF_2O (experimental): □; CF_2O (WB++): ·····; CF_2HCl (experimental): Δ; CF_2HCl (WB++): — - - —.

puted along the same mechanism (WB+) for the lean flame (FP2) using the experimental temperature profile recorded previously [11]. As is illustrated in Fig. 5, the agreement remains quite satisfactory, although the mechanism underestimates the final CO_2 concentration.

Mechanism of CF_2HCl Decay:

The mechanism used for the modeling of the CF_2HCl decay is listed in Table 3. Rate coefficient k_{15} is the same as for the CF_3H decay. The estimate of the rate coefficients k_{18} and k_{19} will be discussed now, since no data are available in the literature.

From previous studies [14,19], we know that about 85% of the CF_2HCl is consumed in flame FS2 by Reaction (10) $CF_2HCl + H \rightarrow CF_2H + HCl$. We will assume therefore that Reaction (19) $CF_2H + O \rightarrow CF_2O + H$ is mainly responsible for the formation of CF_2O. The rate coefficient k_{18} has been estimated to 2×10^{13} cm^3 mol^{-1} s^{-1}. The value of k_{19} has been selected by varying k_{19} in such a manner as to obtain the best agreement between the experimental and the computed CF_2O profiles, using Westbrook's H_2/O_2 mechanism supplemented with the reactions of Table 3. This mechanism is named (WB++). The best agreement is reached for $k_{19} = 1 \times 10^{13}$ cm^3 mol^{-1} s^{-1}. It corresponds to a ratio $k_{18}/k_{19} = 2$. The rate coefficients k_{20} and k_{21} have been determined in a similar way by studying a flame seeded by CF_2Cl_2 traces, discussed previously [19]. A few typical profiles are presented in Figs. 6 and 7. The profiles exhibit good agreement, but they are shifted toward the burned gases. It could be due to a slight shift of the

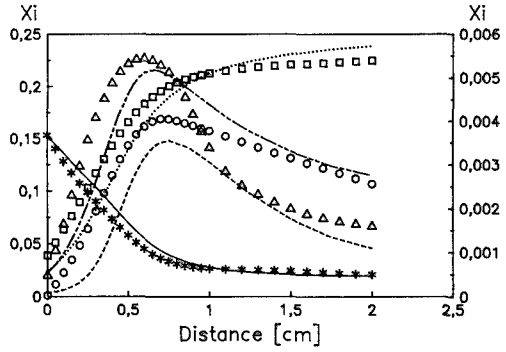

FIG. 7. Profiles of H_2, H_2O (left scale), O and CO (right scale) in the stoichiometric flame (FS3): H_2 (experimental): •; H_2 (WB + +): ———; O (experimental): ○; O (WB + +): - - - - - -; H_2O (experimental): □; H_2O (WB + +): · · · · · ·; CO (experimental): Δ; CO (WB + +): — - - —.

temperature profile. The discrepancy between the computed and the experimental HCl mole fraction profiles can be ascribed to the contribution of atomic chlorine not taken into account. As a matter of fact, in the calibration procedure, it indeed was assumed that large amounts of chlorine atoms are not present in the flame. However, from the computation, it comes out that the mole fraction of atomic chlorine is about 0.005, i.e., equivalent to the noted difference (Fig. 6).

The Inhibiting Effect

The overall inhibiting effects of CF_3H and CF_2HCl have also been studied by measuring the burning velocities [23] of two stoichiometric $CO/H_2/O_2/Ar$ flames, one containing 30% Ar and 2.33% H_2, the other with 50% Ar and 1.67% H_2. The flames have been seeded with variable amounts of CF_3H or CF_2HCl. The inhibiting effect is described quantitatively by using the inhibition parameter $\phi_i = [O_2]_0(V_0 - V_{0i})/([Inh]_0V_0$ suggested by Fristrom and Sawyer [24]. The terms V_0 and V_{0i} are the burning velocities, with and without inhibitor, respectively. $[O_2]_0$ and $[Inh]_0$ are the initial oxygen and inhibitor concentrations. The mean inhibition parameter of 3.20 ± 0.2 for CF_3H corroborates the previous work of da Cruz et al. [2]. In the case of CF_2HCl, we measured a mean value of 2.25 ± 0.2. CF_2HCl is a less efficient inhibitor than CF_3H in spite of the presence of a chlorine atom in the molecule, which is considered generally as more efficient than a fluorine atom for inhibition [2]. This observation can be ascribed to the role of Reaction (19) $CF_2H + O \rightarrow CF_2O + H$ already included in the mechanism. It reinjects, indeed, H atoms essential for the branching reaction (5).

Conclusions

This paper discusses the chemical decay mechanisms for CF_3H and CF_2HCl in $H_2/O_2/Ar$ flames. Modeling with the PREMIX code using the H_2/O_2 Westbrook mechanism supplemented by reactions characteristic for the additives exhibits a good agreement with the experimental results. The suggested mechanism can be used to explain the decay of CF_2XY species (with X, Y: H, F, Cl, or Br) in H_2/O_2 flames, provided that the rate coefficients of the initial attack are known.

Acknowledgments

The authors are grateful to the Fonds National de la Recherche Fondamentale et Collective for its financial support (Contracts Nos. 2.9006.88 and 1.5.140.90F) and the European Communities for the contract SUBSTHAL (EV5V-CT92-0230). They are also grateful to Dr. R. J. Kee for supplying the PREMIX code. One of the authors (H. R.) thanks the Deutscher Akademischer Austauschdienst (DAAD) for its financial support in the beginning of this research.

REFERENCES

1. Molina, M. J., and Rowland, R., *Nature* 249:810 (1974).
2. da Cruz, F. N., Vandooren, J., and Van Tiggelen, P. J., *Bull. Soc. Chim. Belg.* 97:1011 (1988).
3. Biordi, J. C., Lazarra, C. P., and Papp, J. F., *ACS Symposium Series* 16:256 (1975).
4. Safieh, H. Y., Vandooren, J., and Van Tiggelen, P. J., *Nineteenth Symposium (International) on Combustion,* The Combustion Institute, Pittsburgh, 1982, p. 117.
5. Vandooren, J., da Cruz, F. N., and Van Tiggelen, P. J., *Twenty-Second Symposium (International) on Combustion,* The Combustion Institute, Pittsburgh, 1988, p. 1587.
6. Day, M. J., Stamp, D. V., Thompson, K., and Dixon-Lewis, G., *Thirteenth Symposium (International) on Combustion,* The Combustion Institute, Pittsburgh, 1971, p. 705.
7. Dixon-Lewis, G., and Simpson, R. J., *Sixteenth Symposium (International) on Combustion,* The Combustion Institute, Pittsburgh, 1977, p. 1111.
8. Westbrook, C. K., *Nineteenth Symposium (International) on Combustion,* The Combustion Institute, Pittsburgh, 1982, p. 127.
9. Westbrook, C. K., *Combust. Sci. Technol.* 34:201 (1983).
10. Peeters, J., and Mahnen, G., *Fourteenth Symposium (International) on Combustion,* The Combustion Institute, Pittsburgh, 1973, p. 133.
11. Richter, H., Vandooren, J., and Van Tiggelen, P. J., *Bull. Soc. Chim. Belg.* 99:491 (1990).

12. Chase, M. W., Jr., Davies, C. A., Downey, J. R., Jr., Frurip, D. J., McDonald, R. A., and Syverud, A. N., *JANAF Thermochemical Tables*, 3rd ed., 1985, J. Phys. Chem. Ref. Data, Vol. 14, Supplement No. 1.
13. Wagner, H. Gg., Bonne, U., and Grewer, T., *Z. Phys. Chem.* 26:93 (1960).
14. Richter, H., Vandooren, J., and Van Tiggelen, P. J., accepted for publication in *J. Chim. Phys. (Paris)*.
15. Kee, R. J., Miller, J. A., and Jefferson, T. H., Sandia Laboratories Report, SAND 80-8003, 1980.
16. Kee, R. J., Rupley, F. M., and Miller, J. A., Sandia Laboratories Report, SAND 87-8215 · UC-4, 1987.
17. Burcat, A., and McBride, B. J., Israel Institute of Technology (TECHNION) T.A.E. 675, 1992.
18. Miller, J. A., Smooke, M. D., Green, R. M., and Kee, R. J., *Combust. Sci. and Technol.* 34:149 (1983).
19. Richter, H., Ph.D Thesis, Université Catholique de Louvain, Louvain-la-Neuve, Belgium, 1993.
20. a) Tsai, C., and McFadden, D. L., *J. Phys. Chem.* 93:2471 (1989). b) Tsai, C., Belanger, S. M., Kim, J. T., Lord, J. R., and MacFadden, D. L., *J. Phys. Chem.* 93:1916 (1989).
21. Jeong, K. M., and Kaufman, F., *J. Phys. Chem.* 86:1808 (1982).
22. Baulch, D. L., Duxbury, J., Grant, S. J., and Montague, D. C., *J. Phys. Chem. Ref. Data* 10:1–212 (1981).
23. Van Tiggelen, A., Balaceanu, J. C., Burger, J., De Soete, G., Sajus, L., Salé, B., and Van Tiggelen, P. J., *Oxydations et Combustion*, Technip Paris, 1968.
24. Fristrom, R. M., and Sawyer, R. F., *AGARD Conference Proceeding* 84:12–1 (1971).

Twenty-Fifth Symposium (International) on Combustion/The Combustion Institute, 1994/pp. 833–840

HIGH-TEMPERATURE REACTIONS OF PHENYL OXIDATION

P. FRANK, J. HERZLER, TH. JUST AND C. WAHL
Institut für Physikalische Chemie der Verbrennung
Deutsche Forschungsanstalt für Luft-und Raumfahrt
70569 Stuttgart, Pfaffenwaldring 38–40, Germany

The reactions of phenyl radicals with molecular and atomic oxygen have been studied in the temperature range 900–1800 K behind reflected shocks. The total pressure ranged from 1.3 to 2.5 bar. Phenyl radicals were generated by the fast thermal decomposition of nitroso- or iodobenzene. Resonance absorption was used to record the temporal concentration profiles of H, O, and I atoms and of CO molecules. This sensitive technique allowed study of the reaction systems under favorable conditions by applying very low initial concentrations (0.5–250 ppm). Due to the complexity of the system, it was necessary to study in a separate series of experiments the dissociation reactions of intermediates like phenoxy radicals and *p*-quinone. For the initiation reaction $C_6H_5 + O_2$, two product channels were found:

$$C_6H_5 + O_2 \rightarrow C_6H_5O + O \qquad \text{(R1)}$$

and a fast channel, producing H-atoms,

$$C_6H_5 + O_2 \rightarrow C_6H_4O_2 + H \qquad \text{(R2)}$$

with a branching ratio k_1/k_2 of about 3 in the investigated temperature range. Reaction (R2) seems plausible; however, it presently has the status of a working hypothesis.

For

$$C_6H_5 + O \rightarrow C_5H_5 + CO \qquad \text{(R5)}$$

a rate constant of about 10^{14} cm^3 mol^{-1} s^{-1} was deduced.

From the evaluated data, a reaction scheme for phenyl radicals is given, which is expected to improve the modeling results of practical flames containing benzene or other aromatics.

Introduction

The formation and destruction of aromatic hydrocarbons in combustion processes is still far from being quantitatively understood. Recently, we undertook some systematic investigations on the high temperature decomposition of selected aromatic molecules and on the pertinent radicals phenyl and benzyl [1,2]. Especially, phenyl radicals are considered to play an important role as intermediates in high-temperature reactions leading to the formation of PAH (see e.g., Ref. 3). Their reaction with acetylene leads to phenylacetylene [4,5]. This species is assumed to start inception of PAH formation (see e.g., Ref. 6) as a possible pathway to soot. As a competitive process, the reaction of O, O_2, or OH with phenyl radicals reduces the tendency for soot precursor formation. The reaction route of phenyl oxidation by O and O_2 has been investigated in the present study.

Experimental

The high-purity stainless steel shock tube consists of a test section of 6 m and a driver section of 4 m in length. The internal diameter is 7.2 cm. The test section was evacuated by a turbomolecular pump to about 10^{-7} mbar before each experiment. Mixtures were prepared and stored in a 50 L stainless steel tank, which was bakeable up to 250 °C. The measurements were performed behind the reflected shock front close to the end flange. The temperature behind the reflected shock was calculated from the measured speed of the incident shock and by solving the appropriate conservation equations. A detailed description of the apparatus is given elsewhere [7]. Atomic (ARAS) and molecular resonance absorption spectrometry (MRAS) were used to monitor the temporal concentration profiles of H, O, and I atoms and of CO molecules in the wavelength range 121–165 nm. The light sources for the absorption measurements were microwave-excited discharge lamps containing the appropriate gas diluted in helium. Hydrogen atoms (using an oxygen spectral filter) and one of the other species (using a vuv monochromator) can be monitored simultaneously. The transmitted intensity signals were recorded by a two-channel storage oscilloscope and fed to a personal computer for computation. The atomic and molecular concen-

tration profiles reported here are based on calibration experiments. Hydrogen- and O-atom calibration were performed by shock-heating H_2-N_2O-Ar and N_2O-Ar mixtures [7]. Iodine- and CO-calibration curves were evaluated from shock-heated mixtures of CH_3I-Ar [8] and CO-Ar [9], respectively.

For the series of experiments concerning phenyl oxidation, the phenyl radicals were produced by the thermal decay of nitrosobenzene (C_6H_5NO) or iodobenzene (C_6H_5I). The precursor concentration ranged from 6 to 100 ppm. O_2 mole fractions of 40–250 ppm were used. Phenoxy radicals (C_6H_5O) were produced from the thermal decomposition of anisole (methyl phenyl ether: $C_6H_5OCH_3$) or of allyl phenyl ether ($C_6H_5OC_3H_5$) with mole fractions of 25 to 90 ppm. The diluent in all experiments was highly purified argon (Ar = 99.9999%). The purity of all these species was checked by mass spectrometry. The initial concentrations of nitroso- and iodobenzene, anisole, allyl phenyl ether, and *p*-quinone were routinely measured by uv absorption in samples drawn from the shock tube.

The sensitive ARAS and MRAS techniques allowed us to study the high-temperature reactions in highly diluted mixtures. The concentrations are so low that temperature effects other than those stemming from the nonideality of the flow in the shock tube are of no importance. Further, these low initial concentrations reduce strongly, within the timescale of the experiments ($t \leq 800\ \mu s$), the number of important subsequent reactions that had to be considered for the evaluation of the measured concentration profiles.

Results and Discussion

Phenoxy Decomposition:

The dominant reactions of C_5 and C_6 species in a benzene flame—as assumed prior to the present study—are given in Fig. 1 [6,10]. The reaction of phenyl radicals with O_2 is assumed to give phenoxy radicals and oxygen atoms:

$$C_6H_5 + O_2 \rightarrow C_6H_5O + O \qquad \text{(R1)}$$

followed by decomposition of the phenoxy radical to cyclopentadienyl (C_5H_5) and CO.

Due to the scarce data on the high temperature decomposition of the phenoxy radical [11], we investigated first the thermal decay of phenoxy by monitoring the H and the CO absorption. As phenoxy precursors, anisole and allyl phenyl ether were used. Anisole decomposition experiments resulted in some H-atom production. This could be explained quantitatively by the CH_3 submechanism:

$$CH_3 + CH_3 + M \rightarrow C_2H_6 + M \quad [12]$$

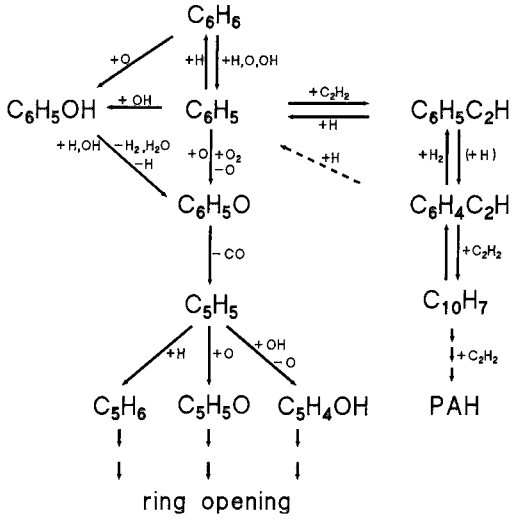

FIG. 1. Dominant reactions of C_5 and C_6 species in a benzene flame, as assumed prior to the present study.

$$C_2H_5 \rightarrow C_2H_4 + H. \quad [13]$$

From these results, we concluded that phenoxy and cyclopentadienyl do not produce H atoms at temperatures $T \leq 1500$ K. Similar conclusions from the allyl phenyl ether decomposition could not be drawn because the simulation of the H-atom concentration profiles was not possible due to the scarce data on high-temperature reactions of allyl radicals. At temperatures $T > 1300$ K, the unimolecular decomposition of the phenoxy radical is very fast and an immediate increase to a constant CO-level is observed. Independent of the precursor and the temperature (1300–1800 K), we found:

$$[CO]_{end}/[C_6H_5O]_0 = 1.0 \pm 0.1.$$

Therefore, we have to assume

$$C_6H_5O \rightarrow C_5H_5 + CO \qquad \text{(R3)}$$

is the only or the major ($\geq 90\%$) decomposition channel.

Because the phenoxy decomposes very fast, the temperature interval under investigation was only 1020–1190 K. A typical CO profile, measured during the thermal decay of allyl phenyl ether, is shown in Fig. 2.

The dissociation of the radical precursor anisole has to be taken into account at temperatures $T <$ 1200 K [11,14,15], whereas allyl phenyl ether decomposes instantaneously at temperatures $T = 1060$ K [11,16]. The evaluation of the CO profiles gave for

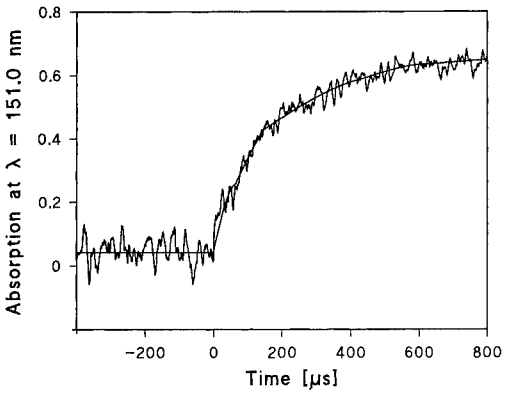

FIG. 2. CO-MRAS signal from thermal decay of allyl phenyl ether: $X(C_6H_5OC_3H_5)$ = 41 ppm; T_5 = 1090 K; p_5 = 2.36 bar.

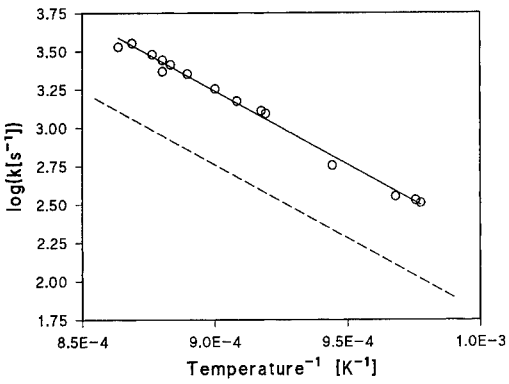

FIG. 3. Arrhenius diagram for the phenoxy decomposition. ○: measured rate coefficients; solid line: best linear fit of these values; dashed line: Arrhenius expression of Lin and Lin [11].

both precursors the same kinetic results. The resulting Arrhenius expression for reaction (R3) is depicted in Fig. 3. The only other available data on phenoxy above 1000 K, which have been deduced from shock-tube experiments, are those by Lin and Lin [11], (Fig. 3). The experimental method applied by Lin and Lin is comparable to that of the present work, but the measurement of CO concentrations by IR-laser absorption had to occur at higher concentrations. The rate constant values of Ref. 11 are about a factor of 3 smaller than those of the present work. This discrepancy compared to our work may be caused by a relatively strong influence of subsequent reactions on the evaluation of data due to the larger initial concentrations applied by Lin and Lin [11].

Phenyl + O_2/Phenyl + O:

Due to the relatively fast thermal decay of phenyl radicals (Braun-Unkhoff et al. [1]) at temperatures T

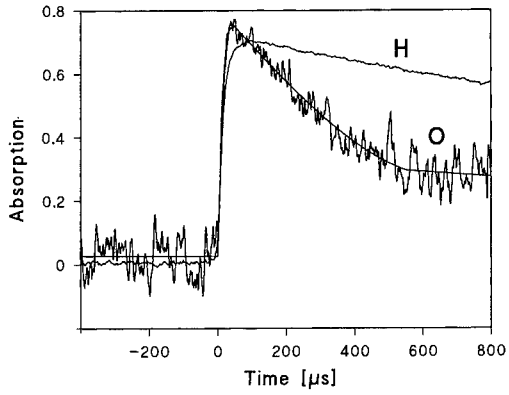

FIG. 4. H- and O-ARAS signals from the reaction of phenyl + O_2: $X(C_6H_5NO)$ = 15 ppm; $X(O_2)$ = 250 ppm; T_5 = 1320 K; p_5 = 2.36 bar.

≥ 1500 K, the investigation of the reaction of phenyl radicals with O_2 was restricted to the temperature range from 1000 to about 1500 K. Figure 4 shows typical experimental profiles of H and O atoms, produced in the reaction system of nitrosobenzene with excess oxygen.

The initial increase and the maximum of the O-atom concentration profiles can be simulated by the production of O atoms accordingly to

$$C_6H_5 + O_2 \rightarrow C_6H_5O + O \qquad \text{(R1)}$$

and by the consumption of O atoms due to the fast reaction

$$C_6H_5 + O \rightarrow C_5H_5 + CO. \qquad \text{(R5)}$$

Model calculations executed by varying the rate constant values for reactions (R1) and (R5) (see Fig. 5) show that the very fast increase of the O-concentration profiles could only be explained by a rate constant for reaction (R1) that is about a factor of 25 larger than preliminary data that Lin and Lin [17] (see Fig. 5) suggest. Using this high value for the O-production reaction (R1), a very high but plausible value of about $1.1 * 10^{14}$ cm^3 mol^{-1} s^{-1} for reaction (R5) is necessary to model the maximum and the following decrease.

Measurements of the oxidation of chlorobenzene [18] as well as the addition of benzene to slowly reacting mixtures of hydrogen and oxygen [19] at lower temperatures show good agreement with our value for the rate coefficient of the reaction of phenyl + O_2 to phenoxy and O. Recent flow reactor measurements of Hoyermann [20] at room temperature on phenyl + O indicate a high value of about $8 * 10^{13}$ cm^3 mol^{-1} s^{-1} for the rate coefficient as well. This is in good agreement with our data.

The energy diagram of reaction (R5), phenyl +

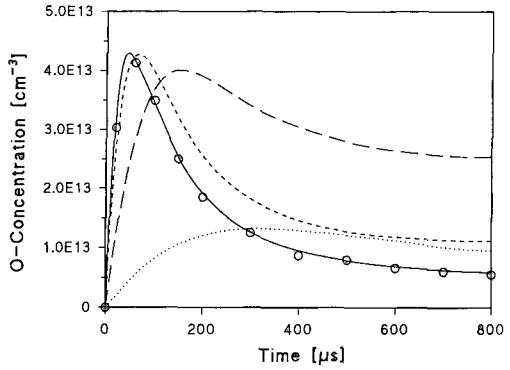

FIG. 5. Simulation of the O concentration profiles (experimental conditions of Fig. 4) by varying R1 and R5: Circles: experimental data; full line: best fit using mechanism of Table 1; dotted curve: using k of Ref. 17 for R1 and $1.0 \cdot 10^{13}$ cm^3 mol^{-1} s^{-1} for R5; long-dashed curve: using $6 \cdot k$ of Ref. 17 for R1 and $1.0 \cdot 10^{13}$ cm^3 mol^{-1} s^{-1} for R5; short-dashed curve: using $17 \cdot k$ of Ref. 17 for R1 and $6.0 \cdot 10^{13}$ cm^3 mol^{-1} s^{-1} for R5.

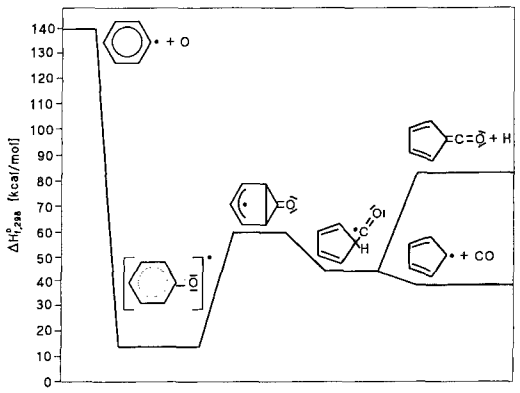

FIG. 6. Energy diagram of phenyl + O. This is a simplified diagram. Small barriers that likely occur along the reaction paths are not shown. The heats of formation of some molecules are estimated values. Necessary group increments were based upon Benson [22] and Melius [23].

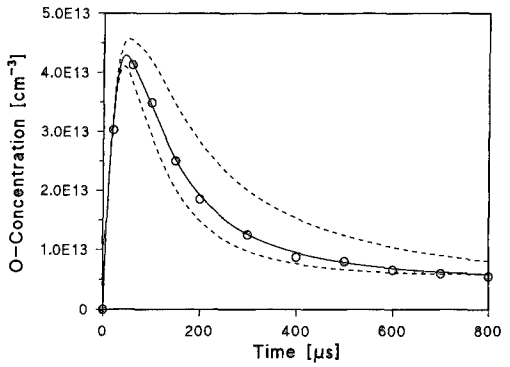

FIG. 7. Sensitivity of the measured O-atom concentration profile (experimental conditions of Fig. 4) with respect to the reaction mechanism of Table 1. Variation of k_6 (C_5H_5 + O) by factors of 1.5 and 0.5: Circles: experimental data; full line: best fit using mechanism of Table 1; dashed line: $k_6 \pm 50\%$.

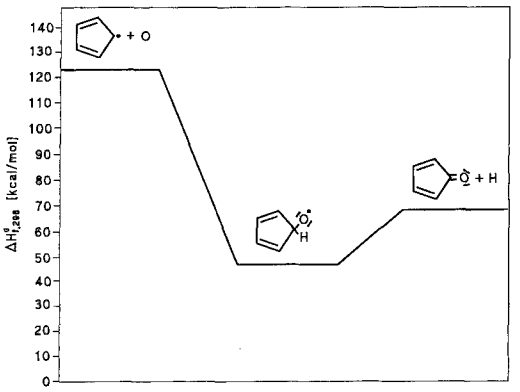

FIG. 8. Energy diagram of cyclopentadienyl + O. This is a simplified diagram. Small barriers that likely occur along the reaction paths are not shown. The heats of formation of some molecules are estimated values.

O, (Fig. 6) indicates that the produced phenoxy is highly excited due to the high exothermicity of the addition reaction ($\Delta H^0_{r,298}$ = 127 kcal/mol). Therefore, it dissociates immediately to cyclopentadienyl and CO. The second possible product pathway (R5a) to a ketene and H is of minor importance due to the barrier of 45 kcal/mol, relative to the C_5H_5 + CO exit (R5). The barrier results in $k_5(E) >> k_{5a}(E)$ for the decomposing transition states, which in turn means that the branching is likely in favor of C_5H_5 + CO.

At longer reaction times, the O-consumption reaction

$$C_5H_5 + O \rightarrow C_5H_4O + H \qquad \text{(R6)}$$

must be considered, too. Figure 7 shows that reaction (R6) has a strong influence on the O consumption at $t > t_{max}$, so a sensitive determination of k_6 was possible. There are, to our knowledge, no literature values available for this rate coefficient.

The energy diagram of reaction (R6), cyclopentadienyl + O, (Fig. 8) shows that the adduct C_5H_5O is highly excited due to the high exothermicity of about $\Delta H^0_{r,298}$ = 74 kcal/mol. Due to this instability, it decomposes rapidly to cyclopentadienone and H.

The very fast occurrence of H atoms in the system phenyl + O_2 (see Fig. 4) cannot be explained by the reaction sequence (R1), (R3), (R5), and (R6), because reaction (R6), which is the only H-producing

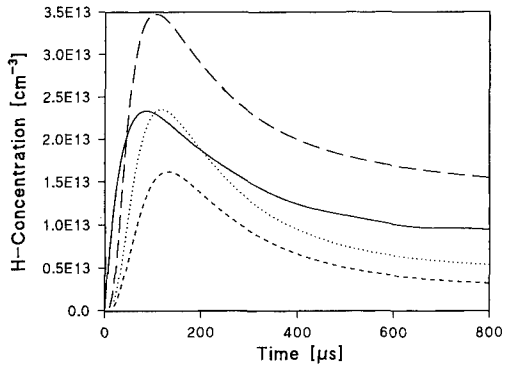

FIG. 9. Calculation of the H-atom concentration profiles (experimental conditions of Fig. 4) with k_1, k_3, k_5 from Table 1, and variation of k_6. Full curve: smoothed measured values; short-dashed curve: $k_6 = 7 \cdot 10^{13}$ cm^3 mol^{-1} s^{-1}; dotted curve: $k_6 = 1.5 \cdot 10^{14}$ cm^3 mol^{-1} s^{-1}; long-dashed curve: $k_6 = 5 \cdot 10^{15}$ cm^3 mol^{-1} s^{-1}.

step, is a reaction of products of (R1), (R3), and (R5), respectively. The short-dashed curve of Fig. 9 shows the calculated H-concentration profiles using the rate coefficients for (R1), (R3), (R5), and (R6), which were deduced from modeling the O profiles and from the phenoxy decomposition measurements. It can be seen that the increase is much too slow and that the calculated concentrations are at all times lower than the measured ones. By increasing k_6 by a factor of 2.2, it is possible to fit the maximum (see the dotted line of Fig. 9), but the initial increase still remains too slow. Even with an extremely large rate coefficient $k_6 = 5 * 10^{15}$ cm^3 mol^{-1} s^{-1} close to collision frequency, we predict much too high H and much too low O concentrations at $t > 50$ μs. The initial increase of the H-concentration profiles is still too slow (see the long-dashed curve of Fig. 9). We conclude that the very fast increase cannot be explained by a bimolecular reaction of two products. Further, the H production cannot originate from unimolecular decomposition reactions, because from the preceding work of Braun-Unkhoff et al. [1], it is known that the thermal decay of phenyl below 1500 K is much too slow to account for measurable H-atom concentrations and because phenoxy decomposition does not produce H atoms under the present experimental conditions. In a separate series of experiments, it was also verified that neither impurities nor reaction products, possibly generated during long residence times of the nitrosobenzene-O_2 mixtures in the mixing vessel, could be the sources of the observed immediate H-atom production.

Therefore, we are forced to assume that only a second initial reaction step can account for the fast observed H-production rate. Thermochemical arguments lead us to a working hypothesis that the product channel

$$C_6H_5 + O_2 \rightarrow C_6H_4O_2 + H \qquad \text{(R2)}$$

which produces H atoms and *p*-quinone or *o*-quinone (see Fig. 10), is likely responsible for the very fast initial H production. Our analysis is based upon the assumption of *p*-quinone being the major product, because *p*-quinone stems from a transition state with a 1,4 bridge of O_2, which is subjected to less stress than the corresponding transition state for *o*-quinone. From Fig. 11, it is to be seen that excellent agreement between measured and calculated H profile is achieved by introducing (R2) into the reaction scheme. The calculated H-concentration profiles mainly depend on three reactions: the H-producing reactions (R2) and (R6) and the H-consuming reaction

$$C_5H_5 + H \rightarrow C_5H_6. \qquad \text{(R7)}$$

A sensitive determination of the rate coefficients of

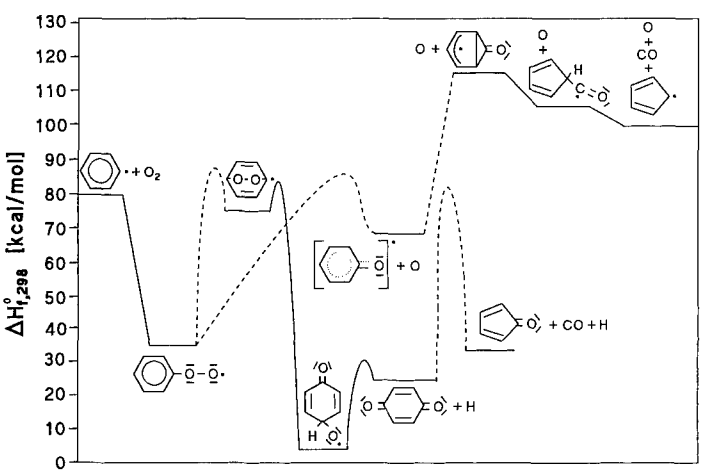

FIG. 10. Energy diagram of phenyl + O_2. This is a simplified diagram. Small barriers that likely occur along the reaction paths are not shown. The heats of formation of some molecules are estimated values. Dashed lines: barrier heights deduced from our measurements.

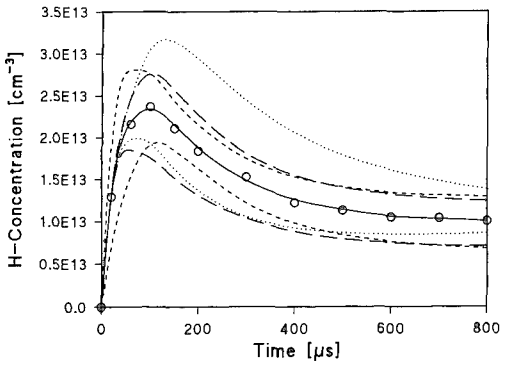

FIG. 11. Sensitivity of the measured H-atom concentration profile (experimental conditions of Fig. 4) with respect to the reaction mechanism of Table 1. Variation of k_2, k_6, and k_7 by factors of 1.5 and 0.5. Circles: experimental data; full line: best fit using mechanism of Table 1; short-dashed line: $k_2 \pm 50\%$; long-dashed line: $k_6 \pm 50\%$; dotted line: $k_7 \pm 50\%$.

these three reactions is possible (Fig. 11). The rate coefficient of (R2) exhibits only weak interdependence with reactions (R6) and (R7) for observation times ≤ 60 μs. The rate coefficient of (R6) can be determined by modeling the O (see Fig. 7) and the H profiles. This rate coefficient, evaluated from two different measured species profiles, shows very good agreement.

With k_2 and k_6, it is now possible to determine k_7. The dotted line of Fig. 11 shows that the calculated H-concentration profiles are very sensitive to variations of k_7. There are no literature values available of this rate coefficient. The observed value of $1.0 \cdot 10^{14}$ $cm^3\ mol^{-1}\ s^{-1}$ is what one would expect for such a recombination at our experimental conditions.

Less important H-consuming reactions are

$$C_6H_5 + H \rightarrow C_6H_6 \qquad (R8)$$

and

$$H + O_2 \rightarrow O + OH. \qquad (R9)$$

The literature values [1,12] for the rate coefficients of these reactions were used. In the present study, OH-concentration measurements have not been carried out. OH radicals are mainly produced by reaction (R9), with maximum values of about $1.5 \cdot 10^{13}$ $cm^3\ mol^{-1}$ at the end of the observation time interval. As there are nearly no data available for high-temperature OH reactions with the C_6 and C_5 species of the investigated reaction system, the modeling studies had to be carried out by using estimated rate constants. Even with k values on the order of $5 \cdot 10^{13}$ $cm^3\ mol^{-1}\ s^{-1}$, the calculated concentration profiles for H, O, and CO were influenced only marginal. Therefore, the influence of the OH radicals reacting in the system with hydrocarbons is negligible with respect to the deduced data in this study.

p-Quinone Decomposition:

In a separate series of experiments, the thermal stability of *p*-quinone was checked. The temporal absorption of H, O, and CO was monitored during the unimolecular decomposition of low initial concentrations (X_0 = 36–72 ppm) of *p*-quinone. Only CO was measurable in appreciable quantities. From the pseudo-first-order increase of CO and from the constant CO absorption ($[CO]_{end} = [C_6H_4O_2]_0$) at $T \geq 1750$ K within the observation interval, it was deduced that the main decomposition channel is

$$C_6H_4O_2 \rightarrow C_5H_4O + CO. \qquad (R4)$$

Under the applied experimental conditions, only

TABLE 1
Reaction mechanism and rate constants

		A	E_a/R	Ref.
R1	$C_6H_5 + O_2 \rightarrow C_6H_5O + O$	2.6×10^{13}	3,080	p.w.
R2	$C_6H_5 + O_2 \rightarrow C_6H_4O_2 + H$	3.0×10^{13}	4,520	p.w.
R3	$C_6H_5O \rightarrow C_5H_5 + CO$	7.4×10^{11}	22,070	p.w.
R4	$C_6H_4O_2 \rightarrow C_5H_4O + CO$	7.4×10^{11}	29,700	p.w.
R5	$C_6H_5 + O \rightarrow C_5H_5 + CO$	$(9–11) \times 10^{13}$		p.w.
R6	$C_5H_5 + O \rightarrow C_5H_4O + H$	7.0×10^{13}		p.w.
R7	$C_5H_5 + H \rightarrow C_5H_6$	1.0×10^{14}		p.w.
R8	$C_6H_5 + H \rightarrow C_6H_6$	7.5×10^{13}		1
R9	$H + O_2 \rightarrow O + OH$	2.0×10^{14}	8,460	12

Units: cm^3, mol, s, kcal.
$k = A \cdot T^n \exp(-E_a/RT)$.
p.w. = present work.

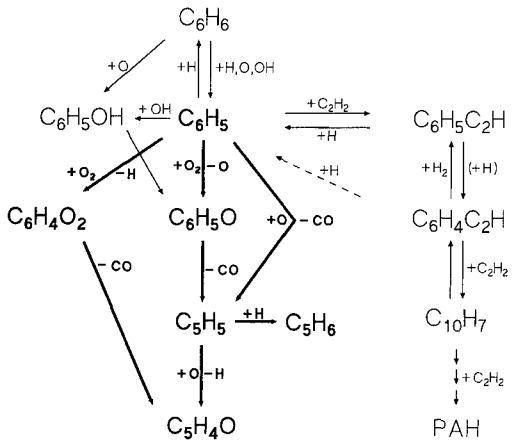

FIG. 12. Dominant reactions of C_5 and C_6 species in a benzene flame, including the new reaction pathways (bold arrows) deduced from this study.

marginal H absorption was detectable, indicating a global rate constant that is at least a factor of 50 smaller than k_4.

The measured ratio $[CO]_{end}/[C_6H_4O_2]_0 = 1.0 \pm 0.1$ between 1550 and 1900 K and the very slow H-atom production points to a rather high thermal stability of the product C_5H_4O at $T \leq 1900$ K.

Conclusions

From CO measurements during the thermal decay of phenoxy, it was verified that the formation of cyclopentadienyl and CO (reaction (R3)) is the main pathway, which proceeds in the investigated temperature interval by a factor of about 3 faster compared with the results of Lin and Lin [11].

The present experimental data indicate that in the reaction system of phenyl radicals with molecular oxygen, two product channels occur with a branching ratio of about 3 to 1 for R1/R2 in the temperature regime 1000–1500 K. A plausible hypothesis for the H-atom channel is presented.

An uncertainty of ±30% was estimated for the rate coefficient of

$$C_6H_5 + O \rightarrow C_5H_5 + CO \qquad \text{(R5)}$$

which was deduced from modeling the O-atom profiles.

The above scheme (Fig. 12) shows qualitatively the reaction routes of phenyl radicals as deduced from the present results. It is expected that the chemical kinetic data, evaluated in the present study (see Table 1), may improve in particular the attempts to model benzene and similar flames, as carried out recently by Chevalier and Warnatz [21], and the modeling of PAH and soot formation in flames.

Acknowledgments

The authors wish to thank N. Ackermann, M. Kallfass, and M. Kapernaum for technical assistance and for analyzing the radical precursors. We are also grateful to the Commission of the European Communities and the German-Israeli-Foundation for financial support.

REFERENCES

1. Braun-Unkhoff, M., Frank, P., and Just, Th., *Twenty-Second Symposium (International) on Combustion,* The Combustion Institute, Pittsburgh, 1988, pp. 1053–1061.
2. Braun-Unkhoff, M., Frank, P., and Just, Th., *Ber. Bunsenges. Phys. Chem.* 94:1417–1425 (1990).
3. Frenklach, M., Clary, D. W., Gardiner, W. C., Jr., and Stein, S. E., *Twenty-First Symposium (International) on Combustion,* The Combustion Institute, Pittsburgh, 1986, pp. 1067–1076.
4. a) Fahr, A., Mallard, W. G., and Stein, S. E., *Twenty-First Symposium (International) on Combustion,* The Combustion Institute, Pittsburgh, 1986, pp. 825–831. b) Fahr, A., and Stein, S. E., *Twenty-Second Symposium (International) on Combustion,* The Combustion Institute, Pittsburgh, 1988, pp. 1023–1029.
5. Herzler, J., and Frank, P., *Ber. Bunsenges. Phys. Chem.* 96:1333–1338 (1992).
6. Frenklach, M., Clary, D. W., Gardiner, W. C., Jr., and Stein, S. E., *Twentieth Symposium (International) on Combustion,* The Combustion Institute, Pittsburgh, 1984, pp. 887–901.
7. Frank, P., and Just, Th., *Ber. Bunsenges. Phys. Chem.* 89:181–187 (1985).
8. Frank, P., and Braun-Unkhoff, M., *Sixteenth International Symposium on Shock Tubes and Shock Waves,* VCH, Weinheim, 1987, pp. 379–385.
9. Frank, P., Bhaskaran, K. A., and Just, Th., *Twenty-First Symposium (International) on Combustion,* The Combustion Institute, Pittsburgh, 1986, pp. 885–893.
10. Brezinsky, K., *Prog. Energ. Combust. Sci.* 12:1–24 (1986).
11. Lin, C. Y., and Lin, M. C., *J. Phys. Chem.* 90:425–431 (1986).
12. Baulch, D. L., Cobos, C. J., Cox, R. A., Esser, C., Frank, P., Just, Th., Kerr, J. A., Pilling, M. J., Troe, J., Walker, R. W., and Warnatz, J., *J. Phys. Chem. Ref. Data* 21:411–734 (1992).
13. Lifshitz, A., Tamburu, C., Frank, P., and Just, Th., *J. Phys. Chem.* 97:4085–4090 (1993).
14. Mackie, J. C., Doolan, K. R., and Nelson, P. F., *J. Phys. Chem.* 93:664–670 (1989).
15. Suryan, M. M., Kalafi, S. A., and Stein, S. E., *J. Am. Chem. Soc.* 111:1423–1429 (1989).

16. Colussi, A. J., Zabel, F., and Benson, S. W., *Int. J. Chem. Kinet.* 9:161–178 (1977).
17. Lin, C. Y., and Lin, M. C., "Eastern States Section of the Combustion Institute," Paper No. 7, 7/1–7/4, 1987.
18. Louw, R., University of Leiden, Netherlands, private communication, 1993.
19. Baldwin, R. R., Scott, M., and Walker, R. W., *Twenty-first Symposium (International) on Combustion,* The Combustion Institute, Pittsburgh, 1986, pp. 991–1000.
20. Hoyermann, K., University of Göttingen, Germany, private communication, 1993.
21. Chevalier, C., and Warnatz, J., *Prepr. Div. Fuel Chem. Am. Chem. Soc.* 36:1486–1493 (1991).
22. Benson, S. W., *Thermochemical Kinetics,* J. Wiley, New York, 1976.
23. Melius, C. F., *Heats of Formation,* Sandia Report BAC-MP4, Sandia National Laboratories, Livermore, USA, 1993.

COMMENTS

M. C. Lin, Emory University, USA. In your kinetic modeling of O and H concentration profiles, did you include the reverse reactions of all processes considered? We attempted to simulate the H profiles with your mechanism; we could not duplicate the profiles until the reverse reactions were included. Specifically, I am concerned about the effectiveness of $H + C_5H_5 \rightarrow C_5H_6$ as a radical termination step.

Author's Reply. In the simulation calculations, the reverse reactions of all processes were always included. The difference between your and our modeling of the H profiles results from using different values for the heat of formation of the cyclopentadienyl radical. The value you used is about 6 kcal/mol lower than our data for $\Delta H_f^\circ = 63.6$ kcal/mol [1]. Therefore, using your data, the equilibrium is at the $C_5H_5 + H$ side, so that the reaction of cyclopentadienyl + H (which is the most important H-consuming reaction of $T \leq 1320$ K) in our simulation of the phenyl + O_2 system yields higher H concentrations. However, our measurements of cyclopentadiene decomposition [2] show good agreement with the data calculated from the higher value for the heat of formation of the cyclopentadienyl radical.

REFERENCES

1. Burcat, A., Zeleznik, F. J., and McBride, B. J., NASA TM-83800, 1985.
2. Herzler, J., unpublished results.

•

Tibor Berces, Hungarian Academy of Sciences, Hungary. You determined concentration-time profiles for H, O, and CO. Did you attempt to fit all three types of profiles simultaneously with one set of kinetic parameters?

Author's Reply. Only H- and O-atom profiles were measured simultaneously in the phenyl + O_2 experiments. We were able to fit the H and O profiles of each experiment simultaneously with one set of kinetic parameters. CO concentrations have not been measured in all experiments because the CO-MRAS method is about one order of magnitude less sensitive. In this case, definitely higher initial concentrations would have been used, and the modeling would have been much more complicated due to the increasing influence of subsequent reactions.

Twenty-Fifth Symposium (International) on Combustion/The Combustion Institute, 1994/pp. 841–849

REACTIONS OF PHENOXY RADICALS IN THE GAS PHASE

RAINER BUTH, KARLHEINZ HOYERMANN AND JOHANN SEEBA
Institut für Physikalische Chemie
Universität Göttingen
Tammannstr. 6, D-37077 Göttingen, Germany

The mechanisms and rates of the formation and the reactions of the phenoxy radical with atoms and radicals in the gas phase have been studied at room temperature (around 295 K) and low pressure (1–5 mbar) using the discharge flow technique. Samples were withdrawn continuously by a molecular-beam-sampling system coupled to a mass spectrometer with electron impact ionization for a specific and sensitive detection by applying low ionization energy and single-ion counting.

Phenoxy radicals were produced by the reaction of phenol with chlorine atoms

$$C_6H_5OH + Cl \rightarrow C_6H_5O + HCl \tag{1}$$

and the rate coefficient k_1 was determined to be

$$k_1 = (1.43 \pm 0.25) \cdot 10^{14}\ \mathrm{cm^3/mol\ s}$$

(relative to the reference reaction $C_2H_6 + Cl$, $k_0 = 3.4 \cdot 10^{13}$ cm³/mol s).

Phenoxy radicals react with atoms according to

$$C_6H_5O + O \rightarrow C_6H_4O_2\ (\text{quinone}) + H \tag{2a}$$

$$\rightarrow C_5H_5 + CO_2 \tag{2b}$$

with reaction (2a) being the main pathway, and a rate coefficient of

$$k_2 = (1.68 \pm 0.35) \cdot 10^{14}\ \mathrm{cm^3/mol\ s}$$

(measured relative to the standard reaction (01) $C_2H_5 + O$, $k_{01} = 1.31 \cdot 10^{14}$ cm³/mol s) and

$$C_6H_5O + H \rightarrow C_6H_6O/C_6H_5OH \tag{3}$$

with C_6H_6O being cyclohexadienone, and a rate coefficient

$$k_3 = 4 \cdot 10^{13}\ \mathrm{cm^3/mol\ s}.$$

(The reference reaction was (02) $C_2H_5 + H$, $k_{02} = 3.6 \cdot 10^{13}$/mol s, and the ratio of the rate constants was determined as $k_3/k_{02} = 1.12 \pm 0.03$.)

Phenoxy radicals combine with the alkyl radicals C_2H_5 and CH_3 in two different pathways with comparable efficiency:

$$C_6H_5O + C_2H_5 \rightarrow C_6H_5OC_2H_5\ (\text{phenetol}) \tag{4a}$$

$$\rightarrow C_2H_5C_6H_4OH\ (\text{ethylphenol}) \tag{4b}$$

$$C_6H_5O + CH_3 \rightarrow C_6H_5OCH_3\ (\text{anisol}) \tag{5a}$$

$$\rightarrow CH_3C_6H_4OH\ (\text{cresol}) \tag{5b}$$

((4a):(4b) = 63:37; (5a):(5b) = 59:41.)

The combination reaction of phenoxy radicals is fast:

$$C_6H_5O + C_6H_5O \rightarrow (C_6H_5O)_2$$

$$k_6 = (2 + 2/-1) \cdot 10^{13}\ \mathrm{cm^3/mol\ s} \tag{6}$$

Introduction

The phenoxy radical is one of the key radicals in the oxidation of aromatics and the pyrolysis of partially oxidized aromatic compounds in the gas phase. In the context of the combustion of aromatics, this may be exemplified by the chemical mechanisms—discussed in the literature—for the conversion of fuels to final products in hot reaction zones. The oxidation of the classical aromatic compound, benzene, at high temperature is initiated by a hydrogen atom abstraction via atoms (O,H) and radicals (OH,CH_3) leading to the phenyl radical C_6H_5. At low temperatures, the complex-forming reaction $C_6H_5 + O_2 \rightarrow C_6H_5O_2$ is slow, whereas at higher temperatures, the chain reaction $C_6H_5 + O_2 \rightarrow C_6H_5O + O$ dominates, thus asking for kinetic data on the further reactions of the phenoxy radicals. (For a review of the high-temperature oxidation of aromatic hydrocarbons, see Refs. 1 and 2.) The decomposition of the phenyl-alkyl ethers and phenols, being present as products in the oxidation of side-chain-substituted benzenes, have been studied extensively, especially with respect to the heat of formation of the primarily formed phenoxy radical [3–9]. The most recent values of the heat of formation of the phenoxy radicals range from 40.4 kJ/mol [10] to 55.3 kJ/mol [9]. Direct studies of the elementary reactions of the phenoxy radicals in the gas phase are scarce. The thermal decomposition of the radical ($C_6H_5O \rightarrow c\text{-}C_5H_5 + CO$) shows an interesting mechanism of CO elimination under ring contraction by the formation of the cyclopentadienyl radical [3,4]. The interaction of the phenoxy radical with hydrogen atoms and methyl radicals are described as a combination to yield phenol [6] (by $C_6H_5O + H \rightarrow C_6H_5OH$) and cresols [11,12,4,5,6,8] ($C_6H_5O + CH_3 \rightarrow C_6H_4CH_3OH$) and ether [11,12] ($C_6H_5O + CH_3 \rightarrow C_6H_5OCH_3$). The structure of the phenoxy radical can be presented by different limiting mesomeric structures, chemically seen as an oxygen-centered and/or a carbon-centered radical. Naturally, the phenoxy radical has only one definite molecular structure, but the reactions of the phenoxy radicals with an alkyl radical (as derived from the complex reaction systems of phenol and hydrochinon oxidation [11,12] or pyrolysis [8]) show formation of phenyl alkyl ethers as well as alkyl substituted phenols. This is described in a shorthand notation simply via an oxygen-centered as well as a carbon-centered phenoxy radical, which facilitates the construction of reduced chemical reaction mechanisms incorporated increasingly in combustion modelling.

The objectives of this study are (1) to establish a phenoxy radical source via the reaction of phenol with chlorine atoms for high radical concentrations in the study of product formation in subsequent (radical + atom) reactions, (2) to determine the rate coefficients for the formation reaction of phenoxy radicals, and, for the reactions of phenoxy radicals with hydrogen and oxygen atoms, (3) to ascertain the primary products of the phenoxy radical reactions and to elucidate mechanistic concepts (oxygen- and/or carbon-centered radical).

Experimental

The experimental arrangement consists of a combination of two conventional discharge flow reactors, a molecular-beam sampling system, a mass spectrometer, and a gas preparation and handling system. As the parts of the apparatus have been assembled from two different experimental arrangements, both described in previous combustion symposia [13,14], only the essentials are summarized. The phenoxy radicals were produced at low pressure (0.5–10 mbar) and low temperature (290–300 K) in a flow reactor A (inner diameter: 20 mm), where Cl atoms (from a microwave discharge in Cl_2/He mixtures) were mixed with a phenol/He flow by a movable inlet probe. This inner discharge flow reactor A was surrounded by a second discharge flow reactor B (inner diameter: 40 mm), where the atoms H, D, O, and F were produced by discharging highly diluted mixtures of H_2/He, D_2/He, O_2/He, and F_2/He, respectively, and the radicals CH_3 or C_2H_5 by the subsequent reactions of F atoms with CH_4/He or C_2H_6/He. In order to meet the experimental conditions for the residence times in the kinetic and the product formation studies, the linear flow velocities (5–50 m/s) and the admixture points of the different reactants were varied independently. The actual concentrations are given in the figure captions. Reliable and reproducible results could be obtained only by frequent and careful cleaning of the arrangement of flow reactors, as to be expected in the work with aromatic compounds.

Samples were withdrawn continuously by a molecular-beam sampling system, differentially pumped by two large diffusion pumps (2 × 2000 L/s), and were crossing the electron impact (EI) ion source of a mass spectrometer (pumped by a 450 L/s turbomolecular pump). A specific detection of labile and stable species was performed either by the mass spectrum at low-energy electron-impact ionization, by the mass spectrum with the fragmentation pattern of the parent ion, or by a high-resolution mass spectrum. A sensitive detection was realized by conventional (analog) direct current (dc) amplification, by (digital) single-ion counting, and by synchronous (reaction "on"/"off") ion counting.

The gas mixtures were prepared by mass flow controllers from commercially available chemicals. Constant flows of phenol/He were obtained by passing He through a long pipe filled with highly dispersed phenol on glass wool as the support. The purity of the chemicals was He (99.996%), H_2 (99.996%), D_2

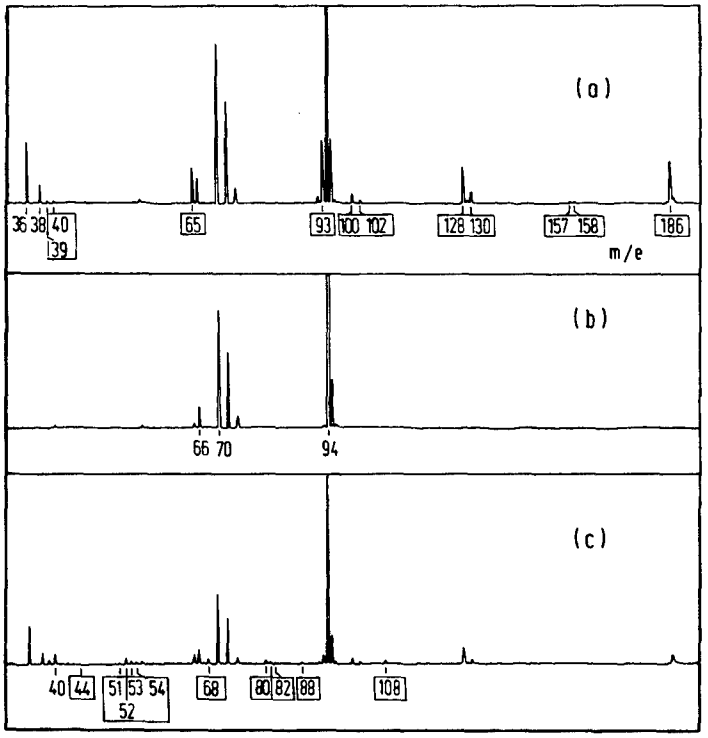

FIG. 1. Mass spectra of the products of the reactions $C_6H_5OH + Cl \rightarrow C_6H_5O + HCl$ and $C_6H_5O + O \rightarrow$ products: (a) $C_6H_5OH + Cl$, reaction (1) (p = 2.7 mbar, 295 K; $[C_6H_5OH]_0 = 2 \cdot 10^{-10}$ mol/cm^3; $[Cl]_0 = 5 \cdot 10^{-11}$ mol/cm^3; residual $[Cl_2]_0 > [Cl]_0$); m/e in boxes: parent ions and fragment ions of products; (b) $C_6H_5OH + Cl_2$: background; and (c) $C_6H_5O + O$, reaction (2) (m/e in boxes: parent ions and fragment ions from reaction (2); mass spectrometer: electron impact ionisation, 17.5 eV).

(99.7%), Cl_2 (99%), F_2 (99%), O_2 (99.995%), CH_4 (99.99%), C_2H_6 (99%), and Phenol (99.5%).

Results

Phenoxy Radical Formation: The Reaction C_6H_5OH + Cl:

The hydrogen atom abstraction of the OH group in phenol by Cl atoms is exothermic by $\Delta_r H^\circ$ (298) = −70 kJ/mol;

$$C_6H_5OH + Cl \rightarrow C_6H_5O + HCl \qquad (1)$$

whereas substitution reactions

$$C_6H_5OH + Cl \rightarrow C_6H_5Cl + OH$$

$$C_6H_5OH + Cl \rightarrow C_6H_4ClOH + H$$

are endothermic (+47 and 68 kJ/mol, respectively). Therefore, reaction (1) was studied with respect to being a possible source for phenoxy radicals.

In Fig. 1a, a mass spectrum of the reaction products of reaction (1), together with the unreacted reactants and the products from subsequent reactions, is shown for an excess of C_6H_5OH over Cl atoms and residual Cl_2 molecules. A moderately low ionization energy (17.5 eV) was chosen in order to avoid a complex mass spectrum due to ion fragmentation. The m/e values, characteristic for products of reaction (1), are shown in boxes in Fig. 1a, and those for $C_6H_5OH + Cl_2$ (background) in Figure 1b, are shown for comparison. Phenoxy radicals are detected directly at the parent ion at m/e = 93 (not obscured by a fragment ion of the excess of C_6H_5OH) and a fragment ion at m/e = 65, which is further suppressed by working at lower ionization energies. A prominent product mass peak is found at m/e = 186, attributed to a recombination product $(C_6H_5O)_2$. The signals at the mass peak at m/e = 128/130 show the intensity ratio (3:1) of the chlorine isotopes $^{35}Cl/^{37}Cl$, pointing to the formation of C_6H_5OCl along the reaction

$$C_6H_5O + Cl_2 \rightarrow C_6H_5OCl + Cl.$$

This was substantiated by the addition of increasing amounts of molecular Cl_2, leading to an increase of signals at m/e = 128/130 at the expense of the $(C_6H_5O)_2$ dimer. (The structure of the formed product, described by the formula C_6H_5OCl, is attributed to p-chlorophenol on the basis of the ion fragmentation pattern of o-, m-, p-chlorophenol at different ionization energies. This $C_6H_5O + Cl_2$ reaction is out of the scope of this paper.)

Small ion signals at m/e = 157/158; m/e = 100/102; m/e = 39/40 cannot be explained unam-

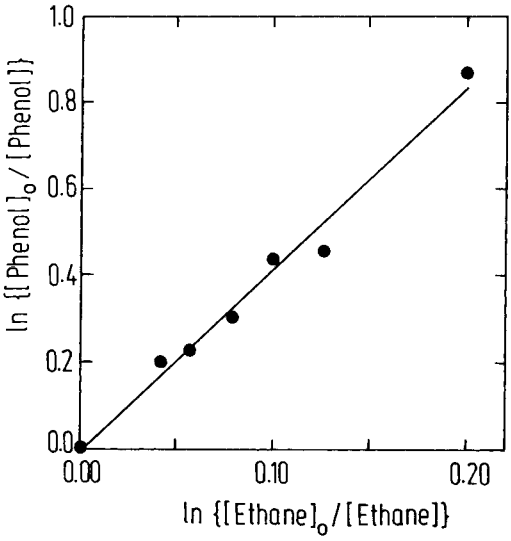

FIG. 2. Ratio of the rate constants of reaction (1) $C_6H_5OH + Cl \rightarrow C_6H_5O + HCl$ and reaction (0) $C_2H_6 + Cl \rightarrow C_2H_5 + HCl$. (Experimental conditions: $p = 2.7$ mbar, 295 K; $[C_6H_5OH]_0 = (1\text{–}20) \cdot 10^{-11}$ mol/cm^3; $[C_2H_6]_0 = (2\text{–}5) \cdot 10^{-10}$ mol/cm^3; mass spectrometer: electron impact ionisation at 17 and 22 eV.)

biguously. It is assumed that fragment ion formation of the unknown structure of the dimer $(C_6H_5O)_2^+ \rightarrow C_{11}H_{10}O^+$ ($m/e = 158$) + CO gives rise to $m/e = 158$, as CO elimination is a common ion fragmentation route in aromatic oxygenated ions. (This is also assumed for $m/e = 100/102$ along $C_6H_5ClO^+ \rightarrow C_5H_5Cl^+$ ($m/e = 100/102$) + CO.)

The rate constant of reaction (1) was measured relative to the standard reaction

$$C_2H_6 + Cl \rightarrow C_2H_5 + HCl. \qquad (0)$$

In the absence of secondary reactions (i.e., no reformation of C_6H_5OH and C_2H_6 and no additional attack on C_6H_5OH or C_2H_6 by products of the reactions (0) and (1), the ratio of the rate constants follows from the relative consumption of C_6H_5OH and C_2H_6 in the presence and the absence of Cl atoms (see Ref. 13):

$$k_1 = k_0 \cdot \ln\{[C_6H_5OH]_0/[C_6H_5OH]\} \div \ln\{[C_2H_6]_0/[C_2H_6]\}.$$

The experimental results are shown in Fig. 2, where the data points are averaged values (from 3 to 5 measurements), the size of the data points reflects approximately one standard deviation reproducibility, and the slope by a linear regression analysis (95% confidence level) is deduced as 4.22 ± 0.42. Adopting the recommended rate constant of reaction (0) ($k_0 = (3.4 \pm 0.5) \cdot 10^{13}$ cm^3/mol s [15]), the absolute value of k_1 is obtained

$$k_1 = (1.43 \pm 0.14) \cdot 10^{14} \text{ cm}^3/\text{mol s}.$$

As the reference reaction (0) is given an uncertainty of $\pm 15\%$ in the recommendation [15], and as our measured confidence interval is $\pm 10\%$, an overall error of 18–20% seems to be realistic;

$$k_1 = (1.43 \pm 0.25) \cdot 10^{14} \text{ cm}^3/\text{mol s}.$$

Thereby, the reaction of phenol with chlorine atoms is a suitable source for phenoxy radicals, as the reaction is fast and shows only formation of phenoxy in a single-reaction channel.

The Reaction $C_6H_5O + O$:

The reaction of phenoxy radicals with oxygen atoms was studied with respect to the formation of products at high and low excess of phenoxy radicals over oxygen atoms and at different mass spectrometric detection conditions (ionization energy). In Fig. 1c, only one example is given as an illustration for the formation of products (m/e in boxes). Moreover, the suppression of the typical phenoxy radical self-reaction is obvious by comparing Figs. 1c and 1a (phenoxy radical production).

The results of the product formation studies are summarized by the reaction scheme

$$C_6H_5O + O \rightarrow C_6H_4O_2 + H \qquad (2a)$$

$$\rightarrow C_5H_5 + CO_2. \qquad (2b)$$

The benzoquinone (presumably 1,4-$C_6H_4O_2$) was identified by its cracking pattern at high ionization energy (70 eV; $m/e = 108$, 54, 82, and 80) and c-C_5H_5 [cyclopentadienyl radical at low ionization energy (15 eV, $m/e = 65$)] and by the study of the secondary reactions c-$C_5H_5 + O$, leading finally to CO and C_2H_2. (The reaction of c-$C_5H_5 + O$ was studied separately and will be published elsewhere.) The calibration of the reaction channels (a) and (b) by the quantitative and simultaneous determination of the consumption of the C_6H_5O radical and the formation of $C_6H_4O_2$, C_5H_5, and CO_2 was incomplete, as only a 35% recovery rate could be established. As CO_2 was detected, only as a minor component (compared to $C_6H_4O_2$: below 15%), and as CO_2 is not absorbed at the reactor wall, reaction (2a) is assigned as the major channel.

The rate constant of reaction (2) was measured relative to reaction (01):

$$C_2H_5 + O \rightarrow \text{products}. \qquad (01)$$

The experimental conditions were chosen such that the C_2H_5 radicals, formed by

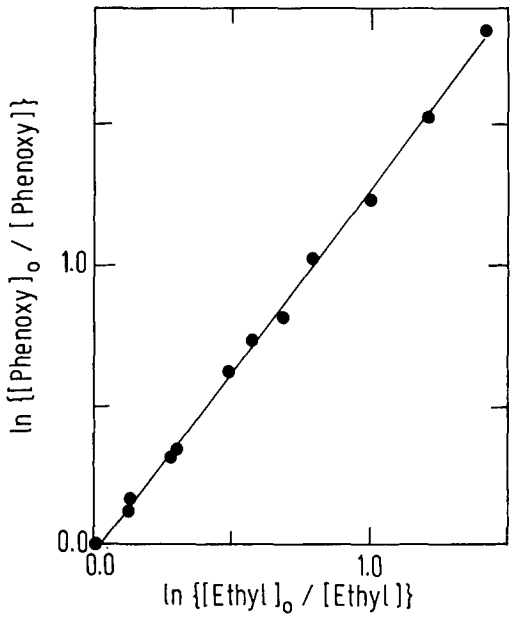

FIG. 3. Ratio of the rate constants of reaction (2) $C_6H_5O + O \rightarrow$ products and reaction (01) $C_2H_5 + O \rightarrow$ products. (Experimental conditions: p = 2.5 mbar, 295 K; $[C_6H_5O]_0 = (0.5\text{–}1) \cdot 10^{-11}$ mol/cm^3; $[C_2H_5]_0 = (0.5\text{–}1) \cdot 10^{-11}$ mol/cm^3; $[O]_0 = (1\text{–}5) \cdot 10^{-11}$ mol/cm^3; mass spectrometer: electron impact ionization at 13.2 and 14.5 eV.)

$$C_2H_6 + Cl \rightarrow C_2H_5 + HCl$$

did not recombine or combine with phenoxy radicals. In Fig. 3, the relative consumption of the C_6H_5O and C_2H_5 by the reaction with oxygen atoms is displayed, from which the relative rate constant is derived simply by the equation

$$k_2 = k_{01} \cdot \ln\{[C_6H_5O]_0/[C_6H_5O]\} \div \ln\{[C_2H_5]_0/[C_2H_5]\}$$

($[C_6H_5O]_0$ and $[C_2H_5]_0$ denote the concentrations in the absence of O atoms, and $[C_6H_5O]$ and $[C_2H_5]$ denote the concentrations, in the presence of O atoms). A linear regression analysis (95% confidence level) yields the expected straight line that intercepts the origin with a slope of 1.28 ± 0.03. Using the reported rate constant for the reaction (01) $k_{01} = (1.31 \pm 0.24) \cdot 10^{14}$ cm^3/mol s [16], the absolute value k_2 is derived:

$$k_2 = (1.68 \pm 0.04) \cdot 10^{14} \text{ cm}^3/\text{mol s}.$$

The small error margin of 3% reflects only the reproducibility. Considering systematic errors and the uncertainty of the rate constant k_{01} (18%), a value with a 20% error seems to be realistic:

$$k_2 = (1.68 \pm 0.35) \cdot 10^{14} \text{ cm}^3/\text{mol s}.$$

The Reaction C_6H_5O + H/D:

The mechanism of the reaction of phenoxy radicals with hydrogen atoms was deduced from the identification of the products by the different ion fragmentation patterns and by the use of deuterium atoms. Postulating two reaction sites of the phenoxy radical (oxygen-centered, carbon-centered) in the course of the reaction with hydrogen atoms, two different products are to be expected:

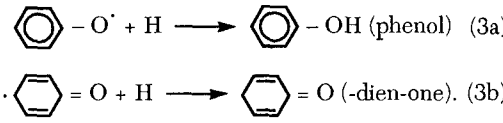

As the C_6H_5O radicals were produced via C_6H_5OH (reaction (1)) and as the C_6H_5O radicals react very fast with H atoms by combination (C_6H_5OH/C_6H_6O), a sensitive phenol product identification was feasible (consumption of phenol, reaction (1), vs formation of phenol, reaction (3a). This is exemplified by Fig. 4. In Fig. 4c, the mass spectrum of phenol is shown: m/e = 95 ($^{13}CC_5H_5OH$); m/e = 66 from ion fragmentation $C_6H_5OH^+ \rightarrow C_5H_6^+ + CO$; no m/e = 93. In Fig. 4b, the additional mass spectrum of the phenoxy radical (besides the residual phenol) is shown: m/e = 93 (parent ion of phenoxy) m/e = 65 from the ion fragmentation $C_6H_5O^+$ (m/e = 93) $\rightarrow C_5H_5^+$ (m/e = 65) + CO. The results for the reaction with D atoms,

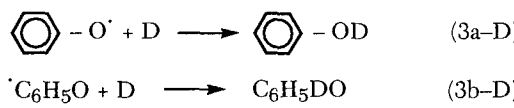

are given in Fig. 4a: phenoxy radicals (m/e = 93, 65) are consumed; products [m/e = 95 ($C_6H_5OD^+/C_6H_5DO^+$) and m/e = 67 ($C_5H_5D^+$)] are formed. But the fingerprint of the deuterated phenol C_6H_5DO, ion abundance ratio (m/e = 95) (m/e = 67) about 16:1, is not observed in the product(s), as a much higher ion intensity is observed at m/e = 67; the analysis with corrections of the phenoxy contribution yields a ratio of (m/e = 95)/(m/e = 67) about 2:1. These experimental findings rule out reaction (3a) as the only channel of reaction (3). The formation of cyclohexadienone (reaction of a carbon-centered C_6H_5O radical) and its assignment to the mass spectra of Fig. 4 is based on the high ion signal at m/e = 67 ($C_5H_5D^+$) (m/e = 66 ($C_5H_6^+$) if normal hydrogen atoms are used for reaction (3)). No mass spectrum of the *c*-hexadienone is available for a direct product identification. But, it is known that the phenolic ion $C_6H_5OH^+$ and the cyclohexadienone ion $C_6H_6H^+$ have different ion structures, as they

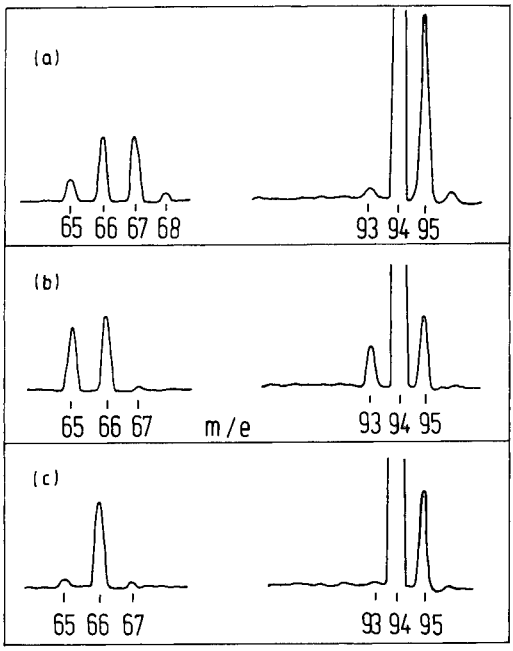

FIG. 4. Mass spectra of the products of reaction (3b–D): $C_6H_5O + D \rightarrow C_6H_5DO/C_6H_5OD$: (a) the reaction $C_6H_5O + D \rightarrow C_6H_5DO/C_6H_5OD$ (discharge "Cl_2/He" on: phenoxy radicals present; discharge "D_2/He" on: D atoms present); (b) reaction (1) $C_6H_5OH + Cl \rightarrow C_6H_5O + HCl$ (discharge "Cl_2/He" on: phenoxy radicals present; discharge "D_2/He" off: no D atoms present); and (c) background: $C_6H_5OH + Cl_2 + D_2$ (both discharges off) (mass spectrometer: 16.5 eV).

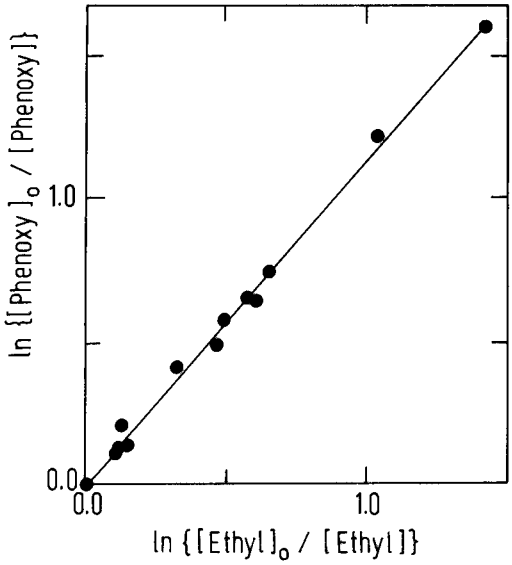

FIG. 5. Ratio of the rate constants of reaction (3) $C_6H_5O + H$ and reaction (02) $C_2H_5 + H$.

show a different mass spectrometric fragmentation pattern with a more frequent decomposition of $C_6H_6O^+$ to $C_5H_6^+ + CO$ than the phenolic ion $C_6H_5OH^+$. (See for example Refs. 17 and 18.) As no absolute mass spectrometric sensitivity for the cyclohexadienone and no quantitative ion abundance at $m/e = 94$ (interference with phenol, $m/e = 94$) is known, no branching ratio of the reaction channels (3a) : (3b) can be derived, but the presence of channel (3b) is obvious.

The rate constant of reaction (3) was determined with respect to the reference reaction

$$C_2H_5 + H \rightarrow 2CH_3. \qquad (02)$$

The measured relative consumptions of the C_6H_5O and the C_2H_5 radicals for different H-atom concentrations are shown in Fig. 5. A linear regression analysis gives the expected straight line through the origin and a slope of (1.12 ± 0.033) (95% confidence level). Adopting the recommended value [19] of the rate constant $k_{02} = 3.6 \cdot 10^{13}$ cm^3/mol s (with an uncertainty factor of 3), the room temperature value of k_3 is given by

$$k_3 = (4.04 \pm 0.12) \cdot 10^{13} \text{ cm}^3/\text{mol s}.$$

As the uncertainty of the reference reaction is high compared to reproducibility of our measurement (3%), no realistic error margins to the absolute rate constant k_3 can be assigned.

No reactions like the isotopic exchange reaction

$$C_6H_5OH + D \rightarrow C_6H_5OD/C_6H_4DOH + H$$

and the Cl_2 attack

$$C_6H_5OH + Cl_2 \rightarrow \text{products}$$

were observed under our experimental conditions.

The competing reaction

$$H + Cl_2 \rightarrow HCl + Cl$$

(small amounts of Cl_2 from incomplete dissociation and by wall recombination) does not influence the determination of the products of reaction (3). For the measurements of the relative rate constants (k_3/k_{02}), low absolute concentrations were applied, and the influence of increasing amounts of Cl_2 addition on these measurements were studied independently. Simulations of the influence of secondary reactions and of competing reactions (like $H + Cl_2$) and of wall reactions ($k_w(C_6H_5O) = 300$–800 s^{-1}) lead to corrections of k_3 below 10%.

The products of the reference reaction (02) at low pressure are $2CH_3$ radicals (see Ref. 14). As the products of the reactions $C_2H_5 + C_6H_5O$ (4) and $CH_3 + C_6H_5O$ (5) are known from our independent study (see below), the suppression of these competing reactions could be verified experimentally.

The Reactions $C_6H_5O + C_2H_5/CH_3$:

The reactions of phenoxy radicals with ethyl and methyl radicals were studied with respect to the formation of products stemming from a C—O and/or C—C linkage:

$$C_6H_5O. + C_2H_5 \rightarrow C_6H_5OC_2H_5 \text{ (phenetol)} \quad (4a)$$

$$.C_6H_5O + C_2H_5 \rightarrow C_2H_5C_6H_4OH \text{ (ethylphenol).} \quad (4b)$$

The assignment of the products of reactions (4b) and (5b) to ethylphenol and cresol, respectively, follows the work of Refs. 11 and 12, as no mass spectra of the alternate products ethyl- and methyl-hexadienone, respectively, were at hand. (Possible isomerization reactions are not the topic of this paper.)

The mass spectra of the different ethylphenols (2-(ortho), 3-(meta), 4-(para)-ethyl-phenol) are similar but different from the phenyl-ethyl-ether (phenetol), especially at the masses m/e = 107 and 122. In Fig. 6a, the mass spectrum of products of reaction (4) is shown together with the mass spectra of the pure substances 2-ethylphenol (Fig. 6b) and phenetol (Fig. 6c). An equimolar mixture of 2-ethylphenol and phenetol in the gas phase was prepared by mixing 9.7-g ethylphenol with 1.54-g phenetol in a thermostated saturator (25 °C) and was analyzed mass spectrometrically (see Fig. 6d). A comparison between the reaction products (Fig. 6a) and the mixture (Fig. 6d) shows the presence of comparable amounts of the ether and the phenol. The quantitative evaluation leads to a ratio of the product channels (reaction (4a):(4b)) of 63:37% with error margins of (57–70):(43–30). They are mainly due to the calculation of the gas-phase composition from the data of the pure substances, assuming nearly ideal solution behavior with small corrections [20].

Similar results were obtained for the reaction with methyl radicals:

$$C_6H_5O. + CH_3 \rightarrow C_6H_5OCH_3 \text{ (anisol)} \quad (5a)$$

$$.C_6H_5O + CH_3 \rightarrow CH_3C_6H_4OH \text{ (cresol).} \quad (5b)$$

The evaluation was based on the ion signals at the noninterfering masses m/e = 107 and 108 for the products, the anisol, the cresol, and the equimolar mixture of anisol/cresol. Here, the channel ratio (5a):(5b) of 59% (±5):41% (±4) was deduced.

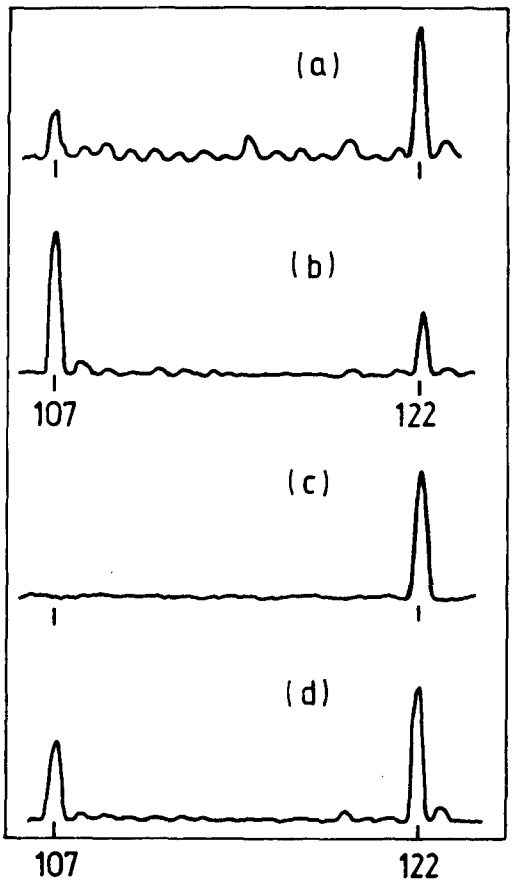

FIG. 6. Mass spectra of the products of reaction (4) $C_6H_5O + C_2H_5 \rightarrow C_6H_5OC_2H_5/C_6H_4(C_2H_5)OH$: (a) reaction (4) products (discharge A "Cl_2/He" on and C_6H_5OH addition: phenoxy radicals present; discharge B "Cl_2/He" on and C_2H_6 addition: ethyl radicals present); (b) mass spectrum of 2-ethylphenol (2-ethyl-2-hydroxy-benzene); (c) mass spectrum of phentole (ethoxy-benzene); and (d) mass spectrum of an equimolar gas mixture of 2-ethylphenol and phenetole.

The Reaction $C_6H_5O + C_6H_5O$:

By the combination of phenoxy radicals (a striking feature in Fig. 1a), a dimer is formed whose structure could not be elucidated. No characteristic fragment ions with high intensity (besides those from phenol and phenoxy) could be detected. Moreover, a search for trimers and tetramers was negative, but, as stated in the experimental section, polymeric material was easily formed.

The rate of the combination reaction

$$C_6H_5O + C_6H_5O \rightarrow (C_6H_5O)_2 \quad (6)$$

was determined indirectly by adding increasing

amounts of oxygen atoms (reaction (3)) at a constant reaction time. The consumption of the C_6H_5O radicals and the increasing suppression of the $(C_6H_5O)_2$ concentration was measured by the mass spectrometer as a function of the oxygen concentration. A numerical integration of the rate equations including reactions (6) and (3) (wall recombination) was performed. This leads to a rate constant of

$$k_6 = (2 + 2/-1) \cdot 10^{13} \text{ cm}^3/\text{mol s}.$$

The large error margin reflects the uncertainty in the phenoxy wall loss reaction.

Discussion

The reactive structure of the phenoxy radical is presented by simplification both as an oxygen-centered and a carbon-centered (ortho, para) radical, when considering the primary products of the reactions with atoms (H and O) and radicals (CH_3 and C_2H_5). The hydrogen-atom addition reaction (2) (abstraction/elimination reactions are endothermic) leads also to the cyclohexadienone reaction (2b) and, thereby, does not represent in total the reverse reaction of phenol decomposition (C_6H_5O + H). The methyl radical addition (5) shows also two pathways. This has been derived by Mulcahy and Williams [11,12] from the study of C_6H_5OH + CH_3 too, where the reactions at the para and the ortho site and less at the oxygen site were assigned from a final product analysis by vapor-phase chromatography. The oxygen-atom reaction (3) is understood mechanistically by addition to the ortho or para carbon atom, forming the highly excited adduct, which decomposes to form quinone + H; the addition to the oxygen site, followed by the dissociation to phenyl + O_2, is endothermic. For the self-reaction of phenoxy radicals in the liquid phase, the C-C linkage is the major and the C-O linkage is the minor pathway. The reactions of phenoxy radicals in the liquid phase may not be compared directly to the gas phase, but for mechanistic studies, see for example Refs. 21 and 22–24.

The rate constant k_3 has been estimated by He et al. [6] from the phenol decomposition and the absence of a temperature dependence of k_3 to be $2.5 \cdot 10^{14}$ cm^3/mol s. The discrepancy to our value (factor 6) is not severe considering the assumptions involved [reaction mechanism, only reaction (3a); no temperature dependence for the extrapolation to 300 K; uncertainty in H_f° (C_6H_5O)].

It has to be stressed that the results (rates and products) have been determined experimentally at low pressure (around 1 mbar) and low temperature (around 300 K). Nevertheless, these findings on the radical + atom/radical interactions are relevant to combustion situations (low temperature and ignition), where the radical decomposition (i.e., $C_6H_5O \rightarrow C_5H_5$ + CO) is not a main radical sink. No large pressure dependence of k_3 is to be expected, considering the large number of degrees of freedom in the combination products C_6H_5OH/C_6H_6O. (This is similar to the reaction C_7H_7 + H $\rightarrow C_7H_8$ [25,26].) As reaction (2) is highly exothermic at 300 K, a similar elementary reaction is to be expected at higher temperature (i.e., 1000 K). Nevertheless, high-temperature studies would complement the low-temperature measurements.

Acknowledgments

The continued interest of Professor H. Gg. Wagner is gratefully acknowledged. Thanks are due to the Deutsche Forschungsgemeinschaft (Sonderforschungsbereich 357 "Molekulare Mechanismen unimolekularer Prozesse") and to the Fonds der Chemischen Industrie for financial support.

REFERENCES

1. Brezinsky, K., *Progr. Energy Combust. Sci.* 12:1–24 (1986).
2. Venkat, C., Brezinsky, K., and Glassman, I., *Nineteenth Symposium (International) on Combustion*, The Combustion Institute, Pittsburgh, 1982, pp. 143–152.
3. Colussi, A. J., Zabel, F., and Benson, S. W., *Int. J. Chem. Kinet.* 9:161–178 (1977).
4. Lin, C.-Y., and Lin, M. C., *Int. J. Chem. Kinet.* 17:1025–1028 (1985).
5. Lin, C.-Y., and Lin, M. C., *J. Phys. Chem.* 90:425–431 (1986).
6. He, Y. Z., Mollard, W. G., and Tsang, W., *J. Phys. Chem.* 92:2196–2201 (1988).
7. Suryan, M. M., Kalafi, S. A., and Stein, S. E., *J. Am. Chem. Soc.* 111:1423–1429 (1989).
8. Mackie, J. C., Doolan, K. R., and Nelson, P. F., *J. Phys. Chem.* 93:664–670 (1989).
9. Walker, J. A., and Tsang, W., *J. Phys. Chem.* 94:3324–3327 (1990).
10. Back, M. H., *J. Phys. Chem.* 93:6880–6881 (1989).
11. Mulcahy, M. F. R., and Williams, D. J., *Nature* 199:761–762 (1963).
12. Mulcahy, M. F. R., and Williams, D. J., *Aust. J. Chem.* 18:20–38 (1965).
13. a) Buth, R., Hoyermann, K., and Rohde, G., *Twenty-Fourth Symposium (International) on Combustion*, The Combustion Institute, Pittsburgh, 1992, pp. 669–674. b) Edelbüttel-Einhaus, J., Hoyermann, K., Rohde, G., and Seeba, J., *ibid.*, pp. 661–668.
14. Bartels, M., Edelbüttel-Einhaus, J., and Hoyermann, K., *Twenty-Third Symposium (International) on Combustion*, The Combustion Institute, Pittsburgh, 1990, pp. 131–138.
15. Atkinson, R., Baulch, D. L., Cox, R. A., Hampson,

R. F., Jr., Kerr, J. A., and Troe, J., *J. Phys. Chem. Ref. Data* 18:881–1097 (1989).

16. Slagle, I. R., Sarzynski, D., Gutman, D., Miller, J. A., and Melius, C. F., *J. Chem. Soc. Faraday Trans. 2* 84:491–503 (1988).
17. Borchers, F., Levsen, K., Theissling, C. B., and Nibbering, N. M. M., *Org. Mass Spectrom.* 12:746–750 (1977).
18. Theissling, C. B., and Nibbering, N. M. M., in *Advances in Mass Spectrometry* (N. R. Daly, Ed.) Heyden and Son, London, 1978, Vol. 7b, pp. 1287–1295.
19. Tsang, W., and Hampson, R. F., *J. Phys. Chem. Ref. Data* 15:1087–1279 (1986).
20. Reid, R. C., Prausnitz, J. M., and Poling, B. E., *The Properties of Gases and Liquids*, 4th ed., McGraw-Hill, New York, 1986, p. 241.
21. Laatsch, H., *Liebigs Ann. Chem.* 319–339 (1984).
22. Weiner, S. A., *J. Am. Chem. Soc.* 94:581–584 (1972).
23. Mahoney, L. R., and Weiner, S. A., *J. Am. Chem. Soc.* 94:585–590 (1972).
24. Mahoney, L. R., and Da Rooge, M. A., *J. Am. Chem. Soc.* 97:4722–4731 (1975).
25. Hippler, H., and Troe, J., *J. Chem. Phys.* 94:3803–3806 (1990).
26. Bartels, M., Edelbüttel-Einhaus, J., and Hoyermann, K., *Twenty-Second Symposium (International) on Combustion*, The Combustion Institute, Pittsburgh, 1988, pp. 1041–1051.

Twenty-Fifth Symposium (International) on Combustion/The Combustion Institute, 1994/pp. 851–858

A DIRECT STUDY OF THE REACTION OF BENZYL RADICALS WITH MOLECULAR OXYGEN: KINETICS AND THERMOCHEMISTRY

KARLHEINZ HOYERMANN AND JOHANN SEEBA
Institut für Physikalische Chemie
Universität Göttingen
Tammannstr. 6, D-37077 Göttingen, Germany

The reaction of benzyl radicals with molecular oxygen was studied at low temperature (243–373 K) and low pressure (1–4 mbar) in an isothermal discharge flow reactor with mass spectrometric detection. Benzyl radicals were prepared by the reaction of Cl atoms with toluene and detected by multiphoton ionization at 502.5 nm combined with mass spectrometry.

For the reaction

$$C_7H_7 + O_2 \rightarrow C_7H_7O_2 \tag{1}$$

a temperature-independent rate constant was found:

$$k = (4.44 \pm 1.3) \cdot 10^{11}\ \mathrm{cm^3/mol\ s}$$

$(246 \leq T\ (\mathrm{K}) \leq 300)$.

The equilibration of reaction (1) and reaction (1′),

$$C_7H_7O_2 \rightarrow C_7H_7 + O_2 \tag{1'}$$

was studied at 300–343 K by the determination of the stationary benzyl concentration, leading to the reaction enthalpy ((1)/(1′)) and the equilibrium constant K_p. The modified van't Hoff plot yields

$$\Delta_r H^\circ = -(64.0 \pm 0.8)\ \mathrm{kJ/mol}$$

$$K_p(300\ \mathrm{K}) = 57{,}200\ \mathrm{bar}^{-1}.$$

Adopting two recent values of the enthalpy of formation of the benzyl radical (H_f° (C_7H_7) = 210.5 and 203.0 kJ/mol), the enthalpy of formation of the benzyl peroxy radical followed as

$$H_f^\circ(C_7H_7O_2) = 146\ (139)\ \mathrm{kJ/mol}.$$

The rate constant for the dissociation of the benzyl peroxy radical (reaction (1′)) is given in the studied temperature range as

$$k' = 4.36 \cdot 10^{13} \exp(-7700/T)\ \mathrm{s}^{-1}$$

$$(246) \leq T\ (\mathrm{K}) \leq 343).$$

The influence of heterogeneous reactions on the evaluated kinetic and thermodynamic data was estimated by the simulation of concentration profiles of complex reaction mechanisms, supporting the reported values.

Introduction

Combustion phenomena of hydrocarbons, as cool flames, engine knock, ignition, and induction times, are directly linked to the reactions of molecular oxygen with hydrocarbon radicals (R). At low temperature, complex formation and equilibration is important ($R + O_2 \leftrightarrow RO_2$); at high temperature, isomerization, dissociation, and OH radical formation takes over ($RO_2 \rightarrow ROOH \rightarrow RO + OH$). For a comprehensive review of the interplay of chemical kinetics, thermochemistry, and combustion, see Refs. 1 through 3. Direct measurements of the rates and the thermochemistry of the reactions of saturated and unsaturated hydrocarbon radicals with molecular oxygen have been performed in recent years, notably by Gutman and coworkers ([4,5]). The benzyl radical (C_7H_7) is of special interest, as it is a key radical in side-chain oxidation aromatics [6], and as it, as an unsaturated resonance-stabilized radical, stands out from other unsaturated hydrocarbon radicals [3].

The rate constant for the reaction

$$C_7H_7 + O_2 \rightarrow C_7H_7O_2 \qquad (1)$$

is reported as $6.0 \cdot 10^{11}$ (300 K [7]), $9.0 \cdot 10^{11}$ (295–373 K [8]), and as a lower limit $\geq 3 \cdot 10^{11}$ cm³/mol s [9], showing a sufficient agreement considering the different techniques. However, the thermochemistry shows discrepancies, as can be seen from the reported values of the equilibrium constant K_p of reaction (1) at 298 K ranging from 830 atm^{-1} (estimation [3]), $5.2 \cdot 10^5$ atm^{-1} (estimation [10]), and $3.5 \cdot 10^8$ atm^{-1} (extrapolation [11]). In continuation of our recent work [9] on reaction (1), the objectives of this study are (1) the direct determination of the rate constant k and its temperature dependence and (2) the determination of the equilibrium constant K_p as a function of temperature, the reaction enthalpy $\Delta_r H°$, and thereby, an estimation of the heat of formation of the benzylperoxy radical $C_7H_7O_2$.

Experimental

The experimental arrangement of an isothermal discharge flow reactor (−40 °C to 100 °C), a molecular-beam sampling system, and a multiphoton-ionization-TOF mass spectrometer has been described essentially in a previous paper [9], also dealing with the reactions of benzyl radicals. Therefore, only a summary is given here. Benzyl radicals were prepared by the reaction of toluene and chlorine atoms, produced by a microwave discharge in highly diluted Cl_2/He flows. Molecular oxygen was added by a movable inlet probe at different positions (z) in the flow reactor. By varying the distance from the inlet probe to the sampling nozzle, different reaction times were realized, calculated from the linear flow velocity and the corrections for Poiseuille flow (see e.g. Ref. 12). In order to achieve reproducible conditions in the flow reactor when changing O_2 concentrations, equal amounts of Ar were used as substitute. Benzyl radicals were detected by mass spectrometry after multiphoton ionization (REMPI) at 502.5 nm. As formation of the benzyl peroxy radical $C_7H_7O_2$ was to be expected and no REMPI spectrum of $C_7H_7O_2$ is known from the literature, a possible interference of C_7H_7 and $C_7H_7O_2$ at 502.5 nm was tested by varying the laser intensity and by changing the wavelength out of reasonance; no indication of a REMPI/mass spectrometric interference of C_7H_7 and $C_7H_7O_2$ was found. Mixture composition, impurities, and products of wall reactions were controlled by electron impact ionization (EI) mass spectrometry simultaneously.

Typical experimental conditions were pressure (1–4 mbar), temperature (243–373 K), concentrations ($[C_7H_8]_0$ around $3 \cdot 10^{-10}$ mol/cm³; $[C_7H_7]_0$ around $1 \cdot 10^{-11}$ cm³/mol s; $[O_2]_0 = (5–45) \cdot 10^{-10}$ mol/cm³), and reaction times (1–4 ms). The chemicals were of commercial grade: He (99.996%), Ar (99.996%), O_2 (99.995%), C_7H_8 (99.5%), and Cl_2 (99.8%).

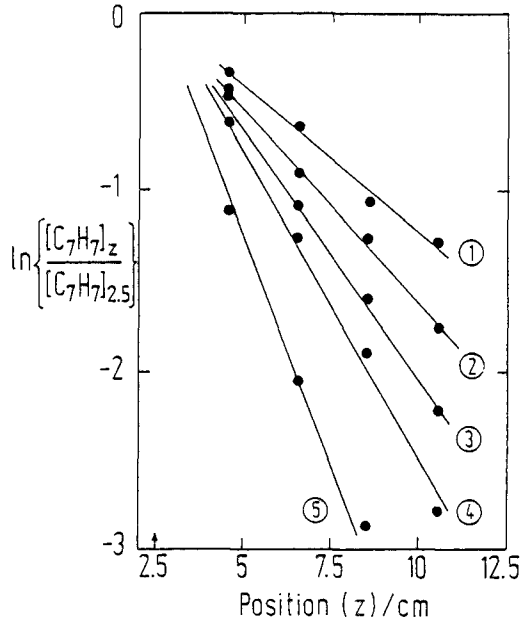

FIG. 1. Reaction (1) $C_7H_7 + O_2$: benzyl concentration profiles in the flow reactor as a function of the position z (= reaction time) for different O_2 concentrations (T = 258 K; p = 1.20 mbar; $[C_7H_8]_0 = 2.0 \cdot 10^{-10}$; $[Cl]_0 = 6.3 \cdot 10^{-11}$; $[O_2] = 0$ (1); $6.2 \cdot 10^{-10}$ (2); $14.9 \cdot 10^{-10}$ (3); $25.8 \cdot 10^{-10}$ (4); $39.8 \cdot 10^{-10}$ (5) in units mol cm^{-3}).

Results

Kinetics: Rate Constant:

The rate constant k for the forward reaction (1) (benzyl radical $C_7H_7 = R$),

$$R + O_2 \rightarrow RO_2 \qquad (1)$$

$$RO_2 \rightarrow R + O_2 \qquad (1')$$

was determined under first-order conditions ($[R]_0 << [O_2]_0$) by measuring the R concentrations for different distances (z) between the O_2 inlet probe and the sampling nozzle and for different excess O_2 concentrations. The measurements of the relative benzyl concentrations (Fig. 1) show the expected logarithmic decay plots for a first-order reaction and the increase in the slope for increasing amounts of O_2 added. The evaluated first-order decay rates as functions of applied O_2 concentration are given for the

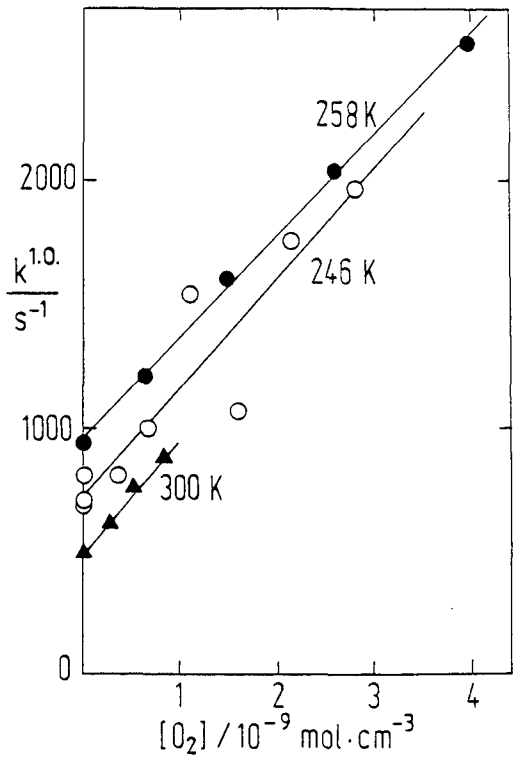

FIG. 2. Reaction (1) $C_7H_7 + O_2$: first-order decay rates as a function of O_2 concentration for the temperature 246 K (p = 1.13 mbar), 258 K (p = 1.20 mbar), and 300 K (p = 1.13 mbar).

temperatures 246, 258, and 300 K in Fig. 2, illustrating the strict proportionality of the first-order rate constants $k^{1.0} = k \cdot [O_2]$. (Large intercepts of the straight lines at $[O_2]_0 = 0$ are observed due to heterogeneous radical reactions. They have been studied separately by applying different residence times in the absence of O_2, leading to comparable wall loss constants k_w. The influence of the wall losses on the determined values of k and K_p are discussed below.) An analysis by linear regression and the 95% confidence criterion leads to $k(246\ \mathrm{K}) = (4.42 \pm 1.3) \cdot 10^{11}$; $k(258\ \mathrm{K}) = (4.10 \pm 0.2) \cdot 10^{11}$; $k(300\ \mathrm{K}) = (4.80 \pm 0.5) \cdot 10^{11}$ in units cm^3/mol s. Within the error limits, no temperature dependence is observed, and an averaged value with the largest error limit from measured values is deduced:

$$k = (4.44 \pm 1.3) \cdot 10^{11}\ \mathrm{cm^3/mol\ s}.$$

At higher temperatures and at reaction times larger than 1 ms, only stationary benzyl concentrations are observed, depending on the O_2 concentration. Such measurements are given in Fig. 3 for 333

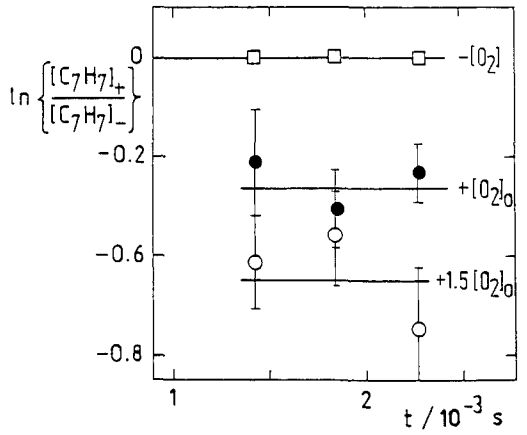

FIG. 3. Reactions (1) and (1′) $C_7H_7 + O_2 \rightleftarrows C_7H_7O_2$: benzyl concentration time profile as a function of O_2 concentration (T = 333 K; p = 1.03 mbar; $[O_2]_0 = 1.45 \cdot 10^{-9}$ mol cm^{-3}; 1.5 $[O_2] = 2.50 \cdot 10^{-9}$ mol cm^{-3}).

K. The stationary C_7H_7 concentrations are interpreted as the C_7H_7 concentration for $t \to \infty$, i.e., the equilibrium concentrations.

Thermochemistry: Equilibrium Constant K_p:

In Fig. 3, the stationary C_7H_7 concentrations (R) (approaching the equilibrium reactions (1)/(1′)) are shown as functions of the O_2 concentration. Although there is a large scatter of the relative C_7H_7 concentrations, no systematic variation with reaction time was observed; secondary reactions seem to be negligible. The equilibrium constant is derived from the well-known integrated rate expression for reactions (1) and (1′), assuming $[R] << [O_2]_0$ = constant:

$$[R]/[R]_0 = \{k[O_2]/(k[O_2] + k')\} \cdot \exp\{-(k' + k[O_2])t\} + k'/(k[O_2] + k').$$

For $t \to \infty$ $(k' + k[O_2])t << 1)$, this expansion leads to

$$[R]_0/[R] = (k/k')[O_2] + 1 = K_p\,[O_2] + 1.$$

In Fig. 4, the straight line is observed with the ordinate value 1 and the constant slope equal to K_p. The measured values of K_p for different temperatures are given in Table 1, showing larger error margins for the conditions where the accuracy of the radical concentration measurements enter into the determination of the equilibrium constant.

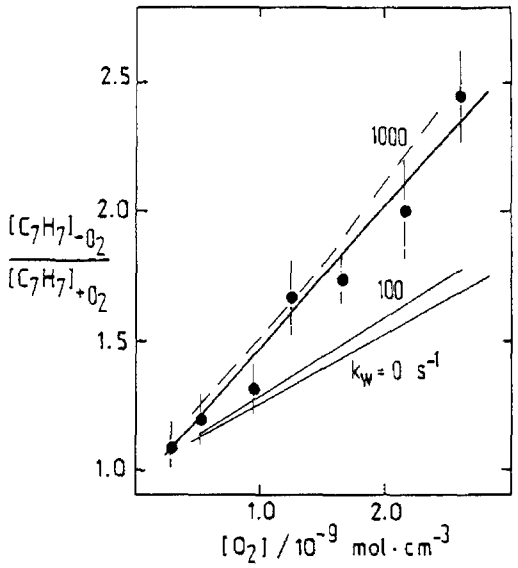

FIG. 4. Reactions (1) and (1′) $C_7H_7 + O_2 \rightleftarrows C_7H_7O_2$: the relative stationary C_7H_7 concentration as a function of O_2 addition ($[C_7H_7]_+ = C_7H_7$ with O_2 addition; $[C_7H_7]_- = C_7H_7$ without O_2 addition): $T = 300$ K; $p = 1.0$ mbar; reaction time: (2.7–3.4 ms; ● : evaluation after reactions (1) and (1′); —: numerical simulation of the relative stationary C_7H_7 concentration including wall loss rates (reaction (2); C_7H_7; $C_7H_7O_2 \rightarrow$ wall; variation of $k_w(2) = 0$, 100, and 1000 s^{-1}.

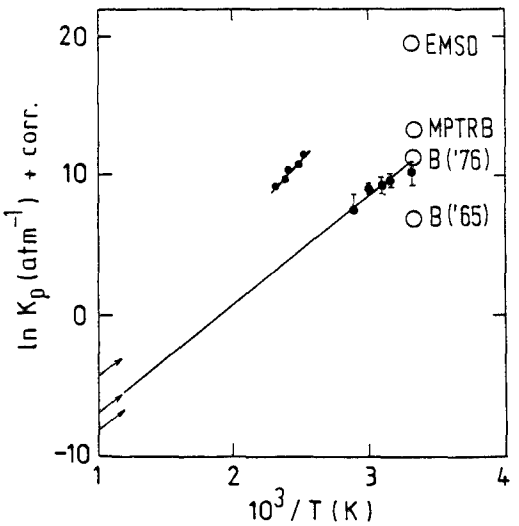

FIG. 5. Modified van't Hoff plot for the reactions $C_7H_7 + O_2 \rightleftarrows C_7H_7O_2$ for $T = 300$–343 K (EMSD = Ref. 11; MPTRB = Ref. 10; B ('65) = Ref. 3; B ('76) = Ref. 16; arrows indicate extrapolation from $T^{-1} \rightarrow 0$ with $\Delta_r S°/R = -14.7$, Ref. 10).

In Fig. 5, the equilibrium constants are shown in a van't Hoff plot, including the extrapolation to $1/T \rightarrow 0$ (third-law plot). This procedure has been extensively described in Refs. 4 and 10, and especially for reaction (1) in Ref. 11 and, therefore, will not be repeated here. The slope from this graph yields the reaction enthalpy $\Delta_r H° = -64.0$ kJ/mol and the value of $K_p(300\text{ K}) = 57{,}200\text{ bar}^{-1}$ with higher accuracy than the values derived from the limited temperature range. As k' is the rate constant for the decomposition reaction of RO_2 (reaction (1′)) in the high-pressure limit, k' can be deduced from the temperature-independent rate constant k by $k' = k/K_p$. Those values are given also in Table 1.

The evaluation of K_p (see Fig. 4) was based on the simple mechanism of reactions (1) and (1′), excluding wall reactions. By a numerical simulation of reactions (1), (1′), and the wall reactions (2.1) and (2.2),

$$R \rightarrow \text{wall} \tag{2.1}$$

$$RO_2 \rightarrow \text{wall} \tag{2.2}$$

TABLE 1
The equilibrium $C_7H_7 + O_2 \rightleftarrows C_7H_7O_2$[a]

T (K)	300	316	323	333	343
$K_p/10^4$ bar^{-1}	2.3 ± 1.4	1.44 ± 0.5	0.91 ± 0.2	0.82 ± 0.2	0.17 ± 0.38
ln K_p	10.04	9.57	9.12	9.01	7.44
	$\Delta_r H° = -64.0$ kJ/mol, ($\Delta_r S°/R = -14.7$) K_p (300 K) = 57,200 bar^{-1}				
k' (s^{-1})	310	1140	1930	3960	7760
	$k' = 4.36 \cdot 10^{13} \exp\{-7700/T\}$ s^{-1}				

the influence of the destruction of C_7H_7 and $C_7H_7O_2$ on the K_p values was analyzed. The wall removal rate constant $k_w(2.1)$ of the C_7H_7 radical follows from the measurements (see Figs. 1 and 2). The measured C_7H_7 concentration ratios (see Fig. 4) are represented best by a wall removal rate constant for the $C_7H_7O_2$ of $k_w(2.2) \sim 800\ s^{-1}$, well within the range of the theoretical limits for our reactor, $0 \leq k_w(2.2)/s^{-1} \leq 7000$ (see below). In order to illustrate the sensitivity of $k_w(2.2)$ on the evaluation of K_p from the C_7H_7 concentration measurements, several situations are given in Fig. 4: (1) the extreme value $k_w = 0$ would require a value of K_p, twice that given in Table 1 ("best experimental values"); (2) $k_w = 1000\ s^{-1}$ would lead to a lower value of K_p. The equivalent simulations ($k_w(2.2) = 1000\ s^{-1}$) for the other temperatures lead to a maximum deviation of K_p of 40%, resulting in $\Delta_r H° = -63.2$ kJ/mol. As seen from Fig. 5, our values are lower than the reported values in the literature. This discrepancy becomes even more pronounced by higher values of $k_w(2.2)$ ($<1000\ s^{-1}$; up to $7000\ s^{-1}$) and by additional reactions of $C_7H_7O_2$.

Adopting the heat of formation of the benzyl radical from the literature $\Delta_f H° = 210.5$ kJ/mol [13]; $\Delta_f H° = 203.0$ kJ/mol [14]), the heat of formation of the benzyl-peroxy radicals follows as $H_f°(C_7H_7O_2) = 146$ and 139 kJ/mol.

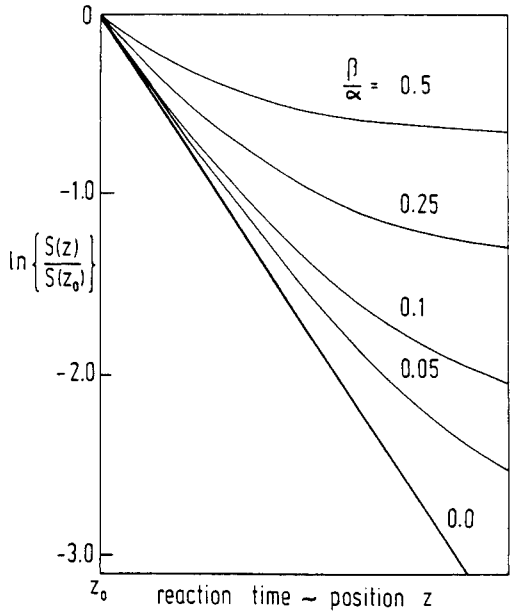

FIG. 6. Reaction (1) $C_7H_7 + O_2 \rightarrow C_7H_7O_2$: schematic ion signal profiles at $m/e = 91$, assuming an ionization cross-section a for C_7H_7 and β for $C_7H_7O_2$ (see text and Fig. 1, line 4).

Discussion

The absence of overlap in the REMPI spectrum between benzyl and benzyl-peroxy radicals is critical to the determination of the benzyl radical concentration, both in the evaluation of the rate constant k and the equilibrium constant. Several checks have been performed. The REMPI spectrum of C_7H_7 is well characterized in the wavelength region of 500–517 nm, and the ionization processes is assigned to a 2 + 2 process, as studied by Hoffbauer and Hudgens [15]. In our study, the ionization spectrum ($498 \leq \lambda/\text{nm} \leq 520$) of pure C_7H_7 (condition: see Fig. 1, line 1, position $z = 10.5$ cm) and of the mixture $C_7H_7/C_7H_7O_2$ (condition: see Fig. 1, line 4, position $z = 10.5$ cm) was identical. A reduction of the laser fluence by a factor of 3 lowered the ion yield correspondingly to the 2 + 2 ionization process of C_7H_7 but did not influence the wavelength dependence. Both observations (wavelength and fluence dependence) do not prove the absence of a contribution of $C_7H_7O_2$ to the C_7H_7 REMPI spectrum, although this complete coincidence seems to be purely accidental. An indication of the absence of the contribution of fragmentation/ionization of $C_7H_7O_2$ to the C_7H_7 radical ionization yield comes from the kinetic studies presented in Fig. 1. Here, a strict linear relation is observed between ln [ion signal S ($m/e = 91$), high C_7H_7 conversion to $C_7H_7O_2$/ion signal S_0 ($m/e = 91$), and low C_7H_7 conversion] and reaction time, i.e., position z in the flow reactor (see for example Fig. 1, line 4: S_0 ($z = 2.5$ cm, high $[C_7H_7]$), S ($z = 10.5$ cm, low $[C_7H_7]$), $S \sim 0.06\ S_0$). This is to be rationalized semiquantitatively. The ion signal S at $m/e = 91$ of the pure radical C_7H_7 is to be related to the concentration of C_7H_7 by an ionization cross-section a ($S = a[C_7H_7]$) and that of $C_7H_7O_2$ (hypothetically) at $m/e = 91$ by the fragmentation /ionization cross-section β ($\beta[C_7H_7O_2]$). Then the measured ion signal S at $m/e = 91$ in the absence of O_2 is $S_0 = a[C_7H_7]_0$ and in the presence of O_2 is $S = a[C_7H_7] + \beta[C_7H_7O_2]$ (For simplification, wall removal of C_7H_7 and $C_7H_7O_2$ is neglected; $[C_7H_7]_0 = [C_7H_7] + [C_7H_7O_2]$.) This analysis leads to

$$\ln\{S/S_0\} = \ln\{([C_7H_7]/[C_7H_7]_0)(1 - \beta/a) + \beta/a\}.$$

If reaction (1) is strictly first order and if $C_7H_7O_2$ does not fragment or ionize at $m/e = 91$ ($\beta = 0$; $\beta/a = 0$), the simple first-order evaluation is valid:

$$\ln\{S/S_0\} = \ln\{[C_7H_7]/[C_7H_7]_0\} = -k[O_2]\cdot t.$$

Otherwise, if $\beta/a > 0$, no straight lines are to be expected in the usual plots of $\ln\{S/S_0\}$ vs t. This is shown schematically for different β/a ratios in Fig. 6, choosing as reference the decay rate of Fig. 1, line 4. An inspection of the measured decay rates (Fig. 1)

(straight lines within experimental scatter) and the systematically curved lines in Fig. 6 points to a low β/a ratio (<0.05), i.e., the absence of a large overlap in the REMPI spectrum between benzyl and benzylperoxy radicals. Therefore, the reliable determination of the C_7H_7 concentration by the REMPI spectrum at 502.5 nm is assumed.

Wall effects are considered next. As shown in the kinetic run in Fig. 1, line 1, (absence of O_2; O_2 replaced by Ar) appreciable C_7H_7 consumption is observed, which follows a first-order rate law and which is attributed to reaction (2.1):

$$\ln\{[C_7H_7]/[C_7H_7]_0\} = -k_w(2.1)\cdot t.$$

The values of $k_w(2.1)$ in different reactors and at different temperatures are included in Fig. 2 (ordinate at $[O_2] = 0$). A simplified equation relates k_w to the geometry of the reactor (surface/volume ratio; $S/V = 2/R$ for a tubular reactor of radius R), the mean velocity of the particle i ($\bar{v}_i \sim (3RT/M)^{0.5}$), and the wall accommodation coefficient γ ($\gamma = 1$: every collision leads to destruction of the radical, $\gamma = 0$: no destruction) (see for example Ref. 12):

$$k_w = \gamma\cdot\bar{v}_i/2R.$$

The measurements at 300 K were performed using a tubular reactor of 3.6-cm inner diameter, and the measurements at 246 and 258 K were performed by a 2.0-cm inner-diameter reactor. Assuming no temperature dependence of γ, a slightly higher value of k_w(258 K) compared to k_w(246 K) is expected along the temperature dependence of $\bar{v}_i$, and the scatter of the values k_w(246 K) represents the reproducibility after different cleaning procedures. The lower value of k_w(300 K) $\sim$ 500 s^{-1} is explained by the larger reactor: the change of the surface/volume ratio (1/2.0 cm (258 K): 1/3.6 cm (300 K) = 1.8) would result in k_w(258 K) $\sim k$(300 K)$\cdot$1.8 = 900 s^{-1}, as observed experimentally. An evaluation of γ leads to $\gamma \sim 0.06$ on the basis of this simplified model.

No direct removal rate coefficient $k_w(2.2)$ of the $C_7H_7O_2$ radical could be deduced, as no direct measurements of the $C_7H_7O_2$ radical concentrations were feasible. However, upper and lower bounds can be given for our reactor at 300 K, as used below in the simulation of the total reaction. For the limiting cases $\gamma = 1$ and $\gamma = 0$, it follows that $7000 \geq k_w(C_7H_7O_2)/s^{-1} \geq 0$.

The kinetic and thermodynamic data were derived from experiments in the limiting cases where negligible interference of the forward and reverse reaction is observed, thus avoiding complicated evaluation procedures like bi-exponential fitting. No temperature dependence of k was observed at T = 246–300 K here, as in the experiments of Ref. 8 (T = 295–372 K). There is an excellent agreement of our k with the absolute value of Ref. 7. Therefore, a

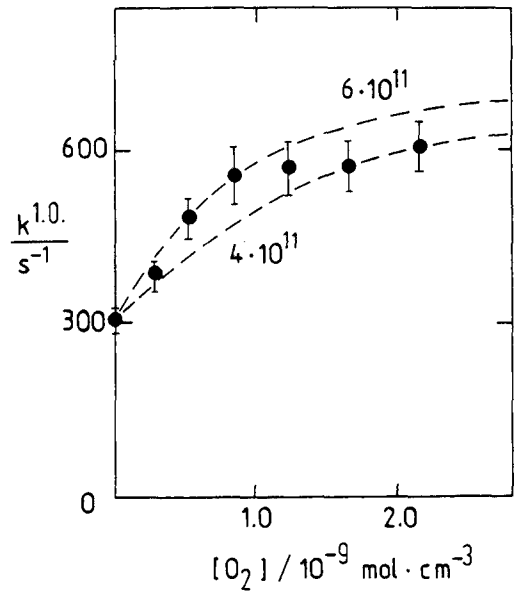

FIG. 7. Reactions (1) and (1′) $C_7H_7 + O_2 \rightleftarrows C_7H_7O_2$ at 300 K (● = measurements; — —: numerical simulation of the first-order rate constant of the disappearance of C_7H_7, full mechanism (see text), variation of k = (4–6)$\cdot 10^{11}$ cm^3 mol^{-1} s^{-1}).

temperature-independent rate constant of k = (4.45 ± 1.3)$\cdot 10^{11}$ cm^3/mol s in the range T = 246–393 K is probable. The derived heat of reaction ($\Delta_r H°$ = −64 kJ/mol) matches the estimated values of Benson ($\Delta_r H°$ = −54.8 kJ/mol [3], −64.9 kJ/mol [16]) and that of Morgan et al. [10] (−70 kJ/mol) perfectly, but it is out of the error ranges quoted by Elmaimouni et al. [11] (−83.7 ± 8.3 kJ/mol). The reasons for the difference in the measured value of Ref. [11] and ours are not obvious. The values of K_p(300 K) reported so far in the literature are included in Fig. 5 for a comparison.

A critical test of consistency of the predicted C_7H_7 concentration based on the derived kinetic (k) and thermodynamic ($k' = k/K_p$) values and of the measured C_7H_7 concentrations in the transition region of the forward/reverse reaction at 300 K is shown for a wide range of O_2 concentration in Fig. 7. The underlying reaction scheme was that of reactions (1), (1′), (2), and

$$C_7H_8 + Cl \rightarrow C_7H_7 + HCl \quad (3)$$

$$C_7H_7 + Cl_2 \rightarrow C_7H_7Cl + Cl \quad (4)$$

$$C_7H_7 + Cl \rightarrow C_7H_7Cl \quad (5)$$

$$C_7H_7 + C_7H_7 \rightarrow (C_7H_7)_2 \quad (6)$$

($k_3 = 3.5 \cdot 10^{13}$ [9], $k_4 = 7 \cdot 10^{11}$ [8], $k_5 = 1 \cdot 10^{14}$ [17], and $k_6 = 2 \cdot 10^{12}$ [18] in units $cm^3/mol\ s$). Rate constants were varied as $k_1 = (4–6) \cdot 10^{11}\ cm^3/mol\ s$ and $k_2 = 300–1500\ s^{-1}$. (The measured rate constant $k_w(2.1) \sim 500\ s^{-1}$, Figs. 1 and 2, and the derived rate constant $k_w(2.2) \sim 800\ s^{-1}$, Fig. 4, are within this range. A variation by a factor of 0.5–2 does not influence the choice of k.) The sensitivity to the variation of the rate constant k and the agreement between prediction and measurement in the transition region is understood as a support of the evaluation at low and high temperatures.

In the context of the equilibration of reactions (1) and (1′), the "ceiling temperature" [3] is often evaluated (temperature at which $[C_7H_7] = [C_7H_7O_2]$ at $[O_2] = 0.1$ atm). From Table 1, the ceiling temperature of 455 K is derived.

Acknowledgments

The continued interest of Professor H. Gg. Wagner is gratefully acknowledged. Thanks are due to the Deutsche Forschungsgemeinschaft (Sonderforschungsbereich 357 "Molekulare Mechanismen unimolekularer Prozesse") and to the Fonds der Chemischen Industrie for financial support.

REFERENCES

1. Benson, S. W., *Twenty-First Symposium (International) on Combustion*, The Combustion Institute, Pittsburgh, 1986, pp. 703–711.
2. Benson, S. W., *Prog. Energy Combust. Sci.* 7:125–134 (1981).
3. Benson, S. W., *J. Am. Chem. Soc.* 87:972–979 (1965).
4. Slagle, I. R., Bencsura, A., Xing, S.-B., and Gutman, D., *Twenty-Fourth Symposium (International) on Combustion*, The Combustion Institute, Pittsburgh, 1992, pp. 653–660.
5. Russell, J. J., Seetula, J. A., Gutman, D., Melius, C. F., and Senkan, S. M., *Twenty-Third Symposium (International) on Combustion*, The Combustion Institute, Pittsburgh, 1990, pp. 163–170.
6. Brezinsky, K., *Progr. Energy Combust. Sci.* 12:1–24 (1986).
7. Ebata, T., Obi, K.-I., and Tanaka, I., *Chem. Phys. Lett.* 77:480–483 (1981).
8. Nelson, H. H., and McDonald, J. R., *J. Phys. Chem.* 86:1242–1244 (1982).
9. Bartels, M., Edelbüttel-Einhaus, J., and Hoyermann, K., *Twenty-Second Symposium (International) on Combustion*, The Combustion Institute, Pittsburgh, 1988, pp. 1041–1051.
10. Morgan, C. A., Pilling, M., Tulloch, J. M., Ruiz, R. P., and Bayes, K. D., *J. Chem. Soc. Faraday Trans. 2* 78:1323–1330 (1982).
11. Elmaimouni, L., Minetti, R., Sawerysyn, J. P., and Devolder, P., *Int. J. Chem. Kinet.* 25:399–413 (1993).
12. Hoyermann, K., in *Physical Chemistry, An Advanced Treatise* (W. Jost, Ed.), Academic Press, New York, 1975, Vol. VI B, pp. 931–1006.
13. Hippler, H., and Troe, J., *J. Chem. Phys.* 94:3803–3806 (1990).
14. Walker, J. A., and Tsang, W., *J. Phys. Chem.* 94:3324–3327 (1990).
15. Hoffbauer, M. A., and Hudgens, J. W., *J. Phys. Chem.* 89:5152–5154 (1985).
16. Benson, S. W., *Thermochemical Kinetics* 2nd Ed., John Wiley, New York, 1976.
17. Benson, S. W., and Weissman, M., *Int. J. Chem. Kinet.* 14:1287–1304 (1982).
18. Müller-Markgraf, W., and Troe, J., *J. Phys. Chem.* 92:4899–4905 (1988).

COMMENTS

John H. Kiefer, University of Illinois at Chicago, USA. These are at least three possible isomers of your $C_7H_7O_2$ adduct. Which do you think dominates, or do you think a mixture is formed?

Author's Reply. This important structural information cannot be deduced from our experiments by mass spectrometry. Experiments are underway in this laboratory using in situ FT-IR spectroscopy. Our speculation (!) starts from C_7H_7 being a phenyl-substituted methyl radical leading to the $PhCH_2O_2$ radical, similar to the mechanism of the O- and H-atom attack to C_7H_7. However, as shown in the study of the reactions of the phenoxy radical ("cyclic," "aromatic") with alkyl radicals (CH_3, C_2H_5, see this Symposium), structurally different products are possible, formally described by the alkyl radical addition both to the oxygen site and the phenyl ring.

•

Horst-Henning Grotheer, DLR, Germany. Your large wall loss coefficients seem to indicate that you are close to the limitations of the flow reaction method. How did you make sure that the wall effects did not change in the course of your experiment? What is the sensitivity of your deduced rate coefficients for an assumed change of the walls?

Author's Reply. Unfortunately, wall effects in flow reactor studies cannot be quantified directly under the $C_7H_7 + O_2$ condition. Reproducibility and consistency of the

measurements under different experimental conditions were taken as indirect proofs for the assignment to the gas-phase reaction. This includes different cleaning procedures, aging and coating (Teflon) of the reactor surface, variation of the diameter of the flow tube, and measuring the pure wall loss rate (C_7H_7 + Ar/He) before and after each run for the homogeneous reaction rate (C_7H_7 + O_2). A more extensive discussion of the wall reactions and the influence on the derived data (especially K_p and $\Delta_r H$) is given in the paper.

Twenty-Fifth Symposium (International) on Combustion/The Combustion Institute, 1994/pp. 859–866

THE REACTIONS OF PHENYLACETYLENES WITH O(^{3}P) IN THE GAS PHASE

M. EICHHOLTZ, A. SCHNEIDER, D.-V. STUCKEN, J.-T. VOLLMER AND H. GG. WAGNER
Institut für Physikalische Chemie
Universität Göttingen
Tammannstr. 6, D-37077 Göttingen, Germany

For the understanding of combustion chemistry and soot formation, it is necessary to know the elementary reactions of the phenylacetylenes. In this paper, we present kinetic data and results of product analyses of the reactions of oxygen atoms (O(^{3}P)) with (1) phenylacetylene (C_6H_5—C≡C—H), (2) phenyldeuteroacetylene (C_6H_5—C≡C—D), and (3) 1-phenylpropyne (methylphenylacetylene, C_6H_5—C≡C—CH_3).

A continuous-flow reactor was used with molecular-beam sampling and mass spectrometric detection. Oxygen atoms were produced by chopped microwave discharges in a mixture of oxygen and helium as carrier gas; in all cases the reactions took place under pseudo-first-order conditions in oxygen atom excess. The kinetic measurements were carried out in the temperature range between 298 and 873 K. The kinetic investigations show that for all three compounds, two main reaction centers have to be considered: the phenyl group and the side chain. The electrophilic addition of O(^{3}P) to the aromatic ring of these compounds is only important at high temperatures (above 500 K). The following Arrhenius expressions were obtained ($k = k_{\text{aromatic}} + k_{\text{side chain}}$ in cm^3/mol × s).

$$k_1(T) = (2.3 \pm 0.5)10^{13} \times \exp\left(-\frac{(2400 \pm 240)\ \text{K}}{T}\right) + (3.6 \pm 0.7)10^{12} \times \exp\left(-\frac{(320 \pm 30)\ \text{K}}{T}\right)$$

$$k_2(T) = (2.3 \pm 0.5)10^{13} \times \exp\left(-\frac{(2400 \pm 240)\ \text{K}}{T}\right) + (3.3 \pm 0.6)10^{12} \times \exp\left(-\frac{(290 \pm 30)\ \text{K}}{T}\right)$$

$$k_3(T) = (2.1 \pm 0.5)10^{13} \times \exp\left(-\frac{(2300 \pm 240)\ \text{K}}{T}\right) + (3.0 \pm 0.5)10^{12} \times \exp\left(-\frac{(210 \pm 20)\ \text{K}}{T}\right)$$

The product analyses at room temperature show that in the case of the reactions of phenylacetylene and phenyldeuteroacetylene with O(^{3}P), the main stable products formed are benzene (C_6H_6) and deutero benzene (C_6H_5D). Toluene was not detected in the reaction of methylphenylacetylene with oxygen atoms.

Introduction

Phenylacetylene seems to be an important intermediate for the soot formation process in combustion. Frenklach et al. [1,2] computed the formation of polyaromatic hydrocarbons (soot formation) proceeding via the formation of aromatic hydrocarbons with acetylenic side chains. Experiments in low-pressure flat flames with various hydrocarbons [3] give evidence for this mechanism. Therefore, the quantitative investigation of elementary reactions of phenylacetylene and its derivatives with radicals is of interest for combustion research. There are only a few kinetic data of reactions with phenylacetylene in the literature [4,5,6]. For the reaction of phenylacetylene with O(^{3}P), no kinetic data and only two product analyses [7,8] are reported. Here, we therefore present results of product analyses and kinetic measurements of the reactions of O(^{3}P) with three phenylacetylenes, namely phenylacetylene, phenyldeuteroacetylene, and methylphenylacetylene.

The obtained results are compared with the oxidation mechanism of styrene and ethylbenzene with O(^{3}P).

Experimental

The reactions were investigated in a low-pressure discharge flow system with molecular-beam sampling and a quadrupole mass spectrometer for detection. A detailed description of the experimental setup used is given in Refs. 9 through 11. The ionization of the compounds in the quadrupole mass spectrometer was performed by using electron impact ionization with an ionization energy of 25 eV. The quartz reactor can be heated up to 873 K by an electric furnace. The oxygen atoms were produced in two sidearms by computer-controlled, pulsed microwave discharges in an O_2/He mixture at room temperature (microwave power output 65–75 W in each resonator). The aromatic hydrocarbons were introduced

TABLE 1
Excerpt of the experimental results of the reaction $O(^3P)$ with phenylacetylene (those results that are not listed fall within the error limits of those indicated)

T (K)	p (mbar)	$[O] \times 10^{10}$ (mol/cm^3)	$[O]/[HC]^a$	v (cm/s)	$k_{2,O} \times 10^{-12}$ (cm^3/mol × s)	$\lg k_{2,O}$
298	2.1	6.0	100	3470	1.31	12.12
298	4.4	9.5	80	4020	1.05	12.02
323	2.8	7.1	190	3830	1.29	12.11
323	2.8	7.7	190	3910	1.21	12.08
373	2.9	5.5	90	3740	1.52	12.18
373	3.3	4.0	110	3340	1.53	12.18
423	3.2	3.9	150	3330	2.00	12.30
423	4.5	3.9	150	3900	1.68	12.23
473	4.7	4.8	220	3800	2.04	12.31
473	4.6	5.8	260	3870	2.14	12.33
573	3.3	5.2	170	3270	2.24	12.35
573	4.8	4.5	270	3730	2.93	12.47
673	4.9	3.2	150	3660	2.45	12.39
673	3.3	2.9	130	3280	2.63	12.42
773	3.7	4.0	140	2900	4.17	12.62
773	5.3	4.5	230	3400	3.09	12.49
873	6.4	3.0	180	3450	3.32	12.52
873	5.6	4.5	250	3250	3.99	12.60

[a]The phenylacetylene concentration was followed on the parent peak on mass $m/e = 102$ as well as on a fragment peak on mass $m/e = 76$.

into the reactor by an axial movable injector probe with helium as carrier gas. At the end of the injector probe, the oxygen atoms and the aromatic hydrocarbons were mixed and the reaction started. For each measurement, the intensity of the background (without reactant flow) was determined. The number of produced oxygen atoms was measured by the difference of the mass signal at $m/e = 32$ with and without microwave discharge. Also, the intensity of the background of this mass was taken into account. The walls of the reactor and the injector probe were rinsed with 10% HF to reduce wall reactions. The purity of the gases used (helium and oxygen; both from Messer Griesheim) was >99.99%. Phenylacetylene and methylphenylacetylene were purchased from Aldrich (purities >98%). The C_6H_5—C≡C—D was prepared by H. Ihmels [12] (purity >97%) by deprotonation of phenylacetylene with n-butyl-lithium in n-hexane/diethylether and addition of D_2O afterwards.

For the measurements, an excess of oxygen atoms over hydrocarbons was applied with excess ratios between 50 and 260. Therefore, the investigations took place under pseudo-first-order conditions. The plots of the measured pseudo-first-order rate constants vs the concentration of oxygen atoms gave straight lines through the origin. This indicates that the wall reaction between the hydrocarbons and the reactor wall was negligible. The obtained rate constants were not pressure dependent in the observed pressure range between 2.0 and 6.4 mbar. A correction of the oxygen-atom concentration was performed as in Ref. 10. The correction values ranged from 1.03 (low temperature and low pressure) to 1.13 (high temperature and high pressure). A second correction for diffusion effects using the expressions given by Taylor [13] and Aris [14] resulted in a maximum correction factor of 1.20.

Experimental Results

All reactions were investigated here in the temperature range between 298 and 873 K. The concentrations of the three acetylenes were followed on the respective parent peaks as well as on a fragment peak. For both sets of investigations, the obtained rate constants were equal each time. Further information and some results are given in Tables 1 through 3.

Product Analyses

For the product analyses, similar conditions of pressure and excess concentrations of oxygen atoms over hydrocarbons have been used as in the kinetic measurements. Therefore, the product analyses can

TABLE 2
Excerpt of the experimental results of the reaction O(³P) with phenyldeuteroacetylene (those results that are not listed fall within the error limits of those indicated)

T (K)	p (mbar)	$[O] \times 10^{10}$ (mol/cm³)	[O]/[HC][a]	v (cm/s)	$k_{2,O} \times 10^{-12}$ (cm³/mol × s)	lg $k_{2,O}$
298	3.3	9.3	100	3340	1.26	12.10
298	4.1	8.3	100	3560	1.23	12.09
323	3.5	11.2	70	3140	1.31	12.12
323	4.8	8.7	60	3700	1.45	12.16
373	4.3	7.2	80	3380	1.79	12.25
373	4.9	7.9	100	3600	1.46	12.16
423	5.0	7.0	90	3540	1.66	12.22
423	3.6	6.0	130	3020	2.00	12.30
473	3.7	5.1	60	2920	1.58	12.20
473	4.5	5.7	80	3210	1.84	12.37
573	4.7	6.2	100	3050	2.24	12.35
573	4.8	8.2	190	3050	2.57	12.41
673	5.8	5.3	170	3110	2.40	12.38
673	5.1	5.9	170	2870	3.16	12.50
773	5.3	5.1	130	2730	2.75	12.44
773	6.1	3.5	100	2940	3.80	12.58
873	4.3	2.3	90	3270	3.47	12.54
873	5.6	4.5	120	3250	4.07	12.61

[a]The phenyldeuteroacetylene concentration was followed on the parent peak on mass $m/e = 103$ as well as on a fragment peak on mass $m/e = 76$.

TABLE 3
Excerpt of the experimental results of the reaction O(³P) with methylphenylacetylene (those results that are not listed fall within the error limits of those indicated)

T (K)	p (mbar)	$[O] \times 10^{10}$ (mol/cm³)	[O]/[HC][a]	v (cm/s)	$k_{2,O} \times 10^{-12}$ (cm³/mol × s)	lg $k_{2,O}$
298	4.7	10.6	160	3790	1.35	12.13
298	3.3	10.2	210	3260	1.64	12.21
323	4.7	7.5	190	3760	1.58	12.20
323	4.0	8.6	200	3570	1.58	12.20
373	4.2	6.7	180	3470	1.83	12.26
373	4.1	10.0	160	3490	1.56	12.19
423	4.3	6.5	190	3340	2.00	12.30
423	5.0	5.1	160	3538	1.74	12.24
473	3.7	3.2	90	2960	2.24	12.35
473	4.5	4.3	140	3230	1.86	12.27
573	5.5	5.1	120	3290	2.57	12.41
573	3.9	6.7	140	2820	2.29	12.36
673	5.0	2.1	60	2960	2.63	12.42
673	4.9	2.9	80	2970	3.16	12.50
773	5.9	3.4	110	3040	3.80	12.58
773	4.3	4.7	130	2540	2.88	12.46
873	5.4	5.4	150	2670	4.07	12.61
873	6.0	5.3	150	2760	3.72	12.57

[a]The methylphenylacetylene concentration was followed on the parent peak on mass $m/e = 116$ as well as on a fragment peak on mass $m/e = 115$.

be compared directly with the kinetic measurements. The product analyses were only performed at room temperature. At high temperatures, no stable primary products were found because the consecutive reactions are too fast. The procedure used was as follows. (1) Two mass spectra were taken under the same experimental conditions: spectrum 1 without O atoms (microwave discharge off), and spectrum 2 with O atoms (microwave discharge on). (2) The "*product spectrum*" results from subtraction of the signal intensities of spectrum 1 from spectrum 2. Positive signals indicate the parent and fragmentation peaks of the formed product(s). Negative signals indicate the parent and fragmentation peaks of the initial reactants. To eliminate contamination signals in the product spectrum, background spectra were measured in the same manner.

For the product analysis of the reaction of oxygen atoms with phenylacetylene, two main products could be identified: CO (mass 28 u) and benzene (masses 78, 77, 52, 51, and 50 u). At higher masses (78 to 200 u), no formation of products could be detected. The ratio of the product peak intensities to each other is constant, independent of different experimental conditions like reaction time, pressure, and concentration of oxygen atoms.

A similar result shows the product analysis of the reaction of phenyldeuteroacetylene with $O(^3P)$. Besides a strong increasing signal on the mass 28 u, fragment signals were also found on the masses 79, 53, 52, and 51 u, a clear indication for the formation of C_6H_5D (parent mass = 79 u).

Product analyses of the reaction of methylphenylacetylene with $O(^3P)$ show that toluene is not formed in this reaction in detectable quantities. The measured mass spectrum of toluene shows that beside the signal on mass 91 u there is also a signal on mass 92 u. The intensity ratio of both signals is 100 (mass 91 u) to 73 (mass 92 u). The ratio of these two signals in the product spectrum is, however, 100 (mass 91 u) to 34 (mass 92 u). Therefore, one can exclude the formation of toluene as main reaction product.

The main product signals of the product spectrum are 28, 89, 90, 91, 92, and 120 u. A comparison of these "*product signals*" (without the signal on 28 u) with the measured mass spectrum of styreneoxide shows a similar fragmentation with similar intensity ratios of the fragments. This is a hint for the formation of styreneoxide. Because of the very small intensities of the fragments, it is not possible to extract quantitative information about the formed styreneoxide.

Discussion of the Kinetics Results

The phenylacetylene derivatives have two different functional groups, the aromatic ring and the acetylene group. The $O(^3P)$ as an electrophilic species may attack either of them. For the reaction of benzene with $O(^3P)$ in the temperature range between 298 and 1450 K [15] and for the reaction of toluene with $O(^3P)$ in the range between 298 and 1350 K [16], linear Arrhenius expressions are described. In the case of the reaction of alkylacetylenes with $O(^3P)$, linear Arrhenius expressions in the range 300 to 1300 K are also reported [17]. In the present investigation, the Arrhenius plot of the measured rate constants is nonlinear in the temperature range investigated here. This can be explained, as for other O-atom reactions with substituted aromatics, with the occurrence of two important reaction channels, the attack of $O(^3P)$ at the acetylene group and at the aromatic ring. The upward bending in the Arrhenius plot indicates that the total rate constant may be split in two different channels, k_{ar} for addition to the aromatic ring and k_{ac} for the reaction with the side chain.

As known from previous experiments performed up to temperatures higher than those here, the Arrhenius parameters for the addition of $O(^3P)$ to the ring in mono-substituted aromatic hydrocarbons can be well correlated in Hammett plots. It is assumed that the phenylacetylenes behave like other substituted aromatics. For the estimation of the contribution of the ring to the rate constant, two Hammett plots for the addition of $O(^3P)$ to aromatic hydrocarbons [11] were used: the plot of the obtained activation energies and the plot of the relative rate constants ($\log k_{298}/k_0$ with $k_0 = k_{298}$ of benzene) vs the substituent constant (σ^+). For the reaction of $O(^3P)$ with aromatic hydrocarbons we used the σ^+ values because they take the electronic density effects of the substituent on the aromatic ring into account [18]. The σ^+ values are taken from Ref. 19.

From this calculated k_{ar} and the experimentally determined total rate constants, the rate constants for the attack of $O(^3P)$ on the C≡CH side chain were obtained ($k_{ac} = k_{exp} - k_{ar}$). The Arrhenius plot for $O(^3P)$ + phenylacetylene is shown in Fig. 1. The Arrhenius parameters of the two reaction channels are listed in Table 4. Towards lower temperatures (<500 K), the contribution of the "aromatic rate constants" to the total rate constants becomes small.

For the reactions of C_6H_5—C≡C—D and C_6H_5—C≡C—CH_3 with $O(^3P)$, the σ^+ values are not reported in the literature. They should, however, be similar to the σ^+ values of phenylacetylene because the electronic effects of these three substituents are quite similar. Therefore, the Arrhenius parameters referring to the aromatic reaction channel of the reactions phenylacetylenes with $O(^3P)$ are expected to be nearly equal. This is confirmed when those values are calculated as mentioned below (see Table 4) and by preliminary experiments at higher temperatures.

The contribution of the "aromatic reaction" should

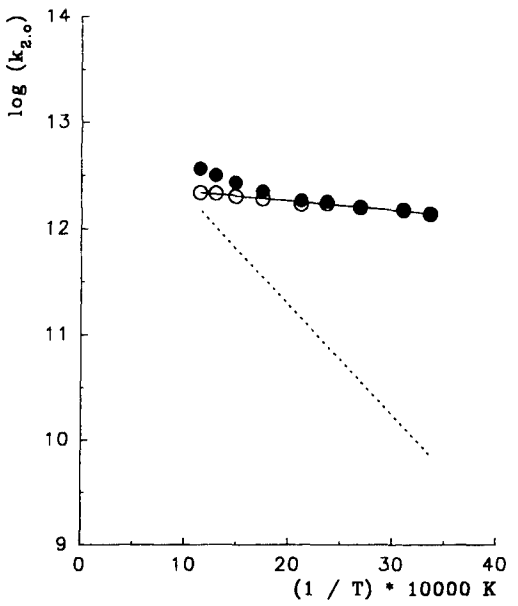

FIG. 1. Arrhenius plot of the reaction of O(³P) with phenylacetylene. Each filled circle is the average value of four measurements of $k(T)$. The open circles and the regression line represent $k_{ac}(T) = k(T)_{exp} - k_{ar}(T)$. The dotted line represents the estimated rate constants of the reaction with the aromatic ring (Hammett correlation) [24].

therefore become negligible at temperatures below 500 K (see Fig. 1). For the reactions of C_6H_5—C≡C—D and C_6H_5—C≡C—CH_3 with O(³P), the Arrhenius parameters of the side-chain reaction were determined by using the rate constants below 500 K. The rate constants at higher temperatures (>500 K) for the addition to the aromatic ring (k_{ar}) for these reactions were estimated by subtracting k_{ac} from k_{exp} ($k_{ar} = k_{exp} - k_{ac}$). The Arrhenius parameters obtained are listed in Table 4.

These kinetic results of the reaction of O atoms with the side chain can be compared with the results of the reaction of alkylacetylenes with O(³P) [17,20]. The activation energies for these acetylenes are higher than those for phenylacetylenes. This can be explained by an activating influence of the phenyl group on the acetylene group. Figure 2 shows a plot of the activation energies of O-atom reactions with different acetylenes vs the ionization potential [21]. The correlation looks quite good.

Discussion of the Product Analyses

The formation of benzene in the reaction of phenylacetylene with O(³P) can hardly be explained by only one reaction step. Following the results of Blumenberg et al. [7] and Sloan and Brudzynski [8]; the primary reaction step should be the addition of O(³P) to the side chain to form a triplet biradical. Afterwards, the H atom from the side chain is migrating to the carbon that is close to the aromatic ring and a CO molecule is eliminated: CO and phenylcarbene result as main products. This leads to the assumption that benzene is formed by a second attack of an oxygen atom under elimination of a further CO molecule.

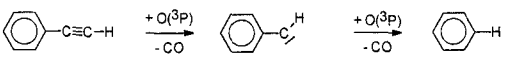

The product analysis of the reaction of phenyldeuteroacetylene (C_6H_5—C≡C—D) with O(³P) supports the proposed mechanism. In this reaction, deuterobenzene (C_6H_5—D) was found in the product spectrum, which should be formed in an analogous

TABLE 4
Arrhenius parameters of the reaction of O(³P) with the investigated acetylenes (*ac* = O(³P) attack at the side chain; *ar* = aromatic reaction channel)

Compound		Preexp. Factor A (cm³/mol × s)	Activation Energy E_a (kJ/mol)	$k_{(298\ K)}$ (cm³/mol × s)
$C_6H_5C{\equiv}CH$	*ar*[a]	2.3×10^{13}	20.0	7.3×10^{9}
	ac	3.6×10^{12}	2.65	1.2×10^{12}
$C_6H_5C{\equiv}CD$	*ar*[b]	2.3×10^{13}	20.0	7.3×10^{9}
	ac	3.3×10^{12}	2.44	1.2×10^{12}
$C_6H_5C{\equiv}CCH_3$	*ar*[b]	2.1×10^{13}	19.1	9.5×10^{9}
	ac	3.0×10^{12}	1.78	1.5×10^{12}

[a]Estimated by the Hammett correlation.
[b]Estimated by $k_{ar} = k - k_{ac}$.

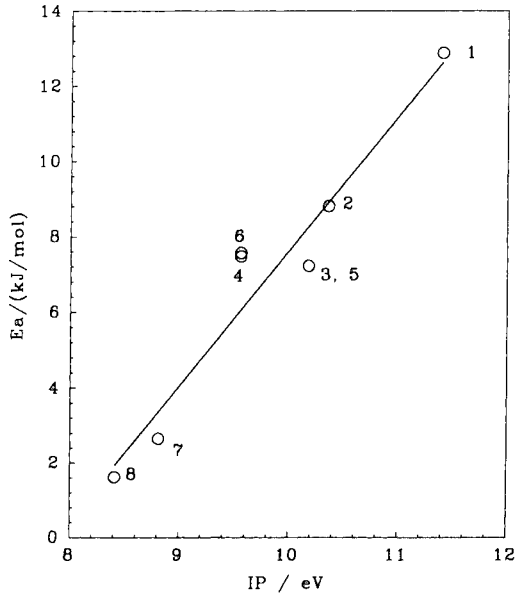

FIG. 2. Correlation between the activation energies for the reaction with atomic oxygen and the ionization potentials for some acetylene compounds: (1) acetylene [17]; (2) propyne [17]; (3) 1-butyne [17]; (4) 2-butyne [20]; (5) 1,3-butadiyne [17]; (6) but-1-en-3-yne [17]; (7) phenylacetylene, and (8) methylphenylacetylene at a lower temperature (<500 K) [this work].

way as benzene in the reaction of O atoms with phenylacetylene.

A detectable contribution of a direct attack of O_2 on the carbene, forming CO_2, could not be found in the product analysis. Besides the formation of benzene and CO, no other products could be found in appreciable amounts for the reaction of C_6H_5—C≡C—H with $O(^3P)$ at room temperature. The rate constants for the formation of benzene and of CO and the consumption of phenylacetylene at room temperature were found to be equal within the error limits.

Thermochemical calculations based on the group additivity method [22] further support this reaction channel. The two possible H-atom abstraction channels are endothermic (H-atom abstraction from the side chain equals +120 kJ/mol, H-atom abstraction from the aromatic ring equals +30 kJ/mol). The addition of $O(^3P)$ to the aromatic ring, forming a triplet biradical by destruction of the aromatic π-system, leads to a reaction enthalpy of −50 kJ/mol. In comparison, the most exothermic reaction with −340 kJ/mol is the attack of $O(^3P)$ on the triple bond of the side chain to form a triplet biradical. Then follows the formation of the phenylcarbene (C_6H_5—C—H) by elimination of CO with an enthalpy of 0 kJ/mol. The consecutive reaction (C_6H_5—C—H plus $O(^3P)$) leads to benzene and CO and is very exothermic (−630 kJ/mol).

The analysis of the reaction product of methylphenylacetylene shows that the methyl group does not migrate like the H or D atom. If the methyl group migrated, toluene should have been found, but it was not. Instead, styrene was detected as the main product. This may be explained by the following reaction mechanism. The first reaction step is the attack of $O(^3P)$ to the triple bond of the side chain, followed by the formation of the phenylmethylcarbene under elimination of CO. In the case of this reaction, the methyl group would have to move to the next carbon atom. Then—by H-atom migration—styrene could be formed:

$$C_6H_5\text{—C}\equiv\text{C—CH}_3 + O(^3P) \rightarrow [C_6H_5\text{—C—CH}_3 + CO] \rightarrow C_6H_5\text{—CH}{=}\text{CH}_2 + CO.$$

A similar mechanism was proposed [23] in the case of dimethylacetylene. The reaction enthalpy of this reaction channel is −500 kJ/mol. Because of the very fast reaction of styrene with $O(^3P)$ [24], one should expect styreneoxide as the main stable product. This is confirmed by the product analysis.

Comparison of Phenylacetylene with Styrene and Ethylbenzene

A comparison of the reactions of phenylacetylenes with oxygen atoms with the respective reactions of styrene and ethylbenzene seems worthwhile. The principal structure of these hydrocarbons is similar. One important difference is the character of the C—C bonds in the side chain: a single bond in ethylbenzene, a double bond in styrene, and a triple bond in phenylacetylene.

The kinetic investigations of the reactions of these three hydrocarbons with oxygen atoms show that the reaction of styrene [24] is the fastest and that of ethylbenzene [25] the slowest. The activation energies of these three reactions are clearly different. The activation energy for ethylbenzene is 15.3 kJ/mol ($k_{298} = 3.6 \times 10^{10}$ cm^3/mol × s) [25], followed by that of phenylacetylene (2.7 kJ/mol; $k_{298} = 1.2 \times 10^{12}$ cm^3/mol × s). For the reaction of styrene with oxygen atoms, the apparent activation energy of the reaction at the side chain is negative (−1.7 kJ/mol; $k_{298} = 2.7 \times 10^{12}$ cm^3/mol × s [24]). The room-temperature rate constants for these three reactions are indeed quite different.

The different kinetic behavior of these hydrocarbons can be seen from the different main reaction channels in the investigated temperature range. At lower temperatures, the oxygen atom attacks the side chain of phenylacetylene and styrene more than the aromatic ring. At room temperature, the aromatic

channel is negligible for both hydrocarbons. In the case of ethylbenzene, the oxygen atom mainly attacks the phenyl group and H-atom abstraction plays only a minor role.

This is shown by product analyses at room temperature (main channels):

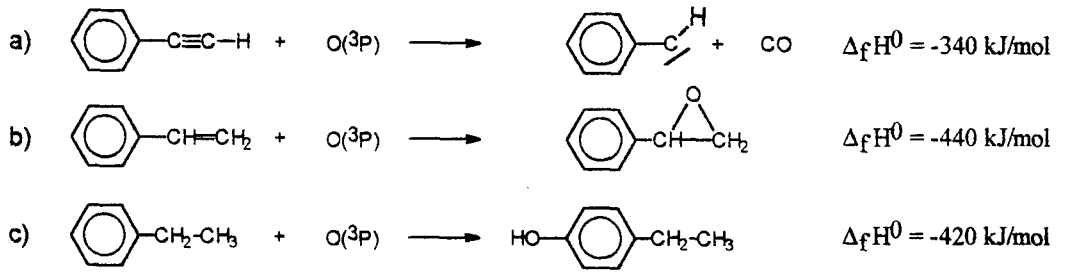

The formation of phenylcarbene and CO in reaction a) is explained above. In the case of reaction b) the oxygen atom attacks one carbon of the side chain, forming a triplet biradical. This radical can be stabilized by formation of styreneoxide, which was found in the product analysis [24]. In the case of reaction c), the O(³P) mainly attacks the π-system of the aromatic ring. The first reaction step leads to a triplet biradical, which can be stabilized by the formation of the phenolic product [25]. In all three cases, the above shown reaction is the most exothermic reaction of the respective reaction system.

At high temperatures (over 1000 K), the addition of the oxygen atom to the aromatic ring of phenylacetylene and styrene becomes more important. Therefore, the rate constants of these three reactions become similar at high temperatures.

Conclusion

Investigations of the reactions of oxygen atoms with phenylacetylene, phenyldeuteroacetylene, and methylphenylacetylene reported here show that the rate constants of these three fast reactions are similar. The nonlinear Arrhenius plots can be described by two reaction channels (the reaction of O(³P) with the side chain and with the aromatic ring). Therefore, the investigated Arrhenius expressions are given as the sum of the Arrhenius expressions of these two channels. At room temperature, the side chain reaction is the important reaction channel. The aromatic reaction channel is becoming important at higher temperatures (>500 K). The product analyses show that the first reaction step is the addition of the oxygen atom to one of the triple-bonded carbons of the respective acetylene with elimination of CO. In the cases of phenylacetylene and phenyldeuteroacetylene, a second attack of an oxygen atom leads to the elimination of a further CO by formation of the respective benzene. In the case of methylphenylacetylene, this second reaction is negligible. Here, the main following reaction is supposed to be the formation of styrene.

Acknowledgment

The support of this work by the Fond der Chemischen Industrie is gratefully acknowledged.

REFERENCES

1. Frenklach, M., Clary, D. W., Gardiner, Jr., W. C., and Stein, S. E., *Twentieth Symposium (International) on Combustion,* The Combustion Institute, Pittsburgh, 1984, p. 887.
2. Frenklach, M., Clary, D. W., Gardiner, Jr., W. C., and Stein, S. E., *Twenty-First Symposium (International) on Combustion,* The Combustion Institute, Pittsburgh, 1986, p. 1067.
3. Bockhorn, H., Fetting, F., and Wenz, H. W., *Ber. Bunsenges. Phys. Chem.* 87:1067 (1983).
4. Herzler, J., and Frank, P., *Ber. Bunsenges. Phys. Chem.* 96:333 (1992).
5. James, F. C., Choi, J., Strausz, O. P., and Bell, T. N., *Chem. Phys. Lett.* 53:206 (1978).
6. Kerr, J. A., and Parsonage, M. J., *Evaluated Kinetic Data on Gas Phase Addition Reactions,* Butterworths, London, 1972.
7. Blumenberg, B., Hoyermann, K., and Sievert, R., *Sixteenth Symposium (International) on Combustion,* The Combustion Institute, Pittsburgh, 1977, p. 841.
8. Sloane, T. M., and Brudzynski, R. J., *J. Am. Chem. Soc.* 101:1495 (1979).
9. Homann, K. H., Mochizuki, M., and Wagner, H. Gg., *Z. Phys. Chem. Neue Folge* 37:299 (1963).
10. Tappe, M., Schliephake, V., and Wagner, H. Gg., *Z. Phys. Chem. Neue Folge* 162:129 (1989).
11. Koch, R., Stucken, D.-V., and Wagner, H. Gg., *Twenty-Fourth Symposium (International) on Combustion,* The Combustion Institute, Pittsburgh, 1992, p. 675.

12. Ihmels, H., private communication, Institut für Organische Chemie der Universität Göttingen.
13. Taylor, G., *Proc. R. Soc. London A* 219:186 (1953).
14. Aris, R., *Proc. R. Soc. London A* 235:67 (1956).
15. Leidreiter, H. I., and Wagner, H. Gg., *Z. Phys. Chem. Neue Folge* 165:1 (1989).
16. Hoffmann, A., Klatt, M., and Wagner, H. Gg., *Z. Phys. Chem. Neue Folge* 168:1 (1990).
17. Homann, K. H., and Wellmann, Ch., *Ber. Bunsenges. Phys. Chem.* 87:527 (1983).
18. Exner, O., *Correlation Analysis of Chemical Data*, Plenum Press, New York, 1988.
19. Exner, O., *Correlation Analysis in Chemistry*, (N. B. Chapman and J. Shorter, Eds.), Plenum Press, New York, 1978, p. 439.
20. Herbrechtsmeier, P., and Wagner, H. Gg., *Ber Bunsenges. Phys. Chem.* 79:673 (1975).
21. Lias, S. G., Bartmess, J. E., Liebman, J. F. Holmes, J. L., Levin, R. D., and Mallard, W. G., *J. Phys. Chem. Ref. Data* 17:(1) (1988).
22. Benson, S. W., *Thermochemical Kinetics*, 2nd ed., Wiley, New York, 1976.
23. Huie, R. E., and Herron, J. T., *Prog. Reaction Kinetics*, 8(1):1 (1975).
24. Buchta, Chr., Frerichs, H., Stucken, D.-V., Tappe, M., and Wagner, H. Gg., *Ber. Bunsenges. Phys. Chem.* 97:658 (1993).
25. Frerichs, H., Stucken, D.-V., Tappe, M., and Wagner, H. Gg., *Z. Phys. Chem. Neue Folge*, 174:1 (1991).

COMMENTS

Alan Doughty, Oxford University, UK. You show that the reaction of $O(^3P)$ atoms with phenylacetylene yields phenylcarbene + CO. It has been shown that phenylcarbene can rearrange to yield acetylene-substituted 1,3-cyclopentadiene (Crow and Wentrup, University of Queensland, Australia). Do you see any evidence for any five-membered-ring species in your product?

Author's Reply. In our product analysis, we found no hint of five-membered-ring species. The product analysis mentioned here was performed with an excess of oxygen atoms over the investigated hydrocarbons. In this case, we cannot find reactive intermediates because the consecutive reactions of these intermediates with O atoms or O_2 molecules are too fast. Therefore, it might be that 1,3-cyclopentadiene-acetylene reacts so rapidly that it cannot be detected. The corresponding epoxide of the 1,3-cyclopentadiene-acetylene also could not be detected.

Twenty-Fifth Symposium (International) on Combustion/The Combustion Institute, 1994/pp. 867–874

HYDROGEN-ATOM ATTACK ON 1-PHENYLPROPENE AT HIGH TEMPERATURES

WING TSANG AND JAMES A. WALKER
Chemical Kinetics and Thermodynamics Division
National Institute of Standards and Technology
Gaithersburg, MD 20899, USA

The reactions of hydrogen atom with 1-phenylpropene (1PP) have been studied in single-pulse shock-tube experiments. Contribution from a large number of the possible reactive channels has been observed. The prime channels are the displacement of the methyl group resulting from addition to the olefinic structure and abstraction of a hydrogen from the methyl group followed by internal displacement of the hydrogen, forming indene. Displacement from the ring is less favored. The following rate expressions at temperatures of 990–1100 K and pressures of 1.4–2.0 atm have been determined.

$$k(\mathrm{H} + \text{1-phenylpropene} \rightarrow \text{styrene} + \text{methyl}) = 10^{13.6\pm0.5} \exp(-1200 \pm 1000/T)$$

$$k(\mathrm{H} + \text{1-phenylpropene} \rightarrow \text{propene} + \text{phenyl}) = 10^{14.0\pm0.7} \exp(-5300 \pm 1500/T)$$

$$k(\mathrm{H} + \text{1-phenylpropene} \rightarrow \text{propenyl} + \text{benzene}) = 10^{14.2\pm0.7} \exp(-6300 \pm 1500/T)$$

$$k(\mathrm{H} + \text{1-phenylpropene} \rightarrow \text{3-phenylallyl} + \mathrm{H_2} + \mathrm{H_2}) \leq 10^{14.2\pm0.5} \exp(-5600 \pm 1000/T)$$

in units of $cm^3\ mol^{-1}\ s^{-1}$, where the relative and absolute uncertainties in the rate constants are factors of 1.10 and 1.25, respectively. An attempt has been made to relate these rate expressions to basic thermal processes, and similarities to those for the appropriate smaller olefins have been noted. Displacement rate constants are made smaller by the reversibility of the hydrogen addition reaction, and together with possible isomerizations, they represent an additional complicating feature.

Introduction

Hydrogen-atom reactions with unsaturated compounds are of great importance in combustion. This paper reports on single-pulse shock-tube experiments involving hydrogen-atom attack on 1-phenylpropene (1PP). A summary of earlier work on simpler compounds and pertinent lower-temperature data can be found in Table 1 [1–9]. Quantitative determination of mechanisms and rates for these reactions are difficult because there are numerous channels for reaction: addition to the sites of unsaturation, followed by decomposition of the radical and hydrogen-atom abstraction. The latter will lead to the formation of a large radical, which if not oxidized, can grow while the former may lead to the breakdown of the molecule to smaller fragments. The significance of such branching ratios to combustion chemistry is clear.

1-Phenylpropene is a more complicated molecule than those which have been studied. It contains both aromatic and olefinic structures. The large number of such species present during combustion creates the need for defining how information on simpler molecules can be extended. Figure 1 contains possible reaction pathways. The numbers are the channels of primary interest. The letters refer to subsequent fast reactions that may lead to the observed products. Although the mechanism is complex, the conditions in single-pulse shock-tube studies lead to simplifying features. Kinetics and thermodynamics drive reactions to completion, and many other possible pathways and products are eliminated.

The experimental approach is to use the decomposition reactions of a very labile organic compound, hexamethylethane (HME), as a source of hydrogen atoms. The processes are [10]

$$\mathrm{HME} = 2\ t\text{-butyl} = \text{isobutene} + \mathrm{H} \qquad (1)$$

with $k_1 = 3 \times 10^{16} \exp(-34{,}500/T)\ s^{-1}$. The subsequent breakdown of t-butyl is rapid under the high-temperature conditions of single-pulse shock-tube studies. Other reaction possibilities are unimportant. The general instability of nearly all large organic radicals (certain resonance stabilized radicals are exceptions to this rule) under the conditions of these studies (high temperatures and high dilutions of molecule undergoing unimolecular decomposition) facilitates the interpretation of the data. Referring to Fig. 1, one sees the possibility of associating reaction pathways with particular unsaturated stable products.

TABLE 1
Past work on hydrogen-atom attack on organics at high and low temperatures

Compound attacked by H [Ref.]	Rate expression Rate constant (1100 K) (cm mol^{-1} s^{-1}) Displacement [group]	Abstraction/H
A. High Temperature Results		
Isobutene [2]	$1.7 \times 10^{13} \exp(-1808/T)[CH_3]$	$1.7 \times 10^{14} \exp(-4024/T)$
	3.3×10^{12}	0.7×10^{12}
Mesitylene [3]	$6.7 \times 10^{13} \exp(-3255/T)[CH_3]$	$3.7 \times 10^{14} \exp(-4342/T)$
	$1.2 \times 10^{12}/CH_3$	0.8×10^{12}
p-Chlorotoluene [4]	$3.5 \times 10^{13} \exp(-3710/T)[CH_3]$	$9.6 \times 10^{13} \exp(-4265/T)$
	1.2×10^{12}	0.6×10^{12}
	$4.8 \times 10^{13} \exp(-4795/T)[Cl]$	
	0.6×10^{12}	
Toluene [1]	$1.2 \times 10^{13} \exp(-2578/T)[CH_3]$	$1.2 \times 10^{14} \exp(-4138/T)$
	1.2×10^{12}	0.9×10^{12}
Phenol [5]	$2.2 \times 10^{13} \exp(-3990/T)[OH]$	$1.1 \times 10^{14} \exp(-6240/T)$
	0.6×10^{12}	0.4×10^{12}
Chlorobenzene [6]	$2.2 \times 10^{13} \exp(-4531/T)[Cl]$	
	0.4×10^{12}	
B. Lower-temperature results: rate constants are derived from rate expression and refer to addition without displacement.		
Butadiene [8]	$4.1 \times 10^{13} \exp(-655/T)$ (2 sites)	
300	4.5×10^{12}	
1100	2.3×10^{13}	
t-Butene-2 [9]	$2.1 \times 10^{13} \exp(-1046/T)$	
300	6.3×10^{11}	
1100	0.8×10^{13}	
Isobutene [9]	$3.7 \times 10^{13} \exp(-849/T)$ (terminal addition)	
300	2.2×10^{12}	
1100	1.7×10^{13}	
Benzene [7]	$4 \times 10^{13} \exp(-2170/T)$ (6 sites)	
300	2.9×10^{10}	
1100	5.6×10^{12}	

Every isobutene that is generated implies a hydrogen released into the system. By carrying out the reactions in a vast excess of 1PP and mesitylene(1,3,5-trimethylbenzene) (MES) in comparison to HME (ratio of these two compounds to HME is in excess of 100 to 1), with the latter present in concentrations near 100 ppm, practically all the hydrogen atoms will react with 1PP and MES. For MES [3], the result of hydrogen-atom attack are displacement of methyl leading to meta-xylene formation,

$$H + MES = \text{meta-xylene} + CH_3 \qquad (2)$$

and abstraction of benzylic hydrogens,

$$H + MES = \text{3,5dimethylbenzyl} + H_2$$

with the rate expressions given in Table 1. Since 1PP and MES are much more stable than HME (in the unimolecular sense), rate constants for products from 1PP and MES can be determined from the following relation:

$$[\text{product}_i/1PP]/[\text{m-xylene}/MES] = k(\text{product}_i)/k_2.$$

Substitution of the rate expression for k_2 will then yield rate constants for the process initiated by hydrogen-atom attack on 1PP.

The yields of isobutene also serve as an internal thermometer for the determination of the temperature of the system. The relations are

$$1/T = [38 - \ln(k_1)]/34{,}500$$

with

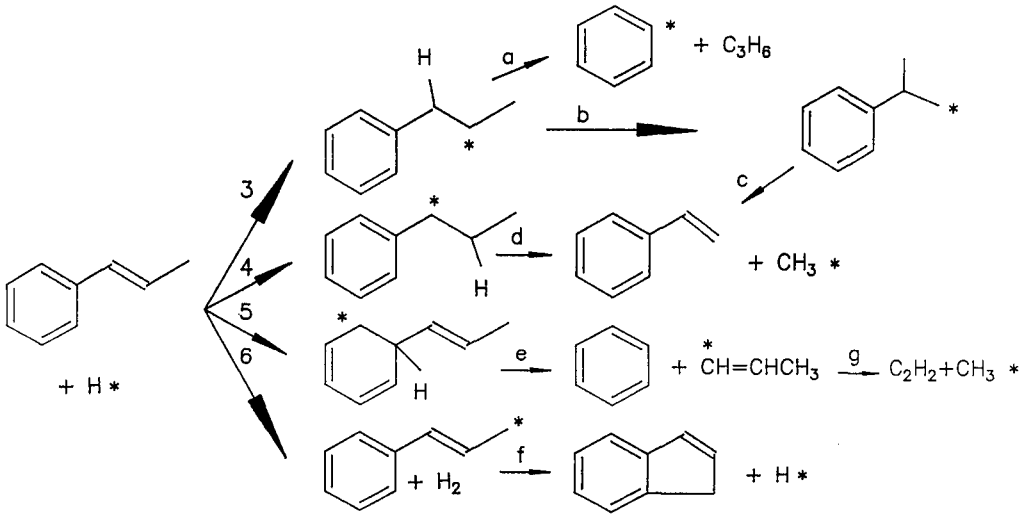

FIG. 1. Mechanism for the hydrogen atom–induced decomposition of 1PP.

$$k_1 = t^{-1} \cdot \ln[1 - (1.03 \cdot \text{isobutene/HME}_i)$$

where t is the heating time of 500 μs and the factor of 1.03 refers to the propene formed during isobutene decomposition. The use of the internal temperature removes the chief uncertainty in such experiments. It depends on HME being present in small amounts relative to other reactants and short chain lengths for reactions involving the main components.

Despite the large number of studies on hydrogen-atom reactions with unsaturated organic compounds, there are no data on hydrogen-atom attack on 1PP or even related molecules. The most pertinent results are lower-temperature data on hydrogen-atom attack on the C_4 olefins and benzene. These are summarized in Table 1. The values at 1100 K from the low-temperature data are extrapolations. At room temperature, the main process is addition. Displacement does not occur, since the low temperatures prevent radical decomposition. There are large differences in rate constants. These can arise from small differences in activation energy. The data in Table 1 suggest that rate constants for addition to the aromatic ring may be an order of magnitude or more smaller than addition to an olefinic structure under the present reaction conditions. An important thrust of this work is to determine this branching ratio for 1PP.

For olefins, relative rate constants for addition to a molecule are affected by the stability of the radicals [11] that are formed. Hence, the propensity for terminal addition. Terminal addition to butadiene will lead to a radical that is stabilized by allylic resonance, and one would expect that this will be the preferred mode. There are no data as to whether the full effect of the allylic resonance energy, of the order of 50 kJ/mol [12], is reflected in the rate constant. The data on butadiene and the butenes demonstrate that such effects do not occur between molecules. The same issue arises in the present system, except that benzylic resonance is substituted for allylic resonance. The values of the two resonance energies are similar. The differences in rate constants between *trans* butene-2 and the *cis* compound at room temperature are small.

Fahr and Stein [13] have reported on the rate constants for phenyl and vinyl addition to benzene and ethylene at temperatures very close to those used here. Their data can be related to some of the present results through the thermodynamics. It will also be used to obtain information on the specificity of addition to the olefinic portion of 1PP.

Experimental

Experiments are carried out in a heated single-pulse shock tube. This permits studying the reactions of high-boiling organic compounds. Details of the experimental procedures have been given in earlier publications [1]. Analysis of reactants and products was by gas chromatography with flame ionization detection. A 6-ft Poropak N column was used to analyze all substances up to propene and was operated at 90 °C. All substances with boiling points higher than isobutene were analyzed with a 30-m dimethylsiloxane wide bore capillary column operated in the programmed temperature mode. *Trans* and *cis*-1PP and

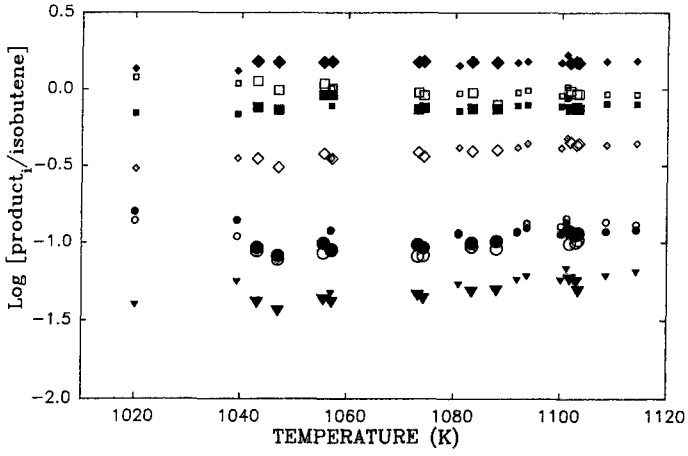

FIG. 2. Product distribution from the hydrogen atom–induced decomposition of 1PP. Large symbols are for reactions with *trans*-1PP. Results from mixture A. Small symbols are for reactions with *cis*-1PP. Results from mixture B: (♦) styrene; (□) methane, (■) indene; (◇) ethane; (○) benzene; (●) propene; and (▼) acetylene. Pressures range from 1.4–2 atm argon.

MES were purchased from Chemical Samples;* HME was from Aldrich Chemicals and, except for vigorous degassing, were used without further purification. Argon was ultrapure grade from Matheson. The only impurity was trace amounts of methane and was corrected for in the subsequent analysis. The major lower boiling point impurity in 1PP was allylbenzene. There are also some unidentified higher-boiling impurities in much smaller amounts than the allylbenzene in *trans*-1PP. The concentration of allylbenzene in the *trans* compound was about 0.2% in comparison to 1% in the *cis* mixture. A majority of the data and all the quantitative results on rate constants were derived from experiments with the *trans* compound. The results on the *cis* compound served as a convenient check of the effect of impurities on the integrity of the results. Four sets of experiments were carried out. The compositions of the mixtures were as follows:

1. 100 ppm HME in 1% *trans*-1PP in argon;
2. 100 ppm HME in 1% *cis*-1PP in argon;
3. 136 ppm HME in 0.5% *trans*-1PP and 1.2% MES in argon; and
4. 100 ppm HME in 0.5% *cis*-1PP and 1.0% MES in argon.

The invariance of the experimental results with changes of relative concentrations of HME, 1PP, and MES testifies to the absence of contributions of 1PP and MES decomposition in these studies and the validity of the postulated mechanism. This is a powerful test. The experiments were carried out at 1.4–2.0 atm pressure and in the temperature range 990–1100 K.

*Certain commercial materials and equipment are identified in this paper in order to specify adequately the experimental procedure. In no case does such identification imply recommendation of endorsement by the national Bureau of Standards, nor does it imply that the material or equipment is necessarily the best available for the purpose.

Results

Data from studies with the first two mixtures can be found in Fig. 2. The yields have been normalized in terms of per hydrogen atom introduced into the system. There is very little difference in the data from the *trans*- and *cis*-1PP mixtures, except that at the lower temperatures, there are more propene and benzene from the *cis* results. This is probably due to the presence of impurities. Otherwise, it is not necessary to draw a distinction between the two sets of results. *Trans* ↔ *cis* isomerization is observed. This has no consequence in this work.

Styrene is the main product. Indene is the next product of importance. All other products are in much smaller concentrations. Quantitative interpretation of the latter will have larger errors than that for the major products since there may be contributions from labile impurities or small side reactions that have been neglected in the analysis. They are a reflection of the "noise" in such studies. Uncertainties in the relative concentrations of the major products are expected to be in the range for standard gas chromatographic analysis or of the order of ±3%. For the minor products, this should be increased by a factor of 2. The presence of allylbenzene as an impurity prevented determination of contributions from this channel. The propene concentrations used here have been corrected for its formation from *t*-butyl decomposition.

Large yields of methane and ethane are found. These are from fragments formed during styrene formation. The sum of methane plus twice the ethane is slightly larger than the styrene and other compounds, acetylene and propene from isobutene, whose presence imply simultaneous ejection of methyl. If the system is behaving as assumed, these should be exactly equal. This may be a reflection of small side reactions that have been neglected. From the propene yields, it is clear that only small amounts

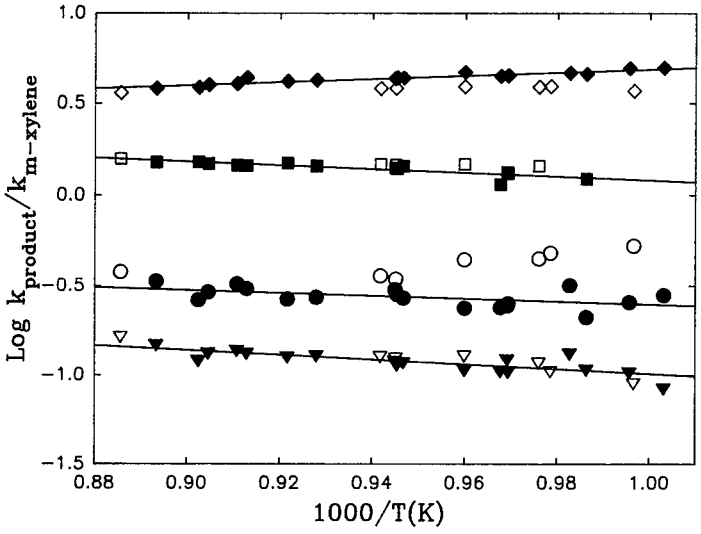

FIG. 3. Ratio of rate constants for the production of styrene (◆), indene (■), propene (●), and acetylene (▼), respectively, vs that for meta-xylene generation during the reaction of hydrogen atoms vs 1PP. Filled symbols are data for *trans*-1PP and mesitylene, mixture C. Open symbols are data for *cis*-1PP and mesitylene, mixture D. Pressures range from 1.4–2 atm argon.

TABLE 2
Summary of experimental rate expressions

Product channel	k(Product channel) / k(Mesitylene)	k(Product channel) ($cm^3\ mol^{-1}\ s^{-1}$)	1100 K
Styrene	$0.65 \times \exp(2000 \pm 190/T)$	$4.4 \times 10^{13} \exp(-1200 \pm 1000/T)$	1.4×10^{13}
Indene (from 3-phenylallyl)	$12.6 \times \exp(-2400 \pm 300/T)$	$8.5 \times 10^{14} \exp(-5600 \pm 1000/T)$	5.2×10^{12}
Acetylene (from propenyl)	$2.2 \times \exp(-3100 \pm 510/T)$	$1.5 \times 10^{14} \exp(-6300 \pm 1500/T)$	4.7×10^{11}
Propene	$1.6 \times \exp(-2000 \pm 750/T)$	$1.1 \times 10^{14} \exp(-5300 \pm 1500/T)$	9.1×10^{11}
Styrene + propene	$0.85 \times \exp(1800 \pm 200/T)$	$5.7 \times 10^{13} \exp(-1400 \pm 1000/T)$	1.5×10^{13}

Uncertainties in column 2 are least-squares values, while those in column 3 are estimates and include 4.2 kJ/mol uncertainty in the rate expression for displacement of methyl from mesitylene. The uncertainties in the relative and absolute rate constants are factors of 1.1 and 1.25, respectively. Variations in the A factors are commensurate with these values. See text for further details.

of phenyl radicals are formed. Together with its high reactivity, this is the reason for the absence of addition products such as toluene.

The normalized yields of styrene are greater than 1. When all other products directly derivable from hydrogen reactions with 1PP are summed, the chain length is near 2.5. When MES is added, the chain length is reduced to 1.5. Figure 3 contains rate data pertaining to the ratio of rate constants for the formation of the appropriate product from 1PP and the rate constants for the displacement of the methyl group from mesitylene-forming meta-xylene. Also included are data from the *cis*-compound. They track that of the *trans* mixture except for propene where, as noted earlier, there appears to be an extraneous source.

Table 2 contains a summary of the rate expressions and constants derived from this study. The rate expressions in the second column in Table 2 are given in terms of the production of particular compound(s) compared to that of meta-xylene from MES and are a quantitative summary of the experimental results. The results in the third column are from multiplying those in the second column by k_2. Also given in Table 2 are rate constants at 1100 K. This serves as a convenient reference point for comparisons. The value of the rate constants cover a wide range. For the less important channels, the rate constants, instead of rate expressions, are probably more meaningful. Estimated uncertainties for the relative rate expressions are 4.2 kJ/mol in the activation energy and a factor of 1.6 in the pre-exponential factor for styrene and

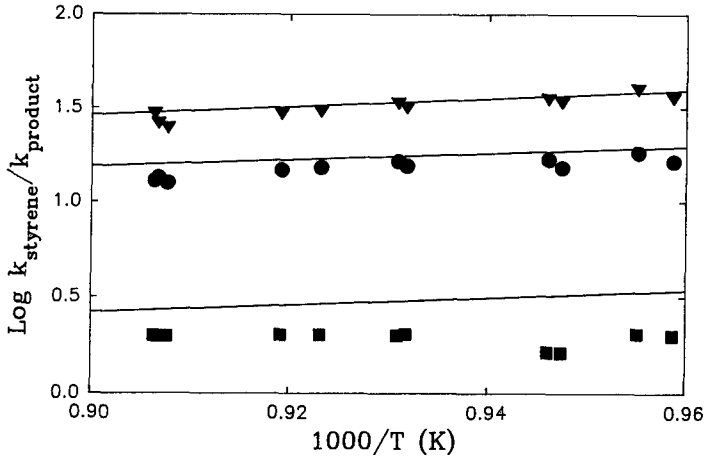

FIG. 4. Ratio of rate constants for the production of indene (■), propene (●), and acetylene (▼), respectively, vs styrene generation during the hydrogen atom–induced decomposition of 1PP in the absence (mixture A, symbols) and presence (mixture C, lines) of mesitylene. Pressures range from 1.4 to 2 atm argon.

indene and 8.4 kJ/mol in the activation energy and a factor of 2.5 in the A factor for acetylene and propene. In absolute terms, the uncertainty in the rate expression of the methyl displacement reaction from MES leads to an additional uncertainty of 4.2 kJ/mol in the activation energy and a factor of 1.6 in the A factor. These uncertainties are larger than that derived from the statistical scatter. They are based on experience from the consistency of earlier studies [10,14]. The relative and absolute uncertainties in the rate constants should be factors of 1.10 and 1.25, respectively.

Figure 4 contains data on the ratio of products from hydrogen-atom attack on 1PP as compared to that producing styrene and demonstrate the effect of MES addition. For propene and acetylene, the results match. In the case of indene, the inhibiting effect of mesitylene leads to the observed lower yields. The additional mode for indene production in the absence of mesitylene is probably the abstraction by methyl of a hydrogen from 1PP, leading to the 3-phenylallyl radical. Only hydrogen-atom attack and the consequences were considered in Fig. 1. Methyl addition processes are reversed and will not make any contributions.

Discussion

The observations summarized in the third column of Table 2 will now be correlated with the thermal processes given in Fig. 1. Under the present conditions, the thermal instability of the larger radicals formed from hydrogen reactions simplify mechanistic possibilities. The only reaction they can undergo is unimolecular decomposition. Figure 1 lists four reaction channels. Two of these involve addition (channels 3 and 4) to the olefinic portion of 1PP. Another process is addition to the propenyl site (channel 5) on the ring and the last is hydrogen abstraction (channel 6) from the methyl group. Other reactions are not included since they are much more endothermic or can readily be reversed.

Addition of hydrogen at the methyl site of olefinic portion of 1PP (channel 4) followed by ejection of methyl (reaction d) must lead to styrene and methyl. Addition at the phenyl site (channel 3) will lead (reaction 2) to propene and phenyl. The possibility of a neophyl rearrangement [15] (channel b) can lead to the formation of 2-phenylpropyl-1 radical, which will decompose readily (channel c) to form methyl and additional styrene. Thus, the present data does not yield independent information on the specificity of H addition to the olefin. The sum of styrene and propene may be a measure of addition to both sites of the double bond ($k_3 + k_4$). Ambiguity arises from the possibility that the addition reaction (channel 3) may be reversed. Thus, $k_3 + k_4$ so deduced must be a lower limit. However, the H + 1PP → phenyl + propene reaction is approximately thermoneutral at 1000 K [16–18]. Rate constants for hydrogen and phenyl bond cleavage may be not be far apart. Propene, a measure of the phenyl released into the system, is only 7% of the styrene. Thus, little error is introduced into the addition rate constant by the neglect of the hydrogen ejection channel. At 1100 K, the sum of rate constants for styrene and propene formation is 1.4×10^{13} $cm^3\ mol^{-1}\ s^{-1}$ or very close to 0.5 times the value for butadiene given in Table 1.

The results of Fahr and Stein can be used to arrive at an estimate of the specificity of hydrogen addition to the olefinic part of 1PP (channels 3 and 4). They found $k(C_6H_5 + C_2H_4 \rightarrow \text{styrene} + H) = 2.5 \times 10^{12} \exp(-3121/T)$ $cm^3\ mol^{-1}\ s^{-1}$. Assuming that this will also hold for terminal addition to propene and accounting for the reaction degeneracy of 2, one finds through detailed balance $k(H + 1PP \rightarrow C_6H_5 + C_3H_6) = 9.5 \times 10^{13} \exp(-3222/T)$ $cm^3\ mol^{-1}\ s^{-1}$. This is equal to 5×10^{12} $cm^3\ mol^{-1}\ s^{-1}$ at 1100 K. Combining this with the overall rate constant for

addition given earlier, the ratio of rate constants for hydrogen addition to the methyl and phenyl sites in 1PP is 1.8. This value is strongly dependent upon the thermodynamic properties of phenyl and its combination rate constant. For the former, the number used here, 328.5 kJ/mol, is from Burcat [18]. A slightly higher value of 340.5 kJ/mol [19] had been suggested and will lead to a rate constant of 1.5×10^{12} cm^3 mol^{-1} s^{-1} for propene formation. Fahr and Stein assume a combination rate constant for phenyl of 3×10^{12} cm^3 mol^{-1} s^{-1}. A value of 10^{13} cm^3 mol^{-1} s^{-1} will raise the original value to 8.5×10^{12} cm^3 mol^{-1} s^{-1}. The corresponding ratios are now 8 and 0.8. Although the results have wide scatter, these considerations demonstrate that a significant portion (although less than half) of the hydrogen atoms may add to the phenyl site of 1PP. Benzyl resonance energy is not a large influence on the position of hydrogen addition on the olefinic portion of 1PP. This sets a limit of 10–40% on the error introduced in assigning styrene and propylene yields to $k_3 + k_4$.

The acetylene yield can be a measure of propenyl formed (channel g) if isomerization to allyl is not important. Results on methyl attack on acetylene [8] and the thermodynamics leads to 4.5×10^{13} $\exp(-15{,}900/T)$ s^{-1} as the rate expression for propenyl decomposition. The thermodynamic properties of propenyl are based on a vinyl C—H bond energy of 459 kJ/mol [20] and molecular parameters estimated in the usual manner. Such isomerization processes can be treated as an internal abstraction with an additional contribution to the activation energy from the ring strain in the transition state [21]. For abstraction of allylic or benzylic hydrogens, the resonance energy has only a small effect on the rate constants [1]. The strain energy for a four-membered ring structure is 125 kJ/mol [22]. The transition state must be tight. A likely rate expression for isomerization is [20] 3×10^{11} $\exp(-17{,}500/T)$ s^{-1} and should be unimportant compared to decomposition.

Acetylene yields are not a measure of hydrogen addition to the propenyl site of the ring structure in 1PP (channel 5), since the reverse reaction is likely to be competitive with propenyl ejection (channel e). It represents instead a minimum value for k_5. The activation energy for acetylene formation is higher than those for the displacement processes in Table 1. This suggests that the barrier for propenyl ejection is higher than the hydrogen addition barrier. Nevertheless, the rate constant is only a factor of 2.5 smaller than that for hydrogen addition to toluene, where displacement is a measure of hydrogen addition. Thermodynamic factors favor the displacement of methyl from the olefinic part of 1PP or the abstraction of a hydrogen by H atoms or a radical such as phenyl in comparison to displacement of propenyl. The ratio (styrene + propene)/acetylene is an upper limit to the ratio of rate constants, $(k_3 + k_4)/k_5$, which defines H-atom addition to the olefinic and ring structures in 1PP. The data in Table 2 lead to a factor of 33 at 1100 K. The actual value of $(k_3 + k_4)/k_5$ must be lower. If displacement of methyl from toluene is equivalent to addition at the propenyl site, one obtains a value of 12. This is the same value from the data on Table 1, using butadiene and benzene as a basis.

Fahr and Stein [13] found the rate expression for vinyl addition to benzene to be $k(C_2H_3 + C_6H_6 \rightarrow \text{styrene} + H) = 1.5 \times 10^{12} \exp(-3222/T)$ cm^3 mol^{-1} s^{-1} or 8×10^{10} cm^3 mol^{-1} s^{-1} at 1100 K. These are different (factor of 1.8) from the original estimate [13] since a newer value for vinyl combination from Fahr et al. [23] has been used. The thermodynamics and the rate expression for propene yield obtained here gives $k(\text{propenyl} + C_6H_6 \rightarrow 1PP + H) = 1.6 \times 10^{13} \exp(-5940/T)$ cm^3 mol^{-1} s^{-1} or 7.3×10^{10} cm^3 mol^{-1} s^{-1} at 1100 K. Despite the differences in the rate expressions, agreement in the rate constants at 1100 K where both measurements were made is good. Fahr and Stein caution their readers on the use of their rate expression beyond the measurement range. The estimated uncertainty in the activation energy in this study is 13 kJ/mol. Thus, the disagreement may not be significant.

Abstraction of a hydrogen from the methyl group (channel 6) will lead to the formation of 1-phenylallyl radical. The resonance energy of this radical is 66 or 18 kJ/mol higher than those for benzyl or allyl [24]. Internal displacement of a hydrogen will lead to the quantitative formation of indene [25] (channel f). Hydrogen, as well as methyl and phenyl, can be a abstracting radical. Thus, indene concentration sets an upper limit for the rate constant of hydrogen abstraction (k_6). The rate expression given here can be compared with others leading to the formation of other resonance-stabilized radicals. From Table 1, it appears that the value from indene concentration is about a factor of 2 larger. A larger rate constant may be consistent with the 18 kJ/mol extra resonance energy. However, earlier studies indicate that resonance energy has very small effects on rate constants for abstraction [1]. The values given here may have additional contributions from methyl abstraction. This is supported by the rate expression, where the A factor is larger than that for other hydrogen-abstraction processes.

These results demonstrate that the main role of hydrogen atoms is to strip alkyl groups from the olefinic portions of large unsaturated compounds containing olefinic and aromatic groups. Abstraction also makes a contribution. Next in order of reactivity is the removal of alkyl structures from the ring. The reversibility of hydrogen addition to these systems makes removal of phenylic and vinylic structures more difficult. Under combustion conditions, most of these effects can be almost quantitatively inferred from data on simpler molecules. There would appear to be a good basis for making estimates. Complicat-

ing factors are the isomerization pathways and uncertainties in the rate constants for decomposition of radicals that involve removal of phenyl and vinyl groups as a result of the reversibility of the initial addition process.

REFERENCES

1. Robaugh, D., and Tsang, W., *J. Phys. Chem.* 90:4159–4163 (1986).
2. Tsang, W., and Walker, J. A., *Twenty-Second Symposium (International) on Combustion,* The Combustion Institute, Pittsburg, 1989, pp. 1091–1097.
3. Tsang, W., Cui, J. P., and Walker, J. A., "Single Pulse Shock Tube Study of the Reactions of Hydrogen Atoms with Complex Aromatics," *Proceedings of the 17th International Symposium on Shock Tubes and Waves,* AIP Conference Proceedings 208, American Institute of Physics, New York, 1990, p. 63–74.
4. Tsang, W., He, Y. Z., Mallard, W. G. and Cui, J. P., "Single Pulse Shock Tube Study of the Reactions of Hydrocarbons with Aromatics, IV: Chlortoluenes," *Proceedings of the 16th International Symposium on Shock Tubes and Waves,* VCH, New York, 1988, pp. 467–474.
5. He, Y. Z., Mallard, G. W., and Tsang, W., *J. Phys. Chem.* 92:2196–2201 (1988).
6. Cui, J. P., He, Y. Z., and Tsang, W., *J. Phys. Chem.* 93:724–727 (1989).
7. Nicovich, J. M., and Ravishankara, A. R., *J. Phys. Chem.,* 88:2534–2541 (1984).
8. Kerr, J. A., and Parsonage, M. A., *Evaluated Kinetic Data on Gas Phase Addition Reactions: Reactions of Atoms and Radicals with Alkenes, Alkynes and Aromatic Radicals,* Butterworths, London, 1972.
9. Harris, G. W., and Pitts, J. N., *J. Chem. Phys.* 79:3994–3987 (1982).
10. Tsang, W., "Comparative Rate Single Pulse Shock Tube in the Thermal Stability of Polyatomic Molecules," in *Shock Tubes in Chemistry* (A. Lifshitz, Ed.), Marcel Dekker, New York, 1981, pp. 59–99.
11. Falconer, W. E., and Sunder, W. A., *Int. J. Chem. Kinet.* 3:395–410 (1971).
12. McMillen, D. F., and Golden, D. M., *Ann. Rev. Phys. Chem.* 33:493–532 (1982).
13. Fahr, A., and Stein S. E., *Twenty-Second Symposium (International) on Combustion,* The Combustion Institute, Pittsburgh, 1988, pp. 1023–1029.
14. Tsang, W., and Lifshitz, A., *Annu. Rev. Phys. Chem.* 41:559–599 (1990).
15. Wilt, J., in "Free Radical Rearrangements" *Free Radicals* (J. Kochi, Ed.) Wiley-Interscience, New York, 1973, Vol. 1, pp. 333–502.
16. Stull, D. R., Westrum, E. F., and Sinke, G. C., *The Thermodynamics of Organic Compounds,* John Wiley and Sons, Inc., New York, 1969.
17. Stull, D. R., and Prophet, H., JANAF Thermochemical Tables, 2nd Edition, NSRDS-NBS37, U.S. Government Printing Office, Washington, DC 20402, 1971.
18. Burcat, A., Zelenik, F. J., and McBride, B., "Ideal Gas Thermodynamic Properties of Phenyl, Phenoxy and o-Biphenyl Radicals" NASA Technical Memorandum 83880, National Aeronautics and Space Administration, Lewis Research Center, Cleveland OH, 44155, (1985).
19. Robaugh D., and Tsang, W., *J. Phys. Chem.* 90:5363–5367 (1986).
20. Cui, J. P., He, Y. Z., and Tsang, W., *Energy Fuels* 2:614–618 (1988).
21. Walsh, R., *Int. J. Chem. Kinet.* 2:71–74 (1971).
22. Benson, S. W., *Thermochemical Kinetics,* John Wiley, New York, 1974.
23. Fahr, A., Laufer, A. H., Klein, R., and Braun, W., *J. Phys. Chem.* 95:3238–3242 (1991).
24. Robaugh, D. A., and Stein, S. E., *J. Am. Chem. Soc.* 108:3224–3229.
25. Tsang, W., and Walker, J. A., in preparation.

COMMENTS

John H. Kiefer, University of Illinois at Chicago, USA. Your agreement with the Fahr and Stein rate for C_6H_5 + C_2H_2 depends very much on the chosen 108.5 kcal/mol for the CH bond energy in ethylene. If you use the "latest" value of 111.2 [Berkowitz, J., Ellison, G. B. and Gutman, D., *J. Phys. Chem.* 98:2744 (1994)] you would not agree at all.

Author's Reply. We are in agreement with Dr. Kiefer's conclusion. Use of the higher value would have led to a discrepancy of a factor of 4 in the equilibrium constant. We believe that the equilibrium constant derived from the experimental numbers is accurate to within a factor of 2. It suggests to us that the "higher" value for the heat of formation derived from nonkinetic methods is in error. Note that the number derived from kinetic methods, as given in Dr. Kiefer's reference, is near 107 kcal/mol.

•

R. W. Walker, Hull University, England. Do you have any comment on the apparently large *A* factor for the H-abstraction reaction at the allylic position in *1*-phenylpropene? As a rotation is lost in the transition state, a value nearer 10^{13} might be expected.

Author's Reply. As noted in the text, the rate expression for the abstraction of the resonance stabilized hydrogen contains components from abstraction by methyl. Therefore it is a maximum value. This is probably the reason for the somewhat larger than expected *A* factor.

Twenty-Fifth Symposium (International) on Combustion/The Combustion Institute, 1994/pp. 875–882

PYROLYSIS OF *p*-XYLENE AND OF 4-METHYLBENZYL RADICALS

H. HIPPLER, S. SEISEL AND J. TROE
Institut für Physikalische Chemie der Universität Göttingen
Tammannstraße 6, D-37077 Göttingen, Germany

The thermal decomposition *p*-xylene (+ Ar) → 4-methylbenzyl + H (+ Ar) (1) was studied in shock waves between 1000 and 1800 K by monitoring UV absorptions of *p*-xylene and 4-methylbenzyl. A high-pressure limiting rate constant of $k_1 = 10^{15.7} \exp(-355 \text{ kJ mol}^{-1}/RT) \text{ s}^{-1}$ was derived. The experiments also allowed measurement of a rate constant $k_2 = 10^{14.6} \exp(-35 \text{ kJ mol}^{-1}/RT) \text{ cm}^3 \text{ mol}^{-1} \text{ s}^{-1}$ for the secondary reaction H + *p*-xylene → 4-methylbenzyl + H_2. Using 4-methylbenzyl iodide as a precursor, the decomposition of 4-methylbenzyl was investigated separately, leading to a rate constant of $10^{16.0} \exp(-360 \text{ kJ mol}^{-1}/RT) \text{ s}^{-1}$ over the range 1200–1600 K.

Introduction

In spite of their general importance as fuel molecules, aromatic hydrocarbons are not yet well characterized with respect to their pyrolysis and oxidation kinetics. In the case of alkyl-substituted aromatics, various C—C and C—H bond splits outside the ring may compete before the ring opens. The relative rates of these reactions often are still under dispute. Likewise, the oxidation mechanism with alternative routes via intermediate peroxide formation or attack by HO, HO_2, and O radicals is not understood in detail. Summaries of previous results are given, e.g., in Refs. 1 through 4, as well as in rate constant compilations such as Ref. 5.

In previous work, we have investigated in detail the high-temperature pyrolysis [6–9] and oxidation [10] of toluene as well as of benzyl radicals. By a combination of thermal and laser excitation experiments, the primary C—H [11] and C—C [12] bond ruptures in toluene, as well as the reverse combination of H with benzyl [13], could be measured. A redetermination of the equilibrium constant for toluene dissociation also was necessary [14]. Secondary processes such as the attack of toluene by H and benzyl dissociation completed our study. The oxidation of benzyl by O_2 at high temperatures apparently is not an efficient process. Instead, the oxidation involves benzyl dissociation forming H atoms, which react with O_2 such that a later attack of benzyl by OH opens the major pathways for oxidation [10].

As xylenes like toluene form important components of B-T-X (benzene-toluene-xylene) fuels, it is of importance to obtain similarly extensive kinetic information on xylene pyrolysis and oxidation as for toluene. It appears attractive to establish analogies or identify differences. An analysis of earlier laser and thermal excitation experiments in Refs. 7 and 11 suggests a markedly larger dissociation rate for *p*-xylene than for toluene, e.g., $k(1100 \text{ K}) = (3.6\text{–}7.4) \times 10^{-2} \text{ s}^{-1}$ and $k(1600 \text{ K}) = 1.6 \times 10^4 \text{ s}^{-1}$ for *p*-xylene as compared to $k(1100 \text{ K}) = 7.9 \times 10^{-3} \text{ s}^{-1}$ and $k(1600 \text{ K}) = 2.5 \times 10^3 \text{ s}^{-1}$ for toluene. The origin of these differences at present cannot be traced uniquely; probably slightly smaller dissociation energies and higher pre-exponential factors of the high-pressure bond dissociation rate constants in *p*-xylene work together. However, a high-temperature dissociation study, in similar detail as for toluene, was still missing. Apart from the primary C—H bond splits, other differences between toluene and *p*-xylene may be located in the competing C—C bond splits, the thermal dissociation of the benzyl and 4-methylbenzyl radicals, the H attack on the parent molecules, etc. First shock wave studies in our laboratory of *p*-xylene decomposition, monitoring the UV absorptions of the parent and the 4-methylbenzyl radicals in Refs. 7, 11, and 15, showed a strong superposition of 4-methylbenzyl formation and disappearance that could not be analyzed in a unique way before extensive complementary measurements were made. Having explored in the meantime optimum strategies for unravelling toluene decomposition with its complex mechanism of competing primary bond ruptures, reverse, and secondary processes, we were now in a position to approach the xylene pyrolysis again. With the results of the present work, we can provide an analysis of the primary fragmentation rate from flow system (near 1100 K) [16,17] to shock wave (1200–1800 K) conditions that is consistent with laser fragmentation rates [11]. Information on secondary reactions is also available such that the differences between the toluene and *p*-xylene pyrolysis systems can well be localized.

Experimental Technique

Our experiments were performed in reflected shock waves over the temperature range 1200–1800

K. Our aluminium shock tube had an inner diameter of 10 cm and a length of the test section of 4.20 m. The progress of reaction was followed by UV-absorption spectroscopy using a Xe-Hg arc lamp (Osram XBO-250) as the light source, a GCS/McPherson (Modell 216.5) monochromator, a Hamamatsu (1P28A) photomultiplier, and a microcomputer for data recording. All further details of our technique have been described in earlier articles such as Refs. 6 through 10. Absorption measurements were made over the spectral range 210–350 nm. In this range, the broad absorption continua of *p*-xylene and of 4-methylbenzyl radicals overlap; however, the spectra can easily be separated (see below). Experimental studies of *p*-xylene decomposition were done with mixtures of *p*-xylene in Ar, either with very low relative concentrations of *p*-xylene (of the order of 10 ppm) or with very high concentrations (of the order of 0.5%). The absolute concentrations of Ar behind reflected shocks were varied between 10^{-6} and 10^{-5} mol cm^{-3}. For separate studies of 4-methylbenzyl spectra and decomposition rates, we used 4-methylbenzyl iodide as a precursor molecule. In further studies of the reaction of H atoms with *p*-xylene, ethyl iodide was used as a thermal source of H atoms.

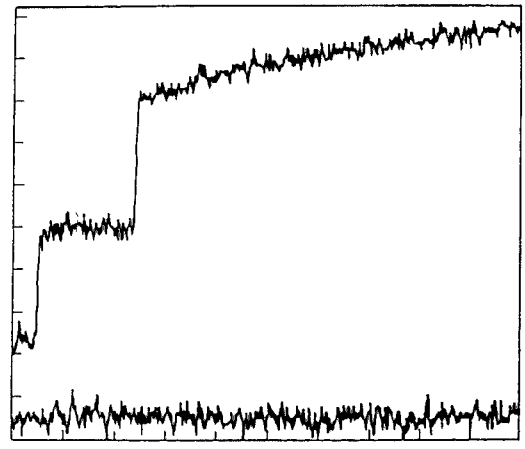

FIG. 1. Absorption signal recorded at 265 nm in the pyrolysis of *p*-xylene in Ar at high xylene concentrations (base line = no absorption; first step: incident shock; second step: reflected shock; horizontal time scale: 90 μs/mark; conditions behind reflected shock: T = 1227 K, [Ar] = 5.6×10^{-6} mol cm^{-3}, $[C_8H_{10}]/[Ar] = 4.67 \times 10^{-3}$).

Results

Absorption Spectra:

The room-temperature spectrum of *p*-xylene is characterized by an absorption band centered around 210 nm with an absorption coefficient ε = 3500 L mol^{-1} cm^{-1} that sharply drops near 225 nm. At shorter wavelengths a much stronger band is located. With increasing temperature, the spectrum broadens towards the red with strong contributions from both bands. However, near 1600 K there is still a very strong decrease of the absorption coefficient at $\lambda > 240$ nm such that values only of the order of 250 L mol^{-1} cm^{-1} are observed near 265 nm. The 4-methylbenzyl radicals have a broad absorption continuum centered around 265 nm [11]. Maximum absorption coefficients of 7500 L mol^{-1} cm^{-1} at this wavelength and temperatures around 1600 K were determined in the present work, in excellent agreement with the laser excitation results from Ref. 11. The comparison of the given data clearly indicates that 4-methylbenzyl radicals can be studied separately from *p*-xylene at 265 nm with large sensitivity. At the same time, a superposition of the two species can be monitored at shorter wavelengths, with dominating *p*-xylene absorption at $\lambda < 230$ nm. (It should be mentioned that the present work supersedes our earlier study [7], in which *p*-xylene and 4-methylbenzyl spectra could not be separated properly. Also, the strong differences between benzyl and 4-methylbenzyl absorption spectra reported in Ref. 7 are incorrect, being due to the previous interpretation with an incorrect toluene dissociation equilibrium constant, which was revised in the meantime.)

Dissociation of p-Xylene at 1200–1500 K:

In a first set of decomposition studies, we followed the strategy of Ref. 9, employing large initial concentrations of *p*-xylene. Because of the very large absorption coefficient of 4-methylbenzyl at 265 nm, very small conversions of *p*-xylene (C_8H_{10}) lead to measurable absorption increases such as demonstrated in Fig. 1. The signals initially rise linearly with time, and by means of the known absorption coefficient of 4-methylbenzyl radicals (C_8H_9), the rate coefficient k of the time law

$$\frac{d[C_8H_9]}{dt} = +k[C_8H_{10}] \qquad \text{(a)}$$

can be determined. Following the analogous discussion for the toluene system [9], under the chosen conditions of very large *p*-xylene concentrations, one may safely assume that the competing primary decomposition steps

$$p\text{-xylene} + \text{Ar} \rightarrow \text{4-methylbenzyl} + \text{H} + \text{Ar} \qquad \text{(1a)}$$

$$p\text{-xylene} + \text{Ar} \rightarrow \text{4-methylphenyl} + \text{CH}_3 + \text{Ar} \qquad \text{(1b)}$$

are rapidly followed by the reactions of the type

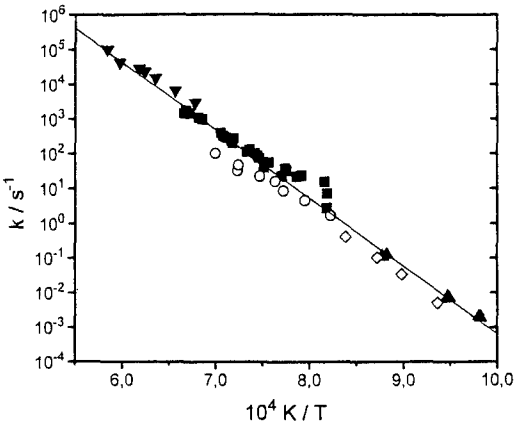

FIG. 2. First-order rate constants of p-xylene decomposition (▼: Ref. 15, reported in the present work; ■: this work; ○: Ref. 17; ◇: Ref. 18; ▲: Ref. 16; $k = k_{1a} + k_{1b}$, see text; data from Ref. 15 and this work at [Ar] = 10^{-5}–10^{-4} mol cm^{-3}, i.e., close to the high-pressure limit of the unimolecular reaction).

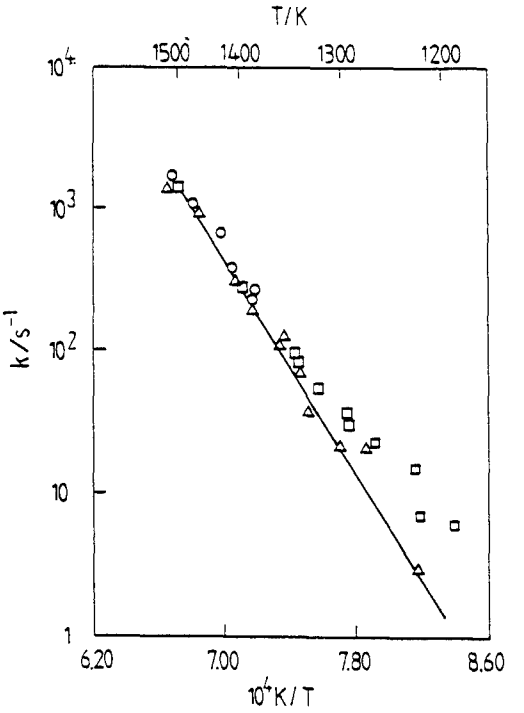

FIG. 3. As Fig. 2, dependence of the apparent k value on [C_8H_{10}] (see text; [C_8H_{10}]/[Ar] = 1.76×10^{-3} (○), 4.67×10^{-3} (□), and 7.42×10^{-3} (△)).

$$\text{H} + p\text{-xylene} \rightarrow \text{4-methylbenzyl} + \text{H}_2 \quad (2)$$

$$\text{CH}_3 + p\text{-xylene} \rightarrow \text{4-methylbenzyl} + \text{CH}_4 \quad (3)$$

$$\text{4-methylphenyl} + p\text{-xylene} \rightarrow \text{4-methylbenzyl} + \text{toluene} \quad (4)$$

such that, for each decomposing p-xylene, two 4-methylbenzyl radicals are formed. Therefore, the rate coefficient k from Eq. (a) corresponds to

$$k = 2(k_{1a} + k_{1b}). \quad (b)$$

Figure 2 shows the obtained results in comparison with earlier data from flow system studies at lower temperatures of Refs. 16 through 18. The data at $T > 1300$ K fit very consistently to an extrapolation of the low-temperature results. At 1200–1300 K, a deviation towards higher values is observed for lower p-xylene concentrations where the p-xylene excess apparently was not high enough to "quench" all other reaction pathways that accelerate the overall reaction. This concentration effect is demonstrated in Fig. 3.

Dissociation of p-Xylene at 1500–1800 K:

In previous decomposition studies from our laboratory [7,15] at higher temperatures, the smallest possible initial p-xylene concentrations were employed. Because of the large absorption coefficient of 4-methylbenzyl, relative concentrations of 15 ppm could easily be used. Under the applied conditions, 4-methylbenzyl formation [Eq. (1a)] was followed by 4-methylbenzyl decomposition

$$\text{4-methylbenzyl} + \text{Ar} \rightarrow \text{CH}_2\text{C}_6\text{H}_4\text{CH}_2 + \text{H} + \text{Ar} \quad (5)$$

and subsequent fragmentation of $CH_2C_6H_4CH_2$, possibly leading to further formation of H atoms by decomposition of $CH_2C_6H_4CH_2$ in analogy to benzyl decomposition. It appears plausible to assume that the spectra of 4-methylbenzyl and of $CH_2C_6H_4CH_2$ are similar. Therefore, the absorption signals from Ref. 7 were more difficult to analyze than the signals from the present work. At the concentrations employed, also reverse processes such as

$$\text{H} + \text{4-methylbenzyl} + \text{Ar} \rightarrow p\text{-xylene} + \text{Ar} \quad (-1a)$$

would contribute to the absorption decay. Reanalyzing the data from Ref. 7, one obtains k_{1a} values such as also shown in Fig. 2. At $T > 1500$ K, the results very well continue the data obtained at lower temperatures.

Figure 2 only includes measurements with high Ar concentrations near 2×10^{-4} mol cm^{-3}. Working at lower pressures, down to Ar concentrations of $2 \times$

10^{-6} mol cm^{-3}, some falloff was observed. The value of k_{1a} near 1650 K drops by a factor of 2 when [Ar] is decreased from 2×10^{-4} to 2×10^{-6} mol cm^{-3}. A comparison with modelled falloff curves shows [7,15] that only minor further increases of k_{1a} should occur at [Ar] $> 2 \times 10^{-4}$ mol cm^{-3}, the limiting high-pressure value being not more than about 30% above the values given in Fig. 2. Neglecting this minor "correction," all data of Fig. 2 between 1000 and 1800 K can well be represented by an Arrhenius expression

$$k_1 = 10^{15.7} \exp(-355 \text{ kJ mol}^{-1}/RT) \text{ s}^{-1}. \quad \text{(c)}$$

The analysis of laser excitation rate constants and their conversion into thermal dissociation rate constants in Ref. 11 led to

$$k_1 = 10^{16.25} \exp(-369 \text{ kJ mol}^{-1}/RT) \text{ s}^{-1}. \quad \text{(d)}$$

Equation (c) at 1650 K gives $k_1 = 2.9 \times 10^4$ s^{-1}, whereas Eq. (d) gives $k_1 = 3.7 \times 10^4$ s^{-1}. In view of the individual uncertainties of the two sets of experiments using completely different techniques, the agreement is excellent, in particular if one takes into account that minor falloff corrections (+30%) have not yet been included in Eq. (c).

A theoretical calculation of specific dissociation rate constants $k(E, J)$ for *p*-xylene decomposition in comparison to thermal dissociation rate constants k_∞ was given in Ref. 11. This analysis depends somewhat on the accurate bond energy of reaction (1a). The modelled expression of Eq. (d) was based on a bond energy (at 0 K) of $E_0 = 358.9$ kJ mol^{-1}, i.e., a value somewhat lower than that of toluene of 371.8 kJ mol^{-1}. The differences between toluene and *p*-xylene bond energies are not yet well established, differences between (1.3–1.7) kJ mol^{-1} [19] and 2.5 kJ mol^{-1} [20] being discussed. Replacing $E_0 = 358.9$ kJ mol^{-1} used for Eq. (d) by $E_0 = 370.2$ kJ mol^{-1}, instead of Eq. (d), one obtains from statistic adiabatic channel model (SACM) calculation [11]

$$k_1 = 10^{16.71} \exp(-382 \text{ kJ mol}^{-1}/RT) \text{ s}^{-1} \quad \text{(e)}$$

which leaves the values near 1650 K and the general agreement between all thermal experiments essentially unchanged. The accuracy of the thermal experiments is not sufficient to distinguish between such small differences of the bond energies.

For completeness, we give the additional falloff parameters required for modelling full falloff curves and falloff corrections such as obtained in Ref. 15. Using the F_{cent} notation of Ref. 21, at 1500 K we have $k_0 \approx$ [Ar] 2×10^{10} cm^3 mol^{-1} s^{-1} and $F_{cent} = 0.071$, and at 1700 K, we have $k_0 \approx$ [Ar] 2×10^{11} cm^3 mol^{-1} s^{-1} and $F_{cent} = 0.034$. Strong and weak collision broadening effects are included in this representation of falloff effects.

As in toluene dissociation, it appears very difficult to determine in thermal decomposition studies the branching ratio $Y_{1b} = k_{1b}/(k_{1a} + k_{1b})$ between C—H and C—C bond splits in *p*-xylene. For this purpose, by analogy to toluene [12], in separate laser excitation experiments [22] with in situ product analysis, we have measured branching ratios at specific excitation energies of *p*-xylene. After conversion to thermal branching ratios using SACM unimolecular rate theory, somewhat smaller branching ratios than in toluene were obtained. Values of $Y_{1b} = 0.05$ at 1000 K, 0.1 at 1200 K, 0.15 at 1500 K, 0.2 at 1750 K, and 0.25 at 2000 K were calculated. These small values indicate that Fig. 2 essentially corresponds to k_{1a} only. Nevertheless, in modelling more complex reaction situations with equilibration of reactions (1a) and (−1a), reaction (1b) should also be included.

Reaction of p-Xylene with Added H Atoms:

In separate experiments, we studied reaction (2) in mixtures of *p*-xylene with excess ethyl iodide. In this case, by the rapid dissociations

$$C_2H_5I + Ar \rightarrow C_2H_5 + I + Ar \quad (6)$$

$$C_2H_5 + Ar \rightarrow C_2H_4 + H + Ar \quad (7)$$

known amounts of H atoms are produced; the molecular elimination of HI was earlier shown to be only of minor importance under high-temperature conditions [9]. Reactions of I with benzyl iodide are much slower than reactions of H with toluene [9], so that one may safely assume that I atoms also react much more slowly with *p*-xylene than H atoms. The H atoms, formed very rapidly behind the shock wave, react with *p*-xylene via reaction (2). With increasing 4-methylbenzyl concentrations, reaction (−1a) increasingly consumes H atoms until 4-methylbenzyl reaches a "steady state." Later on, 4-methylbenzyl also decomposes or is consumed by other reactions. Figure 4 shows a typical 4-methylbenzyl signal from these experiments. At established steady state, the relationship

$$k_2/k_{-1a} = ([C_8H_9]/[C_8H_{10}])_{st.st.} \quad \text{(f)}$$

applies. With the measured signals and an assumed temperature-independent value of

$$k_{-1a} = 2 \times 10^{14} \text{ cm}^3 \text{ mol}^{-1} \text{ s}^{-1} \quad \text{(g)}$$

as measured for H + benzyl + Ar → toluene + Ar between 300 and 1700 K, the results of Fig. 5 are obtained. So far, a value of $k_{-1a} = 1.5 \times 10^{14}$ cm^3 mol^{-1} s^{-1} has been only measured at 300 K [23]. However, the SACM modelling of Ref. 11 for *p*-xylene as for toluene only gives small positive temperature coefficients of k_{-1a} in agreement with the H +

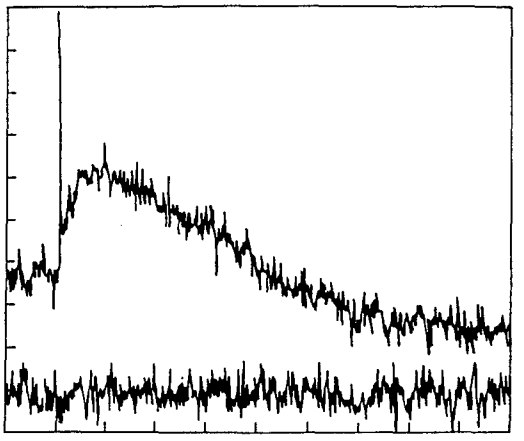

FIG. 4. Absorption signal recorded at 265 nm in the pyrolysis of p-xylene/ethyl iodide mixtures in Ar (T = 1520 K, $[C_8H_{10}] = 1.0 \times 10^{-10}$ mol cm^{-3}, $[C_2H_5I] = 7 \times 10^{-9}$ mol cm^{-3}; horizontal time scale: 135 μs/mark).

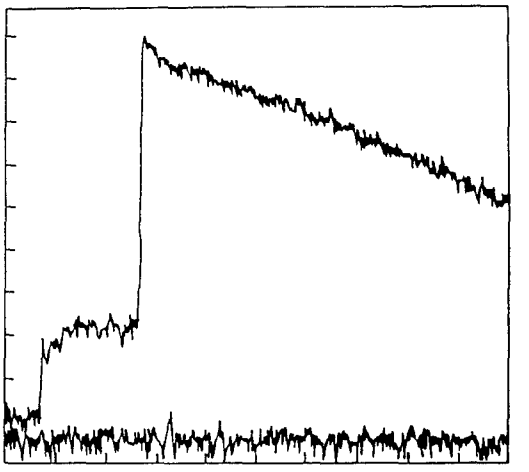

FIG. 6. Absorption signal recorded at 265 nm in the pyrolysis of 4-methylbenzyl iodide (conditions behind reflected shock: T = 1430 K, $[C_8H_9I] = 1.5 \times 10^{-9}$ mol cm^{-3}; horizontal time scale: 115 μs/mark).

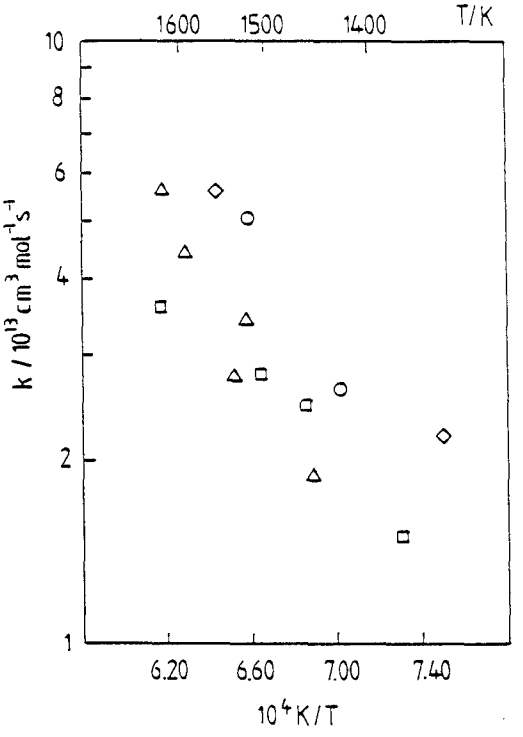

FIG. 5. Rate constant for the reaction H + p-xylene → H_2 + 4-methylbenzyl ($[C_8H_{10}]/[Ar] = 7.4 \times 10^{-5}$ (○), 1.0×10^{-4} (◇), 2.5×10^{-4} (□), 3.4×10^{-4} (△)).

benzyl experiments of Ref. 13. Therefore, the value of Eq. (g) appears well established [unless a larger value up to 6×10^{14} cm^3 mol^{-1} s^{-1} applies such as derived for k_{1a} from Eq. (e)]. With Eqs. (f) and (g), the data of Fig. 5 are represented by

$$k_2 = 10^{14.6} \cdot \exp(-35 \text{ kJ mol}^{-1}/RT) \text{ cm}^3 \text{ mol}^{-1} \text{ s}^{-1}. \quad \text{(h)}$$

The small temperature range of the present experiments does not allow reliable separation of k_2 into pre-exponential and exponential factor. Therefore, Eq. (h) is a tentative expression. (At lower temperatures, the rate of addition of H to xylene [13] exceeds that of abstraction.)

Dissociation of 4-Methylbenzyl Radicals:

The 4-methylbenzyl radicals, formed in the pyrolysis of p-xylene, will soon lose a second H atom from the second methyl group outside the aromatic ring. In order to learn more about this important secondary reaction of the pyrolysis, in separate experiments we studied the dissociation of 4-methylbenzyl radicals. We used the pyrolysis of 4-methylbenzyl iodide in order to prepare these radicals in a clean way. We synthesized this molecule and, because of its sensitivity to light, heat, and oxygen, carefully controlled its purity by ^{1}H-NMR spectroscopy. At first, we monitored the pyrolysis of 4-methylbenzyl iodide at 265 nm; temperatures between 750 and 1600 K and initial reactant concentrations between 2×10^{-10} and 4×10^{-9} mol cm^{-3} were applied. At 265 nm, the absorption coefficient of 4-methylbenzyl (ε = 7500 L mol^{-1} cm^{-1}) is markedly larger than that of the

parent molecule (ε = 1500 L mol^{-1} cm^{-1}). The absorption-time profiles, therefore, behind the incident shock show a rise of the signal (see Fig. 6). The signals behind the reflected shock have a specific structure that is due to contributions from several reactions such as the primary dissociation and its reverse (particularly important behind the incident shock),

4-methylbenzyl iodide + Ar
→4-methylbenzyl + I + Ar (8)

4-methylbenzyl + I + Ar
→ 4-methylbenzyl iodide + Ar (−8)

the dimerization of 4-methylbenzyl and its reverse,

2 (4-methylbenzyl) + Ar
→ 4,4′-dimethyldibenzyl + Ar (9)

4,4′-dimethyldibenzyl + Ar
→ 2 (4-methylbenzyl) + Ar (−9)

and the final dissociation of 4-methylbenzyl

4-methylbenzyl + Ar
→ $CH_2C_6H_4CH_2$ + H + Ar (5)

which is rapidly followed by the recombination

H + 4-methylbenzyl + Ar
→ *p*-xylene + Ar. (−1a)

Estimating k_{-8} and k_{-9} to be equal to the corresponding values in the benzyl iodide system [24], absorption profiles like Fig. 6 over a wide range of conditions could completely be analyzed, leading to values for k_8 of [25]

$$k_8 = 10^{14.8} \exp(-184 \text{ kJ mol}^{-1}/RT) \text{ s}^{-1} \quad \text{(i)}$$

over the range 790–870 K and for k_5 of

$$k_5 = 10^{16.0} \exp(-360 \text{ kJ mol}^{-1}/RT) \text{ s}^{-1} \quad \text{(j)}$$

over the range 1350–1600 K. The rate coefficient k_8 is practically identical to the rate constant of decomposition of benzyl iodide from Ref. 24. Analogous to this result, agreement between the dissociation rate constants for benzyl bromide and 4-methylbenzyl bromide was also found in Ref. 26. Our values for k_5 in Fig. 7 are compared with data from Ref. 17 obtained at lower temperatures in a flow system. The values well fit together. Pre-exponential factor and activation energy of k_5 well fit to the corresponding rate constant for C—H bond split in toluene [9].

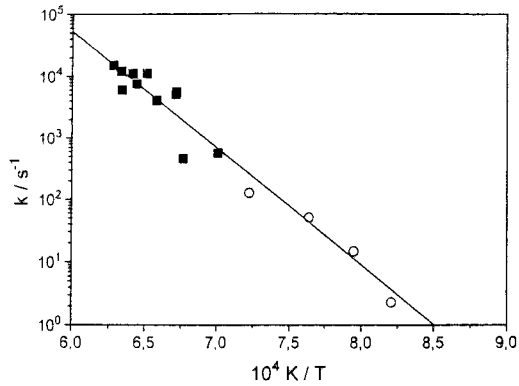

FIG. 7. First-order rate constants of dissociation of 4-methylbenzyl (■: shock wave results from this work; ○: flow system results from Ref. 17).

However, as spectra of $CH_2C_6H_4CH_2$ are not known and as the derived value for k_5 is similar to the corresponding value for benzyl decomposition, we cannot distinguish reaction (5) from the decomposition of $CH_2C_6H_4CH_2$ (whose products by analogy to benzyl decomposition could be H atoms with a stoichiometry of unity and other fragments).

Comparison of Toluene and p-Xylene Decomposition:

Toluene and *p*-xylene decompositions differ in the rates of the primary C—H bond splits, *p*-xylene dissociating five times faster than toluene. This difference can be attributed to the presence of two CH_3 groups outside the ring in *p*-xylene instead of the one group in toluene as well as to a slightly smaller dissociation energy (slightly smaller centrifugal barriers and less rigid CH_2 torsions in *p*-xylene may also contribute to some extent). The reaction of H atoms with *p*-xylene is twice as fast as that of H atoms with toluene. In contrast to these differences, the rate constants for benzyl and 4-methylbenzyl decomposition are very similar. However, this similarity may be misleading. While benzyl dissociates to H and to other fragments not well characterized so far, 4-methylbenzyl may dissociate to $CH_2C_6H_4CH_2$ biradicals or to $CH_2C_6H_4CH_2$ (*p*-chinodimethane) molecules [16–18,26]. Both in toluene and *p*-xylene decomposition, recombination reactions of H atoms with all radicals formed are very fast, rate constants being close to 2×10^{14} cm^3 mol^{-1} s^{-1} only with smaller radicals such as CH_3, falloff effects reduce this value to some extent [5]. The rate of the reaction of H atoms with aromatic radicals in previous work has often been underestimated [1], which had serious consequences on modelled concentration profiles. It finally should be mentioned that the C—C bond split [Eq. (1b)] in *p*-xylene followed by $C_6H_4CH_3$ + H →

TABLE 1
Rate constants for p-xylene pyrolysis from this work[a]

Reaction		k (s^{-1})	T (K)
p-xylene → C_8H_9 + H	1a	$k_{1a} + k_{1b} = 10^{15.7} \exp(-355/RT)$	1200–1800
p-xylene → C_7C_7 + CH_3	1b	$k_{1b}/k_1 = 0.10/0.15/0.2$	1200/1500/1750
H + C_8H_9 → C_8H_{10}	−1a	$k_{-1a} = 2 \times 10^{14}$	300–1700
H + C_8H_{10} → H_2 + C_8H_9	2	$k_2 = 10^{14.6} \exp(-35/RT)$	1350–1600
C_8H_9 → C_8H_8 + H	5	$k_5 = 10^{16.0} \exp(-360/RT)$	1350–1600

[a]Activation energy in kJ mol^{-1}; k in cm^3 mol^{-1} s^{-1}; results from Refs. 15 and 22 included, $k_1 = k_{1a} + k_{1b}$.

toluene may introduce toluene decomposition kinetics into p-xylene pyrolysis. A summary of the rate constants relevant for p-xylene decomposition, such as determined in our laboratory, is given in Table 1. Together with previously determined data for the toluene system, this set was sufficient to reproduce all observations of the present work.

Acknowledgment

Financial support of this work by the Deutsche Forschungsgemeinschaft (SFB 357 "Molekulare Mechanismen unimolekularer Prozesse") is gratefully acknowledged.

REFERENCES

1. Kern, R. D., Chen, H., Singh, H. J., Xie, K., Kiefer, J. H., and Sidhu, S. S., *Turbulence and Molecular Processes* (T. Takeno, Ed.) Elsevier Science Publishers, Amsterdam, 1993, pp. 117–132.
2. Emdee, J. L., Brezinsky, K., and Glassman, I., *J. Phys. Chem.* 96:2151–2161 (1992).
3. Rao, V. S., and Skinner, G. B., *J. Phys. Chem.* 93:1864–1869 (1989).
4. Braun-Unkhoff, M., Frank, P., and Just, Th., *Twenty-Second Symposium (International) on Combustion*, The Combustion Institute, Pittsburgh, 1989, pp. 1053–1061.
5. Baulch, D. L., Cobos, C. J., Cox, R. A., Esser, C., Frank, P., Just, Th., Kerr, J. A., Pilling, M. J., Troe, J., Walker, R. W., and Warnatz, J., *J. Phys. Chem. Ref. Data* 21:411–734 (1992).
6. Astholz, D. C., Durant, J., and Troe, J., *Eighteenth Symposium (International) on Combustion*, The Combustion Institute, Pittsburgh, 1981, pp. 885–892.
7. Brouwer, L., Müller-Markgraf, W., and Troe, J., *Twentieth Symposium (International) on Combustion*, The Combustion Institute, Pittsburgh, 1984, pp. 799–806.
8. Müller-Markgraf, W., and Troe, J., *Twenty-First Symposium (International) on Combustion*, The Combustion Institute, Pittsburgh, 1988, pp. 815–824.
9. Hippler H., Reihs, C., and Troe, J., *Z. Phys. Chem. NF* 167:1–16 (1990).
10. Hippler, H., Reihs, C., and Troe, J., *Twenty-Third Symposium (International) on Combustion*, The Combustion Institute, Pittsburgh, 1990, pp. 37–43.
11. Brand, U., Hippler, H., Lindemann, L., and Troe, J., *J. Phys. Chem.* 94:6305–6316 (1990).
12. Luther, K., Troe, J., and Weitzel, K.-M., *J. Phys. Chem.* 94:6317–6320 (1990).
13. Ackermann, L., Hippler, H., Pagsberg, P., Reihs, C., and Troe, J., *J. Phys. Chem.* 94:5247–5251 (1990).
14. Hippler, H., and Troe, J., *J. Phys. Chem.* 94:3803–3806 (1990).
15. Brouwer, L., Master's and Ph.D. Thesis, University of Göttingen, 1980 and 1984.
16. Swarc, M., *J. Chem. Phys.* 16:128–136 (1948).
17. Errede, L. A., and DeMaria, F., *J. Phys. Chem.* 66:2664–2672 (1962).
18. Schaefgen, J. R., *J. Polym. Sci.* 203–219 (1955).
19. Barton, B. D., and Stein, S. E., *J. Phys. Chem.* 84:2141–2145 (1980).
20. Hayashibara, K., Krupa, G. H., and Beauchamp, J. C., *J. Am. Chem. Soc.* 108:5441–5443 (1986).
21. Gilbert, R. G., Luther, K., and Troe, J., *Ber. Bunsenges. Phys. Chem.* 87:169–177 (1983).
22. Lange, S., Luther, K., Rech, T., Schmoltner, A. M., and Troe, J., *J. Phys. Chem.*, 1994, accepted for publication.
23. Lindemann, L., Ph.D. Thesis, University of Göttingen, 1987.
24. Müller-Markgraf, W., and Troe, J., *J. Phys. Chem.* 92:4899–4905 (1988).
25. Seisel, S., Master's Thesis, University of Göttingen, 1992.
26. Levy, M., Swarc, M., and Throssell, J., *J. Chem. Phys.* 22:1904–1911 (1954).

COMMENTS

David M. Golden, SRI International, USA. How do you rationalize the high ($\geq 10^{16}$ s^{-1}) *A* factors for C—H bond scissions? Transition state theory implies an entropy increase of approximately 9 eu, even though it is only a light H atom leaving a large molecule and the rotor is being tied up as a result of benzyl resonance.

Author's Reply. The *A* factor is not unusually high for an H atom leaving a radical in a simple bond fission reaction. As *A* factors always depend on the partitioning of the rate constant between Boltzmann factor and *A* factor, it is easier to rationalize the result by looking at the rate constant of the reverse reaction, i.e., the H addition to the radical. Here, one obtains 2×10^{14} cm^3 mol^{-1} s^{-1}, which is normal. Compared with the prediction by phase space theory (i.e., completely loose transition state theory), which, e.g., for H + benzyl → toluene gives $k^{PST}_{rec,\infty} = 10^{16}$ cm^3 mol^{-1} s^{-1} (see Troe, J., *J. Chem. Soc. Faraday Trans.* 87:2299, 1991), this is even a low value. Other H-atom additions to radicals have similar rate constants such as $H + CH_3 \rightarrow CH_4$ ($k_{rec,\infty} = 2 \times 10^{14}$ cm^3 mol^{-1} s^{-1}).

•

John C. Mackie, University of Sydney, Australia. Did you observe any high molecular weight material? If so, could the postulated biradical really be a carbene, which could undergo ring enlargement and contraction. These carbene reactions could lead to high molecular weight products often observed in pyrolysis of toluene and other methyl-substituted aromatics.

Author's Reply. In our experiments, we only used time-resolved UV absorption spectroscopy as a detection tool. However, it has previously been shown that *p*-chinodimethane (C_8H_8), obtained via loss of two hydrogen atoms, one from each methyl group, is an essential product in the *p*-xylene (C_8H_{10}) pyrolysis. The dimer ($C_{16}H_{16}$) together with a C_8H_8 polymer have been identified as reaction products [1–4]. For C_8H_8, there exist two mesomeric structures, e.g., the chinoidal or the biradical form, where the chinoidal structure is likely to be more stable by about 10 kcal/mol [5]. To our knowledge, there is no indication for the formation of the carbene isomer of the C_8H_8 which might be obtained through intermolecular H-atom migration. The product analysis did not show specific products from ring enlargement and contraction that are typical for carbenes.

REFERENCES

1. Szware, M., *J. Chem. Phys.* 16:128 (1948); Levy, M., Szware, M., and Throsell, J., *J. Chem. Phys.* 22:1904 (1954).
2. Schaefgen, J. R., *J. Polym. Sci.* 75:203 (1955).
3. Cram, D. J., and Steinberg, H., *J. Am. Chem. Soc.* 73:5691 (1951).
4. Errede, L. A., Gregorian, R. S., and Hoyt, J. M., *J. Am. Chem. Soc.* 82:5218 (1960).
5. Coulson, C. A., Craig, D. B., Maccoll, A., and Pullman, A., *Discuss. Faraday Soc.* 2:36 (1967).

Twenty-Fifth Symposium (International) on Combustion/The Combustion Institute, 1994/pp. 883–891

REACTION MECHANISMS FOR TOLUENE PYROLYSIS

M. B. COLKET AND D. J. SEERY
United Technologies Research Center
East Hartford, CT 06108, USA

The rich chemistry occurring during the pyrolysis of toluene has been investigated by studying its decomposition in a single-pulse shock tube coupled with detailed chemical kinetic modeling to describe product formation. This work provides information on the initial decomposition steps of toluene and its primary radical benzyl as well as the detailed steps leading to the formation of polyaromatic hydrocarbons. Temperatures ranged from approximately 1200 to 1850 K for 1% toluene in argon, total pressures of approximately 10 atm, and residence times near 600 μs. Pyrolysis products were collected and analyzed using gas chromatography. Profiles of hydrogen and hydrocarbons ranging from methane to pyrene were obtained. These semiquantitative data have been interpreted to help resolve many of the existing uncertainties involving the pyrolytic process. In particular, this work supports arguments for a low activation energy process for benzyl radical decomposition as evidenced by the low-temperature formation of cyclopentadiene and the radical recombination product, benzyl-cyclopentadienyl (b-cpd). Also, the data support suggestions for an important role of the methylphenyl radical, specifically in the formation of isomers of dimethyldiphenyl and as a key intermediate in the production of anthracene. Minimal evidence for rapid toluene decomposition to phenyl and methyl was found. Importantly, the data support general mechanisms proposed for ring growth sequences, although an additional important step involving ring closure and direct H_2 elimination is suggested by the data. In addition, the data indicate rapid anthracene/phenanthrene isomerization above 1600 K.

Introduction

The pyrolysis of toluene and related chemistry have been studied by many authors [1–13]. The principal reason for the more recent studies has been that toluene is one of the smallest aromatic molecules implicated in both soot inception and soot growth. Most of these studies have been limited to the initial decomposition steps with little work on subsequent processes, particularly those involving polyaromatic hydrocarbon (PAH) growth mechanisms. Furthermore, there remains a substantial rift between European [9,12,13] and U.S. [8,10,11] authors regarding the relative importance of the primary initiation steps in toluene decomposition, and definitive evidence identifying benzyl radical reaction products is lacking.

It is the objective of this study to present some new data and interpretations that will clarify these primary uncertainties and provide new information on PAH formation.

Toluene pyrolysis studies were initiated in this laboratory using a single-pulse shock tube (SPST) more than 10 years ago [8]. Only trace concentrations of odd carbon species (except for methane) were observed, yet proposed mechanisms included initial formation of C_5 and C_3 species from fragmentation of benzyl radicals. In addition, recovery of carbon was less than 25% near temperatures at which toluene decomposes rapidly (above 1500 K). Subsequently, additional work was performed, including (1) pyrolyzing compounds such as allene, cyclopentadiene, norbornadiene, and phenylacetylene, and (2) collection and identification of high molecular weight species [14] using a gas chromatograph/mass spectral detection. The allene work was described previously [8] and helped to identify rapid formation of benzene from C_3 species. In this paper, the recent results on the pyrolysis of toluene will be presented and interpreted.

Experimental Apparatus and Procedures

Experiments were performed in a 3.5-cm single-pulse shock tube using hardware and procedures previously described [15]. Modifications were made to the gas sampling and analysis systems to collect and more readily identify high molecular weight species. The modifications included higher sample line temperatures (150 °C) and use of a thermal conductivity detector for hydrogen analysis and a mass selective detector for identification. A flame ionization detector was used for quantification. Concentrations of the larger PAH's reported in this study may be in error by as much as a factor of 2 as a result of uncertainties in collection efficiencies and calibration procedures. More than 50 individual peaks were identified as

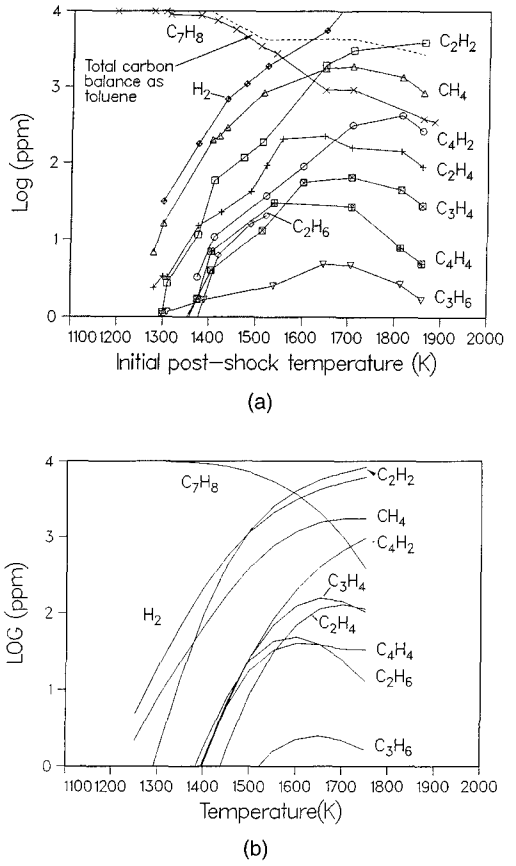

FIG. 1. (a) Formation of aliphatic products during SPST pyrolysis of 1% toluene at 10 atm and 600 μm. (b) Model predictions of aliphatic products during pyrolysis of toluene.

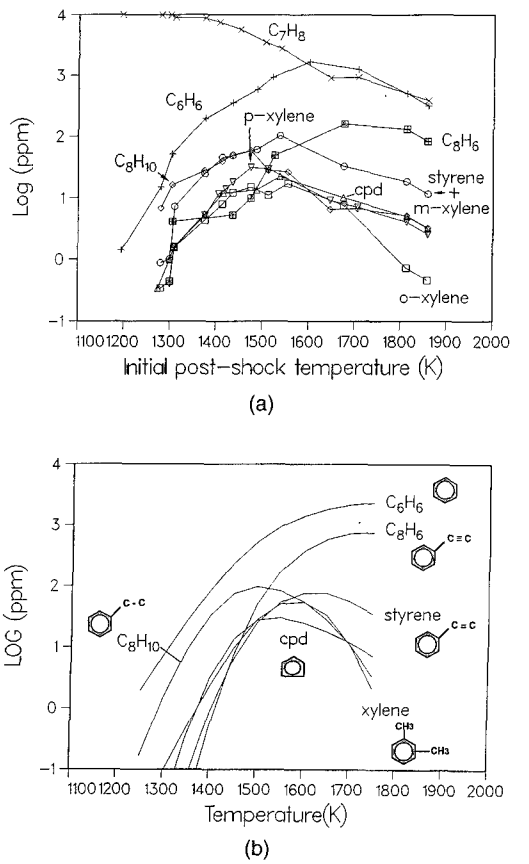

FIG. 2. (a) Formation of single-ringed species during pyrolysis of toluene. (b) Model predictions of single-ringed species during pyrolysis of toluene.

products, and the more dominant are reported. Benzyl-cyclopentadienyl (b-cpd) was identified by its total mass (156) and two very strong peaks at 91 (benzyl) and 65 (cyclopentadienyl). The seven isomers of dimethyldiphenyl were not individually identified. The data reported here are the combination of all the isomers (total, not average). Five isomers of diphenylmethane at 168 amu and four isomers of pyrene at 202 amu were similarly combined. The data presented in Figs. 1a through 4a were obtained from two separate series of experiments, although some of the data were averaged to clarify the figures.

Description of Results

Toluene (1% in argon) has been pyrolyzed at total pressures of about 10 atm for approximately 600 μs. Final products for a series of individual runs are presented in Figs. 1a through 4a for initial post-shock temperatures ranging from about 1200 to 2000 K. Many features of these data have been reported in previous studies using a variety of experimental techniques [1,4–6,11,16]. Methane, acetylene, diacetylene, and benzene are dominant low molecular weight products. Ethylene has been reported [11], but also observed here are vinylacetylene, propene, C_3H_4's and cyclopentadiene. Most of the high molecular weight species observed here have been reported previously [2,6,16]. Of particular note is the new observation of b-cpd presumably formed as a result of the simultaneous presence of benzyl and cyclopentadienyl radicals. It should be recognized that some products (such as b-cpd) may have been formed at least in part during the quenching process in the SPST.

Discussion

A detailed chemical kinetic mechanism has been constructed for comparison with these data. This

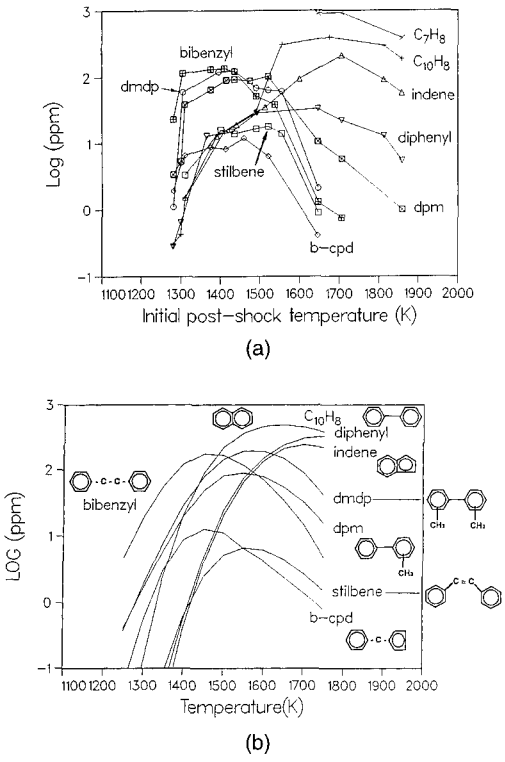

FIG. 3. (a) Formation of two-ring aromatics during pyrolysis of toluene. (b) Model predictions of two-ring aromatics during pyrolysis of toluene.

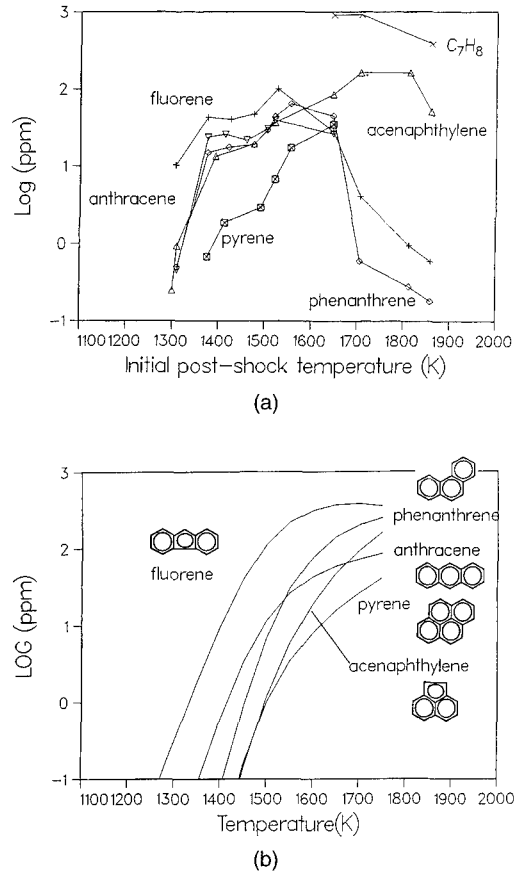

FIG. 4. (a) Formation of PAH hydrocarbons during pyrolysis of toluene. (b) Model predictions of PAH hydrocarbons during pyrolysis of toluene.

mechanism is reproduced in Ref. [17]. Because of space limitations, only key reactions and their associated rate constants are listed in Table 1. The reaction sequence was constructed initially from that reported by Brouwer et al. [12] but was modified substantially to include steps describing the formation of aromatics and other species. Also, reactions involving the methylphenyl radical, as earlier suggested by Rao and Skinner [10] and by Pamidimukkala et al. [11], and related steps were included. The reaction sequence involving light species is similar to those reported in Refs. 16, 18, and 19. Thermodynamic data for several aromatic species were obtained from the literature, and unavailable thermodynamics were estimated using group additivity techniques. Thermodynamic data for selected (aromatic and polyaromatic) species are also provided in Ref. 17. CHEMKIN II [20] and a modified version of the Sandia shock-tube code [21] were used to perform the kinetic calculations. Modifications enabled inclusion of experimental pressure decays (along with temperature decays assuming isentropic, adiabatic expansion) to estimate the effects of the quenching process. Predictions are plotted in Figs. 1b through 4b. In order to understand the behavior of this kinetic set, both a reaction path analysis and SENKIN [22] were used.

Identification of the decomposition pathways of toluene and its initial radicals remains a significant uncertainty in recent literature. Brouwer et al. [12] suggest that $k_2 \approx 0.1k_1$, whereas Pamidimukkala et al. [11] require $k_2 \approx 2.5k_1$ in order to interpret laser schlieren data. The primary formation of benzyl vs phenyl leads to substantially different decomposition pathways. The conclusion in Ref. 11 that k_2 is faster than k_1 seems to be unusual in light of the endothermicities of the two reactions (about 88 and 102 kcal/mole for Reactions 1 and 2, respectively). The 14 kcal/mole differential represents two orders of magnitude in the Boltzmann term and would be difficult to overcome by differences in the A factor. Tsang [23] has recently offered a possible interpretation that, following Reaction 1, subsequent thermal equilibration and recombination of the products, H + benzyl $\Rightarrow (C_7H_8)^*$, lead to formation of a thermally excited toluene molecule with sufficient energy

TABLE 1
Proposed Mechanism for Toluene Pyrolysis
($\log k = \log A - E/R/T/2.303$; units: cm^3 mole s kcal)

Reactions	Forward rate constant		Reverse rate constant	
	$\log A$	E	$\log A$	E
1 C_7H_8 = benzyl + H	15.45	88.9	14.24	−0.2
2 C_7H_8 = phenyl + CH_3	16.00	97.0	12.92	−0.8
3 C_7H_8 + H = benzyl + H_2	14.10	8.4	13.50	23.7
4 C_7H_8 + CH_3 = CH_4 + benzyl	12.20	11.1	13.08	27.1
5 C_6H_6 = phenyl + H	16.76	116.0	14.46	6.4
6 C_6H_6 + H = phenyl + H_2	14.40	16.0	12.71	10.7
7 C_6H_6 + CH_3 = phenyl + CH_4	13.30	16.0	13.10	11.5
8 C_7H_8 + H = C_6H_6 + CH_3	13.08	5.1	12.30	17.0
9 2 benzyl = bibenzyl	12.70	0.5	14.93	60.0
10 benzyl = c-C_5H_5 + C_2H_2	13.78	70.0	11.57	8.3
11 benzyl = C_4H_4 + C_3H_3	14.30	83.6	8.28	−15.6
12 benzyl + c-C_5H_5 = b-cpd	12.70	0.0	13.81	49.3
13 c-C_5H_5 = C_2H_2 + C_3H_3	15.00	71.0	9.75	−3.2
14 C_3H_3 + benzyl = naphthalene + 2H	11.78	0.0	0.0	0.0
15 naphthalenyl + C_6H_6 → pyrene + H + H_2	12.00	5.0	0.00	0.0
16 naphthalene + phenyl → pyrene + H + H_2	11.00	5.0	0.00	0.0
17 DPM = fluorene + H_2	8.00	32.0	10.24	18.3
18 *o*-benzyltoluene = dihydroanthracene + H_2	8.00	40.0	9.67	10.7
19 anthracene = phenanthrene	12.90	65.0	12.73	67.0

to decompose to any of a variety of products. At low pressures, this process might be likely since collisional deactivation is slow. For the high pressures in this study, the Tsang suggestion appears less likely.

At low temperatures (~1200–1300 K in this study), benzene, methane, hydrogen, and bibenzyl are dominant products. The first two products could be the result of initiation by Reaction 2, but we favor Price's [4] interpretations that these products are due principally to the sequence 1,8,4, whereas hydrogen and bibenzyl are formed from Reactions 3 and 9, respectively. Indeed, reaction pathway and sensitivity analysis support this interpretation, at least for the mechanism used in this study. In Ref. 11, contributions from Reaction 8 were not included, since this reaction is nearly thermally neutral and should not by itself influence the laser schlieren data.

Use of the high value for k_2 obtained in Ref. 11 led to substantial overpredictions for methane, ethane, benzene, and ethylbenzene, as well as further increasing the otherwise high prediction for diphenyl production (see Figs. 3a and 3b). Use of the alternative reaction set [12], with its high relative rate for initiation of toluene to benzyl + H, leads to high acetylene predictions, as shown in Fig. 1b. Much of this acetylene is lost to further molecular weight growth that is not accounted for by the limited mechanism used in this study.

Two low-temperature products coincident with the formation of acetylene (presumably a decomposition product of benzyl or phenyl) are cyclopentadiene (cpd) and benzyl-cyclopentadienyl (b-cpd). This latter product is almost entirely formed during the quenching process via the recombination of the two stable radicals, benzyl and cyclopentadienyl. Traces of several other C_5 species at masses 66 and 68 were observed at levels typically 5–10 times below those of cpd. The presence of the C_5 compounds supports arguments for decomposition of benzyl radical. Cyclopentadienyl is preferred since cpd offers the lowest energy path for decomposition (64 kcal/mole). The mechanism for this process has not been described well. Thus, we explored the reverse process by comparing results from cpd pyrolysis with those of cpd/C_2H_2 pyrolysis [24]. The rate of toluene formation was enhanced by about an order of magnitude in the presence of acetylene. Following a suggestion [25], the toluene formation may arise from

$$\text{c-}C_5H_6 + C_2H_2 \Leftrightarrow \text{norbornadiene} \Leftrightarrow \text{toluene} \quad \text{(A)}$$

or

$$\text{c-}C_5H_5 + C_2H_2 \Leftrightarrow \text{norbornadienyl} \Leftrightarrow \text{benzyl} \quad \text{(B)}$$

Known rates [26] for (A) do not account for the high-temperature dependence (60 kcal/mole) of tol-

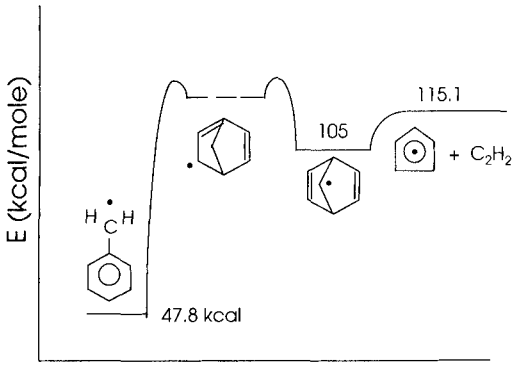

FIG. 5. Low temperature route for decomposition of benzyl radical.

uene formation observed in our cpd/C_2H_2 experiments. We favor (B), which had been suggested [27] for the reverse of benzyl decomposition. Norbornadiene was also shock heated; only traces of the parent remained even at 1100 K, along with the products, cpd, toluene, cycloheptatriene, and acetylene, consistent with known isomerization and decomposition.

Consequently, Reaction 10 was adopted as the preferred low-temperature benzyl decomposition path. A schematic representation of this process is depicted in Fig. 5. The cpd and b-cpd production were used to help determine a rate for benzyl radical decomposition. Unfortunately, a sensitivity analysis indicates that the concentrations of these species are dependent on both the rates for decomposition of benzyl (Reaction 10) and for cyclopentadienyl radicals (Reaction 13).The rates suggested in Table 1 for these two reactions should be considered accurate to about a factor of 3 in the temperature range of 1300–1500 K. The activation energies used here (70 and 71 kcal/mole) are significantly higher than some values reported previously (44.7 and 40, respectively [12]).

In another decomposition path, norbornadienyl could isomerize to cycloheptatrienyl and subsequently decompose. Alternatively, cycloheptatriene could be formed directly from a thermally excited benzyl by bridging of the CH_2 group to the *ortho* position, followed immediately by ring enlargement and decomposition directly into two acetylenes and a propargyl radical. This overall process requires 142 kcal/mole and therefore appears unlikely.

As indicated in Table 1, an alternative mechanism for benzyl decomposition was included in part because of the results of Refs. 6, 16, and 28 suggesting two competitive decomposition processes, and the observations of vinylacetylene in this study. Predictions of vinylacetylene were found to be nearly directly proportional to the rate constant selected for benzyl decomposition to C_4H_4 + C_3H_3. The initial step for this process may be similar to that suggested by Rao and Skinner [29], although the final products suggested here differ from the previous proposal. C_4H_3 + C_3H_4 was not included since it is endothermic by 120 kcal/mole compared with about 60 and 100 kcal/mole for Reactions 10 and 11, respectively. The rate selected in Table 1 was selected principally by the peak production of vinylacetylene.

Other steps for decomposition of toluene/benzyl could involve the methylphenyl ($CH_3C_6H_4$) radical(s). Pamidumukkla et al. [11] suggested the formation of such radicals by H abstraction from the ring. They then allowed its subsequent decomposition following rate kinetics of the phenyl radical. Although this is probably a low limit estimate of the decomposition rate constant, the use of this rate leads to a negligible contribution to overall ring fracture relative to the direct decomposition of benzyl radical.

Growth steps have been nearly ignored by most of the recent kinetic studies despite substantial documentation of PAH production at lower [2,3,5] as well as comparable temperatures [16]. Brouwer et al. [12] included bibenzyl and *trans*-stilbene in their model; however, the SPST results indicate that the spectrum of products is much richer. Some of these high molecular weight species are products of combining stable, long-lived radicals, such as benzyl, cyclopentadienyl, and indenyl, partially or wholly in the rarefaction wave. Condensed ring aromatics and other species such as diphenyl and diphenylmethane (dpm) are principally formed during the period of high-temperature pyrolysis, although concentrations can be altered by about 10% as the reacting gases begin to cool.

Figure 3 indicates that, although bibenzyl is the dominant high molecular weight species at low temperature (and presumably at early pyrolysis times), the combination of dmdp (dimethyldiphenyl) isomers and dpm isomers each attain nearly comparable levels. These high relative levels of dmdp are comparable to those obtained by Brooks et al. [5]. The dmdp production steps included in Table 1 are logical extensions of the reactions involving the methylphenyl radical, whose possible role in toluene pyrolysis was discussed [11]. Some dmdp can also be formed by benzyl addition to toluene. Diphenylmethane could be formed by H-atom substitution on dmdp or benzyl radical addition to benzene.

As shown in Fig. 4a, several three-ringed species eventually attain levels similar to those of bibenzyl, including fluorene, anthracene, phenanthrene, and acenaphthylene. Two unusual features are apparent. First, fluorene was produced at fairly high levels for the low-temperature pyrolysis. Second, anthracene was initially produced at levels substantially greater than its more stable isomer, phenanthrene. Several attempts were made to model fluorene production. Following dpm production, abstraction of an *ortho* H atom should lead to rapid ring closure and H-atom elimination. Unfortunately, unless an unreasonably

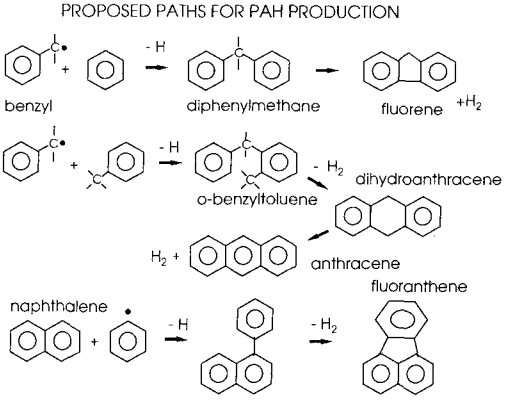

FIG. 6. Proposed paths for PAH production.

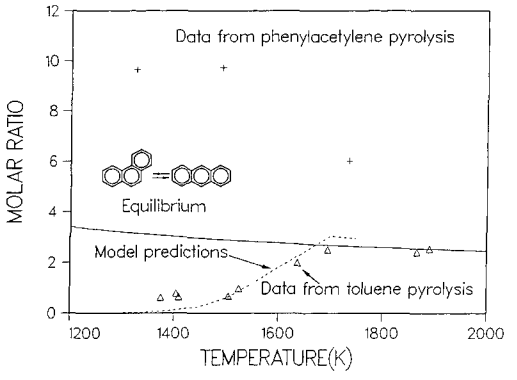

FIG. 7. Experimental and equilibrium phenanthrene/anthracene ratios as a function of temperature. + Ratios determined from pyrolysis of phenylacetylene; Δ ratios determined during pyrolysis of toluene; —— equilibrium ratio; --- predictions from chemical kinetic model.

low activation energy was assigned to the H-atom abstraction process, fluorene production was more than an order of magnitude too slow. As an alternative, a direct four-center elimination of H_2 and ring closure is proposed (see Fig. 6). The low preexponential (10^8 s^{-1}) and the activation energy (32 kcal/mole) seem acceptable. Calculations [30] indicate that reorientation of dpm, so that the *ortho* H atoms are within close proximity, requires only 5–10 kcal/mole. Previously, Badger and Spotswood [2] implicated recombination of phenyl and benzyl as a precursor to fluorene formation.

Low-temperature production of anthracene led to unusually low phenanthrene/anthracene ratios; typically, equilibrium levels had been attained in other SPST pyrolyses at elevated temperatures. In contrast, the opposite trend was observed during phenylacetylene pyrolysis in the SPST. In Fig. 7, experimental and equilibrium phenanthrene/anthracene ratios are plotted as a function of temperature. The ratios from phenylacetylene pyrolysis are near 10 at low temperatures, but from toluene pyrolysis are about 0.5. As temperature increases above 1600 K, the ratios are both driven to equilibrium levels near 2.5. To explain the disparate results at low temperatures, the middle reaction depicted in Fig. 6 is proposed. Anthracene is assumed to be formed from a specific isomer of dimethyldiphenyl, i.e., $C_6H_5CH_2C_6H_4CH_3$ or *o*-benzyltoluene, where the attached methyl group is located in the *ortho* position. Dihydroanthracene can be formed by abstraction of the benzyl H from the *ortho* methyl group, subsequent ring closure, and H-atom elimination, or by direct ring closure and H_2 elimination. Dehydrogenation of dihydroanthracene is assumed to occur at a rate comparable to that for dehydrogenation of 1,4-cyclohexadiene [26]. Several authors have reported the early formation of anthracene [3,31]. The proposed mechanism for formation of anthracene is similar to a previous suggestion [32]. The facile conversion of *o*-benzyltoluene has been demonstrated by Errede and Cassidy [3], who found a 91% conversion of *o*-benzyltoluene to anthracene.

The rapid formation of phenanthrene during the phenylacetylene pyrolysis presumably is due to phenyl addition to phenylacetylene followed by a cyclization process. This sequence is likely similar to the conversion of *cis*-stilbene to phenanthrene plus H_2.

The fastest step for forming naphthalene is assumed to be Reaction 14, isomerization of the recombination product of benzyl and propargyl. There is little previous evidence for this step, but more conventional processes (i.e., sequential addition of acetylene to phenyl [33] and methyl addition to indene) did not result in reasonable naphthalene production rates. A variety of steps have been included in an attempt to describe pyrene formation. By far the most important is phenyl addition to naphthalene (or naphthalenyl addition to benzene) followed by a four-centered H_2 elimination and ring closure to form fluoranthene (see Fig. 6). Subsequently, fluoranthene may isomerize to pyrene or one of the other isomers at mass 202.

Conclusions

Single-pulse shock-tube pyrolysis of toluene and detailed chemical kinetic modeling have been used to clarify several uncertain features of the decomposition path and PAH growth processes. Initiation of the reaction occurs principally by decomposition of toluene to benzyl + H. Primary C-C cleavage also occurs, more slowly. Benzyl radical decomposition to acetylene plus cyclopentadienyl radical was estimated to have a rate constant of 6×10^{13} $\exp(-70{,}000/RT)$ s^{-1} in support of Ref. 12, but four times above the revised determination [13] at 1400

K. Formation of norbornadienyl is proposed as an intermediate in this decomposition process. The large concentrations of dimethyldiphenyl isomers are consistent with earlier results [2] and support the suggestion [12] of the importance of the methylphenyl radical. Mechanisms and associated rate constants for formation of fluorene and anthracene are proposed, and evidence for the anthracene ⇔ phenanthrene isomerization is presented. An estimated rate constant $8 \times 10^{12} \exp(-65{,}000/RT)\ s^{-1}$ is suggested. Ring growth steps follow similar paths and rates as indicated in previous studies [33], except that additional possible processes have been identified. First, four-centered, concerted reactions involving direct H_2 elimination and ring closure with rate constants of $10^8 \exp(-E/RT)\ s^{-1}$, where $30 < E < 40$ kcal/mole, are suggested. Second, phenyl addition to naphthalene leading to fluoranthene formation and isomerization to pyrene is indicated by the data.

Acknowledgments

This work has been supported in part by the Air Force Office of Scientific Research (AFSC) under Contract Nos. F49620-85-C-0012, F49620-88-C-0051, and F49620-91-C-0056. The encouragement by J. Tishkoff is greatly appreciated. This work would not have been performed without the able technical assistance of D. Kocum of United Technologies Research Center. Detailed technical discussions with H. Palmer, J. Kiefer, R. D. Kern, J. Troe, T. Just, M. Frenklach, and W. Tsang have been instrumental in directing this research.

REFERENCES

1. Szwarc, M., *J. Chem. Phys.* 16:128 (1948).
2. Badger, G. M., and Spotswood, T. M., *J. Chem. Soc.* 4220 (1960).
3. Errede, L. A., and Cassidy, J. P., *J. Am. Chem. Soc.* 82:3653 (1960).
4. Price, S. J., *Can. J. Chem.* 40:1310 (1962).
5. Brooks, C. T., Cummins, C. P. R., and Peacock, S. J., *Trans. Faraday Soc.* 67:3265 (1971).
6. Smith, R. D., *J. Phys. Chem.* 83:1553 (1979).
7. Astholtz, D. C., Durant, J., and Troe, J., *Eighteenth Symposium (International) on Combustion*, The Combustion Institute, Pittsburgh, 1981, pp. 885–891.
8. Colket, M. B., and Seery, D. J., Presented at Twentieth Symposium (International) on Combustion, Ann Arbor, MI, 1984.
9. Braun-Unkoff, M., Frank, P., and Just, Th., *Twenty-Second Symposium (International) on Combustion*, The Combustion Institute, Pittsburgh, 1988, pp. 1053–1061.
10. Rao, S. V., and Skinner, G. B., *J. Phys. Chem.* 88:4362 (1984).
11. Pamidimukkala, K. M., Kern, R. D., Patel, M. R., Wei, H. C., and Kiefer, J. H., *J. Phys. Chem.* 91:2148 (1987).
12. Brouwer, L. D., Muller-Markgraf, W., and Troe, J., *J. Phys. Chem.* 92: 4905 (1988).
13. Hippler, H., Reihs, C., and Troe, J., *Z. Phys. Chem. Neue Fo.* 167:1 (1990).
14. Colket, M. B., Hall, R. J., Sangiovanni, J. J., and Seery, D. J., *The Determination of Rate-Limiting Steps During Soot Formation*, United Technologies Research Center Report No. UTRC89–13, 1989.
15. Colket, M. B., *Twenty-First Symposium (International) on Combustion*, The Combustion Institute, Pittsburgh, 1986, pp. 851–864.
16. Smith, R. D., *Combust. Flame* 35:179 (1979).
17. Colket, M. B., Hall, R. J., and Smooke, M. D., *Mechanistic Models of Soot Formation*, United Technologies Research Center Report No. UTRC94-28, 1994.
18. Kiefer, J. H., Mitchell, K.I., Kern, R. D., and Yong, J. N., *J. Phys. Chem.* 92:677 (1988).
19. Wu, C. H., and Kern, R. D., *J. Phys. Chem.* 91:6291 (1987).
20. Kee, R. J. Rupley, F. M., and Miller, J. A., *CHEMKIN II: A Fortran Chemical Kinetics Package for the Analysis of Gas-Phase Chemical Kinetics*, Sandia Report SAND89-8009, 1989.
21. Mitchell, R. E., and Kee, R. J., *A General -Purpose Computer Code for Predicting Chemical Kinetic Behavior Behind Incident and Reflected Shocks*, Sandia Report SAND82-8205, 1982.
22. Lutz, A. E., Kee, R. J., and Miller, J. A., *SENKIN: A Fortran Program for Predicting Homogeneous Gas Phase Chemical Kinetics with Sensitivity Analysis*, Sandia Report SAND87-8248, 1991.
23. Tsang, W., *Chemical and Physical Processes in Combustion*, Paper No. 19, Princeton University, 1993, pp. 121–124.
24. Colket, M. B., Hall, R. J., Sangiovanni, J. J., and Seery, D. J., *The Determination of Rate-Limiting Steps During Soot Formation*, United Technologies Research Center Report Nos. UTRC90–23 and UTRC91–21, 1990 and 1991.
25. Kiefer, J. H., personal communication.
26. Benson, S. W., and O'Neal, H. E., *Kinetic Data on Gas Phase Unimolecular Reactions*, National Bureau of Standards, 1970.
27. Golden, D., personal communication.
28. Muller-Markgraf, W., and Troe, J., *Twenty-First Symposium (International) on Combustion*, The Combustion Institute, Pittsburgh, 1986, pp. 815–824.
29. Rao, S. V., and Skinner, G. B., *Twenty-First Symposium (International) on Combustion*, The Combustion Institute, Pittsburgh, 1986, pp. 809–814.
30. Montgomery, J. A., personal communication.
31. Hurd, C. D., Levetan, R. V., and Macon, A. R., *J. Am. Chem. Soc.* 84:4515 (1962).
32. Hurd, C. D., Macon, A. R., Simon, J. I., and Levetan, R. V., *J. Am. Chem. Soc.* 84:4509 (1962).
33. Frenklach, M., Clary, D. W., Gardiner, W. C., and Stein, S. E., *Twentieth Symposium (International) on Combustion*, The Combustion Institute, Pittsburgh, 1984, pp. 887–901.

COMMENTS

John C. Mackie, University of Sydney, Australia. Can you rule out the seven-membered ring cycloheptatrienyl intermediate rather than the bridging methylene intermediate in the decomposition of benzyl?

Author's Reply. Benson and O'Neal [26] cited the known transitions of norbornadiene to the three (sets of) products: (1) toluene, (2) cyclopentadiene plus acetylene, and (3) cycloheptatriene. Assuming these processes to be reversible, it is reasonable to assume that benzyl radical could decompose via any of the analogous pathways, especially since barriers to the isomerizations would be lower because fewer H-atom transfers would be required. The exact path for acetylene elimination from the C_7 moiety is perhaps speculative. We favor norbornadienyl as the key intermediate, not only because of the analogy to a straightforward Diels–Alder decomposition, but because a path involving a cyclic C_7 species would likely require another intermediate, a linear C_7 species, before acetylene elimination can occur. Our estimate for the heat of formation for this linear species is about 130 kcal/mole, which is 82 kcal above benzyl and 15 kcal/mole above the cyclopentadienyl product. The 82-kcal barrier is about 10 kcal above the observed (overall) values for benzyl decomposition from this work although it is more consistent with the values from Ref. 13. Despite our preference, accurate estimates for the thermodynamics of intermediates and transition states depicted in Fig. 5 have not been obtained, and so we cannot argue exclusively against a cyclic C_7 intermediate. Likely, as temperatures increase above 1600 K, both decomposition paths contribute.

•

Chava Lifshitz, The Hebrew University of Jerusalem, Israel. We suggest that acenaphthylene is formed from phenanthrene by acetylene elimination. This leads to a five-membered ring motif which appears in fullerenes and may form a connection between PAHs, fullerenes, and soot formation.

Author's Reply. We have not included decomposition of phenanthrene as a source of acenaphthylene in our mechanism, perhaps in large part since we focused on modeling growth of PAHs rather than their decomposition. Acenaphthylene was assumed to be formed by acetylene addition to the naphthalen-1-yl radical. As can be seen by comparing Figs. 4a and 4b, acenaphthylene predictions are low relative to the experimental data, and the data could support arguments that acenaphthylene formation is linked or is parallel to the formation (not the destruction) of phenanthrene and anthracene. At 1400 K, it seems unlikely that large amounts of phenanthrene could decompose over the residence time of these experiments (0.6 ms) although at higher temperatures, your suggestion may likely occur. Nevertheless, it is apparent that the acenaphthylene formation model used in this paper is probably incomplete.

•

Jürgen Troe, University of Göttingen, Germany. 1. Is it possible that diphenyl methane is also formed by combination of phenyl with benzyl such as dibenzyl is formed by combination of two benzyl radicals?

2. The dissociation of benzyl is not any longer so badly characterized as you suggest [see H. Hippler, C. Reihs, and J. Troe, *Z. Phys. Chem. NF* 167:1 (1990)]. Above 1500 K clearly a high activation energy (350 kJ mol^{-1}) is observed which probably corresponds to the high-energy ring-opening + chain-breaking pathway. At lower temperatures, other pathways appear, which all seem to be of bimolecular nature but often conserve the high-temperature stoichiometry of one H atom formed per benzyl consumed. For example, we investigated (S. Frisch, H. Hippler, and J. Troe, *Z. Phys. Chem.*, in press) the "stilbene pathway" in which two benzyls combine to dibenzyl, a hydrogen is abstracted from dibenzyl by benzyl or other radicals, and the remaining radical splits off a hydrogen atom.

Author's Reply. 1. We did not include the phenyl-benzyl radical recombination as a source of diphenylmethane in our model. Your suggestion is quite reasonable. We have quickly estimated the rate of this recombination relative to our predicted rate of diphenylmethane formation. At 1300–1400 K, this recombination should increase the predicted rate by 20–40%, and its relative contribution should increase at higher temperatures as the benzyl/toluene ratio increases. Thank you for the observation; we will include this step in our future work.

2. We agree that the work performed in Germany by many authors and in different laboratories now seems well characterized and the results seem consistent with each other. In fact, we tend to agree with most conclusions drawn from those laboratories. However, competent work has also been performed elsewhere (Ref. 11) also using shock tubes but with significantly different diagnostic approaches. These alternative approaches have yielded a different recommended decomposition pathway and necessarily different conclusions regarding the rate constants for individual reactions. Some of the uncertainties regarding these differing interpretations remain to be resolved. For example, the production of one H atom per benzyl decomposed might be questioned from the results of our work since cyclopentadienyl radical appears to be the preferred decomposition product. This radical doesn't lose H atoms readily and in fact may be an H-atom sink rather than a source. The formation path for stilbene production to which you refer is the most dominant path we observed as well; thus we are in agreement with your earlier conclusions regarding the source of stilbene.

•

Phillip R. Westmoreland, University of Massachusetts, Amherst, USA. It will be of interest that we have observed many of the same aromatics in toluene/O_2 flames [1]. Whole exhausts of sooting, 1-atm flat flames were trapped for soot with a filter and for vapor-phase hydrocarbons with XAD-2 resin. Extracts in CH_2Cl_2 were analyzed by GC-MS. Whether from radical addition or combination in the flame, exhaust, or sampling, many species appeared which could be benzyl, phenyl, and toluyl combination (bibenzyl, diphenylmethane, etc.). However, phenanthrene and anthracene were closer to an equilibrium ratio.

REFERENCE

1. Prado, G., et al., "Formation of Polycydic Aromatic Hydrocarbons in Premixed Flames, Chemical Analysis and Mutagenicity," in *Analytical Chemistry and Biological Fate* (M. Cooke and A. J. Dennis, Eds.), Battelle Memorial Institute, Columbus, OH, 1981, p. 189.

Author's Reply. Thank you for the information. It is always a comfort to learn of similar results obtained using different approaches. The nonequilibrium phenanthrene/anthracene ratios obtained here presumably are due to the lower temperatures (1400–1500 K) and the shorter times (0.6 ms) of the present work.

Twenty-Fifth Symposium (International) on Combustion/The Combustion Institute, 1994/pp. 893–900

KINETICS OF THE THERMAL DECOMPOSITION AND ISOMERISATION OF PYRAZINE (1,4 DIAZINE)

ALAN DOUGHTY,* JOHN C. MACKIE AND JACQUELINE M. PALMER
Department of Physical and Theoretical Chemistry
University of Sydney
NSW 2006, Australia

The isomerisation and decomposition of pyrazine have been studied over the temperature range 1200–1480 K. The major products of decomposition were found to be acetylene and HCN, with cyanoacetylene and acrylonitrile also being significant products, although lower yields of these products were observed. The decomposition has been successfully modeled using a free radical mechanism, with the major chain carriers being CN radicals and H atoms. The initiation reaction was found to be C—H bond fission, to yield H atoms and pyrazyl radicals. Kinetic modeling allowed the rate of initiation to be determined, yielding a first-order rate constant given by the expression $k = 10^{15.7} \exp(-96.5 \text{ kcal mol}^{-1}/RT) \text{ s}^{-1}$. The importance of CN radicals as chain carriers appears to be a significant difference in the decomposition of the diazines compared with pyridine or 2-picoline.

Accompanying the decomposition of pyrazine was the isomerisation of pyrazine to pyrimidine. By kinetic modeling, the isomerisation of pyrazine to pyrimidine was found to occur via a fulvenelike intermediate. The rate and mechanism of the isomerisation are analogous to the isomerisation of fulvene to benzene described by Melius and Miller.

Introduction

This study of the thermal decomposition and isomerisation of pyrazine is part of a systematic study of the thermal reactions of N-containing heterocycles. The thermal reactions of these species are being studied because of their relevance to the mechanism of formation of NO_x through the oxidation of fuel-bound nitrogen (FBN) in coal during the combustion of coal and heavy fuels.

Previous XPS (X-ray photoelectron spectrometry) studies of coal [1,2] have indicated that nitrogen in coal is principally in the form of five- and six-membered rings. Analysis of coal tars [3] suggests that N heterocycles containing two nitrogen atoms (such as the diazines) in the aromatic ring could be a significant source of coal nitrogen. Of the diazines, pyrimidine would be expected to be the most likely to be present in material of biological origin, because of the positioning of the nitrogen atoms *ortho* to each other, as is the case for the DNA base pairs. This study of pyrazine complements our study of pyrimidine [4] by further exploring the thermal decomposition reactions of the diazines.

The present study of the decomposition and isomerisation of pyrazine is also of significance since pyrazine is a molecule in which the thermally induced migration of aromatic ring atoms can be observed. In the case of benzene and pyridine, ring atom migration would only be detectable by studying isotopically labeled nitrogen or carbon atoms. The pyrazine case differs in that the products of ring atom migration can be simply detected as the distinct chemical species, pyrimidine or pyridazine. Observation of the migration of ring atoms in pyrazine could be seen as support for the facile rearrangement of fulvene to benzene studied theoretically by Melius and Miller [5] and experimentally by Stein et al. [6].

A major aim of this study has been to develop a detailed reaction mechanism describing the decomposition and isomerisation reactions of pyrazine. A 36-step mechanism for the decomposition and isomerisation of pyrazine has been developed using the CHEMKIN [7] kinetic modeling code. The kinetic model has been shown to successfully reproduce the expermental data over the temperature range 1200–1480 K.

Experimental

The thermal decomposition and isomerisation of pyrazine have been studied over the temperature range 1200–1480 K using the single-pulse shock tube technique. Typical reaction pressures were 13–14 atm, with an average residence time behind the reflected shock front of 850 ($\pm$50) μs. Reactant con-

*Present address: Oxford Centre for Applied Kinetics, Physical Chemistry Laboratories, Oxford University, South Parks Rd., Oxford, UK OX1 3QZ.

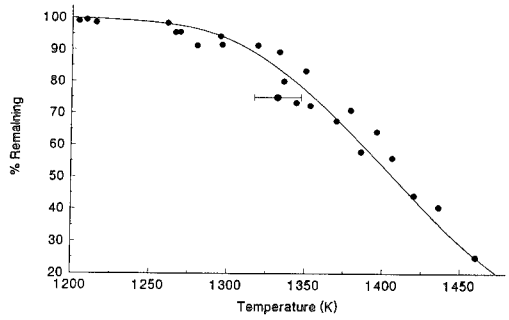

FIG. 1. Temperature dependence of percent pyrazine remaining in the pyrolysis of pyrazine (0.2–0.4 mol%). ●, represent experimental points; curve represents model predictions. Data point given with temperature error bar refers to typical run conducted in 1:4 H_2/Ar.

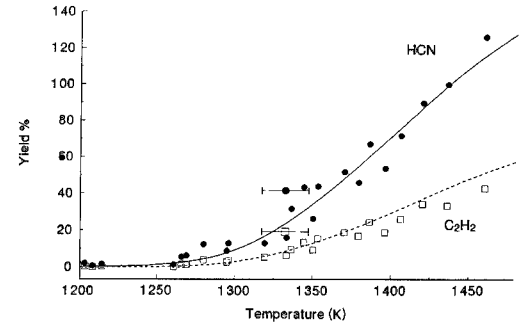

FIG. 2. Temperature dependence of the yield of HCN (●) and acetylene (□) from pyrolysis of pyrazine (0.2–0.4 mol%). Solid curves represent model predictions for the yield of HCN; dashed curves represent model predictions for the yield of acetylene. Data points given with temperature error bar refer to typical run conducted in 1:4 H_2/Ar.

centrations were measured accurately immediately prior to each run using high-resolution gas chromatography (HRGC), utilising a flame ionisation detector (FID). Product analysis was carried out using HRGC/FID. Products were identified by gas chromatography/mass spectrometry and confirmed by retention time matching with samples of known composition. Hydrogen was measured using packed column gas chromatography (GC) and thermal conductivity detector (TCD). Details of the shock tube and quantitative GC analysis have been given elsewhere [8].

Pyrazine (Fluka, >98%) was used without further purification to prepare, by sublimation, mixtures of the vapour dilute in argon of concentrations beween 0.2–0.4 mol%. The only impurity detected in the reactant mixtures was pyrimidine, present at a level of <0.1% of the pyrazine concentration. To gain insight into the modes of formation of products, some experiments were carried out using 0.2–0.4 mol% pyrazine dilute in a mixture of 1:4/H_2:Ar.

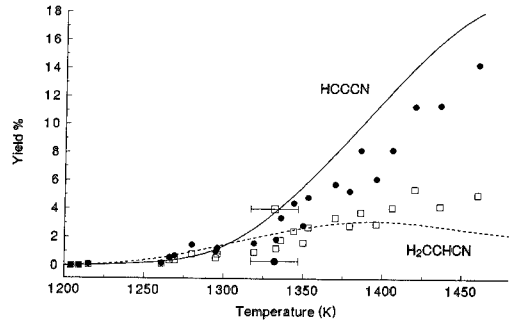

FIG. 3. Temperature dependence of the yield of cyanoacetylene (●) and acrylonitrile (□) from pyrolysis of pyrazine (0.2–0.4 mol%). Solid curves represent model predictions for the yield of cyanoacetylene; dashed curves represent model predictions for the yield of acrylonitrile. Data points given with temperature error bar refer to typical run conducted in 1:4 H_2/Ar.

Results

Pyrazine was found to decompose over the temperature range 1200–1500 K. The major products of decomposition were acetylene and HCN. Cyanoacetylene and acrylonitrile were also present in significant, although considerably lower, concentrations. Hydrogen was present as a major product at high extents of decomposition. Temperature profiles for the disappearance of the reactant and formation of products are given in Figs. 1 through 3. Although the concentration of pyrazine in the reaction mixture was varied between 0.2 and 0.4 mol%, the yields of all major products, and the overall rate of pyrazine decomposition, were only dependent on the reflected shock temperature. It could therefore be concluded that the decomposition of pyrazine is approximately first order with respect to reactant concentration.

Relatively few minor products were detected. At moderate to high extents of decomposition, traces of cyanogen, methane, ethylene, and vinylacetylene were detected. Most interestingly, one of the diazine isomers of pyrazine, pyrimidine, was observed as a minor product. Although only present at a maximum yield of 2%, pyrimidine was present at considerably higher levels in the products' mixture than the very small impurity level (<0.1% of the initial reactant) of pyrimidine in the reactant mixture.

Experiments carried out in a bath gas of 1:4/H_2:Ar showed no change in the product distributions except for the ratio of cyanoacetylene/acrylonitrile. Experiments conducted in hydrogen showed a greatly in-

creased yield of acrylonitrile, to the extent that acrylonitrile concentrations were a factor of 5 greater than those of cyanoacetylene. The total yield of cyanoacetylene and acrylonitrile, however, did not change relative to the other products in the presence of hydrogen. Product yields from a typical run in H_2/Ar are included in Figs. 1 through 3.

For each experimental run conducted, the total concentration of nitrogen in the product mixtures was calculated as a percentage of the nitrogen present in the reactant mixture. The calculation showed that the percent N recovered lay between 90 and 120%, and there was no systematic change in the percent N recovered with temperature. The N-balance calculations therefore show that there were no major involatile products formed in the decomposition of pyrazine.

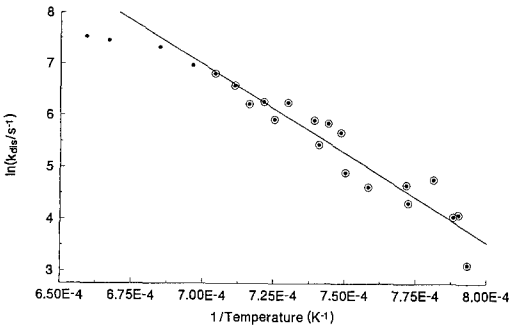

FIG. 4. Arrhenius plot for the rate constant k_{dis} for overall disappearance of pyrazine. ●, k_{dis} from end-product analysis; ○, points used in regression fit; solid line, regression fit.

Discussion

The pyrolysis of pyrazine yields a number of products that are not related in concentration to each other by any simple whole-number ratio. This type of product distribution is typical of that produced from free radical decomposition. The presence of cyanogen, HCN, and hydrogen also suggests that the decomposition of pyrazine is free radical, as these products would be expected to form in the radical abstraction and recombination reactions of the likely chain carriers, H atoms and CN radicals.

Since all four hydrogen atoms of pyrazine are equivalent, the only possible initiation would be fission of a C—H bond to yield pyrazyl radicals. If the C—H bond in pyrazine is of similar energy to the C—H bond in the *ortho-* position of pyridine, an activation energy for the initiation reaction [9,10,11] would be expected to be close to 100 kcal mol^{-1}.

For the decomposition of pyridine [10] and 2-picoline [8,12], the Arrhenius parameters for the overall rate of decomposition of reactant were found to correspond to the parameters for the major initiation reaction, viz., C—H bond fission. Arrhenius parameters for the rate of disappearance of pyrazine obtained by regression analysis of the data of Fig. 4 are as follows:

$$k_{dis} = 10^{13.5(\pm 0.9)} \cdot \exp[-68.3(\pm 5.3)\ \text{kcal mol}^{-1}/RT]\ \text{s}^{-1}.$$

Fission of the C—H bond in pyrazine would be expected to possess an A factor of at least $10^{14.5}$ s^{-1} and an activation energy close to the C—H bond dissociation energy (100 kcal mol^{-1}). If the pressure dependence of the rate constant for pyrazine decomposition is similar to that of pyridine, from the falloff curves of Leidreiter and Wagner [9], it can be concluded that the initiation reaction of pyrazine should be in the high-pressure limit under the conditions of this study. For the thermal decomposition of pyrimidine [4], Arrhenius parameters for the rate of disappearance of reactant were also found to be considerably lower than that expected for the principal initiation reaction. This suggests that the decomposition kinetics of the diazines are strongly influenced by the rates of propagation steps.

Pyrazyl radicals are the likely products of a C—H fission of pyrazine and of ring abstraction by H and CN radicals. Decomposition of the pyrazyl radical would be expected to lead to the observed products. The heat of formation of pyrazyl would therefore be important in determining the decomposition kinetics of pyrazine.

The pyrazyl radical possesses a radical centre *ortho* to a nitrogen atom. Interaction between the nitrogen lone pair and a radical centre *ortho* to the N atom has been shown in studies of the thermal decomposition of pyridine to lower the heat of formation of the radical. This conclusion is supported by *ab initio* molecular orbital calculations [13] on *ortho*-pyridyl. In the study of the initiation reaction of pyridine by Leidreiter and Wagner [9], the *ortho* C—H bond dissociation energy was found to be 100 kcal mol^{-1}. In the study of Mackie et al. [10] on the pyrolysis of pyridine, the bond dissociation energy was optimised using kinetic modeling and determined to be 98 (± 3) kcal mol^{-1}. If the C—H bond energy in pyrazine is estimated as being the same as the *ortho* C—H bond energy in pyridine, a heat of formation for the pyrazyl radical close to 95 kcal mol^{-1} would result.

Through the optimisation of the kinetic model for pyrazine decomposition, discussed below, to best fit the experimental data, a heat of formation of 92 (± 3) kcal mol^{-1} was obtained. This represents a bond dissociation energy of 96.5 kcal mol^{-1}, which falls within the error limits of the C—H bond energy found for pyridine [10]. It therefore appears that the

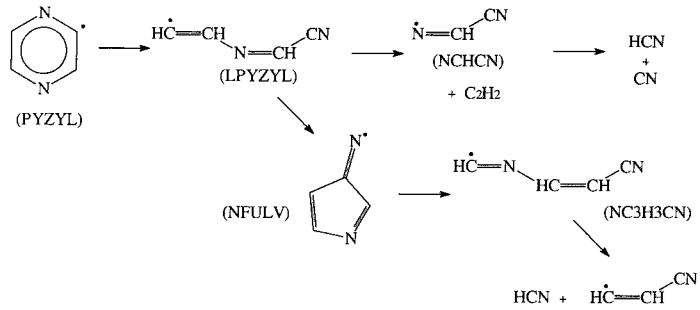

SCHEME 1. Reaction scheme for decomposition of the pyrazyl radical. Species symbols used in Table 1 are included in brackets.

pyrazyl radical is stabilised to a similar extent to the *ortho*-pyridyl radical. The optimised rate constant for the initiation reaction yielding pyrazyl and H atoms from pyrazine was found to be $10^{15.7}$ exp(− 96.5 kcal mol^{-1}/RT) s^{-1}.

The pyrazyl radical could undergo β cleavage to yield either a cyano-substituted vinyllic radical or an acetylenic imino radical. Using group additivity [14], the vinyllic cyano radical was estimated to be 125 kcal mol^{-1}, 35 kcal mol^{-1} more stable than the acetylenic amino radical. The dominant pathway for the decomposition of pyrazyl would therefore be expected to be ring fission to yield the vinyllic cyano-radical.

The major products, acetylene and HCN, can easily be explained by a series of simple fission steps of the open chain radical formed from pyrazyl. These reactions are illustrated in Scheme 1. The final step in the series of fission reactions generates the CN radical, which could H-abstract from pyrazine to form HCN and the pyrazyl radical. The chain carrier in this important radical chain is therefore the CN radical. This differs from the previously studied N heteroaromatics pyridine [10] and 2-picoline [8,12], where the radical chain carriers are H atoms or methyl radicals. In the study of the decomposition of pyrimidine [4], CN radicals were also found to be important radical chain carriers, suggesting that decomposition by a CN radical chain is a characteristic of the mechanism for decomposition of the diazines.

The reason for the importance of CN radicals in the decomposition of pyrazine can be attributed to the higher heat of formation of the diazines compared with the pyridines, coupled with the lower heat of formation of the products formed from this route. The total endotherm for the generation of acetylene, HCN, and CN radicals from pyrazyl is 100 kcal mol^{-1}. For pyridine decomposition, the analogous process would be the generation of two acetylenes and a CN radical of total endotherm 130 kcal mol^{-1}.

In contrast to pyridine, Arrhenius parameters for the rate of overall decomposition of pyrazine have been shown to be influenced by the propagation steps of the chain mechanism. A possible explanation for this difference in behaviour between pyrazine and pyridine could be associated with the different chain carriers in the two cases. CN chains could be more efficient than H chains, and hence where a CN chain is dominant, different overall kinetics might be observed.

Although β-fission steps can explain the mode of formation of HCN and acetylene, simple fission, however, cannot explain the products cyanoacetylene, acrylonitrile, or pyrimidine. These products contain three contiguous carbon atoms and therefore can only form from pyrazine if a rearrangement of the carbon skeleton occurs.

Scheme 1 includes a possible mechanism for the rearrangement of the open chain radical formed from pyrazyl to yield an intermediate radical that could decompose to form a precursor of acrylonitrile and cyanoacetylene. The novel step in the mechanism involves the 1,4 transfer of a CN group. The rearrangement of saturated nitrile radicals in solution [15] has been observed, and it is therefore reasonable to expect that unsaturated species would undergo a similar rearrangement, provided the strain of the cyclic intermediate does not result in a prohibitively high activation energy. The cyclic intermediate shown in Scheme 1 would be expected to possess a relatively small ring strain. The rate of the ring-closing reaction in the rearrangement would be similar to the rate of ring closure for a saturated nitrile radical that has been measured previously [16].

The 1,4-CN transfer reaction would yield a C_3H_3NCN radical, which has been shown to be important in the decomposition mechanism of pyrimidine [4]. In the pyrimidine mechanism, this species was postulated to decompose to HCN and cyanovinyl radicals. Cyanovinyl radicals either decompose to cyanoacetylene and H atoms or H-abstract from the reactant to yield acrylonitrile and pyrazyl.

Experiments in which pyrazine was pyrolysed in the presence of hydrogen give support for this mechanism of formation of acrylonitrile and cyanoacetylene from cyanovinyl radicals. In the presence of a large excess of hydrogen, the cyanovinyl radical could react directly with hydrogen to yield acrylonitrile and H atoms. The experimental results showed that, in the presence of hydrogen, the yield of acrylonitrile is greatly increased and that of cyanoacetylene decreased. This suggests that these two products are

formed from a common precursor, probably cyanovinyl.

Isomerisation of Pyrazine to Pyrimidine

The detection of pyrimidine in the products of pyrazine decomposition shows that there must be a route for the migration of aromatic ring atoms in pyrazine. Although the yield of pyrimidine was always less than 2%, the observation is significant since it poses the question as to the mechanism of the rearrangement.

The mechanism for formation of pyrimidine from pyrazine could be related to the mode of formation of cyanoacetylene and acrylonitrile in the decomposition of pyrazine. In the formation of pyrimidine, cyanoacetylene, and acrylonitrile, the carbon skeleton of pyrazine must be rearranged. The C_3H_3NCN radical, which is the precursor of cyanoacetylene and acrylonitrile in the decomposition of pyrazine, could undergo ring closure to yield *para*-pyrimidyl. This reaction is the reverse of the ring-opening reaction of *para*-pyrimidyl, which was postulated to be important in the decomposition of pyrimidine [4]. The recombination of *para*-pyrimidyl with H atoms would yield pyrimidine. This possible mechanism for the formation of pyrimidine from pyrazine is illustrated in Scheme 2 and is labeled mechanism A.

The proposed mechanism of formation of acrylonitrile and cyanoacetylene in the decomposition of pyrimidine involves a cyclic radical that is of the same empirical formula as the pyrimidyl radicals (see Scheme 1). Ring expansion of this cyclic radical would yield *para*-pyrimidyl. Recombination of H atoms with *para*-pyrimidyl would yield pyrimidine. The mechanism for the formation of pyrimidine via a ring-expansion pathway is illustrated in Scheme 2 and is denoted as mechanism B. Although this pathway involves a tight three-membered ring as a transition state and would therefore possess a relatively large barrier and low *A*-factor, this pathway may be faster than mechanism A since the concentration of the cyclic radical may be higher than that of C_3H_3NCN. The ring-closing reaction of C_3H_3NCN to yield *para*-pyrimidyl would have to compete with the faster fission reaction of C_3H_3NCN, possibly limiting the likely yield of pyrimidine from this pathway.

An alternative to the above free radical mechanisms would be the direct unimolecular rearrangement of pyrazine to pyrimidine. The pathway for such a unimolecular rearrangement would be analogous to the mechanism of benzene ⇄ fulvene rearrangement studied by Melius and Miller [5] and also postulated as a pathway to benzene in flames by Stein et al. [6]. The analogous rearrangement of pyrimidine to pyrazine via a di-imino fulvene analogue is shown in Scheme 2 as mechanism C. The reaction rate estimates for the process were taken from the

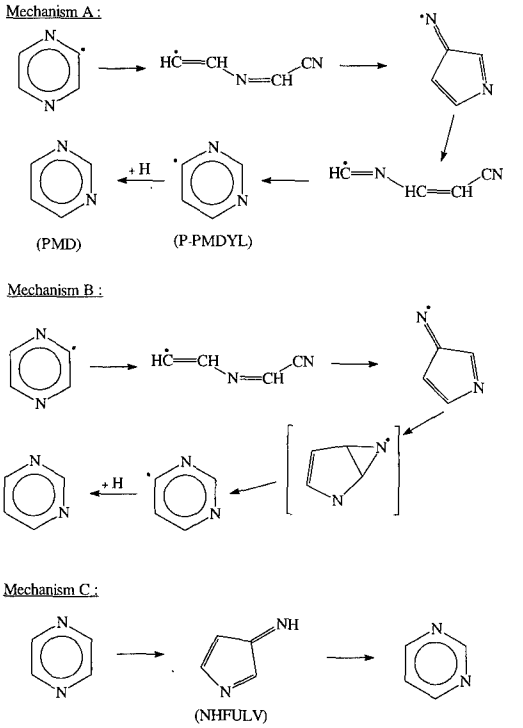

SCHEME 2. Reaction scheme of possible mechanisms of isomerisation of pyrazine to pyrimidine. Species symbols used in Table 1 are included in brackets.

rate constants given by Melius and Miller [5]. Thermochemical estimates for the heat of formation of the di-imino fulvene analogue were made by group additivity [14]. The entropy and heat capacity of this species were estimated using an approximate statistical thermodynamic method, wherein the vibrational modes were estimated by analogy with the vibrational and rotational spectrum of fulvene [17,18].

In the kinetic model, the isomerisation pathway is simplified to two steps consisting of ring contraction of pyrazine, followed by ring expansion to pyrimidine (see Table 1, reactions 11 and 12).

Concentrations of pyrimidine predicted by the three mechanisms of formation from pyrazine are compared with the experimental results in Fig. 5. The figure shows that mechanisms A and B grossly underestimate the yield of pyrimidine observed. The only mechanism that shows agreement with the experimental data is mechanism C, the intramolecular isomerisation of pyrazine to pyrimidine via the di-imino fulvene analogue. The comparison in Fig. 5 suggests that formation of pyrazyl via mechanisms involving radical recombination would be too slow to account for the concentrations of pyrimidine observed.

TABLE 1
Reaction model for pyrazine isomerisation and pyrolysis[a]

	Reactions	Forward reaction			Reverse reaction			Ref.
		log A	n	E	log A	n	E	
1	PYZYL + H ⇔ PYZ	13.60	0.00	0.00	15.72	0.00	96.45	*S*
2	PYZ + CN ⇔ PYZYL + HCN	13.78	0.00	3.00	12.80	0.00	29.19	est.
3	PYZ + H ⇔ PYZYL + H_2	13.00	0.00	4.00	11.50	0.00	11.97	*S*
4	HCCHCN + PYZ ⇔ PYZYL + H_2CCHCN	11.78	0.00	5.00	11.56	0.00	14.42	*S*
5	LPYZYL ⇔ PYZYL	11.30	0.00	5.00	15.12	0.00	40.33	est.
6	C_2H_2 + NCHCN ⇔ LPYZYL	12.90	0.00	2.00	14.36	0.00	29.19	*S*
7	HCN + CN ⇔ NCHCN	13.48	0.00	0.00	14.12	0.00	30.68	est.
8	LPYZYL ⇔ NFULV	12.00	0.00	15.00	15.24	0.00	17.27	*S*
9	NFULV ⇔ NC_3H_3CN	14.95	0.00	14.00	11.72	0.00	12.05	est.
10	NC_3H_3CN ⇔ HCN + HCCHCN	14.00	0.00	10.00	12.83	0.00	9.10	4
11	PYZ ⇔ NHFULV	14.00	0.00	80.00	13.26	0.00	56.65	*S*
12	NHFULV ⇔ PMD	13.48	0.00	58.00	13.92	0.00	82.08	*S*
13	*O*-PMDYL + H ⇔ PMD	13.56	0.00	0.00	15.11	0.00	95.24	4
14	*P*-PMDYL + H ⇔ PMD	13.58	0.00	0.00	15.44	0.00	102.24	4
15	H + PMD ⇔ *O*-PMDYL + H_2	12.70	0.00	8.00	11.76	0.00	17.18	4
16	CN + PMD ⇔ HCN + *O*-PMDYL	13.30	0.00	6.00	12.89	0.00	33.40	4
17	HCCHCN + PMD ⇔ H_2CCHCN + *O*-PMDYL	11.30	0.00	10.00	11.65	0.00	20.64	4
18	H + PMD ⇔ *P*-PMDYL + H_2	12.78	0.00	10.00	11.53	0.00	12.18	4
19	CN + PMD ⇔ *P*-PMDYL + HCN	13.30	0.00	9.00	12.59	0.00	29.40	4
20	HCCHCN + PMD ⇔ *P*-PMDYL + H_2CCHCN	11.48	0.00	11.00	11.52	0.00	14.64	4
21	C_3H_3NCN ⇔ *O*-PMDYL	11.00	0.00	5.00	15.08	0.00	41.94	4
22	C_2H_2 + HCNCN ⇔ C_3H_3NCN	12.48	0.00	4.00	14.46	0.00	36.32	4
23	CN + HCN ⇔ HCNCN	13.00	0.00	2.00	13.13	0.00	27.87	4
24	C_3H_3NCN ⇔ $BC_4H_3N_2$	12.85	0.00	24.50	12.84	0.00	29.50	4
25	H_2CCHCN + CN ⇔ $BC_4H_3N_2$	13.60	0.00	5.00	14.02	0.00	27.66	4
26	*P*-PMDYL ⇔ NC_3H_3CN	14.90	0.00	37.00	11.13	0.00	7.06	4
27	HCCHCN + M ⇔ HCCCN + H + M	15.85	0.00	43.00	16.62	0.00	3.99	8
28	H + HCCHCN ⇔ H_2CCHCN	13.30	0.00	0.00	15.20	0.00	105.88	est.
29	H + H_2CCHCN ⇔ C_2H_3 + HCN	13.00	0.00	7.00	11.03	0.00	6.85	est.
30	H + H_2CCHCN ⇔ H_2 + HCCHCN	13.00	0.00	8.00	11.72	0.00	6.55	est.
31	H + C_2H_2 (+M) ⇔ C_2H_3 (+M)	13.00	0.00	2.70	12.73	0.00	43.07	21
32	2H + M ⇔ H_2 + M	18.00	−1.00	0.00	15.05	0.00	101.76	22
33	CN + HCN ⇔ C_2N_2 + H	7.58	1.57	0.09	14.60	0.00	11.22	23
34	CN + H_2 ⇔ HCN + H	5.69	2.44	2.12	14.91	0.00	26.84	24
35	C_2N_2 + M ⇔ 2CN + M	16.86	0.00	100.40	14.29	0.00	−29.18	25
36	HCN + M ⇔ H + CN + M	15.66	0.00	105.30	14.52	0.00	−17.33	25

[a]Units for A, $cm^3\ mol^{-1}\ s^{-1}$ or s^{-1} as appropriate. Units for E, kcal mol^{-1}. In col. 8, *S* indicates rate constant to which the model predictions are sensitive; est. indicates rate constant to which model predictions are not sensitive. $\Delta H^{\circ}_{f,300}$ estimates in parentheses following species (units kcal mol^{-1}): PYZ = pyrazine (46.9, Ref. 26), PYZYL (92), LPYZYL (125), NCHCN (102), NFULV (124), NHFULV (70.0), NC_3H_3CN (125). Refer to Ref. 4 for thermochemistry of pyrimidine submechanism species.

Experiments carried out in 1:4/H_2:Ar bath gas give qualitative support for the formation of pyrimidine through the intramolecular isomerisation of pyrazine. Yields of pyrimidine were unaffected by the presence of hydrogen. If pyrimidine were formed from *para*-pyrimidyl, the presence of hydrogen would greatly increase the yield of pyrimidine over that observed in the hydrogen-free mixtures.

Kinetic Modeling

The pathways for decomposition of pyrazine discussed above have been used to generate a reaction model for the decomposition of pyrazine. The model is given in Table 1. Where necessary, thermochemical estimates were made of intermediates using group additivity [14]. Initial estimates of reaction

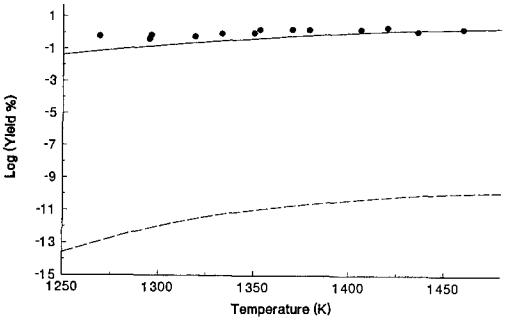

FIG. 5. Temperature dependence of the log (yield) of pyrimidine (●) from pyrolysis of pyrazine (0.2–0.4 mol%). Dashed curve represents model predictions obtained using mechanisms A and B. Solid curve represents the model predictions obtained using mechanism C.

rates where data were unavailable were made by analogy with known reaction rates of similar species.

Included in the mechanism of pyrazine decomposition is a submechanism for the decomposition of pyrimidine. This was necessary to adequately describe the concentration of pyrimidine at high extents of pyrazine decomposition, where decomposition of the pyrimidine formed by isomerisation of pyrazine became significant.

The model predictions included in Figs. 1 through 4 were obtained using the CHEMKIN [7] kinetic modeling code, the shock tube code [19], modified for cooling, and the ordinary differential equation solver LSODE [20]. As can be gleaned from the figures, the model gives an adequate prediction of the experimental yields of product species and the rate of disappearance of the reactant over the temperature range of 1200–1480 K.

Rate of production analysis showed the decomposition of pyrazine to occur almost entirely through H-abstraction by CN and H atoms. At low extents of decomposition (1300 K), 89% of the reacted pyrazine in the reaction model was consumed by H-abstraction reactions, two-thirds of which was due to abstraction by CN, rising to 99% at intermediate extents of decomposition (1400 K). The predicted importance of the propagation reactions is consistent with the low Arrhenius parameters observed for pyrazine decomposition.

REFERENCES

1. Clarke, D. T., and Wilson, R., *Fuel* 62:1034 (1983).
2. Wallace, S., Bartle, K. D., and Perry, D. L., *Fuel* 68:1450 (1989).
3. Palmer, S. R., Hippo, E. J., Kruge, M. A., and Crelling J. C., *Proceedings of International Conference on Coal Science,* Butterworth-Heinemann, Oxford, 1991, p. 993.
4. Doughty, A., and Mackie, J. C., *J. Chem. Soc. Faraday Trans.* 90:541 (1994).
5. Melius, C. F., and Miller, J. A., *Twenty-Fourth Symposium (International) on Combustion,* The Combustion Institute, Pittsburgh, 1992, pp. 621–628.
6. Stein, S. E., Walker, J. A., Suryan, M. M., and Fahr, A., *Twenty-Third Symposium (International) on Combustion,* The Combustion Institute, Pittsburgh, 1990, pp. 85–90.
7. Kee, R. J., Miller, J. A., and Jefferson, T. H., *CHEMKIN: A General Purpose, Problem Independent, Transportable FORTRAN Chemical Kinetics Codes Package,* SANDIA National Laboratories Report No. SAND80-003, 1980.
8. Terentis, A., Doughty, A., and Mackie, J. C., *J. Phys. Chem.* 96:10334 (1992); also see Doughty, A., and Mackie, J. C., *J. Phys. Chem.* 96:10339 (1992).
9. Leidreiter, H. I., and Wagner, H. G., *Z. Phys. Chem. Neue Folge* 153:99 (1987).
10. Mackie, J. C., Colket, M. B., and Nelson, P. F., *J. Phys. Chem.* 94:4099 (1990).
11. Kern, R. D., Yong, J. N., Kiefer, J. H., and Shah, J. N., *16th Symposium (International) on Shock Tubes and Waves,* VCH, Weinheim, Germany, 1988, p. 437.
12. Doughty, A., and Mackie, J. C., *J. Phys. Chem.* 96:10339 (1992).
13. Kikuchi, O., Hondo, Y., Morihashi, K., and Nakayama, M., *Bull. Chem. Soc. Jpn.* 61:291 (1988).
14. Benson, S. W., *Thermochemical Kinetics,* John Wiley, New York, 1976.
15. Beckwith, A. L. J., O'Shea, D. M., and Westwood, S. W., *J. Am. Chem. Soc.* 110:2565 (1988).
16. Griller, D., Schmid, P., and Ingold, K. I., *Can. J. Chem.* 57:831 (1979).
17. Domaille, P. J., Kent, J. E., and O'Dwyer, M. F., *Aust. J. Chem.* 27:2463 (1974).
18. Baron, P. A., Brown, R. D., Burden, F. R., Domaille, P. J., and Kent, J. E., *J. Mol. Spec.* 43:401 (1972).
19. Mitchell, R. E., and Kee, R. J., *A General Purpose Kinetic Code for Predicting Chemical Kinetic Behaviour Behind Incident and Reflected Shocks.* Sandia National Laboratories No. SAND82-8205, 1982.
20. Hindmarsh, A. C., "ODEPACK, a Systematized Collection of ODE Solvers," in *Scientific Computing* (R. S. Stepleman et al., Eds.), North-Holland, Amsterdam, 1983, pp. 55–64.
21. Payne, W. A., and Stief, L. J., *J. Chem. Phys.* 64:1150 (1976).
22. Dixon-Lewis, G., *Philos. Trans. R. Soc. Lond. A* 303:181 (1981).
23. Zabarnick, S., and Lin, M. C., *Chem. Phys.* 134:185 (1989).
24. Atakan, B., Jacobs A., Wahl, M., Weller, R., and Wolfrum, J., *Chem. Phys. Lett.* 154:449 (1989).
25. Mallard, W. G., Westley, F., Herron, J. T., Hampson, R. F., and Frizzell, D. H., *NIST Chemical Kinetics Database-Ver. 5.0,* NIST Standard Reference Data, Gaithersburg, MD, 1993.
26. Tjebbes, J., *Acta. Chem. Scand.* 16:916 (1962).

COMMENTS

John Kiefer, University of Illinois at Chicago, USA. There is evidence that the higher heterocycles like *s*-triazine and *s*-tetrazine decompose by a concerted path to 3HCN and 2HCN + N_2, respectively. Is it possible some concerted decomposition also occurs (to 2HCN + C_2H_2) in pyrazine?

Author's Reply. The observation that the major products are not in simple proportion to one another together with the observation of products of the propagating radicals' recombination—especially cyanogen—is strong evidence in favor of the postulated chain decomposition mechanism involving CN and H radicals as the major decomposition route. We cannot completely rule out the possibility of a simultaneous minor concerted route. However, we have carried out ab initio quantum chemical calculations [1] to search for possible transition states involving concerted decomposition paths in the diazines. For pyrimidine (1,3-diazine) and pyrazine (1,4-diazine), the calculations indicate that a concerted path would have too high an activation energy to compete with C-H fission. Nevertheless, with the 1,2-diazine, pyridazine, a concerted path might possibly be able to compete with bond fission. This apparent lowering of the activation energy for a concerted path would appear to be associated with the juxtaposition of the two nitrogen atoms in the ring. This would suggest that in the higher azines, especially *s*-tetrazine, where there are two pairs of adjacent N atoms, a concerted path is a real possibility.

REFERENCE

1. Jones, J., Bacskay, G. B., Mackie, J. C., and Doughty, A., to be published; Jones, J., B. Sc. (Hons.) Thesis, University of Sydney, Australia, 1993.

•

Assa Lifshitz, The Hebrew University of Jerusalem, Israel. What is the ratio of C_2N_2/HCN that was found in the postshock mixtures? According to your suggested mechanism, you should have gotten a relatively high concentration of C_2N_2 as a result of CN recombination.

Author's Reply. The maximum yield of cyanogen was observed to be 2(±)1 yield %, corresponding to a ratio of C_2N_2/HCN of 1:50. This concentration is relatively low considering the importance of the CN radical in the reaction mechanism, but can be explained by the high rate of H abstraction by CN, resulting in the concentration of CN radicals being relatively low compared to the concentration of chain carriers in H or methyl chains. The CN recombination is also well into the falloff at the pressures of the study.

Twenty-Fifth Symposium (International) on Combustion/The Combustion Institute, 1994/pp. 901–908

AN EXPERIMENTAL AND COMPUTATIONAL STUDY OF METHANOL OXIDATION IN THE INTERMEDIATE- AND HIGH-TEMPERATURE REGIMES

T. J. HELD AND F. L. DRYER
Department of Mechanical and Aerospace Engineering
Princeton University
Princeton, New Jersey 08544-5263, USA

Methanol oxidation has been studied experimentally in a variable-pressure flow reactor, from 1 to 20 atmospheres and from 752 to 1043 K. These conditions encompass both the high- and intermediate-temperature chemical kinetic regimes, as defined by the transition between $H + O_2$ branching and recombination. The overall consumption path of methanol is unaffected by this transition; however, the data indicate an increasing trend toward molecular hydrogen formation at the high-temperature conditions, with an accompanying delay in energy release.

A detailed chemical kinetic model has been developed that successfully reproduces most of the features of methanol oxidation over the conditions studied. Reaction path and sensitivity analyses clearly indicate the importance of the hydroperoxyl radical throughout the conditions, predominantly through the branching reaction path $RH + HO_2 \rightleftharpoons R + H_2O_2$, $H_2O_2\ (+M) \rightleftharpoons 2\ OH\ (+M)$. Under high-temperature conditions, HO_2 also provides a strong termination effect through its reaction with atomic hydrogen. The formaldehyde mole fraction is very sensitive to the rate constant ratio, k_{CH_2O+X}/k_{CH_3OH+X}, where X = H and OH. Optimal results are obtained with a rate constant for $CH_2O + X$ approximately 4.7 times faster than $CH_3OH + X$, for both H and OH.

Introduction

The use of methanol as an automotive fuel has attracted considerable interest in the past decade, for a number of economic, ecological, and political reasons [1]. The likelihood of its implementation in this capacity requires a higher level of understanding and knowledge of the oxidation processes occurring in a spark-ignition engine cylinder.

Preflame reactions are controlling factors in at least two phenomena of vital interest to the automotive and fuel industries: autoignition and unburned hydrocarbon emissions. Both are strongly influenced by the chemistry occurring during compression by the piston and advancing flame front. Figure 1 shows, as symbols, the measured intake conditions and knock points on a temperature-pressure plane from two studies, one using alkane fuels and one using methanol, with polytropic fits to the extremes of the data. The fuel/air mixture follows a similar trajectory during the compression process. Also indicated on the figure, the dividing line between the intermediate- and high-temperature chemical kinetic regimes is defined by the density at which the ratio of the rates of

$$H + O_2 \rightleftharpoons OH + O$$

and

$$H + O_2 + M \rightleftharpoons HO_2 + M$$

is a constant value (also referred to as the "extended second explosion limit" for hydrogen oxidation [5]). Clearly, the mixture does not reach the high-temperature regime prior to either flame passage or autoignition.

To gain a more detailed understanding of methanol oxidation in the intermediate-temperature regime, experiments have been performed in a variable-pressure flow reactor (VPFR) over a wide range of temperatures and pressures. A detailed chemical kinetic model has been constructed and validated by comparison to these data. The controlling kinetics in both the high- and intermediate-temperature chemical kinetic regimes are examined using reaction path and sensitivity analyses.

Experimental

The construction and operation of the VPFR have been discussed in detail in earlier work [6,7]; thus, only a brief description is given here. Nitrogen carrier gas (Liquid Carbonics, >99.998%) is preheated by an electric resistance or electric arc heater to the desired reaction temperature and mixed with a small

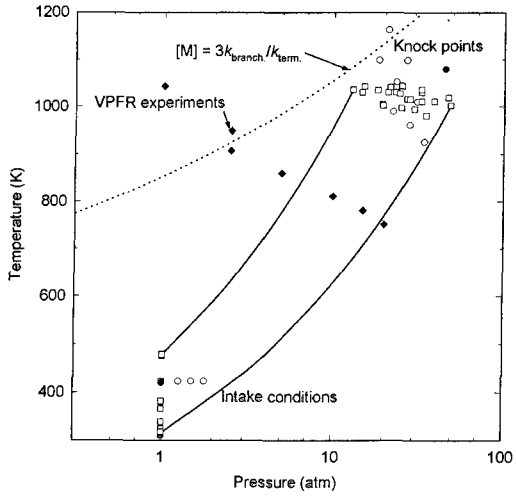

FIG. 1. Spark-ignition-engine end-gas trajectories in two knocking engines. Open circles: Gluckstein and Walcutt [2]; open squares: Smith et al. [3]; filled circles: Driver et al. [4].

amount of oxygen (Airco, 99.993%) at the heater exit. The mixture enters a 10.2-cm-diameter quartz tube, which forms the reactor volume. Liquid methanol (Aldrich, HPLC grade, 99.9%) is vaporized into a diluent nitrogen flow (approximately 5% of the total flow). The fuel vapor/diluent stream enters the reactor through a 2.0-m-long, radiation-shielded injector tube. At the exit of the injector, the fuel/diluent flows radially outward through sixteen 250-μm-diameter holes. The main carrier gas/oxidizer flow is forced radially inward through a 0.6-cm gap between a quartz baffle plate and the upstream edge of a 10°-divergence-angle silica diffuser. Recent experiments demonstrate that mixing is complete within 5% of the total available reaction time in the experiment [8]. The residence time is varied by moving the point of fuel injection with respect to the fixed sampling position, where a small fraction of the reacting gases is extracted for analysis by a water-cooled, convection-quenching, stainless-steel probe. The sampling process has been demonstrated to have a negligible effect on stable species mole fractions [7]. At the same axial location, a silica-coated type R thermocouple measures the gas temperature to an accuracy of approximately ± 2 K.

Infrared spectra of the quenched sample gas are collected by a Fourier transform infrared spectrometer (Nicolet 730), with an 8.6-m-pathlength multipass gas cell. Individual species identification and quantification are performed by partial least-squares fitting to reference spectra [9]. Also, CO and CO_2 are measured by nondispersive infrared analyzers (Horiba PIR-2000), O_2 is measured by an electrochemical analyzer (Infrared Industries, IR 2200), and H_2 is measured by a selective thermal-conductivity detector. The accuracy of the individual species measurements is approximately $\pm 5\%$ [7]. In all experiments, the carbon balance is constant to within $\pm 3\%$ of the mean value.

The distance from the fuel injection point to the sampling location is converted to time by integration of the centerline axial velocity. The velocity profiles are measured by pitot tube at ambient conditions and Reynolds numbers similar to the experimental conditions.

Experimental Results

The initial conditions for the methanol experiments are listed in Table 1. Data for three representative experiments are shown as the symbols in Figs. 2 through 4. The primary intermediate species detected were formaldehyde, carbon monoxide, and hydrogen. Formic acid was detected in relatively small quantities (20–50 ppm), as was methane ($\lesssim 10$ ppm), in all experiments. For the fuel-rich, high-pressure experiments, a small spectral absorption feature, attributed to 1,2-ethanediol (ethylene glycol, <10 ppm), appeared after the oxygen was consumed.

In agreement with previous studies [10], methanol reacts via a relatively simple dehydrogenation path, $CH_3OH \rightarrow CH_2O \rightarrow CO$, followed by carbon monoxide oxidation at high temperatures. At the lower temperatures of the high-pressure studies, the CO oxidation proceeds at a very slow rate. In contrast to methanol's alkane homologue, methane, very few recombination products are measurable. Formic acid is likely to be an oxidation product of the hydroxymethyl radical (CH_2OH), while 1,2-ethanediol is clearly a self-recombination product of hydroxymethyl [7].

One objective of this study is the examination of the shifts in reaction paths between the high- and intermediate-temperature chemical kinetic regimes. Besides the obvious change in the overall reaction rate, some of the species profiles and the energy release patterns change dramatically below the extended second explosion limit. These trends are shown in Figs. 5 and 6, where the time axis has been replaced by the fractional fuel consumption. The carbon-containing species distributions are relatively insensitive to the kinetic regime, although the rate of carbon monoxide oxidation late in the reaction decreases sharply as the conditions become nonexplosive. The relative amount of molecular hydrogen formed is greatly reduced at the expense of water formation at the lower-temperature conditions. The energy release patterns reflect this trend as well—the partial oxidation of methanol to CO and H_2O is responsible for almost 60% of the available chemical enthalpy. The delayed oxidation of H_2 and CO at the

TABLE 1
Initial Conditions

Pressure (atm)	Initial temperature (K)	Initial CH_3OH mole fraction $\times 10^3$	Equivalence ratio	Residence time (s)
1.0	1043	3.44	0.86	0.12
2.5	949	3.33	0.83	0.33
2.5	907	3.33	0.33	0.35
2.5	911	3.33	2.17	0.35
5.0	860	3.72	0.93	0.75
5.0	858	3.72	0.37	0.73
5.0	857	3.72	2.32	0.75
10.0	810	4.15	1.04	1.6
10.0	810	4.15	0.42	1.5
10.0	811	4.15	2.60	1.6
15.0	783	4.15	1.04	2.4
15.0	781	4.15	2.59	2.4
20.0	752	3.64	0.93	3.8

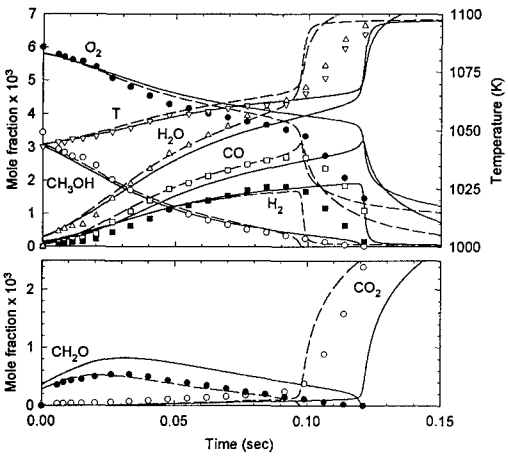

FIG. 2. Methanol oxidation: $\varphi = 0.86$; $T_i = 1043$ K; $p = 1$ atm; $X_{CH_3OH,i} = 0.00344$. Symbols represent data points; solid lines are calculations of base mechanism; dashed lines are modified mechanism, as described in text. Calculations are shifted -0.055 s.

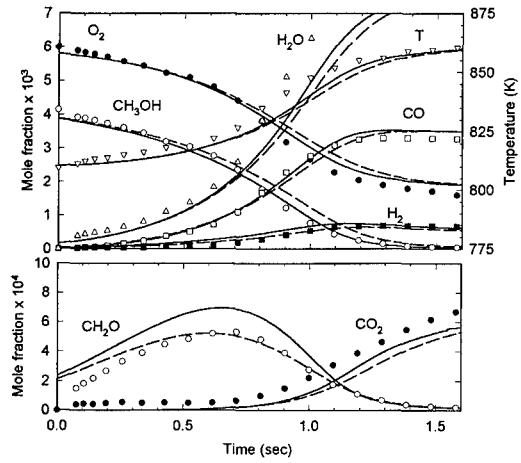

FIG. 3. Methanol oxidation: $\varphi = 1.04$; $T_i = 810$ K; $p = 10.0$ atm; $X_{CH_3OH,i} = 0.00415$. Symbols represent data points; solid lines are calculations of base mechanism; dashed lines are modified mechanism, as described in text. Calculations are shifted -0.75 s.

high-temperature conditions is responsible for the delayed energy release.

Computational

The development of detailed chemical kinetic models serves two primary purposes. First, they may be used to simulate reacting systems at conditions similar to the models' range of validity. More importantly for this work, detailed models allow interpretation of the kinetic behavior of the experiments used in their validation. Recently, a detailed, comprehensive model for methanol oxidation has been developed for and validated against flow reactor, static reactor, shock tube, and flame speed experiments [7]. Space limitations preclude a full listing of the mechanism; however, a brief description follows.

The mechanism is developed hierarchically, based on the $CO/H_2/O_2$ model of Yetter and Dryer [11], with minor modifications based on more recent work [12]. The formaldehyde submechanism is from the comprehensive study of Hochgreb and Dryer [13]. The methanol submechanism is a substantial revision of Norton and Dryer's mechanism [10,14]. To account for potential effects of the small CH_3 levels in

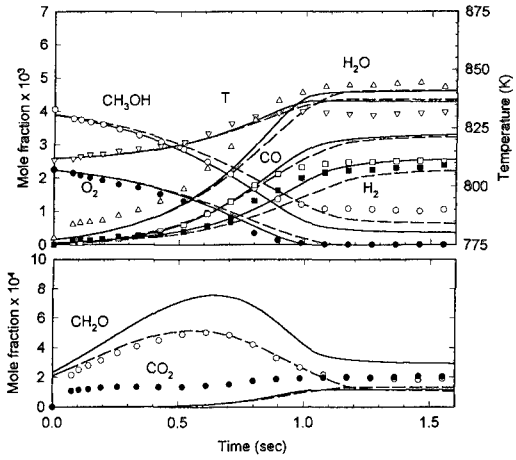

FIG. 4. Methanol oxidation: $\varphi = 2.60$; $T_i = 811$ K; $p = 10.0$ atm; $X_{CH_3OH,i} = 0.00415$. Symbols represent data points; solid lines are calculations of base mechanism; dashed lines are modified mechanism, as described in text. Calculations are shifted -0.72 s.

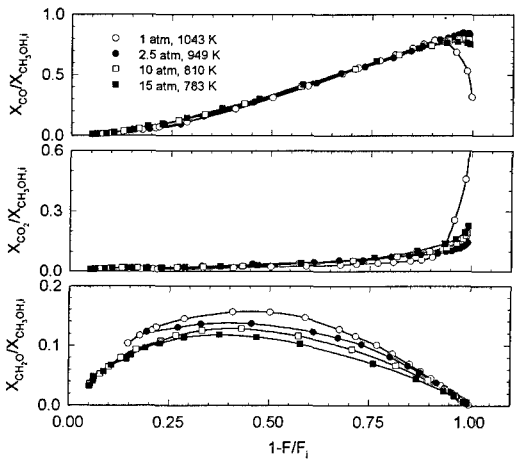

FIG. 5. Mole fraction profiles of carbon monoxide, carbon dioxide, and formaldehyde for several different pressures and initial temperatures. Mole fractions are normalized by initial methanol mole fraction; x axis is fraction of methanol consumed.

methanol oxidation, a C_2 submechanism was added, based primarily on the compilation of Tsang and Hampson [15]. Because the C_2 submechanism had no significant effect on any of the oxidation conditions studied, it is not used for the present work.

Recently, two other detailed mechanisms for methanol oxidation have been reported [16,17]. These other mechanisms are fairly similar to the present work and predict roughly the same species profiles for the experimental conditions reported here.

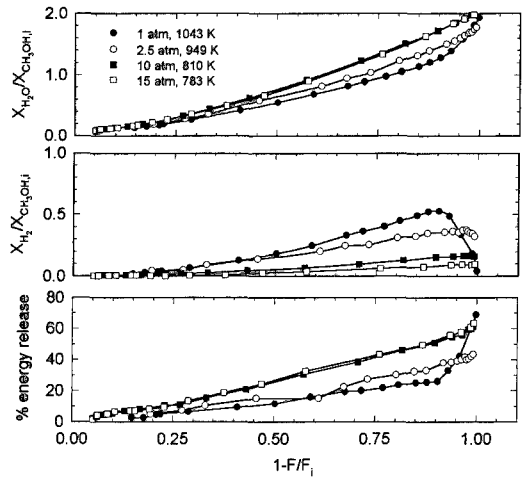

FIG. 6. Mole fraction profiles of water, molecular hydrogen, and fraction of total energy released by reaction, as measured by temperature rise, for several different pressures and initial temperatures. Mole fractions are normalized by initial methanol mole fraction; x axis is fraction of methanol consumed.

The treatment of the important CH_3OH + OH reactions differs substantially among the three, however. The mechanism of Egolfopoulos et al. [16] uses the estimated rate coefficient of Bowman [18], with 50% of the abstraction reaction occurring at the hydroxyl site. Direct measurements of this reaction rate are in excellent agreement with one another [19,20] and yield rate coefficients roughly a factor of 3 higher than Bowman's value. Grotheer et al. [17] use Hess and Tully's rate coefficient [19] but assign only 15% of the abstraction rate to the hydroxyl site, in contradiction to experimental and theoretical evidence that supports an increasing contribution from this site at high temperatures.

A zero-dimensional, adiabatic and isobaric experiment is simulated using the SENKIN code [21]. The adiabatic assumption is approximated by the externally heated and insulated reactor tube, and its low pressure drop permits the isobaric assumption. Because of the high convective velocities and large width of the reaction zone, diffusion in the axial direction is usually negligible compared to the convective and reactive terms in the governing equations. The negligibility of radial diffusion has been demonstrated in a flow-tube experiment operating in a similar configuration [22]. Omission of the diffusive terms permits the zero-dimensional approximation.

Mixing and fluid mechanical processes in a flow-tube experiment can be quite complex, and diffusive terms become non-negligible near the mixing point. Thus, zero-dimensional calculations often predict a relatively long chemical induction time not apparent in the experiments. Postinduction chemistry has

been shown to be very insensitive to initial condition perturbations [7], however. Thus, the timescale of the calculated profiles is offset to match the experimental fuel profile at the point where 50% of the initial fuel has been consumed. The exact amount of the applied "time shift" is noted in the figure captions.

Sensitivity analysis is used extensively in the determination of kinetically important reactions and rate coefficients. The sensitivity of τ_{20-80}, defined as the time between 20 and 80% of the fuel consumption, to individual reaction rate coefficients is calculated from the gradient sensitivity coefficients returned by SENKIN [7]. This factor represents the sensitivity of the overall fuel consumption rate to the reaction rate coefficients. The sensitivity of intermediate species yield at a constant fractional fuel consumption is calculated by a brute-force method, in which reaction rate coefficients are individually perturbed by a factor of 1.1. The response of the calculated species mole fraction approximates the normalized sensitivity coefficient, $d\ \ln(X_i)/d\ \ln(k_j) \approx \Delta\ \ln(X_i)/\Delta\ \ln(k_j)$, where X_i is the mole fraction of species i, and k_j is the rate coefficient of reaction j.

Results

The calculated species profiles for the flow reactor experiments, using the baseline mechanism, are depicted as the solid curves in Figs. 2 through 4. In general, the agreement with overall rate of reaction and intermediate species yield is within experimental error with two exceptions. The calculated formaldehyde yield is always higher than the experimental values by factors of 1.3–1.6, and in the fuel-rich cases, the amount of methanol remaining after total oxygen consumption is calculated to be less than half the measured value. The major reasons for these disparities will be discussed in a following section.

The agreement between model and experiment for the full parameter range is comparable to that shown in Figs. 2 through 4. At the highest-pressure condition (not shown), the calculated overall reaction rate is approximately 50% slower than the experimental value, most likely due to deficiency in the hydrogen peroxide submechanism [7]. At atmospheric pressure (Fig. 2), the calculated rate of CO/H_2 oxidation is much faster than the observed rate. At this point, the rapid decrease in local chemical characteristic time invalidates the zero-dimensional assumption (i.e., axial diffusion is no longer negligible).

Overview:

As the pressure and temperature conditions change from the high- to intermediate-temperature regime, the sequence of reactions responsible for the conversion of methanol to CO remains essentially unchanged:

$$CH_3OH + X \rightleftharpoons CH_2OH/CH_3O + XH$$

$$CH_2OH + O_2 \rightleftharpoons CH_2O + HO_2$$

$$CH_3O(+\ M) \rightleftharpoons CH_2O + H(+\ M)$$

$$CH_2O + X \rightleftharpoons HCO + XH$$

$$HCO + \{M/O_2\} \rightleftharpoons CO + \{(H + M)/HO_2\}$$

where X represents an active radical, primarily OH, H, and HO_2. Methanol is unusual in that thermal decomposition of the primary fuel radical, hydroxymethyl (CH_2OH), is relatively unimportant below about 1500 K. Because of its high production rate from the $CH_2OH + O_2$ reaction, the hydroperoxyl radical (HO_2) plays a significant role in methanol oxidation well above the extended second explosion limit.

The different consumption paths of the two fuel radicals, hydroxymethyl and methoxy (CH_3O), require consideration of abstraction from both sites. Hydroxymethyl formation is generally favored, due to the relative weakness of the C-H bond (94 kcal/mol, vs 104 kcal/mol for O-H). However, isotopic substitution experiments with OH as an abstractor suggest an increasing contribution from the hydroxyl site at high temperatures, with nearly equal rates for the two sites as the temperature exceeds 700 K [19]. The H atom formed by methoxy decomposition contributes to chain branching above the extended second explosion limit, making the abstraction branching ratio a sensitive parameter. Below the extended second explosion limit, the H atom formed by methoxy decomposition rapidly either recombines with O_2 or abstracts a hydrogen from a stable species. Thus, abstraction from either site yields equivalent products. For this study, the rate and branching ratio of Hess and Tully [19] were used for $CH_3OH + OH$.

High-Temperature Conditions:

Although the mechanism responsible for the consumption of carbon-containing species is not strongly affected by the temperature and pressure conditions, the underlying radical kinetics undergo a fundamental shift near the extended second explosion limit. The sensitivity of τ_{20-80} to the reaction rate coefficients is shown in Fig. 7 for the 1 atm, 1043 K (high-temperature) and 10 atm, 810 K (intermediate-temperature) conditions.

The high-temperature kinetic regime is dominated by the chain-branching $H + O_2$ reaction, demonstrated by the high sensitivity of τ_{20-80} to its rate coefficient. Many reactions with large sensitivity coefficients in the high-temperature regime affect supplies or sinks of the H radical.

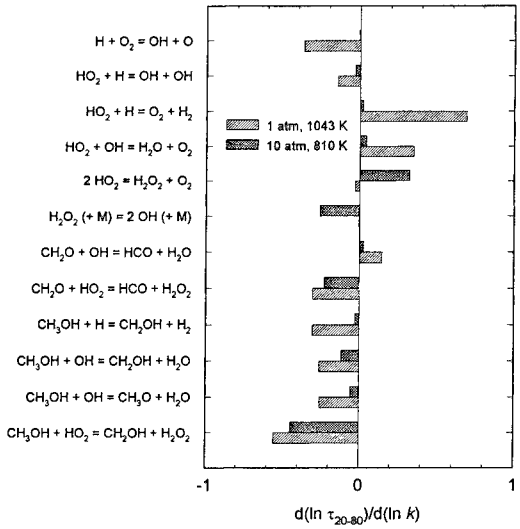

FIG. 7. Sensitivity coefficients of τ_{20-80} at near stoichiometric conditions, 1 atm, 1043 K; 10 atm, 811 K.

The hydroperoxyl radical exerts two opposing influences in the high-temperature regime. As mentioned previously, hydroperoxyl is rapidly produced by the reaction of O_2 with CH_2OH. The HO_2 subsequently reacts via

$$HO_2 + H \rightleftharpoons O_2 + H_2 \qquad 15\%$$

$$HO_2 + OH \rightleftharpoons O_2 + H_2O \qquad 5.7\%$$

$$HO_2 + H \rightleftharpoons 2OH \qquad 45\%$$

$$2HO_2 \rightleftharpoons O_2 + H_2O_2 \qquad 22\%$$

$$RH + HO_2 \rightleftharpoons R + H_2O_2, \qquad 5.5\%$$

$$RH = CH_3OH, CH_2O$$

The numbers in the right-hand column represent the fraction of HO_2 consumed by the corresponding reaction. The first two reactions are strongly chain terminating and display positive sensitivity coefficients for τ_{20-80} (Fig. 7). The termination reaction involving H has a particularly strong effect, since it also depletes the system of an important branching agent. The third and fourth reactions are chain propagating once the decomposition of H_2O_2 to two hydroxyl radicals is taken into account. Very little HO_2 or RH is consumed by the abstraction reactions. However, τ_{20-80} is very sensitive to their rate coefficients because the overall reaction path is chain branching, due to hydrogen peroxide decomposition.

Intermediate-Temperature Conditions:

As previously mentioned, the overall reaction path for methanol oxidation remains unchanged across the extended second explosion limit. However, the radical kinetics shift dramatically. Below the second limit, the hydrogen radical quickly loses importance, due to the dominance of the pseudotermination reaction:

$$H + O_2 + M \rightleftharpoons HO_2 + M$$

over the branching step. Also, the primary source of H atoms is thermal decomposition of the formyl radical. Below about 1000 K, at 0.6% oxygen, the lower activation energy reaction $HCO + O_2$ is much faster than decomposition. Evidence of the decreased H atom levels is seen both experimentally and computationally in the depressed levels of molecular hydrogen, produced by

$$RH + H \rightleftharpoons R + H_2 \ (RH = CH_3OH, CH_2O).$$

Without the influence of the $H + O_2$ branching reaction, the overall rate of methanol consumption becomes almost entirely controlled by HO_2 kinetics. At high temperatures, competition for the H atom dominates the list of sensitive reactions, while the competition for HO_2 between branching and straight-chain paths is important at intermediate temperature:

$$RH + HO_2 \rightleftharpoons R + H_2O_2$$

$$2HO_2 \rightleftharpoons O_2 + H_2O_2.$$

Finally, the thermal decomposition rate of hydrogen peroxide is beginning to become a sensitive parameter. At the conditions of the 1-atmosphere, high-temperature experiment, its characteristic decomposition time is 3.2 ms, while it is 0.25 s at the 10-atmosphere conditions. Because this time is comparable to the experimental time, significant H_2O_2 accumulates. Other, nonbranching reactions, such as

$$H_2O_2 + OH \rightleftharpoons H_2O + HO_2$$

can now compete with the decomposition reaction, making its rate coefficient a more sensitive parameter.

Formaldehyde:

The relative amount of formaldehyde present as an intermediate species is important, particularly due to concerns over its presence as a toxic emission product in methanol-fueled vehicles. However, it is precisely this point where the model disagrees systematically with the experiments. Possible causes for the discrepancy are discussed below.

Sensitivity coefficients (Fig. 8) clearly indicate a strong relationship between formaldehyde mole fraction and the abstraction rates of $CH_3OH + X$ and

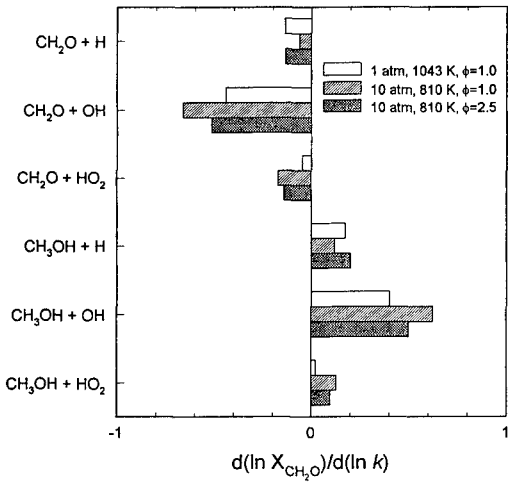

FIG. 8. Normalized sensitivity coefficients of the formaldehyde mole fraction at a constant methanol mole fraction (50% of initial value). Abstraction rate constants from both sites on methanol were varied simultaneously; thus, coefficients represent both product paths at constant branching ratio.

CH_2O + X, where X is primarily OH and, to a lesser degree, H. The coefficients for the reactions with methanol and formaldehyde are approximately equal in absolute value and opposite in sign, indicating that the ratio, rather than magnitude, of their rate constants controls the formaldehyde level.

This disagreement between model and experiment increases with temperature and equivalence ratio, conditions that are more sensitive to the ratio of H-atom abstraction rate constants. Systematic variation of the OH and H rate constant ratios, while holding the total rate constant fixed, provides a best fit of the data with the ratio of $k_{CH_2O+X}/k_{CH_3OH+X} \approx 4.7$ for both H and OH. The values in the baseline mechanism are 1.1 and 3.4, respectively.

The expression of Hess and Tully [19] for CH_3OH + OH, used in the baseline mechanism, is in excellent quantitative agreement with the measurement of Bott and Cohen [20] at 1200 K. Bott and Cohen also provide a direct measurement of CH_2O + OH at 1200 K that is 20% lower than Tsang's expression, as used in Ref. 13 and the present mechanism. The required adjustments are probably within the uncertainty level of either rate constant.

The H-atom reactions are less well defined. The expressions of Tsang [15,23] for both formaldehyde and methanol are considerably in excess of more recent measurements. The base model uses the rate constant recommended by Warnatz [24] for methanol. This expression is in good agreement with the more recent results of Cribb and Dove [25] at their high temperatures. No direct measurements of the rate constant of CH_3OH + H have been conducted at elevated temperatures.

The formaldehyde reaction with H has only recently been measured at high temperature. The results of Choudury and Lin [26] indicate a rate constant for CH_2O + H three times slower than Tsang's rate at 1000 K. Their values rely heavily upon the rate constants for HCO + M $\rightleftharpoons$ H + CO + M and HCO + H $\rightleftharpoons$ H_2 + CO. Because these were measured at much lower temperatures than the formaldehyde study, the quoted uncertainty factor of ± 0.6 for the CH_2O + H rate constant may be optimistic.

By multiplying the rate constant of CH_2O + OH by 1.4, CH_2O + H by 2.2, and CH_3OH + H by 0.45, excellent agreement with the measured formaldehyde is obtained (dashed lines in Figs. 2 through 4). To decrease the methanol consumption rate for the high-temperature conditions, the rate constant of HO_2 + H is returned to its literature value [15], in contrast to earlier work [7] that suggested an increase of 50% was necessary.

Summary

The oxidation of methanol has been studied over wide pressure (1–20 atmospheres), temperature (752–1043 K), and equivalence ratio (0.4–2.6) ranges in a variable-pressure flow reactor. The atmospheric-pressure results are consistent with earlier atmospheric-pressure flow reactor data [10], while the high-pressure results represent the first data of their kind in this pressure-temperature regime. In addition to species previously observed in methanol kinetic studies, small amounts of formic acid and 1,2-ethanediol were detected. The relative amount of energy released during the reaction does not correlate well with the amount of carbon monoxide formed. A considerable fraction of the "late heat release" reported for high-temperature methanol oxidation [10] is due to delayed hydrogen oxidation, in addition to carbon monoxide oxidation.

The detailed kinetic model demonstrates good agreement with most of the flow reactor data, including those of previous studies [10]. Disagreement in peak formaldehyde levels between the model and experiment is indicative of errors in the relative hydrogen abstraction rates from methanol and formaldehyde. Reaction path and sensitivity analyses allow identification of important kinetic routes and reaction rates that strongly affect the calculated profiles. The hydroperoxyl radical plays a dominant role in methanol oxidation through its effect on radical branching and termination, even at temperatures where H + O_2 branching dominates H + O_2 + M termination.

Acknowledgments

The authors are grateful to Paul Michniewicz and Yolanda Stein for their technical assistance with the experimental work. This work was supported by a National Science Foundation Graduate Fellowship (TJH) and by the United States Department of Energy, Chemical Sciences Division, Office of Basic Energy Sciences, under Contract No. DE-FG02-86ER-13503.

REFERENCES

1. Gray, C. L., Jr., and Alson, J. A., *Sci. Am.* (November):108–114 (1989).
2. Gluckstein, M. E., and Walcutt, C., *SAE Trans.* 69:529–553 (1961).
3. Smith, J. R., Green, R. M., Westbrook, C. K., and Pitz, W. J., *Twentieth Symposium (International) on Combustion*, The Combustion Institute, Pittsburgh, 1984, pp. 91–100.
4. Driver, H. S. T., Hutcheon, R. J., Lockett, R. D., Robertson, G. N., Grotheer, H. H., and Kelm, S., *Ber. Bunsenges. Phys. Chem.* 96:1376–1387 (1992).
5. Yetter, R. A., Rabitz, H., and Hedges, R. M., *Int. J. Chem. Kinet.* 23:251–278 (1991).
6. Vermeersch, M. L., "A Variable Pressure Flow Reactor for Chemical Kinetic Studies: Hydrogen, Methane and Butane Oxidation at 1 to 10 Atmospheres and 880 to 1,040 K," Ph.D. Thesis, Princeton University, Princeton, NJ, 1991.
7. Held, T. J., "The Oxidation of Methanol, Isobutene and Methyl Tertiary-Butyl Ether," Ph.D. Thesis, Princeton University, Princeton, NJ 1993.
8. DeGraaff, D., and Zimmitti, E., "A Study of the Mixing Characteristics of the Variable Pressure Flow Reactor," Undergraduate Independent Research Project Report, Princeton University, Princeton, NJ, 1993.
9. Haaland, D. M., and Easterling, R. G., *Appl. Spectrosc.* 36:665–673 (1982).
10. Norton, T. S., and Dryer, F. L., *Combust. Sci. Technol.* 63:107–129 (1989).
11. Yetter, R., Dryer, F. L., and Rabitz, H., *Combust. Sci. Technol.* 79:97–128 (1991).
12. Kim, T. J., "Gas Phase Kinetic Studies of the Hydrogen-Oxygen and Carbon Monoxide-Hydrogen-Oxygen Systems," M.S.E. Thesis, Princeton University, Princeton, NJ, 1993.
13. Hochgreb, S., and Dryer, F. L., *Combust. Flame* 91:257–284 (1992).
14. Norton, T. S., and Dryer, F. L., *Int. J. Chem. Kinet.* 22:219–241 (1990).
15. Tsang, W., and Hampson, R. F., *J. Phys. Chem. Ref. Data* 15:1087–1279 (1986).
16. Egolfopoulos, F. N., Du, D. X., and Law, C. K., *Combust. Sci. Technol.* 83:33–75 (1992).
17. Grotheer, H. H., Kelm, S., Driver, H. S. T., Hutcheon, R. J., Lockett, R. D., and Robertson, G. N., *Ber. Bunsenges. Phys. Chem.* 96:1360–1376 (1992).
18. Bowman, C. T., *Combust. Flame* 25:343–354 (1975).
19. Hess, W. P., and Tully, F. P., *J. Phys. Chem.* 93:1944–1947 (1989).
20. Bott, J. F., and Cohen, N., *Int. J. Chem. Kinet.* 23:1075–1094 (1991).
21. Lutz, A. E., Kee, R. J., and Miller, J. A., *SENKIN: A Fortran Program for Predicting Homogeneous Gas Phase Chemical Kinetics with Sensitivity Analysis*, Sandia National Laboratories Report No. SAND87-8248, 1987.
22. Seeley, J. V., Jayne, J. T., and Molina, M. J., *Int. J. Chem. Kinet.* 25:571–594 (1993).
23. Tsang, W., *J. Phys. Chem. Ref. Data* 16:471–508 (1987).
24. Warnatz, J., in *Combustion Chemistry*, Chap. 5 (W. C. Gardiner, Ed.), Springer-Verlag, New York, 1984.
25. Cribb, P. H., Dove, J. E., and Yamazaki, S., *Combust. Flame* 88:169–185 (1992).
26. Choudhury, T. K., and Lin, M. C., *Combust. Sci. Technol.* 64:19–28 (1989).

Twenty-Fifth Symposium (International) on Combustion/The Combustion Institute, 1994/pp. 909–917

C_1/C_2 CHEMISTRY IN FUEL-RICH POST-FLAME GASES: DETAILED KINETIC MODELLING

I. T. WOODS* AND B. S. HAYNES
Department of Chemical Engineering
University of Sydney
New South Wales 2006, Australia

Measurements have been made of concentrations of hydrocarbons from C_1 to C_4 in sooting and nonsooting postflame gases at atmospheric pressure. The experimental results have been compared with the predictions of the detailed Miller–Melius mechanism for the interactions of hydrocarbons up to C_6.

The modelling of the postflame behaviour of small hydrocarbons is extremely sensitive to the rates and mechanisms of oxidation of C_2H_2 and CH_3 by OH. The Miller–Melius mechanism underpredicts the rates of both processes by a large amount but needs modification of only a few reactions for it to be accurate for postflame hydrocarbons up to at least C_4.

The oxidation of acetylene by OH is effectively irreversible and may be described simply as

$$C_2H_2 + OH \leftrightarrow CH_2CO + H \qquad \text{(R113)}$$

with $k_{113} = 1.1 \times 10^{13} \exp(-7170 \text{ cal mol}^{-1}/RT)$ cm^3 mol s ($\pm 30\%$).

The underprediction of the rate of CH_3 oxidation (via $CH_3 + OH \leftrightarrow CH_2OH + H \rightarrow CH_2O$) in the Miller–Melius mechanism derives mainly from the reversibility of the process under postflame conditions. A substantial increase in the rate constant assumed for the unimolecular decomposition of CH_2OH is indicated. The rate constant for

$$CH_3 + OH \leftrightarrow CH_2OH + H \qquad \text{(R-32)}$$

is found to be $k_{32} = 1.9 \times 10^{13}$ cm^3 mol s ($\pm 30\%$).

An additional process is responsible for substantial destruction of C_1's in the richest flames. This is suggested to be

$$CH_2CO + CH_3 \leftrightarrow C_2H_5 + CO \qquad \text{(R220)}$$

with $k_{220} = 5 \times 10^{12}$ cm^3 mol s ($\pm 50\%$).

The modelling of the concentrations of the higher hydrocarbons is governed by a tendency towards partial equilibria with the C_1's and C_2's. Despite good agreement between measurement and prediction, the present results do not allow a detailed assessment of the mechanistic details in the model.

Introduction

Hydrocarbons, chiefly methane and acetylene, break through the primary reaction zones of sufficiently fuel-rich flames. In the postflame gases, these hydrocarbons catalyse the recombination of flame radicals such as H and OH, react with NO to form HCN, may react to produce larger hydrocarbons and aromatics, and, in the presence of soot, may increase the soot mass by surface growth.

Despite the relative simplicity of the postflame zone, combustion models developed for describing flame-zone phenomena have generally performed poorly in describing postflame behaviour [1,2]. The free radical concentrations in fuel-rich postflame gases are low, and the species O and O_2, in particular, are at such low concentrations that they cannot contribute significantly to the overall post-flame hydrocarbon oxidation, which is determined more by OH reactions.

In an earlier paper [2], we reported an experimental study of the behaviour of methane and acetylene in the postflame region of the laminar, premixed, fuel-rich, nonsooting flames, at atmospheric pressure. Through identification of appropriate species pools, the kinetics of the key C_1/C_2 hydrocarbon reactions in these flames were established. The objective in the present work is to develop complete chemical kinetic mechanisms that describe the behaviour of hydrocarbons up to C_4 in the postflame gases of premixed fuel-rich ethylene/air flames under both nonsooting and sooting conditions. We employ the

*Presently at Dames and Moore Pty Ltd, Sydney.

mechanism, presented recently by Miller and Melius [3], for the formation of higher aliphatic hydrocarbons and benzene under very fuel-rich conditions, as the basis for comparison with our experimental measurements.

Method

The experimental apparatus and procedure have been described previously [2,4]. Briefly, laminar, premixed ethylene/air (+oxygen) flames were stabilised at atmospheric pressure on a water-cooled Meker-type flat-flame burner. The nonsooting flames [2] ranged in temperature from 1950 K near the flame zone to 1760 K far downstream ($t \sim 30$ ms). The sooting flames [4] had initial temperatures in the range of 1780–1920 K and downstream temperatures of 1640–1800 K; final soot volume fractions ranged from 1 to 5×10^{-7}.

Concentration profiles for major species and C_1 to C_4 were determined by gas chromatography of samples withdrawn from the postflame gases via a water-cooled aerodynamic-quench probe. The concentration of hydrogen atoms was determined by the Li/LiOH method and temperature by the sodium line-reversal and Kurlbaum methods.

The sooting flames required some special treatment. In particular, the exit of the sampling probe was equipped with a glass fibre filter to trap soot ahead of the analysis train. The soot volume fraction and particle number density within the flame were determined by conventional scattering and extinction methods. The measured Li absorbance was corrected for the extinction due to soot—the necessity for this correction limited the maximum soot volume fraction in the test flames to less than 5×10^{-7}.

Results

Experimental:

The experimental results obtained in the nonsooting flames have been presented in detail in previously [2]. The dominant species initially is C_2H_2, which subsequently decays to very low concentrations, at a rate depending on the postflame conditions. The C_1's (CH_4 + CH_3) are initially present at much lower concentrations than C_2H_2, but their concentration begins to increase as acetylene decays, before falling off further into the postflame gases. The concentrations of hydrogen atoms are within 15% of the equilibrium appropriate to $H_2 \leftrightarrow 2H$, except in the early postflame regions where $[H] \sim 3 \times [H]_{eq}$. Only the results for $[C_2H_2]$, $[C_1$'s$]$, and $[H]$ in flame N2 ($T_{initial}$ = 1950 K, T_{final} = 1850 K) are reproduced here (Fig. 1).

In sooting flames, the hydrocarbon concentrations

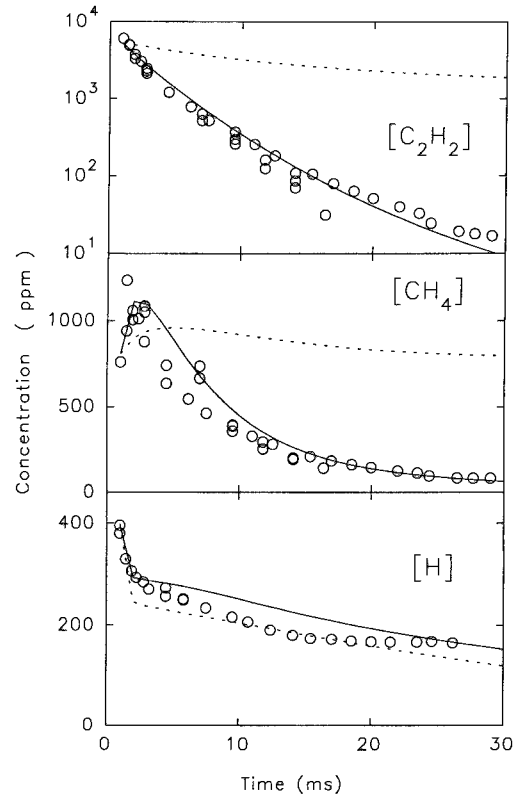

FIG. 1. Concentrations of C_2H_2, C_1's (chiefly CH_4), and H-atoms in nonsooting flame N2 (T_0 = 1950 K, T_{final} = 1850 K). The dashed lines represent the predictions of the original Miller–Melius model; the solid lines are the results obtained with the modified model described in Table 1.

are substantially higher, and their rates of change much lower, as shown for flame S1 ($T_{initial}$ = 1800 K, T_{final} = 1670 K) in Fig. 2. It is characteristic of these very rich flames that $[C_2H_2] > [CH_4]$ throughout the flame and that there is no obvious increase in $[CH_4]$ as C_2H_2 decays. As is also found in the nonsooting flames, the [H] is within 15% of the equilibrium concentration appropriate to $H_2 \leftrightarrow 2H$, except in the earliest postflame regions. The results for the other sooting flames not shown are qualitatively similar to those shown in Fig. 2.

Higher aliphatic hydrocarbons (allene, C_3H_4; diacetylene, C_4H_2, and vinylacetlyene, C_4H_4) are found in the gases sampled from the sooting flames. The grouped concentrations of "C_3's" (= $[C_3H_4]$) and "C_4's" (= $[C_4H_2]$ + $[C_4H_4]$) found in Flame S1 are shown in Fig. 2.

Computer Modelling:

The base mechanism of 218 reactions was taken from Miller and Melius [3]. Their reaction

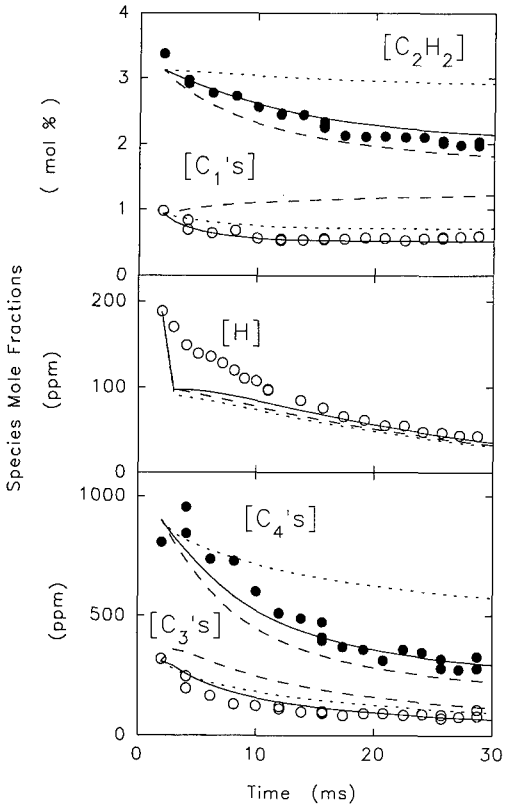

FIG. 2. Concentrations of C_2H_2, C_1's (chiefly CH_4), H-atoms, C_3's, and C_4's in sooting flame S1 (T_0 = 1800 K, T_{final} = 1670 K). The dashed lines represent the predictions of the original Miller–Melius model; the dotted lines are the results for the modified model (Table 1) without reaction R220; the solid lines are for the complete modified model described in Table 1.

identification numbers are employed in this paper, and the mechanism is not tabulated here. Computer-kinetic modelling was carried out using the Sandia SENKIN/CHEMKIN II package [5,6]. All reactions were treated as reversible, with reverse rates being calculated from the forward rates and the Sandia thermodynamic database [7].

No allowance was made in the modelling for diffusional transport. The largest diffusion velocities arising in this system were determined to be due to the initial concentration gradients for [H] in all flames and for $[C_2H_2]$ in the leanest nonsooting flames. In no case did these initial diffusional velocities exceed 15% of the bulk gas velocity; diffusion always contributed less than 5% of the species fluxes for $t > 3$ ms.

The experimental temperature profiles were used in the modelling. The initial values of the concentrations for the simulations were taken as the earliest measured values for [H], $[C_2H_2]$, $[C_3H_4]$, $[C_4H_2]$, [CO], $[CO_2]$, $[H_2]$, $[H_2O]$, and $[N_2]$. The measured initial CH_4 concentration was distributed as $[CH_3]$ and $[CH_4]$ (approximately 90%) according to the partial equilibrium $CH_3 + H_2 \leftrightarrow CH_4 + H$. Initial estimates of [OH] were determined from the partial equilibrium $H + H_2O \leftrightarrow OH + H_2$. The justification for these partial equilibrium assumptions is the fact that the characteristic times for their establishment were determined from the model to be <0.1 ms; it should also be noted that, since [OH] << [H] and $[CH_3]$ << $[CH_4]$, the model results are not significantly sensitive to the precise initial values of [OH] and $[CH_3]$.

The measured initial $[C_3$'s$]$ were distributed approximately according to partial equilibria amongst $\{C_3H_2$, H_2CCCH (propargyl), C_3H_4 (allene)$\}$ and the C_4's amongst $\{C_4H_2$ and $H_2CCCCH\}$, with the starting concentrations of the remaining C_3 and C_4 species in the mechanism being taken as zero. Initial concentrations of all other species were taken as zero.

The dashed lines in Figs. 1 and 2 represent the predictions of the Miller–Melius mechanism. The solid lines in the figures are the predictions of the model when modified, as shown in Table 1. The nondimensional sensitivity coefficients for the dependence of the predicted mole fractions on the values of the rate constants at constant temperature, $S_{ij} = \partial \ln x_i / \partial \ln A_j$, are shown for C_2H_2 and CH_4 in Figs. 3 and 4, respectively. These coefficients pertain to the modified model (Table 1), and only reactions exhibiting a significant coefficient (>0.1) are identified in the plots.

Discussion

The Miller–Melius mechanism grossly underpredicts the observed extent of C_2H_2 decay in both the sooting and the nonsooting flames. The downstream decay of the C_1's in the nonsooting flame is also greatly underpredicted, and in this light, the reasonable fit of the nearly constant $[C_1$'s$]$ profile in the sooting flame appears simply coincidental. In both flames, the tendency of the initial superequilibrium [H] to relax quickly to equilibrium is confirmed by the modelling.

Acetylene Decay:

The modelling of the decay of acetylene under our fuel-rich conditions in the Miller–Melius mechanism depends on the theoretical analysis by Miller and Melius [8] of the oxidation of C_2H_2 by OH:

$$C_2H_2 + OH \leftrightarrow HCCOH + H \quad (R112^*)$$

$$\rightarrow CH_2CO + H \quad (R113^*)$$

$$\rightarrow CH_3 + CO. \quad (R114^*)$$

TABLE 1
Summary of changes to the Miller–Melius mechanism. The modified parameters were used to generate the predictions shown by solid lines in Figs. 1 and 2. Parameters in cm³ mole sec cal units. $k = AT^n \exp(-E/RT)$.

		Original rate parameters			Modified rate parameters		
		A	n	E	A	n	E
32	$CH_2OH + H \leftrightarrow CH_3 + OH$	1.00×10^{14}	0	0	2.00×10^{14}	0	0
37	$CH_2OH + M \leftrightarrow CH_2O + H + M$	1.00×10^{14}	0	25,000	4.40×10^{15}	0	30,000
112	$C_2H_2 + OH \leftrightarrow HCCOH + H$	5.04×10^{5}	2.3	13,500	—	—	—
113	$C_2H_2 + OH \leftrightarrow CH_2CO + H$	2.18×10^{-4}	4.5	−1,000	1.10×10^{13}	0	7,170
114	$C_2H_2 + OH \leftrightarrow CH_3 + CO$	4.83×10^{-4}	4.0	−2,000	—	—	—
219	$CH_2CO + OH \leftrightarrow CH_2O + HCO$	—	—	—	2.80×10^{13}	0	0
220	$CH_2CO + CH_3 \leftrightarrow C_2H_5 + CO$	—	—	—	5.00×10^{12}	0	0

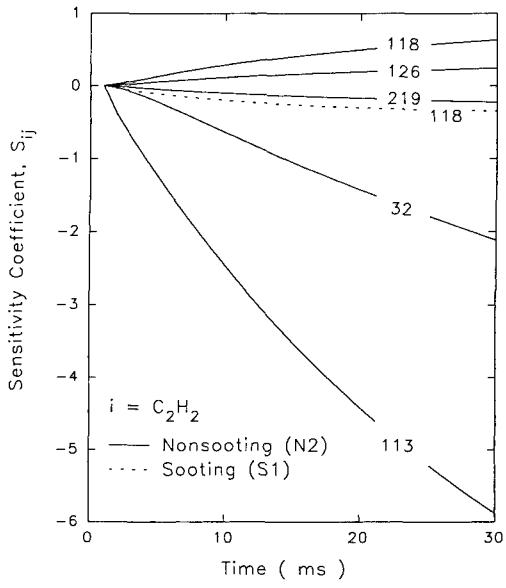

FIG. 3. Nondimensional sensitivity coefficients ($S_{ij} = \partial \ln x_i / \partial \ln A_j$) for prediction of $[C_2H_2]$ with the modified mechanism (Table 2) in the nonsooting (solid line) and sooting (dashed line) flames. Results are shown only for reactions with $|S_{ij}| > 0.1$.

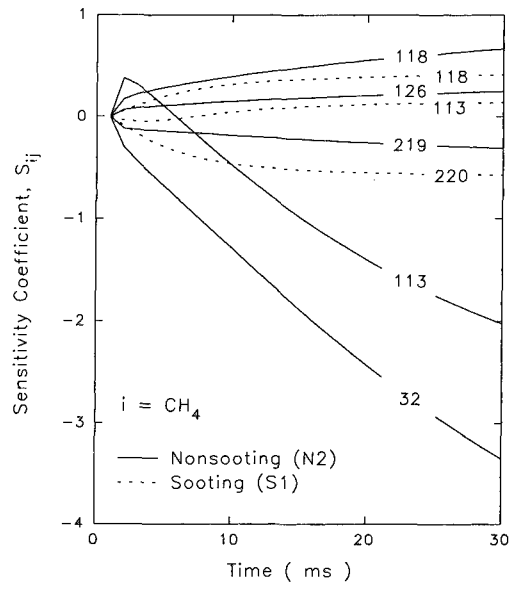

FIG. 4. Nondimensional sensitivity coefficients ($S_{ij} = \partial \ln x_i / \partial \ln A_j$) for prediction of $[CH_4]$ with the modified mechanism (Table 2) in the nonsooting (solid line) and sooting (dashed line) flames. Results are shown only for reactions with $|S_{ij}| > 0.1$.

The sum of the forward rate constants of reactions R.112–114 is 4.9×10^{11} cm³/mol/s, at 1800 K, with fractional contributions 0.72, 0.26, and 0.02, respectively. All the reactions are nominally reversible, but only the reverse of reaction R112 is fast enough to be significant under the present conditions.

*The numbering of the reactions follows that of Miller and Melius [3]. While all reactions in the model are treated as reversible, some are effectively irreversible under the present conditions. These reactions are written as irreversible (→) in the text.

We [2] have previously analysed our results for the nonsooting flames in terms of the decomposition of the total hydrocarbon pool, {$[C_2H_2]$ + $[C_1$'s]}, and found that the rate constant for the reaction C_2H_2 + OH at 1800 K is 1.5×10^{12} cm³/mol/s and that the reaction is effectively irreversible. This rate constant is a factor of three higher than that used by Miller and Melius [3], but even that difference is not enough to account for the discrepancy between the measurements and the Miller–Melius predictions shown in Figs. 1 and 2. This discrepancy derives chiefly from the fact that R112 is reversible ($k_{-112} \sim$

5×10^{13} cm³/mol/s) and that it is removal of hydroxyacetylene (HOCCH), which is rate controlling. According to the mechanism, decomposition of HCCOH occurs via

$$HOCCH + H \leftrightarrow CH_2CO + H. \quad (R115)$$

The rate constant for this process would have to exceed 10^{15} cm³/mol/s for R112 to be rate controlling in flame N2 (Fig. 1). Even if a plausible route for the extremely rapid rearrangement of hydroxyacetylene to ketene could be found, the net result would be that R112 effectively forms ketene irreversibly under postflame conditions. We have, therefore, chosen to model the overall reaction in these terms.

Our pool analysis of the results for the nonsooting flames, coupled with an evaluation of other data on the reaction C_2H_2 + OH, led to an estimate of the rate constant, for the formation of ketene, of $1.1 \times 10^{13} \exp(-7170 \text{ cal mol}^{-1}/RT)$ cm³/mol/s [2]. This is the value that has been used in the modified model as k_{113}, as described in Table 1. Clearly, there is now very good agreement between experiment and prediction, extending over nearly three orders of magnitude in $[C_2H_2]$ in the nonsooting flame N2.

Examination of the sensitivity coefficients for C_2H_2 in Fig. 3 confirms the importance of the modified reaction R113 in determining the $[C_2H_2]$ profiles, at least in the nonsooting flames. The ability of the model to describe accurately the experimental observations when the sensitivity coefficient is as high as six also suggests that the overall rate constant for the reaction of C_2H_2 + OH to form ketene is very precisely determined. Similar results are obtained for the other nonsooting flames, without the need for any adjustments to the values of any of the rate constants in the model. Within the context of the model, the uncertainty in the value of k_{113} is less than 10%; the absolute uncertainty is estimated to be ±30%.

In the sooting flames, the rate of decomposition of acetylene is relatively slow, and the predictions are not particularly sensitive to the assumed rate of C_2H_2 + OH, $S_{C_2H_2,113} < 0.1$. The loss of C_2H_2 by surface growth reactions on the soot particles is negligible, and the differences between the original Miller–Melius mechanism and the present modification is very clear. In these flames, the reversibility of R112 makes this route practically inoperative, and the effective rate according to the Miller–Melius mechanism is at least one order of magnitude lower than given by the revised expression for R113.

Other reactions to which the predictions of $[C_2H_2]$ are sensitive relate to the decomposition of ketene (R118, R126, and R219) and C_1's (R32).

Methane Decay:

The Miller–Melius mechanism includes a number of reactions capable of destroying the ketene produced by the initial oxidation of C_2H_2:

$$CH_2CO + H \rightarrow CH_3 + CO \quad (R118)$$

$$CH_2CO + M \rightarrow {}^3\dot{C}H_2 + CO + M \quad (R122)$$

$$CH_2CO + H,OH,O \leftrightarrow HCCO + H_2,H_2O,OH \quad (R119–R121)$$

The H-atom abstractions, R119–R121, tend to be balanced under the present postflame conditions. Therefore, it is the further reaction of the ketyl radical, HCCO, that determines the effective rates of ketene destruction by R119–R121. Destruction of the ketyl radical occurs almost exclusively via R126, leading to the formation of a C_1 species:

$$HCCO + H \rightarrow {}^1CH_2 + CO. \quad (R126)$$

Reactions R118 and R122 also give rise to C_1's so that there is predicted to be approximately one C_1 formed for each C_2H_2 oxidised. However, while the experimental results show a clear increase in [C_1's] early in the nonsooting flames when acetylene decay is most rapid, this is clearly much less than 1:1.

The Miller–Melius mechanism does not allow for the oxidation of ketene by OH, which is generally presumed to occur in atmospheric and combustion systems [9,10]. Although there is some uncertainty as to the precise nature of the oxidation products [11], the reaction may be presumed to remove ketene without forming C_1 species. This process is included in the modified model as reaction 219, where HCHO and HCO do not count as C_1 species because of their C=O bond [2]:

$$CH_2CO + OH \rightarrow HCHO + HCO. \quad (R219)$$

In including this reaction in the mechanism, we have taken the rate of Vandooren and Van Tiggelen [9] ($k_{219} = 2.8 \times 10^{13}$ cm³/mol/s), which lies well within the range of $10^{13\pm1}$ suggested by Baulch et al. [11].

Oxidation of the C_1 species also limits the extent of increase in [C_1's]. This occurs almost exclusively via R-32:

$$CH_3 + OH \leftrightarrow CH_2OH + H. \quad (R\text{-}32)$$

As shown by the dashed lines in Fig. 1, the Miller–Melius mechanism predicts relatively little C_1 oxidation, despite employing a very high value of $k_{32} = 1.0 \times 10^{14}$ cm³/mol/s. This is because, in the mechanism, the decomposition of CH_2OH, which occurs almost entirely via R37, is rate limiting:

$$CH_2OH + M \rightarrow CH_2O + H + M. \quad (R37)$$

Despite the importance of reaction 37 in the combustion kinetics of methanol, there remains considerable uncertainty in the value of the rate constant. Recent estimates [12] have been higher than the value employed in the Miller–Melius mechanism by one to two orders of magnitude. In modifying the original mechanism, the value reported by Hidaka et al. [13] has been assumed—this is approximately 10 times faster than the Miller—Melius rate under the present conditions. With this assumption, the removal of C_1's proceeds much faster and is determined only by k_{-32}.

The sensitivity of the predicted [C_1's] profile in the nonsooting flames to the value of k_{-32} is very high (Fig. 4), and a precise estimate of this value can be obtained by fitting the experimental data. As shown in Fig. 1, the data are accurately modelled when the rate constant for the reverse reaction (CH_3 + OH) is taken as $k_{-32} = 1.9 \times 10^{13}$ cm^3/mol/s (Table 1). This confirms the estimate of $1.7(\pm 0.4) \times 10^{13}$ obtained from our earlier pool analysis of the nonsooting flames [2] and is in good agreement with other values that have been reported for the rate of this reaction—Roth and Just [14] obtained $k_{-32} = 2(\pm 1) \times 10^{13}$ in the temperature range 1800–2300 K; Dombrowsky et al. [15] reported $1.5(\pm 0.5) \times 10^{13}$. In the context of the revised model, our value of k_{-32} is uncertain by no more than 20%.

The value of k_{32} employed in the modified mechanism (Table 1) is determined from k_{-32} and the equilibrium constant for the reaction. The thermochemistry of CH_2OH is uncertain, but the value for $\Delta H^\circ_{f298}(CH_2OH) = -4.21$ kcal mol^{-1} in the Sandia database [7] is close to the value of -4.5 kcal mol^{-1} determined recently by Traeger and Holmes [16]. Using the Sandia data, the equilibrium constant for R-32 is approximately 10.5 at flame temperatures, giving $k_{32} = 2.0 \times 10^{14}$ cm^3/mol/s, or twice the value used in the original mechanism. This very high value is barely acceptable on kinetic grounds, and it may be that the reaction CH_3 + OH proceeds to other primary products. However, the QRRK study of Dean and Westmoreland [17] found the path to CH_2OH + H (R-32) to be the most likely at higher temperatures. The alternative products CH_3O + H (R-33) are frequently invoked, but this channel is unlikely to contribute significantly, as it is thermodynamically even more unfavourable than R-32. The H-atom abstraction routes to $^3CH_2 + H_2O$ (R34) or $^1CH_2 + H_2O$ (R141) do not lead to C_1 oxidation and have no influence on the predictions.

In the sooting flames, the oxidation of CH_3 is predicted to be insignificant, as shown by the dotted line in Fig. 2a, but the experimental [C_1's] decrease nevertheless. The amount of acetylene taken up as soot by surface growth reactions is negligible, and no realistic combination of rate constants for the decomposition of ketene (R118, R119, R219) could be found to provide an alternative explanation, over the whole range of conditions studied, for the removal of acetylene without concomitant C_1 formation.

Our pool analysis of the nonsooting flames [2] led to the conclusion that some additional process must be capable of limiting C_1 formation from ketene. This was suggested to be R220 ($\Delta H^\circ_{298} = -21$ kcal mol^{-1})

$$CH_2CO + CH_3 \rightarrow C_2H_5 + CO. \quad (R220)$$

As shown by the solid lines in Figs. 1 and 2, the inclusion of R220, with $k_{220} = 5 \times 10^{12}$ cm^3/mol/s, in the modified mechanism leads to very good agreement between experiment and prediction over the whole range of conditions studied here. The same results are obtained if the products of R220 are alternatively assumed to be C_2H_4 + HCO. The sensitivity coefficients in Figs. 3 and 4 reveal that variations in the value of k_{220} strongly affect only the predictions of [C_1's] in the sooting flames. Despite the relatively high value of the sensitivity coefficient, no adjustment in k_{220} is required to fit all the sooting flames. The estimated uncertainty in the magnitude of k_{220} is $\pm 50\%$.

There have been no reports in the literature with which to compare k_{220}. Methyl additions to alkenes generally have A factors around 3×10^{11} cm^3/mol/s, reflecting a tight transition state; they also have activation barriers around 8 kcal mol. Since R220 probably proceeds via the addition complex CH_3CH_2CO, our value for k_{220} seems high. However, the occurrence of the =O substituent may affect these class rules—at the very least, the exothermicity of the addition step in this case (-34 kcal/mol) is such that the activation barrier is likely to be very small [18]; also, the transition state will occur much earlier and may be quite loose compared to the usual case [19].

Radical Equilibrium:

The model reproduces the experimental observation that [H] falls rapidly from its initial superequilibrium value to a value near to that corresponding to the equilibrium $H_2 \leftrightarrow 2H$. In the nonsooting flames, this behaviour is due primarily to the catalytic cycle of the balanced reactions as also found by Kaiser [20]:

$$CH_4 + H \leftrightarrow CH_3 + H_2 \quad (R25)$$

$$CH_3 + H + M \leftrightarrow CH_4 + M. \quad (R23)$$

In the sooting flames, the higher concentrations of CH_4, and the involvement of many other hydrocarbon pairs such as H_2CCH/C_3H_2 in the catalysis of the radical recombination, reinforce the equilibration of the radicals. Now, however, the calculated

initial approach to equilibrium is substantially faster than observed experimentally—the reason for this discrepancy is not clear, but its impact on overall ability of the model to describe our results is not significant.

Higher Hydrocarbons:

The modified mechanism describes accurately the behaviour of the C_3's and C_4's in the sooting flames. For the C_4's, this is more a reflection of the fact that the various hydrocarbons are largely equilibrated among themselves than a testament to the accuracy of the mechanism as such. For example, the balanced reactions R-101 and R124 have long been known to tie the major C_2 and C_4 components to their equilibrium proportions [21]:

$$C_2H_2 + H \leftrightarrow C_2H + H_2 \qquad \text{(R-101)}$$

$$C_2H + C_2H_2 \leftrightarrow C_4H_2 + H. \qquad \text{(R124)}$$

Partial equilibria are not so clearly established between the C_3's and either the C_2's or the C_4's. Nevertheless, the reversible addition of C_1's to C_2's to form C_3's (e.g., R160) and to C_3's to form C_4's (e.g., R171) does ensure strong coupling between these various classes of species [20]:

$$^3CH_2 + C_2H_2 \leftrightarrow H_2CCCH + H \qquad \text{(R160)}$$

$$H_2CCCH + {}^3CH_2 \leftrightarrow CH_2CHCCH + H. \qquad \text{(R171)}$$

Because of these effects, the predictions for both [C_3's] and [C_4's] are insensitive to the detailed kinetics and are determined more by the factors influencing the [C_2H_2] and [C_1's] profiles than by the reactions of the C_3's and C_4's themselves.

Conclusions

The modelling of the postflame behaviour of small hydrocarbons is extremely sensitive to the rates and mechanisms of oxidation of C_2H_2 and CH_3 by OH. The Miller–Melius mechanism underpredicts the rates of both processes by a large amount but needs modification of only a few reactions for it to be accurate for postflame hydrocarbons up to at least C_4.

The oxidation of acetylene by OH is effectively irreversible and may be described simply as

$$C_2H_2 + OH \leftrightarrow CH_2CO + H \qquad \text{(R113)}$$

with $k_{113} = 1.1 \times 10^{13} \exp(-7170 \text{ cal mol}^{-1}/RT)$, $\pm 30\%$. The Miller–Melius description of this process is not suitable both because the rate constant is too low and because their primary channel (C_2H_2 + OH $\leftrightarrow$ HCCOH + H $\rightarrow CH_2CO$) is reversible under postflame conditions.

The underprediction of the rate of CH_3 oxidation (via $CH_3 + OH \leftrightarrow CH_2OH + H \rightarrow CH_2O$) in the Miller–Melius mechanism also derives mainly from the reversibility of the process under postflame conditions. A substantial increase in the rate constant assumed for the unimolecular decomposition of CH_2OH is supported by other estimates for this rate and removes the bottleneck limiting the overall rate of CH_3 oxidation. The rate constant for

$$CH_3 + OH \leftrightarrow CH_2OH + H \qquad \text{(R-32)}$$

is found to be $k_{-32} = 1.9 \times 10^{13}$ cm^3 mol s ($\pm 30\%$).

An additional process is responsible for substantial destruction of C_1's in the richest flames. This is suggested to be

$$CH_2CO + CH_3 \leftrightarrow C_2H_5 + CO \qquad \text{(R220)}$$

with $k_{220} = 5 \times 10^{12}$ cm^3 mol s ($\pm 50\%$).

The modelling of the concentrations of the higher hydrocarbons is governed by a tendency towards partial equilibria with the C_1's and C_2's, and the present results do not allow a detailed assessment of the mechanistic details in the model.

Acknowledgments

The authors acknowledge the financial support of the University of Sydney Research Grant Scheme; ITW acknowledges the support provided by the Chemical Engineering Foundation of the University of Sydney and by the Commonwealth Scholarship Scheme.

REFERENCES

1. Levy, J. M., and Sarofim, A. F., *Combust. Flame* 53:1–15 (1983).
2. Woods, I. T., and Haynes, B. S., *Combust. Sci. Technol.* 87:199–215 (1993).
3. Miller, J. A., and Melius, C. F., *Combust. Flame* 91:21–39 (1992).
4. Woods, I. T., and Haynes, B. S., in *Mechanisms and Modelling of Soot Formation* (H. Bockhorn, Ed.), Springer-Verlag, in press.
5. Kee, R. J., Rupley, F. M., and Miller, J. A., Chemkin-II: A Fortran Chemical Kinetics Package for the Analysis of Gas-Phase Chemical Kinetics, Sandia National Laboratory, Sandia Report SAND89-8009, 1989.
6. Lutz, A. E., Kee, R. J., and Miller, J. A., SENKIN: A Fortran Program for Predicting Homogeneous Gas-Phase Chemical Kinetics with Sensitivity Analysis, Sandia National Laboratory, Sandia Report SAND87-8248, 1987.
7. Kee, R. J., Rupley, F. M., and Miller, J. A. The

Chemkin Thermodynamic Database, Sandia Report SAND87-8215, 1987.
8. Miller, J. A., and Melius, C. F., *Twenty-Second Symposium (International) on Combustion,* The Combustion Institute, Pittsburgh, 1988, pp. 1031–1039.
9. Vandooren, J., and Van Tiggelen, P. J., *Sixteenth Symposium (International) on Combustion,* 1977, pp. 1133–1144.
10. Oehlers, C., Temps, F., Wagner, H. Gg., and Wolf, M., *Ber. Bunsenges. Phys. Chem.* 96:171–175 (1992).
11. Baulch, D. L., Cobos, C. F., Cox, R. A., Esser, C., Frank, P., Just, Th., Kerr, J. A., Pilling, M. J., Troe, J., Walker, R. W., and Warnatz, J., *J. Phys. Chem. Ref. Data* 21:411–734 (1992).
12. Mallard, W. G., Westley, F., Herron, J. T., Hampson, R. F., and Frizzell, D. H., *NIST Chemical Kinetics Database: Version 5.0,* National Institute of Standards and Technology, Gaithersburg MD, 1993.
13. Hidaka, Y., Oki, T., and Kawano, X., *Int. J. Chem. Kinet.* 21:689–692 (1989).
14. Roth, P., and Just., Th., *Twenty-First Symposium (International) on Combustion,* The Combustion Institute, Pittsburgh, 1988, pp. 807–818.
15. Dombrowsky, Ch., Hoffmann, A., Klatt, M., and Wagner, H. Gg., *Ber. Bunsenges. Phys. Chem.* 95:1685–1687 (1991).
16. Traeger, J. C., and Holmes, J. L., *J. Phys. Chem.* 97:3453–3455 (1993).
17. Dean, A. M., and Westmoreland, P. R., *Int. J. Chem. Kinet.* 19:207 (1987).
18. Wong, M. W., Pross, A., and Radom, L., *J. Am. Chem. Soc.,* 115:11050–11051 (1993).
19. Arnaud, R., and Vidal, S., *N. J. Chem.,* 16:471–474 (1992).
20. Kaiser, E. W., *J. Phys. Chem.,* 94:4493–4499 (1990).
21. Bonne, U., Homann, K. H., and Wagner, H. Gg., *Tenth Symposium (International) on Combustion,* The Combustion Institute, Pittsburgh, 1965, pp. 503–512.

COMMENTS

J. Warnatz, ITV, Stuttgart University, Germany. What is the role of C_5 and C_4 species in oxidation by OH at the conditions of your work?

Author's Reply. The Miller–Melius mechanism does not include any OH-oxidation reactions for species larger than C_4's. Of the C_3's and C_4's, only C_3H_2 and C_4H_2 are oxidized by OH, with rate constants approaching gas-kinetic limits. Since these species are the dominant forms of the C_3 and C_4 species, respectively, the model tends therefore to give something approaching an upper-limit estimate of the importance of the oxidation of C_3's and C_4's by OH.

In the modelling of our flames, <10% of C=O bonds are formed by oxidation of C_3H_2 and C_4H_2, resulting in negligible additional uncertainty in the analysis of the overall rate of hydrocarbon oxidation. Oxidation of higher hydrocarbons would be negligible if it were included, because of the very low concentrations of these species under our conditions.

•

Horst-Henning Grotheer, DLR, Germany. You describe a fast reaction of CH_3 + OH into oxidative channels with a rate coefficient of 1.9×10^{13} cm³/mole-s obtained with a high sensitivity. On thermochemical grounds, you doubt that this number refers solely to the channel CH_2OH + H since in this case the reverse reaction would be close to or even larger than collision frequency. This argumentation is supported by new measurements of Dó bé et al. [1] leading to ΔH_f (CH_2OH) = −2.5 kcal/mole at 300 K. This conflict might be resolved by inclusion of the product channel HCOH + H_2 (this Symposium) with a tentative rate coefficient of $5.5 \times 10^{13}\ e^{-1500/T}$ cm³/mole-s which is oxidative in nature as well as exothermic.

REFERENCE

1. S. Dó bé et al., Gas Kinetics Symposium, Dublin, September, 1994.

•

James A. Miller, Sandia National Laboratories, USA. How would it have affected your analysis if our mechanism had included fairly rapid reactions in which hydroxyl and hydrogen atoms abstract a hydrogen from the OH end of hydroxy-acetylene, i.e., OH + $HOC_2H \rightleftarrows$ HCCO + H_2O and H + $HOC_2H \rightleftarrows$ HCCO + H_2? The ketenyl radical would naturally feed into the rest of the mechanism. I think this is the most likely way of breaking the "bottleneck" to which you refer in your paper.

Author's Reply. The rate of removal of HOC_2H to oxidation products needs to be higher by one to two orders of magnitude to enable us to describe the overall oxidation of C_2H_2 via HOC_2H.

The reaction H + $HOC_2H \rightarrow CH_2CO$ + H is already in the mechanism with $k = 10^{13}$ cm³/mol·s. Addition of the parallel channel H + $HOC_2H \rightarrow$ HCCO + H_2, with a similar rate constant, would therefore do little to resolve the bottleneck observed under our conditions. However, if one, or both, of these reactions were taken to have a rate constant of 2–5 × 10^{14} cm³/mol·s, the bottleneck would

indeed be removed. Of course, the rate constant for the overall reaction C_2H_2 + OH would still have to be as reported here, rather than as found described by Miller and Melius.

•

Stephen Niksa, SRI International, USA. Did you check to see if the changes you made to the rate constants will adversely affect other predictions of the Miller–Melius mechanism?

Author's Reply. The modelling of any situation where oxidation is driven mostly by O or O_2 is unlikely to be affected by the changes we propose. Such situations include very fuel-rich flame zones, as modelled by Miller and Melius in their original paper (our Ref. 3). We have in fact confirmed, using the PREMIX code, that the changes proposed do not significantly influence the predictions shown in that original paper.

Twenty-Fifth Symposium (International) on Combustion/The Combustion Institute, 1994/pp. 919–926

KEROSENE COMBUSTION AT PRESSURES UP TO 40 ATM: EXPERIMENTAL STUDY AND DETAILED CHEMICAL KINETIC MODELING

PHILIPPE DAGAUT, MARCELLINE REUILLON, JEAN-CLAUDE BOETTNER AND MICHEL CATHONNET
Laboratoire de Combustion et Systèmes Réactifs—C.N.R.S.
1 C, Avenue de la Recherche Scientifique
45071 Orleans, Cedex 2, France

The oxidation of TR0 kerosene (jet A1 aviation fuel) was studied in a jet-stirred reactor (JSR) at pressures extending from 10 to 40 atm, in the temperature range 750–1150 K. A large number of reaction intermediates were identified, and their concentrations were followed for reaction yields ranging from low conversion to the formation of the final products. A reference hydrocarbon, *n*-decane, studied under the same experimental conditions gave very similar experimental concentration profiles for the main oxidation products.

Because of the strong analogy between *n*-decane and kerosene oxidation kinetics, a detailed chemical kinetic reaction mechanism describing the oxidation of *n*-decane was built to reproduce the present experimental results. This mechanism includes 573 elementary reactions, most of them being reversible, among 90 chemical species. A reasonably good prediction of the concentrations of major species was obtained by computation, covering the whole range of temperatures, pressures, and equivalence ratios of the experiments.

A kinetic analysis performed to identify the dominant reaction steps of the mechanism shows that, under the conditions of the present study (intermediate temperature and high pressure), HO_2 radicals are important chain carriers leading to the formation of the branching agent H_2O_2.

Introduction

Numerical modeling has become an essential part of combustion research for a better prediction of performances and emissions of many combustion systems. In combustion models, the importance of chemical kinetics has increased continuously. It has been proved, in fact, that a good representation of chemistry interactions is essential for the predictive capabilities of numerical models. Moreover, the validity domain of a given model and of its chemical kinetic submodel in terms of temperature, pressure, and equivalence ratio has to be large enough in order to include the wide range of operating conditions of many combustion systems. This is particularly true for the simultaneous prediction of carbon monoxide and unburnt hydrocarbons, which are intermediate products of combustion in engines, mainly formed at low ratings, and of nitrogen oxides, which are mostly produced at high temperature. Numerous studies in the field of chemical kinetics have been done in the past, leading to the conception of reaction mechanisms with growing complexity to describe the oxidation of a great variety of fuels. However, the models used for the combustion of commercial fuels are restricted to single-step empirical expressions or global multistep schemes.

In a previous study [1] on kerosene oxidation in a jet-stirred reactor (JSR) at atmospheric pressure, a quasi-global model was proposed to reproduce the concentration profiles of the major chemical species. However, the validity of such a quasi-global mechanism cannot be extended to the whole range of operating conditions of an engine, particularly at high pressure. Because of the superiority of detailed chemical kinetic mechanisms over quasi-global models for predicting combustion chemistry features, we have begun to develop detailed mechanisms for the oxidation of higher alkanes in the intermediate- and high-temperature ranges [2,3].

In the present study, new experimental data have been obtained for the oxidation of kerosene in a JSR at 10, 20, and 40 bars. A detailed chemical kinetic reaction mechanism built for the oxidation of *n*-decane was tentatively used to model the present experiments in order to show that, to some extent, major experimental species concentration profiles obtained in kerosene oxidation in a JSR from 10 to 40 bars can reasonably be predicted.

Experimental Study

Experimental Details:

A new experimental setup was built for the study of liquid fuel oxidation at high pressure. It is derived from previous jet-stirred reactor experiments in this

laboratory [2,4] and has been described elsewhere [5]. The quartz jet-stirred reactor is enclosed in a stainless steel pressure-resistant jacket filled with insulating material. A regulated nitrogen flow in the outer part of the reactor balances the pressure inside the reaction cell, allowing operation at pressures as high as 40 bars. The reactor is heated by a regulated electrical resistance system.

Before its introduction into the reactor, the liquid fuel is atomized through a small annular orifice in a nitrogen flow and prevaporized in a heated vaporizer. The vapors are mixed with a preheated nitrogen and oxygen flow at the entrance of the injectors. The fuel is delivered at a precise flow rate into the vaporizer by a high-pressure liquid chromatography pump, and the flow rates of the gases are measured and regulated by mass flow controllers. All the gases are preheated before injection by a regulated 12.5-kW induction heating system.

The temperature of the gases inside the reactor is measured by moving an uncoated chromel-alumel thermocouple of 0.16-mm diameter along a whole diameter. Heat losses by radiation are neglected since the reactor wall temperature is nearly identical to that of the gases. Heating of the entering gases and of the reactor permitted operation up to ≈1300 K with temperature gradients across the reactor of less than 10 K. Because of the high dilution of the fuel (0.1% or less by volume), no flame occurs in the reactor, and operation at steady state is possible.

Gas samples are collected at low pressure (20–30 torr) through a sonic quartz probe. In this study, in order to follow the fuel oxidation from low to high conversion, the temperature of the gases in the reactor was varied stepwise at a constant mean residence time.

Several gas chromatographs equipped with capillary columns and a GC/MS system were used for the analysis of the samples, as described elsewhere [5]. Carbon balance was checked for every sample and was found good within ≤5%.

Experimental Results:

The oxidation of TR0 kerosene (Jet A1 aviation fuel) was studied in the temperature range 750–1150 K for an initial fuel concentration ranging from 0.025 to 0.1% at equivalence ratios extending from 0.5 to 1.5. The concentration profiles of stable species were obtained for different mean residence times in the reactor (0.5–2 s), corresponding to reaction yields ranging from low conversion to the formation of the final products.

The experimental procedure used allowed investigation of a very large temperature interval and showed that, at temperatures lower than 750 K, the oxidation is governed by low-temperature chemistry, as described elsewhere for *n*-heptane [5]. In the temperature range considered, as shown previously [1], the main intermediate molecular products of kerosene oxidation are carbon monoxide, lower alkenes (ethylene, propene, 1-butene), methane, and lower unsaturated hydrocarbons (acetylene, propadiene, propyne). Among other products, we detected C_6–C_9 alkenes and aromatics (benzene, toluene, and xylenes). Figure 1 shows an example of the concentration profiles of major products and intermediates from low to high reaction extent.

A previous study [6] on *n*-decane oxidation at atmospheric pressure showed that the main products identified were also found in kerosene oxidation [1]. *n*-Decane oxidation was examined again, under the experimental conditions of the present study, i.e., at higher pressure and reaction yield than before, and these new experiments showed that, in *n*-decane and kerosene oxidation, most of the products are the same. The main difference between the two fuels is the presence of aromatics in significant amounts in kerosene oxidation. These aromatics are mostly produced from the aromatic fraction of kerosene. In addition, our experiments show that the reactivities of *n*-decane and TR0-kerosene are very similar, as can be seen in Fig. 2, where the concentration profiles of the main products of kerosene and *n*-decane oxidation have been plotted vs the temperature for identical initial conditions. This similarity between the reaction products of kerosene and *n*-decane is not restricted to our experimental conditions, since it was also observed in a low-pressure flat-flame experiment [7].

Chemical Kinetic Modeling

The strong analogy between kerosene and *n*-decane oxidation led us to represent kerosene oxidation by a detailed chemical kinetic mechanism built for *n*-decane oxidation.

Elaboration of a Detailed Reaction Mechanism:

The main sequences of reactions occurring in the oxidation and ignition of higher alkanes have been described in several papers [8,9,10,11,12,13]. Because many small hydrocarbons are found as intermediate products in the oxidation of large hydrocarbon fuels, a detailed chemical kinetic reaction mechanism for large hydrocarbons has a hierarchical structure. The basis of the detailed mechanism developed for *n*-decane oxidation was the mechanism previously written for *n*-heptane oxidation [3], and validated by extensive comparison between experiments and simulations for lower hydrocarbons. Reactions of species with more than seven carbon atoms were added, using the procedure described in Refs. 10 and 11 for reaction classification and rate constant values. However, the present study is restricted to the intermediate-temperature regime, and conse-

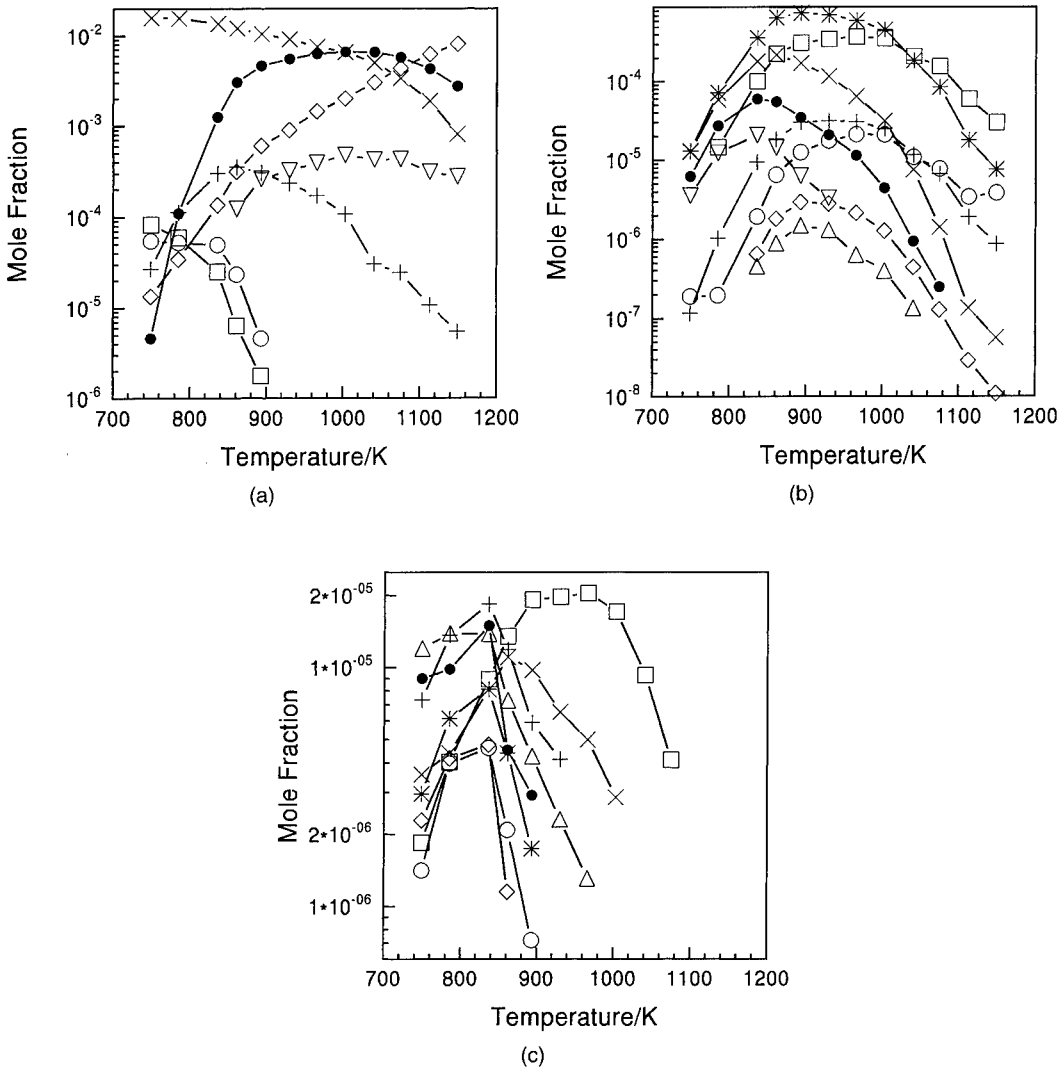

FIG. 1. Experimental concentration profiles obtained for the oxidation of kerosene at 10 atm. Initial mole fractions were 10^{-3} for kerosene and 1.65×10^{-2} for O_2; equivalence ratio = 1; residence time = 0.5 s. (a): × O_2, ● CO, ◇ CO_2, ▽ H_2, + CH_2O, □ *n*-decane, ○ 1,2,4-trimethylbenzene; (b): * C_2H_4, □ CH_4, × C_3H_6, ● 1-butene, + C_2H_6, ○ C_2H_2, ▽ 1-pentene, ◇ propyne, △ propadiene; (c): + 1-hexene, * 1-heptene, ○ 1-octene, ◇ 1-nonene, □ benzene, × toluene, △ *o*-xylene, ● *p*-xylene.)

quently, the chemical mechanism is simpler than the one developed in Ref. 11, since low-temperature reactions can be neglected.

The first part of the mechanism consists of reactions consuming *n*-decane: initiation and reaction with radicals. Initiation occurs mainly through thermal decomposition forming two alkyl radicals, but also through H-atom abstraction by O_2. Reactions with radicals consist of the abstraction of an H atom from *n*-decane to form five different *n*-decyl radicals depending on the site of the abstracted H atom. Each *n*-decyl radical then thermally decomposes to give an alkyl radical plus an alkene, as described for octyl radicals by Dryer and Brezinsky [8]. Isomerization of *n*-decyl radicals must also be taken into account, mainly by H-atom migration across five carbon atoms, but also across four and six carbon atoms. In the present mechanism, these reactions (thermal decomposition and isomerization) have been written for alkyl radicals from C_4 to C_{10}. They control the distribution of intermediate hydrocarbons. The elaboration of the $>C_7$ mechanism subset was not subject to kinetic parameter tuning as was necessary in the quasi-global scheme.

The complete mechanism includes 573 elementary reactions, most of them being reversible, among 90 chemical species. The rate constants for reverse reactions were computed from the forward rate constants and the appropriate equilibrium constants, which were calculated from the sources listed in Ref. 3. In addition, the pressure dependence of unimolecular reactions and of some pressure-dependent bimolecular reactions was taken into account when information was available, as described in Ref. 14.

Comparison with Experiments:

The chemical kinetic reaction mechanism used in this study was first checked against experimental profiles obtained in a study of *n*-decane oxidation at 1 and 10 atm for several equivalence ratios (0.1–1.5). A good agreement was observed for major species (*n*-decane, oxygen, carbon oxides, ethylene, and methane). Although minor species concentrations are not so closely reproduced, it was not attempted at this stage to tune some rate constant values for a better agreement between computations and experiments.

The same mechanism was then used for the prediction of kerosene experiments. As expected from the similarity between *n*-decane and kerosene oxidation under the present experimental conditions, the *n*-decane mechanism can predict with sufficient accuracy the observed reactivity of kerosene up to 40 atm: the concentration profiles of oxygen, CO, and CO_2 are well reproduced, as can be observed in Figs. 3 through 7. Concerning other products, most of them are reproduced within an order of magnitude or better (Figs. 3 through 7). A similar agreement was observed [15] for the prediction of previous experimental results obtained at 1 atm [1].

Kinetic Analysis:

Kinetic analysis is useful to understand the main frame of a complex mechanism and to determine the most important reaction routes, in particular when the mechanism has to be reduced. Such kinetic analyses have been described in detail in our previous studies on large alkanes (*n*-pentane [2] and *n*-heptane [3]) oxidation. They showed some differences in the predominant reaction steps near 1000 K under the conditions of our jet-stirred reactor experiments with the high-temperature regime (shock-tube experiments, or higher temperature well-stirred reactor experiments [16]), although some reaction processes play an important role in both cases. However, these experimental studies on higher alkanes [2,3] have been performed at atmospheric pressure, and those on hydrocarbons up to C_4 [17–20] were restricted to 10 atm. Since the present work extends to 40 atm, it is interesting to investigate the predominant reaction routes under the present experimental conditions.

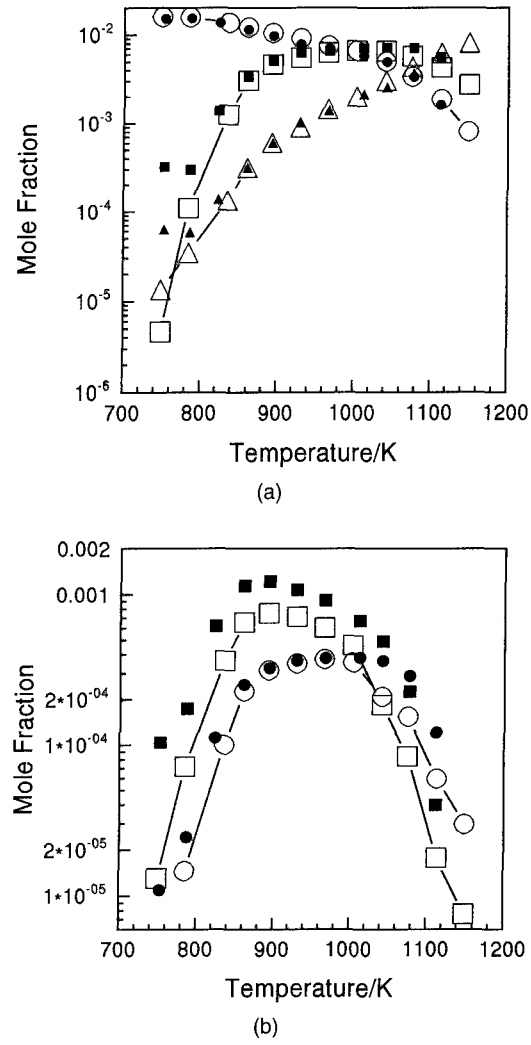

Fig. 2. Comparison between the experimental concentration profiles obtained for the oxidation of *n*-decane (filled symbols) and of kerosene (open symbols) at 10 atm. Initial fuel mole fraction = 10^{-3}; equivalence ratio = 1; residence time = 0.5 s. (a): ●-○ O_2; ■-□ CO; ▲-△ CO_2; (b): ■-□ C_2H4; ●-○ CH_4.)

It is clear that the conditions of the present study (pressure higher than 1 atm and temperature between 800 and 1100 K) are those of the intermediate temperature range where HO_2 radicals play a significant role [12]. Kinetic analysis shows that these radicals are mainly formed by reaction of alkyl radicals with O_2:

$$R + O_2 = \text{alkene} + HO_2. \qquad (a)$$

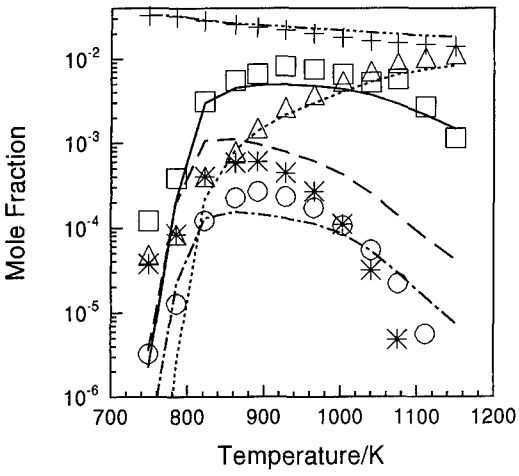

FIG. 3. Comparison between computation (lines) and experiments (symbols) under the following conditions: P = 10 atm; initial fuel mole fraction = 10^{-3}; equivalence ratio = 0.5; residence time = 0.5 s. +—···— O_2; □— CO; △--- CO_2; ○—·— CH_4; *—— C_2H_4.

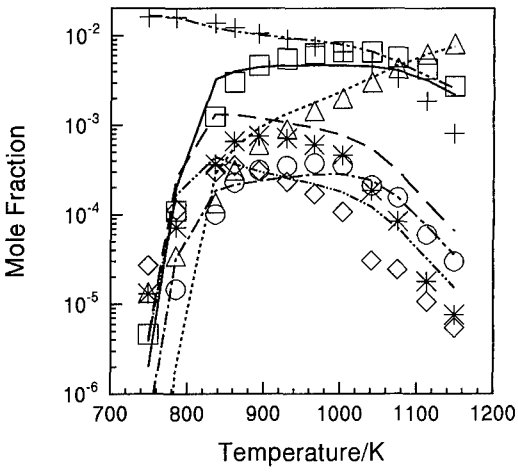

FIG. 4. Comparison between computation (lines) and experiments (symbols) under the following conditions: P = 10 atm; initial fuel mole fraction = 10^{-3}; equivalence ratio = 1.0; residence time = 0.5 s. +—···— O_2; □— CO; △--- CO_2; ○—·— CH_4; *—— C_2H_4; ◇—··— CH_2O.

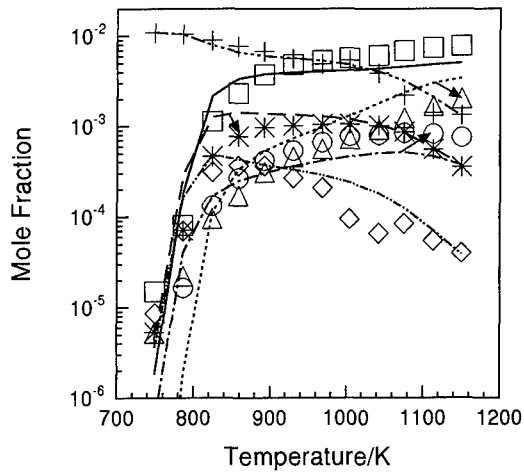

FIG. 5. Comparison between computation (lines and small symbols) and experiments (large symbols) under the following conditions: P = 10 atm; initial fuel mole fraction = 10^{-3}; equivalence ratio = 1.5; residence time = 0.5 s. + —···— O_2; □— CO; △--- CO_2; ○—·— CH_4; *—— C_2H_4; ◇—··— CH_2O.

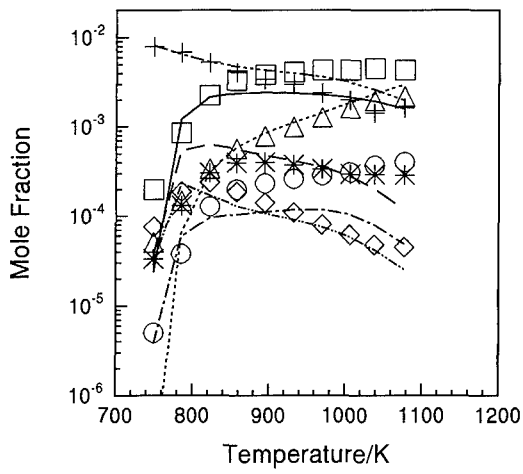

FIG. 6. Comparison between computation (lines and small symbols) and experiments (large symbols) under the following conditions: P = 20 atm; initial fuel mole fraction = 5×10^{-4}; equivalence ratio = 1; residence time = 1.0 s. + —···— O_2; □— CO; △--- CO_2; ○—·— CH_4; *—— C_2H_4; ◇ —··— CH_2O.

However, since we measured decenes only at trace levels in n-decane oxidation, the major pathways for large alkyl radicals are thermal decomposition and isomerization; consequently, reaction (a) was only written for radicals with seven carbon atoms or less.

Kinetic analysis shows an important contribution of ethyl, propyl, butyl, and pentyl radical reactions with O_2 at high pressure with the formation of alkenes through reaction (a). However, at high reaction extent, HCO radicals become the main source of HO_2 radicals through reaction (b):

$$HCO + O_2 = CO + HO_2. \qquad (b)$$

When pressure increases, the importance of reaction (b) decreases because of the competitive process (c):

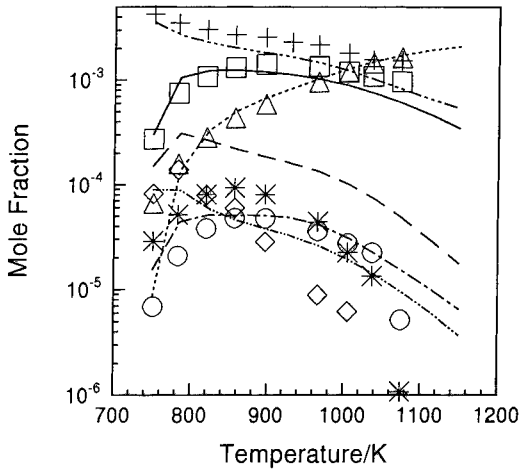

FIG. 7. Comparison between computation (lines and small symbols) and experiments (large symbols) in the following conditions: P = 40 atm; initial fuel mole fraction = 2.5×10^{-4}; equivalence ratio = 1; residence time = 2.0 s. + —···— O_2; □— CO; △--- CO_2; ○—·— CH_4; *—— C_2H_4; ◇ —··— CH_2O.

$$HCO + M = H + CO + M \qquad (c)$$

and a growing fraction of HO_2 radicals is formed from H atoms through reaction (d):

$$H + O_2 + M = HO_2 + M. \qquad (d)$$

Reactions of HO_2 radicals form H_2O_2, which is mainly produced at low reaction extent, by reaction with n-decane:

$$C_{10}H_{22} + HO_2 = C_{10}H_{21} + H_2O_2 \qquad (e)$$

As soon as HO_2 radicals concentration begins to grow, their self reaction becomes the main source of H_2O_2:

$$HO_2 + HO_2 = H_2O_2 \qquad (f)$$

with a small contribution of H-donor intermediates:

$$XH + HO_2 = X + H_2O_2. \qquad (g)$$

In the temperature range of the present study, H_2O_2 decomposes to form two OH radicals:

$$H_2O_2 + M = OH + OH + M. \qquad (h)$$

Under the present experimental conditions, the OH radical was found to be the most important chain carrier for the consumption of n-decane and of intermediates, including CH_2O and CO.

Even at the highest temperature (1150 K) of the present study, reaction (d) dominates over the high-temperature chain-branching process:

$$H + O_2 = OH + O \qquad (i)$$

since, at 1150 K, the ratio of the rates of these two reactions, R_d/R_i, is equal to 10 at 40 atm and to 2.5 at 10 atm. However, its value at 1 atm and 1150 K is only 0.25, showing that, under the conditions of our previous study [1] (1 atm and around 1000 K), reaction (i) competes with reaction (d), which is also the case at higher temperatures than those of the present study for pressures above 1 atm [12].

Finally, the chain-branching process under the present experimental conditions is controlled by the reaction sequence (g) + (h), which forms two OH radicals from a single HO_2 radical through H_2O_2 decomposition. This statement is confirmed by sensitivity analysis, which shows that, in the major portion of the temperature range of this study, the computation is very sensitive to the rate constant of reaction (h). However, at 1150 K, although reaction (d) is largely dominant over reaction (i) in the range 10–40 atm, with large amounts of HO_2 and H_2O_2 being formed as shown above, the most sensitive reaction is reaction (i).

Discussion

Our modeling study shows that the oxidation mechanism of a single alkane, n-decane, can predict the overall combustion behavior of a commercial fuel like TR0 (Jet A1) kerosene. This result can be explained by the composition of this aviation fuel where alkanes constitute the major fraction. It also means that aromatics, which represent less than 20% in volume of this fuel, do not have a pronounced effect on the overall combustion chemistry of the alkane fraction under the conditions of this study.

The present kinetic analysis confirms earlier observations on the chemistry of higher alkane oxidation [2,3,12,15] and the effect of pressure [19,20,21,22] in the intermediate-temperature range. In this oxidation regime, at high pressure, the oxidation process is dominated by HO_2 and H_2O_2 chemistry. In the same temperature range, the main reaction paths of large alkyl radicals are their thermal decomposition and isomerization, a reaction that also prevails in the high-temperature regime. In addition, sensitivity analyses show that the high-temperature branching process through H atoms, reaction (i), controls the oxidation sequence at 1 atm and for the highest temperature of the present studies. For this reason, the same mechanism could be used for kerosene oxidation in the high-temperature range in shock tubes, as shown for n-pentane [2] and n-heptane [3] oxidation, or in flames.

This kinetic analysis thus demonstrates the impor-

tance of experimental studies at high pressure for extending the validity domain of detailed mechanisms. Our experimental technique was shown to be useful for such studies in a large temperature range, including the intermediate- and low-temperature ranges corresponding to the ignition domain in internal combustion engines [23].

Conclusion

This study provides new experimental kinetic data on kerosene oxidation from 10 to 40 bars. A detailed chemical kinetic reaction mechanism written for *n*-decane oxidation was used to predict with reasonable accuracy the main combustion characteristics of kerosene in the conditions of this study. A kinetic analysis was performed in order to identify the controlling steps of the chemistry.

As demonstrated by previous studies of light hydrocarbon oxidation [24], the use of a detailed mechanism involving a great number of chemical intermediates validated on JSR data gives the warranty of the mechanism's predictive capability in a wide range of temperature, pressure (up to 40 bars in the present case), and equivalence ratios and the possible extension to higher temperature conditions. For this reason, although most of the experimental data used for the mechanism's validation were obtained in the intermediate-temperature range, it could also apply with a reasonable degree of confidence to the high-temperature regime. However, this study shows that more precise modeling of kerosene combustion requires some improvements of this mechanism. Including the aromatic hydrocarbon chemistry is probably necessary. The inclusion of soot precursor reactions validated for simple fuels is in progress. The validation (including flame structure predictions) of a more precise and comprehensive kerosene oxidation mechanism is underway.

Acknowledgments

Financial support from DRET is gratefully acknowledged.

REFERENCES

1. Guéret, C., Cathonnet, M., Boettner, J.-C., and Gaillard, F., *Twenty-Third Symposium (International) on Combustion*, The Combustion Institute, Pittsburgh, 1990, p. 211.
2. Chakir, A., Bellimam, M., Boettner, J.-C., and Cathonnet, M., *Combust. Sci. Technol.* 77:239 (1991).
3. Chakir, A., Bellimam, M., Boettner, J.-C., and Cathonnet, M., *Int. J. Chem. Kinet.* 24:385 (1992).
4. Dagaut, P., Cathonnet, M., Rouan, J.-P., Foulatier, R., Quilgars, A., Boettner, J.-C., Gaillard, F., and James, H., *J. Phys. E: Sci. Instrum.* 19:207 (1986).
5. Dagaut, P., Reuillon, M., and Cathonnet, M., *Combust. Sci. Technol.* 95:233 (1994).
6. Balès-Guéret, C., Cathonnet, M., Boettner, J.-C., and Gaillard, F., *Energy Fuels* 6:189 (1992).
7. Vovelle, C., Delfau, J.-L., Reuillon, M., Akrich, R., Bouhria, M., and Sanogo, O., *202nd ACS National Meeting*, American Chemical Society, Washington, DC, 1991, Vol. 36, no. 4, p. 1456.
8. Dryer, F. L., and Brezinsky, K., *Combust. Sci. Technol.*, 45:199 (1985).
9. Warnatz, J., *Twentieth Symposium (International) on Combustion*, The Combustion Institute, Pittsburgh, 1985, p. 845.
10. Axelsson, E. I., Brezinsky, K., Dryer, F. L., Pitz, W. J., and Westbrook, C. K., *Twenty-First Symposium (International) on Combustion*, The Combustion Institute, Pittsburgh, 1987, p. 783.
11. Westbrook, C. K., Warnatz, J., and Pitz, W. J., *Twenty-Second Symposium (International) on Combustion*, The Combustion Institute, Pittsburgh, 1988, p. 893.
12. Dryer, F., in *Fossil Fuel Combustion* (W. Bartok and A. F. Sarofim, Eds.), John Wiley & Sons, Inc., New York, 1991, p. 121.
13. Warnatz, J., *Twenty-Fourth Symposium (International) on Combustion*, The Combustion Institute, Pittsburgh, 1992, p. 553.
14. Dagaut, P., Cathonnet, M., and Boettner, J.-C., *Int. J. Chem. Kinet.*, 23:437 (1991).
15. Cathonnet, M., Balès-Guéret, C., Chakir, A., Dagaut, P., Boettner, J.-C., and Schultz, J.-L., *Third European Propulsion Forum*, Association Astronautique et Aéronautique de France, Paris, 1991, p. 313.
16. Westbrook, C. K., Pitz, W. J., Thornton, M. M., and Malte, P. C., *Combust. Flame* 72:45 (1988).
17. Dagaut, P., Cathonnet, M., Boettner, J.-C., and Gaillard, F., *Combust. Sci. Technol.*, 56:23 (1987).
18. Dagaut, P., Cathonnet, M., and Boettner, J.-C., *J. Phys. Chem.* 92:661 (1988).
19. Chakir, A., Cathonnet, M., Boettner, J.-C., and Gaillard, F., *Twenty-Second Symposium (International) on Combustion*, The Combustion Institute, Pittsburgh, 1988, p. 873.
20. Chakir, A., Cathonnet, M., Boettner, J.-C., and Gaillard, F., *Combust. Sci. Technol.*, 65:207 (1989).
21. Pitz, W. J., and Westbrook, C. K., *Combust. Flame* 63:113 (1986).
22. Dagaut, P., Boettner, J.-C., and Cathonnet, M., *Int. J. Chem. Kinet.*, 24:813 (1992).
23. Cavaliere, A., Ciajolo, A., D'Anna, A., Mercogliano, R., and Ragucci, R., *Combust. Flame* 93:279 (1993).
24. Dagaut, P., Tan, Y., Revel, J., Boettner, J.-C., and Cathonnet, M., *J. Chim. Phys.* 89:1373 (1992).

COMMENTS

Timothy J. Held, Princeton University, USA. In the 10-atm *n*-decane experiment, a small increase in reactivity at low temperature could be noted, consistent with the high-temperature side of the negative temperature coefficient regime. This feature was absent from the kerosene experiments. Have you conducted experiments on *n*-decane oxidation with an appropriate amount of a representative aromatic compound added, to determine whether the aromatic fraction of kerosene is responsible for the difference?

Author's Reply. In kerosene oxidation, the negative temperature coefficient was observed: It is less marked than in *n*-decane oxidation. This is due to the fact that kerosene reactivity in the lower temperature range (<750 K in the conditions of our experiments) is lower than *n*-decane reactivity, probably because of the presence in kerosene of aromatic hydrocarbons. However, we have not performed, in this temperature range, experiments on *n*-decane oxidation with some amount of aromatics added.

•

Vladimir Zamansky, Energy and Environmental Research Corp., USA. Kerosene includes significant amounts of aromatic, cyclic, and nonsaturated hydrocarbons. Could you comment on why there is no visible difference between the major oxidation products of kerosene and *n*-decane.

Author's Reply. The chemical composition (in weight) of the TR0 kerosene (Jet A1 aviation fuel) used in the present study is the following: 79% alkanes, 10% naphtenes, and 11% aromatics. Unlike gasoline, kerosene contains almost no unsaturated hydrocarbons. Since alkanes are the main constituents of kerosene, and since they are more reactive than naphtenes and aromatics, it is not surprising that the concentration profiles of the main oxidation products of kerosene are similar to those of a parent alkane, *n*-decane. However, Fig. 2 shows that kerosene oxidation forms slightly less ethylene than *n*-decane oxidation. The reason is that many of the paraffinic constituents of kerosene are branched alkanes, and their oxidation forms less ethylene than linear alkanes do. The same is true for the oxidation of naphtenes and aromatics. Nevertheless, it appears that the difference in the concentration levels of ethylene in the oxidation of *n*-decane and kerosene is much smaller than that we observed in the comparison between the oxidation of a linear alkane like *n*-heptane and that of a branched alkane with many tertiary C atoms like iso-octane [1]. This justifies the choice of a linear alkane, *n*-decane, as representative of kerosene.

REFERENCE

1. Dagaut, P., Reuillon, M., and Cathonnet, M., *Combust. Sci. Technol.* 95:233 (1994).

•

A. E. Jacob Akanetuk, Stanford University, USA. Results were presented showing concentration vs temperature at fixed residence times. How do these residence times compare to the characteristic reaction times? If the residence times were longer than characteristic reaction times, then how effective was the model used in describing transient evolution of species profiles?

Author's Reply. The working conditions in the reactor are such that the characteristic reaction times are longer than the residence times. This is verified by the facts that the reaction never goes to completion and that the reaction yield varies with the mean residence time. The control of the chemical time is obtained by keeping the fuel mole fraction at a low level, using nitrogen as diluent, and by limiting the experimental temperature to 1200 K.

Twenty-Fifth Symposium (International) on Combustion/The Combustion Institute, 1994/pp. 927–932

COOL FLAMES AND OSCILLATIONS IN HYDROCARBON OXIDATION

A. A. MANTASHYAN
Institute of Chemical Physics NAS of Armenia
375044 Yerevan, P. Sevak str. 5/2, Armenia

Stabilized cool flames and oscillations of propane and butane have been studied. An experimental technique has been developed, which enabled for the first time the detection of free radicals in stabilized cool flames of hydrocarbons. For this purpose, a two-section flow reactor has been constructed. Cool flame appears in the second section and stabilizes there.

In order to detect free radicals and examine their behaviour, a small part of the gas flow was sampled from each section continuously and directed at low pressure to a freezing pin at liquid nitrogen temperature inside the cavity of an electron paramagnetic resonance (EPR) spectrometer.

It has been shown that when passing from the first section (preflame zone) to the stabilized cool flame zone, the concentration of radicals increases abruptly. For example, in the case of propane (C_3H_8:O_2 = 1:1; P = 270 torr; T = 320 °C), the radical concentration makes up $6 \cdot 10^{12}$ molecules/cm^3, whereas in the cool flame zone it is $3 \cdot 10^{14}$ molecules/cm^3 at the same temperature. This abrupt change of radical concentration is caused by the self-accelerated chain process.

The temperature increase in the cool flame zone results in an increase of the radical quantity. The further temperature increase leads to the decrease of radical quantity, and the flame fades at T = 370 °C to 380 °C.

Asymmetric profiles of temperature, radical concentration, and stable products appear in the cool flame zone along the vertical cross section of the reactor.

It is shown that the regularities observed are the results of nonlinear processes with the participation of free radicals. The same results are obtained for other hydrocarbons and mixtures.

By changing the process parameters, damped and stable oscillations are observed, which are correlated to cool flame characteristics.

Stabilized cool flames of propane and butane have been studied in a special two-section reactor.

Direct experimental data have been obtained on the behaviour and nature of free radicals in the stabilized cool flame. It has been ascertained that the appearance and stabilization of the cool flame are accompanied by an abrupt increase of radical concentration caused by the rapid self-accelerated chain process. The temperature increase above 350 °C to 360 °C adversely affects the process development. The radical concentration is decreased, and the cool flame is damped.

The oscillation regimes of the oxidative process have also been studied in the two-section reactor.

A correlation between the cool flame phenomenon and the oscillations has been verified.

Introduction

Direct experimental data on free radicals in the chain reaction of hydrocarbon oxidation obtained for the first time in Refs. 1 through 9 confirmed, in many respects, our ideas about a mechanism of these complex chemical reactions. At the same time, a necessity was revealed to study cool flames, oscillatory processes, and combustion chemistry as a whole on a new level. In the present report, the results of studies performed at the Laboratory of Hydrocarbon Oxidation of the Institute of Chemical Physics NAS of Armenia are summarized.

These results permit evaluation of a mechanism of cool flames and oscillations on the base of direct experimental data on free radicals.

Experimental

A special two-sectional flow reactor [10,11] was developed to study stabilized cool flames with measurement of free radicals. In such a system, it is possible also to realize and study the oscillatory oxidation regimes [12,13]. The reactor sections consist of two cylindrical vessels of the same diameter ($d_1 = d_2$ = 6.1 cm), made from glass or silica, and different lengths (l_1 = 28 cm; l_2 = 11.5 cm), connected to each other through a narrow tube (d = 0.7 cm) [10,11] (Fig. 1). Each section was heated separately. The temperature profiles in the zone of stabilized cool flame were measured by means of thin chromel-alumel thermocouples. Samples of the reacting gas mixture were taken from the stabilized cool flame zone for chromatographic analysis.

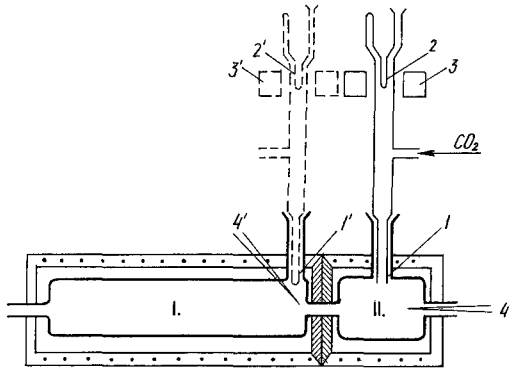

FIG. 1. Schematic diagram of reaction system. I: preflame region; II: stabilized cool flame region; 1,1': slit diaphragm; 2,2': pin for radical accumulation; 3,3': EPR spectrometer cavity; 4,4': thermocouple.

In order to measure free radical concentrations and to examine their behaviour, a small part of the gas flow was sampled continuously from each section of the reactor through a diaphragm. Gases were collected at low pressure for freezing at liquid nitrogen temperature. Paramagnetic specimens accumulated in a freezing pin placed into the cavity of an EPR spectrometer. Registration of EPR spectra was performed during the course of free radical accumulation. Only about 3% of the total amount of gases passed through the reactor was sampled through the diaphragm. Therefore, the process was essentially not disturbed. The kinetic method of radical freezing is described in detail in Refs. 1 and 2.

Cool flames were studied for the oxidation of hydrocarbons with different structure: propane [10,11,16–18], propylene [19], normal and iso-butanes [20–23], and also their mixtures [23]. Weak blue luminescence, well visible in a dark room, is typical for stabilized cool flames. The technique enables one to change the temperature of a stabilized cool flame by changing the heating of the second section keeping the temperature of the first one constant. In this way, it is possible to study the structure of stabilized cool flame at the different temperatures and therefore to obtain information for all conditions appearing in cool flame flash in an isolated reaction vessel.

The two-sectional reactor also enables the study of the oscillatory oxidation regime under definite conditions [12,13] (velocity of gas flow, temperature, etc.). Oscillations were observed as the temperature changes in time. A differential thermocouple was used to determine the oscillations of the radical concentration. Each joint of the thermocouple was placed in thin-wall covers made from silica [24]. A surface of one of the covers was treated by diethylether of ortho-silic acid. Such treatment enables to change the probability of the radical termination on the surface. As a result, two different probabilities of the radical termination were realized on the two covers of differential thermocouple and, therefore, different heat releases on these surfaces. The differential thermocouple registers the change in temperature difference-ΔT, which is related to the changing radical concentration in time.

The study of stabilized cool flames was carried out at pressures in the range 250–350 torr and $RH:O_2$ = 1:1.

It should be noted that for all the systems studied, cool flame appearance is accompanied by an abrupt temperature increase in the second section of the reactor. It takes place at well-defined residence times in the preflame zone. At the given temperature, the flame is stabilized, and the definite heat regime is established. Experimental results obtained for propane-oxygen mixture show that at a pressure of about 270 torr and at the same initial temperature in the first and second sections ($T_1 = T_2 = 609$ K), cool flame appears at a residence time $\tau = 28$ s in the first section.

It has been shown that an abrupt increase of free radical concentration compared to that in the preflame takes place in the stabilized cool flame zone. At the above-mentioned conditions, the concentration of free radicals in the first section is about $6 \cdot 10^{12}$ molecules/cm^3, whereas in the stabilized cool flame zone it is $2.3 \cdot 10^{14}$ molecules/cm^3 at approximately the same temperature [10,11]. In this case, propane conversion does not exceed 5%. The temperature near the reactor wall in the second section is 618–619 K, and in the middle of the reactor, it is about 624 K. As a result, the temperature of the stabilized cool flame is higher by only 20°–24° than that of the first section. Thus, the abrupt increase of the rate of oxidation reaction cannot be caused by such small overheating. The rate of propane oxidation would only be changed negligibly due to such temperature change, in accordance with Arrhenius law. The observed abrupt increase of the radical quantity may be caused by a self-accelerated chain process.

To examine the temperature dependences of the radical concentration in the cool flame, its temperature was changed by changing the heating of the second reaction section.

In the stabilized cool flame zone, the nonuniform temperature field is established, and the temperature was also measured at the radical sampling point [11]. It should be noted that EPR spectra of free radicals detected before the appearance of cool flame (in the first section) and that the spectra of the radicals frozen out from the cool flame zone are identical over the whole temperature range studied (T = 603–663 K; Fig. 2) [11]. The registered spectra correspond to EPR spectra of alkylperoxy radicals RO_2 or the mixture of HO_2 and RO_2 radicals. The temperature dependences of the radical concentration at constant

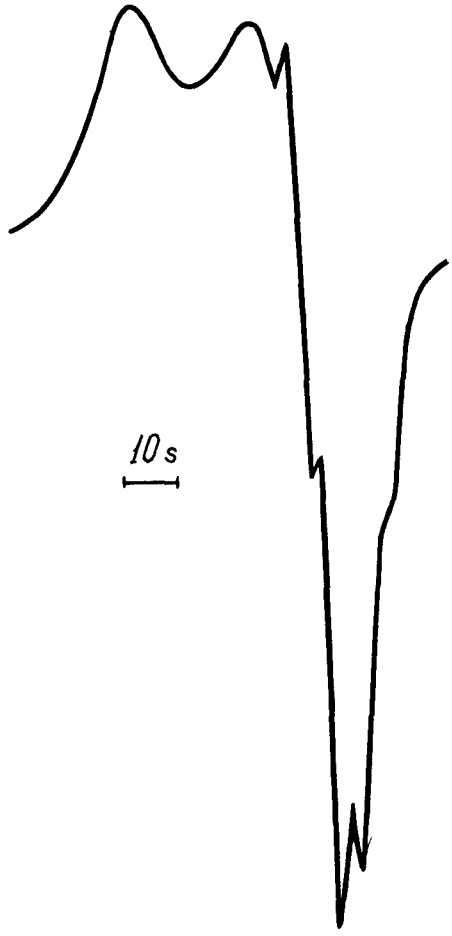

FIG. 2. EPR spectrum of peroxy radicals frozen from propane oxidation reaction.

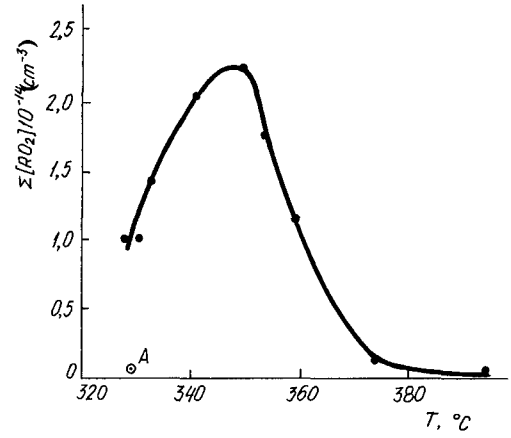

FIG. 3. Temperature dependence of radical concentration in a stabilized cool flame. A: concentration of radicals in the preflame zone (P = 270 torr; C_3H_8:O_2 = 1:1)

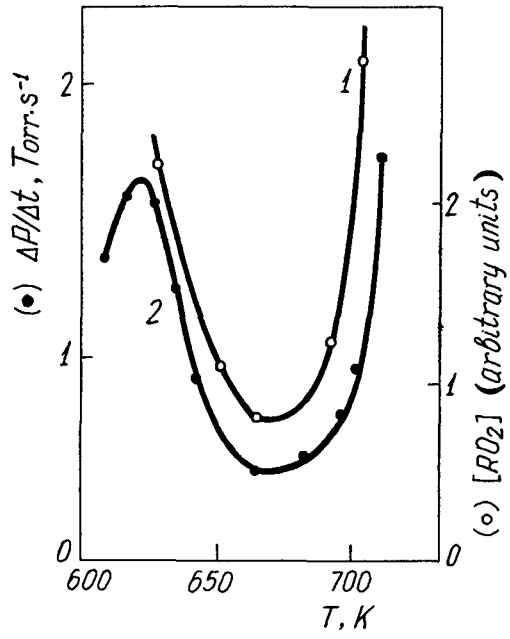

FIG. 4. (1) Dependence of the maximum radical concentrations on temperature and (2) dependence of the maximum of propane oxidation rates on temperature.

temperature (T = 600–603 K) in the preflame zone (in the first section) are presented in Fig. 3.

As can be seen, with the temperature increase to 620–630 K, the concentration of the radicals also increases and then abruptly decreases. At 660–680 K, the radical concentration decreases to a level of slow oxidation reaction, and the flame dies out. The same picture is observed for the brightness of cool flame luminescence.

Using the radical freezing method, other authors [25,26] showed that in a cool flame of ether [25] and n-heptane [26], the radical concentrations decrease as the temperature increases, while no rise in concentration has been observed. It must be noted that these authors performed the experiments in a very narrow range of the cool flame.

In our previous work [27], the behaviour of the radicals in propane oxidation in the negative temperature coefficient (NTC) region had been studied. The temperature dependence of the radicals in this case was the same as for stabilized cool flame. The temperature suppresses a development of the cool flame like as if it suppresses the slow reaction under conventional conditions of thermal oxidation (Fig. 4).

Temperature dependences of the radical concentration in stabilized cool flames of n- and iso-butanes and propylene [13] are presented in Fig. 5.

In all the cases studied, the appearance of cool

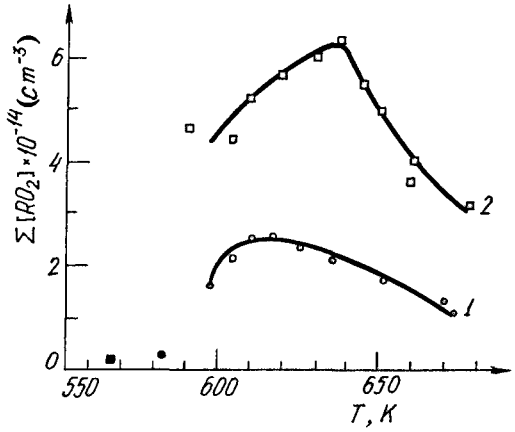

FIG. 5. Dependence of the concentration of radicals in stable cool flame on temperature. 1-iso-C_4H_{10} + O_2 at P = 280 torr; 2-n-C_4H_{10} + O_2 at P = 216 torr (dark symbols = concentrations of radicals in preflame zone).

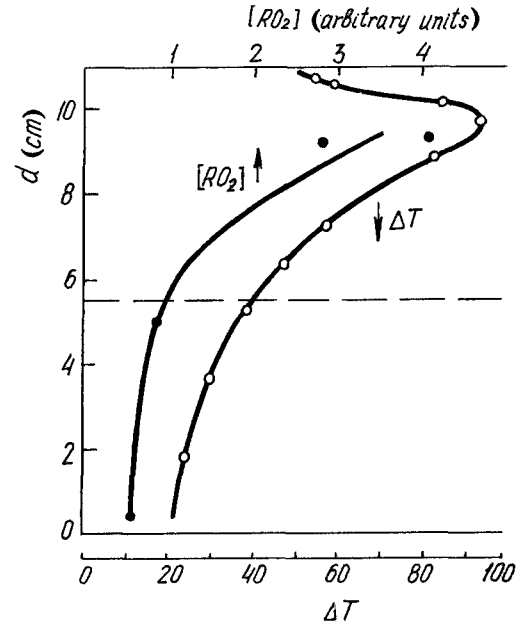

FIG. 6. Temperature profiles and radical concentrations along the vertical axis of the reactor.

flame is accompanied by the abrupt increase of radical concentrations. The self-heating is higher than those in the preflame zone, while the initial temperature in both sections was kept the same [18,22].

Temperature profiles were studied in detail both in slow reaction and in the stabilized cool flame of propane [18] and butanes [22]. It has been shown that the temperature is constant along the horizontal reactor axis, whereas it is changing along its vertical axis. Asymmetric temperature profiles with the maximum temperature above the horizontal axis of the reactor are established (Fig. 6) [23].

The maximum temperature in these profiles increases with the increase of radical concentration, and then decreases at the higher temperatures in the NTC region [23]. The appearance of such high self-heating in the cool flame is obviously connected with the abrupt increase of free radical concentration. Taking into account a small conversion of hydrocarbon, it is natural to assume that the high values of heat release may be caused by the mutual interaction of the radicals.

1. $RO_2 + RO_2 \rightarrow 2RO + O_2 - \Delta H_1$
2. $RO_2 + RO_2 \rightarrow$ aldehyde + alcohol + $O_2 - \Delta H_2$
3. $RO + RO_2 \rightarrow ROOH$ + aldehyde $- \Delta H_3$
4. $RO + RO \rightarrow$ aldehyde + alcohol $- \Delta H_4$
5. $RO_2 + HO_2 \rightarrow ROOH + O_2 - \Delta H_5$.

According to thermochemical data, the value for ΔH for reactions (3) and (4) may be equal to 65–95 kcal/mol depending on RO radical structure. In these reactions, particularly in reaction (4), there is a possibility of the generation of excited formaldehyde molecules, which, as it is known [28], are responsible for the luminescence in cool flame. It has been shown [29] that the excited formaldehyde molecules are formed by the mutual interaction of RO radicals.

Concentration profiles of free radicals, as well as the stable reaction products (aldehydes, alcohols, peroxides, CO, CO_2, and others) coincide with the temperature profiles (Fig. 6). Thus, the cool flame may be considered as a complex chain process.

As it has been shown [12–15], the different regimes of oscillatory oxidation may be realized in a two-section reactor under certain flow conditions.

The oscillatory oxidation has been studied by other researchers [30–32] in the well-stirred flow reactor. Data obtained in this two-section reactor evidence that the oscillations may also appear under conventional flow conditions without special stirring. Factors such as gas flow velocity, equalizing of concentration and temperature profiles due to stirring, rate of heat removal, and so on are only able to vary the parameters at which the different types of oscillations may occur. But the phenomenon itself is connected with the chemistry of the process.

It has been shown for propane [12,13], propylene, and propylene-propane mixtures [13,14] that two types of oscillations—damped and stable—occur in the course of oxidation (Figs. 7 and 8). Oscillations occur during the cool flame stabilization. Temperature oscillations are observed after the abrupt temperature increase in the second section of the reactor up to the cool flame stabilization (Fig. 7). Cool flame stabilization takes place with a damping of oscillations. The duration, frequency, and amplitude of damped oscillations are dependent on initial experimental conditions—initial temperature in the first

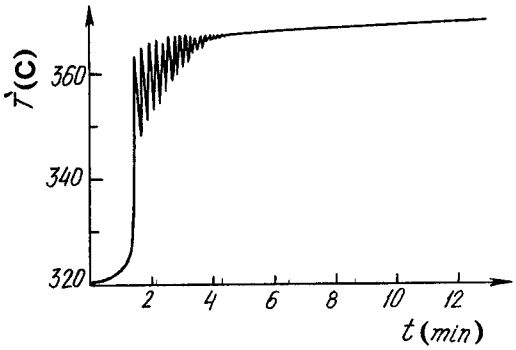

FIG. 7. Damped oscillations at T_2 = 593 K and residence time at τ = 13 s.

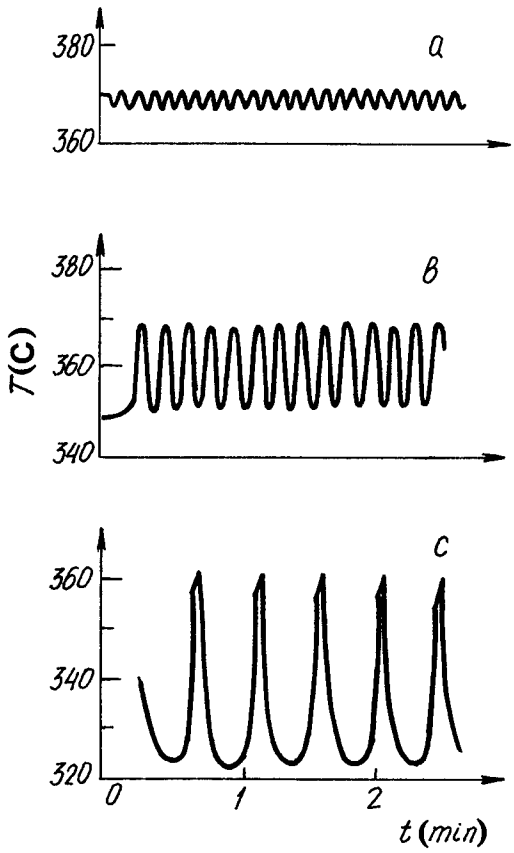

FIG. 8. Different types of oscillations at τ = 12 s: (a) T_2 = 586 K; (b)T_2 = 584 K; and (c) T_2 = 581 K.

and second sections, gas flow velocity, and pressure. Damped oscillations may transform to the stable ones with the constant amplitude and frequency dependent on initial parameters. One can obtain stable oscillations by varying pressure, gas flow velocity, or

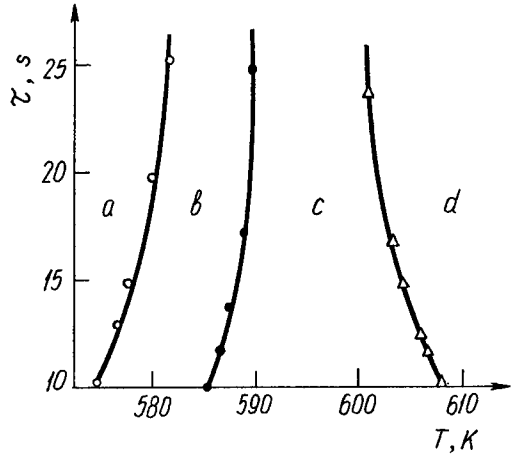

FIG. 9. Regions of existence of different regimes of oxidation of the mixture $C_3H_8:O_2$ = 1:1 at P = 320 torr: (a) slow reaction; (b) nondamped oscillations; (c) damped oscillations; and (d) stable cool flame.

temperature of the stabilized cool flame. Different types of stable oscillations, harmonic, quasiharmonic, and relaxational (Fig. 8) [13], have been observed. For the last case, the time between two flashes is considerably higher than that in the case of harmonic oscillations which are sinusoidal. In addition, the amplitudes of relaxational oscillations considerably exceed those of harmonic ones, reaching up to 40–50°, while the amplitudes of harmonic oscillations are only a few degrees, sometimes only fractions of a degree. Maximum amplitudes typical for harmonic oscillations do not exceed 10–15°.

Oscillations of free radical concentrations [24] for the oscillation regimes studied were detected by means of a differential thermocouple. The difference in temperature can reach up to 10–15° depending on the absolute concentration of the radicals in the oxidation process. Under oscillatory regime, the differential thermocouple registers the oscillations of free radical concentrations. Oscillations of the radical concentration during propane oscillatory oxidation have been detected in this manner [24].

The regions of parameters for different regimes of oxidation in the case of propane-oxygen mixture at P = 4.2 · 10^4 Pa are shown in Fig. 9 [13].

The whole set of the experimental data indicates that there is a firm correlation between the phenomenon of cool flames and oscillations.

Conclusions

1. A new method of cool flame stabilization in a two-section reactor has been developed. The method

enables the study of free radical behaviour in cool flame by using the EPR method.

2. The behaviour of free radicals in propane and butanes oxidation has shown that the cool flame appears as a result of self-acceleration of the chain reaction of hydrocarbon oxidation.
3. The temperature increase due to self-heating or increased heating of a stabilized cool flame leads to the decrease of radical concentrations in the temperature interval 350 °C to 400 °C followed by cool flame disappearance.
4. The phenomenon of oscillations had been studied. It has been shown that there is a relationship between the cool flames and oscillations. Small variations of the process parameters lead the stabilized cool flame into oscillatory regime.

REFERENCES

1. Mantashyan, A. A., and Nalbandyan, A. B., *Zh. Fiz. Chim.* 46:3030 (1972).
2. Nalbandyan, A. B., and Mantashyan, A. A., "Elementary Processes in Slow Gas Phase Reactions," *Izd. Akad. Nauk Arm. SSR*, Yerevan, 1975.
3. Mantashyan, A. A., Beibutyan, M. A., Sahakyan, A. S., and Nalbandyan, A. B. *Dokl. Akad. Nauk SSSR* 202:120 (1975).
4. Poladyan, E. A., Grigoryan, G. L., Khachatryan, L. A., and Mantashyan, A. A., *Kinet. Kataliz.* 17:304 (1976).
5. Mantashyan, A. A., Khachatryan, L. A., and Niazyan, O. M., *Zh. Fiz. Chim.* 51:341 (1977).
6. Arsentiev S. D., and Mantashyan A. A., *Arm. Chim. Zh.* 31:693 (1978).
7. Mantashyan, A. A., and Arsentiev, S. D. *Kinet. i Kataliz.* 4:898 and 1389 (1981).
8. Mantashyan, A. A., Khachatryan, L. A., Niazyan, O. M., and Arsentiev, S. D., *Combust. Flame* 43:221 (1981).
9. Khachatryan, L. A., Niazyan, O. M., Mantashyan, A. A., Vedeneev, V. I., and Teitelboim, M. A. *Intern. J. Chem. Kinet.* 14:1231 (1982).
10. Gookasyan, P. S., Mantashyan, A. A., and Sayadyan, R. H., *Fiz. Goreniya i vzryva* 12:789 (1976).
11. Mantashyan, A. A., and Gookasyan, P. S. *Dokl. Akad. Nauk. SSSR* 234:379 (1977).
12. Bernatosyan, S. G., and Mantashyan, A. A. *Arm. Khim. Zh.* 36:28 (1983).
13. Mantashyan, A. A., Bernatosyan, S. G., and Simonyan, T. R. Oxidation Communic. 5:207 (1983).
14. Mantashyan, A. A., and Bernatosyan, S. G., *Khim. Fiz.* 8:1064 (1983).
15. Bernatosyan, S. G., Grigoryan, R. R., Arsentiev, S. D., and Mantashyan, A. A., *Arch. Combust.* 4:237 (1984).
16. Mantashyan, A. A., Gookasyan, P. S., and Sayadyan, R. H., *Arch. Thermodyn. Combust.* 9:273 (1978).
17. Mantashyan, A. A., Gookasyan, P. S., and Sayadyan, R. H., *React. Kinet. Catal. Lett.* 11:225 (1979).
18. Sayadyan, R. H., Gookasyan, P. S., and Mantashyan, A. A., *Fiz. Gorenia i vzriva.* 16:135 (1980).
19. Simonyan, T. R., and Mantashyan, A. A. *React. Kinet. Katal. Lett.* 17:319 (1981).
20. Simonyan, T. R., and Mantashyan, A. A. *Fiz. Gorenia i vzriva.* 15:165 (1979).
21. Simonyan, T. R., and Mantashyan, A. A. *Arm. Khim. Zh.* 32:757 (1979).
22. Simonyan, T. R., and Mantashyan, A. A. *Arm. Khim. Zh.* 32:691 (1979).
23. Mantashyan, A. A., Gookasyan, P. S., Simonyan, T. R. and Sayadyan, R. H., *Arch. Combust.* 2:13 (1982).
24. Pogosyan, M. J., Bernatosyan, S. G., and Mantashyan, A. A. *Khim. Fiz.* 8:1433 (1989).
25. Carlier, M., and Sochet, L. R. *Combust. Flame* 33:1 (1978).
26. Sahetchian, K. A., Heiss, A., Dumas, G. M. L., and Ben-Aim, R. I., *Combust. Flame* 34:153 (1979).
27. Mantashyan, A. A., Grigoryan, G. L., Sahakyan, A. S., and Nalbandyan, A. B., *Dokl. Akad. Nauk. SSSR* 204:1392 (1977).
28. Kondratiev, V. N., *Acta Physicochem. URSS* 4:556 (1936).
29. Zaslonko, I. S., and Kogarko, S. M., *Kinet. Kataliz.* 11:296 (1970).
30. Lignola, P. G., Caprio, V., Insola, A., and Mondini, G., *Ber. Buns. Ges. Phys. Chem.* 84:369 (1980).
31. Gray, P., Griffiths, J. F., Gasko, Z. M., and Lignola, P. G., *Proc. R. Soc. A* 374:313 (1981).
32. Gray, P., Griffiths, J. F., and Moule, R. J., *Faraday Symp. Chem. Soc.* 9:103 (1974).

Twenty-Fifth Symposium (International) on Combustion/The Combustion Institute, 1994/pp. 933–940

A REDUCED THERMOKINETIC MODEL FOR THE AUTOIGNITION OF FUELS WITH VARIABLE OCTANE RATINGS

M. SCHREIBER, A. SADAT SAKAK AND A. LINGENS
Lehrstuhl für Technische Thermodynamik
RWTH Aachen, D-52056 Aachen, Germany

AND

J. F. GRIFFITHS
School of Chemisty
University of Leeds
Leeds LS2 9JT, United Kingdom

The autoignition characteristics of the reference fuels *i*-octane, *n*-heptane, and their mixtures at temperatures 600–1500 K and pressures ranging 0.3–4.2 MPa are studied by means of a reduced kinetic mechanism comprising five species in six reactions altogether. The scheme is readily adaptable to mixtures of the primary reference fuels via input of an octane number between 0 (= *n*-heptane) and 100 (= *i*-octane). Emphasis is placed on the dependence of ignition delay on gas temperature, on the evolution of reaction as portrayed in the temperature-time records, and on the multitude of dynamic features, e.g., two-stage (or multistage) ignition and negative temperature coefficient characteristics inherent to alkane combustion.

The reduced model was fitted to numerical results derived from quantitative kinetic modelling and validated against currently available data from experimental systems. It was originally designed for application in a computational fluid dynamics code based on a transport equation for the joint probability density function (PDF) of the reacting species. Flame propagation and engine "knock" may thus be described by one consistent model.

Introduction

The autoignition characteristics of higher hydrocarbons—the main constituents of Otto-engine fuel—are usually expressed in terms of an empirically derived octane number (which describes the "knock" properties of an appropriate mixture consisting of *n*-heptane and iso-octane). Thus, mixtures of *n*-heptane and iso-octane are the natural choice for substituting the kinetics of the extremely complex and virtually impossible to model, "real" fuels. However, a cautionary note has to be added, since real fuels contain aromatics and olefins, which have distinctly different autoignition chemistries than do paraffins. In this case, the Research and Motor octane qualities may differ by 5–10 points (for the primary reference fuels, they are equal by definition).

Recently, there has been remarkable progress in understanding the ignition behaviour of these fuel substitutes, thanks to excellent experimental and theoretical work [1–7]. However, in most of the cases, the experiments were limited to comparatively low pressures (<1 MPa) and/or covered only a small range of temperature, pressure, and mixture composition. This makes modelling quite speculative insofar that an extrapolation to engine operation conditions of the models that are validated against these results has to be on the basis of ill-defined reactant pressure or concentration dependences. The most notable exception are the extensive shock-tube studies of *n*-heptane and iso-octane ignition at pressures up to 4.2 MPa, as reported in Refs. 4 and 5.

Due to the very long ignition delays of iso-octane, the available residence time ($<10^{-2}$ s) of the reactive gas mixture in the "control volume" of shock tubes is not sufficient to allow for a satisfactory resolution of the low-temperature range ($T < 1000$ K). On the other hand, rapid compression machines (RCM) face the problem of prereactions occuring during the compression stroke. The characteristics of heat dissipation, as pertaining to the particular experimental device employed, play a major role in determining the overall ignition delay. In order to avoid unacceptable distortions, these effects would have to be corrected most accurately in all modelling approaches [8]. We therefore chose to derive the general properties of the reduced five-step scheme directly from results obtained by a more comprehensive kinetic modelling approach [7], thus avoiding ambiguous boundary conditions. Only then was the

TABLE 1
Five-step reduced scheme for *i*-octane (*n*-heptane)

	Reaction	H°_{300} (kJ/mol)	A (mol m^3 s)	E/R (K)
1	$F \rightarrow X$	709.9	5.0×10^8	18,050
2	$X + 12.5\,(11)\,O_2 \rightarrow P$	−4709.9	7.0×10^6	7,200
3^+	$F + 2O_2 \rightarrow I$	−53.9	3.5×10^9 (3.85×10^{10})	19,500
3^-	$I \rightarrow F + 2O_2$	53.9	6.0×10^{27}	37,500
4	$I \rightarrow 2Y$	−60.0	6.0×10^7 (2.0×10^8)	5,000
5	$Y + 0.5F + 11.5(10)O_2 \rightarrow P$	−3913.1	1.0×10^9	16,500

Arrhenius parameters for the rate constants $k_i = A_i \exp(-E/RT)$ of the five-step scheme. The stoichiometric coefficients apply to *i*-octane combustion; the appropriate values for *n*-heptane oxidation are in parentheses. Coefficients for mixtures must be interpolated.

model validated—as far as possible—against specific experimental combustion studies.

Several reduced models of the chemical kinetics of hydrocarbon fuel autoignition exist to date. The first was the so-called Shell model [9], which takes a very generalized form. It was made more explicit by Cox and Cole [10] and Cowart et al. thereafter [11]. All these models have in common that only those reaction paths in the low-temperature range, which have a direct impact on the time of occurrence of autoignition, are included. As a result, the high-temperature ($T > 1000$ K) chemistry, important for describing, e.g., flame propagation, are excluded. Müller et al. [12] discuss a global kinetic model to represent the oxidation of *n*-heptane over the entire temperature range 600–1500 K. The concept of a model that has a minimal number of variables is extremely attractive, e.g., in multidimensional computational fluid dynamics (CFD) calculations, but it is essential that the underlying kinetic and thermal properties of the combustion system must be encapsulated in the structure, if the model is to have the potential for practical application. Unfortunately, difficulties arise with the model of Müller et al. [12] because the prediction of ignition throughout the entire temperature range rests exclusively on thermal feedback [13]. This results in a qualitative failure to predict a negative temperature dependence of ignition delay, as is manifested by many hydrocarbons and measured in the experiments against which the scheme was validated [4]. There is no possibility of recovering the negative temperature coefficient (ntc) in the absence of some form of chemical autocatalysis coupled to competitive nonbranching reaction modes that are favoured as the temperature is increased. For details, the reader should consult the definitive, mathematical analysis by Gray and Yang [14].

The purpose of this paper is (1) to develop the thermal scheme [12] in a more satisfactory form by introducing chemical autocatalysis, (2) to extend its applicability to fuels other than *n*-heptane via input of a variable octane-number, while retaining its general simplicity, and (3) to explore the pressure dependences of the autoignition delay predicted by a very simple formal structure.

When comparing the numerically obtained results with experiments, we emulated the specific conditions as far as possible, e.g., by considering the compression stroke in a rapid compression machine.

Kinetic Model and Its Application to Primary Reference Fuels or Their Mixtures

The basic structure of the reduced kinetic model is shown in Table 1. The first two reactions ((1) and (2)), which govern the high-temperature oxidation, correspond to the original model [12], whereas the low-temperature steps ((3) through (5)) were modified to represent the degenerate branching characteristics of hydrocarbons in a most simple, albeit qualitative manner. We applied a sensitivity analysis to the more detailed reference scheme and thus extracted the main constituent species [product species, comparatively stable intermediates (i.e., HO_2QO, which initiates low-temperature chain branching), and "representative" radicals]. Consequently, we derived a somewhat larger set of "global" reactions for the entire reaction regime. The high-temperature chemistry could readily be summarized by only two global reactions [12]. Empirical modifications, motivated by the structure of the previously derived global reactions, were necessary to reduce the low-temperature part to only three reactions. By identifying the rate-determining reactions, we had an estimate of the order of magnitude of the reaction rates.

In the revised form, chemical autocatalysis (reaction (4)) occurs in competition with the reverse reaction (3^-), e.g., of the "O_2QOOH-type equilibrium." In reaction (3^+), both the first and the second O_2 addition are subsumed, the product oxygenated radical being represented as species *I*. The variable

Y represents a chain-propagating species, which would for many be considered to be OH. Although there is no need to specify a particular identity for Y, in order to maintain element and enthalpy balances, Y might be regarded to include additional intermediates, such as O-heterocyclic compounds or other partially oxygenated products. Low-temperature oxidation is completed in reaction (5). The kinetic "switch" from the branching to the nonbranching mode—responsible for the ntc of reaction rate—rests exclusively on the reversibility of reaction (3). The activation energy of the backward reaction (3^-) is taken to be much larger than that of the forward reaction (3^+). Branching via reaction (4) can only take place at low temperatures, when (3^-) is unimportant, thus opening the route to the low-temperature oxidation step (5). Higher temperatures, however, preclude this route since the backward reaction (3^-) dominates over the forward reaction.

While retaining a constant value for the heat capacity (36 J/mol K), the reaction enthalpies were adapted to ensure that the adiabatic flame temperature was reached at the end of combustion. In accord with Hess's Law, the overall enthalpies of the high-temperature (reactions (1) and (2)) and low-temperature oxidation paths ((3) through (5)) are identical: $2(\Delta H_1 + \Delta H_2) = \Delta H_3 + \Delta H_4 + 2\Delta H_5$. The reaction rates are given by

$$R_1 = k_1[F](p/p_0)^{0.5} \quad (1)$$

$$R_2 = k_2[X][O_2][M] \quad (2)$$

$$R_{3+} = k_{3+}[F][O_2][M](p/p_0)^{-2.2}\, C_{3+} \quad (3)$$

$$R_{3-} = k_{3-}[I](p/p_0)^{-3.5} \quad (4)$$

$$R_4 = k_4[I]C_4 \quad (5)$$

$$R_5 = k_5[O_2][Y] \quad (6)$$

where $[M] = p/RT$ represents the total concentration of all species (C_{3+} and C_4 are defined below). Since the mechanism is aimed at predicting alkane oxidation over a wide range of pressure, a corrective term (p/p_0) had to be introduced, in which the exponents were chosen such that the region of negative temperature dependence shifts to higher temperatures as the pressure increases. Thus, the consistent (and more meaningful) kinetic structure of the reduced scheme was retained, and the inevitable quantitative "fitting" was diverted to the corrective terms. The reference pressure p_0 corresponds to 10 bar (1 MPa).

Using a recently developed, more comprehensive kinetic model of alkane oxidation, as in Ref. 7, we set out to adjust the five-step model. Thereby, all calculations were performed assuming spatially homogenous conditions, while the boundary conditions were matched to those of typical shock-tube experiments. The resulting system of ordinary differential equations for concentrations and temperature was solved by an adaptation to the LSODAR integration package [15].

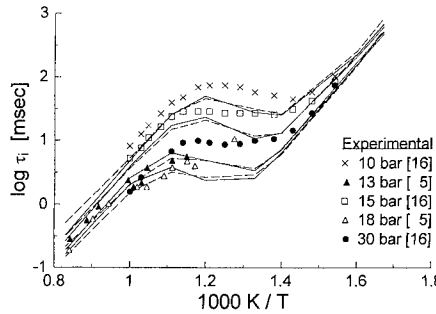

FIG. 1. Total ignition delay times of stoichiometric *i*-octane/air mixtures plotted against the inverse temperature. Four pressures, 10, 15, 30, and 40 bar (top to bottom), were investigated. Combustion occurs at constant volume. The solid lines are the results obtained from the five-step scheme. The broken lines represent calculations with a quantitative kinetic reference model [7]. The symbols refer to high-pressure rapid compression studies by Voinov and Skorodelov [16] and to shock-tube studies of Adomeit and Fieweger [5].

Iso-Octane:

The reduced kinetic model, as shown in Table 1, along with the Arrhenius parameters, emulates the oxidation of $i\text{-}C_8H_{18}$ (F), yielding the intermediates $3C_2H_4 + CH_2 + CH_3 + H(X)$ at high temperatures, and the free radicals $OC_8H_{15}O_2H + H_2O$ (I) and (Y) at low temperatures. The final products (P) are assumed to be $8CO_2 + 9H_2O$.

The ignition delay times (defined by the maximum pressure gradient) for stoichiometric *i*-octane/air mixtures at different pressures are shown in Fig. 1. The adjustment of the five-step model to the more detailed model appears to be excellent. Furthermore, some experimental results have been included in Fig. 1. While the calculated low-temperature branch agrees well with the rapid compression studies [16], there are discrepancies at intermediate and high temperatures. Experimentally determined ignition delays tend to be longer than those derived numerically. Nonetheless, at least the transition from the high-temperature branch to the ntc branch is in good accord with the calculations. The shock-tube studies of Ref. 5 are limited to the high-temperature branch, because of the comparatively short residence times available (e.g., <10 ms).

The evolution of the calculated temperature and concentration profiles of F, X, I and Y are shown in

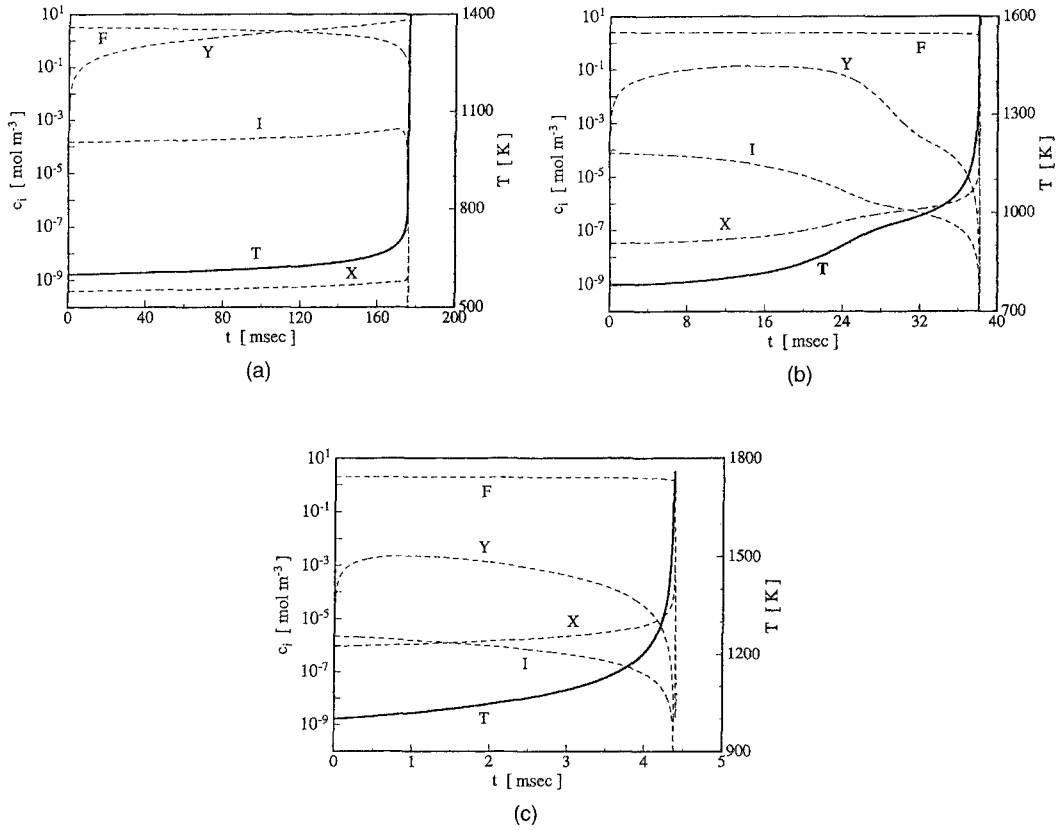

FIG. 2. Calculated temperature- and concentration-time profiles for the combustion of a stoichiometric *i*-octane-air mixture at three different temperatures and constant volume conditions (p_0 = 10 bar). (a) T_0 = 600 K: At low temperatures, ignition is the result of chain branching. Note that I is in steady state, while the total species concentration represented by Y increases continuously. It exceeds the fuel concentration after approximately 110 ms. (b) T_0 = 780 K: At intermediate temperatures, ignition evolves in two stages. While the first stage has kinetic origins (note the rise of Y up to the first stage), "hot" ignition is thermal. (c) T_0 = 1000 K: On further increasing the initial temperature, the concentration of Y diminishes right after the start. There is no scope for a chain-branching explosion. However, the steady temperature increase finally leads to thermal runaway. Note that the product of fuel pyrolisis, X, follows the temperature.

Fig. 2 for three different initial temperatures, 600, 780, and 1000 K, respectively. At T_0 = 600 K, ignition is a one-stage event (Fig. 2a). Its nature is *chain thermal*, with chain branching occuring via reaction (3^+) in conjunction with reaction (4). The reverse reaction (3^-) does not come into play, and since reaction (4) evolves on a much faster timescale than reaction (3^+), c.f. Fig. 6 below, the intermediate I is in steady state throughout most of the induction period. The species concentration Y grows continuously, finally leading to ignition. (Note that the total species concentration represented by Y exceeds that of F halfway through the induction period.) The same applies to X: since production via reaction (1) occurs on a much slower timescale than depletion via reaction (2), it remains in steady state, too. The high-temperature route plays no part until a very late stage of the development of ignition from T_0 = 600 K.

At T_0 = 780 K, a two-stage ignition occurs, and the kinetics are at their most complex (Fig. 2b). While the first stage again has its origin in branching reactions (3^+) + (4), the reverse reaction (3^-) can no longer be neglected. This is borne out, e.g., in the decrease of I. After the first stage, Y decreases continuously, since there is no replenishment of I. However, the temperature at the end of the first stage is sufficiently high to bring about thermal ignition via reactions (1) + (2). (Note that the increase of T precedes the rise of X.)

Finally, at T_0 = 1000 K, a single-stage ignition occurs (Fig. 2c). Oxidation of Y (and, initially to a lesser extent, X) causes the temperature to rise, thus

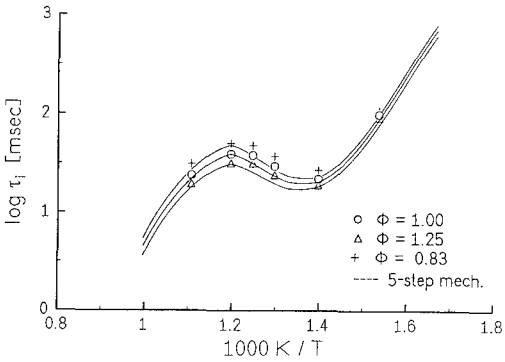

FIG. 3. Dependence of ignition delay on fuel/air equivalence ratio. Solid lines represent calculations with the five-step model. The symbols denote results obtained from the kinetic reference model [7], $p_0 = 11.2$ bar.

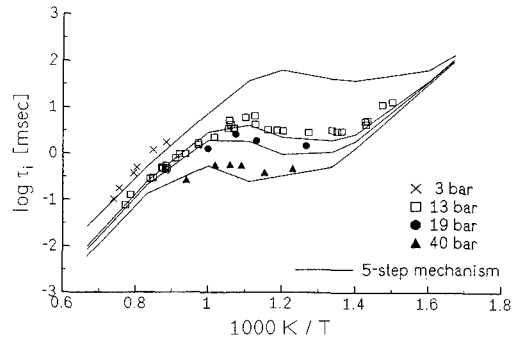

FIG. 4. Ignition delays of stoichiometric n-heptane/air mixtures at different initial pressures. Results from the five-step model are marked by solid lines, while symbols represent the shock-tube experimental data [4].

paving the way for the high-temperature combustion to occur via reaction (1) + (2). Reactions (3^+) and (3^-) are in equilibrium throughout the entire induction period. Another interesting point is that the maxima of I and Y in Fig. 2c are close to their concentrations at the end of the first stage in Fig. 2b.

The dependence of ignition delay times on the fuel/air equivalence ratio Φ ($p = 11$ bar) is depicted in Fig. 3. Ignition delays are shorter for rich mixtures and grow longer for lean mixtures. The five-step scheme and the more detailed model are in excellent agreement, and there are some tentative experimental results that seem to verify these findings [17]. However, at elevated temperatures ($T > 1300$ K), the reverse trend is observed experimentally, i.e., lean mixtures ignite more rapidly. This feature is not reproduced appropriately by the reduced mechanism. Further tests on experimental data, such as in rich mixtures of shock-heated gases and also experiments other than shock tubes, e.g., CFR engine studies or flow reactors (cool flames) are to be performed [18–20].

n-Heptane:

The five-step scheme was adapted to n-heptane oxidation with reference to a more detailed mechanism [21,22] from which the generalized scheme [7] was derived.

The only qualitative differences of the five-step structure pertained to stoichiometric factors required to maintain element balances (given in parenthesis in Table 1). Following Ref. 12, one may associate the intermediates $3C_2H_4 + CH_3 + H$ with X and $OC_7H_{13}O_2H + H_2O$ with I; P, obviously, corresponds to $7CO_2 + 8H_2O$.

The structure of the fuel molecule (i.e., branched or straight chain) strongly affects the likelihood of internal H-atom abstraction and thus of low-temperature branching. We adapted the scheme to the higher reactivity of n-heptane (ON = 0) by modifying the pre-exponential factors of the branching sequence (3^+) + (4).

The ignition delays for stoichiometric n-heptane-air mixtures calculated with the adjusted scheme are shown in Fig. 4 along with the shock-tube results of Ref. 4. The reference-model results were left out for clarity (they are virtually congruent with the five-step scheme values). However, at $p = 3$ bar, the five-step scheme tends to overestimate ignition delays on the low-temperature branch. The overall agreement between experiment and calculation appears to be excellent.

Mixtures of i-Octane + n-Heptane

The reference fuels i-octane and n-heptane set the limits for the ignition delays of any arbitrary fuel mixture with an octane number $0 < \mathrm{ON} < 100$. However tempting, it is not permissible to linearly "interpolate" the frequency factors of reactions (3^+) and (4) between the respective values for i-octane and n-heptane. As demonstrated by Park and Keck [1], the ignition retarding effect of a fuel grows progressively with its octane rating. Our choice of C_{3+} and C_4 as controlling parameters for the low-temperature oxidation rates ensures a replication of this behaviour in the five-step scheme. For convenience, the corrective factors C_{3+} and C_4 were parameterized with the octane number of the fuel:

$$C_{3+} = [(110 - \mathrm{ON})/10] \quad \text{and} \qquad (7)$$
$$C_4 = [(110 - \mathrm{ON}/10]^{1/2}.$$

Thus, if ON = 100, $C_{3+} = C_4 = 1$, and the original frequency factors for i-octane are recovered. On the other hand, if ON = 0, branching is strongly em-

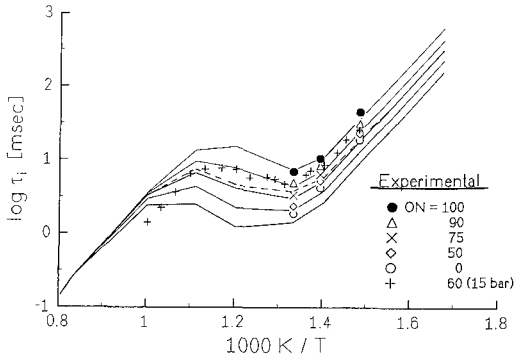

FIG. 5. Calculated ignition delays vs results from rapid compression studies [1] for fuels with different octane numbers (i.e., different *i*-octane/*n*-heptane ratios). The pressure of the charge was approximately $p_c = 18$ bar at TDC. The symbols represent the experimentally derived ignition delays, while the solid lines mark the calculated results (five-step scheme). "+" refers to the rapid compression experiments by Voinov et al. [23], which were performed at a slightly lower pressure, $p_c = 15$ bar. The corresponding calculations are represented by the broken line.

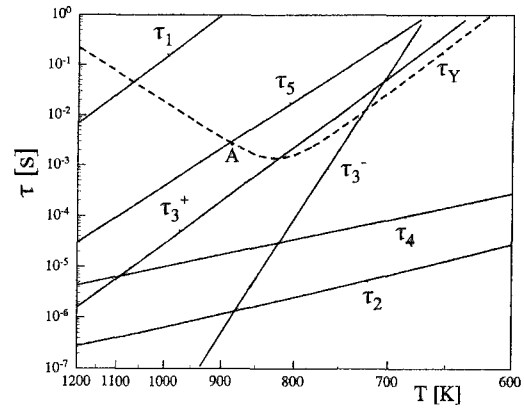

FIG. 6. Characteristic times for the reactions of the five-step model at $p_0 = 10$ bar in an Arrhenius diagram (solid lines). The broken line represents a characteristic time for the branching sequence. It exhibits a local minimum, which marks the onset of a negative temperature dependence of reaction rate. Beyond the point marked "A," chain-branching runaway is not possible.

phasized, and the A-factors for *n*-heptane are in effect.

Fig. 5 shows the calculated ignition delays of different primary reference fuels (PRFs) along with the values obtained by Park and Keck [1] in a rapid compression machine (RCM) at a pressure of 18.5 bar at top dead center (TDC). The agreement is excellent, at least as far as the experimentally investigated low-temperature branch is concerned (most certainly the result of the near-adiabatic RCM operating conditions). The ignition delays of a 60 PRF at approximately 15 bar examined by Voinov et al. [23] are also included. Given the uncertainties in initial conditions of the experiments, the agreement is very good. Note that the model was left unaltered after calibration.

Kinetic Foundation of the Negative Temperature Dependent Region

Degenerate branching via reactions (3) and (4) is responsible for the negative temperature dependence of reaction rate at intermediate temperatures. In order to understand the nature of this phenomenon in terms of the five-step mechanism, it is helpful to have a closer look at the development of the low-temperature branching agent Y. Only if a net growth in Y can be sustained throughout the induction period is there a chance for a branched chain explosion. At low temperatures, this certainly is the case, since the characteristic time τ_{3-} of reaction (3^-) is much longer than the characteristic time τ_{3+} of reaction (3^+), shown in Fig. 6 as a function of T_0 (at $p_0 = 1.5$ MPa). We calculated the characteristic times of the reaction following Ref. 12. The reaction rates are estimated by setting the concentrations of F, O_2, and T equal to their initial values and taking the concentrations of the intermediates X, I, and Y to be (constant) fractions of the initial fuel concentration $[F_0]$. All reaction rates were normalized with $[F_0]$, thus yielding, e.g., $(\tau_2)^{-1} \propto k_2[O_{2,0}][M]$.

The conservation equations for I and Y can be written as

$$\begin{aligned} d[I]/dt &= R_{3+} - R_{3-} - R_4 \\ &= k_{3+}[F][O_2][M] \\ &\quad - (k_{3-} + k_4)[I] \end{aligned} \tag{8}$$

$$\begin{aligned} d[Y]/dt &= 2R_4 - R_6 \\ &= 2k_4[I] - k_5[O_2][Y]. \end{aligned} \tag{9}$$

(For simplicity, the pressure correction term and octane rating are neglected.) At sufficiently low temperatures ($T < 800$ K at 1.5 MPa), I can be assumed to be in quasi-steady state. Then, we obtain from Eq. (8) the following:

$$[I]_{ss} = k_{3+}[F][O_2][M]/(k_{3-} + k_4). \tag{10}$$

The characteristic time of $(2k_4[I]_{ss})$ is plotted as broken line τ_Y) in Fig. 6. A necessary condition for a chain explosion to be possible is that the net branching factor be greater than zero, meaning $d[Y]/dt > 0$

in Eq. (9). The intersection of τ_Y and τ_5 (marked as "A" in Fig. 6) marks the upper temperature limit. If a chain explosion can be thus ruled out, ignition is thermal and governed by reactions (1) + (2).

Since k_{3-} has a very high activation energy and τ_{3+} decreases faster than τ_4 with increasing T (Fig. 6), τ_Y exhibits a local minimum at approximately 800 K. At higher (but not too high) temperatures, chain branching is still possible but evolves on a slower timescale—this is the negative coefficient of reaction rate. Note that it is solely governed by the low-temperature oxidation sequence (reactions (3) through (5)).

The dashed line in Fig. 6 is actually made up of two asymptotes. At low temperatures ($T < 800$ K), $R_{3+} = R_4$, while R_{3-} is neglible:

$$[I] = k_{3+}[F][O_2][M]/k_4. \tag{11}$$

We thus obtain the branch of τ_Y with a "positive" temperature dependence of rate ($E_5 < E_{3+}$ and thus $d[Y]/dt > 0$, cf. Eq. (9)). On raising the temperature further, we reach a crossover at $\tau_{3+} = \tau_{3-}$, where reaction (3) is in partial equilibrium. From $R_{3+} = R_{3-}$ it follows that

$$[I] = k_{3+}[F][O_2][M]/k_{3-}. \tag{12}$$

Since $E_{3-} >> (E_{3+} + E_4)$, the first term in Eq. (9) decreases with increasing temperature. This condition reflects the situation where the ntc of reaction rate is exhibited, i.e., the high-temperature branch of τ_Y.

Conclusion

The five-step model is currently in use in a recently developed Monte Carlo PDF code (MCPDF) to model autoignition and knock in SI engines [24]. In contrast to conventional approaches, this procedure offers the advantage of treating the high-temperature flame regime and the low-temperature reactions consistently with only one mechanism. Arbitrary "switching" algorithms are thus avoided [25]. It seems that the heavy computational burden arising from Monte Carlo methods (reactions of approximately 5×10^5 stochastic particles have to be treated per physical time step) is tractable only if a sufficiently fast mechanism is employed. While knowledge of hydrocarbon combustion is rapidly expanding, the CFD community will nevertheless have to rely on reduced kinetic mechanisms, which try to capture the essential features in a more or less empirical fashion.

Finally, it may be noted that the five-step scheme can easily be adapted to newly emerging—perhaps more reliable experimental and/or numerical—data should the need arise. The approach may also be used to deal with the more complex mixtures of other fuel components. However, in this case, the octane rating alone may not be a sufficiently accurate characterization of autoignition behaviour.

Acknowledgment

The authors wish to thank DFG and SERC for financial support.

REFERENCES

1. Park, P., and Keck, J. C., SAE Paper 900027 1990.
2. Westbrook, C. K., Pitz, W. J., and Leppard, W. R., SAE Paper 912314 1991.
3. Warnatz, J., *Twenty-Fourth Symposium (International) on Combustion*, The Combustion Institute, Pittsburgh, 1992, p. 553.
4. Ciezki, H. and Adomeit, G., *Combust. Flame* 93:421 (1993).
5. Adomeit, G., and Fieweger, K., personal communication, 1993.
6. Griffiths, J. F., Halford-Maw, P. A., and Rose, D. J., *Combust. Flame*, in press.
7. Griffiths, J. F, Hughes, K. J., Schreiber, M., and Poppe, C., to be published, *Twenty-Fifth Symposium (International) on Combustion*, 1994.
8. Griffiths, J. F., Jiao, Q., Schreiber, M., Meyer, J., and Knoche, K. F., *Twenty-Fourth Symposium (International) on Combustion*, The Combustion Institute, Pittsburgh, 1992, p. 1809.
9. Halstead, M. P., Kirsch, L. J., and Quinn, C. P., *Combust. Flame* 30:45 (1977).
10. Cox, R. A., and Cole, J. A., *Combust. Flame* 60:109 (1985).
11. Cowart, J. S., Keck, J. C., Heywood, J. B., Westbrook, C. K., and Pitz, W. J., *Twenty-Third Symposium (International) on Combustion*, The Combustion Institute, Pittsburgh, 1990, p. 1055.
12. Müller, U. C., Peters, N., and Lian, A., *Twenty-Fourth Symposium (International) on Combustion*, The Combustion Institute, Pittsburgh, 1992, p. 777.
13. Griffiths, J. F., *Combust. Flame* 93:203 (1993).
14. Gray, B. F., and Yang, C. H., *Trans. Farad. Soc.* 69:1614 (1969).
15. Petzold, L. R., and Hindmarsh, A. C., *SIAM J. Sci. Stat. Comput.* 4:136–148 (1983).
16. Voinov, A. N., and Skorodelov, D. I., *Kinetika i Kataliz*, 1965, Vol. 8 (2), pp. 252–260.
17. Ribacour, M. "Autoinflammation et Cliquetis de le Moteurs Etude en Machine a Compression Rapide de L'influence de la Structure de Hydrocabure sur le Delais D'autoinflammation," Ph.D. Thesis, University of Lille, 1992.
18. Blin-Simiand, N., Rigny, R., Viossat, V., Circan, S., and Sahetchian, K., *Combust. Sci. Technol.* 88:329 (1993).
19. Ciajolo, A., D'Anna, A., and Mercogliano, R., *Combust. Sci. Technol.* 90:357 (1993).
20. Filipe, D. J., Li, H. L., Miller, D. L., and Cernansky, N. P., SAE Paper 920807 1992.

21. Schreiber, M., Poppe, C., Meyer, J., Griffiths, J. F., and Hughes, K., *Fifth International Conference on Numerical Combustion*, Sept. 29–Oct. 1, 1993, Garmisch-Partenkirchen.
22. Poppe, C., Schreiber, M., and Griffiths, J. F., *Joint Meeting of the British and German Sections of the Combustion Institute*, Cambridge, 1992, pp. 360–363.
23. Voinov, A. N., Skorodelov, D. I., Borisov, A. A., and Lyubimov, A. V., *Russian J. Phys. Chem.* 5:605 (1967).
24. Schreiber, M., and Sadat Sakak, A., to be submitted to *Combust. Flame* (1994).
25. Schreiber, M., Sadat Sakak, A., Poppe, C., Griffiths, J. F., Halford-Maw, P., and Rose, D. J., SAE Paper 932758 1993.

COMMENTS

F. L. Dryer, Princeton University, USA. (Similar question asked by Omer L. Gülder, National Research Council of Canada, Canada.) Regarding your conclusion that your method can easily be extended to include other fuel species and complex mixtures:

1. Does your model reproduce the well-known nonlinearity in octane effects of blending reference components above ON = 87 (i.e., typical of conventional unleaded gasolines), and the much more linear behavior at ON ~ 50 – 60?

2. Does your model have the ability to more generally include octane blending number effects, particular those associated with aromatics, oxygenates, and diolefins?

Author's Reply. The results presented are at conditions that match experimental studies of PRF fuel blends in experimental systems that are more simple than engines (e.g., shock tube, rapid compression machine). The model does reproduce the nonlinearity in octane effects in terms of the factors C_{3+} and C_4. The ignition-retarding effect of a fuel grows progressively with iso-octane rating [1]. It can be taken from Fig. 5—where the ignition delays are plotted on a logarithmic scale—that the ignition-retarding effect becomes stronger with increasing octane numbers. However, more detailed examinations of the intermediate ranges (ON = 90–100, ON = 50–60) would be an interesting exploration. We require experimental results for ignition delay in fuel mixtures of the kinds that you mention in order to test the applicability of the model. It is possible to tune the model *empirically* to reproduce the ignition delay times of more complex fuels. The question remains, to what extent empiricism can be replaced by physically more meaningful numbers. We have no reason to change the structure of the model, since such fuels are still calibrated in PRF reference engines.

•

Nicholas P. Cernansky, Drexel University, USA. While the "shell" model and its later extensions by Keck and coworkers could be "tuned" to match ignition delay data, the models give unrealistically high fuel consumption (near 100%) with too little specific energy release prior to autoignition. What are the typical fuel consumption and specific energy release ranges predicted by your model, and do you consider them reasonable?

Author's Reply. The "shell" model and its extensions were set up to reproduce the autoignition delay times of particular PRF blends. Therefore, only those reaction paths in the low-temperature range that have a direct impact on the time of occurrence of autoignition are included while high-temperature reactions were virtually excluded (c.f. introductory section of the paper). The model as presented here has been designed to describe the *entire* autoignition process up to the adiabatic flame temperatures reached directly after autoignition. In the first (chain-thermal) stage of ignition, only 5–20% of the fuel is consumed. In the second (thermal—or "hot") stage, the remaining fuel and intermediates are oxidized, thus leading to temperatures above 2300 K. Given the restrictions imposed by the model's low dimensionality, we believe the fuel consumption and energy release rates to be quite reasonable (c.f. second paragraph of the paper).

•

I. Glassman, Princeton University, USA. It would appear that your figure which shows agreement between octane number and ignition time could be fortuitous. Octane numbers are measured after the compression stroke. The temperature of the intake charge in a SI engine is about 500 K. For most compression ratio ranges, the temperature just before firing is about 1200 K. It is in this temperature range that essentially the octane rating is made. Yet your ignition times were measured at a much lower temperature.

Author's Reply. Obviously, you refer to the measurements made by P. Park and J. C. Keck [1]. The temperature of the intake charge of typical SI engines lies in the range 300–360 K, thus far below the suggested 500 K. Assuming the compression ratio to be $CR = 10$ and an isentropic compression ($\gamma \approx 1.3$, stoichiometric octane-air mixture), a maximum compression temperature $T_c \approx 720$ K is reached. Certainly, 1200 K is not a realistic assumption for the charge temperature in SI engines *just before* firing! However, CARS experiments performed at our Institute [1] show that the *end-gas temperature in the late stages of combustion* in a SI engine may reach 1200 K prior to autoignition (which may then lead to the onset of knock).

REFERENCE

1. Brüggemann, D., Wies, B., and Zhang, X. X., "CARS-Messungen in einem klopfenden Motor bei gleichzeitiger Beobachtung der Flammenausbreitung," *VDI Berichte* 765:493–503 (1989).

Twenty-Fifth Symposium (International) on Combustion/The Combustion Institute, 1994/pp. 941–948

REDUCED MECHANISM OF SOOT FORMATION—APPLICATION TO NATURAL GAS–FUELED DIESEL COMBUSTION

Y. YOSHIHARA,* A. KAZAKOV, H. WANG AND M. FRENKLACH
Fuel Science Program, Department of Materials Science and Engineering
The Pennsylvania State University, University Park, PA 16802, USA

Stochastic simulations of soot formation were performed for the combustion of natural gas in a glow-assisted direct-injection diesel engine. A simple fluid dynamic method was employed, which describes turbulent mixing by random collision and coalescence of individual fluid cells. The composition of each fluid cell is homogeneous and changes with time under the control of the chemical kinetics. The reaction mechanism was comprised of three parts, each reduced with a different method, keeping the chemistry and physics as uncompromised as possible. The computational results demonstrate that the model of soot formation, developed and tested on laminar premixed flames, is capable of predicting the right amount of soot produced under the conditions of turbulent combustion. The model predicts that soot mass is mostly gained at rather high temperatures, 2100–2400 K, and a narrow range of fuel-air equivalence ratios, 2.6–2.8. The production of soot in diesel combustion was found to be controlled by particle nucleation, mass growth by surface reactions of acetylene, and surface oxidation by OH.

Introduction

Although many questions on physical and chemical details of soot formation remain unanswered [1], attempts to model the process in more practical environments have been increasing [2]. Most of these computational efforts have focused on a more accurate description of the fluid dynamics but at the cost of greatly oversimplified chemistry. In this study, we attempt the opposite: to use a simple model for turbulent mixing but with chemistry and physics as uncompromised as possible. Similar ideas have been pursued by others in different areas of turbulent combustion [3].

We present computer simulations of soot formation for the combustion of natural gas in a glow-assisted direct-injection diesel engine. The computations were carried out under the conditions of an actual experiment [4]: engine speed 1800 rpm, single cylinder, water-cooled, naturally aspirated, four-cycle, swirl ratio 2.7, compression ratio 16, fuel-air equivalence ratio 0.65, and the composition of natural gas 88% CH_4 – 6% C_2H_6 – 4% C_3H_8 – 2% C_4H_{10}. The measurement of soot was performed only at the engine exhaust, with the soot mass fraction estimated to be 5×10^{-5}.

Computational Model

A stochastic approach developed for turbulent combustion [5] was employed in the present study. This approach is based on the method of Curl [6], which describes turbulent mixing by random collision and coalescence of individual fluid cells. The composition of each fluid cell is homogeneous and changes with time under the control of the chemical kinetics. At the onset of combustion, only fuel and air cells exist. Their proportion is determined by the equivalence ratio. A total of 197 cells of equal mass, 190 of air and 7 of fuel, were considered in the present study. The composition of the initial fuel was assumed to be 88% CH_4 – 6% C_2H_6 – 6% C_3H_8, which differs slightly from the experimental composition. The small amount of C_4H_{10} present in the experiment was incorporated into C_3H_8, in order to restrict the size of the reaction set.

The stochastic process of mixing was modeled as a Markovian sequence of "collisions" between two cells chosen at random. The collisions occurred with a constant frequency, 2.5 μs during the fuel injection and 10 μs after the injection. The injection period was from $-20°$ to $-5°$ crank angle. The collision frequency was obtained by fitting the rate of heat release (Fig. 1b). Upon each collision, an instantaneous mixing was assumed: The two colliding cells were replaced with two new identical cells whose composition and temperature were determined by averaging the corresponding properties of the initial cells.

Between the collisions, the time evolution of each cell was modeled as a zero-dimensional process. A set of ordinary differential equations, repeated for all differing cells, each with appropriate initial conditions, was integrated using either an implicit Euler

*On leave from the Department of Mechanical Engineering, Ritsumeikan University, Kita-Ku Kyoto 603, Japan.

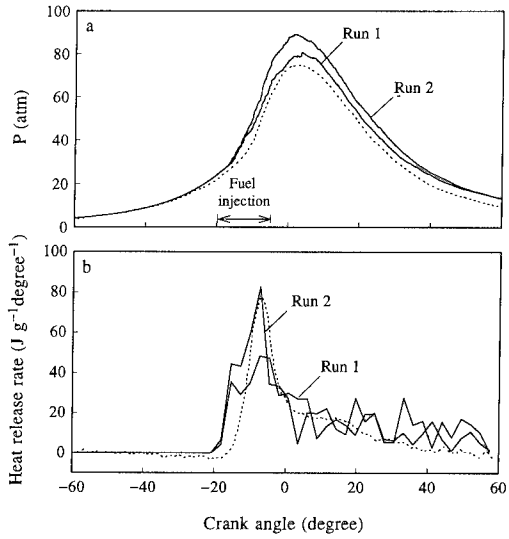

FIG. 1. Experimental (dotted lines) and calculated (solid lines) (a) pressure and (b) rate of heat release. Run 1 and Run 2 represent two different collision histories.

or, for soot-producing cells, Livermore solver for ordinary differential equations (LSODE) methods. When the number of moles of OH in a cell exceeded 10^{-7} and that of CH4 was below 10^{-6}, a state of partial equilibrium was assumed for all species smaller than benzene.

The initial temperature of all fluid cells was 500 K, with the exception of three, which were kept at 1350 K during the injection time to simulate the glow assistance. Heat losses were estimated with Annand and Mas empirical formula [7]. The system pressure was adjusted at every integration step. Two sources of the pressure change were accounted for: the motion of the engine piston and the energy release in reacting cells. The pressure increments computed for the individual cells were averaged over the entire system, as the pressure redistribution was assumed to occur instantaneously. The computed and experimental pressure profiles are shown in Fig. 1a. The calculations were performed using an IBM RISC 6000-580 workstation, with a typical run taking about 20 CPU hours.

Reaction Mechanism

The entire reaction mechanism—from methane to soot particles—was divided into three parts, each reduced with a different method: small-molecule reactions describing the main combustion environment and the formation of benzene; growth of benzene to pyrene; and nucleation, growth, and oxidation of soot particles. The details of these submodels are given below.

Main Combustion Reactions

Although the primary concern of the present study is the formation of soot, accurate prediction for several of the principal gaseous species—H, OH, O_2, C_2H_2, and benzene—is critical for quantitative modeling of soot formation.

These considerations underlie our interest in maintaining this part of the chemical model as truthful as possible, while keeping its size at a bare minimum. We approached this goal with a technique called detailed reduction [8]. The initial, "full" reaction mechanism for methane combustion was taken from Ref. 9. It was reduced in size at the conditions typical of diesel combustion to a 21-species mechanism, listed as reactions 1 through 70 in Table 1. The reduction was performed at the level of $\varepsilon = 0.02$ [8], after which two additional reactions were added to account for the oxidation of acetylene, $C_2H_2 + O \rightarrow {}^3CH_2 + CO$ (reaction 105 in Ref. 9) and $C_2H_2 + O \rightarrow {}^1CH_2 + CO$ (combination of reactions 102 and 106 in Ref. 9). This reduced mechanism in combination with a set of NO_x reactions taken from Miller and Bowman [24] was able to predict the exhaust concentration of NO in similar diesel engine simulations to within a factor of 2 [25]. The set of reactions 1 through 70 was augmented with dissociation of propane, reactions 71 and 72, and formation of C_3H_x species and benzene, reactions 73 through 78 (Table 1).

PAH Growth

A reaction sequence leading from benzene to pyrene, adopted for the present study, is shown in Fig. 2. This reaction scheme is based on both past results [20,26–28] and on a reaction flux analysis performed in the present study, using a more extensive reaction set under the conditions typical of high-pressure turbulent combustion. The nomenclature for chemical species used in Fig. 2 and throughout the manuscript has been introduced previously [16]. Briefly, A_i represents a species composed of i-fused aromatic rings; e.g., A_1 is benzene and A_4 is pyrene. A_iC_2H is an A_i aromatic with one of its H atoms substituted with C_2H. A_i- denotes a radical formed from A_i, and $A_iC_2H^\bullet$ denotes a radical of A_iC_2H with the unpaired electron located next to the C_2H group. P_2 represents biphenyl, an aromatic molecule with nonfused rings, whose importance was predicted for the conditions rich in benzene [29]. As will be demonstrated later in the text, the P_2 channel plays a key role under the conditions tested in the present study.

Assuming steady state for all the radicals in the sequence shown in Fig. 2 and partial equilibrium for reactions 85 and 86 (see Table 1), we obtain an analytical expression relating the concentrations of pyrene and benzene,

TABLE 1
Mechanism of Methane Oxidation and Aromatics Formation

No.	Reaction[a]	$k = AT^{-n}e^{E/RT}$ A (cm, mol, s)	n	E (kJ mol^{-1})	References/ Comments
	Methane oxidation				
1–70	1–4, 8–10, 12–15, 19, 22–25, 32, 35, 36, 38, 40, 44, 46, 51, 52, 57–63, 65–72, 74, 76–82, 86–88, 105, 106, 117, 120, 121, 125, 128–132, 139, 143–149				*b*
	Propane reactions				
71	$C_3H_8 \rightleftharpoons CH_3 + C_2H_5$	7.90 (+22)	−1.79	371.0	10
72	$C_3H_8 + H \rightarrow C_2H_4 + CH_3 + H_2$	1.33 (+06)	2.54	28.3	11
	Benzene formation				
73	$^3CH_2 + C_2H_2 \rightleftharpoons C_3H_3 + H$	1.20 (+13)		27.7	11
74	$CH_3 + C_2H_2 \rightleftharpoons C_3H_4 + H$	2.72 (+18)	−1.97	84.6	12
75	$C_3H_4 + M \rightleftharpoons C_3H_3 + H + M$	4.70 (+18)		334.7	13
76	$C_3H_4 + H \rightleftharpoons C_3H_3 + H_2$	1.00 (+12)		6.3	14
77	$C_3H_4 + OH \rightleftharpoons C_3H_3 + H_2O$	2.20 (+07)	1.9	4.7	*c*
78	$C_3H_3 + C_3H_3 \rightarrow$ benzene	1.00 (+11)			15
	PAH growth				
79.*i*	$A_i + H \rightleftharpoons A_{i-} + H_2$	2.50 (+14)		66.9	*d,e*
80.*i*	$A_i + OH \rightleftharpoons A_{i-} + H_2O$	2.10 (+13)		19.1	*d,f*
81.*i*	$A_{i-} + H \rightleftharpoons A_i$	5.80 (−12)	8.29	−33.8	*g,h*
82.*i*	$A_i + OH \rightarrow$ products	1.00 (+11)			*d,i*
83.*i*	$A_{i-} + O_2 \rightarrow$ products	2.00 (+12)		31.3	*g,j*
84	$A_{1-} \rightarrow$ linear products	1.04 (+29)	−4.26	324.0	*k*
85	$A_{1-} + C_2H_2 \rightleftharpoons A_1C_2H + H$	2.34 (+34)	−5.71	129.4	*l*
86	$A_{2-} + C_2H_2 \rightleftharpoons A_2C_2H + H$	4.63 (+31)	−5.05	123.0	*l*
87.*i*	$A_iC_2H^\bullet + C_2H_2 \rightleftharpoons A_{i+1-}$	3.31 (+50)	−10.95	112.8	*l,m*
88	$A_{3-} + C_2H_2 \rightarrow A_4 + H$	1.27 (+44)	−8.71	138.2	*l*
89	$A_1 + A_{1-} \rightleftharpoons P_2 + H$	1.30 (+03)	2.72	11.3	*n*
90	$P_{2-} + C_2H_2 \rightleftharpoons A_3 + H$	1.27 (+44)	−8.71	138.2	$k_{90} = k_{88}$

[a]The rate coefficients for the reverse directions were determined via equilibrium constants.

[b]Reactions 1–70 were obtained by a detailed reduction of the methane oxidation mechanism in Ref. 9. The numbers shown under the "Reaction" column indicate the reaction number in Table 1 of Ref. 9.

[c]$k_{77} = k(C_2H_6 + OH \rightleftharpoons C_2H_5 + H_2O)$.

[d]A_i represents A_1, A_1C_2H, A_2, A_2C_2H, A_3, and P_2 [16].

[e]Taken from Kiefer et al. [17] for the analogous reaction of benzene.

[f]Taken from Madronich and Felder [18] for the analogous reaction of benzene.

[g]A_{i-} represents A_{1-}, $A_1C_2H^\bullet$, A_{2-}, $A_2C_2H^\bullet$, A_{3-}, and P_{2-} [16].

[h]Based on RRKM calculations for the phenyl and hydrogen atom association reactions at 10 bar with the parameters taken from Rao and Skinner [19]. The forward rate coefficient $k = AT^n \exp(-E/RT - 2.77 \times 10^{-3}\,T - 5.58 \times 10^{-7}\,T^2)$.

[i]For $i = 1$, a linear hydrocarbon product is assumed; for $i > 1$, the product is an aromatic molecule with two carbon atoms less than A_i. The rate coefficient is estimated [20].

[j]For $i = 1$, a linear product is assumed; for $i > 1$, the product is an aromatic radical with two carbon atoms less than A_i. The rate parameters were taken from Lin and Lin [21] for the analogous reaction of phenyl.

[k]Assigned the rate coefficient of the ring opening reaction $A_{1-} \rightarrow n\text{-}C_6H_5$.

[l]Based on RRKM calculations at 10 bar with parameters taken from Ref. 15.

[m]$i = 1, 2$.

[n]The rate coefficient expression was obtained using RRKM calculations, fitted to the experimental data of Fahr and Stein [22] and Scaiano and Stewart [23].

$$\frac{d[A_4]}{dt} = k_{88}[C_2H_2] \cdot \left([A_1]\prod_{i=1}^{7} B_i + B_1E + D\right) \quad (1)$$

where

$$B_1 = k_{87}[C_2H_2]\{k_{-87,2} + k_{88}[C_2H_2] + k_{83}[O_2] + Z_{2,5}k_{82}[OH]/(Z_{1,5} + k_{82}[OH])\}^{-1}$$

$$B_2 = Z_{1,4}(Z_{2,4} + k_{87}[C_2H_2] + k_{83}[O_2] - k_{-87,2}B_1)^{-1}$$

$$B_3 = k_{86}[C_2H_2]/(k_{-86}[H])$$

$$B_4 = k_{87}[C_2H_2](k_{-87,1} + k_{83}[O_2] + Z_{2,3})^{-1}$$

$$B_5 = Z_{1,2}(Z_{2,2} + k_{87}[C_2H_2] + k_{83}[O_2] - k_{-87,1}B_4)^{-1}$$

$$B_6 = k_{85}[C_2H_2]/(k_{-85}[H])$$

$$B_7 = Z_{1,1}\{Z_{2,1} + k_{83}[O_2] + k_{84} + Z_{1,6}k_{89}[A_1]/[Z_{1,6} + k_{-89}[H] + Z_{2,6}k_{-89}[H]/(k_{90}[C_2H_2])]\}^{-1}$$

$$C = Z_{1,6}B_7k_{90}k_{89}[C_2H_2][A_1]^2\{Z_{1,6}k_{90}[C_2H_2] + k_{-89}[H](Z_{2,6} + k_{90}[C_2H_2])\}^{-1} + k_{82}[OH][A_4]$$

$$D = Z_{1,5}C\{(k_{-87,2} + k_{88}[C_2H_2] + k_{83}[O_2])(Z_{1,5} + k_{82}[OH]) + Z_{2,5}k_{82}[OH]\}^{-1}$$

$$E = k_{-87,2}D\{Z_{2,4} + k_{87}[C_2H_2] + k_{83}[O_2] - k_{-87,2}B_1\}^{-1}$$

$$Z_{1,i} = k_{79,i}[H] + k_{80,i}[OH] + k_{-81,i}$$

$$Z_{2,i} = k_{-79,i}[H_2] + k_{80,i}[H_2O] + k_{81,i}[H].$$

The rate coefficients appearing in the above equations are given in Table 1 (reactions 79 through 90). They were obtained from RRKM calculations [28] for a pressure of 10 bar and temperatures from 500 to 3000 K. The rate coefficients evaluated at 10 bar are within a factor of 2 from the values at 100 bar and were, therefore, assumed to be pressure independent in the present calculations.

The accuracy of the reduced model of PAH growth, Eq. (1), was tested by performing kinetic calculations on an individual fluid cell whose initial conditions were typical of those producing the most soot in the stochastic diesel simulations. The results, shown in Fig. 3, indicate that the reduced model overpredicts the pyrene concentration in the beginning, but gets closer to it at times around 1 ms, the average cell reaction time. The difficulty of obtaining

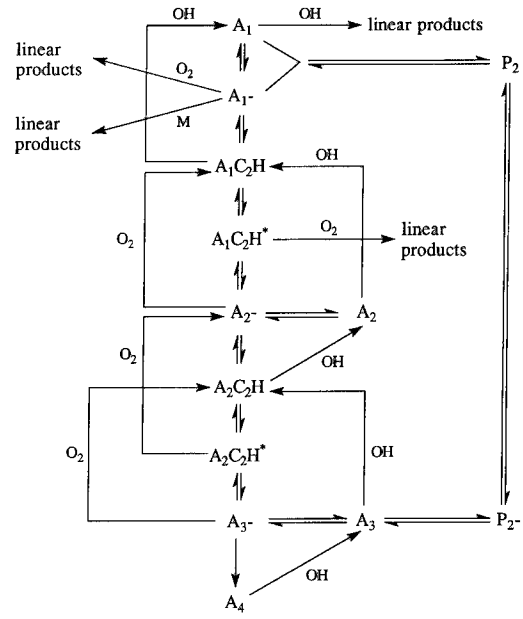

FIG. 2. Reaction scheme of PAH growth.

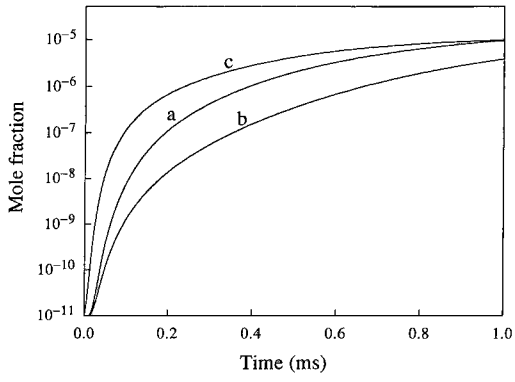

FIG. 3. Calculated mole fraction of A_4 for the conditions of a single fluid cell: $P_0 = 39$ atm, $T_0 = 1954$ K, $\phi = 3.68$, and initial mole fraction of A_4 9.3×10^{-12}. (a) Computed with the full reaction scheme for PAH growth (Fig. 2 and reactions 79–90 in Table 1). (b) The same as (a) but without the P_2 reaction channel (i.e., without reactions 89 and 90). (c) Computed with the reduced model of PAH growth, Eq. 1.

a more accurate reduced model for the reaction scheme in Fig. 2 resides in the complex behavior of A_2 and A_3. Assuming their formation irreversible and omitting the P_2 channel predicts well the initial part of the A_4 profile but greatly underpredicts it in the range of interest. Assuming A_2 is in a steady state or neglecting A_2 altogether overpredicts the A_4 concentration at all reaction times. The physical reason for this is the compound kinetics of A_2: It accumulates

at first, and then reacts at the later stages of reaction. A compromise solution was obtained by assuming the formation of A_2 irreversible, neglecting the formation of A_1C_2H in the oxidation of A_2 by OH, and including the P_2 channel, whose importance in this case was evident (compare, e.g., curve b with a in Fig. 3). In doing so, species P_2, P_2-, and A_3 were assumed to be in steady state.

Soot Particle Model:

The physical model adopted for soot particle formation, growth, and destruction is as follows. The nucleation of particles is described by coalescence of pyrene into dimers. We ignore in the present study the growth of PAHs beyond pyrene, included in our detailed model [20,26–28]. This was done to shorten the computational time, as it has been our experience that the difference in the final amount of soot caused by this assumption does not exceed a factor of 2, which is not critical for the present study.

The dimers formed by the PAH coalescence collide with each other, thus initiating particle coagulation. The particle coagulation was treated as free molecular. Simultaneously with coagulation, particles undergo surface processes: physical condensation of gaseous pyrene, chemical growth by the H-abstraction—C_2H_2-addition (HACA) reaction sequence, and oxidation by O_2 and OH. The particle dynamics were modeled by the method of moments [30], which reduces the corresponding detailed description to a small number of differential equations for the moments of the particle size distribution function (PSDF). Solution of these equations determines all the necessary properties of the particle cloud. The mathematical closure, which requires the knowledge of fractional-order moments, is accomplished in our method by interpolation among the computed whole-order moments, i.e., without a priori specification of PSDF.

A fifth-order model, the same as in our previous studies [20,26–28], was employed in the present computations. The specific equations used are reported in detail in Ref. 27 and, hence, will not be repeated here. As previously described [20,26–28], the surface growth by HACA and oxidation by O_2 were described in terms of elementary surface reactions, whose rates were given as

$$k_s\, C_g\, a \chi_s S \tag{2}$$

where k_s is the per-site rate coefficients; C_g is the concentration of the colliding gaseous species; a is the fraction of surface sites available for a given reaction, assumed to be unity in the present study; χ_s is the number density of corresponding surface sites; and S is the total surface area of the soot particle cloud. The surface reactions and per-site rate coefficients, based on analogous gas-phase reactions of

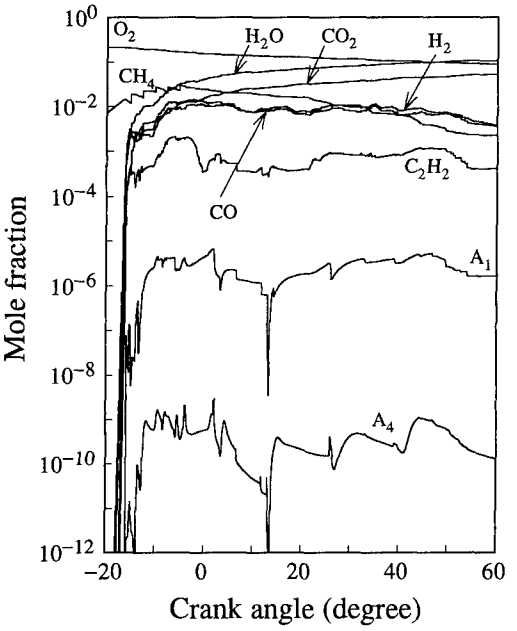

FIG. 4. Species mole fractions averaged over all the fluid cells calculated during Run 1.

one-ring aromatics, benzene, and phenyl, are specified in Refs. 19,26–28.

A detailed understanding of soot particle oxidation by OH is still lacking, and hence, it was described, as was done previously [19,26–28], following Neoh et al. [31], by the probability of reaction upon a collision of OH with the particle surface, γ_{OH}. For its value, we used the following expression:

$$\gamma_{OH} = 0.42\left[\tanh\left(\frac{2664}{T} - 2.80\right) + 1\right] \tag{3}$$

which was obtained by fitting a hyperbolic tangent switch function to new experimental data [32]. The sensitivity of the model predictions to the choice of γ_{OH} was investigated and will be discussed in the next section.

Results and Discussion

The numerical predictions of the model for several selected species, those of interest to modeling soot formation, are shown in Fig. 4. The predictions for the amount of soot computed in a number of runs are displayed in Fig. 5. Inspection of these results indicates that the time history of the soot formed exhibits a distinct maximum, characteristic of diesel engine combustion [33]. We observe that the final soot mass fractions computed in the base-case runs, denoted as Runs 1 and 2 in Fig. 5, are very close to

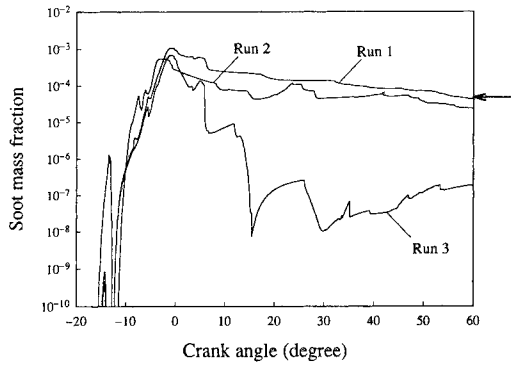

FIG. 5. Soot mass fractions summed over all the fluid cells. Solid lines: calculated with γ_{OH} given by Eq. (3); dotted line: computed using the same collision history as Run 1 but with $\gamma_{OH} = 0.13$ [31]. The arrow on the right vertical axis marks the experimental soot mass fraction, 5×10^{-5}, determined in the engine exhaust [4].

the experimental value of 5×10^{-5} [4] (perhaps fortuitously so, in light of the model uncertainties). The base-case runs 1 and 2 were performed under identical conditions, except for different stochastic sequences of cell collisions, originating from different "seed" numbers for the random number generator. These two runs test the "reproducibility" of the stochastic simulations. The close proximity in the time profiles obtained indicates that the 197 cells seem to provide an acceptable level of statistical variance for the present study.

The oxidation of soot particles by OH was tested computationally. With this reaction switched off, i.e., $\gamma_{OH} = 0$, the calculated mass fraction increases, without displaying a maximum, to a value ~40 times larger than computed in the base cases. The oxidation by O_2 is on the average $\sim 10^2$ slower than by OH. Assigning, following Neoh et al. [31], the OH reaction probability a constant value, $\gamma_{OH} = 0.13$, instead of the temperature-dependent function used in the base case, Eq. (3), the soot mass fraction appears to drop dramatically at larger crank angles, as shown by the curve marked Run 3 in Fig. 5.

Figure 6 presents the distribution of particle mass obtained in the base-case calculation, run 1. Inspection of these data indicates that in time (i.e., with the increase in the crank angle), the particle mass distribution narrows and is shifted to smaller average particle mass. Both of these trends are the result of soot particle oxidation by OH and fluid cell mixing.

Examination of the numerical results of base-case run 1 indicated that soot is mostly produced at rather high temperatures, 2100–2400 K, and a narrow range of fuel-air equivalence ratios, 2.6–2.8. The growth of soot mass occurs predominantly by the acetylene (i.e., HACA) surface reactions with the A_4 condensation being 10^2–10^3 times slower. Although most of the soot mass is gained at these high temperatures, the nucleation of soot particles takes place at temperatures around 1800 K, similar to the nucleation temperatures computed with essentially the same model for laminar premixed flames [20,26–28].

Under the conditions of diesel engine combustion, the model predicts that the initial soot forms in a small number of fluid cells. The fate of this soot is determined by the subsequent history of mixing. A soot-producing fluid cell has only a limited amount of time for reaction, on the average 1 ms (10.8° of the crank angle), before it collides with another fluid cell. Such collisions alter the cell environment, most often to the degree that the soot production is stopped and replaced by the soot oxidation. Only when the initial soot-producing fluid cell collides with fuel-rich cells or with cells containing cold-burned gases does soot survive until the exhaust. In run 1, for example, about 70% of the final soot mass came from such a single soot-producing "survivor" cell.

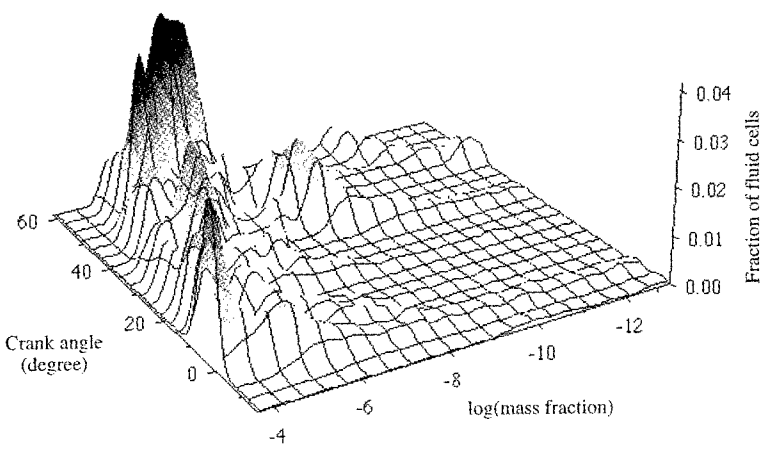

FIG. 6. Smoothed particle mass distribution obtained in Run 1.

Conclusions

Stochastic simulations of soot formation were performed for the combustion of natural gas in a glow-assisted direct-injection diesel engine. The simple fluid dynamic method of Curl [6] was employed, which describes turbulent mixing by random collision and coalescence of individual fluid cells. The composition of each fluid cell is homogeneous and changes with time under the control of the chemical kinetics. The reaction mechanism was comprised of three parts, each reduced with a different method. A set of small-molecule reactions describing the main combustion environment and the formation of benzene was reduced in size using the technique of detailed reduction [8]. Growth of benzene to pyrene was described by an analytical expression based on the assumptions of steady states and partial equilibria. Nucleation, growth, and oxidation of soot particles was modeled by the method of moments [30].

The computational results demonstrate that our model of soot formation, developed and tested on laminar premixed flames [20,26–28], is capable of predicting the right amount of soot produced under the conditions of turbulent combustion. The model predicts that soot mass is mostly gained at temperatures of 2100–2400 K and under a narrow range of fuel-air equivalence ratios, 2.6–2.8. The production of soot in diesel combustion was found to be controlled by particle nucleation, mass growth by the acetylene (i.e., HACA) surface reactions, and surface oxidation by OH.

The present experience indicates that further reduction in the model size can be attempted by using a Peters–Williams type [34] reduced mechanism for main combustion chemistry and a simpler, three-moment model (Method I in Ref. 30) for particle dynamics. Also, the present model of turbulent mixing can be improved by increasing the number of the fluid cells and introducing a finite time for their mixing.

Acknowledgments

The research at PSU was sponsored by the NASA-Lewis Research Center, under Grant No. NAG3-991, the Gas Research Institute, under Contract No. 5092-260-2454, and the Air Force Office of Scientific Research, Air Force Systems Command, USAF, under Grant No. 91-0129. The US Government is authorized to reproduce and distribute reprints for Governmental purposes notwithstanding any copyright notation thereon.

REFERENCES

1. *Proceedings of the International Workshop on Mechanisms and Models of Soot Formation* (H. Bockhorn, Ed.), Springer-Verlag, Heidelberg, in press.
2. Villasenor, R., and Kennedy, I. M., *Twenty-Fourth Symposium (International) on Combustion,* The Combustion Institute, Pittsburgh, 1992, pp. 1023–1030; Honnery, D. R., and Kent, J. H., ibid. pp. 1041–1047; Fairweather, M., Jones, W. P., Ledin, H. S., and Lindstedt, R. P., ibid. pp. 1067–1074; Leung, K. M., Lindstedt, R. P., and Jones, W. P., *Combust. Flame* 87:289–305 (1991); Kennedy, I. M., Wolfgang, K., and Chen, J.-Y., *Combust. Flame* 81:73–85 (1990).
3. Pratt, D., *Prog. Energy Combust. Sci.* 1:73–86 (1976); Correa, S. M., *Combust. Flame* 94:41–60 (1993); Correa, S. M., and Braaten, M. E., *Combust. Flame* 94:469–486 (1993).
4. Ikegami, M., Shioji, M., Zhu, Q.-M., Hotta, Y., and Endo, H., *JSAE* 24:64–69 (1993).
5. Ikegami, M., Shioji, M., and Koike, M., *Twentieth Symposium (International) on Combustion,* The Combustion Institute, Pittsburgh, 1985, pp. 217–224.
6. Curl, R. L., *AIChE J.* 9:175–181 (1963).
7. Annand, W. J. D., and Ma, T. H., *Proc. Inst. Mech. Eng.* 185:976–986 (1970).
8. Frenklach, M., Kailasanath, K., and Oran, E. S., *Prog. Astronaut. Aeronaut.* 105 (2):365–376 (1986); Wang, H., and Frenklach, M., *Combust. Flame* 87:365–370 (1991).
9. Frenklach, M., Wang, H., and Rabinowitz, M. J., *Prog. Energy Combust. Sci.* 18:47–73 (1992).
10. Tsang, W., *J. Phys. Chem. Ref. Data* 17:887–951 (1988).
11. Böhland, T., Temps, F., and Wagner, H. Gg., *Twenty-First Symposium (International) on Combustion,* The Combustion Institute, Pittsburgh, 1988, pp. 841–850.
12. Dean, A. M., and Westmoreland, P. R., *Int. J. Chem. Kinet.* 19:207–228 (1987).
13. Hidaka, Y., Nakamura, T., Miyauchi, A., Shiraishi, T., and Kawano, H., *Int. J. Chem. Kinet.* 21:643–666 (1989).
14. Kiefer, J. H., Al-Alami, M. Z., and Budach, K. A., *J. Phys. Chem.* 86:808–813 (1982).
15. Wang, H., Ph.D. Thesis, The Pennsylvania State University, University Park, PA, 1992.
16. Frenklach, M., Yuan, T., and Ramachandra, M. K., *Energy Fuels* 2:462–480 (1988).
17. Kiefer, J. H., Mizerka, L. J., Patel, M. R., and Wei, H. C., *J. Phys. Chem.* 89:2013–2019 (1985).
18. Madronich, S., and Felder, W., *J. Phys. Chem.* 89:3556–3561 (1985).
19. Rao, V. S., and Skinner, G. B., *J. Phys. Chem.* 92:2442–2448 (1988).
20. Markatou, P., Wang, H., and Frenklach, M., *Combust. Flame* 93:467–482 (1993).
21. Lin, C.-Y., and Lin, M. C., Fall Technical Meeting of the Eastern States Section of the Combustion Institute, Gaithersburg, Maryland, November 1987, Paper 7.
22. Fahr, A., and Stein, S. E., *Twenty-Second Symposium (International) on Combusiton,* The Combustion Institute, Pittsburgh, 1989, pp. 1023–1029.
23. Scaiano, J. C., and Stewart, L. C., *J. Am. Chem. Soc.* 105:3609–3614 (1983).

24. Miller, J. A., and Bowman, C. T., *Prog. Energy Combust. Sci.* 15:287–338 (1989).
25. Yoshihara, Y., Wang, H., and Frenklach, M., "Modeling of NO_x Formation in Natural Gas Fueled Diesel Combustion," accepted to COMODIA 94.
26. Frenklach, M., and Wang, H., *Twenty-Third Symposium (International) on Combustion,* The Combustion Institute, Pittsburgh, 1991, pp. 1559–1566.
27. Frenklach, M., and Wang, H., in "Detailed Mechanism and Modeling of Soot Particle Formation," *Proceedings of the International Workshop on Mechanisms and Models of Soot Formation* (H. Bockhorn, Ed.), Springer-Verlag, Heidelberg, in press.
28. Kazakov, A., Wang, H., and Frenklach, M., *Combust. Flame*, in press.
29. Frenklach, M., Clary, D. W., Gardiner, W. C., Jr., and Stein, S. E., *Twenty-First Symposium (International) on Combustion,* The Combustion Institute, Pittsburgh, 1988, pp. 1067–1076.
30. Frenklach, M., and Harris, S. J., *J. Colloid Interface Sci.* 118:252–261 (1987).
31. Neoh, K. G., Howard, J. B., and Sarofim, A. F., in *Particulate Carbon: Formation during Combustion* (D. C. Siegla and G. W. Smith, Eds.), Plenum, New York, 1981, p. 261.
32. Puri, R., Santoro, R. J., and Smyth, K. C., *Combust. Flame* 97:125–144 (1994).
33. Smith, O. I., *Prog. Energy Combust. Sci.* 7:275–291 (1981).
34. Peters, N., and Williams, F. A., *Combust. Flame* 68:185–207 (1987).

COMMENTS

F. L. Dryer, Princeton University, USA. Not to discount the certain significance of OH oxidation of carbon surfaces, I wonder if under diesel conditions CO_2 and H_2O may also be significant oxidizers. The activation energies for the overall reaction rate of carbon with these oxidizers are of the order of 70–80 kcal/mole-K. We have recently verified the activation energies and compared them with that for O_2 at temperatures from 800 to 1200 K. The reaction rates in pure oxidizer/nitrogen mixtures are comparable between 1450 and 1500 K. Are you planning on considering or have you considered the alternative sources of oxidizing species (of H_2O and CO_2) at the much higher temperatures in which you are interested?

Author's Reply. In our previous studies [1] of soot formation in laminar premixed flames, using essentially the same model, surface reactions with H_2O, CO_2, and CO were found to be insignificant. Similarly, low contributions to soot oxidation by H_2O and CO_2 are reported in experimental studies of laminar diffusion flames [2]. Based on these results and relatively high overall activation energies you report, the role of H_2O and CO_2 in soot oxidation is probably minor. However, your suggestion is well taken, and we will test these reactions under the conditions of turbulent combustion in future studies.

REFERENCES

1. Frenklach, M., and Wang, H., *Twenty-Third Symposium (International) on Combustion,* The Combustion Institute, Pittsburgh, 1991, p. 1559.
2. Sunderland, P. B., Köylü, U. O., and Faeth, G. M., this Symposium.

•

Yiguang Ju, Tohoku University, Japan. If reaction j was removed according to the following rules

$$|R_j| < \varepsilon_r R_{\text{ref}}$$
$$|R_j Q_j| < \varepsilon_q \max\{R_j Q_j\}$$

and if the flame condition, such as temperature, was changed, reaction j may become important again, so you need to include this reaction in the reaction scheme again. Did you consider this in your procedure of reaction mechanism reduction?

Author's Reply. Yes, the above conditions were applied to the entire space of conditions. That is, reaction j is removed only if the above two inequalities are satisfied at *every* grid of the integration procedure. Further details of our reduction method can be found in Ref. 8 of the paper.

Twenty-Fifth Symposium (International) on Combustion/The Combustion Institute, 1994/pp. 949–955

APPLICATION OF REPRO-MODELING FOR THE REDUCTION OF COMBUSTION MECHANISMS

T. TURÁNYI
Central Research Institute for Chemistry
P.O. Box 17, H-1525 Budapest, Hungary

The basic problem of mechanism reduction methods is to find functional relationships between selected state variables (e.g., some concentrations and temperature) and their rates. However, this information is present during the simulations with the full chemical model.

As a new application of the repro-modeling approach, information for rates is extracted from detailed chemical calculations and stored in the form of high-order multivariate polynomials. For an efficient utilization of the polynomials, a computer program was written that rearranges them to the form of multivariate Horner equations. The repro-modeling method is an alternative to the application of the quasi-steady-state approximation (QSSA) and of the low-dimensional manifold method. Pros and cons of these three methods are discussed in detail considering the preparations required, the accuracy attainable, the yield in computer time, and the limitations of the techniques.

Simulations of the combustion of wet CO using two-variable and three-variable repro-models were 24,000 and 11,700 times faster, respectively, than the SENKIN calculation using the full model. These calculations represent the first use of repro-modeling for combustion mechanism reduction.

Introduction

Due to rapid progress in the research of elementary gas reactions, more and more information has become available for the rate coefficients and stoichiometry of reaction steps. When these data are incorporated into detailed models, the mechanisms obtained reproduce the ignition times and species profiles of flames with fair accuracy for most practically important fuels. These mechanisms typically contain 20–50 species and 70–200 reactions. Applying detailed chemistry, the calculation of spatially homogeneous systems and one-dimensional flames is straightforward using generally available hardware and software, while calculation of two-dimensional laminar flames requires several hundred hours of supercomputer time and the simulation of three-dimensional deflagrations is not possible. Also, it is still impossible to do turbulent flame calculations with detailed chemistry.

The elimination of redundant species and redundant reactions from detailed mechanisms may speed up the calculations by a factor of 10 [1], but it is still not enough in most cases.

Fortunately, in chemical kinetic systems, the chemical changes span very diverse timescales. Starting with arbitrary initial conditions in composition space, the concentration of fast variables (i.e., QSSA species) is determined soon by the concentration of slow variables (non-QSSA species). Although this behavior of chemical systems was observed very early [2], the basis of this phenomenon was frequently misinterpreted (see Ref. 3 for a brief history of QSSA).

Three methods are available for the identification of fast variables. According to a "chemical" rule, a QSSA species has a low net production rate compared to its production and consumption reaction rates [4]. The "mathematical" methods are based on the eigenvalue analysis of the Jacobian of the kinetic ordinary differential equations (ODEs). The method of computational singular perturbation (CSP) [5,6] provides a list of fast variables (called CSP radicals). Recently, a method was published [3] for the identification of QSSA species and for the calculation of QSSA errors. According to this article, the error of a QSSA species is equal to the product of its lifetime and net production rate.

After a transition time, concentration changes in a chemical system are determined by $n = n_t - n_f - n_c$ variables, where n_t is the total number of state variables (e.g., concentrations and temperature), n_f is the number of fast variables, and n_c is the number of conservation equations such as atomic conservation relations.

Having selected this minimal number of variables, the next step is to correlate their values to their rates, allowing the simulation of a system containing only n variables. Two basically different methods have been proposed for the calculation of such relations:

1. Quasi-steady-state approximation: In each step of the simulation, the concentrations of QSSA species are calculated from the concentrations of

non-QSSA species, and the production rates of non-QSSA species are calculated using the original system of kinetic ODEs.

2. The intrinsic low-dimensional manifold method [7,8]: n variables are selected, and the values of other variables are determined on the basis of the Jacobian. Production rates for the n variables are calculated using the original system of kinetic ODEs in each point of an n-dimensional grid and tabulated. In each step of the solution of kinetic ODEs, the nearest values in the table are looked up, and the production rates are estimated using multilinear regression.

In this paper, a third method is described for the generation of reduced models, which is also based on the existence of diverse timescales in chemical kinetic models:

3. Repro-modeling: Several hundred simulations of the original mechanism are carried out, and the values of n variables and the rate information corresponding to these variables are collected. The data are fitted using high-order multivariate polynomials. Then, in each step of the simulation, these polynomials are evaluated.

The Repro-Modeling Approach

Very frequently, complex computational models have CPU time-consuming submodels, which may be used several million times during a single simulation. The input of such submodels usually covers a well-defined region. Based on several thousand simulations with typical input data, the input-output relations of the submodel can be approximated by explicit empirical equations. This approach is called repro-modeling [9] and was successfully applied to, for example, the modeling of freeway control. As the evaluation of explicit equations is much faster than the simulation of the submodel, the simulation of the original model can be sped up significantly.

Models of reactive flows have a similar structure, as the calculation of chemical rates is a very time-consuming submodel of the transport model. The spread of air pollution is one of the applications of reactive flow models, and repro-modeling has been applied to atmospheric chemical problems [10–12]. Repro-modeling has also been applied to a liquid-phase chemical reaction [13]. A similar approach was used for the modeling of electronic circuits [14].

The approximating empirical function has to be simple for a fast evaluation and flexible to mimic well the submodel. Continuous piecewise linear functions [9], second order polynomials [10,11], and high-order polynomials, evaluated in Horner form, [12,13] have been successfully used.

Application of Repro-Modeling for Combustion Simulations

Reactive flow problems can be characterized by the following system of partial differential equations deduced from the conservation equations:

$$d\mathbf{U}/dt = A(\mathbf{U}) + B(\mathbf{U}) \tag{1}$$

where $\mathbf{U}$ is the vector of state variables (e.g., species mass fractions, temperature, density, and velocity field), A is the rate of state variables due to transport (advection and diffusion), and B is the rate of state variables due to chemical reaction. Inputs of function B are the temperature and the species concentrations and the output is their rates.

While Eq. (1) has a simple form, it is difficult in most cases to solve it numerically. In the case of two- and three-dimensional systems, the method of operator splitting is common for the solution of Eq. (1). Using this method, the changes of state variables during time interval Δt are calculated from

$$\mathbf{U}(t + \Delta t) - \mathbf{U}(t) = T(\mathbf{U},\Delta t)C(\mathbf{U},\Delta t) \tag{2}$$

where T is the operator of changes of state variables due to transport and C is the operator of changes of concentrations and temperature due to chemical reaction. The inputs of operator C are the concentrations and temperature at time t and the outputs are the same variables time Δt later. It has been shown that the method of operator splitting is well applicable for the calculation of deflagrations (see Ref. 15 and citations therein). Operator C is also well applicable in turbulent flame calculations using the probability density function (PDF) approach (see e.g., Ref. 16).

The concentrations of all those species have to be calculated by Eq. (1), which are interesting for the purposes of the simulation. The chemical term B usually determines other species, which have an influence on the concentration of important species (and temperature) and which have to be calculated as well. The fewer chemical substances considered, the faster the calculation of transport. The chemical term is also the source of another problem. The chemical equations are usually very stiff, and therefore, a small time step has to be used for the solution of Eq. (1), even if the accuracy and stability of transport equation allowed a longer time step. This problem is eliminated when the operator-splitting method is used, but evaluation of operator C is time-consuming due to the stiffness of the kinetic equations.

The repro-modeling technique can be used for the calculation of both chemical rates B and operator C. The repro-model uses the minimal number of state variables, which influence the selected state variables. Creation of the repro-model starts with the

creation of a big table, which consists of some selected state variables and information about their rates. The procedure can be summarized by the following steps.

Tabulation of Variable Value-Rate Relationships

Due to the existence of diverse timescales and conservation relations, chemical changes in a longer timescale have much less degree of freedom than the number of species. As a first guess, $n = n_t - n_f - n_c$ slow variables have to be selected from the state variables. Since some of the slow variables may be redundant in the original chemical mechanism, the final repro-model may contain even less variables. A good fit can be obtained if the repro-model has equal to or more variables than the degree of freedom of the mechanism. This provides a suggestion for the degree of freedom in an indirect way. However, a repro-model with less variables is not senseless since the error induced by the inadequate number of variables is minimized as a consequence of the least-squares fit.

Proper preparation of the table is the crucial step of repro-modelling. Values of the selected n state variables (e.g., temperature and some concentrations) have to cover the whole region where the mechanism is intended to be used. In the case of a working reactive flow model, a possible solution is to use the model with several representative input data and record the input and output of chemical kinetic calculations, i.e., the values and rates of selected variables. If the construction of the final model is impossible, then probing the chemical mechanism with similar concentrations and temperatures can be carried out using spatially homogeneous or one-dimensional calculations. It is important that the recorded rates must belong to relaxed values of fast variables, and therefore, the rates obtained, for example, from spatially homogeneous calculations, have to be recorded only after some initial induction time.

The rate information collected may be either the time derivative of the variables or the changes of variables during time Δt. In the first case, the repro-model can be used for the calculation of chemical rates B in Eq. (1). In the second case, the repro-model is applied as chemical operator C in Eq. (2). In this case, the table has to contain the values of state variables at time t and their values Δt time later. Time interval Δt has to be chosen according to the stability and accuracy requirements of the transport calculations and to keep the error induced by the operator splitting low.

The table obtained resembles the table that is the final result of the intrinsic low-dimensional manifold method. The main difference is that the input variables do not form a grid, and therefore, a fast search in the table is impossible. If the table is prepared carefully, it contains rate information for all regions where the repro-model is intended to be used. The table of the low-dimensional manifold method also contains information for nonrealistic combinations of state variables.

Fitting a Polynomial to the Data of the Table

If the physical model suggests some special functions, then these functions have to be used for fitting the table. In our case, there are no such "natural" functions, and any function is good, which is simple and flexible. Our choice is the application of high-order multivariate polynomials. As a general tenth-order five-variable polynomial has 3003 coefficients, application of such polynomials is only feasible if most of the parameters are set to zero, and there are at most a few dozen nonzero parameters. The fitting procedure has to be suitable for fitting a polynomial to tens of thousands of data points, determining the noneffective parameters of the polynomial and fitting the remaining parameters using the method of least squares. An algorithm, which meets these requirements, was described in detail in a recent article [13]. A series of polynomials, having a discrete orthonormal property on the input data set, is constructed and used for the least-squares approximation. Orthonormal polynomials, which do not decrease the root-mean-square error more than a predefined limit, are rejected, and only the effective orthonormal polynomials are used for the construction of the approximating polynomial. In the final step, the sum of orthonormal polynomials is converted into a single multivariate polynomial.

It is well known that the evaluation of polynomials can be made faster using appropriate factorization. In the case of a single variable, the generation of a Horner equation is straightforward. An algorithm was given in Ref. 13 for the construction of multivariate Horner equations, and a FORTRAN program was provided, which produced a FORTRAN function including the multivariate Horner equation. Evaluation of such functions is very effective on computers with scalar processors. However, this function is not easy to parallelize, and therefore, a new variant for the construction of FORTRAN functions is also used here. In this version, the powers of variables are calculated sequentially and these values are used during the calculation of monomials. While this version is less effective on scalar computers, the calculation of monomials is independent here, and therefore, it is expected to be faster on multiprocessor computers.

The set of FORTRAN functions obtained represents the reduced mechanism.

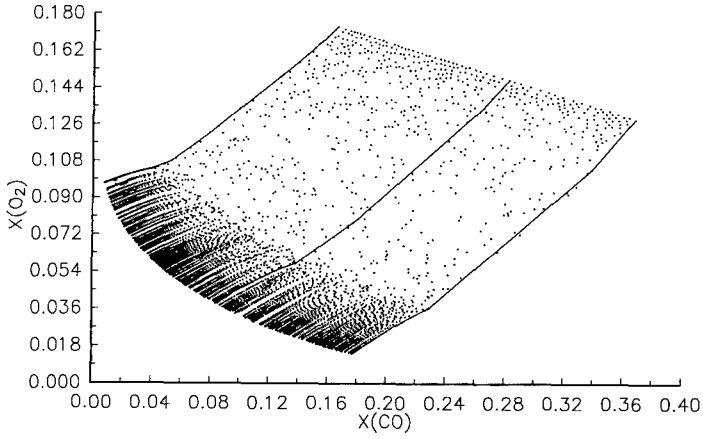

FIG. 1. Carbon monoxide–oxygen phase plane. The solid lines give the trajectories corresponding to a starting temperature of 1000 K and fuel-to-air ratios 0.5, 1.0, 1.5, respectively, until simulation time 0.01 s. The upper ends of the lines belong to the initial unburned mixture. In the case of the simulations applied for the preparation of the table, the initial composition of the mixture was uniformly distributed between $\phi = 0.5$ and 1.5. Dots represent the dependent variables CO and O_2 used in the table. Only a part of 30,000 data points are plotted on the figure for clarity.

Example: Ignition of a Wet Carbon Monoxide-Air Mixture

To promote a direct comparison with the results described in the papers by Maas and Pope [7,8], the mechanism used in those papers is used here without modification. In accordance with Ref. 7, the repro-modeled process is the ignition of a carbon monoxide–hydrogen air mixture at 1-atm constant pressure with a hydrogen-to-carbon atom mole ratio of 1:10.

Our aim was to create a repro-model that describes the combustion of wet CO at ambient temperatures between 990 and 1010 K and fuel-to-oxygen ratios from 0.5 to 1.5. The choice of these limits is arbitrary. Wider limits can also be chosen or different repro-models can be used for different regions of ambient temperature and concentrations. As Maas and Pope have successfully used tables with one and two chemical species concentrations, as a first step, two species concentrations and temperature were selected as variables of the repro-model.

All in all, 300 initial conditions, uniformly distributed within the above limits, were selected by a random number generator and used in spatially homogeneous simulations. The calculations were carried out by program SENKIN [17]. Temperature and mole fractions of CO and O_2, together with their rate information, were recorded at every 10^{-4} s until the final simulation time of 0.01 s. The distribution of the input variables of the table is illustrated in Fig. 1. The rate information was the values of these three variables one time step (10^{-4} s) later. The table contained $300 \times 100 = 30{,}000$ entries, but the rate information belonging to the initial induction time, when the concentrations of QSSA species have not reached their quasi-stationary value, was not used. Therefore, data with a temperature above 1100 K were used only, and these approximately 20,000 data were fitted by the polynomial.

Fitting fourth-order polynomials to the data took about 25 s on an IBM RISC 6000/340 workstation. For the rates of the three variables, polynomials with 22–25 nonzero parameters were fitted. The average deviations between the tabulated rates and the fitted values were below 0.26%.

```
 function h31(y)
 implicit real*8(a-h,o-z)
 dimension y(*), a(22)
 data a/        1.25887E+04,-9.64505E+00,-4.77828E+04, 6.51249E+01,
*-1.27202E+01,-1.73475E+04,-2.09878E+04,-8.07198E+04, 1.70698E-06,
*-2.62401E-02, 1.73978E-02, 2.16879E+01, 1.51500E+04,-1.13259E+06,
*-3.28281E-10, 3.26475E-06,-4.65053E-06, 1.36031E-03, 3.39191E+02,
* 7.03503E+04, 1.98323E+06, 3.01339E+06/
 h31    =a(1)+y(3)*y(3)*a(8)+y(2)*(a(3)+y(3)*(a(7)+y(3)*(a(14)+y(3)*
*a(22)))+y(2)*(a(6)+y(3)*y(3)*a(21)+y(2)*(a(13)+y(3)*a(20))))+y(1)*
*(a(2)+y(3)*(a(5)+y(3)*a(12))+y(2)*(a(4)+y(3)*y(3)*a(19))+y(1)*(y(3
*)*a(11)+y(2)*(a(10)+y(2)*a(18))+y(1)*(a(9)+y(3)*a(17)+y(2)*a(16)+y
*(1)*a(15))))
 return
 end
```

FIG. 2. An example for a computer-generated multivariate Horner equation. The repro-model obtained consists of a set of such FORTRAN functions. This function calculates the temperature 10^{-4} s later, given the temperature and mole fractions of CO and O_2.

The fitting program provided the powers of variables in each monomial and the corresponding coefficients. These data were converted to a FORTRAN function by the appropriate program that created multivariate Horner equations. An example for the obtained function is given in Fig. 2. Another program produced alternative FORTRAN functions. In these functions, the powers of variables are calculated sequentially and then applied for the independent calculation of monomials.

Recursive calculation of the values of variables resulted in temperature-time and concentration-time curves. A sample result for such a calculation is given in Fig. 3. The repro-model was randomly checked using other initial conditions within the limits applied in the preparation of the repro-model, using initial temperatures greater than 1100 K only. In a series of such calculations, similarly good agreement was obtained to the SENKIN solution.

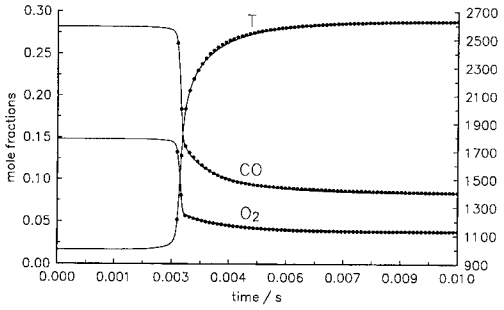

FIG. 3. Concentration-time and temperature-time curves for 1000 K initial temperature and a stoichiometric mixture. Solid lines represent the SENKIN solution, and dots were calculated using a three-variable repro-model. Calculation of the curves with the repro-model was 11,700 times faster.

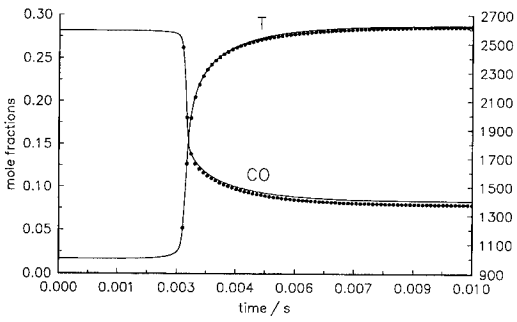

FIG. 4. Concentration-time and temperature-time curves for the same initial concentrations as in Fig. 3. Solid lines represent the SENKIN solution, and dots were calculated by a two-variable repro-model. Calculation of the curves with the repro-model was 24,000 times faster.

When the polynomials were calculated without any factorization, the repro-model calculation was 68 times faster than the SENKIN simulation. Applying independently calculated monomials, the repro-model was already 2220 times faster. Using the multivariate Horner equations, calculation of time curves with the repro-model was 11,700 times faster than the simulations with the full mechanism using program SENKIN.

In a similar way, a two-variable repro-model was also prepared. The two variables selected were temperature and mole fraction of CO. In this case, fifth-order polynomials gave a better fit to the tabulated data. The temperature-time and CO concentration-time curves obtained are given in Fig. 4. Now, the agreement is not as perfect as in the previous case, but it is still good. In this case, the repro-model calculation was 162, 5300, and 24,000 times faster than the SENKIN simulation, using the direct calculation of polynomials, the independently calculated monomials, and the multivariate Horner equations, respectively.

Comparison of the Features of the Three Methods

QSSA:

Preparations

Setting the left-hand side of the kinetic ODEs for the QSSA species to zero always provides algebraic equations for the concentrations of QSSA species. The numerical solution of these equations is very time-consuming [3], and therefore, in practical applications, explicit expressions have to be derived for the calculation of the concentration of QSSA species. Since the conversion of a system of algebraic equations to explicit expressions is not always possible even using algebraic manipulation programs [3], in most cases, the algebraic equations have to be truncated [18]. Note that the CSP can provide hints for such a truncation. Explicit expressions can be supplemented by inner iteration for some QSSA species [19]. Anyhow, the generation of a reduced model containing explicit QSSA expressions always requires significant human effort. On the other hand, identification of QSSA variables provides a physical insight into the model.

Accuracy

It is well known that the QSSA is a first-order approximation only [20]. In principle, much more accurate higher-order QSSAs can be derived as well [21], but generation of such approximations is only possible in the case of small systems.

Further errors are induced when the algebraic equations are truncated. Application of partial equilibrium for some species can also be considered as a truncated QSSA equation.

Yield in computer time

Although the calculation of rates requires the previous calculation of the concentration of QSSA species, the evaluation of the rate equations is very fast. Unfortunately, there are no data for computer time yield for this system, but in the case of mechanisms of similar size, application of QSSA usually results in 20–50 times increase in calculation speed.

Limitations

As in the case of the other two methods, the QSSA is not applicable until the radical concentrations have approached their QSSA values, i.e., a short time interval after the ignition. It has been demonstrated in several cases that the same QSSA equations are applicable for a wide range of conditions.

The Intrinsic Low-Dimensional Manifold Method:

Preparations

Generation of the tables has not been automated and requires considerable human effort. The rates are calculated by a special program that has not been published.

Accuracy

The calculated rates correspond to a high-order QSSA and, therefore, can be more accurate than the rates calculated by the QSSA. This feature becomes apparent at low temperatures. Using adaptive gridding in the preparation of the table, the interpolated values can also be accurate, but at the expense of significantly increased size of the tables.

Yield in computer time

Finding the nearest entries in the big table is very time-consuming, and therefore, the calculation of the rates is much slower than by the QSSA. Note that this drawback of the method could have been eliminated if the information of the table were stored in multivariate polynomials. For the wet CO ignition example, this method was 16 times faster than the simulation of the full mechanism [8].

Limitations

The table contains information for every combination of species concentrations, provided that they remain within predefined limits. The table becomes too big if the number of variables is more than five. In case of reaction diffusion systems, this limit seems to be too tight. Application of polynomials, instead of tables would also solve this problem. Note that application of polynomials instead of look-up tables is a good alternative in the case of turbulent-flame calculations as well.

Repro-Modeling:

Preparations

The original simulation program with minor modifications can be used for the generation of the table. The table has to contain data for all realistic combinations of the state variables, and preparation of such a table requires attention. Fitting of the polynomials and conversion of the polynomials to a Horner form requires small programs, which are available from the author.

Accuracy

The table contains not approximated rates but the "real" rates of variables. The polynomials approximate the tabulated values with an accuracy well below 1%.

Yield in computer time

When the repro-model provides the rates of state variables, these rates are calculated from the values of variables in one step and not in two stages like in the case of QSSA calculations. Calculation of QSSA concentrations might involve time-consuming calculation of square roots, while the equations of the repro-model are always polynomials, which can be evaluated very quickly using their Horner form. Therefore, application of repro-models allows faster calculations of rates than using the quasi-steady-state approximation. Then, the calculated rates are used in the usual simulation models.

When the repro-model provides the changes of state variables over time Δt due to chemical reactions, the solution of stiff kinetic equations is replaced by the evaluation of polynomials. This version allows a several thousand time increase in the speed of the calculation of chemical changes.

Limitations

The repro-model contains information only for the conditions of the simulations used for the generation of the tables. However, these conditions can be very wide, and also, different sets of polynomials can be used for different conditions.

There is very little experience on the maximum applicable number of variables in a repro-model. Repro-models with 13 and 15 variables have been reported (see Refs. 12 and 11, respectively). This limit seems to be rather high, which might allow the application of repro-modeling in reaction-diffusion calculations for most of the fuels.

Conclusions

This paper represents the first application of repro-modeling to combustion simulations. Several other variants of this technique have been used in other areas of computer modeling, especially in air quality simulations. Repro-modeling seems to be competitive to previous mechanism reduction procedures, considering the human effort needed and the accuracy compared to the full mechanism. Furthermore, repro-models allow about two orders of magnitude faster calculation of chemical changes than the reduced mechanisms obtained in the usual way.

Further work is needed for a detailed assessment of the possibilities of repro-modeling in combustion. A series of repro-models has to be produced for the combustion of other fuels and for other reaction conditions. In each case, the relation of efficiency and accuracy to the number of variables and parameters of the repro-model has to be investigated. Potentially, the most important field of application of repro-modeling is the simulation two- and three-di-

mensional deflagrations and of turbulent flames. Insertion of repro-models into laminar and turbulent flame codes also requires further work. These planned calculations will reveal the scope and limitations of repro-modeling in combustion science.

Acknowledgment

The author is thankful for the helpful discussions with Drs. J. Tóth, A. S. Tomlin, D. A. Goussis and with Professor G. Stoyan. The work was partially supported by the Hungarian Science Foundation (OTKA Project No. F014481).

REFERENCES

1. Turányi, T., *New. J. Chem.* 14:795–803 (1990).
2. Bodenstein, M., and Lütkemeyer, H., *Z. phys. Chem.* 114:208–236 (1924).
3. Turányi, T., Tomlin, A. S., and Pilling, M. J., *J. Phys. Chem.* 97:163–172 (1993).
4. Williams, F. A., *Combustion Theory*, 2nd ed., Addison-Wesley, Redwood City, 1985, p. 566.
5. Lam, S. H., and Goussis, D. A., *Twenty-Second Symposium (International) on Combustion*, The Combustion Institute, Pittsburgh, 1989, p. 931.
6. Lam, S. H., *Combust. Sci. Technol.* 89:375–404 (1993).
7. Maas, U., and Pope, S. B., *Combust. Flame* 88:239–264 (1992).
8. Maas, U., and Pope, S. B., *Twenty-Fourth Symposium (International) on Combustion*, The Combustion Institute, Pittsburgh, 1993, p. 103.
9. Meisel, W. S., and Collins, D. C., *IEEE Trans. Syst. Man. Cyber.* 3:349–358 (1973).
10. Dunker, A. M., *Atm. Environ.* 20:479–486 (1986).
11. Marsden, A. R., Jr., Frenklach, M., and Reible, D. D., *JAPCA* 37:370–376 (1987).
12. Spivakovsky, C. M., Wofsy, S. C., and Prather, M. J., *J. Geophys. Res.* 95D:18433–18439 (1990).
13. Turányi, T., *Comput. Chem.* 18:45–54 (1994).
14. Yanilmaz, M., *Comput. Elect. Eng.* 17:267–282 (1991).
15. Wichman, I. S., *Combust. Flame* 83:240–252 (1991).
16. Sion, M., and Chen, J.-Y., *Combust. Sci. Technol.* 88:89–114 (1992).
17. Lutz, A. E., Kee, R. J., and Miller, J. A., "SENKIN: A Fortran Program for Predicting Homogeneous Gas Phase Chemical Kinetics With Sensitivity Analysis," Sandia National Laboratories, Sandia Report No. SAND87–8248, 1988.
18. Mauss, F., and Peters, N., in *Reduced Kinetic Mechanisms for Applications in Combustion Systems* (N. Peters and B. Rogg, Eds.), Springer, Berlin, 1992, p. 64.
19. Wang, W., and Rogg, B., in *Reduced Kinetic Mechanisms for Applications in Combustion Systems* (N. Peters and B. Rogg, Eds.), Springer, Berlin, 1992, p. 82.
20. Bowen, J. R., Acrivos, A., and Oppenheim, A. K., *Chem. Eng. Sci.* 18:177–188 (1963).
21. Li, G., Tomlin, A. S., Rabitz, H., and Tóth, J., *J. Chem. Phys.* 99:3562–3574 (1993).

Twenty-Fifth Symposium (International) on Combustion/The Combustion Institute, 1994/pp. 957–963

ANALYSIS OF A SYSTEMATICAL REDUCTION TECHNIQUE

L. M. T. SOMERS AND L. P. H. DE GOEY
Faculty of Mechanical Engineering (WOC)
Eindhoven University of Technology
PO Box 513, 5600 MB Eindhoven, The Netherlands

The systematical reduction of chemical reaction mechanisms is studied by using a first-order sensitivity analysis. Two important aspects in the reduction strategy are considered here: the identification of the steady-state species and the truncation of the resulting algebraic equations for these species. The analysis is applied to the four-step model of Peters et al. based on the skeletal mechanism for lean methane-air combustion.

The identification of the steady-state species with the sensitivity analysis confirms the choices made by Seshadri and Peters. Even more, with the analysis it is predicted that the differences in burning velocity between the four-step mechanism and the skeletal mechanism can be reduced, by taking CH_3 not in steady state, effectively yielding a five-step model.

The effect of truncation is also investigated, and the differences of several approximations in the four-step model are studied systematically. With the sensitivity analysis introduced here, we are able to predict the qualitative effect of truncation. Applied to the truncation of the expression for OH mole fraction, it shows that the performance of the four-step model can be improved considerably if another reaction is included in this expression. The computations of the burning velocity with this "extended" OH expression confirm the prediction.

It can be concluded that the presented sensitivity analyses can be used effectively to analyze and determine systematically reduced mechanisms.

Introduction

Currently, simple flame systems are easy to model for almost any fuel as long as the detailed chemical mechanism is known. Some simple more-dimensional systems (see Ref. 1) can be modeled using complex chemical reaction mechanisms. These calculations give large sparse matrix equations, with a leading dimension proportional to $N_s \times N_p$, where N_s is the number of species and N_p is the number of mesh points. However, for the development of engineering tools to model realistic (domestic) burner systems or for the direct computation of large-scale reactive flow configurations, detailed models are still impractical. To perform modeling studies of this type, reducing the problem size (through N_s) and reducing the stiffness in the equations is the best way to proceed.

In the early years of combustion modeling, so-called global reaction models were used frequently. Today, most modeling studies on more-dimensional reactive flows still use a global reaction model [2,3]. However, these global reaction models suffer from important drawbacks. The fitting parameters are specific for the composition of the fuel for which they are obtained and cannot be guaranteed to apply for different types of flames. Furthermore, these global models cannot provide information for species like NO. Since exhaust limitations due to governmental regulations become more and more important, this limits the use of a global reaction model as an engineering tool for commercial purposes. In recent years, new approaches have been introduced to reduce the problem size (and stiffness) of the reactive flow equations, still keeping the essential information of the detailed chemical model (computational singular perturbation [9,10] and mathematical reduction techniques [5,6]).

In this paper, we present a study of the so-called systematic reduction of detailed chemical mechanisms [12]. This technique reduces the size of the matrix equations to be solved, is less specific for the type of flame considered, and retains the information on specific species. Unfortunately, much of the effort necessary to deduce a reduced mechanism is related to the experience of the researcher.

A systematic approach to deduce a systematically reduced mechanism, using first-order sensitivity analysis, is presented. The concepts of the systematical reduction technique are briefly introduced in the next section. In the subsequent section, the specific implementation of a sensitivity analysis is introduced. The method is applied to the four-step premixed methane-air mechanism of Seshadri and Peters [12]. Finally, it will be shown that effects of steady-state approximations and truncation of the steady-state ex-

pressions can be analyzed using special sensitivity analyses. These analyses are confirmed by the premixed flame computations.

General Principles

Generally reactive flows are described by the conservation of mass, momentum, and energy together with balance equations for every species in the mixture and the equation of state. For the isobaric premixed adiabatic one-dimensional flame, these can adequately be approximated by the set of equations given by Smooke et al. [14].

To tackle the equations numerically, we apply a finite-volume discretization, as proposed by Thiart (or Ghilani and Larrouturou) [8,7], and put all equations in a residual formulation, yielding

$$r_{ij} = s_{ij} + a_{ij}y_{i(j-1)} - b_{ij}y_{ij} + c_{ij}y_{i(j+1)} \tag{1}$$

where j is the mesh index and $y_i (i = \ldots N_s + 2)$ is a compact notation for the species mass fraction $i \in [1, N_s]$, the temperature $i = N_s + 1$, and the mass flow rate $i = N_s + 2$. The source terms s_{ij} are equal to $M_i\omega_i$ for the species and $-\sum_{i=1}^{N} h_i\omega_i$ for the temperature variable, where M_i is the molar mass and h_i is the molar enthalpy of species i. To find the steady-state solutions of these coupled equations, we employ a modified damped Newton–Raphson method:

$$\Delta \mathbf{y}^{n+1} = -\lambda^n \mathbf{J}^{-1}\mathbf{r}^n \tag{2}$$

where n is the iteration index and the Jacobian matrix $\mathbf{J} = \partial\mathbf{r}/\partial\mathbf{y}$, combined with a time-stepping algorithm whenever Newton's method fails. The Jacobian is only re-evaluated periodically. The structure of this matrix equation is determined by the ordering of the variables in the vector $\mathbf{y}$. Grouping the variables and residuals per mesh point leads to the well-known block-tridiagonal Jacobian matrix equation [11], which can be solved easily. The computations with the four-step and detailed chemical models are performed with this approach.

Effectively, the objective of the systematic reduction strategy will be the replacement of the (partial) differential equations for some species by algebraic expressions that, in principle, reduces the computational effort. In general, the reduction strategy is based on two distinctive tasks. First, there is the actual reduction of the number of differential equations that has to be solved. This directly leads to a quadratic decrease of the dimension of the Jacobian matrix, which now will contain $(N_s^n + 2) \times (N_s^n + 2)$-blocks instead of $(N_s + 2) \times (N_s + 2)$ for detailed computations. Here we introduced N_s^n for the number of species that are not considered to be in steady state. Almost as important is the second aspect in these models: the so-called truncation of the algebraic expressions for the species that are to be considered in steady state.

Two important features in the systematic reduction of the detailed chemical mechanisms are the steady-state approximation and the partial equilibrium approximation. The application of both assumptions is straightforward. The only difficulty is the identification of the species for which the steady-state assumption applies best and the manipulation of the resulting algebraic set of equations [12,14,15].

The Use of Sensitivity Analysis to Identify Steady-State Species:

The success of reducing the detailed chemical model is strongly related with the ability of applying the steady-state assumptions to the proper set of species. Classically, this is done by simply comparing the contributions of the different parts (convective, diffusive, and reactive terms) in the balance equation and a detailed investigation of the magnitude of the chemical source term. Many authors simply refer to the maximum weighted mole fraction of the intermediate species for the flame under consideration (see e.g., Ref. 12). For a group of intermediates, the weighted maximum mole fraction stays below 1 %. It is now common practice to consider this group to be in a steady state. The main argumentation for this observation is that due to fast reactions involving these species, reactions creating these species are effectively balanced with a set of reactions consuming it. Therefore, the maximum mole fraction stays low and the steady-state assumption applies.

Although this heuristic reasoning is often used, it is unsatisfactory since it gives no direct indication of the effect of the steady-state assumption on the flame structure or flame properties (such as the burning velocity). Here, we present a first-order sensitivity analysis that gives an indication of these effects. A sensitivity analysis, often used in combustion studies (see e.g., Ref. 13), deals with predicting the effect of a vector of parameters $\mathbf{k}$ on the observables $\mathbf{y}$, shortly written as $\partial\mathbf{y}/\partial\mathbf{k}$. Simple algebra now leads to

$$\mathbf{J}\frac{\partial \mathbf{y}}{\partial \mathbf{k}} = -\frac{\partial \mathbf{r}}{\partial \mathbf{k}} \tag{3}$$

where we used $d[\mathbf{r}(\mathbf{y}|\mathbf{k})]/d\mathbf{k} = 0$. Typically, this analysis can be performed as a postprocessor since the Jacobian $\mathbf{J}$ is already available and very little effort is needed to evaluate the sensitivities $\partial\mathbf{y}/\partial\mathbf{k}$ or the related weighted or logarithmic sensitivity matrix $\mathbf{S}_{\mathbf{y}}^{\mathbf{k}} = \partial \ln(\mathbf{y})/\partial \ln(\mathbf{k})$.

The use of a sensitivity analysis with respect to the systematic reduction of the detailed chemistry will be treated here. We will introduce a vector of

dummy parameters $\mathcal{T}$ in the residual formulation of the discretized equations, according to

$$r_{ij} = \mathcal{T}_i s_{ij} + a_{ij} y_{i(j-1)} - b_{ij} y_{ij} + c_{ij} y_{i(j+1)} \quad (4)$$

thus yielding the set $\mathcal{T}_i, i \in [1, N_s + 2]$ corresponding to the variables y_i. In the course of the flame calculation, these parameters are all fixed and equal to one and do not affect the solution. After the flame calculation, however, the sensitivity matrix $\mathbf{S}_{\mathbf{y}}^{\mathcal{T}}$ is evaluated. For any observable y_i, the smallest sensitivity coefficients, $\mathbf{S}_{y_{ij}}^{\mathcal{T}_{i'}}$, correspond to the variables $y_{i'}$, which can be considered in steady state. Specifically, if the main objective of the reduced mechanism to be derived is to predict the burning velocity and temperature profile well, the sensitivity coefficients $\mathbf{S}_{(S_L)}^{\mathcal{T}_{i'}}$ and $\mathbf{S}_{(T_j)}^{\mathcal{T}_{i'}}$ are to be considered, where the latter is a function of position (through j). The choice of the species $y_{i'}$ to be considered in a steady state will then be the ones that yield the smallest sensitivity $\mathbf{S}_{(S_L)}^{\mathcal{T}_{i'}}$ and $\mathbf{S}_{(T_j)}^{\mathcal{T}_{i'}}$.

The basic idea behind this method is observed in the following. It can be understood that a scaling of the residual r_{ij} according to

$$r_{ij} = \mathcal{T}_i [s_{ij} + a_{ij} y_{i(j-1)} - b_{ij} Y_{ij} + c_{ij} y_{i(j+1)}]$$

has no effect on the solution, as it is a global scaling. Therefore, a low sensitivity to the scaling applied in Eq. (4) indicates that the residual in good approximation behaves like

$$r_{ij} = s_{ij} \quad (5)$$

for species i, which is precisely the implementation of the residual of a steady-state species. Physically, this means that the mole fraction is determined by the balance of chemical production (ω_i^+) and chemical consumption ω_i^-, rather than a balance of diffusive, convective fluxes and the net chemical source term ω_i ($= \omega_i^+ - \omega_i^-$). We will refer to this type of analysis as the steady-state sensitivity in the following. Note that inerts will yield steady-state sensitivities that are small as well, although the physical reasoning sketched above is not valid in that case. However, like for reactants, steady-state assumptions never apply to species that are present in the fresh mixture, and the sensitivity for these species does not have to be considered. In fact, this steady-state sensitivity analysis should only be applied to species that are possible candidates, i.e., intermediates and product species.

The method is tested for the deduction of the earlier-mentioned four-step model based on the skeletal mechanism. We performed the sensitivity analysis for the adiabatic burning velocity and the temperature profile. In Fig. 1, we plotted the sensitivity of the burning velocity for some equivalence ratios between $\varphi = 0.6$ and $\varphi = 1.1$. Because of the large variation

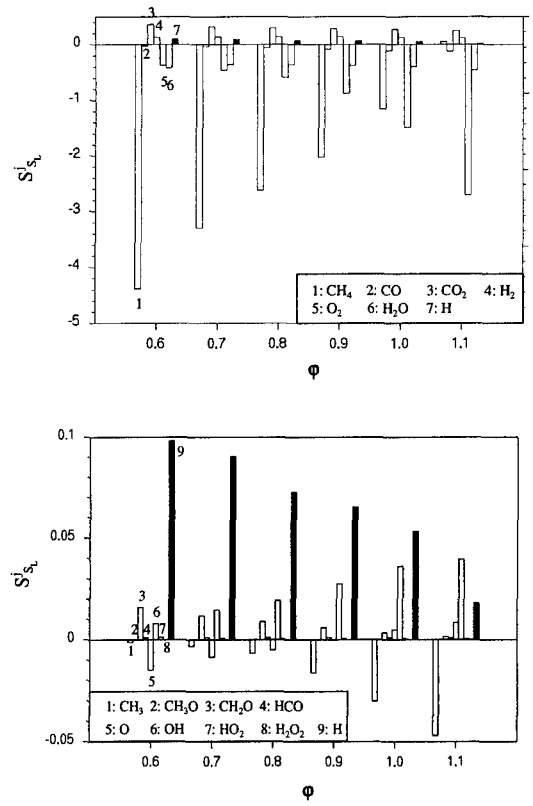

FIG. 1. The steady-state sensitivity of the burning velocity for lean flames. In the top figure, the major species are plotted. The steady-state species are given in the bottom figure. The sensitivity of the atomic hydrogen is plotted in both figures with a solid bar.

in magnitude, the values are separated in two groups, one involving only the species that are taken in steady state later on and one involving the others. For all equivalence ratios, the species that are chosen to be in steady state by Seshadri and Peters show the smallest steady-state sensitivity on the burning velocity. The steady-state sensitivity of the temperature profile for $\varphi = 0.9$ gives the same picture. We plotted only the steady-state species in Fig. 2. The sensitivities of the non-steady-state species are larger by orders of magnitude.

Both the steady-state sensitivity analysis of the burning velocity and the temperature profile confirm the choice for the steady-state species based on the weighted maximum mole fraction. However, this method gives a more straightforward approach to select the steady-state species and can in principle be "tuned" for these observables that are chosen to be predicted well by the reduced mechanism. The implementation is as easy as any "ordinary" sensitivity analysis at almost no extra costs.

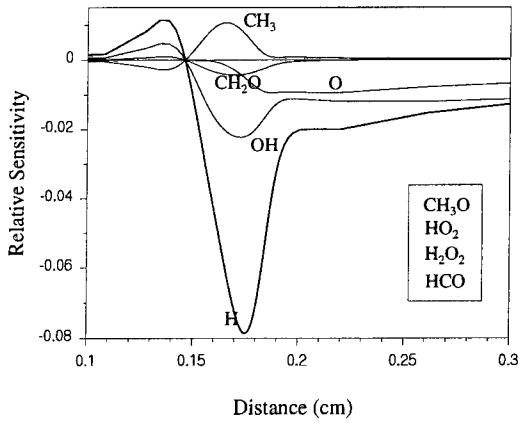

FIG. 2. The steady-state sensitivity of the temperature for $\varphi = 0.9$. Only the species for which a steady-state assumption is applied in the four-step model are presented. The profile of H is included as a reference. The species in the caption are not plotted since they are too low.

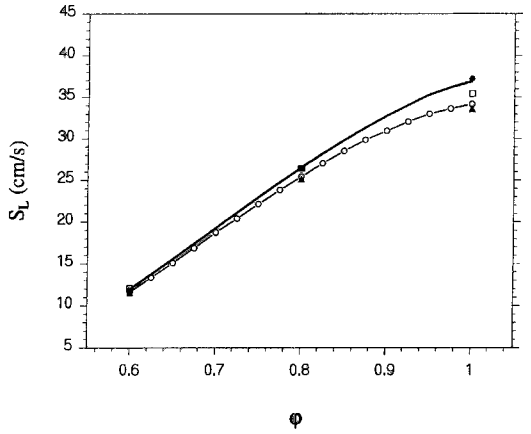

FIG. 3. Burning velocity S_L as a function of φ. The solid line is the full scheme calculation with constant Lewis numbers. The dotted line indicates the results of the computations with eight steady-state approximations and without any truncation (four-step scheme). At $\varphi = 0.6$, 0.8, and 1.0 computations are included where the steady-state assumption for CH_3 (●), O (open square), or OH (solid triangle) has been dropped, respectively (five-step model).

Results and Discussion

If the steady-state assumptions are applied to the skeletal mechanism to obtain a four-step model, we can eliminate at least one reaction rate for the eight species that are considered in a steady state. This process then gives the well-known four-step global mechanism with the reaction rates given by Seshadri and coworkers [12,14]. The set of algebraic equations that determine the mole fractions of the steady-state species are truncated and approximated in such a way that they yield an easy-to-evaluate explicit set of expressions. Here, we will investigate and predict the effect of several levels of approximation within the Peters model. First, we will study the effect of applying the steady-state assumption alone. The effects of truncation will be presented subsequently. It will be shown that a sensitivity analysis can be used to systematically analyze the effect of the different levels of approximation, for the application of the steady-state assumption as well as for the truncation of the steady-state expressions.

Analysis of the Effect of the Steady-State Assumption:

Normally, the objective of the reduced chemical model is to reduce the memory and CPU demand of a flame computation. However, if no truncation is used, the resulting set of algebraic equations for the steady-state species is nonlinear as well and is not easy to solve. Therefore, these expressions are often truncated in such a way that they form an easy-to-evaluate (sometimes explicit) set of equations. This procedure, however, introduces an extra approximation apart from the steady-state assumption, which may affect the solution.

To circumvent this and deduce the effects of the steady-state approximations alone, we modified our detailed flame code. For the steady-state species, we implemented approximation (5) directly. Since there is no other assumption introduced, this is the most accurate four-step model possible based on the skeletal mechanism and for the given steady-state assumptions. In Fig. 3, the resulting burning velocity is compared with the full calculation [using Eq. (1) instead of approximation (5)] as a function of the equivalence ratio φ. On the lean side, the four-step model predicts the burning velocity well. Near the stoichiometric point, the difference increases to approximately 3 cm/s. The calculations with the five-step model (indicated with symbols at $\varphi = 0.6$, 0.8, and 1.0) show that this difference can be reduced by taking CH_3 not in steady state. This effect can be predicted with the use of the sensitivity analysis. In Fig. 1, it can be seen that the steady-state sensitivities at stoichiometric conditions for CH_3 and O are comparable with that of H. However, the sensitivity of the methyl radical, with respect to the burning velocity, has a negative value. This indicates that applying the steady-state assumption to CH_3 will lower S_L. Obviously, taking CH_3 not in steady state will increase it, which is confirmed by the results of the five-step calculation. Similarly, since the sensitivity of the hydroxyl radical has a positive sign, leaving OH out of the set of steady-state species will lead to a further decrease of the burning velocity. This is con-

firmed by the direct calculation. For matters of completeness, we included results of the five-step model with the O radical excluded as well in Fig. (3). Since the magnitude of the steady-state sensitivity of this species is much lower than that of OH and CH_3, we observe a smaller effect in Fig. (3).

It should be stressed that this implementation of a four-step model does not lead to a reduction of the problem size. For modeling purposes, it does not perform "better" than a detailed calculation. It is, however, easy to implement and gives an ideal tool to predict the fundamental limits of any systematically reduced model.

Analysis of the Effect of Truncation:

To have any advantage of the implementation of a four-step model, the set of coupled algebraic nonlinear relations for the steady-state species have to be replaced by easy-to-evaluate, preferably explicit equations. For the skeletal mechanism, Seshadri and Peters truncate this set of algebraic equations. The numbering of the reaction rates $k_i^{f,r}$ that is used corresponds to one introduced by Smooke [14]. For future use, we slightly modify the original expression for the OH radical:

$$[\mathrm{OH}] = \frac{[\mathrm{H_2O}][\mathrm{H}]k_3^r + [\mathrm{H}][\mathrm{O_2}]k_1^f}{[\mathrm{H_2}]k_3^f + [\mathrm{O}]^* k_1^r}. \qquad (6)$$

The other expressions are identical to the ones given by Seshadri and Peters [14]. The set of equations is explicit, for known temperature and concentrations of non-steady-state species, only if partial equilibria (r_3 and r_4) are used for the expression for $[\mathrm{O}]^*$ in Eq. (6), yielding

$$[\mathrm{O}]^* = \mathrm{K}_3^2/\mathrm{K}_4 \frac{[\mathrm{H_2O}][\mathrm{H}]^2}{[\mathrm{H_2}]^2}. \qquad (7)$$

To systematically analyze the effect of this last assumption alone on the flame properties, we performed calculations for the expression for $[\mathrm{O}]^*$ with the complete expression for [O] as given by Seshadri and Peters also. Furthermore, from a sensitivity analysis, it was found that the inclusion of reaction 15 in the expression for OH would lead to an improved prediction of the burning velocity; we performed calculations with this reduced model as well. The studies we will perform differ only in the expression for [OH], which is applied. The equations for the other steady-state species remain unaltered. The three test cases are briefly summarized below.

Test case A: expression (6) + partial equilibrium expression (7) for $[\mathrm{O}]^*$.

Test case B: expression (6) + $[\mathrm{O}]^*$ equal to [O] given by Seshadri and Peters [14].

Test case C: like test case B with r_{15} included in expression for [OH].

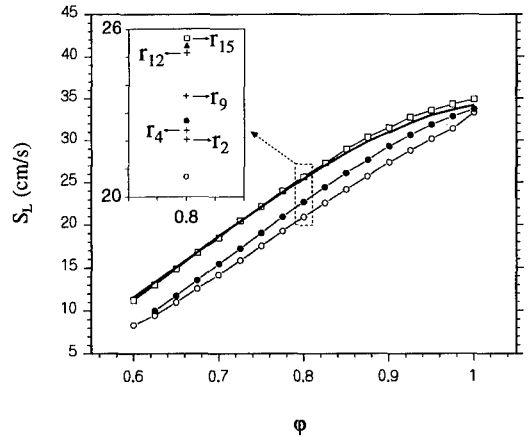

FIG. 4. Burning velocity S_L as function of φ. The solid line is a full four-step reference calculation without truncation. The dotted (○) line refers to test case A. The dotted (●) line represents the results obtained with the model defined in test case B. Test case C is indicated with the square symbols (□). The $\varphi = 0.8$ results are represented again in the upper part of the figure. The effect of inclusion of reactions r_2, r_4, r_9, r_{12} (+ marks), and r_{15} (□) in the expression for [OH] is presented. The "untruncated" four-step calculation is now indicated with the solid triangle.

Obviously, test cases B and C are not explicit, and the resulting set of coupled equations for the steady-state species has to be solved with some kind of iteration process. We use the so-called "inner iteration" procedure [4]. The other species and the temperature are modeled by using the Newton/time-iteration method mentioned earlier.

In Fig. 4, the burning velocities of the three test cases are compared with the values resulting from the "untruncated" four-step model mentioned in the previous section. The results show that due to the truncation of the steady-state expressions alone (●), a decrease of approximately 10% in S_L is introduced. Furthermore, if the partial equilibria (7) are introduced to render the expressions explicit, a further deviation (○) from the theoretical four-step model without truncation is introduced. The results obtained with test case C (□) indicate that the effect of the classical truncation can be canceled if reaction 15,

$$\mathrm{CH_2O} + \mathrm{OH} \rightarrow \mathrm{HCO} + \mathrm{H_2O}$$

is included in the expression for OH.

This effect can be predicted if an approach is used very similar to the steady-state sensitivity analysis. We computed the sensitivities S_{SL}^{gj} for all steady-state species in the "untruncated" four-step model implementation. In Fig. 5, we plotted these for the OH radical with respect to the reactions j for three equiv-

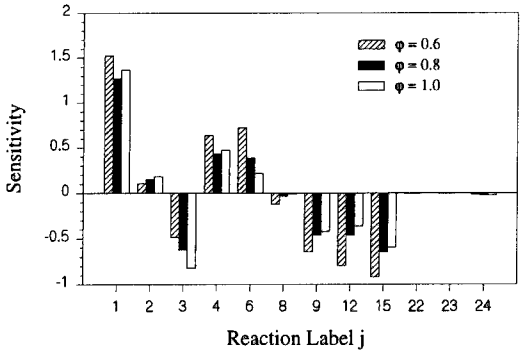

FIG. 5. The sensitivities $S_{S_L}^{\nu_{ij}}$ for the OH radical (i index) for the reactions j present in its source term $s_i = \Sigma_j \nu_{ij} q_j$ for three values of φ.

alence ratios. It is shown that reaction r_1 and r_3 show the largest sensitivities, which is in accordance with the assumptions made by Seshadri and Peters [12] [see also Eq. (6)]. For all three selected equivalence ratios, the sensitivity of reaction (15) is large as well. It is even larger than that of r_3 at $\varphi = 0.6$. To illustrate the implication of the value of the sensitivities $S_{S_L}^{\nu_{ij}}$, we performed several simulations at $\varphi = 0.8$. Starting with the result of test case B (●), for each simulation we included one of the reactions r_2, r_4, r_9, r_{12}, and r_{15} in the truncated expression for [OH]. To show the effect, we magnified the region around $\varphi = 0.8$ in Fig. 4 and inserted the simulations with cross marks + (r_{15}, (□)) in the left upper corner. It shows that a negative sensitivity has a positive effect on the burning velocity. Furthermore, there is a direct correlation between the magnitude of the sensitivity coefficient $S_{S_L}^{\nu_{ij}}$ and the effect of the inclusion of reaction j in the expression for species i on the burning velocity S_L. Since reaction (15) shows a large sensitivity for all three computed equivalence ratios (Fig. 5), this suggests that the inclusion of reaction (15) will lead to a higher burning velocity for the complete φ range that is found indeed.

From a numerical point of view, the use of reduced chemical models is justified only by the decrease of the computational effort. Since in most flame applications by far most of the CPU time is needed to evaluate the Jacobian, we will, therefore, consider this process in more detail. The leading dimension of the matrix Eq. (2) is reduced considerably. Now, 10×10 sub-blocks appear in the Jacobian instead of 18×18 sub-blocks for the full detailed model. This leads to a decrease in the (CPU expensive) Jacobian evaluation time, equal to 0.46, 0.52, and 0.53 for test cases A, B, and C, respectively. Although there is a decrease in the evaluation times, the reduction is not quadratic in the number of variables as might be expected. This is related with the implementation of the reduced model. We still calculate the rates of all the reactions present in the basic detailed chemical scheme. Furthermore, the transport and thermodynamical properties are still formulated in terms of all species. The steady-state species are evaluated prior to any residual computation, including the ones needed for the numerical evaluation of the Jacobian. Due to these reasons, the evaluation time t_f for one residual vector $\mathbf{r}$ will only be marginally shorter than that of the detailed chemistry implementation. It can thus be shown that the amount of work is then proportional to $(N_s^n + 2) \times t_f$, where N_s^n equals the number of non-steady-state species. Since in the detailed computation the effort is proportional to $(N_s + 2) \times t_f$, an implementation of a reduced model will lead only to a linear decrease in computation time, approximately equal to 10/18 ≈ 0.56, which indeed is observed previously. The difference between test cases A and B and C originates from the application of the "inner iteration" procedure applied in test cases B and C. Since test case A uses explicit expressions, only one "sweep" in the inner iteration loop is necessary to evaluate the steady-state species accurately. For both cases B and C, the steady-state equations are processed several times to obtain a sufficiently accurate solution for the steady-state expressions.

From a numerical point of view, this reduction of work remains the main advantage of the reduced model. The gain in CPU time might be increased if the evaluation of the chemical source terms is tuned to the reduced chemical model. It is worth mentioning that the so-called "Partial Explicit" approach proposed by Wang and Rogg [4] will only lead to a minor decrease in CPU time necessary to evaluate the Jacobian (a factor of 0.43 instead of 0.46 was found).

Conclusions

We presented two implementations of a first-order sensitivity analysis that can be used to deduce and analyze systematically reduced reaction schemes. The sensitivity analysis was applied to the four-step methane-air mechanism of Seshadri and Peters [12] and confirmed the choices made for the steady-state species. The steady-state sensitivities can be used to analyze the differences with the original detailed chemical model systematically. Even more, it can be used to minimize the differences between the original model and the reduced scheme.

A second implementation of the sensitivity analysis is described to predict the effects of the truncation of the expressions for the steady-state species. Using this analysis, we have shown that a slight modification to the truncated expressions for the [OH] radical could improve the predicted burning velocity by the four-step model for all modeled equivalence ratios in the range $0.6 \leq \varphi \leq 1.0$. Computations with the modified expression confirm this assumption.

It can be concluded that sensitivity analysis can be used to deduce and improve systematically reduced mechanisms. Both aspects, the identification of the steady-state species and the truncation of the resulting algebraic expressions, can be analyzed successfully.

Acknowledgments

The support of Gastec N.V. and NOVEM, The Netherlands, is gratefully acknowledged. The authors thank Professor J. K. Nieuwenhuizen for stimulating discussions and useful suggestions.

REFERENCES

1. Smooke, M. D., *Twenty-Fourth Symposium (International) on Combustion*, The Combustion Institute, Pittsburgh, 1992, p. 813.
2. Larrouturou, B., "An Introduction to Numerical Combustion," Paper No. ERCOF TAC Summerschool 1992, Aachen, Germany.
3. de Lange, H. C., Modelling of Premixed Flames., Ph.D. Thesis, Eindhoven Üniversity of Technology, The Netherlands, 1992.
4. Wang, W., and Rogg, B., in *Reduced Kinetics Mechanisms for Applications in Combustion Systems* (N. Peters and B. Rogg, Eds.), Springer-Verlag, Berlin, 1993, p. 76.
5. Maas, U., and Pope, S. B., *Combust. Flame* 88:239 (1992).
6. Eggels, R. L. G. M., and de Goey, L. P. H., "Mathematically Reduced Reaction Mechanisms Applied to Adiabatic Flat Hydrogen/Air Flames," *Combust. Flame* in press (1994).
7. Ghilani, M., and Larrouturou, B., *Math. Mod. Num. Anal.* 25:67–92 (1991).
8. Thiart, G. D., *Num. Heat Trans. B*, 17:43–62 (1990).
9. Lam, S. H., and Goussis, D. A., *Twenty-Second Symposium (International) on Combustion*, The Combustion Institute, Pittsburgh, 1988, p. 931.
10. Goussis, D. A., and Lam, S. H., *Twenty-Fourth Symposium (International) on Combustion*, The Combustion Institute, Pittsburgh, 1992, p. 113.
11. Smooke, M. D., Miller, J. A., and Kee, R. J., *Combust. Sci. Technol.* 34:79 (1983).
12. Seshadri, K., and Peters, N., *Combust. Flame* 81:96–118 (1990).
13. Rabitz, H., Kramer, M. A., and Dacol, D., *Ann. Rev. Phys. Chem.* 34:419–461 (1983).
14. Smooke, M. D., in *Reduced Kinetic Mechanisms and Asymptotic Approximations for Methane-Air Flames* (M. D. Smooke, Ed.), Springer-Verlag, Berlin, 1991, pp. 1–28.
15. Mauss, F., and Peters, N., in *Reduced Kinetic Mechanisms for Applications in Combustion Systems* (N. Peters and B. Rogg, Eds.), Springer-Verlag, Berlin, 1993, pp. 58–75.

Twenty-Fifth Symposium (International) on Combustion/The Combustion Institute, 1994/pp. 965–974

ANALYSIS OF THE REACTIONS H + N_2O AND NH + NO: PATHWAYS AND RATE CONSTANTS OVER A WIDE RANGE OF TEMPERATURE AND PRESSURE

JOSEPH W. BOZZELLI, ALBERT Y. CHANG AND ANTHONY M. DEAN
Corporate Research Labs
Exxon Research and Engineering
Annandale, NJ 08801, USA

We have analyzed H + N_2O by considering formation of chemically activated adducts with a master equation formalism to account for collisional stabilization. We consider four product channels for the addition of H atoms to N_2O:

$$H + N_2O = HNNO \tag{1a}$$

$$H + N_2O = N_2 + OH \tag{1b}$$

$$H + N_2O = NH + NO \tag{1c}$$

$$H + N_2O = NNH + O. \tag{1d}$$

The calculations are in good agreement with the available data. At higher temperatures, the NH + NO channel is predicted to be comparable to the N_2 + OH channel, while the NNH + O channel is less important but still significant. An interesting feature of the calculations is the suggestion that HNNO formation could be important at lower temperatures.

This same potential energy surface is also used to analyze the reaction between NH and NO. There are three principal product channels:

$$NH + NO = N_2 + OH \tag{2a}$$

$$NH + NO = N_2O + H \tag{2b}$$

$$NH + NO = NNH + O. \tag{2c}$$

Our predictions are in good agreement with the available data. Below 3000 K, H + N_2O is predicted to be the major channel for the NH + NO reaction. However, the NNH + O channel is predicted to be important at combustion temperatures and should be considered for inclusion in combustion models.

We recommend use of the following rate constants, in units of $cm^3\ mole^{-1}\ s^{-1}$ (T = 300–4000 K, unless specified otherwise):

$$k_{1a} = 8.0 \times 10^{24}\, T^{-4.39} \exp(-5300/T), \text{ for } T = 300\text{–}1200 \text{ K}, P = 1 \text{ atm } N_2$$

$$k_{1b} = 2.2 \times 10^{14} \exp(-8430/T), \text{ for } T = 1000\text{–}2000 \text{ K}$$

$$k_{1c} = 6.7 \times 10^{22}\, T^{-2.16} \exp(-18{,}700/T)$$

$$k_{1d} = 5.5 \times 10^{18}\, T^{-1.06} \exp(-23{,}800/T)$$

$$k_{2a} = 6.1 \times 10^{13}\, T^{-0.50} \exp(-60/T)$$

$$k_{2b} = 2.5 \times 10^{16}\, T^{-1.03} \exp(-420/T)$$

$$k_{2c} = 5.6 \times 10^{12}\, T^{0.21} \exp(-5470/T).$$

Introduction

The reaction between H and N_2O is quite interesting in combustion chemistry. For example, N_2O is an important intermediate formed during propellant combustion [1]. The reaction between H and N_2O is a key reaction in N_2O flames and one of the few that can convert N_2O into N_2, thus avoiding pro-

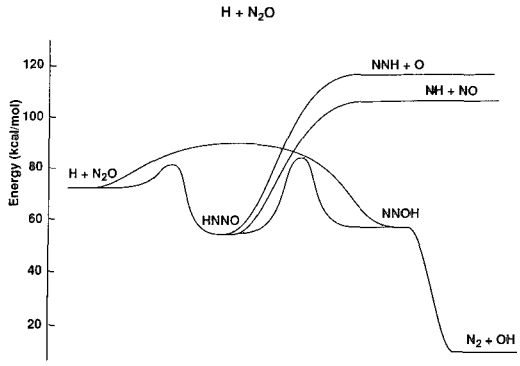

FIG. 1. Potential energy diagram for H + N_2O. Note that both adducts (HNNO and NNOH) can be formed directly from the reactants.

duction of undesirable nitrogen oxides in the atmosphere. However, an alternate channel produces NH + NO, thus serving as a source of NO. In addition, N_2O is an important greenhouse gas. As a result, it is important to understand the temperature and pressure dependence of these reactions so that appropriate rate constants can be included in combustion models.

A potential energy diagram, following Marshall et al. [2], for this reaction is shown in Fig. 1. Aspects of this system have also been addressed in several recent calculations [3–6]. Although some of these make the distinction between cis- and trans-HNNO, the overall features are reasonably similar to that shown in Fig. 1. We selected a barrier height of 9 kcal/mole for addition to form HNNO, since this value is representative of that calculated in the recent work. We use 18 kcal/mole for addition to form NNOH, since this is close to that obtained in all the calculations. Following Melius [5], we use a barrier of 29 kcal/mole for the isomerization.

There are four product channels for this reaction:

$$H + N_2O = HNNO \quad (1a)$$

$$H + N_2O = N_2 + OH \quad (1b)$$

$$H + N_2O = NH + NO \quad (1c)$$

$$H + N_2O = NNH + O. \quad (1d)$$

Figure 1 suggests that the major channels, particularly at lower temperatures, would be HNNO or N_2 + OH. At higher temperatures, the initially formed adduct could have sufficient energy to dissociate to one of the higher-energy exit channels. This reaction has a variety of interesting features. First, the H atom can add to either end of N_2O, which leads to different products. Also, the low entropy of H atoms leads to unusual equilibrium constants between the adducts, HNNO and NNOH, and the reactants, which is manifested as a relatively low A factor for dissociation of the adducts to reactants. Finally, there are data available for this reaction in both directions, providing a good opportunity to test application of chemical activation theory to this system. The goal of such an analysis is to understand the observed effects of temperature and pressure and then to use this understanding to extrapolate measured rate constants to other temperatures and pressures of interest.

Experimental Measurements

Reaction (1b) has been reasonably well characterized. Hidaka et al. [7] used a computer model in conjunction with their shock tube observations in N_2O/Ar and N_2O/H_2/Ar mixtures, while Marshall and coworkers [2,8] measured the reaction directly in a high-temperature photochemical experiment. There is a difference in the higher-temperature rate constants in the two photochemical studies. The authors point out that their earlier work employed a capped inlet that might have led to premature dissociation of some of the N_2O, thus introducing some error. As a result, we only consider the later data. These rate constants, as well as an earlier shock-tube modeling analysis by Dean et al. [9], are compared to the recommended values given by Hanson and Salimian [10] and Tsang and Herron [11] in Fig. 2.

Data for reaction (1c) are more scattered. The more recent information is shown in Fig. 3. Cattolica et al. [12] used measured NH and OH flame profiles in N_2O/H_2 flames to obtain estimates for this rate constant. The two shock-tube measurements of the reverse reaction [13,14] report markedly different values. Also included in this plot is the value obtained by using the recommended value given by Miller and Bowman [15] for the reverse reaction; their assignment is based primarily upon comparison of computed and experimental N_2O profiles in ammonia flames.

A confusing aspect of the NH + NO reaction is that it can yield multiple products:

$$NH + NO = N_2 + OH \quad (2a)$$

$$NH + NO = H + N_2O \quad (2b)$$

$$NH + NO = NNH + O. \quad (2c)$$

Mertens et al. [14] report a branching fraction for the N_2 channel $[k_{2a}/k_{tot}] = 0.19 \pm 0.10$ at 3000 K from measurements of NH and OH. Shock-tube measurements of emissions from electronically excited OH and NH in mixtures of HNCO/NO/Ar [16,17] were used with a complex model to infer a branching fraction of 0.32 ± 0.07 for the N_2 channel at 3500 K. However, an analysis of ammonia flames

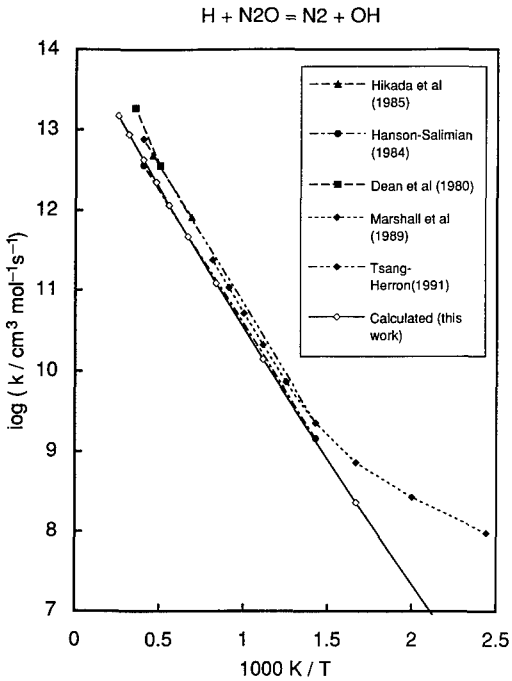

FIG. 2. Comparison of calculated and measured values for the rate constant for H + N_2O = N_2 + OH. The recommended value is that of Marshall et al., for temperatures above 1000 K. The calculations (P = 1 atm N_2) include contributions to this channel from both the HNNO and the NNOH adducts.

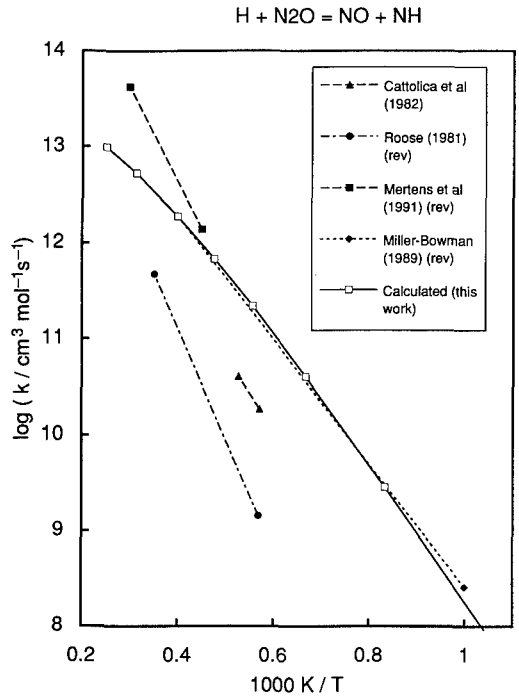

FIG. 3. Comparison of calculated and measured values for the rate constant for H + N_2O = NO + NH. (rev) signifies that the rate constant was obtained via the equilibrium constant from measurement of the reverse reaction. The calculated values are independent of pressure.

[18] suggests that the N_2 channel is 4–6 times larger than the N_2O channel at 2000 K. The more direct nature of the Mertens et al. experiments suggest that their data are the most reliable. At low temperatures, Harrison et al. [19] suggest that their measurements best be interpreted with the N_2 channel as being the dominant one. Yamasaki et al. [20] report direct measurements of OH at 300 K and claim that this is the exclusive channel. They also reported failure to detect H, confirming this assignment. However, very recent work by Durant [6] indicates H + N_2O is the dominant channel at room temperature, with a branching ratio of 0.8 ± 0.4. Calculations by Harrison and Maclagen [21] have been used to support the claim of OH + N_2 as the dominant channel. However, other calculations by Melius and Binkley [22] and by Miller and Melius [3] indicate that the N_2O channel is the predominant one over the entire temperature range. Recent modeling efforts in low-pressure, stoichiometric $H_2/N_2O/Ar$ flames [1] have used the branching fraction reported by Miller and Melius. Given this ambiguity concerning the low-temperature branching fractions, we have plotted the various reported values for the total rate constant for NH + NO in Fig. 4. Although the reported rate constants span a relatively narrow range of about 1 × 10^{13} cm^3 $mole^{-1}$ s^{-1}, there is a dramatic variation in reported temperature dependence. The high-temperature shock tube results exhibit a substantially different temperature dependence than the lower-temperature data or the calculations of Miller and Melius.

Calculations

A method to treat chemical activation systems was developed by Dean [23]. This provides a simple framework by which the effects of temperature and pressure can be readily understood and evaluated. This approach is based on the quantum version of the Kassel theory to estimate the dissociation rate of the energized adduct, often described as QRRK theory. The quantum Kassel approach has been used to analyze a variety of chemical activation reaction systems [24–28], where there was ample literature data to evaluate the predictions. It was shown to be successful in these applications.

Since this approach can use Arrhenius A factors from the literature, there is significantly less opportunity (or temptation) to adjust the input parameters.

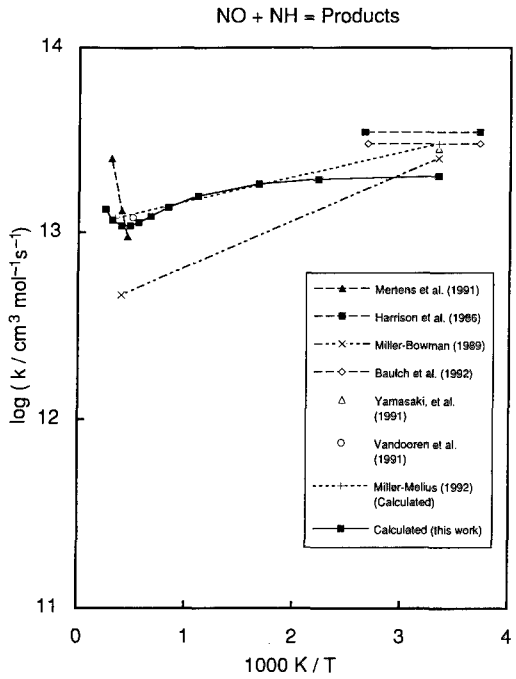

FIG. 4. Comparison of calculated and measured values for the rate constant for NO + NH = products. Note that our calculations indicate an increase in the rate constant at very high temperatures, in qualitative agreement with the data of Mertens et al.

Data required include high-pressure-limit A factors for dissociation of the adduct, which can be based on measured values or transition state theory (TST) estimates based on isoelectronic or structurally similar reactants with known kinetic parameters. We recommend use of the equilibrium constant in conjunction with the reverse reaction rate constant, since there is usually more data available for the reverse (bimolecular) reaction, or it is easier to provide a reliable estimate for this rate constant. This avoids the use of any adjustable parameters for the unimolecular dissociation and guarantees thermodynamic consistency. The information required for the quantum Kassel reaction analysis is available from the literature, from thermodynamic parameter estimation codes [29], TST calculation codes [30], and transport property estimation methods [31]. The reader is referred to a recent review [32] for further discussion of the QRRK technique.

Our initial analysis employed a single geometric-mean frequency for describing the energy distribution of the chemically activated adduct. Our most recent analysis [27] incorporated a three-frequency model to better represent the vibrational energy distribution of the adduct. The three frequencies and the associated degeneracies are computed from fits to heat capacity data, as described by Ritter [33]. These have been shown by Ritter to accurately reproduce molecular heat capacities and vibrational state densities. This approach offers the advantage of avoiding the specification of the complete frequency distribution of the adduct; for many of the molecules of interest, such information is unavailable. We believe that this three-frequency model provides a suitable approach to analyze both unimolecular falloff and bimolecular chemical activation reactions. The code has also recently been generalized to allow multiple wells to be connected in many ways.

The calculations reported herein are done using a master equation analysis to account for collisional stabilization, as opposed to use of the modified weak-collision assumption in our earlier work. In general, results for the major product channels are virtually identical. A detailed comparison will be the subject of a separate paper. The three-frequency model has been retained. However, the constant A term in the QRRK expression for $k(E)$ has been replaced by a temperature-dependent A factor. This accounts for curvature in $k^{\infty}(T)$. Although this approach is not rigorously correct, it gives comparable results to a more general inverse Laplace transform approach. Comparisons of these two methods to RRKM will be described in a forthcoming paper [34].

Results

The input parameters are listed in Table 1. (Note the use of a more complex form for $k(T)$; this was chosen to more accurately fit the rate constant over the extended temperature range of 300–4000 K.) We also explored use of a more complex system, with separate cis- and trans-isomers of HNNO, as described by both Walch [4] and Durant [6]; these results were very similar to those presented below. We prefer the simpler analysis, since there remains considerable ambiguity as to the relative energies of the isomers, cf. Walch. This reaction system is unusual in that the addition reaction to form HNNO has a higher effective A factor than the reverse unimolecular dissociation. This unusual case of a higher A factor for addition than for the (reverse) dissociation is a result of the low entropy of the reactants H + N_2O, combined with loss of a rotor in the dissociation. Thus, the HNNO adduct will have a significantly longer lifetime, leading to a higher probability of stabilization.

$H + N_2O = N_2 + OH$ and $H + N_2O = HNNO$

$N_2 + OH$ can be formed via both adducts. Addition of H to form NNOH will lead immediately to $N_2 + OH$, and the rate constant for production of $N_2 + OH$ via this channel is simply the rate of formation of the complex; no chemical activation cal-

TABLE 1
H + NNO = products

Reaction[a]	A (s^{-1} or cm^3/mole s)	n	a	E_a (kcal/mole)
H + NNO = HNNO[b]	8.46*E*13	0.0	0.0	9.0
HNNO = H + NNO[c]	4.19*E*12	0.306	2.62*E*-04	24.8
H + NNO = NNOH = N_2 + OH[d]	1.26*E*14	0.0	0.0	18.3
HNNO = NH + NO[e]	1.32*E*16	0.0	5.42*E*-04	50.9
HNNO = O + NNH[f]	1.13*E*16	0.0	3.82*E*-04	62.2
HNNO = NNOH = N_2+ OH[g]	6.80*E*12	0.0	0.0	29.4
HNNO: ν_1 = 567 cm^{-1} (degen = 1.99); ν_2 = 1174 cm^{-1} (2.49); ν_3 = 2517 cm^{-1} (1.53); σ = 3.77 Å, ε/k = 280; ΔE_{down} = 1000 cal (N_2), 750 cal (Ar).				

[a]$k = AT^n \exp(-aT) \exp(-E_a/RT)$.
[b]This study, E_a consensus value (cf. text).
[c]Microscopic reversibility (MR).
[d]This study, E_a consensus value (cf. text); A based upon H + NO_2 from Ko and Fontijn [37]. (This channel is effectively a direct route to N_2 + OH. This component is added to that calculated in the chemical activation analysis (cf. text).)
[e]Via k_{rev} and MR with k_{rev} = 3.46*E*13, Harrison et al. [19].
[f]Via k_{rev} and MR with k_{rev} = 7.5*E*13 (based upon O + C_2H_5, Tsang and Hampson [38]).
[g]Transition state theory, ΔS = −3.3 (lose 1 rotor), E_a from Melius [5] (rate-controlling step for N_2 + OH).

culation is needed. This rate constant is added to that obtained from the chemical activation analysis for addition of H to form HNNO to obtain the total for this channel. The high-temperature predictions, above 1000 K, are in good agreement with the data for the N_2 + OH channel (cf. Fig. 2). This is particularly encouraging since no parameters were adjusted in the calculation. However, this prediction does not account for the observed rate constant at lower temperatures. This strongly non-Arrhenius temperature dependence has been attributed to tunneling by Marshall et al. [2]. They point out that tunneling is also consistent with the observed isotope effects in their rate constant measurements for the D + N_2O reaction [8]. Although these researchers rule out stabilization as a major pathway on the basis of their observed lack of pressure dependence, our calculations suggest that stabilization is an alternate explanation for the lower-temperature data.

In Fig. 5, we compare our predictions for all the channels to the data of Marshall et al. [8]. The calculations used a pressure of 0.5 atm Ar, conditions typical of those used in the experiments. Below 900 K, the stabilization of the HNNO adduct is predicted to become important. (As discussed above, the low A factor for dissociation of this adduct back to reactants makes this channel particularly susceptible to stabilization.) The temperature range over which stabilization dominates coincides with the region of significant non-Arrhenius behavior seen in the experiments of Marshall et al. and might account for the unusual behavior. The degree of stabilization should be viewed qualitatively, because the calculated amount of stabilization depends critically upon the amount of energy transferred per collision. To illustrate this, we include two calculations in Fig. 5; in the first, ΔE_{down} is fixed at 0.75 kcal/mole, which yields a room-temperature value of $\Delta E_{average}$ consistent with those tabulated [35]. In the second, ΔE_{down} is assumed to scale linearly with temperature [36], with a value of 0.75 kcal/mole at 300 K. As expected, the latter case shows increasing stabilization at higher temperatures. Nevertheless, the correspondence between the predicted temperature where stabilization dominates and that at which the data of Marshall et al. depart from linearity is striking. Moreover, we point out that the strong temperature dependence of the data, as well as limited number of experiments at constant temperature and various pressures by Marshall et al., might not preclude some experimental dependence on pressure. We feel that additional experiments are needed to identify the source of the higher observed rate at lower temperatures. In the interim, we cautiously suggest use of a calculated stabilization rate constant. At 1 atm N_2,

$$k_{1a} = 8.0 \times 10^{24}\, T^{-4.39} \cdot \exp(-5300/T)\ \mathrm{cm^3\ mole^{-1}\ s^{-1}},$$
$$\text{for } T = 300\text{–}1200\ \mathrm{K}.$$

Over the interval 600–900 K, where this reaction might be important, it is approximately in the low-pressure limit so that the rate constant can be scaled linearly with pressure.

Given the ambiguity concerning the lower-temperature behavior, we are reluctant to conclude that all of the observed loss of reactant in this regime can be attributed to production of N_2 + OH. However, above 1000 K, it appears that the measurements of

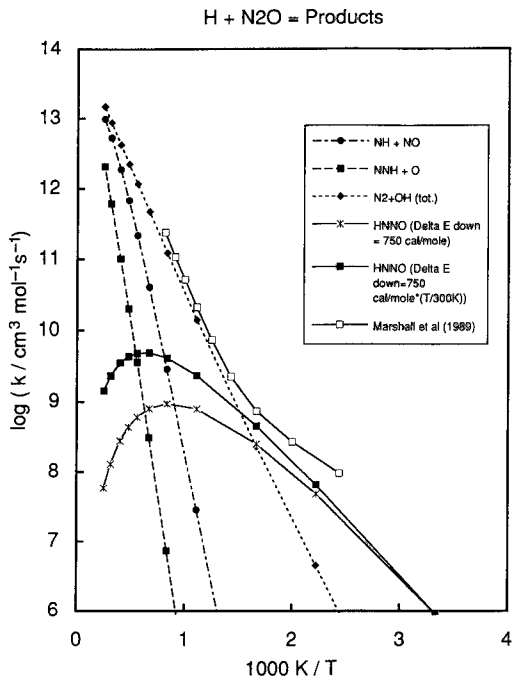

FIG. 5. Arrhenius plot for the various channels of H + N_2O = products, as predicted by the calculations (for P = 0.5 atm Ar, representative of the conditions used by Marshall et al.). Two calculations are included for the stabilization channel, using different expressions for ΔE_{down} (cf. text). Also included are the measurements of Marshall et al. for the total rate constant. Note the importance of the HNNO stabilization channel at lower temperatures, leading to upward curvature in the Arrhenius plot, similar to that seen in the measurements. At high temperatures, the NH + NO channel has grown to become almost as important as N_2 + OH, and NNH + O is also predicted to be important.

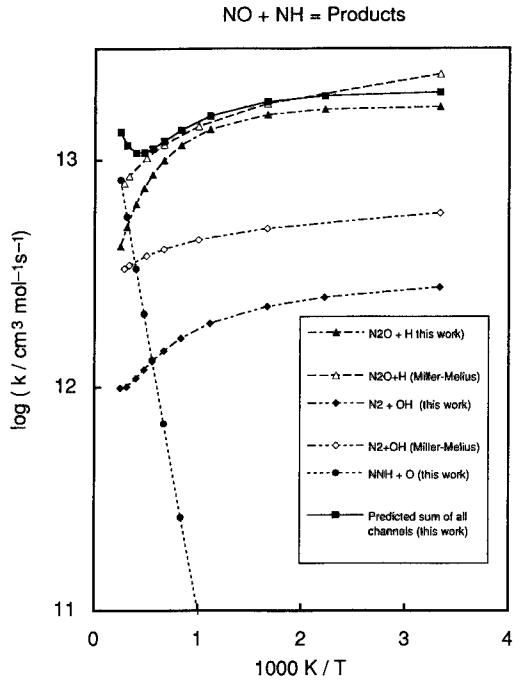

FIG. 6. Arrhenius plot for the various channels of NH + NO = products, as predicted in this work and that of Miller and Melius. Also included is the total rate constant predicted in our calculations. The change in temperature dependence near 2500 K in our predicted total is due to the increasing importance of O + NNH. At lower temperatures, H + N_2O is predicted to be dominant, in agreement with the calculations of Miller and Melius.

Marshall et al. [8] describe this reaction (cf. Fig. 5). Thus, we recommend use of the high-temperature component of their rate expression:

$$k_{1b} = 2.2 \times 10^{14} \exp(-8430/T)\ \mathrm{cm^3\ mole^{-1}\ s^{-1}},$$

for T = 1000–2000 K.

(We have extended the high-temperature range since that value is consistent with the shock-tube data.) Our analysis suggests that there should be virtually no effect of pressure (or collision partner) on this channel above 1000 K and below 100 atm.

H + N_2O = NH + NO

The predicted rate constant for the NH + NO channel is compared to the measurements in Fig. 3. We predict this channel to be independent of pressure over the range 10^{-3}–100 atm. These calculations indicate that, at the higher temperatures, the NH + NO channel becomes increasingly important and is comparable to the N_2 + OH channel near 2500 K (cf. Fig. 5). Selection of a preferred rate constant here is difficult. The data of Mertens et al. [14] are obtained from the measurement of the reverse reaction, and we suspect there might be some ambiguity in assignment of product channels (see below). This would lead to a lower activation energy for k_{1c}, bringing that value closer to that obtained from detailed modeling (of the reverse reaction) by Miller and Bowman [15], as well as that calculated in this work. Our analysis is remarkably similar to the Miller–Bowman value, and we suggest using our calculated value:

$$k_{1c} = 6.7 \times 10^{22}\, T^{-2.16} \cdot \exp(-18{,}700/T)\ \mathrm{cm^3\ mole^{-1}\ s^{-1}},$$

for T = 300–4000 K.

H + N_2O = NNH + O

There is very little information available on reaction (1c). The results in Fig. 5 suggest that this channel becomes important at higher temperatures. The O + NNH channel has a smaller rate constant, due to the higher barrier for this reaction. Our results can be described by the following expression:

$$k_{1d} = 5.5 \times 10^{18}\, T^{-1.06} \cdot \exp(-23{,}800/T)\ \mathrm{cm^3\ mole^{-1}\ s^{-1}},$$

$$\text{for } T = 300\text{–}4000\ \mathrm{K}.$$

This value is lower than that used by Miller and Bowman [15], which is based on an estimate for the reverse reaction. The calculations indicate that this channel has no pressure dependence.

NH + NO = products

We have then used this same potential energy surface to consider the reverse reaction of NH + NO = products. These results are compared to the observations in Fig. 4. The parameters for this calculation were all fixed at the same values used for the H + N_2O reaction, and they seem to account for most of the features reported in the experiments, including the increase in rate at high temperature. Predictions for the various channels are shown in Fig. 6; also included are the results of Miller and Melius [3]. The stabilization channels are predicted to be unimportant, even at the lowest temperatures. The major product channel, except at the highest temperatures, is predicted to be H + N_2O and agrees well with the calculations of Miller and Melius. Our analysis leads to somewhat less of the N_2 + OH product channel than predicted by Miller and Melius. At 3000 K, we predict that k_{2a}/k_{tot} = 9%, as compared to 19 ± 10% measured by Mertens et al. [14]; Miller and Melius report 29%. We note that the reports of N_2 + OH as the dominant channel at lower temperatures would suggest that the barrier to the HNNO = NNOH isomerization used in both this work and Miller and Melius is too high. While a detailed evaluation of the effect of this barrier on the product distribution is beyond the scope of this paper, we note that changes of the magnitude needed would require a substantial decrease in the barrier height, well beyond the expected uncertainty in the Melius calculation. Such a conclusion is consistent with the recent data of Durant [6], who reports that the N_2O channel is dominant at room temperature.

An additional feature of interest in Fig. 6 is the predicted importance of the NNH + O channel at the highest temperatures. These results suggests that the NNH + O channel is a major product in the Mertens et al. shock-tube experiments. This channel is more important for the NH + NO reaction than the H + N_2O reaction since the available energy is appreciably higher for the NH + NO reaction, thus allowing easier access to the endothermic NNH + O channel. This seems to be the most plausible explanation for the observed temperature dependence in the shock-tube experiments. This reaction should be included in high-temperature models, as it provides an efficient route to convert both NO and NH to N_2 (via the very rapid dissociation of NNH to N_2 + H).

None of these channels are predicted to have any pressure dependence. Given the amount of energy in the adducts, as well as the low-energy dissociation channels, this behavior is expected—the unimolecular dissociation events are much too rapid to be intercepted by collisions. Our predicted rate constants, in units of $\mathrm{cm^3\ mole^{-1}\ s^{-1}}$, are

$$k_{2a} = 6.1 \times 10^{13}\, T^{-0.50} \exp(-60/T)$$

$$k_{2b} = 2.5 \times 10^{16}\, T^{-1.03} \exp(-420/T)$$

$$k_{2c} = 5.6 \times 10^{12}\, T^{0.21} \exp(-5470/T)$$

These are applicable over the range 300–4000 K.

Conclusion

We observe that the chemical activation calculations for the reaction H + N_2O are consistent with what little information is available concerning the branching ratio. At higher temperatures, the NH + NO channel is predicted to be comparable to the N_2 + OH channel, while the NNH + O channel is less important. A particularly interesting feature of the calculations is the suggestion that the upward curvature in the Arrhenius plot at lower temperatures could be due to stabilization, as opposed to tunneling. One expects stabilization to be much more important than usual in this system, given the unusually low A factor for dissociation of HNNO back to reactants.

H + N_2O is predicted to be the major channel for the NH + NO reaction. It is difficult to reconcile this result with the experiments of Yamasaki et al. [20], but the very recent data of Durant [6] are consistent with this conclusion. At high temperatures, one expects the O + NNH channel to become important, and this is consistent with the temperature dependence reported in the shock-tube work by Mertens et al. [14]. This is a product channel that should be considered for inclusion in combustion models.

A particularly encouraging feature of these calculations is the agreement with a wide range of experiments on both forward and reverse reactions. This gives us reasonable confidence that the predictions for the various channels at other temperatures and pressures should be sufficiently accurate for use in combustion models, until additional experimental data become available.

REFERENCES

1. Sausa, R. C., Anderson, W. R., Dayton, D. C., Faust, C. M., and Howard, S. L., *Combust. Flame* 94:407–425 (1993).
2. Marshall, P., Fontijn, A., and Melius, C. F., *J. Chem. Phys.* 86:5540–5549 (1987).
3. Miller, J. A., and Melius, C. F., *Twenty-Fourth Symposium (International) on Combustion*, The Combustion Institute, Pittsburgh, 1992, pp. 719–726.
4. Walch, S. P., *J. Chem. Phys.* 98:1170–1177 (1993).
5. Melius, C. F., *BAC-MP4 Heats of Formation and Free Energies*, private communication, 1993.
6. Durant, J. L., *J. Phys. Chem.* 98:518–521 (1994).
7. Hidaka, Y., Taskuma, H., and Suga, M., *Bull. Chem. Soc. Jpn.* 58:2911–2916 (1985).
8. Marshall, P., Ko, T., and Fontijn, A., *J. Phys. Chem.* 93:1922–1927 (1989).
9. Dean, A. M., Johnson, R. L., and Steiner, D. C., *Combust. Flame* 37:41–62 (1980).
10. Hanson, R., and Salimian, S., in *Combustion Chemistry* (W. C. Gardiner, Jr., Ed.), Springer-Verlag, New York, 1984, p. 173.
11. Tsang, W., and Herron, J. T., *J. Phys. Chem. Ref. Data* 20:609–663 (1991).
12. Cattolica, R. J., Smooke, M. D., and Dean, A. M., *A Hydrogen-Nitrous Oxide Flame Study*, Sandia Report, SAND82–8776, Sandia National Laboratories, 1982.
13. Roose, T. R., Ph.D. Thesis, Stanford University, Stanford, CA, 1981.
14. Mertens, J. D., Chang, A. Y., Hanson, R. K., and Bowman, C. T., *Int. J. Chem. Kinet.* 23:173–196 (1991).
15. Miller, J. A., and Bowman, C. T., *Prog. Energy Combust. Sci.* 15:287–338 (1989).
16. Yokoyama, K., Takane, S., and Fueno, T., *Bull. Chem. Soc. Jpn.* 64:2230–2235 (1991).
17. Yokoyama, K., Sakane, Y., and Fueno, T., *Bull. Chem. Soc. Jpn.* 64:1738–1742 (1991).
18. Vandooren, O. M., Sarkisov, O. M., Balakhnin, V. P., and Van Tiggelen, P. J., *Chem. Phys. Lett.* 184:294–300 (1991).
19. Harrison, J. A., Whyte, A. R., and Phillips, L. F., *Chem. Phys. Lett.* 129:346–352 (1986).
20. Yamasaki, K., Okada, S., Koshi, M., and Matsui, H., *J. Chem. Phys.* 95:5087–5096 (1991).
21. Harrison, J. A., and Maclagan, R. G. A. R., *J. Chem. Soc. Faraday Trans.* 86:3519–3523 (1990).
22. Melius, C. F., and Binkley, J. S., *Twentieth Symposium (International) on Combustion*, The Combustion Institute, Pittsburgh, 1984, pp. 575–583.
23. Dean, A. M., *J. Phys. Chem.* 89:4600–4608 (1985).
24. Westmoreland, P. R., Howard, J. B., Longwell, J. P., and Dean, A. M., *AIChE J.* 32:1971–1979 (1986).
25. Bozzelli, J. W., and Dean, A. M., *J. Phys. Chem.* 93:1058–1065 (1989).
26. Bozzelli, J. W., and Dean, A. M., *J. Phys. Chem.* 94:3313–3317 (1990).
27. Bozzelli, J. W., and Dean, A. M., *J. Phys. Chem.* 97:4427–4441 (1993).
28. Dean, A. M., and Westmoreland, P. R., *Int. J. Chem. Kinet.* 19:207–228 (1987).
29. Ritter, E. R., and Bozzelli, J. W., *Int. J. Chem. Kinet.* 23:767–778 (1991).
30. Bozzelli, J. W., and Ritter, E. R., Radicalc—Computer code to calculate entropy and heat capacity contributions to transition states and radical species from changes in vibrational frequencies, barriers, moments of inertia, and internal rotations. *Chemical and Physical Processes in Combustion*, The Combustion Institute, Pittsburgh, 1993, p. 459.
31. Reid, R. C., Prausnitz, J. M., and Poling, B. E., *Properties of Gases and Liquids*, 4th ed., McGraw Hill, New York, 1987.
32. Dean, A. M., Bozzelli, J. W., and Ritter, E. R., *Combust. Sci. Technol.* 80:63–85 (1991).
33. Ritter, E. R., Ph.D. Thesis, New Jersey Institute of Technology, New Jersey, 1989.
34. Chang, A. Y., Bozzelli, J. W., Green, W. H., and Dean, A. M., (to be published).
35. Gardiner, W. C., Jr., and Troe, J., in *Combustion Chemistry*, (W. C. Gardiner, Jr., Ed.), Springer-Verlag, New York, 1984, pp. 173–196.
36. Feng, Y., Niiranen, J., Bencsura, A., Knyazev, V. D., Gutman, D., and Tsang, W., *J. Phys. Chem.* 97:871–880 (1993).
37. Ko, T., and Fontijn, A., *J. Phys. Chem.* 95:3984–3987 (1991).
38. Tsang, W., and Hampson, R. F., *J. Phys. Chem. Ref. Data* 15:1087–1279 (1986).

COMMENTS

Thomas Just, DLR, Germany. The channel NH + NO to NNH + O should show a rather strong pressure dependence. Did you investigate that?

Author's Reply. Our calculations show no pressure effect for this channel. This is consistent with the fact that the activated adduct has so much energy, relative to the low-lying exit channels, that the unimolecular reaction rates dominate collisional stabilization for all conditions of interest. In this case, the competitions are among all the unimolecular pathways of the adduct, since the sum of unimolecular rate constants for these channels completely dominates the stabilization pathway. Thus, none of these channels, even the higher energy one to O + NNH, show any significant pressure effects for $P \leq 60$ atm. The reason O + NNH is important, in spite of its higher energy, is

that the A factor for this pathway is higher than the other routes, so that this becomes increasingly important at higher temperatures.

•

J. R. Richard, CNRS/LCSR-Orleans, France. One of the goals of your analysis was to give values or trends over a wide range of temperature and pressure for the reactions H + N_2O and NH + NO. Unfortunately, no data are given for the pressure dependency of the above reactions, explaining for instance the experimental fact that an increase in the pressure decreases N_2O and NO. Do you think that the different routes you proposed can explain the experimental observation of the pressure influence?

Author's Reply. We have not attempted to incorporate our rate constants into a kinetic model to test the effect of pressure on a specific system. For this system, the only channel that we expect to have a significant pressure dependence over the normal range of pressures for combustion is that for formation of HNNO from H + N_2O. We would need more information about the specific system to address the issue as to whether use of the rate constants discussed in this paper (as well as all the others needed for such a model) could explain the observed pressure effects. However, we do expect that there will be systems where there is a need to account explicitly for the pressure effects on the branching ratios of chemically activated reactions. One of the purposes of this paper was to illustrate a method by which these pressure effects can be estimated in a straightforward manner. These rate constants can then be incorporated into mechanisms that should permit better descriptions of pressure effects on systems of interest.

•

Joseph Durant, Sandia National Laboratories, USA. Can you comment on the isotope effect that you would expect for the H + N_2O reaction given the fact that your model invokes collisional stabilization to explain the observed curvature in the Arrhenius plot?

Author's Reply. Our original calculations did not address the effects of isotopic substitution on the H + N_2O reaction. To address this question, we have calculated the heats of formation, entropy, and $C_p(T)$ to reflect deuterium substitution in order to explore the effect on the stabilization channel. We assume the same k_1 as the H + N_2O case and use microscopic reversibility to obtain k_{-1} for dissociation of DNNO to D + N_2O. These changes result in a slightly deeper well (~1.8 kcal/mole), with a slightly larger preexponential term for DNNO dissociation. These changes resulted in a ~20% increase in stabilization for DNNO at 600 K and 0.5 atm Ar relative to HNNO. Under these conditions, the experiments (cf. Ref. 8) showed a slight decrease in overall rate with the deuterium substitution, which would suggest stabilization is not important. On the other hand, Prof. Lin's comment concerning his unpublished results suggests that both tunneling and stabilization might be important in this system. We simply point out that our calculations suggest that stabilization might play a role in this system and we feel additional experiments are needed to resolve this issue.

•

V. M. Zamansky, Energy and Environmental Research Corporation, USA. I think this work is very important for comparison of different channels for the H + N_2O reaction. There are many experimental measurements for the major channel (into N_2 + OH), but I am aware of only one experimental high-temperature measurement [1] for the NH + NO channel. As a comment, I would like to compare the calculated rate constant with the experimental one. We measured the rate constant of the reaction H + $N_2O \rightarrow$ NH + NO experimentally, $k = 10^{14.8} \exp(-14{,}500/T)$ cm³/mol s, by studying ignition delays in N_2O/H_2 mixtures at T = 850–2000 K. That time we considered only two channels in our mechanism: into N_2 + OH and NH + NO. The comparison shows that the calculated rate constant in your work is about three times lower at 1000 K and two times lower at 2000 K than the experimental value.

REFERENCE

1. Borisov, A. A., Zamansky, V. M., and Skachkov, G. I., *Kinet. Catal.* 19(1):26–32 (1978) (transl. from Russian).

Author's Reply. The agreement between our calculated value for H + N_2O = NH + NO and the measurements of Borisov et al. is even better than cited in the comment. Our calculations are about a factor of 2 low at 1000 K and within 5% at 2000 K.

•

J. R. Pels, Delft University of Technology, The Netherlands. Do your results simply show that at low temperature, e.g., in SNCR or FBC of coal, the reduction of NO by NH (from NH_3) goes primarily through NO + NH $\rightarrow N_2O$ + H $\rightarrow N_2$ + OH rather than directly NO + NH $\rightarrow N_2$ + OH?

Is N_2O + OH $\rightarrow N_2$ + HO_2 or NO + OH $\rightarrow$ NH + O_2 an important channel at these low temperatures?

Author's Reply. 1. Our analysis suggests that the major product channel for NH + NO at low temperatures is H + N_2O, not N_2 + OH. As pointed out in the text, this conclusion is consistent with recent experimental measurements of Durant. This could have significant implications in the modeling of lower temperature systems, like SNCR or FBC of coal. The N_2O formed via NH + NO could react with H to form N_2 + OH, the major low-temperature channel for this reaction, but there are many other reactions of N_2O, such as those with atomic oxygen, that also need to be considered.

2. There is recent evidence that the rate constant for $N_2O + OH = N_2 + HO_2$ is appreciably slower than earlier literature reports. An analysis of N_2O decomposition by Allen et al. [1] reports that use of the Miller–Bowman value results in much too high a yield of NO_2 with too little NO. Their kinetic analysis showed that a much better fit to the data could be obtained if this rate constant were lowered by a factor of 160. [This change reduces the amount of HO_2 formed, which is responsible for converting NO to NO_2 under their conditions.]

The reaction $NO + OH = NH + O_2$ is ~52 kcal/mole endothermic, and is unlikely to be important. A more likely reaction is $NO + OH + M = HONO + M$. This reaction has the potential to serve as a sink for OH, as well as a route to NO_2 via the reaction $X + HONO = HX + NO_2$, where X is a radical such as H, OH, etc.

REFERENCE

1. Allen, M. T., Yetter, R. A., and Dryer, F. L., "The Decomposition of Nitrous Oxide at Elevated Pressures," Spring Western States Section Meeting of the Combustion Institute, 1994, Paper #94-012.

•

James A. Miller, Sandia National Laboratories, USA. Contrary to the statement you made in your presentation, our paper at the last Symposium (Miller, J. A., and Melius, C. F., *Twenty-Fifth Symposium,* p. 719) discusses the effect of the $NH + NO \rightarrow NNH + O$ reaction prominently. We also attributed the rise in the total rate coefficient observed by Mertens et al. [Int. J. Chem Kinet. 23:173 (1991)] to the influence of this channel. We assumed a rate coefficient of 5×10^{13} cm³/mole-s for the reverse reaction occurring on the $^2A''$ surface and computed the forward rate coefficient from the thermochemistry.

Author's Reply. We are sorry if we did not properly acknowledge the previous work by Miller and Melius on the O + NNH channel. We appreciate this opportunity to discuss the significant differences between our results and those referred to by Miller. For example, they concluded that the O + NNH channel only occurs via the excited state surface, and that "on the ground state surface this channel cannot compete with the $N_2O + H$ and $N_2 + OH$ channels, which are much more readily accessible energetically." Our calculations show that reaction to O + NNH *on the ground state surface* is important. They also conclude that the O + NNH channel is negligible compared to the other two channels below about 2000 K, while our value at 2000 K is $\sim 2 \times 10^{12}$, clearly a nonnegligible value. Perhaps more importantly, our value was derived from an explicit chemical-activation analysis with a master equation approach to treat collisional stabilization, where all of the channels are included, rather than an isolated calculation, based on an estimate for the reverse rate constant.

Twenty-Fifth Symposium (International) on Combustion/The Combustion Institute, 1994/pp. 975–981

THE REACTIONS OF NH($X^3\Sigma^-$) WITH THE WATER GAS COMPONENTS CO_2, H_2O, AND H_2

MICHAEL RÖHRIG AND HEINZ GEORG WAGNER
Georg-August-Universität Göttingen
Institut für Physikalische Chemie
Tammannstraße 6, 37077 Göttingen, Germany

In the combustion of nitrogen-containing systems and fuels, the radical NH can play an important role. Many reactions of this radical in its electronic ground state are supposed to be very slow at room temperature. Therefore, experiments have been performed behind shock waves to study some reactions of NH($X^3\Sigma^-$) that are of interest in combustion processes.

As a source of NH($X^3\Sigma^-$), HN_3 was used, which dissociates sufficiently fast above 1000 K. In order to achieve high sensitivity, NH($X^3\Sigma^-$) concentration was measured with a ring dye laser.

The reactions of NH($X^3\Sigma^-$) with the water gas components H_2 (2), H_2O (3), and CO_2 (4) were investigated in the temperature range of 1100–2000 K. The reactions of NH($X^3\Sigma^-$) with H_2O and CO_2 proved to be rather fast. The rate constants obtained were as follows:

$$k_2 = 10^{14.0\pm0.2} \exp[-(10{,}100 \pm 200)\ K/T]\ \text{cm}^3/\text{mol s}$$

$$k_3 = 10^{13.3\pm0.2} \exp[-(6970 \pm 200)\ K/T]\ \text{cm}^3/\text{mol s}$$

$$k_4 = 10^{13.0\pm0.2} \exp[-(7220 \pm 200)\ K/T]\ \text{cm}^3/\text{mol s}$$

Rate constants for the reverse reactions are also given. While the reaction of NH($X^3\Sigma^-$) with H_2 proceeds in the expected way, the reactions of CO_2 and H_2O rapidly form species with N—O bonds like HNO.

Introduction

Methods for the reduction of NO_x in the burned gases of combustion processes such as, e.g., thermal $DeNO_x$ [1] or $RAPRENO_x$ [2] use the addition of certain substances that form essentially NH_2 to remove NO. The NH_2 radical reacts rapidly with NO in a well-known reaction forming N_2 [3]. It is very important for these processes that the NH_2 is available under certain well-defined conditions in the combustion process [4]. The important reactions of NH_2 with many different species possibly present in the combustion process have been investigated in some detail (see, e.g., Ref. 5). Much less quantitative information is available about reactions of NH with these species. Usually, when NH_2 is present in flames, NH can also be formed. If HNCO is used as an additive for NO_x reduction, the NH may even be generated directly to some extent. The reactions of NH are also of importance in combustion of nitrogen-containing fuels.

The reactants to be considered for NH-consuming reactions in flames are of course O_2, hydrocarbons (especially saturated ones), and also the main combustion products, the water gas components H_2, H_2O, CO_2, and CO, as well as the radicals H, O, and OH.

Besides that, the reactions of NH are of general interest in chemistry. The NH radical is isoelectronic to CH_2 radicals and to O atoms. These three species have triplet ground states and singlet first excited electronic states that show a very special reaction behaviour with respect to the elementary reaction mechanisms. In addition, the singlet states of these radicals exhibit high reaction rates already at room temperature, which are partly due to electronic deactivation but in many cases nearly completely to chemical reactions [5]. This is of practical importance in combustion processes, e.g., for CH_2. The energy difference between the triplet and singlet states of NH is 151 kJ/mol [6]. Therefore, rather high temperatures are required for electronic excitation of NH($X^3\Sigma^-$) to NH($a^1\Delta$) except in cases when NH($a^1\Delta$) is formed as reaction product.

In the present paper, we will report experimental results about the reactions of NH($X^3\Sigma^-$) with H_2, H_2O, and CO_2. These results will be discussed in connection with other NH-consuming reactions with species that might be present in the domain where NO_x can be removed [7,8,9,10].

There are only a few rough estimates available in the literature about the rates of NH reactions in its electronic ground state with most of the species mentioned. This indicates that the NH($X^3\Sigma^-$) reactions

with these components are very slow at room temperature [11,12]. For the rate constant of the reaction of $NH(X^3\Sigma^-)$ with H_2 in the temperature range of 2600–2800 K, a directly measured value has been reported by Dove and Nip [13].

Here measurements of NH reaction rates behind shock waves in the temperature range of 1000–2000 K are described. In order to reduce secondary reactions, a very sensitive detection method for $NH(X^3\Sigma^-)$ is required. For the determination of the reaction products, the often-used method of photolysis at room temperature was not very useful because the reactions proved to be very slow indeed. Fortunately, thermodynamic data allow selection of the reaction channels in some cases. Otherwise, product measurements in shock tubes had to be performed.

Source of $NH(X^3\Sigma^-)$ was HN_3, which decomposes sufficiently fast above 1000 K and which was established as a well-suited source for $NH(X^3\Sigma^-)$.

Experimental

The experiments were performed behind incident shock waves using an aluminium shock tube with an internal diameter of 20 cm, described in Ref. 14. The light source for the absorption measurements was an Ar^+ laser (Innova 200-15, Coherent) pumped ring dye laser (899–21, Coherent) with internal frequency doubling unit (8100, Coherent). The bandwidth of the laser was smaller than 1 GHz, which is sufficient for high-temperature, atmospheric pressure measurements, where linewidths typically are about 10 GHz.

A part of the UV beam passed an ammonia/oxygen flame as a stationary NH source. The laser wavelength was adjusted to the maximum of $Q_1(0,0)$ bandhead of the $A^3\Pi \leftarrow X^3\Sigma^-$ transition of NH at 336.100 nm. Then the UV beam was divided into reference and analysis beams. The analysis beam passed through the shock tube. The difference between the two beams was amplified electronically and recorded on a digital storage oscilloscope (9484, LeCroy).

The substances used for the experiments were Ar (99.998%), H_2 (99.999%), and CO_2 (99.995%). The gases were obtained from Messer-Griesheim and were used without further purification. Water was distilled twice and passed directly into the tube via a double saturator in the carrier gas flow.

The HN_3 was prepared by heating a mixture of NaN_3 (99%, Merck, Germany) with an excess of stearic acid (97%, Merck, Germany) to 140 °C. The formed gas passed a U tube, filled with $CaCl_2$ to remove water, into a 20-L glass flask. The HN_3 was then diluted with Ar to concentrations of about 2500 ppm. The purity of HN_3 was checked, and impurities of less than 0.3% were found [6]. The test gas mixtures were prepared before each experiment using a flow system with mass flow controllers (MKS).

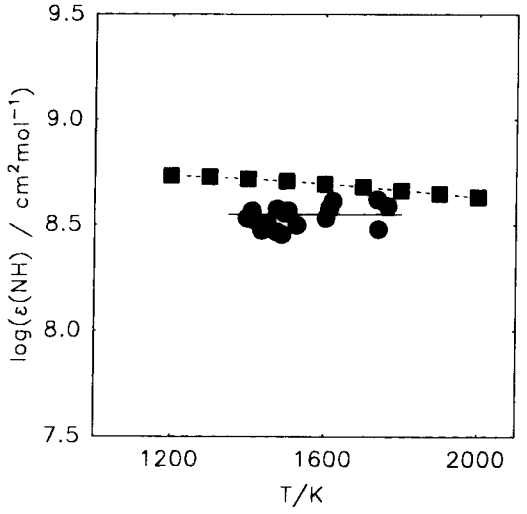

FIG. 1. Absorption coefficient of NH at the $Q_1(0,0)$ bandhead of the $A^3\Pi \leftarrow X^3\Sigma^-$ transition at 336. 100 nm; ■, Chang and Hanson [15]; ●, this work.

A flow of about 10 cm^3/min (298 K, 1.013 bar) of the HN_3 mixture was diluted with a flow of about 5000 cm^3/min of a 0.5–2.5% mixture of the other reactants in Ar. With this device, the initial concentration of HN_3 could be varied between 1 and 30 ppm.

The absorption coefficient of NH at 336.100 nm was determined by absorption measurements with highly diluted HN_3/Ar mixtures (<2 ppm) in the temperature range of 1400–1800 K where HN_3 decomposes completely into $NH(X^3\Sigma^-)$ and N_2. The known initial concentration $[HN_3]_0$ and the measured light intensity at the end of the reaction I_∞ were used to calculate the absorption coefficient:

$$\varepsilon = \ln(I_0/I_\infty)/[HN_3]_0\, d.$$

The term d is the shock tube diameter. The results of these experiment are summarised in Fig. 1. Additionally, the value given by Chang and Hanson [15] for the maximum of the $Q_1(0,0)$ bandhead is outlined. They calculated ε using spectroscopic data and measured broadening coefficients that were found to be independent from the rotational quantum number. The measured and the calculated absorption coefficients are in reasonable agreement. For the conversion of the absorption profiles into $NH(X^3\Sigma^-)$ concentration profiles, a temperature-independent averaged value of $3.4 \cdot 10^8$ cm^2/mol (base e) was used.

Results

For the detailed investigation of the $NH(X^3\Sigma^-)$ reactions, it was necessary to inspect the thermal

decomposition of HN_3 and to check whether the spin-allowed but thermodynamically less favourable reaction channel leading to NH($a^1\Delta$) shows a pronounced influence. For details, see Ref. 16. Briefly, it was found that, under the conditions of interest, NH($a^1\Delta$) formation in the thermal decomposition can be neglected. For the rate constant of HN_3 decomposition, which is equal to the rate constant of NH($X^3\Sigma^-$) formation, a value of $k = (8 \pm 4)\cdot 10^{14}$ $\exp(-18{,}280\ K/T)$ $cm^3\ mol^{-1}\ s^{-1}$ in Ar as carrier gas was obtained. This result is in excellent agreement with the value given by Kajimoto et al. [17] and fits to the data of Zaslonko et al. [18] obtained at higher pressures.

Using these data, the HN_3/reactant system for the species investigated in this work can be described by the following simple reaction mechanism:

$$HN_3 + M \rightarrow NH(X^3\Sigma^-) + N_2 + M \quad (1)$$

$$NH(X^3\Sigma^-) + R \rightarrow \text{Prod.}$$

$$R = H_2(2),\ H_2O(3),\ CO_2(4).$$

This simple mechanism results in an analytical expression that can easily be used to evaluate the experimental results [9]. Because of the low initial concentrations of HN_3 and therefore of NH($X^3\Sigma^-$), secondary reactions of primary reaction products should hardly play any role at the experimental conditions chosen here. The corresponding rate law was checked by experiments with different initial concentrations of HN_3 and especially of CO_2, H_2O, and H_2 (not shown here).

A comparison of measured with calculated NH($X^3\Sigma^-$) concentration profiles for the reaction of NH($X^3\Sigma^-$) with H_2O is shown in Fig. 2. The dashed line represents the measured profile. After the schlieren signal, the NH($X^3\Sigma^-$) concentration rises as a result of the decomposition of HN_3 and then decreases. This decay can be attributed to the reaction of NH($X^3\Sigma^-$) with water. The signals were fitted using the rate constant of HN_3 decomposition given above and by varying the rate constant of the reaction of NH($X^3\Sigma^-$) with the reactants. The measured profile can be approximated well with this simple mechanism given above.

The Reaction NH($X^3\Sigma^-$) + H_2 (2):

For this reaction, the mechanism is

$$NH(X^3\Sigma^-) + H_2 \xrightarrow{M} NH_3 \qquad \Delta_r H^\circ_{298} = -410.4\ \text{kJ/mol} \quad (2a)$$

$$\rightarrow NH_2 + H \qquad \Delta_r H^\circ_{298} = 46.3\ \text{kJ/mol}. \quad (2b)$$

The experimental conditions and the rate constants obtained for this reaction are given in Table 1, part (a) and in Fig. 3 in an Arrhenius plot. A temperature range of 1100–1700 K was covered. In this case data for the reverse reaction (−2b) are available [19–23], and there is also one direct determination in a NH_3 pyrolysis study in the presence of H_2 in Ref. 13.

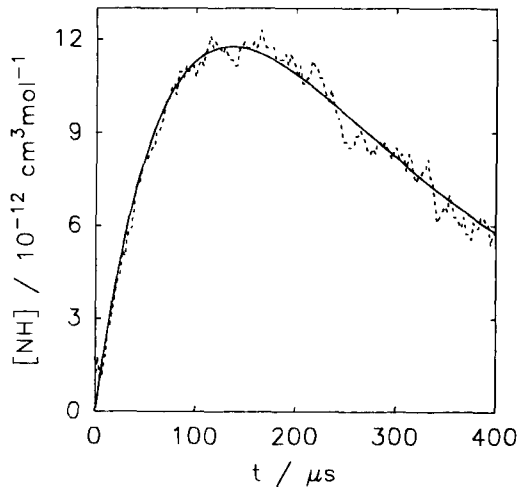

FIG. 2. Typical NH($X^3\Sigma^-$) concentration profile of the reaction of NH($X^3\Sigma^-$) with H_2O; T = 1491 K; ρ = $3.8\cdot 10^{-6}$ mol/cm³; $[HN_3]_0$ = 6 ppm; $[H_2O]$ = 0.6%; ----, experiment; ——, calculation.

The results obtained in this work are in good agreement with the data given in Ref. 13 and can be described in the temperature range of 1100–1800 K by the following Arrhenius expression:

$$k_2 = (1 \pm 0.5)\cdot 10^{14} \cdot \exp([-10{,}100 \pm 200)\ K/T]\ cm^3/mol\ s.$$

The Reaction NH($X^3\Sigma^-$) + H_2O (3):

For this reaction, the following reaction channels may be considered:

$$NH(X^3\Sigma^-) + H_2O$$

$$\rightarrow H_2NOH \qquad \Delta_r H^\circ_{298} = -173.6\ \text{kJ/mol} \quad (3a)$$

$$\rightarrow H_3NO \qquad \Delta_r H^\circ_{298} = -38.7\ \text{kJ/mol} \quad (3b)$$

$$\rightarrow HNO + H_2 \qquad \Delta_r H^\circ_{298} = -24.6\ \text{kJ/mol} \quad (3c)$$

$$\rightarrow NH_3 + O \qquad \Delta_r H^\circ_{298} = 80.4\ \text{kJ/mol} \quad (3d)$$

$$\rightarrow NH_2 + OH \qquad \Delta_r H^\circ_{298} = 110.0\ \text{kJ/mol} \quad (3e)$$

$$\rightarrow NH_2O + H \qquad \Delta_r H^\circ_{298} = 161.8\ \text{kJ/mol} \quad (3f)$$

$$\rightarrow NO + H_2 + H \qquad \Delta_r H^\circ_{298} = 186.0\ \text{kJ/mol}. \quad (3g)$$

The thermodynamic data indicate that most of

TABLE 1
Experimental Conditions and Results for the Reactions of $NH(X^3\Sigma^-)$ with H_2, H_2O, and CO_2 (= R)

Experiment no.	T (K)	$10^{-6}\,\rho$ (mol cm^{-3})	$10^{11}\,k_i$ (cm^3 mol^{-1} s^{-1})	$x(HN_3)$ (ppm)	$x(R)$ (%)
(a) $NH(X^3\Sigma^-) + H_2$					
H_2 – 1	1685	2.7	2.6	9	2
H_2 – 2	1684	3.0	2.3	9	2
H_2 – 3	1582	3.5	1.2	9	2
H_2 – 4	1397	4.1	0.7	9	2
H_2 – 5	1319	4.9	0.4	9	2
H_2 – 6	1233	5.1	0.3	9	2
H_2 – 7	1156	5.6	0.2	9	2
H_2 – 9	1280	4.1	0.4	9	2
(b) $NH(X^3\Sigma^-) + H_2O$					
H_2O – 1	1681	2.6	3.2	6	0.6
H_2O – 2	1683	2.7	3.5	6	0.5
H_2O – 3	1906	2.5	4.8	6	0.7
H_2O – 4	1586	3.3	2.2	6	0.7
H_2O – 5	1491	3.7	1.7	6	0.6
H_2O – 6	1448	3.9	1.4	6	0.7
H_2O – 7	1329	4.5	1.1	6	0.7
H_2O – 8	1670	2.9	2.8	6	0.6
(c) $NH(X^3\Sigma^-) + CO_2$					
CO_2 – 1	1736	2.7	1.7	6	1.5
CO_2 – 2	1615	3.0	1.2	6	1.5
CO_2 – 3	1583	3.4	1.0	6	1.5
CO_2 – 4	1431	4.0	0.7	6	1.5
CO_2 – 5	1834	2.5	1.8	6	1.5
CO_2 – 6	1893	2.2	2.0	6	1.5
CO_2 – 7	1912	2.2	2.0	6	1.5
CO_2 – 8	1201	5.1	0.3	12	2.0

these reaction channels are rather strongly endothermic. A range of 1300–1900 K was covered for the measurements of reaction (3). The experimental results are given in part (b) of Table 1, and the temperature dependence of the rate constants is shown in Fig. 3. From these measurements, the following rate expression results:

$$k_3 = (2 \pm 1)\cdot 10^{13} \cdot \exp[(-6970 \pm 200)\,K/T]\ \text{cm}^3/\text{mol s}.$$

The apparent energy of activation of 58 kJ/mol for the temperature range covered indicates that the main reaction channel cannot be H abstraction (3e). Depending on pressure, one of the three first reactions must take place, probably mainly (3c). This needs further clarification. In any case, H atoms will be formed at elevated temperatures in consecutive reactions and—more important—the reaction leads to the formation of a N—O bond.

The Reaction $NH(X^3\Sigma^-) + CO_2$ (4):

For this reaction, all reaction channels are endothermic. The least endothermic channels are

$$NH(X^3\Sigma^-) + CO_2$$

$$\rightarrow HNO + CO \quad \Delta_r H^\circ_{298} = 6.61\ \text{kJ/mol} \qquad (4a)$$

$$\rightarrow HNCO + O \quad \Delta_r H^\circ_{298} = 158.6\ \text{kJ/mol} \qquad (4b)$$

$$\rightarrow NO + HCO \quad \Delta_r H^\circ_{298} = 158.8\ \text{kJ/mol} \qquad (4c)$$

$$\rightarrow HCN + O_2 \quad \Delta_r H^\circ_{298} = 162.6\ \text{kJ/mol} \qquad (4d)$$

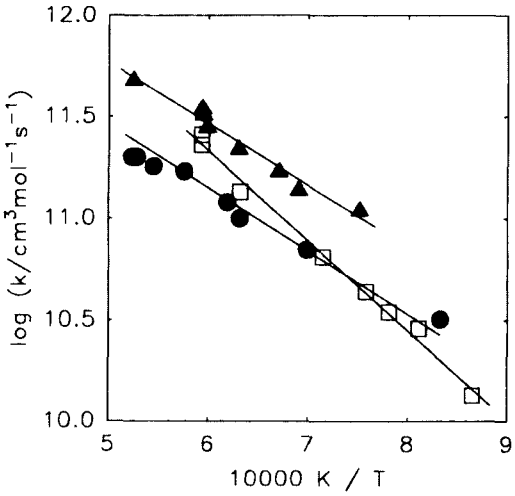

FIG. 3. Temperature dependence of the rate constants of the reactions NH($X^3\Sigma^-$) + H_2 (2), □; NH($X^3\Sigma^-$) + H_2O (3), ▲; and NH($X^3\Sigma^-$) + CO_2 (4), ●; ——, least-squares fit to the data points.

$$\rightarrow \text{HON} + \text{CO} \quad \Delta_r H^\circ_{298} = 164.4 \text{ kJ/mol} \quad (4e)$$
$$\rightarrow \text{OCN} + \text{OH} \quad \Delta_r H^\circ_{298} = 203.9 \text{ kJ/mol} \quad (4f)$$
$$\rightarrow \text{HNC} + \text{O}_2 \quad \Delta_r H^\circ_{298} = 213.2 \text{ kJ/mol} \quad (4g)$$
$$\rightarrow \text{NO} + \text{CO} + \text{H} \quad \Delta_r H^\circ_{298} = 217.2 \text{ kJ/mol.} \quad (4h)$$

The rate measurements of this reaction covered a temperature range of 1200–1900 K. The experimental results for the rate constants are given in Table 1, part (c), and the temperature dependence is shown in Fig. 3. The measured rate constants can be represented by an Arrhenius expression

$$k_4 = (1 \pm 0.5)\cdot 10^{13} \cdot \exp[(-7220 \pm 200)\, K/T] \text{ cm}^3\text{/mol s}$$

with an apparent energy of activation of 60 kJ/mol. It is worthwhile noticing that the apparent energy of activation of this reaction is similar to that of reaction (3). As the thermodynamic data indicate, the main reaction channel must be reaction (4a) with the formation of a N—O bond and at elevated temperatures of H atoms via HNO dissociation. All other reaction channels are too endothermic to be of practical importance in combustion processes.

Discussion

As mentioned above, the role of subsequent reactions was assumed to be unimportant under the experimental conditions in this work. To check the influence of possible consecutive reactions, the signals were also evaluated using computer simulations with an extended reaction mechanism. Most of the reactions had hardly any influence for HN_3 initial concentrations below 10 ppm. For higher HN_3 concentration, the signals could be fitted somewhat better by including these reactions—especially NH + NH—in the evaluation. The rate constants obtained by these computer simulations agreed, however, with those of the analytical evaluation.

As mentioned above, the rate constants of reaction NH($X^3\Sigma^-$) + $H_2 \rightarrow NH_2$ + H (2b) are in good agreement with the results obtained in a less direct way in Ref. 13. For the reverse reaction NH_2 + H $\rightarrow$ NH($X^3\Sigma^-$) + H_2 (−2b), the rate constant obtained from k_{2b} and the thermodynamic data given in Ref. 23 lead to $k_{-2b} = 6.3\cdot 10^{13} \exp(-4450\, K/T)$ cm³/mol s. This reaction is of interest, because it may be a source of NH in some gas phase NO_x-reducing mechanisms. At room temperature, it is quite slow, but at the temperatures of interest here, the rate constant is high. This value for k_{-2b} is in fair agreement with the results obtained in shock tube studies of ammonia [22] and hydrazine [19] pyrolysis by fitting to a complex mechanism. The other possible reaction channel of the reverse reaction NH_2 + H + $M \rightarrow NH_3$ + M gains importance only at elevated pressures.

It should be mentioned that the apparent energy of activation of 84 kJ/mol obtained for the "H atom abstraction" reaction NH($X^3\Sigma^-$) + $H_2 \rightarrow NH_2$ + H here fits well into the Evans–Polanyi plot for the hydrogen abstraction reactions from hydrocarbons by NH($X^3\Sigma^-$). These reactions have been investigated in some detail recently [10]. The main reaction channel is the formation of NH_2. The temperature range that could be covered for these investigations became smaller with increasing number of C atoms because self-reactions of the alkanes become increasingly important. For the reaction of NH($X^3\Sigma^-$) with methane, ethane, propane, and, as a species with a low C—H bond energy, acetaldehyde, the following rate constants were obtained:

$$k_{\text{meth}} = (9 \pm 3)\cdot 10^{13} \cdot \exp[-(84 \pm 5) \text{ kJ mol}^{-1}/RT] \text{ cm}^3\text{/mol s}$$
$$k_{\text{eth}} = (7 \pm 3)\cdot 10^{13} \cdot \exp[-(70 \pm 5) \text{ kJ mol}^{-1}/RT] \text{ cm}^3\text{/mol s}$$
$$k_{\text{prop}} = (6 \pm 3)\cdot 10^{13} \cdot \exp[-(61 \pm 5) \text{ kJ mol}^{-1}/RT] \text{ cm}^3\text{/mol s}$$
$$k_{\text{acet}} = (5 \pm 3)\cdot 10^{13} \cdot \exp[-(48 \pm 5) \text{ kJ mol}^{-1}/RT] \text{ cm}^3\text{/mol s.}$$

The apparent energies of activation of these reactions fit well into an Evans–Polanyi plot. Thus, it becomes possible to extrapolate to higher alkanes

and to compare their reactivity with other possible abstraction reactions by $NH(X^3\Sigma^-)$.

For the reactions of $NH(X^3\Sigma^-) + H_2O$ (3), this Evans–Polanyi plot would require an apparent energy of activation of about 150 kJ/mol for the formation of NH_2. The enthalpy of reaction of step (3e) is 110 kJ/mol. The experimental results give an activation energy of 58 kJ/mol that is definitely much lower. In fact, it is so low that only reaction channels (3a,b,c) are thermodynamically feasible. Already the next channel giving NH_3 and O (3d) can be excluded on the basis of the present thermodynamic data. Therefore, the rate constant of reaction (3) in the temperature range of interest for combustion is not only quite high, but it also leads to a direct formation of a N—O bond. One may consider a reaction mechanism that forms an $[H_2ONH]^*$ complex that probably undergoes an a-a H_2 elimination, so that (3c) seems to be the main channel under normal combustion conditions. In that case, a rate constant of about $k_{-3c} = 1 \cdot 10^{14} \exp(-8055\ K/T)$ cm³/mol s in the temperature range reported here with an apparent energy of activation of 67 kJ/mol for the reverse reaction (−3c) would result. These data for the reverse reactions also depend, of course, on the accuracy of the thermodynamic data.

A similar situation is found for the reaction of $NH(X^3\Sigma^-)$ with CO_2 (4). Based on the thermodynamic data, the only reaction channel that is thermodynamically feasible in the temperature range employed here and consistent with the apparent energy of activation of 60 kJ/mol is the formation of HNO and CO (4a). The $NH(X^3\Sigma^-)$ reacts like the isoelectronic $O(^3P)$ atom but with more favourable thermodynamics and a rather high rate constant for this reaction. For the reverse reaction (−4a), a rate constant of about $k_{4a} = 2.10^{12} \exp(-6192\ K/T)$ cm³/mol s is obtained.

The reaction of $NH(X^3\Sigma^-)$ with CO should not play an important role in the temperature range of interest for combustion processes. It proceeds via the intermediate NHCO, which might have a minor channel leading to NCO.

The rate data and mechanisms of the reactions of $NH(X^3\Sigma^-)$ with the water gas components discussed here do have rate constants that are rather high and that might not have been expected to be so high. Let us for the reason of simplicity discuss the situation for a temperature around 1000 K, where NO_x is often removed in combustion processes. The influence of higher or lower temperatures can easily be judged using the data reported. For combustion at atmospheric pressure the mean concentrations of CO_2 and H_2O in the burned gases at temperatures around 1000 K are approximately a few times 10^{-6} mol/cm³. The rate constants for the reactions considered here are near or above 10^{10} cm³/mol s (see Figs. 3 and 4). Therefore, the lifetime of $NH(X^3\Sigma^-)$ with respect to

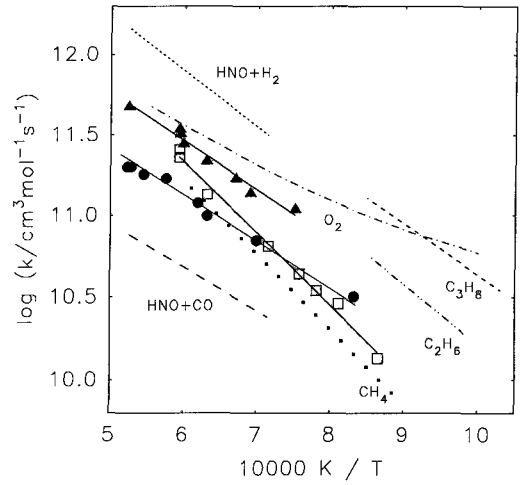

FIG. 4. Rate constants of some $NH(X^3\Sigma^-)$ reactions: □, reaction (2); ▲; reaction (3); ●, reaction (4); $NH(X^3\Sigma^-) + CH_4$ [10]; $NH(X^3\Sigma^-) + C_2H_6$ [10]; $NH(X^3\Sigma^-) + C_3H_8$ [10]; $NH(X^3\Sigma^-) + O_2$ [9]; reverse reactions: $HNO + CO \rightarrow NH(X^3\Sigma^-) + CO_2$; $HNO + H_2 \rightarrow NH(X^3\Sigma^-) + H_2O$.

these reactions and the formation of NO under the conditions mentioned is about 10^{-5} s.

The influence of fuel molecules or oxygen present in the burned (or mostly burned) gases can also be determined using the rate constants given in Fig. 4. The rate constant for $NH(X^3\Sigma^-) + O_2$ is taken from Ref. 9, for $NH(X^3\Sigma^-)$ with methane, ethane, and propane, from Ref. 10. The rate constants of the higher hydrocarbons are, as expected, somewhat higher. For the reactions of $NH(X^3\Sigma^-)$ with unsaturated hydrocarbons—mainly addition reactions—the situation is similar.

For a combustion situation on the lean side, the remaining oxygen in the burned gases may have some influence on the NH consumption, which can be estimated using Fig. 4, but H_2O and CO_2 should remain the more important reactants except in an extremely lean situation.

On the fuel-rich side, the hydrocarbon concentration on the burned-gas side will be definitely lower than the concentrations of the water gas components CO_2, H_2O, H_2, and CO. The influence of these hydrocarbons on NH consumption should therefore remain small. In addition, the product of the NH reactions with alkanes and H_2 is, however, NH_2 and no NO is formed directly. The rate constants for the reactions (−3c) and (−4a) given above are also high enough to compete with HNO dissociation and may break the NO bond, at least towards higher temperatures.

In the case where unburned gas volumes rich in fuel or oxygen or both are mixed into the burned gas, the situation is not as simple as discussed above, but

the rate constants needed for computer modelling of these processes are now available.

Acknowledgments

The support of this work by DFG is gratefully acknowledged.

REFERENCES

1. Lyon, R. K., "Method for Reduction of the Concentration of NO in Combustion Effluents Using Ammonia," U.S. Patent No. 3,900,554, 1975.
2. Perry, R. A., "NO Reduction Using Sublimation of Cyanuric Acid," U.S. Patent No. 4,731,231, 1988.
3. Gehring, H., Hoyerman, K., Schacke, H., and Wolfrum, J., *Fourteenth Symposium (International) on Combustion,* The Combustion Institute, Pittsburgh, 1973, p. 99.
4. Miller, J. A., and Bowman, C. T., *Int. J. Chem. Kinet.* 23:289 (1991).
5. Hack, W., in *Gmelin Handbook of Inorganic and Organometallic Chemistry,* Springer-Verlag, Heidelberg, 1993, Supplement Vol. B1, "Nitrogen," pp. 209–237.
6. Hack, W., and Wilms, A., *J. Phys. Chem.* 93:3540 (1989).
7. Hack, W., Kurzke, H., and Wagner, H.Gg., *J. Chem. Soc. Faraday Trans.* 2 81:949 (1985).
8. Mertens, J. D., Chang, A. Y., Hanson, R. K., and Bowman, C. T., *Int. J. Chem. Kinet.* 23:173 (1991).
9. Hennig, G., Röhrig, M., and Wagner, H.Gg., *Ber. Bunsenges. Phys. Chem.* 97:830 (1993).
10. Röhrig, M., and Wagner, H.Gg., *Ber. Bunsenges. Phys. Chem.* 98 (1994), p. 858.
11. Cox, J. W., Nelson, H. H., and McDonald, J. R., *Chem. Phys.* 96:175 (1985).
12. Cornell, D. W., Berry, R. S., and Lwowski, W., *J. Am. Chem. Soc.* 88:544 (1966).
13. Dove, J. E., and Nip, W. S., *Can. J. Chem.* 57:689 (1979).
14. Holzrichter, K., and Wagner, H.Gg., *Eighteenth Symposium (International) on Combustion,* The Combustion Institute, Pittsburgh, 1981, p. 769.
15. Chang, A. Y., and Hanson, R. K., *J. Quant. Spectros. Radiat. Transfer* 42:207 (1989).
16. Röhrig, M., and Wagner, H.Gg., *Ber. Bunsenges. Phys. Chem.* 98 (1994), p. 864.
17. Kajimoto, O., Yamamoto, T., and Fueno, T., *J. Phys. Chem.* 83:429 (1979).
18. Zaslonko, I. S., Kogarko, S. M., and Mozzhukin, E. V., *Kinet. Katal.* 13:829 (1972).
19. Yumura, M., and Asaba, T., *Eighteenth Symposium (International) on Combustion,* The Combustion Institute, Pittsburgh, 1980, p. 863.
20. Dean, A. M., Hardy, J. E., and Lyon, R. K., *Nineteenth Symposium (International) on Combustion,* The Combustion Institute, Pittsburgh, 1982, p. 97.
21. Mayer, S. W., and Schieler, L., *J. Phys. Chem.* 72:236 (1968).
22. Davidson, D. F, Kohse-Höinghaus, K., Chang, A. Y., and Hanson, R. K., *Int. J. Chem. Kinet.* 22:513 (1990).
23. Melius, C. F., *BAC-MP4 Heats of Formations and Free Energies,* Sandia National Laboratories, Livermore, CA, 1986.

Twenty-Fifth Symposium (International) on Combustion/The Combustion Institute, 1994/pp. 983–991

A SHOCK TUBE STUDY OF THE REACTIONS OF CN AND NCO WITH NO_2

STEVEN T. WOOLDRIDGE, JOHN D. MERTENS,* RONALD K. HANSON AND CRAIG T. BOWMAN
High Temperature Gasdynamics Laboratory
Department of Mechanical Engineering
Stanford University, Stanford, CA 94305, USA

The total rate coefficients for the reactions

$$CN + NO_2 \rightarrow \text{products} \quad (1)$$

$$NCO + NO_2 \rightarrow \text{products} \quad (2)$$

were measured at temperatures between 1000 and 1600 K and pressures near 1.4 atm in a shock tube. Narrow-line laser absorption was utilized to record time histories of CN and NCO radicals in $C_2N_2/NO_2/Ar$ laser photolysis experiments. In the experiment, CN production is nearly instantaneous via photolysis of C_2N_2; production of NCO radicals follows from the main product channel of reaction (1). A least-squares fit to the results for reaction (1) is given by the expression

$$k_1 = 1.59 \times 10^{13} \exp(570/T\,[\mathrm{K}])\ \mathrm{cm^3\ mol^{-1}\ s^{-1}}$$

with corresponding uncertainty factors of $f = 0.91$ and $F = 1.09$ at the low-temperature extreme; $f = 0.84$ and $F = 1.17$ result at the high-temperature extreme. The uncertainty factors give the limiting values of the rate coefficient: $k_{min} = fk_{best\,fit}$, $k_{max} = Fk_{best\,fit}$. The rate coefficient of reaction (2) was measured as $k_2 = 4.5 \times 10^{12}\ \mathrm{cm^3\ mol^{-1}\ s^{-1}}$ ($f = 0.75$, $F = 1.27$) for temperatures near 1250 K. Incorporating the data from the present study with the results from lower-temperature studies gives the following empirical expressions for the total rate coefficients valid for temperatures ranging from 300 to 1600 K:

$$k_1 = 6.16 \times 10^{15}\, T\,[\mathrm{K}]^{-0.752} \exp(-173/T\,[\mathrm{K}])\ \mathrm{cm^3\ mol^{-1}\ s^{-1}}$$

$$k_2 = 3.25 \times 10^{12} \exp(356/T\,[\mathrm{K}])\ \mathrm{cm^3\ mol^{-1}\ s^{-1}}.$$

Introduction

Nitrogen dioxide, NO_2, is an important oxidizing species in the combustion of nitramine-based propellants [1,2]. Oxidation of HCN, which is present in the system in high concentrations, leads to the formation of CN and NCO radicals; therefore, the reactions of CN and NCO with NO_2 are important in models of these combustion processes.

In this study, these reactions are studied in reflected shock experiments using C_2N_2/NO_2 mixtures dilute in argon. The reflected shock conditions span the temperature range 1000–1600 K and the pressure range 1.2–1.5 atm. In order to produce measurable concentrations of CN and NCO at low reflected shock temperatures, 193-nm excimer photolysis of C_2N_2 is employed. The photolysis scheme produces CN radicals nearly instantaneously; rapid kinetic production of NCO radicals via the main product channel of the $CN + NO_2$ reaction follows. Narrow-line continuous-wave (cw) laser absorption diagnostics are utilized to monitor the concentration time histories of CN and NCO. The measured concentration profiles are analyzed using a detailed kinetics model in order to determine the total rate coefficients (to all product channels) for the two elementary reactions

$$\begin{aligned} CN + NO_2 &\rightarrow NCO + NO \\ &\qquad \Delta H_{1000K} = -243\ \mathrm{kJ\ mol^{-1}} \\ &\rightarrow N_2O + CO \\ &\qquad \Delta H_{1000K} = -495\ \mathrm{kJ\ mol^{-1}} \\ &\rightarrow CO_2 + N_2 \\ &\qquad \Delta H_{1000K} = -861\ \mathrm{kJ\ mol^{-1}}. \quad (1) \end{aligned}$$

$$\begin{aligned} NCO + NO_2 &\rightarrow N_2O + CO_2 \\ &\qquad \Delta H_{1000K} = -476\ \mathrm{kJ\ mol^{-1}} \\ &\rightarrow NO + NO + CO \\ &\qquad \Delta H_{1000K} = -95.9\ \mathrm{kJ\ mol^{-1}}. \quad (2) \end{aligned}$$

*Assistant Professor at Trinity College, Hartford, CT 06106, USA.

Existing high-temperature data for these reactions are scarce. Wang et al. [3] measured the total rate coefficient for reaction (1) using a two-laser pump-probe technique with ICN/NO_2 mixtures for temperatures between 297 and 740 K, and obtained the least-squares expression for the rate coefficient $k_1 = 8.12 \times 10^{18}\ T\,[K]^{-1.78} \exp(-591/T\,[K])$ $cm^3\ mol^{-1}\ s^{-1}$. They found the reaction to be pressure independent for total pressures ranging from 50 to 322 torr and also observed a negative temperature dependence. You and Wang [4] used a similar pump-probe technique to measure the rates of both reactions at room temperature and obtained $k_1 = 4.3 \times 10^{13}$ and $k_2 = 1.3 \times 10^{13}$ $cm^3\ mol^{-1}\ s^{-1}$. In two recent studies, Park and Hershberger [5,6] used laser photolysis and infrared diode laser absorption spectroscopy to monitor time histories of CN, NCO, CO, CO_2, NO, and N_2O in ICN/NO_2 and $BrNCO/NO_2$ mixtures. They measured the overall rate coefficients and the product branching ratios of both reactions for temperatures between 298 and 500 K and obtained $k_1 = 3.02 \times 10^{13} \exp(171/T\,[K])$ and $k_2 = 2.51 \times 10^{12} \exp(441/T\,[K])$ $cm^3\ mol^{-1}\ s^{-1}$. The measured room-temperature branching ratios were 87% for the NCO + NO channel of reaction (1) and 92% for the N_2O + CO_2 channel of reaction (2).

The present experiments are conducted in three phases. First, vibrational relaxation and recombination rates of the CN photolysis fragments are measured in baseline photolysis experiments involving C_2N_2/Ar mixtures. Next, photolysis of C_2N_2 in the presence of NO_2 is used in order to measure k_1. Finally, NCO absorption is measured for the determination of k_2.

Experimental Apparatus

The experimental configuration, shown in Fig. 1, consists of three main components: the shock tube, the cw ring dye laser system, and the excimer photolysis laser.

The pressure-driven shock tube is composed of a 6-m driven section (14.3-cm internal diameter) and a 2.4-m driver section (5-cm internal diameter). To minimize the effect of impurities on the experiments, the shock tube is evacuated with a Varian V 1000 turbomolecular pump for at least 1 h between shocks, resulting in leak plus out-gassing rates of less than 2×10^{-6} torr/min. Reflected shock conditions are calculated assuming frozen chemistry and vibrational equilibrium. Gas mixtures of C_2N_2/NO_2 in argon are prepared in a 20-L stainless steel mixing tank. Research-grade argon (99.9995%) from Liquid Carbonic, 1.09% C_2N_2 in argon (Matheson Certified Standard), and 529 ppm NO_2 in argon (Liquid Carbonic Certified Standard) are used without further purification. Pure NO_2 (99.5%) from Matheson is also used after purification via vacuum distillation at 195 K.

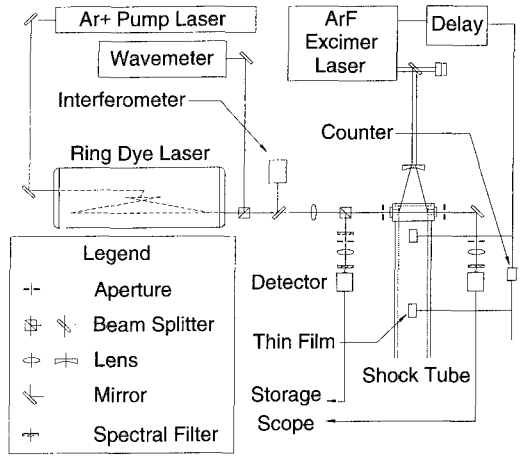

FIG. 1. Experimental configuration for shock tube photolysis experiments.

The laser diagnostic system for CN and NCO detection is described in detail in Ref. 7. Exalite 392E laser dye is used for the CN diagnostic, and Stilbene 420 is used for the NCO diagnostic. Briefly, CN is probed at the P-branch bandhead of the $B \leftarrow X\,(0,0)$ transition at 388.444 nm (vacuum). NCO is monitored at the $P_2 + {}^PQ_{12}$ bandhead of the $A(00^00) \leftarrow X(00^10)$ transition at 440.479 nm (vacuum). The CN absorption coefficients are calculated for the reflected shock test conditions using the methods described by Wooldridge et al. [7,8].

A Lambda Physik model EMG 150 MSC excimer laser operating at 193 nm (ArF) in the single-pulse mode is used to produce CN radicals from the C_2N_2 precursor. As illustrated in Fig. 1, an end wall illumination scheme is used in the experiments. Two 95% reflectors (fused silica substrate, Acton 193/FR/45 coating) are used to turn and rotate the vertically aligned laser pulse onto the UV-grade fused silica window mounted horizontally in the shock tube end wall. A 500-mm focal length MgF_2 cylindrical lens expands the horizontal dimension of the photolysis beam from 2.5 cm to approximately 14 cm. The vertical dimension of the beam is 6 mm. The diagnostic port centerline is approximately 1 cm from the end wall. A typical pulse energy/duration is 40 mJ/15 ns incident on the test gas. Relative pulse energies for the experiments are measured with a Molectron J50HR pyroelectric joule meter located behind the first turning reflector to monitor the 5% transmitted fraction. The photolysis pulse is timed to occur approximately 50 μs after the reflected shock passes the diagnostic port by utilizing a time delay generator connected to the last thin-film amplifier circuit.

Verification of minor photolysis of the NO_2 in the

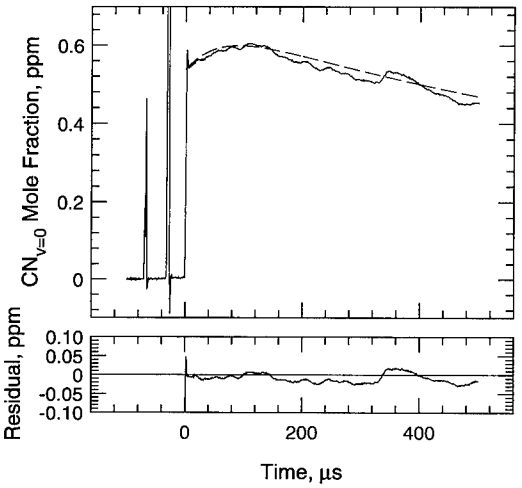

FIG. 2. Baseline CN absorption trace (———) from the photolysis of 587 ppm C_2N_2 in Ar compared with a Chemkin-II calculation (------). Shock conditions are T = 1084 K and P = 1.58 atm. The two signal spikes preceding the photolysis pulse are effects of beam steering due to the passage of the incident and reflected shock waves.

reactant mixtures was accomplished by performing a set of 130.5-nm O-atom ARAS experiments on NO_2/Ar mixtures. For NO_2 mixtures of approximately 580 ppm, a calibrated photolysis yield of less than 0.1 ppm O atoms was observed for the pulse densities typical of the kinetics experiments. Therefore, photolysis of NO_2 is neglected in the data analysis.

Results

CN Absorption Measurements:

ArF excimer photolysis of C_2N_2 results in the production of vibrationally hot CN fragments, with the majority of the CN produced in the electronic ground state [9]. The nonthermal vibrational population of CN relaxes to a Boltzmann distribution through vibrational-translational (V-T) and vibrational-vibrational (V-V) energy transfer between the CN molecules and the other species present in the gas mixture (primarily C_2N_2, NO_2, and Ar). In order to characterize the vibrational relaxation process, a set of baseline C_2N_2 photolysis experiments was conducted. Since ground-state CN is probed, one expects the CN absorption signal to rise instantaneously because of the photolytic production of $CN_{v=0}$, followed by an increase in signal over the time frame of vibrational relaxation. Figure 2 shows this scenario. For all CN absorption experiments, the absorption signal is converted to $CN_{v=0}$ mole fraction via the Beer–Lambert law for narrow-line radiation. Division by the equilibrium fraction of the ground vibrational state converts the absorption coefficient for total CN concentration to a $CN_{v=0}$ absorption coefficient. As Fig. 2 illustrates, the photolytic production and relaxation rise are present in the experimental trace, as well as a long-time decay due to CN recombination. The short time scale of the signal rise observed in all baseline traces suggests that a very efficient, near-resonant V-V energy transfer between CN and C_2N_2 controls the relaxation process. The observation that an increase in the initial C_2N_2 concentration reduces proportionally the relaxation time constant supports this conclusion.

The calculated CN trace, shown in Fig. 2, is produced using Chemkin-II [10], the Chemkin Thermodynamic Data Base [11], and the reaction mechanism shown in Table 1. The NCO heat of formation of $\Delta H^{\circ}_{f,298K}$ = 31.5 kcal mol^{-1} [12] is used in all kinetic modeling; this value is significantly lower than the JANAF recommendation of 38.1 kcal mol^{-1}. The mechanism in Table 1 was pared from a 43-reaction mechanism using sensitivity and contribution factor analyses to identify reactions important to the C_2N_2/NO_2/CN system. For the baseline experiments, only reaction (4) contributes to a kinetic perturbation of the CN profile. Conversion of the calculated CN profile to a $CN_{v=0}$ profile is accomplished by multiplication by a time-evolving fraction of the ground vibrational state. This fraction initially starts at the level produced by the photolysis pulse [$F_{v=0}(t = 0)$] and relaxes to the equilibrium fraction. The nonequilibrium vibrational condition is solely a probing concern; no vibrational enhancement of the CN kinetics is assumed. Consequently, two parameters are adjustable in modeling the baseline traces: $F_{v=0}(t = 0)$ and the relaxation time constant τ_v. The measured level of $CN_{v=0}$, combined with $F_{v=0}(t = 0)$, gives the photolysis yield of CN from C_2N_2; hence, the photolysis yield is directly determined by the value of $F_{v=0}(t = 0)$. Variations of the parameters alter the calculated trace in two ways: a shift in magnitude of the equilibrated level of $CN_{v=0}$, or a change in the time scale required to reach the equilibrated level. For conditions spanning the temperature range 1084–1667 K, the vibrational relaxation parameters are $F_{v=0}(t = 0) = 1.107 - 3.244 \times 10^{-4}\,T$ and $\log_{10}(P_{C_2N_2}\,\tau_v\,[\text{atm}\,\mu s]) = -3.295 + 19.45/T^{1/3}$. For a single experiment, the parameters could be determined to a precision of ±25% for τ_v, and ±10% for $F_{v=0}(t = 0)$.

Figure 3 is a representative data trace from the CN + NO_2 experiments and includes the absorption measurement, the calculated CN profile, and the mole fraction residual. The residual is the experimental profile minus the calculated profile and aids the determination of the "best-fit" value for the total rate coefficient of reaction (1) for each experiment. The fast decay of the CN absorption signal after photolysis is due to reaction with NO_2. Figure 4 shows

TABLE 1
Reaction mechanism

	Reaction	$\log_{10}(A)$	B	θ	Ref.
1	$CN + NO_2 \leftrightarrow$ products	13.20	0	−570	[a]
2	$NCO + NO_2 \leftrightarrow$ products	12.65	0	0	[a]
3	$NO_2 + M \leftrightarrow NO + O + M$	16.04	0	33,000	13
4	$C_2N_2 + M \leftrightarrow CN + CN + M$	34.03	−4.32	65,420	14
5	$C_2N_2 + O \leftrightarrow CN + NCO$	14.11	0	7,130	15
6	$C_2N_2 + CN \leftrightarrow C_3N_3$	12.35	−0.28	1,568	16
7	$NO_2 + O \leftrightarrow NO + O_2$	13.00	0	300	13
8	$NCO + NO \leftrightarrow N_2O + CO$	18.15	−1.73	384	17
9	$NCO + O \leftrightarrow NO + CO$	13.67	0	0	17
10	$CN + O \leftrightarrow CO + N$	13.89	0	0	18
11	$CN + NCO \leftrightarrow NCN + CO$	13.26	0	0	19

Rate coefficients are in the form $k = AT^B \exp(-\theta/T)$ cm^3 mol^{-1} s^{-1}, (θ and T in [K]).
[a]This work.

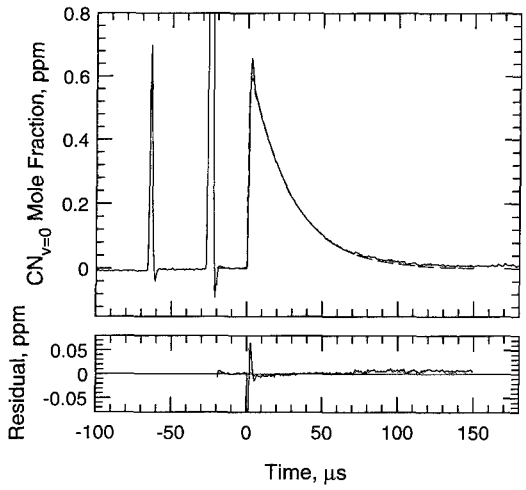

FIG. 3. CN absorption trace (———) from the photolysis of 585 ppm C_2N_2, 80 ppm NO_2 in Ar and the Chemkin-II calculation (------). Shock conditions are T = 1073 K and P = 1.54 atm.

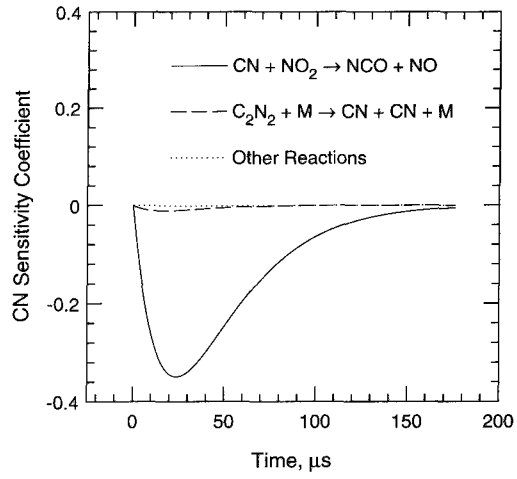

FIG. 4. Calculated CN sensitivity coefficient profile for the conditions of Fig. 3. The sensitivity coefficient for reaction (i) is defined as $a_{i,CN} = (A_i/\chi_{CN,max}) \times (\partial\chi_{CN}/\partial A_i)$.

the sensitivity plot generated from SENKIN [20] for the conditions of Fig. 3. The CN time history is dominated by reaction (1), with a minor contribution from the CN recombination reaction.

The data reduction scheme consists of converting the absorption signal to $CN_{v=0}$ mole fraction and then adjusting the magnitude of k_1 in the model until the residual is minimized. The input conditions to the model are the test gas temperature, pressure, C_2N_2 and NO_2 mole fractions, and the initial mole fraction of CN produced by photolysis. Table 2 shows the experimental conditions and results for this set of experiments. Interference from secondary reactions at high temperatures and the influence of CN vibrational relaxation preclude the use of a pseudo-first-order scheme for data reduction.

The results from Table 2 are plotted in Fig. 5. The expression

$$k_1 = 1.59 \times 10^{13} \exp(570/T\ [\mathrm{K}])\ \mathrm{cm}^3\ \mathrm{mol}^{-1}\ \mathrm{s}^{-1}$$

fits the data to within 6% for temperatures between 1073 and 1582 K.

NCO Absorption Measurements:

Figure 6 shows a sample NCO absorption trace used for the determination of k_2. For the NCO ab-

TABLE 2
Results for CN absorption experiments

T (K)	P (atm)	NO_2 (ppm)	C_2N_2 (ppm)	$k_1 \times 10^{-13}$ ($cm^3\ mol^{-1}\ s^{-1}$)
1073	1.54	80	585	2.85
1097	1.48	468	2165	2.5
1114	1.42	233	2215	2.7
1136	1.56	151	1099	2.6
1181	1.42	80	585	2.7
1240	1.44	80	585	2.45
1289	1.52	468	2165	2.25
1311	1.45	233	2215	2.6
1346	1.35	468	2165	2.3
1347	1.37	233	2215	2.55
1415	1.35	468	2165	2.25
1430	1.36	233	2215	2.5
1562	1.28	468	2165	2.25
1582	1.26	80	585	2.35

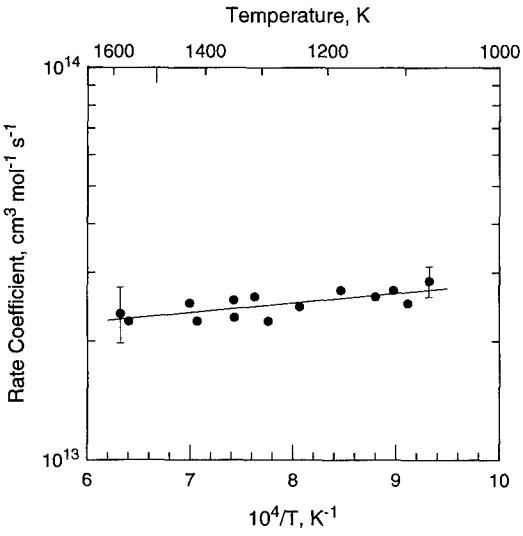

FIG. 5. Arrhenius diagram for reaction (1), CN + NO_2 → products. The solid line is a least-squares fit to the data: $k_1 = 1.59 \times 10^{13} \exp(570/T\ [K])\ cm^3\ mol^{-1}\ s^{-1}$.

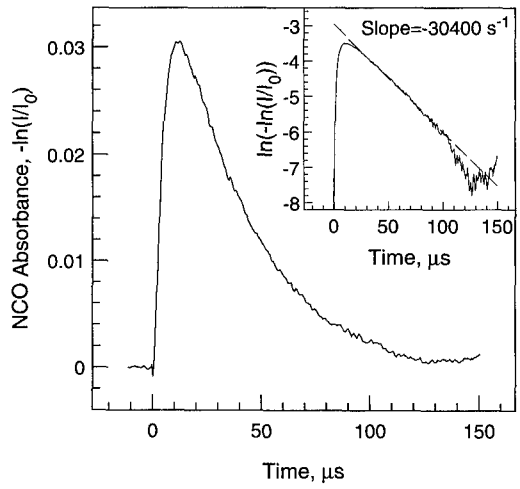

FIG. 6. NCO absorption trace from the photolysis of 0.98% C_2N_2, 500 ppm NO_2 in Ar. Shock conditions are $T = 1221$ K, $P = 1.34$ atm. The slope of the inset figure is equal to $-k_2 \times [NO_2]$.

sorption experiments, the decay of the signal is pseudo-first-order after the initial production of NCO via reaction (1), as confirmed in the sensitivity plot of Fig. 7. The photolysis yield of 30 ppm CN used in the sensitivity analysis is derived from the measured pulse energy relative to the C_2N_2 baseline traces. The yield observed in the baseline experiment for conditions near the NCO experiment is scaled by the pulse energy and initial C_2N_2 mole fraction. The value of k_2 is obtained from the expression

$$k_2 = -\Delta \ln\{-\ln(I/I_0)\}/(\Delta t[NO_2]).$$

The inset in Fig. 6 displays the rate coefficient determination from the decay of the NCO trace. Table 3 gives the results and experimental conditions for the NCO + NO_2 reaction. No temperature dependence of the total rate coefficient is discernible within the scatter of the data. Therefore, an average value of $k_2 = 4.5 \times 10^{12}\ cm^3\ mol^{-1}\ s^{-1}$ for temperatures near 1250 K is reported.

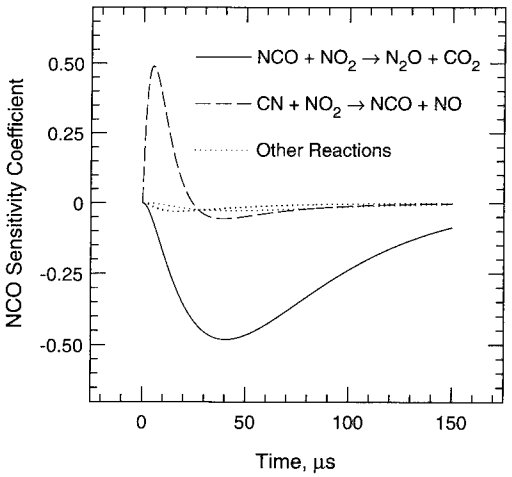

FIG. 7. Calculated NCO sensitivity coefficient profile for $T = 1221$ K, $P = 1.34$ atm, 0.98% C_2N_2, 500 ppm NO_2, and 30 ppm CN.

Discussion

Uncertainty Analysis:

The total uncertainties at the temperature extremes for k_1, estimated using independent error propagation analysis, are given in Table 4. Different sources of uncertainty are important at high or low temperatures. For low temperatures, only the vibrational relaxation parameters influence the results, whereas at high temperatures, interference from secondary reactions emerges. The uncertainties associated with the vibrational relaxation parameters are based on the scatter observed for the entire data set, not the fit precision associated with a particular baseline experiment. The uncertainty factors of $f = 0.91$ and $F = 1.09$ are derived for the low-temperature extreme; for the high-temperature extreme, $f = 0.84$ and $F = 1.17$ are determined. The value of k_1 falls between $f \times k_1$ and $F \times k_1$.

The primary contributors to the uncertainty of k_2

TABLE 3
Results for NCO absorption experiments

T (K)	P (atm)	NO_2 (ppm)	C_2N_2 (ppm)	$k_2 \times 10^{-12}$ ($cm^3\ mol^{-1}\ s^{-1}$)
1147	1.39	500	9810	3.9
1148	1.40	432	2001	4.7
1221	1.34	500	9810	4.6
1245	1.34	432	2001	4.5
1334	1.26	432	2001	4.8

TABLE 4
Uncertainty analysis for k_1

Parameter	Uncertainty (%)	Effect on k_1 (%)	
Low-temperature:			
τ_v	factor of 1.7	−5	+5
$F_{v=0}(t = 0)$	+10	−5	
	−10		+5
Least-squares fit		−5	+6
Total uncertainty = $[\Sigma(\text{uncertainty})^2]^{0.5}$		−9	+9
High-temperature:			
τ_v	factor of 1.7	−10	+7
$F_{v=0}(t = 0)$	+10	−10	
	−10		+7
k_3	+40		+10
	−40	−5	
k_5	+20		+7
Least-squares fit		−5	+6
Total uncertainty = $[\Sigma(\text{uncertainty})^2]^{0.5}$		−16	+17

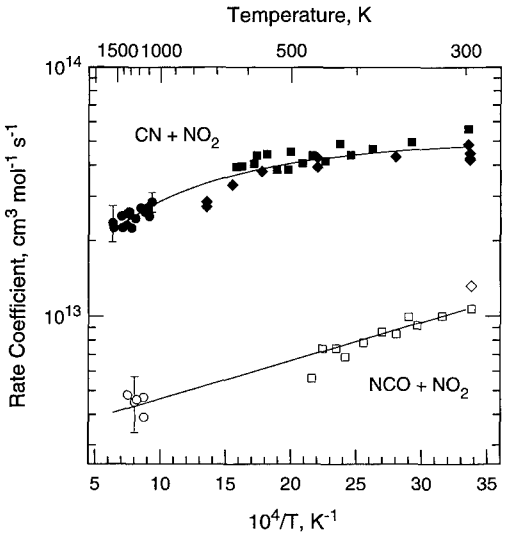

FIG. 8. Arrhenius diagram for the total rate coefficients of reactions (1) and (2). Data for reaction (1) are represented by filled symbols, and data for reaction (2) are represented by open symbols. ●, ○ this study; ♦ Ref. 3; ◇ Ref. 4; ■, □ Refs. 5 and 6. The least-squares data fits are given by $k_1 = 6.16 \times 10^{15}\, T\,[\mathrm{K}]^{-0.752} \exp(-173/T\,[\mathrm{K}])$ and $k_2 = 3.25 \times 10^{12} \exp(356/T\,[\mathrm{K}])\ \mathrm{cm^3\ mol^{-1}\ s^{-1}}$.

are the decrease of the NO_2 concentration due to reactions with CN and NCO, and the uncertainty of the least-squares fit to the pseudo-first-order region of the data trace. Exact quantification of the NO_2 decay is difficult because of branching ratio and diagnostic uncertainties, but as much as 10% could be consumed. Under the pseudo-first-order assumption, a low determination of k_2 occurs. Combination of this uncertainty with the $\pm 25\%$ uncertainty of the pseudo-first-order linear curve fit results in uncertainty factors of $f = 0.75$ and $F = 1.27$.

Reaction (1) Product Channel:

The assumed product channel for reaction (1) in the analysis of the CN absorption data is NCO + NO. Two other channels are active at room temperature: N_2O + CO and CO_2 + N_2 [5]. The choice of branching fractions has no effect on the determination of k_1. However, some information can be extracted from the NCO data concerning the importance of this channel. The rapid rise of the NCO signal indicates that the NCO + NO channel is active at 1250 K; however, the magnitude cannot be quantified until an accurate measurement of the NCO absorption coefficient at the conditions of the present study is available.

Comparison with Low-Temperature Studies:

Figure 8 shows the results of the current study for k_1 and k_2 and the low-temperature results from Refs. 3 through 6. A least-squares analysis of the data yields the following empirical expressions for the total rate coefficients of reactions (1) and (2) valid for temperatures between 300 and 1600 K:

$$k_1 = 6.16 \times 10^{15}\, T\,[\mathrm{K}]^{-0.752} \cdot \exp(-173/T\,[\mathrm{K}])\ \mathrm{cm^3\ mol^{-1}\ s^{-1}}$$

$$k_2 = 3.25 \times 10^{12} \cdot \exp(356/T\,[\mathrm{K}])\ \mathrm{cm^3\ mol^{-1}\ s^{-1}}.$$

The apparent negative temperature dependence of both reactions can be explained via analogy with the reaction mechanism associated with the NCO + NO reaction [21,22]. Park and Hershberger interpret their branching ratio results for reaction (1) in terms of the formation and dissociation of a NC-ONO collision complex [5]. Isomerization of this complex to the OCN-NO intermediate associated with the NCO + NO reaction was postulated as the mechanism responsible for the minor N_2O + CO and CO_2 + N_2 channels. The observed temperature dependence of k_1 results from a redissociation of the NC-ONO complex into CN and NO_2 at higher temperatures, which is similar to the NCO + NO reaction [21]. The barrier height for the primary dissociation channel (NCO + NO) is likely to be somewhat smaller than that associated with the isomerization channel; both barriers are less than the energy of the transition state of the redissociation process.

Conclusions

The total rate coefficients for the reactions

$$\mathrm{CN} + \mathrm{NO_2} \rightarrow \text{products} \qquad (1)$$

$$\mathrm{NCO} + \mathrm{NO_2} \rightarrow \text{products} \qquad (2)$$

were measured using narrow-line laser absorption of CN and NCO radicals in $C_2N_2/NO_2/Ar$ photolysis experiments. Empirical expressions for the rate coefficients valid for temperatures ranging from 300 to 1600 K were derived from available data:

$$k_1 = 6.16 \times 10^{15}\, T\,[\mathrm{K}]^{-0.752} \cdot \exp(-173/T\,[\mathrm{K}])\ \mathrm{cm^3\ mol^{-1}\ s^{-1}}$$

$$k_2 = 3.25 \times 10^{12} \cdot \exp(356/T\,[\mathrm{K}])\ \mathrm{cm^3\ mol^{-1}\ s^{-1}}.$$

Uncertainties concerning the products of both re-

actions still exist. However, correlation of the results from this study with previous studies conducted at different temperatures suggests that reaction (1) proceeds primarily toward the NCO + NO channel, and reaction (2) most likely results in N_2O + CO_2 products.

Acknowledgment

This work is supported by the Office of Naval Research under Contract No. N00014-90-J-1883, with Dr. Richard Miller as technical monitor.

REFERENCES

1. Melius, C. F., *Proceedings of the 24th JANAF Combustion Meeting*, 1987.
2. Melius, C. F., in *Chemistry and Physics of Energetic Materials* (S. N. Bulusu, Ed.), NATO ASI Series, Kluwer Academic Publishers, Dordrecht, The Netherlands, 1990, p. 51.
3. Wang, N. S., Yang, D. L., and Lin, M. C., *Chem. Phys. Lett.* 163:480–484 (1989).
4. You, Y., and Wang, N. S., *Third International Conference on Chemical Kinetics: Program and Abstracts*, National Institute of Standards and Technology, Gaithersburg, MD, 1993, p. 108.
5. Park, J., and Hershberger, J. F., *J. Chem. Phys.* 99:3488–3493 (1993).
6. Park, J., and Hershberger, J. F., *J. Phys. Chem.* 97:13647–13652 (1993).
7. Wooldridge, S. T., Hanson, R. K., and Bowman, C. T., *J. Quant. Spectrosc. Radiat. Transfer* 50:19–34 (1993).
8. Wooldridge, S. T., Hanson, R. K., and Bowman, C. T., in preparation.
9. Halpern, J. B., and Jackson, W. M., *J. Phys. Chem.* 86:973–976 (1982).
10. Kee, R. J., Rupley, F. M., and Miller, J. A., *Chemkin-II: A Fortran Chemical Kinetics Package for the Analysis of Gas-Phase Chemical Kinetics*, Sandia National Laboratories Report No. SAND89-8009, 1989.
11. Kee, R. J., Rupley, F. M., and Miller, J. A., *The Chemkin Thermodynamic Data Base*, Sandia National Laboratories Report No. SAND87-8215B, 1990.
12. East, A. L. L., and Allen, W. D., *J. Chem. Phys.* 99:4638–4650 (1993).
13. Hanson, R. K., and Salimian, S., in *Combustion Chemistry* (W. C. Gardiner, Ed.), Springer, New York, 1984, p. 361.
14. Natarajan, K., Thielen, K., Hermanns, H. D., and Roth, P., *Ber. Bunsenges. Phys. Chem.* 90:533–539 (1986).
15. Roth, P., Louge, M. Y., and Hanson, R. K., *Combust. Flame* 64:167–176 (1986).
16. Yang, D. L., Yu, T., Lin, M. C., and Melius, C. F., *J. Chem. Phys.* 97:222–226 (1992).
17. Mertens, J. D., Dean, A. J., Hanson, R. K., and Bowman, C. T., *Twenty-Fourth Symposium (International) on Combustion*, The Combustion Institute, Pittsburgh, 1992, pp. 701–710.
18. Davidson, D. F., Dean, A. J., DiRosa, M. D., and Hanson, R. K., *Int. J. Chem. Kinet.* 23:1035–1050 (1991).
19. Tsang, W., *J. Phys. Chem. Ref. Data* 21:753–791 (1992).
20. Lutz, A. E., Kee, R. J., and Miller, J. A., *SENKIN: A Fortran Program for Predicting Homogeneous Gas Phase Chemical Kinetics with Sensitivity Analysis*, Sandia National Laboratories Report No. SAND87-8248, 1988.
21. Lin, M. C., He, Y., and Melius, C. F., *J. Phys. Chem.* 97:9124–9128 (1993).
22. Cooper, W. F., Park, J., and Hershberger, J. F., *J. Phys. Chem.* 97:3283–3290 (1993).

COMMENTS

M. C. Lin, Emory University, USA. The reaction of CN with NO_2 may take place via three possible intermediates: NCONO, $NCNO_2$, and $CNNO_2$. The first intermediate, which you proposed, may not undergo rearrangement to produce other products (than the direct decomposition products, NCO + NO). The third intermediate $CNNO_2$, however, may rearrange to give OCNNO, leading to the production of N_2O + CO and N_2 + CO_2, similar to the NCO + NO reaction.

Author's Reply. Assuming that the $CNNO_2$ intermediate isomerizes to OCNNO, calculations of the branching fractions for CN + NO_2 using the QRRK treatment for chemically activated reactions [1] indicate that the NCO + NO product channel is dominant for the NCONO and $CNNO_2$ intermediate pathways. The measured room-temperature branching fractions for N_2O + CO (7.6 ± 3.2%) and CO_2 + N_2 (5.6 ± 6.0%) (Ref. 5 of our paper) can be recovered only when the reaction is assumed to proceed entirely through the $CNNO_2$/OCNNO channel. These results are not surprising if the underlying processes associated with OCNNO decomposition are considered. According to Lin et al. (Ref. 21 of our paper), the transition states for OCNNO decomposition to N_2O + CO and CO_2 + N_2 are very tight, while decomposition to NCO + NO occurs through a loose transition state. As a result, if the reaction of CN with NO_2 occurs via the formation of $CNNO_2$ and its subsequent isomerization to OCNNO, the dominant products will be NCO + NO.

REFERENCE

1. Dean, A. M., Bozzelli, J. W., and Ritter, E. R., *Combust. Sci. Technol.* 80:63–85 (1991).

•

John H. Kiefer, University of Illinois at Chicago, USA. What are the products of your second reaction, NCO + $NO_2 \rightarrow$ products?

Author's Reply. The high-temperature products of the NCO + NO_2 reaction are not established. At room temperature, Park and Hershberger (Ref. 6 of our paper) report that the branching fraction of the N_2O + CO_2 channel is 92%. They propose that these products are formed from an O_2NNCO intermediate, while the minor product channel of NO + NO + CO occurs through an ONONCO intermediate. The choice of products does not affect our determination of the overall rate of reaction (2).

Twenty-Fifth Symposium (International) on Combustion/The Combustion Institute, 1994/pp. 993–1001

KINETIC STUDIES OF THE REACTIONS $NH(X^3\Sigma^-)$ + NO AND $NH(X^3\Sigma^-)$ + O_2 AT ELEVATED TEMPERATURES

HANNELORE LILLICH, ALEXANDER SCHUCK, HANS-ROBERT VOLPP AND JÜRGEN WOLFRUM
Physikalisch-Chemisches Institut der Universität Heidelberg
Im Neuenheimer Feld 253, 69120 Heidelberg, Germany

AND

PRAKASH D. NAIK
Chemistry Division, Bhabha Atomic Research Centre
Bombay-400 085, India

Absolute rate coefficients for the reaction of $NH(X^3\Sigma^-)$ + NO → products (k_1) and $NH(X^3\Sigma^-)$ + O_2 → products (k_2) were measured as a function of temperature in a heatable quartz reactor by means of the laser photolysis/laser-induced fluorescence (LP/LIF) pump-probe technique. $NH(X^3\Sigma^-)$ radicals were produced by the 193 nm photolysis of isocyanic acid in the presence of a large excess of xenon. The measured rate coefficients can be described by the following expressions: $k_1(293 < T < 1085\ K) = 10^{14.18} \times (T/298\ K)^{(-1.60\pm0.01)} \exp(-3.8 \pm 0.2\ kJ\ mol^{-1}/RT)\ cm^3\ mol^{-1}\ s^{-1}$; $k_2(293 < T < 793\ K) = 10^{9.38} \times (T/298\ K)^{(3.34\pm0.15)} \times \exp(2.3 \pm 0.4\ kJ\ mol^{-1}/RT)\ cm^3\ mol^{-1}\ s^{-1}$. For the reaction $NH(X^3\Sigma^-)$ + NO (1), the branching ratio $\beta = k_{1a}/k_1$ into the OH product channel—$NH(X^3\Sigma^-)$ + NO → OH + N_2 (1a)—was measured by means of a calibration method to be $\beta = (0.15 \pm 0.05)$ at 300 K. In addition, the following temperature-dependent removal rate coefficient for $NH(X^3\Sigma^-, v = 1)$ by NO was measured: $k_{1(v=1)}(293 < T < 922\ K) = 10^{13.68} \times (T/298\ K)^{-0.71} \times \exp(0.27 \pm 0.01\ kJ\ mol^{-1}/RT)\ cm^3\ mol^{-1}\ s^{-1}$.

Introduction

The reactions of $NH(X^3\Sigma^-)$ with NO (1) and O_2 (2) are important in a variety of combustion processes including the oxidation of ammonia, the Thermal $DeNO_x$, and the $RAPRENO_x$ process [1–4].

$$NH(X^3\Sigma^-) + NO \rightarrow N_2 + OH \quad (1a)$$

$$\rightarrow N_2O + H \quad (1b)$$

$$NH(X^3\Sigma^-) + O_2 \rightarrow \text{products} \quad (2)$$

Several experimental studies on the kinetics of the reactions (1) and (2) were carried out, but there is still a lack of rate constant data in the temperature range relevant to combustion.

For reaction (1), values between $2.3 \times 10^{13}\ cm^3\ mol^{-1}\ s^{-1}$ and $3.6 \times 10^{13}\ cm^3\ mol^{-1}\ s^{-1}$ were measured for the room-temperature rate coefficients [5–10]. Harrison et al. found the rate constant of reaction (1) to be temperature independent between 269 and 377 K [8]. In a room-temperature study, Harrison et al. could not detect OH as a product of reaction (1) [8]. By way of contrast, Yamasaki et al. reported N_2 + OH to be exclusively formed in reaction (1) at room temperature [9]. High-temperature branching ratios $\beta = k_{1a}/k_1$ for reaction (1) into the OH-producing channel reaction (1a) were measured, and values of $\beta = (0.19 \pm 0.10)$ at 3000 K [11] and $\beta = (0.32 \pm 0.07)$ at 3500 K [12] were reported. Very recently, Durant measured a room-temperature branching ratio of (0.8 ± 0.4) into the N_2O + H channel of reaction (1) [13]. Also very recently, Hack et al. [10] determined values of $k_1(298\ K) = 3.6 \times 10^{13}\ cm^3\ mol^{-1}\ s^{-1}$ and $k_{1a}(298\ K) = 3 \times 10^{12}\ cm^3\ mol^{-1}\ s^{-1}$ from which a value of $\beta = 8.3 \times 10^{-2}$ can be derived. Reaction dynamics studies were carried out by Patel-Misra and Dagdigian [14], who measured the vibrational and rotational state distributions of OH radicals produced in reaction (1). For reaction (1), several theoretical studies were carried out [15–18]. Although the results of these studies vary widely, they agree that the transition state for the formation of H + N_2O is lower in energy than the one leading to N_2 + OH. Miller and Melius reported expressions for the rate coefficients of reactions (1) and (2) for the temperature range 300–3300 K, and a value of $\beta = 0.19$ at 300 K [19] was found for reaction (1).

For reaction (2), Hack et al. determined that at room temperature the OH-producing channel is the main channel [20] and that room-temperature measurements yielded values of $5.6 \times 10^9\ cm^3\ mol^{-1}\ s^{-1}$ and $5.1 \times 10^9\ cm^3\ mol^{-1}\ s^{-1}$ [20,21]. An upper limit of $2 \times 10^{10}\ cm^3\ mol^{-1}\ s^{-1}$ for k_2 was determined at room temperature by Pagsberg et al. [22],

and Hack et al. found that k_2 increases in going from room temperature to 543 K [20].

High-temperature data for reactions (1) and (2) were obtained in flame [23–25] and shock tube studies [11,12,26]. For reaction (2), rate constants have also been determined at intermediate temperatures $985 < T < 1729$ K by Henning et al. [27].

In the present study, rate constant measurements for reactions (1) and (2) were carried out at elevated temperatures that allow a direct comparison in particular with the results of the calculations carried out by Miller and Melius [19] and Fueno et al. [28]. In addition, the branching ratio β was measured for reaction (1) at room temperature using a calibration method.

Experimental

The measurements of the absolute rate coefficients for reactions (1) and (2) in the temperature range between 293 and 1085 K and between 293 and 793 K, respectively, were carried out in a heatable quartz reactor (depicted schematically in Fig. 1), which has been described in detail elsewhere [29], using the laser photolysis/laser-induced fluorescence (LP/LIF) pump-probe technique. In the present study, $NH(X^3\Sigma^-)$ radicals were generated by laser photolysis of HNCO at 193 nm, which is known to proceed predominantly via C-N bond breaking leading to $NH(a^1\Delta)$ + CO [30,31]. Recently, the branching ratio into the H + NCO channel was measured to be 0.05 ± 0.006 [32]. The present experiments were carried out in a large background of xenon in order to ensure the rapid quenching of the initially formed $NH(a^1\Delta)$. Detailed studies are reported on the electronic quenching of $NH(a^1\Delta)$ with various collision partners [33,34], in which xenon was found to be an efficient quencher for $NH(a^1\Delta)$ [35–38]. A quenching rate coefficient of 7×10^{12} cm^3 mol^{-1} s^{-1} was measured, and the rate was found to be almost temperature independent between 298 and 476 K [35]. The formation of vibrational-excited $NH(a^1\Delta)$ in the 193-nm photolysis of HNCO was also observed. Bohn and Stuhl determined the $(v = 1)/(v = 0)$ vibrational population ratio to be 0.26 ± 0.05 [39], and the total population of higher vibrational states was reported to be less than 3%. Investigations of the electronic quenching of $NH(a^1\Delta)$ by xenon showed that this process occurs predominantly vibrationally adiabatic [14,36–38]. Due to the slow vibrational relaxation rate ($k_{rel} < 10^8$ cm^3 mol^{-1} s^{-1}) of $NH(X^3\Sigma, v = 1)$ by xenon [36], it was also possible to measure the rate constants for $NH(X^3\Sigma^-, v = 1)$ removal by NO.

HNCO was photodissociated at 193 nm using the output of an ArF* excimer laser (Lambda LPX 205). A XeCl excimer laser (Lambda EMG 210 MSC) pumped dye laser (Lambda FL 2002 EC) operated with p-Terphenyl dye was used to detect $NH(X^3\Sigma^-, v = 0, 1)$ radicals by LIF at the $NH(A^3\Pi - X^3\Sigma^-$; 0-0, 1-1) transition around 336 nm. The frequency-doubled output of a second dye laser (Lambda FL 2002 EC, operated with Rhodamine B dye)—pumped by the same XeCl excimer laser—was used to detect $OH(v = 0)$ radicals by LIF in the $OH(X^2\Pi - A^2\Sigma^+$; 0-0) system around 308 nm. In the 193 nm photolysis of H_2O_2, OH is produced almost exclusively in the vibrational ground state [40]. Under our experimental conditions—due to the large OH vibrational quenching rate of NO—vibrationally excited OH produced in reaction (1) was completely quenched to the OH vibrational ground state [41]. The photolysis and the probe laser beams propagated in opposite directions through the side arms of the reactor. Both dye laser beams were attenuated until the measured fluorescence signal showed a linear dependence on the probe laser intensity. NH and OH fluorescence was collected by a lens perpendicular to the laser beams direction and focused upon the cathode of a photomultiplier (EMI 9781). To reduce the NO background fluorescence generated by the photolysis laser pulse, a filter (Schott KG 4 or UG 5) was used in front of the photomultiplier when NH or OH was detected, respectively. The photomultiplier signal was measured by a Boxcar integrator (SR 250) and transferred to a microcomputer (Hewlett Packard series 9000, model 320), which was also used to control the timing of the whole experiment by means of a delay generator (SR DG 535). Fluorescence signals were normalized to both probe and photolysis laser intensities, which were measured by photodiodes. Mixtures of HNCO and Xe were prepared in a 101 storage vessel by evaporating 7 torr of HNCO and adding 753 torr Xe. The gas flows were regulated by calibrated mass flow controllers (Tylan). The total pressure in the reactor was measured by means of a MKS Baratron. Typical partial pressures of the gases used are listed in Tables 1 and 2. The gases used had the following purities: Xe > 99.99%, NO > 99.8%, and O_2 > 99.999% (all Messer Griesheim). To remove NO_2 impurities, which could lead to additional formation of OH by reacting with the H atoms generated in the HNCO photolysis, the NO flow was passed through a two-stage methanol-dry ice trap and over KOH before entering the reactor. In addition, a mixture of HCl (1.5 mbar) and NO (3 mbar) was photolyzed at 193 nm, and no OH radicals could be detected, verifying that the NO used in the experiments was free from NO_2. The H_2O_2 (PEROXID Chemie) used in the calibration measurements for the OH radicals was pumped through the reactor for at least 48 hours until it reached a final concentration of more than 99% (determined by titration). Typically, H_2O_2 partial pressures of 200 mtorr were used in the calibration measurements.

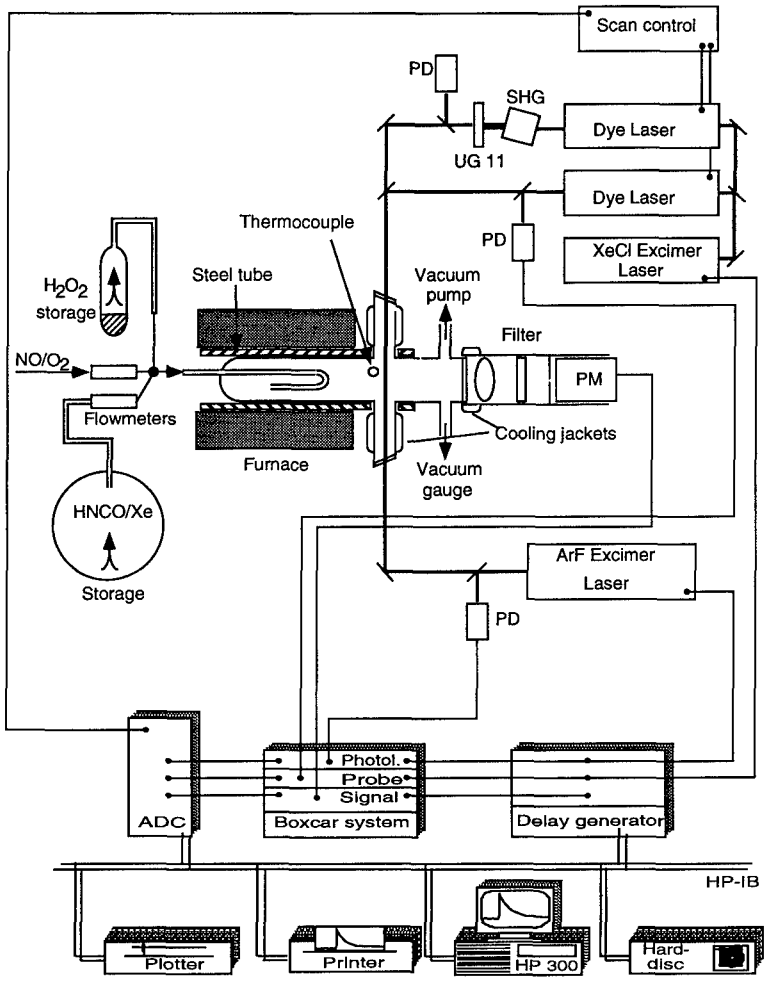

FIG. 1. Schematical description of the experimental setup of the LP/LIF apparatus: PD, photodiode; PM, photomultiplier; ADC, analog-to-digital converter; HP-IB, Hewlett-Packard interface-bus IEEE-488; SHG, second harmonic generation crystal.

Experimental Results and Discussion

Experimental conditions for all measurements are listed in Tables 1 and 2. As it can be seen, in all experiments, high concentrations of xenon were present to ensure the fast electronic quenching of the NH($a^1\Delta$) in order to minimize the loss of NH($a^1\Delta$) radicals via the fast reaction (3) [42]:

$$NH(a^1\Delta) + HNCO \rightarrow NH_2 + NCO \quad (3)$$

Under the conditions listed in Tables 1 and 2, even in the case of the fastest reactive removal of NH($X^3\Sigma^-$), NH($a^1\Delta$) quenching was faster by at least a factor of 10. All experiments were carried out under pseudo-first-order conditions. NO and O_2 concentrations were typically between two and four orders of magnitude higher than the NH concentration generated in the HNCO photodissociation at the photolysis laser intensities used in our study. A biexponential expression

$$I_{fl}(t) = A\,[\exp(-k_{decay}\,t) - \exp(-k_{rise}\,t)] \quad (4)$$

was fitted (using a least-squares procedure) to the measured NH($X^3\Sigma^-$) fluorescence vs time profiles, with A, k_{decay}, and k_{rise} as fit parameters. From the slope of k_{decay} ($k_{decay} = k\,[X] + k_D$, where k_D accounts for additional NH loss processes mainly caused by diffusion of NH radicals out of the detection volume) vs [X] (X = NO and O_2, respectively) plots, the bimolecular rate constant k was determined, as shown in Figs. 2 and 3.

TABLE 1
Experimental Conditions and Results from the Study of Reaction (1). The Reported Errors of k Represent Two Standard Deviations.

T [K]	P [torr]	[Xe]	[HNCO] [10^{-8} mol cm^{-3}]	$[NO]_{min-max}$	$k_{decay}^{min-max}$ [10^4 s^{-1}]	k [10^{13} cm^3 mol^{-1} s^{-1}]
293	26	139	1.3	0.68–4.30	18–134	3.29 ± 0.17
558	26	73	0.7	0.30–1.20	5.5–27	2.33 ± 0.15
752	28	58	0.6	0.24–1.14	4.3–22	2.01 ± 0.12
943	29	48	0.5	0.15–0.94	2.8–15	1.50 ± 0.10
1085	29	42	0.4	0.17–0.76	2.2–8.4	1.23 ± 0.17
293[a]	27	144	1.3	0.44–1.40	14–54	4.27 ± 0.46
560[a]	27	75	0.7	0.33–0.65	8.0–17	2.84 ± 0.21
751[a]	27	56	0.5	0.23–0.92	5.8–21	2.34 ± 0.26
941[a]	24	40	0.4	0.15–0.43	1.7–7.2	2.01 ± 0.18

[a]$NH(X^3\Sigma^-, v = 1) + NO$

TABLE 2
Experimental Conditions and Results from the Study of Reaction (2). The Reported Errors of k Represent Two Standard Deviations.

T [K]	P [torr]	[Xe]	[HNCO] [10^{-8} mol cm^{-3}]	$[O_2]_{min-max}$	$k_{decay}^{min-max}$ [10^3 s^{-1}]	k [10^9 cm^3 mol^{-1} s^{-1}]
293	55	87	0.8	41–194	5.9–15	5.68 ± 0.46
397	45	59	0.6	20–131	3–20	14.8 ± 2.0
464	50	53	0.5	12–125	4.1–24	16.8 ± 0.9
563	45	63	0.6	13–64	4.8–23	32.2 ± 6.1
640	45	55	0.5	11–56	7.5–27	46.4 ± 11.0
716	46	50	0.5	4.1–18	5.4–15	70.7 ± 13.0
793	51	31	0.3	2.2–19	10–28	87.9 ± 6.8

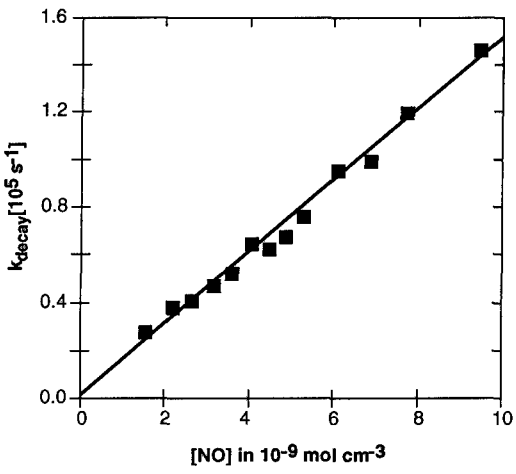

FIG. 2. Plots of pseudo-first-order rate constants (k_{decay}) for reaction (1) at 943 K.

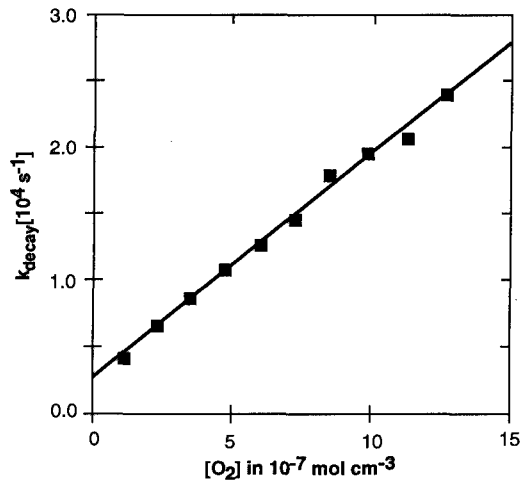

FIG. 3. Plots of pseudo-first-order rate constants (k_{decay}) for reaction (2) at 464 K.

Possible reactions that could contribute to $NH(X^3\Sigma^-)$ removal are as follows:

$$NH(X^3\Sigma^-) + HNCO \rightarrow NH_2 + NCO \quad (5)$$

$$NH(X^3\Sigma^-) + OH \rightarrow \text{products} \quad (6)$$

$$NH(X^3\Sigma^-) + N_2O \rightarrow \text{products} \quad (7)$$

$$NH(X^3\Sigma^-) + H \rightarrow \text{products} \quad (8)$$

However, with $k_5 = 2 \times 10^{13} \times \exp(-12{,}000\ K/T)$ taken from the literature [43], at the conditions of the present study, reaction (5) could not significantly compete with the title reactions, due to its high activation energy. The subsequent reactions (6) through (8) of $NH(X^3\Sigma^-)$ radicals with reaction products formed in reactions (1) and (2) can be neglected due to the low concentration of the reactants employed in the study.

The branching ratio β for the OH-producing channel of reaction (1) was determined at room temperature by calibrating the OH signal from reaction (1) against well-defined OH concentrations from the H_2O_2 photolysis [44]. For this purpose, the location of the maximum I_{max}(OH reaction) in the OH LIF vs time profile in reaction (1) was determined. The branching ratio was calculated using the following equation [45]:

$$\beta = \{I_{max}(OH, react)/I(OH, calib)\} \times \{[OH]_{calib}/[NH(X^3\Sigma^-)]_{init}\} \quad (9)$$

Here, I(OH,calib) is the OH LIF signal measured in the H_2O_2 photolysis, and $[OH]_{calib}$ is the corresponding OH radical number density. The term I_{max}(OH, react) is the OH LIF signal (both OH LIF signals were corrected to account for the different fluorescence lifetimes arising from the different fluorescence quenching conditions) measured in reaction (1), and $[NH(X^3\Sigma^-)]_{init}$ is the initial number density of $NH(X^3\Sigma^-)$ radicals. At the low photolysis laser intensities, I_{photo}, used in our experiment, $[OH]_{calib}$ can be calculated using the linear relationship $[OH]_{calib} = \phi_{OH}\, \sigma_{H_2O_2}\, [H_2O_2]\, I_{photo}$, where ϕ_{OH} denotes the OH quantum yield of the H_2O_2 photolysis at 193 nm and $\sigma_{H_2O_2}$ is the corresponding absorption cross section [46]. $[NH(X^3\Sigma^-)]_{init}$ is given by the following similar expression: $[NH(X^3\Sigma^-)]_{init} = a\, \phi_{NH(a^1\Delta)}\, \sigma_{HNCO}\, [HNCO]\, I_{photo}$. Here, $\phi_{NH(a^1\Delta)}$ is the $NH(a^1\Delta)$ quantum yield of the HNCO photolysis at 193 nm and σ_{HNCO} is the corresponding absorption cross section [31]. The parameter a accounts for the fact that a certain amount of the initially formed $NH(a^1\Delta)$ radicals can react with HNCO—via reaction (3)—or with NO—via reaction (10)—before being quenched to $NH(X^3\Sigma^-)$:

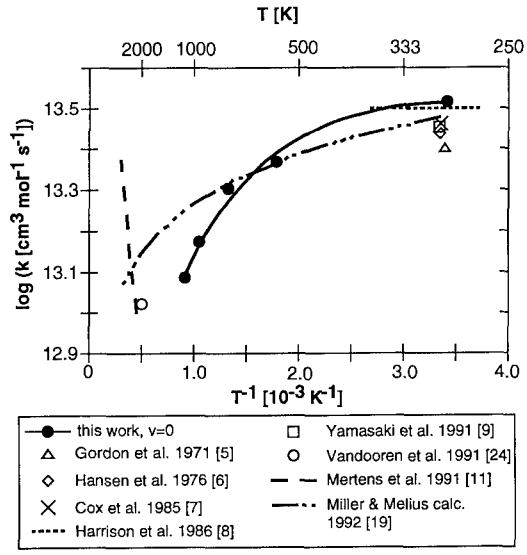

FIG. 4. Arrhenius plot for the reaction of $NH(X^3\Sigma^-)$ radicals with NO.

$$NH(a^1\Delta) + NO \rightarrow N_2O + H \quad (10a)$$

$$\rightarrow N_2 + OH \quad (10b)$$

The value of a was determined by numerical modeling of the reaction system (1), (5–8) on a computer including the physical quenching by NO and Xe and the $NH(a^1\Delta)$ consuming reactions (3) and (10). For the experimental conditions used in our calibration measurement, we determined a value of about 0.95 for a. With this value, we calculated a branching ratio of $\beta = (0.15 \pm 0.05)$ for the OH-producing channel of reaction (1) at room temperature, which is within the experimental error limits in good agreement with the theoretical value of $\beta = 0.19$ reported by Miller and Melius [19]. Within the combined error limits, our value is also in reasonable agreement with the result of Hack et al. [10]. The measured OH concentration vs time profiles clearly showed that OH removal is too slow to influence the measured β value significantly. Computer simulation of the reaction system (1), (6–8) including the OH-producing reactions (10b) and (3) and (5) followed by (11) [45,47].

$$NH_2 + NO \rightarrow N_2 + OH + H. \quad (11)$$

showed that under our experimental conditions, these reactions can only lead to a OH production of less than 1%.

In Figs. 4 and 6, the measured temperature-dependent rate coefficients of reactions (1) and (2), which can be described by the following modified Arrhenius expressions

$$k_1(293 < T < 1085\ \mathrm{K}) = 10^{14.18} \times (T/298\ \mathrm{K})^{(-1.60\pm0.01)} \exp(-3.8 \pm 0.2\ \mathrm{kJ\ mol^{-1}/RT})\ \mathrm{cm^3\ mol^{-1}\ s^{-1}}$$

and

$$k_2(293 < T < 793\ \mathrm{K}) = 10^{9.38} \times (T/298\ \mathrm{K})^{(3.34\pm0.15)} \times \exp(2.3 \pm 0.4\ \mathrm{kJ\ mol^{-1}/RT})\ \mathrm{cm^3\ mol^{-1}\ s^{-1}}$$

respectively, are shown and compared with earlier experimental results, as well as with the theoretical results reported by Miller and Melius [19] and Fueno et al. [28]. The above-listed Arrhenius expressions were obtained by fitting (using a least-squares procedure) the measured rate constant values according to

$$k(T) = A \times (T/298)^n \times \exp(-E_A/\mathrm{RT}). \quad (12)$$

The error bars in Fig. 4 represent two standard deviations (2σ) of the least-squares fit shown in Fig. 2. We suggest that this value is a reasonable estimate of the overall accuracy of our measurements (see Tables 1 and 2).

In the case of reaction (1), our values are in reasonable agreement with earlier low-temperature measurements [5–10]. In qualitative agreement with theory [19], our results show that the rate coefficient decreases significantly with increasing temperature between 293 and 1085 K. This together with the high-temperature results [24,25] suggests that the rate constant has a minimum somewhere between 1000 and 2000 K. The following increase of the rate coefficient between 2220 and 3350 K, as observed by Mertens et al. [11], was attributed to the opening of the NNH + O channel in reaction (1) at high temperatures [19]. In order to find the exact location of the minimum in the rate constant of reaction (1), additional high-temperature measurements that bridge the gap between our present results and the flame studies [24] and the shock tube studies [11] are clearly desirable. From Fig. 5, it can be seen that the total removal rate for $NH(X^3\Sigma^-, v = 1)$ by NO, which can be described by the following Arrhenius expression

$$k_{1(v=1)}(293 < T < 922\ \mathrm{K}) = 10^{13.68} \times (T/298\ \mathrm{K})^{-0.71} \times \exp(0.27 \pm 0.01\ \mathrm{kJ\ mol^{-1}/RT})\ \mathrm{cm^3\ mol^{-1}\ s^{-1}}$$

is only slightly higher than the rate constant for the reaction of $NH(X^3\Sigma^-, v = 0)$ with NO (vibrational quenching by Xe can be neglected even with the large Xe background present in our experiments

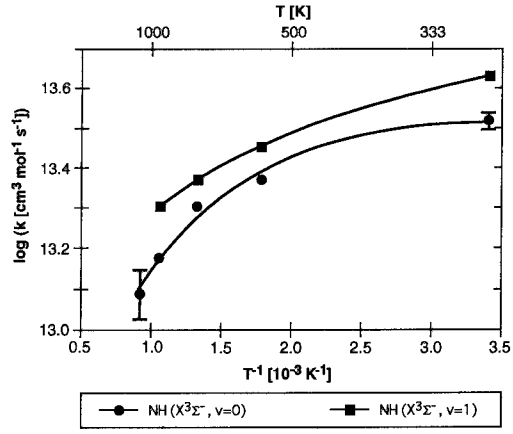

FIG. 5. Arrhenius plot for the reaction of $NH(X^3\Sigma^-, v = 0)$ and $NH(X^3\Sigma^-, v = 1)$ radicals with NO.

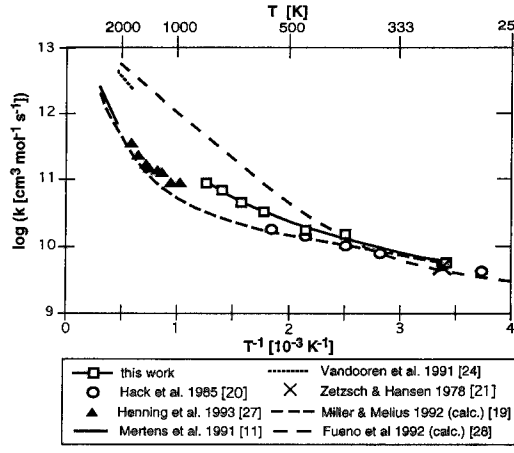

FIG. 6. Arrhenius plot for the reaction of $NH(X^3\Sigma^-)$ radicals with O_2.

[35]), indicating that in reaction (1), reactivity is not significantly enhanced by vibrational excitation of NH.

As shown in Fig. 6, in the case of reaction (2), our present results are in good agreement with earlier measurements at lower temperatures [20,21]. In addition, the results of the high-temperature flame studies by Vandooren et al. [24] and the shock tube studies of Mertens et al. [11] seem to coincide also with the values that could be extrapolated from our Arrhenius expression. However, at this point, it should be noted that our Arrhenius expression has been derived only in order to represent our measured values most accurately (without attributing any physical meaning to the parameters). To derive a reliable expression for extrapolation to the high-temperature range, additional theoretical considerations

(as described in detail in Refs. 48 and 49) would be necessary.

In the temperature range $400 < T < 793$ K, our measured values are clearly higher than the values calculated by Miller and Melius (taken from Table III of Ref. 19). Measurements in the intermediate temperature range $985 < T < 1729$ K [27] gave also values that are slightly higher than the results obtained in Ref. 19. On the other hand, the present experimental results for $T > 400$ K are considerably lower than the results of the calculations carried out by Fueno et al. [28]. In any case, as shown in Fig. 6, the available experimental data clearly indicate that the Arrhenius plot for the rate of reaction (2) is strongly curved at $T > 400$ K.

Conclusion

In agreement with the calculations of Melius and Binkley [15], our measurements show that the rate constant of reaction (1) has a negative temperature dependence in the temperature range $293 < T < 1085$ K, indicating that the reaction proceeds via the formation of an HNNO intermediate [15]. In addition, our measured value of the branching ratio $\beta = (0.15 \pm 0.05)$ into reaction channel (1a) at room temperature is consistent both with the recently measured value of (0.8 ± 0.4) [13] and the recently calculated value of 0.89—quoted in Ref. 13 as a private communication from J. A. Miller—for the branching ratio into reaction channel (1b). This good agreement between the results of the experiments and the results of Miller's calculations supports the prediction that in reaction (1), $H + N_2O$ products are predominately formed with the branching ratio being described by the products of dissociation of cis-$HNNO(^2A')$ [13].

In the case of reaction (2), our measured rate constants are markedly higher in the temperature range $293 < T < 793$ K than the rate constants calculated by Miller and Melius [19]. In the above-mentioned temperature range for reaction (2), reaction on the $HNOO(^1A')$ surface is dominant with the three-membered ring formation from the initial HNOO adduct being the rate-limiting step [19]. Therefore, additional ab initio studies of the transition state for this process are clearly desirable, which could possibly lead to a better agreement between the present experimental results and theory.

On the experimental side for reaction (2), measurements at higher temperatures ($800 \text{ K} < T < 1100$ K) are under way to bridge the gap between the temperature range investigated in the present work and the temperature range investigated in Ref. 27. In addition, for reactions (1) and (2), measurements of the temperature dependence of the branching fraction into $OH + N_2$ and $NO + OH$, respectively, are planned for the near future in our laboratory. A comparison between the results of these investigations and the results from Ref. 19 will allow a rigorous test of the currently available potential energy surfaces for reactions (1) and (2).

Acknowledgments

The financial support of the research association TECFLAM and the EC in the framework of the JOULE(CHEMCOM) project is gratefully acknowledged. Thanks are due to Paul Dagdigian and Joseph L. Durant, Jr. for sending preprints of their publications. We also wish to thank George Schatz for helpful discussion. One of the authors (PDN) thanks the KFA Jülich for a fellowship under the Indo-German bilateral agreement.

REFERENCES

1. Miller, J. A., and Bowman, C. T., *Prog. Energy Combust. Sci.* 15:287–338 (1989).
2. Perry, R. A., and Siebers, D. L., *Nature* 324:657–658 (1986).
3. Miller, J. A., and Bowman, C. T., *Int. J. Chem. Kinet.* 23:289–313 (1991).
4. Muris, S., Ph.D. Thesis, University of Heidelberg, Heidelberg, 1993.
5. Gordon, S., Mulac, W., and Nangia, P., *J. Phys. Chem.* 75:2087–2093 (1971).
6. Hansen, I., Höinghaus, K., Zetzsch, C., and Stuhl, F., *Chem. Phys. Lett.* 42:370–372 (1976).
7. Cox, J. W., Nelson, H. H., and McDonald, J. R., *Chem. Phys.* 96:175–182 (1985).
8. Harrison, J. A., Whyte, A. R., and Phillips, L. F., *Chem. Phys. Lett.* 129:346–352 (1986).
9. Yamasaki, K., Okada, S., Koshi, M., and Matsui, H., *J. Chem. Phys.* 95:5087–5096 (1991).
10. Hack, W., Wagner, H. Gg., and Zasypkin, A., *Ber. Bunsenges. Phys. Chem.* 98:156–164 (1994).
11. Mertens, J. D., Chang, A. Y., Hanson, R. K., and Bowman, C. T., *Int. J. Chem. Kin.* 23:173–196 (1991).
12. Yokoyama, K., Sakane, Y., and Fueno, T., *Bull. Chem. Soc. Jpn.* 64:1738–1742 (1991).
13. Durant, J. L., Jr., *J. Phys. Chem.* 98:518–521 (1994).
14. Patel-Misra, D., and Dagdigian, P. J., *J. Phys. Chem.* 96:3232–3236 (1992).
15. Melius, C. F., and Binkley, J. S., *Twentieth Symposium (International) on Combustion*, The Combustion Institute, Pittsburgh, 1984, pp. 575–583.
16. Fueno, T., Fukada, M., and Yokoyama, K., *Chem. Phys.* 124:265–272 (1988).
17. Harrison, J. A., and Maclagan, R. G. A. R., *J. Chem. Soc. Faraday Trans.* 86:3519–3523, (1990).
18. Walch, S. P., *J. Chem. Phys.* 98:1170–1177 (1993).
19. Miller, J. A., and Melius, C. F., *Twenty-Fourth Symposium (International) on Combustion*, The Combustion Institute, Pittsburgh, 1992, pp. 719–726.
20. Hack, W., Kurzke, H., and Wagner, H. Gg., *J. Chem. Soc. Faraday Trans. II* 81:949–961 (1985).

21. Zetzsch, C., and Hansen, I., *Ber. Bunsenges. Phys. Chem.* 82:830–833 (1978).
22. Pagsberg, P. B., Eriksen, J., and Christensen, H. C., *J. Phys. Chem.* 83:582–590 (1979).
23. Morley, C., *Eighteenth Symposium (International) on Combustion*, The Combustion Institute, Pittsburgh, 1981, pp. 23–32.
24. Vandooren, J., Sarkisov, O. M., Balakhin, V. P., and Van Tiggelen, P. J., *Chem. Phys. Lett.* 184:294–300 (1991).
25. Dean, A. M., Chou, M.-S., and Stern, D., *Int. J. Chem. Kin.* 16:633–653 (1984).
26. Roose, T. R., Hanson, R. K., and Kruger, C. H., *Eighteenth Symposium (International) on Combustion*, The Combustion Institute, Pittsburgh, 1981, pp. 853–862.
27. Henning, G., Röhrig, M., and Wagner, H. Gg., *Ber. Bunsenges. Phys. Chem.* 97:830–832 (1993).
28. Fueno, T., Yokoyama, K., and Takana, S., *Theor. Chim. Acta* 8:299–308 (1992).
29. Atakan, B., and Wolfrum, J., *Chem. Phys. Lett.* 178:157–162 (1991).
30. Drozdoski, W. S., Baronavski, A. P., and McDonald, J. R., *Chem. Phys. Lett.* 64:421–425 (1979).
31. Spiglanin, T. A., Perry, R. A., and Chandler, D. W., *J. Phys. Chem.* 90:6184–6189 (1986).
32. Yi, W., and Bersohn, R., *Chem. Phys. Lett.* 206:365–368 (1993).
33. Rohrer, F., and Stuhl, F., *Chem. Phys. Lett.* 111:234–237 (1984).
34. Bower, R. D., Jacoby, M. T., and Blauer, J. A., *J. Chem. Phys.* 86:1954–1956 (1987).
35. Hack, W., and Wilms, A., *J. Phys. Chem.* 93:3540–3546 (1989).
36. Nelson, H. H., McDonald, J. R., and Alexander, M. H., *J. Phys. Chem.* 94:3291–3294 (1990).
37. Adams, J. S., and Pasternack, L., *J. Phys. Chem.* 95:2975–2982 (1991).
38. Hack, W., and Rathman, K., *J. Phys. Chem.* 96:47–52 (1992).
39. Bohn, B., and Stuhl, F., *J. Phys. Chem.* 97:4891–4898 (1993).
40. Jacobs, A., Wahl, M., Weller, R., and Wolfrum, *J., Appl. Phys. B* 42:173–179 (1987).
41. Smith, I. W. M., and Williams, M. D., *J. Chem. Soc. Faraday Trans. II* 81:1849–1860 (1985).
42. Bohn, B., and Stuhl, F., *J. Phys. Chem.* 97:7234–7238 (1993).
43. Mertens, J. D., Kohse-Höinghaus, K., Hanson, R. K., and Bowman, C. T., *Int. J. Chem. Kin.* 23:655–668 (1991).
44. Jacobs, A., Volpp, H.-R., and Wolfrum, J., *Twenty-Fourth Symposium (International) on Combustion*, The Combustion Institute, Pittsburgh, 1992, pp. 605–611.
45. Atakan, B., Jacobs, A., Wahl, M., Weller, R., and Wolfrum, J., *Chem. Phys. Lett.* 155:609–613 (1989).
46. Schiffman, A., Nelson, Jr., D. D., and Nesbitt, D. J., *J. Chem. Phys.* 98:6935–6946 (1993).
47. Stephens, J. W., Morter, C. L., Farhat, S. K., Glass, G. P., and Curl, R. F., *J. Phys. Chem.* 97:8944–8951 (1993).
48. Cvetanovic, R. J., Singleton, D. L., and Paraskevopoulos, G., *J. Phys. Chem.* 83:50–60 (1979).
49. Jeong, K.-M., Hsu, K.-J., Jeffries, J. B., and Kaufman, F., *J. Phys. Chem.* 88:1222–1226 (1984).

COMMENTS

John Hershberger, North Dakota State University, USA. You quoted slightly higher decay rates for vibrationally excited states of NH relative to the ground vibrational state in the NH + NO reaction. Is this effect a true increase in the reaction rate constant, or a vibrational relaxation effect?

Author's Reply. We cannot rule out completely that the slightly higher decay rates for vibrationally excited $NH(^3\Sigma^-)$ in the $NH(^3\Sigma^-)$ + NO reaction are a vibrational relaxation effect. But from the fact that the measured overall rate for $NH(^3\Sigma^-; v = 1)$ is only slightly higher than the rate of reaction of the $NH(^3\Sigma^-)$ radical in the vibrational ground state, we can see that vibrational excitation of the NH bond does not increase reactivity in the $NH(^3\Sigma^-)$ + NO reaction very much. Actually, this is what one expects for a reaction for which a "loose" NH–NO transition state (for which the bond lengths and frequencies are close to those for NH and NO) determines the total rate coefficient.

•

Joseph Durant, Sandia National Laboratories, USA. Can you comment on the pressure dependence of the product branching fractions you observed in this work?

Author's Reply. We have not yet studied the pressure dependence of the product branching fractions in the reactions $NH(^3\Sigma^-)$ + NO and NH $(^3\Sigma^-)$ + O_2. In very recent experiments carried out in our laboratory, we found that at room temperature the rate constant for the reaction $NH(^3\Sigma^-)$ + NO → products and $NH(^3\Sigma^-)$ + O_2 → products is pressure independent.

•

M. C. Lin, Emory University, USA. The formation of H + NO_2 from NH + O_2 is exothermic by about 30 kcal/mole. Did you attempt to detect H or NO_2 in this reaction?

Author's Reply. We have not yet investigated the different possible product channels in the reaction $NH(^3\Sigma^-) + O_2$ at higher temperature. Experiments in which we will investigate the formation of H atoms and O atoms from the reaction $NH(^3\Sigma^-) + O_2$ as a function of temperature are underway. Very recent experiments carried out in our laboratory indicate that at room temperature the OH + NO producing channel clearly dominates. By means of a calibration method, we determined the OH yield from the reaction $NH(^3\Sigma^-) + O_2$ to be (1.05 ± 0.15) at $T = 294$ K.

Twenty-Fifth Symposium (International) on Combustion/The Combustion Institute, 1994/pp. 1003–1010

HYDROCARBON-NO_x INTERACTIONS AT LOW TEMPERATURES—1. CONVERSION OF NO TO NO_2 PROMOTED BY PROPANE AND THE FORMATION OF HNCO

P. F. NELSON
CSIRO Division of Coal and Energy Technology
P.O. Box 136, North Ryde 2113, Australia

AND

B. S. HAYNES
Department of Chemical Engineering
University of Sydney
Sydney 2006, Australia

Reactant conversions and product distributions for reactions between NO (0–350 ppm), propane (425–1000 ppm), and O_2 (2.3–16%) in a laminar flow reactor at temperatures in the range 500 °C–800 °C have been determined by long–path-length Fourier transform infrared (FTIR) spectroscopy. Addition of NO significantly decreases the temperature at which oxidation of propane commences, but the formation of intermediate products (the olefins, ethylene and propylene, and formaldehyde) occurs over a wider temperature range than does the formation of these products in the absence of added NO. Oxidation of the propane coincides with NO to NO_2 conversion, although significant NO to NO_2 conversion occurs before substantial oxidation of the hydrocarbon. The NO to NO_2 conversion occurs in stages and increases when the intermediate carbon-containing products begin themselves to oxidise. For experiments in the presence of added NO, CH_4 is not observed as a product, implying that steady-state concentrations of CH_3 radicals are low; rapid conversion of CH_3 to CH_3O_2 followed by reaction of CH_3O_2 with NO is a probable reason for this observation. At high NO and propane concentrations (350 and 1000 ppm, respectively), HNCO was detected as a product of these reactions. Formation of HNCO coincides with NO to NO_2 conversion. These observations provide evidence for hydrocarbon-NO interactions that result in the formation of species containing C—N bonds occurring at lower temperatures than previously reported.

Introduction

The oxidation of NO to NO_2 in the presence of oxygen has been shown to be strongly promoted, at temperatures as low as 300 °C, by the presence of low concentrations of hydrocarbons, CO and H_2 [1–4]. At the same time, the oxidation of the hydrocarbon is greatly sensitised, giving rise to the formation of oxygenated species, such as aldehydes, and unsaturated hydrocarbon compounds.

Emissions of NO_2 from combustion appliances such as gas cookers and heaters [5] and gas turbines [6] are most probably the result of these interactions. It has also been demonstrated [3] that trace concentrations of NO (as little as 0.02 ppm, similar to that often found in urban air) have a profound promoting effect on the oxidation of *n*-butane, suggesting that hydrocarbon-NO interactions may also be important in experimental studies of low-temperature ignition and in ignition phenomena in automotive and other engines.

The facile and, under some conditions, near-complete conversion of NO to NO_2 also suggests a possible control technology for NO_x emissions from stationary combustion sources since NO_2 is significantly more soluble than NO, and may therefore be removed by scrubbing processes. These processes may be profitably combined with the removal of SO_2 from flue gases using similar means. A number of studies [7,8] have reported the use of methanol to promote the conversion of NO to NO_2 for this purpose.

Addition of hydrocarbons, H_2 and H_2O_2 has also been used to modify the range of temperatures [9,10] for which the selective noncatalytic reduction (SNCR) of NO with NH_3 is effective in achieving acceptable reductions in NO emissions. Clearly, interactions between the added hydrocarbon and NO will be important in determining the overall efficiency and product distributions in industrial applications of hydrocarbon-promoted SNCR.

The ability of hydrocarbon fragments such as CH, CH_2, and, possibly, CH_3, to reduce NO to HCN is employed in "reburning," or fuel staging, when hydrocarbons are injected into hot combustion gases.

The subsequent reoxidation of HCN (and the injected hydrocarbon) results, under appropriate conditions of air/fuel ratios, in substantial formation of N_2 and thus leads to a net reduction in the overall NO emissions. While the reburning process is generally carried out at high temperatures, similar interactions could be expected if reactive hydrocarbon fragments were available at lower temperatures.

It has also recently become apparent that some selective catalytic reduction (SCR) catalysts, such as Cu- or Co-exchanged ZSM-5, effect the reduction of NO to N_2 in the presence of hydrocarbons at temperatures in the vicinity of 300 °C–400 °C [11–13]. The relative contributions of gas- and surface-phase reactions are unknown. There is evidence [12,14,15] that these reactions proceed via an NO_2 intermediate; hence, gas-phase reactions producing NO_2 may play an important role in the overall conversion of NO to N_2.

There is thus considerable justification for both experimental and modelling studies of reactions between hydrocarbons and NO, in the presence of O_2, for the temperature range of 300 °C–800 °C. Previous work has concentrated on rather low concentrations of NO [3], typical of those found in household appliances and/or gas turbines. In this work, we have investigated the interaction of propane with NO in the presence of oxygen, at somewhat higher concentrations more relevant to those found in flue gases from coal-fired power stations.

The major aim of this study was to identify the hydrocarbon and nitrogen-containing products arising in this system. The detection of NO_2 in most previous studies has been performed by the indirect technique of NO and NO_x analysis by chemiluminescence. In this study, we report direct measurements of NO_2, and of other hydrocarbon and nitrogen-containing species, by long–path-length Fourier transform infrared (FTIR) spectroscopy.

Experimental

Experiments were conducted in a ceramic tube reactor (Alsint, 4-mm i.d.) heated electrically. Two ceramic thermocouple sheaths were positioned in the reactor above and below the heated zone, and temperatures were measured at the top and bottom of this region. The length of the approximately isothermal (±5 °C) heated zone was 200 mm. Based on previous work with *n*-butane and other hydrocarbons [3,5] in which reactor materials and geometry were varied with little effect on results, heterogeneous effects are unlikely to play a significant role in this system, particularly at the temperatures and residence times employed here.

Gas mixtures were prepared by mixing flows of the gases propane in He (1570 ppm), NO in He (3600 ppm), O_2 in He (7.6%), or O_2 in N_2 (21%) using mass flow controllers. Total gas flows were of the order of 40–80 mL/min, with resultant residence times of the order of 0.6–1.3 s. Experiments were performed by establishing the required gas composition and then varying the reactor temperature.

Experiments were performed under the same conditions of temperature range and residence time with and without added NO. Reactant and product gas compositions were determined on line by long–path-length FTIR spectroscopy. The entire gas flow was passed through a multipass cell (Infrared Analysis Model 3.2, total path length 3.2 m on a base length of 10 cm, volume 100 mL). The residence time of the sample in the tubing (stainless steel, 1/16-in. o.d.) connecting the reactor to the cell was less than 1 s at a flow rate of 80 mL/min, and the average residence time of the gas in the cell at this flow rate was approximately 2 min. Calculations and measurements at much shorter cell residence times demonstrated that negligible conversion of NO to NO_2 by the thermal (Bodenstein) oxidation reaction occurred under these conditions.

Most of the species of interest can be determined by this technique apart from O_2 and H_2. Concentrations of O_2 were always in large excess compared with those of propane or NO, and the concentrations of O_2 would not have been significantly different in reactants or products.

Spectra were collected at a spectral resolution of 0.25 cm^{-1} by the coaddition of 64 or 256 scans. The species determined and the features used for quantitative analysis were as follows: C_3H_8 (2968 cm^{-1}), C_3H_6 (912 cm^{-1}), C_2H_4 (949 cm^{-1}), CH_4 (3086 cm^{-1}), HCHO (1746 cm^{-1}), CO (2120 cm^{-1}), CO_2 (721 cm^{-1}), NO (1876 cm^{-1}), NO_2 (1615 cm^{-1}), and HNCO (2269 cm^{-1}). Acetaldehyde (CH_3CHO), reported as a product of the reaction of hydrocarbons and NO at somewhat lower temperatures [3], was not detected in the present experiments (detection limit 5 ppm). Other products whose features did not appear in the spectra were HONO, HNO_3, ethylene oxide, propylene oxide, and acetone. A weak feature was observed under some conditions at 712 cm^{-1} and may have been due to HCN. For some of these products, particularly HNO_3, the sampling arrangements may not have been appropriate to ensure transport of the material to the cell, and so caution is required in the conclusions drawn from these null observations. Nitrous oxide (N_2O) was present in trace quantities in the NO reactant gas; no additional N_2O was produced by the reaction.

The concentrations of the hydrocarbons, carbon oxides, and nitrogen oxides were determined by calibrating the FTIR using the same gas cell and mixtures prepared from standard gas mixtures. The standards were diluted with N_2 and/or He using mass flow controllers to give a range of concentrations covering that observed in the experiments. The effects of differential broadening due to different dilution

gases were evaluated, and the calibrations were extended to high concentrations to determine the extent to which the Beer–Lambert absorption law applied.

The calibration for HCHO was obtained from the USEPA Technology Transfer Network [16] and is based on duplicate analyses of 100 ppm HCHO in an 11.25-m cell at the same resolution as used in this study. An estimate of the concentration of HNCO is based on published spectroscopic data [17,18].

Results and Discussion

Product Distributions from the Oxidation of Propane with and without Added NO:

Mixtures of propane (425 ppm) and O_2 (16%) were prepared with and without added NO (67 ppm) and propane conversions and product formation determined for temperatures in the range 500 °C–800 °C. The results, shown in Fig. 1a, demonstrate that NO addition reduces the temperature at which C_3H_8 begins to oxidise by approximately 100 °C. Figure 1b shows concentrations of the major carbon-containing products, CO and C_2H_4. In the presence of added NO, formation of these products obviously commences at lower temperatures, but perhaps of more interest is the fact that the concentration profiles as a function of temperature are much broader in the case of the experiment with added NO. In the absence of NO, ethylene is observed only over a very narrow temperature range, and the formation of CO is similarly much more sensitive to temperature. Without NO, the behaviour is akin to an ignition experiment, with intermediate products only apparent over a very narrow temperature range and CO_2 and CO being the ultimate carbon-containing products.

Figure 2 shows some additional results from the experiment with added NO and provides some insight into the means by which NO changes the oxidation of the propane. Measurements of NO, shown in the bottom section of Fig. 2, reveal that the onset of oxidation of the propane is accompanied by a decrease in the NO concentration and a corresponding increase in concentrations of NO_2. The decrease in NO is greater than the increase in NO_2. There are a number of possible explanations for this observation. Additional nitrogen-containing products may have been produced; however, none were detected under these conditions by FTIR spectroscopy. An alternative explanation is that the calibrations for NO and NO_2 (based on separate standards of NO and NO_2) are not internally consistent.

A high correlation is evident in Fig. 2 between the small changes in NO and NO_2 concentration after the initial major adjustment in the NO/NO_2 ratio. In particular, Fig. 2 also reveals that the onset of oxidation of product ethylene coincides with additional

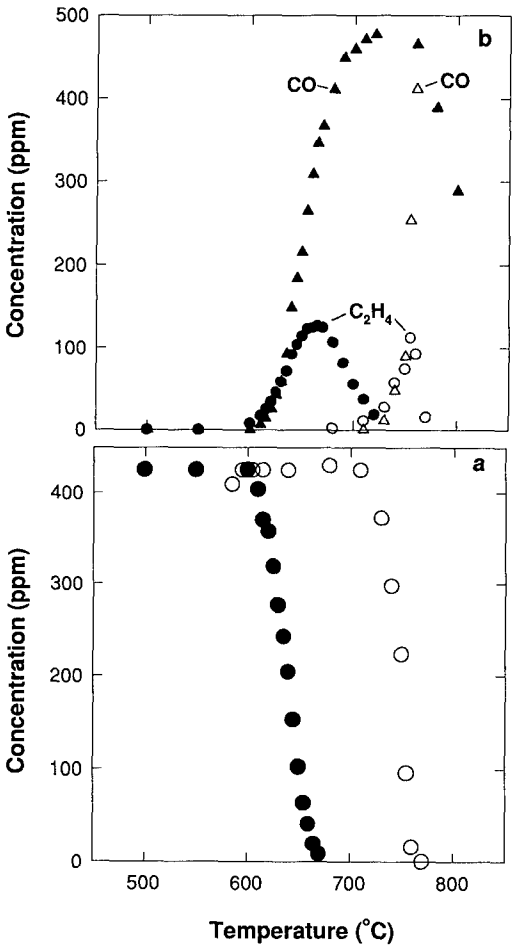

FIG. 1. Concentrations of (a) C_3H_8 and (b) CO and C_2H_4 as a function of temperature. Inlet conditions: filled symbols: C_3H_8 (425 ppm), NO (67 ppm), O_2 (16%), balance N_2 (76%), He (8%); open symbols: C_3H_8 (425 ppm), O_2 (16%), balance N_2 (76%), He (8%). Residence time 0.7 s.

conversion of NO to NO_2. This phenomenon is much more evident at higher NO and propane concentrations and will be discussed below.

The major carbon-containing products of the reaction in the presence of NO are CO, HCHO, C_2H_4, and C_3H_6. In fact, up until the completion of oxidation of the propane, these products account for at least 90% of the carbon-containing products. At higher temperatures, CO_2 becomes an important product. Hence, the majority of the reacted propane is converted to four simple products, and more complex organic oxygenates and/or nitrogen-containing organic species must contribute, at most, a minor part of the products.

The fate of the reacted C_3H_8 may be further investigated by the calculation of carbon selectivities.

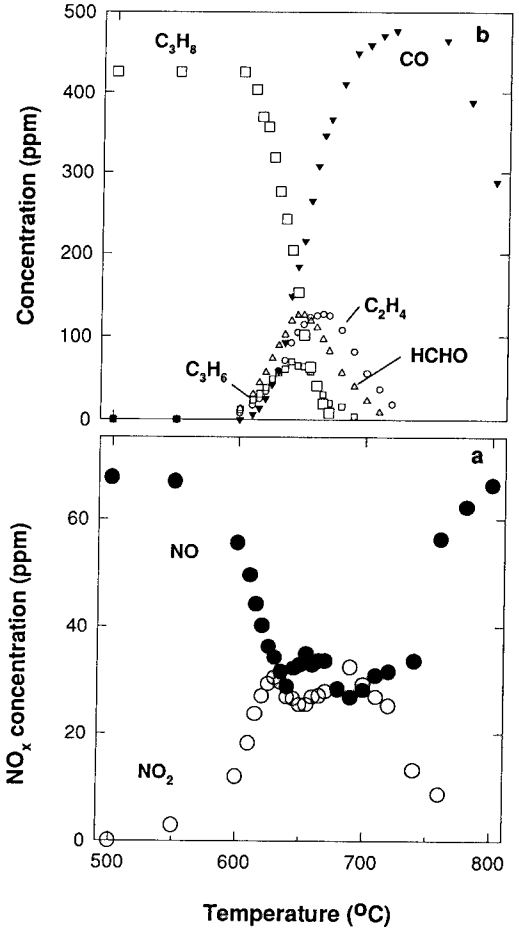

FIG. 2. Concentrations of (a) NO and NO_2, and (b) designated products as a function of temperature. Conditions as for Fig. 1, with NO addition.

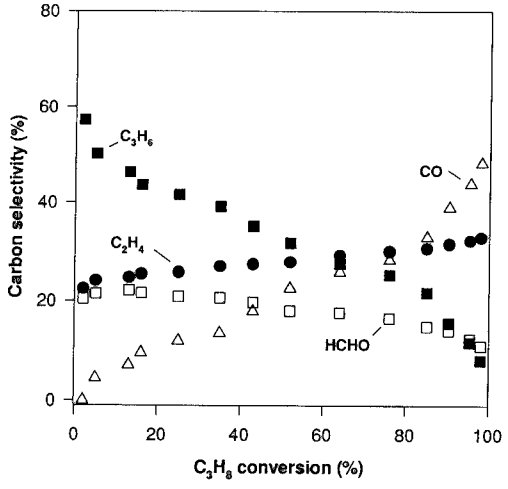

FIG. 3. Carbon selectivities for carbon-containing products as a function of C_3H_8 conversion. Conditions as for Fig. 1, with NO addition.

The basis for this is that the amount of C appearing in each of the four major products as a proportion of the C reacted from C_3H_8 is calculated as a function of propane conversion. It should be noted that the propane oxidation occurs over a temperature range of 50 °C, so that a temperature effect is also included in the functional dependence of the selectivities on conversion. Results for this calculation are given in Fig. 3. From this it can be seen that C_3H_6 is the predominant initial product, and for conversions less than 10% accounts for more than 50% of the products on a C basis. Propylene was also observed [5] as the major initial hydrocarbon product of the C_3H_8/NO/O_2 system at lower temperatures, lower inlet NO concentrations, and longer residence times. It is also instructive to consider the selectivities in conjunction with the NO and NO_2 data of Fig. 2. Most of the NO to NO_2 conversion occurs for C_3H_8 conversions of less than 10%. More than 75% of the reacted C under these conditions appears as olefins, C_3H_6, and C_2H_4, and the bulk of the remainder as HCHO.

Previous workers (1–5) have discussed mechanisms for the conversion of low concentrations of NO to NO_2 promoted by hydrocarbons. It is generally agreed that the conversion is a result of reactions of the general type:

$$NO + RO_2 \rightarrow NO_2 + RO \qquad (1)$$

where R = H, CH_3, C_2H_5, . . . , C_nH_{2n+1}, and that the addition of NO significantly perturbs the steady-state concentration of the reactive OH radical. It is generally accepted that this class of reactions is also responsible for the conversion of NO to NO_2 in the free atmosphere, where subsequent photolysis of the NO_2 results in ozone production and photochemical smog formation.

Detection or nondetection of minor products in this system also provides insight into the likely mechanism of the reaction. The FTIR measurements showed that, for the experiments with added NO, no CH_4 or C_2H_6 (detection limits 2 ppm) was formed. By contrast, small but significant concentrations of CH_4, reaching a maximum of 22 ppm at about 750 °C, were determined in the experiments without added NO. This implies that steady-state concentrations of CH_3 in the $C_3H_8/NO/O_2$ system are very low as a consequence of rapid conversion of CH_3 to CH_3O_2 and reaction of CH_3O_2 with NO:

$$CH_3 + O_2 \rightarrow CH_3O_2 \qquad (2)$$

$$CH_3O_2 + NO \rightarrow CH_3O + NO_2. \qquad (3)$$

Reaction (3) is, of course, a special case of reaction

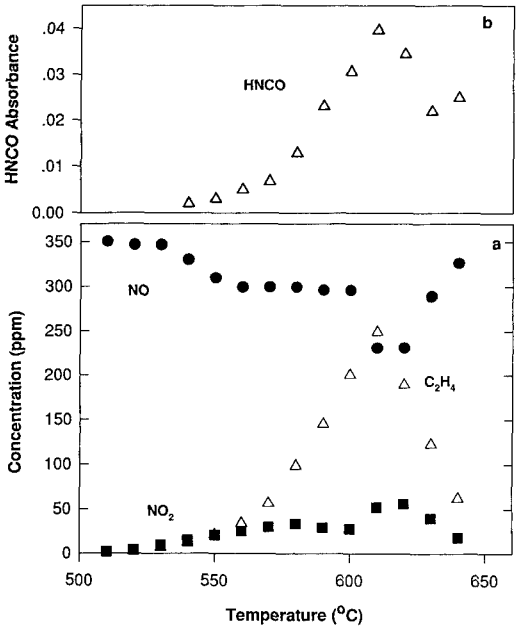

FIG. 4. (a) Concentrations of designated species as a function of temperature. (b) HNCO absorbance, measured at the maximum of the *R* branch of the feature centred at 2269 cm^{-1}. Inlet conditions: C_3H_8 (1000 ppm), NO (350 ppm), O_2 (2.25%), balance He. Residence time 0.6 s.

(1). In the absence of added NO, the reverse of reaction (2) will provide sufficient CH_3 for the formation of CH_4.

Bromly et al. [3] reported results for interactions between NO and *n*-butane in air at temperatures from 330 °C–450 °C and postulated the reaction

$$NO + OH + M \rightleftarrows HONO + M \qquad (4)$$

as an important mechanism for the scavenging of reactive radicals by NO, particularly at high [NO]/[*n*-butane] ratios. In the present experiments, no HONO was detected (detection limit ~0.5 ppm). However, the higher temperatures and lower [NO]/[propane] ratios of the present study may be the reason for the failure to detect HONO.

Evidence for Reburning Reactions at Temperatures between 550 °C and 650 °C:

Similar experiments were also conducted with a reactant mixture comprising C_3H_8 (1000 ppm), NO (350 ppm), and O_2 (2.25%). This NO concentration is more typical of that which may be found in the flue gases from a coal-fired power station. A selection of the results for this experiment is given in Fig. 4a, which shows NO and NO_2 concentrations as a function of reaction temperature. Between 525 °C and 550 °C, NO concentrations decrease by about 15%. As for the previous experiment, the increase in NO_2 concentration is less than the decrease in the NO, but in this case, another nitrogen-containing species was detected; the identity and concentration of this species will be discussed below.

At higher temperatures (>600 °C), there is an additional decrease of about 17% in NO, resulting in a total decrease of 32% of the inlet concentration. As was the case with the previous experiment, this additional decrease corresponds with the onset of C_2H_4 oxidation and is accompanied by a corresponding increase in NO_2 concentrations. At higher temperatures, the NO concentration returns to the inlet value, and C_3H_8 conversion is largely to CO_2.

The identity of the additional nitrogen-containing species was established on the basis of its FTIR spectrum. Figure 5a shows a section of the spectrum in the range from 2300–1500 cm^{-1}, with absorption features due to CO, NO, HCHO, NO_2, and H_2O. A characteristic additional feature is evident, centred at about 2269 cm^{-1}, and Fig. 5b shows an expanded version of this spectrum in the range from 2300–2220 cm^{-1}. Based on previous spectroscopic investigations [17,18] and kinetic experiments [19] on pure components, this feature may be positively assigned to HNCO, which, to our knowledge, has not previously been reported in combustion systems at this temperature.

Data reported in Herzberg and Reid [17] and Steiner et al. [18] enable an absorption coefficient of 25 ± 10 cm^{-1} atm^{-1} to be calculated for the maximum of the *R* branch of this feature. Based on this value for the absorption coefficient, the peak absorbance for HNCO of 0.04 (see Fig. 4b) corresponds to a concentration of 3.6–8.3 ppm. This calculated concentration should, however, be treated as a guide only, since the reported spectra [17,18] were obtained at low pressures of pure HNCO.

The results provide evidence for hydrocarbon-NO interactions at low temperatures that result in the formation of species containing C—N bonds. The formation of HNCO is of particular interest given its high toxicity, which could have substantial impacts on the use of hydrocarbons in NO_x reduction technologies and on air quality. At present, kinetic investigations of reactions between hydrocarbon fragment radicals and NO [20], detailed kinetic models of hydrocarbon oxidation [21–23], and NO formation and destruction [21] are unable to account for these observations. Here we simply raise a number of possibilities.

Reburning reactions are thought to proceed through reactions of the general type

$$CH_i + NO \rightarrow \text{products} \quad (\text{e.g., HCN, CN, ...}) \qquad (5)$$

where $i = 0$–3. Although the rates of the most important of these reactions are now known reasonably

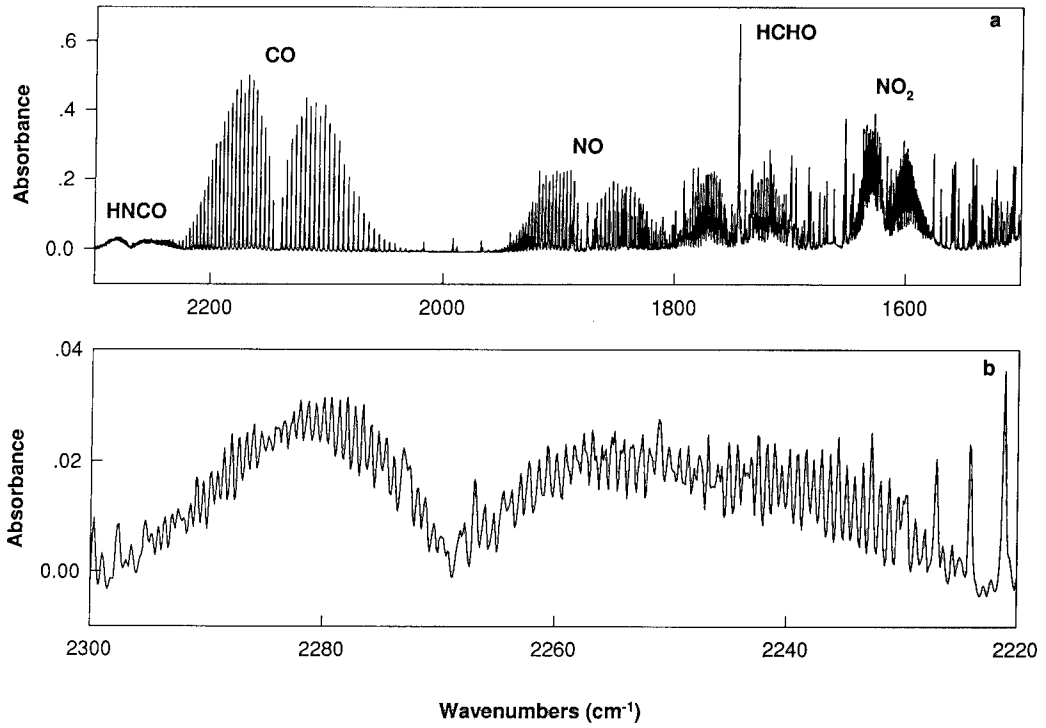

FIG. 5. FTIR spectra in the region (a) 2300–1500 cm^{-1}, (b) 2300–2220 cm^{-1}. Spectra recorded at 0.25-cm^{-1} resolution.

well [20], inadequate information is presently available for the product branching ratios, particularly at intermediate and higher temperatures. Recently, for example, the reaction between CH_2 and NO was shown [24] to proceed through formation of the addition complex CH_2NO; rearrangement or reaction of this complex to form HNCO may be possible.

Concentrations of C and CH would probably be too low at these temperatures for these species to participate. However, some CH_2 may be formed from decomposition of the intermediate oxidation product, ketene (C_2H_2O), for example. Detection of small but significant concentrations of C_2H_2 in the present experiments, conceivably formed from recombination of CH_2, makes this a not impossible pathway to HNCO production.

Reactions between methyl radicals and NO are also a potential source of HNCO. The reaction

$$CH_3 + NO \rightarrow \text{products} \qquad (6)$$

has been extensively studied at room temperature [20], where it yields CH_3NO. A recent shock tube study [25] of this reaction demonstrates that the rate of this reaction may be significantly higher at combustion temperatures than previous estimates and measurements [20] suggest. Theoretical calculations predict [26] that the products of this reaction at higher temperatures would most likely be HCN + H_2O and/or H_2CN + OH, but clearly, direct determinations of product branching ratios for this reaction are required.

Finally, the reaction

$$HCCO + NO \rightarrow HCNO + CO \qquad (7)$$

could conceivably play a role, although it is more likely to be important for fuel-rich conditions [21], unlike those pertaining to this experiment.

The present results clearly require the modification and further development of models for hydrocarbon-NO interactions, particularly at intermediate temperatures. A model recently developed for the $H_2/O_2/NO$ system [27] represents initial progress in the development of such models.

Conclusions

Results of experiments performed in a laminar flow reactor at temperatures in the range 500 °C–800 °C with NO (0–350 ppm), propane (430–1000 ppm), and O_2 (2.3–16%) lead to the following conclusions.

1. Addition of NO significantly decreases the temperature at which oxidation of propane commences, and the formation of intermediate prod-

ucts (the olefins, ethylene and propylene, and formaldehyde) occurs over a wider temperature range than does the formation of these products in the absence of added NO.

2. Oxidation of the propane coincides with NO to NO_2 conversion. The NO to NO_2 conversion occurs in stages, commencing before significant oxidation of the propane but increasing when the intermediate products begin themselves to react. The major part of the reacted propane is initially converted to olefins (C_3H_6 and C_2H_4), and C_3H_6 is the major carbon-containing product during the period when most of the NO is converted to NO_2.
3. In experiments with added NO, CH_4 is not observed as a product, implying that steady-state concentrations of CH_3 radicals are very low; rapid conversion of CH_3 to CH_3O_2 followed by reaction of CH_3O_2 with NO probably accounts for this observation.
4. At high NO and propane concentrations (350 and 1000 ppm, respectively), HNCO was detected as a product of reactions in the $C_3H_8/NO/O_2$ system. Formation of HNCO coincides with NO to NO_2 conversion. These observations provide evidence for hydrocarbon-NO interactions at lower temperatures than previously reported, which result in the formation of species containing C-N bonds. The source of the HNCO is at present unknown, but reactions involving CH_3 or CH_2 radicals with NO are plausible suggestions.

REFERENCES

1. Hori, M., *Twenty-First Symposium (International) on Combustion,* The Combustion Institute, Pittsburgh, 1986, pp. 1181–1188.
2. Bromly, J. H., Barnes, F. J., and Little, L. H., *J. Inst. Energy* 61:89–97 (1988).
3. Bromly, J. H., Barnes, F. J., Mandyczewski, R., Edwards, T. J., and Haynes, B. S., *Twenty-Fourth Symposium (International) on Combustion,* The Combustion Institute, Pittsburgh, 1992, pp. 899–907.
4. Hori, M., Matsunaga, N., Malte, P. C., and Marinov, N. M., *Twenty-Fourth Symposium (International) on Combustion,* The Combustion Institute, Pittsburgh, 1992, pp. 909–916.
5. Bromly, J. H., *"The Formation of Nitrogen Oxides in Gas Combustion,"* Ph.D. Thesis, Murdoch University, Western Australia, 1991.
6. Johnson, G. M., and Smith, M. Y., *Combust. Sci. Technol.* 19:67–70 (1978).
7. Murakami, N., and Izumi, J., U.S. Patent 4,350,669, 1982.
8. Lyon, R. K., Cole, J. A., Kramlich, J. C., and Chen, S. L., *Combust. Flame* 81:30–39 (1990).
9. Lyon, R. K., and Hardy, J. E., *Ind. Eng. Chem. Fundam.* 25:19 (1986).
10. Pohl, J. H., Yang, S.-C., Sowa, W. A., and Dill, J. W., *ACS Div. Fuel Chem. Preprints* 38:708–717 (1993).
11. Truex, T. J., Searles, R. A., and Sun, D. C., *Platinum Met. Rev.* 36:2–11 (1992).
12. Iwamoto, M., and Mizuno, N., *Proc. Inst. Mech. Eng. D* 207:23–33 (1993).
13. Li, Y., and Armor, J. N., *Appl. Catal. B* 1:L31 (1992).
14. Valyon, J., and Hall, W.K., *J. Phys. Chem.* 97:1204–1212 (1993).
15. Petunchi, J. O., and Hall, W. K., *Appl. Catal. B* 2:L17–L26 (1993).
16. USEPA Office of Air Quality Planning and Standards (OAQPS) Technology Transfer Network (TTN), EMTIC Bulletin Board, Innovative Technologies Section, node name: ttnbbs.rtpnc.epa.gov.
17. Herzberg, G., and Reid, C., *Discuss. Faraday Soc.* 9:92–99 (1950).
18. Steiner, D. A., Polo, S. R., McCubbin, T. K., Jr., and Wishah, K. A., *J. Mol. Spectrosc.* 98:453–483 (1983).
19. He, Y., Liu, X., Lin, M. C., and Melius, C. F., *Int. J. Chem. Kinet.* 23:1129–1149 (1991).
20. Mallard, W. G., Westley, F., Frizzell, D. H., Herron, J. T., and Hampson, R. F., *NIST Chemical Kinetics Database Version 5.0,* National Institute of Standards and Technology, Gaithersburg, MD, 1993.
21. Miller, J. A., and Bowman, C. T., *Prog. Energy Combust. Sci.* 15:287–338 (1989).
22. Wilk, R. D., Green, R. M., Pitz, W. J., Westbrook, C. K., Addagarla, S., Miller, D. L., and Cernansky, N. P., SAE Technical Paper Series No. 900028, 1990.
23. Warnatz, J., *Twenty-Fourth Symposium (International) on Combustion,* The Combustion Institute, Pittsburgh, 1992, pp. 553–579.
24. Atakan, B., Kocis, D., Wolfrum, J., and Nelson, P. F., *Twenty-Fourth Symposium (International) on Combustion,* The Combustion Institute, Pittsburgh, 1992, pp. 691–699.
25. Yang, H., Lissianski, V., Okoroanyanwu, J. U., Gardiner, W. C., Jr., and Shin, K. S., *J. Phys. Chem.* 97:10042–10046 (1993).
26. Melius, C. F., unpublished data, cited by Hoffman, A., Wagner, H. Gg., Wolff, Th., and Hwang, S. M., *Ber. Bunsenges. Phys. Chem.* 94:1411 (1990).
27. Bromly, J. H., Barnes, F. J., Nelson, P. F., and Haynes, B. S., *Int. J. Chem. Kinet.*, to be submitted.

COMMENTS

J. Houston Miller, George Washington University, USA. These questions concern the band centered at 2269 cm^{-1}. First, is there evidence for CO_2 in your spectra? Secondly, what is the rotational constant observed as fine structure in the band and is that consistent with HNCO?

Author's Reply. Spectral features due to CO_2 are observed at higher temperatures when oxidation of the propane proceeds to completion. Under these conditions, the region around 2269 cm^{-1} is obscured by lines due to $^{13}CO_2$. Measurements of the rotational constant of the band give a value of 0.36 ± 0.03 cm^{-1}, in good agreement with the value reported by Steiner et al. [1] of 0.37 cm^{-1}.

REFERENCE

1. Steiner, D. A., Polo, S. R., McCubbin, T. K., Jr., and Wishah, K. A., *J. Mol. Spectrosc.* 98:453–483 (1983).

•

M. C. Lin, Emory University, USA. Your observation of HNCO is interesting. Aside from what you have proposed, there are other possibilities for its formation: (1) HNC + $NO_2 \rightarrow$ HNCO + NO, if both HCN and NO_2 are present, and (2) HCO + HNO $\rightarrow$ HC(O)N(H)O $\rightarrow$ HNCO + OH, if CH_2O and NO are present. The former process was found to occur in our study of the thermal reaction of HCN with NO_2 below 800 K. The latter was observed to take place when we pyrolyzed CH_2O and NO above 700 K. Ab initio molecular orbital calculations have been made for both processes, collaborating with C. F. Melius of Sandia National Laboratories.

Author's Reply. The additional mechanisms for HNCO production suggested are interesting. In the case of the first suggestion

$$HNC + NO_2 \rightarrow HNCO + NO$$

there is still a problem with the reaction that gives rise to HNC (or HCN) at these rather low temperatures. In the case of the second suggestion, we find significant amounts of HNCO at temperatures where the concentration of HCHO is continuing to increase, but clearly this reaction offers a plausible route to HNCO at these temperatures.

•

A. E. Jacob Akanetuk, Stanford University, USA. The experimental regime of 500 °C–800 °C corresponds to conditions in the flue stream in a practical combustor. How realistic is 16% excess oxygen, which was one of the experimental conditions?

Author's Reply. This study was not attempting to simply investigate NO to NO_2 conversion catalysed by propane under conditions similar to those found in the flue gases from practical combustors. Oxygen concentrations in coal-fired power stations are usually less than 10%, and some of the experiments in our study were done at 2.25% O_2, typical of flue gas concentrations. Effects of systematic variations in O_2 concentration are part of our ongoing studies.

Twenty-Fifth Symposium (International) on Combustion/The Combustion Institute, 1994/pp. 1011–1018

ASPECTS OF NITROGEN FLAME CHEMISTRY REVEALED BY BURNING VELOCITY MODELLING

MARTIN J. BROWN AND DAVID B. SMITH
British Gas (plc)
Gas Research Centre
Ashby Road, Loughborough LE11 3QU, UK

By using detailed modelling of flames, previous burning velocity data of Gray and coworkers have been corrected to yield a reliable and consistent set of data for the four systems: H_2-N_2O, NH_3-O_2, NH_3-NO, and NH_3-N_2O.

The original measurements were made from flame radius vs time records of expanding spherical flames, burning at low pressure (70 torr (92 mbar)) and 60 °C. Expanding flame computations reproduce the broad features of the experiments, allowing flame speeds to be derived by the same means as used in the experiments. But from planar one-dimensional (1D) computations, true 1D burning velocities were also obtained. The ratio of the two computed values gives a correction factor that is then applied to the experimental data. Corrections range from 10% in the most favourable cases up to a factor of 2 in mixtures where the original flame radius/time records were markedly nonlinear.

Planar 1D-computed burning velocities were then compared with the corrected experimental data, with modifications made to the kinetics to improve the agreement. For H_2-N_2O, excellent agreement was obtained after relatively modest changes to the H + N_2O and N_2O decomposition reactions. For NH_3-O_2, reasonable agreement was found with changes to HNO + OH and HNO decomposition reactions. The NH_3-NO system was sensitive to both the overall rate and branching ratio of the NH_2 + NO reaction:

$$NH_2 + NO \rightarrow N_2 + H + OH$$
$$\rightarrow N_2 + H_2O.$$

A satisfactory simulation of burning velocities required adjustment of the total rate, while reproduction of gross flame features required the contribution from the first reaction to be approximately 80% at the high temperatures of these flames. Finally, burning velocities for NH_3-N_2O mixtures were sensitive to all the above-mentioned reactions, and an excellent simulation was achieved without further changes.

Introduction

There is continuing interest in the combustion chemistry of nitrogen-containing fuels and oxidants, straddling propellant chemistry, the formation of NO in flames, and operation of various NO control methods. In this paper, we examine aspects of the flame chemistry of four systems, H_2-N_2O, and NH_3 with O_2, NO, and N_2O, by comparing experimental burning velocities with the results of modelling using detailed kinetics. Since burning velocities are normally sensitive to few reactions, this exercise may be regarded as providing a rigorous partial test of the kinetic model.

Despite relatively simple chemistry, the H_2-N_2O mechanism is still not fully resolved. In an earlier modelling study of H_2-N_2O, Coffee [1] was hindered in the validation of his reaction scheme by the lack of experimental data. He concluded that the most useful contribution would be reliable burning velocities. This view receives support, perhaps unwitting, from the recent work of Sausa et al. [2], in which detailed modelling was compared with experimental flame structure data obtained by molecular beam-mass spectrometry. Despite a thorough study, they were unable to unravel significant issues in the chemistry.

The NH_3-NO/N_2O systems are particularly interesting because of the spotlight they throw on the reaction: NH_2 + NO → products, which is thought to be the key to the operation of the Thermal De-NO_x process [3,4]. The critical issue is the branching ratio between the possible product channels:

$$NH_2 + NO \rightarrow N_2 + H + OH \quad (36)$$
$$\rightarrow NNH + OH \quad (36a)$$
$$\rightarrow N_2 + H_2O \quad (37)$$

(reaction numbers taken from listing in Table 1) with

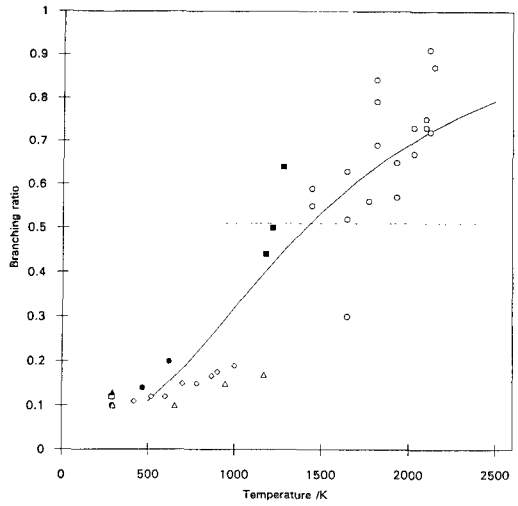

FIG. 1. Compilation of available data on branching ratio $[k_{36}/(k_{36} + k_{37})$, where 36 may include 36a] for the NH_2 + NO reaction: · · · · Miller and Bowman [4]; ——— ○ Vandooren et al. [5]; ▲ Hall et al. [6]; ■ Kimball-Linne and Hanson [7]; □ Silver and Kolb [8]; ● Bulatov et al. [9]; ◇ Atakan et al. [10]; and △ Stephens et al. [11].

channels (36) or (36a) producing reactive species, while channel (37) is terminating. The various determinations of the branching ratio, shown in Fig. 1, clearly demonstrate the lack of consensus. Miller and Bowman [4] favoured a temperature-independent value of 0.51, largely to suit the needs of their thermal de-NO_x model. Vandooren et al. [5] also derived high branching ratios, based on NH_3-flame structure studies. On the other hand, the three most direct determinations [9–11] yield significantly lower values. Although the results of Bulatov et al. [9] may be compatible with the Miller-Bowman value [4], the other two are not. They cover wider temperature ranges than Bulatov, are in excellent agreement with each other, and appear to offer persuasive evidence in favour of a lower branching ratio, which, as Stephens et al. [11] argue, has considerable implications for the thermal de-NO_x chemistry. However, the overlap of the Stephens et al. study with the operating range of thermal de-NO_x is small. As demonstrated later, burning velocities of the NH_3-NO system in particular are overwhelmingly sensitive to this reaction and can help to fix the branching ratio at high temperature.

Modelling Details

Two types of flame were modelled: planar one-dimensional (1D) and expanding spherical. Mixture-averaged transport properties were used in all computations. For planar flames, the Sandia Laboratory PREMIX program [12] was used, slightly modified to ensure strict conservation of mass and energy.

For expanding spherical flames, the unsteady 1D conservation equations at constant pressure are solved, using a program developed at British Gas but derived from PREMIX and retaining its CHEMKIN and transport property routines [13,14]. Adaptive regridding was used, with the grid being checked after each time step and recomputed when necessary to achieve maximum computational efficiency. To initiate the expanding flame calculations, a high temperature (3000–4000 K) was set in a central core having a width of 2–12.5 mm, depending on ease of ignition, equivalent to 1–75 mJ. Repeat runs were performed to locate the minimum ignition energy, although, except in its earliest stages, flame growth showed little dependence on ignition energy.

The base mechanism largely follows that of Miller and Bowman [4], with their rate data used for the nitrogen steps. Two further reactions (NH_3 decomposition and $NH_3 + O_2 \rightarrow NH_2 + HO_2$, reactions (73) and (74)) were added to assist the initiation of NH_3-O_2 flames. For the H_2/O_2 reactions, rate data mainly from the recent evaluation of Baulch et al. [15] were used together with minor refinements to certain rate coefficients by the same authors, as detailed by McLean et al. [16]. Modifications were made to the model to improve its performance, as described in the Discussion. This optimised mechanism is shown in Table 1; for brevity, the H_2/O_2 reactions are omitted but are listed elsewhere [16].

Methodology

In order to validate a kinetic model using burning velocity data, such data must obviously be reliable, although in practice this requirement proves hard to meet. There have been several determinations of burning velocity for the systems of interest [17–21], though none in recent years. We have chosen to use the data set provided by Gray and coworkers [17,18] for three reasons: (1) it provides a consistent set of data for the systems of interest; (2) we believe their data can yield accurate burning velocities *after corrections are applied*, as described below; and (3) burner methods also need significant correction [16,22], but because of the more complex geometry, the factors are much harder to quantify.

The technique Gray and coworkers used [17,18] was to burn expanding spherical flames and determine the flame speed at constant pressure from radius vs time data obtained from the schlieren image of the flame. Although for many experiments the flames apparently settled to a constant speed after only a short initial acceleratory period, in some (mainly rich) mixtures, more prolonged acceleration was observed. They followed the traditional approach by assuming that flames travelled at constant speed.

TABLE 1
Optimised reaction mechanism

Number	Reaction	A	n	E
19	$NH + O_2 = HNO + O$	1.00E + 13	0.00	12000.0
20	$NH + O_2 = NO + OH$	7.60E + 10	0.00	1530.0
21	$NH + NO = N_2O + H$	3.34E + 14	−0.46	0.0
22	$N_2O + OH = N_2 + HO_2$	2.00E + 12	0.00	10000.0
23	$N_2O + H = N_2 + OH$	2.23E + 14	0.00	16946.0
24	$N_2O + M = N_2 + O + M$	1.60E + 14	0.00	51600.0
	Enhancement factors: $H_2O = 5$, $H_2 = 1.5$, $N_2O = 10$.			
25	$N_2O + O = N_2 + O_2$	1.00E + 14	0.00	28200.0
26	$N_2O + O = NO + NO$	1.00E + 14	0.00	28200.0
27	$NH + OH = HNO + H$	2.00E + 13	0.00	0.0
28	$NH + OH = N + H_2O$	5.00E + 11	0.50	2000.0
29	$NH + N = N_2 + H$	3.00E + 13	0.00	0.0
30	$NH + H = N + H_2$	1.00E + 14	0.00	0.0
31	$NH + O = NO + H$	2.00E + 13	0.00	0.0
32	$NH_2 + O = HNO + H$	6.63E + 14	−0.50	0.0
33	$NH_2 + O = NH + OH$	6.75E + 12	0.00	0.0
34	$NH_2 + OH = NH + H_2O$	4.00E + 06	2.00	1000.0
35	$NH_2 + H = NH + H_2$	6.92E + 13	0.00	3650.0
36	$NH_2 + NO = N_2 + H + OH$	6.51E + 11	0.00	0.0
37	$NH_2 + NO = N_2 + H_2O$	1.40E + 20	−2.60	924.0
38	$NH_3 + OH = NH_2 + H_2O$	2.04E + 06	2.04	566.0
39	$NH_3 + H = NH_2 + H_2$	6.36E + 05	2.39	10171.0
40	$NH_3 + O = NH_2 + OH$	2.10E + 13	0.00	9000.0
41	$NNH + M = N_2 + H + M$	2.00E + 14	0.00	19870.0
42	$NNH + NO = N_2 + HNO$	5.00E + 13	0.00	0.0
43	$NNH + H = N_2 + H_2$	1.00E + 14	0.00	0.0
44	$NNH + OH = N_2 + H_2O$	5.00E + 13	0.00	0.0
45	$NNH + NH_2 = N_2 + NH_3$	5.00E + 13	0.00	0.0
46	$NNH + NH = N_2 + NH_2$	5.00E + 13	0.00	0.0
47	$NNH + O = N_2O + H$	1.00E + 14	0.00	0.0
48	$HNO + M = H + NO + M$	6.02E + 20	−1.61	50837.0
	Enhancement factors: $H_2O = 10$, $O_2 = 2$, $N_2 = 2$, $H_2 = 2$.			
49	$HNO + OH = NO + H_2O$	4.80E + 13	0.00	1000.0
50	$HNO + H = H_2 + NO$	5.00E + 12	0.00	0.0
51	$HNO + NH_2 = NH_3 + NO$	2.00E + 13	0.00	1000.0
52	$N + NO = N_2 + O$	3.27E + 12	0.30	0.0
53	$N + O_2 = NO + O$	6.40E + 09	1.00	6280.0
54	$N + OH = NO + H$	3.80E + 13	0.00	0.0
55	$HO_2 + NO = NO_2 + OH$	2.11E + 12	0.00	−479.0
56	$NO_2 + H = NO + OH$	3.50E + 14	0.00	1500.0
57	$NO_2 + O = NO + O_2$	1.00E + 13	0.00	600.0
58	$NO_2 + M = NO + O + M$	1.10E + 16	0.00	66000.0
59	$NH_2 + NH = N_2H_2 + H$	5.00E + 13	0.00	0.0
60	$NH + NH = N_2 + H + H$	2.54E + 13	0.00	0.0
61	$NH_2 + N = N_2 + H + H$	7.20E + 13	0.00	0.0
62	$N_2H_2 + M = NNH + H + M$	5.00E + 16	0.00	50000.0
	Enhancement factors: $H_2O = 10$, $O_2 = 2$, $N_2 = 2$, $H_2 = 2$.			
63	$N_2H_2 + H = NNH + H_2$	5.00E + 13	0.00	1000.0
64	$N_2H_2 + O = NH_2 + NO$	1.00E + 13	0.00	0.0
65	$N_2H_2 + O = NNH + OH$	2.00E + 13	0.00	1000.0
66	$N_2H_2 + OH = NNH + H_2O$	1.00E + 13	0.00	1000.0
67	$N_2H_2 + NO = N_2O + NH_2$	3.00E + 12	0.00	0.0
68	$N_2H_2 + NH = NNH + NH_2$	1.00E + 13	0.00	1000.0
69	$N_2H_2 + NH_2 = NNH + NH_3$	1.00E + 13	0.00	1000.0

TABLE 1
(continued)

Number	Reaction	A	n	E
70	$NH_2 + NH_2 = N_2H_2 + H_2$	$5.00E + 11$	0.00	0.0
71	$NH_2 + O_2 = HNO + OH$	$4.50E + 12$	0.00	25000.0
72	$NH_2 + HO_2 = NH_3 + O_2$	$3.00E + 13$	0.00	3011.0
73	$NH_3 + M = NH_2 + H + M$	$2.50E + 16$	0.00	93791.0
74	$NH + NO = N_2 + OH$	$2.16E + 13$	−0.23	0.0

Rates in the form $k = AT^n \exp(-E/RT)$, in units of cm, mol, s, cal. (For brevity, reactions (1) through (18) are omitted, but they can be found in Ref. 16.)

There are two reasons why this is not strictly correct: flame stretch and finite flame thickness. Our own studies [16,22] of spherically expanding flames show that the assumption of constant flame speed will not yield accurate burning velocities. Thus, the burning velocities as reported must be suspect.

The method adopted for correcting the data has four stages. First, expanding spherical flames were computed, using the base mechanism, with no adjustments made to bring the computed radius vs time plots into close agreement with the experimental. However, it is worth noting that the main features of the experiments were reproduced, with lean mixtures settling down fairly quickly to apparently constant speeds and rich mixtures being subject to pronounced acceleration. These computed radius/time plots were then analysed by the same procedure as used in the experiments. That is, flame speeds were determined at a radius of 3 cm or slightly larger when prolonged acceleration occurred.

The second stage was to compute planar 1D flame speeds, using the same kinetic mechanism and transport properties. The ratio of the flame speed derived from the expanding flame to the 1D value provides a correction factor, which is then applied to the real experimental data to convert them into 1D values.

These corrected experimental data can then be compared with the results of 1D computations. Since, up to this point, all computations had used the base scheme with no attempt at optimisation, significant differences between experimental and computed velocities were anticipated and indeed found. Therefore, the third stage of the methodology was to modify the kinetic mechanism to improve the agreement. A simple optimisation routine, using sensitivity coefficients from 1D modelling and uncertainties in rate constants as inputs, was employed to identify appropriate changes. However, the results of the optimisation were not then applied in an automatic fashion but were rather used as a guide to the preferred kinetic modifications.

The fourth stage was to rerun the spherical cases using the optimised scheme, to check whether the correction factors obtained in stage two were still valid. In general, they were, except where the corrections were particularly large (lean H_2-N_2O, for example), in which case, a further iteration of stages 2 through 4 was carried out. The reason for this staged approach is that 1D computations are much quicker (typical central processing unit (CPU) time of a few seconds or minutes for 1D, compared with many hours for the expanding flame cases).

Errors in the original experimental data were assessed [17] to be about 2%, increasing to 5% when acceleration occurred, i.e., in rich mixtures. The correction procedure introduces additional uncertainties. We estimate the combined errors in the corrected data lie in the range of 3% in favourable cases up to 15% in the worst (i.e., accelerating) cases, when the radius at which the speed was originally determined is imprecise, making the match with experiment more uncertain.

Results and Discussion

Representative results of the expanding flame code are shown in Fig. 2 for the H_2-N_2O system. Over much of the stoichiometric range, the radius vs time plots, after a settling period, appear fairly linear, as shown in Fig. 2a. But even in these cases, the speed vs radius plots (Fig. 2b) reveal that the speed is not quite constant at 3 cm, though differences from 1D values are small (within 25%). Thus in these cases, the experimental data need only modest correction. Towards the lean and rich composition extremes, marked nonlinearities were observed. Flames in lean mixtures were decelerating up to and beyond the region of measurement. The deceleration is a manifestation of flame stretch with a negative Markstein length and is expected in lean mixtures of a light fuel with a heavy oxidant [22]. In rich mixtures, on the other hand, computations showed flames to have a very pronounced acceleration characteristic of stretch with normal Markstein behaviour (Fig. 2a). The first case is not commented on by the experimenters, though the second is specifically referred to [18]. In both cases, as shown in Fig. 2b,

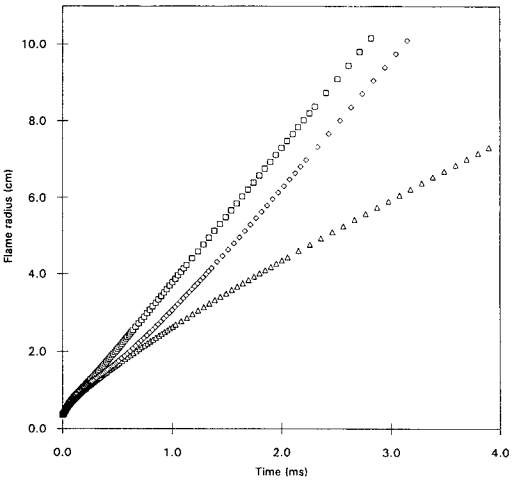

(a)

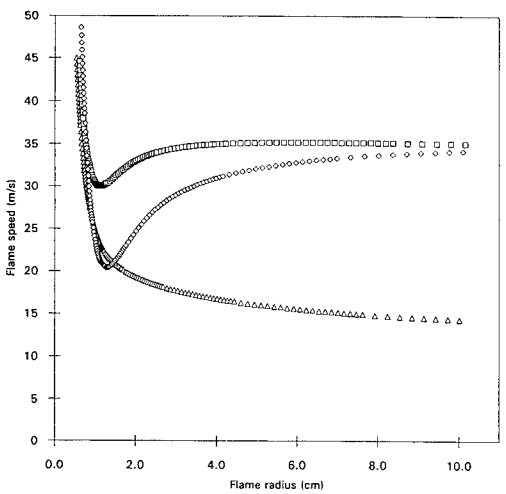

(b)

FIG. 2. (a) Computed flame radius vs time data for H_2-N_2O expanding flames. Percent H_2 in mixture: △ 30%; □ 50%; ◇ 60%. (b) Flame speed vs radius data for flames shown in (a).

speeds at 3 (or 4) cm are very different from 1D values. Corrections to experimental data are now large, up to a factor of 2.

For the ammonia systems, over most of the composition range, radius vs time records were reasonably linear, showing that the experimental data need only 10–20% adjustment. Towards the limits (particularly rich), larger corrections were again needed. However, in the case of NH_3-NO, achieving such behaviour put significant constraints on the kinetic mechanism, as discussed later.

The four systems are now discussed in turn. The systems are treated in the following order: H_2-N_2O, NH_3-O_2, NH_3-NO, and NH_3-N_2O, since they form a hierarchical set progressing from H_2-N_2O, as the simplest, up to NH_3-NO/N_2O, as the most complex.

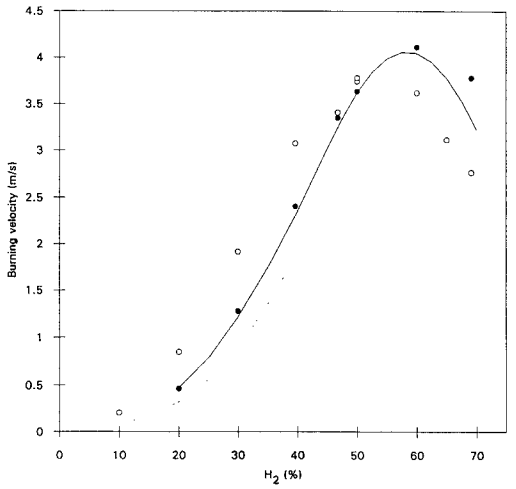

FIG. 3. Burning velocity of hydrogen/nitrous oxide as a function of stoichiometry at 60 °C and 70 torr (92.05 mbar); ○ experimental data [18]; ● corrected experimental; ···· computed values using base model; and ——— computed values with adjusted rates.

All the experiments were carried out at initial conditions of 60 °C temperature and 70 torr (92.05 mbar) pressure. Although the original experimental data were reported as S_b, in the following discussion, velocities have been converted into the more conventional S_u by multiplying by the burned to unburned gas density ratio. Since the correction procedure yields 1D values, this is a valid procedure.

Hydrogen-Nitrous Oxide:

The original experimental and corrected burning velocities are shown in Fig. 3. After correction, the stoichiometric burning velocity is 3.63 m/s, and the maximum value is 4.11 m/s. Because the correction factors vary with stoichiometry, the position of the maximum is shifted from 50% H_2, as found in the original experiments, to 60%.

As shown in Fig. 3, the base mechanism provides a poor simulation of burning velocity, always underpredicting the corrected experimental values. Sensitivity analysis reveals that the most sensitive reactions are

$$H + N_2O \leftrightarrow N_2 + OH \qquad (23)$$

$$H + N_2O \leftrightarrow NNH + O \qquad (-47)$$

$$N_2O + M \leftrightarrow N_2 + O + M \qquad (24)$$

with reaction (24) exerting its main influence in lean

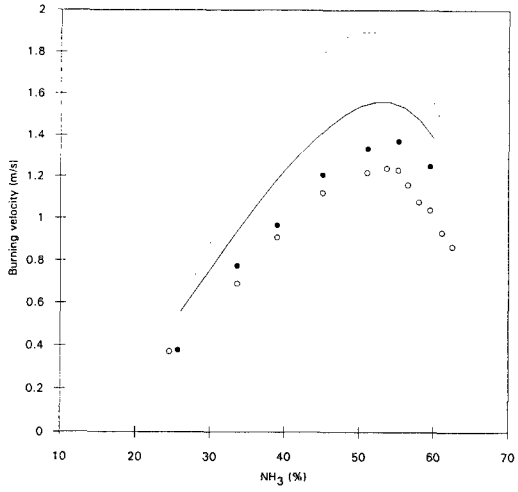

FIG. 4. Burning velocity of ammonia/oxygen as a function of stoichiometry at 60 °C and 70 torr (92.05 mbar): ○ experimental data [17]; ● corrected experimental; ···· computed values using base model; and ——— computed values with adjusted rates.

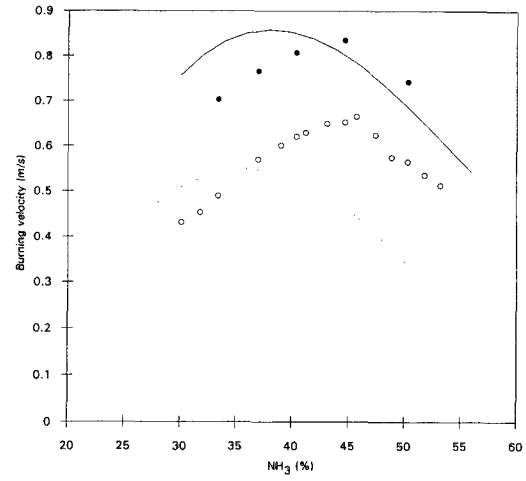

FIG. 5. Burning velocity of ammonia/nitric oxide as a function of stoichiometry at 60 °C and 70 torr (92.05 mbar): ○ experimental data [17]; ● corrected experimental; ···· computed values using base model; and ——— computed values with adjusted rates.

mixtures. The following changes were introduced: a higher rate for reaction (23) taken from Marshall et al. [23]; and varying the collision efficiencies for reaction (24) to 5 for H_2O, 1.5 for H_2, and 10 for N_2O. These efficiencies are not well characterised [24], a point made previously by both Coffee [1] and Sausa et al. [2]. Sausa et al. found the reaction with N_2O as partner to be particularly significant.

With these relatively modest changes, the mechanism provides an excellent simulation of the burning velocities. Agreement between corrected experiment and model is within 5%, except for the richest point, where the difference reaches 15%. But in this case, the marked curvature found in both experimental and computed radius/time records increases the uncertainty in the corrected burning velocity, to a value possibly as high as 15%, as described in the earlier section on Methodology.

Ammonia-Oxygen:

The original experimental and corrected burning velocities are shown in Fig. 4. After correction, the maximum velocity is 1.37 m/s in a mixture containing 55% NH_3, very close to stoichiometric.

The base mechanism overpredicted the burning velocities for all mixtures (see Fig. 3). The sensitive reactions are

$$HNO + M \leftrightarrow H + NO + M \quad (48)$$

$$HNO + OH \leftrightarrow NO + H_2O \quad (49)$$

$$H + O_2 \leftrightarrow OH + O \quad (1)$$

HNO reactions are important, particularly under lean conditions, because NH_3 oxidation is channelled through the reaction $NH_2 + O_2 \rightarrow HNO + OH$. Reaction (48) then acts as a source of H atoms and has positive sensitivity, while reaction (49) is terminating.

Using the recommendations of Tsang and Herron [25] (which represent a significant decrease in the rate of reaction (48), particularly at higher temperatures, and a slight increase in that of reaction (49)) improved the simulation significantly, although differences are still in the region of 20–25%. Given the uncertainties in the high-temperature rates of the three sensitive reactions (factors of 3 for reactions (48) and (49) [25] and 2 for reaction (1) [15]), judicious selection of rates would undoubtedly improve the fit, but such an exercise seems unjustified. We conclude that the modified mechanism provides an adequate simulation of the burning velocities of the NH_3-O_2 system.

Ammonia-Nitric Oxide:

The original experimental and corrected burning velocities are shown in Fig. 5. After correction, the maximum velocity is 0.84 m/s in a 45% NH_3 mixture; the stoichiometric value is 0.81 m/s.

The NH_3-NO system proved to be the most interesting, because gross features of flame propagation depended markedly on the branching ratio of the NH_2 + NO reaction:

$$NH_2 + NO \rightarrow N_2 + H + OH \quad (36)$$

$$\rightarrow NNH + OH \quad (36a)$$

$$\rightarrow N_2 + H_2O \quad (37)$$

while burning velocity was overwhelmingly sensitive to the overall reaction (36) + (37). Modelling confirms that, for these high-temperature flames where NNH is unstable, the choice of channel (36) or (36a) makes essentially no difference to the computed flame structure or burning velocity.

Stoichiometric requirements for the overall oxidation of NH_3 by NO [5] dictate that there must be a dissociation reaction, and this is provided mainly by reaction (36). Using the Miller–Bowman branching ratio of 0.51 [4], too much is routed into reaction (37). Temperatures and H_2 and H_2O concentrations reach transient levels well in excess of equilibrium. And, although this behaviour was found to some extent in the other systems, it was particularly noticeable here—with temperature excursions greater than 200 K. The final phase of the flame is then a slow, endothermic process (mainly dissociation of water) delaying the attainment of equilibrium. The overall effect is to cause radius vs time records to become grossly curved, to such an extent that correction factors could not sensibly be assigned.

On the other hand, the rate constants of Vandooren et al. [5] (with a higher branching ratio) prevented these adverse features (temperature overshoot of only 30 K) and yielded much more linear radius vs time behaviour. This puts a significant constraint on the branching ratio, since Andrews and Gray [17] make no comment about anomalous radius/time behaviour. While this does not of itself justify the Vandooren et al. value, the clear implication is that the branching ratio must be high enough to allow sufficient dissociation to prevent the slow attainment of equilibrium.

Our study does not allow a precise temperature to be determined over which the NH_2 + NO reaction exerts its greatest influence on burning velocity, although it should be noted that these are hot flames, having final temperatures up to 2700 K. Even so, it is clear from Fig. 1 that for a high-temperature branching ratio around 0.8 to be compatible with the low-temperature data [10,11] requires the ratio to be markedly temperature dependent above 1000 K. It also seems to rule out the value adopted by Miller and Bowman [4].

In addition to the radius/time behaviour being dependent on the branching ratio, the burning velocity of NH_3-NO mixtures is overwhelmingly sensitive to the overall rate of reaction (36) + (37). Using the values of Vandooren et al. [5] [k_{36} = 9.3E11 cm^3 mol^{-1} s^{-1}; k_{37} = 2.0E20 $T^{-2.6}$ exp($-$924 cal mol^{-1}/RT) cm^3 mol^{-1} s^{-1}] overpredicted burning velocities by at least 20%. In comparison, the Miller–Bowman rates gave burning velocities that were too low, largely a result of their low branching ratio. A satisfactory simulation was provided by reducing the Vandooren values for reactions (36) and (37), both by 30% to maintain their high branching ratio. This yields the adjusted fit shown in Fig. 5. This modified rate agrees reasonably well with the Atakan et al. data (which are the most reliable up to 1000 K) but has a different temperature dependence above 1000 K.

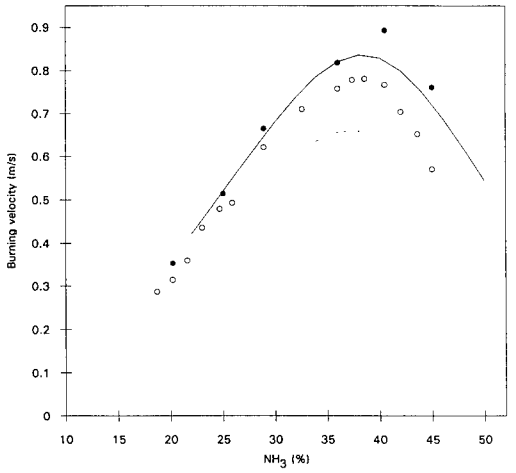

FIG. 6. Burning velocity of ammonia/nitrous oxide as a function of stoichiometry at 60 °C and 70 torr (92.05 mbar): ○ experimental data [17]; ● corrected experimental; · · · · computed values using base model; and ——— computed values with adjusted rates.

Ammonia-Nitrous Oxide:

The original experimental and corrected burning velocities are shown in Fig. 6. After correction, the maximum velocity is 0.89 m/s in a stoichiometric (40% NH_3) mixture. In this case, the stoichiometric mixture lies in the region of marked acceleration in flame propagation, resulting in an uncertainty in this burning velocity of around 15%.

The burning velocities for this system are sensitive to five reactions: H + N_2O (reaction (23)), N_2O decomposition (reaction (24)), HNO decomposition (reaction (48)), and NH_2 + NO (reactions (36) and (37)). Incorporating the modifications to these reactions as required for the other systems produced the adjusted fit shown in Fig. 6. The result is seen to be an excellent simulation. The worst agreement is 8% in a stoichiometric mixture that, as indicated above, is the most imprecise measured/corrected value. Over most of the range, agreement is within 3%.

Conclusions

1. Modelling of expanding flames allows the experimental burning velocities of Gray and coworkers

to be corrected, to yield reliable 1D burning velocities. Corrected data are reported for four systems: H_2-N_2O, NH_3-O_2, NH_3-NO, and NH_3-N_2O and compared with the predictions of 1D simulation.

2. Comparison of experimental and computed burning velocities suggests that the following changes are needed to the Miller–Bowman scheme [4]:
   a. a higher rate for H + N_2O (reaction (−47)), as reported by Marshall et al. [23];
   b. modifications to the collision efficiencies for N_2O decomposition reaction (24);
   c. a lower rate for HNO decomposition reaction (43) and a slightly higher rate for HNO + OH (reaction (49)), in line with Tsang and Herron's recommendations [25]; and
   d. modification to the total rate and branching ratio of the NH_2 + NO reactions (36) and (37). The branching ratio conclusion has significant implications for the operation of the thermal de-NO_x mechanism.

Acknowledgments

The authors are grateful to British Gas (plc) for permission to publish this paper. They also acknowledge, with thanks, contributions from Drs. S. C. Taylor and J. K. Worrell for assistance with the early stages of this work.

REFERENCES

1. Coffee, T. P., *Combust. Flame* 65:53–60 (1986).
2. Sausa, R. C., Anderson, W. R., Dayton, D. C., Faust, C. M., and Howard, S. L., *Combust. Flame* 94:407–425 (1993).
3. Lyon, R. K., and Hardy, J. E., *Ind. Eng. Chem. Fundam.* 25:19–24 (1986).
4. Miller, J. A., and Bowman, C. T., *Prog. Energy Combust. Sci.*, 15:287–338 (1989).
5. Vandooren, J., Bian, J., and van Tiggelen, P. J., *Proceedings of the Anglo-German Combustion Symposium*, Cambridge, 1993, pp. 208–211.
6. Hall, J. L., Zeitz, D., Stephens, J. W., Kasper, J. V. V., Glass, G. P., Curl, R. F., and Tittel, F. K., *J. Phys. Chem.* 90:2501–2505 (1986).
7. Kimball-Linne, M. A., and Hanson, R. K., *Combust. Flame* 64:337–351 (1986).
8. Silver, J. A., and Kolb, C. E., *J. Phys. Chem.* 91:3713–3714 (1987).
9. Bulatov, V. P., Ioffe, A. A., Lozovsky, V. A., and Sarkisov, O. M., *Chem. Phys. Lett.* 161:141–146 (1989).
10. Atakan, B., Wolfrum, J., and Weller, R., *Ber. Bunsenges. Phys. Chem.* 94:1372–1375 (1990).
11. Stephens, J. W., Morter, C. L., Farhat, S. K., Glass, G. P., and Curl, R. F., *J. Phys. Chem.* 97:8944–8951 (1993).
12. Kee, R. J., Grcar, J. F., Smooke, M. D., and Miller, J. A., *A Fortran Program for Modeling Steady Laminar One-Dimensional Premixed Flames*, Sandia Report SAND85-8240, 1985.
13. Kee, R. J., Rupley, F. M., and Miller, J. A., *Chemkin II: A Fortran Chemical Kinetics Package for the Analysis of Gas-Phase Chemical Kinetics*, Sandia Report SAND89-8009, 1989.
14. Kee, R. J., Dixon-Lewis, G., Coltrin, M. E., and Miller, J. A., *A Fortran Computer Code Package for the Evaluation of Gas-Phase Multicomponent Transport Properties*, Sandia Report SAND86-8246, 1986.
15. Baulch, D. L., Cobos, C. J., Cox, R. A., Esser, C., Frank, P., Just, Th., Kerr, J. A., Pilling, M. J., Troe, J., Walker, R. W., and Warnatz, J., *J. Phys. Chem. Ref. Data* 21:411–734 (1992).
16. McLean, I. C., Smith, D. B., and Taylor, S. C., *Twenty-Fifth Symposium (International) on Combustion*, The Combustion Institute, to be published.
17. Andrews, D. G. R., and Gray, P., *Combust. Flame* 8:113–125 (1964).
18. Gray, P., Holland, S., and Smith, D. B., *Combust. Flame* 14:361–374 (1970).
19. Ausloos, P., and van Tiggelen, A., *Bull. Soc. Chim. Belg.*, 60:433 (1951).
20. Parker, W. G., and Wolfhard, H. G., *Fourth Symposium (International) on Combustion*, Williams and Wilkins, Baltimore, MD, 1953, pp. 420–428.
21. Duval, A., and van Tiggelen, P. J., *Bull. Acad. Roy. Belges* 53:366–402 (1967).
22. Dowdy, D. R., Smith, D. B., Taylor, S. C., and Williams, A., *Twenty-Third Symposium (International) on Combustion*, The Combustion Institute, Pittsburgh, 1990, pp. 325–332.
23. Marshall, P., Ko, T., and Fontijn, A., *J. Phys. Chem.* 93:1922–1927 (1989).
24. Baulch, D. L., Drysdale, D. D., and Horne, D. G., *Evaluated Kinetic Rate Data for High Temperature Reactions*, Butterworths, London, 1973, Vol. 2, p. 89.
25. Tsang, W., and Herron, J. T., *J. Phys. Chem. Ref. Data* 20:609–663 (1991).

Twenty-Fifth Symposium (International) on Combustion/The Combustion Institute, 1994/pp. 1019–1026

NO_x FORMATION IN LEAN PREMIXED NONCATALYTIC AND CATALYTICALLY STABILIZED COMBUSTION OF PROPANE

A. SCHLEGEL, S. BUSER AND P. BENZ
Paul Scherrer Institute, Combustion Technology Section
CH-5232 Villigen-PSI, Switzerland

AND

H. BOCKHORN AND F. MAUSS
Universität Kaiserslautern, Fachbereich Chemie
Erwin Schrödinger-Str. 53, D-67663 Kaiserslautern, Germany

NO_x formation in catalytically stabilized and noncatalytic combustion of lean, premixed, atmospheric, propane/air mixtures is experimentally and numerically investigated. For this, the combustion of preheated (400 °C) mixtures with adiabatic flame temperatures from 1300 to 1500 °C is stabilized by catalytically active and inactive ceramic foam structures in an adiabatic combustion chamber. To study catalytically stabilized combustion, a fraction of the fuel is converted catalytically within the active foam. In noncatalytic combustion, no fuel is converted within the inactive foam. In both cases, a complete burnout is accomplished downstream of the foams in a homogeneous combustion zone. For the modelling, the homogeneous combustion is represented by a one-dimensional, adiabatic, premixed, laminar flame. A detailed chemical mechanism for propane combustion and NO_x formation is included.

Experimental and numerical results for NO_x emissions are presented, and the channels of NO_x formation are identified. The numerically obtained NO_x emissions compare well with the experimental data. The calculations show that only little thermal NO_x is formed in the burnt gas by the Zeldovich mechanism because of the low flame temperatures. The NO_x emitted is mainly prompt-NO formed within the combustion zone by the Fenimore, the Zeldovich, and the N_2O mechanisms. Under the conditions above, the formation of NO reacts most sensitively with respect to the reaction rates of the reactions $CH + N_2 \rightarrow HCN + N$ and $CH + O_2 \rightarrow O + CHO$.

The NO emissions of the catalytically stabilized flames are remarkably lower than those of the noncatalytic flames and depend on the fraction of catalytically converted fuel. The higher this fraction is, the lower the NO_x emissions are. The calculations indicate that the reduction of prompt-NO formation in catalytically stabilized combustion is due to a decrease in the NO formation via the Fenimore and the N_2O mechanisms, whereas NO formation via the Zeldovich mechanism is scarcely influenced.

Introduction

In catalytically stabilized thermal (CST) combustion, hydrocarbons are consumed simultaneously by heterogeneous reactions on a catalyst surface and by homogeneous gas-phase reactions. The combination of these two reaction mechanisms allows stable and complete combustion of lean premixed fuel/air mixtures at high power density and low NO_x emissions. Little thermal NO is formed because of the low combustion temperatures [1–4].

CST combustion is applicable in gas turbines. The combustion temperature must be at least as high as the turbine inlet temperature, which lies currently above 1200 °C. To improve gas turbine efficiency, the desired turbine inlet temperature will increase in the future. Since present-day catalysts are not stable enough at these temperatures, catalytic combustion concepts have to be designed whereby the catalyst is kept at significantly lower temperatures than the flame temperature. This can be achieved by burning part of the fuel within the catalyst while combustion is completed behind the catalyst (see also Ref. 5). The catalyst acts as a preconverter/stabilizer for the subsequent homogeneous combustion process.

A different technology already in practice is the noncatalytic, lean premixed combustion [6,7]. The stabilization of this type of combustion is difficult at low combustion temperatures.

CST combustion and noncatalytic, lean premixed combustion are both applicable in a range of combustion temperatures from 1300 °C to 1500 °C. The question arises as to what mode of combustion shows lower NO_x emissions under otherwise equivalent operating conditions.

It must therefore be ascertained to what extent the

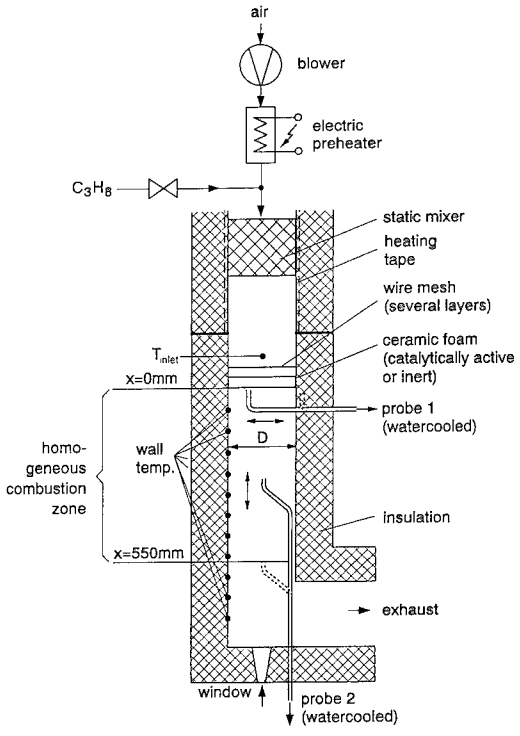

FIG. 1. Schematic of flow system and combustion chamber.

ratio of catalytically/homogeneously converted fuel affects NO_x production. Catalytic (heterogeneous) and homogeneous reaction mechanisms differ in principle. It is evident that the use of a catalyst affects NO_x production rates in the flame zone, whereas no influence on the NO_x formation in the "postflame zone" is to be expected.

In this work, NO_x formation in CST combustion and noncatalytic, lean premixed combustion is investigated both experimentally and numerically. Burner inlet temperatures of 400 °C and adiabatic combustion temperatures from 1300 °C to 1500 °C correspond to those of modern gas turbines. The investigations are carried out under atmospheric conditions. Propane is used as fuel since it is easy to ignite catalytically and produces, compared with methane, more prompt-NO during the homogeneous combustion.

Experimental

Experimental Setup:

The flow system and the combustion chamber are shown schematically in Fig. 1. By means of an electric preheater, the air flow is heated to an inlet temperature T_{in} of 400 °C. Via a mass flow controller, pure propane (>99.95% C_3H_8) is injected. The static mixer generates a homogeneous fuel and temperature distribution. To prevent the development of radial temperature profiles, all tubing is maintained at T_{in} by a heating tape. The combustion chamber is strongly insulated to obtain approximately adiabatic conditions.

The combustion process is stabilized by ceramic foam structures made of Mullite ($3Al_2O_3 \cdot 2SiO_2$) with 20 pores per inch. To investigate CST combustion, these foams are coated with platinum on an Al_2O_3 washcoat. Ceramic foams allow better radial mass and heat transfer than honeycomb monoliths and thereby produce homogeneous concentration and temperature profiles [8,9].

At the inlet of the combustion chamber, a fine wire mesh in several layers guarantees constant velocity over the cross section. The upstream radiation heat losses from the foam are absorbed by the mesh and uniformly transferred to the incoming fuel/air mixture.

The wall temperatures of the combustion chamber are measured with Pt/Rh thermocouples located close to the surface. The cross-section diameter D open to fluid flow is 90 mm.

Concentrations of CO, CO_2, O_2, C_xH_y, NO, and NO_x at different positions inside the combustion chamber are sampled by means of two water-cooled stainless steel probes. Probe 1 is adjustable in radial position and enables the measurement of gas concentrations immediately after the catalyst ($x = 0$ mm). Probe 2 is adjustable along the axis from $x = 0$ to $x = 550$ mm. Probe 1 is completely removable to avoid biasing of the measurements at the position of probe 2. Both probes are cooled with water of 60 °C, and all tubings to the analyzers are heated; thus, the condensation of water vapour in the sampled gas is prevented. NO_x measurements are made on a wet basis with a TECAN (CLD 700 EL ht) chemiluminescence NO/NO_x analyzer.

Procedure and Conditions of Experiments:

In the CST combustion experiments, part of the fuel is converted within the catalyst. The remaining fuel is burnt homogeneously downstream of the catalyst.

To vary the part of fuel converted within the catalyst, the flow velocity, the catalyst length (14–35 mm), and the activity of the catalyst have been varied. The activity of the catalyst has been reduced stepwise by exposing it repeatedly for a short time to temperatures well above 1300 °C.

The amount of fuel converted within the catalyst was evaluated at the outlet of the catalyst bed ($x = 0$) by measuring the gas composition with probe 1 at different radial positions and determining an area-weighted average.

The inlet temperature was fixed at $T_{in} = 400$ °C,

and the adiabatic flame temperatures T_{ad} were 1300 °C, 1400 °C, and 1500 °C, corresponding to equivalence ratios of $\phi = 0.379$, 0.428, and 0.478.

The experiments in noncatalytic mode were carried out with a catalytically inactive ceramic foam, so that the total conversion occured homogeneously downstream of the foam. Ignition was accomplished with a spark plug. The inlet temperatures were fixed at $T_{in} = 400$ °C as well, and the adiabatic combustion temperatures were varied from 1290 °C to 1540 °C.

All experiments were carried out at stationary conditions and with complete burnout at the outlet of the combustion chamber (probe 2, $x = 550$ mm: $[C_xH_y] < 1$ ppm, $[CO] < 10$ ppm). The adiabatic flame temperatures were evaluated from the measured gas composition of the completely burnt gas.

Modelling

For the modelling of catalytically stabilized combustion, the following assumption is made: The catalyst converts a part of the fuel heterogeneously to the oxidation products CO_2 and H_2O according to $C_3H_8 + 5O_2 \rightarrow 3CO_2 + 4H_2O$. No intermediates and, in particular, no NO_x are desorbed from the surface. To simulate varying degrees of catalytic conversion, the associated partially reacted gas mixture and temperature are used as inlet conditions for the calculation of the homogeneous combustion zone.

A complete description of the homogeneous combustion zone for both the noncatalytic and the catalytically stabilized combustion would require a two-dimensional model describing all chemical and physical mechanisms that occur in the practical combustion system used for the experiments. In particular, the influence of the combustion chamber walls on the processes in the gas phase should be considered. This work, however, is focused on the effect of catalytic conversion on NO formation, which can be described with a simpler model. Therefore, the homogeneous combustion along the centerline of the combustion chamber is assumed to be represented by a one-dimensional, adiabatic, laminar, premixed, and freely propagating flame including detailed chemistry with special regard to NO formation mechanisms.

The governing equations for this model are described elsewhere [10]. The transport properties are evaluated according to Curtis and Hirschfelder [11]. The differential equations are transferred into a system of algebraic equations by finite-difference approximations. This system is solved by a combination of time integration and the damped modified Newton algorithm [12].

Reaction Mechanism:

The calculations were performed using a detailed reaction scheme for the C/H/N/O system [13], which includes recently evaluated kinetic data of the CEC evaluation group [14]. The NO mechanism is taken from Bockhorn et al. [15a,b], completed with the latest data for the "reburn reaction" $CH_3 + NO \rightarrow HCN + H_2O$ from Gardiner et al. [16], and extended by $NO_2 \leftrightarrow NO$ reactions from Miller and Bowman [17]. The complete mechanism comprises 488 elementary reactions among 53 chemical species.

Results and Discussion

Noncatalytic Premixed Combustion:

Calculated and measured NO_x emissions in dependence on the adiabatic flame temperature are shown in Fig. 2 for noncatalytic combustion. The computations were performed for residence times of 60 and 80 ms, corresponding to the experimental residence times. The calculated NO_2 concentrations are negligibly small, whereas the measurements occasionally show significant NO_2 concentrations. The observed NO_2 is formed from NO as a result of probe effects [18,19]. Therefore, it is assumed that the sum of the detected NO and NO_2, reported here as NO_x, represents the true emissions of NO in the experiment.

Measurements of axial concentration profiles with probe 2 showed that the combustion zone was located at or near the outlet face of the noncatalytic foam over the whole cross section [20]. This validates the assumption of a flat flame for the modelling. Because of the size and the cooling effects of the probe and nonisokinetic sampling, the resolution of the axial concentration profiles is not accurate enough to be compared with the calculations.

The measured NO_x values in the exhaust gas up to 7 ppm are slightly lower than the predicted NO_x values, showing generally good agreement. The differences calculated for the highest and lowest residence times are within the variance of the experiments.

In Fig. 3, NO formation rates and the gas temperature for a noncatalytic propane/air flame ($T_{in} = 400$ °C, $T_{ad} = 1500$ °C) are plotted vs residence time. NO is formed via the Fenimore mechanism [initial reaction: $CH + N_2 \rightarrow HCN + N$, $k_{r459} = 4.4 \cdot 10^{12} \exp(-92{,}000/RT)$], the Zeldovich mechanism [initial reaction: $O + N_2 \rightarrow N + NO$, $k_{r457} = 1.8 \cdot 10^{14} \exp(-319{,}000/RT)$], and the N_2O mechanism (formation of NO via N_2O). NO formed within the flame diffuses in the upstream direction into cooler flame zones where it is oxidized to NO_2 via

$$O + NO + M \rightarrow NO_2 + M$$

$$k_{r481} = 2.75 \cdot 10^{15} \exp(7820/RT)$$

and

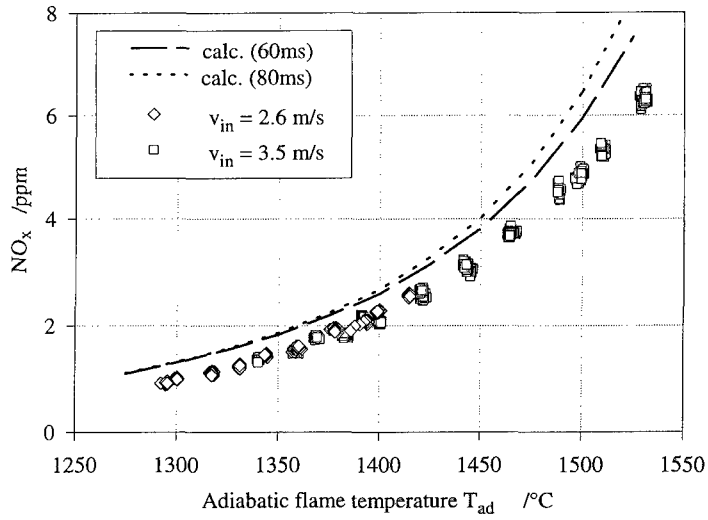

FIG. 2. Measured and calculated NO_x concentrations at combustion chamber outlet (x = 550 mm) in dependence on the adiabatic flame temperature T_{ad} for noncatalytic premixed propane/air combustion; T_{in} = 400 °C, atmospheric pressure.

$$HO_2 + NO \rightarrow OH + NO_2$$

$$k_{r483} = 2.11 \cdot 10^{12} \exp(2000/RT).$$

The NO_2 moving downstream into hotter flame zones is then "recycled" back to NO via

$$H + NO_2 \rightarrow OH + NO$$

$$k_{r485} = 3.5 \cdot 10^{14} \exp(-6300/RT).$$

Figure 4 shows for the same flame the NO concentrations and the contribution of the different formation mechanisms vs residence time. NO is mainly formed within the flame zone as prompt-NO. All three mechanisms contribute to the formation of prompt-NO (at t = 12 ms: total-NO = 4.6 ppm, via Fenimore: 57%, via Zeldovich: 21%, via N_2O: 19%). In the postflame zone, the NO concentration increases linearly with residence time. Here, NO is mainly formed via the Zeldovich mechanism and a small part via the N_2O mechanism. In this flame, the contribution of postflame-NO to total-NO is relatively small. Figure 4 again indicates that there is only little variation of NO with residence time. For lower adiabatic flame temperatures, Figs. 3 and 4 do not change qualitatively. However, NO formation in the postflame zone via the Zeldovich mechanism is negligible.

In Fig. 5, the 10 largest, absolute, first-order sensitivities of the mole fraction of NO are plotted against residence time. The absolute sensitivity of NO with respect to a reaction j is defined as the change in the mole fraction of NO if the rate of reaction j (and its backward reaction) is increased by 10%.

The NO mole fraction is most sensitive to the initial reaction of the Fenimore mechanism

$$CH + N_2 \rightarrow HCN + N \text{ (r459)}.$$

The CH radicals are formed mainly via (r53)

$$OH + {}^3CH_2 \rightarrow CH + H_2O$$

which explains the high positive sensitivity of this reaction. Reaction 49, on the other hand, removes CH radicals via

$$CH + O_2 \rightarrow O + CHO$$

so that the Fenimore mechanism is suppressed. Therefore, the mole fraction of NO is very (negative) sensitive to changes in the rate coefficient of reaction 49 (compare Bockhorn [15a,b]). Yet, the experimentally determined rate coefficients of reactions 459 and 49 are somewhat uncertain.

The rate coefficient of reaction 459 used in this work, $k_{r459} = 4.4 \cdot 10^{12} \exp(-92{,}000/RT)$, corresponds to the value reported from Dean et al. [21]. Different values for this reaction are given, for example, from Glarborg et al. [22], $k_{r459} = 4.0 \cdot 10^{11} \exp(-56{,}900/RT)$, from Lindackers et al. [23], $k_{r459} = 6.1 \cdot 10^{11} \exp(-58{,}200/RT)$, and from Miller and Bowman [17], $k_{r459} = 3.0 \cdot 10^{11} \exp(-56{,}940/RT)$. The rate coefficient for reaction 49, $k_{r49} = 3.0 \cdot 10^{13}$, is close to the recommended value $k_{r49} = 3.3 \cdot 10^{13}$ from Baulch et al. [14]. The confidence region of this rate coefficient covers the range from $1.0 \cdot 10^{13}$ to $1.0 \cdot 10^{14}$ [14].

The uncertainties in these two rate coefficients could explain the differences of the measured and calculated NO concentrations (The change in NO mole fraction if the rate of one of these two reactions is increased by only 10% is shown in Fig. 5.)

The sensitivity of the mole fraction of NO against the initial reaction of the Zeldovich mechanism

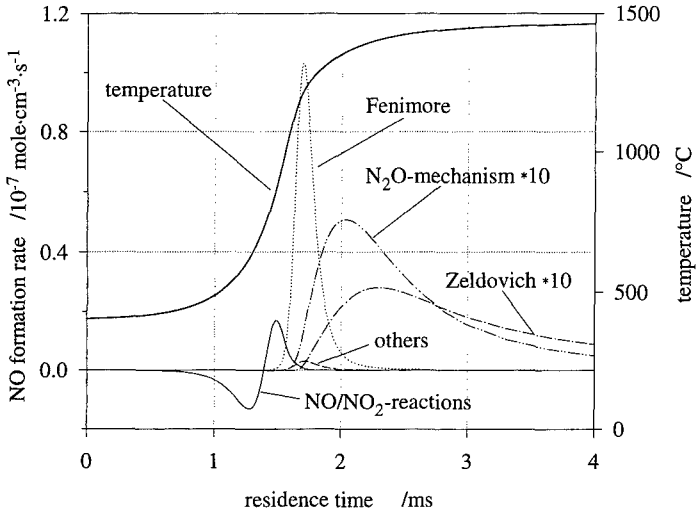

FIG. 3. Calculated NO formation rates of the different mechanisms and gas temperature vs residence time of a noncatalytic propane/air flame (T_{in} = 400 °C, T_{ad} = 1500 °C, atmospheric pressure).

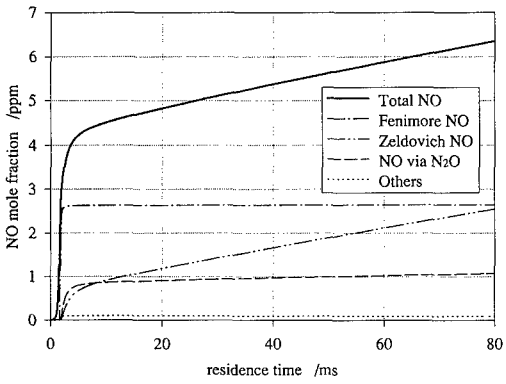

FIG. 4. Calculated contribution of the different NO formation mechanisms to total NO vs residence time for the flame of Fig. 3.

$$O + N_2 \rightarrow N + NO$$

(r457) is considerably lower within the flame front, but it is increasing linearly with increasing residence time in the postflame zone. After 80 ms, the sensitivity of reaction 457 is as large as that of reaction 459. The (positive) sensitivity of reaction 473,

$$O + N_2O \rightarrow NO + NO$$

is slightly increasing in the postflame zone as well.

Figure 6 shows the main channels for the formation of NO in the same propane/air flame. The thickness of the arrows corresponds with the total mole fraction of NO formed over a residence time of 20 ms. The figure reveals as important channels the conversion of N_2 via HCN and NCO to NO, of N_2 via N to NO, of N_2O to NO (N_2O mechanism), and of N_2 directly to NO. The Zeldovich mechanism, which is opened by $O + N_2 \rightarrow N + NO$ (r457), forms NO directly from N_2 but also via N radicals. The amount of N radicals formed either by the Fenimore or the Zeldovich mechanism is indicated by dotted lines in Fig. 6. About 78% of total N_2O is formed from N_2 through the reaction

$$O + N_2 + M \rightarrow N_2O + M$$

$$k_{r468} = 4.36 \cdot 10^{12} \exp(-60{,}380/RT)$$

and 22% via N_2H by the reaction chain

$$H + N_2 + M \rightarrow N_2H + M$$

$$k_{r454} = 7.08 \cdot 10^{14} \exp(-108{,}280/RT)$$

$$O + N_2H \rightarrow H + N_2O$$

$$k_{r465} = 1.0 \cdot 10^{14}.$$

However, the destruction of N_2O to N_2 through reactions

$$H + N_2O \rightarrow OH + N_2$$

$$k_{r469} = 7.6 \cdot 10^{13} \exp(-63{,}590/RT)$$

$$OH + N_2O \rightarrow HO_2 + N_2$$

$$k_{r471} = 2.0 \cdot 10^{12} \exp(-41{,}840/RT)$$

$$O + N_2O \rightarrow O_2 + N_2$$

$$k_{r475} = 1.0 \cdot 10^{14} \exp(-118{,}000/RT)$$

is predominant over the formation of N_2O from N_2

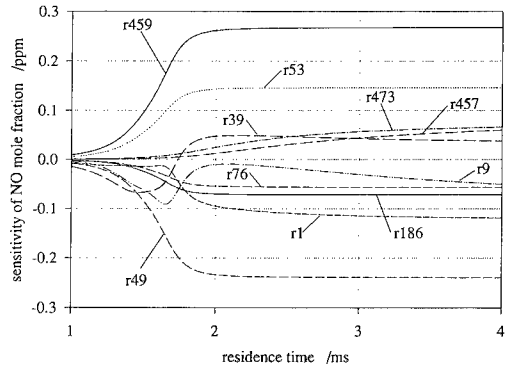

FIG. 5. Absolute, first-order sensitivities of the mole fraction of NO for the 10 most sensitive reactions vs residence time for the flame of Fig. 3 (see text). Reaction rate coefficients are in the form $k_j = k_0 T^{\beta} \exp(-E_a/RT)$.

	reaction	k_0 (cm mol s)	β (−)	E_a (kJ/mol)
r459:	$CH + N_2 \rightarrow HCN + N$	$4.4 \cdot 10^{12}$	0.0	92.0
r457:	$O + N_2 \rightarrow N + NO$	$1.8 \cdot 10^{14}$	0.0	319.0
r49:	$CH + O_2 \rightarrow O + CHO$	$3.0 \cdot 10^{13}$	0.0	0.0
r1:	$H + O_2 \rightarrow O + OH$	$2.0 \cdot 10^{14}$	0.0	70.3
r53:	$^3CH_2 + OH \rightarrow CH + H_2O$	$1.91 \cdot 10^{12}$	0.0	−77.5
r473:	$O + N_2O \rightarrow NO + NO$	$1.0 \cdot 10^{14}$	0.0	118.0
r9:	$H + O_2 + M \rightarrow HO_2 + M$	$2.3 \cdot 10^{18}$	−0.8	0.0
r186:	$O + CHCO \rightarrow H + CO + CO$	$9.6 \cdot 10^{13}$	0.0	0.0
r39:	$OH + CO \rightarrow H + CO_2$	$6.0 \cdot 10^{06}$	1.5	−3.1
r76:	$^3CH_2 + O_2 \rightarrow H + OH + CO$	$1.3 \cdot 10^{13}$	0.0	6.2

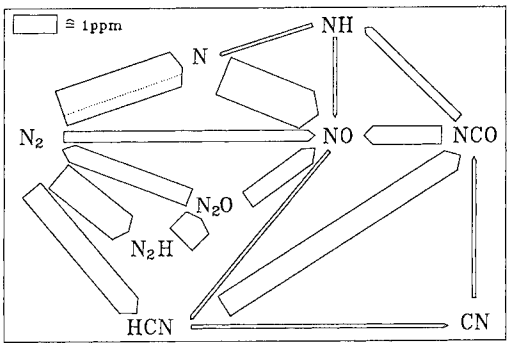

FIG. 6. Main reaction channels for the formation of NO for the flame of Fig. 3 (residence time = 20 ms).

through reaction 468. Thus, a net flux of N_2O to N_2 appears in Fig. 6. N_2O forms NO via

$$O + N_2O \rightarrow NO + NO$$

$$k_{r473} = 1.0 \cdot 10^{14} \exp(-118{,}000/RT)$$

In this flame, at a pressure of 0.1 MPa, about 20% of NO is formed via the N_2O mechanism. Since the N_2O formation via reaction 468 from N_2 and the N_2H formation via reaction 454 are both "third-body reactions," it is evident that the N_2O mechanism will be more important at higher pressure.

Destruction of NO occurs mainly by the reaction

$$CH_3 + NO \rightarrow H_2O + HCN$$

$$[k_{r418} = 1.2 \cdot 10^{14} \exp(-121{,}200/RT)]$$

Subsequently, the HCN reacts to NO through the Fenimore mechanism. However, this "reburning mechanism" of NO is not important in this flame.

Catalytically Stabilized Combustion:

In Figs. 7A through 7C, calculated and measured NO_x concentrations for adiabatic flame temperatures of 1300 °C, 1400 °C, and 1500 °C in dependence on the fuel conversion within the catalyst are given. The calculations for the different adiabatic flame temperatures were carried out for both the upper and lower limits of residence times (corresponding to the flow velocities) of the experiments.

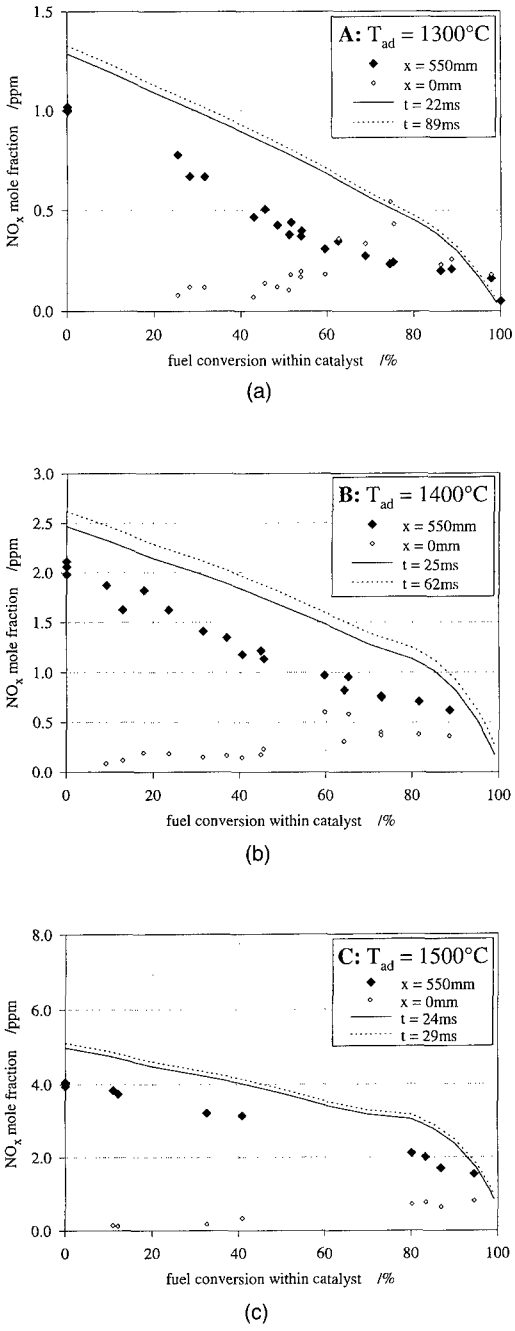

FIG. 7. Measured and calculated NO_x mole fractions in dependence on fuel conversion within catalyst for different adiabatic flame temperatures T_{ad}. Propane/air, T_{in} = 400 °C, atmospheric pressure, flow velocity at inlet: A: 2.7–10.6 m/s; B: 3.5–8.9 m/s; C: 7.1–8.7 m/s. [Lines: calculations with t = corresponding residence time for minimum and maximum flow velocity; symbols: measurements at combustion chamber outlet (x = 550 mm) and at catalyst outlet (x = 0 mm).]

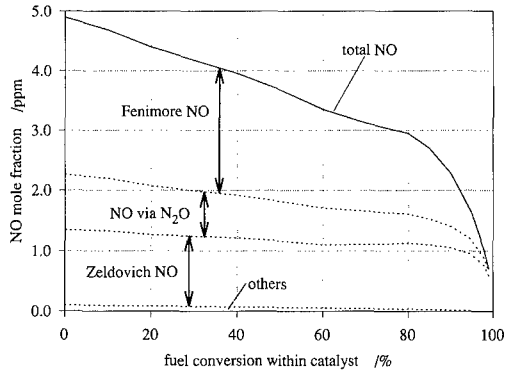

FIG. 8. Calculated contribution of the different NO formation channels to total-NO vs fuel conversion within catalyst (propane/air, T_{in} = 400 °C, T_{ad} = 1500 °C, residence time = 20 ms, atmospheric pressure).

The NO_x emission decreases with increasing conversion within the catalyst. The calculated dependence is not linear, however. At high conversion within the catalyst, the dependence on conversion is stronger than at low conversion. This nonlinearity is more pronounced at high adiabatic flame temperatures.

Measured NO_x values at the catalyst outlet larger than zero come from interferences with C_xH_y and CO of the analyzer used for the measurements. At low conversion within the catalyst, only interference of C_xH_y is present, whereas, at higher conversion, interference from CO may be present as well. In addition, probe effects could contribute to the measured values, since the sampled gas at higher conversions is extremely reactive. However, the good agreement of measured and calculated NO_x concentrations at the outlet of the combustion chamber shows that the assumption of vanishing NO formation within the catalyst holds.

Apart from this, NO formation due to homogeneous reactions within the catalyst, which may be relevant at higher catalyst temperatures (i.e., high fuel conversion within catalyst at high adiabatic flame temperatures) needs further investigation.

Figure 8 shows the calculated NO concentrations for adiabatic flame temperatures of 1500 °C and residence times of 20 ms vs fuel conversion within the catalyst. The contribution to total-NO of each of the main NO formation mechanisms is shown as well. The decrease of total-NO, which is more or less linear up to about 80% fuel conversion within catalyst, is mainly due to the decrease of the contributions of the Fenimore and the N_2O mechanisms. The contribution of the Zeldovich mechanism remains almost constant. For fuel conversions within the catalyst higher than 80%, the contribution of the Fenimore and the N_2O mechanisms decrease rapidly, so that most of the total-NO is formed via the Zeldovich mechanism.

Conclusion

In noncatalytic, premixed combustion of lean propane/air mixtures with adiabatic flame temperatures of 1300 °C–1500 °C (burner inlet temperature 400 °C, pressure 0.1 MPa, residence time <80 ms), the NO_x formation in the flame zone (prompt-NO) is predominant over the thermal NO_x generated in the postflame zone.

The calculations, which compare well with the experiments, show a substantial contribution of the Fenimore, the Zeldovich (enhanced by superequilibrium O), and the N_2O mechanisms to the formation of prompt-NO. The reactions $CH + N_2 \rightarrow HCN + N$ (initial reaction of the Fenimore mechanism) and $CH + O_2 \rightarrow O + CHO$ (removal of CH radicals) are identified as the most sensitive reactions for the NO_x emissions. N_2H is identified as an important intermediate species for the NO formation via N_2O at atmospheric pressure.

In a catalytic burner under the same operating conditions, where part of the fuel is converted within the catalyst and the remaining fuel is burnt homogeneously downstream, less prompt-NO is formed. The NO_x emissions decrease with increasing part of the fuel converted within the catalyst. Therefore, the highest possible conversion of the fuel within the catalyst bed must be pursued. This can be limited by the thermal stability of the catalyst bed.

The calculations show that the reduction of prompt-NO formation in catalytically stabilized combustion is due to a decrease in the NO formation via the Fenimore and the N_2O mechanisms, whereas NO formation via the Zeldovich mechanism is hardly influenced.

Gas turbines are the most important application for lean premixed combustion. As far as burner inlet temperatures and combustion temperatures are concerned, our investigation matches gas turbine conditions. Likewise, at high pressures (typically 1.0–1.5 MPa) and using natural gas instead of propane, it is expected that the tendency of the catalyst influence on NO_x formation remains the same.

Acknowledgment

We thank the Swiss Federal Office of Energy (BEW) for financial support of this work.

REFERENCES

1. Pfefferle, W. C., Carrubba, R. V., Heck, R. M., and Roberts, G. W., ASME Paper 75WA/FU-1, 1975.
2. Bruno, C., Walsh, P. M., Santavicca, D. A., Sinha, N., Yaw, Y., and Bracco, F. V., *Combust. Sci. Technol.* 31:43–74 (1983).
3. Pillsbury, P. W., ASME Paper 84-GT-54, 1984.
4. Kajita, S., Tanaka, Y., and Kitajima, J., ASME Paper 90-Gt-89, 1990.
5. Scherer, V., Weisenstein, W., Griffin, T., Benz, P., Buser, S., and Schlegel, A., *Proceedings of the Second International Conference on Combustion Technology for a Clean Environment*, 19–22 July 1993, Portugal.
6. Aigner, M., Mayer, A., Schiessel, P., and Strittmatter, P., ASME Paper 90-GT-308, 1990.
7. Lovett, J. A., and Abuaf, N., ASME Paper 92-GT-120, 1992.
8. Schlegel, A., Benz, P., and Buser, S., *Wärme- und Stoffübertragung* 28:259–266 (1993).
9. Benz, P., Hütter, P., and Schlegel, A., *Wärme- und Stoffübertragung* 29:125–127 (1993).
10. Smooke, M. D., Miller, J. A., and Kee, R. J., in *Numerical Methods in Laminar Flame Propagation* (N. Peters and J. Warnatz, Eds.), Vieweg, Wiesbaden, 1982.
11. Curtis, C. F., and Hirschfelder, J. O., *J. Chem. Phys.* 17:550 (1949).
12. Grcar, J. F., Kee, R. J., Smooke, M. D., and Miller, J. A., *Twenty-First Symposium (International) on Combustion*, The Combustion Institute, Pittsburgh, 1986, pp. 1773–1782.
13. Warnatz, J., in *Combustion Chemistry* (W. C. Gardiner, Jr., Ed.), Springer, Berlin, 1984.
14. Baulch, D. L., Cobos, C. J., Cox, R. A., Esser, C., Frank, P., Just, Th., Kerr, J. A., Pilling, M. J., Troe, J., Walker, R. W., and Warnatz, J., *J. Phys. Chem. Ref. Data* 21:411 (1992).
15. a) Bockhorn, H., Chevalier, Ch., Warnatz, J., and Weyrauch, V., *ASME HTD Vol. 166*, Book No. G00629, 1991. b) Bockhorn, H., Chevalier, Ch., Warnatz, J., and Weyrauch, V., *VDI Berichte* No. 922, VDI Verlag, Düsseldorf, 1991.
16. Gardiner, W., Lissianski, V., Okoroanyanwu, U., Yang, H. X., Zhao, M., and Shin, K. S., *Proceedings of the Second International Conference Combustion Technology for a Clean Environment*, 19–22 July 1993, Portugal.
17. Miller, J. A., and Bowman, C. T., *Prog. Energy Combust. Sci.* 15:287–338 (1989).
18. Johnson, G. M., Smith, M. Y., and Mulcahy, M. F. R., *Seventeenth Symposium (International) on Combustion*, The Combustion Institute, Pittsburgh, 1979, pp. 647–660.
19. Kramlich, J. C., and Malte, P. C., *Combust. Sci. Technol.* 18:91–104 (1978).
20. Sathe, S. B., Peck, R. E., and Tong, T. W., *Combust. Sci. Technol.* 70:93–109 (1990).
21. Dean, A. J., Hanson, R. K., and Bowman, C. T., *Twenty-Third Symposium (International) on Combustion*, The Combustion Institute, Pittsburgh, 1990, pp. 259–265.
22. Glarborg, P., Miller, J. A., and Kee, R. J., *Combust. Flame* 65:177–202 (1986).
23. Lindackers, D., Burmeister, M., and Roth, P., *Twenty-Third Symposium (International) on Combustion*, The Combustion Institute, Pittsburgh, 1990, pp. 251–257.

Twenty-Fifth Symposium (International) on Combustion/The Combustion Institute, 1994/pp. 1027–1034

NO_x FORMATION IN GEOMETRICALLY SCALED GAS-FIRED INDUSTRIAL BURNERS

A. D. AL-FAWAZ, L. M. DEARDEN, J. T. HEDLEY, M. MISSAGHI,°°
M. POURKASHANIAN, A. WILLIAMS AND L. T. YAP°

Department of Fuel and Energy
The University of Leeds
Leeds, LS2 9JT, UK

Scaling of NO_x formation from two geometrically similar 0.067-MW and 0.266-MW industrial-type natural-gas-fired burners was investigated experimentally and theoretically. The scaling criterion employed in this study was constant-velocity scaling. Detailed in-flame measurements are presented for baseline flames produced from both burners. In-furnace measurements were taken from a refractory-lined rapid-heating furnace for an excess air level of 12%. Comparisons of temperature and species concentration measurements were made and were corroborated by theoretical predictions from computational fluid-dynamic calculations. The mean turbulent NO production rate is obtained using the probability density function (pdf) formulations. Theoretical results are used as a platform to interpret the increase in the baseline NO_x emission. The theoretical results are explained in terms of differences in flame characteristics leading to differences in contribution from thermal- and prompt-NO due to velocity scaling. Furthermore, there was reasonably good agreement of the experimental as well as the numerically calculated exhaust NO_x emissions of these complex burners when using a flamelet-based scaling correlation for simple turbulent diffusion flames. Additionally, the lower prompt-NO contribution compared with thermal-NO formation predicted by the detailed calculations for the larger burner was in noteworthy agreement with the flamelet-based scaling arguments.

Introduction

When designing a new burner for industrial use, it is often preferable to use a significantly smaller scaled version to ascertain its characteristics. Financial constraints and overall practicality are the usual reasons for this approach [1]. It is therefore necessary to know how various flame characteristics scale as a result of different geometrical scales of the burner. Currently, with increasing emphasis being placed on decreasing NO_x emissions, the need for reliable scaling relationships is becoming an economic necessity.

The use of dimensional analysis and of similarities has proven to be of considerable value in the investigation of many physical problems. However, dimensional analysis is too ambiguous to be successfully applied to the analytical study of combustion problems, which typically contain a large number of variables. For many years, similarity techniques have been applied in the combustion field [2,3,4]. Here, the ultimate goal of similarity considerations is to provide a quick and economical route to full-scale burner systems. However, detailed understanding of pollutant formation processes, as well as understanding of fluid-dynamic and thermochemical aspects of the combustion system, is required to develop scaling as an appropriate design tool. It has been recognised that the flow fields and scalar fields of bench-scale experiments are not related to the full-scale version in a simple manner [1]. This is a result of the complex manner in which various nonlinear physical and chemical phenomena interact. Despite these hurdles, the identification of significant dimensionless numbers and correlations that may be found between these quantities can be invaluable to burner designers.

Experimental and theoretical temperature and species profiles generated by two geometrically similar burners are presented here. The constant inlet-velocity scaling approach is employed to examine NO formation in turbulent flows. NO concentrations generally form only in trace quantities. Hence, the NO formation does not affect the thermochemistry of the flow field significantly. As a result, the NO formation rate calculations can be decoupled from the calculations for the flow field and solved separately by postprocessing. Detailed NO predictions were accomplished utilising reduced reactions for the complex chemical mechanisms of thermal- and prompt-NO formation. A joint probability density function (pdf) approach was employed to address the interaction of chemistry and turbulence.

°BOC Group Technical Center, Murray Hill, NJ, USA.
°°FLUENT Inc., NH, USA.

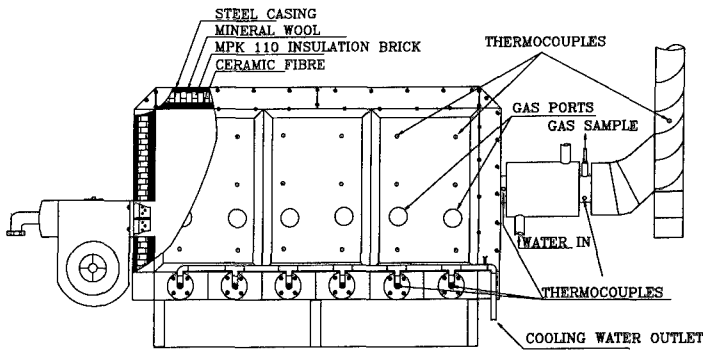

FIG. 1. Schematic diagram of the experimental apparatus.

Experimental Method

The Experimental Furnace:

Experimental tests were performed in a 1.8-m by 0.9-m by 0.6-m refractory-lined rapid-heating furnace, shown in Fig. 1. A multisectioned water-cooled base provided an adjustable load that could be tailored in a longitudinal direction. Six ports were located along the length of the furnace, enabling measurements of species and gas temperature. A water-cooled quartz-lined probe was employed for on-line analysis of the in-furnace combustion gases CO, CO_2, NO, NO_2, and O_2. The CO and CO_2 concentrations were measured using nondispersive infrared analysers. A chemiluminescence detector was used to determine NO and NO_2 concentrations. In addition, Pt-Pt-13% Rh (25 μm) thermocouples were used to monitor flame and wall temperatures, and water inlet and outlet temperatures were measured with K-type thermocouples.

The Experimental Burners:

The natural-gas burners of 0.067 MW (burner A) and 0.266 MW (burner B) were designed for use in compact industrial boilers. Both burners are characterised by an adjustable gas nozzle that provides stable firing over a large range. Combustion air is provided by a centrifugal impeller fan. Details of the burners are summarised in Table 1.

Velocities were effectively maintained constant: the primary combustion-air velocity, u_p = 11.9 m/s, the secondary combustion-air velocity, u_s = 10.5 m/s, and the natural-gas flow velocity, u_g = 19.5 m/s. For each flame, the burner was fired at the rated thermal input, and the furnace was allowed to reach thermal equilibrium (3–5 h). For each condition, in-flame measurements of gas composition and gas temperature were made. In the furnace exhaust, gas samples were extracted with a stationary water-cooled probe. A flow-rate correction was carried out according to the velocity profile of the exhaust gas.

TABLE 1
Burner Characteristics and Experimental and Predicted Measurements of Temperature, NO_x, and EI_{NO_x} in the exhaust

	Burner A	Burner B
Thermal output (MW)	0.067	0.266
Gas flow rate (m^3/h)	6.75	27.00
Air flow rate (m^3/h)	72.72	290.16
Fr_{eq} (Froude number)	3,504	1,797
Re_{eq}	13,028	26,188
Measured exhaust temperature (°C)	885	1,201
Measured exhaust NO_x and {NO} concentration (ppm)	56 {49}	91 {70}
Predicted exhaust-NO concentration (ppm)	58	81
EI_{NO_x} based on the measurement of total NO_x in the exhaust gases (g/kg)	1.179	1.940
EI_{NO_x} based on the prediction of total NO_x in the exhaust gases (g/kg)	1.469	2.071
EI_{NO_x} based on the prediction of prompt-NO in the exhaust gases (g/kg)	0.383	0.464

Numerical Simulation

Identifying the important scaling parameters is crucial for scale-up of research data obtained for small prototype burners. However, even for a relatively simple combustion process involving gaseous fuels, the number of important dimensionless numbers can be prohibitive. Generally, it is not possible to maintain more than one of these dimensionless numbers constant.

However, using a flamelet-based model for buoyancy-dominated turbulence flames, Røkke et al. [5] derived a simple scaling correlation:

$$\frac{EI_{NO_x}\rho_0 u_0}{d_0} \approx 44Fr^{3/5} \approx \frac{11u_0^{1.2}}{d_0^{0.6}} \quad (1)$$

which collapsed the NO_x emission measurements for various fuels from different studies over five orders of magnitude of Froude number. In this equation, ρ_0 = fuel density (kg/m^3), u_0 = average exit velocity (m/s), d_0 = exit diameter (m), and Fr = Froude number.

In this investigation, the emission index of NO_x (EI_{NO_x}), expressed as g NO_x/kg natural gas, was calculated from the expression

$$EI_{NO_x} = \frac{(X_{NO}MW_{NO}) + (X_{NO_2}MW_{NO_2})}{X_{CO_2}MW_{CH_4}} \times 1000 \quad (2)$$

where X_i is the mol fraction of species i and MW_i is the molecular weight of species i. The above equation assumes that all the carbon from natural gas is oxidised to CO_2, which is a reasonable assumption in postflame and exhaust gases.

In this study, the effect of scaling on the prompt- and thermal-NO emissions was investigated. In the present study, the burner was scaled in accordance with the following: (1) the geometric similarity that was achieved by fixing all geometric dimensions in proportion with each other, and (2) kinematic or aerodynamic and mixing similarity. In general, mixing depends on the pattern of flow, which, in turn, will depend on the forces that influence the flow pattern producing parameters. The ratio of momentum flux at source can be kept constant by maintaining the primary and secondary air velocities constant. This will lead to a similarity in initial mixing characteristics for both burners under investigation.

The flow-field predictions are obtained by solving the Reynolds-averaged conservation equations using the SIMPLE algorithm of Patanker [6] for the pressure/velocity coupling. Turbulence closure was obtained using the k-ε model. Concentrations of NO are small in comparison with other stable species formed during the combustion process. Therefore, the NO formation mechanism has no significant effect on the flow field and the flame chemistry. Here, NO concentrations are calculated using a postprocessing code [7,8]. In the first stage of numerical analysis, grid dependency of the solution of the numerical model for the baseline flame was determined. The finer mesh produced significantly smaller differences in the results.

In general, during natural-gas combustion, the NO formation is controlled by (1) thermal-NO, (2) prompt-NO, and (3) N_2O to NO route [9]. In this investigation, burners were operated under fuel-lean conditions (12% excess air). Formation of NO through the N_2O route was considered to be negligible, since N_2O can only contribute significantly to the total-NO concentration at high pressures resulting from more effective three-body reactions. Therefore, in this study, only thermal- and prompt-NO pathways were considered. The postprocessing code [7,8] employs a joint variable pdf technique to address the interaction of turbulence and chemistry. In addition, partial-equilibrium radical atom formation for O and other species such as OH is considered, giving a result for [O] and [OH] that would be wrong by a factor of 2.

Thermal-NO is formed via the extended Zeldovich mechanism [10]:

$$O + N_2 \underset{k_{-1}}{\overset{k_1}{\rightleftharpoons}} NO + N \quad (R_1)$$

$$N + O_2 \underset{k_{-2}}{\overset{k_2}{\rightleftharpoons}} NO + O \quad (R_2)$$

and when OH >> H > O (i.e., for rich mixtures):

$$N + OH \underset{k_{-3}}{\overset{k_3}{\rightleftharpoons}} NO + H. \quad (R_3)$$

The rate of formation of NO is obtained as a function of the rate constants (k_1–k_3) and (k_{-1}–k_{-3}). With the "quasi–steady-state" assumption for nitrogen atom concentration [10], the rate-limiting step is determined by

$$\frac{d[NO]_T}{dt} = 2k_1[O][N_2]\left\{\frac{1 - [NO]^2/K[O_2][N_2]}{1 + k_{-1}[NO]/k_2[O_2] + k_3[OH]}\right\} \quad (3)$$

where $K = (k_1/k_{-1})(k_2/k_{-2})$ is the equilibrium constant for the reaction between N_2 and O_2.

Here,

$$k_1 = 1.84 \times 10^{14} \cdot \exp(-76{,}250/RT) \quad \text{cm}^3/\text{mol s} \quad (4)$$

in which R is the universal gas constant and T is the temperature.

Prompt-NO is produced by reactions of N_2 with fuel-derived radicals in fuel-rich regions. These fuel-rich zones generally occur in the vicinity of the burner in low-temperature regions. Various species, for example, CH, CH_2, etc., resulting from fuel degradation have been proposed as precursors for prompt-NO formation [10], but the major route is via CH.

The amount of prompt-NO produced in combustion systems is relatively small compared with the

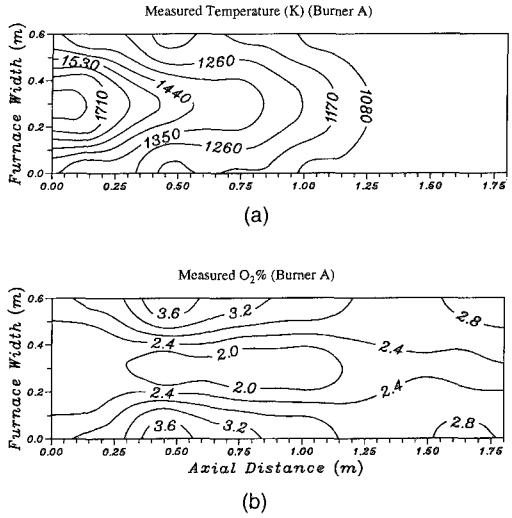

FIG. 2. Contours of temperature (a) and O_2 (b) for burner A.

total NO_x formation. Here, a global kinetic rate was used to predict prompt-NO emissions [7]:

$$\frac{d[\mathrm{NO}]_p}{dt} = f\, T^{\beta} A_{Pr}\, [\mathrm{O_2}]^a [\mathrm{N_2}][\mathrm{fuel}]^b \exp(-E_a/RT) \tag{5}$$

where f is a correction factor applicable for all aliphatic alkane hydrocarbon fuels and for air/fuel ratios of 0.75–1.56. The term T^{β} represents the non-Arrhenius behaviour of Eq. (5) at experimental conditions where the maximum flame temperature is very high (e.g., oxy-fuel combustion) or very low. In this investigation, a β value of zero was used, indicating normal air–natural-gas combustion. The preexponential factor A_{Pr} has a value of $6.4 \times 10^6 (RT/P)^{a+1}$ where P is pressure. The terms a and b are the reaction order for oxygen and fuel, respectively, and vary between 0 and 1 depending on the rate of consumption of oxygen and fuel. Finally, the activation energy has a value of 303 kJ/mol.

In order to apply Eq. (5) for different hydrocarbon fuels and different air/fuel ratios, a correction factor of $f = 4.75 + C_1 n - C_2\theta + C_3\theta^2 - C_4\theta^3$ was used where C_1–C_4 are constants with values of 8.19×10^{-2}, 23.2, 32, and 12.2, respectively. Here, n is the number of carbon atoms per molecule for the hydrocarbon fuel type, and θ is the equivalence ratio. The correction factor f is based on experimental values by investigation, and full details are given elsewhere [7].

In most practical combustion systems, the flow is highly turbulent, suggesting that temporal variations in species concentration and temperature will influence flame properties. Because of the high activation energy chemistry of NO, NO-formation time scales may interact with fluid-mechanical time scales. Hence, considerable errors may result when calculating mean NO reaction rates using mean temperature and species concentrations. Therefore, the transport equation for NO was solved in which the source term included the effects of turbulence/chemistry interaction.

The present work employs a joint two-variable pdf, which has proved successful in previous studies [7,8,11]. The turbulent rate is computed by using an assumed-shape pdf closure assumption. The pdf is based on two parameters: temperature and oxygen, and temperature and mean fuel mass fraction. These were chosen as the two variables for thermal- and prompt-NO production, respectively. The shape of the pdf is assumed to take the beta function form.

The mean turbulent reaction rate $\overline{w}$ is described in terms of the instantaneous rate w and a joint pdf of various variables:

$$\overline{w} = \int w\,(\upsilon_1,\upsilon_2)\, P\,(\upsilon_1,\upsilon_2)\, d\upsilon_1,\upsilon_2 \tag{6}$$

where υ, υ_2 are temperature and mixture fraction and P is the joint probability density function. For statistically independent variables, the two-variable pdf, $P\,(\upsilon_1,\upsilon_2)$, can be expressed as

$$P\,(\upsilon_1,\upsilon_2) = P_1\,(\upsilon_1)\, P_2\,(\upsilon_2) \tag{7}$$

where P_1 and P_2 are two-moment beta functions. The equation for the beta function $P(\upsilon)$ depends on the mean value of the appropriate quantities, $(\overline{\upsilon}_1)$ and its second moment $(\overline{\upsilon_i'^2})$. The second moment $(\overline{\upsilon_i'^2})$ is assumed to be related to the first by

$$\overline{\upsilon_i'^2} = S(\overline{\upsilon_i} - \overline{\upsilon}_i^2) \tag{8}$$

where S is a coefficient that represents fluctuation intensity and $i = 1$ and 2. High S values correspond to high Damkohler numbers. In this study, S parameters are selected based on sensitivity analysis of the variation of NO_x concentrations with the S parameter. A full description of the code is given elsewhere [11].

Results and Discussion

Experimental Results:

In this study, the constant-velocity scaling method was examined by performing in-flame measurements on geometrically similar 0.067-MW (A) and 0.266-MW (B) natural-gas burners. Under these conditions, the flue gas temperature was measured to be approximately 915 K for burner A and 1220 K for burner B.

The experimental results are presented in Figs. 2

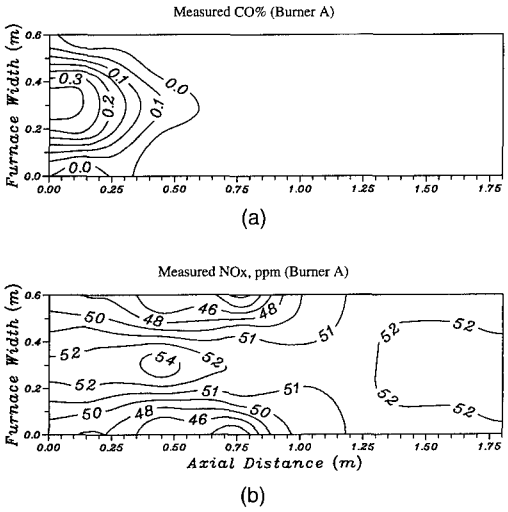

FIG. 3. Contours of CO (a) and NO_x (b) for burner A.

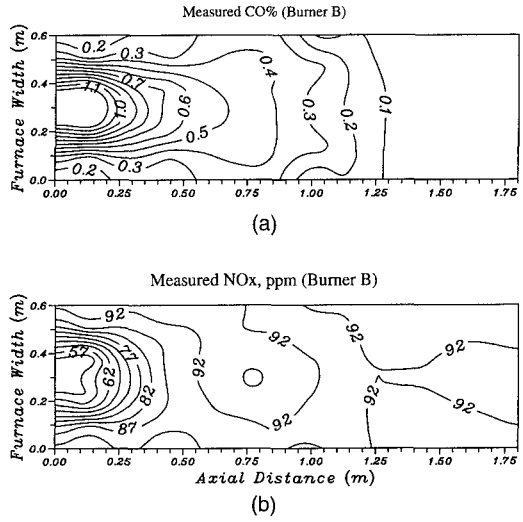

FIG. 5. Contours of CO (a) and NO_x (b) for burner B.

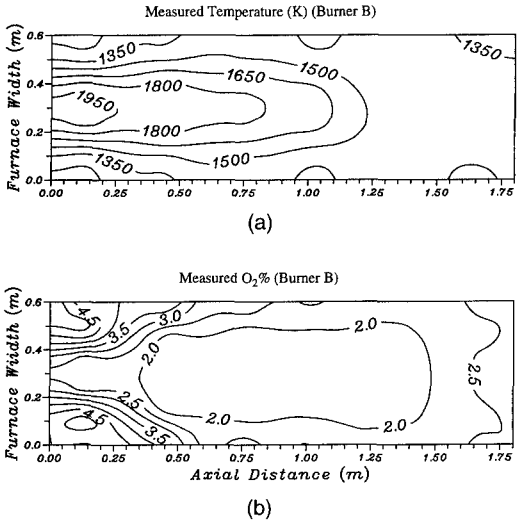

FIG. 4. Contours of temperature (a) and O_2 (b) for burner B.

through 5 for the individual burners, which show the temperature and species concentrations. The boundaries of the combustion zone and an approximate flame length can be estimated from the temperature contours. Estimated flame lengths of 0.8 and 1.2 m were obtained for the small (A) and large burner (B), respectively, when taking 1400 K as the ad hoc minimum temperature boundary for the flame. Visual observation and video photographs indicated an approximate flame length of 0.76 m for burner A and 1.26 m for burner B.

Exhaust O_2 concentrations of 2.6% were obtained for both burners, as shown in Figs. 2b and 4b. These values show that the amount of excess air utilised was 12%. Lower concentrations of O_2 in the initial part of the furnace for the small burner (Fig. 2b) indicate consumption of O_2 in a reduced volume evidenced by the small flame length.

Figures 3a and 5a show the CO concentrations for the respective burners. Exhaust CO produced by the small burner is negligible, indicating that there was sufficient time for CO to be completely oxidised to CO_2. With the presence of a much longer flame from the larger burner, CO levels were significantly greater, highlighting the lower efficiency of the 0.266-MW burner within this furnace.

Figures 3b and 5b confirm that the areas of highest NO_x concentration occur in the highest temperature regions. The spacial maxima of NO_x concentrations are found close to but downstream of the maximum temperature zones. This indicates that NO_x formation rates are highest in the high-temperature zones. As a result, NO_x emissions are suggested to be dominated by thermal-NO. The higher NO_x concentration from burner B can be attributed to the elevated temperatures within the combustion chamber.

To examine geometrical scaling, ratios of temperature, NO_x concentration, and EI_{NO_x} indices of the large to small burners are plotted in Fig. 6 in burner-size nondimensionalised coordinates (x/d_o and r/d_o, where d_o is the burner diameter). The NO_x concentration ratio, close to unity up to $x/d_o = 3$, suggests the dominance of the prompt-NO contribution in the near-burner zone (NBZ). Downstream, the NO_x concentration ratio and the temperature ratio increase over unity to 1.9 and 1.3, respectively, emphasising the greater contribution of thermal-NO. These results appear to indicate a greater contribution of

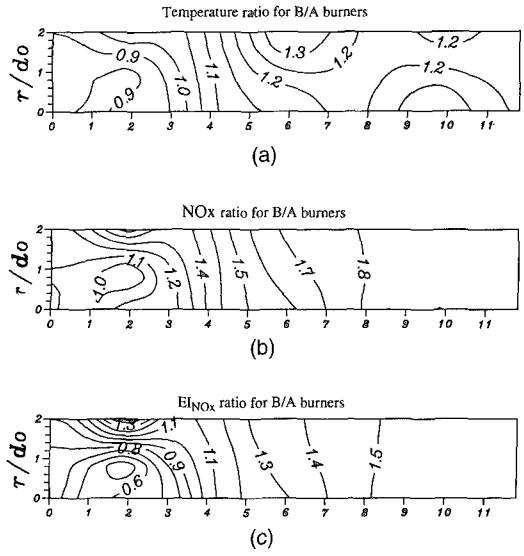

FIG. 6. Contours of the normalised temperature (a), NO_x (b), and EI_{NO_x} (c) ratio for burner B/burner A.

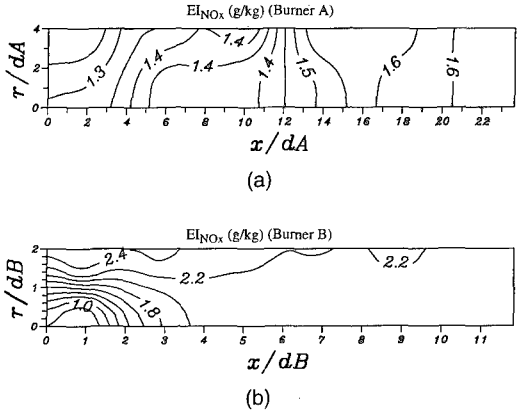

FIG. 7. Contours of EI_{NO_x} for burner A (a) and burner B (b).

prompt-NO to the total NO_x emissions for the smaller burner.

Figure 7 shows the EI_{NO_x} from simultaneous local measurements of NO, NO_2 and CO_2 concentration for both burners. It is evident that EI_{NO_x} remains fairly constant where combustion is complete, highlighting that, in these areas, NO_x is neither formed nor destroyed in postflame regions. Figure 7b indicates that the EI_{NO_x} for the large burner is lower in the NBZ region, again indicating the high contribution of prompt-NO to total NO_x for the small burner.

Numerical Calculations:

The combustion model employed in this investigation uses a two-step reaction mechanism used previously by the authors [7]. Figures 8 and 9 present the predicted thermal-, prompt-, and total-NO concentrations for burners A and B. Computer predictions indicate that the thermal-NO (Figs. 8a and 9a) is produced mainly in the flame front, and its concentration follows closely the temperature profiles. Prompt-NO contributes (Figs. 8b and 9b) approxi-

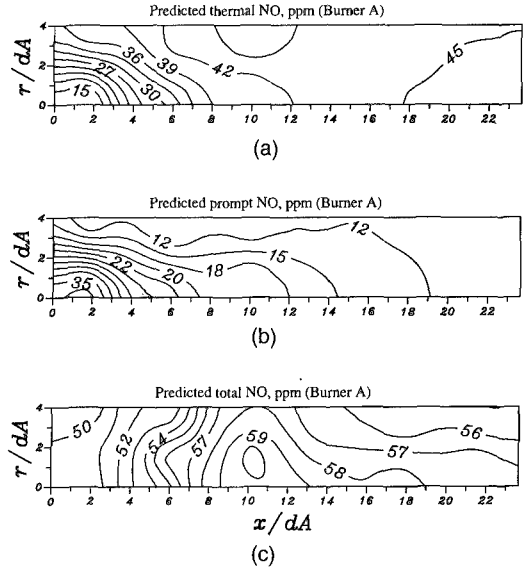

FIG. 8. Predicted thermal- (a), prompt- (b) and total-NO (c) for burner A.

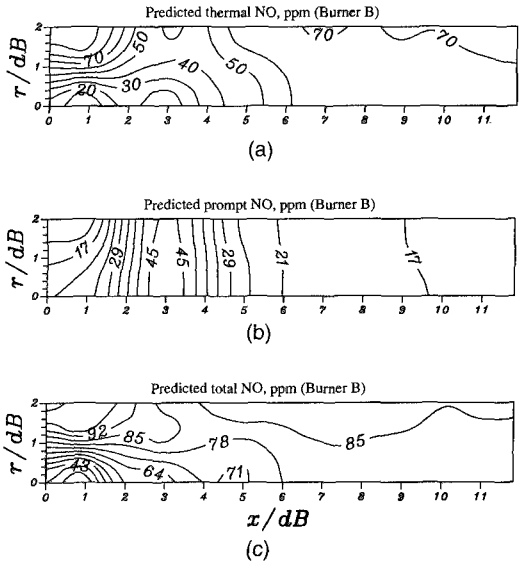

FIG. 9. Predicted thermal- (a), prompt- (b) and total-NO (c) for burner B.

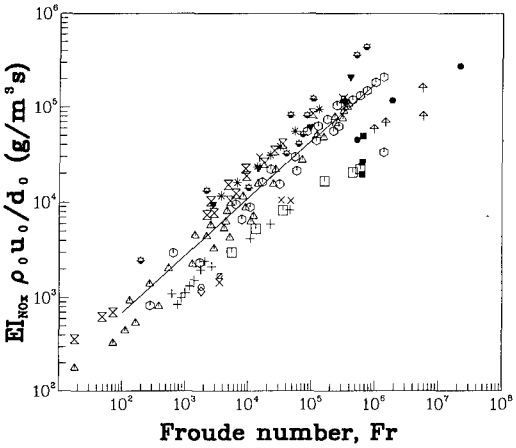

FIG. 10. Correlation of EI_{NO_x} for different flames (as presented in Ref. 5) and data obtained during this study: Røkke et al. (△, C_3H_8, + CH_4), Turns and Myhr (CH_4, ▼ C_2H_4, □ CO/H_2, C_3H_8), Chen and Driscoll (× CH_4, H_2), Lavoie and Schlader (● H_2), Bilger and Beck (■ H_2), Buriko and Kuznetsov (Y C_3H_8), Takagi et al. (C_3H_8) Turns and Lovett (C_3H_8), Burner A (× experimental, ∅ theoretical), Burner B (○ experimental, ◇ theoretical), and —— $44Fr^{3/5}$.

mately 15–21% to the total-NO emitted in the postflame, in comparison with 50–70% in the NBZ.

The predicted and measured exhaust-NO emissions are summarised in Table 1. In general, predicted NO concentrations are approximately 10–18% higher. Figure 10 shows the results of a flamelet-based scaling correlation for EI_{NO_x} [5]. This correlation was based on the derivation of explicit expressions for local instantaneous NO production rates using 14 elementary steps in a two-reaction-zone laminar flamelet model. Average NO production rates were obtained using asymptotics in the approximation of a joint pdf for mixture fraction and scalar dissipation. The current experimental results for various turbulent diffusion flames are well correlated.

Adopting an equivalent-area-diameter single-jet similarity for the complex burner, the NO_x emission index is well correlated. It appears that, to a leading order, for these flames, orientation of firing is not important. As with other natural-gas data, the burner similarity data obtained here also fall low. This is the result of a higher stoichiometric mixture fraction for CH_4 than adopted in the Røkke et al. [5] derivation of the scaling correlation. In essence, the scaling law somewhat overestimates the size of the methane flame volume. In addition, adopting a turbulent flame similarity based on the individual fuel jets in the complex burners, the NO_x emission index numbers measured also fall well within the bank of experimental observations by these and other researchers (Fig. 10). The detailed NO calculations indicate a decrease in the ratio of exhaust prompt- to exhaust thermal-NO emission indices from burner A to burner B. This decrease was anticipated by the flamelet-based correlation within 12%.

The correspondence of the trends between measurements, calculations, and the scaling correlation of Røkke et al. [5] suggests that the decreased contribution of prompt-NO in burner B can be attributed to the lower level of scalar dissipation rates in the flame. Lower scalar dissipation rates result in higher temperatures, increasing the high-activation-energy thermal-NO formation in the oxygen consumption zone, while leaving the low-activation-energy prompt-NO formation rate unaffected in the thin fuel-consumption zone. Considering the large range of phenomena involved in developing the scaling correlations, which are not well understood, the agreement between our complex burner data and the scaling laws, developed for "simple" turbulent diffusion flames, is encouraging.

Conclusions

In-flame measurements of O_2, CO, and NO_x are presented for 0.067-MW and 0.266-MW geometrically similar burners firing in a rapid-heating furnace. In the near-burner zone, the prompt mechanism dominated NO_x formation, while downstream, thermal-NO contributed more for the larger burner. Calculations suggest prompt-NO contributions to the total exhaust-NO for the small and large burners of 21 and 16%, respectively. This demonstrates the importance of prompt-NO even with high-temperature processes.

The results of the experiments as well as the detailed calculations are in reasonable qualitative agreement with scaling correlations developed from a laminar flamelet model [5]. The agreement is encouraging and may allow the wealth of scientific data on NO_x emissions in turbulent flames to be used more effectively in the development of complex industrial burner systems.

Acknowledgments

The authors wish to thank MEPA, Saudi Arabia, for the studentship (ADA), The Institution of Gas Engineers, UK, for a Fellowship (LMD), BOC Technical Center, USA, for financial support (JTH), and Mr. G. Cole for technical support.

REFERENCES

1. Smart, J. P., Van der Kamp, W. L., and Morgan, M. E., *Report on the AP17 Experiments IJmuiden*, IFRF Doc. No. F37/y/19, December 1989, pp. 1, 3.
2. Thring, M. W., and Newby, M. P., *Fourth Symposium*

(International) on Combustion, The Combustion Institute, Pittsburgh, 1953, p. 789.
3. Bilger, R. W., *Combust. Flame* 26:115 (1976).
4. Peters, N., and Donnerhack, S., *Eighteenth Symposium (International) on Combustion*, The Combustion Institute, Pittsburgh, 1981, p. 33.
5. Røkke, N. A., Hustad, J. E., Souju, K. O., and Williams, F. A., *Twenty-Fourth Symposium (International) on Combustion*, The Combustion Institute, Pittsburgh, 1992, p. 385.
6. Patanker, S. V., *Numerical Heat Transfer and Fluid Flow*, Hemisphere, Washington, DC, 1980.
7. Missaghi, M., Pourkashanian, M., Yap, L. T., and Williams, A., *Proceedings of the American Flame Foundation Conference*, San Francisco, October 1990, IFRF Publications, The Netherlands.
8. Missaghi, M., Yap, L. T., Ahmadi, S. H., Al-Fawaz, A. D., Hampartsoumian, E., Pourkashanian, M., and Williams, A., *Proceedings of the 1992 International Gas Conference*, Orlando.
9. Michaud, M. G., Westmoreland, P. R., and Feitelberg, A. S., *Twenty-Fourth Symposium (International) on Combustion*, The Combustion Institute, Pittsburgh, 1992, p. 879.
10. Bowman, C. T., and Miller, J. A., *Prog. Energy Combust. Sci.* 15:1 (1989).
11. Missaghi, M., Nimmo, W., Pourkashanian, M., and Williams, A., *Combust. Sci. Technol.* 93:153–172 (1993).

COMMENTS

Roman Weber, International Flame Research Foundation, The Netherlands. Your two flames possess very different thermal characteristics. The in-flame temperatures of the 67-kW flame are around 300 °C lower than those for the 266-kW flame. The furnace exit temperatures (885 °C vs 1201 °C) indicate that for the first flame around 60% of the thermal input was extracted, and for the second flame around 40%. Consequently, the 67-kW flame jet entrains much cooler combustion products than the 266-kW flame. In a paper by Sayre et al. (this volume), you can find that for nonsooty flames such a difference in the energy entrained into the flame jets can alter the NO_x emissions by as much as 30%. Your flames were sooty and of substantially different surface to volume ratio. Furthermore, the confinement, defined as ratio of furnace to burner diameter, is very different for both flames and therefore, in-furnace fluid dynamic similarity may not hold. To my understanding, you have clustered all these effects into the Froude number and did not make any attempt to deconvolute them. The correlation shown in Fig. 6 is practically useless due to the logarithmic scale, which masks a very wide spread in the data. The spread will remain wide until a series of systematic measurements is carried out to deconvolute the effects discussed above.

Author's Reply. Indeed, not geometrically scaling the furnace confinement with burner size may affect some of the flame characteristics. As shown in the paper, detailed calculations were necessary to extract detailed scaling information. No simple substitutes for this are apparent. However, as argued in the discussion, to a leading order, the NO_x emissions from as complex a burner can indeed be interpreted in terms of "simple" turbulent diffusion flames. In this respect, the corroboration of our computational and experimental results with an analytical flamelet-based model for NO_x emissions is very encouraging.

Twenty-Fifth Symposium (International) on Combustion/The Combustion Institute, 1994/pp. 1035–1041

INFLUENCE OF GASDYNAMICS ON NO_x EMISSION FROM LARGE DIFFUSION NATURAL GAS FLAMES

JERZY TOMECZEK, JAN GÓRAL AND BOGUSŁAW GRADOŃ
Department of Process Energy
Silesian Technical University
40-019 Katowice, Krasińskiego 8, Poland

This paper presents the influence of gasdynamic parameters on NO_x emissions from large diffusion type flames with coaxial air and gas flow. The objective of this study was to explain the observed differences in NO_x emissions with changes in air to gas velocity ratio (w_a/w_g) for natural gas flames, and to understand the interrelations among NO_x and flow conditions at burner outflow. A broad range of parameters was used: sevenfold velocity variation for both air and gas flows, air preheating up to 450 °C, and furnace wall temperatures up to 1100 °C. It was found that the largest values of NO_x were obtained for the ratio of air to gas velocity (w_a/w_g) close to 0.8, which separates the luminous $[(w_a/w_g) < 0.8]$ from non-luminous flames $[(w_a/w_g) > 0.8]$. For luminous flames, NO_x increases, while, for non-luminous flames, NO_x decreases with the (w_a/w_g) ratio. It has been shown also that NO_x formation is mainly a burner phenomenon; the value of air ratio λ_{max} at which NO_x reaches its maximum depends on the furnace temperature. The influence of air preheating on NO_x was established to be dependent on the air to gas velocity ratio (w_a/w_g), so that, for high values of this ratio, NO_x is much more sensitive to air temperature. The most important finding is that, for coaxial air-gas flow flames, it is possible to scale the NO_x emission with two dimensionless parameters, $(\rho_g w_g/\rho_a w_a)$ and (w_a/w_g), combining both the air preheating and the flame gasdynamics.

Introduction

Energy savings in high-temperature industrial processes favour high combustion air temperature in furnaces, which is commonly believed to be the main reason for large NO_x emission. It has already been shown that, even in furnaces with air preheating as high as 1000 °C and combustion chamber temperature up to 1400 °C (measured as flue gas temperature at chamber outlet), the emission of NO_x can be reduced well below 200 ppm [1]. Although the formation of NO_x is mainly a burner phenomenon, the combustion chamber has substantial influence on the amount of NO_x produced [2,3]. For gaseous fuels, it is believed that control of the thermal mechanism will lead to reduction of NO_x emission. The most effective way of designing low NO_x industrial gaseous burners is to guarantee good mixing of the combustion air with the flue gases before the flame reaches its maximum temperature. In the case of external recirculation of the flue gases, the degree of mixing with the combustion air is determined by the recirculation device only, but in the case of internal recirculation, the degree of mixing depends on many parameters whose quantitative influence is not well known. The NO_x scaling relations can be developed only by proper understanding of the detailed flame structure, considering chemical kinetics, fluid mechanics, and radiative heat transfer.

There is experimental evidence that the burner design and combustion parameters at the burner outflow influence the level of NO_x emission from diffusion flames. Because of the complex geometry of industrial burner nozzles, a full-scale experiment is required for determination of NO_x. A compounding factor is the lack of reliable theoretical design criteria for low NO_x burners. These full-scale tests gathered much valuable data on NO_x from flames produced by a variety of burners, as a function of the combustion air ratio, swirl number, combustion air preheat, and furnace temperature [2–6]. Despite the enormous practical importance of these data, it is very difficult to utilize them for testing of mathematical models due to the three-dimensional flow in industrial furnaces, difficulties in determination of boundary conditions, and the complex chemical kinetics of hydrocarbon combustion.

The above-mentioned difficulties, among others, were the main reasons that a simple diffusion jet flame in still air has been the subject of many investigations. Bilger and Beck [7] related the level of NO_x emission to the Reynolds number at constant Froude number at the fuel gas nozzle outlet. Peters and Donnerhack [8] have shown that there exists a Reynolds and Froude numbers dependence of the NO_x emission index. Chen and Driscoll [9] found that, using both Reynolds and Damköhler numbers, it is possible to correlate the NO_x emission from hydrogen

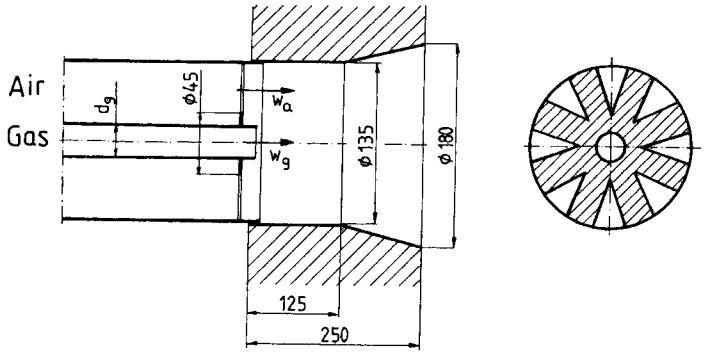

FIG. 1. Burner diagram.

flames. The observed (for hydrogen flames) "fuel-rich" shift of nitric oxide formation [7,10] was not confirmed for hydrocarbon flames where the shift was towards the "fuel-lean"–reaction-zone side [11]. As a possible explanation, the soot radiation cooling of the flame was presented [11]. A significant role of radiative heat losses by high-temperature flames has been ascribed to gas molecular radiation rather than to soot radiation [12,13]. For low-temperature luminous flames, the chemical interactions between soot and NO also can influence the NO_x emission [12,14].

In practical combustors in which both the fuel and air are forced to flow out of the burner nozzles, the NO_x emission predictions must include the air flow conditions because the shape, volume, and properties of diffusion flames are controlled by the gasdynamics of the air stream. For coaxial air-gas diffusion flames, a ratio of the air to gas velocity (w_a/w_g), determining the forced air mixing, together with the Reynolds number, which determines the Kolmogorov time scale, were proposed by Chen and Driscoll [9] to be important for NO_x prediction in small diffusion flames. Using a simple theoretical model by Peters and Donnerhack [8] and a Dahm and Mayman [15] equation for flame length of coaxial air-gas diffusion flames, they were able to predict a decrease of NO_x level with the ratio of (w_a/w_g) in hydrogen flames. This was explained by a reduction of the reaction zone volume at higher air velocity. This simple modelling has failed, however, for coaxial air-methane flames in which the NO_x emission increased with the ratio (w_a/w_g), despite a decrease in the flame length [9]. In natural gas diffusion flames, Chen and Driscoll [9] have found that coaxial air cannot be used to reduce NO_x emissions if $(w_a/w_g) < 0.15$. They have anticipated, however, that NO_x reduction in methane-air flames would require larger values of (w_a/w_g). Literature results for industrial-type natural gas burners show in all cases a decrease of NO_x emission with the increased air velocity [2,5].

There are very limited data concerning the influence of gasdynamics on NO_x emissions for high-temperature combustion air [2] because most of the experiments for preheated air were carried out with one size of the air nozzle [5,6]. In the last case, it is difficult to distinguish the influence of the combustion air preheating from the influence of the increased air velocity due to higher temperature.

Analysis has shown that systematic experiments in which both the air and fuel gas outflow parameters will be varied appear to be necessary to establish the influence of gasdynamics on NO_x emissions. A coaxial air-gas burner has been chosen, because for long diffusion flames it gives the lowest NO_x emission. The aim of the present research was to determine possibilities for minimization of NO_x from industrial flames produced by such burners and to separate the effects of air preheating from fluid mechanics.

Experimental

Investigations were carried out in a horizontal refractory-lined combustion chamber of inner dimensions 3.3 × 1 × 1 m. The temperature of the walls was measured by means of PtRh-Pt thermocouples. NO_x emissions were measured at the chamber outflow using a water-cooled stainless steel sampling probe. The cooling of sampled gases was adequate to quench NO_x reactions. After removing the condensed water vapour, the sampled gases were passed through a calibrated (Testoterm testo 33) analyzer.

The burner used in experiments is presented in Fig. 1. The uncooled burner stone placed in front of the burner has a length of 250 mm and outflow diameter of 180 mm. The burner enables changes of the cross-section areas of the gas and air nozzles, so various velocity ratios (w_a/w_g) could be obtained at constant burner load without interference in the shapes of the jets. The range of parameters used in the experiments is presented in Table 1, encompassing six values of air nozzle cross sections and seven gas nozzle diameters. Both gas and air velocity could be varied by a factor of 7. The combustion air could be preheated up to 450 °C. All investigations were conducted for three values of the combustion chamber wall temperature, 100 °C, 500 °C, and 1100 °C.

TABLE 1
Range of investigated parameters

Parameter	Value	Dimension
Thermal power—P	290	kW
Gas nozzle diameter—d_g	9.5–25	mm
Air nozzle cross-section area	(1.35–5.4) 10^{-3}	m^2
Air velocity—w_a	15.5–111	m/s
Gas velocity—w_g	17–119	m/s
Air ratio—λ	1.09	—
Air temperature—T_a	20–450	°C
Furnace temperature—T_f	100, 500, 1100	°C
Gas temperature	20	°C
Gas density	0.74	kg/m^3
Gas heating value (lower)	34.7	MJ/m^3

The wall temperature is a mean value of 13 measurements along the chamber. The largest difference between the individual points was below 100 K.

The composition of the natural gas during the experiments was fairly constant, and the heating value did not vary by more than 2%. Within the period of investigation, the average gas composition was as follows: CH_4 = 95.5%, C_2H_6 = 0.6%, O_2 = 0.2%, N_2 = 3.7%.

The evaluation of experimental results depends on the main parameters influencing the NO_x formation: air and natural gas streams as a base for the air ratio λ calculation, combustion chamber temperature T_f, and air temperature T_a. During the tests, the air ratio λ was controlled through oxygen measurement at the chamber outflow. The air ratio determined on basis of oxygen measurements (O_2 = 2.5% in flue gas) did not differ by more than 2.5% from the value determined by means of the air and natural gas streams. The combustion air temperature was not influenced by the conditions during the tests, because the air was preheated in a separate furnace. At the high chamber wall temperatures (1100 °C) of the experiments, substantial influence of this temperature on NO_x emission could be expected. For this reason, special precautions were taken to keep this temperature in a range as narrow as possible. The largest variation of the chamber wall temperature during the test series was less than 50 K, which, on the basis of our initial tests and the literature information [2,3], would give an error in NO_x measurement within 3–5%.

Results

It was found that coaxial air strongly influenced the NO_x level for a constant gas velocity (Fig. 2) and for a constant air velocity (Fig. 3). Increasing the ratio of air to gas velocity (w_a/w_g), we observe a considerable increase in NO_x emissions until a maximum at (w_a/w_g) ≈ 0.7–0.9. Further increase of this ratio causes a sharp fall of the NO_x level, until (w_a/w_g) ≈ 1.5–2.0, when NO_x increases again. To confirm this observation, experiments were reproduced for three different gas velocities (Fig. 2). This unexpected result also was confirmed when the ratio (w_a/w_g) was varied at three different air velocities (Fig. 3). During these experiments, the value of the air ratio λ = 1.09 was constant. The measurements confirm the findings by Chen and Driscoll [9] that, for methane-air flame, the NO_x level increases with the (w_a/w_g) ratio

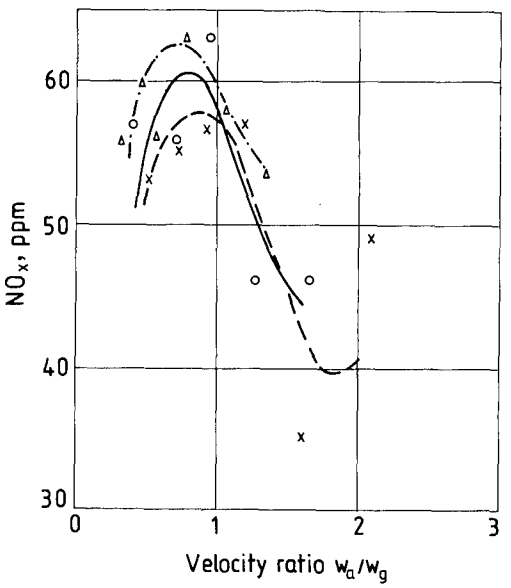

FIG. 2. NO_x as function of velocity ratio (w_a/w_g) for P = 290 kW, λ = 1.09, T_f = 1100 °C, T_a = 20 °C, and Δ —·— w_g = 45.3 m/s, ○ — w_g = 37.4 m/s, × --- w_g = 29 m/s.

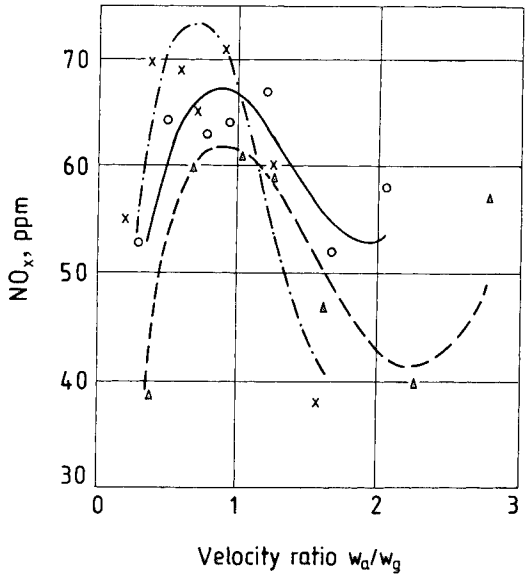

FIG. 3. NO_x as function of velocity ratio (w_a/w_g) for P = 290 kW, λ = 1.09, T_f = 1100 °C, T_a = 20 °C, and Δ --- w_a = 48 m/s, ○ – w_a = 35 m/s, × –·– w_a = 27 m/s.

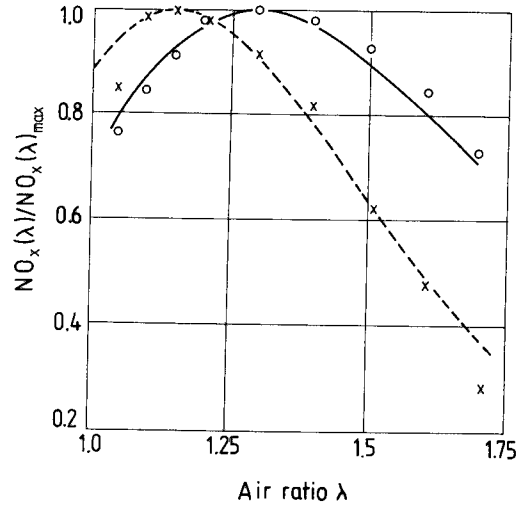

FIG. 4. $NO_x(\lambda)/NO(\lambda)_{max}$ as function of air ratio λ for P = 290 kW, T_a = 20 °C, w_g = 37.4 m/s, and ○ – T_f = 1100 °C (one air nozzle), × --- T_f = 100 °C (three air nozzles).

for small values of this ratio. For higher values of the ratio (w_a/w_g), the results are also in agreement with the observed decrease of NO_x with the increased air velocity [2,5]. The present conditions did not allow exploration of the range of $(w_a/w_g) > 1.5$ sufficiently with other parameters constant.

For enclosed flames, NO_x is often presented as a function of the air ratio λ. The function $NO_x(\lambda)$ has a maximum at λ above unity. For a given type of burner, the position of this maximum is related to the combustion air temperature [2]. Both thermodynamic equilibrium calculations and experiments have shown that the position of $NO_x(\lambda)_{max}$ shifts towards larger values of λ as the combustion air temperature increases [2,3,16]. We are aware of only one experiment in which the influence of the combustion chamber temperature on the position of the maximum was investigated; however, the results were unclear [3]. Figure 4 presents two normalized profiles $NO_x(\lambda)$ for two levels of the furnace temperature T_f. During these experiments, the gas flow was constant, and the value of λ was varied only by means of the air flow, so that velocity ratio (w_a/w_g) varied from 0.89 to 1.45. It can be seen that the position of maximum NO_x shifts towards higher λ with the furnace wall temperature.

Discussion

Chen and Driscoll [9] have shown that, in coaxial methane-air diffusion flames, the influence of gasdynamics on NO_x cannot be explained by means of the Peters and Donnerhack [8] model with Dahm and Mayman's [15] flame length equations. Following the proposal by Buriko and Kuznetsov [11] on the role of flame radiation, it is believed that the mode of methane combustion should help to explain the results presented in Figs. 2 and 3. The influence of gasdynamics on the properties of large natural gas diffusion flames has been reported by Tomeczek and Gebhardt [17], where the ratio of the air to gas momentum determined the crossover between the luminous and non-luminous flames. When this ratio is 13, the flame can vary its properties in a steplike manner from luminous to non-luminous and vice-versa. For the natural gas used (3.7% N_2) and the value λ = 1.09 from Figs. 2 and 3, (w_a/w_g) = 0.8 at the luminous–non-luminous border. This agrees surprisingly well with the position of the maxima in Figs. 2 and 3. Hence, it is anticipated that, for luminous flames, the NO_x emission increases with the ratio (w_a/w_g), while, for non-luminous flames, NO_x decreases. For the value of the ratio $(w_a/w_g) > 2$ within the non-luminous flames, a second increase is evident.

Because the level of NO_x is very sensitive to (w_a/w_g), as can be seen in Figs. 2 and 3, it must be considered in the presentation of results in which both the air and gas velocities are varied. Thus, we have taken from experimental results only those which have at least five points of exactly the same (w_a/w_g). The attempts to apply the air and gas Reynolds numbers gave poor collapse of the experimental data. The problem was caused by data at the highest values of gas velocity, about 100 m/s. If the gas ve-

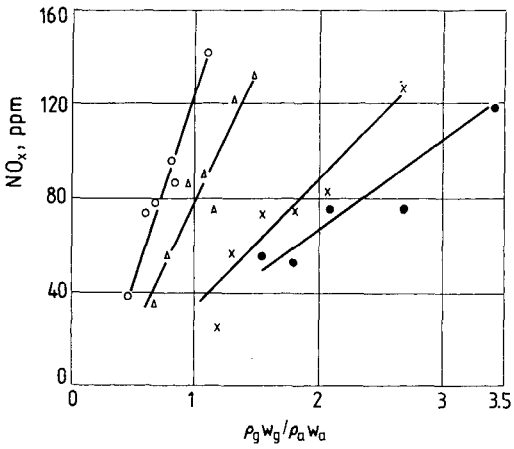

FIG. 5. NO_x as function of momentum density ratio $(\rho_g w_g/\rho_a w_a)$ for P = 290 kW, λ = 1.09, T_f = 500 °C, T_a = 20 °C–450 °C, and ● – w_a/w_g = 0.41, × – w_a/w_g = 0.53, Δ – w_a/w_g = 0.94, ○ – w_a/w_g = 1.3.

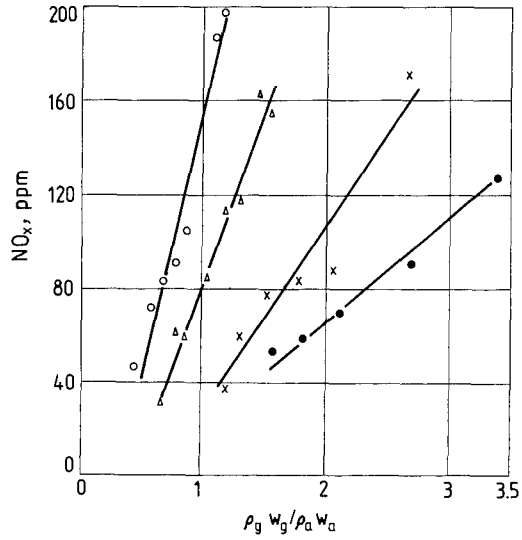

FIG. 6. NO_x as function of momentum density ratio $(\rho_g w_g/\rho_a w_a)$ for P = 290 kW, λ = 1.09, T_f = 1100 °C, T_a = 20 °C–450 °C, and ● – w_a/w_g = 0.41, × – w_a/w_g = 0.53, Δ – w_a/w_g = 0.94, ○ – w_a/w_g = 1.3.

locity was limited to only 67 m/s, then the dependence of NO_x emission on air and gas Reynolds numbers was acceptably described by

$$NO_x = A + B\frac{Re_g}{Re_a}\left(\frac{w_a}{w_g}\right)^{0.5} \tag{1}$$

where, for a constant furnace wall temperature T_f, the values of A and B could be determined with correlation coefficient 0.98 for T_f = 500 °C and 0.94 for T_f = 1100 °C. Unfortunately, with all experimental points, including these for gas velocity up to 119 m/s, the correlation coefficient droped to only 0.76. However, we did not want to reject these points, which may have practical significance, so we decided that the relation NO_x (Re_a, Re_g) is not satisfactory. The best presentation of the experimental data is obtained in terms of two dimensionless parameters: the velocity ratio (w_a/w_g) and the momentum density ratio $(\rho_g w_g/\rho_a w_a)$. Figure 5 presents the NO_x emission for furnace temperature T_f = 500 °C and Fig. 6 for T_f = 1100 °C. The experimental points include results for various air preheat temperatures within the range T_a = 20 °C–450 °C. The lines at constant velocity ratio (w_a/w_g) present the influence of combustion air temperature on NO_x emission separated from the gasdynamics. It can be seen that, for low (w_a/w_g), the influence of combustion air temperature is relatively small, while, for high (w_a/w_g), the NO_x emission is much more sensitive to air temperature. The reason for such behaviour is radiation heat exchange between the flame and the furnace walls. High combustion air temperatures can give only a moderate increase in the luminous flame temperature, while, for non-luminous flames, the increase is much higher. For lower furnace wall temperatures, the curves have a slightly smaller slope, which can be seen by comparing Figs. 5 and 6.

The relation between the NO_x level and the thermal and gasdynamical parameters allows us to analyze the influence of burner parameters. The correlation lines in Figs. 5 and 6 can be presented in a form

$$\begin{aligned} NO_x &= C\left(\frac{w_g}{w_a}\right) + f\left(\frac{w_g}{w_a}\right)(\rho_g w_g/\rho_a w_a)^N \\ &= C\left(\frac{w_g}{w_a}\right) + F\left(\frac{w_g}{w_a}\right)(\rho_g/\rho_a)^N. \end{aligned} \tag{2}$$

The influence of the air to gas velocity ratio (w_a/w_g) on NO_x can be found from Eq. (2). An analytical solution is possible for the coefficient N = 1 in Eq. (2). If the functions $F(w_g/w_a)$ and $C(w_g/w_a)$ are known, then we can find the derivative at constant combustion air temperature (ρ_a = const)

$$\left.\frac{dNO_x}{d\left(\frac{w_g}{w_a}\right)}\right|_{(\rho_g/\rho_a)} = \frac{dC}{d\left(\frac{w_g}{w_a}\right)} + \frac{dF}{d\left(\frac{w_g}{w_a}\right)}. \tag{3}$$

The ratio (w_a/w_g) at which the increase of air velocity at constant gas velocity causes the NO_x decrease can be found from the condition

$$\left.\frac{dNO_x}{d\left(\frac{w_g}{w_a}\right)}\right|_{(\rho_g/\rho_a)} > 0. \tag{4}$$

A good correlation for the function $f(w_g/w_a)$ in Eq. (2) can be obtained in a linear form, and the function $F(w_g/w_a)$ can be written as

$$F\left(\frac{w_g}{w_a}\right) = f\left(\frac{w_g}{w_a}\right)\frac{w_g}{w_a} = \left(A - B\frac{w_g}{w_a}\right)\frac{w_g}{w_a}. \quad (5)$$

The function $C(w_g/w_a)$ can be described by a linear form

$$C\left(\frac{w_g}{w_a}\right) = a - b\left(\frac{w_g}{w_a}\right). \quad (6)$$

We can find then, that for the ratio

$$\frac{w_a}{w_g} > \frac{2B}{A - b(\rho_a/\rho_g)} \quad (7)$$

increase of air velocity at constant gas velocity leads to a NO_x decrease.

The experimental points in Figs. 5 and 6 allow us to determine the coefficients A and B in Eq. (5) and b in Eq. (6). Using Eq. (7), we obtain the limit ratio values

$$\frac{w_a}{w_g} > 0.63 \quad \text{for } T_a = 20\ °C \quad (8)$$

$$\frac{w_a}{w_g} > 0.68 \quad \text{for } T_a = 450\ °C \quad (9)$$

for both furnace temperatures $T_f = 500$ °C and for $T_f = 1100$ °C, which confirm for the entire air temperature range the position of NO_x maximum (presented in Figs. 2 and 3 for air temperature $T_a = 20$ °C).

From a practical point of view, the dependence of $NO_x(\lambda)$ can be used for operational air ratio control. The normalized curve can be described by a formula

$$\frac{NO_x(\lambda)}{NO_x(\lambda)_{max}} = \exp[-K(\lambda - \lambda_{max})^2/\lambda] \quad (10)$$

where, for combustion air temperature $T_a = 20$ °C, the constants are equal to $\lambda_{max} = 1.15$, $K = 5.5$ for $T_f = 100$ °C and $\lambda_{max} = 1.3$, $K = 3.8$ for $T_f = 1100$ °C. The normalized curves calculated by Eq. (10) are presented in Fig. 4, along with experimental points. It is worth noting that the points for the low-temperature furnace were obtained by means of three air nozzles. For the natural gas flames presented by Flamme et al. [18], the constants in Eq. (10) are equal to $K = 6$, $\lambda_{max} = 1.1$ for $T_a = 25$ °C and $T_f \approx 1000$ °C [19].

Conclusions

The ratio of the coaxial air to gas velocity is an important parameter determining NO_x emissions from turbulent diffusion natural gas flames. The increase of air velocity at constant gas velocity and constant air ratio leads to a decrease in NO_x emissions if $(w_a/w_g) > 0.63$ for combustion air temperature 20 °C and $(w_a/w_g) > 0.68$ for 450 °C.

The influence of gasdynamics on NO_x emissions from large coaxial air-gas diffusion flames can be described well by the velocity ratio (w_a/w_g) and the momentum density ratio $(\rho_a w_a/\rho_g w_g)$ at constant air ratio $\lambda = 1.09$ and within the velocity ratio $(w_a/w_g) = 0.41 - 1.3$. At constant (w_a/w_g), the emission of NO_x from luminous flames is less sensitive to combustion air preheating than from non-luminous flames.

The air ratio λ at which $NO_x(\lambda)$ reaches its maximum shifts towards higher values with the increased furnace wall temperature. This shift is caused by a reduced flame cooling effect due to heat radiation and recycled flue gases (in furnaces with hot walls).

REFERENCES

1. Flamme, M., and Kremer, H., *Proceedings of the European Conference on Natural Gas Policies and Technologies*, Athens, Greece, October 14–16, 1992.
2. Flamme, M., Ph.D. Thesis, Ruhr-Universität Bochum, Bochum, Germany, 1989.
3. Lehmkühler, Th., Fritz, H., van Heyden, L., and Vissel, Fr., BFI-Forschungsbericht Nr. 694a, Düsseldorf, Germany, 1978.
4. Heap, M. P., Lowes, T. M., and Walmsley, R., *Fourteenth Symposium (International) on Combustion*, The Combustion Institute, Pittsburgh, 1973, pp. 883–894.
5. Lowes, T. M., Bartelds, H., Heap, M. P., and Walmsley, R., *Brennstoff-Wärme-Kraft* 26(1):26–31 (1974).
6. Michelfelder, S., *Glastechnik, Ber.* 51(7):167–175 (1978).
7. Bilger, R. W., and Beck, R. E., *Fifteenth Symposium (International) on Combustion*, The Combustion Institute, Pittsburgh, 1975, pp. 541–552.
8. Peters, N., and Donnerhack, S., *Eighteenth Symposium (International) on Combustion*, The Combustion Institute, Pittsburgh, 1981, pp. 33–42.
9. Chen, R.-H., and Driscoll, J. F., *Twenty-Third Symposium (International) on Combustion*, The Combustion Institute, Pittsburgh, 1990, pp. 281–288.
10. Kent, J. H., and Bilger, R. W., *Fourteenth Symposium (International) on Combustion*, The Combustion Institute, Pittsburgh, 1973, pp. 615–625.
11. Buriko, Y. Y., and Kuznetsov, V. R., *Fiz. Gorenija Vzrywa* 14(3):296–303 (1978).

12. Turns, S. R., and Myhr, F. H., *Combust. Flame* 87:319–335 (1991).
13. Turns, S. R., and Lovett, J. A., *Combust. Sci. Technol.* 66:233–249 (1989).
14. Cheng, M. T., Kirsch, M. J., and Lester, T. W., *Combust. Flame* 77:213–217 (1989).
15. Dahm, W. J. A., and Mayman, A. G., *AIAA J.* 28(7):1157–1162 (1990).
16. Kremer, H., *Gas Wärme Int.* 35(4):239–246 (1986).
17. Tomeczek, J., and Gebhardt, Z., *Gas Wärme Int.* 35(1):39–42 (1986).
18. Flamme, M., Beckervordersandforth, C. B., and Kremer, H., *Chem. Eng. Technol.* 11:104–112 (1988).
19. Tomeczek, J., *Final Report for the EC*, Contract ERB-CIPA-CT-92-0083, Bochum, Germany, 1993.

Twenty-Fifth Symposium (International) on Combustion/The Combustion Institute, 1994/pp. 1043–1049

STUDY OF NO_x EMISSION CHARACTERISTICS IN PRESSURIZED STAGED COMBUSTOR CONCEPTS

J. MEISL, R. KOCH, R. KNEER AND S. WITTIG
Lehrstuhl und Institut für
Thermische Strömungsmaschinen
Universität Karlsruhe
Kaiserstrasse 12, 76128 Karlsruhe, Germany

The rich-quench-lean (RQL) combustor technology is a promising concept for advanced low-emission aeroengines. In the present study, the RQL concept has been investigated with primary emphasis on the influence of elevated pressure levels and inlet air temperatures on NO_x emissions. Supporting the experimental study utilizing a model combustor, a detailed numerical simulation of the chemical kinetics has been performed. The RQL combustor consists of two stages, in which fuel is burnt first under fuel-rich and subsequently under fuel-lean conditions.

It was found that—in contrast to the final emissions—the primary stage emissions are widely unaffected by pressure, a result which is in good agreement with predictions from the chemical kinetics simulation. The lowest concentrations of totally fixed nitrogen (TFN) produced in the primary zone are obtained with air fuel ratios of $\lambda_{prim} \approx 0.63$. The minimum NO_x emissions at the combustor exit were observed at higher primary air fuel ratios ($\lambda_{prim} \approx 0.67$–$0.73$). As the pressure level increases, the minimum is shifted toward higher NO_x concentrations and higher primary air fuel ratios. Both effects are mainly determined by the mixing of dilution air to the primary stage exhaust gas.

Thus, it can be concluded that a suitable approach to achieve low total NO_x emissions is to optimize the quenching zone in such a way that the mixing-induced emission minimum of the quenching zone occurs at the same value of the air fuel ratio as that of the primary stage.

Introduction

The reduction of NO_x emissions is a major issue in gas turbine combustor development. Since the NO formation is strongly promoted by elevated temperatures, the improvement of the thermodynamic efficiency of gas turbines by increasing combustion pressure and temperature has an adverse effect on the efforts in NO_x reduction. To overcome this discrepancy, advanced low-emission combustor technologies are required. In preliminary studies of the NO_x reduction potential of several low-emission combustor technologies [1], a reduction potential of 70–80% is assigned to the lean premixed combustion and 70% to the staged or rich-quench-lean (RQL) combustion. While the concept of lean premixed combustion is already applied in modern stationary gas turbines and well documented in the literature [2], the RQL concept has not been sufficiently investigated for gas turbine applications.

Typically, the RQL combustor concept consists of a fuel-rich primary zone, a quenching zone, where additional dilution air is injected, and a fuel-lean secondary zone. In both, the primary zone and the secondary zone, the NO formation rates are low due to nonstoichiometric conditions and relatively low temperatures. However, the critical factor in achieving very low NO_x emissions is a uniform and rapid mixing of the dilution air to the main flow. Otherwise, regions of stoichiometric conditions and locally high temperatures are formed promoting an extensive formation of thermal NO. Successful applications of staged combustion at moderate temperatures are reported in literature elsewhere [3,4], with special emphasis on fuels with nitrogen content.

However, with respect to gas turbine applications, two major issues have to be addressed: the elevated combustor inlet and dilution air temperature and the elevated pressure level. It is well known that both enhance the NO formation rate. Therefore, the objective of the present study was to evaluate the influence of the pressure level on NO_x emissions in the staged combustion process at typically high combustor inlet temperatures. The influence of the pressure level on thermal NO formation under fuel-rich conditions is different from fuel-lean conditions [5]. Generally, in the fuel-rich environment, thermal NO formation is hardly affected by pressure, while it increases significantly with growing pressure levels under fuel-lean conditions. Due to this different impact of pressure on the NO formation, the total NO_x emission of an RQL combustor might be a complex function of the pressure level.

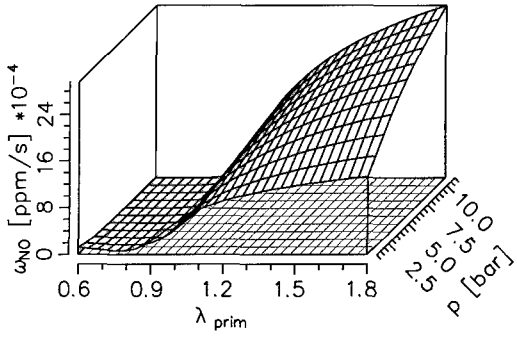

FIG. 1. Calculation of NO production rates in a perfectly stirred reactor as a function of air fuel ratio and pressure level at a temperature of $T = 2000$ K and at a residence time of 10 ms.

Influence of Pressure in Staged Combustion

NO-Formation Processes:

Generally, from nitrogen-free fuels, two different mechanisms have to be considered in analyzing the NO formation in staged combustors: the well-known Zeldovich mechanism, and—in fuel-rich zones—the prompt NO mechanism [6,7]. In order to demonstrate the dependence of NO production rates on the pressure, a calculation was carried out using the perfectly stirred reactor (PSR) model of the CHEMKIN code [8] and implementing the NO formation mechanism of Miller and Bowman [9]. This calculation was performed for several air fuel ratios $\lambda[\lambda = (\dot{m}_{air}/\dot{m}_{fuel})/(\dot{m}_{air}/\dot{m}_{fuel})_{stoich}]$. A residence time of 10 ms was selected to reach the state of equilibrium of oxidative radicals. In addition, a constant temperature of $T = 2000$ K was chosen to illustrate exclusively the influence of pressure on the NO formation rate. Obviously, this approach is limited to a theoretical consideration, since in reality a variation of λ causes a change in temperature.

Figure 1 illustrates the different NO production rates under fuel-rich and fuel-lean conditions as a function of the pressure level. It is found that the production rates increase significantly with growing pressure at air fuel ratios $\lambda > 1$, while a slight decrease is observed with a growing pressure level at fuel-rich air fuel ratios.

Mixing Effects:

Our own studies [10] as well as investigations of jet mixing in nonreacting and also in reacting flows [11,12] revealed that the mixing effectiveness in case of an invariable geometry mainly depends on the momentum flux ratio of the mixing jets and the main flow at constant main flow Reynolds numbers. Therefore, the mixing effectiveness can be used as a criterion for the uniformity of the temperature distribution in the mixing zone. Analyzing the basic contributions of the different parameters influencing the momentum flux ratio, the following expression can be derived:

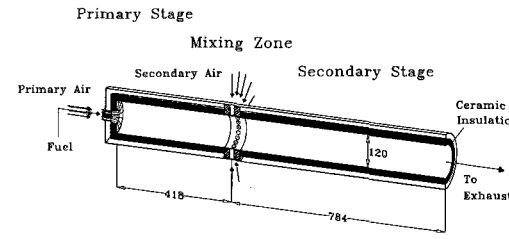

FIG. 2. Scheme of the experimental combustor.

$$J = \left(\frac{\lambda_{total} - \lambda_{prim} - \left(\frac{\dot{m}_{fuel}}{\dot{m}_{air}}\right)_{stoich}}{\lambda_{prim}} \right)^2 \cdot \frac{T_{Jets}}{T_{prim}} \left(\frac{A_{prim}}{A_{Jets}}\right)^2. \quad (1)$$

For a given geometry, J is mainly influenced by the primary air fuel ratio λ_{prim}. The effect of the overall air fuel ratio λ_{total} and temperatures is of minor significance. It is also obvious that J is independent of pressure.

Model Combustor and Measurement Techniques

The test combustor used in this study was installed in the high-pressure/high-temperature test facility of the "Institut für Thermische Strömungsmaschinen." This facility, which has been described in detail earlier [13], is capable of supplying preheated nonvitiated air up to 1123 K at a maximum pressure level of 10 bar.

A scheme of the cylindrical model combustor is shown in Fig. 2. The preheated primary air enters the combustor with a strong swirl through a dump diffusor (aperture angle of 15°). The fuel nozzle is located at the center of the diffusor. The inner diameter D of the combustor is 120 mm. In order to obtain a nominal residence time of 100 ms at $\lambda_{prim} = 0.7$, a length of $l_{prim} = 418$ mm was selected for the primary zone.

Secondary air is injected into the mixing zone through 20 mixing holes arranged in one row along the perimeter. The diameter of the holes can be varied by inserting new casings. The residence time in the secondary stage (length $l_{sec} = 784$ mm) was chosen to be 100 ms at an overall air fuel ratio of λ_{total}

TABLE 1
Test conditions

Pressure level	p	2–5	bar
Inlet temperature	T	673–823	K
Primary air fuel ratio	λ_{prim}	0.5–0.95	
Thermal power	P	50–100	kW
Mixing jet diameter	d	12–14	mm

= 2.4 to ensure complete CO oxidation. The inner walls of the primary and the secondary stage are insulated by means of cylindrical ceramic tubes to minimize heat losses.

For the sampling of the exhaust gases, multihole probes are located at the end of each stage, respectively. Multihole probes were used to get average values of the species concentration over the cross section. For suppression of secondary chemical reactions, the probes are water cooled. The dry exhaust gas was analyzed by a chemiluminescence NO/NO_x meter and a chemical cell O_2 meter.

The NO/NO_x meter was also used to evaluate the totally fixed nitrogen (TFN) concentrations in the exhaust gas of the primary stage. The TFN comprises the stable nitrogen species NO, NH_3, and HCN. According to the data provided by the manufacturer of the NO/NO_x meter, the conversion rate of TFN to NO has been estimated to be about 80%. Therefore, the measured TFN values represent a lower limit of the real values.

Results and Discussion

The present investigation was directed toward the evaluation of the staged combustion concept for gas turbine applications. Particular emphasis was put on the influence of the pressure level, the air inlet temperature, and the geometry of the mixing zone on NO_x emissions. Therefore, the operating conditions of the combustor have been varied over a wide range (Table 1).

For all series of experiments, the residence time in both the primary and the secondary stage was kept constant at the same value of λ_{prim}. This was achieved by adjusting the appropriate air mass flow and thermal power corresponding to the pressure level. Therefore, the variables remaining were the pressure level, the air inlet temperature, the diameter of the mixing holes, and the primary air fuel ratio. Thus, λ_{prim} was varied while keeping the total air fuel ratio constant at λ_{total} = 2.4. According to this approach, the Reynolds number characterizing the primary stage flow increased with growing pressure and primary air fuel ratio.

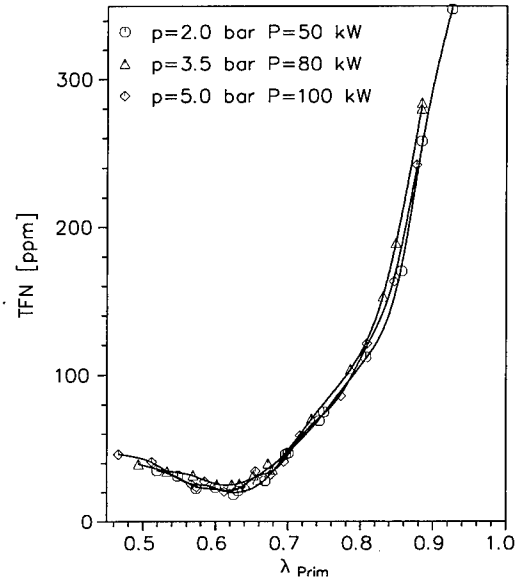

FIG. 3. Effect of pressure level on TFN concentrations in the primary stage for T_{inl} = 673 K and d = 14 mm.

Primary Stage:

The results plotted in Fig. 3 illustrate the influence of the pressure level on the TFN emissions at the end of the primary stage (T_{inl} = 673 K). The diameter of the mixing holes was adjusted to d = 14 mm. Because of the relatively large diameters of the holes, a backflow of dilution air into the primary stage can be excluded. For all test cases, a characteristical TFN-minimum was found at a primary air fuel ratio of about λ_{prim} = 0.63. The increase of TFN in direction to higher air fuel ratios is an effect of pronounced thermal NO formation. On the other hand, the occurrence of the intermediates HCN and NH_3 is responsible for the increase at more fuel-rich conditions. Furthermore, it can be noticed that over the entire air fuel ratio range, the TFN-concentrations of the three test series differ only slightly from each other. As a final result, a pronounced influence of pressure on primary stage TFN-emissions was not found. The absolute level of NO_x-emissions also depends on the heat losses of the combustor. The evaluation of the magnitude of this effect is presently under investigation.

Secondary Stage:

The influence of pressure on overall NO_x-emissions at the combustor exit is shown in Fig. 4 for the same operating conditions as considered in Fig. 3. In order to eliminate dilution effects by excess air, the NO_x concentrations are corrected to 15% excess oxygen, as it is convenient for gas turbine emission measurements.

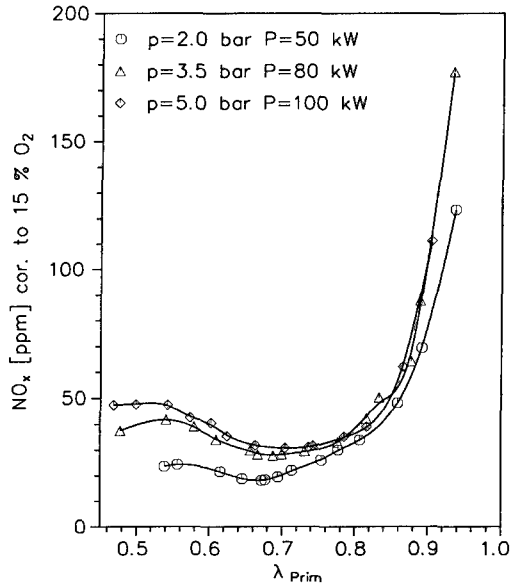

FIG. 4. Effect of pressure level on overall NO_x emissions for T_{inl} = 673 K and d = 14 mm.

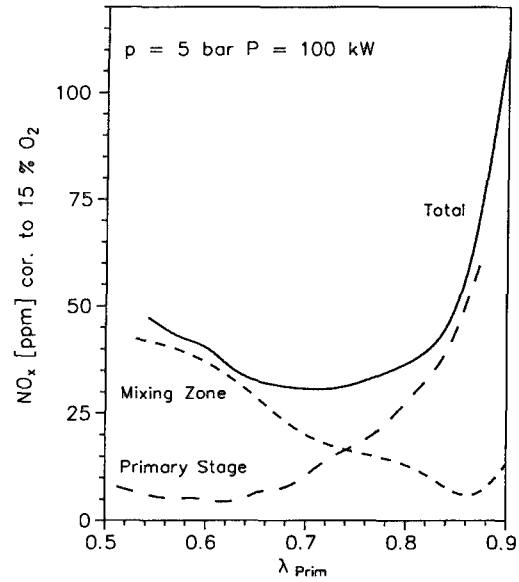

FIG. 5. Contributions of the primary stage and the mixing zone to the overall NO_x formation for the case p = 5 bar and d = 14 mm.

Typically, a minimum in NO_x-concentrations for each of the three conditions exists. Remarkably, these minima occur at higher air fuel ratios than the TFN minima of the primary stage. Furthermore, with growing pressure, the NO_x concentrations increase at $\lambda_{prim} < 0.75$, and the minima are shifted toward higher primary air fuel ratios. As these effects cannot be explained by the primary stage TFN emissions, the enhancement of the overall NO_x emissions and the shift of the minima with increasing pressure have to be attributed to the NO formation during the mixing process.

To achieve a more detailed understanding of the NO_x emission characteristics of the primary and mixing zones, the contributions from both zones are plotted in Fig. 5 together with the total emissions for the conditions of p = 5 bar and P = 100 kW. The TFN concentrations of the primary stage also are corrected to an exhaust volume corresponding to 15% excess oxygen. The NO_x concentrations formed in the mixing zone have been derived from the difference of the total and the primary stage emissions. The diagram demonstrates that the minima of the emissions of the primary stage and mixing zone are found at different λ_{prim}. Since the variation of λ_{prim} was achieved by decreasing the primary stage air flow and simultaneously increasing the dilution air flow, the momentum flux ratio of both air flows was altered (see Eq. (1)). Therefore, the minimum of NO_x formation in the mixing zone can be attributed to optimum mixing conditions. The location of the total NO_x emission minimum results from the superposition of both partial emissions. The shift of the overall

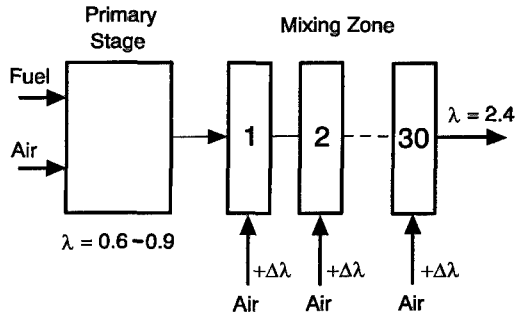

FIG. 6. Scheme of the mixing model. Each box corresponds to a single PSR.

minimum for the NO_x concentrations to higher λ_{prim} causes advantages in the operation of the RQL concept, as the soot formation in the primary stage is not quite as pronounced. On the other hand, to achieve lower emissions using this combustor concept, the lowest NO_x concentrations formed in the mixing zone must occur at the same λ_{prim}, at which the primary stage produces the lowest emissions.

In analyzing the effect of pressure on chemical kinetics in the mixing zone and on the shift of the secondary zone NO_x minimum, the mixing process is simulated simply by using 30 subsequent PSR (Fig. 6), with the outlet of one PSR connected to the inlet of the next one. Additional air is added in every PSR to enhance linearly the air fuel ratio until the overall air fuel ratio of λ = 2.4 is reached in the last PSR.

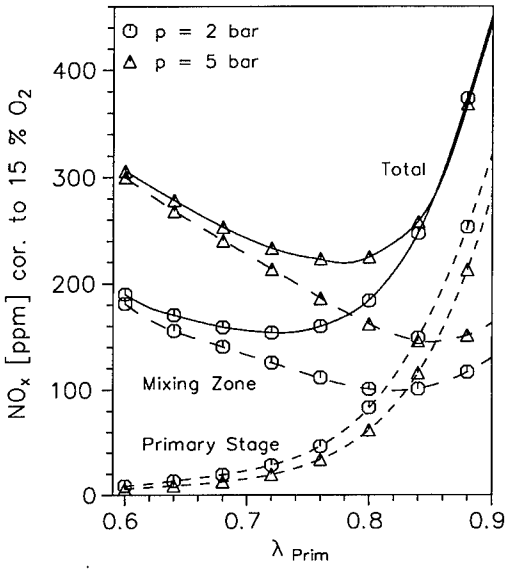

FIG. 7. Calculated effect of pressure level on NO_x formation using the mixing model. The point of fastest mixing is assumed to occur at $\lambda_{prim} = 0.85$.

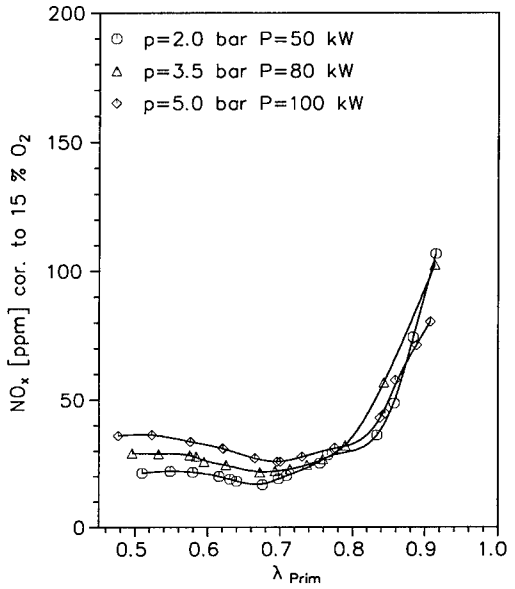

FIG. 8. Effect of pressure level on overall NO_x emissions for $T_{inl} = 673$ K and $d = 10$ mm.

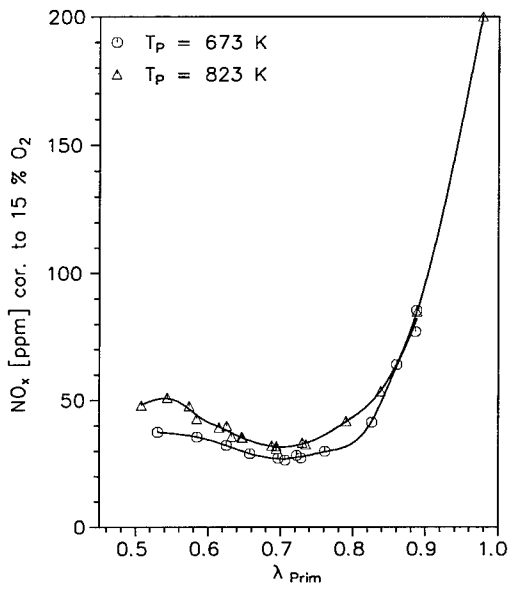

FIG. 9. Effect of air inlet temperature on overall NO_x emissions for $p = 3.5$ bar and $d = 14$ mm.

The reaction is started in the first PSR under fuel-rich conditions representing the primary zone conditions. In this model, the residence time in the mixing zone (consisting of 30 PSR) is a degree for the mixing effectiveness. According to the experimental observations ($p = 5$ bar; $P = 100$ kW) the best mixing, i.e., the smallest mixing time, was assigned to $\lambda_{prim} = 0.85$. Because the momentum flux ratio is relatively unaffected by pressure (see Eq. (1)), it is assumed that the mixing time does not depend on pressure.

Figure 7 shows the result of this simulation. As pressure increases, the total NO_x minima are clearly shifted toward a value of $\lambda = 0.85$, representing the air fuel ratio of best mixing. In agreement with the experimental results, NO formation under fuel-lean conditions (mixing zone) is promoted by pressure, while TFN formation (primary zone) is influenced only slightly by pressure. Therefore, at this high inlet air temperature, the NO formation in the mixing zone becomes more and more dominant with increasing pressure and determines the overall NO_x emissions. Therefore, the location of the NO_x minimum at high-pressure levels is found close to the air fuel ratio of best mixing. This interrelation reveals that the minima of the total emissions are shifted to higher λ_{prim} due to the pressure dependence of the NO formation in the mostly fuel-lean mixing zone, even if the mixing effectiveness is not influenced by pressure.

To check this effect, additional investigations using a slightly different mixing configuration were carried out. The overall NO_x concentrations are shown in Fig. 8 for the operating conditions discussed in Fig. 4, except for a smaller mixing hole diameter of $d = 10$ mm. Because of the smaller diameter of the mixing jets, the momentum flux ratio at the same λ_{prim} is higher than for the larger diameter. But also the

spacing between the edges of the orifices is enlarged. Despite of the significant differences in the mixing configuration, a similar effect of pressure on the NO_x-emissions is found. But due to the modification, the NO_x-concentrations at low air fuel ratios are reduced for this jet diameter. This effect indicates, that the mixing effectiveness is obviously improved by this configuration, because the TFN-formation in the primary stage was not affected by this modification. The pronounced influence of pressure also represents a comparison of the results between both mixing configurations. It is found that the differences in concentrations and the location of the minimum are quite small for $p = 2$ bar, while these are more significant at the elevated pressure levels.

The influence of enhanced air inlet temperature on total NO_x-emissions, which is a major issue for gas turbine applications, was also studied (Fig. 9). The test conditions selected were $p = 3.5$ bar and $d = 14$ mm. As expected, the higher temperature ($T_{inl} = 823$ K) leads to higher NO_x-concentrations, but also a shift to lower λ_{prim} is observed. The same tendency was found for the other pressure levels investigated. The shift of the minimum leads to the conclusion, that the NO-formation in the primary stage, which determines to a great degree the total emissions at high air fuel ratios, is more promoted by the elevated temperature than the NO-formation during the mixing process. Thus, in contrast to the effects caused by increasing pressure, an increase of inlet temperature tends to shift the emission minimum to lower air fuel ratios.

Conclusions

With respect to gas turbine application, the concept of staged combustion (RQL) has been studied with special emphasis on the influence of elevated pressure and high air inlet temperatures. As expected, the results show a pronounced influence of pressure level on NO_x emissions. By varying simultaneously the primary and secondary air fuel ratio in opposite directions at constant pressure conditions, an operating point was found providing lowest NO_x emissions. At higher pressure levels, minimum NO_x concentrations are found at higher primary air fuel ratios. Moreover, the level of NO_x concentrations is increased. This effect was observed for the two configurations of the mixing zone tested. The measured emissions at the end of the primary stage and at the combustor exit clearly demonstrate that the TFN level formed in the fuel-rich primary zone is widely unaffected by pressure. The NO formation in the mostly fuel-lean mixing zone, however, is promoted by pressure and, therefore, is primarily responsible for the pressure dependence of the total NO_x emissions of this combustor concept.

The detailed analysis of the data reveals the emission characteristics of the mixing zone that shows an opposite tendency compared to the primary stage. At the optimum operating point of the primary stage, NO is extensively formed in the mixing zone and vice versa. Therefore, the major conclusion of the present study is that the NO formation in the mixing zone is critical for the overall emissions under extreme combustor inlet conditions. Significantly lower NO_x emissions of the staged combustion concept can be achieved by adapting and tuning the mixing zone.

Nomenclature

A	cross section (m^2)
J	momentum flux ratio (−)
P	thermal power (kW)
T	temperature (K)
d	mixing jet diameter (m)
p	pressure (bar)
$\dot{m}$	mass flow (kg/s)
λ	air fuel ratio (−)

Subscripts

prim	primary stage
sec	secondary stage

Acknowledgments

The research program has been supported by the Forschungsvereinigung Verbrennungs kraftmaschinen e.V. (FVV) of the Arbeitsgemeinschaft Industrieller Forschungsvereinigungen e.V. (AIF-Nr. 7375). Thanks are due to the chairman of the working group, Dr. C. Coulon from the "Daimler Benz AG Stuttgart," for his continuing assistance. The overall design of the model combustor was provided by Professor W. Leuckel and Dipl.-Ing. K. Knapp from the "Engler-Bunte-Institut" in Karlsruhe.

REFERENCES

1. *BRITE EURAM: Low Emission Combustor Technology, AERO/1019—Task 3*, Technical Report: Summary of Pollutant Reduction Methods, 1991.
2. Sattelmayer, T., Felchlin, M. P., Haumann, J., Hellat, J., and Styner, D., *J. Eng. Gas Turbines Power* 114:118–125 (1992).
3. Rizk, N. K., and Mongia, H. C., *ASME*, 1990, 90-GT-87.
4. Hirai, T., Nagai, N., and Takado, J., *JSME Int. J.* 30:303–309 (1987).
5. Knapp, K., Meisl, J., Leuckel, W., and Wittig, S., 16. *Deutscher Flammentag, VDI-Berichte—1090*, 1993, pp. 587–594.
6. Zeldovich, Y. B., *Acta Phys. Chem.* USSR 21 (1946).
7. Fenimore, C. P., *Thirteenth Symposium (International) on Combustion*, The Combustion Institute, Pittsburgh, 1971, p. 373.

8. Glarborg, P., Kee, R. J., Grcar, J. F., and Miller, J. A., Sandia National Laboratories Report No. SAND86-8209, 1986.
9. Miller, J. A., and Bowman, C. T., *Prog. Energy Combust. Sci.* 15:287–338 (1989).
10. Wittig, S., Elbahar, O., and Noll, B., *J. Eng. Gas Turbines Power* 106:193–197 (1984).
11. Dörr, T., and Hennecke, D. K., AGARD-CP-536, 39_1–39_9 (1993).
12. Talpallikar, M. V., Smith, C. E., Lai, M. C., and Holdeman, J. D., *J. Eng. Gas Turbines Power*, 114:416–424 (1992).
13. Pfeiffer, A., Schulz, A., and Wittig, S., *ASME* 91-GT-63 (1991).

Twenty-Fifth Symposium (International) on Combustion/The Combustion Institute, 1994/pp. 1051–1059

EFFECT OF NO AND O_2 CONCENTRATION ON N_2O FORMATION DURING COAL COMBUSTION IN A FLUIDIZED-BED COMBUSTOR: MODELING RESULTS

SHAKTI K. GOEL, ATSUSHI MORIHARA,* CLAES J. TULLIN** AND ADEL F. SAROFIM

Department of Chemical Engineering
Massachusetts Institute of Technology
Cambridge, MA 02139, USA

This paper addresses the issue of understanding the NO and N_2O formation kinetics during char combustion in a fluidized-bed combustor. A single-particle numerical model that simulates the combined internal diffusion and reaction equations is developed. Kinetic parameters for the char oxidation, CO and CO_2 formation, NO formation and destruction both by char and by a char-catalyzed CO reaction, and N_2O formation and destruction reactions have been estimated using fractional order kinetics. Modeling results have been compared with the experimental data. Primarily, N_2O is formed by the reaction of NO with char nitrogen in the presence of O_2. Formation of N_2O increases with increases in the bulk NO concentration. N_2O, however, is not formed in the absence of oxygen, as oxygen is required to release the char nitrogen bound in aromatic rings. A higher O_2 concentration in the feed gas gives higher concentrations of NO and N_2O. The instantaneous conversion of char nitrogen to N_2O increases, whereas the conversion to NO decreases, with increases in bulk O_2 concentration. The char-catalyzed NO/CO reaction at low temperatures and high O_2 concentrations is the dominant destruction mechanism for NO. At high temperature, NO is destroyed mainly by its heterogeneous reaction with char.

Introduction

Increases in coal consumption continue to be constrained by the emission of the acid rain precursors SO_2 and NO, and the greenhouse gas CO_2. One of the promising technologies that can utilize coal efficiently and minimize the impact on the environment is pressurized fluidized-bed combustion. Pressurized fluidized-bed combustors, when used as part of a power generation cycle, increase the thermal efficiency, provide in-bed capture of sulfur oxides, and reduce nitric oxide emissions. One of the potential problems of fluidized-bed combustors, however, is the formation of N_2O. N_2O is known to be a greenhouse gas and is formed in the temperature window in which fluidized-bed combustors are operated. N_2O has a lifetime of 150 years and can possibly contribute to the ozone destruction chemistry in the stratosphere. It is produced by the oxidation of nitrogen organically bound in coal, with the contribution from char oxidation being somewhat larger than that from the volatiles [1]. Though the homogeneous gas phase chemistry of N_2O has been studied in detail [2], the heterogeneous chemistry is relatively poorly understood. An analytical model based on lumped reaction rates derived from a 15-step heterogeneous kinetic mechanism was reported in an earlier paper [3]. However, lumping of the reactions could not explain the effects of NO on N_2O formation in the absence of ambient O_2. Therefore, the present paper attempts to develop a single-particle model based on more elaborate rate formulations. Kinetic parameters of the reactions involved in the NO and N_2O formation have been estimated using inverse optimization techniques. The model is then used to explain the following experimental effects of bulk NO and O_2 concentrations on NO and N_2O formation from char:

1. the increase in N_2O formation with increases in NO concentration in the presence of O_2, and
2. the increase in N_2O formation and decrease in NO formation with increases in O_2 concentration.

Experimental

Batch combustion experiments were performed in a small-scale quartz glass bubbling fluidized-bed reactor with an inner diameter of 57 mm. A bed of silica sand (particle size 150–212 μm) with a bed height of approximately 50 mm was fluidized by O_2 or O_2 and NO in helium. The oxygen concentration in the inlet gas stream was varied from 1 to 12% and NO from 0 to 700 ppm. The composition and flow

*Hitachi Research Laboratory, Japan.
**Chalmers University of Technology and University of Göteborg, S-412 96, Göteborg, Sweden.

rate were controlled using mass flow controllers. The flow rate was set to 2.5 L/min at STP conditions. Coal particles, 4 mm in diameter, were burned at three different temperatures of 750 °C, 800 °C, and 850 °C, and the concentrations of the combustion products, viz., N_2O, NO, O_2, CO_2, CO, and CH_4, were measured using a Fourier transform infrared (FTIR) spectrometer equipped with an MCT detector and a low-volume gas cell of 223 cm^3. The path length was set to 7.25 m. A detailed description of the reactor and the experimental setup can be found in Refs. 4 and 1. The experimental raw data for NO and N_2O in the form of concentration vs time were converted into instantaneous and net conversion of char nitrogen to NO and N_2O data using Eqs. (1) and (2).

$$f_{N_2O} = \frac{2([N_2O]_e - [N_2O]_{in})}{\frac{N}{C}([CO] + [CO_2] + [CH_4])} \quad (1)$$

$$F_{N_2O} = \frac{\int_0^t 2([N_2O]_e - [N_2O]_{in})\, dt}{\frac{N}{C}\int_0^\infty ([CO] + [CO_2] + [CH_4])\, dt} \quad (2)$$

where N/C is the ratio of nitrogen to carbon present in char and $[\cdot]_e$ and $[\cdot]_{in}$ are the concentrations of species "i" in the effluent and inlet to the reactor, respectively. An equation similar to Eq. (1) was used to evaluate f_{NO}. The following sections present the heterogeneous kinetic mechanism, the single-particle model, parameter determination studies to calculate the rate constants, and the modeling results explaining the experimental observations.

Heterogeneous Kinetic Mechanism

A 15-step mechanism for NO and N_2O surface kinetics was proposed in an earlier paper [3]. Based on this mechanism, an analytical single-particle model that used lumped chemistry was developed. However, due to lumping of the reactions, the predictive ability of the analytical model was limited. Therefore, in this section more thorough rate formulations based on the 15-step mechanism given below are developed.

Formation of CO and CO_2

$$\left.\begin{array}{c} \frac{1}{2}O_2 + (-C) \xrightarrow{1} (-CO) \\ (-CO) \xrightarrow{2} CO + -C \\ \frac{1}{2}O_2 + (-CO) \xrightarrow{3} (-CO_2) \\ (-CO_2) \xrightarrow{4} CO_2 + -C \end{array}\right\} a \quad (3)$$

Formation of NO

$$\left.\begin{array}{c} \frac{1}{2}O_2 + (-CN) \xrightarrow{5} (-CNO) \quad \text{or } (-NCO) \\ (-NCO) \xrightarrow{6} CO + (-N) \\ (-CNO) \xrightarrow{6'} NO + (-C) \\ \frac{1}{2}O_2 + (-N) \xrightarrow{7} (-NO) \\ (-NO) \xrightarrow{8} NO + -C \end{array}\right\} b \quad (4)$$

Destruction of NO and Formation of N_2O

$$NO + (-C) \xrightarrow{9} \frac{1}{2}N_2 + (-CO)\}c$$

$$\left.\begin{array}{c} NO + -C \xrightarrow{10} (-NO) \\ CO + -C \xrightarrow{11} (-CO) \\ (-NO) + (-CO) \xrightarrow{12} \frac{1}{2}N_2 + CO_2 + 2 - C \end{array}\right\} d$$

$$\left.\begin{array}{c} NO + (-N) \xrightarrow{13} (-N_2O) \\ NO + (-NCO) \xrightarrow{13'} (-N_2O) + (-CO) \\ (-N_2O) \xrightarrow{14} N_2O + -C \end{array}\right\} e \quad (5)$$

Destruction of N_2O

$$N_2O + (-C) \xrightarrow{15} N_2 + (-CO)\}f \quad (6)$$

where "$-C$" is a free site and other "$-X$" denotes the surface bound species, X. The mechanism outlined above is tentative and is developed from the experimental observations of Refs. 5 and 1. The reaction rate formulations are linked to the mechanism via the superscripts a–f and are presented in Table 1. The analytical model [3] uses the equivalent pseudo–first-order reaction rates obtained by lumping the reaction rates (a–f) of the numerical model. The mechanism proposes that O_2 first reacts with char carbon to form CO and CO_2. O_2 also breaks the aromatic rings bound to the char surface and forms an active intermediate, I, such as $-CNO$ or $-NCO$. This active intermediate, I, decomposes to form NO or reacts with NO to form N_2O. The fraction $k_1/(k_1 + k_2[NO])$ as in R_{NO} denotes the probability that the reactive intermediate, I, forms NO, and $k_2[NO]/(k_1 + k_2[NO])$ as in R_{N_2O} gives the probability that it reacts with NO to form N_2O. An earlier study [5] has reported that N_2O is not formed in the absence of O_2. Therefore, the N_2O formation term in R_{N_2O} has a dependence on $[O_2]$. A single-particle numerical model that uses the kinetic rate expressions given above is developed in the next section.

TABLE 1
Expressions for the net rates of formation and destruction for O_2, CO, CO_2, NO, and N_2O used in the numerical model

Rate	Expressions
R_{O_2}	$-\frac{1}{2}k_{O_2}[O_2]^a - \frac{1}{2}k_{CO}[CO][O_2]^{a1/2}$
R_{CO}	$k_{O_2}[O_2] - k_{CO}[CO][O_2]^{1/2}$
R_{CO_2}	$k_{CO}[CO][O_2]^{1/2}$
R_{NO}	$\frac{N}{C}k_{O_2}[O_2]\left(\frac{k_1}{k_1 + k_2[NO]}\right)^b - k_{NO}[NO^c] - k_{NO-CO}[NO][CO^d] - \frac{N}{C}k_{O_2}[O_2]\left(\frac{k_2[NO]}{k_1 + k_2[NO]}\right)^e$
R_{N_2O}	$\frac{N}{C}k_{O_2}[O_2]\left(\frac{k_2[NO]}{k_1 + k_2[NO]}\right)^e - k_{N_2O}[N_2O^f]$

The superscripts *a–f* relate the rate expressions to the proposed mechanism. k_j is the reaction rate constant for reaction "*j*" and R_i is the net rate of formation and destruction of species "*i*," viz., O_2, CO, CO_2, NO, and N_2O.

The rate parameters are then estimated from the parameter determination studies.

Model Development

The single-particle model solves for the diffusive transport and the kinetics of reactants and products in a shrinking char sphere. The model is based on the following assumptions.

1. The char particle is spherically symmetric;
2. The system is in pseudo steady state; and
3. Ash falls off from the particle surface under the fluidizing conditions.

The governing mass conservation equations are

$$\mathcal{D}_{p_i}\left(\frac{\partial^2[\cdot]}{\partial r^2} + \frac{2}{r}\frac{\partial[\cdot]}{\partial r}\right) + R_i([\cdot]) = 0 \qquad (7)$$

The boundary conditions are

$$@ \quad r = 0 \qquad \left.\frac{\partial[\cdot]}{\partial r}\right|_{\text{center}} = 0 \qquad (8)$$

$$@ \quad r = R \qquad \mathcal{D}_{p_i}\left.\frac{\partial[\cdot]}{\partial r}\right|_{\text{surface}} = k_g([\cdot]_\infty - [\cdot]_s) \qquad (9)$$

where $\mathcal{D}_{p_i}$ is the particle diffusivity and $[\cdot]_\infty$ and $[\cdot]_s$ are the concentrations of species "*i*" in the bulk and the particle surface, respectively, k_g is the external mass transfer coefficient, and r is the radial position inside the particle. The term R_i is the same as defined in Table 1. We have five equations in the form of Eq. (7) for five species, viz., O_2, CO, CO_2, NO, and N_2O. These five equations, which are second-order nonhomogeneous ordinary differential equations involving nonlinear terms, are then solved simultaneously using a finite-element code that allocates the node points using the collocation method.

Parameter Determination

The model developed in the previous section was used to obtain the kinetic rate parameters by fitting the model to the experimental data of Ref. 1. The concentration vs time raw data for NO and N_2O were transformed into instantaneous conversion of char nitrogen data as a function of instantaneous particle radius using Eqs. (1) and (10).

$$R(t) = R_0(1 - X_c(t))^{1/3} \qquad (10)$$

where $R(t)$ is the particle radius at any given time and $X_c(t)$ is the conversion of char carbon on a mol/mol basis. The objective function, $\mathcal{L}_2$, minimized was a weighted least-square error norm [Eq. (11)] for the observed and predicted instantaneous conversion data. Minimization of $\mathcal{L}_2$ was done with respect to the rate constants, viz., k_{O_2}, k_{CO}, k_{NO}, k_{NO-CO}, k_{N_2O}, k_2/k_1, and the effective diffusivity, $\mathcal{D}_p$, of char treated here as a constant during reaction.

$$\mathcal{L}_2 = \left\{w_{NO}\sum_j^N (f_{NO_{exp}} - f_{NO_{model}})_j^2 + w_{N_2O}\sum_j^N (f_{N_2O_{exp}} - f_{N_2O_{model}})_j^2\right\}^{1/2} \qquad (11)$$

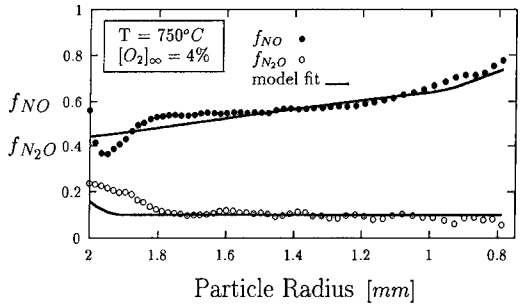

FIG. 1. Comparison of the experimental and model predicted f_{NO} and f_{N_2O} profiles for three particle temperatures of 750 °C, 800 °C, and 850 °C, two oxygen concentrations of 4 and 8% in helium, and one initial particle radius of 2 mm. Comparisons for only four of the six experimental data sets used for the study are shown here.

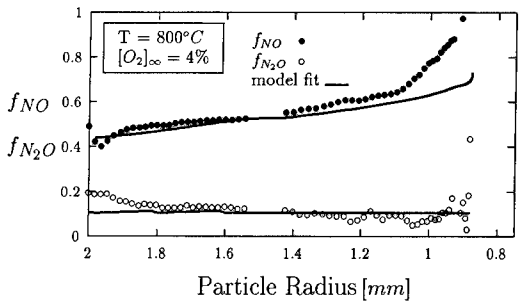

FIG. 2. See Fig. 1 caption.

where N is the total number of data points for a given experimental condition. The f_{NO} and the f_{N_2O} profiles exhibit random variation and were used to test the more elaborate chemistry of the model. The search for the optimal parameter values was carried out using the Davidson, Fletcher, Powell [6] optimizer and six experimental data sets (three temperatures of 750 °C, 800 °C, and 850 °C for each of the two O_2 concentrations of 4 and 8%). The weights w_{NO} and w_{N_2O} were chosen in such a way that the search path took minimum CPU time to find the point of minima. Figures 1 through 4 show the comparison for four of the six experimental data sets used for the study. This suggests that the more elaborate kinetic model is able to explain the experimental observations and that it can be used as a predictive tool for other experimental observations. Table 2 shows the optimal values of the rate parameters estimated and their comparison with other values reported in the literature [5]. The optimal activation energy for the char oxidation reaction is close to the values reported in Ref. 7 for different coal types.

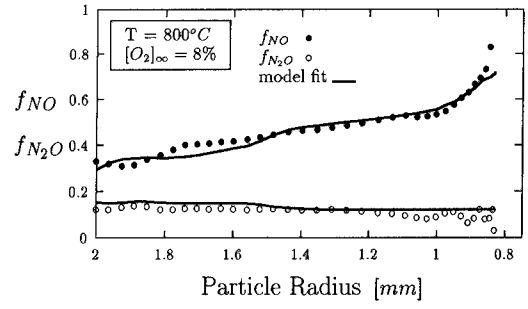

FIG. 3. See Fig. 1 caption.

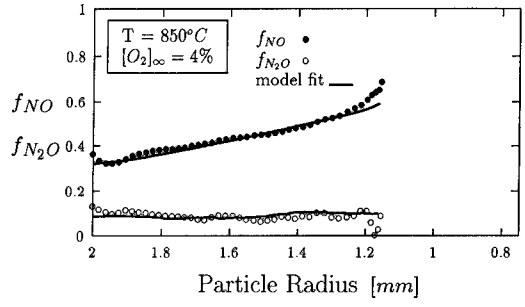

FIG. 4. See Fig. 1 caption.

Effect of $[O_2]_\infty$ and $[NO]_\infty$ on NO/N_2O Formation: Modeling Results

Having done the experiments, developed the model, and estimated the rate parameters, we then explored the model performance over a wider range of operating conditions. The analyses of the additional experimental data that were not used for the parameter determination studies are divided into two sections, as follows: (1) the effect of NO concentration on N_2O formation, and (2) the effect of O_2 concentration on NO and N_2O formation.

Effect of NO Concentration on N_2O:

Figure 5 shows the comparison of the model results and the experimental data for the instantaneous conversion profiles of char nitrogen to N_2O. The comparison is carried out for three different concentrations of NO, viz., 723, 205, and 0 ppm, in a gaseous feed of 2% oxygen in helium, and one particle size of 4 mm burning at 750 °C. The results show that the presence of NO in the feed augments the formation of N_2O. The f_{N_2O} values for all values of carbon conversion increase with increases in NO concentration. NO present in the feed diffuses into the char particle. It then reacts with the char nitrogen sites formed during the opening of aromatic rings by the oxidation reactions to form N_2O. Since the N_2O

TABLE 2
Estimated pre-exponential factors and activation energies for the rate constants shown in Table 1

Rate constant (units)	$A \exp\left(-\frac{E_a}{RT}\right)$	Standard error $\ln(A)$ and $\frac{E_a}{R}$	Coal type	Reference
k_{O_2}(1/s)	$1.24\ 10^6 \exp\left(-\frac{6253}{T}\right)$	(±0.36), (±400)	Newlands	present work
$k_{CO}\left(\frac{m^{3/2}}{mol^{1/2}\ s}\right)$	$1.20\ 10^8 \exp\left(-\frac{13{,}454}{T}\right)$	(±0.97), (±1041)	Newlands	present work
k_{NO}(1/s)	$2.09\ 10^8 \exp\left(-\frac{14{,}455}{T}\right)$	(±0.79), (±860)	Newlands	present work
$k_{NO}\left(\frac{g_N}{g_C sPa}\right)$	$9.3\ 10^{-1} \exp\left(-\frac{16{,}900}{T}\right)$	(−), (−)	Cedar Grove char (35–50 μm)	deSoete [5]
$k_{NO}\left(\frac{g_N}{g_C sPa}\right)$	$1.2\ 10^0 \exp\left(-\frac{16{,}600}{T}\right)$	(−), (−)	Prosper char (35–50 μm)	deSoete [5]
$k_{NO}\left(\frac{g_N}{g_C sPa}\right)$	$5.8\ 10^0 \exp\left(-\frac{17{,}800}{T}\right)$	(−), (−)	Eschweiler char (35–50 μm)	deSoete [5]
$k_{NO-CO}\left(\frac{m^3}{mol\ s}\right)$	$3.68\ 10^7 \exp\left(-\frac{13{,}097}{T}\right)$	(±1.11), (±1083)	Newlands	present work
$\frac{k_2}{k_1}\left(\frac{m^3}{mol}\right)$	$9.0\ 10^2 \exp\left(-\frac{3551}{T}\right)$	(±0.16), (±171)	Newlands	present work
$k_{N_2O}(s^{-1})$	$4.8\ 10^8 \exp\left(-\frac{16{,}983}{T}\right)$	(±0.764), (±818)	Newlands	present work
$k_{N_2O}\left(\frac{g_N}{g_C sPa}\right)$	$0.68 \exp\left(-\frac{12{,}200}{T}\right)$	(−), (−)	Prosper char	deSoete [5]
$k_{N_2O}\left(\frac{g_N}{g_C sPa}\right)$	$0.9 \exp\left(-\frac{13{,}900}{T}\right)$	(−), (−)	Cedar char	deSoete [5]
$k_{N_2O}\left(\frac{g_N}{g_C sPa}\right)$	$0.14 \exp\left(-\frac{10{,}000}{T}\right)$	(−), (−)	Eshweiler char	deSoete [5]

formation rate depends on the NO concentration, it increases with increases in NO concentration. Consequently, more N_2O is produced as the NO concentration in the feed is increased. This behavior is observed throughout the particle burnout. As the carbon conversion reaches unity, the f_{N_2O} profile drops to zero when $[NO]_\infty = 0$ ppm, for the 205-ppm case decreases but does not go to zero, and exhibits a steep increase when $[NO]_\infty = 723$ ppm. The change in f_{N_2O} with changes in conversion can be understood by noting that the NO concentration to which a char particle is exposed is determined by the balance between NO diffusing into a pore and getting partially reduced, and NO being formed in the pore and diffusing out of a particle. When $[NO]_\infty =$ 0 ppm, only the NO formed in the pore diffuses out. As the particle shrinks with increasing burnout, the diffusion path decreases and the N_2O concentration within a pore decreases, approaching zero in the limit of complete burnout. The decrease in f_{N_2O} with increasing burnout is consistent with this behavior. On the other hand, when $[NO]_\infty = 723$ ppm, the balance between the NO formation and destruction reactions within the pores apparently gives a concentration that is initially less than that in the free stream. In other words, at high conversions, the net diffusion of NO is out of the pore for $[NO]_\infty = 0$ ppm and into the pore for $[NO]_\infty = 723$ ppm. The increase or decrease in the f_{N_2O} profiles reflects the increase or decrease in NO concentration within the pores. The

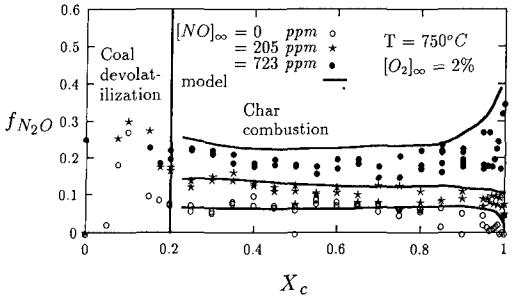

FIG. 5. Comparison of the experimental and model predicted profiles for instantaneous conversion of char nitrogen to N_2O at three bulk NO concentrations of 0, 205, and 723 ppm at a temperature of 750 °C and an oxygen concentration of 2% in helium.

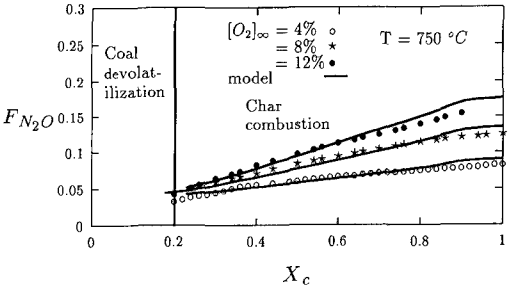

FIG. 6. Comparison of the experimental and model predicted profiles for the cumulative conversion of char nitrogen to N_2O for different bulk oxygen concentrations of 4, 8, and 12% in helium at a temperature of 750 °C.

fractional conversion to N_2O is, therefore, a minimum at complete burnout when $[NO]_\infty = 0$, and a maximum when $[NO]_\infty = 723$ ppm.

Effect of $[O_2]_\infty$ on NO and N_2O Formation:

Experimental observations of Refs. 5, 8, and 9 suggest that N_2O is formed from NO but only in the presence of oxygen. This fact was incorporated into the kinetic mechanism and the rate expressions developed earlier. The effects of bulk O_2 concentration levels on cumulative N_2O, F_{N_2O}, and instantaneous NO, f_{NO}, formation in absence of ambient NO are shown in Figs. 6 and 7. The F_{N_2O} values at a given value of carbon conversion increase as oxygen concentration increases. These effects can be explained by noting that, with increasing $[O_2]_\infty$, the rate of NO production increases, and therefore, the concentration of NO in the pores increases to provide the driving force for NO removal by either diffusion or reaction with the char. The increase in instantaneous conversion of char nitrogen to N_2O and the decrease to NO are, therefore, partly due to the increase in

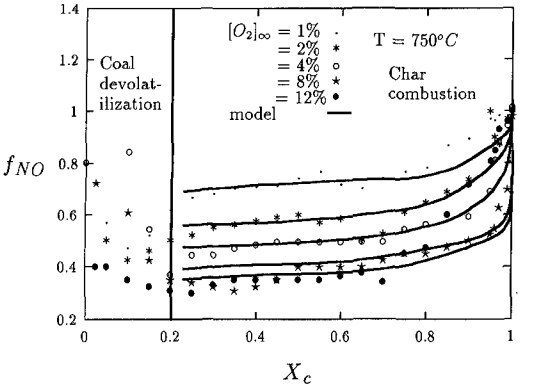

FIG. 7. Comparison of the experimental and model predicted profiles for the instantaneous conversion to NO for different bulk oxygen concentrations of 1, 2, 4, 8, and 12% in helium at a temperature of 750 °C.

the rate of fraction of char nitrogen intermediate reacting with NO and forming N_2O. Increasing $[O_2]_\infty$ also increases the CO concentration in the pores and consequently the rate of destruction of NO with CO on char surface. The NO/CO char-catalyzed reaction is found to be important as the sum of f_{NO} and f_{N_2O} (instantaneous conversion of char nitrogen to NO and N_2O) at a given carbon conversion decreases as the O_2 concentration in the bulk increases. Had the increase in NO destruction rate with increase in $[O_2]_\infty$ been due to the NO + (*I*) reaction only, all of it should have formed N_2O, keeping $f_{NO} + f_{N_2O}$ constant. On the contrary, both the experimental and modeling results show a decrease in the fractional conversion of char nitrogen to the sum of the nitrogen oxides. For example, the modeling results show that, at a carbon conversion of 40%, $f_{NO} + f_{N_2O} = 0.585$ for $[O_2]_\infty = 2\%$, and 0.395 for $[O_2]_\infty = 12\%$. Figure 8 shows that instantaneous conversion of char nitrogen to free molecular N_2, f_{N_2}, increases with increases in bulk O_2 concentration at a given bed temperature. At low temperatures, NO is destroyed mainly by the char-catalyzed NO/CO reaction. The reaction becomes more important with increases in $[O_2]_\infty$. At high temperatures, the reaction of NO with char (carbon and nitrogen) becomes the dominant destruction mechanism. These observations suggest that the decrease in f_{NO} with increases in $[O_2]_\infty$ is due to increases in rates of formation of NO and CO and, therefore, in their concentrations in the pores. It should be noted that, though f_{NO} decreases with increases in $[O_2]_\infty$, the NO concentration in the pores still increases. At high carbon conversions, the fraction of the char nitrogen converted to NO is underpredicted and that converted to N_2O overpredicted. These deviations are possibly due to an increase in the effective diffusivity as a consequence of increase in porosity at high conversions. Such an increase

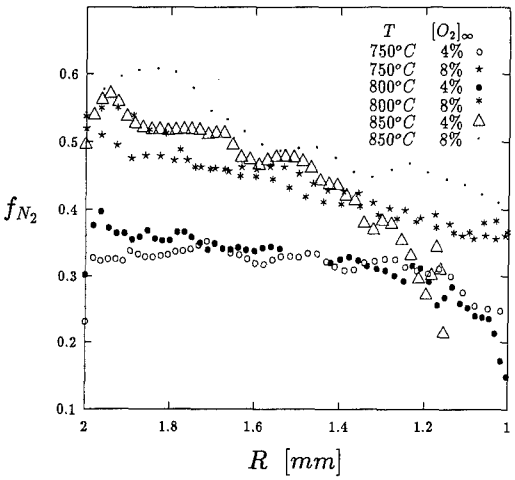

FIG. 8. Experimental profiles for instantaneous conversion of char nitrogen to N_2 for three temperatures of 750 °C, 800 °C, and 850 °C and two oxygen concentrations of 4 and 8%. This figure highlights the importance of the char-catalyzed NO/CO reaction.

would allow the reaction products, including NO, to diffuse out of the particles more rapidly, reducing their concentration in the pores. The fraction of the char nitrogen converted to N_2O will, therefore, decrease as the NO concentration decreases.

Concluding Comments

Previous studies [5] have provided a solid foundation for understanding the formation of NO and N_2O during the oxidation of char nitrogen. The present study shows that a model modified to include the reaction of an oxidized char nitrogen intermediate, I, with NO to form N_2O provides a good fit of the experimental data over a range of oxygen concentrations and with varying levels of NO in the fluidizing gas stream. The parallel reactions of the intermediate can be represented by

$$\text{char} - \text{N} \xrightarrow{O_2} -I \begin{cases} \nearrow \text{NO} \\ \xrightarrow{\text{NO}} \searrow N_2O \end{cases}$$

The path to N_2O is favored by high local NO concentrations. This explains the increase in F_{N_2O} and f_{NO} when NO is added in the feed, or when the local NO concentration in the pore is increased by increasing $[O_2]_\infty$. This reaction also explains the decrease in f_{N_2O} at high conversions when the NO concentration falls as NO diffuses out of the particle rapidly in the absence of NO in the free stream.

The rate of surface catalyzed NO/CO reaction is enhanced by increases in the oxygen concentration, which explains the experimental decrease in instantaneous conversion of bound nitrogen to NO and N_2O. The understanding of the major global pathways to NO and N_2O formation can be used to improve strategies for the control of the emissions.

Nomenclature

A	pre-exponential factor (units depend on the order of the reaction)
E_a	activation energy (J/mol or cal/mol)
$\mathcal{D}_{p_i}$	effective diffusivity of species "i" inside the particle pores (m^2/s)
$f_{NO}, f_{N_2O}, f_{N_2}$	instantaneous fractional conversion of char nitrogen to NO, N_2O, and N_2, respectively
F_{N_2O}	cumulative conversion of char nitrogen to N_2O
k_j	rate constant for reaction "j" (units depend on the order of the reaction)
k_g	external mass transfer coefficient (m/s)
$\mathcal{L}_2$	least-square norm used in parameter estimation
N/C	ratio of nitrogen to carbon content in char
$[\cdot]_{e,in,s,\infty}$	concentration of species "i" in the effluent and inlet gas stream, at the surface of the particle, and the bulk, respectively (mol/m^3)
r	radial distance inside the char particle (m)
$R(t)$	particle radius at any given time, t (m)
R_i	net rate of formation of species "i" = O_2, CO, CO_2, NO, and N_2O (mol/m^3s)
R_0	initial radius of the char particle (m)
T	temperature of the char particle (K)
w_{NO}, w_{N_2O}	weights with respect to f_{NO} and f_{N_2O}, respectively, in the evaluation of the objective function
$X_c(t)$	fractional conversion of char carbon at any given time t (mol/mol)

Acknowledgments

Financial support for this research was provided by the Hitachi Research Laboratory and the Martin Foundation. SKG wishes to thank Dr. Narsimha Acharya for his help in developing the finite-element code.

REFERENCES

1. Tullin, C. J., Sarofim, A. F., and Beér, J. M., *J. Instit. Energy* 66:207–215 (1993).
2. Kilpinen, P., and Hupa, M., *Combust. Flame* 18:94–104 (1991).
3. Goel, S. K., McRae, G. J., and Sarofim, A. F., *Symposium on Fundamental Chemical and Physical Processes in Combustion/Incineration*, AIChE Annual Meeting, St. Louis, MO, Paper 161g, 1993.
4. Tullin, C. J., Goel, S., Morihara, A., Sarofim, A. F., and Beér, J. M., *Energy Fuels* 7:796–802 (1993).
5. de Soete, G. G., *Twenty-Third Symposium (International) on Combustion*, The Combustion Institute, Pittsburgh, 1990, pp. 1257–1264.
6. Press, W. H., Flannery, B. P., Teukolsky, S. A., and Vetterling, W. T., *Numerical Recipes in C*, Cambridge University Press, Cambridge, UK, 1988.
7. Smith, I. W., *Nineteenth Symposium (International) on Combustion*, The Combustion Institute, Pittsburgh, 1982, pp. 1045–1065.
8. Krammer, G. F., and Sarofim, A. F., *Combust. Flame* 97:118–124 (1994).
9. Kramlich, J. C., Cole, J. A., McCarthy, J. M., Lanier, W. S., and McSorley, J. A., *Combust. Flame* 77:375 (1989).

COMMENTS

John Kramlich, University of Washington, USA. In this paper, and in other recent publications by your group, you make a convincing argument that significant N_2O is formed from the NO + char nitrogen reaction only if free oxygen is available to activate the char nitrogen. This offers a plausible mechanism explaining the appearance of N_2O in combustion fluidized beds. Pilot-scale data on a circulating fluidized bed, however, show that the addition of 360 ppm NO to the combustion air failed to yield any change in N_2O profiles through the bed (Moritomi, H., and Suzuki, Y., "N_2O Emissions from Circulating Fluidized Bed Combustion," 4th China-Japan Fluid Bed Symposium, 1991). On the surface, these data do not appear to support the importance of your mechanism in practical systems. Could you comment on the role of your mechanism for N_2O formation in fluidized beds, and on the broader issues of homogeneous vs heterogeneous formation?

Author's Reply. In a practical bed, a large number of the nitrogen oxides produced by the particles are destroyed later by carbon and bed material. It is, therefore, difficult to draw any inferences on the formation mechanism from experiments such as those of Moritomi and Suzuki. The char nitrogen we believe must be released by the mechanism we propose although the net emissions will be governed by the destruction mechanism. No simple answer can be given on the role of volatiles in a practical bed since it is complicated by the extent to which combustion occurs in the bed, bubbles, or the freeboard and the volatiles can reduce the nitrogen oxides as well as contribute to their formation [see, e.g., Amand, L. E., and Leckner, B., *Twenty-Third Symposium (International) on Combustion*, The Combustion Institute, Pittsburgh, 1990, pp. 927–933]. For single particles, the role of volatiles can be established, and they contribute less to the formation of NO and N_2O than does the char [1].

•

Jari Stenberg, Tampere University of Technology, Finland. In your paper, you estimated the temperature of a burning char particle of ~1-mm diameter to be 5 °C–30 °C above bed temperature when $[O_2]$ is between 5 and 12%. According to pyrometric measurements that we have made, the temperature rise would rather be 50 °C–150 °C under these conditions. Do you have some comment on this?

Author's Reply. The temperature difference between a coal particle and the bed is a complicated function of both inert and active (coal) particle sizes, fluidizing velocity, difference of active and inert particle densities, residence time of the active particle in the bubble and the emulsion phases, and bed temperature. In our experiments, the inert and active particle sizes were 212 μm and 2 mm (on average), respectively. Modeling results based on the work of Agarwal, P. K., [*Twenty-Second Symposium (International) on Combustion*, The Combustion Institute, Pittsburgh, 1988, pp. 279–286] show that this difference at a bed temperature of 750 °C and 2% oxygen concentration is 5 °C and 35 °C for 12% oxygen in the feed. As the inert and active particle sizes increase (much higher than our experiments), the temperature difference also increases and may be as high as 100 °C–300 °C [see, e.g., Linjewile, T. M., and Agarwal, P. K., *Twenty-Third Symposium (International) on Combustion*, The Combustion Institute, Pittsburgh, 1990, pp. 917–925]. Possibly the differences between the bed particle sizes and fluidization velocity in the experiments you report and those in our laboratory are responsible for the differences in the observed temperature difference.

•

Jürgen Warnatz, Stuttgart University, ITV, Germany. Your way to determine rate parameters by inverse optimization looks very optimistic to me. What you are looking for are global minima, but what you are finding are local minima. Could you comment on that?

Author's Reply. The minimization exercise was aimed at finding the best estimates of the kinetic parameters. In or-

der to achieve this aim, the reported values in the literature for these parameters were taken as initial guess and a point of minima was obtained. This point was perturbed and again used as an initial guess for the minimization exercise. This step was iterated until the initial point converged to the optimal estimates. Secondly, the span of search for optimal parameters included the entire feasible domain of kinetic parameters. On further broadening the domain, the optimal rate parameters were found to be infeasible (either very high or very low activation energies). Therefore, the domain of search was also kept optimal for the search of the parameters. To countercheck that the rate constants calculated were indeed the optimal ones, the conversion data were subjected to fractional factorial design studies. In these studies, the search parameters were normalized over small domains to lie between -1 and 1. The value of the objective function was then calculated for each parameter at its extreme values of -1 and 1. A second-order polynomial was then fitted through the values of the objective function, and its point of minima was calculated analytically. This exercise was repeated over the entire domain of search and the parameters thus calculated were compared with the ones obtained using the optimizer. It is not necessary that we look for the global minima but the best minima in the domain of search. The global minima may lie outside the practical domain and hence may not be of any significance. Further details of the optimization exercise may be found in Ref. 3.

•

Robert Hurt, Sandia National Laboratories, USA. 1. Have you performed sensitivity analyses to see if each of your model parameters can be accurately determined by your approach? Are additional separate experiments necessary to uniquely define some of the kinetic constants?

2. What value for the effective diffusivity does your optimization routine yield, and is it determined with sufficient accuracy (i.e., is the model prediction sufficiently sensitive to diffusivity) to allow you to attach a physical interpretation to it? If so, what pore classes and diffusional processes govern here?

Author's Reply. 1. The rate constants were calculated for five global reactions representing the formation of CO and CO_2, and formation and destruction of NO and N_2O. These reactions are indeed necessary to represent the entire mechanism. A study on the sensitivity analyses done for these reactions is reported in Ref. 3. Separate experiments like the ones to calculate the rate constants for NO and N_2O destruction reactions can be done separately. Moreover, further experiments are required to determine the rate constants of the elementary reactions of the mechanism. The minimization exercise can then be performed to calculate the rate constants.

2. The effective diffusivity D_p was calculated to lie between 10^{-5} and 10^{-6} m²/s. The term D_p determines Bi_{mt} which, in turn, determines the external mass transfer rates. Since the surface boundary condition for the model is based on external mass transfer, the model predictions are very sensitive to effective diffusivity. The calculated value of D_p corresponds to Knudsen diffusion in mesopores.

•

Stephen Niksa, SRI International, USA. How many parameters were adjusted freely in your minimization, and how many were specified from reports in the literature? Are the assigned magnitudes consistent with expected values?

Author's Reply. The kinetic parameters were estimated for global reactions of char oxidation, CO oxidation, NO destruction on char and by CO on the char surface, and N_2O destruction. All of these rate constants were estimated in the minimization exercise, and none were specified from literature. The values of the activation energies for different reactions are given in Table 2 and are compared with the values reported in literature. The comparison shows that the activation energies for different chars are in close agreement.

Twenty-Fifth Symposium (International) on Combustion/The Combustion Institute, 1994/pp. 1061–1073

INVITED LECTURE

TRANSITION AND STRUCTURE OF JET DIFFUSION FLAMES

TADAO TAKENO
Department of Mechanical Engineering
Nagoya University
Chikusa-ku, Nagoya, 464-01, Japan

The transition behavior from laminar to turbulent flames of fuel jet diffusion flames, observed experimentally, is described and compared with the behavior of unignited cold jets. The transition is caused by Kelvin–Helmholtz instability of the jet flow, and the mechanism is essentially the same as that which causes transition of cold jets. The effects of the flame on this mechanism are discussed. Next, the successful application of a numerical experiment, combined with the flame surface model, to reveal the significant roles played by the density change and the increase in transport coefficients in the flame is described. The concept has been applied further to understand the flame structure in the transitional region from laminar to turbulent jet diffusion flames, where large-scale vortex motion dominates the mixing process and the laminar flamelet concept can be applied safely. Finally, numerical modeling of interactions between flow fields and chemical reactions in turbulent diffusion flames in the laminar flamelet regime is discussed. It is shown that the concept of local scalar dissipation rate, combined with a flame surface model, is very useful for numerical modeling of the interactions.

Introduction

The diffusion flame between a fuel jet and a coflowing air stream is an important flame of fundamental and practical interest and has been the subject of many investigations. Especially when the jet velocity is increased and the flow becomes turbulent, we have a turbulent jet diffusion flame, which is frequently used in industry. Understanding the structure of turbulent jet diffusion flame is a very popular subject of combustion research at present, and three excellent reviews of these studies have appeared in past Symposia [1–3]. One point common to these reviews is that they are all concerned with the fully developed turbulent flame, and they do not mention the transition problem from a laminar to a turbulent flame. However, this transition is very interesting, and understanding it provides clues about fully developed flame structure. This is the reason why transition characteristics, observed experimentally, are described in the first part of this review.

In the course of studies on transition, we have found that numerical experiments are effective for understanding the underlying physics of the phenomenon. We believe that the accuracy of numerical calculations has reached a level where the approach can be applied to combustion problems, and that this approach will be powerful for certain problems. Then, in the next part of this review, we shall describe how the approach has successfully been applied to understand transition behavior, and flame structure in the transitional region from laminar to turbulent of jet diffusion flames, where large-scale coherent structures dominate the mixing process and the concept of laminar flamelet model [1] can safely be applied. Finally, the discussion will be extended to numerical modeling of the interaction between flow fields and chemical reactions in turbulent flames. Modeling is another popular aspect of combustion, with many researchers concerned with developing appropriate models [4,5].

In the formation of pollutants such as NO_x and soot, chemical kinetics will play a significant role, and the description of the formation processes in turbulent reacting flow requires calculations based on detailed kinetics, on the one hand, and includes effects of fluctuating three-dimensional velocity, temperature, and concentration fields on the other. The simultaneous calculation of both these aspects is not feasible at present, so physical models are needed to separate the kinetics calculations from the fluctuation calculations. In the final part of the present review, one possible approach in this direction will be described.

Transition in Fuel Jet Diffusion Flame; Experimental Observation

Transition in Cold and Flame Jets:

The transition in fuel jet diffusion flames, as well as in unignited cold jets, was reported, and its practical importance was pointed out, in two early pioneering works [6,7]. Above a certain fuel injection velocity, there appeared along the flame a definite

point where a sudden breakdown of laminar flow occurred, and the flame became blurred downstream of this point. The flow and flame became turbulent downstream. On the basis of these findings, Scholefield and Garside [7], and later Gaydon and Wolfhard [8], suggested correctly that there might exist two turbulence-generating mechanisms: pipe flow turbulence inside the injector and the friction of fuel and air at the boundary of free jet. In general, the transition behavior depends crucially on the flow characteristics of pipe flow in the injector and of the coflowing air stream. In many cases, in practical burners in industry, or even in laboratory burners, the transition is masked by accompanying turbulent flows and is seldom observed. In addition, to observe the transition, the flame should be stable enough at the injector rim to sustain the flame up to a certain fuel injection velocity. Systematic studies on the transition are very limited, and some early and recent studies are reviewed, respectively, by Lewis and von Elbe [9], Gaydon and Wolfhard [8], and Chigier [10]. In a series of studies [11–14], we made careful experiments in which a low turbulence level was maintained within the pipe flow and the coflowing air stream, to study the transition mechanism by varying the type of fuel and the fuel injection velocity. A long narrow injector was used, and the transition behavior was studied as related to the pipe flow characteristics by using instantaneous (1 μs) schlieren pictures and high-speed–motion schlieren movies (10,000 pps). Some characteristic features of the transition of jet diffusion flames found from this work will be described in the following.

Hydrogen and acetylene flames were very stable, and we could sustain the flame up to very high injection velocities without any additional stabilization mechanisms. In the case of city gas (a mixture of H_2, CH_4, CO, and other gases), we used a heated coflowing air flow to stabilize the flame. The flame configuration depended on the injection Reynolds number $Re = \rho_o u_o d/\mu_o$, where ρ_o, u_o, d, and μ_o are fuel density, fuel injection velocity, injector diameter, and viscosity coefficient of fuel, respectively. Figure 1 compares the instantaneous schlieren picture of the ignited hydrogen flame jet with that of the unignited cold jet for $Re = 1074$. The flame jet is laminar through the whole flow field, whereas there exists a transition point along the cold jet, and downstream of this point, the flow becomes turbulent. As Re was increased, the transition point in the cold jet moved upstream, and it appeared along the flame jet as well. Then the flame took the characteristic configuration comprised of the upstream slender laminar flame and the downstream blurred turbulent flame. An example of this configuration for the city gas flame is shown in Fig. 2. Hydrogen flames were difficult to photograph, and Fig. 3 shows a schlieren picture of this configuration of hydrogen flame for $Re = 1345$. A sinusoidal small-scale fluctuation is observed at the transition point in the jet very near the axis, whereas large-scale fluctuations are observed outside the flame.

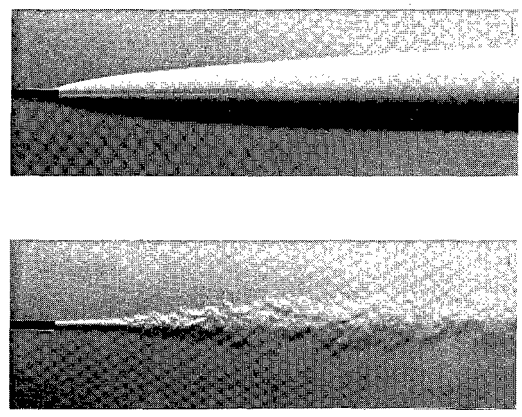

FIG. 1. Instantaneous schlieren pictures of a hydrogen flame jet and a cold jet for $Re = 1074$, $u_o = 106$ m/s.

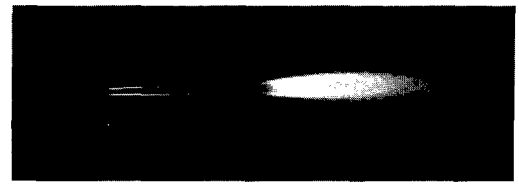

FIG. 2. City gas jet flame with a characteristic configuration comprised of an upstream slender laminar flame and a downstream blurred turbulent flame.

FIG. 3. Instantaneous schlieren picture of a hydrogen flame jet for $Re = 1345$, $u_o = 133$ m/s.

When Re was increased further, the transition point in the flame jet, as well as in the cold jet, moved upstream, as shown in Fig. 4. In the figure, the transition length X_L from the injector exit to the transition point, observed in the schlieren pictures and made nondimensional by d, is plotted against Re for both the hydrogen flames and the cold jets. When Re reached the critical value of 1950, where pipe flow inside the injector entered into the transition region, intermittent flow fluctuations begin to be ejected into the jet from the injector. Then the transition point

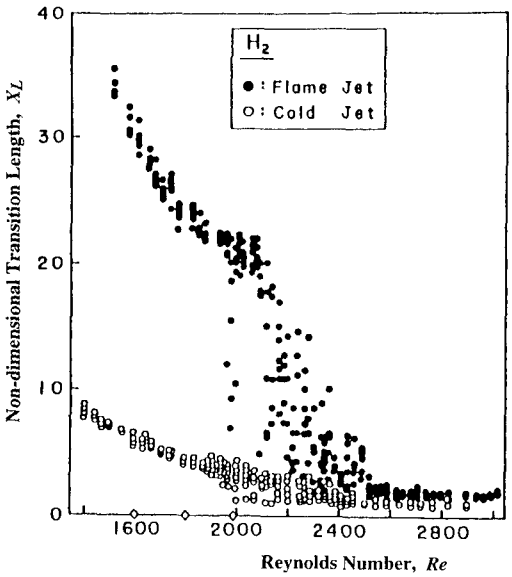

FIG. 4. Nondimensional transition length of hydrogen flames and cold jets.

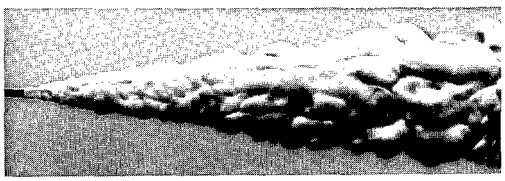

FIG. 5. Instantaneous schlieren picture of a fully turbulent hydrogen flame jet for $Re = 3016$, $u_o = 299$ m/s.

in the flame began to shift back and forth, in accordance with the ejection of fluctuations, and the transition length depended on the instant when the schlieren picture was taken. As Re was increased further, the frequency of the shift, and hence the fraction of time when the transition point is located at the upstream position, increased. Finally, when Re reached 2500, the pipe flow now entered into the fully developed turbulent region, the shift occurred almost continuously, and the transition point was always located at the upstream position. Then it would not move for a further increase of Re. The flame became fully turbulent, and the whole flame was blurred except the small portion immediate downstream of the injector exit. A typical schlieren picture of this state is shown in Fig. 5.

Acetylene flames did not take the characteristic configuration, comprised of the upstream laminar and downstream turbulent flames, when Re was smaller than the critical value of 1950. The transition point appeared in the cold jet, but the whole flame and flow remained laminar in the flame jet. This

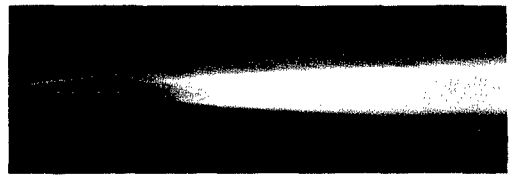

FIG. 6. Instantaneous schlieren picture of a fully turbulent acetylene flame jet with superimposed direct images of a luminous flame for $Re = 3479$ and $u_o = 31.3$ m/s.

makes a sharp contrast to hydrogen and city gas flames, and the difference can be explained in terms of a large increase in kinematic viscosity in the flame [13]. When Re reached 1950, the flame became turbulent suddenly, and the whole flame began to fluctuate incessantly. Figure 6 shows a typical schlieren picture of the fully developed turbulent flame with superimposed direct images of luminous flame. It is interesting to note that the luminous flame is turbulent with rather large-scale fluctuations, in contrast to the original small-scale fluctuations ejected from the injector.

Effects of Flame on Transition:

The above-described recent experimental studies have confirmed the old suggestion of two distinct transition mechanisms: hydrodynamic instability of the fuel jet very near the axis and pipe flow turbulence inside the fuel injector. The latter mechanism is easy to understand, and the transition can be predicted in terms of Re. On the other hand, the transition by the former mechanism is rather complicated, and now we shall concentrate on this mechanism. This is essentially the same as that which causes transition in cold jets and is called Kelvin–Helmholtz instability of the jet velocity distribution. The physics of this instability is clear, yet no theory has successfully been developed so far to predict the transition point. The presence of the flame further complicates the phenomenon. The above-described experimental observations, and those by other investigators [15–18], have shown that the transition is delayed remarkably by the presence of the flame. Then one problem to be solved is the question of how the flame delays the transition. Another experimental observation is that there are two types of fluctuations in the flame jet: a small-scale sinusoidal fluctuation near the jet axis and a large-scale fluctuation outside the flame. The former fluctuation is caused by Kelvin–Helmholtz instability. The second problem to solve is to determine the origin of the outer fluctuation. We [12–14] and Takahashi et al. [16] suggested that the outer fluctuation is triggered by the internal one and they are of the same origin. However, there were some arguments [15,17,18] that the outer fluc-

tuation is caused by mechanisms other than Kelvin–Helmholtz instability.

One suggestion was that fluctuation can be attributed to another hydrodynamic instability that develops in the interfacial zone between the hot combustion gas and the surrounding air [18]. This makes the argument somewhat confusing. It has long been known [9] that, in any vertical jet diffusion flame with slow fuel injection velocity, the buoyancy induces a low-frequency instability at the interface, which causes flame flickering. The most familiar example is the flickering of a candle flame. Recent experimental and numerical studies have shown that this is, in fact, the case [19–21]. The fluctuation at issue is observed for jets having high injection velocity in horizontal flow configurations, and has nothing to do with this buoyancy-driven instability. Are there any new instability mechanisms other than this instability and Kelvin–Helmholtz instability? This is the second question, and we have to answer these two questions.

Transition in Jet Diffusion Flames; Numerical Experiment

Numerical Approach:

In order to answer these questions, we have to know details of velocity, temperature, and concentration fields in the very narrow region just downstream of the injector rim. In addition, we want to know, if possible, the separate effects of the various parameters on these fields. An experimental approach would be very difficult, and the fields are too complicated for a theoretical analysis such as linear stability theory [22]. This suggests a numerical approach. It has been stressed in our experimental studies that the structure of the laminar portion of the flame is suitably described in terms of a flame surface model of infinite reaction rate. In addition, in the transition problem, the direct effect of chemical reactions on the flow instability is not important. It is the resulting variations of density and transport properties that are expected to play a decisive role in the flow-stabilizing effect. This can well be studied in terms of the flame surface model, provided the temperature dependence of the density and transport coefficients is fully taken into account [12–14]. We can study the transition problem by adopting this model without being involved in the complicated chemical reaction mechanisms. In addition, the Lewis number may be assumed unity to make full use of Shvab–Zeldovich formulation of the conserved scalar, z [23].

In our numerical study [24], the transition from a laminar to a turbulent flame within a plane two-dimensional fuel jet is studied in terms of a flame surface model. The fuel selected was methane, and the value, z^*, of conserved scalar at the flame surface, given by the following equation, is 0.05504.

$$z^* = Y_{O,\infty}/(jY_{F,O} + Y_{O,\infty}) \tag{1}$$

where $Y_{O,\infty}$ and $Y_{F,O}$ are mass fractions of oxygen in coflowing air stream and of fuel in the fuel jet, respectively. The term j is the mass of oxygen required to burn a unit mass of fuel completely. The air and fuel are at room temperature, $T_O = T_\infty = 300$ K. The adiabatic flame temperature is $T^* = 2225.9$ K, and the resulting nondimensional flame temperature $\theta^* = T^*/T_O = 7.419$. The time-dependent Navier–Stokes equations for a variable density, with the equation for the conserved scalar, were solved numerically using a finite-difference method in order to study the time-dependent flame surface behavior. The temperature dependence of the transport coefficients was taken into account, and the results were compared with results for constant transport coefficients, to study the effect of property variation on the flame surface behavior. The approach may appear to be somewhat different from usual numerical calculations. We did not intend to simulate exactly or to reproduce, we should say, the actual phenomenon. We only tried to find out the underlying physics by making a numerical experiment. That is, if the calculation is accurate enough to reproduce the essential features of the real phenomenon, then we can make use of the calculation to understand the underlying physics. A two-dimensional calculation was made, in spite of the fact that actually there are no two-dimensional jets, since we believe that the underlying physics should remain the same for planar and axisymmetric jet flames. We adopted some unrealistic assumptions concerning the transport coefficients in order to clarify their individual effects. Once we admit this concept of numerical experiment, we will find several advantages over actual experiments, since we can very easily control the respective parameters involved.

Some examples of the calculated results will be described in the following. Figure 7 compares the instantaneous temperature distribution with the time-averaged distribution for $Re = 2000$. Each color represents the value of the non-dimensional temperature explained in the scales below each figure. The flame takes a familiar configuration comprised of a upstream laminar and downstream turbulent flame. In the laminar portion, the cold fuel jet in blue is on the axis and is surrounded by the hot burned gas produced by the flame surface. It should be noted that the temperature gradient is steep in the outward direction, but is quite gradual in the inward direction, which produces thick high-temperature strips. The instantaneous distribution shows that a small-scale sinusoidal fluctuation of the fuel jet appears at the coldest temperature (blue color) on the axis, and develops into a large-scale eddy motion

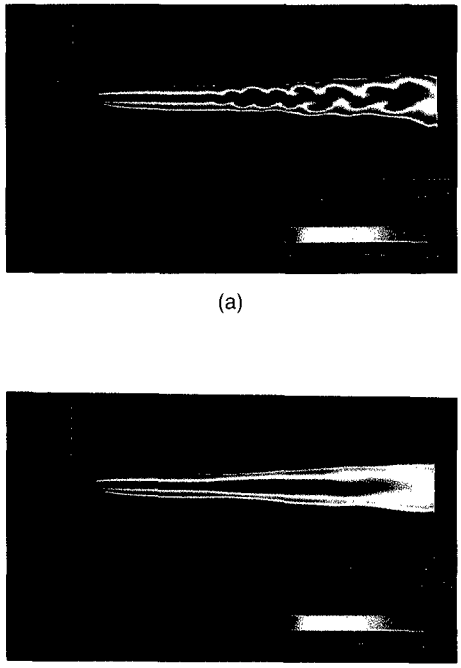

FIG. 7. Comparison of (a) instantaneous and (b) time-averaged temperature distributions for $Re = 2000$.

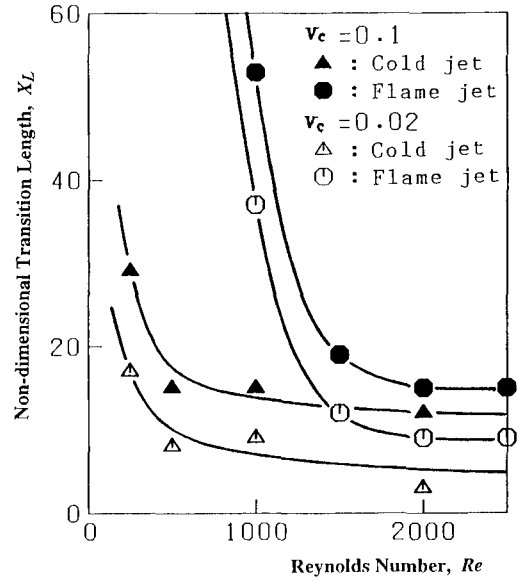

FIG. 8. Calculated dependence of transition length on Reynolds number: comparison of cold jets and flame jets.

downstream. The outer large-scale fluctuation, on the other hand, starts downstream of the incipient point of the inner fluctuation and merges with it to produce large-scale eddy motion along the flame surface downstream. In the time-averaged distribution, the points of incipient instability for the inner and outer fluctuations are more apparent, since the distributions start to diverge at these points. In the downstream turbulent region, the averaged flame temperature becomes lower than the adiabatic flame temperature because of mixing with the cold air. It is interesting to note that the time-averaged flame surface shrinks and then diverges again at the outer transition point because of the sudden increase in radial transport of heats and mass. This behavior corresponds well to experimental observations using direct photography [11,12].

The numerical calculation described above made it possible to define the transition length, and to compare this length for the flame jet and the cold jet. The calculation revealed that the quantity most sensitive to fluctuations is the transverse velocity, and then we introduced a probability density function (PDF), which represents the number of times that the nondimensional transverse velocity v exceeds a certain critical value v_c along the axial distance for constant transverse distance [24]. The transition point was defined as the point where the PDF starts to increase on the axis. Figure 8 shows the calculated dependence of the nondimensional transition length on Reynolds number, Re. For the purpose of comparison, results for the two cases when v_c was taken to be 0.02 and 0.1 are shown. Although the curve is shifted with the critical values, the qualitative behavior correlates quite well with the experimental observations shown in Fig. 4. The transition in the jet is delayed by the presence of the flame. The above-described results of the calculations correlate with the experimentally observed flame behavior, and now we believe that the numerical calculation is accurate enough to reproduce the transition phenomenon. Therefore, we can make use of the calculation to carry out numerical experiments to answer the two questions mentioned before.

Origin of Large-Scale Fluctuations:

The first question is, what is the origin of the large-scale fluctuation outside the flame. To answer this question, another PDF was introduced to represent the number of times the flame surface is situated at a particular position. Figure 9(a) is an illustration of the color representation of this PDF, which shows that, at nondimensional axial distance $x = 22$, the PDF begins to widen to represent incipient flame fluctuations. On the other hand, Fig. 9(b) shows the root-mean-square (rms) of the transverse velocity. The upstream end of the blue color region represents the transition point of the inner fluctuation, and this region begins to widen downstream, suggesting that the inner fluctuation is transferred outward. Figure

9(c) is the superposition of (a) and (b), and shows clearly how the flame surface begins to fluctuate when the inner velocity fluctuation reaches the flame surface at $x = 22$. This suggests that the outer flame fluctuation is eventually induced by an instability originating on the axis as a result of Kelvin–Helmholtz instability. That is, the small-scale fluctuation near the jet axis and the large-scale fluctuation outside the flame are of the same origin.

Effects of Variable Density and Transport Coefficients:

The second question is, how does flame delay the transition? In order to study the effects of variable density and transport coefficients, calculations were done for the following six cases, and comparison was made of the flow stability: (A) fuel to fuel jet, no density and temperature distributions, constant transport properties; (B) frozen jet, density distribution due to mixing, constant transport properties; (C) normal flame jet, density, and temperature distributions, increase in viscosity and diffusion coefficients; (D) hypothetical flame jet, density, and temperature distributions, constant viscosity coefficient; (E) hypothetical flame jet, density, and temperature distributions, constant diffusion coefficient; and (F) hypothetical flame jet, density, and temperature distributions, constant viscosity and diffusion coefficients. The results showed that the flow is stable in the order of C, D, A, B, E, and F. That is, the normal flame jet is most stable. Figure 10 shows the transverse distributions of mass fraction of species i, nondimensional density, temperature, diffusion coefficient, viscosity, kinematic viscosity, axial and transverse velocities at the upstream laminar portion ($x = 10.7$) of the normal flame jet. The flame surface is located at the position where $Y_F = Y_O = 0$, and θ becomes maximum. There are four characteristic features to be noted: as follows. (1) At the flame surface, the temperature gradient is steep in the outward direction and gradual in the inward direction. (2) The transport coefficients become very large at the flame surface. (3) Thick viscous layers are produced just inside the flame surface. (4) The flame surface is located outside the axial velocity distribution.

The thick viscous layer of (3) is the result of (1) and (2), and the shift of flame surface outside the shear layer is the result of increases in the diffusion coefficient. In this way, we notice that the increase in transport coefficients has profound effects on transverse distributions. The comparison of the transverse distributions and the degree of flow stability of six cases has brought about the following three conclusions. (i) Jet flow of lower density is more unstable, and hence, the large density decrease in the flame tends to make the jet unstable if there are no additional stabilization mechanisms. (ii) The increase in viscosity has a considerable stabilizing effect, but is not very significant as long as the highly viscous layer remains thin. (iii) The increase in diffusion coefficient has a most important stabilizing effect through the shift of flame outside the shear layer and the production of a thick viscous layer. The last two stabilizing mechanisms will be especially important in most hydrocarbon flames in which j is large and z° is very small. Large j will decrease the inner temperature gradient at the flame surface and thus contribute to produce a thick viscous layer, while small z° will locate the flame surface at the outer edge of the shear layer so that it is more readily affected by such influences.

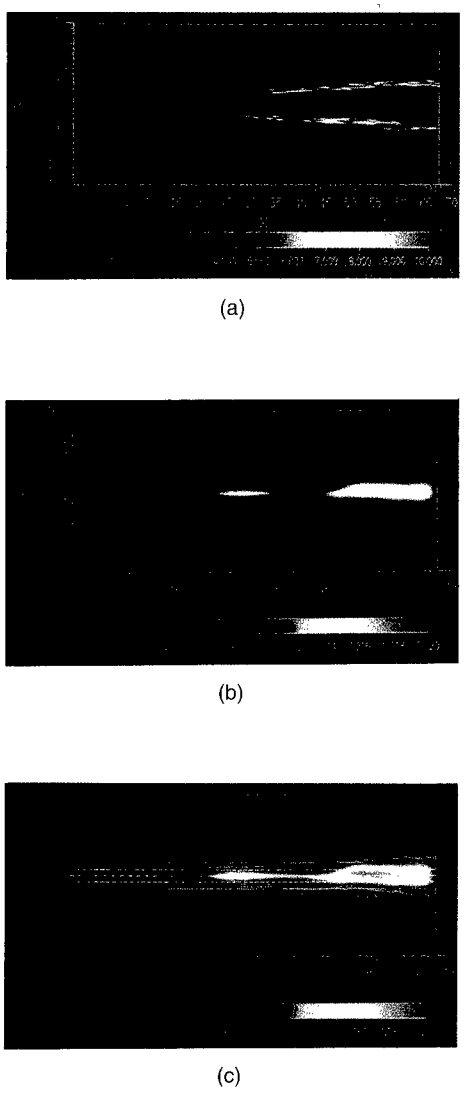

FIG. 9. Relation between (a) flame surface PDF and (b) root-mean-square transverse velocity for $Re = 2000$. (c) shows superposition of (a) and (b).

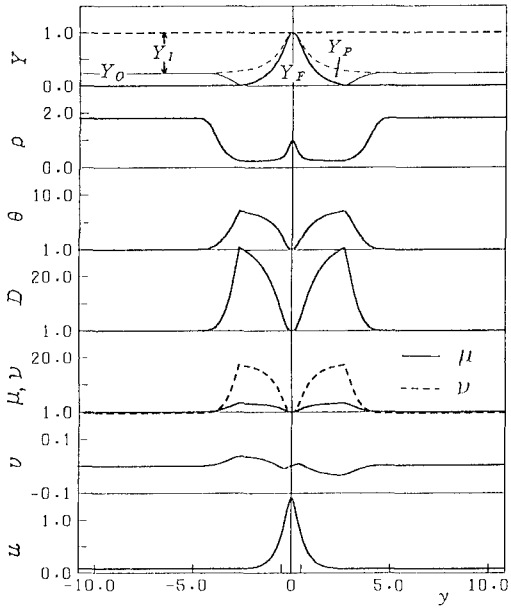

FIG. 10. Transverse distributions of mass fractions Y_i, nondimensional density ρ, temperature θ, diffusion coefficient D, viscosity coefficient μ, kinematic viscosity ν, transverse velocity v, and axial velocity u for $Re = 2000$ at a nondimensional axial distance of $x = 10.7$.

Effects of Fuel Properties:

Further numerical experiments were conducted to study the effects of fuel properties on transition [25,26]. When fuel is changed in usual experiments, properties such as density, transport coefficients, adiabatic flame temperature θ°, and j change simultaneously, and it is difficult to distinguish the respective effects of these properties. In the numerical experiment, on the other hand, the parametric study can easily be done to study the separate effects of each of these properties. This study has revealed that an increase in θ° contributes to suppression of the instability through an increase of the viscosity. One interesting finding was the effect of z° given by Eq. (1). This quantity depends not only on fuel properties but also on the dilution of fuel and air, and is very important since the value determines the location of the flame surface relative to the axial velocity distribution. In a case where pure methane is injected into a coflowing air stream, z° is as small as 0.05504, and in this case, the flame surface is situated outside the shear layer of jet velocity distribution, as seen in Fig. 10. What happens if the flame surface is located inside the shear layer? As z° is increased for a constant flame temperature θ°, the flow was found to become more stable. This occurs because the highly viscous layer is located just at the very position where the axial velocity is changing. That is, the suppressing ability of the viscous layer becomes more powerful as the layer moves into the shear layer.

In the past, there has been some confusion about the explanation of flame-stabilizing effects. This can be attributed to the complex combination of the above-described stabilizing and unstabilizing effects. The numerical experiment has shown very clearly the respective contributions of these effects, and the importance of the increases in viscosity and diffusion coefficients. Although the finding is based on results for a specific case, the implications seem quite plausible and universally important.

Flame Structure in Transitional Region

Gasdynamic Aspects of Heat Release:

The modeling of turbulent reacting flow is a very popular subject, and most models are concerned with how to describe the effects of finite-rate chemistry [4,5]. However, it seems that some important aspects of gasdynamics associated with heat release in turbulent flows have not been properly understood as yet. The above-described approach using numerical experiment in terms of a flame surface model can easily be extended to study these aspects of the transitional region of jet diffusion flames, without being involved with the complicated interactions between reactions and turbulence. In addition, we can study the behavior of large-scale coherent structures in two-dimensional flow calculations, since they remain two-dimensional in the transitional region. The small-scale three-dimensional turbulence may modify their evolution process, but will not alter their essential characteristics [30]. In general, the heat release will affect the flow field through a reduction in the density, and an increase in the transport coefficients, due to the temperature increase. In the following, some results of the numerical experiments [25–29] on the effects of heat release will be described.

Effects of Decreased Density:

It has been found that the density reduction has no remarkable effect on the axial velocity distribution in the laminar portion of the flame jet [24,29]. The flame jet is a free jet, in which the pressure remains almost constant through the whole flow field. Only the transverse velocity toward the jet axis is accelerated because of the entrainment of coflowing air into the jet. The smaller density is favorable for increasing the entrainment [29]. In the downstream transitional region of the flame, on the other hand, the reduced density tends to suppress the lateral expansion of the induced fluctuating flame surface. This is because the momentum of transverse velocity fluctuation becomes relatively small as compared with the momen-

tum of the coflowing air stream, which makes it difficult for the fluctuation to expand laterally [28]. That is, the blurred turbulent flame width becomes smaller than might have been expected from the lateral expansion of the cold jet.

Effects of Increased Viscosity:

The time-dependent flame surface behavior in the transitional region is closely related to the transverse velocity fluctuations [24]. It has been found that, at any instant, most of the velocity fluctuations are confined inside the instantaneous flame surface, although some small fluctuations survive outside the flame surface [28]. In other words, the velocity fluctuations disappear quickly as they approach the flame surface and enter the highly viscous layer. Since the flame surface is always located at the outer edge of the distribution of the conserved scalar, z, this suggests that its lateral movement is mostly determined by the transverse velocity fluctuation. That is, the transverse velocity fluctuation is mostly responsible for fuel transport to the flame surface, and the flame surface is always located at the outer edge of the velocity fluctuation. Another effect of the increased viscosity in the viscous layer, just inside the flame surface, is to suppress the development of the amplitude of flame surface fluctuations. That is, the amplitude of fluctuations would diverge quickly if there were no such highly viscous layers, and it is much smaller than might have been expected from the behavior of the corresponding cold jet [28].

Breakoff of Flame Surface:

Another interesting finding was the behavior of the flame at the downstream end, or the flame tip. In the present numerical experiment, the computational domain is restricted to the upstream portion of the turbulent flame. This is the reason why we use the expression "transitional region," and we do not mention the fully developed turbulent flame structure farther downstream. When pure fuel is injected, the flame length becomes much longer than the downstream end of the computational domain, and we cannot study the flame tip behavior. However, if the injected fuel is diluted by an inert gas, z° becomes larger and the flame tip shifts upstream. When methane is diluted by a hypothetical inert gas of the same molecular weight up to $Y_{F,O} = 0.1$, z° becomes as large as 0.36809. The adiabatic flame temperature θ° is decreased to 5.292. Figure 11 shows the instantaneous distribution of the conserved scalar z for $Re = 2000$. The instantaneous flame surface is superimposed and is shown by white lines. As is seen in the figure, the flame surface is pinched off at the tip to produce several flame islands. The details of the process leading to this pinched-off behavior are shown in Fig. 12, in which the instantaneous local velocity

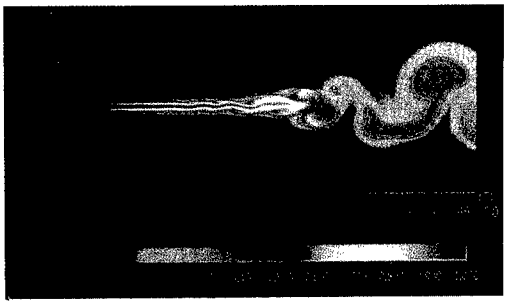

FIG. 11. Instantaneous distribution of conserved scalar for $Re = 2000$ with a white line superimposed upon the flame surface.

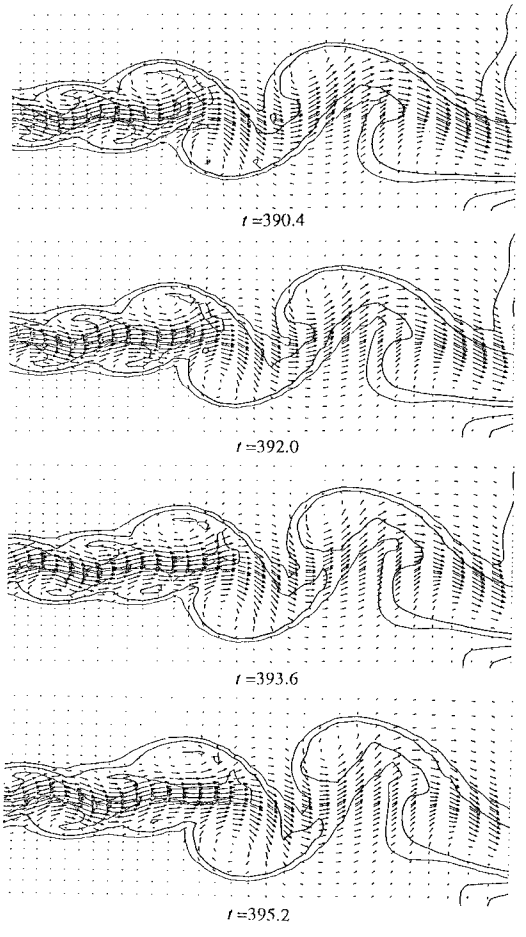

FIG. 12. Instantaneous local velocity vector and flame surface z° with $0.5z^\circ$ and $2.0z^\circ$ contours.

vector, relative to the outer uniform air flow, and the flame surface z^*, with $0.5z^*$ and $2.0z^*$ contours, are shown with a nondimensional time interval of 1.6. The dimensional time t^* is made nondimensional by d/u_o. This is the same phenomenon as the one observed before for the oscillating flame [27]. Since we have assumed an infinite reaction rate, the breakoff of the flame surface at $t = 393.6$ has nothing to do with finite-rate chemistry. This is caused as a result of fuel shortage in the vicinity of the flame surface at the instant when a large amount of air is entrained by large-scale vortex motions. In the vicinity of the flame tip, the concentration gradient of fuel is very small, and hence, the supply of fuel to the flame surface by molecular diffusion is very slow. If the air entrainment is rapid enough, the convective air flow is faster than the molecular diffusion, which produces a point along the flame surface where no fuels are present momentarily, leading to the breakoff of the flame surface.

Although the above-described flame tip behavior is observed for the rather special case of large fuel dilution, there is a fair chance that similar breakoff should occur even at the flame tip of the undiluted normal flame. The fuel concentration gradient becomes very small in the same way, and the flame surface is very likely to be affected by large-scale convective air motions. Of course, whether or not the fully developed turbulent flame structure in the downstream region is in the laminar flamelet regime would be controversial. We believe, however, that the above explanation seems very plausible and universally applicable. Even when the structure is not in the laminar flamelet regime, this process will actually happen, and some of the local interruptions and extinctions of OH and CH distributions observed experimentally [31] may be explained by this mechanism, and are not caused by finite-rate chemistry.

Interaction between Flow Fields and Chemical Reactions in the Laminar Flamelet Regime

Introduction of Physical Model:

The computational work needed for the numerical experiment described above is not so large and can be handled very easily by any common large computer. The approach seems very successful for understanding the gasdynamic aspects of fuel jet diffusion flames in the transitional region, as well as in the laminar region. However, it should be remembered that any turbulence models are not included in the approach, and that it is based on the extremely simplified assumption of infinite reaction rate. If we want to describe the flame behavior in which three-dimensional turbulence plays a significant role, then the calculation required for direct numerical simulation becomes too large to be handled even by most sophisticated supercomputers [3,32]. In addition, if we want to include the detailed kinetics, the computational work becomes so enormous that implementing the calculation is out of the question. This is the reason why we need to develop a physical model to make the numerical calculation actually possible. There are many models proposed at present, and excellent reviews of these models are given by Williams [4]. In the following, we shall describe the model developed in our studies.

Effects of Chemical Reactions on the Flow Field:

The key to success of the model is how to separate the kinetics calculation from the flow calculation. In the following, we shall concentrate on the turbulent diffusion flame in the laminar flamelet regime [33–35]. We shall consider how to describe the interaction between the flow field and chemical reactions in this regime. In the beginning, we have to consider how to describe the effects of chemical reactions on the flow field. The respective elementary reactions themselves are not important for the local flow field, and what is important is the resultant heat release and the density change produced through it. That is, the reactions will affect local flow field only through the density change. In the laminar flamelet regime, most chemical reactions are concentrated in a rather narrow high-temperature region, and the heat is released only in this narrow region. In general, the width of this zone is smaller than the representative scale of flow fluctuations, and therefore, the density change produced can be predicted well in terms of the flame surface model with simplified one-step kinetics. Then the time-dependent flow field can be predicted by solving the Navier–Stokes equation with variable density, simultaneously with the equation of conserved scalar, in the same way as described above.

Effects of Local Flow Field on Chemical Reactions:

The next problem is how to describe the effects of the local flow field on chemical reactions in the thin reaction zone. The asymptotic analysis predicts that, in the species conservation equation, the contribution of the convective term is not important in this thin zone, and the chemical reaction must be balanced by the molecular diffusion [23]. Figure 13 shows the contribution of the respective terms in the thin reaction zone, compared to contributions in the outer diffusion layer. The available reaction time for the reaction in the zone is determined by the characteristic diffusion time in this zone. In the outer diffusion layer, on the other hand, there are no chemical reactions, and the molecular diffusion is balanced by convection. Hence, the local flow field affects the concentration distribution. Since the concentration must be continuous at the boundary, the distribution in the outer layer will mostly determine the charac-

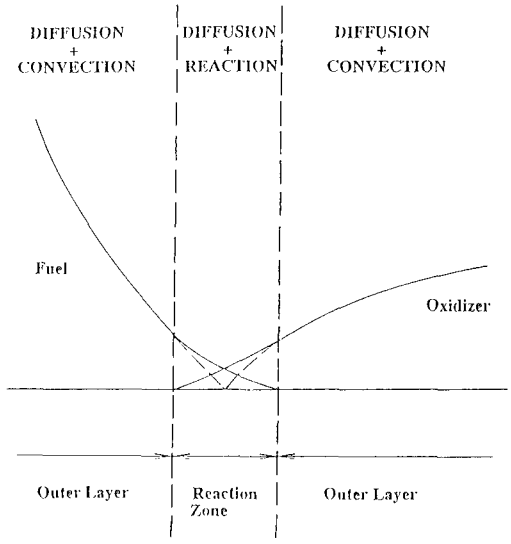

FIG. 13. Contribution of respective terms in the thin reaction zone and in the outer diffusion layer.

teristic molecular diffusion time in the thin reaction zone. In this way, the local flow field affects the reactions in the thin reaction zone through the characteristic diffusion time. The latter, in turn, may be evaluated in terms of the local scalar dissipation rate [23] at the thin reaction zone.

Prediction of NO Emission Index of Turbulent Diffusion Flame:

On the basis of these considerations, we have developed a numerical method to predict the emission index of NO for turbulent diffusion flames [33–35]. The procedure for the actual calculation is as follows. First, we calculate the emission index of a counterflow laminar diffusion flame as a function of velocity gradient by using detailed kinetics of large mechanism [36]. It should be remembered that, within the thin reaction zone, the chemical reaction is balanced by only the molecular diffusion, and hence, the relation between the representative reaction time and molecular diffusion time is independent of flow field. Therefore, we can calculate the relation in any flow field, and we may do it in the counterflow flame, for which we can adopt a similarity solution to simplify the calculation. In the calculation, we can study the heat release rate distribution in the reaction zone. Usually, the distribution gives a sharp peak at a certain position, which we can define as the apparent flame surface position. On the other hand, we can introduce the conserved scalar in terms of nitrogen concentration and then obtain the scalar dissipation rate. Then we can evaluate the values of this scalar z_q and the scalar dissipation rate at the apparent

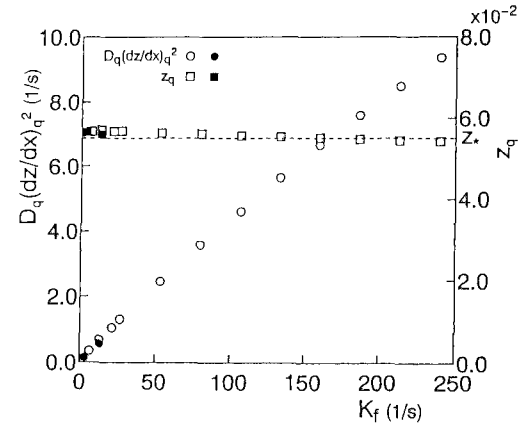

FIG. 14. Dependence of conserved scalar, z_q, and scalar dissipation rate, $D_q(dz/dx)_q^2$, at the apparent flame surface position, on the velocity gradient K_f in methane/air counterflow diffusion flames.

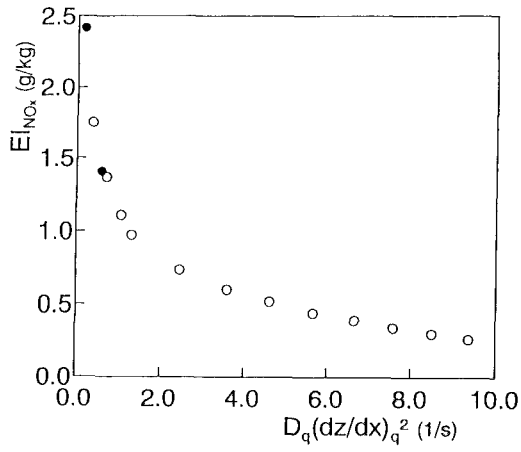

FIG. 15. Dependence of NO emission index on scalar dissipation rate, at an apparent flame surface position in a methane/air counterflow diffusion flame.

flame surface position. These values change with the velocity gradient, as shown in Fig. 14. It can be seen that z_q remains almost constant at a value nearly equal to $z^* = 0.05504$ calculated for simple one-step kinetics. On the other hand, the scalar dissipation rate increases almost linearly with the velocity gradient. This suggests that the characteristic diffusion time is almost proportional to the representative flow time. Figure 15 shows how the emission index decreases with the scalar dissipation rate.

The second step of the calculation is to make the jet flame calculation in terms of the flame surface model, in the same way as described in the transition problem. Then we can calculate the scalar dissipation

FIG. 16. Instantaneous distribution of scalar dissipation rate with a superimposed flame surface.

rate distribution at any instant and evaluate the rate at the flame surface. Figure 16 shows the instantaneous distribution with the instantaneous flame surface superimposed. The time ensemble of these distributions makes it possible to calculate the probability density function (PDF) of the rate at flame surface position. The combination of this PDF and the result shown in Fig. 15 makes it possible to obtain the average value of the emission index of the whole flame. The derived index was found to correlate rather satisfactorily with the experimental data obtained by Driscoll et al. [37].

We think that the above-described method is very useful for numerical modeling of interactions between flow fields and chemical reactions in turbulent diffusion flames in the laminar flamelet regime. The laminar flamelet model is popular as well in the modeling of premixed flames [4,5], and we hope that the same method can be applied to numerical modeling of turbulent premixed flames in this regime [38].

Conclusions

Combustion is a complicated phenomenon involving simultaneous chemical reactions, heat and mass transfer, and gaseous motion, and it is very difficult to elucidate scientifically the essential nature of the phenomenon. There are many parameters involved, and it is quite difficult to make experiments that control these parameters in order to find their separate effects. Numerical experiments, on the other hand, can very easily control the various parameters involved to identify their separate effects. We believe that the accuracy of numerical calculation has now reached the point where the essential features of some combustion phenomena can correctly be reproduced by calculations. Then the concept of numerical experiment is very effective, provided that it is accompanied by the appropriate physical models. Specifically, in the study of turbulent flames in the laminar flamelet regime, the combination of flame surface models and the local scalar dissipation rate at the flame surface provides a powerful means to understand, and hence to predict, flame behavior.

Acknowledgments

The present study was supported in part by Tanikawa Thermal Engineering Promotion Foundation and General Sekiyu Research and Development Foundation. The author would like to extend his sincere thanks to his former and present colleagues, and former graduate students, for their help in the present study. Special thanks go to Mr. Y. Kotani and Profs. H. Yamashita and G. Kushida for their contributions to the present study.

REFERENCES

1. Peters, N., *Twenty-First Symposium (International) on Combustion*, The Combustion Institute, Pittsburgh, 1986, pp. 1231–1250.
2. Bilger, R. G., *Twenty-Second Symposium (International) on Combustion*, The Combustion Institute, Pittsburgh, 1988, pp. 475–488.
3. Pope, S. B., *Twenty-Third Symposium (International) on Combustion*, The Combustion Institute, Pittsburgh, 1990, pp. 591–612.
4. Williams, F. A., in *Turbulence and Molecular Processes in Combustion* (T. Takeno, Ed.), Elsevier, Amsterdam, 1993, p. 1.
5. Libby, P. A., and Williams, F. A. (Eds.), *Turbulent Reacting Flows*, Academic Press, London, 1994, p. 1.
6. Hottel, H. C., and Hawthorne, W. R., *Third Symposium (International) on Combustion*, Williams & Wilkins, Baltimore, 1953, pp. 254–266.
7. Scholefield, D. A., and Garside, J. E., *Third Symposium (International) on Combustion*, Williams & Wilkins, Baltimore, 1953, pp. 102–110.
8. Gaydon, A. G., and Wolfhard, H. G., *Flames, Their Structure, Radiation and Temperature*, 3rd ed., Chapman and Hall, London, 1970, pp. 137–139.
9. Lewis, B., and von Elbe, G., *Combustion, Flames and Explosions of Gases*, 3rd ed., Academic Press, Orlando, 1987, pp. 479–488.
10. Chigier, N., *Energy, Combustion and Environment*, McGraw-Hill, New York, 1981, pp. 230–233.
11. Takeno, T., and Kotani, Y., *Combust. Sci. Technol.* 10:45–57 (1975).
12. Takeno, T., and Kotani, Y., *Acta Astronaut.* 2:999–1008 (1975).
13. Takeno, T., and Kotani, Y., *Progress in Astronautics and Aeronautics*, AIAA Inc., New York, 1978, Vol. 58, pp. 19–35.
14. Takeno, T., and Kotani, Y., *Acta Astronaut.* 6:1009–1010 (1979).
15. Yule, A. J., Chigier, N. A., Ralf, S., Boulderstone, R., and Ventura, J., *AIAA J.* 19:752–760 (1981).
16. Takahashi, F., Mizomoto, M. and Ikai, S., *Combust. Flame* 48:85–95 (1982).

17. Savas, O., and Gollahalli, S. R., *AIAA J.* 24:1137–1140 (1986).
18. Coats, C. M., and Zhao, H., *Twenty-Second Symposium (International) on Combustion*, The Combustion Institute, Pittsburgh, 1988, pp. 685–692.
19. Davis, R. W., Moore, E. F., Roquemore, W. M., Chen, L.-D., Vilimpoc, V., and Goss, L. P., *Combust. Flame* 83:263–270 (1991).
20. Ellzey, J. L., and Oran, E. S., *Twenty-Third Symposium (International) on Combustion*, The Combustion Institute, Pittsburgh, 1990, pp. 1635–1640.
21. Chen, L.-D., Vilimpoc, V., Goss, L. P., Davis, R. W., Moore, E. F., and Roquemore, W. M., *Twenty-Fourth Symposium (International) on Combustion*, The Combustion Institute, Pittsburgh, 1992, pp. 303–310.
22. Michalke, A., and Hermann, G., *J. Fluid Mech.* 53:343–359 (1982).
23. Williams, F. A., *Combustion Theory*, 2nd ed., Benjamin/Cummings, Menlo Park, CA, 1985, pp. 73–80.
24. Yamashita, H., Kushida, G., and Takeno, T., *Proc. R. Soc. London A* 431:301–314 (1990).
25. Idota, T., Yamashita, H., Kushida, G., and Takeno, T., "Numerical Simulation of Fuel Jet Diffusion Flame," *Thirtieth Japanese Symposium on Combustion*, 1992, pp. 430–432 (in Japanese).
26. Yamashita, H., Idota, T., and Takeno, T., "Effect of Fuel Properties on Transition of Fuel Jet Diffusion Flame," *The 70th JSME Spring Annual Meeting*, 1993, pp. 807–809, (in Japanese).
27. Yamashita, H., Kushida, G., and Takeno, T., *Progress in Astronautics and Aeronautics*, AIAA Inc., New York, 1991, Vol. 131, pp. 193–219.
28. Yamashita, H., Kushida, G., and Takeno, T., *Twenty-Fourth Symposium (International) on Combustion*, The Combustion Institute, Pittsburgh, 1992, pp. 311–316.
29. Yamashita, H., Kushida, G., and Takeno, T., "Flow Field of Fuel Jet Diffusion Flame," *Twenty-Eighth Japanese Symposium on Combustion*, 1990, pp. 40–42, (in Japanese).
30. Fedorchenko, A. T., *Sov. Phys. Dokl.* 33:717–721 (1988).
31. Starner, S. H., Bilger, R. W., Dibble, R. W., Barlow, R. S., Fourguette, D. C., and Long, M. B., *Twenty-Fourth Symposium (International) on Combustion*, The Combustion Institute, Pittsburgh, 1992, pp. 341–349.
32. Oran, E. S., and Boris, J. P., *Numerical Simulation of Reactive Flow*, Elsevier, New York, 1987, pp. 455–476.
33. Takeno, T., Nishioka, M., and Yamashita, H., in *Turbulence and Molecular Processes in Combustion* (T. Takeno, Ed.), Elsevier, Amsterdam, 1993, p. 375.
34. Takeno, T., Nishioka, M., and Yamashita, H., "Prediction of NO_x Emission Index of Turbulent Diffusion Flame," *Fifth International Conference on Numerical Combustion*, 1993, p. 115.
35. Takeno, T., Nishioka, M., and Yamashita, H., "Effects of Local Flow Field on NO_x Emission Index of Turbulent Diffusion Flame," *Third Tsukuba International Workshop on Chaos/Turbulence*, 1993, p. 83; also in *The 71st JSME Spring Annual Meeting*, 1994, Vol. III pp. 618–620 (in Japanese).
36. Nishioka, M., Nakagawa, S., Ishikawa, Y., and Takeno, T., "NO Emission Characteristics of Methane Air Double Flame," *Combust. Flame*, in press.
37. Driscoll, J. F., Chen, R., and Yoon, Y., *Combust. Flame* 88:37–49 (1992).
38. Takeno, T., Nishioka, M., Zhu, X. L., and Yamashita, H., "Effects of Local Flow Field on Chemical Reactions in Thin Reaction Zone of Premixed Flame," paper to be presented at U.S.-Japan Seminar "Modeling in Combustion Science," Hawaii, July 1994.

COMMENTS

Ruey-Hung Chen, University of Central Florida, USA. Congratulations on your predicted results comparing favorably with experimental results. Interaction between (turbulent) fluid flows and finite rate kinetics such as NO_x formation is certainly a difficult subject to tackle. Was the comparison done only for transitional flames? For fully developed turbulent jet diffusion flames, $EINOx/[L_f^2/(D_f^2 U_f)] \propto Da^{-1/2}$ for thermal NO_x was demonstrated [1]. Such dependence had been predicted using a pdf approach [2]. Would you please comment on the relative merits of your approach and the pdf approaches?

REFERENCES

1. Chen, R.-H., and Driscoll, J. F., *Twenty-Third Symposium (International) on Combustion*, The Combustion Institute, Pittsburgh, 1991, p. 281.
2. Chen, J.-Y., and Kollmann, W., *Combust. Flame* 88:397 (1992).

Author's Reply. Our method of prediction is based on the laminar flamelet concept, and the method can be applied to fully developed turbulent flames as well, if the flames are in the laminar flamelet regime. In the prediction, we use the response of $EINO_x$ to characteristic molecular diffusion time of laminar diffusion flames, and we try to derive the probability density function of this diffusion time in the turbulent flame by the direct numerical simulation.

•

A. Gohoniem, Massachusetts Institute of Technology, USA. 1. What was the buoyancy effect on this flame, and how was it eliminated in the experiment?

2. The departure of the reaction zone from the vorticity

structure was also observed in our reacting shear layer computation even with constant temperature-independent diffusivities, and therefore we suspect that the destabilization of the flame is due to the vorticity and not the temperature-dependent diffusivities.

3. What was the initial perturbation imposed on the jet?

Author's Reply. 1. The experiment was done in the horizontal flow configuration with coflowing air stream of 5.0 m/s. Only when the fuel injection velocity was extremely low, and the whole flame remained laminar, was the downstream portion of the flame caused to curve upward slightly as a result of buoyancy.

2. I am not sure if the stabilization mechanisms suggested in the present paper always play dominant roles in any conditions. Another mechanism may come to play some roles in other conditions.

3. No artificial disturbances were introduced, and if the flow was unstable, the fluctuations were generated spontaneously.

Twenty-Fifth Symposium (International) on Combustion/The Combustion Institute, 1994/pp. 1075–1089

INVITED TOPICAL REVIEW

MODELING TURBULENT FLAME PROPAGATION

WM. T. ASHURST
Combustion Research Facility
Sandia National Laboratories
Livermore, CA 94551–0969, USA

Laser diagnostics and flow simulation techniques are now providing information that, if available 50 years ago, would have allowed Damköhler to show how turbulence generates flame area. In the absence of this information, many turbulent flame speed models have been created, most based on Kolmogorov concepts that ignore the turbulence vortical structure. Over the last 20 years, the vorticity structure in mixing layers and jets has been shown to determine the entrainment and mixing behavior, and these effects need to be duplicated by combustion models. Turbulence simulations reveal the intense vorticity structure as filaments and simulations of passive flamelet propagation show how this vorticity creates flame area and defines the shape of the expected chemical reaction surface. Understanding how volume expansion interacts with flow structure should improve experimental methods for determining turbulent flame speed. Since the last decade has given us such powerful new tools to create and see turbulent combustion microscopic behavior, it seems that a solution of turbulent combustion within the next decade would not be surprising in the hindsight of 2004.

Introduction

Forman Williams, in the last Hottel lecture, described the role of theory in combustion science. He excluded modeling and simulation based on computation, and this is the theme of our review. One area of combustion modeling that has grown since Williams's lecture [1] and the book with Liñán [2] is the linear eddy work by Kerstein and coworkers. This model uses random stirring with a deterministic structure in scalar diffusion and reaction, but details of this work will be left to their symposium papers. Computer capability has also grown, and there are simulation papers within these proceedings that should be consulted: Grinstein and Kailasanath have simulated reaction in a jet that starts with a square cross section, and the vorticity dynamics are related to the entrainment and the resulting reaction; Kaplan and coworkers have included radiation in a reacting jet and investigate the stabilization mechanism of a lifted jet; and Patnaik and Kailasanath simulate detailed chemistry in microgravity. Also, the current Hottel lecture by Frank Marble on *Gasdynamic Enhancement of Nonpremixed Combustion* provides another reason for ignoring non-premixed combustion in this review.

Therefore, which new aspects of combustion science should concern modeling premixed combustion? My favorite is the structure of turbulence. Numerical simulations of turbulence have revealed an intense vorticity structure that is tubelike at a low Mach number and sheetlike at larger flow speeds [3]. How will a premixed flame move through this structure? Since the simulation of turbulence and combustion combined is too much for computers of today, we look for ways to separate these two problems and focus the computer power on just one aspect. From personal experience, my viewpoint is that vorticity and its structure are vital to entrainment and molecular mixing and, therefore, vital to combustion models. In jets and mixing layers, these moving structures produce a smooth time-average Eulerian velocity field which does not resemble the Lagrangian flow pattern around the structure. The important point is that flame motion occurs in the Lagrangian frame, and the historical difficulty is that experimental information was acquired in the Eulerian frame. Grasping how these views differ is now easier with simulation techniques and with global information given by laser sheet techniques. When viewed in its reference frame, the local swirling motion around a vortex is a simple flow pattern; the experimental difficulty is finding that reference frame.

A complete review of combustion modeling is not possible within the given space limitations, and so, in this review, we give a brief description of flow vorticity structure and a more detailed presentation of computed turbulence structure. We then discuss flamelet Pmodels that are used to decouple chemistry from turbulence. The propagation of flamelets through this structure has provided concepts for modeling turbulent, spherically expanding flames and steady planar flames. A recent example of detailed chemistry with simulated two-dimensional turbulence shows what will become common with the larger and faster computers of tomorrow.

Flow Vorticity Structure

It has been 20 years since the Brown and Roshko publication on the vortical structure of a mixing layer [4]. In these layers, the Kelvin–Helmholtz instability creates spanwise vortical rollers, and these structures pair together and form larger structures; this process continues as long as the outer flow conditions maintain a velocity difference across the layer. Between these rollers, there appears counter-rotating vortex pairs orientated in the streamwise direction. Pairs of opposite rotation will form, if the spanwise vorticity is pulled into the flow direction, acquiring a horseshoe shape. A straight vortex tube has a symmetric rotation about its axis and, therefore, no net flux in any plane containing the axis. However, a counter-rotating pair, similar to a vortex loop, will create a net flux of momentum and scalar normal to the plane of the loop. The loop shape may not remain in the initial plane because the self-induced velocity depends on the curvature magnitude, and this will form curved vortex sections in planes normal to the initial plane. The topology may also change via a reconnection process [5]; a common sight are the loops formed in the contrails behind a high-altitude jet—these loops often form a regular structure with downward motion.

The current understanding [6] of the mixing behavior in these flows is that the second vortex pairing creates a mixing transition (the streamwise vortical structure has formed), and at this flow location, there is a scalar distribution, which does not change shape with location across the layer; the third vortex pairing creates a broad-marching distribution, that is, the peak scalar value changes with location. The large-scale structures affect the overall mixing process, and the number of pairings, rather than the Reynolds number by itself, characterizes the mixing behavior. From direct numerical simulations of a mixing layer, Lopez and Bulbeck [7] have examined the vorticity structure in the streamwise direction and find that the Burgers' vortex is a valid solution where the axial strain is extensional, but where it is compressional, the vorticity spirals opposite its own swirl direction. This vortex breakdown mechanism may set the length scale of the vortex.

The streamwise vorticity structure in a jet has been determined by Liepmann and Gharib [8]; using the DPIV technique, they find that these structures drastically alter the entrainment process and become more dominant than the ring mode of vorticity; simulations are given in Ref. 9. Jets with a non-round orifice have been used to enhance entrainment via the deformation of the vortex structures; Hertzberg and Ho [10] have examined a rectangular jet in which the downstream wall confinement is a constant distance from the orifice perimeter. Freely expanding non-round jets exhibit a larger spreading in the minor axis plane; in this confined flow, the three-dimensional effects combined with this spreading create no backflow in the minor axis plane. Understanding and then controlling these three-dimensional structures offers a way to control mixing and, hence, combustion. Jets with axial forcing controlling the lifted flame behavior are in Ref. 11, and additional azimuthal perturbations are in the study by Lasheras et al. [12]. Details of a swirling jet flow are given next [13].

Swirling flows are often used to promote mixing with controlled residence times, yet the analysis of the instantaneous flow structure has not developed to the point that even mean spreading angle of the flow can be predicted. While some success has been achieved with a second-order closure of the Reynolds-averaged Navier–Stokes equations, there is concern regarding the use of the Reynolds' decomposition in this swirling flow, especially when dispersion of spray droplets and the resulting unsteady evaporation must be included for combustion applications.

In this swirl flow, there is a center body, which houses the spray mechanism, and so, the axial flow is an annular jet with reverse flow along the centerline near the exit plane. All components of the mean velocity indicate an axisymmetric pattern, with large fluctuation values compared to the mean values. However, instantaneous images of the swirling jet fluid do not resemble an axisymmetric pattern but indicate a Kelvin–Helmholtz roll-up on the outer edge, which is not symmetric with respect to the centerline. These outer structures form an eddy of very large scale, and this eddy moves downstream along a path with increasing radius. Images taken normal to the axial flow give the impression of a helical structure, a left-handed helix with a pitch corresponding to the jet diameter; the flow swirl is right-handed, see Fig. 1. Thus, the instantaneous flow pattern does not resemble the time-average mean flow, and so, the motion of drops as calculated from the Reynolds-decomposition may not resemble the actual drop motion. In particular, measurements indicate regions where the average radial velocity is outward, as are drops above a certain size ($\sim 20\ \mu m$), but smaller drops are moving inward at this location. The formation of these structures creates a fluctuation velocity that is larger than the mean velocity, and so, in this spatial region, the mean velocity no longer has much meaning.

Vorticity Structure in Turbulence

The equations of motion were developed by Newton in 1686 and those for a viscous fluid by Navier in 1822 and Stokes in 1845. Just 100 years ago this spring, Reynolds suggested a decomposition into a mean velocity and the temporal fluctuation about that mean to describe turbulence. Taylor, in 1935, developed a statistical approach. In 1941, Kolmogo-

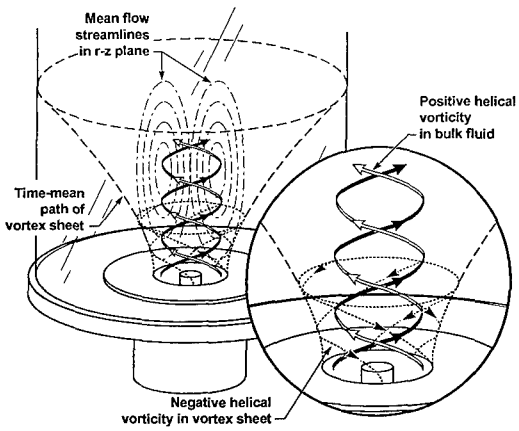

FIG. 1. Sketch of swirling vortex structure; the vorticity lines are wound in a left-hand helix, which creates a right-hand flow rotation. This unsteady Lagrangian structure convects spray droplets to different locations depending upon droplet size and instantaneous location of the vorticity, and this dispersion pattern does not correlate very well with the time-average axisymmetric flow pattern.

rov assumed that the velocity difference between two points separated by the distance r would depend on that distance, viscosity, and energy dissipation in the turbulent flow. When the distance grew large, the effect of viscosity would disappear, leaving only the energy dissipation to characterize a turbulent flow. This implies (though not contained within the 1941 paper) the $-5/3$ power law wave number dependence of the energy spectrum.

The experimental techniques and, thereby, the conceptual view promoted the Fourier description of the flow, and hence, the energy spectrum was the focus. The physical flow pattern was dismissed as too complicated: it was turbulent. Also, the phase angle of the Fourier modes was too much to deal with. Only with the decade of the 1980s were computers and computer graphics advanced enough so that simulated turbulence and the flow pattern could be easily examined. The critical importance of phase angle is shown by She et al. [14] in which the computed flow vorticity is imaged along with "vorticity" from the same Fourier modes but with random phase angles. The two flows have exactly the same spectrum but do not look alike in physical space. For combustion models, which need entrainment and molecular mixing, the physical flow pattern is of vital concern, and not just any phase angle with a given energy spectrum will do.

The structure of vorticity and its role in stability has recently been recognized as being more essential than previously assumed. A significant concept change is the use of three-dimensional, nonmodal fluid motion which leads to finite amplitude deformation via interactions between eigenfunctions that are not orthogonal to one another. The review by Trefethen et al. [15] describes the effect of a streamwise vortex in a shear flow, in which the fluid motion amplifies in an inviscid manner before the effect of viscosity occurs. "Such behavior is physically straightforward, appearing complicated only when interpreted in the basis of eigenmodes."

Status of the Largest Turbulence Simulations:

Using a parallel computer (CM-2 at Los Alamos National Laboratory), simulations of forced and decaying turbulence have been performed with a grid mesh of 512^3; the largest Reynolds number is $\mathrm{Re}_\lambda \sim 200$, see Chen et al. [16] and She et al. [17]. The focus of these large simulations is understanding the intermittent turbulence structure. Kolmogorov added a third hypothesis in 1962 to account for fluctuations in the energy dissipation, but until recently, this intermittency effect eluded theory and experimentation. Their 512^3 results are (1) energy spectra scaled by k_p and $E(k_p)$ collapse and agree with experimental results at much higher Reynolds number; (2) variation of k_p, which is the peak wave number in the dissipation spectrum, is consistent with the 1941 Kolmogorov theory in that k_p has a linear relation to k_d, the Kolmogorov wave number ($k_d^4 = \varepsilon/\nu^3$); and (3) velocity increment results indicate intermittency growth with decrease in distance. Given results 1 and 2 in contrast to 3, why is the Kolmogorov theory so good for the energy spectrum but not for the higher powers of the velocity increments? She suggests [17] that structures that dominate intermittency do not have a large contribution to the mean transfer of energy. However, the swirling flow about these structures creates flame area and curvature, and for this reason, we concentrate on their features in this review.

Models of Turbulence Structure:

Experimental measurement of higher powers of the velocity difference do not agree with the 1941 theory, which gives a spatial scaling with exponent of $p/3$ for the power p of the velocity difference, or increment. She [18] has used the filament shape of the intense vorticity, revealed by direct numerical simulations of turbulence, in order to develop a universal scaling of the velocity increments without adjustable parameters. There are two assumptions: (1) successive moments of the energy dissipation averaged over a volume of size l have a universal relation to the infinite moment of the dissipation and (2) the structures that give the most intermittent events are filaments of vorticity. The filamentary nature sets a codimension in the model and the resulting exponents of the velocity increment to the power p are $\zeta_p = p/9 + 2[1 - (2/3)^{p/3}]$. The correction to the energy

spectrum with this scaling model is small, $\approx k^{-(5/3)-0.03}$, but the departure from higher exponents of the Kolmogorov theory is large, and this new scaling gives values of ζ_p, which are within experimental uncertainty; for example, the tenth power model result is 2.593, the experimental value is 2.60, and the Kolmogorov is 3.33.

Computed Vortical Structure:

Jiménez et al. [19] have performed direct numerical simulations with four grid sizes, 64^3–512^3, with $35 < \mathrm{Re}_\lambda < 170$, where the Reynolds number is based on the Taylor scale λ. These simulations are at constant dissipation; the forcing used a negative viscosity in the lowest wave numbers so that $K\eta \approx 2$, where K is the largest resolved wave number. The dissipation is determined from the energy spectrum, and this, in turn, defines the Kolmogorov length as $\varepsilon = \nu^3/\eta^4$, and the Taylor microscale is defined by $\varepsilon = 15\ \nu u'^2/\lambda^2$. The energy dissipation, reduced by integral scales, is $\varepsilon\Lambda/u'^3 \sim 6.5/\sqrt{\mathrm{Re}_\lambda}$, for $\mathrm{Re}_\lambda < 100$. Figure 2b of Ref. 19 indicates nonisotropic behavior for the small scales, which may be caused by the deterministic forcing scheme (the negative viscosity imposes a ∇^2 pattern). Large scales creating deterministic small-scale structure have been examined by Yeung and Brasseur [20].

From distributions of vortex size and circulation, they [19] find intense vorticity with an apparent Gaussian radial distribution. The $1/e$ radius is approximately 4η, and the estimated circulation is $\Gamma \approx 22\sqrt{u'\lambda\nu}$. They suggest that a square-root behavior develops from shear layers that have a velocity difference of u' and a layer thickness that has been squeezed down to the Kolmogorov length. This gives $u' \sim \Gamma/\eta$, and so, $u'\eta/\nu \sim \Gamma/\nu$, and with the relation $\lambda/\eta \sim 2\sqrt{u'\lambda/\nu}$, they obtain

$$\frac{u'\eta}{\nu} \sim \frac{\Gamma}{\nu} \sim \sqrt{\frac{u'\lambda}{\nu}} \tag{1}$$

and thus, pieces of these thin shear layers that roll up into vortex tubes will have the square-root circulation behavior. They comment that these tubes appear on the edges of regions which are nearly uniform in their velocity values—this feature would imply that collisions between fluid volumes creates shear layers that sometimes roll up into vortex tubes. This mechanism may require an oblique impact angle between the two fluid volumes, according to Ruetsch and Maxey [21]. The collision process may create an extensional strain rate in the direction of the vorticity, and it is this axial strain rate that can maintain the Burgers' vortex as a steady, viscous solution. As a footnote in a 1939 meeting paper [22], Burgers presented this solution in response to Taylor's 1938 paper which stated that vortex stretching

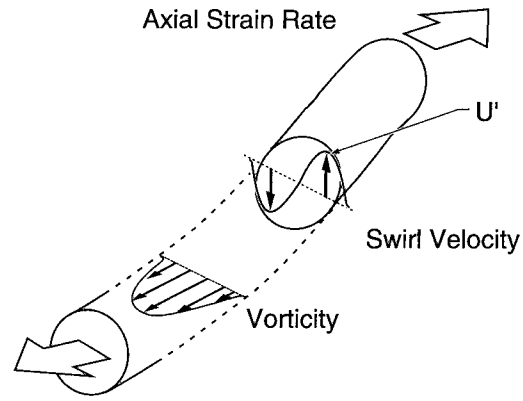

FIG. 2. In a Burgers' vortex, the axial strain rate maintains a Gaussian vorticity distribution; from the simulations, the $1/e$ radius is 4η, and the circulation is $22\nu\sqrt{\mathrm{Re}_\lambda}$, which gives a maximum swirling velocity of u'. Passive propagation normal to the vortex axis is shown in Fig. 3.

might be important in the dissipation of mechanical energy. Replacing the time variable in Oseen's vortex with an axial strain, Burgers shows the balance between strain rate s, and kinematic viscosity ν creates a Gaussian radial distribution of vorticity which creates a swirling velocity around the vortex axis of

$$u_\theta = \frac{\Gamma}{2\pi r}\,[1 - \exp(-sr^2/4\nu)] \tag{2}$$

where r is the radial distance. A constant axial strain rate of u'/λ would be consistent with the $1/e$ radius of 4η. When the axial strain ceases, then the vortical core expands but expands slowly as $\sqrt{4\nu t}$, and while it is expanding, any radial location outside the decaying core still responds to the circulation Γ contained within that radial location. Therefore, while the vortex is decaying, the swirling flow outside the decay region does not yet realize that the axial strain rate has disappeared.

The maximum swirling velocity U_θ produced by the Burgers vortex is close to the $1/e$ radial location, and with $u'\eta/\nu = \sqrt{u'\lambda/4\nu}$, we obtain

$$\frac{U_\theta}{u'} = \frac{0.63\ \Gamma/\nu}{8\pi\eta u'/\nu} = \frac{0.63[2(\Gamma/\nu)/\sqrt{u'\lambda/\nu}]}{8\pi} \approx 1 \tag{3}$$

when $\Gamma = 22\sqrt{u'\lambda\nu}$ is used. Thus, the maximum swirling velocity is the root mean square velocity. This observation may explain why much of the experimental turbulent flame speed data has $S_T/S_L \sim u'/S_L$, because this swirling motion around the vortex tube axis creates flame area, see Figs. 2 and 3. (This intense vortex tubestructure and its effect on flame shape and propagation is theessential concept of this review.)

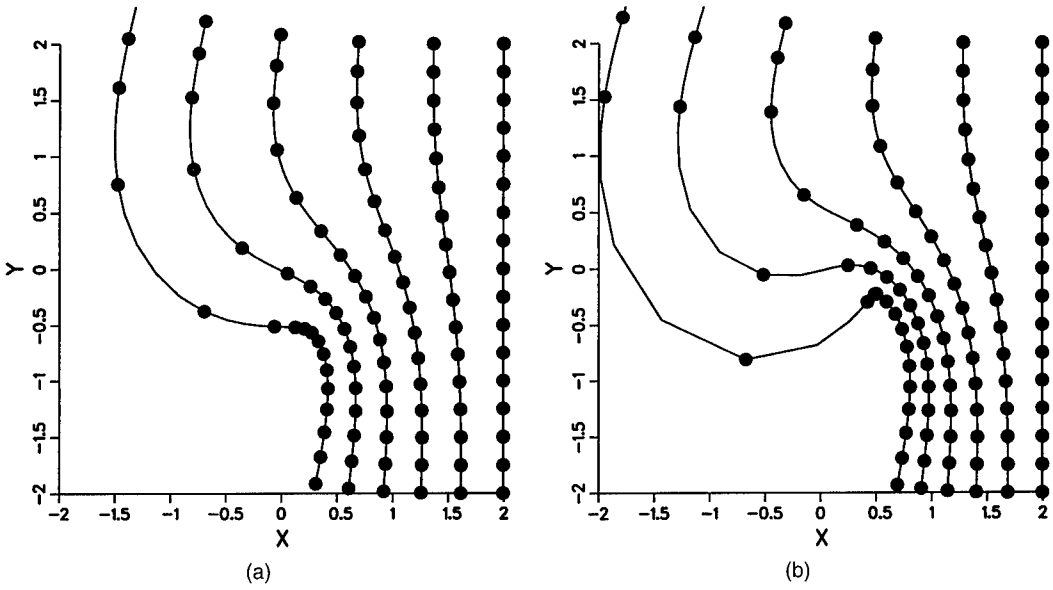

FIG. 3. Passive propagation in the swirling flow shown in Fig. 2, $u_\theta = (7/4)(u'/r)[1 - \exp(-r^2)]$, where the radial distance is in units of 4η. The time interval between images is $2\eta/S_L$. The filled circles are points which are moved in the direction normal to the local flame surface, and the change in their spacing indicates the flame stretch (excessive positive stretch also shows the segments used to define the motion). (a) $u' = 0.5\ S_L$; the sixth image shows a compression region, but with $u_\theta < S_L$, there is no cusp at this time. (b) $u' = 0.8\ S_L$; the sixth image does show a cusp formation. From passive turbulence simulations, approximately 30% of the flame surface has compressive strain. Generation of flame area may exhibit a different functional behavior when cusp formation is possible, and so, extrapolation of S_T vs u' from $u' > S_L$ towards u' of zero may require different functions. These images neglect the radial strain rate; to include it would require specification of Re_λ (in order to define λ compared to η).

Flow around a vortex may also describe a behavior found in direct simulations of particles within a turbulent flow. Yeung and Pope [23] computed trajectories of Lagrangian particles, and they found that the time correlation of an acceleration component goes through zero in 2.2 Kolmogorov time units, independent of the Reynolds number. If the particle is going around the vortex axis, at the maximum swirling radius, then the acceleration would correspond to the centrifugal force, and this acceleration in Cartesian coordinates would appear as sinusoidal in time—the period from maximum to zero would be one-quarter of a rotation around the vortex axis. The time for one rotation is $t_u = 2\pi R/U_\theta$, where R is the location of maximum swirling velocity, $\approx 4\eta$. Scaling one-fourth of this time with the Kolmogorov time τ_η gives $t_u/4\tau_\eta = \pi \mathrm{Re}_{r\theta}/2U_\theta$, where we assume that $\tau_\eta e_{r\theta} \sim 1$. The shear $e_{r\theta}$ and the angular velocity U_θ/R have the same dependence upon Γ/R^2 and, thus, have the same Reynolds number dependence. Therefore, this acceleration time period has no Reynolds number dependence.

Another particle behavior that might be related to vortex structure is the condensation of Stokes particles within computed turbulence [24]. Capture of a particle might result from the balance of inward strain rate normal to vortex axis and the outward centrifugal force. A certain range of Stokes number would allow the particle to ride around the vortex at the maximum swirling location. Smaller values would spiral inward, and larger values would be affected by neighboring structures. Fully interacting simulations, but with decaying turbulence, have been performed in Ref. 25, and within a two-dimensional periodic vortex field, the dynamics of buoyant and heavy particles has been simulated [26].

Summary of Structure

The numerical simulations of turbulence allow examination of microscopic flow patterns which affect turbulent combustion. These simulations are large enough to show agreement with experimental results, and so, models of the vortical structure should be developed in order that their effect upon turbulent combustion can be modeled. Turbulent combustion models based on the energy-cascade concept of Kolmogorov have been reviewed by Bray and Cant [27]; in the following, we give new concepts about propagation through this vortical structure and the resulting turbulent flame speed models that can be created.

Flamelet Models

To investigate flame stability, Markstein wrote a flame evolution equation in 1964, but without a nonlinear tool, he was restricted to a stability analysis [28]. Osher and Sethian developed a technique [29] to follow a front as one level surface in a continuous field, and thereby, topology changes are easily treated. Passive front propagation through a flow structure can be done if volume expansion is ignored, but these constant-density flames appear so artificial that one hesitates to use them; however, we find they reveal concepts of turbulent propagation. Therefore, the flamelet assumption has been exploited in order to decouple the complexity of chemistry from that of turbulence. Markstein's notation was f for a flame with volume expansion; while a passive formulation [30] has acquired the letter G; we distinguish between these flamelet models by using f when volume expansion is considered and G when it is not. The special initial condition formulated by Kerstein is $G = x$ for the evolution equation

$$\frac{\partial G}{\partial t} + \mathbf{u}\cdot\nabla G = S_L|\nabla G| \tag{4}$$

where the right side describes Huygens' propagation. This nonlinear term makes the initial condition very special: It provides a connection between flame area and the gradient of G. The scalar gradient corresponds to the flame surface density, that is, flame area per unit volume. This formulation allows a numerical simulation that follows Damköhler's idea: Creation of flame area by turbulent motion causes the larger consumption rate. Now, with the passage of 50 years, the computer tool can easily determine passive flame area within a turbulence simulation, and the motion can be forced so that a statistically steady propagation is obtained.

The G Equation and the Z Equation:

Flamelets within non-premixed combustion have a long history, and now with the scalar G equation, Peters [31] has unified the procedure to obtain a one-dimensional temperature equation for a premixed and nonpremixed reaction, the latter using the mixture fraction Z and the former using the G equation. The temperature equation for a premixed flamelet is obtained by a transformation from physical space to G space. Using a coordinate normal to the flame surface, $x_n = G/|\nabla G|$, and the propagation equation, the one-dimensional temperature equation is

$$\rho\frac{\partial T}{\partial t} + \rho S_L\frac{\partial T}{\partial x_n} = \frac{\partial}{\partial x_n}\left(\rho D\frac{\partial T}{\partial x_n}\right) + w \tag{5}$$

where the burning velocity S_L replaces the convection velocity and w is the reaction term. For premixed combustion, this results in a flame zone that should be thin in physical space, while for nonpremixed reaction, the chemistry should occur within a narrow range of mixture fraction.

Neither flamelet equation has a chemical source term. Since Z is a conserved scalar with respect to chemical reaction, it is clear why there is no source term for Z. But this is less clear for the G equation, where the gradient of G times the burning velocity appears. This scalar has been created in order to track a front; the scalar gradient defines the flame normal as $\mathbf{n} = -\nabla G/|\nabla G|$ and is used in the kinematic balance describing Huygens' propagation. This scalar gradient has a smooth variation through the thin reaction zone, and so, in this sense, the right side of the G equation is not a chemical source term, but it is a kinematic source term for Huygens' propagation. Note that this propagation is not a diffusive one, and therefore, there is no diffusive term in the G equation.

We now describe G-equation simulations with computed three-dimensional Navier–Stokes turbulence; the turbulent kinetic energy has been maintained at a constant value so that steady propagation can be observed within a periodic domain.

Geometry of the G Surface:

The curvature of computed G surfaces has been taken in two-dimensional slices that mimic laser-produced flame images. Comparison throughout a turbulent flame zone [32] shows that one length scale normalizes experimental results into agreement with computed curvature distributions. The mean positive curvature does not change with location, but the mean negative curvature increases with distance from the leading edge of the zone.

A full surface definition is given by the normal vector $\mathbf{n}$ and two eigenvectors of curvature h_1 and h_2, where $|h_1| \leq |h_2|$. The ratio of these two eigenvalues h_1/h_2, the shape factor introduced by Pope [27], indicates the most likely shape is that of a cylinder. This cylindrical feature is caused by the swirling velocity around the intense vorticity; Fig. 3 shows how this swirling motion distorts the flame and creates an alignment between $\mathbf{h}_1$ and the vorticity vector [33]. Previous results have shown that vorticity aligns with the intermediate strain direction β (where the eigenvalues are $\alpha \geq \beta \geq \gamma$), and Fig. 4 shows that the alignment probability of the flame cylinder axis is very similar to the alignment of intermediate strain with vorticity. The extensional strain rate in the plane of the flame is usually smaller than the rms estimate of $\sqrt{7.5u'^2/\lambda^2}$; the former is closer to $u'/2.5\lambda$.

G-Fluctuations and the Mean Progress Variable:

The initial condition $G = x$ allows fluctuations of G to describe the flame spatial displacement, and this

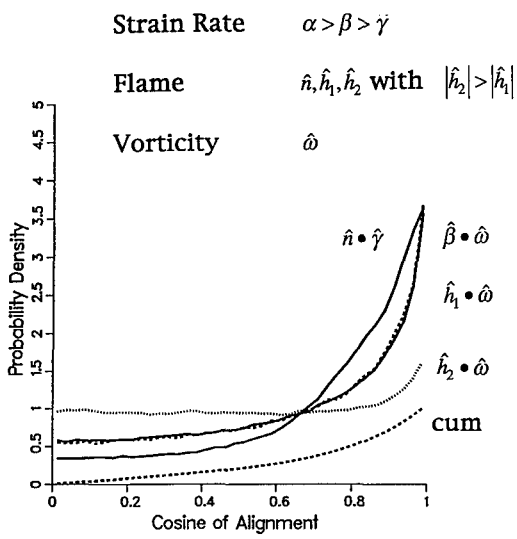

FIG. 4. Flame surface alignment with the compressive strain rate is given by $\mathbf{n} \cdot \gamma$; the cumulative probability of this distribution shows that more than half of the flame surface is within 37° of the γ direction. The intermediate strain rate β and the smallest curvature eigenvalue $\mathbf{h}_1$ align with the vorticity direction, which is consistent with the large probability for a cylindrical flame shape.

information can be related to the mean progress variable, and so, contact with flamelet models based on a progress variable can be made [27]. In the G simulation, the initial mean gradient is maintained with a jump periodic boundary condition in the x direction, the mean propagation direction. The average of G over a constant x plane is $\langle G(x_p) \rangle$, and the scalar fluctuations on that plane, $G' = G(x_p, y, z) - \langle G(x_p) \rangle$. These scalar functions correspond to the flame displacement from its mean location $G' = -x_d$, where x_d is the displacement of the surface. From simulations [32], the probability distribution of scalar fluctuations determine the mean progress variable as

$$\bar{c}(x) = \int_{G'=-x}^{\infty} P(G')\, dG' \tag{6}$$

where the total integral of the probability density $P(G')$ is unity. The value of $\bar{c}(x)$ can also be computed by measuring the displacement of selected G surfaces; the direct result agrees with the G' result. The mean progress variable is also given by a traveling wave solution to a nonlinear reaction diffusion mechanism, the KPP equation:

$$\frac{\partial \bar{c}}{\partial t} = w\bar{c}(1 - \bar{c}) + D\frac{\partial^2 \bar{c}}{\partial x^2} \tag{7}$$

where w is the reaction rate and D is the turbulent diffusivity. A first approximation [34] for the spatial gradient of the mean progress variable is

$$\frac{d\bar{c}(x)}{dx} = a\bar{c}(x)[1 - \bar{c}(x)] \tag{8}$$

and in the full numerical solution, the variation in the a coefficient is only noticeable near $\bar{c} \sim 0$. Therefore, with a constant coefficient, the spatial distribution is $\bar{c}(x) = [1 + \exp(-ax)]^{-1}$, and by differentiation of Eq. (6), the approximate distribution for scalar fluctuations is

$$P(G') = \frac{a \exp(aG')}{[1 + \exp(aG')]^2} \tag{9}$$

and this approximation agrees with the simulation results. These $P(G')$ distributions have a larger probability near the origin than the Gaussian distribution. These G simulations, which are based on Huygens' propagation into the unburnt gas, give ensemble results which are well described by the reaction-diffusion balance in the KPP model. Yet, the microscopic flame dynamics are not diffusive. Therefore, even though the ensemble behavior is given by a diffusive model, diffusion-based models of microscopic dynamics may give the wrong combustion dynamics. Hence, in a Large Eddy Simulation, how large must the space and time domain be for a diffusive subgrid model vs a nondiffusive one?

Partially Premixed Flamelets:

Early injection of fuel into the diesel engine may create regions of partially premixed fuel and air, and after ignition, there will be flame propagation through the regions which are connected and within the flammability limits. The remaining charge may be considered as a nonpremixed reaction. The burning velocity exhibits a large variation within the flammability limits, and this variation may affect the premixed flame shape. Near stoichiometric conditions, the flame normal should be normal to the mixture fraction gradient, but near lean and rich pockets, the gradient of G aligns with the gradient of Z. Propagation along a stoichiometric contour may be sensitive to heat loss when the flame dimension normal to the contour approaches the flame thickness: A gap-quenching mechanism might occur. Ignoring some of these complications at this time, Peters [31] has formulated a passive partially premixed flame propagation based on the G equation and the Z equation. From the known behavior of $S_L(Z)$, the Huygens' propagation is simulated in a Z field, which has a constant variance in addition to a constant turbulent kinetic energy. Pockets of Z that are too rich or too lean in comparison to Z_{st} retard the local propagation of a G surface. Some dynamics of these pockets will

depend on volume expansion effects, which are not included in this passive formulation. The burnout of a rich pocket should be important in soot production.

G-Equation Applications:

Collins [35] has used two-dimensional spectral simulations to obtain the correlations given in the analysis by Peters [36] for the spatial correlation of scalar fluctuations. By choice, the simulation forcing style suppresses coherent flow structures, and the location of the forcing wave number creates an energy spectrum with either a $-5/3$ or a -3 power law. In the x, y domain, the mean scalar gradient is enforced by using $G = x + g$, where g is the scalar fluctuation, and it is periodic in all directions. The propagation equation is

$$\frac{\partial g}{\partial t} + w' + \mathbf{u}\cdot\nabla g = S_L \sqrt{\left(\frac{\partial g}{\partial x} + 1\right)^2 + \left(\frac{\partial g}{\partial y}\right)^2} \tag{10}$$

where w', the velocity fluctuation in the mean propagation direction, $= \mathbf{u}\cdot\mathbf{i}$ (this is Eq. (5) in Ref. 30). The mean scalar gradient makes the scalar fluctuations anisotropic via the $w'w'$ term in the equation for $\langle w'g\rangle$. This makes $\langle w'g\rangle$ negative in value, and it is the principal source term for the scalar spatial correlation $\langle g(\mathbf{x})g(\mathbf{x} + \mathbf{r})\rangle$. The current simulations by Collins yield a scalar spectrum with a power-law behavior, and the power depends upon the shape of the energy spectrum. Peters uses a different approach; he considers a field in which flamelets travel from all directions into a certain spatial domain, and so, the mean gradients cancel, and the scalar fluctuations are those of an isotropic field. The scalar spectrum obtained by Peters has a $-5/3$ power law modified by exponential factors, one of which contains the Gibson length scale. Wirth and Peters [37] have obtained the scalar spectrum from two-dimensional flame images within an engine by a complex Fourier transform of the image geometry in terms of the arc length along the flame. These experimental results are then used to determine the Gibson length by a fitting process using the analytical expression.

Zhu and Ronney [38] have performed what they call a Huygens-DNS simulation (specified flame velocity within a computed flow) of a Taylor-Couette flow with a single scale of counter-rotating eddies. This flow with liquid flames can produce propagation with u' a thousand times S_L, and the resulting observed behavior is $S_T \ln(S_T/S_L) \sim u'$. This relationship indicates a flame perimeter that grows in proportion to its length over the time period in which the advancing flame engulfs the vortex; that is $dL/L \sim dt/\tau$, where $\tau \sim L/u'$ is the eddy rotation time and the engulfment time period is L/S_T. The computed and experimental flow-flame pattern exhibits a diminishing row of unburnt pockets behind the leading front when $u' >> S_L$, but the flame advancement appears to depend upon how the flame reaches the next eddy; thus, variations in the shape of the computed eddy do yield large variations in S_T.

Turbulent Flame Speed

Is there a generic "Turbulent Flame Speed" or is it the net result of many interacting effects? Consider the possible effects in the reaction-sheet regime: the laminar burning velocity S_L, the volume expansion T_b/T_u, the turbulence structure u', λ, the change in S_L due to strain rate and curvature, the Lewis number, the flame shape and size, and the flow confinement. To emphasize these many effects, we call S_T the turbulent flame speed rather than a burning velocity. Variations in the unburnt gas flow structure, which have usually not been measured, may explain part of the historical confusion regarding turbulent flame speed data. Another part is knowing the actual mass flux that is entering the flame zone. For example, the double-kernel method has been used in a fan-stirred chamber with the assumption [39] that as the two flames meet, they will approach each other at twice the S_T value. However, if the flow induced by volume expansion is considered, then as Shepherd illustrates [40], the mass flux away from the line joining the two flames is not entering the flames, and so, this method yields an overestimate of S_T. Variations in flame shape and size as the two flames meet could produce large variations in the ignored mass flux, and this may partly explain the large scatter in the S_T values given by this technique. The concept of a turbulent flame speed has generated many model approaches and many functional forms—most have been based on the Kolmogorov cascade concept and not on particular flow patterns creating flame area. Within the engine community, the current practice is a two-zone model of flame propagation; the burnt zone is separated from the unburnt zone by a spherical surface and a simple cutoff is used where the sphere extends beyond the piston-cylinder walls. Thus, volume expansion is not allowed to interact with the walls and deform the flame surface (the tulip flame deformation has been numerically examined by Gonzalez et al. [41]). These methods require a turbulent flame speed model, and we now describe some of the current models.

Engine Combustion Models:

The February SAE meeting papers and the work presented at the KIVA Users meeting reveal the current models used in engine combustion analysis. Commerical codes are available, and with 10^4–10^5

elements, very realistic engine flow geometry can be computed. Computation times range from hours to tens of hours. The turbulence model is usually $k - \varepsilon$, and the Magnussen model of ε/k for the reaction rate is a popular choice. The next level of flame description is the Coherent Flame Model, which uses a balance equation [42] with assumed flame area growth and destruction terms. Another approach is the Fractal Flame Model, which uses the experimental fractal dimension of flame contours to produce the total flame area [43]. Bielert et al. [44] have constructed a two-dimensional flame model in which the leading edge of the flame front is tracked, and consumption of eddies behind this front, over a finite time period, gives a turbulent flame zone with finite thickness. Concentrating on only the early flame growth and using measurements of flame radii from 3 to 11 mm, Boulouchos et al. [45] have constructed a spectral model that allows the range of flow scales that create flame area to grow with the flame size. They also use a two-step model: laminar growth with a step change to turbulent propagation. Both these models can describe the rather sparse data set of flame radii. They have also considered the Gibson scale idea—that scale being the minimum scale that wrinkles the flame—but they find it gives unrealistic behavior over the conditions of the data set.

Within the engine community, there has been a debate on the existence of a steady turbulent flame speed. To answer this question, Checkel has constructed a 5-in. cube [46], within which turbulence is created by pushing a perforated plate through the chamber before ignition. The flame radius can then be observed as a function of time. The results of Ting et al. [47] reveal continual flame speed growth for flame radii up to 55 mm, and so, for dimensions typical of a car engine, the turbulent burning rate does not seem to have a constant value. A model of this engine-type propagation has been developed [48], and even though the current model may not be correct in all aspects, the concepts do illustrate how flamelet simulations, combined with turbulence simulations and experimental information, can lead to a propagation mechanism that is based on realistic flow patterns rather than assumed flow concepts.

Flame Speed and Flame Size:

The experimental results yield a turbulent flame speed which increases with the size of the flame ball, whereas a spherical laminar flame ball has a constant speed of $S_L + \tau S_L$, where the first term is the burning velocity advancement into the gas ahead of the flame, the second term is the velocity created by volume production, and the heat release parameter τ is the temperature ratio minus unity. The velocity field created by volume expansion confined to a spherical surface, with radius R_s, is

$$V_s = \tau S_L \frac{R_s^2}{R^2} \tag{11}$$

for $R \geq R_s$; there is no velocity effect within the sphere, and the surface velocity does not depend upon size. However, if the flame is wrinkled and not confined to the sphere surface, then the volume expansion effect at the largest flame radii will be different than at smaller radii. To estimate this effect, assume a spherical shell with a constant flame density; this corresponds to a uniform distribution of volume expansion within a shell of finite thickness. The assumed flame surface density is

$$\langle |\nabla G| \rangle \sim \frac{1}{2\pi\lambda} \sqrt{\frac{u'}{S_L}} \tag{12}$$

based on passive G-equation simulations. When $u' >> S_L$, the heat release should limit the flame area, but this effect is neglected. The inner radius R_i and outer radius R_o define the flame zone, and this distributed volume production will create a flow velocity of

$$V_R = \tau S_L \sqrt{\frac{u'}{S_L}} \int_{R_i}^{R_o} \frac{R_s^2}{R^2} \frac{dR_s}{2\pi\lambda} \tag{13}$$

for $R \geq R_o$. Integration gives

$$V_o = \frac{\tau S_L R_o}{6\pi\lambda} \sqrt{\frac{u'}{S_L}} [1 - (R_i/R_o)^3] \tag{14}$$

for the flow velocity at the largest flame radius R_o. When the inner radius is a small fraction of the outer radius (a thick flame zone), then the velocity of the outer flame ball will depend upon the flame size. However, if the flame zone is thin ($R_i \sim R_o$), then the bracketed term will vanish, and the velocity will be independent of flame size, as in the laminar case. (Thus, the turbulent flame speed growth with size is aconsequence of volume expansion distributed throughout theflame ball.) The turbulent flame speed estimate is

$$\frac{S_T}{S_L} - 1 \sim C_R \frac{R}{6\pi\lambda} \sqrt{\frac{u'}{S_L}} \tag{15}$$

where C_R is the bracketed term value. Now, we replace the Taylor scale with the integral scale Λ and find a linear dependence upon the ratio u'/S_L. By using $\Lambda/\lambda = \sqrt{u'\Lambda/15\nu}$ and replacing the kinematic viscosity with the thermal diffusivity, $\nu = 0.7\ a$, and by using an estimated flame thickness, $\delta_f = 7.4\ a/S_L$, we obtain

$$\frac{S_T}{S_L} - 1 \sim \frac{0.045 C_R R}{\sqrt{\Lambda \delta_f}} \frac{u'}{S_L} \tag{16}$$

and so, the linearity in u'/S_L is the product of two square root terms. The data indicate that C_R is near unity, which implies that R_i is about half the flame radius, if the $2\pi\lambda$ factor is correct. A flame zone that grows, $L \sim R_o/2$ also implies a constant burnout time, as used in Ref. 44.

In a numerical study of flame-ball development, Kwon et al. [49] assumed that the velocity field created by volume expansion confined to a single spherical surface could be combined with velocity fluctuations in order to simulate the flame dynamics. This single sphere with a thin flame-zone assumption restricted their results to a turbulent flame speed that does not grow with flame size, except through the creation of extra flame area by the fluctuation velocities.

How many phases does the flame-ball growth have? After spark ignition, the early flame surface may encounter flow structures that are large in comparison to the burnt volume at that instant, and so, the flame-flow interaction in that case may not resemble the spherical velocity distribution used above. After the flame ball has developed to a size where there are many flow structures interacting with the flame at once, then the uniformly distributed volume source solution may be reasonable. Changes from the spherical shape are observed, indicating that the spherical shape may not be a stable one. Indeed, an ellipsoid will create a larger flow velocity in the major axis direction, but while making the flame motion faster, this expanison effect will increase the unburnt gas divergence, and this may restore the spherical shape. As mentioned above, the heat release parameter could also determine an upper limit for the flame-surface density.

Steady, Planar Flame Speed:

Given a spherically expanding flame, can we extract a value for steady propagation in other configurations? Normalizing the flame radius with $\sqrt{\lambda \Lambda}$, the geometric mean of the two length scales, which can distort the flame surface, we have from Eq. (15)

$$\frac{S_T}{S_L} \sim \frac{R}{\sqrt{\lambda \Lambda}} \sqrt{\frac{u'}{S_L} \frac{\Lambda}{\lambda}} \tag{17}$$

and the last term, by itself, collapses experimental data of steady, planar turbulent flame speeds [50]. Changing the length scale ratio into Re_λ, this same relation fits the data of Liu and Lenze [51]:

$$\frac{S_T}{S_L} - 1 = 1.75 \sqrt{\frac{u'}{S_L} \frac{\mathrm{Re}_\lambda}{15}} \tag{18}$$

and by making small changes in some of their λ estimates, the above relation describes all their data points. A different estimate, also based on passive G-equation simulations, is given by Wirth and Peters [37] as

$$S_T = (S_L + 0.8\sqrt{S_L u'} + 1.5u') \cdot \left(1 - 1.4 \frac{L_M}{\Lambda} \frac{u'}{S_L}\right) \tag{19}$$

where the square root term is the G-equation result and the term with u' is the assumed large intensity limit, but modified by the last factor, which includes the flame thickness compared to the flow length scale.

S_T vs u'—The Bending:

We now discuss the "bending" feature of S_T vs u'. The linearity of S_T with respect to u' may depend on how the length scales change as u' is increased in an experimental configuration. The passive G-equation simulations imply that variation of S_T with u' depends upon S_L and Re_λ, where the Reynolds number dependence is related to flame propagation through a nonspace-filling vortical structure [52]. Thus, the bending effect could be a structural effect of the turbulence. This vortical structure concept differs from that of Bradley [39], who considers bending to be a strain-rate reduction of S_L, and so, flame stretch is the key parameter that causes bending. The Karlovitz stretch factor is

$$K = 0.157 \frac{(u'/S_L)^2}{\sqrt{\mathrm{Re}_\Lambda}} \tag{20}$$

but using this stretch relation to define Re_λ in Eq. (18), we find agreement [48] with the summary plot of S_T given in Figure 4 of [39] for $u' < 6S_L$. Thus, flame stretch may not be the only cause of bending. Models which incorporate the statistical behavior of flame stretch found in simulation results are given by Kostiuk and Bray [53].

Another possible contribution to bending is the reduction in flame folding when volume expansion is included; that is, the flame surface will interact with itself through the Biot–Savart interaction, and this interaction will inhibit the folding seen in a passive flame simulation. Additionally, the flame shape may induce a mass flux away from the flame, and thereby, reduce the burning rate.

To resolve the relative importance of vortical structure vs strain rate vs volume expansion, we need simulations with heat release and over a range of Reynolds numer, say for example $30 < \mathrm{Re}_\lambda < 150$ with values of u' up to 10 times the burning velocity. The questions to be explored are as follows: (1) As

Re_λ is increased, does the vortical structure have gaps that cause bending, or are there many little tubes that fill in the gaps and yield a more linear behavior in S_T vs u'? (2) Given this vortical structure, for various mixture fractions and Lewis numbers, how large is the effect of flame stretch upon the total flame area? (3) How does total flame area change with increasing heat release?

Vortex-Flame Interaction

Creating a known vortex structure and letting it interact with a flame has recently been performed by several groups. Santavicca et al. [54] used a V-shaped flame interacting with a Kármán vortex street. Ground state OH is imaged in a plane of laser light. Samaniego [55] puffed a vortex pair from a slot into a V-shaped flame and observed a quenching, reignition process. Roberts et al. [56] created vortex rings which meet a propagating flame and determined the vortex strength/size combinations that wrinkle the flame and those that locally quench the flame. Their definition of quenching is any local flame section that exhibits a peak OH intensity, which is less than 0.01 of the undisturbed flame intensity. Their configuration is a vertical tube with premixed methane air in which a nearly flat flame propagates upward, while the vortex ring moves down; the resulting interaction may quench the flame or create unburnt pockets, or not even wrinkle the flame. The observed minimum vortex size that wrinkles the flame is $U_\theta/S_L = 2.5\delta/d_c$, where the flame thickness δ is estimated as being $7.4a/S_L$, with a the thermal diffusivity, and the estimated core size d_c is $0.2D$, where D is the orifice diameter that creates the ring. To quench a thin flame, the effect of flame stretch upon quenching is thought to be a function of the Karlovitz relation, which for this vortex-ring case is $(U_\theta/d_c)(\delta/S_L)$. However, as the vortex size is changed, their single vortex-ring quenching data do not exhibit a constant value of this Karlovitz parameter until the core size becomes large, $d_c > 10\delta$, and then, the value is 2.2. They conclude that small vortices are not as effective in quenching the flame as the Karlovitz concept would predict.

However, a Péclet number is constant along their quenching boundary. We see that the vortex-ring parameters that cause quenching are $U_\theta/S_L \sim 9.2\delta/d_c$, and this expression is also a Péclet number by replacing the flame thickness with $7.4a/S_L$. Thus, the quenching Péclet number is $U_\theta d_c/a = 68$. The ratio of (U_θ/d_c) to (d_c^2/a) could reflect a flow timescale relative to a heat transfer timescale. In summary, in their single vortex-ring flame interaction, a Péclet number below 20 causes no flame distortion, and a Péclet number above 70 creates a local quenching. Noteworthy is that a two-dimensional, single reaction step flame simulation has the same quenching trends as seen in the experiments, and therefore, more study of this flow should provide the quenching concepts for this vortex-flame interaction.

A direct numerical simulation of two-dimensional, decaying turbulence interacting with a $H_2/O_2/N_2$ system has been performed by Baum et al. [57]. They have selected the 9-species, 19-reaction scheme devised by Miller, Mitchell, Smooke, and Kee, and so, this should be considered a "full" kinetics flow simulation by comparison to previous efforts. While very costly in computer resources, this type of work provides a standard against which reduced-kinetic models may be judged. For example, the peak H atom is near the flame, i.e., the peak heat release, but there is a long diffuse region in the products. The peak OH is well behind the flame and does not remain as a connected contour, and so, images of this species would not be a valid experimental indicator of the heat-release connectivity.

These simulations with volume expansion require inflow/outflow boundary conditions, and as discussed by Poinsot [58], the compressible formulation with its explicit tracking of acoustic wave motion allows an easier boundary treatment. The acoustic time-step restriction does make this formulation more costly if a near-zero Mach number system is considered, but acoustic effects are needed if combustion stability questions are to be included. Currently, simulations in two-dimensions, which include detailed chemistry and heat release, are at the limit of computer capability and, therefore, are done for that reason [58]. However, as discussed by Collins [35], details of the forcing scheme may encourage the formation of vortical flow structures, and it would be good to exploit the two-dimensional system so that it mimics some features of the three-dimensional vortex structure. For example, as a function of Reynolds number, the vortex circulation and core diameter and the spacing between the vortices could be made to match the three-dimensional structure.

The Turbulent Future

When will the turbulence problem be solved? Since the flow is a nonlinear problem, then progress before the computer, the tool for developing nonlinear solutions, was limited. Additionally, before the laser-slice technique, the experimental information was also obscured by line of sight information and pointwise, random-looking signals. Growth in the computer tool has occurred during my career: 30 years ago, I used an IBM 1620 with card input and card output; 20 years ago, I used 1000 CDC 6600 hours to generate molecular dynamics simulations that reproduced the shear viscosity of liquid argon; 10 years ago, other people were using 50 h on a CRAY-1 to simulate turbulence with a million grid points; today, the CM-2 produces flow fields with 64

Giga-bytes of information, and 10 years from now, turbulence will be solved! The explosive growth in the nonlinear tool, combined with its widespread use and experimental flow images, means that sooner or later someone will create a model with the right perspective and, thereby, capture the essence of turbulent combustion.

For premixed flame propagation, where do we stand? Will we understand the dynamics of the reaction-sheet regime? For passive propagation, I think the understanding has started with the use of the G equation: The constant energy turbulence simulations allow a statistically steady flame motion to develop, and the probing of that flow allows models to be built, and, hence, understanding gained. Currently, we find that a two-dimensional flame-vortex interaction is a good configuration for exploring the effects of turbulence upon detailed flame structure. Going beyond these passive simulations requires the inclusion of heat release, and this calls for an adaptive grid in order to resolve the desired thin flame zone with large density change. The questions to be answered are as follows: Does the baroclinic production of vorticity change the flame surface geometry in a significant way from the passive flame? Does angular momentum within the vortex tube respond to the density change across the flame in ways that change propagation? Does the volume expansion affect the unburnt vortical structure? Does the pollutant formation depend upon flame shape?

Acknowledgments

This work was supported by the United States Department of Energy through the Office of Basic Energy Sciences, Division of Chemical Sciences. Their support of fundamental work without imposing specific short-range goals has allowed a very open approach, and by looking back, one can see many interconnections that were not visible when thinking ahead.

I met Norbert Peters at the 1979 Shear Flow conference, and although I was 48 hours ahead at birth, he clearly has led me into the combustion world. During a 1980 CRF research visit, Bob Bilger suggested that the premixed problem was in great need in comparison to non-premixed. Interactions with Forman Williams started in 1980 and have always been enjoyable and encouraging, as have the many trips to Cal Tech since the 1983 invitation by Paul Dimotakis. Alan Kerstein joined the group in 1981, and the many wild-idea, bad-pun sessions produced some of the work given above. By sharing their computer results, Parviz Moin and Mike Rogers got us into the DNS world. By creating the Center for Turbulence Research, Moin and Reynolds will continue to aid the whole combustion community.

REFERENCES

1. Williams, F. A., *Twenty-Fourth Symposium (International) on Combustion,* The Combustion Institute, Pittsburgh, 1992, p. 1.
2. Liñán, A., and Williams, F. A., *Fundamental Aspects of Combustion*, Oxford University Press, Oxford, 1993.
3. Chen, J. H., *Turbulent Shear Flows,* Springer-Verlag, New York, 1992, Vol. 8, p. 297; Chen, J. H., et al., *Proc. Summer Program 1990,* Center for Turbulence Research, NASA-Ames/Stanford University, 1990 (compare Figure 10 with 14).
4. Roshko, A., "Instability and Turbulence in Shear Flows." In *Theoretical and Applied Mechanics 1992,* (S. R. Bodner, et al., Eds.), Elsevier Science Publishers B. V., Amsterdam, 1993.
5. Boratav, O. N., Pelz, R. B., and Zabusky, N. J., *Phys. Fluids A* 4:581 (1992).
6. Karasso, P. S., and Mungal, M. G., "LIF Measurements of Mixing in Turbulent Shear Layers." *Sixth International Symposium on Applications of Laser Techniques to Fluid Mechanics*, Lisbon, Portugal, July, 1992; Karasso, P. S., "Experiments on Scalar Mixing and Reaction in Plane and Curved Turbulent Shear Layers," Thesis, Stanford University, Stanford, CA, 1994.
7. Lopez, J. M., and Bulbeck, C. J., *Phys. Fluids A* 5:1694 (1993); erratum 3013.
8. Liepmann, D., and Gharib, M., *J. Fluid Mech.* 245:643 (1992).
9. Abid, M., and Brachet, M. E., *Phys. Fluids A* 5:2582 (1993).
10. Hertzberg, J. R., and Ho, C. M., *AAIA J.* 30:2420 (1992).
11. Chao, Y.-C., and Jeng, M.-S., *Twenty-Fourth Symposium (International) on Combustion,* The Combustion Institute, Pittsburgh, 1992, p. 333.
12. Lasheras, J. C., Liñán, A., Lecuona, A., and Rodriguez, P., *Twenty-Fourth Symposium (International) on Combustion,* The Combustion Institute, Pittsburgh, 1992, p. 325.
13. Edwards, C. F., *Fuel* 72:1151 (1993).
14. She, Z.-S., Jackson, E., and Orszag, S. A., *Nature* 344:226 (1990).
15. Trefethen, L. N., Trefethen, A. E., Reddy, S. C., and Driscoll, T. A., *Science* 261:578 (1993).
16. Chen, S., Doolen, G. D., Kraichnan, R. H., and She, Z.-S., *Phys. Fluids A* 5:458 (1993).
17. She, Z.-S., Chen, S., Doolen, G., Kraichnan, R. H., and Orszag, S. A., *Phys. Rev. Lett.* 70:3251 (1993).
18. She, Zhen-Su, and Leveque, Emmanuel, *Phys. Rev. Lett.* 72:336 (1994).
19. Jiménez, J., Wray, A. A., Saffman, P. G., and Rogallo, R. S., *J. Fluid Mech.* 255:65 (1993); Jiménez, J., and Wray, A. A., *Meccanica* Sept. (1994).
20. Yeung, P. K., and Brasseur, J. G., *Phys. Fluids A* 3:884 (1991).
21. Ruetsch, G. R., and Maxey, M. R., *Phys. Fluids A* 4:2747 (1992).

22. Burgers, J. M., *Verhandel. Kon. Nederl. Akad. Wetenschappen Amsterdam, Afdeel. Naturkunde* 1940, Vol. 43, pp. 2–12; Burgers, J. M., *Advances in Applied Mechanics* Academic Press, New York, 1948, Vol. 1, p. 171.
23. Yeung, P. K., and Pope, S. B., *J. Fluid Mech.* 207:531 (1989).
24. Squires, K. J., and Eaton, J. K., *Phys. Fluids A* 2:1191 (1990).
25. Elghobashi, S., and Truesdell, G. C., *Phys. Fluids A* 5:1790 (1993).
26. Tio, K.-K., Liñán, A., Lasheras, J. C., Gañán, A. M., *J. Fluid Mech.* 254:671 (1993).
27. Bray, K. N. C., and Cant, R. S., *Proc. R. Soc. London A* 434:217 (1991).
28. Markstein, G. H., *Nonsteady Flame Propagation*, Pergamon Press, Oxford, 1964, p. 8.
29. Osher, S., and Sethian, J. A., *J. Compos. Phys.* 79:12 (1988).
30. Kerstein, A. R., Ashurst, W. T., and Williams, F. A., *Phys. Rev. A* 37:2728 (1988).
31. Peters, N., "Premixed, Non-Premixed and Partially Premixed Turbulent Combustion with Fast Chemistry," *Proceedings of Joint Meeting of the British and German Sections of The Combustion Insititute*, Cambridge, March, 1993.
32. Ashurst, Wm. T., and Shepherd, I. G., *Combust. Sci. Technol.*, to be submitted (1994).
33. Ashurst, Wm. T., "Constant-Density Markstein Flamelet in Navier-Stokes Turbulence," *Combust. Sci. Technol.*, in press (1994).
34. Murray, J. D., *Mathematical Biology*, (Springer-Verlag, New York, 1989, p. 282.
35. Collins, L. R., "Spectral Analysis of a Simulated Premixed Flame Surface in Two Dimensions," submitted to *Computers and Fluids*, 1994.
36. Peters, N., *J. Fluid Mech.* 242:611 (1992).
37. Wirth, M., and Peters, N., *Twenty-Fourth Symposium (International) on Combustion*, The Combustion Institute, Pittsburgh, 1992, p. 493.
38. Zhu, J., and Ronney, P. D., "Simulation of Front Propagation at Large Non-dimensional Flow Disturbance Intensities." *Combust. Sci. Technol.*, in press (1994).
39. Bradley, D., *Twenty-Fourth Symposium (International) on Combustion*, The Combustion Institute, Pittsburgh, 1992, p. 247.
40. Shepherd, I. G., *Some Effects of Heat Release in Premixed Flames*, Western States, March, 1994; Shepherd, I. G., and Kostiuk, L. W., *Combust. Flame* 96:371 (1994).
41. Gonzalez, M., Borghi, R., and Saouab, A., *Combust. Flame* 88:201 (1992).
42. Duclos, J. M., Veynante, D., and Poinsot, T., *Combust. Flame* 95:101 (1993).
43. Chin, Y.-W., Matthews, R. D., Nichols, S. P., and Kiehne, T. M., *Combust. Sci. Technol.* 86:1 (1992).
44. Bielert, U., Klug, M., and Adomeit, G., SAE 940211, 1994.
45. Boulouchos, K., Steiner, T., and Dimopoulos, P., SAE 940476.
46. Checkel, M. D., and Thomas, A., *Combust. Flame* 96:351 (1994).
47. Ting, S.-K., Checkel, M. D., Haley, R., and Smy, P. R., SAE 940687. Flame radii up to 84 mm are in Palm-Leis, A., and Strehlow, R. A., *Combust. Flame* 13:111 (1969).
48. Ashurst, Wm. T., Checkel, M. D., and Ting, D. S.-K., "The Eddy Structure Model of Turbulent Flamelet Propagation, the Expanding Spherical and Steady Planar Cases." *Combust. Sci. Technol.*, 99:51 (1994).
49. Kwon, S., Wu, M.-S., Driscoll, J. F., and Faeth, G. M., *Combust. Flame* 88:221 (1992).
50. Gülder, Ö. L., *Twenty-Third Symposium (International) on Combustion*, The Combustion Institute, Pittsburgh, 1991, p. 743.
51. Liu, Y., and Lenze, B., *Twenty-Second Symposium (International) on Combustion*, The Combustion Institute, Pittsburgh, 1988, p. 747.
52. Ashurst, Wm. T., *Combust. Sci. Technol.* 92:87 (1993).
53. Kosiuk, L. W., and Bray, K. N. C., *Combust. Sci. Technol.* 95:193 (1994).
54. Lee, T.-W., Lee, J. G., Nye, D. A., and Santavicca, D. A., *Combust. Flame* 94:146 (1993).
55. Samaniego, J.-M., "Stretch-Induced Quenching in Flame-Vortex Interactions," Center for Turbulence Research, Annual Research Briefs 205, 1993.
56. Roberts, W. L., Driscoll, J. F., Drake, M. C., and Goss, L. P., *Combust. Flame* 94:58 (1993).
57. Baum, M., Poinsot, T. J., Haworth, D. C., and Darabiha, N., "Using Direct Numerical Simulation to Sturdy $H_2/O_2/N_2$ Flames with Complex Chemistry in Turbulent Flows," *J. Fluid Mech.*, in press (1994).
58. Poinsot, T. J., "The Combustion Program at CTR," Center for Turbulence Research, Annual Research Briefs 195, 1993.

COMMENTS

Paul Ronney, University of Southern California, USA. Do you think the flamelet regime is the most relevant one? Do you have an opinion as to what happens at high Karlovitz numbers, where nonflamelet behavior might occur? This might be a useful issue to consider, since you refer back to Damköhler, who also proposed the relation $S_T/S_L = \sqrt{D_T/D_L}$, where D is a relevant diffusivity, in the limit of very high Ka.

Author's Reply. Damköhler did suggest the above form when the fine-body turbulence is judged to be more important than the coarse-body effect. Formation of opinions should be based on numerical simulations and comparable experimental results. Calculations that include detailed chemical structure, such as given in Ref. 57 (to appear in *J. Fluid Mech.*), are needed. Three-dimensional simulations, with a simple nonpremixed reaction, are given in Nomura and Elghobashi [*Theor. Comput. Fluid Dyn.* 5:153 (1993)].

•

Matt Hall, University of Texas, USA. Your rule of thumb estimate of the diameter of a vortex tube as approximately 4η would lead to diameters as large as 200 μm based upon typical Kolmogorov scales of 10–50 μm. Within engines, PIV and LDA measurements give integral scales of 2–4 mm. In view of this order of magnitude difference, with what turbulent length scale would you associate the vortex tube size?

Author's Reply. From the cited simulations, the mean vortical radius is approximately 4η [see text above Eq. (1)]. Using the apparent values of $\varepsilon\Lambda/u'^3 \sim 6.5/\sqrt{Re_\lambda}$, then the ratio of integral scale to vortex diameter, $\Lambda/8\eta$, would be two for Re_λ of 25 and 10 for Re_λ of 81; this range corresponds to low-speed engine results. The Taylor scale has less variation over this Reynolds number range: $\lambda/8\eta$ is 1.3 and 2.1, and so the Taylor scale may approximate the vortex diameter over a restricted range of test-engine results. A caution about the simulation results should be noted: The resolution of the integral scale is not as good as the Kolmogorov scale because the large scales are undersampled in comparison with the small scales. A further caution: Does the simulated box turbulence also exist within an engine chamber? PIV determination of engine flow structure should be compared with computed vortex structure.

•

S. B. Pope, Cornell University, USA. In a previous modelling study [Pope, S. B., and Cheng, W. K., *Twenty-First Symposium (International) on Combustion,* The Combustion Institute, Pittsburgh, 1986, p. 1473], the increase of turbulent flame speed with flame-ball radius was observed in accord with experiments. But for large times, the model predicts that S_T is asymptotic to a constant times u'. Your model formula for S_T appears to have a linear dependence upon R, so that S_T can become arbitrarily large compared to u'.

Author's Reply. In the Pope and Cheng work, the largest flame radius was 20 mm, whereas the experiments cited in Ref. 47 indicate a radial growth up to the maximum observed radius of 84 mm. Additionally, in the Pope and Cheng model the inclusion of volume expansion appears to be in the same manner as that done by Kwon et al. [49], that is, with respect to a laminar flame ball the model allows turbulence to create more flame area but the model does not include the integrated effect of distributed volume expansion [see Eq. (14) and the following discussion]. With regard to an arbitrarily large S_T value, the discussion notes that changes in the turbulent flame zone thickness would modify S_T as indicated by the ratio of R_i/R_o in Eq. (14). A similar inner and outer flame-ball radius ratio has been included as an empirical modification by Groff to the Blizard–Keck–Tabaczynski entrainment model of turbulent flame propagation [*Combust. Flame* 67:153 (1987)]. Inclusion of this radius ratio improves the model result for flame acceleration compared with experimental results for radii up to 40 mm in a fan-stirred chamber. It is *very* interesting to see what this empirical modification does to the entrainment model: The burnt radius velocity is given as $dr_b/dt = (dm_b/dt)(3/4\pi\rho_b r_b^2)$, and the assumed mass burning rate is $(m_e - m_b)S_L/\lambda$ where m_e is the entrained mass enclosed within radius r_e and the time constant assumes eddies of Taylor size burning at the laminar burning velocity. The burnt radius velocity becomes $dr_b/dt = (m_e - m_b)(S_L/\lambda)(3/4\pi\rho_b r_b^2)$. Now, even though the flame surface is known to be greatly distorted so that a spherical shell between r_b and r_e includes both burnt and unburnt mass, we assume that r_e can be defined as a spherical shell outside the burnt volume and use $m_e - m_b = 4\pi\rho_u(r_e^3 - r_b^3)/3$. The burnt radius velocity is then $dr_b/dt = (\rho_u S_L/\rho_b)(r_e^3 - r_b^3)/r_e^3](r_e^2/r_b^2)$ where a factor of r_e^3 has been multiplied and divided on the right side. Now the *interesting* part is that Groff's inclusion is the additional term of r_b^2/r_e^2 to the entrainment velocity. By including this factor in the above equation for the burnt radius velocity, we obtain the functional form given in Eq. (14)—with the minor difference of density ratio instead of temperature ratio minus unity! Thus, distributed volume expansion may cause flame acceleration—until limited by turbulence decay and/or by an upper limit on flame surface density due to volume expansion.

•

J. Chomiak, Chalmers University of Technology, Sweden. In your presentation, you have emphasized the role of concentrated vortex structures in turbulent flame development. The current DNS simulations of turbulence show indeed that they are permanent, long lasting (typical lifetimes of the order of five large eddy turnover times), and extending over several integral length scales so they are the true coherent structures of large *Re* number turbulence. However, their distribution is random in space, and so on average their inclination angle to the flame has to be about 45°. In your model, you assume that they are always parallel to the flame. Can you comment on the accuracy of the assumption.

Author's Reply. The current modeling viewpoint does not assume a particular flame-vortex configuration, but

does assume that the vortex structure may determine the flame surface density and that the integrated effect of volume expansion determines the turbulent flame speed. The passive flame simulations and experimental results that led to this viewpoint, Refs. 47 and 48, do not rule out the vortex bursting mechanism proposed by you in the Sixteenth Symposium. Simulations and experiments that provide known flame-vortex interactions along with the resulting flame speed are now possible, and it is this new work that will determine which modeling concepts are viable.

Twenty-Fifth Symposium (International) on Combustion/The Combustion Institute, 1994/pp. 1091–1098

DYNAMICS OF THE FLAME SURFACE AREA IN TURBULENT NON-PREMIXED COMBUSTION

W. KOLLMANN
MAE Department
University of California at Davis
Davis, CA 95616, USA

AND

J. H. CHEN
Combustion Research Facility
Sandia National Laboratories
Livermore, CA 94551-0969, USA

The dynamic equations for integral quantities relevant to turbulent flames are developed based on a theorem of geometric measure theory. The total area of level surfaces is considered in detail using mixture fraction, a quantity which is important for non-premixed combustion, to define the level surfaces. The level surface corresponding to its stoichiometric value is defined as the flame surface. It is shown that the rate of strain generated by the motion of the fluid, coupled with molecular diffusion and source terms of the scalar variable defining the level surface, determines the evolution of the surface properties. Direct numerical simulation (DNS) results obtained for a low-Reynolds-number turbulent non-premixed flame are used to evaluate the effects of strain rate and scalar dynamics on the surface area of level surfaces, including the flame surface.

Introduction

Global properties of turbulent flames are of significant practical interest. For instance, the emission index for NO in turbulent flames is defined as the ratio of the total NO flux to the fuel mass flux. The total NO flux depends essentially on the reactive volume (see Chen and Kollmann [1]), which, in turn, is defined as the instantaneous volume bounded by the two iso-surfaces $\zeta(\underline{x},t) = z_{st} + \Delta z$ and $\zeta(\underline{x},t) = z_{st} - \Delta z$, where ζ denotes the mixture fraction, z_{st} its stoichiometric value, and Δz the thickness of the reactive zone. The propagation of the two bounding level surfaces determines the statistics of the reactive zone and thus the expectation of the NO flux. It follows that the dynamics of iso-surfaces are at the heart of the prediction problem for the NO-emission index.

Iso-surfaces are known to be smooth for almost all level values if the generating scalar field is infinitely often differentiable (see Maz'ja [2], Chap. 1.2, p. 35). It is clear that the extremal level values of Φ do not necessarily correspond to surfaces, but may produce sets of isolated points or subsets of the flow field $\mathfrak{D}$ with positive volume. If such level values are avoided, the iso-surfaces are accessible to analysis using classical topology and differential geometry [3,4]. A theorem of geometric measure theory [2] provides the bridge between volume integrals and iso-surfaces, and it is the main tool for the derivation of transport equations governing global properties of iso-surfaces such as surface area.

Velocity and scalar fields generated by direct numerical simulation of a non-premixed flame in decaying turbulence [5,6] are used to evaluate the terms in the transport equation for the surface area of level surfaces. It is verified that the curvature term is not negative definite and that the in-plane stretching term produces significant increase in the area of the iso-surfaces as the upper and lower limits for mixture fraction are approached.

The Relation of Iso-Surfaces to Mixing and Chemical Reactions

A major obstacle in the development of a closure scheme for turbulent combustion is the construction of a realistic model for mixing that satisfies all mathematical constraints [7,8]. Several models for mixing in turbulent flows have been developed so far [7,9–13], but none of them is perfect. For instance, the model based on the notion that pairwise interaction of fluid volumes, small compared to the relevant scales of the flow in a continuous medium [9,10], is oversimplified for the following reasons, and more-

over, is incorrect in the asymptotic limit $t \to \infty$ [14]. First, it should be noted that discretization of the scalar space into regular and local grid cells corresponds to a discretization of physical space determined by families of iso-surfaces. These iso-surfaces do not provide a discretization of physical space into local cells but into highly complicated subregions, which may be distributed over the entire flow field. Consider such a subregion determined as the set of points $\mathcal{A}_n(t) \equiv \{\underline{x} | \varphi_n \leq \Phi(\underline{x},t) \leq \varphi_{n+1}\}$. This set $\mathcal{A}_n$ is bounded by two iso-surfaces, $\Phi(\underline{x},t) - \varphi_n = 0$ and $\Phi(\underline{x},t) - \varphi_{n+1} = 0$, which do not intersect as long as the scalar Φ is at least a continuous function of location $\underline{x}$. The set $\mathcal{A}_n$ may be the union of a finite number of disjoint sets, each of which may have nontrivial topological properties (intrinsic properties as given by the Euler–Poincaré characteristic and the number of disjoint pieces and embedding properties such as braiding, linkage, and knottedness). Furthermore, the set $\mathcal{A}_n$ may be closed or it may intersect with the boundary of the flow domain. The evolution of this set for a short time interval (short compared to the time scales of the flow; for larger time intervals, self-intersection of iso-surfaces may occur) is completely determined by the motion of the bounding iso-surfaces. If the scalar $\Phi(\underline{x},t)$ is nondiffusive and conserved, the iso-surfaces are materially invariant and, therefore, cannot change their topology, and no mixing takes place. It follows that mixing is due to the motion of the iso-surfaces relative to the fluid (the fluid velocity $\underline{v}$ is the macroscopic average of molecular motion without regard to species), and the amount of mixing is given locally by the relative progression velocity V of the interfaces in the direction normal to them. This relative progression velocity $V\underline{n}$, which is the difference between the velocity $\underline{v}^s$ of the level surface and the fluid velocity $\underline{v}$, is by no means constant on the iso-surface. It varies with the curvature of the iso-surface, as can be deduced from the relation to the scalar Φ defining the iso-surface [4,15,16]

$$V = \frac{1}{|\nabla\Phi|}\left\{\frac{1}{\rho}\frac{\partial}{\partial x_a}\left(\rho\Gamma\frac{\partial\Phi}{\partial x_a}\right) + \dot{W}_\Phi(\Phi)\right\} \quad (1)$$

where the equation for the iso-surface is given implicitly by

$$S(\underline{x},t,\varphi) = \Phi(\underline{x},t) - \varphi \quad (2)$$

and the scalar Φ defining the iso-surface is governed by

$$\rho\left(\frac{\partial\Phi}{\partial t} + v_a\frac{\partial\Phi}{\partial x_a}\right) = \frac{\partial}{\partial x_a}\left(\rho\Gamma\frac{\partial\Phi}{\partial x_a}\right) + \rho\dot{W}_\Phi(\Phi). \quad (3)$$

The unit normal vector of the iso-surface is defined by

$$n_a \equiv -\frac{1}{|\nabla\Phi|}\frac{\partial\Phi}{\partial x_a} \quad (4)$$

pointing into the region where $\Phi(\underline{x},t) < \varphi$ holds. The divergence of the unit normal vector of a level surface can be shown to be determined by the mean curvature H of the level surface [4]

$$\left(\frac{\partial n_a}{\partial x_a}\right)_{\Phi=\varphi} = -2H \quad (5)$$

where $H \equiv 1/2(k_1 + k_2)$ and k_1, k_2 are the principal curvatures of the surface (see Do Carmo [3] for definition). It follows that the relative progression velocity V is determined by three distinct phenomena

$$V = 2\Gamma H + \frac{1}{|\nabla\Phi|}\left\{\frac{1}{\rho}\frac{\partial}{\partial n}\left(\rho\Gamma\frac{\partial\Phi}{\partial n}\right) + \dot{W}_\Phi\right\} \quad (6)$$

where $\partial/\partial_n \equiv n \cdot \nabla$. The first contribution is purely geometric, as it is proportional to the mean curvature of the level surface, the second is due to the diffusive flux normal to the level surface, and the last term represents the motion of the level surface due to the production or destruction of the scalar Φ.

It is easy to see that the relation (1) for the relative progression velocity follows at once from the dynamic equation (3) for the scalar defining the level surface if Eq. (3) is written as [17]

$$\frac{\partial\Phi}{\partial t} + \left(v_a - \frac{V}{|\nabla\Phi|}\frac{\partial\Phi}{\partial x_a}\right)\frac{\partial\Phi}{\partial x_a} = 0. \quad (7)$$

This equation can be regarded as the dynamic equation for the scalar Φ that is convected with the surface velocity

$$v_a^s \equiv v_a - \frac{V}{|\nabla\Phi|}\frac{\partial\Phi}{\partial x_a} \quad (8)$$

where the superscript s refers to the iso-surface. Equation (8) simply states that the iso-surface $\Phi = \varphi$ moves relative to the fluid with the speed V in its normal direction. It is important to notice that the fluid velocity and the modified velocity are fundamentally different. The fluid velocity induces a smooth one-to-one mapping of the flow field, which is the solution of the kinematic equations (Lagrangian frame, $\underline{a}$ is the label variable defined as the location of a material point at the reference time zero)

$$\frac{dX_a}{dt} = v_a\,[\underline{X}(\underline{a},t),t], \qquad \underline{X}(\underline{a},0) = \underline{a} \quad (9)$$

but the surface velocity $\underline{v}^s$ does not. It is well known that the surface velocity $\underline{v}^s$ determined by V = constant leads to cusp singularities, and self-intersection

of iso-surfaces is possible. If the relative progression velocity V is given by the diffusion and source in Eq. (3), no self-intersection is observed, but topological change of iso-surfaces can occur.

The spreading of the iso-surface relative to the fluid is proportional to the scalar dissipation rate, as can be seen from [18]

$$\langle V|\nabla\Phi|\delta(S)\rangle(\varphi) = \frac{\partial}{\partial_\varphi}(\langle\varepsilon_\Phi|\Phi = \varphi\rangle f_\Phi) + \dot{W}_\Phi(\varphi)f_\Phi \tag{10}$$

where f_Φ denotes the Eulerian pdf of the values of Φ at $\underline{x}$ and time t. The relation (10) shows that transport in scalar space must occur if mixing and chemical reactions are to take place. It also shows that mixing and chemical reactions are local in scalar space depending on the local values of the conditional dissipation rate and the scalar pdf.

Transport Equations for Global Properties of Level Surfaces

The principal tool for the derivation of transport equations for integral properties of scalar fields is the relation

$$\int_{\mathcal{D}} d\underline{x} f(\underline{x})\delta(\Phi(\underline{x}) - \varphi)|\nabla\Phi| = \int_{S_\Phi(\varphi)} dA(\underline{x})f(\underline{x}) \tag{11}$$

valid for differentiable functions $f(x)$. It is a consequence of the general theorem 1.2.4 in Maz'ja [2] (Chap. 1.2.4, p. 37) for nonnegative $f(\underline{x})$; the condition $f \geq 0$ can be removed easily for differentiable functions. The surface area $\mathcal{A}_\Phi(\varphi)$ is an important special case that follows at once from relation (11) by setting $f(\underline{x}) = 1$ as

$$\mathcal{A}_\Phi(\varphi) = \int_{\mathcal{D}} dx\delta(\Phi(\underline{x}) - \varphi)|\nabla\Phi|. \tag{12}$$

All relations hold under the condition that the level surfaces $S_\Phi(\varphi)$ are contained in the domain $\mathcal{D}$.

Kinematic Relations:

Transport equations for global (integral) properties follow from the representation (11) by differentiation with respect to time. The nature of the resulting equation to be established in the present section will be kinematic, expressing the time rate of change of global variables in terms of the progression velocity and geometric parameters of the level surfaces. The dynamic aspect will be considered in the following section.

A global variable is defined by

$$\mathfrak{F}_\Phi(\varphi,t) \equiv \int_{S_\Phi(\varphi)} dA(\underline{x})f(\underline{x},t) \tag{13}$$

where $f(\underline{x},t)$ is a smooth function of location and time to allow differentiation. Application of Eq. (11) to Eq. (13), differentiation with respect to time, and using the properties of the Dirac function lead to

$$\frac{\partial\mathfrak{F}_\Phi}{\partial t} + \frac{\partial}{\partial\varphi}\int_{\mathcal{D}} d\underline{x}\delta(\Phi - \varphi)|\nabla\Phi| f\frac{\partial\Phi}{\partial t} = \int_{\mathcal{D}} d\underline{x}\delta(\Phi - \varphi)|\nabla\Phi\frac{\partial f}{\partial t} + \int_{\mathcal{D}} d\underline{x}\delta(\Phi - \varphi)f\frac{\partial|\nabla\Phi|}{\partial t}. \tag{14}$$

Three contributions to the time rate of change of the global variable $\mathfrak{F}_\Phi(\varphi,t)$ emerge: a convective transport term in scalar space and two source terms determined by the evolution of f and $|\nabla\Phi|$. It is straightforward to establish equations equivalent to Eq. (14) using the surface velocity $\underline{v}^s$ defined in Eq. (8) and the relation (11). It follows that

$$\frac{\partial\mathfrak{F}_\Phi}{\partial t}(\varphi,t) = \int_{\mathcal{D}} dx\delta(\Phi - \varphi)\cdot\left\{\frac{\partial}{\partial t}(f(\underline{x},t)|\Delta\Phi|) + \nabla\cdot(\underline{v}^s f(\underline{x},t)|\nabla\Phi|)\right\}. \tag{15}$$

holds. The relation (11) can be applied once more to Eq. (15), and a third equivalent version emerges in terms of surface integrals only,

$$\frac{\partial\mathfrak{F}_\Phi}{\partial t}(\varphi,t) = \int_{S_\Phi(\varphi)} dA\left\{\frac{D^s f}{Dt} + f\frac{D^s}{Dt}\log(|\nabla\Phi|) + f\frac{\partial v_a^s}{\partial x_a}\right\} \tag{16}$$

where $D^s/Dt \equiv \partial/\partial t + v_a^s\,\partial/\partial x_a$ denotes the time rate of change following points on the level surface. The time rate of change of the global variable $\mathfrak{F}$ is caused by the change of the function $f(\underline{x},t)$ on the level surface and the time rate of change of $\log(|\nabla\Phi|)$ on the level surface.

It is straightforward to show that the transport equations (15), (19), (20) are equivalent to the theorem stated by Candel and Poinsot [19] in the form

$$\frac{d}{dt}\int_{S\Phi(\varphi)} dA\underline{G}\cdot\underline{n} = \int_{S\Phi(\varphi)} dA\left\{\frac{\partial \underline{G}}{\partial t} + (\underline{v}^s\cdot\nabla)\underline{G} - (\underline{G}\cdot\nabla)v^s + \underline{G}(\nabla\cdot\underline{v}^s)\right\}\cdot\underline{n}$$

if the function $f(x)$ is regarded as the flux normal to the level surface $f \equiv \underline{G}\cdot\underline{n}$. This result builds the bridge to the equations for surface quantities obtained by Candel and Poinsot [19] and Bideaux et al. [20].

Dynamic Relations:

The main tools for the derivation of dynamic equations governing the evolution of global variables are one of the kinematic relations (14), (15), (16) and the dynamic equation (3) for the defining variable $\Phi(\underline{x},t)$. The scalar $f(\underline{x},t)$ appearing in the global variable is governed by

$$\rho\left(\frac{\partial f}{\partial t} + v_a\frac{\partial f}{\partial x_a}\right) = \frac{\partial}{\partial x_a}\left(\rho\lambda\frac{\partial f}{\partial x_a}\right) + \rho\dot{W}_f(f). \quad (17)$$

The kinematic relations (1) and (8) express the progression velocity V of the level surfaces in terms of the scalar field Φ and fluid and surface velocities. It is straightforward to establish the dynamic equation for the global variable $\mathfrak{F}_\Phi$ using relation (15) in the form

$$\frac{\partial\mathfrak{F}_\Phi}{\partial t} = \int_{S\Phi(\varphi)} dA\left\{\frac{1}{\rho}\frac{\partial}{\partial x_a}\left(\rho\lambda\frac{\partial f}{\partial x_a}\right) + \dot{W}_f + f\left(\frac{\partial v_a}{\partial x_a} - n_a n_\beta\frac{\partial v_\beta}{\partial x_a}\right) + \frac{1}{|\nabla\Phi|}\left[\frac{1}{\rho}\frac{\partial}{\partial x_a}\left(\rho\Gamma\frac{\partial\Phi}{\partial x_a}\right) + \dot{W}_\Phi\right]\frac{\partial}{\partial x_a}(n_a f)\right\} \quad (18)$$

which is valid if the area of the level surface satisfies $\mathcal{A}_\Phi \geq 0$. This is one of several equivalent versions of the dynamic equation for the global variable $\mathfrak{F}_\Phi(\varphi,t)$. As a special case the equation for the surface area $A_\Phi(\varphi,t)$ is also given:

$$\frac{\partial\mathcal{A}_\Phi}{\partial t} = \int_{S\Phi(\varphi)} dA\left\{\frac{\partial v_a}{\partial x_a} - n_a n_\beta\frac{\partial v_\beta}{\partial x_a} + \frac{1}{|\nabla\Phi|}\left[\frac{1}{\rho}\frac{\partial}{\partial x_a}\left(\rho\Gamma\frac{\partial\Phi}{\partial x_a}\right) + \dot{W}_\Phi\right]\frac{\partial n_a}{\partial x_a}\right\}. \quad (19)$$

The surface area changes as a result of the deformation caused by the motion of the fluid and the dynamic change of the scalar field defining the level surface. In particular, the surface area changes because of the rate of strain acting in the tangential plane and the change of the scalar variable Φ defining the level surface, but both phenomena may increase or decrease the surface area. The strain rate has eigenvalues that add to zero for incompressible flows or to the rate of volume expansion for reacting flows, but in both cases, positive and negative eigenvalues may be present. Suppose the coordinate system is rotated such that the third direction is parallel to the surface normal; then we obtain

$$\frac{\partial v_a}{\partial x_a} - n_a n_\beta\frac{\partial v_\beta}{\partial x_a} = -\frac{\partial v_1}{\partial x_1} - \frac{\partial v_2}{\partial x_2}$$

which shows that the change of surface area is indeed due to the in-plane strain rates. As can be seen from Eq. (19), expansion in the tangential plane will increase the surface area and compression will decrease it. The dynamics of the scalar variable defining the level surface appear in Eq. (19) as molecular diffusion and source term. It is clear that both may be positive or negative and, hence, increase or decrease the surface area as time evolves. The molecular diffusion term can be analyzed in more detail if the variation of density is disregarded and the diffusivity is assumed constant. It follows then that it is given by

$$\frac{1}{|\nabla\Phi|}\Delta\Phi\frac{\partial n_a}{\partial x_a} = \frac{\partial n_a}{\partial x_a}\frac{\partial n_\beta}{\partial x_\beta} + \frac{\partial n_\gamma}{\partial x_\gamma}\frac{n_a n_\beta}{|\nabla\Phi|}\frac{\partial^2\Phi}{\partial x_a\partial x_\beta}. \quad (20)$$

The first term on the right side is purely geometrical since it only depends on the mean curvature H

$$\frac{\partial n_a}{\partial x_a} = -2H$$

whereas the second term depends on the variation of the defining scalar normal to the level surface $\partial\Phi/\partial_n = n\cdot\nabla\Phi$. It is easy to see that Eq. (20) can be recast in the form

$$\frac{1}{|\nabla\Phi|}\Delta\Phi\frac{\partial n_a}{\partial x_a} = 4H^2 - 2\frac{H}{|\nabla\Phi|}\frac{\partial^2\Phi}{\partial n^2} \quad (21)$$

which proves that the effect of molecular diffusion on the surface area is not definite: The first term on the right side in Eq. (21) always decreases the surface area [note the negative sign in Eq. (19)] if the mean curvature H is nonzero, but the second term may decrease or increase it depending on the signs of the normal derivative and the mean curvature.

Direct Simulation Method

Direct numerical simulations (DNS) of a turbulent non-premixed flame are performed for the study of the dynamics of level surfaces by solving the compressible reacting Navier–Stokes species and energy equations. The present formulation includes variable density, variable dynamic viscosity, and heat release effects. An Arrhenius two-step chemical kinetics model is used in the present DNS, chosen to study the effect of a fast-diffusing radical-like species such as OH. In the model, a radical I is produced in the first step and then consumed in the second step

$$A(\text{fuel}) + B(\text{oxidiser})$$

$$\rightarrow I(\text{intermediate, radical-like species}) \quad (22)$$

$$A(\text{fuel}) + I(\text{intermediate}) \rightarrow P(\text{product}). \quad (23)$$

The values of the parameters in the two-step mechanism are chosen to correspond to global methane-air combustion. The effect of differential molecular diffusion is studied by varying the Schmidt number of the intermediate species between unity and one-half (Chen et al. [5]) while taking the Schmidt number of all other species to be unity. In the present study, for the purpose of studying the effects of strain rate and scalar dynamics on the flame surface area, the effect of differential diffusion is neglected, and the Schmidt number of all of the species is taken to be unity.

The initial distribution of reactants and product concentrations are obtained from a onedimensional computation of an unstrained plane laminar non-premixed flame. Subsequently, an initial turbulent kinetic energy spectrum is prescribed, and the plane laminar flame is allowed to interact with the isotropic turbulence field. The initial Reynolds number based on the Taylor scale and cold fluid viscosity is 50, and the ratio of the initial reaction zone thickness to the Kolmogorov scale is 10. The effect of the turbulence on the flame is to convect, distort, and stretch the flame, whereas the effect of the flame on the turbulence, through increases in dynamic viscosity and through dilatational effects, is to dampen the turbulence in the vicinity of the high-temperature reaction zone. If the chemical kinetics are fast in comparison to characteristic flow times, then the flame burns fully. However, if the chemistry and the fluid mechanical time scales are of the same order of magnitude, then local extinction occurs in regions that are unable to sustain the large tangential strain rates.

In the present study, the level surface defined by the mixture fraction is used to study the dynamics of the flame surface area. For the two-step DNS, the mixture fraction, defined for our choice of stoichiometric coefficients, molecular weights, and unmixed stream concentrations, is given by

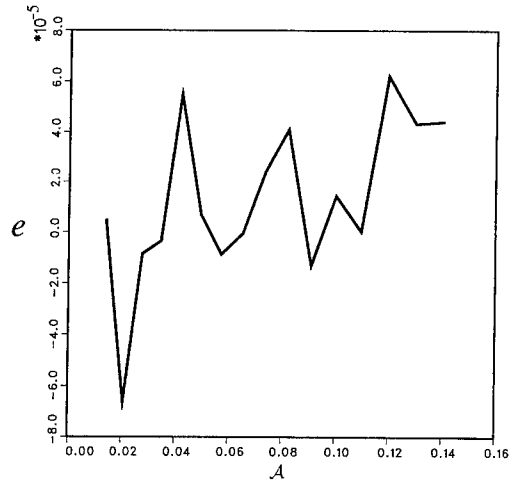

FIG. 1. Error e as defined in section V ("Triangulation Procedure for Iso-Surfaces") in the surface integral computation for a sphere with the analytic velocity field given in section V as a function of the surface area. The exact value for the integral is zero.

$$Z = \frac{2Y_A - Y_I - 2Y_B + 2}{4} \quad (24)$$

such that in the unmixed A stream, $Z = 1$, and in the unmixed B stream, $Z = 0$. When all the molecular diffusion coefficients are equal, Z is a conserved scalar. In the limit of infinitely fast chemistry, at the flame $Y_A = Y_B = Y_I = 0$, giving $Z_{c1} = 1/2$, whereas if the second step is relatively slow compared with the first step, at the flame $Y_A = Y_B = 0$, $Y_I = 1$, giving $Z_{c2} = 1/4$. Thus, these two limits of Z identify the locations of the reaction zones under these limiting cases.

Triangulation Procedure for Iso-Surfaces

A numerical procedure based on linear interpolation of scalar field data given on a threedimensional lattice of grid points and triangulation of the level surface defined by a prescribed level value has been developed (see Chen and Kollmann [21] for a detailed description). Once the triangulated surface is established, surface integrals such as surface area and the terms in the transport equation (19) can be computed. However, the accuracy of this numerical integration procedure must be established before the application to turbulent reacting flows can be attempted. The computation of the strain rate term

$$I_1 \equiv \int_{S\Phi(\varphi)} dA \left\{ \frac{\partial v_\alpha}{\partial x_\alpha} - n_\alpha n_\beta \frac{\partial v_\beta}{\partial x_\alpha} \right\}.$$

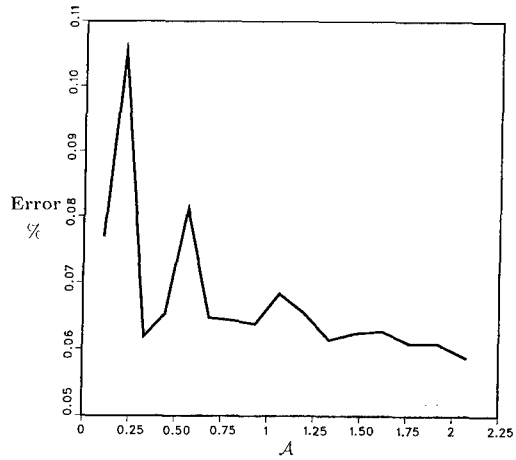

FIG. 2. Percent error in the surface integral for the curvature term for diffusion from a point source as a function of the surface area of the spherical level surfaces.

can be tested using the Gauss divergence theorem if the vector field $b_\alpha = n_\beta\, \partial v_\beta/\partial x_\alpha$ is solenoidal. It follows then that I_1 must be zero for all level values. The scalar field is defined for this test as the solution

$$\Phi(\underline{x},t) = \frac{1}{(2\sqrt{\pi\Gamma t})^3} \exp\left\{-\frac{x_\alpha x_\alpha}{4\Gamma t}\right\}. \tag{25}$$

of the initial value problem of

$$\frac{D\Phi}{Dt} = \frac{\partial\Phi}{\partial t} = \Gamma\Delta\Phi$$

where the fluid velocity is zero and the domain $\mathcal{D} = R^3$ with the initial condition $\Phi(\underline{x},0) = \delta(\underline{x})$. The vector field b is given by

$$b_\alpha(\underline{x}) = \begin{pmatrix} \sin\left(\pi \dfrac{k_1 x_1}{L_1}\right) \sin\left(\pi \dfrac{k_2 x_2}{L_2}\right) \sin\left(\pi \dfrac{k_3 x_3}{L_3}\right) \\ \cos\left(\pi \dfrac{k_1 x_1}{L_1}\right) \cos\left(\pi \dfrac{k_2 x_2}{L_2}\right) \cos\left(\pi \dfrac{k_3 x_3}{L_3}\right) \\ \dfrac{k_1 L_3}{k_3 L_1} \cos\left(\pi \dfrac{k_1 x_1}{L_1}\right) \sin\left(\pi \dfrac{k_2 x_2}{L_2}\right) \cos\left(\pi \dfrac{k_3 x_3}{L_3}\right) + \dfrac{k_2 L_3}{k_3 L_2} \cos\left(\pi \dfrac{k_1 x_1}{L_1}\right) \sin\left(\pi \dfrac{k_2 x_2}{L_2}\right) \sin\left(\pi \dfrac{k_3 x_3}{L_3}\right) \end{pmatrix}.$$

The result ($k_1 = k_2 = k_3 = 4.0$ and $L_1 - L_2 = L_3 = 1.0$) of the integration over the spherical level surfaces defined by Eq. (25) is shown in Fig. 1, where the error

$$e \equiv \frac{\displaystyle\int_{S\Phi(\varphi)} dA n_\alpha b_\alpha}{\displaystyle\int_{S\Phi(\varphi)} dA |\underline{b}|}$$

is plotted as a function of the level value. It is evident that accuracy of the numerical integration over the spherical level surfaces is satisfactory.

The accuracy of the numerical calculation of the curvature term on the right side of Eq. (19)

$$I_2 \equiv -\int_{S\Phi(\varphi)} dA \frac{1}{|\nabla\Phi|} \Gamma\Delta\Phi \frac{\partial n_\alpha}{\partial x_\alpha}$$

can be tested using the same solution (25) of the diffusion equation. A simple calculation shows that $I_2 = -8\pi\Gamma\{3 + 2\log[\varphi(2\sqrt{\pi\Gamma t})^3]\}$ holds. The relative error between numerical and analytic integration is plotted in Fig. 2 for the spherical level surfaces defined by the solutions of Eq. (25). It is seen that the accuracy is satisfactory.

Results for a Non-Premixed Turbulent Flame

Velocity and scalar fields obtained by direct numerical simulation of a non-premixed flame in decaying turbulence allow the calculation of surface area and the terms in its transport equation (19). The strain rate term I_1 is shown in Fig. 3 as a full line together with the incompressible part, $I_1^i = -\int_{S\Phi(\varphi)} dA n_\alpha n_\beta\, \partial v_\beta/\partial x_\alpha$, as a broken line. The minimum of generation of surface area occurs close to the stoichiometric value ($\zeta_{st} = 0.5$ in the present case), and it appears that the expansion rate due to the heat release of the reactions has no effect at this value of mixture fraction since both curves agree. The effect of heat release is significant at lean and rich mixtures, and I_1 and I_1^i approach each other as the limits of the range of mixture fraction are reached. The rapid increase of production of surface area near these limits is due to the fact that those limit values are maintained at the upstream and downstream boundaries of the flow domain. The actual production rate of surface area due to straining and the effect of the curvature term in Fig. 4 is flat in the center of the range of level values, and destruction of surface area becomes significant only near the limits zero and unity for the level value. It is evident that the curvature term is positive for level values between 0.1 and 0.8, verifying that the curvature term is not negative definite. The surface area for mixture fraction is shown in Fig. 5 for two times as a function of the level value, illustrating that it in-

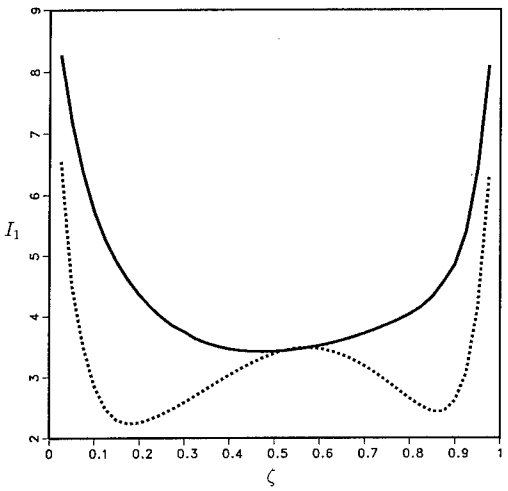

FIG. 3. In-plane stretching terms I_1 (full line) and I_1^i (broken line) in the equation for the surface area of the level surfaces of mixture fraction. Velocity and scalar fields are taken from DNS results for a non-premixed flame in decaying turbulence.

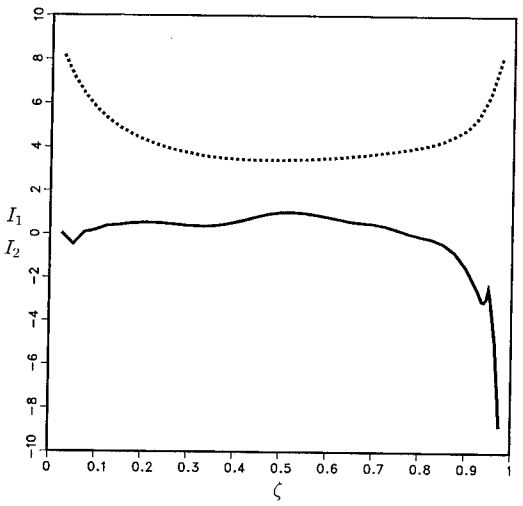

FIG. 4. In-plane stretching (broken line) and curvature (full line) terms in the equation for the surface area of level surfaces of mixture fraction. Velocity and scalar fields are DNS data for a non-premixed flame in decaying turbulence.

creases in time consistent with the time rate of change (the sum of the curves) in Fig. 4. The level surface at $t = 13.2$ and the level value $\zeta = 0.025$ in Fig. 6 illustrate the amount of wrinkling for a level value close to the lower bound zero of mixture fraction.

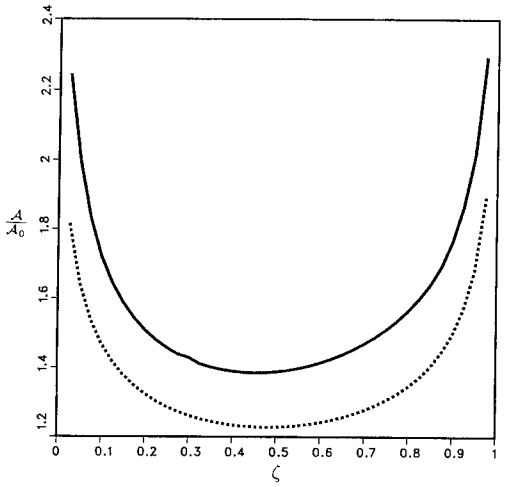

FIG. 5. Surface area of level surfaces of mixture fraction at times $t = 8.75$ (broken line) and $t = 13.2$ (full line) as a function of the level value.

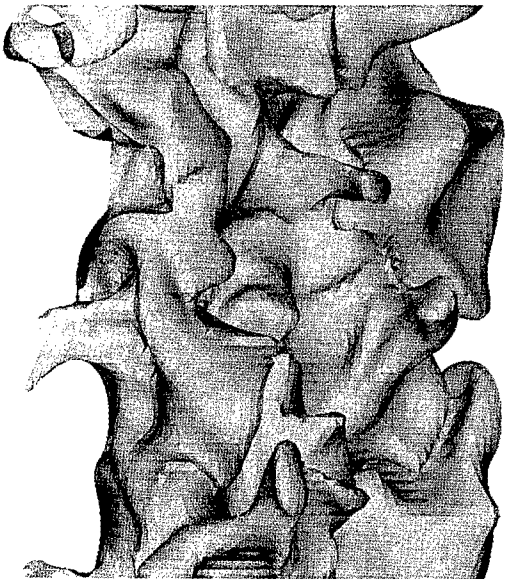

FIG. 6. Iso-surface of mixture fraction at time $t = 13.2$ and the level value $\zeta = 0.025$.

Conclusions

The transport equation for integral variables such as surface area was established using a theorem of geometric measure theory. The equation for the surface area was considered in detail, and it was shown that the rate of strain produces surface area, and the term arising from the diffusive flux of the scalar defining the level surface is able to destroy and produce

surface area. DNS results for a non-premixed flame in low Reynolds number turbulence were used to evaluate the terms in the equation for the surface area. The simulation started with a plane flame front and it was found that the surface area increases with time even though the turbulence decays. The wrinkling of the level surfaces is much more pronounced for level values near the limits zero and unity than near the stoichiometric value.

Future work will include a new simulation with a random distribution of burning reactants to investigate the possibility of interactions between flamelets that could lead to mutual annihilation and topological change of the level surfaces for mixture fraction. Furthermore, the influence of differential molecular diffusion between species on the dynamics of the flame surface area and the differences in the flame surface area defined by a conserved scalar quantity such as the mixture fraction and by a reactive scalar field such as the intermediate species I mass fraction will be investigated.

Acknowledgment

This research was supported by the Department of Energy's Office of Basic Energy Sciences, Division of Chemical Sciences.

REFERENCES

1. Chen, J.-Y., and Kollmann, W., *Combust. Flame* 88:397 (1992).
2. Maz'ja, V. G., *Sobolev Spaces*, Springer-Verlag, Berlin, 1985.
3. Do Carmo, M. P., *Differential Geometry of Curves and Surfaces*, Prentice-Hall, Englewood Cliffs, NJ, 1976.
4. Pope, S. B., *Int. J. Eng. Sci.* 26:445 (1988).
5. Chen, J. H., Mahalingam, S., Puri, I. K., and Vervisch, L., "Structure of Turbulent Non-premixed Flames Modeled with Two-step Chemistry," Paper WSS/CI 92-51, Western States Section of the Combustion Institute Fall Meeting, Berkeley, 1992.
6. Vervisch, L., Chen, J. H., Mahalingam, S., and Puri, I., "Numerical Study of Finite Rate Chemistry Effects and Unequal Schmidt Numbers on Turbulent Non-premixed Flames," Ninth Symposium on Turbulent Shear Flows, Kyoto, Japan, 1993.
7. Pope, S. B., *Prog. Energy Combust. Sci.* 11:119 (1985).
8. Kollmann, W., and Chen, J. -Y., in *Major Research Topics in Combustion*, (M. Y. Hussaini, A. Kumar, and R. G. Voigt, Eds.), Springer-Verlag, New York, 1992, p. 359.
9. Janicka, J., Kolbe, W., and Kollmann, W., *J. Non-Equilib. Thermodyn.* 4:27 (1979).
10. Dopazo, C., *Phys. Fluids* 22:20 (1979).
11. Kerstein, A. R., *Combust. Sci. Technol.* 60:391 (1988).
12. Vervisch, L., Garreton, D., Borghi, R., and Vandromme, D., *Computation of a Diffusion Flame Experiment Using Two pdf Methods*, 1994, to be published.
13. Vervisch, L., *A Proposition to Improve the Simplified pdf Method Hades-Peul Used in Turbulent Diffusion Flame Combustion Modelling*, CTR-Notes, Stanford University, Stanford, CA, 1992.
14. Pope, S. B., *Combust. Sci. Technol.* 28:131 (1982).
15. Gibson, C. H., *Phys. Fluids* 11:2305 (1968).
16. Byggstoyl, S., and Kollmann, W., *Phys. Fluids* 29:1423 (1986).
17. Kerstein, A. R., Ashurst, W. T., and Williams, F. A., *Phys. Rev. A* 37:2728 (1988).
18. Chen, J.-Y., and Kollmann, W., "Comparison of Prediction and Measurement in Non-premixed Turbulent Flames," in *Turbulent Reacting Flows*, P. A. Libby and F. A. Williams, Eds., Academic Press, 1994, pp. 211–308.
19. Candel, S. M., and Poinsot, T. J., *Combust. Sci. Technol.* 70:1 (1990).
20. Bideaux, E., Vervisch, L., and Bray, K. N. C., *Study of the Transport Equation for a Surface Density Function and Some Implications for Turbulent Combustion Modelling*, 1993, to appear.
21. Chen, J. H., and Kollmann, W., *Topological and Geometrical Properties of Turbulent Flames*, AIAA 94-0098, 1994.

COMMENT

Cavaliere Antonio, DIP.ING. Chimica, Italy. Did you observe any annihilation of iso-level surface in your DNS?

Author's Reply. The annihilation of iso-surfaces would lead to a change of the genus of the surfaces, which was computed for all level values at several time steps. A change of genus was observed a few times for level values close to zero. The reason for the rare occurrence of annihilation is due to the initial conditions, where a single-plane laminar flame is embedded in homogeneous turbulence, and the moderate turbulence level.

Twenty-Fifth Symposium (International) on Combustion/The Combustion Institute, 1994/pp. 1099–1106

PARTIALLY PREMIXED TURBULENT FLAME PROPAGATION IN JET FLAMES

C. M. MÜLLER, H. BREITBACH AND N. PETERS
Institut für Technische Mechanik
Rheinisch-Westfälische Technische Hochschule Aachen
Templergraben 64, 52056 Aachen, Federal Republic of Germany

Flamelet formulations for premixed and non-premixed combustion are combined in order to treat partially premixed combustion in the fast chemistry limit. The flamelet concept for non-premixed combustion is based on the equation for the mixture fraction $Z(\mathbf{x},t)$, while that for premixed combustion uses a field equation for the scalar field $G(\mathbf{x},t)$, whose level surfaces $G = G_0$ represent the flame surface. The laminar burning velocity appearing in this equation is assumed to depend on the local mixture fraction field $Z(\mathbf{x},t)$ and the scalar dissipation rate χ. The formulation is used to determine flame propagation and liftoff heights in turbulent jet diffusion flames of methane. The analysis is viewed as a first step to resolve the previous controversy about the stabilization mechanism—premixed flame propagation vs diffusion flame quenching—since both effects are found to be important and to influence the liftoff height.

Introduction

If chemistry is fast compared to the characteristic timescales of turbulence, combustion tends to occur in thin layers called flamelets. The flamelet concept views a turbulent flame as an ensemble of thin flamelets, whose structures are essentially one-dimensional [1,2]. For non-premixed combustion, an equation for a conserved scalar, the mixture fraction $Z(\mathbf{x},t)$, is solved, and the flamelets are located on the surfaces $Z(\mathbf{x},t) = Z_{st}$, with the stoichiometric value Z_{st} being fixed. Similarly, in a recently developed flamelet formulation for premixed turbulent combustion [3], a field equation of the scalar $G(\mathbf{x},t)$ is used, where level surfaces $G(\mathbf{x},t) = G_0$ represent the flame surface. The latter formulation can be derived from first principles and has much of the essential physics in common with the Bray–Moss–Libby model [4]. In this paper, we present a unified approach based on the two scalar fields $Z(\mathbf{x},t)$ and $G(\mathbf{x},t)$. At the intersection of isolines, $G(\mathbf{x},t) = G_0$ and $Z(\mathbf{x},t) = Z_{st}$, two-dimensional flamelet structures occur, corresponding to triple flames that have been analyzed in a series of papers by Dold and coworkers [5–8], by Buckmaster and Matalon [9], by Wichman [10], and recently by Kioni et al. [11]. Such triple flamelets may be viewed as typical structures responsible for flame propagation in a partially premixed turbulent flow field.

There has been a long-term controversy about the stabilization mechanism in lifted turbulent diffusion flames. The mechanism proposed by Vanquickenborne and van Tiggelen [12] suggests that flame stabilization occurs on the contour of mean stoichiometric mixture at the position where the axial mean velocity equals the turbulent burning velocity. This model has been followed by Eickhoff et al. [13] and Kalghatgi [14]. On the contrary, Peters and Williams [15] have argued that in a non-premixed flow field, flame propagation will proceed along instantaneous surfaces of stoichiometric mixtures up to the point where the flame is quenched. Since the flame at the surface of stoichiometric mixture was viewed as a diffusion flamelet, flamelet quenching was thought to be the essential mechanism. Broadwell et al. [16], Miake-Lye and Hammer [17], Schefer et al. [18], and recently Chao and Jeng [19] have presented additional and complementary interpretations. A thorough review on the liftoff problem has been given by Pitts [20].

A Laminar Flamelet Model for Partially Premixed Combustion

We will start from the flamelet model for premixed combustion [21] based on the equation for the scalar G:

$$\frac{\partial G}{\partial t} + \mathbf{v}^c \nabla G = s_L |\nabla G|. \tag{1}$$

The flame position is defined by $G(\mathbf{x},t) = G_0$, where G_0 is an arbitrary constant. Values of $G > G_0$ define the region of burnt gas, and $G < G_0$ define that of the unburnt mixture. Equation (1) was first written down by Markstein [22] and was independently formulated by Williams [23]. It may be derived from a

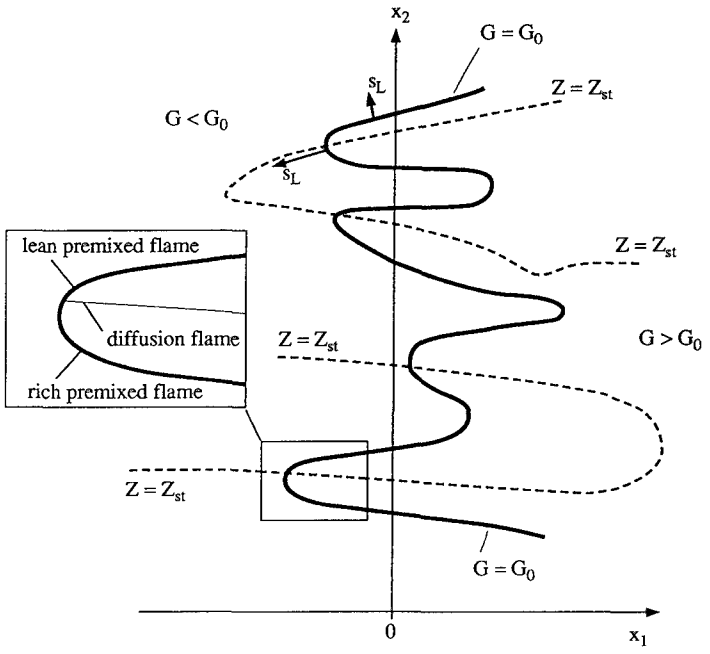

FIG. 1. Flame propagation through a nonuniform mixer described by the two scalar fields $Z(\mathbf{x},t)$ and $G(\mathbf{x},t)$.

kinematic balance between the flame propagation velocity, the flow velocity, and the burning velocity normal to the instantaneous premixed flame front [3]. Therefore, the velocity $\mathbf{v}^c$ is the conditioned velocity immediately upstream of the front, if s_L is defined as the burning velocity with respect to the unburnt mixture.

In a non-premixed flow field, the burning velocity will depend predominantly on the local fuel-air equivalence ratio Φ, which is related to the mixture fraction by

$$\Phi = \frac{Z\,(1 - Z_{st})}{Z_{st}\,(1 - Z)}. \tag{2}$$

The equation for the mixture fraction field is written as

$$\rho \frac{\partial Z}{\partial t} + \rho \mathbf{v} \nabla Z = \nabla(\rho D \nabla Z). \tag{3}$$

Here, ρ is the density and D is the diffusion coefficient, assumed to be equal for all species and the enthalpy. For illustration purposes, we assume the scalar fields of $G(\mathbf{x},t)$ and $Z(\mathbf{x},t)$ to be given within a spatially slowly varying velocity field and try to construct a flame front. Since the laminar burning velocity is the largest close to $Z = Z_{st}$ (or $\Phi = 1$), flame propagation will be faster in regions close to Z_{st} than in regions where the mixture is either very rich or very lean. This is shown schematically by the length of the arrows for s_L in Fig. 1. A key element of the analysis of flame propagation in nonhomogeneous mixtures is the so-called triple flame, which is blown up in Fig. 1. This is a flame structure that propagates within a non-premixed mixing field essentially following a surface of stoichiometric mixture. The structure of a triple flame is composed of a fuel-rich premixed flame branch that leaves unburnt fuel, carbon monoxide, and hydrogen behind it; a fuel-lean branch that leaves excess oxygen behind it; and a diffusion flame that is located at $Z = Z_{st}$. Such elementary flame structures are being observed experimentally in layered mixtures [11]. Their structure and dynamics are influenced by a number of external conditions such as the local strain rate and the mixture fraction gradient.

We will outline the general features of a theory of partially premixed flamelets by assuming that the local burning velocity depends only on the local mixture fraction and the mixture fraction gradient, expressed in terms of the scalar dissipation rate

$$\chi = 2D|\nabla Z|^2. \tag{4}$$

The burning velocity s_L is expected to decrease with increasing χ and to vanish at a value χ_q, which should be of the same order of magnitude as the dissipation rate at quenching for a non-premixed diffusion flamelet [1]. Assuming a linear decrease, one may express the dependence of the burning velocity on Z and χ as

$$s_L(Z,\chi) = s_L(Z)\left(1 - a\,\frac{\chi}{\chi_q}\right) \tag{5}$$

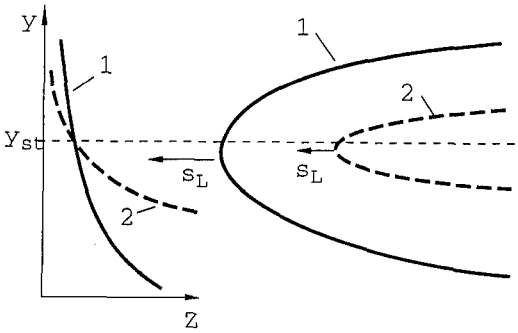

FIG. 2. A schematical illustration of triple flamelets for two different mixture fraction gradients.

where a is assumed to be constant. For two different presumed mixture fraction gradients in the y direction, the corresponding triple flamelet structure is schematically shown in Fig. 2. If, as in case 1, the mixture fraction gradient in the vicinity of Z_{st} is small (and therefore, χ is small), the triple flamelet is broad in physical space, and its propagation speed relative to the flow is mainly determined by the premixed burning velocity $s_L(Z_{st})$. If, on the other hand, as in case 2, the mixture fraction gradient and χ are large, the triple flamelet structure is narrow. Its leading edge will propagate with a lower burning velocity since it looses heat not only by preheating the unburnt mixture upstream but also that on both sides in the y direction. As χ approaches χ_q, the heat loss mechanism toward the sides becomes dominant, and the triple flamelet structure is quenched in a similar way as a one-dimensional diffusion flamelet.

We now want to derive an equation for the mean scalar field $\bar{G}$. As in Ref. 21, we may split the scalar G into a mean value $\bar{G}$ and a fluctuation G'

$$G(x,t) = \bar{G}(\mathbf{x},t) + G'(\mathbf{x},t). \tag{6}$$

It may be shown [4] that scalar level fluctuations G' correspond to spatial flame displacements around the mean flame contour located at $G = G_0$. The turbulent counterpart of Eq. (1), the equation of the mean scalar G, is then written as

$$\frac{\partial \bar{G}}{\partial t} + \overline{\mathbf{v}}^c \nabla \bar{G} = \overline{s_L|\nabla G|}. \tag{7}$$

In this equation, no turbulent scalar flux terms appear. However, the conditioned mean velocity $\mathbf{v}^c$ needs to be modeled. We have adopted the formulation

$$\overline{\mathbf{v}}^c = \frac{\overline{\rho \mathbf{v}}}{\rho_u} = \frac{\bar{\rho}\tilde{\mathbf{v}}}{\rho_u} \tag{8}$$

where $\rho_u = \rho_u(\tilde{Z})$. Due to expansion effects, the Favre averaged velocity $\tilde{\mathbf{v}}$ is expected to slow down in front of the flame and to accelerate after passing the flame front. The use of Eq. (8) for the conditioned velocity guaranties that this velocity continues to decrease during the passage through the flame front. This may be justified by observing that in the case of a steady one-dimensional flame where $d\bar{G}/dx = 1$, $\bar{\rho}\tilde{v}$ is the mass flux through the mean flame surface, whereas $\rho_u s_L$, now multiplying $|\overline{\nabla G}|$ on the right-hand side (rhs), is the mass flux through the instantaneous flame surface area represented by $|\overline{\nabla G}|$.

The remaining problem is the modeling of the rhs of Eq. (7). Denoting the scalar gradient $|\nabla G|$ by σ, the ensemble average of the source term in Eq. (7) is

$$\overline{s_L(Z,\chi)|\nabla G|} = \int_0^\infty \int_0^\infty \int_0^1 s_L(Z,\chi)\sigma P(Z,\chi,\sigma)\, dZ\, d\chi\, d\sigma. \tag{9}$$

Here, $P(Z,\chi,\sigma)$ is a joint probability density of Z, χ, and σ. In general, one may not assume these to be statistically independent. In fact, scalar gradients of G will tend to align with gradients of Z in very lean and rich parts of the mixture, while the gradient of G is nearly normal to that of Z around $Z = Z_{st}$.

We will for simplicity, however, assume statistical independence and, furthermore, neglect fluctuations of χ. The joint probability density function (PDF) is then written

$$P(Z,\chi,\sigma) = P(Z)P(\sigma)\delta(\chi - \bar{\chi}). \tag{10}$$

Then, the integral in Eq. (9) takes the form

$$\overline{s_L(Z,\chi)|\nabla G|} = \overline{|\nabla G|}\left(1 - a\frac{\bar{\chi}}{\chi_q}\right) \cdot \int_0^1 s_L(Z)P(Z)\, dZ. \tag{11}$$

Here, one may exploit the fact that the burning velocity $s_L(Z)$ has a strong peak in the vicinity of Z_{st} and decreases rapidly for $Z < Z_{st}$ toward the lean side and for $Z > Z_{st}$ toward the rich side. A convenient approximation for the integral in Eq. (11) is, therefore,

$$\int_0^1 s_L(Z)P(Z)\, dZ = s_L(Z_{st})P(Z_{st})(\Delta Z)_{s_L} \tag{12}$$

which defines the width $(\Delta Z)_{s_L}$. This is essentially the range in mixture fraction space where the burning velocity is a significant fraction of the maximum burning velocity. It will depend on the shape of $s_L(Z)$ and via $P(Z)$ on $\tilde{Z}$ and $\widetilde{Z''^2}$. For simplicity, we have

assumed $(\Delta Z)_{sL}$ to be constant in the calculations below.

If Eq. (12) is inserted into Eq. (11), the product $s_L(Z_{st})\ \overline{|\nabla G|}$ appears. For premixed turbulent combustion, it has been argued [21] that

$$s_L\overline{|\nabla G|} = s_T|\nabla \bar{G}| \tag{13}$$

where s_T is the turbulent burning velocity and $|\nabla \bar{G}|$ is the absolute gradient of the mean G field. This is equivalent to Damköhler's suggestion that the ratio of the turbulent to the laminar burning velocity should be proportional to the flame surface area to the cross-sectional area of the mean flame. For the turbulent burning velocity, an ansatz of the form

$$s_T = s_L + b_2(s_L v')^{1/2} + b_1 v' \tag{14}$$

has been used [21] when stretch effects are neglected. It describes the increase of s_T due to turbulent fluctuations. Inserting Eqs. (12) through (14) into Eq. (11) leads with $s_L = s_L(Z_{st})$ to

$$\overline{s_L(Z,\chi)|\nabla G|} = s_T|\nabla \bar{G}| \tag{15}$$

where

$$s_T = \underbrace{\{s_L(Z_{st}) + b_2[s_L(Z_{st})v']^{1/2} + b_1 v'\}}_{\text{premixed flame propagation}}\ \underbrace{P(Z_{st})(\Delta Z)_{sL}}_{\text{partial premixing}}\ \underbrace{\left(1 - a\frac{\bar{\chi}}{\chi_q}\right)}_{\text{flamelet quenching}}. \tag{16}$$

This formulation contains three contributions:

1. A term accounting for premixed flame propagation with the maximum laminar burning velocity $s_L(Z_{st})$, which is enhanced by turbulent velocity fluctuations.
2. A term due to partial premixing, which restricts flame propagation to regions where the probability for stoichiometric conditions is large. Therefore, the first term in Eq. (16) is multiplied by $P(Z_{st})$. This conditioning is less severe if $(\Delta Z)_{sL}$ is larger.
3. A term accounting for flamelet quenching. The turbulent burning velocity decreases if the mean scalar dissipation rate increases, indicating that laminar triple flamelets are less able to propagate due to increasing local mixture fraction gradients.

Experiments on Downward Flame Propagation in Vertical Jet Flames

To determine instationary propagation velocities in turbulent jets, we use a simple experimental setup that consists of a burner, an ignition device, a high-speed camera, and an argon-ion laser. As nozzles, we used cylindrical brass tubes with a sharp upper edge, a length of 115 mm, and inner diameters D of 4, 6, and 8 mm. A stainless steel mesh was installed in the inlet of the tubes. Methane with a purity of 99.5% was used as fuel, the fuel mass flow was measured by flowmeters. The exit velocity U_0 was defined as the area-averaged velocity at the nozzle.

To visualize the flame front, the fuel flow was seeded with club moss spores and illuminated with a laser light sheet. The club moss spores scatter the laser light in the unburned mixture and burn in the flame front; thus, there is no light scatter in the burned gas. As a light source, we use a 20-W argon-ion laser; the light sheet is focused through the axis of the burner. Flame propagation is recorded with a HYCAM high-speed camera at 200 frames per second perpendicular to the laser light sheet. An electric spark from a conventional transistor ignition system is used to ignite the flame. The spark is positioned on the axis of symmetry at a height, where a fuel lean mixture is expected.

In order to determine the burning velocities, the lowest visible flame front position on each image of the film is marked. From the images, it can be seen that local propagation velocities are influenced by three-dimensional structures moving sometimes in spirals around the axis of symmetry. By the two-dimensional laser light sheet, this effect cannot be resolved in the measurements but is visible since the lowest flame front position often switches from the right to the left side of the jet's axis.

Numerical Calculation of Flame Propagation and Liftoff

The model described in paragraph 2 has been used to calculate the unsteady flame propagation and the stabilization in turbulent jet flames. For this purpose, the KIVA II code [24] was modified to include Eq. (7) with Eqs. (15) and (16). The second set of constants from Ref. 25 was used for the k-ε model and the mixture fraction equation and its variance. The $\bar{G}$ field was initialized with $\bar{G} = 0$ for unburnt conditions. Combustion was initiated by setting $\bar{G} = 0.1$ in one cell. The evolution of the $\bar{G}$ field then led to values $\bar{G} > G_0$, where G_0 was chosen as $G_0 = 1.0$. If $\bar{G}$ increases beyond $\bar{G} = 2.0$, it is set equal to that value.

The combustion model of KIVA was removed, but equations for the mean mixture fraction $\bar{Z}$ and its

variance $\widetilde{Z''^2}$ were included. In addition, an equation for the mean total enthalpy $\tilde{h}$ was solved:

$$\frac{\partial \bar{\rho}\tilde{h}}{\partial t} + \nabla(\bar{\rho}\mathbf{v}\tilde{h}) = \frac{\partial \bar{p}}{\partial t} + \mathbf{v}\nabla\bar{p} + \nabla\left(\frac{\mu_t}{\sigma_t}\nabla\tilde{h}\right). \quad (17)$$

This was necessary because KIVA II is a compressible code, which uses a Arbitrary Lagrangian Eulerian (ALE) algorithm, where in a first Lagrangian step, the diffusion and acoustic terms are solved implicitly. In the second Eulerian step, the convection terms are treated explicitly by subcycling the implicit time step. Therefore, the enthalpy equation cannot be coupled to the mixture fraction equation, but must contain the first two acoustic terms on the rhs of Eq. (17).

The mass fraction of the chemical species were determined by using a flamelet library for laminar counterflow diffusion flames for different velocity gradients [25]. There are two possible states for a diffusion flamelet that are conditioned by the value of $\bar{G}$: If in a computational cell $\bar{G} >> G_0$, it is considered to be completely burnt and the mass fractions are determined by

$$Y_{i,b}(\tilde{Z}, \widetilde{Z''^2}, \bar{a}) = \int_0^1 Y_i(Z,a)P(Z)\,dZ \quad (18)$$

where $Y_i(Z,a)$ is taken from the library of burning flamelets setting the velocity gradient a of the flamelet equal to the local strain rate

$$\bar{a} = \frac{\tilde{\varepsilon}}{\tilde{\kappa}} \quad (19)$$

of the turbulent flow. In Eq. (18), a beta function PDF [25] was used. The integration was performed in advance, and values for $\tilde{Y}_{i,b}$ were tabulated as functions of $\tilde{Z}$, $\widetilde{Z''^2}$, and $\bar{a}$.

If $\bar{G} << G_0$ in a computational cell, the mass fractions are those of fuel and air in an unburnt mixture at the local value $\tilde{Z}$

$$\tilde{Y}_{i,u} = Y_{i,u}(\tilde{Z}) \quad (20)$$

If the computation cell is located within the flame brush thickness, the weighted sum

$$\tilde{Y}_i = f\tilde{Y}_{i,b} + (1 - f)\tilde{Y}_{i,u} \quad (21)$$

is used. The fraction of burnt flamelets in each cell calculated by assuming that G fluctuations are Gaussian distributed [4]. Then,

$$f = \int_{G=G_0}^{\infty} \frac{1}{\sqrt{2\pi\overline{G'^2}}} \exp\left\{-\frac{(G - \bar{G})^2}{2\overline{G'^2}}\right\} dG \quad (22)$$

where the variance $\overline{G'^2}$ is assumed proportional to the square of the integral length scale [4] $l_t = \tilde{k}^{3/2}/\varepsilon$. The proportionality factor was varied between 0.5 and 1.0, depending on the numerical grid size, in order to obtain stable solutions.

The temperature $\tilde{T}$ in the cell was calculated from the mean enthalphy by

$$\sum_{i=1}^{n} \tilde{Y}_i h_i(\tilde{T}) = \tilde{h}(\mathbf{x},t) \quad (23)$$

where the specific enthalpies are taken from NASA polynomials. The numerical constants used in Eq. (16) were $b_2 = 0.20$ and $b_1 = 0.46$ and $a = 3.8$ with $s_L\,(Z_{st}) = 39$ cm/s, $(\Delta Z)_{sL} = 0.23$ and $\chi_q = 5$/s [1]. The rather large value for $(\Delta Z)_{sL}$ was necessary in order to obtain sufficiently large turbulent burning velocities that were able to compete with the flow velocity. The scalar dissipation rate $\bar{\chi}$ in Eq. (16) does not take mixture fraction variations into account [4] but was defined as

$$\bar{\chi} = 2\frac{\tilde{\varepsilon}}{\tilde{\kappa}}(\Delta Z)_F^2 \quad (24)$$

where $(\Delta Z)_F$ is the flame width in mixture fraction space, assumed here as $(\Delta Z)_F = 2Z_{st}$. The velocity fluctuations were modeled in the same way as the conditioned mean velocity by $v' = \bar{\rho}/\rho_u\sqrt{2/3\tilde{k}}$. The conditioned mean velocity and the conditioned velocity fluctuation were taken at the mean flame front. The temperature profile and, due to thermal expansions, the velocity change at the flame front $\bar{G} = G_0$ are continuous over a few grid points due to the weighting used in Eq. (21).

Results

Propagating Flame Fronts:

In order to simulate a propagating flame front through a turbulent methane jet into still air, one computational cell of the steady cold flow field was initiated with $\bar{G} = G_0$ on the centerline downstream of the position of mean stoichiometric mixture. The flame ignition and propagation is then driven by the G gradient toward the neighboring cells, which were originally set to $G = 0$. An example calculation is shown in Fig. 3, where the axial distance between the flame base and the nozzle is plotted vs time. The solid line denotes the calculation, and the dashed line represents the ensemble average of the measured values from different experimental runs. Error bars identify the maximum scatter of the experimental data.

It is seen that the slope of the calculated curve and, therefore, the propagation velocity agree well

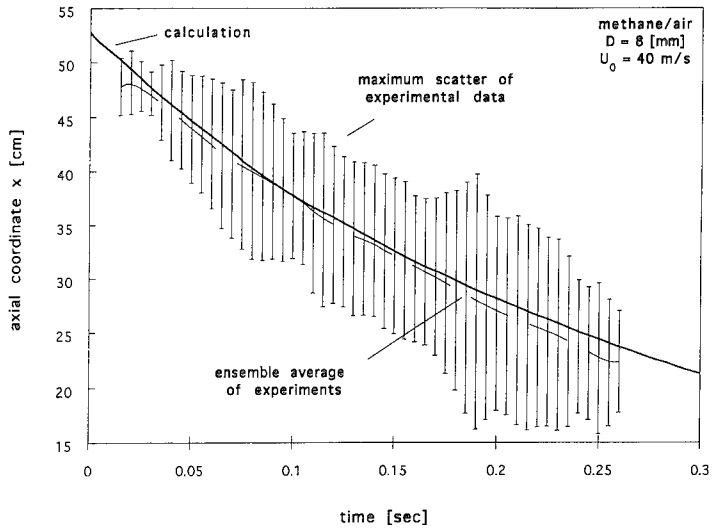

FIG. 3. Axial coordinate of the flame base over time during unsteady propagation of a flame burning in an ignited turbulent cold jet of methane into still air.

with that of the experimental runs. A closer inspection of the calculations shows that flame propagation follows the surface of mean stoichiometric mixture and depends on the velocity fluctuations there. The experiments, seem to show a transport of the flame by the large structures at the edge of the jet. Therefore, there remains a substantial difference between the very crude turbulence modeling based on the k-ε model and the large-scale dynamics in a jet. Modeling of these features goes beyond the scope of this paper.

Liftoff Heights:

When the unsteady flame front propagation reaches a steady state, the liftoff height can be determined. Figure 4 shows a blowup of the stabilization region in a turbulent methane jet flame with a diameter $D = 4$ mm and a fuel exit velocity U_0 of 20 m/s. The shadowed area indicates the burnt gas region $\bar{G} > G_0$, and the solid lines are isocontours of the mixture fraction. The expansion by the flame deflects the stream lines and, thereby, the mixture fraction isocontours at the flame base.

Figure 5 shows a schematic presentation of profiles of the Favre mean velocity $\tilde{\mathbf{v}}$, the conditioned mean velocity $\overline{\mathbf{v}^c}$, and the mean scalar $\bar{G}$ normal to the flame front at the leading edge. The expansion effect leads first to a decrease of the Favre mean velocity $\tilde{\mathbf{v}}$ with a local minimum in front of the flame and to an acceleration further downstream. The conditioned velocity $\overline{\mathbf{v}^c}$, however, continues to decrease through the front. Therefore, flame propagation always proceeds toward an increasing velocity reaching a stable position when flow velocity and burning velocity are equal. The burning velocity decreases due to the flamelet quenching term in Eq. (16) as the

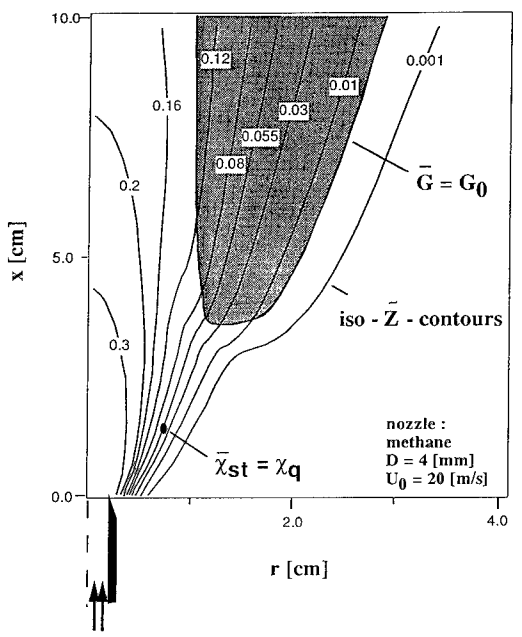

FIG. 4. Stabilization region of a lifted turbulent jet diffusion flame.

flame moves upstream. This term takes a value of 0.9 downstream but reaches 0.3 when the stabilization height is approached. This indicates that flamelet quenching is rather unimportant during the flame propagation phase but becomes the dominant mechanism for flame stabilization.

In Fig. 6, calculated nondimensional liftoff heights H/D of turbulent methane jet diffusion flames are plotted vs the jet exit velocity. They are compared

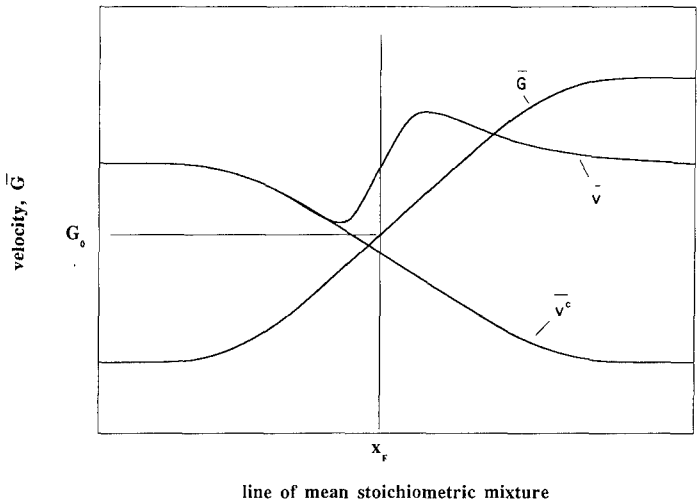

FIG. 5. A cut following the line of mean stoichiometric mixture at the stabilization height.

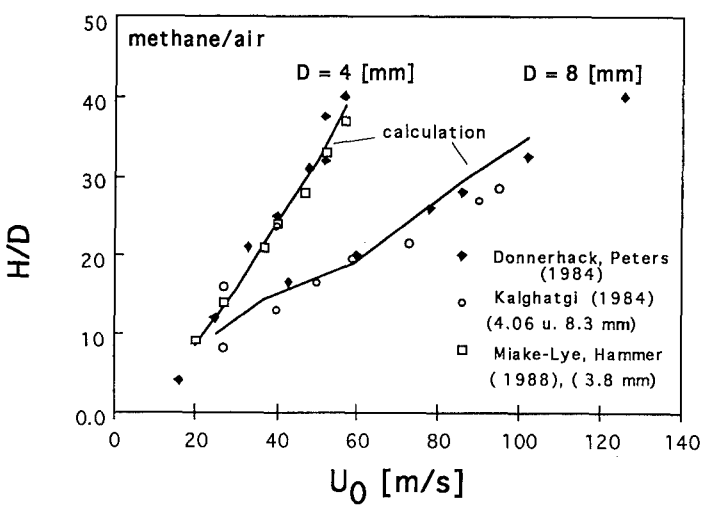

FIG. 6. Measured and calculated liftoff heights of methane/air jet diffusion flames.

with experiments of different authors. The calculations have been performed for two nozzle diameters, $D = 4$ and 8 mm, and a wide range of jet exit velocities. The computed liftoff heights depend on the value of the parameter a, which was fitted as $a = 3.8$ for these calculations. If the stabilization height was determined by $\bar{\chi} = \chi_q$, as by the flamelet quenching criterion, the liftoff height is underpredicted. This is also evident from Fig. 4, where the position of $\bar{\chi} = 5.0/s$ lies upstream of the stabilization region. Therefore, both effects, premixed flame propagation and flamelet quenching, add to the stabilization mechanism.

Conclusions

A flamelet formulation for partially premixed turbulent combustion has been used to predict flame propagation and liftoff in jet diffusion flames. The resulting expression for the turbulent burning velocity combines the two different stabilization mechanisms, partially premixed flame propagation along the surface of mean stoichiometric mixture and flamelet quenching. While the unsteady flame propagation is essentially dominated by the first mechanism, the flame is stabilized close to but downstream of the position $\bar{\chi} = \chi_q$, indicating that flamelet quenching is important for flame stabilization of lifted flames.

Acknowledgment

The measurements of flame propagation have been carried out by Ms. Mechthild Hesselt in a diploma thesis.

REFERENCES

1. Peters, N., *Prog. Energy Combust. Sci.* 10:319–339 (1984).
2. Peters, N., *Twenty-First Symposium (International) on Combustion*, The Combustion Institute, Pittsburgh, 1986, pp. 1231–1256.
3. Peters, N., *J. Fluid Mech.* 242:611–629 (1992).
4. Bray, K. N. C. and Peters, N., in *Turbulent Reactive Flows* (P. A. Libby and F. A. Williams, Eds.), Academic Press, New York, 1994.
5. Dold, J. W., *Prog. Astronaut. Aeronaut.* 113:240–248 (1988).
6. Dold, J. W., *Combust. Flame* 76:71–88 (1989).
7. Hartley, L. J., and Dold, J. W., *Combust. Sci. Technol.* 80:23–46 (1991).
8. Dold, J. W., Hartley, L. J., and Green, D., in "Dynamical Issues in Combustion Theory." *IMA Volumes in Mathematics and its Applications* (P. C. Fife, A. Linan, and F. A. Williams, Eds.), Springer, New York, 1990, pp. 83–105.
9. Buckmaster, J., and Matalon, M., *Twenty-Second Symposium (International) on Combustion*, The Combustion Institute, Pittsburgh, pp. 1527–1535.
10. Wichman, I. S., *Combust. Sci. Technol.* 64:295–313 (1989).
11. Kioni, P. N., Rogg, B., Bray, K. N. C., and Linan, A., *Combust. Flame* 64:276–290 (1993).
12. Vanquickenborne, L., and van Tiggelen, A., *Combust. Flame* 10:59 (1966).
13. Eickhoff, H., Lenze, B., and Leukel, W., *Twentieth Symposium (International) on Combustion*, The Combustion Institute, Pittsburgh, 1985, p. 311.
14. Kalghatgi, G. T., *Combust. Sci. Technol.* 41:17 (1984).
15. Peters, N., and Williams, F. A., *AIAA J.* 21:423 (1983).
16. Broadwell, J. E., Dahm, W. J. A., and Mungal, M. G., *Twentieth Symposium (International) on Combustion*, The Combustion Institute, Pittsburgh, 1985, p. 303.
17. Miake-Lye, R. C., and Hammer, J. A., *Twenty-Second Symposium (International) on Combustion*, The Combustion Institute, Pittsburgh, 1989, p. 817.
18. Schefer, R. W., Namazian, M., and Kelly, J., *Twenty-Second Symposium (International) on Combustion*, The Combustion Institute, Pittsburgh, 1989, p. 833.
19. Chao, Y.-C., and Jeng, M.-S., *Twenty-Fourth Symposium (International) on Combustion*, The Combustion Institute, Pittsburgh, 1992, pp. 333–340.
20. Pitts, W. M., *Twenty-Second Symposium (International) on Combustion*, The Combustion Institute, Pittsburgh, 1989, pp. 809–816.
21. Wirth, M., and Peters, N., *Twenty-Fourth Symposium (International) on Combustion*, The Combustion Institute, Pittsburgh, 1992, pp. 493–501.
22. Markstein, G. H., *Nonsteady Flame Propagation*, Pergamon Press, Oxford, 1964, p. 8.
23. Williams, F. A., in *The Mathematics of Combustion* (J. Buckmaster, Ed.) SIAM, Philadelphia, 1985, pp. 97 ff.
24. Amsden, A. A., O'Rourke, P. J., and Butler, T. D., *KIVA II: A Computer Program for Chemically Reactive Flows with Sprays*, Los Alamos National Laboratory, Report LA-11560-MS, 1989.
25. Janicka, J., and Peters, N., *Nineteenth Symposium (International) on Combustion*, The Combustion Institute, Pittsburgh, 1982, p. 367.

COMMENTS

R. W. Bilger, University of Sydney, Australia. In 1978, Sir William Hawthorne proposed to set the following problem for John Moore's Combustion class at Cambridge University. "A slab of combustible mixture lies between semi-infinite inert gases. What will be the propagation speed of the laminar combustion wave through the mixture?" The students were expected to recognize this as an application of Actuator Disc Theory and show that the speed was the laminar flame speed times the square root of the density ratio. The flow diverges ahead of the flame, slowing the unburnt mixture so that overall the flame travels faster than the planar laminar flame speed. This effect is evident in your modelling of the lifted diffusion flame. It seems to be an important component of the stabilization mechanism.

Author's Reply. I agree that this effect is very important also for the turbulent flame propagation process and flame stabilization. It is this effect that explains the relatively large upstream propagation velocities that we have measured in these flames.

•

Ralph C. Aldredge, University of California, Davis, USA. Does your model assume that variations of G occur over a much larger scale than that over which the mixture fraction variable changes by amounts of order unity?

Author's Reply. No, because changes of the mixture fraction will only modify the turbulent burning velocity that is assumed to be a known quantity for the solution of the G equation. Variations of G occur over a scale that is of the order of the integral length scale.

•

Robert Dibble, University of California, Berkeley, USA. Does your model predict the effect of coflow air velocity and also addition of air to the fuel? Coflows in excess of 1 m/s cause a lifted flame to blow off.

Author's Reply. The model would predict the effect of coflow air velocity and of premixing the fuel jet with air. Blow-off will occur when the flame propagation velocity in the laboratory frame of reference is smaller than the coflow velocity.

Twenty-Fifth Symposium (International) on Combustion/The Combustion Institute, 1994/pp. 1107–1113

A LAGRANGIAN MODEL FOR PREDICTING TURBULENT DIFFUSION FLAMES WITH CHEMICAL KINETIC EFFECTS

M. OBOUNOU, M. GONZALEZ AND R. BORGHI
University of Rouen,
URA CNRS 230/Coria, France

The present study is a new step in the development of a lagrangian turbulent combustion model devoted to the prediction of non-premixed flames in which kinetic effects occur. Taking into account, in a refined manner, the interaction between chemical reaction and turbulence, the model includes a spectrum of turbulent timescales instead of a single mean timescale. The more recent improvement of the model consists in including a library of chemical delay times derived from a six-step reduced reaction mechanism for methane-air combustion, which is valid over a wide range of equivalence ratio. The predictions of the combustion model in which the library was implemented were compared with experimental data on turbulent jet diffusion flames near extinction. These calculations were performed with a finite volume technique devoted to variable density Navier–Stokes equations. A standard two-equations turbulence model was used and provided reliable results for dynamic variables (mean velocity and kinetic energy of turbulence). Comparisons between computed and measured mean mixture fraction and mixture fraction root mean square (rms) are quite satisfactory, proving that scalar transport is correctly modeled. The more salient point is the prediction of partial extinction and reignition phenomena, in agreement with experiments. This result clearly demonstrates the ability of the turbulent combustion model to simulate the interaction between turbulence and chemical reactions, which occurs in flames displaying kinetic effects.

Introduction

The prediction of extinction (or partial extinction) regimes requires refined modeling of the interaction taking place between turbulence and chemical reactions. Kinetic effects appear when some chemical reactions are not too fast with respect to turbulent strain. Overlapping between chemical and turbulent timescales may thereby occur, for they reach comparable orders of magnitude. Chemical rates are therefore altered by the exact shape of the turbulent timescales spectrum, which spreads from the small dissipative scales up to those of large structures. Then, knowing the relevant turbulent scales that interact with combustion reactions turns out to be a more acute problem than in the case of fast reactions. Indeed, fast chemistry implies that chemical and turbulent timescales are quite separated, and in that case, a single mean turbulent timescale provides sufficient information to the model. On the contrary, when kinetic effects are present, the turbulent entry required by the combustion model is not likely to be a single timescale but has to include a distribution of turbulent timescales. A number of previous models [1–3] neglected this point. The approach of laminar flamelets models [4,5] addresses the problem by considering a distribution of strain but is restricted to the domain of wrinkled flames. On the other hand, Pope and Chen [6] proposed an equation for the joint probability density function (pdf) of composition, velocity and dissipation that should provide information on the turbulent scales. However, this method has not been applied to practical calculations up to now.

Following the ideas previously presented in Ref. 7, the Modèle Intermittent Lagrangien (MIL) was devised [8]; it includes a distribution of turbulent time scales and is devoted to the thickened-wrinkled flames domain. This model requires the knowledge of a local "chemical delay time," the nature of which will be discussed further and which, in the early version, had been approximately estimated using an Arrhenius law. At that time, comparisons with experimental data on flames near extinction showed that the model had the capability to display kinetic effects but that it did not succeed in predicting reignition. We have improved the chemical delay time calculation by means of a six-step and ten-species reduced reaction mechanism that has been derived under consideration of atomic flux graphs [9]. It was used for building a library in which the local chemical delay time is given as a function of the instantaneous mixture fraction, provided that two parameters related to local mixing, i.e., mean mixture fraction and oxygen mean mass fraction are known.

Finally, the predictions of the extended MIL model were tested against experimental results on turbulent jet diffusion flames near extinction obtained by Masri et al. [10]. Since the model appears

to simulate extinction-reignition effects, these comparisons are satisfactory and prove that the refinement in computing the chemical delay time is a decisive improvement.

It is to be noted that other attempts [11–13] were made to calculate the flames investigated by Masri et al. [10]. Chen et al. [12] used a second-order moment procedure for flow computation and a joint pdf equation for scalar transport. They tested two reduced reaction mechanisms but did not succeed in simulating the kinetic effects and suspected an artifact of the current Monte-Carlo procedure. Masri and Pope [11] solved a velocity-composition joint pdf equation by the Monte-Carlo method. Their results were satisfactory only for flames far from extinction, for their simple thermochemical model did not account for kinetic effects. Vervisch [13] tested the lagrangian PEUL model [15] as well as a pdf procedure. Both methods, implemented in a k-ε flow calculation, provided correct predictions.

The MIL model consists, as well as the PEUL model, in approximating the joint pdf of reactive species by its skeletal shape in the composition space. However, there exists a twofold difference between these models. On one hand, MIL assumes high global activation energy combustion that, although including some restriction, is realistic for reactants consumption, formation of main products, and heat release; it will be seen below that this hypothesis simplifies the determination of the joint pdf shapes in the composition space. On the other hand, the allowance for a distribution of turbulent timescales is an essential feature of MIL, which is not considered in the PEUL model.

The Turbulent Combustion MIL Model

The MIL model originates from the IEM (Interaction by Exchange with Mean) model [14] in which the diffusion term in the lagrangian equation for the reactive species mass fractions is modeled as an exchange with the mean value

$$\frac{d\,Y_i}{dt} = \frac{\tilde{Y}_i - Y_i}{\tau} + \dot{w}_i(Y_{j,j=1,\ldots,N}, T) \qquad (1)$$

where Y_i is the instantaneous mass fraction of species i and $\tilde{Y}_i$ is its statistical mean value; $\dot{w}_i$ is the instantaneous reaction rate of species i, depending on the mass fractions of all other species and temperature; $1/\tau$ is the frequency of exchange that, in the IEM model for homogeneous media, is unique and related to the kinetic energy of turbulence k and its dissipation ε by stating $\tau ak/\varepsilon$. Borghi [15] extensively discussed this model and demonstrated that Eq. (1) allows to derive the classical equations for $\tilde{Y}_i$ and

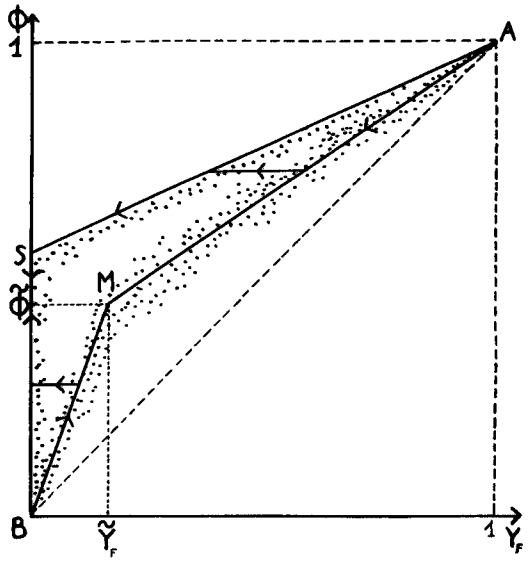

FIG. 1. Trajectories of fluid particles in the phase plane fuel (Y_F)/mixture fraction (ϕ) in the case of a diffusion flame.

$\widetilde{Y_i''Y_j''}$ as well as the modeled pdf equation of Dopazo and O'Brien [1].

In the framework of MIL, the exchange time τ, instead of being unique, is assumed to obey a turbulent timescales distribution that will be discussed later.

Assuming "sudden combustion," i.e., high global activation energy is the second main hypothesis of the model. Sudden combustion implies that chemical reaction starts with quasi-negligible consumption of reactants and very low heat release and, after an "ignition delay," terminates rapidly, most of the consumption of reactants and heat release occurring in a short time interval compared to the ignition delay. This picture differs radically from the infinitely fast chemistry hypothesis that states any chemical timescale to be negligible in comparison of all turbulent timescales and that, thereby, precludes considering a chemical delay.

We consider the case of non-premixed combustion. Let us depict the history of fluid particles in a phase space (ϕ, Y_F) (Fig. 1), where ϕ is a mixture fraction defined such that $\phi = 1$ in the fuel inlet (point A) and $\phi = 0$ in the oxidizer inlet (point B) and Y_F is the fuel mass fraction. On Fig. 1, M is the point the mean value ($\tilde{\phi}$, $\tilde{Y}_F$) is located in the phase space and S is the point corresponding to stoichiometric conditions. In a homogeneous turbulent medium and assuming sudden combustion, Eq. (1) implies that the trajectories on which fluid particles move are made with paths along the mixing lines AM and BM when weak reaction occurs or paths along

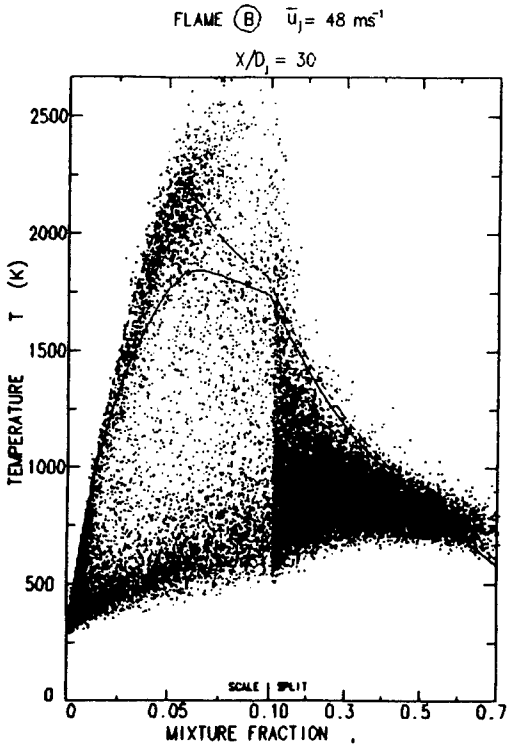

FIG. 2. Scatter plot of the instantaneous temperature vs mixture fraction in a jet diffusion flame of methane near extinction (from Masri et al. [16]).

AS and BS when reaction is very fast. The fluid particles skip from the former to the latter as soon as ignition conditions are fulfilled. Jumps from mixing to equilibrium lines are very fast, and thus, the probability to find a fluid particle elsewhere than along AM, BM, AS, and BS is quite small. Consequently, the projection of the joint pdf $\tilde{P}_{\phi,yF}(\phi, Y_F)$ on the (ϕ, Y_F) plane lies only on AM, BM, AS, and BS.

In actual fact, we deal with nonhomogeneous flows, and as a consequence, the projection of $\tilde{P}_{\phi,yF}(\phi, Y_F)$ rather looks like a picture made with the equilibrium lines and one cloud of points around the mixing lines. This approximated shape of the joint pdf that arises from the MIL model is far from being unrealistic. Scatter plots in a mixture fraction/temperature plane provided by the Masri et al. experiments [16] indeed show that, in flame zones near extinction, such a description holds, at least for lean to slightly rich mixtures (Fig. 2). In regions that are further from extinction, the measured scatter plots display dense clouds of points in the vicinity of the equilibrium lines, a picture that, obviously, also supports the MIL model assumptions.

The mean consumption rate of fuel, in the framework of a global one-step reaction approximation, is derived considering the trajectories described on Fig. 1 together with the equations of IEM for ϕ and Y_F. Mathematical details are given in Ref. 8; then, the mean reaction rate writes

$$\tilde{\dot{w}}_F = \int_0^1 \tilde{P}\varphi(\phi) \int_{\tau_{ig}(\phi)}^{+\infty} \dot{w}_F^c P(\tau) d\tau d\phi \qquad (2)$$

where

$$\dot{w}_F^c = -\tilde{Y}_F/\tau \quad \text{for } \phi \leqslant \phi_s$$
$$\dot{w}_F^c = -[\tilde{Y}_F(1 - \phi_s) + (\tilde{\phi} - \phi_s)]/\tau(1 - \phi_s) \quad \text{for } \phi \geqslant \phi_s \qquad (3)$$

where ϕ_s is the stoichiometric value of mixture fraction, $\tilde{P}_\varphi(\phi)$ is the pdf of ϕ, and $P(\tau)$ is the distribution of turbulent timescales; as far as we know, neither theoretical nor experimental works have been carried out for determining $P(\tau)$. Direct numerical simulation of non-premixed flames [17] could be a valuable guidance for getting more insight into such a distribution and, also, for including chemistry effects in the modelling of the micromixing process. Here, we follow the experimental study of Bray et al. [18] and assume an exponential function:

$$P(\tau) = \exp[-(\tau - \tau_K)/(\tau_t - \tau_K)]/(\tau_t - \tau_K) \quad \text{for } \tau \geqslant \tau_K \quad \text{and } P(\tau) = 0 \quad \text{for } \tau < \tau_K \qquad (4)$$

where τ_K is the Kolmogorov timescale and τ_t *a* k/ε; $\tau_{ig}(\phi)$ is the chemical delay time; a way of computing this parameter is shown in the next section.

Building the Library of Chemical Delay Times for Methane/Air Combustion

The reaction rates are given by a six-step reaction mechanism that was derived by means of the atomic flux graphs technique [9]. This chemical scheme includes 10 species and writes

$$CH_4 \rightarrow CH_3 + 1/2\ H_2 \qquad (R1)$$
$$CH_3 + 1/2\ O_2 \rightarrow CH_2O + 1/2\ H_2 \qquad (R2)$$
$$CH_2O + 1/2\ O_2 \rightarrow CO + H_2O \qquad (R3)$$
$$H_2 + 1/2\ O_2 \rightleftarrows H_2O \qquad (R4)$$
$$CO + 1/2\ O_2 \rightleftarrows CO_2 \qquad (R5)$$
$$N_2 + O_2 \rightleftarrows NO + NO \qquad (R6)$$

The corresponding reaction rates are reported in Ref. 9. This scheme was fitted for equivalence ratio and temperature ranging, respectively, from 0.2 to 2 and 900 to 1500 K. It provides quite a good predic-

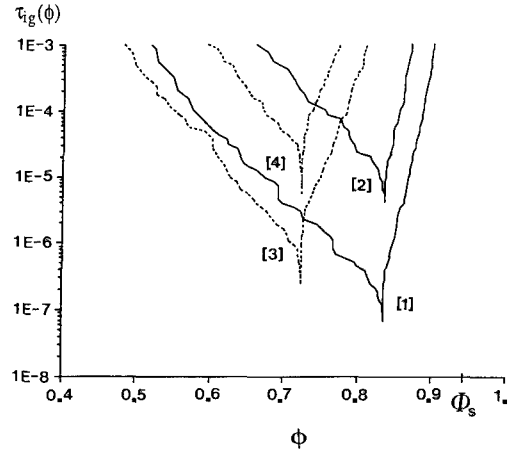

FIG. 3. Sample of the chemical delay time library for different couples ($\tilde{\phi}$, $\tilde{Y}_{O_2}$).

tion of ignition times [9]. Since nitric oxide production is only weakly coupled with other reactions, the chemical reaction (R6) is neglected in the computation of chemical delay times.

The chemical delay time that is considered in the model is not the ignition time of a mixture at given initial equivalence ratio and temperature. In point of fact, our chemical delay time, in addition to kinetic processes, takes into account local mixing effects. More precisely, it has to be viewed as the delay time during which a fluid particle proceeds to ignition while experiencing mixing.

Then, the chemical delay times library is built up as follows. Reaction rates being known due to the reduced scheme (R1 through R5) system (1) (including an equation for temperature) can be solved provided that the mean values $\tilde{Y}_i$, $\tilde{T}$, as well as the exchange time τ are given. Notice that the solution of the lagrangian equation for an inert species (e.g., mixture fraction ϕ) is analytical. The under mentioned procedure is used:

1. Selecting values for $\tilde{Y}_{O_2}$ and $\tilde{\phi}$ allows to determine the main species mean mass fractions, $\tilde{Y}_{CH_4}$, $\tilde{Y}_{CO_2}$, and $\tilde{Y}_{H_2O}$ and the mean temperature $\tilde{T}$, assuming global reaction, adiabaticity and equal diffusivities.
2. Minor species, including carbon monoxide, hydrogen, and radicals are neglected as far as their mean mass fractions are concerned: $\tilde{Y}_{CO} \simeq 0$, $\tilde{Y}_{H_2} \simeq 0$, $\tilde{Y}_{CH_3} \simeq 0$, and $\tilde{Y}_{CH_2O} \simeq 0$. It is to be noticed that in the present scheme, CH_3 and CH_2O stand for the radical pool of the detailed scheme, i.e., O, H, OH, CH_3, ... Although production of radicals during the ignition process is duly taken into account, the previous hypothesis implies that we will compute chemical delay times in mixtures that would be initially free of radicals. This restriction is, of course, questionable since we know that mixing with radicals may strongly influence ignition. However, the library we build accounts for mixing with hot products through $\tilde{Y}_{O_2}$ (and then $\tilde{T}$) and, consequently, for radicals production through the increase in temperature. Accounting for the presence of radicals in the mean mixture requires extending the library to include $\tilde{Y}_{CH_3}$ and $\tilde{Y}_{CH_2O}$ as two additional parameters and solving their respective transport equations. Although quite tractable, this task (especially the derivation and the implementation of a five-parameters library) is rather tedious. This is the reason why this improvement, which is at present seriously considered, is still under progress. It will also be shown below that the already implemented three-parameters libary leads to quite reliable results.
3. System (1) is solved for temperature, mixture fraction, and $Y_i's$ (i = CH_4, O_2, CO_2, H_2O, CO, H_2, CH_3, CH_2O). One couple ($\tilde{Y}_{O_2}^{(k)}$, $\tilde{\phi}^{(k)}$) being given, integration is performed for one value τ^* of τ. Ignition is detected whenever temperature experiences a sudden increase (e.g., at time t_{ig}); then, integration is stopped and one value of the chemical delay time t_{ig} is stored in the library as $\tau_{ig} \equiv \tau^*(\tilde{Y}_{O_2}^{(k)}, \tilde{\phi}^{(k)}, \phi_{ig})$ where ϕ_{ig} is the mixture fraction at time t_{ig}. Afterward, the system is integrated again for another value of τ, providing another τ_{ig}, and so on. The library is completed using the above technique for a number of couples ($\tilde{Y}_{O_2}^{(k)}$, $\tilde{\phi}^{(k)}$) in the domain $[0 \leq (\tilde{Y}_{O_2}^{(k)}, \leq Y_{O_{2B}}, 0 \leq \tilde{\phi}^{(k)} \leq 1]$ (where $Y_{O_{2B}}$ is the oxygen mass fraction in air inlet) and various values of τ ranging from 10^{-6} to 10^{-2} s.

Since for each value of τ, integration of (1) is performed with initial conditions corresponding once to pure fuel and once to pure air, two ignitions may be found, one on the rich side and the other on the lean side. For this reason, $\tau_{ig}(\phi)$, for given values of $\tilde{Y}_{O_2}$ and $\tilde{\phi}$, is represented by U-shaped curves (which take a V shape in a semilog plot), as displayed by Fig. 3.

Finally, the chemical delay times library completes the MIL model. This model is used with a global reaction assumption for heat release and main species but includes complex chemistry through the chemical time τ_{ig}.

Comparison of MIL Predictions with Experimental Data

MIL was used for predicting turbulent diffusion flames near extinction investigated experimentally by Masri et al. [10]. Their experimental setup consists of a burner with a central jet of methane in a coflowing air stream. The burner stability is ensured due to a burnt gas flow provided by a pilot flame surrounding the methane jet. Experimental conditions are as follows: air coflow: $U_e = 15\ \mathrm{m \cdot s^{-1}}$; pilot burnt gas $U_{pb} = 24\ \mathrm{m \cdot s^{-1}}$; $T_{pb} = 2400$ K. Flame characteristics are varied by changing the methane bulk velocity: $U_j = 36\ \mathrm{m \cdot s^{-1}}$ (flame A), $U_j = 41\ \mathrm{m \cdot s^{-1}}$ (flame L), $U_j = 48\ \mathrm{m \cdot s^{-1}}$ (flame B), $U_j = 55\ \mathrm{m \cdot s^{-1}}$ (flame M). The diameter of the central jet is $D_j = 7.2$ mm.

The flow was computed by a numerical procedure for two-dimensional compressible flows [19,20]. Spatial discretization is performed with a finite volume technique and time integration with a semi-implicit factored scheme. The main equations to be solved are the Favre averaged transport equations for mass, momentum, energy, and fuel; in addition, this set includes an equation of state. Transport equations for kinetic energy of turbulence and its dissipation are also needed since the k-ε model is used. The pdf of mixture fraction $\tilde{P}_\varphi(\phi)$ in Eq. (2) is approximated by means of a presumed pdf method [2] that requires solving equations for the mean mixture fraction and mixture fraction variance.

The fuel mean reaction rate $\tilde{\dot{w}}_F$ of the MIL model is implemented in the fuel-averaged equation. At each point, the oxygen mean mass fraction $\tilde{Y}_{O_2}$ is computed from $\tilde{Y}_F$ and $\tilde{\phi}$ and the couple $(\tilde{Y}_{O_2}, \tilde{\phi})$ provides the entry in the chemical delay times library for determining $\tau_{ig}(\phi)$.

The boundary conditions for velocity and kinetic energy of turbulence at the burner inlet are taken from the actual ones [11].

Experimental data on velocity and turbulent kinetic energy were available for flame L only. Numerical predictions of these variables (not shown here) are almost satisfactory and consistent with the middling ability of the standard k-ε model to predict variable density jet flows.

Figure 4 shows mean and root mean square (rms) mixture fraction calculations in flame B. The dissipation of mixture fraction fluctuations, ε_ϕ, was modeled in a usual way, assuming $\varepsilon_\phi \equiv C_D\, \varepsilon/k\ \widetilde{\phi''^2}$ (with $C_D = 2$ as recommended by Béguier et al. [21] for jet flows). The numerical results are rather good for

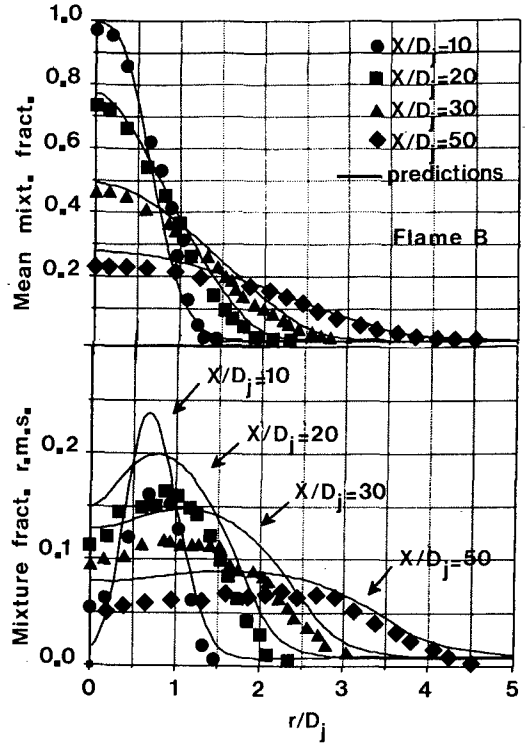

FIG. 4. Radial profiles of mean mixture fraction and mixture fraction rms at axial locations $x/D_j = 10$, 20, 30, and 50 (flame B).

the mean mixture fraction. For rms mixture fraction, the agreement is not perfect, but the main behavior is correctly captured. Moreover, these results are substantially better than those obtained by Chen et al. [12] who used a second-order modeling.

Flame A, although not fast burning, does not experience extinction. Despite slight underestimation, calculations display a correct temperature evolution (Fig. 5).

Comparison with experimental data from flame B is more fruitful. First, Fig. 6 shows that methane mean mass fraction is quite well predicted. Similar results were obtained in flames A and L but are not reported here.

The salient phenomenon that was experimentally put into evidence in flame B is the partial extinction occurring in the region located between 10 and 20 jet diameters and further reignition [10,16]. Indeed, measurements clearly show (Fig. 7) that the maximum temperature reaches 1400 K at $x/D_j = 10$, decreases to 800 K at $x/D_j = 20$, and afterward, increases progressively downstream (1000 K at $x/D_j = 30$, 1400 K at $x/D_j = 50$). It seems that such a behavior is not easy to explain, at first sight. Nevertheless, pdf measurements [16] support the idea that although high strain drives the flame to be extin-

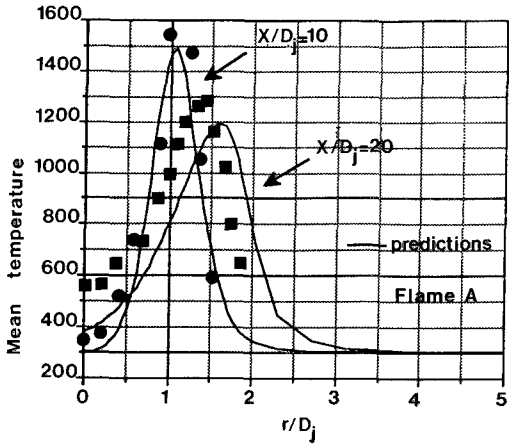

FIG. 5. Radial profiles of mean temperature at axial locations $x/D_j = 10$ and 20 (flame A).

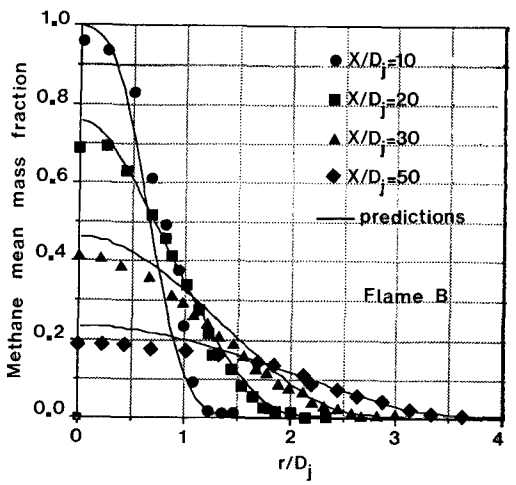

FIG. 6. Radial profiles of methane mean mass fraction at axial locations $x/D_j = 10$, 20, 30, and 50 (flame B).

guished, pockets of burnt fluid are still encountered and are helping to keep chemical reaction alive further downstream. Thereby, close to extinction, combustion occurs in a quasi-bimodal regime, and the flow displays either burnt gas or mixing fluid. This picture is in agreement with the "intermittent" nature of the MIL model previously reported (Fig. 1). Moreover, in the framework of MIL, strain effects as well as thermal influence over chemical reaction are taken into account, the former via the turbulent timescales distribution (which includes the turbulence Reynolds number $(\tau_t/\tau_K)^2$) and the latter via the chemical delay time τ_{ig}. It is also clear that the two Damköhler numbers τ_K/τ_{ig} are key parameters of the model (formula 2).

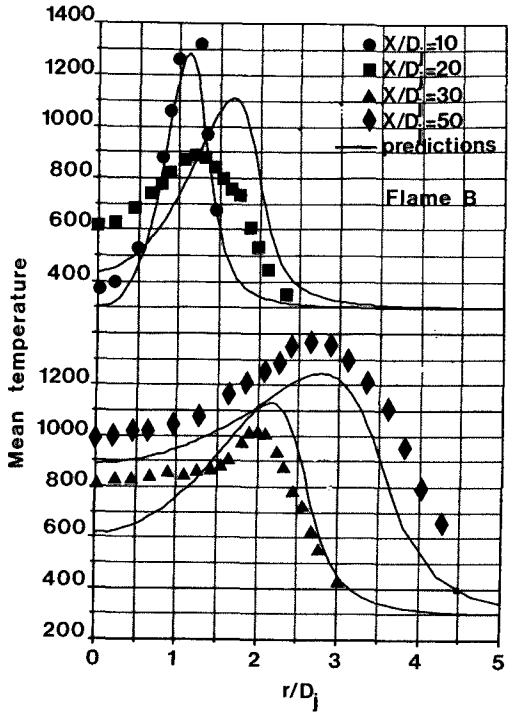

FIG. 7. Radial profiles of mean temperature at axial locations $x/D_j = 10$, 20, 30, and 50 (flame B).

Mean temperature is reasonably well predicted in flame B (Fig. 7). The shift of the calculated profile toward the periphery of the jet at $x/D_j = 20$ is rather surprising, for this trend is not displayed at other sections. This discrepancy could be explained by possible inaccuracies in flow computation but, unfortunately, experimental dynamic variables were not available for flame B.

The computed temperature profiles of Fig. 7 have been put together on Fig. 8. Then, looking at the longitudinal evolution of the maximum temperature, it clearly appears that partial extinction (between $x/D_j = 10$ and 20) and further reignition ($x/D_j = 30$ and 50) are predicted. These results demonstrate the ability of the model to calculate the main trends of flames near extinction.

Conclusion

Additional extension of a lagrangian model devised for predicting turbulent diffusion flames that display kinetic effects has been achieved. The model assumes high activation temperature reaction and requires two main entries: a distribution of turbulent timescales and a chemical delay time. This formulation allows accounting for turbulence/chemistry in-

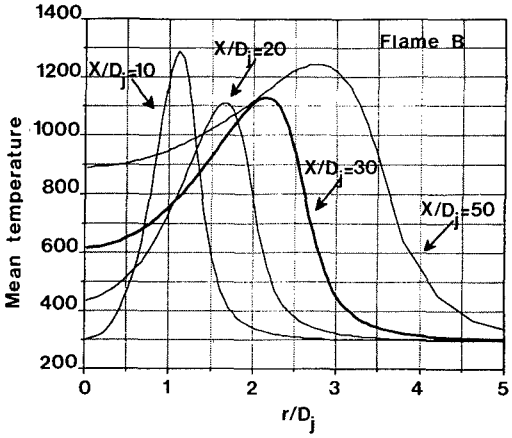

FIG. 8. Computed radial profiles of mean temperature at axial locations $x/D_j = 10, 20, 30$, and 50, showing partial extinction and reignition (flame B).

teraction in a refined manner since the model is likely to display the right parameters to this purpose, i.e., the nondimensional ratios τ_K/τ_{ig}, τ_t/τ_{ig}, τ_t/τ_K. The recent development consisted in deriving a library of such chemical delay times from a six-step reduced mechanism for methane-air combustion. Comparison of numerical predictions with experimental data from turbulent diffusion flames near extinction proved that the model is well suited for addressing such combustion regimes; in particular, the computations appeared to predict extinction-reignition phenomena.

Acknowledgments

The authors would like to acknowledge the Centre National de la Recherche Scientifique and Gaz de France for supporting this study.

REFERENCES

1. Dopazo, C., and O'Brien, E. E., *Acta Astronaut.* 1:1239–1255 (1974).
2. Borghi, R., and Moreau, P., *Acta Astronaut.* 4:321–341 (1977).
3. Pope, S. B., *Prog. Energy Combust. Sci.* 11:119–192 (1985).
4. Cant, R. S., and Bray, K. N. C., *Twenty-Second Symposium (International) on Combustion,* The Combustion Institute, Pittsburgh, 1988, pp. 791–799.
5. Peters, N., *Prog. Energy Combust. Sci.* 10:319–339 (1984).
6. Pope, S. B., and Chen, Y. L., *Phys. Fluids A* 2:1437–1449 (1990).
7. Borghi, R., and Gonzalez, M., *Combust. Flame* 63:239–250 (1986).
8. Gonzalez M., and Borghi, R., in *Selected Papers from Turbulent Shear Flows* 7 (F. Durst and B. E. Launder, Eds.), Springer-Verlag, Berlin, 1991, p. 293.
9. Revel, J., Boettner, J. C., Cathonnet, M., and Bachman, J. S., *J. Chim. Phys.* 91:365–382 (1994).
10. Masri, A. R., Bilger, R. W., and Dibble, R. W., *Combust. Flame* 71:245–266 (1988).
11. Masri, A. R., and Pope, S. B., *Combust. Flame* 81:13–29 (1990).
12. Chen, J. Y., Kollmann, W., and Dibble, R. W., *Combust. Sci. Technol.* 64:315–346 (1989).
13. Vervisch, L., Ph.D. Thesis, University of Rouen France, 1991.
14. Villermaux, J., *Encyclopedia of Fluid Mechanics,* Gulf Publishing Co., West Orange, NJ, 1986, p. 707.
15. Borghi, R., *Prog. Energy Combust. Sci.* 14:245–292 (1988).
16. Masri, A. R., Bilger, R. W., and Dibble, R. W., *Combust. Flame* 73:261–285 (1988).
17. Vervisch, L., *Annual Research Briefs,* Center for Turbulent Research, Stanford, 1992, p. 411.
18. Bray, K. N. C., Libby, P. A., and Moss, J. B., *Twentieth Symposium (International) on Combustion,* The Combustion Institute, Pittsburgh, 1984, pp. 421–427.
19. Dutoya, D., and Michard, P. J., *Rech. Aérospat.* 1980–2:123–129 (1980).
20. Dupoirieux, F., and Dutoya, D., *Rech. Aérospat.* 1987–6:15–22 (1987).
21. Béguier, C., Dekeyser, I., and Launder, B. E., *Phys. Fluids* 21 (3):307–310 (1978).

COMMENT

J. Chomiak, Chalmers University of Technology, Sweden. For your model to be applicable, you must be sure that there are no flamelets in the reaction domain or that the flamelet combustion is negligible as compared with the distributed reaction combustion. Do you have an estimate of the importance of the flamelet combustion on the predictions?

Author's Reply. After the pdf's measurements of Masri et al. [16], it is not clear to what extent flamelets take part in the flame structure. Furthermore, their results on conditional pdf's indicate that the partial extinction and reignition phenomenon may be explained through the existence of fully burned pockets that provide possible reignition in regions close to extinction [1]. Clearly, this behavior may be simulated through the intermittent nature of our model which takes into account turbulent exchanges with the environment.

REFERENCE

1. Masri, A. R., Bilger, R. W., and Dibble, R. W., *Combust. Flame* 74:267–284 (1988).

Twenty-Fifth Symposium (International) on Combustion/The Combustion Institute, 1994/pp. 1115–1123

TWO-DIMENSIONAL NONSTATIONARY CAUSAL STOCHASTIC MODEL FOR TURBULENCE/RADIATION INTERACTIONS IN FLAMES

S. H. CHAN,* X. C. PAN** AND J. ZHANG†

Department of Mechanical Engineering
University of Wisconsin-Milwaukee
Milwaukee, Wisconsin 53201, USA

A new stochastic method is presented to treat turbulence/radiation interactions. In order to simulate the random field of instantaneous mixture fraction distributions along the radiation path, a two-dimensional (2D) nonstationary causal stochastic model is proposed. The model can account for not only the first-order correlations both in time space and geometric space but also the first-order cross correlation. Also presented is a general proof that in the simulation of the mixture fraction, the contributions from the first-order correlations in time and geometric spaces are important and so is the contribution from the first-order time-geometric space cross correlation. Furthermore, the second- and higher-order correlation terms are proved to be negligibly small. They provide the foundation for the general development of the present two-dimensional and future three-dimensional stochastic models for turbulence-radiation interactions. Finally, application of the proposed two-dimensional causal model to simulate the radiation process in turbulent carbon monoxide/hydrogen/air flames is illustrated. The predicted mean and fluctuating radiation properties are found to be in good agreement with experimental data.

Introduction

Theoretical and experimental studies have shown that turbulence/radiation interactions in turbulent diffusion flames have a significant influence on radiation. This is due to temperature and species concentration fluctuations and the strong nonlinear relationship between radiation and temperature. Cox [1], Kabashnikov and coworkers [2,3], and Grosshandler and Joulain [4] studied the turbulent effects on radiation by using simplified flame radiation models. The results showed that turbulent fluctuations increase mean radiation properties from the level based on the mean scalar property distribution profiles in a flame. Nelson [5] used a simple band radiation model to evaluate the importance of mean and fluctuation parameters. It was illustrated that the importance of fluctuations is largely confined to variation in the Planck function. Chan and Chern [6] proposed a method to consider the turbulence/radiation interactions for multiphase diffusion flames, by solving the energy equation with a radiative source term. A linear relationship assumption between enthalpy and mixture fraction and a PDF method with three-dimensional (mixture fraction, enthalpy, and scalar properties) state relationships were used.

Generally, the turbulence/radiation interaction can be better simulated and studied by a stochastic approach. If the instantaneous mixture fraction distribution along a radiation path is simulated stochastically as a two-dimensional (2D) (time space t, geometric space s) random field (see Fig. 1), radiation intensities can be calculated by solving the radiative transfer equation along the radiation path since the radiation properties such as temperature and species concentrations can be considered as functions of mixture fraction, and the radiation statistics can be readily computed from the instantaneous radiation intensities. Therefore, radiation statistics can be calculated simply from the simulation of instantaneous mixture fraction distributions along the radiation path. Jeng et al. [7] provided a first attempt to use a stochastic approach to study the turbulence/radiation interactions. It was assumed that the flow field consists of numerous statistically independent turbulent eddies, each of them having uniform properties, which are only a function of mixture fraction. The cumulative distribution function of mixture fraction was randomly sampled by selecting a random number in the range of 0–1 to find the instantaneous mixture fraction. That is, the mixture fraction at (m,n) was simulated independent of the mixture fraction in t and s directions (Fig. 1a). There was no temporal or spatial correlation consideration. Using the time-series technique for a first-order autoregressive process, Kounalakis et al. [8] modified the approach to account for temporal correlations of mixture fraction, whereby the mixture fraction at (m,n) was simulated

*Wisconsin Distinguished Professor.
**Graduate Student.
†Assistant Professor.

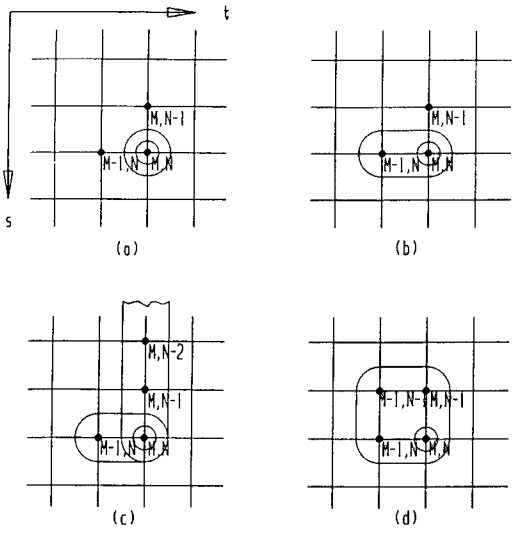

FIG. 1. The two-dimensional random field for the existing and present models.

by correlating with previous time space in the t direction (Fig. 1b). There was no spatial correlation consideration. Following the time-series technique to consider both temporal and spatial correlations of mixture fraction, Kounalakis et al. [9] later assumed that the mixture fraction could be constructed as an additive function of a first-order autoregressive process in time space and a pth-order ($p \geq 1$) moving average process in geometric space. That is, the mixture fraction at (m,n) was simulated using the correlation with the mixture fraction at the previous time in the t direction and, with that, at all previous locations in the s direction (Fig. 1c). It was simply based on the assumption that the one-dimensional random processes in the t and s directions are additive. The prediction of mixture fraction at (m,n) was only expressed as the sum of the one-dimensional predictions of mixture fraction in each direction, namely, the prediction at $(m - 1, n)$ in the t direction and at $(m, n - 1)$, $(m, n - 2)$, etc. in the s direction. Consequently, the contribution from cross locations, such as $(m - 1, n - 1)$, cannot be accounted for since there was no temporal-spatial correlation consideration. As to be seen later, in the simulation of mixture fraction at (m,n), the contribution from the cross location at $(m - 1, n - 1)$ is in fact more significant than from the second-order location at $(m, n - 2)$ or $(m - 2, n)$.

In summary, the above review reveals lack of a systematic formulation and rigorous model to simulate radiation-turbulence interactions. There is a need to develop a general two-dimensional stochastic model to simulate a radiation field in turbulent flames. Also needed is the assessment of the relative significance of the contribution from cross- and non-cross-correlation terms. Therefore, the objectives of the present study are several. First, a general two-dimensional causal stochastic model for the simulation of mixture fraction in turbulent reacting flows is presented. The model can account for precorrelations in time and geometric spaces as well as the cross correlations (Fig. 1d). This makes possible a straightforward extension of the present 2D model to a three- or higher-dimensional model. Second, it aims to provide a proof that, in the mixture fraction simulation, the contributions from the first-order correlations in the time and geometric spaces and the first-order cross correlation are significant, but not from the higher-order correlations. This provides a useful rule for the development and considerable simplification of the present and any stochastic models for the analysis of turbulence-radiation in flames. Finally, for illustration, the proposed two-dimensional nonstationary causal model is used to predict mean and fluctuating spectral radiation intensities of carbon monoxide/hydrogen/air turbulent diffusion flames, and the results are compared to the existing experimental data to show the validity of the model.

Two-Dimensional Stochastic Model

The existing stochastic models are essentially based on the concept of the time-series technique intended for a one-dimensional process. The present work, however, is based on the recent advances in the field of image processing, which has developed a model capable of simulating a two-dimensional random field [10]. Nevertheless, the latter is for a stationary field; namely, the mean and variance of a scalar are treated as constant in the field. In combustion, the mean and variance of mixture fraction are a function of position. Therefore, a two-dimensional model for a nonstationary random field suitable for general use in turbulent combustion is developed below.

Consider the instantaneous mixture fraction distributions along a radiation path as a two-dimensional (time space–geometric space) random field. Let $z(m,n)$ be such a two-dimensional random field with a mean value $\bar{z}(m,n)$ and covariance $r(m,n; m - k, n - l)$. For the simulation of mixture fraction, m and n represent the location of time space and the location of geometric space, respectively. It is noted that m can also designate the location of another geometric space. For a two-dimensional nonstationary random field, the linear prediction of $z(m,n)$ under minimum variance representations is simulated as

$$z(m,n) = \sum_{(k,l)} \sum_{\in \hat{S}} a(m - k, n - l) z \cdot (m - k, n - l) + \varepsilon(m,n) \qquad (1)$$

in which $\hat{S}$ is the prediction region, and the predictor

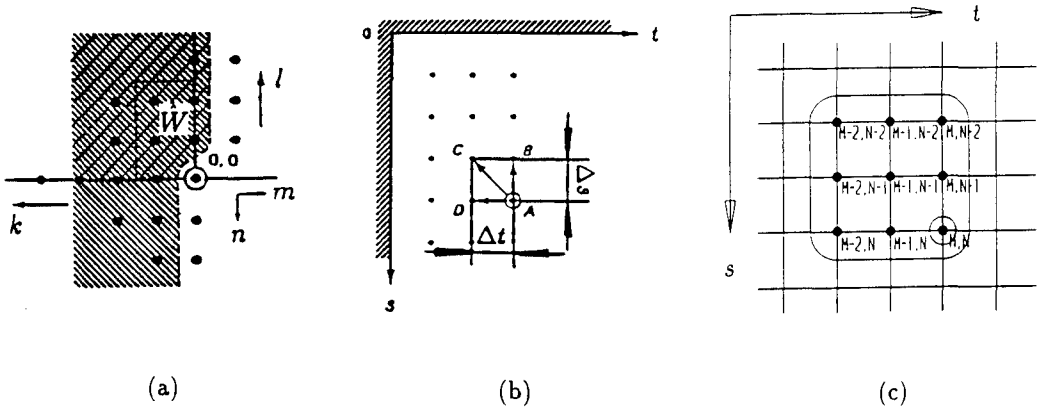

FIG. 2. (a) The causal prediction region $\hat{S}$ and the corresponding finite prediction region $\hat{W}$, (b) initial conditions for a causal system (Δt: time-space increment; Δs: geometric-space increment), and (c) the two-dimensional random field for the second-order causal model.

coefficients a's, unlike the prior work [10], are now allowed to be a function of $m - k$ and $n - l$. The term $\varepsilon(m,n)$ is the zero mean prediction error that is governed by the present state (m,n) and is independent of all the other states such that the following expectations hold:

$$E[\varepsilon(m,n)] = 0,$$

$$E[\varepsilon(m,n)z(m - k, n - l)] = \beta^2_{m,n}\delta(k,l) \quad (2)$$

in which $\beta^2_{m,n} \equiv E[\varepsilon(m,n)\varepsilon(m,n)]$ is the variance of $\varepsilon(m,n)$, and $\delta(k,l) = 0$ when $k \neq 0 \cup l \neq 0$ and $\delta(k,l) = 1$ when $k = l = 0$. Decomposing $z(m,n)$ into mean and fluctuating parts as

$$z(m,n) = \bar{z}(m,n) + z'(m,n) \quad (3)$$

and substituting Eq. (3) into Eq. (1),

$$\bar{z}(m,n) + z'(m, n) = \sum_{(k,l)} \sum_{\in \hat{S}} a(m - k, n - l)\bar{z} \cdot (m - k, n - l) + \sum_{(k,l)} \sum_{\in \hat{S}} a(m - k, n - l)z' \cdot (m - k, n - l) + \varepsilon(m,n). \quad (4)$$

Taking the time average of Eq. (4) yields

$$\bar{z}(m,n) = \sum_{(k,l)} \sum_{\in \hat{S}} a(m - k, n - l)\bar{z} (m - k, n - l). \quad (5)$$

By substituting Eq. (5) into Eq. (4), we have

$$z'(m,n) = \sum_{(k,l)} \sum_{\in \hat{S}} a(m - k, n - l)z' (m - k, n - l) + \varepsilon(m,n) \quad (6)$$

which shows that $z'(m,n)$ is another two-dimensional nonstationary random field with zero mean and covariance $r(m,n;m - k, n - l)$. Therefore, the simulation of $z(m,n)$ can be shifted to the simulation of $z'(m,n)$. This is the approach used in the present study.

Causal Prediction:

A causal predictor is characterized in terms of previous predictions. The proposed two-dimensional stochastic model is causal in both dimensions, and its prediction region is (Fig. 2a)

$$\hat{S} = \{k \geq 1, \forall l\} \cup \{k = 0, l \geq 1\}. \quad (7)$$

The special case of the single-quadrant causal prediction region is

$$\hat{S} = \{k \geq 0, l \geq 0, (k,l) \neq (0,0)\} \quad (8)$$

which is called a strongly causal predictor and is used in the present simulation.

In practice, only a finite neighborhood $\hat{W}$, $\hat{W} \subset \hat{S}$, is used in the prediction process, so Eq. (6) becomes

$$z'(m,n) = \sum_{(k,l)} \sum_{\in \hat{W}} a(m - k, n - l)z' \cdot (m - k, n - l) + \varepsilon(m,n) \quad (9)$$

in which $\hat{W}$ (Fig. 2a) can generally be described by

$$\hat{W} = \{0 \leq k \leq p, 0 \leq l \leq q, (k,l) \neq (0,0)\}. \quad (10)$$

For the causal simulation, the prediction output

$z'(m,n)$ can be uniquely computed recursively from the past outputs $\{z'(m-k, n-l), (k,l) \in \hat{W}\}$ and the present input $\varepsilon(m,n)$. Therefore, the causal simulations are recursive.

First-Order Causal Model:

The first-order causal model for the simulation of the two-dimensional nonstationary random field is presented next. By setting $p = q = 1$ in Eq. (9),

$$\begin{aligned} z'(m,n) = {} & a(m-1, n)z'(m-1, n) \\ & + a(m, n-1)z'(m, n-1) \\ & + a(m-1, n-1)z'(m-1, n-1) \\ & + \varepsilon(m,n). \end{aligned} \tag{11}$$

Multiplying both sides of Eq. (11) by $z'(m-k, n-l)$ and then taking expectations yield

$$\begin{aligned} r(m,n; m-k, n-1) = {} & a(m-1, n)r \\ & \cdot(m-1, n; m-k, n-l) + a(m, n-1)r \\ & \cdot(m, n-1; m-k, n-l) + a(m-1, n-1)r \\ & \cdot(m-1, n-1; m-k, n-l) \\ & + r_\varepsilon(m,n; m-k, n-l) \end{aligned} \tag{12}$$

where

$$r(m,n; m-k, n-l) \equiv E[z'(m,n)z'(m-k, n-l)] \tag{13}$$

$$r_\varepsilon(m,n; m-k, n-l) \equiv E[\varepsilon(m,n)\varepsilon(m-k, n-l)]. \tag{14}$$

It is noted that

$$E[\varepsilon(m,n)z'(m-k, n-l)] = E[\varepsilon(m,n)\varepsilon(m-k, n-l)] = \beta_{m,n}^2\delta(k,l) \tag{15}$$

Using Eq. (15) and the definition of the correlation at lags k and l,

$$\rho_{m,n;m-k,n-l} \equiv \frac{E[z'(m,n)z'(m-k, n-l)]}{\sqrt{E[z'^2(m,n)]E[z'^2(m-k, n-l)]}} = \frac{r(m,n; m-k, n-l)}{\sigma_{m,n}\sigma_{m-k,n-l}} \tag{16}$$

where $\sigma_{m,n}^2$ is the variance of $z'(m,n)$; Eq. (12) is expressed as

$$\begin{aligned} \sigma_{m,n}\rho_{m,n;m-k,n-l} = {} & a(m-1, n)\sigma_{m-1,n} \\ & \rho_{m-1,n;m-k,n-l} + a(m, n-1)\sigma_{m,n-1}\rho_{m,n-1;m-k,n-l} \\ & + a(m-1, n-1)\sigma_{m-1,n-1}\rho_{m-1,n-1;m-k,n-l} \\ & + r_\varepsilon(m,n; m-k, n-l). \end{aligned} \tag{17}$$

Applying the above to the three nodal points next to (m,n) in Fig. 1d and using Eqs. (15) and (16) yield

$$\begin{aligned} \sigma_{m,n}\rho_{m,n;m-1,n} = {} & a(m-1, n)\sigma_{m-1,n} \\ & + a(m, n-1)\sigma_{m,n-1}\rho_{m,n-1;m-1,n} \\ & + a(m-1, n-1)\sigma_{m-1,n-1} \\ & \cdot \rho_{m-1,n-1;m-1,n}, \qquad (k = 1, l = 0) \\ \sigma_{m,n}\rho_{m,n;m,n-1} = {} & a(m-1, n)\sigma_{m-1,n}\rho_{m-1,n;m,n-1} \\ & + a(m, n-1)\sigma_{m,n-1} \\ & + a(m-1, n-1)\sigma_{m-1,n-1} \\ & \cdot \rho_{m-1,n-1;m,n-1}, \qquad (k = 0, l = 1) \\ \sigma_{m,n}\rho_{m,n;m-1,n-1} = {} & a(m-1, n)\sigma_{m-1,n} \\ & \cdot \rho_{m-1,n;m-1,n-1} + a(m, n-1)\sigma_{m,n-1} \\ & \cdot \rho_{m,n-1;m-1,n-1} + a(m-1, n-1) \\ & \cdot \sigma_{m-1,n-1}, \qquad (k = 1, l = 1) \end{aligned} \tag{18}$$

from which the predictor coefficients $a(m-k, n-l)$ can be readily solved in terms of variance $\sigma_{m,n}$ and correlation $\rho_{m,n;m-k,n-l}$. As in image processing [10], the correlation function $\rho_{m,n;m-k,n-l}$ is taken as separable,

$$\rho_{m,n;m-k,n-l} = \rho_{m,m-k}\rho_{n,n-l}. \tag{19}$$

Substituting Eq. (19) into Eq. (18) and then solving for the coefficients,

$$\begin{aligned} a(m-1, n) &= \frac{\sigma_{m,n}}{\sigma_{m-1,n}}\rho_{m,m-1} \\ a(m, n-1) &= \frac{\sigma_{m,n}}{\sigma_{m,n-1}}\rho_{n,n-1} \\ a(m-1, n-1) &= -\frac{\sigma_{m,n}}{\sigma_{m-1,n-1}}\rho_{m,m-1}\rho_{n,n-1}. \end{aligned} \tag{20}$$

Here, $\rho_{m-k,m} = \rho_{m,m-k}$ and $\rho_{n-l,n} = \rho_{n,n-l}$ have been used. Therefore, the two-dimensional nonstationary first-order causal model is expressed as

$$z'(m,n) = \frac{\sigma_{m,n}}{\sigma_{m-1,n}} \rho_{m,m-1} z'(m-1,n) + \frac{\sigma_{m,n}}{\sigma_{m,n-1}} \rho_{m,n-1} z'(n,n-1) - \frac{\sigma_{m,n}}{\sigma_{m-1,n-1}} \rho_{m,m-1}\rho_{n,n-1} z' \cdot (m-1, n-1) + \varepsilon(m,n) \quad (21)$$

and the covariance function of ε is obtained by multiplying $\varepsilon(m-k, n-l)$ on both sides of Eq. (21) and by taking the expectation of the resulting equation,

$$r_\varepsilon(m,n; m-k, n-l) = \sigma^2_{m,n}(1-\rho^2_{m,m-1})(1-\rho^2_{n,n-1})\delta(k,l). \quad (22)$$

It is noted that in the limit when the variances are assumed to be constant, $\sigma_{m,n} = \sigma_{m-1,n} = \sigma_{m,n-1} = \sigma_{m-1,n-1} = \sigma$, Eqs. (21) through (22) do reduce correctly to the stationary model [10].

Mixture Fraction Stochastic Simulations

As in Eq. (3), the instantaneous mixture fraction distributions along the radiation path $z(s,t)$ can be decomposed as

$$z(t,s) = \bar{z}(s) + z'(t,s). \quad (23)$$

It is noted that the mean value of mixture fraction $\bar{z}$ depends on location s only. When $z'(s,t)$ is considered as a first-order causal field and the correlation function is treated as separable, the above two-dimensional nonstationary first-order causal model, Eq. (21), can be simplified as

$$z'(t,s) = R(\Delta t)z'(t-\Delta t, s) + \frac{\sigma_s}{\sigma_s - \Delta s} R(\Delta s) z'(t, s-\Delta s) - \frac{\sigma_s}{\sigma_s - \Delta s} R(\Delta t)R(\Delta s) z' \cdot (t-\Delta t, s-\Delta s) + \varepsilon(t,s) \quad (24)$$

since the variance of mixture fraction σ^2 is only a function of location s; that is, $\sigma_{t-\Delta t,s} = \sigma_{t,s} = \sigma_s$. In Eq. (24), the temporal correlation $R(\Delta t) \equiv \overline{f'(t)f'(t-\Delta t)}/\overline{f'^2}$, the spatial correlation $R(\Delta s) \equiv \overline{f'(s)f'(s-\Delta s)}/[\sqrt{\overline{f'^2(s)}}\sqrt{\overline{f'^2(s-\Delta s)}}]$ are equivalent to $\rho_{m,m-1}$ and $\rho_{n,n-1}$ in Eq. (21), respectively. As shown experimentally by Becker et al. [12], Wygnanski and Fiedler [13], and Frenkiel and Klebanoff [14], the temporal and spatial correlations are expressed generally in terms of exponential forms. The prediction error, $\varepsilon(t,s)$, is chosen to be an uncorrelated Gaussian random variable with a zero mean and a variance given by

$$\beta_s^2 = \sigma_s^2[1 - R^2(\Delta t)][1 - R^2(\Delta s)] \quad (25)$$

which is obtained from Eq. (22) by setting $k = l = 0$.

Equation (24) can be solved recursively, if $\varepsilon(t,s)$ and the initial values $z'(0,s)$, $z'(t,0)$, and $\varepsilon(t,s)$ are known. To obtain the solution at location A, we only need the previously determined solutions at locations B, C, and D and the random variable ε at location A (Fig. 2b). The initial values $z'(0,s)$ and $z'(t,0)$ can be simulated by using the one-dimensional time-series technique.

Since the mixture fraction has a clipped Gaussian probability density function, it can be obtained from the causal simulation of Eqs. (23) through (25) with the following stipulation:

$$f = z, \quad 0 \le z \le 1; \qquad f = 0, \quad z \le 0; \qquad f = 1, \quad z \ge 1. \quad (26)$$

Carbon Monoxide/Hydrogen/Air Flames

The present causal model is applied to buoyant turbulent round jet diffusion flames of a carbon monoxide/hydrogen mixture burning in still air. The experimental data of such flames are available from Kounalakis' work [11]. Two flames were considered. Their Reynolds numbers at the burner exit were 7,400 and 12,700. The radial radiation paths were at x/d = 30, 40, and 50. The measured time-averaged mean and variance of mixture fraction distributions for the three radiation paths in each flame were given. The measured temporal and spatial correlations, the integral length, and timescales along the radiation paths of two flames were also available. Those measured quantities are useful in the later validation of the proposed two-dimensional stochastic model.

The prediction of radiation statistics began with the simulation of instantaneous mixture fraction distributions along a radiation path, which was performed by using the two-dimensional nonstationary first-order causal model. It was required to generate a set of random numbers ranging 0–1. The random numbers were chosen to be equal to the cumulative distribution function of the unclipped Gaussian powder diffraction file (PDF) of $\varepsilon(s,t)$ with zero mean and a variance given by Eq. (25). The measured correlations, $R(\Delta t)$ as a function of x/d and Δt, and $R(\Delta s)$ as a function of x/d and Δs, and the variance of mix-

TABLE 1
Predicted and measured radiation properties

	$\bar{i}_\lambda$ (Kw/m^2 μm sr)			$\sqrt{\overline{i'^2_\lambda}}/\bar{i}_\lambda$ (%)		
x/d	Data	Predicted 2D Causal	Predicted [9]	Data	Predicted 2D Causal	Predicted [9]
			(Re = 7,400, λ = 4.5 μm)			
30	8.7	8.6	9.8	20	21	16
40	11.2	11.0	10.3	18	20	19
50	11.0	11.2	9.7	26	24	27
			(Re = 7,400, λ = 2.8 μm)			
30	2.6	2.2	2.3	24	25	23
40	2.9	2.5	2.7	27	30	29
50	2.8	2.7	2.5	35	33	36
			(Re = 12,700, λ = 4.5 μm)			
30	9.2	9.0	10.1	15	19	15
40	11.4	10.8	12.0	13	17	13
50	12.4	11.8	11.7	16	16	16
			(Re = 12,700, λ = 2.8 μm)			
30	2.2	1.8	2.5	25	26	21
40	3.3	2.4	3.4	22	26	21
50	3.6	2.9	3.3	26	27	27

ture fraction σ_ξ^2, taken from Kounalakis [11], were used in evaluating Eq. (25). With $\varepsilon(s,t)$, Eq. (24) was solved to yield $z'(t,s)$. Then the unclipped instantaneous mixture fraction z was computed from Eq. (23), in which the measured values [11] of the mean mixture fraction $\overline{f(s)}$ were used. The clipped f was finally determined from Eq. (26). The corresponding instantaneous species concentrations and temperature of the reacting mixture were calculated from the state relationships of a radiating flamelet with a scalar dissipation rate of $\chi = 1.0$, as shown in Ref. [15]. The relationships were obtained by solving flamelet conservation equations using a reduced three-step chemical kinetic mechanism and an energy equation with an optically thin radiation model [15]. The flamelet with $\chi = 1.0$ corresponds to a 10% loss of heat of reaction by radiative transfer [15].

This simulation was made for the two carbon monoxide/hydrogen/air turbulent diffusion flames specified above. The radiation paths were discretized into 37 segments. The sampling frequency for the stochastic simulation was 20,000 Hz so that the frequency of experimental data up to 10,000 Hz could be resolved. Therefore, $\Delta t = 1/20{,}000$ s was used. The space increment was chosen to coincide with data location; i.e., $\Delta s = 0.3$, 0.4, and 0.5 d for $x/d =$ 30, 40, and 50, respectively. The total number of realizations was 2000 to yield stable radiation statistics. The spectral radiation intensities were calculated using the RADCAL algorithm of Grosshandler [16], which was based on a narrow-band model.

The two-dimensional nonstationary first-order causal predictions of the mean and fluctuating spectral radial radiation intensities are summarized in Table 1 together with the experimental data. The results are given at two spectral wavelengths: $\lambda = 2.8$ μm and $\lambda = 4.5$ μm. For each wavelength, the intensity at three axial locations of $x/d = 30$, 40, and 50 are given. The comparison between the present prediction and the measured mean spectral radiation intensities in Table 1 shows a good agreement, with an average error of about 10%. Similarly, the predicted fluctuations of spectral radiation intensities given in Table 1 are close to the measurement values with an average discrepancy less than 10%. This small difference may be attributed to the use of the predicted flamelet state relationships since the state relationship data for the experimental conditions are unavailable. For completeness, the prediction by Kounalakis et al. [9] is also listed. However, it should be pointed out that they used equilibrium state relationships with a 10% radiative heat loss. Furthermore, for CO/H_2/air flames, radiative transfer is relatively weak, and thus, no great difference is expected between the present results and Kounalakis' results.

Higher-Order Model

The causal model presented above is of the first-order realization. In practice, the higher-order correlation predictors can be neglected since they have little effect on simulation when compared to the contributions from the first-order correlation predictors.

This is proved next by the presentation of the second-order realization.

In reference to Fig. 2c, the two-dimensional nonstationary second-order causal model can be obtained by setting $p = q = 2$ in Eq. (9):

$$z'(m,n) = \sum_{i=1}^{2} a(m-i,n)z'(m-i,n) + \sum_{i=0}^{2} a(m-i,n-1)z'(m-i,n-1) + \sum_{i=0}^{2} a(m-i,n-2)z'(m-i,n-2) + \varepsilon(m,n). \tag{27}$$

Multiplying both sides of Eq. (27) by $z'(m-k, n-l)$ and then taking expectation yield

$$r(m,n;m-k,n-l) = \sum_{i=1}^{2} a(m-i,n)r(m-i,n;m-k,n-l) + \sum_{i=0}^{2} a(m-i,n-1)r \cdot (m-i,n-1;m-k,n-l) + \sum_{i=0}^{2} a(m-i,n-2)r \cdot (m-i,n-2;m-k,n-l) + r_\varepsilon(m,n;m-k,n-l). \tag{28}$$

As in the first-order model, we assume that the correlation function is treated as separable. By substituting Eqs. (16) and (19) into Eq. (28),

$$\sigma_{m,n}\rho_{m,m-k}\rho_{n,n-l} = \sum_{i=1}^{2} a(m-i,n)\sigma_{m-i,n}\rho_{m-i,m-k}\rho_{n,n-l} + \sum_{i=0}^{2} a(m-i,n-1)\sigma_{m-i,n-1}\rho_{m-i,m-k}\rho_{n-1,n-l} + \sum_{i=0}^{2} a(m-i,n-2)\sigma_{m-i,n-2}\rho_{m-i,m-k}\rho_{n-2,n-l} + r_\varepsilon(m,n;m-k,n-l). \tag{29}$$

Using Eqs. (15) and (29) for different values of k and l ($k = 0, l = 1$; $k = 0, l = 2$; $k = 1, l = 0$; $k = 1, l = 1$; $k = 1, l = 2$; $k = 2, l = 0$; $k = 2, l = 1$; $k = 2, l = 2$) yields a set of eight long equations similar to Eq. (18). Then, solving simultaneously with considerable manipulation yields

$$\begin{aligned}
a(m-1,n) &= \frac{\sigma_{m,n}}{\sigma_{m-1,n}}\phi_{m1},\\
a(m-1,n-1) &= -\frac{\sigma_{m,n}}{\sigma_{m-1,n-1}}\phi_{m1}\phi_{n1}\\
a(m-2,n) &= \frac{\sigma_{m,n}}{\sigma_{m-2,n}}\phi_{m2},\\
a(m-1,n-2) &= -\frac{\sigma_{m,n}}{\sigma_{m-1,n-2}}\phi_{m1}\phi_{n2}\\
a(m,n-1) &= \frac{\sigma_{m,n}}{\sigma_{m,n-1}}\phi_{n1},\\
a(m-2,n-1) &= -\frac{\sigma_{m,n}}{\sigma_{m-2,n-1}}\phi_{m2}\phi_{n1}\\
a(m-2,n) &= \frac{\sigma_{m,n}}{\sigma_{m-2,n}}\phi_{n2},\\
a(m-2,n-2) &= -\frac{\sigma_{m,n}}{\sigma_{m-2,n-2}}\phi_{m2}\phi_{n2}
\end{aligned} \tag{30}$$

where

$$\phi_{i1} = \frac{\rho_{i,i-1} - \rho_{i-1,i-2}\rho_{i,i-2}}{1-\rho_{i-1,i-2}^2},\quad \phi_{i2} = \frac{\rho_{i,i-2} - \rho_{i,i-1}\rho_{i-1,i-2}}{1-\rho_{i-1,i-2}^2},\quad i = m,n. \tag{31}$$

Therefore, the two-dimensional nonstationary second-order causal model can be expressed as

$$\begin{aligned}
z'(m,n) = {} & \frac{\sigma_{m,n}}{\sigma_{m-1,n}}\phi_{m1}z'(m-1,n) + \frac{\sigma_{m,n}}{\sigma_{m-2,n}}\phi_{m2}z'(m-2,n)\\
& + \frac{\sigma_{m,n}}{\sigma_{m,n-1}}\phi_{n1}z'(m,n-1) + \frac{\sigma_{m,n}}{\sigma_{m,n-2}}\phi_{n2}z'(m,n-2)\\
& - \frac{\sigma_{m,n}}{\sigma_{m-1,n-1}}\phi_{m1}\phi_{n1}z'(m-1,n-1) + \frac{\sigma_{m,n}}{\sigma_{m-1,n-2}}\phi_{m1}\phi_{n2}z'(m-1,n-2)
\end{aligned}$$

$$+ \frac{\sigma_{m,n}}{\sigma_{m-2,n-1}} \phi_{m2}\phi_{n1} z'(m-2, n-1)$$

$$+ \frac{\sigma_{m,n}}{\sigma_{m-2,n-2}} \phi_{m2}\phi_{n2} z'(m-2, n-2)]$$

$$+ \varepsilon(m,n). \tag{32}$$

As in Eq. (24), for the simulation of mixture fraction fluctuations, Eq. (32) can be simplified as

$$\begin{aligned} z'(t,s) = {} & \underbrace{\phi_{t1} z'(t-\Delta t, s)}_{\mathrm{I}} + \underbrace{\phi_{t2} z'(t-2\Delta t, s)}_{\mathrm{II}} \\ & + \underbrace{\frac{\sigma_s}{\sigma_{s-\Delta s}} \phi_{s1} z'(t, s-\Delta s)}_{\mathrm{III}} + \underbrace{\frac{\sigma_s}{\sigma_{s-2\Delta s}} \phi_{s2} z'(t, s-2\Delta s)}_{\mathrm{IV}} \\ & - \underbrace{\left[\frac{\sigma_s}{\sigma_{s-\Delta s}} \phi_{t1}\phi_{s1} z'(t-\Delta t, s-\Delta s)\right.}_{\mathrm{V}} \\ & + \underbrace{\frac{\sigma_s}{\sigma_{s-2\Delta s}} \phi_{t1}\phi_{s2} z'(t-\Delta t, s-2\Delta s)}_{\mathrm{VI}} \\ & + \underbrace{\frac{\sigma_s}{\sigma_{s-\Delta s}} \phi_{t2}\phi_{s1} z'(t-2\Delta t, s-\Delta s)}_{\mathrm{VII}} \\ & + \underbrace{\left.\frac{\sigma_s}{\sigma_{s-2\Delta s}} \phi_{t2}\phi_{s2} z'(t-2\Delta t, s-2\Delta s)\right]}_{\mathrm{VIII}} + \underbrace{\varepsilon(t,s)}_{\mathrm{IX}} \end{aligned} \tag{33}$$

where

$$\phi_{i1} = \frac{R(\Delta i)[1 - R(2\Delta i)]}{1 - R^2(\Delta i)},$$

$$\phi_{i2} = \frac{R(2\Delta i) - R^2(\Delta i)}{1 - R^2(\Delta i)}, \qquad i = t, s \tag{34}$$

and the time-space increment and the geometric-space increment are taken as constant. As noted before, both the spatial and temporal correlations often have exponential form, $R(\Delta t) = \exp(-\Delta t/\tau)$ and $R(\Delta s) = \exp(-\Delta s/\Gamma)$, in which Γ and τ are the spatial integral scale and the temporal integral scale, respectively. Therefore,

$$R(2\Delta t) = \exp(-2\Delta t/\tau) = R^2(\Delta t),$$

$$R(2\Delta s) = \exp(-2\Delta s/\Gamma) = R^2(\Delta s). \tag{35}$$

Upon substituting Eq. (35) into Eq. (34) yields $\phi_{t2} = 0$ and $\phi_{s2} = 0$. Thus, the terms II, IV, VI, VII, and VIII of Eq. (33) become zero. Equation (33) is then reduced to

$$\begin{aligned} z'(t,s) = {} & \phi_{t1} z'(t-\Delta t, s) \\ & + \frac{\sigma_s}{\sigma_{s-\Delta s}} \phi_{s1} z'(t, s-\Delta s) \\ & + \frac{\sigma_s}{\sigma_{s-\Delta s}} \phi_{t1}\phi_{s1} z'(t-\Delta t, s-\Delta s) \\ & + \varepsilon(t,s) \end{aligned} \tag{36}$$

which is identical to Eq. (24), the two-dimensional nonstationary first-order causal model by noting that $\phi_{t1} = R(\Delta t)$ and $\phi_{s1} = R(\Delta s)$.

It is therefore concluded that the terms involving second-order correlations, namely, terms II, IV, VI, VII, and VIII and Eq. (33) can be neglected in the mixture fraction simulation and that the contributions from the first-order correlation predictors and the first-order cross-correlation predictor are more important than that from the second-order correlation predictors or second-order cross-correlation predictors. It can be proven that the same conclusion is also valid for higher-order realizations. The consequence of negligible second- and higher-order terms is caused primarily by the exponential form of the spatial and temporal correlations. Comparing to the recent Kounalakis' approach [9], it assumes the mixture fraction as an additive function of a first-order autoregressive process in time space and a pth-order moving average process in geometric space. In view that the pth-order moving average process is a finite form of a higher-order autoregressive process since the latter can be expressed as an infinite weighted sum of prediction errors, the approach includes the relatively insignificant higher-order spatial correlation predictors but cannot include the much more important first-order cross-correlation predictor. In contrast, the present two-dimensional nonstationary first-order causal model purposely ignores the higher-order spatial correlation terms but includes the first-order cross-correlation term. Thus, the proposed model is more realistic and theoretically sound.

Conclusions

1. The instantaneous mixture fraction distributions along a radiation path has been considered as a two-dimensional (time space–geometric space) nonstationary random field, and has been simulated on the basis of the realization of its fluctuation.
2. In the simulation of mixture fraction, it is proved that the contributions from the first-order correlation predictors in time and geometric spaces and from the first-order cross-correlation predictor

are important, but not from higher-order predictors. This conclusion is also valid for other turbulent quantities, such as velocity, since their correlations exhibit an exponential functional form.

3. A two-dimensional nonstationary causal model has been proposed. It accounts for not only the first-order correlation predictors in time space and geometric space but also the first-order cross-correlation predictor. It is more general than the existing models and provides a more realistic and accurate approach for the simulation.
4. The two-dimensional nonstationary causal model has been successfully used in the mixture fraction simulation for turbulent diffusion carbon monoxide/hydrogen/air flames. The predicted and measured values of the mean and fluctuating radiation intensities are found in good agreement.

Nomenclature

$a(m-k, n-l)$	predictor coefficients of random field
d	burner exit diameter
$E[\cdot]$	expectation
f	mixture fraction
i_λ	spectral radiation intensity
p,q	order of prediction
r	covariance of random field
$R(\Delta s)$	spatial correlation
$R(\Delta t)$	temporal correlation
s	geometric-space coordinate
$\hat{S}$	prediction region
t	time-space coordinate
$\hat{W}$	finite prediction region
x	axial distance from the burner exit
$z(m,n)$	random field
$z(t,s)$	unclipped mixture fraction distribution
β^2	variance of prediction error
Γ	integral length scale
δ	Knonecker delta function
Δs	geometric-space increment
Δt	time-space increment
ε	prediction error
λ	wavelength
ρ	correlation
σ^2	variance
τ	integral timescale
ϕ_{i1}, ϕ_{i2}	prediction coefficients

Subscripts:

s	geometric-space coordinate
t	time-space coordinate
ε	prediction error

Superscripts:

$(\cdot)'$	instantaneous fluctuation from time-averaged mean value
$\overline{(\cdot)}$	time-averaged mean quantities
$\sqrt{\overline{(\cdot)'^2}}$	root-mean-squared fluctuating quantities

Acknowledgments

This research was sponsored by the Gas Research Institute. We would like to thank James Kerzerle and Dr. Robert Serauskas for their interest in our research.

REFERENCES

1. Cox, G., *Combust Sci. Technol.* 17:75–78 (1977).
2. Kabashnikov, V. P., and Kimt, G. I., *J. Appl. Spect.* 31:963–967 (1979).
3. Kabashnikov, V. P., and Myasnikova, G. I., *Heat Transfer-Soviet Res.* 17:116–125 (1985).
4. Grosshandler, W. L., and Joulain, P., *10th Int. Colloquium on Dynamics of Explosion and Reactive Systems* (J. R. Bowell et al., Eds.), AIAA Publication, New York, 1987.
5. Nelson, D. A., *J. Heat Trans.* 111:131–134 (1989).
6. Chan, S. H., and Chern, C. F., *Int. Heat Transfer Conference*, Jerusalem, 1990, Vol. 4, pp. 143–148.
7. Jeng, S.-M., Lai, M.-C., and Faeth, G. M., *Combust. Sci. Technol.* 40:41–52 (1984).
8. Kounalakis, M. E., Gore, J. P., and Faeth, G. M., *Twenty-Second Symposium (International) on Combustion*, The Combustion Institute, Pittsburgh, 1988, pp. 1281–1290.
9. Kounalakis, M. E., Sivathanu, Y. R., and Faeth, G. M., *ASME/JSME Thermal Engineering Proceedings*, 1991, Vol. 5, pp. 3–12.
10. Jain, A. K., *Fundamentals of Digital Image Processing*, Prentice-Hall, Englewood Cliffs, NJ, 1989.
11. Kounalakis, M. E., Ph.D. Thesis, The University of Michigan, Ann Arbor, MI, 1990.
12. Becker, H. A., Hottel, H. C., and Williams, G. C., *J. Fluid Mech.* 30:285–303 (1967).
13. Wygnanski, I., and Fiedler, H., *J. Fluid Mech.* 38:577–612 (1969).
14. Frenkiel, F. N., and Klebanoff, P. S., *Phys. Fluids* 16:725–737 (1973).
15. Chan, S. H., Pan, X. C., and Abou-Ellail, M. M. M., 1993 Fall Technical Meeting, Eastern States Section of the Combustion Institute, Princeton, NJ, 1993, pp. 85–88.
16. Grosshandler, W. L., *Int. J. Heat Mass Trans.* 23:1447–1459 (1980).

Twenty-Fifth Symposium (International) on Combustion/The Combustion Institute, 1994/pp. 1125–1131

EFFECTS OF MOLECULAR TRANSPORT ON TURBULENCE-CHEMISTRY INTERACTIONS IN A HYDROGEN-ARGON-AIR JET DIFFUSION FLAME

SURESH MENON, WILLIAM H. CALHOON, JR. AND GRAHAM GOLDIN
Georgia Institute of Technology
Atlanta, GA 30332, USA

AND

ALAN R. KERSTEIN
Sandia National Laboratories
Livermore, CA 94551, USA

A numerical simulation of entrainment, turbulent advection, molecular transport, and chemical kinetics in a turbulent diffusion flame is used to investigate effects of molecular transport on turbulence-chemistry interactions. The simulation is implemented on a one-dimensional domain representing the jet centerline. Turbulent eddies are represented by rearrangement events that capture the folding and compressive-strain effects of vortical motion. A full finite-rate chemical mechanism is used to represent the combustion of a hydrogen-argon mixture issuing into air. Results based on incorporation of differential diffusion and variable Lewis number are compared to cases with the former effect, or both effects, suppressed. Significant impact on radical species production and on NO emission index (based on a reduced mechanism for thermal NO) is found. A reduced mechanism for hydrogen-air combustion, omitting both effects and incorporating other simplifications, performs comparably except that its NO predictions agree well with the case of full chemistry and molecular transport, possibly due to cancellation of errors.

Introduction

There is increasing experimental evidence [1–3] of the sensitivity of combustion chemistry in turbulent diffusion flames to molecular transport mechanisms in the flame zone. Previous models of the three-way coupling of flow, chemistry, and molecular transport mechanisms have involved idealized laminar configurations [4,5] or turbulence models [1,6,7] that do not account for the local time scales governing molecular mixing. To represent this coupling quantitatively in a model, the minimal requirements are (1) a validated chemical mechanism, (2) a mechanistically literal treatment of molecular transport, and (3) an accurate representation of the length and time scales governing the formation and strain history of the flame.

A model conforming to these requirements is applied here to the combustion of a turbulent jet of hydrogen-argon issuing into air. The chemical mechanism for this system is well established [8]. The treatment of turbulent flow and molecular transport is based on the linear-eddy model [9,10]. The formulation applied here incorporates the entrainment of air parcels into the jet, their breakdown by turbulent eddies, the molecular mixing of fuel and air, chemical conversion, thermal transport, and the coupling of density variations in the jet interior to the entrainment process [9]. Representation of all these processes is achieved by performing a stochastic simulation on a line corresponding to the jet centerline, with sufficient spatial and temporal resolution to allow mechanistically literal implementation of species and enthalpy transport. Limitation of the simulation to one spatial dimension allows computationally affordable simulation at full resolution for Reynolds numbers (*Re*) corresponding to typical laboratory experiments (jet *Re* of order 10^4).

To investigate the three-way coupling of flow, chemistry, and molecular transport, results based on a full implementation of the model are compared to cases in which the molecular transport mechanisms are simplified, either by suppressing differential molecular diffusion or by suppressing both differential diffusion and Lewis-number (*Le*) variations. A reduced chemical scheme [8] that omits differential diffusion and *Le* variations is also considered. Sensitivity of species concentrations, temperature, and NO emission index to the alternative formulations is examined.

Model Formulation and Numerical Method

The simulation model is based on Kerstein's linear-eddy model [9–11], which preserves the basic

mechanistic distinction between convective transport and molecular transport by incorporating them as two concurrent processes along a one-dimensional line representing the centerline of the jet. Molecular transport (and chemical production) is incorporated by the finite-difference solution of the diffusion equation:

$$\frac{\partial Y_k}{\partial t} = \frac{w_k W_k}{\rho} - \frac{1}{\rho A}\frac{\partial}{\partial x}(\rho A Y_k V_k) \qquad (1)$$

where Y_k, W_k, V_k, and w_k are, respectively, the kth species mass fraction, molecular weight, diffusion velocity, and molar production rate. Here, ρ is the mixture density, and A is the jet area. The diffusion velocity is approximated by [12] $V_k = -(D_k/X_k)\partial X_k/\partial x$, where X_k and D_k are, respectively, the kth species mole fraction and mixture-averaged diffusion coefficient. For the cases with finite-rate kinetics, a one-dimensional thermal diffusion equation is also solved along with the molecular diffusion equation. Since chemical reactions and diffusion/mixing occur at the small scales, the strategy is to resolve all relevant length scales by using a one-dimensional representation of the streamwise evolution of the jet at its centerline. More details of this approach are given elsewhere [11,13].

Turbulent convection is represented by randomly occurring rearrangement events that punctuate the ongoing molecular transport and chemical kinetic processes. Each event is the model analog of a turbulent eddy. The event is a "triplet map" applied to a randomly chosen segment of the computational domain, representing the folding and compressive strain effects of an eddy of that size on the concentration and thermal fields. The rearrangement process is formulated so that the sequence of events reproduces the eddy size-vs-frequency distribution for inertial-range turbulence, based on the Kolmogorov cascade picture. Again, for brevity, details discussed in the cited references are omitted.

The basic processes of convective and molecular (mass and thermal) transport and chemical kinetics are supplemented by application-specific processes that are designed to incorporate the specific aspects of the problem under study. The present formulation incorporates two application-specific processes: air entrainment and streamwise flow. Air is entrained in discrete parcels introduced at randomly chosen times and locations. The dependence of parcel size and entrainment event frequency on location is determined by an empirical entrainment law [9] based on data correlations developed by Becker and Yamazaki [14]. The entrainment law incorporates buoyancy effects caused by combustion-induced density variations, thus introducing dynamic coupling of chemical heat release and turbulent mixing. The streamwise motion caused by thermal expansion (due to heat release), air entrainment, and fuel feed from the jet is incorporated as described earlier [9,11].

This formulation embodies the principal mechanisms causing large-scale and small-scale unsteadiness of the flow and of the combustion process, and the couplings among these mechanisms. The model is implemented as a Monte Carlo simulation, starting from an initial jet of air into air, switching to fuel feed at time zero, and igniting a few cells near the nozzle. After an initial transient, statistical stationarity is achieved. Species and temperature data are subsequently collected and reduced in a format akin to data collection and reduction in laboratory experiments.

Hydrogen-air kinetics is modeled [8] using a 10-step reaction mechanism supplemented by a three-step Zeldovich mechanism for thermal NO production. In all, there are 11 species (H_2, O_2, O, H, H_2O, OH, HO_2, N_2, N, NO, and Ar) diffusion equations and one equation for temperature that are solved simultaneously. Using simplifications such as equal diffusivity, $Le = 1$, and partial equilibrium of the bimolecular reactions, a reduced mechanism [8] in terms of a mixture fraction and progress variable has also been investigated.

The solution procedure for simulating both the full and reduced kinetics has been discussed elsewhere [13]. The reduced mechanism was implemented using a look-up table approach [8], while for the full kinetics, the CHEMKIN software package [12] was employed. An implicit predictor-corrector scheme was employed to advance the solution in time. To reduce the computational time, the code was implemented efficiently on a massively parallel computer, Kendall Square Research (KSR1) [13]. All finite-rate calculations were carried out on a 32-processor KSR1.

Results and Discussion

The effects of molecular transport on the finite-rate kinetics of a H_2-22%Ar jet flame are investigated. The test geometry is similar to a previous experiment [15] with fuel nozzle diameter $d_o = 0.0052$ m, fuel jet velocity of 75 m/s, and Reynolds number (based on nozzle diameter) of 9000. The fuel and ambient air temperature are initially 300 K, and the pressure is 1 atm. A streamwise domain extending to $x/d_o = 228$ has been discretized into 1250 cells, with the resolution scale increasing linearly with x. This discretization does not resolve the cold-flow Kolmogorov scale but is adequate for the combustion application involving temperature-dependent viscosity. Adequacy of resolution is verified by examining instantaneous spatial profiles of species concentration and temperature in flame zones within the simulation.

Four cases are discussed here: (1) the reduced

mechanism, and three cases with full finite-rate chemical mechanisms (2) $Le = 1$, no differential diffusion (case A), (3) variable Le, no differential diffusion (case B), (4) variable Le and differential diffusion (case C). Thus, the effect of the partial equilibrium assumption in the reduced mechanism can be addressed by comparing with case A. Lewis number (i.e., thermal conductivity) effects can be investigated using case B results, while both thermal and molecular differential diffusion effects can be studied using case C results.

Both time-averaged axial profiles and scatter plots at a chosen location are examined. Care needs to be taken when interpreting the time-averaged data because of the complex nonlinear interaction between air entrainment, mixing, heat release, and thermal expansion processes simulated here. Differences between heat release in different cases must precede differences in mixing and entrainment, because variations in the mixing process are caused by thermally induced viscosity changes and entrainment rate variations are caused by thermally induced density changes [9]. Thus, when flow properties are time averaged, differences among cases at small x must reflect differences in time-averaged heat release due to different transport mechanisms (cases A through C) and chemistry (reduced case).

Keeping this in mind, we consider the streamwise variation of the time-averaged temperature (Fig. 1a) and density (Fig. 1b). High temperature (for cases A and B) causes lower density (Fig. 1b), which in turn causes enhanced buoyancy and entrainment. The mechanism leading from this to a faster temperature falloff for cases with higher peak temperature (cases A and B) can be interpreted as follows. The air entrainment flux at locations farther downstream is increased, increasing the dilution rate of the fuel and thus moving the crossover point from overall fuel-rich to overall fuel-lean mixture to smaller x. After this crossover, the main effect of dilution is to lower temperature and increase density. This explains the more rapid falloff of temperature for cases A and B than for case C. However, in Fig. 1b, for large x, there is a recrossing because the higher density for cases A and B in the range $40 < x/d_o < 120$ eventually decreases the entrainment such that case C catches up and overtakes them. This occurs because the empirical entrainment law used here is nonlinear and time lagged, and an additional time lag is introduced by the mixing process [9]. Although the entrainment law is based on time-averaged correlations that may not fully reflect the unsteady dynamics, it is at least indicative of the flow-chemistry interactions that are likely to occur.

Thus, the near-field sensitivity of the flow properties to transport is a direct effect of the molecular transport and chemical kinetics assumptions in cases A through C and the reduced mechanism, but the

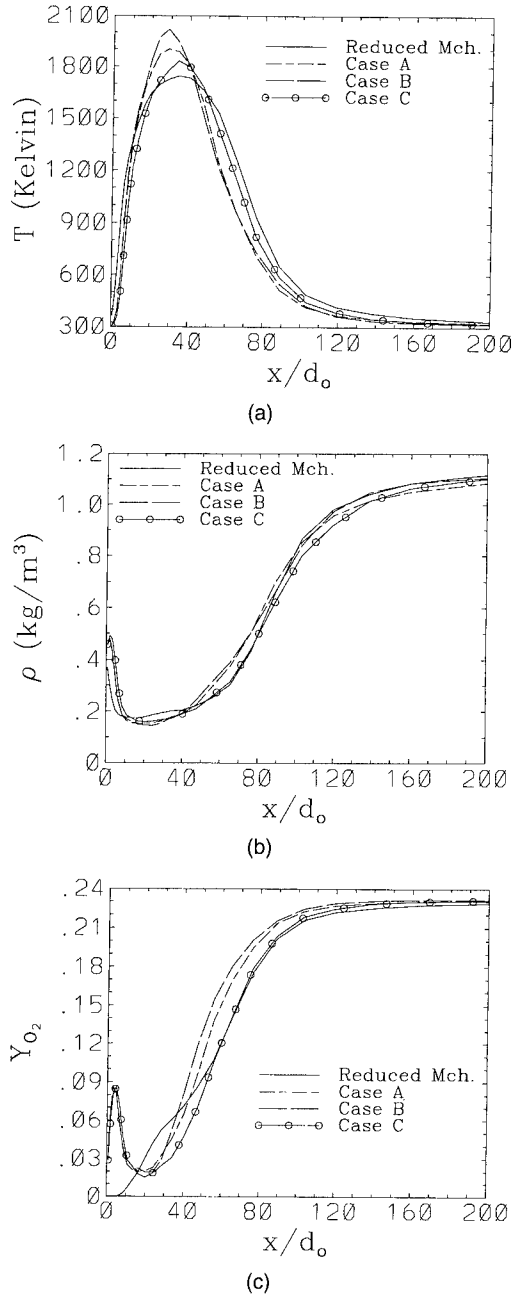

FIG. 1. Time-averaged axial profiles of flow properties in a H_2-22%Ar-air turbulent jet diffusion flame. Fuel jet velocity is 75 m/s, and Reynolds number (based on jet diameter, $d_o = 0.0052$ m) is 9000. Four cases are shown: (1) reduced mechanism, (2) $Le = 1$, no differential diffusion (case A), (3) variable Le, no differential diffusion (case B), and (4) variable Le, differential diffusion (case C). (a) Temperature variation as a function of x/d_o, (b) density variation as a function of x/d_o, and (c) molecular oxygen mass fraction (Y_{O_2}) variation as a function of x/d_o.

far-field sensitivity largely reflects differences in overall stoichiometry due to entrainment effects.

The temperature profile for case B reaches a higher maximum than the other cases. The difference from case A is due to a reduction in the thermal conductivity in case B, indicated by a rapid decrease in Le from 0.95 at $x = 0$ to about 0.6 at $x/d_o = 40$. Slower diffusion of heat than for the $Le = 1$ case causes higher temperatures in flame zones, accelerating the exothermic reaction steps. This acceleration increases the average temperature in the near field, affecting entrainment and mixing rates and thereby inducing the far-field effects discussed earlier. Case C, with both variable Le and differential diffusion, has a lower maximum of the temperature than case B, indicating that differential molecular diffusion tends to cancel the thermal conductivity effects.

The density (Fig. 1b) and Y_{O_2} (Fig. 1c) profiles indicate that Le and differential diffusion sensitivities, though magnified in the far field as a result of turbulence-chemistry interaction, are not as important in the near field as the difference between full and reduced chemical-kinetic mechanisms. In the reduced mechanism, fuel and O_2 can react at 300 K, so mixing with hot products is not required for ignition. This causes underprediction of Y_{O_2} concentration in the near field. In fact, the mixing of O_2 and fuel is fast enough so that the fast reaction causes the Y_{O_2} concentration to be negligible initially and causes the density to decrease initially as a function of x. In contrast, both of these quantities increase initially in cases A through C as cold, dense O_2 is entrained and mixed, but is not consumed until it subsequently mixes with hot products. Significant deviations persist until about $x/d_o = 50$, where convergence of the reduced mechanism and case C profiles occurs. In view of the near-field artifacts of the reduced mechanism, and their likely magnification due to turbulence-chemistry interaction, this convergence indicates a cancellation of errors rather than a mechanistically based performance improvement. This interpretation is supported by the persistence of temperature deviations (Fig. 1a) in the far field despite a crossing of the reduced mechanism and case C temperature profiles near $x/d_o = 50$.

A variety of other properties were analyzed. For brevity, only representative results are discussed. The profiles for the principal product Y_{H_2O} (not shown) follow the trend seen in the temperature profiles. In the near field, profiles for cases A through C are nearly identical, while the reduced-mechanism case shows a larger concentration of water due to the instantaneous conversion of the reactants upon mixing.

Radical formation shows much greater sensitivity to molecular transport as well as chemical kinetic assumptions. The reduced mechanism overpredicts by a large amount the formation of H, O, and OH while underpredicting significantly the formation of HO_2.

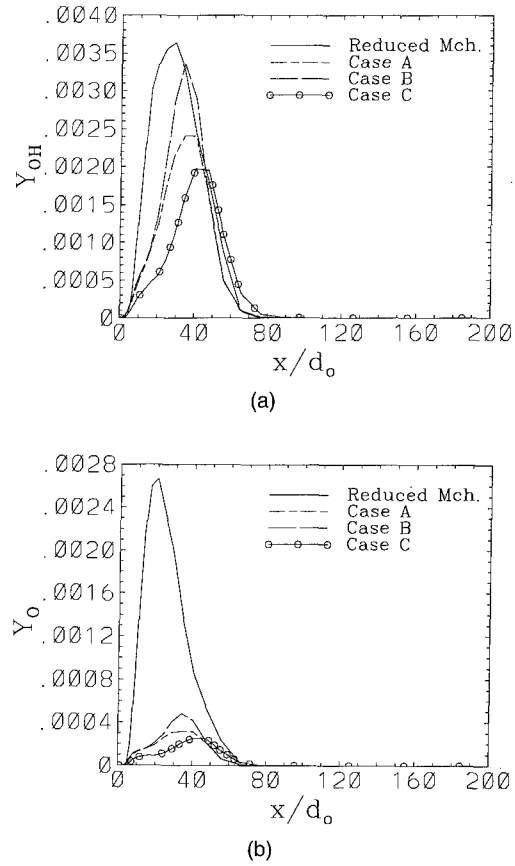

FIG. 2. Time-averaged axial profiles of radical species in a H_2-22%Ar-air turbulent jet diffusion flame. Conditions and cases same as in Fig. 1. (a) Hydroxyl mass fraction (Y_{OH}) as a function of x/d_o, (b) atomic oxygen mass fraction (Y_O) as a function of x/d_o.

The overprediction of H (not shown) by the reduced mechanism is a result of the partial equilibrium assumption, because H radicals are instantaneously generated when fuel and oxidizer are mixed, irrespective of the temperature. This overprediction of H radicals is consistent with earlier partial equilibrium calculations [8].

Figures 2a and 2b show the OH and O mass fraction profiles, respectively. The OH profiles reflect the temperature differences seen earlier. The reduced mechanism overpredicts OH by the largest amount even where it underpredicts the temperature. This is consistent with the overabundance of H and O radicals for this case. Relaxing the partial equilibrium assumption (case A) results in a reduction of OH radical, while relaxing the $Le = 1$ assumption (case B) has a counteracting effect. This is consistent with the increased flame zone temperatures caused by reduced thermal conductivity. The OH production is decreased when both Le and differential diffusion

effects are allowed (case C), indicating a cancellation of the effects of thermal and molecular diffusion on radical formation. The O profiles in Fig. 2b show significant overproduction by the reduced mechanism. Relaxation of partial equilibrium (case A) reduces O production significantly. Case C predicts lower O radical than case B, partly because of reduced temperature and perhaps, as noted above, as a result of a counterbalance between thermal conductivity (*Le*) effects and molecular diffusion effects.

Scatter plots at $x/d_o = 30$ were also analyzed. All variables were conditionally averaged as described elsewhere [1], and the mixture fraction ξ was calculated according to the formula [1,8]

$$\xi = \frac{2[H_2] + 2[H_2O] + 39.9[Ar]}{2[H_2] + 18[H_2O] + 32[O_2] + 28[N_2] + 39.9[Ar]} \tag{2}$$

where [Ar] is assumed to be given by [Ar] = 0.22/0.78 ([H_2] + [H_2O]) as done earlier [1]. With this definition, $\xi = 1$ corresponds to pure fuel and $\xi = 0$ to pure air, with $\xi_{stoic} = 0.1632$.

The scatter data (approximately 6000 data samples) at $x/d_o = 30$ were conditionally averaged as described by Barlow et al. [1] over bin width in mixture fraction space of 0.02. The local equilibrium limit was also determined by volumetrically mixing fuel with air at different values of ξ and allowing the mixture to adiabatically react to its equilibrium composition. Because of volumetric mixing, the adiabatic equilibrium limit implicitly assumes that both molecular diffusion and Lewis number effects are absent. Although the conditionally averaged data for all the properties were analyzed, because of lack of space, only representative results are shown here.

Conditionally averaged temperatures (not shown) for case B indicate a significant superequilibrium of temperature on the fuel-rich side relative to the adiabatic equilibrium line. With differential diffusion included (case C), the temperature values fall below equilibrium [13]. These results suggest that the superequilibrium of temperature is a direct Lewis number effect rather than a differential diffusion effect. For opposed flow, non-premixed laminar flames, Barlow et al. [1] attributed superequilibrium temperature to differential diffusion effects, but they did not separate Lewis number (i.e., thermal conductivity) effects from species diffusion effects.

Strong differential diffusion effects are also seen in conditional averages of Y_{H_2O} [13], with a large departure from equilibrium on the rich side for case C. Figure 3a for OH mole fraction shows that all cases exhibit the experimentally observed [1,3] superequilibrium, with the peak OH occurring near stoichiometric mixture fraction. Superequilibrium occurs on both the lean and rich side, and significant OH is found away from ξ_{stoic}, even at locations where the

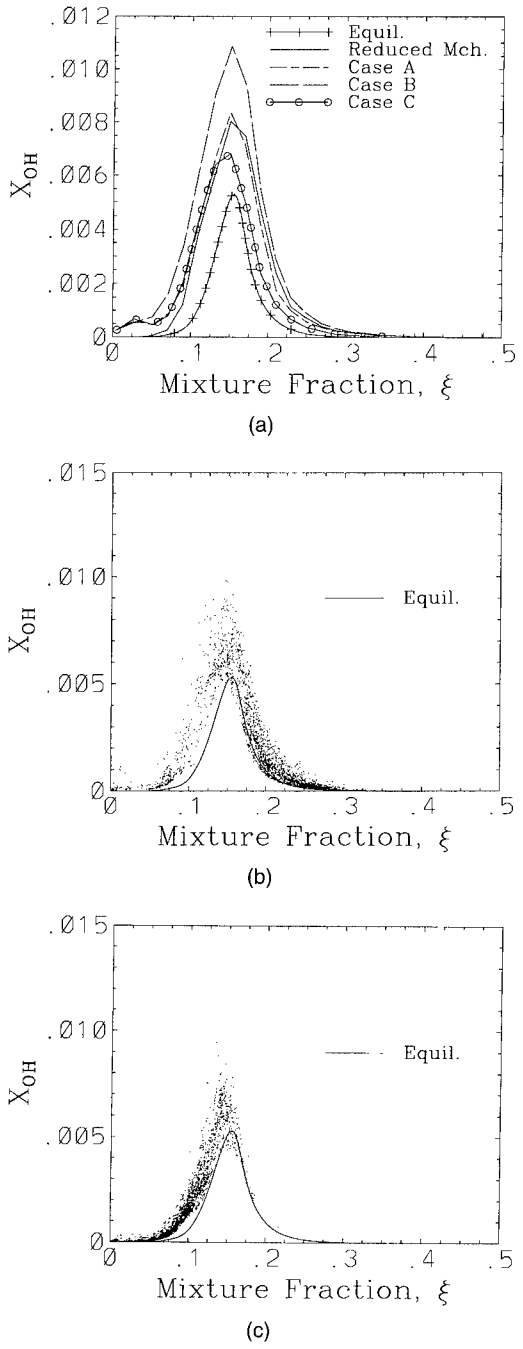

FIG. 3. Conditional average and scatter plots of hydroxyl mole fraction as a function of mixture fraction [Eq. (2)] for conditions and cases noted in Fig. 1. Also shown is the adiabatic equilibrium curve (obtained with $Le = 1$ and no differential diffusion). (a) Conditional average of hydroxyl mole fraction at $x/d_o = 30$, (b) scatter plot of hydroxyl mole fraction at $x/d_o = 30$, and (c) scatter plot of hydroxyl mole fraction at $x/d_o = 50$.

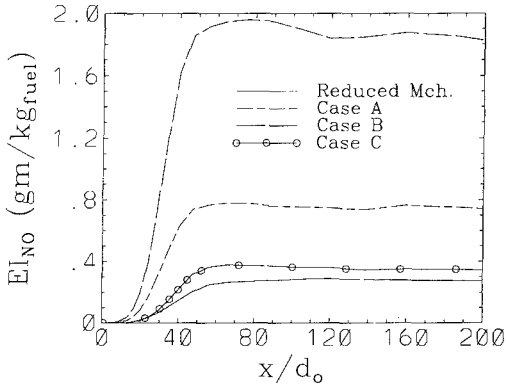

FIG. 4. Emission index of NO (gm/kg of fuel) as a function of axial distance for conditions and cases noted in Fig. 1.

adiabatic equilibrium curve predicts zero OH mole fraction. Case B with variable Lewis number shows the largest departure. This is consistent with the higher temperature seen in this case. Although the reduced mechanism and case A are in good agreement near stoichiometry, they begin to diverge in the lean limit. This is consistent with previous work [1], in which it was determined that partial equilibrium should be a good approximation near ξ_{stoic} while becoming inaccurate as the local temperature drops below 1600 K for off-stoichiometric conditions.

Superequilibrium of OH is observed even farther downstream. Figures 3b and 3c show the scatter plot for case C at $x/d_o = 30$ and 50, respectively. Farther downstream, superequilibrium occurs mostly on the lean side, and the data are closer to equilibrium. These results are consistent with experimental observation [1] and with the notion that the increase of the local turbulent time scale for mixing and of the residence time with axial location allows more time for the radical to approach equilibrium.

The emission index for NO (EINO) is shown in Fig. 4. Both cases A and B show large values of EINO, primarily due to the high peak temperature noted earlier and an abundance of O radical. The EINO for reduced kinetics and case C are surprisingly close. Further analysis shows that the assumption $[NO]/[NO]_{equil} << 1$ used to reduce the Zeldovich mechanism [8] in the reduced kinetics case is satisfied in case C but not in cases A and B. More importantly, the reduced kinetics is based on partial equilibrium assumptions leading to overprediction of O radical (essential to thermal NO production), compensating for the temperature suppression (Fig. 1a) caused by rapid entrainment (reflected in the rapid rise of the Y_{O_2} profile). Thus, it appears that a cancellation of effects accounts for the agreement between the reduced kinetics case and the mechanistically more complete formulation.

Conclusions

A computational model incorporating simplified but plausible representations of molecular transport, convective transport, and chemical kinetic processes in a turbulent jet diffusion flame has been used to investigate the interactions among these processes. For hydrogen-air combustion, it is found that Lewis-number and differential diffusion effects impact the heat release rate in the near field, affecting the buoyancy of the jet and thus the entrainment of air farther downstream. A two-way coupling between molecular processes and the large-scale development of the jet is obtained. The back-coupling is due to the effect of the entrainment rate on the overall stoichiometry at a given streamwise location.

It is shown that this feedback process can either amplify or suppress errors introduced through model simplification. It is not obvious whether the specific trends noted here extrapolate, e.g., to higher Reynolds numbers for which buoyancy effects are reduced. Nevertheless, the results indicate the likelihood that the magnitude of the effects can be significant in practical situations.

Significant superequilibrium of OH mole fraction is obtained, as in experiments. The results for OH and other radicals are sensitive to molecular transport assumptions. Adoption of a reduced chemical kinetic scheme based on partial equilibrium leads to higher concentrations of H, O, and OH radicals and lower HO_2 concentration than obtained with full molecular transport and chemical kinetics (case C). Overprediction of O tends to cause overprediction of NO. Predictions of the NO emissions index based on the full and reduced formulations, respectively, are nevertheless in good agreement because of temperature suppression in the latter formulation, a consequence of the coupling between heat release and entrainment. This cancellation of O overprediction and temperature underprediction is sensitive to the strong couplings among the molecular, convective, and chemical processes determining NO emission.

Acknowledgments

This work was supported by NASA Lewis Research Center and by the Division of Chemical Sciences, Office of Basic Energy Sciences, U.S. Department of Energy.

REFERENCES

1. Barlow, R. S., Dibble, R. W., Chen, J.-Y., and Lucht, R. P., *Combust. Flame* 82: 235–251 (1990).
2. Bilger, R. W., *Annu. Rev. Fluid Mech.* 21:101–135 (1989).
3. Drake, M. C., Pitz, R. W., Lapp, M., Fenimore, C. P., Lucht, R. P., Sweeney, D. W., and Laurendeau, N. M., *Twentieth Symposium (International) on Combustion,*

The Combustion Institute, Pittsburgh, 1984, pp. 327–335.
4. Barlow, R. S., and Chen, J.-Y., *Twenty-Fourth Symposium (International) on Combustion*, The Combustion Institute, Pittsburgh, 1992, pp. 231–237.
5. Gutheil, E., and Williams, F. A., *Twenty-Third Symposium (International) on Combustion*, The Combustion Institute, Pittsburgh, 1990, pp. 513–521.
6. Bilger, R. W., and Dibble, R. W., *Combust. Sci. Technol.* 28: 161–172 (1982).
7. Dibble, R. W., Kollmann, W., and Schefer, R. W., *Combust. Flame* 55:307–321 (1984).
8. Chen, J.-Y., and Kollman, W., *Combust. Flame* 70:75–99 (1990).
9. Kerstein, A. R., *Combust. Sci. Technol.* 81:75–96 (1992).
10. Kerstein, A. R., *J. Fluid Mech.* 216:411–435 (1990).
11. Menon, S., McMurtry, P., Kerstein, A. R., and Chen, J.-Y., *J. Prop. Power* 10:161–168 (1994).
12. Kee, R. J., Dixon-Lewis, G., Warnatz, J., Coltrin, M., and Miller, J. A., Sandia National Laboratories Report SAND86-8246, 1991.
13. Calhoon, W., Menon, S., and Goldin, G., AIAA 94-0676, 1994.
14. Becker, H. A., and Yamazaki, S., *Combust. Flame* 33:123–149 (1978).
15. Magre, P., and Dibble, R. W., *Combust. Flame* 73:195–206 (1988).

COMMENTS

R. W. Bilger, University of Sydney, Australia. The Lewis number effects found are much stronger than expected. Could this be an artefact of the way the chemistry and local molecular diffusion are handled? As I understand it, this is done by a technique similar to operator splitting. Chemistry and local molecular diffusion are not handled simultaneously. Doesn't this lead to errors?

Author's Reply. The strong Lewis number effects were noted only for Case B (variable *Le* without molecular differential diffusion) while for Case C (variable *Le* and differential diffusion) the effects were not that pronounced. In experimental studies of turbulent flames, strong dependence on *Le* number has not been observed; however, the effects of the thermal and molecular differential diffusion were not separated. The Case C results appear to agree with this observation. The numerical scheme is an implicit predictor-corrector method that employs partial decoupling of diffusion and chemistry in the predictor step and then in the corrector step. The final update of the full equations is obtained implicitly using the predicted values to determine the nonlinear coefficients. We believe that this procedure does not introduce any significant errors.

Twenty-Fifth Symposium (International) on Combustion/The Combustion Institute, 1994/pp. 1133–1139

SIMULTANEOUS MEASUREMENT OF CONSERVED AND REACTIVE SCALARS IN TURBULENT DIFFUSION FLAMES FOR ASSESSMENT OF PDF MODELS

T. S. CHENG
Department of Mechanical Engineering
Chung-Hua Polytechnic Institute
Hsin Chu, Taiwan, R.O.C.

AND

R. W. PITZ
Department of Mechanical Engineering
Vanderbilt University
Nashville, TN 37235, USA

Simultaneous measurements of temperature, major species concentrations (H_2, O_2, N_2, H_2O), and OH concentration have been made in turbulent swirled and unswirled hydrogen jet diffusion flames. These quantities are measured nonintrusively by Raman scattering and predissociative fluorescence induced by a KrF narrowband excimer laser. From the experimental results of the major and minor species concentrations, the simultaneous values of the mixture fraction f and the reaction progress variable q are calculated for each laser pulse assuming a partial-equilibrium model. The measured mean and root-mean-square (rms) OH concentrations are compared to equilibrium and partial-equilibrium values predicted from the instantaneous temperature and major species concentration measurements. The comparisons show strong super-equilibrium OH values in both swirled and unswirled flames. Assumed shape joint probability density function (pdf) combustion models commonly assume that f and q are statistically independent. This assumption is evaluated by calculating the correlation coefficient between f and q from simultaneous measurements of f and q in swirled and unswirled turbulent diffusion flames. The mixture fraction and the reaction progress variable are found to be highly correlated in all the flames, suggesting that statistical independence is a poor assumption. Thus, assumed shape joint pdf models of turbulent combustion that assume statistical independence may incorrectly predict radical concentrations and other nonequilibrium effects.

Introduction

The development of engineering computer models for practical combustors holds the potential for computer-aided combustor design with lower development costs, higher combustion efficiencies, lower pollution emissions, and wider fuel specifications. However, to be reliable over a wide range of conditions, such models should be based upon a fundamental, quantitative understanding of the complex interaction of fuel/air mixing and chemical reaction. In many turbulent reacting flows, departures from chemical equilibrium appear at conditions where the characteristic turbulent mixing time becomes comparable with the characteristic chemical reaction time. Significant departures from chemical equilibrium can occur in turbulent flows by intense mixing. Modeling these highly turbulent flames with the fast chemistry assumption may fail to predict the concentrations of radicals that are considerably higher than their equilibrium values [1,2].

Considerable improvement has been made in modeling the fuel/air mixing process using an assumed shape joint probability density function (pdf) of the conserved mixture fraction f and the reactive scalar q to account for turbulence-chemistry interaction in turbulent diffusion flames such as jet flames [2–5], recirculating flames [6], and supersonic flames [7]. With this approach, the main hypothesis is the statistical independence of f and q. Hence, the covariance $\widetilde{f''q''}$ and the correlation coefficient between f and q would be zero. The assumption of statistical independence of the mixing and reacting scalars has been examined by Pope and Correa [8] in a study of a syngas turbulent diffusion flame. Their model predicts the joint pdf by solving a pdf transport equation that does not assume statistical independence of f and q. Pope and Correa's calculations demonstrate that f and q are highly correlated. They compared predictions from both an assumed shape joint pdf model and a joint pdf transport model to OH mea-

surements and found that the pdf transport model gave superior results. Correa and Pope [9] have also extended their joint pdf transport model to predict nonequilibrium chemistry in recirculating bluff-body stabilized syngas diffusion flames. However, the issue of statistical independence of f and q has not been definitively evaluated by direct measurement in a turbulent reacting flame.

Simultaneous measurements of temperature, major species (H_2, O_2, N_2, H_2O), and minor species (OH) concentrations have been made in turbulent unswirled [10] and swirled [11,12] lifted hydrogen jet diffusion flames into still air with Raman scattering and predissociative fluorescence induced by a KrF excimer laser. In this paper, the instantaneous values of f and q are calculated from the concentration and temperature measurements. The measured mean and root-mean-square (rms) OH values are compared to OH equilibrium and partial-equilibrium values calculated from temperature and major species concentrations to assess the amount of superequilibrium in the flames. The simultaneous measurements of the mixing and reactive scalars are also used to evaluate the assumption of statistical independence of f and q commonly used in assumed shape pdf nonequilibrium combustion models.

Hydrogen Jet Flames and Raman System

The multispecies measurements are made in unswirled and swirled hydrogen jet diffusion flames. The jets both have a converging nozzle with a nominal 2-mm exit diameter [10–12]. The actual measured exit diameters are 1.80 and 1.87 mm for the unswirled jet and swirled jet respectively. The unswirled jet flame is formed by injecting hydrogen (0.169 g/s) through a straight tube into atmospheric air. The calculated exit conditions are as follows: a velocity of 750 m/s, a Reynolds number of 14,000 based upon nozzle exit diameter (1.80 mm), and a liftoff height of 8 diameters based on visual observations. The swirled combustor is operated with fuel either axially and/or tangentially supplied to the combustor with each of these flows being controlled separately. The calculated exit conditions are the following: a velocity of 660 m/s, a Reynolds number of 12,500, and a visual liftoff height of 6 diameters. For these conditions, three flow regimes are investigated: an axial jet flame (axial = 0.157 g/s, $S = 0.0$), a mixed jet flame (axial = 0.079 g/s, tangential = 0.079 g/s, $S = 0.12$), and a tangential jet flame (tangential = 0.157 g/s, $S = 0.5$), where S is the geometric swirl number [13]. The swirled jet flame is very similar to that studied by Yuasa [14]. The Mach number is 0.52 and 0.60 for swirled and unswirled jet flames, respectively. The calculations demonstrate that Mach number effects on temperature are not important ($<$20 K). Additional details on the jet combustors can be found elsewhere [10–12].

Using a single narrowband KrF excimer laser at 248 nm, the major species and temperature are determined by Raman scattering, and the OH concentration is determined by laser-induced predissociative fluorescence (LIPF). Under normal conditions, the major contributor to the uncertainties for both concentration and temperature measurements is shot noise resulting from the probabilistic nature of the electron emission from the photomultiplier tube photocathode. The experimental relative standard deviations for single-shot temperature and OH concentration measurements are 11.7 and 13.2% in the stoichiometric flame, respectively. For lower OH concentration measurements ($\leq$0.1% mole fraction), the relative standard deviation can be up to 30%. The spatial resolution of the Raman system is 0.4 mm. This experimental resolution would capture at least 85% of the scalar variance for both swirled and unswirled flames based on the estimation of Mansour et al. [15]. The measurement method and calibration procedure have been described in detail by Cheng et al. [10].

Thermochemical Model

In H_2-air flames, an eight-step reaction mechanism has been widely used in the thermochemical model. The two-body shuffle reactions

$$H + O_2 \rightleftharpoons OH + O \qquad \text{(R1)}$$

$$O + H_2 \rightleftharpoons OH + H \qquad \text{(R2)}$$

$$H_2 + OH \rightleftharpoons H_2O + H \qquad \text{(R3)}$$

$$OH + OH \rightleftharpoons H_2O + O \qquad \text{(R4)}$$

are assumed to be in partial equilibrium.

Therefore, the progress of chemical reactions is determined entirely by the slow three-body recombination reactions:

$$H + OH + M \rightleftharpoons H_2O + M \qquad \text{(R5)}$$

$$H + O + M \rightleftharpoons OH + M \qquad \text{(R6)}$$

$$H + H + M \rightleftharpoons H_2 + M \qquad \text{(R7)}$$

$$H + O_2 + M \rightleftharpoons H\,O_2 + M. \qquad \text{(R8)}$$

The assumption of partial equilibrium of reactions (R1) through (R4) has been justified for temperatures above 1200 K [3]. But detailed kinetic modeling [16] and experiments in premixed H_2-air flames [17] suggest that the assumption is valid for temperatures greater than 1500 K. In this work, experimental data

that have instantaneous temperatures above 1500 K are used in the calculation of f and q.

To reduce the number of conservation equations to be treated, a linear combination of mass fractions is used as proposed by Dixon-Lewis et al. [18]. The combined mass fraction $Y^*_{H_2}$ is given by

$$Y^*_{H_2} = Y_{H_2} + \frac{1}{2}\frac{M_{H_2}}{M_{OH}} Y_{OH} + \frac{M_{H_2}}{M_O} Y_O + \frac{3}{2}\frac{M_{H_2}}{M_H} Y_H \quad (1)$$

where Y_i and M_i are the mass fraction and molecular weight of species i, respectively. The rate of change of $Y^*_{H_2}$ is determined only by the rates of the recombination reactions (R5) through (R8).

Since the mass fractions of major species (H_2, O_2, N_2, H_2O), minor (OH) species, and temperature are simultaneously measured, the mass fractions of O and H atoms and OH molecules can be calculated through the partial-equilibrium assumption by

$$Y_O = M_O K_{e4}\left(\frac{Y_{OH}}{M_{OH}}\right)^2 \frac{M_{H_2O}}{Y_{H_2O}} \quad (2)$$

$$Y_H = M_H \frac{K_{e4}}{K_{e1}}\left(\frac{Y_{OH}}{M_{OH}}\right)^3 \frac{M_{O_2}}{Y_{O_2}}\frac{M_{H_2O}}{Y_{H_2O}} \quad \text{lean} \quad (3)$$

$$Y_H = M_H K_{e3}\frac{Y_{OH}}{M_{OH}}\frac{Y_{H_2}}{M_{H_2}}\frac{M_{H_2O}}{Y_{H_2O}} \quad \text{rich} \quad (4)$$

$$Y_{OH} = M_{OH}\left(\frac{K_{e1}}{K_{e4}} K_{e3}\right)^{1/2}\left(\frac{Y_{O_2}}{M_{O_2}}\frac{Y_{H_2}}{M_{H_2}}\right)^{1/2} \quad (5)$$

where K_{e1}, K_{e3}, and K_{e4} are the equilibrium constants of reactions (R1), (R3), and (R4) evaluated at the measured temperature T. Thus, the values of $Y^*_{H_2}$ and partial equilibrium Y_{OH} can be determined from the concentration and temperature measurements for each laser shot from Eqs. (1) through (5).

The mixture fraction, f, is calculated from the Raman scattering measurements of the major species concentrations for each laser shot as the mass originating from the fuel stream divided by the total mass [19,20]:

$$f = \frac{\dfrac{2[H_2] + 2[H_2O]}{32[O_2] + 28[N_2] + 18[H_2O] + 2[H_2]} - Z_{H,a}}{1 - Z_{H,a}} \quad (6)$$

where $Z_{H,a}$ is the mass fraction of hydrogen atoms in the still air. This is given by $Z_{H,a} = (2/18)[\omega/(1 + \omega)]$ where ω is the specific humidity (kg H_2O/kg dry air) in the ambient air. The OH concentration and $Z_{H,a}$ (<0.001) are not included in the mixture fraction calculation for these experiments, because the error in mixture fraction is small.

Based on the mixture fraction, the OH mole fraction can be determined from adiabatic-equilibrium calculations [10]. The OH equilibrium value for each laser shot can be averaged at a position in the flame to give the average OH value in the fast chemistry limit.

For a given mixture fraction f, the variable $Y^*_{H_2}$ varies between its frozen and its equilibrium value, leading to the definition of the reaction progress variable

$$q = \frac{Y^*_{H_2} - Y^{*u}_{H_2}}{Y^{*e}_{H_2} - Y^{*u}_{H_2}} \quad (7)$$

where the superscripts u and e denote unburnt and completely burnt (i.e., equilibrium) mixtures. The reaction progress variable q has a value of unity when the reactions reach the equilibrium state and a value of zero when there is no reaction. This value is calculated from the concentration and temperature measurements from each laser shot using Eqs. (1) through (4).

The Favre averages and the corresponding rms fluctuations of f and q are calculated from the Raman measurements. The correlation coefficient R between f and q is defined by

$$R \equiv \widetilde{f''q''}[\widetilde{f''f''}\ \widetilde{q''q''}]^{-1/2} \quad (8)$$

where $\widetilde{f''q''}$ is the covariance of f and q. As stated earlier, with a spatial resolution of 0.4 mm, we estimate >85% of the scalar variance is captured by the Raman measurement. We expect the Raman measurement to slightly underestimate the covariance and the correlation coefficient as well.

Results and Discussion

Radial profiles of mean and rms OH mole fractions determined from LIPF measurements, equilibrium calculations, and partial-equilibrium calculations are compared in Fig. 1 at x/D = 33, 111, and 194 in the unswirled turbulent jet flame. At each radial location, 1000 independent laser shots are taken. The mean OH mole fractions from the LIPF measurements shown in Fig. 1a are much larger at x/D = 33 and 111 than the mean equilibrium OH mole fractions calculated from Raman data assuming adiabatic equilibrium. The measured peak values are about 2–2.5 times larger than the calculated equilibrium values. Far downstream (x/D = 194), the measured OH values are nearly equal to the calculated equilibrium values. The partial-equilibrium OH values shown in

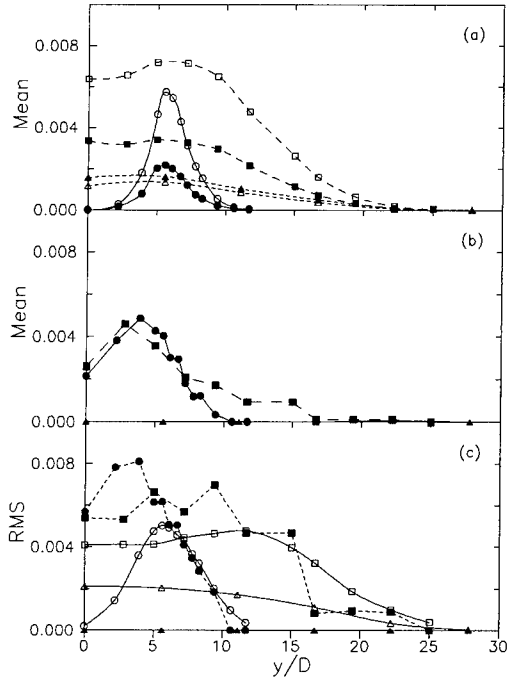

FIG. 1. Comparison of OH mole fraction radial profiles of (a) measured mean (open symbols) and calculated mean equilibrium (closed symbols), (b) calculated mean partial equilibrium, and (c) measured rms (open symbols) and calculated rms partial equilibrium (closed symbols) in an unswirled turbulent flame (Re = 14,000). ○: x/D = 33; □: x/D = 111; △: x/D = 194.

Fig. 1b are calculated from Eq. (5) using the measured mole fractions of H_2 and O_2. Since the mole fraction of either H_2 or O_2 is small (<1%), the Raman scattering signal is weak, and the error in calculating the OH partial-equilibrium value is large. The OH partial-equilibrium values should be viewed as qualitative, and they illustrate the problems of measuring small concentrations with Raman scattering. When compared to Fig. 1a, they are generally smaller (except for x/D = 33) and shifted to the rich core of the jet. The rich shift is probably due to the breakdown of the partial-equilibrium assumption in cold rich gas. At x/D = 194, the partial-equilibrium OH values are unrealistically small from errors associated with measuring small (<1%) H_2 mole fraction. As shown in Fig. 1c, the calculated rms partial-equilibrium OH mole fractions are much larger at x/D = 33 and 111 than the measured rms OH mole fractions in the rich-flame region. These are mainly due to shot noise resulting from the small O_2 values.

Figure 2 shows similar comparisons of the measured and calculated adiabatic-equilibrium OH mole fraction at x/D = 21, 53, and 107 in unswirled (S = 0), low swirl (S = 0.12), and high swirl (S = 0.5)

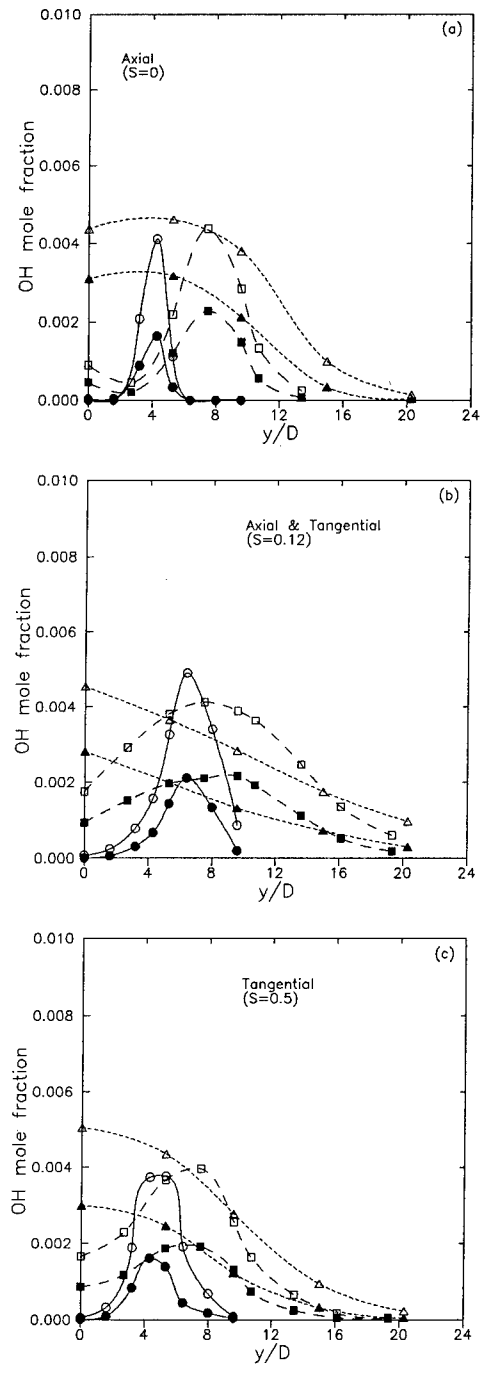

FIG. 2. Comparison of radial profiles of measured average OH mole fractions (open symbols) and calculated average equilibrium OH mole fractions (closed symbols) in (a) unswirled, (b) low swirl, and (c) high swirl turbulent flames (Re = 12,500). ○: x/D = 21; □: x/D = 53; △: x/D = 107.

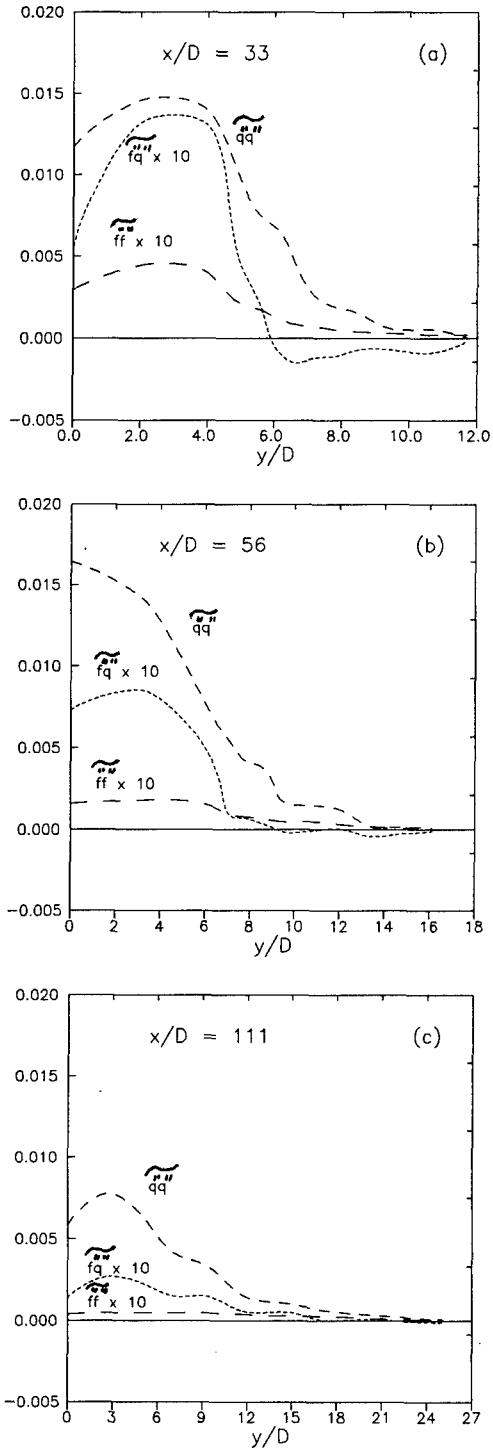

FIG. 3. Favre average variances and covariance of f and q vs y/D at x/D = 33, 56, and 111 in unswirled turbulent flame (Re = 14,000).

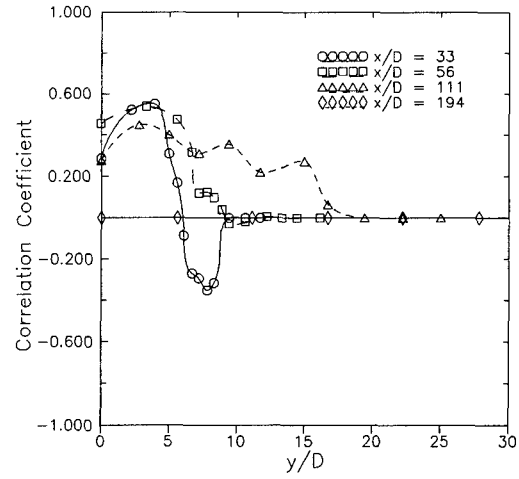

FIG. 4. Correlation coefficient R vs y/D at x/D = 33, 56, 111, and 194 in unswirled turbulent flame (Re = 14,000).

turbulent flames of the swirl combustor. For these three different operating conditions (Figs. 2a, 2b, and 2c), the peak average OH mole fractions determined from radial profiles also show large differences between the LIPF and equilibrium values. These superequilibrium effects, which are similar to that of the unswirled flame as shown in Fig. 1, are large close to the nozzle and smaller downstream.

The superequilibrium OH measurements made in unswirled and swirled turbulent diffusion flames are in qualitative agreement with previous laser saturated fluorescence (LSF) measurements made in a turbulent hydrogen Re = 8500 flame [21]. The comparisons of the measured OH mole fractions with the equilibrium and partial-equilibrium calculations (as shown in Figs. 1 and 2) show that using the fast chemistry or partial-equilibrium assumption in the thermochemical model may fail to predict the concentrations of radicals in turbulent flames.

The results of the variances $\widetilde{f''f''}$ and $\widetilde{q''q''}$ and covariance $\widetilde{f''q''}$ calculations can be used to test the validity of assumed shape joint pdf models. A major assumption made in the assumed joint pdfs is that f and q are statistically independent. If this were true, the covariance $\widetilde{f''q''}$ and the correlation coefficient R between f and q would be zero. In the unswirled flame, the variances $\widetilde{f''f''}$ and $\widetilde{q''q''}$ and covariance $\widetilde{f''q''}$ are shown in Fig. 3. The absolute values of $\widetilde{f''f''}$ and $\widetilde{f''q''}$ are smaller than Pope and Correa's [8] calculations in a syngas flame since the stoichiometric mixture fraction for hydrogen is about 10 times smaller than the syngas flame (0.028 vs 0.3).

The correlation coefficient R for the unswirled flame is shown in Fig. 4 at x/D = 33, 56, 111, and

194. The values of correlation coefficient R are far from zero except at large y/D and far downstream ($x/D = 194$). This indicates that f and q are highly correlated. Fig. 5 represents the correlation coefficient at $x/D = 21$, 53, and 107 in unswirled (Fig. 5a), low swirl (Fig. 5b), and high swirl (Fig. 5c) flames of the swirl combustor. These profiles also demonstrate that f and q are highly correlated and far from being independent.

The correlation calculations deduced from the experimental data of unswirled and swirled hydrogen flames are in qualitative agreement with the joint pdf calculations made by Pope and Correa [8] in a study of a syngas turbulent jet flame. Both our measurements and Pope and Correa's calculations show that the conserved and reactive scalars are not independent. Assumed shape pdf models that assume statistical independence have been used to predict hydrogen jet flames [2,3,5], syngas jet flames [4,6], recirculating flames [6], and supersonic flames [7]. Our results suggest that these assumed shape joint pdf models may incorrectly predict the minor species and subsequent nonequilibrium effects in these turbulent reacting flows. The use of a model that does not assume statistical independence (e.g., Pope and Correa [8]) is necessary to properly predict nonequilibrium effects.

Conclusions

Experimental results of the major and minor species concentrations made in unswirled and swirled turbulent hydrogen diffusion flames are used to compare with the fast chemistry limit and the partial-equilibrium assumption and to test the validity of assumed shape joint pdf models. The comparisons of measured OH concentrations with equilibrium and partial-equilibrium values show that a simple fast chemistry or partial-equilibrium assumption made in some combustion models may fail to predict the superequilibrium concentrations of radicals. The measured covariances of the conserved and reactive scalars $\widetilde{f''q''}$ and their correlation coefficient R in swirled and unswirled turbulent diffusion flames are high, indicating that these scalars are highly correlated. The measured correlation coefficients are in agreement with pdf transport model predictions by Pope and Correa. These measurements suggest that the common assumption used in assumed shape joint pdf models that the mixing and reactive scalars are statistically independent is a poor assumption. Predictions of turbulent reacting flames using assumed shape joint pdf models may incorrectly predict OH concentrations and other nonequilibrium effects. A joint pdf transport model such as Pope and Correa's that does not assume statistical independence of the conserved and reactive scalars must be used to prop-

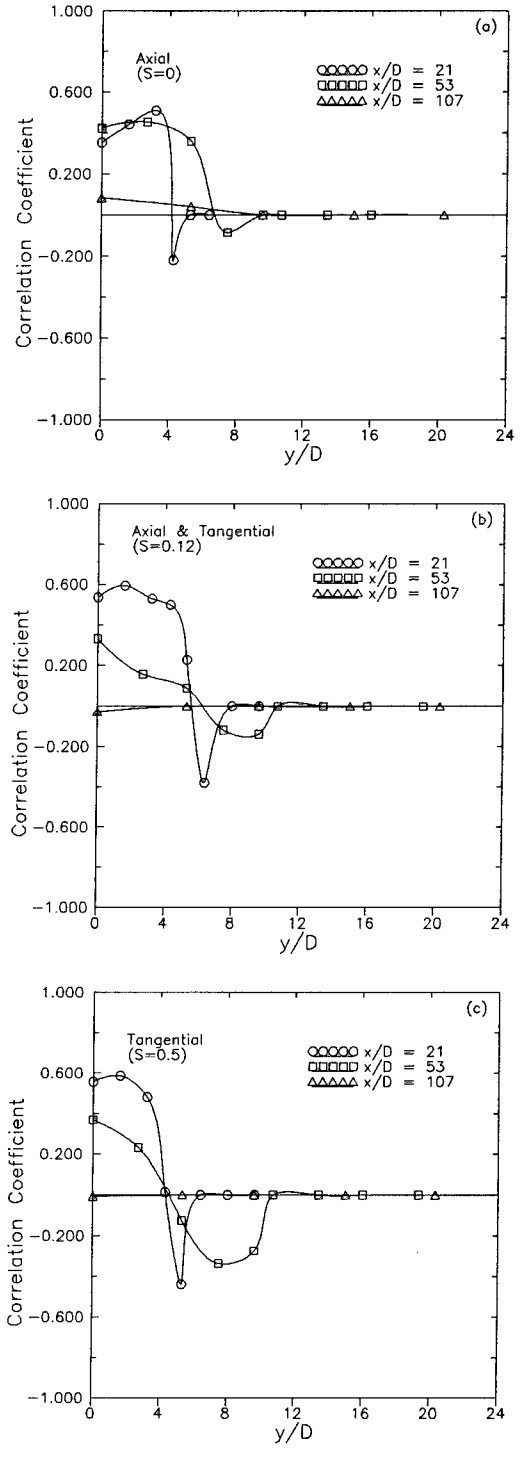

FIG. 5. Correlation coefficient R vs y/D at $x/D = 21$, 53, and 107 in (a) unswirled, (b) low swirl, and (c) high swirl turbulent flames ($Re = 12{,}500$).

erly predict nonequilibrium effects in turbulent diffusion flames.

Acknowledgments

The research at Vanderbilt University was supported by the National Science Foundation (PYI Grant CTS-8657130). The work done at Chung-Hua Polytechnic Institute was partially supported by the National Science Council of the Republic of China (Contract No. NSC 82-0424-E-216-038).

REFERENCES

1. Takagi, T., Ogasawara, M., Fujii, K., and Daizo, M. *Fifteenth Symposium (International) on Combustion*, The Combustion Institute, Pittsburgh, 1975, pp. 1051–1059.
2. Janicka, J., and Kollmann, W., *Combust. Flame* 44:319–336 (1982).
3. Janicka, J., and Kollmann, W., *Seventeenth Symposium (International) on Combustion*, The Combustion Institute, Pittsburgh, 1979, pp. 421–430.
4. Correa, S. M., Drake, M. C., Pitz, R. W., and Shyy, W., *Twentieth Symposium (International) on Combustion*, The Combustion Institute, Pittsburgh, 1984, pp. 337–343.
5. Chen, J.-Y., *Combust. Flame* 69:1–36 (1987).
6. Correa, S. M., and Gulati, A., *Combust. Flame* 89:195–213 (1992).
7. Villasenor, R., Chen, J.-Y., and Pitz, R. W., *AIAA J.* 30, 395–402 (1992).
8. Pope, S. B., and Correa, S. M., *Twenty-First Symposium (International) on Combustion*, The Combustion Institute, Pittsburgh, 1986, pp. 1341–1348.
9. Correa, S. M., and Pope, S. B., *Twenty-Fourth Symposium (International) on Combustion*, The Combustion Institute, Pittsburgh, 1992, pp. 279–285.
10. Cheng, T. S., Wehrmeyer, J. A., and Pitz, R. W., *Combust. Flame* 91:323–345 (1992).
11. March, S. R., Cheng, T. S., Pitz, R. W., Wehrmeyer, J. A., and Debelak, K. A., "Temperature and Species Concentration Measurements in a Swirled Hydrogen Diffusion Flame," 29th Aerospace Science Meeting, AIAA-91–0480, 1991.
12. Pitz, R. W., Cheng, T. S., March, S. R., and Wehrmeyer, J. A., "Effects of Swirl on Finite-Rate Chemistry in Lifted Jet Diffusion Flames," 27th Joint Propulsion Conference, AIAA-91–2319, 1991.
13. Claypole, T. C., and Syred, N., *Eighteenth Symposium (International) on Combustion*, The Combustion Institute, Pittsburgh, 1981, pp. 81–89.
14. Yuasa, S., *Combust. Flame* 66:181–192 (1986).
15. Mansour, M. S., Bilger, R. W., and Dibble, R. W., *Combust. Flame* 82:411–425 (1990).
16. Warnatz, J., *Combust. Sci. Technol.* 26:203–213 (1981).
17. Hynes, A. J., Steinberg, M., and Schofield, K., *J. Chem. Phys.* 80:2585–2597 (1984).
18. Dixon-Lewis, G., Goldsworthy, F. A., and Greenberg, J. B., *Proc. R. Soc. London A* 346:261–278 (1975).
19. Pitz, R. W., and Drake, M. C., *AIAA J.* 24:815–822 (1986).
20. Magre, P., and Dibble, R., *Combust. Flame* 73:195–206 (1988).
21. Drake, M. C., Pitz, R. W., Lapp, M., Fenimore, C. P., Lucht, R. P., Sweeney, D. W., and Laurendeau, N. M., *Twentieth Symposium (International) on Combustion*, The Combustion Institute, Pittsburgh, 1984, pp. 327–335.

COMMENTS

E. P. Hassel, Darmstadt, Germany. As your working group pointed out in earlier publications, there is a certain probability to dissociate the water molecule by a KrF-excimer laser beam with 248 nm. We also observed this in our lab. If this would have happened in the described experiments, it would have had a big impact on the measured OH superequilibrium concentrations and thus on the correlation between mixture fraction and reaction progress variable. Would you please comment on this?

Author's Reply. To minimize two-photon H_2O photodissociation to form H and OH, the laser is tuned to a 248.623-nm wavelength that is away from any strong two-photon H_2O absorption lines. In addition, a long 2-m focussing laser lens limits the laser power density and hence the two-photon photodissociation in the measurement zone. Then the OH fluorescence signal is calibrated in an adiabatic Hencken multielement diffusion flame at a range of fuel/air ratios. The calibration point is downstream (5 cm) where the OH concentration has equilibrated. At rich or lean conditions where we do not expect any OH signal, we do find some fluorescence signal possibly due to production of OH from two-photon H_2O photodissociation. This baseline signal is subtracted out in the calibration and does not affect the OH superequilibrium measurements in the turbulent flame. This is confirmed by OH measurements far downstream in the turbulent jet where the OH concentrations are at equilibrium values.

Twenty-Fifth Symposium (International) on Combustion/The Combustion Institute, 1994/pp. 1141–1147

WIDE-FIELD CONSERVED SCALAR IMAGING IN TURBULENT DIFFUSION FLAMES BY A RAMAN AND RAYLEIGH METHOD

J. B. KELMAN, A. R. MASRI, S. H. STÅRNER AND R. W. BILGER
Department of Mechanical and Mechatronic Engineering
The University of Sydney
NSW 2006, Australia

A new experimental approach to two-dimensional (2D) measurements of mixture fraction and other scalars in turbulent flames has been developed, based on simultaneous fuel Raman and Rayleigh imaging. The inherently weak Raman signal is enhanced by high laser energy, low f-number optics, and a multipass cell. Measurements have been obtained in piloted flames of air-diluted methane, at Reynolds number 28,000–53,000. With the assumptions of unity Lewis number and a one-step reaction, single-shot images of mixture fraction, fuel mass fraction, and temperature have been derived with spatial resolution of about 10 Kolmogorov scales. Advantages and difficulties in the use of the multipass cell are discussed and some early results presented. The wide-field images enable determination of scalar turbulence macroscales that are found to be anisotropic and to vary with radius. The location of the instantaneous stoichiometric mixture fraction contours indicates that there is little reaction in the outer regions where entrainment takes place. Generally, the stoichiometric contour is aligned with regions of high scalar dissipation.

Introduction

Direct mixture fraction and scalar dissipation measurements in fully turbulent jet diffusion flames have been a long-standing requirement of modellers and theorists [1–3], who have hitherto relied largely on data from nonreacting flows for testing of hypotheses and model validation, especially where scalar gradient information is involved. It should be emphasised that only by imaging of a conserved scalar such as the mixture fraction can the structure of flames and nonreacting flows be properly related. The imaging of mixture fraction can, at least in principle, allow the imaging of the (single step) fuel reaction rate, which would give a true representation of where the reaction zone lies within the flame. Recent studies [4–6] have explored a two-scalar method for imaging mixture fraction. This approach has been tested against single-point measurements [7] as regards scalar statistics, but the gradient data needed for determining scalar dissipation (by far the most demanding aspect) are new and require extensive comparisons with data obtained by alternative methods. Among other studies on this topic is the Rayleigh imaging in a H_2 flame at moderate Reynolds number [8], as well as Rayleigh imaging in cold flows [9,10], used to discuss flame structure. The most detailed quantitative imaging work to date [6] uses the same two-scalar approach as in this paper, but with very narrow field ("ribbon") imaging in which a focused laser beam is retroreflected with a slight vertical offset, so that two scalar gradient components may be measured simultaneously. The tight field optimises signal quality, enabling good statistics of mixture fraction and scalar dissipation rate to be calculated, but with the loss of macroscale two-dimensionality.

In this paper, we image a wider field (around four integral lengths), using Rayleigh scattering to derive temperature and spontaneous Raman scattering to record fuel concentration, with a multipass cell to maximise the Raman signal-to-noise ratio (SNR). In other work [4,5], laser-induced fluorescence (LIF) from a special fuel (or a fluorescing marker in the fuel) is used to obtain the rather high SNR required for deriving the scalar dissipation rate, $\chi = 2D\nabla f \cdot \nabla f$ [where D is the diffusivity (calculated as a function of mixture fraction from predictions for opposed-flow laminar flames of the same composition), f the mixture fraction, and ∇ the gradient operator]. These alternative approaches will provide valuable comparisons, although unresolved queries exist as regards the effects of pyrolysis and temperature-dependent LIF cross sections of such markers. Although similar Raman/Rayleigh wide-field imaging has been reported previously [11], this is the first time that a quantitative analysis in terms of a conserved scalar is carried out.

Here we present details of the two-scalar method for mixture fraction measurements applied to full two-dimensional (2D) imaging with a multipass cell. Advantages and difficulties are discussed and early results are shown, with a brief examination of structural features. An analysis of the complete results (including both methane and methanol fuels) is scheduled for a paper to follow.

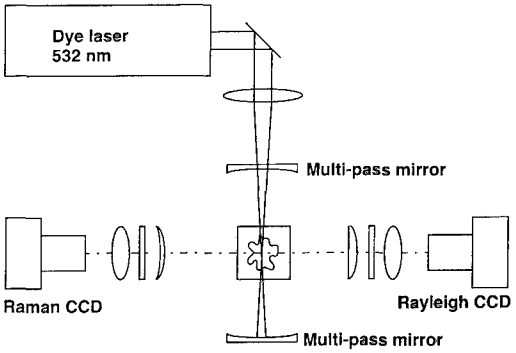

FIG. 1. Plan view of optics layout.

Experimental Arrangement and Data Reduction

The flames chosen as test objects, methane diluted with air (1/3 by volume), have been extensively documented by point Raman/Rayleigh/OH LIF measurements [12,13], which enables validation of the new method, except as regards scalar gradients and length scales. Such validation has been pursued in a companion paper by Stårner et al. [6]. The 7.2-mm jet nozzle, surrounded by an 18-mm pilot annulus, is placed in a vertical coflow of 15 m/s. The premixed pilot composition is such that the C/H ratio equals that of the main jet. Further details may be found in Ref. 13. Jet Reynolds numbers vary from 28,000 to 53,000.

The optics arrangement shown in Fig. 1 is quite simple: 1.3-J pulses, 3-μs long, from a flashlamp-pumped dye laser at 532 nm are formed to a sheet and passed through a multipass cell [11]. The cell mirrors are at 300-mm centres, with a radius of curvature of 150 mm. All C-H stretches in the flame are recorded by vibrational Raman scattering with a lens-coupled, intensified charge-coupled device (CCD) camera, with f/1.1 collection optics. A 10-nm bandwidth, 632-nm centred interference filter is used to reject luminosity and Rayleigh scattering. The Rayleigh data are recorded on a similar camera, but with neutral density filters to attenuate the very high Rayleigh signal level obtained in the multipass cell. This attenuation is needed to enable the intensifier to operate in its design range, and is preferable to reducing the collection aperture, which tends to cause severe vignetting. The resolution of the collection optics is 85 μm. By comparison, the point measurements in Ref. 14 have a spatial resolution around 1 mm, and effective bandwidth is 3–4 nm [14].

The multipass cell serves exclusively to increase the SNR of the Raman data; the SNR of the raw signal on the axis (binned 2 × 2 pixels on transfer to the computer) varies from 9 in the upper part of the multipass cell to 14 at its lowest part, where the maximum number of passes is obtained, and where the stripe effect of the nonuniform incident beam is minimised. The multipass cell has a lower sheet intensity where the beam enters at the top end of the cell, increasing as the laser beam "walks" down the mirrors. For visualisation and calculation of large scales, the whole image can be used (50 × 33 mm in the object plane), whilst only the lowest third of the flame would normally serve for calculation of scalar statistics. The main disadvantage of the multipass cell lies in the broadening of the beam waist due to beam steering in the flame, which causes an increase from 0.6 mm to around 1 mm, thus limiting the spatial resolution. The beam steering also increases the stripiness of the image. Further difficulties encountered in the use of the multipass cell include low-level Rayleigh cross talk to the Raman channel, due to incomplete rejection of the 532-nm scattering by the 632-nm filter; a narrower-bandwidth filter should reduce this interference. Also, the high Rayleigh background, arising from scattering off the cell mirrors, appears to increase with the strength of the refractive index gradients in the flame brush; the many passes through the flame are thought to amplify this effect, which is not easily quantifiable and therefore makes the scalar outputs semiquantitative. It is estimated that errors result in instantaneous temperature and mixture fraction data of up to 15 and 25% of local values, respectively.

The integral length scale varies between 4 and 8 mm at the measurement location chosen, $x/D = 22$ (x being the distance from the nozzle and D the nozzle diameter); we use the procedure described in Ref. 6 to estimate the Kolmogorov scale at 0.2 mm. As argued in Ref. 6, it seems unlikely that all of the scalar dissipation can be captured, especially close to the nozzle and near the axis; however, in the reaction zone, the scales are substantially larger, so the error should be much reduced. To be compatible with the beam waist thickness, the Raman images have been smoothed 5 × 5 pixels, which at worst would correspond to a resolution of 0.85 mm; thus, spatial resolution remains limited by the beam thickness, and the SNR of the Raman data is raised to 35. The similarly processed Rayleigh data (after the usual corrections and smoothing 3 × 3 pixels) have an SNR of 80, measured in cold air on corrected images.

Calibration of the Raman channel is obtained by cold-flow measurements in a uniform field of known concentration. The Raman cross section is assumed to be temperature independent. Interference from all sources, including soot precursors, on the fuel Raman line is believed to be insignificant. Stårner et al. [12,13] found that soot interference in a similar flame and location was small. The Rayleigh field of view is such that unmixed coflow air is present at the edge of each image: this allows shot-to-shot laser energy monitoring and correction of both channels, as well as partial correction for residual stripes in the images.

The data reduction technique is fully described elsewhere [7]. Briefly, we assume that the flow has uniform inlet composition and unity Lewis number, and that the chemistry is in the form of a one-step reaction. A conserved scalar is defined, based on total enthalpy (with radiation neglected): $\beta = Y_{fu} + c_pT/Q$, where Y_{fu} is the fuel mass fraction, c_p the specific heat at constant pressure, and Q the lower heat of combustion. The mixture fraction, f, can then be defined as

$$f = \frac{\beta - \beta_2}{\beta_1 - \beta_2} = \frac{Y_f + c_p/Q(T - T_2)}{Y_{f,1} + c_p/Q(T_1 - T_2)} \quad (1)$$

where subscripts 1 and 2 denote fuel and air streams. With some manipulation, f can then be expressed in terms of the Rayleigh (Ra) and Raman (Rm) signals as

$$f = \frac{C_1 a_T Rm}{WRaRm_{\text{cal}}} + C_2(a_T/Ra - T_2) \quad (2)$$

where C_1 and C_2 are calibration constants, W the mixture mole weight, and a_T proportional to the Rayleigh cross section. Predictions for opposed-flow laminar flames are used to produce the fully reacted state at various strain rates and to determine values for a_T, W, and c_p dependent on f [6]. As a_T, W, and c_p vary somewhat with f, an iterative method is used; typically, convergence to 0.1% is reached within four iterations. A reaction progress variable can then be defined as $b = (T - T_2)/(T_r - T_2)$, subscript r denoting the fully reacted state. This important quantity gives a direct indication of local extinction in highly loaded flames and is readily calculated here.

Results and Discussion

Figures 2 through 4 show representative instantaneous Rayleigh and Raman images (corrected), as well as the corresponding calculated mixture fraction and temperature images, all centred on $x/D = 22$ (x being the distance from the nozzle and D the nozzle diameter), and with jet velocity varying from 50% (Fig. 2) to 95% (Fig 4) of blow-off velocity U_{bo} (defined here as the velocity at which no significant reaction occurs downstream of the flame "neck," around $x/D = 15$; $U_{bo} = 115$ m/s). Figure 2 represents a steadily burning flame without local extinction at the neck. As reported elsewhere [15], the small-scale structure on the axis changes into larger scales in the flame zone (which roughly coincides with the middle of the shear layer at this axial location) because of the increased viscosity that reduces the turbulence Reynolds number Re_t. This scale change is a particular feature of the upstream region of turbulent jet diffusion flames and is quantified in Fig.

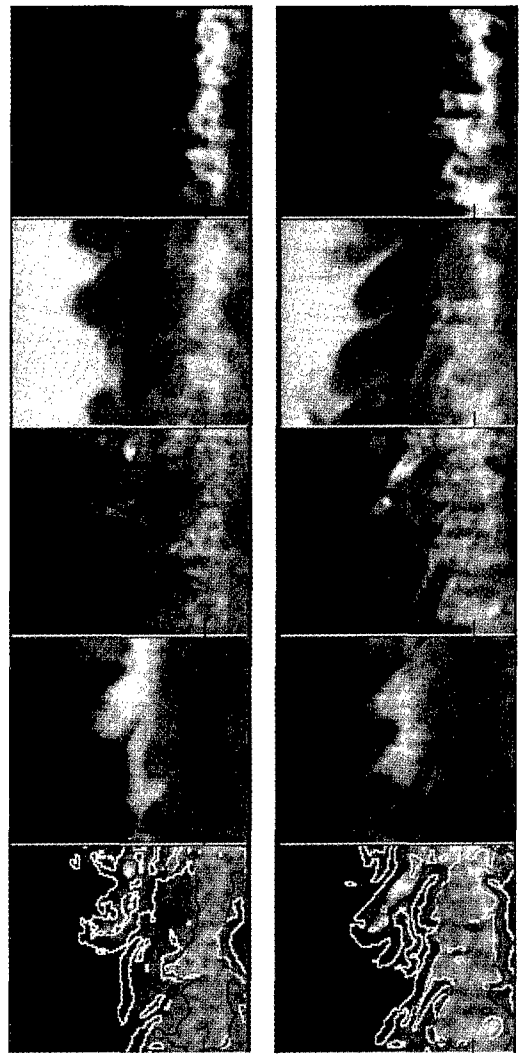

FIG. 2. Two sets of instantaneous images of flame at 50% of blow-off velocity, centred on $x/D = 22$, $Re_{\text{jet}} = 28{,}000$. The flow is upwards; the flame axis marked with a tick. Object size 31 × 26 mm. From above: Raman and Rayleigh intensity (both corrected), mixture fraction, and temperature. The bottom images show the mixture fraction overlaid with the stoichiometric contour f_s (black) and contours of near-peak scalar dissipation χ (white).

5, which shows the variation of the integral length scale $l_{11} = \int_0^\infty R_{11}dx$ with radius for the three velocities of Figs. 2 through 4. The autocorrelation coefficient R_{11} is calculated in the axial direction, using the mixture fraction images. For the fully burning flame, l_{11} grows with radius by almost a factor of 2 from the low on the axis, whilst for the almost extinguished flame of Fig. 4, there is little change in l_{11}. Also, it is

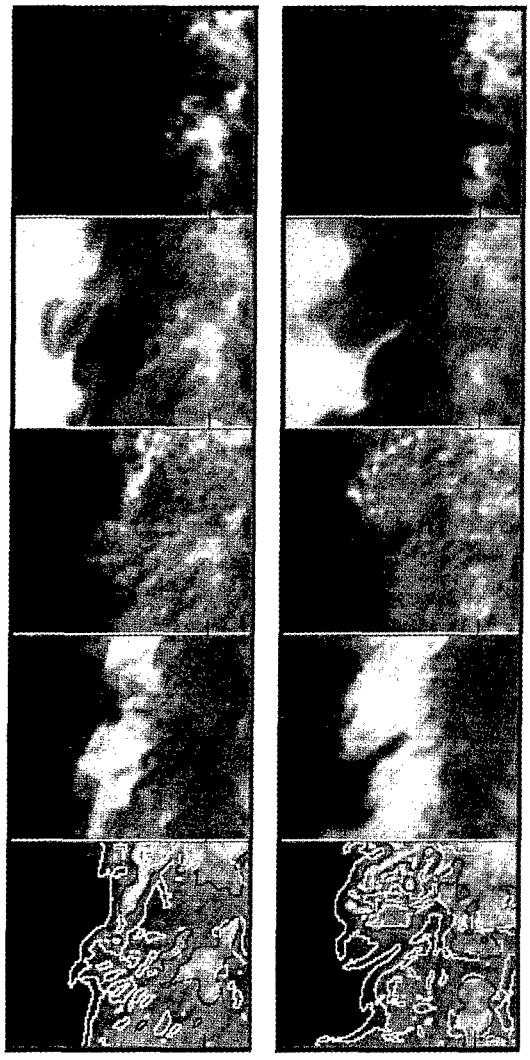

FIG. 3. Flame at 75% of blow-off velocity, Re_{jet} = 42,000. Other data as in Fig. 2.

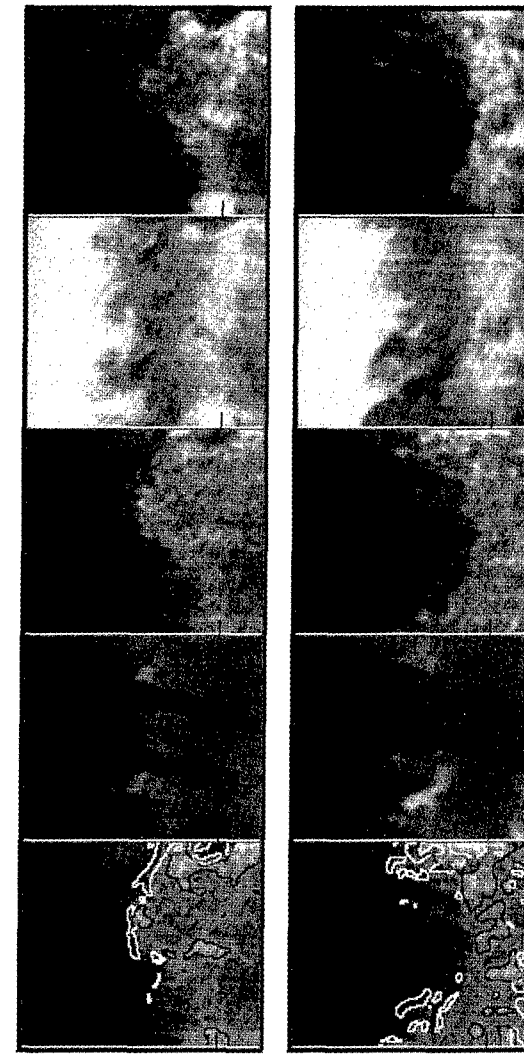

FIG. 4. Flame at 95% of blow-off velocity, Re_{jet} = 53,000. Other data as in Fig. 2.

seen that, on the axis, l_{11} is smaller for the fully burning flame than for the nearly blown-off case; this is interpreted as an indication of how the flame envelope around the central jet impedes the mixing, as also instanced by the 15% higher centreline mean mixture fraction in the case of Fig. 2 than in the colder jet of Fig. 4. (This simply illustrates the fact that the mixture fraction decays less rapidly in a flame than in the corresponding cold jet.) One may expect the growth in l_{11} with radius to be even more pronounced in flames with much lower stoichiometric mixture fraction (e.g., CH_4, f_s = 0.055) since the profile of f_s then lies largely outside the shear layer at this axial location [16]. In the radial direction, the integral length scale $l_{22} = \int_0^\infty R_{22}dr$ is found to be $0.83l_{11}$ near the centreline and $0.58l_{11}$ in the shear layer; this is consistent with results for a lifted jet flame [17].

The high value of f_s here (f_s = 0.353) is likely to have further effects on flame structure: A study of the images reveals that, inside the large eddies surrounded by strands of entrained air, the mean mixture fraction is around 0.18, i.e., well below stoichiometric, with excursions to 0.05 and 0.25. Thus, one does not expect the interface between these eddies and the entrained air to contain much burning fluid. By contrast, in a pure CH_4 flame, with f_s = 0.055, these eddies would typically be surrounded by the

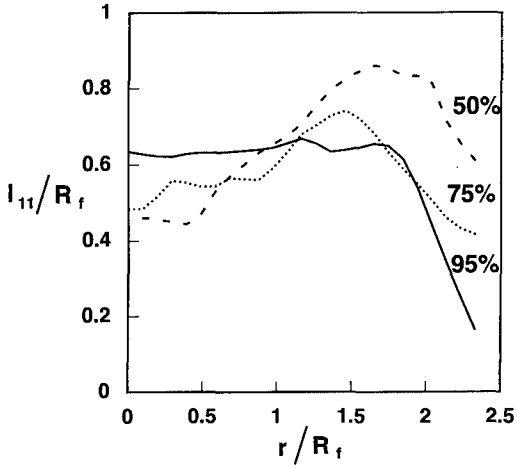

FIG. 5. Radial profiles of integral length scale $l_{11} \approx \int_0^\infty R_{11}dx$ for flames at 50, 75, and 95% of blow-off velocity, normalised by the mixture fraction half-radius R_f.

stoichiometric contour, with the richer interior of each eddy comprising fuel and products. This difference in structure between flames of low and high f_s is likely to be a contributing reason for the observed difference in extinction behaviour [12,13]: A pure CH_4 flame has a wide range of velocity in which local extinction gradually increases, whilst the diluted flame of this paper shows much more abrupt extinction when velocity is increased.

Although the instantaneous scalar dissipation rate (calculated here as $\chi = \chi_x + \chi_r$, neglecting the azimuthal component) is likely to be substantially attenuated by the limited spatial resolution, it can be used to demonstrate adequately the distribution of χ relative to the stoichiometric contour. It is found that there is a clear tendency of χ to align with f_s. The mixture fraction images in Figs. 2 through 4 provide some illustration. In direct numerical simulations of isotropic turbulence [18] at a low Re_t range of 41–85, the overlap of f_s and contours of high χ is more complete than in the results at 50% of blow-off, where $Re_t \approx 250$. Results for a cold jet [9] of $Re_t = 140$ also show that patches of intense χ "are aligned in general with the isopleth . . . surfaces of mixture fraction." Although at first sight these results do not appear to run counter to the flamelet modelling assumption that χ in the reaction zone can be approximated by its value at f_s, it should be stressed that, in the present flame, the reaction zone is very wide, ranging from $f = 0.14$ to 0.69 [12]; this range covers more than half of the turbulent fields in Figs. 2 through 4. As it can be seen that high values of χ are also present well away from the stoichiometric contour, it seems likely that such an assumption is less valid in this flow than in one of low f_s where the reaction zone is narrow. It would be of great interest to determine whether the reaction zone shifts from the stoichiometric contour towards peaks in χ, as argued in Ref. 9 for downstream regions in reacting flows. Although it is possible, at least in principle, to derive the instantaneous single-step reaction rate $w_{fu} = -\rho/2\chi d^2Y_{fu}/df^2$ on the basis of the data collected, the low signal quality of the Raman data in this experiment precludes a meaningful calculation of d^2Y_{fu}/df^2 at present.

Concluding Remarks

This work illustrates that meaningful instantaneous conserved scalar images can be derived from fuel Raman/Rayleigh imaging in a turbulent hydrocarbon flame. It should be stressed that it is not the assumptions in the two-scalar method that render the present wide-field results less than fully quantitative, but a combination of inadequate Raman signal strength and difficulties arising from the use of the multipass cell. There are several ways to improve this situation: Steps are now taken to optimise the Raman diagnostics by the use of a more sensitive image intensifier, better filtering, higher laser energy, increased magnification and possibly replacing the multipass cell with a single retroreflected and cavity-dumped beam (as in Ref. 6 but with a wider field). Estimates, partly based on Ref. 6, indicate that these improvements will enable calculation of full scalar statistics, including mean scalar dissipation, with errors no larger than those inherent in the two-scalar method itself. It may also be possible to derive at least a qualitative instantaneous distribution of w_{fu}.

The alternative two-scalar method for mixture fraction measurements, using fuel/LIF/Rayleigh [4], still presents serious obstacles due to parent fuel pyrolysis (a relatively minor problem in the present work) and LIF cross-section variation with temperature [19]. Although the very strong LIF signal is a major asset in wide-field imaging, present indications are that the simpler and more direct fuel Raman route, when optimised, will yield the more reliable statistics.

It would be most useful to record CH or OH LIF as a reaction zone marker, simultaneously with f and χ; to this end, it is intended to add a third camera and second laser to the existing diagnostic tools.

Acknowledgment

This work is supported by the Australian Research Council.

REFERENCES

1. Peters, N., *Twenty-First Symposium (International) on Combustion*, The Combustion Institute, Pittsburgh, 1988, pp. 1231–1250.

2. Bilger, R. W., in *Instrumentation for Flows with Combustion*, (A. M. P. K. Taylor, Ed.), Academic Press, London, 1993, pp. 1–51.
3. Pope, S. B., *Twenty-Third Symposium (International) on Combustion*, The Combustion Institute, Pittsburgh, 1991, pp. 591–612.
4. Stårner, S. H., Bilger, R. W., Lyons, K. M., Marran, D. F., and Long, M. B., paper presented at the 14th International Colloquium on the Dynamics of Explosions and Reactive Systems, Coimbra, Portugal, August 1993.
5. Long, M. B., Frank, J. H., Lyons, K. M., Marran, D. F., and Stårner, S. H., "A Technique for Mixture Fraction Imaging in Turbulent Nonpremixed Flames," *Int. J. Phys. Chem.*, to appear.
6. Stårner, S. H., Bilger, R. W., Lyons, K. M., Frank, J. H., and Long, M. B., "Conserved Scalar Measurements in Turbulent Diffusion Flames by a Raman and Rayleigh Ribbon Imaging Method," Paper Presented at the Fall Meeting of the Western States Section of the Combustion Institute, 1993. Also to appear in *Combust. Flame* (1994).
7. Stårner, S. H., Bilger, R. W., Dibble, R. W., and Barlow, R. S., *Combust. Sci. Technol.* 86:223–236 (1992).
8. Stepowski, D., and Cabot, G., *Combust. Flame* 88:296–308 (1992).
9. Bilger, R. W., Yip, B., Long, M. B., and Masri, A. R., *Combust. Sci. Technol.* 72:137–155 (1990).
10. Buch, K. A., Dahm, W. J. A., Dibble, R. W., and Barlow, R. S., *Twenty-Fourth Symposium (International) on Combustion*, The Combustion Institute, Pittsburgh, 1993, pp. 295–301.
11. Long, M. B., Levin, P. S., and Fourguette, D. C., *Opt. Lett.* 10:267–269 (1985).
12. Stårner, S. H., Bilger, R. W. Dibble, R. W., and Barlow, R. S., *Combust. Sci. Technol.* 70:111–133 (1990).
13. Stårner, S. H., Bilger, R. W., Dibble, R. W., and Barlow, R. S., *Combust. Sci. Technol.* 72:255–269 (1990).
14. Stårner, S. H., Bilger, R. W., Dibble, R. W., and Barlow, R. S., *Twenty-Third Symposium (International) on Combustion*, The Combustion Institute, Pittsburgh, 1990, pp. 645–651.
15. Townsend, A. A., *J. Fluid Mech.* 26:689–715 (1966).
16. Stårner, S. H., Bilger, R. W., Dibble, R. W., Barlow, R. S., Fourguette, D. C., and Long, M. B., *Twenty-Fourth Symposium (International) on Combustion*, The Combustion Institute, Pittsburgh, 1993, pp. 341–349.
17. Schefer, R. W., Namazian, M., and Kelly, J., *Twenty-Second Symposium (International) on Combustion*, The Combustion Institute, Pittsburgh, 1989, pp. 833–842.
18. Montgomery, C. J., Kosaly, G., and Riley, J. J., *Combust. Flame* 95:247–260 (1993).
19. Frank, J. H., Lyons, K. M., Marran, D. F., Long, M. B., Stårner, S. H., and Bilger, R. W., "Mixture Fraction Imaging in Turbulent Nonpremixed Hydrocarbon Flames," Fall Meeting of the Western States Section of the Combustion Institute, 1993. Also accepted for the Twenty-Fifth Symposium (International) on Combustion, Irvine, CA, 1994.

COMMENTS

S. B. Pope, Cornell University, USA. You observe that the peak scalar dissipation occurs close to the stoichiometric contour. Isn't this conclusion limited to the particular location that you have chosen to image? If you examined the fields further downstream, you would expect to find the peak scalar dissipation at lower values of mixture fraction.

Author's Reply. The peak scalar dissipation does appear to lie close to the stoichiometric contour, and this is limited to the chosen location. Peak scalar dissipation does not necessarily occur at stoichiometric, but more often at the edge of high-temperature regions. At locations further downstream, obviously peak scalar dissipation cannot occur at stoichiometric as mixture fraction values will have reduced. It is expected that scalar dissipation will peak at lower values of mixture fraction and correspond to the high-temperature gradients. Unfortunately, due to soot precursor interference measurements downstream were not possible.

•

J. M. Seitzman, Georgia Institute of Technology, USA. Did you perform measurements with your system in a well-characterized flame with a thin and/or convoluted flame zone in order to determine the systematic errors associated with the measurement, for example with respect to noise, spatial resolution, and camera alignment? If so, what errors were found?

Author's Reply. Yes. Preliminary measurements were carried out in a laminar methane-air (1:3 by volume) flame. This was a laminar jet flame, 1-in. burner diameter. Mixture fraction and temperature results were in good agreement with those from laminar flame computations. Errors in camera alignment, or poor resolution, will show clearly when processed. No errors due to this were observed. The laminar flame did show evidence of interference from soot precursors, close to the tip of the flame. This did limit measurement to axial locations less than 30 jet diameters in the turbulent flames.

•

Godfrey Mungal, Stanford University, USA. Your flames are diluted with air, which contains oxygen; how would your results and interpretations change if you had diluted

with nitrogen (e.g., width of flame zone, shape, convolutions, etc.).

Author's Reply. The fuel was diluted with air for two reasons. One, to reduce soot interference on the Raman measurement, and two, to move the reaction zone into the shear layer. If the flames had been diluted with nitrogen, the stoichiometric mixture fraction would have moved away from the shear layer compared with the air-diluted flame [1]. Attainable Reynolds numbers would have reduced for compatible values of stoichiometric mixture fraction, and this would have led to a generally less convoluted flame. We were interested in a more turbulent flame, and this is why air was chosen as the dilutant.

REFERENCE

1. Stårner, S. H., Bilger, R. W., Dibble, R. W., Barlow, R. S. "Piloted Diffusion Flames of Diluted Methane Near Extinction: Detailed Structure from Laser Measurements," *Combust. Sci. Technol.* 72:255–269 (1990).

Twenty-Fifth Symposium (International) on Combustion/The Combustion Institute, 1994/pp. 1149–1157

SIMULTANEOUS NO AND TEMPERATURE IMAGING MEASUREMENTS IN TURBULENT NONPREMIXED FLAMES

MEHDI NAMAZIAN AND JOHN KELLY
Altex Technologies Corporation
650 Nuttman, Santa Clara, CA 95054, USA

AND

ROBERT SCHEFER
Combustion Research Facility
Sandia National Laboratories
Livermore, CA 94551, USA

A quantitative laser-induced fluorescence imaging technique was developed with sufficient sensitivity to detect low NO concentration levels present in turbulent flames. For this linear fluorescence technique, quenching and population corrections are necessary for quantitative NO imaging. A correction procedure was developed that utilizes temperature measurements and flamelet or distributed reaction model results. The model results showed that the quenching correction can be related to temperature.

Simultaneously with NO imaging, Rayleigh scattering imaging was used to determine the temperature. The measured temperature was combined with model results to estimate the quenching and population corrections for the NO signal. Analysis showed that this data reduction methodology has less than 10% error and the total error is within 25%. The imaging setup uses a multipass cell, to create a thin sheet of laser light, and a $0.8/f$ collection optics for the NO signal. The in-flame detectability of the imaging system is 1 ppm. To validate the technique, NO was measured and compared at two different rotational levels. Imaging results were also compared with NO_X probe and thermocouple temperature measurements. The results of different measurement methods compared well, thus confirming the validity of the technique.

The technique was applied to the flame initiation zone of lifted turbulent non-premixed-methane flames. NO was found to correspond closely to the temperature field. As the turbulence altered the structure of the temperature field, NO was similarly altered. Distributed reaction model results were favorably compared to the imaging data. This further supports the validity of both experimental and model results.

Introduction

Planar imaging of NO provides multipoint statistics needed to relate NO formation to flame zone and local turbulence characteristics. These measurements provide information useful in developing and validating models. The development of an NO imaging technique for turbulent flames has been limited (1) by the low NO concentration present in these flames and a near 1-ppm detectability requirement and (2) by the NO signal dependence on local flame temperature and species concentrations. The experimental and data reduction methodology, described in this paper, overcomes both of these limitations.

Planar imaging of NO has been demonstrated at high (100s ppm) NO concentrations [1–3]. In these experiments, the laser beam is spread into a sheet, thus reducing the laser energy density to orders of magnitude lower than what is available in point measurements. Near 1 ppm, NO detectability has been achieved in NO fluorescence point measurements [4–6]. Therefore, there is no fundamental limitation in achieving the same detectability using imaging techniques. In the current experiments, a multipass cell [7] is used to raise the energy density in the sheet to near what is available in point measurements. This overcomes the first limitation cited above.

The fluorescence signal depends on collisional quenching rates, which vary across the flame and are a function of local temperature and major species concentrations. To obtain quantitative NO measurements from the images, major colliding species concentrations, their respective quenching cross sections, as well as temperature must be known at each point in the image [5]. This is a difficult task in imaging measurements. However, using the current understanding of the turbulent flame structure [8,9] allows the task to be simplified. As shown below, this is achieved by relating the major quenching species concentrations to temperature. Using this data reduction methodology, simultaneous temperature and

NO images are sufficient to correct the NO image for both quenching and population effects. This approach overcomes the second limitation cited above.

As expected, estimating quenching species concentrations from temperature measurements introduces some error. Analytical models and cross-section data [10–12] are utilized in the error analysis section to estimate the magnitude of the error in NO measurements. In the experimental section, a combined NO and Rayleigh imaging system is described and applied to a methane-air laminar flat flame and a methane turbulent-lifted flame. The turbulent flame has been extensively studied by the authors [13,14]. The imaging results are then compared to sampling probe data and model results to validate the technique. Finally, the relationship between the instantaneous NO and temperature fields are discussed.

Error Analysis

In the linear fluorescence regime, the fluorescence signal (S_{fl}), or the number of photons generated, can be related to the NO mole fraction, X_{NO}, by the following relation:

$$X_{NO} = C_{ref} \frac{S_{fl}}{E} \sigma \frac{\sqrt{T}}{F(T)} \tag{1}$$

or in term of a reference $X_{NO_{ref}}$.

$$X_{NO} = X_{NO_{ref}} C_l C_q C_f \tag{2}$$

where C_l, C_q, and C_f are S_{fl}/E, σ, and $\sqrt{T}/F(T)$, respectively, each normalized by the reference values, determined at the stoichiometric mixture condition. Note that in these relations, E is the laser energy per unit frequency per unit area, $F(T)$ is the population fraction in the pumped state, T is the temperature, and σ is the mixture-averaged quenching cross section defined by

$$\sigma = \sum X_i \sigma_i \left(1 + \frac{M_{NO}}{M_i}\right)^{1/2} \tag{3}$$

where X_i, σ_i, and M_i are the mole fraction, the quenching cross section, and the molecular mass of the quenching species i, respectively, and M_{NO} is the NO molecular mass. To quantify the NO signal, the product $C_q \cdot C_f$ or the normalized value of $\sigma\sqrt{T}/F(T)$, must be calculated. Error is introduced when estimated, rather than actual; C_q and C_f values are used in Eq. (2).

It can be shown that the magnitude of this error relative to peak NO is

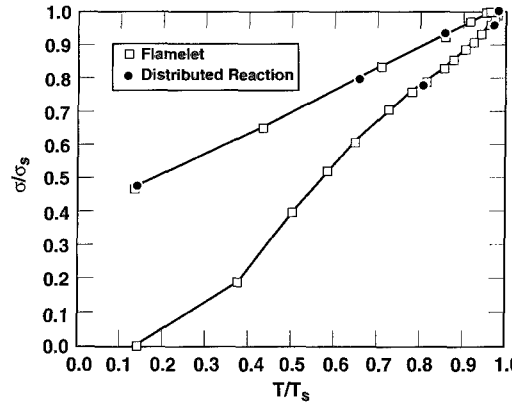

FIG. 1. Quenching cross section (σ), vs temperature (T). Both axes are normalized by the respective stoichiometric values: flamelet $\sigma_s = 15.8\ A^2$, $T_s = 2174$ K; distributed reaction $\sigma_s = 14.9\ A^2$, $T_s = 1990$ K. Fuel is methane.

$$\frac{\Delta(NO)}{NO_{max}} = \frac{(1 - Cq_{est} C_{f_{est}}/Cq_{actual} C_{f_{actual}}) NO_{actual}}{NO_{max}} \tag{4}$$

where NO_{max} is the maximum NO concentration. To determine X_{NO} from the laser fluorescence images, σ, T, and $F(T)$ in Eq. (1) must be estimated. Rayleigh scattering will be used to determine T and $F(T)$. Most importantly, a method will be described where T can also be used to estimate σ.

Flame zones in turbulent combustion have been predicted by flamelets or distributed reaction models. The flamelet model best corresponds to conditions where the turbulence scale is large compared to the flame thickness. In contrast, the distributed reaction model best corresponds to conditions where the turbulence scale is similar to the flame thickness. Therefore, these two models represent the bounding cases for turbulent combustion. Both of these models were utilized to estimate σ and the error in NO. For the model calculations, a modification of the PROF code [15] was used to predict flamelet and distributed reaction cases.

Figure 1 shows the model-derived quenching cross section plotted against the temperature for these two flame cases. Both coordinates are normalized by their corresponding stoichiometric values. Model calculations were used to determine X_i in Eq. (3), and each species' cross section was obtained from Paul et al. [10]. The upper and lower segments of the curve in Fig. 1 correspond to the air and fuel sides of the flame, respectively. Over most of the domain, CO_2 and H_2O represent over 80% of the total quenching cross section. These two species are stable, and their level is similar for a range of flames, from flamelet to distributed reaction limiting cases.

This is the major reason for similarity between the two cases shown in Fig. 1.

The close correspondence of flamelet and distributed reaction results suggests that the cross-section correction procedure can be effectively applied to a broad range of turbulent flame conditions. This is also supported by turbulent flame experimental results. Multispecies and temperature measurements in low- or moderately stretched turbulent non-premixed flames reveal that, in the mixture fraction coordinate, all the major species and temperature data are scattered around flamelet calculation results [16,17]. Furthermore, by conditioning the data on the temperature, Starner et al. [17] shows that there is a deterministic trend in the data. The higher values of the major product species concentrations (e.g., CO_2 and H_2O) are associated with higher temperatures. This is reasonable. In the absence of preferential diffusion and limited radiation heat loss (i.e., early part of flame), it is expected that there will be a relationship between the local temperature and concentration of these two product species and, for that matter, all other stable species. The theoretical framework for this turbulent flame picture has previously been established by Bilger [8].

Given the similarity of the model results in Fig. 1, the supporting experimental evidence in Ref. 17, and theoretical framework support in Refs. 8 and 9, it is concluded that temperature can be used, with the model results in Fig. 1, to correct NO measurements for quenching effects. In addition, the temperature can be used to correct the data for population effects.

The flamelet calculation results were used as a base to estimate the magnitude of the error in temperature and the NO measurements. It is assumed that the temperature will be measured by Rayleigh scattering and that the Rayleigh cross section for air was used uniformly across the flame. The temperature error was found to be within 10% in the flame zone and on the lean side of the flame, where methane concentration is low. The error increases as the center of the jet is approached. The maximum error in the jet flame of interest is 50%, estimated for the cold center of the jet. Therefore, the NO and temperature data, near the center of the jet, should be ignored.

This estimated temperature and the corresponding flamelet model species concentrations were then used to estimate NO quenching cross section (Cq_{est}) and population corrections ($C_{f_{est}}$). Results are shown in Fig. 2, where the error as defined by Eq. (4) is plotted for $J = 18$, which is the line used in the subsequent experiments. The error was found to be insensitive to J. The population and quenching errors partially offset each other, resulting in less than 10% error in NO. Around the stoichiometric conditions ($Z = 0.055$), the error is less than 5%. The local error as defined by $(1 - C_fC_q)_{est}/(1 - C_fC_q)_{actual}$ is also less than 10% for $Z < 0.4$ (corresponding to $Y < -4$ mm, in the results presented below). These are acceptable error levels considering that correction factors (i.e., $C_f \cdot C_q$ in Eq. (2)) can be as high as 5. This analysis support using a combined NO and Rayleigh imaging setup for quantitative NO imaging.

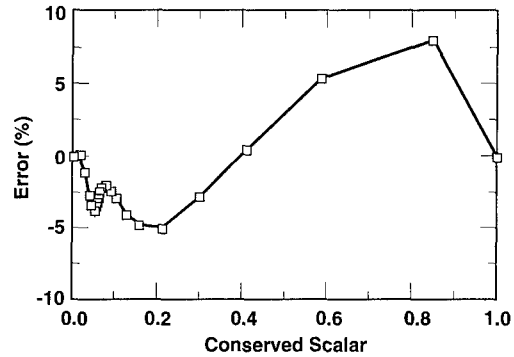

FIG. 2. Estimated error defined by Eq. (4), for combined NO-Rayleigh technique. A conserved scalar value of 0.055 represents stoichiometric condition.

Note that the error levels estimated above represent the error due to the data reduction methodology. The experimental error needs to be combined with this error. Near the peak values, the combined errors are within 15 and 25% for temperature and NO, respectively. For the NO, the shot noise (10–15%, depending on the axial location) is the dominant error. This error can be reduced by increasing the laser energy.

Experimental Setup, Procedure, and Results

The two-camera setup is shown in Fig. 3. Ultraviolet laser light ($\lambda = 225$ nm, $\Delta\nu = 0.3$ cm^{-1}) for the fluorescence excitation of the NO molecule, was provided by an Nd:YAG-pumped dye laser system. The frequency-doubled output of an Nd:YAG laser (6-ns pulse, 500-mJ pulse) was used to pump a pulsed-dye laser with LDS 698 dye with a tunable output around 676 nm. A small fraction of this beam was split and directed to a wavelength meter, for continuous wavelength verification. The remaining portion of the output of the dye laser was frequency doubled and mixed with the dye beam in a BBO crystal. With this configuration, about 0.5 mJ of laser energy was obtained at around 225 nm, which was used to pump the NO $A^2\Sigma(v'' = 0)$, $X^2\Pi(v' = 0)$ electronic band. A polarization rotator was used to adjust the UV beam polarization to eliminate Rayleigh scattering. For the imaging experiments, the beam was formed into a 0.5-mm-thick and 50-mm-high sheet of light by a multipass cell consisting of two cylindrical reflectors coated for high reflectivity (≥99%) at 226 nm. Near 30 overlapping passes were used in

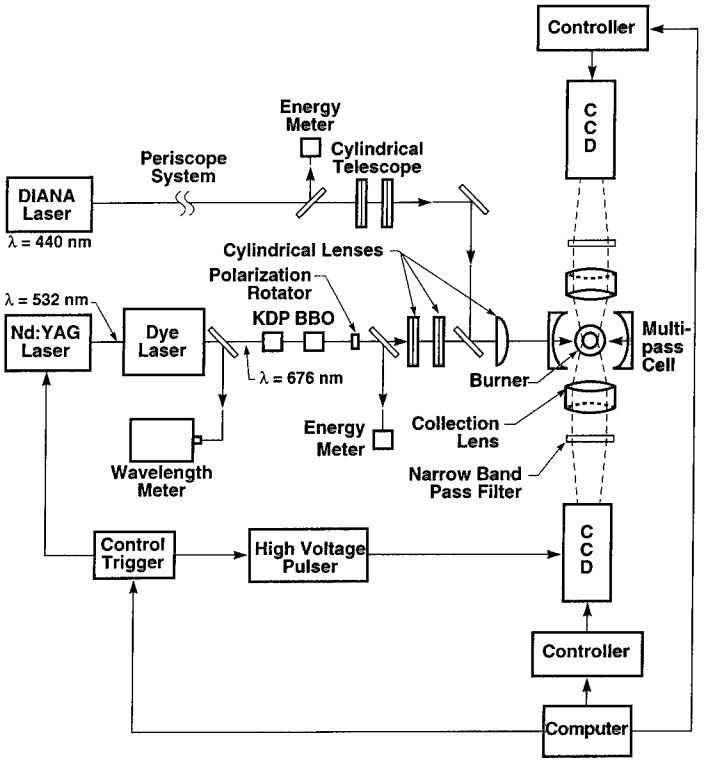

FIG. 3. Schematic of combined NO and Rayleigh imaging system.

the cell, providing near 10^6 W/cm^2/cm^{-1} energy density. The fluorescence signal was collected with an $f/0.8$ lens system and detected at 240 nm (25-nm bandwidth) using an intensified camera. Use of this filter was necessary to block soot emissions and other non-NO signals that are present in the flame. Experiments were performed using the $Q_1(18)$ and $Q_1(26)$ lines of NO.

For the Rayleigh measurements, the Sandia Combustion Research Facility's flash lamp-pumped dye laser (1.8 μs pulse duration, λ = 440) was used. Before combining with the UV beam, the beam divergence was adjusted in a cylindrical telescope, to compensate for different focusing properties of this beam and the UV beam in the multipass cell [14]. The beam was combined with the UV beam using a dichoric reflector and formed into an overlapping sheet in the multipass cell. The cell was also coated for high reflectivity at 444 nm. The Rayleigh signal was collected with a 55-mm camera lens and detected by the second camera, gated for 4 μs. In the initial experiments, two vidicon cameras [13] were used. A majority of the data was obtained using photometric charge coupled device (CCD) cameras, described by Schefer et al. [18]. A 4 × 4 pixel averaging was used, resulting in 0.5-mm nominal resolution.

All of the images were corrected for shot-to-shot variations in laser power. Two approaches were used to normalize the NO data. In the first approach, NO data were normalized by the images obtained from 6.7 and 67 ppm NO uniformly seeded in air for $Q_1(18)$ and $Q_1(26)$, respectively. In the second approach, data were normalized by images obtained from a lean premixed flame (ϕ = 0.7) seeded with 40 ppm NO. Both approaches resulted in the same reduced data set. This indicates that laser broadening and shift is insignificant. The Rayleigh data were converted to temperature by applying the air Rayleigh cross section uniformly across the flame.

The NO signal was corrected for population and quenching effects. The temperature, measured by Rayleigh, was used for this purpose. For the population correction, the Boltzman relation was used. To correct for the quenching effects, the measured temperature was normalized by the corresponding laminar flame stoichiometric mixture temperature (T_s = 1990 K), and results of Figure 1 were used for the correction.

Thermocouple temperature measurements and NO_X sampling were also performed in the jet flame for comparison with the laser-based data. A 0.05-mm (0.002 in.) thermocouple wire was used to minimize the effect of radiation. Since NO can be converted to NO_2 within the probe, only NO_X data are used for comparison. As in Drake et al. [19], an uncooled quartz probe was used for these measurements.

To further support the validity of the laser-based measurements, experiments were performed at two

separate lines, $Q_1(18)$ and $Q_1(26)$. Two different J levels were intentionally chosen that have significantly different population corrections (C_f in Eq. (2)). As an example, the C_f values at $T = 300$ K are 2.87 and 0.216 for $J = 18$ and $J = 26$, respectively. Note that, as in Eq. (2), these values are referenced to the stoichiometric temperature and calculated for the flamelet with $T_s = 2174$ K. The ratio between these two correction factors is around 13. Thus, two substantially different correction factors are applied to each data set. Similarity between the NO data obtained from these two separate lines should verify the approach.

A 50-mm-diameter laminar flat flame burner was used for laminar flame imaging and to obtain calibration images of seeded NO. For the turbulent jet-flame measurements, the burner consisted of a 5.4-mm-diameter tube. Methane was injected through the fuel tube at a velocity of 21 m/s (Reynolds number 7000), creating a lifted flame with 30-mm average liftoff height [13].

Signal Verifications:

Using point measurements, NO spectra were obtained in an NO/N_2 calibration mixture and in premixed laminar flames and, compared to the calculated spectra [20], to verify the signal and to identify the spectral lines. The data demonstrated that saturation is possible in the NO/N_2 mixture at a spectral power density higher than 0.5×10^7 W/cm^2/cm^{-1}, but not in the flame, where only linear fluorescence is possible. In the imaging experiments, the spectral power density is 10^6 W/cm^2/cm^{-1}, which is well into the linear regime. Thus, laser power variation and quenching corrections are necessary to obtain quantitative NO information from fluorescence signals.

Imaging System Detectability:

The detectability of the imaging system was found by imaging 5 ppm of NO seeded in air using $Q_1(18)$. From these images, the signal-to-noise ratio was found to be 5, for 5 ppm NO. This translates into a 0.2-ppm detectability limit for the system in a NO/air mixture. Using the temperature effect and product composition quenching data, it is estimated that the current imaging system has a lower detectability limit of about 1 ppm NO in the flame.

Laminar Flat Flame Data:

To verify the quantitative imaging capability of the current system, it was applied to a laminar flat flame burner. The fuel-to-air equivalence ratio was varied to detect NO levels under different quenching conditions. Figure 4 shows a plot of the measured NO levels along with the sampling probe data and premixed laminar flame calculations [15] for comparison. The sampling data are taken from Fenimore [21]. The correspondence of imaging data with the calculations and sampling measurements is good, verifying the imaging system in laminar premixed flames.

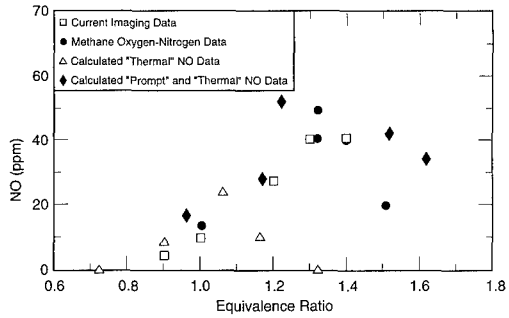

FIG. 4. Comparison between imaging data and calculated and probe NO data in a laminar flat flame. To convert equivalence ration, φ, to conserved scalar, Z, use $Z = \varphi/(17.2 + \varphi)$ for methane.

Turbulent Flame Imaging Data:

To verify the technique in the turbulent jet flames, the mean values obtained from the $Q_1(18)$ and $Q_1(26)$ lines were compared with each other and with the probe sampling data obtained in the jet flame. An example is shown in Fig. 5. The mean profiles were obtained by averaging 200 images. In this figure, $Y = 0$ represents the center of the jet. As shown, the profiles obtained at two J values are similar, except near the centerline, where the temperature measurements and signal corrections are not valid. The peak values for these lines are within 10%. This is typically found to be the case for other axial locations. At some axial locations, up to 20% difference was found. This is reasonable, considering that each line can have 25% error, as discussed above.

The peak NO_X value measured by the sampling probe at $X = 40$ mm is 30 ppm. At higher axial locations, the peak NO_X and NO increased. As an example, at 70 mm, the upper part of the imaging region, the peak NO and NO_X, were 35 and 39 ppm, respectively. These results suggest that NO_X consists of around 80% NO, with the remainder NO_2. This is reasonable [19].

The imaged temperature data and thermocouple data are also presented in Fig. 5. Near the jet centerline ($Y > -4$ mm), the imaged temperature data have a substantial error, as discussed above. However, away from the centerline, i.e., at the left of $Y = -4$ mm, the imaged temperature data compare well with the thermocouple data. These, and other results not presented, show that the average peak flame temperature, obtained from imaging data, is within 100 K of the thermocouple data.

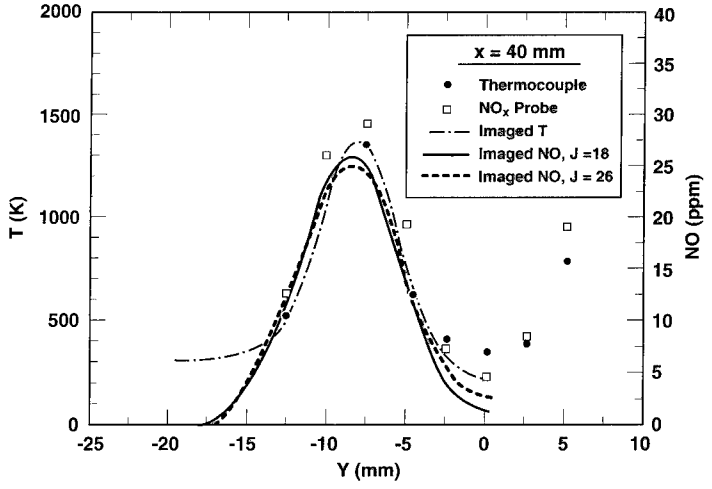

FIG. 5. Comparison between NO imaging data obtained by $Q_1(18)$ and $Q_1(26)$ and probe NO_x in lifted turbulent jet flame. Imaged temperature and thermocouple measurement data are also shown. The average jet liftoff is 30 mm.

The purpose of planar imaging measurements is to capture the instantaneous spatial structure of the temperature and NO fields. As is well known, NO production rates cannot be determined from average temperatures. By measuring instantaneous temperatures and NO concentrations, the relationship of these parameters over the complete field can be determined. Also, the structure of the NO and T fields can be related to large-scale turbulence structures. This will yield important information on how turbulence affects combustion and NO formation. Some imaging data are included below as an example of the type of information provided by this imaging technique.

Figure 6 shows representative instantaneous contour plots of NO and temperature in the jet flame highlighted above. In these images, the 5.4-mm jet is located at $X = 0$ and at $Y = 0$. Only the left side of the flame is contained in the image. The flame is lifted and, in Fig. 6a, NO is below 2 ppm (dotted line) upstream of the 35-mm axial location. The corresponding temperature contour (Fig. 6b) shows that at this axial location, the temperature is around 1500 K, but 2 mm below this location ($X = 32$ mm) the temperature drops below 500 K. Beyond this flame initiation location, both the NO and temperature have a similar structure. The similarity in structure between NO and temperature can also be observed in Figs. 6c and 6d. These images were obtained on the same flame at a different time. Interestingly, the images in Figs. 6c and 6d show separated "islands" of NO and temperature. The presence of a cooler region separating two high-temperature zones is probably a result of local turbulent quenching of the flame.

These images, as well as many others, show the strong correlation of instantaneous NO to temperature. As noted above, instantaneous temperatures are

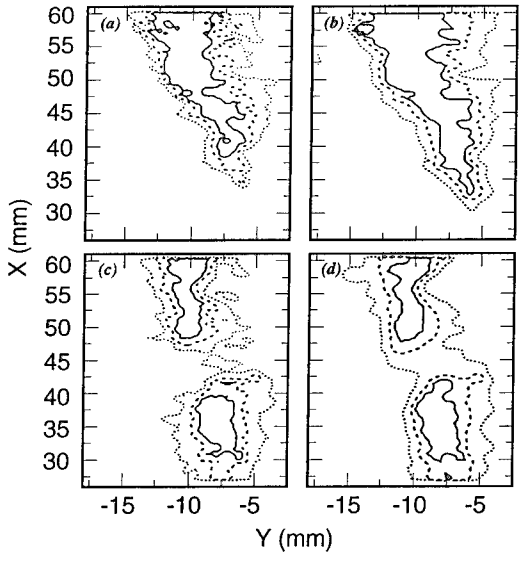

FIG. 6. Instantaneous contour of NO (left) and temperature (right) in the lifted turbulent jet flame. Dot: 2-ppm NO and 500 K; dashed: 5-ppm NO and 1000 K; solid: 10-ppm NO and 1500 K.

needed to correctly predict NO production rates in turbulent flames. To support this, distributed reaction model results, utilized in the quenching correction procedure, were compared to the NO and T imaging data. The good comparison of the distributed reaction model results with CH, CH_4, and OH imaging data [13,14] supports using this model to predict NO and T.

According to the prior experimental and model results [13,14], intense reaction of the lifted flame occurs in a region surrounding the $\phi = 1$ condition. At

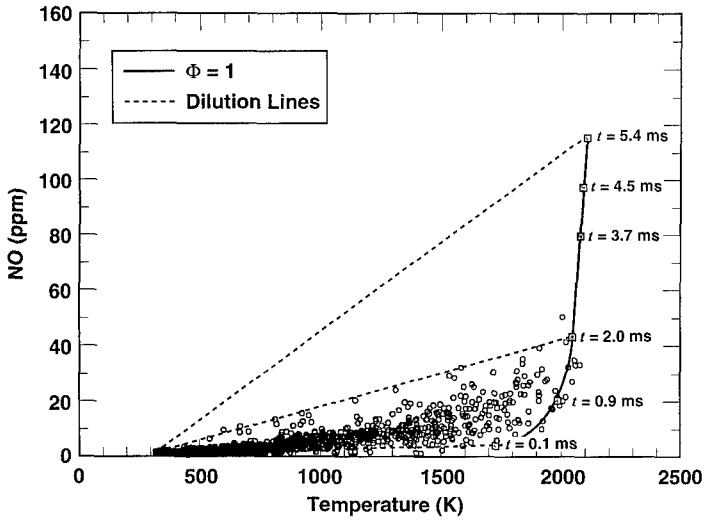

FIG. 7. NO and temperature at the base of the lifted flame. The points are experimental data and lines represent the distributed reaction model. The solid line shows variation of NO-T with residence time at stoichiometric condition. The dashed lines represent dilution.

the flame initiation point, reactions are nearly extinguished. According to the distributed reaction model, the local residence time at this point should be 0.1 ms. If a region that covers up to 10 mm downstream of the initiation point is used in the comparison of model to experimental results, the maximum residence time would be bound by the convective time over the 10-mm domain. For the 5 m/s axial velocity, measured by LDV at the $\phi = 1$ line, the maximum residence time would be 2 ms. Therefore, model results for residence times between 0.1 and 2 ms should bound the data. Furthermore, the model results give the local NO production in the peak temperature zones. As the NO diffuses outward, both NO and temperature will decrease by dilution with surrounding gases. Therefore, predicted dilution results should be considered in combination with the NO production results.

Figure 7 compares the model and imaging results. Points on this figure, taken from the images, are instantaneous NO and temperature data at the base of the lifted flame. The solid line represents the distributed reaction model results for $\phi = 1$, at different residence times. The dashed lines joining the $\phi = 1$ line to the ambient condition ($T = 300$ K, NO $= 0$), represent dilution of the NO produced at $\phi = 1$ and at the specified residence time. As noted above, the data should be bound by the 0.1- and 2-ms residence time model results. This is found to be the case.

From this comparison, it can be concluded that prompt and thermal NO mechanisms used in the model can correctly predict NO production in turbulent flames. Furthermore, the comparison of model results and data gives additional support to the validity of the distributed reaction model in predicting local turbulent flame characteristics.

Conclusions

A quantitative laser-induced fluorescence NO imaging technique has been developed and validated that is capable of measuring low NO levels, characteristic of those found in turbulent flames. The technique uses a simplified quenching and population correction procedure that was developed from the current understanding of turbulent flames. Using turbulent flame models, it was shown that corrections are only a function of temperature. Therefore, by measuring temperature, with Rayleigh scattering, and using turbulent flame models, the NO imaging data can be corrected. Analysis showed that the error using this correction approach is less than 10%. The combined experimental and data reduction approach error is within 25%. Only in the cold center of the jet flame, where fuel concentration is high, do the temperature and NO measurement errors become unacceptable. The technique was validated by imaging NO and temperature and comparing results at two different rotational levels for NO. In addition, good comparisons of time-averaged NO and temperature imaging results with probe and thermocouple data in premixed laminar and turbulent jet flames support the validity of the approach. Instantaneous NO and temperature images illustrate the close correspondence of NO and temperature fields in turbulent non-premixed flames. Good comparison of imaging results with distributed reaction model results, at the flame initiation point, provided further validation of the imaging technique and the model.

Acknowledgments

This work was supported by the Basic Research Department of the Gas Research Institute, through Altex Technologies Corporation, and by the Department of En-

ergy, Office of Basic Energy Sciences, Division of Chemical Sciences, through Sandia National Laboratories in Livermore, CA.

REFERENCES

1. Seitzman, J. M., Kychaakoff, G., and Hanson, R. K., *Optics Lett.* 10:439–441 (1985).
2. Allen, M. G., Parker, T. E., Reinecke, W. G., Lenger, H. H., Foutter, R. R., Rawlins, W. T., and Davis, S. J., *AIAA J.* 31:505–512 (1993).
3. Paul, P. H., and Clement, N., *Opt. Lett.* 18:161 (1993).
4. Wodtke, A. M., Hauwel, L., Schluter, H., Meijer, G., and Anderson, P., *Optics Lett.* 13:910–912 (1988).
5. Barlow, R. S., and Carter, C. D., *Combust. Flame.* 97:261–280 (1994).
6. Reisel, J. R., Carter, C. D., and Laurendeau, N. M., *Combust. Sci. Technol.* 91:271–295 (1993).
7. Long, M. B., Levin, P. S., and Fourguette, D. C., *Optics Lett.* 10:267 (1985).
8. Bilger, R. W., in *Turbulent Reacting Flows* (P. A. Libby, Ed.), Springer-Verlag, Berlin, 1980, Vol. 44, p. 64.
9. Peters, N., *Prog. Energy Combust. Sci.* 10:319–339, (1984).
10. Paul, P. H., Gray, J. A., Durant, J. L., Jr., and Thoman, J. W., Jr., *AIAA J.* 32:1670–1675 (1994).
11. Drake, M. C., and Ratcliffe, J. W., GM Report 7426, General Motors Research Laboratories, July 30, 1991.
12. Heard, D., Jeffries, J. B., and Crosley, D. R., *Chem. Phys. Lett.* 178:553 (1991).
13. Namazian M., Kelly, J., and Schefer, R. W., *Twenty-Second Symposium (International) on Combustion,* The Combustion Institute, Pittsburgh, 1988, pp. 627–634.
14. Schefer, R. W., Namazian, M., and Kelly, J., *Twenty-Third Symposium (International) on Combustion,* The Combustion Institute, Pittsburgh, 1990, pp. 669–676.
15. Knedall, R., and Kelly, J., "Premixed One Dimensional Flame Code User's Manual," Acurex Final Report, 78–278, 1978. Also GRI 88/0168, 1988.
16. Barlow, R. S., Dibble, R. W., Starner, S. H., and Bilger, R. W., *Twenty-Third Symposium (International) on Combustion,* The Combustion Institute, Pittsburgh, 1990, pp. 583–589.
17. Starner, S. H., Bilger, R. W., Dibble, R. W., and Barlow, R. S., *Combust. Sci. Technol.* 72:255–269 (1990).
18. Schefer, R. W., Namazian, M., Filtopoulos, E. E. J., and Kelly. J., *Twenty-Fifth Symposium (International) on Combustion,* The Combustion Institute, Pittsburgh, 1994, pp. 1223–1231.
19. Drake, M. C., Correa, S. M., Pitz, R., Shyy, W., and Fenimore, C. P., *Combust. Flame* 69:347–365 (1987).
20. Seitzman, J. M., Ph.D. Thesis, Stanford University, Stanford, CA, 1991.
21. Fenimore, C. P., *Thirteenth Symposium (International) on Combustion,* The Combustion Institute, Pittsburgh, 1971, pp. 373–380.

COMMENTS

N. M. Laurendeau, Purdue University, USA. What are the confidence limits on the quoted uncertainties in temperature and NO concentration? How does the uncertainty in temperature affect the uncertainty in NO concentration? What are the total uncertainties including the calibration procedure for both temperature and NO concentration?

Author's Reply. The confidence level on the quoted uncertainties (errors) is 99%.

In determining the error in the data reduction methodology for NO, the Rayleigh error is already included.

To determine the sensitivity of NO to temperature error, the model was run for $J = 18$ and assumed 10, 20, and 30% error in peak temperature. The corresponding error in peak NO was found to be 3, 6, and 10%, respectively.

The total relative uncertainties for temperature and NO, for the current experiment, are 15 and 25%, respectively.

•

James F. Driscoll, University of Michigan, USA. Your images were obtained at upstream locations where the flame is nearly vertical and is not significantly wrinkled. Are there fundamental limitations such as the presence of soot, that prevented you from studying the flame tip, where most of the NO is believed to be formed?

Author's Reply. As shown in Fig. 1 of the paper, the quenching correction value is different for the fuel and air sides of the flame. As long as the wrinkling of the flame permits this distinction, the technique can be applied, with the errors cited in the paper. If the fuel and air sides of the flame are not distinguished, due to the extreme wrinkling of the flame, additional error will be involved. This error can be estimated from Fig. 1.

The NO imaging can be performed in the presence of some soot. However, as you are aware, soot interferes with the Rayleigh signal. Alternative temperature measurement techniques need to be considered in this case. Also, the data reduction model needs to include the radiation effect.

•

Houston Miller, George Washington University, USA. Are the quenching corrections in the flamelet model independent of scalar dissipation rate even for high stretch

conditions close to extinction where both temperature and combustion product concentrations (i.e., CO_2 and H_2O) are lower than in low stretch flamelets?

Author's Reply. We do not claim that the absolute quenching corrections are independent of the scalar dissipation. Instead, we claim that, when normalized by the stoichiometric values, the corrections are self-similar and should collapse on Fig. 1 of the paper. We have not tested this theory for highly stretched flames. However, we are reasonably confident that they will collapse on Fig. 1, as the trend of data suggests. As you correctly state, the stretch reduces temperature and CO_2 and H_2O. This results in lower values of quenching correction. A lower quenching correction for a lower temperature is consistent with the trend of Fig. 1 data.

•

James Kelman, University of Sydney, Australia. Has the author considered the effect of variable strain rates in the flame on the quenching correction coefficients of NO? As the strain rate is increased in the laminar flame computations, the stoichiometric temperature will drop and an ambiguity in the quenching rate correction will arise.

Robert W. Pitz, Vanderbilt University, USA. Your NO concentrations are corrected by a mixture average cross section, σ, that is calculated for both a flamelet and a distributed reaction [i.e., perfectly stirred reactor (PSR)]. The stoichiometric temperature, T_s, in the reaction zone will depend on the strain parameter in the case of the flamelet calculation and the residence time in the case of the PSR calculation. In your NO data reduction, what value of T_s was assumed for Fig. 1 and how do variations in the strain parameter and residence time affect the calculated variation of absolute σ with absolute T?

Author's Reply. The variation in the strain rate, or residence time, affects the stoichiometric temperature (T_s) and quenching rate (σ_s) used to extract the quenching corrections from Fig. 1 of the paper. However, the variations are in the same direction and partially offset each other. In the present experiment, assuming a constant T_s and σ_s results in 3% error in NO.

The T_s and σ_s assumed for the data reduction were 1990 K and 14.9 Å^2, respectively. These values are calculated for a stoichiometric well-stirred reactor at approximately 1-ms residence time. These conditions are consistent with the distributed reaction zone model previously developed for the base of this flame (see Refs. 13 and 14 of the paper). Increasing the residence time increases T_s. Accordingly, σ_s increases, which compensates for some of the T_s variation. As an example, at 9-ms residence time, representative of the time scale at the top of the images, T_s and σ_s are 2130 K and 15.5 Å^2, respectively. The ratios between these values to those at the bottom of the image are 1.07 and 1.04, for T_s and σ_s, respectively. Therefore, assuming a constant T_s and σ_s for this flame results in approximately 3% error in σ and NO values.

Twenty-Fifth Symposium (International) on Combustion/The Combustion Institute, 1994/pp. 1159–1166

MIXTURE FRACTION IMAGING IN TURBULENT NONPREMIXED HYDROCARBON FLAMES

JONATHAN H. FRANK, KEVIN M. LYONS, DAVID F. MARRAN AND MARSHALL B. LONG
Department of Mechanical Engineering and Center for Laser Diagnostics
Yale University
New Haven, CT 06520-8284, USA

AND

STEN H. STÅRNER AND ROBERT W. BILGER
Department of Mechanical Engineering
The University of Sydney
NSW 2006, Australia

Three different experimental approaches for making instantaneous, two-dimensional (2D) measurements of the mixture fraction in turbulent nonpremixed hydrocarbon flames are presented. The availability of spatial information on the mixture fraction provided by these techniques makes determination of the scalar dissipation feasible. Each of the techniques to be presented is based on simultaneously imaging fuel concentration and Rayleigh scattering. Measurement of the fuel concentration can be accomplished in a number of ways, including (1) Raman scattering from the fuel, (2) fluorescence from the fuel, or (3) fluorescence from a molecular tag added to the fuel. Preliminary results for experiments utilizing each of these approaches will be presented.

In one experiment, joint Raman/Rayleigh measurements were performed in a turbulent methane flame. This approach worked quite well and was able to provide valuable mixture fraction statistics. However, the weak Raman signal required a tradeoff between signal/noise and spatial resolution. A second experiment involved imaging fuel fluorescence from an acetaldehyde flame. The acetaldehyde fluorescence/Rayleigh images obtained in this experiment were of high quality. On the fuel-rich side of the flame, however, the calculated mixture fraction shows a dip and plateau. These irregularities may be the result of fuel pyrolysis and could represent a limitation of this approach. A third method of mixture fraction measurement was to introduce acetone as a fuel tracer and image its fluorescence. Acetone fluorescence proved to be problematic when excited at a wavelength of 320 nm. Our measurements show indications of a temperature dependence of the fluorescence yield, making it difficult to interpret the signal.

Introduction

In modeling of turbulent nonpremixed flames, the quantity most often used to describe the flow is the mixture fraction. The mixture fraction is defined as the mass fraction of all atoms originating from the fuel stream and is one of many possible conserved scalars that can be defined in the flame. Each of these conserved scalar quantities is independent of the chemical reaction. Under idealized conditions, knowledge of a single conserved scalar can be used to derive essentially all of the scalar quantities of interest in the flow.

In nonreacting flows, determination of the mixture fraction is straightforward since only a single species must be monitored, and quantitative information in two and three dimensions is available [1,2]. Bilger and coworkers [3,4] used cold-flow images of the mixture fraction to infer flame structures in a turbulent nonpremixed H_2 flame. Because image data were available, it was possible to calculate the scalar dissipation as well as infer reaction rates in this zero heat release "flame." The use of cold-flow images to infer nonpremixed flame structure was also employed in a recent study by Buch et al. [5]. In both of these studies, valuable insight was gained. However, since the images that served as a basis for the analysis were from cold flows, the heat release in actual flames is not present, and questions of the generality of the conclusions persist.

Experimentally, the determination of the mixture fraction in flames is difficult since it involves simultaneous monitoring of a large number of species. The mixture fraction has been determined at a single point from measurements of the major species using spontaneous Raman scattering [6], and the results from these studies are among the most complete sets of experimental data available in turbulent nonpre-

mixed flames. The data from single-point measurements are incomplete, however, because of the lack of multidimensional information required to obtain gradients. The scalar dissipation, χ (defined as $\chi = 2D\nabla\xi \cdot \nabla\xi$, with D the diffusivity and ξ the scalar), determines the rate of molecular mixing and is widely used in modeling turbulent reacting flows. Therefore, techniques capable of two-dimensional (2D) or preferably three-dimensional (3D) measurements of the mixture fraction are needed.

Stårner et al. [7] have demonstrated a means of determining the mixture fraction in a flame without measuring all of the major species. In that work, it was shown that the mixture fraction can be determined from simultaneous measurement of only two quantities. The method pursued in the present study involves the simultaneous measurement of fuel concentration and Rayleigh scattering. The method assumes unity Lewis number and a one-step reaction between fuel and oxidizer. The two measured quantities are used to form a conserved scalar from which the mixture fraction is determined in an iterative process. While a complete discussion of the approach is beyond the scope of what can be presented here (see Ref. 7 for details), the basics are outlined below.

A conserved scalar, β, based on the fuel mass fraction (Y_f) and the enthalpy ($H = c_pT/Q$) serves as the basis for determining the mixture fraction:

$$\beta = Y_f + c_pT/Q$$

$$\xi \equiv \frac{\beta - \beta_2}{\beta_1 - \beta_2} = \frac{Y_f + c_p/Q(T - T_2)}{Y_{f,1} + c_p/Q(T_1 - T_2)}$$

where the subscripts denote the fuel (1) and oxidizer (2) streams. The mixture fraction can be expressed in terms of the fuel concentration signal (obtained from Raman or fluorescence techniques), F, and the Rayleigh signal, Ra, as follows:

$$\xi = \frac{C_1 a_T F}{W Ra F_{\text{cal}}} + C_2(a_T/Ra - T_{\text{ambient}})$$

where C_1, C_2, and F_{cal} are calibration constants, a_T is proportional to the local Rayleigh cross section, and W is the local mixture mole weight. Since a_T and W are both functions of ξ, an iterative process must be used on a pixel by pixel basis to derive the temperature and mixture fraction. The procedure converges quickly, usually within less than four iterations.

In the following sections, three different experimental approaches to determining the mixture fraction in turbulent nonpremixed hydrocarbon flames will be explored. Each of these techniques is based on simultaneous monitoring of the fuel concentration and Rayleigh scattering. The main difference in the approaches is the means for determining the fuel concentration. Details of the experimental configuration will be given along with representative results.

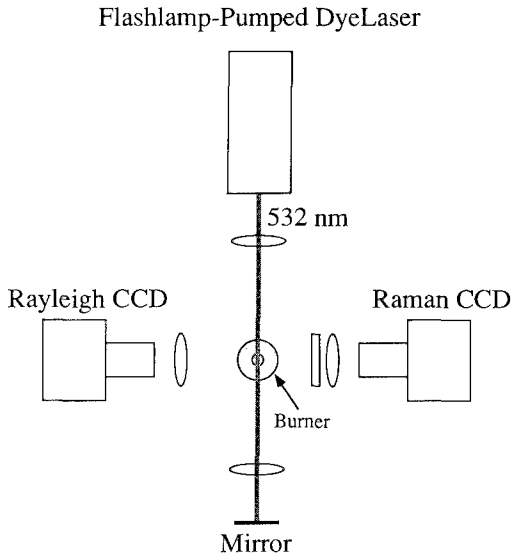

FIG. 1. Experimental configuration for Raman/Rayleigh line imaging.

Experiments

Raman/Rayleigh Line Imaging in a Methane Flame:

In one set of experiments, the concentration of fuel was inferred from the Raman scattering of the vibrational C-H stretch of the hydrocarbon fuel. An advantage of this approach is that no special fuel or fuel tags are required; Raman scattering should be equally applicable to nearly all hydrocarbon fuels. The main drawback to Raman scattering is the extremely small Raman-scattering cross section and, consequently, the difficulty in getting sufficient signals. Raman imaging of the fuel has been used previously in a number of experiments [8,9], and simultaneous Raman and Rayleigh imaging has been demonstrated [10], although the data were not used to determine mixture fraction. Each of these previous Raman imaging experiments made use of a multipass optical cell to form the illumination sheet. In this work, a multipass cell was not used, but a two-pass arrangement allowed two components of the scalar gradient to be determined along a line.

The experimental configuration used for simultaneous Raman and Rayleigh line imaging is shown schematically in Fig. 1. A flashlamp-pumped dye laser (Candela LFDL-20 using pyromethene 546 dye) provided up to 1 J of energy at 532 nm. The laser's 2-μs pulse duration was short enough to freeze the motion in the flames studied. To reduce the beam divergence of the laser and thereby reduce the waist of the focused beam, the laser cavity was lengthened to 3.1 m. The beam was focused into the flame ini-

tially by a 15-cm f.l. spherical lens. After passing through the flame, the beam was recollimated by a 30-cm f.l. lens, reflected from a planar mirror, and refocused into the flame. The two beams were aligned so that the reflected beam passed just over the top of the incoming beam. This two-beam approach allowed gradients to be obtained in both the radial and axial directions. The beam waist was measured to be 0.6 mm, which was roughly 6 times the smallest flow scales [11].

The scattered Raman and Rayleigh light was detected by two intensified charge-coupled device (CCD) detectors oriented perpendicular to the laser beam as shown in Fig. 1. The Raman-scattered light was isolated by an interference filter [center frequency 630 nm, 10 nm full width at half maximum (FWHM)] and focused onto a single-stage image intensifier by an f1.2 camera lens. The output of the intensifier was optically coupled to a cooled CCD detector (Photometrics Star 1). An f4.0 camera lens imaged the Rayleigh scattering onto a two-stage image intensifier, which was optically coupled to the second cooled CCD detector (Photometrics KAF4200). Both image intensifiers were gated coincident with the laser pulse to eliminate flame luminosity. (Note that the use of the intensifiers was primarily for gating rather than for high gain.) The digitized output from both cameras was read into a single lab computer.

The raw Raman and Rayleigh line images were corrected for background and nonuniform detector response. In addition, since the magnification of the two images was slightly different, the necessary rotation, translation, scaling, and cropping were applied to the images to allow them to be compared on a pixel-by-pixel basis. The volume corresponding to each pixel was $0.09 \times 0.09 \times 0.6$ mm^3, with the largest value corresponding to the beam thickness. Since the beam thickness represents the main limitation to the spatial resolution in these measurements, the signals were integrated in the cross beam direction, and 3-pixel smoothing was applied in the radial direction. The resulting images consist of two lines radially across the flow corresponding to the main and reflected beams with a pixel resolution of $0.27 \times 0.45 \times 0.6$ mm^3.

The flame investigated was an axisymmetric, piloted methane-air flame. The main fuel nozzle had a diameter of 3.8 mm. The main jet was surrounded by an annular premixed pilot flame (pilot diameter 15 mm). A low-speed annular coflow of filtered air surrounded the burner to eliminate particles from the flow, which would interfere with the Rayleigh scattering. The methane was diluted 3/1 on a volume basis to eliminate soot. An example of the corrected Raman and Rayleigh images obtained from two different laser shots is shown in Fig. 2. In the figure, the scattered intensity along each of the lines is represented as a false color image, and directly above it,

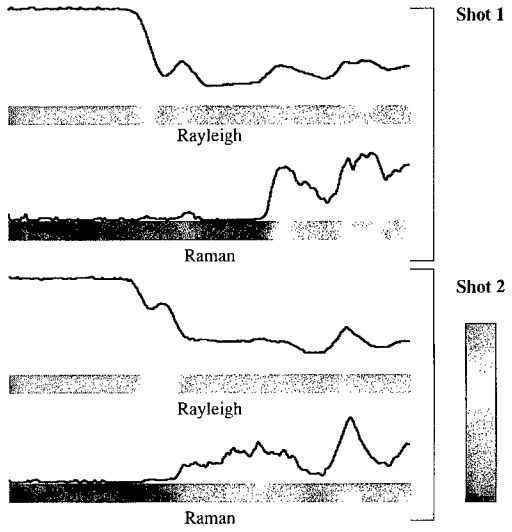

FIG. 2. Two pairs of Raman/Rayleigh images from a turbulent methane-air flame. Scattered intensity along each of the lines is represented as a false color image, and directly above it, the intensity along one of the lines is plotted. For the data shown, the Reynolds number was 20,600, and the beams intersected the flow 25 nozzle diameters downstream.

the intensity along one of the lines is plotted. For the data shown, the Reynolds number was 20,600, and the beams intersected the flow 25 nozzle diameters downstream. The signal/noise for the ambient air in the Rayleigh images is ≈200. Because of the weakness of the Raman signal, the signal/noise for those images is roughly 15. Determination of the error in the mixture fraction and temperature based solely on the signal/noise of the Raman and Rayleigh data is not straightforward because of the iterative procedure involved in calculating these quantities. Probably the best approach for finding the overall uncertainty would be from an ensemble of measurements in laminar flames, where the mixture fraction could be obtained independently. Such a data set is not currently available.

Figure 3 shows the calculated mixture fraction and temperature corresponding to the data from the two laser shots shown in Fig. 2. Again the scalar values are represented as a false color image with the scalar value along one of the lines plotted directly above. Sets of 500 instantaneous shots were taken at a number of different locations within the flame to allow statistical characterization of the mixture fraction and the scalar dissipation. A complete description of the results obtained from this measurement approach is presented elsewhere in this conference [11].

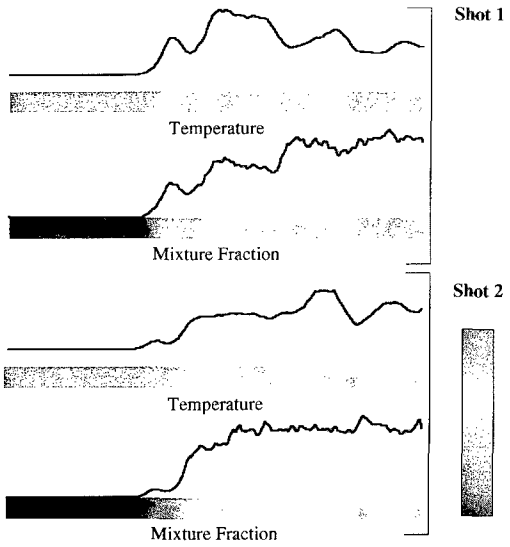

FIG. 3. The calculated mixture fraction and temperature corresponding to the data from the two laser shots shown in Fig. 2. The right side of the image corresponds to the jet centerline and the measured region extends 17 mm in the radial direction.

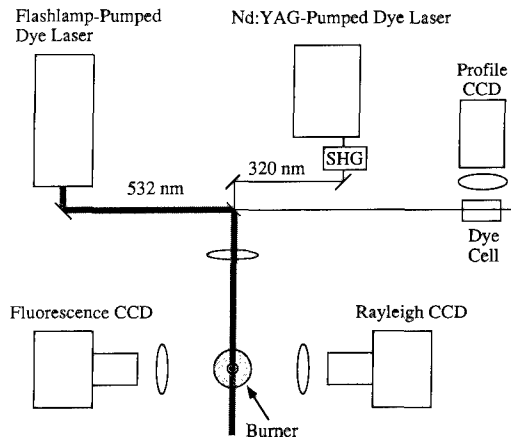

FIG. 4. Optical configuration for fluorescence/Rayleigh experiments.

Fluorescence/Rayleigh Imaging in an Acetaldehyde Flame:

The second approach used for measuring the fuel concentration involved detection of acetaldehyde fluorescence [12,13]. Acetaldehyde (CH_3CHO) was chosen for its relatively high fluorescence yield and small variation of fluorescence yield with temperature, which allows quantitative measurements of the fuel concentration to be made with relatively simple calibrations [14,15].

The experimental configuration used for acetaldehyde fluorescence/Rayleigh imaging is shown schematically in Fig. 4. The flow was illuminated by two overlapping laser sheets. The first, formed from the second harmonic of a Nd:YAG-pumped dye laser (320 nm, 1 mJ per 10-ns pulse, 10-mm sheet height), excited fluorescence from the acetaldehyde fuel. The second illumination sheet, from a flashlamp-pumped dye laser (532 nm, 1 J per 2-μs pulse, 2-cm sheet height), excited Rayleigh scattering. The imaging configuration was similar to that described for the Raman/Rayleigh experiments. The fuel fluorescence was imaged onto a gated image intensifier that was optically coupled to a cooled CCD detector (Photometrics KAF 4200). The Rayleigh scattering was imaged onto a separate gated intensifier that was optically coupled to the second CCD detector (Photometrics Star 1). The two lasers and image intensifiers were fired sequentially with a pulse separation of ~3 μs. This temporal separation ensured that there was no interference between the detected signals from the two laser sheets, but was short compared to the smallest flow time scales. The laser excitation wavelength of 320 nm was chosen to be above acetaldehyde's dissociation wavelength at room temperature [16,17]. Earlier experiments in our laboratory showed that, with 280-nm excitation (near the peak of the acetaldehyde absorption spectrum), a significant amount of temperature-sensitive dissociation occurred in the flame, which caused unacceptable errors in the mixture fraction calculation.

The vessel containing the acetaldehyde, which is supplied as a liquid, was immersed in a liquid bath with a temperature of 40 °C. This provided a sufficient amount of vapor for the experiments described here. The flow lines and rotameters used for the pure acetaldehyde vapor were maintained at an elevated temperature to prevent condensation. Dilution of the pure vapor with air immediately after the rotameter prevented any further condensation problems. The final temperature of the acetaldehyde-air fuel mixture was not significantly above ambient temperature.

The raw fluorescence and Rayleigh images were corrected for background, nonuniform detector response, and differences in magnification. A small fraction of the 320-nm beam was split off, formed into a sheet, and focused into a cell containing a weak solution of fluorescent dye. The fluorescence generated was imaged onto a CCD detector. The image from this detector could be used to compensate for shot-to-shot variations in the UV laser sheet intensity profile. Variations in the intensity profile from the flashlamp-pumped dye laser were measured by making certain that the edge of each image contained a region of ambient air. Rayleigh scattering from this region was used to compensate for profile variations.

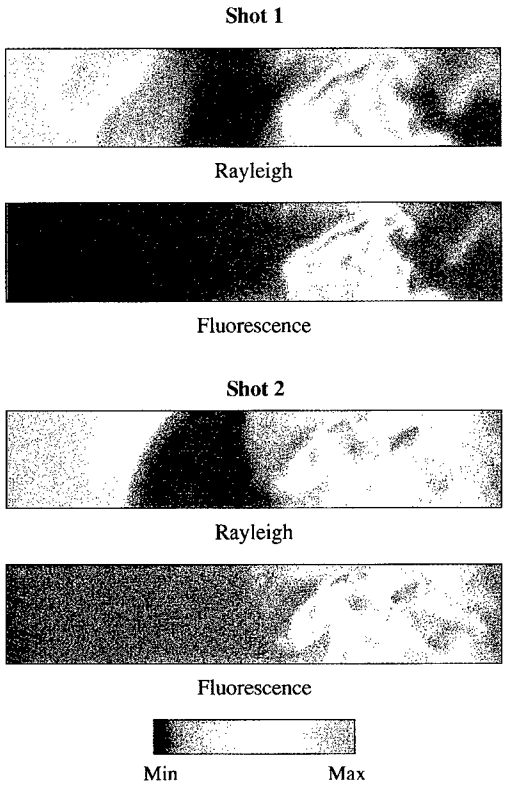

FIG. 5. Images from a piloted, turbulent diffusion flame of acetaldehyde (Re = 18,000). The measurements have been made 25 d downstream (d = 3.8 mm) and cover 4.5 mm in the axial direction by 23 mm in the radial direction. The Rayleigh image shows the distribution of light scattered elastically from the flame and the ambient air, while the fluorescence image is indicative of the distribution of unburned fuel. In each image, the scalar is represented by a linear false color map.

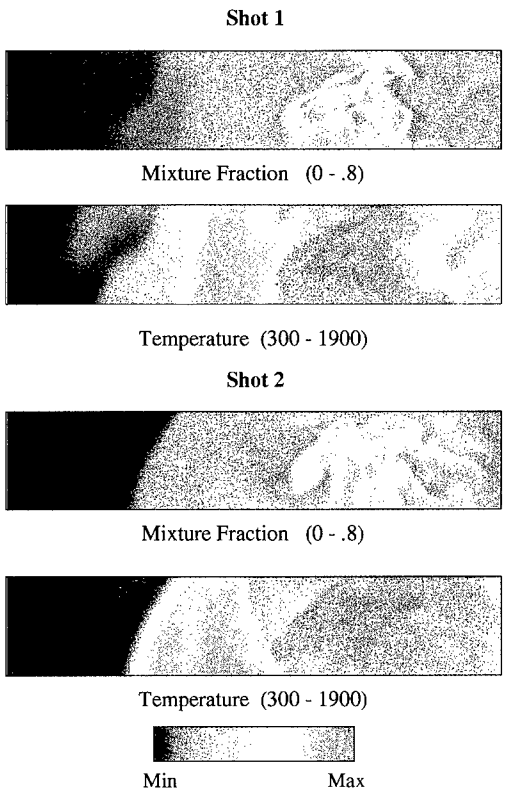

FIG. 6. The conserved scalar and temperature fields calculated from the data of Fig. 5. In each image, the scalar value is represented by a linear false color map.

Figure 5 shows two pairs of matched, corrected fluorescence and Rayleigh images from a turbulent acetaldehyde-air flame. The fuel was a mixture of acetaldehyde diluted 1/1 by air (on a mass basis) to eliminate soot. It emanated from the burner described above with a velocity corresponding to Re = 18,000. The signal/noise for the fluorescence images is 50; for the Rayleigh images, signal/noise is near 200.

Figure 6 shows the calculated temperature and mixture fraction corresponding to the instantaneous fluorescence/Rayleigh images in Fig. 5. Evident in the temperature mappings are the high-temperature zones on the outer edge of the flame. Peaks in the measured temperature are very close to the adiabatic flame temperature (T_{ad} = 1880 K) of our fuel. As expected, the mixture fraction is greatest in the unburned regions near the center of the jet and is near the stoichiometric value where the temperature peaks (ξ_{st} = 0.228). The spatial scales in the mixture fraction images vary significantly, with relatively complex structures in the unreacted center part of the fuel jet and with larger, simpler structures in the outer hot region of the flame. This change of scale due to heat release is not present in mixture fraction images of cold flows.

A closer inspection of the mixture fraction images in Fig. 6 shows a slight decrease in the mixture fraction on the rich side of the stoichiometric value, where the temperature has not yet peaked. A similar dip in the mixture fraction on the rich side of the flame front was noted in measurements performed in a laminar flame. One explanation of this behavior is pyrolysis of the acetaldehyde fuel. To investigate this, experiments were done in which the acetaldehyde fluorescence and fuel Raman scattering were measured simultaneously. The C-H Raman scattering should be relatively insensitive to the breakup of the acetaldehyde into other hydrocarbon fragments. The fluorescence, on the other hand, is expected only

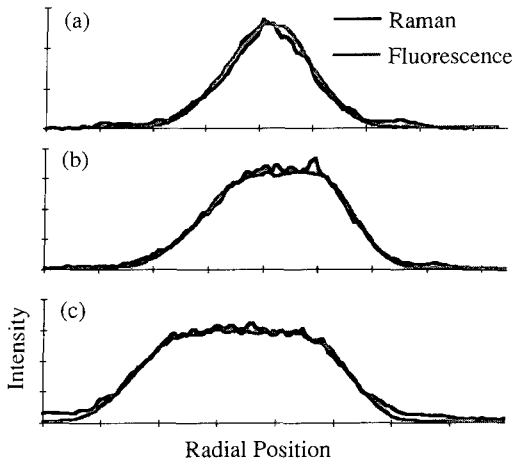

FIG. 7. Comparison of Raman and acetaldehyde fluorescence intensity at various downstream locations in a laminar acetaldehyde-air flame. Shots (a) through (c) correspond to different downstream locations from a 16-mm-diameter nozzle. Downstream locations were (a) 33.5, (b) 23.5, and (c) 13.5 mm. The fluorescence was excited at 320 nm.

from the acetaldehyde molecule itself, so differences in the Raman and fluorescence traces may be indicative of pyrolysis. The experimental configuration was nearly the same as for the fluorescence/Rayleigh experiments. Two changes were required: First, the appropriate interference filter was added in front of the detector used to detect the Raman scattering, and second, the flashlamp-pumped dye laser was focused to a line rather than a sheet to provide increased Raman signal. Figure 7 shows a comparison of acetaldehyde fluorescence and C-H Raman intensity along lines intersecting a laminar flame. The agreement is quite good despite the relatively noisy Raman signal. Experiments in a turbulent flame showed similar agreement. These results support the assertion that acetaldehyde fluorescence is a good alternative to Raman scattering as a means of marking the fuel [13], but do not explain the anomalous dip in the mixture fraction on the fuel-rich side of the stoichiometric value.

A recent calculation of acetaldehyde chemistry in a counterflow flame by Lindstedt and Long [18] sheds considerable light on the mixture fraction obtained in these experiments. Calculation of the mixture fraction from the computed temperature and fuel mass fraction using the two-scalar scheme outlined above results in a dip in mixture fraction on the rich side of the flame similar to those obtained in the experiments. One of the most striking features of the calculation is the high concentration of CO (a maximum mole fraction of nearly 20%) present in the flame. The combustion characteristics of acetaldehyde appear to differ significantly from those of methane, so that the two-scalar approach that worked well for methane and propane may not work as well for acetaldehyde. It is likely that the mixture fraction derived from this technique is apt to be quite satisfactory for mixture fraction values large enough that the fuel is still intact and for mixture fraction less than the stoichiometric value (where ξ is determined from the Rayleigh signal alone). However, for a significant range of mixture fraction values from stoichiometric to the rich side of the flame, errors due to pyrolysis are likely. As one way to check that the results of the calculation are in agreement with the experimental data, the computed results were used to generate plots of the expected Raman and fluorescence signals. The results were in good qualitative agreement with those shown in Fig. 7.

Fluorescence Imaging in an Acetone-Seeded Methane Flame:

Another technique that has been proposed as a way of marking the fuel in hydrocarbon flames is to introduce acetone as a tracer and detect acetone fluorescence [13,19]. Acetone is easily seeded into flows and has only mild toxicity. However, an unresolved issue related to the use of acetone as a fuel tracer in flames relates to the behavior of the fluorescence as a function of temperature. To test the use of acetone as a fuel tracer for determination of mixture fraction, the fluorescence/Raman setup described above was used to investigate laminar and turbulent acetone-seeded methane flames.

The acetone was seeded into the methane fuel by bubbling methane through liquid acetone heated to 30 °C. The methane and acetone vapor were diluted with air, giving a final mixture of 70% air, 25% methane, and 5% acetone by volume. The laminar flame was stabilized on a 16-mm-diameter nozzle, and the gas mixture had a Reynolds number of 700 at the nozzle exit. Results of the fluorescence/Raman comparison in the laminar flame are shown in Fig. 8. A clear departure between the normalized fluorescence and Raman signals is evident, with the fluorescence signal *exceeding* the Raman signal in the fuel-rich region of the flame. This behavior is consistent with the fluorescence increasing as a function of temperature as reported by Tait and Greenhalgh [13]. A comparison of the normalized Raman and fluorescence signals in a turbulent flame showed similar results, with the fluorescence signal greater than the Raman signal in some locations.

Discussion and Conclusions

Three different methods of measuring instantaneous mixture fraction have shown varying poten-

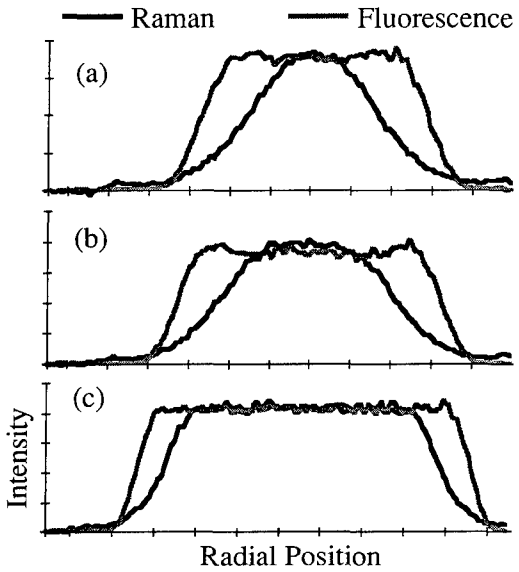

FIG. 8. Comparison of Raman and acetone fluorescence intensity at various downstream locations in a laminar methane-air flame seeded with acetone vapor. Downstream locations were (a) 63.5, (b) 38.5, and (c) 13.5 mm. The fluorescence was excited at 320 nm.

tials. Joint Raman/Rayleigh measurements have been shown to work quite well and can provide valuable mixture fraction statistics. However, the weak Raman signal limits the signal/noise. While line measurements provide a modest signal/noise, it is not without the sacrifice of spatial resolution. Fluorescence from PAHs can also interfere with imaging the Raman scattering. In addition, caution must be used when interpreting Raman scattering of the vibrational C-H stretch for hydrocarbon fuels that produce significant quantities of intermediates during combustion.

Strong fluorescence from acetaldehyde provides good signal/noise, making imaging of fuel concentration possible. The acetaldehyde fluorescence and C-H Raman signals track each other well. On the fuel-rich side of the flame, the calculated mixture fraction shows a dip and plateau. These irregularities may be the result of relatively large concentrations of CO produced as an intermediate in the combustion reaction. If a simple one-step reaction mechanism is assumed when calculating mixture fraction, significant errors could occur in the subsequent computation of scalar dissipation rates. It may be possible to improve the iterative procedure used to calculate mixture fraction by incorporating aspects of a detailed calculation of the reaction mechanism.

The third method of mixture fraction measurement was to introduce acetone as a fuel tracer and image its fluorescence. Acetone fluorescence proved to be problematic when excited at a wavelength of 320 nm. Our measurements show indications of a temperature dependence of the fluorescence yield, making it difficult to interpret the signal. The use of other excitation wavelengths may demonstrate further possibilities for this technique. Even if the temperature-dependence issues can be resolved, it is not clear that the chemistry of acetone is sufficiently close to that of simple hydrocarbon fuels to allow the accurate determination of mixture fraction.

Acknowledgments

The authors gratefully acknowledge the partial support of this research by the Air Force Office of Scientific Research (Grant No. AFOSR-91-0150) and the Australian Research Council.

REFERENCES

1. Yip, B., and Long, M. B., *Opt. Lett.* 11:64 (1986).
2. Yip, B., Lam, J. K., Winter, M., and Long, M. B., *Science* 235:1209 (1987).
3. Bilger, R. W., *Twenty-Second Symposium (International) on Combustion*, The Combustion Institute, Pittsburgh, 1989, p. 475.
4. Bilger, R. W., Yip, B., Long, M. B., and Masri, A. R., *Combust. Sci. Technol.* 72:137 (1990).
5. Buch, K. A., Dahm, W. J. A., Dibble, R. W., and Barlow, R. S., *Twenty-Fourth Symposium (International) on Combustion*,, The Combustion Institute, Pittsburgh, 1992, p. 295.
6. Dibble, R. W., Masri, A. R., and Bilger, R. W., *Comb. Flame* 67:189 (1987).
7. Stårner, S. H., Bilger, R. W., Dibble, R. W., and Barlow, R. S., *Combust. Sci. Technol.* 86:223 (1992).
8. Long, M. B., Fourguette, D. C., Escoda, M.C., and Layne, C. B., *Opt. Lett.* 8:244 (1983).
9. Namazian, M., Schefer, R. W., and Kelly, J., *Opt. Lett.* 16:858 (1991).
10. Long, M. B., Levin, P. S., and Fourguette, D. C., *Opt. Lett.* 10:267 (1985).
11. Stårner, S. H., Bilger, R. W., Lyons, K. M., Frank, J. H., and Long, M. B., *Twenty-Fifth Symposium (International) on Combustion*, The Combustion Institute, Pittsburgh.
12. Arnold, A., Becker, H., Suntz, R., Monkhouse, P., Wolfrum, J., Maly, R., and Pfister, W., *Opt. Lett.* 15:831 (1990).
13. Tait, N. P., and Greenhalgh, D. A., *Twenty-Fourth Symposium (International) on Combustion*, The Combustion Institute, Pittsburgh, 1992, p. 1621.
14. Stårner, S. H., Bilger, R. W., Lyons, K. M., Marran, D. F., and Long, M. B., *Proceedings of the 14th International Colloquium on the Dynamics of Explosions*

and Reactive Systems, Coimbra, Portugal, August 1993.
15. Long, M. B., Frank, J. H., Lyons, K. M., Marran, D. F., and Stårner, S. H., *Ber. Bunsenges. Phys. Chem.*, 97:1555–1559 (1993).
16. Archer, A. S., Cundall, R. B., Evans, G. B., and Palmer, T. F., *Proc. R. Soc. London*, A 333:385 (1973).
17. Ohta, N., Koguchi, T., Takemura, T., and Suzuka, I., *Chem. Phys. Lett.* 191:232 (1992).
18. Lindstedt, P., and Long, M. B., *Comments on the Pyrolysis Properties of Acetaldehyde*, unpublished report, 1993.
19. Lozano, A., Yip, B., and Hanson, R. K., *Exp. Fluids* 13:369 (1992).

COMMENTS

R. V. Serauskas, Gas Research Institute, USA. In using the 320-mm laser wavelength in the acetaldehyde experiments, aren't you already close enough (or beyond) the photodissociation threshold for the higher flame temperatures?

Author's Reply. At higher temperatures, some photodissociation may occur. However, the agreement of the acetaldehyde fluorescence and C-H Raman signals in a laminar flame (see Fig. 7) indicates that photodissociation is not a prominent feature. Any acetaldehyde molecules that dissociate into other hydrocarbons would contribute to the Raman signal, but not the fluorescence. If photodissociation occurred only in regions of elevated temperature, the normalized Raman and fluorescence profiles would not coincide.

•

Nigel Tait, Cranfield University, UK. What would you estimate the error in the measurement of the mixture fraction to be near the stoichiometric contour? Have you tried correcting the measurements with acetone using its known (near linear) temperature dependence? There might be an advantage in this approach since, as the graphs in your paper illustrate, the LIF signal from acetone extends nearer the stoichiometric contour than both the Raman and the acetaldehyde signals. It might, however, still have potential problems due to the differences between its chemistry and that of methane.

Author's Reply. In order to provide an adequate estimate of the accuracy of our mixture fraction measurements, experiments in which mixture fraction can be determined independently using major species concentrations should be conducted. These experiments have not been done as yet.

We have not investigated the possibility of correcting the acetone measurements for the temperature dependence of the fluorescence yield. Even with a correction, it is not clear whether mixture fraction could be unambiguously determined in a turbulent flame. As you point out, imaging a fuel marker rather than the fuel itself has some significant disadvantages.

•

Ian Kennedy, University of California, Davis, USA. Your definition of mixture fraction as a coupling function assumes a Lewis number of 1. The Lewis numbers of acetaldehyde and acetone are probably somewhat greater than 1. Does this have an impact on your interpretation of the data as mixture fractions? Can it account, to some extent, for the anomalous dip you observed in the acetaldehyde experiment?

Author's Reply. The assumption of unity Lewis number is a limitation of this method of determining mixture fraction and may well contribute to the dip in mixture fraction that was observed in the acetaldehyde flame. However, both experiments and calculations indicate that the most significant source of error is from the pyrolysis of acetaldehyde. Pyrolysis causes a loss of the fuel fluorescence signal far to the rich side of stoichiometric. Corrections to this difficulty are not likely with the acetaldehyde fluorescence/Rayleigh technique presented in this paper. The reason is that the Rayleigh signal is not very sensitive to changes in mixture fraction at elevated temperatures on the rich side of stoichiometric where fuel pyrolysis occurs.

•

E. P. Hassel, Darmstadt, Germany. The biggest problem in the application of Raman spectroscopy in hydrocarbon flames is LIF from soot and PAHs. You stated that you diluted your flame to reduce this problem. What are your experiences in dealing with soot? Were you able to measure in all flame regions? What was the percentage of evaluable Raman spectra?

Author's Reply. Valid Raman scattering measurements were obtained both at 25 and 35 nozzle diameters downstream in the air-diluted methane flame reported here. However, LIF interference could be significant further downstream, especially near the flame tip, and in flames with less dilution. In highly sooting flames, the use of joint Raman/Rayleigh imaging for mixture fraction measurements will not be applicable. One case of interest where we have applied this technique to an undiluted flame is in the stabilization region of a nonpremixed lifted methane flame.

Twenty-Fifth Symposium (International) on Combustion/The Combustion Institute, 1994/pp. 1167–1173

RAMAN MEASUREMENTS AND JOINT PDF MODELING OF A NONPREMIXED BLUFF-BODY-STABILIZED METHANE FLAME

SANJAY M. CORREA AND ANIL GULATI
General Electric Research Center
Schenectady, NY 12301, USA

AND

STEPHEN B. POPE
Cornell University
Ithaca, NY 14853, USA

Mixture fraction, temperature, and major species in a recirculation-stabilized nonpremixed methane-air flame are (1) measured using laser Raman scattering and (2) calculated using the joint velocity-composition probability density function (PDF) model, appropriately combined with an elliptic mean flow solver. The Raman system was modified to account for the significant levels of laser-induced fluorescence (LIF) and incandescence encountered in the rich sooty zone of the flame. The joint PDF contains three velocity components, which are modeled by Langevin equations, and five thermochemical scalar variables with mixing given by linear deterministic relaxation to the mean and chemistry by a four-step steady-state reduced scheme. The flame is characterized by significant finite-rate chemistry, including, unlike a $CO/H_2/N_2$ fuel in the same apparatus, strong bimodality in the temperature-mixture fraction scatter plots. Calculations are compared with Raman data on temperature and major species. The agreement is in general reasonable, with the largest discrepancies being caused by the breakdown of the assumption of a chemical steady state for the cool fuel-rich gas at the core of the flame. Large discrepancies are found on the peak CO, as in other similar studies, confirming a need for better measurements of CO than Raman spectroscopy can provide. The model overpredicts the degree of extinction. The radial flux of the mixture fraction calculated directly from the joint PDF is compared with the flux given by an *a posteriori* gradient diffusion calculation, indicating no (radial) counter-gradient diffusion and a "turbulent Schmidt number" of about 0.4.

Introduction

Chemical kinetics and their interactions with turbulence control combustion phenomena such as emissions and the related issue of flame stability, which have become significant technology drivers [1,2]. The pressure-corrected mean Navier–Stokes/*assumed-shape* PDF/k-ε turbulence model does not account rigorously for the turbulence-chemistry aspects of these issues, but affords significant geometric flexibility and rapid convergence for pressure-dominated internal flow [3]. On the other hand, the joint (velocity-composition) probability density function (PDF) transport model includes turbulence and chemistry with single-point closure [4]. The PDF model has been widely used to compute turbulent *jet* flames, both in the composition-only form [5] and in the joint velocity-composition form [6–8]. More recently, the joint PDF model has been extended to "elliptic" (recirculating) flow and applied to the computation of CO/H_2 bluff-body flames [9], marking a step toward the recirculation-stabilized flow fields found in practical burners. Bluff bodies also eliminate the pilot stabilization necessary in jet flames at high Reynolds numbers.

There are other approaches, intermediate in complexity and cost, between the assumed-shape PDF model (No. 1) and the joint velocity-composition PDF transport model (No. 4). The "conditional moment closure" model (No. 2) solves conventional time-averaged field equations for the means of reactive scalars conditioned on the mixture fraction [10] and is applicable only when fluctuations about this conditional mean are small. The scalar PDF model (No. 3) does not treat the velocity part of the PDF, using instead conventional turbulence modeling to supply the scalar (and momentum) fluxes [11]. Arguments of computational cost are usually made to support model numbers 1 through 3; however, the speedup achieved in parallelizing particle tracking PDF computations shows that they can be usable in practical design codes [12].

Methane is of particular interest in this context for scientific reasons, because it affords strong finite-rate

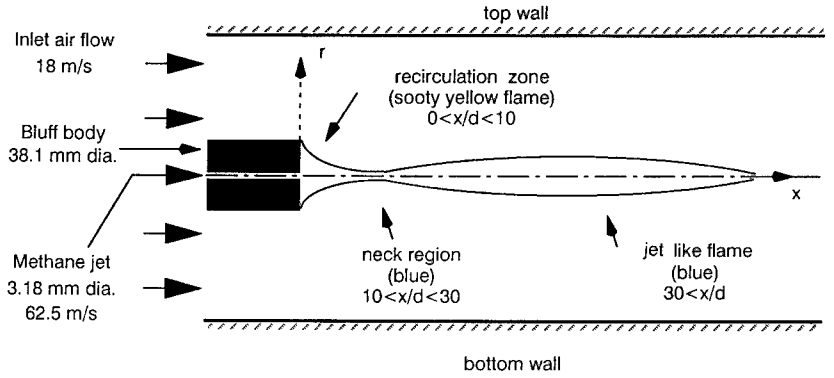

FIG. 1. Non-premixed bluff-body-stabilized methane flame; d is the jet diameter.

chemistry effects and well-studied reduced kinetic schemes, and for practical reasons, because there is a significant worldwide natural-gas economy. For example, about 50 GW of new gas-fired power plants are being sold annually. The development and qualification of predictive tools—with the required geometry, chemistry, and turbulence capabilities—will aid this industry.

Of the many prior bluff-body flame studies, the most closely related is that of Masri et al. [13] who also used fluorescence-corrected Raman spectroscopy of methane-air flames. The present work uses a jet that is twice as big and stresses the jet-dominated regime, which is less susceptible to large-scale shedding off the bluff body; greater degrees of extinction are found. Hence, the new contributions of this paper are Raman temperature and major species measurements in the jet-dominated regime of a bluff body–stabilized nonpremixed methane-air flame, and comparisons with predictions of the joint PDF/elliptic mean flow computational fluid dynamics (CFD) model.

Experimental Setup and the Raman Measurement Technique

The bluff-body burner and the inflow conditions are shown in Fig. 1. The axisymmetric bluff body has an outer diameter of 38.1 mm with an axial jet of 3.18-mm diameter "d" located in the center. It is well known that parts of this flow field—notably, the annular shear layer shed off the bluff body—can be dominated by unsteady effects. Care was taken to operate in a velocity (jet and coflow) regime where the flame was steady. The cold jet Reynolds number is 12,000, based on the jet diameter and jet exit velocity of 62.5 m/s. The coflow air velocity is 18 m/s. The back surface of the bluff body is coated with a thermal barrier material to reduce heat loss. The flame is stabilized by the recirculation zone provided by the bluff body. The tunnel cross section is 15 × 15 cm, large enough not to interfere with the flame. (The calculations are made for a circular duct of the same cross-sectional area.) Visual observations of methane flames at various air and fuel-jet velocities were used to select the conditions for the Raman-scattering measurements reported below. This flame is anchored by the bluff body and is almost extinguished in the neck region, before reigniting further downstream.

The Raman system is based on a flashlamp-pumped dye laser that provides pulses of ≈1 J in 2–4 μs, within a 0.2-nm bandpass at 488 nm at a repetition rate of 10 Hz. The light scattered at right angles is collected by two lenses, separated in frequency by a 0.75-m-spectrometer, and is detected by eight photomultiplier tubes (PMTs). The PMTs detect anti-Stokes vibrational Raman scattering from N_2, Stokes vibrational Raman scattering from N_2, O_2, H_2, H_2O, CO, and CO_2, and Rayleigh scattering. The temporal resolution (2–4 μs) of the technique is limited by the laser pulse length, the spatial resolution (0.2 × 0.2 × 0.6 mm) is limited by the spectrometer entrance slit and the collection optics, and the data acquisition rate is limited by the laser repetition rate. The flame luminescence was broadbanded throughout the visible region and was reduced by a polarization filter in the collection optics. The polarization vector was aligned to pass horizontally polarized Raman- and Rayleigh-scattered light.

The instantaneous temperature on every laser shot was determined in three independent ways: (1) the Stokes-anti-Stokes (SAS) ratio from nitrogen, which yields the temperature directly [14]; (2) an iterative scheme in which an initial temperature is guessed, based on which the mole fractions of all major species are calculated using their measured vibrational intensities. The mole fractions are then corrected using high-temperature correction factors to account for changes in the fraction of the Raman band falling in the exit slits provided for the respective photomultiplier tubes. The iteration process is repeated

until the sum of the mole fractions is unity; and (3) Rayleigh scattering: Raman data on the major species were used to obtain the Rayleigh cross section of the mixture and thus provide temperature in an iterative manner.

The last two methods agreed best, to within 10 K on mean temperature and to within 50 K on a shot-to-shot basis. Hence, method (2), based on the sum of mole fractions of major species, is reported below.

Initial measurements with the Raman system showed that there was significant laser-induced fluorescence (LIF) interference throughout the flame, as has also been reported elsewhere [15,16]. The LIF was fairly broadband and contaminated all Raman channels, but it was negligible in the Rayleigh channel. An additional difficulty encountered in the application of Raman to this flame was the cross talk between CH_4 and other Raman channels, primarily O_2. For the 488-nm excitation used here, the Raman interference in other major species was insignificant. To account for these two additional sources of contamination in the signals, the system and calibration procedures were modified. Additional PMTs were installed in two Raman-free regions of the spectra to monitor the LIF on a shot-to-shot basis. These PMTs, termed F_1 and F_2, were located at 540 nm (between O_2 and CO_2) and at 590 nm (between CH_4 and H_2O), respectively. These two signals were found to correlate very well with each other and with all other Raman signals so that the use of F_1 was found to be sufficient to allow corrections in all other channels.

A calibration procedure was used to correct for the LIF [15]. A 38-mm-diameter honeycomb burner was built to provide laminar diffusion flames of 30% CH_4/70% CO. The flame was visibly sooty and yellow at the downstream end and contained enough soot precursors and LIF at the upstream end to allow calibrations. The calibration factors were obtained by iteration. First, the raw data were used to calculate the temperature (from the sum of mole fractions) and mole fractions of major species. The contamination caused by fluorescence was particularly evident in the fuel-rich regions of the flame. The next step was to estimate correction factors for each of the major species based on the raw data and to subtract a term equal to the product of the correction factor for species i and the value of the fluorescence signal measured in photomultiplier tube F_1. The calculated temperature and mole fraction profiles were then compared with the predicted values. The process was iterated to convergence. Figure 2 shows the temperature and selected species so obtained. The temperature agrees fairly well with the predicted laminar flamelet calculations [5] for an assumed stretch of 5/s; the calculations did not depend strongly on this assumed value. The corrections for N_2, O_2, and CH_4 are substantial, and the corrected species data again agreed with the laminar flame calculations, which are omitted for clarity. The calibration procedures were repeated before and after each set of measurements.

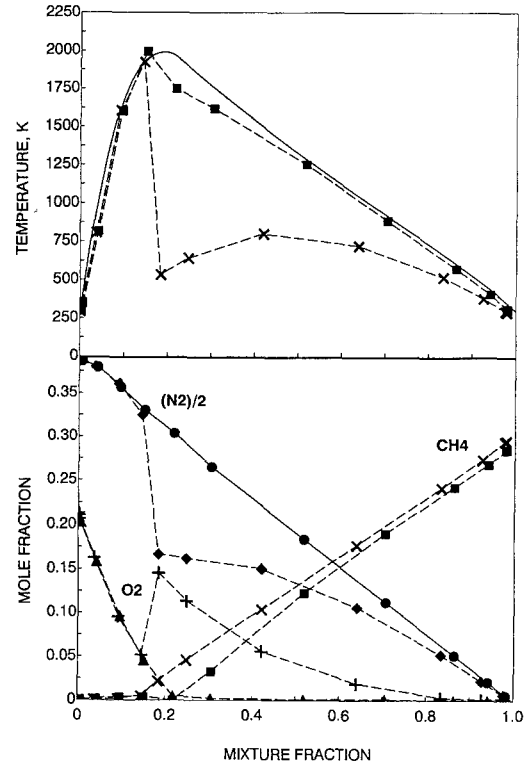

FIG. 2. Raw and fluorescence-corrected Raman data. Temperature: X = raw data; ■ = corrected data; solid line = laminar flame calculation from Ref. 5. Species (raw data): ♦ = N_2; + = O_2; and X = CH_4; corrected data: ● = N_2; ▲ = O_2; and ■ = CH_4.

Radial profiles of temperature and mole fractions of major species were measured at axial locations of x/d = 5, 10, 20, 30, 50, and 70 and along the centerline. Since not all these data can be discussed here, attention will be confined to the region of maximum turbulence, $10 \leqq x/d \leqq 20$.

Joint PDF/Elliptic Mean Flow CFD Model

To extend the PDF model from parabolic to elliptic flows, an iterative PDF/elliptic computational fluid dynamics (CFD) approach has been developed [9]. The highly nonuniform CFD grid accounts for the disparate flow scales imposed by the jet and bluff body dimensions, with enough resolution and with a second-order accurate numerical discretization scheme to eliminate numerical "diffusion" errors [3].

In the joint PDF model, the turbulent flow is described by the velocity U, the mixture fraction ξ, and

the reactive scalars in the system. In the PDF transport equation, these become the independent variables denoted by V, ψ, and $\phi_k (k = 1, \ldots, 4)$, respectively. The joint PDF evolves in this eight-dimensional velocity-composition space as well as in the two-dimensional x-r physical space. A one-point statistical description in terms of the joint PDF of the velocity and these scalars is sought. If the flow is statistically stationary, all one-point statistics depend only on the spatial coordinates. All one-point statistics are recovered from this PDF because the composition is a known function of the above scalars. The velocity-composition joint PDF evolution model relaxes many of the assumptions made in the standard closure, such as PDF shape, statistical independence of scalars, and gradient diffusion of scalars. Closure of the nonlinear chemical source term and the "turbulent fluxes" of scalars are given directly by the PDF.

Turbulent mixing of the scalars is modeled as a linear, deterministic relaxation to the local mean, sometimes called Interaction-by-Exchange-with-the-Mean (IEM) [17]. The IEM model has been isolated and studied in detail in the partially stirred reactor model [12,18]. Regarding the velocity term, the fluctuating component of acceleration (arising from the fluctuating pressure gradient and viscous forces) is modeled by the simplified Langevin model [9,19]. The Seshadri–Peters, four-step reduced scheme is adopted for the kinetics [20]. A look-up table of reaction rates, density, and temperature is constructed on a nonuniform $20 \times 10 \times 10 \times 10 \times 10$ grid.

The axisymmetric elliptic mean flow CFD model and the PDF model communicate with each other iteratively. Details are given in Ref. 9. On each time step, the fields of the mean velocity and the turbulence frequency, obtained from the local turbulence kinetic energy (TKE) and dissipation rate, are passed from the CFD model to the PDF model. A shift and a uniform stretching in V space are applied to the PDF so that the mean velocity and the TKE of the two submodels are in agreement. Thus, the no-slip boundary condition is automatically satisfied at walls. Stochastic Lagrangian particle evolution, per the IEM model and the reduced scheme, occurs at the above frequency. The mean density field is passed back to the CFD model, and the two submodels are iterated to convergence. The 75×60 cell, $\approx 10^5$ particle calculation, was run until a statistical steady-state was achieved. For display purposes, lower moments such as the means were averaged over the last 200 time steps of the PDF evolution, reducing statistical fluctuations in the results. Scatterplots were prepared from the calculations by saving several realizations of the PDF particle array after stochastic convergence and then postprocessing the more than 10^6 particles so obtained.

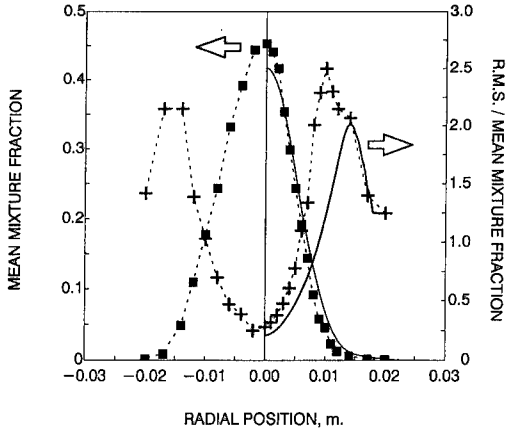

FIG. 3. Comparison of mean and rms mixture fraction profiles at $x/d = 20$. Raman data: ■ and +; Calculations: solid lines.

Discussion

The following discussion focusses on the region of strongest turbulence ($10 \leqq x/d \leqq 20$), where the off-axis recirculation zone provides intense mixing at the edges of the jet.

Computed radial profiles of the mean and root mean square (rms) mixture fraction at $x/d = 20$ compare well with the Raman data (Fig. 3). The measured radial profiles are shown in full, revealing the degree of symmetry, while the computed profiles are by assumption axisymmetric. The comparisons indicate that the calculated mixture fraction field is accurate enough to permit a meaningful evaluation of the reactive quantities. The mean temperature peaks in the recirculation zone with a maximum of less than 1000 K, a result of the strong turbulence. Computations and data agree quite well (Fig. 4), although the temperature is underpredicted by almost 250 K along the centerline. The mean major species profiles also agree quite well (Fig. 5). The mean O_2 is depleted in the wake of the bluff body but coexists with mean CH_4, a consequence of finite-rate chemistry. The O_2 returns to ambient levels at the edge of the bluff body ($r \cong 0.02$ m). The model predicts more mean O_2 than measured at the centerline, which is consistent with underprediction of the mean temperature in Fig. 4.

Scatterplots provide an instructive format in which to study turbulence-chemistry interactions and best utilize the power of the time- and (not quite) space-resolved Raman spectroscopy and the PDF model. The measured temperature-mixture fraction scatterplot using all data from $x/d = 10$ and $x/d = 20$ is shown in Fig. 6a, along with the calculated laminar flame profile for a stretch of 5/s [5]. Unlike in the CO/H_2 flame [9], bimodality is clearly evident. A significant number of points has mixture fraction values

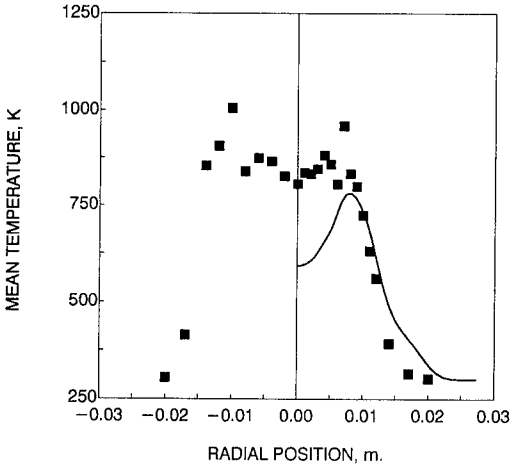

FIG. 4. Comparison of mean temperature profiles at $x/d = 20$.

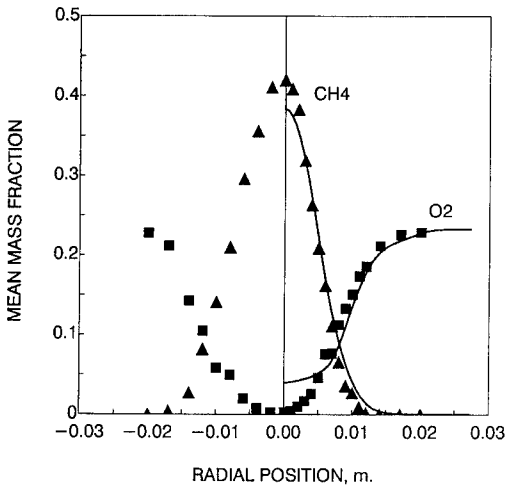

FIG. 5. Comparison of mean CH_4 and O_2 profiles at $x/d = 20$.

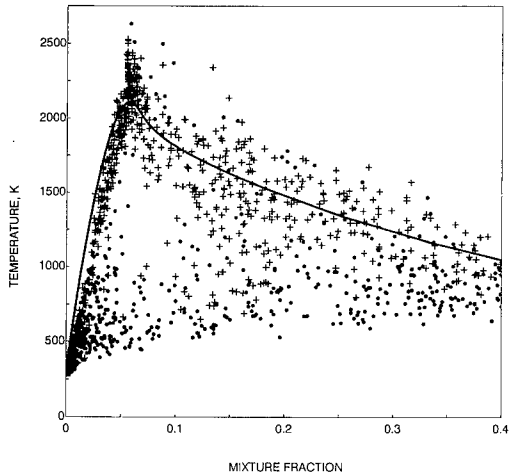

(a)

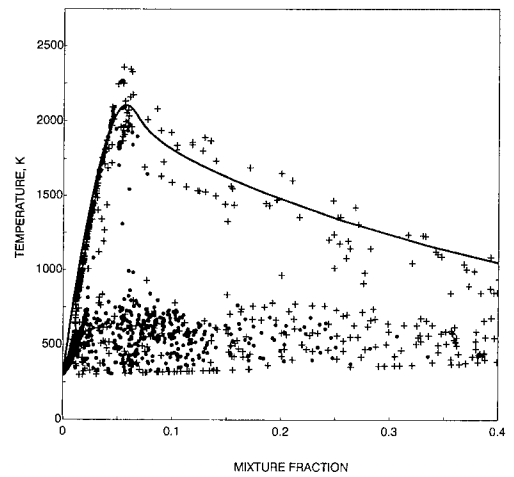

(b)

FIG. 6. Temperature-mixture fraction scatterplot at $x/d = 10$ (plus symbols) and $x/d = 20$ (solid symbols). Solid line is laminar flame calculation, from Ref. 5. (a) Raman data, (b) computed points.

close to stoichiometric but temperatures that manifest localized extinction, while other points are clustered along the line of strained flamelet temperatures. The physical picture that emerges from the scatterplots is that of a recirculation zone (which anchors the turbulent flame), connected to a jetlike region by a narrow neck of high shear with a significant amount of local extinction. The corresponding calculated scatterplot (Fig. 6b) is similar, although the predicted points exhibit a greater trend toward extinction. On a related note, stochastic calculations of lean methane-air combustion in a partially stirred reactor [12] showed that the parent starting scheme used to develop the four-step model agreed with a 77-step scheme reasonably well when the mean temperatures were above 1500 K but prematurely predicted blowout relative to the 77-step scheme. This behavior is similar to the overprediction toward extinction in the present study.

The coexistence of fuel and oxygen is again apparent in Y_{CH_4}-Y_{O_2} scatterplots (not shown), from both the data and the model. The measured and calculated scatterpoints at $x/d = 20$, both of T-ξ and Y_{CH_4}-Y_{O_2}, were closer to the chemically "frozen" line than those at $x/d = 10$, in accordance with Raman data and with visual observations of the flame.

The calculated CO scatterplots have maxima at 3% (inset, Fig. 7), whereas the data peak at about 10%

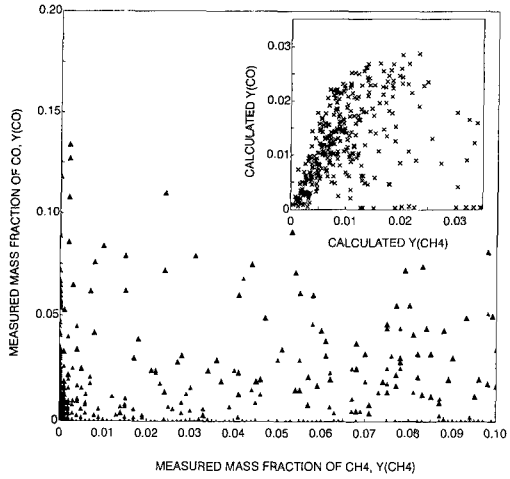

FIG. 7. CO-methane scatterplot at $x/d = 10$ and $x/d = 20$.

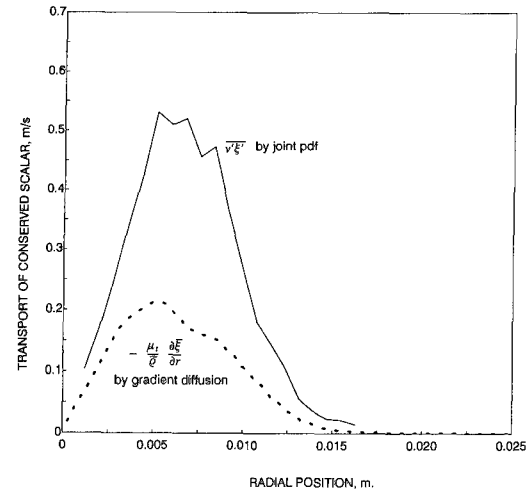

FIG. 8. Radial flux of conserved scalar at $x/d = 20$.

(Fig. 7), well above the flamelet maxima. Similar 10% levels were measured in Masri et al.'s bluff-body flame [13] and in pilot-stabilized flames [5], and 2–3% peaks were predicted in the latter using the four-step scheme within a (scalar) PDF/Reynolds stress model [5]. Hence, this discrepancy on CO maxima has appeared in diverse circumstances (but always in combustion gases that are near local extinction). There are many potential contributors, including (1) the assumption of a steady state for the radicals in the four-step mechanism; (2) the errors in Raman-based CO and CO_2 data, as discussed above and in Refs. 5 and 13 and as seen by direct comparison with predicted mean CO and CO_2 profiles in the CO/H_2 bluff-body flame of Ref. 9; and (3) neglection of phenomena such as unsteady flamelets or micromixed gases (perfectly stirred reactors) that have been shown to lead to high CO [21,22]. In intense turbulence, however, the microscale may be better simulated by the PaSR since it is the degenerate form of the PDF equation for spatially homogeneous systems. For example, at 30 atm, the PaSR indicates that approximately 2% peak CO levels are encountered until the fuel is pyrolyzed and CO oxidation can commence [23]. It seems clear that CO is an important clue to the microstructure of highly turbulent combusting gases and that accurate measurements will be critical.

The very large scatter about the conditional mean indicates that the CMC model [10] is inapplicable to this flow.

Because the joint PDF contains the velocity components of each particle, the scalar fluxes can be examined. Figure 8 shows the computed radial transport $\overline{v'\xi'}$ of the mixture fraction at $x/d = 20$, calculated by summing over particles in 20 radial bins. Also shown is the gradient diffusion flux $-(\mu_t/\bar{\rho})\,\partial\bar{\xi}/\partial r$, the latter computed from the mean fields; μ_t is the turbulent viscosity computed from the k-ε equations. Both fluxes were calculated *a posteriori*, since they were not needed for the main computation. Figure 8 shows that in the presence of the strong radial gradient $\partial\bar{\xi}/\partial r$, (radial) transport of the mixture fraction is consistent with the notion of gradient diffusion; i.e., there is no countergradient diffusion. The magnitude of $\overline{v'\xi'}$ is, however, much greater than that of $-(\mu_t/\bar{\rho})\,\partial\bar{\xi}/\partial r$. The indicated "turbulent Schmidt number" is about 0.4.

Conclusions

Complementary Raman measurements and joint PDF modeling have been used to study a turbulent nonpremixed methane-air flame stabilized behind a bluff body. The study demonstrates several points:

1. The bluff-body burner provides a strongly turbulent field leading to localized extinction, without the need for a pilot flame. Thus, the two-stream nature of the problem is preserved, unlike many piloted jet-flame studies where the composition or the excess enthalpy of the pilot flame can cause modeling difficulties. The present recirculation-stabilized flame is also much closer to practical burners.
2. By correcting for fluorescence, Raman measurements can be made in bluff-body CH_4-air flames; however, the errors in certain species (e.g., CO and CO_2) may be so large that models should not be changed on the basis of such data alone.
3. Given the similarity in scatterplots, it is clear that the *pointwise* structure of the above bluff-body flame and the piloted jet flame are quite similar,

in agreement with previous work. A greater degree of local extinction is measured here.

4. The limitations of PDF shape assumption, statistical independence of scalars, and gradient diffusion are removed from this "elliptic" model. The consequences of these can be seen in joint scatterplots and in convective fluxes.

The acquisition of Raman data and the three-velocity/five-scalar joint PDF calculation in this bluff-body methane flame takes each "discipline" to the limits of the present state of the art. Any significant further progress is likely to require improvements in major species measurements, complementary velocity and minor species measurements, and parallel computers. Reduced chemistry schemes that relax steady-state assumptions (and are likely to require additional scalars) will have to be developed and assessed in simpler contexts.

Acknowledgment

The work at GE is supported in part by the Air Force Office of Scientific Research, Contract No. F49620-91-C-0072, Dr. Julian Tishkoff, Project Manager.

REFERENCES

1. Bowman, C. T., *Twenty-Fourth Symposium (International) on Combustion,* The Combustion Institute, Pittsburgh, PA, 1992, pp. 859–878.
2. Correa, S. M., *Combust. Sci. Technol.* 87:329–362 (1992).
3. Correa, S. M., and Shyy, W., *Prog. Energy Combust. Sci.* 13:249–292 (1987).
4. Pope, S. B., *Twenty-Third Symposium (International) on Combustion,* The Combustion Institute, Pittsburgh, PA, 1990, pp. 591–612.
5. Chen, J.-Y., Kollmann, W., and Dibble, R. W., *Combust. Sci. Technol.* 64:315–346 (1989).
6. Correa, S. M., Gulati, A., and Pope, S. B., *Combust. Flame* 72:159–173 (1988).
7. Taing, S., Masri, A. R., and Pope, S. B., *Combust. Flame* 95:133–150 (1993).
8. Norris, A. T., and Pope, S. B., "Modeling of Extinction in Turbulent Diffusion Flames by the Velocity-Dissipation-Composition PDF Method," submitted to *Twenty-Fifth Symposium (International) on Combustion,* Irvine, CA, July 31–August 5, 1994.
9. Correa, S. M., and Pope, S. B., *Twenty-Fourth Symposium (International) on Combustion,* The Combustion Institute, Pittsburgh, PA, 1992, pp. 279–285.
10. Smith, N. S. A., Bilger, R. W., and Chen, J.-Y., *Twenty-Fourth Symposium (International) on Combustion,* The Combustion Institute, Pittsburgh, PA, 1992, pp. 263–269.
11. Chen, J.-Y., and Kollmann, W., *Twenty-Third Symposium (International) on Combustion,* The Combustion Institute, Pittsburgh, PA, 1990, pp. 751–757.
12. Correa, S. M., and Braaten, M. E., *Combust. Flame* 94:469–486 (1993).
13. Masri, A. R., Dibble, R. W., and Barlow, R. S., *Twenty-Fourth Symposium (International) on Combustion,* The Combustion Institute, Pittsburgh, PA, 1992, pp. 317–324.
14. Drake, M. C., Lapp, M., and Penney, C. M., "Use of Raman Effect for Gas-Temperature Measurement," in *Temperature, Its Measurement in Science and Industry,* (J. F. Schooley, Ed.), 1982, Vol. 5, p. 631.
15. Dibble, R. W., Starner, S. H., Masri, A. R., and Barlow, R. S., *Appl. Phys.* B51:1727–1731 (1990).
16. Masri, A. R., and Dibble, R. W., *Twenty-Second Symposium (International) on Combustion,* The Combustion Institute, Pittsburgh, PA, 1989, pp. 607–618.
17. Borghi, R., *Prog. Energy Combust. Sci.* 14:245–292 (1988).
18. Correa, S. M., *Combust. Flame* 93:41–60 (1993).
19. Pope, S. B., *Ann. Rev. Fluid Mech.* 26:23–63 (1994).
20. Seshadri, K., and Peters, N., *Combust. Flame* 81:96–118 (1990).
21. Mauss, F., Keller, D., and Peters, N., *Twenty-Third Symposium (International) on Combustion,* The Combustion Institute, Pittsburgh, PA, 1990, pp. 693–698.
22. Chen, J.-Y., and Dibble, R. W., *Combust. Sci. Technol.* 84:45–50 (1991).
23. Correa, S. M., "Models for High-Intensity Turbulent Combustion," *Comp. Sys. Eng.* 5 (2):135–145 (1994).

Twenty-Fifth Symposium (International) on Combustion/The Combustion Institute, 1994/pp. 1175–1181

EFFECT OF DILUTION ON THE LIFTOFF OF NON-PREMIXED JET FLAMES

B. J. LEE, J. S . KIM AND S. H. CHUNG
Department of Mechanical Engineering
Seoul National University
Seoul 151-742, Korea

Effects of fuel dilution on the characteristics of lifted, non-premixed jet flames have been studied experimentally by using nitrogen as a diluent in the fuel stream. Depending on the nozzle diameters and the degree of dilution, the liftoff behavior can be classified into three different modes: (1) both the liftoff and blowout happen in the laminar regime, (2) the liftoff occurs in the laminar regime, while the blowout takes place after the fluid undergoes the transition to turbulence, and (3) both the liftoff and blowout occur in the turbulent regime.

For the transition case (i.e., case 2), the flame is lifted off in the laminar regime, and the liftoff height increases rapidly until the height becomes comparable to the breakup length of the jet. At this point, both the liftoff height and breakup length decrease slowly with the jet velocity. As the jet velocity increases further toward the critical Reynolds number for transition to turbulence, there is a sudden decrease in the liftoff height. After this transition, the liftoff height increases linearly with the jet velocity.

In the laminar regime, the liftoff height scaled with the nozzle diameter squared can be correlated with the jet velocity, and the preferential diffusion between the fuel and diluent is observed to play a significant role for a diluted jet. In the turbulent regime, the linear dependence of the liftoff height on nozzle diameter has been shown by a correlation between the nozzle diameter, the level of dilution, and the jet velocity.

Introduction

Liftoff characteristics of non-premixed jet flames have been studied extensively in conjunction with flame stabilization in combustion equipments such as boilers or gas turbines. These investigations have focused either on turbulent or laminar cases. For laminar lifted flames [1,2], it has been demonstrated that the flame near the stabilization point has a tri-brachial structure involving rich and lean premixed flames and a diffusion flame all extending from a single stabilization point; thus, it possesses the characteristics of a stoichiometric premixed flame. Based on this observation, a correlation has been derived from cold jet theories for momentum and mass transports, which relates the liftoff height with the nozzle diameter and the jet velocity. Also, the significant role that the Schmidt number plays on the existence and behavior of lifted flames has been demonstrated for hydrocarbon flames, where propane and butane jets have lifted flames, while methane and ethane jets blowout directly from nozzle-attached flames [2].

For turbulent non-premixed jets, there are many experimental results and several competing theories in explaining the liftoff characteristics [3–11]. These include explanations based on turbulent premixed flames near the flame base [4,5], on the quenching of laminar diffusion flamelets [6], and on the large-scale mixing [7,11].

For all these experiments, laminar and turbulent-lifted flames are separately investigated due to limitations in selecting nozzle diameters and flow velocities. If a continuous transition from laminar- to turbulent-lifted flames can be observed, it will furnish better insights into the understanding of the liftoff characteristics in both regimes. Motivated by this challenge, experimental observations reported here include transition characteristics by diluting the fuel stream using nitrogen. Experimental methods are discussed in the next section followed by results and discussions.

Experiment

The experimental setup consisted of a nozzle, a fuel supply system, and a visualization setup. The nozzles used were stainless steel tubes with i.d.'s of d = 0.74, 1.6, 2.6, and 3.6 mm and lengths of 70 cm to ensure a fully developed flow at the nozzle exit.

Flow rates of the fuel and nitrogen were controlled by microneedle valves and rotameters calibrated using a wet-test gas meter. The fuel used was C.P.-grade propane (>99%). A cathetometer, a 35-mm camera, and schlieren optics were used for visualization and dimension measurements. The schlieren light source used was a 60-W xenon lamp. To minimize disturbances from the ambience for the laminar

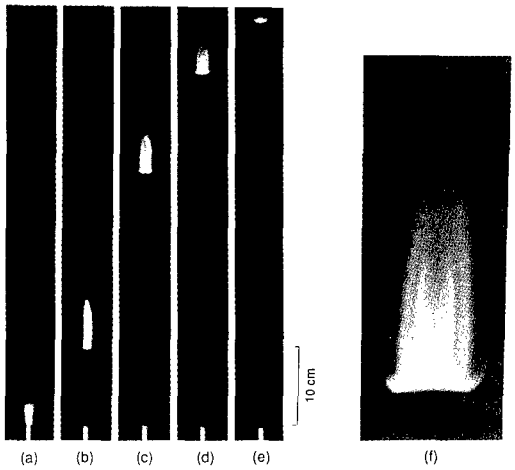

FIG. 1. Photographs showing attached, lifted, and enlarged flame shapes for propane with $Y_{P,o} = 0.28$ and $d = 2.6$ mm, (a) $U_o = 0.60$ m/s, (b) 1.44 m/s, (c) 2.37 m/s, (d) 3.10 m/s, (e) 3.35 m/s, and (f) 3.10 m/s.

cases, a 50 × 50 × 200 cm enclosure having meshes and acryle plates at the sides surrounds the nozzle; the effect of the enclosure on liftoff heights in the laminar regime is found to be negligible.

Experiments were conducted by mixing the fuel and diluent at certain concentrations, and the flow rate was controlled by partial ventings. To prevent the fluctuation of the fuel concentration in a mixture by venting, the pressure at the fuel and nitrogen-mixing junction was kept constant. A gas chromatograph was used to monitor the mixture composition at the nozzle exit.

Liftoff heights were measured by using a cathetometer. For turbulent cases, the height was defined as an average position of the flame base. Various flame dimensions were measured from photographs, and the breakup length of the jet was determined from schlieren images.

Results and Discussions

Various laminar flames are observed for a mass fraction of propane $Y_{P,o} = 0.28$ in a jet with a diameter $d = 2.6$ mm, as shown in Fig. 1, where the subscript P and o indicate propane and the condition at the nozzle exit, respectively. As the average nozzle exit velocity U_o increased, the flame changes from the nozzle attached (a) to stable laminar-lifted flames (b) through (d). Further increases of U_o lead to blowout from the nearly flat flame (e). The enlarged picture (f) shows clearly the *tribrachial* nature of lifted flames near the base. It has rich and lean premixed flames and a faint blue diffusion flame all extending from the same point near the flame base where the flame is stabilized. Both the liftoff and blowout occur in the laminar regime.

Figure 2 shows the schlieren photographs for $Y_{P,o}$

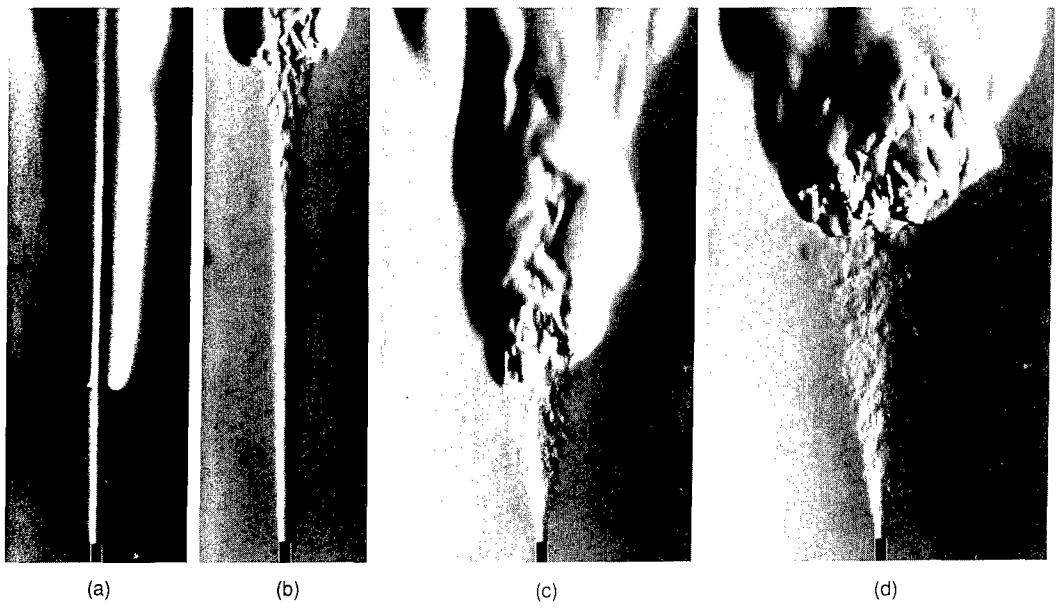

FIG. 2. Schlieren photographs of propane/nitrogen jet for $Y_{P,o} = 0.51$ and $d = 2.6$ mm, (a) $U_o = 4.50$ m/s, (b) 4.80 m/s, (c) 9.56 m/s, and (d) 12.23 m/s.

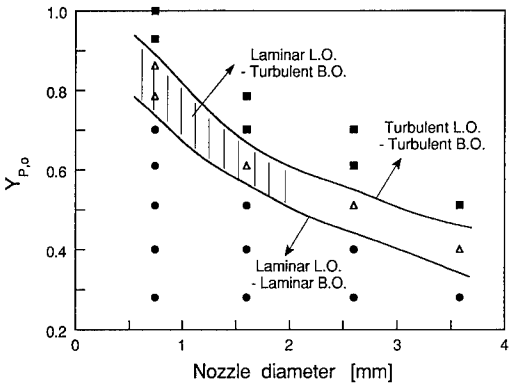

FIG. 3. Boundaries of three different modes of liftoff (B.O.: blowout; L.O.: liftoff; shaded area: after blowout, reigniting stabilize the flame with some increase of flow rate; symbols indicate the experimental conditions).

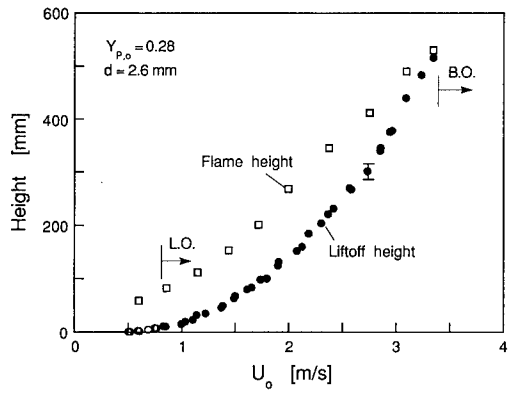

FIG. 4. Flame characteristics with nozzle exit velocity for $d = 2.6$ mm and $Y_{P,o} = 0.28$.

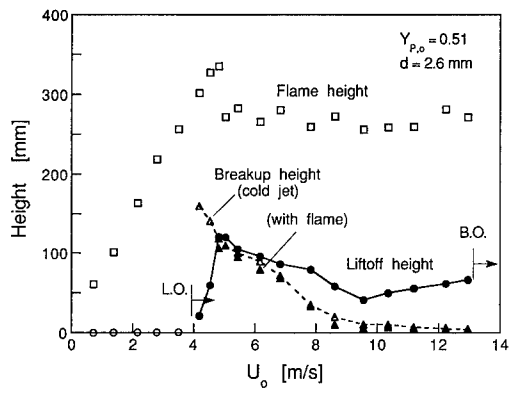

FIG. 5. Flame characteristics with nozzle exit velocity for $d = 2.6$ mm and $Y_{P,o} = 0.51$.

$= 0.51$ and $d = 2.6$ mm. By increasing U_o, the flame changes from a laminar-lifted flame (a) to a lifted flame after the jet breakup (b). Then, the liftoff height decreases with U_o due to the decrease in the breakup height until the Reynolds number Re_d, based on the diameter, reaches a critical value for transition to turbulence (c), and the liftoff height increases with U_o until blowout occurs (d). Case (c) has a Reynolds number of $\mathrm{Re}_d = 3100$, based on the viscosity of the fuel mixture calculated from Wilke's formula.

Depending on d and $Y_{P,o}$, the lifted flames have three different modes, as shown in Fig. 3: (1) liftoff occurs and persists until blowout in the laminar regime, (2) liftoff occurs in the laminar regime and undergoes the transition to the turbulent regime when blowout occurs, and (3) both liftoff and blowout occur in the turbulent regime. The general trend is observed to be that $Y_{P,o}$ of these boundaries decreases with increasing d, which can be influenced by several factors such as the breakup characteristics of the jets, the effect of dilution on the flame speed, and the flame-anchoring mechanism. The shaded area indicates the region where the lifted flame first extinguished in the jet breakup region, and with further increases in U_o, it was reignited by an external source and stabilized the flame again in the turbulent regime.

Liftoff heights, flame heights, and jet breakup heights in the respective modes are plotted in Figs. 4 through 6 for $d = 2.6$ mm. Figure 4 shows results for $Y_{P,o} = 0.28$, where the liftoff and blowout are all observed in the laminar regime. After the blowout at $U_o = 3.35$ m/s, reigniting was unsuccessful. The liftoff height H_L is nonlinear to U_o and will be discussed later. The maximum H_L is higher than 50 cm, which is much larger than previous observations for the laminar and turbulent regimes. In the experiment using pure fuel [2], it was predicted that H_L at the blowout would be proportional to d^2 in the laminar regime. Thus, for the present diluted jets using a much larger nozzle diameter, the observed maximum H_L is expected to be much larger.

For $Y_{P,o} = 0.51$, the flame initially lifts off in the laminar regime, where H_L is rapidly increased with U_o, as is shown in Fig. 5. As U_o is further increased, H_L decreases with U_o in the region of $4.8 < U_o < 7$ m/s. This region corresponds to the jet breakup, as seen in Fig. 2b, where the jet breakup is defined as the location of laminar-to-turbulent transition along the jet [3]. This jet breakup height is plotted in Fig. 5 for both the cold jet and a jet flame, whose difference is negligible because the flame is stabilized above the jet breakup height, and the flame base has a limited influence on the upstream (Fig. 2b). The decrease in H_L in this range can be attributed to the decrease in the breakup height with U_o. For $U_o > 7$

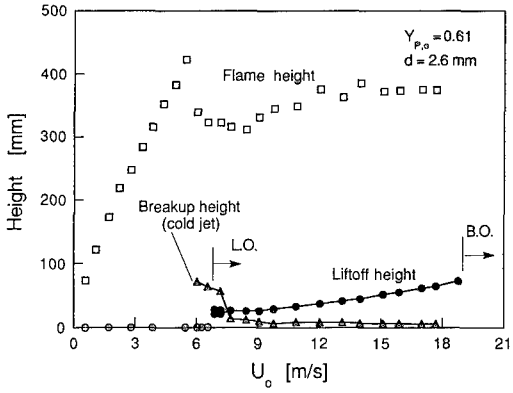

FIG. 6. Flame characteristics with nozzle exit velocity for d = 2.6 mm and $Y_{P,o}$ = 0.61.

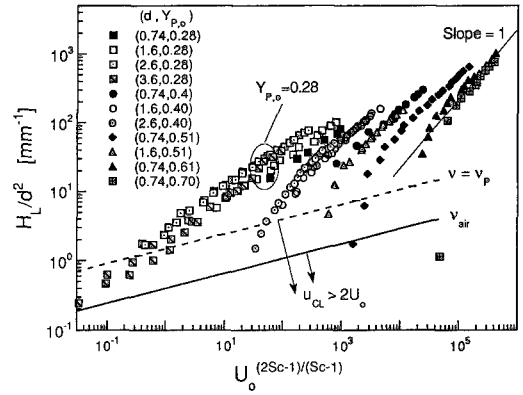

FIG. 7. Liftoff height characteristics for laminar-lifted flames (U_o in m/s) for Sc = Sc_P in abscissa.

m/s, which corresponds to Re_d = 2300, the breakup height decreases rapidly. As U_o is further increased ($8 < U_o < 9.6$ m/s corresponding to $Re_d \approx$ 2600–3100), H_L rapidly decreases with U_o (Fig. 2c). Thus, this rapid decrease in H_L arises from the transition to turbulence inside the nozzle. After this transition, H_L increases slowly and linearly with U_o, as was previously observed [5,10].

For $Y_{P,o}$ = 0.61, the liftoff only occurs in the turbulent regime, as shown in Fig. 6, when U_o = 6.9 m/s, corresponding to Re_d = 2500.

Laminar Liftoff Height:

In the previous work with a pure fuel jet [2], the following relation had been derived:

$$H_L/d^2 \propto U_o^{(2Sc-1)/(Sc-1)} \tag{1}$$

where Sc is the Schmidt number of fuel. This derivation was based on the laminar cold jet theory and the tribrachial nature near the stabilization point [2]; thus, the influence of the flame base to the upstream was O (1 mm) corresponding to the laminar flame thickness. Also, the concentration at the flame base should be stoichiometric, since rich and lean premixed flames as well as a diffusion flame coexisted there. Hence, for the flame to be stationary at the flame-anchoring point, the axial velocity should be equal to the laminar burning velocity of the stoichiometric mixture.

The present experimental data of H_L for the diluted fuel are plotted in Fig. 7 using Eq. (1), where Sc = Sc_p = 1.376 for propane into air has been used in the abscissa. This demonstrates several marked differences from the pure fuel data of Ref. 2, where the slopes were all unity irrespective of d for the pure propane jet. First, the slopes are much larger than unity for small U_o. The reason can be explained as follows. The axial velocity in the jet theory can be written as [2]

$$u = \frac{3}{8\pi\nu x}\frac{J}{\rho}\frac{1}{(1+\eta^2/8)^2} \tag{2}$$

where u is the axial velocity; ν is the kinematic viscosity; ρ is the density; $\eta = \sqrt{1/8}(U_o d/\nu)(r/x)$, the similarity variable; x and r are the axial and radial coordinates, respectively; and J is the momentum flux at the nozzle exit defined as $J = \pi\rho U_o^2 d^2/3$, assuming a fully developed Poiseuille flow at the exit. This can be applied in the far field region, and the centerline velocity $u_{CL} = U_o^2 d^2/(8\nu x)$ should be smaller than the maximum nozzle exit velocity $2U_o$ for the Poiseuille flow, corresponding to $x/d^2 > U_o/(16\nu)$. This criterion is plotted in Fig. 7 for $\nu = \nu_{air}$ and ν_P. Since the far field region is farther away from this criterion, it is clear that the rapid increase of H_L/d^2 for small U_o is outside of the applicability of the jet theory; in other words, the liftoff height is too small for the jet theory to be valid.

In the high-velocity regime, the slope of H_L/d^2 in Fig. 7 is decreasing with the decrease in $Y_{P,o}$ from unity and is weakly dependent on diameter, as can be seen for $Y_{P,o}$ = 0.28. In Fig. 8a, the slope of the curves in Fig. 7 for large U_o is plotted. The slopes are close to unity for $0.6 < Y_{P,o} \leq 1.0$ and decrease rapidly with the decrease in $Y_{P,o}$ for $Y_{P,o} < 0.6$. These slopes can be used in determining an effective Schmidt number for the diluted fuel mixture by using Eq. (1) and treating the fuel mixture as a single component. However, the calculated effective Sc is larger than the Sc of propane or nitrogen, which seems physically unrealistic. Thus, propane and the diluent nitrogen in the fuel stream should be considered separately because of their respective different mass diffusivities; in other words, nitrogen and pro-

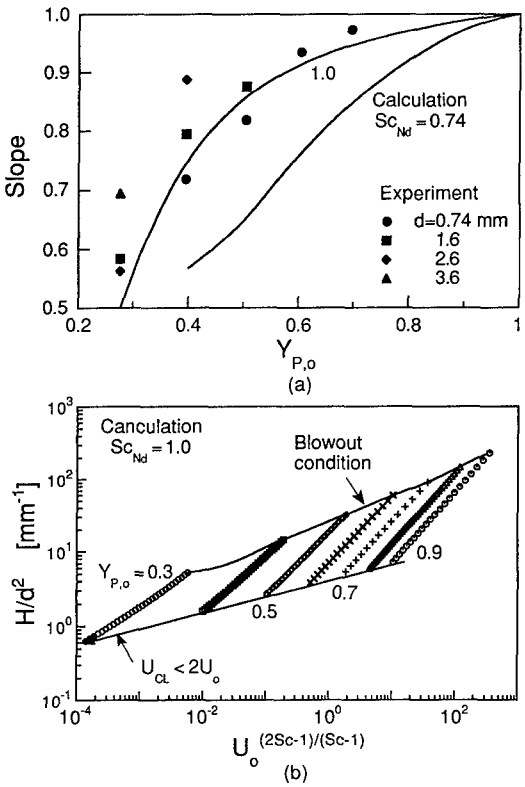

FIG. 8. Liftoff characteristics: (a) slope as functions of dilution from experiment in Fig. 7 and (b) theoretical prediction of flame behavior.

pane have different proportions in the flow field. To demonstrate this preferential diffusion effect, we start from the profiles of species concentrations written as [2]

$$Y_j = \frac{(2Sc_j + 1)}{8\pi\nu x}\frac{I_j}{\rho}\frac{1}{(1 + \eta^2/8)^{2Sc_j}} \tag{3}$$

where I_j is the mass flow rate for jth species defined as $I_j = \pi\rho U_o d^2 Y_{j,o}/4$ and the subscripts $j = P$ and Nd stand for propane and diluent nitrogen, respectively. Here, we have treated the diluent nitrogen and the nitrogen in air separately, and air is treated as a single component in deriving the equation. The effect of the radial velocity is neglected since it is much smaller than u.

Based on the tribrachial nature of the flame, propane and air should be in stoichiometry, and the axial velocity is the laminar flame speed of this mixture. To determine the flame anchor position, flame speed information is needed. The laminar flame speed, u°, of the stoichiometric propane/air with nitrogen dilution is calculated by using Smooke's code [12] and the detailed kinetic mechanism of Peters [13]. The results are normalized and correlated as

$$u^\circ = 17.41Y_P^\circ - 0.602, \qquad 0.045 < Y_P^\circ < 0.060 \tag{4}$$

with the correlation coefficient larger than 0.995 where the superscript $^\circ$ indicates the flame stabilization point. Here, $Y_P^\circ = 0.060$ corresponds to the stoichiometric propane/air without the nitrogen dilution, whose flame speed was adopted to be 0.44 m/s [14].

Considering the tribrachial nature at the stabilization point (x°, r°), where x° is H_L, the axial velocity becomes u° and $Y_{air}^\circ/Y_P^\circ = AF$, where AF is the stoichiometric air to propane mass ratio. In Eq. (2), $(1 + \eta^{\circ 2}/8)^2$ can be expressed by u° and x° and when substituted into Eq. (3), one finds

$$Y_j^\circ = a_j U_o^{1-2Sc_j}(x^\circ/d^2)^{Sc_j - 1}\, u^{\circ Sc_j} Y_j^o \tag{5}$$

where $a_j = (1 + 2Sc_j)8^{Sc_j}\nu^{(Sc_j-1)}/32$. One can express x°/d^2 from Eqs. (4) and (5) and U_o from $Y_P^\circ + Y_{Nd}^\circ + Y_{air}^\circ = 1$ as functions of u° and Y_p°, resulting in

$$x^\circ/d^2 = u^\circ(a_P Y_{P,o}/Y_P^\circ)^{(2Sc_{Nd}-1)/Sc_{Nd}-Sc_P)} \cdot (a_{Nd}Y_{Nd,o}/Y_{Nd}^\circ)^{(2Sc_P-1)/(Sc_P-Sc_{Nd})} \tag{6}$$

$$U_o = u^\circ(a_P Y_{P,o}/Y_P^\circ)^{(Sc_{Nd}-1)/Sc_{Nd}-Sc_P)} \cdot (a_{Nd}Y_{Nd,o}/Y_{Nd}^\circ)^{(Sc_P-1)/(Sc_P-Sc_{Nd})} \tag{7}$$

Since $(1 + \eta^{\circ 2}/8)^2 > 1$ in Eq. (2), $x^\circ/d^2 < U_o^2/(8\nu u^\circ)$, which corresponds to the blowout condition [2] when $u = u^\circ$ and $Y_P = Y_P^\circ$ contours cross on the centerline. Also, $u_{CL} < 2U_o$, as was previously mentioned. Calculations are conducted within these two limits by varying u° and determining Y_P° from Eq. (4), then from Eqs. (6) and (7), x°/d^2 and U_o can be calculated. The air viscosity, $Sc_P = 1.376$ and $Sc_{Nd} = 1$ are used since Sc of nitrogen into air is close to unity. The results are shown in Fig. 8 with linearly fitted slopes. The experimental results and calculations agree well, substantiating the importance of the preferential diffusion and the effect of flame speed variation with nitrogen dilution.

Several points are worth mentioning. First, the derivation shows that x°/d^2 is independent of d, which agrees with the experiment. Another point is that the abscissas in Figs. 7 and 8b are different on the order of 100. Knowing that the jet theory generally has inaccuracies in the absolute velocity prediction, this can easily compensate for the difference of the order of 100, since the abscissa used is $U_o^{4.66}$ for Sc = 1.376. To test the sensitivity of Sc_{Nd}, the data for $Sc_{Nd} = 0.74$, which corresponds to the self-diffusion coefficient of nitrogen [15], are plotted

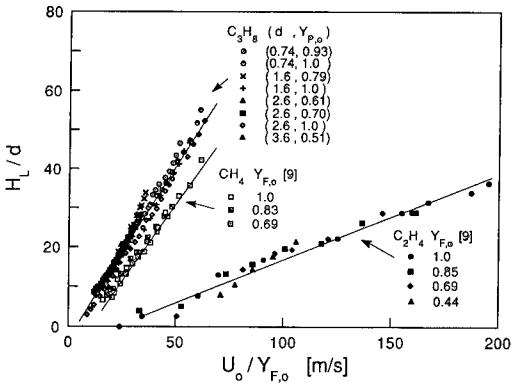

FIG. 9. Turbulent-lifted flame height with nozzle exit velocity.

showing a decreasing slope, which is faster than $Sc_{Nd} = 1$.

Turbulent Liftoff Height:

The present experimental data in the turbulent regime for various nozzle diameters ($0.74 \leq d \leq 3.6$ mm) and degrees of dilution ($0.5 \leq Y_{P,o} \leq 1.0$) are correlated in Fig. 9 in terms of H_L/d vs $U_o/Y_{P,o}$, where the subscript F stands for fuel and P for propane. This plot demonstrates that H_L correlates well with d and the fuel dilution with the correlation coefficient of 0.989. The present experiment was conducted for the nozzle length long enough for the flow to be fully developed, and there was an enclosure surrounding the nozzle. Whereas the nozzle length in Ref. 5 was 10 cm extending from a settling chamber, and the experiment was conducted in an open environment so that the flow pattern is expected to be different. This difference can explain the discrepancy on the diameter dependence found in Ref. 5, where it had suggested the independence of d on H_L. The term $Y_{F,o}$ in the horizontal axis can be conceived as the effect of dilution on the flame speed for the non-premixed jet; however, the linear dependence on diameter cannot be fully explained. Factors affecting this includes the turbulence intensity and the length scale along the jet and the turbulent flame speed.

Using the present correlation, the air-diluted premixed jet experiment with fixed nozzle diameter by Miake-Lye and Hammer [8] is also plotted in Fig. 9 motivated by the fact that lifted non-premixed jet also had the characteristics of premixed nature near the flame stabilization region by the air entrainment [4,10]. As can be seen, the liftoff height correlates well with $U_o/Y_{F,o}$.

Concluding Remarks

Liftoff characteristics of nitrogen-diluted, non-premixed jets have been studied experimentally. The observed liftoff can be classified into three different modes depending on flow characteristics at the liftoff and blowout. For the lifted flame with transition, i.e., where the fluid undergoes the transition from a laminar flow to a turbulent flow, the liftoff height initially grows rapidly in the laminar range until the height becomes comparable to the jet breakup length, then it decreases with the jet velocity. After the sudden decrease at the transition to turbulence inside the nozzle flow, the liftoff height increases linearly in the turbulent regime.

For laminar-lifted flames, the effect of preferential diffusion and flame speed variation by nitrogen dilution has been demonstrated. For turbulent flames, H_L/d vs $U_o/Y_{P,o}$ correlates well for the fully developed nozzle flow conditions in an enclosure employed in this investigation.

Acknowledgment

This work was supported by the Korea Science and Engineering Foundation through the Turbo and Power Machinery Research Center. We are thankful to one of the Publications committee member for his English editing.

REFERENCES

1. Savas, Ö., and Gollahalli, S. R., *J. Fluid Mech.* 165:297–318 (1986).
2. Chung, S. H., and Lee, B. J., *Combust. Flame* 86:62–72 (1991).
3. Scholefield, D. A., and Garside, J. E., *Third Symposium (International) on Combustion*, Williams and Wilkins, Baltimore, 1949, pp. 102–110.
4. Vanquickenborne, L., and van Tigglen, A., *Combust. Flame* 10:59–69 (1969).
5. Kalghatgi, G. T., *Combust. Sci. Technol.*, 41:17–29 (1984).
6. Peters, N., and Williams, F. A., *AIAA J.* 21:423–429 (1983).
7. Eickhoff, H., Lenze, B., and Leuckel, W., *Twentieth Symposium (International) on Combustion*, The Combustion Institute, Pittsburgh, 1986, pp. 311–318.
8. Miake-Lye, R. C., and Hammer, J. A., *Twenty-Second Symposium (International) on Combustion*, The Combustion Institute, Pittsburgh, 1988, pp. 817–824.
9. Yamashita, H., Kushida, G., and Takeno, T., *Twenty-Fourth Symposium (International) on Combustion*, The Combustion Institute, Pittsburgh, 1992, pp. 311–316.
10. Pitts, W. M., *Twenty-Second Symposium (Interna-*

tional) on Combustion, The Combustion Institute, Pittsburgh, 1988, pp. 809–816.

11. Takahashi, F., and Goss, L. P., *Twenty-Fourth Symposium (International) on Combustion*, The Combustion Institute, Pittsburgh, 1992, pp. 351–359.
12. Smooke, M. D., *J. Computat. Phys.* 48:72–105 (1982)
13. Peters, N, in *Reduced Kinetic Mechanisms for Application in Combustion Systems* (N. Peters and B. Rogg, Eds.), Lecture Notes in Physics Series m15, Springer-Verlag, Berlin, 1993, pp. 3–14.
14. Law, C. K., in *Reduced Kinetic Mechanisms for Application in Combustion Systems* (N. Peters and B. Rogg, Eds.), Lecture Notes in Physics Series m15, Springer-Verlag, Berlin, 1993, pp. 15–26.
15. Landolt-Börnstein, *Transportphänomene*, Springer-Verlag, Berlin, Aufl. 6, Bd. II/Teil 5, 1969.

Twenty-Fifth Symposium (International) on Combustion/The Combustion Institute, 1994/pp. 1183–1189

STABILIZATION MECHANISM OF LIFTED JET DIFFUSION FLAMES

CAROLYN R. KAPLAN* AND ELAINE S. ORAN**
*Chemistry Division, **Laboratory for Computational Physics and Fluid Dynamics
Naval Research Laboratory
Washington, D.C. 20375, USA

AND

SEUNG W. BAEK
Department of Aerospace Engineering
Korea Advanced Institute of Science and Technology
Taejon, Korea

Flame lift and stabilization are studied using numerical simulations of diffusion flames resulting from a methane jet injected into an air background. The numerical model solves the time-dependent, axisymmetric, multidimensional Navier–Stokes equations coupled to submodels for chemical reaction and heat release, soot formation and radiation transport. Simulations are conducted for an undiluted methane jet and for two nitrogen-diluted jets ($CH_4:N_2/3:1$ and $CH_4:N_2/1:1$). The jet exit velocities range from 20 to 50 m/s through a 1-cm-diameter nozzle, coflowing into a 30-cm/s air stream. The flame liftoff height increases linearly with jet exit velocity and the stabilization height increases as the nitrogen dilution of the jet increases. The computations show that the flame is stabilized on a vortical structure in the inner shear layer, which is on the stoichiometric surface at a height where the local axial velocity is approximately equal to the turbulent burning velocity. There is no appreciable chemical heat release in the region below the stabilization point, although a stoichiometric surface exists in that region. The flame base moves upward with the vortical structure to which it is attached, and then quickly jumps down to attach to a new, lower vortex, resulting in an oscillating (1–2 cm) flame liftoff height. The results corroborate parts of both the premixedness and extinction stabilization theories, and suggest that the liftoff mechanism is a result of complex fluid-chemical interactions, parts of which are incorporated in the simplified theories.

Introduction

Although a great deal of research has been devoted to the study of liftoff and blowout of turbulent jet diffusion flames, the physical mechanisms responsible for flame stabilization are still controversial. A recent review by Pitts [1] summarized published experimental and theoretical results and has concluded that none of the theories currently available is totally satisfactory. Pitts [1] further concludes that the current experimental characterization of flame stabilization is insufficient to determine the actual physical processes that determine liftoff and blowout.

The phenomenon of liftoff has been experimentally investigated for many decades through flow visualization studies. Vanquickenborne and van Tiggelen [2] provided extensive experimental measurements of nonreacting and reacting turbulent jets of methane over a broad range of jet exit diameters and velocities. Their findings [2] show that lifted flames are stabilized in a turbulent region of the jet near the radial position where the time-averaged fuel mass fraction equals that required for stoichiometric burning. Other measurements of jets of mixtures of natural gas and hydrogen [3,4] showed that the most likely radial position for combustion to occur is along the mass-fraction contour where the laminar flame speed is maximum. Extensive experimental studies by Kalghatgi [5] for a variety of fuels and a wide range of jet diameters and velocities have resulted in empirical correlations between liftoff height, jet velocity, and maximum laminar flame speed. Observations for lifted natural-gas flames have been reported by Eickhoff et al. [6] and Sobiesiak and Brzustowski [7] and for propane flames by Savas and Gollahalli [8].

Analysis of the experimental studies has resulted in the development of theoretical treatments of flame stabilization. Vanquickenborne and van Tiggelen [2] suggested that the stabilization of lifted turbulent jet diffusion flames can be understood by assuming that the fuel-air mixture is fully premixed at the base of the lifted flame. They then define a local flame speed, which is determined by the local turbulence structure. The flame is stabilized at a position where the local time-averaged axial velocity along the stoichiometric mass fraction contour equals the local flame

speed. Results of other experiments [3–7] have supported this premixedness model.

Several more recent theories challenge this by proposing that the stabilization of lifted flames results from flame extinction processes that occur in turbulent structures of the nearby unignited flow. Many different types of extinction processes have been suggested [9–14]. Peters and Williams [9] analyzed the problem in terms of the laminar flamelet model, in which flamelets are extinguished when the local turbulence-induced concentration gradients are sufficient to quench combustion. Flame stabilization occurs at the point where combustion extinction and propagation are balanced. Janicka and Peters [10] considered the effects of assumptions concerning the scalar dissipation on calculated values of liftoff height. Donnerhack and Peters [11] tested a local quenching theory, in which they state that extinction occurs when the rate of heat conduction to the sides of the flame exceeds the rate of heat production due to chemical reaction. Byggstoyl and Magnussen [13] suggest that the extinction occurs in the smallest vortices of the flow, while Broadwell et al. [14] suggest that lifted flames result from flame extinction in large-scale turbulent structures.

In this paper, we describe results from a time-dependent numerical model used to study the unsteady behavior of an axisymmetric coflowing methane-air jet diffusion flame. First, we use a series of calculations with increasing jet exit velocities to demonstrate that the numerical model can, in fact, simulate the phenomenon of flame lift and that the results are consistent with the correct physical behavior. Then we analyze these flames to determine trends in liftoff behavior and make comparisons with some of the current theories of flame stabilization.

Numerical Method

The numerical model solves the time-dependent equations for conservation of mass density, momentum, energy, individual species number densities, soot number density, and soot volume fraction [15]. The solution to the conservation equations includes both radial and axial components of molecular diffusion, thermal conduction, viscosity, radiation transport, and convection; that is, we do not make boundary-layer approximations and do not restrict the Lewis number to unity. These equations are rewritten in terms of finite-volume approximations on an Eulerian mesh and solved numerically for specified boundary and initial conditions. The model consists of separate algorithms for each of the individual processes, which are then coupled together by the method of timestep splitting [15–19].

The different algorithms and how they are applied to solve for the convective [20], diffusive, and radiation transport processes have already been described in detail [15–17], and are not discussed here. However, the algorithms for chemical reaction and soot formation are different than those used previously [15,16], and therefore are described below. We represent the chemical reaction and energy-release process phenomenologically using a finite-rate, single-step, quasi-global Arrhenius expression [21]

$$-\frac{d[\mathrm{CH_4}]}{dt} = 2.3 \times 10^7 \cdot \exp\left[\frac{-30{,}000}{RT}\right][\mathrm{CH_4}]^{-0.3}[\mathrm{O_2}]^{1.3} \tag{1}$$

where T is temperature and R is the universal gas constant. Equation (1) is used to calculate the rate of depletion of CH_4. In order to prevent an infinite reaction rate when the CH_4 is fully depleted, we assume a zero reaction rate when the CH_4 concentration falls below 1.0×10^{-20} moles/cm^3. The concentrations of O_2, CO_2, H_2O, and N_2 are then calculated based on their respective stoichiometric coefficients. The chemical heat release rate is then determined from

$$Q = -\Delta H_c \frac{d[\mathrm{CH_4}]}{dt} \tag{2}$$

where ΔH_c is the heat of combustion for CH_4 oxidation.

The evolution of soot number density and soot volume fraction is represented by two coupled ordinary differential equations derived by Syed et al. [22] based on their experimental measurements in methane-air diffusion flames, and include terms for soot nucleation, surface growth, and coagulation on the soot formation rate.

$$\frac{dn_d}{dt} = N_0 C_a \rho^2 T^{1/2} X_{\mathrm{fuel}} e^{-T_a/T} - \frac{1}{N_0} C_\beta T^{1/2} n_d^2 \tag{3}$$

$$\frac{df_v}{dt} = \frac{1}{\rho_{\mathrm{soot}}}\left[C_\gamma n_d^{1/3}(\rho_{\mathrm{soot}} f_v)^{2/3}\rho T^{1/2} X_{\mathrm{fuel}} e^{-T_\gamma/T} + C_\delta C_a \rho^2 T^{1/2} X_{\mathrm{fuel}} e^{-T_a/T}\right] \tag{4}$$

where n_d is the soot number density, N_0 is Avogadro's number, ρ is the fluid density, X_{fuel} is the fuel mole fraction, and f_v is the soot volume fraction. The constants, C_a, C_β, C_γ, C_δ, T_a, T_γ are taken from Ref. 22, and ρ_{soot}, the density of a soot particle, is assumed to be 1.8 g/cm^3. The soot volume fraction and number densities, as calculated in Eqs. (3) and (4), are further reduced by a soot oxidation algorithm [15].

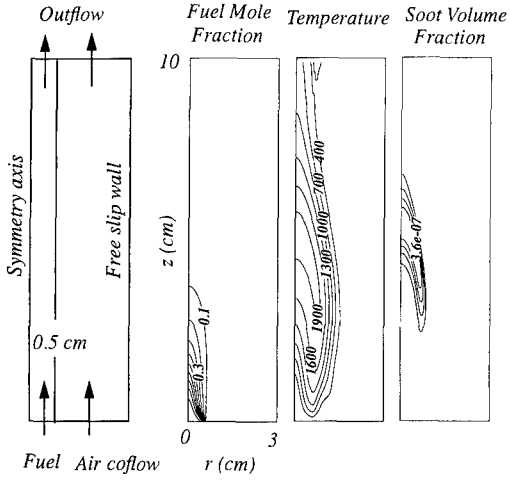

FIG. 1. Initial conditions and computed contours for a laminar methane-air diffusion flame.

Results

Steady Methane-Air Diffusion Flame:

Simulations were first conducted for a steady-state, laminar methane-air diffusion flame for which the experimental data of Mitchell et al. [23] are available. Figure 1 shows a schematic of the computational conditions and results from a simulation in which undiluted methane flows at 5 cm/s through a 1.2-cm-diameter tube, while air flows at 10 cm/s through the outer annular region. The full computational grid is 10 × 20 cm and consists of 128 × 152 cells. Cells of approximately 0.02 × 0.02 cm are concentrated around the jet exit; the grid spacing is then gradually stretched in both the radial and axial directions [15–17]. This time-dependent calculation showed that the flame reached the steady state shown by 12,000 timesteps (0.12 s). The contours of fuel mole fraction, temperature, and soot volume fraction predict that the flame height is approximately 8 cm, based on the height of the sooting layer. The maximum soot volume fraction is 3.6×10^{-7}, and is located on the fuel-rich side of the high-temperature region. Figure 2 compares experimental and computed radial profiles of temperature at selected heights above the burner for which experimental data were presented [23]. The dashed line is the curve drawn by Mitchell et al. [23] through their experimental data points (error bars are not included with the experimental results). In general, the agreement is quite reasonable, although there is a tendency for the simulations to predict a flame sheet thickness that is wider than those observed experimentally at lower heights in the flame.

Unsteady Lifted Methane-Air Diffusion Flame:

Simulations of lifted flames were then conducted for cases in which the fuel mixture flows at a high velocity through a 1.0-cm-diameter jet into a low-velocity (30 cm/s) coflowing air stream. The fuel streams considered included undiluted methane and also nitrogen-diluted ($CH_4:N_2/3:1$ and $CH_4:N_2/1:1$) fuel mixtures. Figure 3 shows contours of temperature, chemical heat release rate, and radial velocity for cases in which the undiluted methane fuel jet velocity varies from 20 to 50 m/s. The location of the stoichiometric surface is shown by the solid line with black circles superimposed. The radial velocity contours show the Kelvin–Helmholtz instabilities, which form in the shear layer between the high- and low-velocity streams. The dashed lines in the radial velocity contours correspond to counterclockwise rotating structures, while the solid lines correspond to clockwise-rotating structures. As shown in

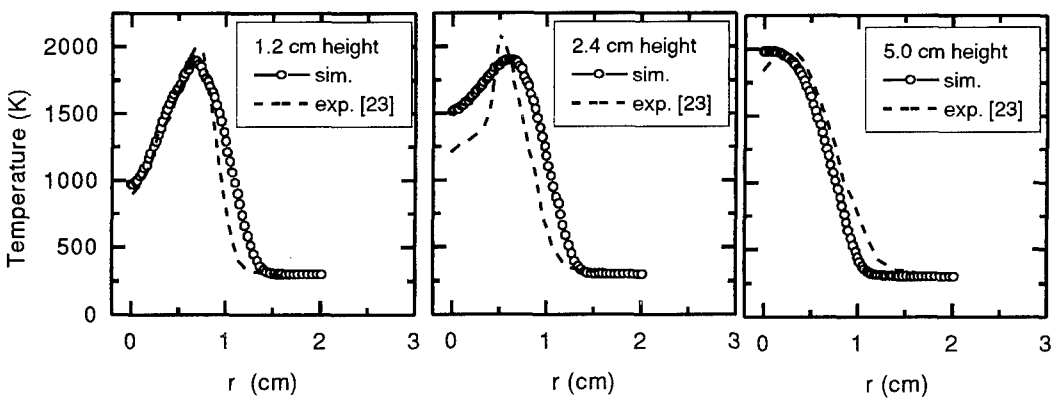

FIG. 2. Comparison between simulation and experimental results [23] for laminar methane-air flame. The dashed line is the curve drawn by Mitchell et al. [23] through their experimental data.

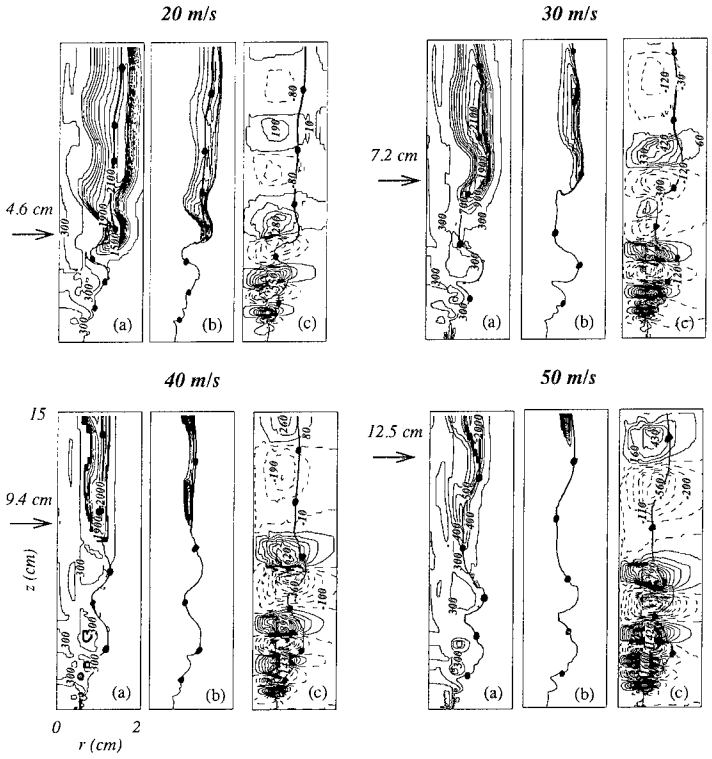

FIG. 3. (a) Temperature (K), (b) chemical heat release rate (ergs/cm^3-s), and (c) radial velocity (cm/s) contours for undiluted methane fuel jet; jet inflow velocities 20–50 m/s. Heavy solid line with solid circular symbols corresponds to the location of the stoichiometric surface. Arrow points to liftoff height.

Fig. 3, the liftoff heights are 4.6, 7.2, 9.4, and 12.5 cm for the 20, 30, 40, and 50 m/s cases, respectively. For all of the cases shown, the base of the lifted flame is situated on the stoichiometric surface, and is attached to a Kelvin–Helmholtz structure; that is, the stoichiometric contour passes through the vortical structure at the flame stabilization location.

Figure 4 shows that there is reasonable agreement between the simulation results and the experimental data of Kalghatgi [5]. Both show a linear relationship between flame liftoff height and jet exit velocity. Figure 4 also shows results from a simulation in which the fuel jet is diluted with nitrogen ($CH_4:N_2/1:1$). As expected, the liftoff height is greater for a given jet inflow velocity for the nitrogen-diluted case, as the residence time (chemical time) is longer when the fuel stream is diluted. For the nitrogen-diluted case, the liftoff height is again a linear function of the jet exit velocity, but the slope of this line is greater than that for the undiluted case. This phenomenon of a steeper slope with increasing nitrogen dilution has also been shown experimentally [11,24] in studies of the effect of jet dilution on liftoff height.

The liftoff heights presented in Fig. 4 were taken from instantaneous temperature images at one particular timestep (15,000 timesteps). However, animations of this unsteady flame show that the liftoff height fluctuates. That is, the base of the flame moves up with the vortical structure to which it is attached,

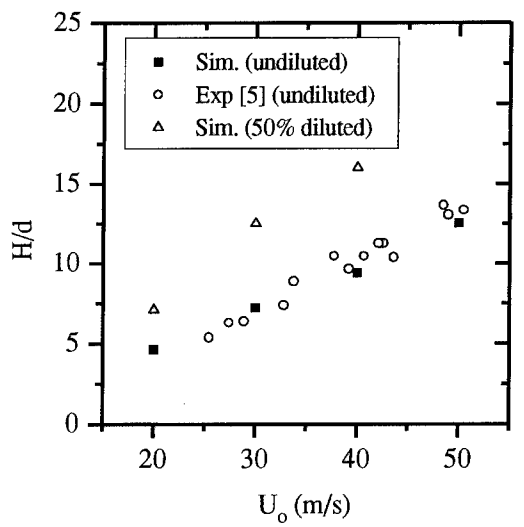

FIG. 4. Liftoff height as a function of jet exit velocity for simulations (undiluted fuel jet and 50% diluted fuel jet) and experimental measurements (undiluted fuel jet).

TABLE 1
Comparison of turbulent burning velocity (S_t) to fluid axial velocity (from the simulations) at the liftoff height. Method used to calculate S_t is outlined at bottom.

Jet velocity (m/s)	Liftoff height (cm)	R_l at liftoff height[a] (approx.)	S_t/S_u[b]	S_t (approx.) at liftoff height[c] (cm/s)	Axial velocity at liftoff height, from simulations (cm/s)
20	4.6	38	1.7–2.6	70–105	60–100
30	7.2	50	1.9–3.0	75–120	80–110
40	9.4	87	2.6–4.0	105–160	110–170
50	12.5	144	3.3–5.1	130–205	140–220

[a]From Eq. (6).
[b]From Eq. (5), and experimental results [5,25].
[c]Based on S_u = 40 cm/s, and S_t/S_u from previous column.

and then quickly jumps down to attach to a new, lower vortex, resulting in an oscillating flame height. The fluctuation in liftoff height due to this movement is approximately 1 to 2 cm.

Tests of Flame Stabilization Theory:

The computations have shown that the numerical model does indeed simulate the phenomenon of flame liftoff, and the results are consistent with published experimental data. Now, we compare the simulation results with some of the current theories of flame lift. One of the important hypotheses from the premixedness theory of Vanquickenborne and van Tiggelen [2] is that the base of the flame stabilizes on the stoichiometric surface at the height where the local axial velocity is equal to the turbulent burning velocity. In order to evaluate this hypothesis, we calculated the ratio of the turbulent burning velocity to the maximum laminar burning velocity (S_t/S_u) at the liftoff height based on a correlation by Kalghatgi [5]

$$\frac{S_t^2}{S_u^2} = R_l \cdot f_4(W_s, \bar{p}) \cdot K \tag{5}$$

where f_4 and K are constants taken from Ref. 5 (f_4 = 0.138, K ranges from 0.56 to 1.3). The term R_l is the turbulent Reynolds number, given by

$$R_l = \frac{u'l}{\nu_s} \tag{6}$$

where u' is the root mean square (rms) fluctuation velocity, l is the turbulent integral length scale in the jet mixing layer, and ν_s is the kinematic viscosity at the base of the flame. In Ref. 5, the values of S_t/S_u as a function of $R_l^{1/2}$ from Eq. (5) are favorably compared with an experimentally determined ratio of turbulent burning velocity to laminar burning velocity as a function of $R_l^{1/2}$ by Smith and Gouldin [25]. That is, the experimental data points of Smith and Gouldin [25] fall within the range of values of S_t/S_u for a given R_l from Eq. (5). Therefore, using values of u' = 2 m/s (simulation results show rms velocity fluctuations on the order of 1 to 2 m/s), and calculating l based on correlations from Abramovich [26] and Davies et al. [27],

$$l = Cz \tag{7}$$

(where C is a constant, and z is the axial height), we calculated values of R_l at the flame lift height from Eq. (6), and used that value to calculate a range of S_t/S_u from Eq. (5). Table 1 lists the values of these quantities for the four cases in which the jet is undiluted. Based on a maximum laminar burning velocity S_u = 40 cm/s for methane-air flames, we calculated the range of turbulent burning velocities, S_t, at the liftoff height, as shown in Table 1.

We then compared these calculated values of S_t with the axial velocity at the liftoff height based on the simulation results. The axial velocity fluctuates considerably (varies from negative to positive values) within the rotating vortical structures to which it is attached. However, the axial velocity is always positive (flowing upwards) in the region immediately below the vortical structure to which the flame is attached. For each of the jet velocities considered, Table 1 shows the range of axial velocity values in the region immediately below the vortical structure to which the flame is attached. As shown, this range of axial velocities based on the simulations is approximately the same as the range of calculated [from Eqs. (5) and (6)] turbulent burning velocities at the liftoff height.

Although the results above show that the simula-

tions do, in fact, corroborate some parts of the premixedness theory [2], this does not imply that the simulations conflict with some of the proposed extinction mechanisms [9–14]. In fact, the computations show that although a stoichiometric surface exists in the region below the stabilization point (as shown in Fig. 3), there is no appreciable chemical heat release or formation of products in that region. This lack of heat release may be due to a local quenching process within the turbulent structures of the jet. The simulation results show that strain rates in the highly turbulent structures near the jet exit are approximately 1000–1400 s^{-1}, then decrease to values of approximately 300–500 s^{-1} at the stabilization point, and continue to decrease with increasing height. Further analysis is planned to fully investigate the strain rates and scalar dissipation in the turbulent structures of the jet.

Summary

A solution of the time-dependent multidimensional reactive flow Navier–Stokes equations has been obtained to study the stabilization mechanism of lifted jet diffusion flames. Although this computation is based on axisymmetric geometry, and hence neglects nonsymmetric turbulence behavior, it is able to capture the fluid-chemical interactions that are important in turbulent flows and contribute to flame lift. The liftoff heights are in reasonable agreement with published experiments; the results show a linear relationship between liftoff height and jet exit velocity, and the liftoff height increases with increasing fuel dilution due to longer residence times. The computations are compared with some of the current theories of flame stabilization, and show that the flame is stabilized on an inner shear layer vortical structure, which is on the stoichiometric surface at a height where the local axial velocity is approximately equal to the turbulent burning velocity. In the region below the stabilization point, strain rates are very high and there is no appreciable chemical heat release, even though a stoichiometric surface exists there. The simulation results corroborate parts of both the premixedness and extinction stabilization theories, and suggest that the liftoff mechanism is a result of complex fluid-chemical interactions, parts of which are incorporated in the simplified theories. Future work includes further investigation of the strain rates and extinction in the turbulent jet region and possible development of a three-dimensional model to fully characterize the effects of nonsymmetric turbulence behavior.

Acknowledgments

This work was sponsored by the Naval Research Laboratory through the Office of Naval Research. Computing time was provided by Numerical Aerodynamic Simulator (NAS), the Pittsburgh Supercomputing Center, and the Naval Research Laboratory. The authors acknowledge Drs. F. Williams, P. Tatem, and J. Boris for providing the necessary resources and environment for the accomplishment of this work.

REFERENCES

1. Pitts, W. M., *Twenty-Second Symposium (International) on Combustion*, The Combustion Institute, Pittsburgh, 1988, pp. 809–816.
2. Vanquickenborne, L., and van Tiggelen, A., *Combust. Flame* 10:59–69 (1966).
3. Hall, L., Horch, K., and Gunther, R., *Brennst.-Warme-Kraft* 32:27–31 (1980).
4. Gunther, R., Horch, K. and Lenze, B., *First Specialist Meeting (International) of the Combustion Institute*, The Combustion Institute, Pittsburgh, 1981, p. 117.
5. Kalghatgi, G. T., *Combust. Sci. Technol.* 41:17–29 (1984).
6. Eickhoff, H., Lenze, B., and Leuckel, W., *Twentieth Symposium (International) on Combustion*, The Combustion Institute, Pittsburgh, 1985, pp. 311–318.
7. Sobiesiak, A., and Brzustowski, T. A., "Some Characteristics of the Stabilization Region of Lifted Turbulent Jet Diffusion Flames," abstract for paper presented at the 1984 Fall Technical Meeting, Eastern Section, The Combustion Institute, Clearwater Beach, FL, December 1984.
8. Savas, O., and Gollahalli, S. R., *AIAA J.* 24:1137–1140 (1986).
9. Peters, N., and Williams, F. A., *AIAA J.* 21:423–429 (1983).
10. Janicka, J., and Peters, N., *Nineteenth Symposium (International) on Combustion*, The Combustion Institute, Pittsburgh, 1982, pp. 367–374.
11. Donnerhack, S., and Peters, S., *Combust. Sci. Technol.* 41:101–108 (1984).
12. Peters, N., *Combust. Sci. Technol.* 30:1–17 (1983).
13. Byggstoyl, S., and Magnussen, B. F., in *Turbulent Shear Flows 4* (L. J. S. Bradbury et al., Eds.), Springer, New York, 1985, p. 381.
14. Broadwell, J. E., Dahm, W. J. A., and Mungal, M. G., *Twentieth Symposium (International) on Combustion*, The Combustion Institute, Pittsburgh, 1984, pp. 303–310.
15. Kaplan, C. R., Baek, S. W., Oran, E. S., and Ellzey, J. L., *Combust. Flame* 96:1–21 (1994).
16. Kaplan, C. R., Baek, S. W., and Oran, E. S., AIAA Paper 93-0109, American Institute of Aeronautics and Astronautics, Washington, D.C., 1993.
17. Ellzey, J. L., Laskey, K. J., and Oran, E. S., *Combust. Flame* 84:249–264 (1991).
18. Ellzey, J. L., and Oran, E. S., *Twenty-Third Symposium (International) on Combustion*, The Combustion Institute, Pittsburgh, 1990, pp. 1635–1640.
19. Oran, E. S., and Boris, J. P., *Numerical Simulation of Reactive Flow*, Elsevier, New York, 1987.

20. Patnaik, G., Guirguis, R. H., Boris, J. P., and Oran, E. S., *J. Comput. Phys.* 71:1–20 (1987).
21. Westbrook, C. K., and Dryer, F. L., *Combust. Sci. Technol* 27:31–43 (1981).
22. Syed, K. J., Stewart, C. D., and Moss, J. B., *Twenty-Third Symposium (International) on Combustion*, The Combustion Institute, Pittsburgh, 1990, pp. 1533–1541.
23. Mitchell, R. E., Sarofim, A. F., and Clomburg, L. A., *Combust. Flame* 37:227–244 (1980).
24. Miake-Lye, R. C., and Hammer, J. A., *Twenty-Second Symposium (International) on Combustion*, The Combustion Institute, Pittsburgh, 1988, pp. 817–824.
25. Smith, K. O., and Gouldin, F. C., *AIAA J.* 17:1243–1250 (1979).
26. Abramovich, G. N., *The Theory of Turbulent Jets*, The M.I.T. Press, Cambridge, MA, 1963.
27. Davies, P. O. A. L., Fisher, M. J., and Barrat, M. J., *J. Fluid Mech.* 15:337 (1963).

COMMENTS

Yei-Chin Chao, National Cheng Kung University, Taiwan, ROC. The lifted flame at the present conditions usually stabilizes downstream of the end of the potential cone where the near-field large coherent structures start to cascade into small eddies and the helical stability modes step in, or dominate the flow. What is the computational grid size at the flame base and how does it compare with the small-eddy scale? How do you take the helical mode into consideration in your computation? The lift-off height fluctuation in your animation indicates the jump of flame base from a vertical structure to another. Did you find "braids" (Ref. 1) formed between vortices before flame jumping?

REFERENCE

1. Chao, Y. C., and Jeng, M. S., *Twenty-Fourth Symposium (International) on Combustion*, The Combustion Institute, Pittsburgh, 1992, pp. 333–340.

Author's Reply. Computational cells are 0.02×0.02 cm near the jet exit, and then are slowly stretched in both the radial and axial directions. At the flame stabilization locations, the cell size is 0.02 cm in the radial direction and varies in the axial direction according to the problem modeled. For the 20 m/s jet, stabilized at $z = 4.6$ cm, $\Delta z = 0.07$ cm, while for the 50 m/s case, stabilized at $z = 12.5$ cm, $\Delta z = 0.15$ cm. These computational cell sizes are substantially smaller than the small-eddy scale, which is about ~0.4 cm.

This computation is a direct numerical simulation that solves the multidimensional, axisymmetric, time-dependent, reactive-flow Navier–Stokes equations. Because it is basically two-dimensional, we cannot see a three-dimensional helical mode.

Contours of fuel mole fraction, temperature, and the stoichiometric surface show significant deformation and stretching as the flame base moves from one vortical structure to another. This stretching is very similar to the "braiding" phenomenon shown in Fig. 4 of the referenced paper.

Twenty-Fifth Symposium (International) on Combustion/The Combustion Institute, 1994/pp. 1191–1197

EFFECT OF TURBULENCE ON EXTINCTION OF COUNTERFLOW DIFFUSION FLAME

HIROSHI TSUJI, AKIRA YOSHIDA AND NOBUYUKI ENDO
Department of Mechanical Engineering
Tokyo Denki University, Tokyo, Japan

A laminar counterflow diffusion flame established in the forward stagnation region of a porous cylinder has been used widely for the laminar flame studies. In the present study, this flame was applied to investigating the extinction of a diffusion flame due to air stream turbulence. Propane or methane was ejected from a 30-mm porous cylinder. The turbulence was given to the counterflowing air stream by perforated plates. The results of this study show that the air stream turbulence causes large-scale distortions with small amplitude on the apparently laminar diffusion flame, and the time-averaged thickness of this flame is three times as large as the purely laminar flame. Even if the air stream becomes turbulent, there exists a critical stagnation velocity gradient beyond which the flame can never be stabilized, however large the fuel ejection velocity is. Local extinction near the stagnation region always leads to global extinction of the whole flame. As expected, the critical velocity gradient decreases as the turbulence intensity increases. This flame is subjected to the sum of the bulk stretch rate exerted by the mean flow and the turbulent stretch rate exerted by small eddies of Kolmogorov scale. The critical total stretch rate at which the extinction occurs is nearly constant for each fuel for all turbulence conditions tested in the present study and coincides with the critical stagnation velocity gradient of the laminar diffusion flame, that is, the total stretch rate without turbulence. This fact suggests that large-scale eddies are not so effective for the local extinction and that the chemical reaction that occurs in molecular scale is not affected by small eddies of the Kolmogorov scale.

Introduction

Extinction of diffusion flames can be caused when the reaction rates of fuel and oxidizer become slower than the rate at which reactants are supplied to the reaction zone by diffusion. The steep velocity gradient and high strain rate associated with flame stretch cause an excess amount of heat convection, which leads to reduction of temperature. As a result, the chemical reaction is retarded, and flame extinction can occur. The extinction of laminar diffusion flames due to flame stretch has been studied mostly by using the counterflow diffusion flame established in the forward stagnation region of a porous cylinder [1–4].

Turbulence provides additional diffusion process and stretch rate through eddy motion. For diffusion flames in the turbulent shear layer, extinction occurs when a large-scale aerodynamic time scale is small compared with the chemical reaction time scale [5]. It is natural that the extinction of such a flame is affected by large eddies rather than by small dissipative eddies, because the flame is at first subjected to shear-generated large eddies that break down to small-scale eddies downstream through the turbulent energy cascade. Even for fully developed turbulent flow, it has been suggested that large-scale eddies play an important role in the lifting off and blowing out of the jet diffusion flame [6]. However, data were scattered, and the extinction mechanism due to large-scale stretch rates is rather inconclusive.

On the other hand, based on the small-scale stretching of laminar diffusion flamelets, a critical value of the scalar dissipation rate has been introduced to predict the liftoff heights of the jet diffusion flame [7]. The importance of the Kolmogorov-scale eddies has been also suggested [8]. In this model, extinction occurs when the mixing rate in Kolmogorov-scale eddies is faster than chemical reaction rates [8]. In the counterflow geometry, the bulk flow stretch rate can be estimated by the velocity gradient of the mean flow. In addition to the bulk flow stretch rate, Kostiuk et al. [9] introduced the small-scale turbulent stretch rate based on the Kolmogorov time scale and showed that the extinction of turbulent premixed flames occurs when the sum of bulk flow stretch rate and small-scale stretch rate exceeds a critical value [10]. Also, for the partially premixed and nonpremixed turbulent flames, extinction limits were found to be correlated by the sum of the bulk flow stretch rate and small-scale stretch rate [11,12]. Total stretch rates when extinction occurs follow a single curve as a function of air volume fraction in the fuel [11].

In the present work, we adopted the counterflow

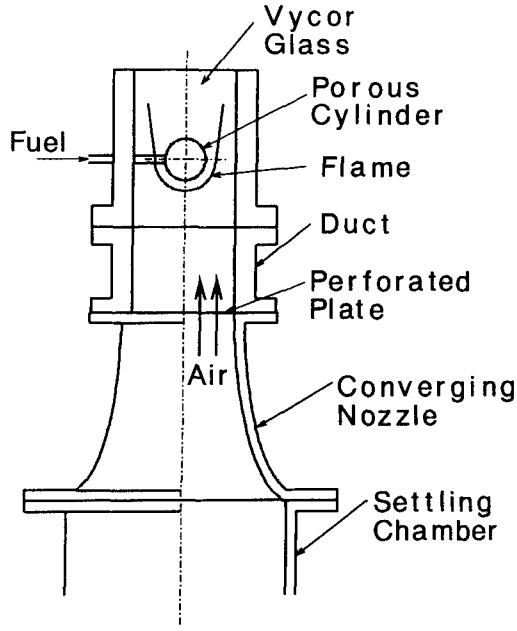

FIG. 1. Burner assembly.

geometry established in the forward stagnation region of a porous cylinder, from which fuel gas was ejected uniformly into the counterflowing air stream. The specific objectives were to measure extinction limits as a function of bulk flow and turbulent stretch rates and to determine which scale of eddies is effective, large scale or small scale, for local flame extinction.

Experimental Apparatus

The experiments were performed using a rectangular chamber of 30-mm × 120-mm cross section and an uncooled porous cylinder 30 mm in diameter and 30-mm long, as shown in Fig. 1. The air stream at the exit of the converging nozzle had a uniform velocity profile and was of low turbulence level. A turbulence-producing grid was installed at the nozzle exit. A constant area extension duct 100 mm in length was placed on the turbulence-producing grid to ensure the establishment of fully developed isotropic turbulent flow. In the present study, three kinds of perforated plates were used to vary the turbulence characteristics.

The porous cylinder was made of sintered bronze of nominal porosity of 2 μm and 5 mm in thickness. The cylinder spanned the short 30-mm dimension of the combustion chamber, and the center of the cylinder was located 170 mm downstream of the turbulence-producing grid. The downstream side of the cylinder surface was coated with heat-resisting paint in order to prevent ejection of the fuel into the wake produced downstream of the cylinder. The ejection velocity was calculated by dividing the volume flow rate of fuel by the ejection area of cylinder surface. It is noted that no turbelence was added to the fuel flow, although the air stream was turbulent. Fuels used were propane (98.7% pure) and methane (99.8% pure).

The configuration of flame stabilized in the forward stagnation region of the cylinder was recorded by means of direct time exposure and instantaneous schlieren photographs. Flame geometry was also recorded on the frame memory of a computer through a charge-coupled device (CCD) camera. The location and the thickness of the flame were measured using the stored data, and the distance from the cylinder surface to the flame was determined. The turbulence characteristics of the air stream were measured by a hot-wire anemometer.

TABLE 1.
Turbulence-Producing Grids and Turbulence Characteristics for V = 2.0 m/s

Grid no.	Hole diameter (mm)	Distance between holes (mm)	v' (m/s)	L (mm)	R_L	a_t (1/s)
None	—	—	0.013	—	—	—
P_1	2.0	3.5	0.266	7.7	130.9	195.3
P_2	3.0	4.0	0.124	5.8	46.0	81.3
P_3	5.0	8.0	0.185	4.8	56.7	165.3

Experimental Results and Discussion

Flow Configuration:

In the present study, when estimating the flow-field parameters, we used the values of the mean velocity, the turbulence intensity, and the length scales at the center of the extension duct exit, 55 mm upstream of the cylinder surface. The flow field was measured under isothermal flow conditions by a hot-wire anemometer. Table 1 shows the specifications of perforated plates used and characteristics of turbulence for the mean velocity V = 2.0 m/s. Hence, v' is the turbulence intensity, L the integral scale of turbulence, and R_L the Reynolds number based on the integral scale. The turbulent stretch rate a_t will be mentioned later. Figure 2 shows the lateral profiles of mean and fluctuating velocities at the extension duct exit for P_2 grid and V = 2.8 m/s. Mean and fluctuating velocities are uniform across the exit cross section except for the boundaries.

Figure 3 shows the mean and fluctuating velocity profiles along the stagnation stream line for the P_2

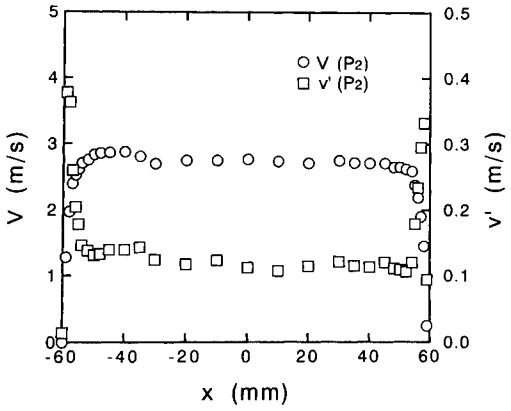

FIG. 2. Lateral profiles of mean and fluctuating velocities for $V = 2.8$ m/s.

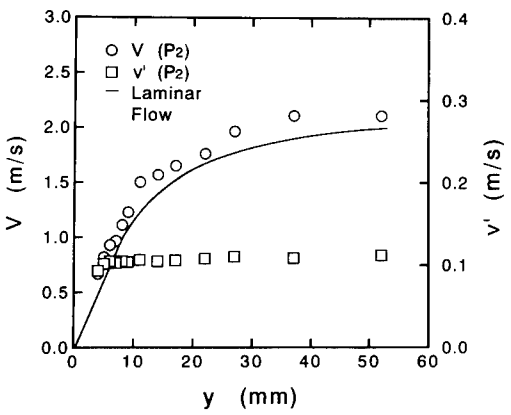

FIG. 3. Mean and fluctuating velocity profiles along stagnation stream line for $V = 2.0$ m/s.

grid and $V = 2.0$ m/s, the origin being placed on the cylinder surface. The velocity profile for the laminar case is also shown by a solid line for comparison. The mean velocity gradually decreases toward the cylinder surface, and the flow field with constant velocity gradient is established near the forward stagnation region. The stagnation point lies on the cylinder surface, because no fuel was ejected in the measurements of flow field. The mean velocity profile for turbulent flow is similar to that for laminar flow. The mean flow is decelerated along the stagnation stream line, whereas the turbulence intensity is fairly constant even near the cylinder surface. This finding is consistent with the results obtained in the stagnating flow toward the flat plate [13,14]. The scale of turbulence was also found to be unchanged along the stagnation stream line except for the vicinity of the stagnation point [13]. The initial turbulence produced by the perforated plate will decay with distance from the plate. This decay of turbulence should

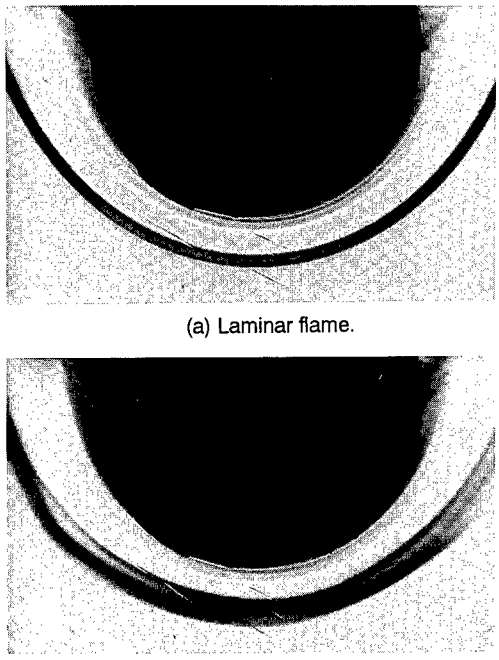

(a) Laminar flame.

(b) Turbulent flame, $v' = 0.13$ m/s.

FIG. 4. Schlieren photographs of laminar and turbulent methane diffusion flames for $V = 1.0$ m/s and $v_w = 0.26$ m/s. (a) Laminar flame, (b) turbulent flame, $v' = 0.13$ m/s.

be compensated by the turbulence production due to the bulk flow stretch [15]. The independence of the mean flow from the turbulence suggested in Figs. 2 and 3 implies that the mean and the turbulent field can be described independently.

Flame Appearance:

Figure 4(a) shows an instantaneous schlieren photograph of a thin laminar diffusion flame of methane for $V = 1.0$ m/s and $v_w = 0.26$ m/s, where v_w is the fuel ejection velocity. The purely laminar diffusion flame is stabilized at some distance from the cylinder surface in the forward stagnation region. When the turbulence producing grid P_1 was installed, the turbulence intensity of the air stream v' was 0.13 m/s, and the flame shape changed as shown in Fig. 4(b). Large-scale distortions with small amplitude were generated on the apparently laminar diffusion flame. The time-averaged flame thickness increases due to these distortions, which move rather rapidly in space and time. The flame thickness measured from the long-exposure photograph by the CCD camera was about 3 mm and trebled compared with that of the laminar flame. It is noted that the stagnation point lies between the flame and the cylinder surface and that the distance between the flame and the cylinder

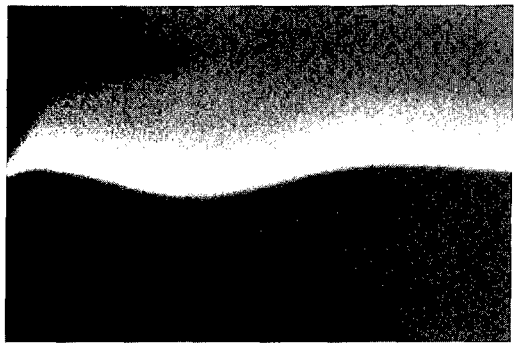

FIG. 5. Instantaneous direct photograph of side view of turbulent methane diffusion flame for $V = 1.0$ m/s, $v_w = 0.26$ m/s, and $v' = 0.13$ m/s.

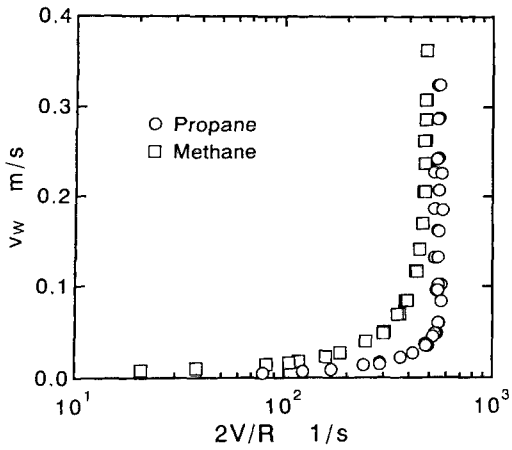

FIG. 6. Extinction limits of laminar methane and propane diffusion flames.

surface is so large that the flame does not come in contact with the cylinder.

Figure 5 shows the instantaneous direct photograph of the side view of the same flame taken with the exposure time of 2 ms. It is clearly shown that the scale of distortions is significantly large compared with the local flame thickness. From these visual observations, the local structure of this contorted flame seems unchanged from the laminar diffusion flame shown in Fig. 4(a), and this comparison gives us an incorrect insight into the extinction mechanism such that only large-scale eddies play a dominant role (see below).

Extinction of Laminar Diffusion Flame:

Figure 6 shows the extinction limits of laminar propane and methane diffusion flames as a function of the fuel ejection velocity v_w and the stagnation velocity gradient $2V/R$, where R is the cylinder radius. The ejection velocity at the extinction limits is small over a wide range of the stagnation velocity gradient and increases slightly with increase of the stagnation velocity gradient. However, if the stagnation velocity gradient becomes a very large value, the ejection velocity at the extinction limits increases steeply, and there exists a critical stagnation velocity gradient $(2V/R)_e$, beyond which the flame can never be stabilized. The extinction of the flame occurred very abruptly at flow rates reproducible to within 3%.

The extinction at small values of the ejection velocity is mainly due to thermal quenching of the flame near the cylinder surface. On the other hand, the extinction at the critical stagnation velocity gradient is due to chemical limitations on the reaction rate in the flame zone, because the temperature gradient becomes zero at the cylinder surface when the fuel ejection velocity is appropriately high [2], and therefore, at this extinction limit, the heat loss from the flame to the cylinder is negligible. As a result, this extinction is clearly discriminated from the extinction due to thermal quenching. Figure 6 shows that the critical stagnation velocity gradient $(2V/R)_e$ of the propane flame is slightly larger than that of the methane flame.

The stagnation velocity gradient has the dimension of the so-called reaction frequency (time^{-1}), and thus, the critical stagnation velocity gradient may be thought to represent a measure of the overall reaction rate or the flame strength for each combination of reactants [1].

Effect of Turbulence on Extinction of Laminar Diffusion Flames:

When the air flow becomes turbulent, the extinction is expected to occur at a smaller stagnation velocity gradient than in the laminar flame, because additional stretch is imposed by turbulence. Figures 7 and 8 show the extinction limits of turbulent methane and propane diffusion flames, respectively. The extinction limits of the laminar diffusion flames are also shown for comparison. In general, it can be found that the higher the turbulence intensity is, the smaller the critical stagnation velocity gradient becomes.

Following Ref. 9, we estimate the nominal total stretch rate a_T acting on the flame as the sum of the bulk flow stretch rate a_b and the turbulent stretch rate a_t.

$$a_T = a_b + a_t. \tag{1}$$

Here, based on potential flow theory for nonreacting stagnation flows, the bulk flow stretch rate in the lateral direction near the forward stagnation region of a cylinder is expressed by $2V/R$.

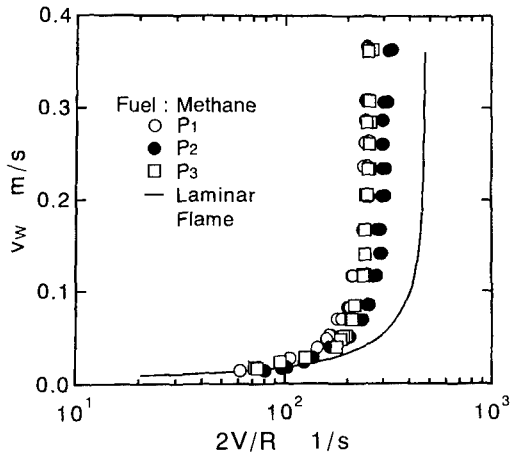

FIG. 7. Extinction limits of turbulent methane diffusion flames.

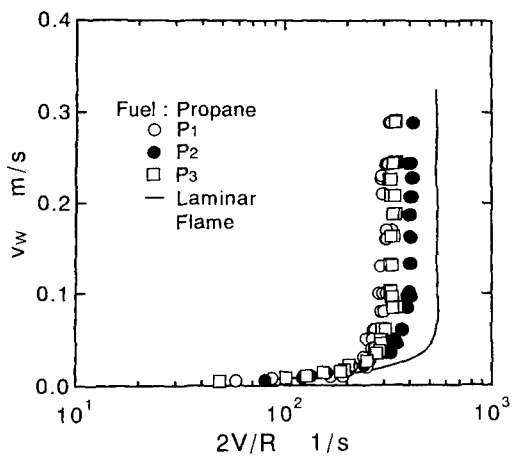

FIG. 8. Extinction limits of turbulent propane diffusion flames.

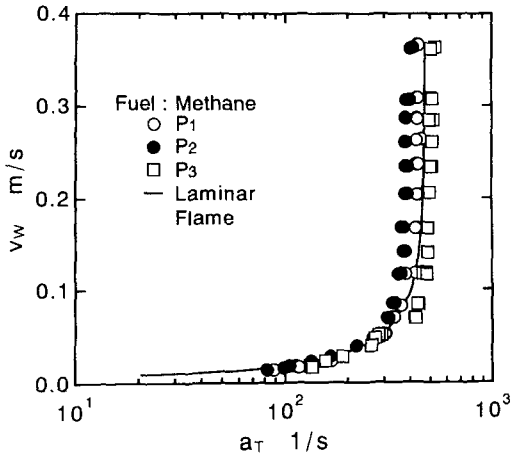

FIG. 9. Extinction limits of turbulent methane diffusion flames as a function of total stretch rate.

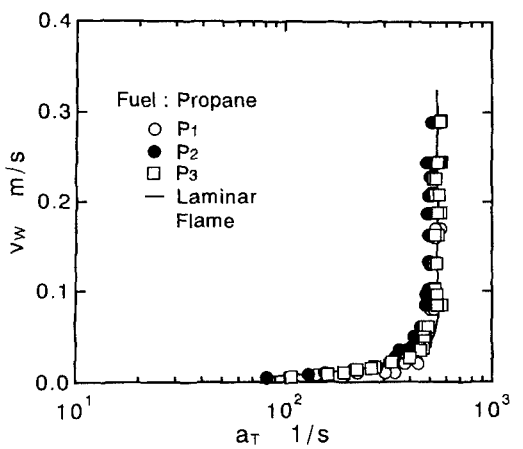

FIG. 10. Extinction limits of turbulent propane diffusion flames as a function of total stretch rate.

$$a_b = 2V/R. \tag{2}$$

Even though the small eddies of the Kolmogorov scale contain less turbulent energy than the large eddies, the stretch rate produced by these eddies is the largest and may lead to local extinction of the reaction zone. The stretch rate due to the small-scale turbulence a_t is assumed to be equal to the inverse of the Kolmogorov time scale.

$$a_t = (\varepsilon/\nu)^{1/2}. \tag{3}$$

Here, ν is the kinematic viscosity and ε the dissipation rate. The dissipation rate ε can be related to the turbulence intensity v' and the Taylor microscale λ by

$$\varepsilon = 15\nu(v'^2/\lambda^2) \tag{4}$$

for isotropic turbulence. Dryden [16] has used experimental data and shown that

$$\lambda^2 = 48.64(L\nu/v'). \tag{5}$$

Therefore,

$$\varepsilon = 0.3084(v'^3/L). \tag{6}$$

The values of a_t for each grid at 55 mm upstream of the cylinder surface are shown in Table 1.

Figures 9 and 10 show the extinction limits as a function of fuel ejection velocity v_w and total stretch rate a_T. In these figures, the extinction limits of laminar diffusion flame are also shown by a solid line for comparison. The total stretch rates at extinction estimated by using the turbulent stretch rate of

small-scale eddies coincide with the critical stagnation velocity gradients at extinction of the laminar diffusion flame. Therefore, it can be concluded that the small-scale eddies play an important role for local extinction of laminar flamelets and that the overall reaction rate or the flame strength is unchanged by turbulence. This fact implies that the chemical reaction in molecular scale is not affected by small-scale turbulence. This can be also conceivable from the fact that the time scale of chemical reaction in molecular scale is much smaller than the turbulent time scale.

When the stagnation region is approached where the flame is produced, anisotropy of turbulence prevails mainly in the large-scale eddies, and the turbulence intensity and also the integral scale change significantly in the vicinity of the stagnation point [13]. Even so, however, it is well established that the small dissipative eddies should be rather isotropic in the inertial subrange.

The stretch rate of large eddies, for example, of the integral scale can be estimated by $a_t = v'/L$ and is found to be much smaller than that of small eddies (see Table 1). It is well known that the flame curvature is another origin of flame stretch. The stretch rate produced by the flame curvature, a_c, was estimated by $a_c = v'/\rho$, where ρ is the mean radius of flame curvature. The flame curvature stretch rate a_c thus estimated ranges from 1 to 25 s^{-1} depending on the flame curvature and is negligibly small compared with the turbulent stretch rate a_t.

Using the counterflow geometry of opposed jet configuration, Mastorakos et al. [11] found that the total stretch rate at which extinction occurs in turbulent flows is close to that of laminar flow; however, it is consistently smaller than the latter. The reason why the discrepancy exists is not yet known. On the other hand, for the turbulent premixed flames, the total stretch rate that causes extinction is 3–5 times larger than the laminar premixed flames [10]. The reason why the turbulent premixed flames are not extinguished even in a flow with a higher stretch rate is due to the statistical nature of turbulence. The turbulent strain exerted by small dissipative eddies is concentrated in local regions of high vorticity, where the local extinction occurs and a hole without flame is formed. This local extinction does not necessarily lead to global extinction of the whole flame, because these holes can be reignited if the total area of holes is small. However, when the mean turbulent strain exceeds some critical value, the total number of these holes increases and global extinction will occur [10]. Global extinction is important from a practical point of view. Transition from local to global extinction is another issue that may include the effect of bulk flow configurations as well as the large-scale eddy motion; the holes where local extinction occurs may be extended, reduced, or reignited depending on bulk flow and large eddy motion.

The same is the case for the turbulent diffusion flame except that the diffusion flame cannot propagate by itself. Therefore, the concept of the total stretch rate cannot be applied directly to predict global extinction in more complicated geometries, such as bluff-body– or swirl-stabilized flames. In these complicated practical geometries, however, a fundamental aspect of the extinction phenomenon, namely, the effect of turbulence on local extinction of laminar flamelets, is obscured, because we can observe only global extinction. In the counterflow geometry formed near the forward stagnation region of the cylinder as used in the present study, extinction occurs very abruptly. The local extinction that occurs in the vicinity of the forward stagnation region where the total stretch rate is the largest leads necessarily to global extinction. The residual flame is blown off by the air flow, because away from the stagnation region, the air flow velocity increases along the interface between fuel and air flow. Therefore, we could extract fundamental aspects of extinction phenomena, the local extinction of flamelets by small-scale turbulence.

Conclusions

In the present study, methane or propane was ejected from a porous cylinder in the counterflowing turbulent air stream, and the extinction process due to turbulence was investigated. Conclusions of the present study are summarized as follows.

1. The air stream turbulence causes large-scale distortions with small amplitude on the apparently laminar diffusion flame, and the time-averaged flame thickness is three times as large as the laminar flame.
2. Even if the air stream becomes turbulent, there exists a critical stagnation velocity gradient beyond which the flame can never be stabilized, however large the fuel ejection velocity is. The local extinction near the stagnation region always leads to global extinction of the whole flame. The critical velocity gradient decreases with increasing turbulence intensity.
3. The counterflow diffusion flame in the turbulent air stream is subjected to the sum of the bulk flow stretch rate exerted by the mean flow and the turbulent stretch rate exerted by small eddies of Kolmogorov scale. The total stretch rate at which the extinction occurs is nearly constant for each fuel for all turbulence conditions tested in the present study and coincides with the critical stagnation velocity gradient of the laminar diffusion flame.
4. Small-scale eddies of Kolmogorov scale are much more effective than large-scale eddies in the local extinction, and the chemical reaction that occurs in molecular scale is not affected by the small eddies of the Kolmogorov scale.

Acknowledgments

We wish to express our thanks to Dr. E. Mastorakos for useful discussions on flame extinction.

REFERENCES

1. Tsuji, H., *Prog. Energy Combust. Sci.* 8:93–119 (1982).
2. Tsuji, H., and Yamaoka, I., *Eleventh Symposium (International) on Combustion*, The Combustion Institute, Pittsburgh, 1966, pp. 979–984.
3. Tsuji, H., and Yamaoka, I., *Twelfth Symposium (International) on Combustion*, The Combustion Institute, Pittsburgh, 1968, pp. 997–1005.
4. Tsuji, H., and Yamaoka, I., *Thirteenth Symposium (International) on Combustion*, The Combustion Institute, Pittsburgh, 1970, pp. 723–731.
5. Miake-Lye, R. C., and Hammer, J. A., *Twenty-Second Symposium (International) on Combustion*, The Combustion Institute, Pittsburgh, 1988, pp. 817–824.
6. Broadwel, J. E., and Mungal, M. G., *Twenty-Second Symposium (International) on Combustion*, The Combustion Institute, Pittsburgh, 1988, pp. 579–587.
7. Peters, N., and Williams, F. A., *AIAA J.* 21:423–429 (1983).
8. Lockwood, F. C., and Megahed, I. E. A., *Combust. Sci. Technol.* 19:77–80 (1978).
9. Kostiuk, L. W., Bray, K. N. C., and Chew, T. C., *Combust. Sci. Technol.* 64:233–241 (1989).
10. Kostiuk, L. W., Bray, K. N. C., and Cheng, R. K., *Combust. Flame* 92:396–409 (1993).
11. Mastorakos, E., Taylor, A. M. K. P., and Whitelaw, J. H., *Combust. Flame* 91:40–54 (1992).
12. Mastorakos, E., Taylor, A. M. K. P., and Whitelaw, J. H., *Combust. Flame* 91:55–64 (1992).
13. Cho, P., Law, C. K., Hertzberg, J. R., and Cheng, R. K., *Twenty-First Symposium (International) on Combustion*, The Combustion Institute, Pittsburgh, 1986, pp. 1493–1499.
14. Liu, Y., and Lenze, B., *Twenty-Second Symposium (International) on Combustion*, The Combustion Institute, Pittsburgh, 1988, pp. 747–754.
15. Kostiuk, L. W., Bray, K. N. C., and Cheng, R. K., *Combust. Flame* 92:377–395 (1993).
16. Dryden, H. L., *Q. Appl. Math.* 1:7–42 (1943).

Twenty-Fifth Symposium (International) on Combustion/The Combustion Institute, 1994/pp. 1199–1205

STRAIN EFFECTS ON THE STRUCTURE OF COUNTERFLOWING TURBULENT PREMIXED FLAMES

CHRISTINE MOUNAÏM-ROUSSELLE AND ISKENDER GÖKALP
Laboratoire de Combustion et Systèmes Réactifs
Centre National de la Recherche Scientifique
45071 Orléans Cédex 2, France

Dynamic and scalar structures of turbulent premixed flames stabilized in the opposed jet configuration are investigated. The opposed jet burner facility allows control of many parameters of turbulent premixed combustion, including the bulk and turbulent strain rates. The main mixture streams are enveloped in coflowing air to reduce flame bouncing, to render the turbulence structure more isotropic and homogeneous at the stagnation plane, and, therefore, to better match the major modelling assumptions. Detailed investigation of the velocity field confirms the strong variation of the initial turbulence parameters as the flow stagnates, and the similarity between nonreacting and reacting flow fields. It is clearly demonstrated that turbulent premixed flames stabilized in the opposed jet configuration are ideal for turbulent combustion model validation, as modification of the turbulence field by the flame is minimized.

Two different extinction regimes of opposed jet turbulent premixed flames are identified. For small and moderate burner separations, the total strain rate causes extinction. For large separation distances, mixing and dilution by the external air are the causes of flame extinction. For the first regime, it is confirmed that bulk and turbulent strain rates should be taken into account simultaneously to establish the robustness of turbulent premixed flames.

For the first time, the scalar structure of opposed jet turbulent premixed flames is explored by laser-induced Rayleigh light-scattering technique. All the relevant parameters of instantaneous flame fronts are determined, and estimates of the flame surface density are proposed. It is shown that, for constant mixture composition and constant initial turbulence structure, the flame surface density increases with the bulk strain rate before its extinction value is closely approached. This result is discussed by using various ingredients of flamelet models.

Introduction

Turbulent premixed counterflow flames stabilized in the vicinity of a stagnation plane, which is formed when two identical gaseous turbulent streams of premixed reactants are opposed to each other, have been recently introduced into turbulent combustion studies, both experimental [1–6] and theoretical [7–10]. Advantages of this laboratory turbulent flame configuration include the absence of any contact with a flame holder or a pilot flame, the possibility of varying the imposed mean velocity gradient within the flame brush and thus approaching global flame extinction, and the possibility of a theoretical analysis based on a similarity formulation of the flow field.

This peculiar turbulent flame configuration is, however, not as simple as these advantages would suggest; it needs a huge amount of control effort to be stabilized correctly, i.e., effectively in the vicinity of the stagnation plane. Optical access, which may seem easier at first glance, is seriously hindered by beam steering and flame radiation. Finally, the interaction between the initial turbulence structure and the stagnating mean flow field is not trivial and needs to be addressed in detail. More specifically, the influence of the mean strain rate on the axial and radial variations of turbulence intensities and time scales has been found to be significant [11,12].

A counterflowing turbulent premixed flame facility has been developed at the CNRS-LCSR. The main difference between this facility and that used by Kostiuk [1] is that our burner provides a coflowing air envelope around the main streams. Previous work has indeed shown that the influence of the coflow on the nonreacting flow characteristics was substantial [13,14].

One objective of the present paper is to widen the existing knowledge on the extinction regimes of turbulent premixed flames by controlling the mean and turbulent strain rates imposed on them. A second objective is to explore the scalar structure of opposed jet flames in order to identify and analyze the effects of stretch on the mean reaction rate, and to provide some input for turbulent combustion modeling efforts based on the flame surface density concept. In the following, the experimental setup and diagnostics

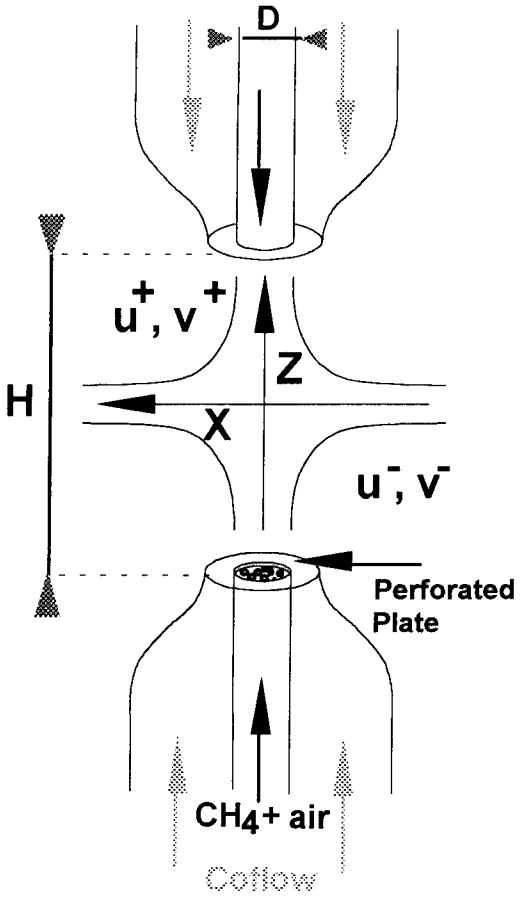

FIG. 1. Experimental apparatus.

are first presented. The structure of the nonreacting flow field with and without coflow and the global characteristics and extinction limits of lean methane-air turbulent flames are discussed next. The last section of the paper concerns the scalar structure of opposed jet flames explored by the Rayleigh light-scattering technique. The effects of the bulk strain rate on flamelet temporal and spatial dynamics and on the flame surface density are discussed.

Experimental Setup and Optical Diagnostics

Two identical burners are opposed to each other vertically and separated by a distance H (Fig. 1). The center nozzle (diameter $D = 25$ mm) is fed by a methane-air mixture. The enveloping nozzle is profiled (exit section diameter 50 mm) and carries the coflowing air. The upper burner is water cooled. The precise control of the mixture equivalence ratio is achieved by regulating the mass flow rates of the air and methane flows. For laser-Doppler anemometry (LDA) measurements, an additional air stream flows through seeders containing aluminum oxide particles. The coflow can also be seeded, and its flow rate is controlled by calibrated sonic nozzles. The burners are mounted on a computer-controlled two-axes traverse system that also commands the burner separation H. The origin of the coordinate system is placed on the actual stagnation plane (Fig. 1).

The turbulence structure of the mixture is varied by using two different perforated plates, fixed 2 mm upstream of the center nozzle exit section. The finer plate PP1 has a mesh size of 1.3 mm and a hole diameter of 0.8 mm, giving a blockage ratio of 0.66. It produces a turbulence intensity of 8% and an integral length scale of 5 mm. The corresponding parameters for the coarser plate PP2 are, respectively, 3.6 mm, 3 mm, 0.37, 13%, and 8 mm. With the turbulence parameters evaluated at the burner exit section and a characteristic chemical time evaluated by using the unstretched laminar flame propagation velocity and the Zeldovich laminar flame thickness, the turbulent Reynolds number based on the integral length scale can be varied between 10 and 60, and the Damköhler number between 10 and 25, so that all the investigated flames lie, a priori, in the flamelet regime [14]. Two-component LDA is used for velocity measurements [13,14].

The instantaneous scalar structure of turbulent opposed jet flames is explored by laser-induced Rayleigh light scattering, which allows the statistics of the presence and passages of instantaneous flame fronts to be determined in the turbulent premixed flame brush [15,16]. The present Rayleigh scattering setup uses the green line (7 W) of a cw Argon-ion laser (20 W). The laser beam is focused down by a 242-mm focal length lens. The scattered light is collected by a photomultiplier through a pinhole of 300-μm diameter. The volume of the measuring probe is about 5.3 10^{-3} mm^3. Many problems due to this peculiar flame configuration had to be solved to optimize the quality of the Rayleigh signal according to flame conditions [14]. They include strong flame radiation, beam steering, and the choice of the appropriate measurement volume dimensions. The data acquisition system collects 500 $\times$ 1024 samples per measuring point with a sampling rate of 100 kHz. The major achievement of the Rayleigh scattering system and the corresponding data-analysis methodology that we developed [16] is the possibility of estimating all the relevant time and space scales of flamelet dynamics. Of particular importance is the estimation of the velocity of the flamelet surface at a point of interest within the turbulent flame brush by determining the transit time of the flamelet over this point. The methodology used to convert this information into an estimate of the flame surface density and of the mean reaction rate is fully explained in Refs. 14 and 16.

TABLE 1
Influence of the coflow on the bulk strain rate

Case			Without coflow		With coflow
No.	U_∞	H	a_b (1/2 du/dz)	a_b (dv/dr)	a_b (1/2 du/dz)
I	4.5	30	210	213	150
II	4.5	60	160	156	115
III	9	60	340	350	300

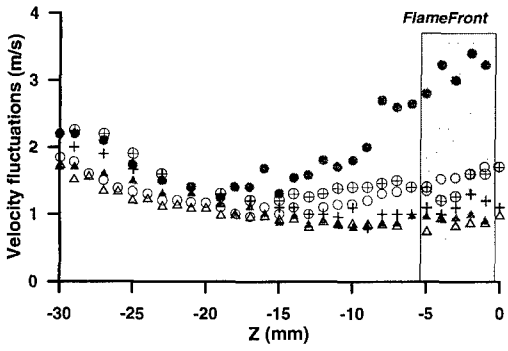

FIG. 2. Variation of the fluctuating velocities vs the axial coordinate. Case III of Table 1. ●: u' without coflow; ○: u' with coflow; ⊕ u' reacting; △: v' without coflow; ▲: v' with coflow; +: v' reacting.

Nonreacting Velocity Field

The knowledge of the structure of the nonreacting flow is needed, as the flow structure at extinction is by definition equivalent to that of the nonreacting case. The influence of the coflow on the mean strain rates is summarized in Table 1 for three combinations of the mean exit velocity and the burner separation distance with PP2. The bulk velocity of the coflow is 1 m/s. For the three cases, the bulk strain rate a_b is lower with coflow, the difference being smaller for larger strain rates. Table 1 compares also the values of a_b obtained from both terms of the continuity equation. The main influence of the coflow is to increase the radial extension of the stagnation plane [14].

Centerline variations of the velocity fluctuations, presented in Fig. 2 for case III of Table 1, show that u' increases strongly in the absence of coflow when the flow stagnates. The coflow exerts different effects on the two fluctuating velocity components: u' decreases strongly, whereas v' is approximately unchanged. Consequently, the isotropy of the turbulence field is largely improved with coflow. The coflow also homogenizes the transverse distributions of turbulence characteristics [13,14]. Therefore, the flames stabilized with coflow better match the hypotheses of modeling attempts. The decrease of the axial fluctuation velocity is directly related to the beneficial effect of the coflow on the instability of the stagnation plane and on flame bouncing. This is also confirmed by the spectral analysis of the axial fluctuating velocity [13]. The detailed study of the turbulence field as the flow stagnate shows that the axial and radial integral time scales increase strongly in all cases, i.e., even in the absence of bouncing for $H < 2D$ [13,14]. The flow stagnation effects on the initial turbulence structure are therefore not trivial and need careful analysis. These observations also indicate that extreme care should be taken in interpreting the structure of turbulent premixed flames stabilized in the vicinity of a stagnation plane, in terms of turbulence data collected far upstream of this region.

General Observations on Opposed Turbulent Jet Flames and Extinction Limits

The flames stabilized between two identical opposed turbulent streams of lean methane-air mixtures are circular in the mean, bluish, and about 80 mm in diameter. Pictures of the flames obtained by laser tomography [14] show that the twin flames are well separated for $H \approx 2D$, and they progressively approach each other for $H < 2D$, at constant exit velocity and equivalence ratio. For $H > 2D$, without coflow, the flames stabilize closer to the upper burner; the low-frequency longitudinal oscillation ("bouncing") of the flame is quite apparent. Also, the flame is not entirely planar, but curved upward at its periphery. With the onset of the coflow, the flames are stabilized much closer to the symmetry plane, larger, more planar, and stable. These observations can be explained in terms of the characteristics of the nonreacting flow with coflow, i.e., larger stagnation plane, more spatially homogeneous and isotropic turbulence, and less energetic low-frequency components of the longitudinal velocity spectrum.

With the present flame configuration, as in Ref. 1, but contrary to stagnation plate experiments [17,18], axial variations of the unconditional mean and fluctuating velocities are quasi-similar to those of the nonreacting counterflow. In particular, as shown in Fig. 2, the fluctuating velocity profiles present no sharp increase through the turbulent flame brush. Bray [9] explains the differences between the two stagnation flame configurations in terms of a Damköhler number defined as $D_T = 1/(a_b t_{cT})$ where t_{cT} is a "turbulent reaction time." It is further argued that smaller values of D_T (corresponding to larger bulk strain rates as in the case of opposed jet flames) lead to smaller mean reaction rates and, therefore,

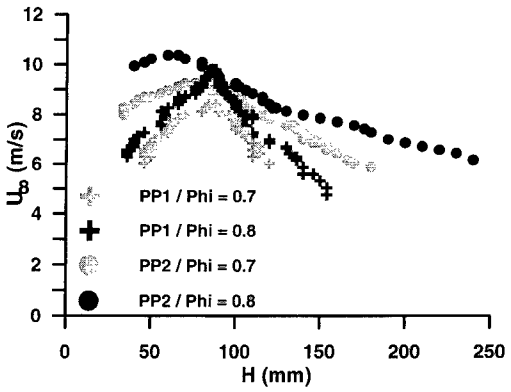

FIG. 3. Extinction limits for lean methane-air mixtures.

to weaker differences in the axial velocity distributions of reacting and nonreacting flows.

It can easily be shown that D_T is a combination of four time scales and can be written as $D_T = gt_f/(a_b t_c \hat{T})$. In this relation, g is a constant depending on the distribution functions of flamelet passage times, t_f the average transit time of flamelets over a given point in the flame brush, t_c the characteristic chemical time estimated as the ratio between the laminar flame thickness and the laminar flame propagation velocity, and $\hat{T}$ the integral time scale of the flamelet crossing time series. With $g = 1$ (see below), it is found that the "turbulent reaction time" t_{cT} is in fact equal to $t_c\hat{T}/t_f$. This is indeed a time scale that combines the characteristic chemical time of the flamelet and its dynamic time scales. This interpretation will be further pursued below during the discussion of extinction limits and the effect of bulk strain rate on the structure of turbulent opposed jet flames.

Figure 3 shows the extinction limits of methane-air flames for two equivalence ratios and two turbulence structures. These limits are only slightly influenced by the coflow and by the mass flow rate of the coflow [14]. For all cases, two regimes of extinction are observed. The regime on the left of the maximum stabilization velocity represents the extinction limit due to the imposed total stretch rate. In this regime, the two unsymmetrical flames move closer to each other as the extinction limit is approached. On the right of this region, for larger burner separation distances, another extinction mechanism due to the dilution of the reactive mixture by mixing with the surrounding air is observed. In this case, before extinction, the flames are well separated but more unstable; increased flame bouncing and individually burning flame parcels are also observed. In the following, we shall only concentrate on the extinction limits due to stretch.

As expected, for both turbulence conditions, flames closer to stoichiometry are more robust. Also, the extinction limits are narrower for flames exposed to smaller-scale turbulence generated by PP1. These results confirm the idea that extinction of turbulent premixed flames is controlled by the combination of bulk and turbulent strain rates [9]. Table 2 presents the bulk strain rates at extinction $a_{b,e}$ deduced from the extinction limits displayed in Fig. 3. The values of $a_{b,e}$ for PP1 indicate that smaller turbulence structures produce flames less resistant to the bulk strain rate. To implement this idea an estimate of the turbulent strain rate can be based on the inverse of the turbulent integral time scale determined on the stagnation plane. Typical values of $a_{t,e}$ for an exit velocity of 7.5 m/s and $H = 2D$ are shown in Table 2 and confirm that higher turbulent strain rates are produced by PP1. It is worth noting that, for all cases, the sum $a_{b,e} + a_{t,e} = a_e$ is of the same order of magnitude and lies between 500 and 600 s^{-1}. However, the total extinction strain rate is lower for the leanest two flames. If the stretch rate $a_{c,e}$ caused by flamelet propagation and curvature is taken into account by estimating $a_{c,e}$ as S_L/R where R is a characteristic flamelet wrinkling scale, two competitive effects can act on $a_{c,e}$. One is the highest S_L for $\phi = 0.8$, which will increase $a_{c,e}$; the other is the increase of u'/S_L for $\phi = 0.7$, which may decrease the characteristic flamelet wrinkling scales. The net effect of this competition remains to be analyzed more fully in order to deepen the notion of total extinction stretch parameter for turbulent premixed flames. Some more evidence on these mechanisms is provided in the next section where the scalar structure of two opposed jet flames, one with moderate and the other with strong bulk strain rates, is explored by the Rayleigh light-scattering technique.

TABLE 2
Values of the strain rates at extinction

	$a_{b,e}$ (s^{-1})		$a_{t,e}$ (s^{-1})		a_e (s^{-1})	
	PP1	PP2	PP1	PP2	PP1	PP2
0.8	350	480	240	60	590	540
0.7	260	450	240	60	500	510

Influence of the Bulk Strain Rate on the Structure of Opposed Jet Flames

The Rayleigh light-scattering technique is used to explore the dynamics of flamelet crossings and the related structural parameters of two flames, A and B, obtained with coflow and with PP2 for an exit centerline velocity of 6 m/s and an equivalence ratio $\phi = 0.8$. They only differ in terms of the bulk strain rate, where $a_b = 240\ s^{-1}$ ($H = 2D$) for flame A, and $a_b = 400\ s^{-1}$ ($H = 1.2D$) for flame B. As

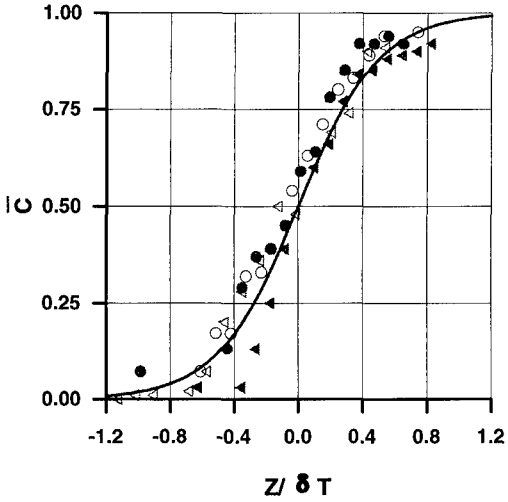

FIG. 4. Variation of the mean progress variable vs the normalized axial coordinate. ●: Flame A; ◀: flame B.

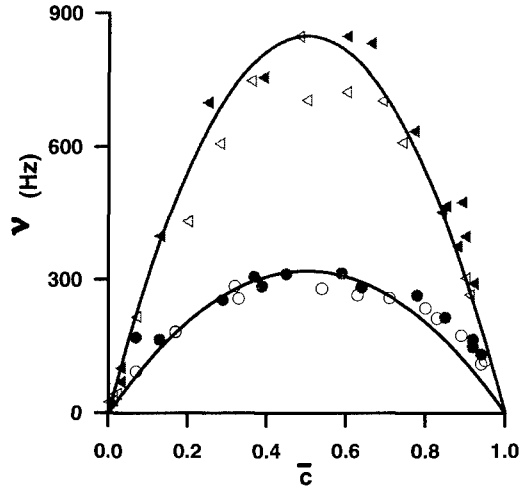

FIG. 5. Variation of the flamelet crossing frequency vs $\bar{c}$ ●: Flame A; ◀: flame B.

documented previously [14–16], the Rayleigh scattering signal can be used to estimate various time scales of instantaneous flame fronts within the flame brush and also the mean progress variable $\langle c \rangle$ defined as $\langle t_p \rangle / (\langle t_r \rangle + \langle t_p \rangle)$ where $\langle t_r \rangle$ and $\langle t_p \rangle$ are the mean time intervals during which the fixed Rayleigh scattering probe stays, respectively, in the reactants or products between two consecutive passages of the flamelet. They are also used to determine the crossing frequency of flamelets in a given point within the flame brush, as $\nu = 2/(\langle t_r \rangle + \langle t_p \rangle)$. Bray [9] has further shown that an estimate of the flame surface density can be obtained as $\Sigma = \nu \langle 1/V_n \rangle$, where $\langle V_n \rangle$ is the average flamelet transit (or convection) velocity over a fixed point within the flame brush. This important parameter can be estimated from the flamelet transit time data provided by the Rayleigh scattering technique [14–16].

The analysis of the probability density functions (pdfs) of flamelet crossing time series, not shown here, indicates bimodal shapes equivalent to those obtained with turbulent Bunsen flames [15]. As shown in Fig. 4, the mean progress variable $\langle c \rangle$ can be satisfactorily normalized for both lower flames (open symbols) and upper flames (dark symbols), by the respective turbulent flame brush thickness δ_T, which is 5–6 mm, as predicted in Wu and Bray [10] for the experiments of Ref. 1. An important feature of the bulk strain effects is depicted in Fig. 5, which shows that the flamelet crossing frequencies are strongly increased for flame B, which has the highest bulk strain rate (400 s^{-1}). Note that the extinction bulk strain rate for these flames is 480 s^{-1} (Table 2). This figure also shows that ν is clearly decreasing toward the products zone for both flames ($\langle c \rangle = 1$), indicating that the twin flames are well separated from each other and well away from extinction conditions. The curves on this figure represent the prediction of ν following the Bray–Moss–Champion–Libby model as $\nu = 4\, \nu_{\max} \langle c \rangle (1 - \langle c \rangle)$. The good agreement confirms that these flames are in the flamelet regime. The independent determination of the integral time scale $\hat{T}$ of the flamelet crossing time series and of ν permits to estimation of the parameter g, which is found nearly equal to unity, as in Ref. 1, indicating smaller probabilities for the occurrence of shortest time intervals between two consecutive flamelet crossings, compared to Bunsen flames [15]. This behavior is also consistent with the observation of much smaller flamelet crossing frequencies found in opposed jet flames compared with conical flames, stabilized with the same initial turbulence structure [15].

As $\hat{T}$ and ν are related to each other by $\hat{T} = g\langle c \rangle (1 - \langle c \rangle)/\nu$ [9], the increase of ν with a_b implies decreasing values of $\hat{T}$, i.e., smaller intervals between two consecutive flamelet crossings. On the other hand, Fig. 6 shows that the amount of mixture reacted per flamelet crossing, $\bar{\omega}_f/\rho_u = S_L/\langle V_n \rangle$, estimated as explained in Ref. 16, is not sensitive to the variation of the bulk strain rate under the present conditions. This indicates that the local flamelet structure is not modified, so that flamelet extinction is not expected. Finally, Fig. 7 shows the variation of the estimated flame surface density, which is higher for the highest strain rate flame B.

The extinction Damköhler number introduced by Bray [9] can be written as $D_T = \bar{\omega}_f / (\rho_u a_{b,e} \hat{T})$ by using the flamelet hypotheses [15,16]. We have shown above that for the same mixture and initial turbulence conditions, increasing a_b decreases $\hat{T}$. Therefore, if the local stretch effects are moderate so that

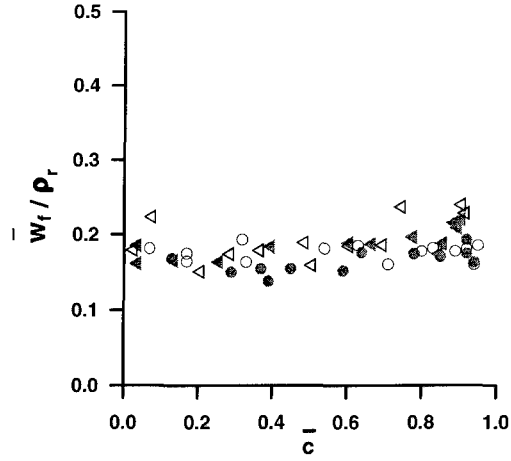

FIG. 6. Variation of $\bar{\omega}_f/\rho_r$ vs $\bar{c}$. ●: Flame A; ◀: flame B.

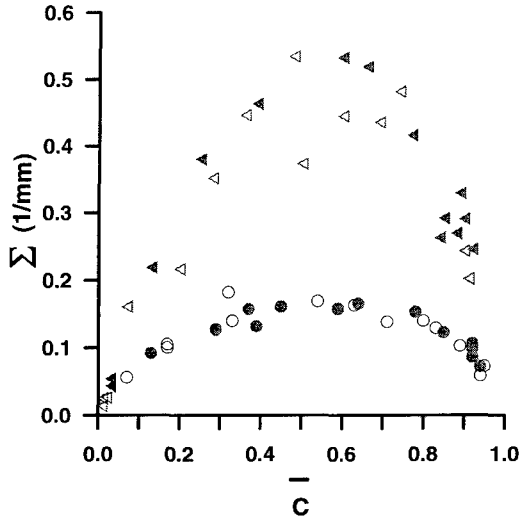

FIG. 7. Variation of the flame surface density vs $\bar{c}$. ●: Flame A; ◀: flame B.

flamelet extinction is not the dominant mechanism (i.e., $\bar{\omega}_f/\rho_u$ is constant as in Fig. 6), this expression of the extinction Damköhler number clearly indicates that the increase of a_b (the reduction of the residence time within the turbulent flame brush) is first balanced by the decrease of the temporal (or spatial) spacings between flamelets so that the turbulent burning rate is maintained and even strengthened. This can be interpreted as the production of additional flame surface area by strain as suggested by the coherent flamelet model [19]. Extinction will therefore occur when flamelet annihilation due to the closeness of successive flamelet crossings will dominate so that the decrease of the reactants' residence time within the turbulent flame brush is no more counterbalanced. It is also worth noting that the bulk strain rate characterizing flame B is equal to 5/6 of $a_{b,e}$; one can therefore speculate that extinction conditions of turbulent premixed flames can be reached for slight modifications of flow and turbulence conditions, so that the approach to extinction is a "catastrophe-like" phenomenon and not a gradual one.

Conclusions

Dynamic and scalar structures of turbulent premixed flames stabilized in the opposed jet configuration have been investigated. The opposed jet burner facility allows control of many parameters of turbulent premixed combustion, including the bulk and turbulent strain rates. The use of a coflow contributes to reduce flame bouncing, to render the turbulence structure more isotropic and homogeneous at the stagnation plane, and, therefore, to better match the major modeling assumptions. Detailed investigation of the velocity field confirms the strong variation of the initial turbulence parameters as the flow stagnates and the similarity between nonreacting and reacting flow fields. It is therefore clearly demonstrated that turbulent premixed flames stabilized in the opposed jet configuration are ideal for turbulent combustion model validation as the modification of the turbulence field by the flame is minimized.

Two different extinction regimes of opposed jet turbulent premixed flames are identified, depending on the separation distance between the burners. For small and moderate separations, the total strain rate causes extinction. For large separation distances, mixing and dilution by the external air are the causes of extinction. For the first regime, the present results confirm that bulk and turbulent strain rates should be taken into account simultaneously to establish the robustness of turbulent premixed flames.

For the first time, the scalar structure of opposed jet turbulent premixed flames is explored by laser-induced Rayleigh light-scattering technique. All the relevant parameters of instantaneous flame fronts are determined by this technique, and estimates of the flame surface density are proposed. It has been shown that, for constant mixture composition and initial turbulence structure, increasing the bulk strain rate to the 5/6 of its extinction value increases the flame surface density. This result has been discussed by using the various concepts of flamelet models, such as the extinction Damköhler number, and the ingredients of the coherent flamelet model.

Acknowledgments

The support of the French Army Research Office, DRET, Groupe 7 and of the Conseil Regional Centre is greatly appreciated. The authors also acknowledge many useful discussions with Ken Bray, Fred Gouldin, Ian Shepherd, Robert Cheng, and Larry Kostiuk.

REFERENCES

1. Kostiuk, L. W., Ph.D. Thesis, Cambridge University, Cambridge, UK, 1991.
2. Kostiuk, L. W., Bray, K. N. C., and Chew, T. C., *Combust. Sci. Technol.* 64:233–241 (1989).
3. Bray, K. N. C., Champion, M., Kostiuk, L. W., and Libby, P. A., *Seventh Symposium on Turbulent Shear Flows*, Stanford University, Stanford, CA, 1989, p. 1.2.1.
4. Kostiuk, L. W., Bray, K. N. C., and Cheng, R. K., *Combust. Flame*, 92:377–395 (1993).
5. Kostiuk, L. W., Bray, K. N. C., and Cheng, R. K., *Combust. Flame* 92:396–409 (1993).
6. Mastorakos, E., Ph.D. Thesis, Imperial College of London, London, UK, 1993.
7. Bray, K. N. C., Champion, M., and Libby, P. A., *Combust. Flame* 84:391–410 (1991).
8. Bray, K. N. C., Champion, M., and Libby, P. A., *Combust. Flame* 91:1653 (1992).
9. Bray, K. N. C., in *Turbulence and Molecular Processes in Combustion* (T. Takeno, Ed.), Elsevier, Amsterdam, 1993, p. 355.
10. Wu, A. S., and Bray, K. N. C., *CUED/ATHERMO/TR60*, Cambridge University Engineering Department, Cambridge, UK, unpublished report, 1993.
11. Gutmark, E., Wolfshtein, M., and Wygnaski, I., *J. Fluid Mech.* 88:737–756 (1978).
12. Britter, R. E., Hunt, J. C. R., and Munford, J. C., *J. Fluid Mech.* 92:269–301 (1979).
13. Mounaïm-Rousselle, Ch., and Gökalp, I., Spring Annual Meeting of the Western States Section of the Combustion Institute, Salt Lake City, UT, March 22–23 1993.
14. Mounaïm-Rousselle, Ch., Ph.D. Thesis, Université d'Orléans, Orléans, France, 1993.
15. Deschamps, B., Boukhalfa, A., Chauveau, C., Gökalp I., Shepherd, G., and Cheng, R. K., *Twenty-Fourth Symposium (International) on Combustion*, The Combustion Institute, Pittsburgh, 1992, pp. 469–475.
16. Mounaïm-Rousselle, Ch., and Gökalp, I., *Ninth Symposium on Turbulent Shear Flows*, Kyoto, Japan, 1993, p. 31–2.1.
17. Cho, P., Law, C. K., Hertzberg, J. R., and Cheng, R. K., *Twenty-Second Symposium (International) on Combustion*, The Combustion Institute, Pittsburgh, 1988, p. 739.
18. Liu, Y., and Lenze, B., *Twenty-Second Symposium (International) on Combustion*, The Combustion Institute, Pittsburgh, 1988, p. 747.
19. Poinsot, T., and Candel, S., *Combust. Sci. Technol.* 70:1–15 (1990).

Twenty-Fifth Symposium (International) on Combustion/The Combustion Institute, 1994/pp. 1207–1214

EXPERIMENTAL INVESTIGATION OF A PREMIXED FLAME IN AN IMPINGING TURBULENT STREAM

S. C. LI, PAUL A. LIBBY AND F. A. WILLIAMS
University of California at San Diego
La Jolla, CA 92093, USA

Flames in stagnating turbulence provide useful vehicles for fundamental studies of turbulent reacting flows. We present here experimental data on premixed flames in a turbulent methane-air mixture impinging on a wall. Turbulence generators with two different hole sizes and therefore resulting in turbulent streams with two different integral scales are employed. Time-resolved axial and radial velocity components are measured at many positions along the axis. Corrections for the density and velocity biasing associated with the different seeding levels in reactants and products are made in terms of particle fluxes. The aerothermochemical conditions are such that the flame is found to be free standing, i.e., separated from the wall. Histograms of the axial velocity within the flame are interpreted so as to yield the progress variable and thus the density with the consequence that the pairs of velocity data are supplemented with state data. Both conventional and Favre-averaged quantities are thereby obtained. Generation and redistribution of turbulent intensities within the flame are observed. The influence of the integral length of the turbulence on the character of the flame is in accord with physical arguments.

Introduction

The experimental results presented here supplement and extend those of Cho et al. [1,2], Liu and Lenze [3], and Asato et al. [4] on premixed flames in a turbulent stream impinging on a nearby wall. The attractiveness for fundamental combustion studies of these flames, and indeed the whole range of flames in stagnating turbulence, is reviewed by Bray et al. [5]; in brief, a relatively simple and convenient setup permits the entire range of behavior from chemical equilibrium to extinction to be studied experimentally. Moreover, the complementary theoretical analysis so important for advancing understanding of the processes involved in turbulent combustion leads to systems of *ordinary differential equations* whose treatment is considerably simpler and therefore less prone to uncertainties than the partial differential description required in many other flows.

The only theory for turbulent flames in impinging reactant streams is due to Bray et al. [6], but it assumes that the flame is adjacent to the wall; i.e., the rate of strain imposed on the flame is large. In this case, reactant is present at the wall some of the time. While this situation is of interest in connection with the study of extinction, it does not permit comparison with the detailed data concerning the velocity and state fields in either the experiments cited earlier or in those reported here. In the experiments in question, the rate of strain imposed on the flame is sufficiently low for the flame to be free standing, i.e., removed from the wall, and thus for products to be present at the wall all of the time. The theory for free-standing flames is under development and will be reported elsewhere.

Although not quantitatively applicable to the present experiments, the theory of Refs. 5 and 6 for thin flames in stagnating turbulence and the Bray–Moss–Libby (BML) theory of premixed turbulent combustion (cf., e.g., Refs. 7 and 8) supply important insights into the characteristics of the flames considered here. In particular, we know that countergradient diffusion arises in free-standing flames because of the drop in mean pressure which prevails within them. We also know that the thickness of the flame, sometimes termed the "brush," is proportional to the integral scale of the turbulence approaching the flame. However, an unexpected and as yet unexplained feature of these flames found by Cho et al. relates to the absence of production of intensity of the axial velocity component. The theory of infinite planar flames (cf. Refs. 7 and 8) predicts that the interaction between density inhomogeneities due to heat release and mean pressure drop results in significant *increases* in the intensity of the normal velocity within the flame. The intensity of the tangential velocity component is predicted to be unchanged. These predictions are confirmed by experiments on unstrained flames in open burners (cf., e.g., Ref. 7). Because this interaction also prevails in the free-standing flames considered here, it is expected that the intensity of the axial velocity in the product stream would be greater than that in the reactant stream and that there would be little change in the intensity of the

radial component. However, the data of Cho et al. [2] do not support these expectations. Clarification would appear to rely on appropriate theoretical considerations.

The present experiments involve two different turbulence generators so that we examine the influence of turbulent scales on the structure of free-standing flames. Measurements along the axis of the axial and radial velocity components determine the mean axial velocity and the intensity of these two components. From the bimodality of the probability density function of the axial velocity within the flame, we deduce values for the progress variable and are therefore able to determine a variety of useful statistical information. Following a discussion of the experimental arrangement and data collection and analysis, we present and interpret the data and draw conclusions.

Experimental Arrangement

The flow under consideration and the duct arrangement establishing that flow are shown schematically in Fig. 1. An axisymmetric duct containing a turbulence grid discharges reactants against a wall. Associated with the coordinates r and z are the velocity components u and w, respectively. The exit plane of the duct is located a distance d from the wall, a value sufficiently small compared with the diameter of the duct so that mixing between the jet and the surrounding ambient negligibly influences the flow in the neighborhood of the axis. The data are conveniently presented in terms of a dimensionless axial coordinate $\zeta \equiv z/d$ so that the wall is $\zeta = 0$ and the exit plane of the jet is $\zeta = 1$. At the exit of the duct, the mean axial velocity has a magnitude W_1.

The exit diameter of the duct is 4.5 cm, the separation distance is $d = 3$ cm, and the mean axial velocity at the exit of the jet has a magnitude W_1 of 3.6 m/s. Perforated grids, each with 50% blockage as a result of holes of either 4- or 6-mm diameter, denoted h, are located 3 cm upstream of the exit plane. These features differ significantly from those in the experiments in Refs. 1 and 2, where $d = 7$ cm or more. The gas stream consists of a mixture of air and methane at an equivalence ratio of 0.89. The value of the heat release parameter $\tau \equiv (T_p/T_r) - 1$ in the BML theory is 6.0. Here T_r and T_p are the temperatures in the reactants and products, respectively. Figure 2 is a photograph viewing the wall from slightly below and showing the flame in the neighborhood of the wall.

Velocity Measurement and Data Processing

The gas stream is seeded with MgO particles with diameters smaller than 1 μm. A two-component

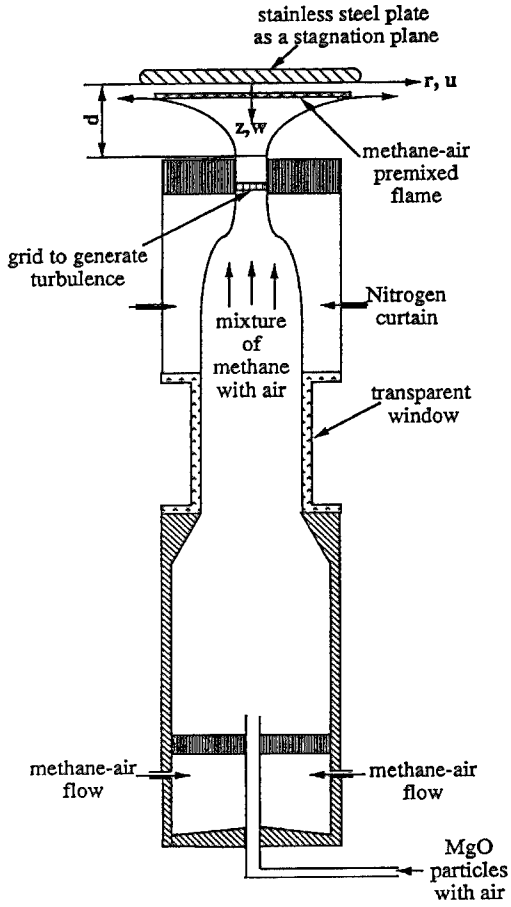

FIG. 1. Schematic representation of the flow and the experimental arrangement.

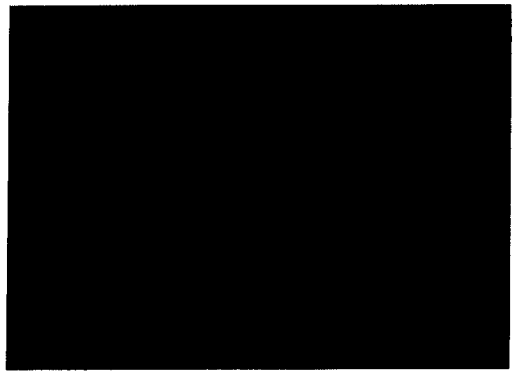

FIG. 2. Photograph of the flame.

phase doppler particle analyzer is used as a laser-Doppler velocimetry to measure the axial and radial velocity components on the axis from the exit plane to the wall. At each measuring location along the axis, approximately 3000 pairs of velocity samples are collected and stored on disc for subsequent processing.

A feature important for data analysis is seen in Fig. 3, which shows histograms of axial velocity at five representative axial stations. The first and last of these histograms correspond to points in the product and reactant streams, respectively, and to nearly Gaussian distributions. On the contrary, the middle three correspond to locations within the flame and are clearly bimodal, with the left mode given by products and the right mode by reactants. To interpret these data, we adopt the thin flamelet approximation according to which each data point corresponds to either reactant or product. Moreover, we associate all points to the left of the minimum in the histogram with product and all to the right with reactant. The significant separation of the maxima in these histograms leads to results for statistics involving state variables within 10% of those given by considerably more elaborate interpretations, e.g., those given by partially overlapping Gaussian approximations for reactants and products separately.

If $a(t; r, z)$ denotes the time history of a generic flow variable at a fixed spatial location, then its conventional mean is

$$\bar{a}(r,z) = \frac{\sum_{i=1}^{N_p} B_{pi}a_{pi} + \sum_{i=1}^{N_r} B_{ri}a_{ri}}{\sum_{i=1}^{N_p} B_{pi} + \sum_{i=1}^{N_r} B_{ri}} \tag{1}$$

while its Favre-averaged mean is

$$\tilde{a}(r,z) = \frac{\rho_p \sum_{i=1}^{N_p} B_{pi}a_{pi} + \rho_r \sum_{i=1}^{N_r} B_{ri}a_{ri}}{\rho_p \sum_{i=1}^{N_p} B_{pi} + \rho_r \sum_{i=1}^{N_r} B_{ri}} \tag{2}$$

where the subscripts r and p denote reactant and product, respectively, and where N_r and N_p are the number of samples in reactant and product, respectively. Finally, in these equations, B_{pi} and B_{ri} are correction parameters to account for density and velocity biasing in the laser-Doppler velocimetry measurements. Such biasing is negligible in the two constant density regions, i.e., outside the flame. On the contrary, within the flame, large changes in velocity and density across flamelets result in corresponding changes in the density of seed particles and in the lower probability of collecting data in product than in reactant [9,10]. Under some circumstances, bias can be removed by weighting each individual datum by the time interval between consecutive samples [1], but this procedure is only accurate if the data rates are suitably high in *both* reactants and products. This is not the case in our experiment: i.e., the seed loading within product is too low. Accordingly, we are forced to an alternative procedure to account for the low density and high velocity in product gas within the flame.

Seed density is expected to be proportional to gas density [9,10] and the number of seed particles passing through the probe volume per unit time to be proportional to gas velocity [11]. Two limiting choices for the correction parameters would be $B_{pi} = B_{ri} = 1$ and $B_{pi} = 1/\rho_p$, $B_{ri} = 1/\rho_r$, the former being appropriate for stationary, unstrained flamelets and the latter for homogeneous, isotropic turbulence. Our flow is intermediate between these limiting cases and can be treated by a seed flux balance based on the approximation that, in the neighborhood of the axis, flux in the axial direction is dominant. We are thus lead to correction parameters $B_{pi} = (\rho_p w_{pi})^{-1}$ and $B_{ri} = (\rho_r w_{ri})^{-1}$, where each datum involves a measured axial velocity. Errors in this procedure are proportional to fluctuations in the radial velocity component. However, since the intensities of the fluctuations of both velocity components are comparable and relatively small, the errors in this procedure can be estimated from the formulas

$$\begin{aligned} B_{pi} &= [\rho_p(\bar{W}_p \pm \overline{w'^2_p}^{1/2})]^{-1} \\ B_{ri} &= [\rho_r(\bar{W}_r \pm \overline{w'^2_r}^{1/2})]^{-1} \end{aligned} \tag{3}$$

where $\bar{W}_r$ and $\bar{W}_p$ are the conditioned mean axial velocity within reactant and product, respectively, and $\overline{w'^2}$ with subscripts r and p denote conditioned intensities of the axial velocity component. The resulting enhanced weighting factor of product data involves multiplication by 2 or 3 rather than by over 6, which would be the case if density weighting alone were employed. In all the following figures, the vertical error bars correspond to the plus and minus signs of Eqs. (3).

Experimental Results

The bimodality in Fig. 3 is expected on the basis of the BML theory and can be understood from the equation for the Favre-averaged intensity of the axial velocity, namely

$$\frac{\overline{\rho w''^2}}{\bar{\rho}} = \tilde{c}(1 - \tilde{c})(\bar{W}_p - \bar{W}_r)^2 + \tilde{c}\overline{w'^2_p} + \overline{w'^2_r} \tag{4}$$

where standard notation applies; here $c(r, z, t)$ is the progress variable, which according to the BML theory has essentially one of two values: zero within re-

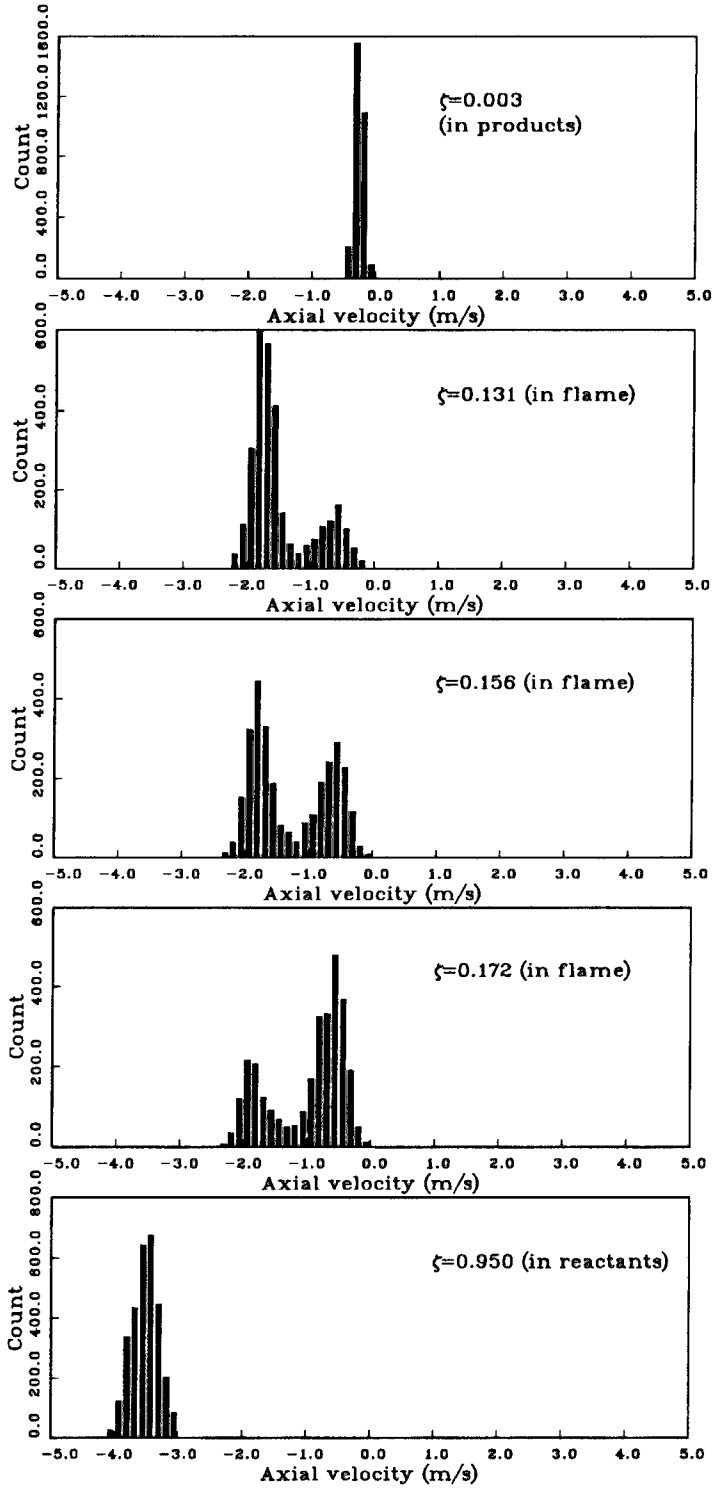

FIG. 3. Histograms of the axial velocity at various axial stations for $h = 4$ mm.

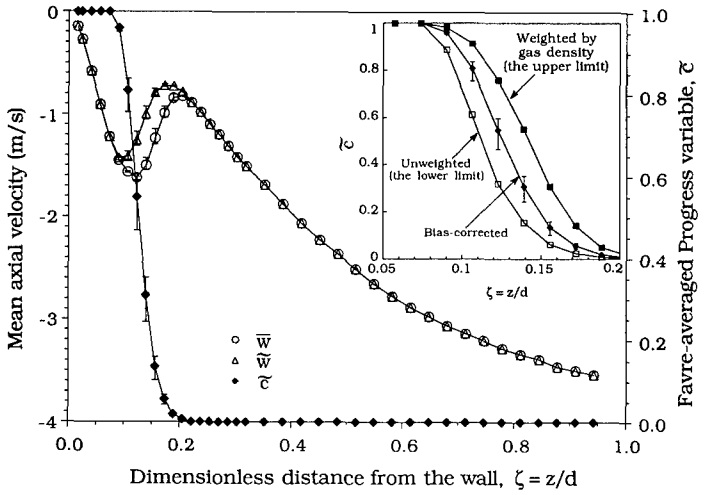

FIG. 4. The mean axial velocities and Favre-averaged progress variable for $h = 4$ mm.

actants and unity within products. It is related to the instantaneous gas density by

$$c = \frac{(\rho_r/\rho) - 1}{\tau}.$$

We see from Eq. (4) that the unconditioned intensity depends on two mechanisms, one due to differences in the conditioned mean velocities within reactants and products and a second due to fluctuations within the two gases. If only the first mechanism were operative, the three histograms in Fig. 3 corresponding to points within the flame would be delta functions at $\bar{W}_r$ and $\bar{W}_p$ with $-W_p > -W_r$, but fluctuations within the two gases result in the observed distributions. We note that the corresponding histograms of the radial velocity (not shown) are symmetric with a zero mean value as expected on the axis. However, the intensity of the fluctuations of the radial velocity reflected in these histograms is greater by a factor of roughly 2 within products than in reactants under the differential influence of the curvature of the mean pressure in the neighborhood of the axis.

The distribution of the mean axial velocity in terms of conventional averaging $\bar{W}(\zeta)$ for the grid with $h = 4$ mm is shown in Fig. 4. We see that initially there is a monotonic decrease in the magnitude of the mean axial velocity until, in the neighborhood of $\zeta \approx 0.2$, there is a significant increase in $-\bar{W}$, followed by a further decrease to zero. The implication from this distribution is that the flame is located in the narrow range between $\zeta = 0.2$ and $\zeta = 0.08$, an implication supported by the Favre-averaged mean velocity $\tilde{W}(\zeta)$. In the reactant and product streams, these mean velocities are, of course, equal since the density is constant there, but within the flame they differ, the BML theory relates these means with other quantities of interest according to

$$\tilde{W} - \bar{W} = -\overline{w''} = -\tau \frac{\overline{\rho w'' c''}}{\bar{\rho}}. \tag{5}$$

That the mean of the Favre-averaged fluctuation $\overline{w''}$ is important is indicated by its appearance multiplying the pressure gradient term $d\bar{p}/dz$ in the z-momentum equation. The implication is that this product describes the interaction between the force field due to the mean pressure gradient and density inhomogeneities. It is this interaction that results in countergradient diffusion and, in infinite planar flames, in turbulence production. The correlation in the last of Eqs. (5) is the mean axial flux of the progress variable.

We see from Fig. 4 that $\tilde{W} > \bar{W}$, implying that $\overline{\rho w'' c''} < 0$, but according to gradient transport,

$$\frac{\overline{\rho w'' c''}}{\bar{\rho}} \propto -\frac{\partial \tilde{c}}{\partial z}.$$

In the coordinate system used here (cf. Fig. 1), the gradient on the right side of this equation is negative, so that gradient transport implies that the flux is *positive*. We thus have clear experimental evidence of the countergradient diffusion shown earlier by Cho et al. [2].

The remaining results in Fig. 4 are the variation of the Favre-averaged progress variable. The $\tilde{c}$ curve in the main figure clearly shows the location of the flame brush within which $0 < \tilde{c} < 1$. The inset in Fig. 4 indicates that the bias-corrected Favre-averaged progress variable lies between the upper limit ($B_{pi} = 1/\rho_p$ and $B_{ri} = 1/\rho_r$) and the lower limit ($B_{pi} = B_{ri} = 1$). Although results in all figures remain qualitatively unchanged even if either limit is employed, the bias correction is considered to improve the accuracy of the results.

Examination of Fig. 4 suggests a significant differ-

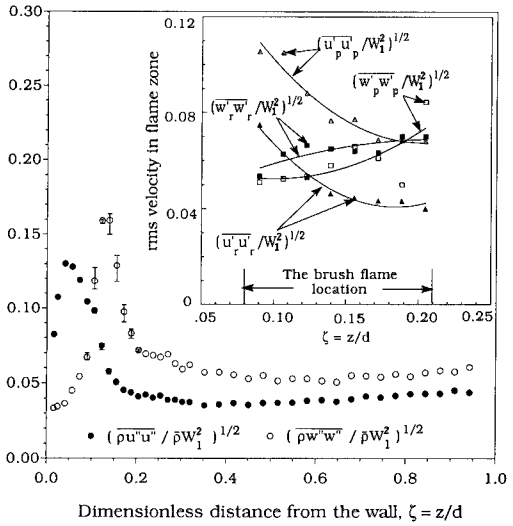

FIG. 5. The root-mean-square (rms) of the intensity of the radial and axial velocity components for $h = 4$ mm.

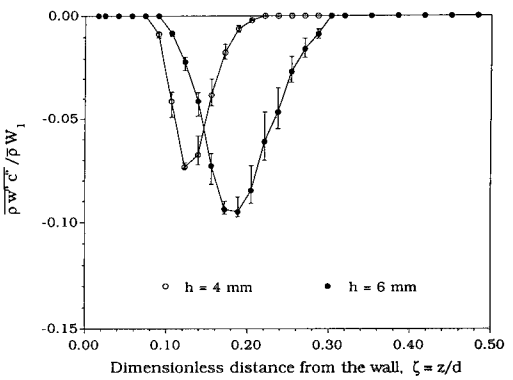

FIG. 6. The mean axial flux of the progress variable for two different values of h.

ence between the flames considered here and unstrained flames dealt with previously. We refer to the increase in the mean axial velocity. In the latter flames, with a representative value of τ of 6, the mean axial velocity increases by that value, but we see from Fig. 4 that $|\bar{W}|$ only increases by a factor of 2.* The implication is that, within the thickness of the flame, the radial gradient of the radial flux of mass, namely

$$\frac{1}{r}\frac{\partial}{\partial r}\overline{\rho u r}$$

*It is interesting to note in this regard that $\bar{W}_p$ is roughly 2.5 times $\bar{W}_r$ *within* the flame, as may be seen from the middle three histograms of Fig. 3.

is sufficiently large so as to balance the mass entering the cold side of the flame with a reduced flux through the hot side. The further implication is that the radial rate of strain generates fluctuations in the radial velocity at the expense of fluctuations in the axial direction. We later discuss this point further.

The distributions of the Favre-averaged intensities of the axial and radial velocity components are shown in Fig. 5. The intensity data indicate that our turbulence generator yields somewhat anisotropic turbulence at the exit plane of the jet with the axial contribution greater than the radial and that this anisotropy increases under the influence of the rate of strain field associated with the stagnating flow and increases further within the flame. However, in the product gas downstream of the flame, as the wall is approached, the intensity of the axial velocity decreases more rapidly than that of the radial component so that, in the product stream, the turbulence is again highly anisotropic but with the two intensities reversed in relative magnitude. Important in terms of our earlier discussion of the radial rate of strain is the observation from the inset in Fig. 5 that the conditioned intensities of the axial velocity within reactants and products are essentially the same throughout the flame and relatively small, the implication being that the unconditioned intensity of the axial velocity is largely associated with differences in the *conditioned* mean velocity within the two gases. We also see from this inset that the intensity of the radial velocity within the light products is higher than within the heavy reactants across the entire flame. The present results for the axial velocity are in agreement with those of Cho et al. [2] but differ with respect to the radial velocity; they show that the difference in the conditioned radial intensities vanishes at the edges of the flame, whereas we find a nearly constant increment. The difference in the two experiments is presumably associated with the higher mean rate of radial strain, i.e., the higher curvature in the radial direction of the mean static pressure, imposed on the flame in the present experiment.

We also note from the main portion of Fig. 5 that there is essentially no increase in the unconditioned intensity of the axial velocity across the flame, while there is a significant increase in the intensity of the radial velocity. This behavior is contrary to that in infinite planar flames, in which there are significant increases in the intensities of the normal velocity and no change in that of the lateral velocities. Again, the radial curvature of the mean static pressure may account for the difference in the two flows. It would be interesting to determine if the observations concerning the unconditioned and conditioned intensities and the differences in strained and unstrained planar flames are supported by appropriate turbulence modeling.

In Fig. 6, we show the mean axial flux of the progress variable, everywhere negative, implying coun-

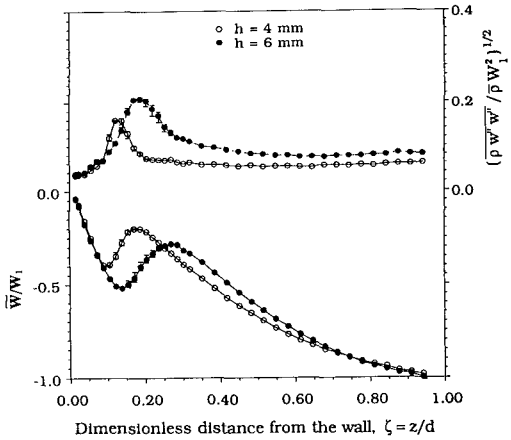

FIG. 7. Comparison of the mean axial velocity $\tilde{W}(\zeta)$ and the root-mean-square (rms) of the axial velocity for two values of h.

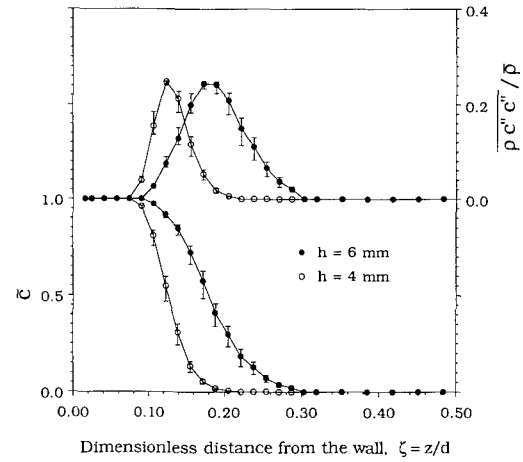

FIG. 8. Comparison of the mean progress variable and the intensity of the progress variable for two values of h.

tergradient diffusion. Note that we are unable to resolve the small edge region where theory and physical considerations indicate that gradient transport should prevail [8].

The Influence of the Integral Scale

The influence of the size of the holes in the turbulence generator is shown in Fig. 6 and in the remaining figures. It is clear from Fig. 6 as well as from Fig. 7 and especially from Fig. 8 that, with an increase in hole diameter in the turbulence generator and therefore with an increase in the integral scale of the turbulence, the thickness of the flame increases. Specifically, when $h = 6$ mm, the flame extends from $\zeta = 0.3$ to $\zeta = 0.1$. Note that, as expected, the increase in thickness is roughly proportional to the increase in h. Figure 7 shows the mean axial velocity in terms of $\tilde{W}(\zeta)/W_1$ and the intensity of the axial velocity in terms of $(\overline{\rho w''^2}/\bar{\rho}W_1^2)^{1/2}$ for both values of h. Again, we see the increase in thickness of the flame. Note that the maximum values of the intensity shown in Fig. 8 in the two cases are equal, in accord with the BML theory, but the smaller thickness for flames with $h = 4$ mm leads to larger gradients. In Figs. 6 through 8, the increase in thickness is accompanied by a shift in position of the cold edge toward the exit plane of the jet and an increase in the intensity and Favre-averaged flux; this could be interpreted as an increase in turbulent flame speed, but in view of the three dimensionality of the flow, such an interpretation is problematic despite its previous use [1–3]. It is also noted from Figs. 6 and 8 that the average gradient of the progress variable decreases while countergradient diffusion increases with increasing turbulent intensity.

Conclusions

We report the results of measurements in two premixed flames in stagnating turbulence arising from the impingement of a reactant stream against a wall. Direct time-resolved measurements of the axial and radial velocity components along the axis are analyzed so that data on the progress variable and therefore on the density are also obtained. Corrections for measurement bias in terms of the flux of seed particles are made. Two turbulence generators with different hole sizes are employed. The aerothermochemical conditions are such that the flame is free standing, i.e., removed from the wall. The intensity of the radial velocity in product is higher than in reactant across the entire flame, a result differing from previous data and from planar unstrained turbulent flames. We provisionally attribute this finding to the radial rate of strain associated with the radial curvature of the mean static pressure in stagnating turbulence, but further consideration of these differences by appropriate analysis is indicated. The intensities of the radial velocity within both reactants and products increase across the flame, so there is turbulence production associated with heat release. It is found, as expected, that the thickness of the flame is proportional to the hole size, i.e., to the integral scale of the turbulence.

Acknowledgments

The research reported here was supported by the Department of Energy, Office of Basic Energy Sciences under Contracts Nos. DE-FG03-86ER13527 and DE-F003-87ER13685.

REFERENCES

1. Cho, P., Law, C. K., Hertzberg, J. R., and Cheng, R., *Twenty-First Symposium (International) on Combustion*, The Combustion Institute, Pittsburgh, 1986, pp. 1493–1499.
2. Cho, P., Law, C. K., Shepherd, I. G., and Cheng, R., *Twenty-Second Symposium (International) on Combustion*, The Combustion Institute, Pittsburgh, 1988, pp. 739–745.
3. Liu, Y., and Lenze, B., *Twenty-Second Symposium (International) on Combustion*, The Combustion Institute, Pittsburgh, 1988, pp. 747–754.
4. Asato, K., Kawamura, T., and Ban, T., *Twenty-Second Symposium (International) on Combustion*, The Combustion Institute, Pittsburgh, 1988, pp. 1509–1515.
5. Bray, K. N. C., Champion, M., and Libby, P. A., *Turbulent Reacting Flows*, Academic Press, London, 1994, pp. 573–607.
6. Bray, K. N. C., Champion, M., and Libby, P. A., *Combust. Flame* 91:165–186 (1992).
7. Bray, K. N. C., Libby, P. A., Masuya, G., and Moss, J. B., *Combust. Sci. Technol.* 25:127–140 (1981).
8. Libby, P. A., *Prog. Energy Combust. Sci.* 11:86–96 (1985).
9. Goss, L. P., in *Instrumentation for Flows with Combustion* (A. M. K. P. Taylor, Ed.), Academic Press, London, 1993, pp. 292–317.
10. Heitor, M. V., Taylor, A. M. K. P., and Whitelaw, J. H., *Exp. Fluids* 3:323–339 (1985).
11. McLaughlin, D. K., and Tiederman, W. G., *Phys. Fluids* 16:2082–2088 (1973).

Twenty-Fifth Symposium (International) on Combustion/The Combustion Institute, 1994/pp. 1215–1222

THE FORMATION AND DESTRUCTION OF AROMATIC COMPOUNDS IN A TURBULENT FLAME

JOHANNES H. THIJSSEN,° MAJED A. TOQAN,°° JÁNOS M. BEÉR AND ADEL F. SAROFIM
Department of Chemical Engineering and Energy Laboratory
Massachusetts Institute of Technology
Cambridge, MA 02140-2390, USA

Systematic, detailed studies of the effects of temperature and fuel type on polycyclic aromatic compound (PAC) emissions from turbulent flames were carried out in a well-controlled, pilot-scale turbulent flame. Benzene and toluene were injected as a secondary fuel into the hot combustion products of a fuel-lean natural gas air flame at 1350 and 1550 K. The experimental results show a strong combined influence of fuel type and temperature on the PAC emissions. At 1350 K, the PAC yield was approximately 10 times higher than that of soot, while at 1550 K, the soot yield was 10 times higher than the PAC yield, indicating a much faster formation and conversion to soot of PACs. At the higher temperature, the product distribution of PACs shifted toward species containing cyclopenta-fused rings.

At 1550 K, the fuel type had virtually no impact on either the total yield of PACs and soot or the product distribution, while at the lower temperature, a large difference in yield and product distribution were found between the experimental fuels. At 1350 K, toluene injection produced up to 25 times more PACs and 30 times more soot than the injection of benzene. Also, the peak concentrations of soot and PACs in the benzene flame occurred later than in the toluene flame. A numerical model based on a segregated flow analysis was used to quantitatively analyze the experimental data. The treatment of the experimental flames by the model showed that the PAC emissions from the flames were affected by both chemistry and mixing. The model correctly predicted the trends of formation, and destruction of most compounds included in the model, and the absolute concentrations of individual species vary from within a factor of 5 (for major species) to within two orders of magnitude (for trace pollutants).

Introduction

Combustion processes may be responsible for the emission of a broad range of pollutants, some of which, including several polycyclic aromatic compounds (PACs), are thought to have adverse health effects [1–3]. The PACs, particularly those with four or five aromatic rings, are known to cause mutations in bacteria and human cells and cancer in rodents [4–6]. Because of this, PACs are among the hazardous air pollutants regulated under the 1990 amendments to the U.S. Clean Air Act, as well as under environmental laws in several other industrialized countries. Because combustion systems are among the prime sources of PACs [7,8], the understanding of their formation and destruction in flames is key to minimization of their anthropogenic emissions. The flames in most practical stationary combustion systems are turbulent diffusion flames. Especially if staged air combustion is applied to reduce NO_x emissions, such flames comprise a high-temperature fuel-rich (pyrolysis) zone, in which conditions are favorable for hydrocarbon molecular weight growth, possibly leading to formation of PACs and soot. This fuel-rich zone is usually followed by a fuel-lean zone, intended for the oxidation of the products of incomplete combustion formed in the previous zone. The survival of PACs and soot will depend on the effectiveness of the oxidation that follows the mixing of combustion products from the fuel-rich zone with the rest of the combustion air. Despite such care, measurable quantities of PACs can be emitted from stationary combustion systems, especially when the temperature distribution or the fuel air ratio deviate from design conditions. The mixing processes in the combustion system, through their effects on the pyrolysis and oxidation reactions, play important roles in the emission of trace concentrations of toxic combustion by-products. Of particular importance is the mixing of "raw" fuel with hot combustion products. Such conditions are purposely caused in staged combustion systems that apply fuel staging as a NO_x reduction strategy. The purpose of the present study was to quantitatively determine combustion process

°Present address: Arthur D. Little, Inc., Acorn Park, Cambridge, MA 02140-2390, USA.

°°Present address: ABB Combustion Engineering, 1000Prospect Hill Road Bldng 301, Windsor, CT 06095-0339, USA.

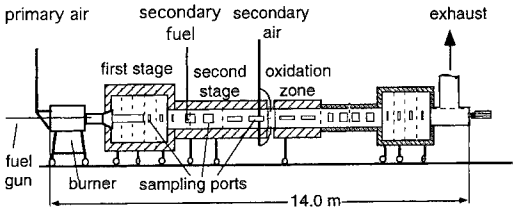

FIG. 1. Configuration of the MIT CRF. The first stage, second stage, and oxidation zone are refractory lined. The CRF has sampling ports for physical and optical access on either side of the furnace.

parameters that lead to the emission of PACs from stationary combustion sources. To investigate the effects of temperature, fuel composition (in particular, aromatic methylation), and turbulent mixing, the hot combustion products of natural gas-air flames were doped with benzene and toluene, at two different temperatures, under well-controlled, turbulent plug flow conditions. Fluid dynamic and detailed chemical kinetic modeling were employed to analyze the data.

Experimental Equipment

The combustion equipment used in this study was the flame tunnel of the MIT Combustion Research Facility (CRF), which had been configured to include a turbulent, near plug-flow test section (Fig. 1). A swirl-stabilized burner [9] was used to introduce a stoichiometric mixture of natural gas and air into the 1.2 × 1.2 × 1.5 m first stage of the flame tunnel. The firing rate of the burner was adjusted to control the temperature at the end of the first stage. As the hot combustion products entered the second stage, they were doped with the liquid secondary fuel, which was injected radially through an eight-hole N_2-assisted atomizer. The contribution of the secondary fuel to the total heat input ranged from 8 to 11%. This arrangement provided near plug-flow conditions in the test section, which consisted of three 0.5-m diameter, 1.0-m-long, refractory-lined, water-cooled cylindrical sections. Ports in the sections allowed sufficient optical and physical access to the furnace for spatially detailed measurements. At the end of the second stage, secondary air was added to the combustion products through eight nozzles, to ensure complete burnout. The operating conditions for the experiments are listed in Table 1.

Measurements of temperature (using a suction pyrometer), velocities (using a five-hole hemispherical impact tube) and major gaseous species concentrations (O_2, CO, CO_2, and NO_x, using paramagnetic, NDIR, and chemiluminescent analyzers) were made to establish the experimental conditions in detail.

Hydrocarbon PAC Measurement:

Since the sampling and analysis of combustion products to determine their concentration of hydrocarbons and PACs is a time-consuming operation, the MIT-LIF system [10] was used to measure the detailed spatial distribution of the sum of PACs in the test section. This PAC map was then used to determine the locations where extractive samples for light hydrocarbon and PAC measurements were to be taken.

Gas samples for light hydrocarbons (C_1 to C_4) were drawn into 0.5 l gas bottles through a water-cooled, stainless steel probe. A fraction of the samples was injected on a Hewlett Packard model 5334 gas chromatograph (GC), fitted with a 4-m Porapak B and a 6-m molesieve (Suppelco) column in series, interfaced with a thermal conductivity detector and a flame ionization detector (FID).

Sampling for PACs was performed using a dichloromethane (DCM) based sampling train [11]. This consisted of a water-quenched, stainless steel, water-cooled sampling probe, a soot trap (collecting soot on a preweighed filter paper), three cooled DCM impingers in series, a flow meter, and a vacuum pump. After sampling, the soot filter and water are extracted with DCM in a Soxhlet apparatus for approximately 16 h. The soot filter was then dried and weighed to determine the soot weight. The DCM solution was then combined with the DCM from the impingers and concentrated in a Kuderna–Danish evaporative concentrator to a volume of approximately 125 mL. If the tar concentration, as determined by evaporation of a 100 μL fraction of the concentrate, was less than 2 mg/mL, the concentrate was further processed in a smaller Kuderna–Danish evaporator.

A fraction of this concentrate was injected on a Varian model 3700 (GC), interfaced to a Finnigan-MAT 211 double-focusing mass spectrometer (MS) for identification. The GC was fitted with a 15-m DB5-fused silica capillary column, having a 0.32-mm diameter and a 0.25-μm film thickness, and was equipped with a cold-on-column injector. It was programmed with an initial hold at 45 °C for 2 min followed by a ramp of 10 °C/min to 280 °C for 5 min. The MS was operated at 70-eV electron energy, 4.5-A filament current, 3000-V acceleration potential, and an ion source temperature of 180 °C.

Another fraction of the concentrate was injected on a GC of the same type and fitted with the same type of column as the one used with the MS, but interfaced to a FID. Quantification of PACs was realized by comparison with a standard mixture of 17 components of known concentrations, consisting of the EPA 16 PAH standard plus cyclopenta(*cd*)pyrene (CPP). For the quantification of monocyclic aromatic compounds (MACs), a special

TABLE 1
Operating conditions of the CRF during tests

First stage	Units	1350 K	1550 K
Thermal input fuel	MW	1.84E − 01	2.77E − 01
Air preheat temperature	K	4.69E + 02	4.83E + 02
Natural gas flow rate	Nm3/s	6.12E − 03	9.22E − 03
Burner air flow rate	Nm3/s	7.53E − 02	1.14E − 01
Fuel equivalence ratio	—	7.70E − 01	7.67E − 01
Exit temperature	K	1.35E + 03	1.54E + 03
Mole fraction CO_2	—	7.48E − 02	7.48E − 02
Mole fraction CO	—	1.40E − 04	2.01E − 05
Mole fraction O_2	—	4.25E − 02	3.46E − 02
Mole fraction H_2O	—	1.50E − 01	1.05E − 01
Flue gas flow rate	m3/s	4.03E − 01	7.00E − 01
Residence time	s	5.37E + 00	3.09E + 00

Second stage	Units	1.350E + 03 K		1.550E + 03 K	
		Toluene	Benzene	Toluene	Benzene
Fuel flow rate	kg/s	7.07E − 04	7.01E − 04	8.77E − 04	7.36E − 04
Fraction of heat input through fuel	—	1.11E − 01	1.10E − 01	9.28E − 02	7.90E − 02
Atomizing fluid flow rate	kg/s	5.83E − 05	5.83E − 05	8.13E − 05	8.13E − 05

standard was prepared, containing benzene, *o*-xylene, phenyl-acetylene, styrene, and toluene.

Finally, a fraction of the concentrate was injected on a high-performance liquid chromatography (HPLC) for qualitative assessment of the concentrations of PACs with molecular weights higher than 300 amu.

Experimental Results and Discussion

Four test series were conducted: operating the primary combustion stage at two firing rates and injecting benzene and toluene, respectively, as secondary fuels into the exhaust from the first stage (Table 1). As the residence time in the first stage was long (3–5 s) and the first stage was operated under fuel-lean comditions, ample time was available for the complete combustion of the fuel. The exhaust of the first stage entering into the second stage was shown to contain no measurable amounts of PACs or small hydrocarbons.

The additional heat input through the secondary fuel was offset by the increased heat extraction caused by strongly increased soot concentrations so that the temperature was not affected significantly (rise of less than 20 K). Spatially detailed mapping (5 cm in radial and 20 cm in axial direction) of the concentrations of major species and temperatures in the flame confirmed that the conditions in the second stage approximated by plug flow in all cases, as the variation in any of these measured quantities was less than 20% over any of the cross sections. This warranted the characterization of the PAC and hydrocarbon concentrations along the flame by centerline measurements only.

The Effect of Fuel Type at 1350 K:

The temperature and major species concentrations distributions in the 1350 K benzene and toluene flames were similar, except for the CO concentrations, which were significantly higher in the benzene flame. The PAC and soot concentrations (Fig. 2a) showed a remarkable dependence upon the fuel type: they were much higher in the toluene than in the benzene flame. The average net production rate of PACs from injection to peak value was 25 $\mu g\ s^{-1}\ cm^{-3}$ in the toluene flame, while in the benzene flame, it was no higher than 1.0 $\mu g\ s^{-1}\ cm^{-3}$. The fractional PAC yields at the peak concentration (based on the amount of secondary fuel injected) were 0.28 and 0.14. The rate of formation of soot in the toluene flame was also higher than in the benzene flame (15 vs 0.5 $\mu g\ s^{-1}\ cm^{-3}$), leading to correspondingly higher soot yields (0.7 vs 0.17). Noteworthy is that in the benzene flame, the ratio of soot to PACs was only half that in the toluene flame. Qualitatively, these results are in good agreement with expectations: under the experimental conditions, toluene is less stable (i.e., more easily oxidized) than benzene. In addition, there exist more direct pathways to PAC

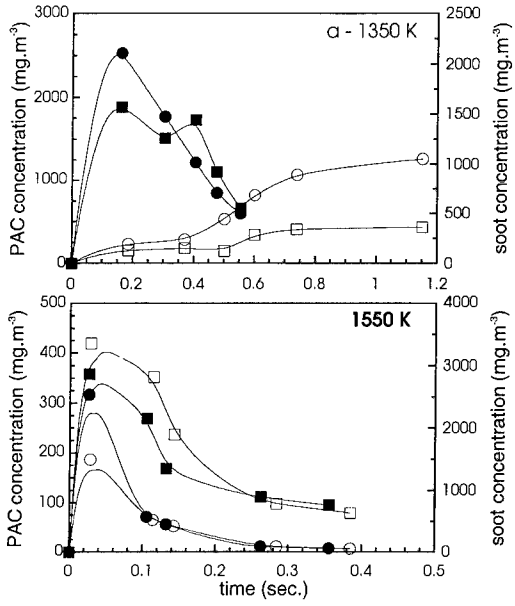

FIG. 2. Concentrations of PACs and soot in the (a) 1350 K and (b) 1550 K flames. Open symbols refer to the benzene flames; closed symbols refer to the toluene flames. ● and ○ represent the total PAC or tar concentrations, as measured by the evaporation of 100 μL of the sample; ■ and □ represent the soot concentrations.

formation from some of the reaction products of fuel-rich toluene oxidation (such as benzyl radical and acetylene) than some of those of benzene oxidation (such as phenol). This is partly aided by the higher concentrations of H atoms occuring in the fuel-rich oxidation of toluene.

The Effect of Fuel Type at 1550 K:

At 1550 K, no substantial difference was found in the concentrations between the major species, PAC, and soot concentrations in the toluene and the benzene flame (Fig. 2b). The PAC concentrations grew rapidly in both flames until a distance of 300 mm (or 20 ms) from the secondary fuel nozzle then dropped with a near exponential decay to values close to the detection limit of the chemical analytical techniques. The formation of soot followed the formation of PACs with approximately a 50-ms delay. The similarity of the soot and PAC concentration profiles may be explained by the fact that the earlier-mentioned higher stability of benzene (compared to toluene) does not play a significant role at 1550 K.

The Effect of Flame Temperature:

Net PAC formation rates were found to be highest in the 1350 K toluene flame, followed by both 1550 K flames (Table 2). The net yield of PACs in the 1550 K flames was substantially lower. The net rate of formation of soot in the 1550 K flames was more than 10 times higher than that in either of the 1350 K flames. Therefore, the lower net production of PACs in the 1550 K flames (compared to the 1350 K toluene flame) is likely to have been a result of a rapid conversion of PACs into soot. The higher temperature is also likely to cause a higher fraction of the PACs to be in the radical form, leading to higher rates of formation of soot [12]. This, together with the fact that the formation of soot from PACs is virtually irreversible, explains that the ratio of PAC to soot concentrations in the 1550 K flames is much smaller than in the 1350 K flame (Table 2).

When contrasting the 1550 and 1350 K flames with respect to the fraction of individual PACs in the DCM extractable material (Fig. 3), the main difference is that in the 1550 K flames, PACs with cyclopenta-fused rings (such as acenaphtylene, fluoranthene, and cyclopenta(*cd*)pyrene) were more prevalent. This is consistent with observations by Bockhorn et al. [13] and Frenklach and Warnatz [14], and more recently by Marr [15] who found cyclopenta-fused PACs to play a key role in the molecular weight growth of PACs. It is also consistent with observations by Mulholland [16] who found increased

TABLE 2

The average PAC and soot production rates and yields in the four flames. Production rates are averaged between the injection of the secondary fuel and the peak concentration of the species of interest. The yield is based on the total PAC concentrations, as measured by evaporation of a 100-μL sample, and on the amount of secondary fuel injected.

Fuel type	T (K)	PAC production (μg s^{-1} cm^{-3})	PAC yield (g/g fuel)	Soot production (μg s^{-1} cm^{-3})	Soot yield (g/g fuel)
Toluene	1350	2.5	0.28	15	0.7
Benzene	1350	1.0	0.14	0.5	0.17
Toluene	1550	15	0.04	150	0.41
Benzene	1550	10	0.03	150	0.48

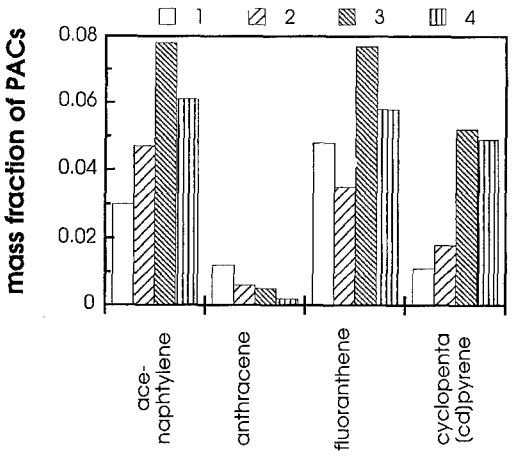

FIG. 3. Comparison of the relative abundance of individual key PACs. The values are a mass fraction of the total amount of PACs that each of the individual PACs account for.

formation of cyclopenta-fused PACs at higher temperatures during pure pyrolysis of both chlorinated and nonchlorinated monocylcic aromatic compounds (MACs). From the point of view of health effects, this is important because various toxicological studies have indicated that cyclopenta(*cd*)pyrene and fluoranthene account for most of the mutagenicity and carcinogenicity of combustion by-products in both bacterial, human cell, and animal tests [5,6,17]. Nevertheless, the total mutagenicity (mutagenic potential of the sample per unit energy associated with the sampled gas) emitted from the 1550 K flames was smaller than that emitted from the 1350 K flames, because the absolute yield of mutagens was still lower in the 1550 K flames than in the 1350 K flames (the total PAC concentrations are approximately 10 times lower). This agrees with earlier findings [4], which suggested that reduction of the total PAC emissions is the most effective way of reducing the mutagenic potential from combustion sources (mutations per unit energy), although the tar emitted is more mutagenic (mutations per gram DCM extractable material).

The destruction of PACs and soot in the second stage of the 1550 K flames also showed strong similarities between the benzene and the toluene flames. The rate of destruction of PACs was, as in the 1350 K toluene flame, substantially higher than the rate of destruction of soot. When the decay part of the concentration curves of soot and PACs was fitted with an exponential function, the time constants obtained for PAC destruction were approximately 0.1 s while the time constants for soot destruction were approximately 0.2 s. The ratio of the rate constants for soot oxidation* in 1550 K flames and the 1350 K toluene flame was 3.2, which would indicate an activation energy of 26 kcal/mol, not too far from the 39 kcal/mol found by Lee et al. [18]. As the temperature was increased, the rate of destruction of PACs increased somewhat more than that of soot.

Quantitative interpretation of the results from the studies described above is greatly facilitated by the use of numerical modeling tools. Because of the nature of the flames of interest and our interest in individual PACs emitted, treatment of both mixing and chemical kinetics in some detail was necessary. Therefore, a combined but decoupled use of a detailed fluid dynamic code and a detailed chemical kinetic mechanism was applied. This is possible because the micropollutants of interest (such as NO_x and PACs) are present in low concentrations (mole fractions typically between 10^{-9} and 10^{-4}) and do not play an important role in branching reactions (such as O, H, and OH radicals do) so that the effect they have on density changes in the flow is minor.

The modeling approach was implemented using the commercial computational fluid dynamics (CFD) package, Fluent, and a chemical kinetic model based on Sandia's CHEMKIN [19,20]. The chemical kinetic model and the thermodynamic database used are drawn from Marr's molecular weight growth model [13] supplemented with the benzene and toluene oxidation reactions from the toluene oxidation model of Emdee et al. [21]. The resulting model contained 127 chemical species and 382 elementary reactions. Of those reactions, 240 described hydrocarbon chemistry up to C_4 and the pyrolysis and oxidation of benzene and toluene; the rest were used to describe the formation and destruction of PACs (and some of their related radicals) up to pyrene. A detailed description of the modeling approach is given elsewhere [22]. Briefly, an axisymmetric representation of the flow with the fluid dynamics package is used to estimate the mixing rate between secondary fuel and the hot combustion products from the first stage, as well as the temperatures in the system. The rate of toluene consumption in the CFD code was assumed to be purely mixing controlled. Mass-weighted averaging of the axial flux of unconverted toluene and of the temperature in radial direction then yielded the mass fraction of unmixed toluene and the temperature as a function of time. These profiles were then fitted by a simple exponential function and a third-order polynomial, respectively, for use with the segregated flow model. The segregated flow model used in this study treats the flow as two discrete phases: one with unmixed fuel and one with a mixture of fuel and combustion gases. At discrete time steps, a fraction of the contents of

*Defined as in k_{soot} in $-\frac{d[\text{soot}]}{dt} = k_{soot} \cdot [\text{soot}] \cdot [O_2]$.

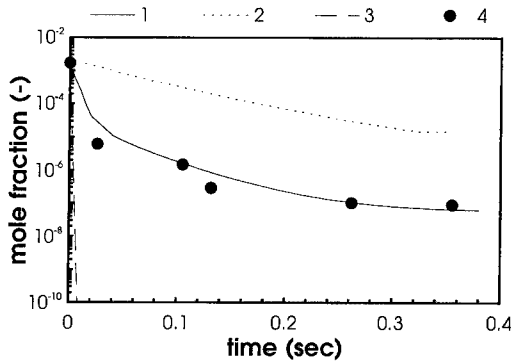

FIG. 4. Relative importance of mixing and chemical kinetics in the system: (1) segregated flow model considering both mixing and chemical kinetics; (2) model assuming mixing control; (3) model assuming chemical kinetic control; and (4) experimental data.

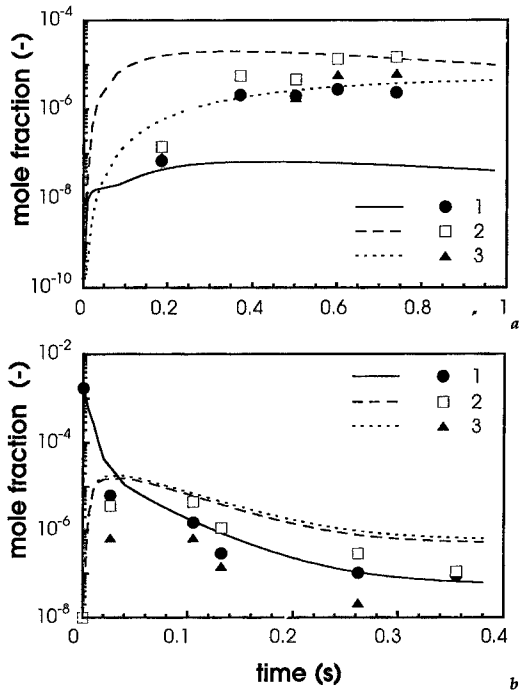

FIG. 5. Selected results of the segregated flow analysis for (a) the 1350 K benzene flame and (b) the 1550 K toluene flame. Lines represent modeling results; symbols represent experimental results; species: (1) toluene; (2) naphthalene; (3) phenanthrene.

the first phase is allowed to mix with contents of the second phase, according to the mixing function described above. The solution of the mixing and chemical kinetic problems are implemented in a FORTRAN computer code, using Sandias CHEMKIN II subroutine library as a basis. The initial mole fractions of the individual species in each of the reactors were calculated by treating the first stage as a PSR (using Sandia's PSR code).

Figure 4 shows a comparison of the measurement of secondary fuel destruction with a mixing model (assuming mixing control), a homogeneous plug-flow model (assuming kinetic control), and the segregated flow analysis. A description of the system by a homogeneous (one-phase) flow would yield a good approximation, if PAC and soot formation and destruction were kinetically controlled, whereas a description of the fuel concentration decay based solely on the mixing rate would describe reality if it were mixing controlled. Clearly, both turbulent mixing and detailed chemistry need to be addressed in order to make accurate predictions. Figure 5 shows the capacity of the model in predicting concentrations of individual PACs. The trends of PAC formation and destruction are predicted correctly over a wide range of concentrations and conditions. The most significant discrepancy between predictions and measurements concerns the larger (three and four ring) PACs, which are overpredicted, especially at 1550 K. The reason for this discrepancy is the absence of the treatment of soot formation in the model; soot serves as a sink for carbon, especially affecting the concentrations of these higher molecular weight species.

Conclusions

Systematic studies of the effects of temperature and fuel type on PAC emissions were carried out in a well-controlled, pilot scale, turbulent flame. The experimental studies of PAC formation and destruction showed strong combined influences of temperature (in the region between 1350 and 1550 K) and fuel type. At 1350 K, the PAC yield was approximately 10 times higher than that of soot, while at 1550 K, the soot yield was 10 times higher than the PAC yield. As expected, the formation of PACs and their conversion to soot occurs much (approximately two times) faster at 1550 K than at 1350 K. At the higher temperature, the product distribution of PACs shifted toward species containing cyclopenta-fused rings, while direct polymerization products of the fuel were found at lower concentrations.

At 1550 K, the fuel type had virtually no impact on either the total yield of PACs and soot or the product distribution, while at the lower temperature, a large difference in yield and product distribution were found between the experimental fuels. At 1350 K, toluene injection produced up to 25 times more PACs and 30 times more soot than the injection of benzene. Also, the peak concentrations of soot and PACs in the benzene flame occurred later (at approximately 1 s) than in the toluene flame (approximately 0.15 s). This difference is consistent with the

relative stability of the two fuels and the pyrolysis pathways that are open to each of the fuels.

The modeling study was the first attempt to quantitatively represent the processes of formation and destruction of PACs by the application of detailed chemical kinetic mechanisms to pilot-scale turbulent-combustion processes. This was achieved by partial decoupling of the solution of the mixing problem from that of the chemical kinetic problem. The model, based on a partially segregated flow analysis, has the turbulence parameters in the CFD code as only adjustable parameters and can, in principle, be used in any turbulent combustion device (modifications may be necessary to account for recirculating flows).

The treatment of the experimental flames by the model showed that the PAC emissions from the flames were affected by both chemistry and mixing. The model was able to predict correctly the trends of formation and destruction of most compounds included in the model: i.e., the slope of the predicted concentration-time curve corresponds to that of the measured curve at any point in time. The prediction of the absolute concentrations of individual species varies from within a factor of 5 (for major species including the secondary fuel) to within two orders of magnitude for the trace pollutants.

Acknowledgments

The authors acknowledge the generous financial support from the U.S. Environmental Protection Agency (Grant No. CR817574-01-3); Eniricerche S.p.A.; Ente Nazionale per l'Energia Elettrica; Lentjes AG./Technolas Indrustrie und Umweltanalytik GmbH; Stadtwerke Düsseldorf; John Zink Co.; and the National Institute for Environmental Health Studies (Grant No. ES01640-16). The authors are grateful to Dr. J. Marr for providing them with early releases of his chemical kinetic models and to Dr. L. Bonfanti (ENEL), Ms. J. Culler, and Dr. A. L. Lafleur (NIEHS/MIT CEHS) for their valuable contribution to the chemical analyses of the flame and the MIT-Combustion Research Facility staff for their participation in the experimental studies. The discussions of hydrocarbon kinetics with Professor J. B. Howard has been most valuable for the formulation of the combined chemical kinetic model and for the interpretation of the experimental data. Dr. J. D. Teare's contribution to the administrative organization of the consortium of industrial sponsors is acknowledged with thanks.

REFERENCES

1. Lewtas, J., in *Toxicological Effects of Emissions from Diesel Engines* (J. Lewtas, Eds.), Elsevier Biomedical, New York, 1982, Vol. 10, pp. 243–264.
2. Grimmer, G., and Misfeld, J., in *Environmental Carcinogens: Polycyclic Aromatic Hydrocarbons* (G. Grimmer, Eds.), CRC Press, Inc., Boca Raton, FL, 1983, pp. 1–25.
3. Schmähl, D.-W., Brune, H., Schneider, P., Mohr, U. D., Habs, M., Pott, F., and Steinhoff, D., in *Environmental Carcinogens: Polycyclic Aromatic Hydrocarbons* (G. Grimmer, Eds.), CRC Press, Inc., Boca Raton, FL, 1983, pp. 157–221.
4. Toqan, M. A., Thijssen, J. H. J., Lafleur, A., and Beér, J. M., *J. Inst. Energy* 66:119–125 (1993).
5. Barfknecht, T. R., Hites, R. A., Cavaliers, E. L., and Thilly, W. G., in *Toxicological Effects of Emissions from Diesel Engines* (J. Lewtas, Eds.), Elsevier Biomedical, New York, 1982, Vol. 10, pp. 277–295.
6. Busby, W. F., Goldman, M. E., Newberne, P. M., and Wogan, G. N., *Carcinogenisis* 5:1311–16 (1985).
7. Forester, J., *J. Am. Stat. Assoc* 75:25 (1980).
8. Grimmer, G., *Environmental Carcinogens: Polycyclic Aromatic Hydrocarbons,* CRC Press, Inc., Boca Raton, FL, 1983.
9. Toqan, M. A., Beér, J. M., Jahnsohn, P., Sun, N., Shihadeh, A., and Teare, J. D., "Low NO_x Emission from Radially Stratified Natural Gas–Air Turbulent Diffusion Flames," *Twenty-Fourth Symposium (International) on Combustion,* The Combustion Institute, Sydney, Australia, 1992.
10. Thijssen, J. H. J., Toqan, M. A., Beér, J. M., and Sarofim, A. F., *Combust. Sci Technol.* 90:101 (1993).
11. Kruzel, E. L., Lafleur, Arthur L., Braun, Andrew G., Longwell, John P., Thilly, William G., and Peters, William A., *Environ. Health Persp.* 90:305–314 (1991).
12. Howard, J. B., "Carbon Addition and Oxidation Reactions in Heterogeneous Combustion and soot Formation," *Twenty-Third Symposium (International) on Combustion,* The Combustion Institute, Orleans, France, 1990.
13. Bockhom, H., Fetting, F., and Wenz, H. W., "Investigation of the Formation of High Molecular Hydrocarbons and Soot in Premixed Hydrocarbon-Oxygen Flames." *Ber. Bunsenges. Phys. Chem.* 87:1067 (1983).
14. Frenklach, M., and Warnatz, J., "Detailed Modeling of PAH profiles in a Sooting Low-Pressure Acetylene Flame." *Combust. Sci. Technol.* 51:265 (1987).
15. Marr, J., Ph.D. Thesis, Massachusetts Institute of Technology, Cambridge, MA, 1993.
16. Mulholland, J. A., Ph.D. Thesis, Massachusetts Institute of Technology, Cambridge, MA, 1992.
17. Kaden, D. A., Hites, R. A., and Thilly, W. G., *Cancer Res.* 39:4152–4159 (1979).
18. Lee, K. B., Thring, M. W., and Beér, J. M., *Combust. Flame* 6:137–145 (1962).
19. Lutz, A. E., Kee, R. J., and Miller, J. A., *SENKIN: A Fortran Program for Predicting Homogeneous Gas Phase Chemical Kinetics With Sensitivity Analysis,* Sandia Report, SAND87-8248.UC-401, Sandia National Laboratories, 1991.
20. Kee, R. J., Rupley, F. M., and Miller, J. A., *Chemkin-*

II: A Fortran Chemical Kinetics Package for the Analysis of Gas-Phase Chemical Kinetics, Sandia Report, SAND87-8009.UC-401, Sandia National Laboratories, 1991.

21. Emdee, J. L., Brezinsky, K., and Glassman, I., *J. Phys. Chem.* 96:2151–2161 (1992).
22. Thijssen, J. H. J., Ph.D., Massachusetts Institute of Technology, Cambridge, MA, 1993.

COMMENTS

A. E. Jacob Akanetuk, Stanford University, USA. What was the actual oxygen level at the injection point of the toluene (as it was not explicitly stated)? It appears that the processes studied in the experiments were pertinent only to the upper furnace and convection section of a utility boiler, and the oxygen level in the experiments should have been stated to be at a value typical of the convection section of a utility boiler.

Author's Reply. The oxygen level at the injection point of toluene was about 4%. We agree that the experimental conditions (temperature and O_2 concentrations) are pertinent to the processes in the upper furnace of an industrial or utility boiler.

•

P. Tesner, All Russian Institute of Natural Gas, Russia. 1. What is the concentration of acetylene as compared with the concentration of PAH?

2. Was the dispersion of soot measured?

Author's Reply. 1. Acetylene concentrations (mol fractions) were generally two orders of magnitude higher than those of the PAHs. (Typically 10^{-4}, compared with 10^{-6}.)

2. The distribution of soot concentration (mg/m^3) has been measured both by laser light scattering and also by sampling along the flame axis.

Twenty-Fifth Symposium (International) on Combustion/The Combustion Institute, 1994/pp. 1223–1231

TEMPORAL EVOLUTION OF TURBULENCE/CHEMISTRY INTERACTIONS IN LIFTED, TURBULENT-JET FLAMES

R. W. SCHEFER
Combustion Research Facility
Sandia National Laboratories
Livermore, CA 94551-0969, USA

AND

M. NAMAZIAN, E. E. J. FILTOPOULOS AND J. KELLY
Altex Technologies Corporation
650 Nuttman Rd., Santa Clara, CA 95054, USA

Flame ignition, extinction, and reignition that control flame stability are inherently time-dependent phenomena. To better understand and quantify these important characteristics, two-pulse images of the instantaneous CH/CH_4 distributions, with a variable time delay between images, were used to study the temporal evolution of turbulence/chemistry interactions in lifted, turbulent CH_4-jet flames. The jet-exit velocity was 21 m/s, corresponding to a jet-exit Reynolds number of 7000. The results are presented to emphasize the interactions between turbulence structure and the flame that lead to the large fluctuations in flame liftoff height observed experimentally. The results show that the flame envelope curves around semiorganized, large-scale vortical structures formed along the periphery of the jet. Interactions between these vortical structures and the flame cause excessive stretch that leads to local flame extinction. Extinction occurs on both the downstream edges of the structures and on the upstream sides. Once the flame is extinguished by a vortical structure, the flame stabilization point can be carried significant distances downstream by the vortex. The return to an upstream stabilization location occurs through turbulent premixed flame propagation. The images clearly show upstream propagation of the flame within the plane of the image. Evidence also exists for the importance of flame propagation in the azimuthal direction normal to the image plane.

Introduction

Flame stabilization theories generally recognize the importance of local ignition, flame propagation, and extinction phenomena as having a major influence on flame stability. These theories have in large part been developed based on experimental observations in turbulent, lifted-jet flames. An understanding of the stabilization mechanism for lifted flames is essential to a better understanding of flame stabilization in general since lifted flames include many of the fundamental mechanisms controlling flame stabilization in practical burners.

Theories for lifted-flame stabilization have been reviewed by Pitts [1]. Early theories were based on the concept of premixed flame propagation. Vanquickenborne and van Tiggelen [2] proposed that, in lifted flames, the fuel and air are premixed prior to ignition and that stabilization occurs where the local flow velocity along the stoichiometric contour is equal to the turbulent flame speed. Flame extinction forms the basis for several more recent theories. Peters and Williams [3] have argued that the fuel and air are not premixed at the flame stabilization point and that liftoff can be explained in terms of laminar flamelets in which extinction occurs where the local value of scalar dissipation exceeds a critical value, and the flame is quenched. The flame is stabilized where scalar dissipation is below this critical value. Extinction has also been proposed by Byggstoyl and Magnussen [4] as the mechanism controlling flame stabilization. In this model, stabilization is determined by extinction at the smallest turbulence scales.

The role of large-scale turbulence structure in lifted-flame stabilization has also been examined [5,6,7]. Miake-Lye and Hammer [5] proposed a model for lifted-jet flame behavior based on large-scale flow dynamics that was consistent with experimental findings for undiluted and slightly diluted fuel mixtures. In the model, large-scale strain imposed on the concentration field determines the stability criterion. Inherent to the model is upstream propagation of the flame from one large-scale structure to the next. Such propagation occurs provided the strain rate between structures is below a critical value. Broadwell et al. [6] consider large-scale motion and

small-scale mixing between the fuel and air. In the proposed model, hot combustion products are carried by large-scale motion from inside the jet to the outer edges where they are subsequently reentrained with outer air. Provided sufficient mixing time is available, the reentrained mixture acts as an ignition source for the fuel, resulting in the formation of flame sheets at near-stoichiometric conditions along the interface between the entrained fluid and fuel-rich jet. While this model gave good agreement with experimentally measured blowout velocities, Pitts [1] has shown that extension of the model to predict lift-off is not consistent with experimental data.

Single-shot images of the instantaneous CH, CH_4, and temperature fields in lifted, turbulent CH_4-jet flames were used in a previous paper [8] to evaluate several of the above theories. The results showed that the magnitude of the scalar dissipation at the flame base is considerably below the critical value that could result in extinction and that scalar dissipation is not important to flame stabilization. This result might be expected since sufficient time is available upstream of the flame stabilization location for fuel from the central jet to mix with air from the surrounding fluid. The low scalar dissipation rates measured reflect the degree of premixing that has occurred upstream of the flame. Alternatively, it was concluded that local stoichiometry and turbulence characteristics are the primary factors controlling flame stability.

Since flame ignition, extinction, and propagation are time-dependent phenomena, time-resolved measurements are needed to more fully understand their role in flame stabilization. Recognizing the importance of such measurements, we have obtained two-pulse images of the CH/CH_4 distributions in a lifted, turbulent CH_4-jet flame. In the remainder of the paper, the experimental system will be described, and selected experimental results will be presented. The data reveal a wide diversity of turbulence/flame interactions that cannot entirely be included in the present paper because of length limitations. We have therefore chosen to focus on those interactions that explain the fluctuations in liftoff height that have been observed experimentally [5–8]. These fluctuations are on the order of the local jet diameter, which has led investigators to conclude that large-scale structure plays an important role in the stabilization mechanism. The present results will attempt to further elucidate this interaction.

Experimental System

The burner consisted of a 5.4-mm diameter fuel jet located in the center of a plate. Methane was injected through the central fuel tube into surrounding still air. Measurements were obtained at a jet-exit velocity of 21 m/s, corresponding to a jet-exit Reynolds number of 7000. The visible flame was lifted and stabilized at an axial position approximately 30 mm downstream of the burner face. This flow has been studied previously using single-shot imaging of CH, CH_4, OH, and temperature [8,10].

The experimental system used here is similar to that used previously with appropriate modifications, as described below, to provide two laser pulses with an adjustable time delay between pulses. For the CH and CH_4 measurements, the laser was tuned to produce a 431.5-nm wavelength beam. The 431.5-nm beam (1.8-μs pulse duration) was used to excite the (0,0) band of the A^2 D-X^2 II system of CH, and the fluorescence of the (0,1) transition was observed at 489 nm. Simultaneously, spontaneous Raman scattering from CH_4 also occurred near 489 nm for the 431.5-nm excitation. The beam was formed into a 0.2-mm thick sheet of light by a multipass cell consisting of two cylindrical reflectors. The combined CH fluorescence and CH_4 Raman-scattering signals were collected at a right angle to the laser sheet by two 55-mm focal length camera lenses (f/1.2) and focused onto intensified Photometrics CCD cameras located on opposite sides of the laser sheet. The light passed through 10-nm bandwidth filters centered at 489 nm that transmitted only the combined fluorescence and Raman signals to the cameras. The camera intensifiers were gated to stay on for 4 μs to reduce flame luminescence and background-scattered light.

When operated in the previous single-pulse mode, the laser consisted of one oscillator and three amplifier stages. To provide two temporally separated pulses, the laser was reconfigured into two separate lasers, each consisting of a single oscillator and amplifier stage. Each laser produced a 300-mJ beam. The beams from the two lasers were orthogonally polarized, which allowed the beams to be combined using a polarizing beamsplitter. Once combined, a Pockel cell was used to rotate the polarization of the horizontally polarized beam to vertical. The time-delayed beams were formed into overlapping sheets in the multipass cell. Timing pulse generators were used to fire both lasers with a variable time delay up to 500 ms specified by the user, and to gate both camera intensifiers so that the first laser shot was recorded on one camera and the second shot on the other camera. Both camera detectors were operated in a 256 × 192-pixel format, providing a spatial resolution of about 200 × 200 μm. This resolution was comparable to the Kolomogorov scale, which varies from 0.1 mm near the flame initiation point to about 0.2 mm at downstream locations.

Calibration in a flow of 100% CH_4 at room temperature and pressure allowed the CH_4 Raman signal to be converted to number density. The shot noise of the system was estimated as 5% of the signal from pure CH_4, based on the calibration data. No attempt was made to quantitatively relate the CH signal to number density. The CH could be differentiated

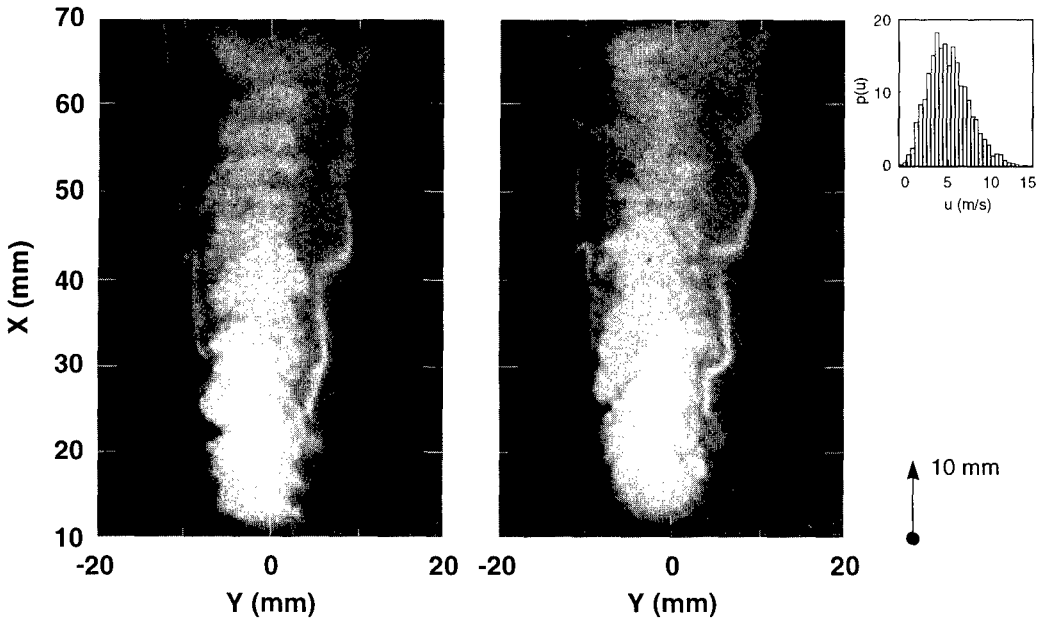

FIG. 1. Two-pulse images of the CH/CH_4 distribution in a lifted, turbulent CH_4-jet flame. Jet velocity is 21 m/s. Figure 1b was taken 1 ms after Fig. 1a.

from CH_4 by both the stronger CH signal and its location [11] and was thus used as a spatial indicator of the flame zone. The combined CH/CH_4 data are presented as a normalized concentration, where the combined CH/CH_4 number density is normalized by the number density of pure CH_4 at room temperature. Each image was corrected for background signal and shot-to-shot variations of laser power.

Results

Previous single-shot images indicate that vortical structures formed in the mixing region adjacent to the fuel jet may play an important role in lifted-flame stabilization [10]. Further evidence supporting this view is provided by the present data, where progression of the vortex rollup can be seen from the images. Figure 1 shows combined CH/CH_4 images obtained in the lifted flame. The CH/CH_4 distribution is presented as a gray scale, with higher concentrations indicated by lighter shades. The size of the imaged area is 60 mm in the axial direction, x, by 40 mm in the radial direction, y, and the fuel-jet exit is located 10 mm below the bottom of the images. The image to the left (Fig. 1a) was taken during the first laser shot, 1 ms before the image to the right (Fig. 1b). The high-CH region can be identified by both its location and magnitude relative to the local CH_4 signal. As described in previous papers, the CH forms in a narrow region along the periphery of the central jet [8]. In Fig. 1, the high-CH region, or flame zone, is located between 5 and 10 mm from the centerline along both sides of the central jet. The exact radial location varies with both axial location and from shot to shot as the flame zone responds to variations in the fuel jet boundaries. The central fuel jet is indicated by the light gray area between the two flame zones. In this upstream region of the flow, reaction is confined to the mixing region adjacent to the central jet. Note that the high-CH region begins several millimeters downstream from the bottom of the image. In Fig. 1a, the flame on the left side of the jet is first seen at about 30 mm downstream, while the flame on the right is at 23 mm. These points correspond to the location where the lifted flame is stabilized, or the flame liftoff height. The liftoff height varies from shot to shot and is typically not the same on both sides of the jet.

The insert in the upper right corner of the figure shows the probability distribution of axial velocity (measured using laser-Doppler velocimetry) along the time-averaged stoichiometric line, which coincides with the maximum CH, at the average flame liftoff height of 30 mm. The velocity distribution extends from slightly negative numbers to about 10 m/s. The arrow below the distribution indicates the distance a structure could travel over the time delay between images if moving at the maximum velocity of 10 m/s.

Vortical structure growth can be seen along the right edge of the jet. In Fig. 1a, the flame zone is

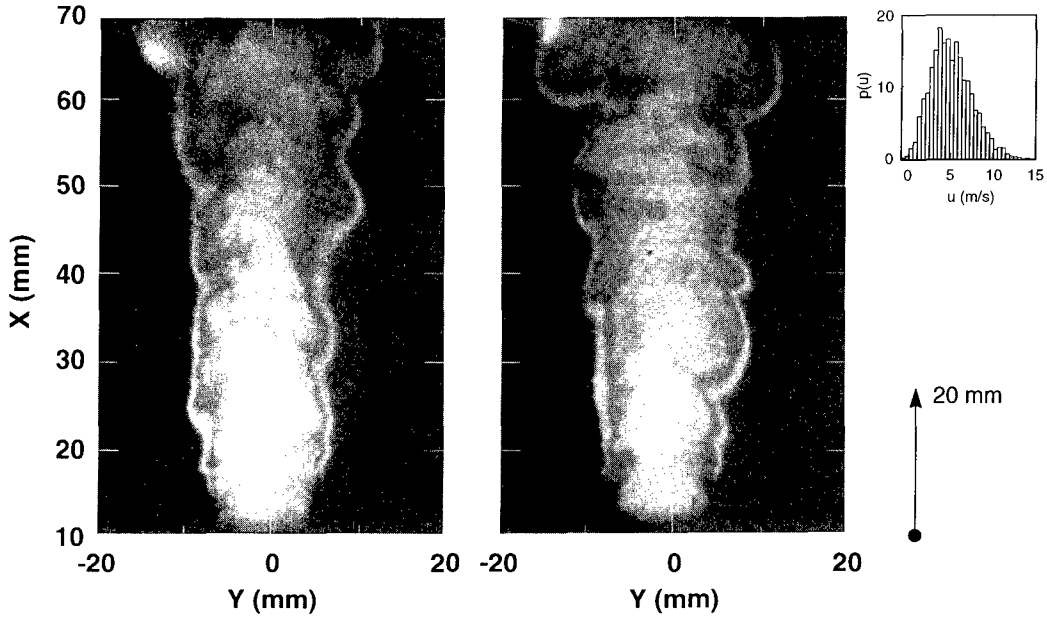

FIG. 2. Two-pulse images of the CH/CH_4 distribution in a lifted, turbulent CH_4-jet flame. Jet velocity is 21 m/s. Figure 2b was taken 2 ms after Fig. 2a.

relatively straight, with only a single outward bulge near the center of the image at $x = 40$ mm. At this location, the flame curves outward around the structure. One millisecond later, Fig. 1b shows the development of three outward bulges, or vortical structures. The structure located in the center continues to roll up and increase in size, while those located at $x = 30$ and 60 mm develop from relatively straight flame regions. The flame zone at these locations is forced outward in response to the structure growth. Note the lack of symmetry in these two images, with vortical structure growth limited to the right side of the flame. The flame zone on the left side remains straight, with a minimum of structure apparent. Figure 2 shows another example of vortical structure growth. In contrast to the asymmetry in Fig. 1, two large vortical structures form nearly symmetrically on both sides of the central jet in the downstream region of the images. This observation is consistent with the axisymmetric stability mode for the jet proposed by Dahm and Dimotakis [12]. Again, the vortical structures develop with time over the 2-ms delay between Figs. 2a and 2b.

Similar flame/vortex interactions were observed in buoyant jet-diffusion flames using planar flow visualization [13]. Two different vortical structures were identified in these flames; small rollup vortices inside the luminous flame zone and larger toroidal vortices outside the flame zone. The small inner vortices were attributed to Kelvin–Helmholtz instability of the jet, while the outer vortices are due to buoyancy-driven instability. At the Reynolds numbers of the present jet, it was found that the outer vortices are no longer well defined, and flame curvature results primarily from interactions between the flame and the inner vortices. Given the close correspondence between the radial location of these inner vortices and the location of the present flame, it is concluded that the flame bulges seen in Figs. 1 and 2 are the result of similar interactions between the flame and these inner vortical structures.

Figures 1 and 2 both show a flame that remains connected from the flame liftoff height to the top of the images, and a connectivity that is not affected by the presence of vortical structures. Figure 3 shows two images with a time delay of 2 ms. The vortex/flame interaction along the right side of the jet is similar to those described previously, with no evidence of flame extinction. In contrast, along the left side of the jet, a single vortical structure with a continuous flame formed around the structure is seen near the center of the image in Fig. 3a. Further development of the structure and some downstream movement are seen in Fig. 3b. However, no CH exists upstream of the structure, and the flame stabilization point coincides with the upstream edge of the vortex. Examination of the entire data set of 900 images shows that extinction of the flame at the upstream edge of the vortex occurs numerous times. Images with longer pulse delay times further show the flame stabilization point can be carried significant distances downstream by the vortex.

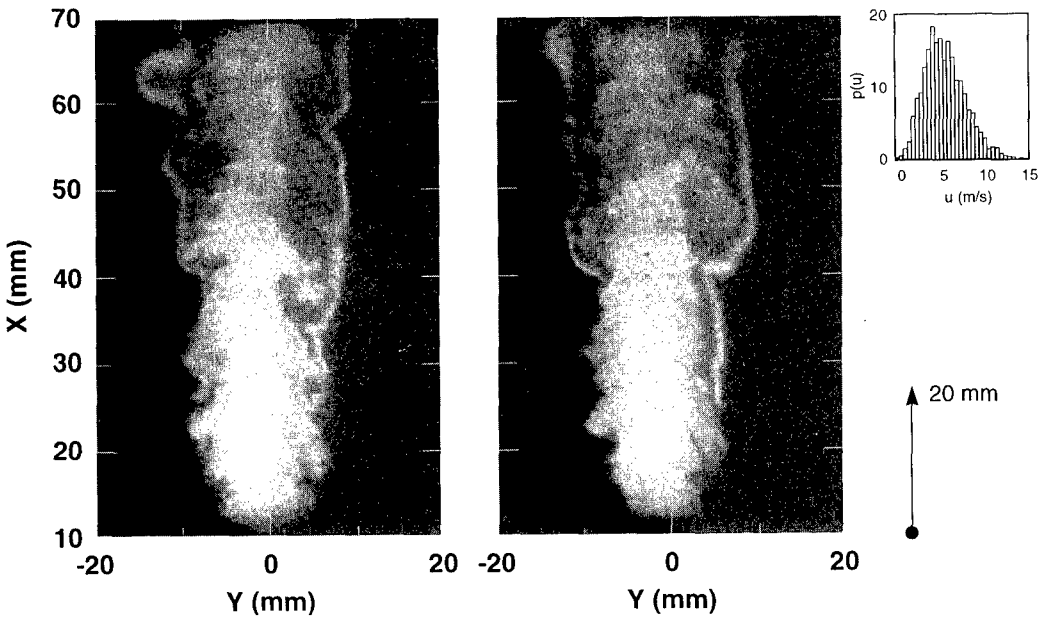

FIG. 3. Two-pulse images of the CH/CH_4 distribution in a lifted, turbulent CH_4-jet flame. Jet velocity is 21 m/s. Figure 3b was taken 2 ms after Fig. 3a.

While the above discussion establishes the importance of large-scale structure in flame stabilization, the data further support the existence of turbulent flame propagation through the fuel/air mixture along the jet periphery. This upstream propagation occurs irrespective of the presence of structure. One example of this is seen along the right side of the jet in Fig. 3a, where the flame zone extends a short distance upstream of the vortical structure in the center of the image. In Fig. 3b, the flame has propagated about 4 mm upstream of its original location. Given the straightness of the flame in this region, this propagation apparently involves no vortical structure. A second example of upstream propagation is shown in Fig. 4, where the flame along the right side of the jet has propagated nearly 10 mm further upstream during the 4-ms pulse delay, again in a region where the jet exhibits no apparent larger-scale structure.

It is noteworthy that, along the left side of the jet in Fig. 4a, no flame exists upstream of $x = 30$ mm. Figure 4b, however, shows the sudden appearance of a flame segment between 15 and 19 mm downstream. Since the sudden upstream appearance of a flame requires an ignition source, this event is taken as evidence of the three dimensionality of the flow. We speculate that this upstream ignition results from flame propagation in the azimuthal direction normal to the image plane. Numerous other examples of upstream ignition can be found in the data.

These observations are consistent with the concepts of Vanquickenborne and van Tiggelen [2], in which a turbulent flame propagates through premixed fuel and air. It is important to note that previous imaging of CH/CH_4 and temperature in the present flames shows that the fuel and air are premixed at the flame stabilization point [10]. This result, taken in conjunction with the present images, supports concepts inherent in the Vanquickenborne and van Tiggelen premixed flame propagation theory.

Interactions between turbulence and the flame also result in local flame extinction and reignition. Two examples of these are shown in Fig. 5. In Fig. 5a, the flame along the right side of the jet is continuous downstream of the flame liftoff position and, in particular, is continuous around the vortical structure located at about 35 mm downstream. The image in Fig. 5b, taken 2 ms later, shows a break in the flame where the vortical structure expands radially outward. Other images show that flame extinction most frequently occurs at the location where a vortical structure results in an outward bulge in the flame. This is an example of flame extinction due to interactions between the flame and large-scale turbulence structure, which result in excessive stretch imposed on the flame. Examples of reignition are also seen. Along the left side of the jet in Fig. 5a, at about 50 mm downstream, a break resulting from an outward bulge in the central jet is seen. Figure 5b shows that

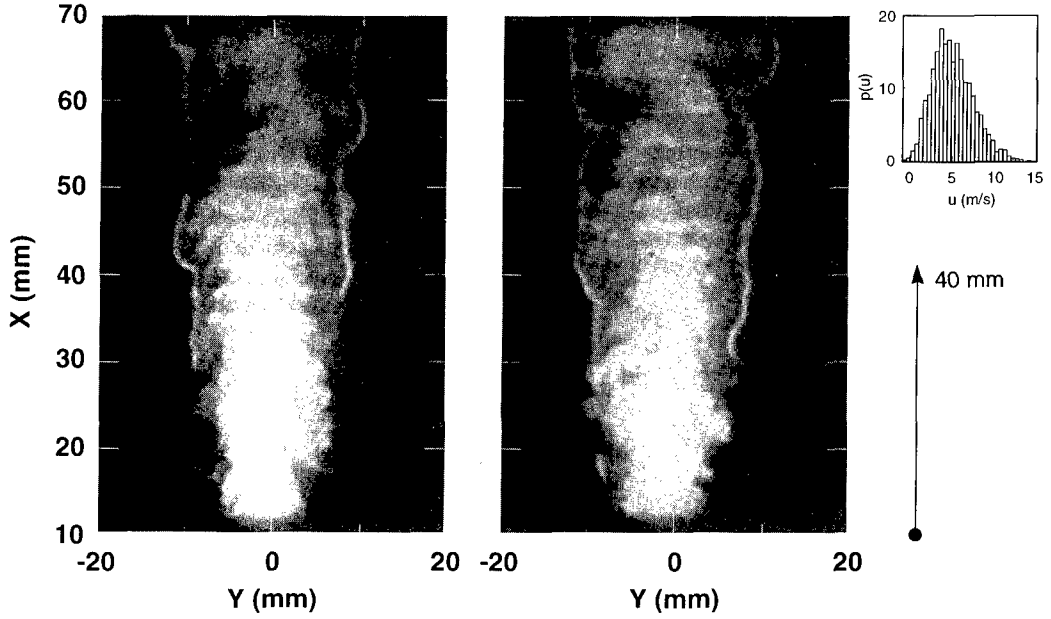

FIG. 4. Two-pulse images of the CH/CH_4 distribution in a lifted, turbulent CH_4-jet flame. Jet velocity is 21 m/s. Figure 4b was taken 4 ms after Fig. 4a.

the flame has reignited and again formed a continuous flame where the break previously existed.

Discussion

Current theories for lifted-flame stabilization can be categorized as to whether they are based on the concept that (1) flame stabilization is controlled by premixed flame propagation, or that (2) extinction due to vortex/flame interactions controls flame stability. It is important to recognize that these theories do not necessarily represent opposing theoretical viewpoints and that the present data show both premixed flame propagation and vortex/flame interactions. In general, the flame burns in a premixed mode and appears to stabilize where the premixed flame velocity just balances the local flow velocity, in agreement with earlier theories of Vanquickenborn and van Tiggelen [2]. However, when large-scale structures interact with the flame, the data show flame extinction that can cause local breaks in the flame surface or result in the flame being carried significant distances downstream by the structure. The presence of mechanisms inherent to both categories of lifted-flame theories perhaps explains to some extent why each theory has demonstrated some degree of success in predicting lifted-flame behavior.

An important objective of the present work is to further elucidate the mechanism whereby large fluctuations in the flame liftoff height occur. As noted previously, the liftoff height varies over a distance comparable to the local jet diameter. In the present flame, the time-average liftoff height is 30 mm, with a rms value of about 25 mm [8]. The magnitude of these fluctuations is comparable with other studies [5,9]. Further analysis of the images shows that the mechanisms controlling these fluctuations can be conceptualized into (1) extinction events resulting in downstream movement in the stabilization point, and (2) premixed flame propagation that results in a return of the stabilization point to an upstream location. Considering extinction events first, it was shown that vortex/flame interactions lead to flame extinction in several ways. From interactions such as shown along the left side of the jet in Fig. 3, extinction can occur at the upstream edge of a vortex, and the stabilization point can be carried considerable distances downstream. Extinction also can occur along the downstream edge, as was seen along the right side of the jet in Fig. 5. In the latter case, it is observed that, once extinction occurs, the upstream segment of the flame is often extinguished, and the stabilization point is carried downstream by the structure. The reason why extinction of this upstream segment occurs requires further study. However, in all images analyzed, large-scale movement of the stabilization point downstream is initiated by an extinction event due to flame/vortex interactions.

Extinction along the downstream edge of vortical structures is consistent with Pitts [7], who concluded that flame extinction is most probable along the

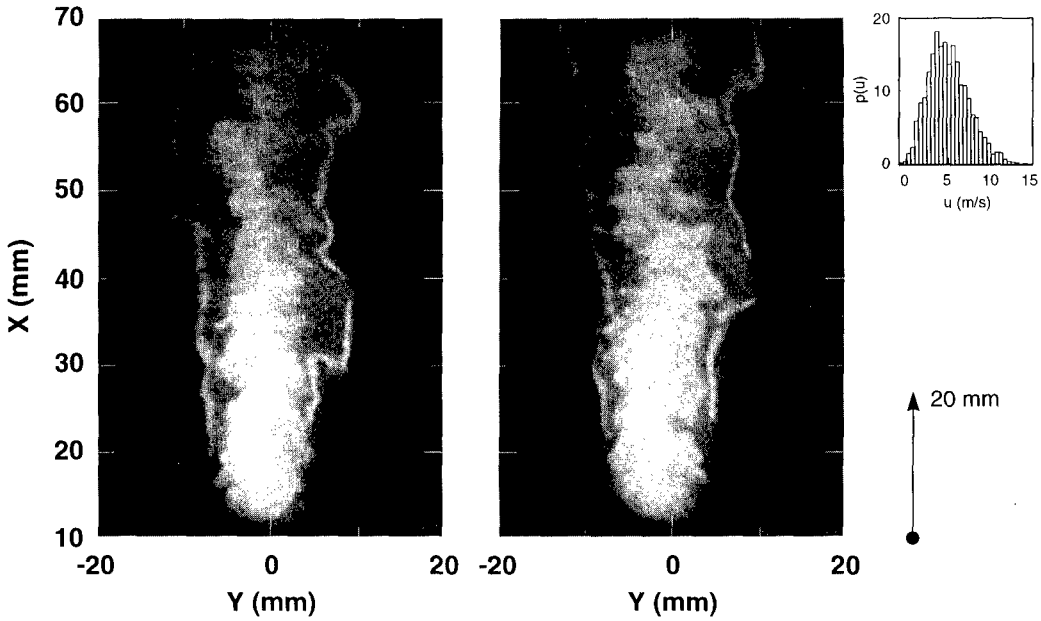

FIG. 5. Two-pulse images of the CH/CH_4 distribution in a lifted, turbulent CH_4-jet flame. Jet velocity is 21 m/s. Figure 5b was taken 2 ms after Fig. 5a.

downstream edge where high shear exists. Flow visualization and numerical simulations that were used to study vortex/flame interactions in a periodically forced jet-diffusion flame further support local flame quenching due to high strain rates along the downstream edge of the vortex [14]. On the other hand, Pitts also concludes that stabilization of the flame is likely on the upstream side of the structure, which is often not the case in the present images.

A possible explanation for these different observations can be found in the model proposed by Broadwell et al. [6]. This model, which is based on a balance between mixing times and chemical reaction times, was developed to predict blowout velocities. Pitts [1] later showed that extension of the model to predict flame liftoff was not consistent with experimental findings. This failure was attributed to assumptions concerning mixing time estimates for reentrained hot combustion products, fuel and entrained air. He further argued that the appropriate mixing time may be the mixing time at the upstream edge of vortical structures. Given these considerations, it is feasible that the present observations are consistent with the Broadwell model and that extinction occurs along the upstream edge of vortical structures when insufficient residence time is available for combustion to be maintained.

The data further show that the primary mechanism by which the flame stabilization point returns upstream is more consistent with upstream propagation of the flame along the jet periphery and is not related to interactions with vortical structures. Examples of upstream propagation of the flame are seen in Figs. 3 and 4. Propagation can occur either along relatively straight jet boundaries when no vortical structures are present, or it can occur along the outer vortex boundaries when strain is below the critical value for extinction. Also note from the discussion of Fig. 4 the potential importance of flame propagation in the azimuthal direction, which can result in rapid upstream jumps in the flame stabilization point. The picture presented by the data is consistent with that proposed by Miake-Lye and Hammer [5], in which the flame can propagate upstream from one structure to the next when the strain between these structures is sufficiently low. Note that this model as developed is two dimensional and does not account for three-dimensional effects.

Summary and Conclusions

Two-pulse images of the instantaneous CH/CH_4 distributions with a variable time delay between images were used to study the temporal evolution of turbulence/chemistry interactions in lifted, turbulent CH_4-jet flames. The results are presented to emphasize the interactions between turbulence structure and flame chemistry that lead to the large fluctuations in flame liftoff height observed experimentally. The results show that the flame envelope curves around semiorganized, large-scale vortical structures

formed along the periphery of the jet. Interactions between these vortical structures and the flame cause excessive stretch that leads to local flame extinction. Extinction occurs on both the downstream edges of the structures and on the upstream sides. Once the flame is extinguished by a vortical structure, the flame stabilization point can be carried significant distances downstream by the vortex. The return to an upstream stabilization location occurs through turbulent premixed flame propagation. The images clearly show upstream propagation of the flame within the plane of the image. Evidence also exists for the importance of flame propagation in the azimuthal direction normal to the image plane.

Acknowledgments

This research was supported by the U.S. Department of Energy, Office of Basic Energy Sciences, Division of Chemical Sciences, through Sandia National Laboratories and by the Physical Science Department of the Gas Research Institute through Altex Technologies Corporation. The authors would also like to acknowledge the work of J. Brandt and G. Wilkerson on the development of the double-pulse laser system.

REFERENCES

1. Pitts, W. M., *Twenty-Second Symposium (International) on Combustion,* The Combustion Institute, Pittsburgh, 1988, p. 809.
2. Vanquickenborne, L., and van Tiggelen, A., *Comb. Flame* 10:59–69 (1966).
3. Peters, N., and Williams, F. A., *AIAA J.* 21:423–429 (1983).
4. Byggstoyl, S., and Magnussen, B. F. *Fourth Symposium on Turbulent Shear Flows* (L. J. S. Bradbury, F. Durst, F. W. Schmidt, and J. H. Whitelaw, Eds.), Karlsruhe, Germany, 1983, Springer-Verlag, Berlin, pp. 10:32–10.
5. Miake-Lye, R. C., and Hammer, J. A., *Twenty-Second Symposium (International) on Combustion,* The Combustion Institute, Pittsburgh, 1988, p. 817.
6. Broadwell, J. E., Dahm, W. J. A., and Mungal, M. G., *Twentieth Symposium (International) on Combustion,* The Combustion Institute, Pittsburgh, 1985, p. 303.
7. Pitts, W. M., *Twenty-Fourth Symposium (International) on Combustion,* The Combustion Institute, Pittsburgh, 1990, p. 661.
8. Schefer, R. W., Namazian, M., and Kelly, J., "Stabilization of Lifted, Turbulent-Jet Flames," *Comb. Flame,* to appear, 1994.
9. Chen, T. H., and Goss, L. P. "Flame Lifting and Flame/Flow Interactions of Jet Diffusion Flames," Paper No. AIAA-89-0156, presented at the AIAA Twenty-Seventh Aerospace Sciences Meeting, Reno, NV, 1989.
10. Schefer, R. W., Namazian, M., and Kelly, J., *Twenty-Third Symposium (International) on Combustion,* The Combustion Institute, Pittsburgh, 1990, p. 669.
11. Namazian, M., Schmitt, R. L., and Long, M. B., *Appl. Opt.* 27:3597–3600 (1988).
12. Dahm, W. J. A., and Dimotakis, P. E., *AIAA J.* 24:1216–1220 (1989).
13. Chen, L. D., Seaba, J. P., Roquemore, W. M., and Goss, L. P., *Twenty-Second Symposium (International) on Combustion,* The Combustion Institute, Pittsburgh, 1988, p. 677.
14. Hsu, K. Y., Chen, L. D., Katta, V. R., Goss, L. P., and Roquemore, W. M., "Experimental and Numerical Investigations of the Vortex-Flame Interactions in a Driven Jet Diffusion Flame," Paper No. AIAA-93-0455, presented at the AIAA Thirty-First Aerospace Sciences Meeting, Reno, NV, 1993.

COMMENTS

R. W. Bilger, University of Sydney, Australia. Experimental and LES (large eddy simulation) studies or round jet mixing indicate that there are at least four other major modes of instability apart from the toroidal vortex mode you seem to favour in your explanations. These other modes include tangential modes and spiral modes. Couldn't some of the events highlighted in your paper result from these other modes?

Author's Reply. The presence of other instability modes in addition to the toroidal vortex (or axisymmetric) instability mode highlighted in the paper is well known. Indeed, similar imaging measurements of the CH_4 concentration in a nonreacting jet flow at the same inlet conditions also provide evidence of helical mode instabilities [1]. The toroidal vortex/flame interactions were highlighted in the paper since these interactions are more easily observed when the image plane is orientated parallel to the jet axis.

REFERENCE

1. Schefer, R. W., Kerstein, A. R., Namazian, M., and Kelly, J. Physics of Fluids 6:652 (1994).

•

Norbert Peters, RWTH, Aachen, Germany. I believe that flame propagation along the surface of stoichiometric mixture occurs by triple flamelets. Would you agree?

Author's Reply. We agree that flame propagation by triple flamelets could be the mechanism for flame propagation. This speculation is supported by the observations that the flame location coincides closely with the stoichiometric surface and that the flame zone width is comparable to the width of the region where the fuel and air are within the methane flammability limits. This flame thickness, which typically varies from 1 to 4 mm, is considerably wider than the expected thickness of a laminar flamelet but is consistent with what one might expect for a triple flame.

Twenty-Fifth Symposium (International) on Combustion/The Combustion Institute, 1994/pp. 1233–1239

FINE STRUCTURE OF SMALL-SCALE AND HIGH-INTENSITY TURBULENT PREMIXED FLAMES

JUNICHI FURUKAWA
Tokyo Metropolitan Technical College
1-10-40 Higashi-Ohi
Shinagawa-Ku, Tokyo 140, Japan

TOSHISUKE HIRANO
University of Tokyo
7-3-1 Hongo
Bunkyo-Ku, Tokyo 113, Japan

The present study has been performed to accumulate reliable experimental data on aspects of the chemically reacting zone of methane-air and propane-air turbulent premixed flames in a regime in which the Kolmogorov scale is 46 μm, which is smaller than the laminar premixed flame thickness. The characteristics of measuring systems adopted in this study are discussed, and the microelectrostatic probe is pointed out to be the most desirable one.

Based on the data obtained by a specially designed microelectrostatic probe with two fine sensors, it is shown that the local reaction zone thickness in the flame brush of a turbulent premixed flame is little different from the thickness of a laminar premixed flame whose equivalence ratio is the same as that of the turbulent flame. Also, the radii of the local reaction zone curvature for methane-air flames are larger than those for propane-air flames. These results imply that the radius increases as the local reaction zone thickness increases. At the same time, by comparing the mean radii under the conditions for the same local reaction zone thickness and different Lewis numbers Le, it can be found that the mean radius for Le > 1 is larger than that for Le < 1.

Introduction

Since Damköhler [1] introduced the hypothesis of a propagation mechanism of premixed flames in small-scale turbulence, a number of flame models [2–10] have been proposed for the fine structure of small-scale and high-intensity turbulent premixed flames. These flame models can be reduced into three ideas: (1) turbulence does not wrinkle the flame front significantly but alters the effective transport properties in the reaction zone, consequently the reaction zone thickness increases [1,2]; (2) local extinction occurs due to the local flame stretch [3,5,6]; and (3) combustion takes place in a vortex tube of a diameter equal to the Kolmogorov scale, subject to stretching by eddies of the Taylor microscale [4,7,10]. These ideas are somewhat contradictory with each other. In addition, most of these ideas have been proposed based on hypotheses. It seems that in the absence of accurate experimental evidence, any idea will continue to be speculative. Therefore, the fine structure of turbulent premixed flames, in a regime in which the Kolmogorov scale of turbulence is smaller than the laminar premixed flame thickness, still remains one of the outstanding problems in turbulent combustion [11].

Under the inconsistent circumstances as mentioned above, it has been shown that the local reaction zone thickness of propane-air turbulent premixed flames, in a regime in which the Kolmogorov scale is smaller than the laminar flame thickness, is similar to that of the laminar premixed flame [12]. However, the result obtained in this study has not been universally accepted because the experimental conditions are limited to a near stoichiometric propane-air flame under different characteristics of turbulence. In order to overcome the inconsistent circumstances and distinguish among various hypotheses, we believe it is indispensable to accumulate accurate experimental data on aspects of the chemically reacting zone of turbulent premixed flames in this category. In our previous studies, the attempts have been made to accumulate accurate experimental data on the configuration of the local reaction zone of near stoichiometric propane-air flames under different characteristics of turbulence [15], the spatial distribution of the local reaction zone curvature in a turbulent flame brush [17], and the configuration of the local reaction zone under different mixture ratios of propane-air flames and burner sizes [18].

In the present study, efforts have been concentrated to accumulate accurate experimental data on

the fine structure of chemically reacting zones of methane-air and propane-air turbulent premixed flames of various mixture ratios in a regime in which the Kolmogorov scale is smaller than a laminar premixed flame.

Time and Spatial Resolutions Required for Diagnostics for Measurement of Fine Structure of Turbulent Premixed Flames

In order to accumulate reliable experimental data on the aspects of chemically reacting zones of small-scale and high-intensity turbulent premixed flames, diagnostics with spatial and time resolutions adequate to detect the fine structure of a chemically reacting zone must be used. It seems that most diagnostics used in the previous studies [2,4,6,8–10] are not accurate enough to study the fine structures mentioned in the previous section. Therefore, discussion on the fine structure of turbulent premixed flames has been based on hypotheses without proof.

Generally, in experimental studies on turbulent flames, the measuring points are fixed at an arbitrary point in the turbulent flame brush. In these cases, the obtained data is a function $P(t)$ of time. In order to discuss the fine structure of turbulent premixed flames, the function $P(t)$ must be transformed into a function of space $Q(\mathbf{r})$, where $\mathbf{r}$ is the position vector. For that purpose, $Q(\mathbf{r})$ must have the spatial resolution of the order of 10^{-2} mm because the fine structure of a chemically reacting zone will be of the order of 10^{-1} mm. Suppose a chemically reacting zone is passing the measuring point at about 10 m/s; the time required for the zone to pass the measuring point is of the order of 10^{-5} s. Therefore, the time resolution required for accurately recording $P(t)$ measurements is of the order of 10^{-6} s.

The time and spatial resolutions of typical diagnostics used in turbulent flame studies are presented in Table 1. Although modern laser diagnostics utilizing a pulsed laser such as CARS have a higher sample hold resolution of the order of 10^{-8} s, the pulse frequency is of the order of 10^2 pulse/s. Consequently, the time resolution for repeated $P(t)$ measurements is of the order of 10^{-2} s. Therefore, an adequate time resolution for $P(t)$ measurements cannot be achieved. The planar laser-induced fluorescence, which might be one of the most promising diagnostics, can conduct two-dimensional measurements. However, the optical detector such as that of charge coupled device (CCD) camera is of a spatial resolution of only the order of 10^{-1} mm/pixel [13], which is not sufficient for measurements of fine structure of turbulent flames too.

It has been reported that the vortex tube structure of the turbulent premixed flame has been successfully examined by using the thermocouple with a compensation system [8–10], the time resolution of which is of the order of 10^{-4} s [14]. Unfortunately, as is obvious, it is not of a necessary resolution to be able to detect the fine structure of typical chemically reacting zones.

TABLE 1
Time and spatial resolutions of typical diagnostics used in turbulent flame studies and their abilities to detect chemically reacting zone

	Time resolution (s)	Spatial resolution (mm)	Detect chemically reacting zone
Rayleigh	10^{-2}	10^{-1}	no
CARS	10^{-2}	?	no
LIF	10^{-2}	10^{-1}	yes
Thermocouple	10^{-4}	10^{-1}	no
Electrostatic probe	10^{-6}–10^{-7}	10^{-2}	yes

CARS: coherent anti-Stokes Raman spectroscopy; LIF: laser-induced fluorescence.

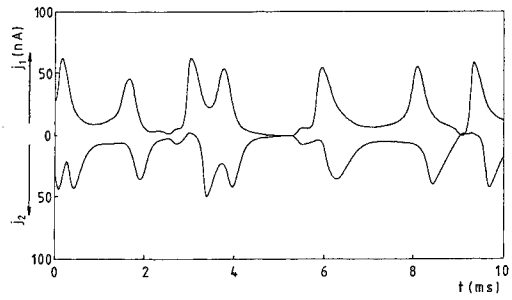

FIG. 1. Typical ion current records obtained by the electrostatic probe with two identical sensors.

In our previous study [15], the electrostatic probe was shown to be able to detect the difference in the local reaction zone thicknesses of turbulent premixed flames whose equivalence ratios were 1.0 and 1.2. We concluded that nothing but a well-designed electrostatic probe can satisfy the time and spatial resolutions required for the measurements of the fine structure of small-scale and high-intensity turbulent premixed flames.

Even though an electrostatic probe has the spatial and time resolution required to measure the local reaction zone structure of turbulent premixed flames, the effect of disturbances caused by inserting the probe on data obtained is frequently questioned. Typical records of ion currents obtained in a turbulent premixed flame by using the microelectrostatic probe with two identical sensors are shown in Fig. 1. The polarity of the ion current obtained by one sensor is made opposite to that obtained by the other. In the figure, j_1 and j_2 represent the ion currents

recorded by the sensors placed upstream and downstream, respectively. The pairs of ion current records indicate that the variation of the ion current to one sensor is very similar to that of the ion current to the other sensor. Therefore, the fine structure of a chemically reacting zone can be inferred to change very little between the two sensors; i.e., the disturbance caused by inserting a probe is negligibly small [16].

In the present study, therefore, a microelectrostatic probe with two identical sensors has been used as the diagnostic to measure the fine structures of chemically reacting zones of turbulent premixed flames.

Experimental Apparatus

The turbulent flame burner used in the present study is a cylindrical burner 26 mm in diameter [15,17,18]. The burner consists of a tube long enough to establish a fully developed turbulent flow. A uniform methane-air or propane-air mixture is supplied at an average velocity of 7.0 m/s to the burner. The equivalence ratios, ϕ, of the mixture are 0.95, 1.15, and 1.23 for methane-air flames and 0.85, 1.10, and 1.37 for propane-air flames. The laminar burning velocities of $\phi = 0.95$ and 1.23 of methane-air flames and $\phi = 0.85$ and 1.37 of propane-air flames are the same, respectively.

The characteristics of turbulence of the unburned mixture stream are examined by using a hot wire velocimeter. The data acquisition system for turbulence measurements is composed of a 10-bit, 32-kHz A/D convertor, a 256-kword buffer memory, and a 16-bit microcomputer. A typical data number processed for a measurement is 5.12×10^6 words. The turbulence intensity u' is 1.41 m/s. The integral scale L_x, obtained from the autocorrelation coefficient, is 6.5 mm. The microscale λ_x, obtained from the power spectrum density function, is 2.1 mm. Therefore, the Kolmogorov scale η is inferred to be 46 μm, and the turbulent Reynolds number R_L based on the integral scale is 587 [18]. The turbulent premixed flames established in such flows under the conditions $u' > S_L$ and $\eta < \delta_L$, where S_L and δ_L represent the laminar burning velocity and the laminar flame thickness, respectively.

The microelectrostatic probe and data acquisition system for ion current measurements are the same as those used in our previous studies [15,17,18]. The typical data number processed for each ion current measurement is 1.28×10^6 words.

Local Reaction Zone Thickness

It has been shown in our previous studies [11,15,19] that the local reaction zone thickness of turbulent premixed flames can be successfully examined by analyzing ion current records [19–21]. The process for determining the local reaction zone thickness is briefly summarized in the following.

The local reaction zone thickness can be measured by assuming that the region where ion density is particularly higher than that of surroundings represents the local reaction zone. It is seen from Fig. 1 that there are various shapes of ion current fluctuations and periods during which no ion current is recorded. The nonion current periods should correspond to the periods during which the sensors are in a space where no chemical reaction occurs, i.e., a space occupied by either an unburned mixture or burned gas. On the other hand, recording a significant ion current must correspond to the period during which the sensors are in zone with appreciable chemical reaction. It has been shown in our previous study that the ion current characteristics represented by the half-value period t_h and the maximum ion current j_m can be expressed as follows [20,21]:

$$t_h = f(\delta_T, V_f, a) \tag{1}$$

$$j_m = g(V_f, a) \tag{2}$$

where δ_T denotes the local reaction zone thickness, V_f denotes the reaction zone velocity when it passes the sensors, and a denotes the angle of the reaction zone to the probe axis. The velocity V_f can be measured by using the microelectrostatic probe with two identical sensors as the average velocity between two sensors. Based on Eq. (1), the local reaction zone thickness δ_T can be estimated by considering the variations of the angle a in the turbulent flame brush. It is clear that the profile of the probability density function of the half-value period t_h depends on the probability density of the angle a and the local reaction zone thickness δ_T. Thus, the local reaction zone thickness can be estimated by comparing the experimentally obtained probability density function for t_h with the predicted ones assuming definite thicknesses of the local reaction zone [11,15,19].

Dependence of t_h on ϕ obtained when an electrostatic probe passes through methane-air and propane-air laminar premixed flames parallel to the sensor axis is shown in Fig. 2 [19,21]. In this case, the relative velocity of the flame to the electrostatic probe V (essentially equals V_f) is 3.0 m/s, and the angle $a = 0$. The flame thickness δ_L, estimated roughly by $\delta_L = t_h V$, is also indicated in Fig. 2. Although the absolute value of the high ion density region thickness, which includes the thickness of ion sheath established around the sensor [20], is approximately 30% larger than the laminar flame thickness predicted on the basis of the laminar burning velocity [22], Fig. 2 clearly shows that the electrostatic probe can detect the difference in flame thickness due to the difference in the fuel and/or mixture ratio. The

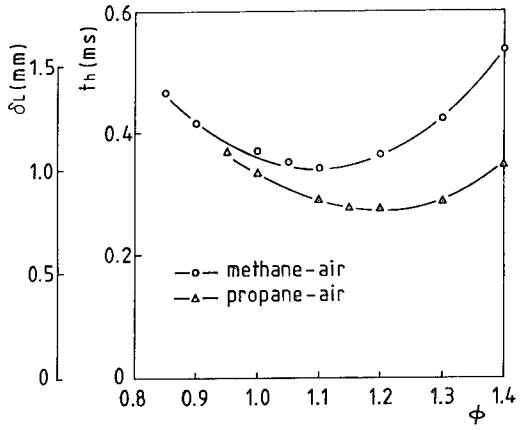

FIG. 2. Dependence of the half-value period of ion current of methane-air and propane-air laminar premixed flame on the equivalence ratio of mixture.

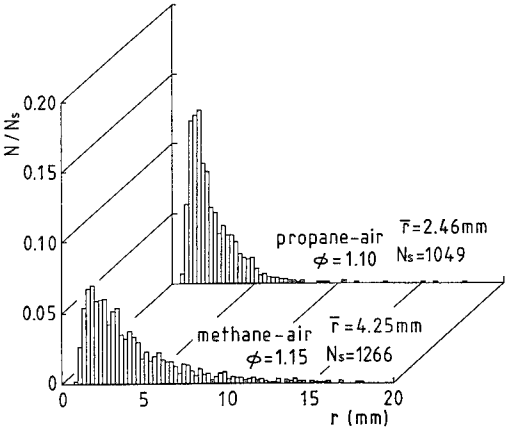

FIG. 4. Frequency distributions of the radii of the local reaction zone curvatures convex toward burned gas of methane-air and propane-air turbulent premixed flames. N: Numbers of r in each 0.25-mm interval; N_s: sample size.

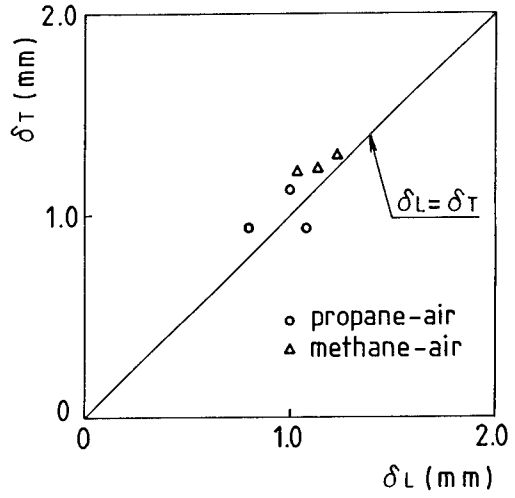

FIG. 3. Comparison between the local reaction zone thickness of turbulent premixed flames and the thickness of laminar premixed flames.

thickness of a methane-air flame is larger than that of a propane-air flame at the same equivalence ratio.

Figure 3 shows predicted local reaction zone thickness δ_T, also estimated roughly by $\delta_T = t_h V_f$, of a turbulent premixed flame plotted against the laminar flame thickness δ_L whose equivalence ratio is the same as that of the turbulent flame. It is seen that $\delta_T = \delta_L$. When the mixture ratio or fuel changes, the laminar flame thickness and the burning velocity change; consequently, the chemical and thermal structures of the flame should change. Even for a variety of conditions, the local reaction zone thickness almost equals the laminar premixed flame thickness whose equivalence ratio is the same as that of the turbulent flame [22].

Local Reaction Zone Configuration

It has been shown in our previous studies [15,17,18] that the local reaction zone configuration of turbulent premixed flames can be successfully examined in terms of the radius of the local reaction zone curvature by analyzing the ion current record [19–21].

The local reaction zone curvatures for both convex toward the burned gas and convex toward the unburned mixture have been examined for methane-air and propane-air turbulent premixed flames. In these cases, the equivalence ratio of the mixture is about 1.1. The measured frequency distribution of radii of local reaction zone curvatures for convex toward the burned gas and the unburned mixture for methane-air (ϕ = 1.15) and propane-air turbulent premixed flames (ϕ = 1.10) are respectively shown in Figs. 4 and 5, where N is the number of curvatures within a 0.25-mm interval and presented in the value normalized with the sample size N_s [14,16,17]. The radii of the local reaction zone curvature of the methane-air flame are distributed over a wider range than those of the propane-air flame. The smallest, the most probable, and the mean radii of the local reaction zone curvature for both convex toward burned gas and unburned mixture of the methane-air flame are larger than those of the propane-air flame. Note that the smallest radius of the local reaction zone curvature of the methane-air flame, as well as in the propane-air flame [18], is much larger than the Kolmogorov scale of turbulence in the unburned mixture stream.

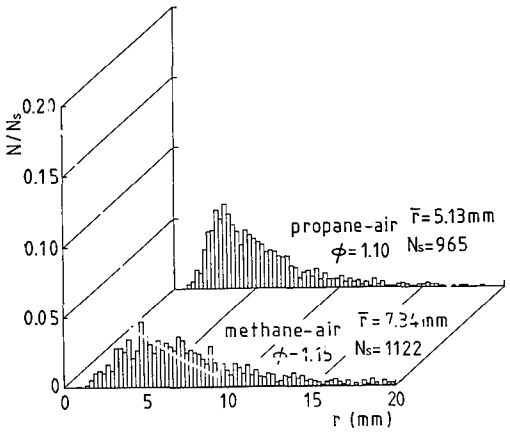

FIG. 5. Frequency distributions of the radii of the local reaction zone curvatures convex toward unburned mixture of methane-air and propane-air turbulent premixed flames. N: Numbers of r in each 0.25-mm interval; N_s: sample size.

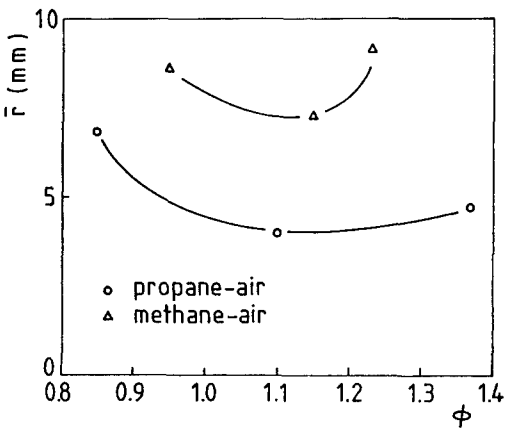

FIG. 6. Mean radii of the local reaction zone curvatures of methane-air and propane-air turbulent premixed flames.

Figure 6 shows the mean radii of the local reaction zone curvatures convex toward unburned mixture of methane-air and propane-air turbulent premixed flames are plotted against mixture ratio. The mean radii for methane-air flames are larger than those for propane-air flames. The mean radius is minimum when the equivalence ratio is about 1.1. This result implies that the mean radius of curvature increases as the local reaction zone thickness increases. At the same time, by comparing the mean radius under the conditions for the same local reaction zone thickness and different Lewis numbers Le, it can be found that the mean radius for Le > 1 is larger than that for Le < 1. The dependence of the radius of the local reaction zone curvature on the local reaction zone thickness and Lewis number is qualitatively the same as in the stretched cylindrical premixed flames [23].

Dominant Transport Mechanism in the Local Reaction Zone

If turbulence within the reaction zone includes small-scale eddies that significantly change transport properties in the reaction zone, the local reaction zone thickness should increase. However, as shown under a variety of conditions, the local reaction zone thickness is little different from the laminar flame thickness whose equivalence ratio is the same as that of the turbulent premixed flame. In addition, the effect of the Lewis number on the radius of the local reaction zone curvature suggests that the molecular transport is dominant even in the local reaction zone.

If a flame would propagate through a vortex tube structure of a diameter close to the Kolmogorov scale, the smallest radius of the local reaction zone should be of the order of the Kolmogorov scale. Although the spatial resolution of the detective system is much higher than the smallest radius, the smallest radius of the local reaction zone curvature observed throughout the present study is much larger than the Kolmogorov scale.

Hypotheses concerning turbulent flame structures have been proposed based on the characteristics of turbulence in an unburned mixture stream. The results of this experimental study imply the need to question the ability of the small-scale turbulent eddies to expand the local reaction zone or survive through the preheat zone.

Conclusions

In the present study, efforts have been concentrated to accumulate reliable experimental data on some aspects of the chemically reacting zone of turbulent premixed flames in a regime in which the Kolmogorov scale is smaller than the laminar premixed flame thickness. The major conclusions obtained throughout the present study are as follows:

1. The local reaction zone thickness in the flame brush of a turbulent premixed flame is little different from the thickness of laminar premixed flames whose equivalence ratio is the same as that of the turbulent premixed flame.
2. The radii of the local reaction zone curvature for methane-air flames are larger than those for propane-air flames. The radius increases as the local reaction zone thickness increases. At the same time, by comparing the mean radius under the conditions for the same local reaction zone thickness and different Lewis numbers Le, the mean radius for Le > 1 is larger than that for Le < 1.

Acknowledgment

The authors would like to express their sincere appreciation to K. Okamoto, graduate student of Sophia University, for her help in conducting the experiments.

REFERENCES

1. Demkohler, G., Z. Elektrochem. 46:601–626 (1940).
2. Summerfield, M., Reiter, S. H., Kebly, V., and Mascolo, R. W., *Jet Propul.* 25:377–384 (1955).
3. Klimov, A. M., *Zh. Prikl. Mekh. Tekh. Fiz.* 3:49–58 (1963).
4. Chomiak, J., *Combust. Flame* 15:319–321 (1970).
5. Williams, F. A., Paper presented at AGARD Conference Proceedings, No. 164, 1975.
6. Ballal, D. R., and Lefebvre, A. H., *Proc. R. Soc. London Ser. A* 344:217–234 (1975).
7. Tabaczynski, R. J., Ferguson, C. R., and Radhakrishnan, K., SAE Paper 770647, 1977.
8. Yoshida, A., *Twenty-Second Symposium (International) on Combustion*, The Combustion Institute, Pittsburgh, 1988, pp. 1471–1478.
9. Katsuki, M., Mizutani, Y., Yasuda, T., Kurosawa, Y., Kobayashi, K., and Takahashi, T., *Combust. Flame* 82:93–105 (1990).
10. Yoshida, A., Narisawa, M., and Tsuji, H., *Twenty-Fourth Symposium (International) on Combustion*, The Combustion Institute, Pittsburgh, 1992, pp. 519–525.
11. Liñán, A., and Williams, F. A., *Fundamental Aspects of Combustion*, Oxford University Press, Oxford, 1993, p. 150.
12. Furukawa, J., Harada, E., and Hirano, T., *Twenty-Third Symposium (International) on Combustion*, The Combustion Institute, Pittsburgh, 1990, pp. 789–794.
13. Dibble, R. W., private communication, 1993.
14. Yoshida, A., Kubozuka, S., and Nakamura, S., *Combust. Sci. Technol.* 65:317–331 (1989).
15. Furukawa, J., Maruta, K., Nakamura, T., and Hirano, T., *Combust. Sci. Technol.* 90:267–280 (1993).
16. Furukawa, J., *Combust. Sci. Technol.* (Japanese Edition) 1(3):207–209 (1993).
17. Furukawa, J., Nakamura, T., and Hirano, T., *Combust. Sci. Technol.* 96:169–181 (1994).
18. Furukawa, J., Maruta, K., Nakamura, T., and Hirano, T., Paper presented at Fourteenth International Colloquium on Dynamics of Explosions and Reactive Systems, 1993.
19. Maruta, K., Furukawa, J., Gomi, T., and Hirano, T., *Trans. Jpn. Soc. Mech. Eng.* (in Japanese) 59 (566):3277–3282 (1993).
20. Furukawa, J., Maruta, K., Nakamura, T., Gomi, T., and Hirano, T., *Jpn. Soc. Mech. Eng. Int. J. Ser. B* 36 (4):682–687 (1993).
21. Furukawa, J., and Okamoto, K., *Nensho Kenkyu* (in Japanese) 93:45–50 (1993).
22. Williams, F. A., *Combustion Theory*, 2nd ed., Addison-Wesley, Menlo Park, CA, 1985, p. 135.
23. Kobayashi, H., and Kitano, M., *Combust. Flame* 76:285–295 (1989).

COMMENTS

Jerzy Chomiak, Chelmers University of Technology, Sweden. 1. The typical recombination time for combustion-generated chemi-ions is about 1 ms, so the technique does not seem to be well suited for internal flame structure studies even if the response of the Langmuir probe is very fast.

2. The turbulence parameters of your burner are such that one expects the flame to be in the laminar flamelet regime, and consequently no flame structure change could be observed as shown.

Author's Reply. 1. The most important requirement for the diagnostics is the temporal and spatial resolution. The temporal results of the electrostatic probe are of the order of 10^{-6} s. The position of the region in which ions exist precisely corresponds to the position of the local reaction zone. Moreover, ions do not exist where no chemical reaction occurs. As shown in Fig. 1, the ion current decreases very rapidly even in the burned gas.

2. In Ref. 12, we measured the local reaction zone thickness under conditions where the turbulence intensity was much higher and the scale was much smaller. The local reaction zone thickness still equaled the laminar flame thickness. This is probably because, as verified by recent studies [1], in turbulent flows small-scale structures with high strain rates are very localized and infrequent events. Consequently, only in very limited regions of space and time are the strain rates high enough to cause local disruption of the laminar flame structure. Or, the small-scale eddies that cause local disruption of the laminar flame structure may not survive in the local reaction zone.

REFERENCE

1. She, Z. S., Jackson, E., and Orzag, S. A., *Proc. R. Soc. (London) A* 434:101 (1991).

•

Benoit Bedat, Lawrence Berkeley Laboratory, USA. The turbulence level that you obtain is about 20%. The value for a fully developed turbulent flow obtained in a pipe is about 5%.

As you mentioned in your talk, the choice of the turbulence measurement location and the fact that the turbulence was measured only in a nonreacting flow indicate that you measured mainly a shear-stress turbulence induced by mixing of a nonreacting jet flow with quiescent air. So the turbulent fluctuation u' of 1.4 m/s is not relevant in reacting conditions. The Taylor and Kolmogorov scales in your study are largely underestimated. I believe that in your experiment the Kolmogorov scales are larger than the flame front thickness.

Author's Reply. The structure of turbulent premixed flame has long been discussed based on the characteristics of turbulence in the cold flow. However, there is no common understanding for estimation of the characteristics of turbulence. For example, at which point should we measure the turbulence? The absence of common understanding causes confusion in comparing the one experimental result with the other.

In our opinion, we should not discuss the structure of turbulent premixed flames based on the characteristics of turbulence in the cold flow but discuss based on the characteristics of turbulence in the local reaction zone or at the leading edge of the local reaction zone.

Twenty-Fifth Symposium (International) on Combustion/The Combustion Institute, 1994/pp. 1241–1248

COMPARATIVE EXPERIMENTAL AND NUMERICAL INVESTIGATION OF A PILOTED TURBULENT NATURAL-GAS DIFFUSION FLAME

T. W. J. PEETERS, P. P. J. STROOMER, J. E. DE VRIES, D. J. E. M. ROEKAERTS AND C. J. HOOGENDOORN
Section Heat Transfer, Department of Applied Physics
Delft University of Technology
P.O. Box 5046, 2600 GA Delft, The Netherlands

A turbulent natural-gas diffusion flame is investigated both experimentally and numerically. Measured quantities involve mean velocity, turbulence characteristics, mean temperatures, visualisation of the OH reaction zone and passive scalar concentration, and statistical analysis of OH concentrations. The configuration is a laboratory-scale piloted diffusion flame with annular coflowing air, placed in a ventilated confinement, of well-defined initial and boundary conditions. The fuel jet velocity is 23.2 m/s, and the annular air velocity is 5.1 m/s.

The techniques used are laser-Doppler anemometry (LDA), thermocouple measurements, and 1D- and 2D-laser induced fluorescence (LIF). The mathematical model is based on a constrained-equilibrium conserved-scalar model, resembling a laminar flamelet model, with a standard k-ε turbulence model and a four-flux radiation model.

Comparisons up to 42 jet diameters downstream of the burner nozzle show good agreement for mean axial velocity and temperatures. The turbulence quantities are qualitatively reproduced by the k-ε turbulence model. The OH radical concentrations are underpredicted because of the lack of superequilibrium effects in the chemistry model. In addition, the profile shapes do not correspond very well. The data support the applicability of a conserved-scalar model with an assumed β-function probability density function (PDF) shape for mean temperature predictions. For OH predictions, however, the conserved-scalar approach does not hold.

Introduction

The investigation of turbulent natural-gas diffusion flames is of practical and fundamental interest. Natural gas is a widely used type of fuel, especially in The Netherlands, in industry as well as household appliances. Dutch natural gas mainly consists of nitrogen-diluted methane. The modelling of methane combustion is fundamentally difficult because of finite-rate chemistry effects, prohibiting the application of so-called conserved-scalar models to describe the interaction between turbulence and chemistry.

The present study compares a conserved-scalar model originally developed by Bilger and Stårner [1] with experimental results obtained for a laboratory-scale diffusion flame. The comparison comprises velocities, turbulence quantities, OH radical concentrations and their statistics, and mean temperatures. The experimental methods used were laser-Doppler anemometry (LDA), 1D- and 2D-laser induced fluorescence (LIF) of OH, 2D-LIF of NO seeded to the fuel, and thermocouple measurements.

The objective of this paper is to compare the measured data with the model predictions, to gain a qualitative insight into the physics and chemistry of this flame, in particular the validity of conserved-scalar approximations. This work is part of a long-term project to construct a database with experimental and numerical results for a large number of relevant quantities in this flame.

Flow Configuration

The burner was designed to yield a turbulent nonpremixed flame. Fuel was natural gas (approximately 81% CH_4, 3% C_2H_6, 15% N_2 by volume); the oxidiser was air. The burner was axisymmetric and consisted of a fuel jet and a primary air annulus (Fig. 1). Two duplicates of the same burner were used in separate LDA and LIF setups, in order not to contaminate the burner used for the LIF experiments. Despite the fact that the burners are exact duplicates, the initial conditions may suffer from slight differences, which we believe to be unimportant. The burner was placed in a throat, and the flame was confined by an enclosure. The low-velocity coflowing air from the throat prevented recirculation in the flame chamber. The fuel jet nozzle was 6 mm in diameter. The burner was 1-m long, ensuring a well-developed turbulent pipe flow at the burner exit. The inner diameter of the annulus was 15 mm and the outer diameter 45 mm. To stabilise the flame, pilot

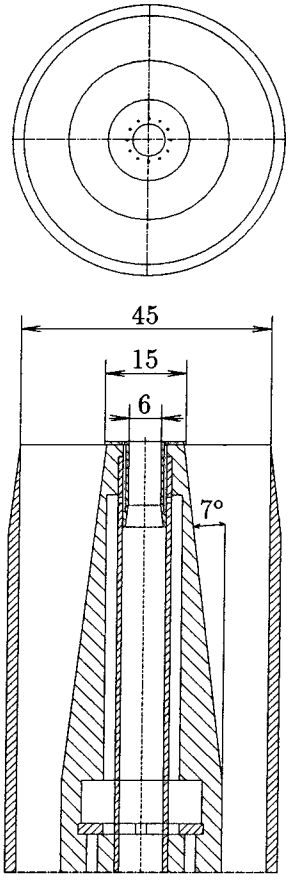

FIG. 1. Schematic representation of burner nozzle; top view and cross section. All measures in mm.

flames issued from the 9-mm-wide burner rim, supplied by twelve 0.5-mm holes located on a 7-mm-diameter ring. The pilot flames consisted of a hydrogen/acetylene/air mixture, with a C to H ratio equal to that of the natural gas [2]. The throat and the flame chamber were octagonal, 0.57 m from side to side, and the flame chamber was 0.90-m high. The mean exit velocity of the fuel jet was 23.2 m/s and of the primary air flow 5.1 m/s. The velocity of the coflowing secondary air was 0.3 m/s. The thermal power of the flame was about 20 kW. The fuel jet Reynolds number and the primary air annulus Reynolds number, based on the respective mean exit velocities and their hydraulic diameters, were both nearly 10^4.

Laser Diagnostics

LDA:

Instantaneous velocity measurements were performed with a two-dimensional laser-Doppler anemometer operating in the dual-beam, backscatter mode. The output of a 4W Ar^+-ion laser was coupled through a fibre-optical system with the LDA optics. The optics were oriented in such a way that the green beams (λ_{gr} = 514.5 nm) measured the axial velocity component of the flow, and the blue beams (λ_{bl} = 488.0 nm) measured the radial velocity component.

In order to eliminate directional ambiguity, an effective frequency preshift was used by means of acousto-optical modulation. Al_2O_3 seeding particles (nominal diameter 1 μm) were provided by cyclone seeders to both the gas jet flow and the air annulus. Light scattered by particles in the probe volume (ellipsoidal shape, diameter 0.15 mm, length 1.9 mm) was collected by two separate photomultipliers. The resulting LDA signals were processed by a TSI, model IFA-750, signal processor. Single-particle detection was ensured by a coincidence window of 10 μs. For each data point, 10,240 individual realisations were averaged to obtain mean velocity components, the corresponding root-mean-square (rms) velocities, and Reynolds shear stresses. No attempts have been made to correct for velocity bias. The accuracy of the measurements was checked by reproduction of independent measurements and found to be better than 5%.

LIF:

In the LIF experiments, the emphasis was on the spatial structure of the OH radical and inert species concentrations. Two-dimensional detection by planar laser induced fluorescence (PLIF) [3] was used for visualisation and one-dimensional detection for the semiquantitative processing of the OH measurements [4]. Broadband fluorescence was detected, so the signal was influenced by collisional processes such as rotational relaxation and quenching [5].

For statistical processing, 5000 one-dimensional OH measurements were used. The one-dimensional OH measurements obtained in the turbulent flame were put on a semiquantitative basis by comparing the measurements with a measurement in a laminar, premixed flat flame, using exactly the same detection configuration. A location of 25 mm above the burner surface was chosen because of small gradients of species and temperature at this position. The flame was operated with methane and air at an equivalence ratio of 0.88. The OH concentration, temperature, and main species concentration profiles were calculated with the PREMIX code [6]. We included heat losses due to radiation of CO_2 and H_2O in this model, which gave an OH concentration equal to 2.13×10^{15} cm^{-3} at x = 25 mm and a temperature of 1760 K. Because of this calibration and the use of broadband detection, the fluorescence profile is systematically affected by about 50%.

The NO-seeding concentration (7400 ppm) was chosen to be orders of magnitude larger than the NO concentrations produced by the flame itself. Since at

the relatively low temperatures the chemical destruction and production rates are sufficiently small, it is assumed that NO serves as a passive scalar, to be interpreted as an inert fuel concentration. However, near the reaction zone quenching, mainly by H_2O, occurs.

OH radicals were excited and detected in the $A - X$ (0,0) band, where the Q_1 (8) line (λ = 309.239 nm) was chosen for minimum temperature sensitivity of the Boltzmann factor. NO was excited in the $A - X$ (0,0) band and detected in the (0,1) band in order not to detect PAH fluorescence, using an interference filter (bandwidth 18 nm, centred at 245 nm). The Q_1 (19) excitation line (λ = 225.806 nm) combined a sufficiently large signal with a small temperature dependence of the Boltzmann factor.

One- and two-dimensional detection of fluorescence was done by means of a diode array OSMA camera (700 pixels) and a Proxitronic charge-coupled device (CCD) camera (720 × 575 pixels), respectively, both gated and enhanced. The gate time of the diode array camera was 40 ns and of the CCD camera 100 μs. The field of view of the diode array camera was 106 mm and of the CCD camera 100 mm horizontal × 80 mm vertical for the OH visualisation and 63 mm × 50 mm for the NO visualisation.

The repetition rate of the Nd:YAG laser was 10 Hz in the one-dimensional measurements and 8.3 Hz in the two-dimensional measurements; the pulse duration was 5 ns, short enough to freeze the turbulent fluctuations in the flame. The laser beam was focussed with a f = 500 mm fused-silica lens in the one-dimensional measurements. For the two-dimensional measurements, a thin laser sheet was created with a f = 1500 mm spherical lens in combination with a cylindrical lens. In both setups, imaging of the fluorescence signal was done by means of a UV Nikkor f = 105 mm camera lens.

Mathematical Model

The mathematical model was based upon the Favre-averaged transport equations for mass, momentum (including buoyancy), and enthalpy, in cylindrical coordinates. Turbulence was modelled by a standard k-ε model with a correction for round-jet development [7]. This model was checked to give the correct spreading rates for velocity and a passive scalar in isothermal turbulent round jets. No further adjustment of constants was performed for this particular flame.

The general transport equation reads as follows:

$$\mathfrak{L}(\tilde{\phi}) = \bar{\rho}\tilde{S}_{\phi} \tag{1}$$

where the elliptic transport operator $\mathfrak{L}$ is given by

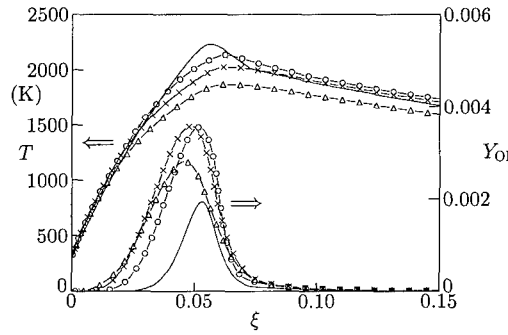

FIG. 2. Temperature and OH mass fraction as a function of the mixture fraction for laminar diffusion flames and the constrained-equilibrium model. Symbols: flamelet ○ a = 10 s^{-1}, × a = 100 s^{-1}, Δ a = 300 s^{-1}, and — constrained equilibrium.

$$\mathfrak{L}(\phi) \equiv \frac{\partial \bar{\rho}\tilde{u}\phi}{\partial x} + \frac{1}{r}\frac{\partial r\bar{\rho}\tilde{v}\phi}{\partial r} - \frac{\partial}{\partial x}\left(\frac{\mu_t}{\sigma_\phi}\frac{\partial \phi}{\partial x}\right) - \frac{1}{r}\frac{\partial}{\partial r}\left(\frac{r\mu_t}{\sigma_\phi}\frac{\partial \phi}{\partial r}\right) \tag{2}$$

and the term on the right-hand side of Eq. (1) represents the mean source term. A four-flux radiation model [8] was used to simulate radiative heat losses.

In the limit of a high Damköhler number, the chemistry will attain equilibrium even within the smallest turbulent eddies, before the turbulent mixing processes will disturb this chemical equilibrium. By the Shvab–Zel'dovich assumptions [9], all thermochemical variables are related to the mixture fraction ξ, which is a conserved scalar. Hence, if the probability density function $\tilde{P}(\xi)$ is known, the mean values of all dependent properties can be determined. In the present model, a β-function PDF is assumed for $\tilde{P}(\xi)$, which is completely determined by the mean $\tilde{\xi}$ and the variance $\widetilde{\xi''^2}$. Transport equations are solved for these moments to calculate the PDF in each grid point.

The assumption of equilibrium chemistry does not hold in methane flames under laboratory conditions, since the burnout of CO and the three-body recombination reactions are not in equilibrium at these relatively low temperatures. As a remedy, the constrained-equilibrium model of Bilger and Stårner [1] was used. This model imposes constraints for the hydrocarbons, thus reducing the CO level on the rich side, whereas the full equilibrium is retained around stoichiometric, where temperatures are highest. Nonadiabaticity was accounted for [10].

Laminar diffusion flame calculations using the OPPDIF code [11] show that the maximum temperature decreases with increasing strain rate, a, but that the OH-radical profile is rather insensitive to the strain rate (Fig. 2). The constrained-equilibrium

model does not account for strain rate variations and therefore predicts rather high temperatures near $\xi = \xi_{st}$. The constrained-equilibrium OH results differ from the laminar flamelet model by a factor of 2. Besides, the laminar flamelet model gives a maximum OH concentration at the lean side of stoichiometry. Differences between the two models are mainly attributed to the superequilibrium OH concentrations in the laminar flamelet model.

Numerical Aspects:

The set of coupled nonlinear elliptic differential equations was solved by a finite-volume discretisation and an alternating-direction implicit (ADI) technique for the resulting set of algebraic equations. The computer code used an upwind discretisation scheme for convection and a 50 × 50 rectilinear nonuniform grid, with many grid points close to the nozzle and the axis of symmetry.

Inlet conditions were prescribed at the nozzle exit plane by using piecewise uniform velocity profiles and a turbulence intensity of 5%. The inlet dissipation rate was estimated from $\tilde{\varepsilon} = \tilde{k}^{3/2}/(0.03D)$, where D is the hydraulic diameter of the respective inlet regions. The inner burner rim was implemented as an impermeable wall, whereas the outer burner rim was taken to be infinitely thin. Other boundary conditions were a symmetry axis at $r = 0$, an impermeable wall with standard wall functions at $r = 0.285$ m, and zero-gradient outlet conditions.

The conserved-scalar model was implemented by constructing a nonuniform table, locally refined to minimise interpolation errors, with $\tilde{\xi}$, $\tilde{h}$, and $\widetilde{\xi''^2}$ as independent variables. All PDF-averaged dependent properties (temperature, mass fractions, molecular transport properties, density) were stored in this table in a preprocessing step. A lookup procedure during the iterative solution process thus saved a large amount of computing time. A typical run took about 30 minutes on a CRAY YMP-4 supercomputer. Successive grid refinement to 100 × 75 grid points showed that results were grid independent.

Results and Discussion

Velocities and Turbulence Characteristics:

The mean axial velocity component $\tilde{u}$, for various radial positions on three different heights, is given in Fig. 3. As in the sequel, the lines correspond to the numerical results, whereas the symbols represent measurement data.

For $x = 50$ mm, the velocity has a maximum on the centreline and then rapidly decays with radial position at the edge of the central jet and increases slightly in the annular jet. The lower experimental values of $\tilde{u}$ between the jet and the annulus flow, near $y = \pm 8$ mm, can be explained by the bluff-body-like character of the burner rim. Consequently, a recirculation zone exists right above the burner nozzle, which is slightly underestimated by the numerical predictions. At $x = 150$ mm, the correspondence between the numerical and experimental results is particularly good. For $x = 250$ mm, the mean velocities are underestimated by the model.

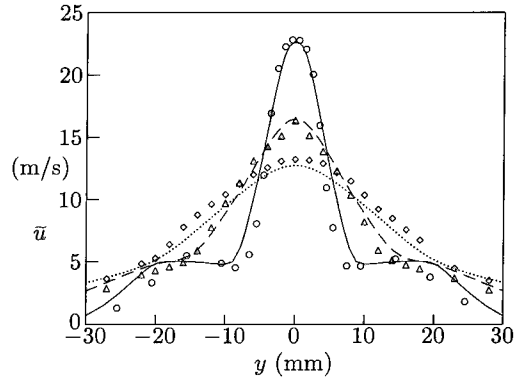

FIG. 3. Comparison of measured mean axial velocity and numerical results, at $x = 50$, 150, and 250 mm. Symbols: experiments ○ $x = 50$ mm, Δ $x = 150$ mm, ◇ $x = 250$ mm. Lines: predictions — $x = 50$ mm, -- $x = 150$ mm, ··· $x = 250$ mm.

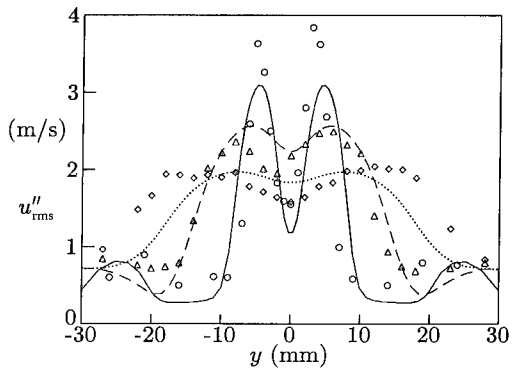

FIG. 4. Comparison of measured axial rms velocity fluctuations and numerical results, estimated from $u''_{rms} = \tilde{k}^{1/2}$. Lines and symbols are the same as those of Fig. 3.

In Fig. 4, the radial profiles of the rms axial velocity u''_{rms} are presented at three x values. The profiles peak at the maximum gradient of the mean velocity. For $x = 50$ mm, the numerical results show lower centreline and peak turbulence than the experiments. Again, for $x = 150$ mm, the correspondence between the LDA results and the model is fairly good, considering the slight asymmetry of the measurements and the limitations of the k-ε model. At $x = 250$ mm,

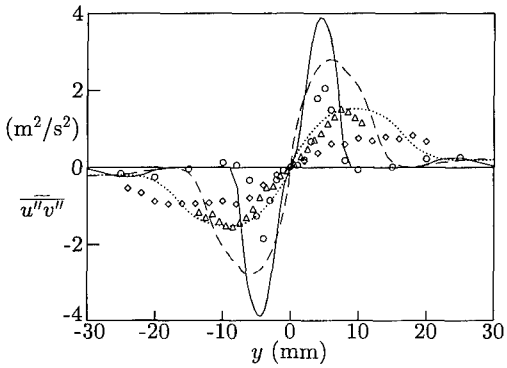

FIG. 5. Comparison of measured shear stress and numerical results, estimated from $\widetilde{u''v''} = -\nu_t(\partial\tilde{u}/\partial r + \partial\tilde{v}/\partial x)$. Lines and symbols are the same as those of Fig. 3.

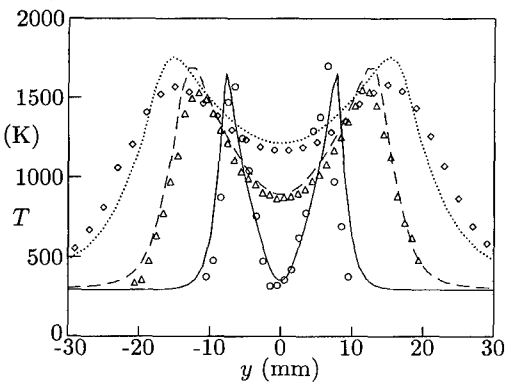

FIG. 6. Comparison of measured mean temperatures and numerical results. Lines and symbols are the same as those of Fig. 3.

FIG. 7. Instantaneous images of OH and NO seeded to the fuel. The OH images (left) cover x = 15–93 mm, and 100–178 mm. The NO images (right) cover 25–75, 75–125, and 125–175 mm. For clarity, in every region the grey level of the NO signal is scaled with the maximum signal.

the rms velocities are underestimated by the model, which may be due to the simple estimation $\widetilde{u''^2} = \tilde{k}$, which is not generally true. Furthermore, it is still disputable whether the LDA experiments yield Reynolds or Favre-averaged velocities.

The measured Reynolds shear stresses $\widetilde{u''v''}$ are shown in Fig. 5. Correspondence with the numerically obtained results is qualitatively correct.

Temperatures:

In Fig. 6, the mean profiles of the measured temperatures are compared with numerical results. Temperatures were measured with a 50-μm Pt-6%Rh/Pt-30%Rh thermocouple and corrected for radiative and conductive heat losses. Correspondence between the measured and simulated temperatures is excellent, taking into account the experimental accuracy of ± 70 K. Inspection of the radial location of maximum temperature reveals that the spreading of the reaction zone is predicted accurately by the model.

The differences between measured and calculated maximum temperatures are small, but seem to increase slowly with x. This is attributed to soot radiation, which was not included in the present model.

OH- and NO-Seed Visualisation:

In Fig. 7, instantaneous images of both OH- and NO-seeded fuel are shown. Close to the burner, our NO visualisations reveal typical Kelvin–Helmholtz instabilities in the fuel flow, whereas downstream

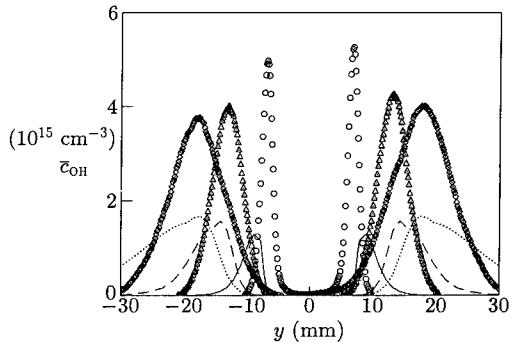

FIG. 8. Radial mean OH concentration profiles. Lines and symbols are the same as those of Fig. 3.

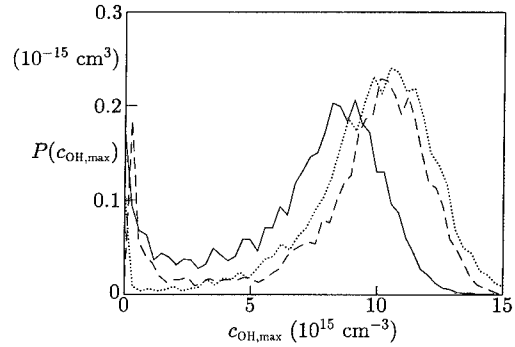

FIG. 9. Distribution of instantaneous maximum OH concentration at various x-values: — x = 50 mm, -- x = 150 mm, ··· x = 250 mm.

well-developed turbulence is found. Figure 7 shows that the NO field is only detected on the rich side of the reaction zone, indicated by OH. This is due to quenching of excited NO molecules by combustion products and O_2. Hence, the NO data could not be used for quantitative conserved-scalar measurements.

OH is produced in the region of the stoichiometric isopleth where temperatures are highest. Near the nozzle, the OH zone is not strongly convoluted by the shear layer turbulence. This is a consequence of the reaction zone not coinciding with the highest shear stresses, because of the low stoichiometric mixture fraction (ξ_{st} = 0.07). The turbulent eddies in the annular air flow are too small to cause a roll-up of the OH zone. With increasing axial distance, the eddies grow and the reaction zone overlaps the shear layer, giving a stronger convolution of the OH zone.

About 10 diameters downstream of the burner nozzle, frequently holes are observed in the OH zone, which is evidence of local extinction. At high strain rates, the reaction zone is stretched, and penetrating eddies cause local extinction. Further experiments showed that local extinction was sensitive to an increase of the annular flow rate. Further downstream, the decreased shear stresses lead to a thicker OH zone with fewer holes.

Statistical Aspects of OH Concentration Fluctuations:

Radial profiles of the average OH concentration $\bar{c}_{OH}$ are shown in Fig. 8, for x = 50, 150, and 250 mm. On the centreline, the average OH concentration and its standard deviation did not increase significantly up to x = 250 mm. Therefore, the reaction zone does not reach the jet axis for x smaller than 250 mm. The measured maximum average OH concentrations were about $4 \times 10^{15}\ \mathrm{cm}^{-3}$ and remained fairly constant with x.

Predictions of the OH concentrations by the constrained-equilibrium model do not take into account superequilibrium levels of OH. The predicted concentrations therefore are too low. The shape of the predicted profiles does not match with the experiments. To investigate the sensitivity of predictions on the assumed PDF shape, we replaced the β-function mixture fraction PDF by a top-hat distribution. This deteriorated the mean temperature as well as the OH predictions: Both the temperature and OH profiles showed lower maximum values, and OH profile shapes deviated even more strongly from the experiments. We conclude that the conserved-scalar model with a β-function PDF performs well for mean temperature predictions, but fails to represent the shape of the measured mean OH profiles. It is unlikely that substituting the β-function PDF by any other PDF shape will significantly improve OH predictions without harming the mean temperature predictions. The observed differences cannot be attributed to the assumed PDF shape, but are inherent to the conserved-scalar chemistry model for OH.

Looking at the trend for larger downstream distance x, the experiments show a decay of maximum average OH values, whereas the conserved-scalar model gives a maximum OH level at the flame tip where $\tilde{\xi} = \xi_{st}$ and fluctuation levels are small. The experiments disagree with such a trend, even for $x > 250$ mm. Soot radiation is held responsible for this effect.

The distribution functions of the peak OH concentration in every instantaneous radial profile exhibited a most probable instantaneous peak concentration of $12 \times 10^{15}\ \mathrm{cm}^{-3}$ (see Fig. 9). The distribution functions all have a bimodal shape, with a peak near $c_{OH,max} = 0$, indicating the existence of local extinction. The low probability of finding peak OH concentrations between 2 and $7 \times 10^{15}\ \mathrm{cm}^{-3}$ suggests that concentration fluctuations at a fixed position in space are mainly due to turbulent displacements of the reaction zone or to local extinction, rather than lower concentration in the reaction zone itself.

Laminar flamelets are believed to describe the OH

chemistry in a more realistic manner than (constrained) equilibrium models. The laminar flamelet data of Fig. 2 are equivalent to peak OH concentrations of 20×10^{15} cm^{-3}, indicating that the measured values may be too low by a factor of 1.6. Despite this difference, the measurements still represent the actual OH distributions of the flame.

Returning to the radial mean OH profiles, it is interesting to see whether the laminar flamelet model would predict the experimental shape of these profiles. In the flamelet model, OH depends on ξ similarly to the constrained-equilibrium model (Fig. 2). Hence, the use of a flamelet model (retaining the scalar mixing model) will not alter the shape of the radial mean OH profiles.

Conclusions

A turbulent natural-gas diffusion flame was investigated numerically and experimentally. The mean velocities were reproduced fairly well, and the turbulence quantities as predicted by the k-ε model yielded qualitative agreement with the experiments.

The temperature predictions agreed excellently with the thermocouple measurements. The assumed PDF model and the k-ε model used therefore reproduced the overall behaviour of the major quantities in the flame.

The fluctuations in the OH concentration are dominated by fluctuations in the location of the OH zone and not by fluctuations of the peak OH concentration inside the OH zone. The OH concentrations were underpredicted compared to the experiments as a result of the absence of superequilibrium OH in the model. Furthermore, the shape of the OH profiles was not reproduced by the model.

Variation of the assumed PDF shape suggests that the β function performs best for this flame, as far as mean temperature is concerned. The laminar flamelet model will yield higher OH concentrations compared to the constrained-equilibrium model. However, correspondence between the predicted and measured OH profiles will not be improved. Hence, we believe that a conserved-scalar model is not appropriate for the description of radical concentrations in this kind of flame.

Nomenclature

a	strain rate of laminar diffusion flame (s^{-1})
c	species concentration (molecules/cm^3)
D	hydraulic diameter (m)
f	focal length (m)
h	enthalpy (J/kg)
k	turbulent kinetic energy (m^2/s^2)
P	probability density function (—)
r	distance from axis of symmetry (m)
T	temperature (K)
u	axial velocity (m/s)
v	radial velocity (m/s)
x	axial position (m)
y	radial position (m)
Y	species mass fraction (—)

Greek symbols

ε	viscous dissipation rate (m^2/s^3)
ξ	mixture fraction (—)
μ_t	turbulent dynamic viscosity [kg/(m · s)]
ν_t	turbulent kinetic viscosity (m^2/s)
ρ	density (kg/m^3)
σ_ϕ	turbulent Prandtl or Schmidt number (—)

Subscripts

st	stoichiometric value
rms	root-mean-square value

Superscripts

$-$	Reynolds-averaged value
$\sim$	Favre-averaged value
$''$	Favre fluctuation

Acknowledgments

The authors gratefully acknowledge financial support from the Dutch Foundation for Chemical Research (SON), the Stichting Nationale Computerfaciliteiten (National Computing Facilities Foundation, NCF) for the use of supercomputer facilities, and the Nederlandse Organisatie voor Wetenschappelijk Onderzoek (Netherlands Organisation for Scientific Research, NWO). Part of this work was performed within SCIENCE project SC1-0459 of the European Community. Financial and material support by Koninklijke/Shell Laboratories Amsterdam is gratefully acknowledged.

REFERENCES

1. Bilger, R. W., and Stårner S. H., "A Simple Model for Carbon Monoxide in Laminar and Turbulent Hydrocarbon Diffusion Flames," *Combust. Flame* 51:155–176 (1983).
2. Stårner, S. H., and Bilger, R. W., "Characteristics of a Piloted Diffusion Flame Designed for Study of Combustion Turbulence Interactions," *Combust. Flame* 61:29–38 (1985).
3. Seitzman, J. M., Paul, P. H., and Hanson, R. K., "PLIF imaging of OH Structures in a Turbulent Nonpremixed H_2-air Flame," in *Proceedings of 28th Aerospace Sciences Meeting, Reno, Nevada*, AIAA 90-0160, 1990.
4. Aldén, M., Edner, H., Holmstedt, G., Svanberg, S., and Högberg, T., "Single-Pulse Laser-Induced OH Fluorescence in an Atmospheric Flame, Spatially Re-

solved with a Diode Array Detector," *Appl. Opt.* 21:1236–1240 (1982).
5. de Vries, J. E., van der Meer, Th. H., and Hoogendoorn, C. J., "OH Concentration Fluctuations in Turbulent Natural Gas Jet Flames," *Chem. Eng. J.* 53:39–46 (1993).
6. Kee, R. J., Grcar, J. F., Smooke, M. D., and Miller, J. A., *A Fortran Program for Modeling Steady Laminar One-Dimensional Premixed Flames*, Technical Report SAND85-8240, Sandia National Laboratories, 1985.
7. Pope, S. B., "An explanation of the turbulent round-jet/plane-jet anomaly," *AIAA J.* 16:279–281 (1978).
8. Khalil, E. E., *Modelling of furnaces and combustors*, Abacus Press, Tunbridge Wells, UK, 1982.
9. Williams, F. A., *Combustion Theory*, 2nd ed., Benjamin/Cummings Publishing Co., Menlo Park, CA, 1985.
10. Peeters, T. W. J., Roekaerts, D., and Hoogendoorn, C. J., *Modelling of turbulent non-premixed flames. Part 1. Conserved-scalar chemistry models*, Technical Report BCWT.93.1, Technische Universiteit Delft, Delft, The Netherlands, 1993.
11. Lutz, A. E., and Kee, R. J., *OPPDIF: Opposed-Flow Laminar Diffusion Flame Code*, Technical report, Sandia National Laboratories, 1992.

COMMENTS

M. A. Delichatsios, FMRC, USA. Buoyancy effects may be important in your case. Can you comment on that?

Author's Reply. The local Richardson number of the jet flow can be defined as $Ri_x = gx\Delta\rho/uj\rho j$ where U_j is the centerline jet velocity, ρ_j the centerline density, $\Delta\rho$ a characteristic density difference, g the constant of gravitational acceleration, and x the height above the burner. For the range of axial distances studied in the paper, $Ri_x < 0.03$, indicating that buoyancy effects can be neglected.

•

A. R. Masri, University of Sydney, Australia. Your coflow velocity is very low, which implies that the OH sits in a laminar scalar layer outside the shear layer. I find it surprising that you get local extinction (visible in the OH profile) at such low velocities.

Author's Reply. In the present configuration, two mixing layers exist: one between the central fuel jet and the annular air flow, and one between the annular air flow and the low-speed coflow. The first mixing layer hardly affects the reaction zone structure, but the second mixing layer interacts with the reaction zone at about 20 jet diameters above the nozzle. In this region, local extinction is found to occur most frequently.

Twenty-Fifth Symposium (International) on Combustion/The Combustion Institute, 1994/pp. 1249–1256

EXPERIMENTAL ANALYSIS OF FLAMELET MODELS FOR PREMIXED TURBULENT COMBUSTION

DENIS VEYNANTE,* JEAN MARC DUCLOS AND JULIEN PIANA
Laboratoire E.M2.C.
Ecole Centrale Paris and C.N.R.S.
Grande Voie des Vignes
92295 Chatenay-Malabry Cedex, France

Flamelet models are now widely used to predict turbulent premixed combustion because they allow the separation of chemical features from the description of the turbulent flow field. Some of them introduce a flame surface density (flame surface per unit volume) modelled either by an algebraic closure (Bray–Moss–Libby model) or from a transport equation. This equation may be exactly written but needs closure assumptions. In the present work, a two-dimensional turbulent premixed propane-air V flame is studied. Velocity profiles are obtained from laser-Doppler velocimetry. Flame front visualizations are achieved by tomography with high-speed cinematography using a copper vapor laser. Images are then processed to extract flame front characteristics (flame surface density, vector normal to the flame front, curvature). The Bray–Moss–Libby model is found to have a good trend but needs a precise closure of the flame wrinkling length scale. Then some terms of the exact transport equation for flame surface density are examined. A simple model is proposed to close the strain rate term acting on the flame surface and due to the mean flow. Curvature and propagation terms are found to act as a source term on the fresh gases side and as a consumption term on the burnt one. This fact points out a lack in the generally used closures of the flame surface density equation where the propagation term is neglected and the curvature term modelled as a destruction one.

Introduction

Flamelet models are now one of the most common approaches for turbulent premixed combustion [1–11]. Under the assumption of a reaction occurring at fast time and short length scales relative to the turbulence, these models are very attractive because they separate the chemical problem from the description of the turbulent flow field. In all flamelet models, the reaction is assumed to take place in thin flame sheets separating unburnt and fully burnt gases. Then, the reaction rate of the mean progress variable $\bar{c}$ may be expressed as $\dot{\bar{\omega}} = w_m \Sigma$, introducing the flame surface density Σ (flame surface per unit volume) and w_m, the mean propagation speed of the flame front. Chemical effects, included in w_m, will not be discussed here. The action of the turbulent flow on the flame surface (convection, distortion, . . .) [12] is described through the flame surface density Σ. Experimental [13], theoretical, and numerical [14] evidences suggest that the domain of validity of the flamelet approach is indeed large, and many practical reacting flows occur in this regime.

Then, the flame surface density has to be obtained. In the current formulation of the Bray–Moss–Libby model (BML) [1,2,4,7], Σ is determined with an algebraic closure

$$\Sigma = \frac{g\bar{c}(1 - \bar{c})}{\sigma_y L_y} \tag{1}$$

where g is a constant of the order of unity, σ_y an orientation factor assumed to be a universal constant of the model, and L_y a length characterizing the flame wrinkling and assumed constant across the turbulent flame brush. This closure is established from a statistical analysis of a random telegraph signal [4].

Another approach is to write a modelled transport equation for the flame surface density Σ [5,6,8,9,11,15–19]. This equation was firstly postulated for turbulent diffusion flames and based on phenomenological analysis [15]. Recent theoretical work has produced a more rigourous approach [10,11,12] that leads to an exact formulation. Splitting the velocity in Favre average and fluctuations $u = \tilde{U} + u''$, the Σ-equation may be written [11]

$$\frac{\partial \Sigma}{\partial t} + \nabla \cdot \tilde{U}\Sigma + \nabla \cdot \langle u'' \rangle_S \Sigma + \nabla \cdot \langle w\mathbf{n} \rangle_S \Sigma = \langle A_T \rangle_S \Sigma + \langle a_T \rangle_S \Sigma + 2\langle wH \rangle_S \Sigma \tag{2}$$

*Also with Centre de Recherche sur la Combustion Turbulence (C.R.C.T.), Ecole Centrale Paris—C.N.R.S.—Institut Français du Pétrole.

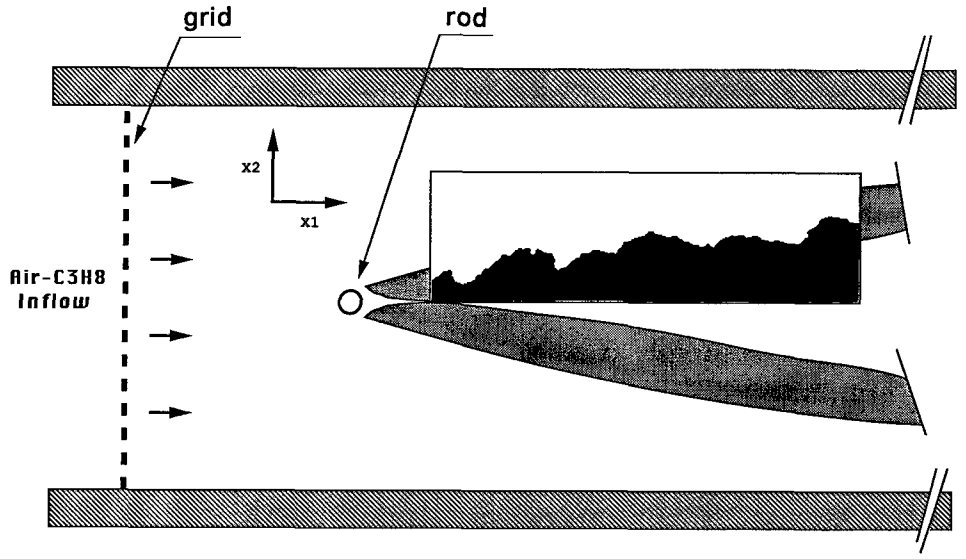

FIG. 1. Experimental combustion chamber. An instantaneous binarized (white in fresh gases, black in burnt gases) view of the flame front is added to the flame sheet and visualizes the zone analysed by tomography.

where **n** is the vector normal to the flame front pointing towards the fresh gases, H the flame front curvature (positive convex towards the fresh gases), and w the local propagation speed of the front. The term $\langle\ \rangle S$ denotes the average along the flame front surface. The last three terms on the left-hand side represent, respectively, convection by the mean flow, turbulent diffusion, and flame propagation. The source terms on the right-hand side correspond, respectively, to the strain rate of flame surface due to the mean flow field, turbulent strain rate, and combined effects of flame curvature and propagation. The two strain rates are given by

$$\langle A_T\rangle_S = \nabla\cdot\tilde{U} - \langle \mathbf{nn}\rangle_S{:}\nabla\tilde{U} = (\delta_{ij} - \langle n_i n_j\rangle_S)\frac{\partial \tilde{U}_i}{\partial x_j} \quad (3)$$

$$\langle a_T\rangle_S = \langle \nabla\cdot u'' - \mathbf{nn}{:}\nabla u''\rangle_S = \left\langle \delta_{ij}\frac{\partial u_i''}{\partial x_j} - n_i n_j \frac{\partial u_i''}{\partial x_j}\right\rangle_S \quad (4)$$

where δ_{ij} is the Kronecker symbol and $\tilde{U}_i$ and n_i are, respectively, the x_i components of the mass average velocity and of the vector normal to the flame front.

Unfortunately, the Σ equation remains unclosed and requires modelling assumptions. A summary and a comparison of various closure schemes may be found in Ref. 20. Information about flame surface density and surface averaged quantities in a turbulent flow is difficult to obtain. Direct numerical simulations are a powerful tool to study the Σ equation terms [11] but are restricted to some well-defined problems. Few experimental data are available: Flame surface densities have been measured by Deschamps et al. [21] in a methane-air conical turbulent premixed flame with a Rayleigh scattering technique, but this work is restricted to the determination of the BML model constants, and no analysis of the Σ equation has been conducted. Santavicca and coworkers have obtained flame statistics such as orientation factor or curvature as functions of the turbulence level or Lewis number from laser-induced fluorescence data [22,23], but flame surface densities are not examined. The aim of the present work is to obtain experimental data on a two-dimensional premixed V flame to analyse flame surface densities and some terms of the Σ equation. Measurements are based on laser-Doppler velocimetry and flame front visualization by high-speed tomography.

Experimental Methods

Experimental Setup and Diagnostics:

The experimental setup is displayed in Fig. 1. A premixed propane/air flow is injected with an upstream velocity of 8 m/s (air mass flow rate of 35 g/s) and an equivalence ratio of 0.7 into a rectangular combustor through a grid. The height, depth, and length of the combustion chamber are, respectively, 50, 80 and, 300 mm. The lateral walls are transparent artificial quartz windows allowing visualization of the whole chamber. The upper and lower walls are made of thick ceramic material including two narrow

windows used for laser sheet. The flame is stabilized by a small cylindrical rod of 3-mm diameter (blockage ratio of 6%) embedded in the lateral windows, allowing measurements upstream from the rod. A two-dimensional V flame with a half angle of about 6° is observed.

Velocities are measured with a two-component laser velocimeter. The measuring volume is 0.3-mm diameter and 1.2-mm length. The flow is seeded with magnesium oxide, and a mean data rate of about 5 kHz is achieved. Transverse mean velocity profiles are measured both for cold and combusting flows for various downstream locations. The upstream flow is found to be established with a turbulence level of about 10% and an integral turbulent length scale, estimated from the Taylor hypothesis and the time autocorrelation function, of about 3 mm corresponding to the grid mesh. The turbulent Reynolds number and the ratio u'/S_L between turbulent fluctuations and laminar flame speed may be estimated, respectively, to 150 and 2.5. The Strouhal frequency of a von Kármán street (about 530 Hz) is clearly apparent in velocity data obtained without combustion.

Flame front is visualized by tomography [24]. The flow is seeded with small droplets of groundnut oil burning at the flame front. Only fresh gases, including droplets, diffuse the laser light whereas burnt gases appear as dark areas. A copper vapor laser (pulse duration about 40-ns repetition rate from 3 to 20 kHz) is synchronized with a high-speed 16-mm camera operating at 5000 frames per second. On these time-resolved visualizations, the combusting flow exhibits strong coherent structures, starting at the rod and growing when moving downstream. Unlike von Kármán streets, these structures are symmetrical between the two flame sheets. Then, only the upper flame sheet is analysed by image processing. Two hundred images are digitized with a charge-coupled device camera (400 × 120 pixels, leading to a pixel resolution of 0.14 mm) and a microcomputer. The zone analysed corresponds to a rectangle 5.6-cm long and 1.68-cm high starting 1.12 cm dowstream the rod, the lower edge corresponding to the combustion chamber axis. The images are then binarized ($c = 0$ in the fresh gases, $c = 1$ in the burnt gases) allowing the determination of the flame front coordinates. An example of a binarized image is displayed in Fig. 1. The Reynolds averaged progress variable $\bar{c}$ is obtained by averaging all the binarized images.

Flame Front Statistics and Data Reduction:

Under the assumption of a two-dimensional instantaneous flow (no evidence of three-dimensional effects has been observed), flame surface statistics may be determined from tomographic images. The distance along the flame front s is computed from the front coordinates. Cubic spline functions are used to provide first and second derivatives of $x_1(s)$ and $x_2(s)$ signals, leading to the flame front normal vector components (n_i) and to the flame curvature H. The measuring domain is divided into overlapping square boxes of 15 × 15 pixels (about 2 × 2-mm square), a good compromise between processing noise appearing with a low pixel number and artificial diffusion introduced by larger boxes. In each box, the arc length of the flame front is computed from s (or is set to zero if no flame is present). Results are then averaged over the 200 available frames, divided by the box surface, leading to a flame surface density affected to the center point of the box. The surface average of all other quantities Q is determined in each box according to

$$\langle Q \rangle_S = \frac{\int_S Q dS}{\int_S dS}. \tag{5}$$

Data reduction procedures have been carefully tested and validated both with synthetic images and experimental data.

Results and Discussion

Velocity Profiles:

Transverse mean velocity profiles are displayed for different downstream locations in Fig. 2. The wake due to the flame holder is progressively reduced with the distance from the rod. An increase in the axial velocity, due to the thermal expansions of hot gases, is apparent on the profiles 0.08 and 0.210 m downstream the rod: The velocity reaches a maximum on the centerline (up to 30 m/s), and the flame brush acts as a convergent wall leading to an increase in fresh gases velocity (up to 20 m/s compared with 8 m/s at the chamber entrance). The thermal expansion also has an important consequence on the flame dynamics, clearly apparent on the high-speed tomographic film: In the first part of the chamber, the coherent structures embedding the flame front turn clockwise (counterclockwise) in the upper (lower) flame sheet, as in classical von Kármán streets, except for their symmetry. When the centerline velocity becomes higher, the upper (lower) coherent structures start to turn counterclockwise (clockwise). This phenomenon probably reduces the increase in flame area density due to mean strain rate.

Mean Progress Variable and Flame Surface Density:

Five transverse flame surface density profiles are displayed in Fig. 3. As the flame sheet becomes larger, the maximum value of Σ decreases slightly

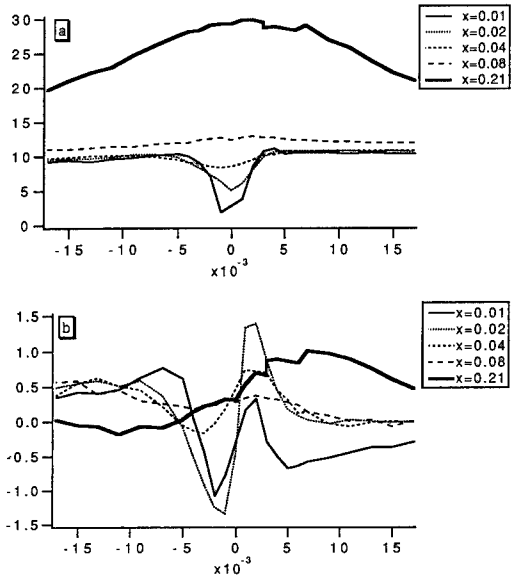

FIG. 2. Transverse velocity profiles for several downstream locations (m/s). (a) mean axial velocity, (b) mean transverse velocity. Downstream locations are in meters from the rod. Transverse locations, in meters, originate at the combustion axis.

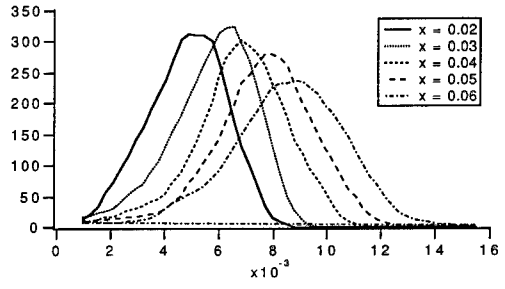

FIG. 3. Transverse mean flame surface density Σ profiles plotted for five x_1 locations (in meters downstream the stabilizing rod) as a function of the transverse coordinates (in meters from the combustion chamber axis). Unit of Σ is m^{-1}. Results are obtained by averaging 200 images.

with the downstream location and is shifted towards the fresh gases. The flame surface density profiles are plotted as a function of the mean progress variable $\bar{c}$ in Fig. 4. Unlike the direct numerical simulation results in a propagating turbulent flame [11], the profiles are symmetrical and look like a parabola as suggested by Eq. (1). Figure 5 displays the computed values of $\Sigma/[\bar{c}(1 - \bar{c})]$, which is $g/[\sigma_y L_y]$ in the Bray–Moss–Libby formulation. This quantity may be assumed to be constant between $\bar{c} = 0.2$ and $\bar{c} = 0.8$. These results are in qualitative agreement with those of Deschamps et al. [25]. Nevertheless, this constant

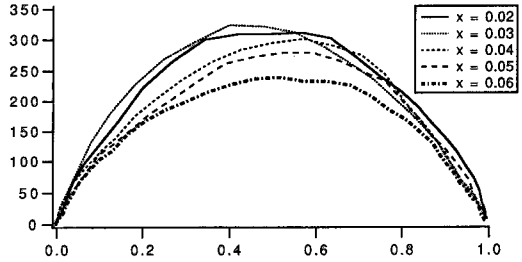

FIG. 4. Transverse flame surface density Σ profiles for five downstream locations plotted as a function of the mean progress variable $\bar{c}$.

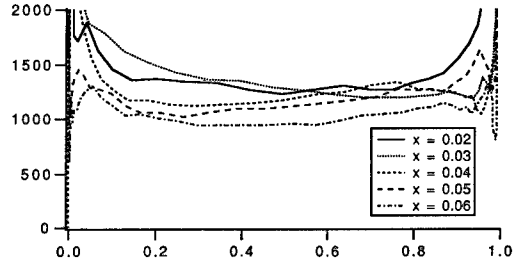

FIG. 5. Transverse profiles of $\Sigma/[\bar{c}(1 - \bar{c})]$ (in m^{-1}), corresponding to $g/[\sigma_y L_y]$ in the Bray–Moss–Libby formulation, plotted as a function of the mean progress variable $\bar{c}$ for five downstream locations.

decreases slightly with the downstream location, corresponding to a flame wrinkling length scale $\sigma_y L_y$ increasing from 0.7 to 0.9 mm, about four times lower than the integral length scale l_t of the cold flow. Deschamps et al. have found that l_t and $\sigma_y L_y$ are equal, but their flame surface densities are about four times lower. This discrepancy may probably be explained by the different nature of the two experiments and shows a limit of the BML approach that requires a precise model for the flame wrinkling length scale, depending on various effects (strain rate, curvature, . . .) included in the Σ equation.

Strain Rate Due to the Mean Flow:

The only unclosed terms in the strain rate $\langle A_T \rangle_S$ due to the mean flow [Eq. (3)] are the surface averaged cross products $\langle n_i n_j \rangle_S$, which act as orientation factors. Following Cant et al. [5], the component of the normal vector may be split between mean and fluctuating parts: $n_i = M_i + m_i$ with $\langle n_i \rangle_S = M_i$ and $\langle m_i \rangle_S = 0$, leading to

$$\langle n_i n_j \rangle_S = M_i M_j + \langle m_i m_j \rangle_S. \tag{6}$$

The mean normal vector to the flame front **M** is a function of the mean progress variable $\bar{c}$ and the flame surface density Σ [5]

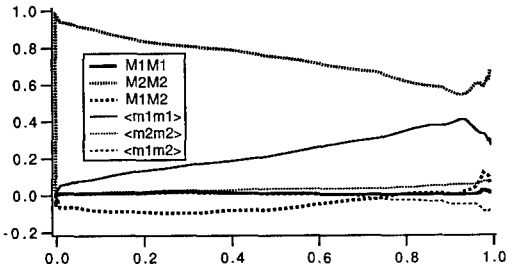

FIG. 6. Profiles of the components of the strain rate due to the mean flow. Mean (M_iM_j) and fluctuating ($\langle m_im_j\rangle_S$) parts are plotted as a function of the mean progress variable $\bar{c}$ for $x_1 = 0.03$ m.

$$\mathbf{M} = -\frac{\nabla\bar{c}}{\Sigma}. \tag{7}$$

Now, only the fluctuating part $\langle m_im_j\rangle_S$ remains unclosed. Cant et al. [5,9] assume isotropic fluctuations and write

$$\langle m_im_j\rangle_S = \frac{\delta_{ij}}{3}(1 - \mathbf{M}\cdot\mathbf{M}). \tag{8}$$

Mantel and Borghi [19] have, indirectly, proposed another closure scheme

$$\langle n_in_j\rangle_S = \frac{\widetilde{u_i''u_j''}}{2k} \tag{9}$$

where k is the turbulent kinetic energy.

Transverse profiles of M_iM_j and $\langle m_im_j\rangle_S$ are plotted as a function of the mean progress variable $\bar{c}$ for $x_1 = 0.03$ m in Fig. 6. A strong dissymmetry is observed: The higher term, $\langle n_2n_2\rangle_S$, is mainly due to the mean vector (M_2M_2). On the other side, $\langle n_1n_1\rangle_S$ comes from its fluctuations ($\langle m_1m_1\rangle_S$). The cross product $\langle n_1n_2\rangle_S$ remains low and may be approximated by its mean value M_1M_2. These results are summarized as

$$\begin{aligned}
&\langle n_1n_1\rangle_S = \langle m_1m_1\rangle_S = 1 - M_2M_2; \qquad M_1M_1 = 0\\
&\langle n_2n_2\rangle_S = M_2M_2; \qquad \langle m_2m_2\rangle = 0\\
&\langle n_1n_2\rangle_S = M_1M_2; \qquad \langle m_1m_2\rangle = 0.
\end{aligned} \tag{10}$$

The same trend is observed for other downstream locations with a slight increase in $\langle m_1m_1\rangle_S$ with the downstream location on the burnt side of the reaction zone (and a corresponding decrease in M_2M_2). Expression (7), connecting $\mathbf{M}$ with $\bar{c}$ and Σ, is found to be very well verified in our results, validating the processing procedure.

Then a simple model may be proposed for $\langle n_in_j\rangle_S$ in the case of a two-dimensional flow involving mixing layers and coherent structures (the previously presented models involve turbulent flame propagation in homogeneous turbulence). Defining direction 1′ tangential to the iso mean progress variable $\bar{c}$ and 2′ normal to this direction, one may write

$$\begin{aligned}
&\langle n_1'n_1'\rangle_S = 1 - M_2'M_2';\\
&\langle n_2'n_2'\rangle_S = M_2'M_2';\\
&\langle n_1'n_2'\rangle_S = 0 \quad \text{with } M_2' = \frac{|\nabla\bar{c}|}{\Sigma}.
\end{aligned} \tag{11}$$

Moving in the laboratory frame, we obtain

$$\begin{aligned}
\langle n_1n_1\rangle_S &= (1 - M_1^2 - M_2^2)\frac{M_2M_2}{(M_1^2 + M_2^2)} + M_1M_1\\
\langle n_2n_2\rangle_S &= (1 - M_1^2 - M_2^2)\frac{M_1M_1}{(M_1^2 + M_2^2)} + M_2M_2\\
\langle n_1n_2\rangle_S &= [2(M_1^2 + M_2^2) - 1]\frac{M_1M_2}{(M_1^2 + M_2^2)}
\end{aligned} \tag{12}$$

where M_1 and M_2 come from Eq. (7).

The velocity gradients may be roughly estimated from velocity data to about 400 s^{-1} for $\partial\tilde{U}_1/\partial x_2$, 150 for $\partial\tilde{U}_2/\partial x_2$, 50 for $\partial\tilde{U}_1/\partial x_1$, and $\partial\tilde{U}_2/\partial x_1$ is negligible. Then, assuming $\langle n_1n_1\rangle_S = 0.2$, $\langle n_2n_2\rangle_S = 0.8$, and $\langle n_1n_2\rangle_S = -0.1$ leads to a contribution of each term, respectively, of about 40, 30, 40, and 0 s^{-1}. The three first terms are of the same order, and the strain rate $\langle A_T\rangle_S$ cannot be reduced to the main gradient $\partial\tilde{U}_1/\partial x_2$. Another important point is that velocity gradients may change sign as $\partial\tilde{U}_1/\partial x_2$ and $\partial\tilde{U}_1/\partial x_1$ do clearly on velocity profiles, and thus, the strain rate contains positive and negative contributions. This point needs further precise investigation.

Curvature and Propagation Terms:

These terms ($2\langle wH\rangle_S\Sigma$ and $\nabla\cdot\langle wn\rangle_S\Sigma$) contain the local propagation speed w that cannot be obtained from our measurements and requires modelling. The term w depends on laminar flame characteristics and includes complex stretch and curvature effects through the Markstein length [25]. We have chosen here to assume a constant value of w. Because of a Lewis number greater than unity (about 1.9) and the measured curvatures, a curvature-dependent propagation speed will slightly reduce the effects observed here, but the general trend will be maintained. This point will be examined in a further work.

Transverse profiles of the mean curvature are plotted as a function of $\bar{c}$ in Fig. 7. Curvatures are positive on the fresh gases side (up to $\bar{c} = 0.6$ or 0.8) and negative on the burnt gases side. These results correspond to the ones obtained by Trouvé and Poinsot

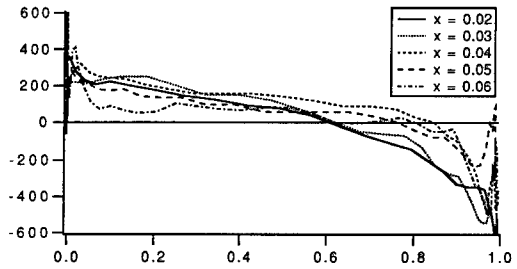

FIG. 7. Transverse profiles of the mean curvature $\langle H \rangle_S$ plotted as a function of the mean progress variable $\bar{c}$ for five downstream locations. Curvatures are positive towards the burnt gases. Unit is m^{-1}.

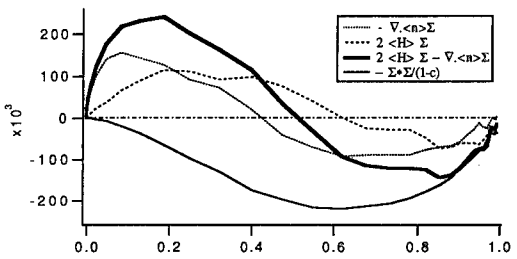

FIG. 8. Transverse profiles of propagation $(-\nabla \cdot \langle n \rangle_S \Sigma)$, curvature $(2\langle H \rangle_S \Sigma)$, and combined $(2\langle H \rangle_S \Sigma - \nabla \cdot \langle n \rangle_S \Sigma)$ terms as a function of the mean progress variable $\bar{c}$ for the downstream location $x_1 = 0.03$ m. The modelled consumption term $-\Sigma^2/(1-\bar{c})$ is also computed. Comparable results are obtained with other downstream locations.

in direct numerical simulations [11]. Accordingly, the third term of the right-hand side in Eq. (2) acts as a source term for fresh gases and a consumption term for burnt gases. The same trend is also observed for the propagation term $(-\nabla \cdot \langle n_S \Sigma \rangle)$. A comparison of propagation $(-\nabla \cdot n_S \rangle \Sigma)$, curvature $(2\langle H \rangle_S \Sigma)$, and combined $(2\langle H \rangle_S \Sigma - \nabla \cdot \langle n \rangle_S \Sigma)$ terms is displayed in Fig. 8 for $x_1 = 0.03$ m. These terms are of the same order. The term $-\Sigma^2/(1-\bar{c})$ is also computed. This term is generally used to model the consumption term in the Σ equation, and Vervisch et al. have shown that it is included in a combination of propagation and curvature terms [26]. This consumption term has a good trend on the burnt gases side $(0.85 \leqslant \bar{c} \leqslant 1)$ but acts too soon on the fresh gases side. Another important failure of classical closure of the flame surface density equation is to neglect the source term due to propagation and curvature for $\bar{c} \leqslant 0.5$, whereas its order is comparable to strain and convective terms.

Conclusion

Velocity and flame surface property measurements have been conducted in a two-dimensional premixed turbulent flame stabilized behind a small rod. Data have been analysed by comparison with flamelet models, both with an algebraic closure and a transport equation for the flame surface density. The main conclusions are as follows:

1. The Bray–Moss–Libby closure provides a good trend for the flame surface density profiles, at least for a mean progress variable $\bar{c}$ lying between 0.2 and 0.8. Nevertheless, the flame surface wrinkling length scale needs to be carefully modelled and depends on the downstream location. Our results are not exactly similar to those of Deschamps et al. [21], and the discrepancy may be explained by differences between experimental geometries and flame characteristics.
2. Orientation factors $\langle n_i n_j \rangle_S$ intervening in the strain rate $\langle A_T \rangle_S$ exhibit a strong anisotropy. This is of importance because the higher velocity gradient $(\partial \tilde{U}_2/\partial x_2)$ is affected by a small coefficient and becomes of the same order as other components. A simple model is proposed for $\langle n_i n_j \rangle_S$ in such two-dimensional mixing layer configurations where the assumption of isotropy of the normal vector fluctuations is no longer valid.
3. As observed by direct numerical simulations [11], the curvature term acts as a source term on the fresh gases side and a consumption term on the burnt one. The propagation term is found to have the same order and the same trend.
4. A lack in the flame surface density transport equation closure lies in the consumption term modelled as $-\Sigma^2/(1-\bar{c})$. By comparison with the exact Σ equation, this term has a good trend on the burnt gases side $(\bar{c} \geqslant 0.85)$ but acts too soon on the fresh gases side where it should be a source term.

Nomenclature

$\langle a_T \rangle_S$	turbulent strain rate acting on the flame tangent plane
$\langle A_T \rangle_S$	strain rate due to the mean flow
c	progress variable (0 in fresh gases, 1 in burnt gases)
$\bar{c}$	Reynolds averaged progress variable
g	constant of the Bray–Moss–Libby model
H	local flame curvature (positive convex towards the fresh gases)
k	turbulent kinetic energy
l_t	integral length scale of the cold flow
L_y	length characterizing the flame wrinkling (BML model)
M_i	mean component of the vector normal to the flame front **M**
m_i	fluctuating component of the vector normal to the flame front
n	vector normal to the flame front (pointing towards the fresh gases)

n_i	component of the vector normal to the flame front
s	distance along the flame front
u	velocity
$\tilde{U}$	Favre averaged (mass weighted) velocity
u''	velocity fluctuations
w	local propagation speed of the flame
x_1	downstream coordinate (origin at the rod)
x_2	transverse coordinate (origin at the combustion chamber axis)
δ_{ij}	Kronecker symbol
σ_y	orientation factor (BML model)
Σ	flame surface density (flame surface per unit volume)
$\langle\ \rangle_S$	averaged quantity along the flame front

Acknowledgments

The authors wish to acknowledge Drs. T. Poinsot, A. Trouvé, and T. Baritaud from C.R.C.T. for many helpful discussions. The financial support of Ecole Centrale Paris, DRET, GSM, SNECMA, and the European Community (BRITE-EURAM ETMA project) is greatly appreciated. Computer support for image processing has been provided by IDRIS (Institut de Développement et de Recherches en Informatique Scientifique)—Orsay (France).

REFERENCES

1. Bray, K. N. C., Libby, P. A., and Moss, J. B., *Combust. Sci. Technol.* 41:143–172 (1984).
2. Bray, K. N. C., Moss, J. B., and Libby, P. A., *Combust. Flame* 61:87 (1987).
3. Peters, N., *Twenty-First Symposium (International) on Combustion*, The Combustion Institute, Pittsburgh, 1986, pp. 1231–1250.
4. Bray, K. N. C., Champion, M., and Libby, P. A., in *Turbulent Reacting flows, Lecture Notes in Eng., Springer Verlag*, New York, 1989, p. 40.
5. Cant, R. S., Pope S. B., and Bray, K. N. C., *Twenty-Third Symposium (International) on Combustion*, The Combustion Institute, Pittsburgh, 1990, pp. 809–815.
6. Candel, S., Veynante, D., Lacas, F., Maistret E., Darabiha, N., and Poinsot, T., in *Recent Advances in Combustion Modeling* (B. E. Larrouturou, Ed.) World Scientific, Singapore, 1990.
7. Bray, K. N. C., *Proc. R. Soc. London A* 431:315–335 (1990).
8. Boudier, P., Henriot, S., Poinsot, T., and Baritaud, T., *Twenty-Fourth Symposium (International) on Combustion*, The Combustion Institute, Pittsburgh, 1992, pp. 503–510.
9. Cant, R. S., *Joint Meeting of the British and German Sections*, The Combustion Institute, Pittsburgh, 1993, pp. 48–51.
10. Candel, S., and Poinsot, T., *Combust. Sci. Technol.* 70:1–15.
11. Trouvé, A., and Poinsot, T., in *Proceedings of the Summer Program*, Center for Turbulence Research, Stanford, 1992. Also *J. Fluid Mech.*, to appear, 1995.
12. Pope, S. B., *International J. Eng. Sci.* 26:445–469 (1988).
13. Roberts, W. L., Driscoll, J. F., Drake, M. C., and Goss, L. P., *Combust. Flame* 94:58–69 (1993).
14. Poinsot, T., Veynante, D., and Candel, S., *J. Fluid Mech.* 228:561–605 (1991).
15. Marble, F. E., and Broadwell, J. E., *Project Squid Technical Report*, TRW-9-PU, 1977.
16. Pope, S. B., and Cheng, W. K., *Twenty-Second Symposium (International) on Combustion*, The Combustion Institute, Pittsburgh, pp. 781–789, 1988.
17. Darabiha, N., Giovangigli, V., Trouvé, A., Candel, S., and Esposito, E., in *Proceedings of the France-USA Joint Workshop on Turbulent Combustion*, Springer Verlag, New York, 1987.
18. Borghi, R., *Combust. Flame* 80:304–312, 1990.
19. Mantel, T., and Borghi, R., *Combust. Flame*, 96:443–457 (1994).
20. Duclos, J. M., Veynante, D., and Poinsot, T., *Combust. Flame* 95:101–117 (1993).
21. Deschamps, B., Boukhalfa, A., Chauveau C., Gökalp, I., Shepherd, I. G., and Cheng, R. K., *Twenty-Fourth Symposium (International) on Combustion*, The Combustion Institute, Pittsburgh, pp. 469–475, 1992.
22. Lee, T.-W., North, G. L., and Santavicca, D. A., *Combust. Flame* 93:445–456 (1993).
23. Lee, T.-W., Lee, J. G., Nye, D. A., and Santavicca, D. A., *Combust. Flame* 94:146–160 (1993).
24. Boyer, L., in *Non Equilibrium Cooperative Phenomena in Physics and Related Fields* (M. G. Velarde, Ed.) Plenum Press, New York, 1983.
25. Clavin, P., and Williams, F. A., *J. Fluid Mech.* 116:251–282.
26. Vervisch, L., Bidaux, E., Bray, K. N. C., and Kollman, W., *Phys. Fluid*, submitted.

COMMENTS

F. C. Gouldin, Cornell University, USA. In turbulent flows, velocity fluctuations and contortions of scalar level surfaces, e.g., isothermal surfaces, are three dimensional. The authors present results for flamelet surface density (Σ), surface radii of curvature, and correlations between components of flamelet surface normal. These results are obtained by analysis of flamelet visualization data obtained, in turn, by laser tomography. Large amounts of data are

obtained, and the data analysis is extensive. However, the tomography method visualizes the lines formed by the intersection of the plane of laser sheet illumination and the flamelet surface. Given that the visualization data do not allow one to find surface properties directly, how do the authors justify the interpretation of their results as surface properties rather than line properties?

Author's Reply. As pointed out in the comment, velocity fluctuations and contortions of scalar level surfaces are three dimensional in turbulent flows. In the present work, the data analysis is based on the assumption of a two-dimensional flow to extract surface properties from quantities that are rigorously line properties. In our experiment, this assumption is not too crude because the flow field and the flame front movement are mainly dominated by large 2D coherent structures. In the cold flow, the classical von Kármán street is clearly apparent with a frequency corresponding to the well-known Strouhal number of 0.2. Of course, the mean flow is also two dimensional. Accordingly, our data may be analyzed as surface properties without the introduction of a too important bias effect.

•

Ian Shepherd, Lawrence Berkeley Laboratory, USA. The curvature determination will be sensitive to many factors: interpolation method, number of points in the fit, etc. Have you investigated such sensitivity in your results?

Author's Reply. The curvature determination is very sensitive to many factors because it required the determination of the second derivatives of the flame front coordinates. The method retained here is based on a smooth of the flame front coordinate signal as a function of the arc length along the front. These two signals are then interpolated using cubic spline functions (from NAG scientific library) providing directly the first and the second derivatives allowing the curvature determination. Of course, various tests have been done, especially with synthetic signals such as circle and sinusoidal functions. This technique is found to be satisfactory. Another approach has also been tested, generally used to process direct numerical simulation data (see Trouvé and Poinsot) and based on the gradient of the progress variable. This method does not require the flame front determination but is somewhat rough with bimodal signals as in our experiment.

Nevertheless, the instantaneous curvature signal is blurred by noise, and only an average over a great number of images leads to a good result. Improvement of the flame front curvature determination is one of our objectives in a next step. One has also to mention that all the processing technique is based on the assumption of a two-dimensional flow.

•

Salah Ibrahim, British Gas, England. You have shown experimental results for the term $\Sigma/[\bar{c}(1 - \bar{c})]$ which is equivalent to $g/[\sigma_y L_y]$, and which is very important in modelling turbulent premixed combustion using the laminar flamelet concept. Have you tried to extract results for the flame scale, L_y, from your experiments? If so, what is the relative behavior of that term at the leading and trailing edge of the flame brush? And how is that compared with Prof. K. N. C. Bray's empirical correlation?

Author's Reply. In fact, this work is mainly focused on an experimental analysis of the flame surface density transport equation. Of course, our data allow a determination of the wrinkling scale L_y used in the Bray–Moss–Libby algebraic closure for the flame surface density, and the ratio $g/\sigma_y L_y$ is plotted on Fig. 5. This ratio is found to be almost constant along a transverse profile for the Reynolds averaged progress variable $\bar{c}$ lying between 0.2 and 0.8. But this constant is found to decrease slightly with the downstream locations, corresponding with a scale $\sigma_y L_y$ increasing from 0.7 to 0.9 mm about four times lower than the integral length scale of the cold flow, which is not in quantitative agreement with the experimental results of Deschamps et al., as pointed out in the text. The wrinkling length scale L_y seems to decrease at the leading and trailing edge of the flame brush. Nevertheless, no precise determination of the wrinkling scale L_y and comparison with the Prof. K. N. C. Bray empirical correlation have been conducted in this work, but will be done in a further analysis, even L_y is probably a very difficult quantity to model through an algebraic closure. But, to our thinking, a flame surface density transport equation provides a more promising way.

Twenty-Fifth Symposium (International) on Combustion/The Combustion Institute, 1994/pp. 1257–1264

LARGE-EDDY SIMULATIONS OF BLUFF BODY STABILIZED FLAMES

C. FUREBY AND C. LÖFSTRÖM
Division of Combustion Physics
Lund Institute of Technology
Lund, Sweden

The objective of this paper is to extend a previously developed large-eddy simulation (LES) model, originally developed for anisochoric high-Reynolds- (Re-) number flows, to include chemically reacting flows as well. The LES model, developed from a physical model founded on modern continuum-mechanical mixture theories, includes a complete treatment of the subgrid stresses and fluxes. Different multistep global reaction schemes have been adopted along with a combustion model that considers the influence of subgrid effects on the effective chemical reaction rates. In order to study the predictive capabilities of this LES model, numerical simulations of the flow behind a two-dimensional generic bluff body in a straight channel have been undertaken, and results are compared with measurements from experimental investigations. In the simulations of reacting flow situations, the fuel was propane, and premixed conditions were enforced. The measurements were done with nonintrusive methods such as the 2λ-CARS technique, giving temperature probability density functions (pdfs) and profiles, as well as traditional gas analysis, giving temperature profiles. Comparison of simulated and measured temperature pdfs and profiles indicates that the LES technique works well for unsteady premixed flows, and it mimics most of the significant flow features, including typical unsteady flow structures and the flame-front dynamics.

Introduction

Turbulent combustion is the dominant process in most practical combustion systems. Although turbulent combustion is widely used, a detailed knowledge and understanding of the process are not yet present. Improvement of current simulation models and development of new simulation models for turbulent reacting flows are of key interest. By combining detailed measurements with detailed numerical simulations, we can learn much more about such complicated dynamic systems.

The objective of the present work is to investigate the predictive capabilities of a large-eddy simulation (LES) model [1]. The study involves numerical experiments of unsteady turbulent wakeflow behind a two-dimensional generic bluff body, as well as comparison with physical experiments made on a similar test rig [2]. The LES methodology has been employed by several groups for nonreacting turbulent flows with success [3,4], but only a few attempts have been made to include combustion, [1,5]. The extension from nonreacting to reacting flow is a difficult task since (1) transport equations for each constituent must be solved. Often computer memory and speed limit the number of constituents possible to handle, and, thus, detailed reaction mechanisms are excluded; (2) it is difficult to formulate accurate reduced reaction mechanisms; and (3) the description of the reaction rate is strongly affected by the turbulent flow field.

A Physical Model for Chemically Reacting Flows

By adopting the principles of Trusdell [6], balance equations for mass, momentum, moment of momentum, and energy can be formulated. To close the set of balance equations, constitutive equations, expressing the physical properties of the mixture and describing the interactions between constituents, must be formulated [1,7]. We further assume that (1) the mixture has only one temperature; (2) the stress tensor is symmetric; (3) body forces and radiation are neglected; and (4) the fluid is linearly viscous with Fourier heat conduction. Thus,

$$\begin{cases} \dfrac{\partial}{\partial t}(\rho Y_A) + \operatorname{div}[\rho Y_A(\dot{\mathbf{x}} + \mathbf{u}_A)] = \hat{m}_A \\ \dfrac{\partial \rho}{\partial t} + \operatorname{div}(\rho\dot{\mathbf{x}}) = 0 \\ \dfrac{\partial}{\partial t}(\rho\dot{\mathbf{x}}) + \operatorname{div}(\rho\dot{\mathbf{x}} \otimes \dot{\mathbf{x}}) = -\operatorname{grad} p + \operatorname{div} \mathbf{S} \\ \dfrac{\partial}{\partial t}(\rho h) + \operatorname{div}(\rho h\dot{\mathbf{x}}) = \dot{p} + \phi - \operatorname{div}[(\kappa/C_p)\operatorname{grad} h] \end{cases} \tag{1}$$

where ρ is the density, Y_A are the mass fractions, $\dot{\mathbf{x}}$ is the velocity, $\mathbf{u}_A$ are the diffusion velocities, m_A are the mass supply terms, p is the thermodynamic pressure, $\mathbf{S}$ is the viscous stress tensor, h is the specific

entropy, $\dot{p}$ is the substantial time derivative of pressure, ϕ is the dissipation function, $\kappa(\rho,\theta)$ is the heat conductivity, and C_p is the specific heat at constant pressure. The thermodynamic pressure and the specific enthalpy h are calculated by the ideal gas law and the caloric equation of state. The equation of motion for each constituent is cast into an algebraic relation, expressing the diffusion velocities in terms of mass fraction gradients and temperature gradients [1],

$$\mathbf{u}_A = \kappa_{YA}\,\mathrm{grad}(\ln Y_A) - \kappa_{\theta A}\,\mathrm{grad}(\ln \theta) \qquad (2)$$

where $\kappa_{YA}(\rho,\theta)$ and $\kappa_{\theta A}(\rho,\theta)$ are material coefficients and θ is the temperature.

The Large-Eddy Simulation Model

The main limitation of numerical simulations of high-Reynolds- (Re-) number flows is the inability to deal simultaneously with the wide range of length scales present. A remedy can be sought so that phenomena occurring at scales smaller than the resolvable scales are separately modeled [3]. This approach has been termed large-eddy simulation (LES), and in comparison with direct numerical simulation, it allows the simulation of flows with practical physical parameters. The methodology involves decomposing the variables into large-scale and subgrid-scale (SGS) components, followed by prefiltering of the fluid dynamics equations (1) by

$$\bar{\rho}\tilde{\phi}(\mathbf{x},t) = \int_D G(\mathbf{x} - \mathbf{z}, \Delta)\rho(\mathbf{z},t)\phi(\mathbf{z},t)d^3\,\mathbf{z} \qquad (3)$$

where $G = G(\mathbf{x} - \mathbf{z}, \Delta)$ is an appropriate filter function with a characteristic width Δ, ϕ represents the filtered variable, and the integration is over the entire computational domain. The remaining portion of ϕ, i.e., ϕ'', is defined as the SGS field. Thus,

$$\begin{cases} \dfrac{\partial}{\partial t}(\bar{\rho}\tilde{Y}_A) + \mathrm{div}[\bar{\rho}\tilde{Y}_A(\tilde{\dot{\mathbf{x}}} + \tilde{\mathbf{u}}_A)] = \tilde{\hat{m}}_A - \mathrm{div}\,\mathbf{b}_{YA} \\ \dfrac{\partial\bar{\rho}}{\partial t} + \mathrm{div}(\bar{\rho}\tilde{\dot{\mathbf{x}}}) = 0 \\ \dfrac{\partial}{\partial t}(\bar{\rho}\tilde{\dot{\mathbf{x}}}) + \mathrm{div}(\bar{\rho}\tilde{\dot{\mathbf{x}}} \otimes \tilde{\dot{\mathbf{x}}}) = -\mathrm{grad}\,\bar{p} + \mathrm{div}(\bar{S} - B) \\ \dfrac{\partial}{\partial t}(\bar{\rho}\tilde{h} + \mathrm{div}(\bar{\rho}\tilde{h}\tilde{\dot{\mathbf{x}}}) = \bar{\dot{p}} + \bar{\phi} - \mathrm{div}[(\kappa/C_p)\mathrm{grad}\,\tilde{h} - \mathbf{b}_h] \end{cases} \qquad (4)$$

where $\mathbf{B} = \mathbf{L} + \mathbf{C} + \mathbf{R}$, $\mathbf{b}_h = \mathbf{l}_h + \mathbf{c}_h + \mathbf{r}_h$, and $\mathbf{b}_{YA} = \mathbf{l}_{YA} + \mathbf{c}_{YA} + \mathbf{r}_{YA}$ in which $\{\mathbf{L},\mathbf{l}_h,\mathbf{l}_{YA}\}$ are the Leonard quantities, $\{\mathbf{C},\mathbf{c}_h,\mathbf{c}_{YA}\}$ are the cross quantities and $\{\mathbf{R},\mathbf{r}_h,\mathbf{r}_{YA}\}$ are the Reynolds quantities; see Ref. 1.

The Leonard quantities can be directly calculated, while the cross quantities and Reynolds quantities must be modeled. Following Ref. 8, we have adopted a scale-similarity model for the cross quantities and calculated, with the aid of Taylor series expansions, the sum of Leonard and modeled cross quantities according to

$$\begin{cases} \mathbf{L} + \mathbf{C} \equiv \bar{\rho}(\widetilde{\tilde{\dot{\mathbf{x}}} \otimes \tilde{\dot{\mathbf{x}}}} - \tilde{\tilde{\dot{\mathbf{x}}}} \otimes \tilde{\tilde{\dot{\mathbf{x}}}}) \approx \bar{\rho}k^2\tilde{\mathbf{L}}\tilde{\mathbf{L}}^T \\ \mathbf{l}_h + \mathbf{c}_h \equiv \bar{\rho}(\widetilde{\tilde{\dot{\mathbf{x}}}\tilde{h}} - \tilde{\tilde{\dot{\mathbf{x}}}}\tilde{\tilde{\mathbf{h}}}) \approx \bar{\rho}k^2\tilde{\mathbf{L}}\,\mathrm{grad}\,\tilde{h} \\ \mathbf{l}_{YA} + \mathbf{c}_{YA} \equiv \bar{\rho}(\widetilde{\tilde{\dot{\mathbf{x}}}\tilde{Y}_A} - \tilde{\tilde{\dot{\mathbf{x}}}}\tilde{\tilde{Y}}_A) \approx \bar{\rho}k^2\tilde{\mathbf{L}}\,\mathrm{grad}\,\tilde{Y}_A \end{cases} \qquad (5)$$

where $k^2 = \int_D G(\mathbf{x} - \mathbf{z}, \Delta)(\mathbf{x} - \mathbf{z})^2 d^3\mathbf{z}$ and $\tilde{\mathbf{L}} = \mathrm{grad}\,\tilde{\dot{\mathbf{x}}}$. Finally, the Reynolds quantities are modeled by

$$\begin{cases} \mathbf{R} \approx \frac{2}{3}c_I\bar{\rho}\Delta^2\|\tilde{\mathbf{D}}\|\mathbf{I} - 2c_D\bar{\rho}\Delta^2\|\tilde{\mathbf{D}}\|\tilde{\mathbf{D}}_D \\ \mathbf{r}_h \approx -2c_H\bar{\rho}\Delta^2\|\tilde{\mathbf{D}}\|\mathrm{grad}\,\tilde{h} \\ \mathbf{r}_{YA} \approx -2c_Y\bar{\rho}\Delta^2\|\tilde{\mathbf{D}}\|\mathrm{grad}\,\tilde{\mathbf{Y}}_A \end{cases} \qquad (6)$$

where $\tilde{\mathbf{D}}_D$ is the deviator of the rate of strain tensor $\tilde{\mathbf{D}}$, $\|\tilde{\mathbf{D}}\|$ is the Frobenius norm of $\tilde{\mathbf{D}}$, while c_I, c_D, $c_H = c_D/Pr_T$, and $c_Y = c_D/Sc_T$ are dimensionless model coefficients; see also Ref. 9.

What remains to be specified is the filter function $G = G(\mathbf{x} - \mathbf{z}, \Delta)$ and a relation between the filter width Δ and the local geometry on the grid. On a nonuniform grid, it is not obvious how to determine the resolved length scale. Several measures have been proposed [3,10]; here we have followed Ref. 3; further, a Gaussian filter function is adopted.

Chemical Reaction Modeling

Chemistry makes itself felt in reactive flows through the mass supply terms $\hat{m}_A$ appearing in the mass balance equations (4_1). To obtain expressions for $\hat{m}_A$, consider a reaction mechanism involving N constituents and M reaction steps of the form

$$\sum_A \upsilon^R_{Aj}\,\Xi_A \underset{k_{jb}}{\overset{k_{jf}}{\leftrightarrow}} \sum_A \upsilon^P_{Aj}\,\Xi_A,$$

$$A \in [1 \ldots N], \qquad j \in [1 \ldots M] \qquad (7)$$

where υ^R_{Aj} and υ^P_{Aj} are the stoichiometric coefficients for reactants and products, respectively, Ξ_A denotes the constituents, and k_{jf} and k_{jb} are the forward and backward rate constants expressed in Arrhenius

form. For constituent A, the contributions of all reactions may be expressed as follows:

$$\begin{cases} \hat{m}_A = M_A \sum_{j=1}^{M} (\upsilon_{Aj}^P - \upsilon_{Aj}^R) w_j \\ w_j = k_{jf} \Pi_{A=1}^N Y_A^{\upsilon_{Aj}^P} - k_{jf} \Pi_{A=1}^N Y_A^{\upsilon_{Aj}^R} \end{cases} \quad (8)$$

where M_A is the molar mass of constituent A and w_j is the reaction rate of reaction j composed of the forward and the backward reaction rates, respectively.

This paper focus on premixed hydrocarbon combustion. The oxidation of a hydrocarbon fuel C_nH_m consists primarily of the sequential fragmentation of the initial fuel molecule into smaller intermediate constituents that are ultimately converted into final products dominated by H_2O and CO_2. We have adopted the following sets of global reaction mechanisms founded on the sequential burning structure of hydrocarbons:

$$C_nH_m + (n + \tfrac{m}{4})O_2 \rightarrow nCO_2 + \tfrac{m}{2} H_2O \quad (9_1)$$

$$\begin{cases} C_nH_m + (\tfrac{n}{2} + \tfrac{m}{4})O_2 \rightarrow nCO + \tfrac{m}{2} H_2O \\ CO + \tfrac{1}{2} O_2 \leftrightarrow CO_2 \end{cases} \quad (9_2)$$

$$\begin{cases} C_nH_m + \tfrac{n}{2} O_2 \rightarrow nCO + \tfrac{m}{2} H_2 \\ CO + \tfrac{1}{2} O_2 \leftrightarrow CO_2 \\ H_2 + \tfrac{1}{2} O_2 \leftrightarrow H_2O. \end{cases} \quad (9_3)$$

Since the reduced mechanisms (9) approximate the effects of many elementary reactions, the reaction rates must represent an appropriate average of the individual kinetic reaction rates involved. We have used kinetic reaction rate expressions from Westbrook and Dryer [11].

In the LES model, the mass supply terms will be filtered by Eq. (3). The calculation of the filtered mass supply terms results in complicated expressions accounting for the alteration of the mass supply terms as given by the product of large and SGS components of rate constants, temperature, and mass fractions. Hence, other avenues, such as phenomenological modeling, should be considered.

Phenomenological models that aim at describing the SGS mixing and chemical reactions together with algorithms responsible for coupling between the SGS activity and the coarsely resolved macroscopic fluid dynamic fields must include a wide range of phenomena such as (1) explicit feedback mechanisms for energy transfer between macroscopic fluid dynamics and SGS mixing, (2) smooth coupling of macroscopic and SGSs at the cell cutoff wave number, and (3) onset of chemical reactions. Based on the energy cascade theory [12], one can assume that the local reaction rate can be influenced by the time scales of the turbulence. One finds eddies with characteristic time scales from the time scale for turbulent mixing to the small Kolmogorov scales. Thus, we have modeled the filtered mass supply terms as the minimum of one kinetically controlled and one mixing-controlled component:

$$\begin{cases} \tilde{\hat{m}}_A = M_A \sum_A (\upsilon_{Aj}^P - \upsilon_{Aj}^R) \min[w_j^{\text{mix}}, w_j^{\text{kin}}] \\ w_j^{\text{mix}} = (\bar{\rho}/\tau_{\text{mix}})\{\min_{A\in(P)}[Y_A/(\upsilon_{Aj} M_A)] - \min_{A\in(R)}[\tilde{Y}_A/(\upsilon_{Aj} M_A)]\}. \end{cases} \quad (10)$$

The kinetically controlled reaction rates w^{kin} of Arrhenius type use the large-scale components. The mixing-controlled mass rate of production, w^{mix}, is assumed inversely proportional to a mixing time, τ_{mix}, determined by the SGS kinetic energy and the SGS dissipation according to

$$\tau_{\text{mix}} \propto q_{\text{SGS}}/\varepsilon_{\text{SGS}} \propto \lambda_{\text{SGS}}/\sqrt{2q_{\text{SGS}}} = c_D \Delta/\sqrt{2q_{\text{SGS}}} \quad (11)$$

where q_{SGS} is the SGS kinetic energy and ε_{SGS} is its dissipation rate. For the calculations presented here, the proportionality constant was chosen to 1.

Numerical Simulation Methods

The governing equations (4) are discretized on a staggered mesh by a finite-volume technique based on the SIMPLER method [13]. For convective terms, the use of central differencing leads to unphysical oscillatory behaviour at low Re numbers and to divergence of the solution as the Re number is increased. We have instead made use of a second-order accurate upwind scheme [14] combined with a flux-corrected transport algorithm [15] giving third-order accuracy. For the diffusive terms, traditional central difference schemes of third-order accuracy have been used. The time advance was made with a second-order accurate implicit scheme with typical time steps of 25–50 μs. For the spatial discretization, two meshes of 30,000 and 90,000 cells, aiming at keeping the grid spacing between 2.0 and 0.1 mm (finer mesh in shear layers and at walls), have been used. For the simulations, workstations and a Cray X-MP/416 have been used; typical run times are about 75 cpu h for the three-step reaction mechanism on the Cray.

Physical and Numerical Experiments

In order to study the predictive capabilities of the LES model, numerical experiments on a test rig [2]

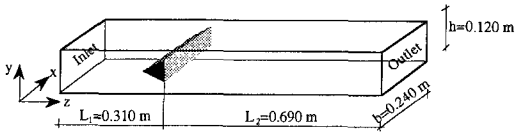

FIG. 1. Validation rig. Outline of the computational domain, coordinate system, and overall dimensions.

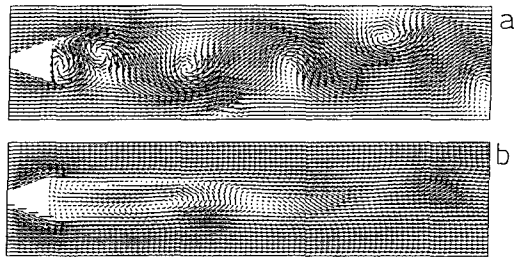

FIG. 2. Snapshots of velocity vectors: (a) nonreacting case, (b) reacting case.

have been carried out. The rig consists of a rectilinear channel, with rectangular cross section, divided into an inlet section containing fuel and air inlets as well as a honeycomb screen, and a combustor section containing a triangular-shaped bluff body (see Fig. 1). The fluid is air, which is assumed to be composed of 79% N_2 and 21% O_2; the pressure is atmospheric. In the nonreacting case, the inlet air was at 298 K, while in the reacting case, it was at 600 K premixed with propane, giving an equivalence ratio of $\phi = 0.61$. The Re number, based on the flame holder height, the inlet temperature, and the inlet velocity, was Re = 45,000 in the nonreacting case and Re = 27,700 in the reacting case. In the simulations, no velocity fluctuations were prescribed; the flow was allowed to evolve naturally. At outflow boundary, zero gradient conditions were used.

As the test rig was a premixed turbulent device, the coherent anti-Stokes Raman spectroscopy (CARS) temperature measurements were done with 2-λ CARS [16]. This method gave a signal strength 34 times higher than a conventional broadband CARS. As the uncertainty in the nonresonant signal was considered a minor problem compared with the uncertainty coming from nonuniform temperature in the probe volume, the higher signal strength was used to decrease the probe volume length. The measurements were done with a measured probe volume having 99% of the signal from a length of 1 mm and a diameter of 0.1 mm. The probe volume was oriented in the x direction. Using the method on a constant-temperature source with known temperature gives in the interval 600–1800 K an uncertainty of 20–60 K. We have estimated an uncertainty due to the nonresonant signal to be 20 K. We get a maximum uncertainty due to nonuniform temperature in the probe volume to be 100 K, when mixing 20% of 600 K with 80% of 1900 K. Mixing with other ratios gives a smaller error. The last uncertainty always underestimates the temperature, but the others can be positive or negative. In the experimental pdfs, the precision of the method has been deconvoluted.

Comparison of Physical and Numerical Experiments

To illustrate the difference between nonreacting and reacting flow situations, instantaneous velocity fields obtained from the simulations are shown in Fig. 2. Unsteady behaviour is due to vortex shedding, with vorticities alternatively shedding from the upper and lower edges of the bluff body, forming a von-Kármán vortex street behind the bluff body. In the nonreacting case, the shedding frequency is 104 Hz (measured 105 Hz), and in the reacting case, frequencies from 20 to 1100 Hz are found (experiments indicate no dominating frequency).

An important effect of heat release, due to chemical reactions, is that the strength of the vortex shedding is much weaker in the reacting case compared with the nonreacting case. As seen in Fig. 3, the vorticity field is more diffuse in the reacting case, and the large-scale vortices are broken up directly after they have been formed. This seems to be a result of the thermal expansion in the vortex cores, as discussed by McMurtry et al. [17]. The heat release has also caused the vorticity field to take on a less structured appearance. Because the simulation is limited to two spatial dimensions, some potentially important physics, e.g., vortex stretching, have been lost. Another effect of heat release in reacting flows will be

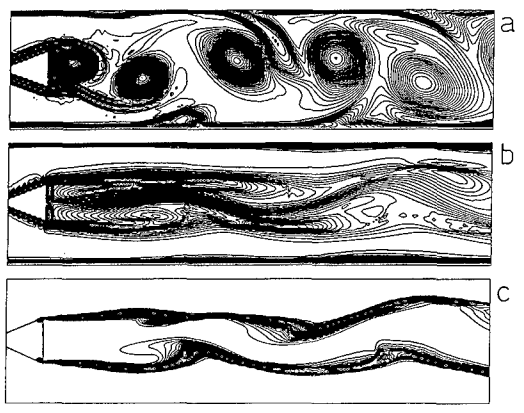

FIG. 3. Snapshot of vorticity and heat release: (a) vorticity in the nonreacting flow situation, (b) vorticity in the reacting flow situation, and (c) heat release in the reacting flow situation.

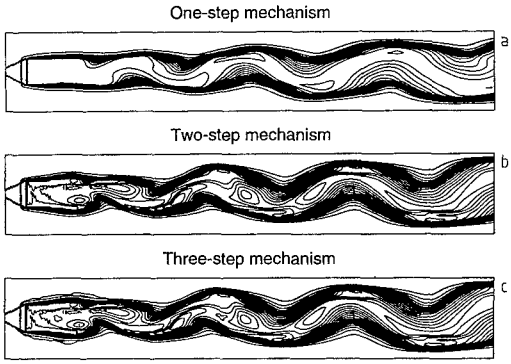

FIG. 4. Instantaneous temperature contours for different reaction mechanisms. Isochors are drawn for each 100 K. (a) One-step chemistry, (b) two-step chemistry, and (c) three-step chemistry.

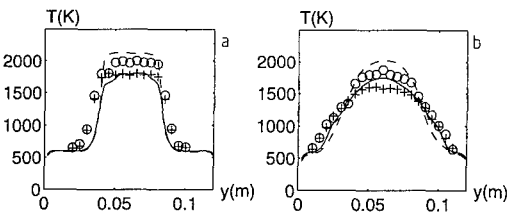

FIG. 5. Temperature profiles in two cross sections downstream of the flameholder: (a) $z = 0.348$ m, (b) $z = 0.686$ m. Crosses (+) represent CARS measurements [2], while circles (○) represent gas analysis based on one-step chemistry [2]. Dashed lines (---) represent simulations with the one-step mechanism; solid lines (——) represent simulations with the three-step mechanism.

to increase the viscosity, thus lowering the Re number and having a stabilizing effect on the flow.

To illustrate the impact of multistep mechanisms, Fig. 4 shows instantaneous snapshots of the temperature field for the one-, two-, and three-step reaction mechanisms. Comparison reveals that the temperature is overpredicted by the one-step mechanism while it is more realistically predicted in the two- and three-step mechanisms, which yield almost identical temperatures. From Fig. 4, we observe that the dynamics of the flame front is strongly affected by the reaction mechanism utilized; this can also be observed from inspecting the temperature profiles of Fig. 5.

Figure 5 shows time-averaged temperature profiles at two different locations downstream of the flameholder. Comparison is made both with CARS measured temperature profiles [2] and temperature profiles obtained from gas analysis based on one-step chemistry [2]. The following features may be observed: (1) Predicted flame propagation compares

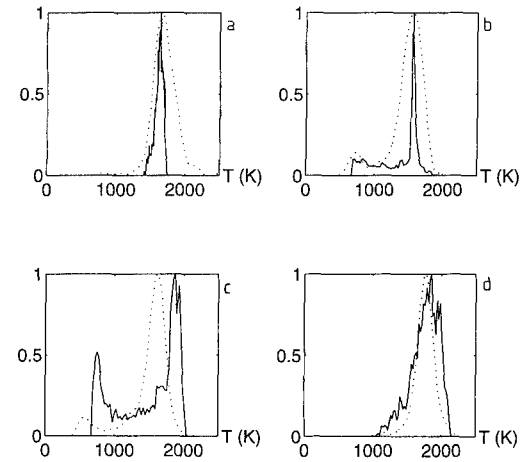

FIG. 6. Temperature probability density functions at the four points (a) (0.080, 0.348), (b) (0.080, 0.460), (c) (0.080, 0.686), and (d) (0.060, 0.460). Measured pdfs are indicated with dotted lines (····), while simulated pdfs (three-step chemistry) are indicated with straight lines (——). The pdfs are normalized with respect to their maximum value.

well in general with measurements; and (2) the one-step mechanism predicts overly high mean temperatures (see also Ref. 16). The overall impression is that the LES method is in good agreement with measurements and that the agreement increases when more accurate chemical reaction mechanisms are adopted.

Figure 6 shows a comparison between predicted (LES) and measured (CARS) temperature probability density functions (pdfs) in some points behind the bluff body. The predicted pdfs were obtained from a time interval of 0.1 s (5000 samplings), while the measured pdfs were obtained by 1000 samplings, at 5 ns, spread out over an interval of 3 min. It is observed that the movement of the flame front is well captured in the LES model and thus gives rise to pdfs that qualitatively are similar to the measured ones. The aberration in Fig. 6c can be explained by the fact that the measurement was probably performed at a lower equivalence ratio, $\phi \approx 0.56$, and that low-frequency noise was observed during this run. In general, we note that the simulated pdfs are narrower than the measured pdfs, mainly because of limited simulation time.

Concluding Remarks

The results indicate that the LES technique works well for unsteady reacting flows. The method mimics most of the significant flow features, including typical unsteady flow structures. From Figs. 5 and 6, it can

be observed that the movement of the flame front is captured by the simulations and thus give rise to temperature pdfs that qualitatively are similar to the measured ones. Although the present simulations of reacting vortex-shedding flows do not provide a complete picture, certain trends can still be discerned. Fine spatial grids, preferably with high grid density in the shear layers, must be used to resolve this particular flow structure since the generation of the instabilities driving the flow mainly occurs in the thin shear layers behind the bluff body. It is believed that two-dimensional LES simulations do not have the capability to accurately mimic the actual physical processes in the flow. Three-dimensional LES, carried out for nonreacting flows, give superior correlations between simulations and experiments, indicating that such flows should be treated as fully three dimensional. Further, the phenomenological models adopted for the filtered mass supply terms seem too simple; current work is aimed at investigating the treatment of these terms.

Acknowledgments

The authors would like to thank E. Lundgren and S.-I. Möller at LTH and Volvo Flygmotor AB for valuable discussions, the NSC in Linköping, Sweden for providing the computational resources, CHAM for providing the code Phoenics in which the LES model and the numerics are implemented, and NUTEK and the Technical Faculty at Lund University for financial support.

REFERENCES

1. Fureby, C., Lundgren, E., and Möller, S. I., "Large Eddy Simulations of Chemcally Reactive Flows," 5th International Conference on Numerical Combustion, Garmisch-Partenkirchen, Germany, 1993.
2. Sjunneson, A., Olovsson, S., and Sjöblom, B., *Validation Rig—A Tool for Flame Studies,* VOLVO Flygmotor AB, S-461 81, Trollhättan, Sweden, 1991.
3. Deardroff, J. W., *J. Fluid Mech.* 41:453 (1970).
4. Zang, T. A., Dahlburg, R. B., and Dahlburg, J. P., *Phys. Fluids A* 4:127 (1992).
5. Menon, S., and Jou, W.-H., *Comb. Sci. Technol.* 75:53 (1991).
6. Trusdell, C., *Rational Thermodynamics,* Springer-Verlag, New York, 1984.
7. Bowen, R. M., in *Continuum Physics* (C. Eringen, Ed.), Academic Press, New York, 1976, Vol. II.
8. Bardina, J., Ferziger, J. H., and Reynolds, W. C., *Improved Turbulence Models based on Large Eddy Simulation of Homogeneous, Incompressible Turbulent Flows,* Stanford, CA, Rep. No. TF-19.
9. Erlbacher, G., Hussaini, M. Y., Speziale, C. G., Zang, T. A., *Toward the Large-Eddy Simulation of Compressible Turbulent Flows,* ICASE Rep. No. 187460, 1990.
10. Moin, P., and Kim, J., *J. Fluid Mech.* 118:341 (1981).
11. Westbrook, C., and Dryer, F., *Comb. Sci. Technol.* 27:31 (1981).
12. Tennekes, H., and Lumly, J. L., *A First Course in Turbulence,* MIT Press, Cambridge, MA, 13th printing, 1990.
13. Patankar, S. V., and Spalding, D. B., *Int. J. Heat Mass Transfer* 15:1787 (1980).
14. Roe, P. L., *J. Comput. Phys.* 49:357 (1981).
15. Boris, J. P., Book, D. L., and Hain, K., *J. Comp Phys.* 18:248 (1975).
16. Löfström, C., Kröll, S., and Aldén, M., *Twenty-Fourth Symposium (International) on Combustion,* The Combustion Institute, Pittsburgh, 1992, p. 1637.
17. McMurtry, P. A., Jou, W. H., Riley, J. J., and Metcalfe, R. W., *AIAA J.* 24:962 (1986).

COMMENTS

Sebastien Candel, CNRS, Ecole Centrale, France. 1. Your LES simulations of the reacting flow show a large-scale motion of a sinusoidal antisymmetric type. This is seldom observed in this configuration. Could you explain this peculiar phenomenon?

2. I noticed that you had reaction taking place on the upstream side of the bluff body. This is at variance with experiments. The flame is stabilized on the downstream side of the body. Could you explain this behavior and evaluate its influence?

Author's Reply. 1. This sinusoidal antisymmetric large-scale motion seems to be closely related to the mass flow through the combustor and the equivalence ratio. By decreasing the mass flow by about 10% or increasing the equivalence ratio by about 20%, a broader symmetric flame is produced; in the latter case, symmetric pulsations are observed and verified by experiments [1].

2. No reactions take place upstream of the flameholder as can be seen from Fig. 4.

REFERENCE

1. Sjunneson, A., Henrikson, P., and Löfström, C., *Cars Measurements and Visualization of Reactive Flows in a Bluff Body Stabilized Flame,* VOLVO Flygmotor AB, S461 81, Trollhättan, Sweden.

●

J. Chomiak, Chalmers University of Technology, Sweden. You were able to predict well the large-scale flapping of the reacting wake behind the flameholder. I wonder however how important this phenomenon is in terms of contribution to the turbulence energy spectrum and reaction dynamics. Have you compared your LES simulations with stationary ones using the same subgrid mechanisms, and what are the results of such comparison?

Author's Reply. We have not compared the results with stationary simulations of the same type for the plain reason that the flow observed from experiments is unsteady. However, we have made comparisons with stationary RANS using the k-ε model and various combustion models (EDC, BML, etc.), and the results indicate that the LES could describe the flow much more accurately than the RANS. For example, the length of the wake was overpredicted by a factor of 2 in the RANS while accurately predicted by the LES. Of course, in this type of flow, most of the kinetic energy is contained in a narrow wave number range corresponding to the large-scale motion.

•

S. Elghobashi, University of California, Irvine, USA. What is the ratio of magnitude of the reaction rate term obtained from the SGS part and the exact (large-scale) part?

A. Ghoniem, Massachusetts Institute of Technology, USA. You model the reaction rate as min (ω_{kin}, ω_{mix}). In this flow, it seems that the burning rate should be governed by mixing. How many times in a typical time step was ω_{kkn} selected over ω_{mix}? What was the ratio of the laminar burning velocity to one incoming flame speed?

Author's Reply. The ratio of magnitude of the SGS mixing controlled reaction rate and the kinetically controlled reaction rate (based on the large or resolved scales) varies strongly over the computational domain. In some parts, the reaction rate is SGS mixing controlled, predominantly along the flame front where the length and time scales are very small, and in some parts it is kinetically controlled, typically outside of the flame front. The ratio of the reaction rate components (w_{kin}/w_{mix}) therefore varies between zero and infinity.

•

Salah Ibrahim, British Gas, England. Your reaction rate is raised on the eddy breakup (EBU) model, which is dominated by the mixing rate term, τ. Have you examined the sensitivity of your results to the filtration scale, Δ, which is a major factor in determining the mixing rate, τ from your SGS (subgrid-scale) model.

Author's Reply. The model for the filtered mass supply terms, $\hat{m}_A$, is based on a combination of the EBU formulation proposed by Magnussen and Hjertager and the large-scale kinetics obtained from the Arrhenius expressions. This means that in some parts of the computation domain the effective reaction rate will be determined by kinetics and in some parts by SGS mixing. From the simulations, we have found that the SGS mixing is rate determining at the flame front and at locally isolated small regions within the flame. The characteristic SGS mixing time, $\tau \propto q/\varepsilon$, is here independent of the filter width, but that depends on how the SGS kinetic energy q is modeled and also on whether or not the simulations are resolved down to the Taylor microscales. The simulations presented here are resolved down to the Taylor scales and thus the $k^{-5/3}$ law together with the SGS model for q can be used to determine the SGS dissipation rate ε. At this resolution, the results are only slightly sensitive to alterations in the filter width, but if the cutoff wave number is much smaller the LES will turn into a coherent scale capturing simulation and then our spectral assumptions on which the SGS model is based are no longer valid.

•

Roman Weber, International Flame Research Foundation, The Netherlands. Could you comment on sensitivity of the predicted temperatures to the constant(s) of the eddy breakup model? Which values did you use? Did you use the same value for all three chemical mechanisms you investigated?

Author's Reply. A complete sensitivity analysis for this particular SGS model has been carried out for the two-step mechanism and will be presented elsewhere in more detail [1]. The value of the constant used for the fuel conversion reaction affects the temperature field, while the ratio of the constants affects the amount of CO formed. The range of the constants can generally be divided into three intervals. At low values, the flame depends strongly on the values of the constants (small values lead to local extinction), at intermediate values only a weak dependence is found (characterized by the shape of the flame), and at high values the dependence is almost negligible. In the simulations presented here, the same value was used for the fuel conversion reactions in the different mechanisms. Another value was used for the CO-conversion reaction in the two- and three-step mechanisms, and yet another value was used for the H_2-conversion reaction in the three-step mechanism.

REFERENCE

1. Fureby, C., and Möller, S.-I., "Large Eddy Simulations of Reacting Flow," in progress.

•

Jay Boris, Naval Research Laboratory, USA. Research at NRL that has been corroborated at Minnesota, Liver-

more, Stanford, and in the weather predictions community has shown that the complex subgrid-scale models can be dropped from a nonreacting large eddy simulation without appreciably changing the result. The monotone CFD model, such as you employ, produces the necessary subgrid mixing intrinsically. Have you done the equivalent "experiment" (turn off your subgrid model), and what was the result in the reacting case?

Author's Reply. Yes, we have done the same "experiment" both in the nonreacting case and in the reacting case. We also found, in both cases, that the SGS terms affect the results only to a limited extent. It is important, however, to recognize that switching off the explicitly provided SGS model means that the truncation error instead acts as an implicit SGS model. For example, using a second-order accurate numerical method having a truncation error of $O(\Delta x_i^2)$ would then, in some sense, be comparable to the Smagorinsky model, which is of $O(\Delta^2)$. Relying on the truncation error to produce the necessary SGS mixing can be dangerous since the amplitude cannot be efficiently controlled. It is also doubtful whether the truncation error can represent backscatter.

•

T. Poinsot, IMF Toulouse and Cerfacs, France. What is the effect of box length on the results? Which boundary conditions were used at the outlet?

Author's Reply. If by box length is meant the width of the kernel $G(x - z,\Delta)$ in the case of a box-shaped filter function, we have tested three different box lengths Δx_i, $2\Delta x_i$, and $4\Delta x_i$ is the grid spacing in direction i. The magnitude of the SGS quantities depends on the box lengths since the effective viscosity increases quadratically in box length. A larger box length then leads to somewhat smoother results. Only small differences were found but a good choice seems to be $2\Delta x_i$, which has been recommended by other investigators as well. At the outlet, Neumann conditions were used for the balance equations of mass, momentum, and energy while Dirichlet conditions were used for the Poisson equation governing the pressure.

Twenty-Fifth Symposium (International) on Combustion/The Combustion Institute, 1994/pp. 1265–1272

THE VORTICITY DYNAMICS OF AN EXOTHERMIC, SPATIALLY DEVELOPING, FORCED, REACTING SHEAR LAYER

MARIOS C. SOTERIOU AND AHMED F. GHONIEM
Department of Mechanical Engineering
Massachusetts Institute of Technology
Cambridge, MA 02139, USA

The effects of combustion exothermicity on the vorticity dynamics of a low Mach number, forced, spatially developing, high Reynolds number, reacting shear layer are investigated using the results of a two-dimensional numerical simulation. The chemical reaction is modeled by single-step, irreversible, Arrhenius kinetics with a high Damkohler number, a moderate Karlovitz number, and significant heat release. The numerical solution is obtained using the Lagrangian transport-element method. Results indicate that a fast exothermic reaction, with the concomitant density variation, modifies the shape, size, speed, and orientation of the large-scale vortical structures and their downstream interactions, leading to an overall reduction of the cross-stream growth of the mixing region. These changes are traced to the two primary mechanisms by which density variation due to heat release modifies vorticity: volumetric expansion and baroclinic generation. It is shown that the weakening of the vorticity due to volumetric expansion diminishes the cross-stream mixing zone by aligning the eddy major axis with the flow direction. Baroclinic vorticity generation, on the other hand, is responsible for the formation of a band of positive vorticity on the outer perimeter of the large eddies, whose vorticity is predominantly negative, which inhibits entrainment and alters the eddy interaction mechanism from pairing of adjacent eddies to tearing of smaller eddies by their larger neighbors. Both mechanisms contribute to the acceleration of the eddies in the streamwise direction.

Introduction

Post-transitional, exothermic, reacting shear layers are encountered in many combustion systems. The flow, which arises due to the intrinsic instability of the shear region between two reacting streams originally moving at different velocities, is endowed with mechanisms that enhance mixing and combustion rates. Experimental studies [1,2] indicate that the essentially two-dimensional (2D) vortical structures, or eddies, which characterize the early stages of the nonreacting flow, persist in their reacting counterpart, despite the significant effects of combustion exothermicity. Moreover, most of the products are found within these structures, exemplifying their importance to the combustion process and motivating further studies into their properties. The latter are essentially controlled by vorticity dynamics.

The effects of combustion exothermicity on a post-transitional shear layer have been the subject of several studies. Experimental investigations [1,3,4] indicate that heat release reduces the shear-layer growth and diminishes the rates of mixing and combustion. Numerical studies, mostly restricted to the idealized temporally evolving flow, have been carried out for both nonpremixed [5,6] and premixed [7] layers and have, to some extent, been able to reproduce this behavior. However, due to the idealized nature of the temporal model, conclusions drawn from these studies must be treated with caution; e.g., it is well known that asymmetric entrainment cannot be reproduced by this model [8–12]. Moreover, the nonpremixed calculations [5,6] were limited to a temperature-independent (zero activation energy) reaction rate, and a low Damkohler number.

On the other hand, numerical studies of spatially evolving layers have been restricted to cases where the effects of combustion on the flowfield are negligibly small [13,14]. An exception is presented in Ref. 15, where a large-scale simulation of a compressible shear layer with variable transport properties and temperature-dependent kinetics was performed. However, combustion heat release was kept low and the effect of the activation temperature was diminished by raising the background temperature.

In this paper, the vorticity dynamics of a forced, spatially developing, exothermic shear layer are investigated, while allowing for temperature-dependent Arrhenius kinetics and significant exothermicity. Results are obtained using direct 2D transport-element simulations. The numerical scheme makes it possible to use a higher activation energy and Damkohler number than previously attempted. The effects of combustion exothermicity on the vorticity dynamics are analyzed in terms of the contributions of the two major mechanisms of vorticity modification,

i.e., volumetric expansion and baroclinic vorticity generation.

The Governing Equations

A two-dimensional reacting shear flow in which gravitational effects are negligible and compressibility effects are limited to the low Mach number regime [5] is considered. We assume that all species behave as perfect gases with equal molecular masses and equal and constant mass diffusivities and specific heats. The momentum and thermal diffusivities are also constant, and the Lewis number is equal to unity. Combustion occurs according to a single-step, irreversible, mole-preserving Arrhenius reaction, i.e., $\phi^\circ\eta_1 + \eta_2 \rightarrow (1 + \phi^\circ)\eta_p$, where η_i denotes species i ($i = 1$ and 2 for the reacting species and $i = p$ for the product) and ϕ is the molar stoichiometric ratio.

We use the Helmholtz decomposition to recast the equations into their vorticity-streamfunction-velocity potential form, and Shvab–Zeldovich (SZ) variables to simplify the scalar-transport equations. The equations of the SZ variables are then transformed into SZ-gradient equations. Since combustion occurs at a finite rate, and thus the SZ variable solutions alone cannot yield the complete reacting field, one reacting variable is solved for in primitive form. The resulting equations, in nondimensional form, are

$$\nabla^2\phi_e = -\frac{1}{\rho}\frac{d\rho}{dt}, \qquad \nabla^2\psi = -\omega,$$

$$\text{and } \nabla^2\phi_p = 0 \qquad \text{(1a,b,c)}$$

$$\frac{d\omega}{dt}\hat{\mathbf{k}} = -(\nabla\cdot\mathbf{u})\omega\mathbf{k} + \frac{\nabla\rho x\nabla p}{\rho^2} + \frac{1}{\mathrm{Re}}\nabla^2\omega\hat{\mathbf{k}} \qquad (2)$$

$$\frac{d\mathbf{g}}{dt} = -\mathbf{g}\cdot\nabla\mathbf{u} - \mathbf{g}x(\omega\hat{\mathbf{k}}) + \frac{1}{\mathrm{Pe}}\nabla^2\mathbf{g} \qquad (3)$$

$$\frac{dY_p}{dt} = \frac{1}{\mathrm{Pe}}\nabla^2 Y_p + (1 + \phi)\frac{\dot{w}}{\rho}. \qquad (4)$$

The velocity vector, $\mathbf{u} = (u,v)$, is reconstructed as $\mathbf{u} = \nabla\phi_e + \nabla\phi_p + \nabla x(\psi\hat{\mathbf{k}})$. To non-dimensionalize, we use the initial thickness of the vorticity layer, d, the velocity difference between the two streams, ΔU, and the initial global temperature and density, T_0 and ρ_0, respectively. $\mathbf{x} = (x,y)$ is a right-handed Cartesian coordinate system, t is time, $\nabla = (\partial/\partial x, \partial/\partial y)$ and $d/dt = \partial/\partial t + \mathbf{u}\cdot\nabla$. ϕ_e is the expansion velocity potential, ϕ_p is the velocity potential related to the boundary conditions, ψ is the streamfunction, $\omega(\omega\hat{\mathbf{k}} = \nabla x\mathbf{u})$ is the vorticity; $\hat{\mathbf{k}}$ is the unit vector normal to the plane of motion, p is the pressure and ρ is the density, which is related to the temperature, T, via $\rho T = 1$. The Reynolds and Peclet numbers are $\mathrm{Re} = \Delta Ud/\nu$ and $\mathrm{Pe} = \Delta Ud/a$, respectively, where ν is the kinematic viscosity and a is the thermal diffusivity. $\mathbf{g} = \nabla\beta$ is the gradient of the SZ-variable $\beta = \lambda$ or γ, where $\lambda = Y_1 - \phi Y_2$ and $\gamma = T - (Q_0\phi/(1 + \phi))Y_p$. The term Y_i is the mass fraction of species i with $Y_1 + Y_2 + Y_p = 1$; ϕ is the mass stoichiometric ratio; $\phi = \phi^\circ \mathrm{M}_1/\mathrm{M}_2$, M_i being the molar mass of species i; $Q_0 = \Delta h_f/c_pT_0$ is the normalized enthalpy of reaction, with c_p being the mixture specific heat; $\dot{w} = A_f\rho^2Y_1Y_2\exp(-T_a/T)$ is the reaction rate, where $A_f = A_f\rho_0 d/\Delta U$ is the frequency factor and $T_a = E_a/RT_0$ is the activation temperature, with E_a and R being the activation energy and the universal gas constant, respectively.

Numerical Solution

We use the transport-element method to perform the numerical simulation (for details, see Ref. 12). In this Lagrangian, grid-free scheme, the vorticity, volumetric expansion, SZ gradients, and product mass fraction are discretized among a large number of elements of finite area and overlapping Gaussian cores. The vortical and expansion contributions to the velocity are computed using convolutions over the fields of vortex and expansion elements, respectively. The SZ variables are obtained from the corresponding discrete gradient fields via a similar convolution. The contribution of the boundary conditions is obtained using conformal mapping and the method of images.

The evolution of the flow and scalar fields is obtained by integrating the governing equations, written for each element, in two fractional steps. In the first step, which includes all processes except diffusion, the elements are advected with the local velocity vector and the relevant source terms are integrated; e.g., the circulation of an element is modified by the baroclinic term according to the cross product of the material acceleration and the density gradient. The SZ-gradient equation is substantially simplified using kinematical relations between the gradient and the stretch of the associated material line. The integration of the product-mass fraction equation, carefully performed to eliminate conventional sources of numerical errors, modifies the local concentrations according to the reaction source term. In the second fractional step, diffusion effects are incorporated via a novel implementation of the core expansion scheme in which after each core expansion, the strength of the elements is recomputed using the original core size [12].

The severe distortion of the flow map, which could lead to insufficient core overlap and deterioration of the numerical accuracy, is accommodated by continuously inserting/removing elements in regions of high tensile/compressive strains, as assessed by the distance between neighboring elements. This inser-

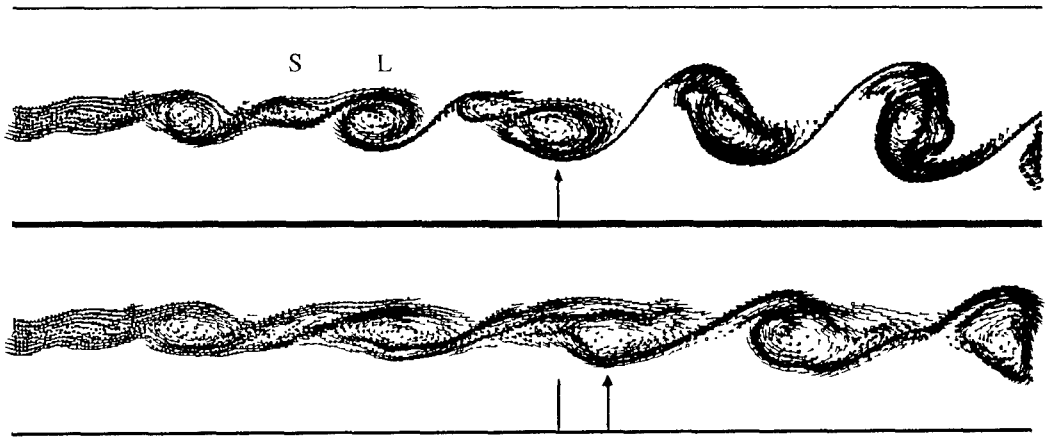

FIG. 1. The flow field in the uniform-density (top) and variable-density (bottom) cases at $t = 64$, depicted using the vortex elements, and their velocity vectors measured with respect to the mean flow. The top and bottom number of elements are 5389 and 4034, respectively. L and S denote examples the fundamental eddies that form during the first and second halves of the subharmonic forcing function. Arrows indicate the location of eddies formed at the same time.

tion/removal of elements is carried out while satisfying local conservation laws.

Geometry and Boundary Conditions

The shear layer evolves downstream of a thin plate in a two-dimensional channel of height H and length $X_{max} = 5H$ between two parallel streams of unequal velocities but same temperature and density (T_0, ρ_0), each stream carrying a single reactant. The top and bottom walls are modeled as rigid, slip, impermeable, and adiabatic planes. At the exit, a condition of vanishing gradient is imposed by deleting the elements as they cross the boundary. At the inlet section, (1) errorfunction profiles with equal thicknesses are assumed for u and λ, rendering the ω and $\nabla\lambda$ profiles Gaussians, with a standard deviation σ; (2) γ is taken to be unity; and (3) a finite amount of product is introduced, in the form of a Gaussian profile with a standard deviation, σ, and a peak value of 0.4 to enforce ignition. The scaling of σ, where $d = 2\sigma$, with H is such that two wavelengths of the most unstable mode of the uniform-density shear layer fit within the channel height.

The calculations are initialized by assuming that the inlet conditions persist throughout the domain. Square elements of side $h = 0.0195H$ are distributed over nine horizontal material layers lying within the support of the discretized quantities. The core radius is such that $\delta/h = 1.2$.

External forcing is implemented at the inlet by displacing the elements in the cross-stream direction. The forcing signal consists of in-phase components of the most unstable mode of the uniform-density layer and its subharmonic, both at an amplitude $Amp_f = Amp_s = 0.32d$. This forcing, which promotes roll-up and pairing in the uniform density flow [16], results in the formation of two eddies of unequal size per cycle. A large eddy, referred to in this text as the L-eddy, forms when the two components of the signal act constructively, and a small eddy, the S-eddy, forms when they act destructively (see Fig. 1).

Results and Discussion

Parameters:

The following parameters are used. The inlet velocity ratio is $r = 0.5$, Re $= 500$, $T_a = 10$, $A_f = 100$, $\phi = 1$, and $Q_0 = 6$, corresponding to a Damkohler number, Da $= \tau_{dif}/\tau_{che} = 1026$, where $\tau_{dif} = d^2/a$ is the diffusion timescale and $\tau_{che} = (T_f/A_f)\exp(T_a/T_f)$ is the chemical reaction timescale, and a Karlovitz number, Ka $= \tau_{che}/\tau_{flw} = 0.49$, where $\tau_{flw} = d/\Delta U$ is the flow timescale. The vorticity dynamics of the reacting layer are investigated by (1) comparing the results of constant-density (CD) and variable-density (VD) simulations, (2) analyzing the distributions of the vorticity modification terms, and (3) comparing results of simulations in which one of the vorticity modification mechanisms is removed. Under the assumptions of our model, the effects of the exothermic energy are confined to density variation.

The Flow Field:

Figure 1 displays a comparison between the CD and the VD layers, both depicted in terms of the vortex elements and their velocity vectors measured with respect to the inlet mean velocity. In agreement

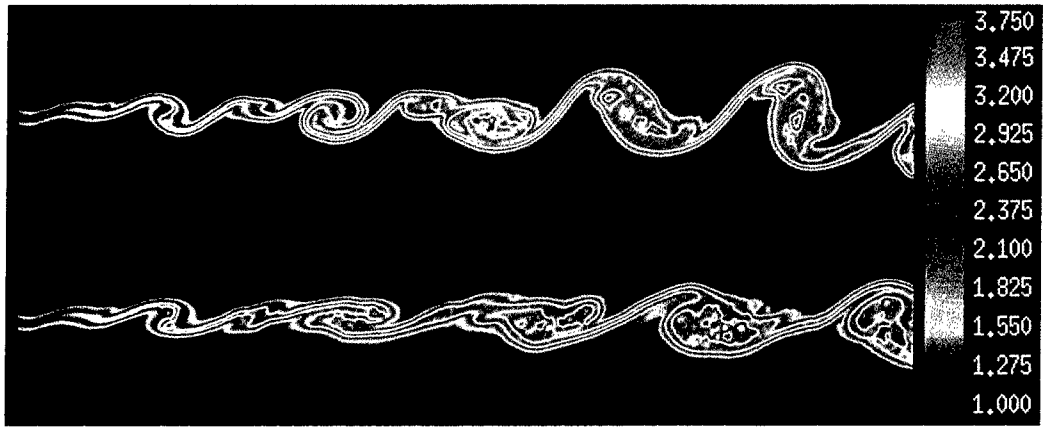

FIG. 2. The temperature fields of the uniform-density (top) and variable-density (bottom) cases at $t = 64$. The blue to red color bar describes the temperature scale: $1 \leq T \leq 3.75$.

with experimental observations, the flow in both cases is dominated by large scale vortical structures that form due to the destabilization of the initial vorticity layer via the amplification of the Kelvin–Helmholtz instability, the rollup of the fundamental eddies and their interactions due to the subharmonic instability. The figure shows that density variation modifies the evolution and interactions of the vortical structures leading to an overall reduction of the cross-stream growth.

In the VD case, the vortical structures accelerate in the streamwise direction. At the initial stages, the fundamental eddies are larger, primarily in the mean flow direction; i.e., they are less rounded. At the later stages, the pairing-merging of fundamental eddies into larger, coherent, and rounded structures observed in the CD case is impaired and replaced by tearing of the S-eddy between its two neighboring L-eddies. This results in subharmonic structures that are less rounded and, in contrast to the CD case, tend to keep their major axis aligned with the streamwise direction. As a result, the layer cross-stream growth is significantly inhibited.

The Temperature Field:

Since the effect of combustion on the flow is felt solely through the density field, one should be able to explain the various phenomena described above by reviewing the density, or temperature, field and the mechanisms by which this field influences the flow. Figure 2 presents instantaneous, 2D maps of the temperature, which in the case of the VD flow is equivalent to inverse density, while in the CD case it is artificially decoupled from the flow, for the two cases of Fig. 1. It is clear that the region of temperature variation is the same as the region where vortical structures exist. This is because these structures control the mixing of the two reactants and, hence, are where combustion takes place. The plot also provides a clear indication that significant phenomena occur at scales smaller than those of the vortical structures. Density variation is more closely related to the rollup of the material layer initially positioned between the two reactants, which for $\phi = 1$, coincides with the vorticity layer. The density experiences a minimum in the vicinity of this layer, confirming that this is where most burning occurs. Thus, analysis of the flow and reaction fields can best be accomplished by investigating the dynamics of the vorticity layer.

Vorticity Dynamics, Preliminaries

The combustion-related density field can influence the dynamics in several ways. Mass conservation implies that a density decrease causes volumetric expansion, which, since the flow is semiconfined, causes a streamwise acceleration. The vorticity equation indicates that in a 2D, VD field, the vorticity of a fluid element is modified by three mechanisms: Volumetric expansion, $-(\nabla \cdot \mathbf{u})\omega$; baroclinic generation, $(\nabla\rho \times \nabla p)/\rho^2$; and viscous diffusion, $(1/\mathrm{Re})\nabla^2\omega$. In an exothermic field, $\nabla \cdot \mathbf{u}$ is generally positive, and volumetric expansion reduces the element vorticity while preserving its circulation; the decrease of the vorticity is equal and opposite to the increase in area, without changes in sign.

Baroclinic vorticity generation arises from the misalignment of the pressure and density gradients and is capable of producing vorticity of both signs. Since the pressure gradient is mainly a manifestation of the fluid acceleration, vorticity is formed as neighboring elements experience differential accelerations due to their different density. Because of its directional na-

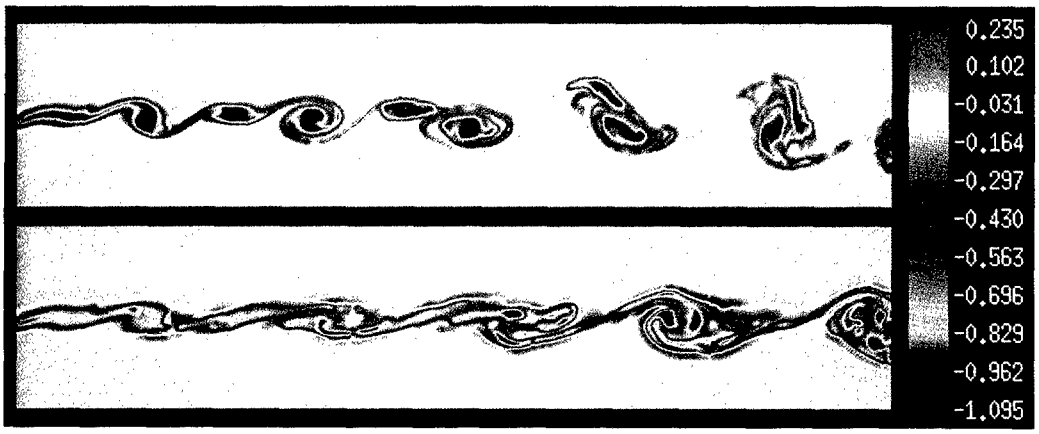

FIG. 3. The vorticity distribution in the uniform-density (top) and variable-density (bottom) cases at $t = 64$. The blue to red color bar describes the vorticity scale: $-1.095 \leq \omega \leq 0.235$.

FIG. 4. The distributions of the rates of vorticity modification by baroclinic generation (top) and volumetric expansion (bottom) at $t = 64$. The blue to red color bar describes the vorticity-rate scale: $-0.02 \leq \dot{\omega} \leq 0.02$.

ture, baroclinic vorticity generation is strongly linked to the geometry of the flow map.

Viscous diffusion acts to smooth out vorticity variations. However, when the Reynolds number is high, viscous diffusion plays a minor role.

Vorticity Distribution:

Figure 3 presents the vorticity distribution of the two cases shown in Fig. 1, with blue and red indicating positive and negative vorticity, respectively. The most striking difference between the two cases is the presence of positive vorticity, in the VD case, on the outer rims of the vortical structures whose vorticity is, primarily, of a negative sign. Most of the negative vorticity has its origin in the incoming flow. Since only the baroclinic torque is capable of producing vorticity of both signs, the positive vorticity must be a manifestation of this mechanism.

Baroclinic Vorticity Generation:

Figure 4 (top) shows the baroclinic vorticity production term at the same time step as before, with red and blue indicating positive and negative rates. The complexity of this figure can be unraveled by considering the action in the neighborhood on a single eddy during rollup. This is done in Fig. 5, where schematic diagrams of the geometric evolution of the layer are drawn, and the corresponding baroclinic term is estimated by considering the cross product of the density gradient and the fluid acceleration.

During rollup, the layer acquires a "Z" configuration. Throughout this process, fluid from the braids

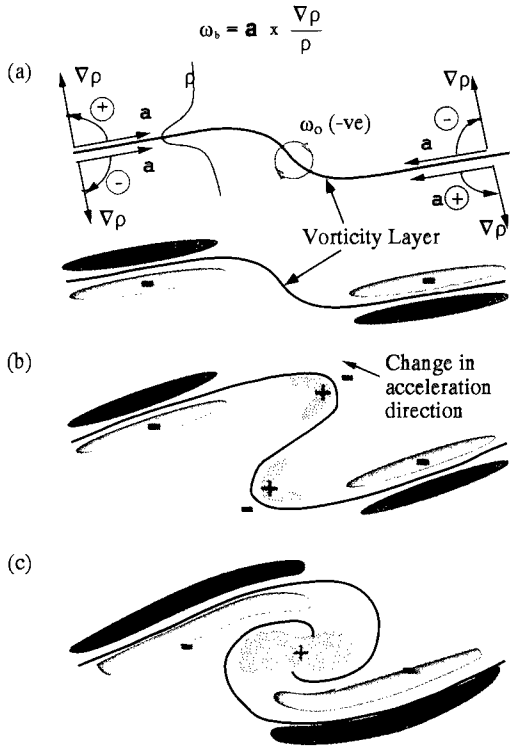

FIG. 5. Schematic illustration of the process of baroclinic vorticity generation. ω_0 is the initial vorticity, and $\dot{\omega}_b$ is the vorticity generation rate. $\nabla\rho$ is the density gradient, and **a** is the material acceleration.

is accelerated in the streamwise direction toward the evolving structure. This acceleration changes its direction as one crosses the stagnation point, defined in the frame of reference moving with the eddy, between the neighboring structures. The density field is such that the density gradient is approximately normal to the layer, changing sign across it, while the local stretch ensures that the magnitude of the gradient stays large. Thus, in the braids, the enhanced density gradient and the fluid acceleration are mutually normal, and the contribution of the baroclinic term is maximum. The arrangement of the vectors involved creates positive and negative vorticity on the upper and lower sides of the braid on the left-hand side of the eddy, respectively, while the opposite occurs on the right-hand side.

Closer to the center of the structure, which in the moving reference frame is also a stagnation point, the acceleration on both sides reverses sign, and so does the generated vorticity. The baroclinic term becomes weaker as the fluid acceleration is increasingly dominated by rotation and the density gradient zone thickens. As rollup continues, a region of negative vorticity is established inside the eddy core, surrounded by a band of strong positive vorticity on the outside, particularly on the upper-left and lower-right sides, as shown in Figs. 4 and 5. Adding an overall negative vorticity to this picture would result in the vorticity field shown in Fig. 3.

This rearrangement of the vorticity has significant implications. For example, positive vorticity around the eddies decreases the entrainment of irrotational fluid into the large structures, since it weakens the field created by the original negative vorticity. Furthermore, it may upset the eddy interaction mechanism that is responsible for pairing in the CD flow.

Divergence:

The effect of the expansion term on the vorticity field can be inferred from the vorticity plots. Figure 3b shows that the vorticity occupies more area and that the negative vorticity is weaker than in the CD case. To highlight the zone where volumetric expansion has the strongest effect on the vorticity, we plot in Fig. 4 (bottom) the distribution of the $-(\nabla \cdot \mathbf{u})\omega$ term, i.e., the rate of vorticity change due to divergence. Since divergence is essentially due to the Lagrangian change in density, this zone can also be considered as where the flame is located. In this regard, the figure indicates that most of the burning occurs within the braids, which is expected since D_a is high, while K_a is moderate. Evidently, the expansion in the braids weakens the vorticity there, and through the roll-up, leads to the formation of less vigorous eddies.

Separating the Mechanisms:

The above discussion indicates that the approach of analyzing the effect of the different mechanisms of vorticity modification using simulations that involve all the terms in the governing equation has the following limitations: (1) it is not obvious how the two mechanisms interact, and (2) it is not clear whether the changes in the evolution of individual eddies, e.g., acceleration, or the shift of the eddy interaction mechanism from pairing to tearing is a result of expansion, baroclinicity, or both. To overcome these limitations, the calculation for the VD case was repeated twice, but at each time, one of the two mechanisms of vorticity modification was eliminated in an attempt to distinguish between the phenomena attributable to each mechanism. These simulations are labeled baroclinicity-only and expansion-only to distinguish the active mechanism in each case.

Figure 6 displays the results of these calculations. The figure shows that the suppression of pairing and the onset of tearing are due to the baroclinic generation, while the alignment of the major axis of the structure with the streamwise direction is due to volumetric expansion. In the expansion-only simulation, Fig. 6 (bottom), pairing occurs in a way similar to that found in the CD flow. In this case, the vorticity

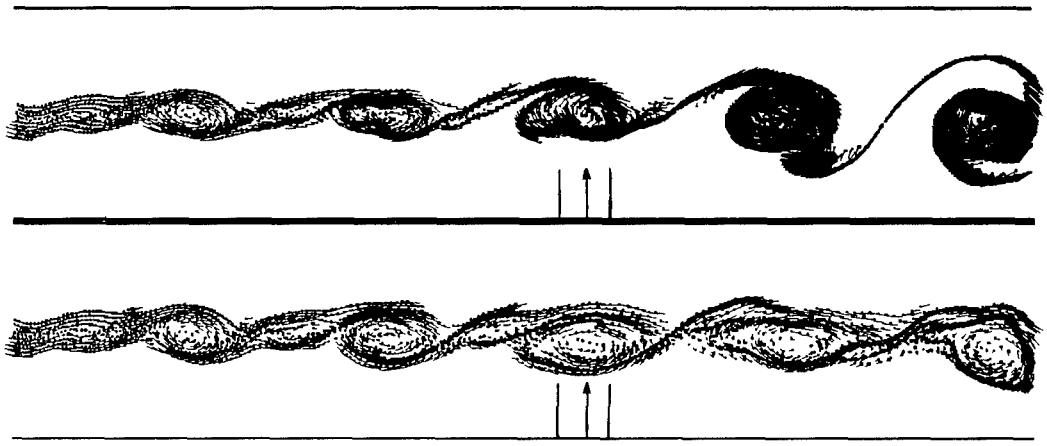

FIG. 6. The baroclinicity-only (top) and expansion-only (bottom) cases at $t = 64$ shown in terms of the vortex elements and their relative velocity. The top and bottom number of elements are 9232 and 3818, respectively. Arrows indicate the location of eddies formed at the same time. The lines on the left and right sides of the arrows correspond to the locations of the same eddies in the uniform and variable density cases, respectively, shown in Fig. 1.

layer thickens due to volumetric expansion, and rollup is slowed down due to the weakened vorticity.

In the baroclinicity-only case (Fig. 6 (top)) on the other hand, the S-eddies are torn between their neighboring L-eddies, similar to the VD case. Positive vorticity surrounding the vortical structures inhibits the spiraling of the fundamental eddies around a common center. This allows enough time for the larger L-eddies to gain fluid at the expense of the S-eddies. The above argument implies, as shown before [17], that in the absence of external forcing, baroclinic vorticity generation suppresses eddy interactions.

Comparisons between the fundamental eddies of the CD and baroclinicity-only case indicate that these eddies are smaller and more elliptical in the latter; i.e., baroclinicity is responsible for reducing entrainment, as mentioned earlier. Figure 6 also reveals that the acceleration of the vortical structures in the streamwise direction is not only due to volumetric expansion but also due to baroclinicity. This has been observed before in the study of the nonreacting VD flow [18]. This acceleration is due to the redistribution of the vorticity inside the structures and the loss of eddy symmetry, which arises from the unequal tearing of the S-eddy toward its neighboring L-eddies.

Finally, the number of elements used to discretize the evolving material layers indicates that baroclinic vorticity generation increases the eddy-induced strain, while volumetric expansion reduces it.

Conclusions

Combustion exothermicity modifies the evolution and interactions of the vortical structures in a spatially developing shear layer. It flattens the eddies and complicates their vorticity distribution, increases their speed, alters their interaction mechanism from pairing to tearing, and keeps their major axis aligned with the flow direction. Consequently, the size of the mixing region is reduced.

The alteration of the eddy shape is a consequence of the baroclinic torque, which significantly complicates the eddy vorticity field and reduces entrainment. Vorticity generation is also responsible for the modification of the eddy interaction mechanism. The alignment of the eddy major axis with the streamwise direction is a manifestation of the weakening vorticity field due to volumetric expansion. The acceleration of the eddies is a combined effect of both mechanisms: volumetric expansion because of confinement and baroclinic generation because it induces vorticity asymmetry within each individual eddy.

At the initial stages, baroclinic generation reduces the eddy size by suppressing entrainment while volumetric expansion increases it while weakening the existing vorticity. Farther downstream, where eddy interactions take place, both mechanisms act to decrease the mixing region: baroclinic generation by resisting pairing and volumetric expansion by aligning the eddy major axis with the flow direction. For forced shear layers, this latter effect is by far the more significant.

Acknowledgment

This work is supported by the Air Force Office of Scientific Research, Grant No. F49620-92-J-0445.

REFERENCES

1. Hermanson, J. C., and Dimotakis, P. E., *J. Fluid Mech.* 199:333 (1989).
2. Brown, G. L., and Roshko, A. J., *J. Fluid Mech.* 64:775 (1974).
3. Keller, J. O., Ph.D. Thesis, University of California, Berkeley, CA, 1982.
4. Mungal, M. G., and Dimotakis, P. E., *J. Fluid Mech.* 148:349 (1984).
5. McMurtry, P. A., Jou, W. H., Riley, J. J., and Metcalfe, R. W., *AIAA J.* 24:962 (1986).
6. McMurtry, P. A., Riley, J. J., and Metcalfe, R. W., *J. Fluid Mech.* 199:297 (1989).
7. Ghoniem, A. F., and Krishnan, A., *Twenty-Second Symposium (International) on Combustion*, The Combustion Institute, Pittsburgh, 1988, p. 665.
8. Grinstein, F. F, Oran, E. S., and Boris, J. P., *J. Fluid Mech.* 165:201 (1986).
9. Givi, P., and Jou, W. H., *Twenty-Second Symposium (International) on Combustion*, The Combustion Institute, Pittsburgh, 1988, p. 635.
10. Sandham, N. D., and Reynolds, W. C., *J. Fluid Mech.* 224:133 (1974).
11. Givi, P., *Prog. Energy Combust. Sci.* 15:1 (1989).
12. Soteriou, M. C., Ph.D. Thesis, Massachusetts Institute of Technology, Cambridge, MA, 1993.
13. Ghoniem, A. F., and Givi, P., *AIAA J.*, 26:690 (1988).
14. Ghoniem, A. F., and Heidarinejad, G., *Combust. Sci. Technol.* 72:79 (1990).
15. Grinstein, F. F., and Kailasanath, K., *Phys. Fluids* 4:2207 (1992).
16. Ghoniem, A. F., and Ng, K. K., *Phys. Fluids* 30:706 (1987).
17. Soteriou, M. C., and Ghoniem, A. F., AIAA Paper 94-0777.
18. Soteriou, M. C., Knio, O. M., and Ghoniem, A. F., AIAA Paper 91-0081.

COMMENTS

J. Chomiak, Chalmers University of Technology, Sweden. To evaluate correctly the baroclinic effects, you have to resolve the flow field down to the local laminar flamelet thickness ($\nabla\rho$) and curvature (∇p). Is this feasible for truly high Reynolds number flow simulations?

Author's Reply. We agree with the comment and add that one of the primary motivations behind developing our Lagrangian scheme is the need to address these issues. As mentioned in the response to an earlier question (see the answer to Elgobashi's question), for a moderate Reynolds number, our scheme resolves scales down to the Kolmogorov scale, i.e., the diffusion thickness of the flame, required to compute $\nabla\rho$, is properly captured, and the local strain field and flame surface curvature needed to obtain the pressure gradient, are well resolved. At higher Reynolds numbers, as articulated earlier, we expect the number of elements required to grow as $Re^{1.5}$.

•

S. Elghobashi, University of California, Irvine, USA. How many elements exist in an eddy of the Kolmogorov length size?

Author's Reply. The total number of computational elements in the simulation increases from less than 1000 at $t = 0$ when the shear layer is laminar up to more than 10,000 after the large eddies have "equilibrated." The increase in the number of elements is to accommodate the small scales that form as a result of the high strain rates exerted by the large eddies. Since the flow is nearly inviscid, the increase in the number of elements corresponds to an equivalent decrease in the size of each element, i.e., the smallest scale. Given that we are simulating a 2D flow, the scale of the element is $\sim 1/\sqrt{N}$, where N is the total number of elements, i.e., the smallest scale is ~0.01. If the same 3D Kolmogorov scaling is used in 2D, and given that our Reynolds number is 500, then the Kolmogorov scale is ~0.01, i.e., we use one element to resolve a Kolmogorov eddy. It should be noted however that the resolution of the schemes is higher than one element size since a core function is used to describe the variation within an element.

•

Rupert Klein, ITM, RWTH Aachen, Germany. You have emphasized that you are using a large but finite rate chemistry model. I have two questions:

1. Where in your mathematical model does the finite rate chemistry model enter?
2. Have you also used an infinite rate model and compared it to the present results?

Author's Reply. The finite rate chemistry model is used in computing the chemical source term in Eq. (4) which, as described in the paper, has an Arrhenius form. Since our Damköhler number is very high, 1026, the burning rate is governed by the mixing, or molecular diffusion rate. We have actually shown in an earlier publication (Soteriou and Ghoniem, 32nd Aerospace Sciences Meeting, January 1994, AIAA-94-9777) that an infinite rate model can be used to obtain similar results, as far as the impact of the combustion heat release on the flow, if the Shvab–Zeldovich formulation is used.

Twenty-Fifth Symposium (International) on Combustion/The Combustion Institute, 1994/pp. 1273–1281

STRAIN RATE MODELLING FOR A FLAME SURFACE DENSITY EQUATION WITH APPLICATION TO NON-PREMIXED TURBULENT COMBUSTION

F. FICHOT, B. DELHAYE, D. VEYNANTE AND S. M. CANDEL
E.M2.C Laboratory, CNRS, Ecole Centrale Paris
92295 Chatenay-Malabry, France

Flamelet models of turbulent combustion have been the subject of continuous interest because they decouple the description of the flamelet structure from that of the turbulent flow field. While these concepts are now widely used to calculate premixed and non-premixed flames, many issues remain unsettled. Formulations based on a transport equation for the flame surface density, like that used in this article, require a set of closure rules that were previously defined from physical considerations. The objective of this article is to show how these rules may be improved by making use of direct numerical simulations. A refined description of the strain rate that effectively produces flame area is proposed and included in the model. Unsteady flamelet effects are also taken into account. Experimental data on flame surface density are obtained by processing a series of instantaneous planar laser-induced fluorescence (PLIF) images of a 2D non-premixed turbulent burner. Results from the model are compared with these experimental measurements of flame surface density. Their excellent agreement shows the accuracy of the new formulation of the strain rate.

Introduction

The flamelet approach is now widely used to model turbulent combustion. One advantage of this concept is that it decouples the description of the local reactive elements from that of the turbulent flow. When this analysis is applicable to non-premixed configurations, the reaction rate may be expressed in terms of the scalar dissipation of the mixture fraction [1,2]. Alternatively, the flame surface density (FSD) Σ may be evaluated and the mean consumption rate calculated as the product of this density by the mean consumption rate per unit flame surface

$$\bar{\omega}_f = V_f \Sigma. \tag{1}$$

Kinetics, transport, and local strain rate effects are included in the determination of V_f while the FSD is suitably described with a transport equation [3,4,5]. The balance equation for the FSD, originally derived from physical arguments, takes the form

$$\frac{\partial \Sigma}{\partial t} + u_i \frac{\partial \Sigma}{\partial x_i} = \frac{\partial}{\partial x_i}\left(\nu_t \frac{\partial \Sigma}{\partial x_i}\right) + E_s \Sigma - \beta\left(\frac{V_f}{Y_f} + \frac{V_o}{Y_o}\right)\Sigma^2. \tag{2}$$

In this equation, β is a constant coefficient that adjusts the level of flame shortening. A single-step, irreversible, and fast reaction is assumed. The three terms on the right-hand side respectively correspond to turbulent diffusion of the flame surface, flame surface production under strain rate E_s, and flame surface annihilation due to reactant consumption. The strain rate may be modelled as the absolute value of the transverse gradient of the mean axial velocity in mixing layer configurations [3] or from the inverse of a turbulent time. An exact equation for the strain rate E_s may be obtained from recent studies [6,7,8,9]. The strain rate has the form $E_s = \langle A_T \rangle_S + \langle a_T \rangle_S$ where

$$\langle A_T \rangle_S = \nabla \cdot \mathbf{U} - \langle \mathbf{nn} \rangle_S : \nabla \mathbf{U} = [\delta_{ij} - \langle n_i n_j \rangle_S] \frac{\partial U_i}{\partial x_j} \tag{3}$$

$$\langle a_T \rangle_S = \langle \nabla \cdot \mathbf{u}' - \mathbf{nn} : \nabla \mathbf{u}' \rangle_S = \left\langle \delta_{ij} \frac{\partial u_i'}{\partial x_j} - n_i n_j \frac{\partial u_i'}{\partial x_j} \right\rangle_S \tag{4}$$

where δ_{ij} is the Kronecker symbol, U_i and n_i are, respectively, the x_i components of the mass average velocity and of the vector $\mathbf{n}$ normal to the flame front, pointing towards the fuel side, and $\langle\ \rangle_S$ denotes the average along the flame front surface. The terms $\langle A_T \rangle_S$ and $\langle a_T \rangle_S$ are the strain rates respectively due to the mean and turbulent flow fields. Our attention is focused on the closure of $\langle A_T \rangle_S$, the strain rate due to the mean flow, which is analyzed using a direct numerical simulation of a two-dimensional reactive

mixing layer. In the second section, a model for the total strain rate is derived. Unsteady effects of the strain rate on the mass consumption rate per unit surface are then taken into account with an additional transport equation as proposed by Haworth et al. [10] (third section). Experimental measurements of the flame surface density are obtained from planar laser-induced fluorescence (PLIF) images of a non-premixed burner (fourth section). Expressions for the strain rate derived from direct simulations are included in a turbulent model. The data are then used to directly evaluate numerical calculations based on this model of the same configuration (fifth section).

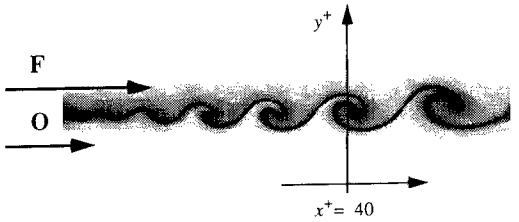

FIG. 1. Shear layer configuration. Instantaneous distribution of product mass fraction calculated by direct numerical simulation.

Modelling of the Strain Rate

We will successively consider the two components that form E_S. The strain rate due to mean flow $\langle A_T \rangle_S$ features a surface average of the cross products $\langle n_i n_j \rangle_S$ that act as orientation factors. Following Cant et al. [8], the normal vector may be split between mean and fluctuating parts: $n_i = M_i + m_i$ with $\langle n_i \rangle_S = M_i$ and $\langle m_i \rangle_S = 0$, leading to

$$\langle n_i n_j \rangle_S = M_i M_j + \langle m_i m_j \rangle_S. \tag{5}$$

Expression (3) may be rewritten

$$\langle A_T \rangle_S = (\delta_{ij} - M_i M_j) \frac{\partial U_i}{\partial x_j} - \langle m_i m_j \rangle_S \frac{\partial U_i}{\partial x_j} \tag{6}$$

To use this, it is necessary to estimate $M_i M_j$ and $\langle m_i m_j \rangle_S$. First, the mean normal vector is parallel to ∇Z. Next, the fluctuations are assumed to be isotropic [8]; thus, the following expression applies:

$$\langle n_i n_j \rangle_S = \frac{\delta_{ij}}{3} (1 - M_i M_i). \tag{7}$$

One may also link $\langle n_i n_j \rangle_S$ to the velocity fluctuations according to Mantel and Borghi [11]

$$\langle n_i n_j \rangle_S = \frac{1}{2} \frac{\overline{u_i' u_j'}}{k}. \tag{8}$$

These two closure schemes essentially assume that the turbulent field is homogeneous and isotropic, which is inadequate for a shear layer configuration. In the following subsection, the values of the orientation factors, and the corresponding strain rate due to the mean flow, are deduced from direct numerical simulations.

Direct Numerical Simulation

Consider a plane mixing layer established between two reactive fluids. The flow is assumed to be incompressible with a constant viscosity. The fuel and oxidizer, initially separated by a splitter plate, react after contact (Fig. 1). The chemical evolution is described by a single-step, infinitely fast irreversible reaction, $F + sO \rightarrow (1 + s) P$, where s designates the mass stoichiometric ratio of oxidizer to fuel.

Under these circumstances, the reaction zone is localized on a thin sheet separating the reactants and essentially controlled by the mixing dynamics. Density variations associated with the reaction heat release are neglected. This thermodiffusive approximation is classically adopted in theoretical studies [12,13] and also used in direct simulations [14,15,16]. It decouples the calculation of the flow field from the determination of the chemical species mass fractions. From the mixture fraction Z, one may deduce the other chemical variables as well as the temperature [1,2,17,18].

We focus on the large-scale vortices resulting from the Kelvin–Helmholtz instability that are typically observed in such configurations. Because of their typical time, the smaller eddies are less efficient and are more rapidly dissipated by viscosity. The simulations are performed in two dimensions, but we are aware that three-dimensional effects are significant at the smallest scales or at high Mach numbers; however, they will not be described here. The Navier–Stokes equations are solved by a 2D finite volume technique using a centered second-order scheme. The mixture fraction equation is resolved with a fourth-order compact implicit scheme. Further details may be found in Braza [19] and Delhaye et al. [20].

Results

A typical distribution of product mass fraction is shown at the top of Fig. 2. Transverse profiles of $M_i M_j$ and $\langle m_i m_j \rangle_S$ are deduced from the simulation. The surface-averaged value of the quantity Q is determined by

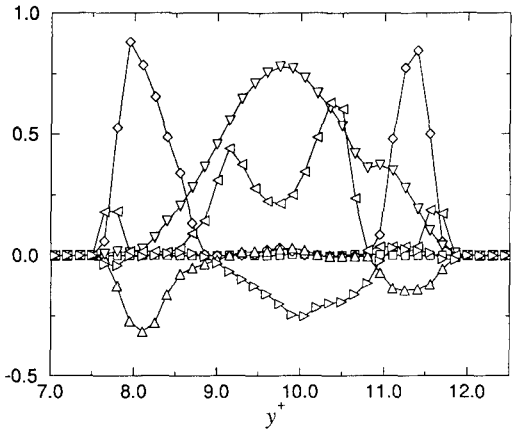

FIG. 2. Mean transverse profiles of the terms M_iM_j and $\langle m_im_j\rangle_S$ deduced from the direct simulation ($x^+ = 40$). (□) M_1M_1; (◇) M_2M_2; (△) M_1M_2; (▽) $\langle m_1m_1\rangle_S$; (◁) $\langle m_2m_2\rangle_S$; (▷) $\langle m_1m_2\rangle_S$.

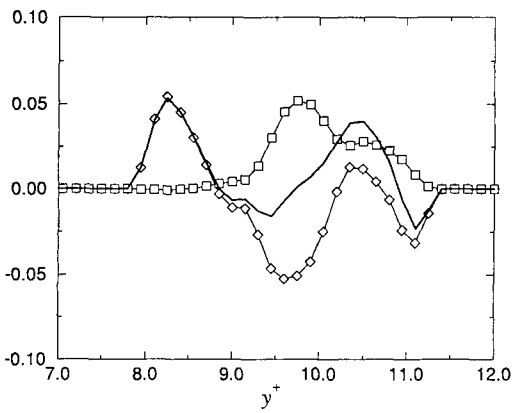

FIG. 3. Mean transverse profiles of the terms of the strain rate equation [Eq. (15)] ($x^+ = 40$). (□) $A = -\langle n_1n_2\rangle_S(\partial U_1/\partial x_2 + \partial U_2/\partial x_1)$; (◇) $B = (\langle n_2n_2\rangle_S - \langle n_1n_1\rangle_S)\,\partial U_1/\partial x_1$. Solid line (——) $A + B = \langle A_T\rangle_S$.

$$\langle Q\rangle_S = \frac{\int_S Q dS}{\int_S dS}. \tag{9}$$

Results are plotted in Fig. 2. They exhibit a strong anisotropy of the fluctuations, and consequently, $\langle m_1m_1\rangle$ and $\langle m_2m_2\rangle$ are quite different. It is found that, everywhere in the mixing layer,

$$\langle n_1n_1\rangle_S \approx \langle m_1m_1\rangle_S, \qquad M_1M_1 << \langle m_1m_1\rangle_S. \tag{10}$$

In the center of the mixing layer, one has

$$\langle n_2n_2\rangle_S \approx \langle m_2m_2\rangle_S, \qquad M_2M_2 << \langle m_2m_2\rangle_S \tag{11}$$

$$\langle n_1n_2\rangle_S \approx \langle m_1m_2\rangle_S, \qquad M_1M_2 << \langle m_1m_2\rangle_S \tag{12}$$

while on the edge of the mixing layer,

$$\langle n_2n_2\rangle_S \approx M_2M_2, \qquad \langle m_2m_2\rangle_S << M_2M_2 \tag{13}$$

$$\langle n_1n_2\rangle_S \approx M_1M_2, \qquad \langle m_1m_2\rangle_S << M_1M_2. \tag{14}$$

Using the mass conservation and the assumption of a constant density, expression (3) may be simplified as

$$\langle A_T\rangle_S = (\langle n_1n_1\rangle_S - \langle n_2n_2\rangle_S)\frac{\partial U_1}{\partial x_1} - \langle n_1n_2\rangle_S\left(\frac{\partial U_1}{\partial x_2} + \frac{\partial U_2}{\partial x_1}\right). \tag{15}$$

The two terms of this equation are plotted in Fig. 3. In the center of the mixing layer, the gradient of mean transverse velocity reaches its maximum value ($|dU_1/dx_2| \approx 0.3$), which is about six times higher than the result provided by direct simulation. This indicates that the assumption commonly used in this configuration to estimate the strain rate due to the mean flow field ($\langle A_T\rangle_S = |dU_1/dx_2|$) is not valid.

To include these results in a turbulent combustion model, one has to define two regions corresponding to the previously described center and edges of the mixing layer. When $\nabla Z = 0$, the vector normal to the flame is assumed to consist only of fluctuations. A modelling similar to that of Mantel and Borghi [11] is chosen because it does not assume the isotropy of the fluctuations. In this case, $\langle n_in_j\rangle_S$ is expressed as in Eq. (8). When ∇Z is not zero, it is assumed that Eqs. (10), (13), and (14) are valid in a frame linked to the mean gradient of Z. To find the five unknowns M_1, M_2, $\langle m_1m_1\rangle_S$, $\langle m_2m_2\rangle_S$, $\langle m_1m_2\rangle_S$, one needs three more equations. A first equation is given by writing that $\mathbf{n}$ is parallel to $\nabla\mathbf{Z}$. The norm of $\mathbf{n}$ is unity ($\mathbf{n}^2 = 1$), which provides another equation. The system is closed by assuming that $\langle n_1n_1\rangle_S = \langle m_1m_1\rangle_S = \overline{u_1'u_1'}/(2k)$ in the previous frame, which refers to the modelling proposed by Mantel and Borghi [11]. The resulting formulation is

$$\langle n_1n_1\rangle_S = \frac{\left(\frac{\partial Z}{\partial x_2}\right)^2}{(\nabla Z)^2} + \gamma^2\left[\frac{\left(\frac{\partial Z}{\partial x_1}\right)^2}{(\nabla Z)^2} - \frac{\left(\frac{\partial Z}{\partial x_2}\right)^2}{(\nabla Z)^2}\right] \tag{16}$$

$$\langle n_2 n_2 \rangle_S = \frac{\left(\frac{\partial Z}{\partial x_1}\right)^2}{(\nabla Z)^2} + \gamma^2 \left[\frac{\left(\frac{\partial Z}{\partial x_2}\right)^2}{(\nabla Z)^2} - \frac{\left(\frac{\partial Z}{\partial x_1}\right)^2}{(\nabla Z)^2} \right] \quad (17)$$

$$\langle n_1 n_2 \rangle_S = (2\gamma^2 - 1) \frac{\frac{\partial Z}{\partial x_1} \frac{\partial Z}{\partial x_2}}{(\nabla Z)^2} \quad (18)$$

with γ^2 defined as

$$\gamma^2 = 1 - \left(\frac{\left(\frac{\partial Z}{\partial x_1}\right)^2}{(\nabla Z)^2} \frac{\overline{u_2' u_2'}}{2k} + \frac{\left(\frac{\partial Z}{\partial x_2}\right)^2}{(\nabla Z)^2} \frac{\overline{u_1' u_1'}}{2k} - \frac{\frac{\partial Z}{\partial x_1} \frac{\partial Z}{\partial x_2}}{(\nabla Z)^2} \frac{\overline{u_1' u_2'}}{k} \right). \quad (19)$$

The strain rate due to velocity fluctuations is modelled as

$$\langle a_T \rangle_S = a\varepsilon/k \quad (20)$$

where a is a constant, k the turbulent kinetic energy, and ε its dissipation.

One should note that the behavior of the moment terms as described above is typical of flows containing well-defined coherent structures. If these structures are weaker, the moment terms may be different. However, comparisons between simulations and experiments indicate that the model will still apply for a realistic class of flows. Another question that may be raised is that of 3D effects. The model devised for the mean strain rate and the experiment is essentially two dimensional while the description of the strain rate associated with the fluctuations is 3D. However, a fully 3D model may be derived along similar lines of reasoning.

Local Consumption Rate of the Flamelets

The local fuel consumption rate per unit of flame area V_f is needed to express the reaction rate in relation (1). The local flamelet is modelled as a counterflow laminar diffusion flame. Under the assumption of infinitely fast chemistry and constant density, this flame element may be described by a single, one-dimensional equation for the passive scalar

$$\frac{\partial Z}{\partial t} - E_s(t)x \frac{\partial Z}{\partial x} = D \frac{\partial^2 Z}{\partial x^2} \quad (21)$$

with the following initial and boundary conditions

$$Z(x, 0) = H(x), Z(-\infty, t) = 0, Z(+\infty, t) = 1 \quad (22)$$

where $E_s(t)$ is the strain rate, D a constant diffusion coefficient, and $H(x)$ is the Heaviside function.

Assuming a constant strain rate $E_s(t) = A$, this equation leads to the classical solution [3], where ϕ is the global equivalence ratio

$$V_f = Y_{f\infty} \left(\frac{DA}{2\pi}\right)^{1/2} \frac{\phi + 1}{\phi} e^{-w^2} \quad (23)$$

with

$$w = \mathrm{erf}^{-1}\left(\frac{\phi - 1}{\phi + 1}\right). \quad (24)$$

In practical applications, the flame element is transported in a field of variable strain, and this parameter changes sometimes quite rapidly. This is the case in the injection zone where the shear takes large values along a flamelet trajectory. It is known (for example, Ref. 10) that the flamelet response time cannot be neglected. Mauß et al. [21] and Thévenin and Candel [22] have shown that variable strain effects should be included to account for local extinction or to describe the ignition of a non-premixed configuration. One may introduce an equivalent strain rate $A(t)$ defined at each time as the strain rate of the stationary flamelet having the same reaction rate as the real one, and one may derive a transport equation for $A(t)$ (Haworth et al. [10])

$$\frac{dA}{dt} = -2A^2(t) + 2E_s(t)\,A(t). \quad (25)$$

This equation describes the relaxation of the strain rate to its local value.

Determination of Flame Surface Density From OH PLIF Imaging

The experimental setup is shown in Fig. 4. An air flow at 10 m/s is injected into a rectangular combus-

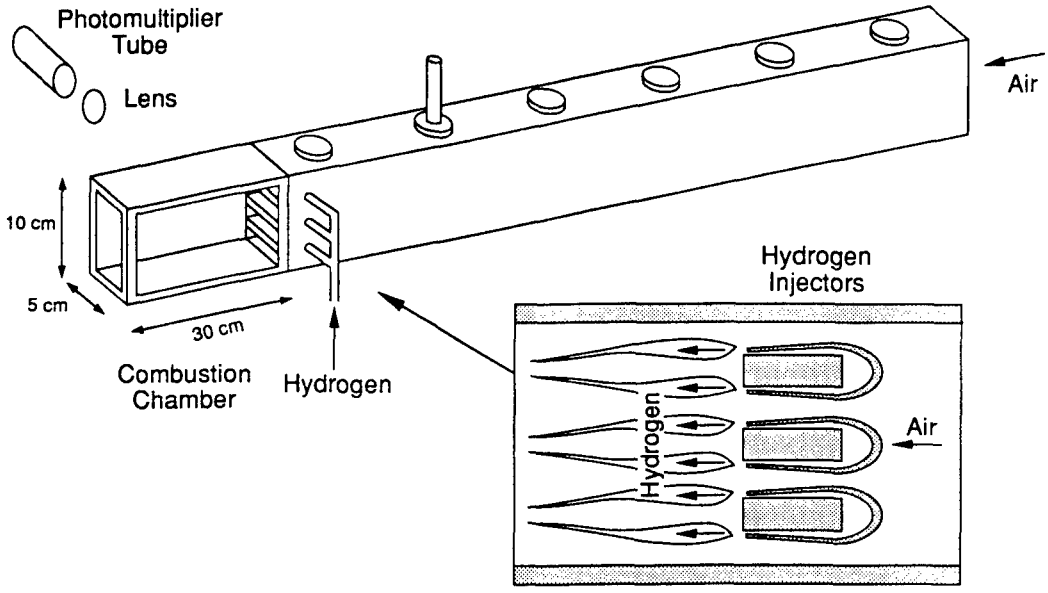

FIG. 4. Schematic view of the experimental setup.

tion chamber. Hydrogen (14 m/s) is introduced through six narrow slots on the upper and lower sides of three injection blocks at the upstream entrance of the chamber. The lateral walls are artificial quartz windows and allow optical imaging. Planar induced fluorescence of the OH radical is conducted and provides flame images recorded with a charge-coupled device camera. The OH radical is assumed to be a good marker of the flame reaction rate in this non-premixed combustion case. Details about the experimental setup and imaging system may be found in McManus et al. [23].

In the example shown in Fig. 5, a well-defined flame front and its distortions are clearly apparent. There is no evidence of local extinction, and the flame looks like a surface distorted by turbulent structures. Accordingly, a flamelet model seems to be well adapted for numerical simulations of such a flame. The flame surface density may be estimated by averaging a sufficient number of images and the result may be compared to model predictions.

On each image, the flame sheet is localized as the maximum OH fluorescence. The flame is represented by a line of pixels, on which a curvilinear abscissa is measured. Tests show that this method is accurate and reliable but limited to cases without front interaction (which does not occur in our data set). Another limitation is due to the pixel size. Any structure smaller than this size (0.26×0.26 mm^2) cannot be detected by the algorithm. Flame fronts are extracted from a set of 30 images. Each image is divided into cells of area S where the flame arc length L is measured. The flame surface density Σ is estimated by averaging over all the set of images

$$\Sigma = \frac{1}{N} \sum_{i=1}^{N} \frac{L(i)}{S} \tag{26}$$

The validity of this expression and influence of the cell size are discussed in Delhaye et al. [20]. The flame surface density is evaluated from 2D slices. At present, this is the only applicable but approximate method.

The observation of the experimental result (Fig. 6) indicates that combustion occurs mainly in a narrow region where flame surface density is high and reaches a maximum about 1.5 cm downstream of the injector. Further downstream, the flame extends over a broader region, and the flame surface density takes lower values. The flame surface density takes small values close to the injector because the diffusion flame is extinguished by the high initial strain rates. The reaction zone is clearly embedded in the mixing layer between the two air and hydrogen streams, justifying the direct numerical simulation used previously to analyse the closure of the strain rate due to the mean flow.

Results and Discussion

The previous model is now examined numerically by solving conservation equations for mass, momentum, enthalpy, chemical species, flame surface density, and turbulent kinetic energy and its dissipation (the $k - \varepsilon$ closure model is used). The equations are discretized and solved with a finite volume technique. A centered scheme is used to compute the

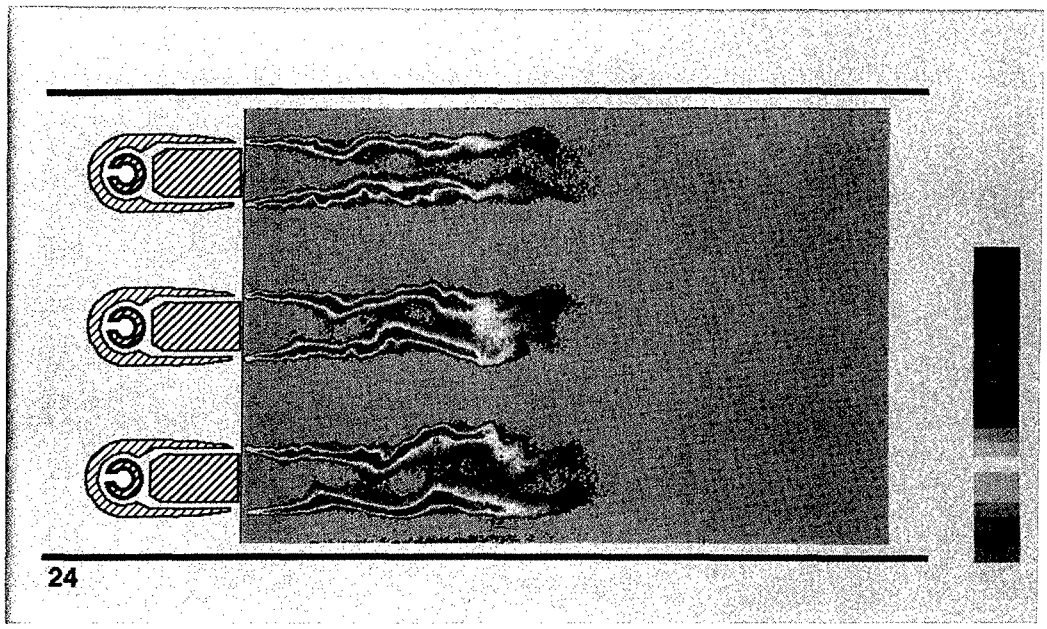

FIG. 5. Example of an OH-PLIF image of the six flames, $V_{air} = 10$ m/s, $V_{H_2} = 14$ m/s. Vertical dimension of combustor 10 cm. Injection slot thickness 0.3 cm (McManus et al. [23]).

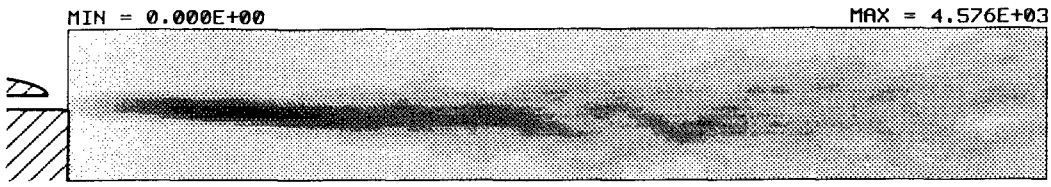

FIG. 6. Experimental flame surface density (m^{-1}), $V_{air} = 10$ m/s, $V_{H_2} = 14$ m/s. The density is plotted on a scale of gray levels; the darkest symbol corresponds to the maximum, which is located at about 1.5 cm.

fluxes, and a semi-implicit fractional step method is adopted to advance the solution in time (ADI method). The domain of computation represents one-sixth of the real combustion chamber, which means that only one flame is calculated and the other ones are assumed to be symmetrical. Mesh size and time step are selected to ensure a low numerical diffusion and a good accuracy of the steady-state solution. Parameters of the model are chosen as follows: $\alpha = 4$ and $\beta = 0.5$.

Figure 7 shows that the turbulent strain rate $\langle a_T \rangle_S$ is larger than the strain rate due to mean flow $\langle A_T \rangle_S$, except on the outer boundaries of the mixing layer where they become comparable. A large peak in $\langle A_T \rangle_S$ shows the position of the hydrogen jet, whereas a smaller peak can be observed on the edge of the recirculation zone. This is consistent with the results of the second section and indicates the importance of the mean velocity gradients in the initial part of the jet. The large peak decreases as one moves down-

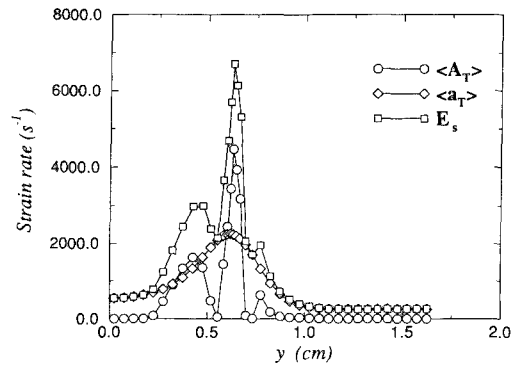

FIG. 7. Cross section of the mean flow ($\langle A_T \rangle_S$), turbulent ($\langle a_T \rangle_S$), and total (E_s) strain rates at 0.75 cm of the injector. Hydrogen is injected between $y = 0.62$ cm and $y = 0.65$ cm and air between $y = 0.65$ cm and $y = 1.62$ cm.

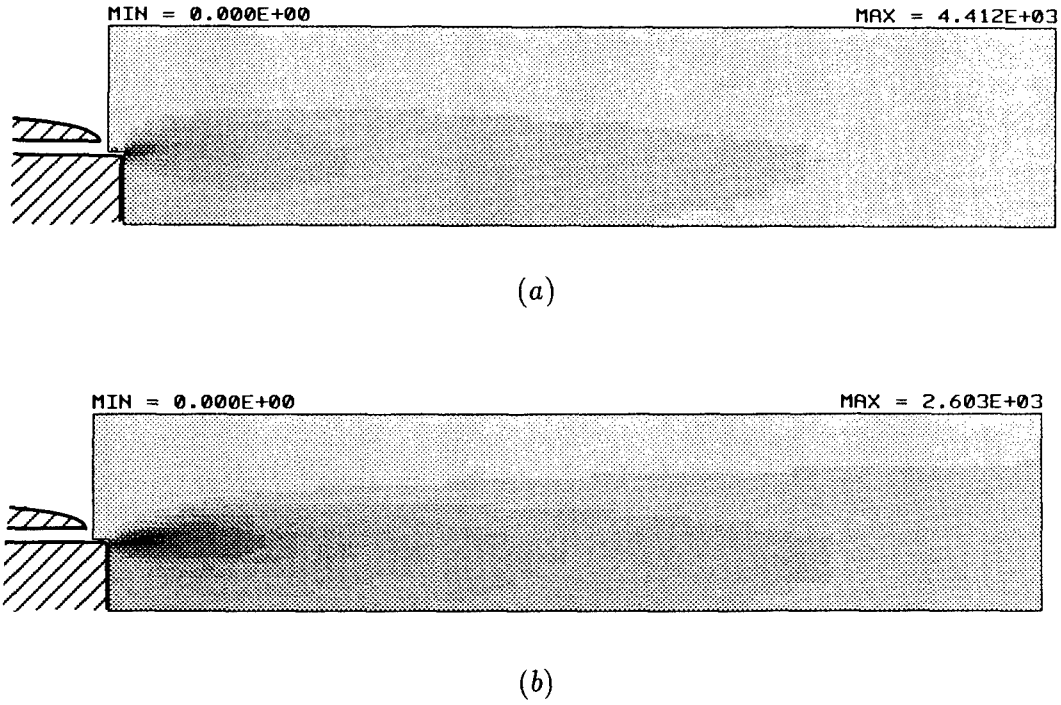

FIG. 8. Local instantaneous turbulent strain rate (a) and equivalent strain rate (b) experienced by the flamelets (s^{-1}).

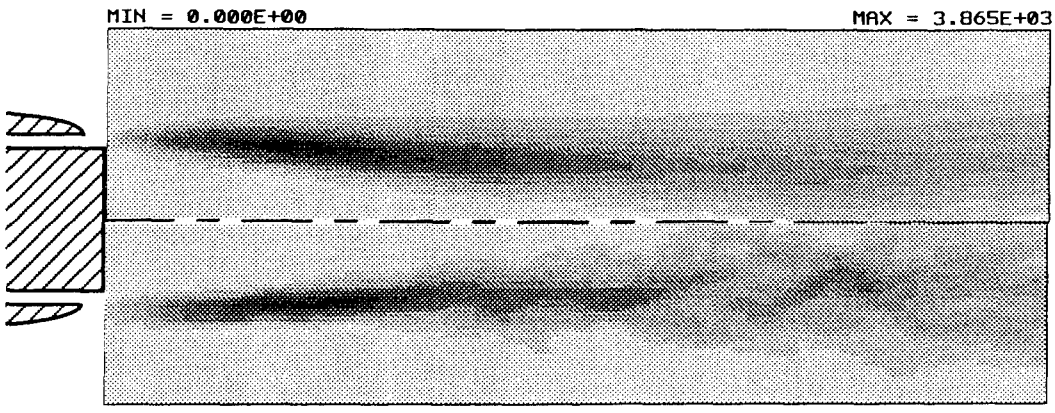

FIG. 9. Comparison between the calculated flame surface density (top) and the experimental data (bottom, this figure is a reverse view of Fig. 6) (m^{-1}), V_{air} = 10 m/s, V_{H_2} = 14 m/s.

stream. At about 2 cm from the injector, only the peak on the edge of the recirculation zone remains.

The strain rate is also an important ingredient of the mean local consumption rate per unit of flame area. As previously described, unsteady effects are taken into account by introducing an equivalent strain rate. In Fig. 8, the local turbulent strain rate $\langle a_T \rangle_S$ is compared with the corresponding equivalent strain rate A intervening in the local consumption rate. The maximum equivalent strain rate is lower than the maximum value of $\langle a_T \rangle_S$. Accordingly, the region of high local reaction rate (i.e., high value of A) is longer and lies further away from the injector. The difference between the local and equivalent strain rates stresses the importance of unsteady flamelet effects in this geometry where large velocity gradients exist near the fuel injector.

The numerical flame surface density field is displayed in Fig. 9. The macroscopic strain notably influences the spreading of flame surface density into

a long and narrow region detached from the injector, which is in good agreement with the experimental observation. The length of the flame is also predicted correctly, and the order of magnitude of the maximum is the same as the experimental one. Because the spatial extent of the heat release is well described, the mean flow variables are also well calculated.

Conclusion

A model has been proposed for the flame surface density transport equation in the case of non-premixed turbulent combustion. Creation of flame surface by stretch may be split in two contributions: creation by the mean strain rate and by the velocity fluctuations. A closure of the former term is devised, based on the results of direct numerical simulation of a 2D mixing layer. It clearly shows a strong anisotropy of the vector normal to the flame. This leads to a general formulation of the strain rate due to the mean velocity gradient.

Experimental profiles of the flame surface density were obtained on a 2D hydrogen-air non-premixed turbulent burner. The model is validated by a numerical simulation of the same burner. Results show an excellent agreement between the experimental data and the numerical values, both on the location and the order of magnitude of the flame surface density. Contribution of the mean strain rate is important, especially on the edges of the shear layer. Unsteady flamelet effects are also observed.

These encouraging results show that other terms of the equation could be studied by direct numerical simulation, for example the stretch due to velocity fluctuations or the curvature effects.

Nomenclature

$\langle A_T \rangle_S$	strain rate due to the mean flow field
$\langle a_T \rangle_S$	strain rate due to the turbulent flow field
E_S	total strain rate
k	turbulent kinetic energy
M_i, m_i	mean and fluctuating parts of n_i
n_i	components of the vector normal to the flame surface
s	mass stoichiometric coefficient
u_i	velocity vector components
U_i	mean velocity vector components
u_i'	turbulent velocity vector components
V_f	fuel laminar mass consumption rate per unit of flame surface
V_o	oxidizer laminar mass consumption rate per unit of flame surface
Y_f	fuel mass fraction
Y_o	oxidizer mass fraction
Z	mixture fraction variable
α, β	coefficients of turbulent combustion model
ε	dissipation rate of the turbulent kinetic energy
ϕ	global equivalence ratio
ν_t	turbulent viscosity
ρ	density
Σ	mean flame surface density
$\bar{\dot{\omega}}_f$	mean consumption rate of fuel
$(\ )^+$	dimensionless variables
$(\ )$	Reynolds averaged variables
$\langle\ \rangle_S$	averaged variables along the flame surface

Acknowledgment

The authors wish to thank SEP (Société Européenne de Propulsion), Vernon, France, for its financial support of this work.

REFERENCES

1. Peters, N., *Twenty-First Symposium (International) on Combustion*, The Combustion Institute, Pittsburgh, 1986, pp. 1231–1250.
2. Bilger, R. W., *Twenty-Second Symposium (International) on Combustion*, The Combustion Institute, Pittsburgh, 1988, pp. 475–488.
3. Marble, F. E., and Broadwell, J. E., *The Coherent Flame Model for Turbulent Chemical Reactions*, Project Squid Report, TRW-9-PU, 1977.
4. Veynante, D., Candel, S. M., and Martin, J. P., in *Complex Chemical Reaction Systems* (J. Warnatz and W. Jäger, Eds.), Springer-Verlag, Berlin, 1987.
5. Veynante, D., Lacas, F., and Candel, S. M., *AIAA J.* 29:848–851 (1991).
6. Candel, S. M., and Poinsot, T., *Comb. Sci. Technol.* 70:1–15 (1990).
7. Pope, S. B., *Int. J. Eng. Sci.*, 26:445–469 (1988).
8. Cant, R. S., Pope, S. B., and Bray, K. N. C., *Twenty-third Symposium (International) on Combustion*, The Combustion Institute, Pittsburgh, 1990, pp. 809–815.
9. Trouvé, A., and Poinsot, T., *Proceedings of the Summer Program*, Center for Turbulence Research, Stanford, 1992. *J. Fluid Mech.*, submitted.
10. Haworth, D. C., Drake, M. C., Pope, S. B., and Blint, R. J., *Twenty-Second Symposium (International) on Combustion*, The Combustion Institute, Pittsburgh, 1988, pp. 589–597.
11. Mantel, T., and Borghi, R., *Thirteenth ICDERS*, 1991.
12. Clavin, P., *Prog. Energy Comb. Sci.*, 11:1–59 (1985).
13. Karagozian, A. R., and Marble, F. E., *Comb. Sci. Technol.* 45:65–84 (1986).
14. Riley, J. J., Metcalfe, R. W., and Orszag, S. A., *Phys. Fluids* 29:406–422 (1986).
15. Chang, C. H. H., Dahm, W. J. A., and Tryggvason, G., *Phys. Fluids A* 3:1300–1311 (1991).
16. Nomura, K. K., and Elghobashi, S. E., *Phys. Fluids A* 4:606–625 (1992).

17. Peters, N., *Comb. Sci. Technol.* 30:1–17 (1983).
18. Williams, F. A., *Combustion Theory*, Benjamin Cummings Publishing Co, Menlo Park, CA, 1985.
19. Braza, M., "Analyse Physique du Comportement Dynamique d'un Écoulement Externe, Décollé, Instationnaire en Transition Laminaire-Turbulente," Doctoral Thesis, INP Toulouse, 1986.
20. Delhaye, B., Veynante, D., Candel, S. M., and Ha Minh, H., *Theoretical and Computational Fluid Dynamics* 6:67–87 (1994).
21. Mauß, F., Keller, D., and Peters, N., *Twenty-Third Symposium (International) on Combustion*, The Combustion Institute, Pittsburgh, 1990.
22. Thévenin, D., and Candel, S. M., *Comb. Sci. Technol.* 91:73–94 (1993).
23. McManus, K., Yip, B., and Candel, S. M., *Proceedings of Third World Conference on Experimental Heat Transfer, Fluid Mechanics and Thermodynamics* (M. D. Kelleher et al., Eds.), Elsevier, Amsterdam, pp. 86–102.

COMMENTS

Baki Cetegen, University of Connecticut, USA. Could you please comment on the contribution of the small turbulent fluctuation length scales to the generation of flame surface area? It appears that length scales smaller than local diffusion flame thickness would not affect the generation of flame surface area.

Author's Reply. It is indeed probable that turbulent fluctuations with scales smaller than the flame thickness will not influence the generation of flame surface area. This is well demonstrated in direct simulations of premixed flames propagating in a turbulent field (see, for example, Poinsot et al. [1]). The same small-scale cut-off mechanism is expected in the case of diffusion flames.

REFERENCE

1. Poinsot, T., Veynante, D., and Candel, S., *J. Fluid Mech.* 228:561–606 (1991).

•

Jerzy Chomiak, Chalmers University of Technology, Sweden. In your model, you simply add the flame surface generation by mean flow and turbulent stretching whereas we know that stretching of the flame by mean flow will damp the perturbation of the flame by turbulence.

Author's Reply. It is certainly true that stretching at the larger scales will influence the amplitude of the perturbations produced by the smaller scales. While this mechanism is not taken into account in the present model, it certainly deserves further analysis. In the present article, we only devise an improved but still approximate model of the effective flame stretch that produces flame area.

Twenty-Fifth Symposium (International) on Combustion/The Combustion Institute, 1994/pp. 1283–1291

NUMERICAL SIMULATION OF LOCAL EXTINCTION EFFECTS IN TURBULENT COMBUSTOR FLOWS OF METHANE AND AIR

I. R. GRAN, M. C. MELAAEN AND B. F. MAGNUSSEN
Division of Thermodynamics
University of Trondheim
Trondheim, Norway

The finite-volume approach together with body-fitted curvilinear nonorthogonal coordinates and a non-staggered grid arrangement is used for investigating turbulent reacting flows inside gas-turbine combustion chambers. The high Reynolds number k-ε turbulence model was employed to model the turbulence. Two different combustion models, the eddy dissipation concept (EDC) and the laminar flamelet model have been employed to account for the turbulence chemistry interaction. An extinction model for the eddy dissipation concept is presented, and a new extinction model for the laminar flamelet model is set forth. First, the combusting flow in a sudden expansion axisymmetric can combustor is studied. The agreement between calculations and measurements is good only when the effects of local extinction are taken into account. Second, the effects of extinction on the combusting flow in an annular gas-turbine combustor with a complex 3D geometry are examined. Significant impact on the reaction rate in the primary and intermediate zones of the combustor due to local extinction effects is predicted.

Introduction

A method for calculation of turbulent reacting flow inside combustors is set forth. The high Reynolds number k-ε model with wall functions is used for modeling the turbulence inside the combustors. Two different combustion models, the eddy dissipation concept (EDC) and the laminar flamelet method, have been used. Inclusion of finite-rate chemical kinetics in turbulent combusting flows increases the computational task substantially compared with calculations based on the fast chemistry assumption [1,2,3]. Thus, models that can account for effects of finite-rate chemistry such as ignition, extinction, and NO_x formation without significantly increasing the computational effort are needed. In the present paper, one extinction model for each of the two combustion models has been tested.

The text is divided into three parts. The first part describes the mathematical models used. In the second part of the paper, it is shown that the extinction models are able to account for important effects of finite-rate kinetics in a confined axisymmetric combustor flow of methane and air. Finally, the effects of local extinction in a complex three-dimensional gas-turbine combustor are studied.

Mathematical Modeling

Governing Equations:

The Favre-averaged equations for steady compressible flow when using the high Reynolds number k-ε model are as follows:

Overall mass conservation

$$\frac{\partial}{\partial x_j}(\bar{\rho}\tilde{u}_j) = 0 \tag{1}$$

Conservation of momentum

$$\frac{\partial}{\partial x_j}(\bar{\rho}\tilde{u}_j\tilde{u}_k) = \frac{\partial}{\partial x_j}\left[\mu_t\left(\frac{\partial \tilde{u}_k}{\partial x_j} + \frac{\partial \tilde{u}_j}{\partial x_k}\right)\right] - \frac{\partial}{\partial x_k}\left(\bar{p} + \frac{2}{3}\bar{\rho}\tilde{k} + \frac{2}{3}\mu_t\frac{\partial \tilde{u}_l}{\partial x_l}\right) \tag{2}$$

Equation for turbulent kinetic energy

$$\frac{\partial}{\partial x_j}(\bar{\rho}\tilde{u}_j\tilde{k}) = \frac{\partial}{\partial x_j}\left(\frac{\mu_t}{\sigma_k}\frac{\partial \tilde{k}}{\partial x_j}\right) + G - \tilde{\varepsilon}\bar{\rho} \tag{3}$$

Equation for the dissipation rate of turbulent kinetic energy

$$\frac{\partial}{\partial x_j}(\bar{\rho}\tilde{u}_j\tilde{\varepsilon}) = \frac{\partial}{\partial x_j}\left(\frac{\mu_t}{\sigma_\varepsilon}\frac{\partial \tilde{\varepsilon}}{\partial x_j}\right) + C_1\frac{\tilde{\varepsilon}}{\tilde{k}}G - C_2\frac{\tilde{\varepsilon}^2}{\tilde{k}}\bar{\rho} \tag{4}$$

where the rate of turbulent kinetic energy production is given as

$$G = \mu_t\left(\frac{\partial \tilde{u}_j}{\partial x_k} + \frac{\partial \tilde{u}_k}{\partial x_j}\right)\frac{\partial \tilde{u}_j}{\partial x_k} \tag{5}$$

and $\mu_t = C_\mu \bar{\rho} \tilde{k}^2/\tilde{\varepsilon}$ is the turbulent eddy viscosity and standard coefficients are selected in the k-ε model. Wall functions are employed for solid boundaries.

The EDC Combustion Model:

The EDC combustion model is an extended version of the well-known combustion model proposed by Magnussen and Hjertager [4]. This model has the ability to handle premixed, partially premixed, and nonpremixed combustion with accuracy [5], and it is currently one of the most popular concepts for modeling local reaction rates in practical turbulent combustion systems.

In the model expressions, the mass fraction of the individual species, $\tilde{Y}_i$, is used. The equations for conservation of individual species for a mixture of N species can be written

$$\frac{\partial}{\partial x_j}(\bar{\rho}\tilde{u}_j\tilde{Y}_i) = \frac{\partial}{\partial x_j}\left(\frac{\mu_t}{\sigma_Y}\frac{\partial \tilde{Y}_i}{\partial x_j}\right) + \bar{\rho}\tilde{\omega}_i \qquad i = 1, \ldots, N \tag{6}$$

where the chemical source term $\tilde{\omega}_i$ expresses the net rate of production of species i due to chemical reaction.

Under certain simplifying assumptions, the energy conservation in terms of enthalpy is

$$\frac{\partial}{\partial x_j}(\bar{\rho}\tilde{u}_j\tilde{h}) = \frac{\partial}{\partial x_j}\left(\frac{\mu_t}{\sigma_h}\frac{\partial \tilde{h}}{\partial x_j}\right). \tag{7}$$

The mean temperature is found from

$$\tilde{h} = \sum_{i=1}^{N} \tilde{Y}_i h_i(\tilde{T}). \tag{8}$$

The mean density is determined from the equation of state for a mixture of perfect gases:

$$\bar{\rho} = \frac{\bar{p}}{\tilde{T}R_u \sum_{i=1}^{N} \frac{\tilde{Y}_i}{M_i}}. \tag{9}$$

Assuming that the combustion can be suitably represented by the single irreversible one-step reaction

$$\{1 \text{ kg fuel } (F)\} + \{r_F \text{ kg oxidizer } (O)\} \rightarrow \{(1 + r_F) \text{ kg product } (P)\} \tag{10}$$

and the following set of normalized species concentrations are defined

$$\hat{Y}_F = \frac{\tilde{Y}_F}{1} \qquad \hat{Y}_O = \frac{\tilde{Y}_O}{r_F} \qquad \hat{Y}_P = \frac{\tilde{Y}_P}{1 + r_F} \tag{11}$$

the eddy dissipation concept expresses the chemical reaction rate as [5,6]

$$\tilde{\omega}_F = -C_\omega \kappa \frac{\tilde{\varepsilon}}{\tilde{k}} \min[\hat{Y}_{\min}, \hat{Y}_P, (\hat{Y}_{\min} + \hat{Y}_P)\gamma_\lambda]$$

$$\hat{Y}_{\min} = \min[\hat{Y}_F, \hat{Y}_O]. \tag{12}$$

The mass fraction occupied by turbulent fine structure regions, γ_λ, is expressed as

$$\gamma_\lambda = C_\gamma\left(\frac{\nu\tilde{\varepsilon}}{\tilde{k}^2}\right)^{1/4} \tag{13}$$

and the correlation factor for nonpremixedness, κ, is written

$$\kappa = \frac{(\hat{Y}_{\min} + \hat{Y}_P)^2}{(\hat{Y}_F + \hat{Y}_P)(\hat{Y}_O + \hat{Y}_P)}. \tag{14}$$

The terms C_ω and C_γ are constants with values 11.1 and 2.1, respectively [5].

The mixture fraction is defined as the mass fraction of burned and unburned fuel:

$$\tilde{f} = \hat{Y}_F + \hat{Y}_P. \tag{15}$$

The EDC Extinction Model:

Local extinction can influence combustion characteristics of main importance for the performance of combustion chambers. Here, a model for predicting local extinction in reacting turbulent flows proposed by Byggstøyl and Magnussen [7] is presented. The model is based on the eddy dissipation concept, and the extinction is assumed to take place in the turbulent fine structures [5]. The characteristic time scale for the turbulent fine structures is determined as

$$\tau^* = 0.41\left(\frac{\nu}{\tilde{\varepsilon}}\right)^{1/2}. \tag{16}$$

This time scale is compared with a chemical time scale, τ_{ch}, in order to establish whether extinction is expected or not. If the turbulent fine structure is treated as a perfectly stirred reactor (PSR), PSR calculations can guide the choice of τ_{ch}. Figure 1 shows PSR results indicating τ_{ch} for methane and air for different inlet temperatures and compositions. Extinction is predicted if $\tau^* < \tau_{ch}$, and the chemical source term $\tilde{\omega}_i$ in Eq. (6) is set equal to zero where such conditions prevail.

According to the extinction model, a lifted diffusion flame will be stabilized at the position where the turbulent fine structure time scale equals the chemical time scale. The extinction model has been tested by performing calculations of jet flows and then ex-

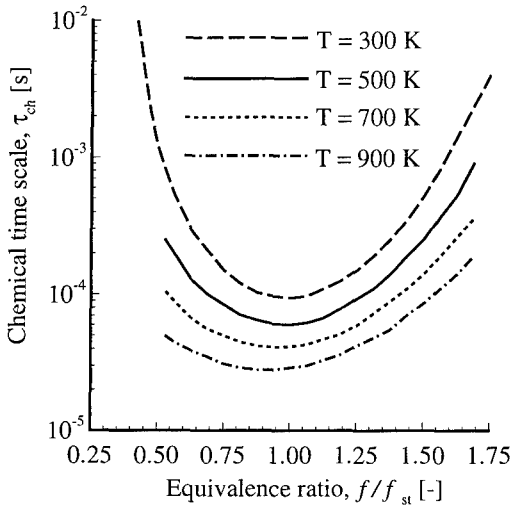

FIG. 1. τ_{ch} for different inlet temperatures and compositions.

tracting the quenching time scales by comparison with experimental data [7]. Excellent agreement between theoretical and measured time scales was achieved.

The Flamelet Combustion Model:

Flamelet methods assume that turbulent reacting flows consist of an ensemble of reaction-diffusion layers that are continuously displaced and stretched within the turbulent medium. The structure of the flamelets can be approximated by employing the flame sheet model or by assuming equilibrium or partial equilibrium. A more detailed description of nonequilibrium effects is achieved by extracting data from measurements or by performing numerical laminar flamelet calculations with detailed chemistry [8, p. 328]. After that, it is necessary to build the turbulent reacting field by a convenient collection of such flamelets. This can be done by tabulating the state, characterized by the *state vector*, $\boldsymbol{\psi}_{fl}$, in the flamelet as a function of the mixture fraction f for different rates of scalar dissipation χ:

$$\boldsymbol{\psi}_{fl} = \boldsymbol{\psi}_{fl}(f,\chi). \tag{17}$$

The instantaneous scalar dissipation rate is defined as

$$\chi = 2D\frac{\partial f}{\partial x_j}\frac{\partial f}{\partial x_j} \tag{18}$$

where D is the diffusion coefficient. The term χ may be interpreted as the inverse of a characteristic diffusion time [8, p. 323].

Mean values can then be found by using the Favre joint probability density function (PDF) $\tilde{P}(f,\chi)$ of the scalar variables:

$$\tilde{\boldsymbol{\psi}} = \int_0^\infty \int_0^1 \boldsymbol{\psi}_{fl}(f,\chi)\tilde{P}(f,\chi)df d\chi. \tag{19}$$

Since Favre averaging is used, special care is taken when evaluating time-averaged quantities [9, p. 73].

In the present study, $\tilde{P}(f,\chi)$ is found from the presumed-shape method. First, it is assumed that f and χ are statistically independent:

$$\tilde{P}(f,\chi) = \tilde{P}_f(f)\tilde{P}_\chi(\chi) \tag{20}$$

where $\tilde{P}_f$ and $\tilde{P}_\chi$ are the marginal PDFs.

The term $\tilde{P}_f$ is then assumed to be a β function:

$$\tilde{P}_f(f) = f^{(\alpha-1)}(1-f)^{(\beta-1)}\frac{\Gamma(\alpha+\beta)}{\Gamma(\alpha)\Gamma(\beta)}. \tag{21}$$

The parameters α and β are related to the first- and second-order moments of f by

$$\tilde{f} = \frac{\alpha}{\alpha+\beta} \qquad \widetilde{f''^2} = \frac{\tilde{f}(1-\tilde{f})}{1+\alpha+\beta}. \tag{22}$$

An equation for the mean mixture fraction $\tilde{f}$ is obtained if Eq. (15) is introduced in Eq. (6).

$$\frac{\partial}{\partial x_j}(\bar{\rho}\tilde{u}_j\tilde{f}) = \frac{\partial}{\partial x_j}\left(\frac{\mu_t}{\sigma_Y}\frac{\partial \tilde{f}}{\partial x_j}\right). \tag{23}$$

The equation for the variance of the mixture fraction $\widetilde{f''^2}$ is written

$$\frac{\partial}{\partial x_j}(\bar{\rho}\tilde{u}_j\widetilde{f''^2}) = \frac{\partial}{\partial x_j}\left(\frac{\mu_t}{\sigma_Y}\frac{\partial \widetilde{f''^2}}{\partial x_j}\right) + c_1\frac{\mu_t}{\sigma_Y}\frac{\partial \tilde{f}}{\partial x_j}\frac{\partial \tilde{f}}{\partial x_j} - c_2\bar{\rho}\frac{\tilde{\varepsilon}}{\tilde{k}}\widetilde{f''^2} \tag{24}$$

where $c_1 = c_2 = 2.0$.

The term χ is assumed to be log-normal distributed:

$$\tilde{P}_\chi(\chi) = \frac{1}{\chi\sigma(2\pi)^{(1/2)}}\exp\left[-\frac{1}{2\sigma^2}(\ln\chi-\mu)^2\right] \tag{25}$$

where μ and σ relate to the mean and variance of χ according to

$$\tilde{\chi} = \exp(\mu+\sigma^2/2) \qquad \widetilde{\chi''^2} = \tilde{\chi}^2[\exp(\sigma^2)-1]. \tag{26}$$

The modeling assumption

$$\tilde{\chi} = c_2(\tilde{\varepsilon}/\tilde{k})\widetilde{f''^2} \tag{27}$$

used in the derivation of Eq. (24) gives an expression for $\tilde{\chi}$. Instead of solving a model equation for $\widetilde{\chi''^2}$, the common assumption of using a fixed value $\sigma^2 = 2.0$ was employed [8, page 333].

In the present work, the instantaneous values of $\boldsymbol{\psi}_{\mathrm{fl}}$ were obtained from the flame-sheet model by Burke and Schumann [8, page 328].

In the Burke–Schumann model, it is assumed that $\boldsymbol{\psi}_{\mathrm{fl}}$ is independent of χ:

$$\boldsymbol{\psi}_{\mathrm{fl}} = \boldsymbol{\psi}_{\mathrm{fl}}(f). \tag{28}$$

This results in a significant computational advantage, since Eq. (19) reduces to

$$\tilde{\boldsymbol{\psi}} = \int_0^1 \boldsymbol{\psi}_{\mathrm{fl}}(f)\tilde{P}_f(f)\,df. \tag{29}$$

Instead of using the assumed-shape method, a transport equation for the velocity-composition joint PDF could have been solved [1,2]. The solution of PDF transport equations is very expensive. The essential advantage of this approach is that the effects of nonlinear chemical kinetics appear in closed form. This advantage is not realized if the state is determined from Eq. (17) or Eq. (28) [2].

A New Flamelet Extinction Model:

At a certain rate of scalar dissipation, the laminar flamelet is extinguished. This scalar dissipation can be characterized by the scalar dissipation rate evaluated at the stoichiometric contour, $\chi_{\mathrm{st}} = \chi(f_{\mathrm{st}})$. Thus, extinction occurs if χ_{st} exceeds the quenching value, χ_q. With this assumption, Eq. (28) can be expressed as [8, page 335]:

$$\boldsymbol{\psi}_{\mathrm{fl}} = \begin{cases} \boldsymbol{\psi}_b(f) & \text{if } \chi_{\mathrm{st}} \le \chi_q \\ \boldsymbol{\psi}_q(f) & \text{if } \chi_{\mathrm{st}} > \chi_q \end{cases} \tag{30}$$

where $\boldsymbol{\psi}_b$ and $\boldsymbol{\psi}_q$ designate the state in a burning and an extinguished flamelet, respectively. Numerical values for χ_q have been deduced from analyzing experimental data and by analytical and numerical calculations. For a methane-air diffusion flamelet, the value $\chi_q = 8.0\ \mathrm{s}^{-1}$ is estimated [8, page 331]. This value has been adopted in the present work.

An approximate relation between χ and χ_{st} can be written [8, page 325]

$$\chi = \chi_{\mathrm{st}}\lambda \tag{31}$$

$$\lambda = \exp\{2[\mathrm{erfc}^{-1}(2f_{\mathrm{st}})]^2 - 2[\mathrm{erfc}^{-1}(2f)]^2\}. \tag{32}$$

By inserting Eqs. (20), (25), (30), and (31) into Eq. (19), the following expression for the mean state $\tilde{\boldsymbol{\psi}}$ appears:

$$\tilde{\boldsymbol{\psi}} = \int_0^1 [\boldsymbol{\psi}_b p_b + \boldsymbol{\psi}_q(1 - p_b)]\tilde{P}_f\,df \tag{33}$$

where

$$p_b = \frac{1}{2} + \frac{1}{2}\,\mathrm{erf}\left[\frac{\ln(\lambda\chi_q/\tilde{\chi}) + \frac{1}{2}\sigma^2}{(2)^{1/2}\sigma}\right]. \tag{34}$$

In the extinction model presented in Ref. 8, Eqs. 5.2 and 5.3, p_b is taken outside the integration in Eq. (33) and evaluated by using mean values. When this is used, the results obtained are significantly different from those obtained with the present extinction model.

Numerical Solution:

To model the complex combustor geometry, a curvilinear nonorthogonal grid arrangement is selected. Based on earlier experience, a nonstaggered (collocated) grid arrangement is preferred [10,11]. The convective terms are discretized by the second-order upwind scheme (SOU), but the numerically more stable power law scheme is employed to start the calculations. For the nonstaggered (collocated) grid arrangement used, the Cartesian velocity components are stored in scalar grid points so that velocity interpolation is needed when the convective flux at the control volume faces is to be estimated. This is achieved by the Rhie and Chow interpolation method [12]. The SIMPLE algorithm is chosen to find updated velocity and pressure fields obeying the discrete momentum and continuity equations for the converged solution. In addition to the $\tilde{k}$ and $\tilde{\varepsilon}$ equations, the $\tilde{h}$ and $\tilde{Y}_i$ equations or the $\tilde{f}$ and $\widetilde{f''^2}$ equations are solved depending on the combustion model used. The equations are solved sequentially by line-by-line TDMA together with block correction, and the process is repeated until convergence. The solution is regarded as converged when the 1-norm of the residuals scaled against a representative inflow flux is less than 10^{-5} for all variables.

Axisymmetric Combustor

The combusting flow investigated experimentally by Lewis and Smoot [13] is studied. In this experiment, nonswirling coaxial streams of natural gas (mainly methane) and pure air are injected into a sudden-expansion chamber (see Fig. 2).

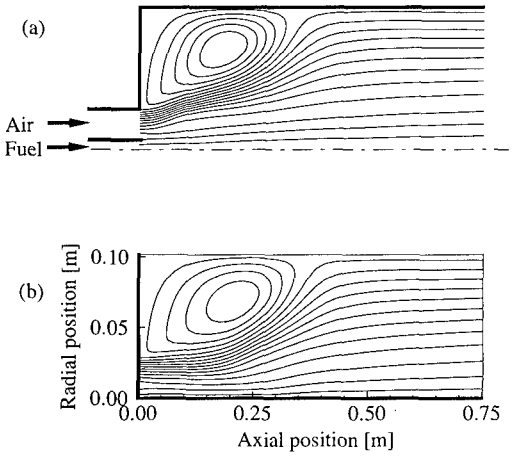

FIG. 2. Streamlines in axisymmetric combustor: (a) without extinction, (b) with extinction.

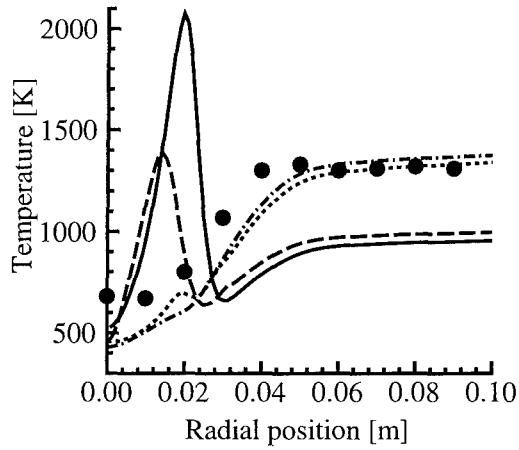

FIG. 3. Temperature profiles at $x = 95$ mm. Solid line: EDC without extinction; dash-dotted line: EDC with extinction; dashed line: flamelet model without extinction; dotted line: flamelet model with extinction.

Previous Simulations:

The computational grid used in the present calculations has 61 × 47 nodes in the axial and radial directions, respectively. The reason for this is to allow comparison with previous numerical predictions of this case presented by Nikjooy [14], who used a similar grid. The results of Nikjooy closely resemble the present results obtained when extinction is not accounted for [6].

Grid Dependency:

To ensure that the calculations are grid independent, additional calculations have been performed with a coarse 22 × 22 grid, a medium grid with 42 × 42 nodes, and a fine grid with 102 × 102 nodes for the flamelet model without extinction. The results obtained using the medium and fine grids were almost impossible to distinguish, and it is therefore concluded that the results obtained with the 61 × 47 grid are grid independent.

Results:

Calculated streamlines without and with extinction are shown in Figs. 2a and 2b, respectively. Figure 3 shows radial temperature profiles 95 mm downstream of the inlet. When extinction is not accounted for, both the EDC model and the flamelet model fail to reproduce the qualitative trends in the measurements. The cause for this discrepancy is that the flame is lifted from the fuel-air inlet. The lowest values for the turbulent fine structure time scale τ^* and, correspondingly, the largest strain rates χ, are found in the shear layer between the fuel and air jets and in the shear zone between the air jet and the recirculating zone.

When extinction is accounted for, however, the correspondence between the calculated and measured temperature is good. As expected, the temperature near the axis is lower when extinction is modeled. The effect that the temperature close to the wall is higher in the calculations with extinction deserves some discussion, however. The outer half of the temperature profiles in Fig. 3 are inside a recirculation bubble (see Fig. 2). The mixture in the recirculation bubble has enough time to react, so the temperature in this region is determined by the amount of fuel that diffuses through the annular air jet and out to the recirculation zone. The expansion between the coannular fuel and air jets when extinction is not modeled does not lead to a significant increase in the turbulence energy production rate, so the kinematic eddy viscosity ν_t is essentially unchanged. Because of the higher temperature without extinction, the density is reduced, leading to a lower dynamic turbulent eddy viscosity, $\mu_t = \rho\nu_t$, and, thus, a slower radial transport of fuel away from the center axis. At the same time, the size of the recirculation bubble is reduced by the expanding gases (see Fig. 2). The calculated reattachment lengths are 410 mm when extinction is modeled and 370 mm when extinction is not modeled.

Figure 4 shows radial profiles of the mixture fraction 327 mm downstream of the inlet. As for the temperature, the calculated results are seen to be in agreement with the measurements only when the effects of extinction are taken into account. The reason for the results seen here is the same as for the temperature results. The larger dynamic turbulent eddy viscosity when local extinction effects are taken into account leads to a faster axial decay of fuel along the

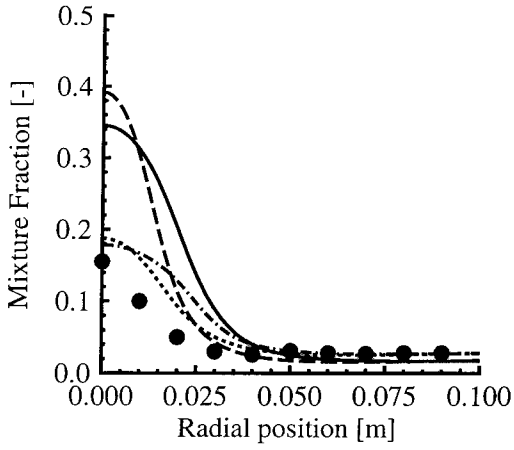

FIG. 4. Mixture fraction profiles at $x = 327$ mm. Solid line: EDC without extinction; dash-dotted line: EDC with extinction; dashed line: flamelet model without extinction; dotted line: flamelet model with extinction.

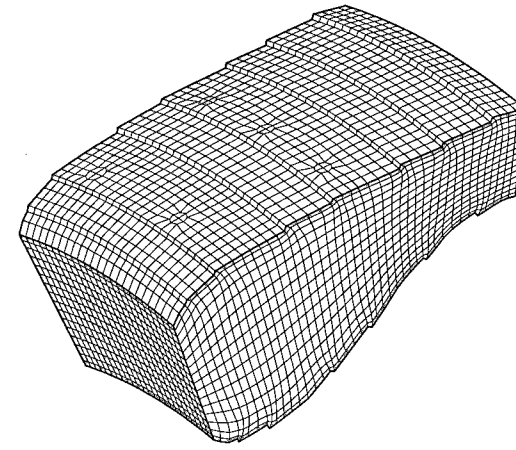

FIG. 5. Perspective of grid system for the annular combustor.

center axis and a higher value for the mixture fraction close to the combustor wall.

The EDC model and the flamelet model give reasonably similar results. Also, when the two extinction models were used, the results were as similar as one would expect from two such different models. This is also the case for other axial positions not presented here. If the reactants are partially premixed prior to entering the calculation domain, the flamelet model used here is inadequate. It is then necessary to add a reactive variable in the formulation that leads to a multidimensional PDF. The EDC model however, has been developed for diffusion, premixed, and partially premixed combustion [5]. Since the results obtained with the two models are essentially similar, the EDC model is preferred since it is simpler, yet more general.

Prediction of an Annular Combustor

The calculated annular gas-turbine combustor is periodic with 20 fuel injectors, so just a single 18° sector of the flame tube was modeled in the calculations. The 46 × 18 × 26 (axial × radial × circumferential) grid system used is shown in Fig. 5. The grid resolution is quite coarse, but it is regarded as sufficient for demonstrating the effects of local extinction in this combustor. Calculations for this combustor have previously been reported in several papers, for example Ref. 15.

Velocity Field:

The velocity fields obtained with the extinction model can hardly be distinguished from the fields obtained without the extinction model. Therefore, only the velocities without extinction are shown. Velocity vectors for side-view plane No. 9 are seen in Fig. 6. Side-view plane No. 9 cuts through the middle of the swirl cup and the primary dilution jets. The flows from the dilution jets are easily identified. Two counter-rotating vortices in the primary zone of the combustor recirculate combustion products and thus provide sufficient reaction time and temperature to anchor the flame.

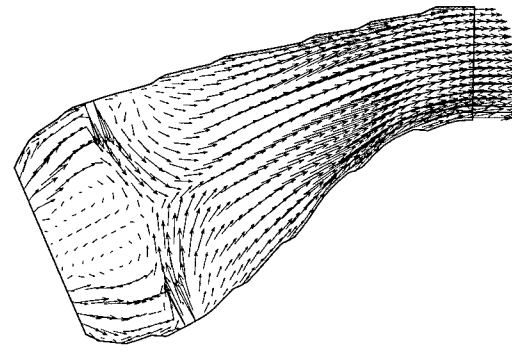

FIG. 6. Velocity vectors at side-view plane No. 9.

Temperature Field:

In Figs. 7 and 8, temperature contours at side-view plane No. 9 are shown. In the simulations, the most profound effect of local extinction is observed where the primary dilution jets that are aligned with the swirl cup impinge. This can be clearly seen by comparing Figs. 7 and 8. This is not unexpected, since the impingement results in a high level of turbulence and, accordingly, a small turbulence time scale τ^*. In

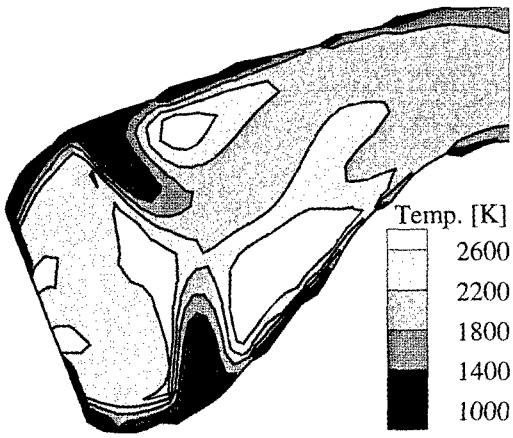

FIG. 7. Temperature field without extinction at side-view plane No. 9.

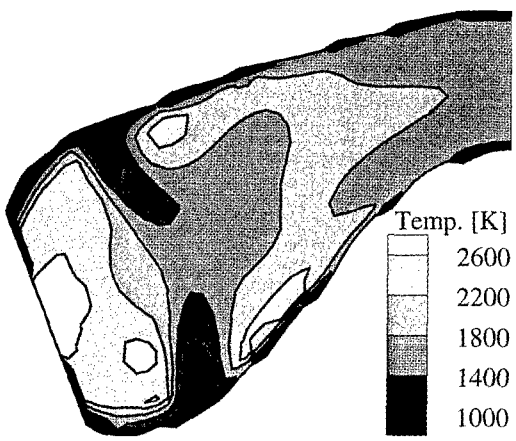

FIG. 8. Temperature field with extinction at side-view plane No. 9.

addition, the dilution jets are cool, so the chemical time scale τ_{ch} is (relatively) large (see Fig. 1).

Discussion:

The effects of extinction on the predicted reaction rate in the primary and intermediate regions of the combustion chamber illustrate the importance of finite-rate chemistry in gas-turbine combustor flows. Since no measurements inside of the combustor are available, it is difficult to assess whether the present extinction model is sufficient to account for the chemical kinetics effects on the heat release. With calculated peak temperatures exceeding 2600 K, the assumption of an irreversible one-step reaction [Eq. (10)] leads to some error. In addition, the effects of radiative heat transfer should be included. With the EDC combustion model, inclusion of a radiation model is straightforward.

Conclusions

The conclusions of this paper are summarized as follows.

1. The EDC and the flamelet combustion models with and without extinction models are compared.
2. In the axisymmetric sudden-expansion combustor studied, the effects of local extinction can be adequately handled by both of the extinction models discussed.
3. The EDC model and the flamelet model give essentially similar results. Therefore, the EDC model is preferred since it is simpler and yet more general than the flamelet model.
4. The very high levels of turbulence in modern gas-turbine combustion chambers lead to kinetically limited reaction rates. The present calculations indicate that the effects of local extinction have a significant impact on the reaction rate.

Nomenclature

f	mixture fraction
h, h_i	enthalpy, enthalpy of species i
k	turbulent kinetic energy
M_i	molecular weight of species i
$\tilde{P}$	joint Favre probability density function (PDF)
$\tilde{P}_f$, $\tilde{P}_\chi$	fractional PDFs for f and χ
p	pressure
p_b	burning probability
R_u	universal gas constant
r_F	stoichiometric oxidizer requirement
T	temperature
u_j	Cartesian velocity component
x_j	Cartesian coordinates
Y_i	mass fraction of species i
$\gamma\lambda$	mass fraction of turbulent fine structures
ε	dissipation rate of turbulent kinetic energy
μ	parameter in log-normal distribution
μ_t, ν_t	dynamic and kinematic turbulent eddy viscosities
ν	kinematic viscosity
ρ	density
σ	parameter in log-normal distribution
σ_h, σ_k, σ_ε, σ_Y	turbulent Prandtl/Schmidt numbers

τ_{ch}	chemical extinction time scale
τ°	turbulence fine structure time scale
χ	scalar dissipation rate
$\boldsymbol{\psi}$	state vector $= (h, p, Y_1, \ldots, Y_N)^T$
ω_i	reaction rate of species i

Subscript

b	burning
F	fuel
fl	flamelet
O	oxidizer
P	product
q	quenched
st	stoichiometric
t	turbulent

Acknowledgments

Financial support from the State R & D Program for Utilization of Natural Gas (SPUNG) is gratefully acknowledged. I. R. Gran and M. C. Melaaen are grateful to the Royal Norwegian Council for Scientific and Industrial Research (NTNF) for doctorate scholarships.

REFERENCES

1. Correa, S. M., and Pope, S. B., "Comparison of a Monte Carlo PDF/Finite-Volume Mean Flow Model with Bluff-Body Raman Data," in *Twenty-Fourth Symposium (International) on Combustion*, The Combustion Institute, Pittsburgh, 1992, pp. 279–285.
2. Masri, A. R., and Pope, S. B., "PDF Calculations of Piloted Turbulent Nonpremixed Flames of Methane," *Combust. Flame* 81:13–29 (1990).
3. Gran, I. R., "Mathematical Modeling and Numerical Simulation of Chemical Kinetics in Turbulent Combustion," Dr. Ing. Thesis, University of Trondheim, Norway, 1994.
4. Magnussen, B. F., and Hjertager, B. H., "On Mathematical Modeling of Turbulent Combustion with Special Emphasis on Soot Formation and Combustion," In *Sixteenth Symposium (International) on Combustion*, The Combustion Institute, Pittsburgh, 1976, pp. 719–729.
5. Magnussen, B. F., "Modeling of Pollutant Formation in Gas Turbine Combustors Based on the Eddy Dissipation Concept," in *Eighteenth International Congress on Combustion Engines*, Tianjin, China, June 1989, International Council on Combustion Engines.
6. Gran, I. R., Melaaen, M. C., and Magnussen, B. F., "Numerical Analysis of Flame Structure and Fluid Flow in Combustors," in *Twentieth International Congress on Combustion Engines*, London, 1993, International Council on Combustion Engines.
7. Byggstøyl, S., and Magnussen, B. F., "A Model for Flame Extinction in Turbulent Flow," in *Fourth International Symposium on Turbulent Shear Flows*, Karlsruhe, 1983, pp. 10.32–10.38.
8. Peters, N., "Laminar Diffusion Flamelet Models in Non-Premixed Turbulent Combustion," *Prog. Energy Combust. Sci.* 10:319–339 (1984).
9. Bilger, R. W., "Turbulent Flows with Nonpremixed Reactants," in *Turbulent Reacting Flows* (P. A. Libby and F. A. Williams, Eds.), Springer-Verlag, Heidelberg, 1980, pp. 65–114.
10. Melaaen, M. C., "Calculation of Fluid Flows with Staggered and Nonstaggered Curvilinear Nonorthogonal Grids—The Theory," *Numer. Heat Transfer, Part B* 21:1–19 (1992).
11. Melaaen, M. C., "Calculation of Fluid Flows with Staggered and Nonstaggered Curvilinear Nonorthogonal Grids—A Comparison," *Numer. Heat Transfer* 21:21–39 (1992).
12. Rhie, C. M., and Chow, W. L., "Numerical Study of the Turbulent Flow Past an Airfoil with Trailing Edge Separation," *AIAA J.* 21:1525–1532 (1983).
13. Lewis, M. H., and Smoot, L. D., "Turbulent Gaseous Combustion, Part I: Local Species Concentration Measurements," *Combust. Flame* 42:183–196 (1981).
14. Nikjooy, M., "On the Modeling of Non-Reactive and Reactive Turbulent Combustor Flows," Ph.D. Thesis, Arizona State University, Tempe, 1987.
15. Shyy, W., Correa, S. M., and Braaten, M. E., "Computation of Flow in a Gas Turbine Combustor," *Combust. Sci. Technol.* 58:97–117, 1988.

COMMENTS

T. W. J. Peters, Delft University of Technology, The Netherlands. 1. In your axisymmetrical combustion chamber case, the measured centerline temperature is significantly higher than the predicted values, even with your extinction model. Did you include nonadiabaticity effects due to radiation, to account for fuel and air preheating?

2. In Fig. 3b, your flamelet prediction shows a wiggle around $r = 0.025$ m. Is this related to the fact that your flamelet library consists of two flamelets only?

Author's Reply. 1. Nonadiabaticity effects due to radiation have not been included in the computations. Another possible reason for the underpredicted centerline temperature is that the fuel is preheated by the coflowing air *before* entering the combustor. We have found that the fuel inlet temperature will be 460 K instead of 300 K, provided that the inner tube is made of metal.

2. The "wiggle" in the flamelet calculations where extinction is accounted for is what is left of the reaction zone around the stoichiometric contour. This wiggle is not a result of a coarse flamelet library, but rather that the extinction model allows for some reaction in the lean region of

the shear layer where the turbulence level is sufficiently low. However, the size of the wiggle would have been smaller if a flamelet library that accounted for the high strain rates in the burning flamelets had been used.

•

Salah S. Ibrahim, British Gas, England. In your gas turbine combustor calculations, the flow is generated from two opposed like jets that generate a strong recirculating complex flow. Have you examined the dependence of your predictions on the computational grid resolution? Also, I would like to know the value of the extinction strain rate χ_q that you have used.

Author's Reply. 1. We have not examined the grid dependence of the predictions of the gas turbine combustor. As pointed out in our paper, we regard the grid resolution as sufficient for demonstrating the predicted effect of extinction.

2. For the axisymmetric combustor, we use $\chi_q = 8.0\ \mathrm{s}^{-1}$ as the extinction strain rate. In the gas turbine combustor, only the eddy dissipation concept (EDC) is applied. In the EDC model, an extinction time scale τ_{ch} rather than a strain rate is used (see Fig. 1 in the paper).

Twenty-Fifth Symposium (International) on Combustion/The Combustion Institute, 1994/pp. 1293–1299

TURBULENT BROADENING OF AUTOIGNITION LIMITS

SANJAY M. CORREA AND ANTHONY J. DEAN
General Electric Research Center
Schenectady, NY 12301, USA

We present a model for calculating the autoignition time in a *turbulent* flow in which fuel and air are being mixed. The model is applied to the 40-atm heptane-air system. Chemical kinetics are described by a four-step reduced mechanism or a 19-step reduced mechanism. Mixing is described by a particle-tracking probability density function (PDF) model. The model requires five dependent variables (temperature and four species) in the four-step mechanism and 14 dependent variables (temperature and 13 species) in the 19-step mechanism for each of the N_p particles used to discretize the PDF. The system is studied for $800 \leq T_{in} \leq 1000$ K, an initial mean equivalence ratio of 0.5 or 1.0, initial fuel-air distributions with a range of variances, and mixing frequencies (ω) from 10 Hz to 10 kHz. If the initial fuel-air PDF approaches a delta function, the predicted autoignition times (τ_{ign}) agree well with published data from shock tubes. Agreement is also obtained regardless of initial fuel-air distribution for $\omega \rightarrow 10$ kHz, because the initial differences are mixed away before the chemical kinetics can act. For $\omega \leq 1$ kHz, τ_{ign} decreases by up to a factor of 2 as the initial variance is increased. Particle locii in phase space are used to indicate the relative roles of mixing and chemistry in lean vs rich gas. The behavior of the four-step mechanism is very similar to that of the 19-step mechanism, across the mixing frequency range 10 Hz to 10 kHz.

Introduction

Autoignition is of interest in spark-ignition engines and in diesel engines, where its relationship to "knock" is widely appreciated. It is also of interest in lean premixed combustion (LPC) for low-NO_x gas turbines; for example, 25 ppm NO_x at 15% O_2 is now routinely attained in utility-class natural gas–fired LPC gas-turbine power plants [1]. More stringent regulations apply in certain areas of the world [2]. Similar performance will be expected with liquid hydrocarbon fuels. At the same time, the pressures and temperatures of the gas-turbine cycle are being increased in the interest of thermal efficiency: compressor discharge (combustor inlet) temperatures and pressures may be as high as 800–1000 K and 30–40 atm, respectively. A major concern in LPC under such conditions is autoignition of the fuel-air mixture during prevaporization and premixing. Since the autoignition time determines the maximum time available for premixing, it is a determinant of the ultimate NO_x emission levels. Hence, it is necessary to understand—and ideally to predict—autoignition times in the turbulent mixing field of a premixer.

Laboratory measurements are usually made in the well-characterized and well-controlled environment of shock tubes [3], flow reactors [4], or rapid compression machines [5]. In practice, however, autoignition can deviate from these laboratory data. Possible explanations for the discrepancies involve flashback through boundary layers, flame stabilization in regions of separated flow [6], temperature rise induced by acoustic waves, "statistical variations," and so on. The first and second of these are not strictly defined as autoignition. The third can be quantified: the temperature rise ΔT caused by a pressure rise Δp is given by linear acoustics as $\Delta T/T_0 = [(\gamma - 1)/\gamma]\Delta p/p_0$, where subscript "0" refers to the base quantity and γ is the ratio of specific heats. A severe combustion pressure oscillation in an LPC gas turbine is 2–3% of the base pressure; hence, the temperature rise is 20 K or less, which is insufficient to lead to dramatically different autoignition behavior. We focus here on the effect of nonuniformities in the fuel-air ratio on the autoignition time.

The notion of "turbulence broadening" of reaction zones has been discussed before; e.g., the broadening of thermal NO_x formation zones by superequilibrium in the oxyhydrogen radical pool was reviewed in Ref. 1. Others have considered the effect of temperature fluctuations specifically on autoignition. Tsuge and Sagara [7] started with the Boltzmann equation and found that, in principle, turbulence would decrease the effective activation energy and so broaden the autoignition limits. Closed-form analyses of single-step Arrhenius law models in the context of turbulent fluctuations gave similar results [8]. It is difficult, however, to relate these studies to the stiff multistep kinetics of practical fuels. Recent advances in chemical kinetic mechanisms [9] and turbulence modeling [10–13] make it worthwhile to revisit this problem.

This paper presents a model for calculating autoignition time in a turbulent flow in which fuel and air are in the process of being premixed. The method

is applied to the 40-atm heptane-air system, which is of interest because (1) autoignition times are on the order of 1 ms, much more relevant here than the 10–20 ms times measured in lower-temperature ranges in rapid compression machines [5], and (2) a four-step reduced kinetic mechanism has been developed for heptane ignition by Muller et al. [9] and compared well with the data of Ciezki and Adomeit [3]. Reduced mechanisms are potentially usable in computational fluid dynamics (CFD) design tools and, hence, merit investigation in the parameter spaces in which they will be used, e.g., turbulent mixing parameters. Finally, although detailed flow-field calculations are not presented here, the turbulence-chemistry interaction submodel is derived from the Monte Carlo/PDF transport closure model used in flow codes [10]. The present calculations can be viewed as a test of the probability density function (PDF) approach within each computational cell of a CFD/PDF calculation, since the subgrid is homogeneous.

The Model

The PDF $P(\mathbf{\Psi})$ denotes the probability density function of the scalar set denoted by the vector $\mathbf{\Psi}$. In a spatially homogeneous but unmixed reacting flow, P evolves according to [10,11]

$$\rho(\mathbf{\Psi})\frac{\partial P}{\partial t} + \frac{\partial[\rho(\mathbf{\Psi})S_a(\mathbf{\Psi})P]}{\partial \psi_a} = \frac{\partial\left[\left\langle \frac{\partial \mathbf{J}_i^a}{\partial x_i}\bigg|_{V,\mathbf{\Psi}}\right\rangle P\right]}{\partial \psi_a} \quad (1)$$

where the density ρ is a function of the scalar variables $\mathbf{\Psi}$, $S_a(\mathbf{\Psi})$ is the reaction rate, and the term in angle brackets is the conditional flux J_i^a of the scalar denoted by a in the direction i. The terms describe, respectively, the evolution of the PDF, the transport of the PDF in composition space ψ_a by reaction $S_a(\mathbf{\Psi})$, and the transport of the pdf in composition space by molecular fluxes. The terms on the left-hand side are exact, while that on the right-hand side requires modeling. Here, the PDF P describes the mass fractions Y_k of chemical species and is represented by the N_p-member ensemble $Y_k^{(n)}$, where $1 \leq k \leq N_s$ and $1 \leq n \leq N_p$; N_s is the number of species, and N_p is the number of particles. Each of the members n is referred to as a "particle." The PDF evolves under the combined influence of mixing and reaction.

The mixing term is modeled by "interaction-by-exchange-with-the-mean" (IEM), which is expected to be accurate if the scalar field is not intermittent in physical space [12,13]. The N_s species conservation equations for the nth particle become [14,15]

$$\frac{dY_k^{(n)}}{dt} = -\omega(Y_k^{(n)} - \bar{Y}_k) + w_k^{(n)}\frac{M_k}{\rho^{(n)}} \quad (2)$$

where ω is the mixing frequency, $w_k^{(n)}$ is the molar production rate of species k per unit volume for the nth particle, M_k is the molecular weight of species k, and $\rho^{(n)}$ is the density of the nth particle. The IEM model is preferred to others such as the Curl model [16,17] because (1) mixing and chemistry are accounted for simultaneously and (2) it is almost perfectly "parallelizable," i.e., suited to parallel computers [15]. The latter feature is not essential here because of the relative simplicity of the kinetics [9] relative to full mechanisms. The calculations reported below are not computationally intensive; thus, no special algorithms or computers are required. The temperature equation is analogous to Eq. (2).

For all $\omega \neq 0$, the effects of mixing and chemistry are simultaneous and cannot be reproduced by summing up N_p plug flow results with the initial conditions for N_p particles; a calculation of the latter kind would not capture the mixing.

To start with, the four-step four-variable mechanism is adopted [9]. This mechanism predicts heptane-air autoignition times in agreement with shock-tube data [3], although the negative temperature-dependence regime is not reproduced. In it, fuel is oxidized as follows:

$$F \rightarrow X \quad \text{(I)}$$

$$X + 11O_2 \rightarrow P \quad \text{(II)}$$

$$F + 2O_2 \leftrightarrows Y \quad \text{(III)}$$

$$Y + 9O_2 \rightarrow P \quad \text{(IV)}$$

where F denotes the fuel (C_7H_{16}), X and Y denote the groups of intermediates $3C_2H_4 + CH_3 + H$ and $HO_2R''O + H_2O$, respectively, and P denotes the group of products $7CO_2 + 8H_2O$. Hence, the dependent variables in Eq. (2) are $Y_F^{(n)}$, $Y_X^{(n)}$ $Y_Y^{(n)}$, and $Y_P^{(n)}$ for each particle n. The source terms $w_k^{(n)}$ for each particle in Eq. (2) are identical to the source terms in Ref. 9, up to factors in molecular weights to convert from mole to mass fractions. Reaction III is reversible, with the reverse rate having a much larger activation energy than the forward rate; however, at the ≥800 K inlet temperatures considered below, the reverse rate is always important and even dominant. In Ref. 9, this mechanism was favorably compared with shock-tube data [3] at the conditions (p, T_{in}, ϕ) considered below. The corresponding equation for the nth particle temperature $T^{(n)}$ is written as in Ref. 9 with $T_1 - T_4$ being constants (the ratios of reaction enthalpies to average specific heats), $k_{\mathrm{I}} - k_{\mathrm{IV}}$ being the rate constants, and X_k being the mole fraction of species k,

$$\frac{dT^{(n)}}{dt} = -\omega(T^{(n)} - \bar{T}) + [T_1k_{\mathrm{I}}X_F + T_2k_{\mathrm{II}}X_XX_O + T_3(k_{\mathrm{IIIf}}X_FX_O - k_{\mathrm{IIIb}}X_Y) + T_4k_{\mathrm{IV}}X_YX_O]^{(n)}$$

where $\bar{T}$ is the ensemble mean temperature. Hence, the model consists of $5 \times N_p$ first-order-coupled ordinary differential equation in time; $N_p \approx 100$ in the calculations reported below. Integration is performed numerically using a Gear method [18]. It should be emphasized that in the Lagrangian frame this is an initial value problem with no inflow or outflow; hence, Monte Carlo operations on the particles are not required. The particle count affects accuracy through discretization of the PDF and not through Monte Carlo operations.

A 13-species/19-step reaction mechanism [19] will also be considered below, in which case the model consists of $14 \times N_p$ equations.

The autoignition delay time can be defined in many ways and is not always stated clearly. The following criteria are used here: (1) With the four-step mechanism, the temperature rises from the beginning of the calculation but accelerates upon passing about 1300 K. Hence, ignition was defined as the time when 25% of the particles attained 1300 K. Changing this fraction had no influence on the trends. (2) With the 19-step mechanism, the criterion is when the (mean) temperature gradient exceeded 5 K/μS. The ignition time is not sensitive to this value because the rise during autoignition is so fast.

Discussion of Results: The Four-Step Mechanism

The particles' compositions and temperatures can be initialized according to any desired PDF. Here, we will prescribe uniform initial temperatures, however, with a Gaussian distribution of fuel-air ratio. The predicted autoignition time, therefore, depends on four inputs to the model, viz., the mean equivalence ratio ($\bar{\phi}$) and the variance (g) of the initial fuel-air distribution, the initial temperature (T_{in}), and the turbulent mixing frequency (ω). In the code, the distribution is specified via the fuel mass fraction (to which "g" refers), but the initial mean will be reported in terms of the equivalence ratio for ease of reading. If the variance is too large, the PDF is clipped to ensure positive initial fuel mass fractions.

Before the parametric study, a single simulation will be analyzed in detail. The conditions are $\bar{\phi} = 1$, $g = 9 \times 10^{-4}$, $T_{in} = 1000$ K, and $\omega = 1000$ Hz. Figure 1 shows the evolution of the temperature of the "richest" and "leanest" particles and of the ensemble, from $t = 0.01$ ms to just before autoignition. [The term richest (leanest) particle describes both the initial and the instantaneous equivalence ratio, because according to the IEM model, the richest (leanest) particle will always remain the richest (leanest); of course, its stoichiometry will decrease (increase) during mixing.] The rich particles lead the ignition process, because the heat and intermediate species generated in the rich particles mix into the leaner particles. Figure 2 shows corresponding locii in the Y_F-Y_X composition subspace. Different effects of mixing and reaction in the richest and leanest particles are readily distinguished in Fig. 2: the lean particle moves up on the Y_F axis, showing that the fuel mass fraction must be increasing, because of mixing, faster than any decrease caused by reaction I. In contrast, the rich particle moves down in Y_F under the

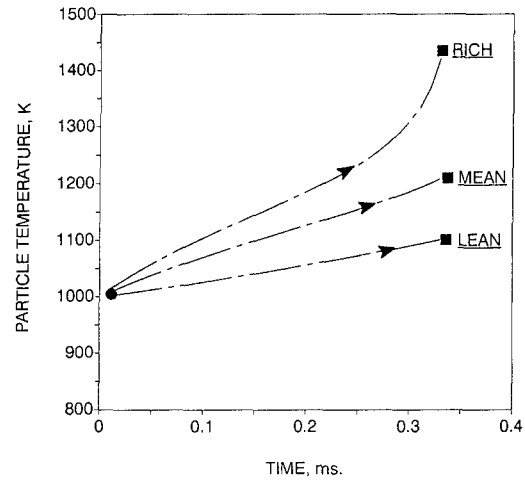

FIG. 1. The evolution of temperature for $\bar{\phi} = 1$, $g = 9 \times 10^{-4}$, $T_{in} = 1000$ K, and $\omega = 1000$ Hz. The richest and leanest particles are shown along with the ensemble mean. The locii start at $t = 0.01$ ms (●) and end just before autoignition at $t = 0.33$ ms (■); the arrows indicate advancing time.

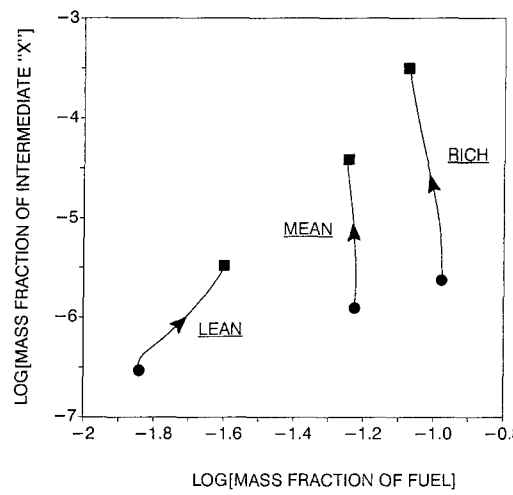

FIG. 2. The evolution of fuel and intermediate X for the conditions of Fig. 1. The richest and leanest particles are shown along with the ensemble mean. Symbols are as in Fig. 1.

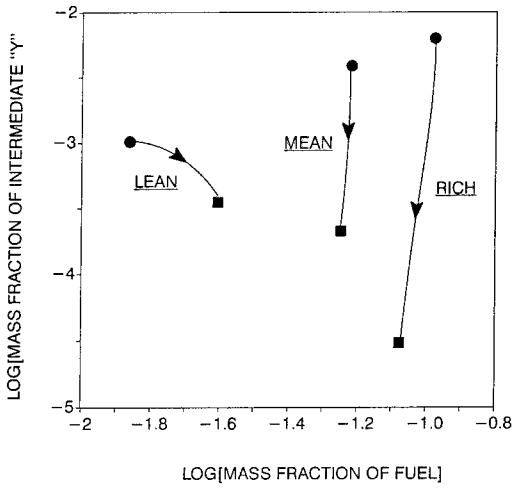

FIG. 3. The evolution of fuel and intermediate Y. Conditions and symbols are as in Fig. 1.

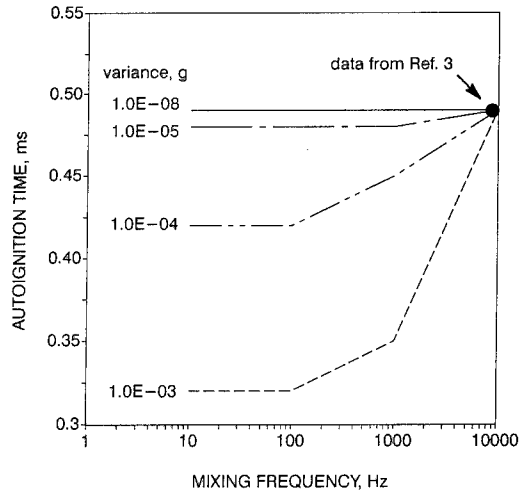

FIG. 4. The effect of mixing frequency on autoignition time. The curves are parameterized by the initial variance. Conditions are $\bar{\phi} = 1$ and $T_{in} = 1000$ K.

combined influence of mixing and reaction I. The projected length of the locus indicates the net change in species, which is greatest for the rich particle. The corresponding locii in Y_F-Y_Y space (Fig. 3) show that there is a rapid ($t < 0.01$ ms) production of intermediate Y, due to reaction III (forward). This reaction does not require radical species and, hence, commences immediately at $t = 0$. The rapid production of Y is followed by a slower decay to products via reaction IV. The fuel tracks are, of course, identical to those in Fig. 2.

The Effects of Mixing Frequency and Nonuniform Initial Distribution:

Figure 4 shows the effects of independent increases in ω and in g of the initial (Gaussian) fuel-air distribution on the autoignition time, τ_{ign}. The mean is stoichiometric ($\bar{\phi} = 1$). Both ω and g are carried to extreme values, as may be expected in the near field of a fuel injector in a premixing tube. For low ω's, the autoignition time drops as the initial g increases, because the richer particles lead the process, as discussed in Figs. 1 through 3. As ω becomes large ($\omega \rightarrow 10$ kHz), the autoignition times approach a common value regardless of the initial g, because the mixing is fast compared to any of the chemical rates. This common value of 0.5 ms compares well with the data [3] and the original computations per the four-step mechanism [9]. The decrease in τ_{ign} with g is greater if the mixture is overall lean ($\bar{\phi} = 0.5$; Fig. 5): a factor of about 2 is apparent.

From the above calculations, the autoignition time τ_{ign} decreases as g increases at *both* values of $\bar{\phi}$. The reason is found in the original shock-tube data: the autoignition times decrease monotonically with in-

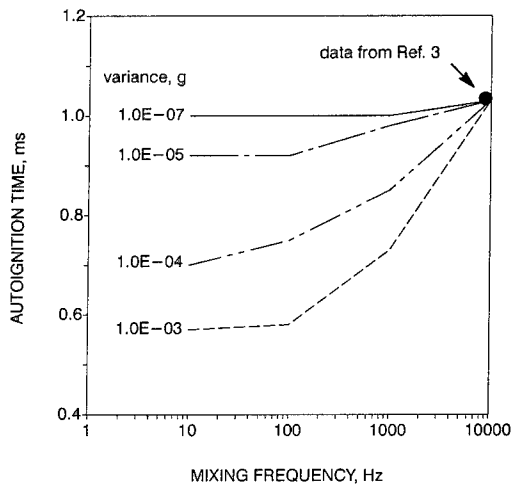

FIG. 5. The effect of mixing frequency on the autoignition time. The curves are parameterized by the initial variance. Conditions are $\bar{\phi} = 0.5$ and $T_{in} = 1000$ K.

crease in ϕ, in the range $0.5 < \phi < 2$ [3]. Hence, in the present study, as g increases at constant $\bar{\phi}$ in the initial PDF, the system is affected by the shorter ignition times of the richer particles.

To understand the behavior of τ_{ign} with mixing frequency, the intrinsic chemical time scales were examined. The evolution of species in a single isolated particle is shown in Fig. 6, prior to autoignition and at initial conditions of 1000 K, 40 atm, and $\phi = 1$. Species Y is formed very rapidly via reaction (IIIf) until the concentration of Y is sufficient for reaction (IIIf) to be nearly balanced by reaction (IIIb). Ini-

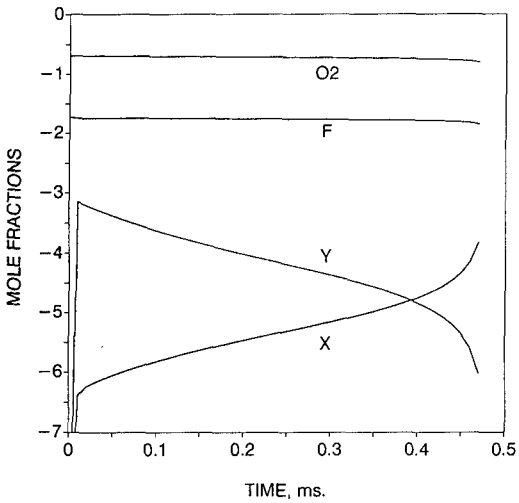

FIG. 6. The evolution of species in a single isolated particle at initial conditions of 1000 K, 40 atm, and $\phi = 1$.

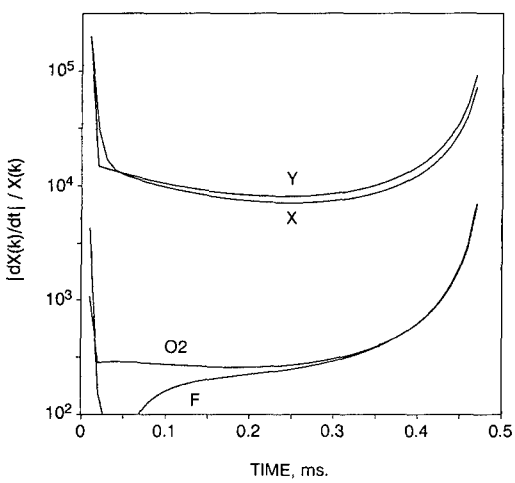

FIG. 7. The evolution of the characteristic inverse time constants, corresponding to Fig. 6. $X(k)$ is the mole fraction of species k.

tially, reaction (I) is very slow. Prior to ignition, the overall temperature gradually increases, the concentration of Y decreases and the concentration of X increases. At about 1300 K, the rate of reaction (I) becomes sufficiently fast for autoignition to occur. For initial temperatures between 700 and 1100 K, the shape of the species time histories are very similar to Fig. 6.

The influence of mixing frequency on the chemistry can be understood by examining the formation or removal frequency (in other words, the chemical frequency) of each species. The chemical frequency for a species is defined as the inverse of the instantaneous time constant of a species $|dX_k/dt|/X_k$. Figure 7 shows the chemical frequencies for each species calculated at the conditions of Fig. 2. Species F, O_2, and Y are removed while species X is formed. The chemical frequencies range from about 300 to 3×10^4 Hz. This range is consistent with the observed effect of mixing frequency on autoignition in Fig. 4. At frequencies at or below 100 Hz, the mixing frequency is lower than any of the chemical frequencies, and so the effect of concentration variation on autoignition is at a maximum. At a high mixing frequency of 10^4 Hz, the mixing frequency is on the same order as the highest chemical frequency, so the influence of the initial concentration variation is effectively eliminated, and autoignition reverts to the well-mixed case. At intermediate mixing frequencies, the chemical frequencies are only slightly faster than the mixing frequency, and so the influence on autoignition is at an intermediate value between the two extremes.

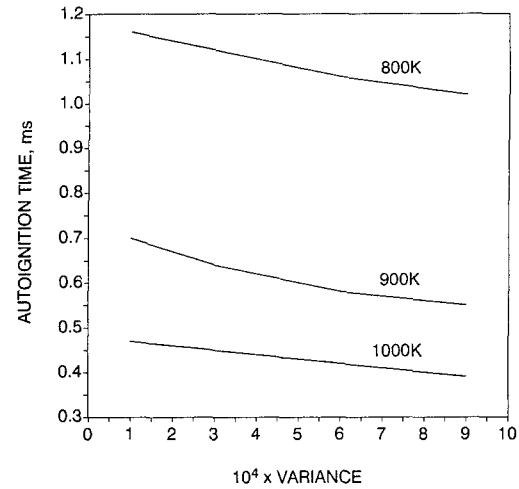

FIG. 8. The effect of the initial temperature and initial distribution of fuel-air ratio on the ignition time. Conditions are $\bar{\phi} = 1$ and $\omega = 1000$ Hz.

The Effects of Initial Temperature and Nonuniform Initial Distribution:

The variation of τ_{ign} with g is shown for $\bar{\phi} = 1$ in Fig. 8. At all temperatures, τ_{ign} decreases in a linear manner as g increases. It is also apparent that τ_{ign} decreases as the inlet temperature T_{in} increases; however, shock-tube measurements (which are relevant for the case $g = 0$) indicate the well-known negative temperature dependence in the range $T_{in} \approx 850$ K to $T_{in} \approx 1000$ K [3]. This discrepancy is intrinsic to the four-step mechanism [9].

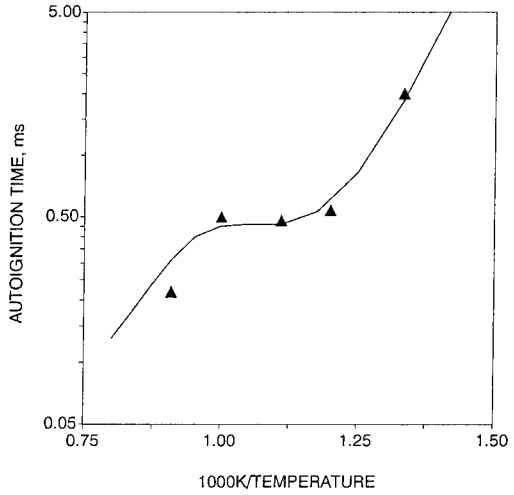

FIG. 9. Comparison of the 19-step (solid line) and the 1011-step mechanisms (▲ symbols). $\phi = 1$.

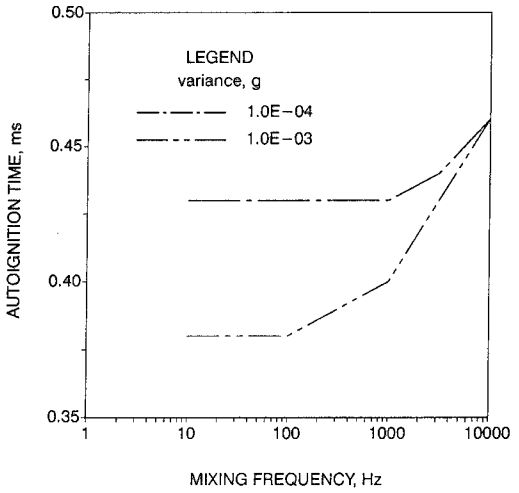

FIG. 10. The effect of mixing frequency on autoignition time, using the 19-step mechanism. The curves are parameterized by the initial variance. Conditions are $\bar{\phi} = 1$ and $T_{in} = 1000$ K.

The 19-Step Mechanism

The diversity of turbulence-chemistry interactions depends on the complexity of the reaction pathway, specifically, on the number of (significantly) different timescales in the chemistry. The four-step mechanism does not have as many timescales as full mechanisms, and hence, the above response to changes in the turbulence may be misleading. To investigate this further, a 13-species/19-step reaction mechanism [19] was applied to the same shock-tube data set. This reduced mechanism is based on the so-called Shell model [20]. It has been modified by other workers to predict autoignition for a variety of fuels in rapid compression machines, successfully reproducing the two-stage ignition observed there.

Here, the 19-step mechanism was further modified. The rates of three reactions involving fuel or fuel fragments (reactions (1), (3), and (8) in Ref. 18), were adjusted in the present work to match the autoignition times predicted by the 1011-step mechanism as reported in Ref. 9. The pre-exponential factors of reactions (3) and (8) were increased by factors of 2 and 3, respectively, while the activation energy of reaction (1) was reduced by 6 kcal/mol. These changes can be justified on the basis of different fuel structure (n-heptane instead of octane) and of different initial heating of the fuel-air mixture. With these modest changes, the predicted autoignition times agree well with those of the 1011-step mechanism, including the negative temperature dependence (Fig. 9). The autoignition time is at a local maximum at $T_{in} = 1000$ K.

The case $T_{in} = 1000$ K was selected for parametric simulations over g and ω (Fig. 10). By direct comparison of Figs. 4 and 10, it is concluded that the four-step mechanism reproduces the results of the 19-step mechanism to a reasonable degree in the range $10 < \omega < 10^4$ Hz. This agreement occurs because although some of the additional species in the 19-step mechanism have timescales as small as 10^{-4} to 10^{-5} s, they are not influential after the preignition stage. Since $10 < \omega < 10^4$ Hz spans the expected turbulence in multidimensional flow [15,21], the four-step mechanism can be regarded as usable for CFD-based studies.

Conclusions

Recent developments in stochastic mixing models and algorithms, combined with developments in reduced chemical kinetic mechanisms, have led to a model for the computation of autoignition in imperfectly premixed systems. The model is used to study the evolution of a nonuniform heptane-air mixture under the simultaneous influence of mixing and ignition chemistry, at high pressures and high initial temperatures. The model behaves according to expected bounds in the limits of (1) very narrow initial PDFs of fuel-air ratio and (2) a very high mixing frequency. The predicted values of autoignition time in these limits agree well with shock-tube data. A computational study of the autoignition time as a function of the initial temperature, of the initial mean and variance of the PDF of the fuel-air ratio, and of the mixing frequency, has been carried out. The four-step mechanism agreed well with a 19-step mechanism in the range 10–10^4 Hz (mixing frequency).

The model based on the four-step mechanism is

computationally inexpensive enough for parametric studies on simple computers. Although it does not capture the negative temperature-dependence regime of autoignition delay time, it may be useful in estimating the spread in measured autoignition times caused by fuel-air nonuniformity, or in applying laboratory data to design. For example, a practical implication of the present study is that a premixer tube at modern aircraft gas-turbine engine conditions can be only about half as long as might be expected from shock-tube data. (Aircraft engines do not yet employ lean prevaporized premixed combustors, for the reasons given earlier.) More importantly, however, since the model is derived from the joint PDF equation, there is a proven way to implement it in multidimensional CFD calculations [21]. Such tools will facilitate design analyses of premixer flows, including regions of separation or other types of recirculation.

Acknowledgment

This work was supported in part by the Air Force Office of Scientific Research, Contract No. F49620-91-C-0072, Dr. Julian Tishkoff, Project Manager.

REFERENCES

1. Correa, S. M., *Combust. Sci. Technol.* 87:329–362 (1992).
2. Bowman, C. T., *Twenty-Fourth Symposium (International) on Combustion,* The Combustion Institute, Pittsburgh, PA, 1992, pp. 859–878.
3. Ciezki, H. K., and Adomeit, G., *Combust. Flame* 93:421–433 (1993).
4. D'Anna, A., Mercogliano, R., Barbella, R., and Ciajolo, A., *Combust. Sci. Technol.* 83:217–232 (1992).
5. Halstead, M. P., Kirsch, L. J., and Quinn, C. P., *Combust. Flame* 30:45–60 (1977).
6. Plee, S. L., and Mellor, A. M., *Combust. Flame* 32:193–203 (1978).
7. Tsuge, S., and Sagara, K., *Combust. Sci. Technol.* 18:179–189 (1978).
8. Tennankore, K. N., *Combust. Sci. Technol.* 28:81–83 (1982).
9. Muller, U. C., Peters, N., and Linan, A., *Twenty-Fourth Symposium (International) on Combustion,* The Combustion Institute, Pittsburgh, PA, 1992, pp. 777–784.
10. Pope, S. B., *Prog. Energy Combust. Sci.* 11:119–192 (1985).
11. Pope, S. B., *Twenty-Third Symposium (International) on Combustion,* The Combustion Institute, Pittsburgh, PA, 1990, pp. 591–612.
12. Borghi, R., *Prog. Energy Combust. Sci.* 14:245–292 (1988).
13. Meyers, R. E., and O'Brien, E. E., *Combust. Sci. Technol.* 26:123–134 (1981).
14. Correa, S. M., *Combust. Flame* 93:41–60 (1993).
15. Correa, S. M., and Braaten, M. E., *Combust. Flame* 94:469–486 (1993).
16. Curl, R. L., *AlCh. E. J.* 9:175–181 (1963).
17. Flagan, R. C., and Appleton, J. P., *Combust. Flame* 23:249–267 (1974).
18. Hindmarsh, A. C., "ODEPACK, A Systemized Collection of ODE Solvers," in *Scientific Computing,* (R. S. Stephen, Ed.), IMACS Trans. on Scientific Computation, North Holland, Amsterdam, 1983, Vol. 1, pp. 55–64.
19. Cowart, J. S., Keck, J. C., Heywood, J. B., Westbrook, C. K., and Pitz, W. J., *Twenty-Third Symposium (International) on Combustion,* The Combustion Institute, Pittsburgh, PA, 1990, pp. 1055–1062.
20. Kirsch, L. K., and Quinn, C. P., *J. Chim. Phys.* 82:459–473 (1985).
21. Correa, S. M., and Pope, S. B., *Twenty-Fourth Symposium (International) on Combustion,* The Combustion Institute, Pittsburgh, PA, 1992, pp. 279–285.

Twenty-Fifth Symposium (International) on Combustion/The Combustion Institute, 1994/pp. 1301–1308

THE STRUCTURE OF THE RECIRCULATION ZONE OF A BLUFF-BODY COMBUSTOR

A. R. MASRI AND B. B. DALLY
Department of Mechanical and Mechatronic Engineering
The University of Sydney
New South Wales 2006, Australia
R. S. BARLOW
Combustion Research Facility
Sandia National Laboratories
Livermore, CA 94550, USA
AND
C. D. CARTER
Systems Research Laboratories, Inc.
Dayton, OH 45440, USA

The instantaneous mixing and reactive scalar fields have been measured in the recirculation zones of turbulent non-premixed flames stabilized on a bluff body, using the spontaneous Raman scattering technique. The measured means and rms fluctuations of mixture fraction, temperature, and the mass fractions of stable species are presented for various axial locations in the recirculation zone of CH_4/CO and CH_4/H_2 flames. The diameters of the bluff body and the central fuel jet are 50 and 2 mm, respectively. Both flames are about 40 cm in length and have a full, luminous recirculation zone that extends for about one bluff-body diameter from the exit plane. Two regions of almost homogenous mixture are identified within the recirculation zone: A large outer region, which on average is fuel lean, and an inner region, which is smaller and closer to the central fuel jet. Combustion is more intense in the inner region, where mean mixture fraction is stoichiometric and the peak values for temperature and mass fractions of combustion products are reached. Finite-rate chemical kinetic effects exist but *not* at high enough levels to cause localized extinction in the recirculation zone.

Introduction

Bluff-body combustors are used in many industrial applications because they provide excellent turbulent mixing characteristics, improved flame stability, and ease of combustion control. Experimental studies of bluff-body stabilized flames [1–5] have identified three main controlling parameters. These are (1) the strength of the circulation vortex, which scales linearly with the coflow air velocity, $\bar{u}_e$; (2) the fuel-jet momentum, which is a function of the fuel-jet velocity, $\bar{u}_j$; and (3) the diameter of the bluff-body, D_B, relative to the fuel-jet diameter, D_J. Two main types of bluff-body flames [2] have also been identified: (1) fuel-jet dominant flames, which are conical in shape and are stabilized to the burner by hot recirculating gases; and (2) coflow-air dominant flames, which have a luminous recirculating flame on the face of the bluff body. The occurrence of these flames depends on the relative fuel-jet velocity and coflow air velocity.

Computing the structure of bluff-body stabilized flames is now the subject of intense research. This is a step forward toward achieving the long-term objective of developing computer codes that may be used as design tools for the optimization of practical combustors. Standard codes using $k - \varepsilon$ turbulence closure models predict the global structure of the flow but are unable of resolving the details of the recirculation zones [5,6]. Reynolds stress closure models perform slightly better but are much more complex, as they require the solution of six modeled equations for the six turbulent stresses [7]. Current efforts are underway to modify the $k - \varepsilon$ approach using renormalization group models of turbulence, where the $k - \varepsilon$ constants will have a functional dependence on the flow [8]. Although problems still exist in computing the flow field, the mixing and reactive scalar fields are even more difficult. Correa and Pope [9] have used a hybrid approach, which combines a Lagrangian Monte Carlo solution technique for the velocity-composition probability density function (PDF) with a finite volume method for the $k - \varepsilon$ model of turbulence.

The main difficulty with these flows lies in the recirculation zone on the face of the bluff body, where the velocity, mixing, and reactive scalar fields are very complex. Current turbulent combustion models do not provide a very good description of even the velocity and mixing fields and need further development in these areas before the reactive scalar fields can be computed with confidence. Such an effort requires extensive measurements in the recirculating regions of the flows. Measurements of the velocity and turbulence fields have been reported by others [1,10,11]. Thermocouple and probe sampling data have been reported for temperature and the compositional structure of recirculation zones [12–15]. It is well known, however, that the flow there is very sensitive to probe interferences. The purpose of this paper is to present nonintrusive, spontaneous Raman measurements of species concentration and temperature in the recirculation zone of bluff-body stabilized non-premixed flames. Maps of the temperature and mixture fraction fields are provided. Fuel mixtures of CH_4/CO and CH_4/H_2 are used to ensure that the recirculation zone is free from soot.

Experimental

Spontaneous Raman scattering measurements of temperature and the concentration of many species are performed in the center of the recirculation zones of two flames. The measurements were performed at the Combustion Research Facility, Sandia National Laboratories, Livermore, CA. The laser beam from the facility dye laser, DIANA (dye: COUMARIN 521, λ = 532 nm, $\Delta\lambda$ = 0.3 nm, 1.0 J/pulse, 2-μs pulse width), is focused to a 500-μm-waist diameter. The laser energy in the probe volume is effectively doubled by reflecting the laser beam back onto itself using a spherical mirror. The signals from the Stokes vibrational Raman scattering from CH_4, CO_2, O_2, CO, N_2, H_2O, and H_2 are collected by photomultiplier tubes placed at the exit plane of the polychromator. Three other photomultiplier tubes are stationed around the Raman signals at 556, 583, and 645 nm. These monitor the fluorescence that interferes, in varying degrees, with each of the Raman signals. More details on the optical setup and the data processing procedure can be found elsewhere [16].

The burner has a bluff-body diameter, D_B = 50 mm and a fuel-jet diameter, D_J = 2.0 mm. Coflowing air is supplied through a shroud with an internal diameter of 86 mm. Both burner and coflowing air shroud are centered in a wind tunnel providing an outer coflowing stream of air at 2.0 m/s. The air through the shroud is supplied by a separate compressor and the coflow velocity is 25 m/s. Two fuel mixtures are used: CH_4/CO = 1/1 (by volume) and CH_4/H_2 = 2/1 (by volume). The stoichiometric values of mixture fraction are ξ_s = 0.114 and 0.052, respectively. The addition of CO or H_2 to the methane is necessary to prevent the formation of soot in the recirculation region. With these fuel mixtures, the ceramic on the face of the bluff body is red hot, and the flame in the recirculation zone appears to be soot free. It should be noted that an inert diluent, like N_2, could replace H_2 or CO, but this will shorten the flame, decrease its temperature, and reduce its stability. The following flames are investigated:

Fuel	$\bar{u}_j$ (m/s)	$\bar{u}_e$ (m/s)	Re_J	ξ_s	Recirculation zone
CH_4/CO	97.6	25	12,156	0.114	light to dark blue
CH_4/H_2	167.1	25	15,183	0.052	blue/pink

The jet Reynolds number, Re_J is based on the central jet exit conditions. The visible length of the flame is about 40 cm, and the length of the recirculation zone is ~5 cm for both fuels. Blowoff occurs at $\bar{u}_{BO} \sim$ 103.4 m/s for the CH_4/CO flame and at $\bar{u}_{BO} \sim$ 186.0 m/s for the CH_4/H_2 flame. At these velocities, the flames blow off in the intense mixing zone, which extends from $x/D_B \sim$ 1.0 to 2.0, while a stable flame still exists in the recirculation region. For each data point, temperature is determined from the sum of the species number densities, and the mixture fraction, ξ, is calculated as follows:

$$\xi = \frac{\dfrac{2(Z_C - Z_{C,O})}{W_C} + \dfrac{(Z_H - Z_{H,O})}{2W_H} - \dfrac{(Z_O - Z_{O,O})}{W_O}}{\dfrac{2(Z_{C,F} - Z_{C,O})}{W_C} + \dfrac{(Z_{H,F} - Z_{H,O})}{2W_H} - \dfrac{(Z_{O,F} - Z_{O,O})}{W_O}} \tag{1}$$

where Z_i is a conserved scalar given by the total mass fraction of element i and W_i is the molecular weight of element i. This formulation preserves the stoichiometric value of the mixture fraction regardless of differential diffusion effects.

Results and Discussion

Measurements have been made at various axial locations in the recirculation region of CH_4/CO and CH_4/H_2 flames. The measured mean values of mixture fraction $\bar{\xi}$ and temperature $\bar{T}$ are shown in Fig. 1 at the corresponding measurement location in the

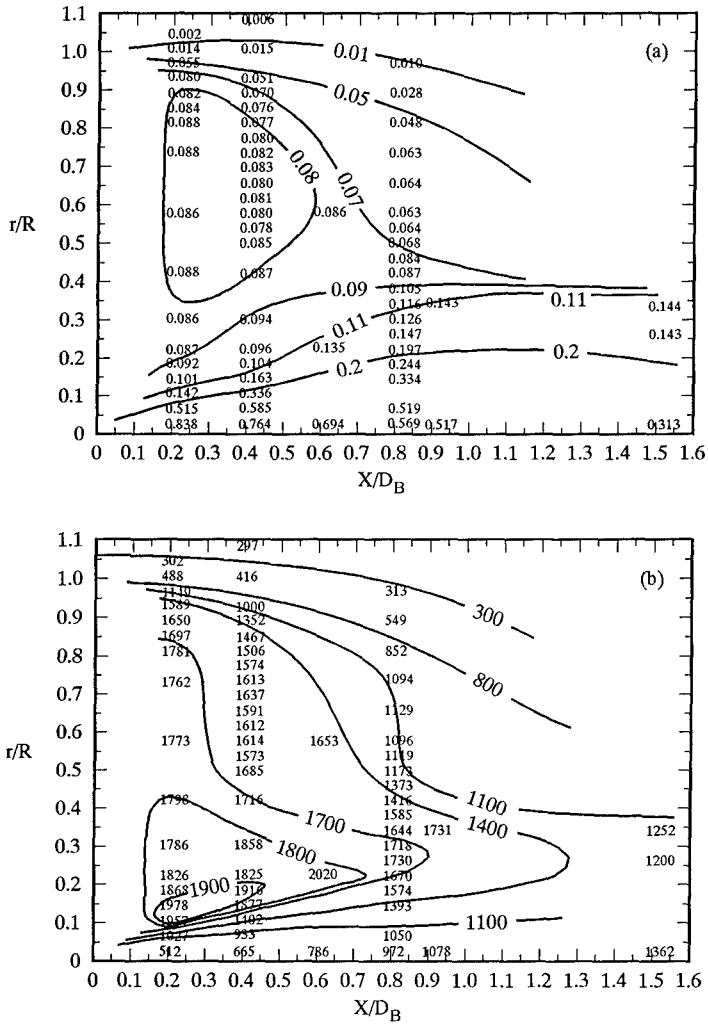

FIG. 1. Contours of (a) isopleths and (b) isotherms in the recirculation zone of the CH_4/CO flame. Also shown are the mean values of (a) mixture fraction and (b) temperature (K) at the corresponding measurement locations.

CH_4/CO flame. Also shown on Fig. 1 are contours of isotherms and isopleths. Interpolation has been used where needed to complete these contours. Two regions of almost-uniform temperature and mixture fraction are identified. A large, outer region on the air side of the flow extends to about $x/D_B \sim 1.0$ and is centered at $r/R = 0.65$, $x/D_B = 0.4$. It has a fuel-lean average mixture fraction with $\bar{\xi} \sim 0.08$ and $\bar{T} \sim 1600$ K. The inner region is much smaller in size, closer to the jet exit plane and centered at $r/R = 0.15$, $x/D_B = 0.3$. It has a mean mixture fraction very close to stoichiometric and a mean temperature of about 1980 K. Contour plots generated for other reactive species (not shown here) reveal a similar structure. These regions correspond closely to the double vortex structure, which has previously been observed [1–6] in the velocity field of such flows. The size and center of these vortices do not necessarily match those identified here from the mean temperature and mixture fraction results. For convenience, however, these inner and outer regions of uniform composition are referred to, in the rest of the paper, as the inner and outer vortices, respectively.

Figure 2 shows scatter plots for the measured temperature and mass fraction of H_2O plotted vs mixture fraction at $x/D_B = 0.4$ and 0.8 in the CH_4/CO flame and at $x/D_B = 0.8$ in the CH_4/H_2 flame. The three profiles shown on each plot represent the computed structure of laminar flames of the same fuel and over three different stretch rates ranging from low to intermediate to close to extinction. The overshoots in the peak temperature and mass fraction of water are mainly due to experimental error and represent only a very small proportion of the number of data points shown on each scatter plot. The data generally follow the laminar flamelet contours. Local extinction is rarely observed, regardless of the axial location within the recirculation zone in both CH_4/CO and

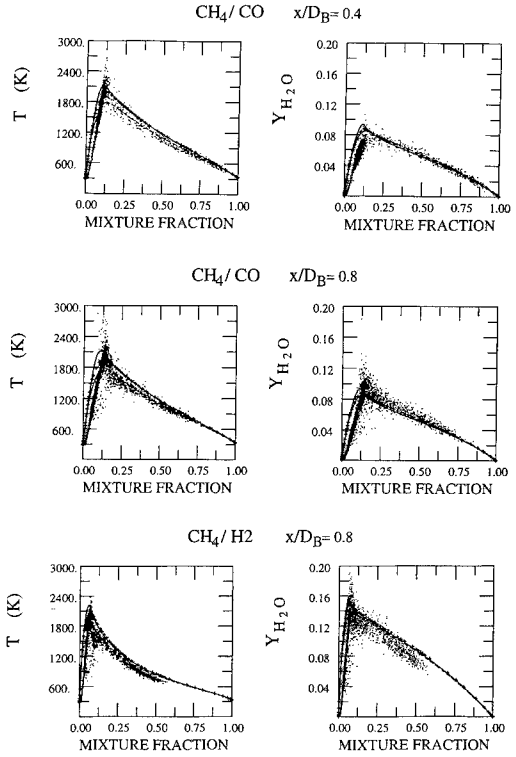

FIG. 2. Scatter plots for temperature, and the mass fraction of H_2O vs mixture fraction measured at $x/D_B = 0.4$ and 0.8 in the CH_4/CO flame and at $x/D_B = 0.8$ in the CH_4/H_2 flame. Solid and broken lines represent "fully burnt" and "fully stretched" flamelets, respectively, while the "intermediate" flamelet is represented by "+."

CH_4/H_2 flames. This is remarkable considering that these flames are at about 95 and 90% of the respective blowoff velocities and show significant localized extinction further downstream of the recirculation zone in the intense turbulent mixing neck. The scatter in the data and the coexistence of fuel and oxygen (not shown here) is evidence of the presence of finite-rate chemistry, albeit not large enough to induce local extinction. This implies that transient extinction/reignition processes need not be considered in modeling combustion in such zones. Although it is still necessary to account for the finite-rate chemistry effects, the next most important step in the computational development is to improve on the calculations of the mixing field in these recirculating zones.

Figures 3 through 5 each show plots for radial profiles of various scalars measured in the recirculation zone of the CH_4/CO and CH_4/H_2 flames. Each plot contains two or more radial profiles. The solid lines represent the measured mean profile. The vertical bars shown with the measurements are *not* error bars, as they represent measured turbulent fluctuations ($\pm\sigma$) of the scalar on each side of the mean. All the results are plotted vs r/R, where R is the radius of the bluff body ($R = 25$ mm).

Figure 3 shows radial profiles of the measured temperature, T, mixture fraction, ξ, and the mass fractions of CH_4 and O_2 measured in the CH_4/CO flame. Figure 4 shows four plots for the mass fractions of CO, CO_2, H_2, and H_2O for the same flame. Each plot shows three radial profiles measured within the recirculation zone at $x/D_B = 0.2$, 0.4, and 0.8. At $x/D_B = 0.2$, the mean-measured mixture fraction decreases from $\bar{\xi} = 0.84$ on the jet centerline to $\bar{\xi} = 0.11$ at $r/R = 0.12$, which is within the inner vortex. For the same respective locations, the mean-measured temperature, $\bar{T}$, increases from 512 to ~2000 K. In the range $0.25 \leq r/R \leq 0.8$, the mean-measured values of temperature and mixture fraction are nearly constant at ~1780 K and 0.087, respectively. At $x/D_B = 0.4$, the region of constant $\bar{\xi}$ is slightly narrower and extends from $r/R = 0.4$ to 0.8, where $\bar{\xi} \sim 0.08$. The mean temperature in the center of this constant $\bar{\xi}$ zone is about 1600 K. The region of constant $\bar{T}$ and $\bar{\xi}$ in the center of both recirculation zones implies that the fluid in both vortex cores is, on average, well mixed and nearly homogeneous. At $x/D_B = 0.8$, which is close to the recirculation zone tip, the rms fluctuations of mixture fraction ξ' are large, causing the high rms of fluctuations in temperature.

At a given axial location, the radial decrease in the mean mass fraction of CH_4 is faster than that for CO. This implies that, while no CH_4 is left in the core of the inner vortex, the mean level of CO is still 2%. At $x/D_B = 0.2$, the mean mass fractions of CO_2 and H_2O reach their peaks of 27 and 7% at $r/R = 0.12$, then decrease to a uniform level of 25.5 and 5.5%, respectively, in the region $r/R = 0.20$–0.85. Further downstream, the peak mean level of CO_2 decreases to 14% at $x/D_B = 0.8$, while that of H_2O increases to 8.3%. The peak mass fractions of CO_2 measured at $x/D_B = 0.2$ and 0.4 are higher than the theoretical limit of 19%, implying that this Raman line is affected by other interferences. Plots of the fluorescence interference on the Raman signals (not shown here) indicate a peak at $r/R = 0.08$ and 0.13 at $x/D_B = 0.2$ and 0.4, respectively. The error on CO_2, however, covers the whole width of the bluff body and implies the existence of extraneous, narrow band interference, which is possibly due to emission from soot precursors or the ceramic on the face of the bluff body.

The measured mass fraction of hydrogen peaks in rich mixtures close to the flame centerline and outside the core of the inner vortex. Oxygen penetration into the recirculation zone is significant, with mean mass fractions reaching 6% at $x/D_B = 0.2$ and increasing to 11% at $x/D_B = 0.8$. Nitrogen penetration (not shown here) in the recirculation zone is consistent with that shown here for oxygen. All measured scalars confirm that the fluid within the core of both inner and outer vortices is, on average, well mixed

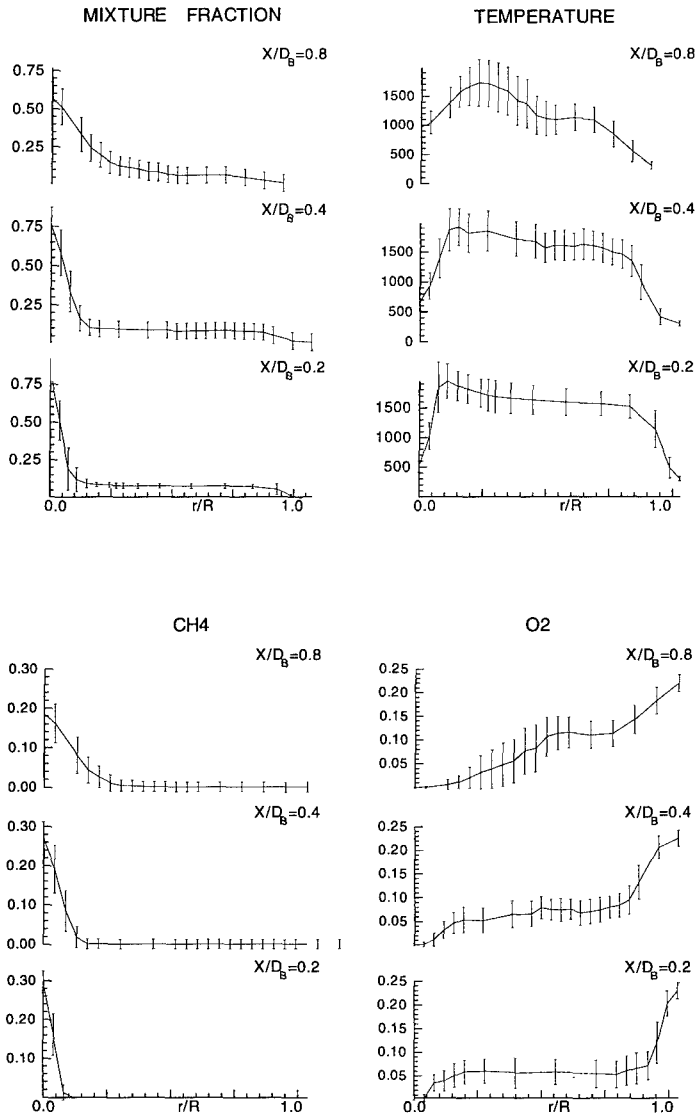

FIG. 3. Radial profiles of the mean temperature, $\bar{T}$, mixture fraction, $\bar{\xi}$, and the mean mass fractions of CH_4, O_2, measured at three axial locations in the recirculation zone of the CH_4/CO flame. The height of each vertical bar represents one rms fluctuation ($\pm\sigma$) of the scalar on each side of the mean.

and nearly homogeneous. The recirculating air mixes with jet fuel to stoichiometric proportions and burns intensely in the inner vortex, where the mean temperature is about 200–300 K higher than that in the outer vortex, where mixture is, on average, fuel lean. The rms fluctuations of all scalars peak in the region $r/R = 0.2$–0.4 at $x/D_B = 0.8$, which is close to the tip of the recirculation zone. It should also be noted that the low rms of fluctuations measured on the air side of the recirculation zone confirms the absence of instabilities, which leads to the periodic shedding of vortices.

Figure 5 shows plots for mixture fraction, temperature, and the mass fractions of H_2, H_2O, O_2, and CO at $x/D_B = 0.3$ and 0.8 in the CH_4/H_2 flame. The vertical bar shown at each measurement location represents one rms fluctuation of the scalar on each side of the mean ($\pm\sigma$). The solid line passes through the mean value. The mixing characteristics here are generally similar to those of the CH_4/CO flame. Although not enough data exist for this flame to generate contour plots, the inner and outer regions of homogeneous mixture can also be identified from the available profiles. At $x/D_B = 0.3$, the mean temperature peaks at 2125 K at $r/R = 0.17$, where $\bar{\xi}$ is almost stoichiometric at 0.05 and the inner vortex is expected to exist. Both $\bar{T}$ and $\bar{\xi}$ decrease to constant levels of ~2050 K and 0.045, respectively, in the

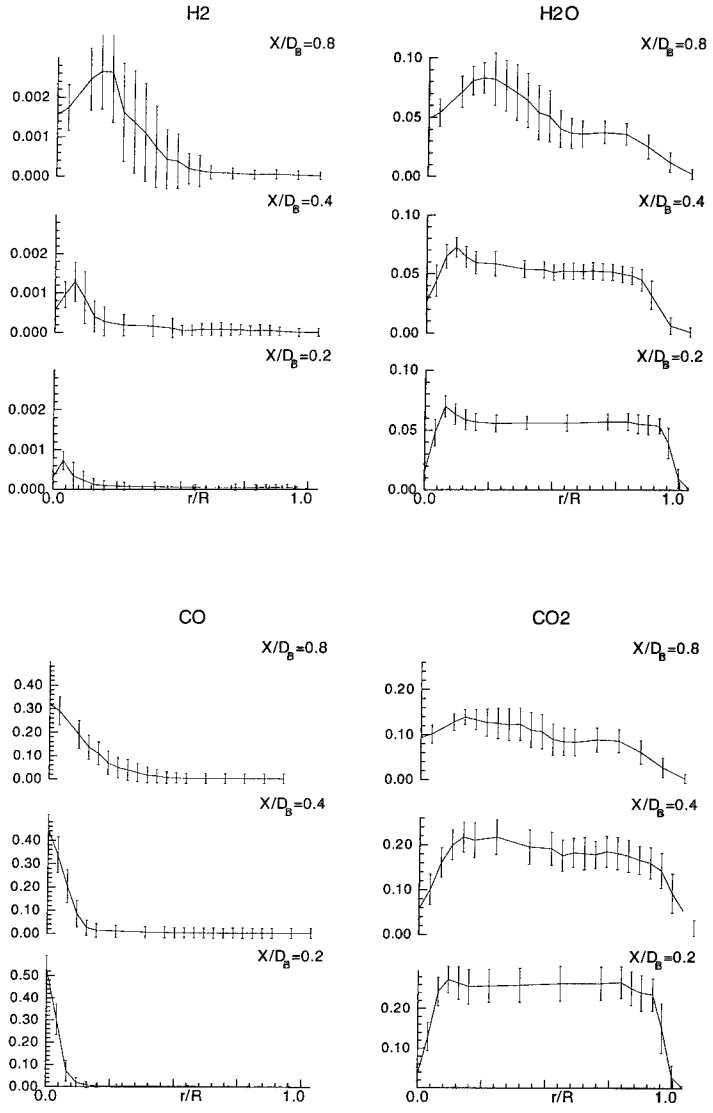

FIG. 4. Radial profiles of the mean mass fractions of H_2, H_2O, CO, and CO_2 measured at three axial locations in the recirculation zone of the CH_4/CO flame. The height of each vertical bar represents one rms fluctuation ($\pm\sigma$) of the scalar on each side of the mean.

range r/R = 0.2–0.9, where the outer vortex is located. Peak mean mass fraction of H_2O increases from 11.8% at x/D_B = 0.3 to 12.4% at x/D_B = 0.8. The peak CO levels occur on the rich side of stoichiometric. As for the CH_4/CO flame, the rms fluctuations peak for all scalars toward the end of the recirculation zone at x/D_B = 0.8.

The mean mass fraction of CH_4 decreases to 1% of its centerline value at $r/R \sim 0.15$, and 0.42 at x/D_B = 0.3 and 0.8, respectively. A slower rate of decay is measured for H_2, where the 1% level of the centerline value is reached at $r/R \sim 0.25$ and 0.58 at x/D_B = 0.2 and 0.8, respectively. The inner vortex, therefore, has some H_2 but no CH_4 left in its core, and this is consistent with the behavior of the CH_4/CO flame. The faster radial decay in CH_4 is a consequence of the chemistry rather than differential diffusion since the mixture fractions calculated from the carbon and hydrogen atomic balances are very close to those determined using Eq. (1).

The results presented here reveal that the outer vortex entrains enough air closer to the fuel jet to produce a combustible mixture in the *inner* vortex, which appears to be responsible for main heat release. Combustion products peak at the inner vortex region and are then carried radially out to the outer vortex. The outer vortex is fuel lean with $\bar{\xi} \sim 0.08$ but is still reactive since the lean reactive limit of the CH_4/CO fuel mixture is $\xi_l \sim 0.05$. It should be noted here that the inner region, although referred to here as a vortex,

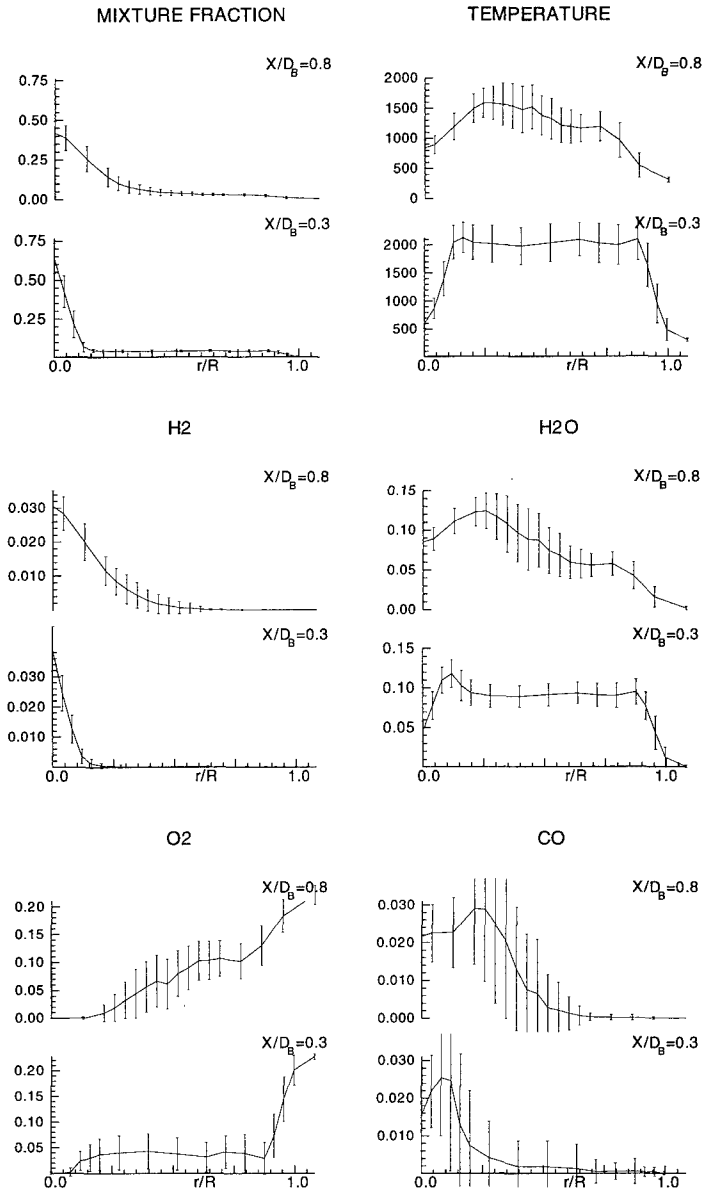

FIG. 5. Radial profiles of the mean mixture fraction, temperature, and the mass fractions of H_2, H_2O, O_2, and CO measured at two axial locations in the recirculation zone of the CH_4/H_2 flame. The height of each vertical bar represents one rms fluctuation ($\pm\sigma$) of the scalar on each side of the mean.

does not necessarily imply a second full recirculating inner zone. The existence of such a zone in these flows must be confirmed from velocity measurements.

Conclusions

The spontaneous Raman scattering technique is successfully used to perform measurements of mixture fraction, temperature, and the concentration of stable species at various axial locations in the recirculation zone of bluff-body stabilized diffusion flames. Two zones of almost homogeneous mixture are identified within the recirculation zone: A large outer region or vortex, which is fuel lean on average, but still within the lean reactive limit. An inner, smaller region that is close to the central fuel jet and has a stoichiometric mean mixture fraction. Peak temperature and mass fractions of combustion products are reached within this inner region. Although chemical kinetic effects are still significant, they are not high enough in the recirculation zone to cause localized extinction, even in flames that are very close to blowoff.

Acknowledgments

This work has been supported by the U.S. Department of Energy, Office of Basic Energy Sciences, Division of Chemical Sciences. Dr. Masri and Mr. Dally are supported by the Australian Research Council. The efforts of T. Prast and G. Wilkerson in operating the laboratory and the laser are acknowledged.

REFERENCES

1. Roquemore, W. M., Bradley, R. P., Stutrud, J. S., Reeves, C. M., Obringer, C. A., and Britton, R. L., "Utilization of Laser Diagnostics to Evaluate Combustor Models," AGARD Propulsion and Energetics Panel, Cesme, Turkey, 1983.
2. Roquemore, W. M., Bradley, R. P., Stutrud, J. S., Reeves, C. M., and Britton, R. L., "AIAA 21st Aerospace Sciences Meeting," Paper AIAA 83-0335, Reno, Nevada, Jan., 1983.
3. Chen, R.-H., Driscoll, J. F., Kelly, J., Namazian, M., and Schefer, R. W., *Combust. Sci. Technol.* 71:197–217 (1990).
4. Brum, R. D., Ikioka, L. M., and Samuelsen, G. S., ASME Publication 82-HT-36, 1982.
5. Correa, S. M., and Gulati, A., *Combust. Flame* 89:195–213 (1992).
6. Strugess, G. J., and McManus, K. R., "AIAA 22nd Aerospace Sciences Meeting," Paper AIAA 84-0372, Reno, Nevada, Jan., 1984.
7. Rodi, W., *PCH Phys. Chem. Hydrodynamics* 7:297–324 (1986).
8. Yakhot, V., Orszag, S. A., Thangam, S., Gatski, T. B., and Speziale, C. G., *Phys. Fluids A* 4(7):1510–1520 (1992).
9. Correa, S. M., and Pope, S. B., *Twenty-Fourth Symposium (International) on Combustion*, The Combustion Institute, Pittsburgh, 1992, pp. 279–285.
10. Schefer, R. W., Namazian, M., and Kelly, J., *Combust. Sci. Technol.* 56:101–138 (1987).
11. Namazian, M., Kelly, J., and Schefer, R. W., *Twenty-Second Symposium (International) on Combustion*, The Combustion Institute, Pittsburgh, 1988, pp. 627–634.
12. Davies, T. W., and Beer, J. M., *Thirteenth Symposium (International) on Combustion*, The Combustion Institute, Pittsburgh, 1971, pp. 631–638.
13. Kimoto, K., Shiraishi, I., and Matsumoto, R., *Combust. Sci. Technol.* 25:31–41 (1981).
14. Masri, A. R., and Bilger, R. W., *Twentieth Symposium (International) on Combustion*, The Combustion Institute, Pittsburgh, 1984, pp. 319–326.
15. Prade, D. B., and Lenze, B., *Twenty-Fourth Symposium (International) on Combustion*, The Combustion Institute, Pittsburgh, 1992, pp. 369–375.
16. Dibble, R. W., Ståner S. H., Masri, A. R., and Barlow, R. S., *Appl. Phys. B: Special Issue on Combustion Diagnostics* 1727–1731 (1990).

Twenty-Fifth Symposium (International) on Combustion/The Combustion Institute, 1994/pp. 1309–1315

RICH METHANE/AIR FLAMES: BURNING VELOCITIES, EXTINCTION LIMITS, AND FLAMMABILITY LIMIT

MARY N. BUI-PHAM AND JAMES A. MILLER
Combustion Research Facility
Sandia National Laboratories
Livermore, CA 94551-0969, USA

A theoretical investigation has been conducted to establish a reliable chemical kinetic mechanism that can determine the extinction limit of opposed-flow, strained, rich premixed methane-air flames. In the process of developing this kinetic representation for rich methane-air flames, we found that a value of 102.5 kcal/mol for the heat of formation at 298 K for singlet methylene, which is 1 kcal/mol higher than the currently available thermochemical data, gives the best agreement with experimental data on burning velocities for equivalence ratios between 0.5 and 1.7. Using this value for $\Delta H_{f^1CH_2}$ in our calculations, the extinction stretch rate, K_{ex}, was found to be $K_{ex} = 2250\ s^{-1}$ for $\phi = 1.0$, $K_{ex} = 2000\ s^{-1}$ for $\phi = 1.1$, and $K_{ex} = 1400\ s^{-1}$ for $\phi = 1.2$. These results agree better with experiments than those using a lower heat of formation of singlet methylene. In comparison with previous calculations made by Kee et al., our predictions are basically the same, except that our extinction stretch rate is slightly higher at $\phi = 1.0$ and that our location of the maximum extinction stretch rate is closer to that found in experiments. In addition, we establish the rich flammability limit using two different criteria to be approximately between $\phi = 1.62$ and $\phi = 1.68$, which agrees very well with an experimental value of $\phi = 1.67$.

Introduction

Understanding the structures and extinction conditions of combustion processes continues to be a challenging problem due to the chemical and fluid mechanical complexities involved. In recent years, thanks to the advance of computing technology, mathematical modeling has become a very useful and even essential tool in predicting the structures and critical conditions, as well as in determining the principal chemical paths, of many combustion systems using detailed chemistry. In this paper, we present our findings in the continuing research on premixed methane-air flames.

Previously, the chemical kinetic mechanism used by Kee et al. [1], which is essentially that of Miller and Bowman [2], produced high burning velocities under rich conditions [3]. As a result of these more robust rich flames, the extinction stretch rates, K_{ex}, calculated by Kee et al. [1] for an opposed-flow, strained premixed flame were significantly higher than those measured by Law et al. [4] (at least this is one possible explanation). These findings provide the impetus for developing a more reliable mechanism to predict accurately the extinction limit for rich methane-air flames. In order to accomplish this goal, we first need to assess how well this mechanism performs in freely propagating systems, since if it cannot determine burning velocities accurately, there is no reason to believe that it will produce correct critical extinction conditions. In the process of constructing this kinetic representation, we discovered that the heat of formation at 298 K of singlet methylene ($\Delta H_{f^1CH_2}$) plays a significant role in the determination of burning velocities and extinction limits of methane-air flames. This occurs because of the very fast reaction $^1CH_2 + H_2O \rightleftharpoons CH_3 + OH$, whose rate coefficient was nearly the collision rate at room temperature, as determined by Hack et al. [5]. In our model, we input the reaction as written with Hack's rate coefficient ($k_f = 1 \times 10^{14}\ cm^3/mol \cdot s$), but the reverse of this reaction actually takes place in methane flames, thus causing the thermochemistry (through the equilibrium constant, which is used to calculate the reverse rate) to have a direct effect on the kinetics. The situation is further complicated by the fact that, using the best available thermochemistry, one would calculate this singlet methylene reaction with water to be about 0.5 kcal/mol endothermic. Clearly, this is not consistent with such a fast reaction.

To address the validity of the new mechanism, we employ mathematical modeling to determine the structure and burning velocity of freely propagating methane-air systems and compare these results with experimental data for a range of equivalence ratios from 0.5 to 1.7 at atmospheric pressure. Sensitivity and reaction rate analyses are also performed to provide further insight into the chemical behavior and principal path of oxidation, as well as the flammability

limit of these rich flames. In our calculations, we test three different values for the heat of formation for $^1CH_2$: (1) the currently accepted value of $\Delta H_{f^1CH_2}$ = 101.5 kcal/mol, (2) a high value of $\Delta H_{f^1CH_2}$ = 104.5 kcal/mol, and (3) an intermediate value of $\Delta H_{f^1CH_2}$ = 102.5 kcal/mol. Comparison with experiments [6,7] reveals that the intermediate value for $\Delta H_{f^1CH_2}$ = 102.5 kcal/mol gives the best agreement for burning velocity predictions. This value of the heat of formation of singlet methylene is then used in extinction limit calculations for an opposed-flow, strained methane-air premixed flame for $\phi = 1.0$, $\phi = 1.1$, and $\phi = 1.2$, and the results are compared with Law's experiments [4]. In addition, we also attempt to establish the flammability limit of rich methane/air flames using two different criteria: (1) the composition that yields $V_u = 5$ cm/s (a qualitative rule proposed by Westbrook [8]) and (2) a kinetic criterion reported by Law and Egolfopoulos [9], where the competition between branching and termination reactions is considered.

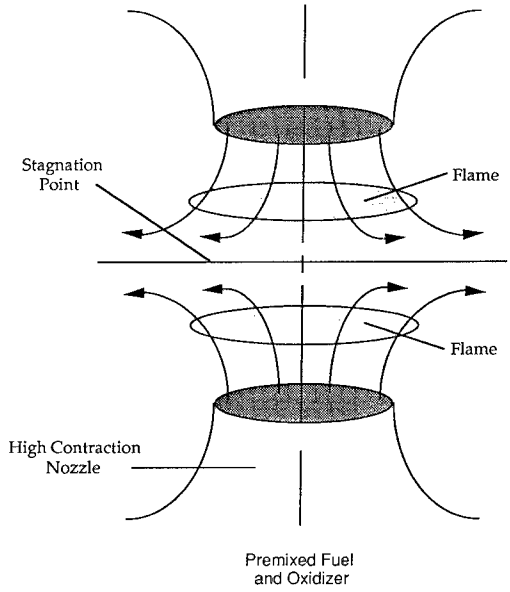

FIG. 1. Configuration used in opposed-flow model with separation distance of 7 mm.

Formulation for the Mathematical Problem

Chemical Kinetic Mechanism:

The present kinetic scheme is derived primarily from Miller and Melius [10] with some improvements. The main modifications are as follows:

1. The new rate used for the reaction OH + O = H + O_2 comes from Masten et al. [11]; this rate coefficient is consistent with Hessler's measurements at very high temperature [12] and also agrees with Miller and Melius's trajectory calculations using Varandas's potential energy surface over a very wide temperature range. The rate expression $k_f = 2.02 \times 10^{14}\ T^{-0.4}$ cm^3/mol·s appears to represent the kinetic data available from below room temperature to above 5000 K [13], where the subscript f denotes the forward direction of the reaction.
2. The inclusion of the methanol subset, which is comprised mostly of compilations by Tsang of the National Institute of Standards and Technology [14] and the European group (CEC) [15], with the use of Choudhury's rate constant for reaction $CH_3O + M = CH_2O + H + M$ ($k_f = 5.45 \times 10^{13} \exp(-13{,}497/RT)$ cm^3/mol·s) [16].

This new scheme consists of 239 reactions involving 53 chemical species (including up to C_6 chemistry). Because of its length, the mechanism is not listed here but can be obtained from the authors.

Governing Equations

Freely Propagating Premixed Flame:

The mathematical formulation for a steady, planar, adiabatic deflagration at low Mach number has been extensively cited in the literature [17,18] and will not be presented here. The mass flow rate $\dot{M}$ is an eigenvalue and must be determined as part of the solution; therefore, in addition to the usual boundary conditions, the location of the flame is chosen to be fixed by specifying the temperature at one point. This is sufficient to obtain the solution for the flame speed eigenvalue. As an improvement over previous calculations, thermal diffusion and multicomponent transport [19] are included, and central differencing techniques are employed.

Strained, Opposed Premixed Flame:

Figure 1 is an illustration of the configuration used in modeling strained, opposed premixed flames; a detailed description can be found in Ref. 1. The mixture composition, temperature, and inlet velocity are specified at the nozzle exit, and symmetry conditions are applied at the stagnation or symmetry plane. The nozzle separation distance for the present calculations is chosen to be 7 mm, because this is one of the separation distances used by Law et al. [4] in their experiments, with which we compare our predictions. In this fixed-domain approach, the inlet velocity is assumed to be purely axial at the nozzle exit,

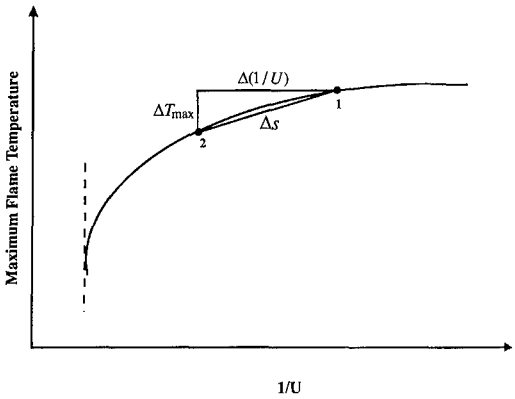

FIG. 2. Illustration of arc length continuation method.

and the radial pressure gradient eigenvalue is computed. The extinction limit is calculated with the aid of the arc length continuation method. Figure 2 illustrates this method using a plot of one component of the solution (maximum flame temperature) as a function of some parameter (velocity). Given a solution at point 1, the goal is to calculate the solution at point 2 efficiently. Using the normalized arc length continuation method, the relationship between point 1 and point 2 can be written as

$$\Delta s = \sqrt{\left(\frac{T_{\max,2} - T_{\max,1}}{T_{\max,1}}\right)^2 + \left(\frac{U_2 - U_1}{U_1}\right)^2}. \quad (1)$$

This procedure involves a change of variables, where the independent parameter (velocity) becomes a dependent variable, and the arc length Δs becomes the parameter. Equation (1) is then solved together with the other governing equations for a specified value of Δs (which decreases in value as the extinction limit is approached). The most important feature of the continuation procedure is its behavior near the extinction limit—a turning point in the solution (where vertical tangency occurs in Fig. 2). At this point, the Jacobian of the original system is singular, whereas the Jacobian of the augmented system is well behaved. Therefore, this method is a great tool in accurately predicting flame extinction limits.

Result and Discussions

Burning Velocity:

Under stoichiometric and slightly rich conditions, reaction with OH is one of the dominant removal paths for methyl radicals; this reaction $CH_3 + OH \Rightarrow$ products has several channels;

$$CH_3 + OH + (M) \rightarrow CH_3OH + (M) \quad (1)$$

$$CH_3 + OH \rightarrow CH_2OH + H \quad (2)$$

$$\rightarrow CH_3O + H \quad (3)$$

$$\rightarrow {}^1CH_2 + H_2O \quad (4)$$

$$\rightarrow {}^3CH_2 + H_2O \quad (5)$$

$$\rightarrow HCOH + H_2. \quad (6)$$

The first five paths are included in our mechanism, and of these, reaction (4) is the most important under flame conditions. Reaction (6) has only recently been introduced by Walch [20] as a possibility from electronic structure calculations. The sensitivity analysis for the mass burning rate of a freely propagating methane-air premixed flame for an equivalence ratio of 1.6 shown in Fig. 3 reveals that the reaction $CH_3 + OH = {}^1CH_2 + H_2O$ plays an important role. Hack et al. [5] measured the reverse rate of this reaction, i.e., ${}^1CH_2 + H_2O \rightarrow CH_3 + OH$, in a quasi-static flash photolysis system and found it to be approximately gas kinetic at room temperature (on the order of $\sim 10^{14}$ cm^3/mol. s). In our model, we include this reaction, as measured by Hack, in the (-4) direction; however, in methane flames, this reaction actually proceeds in the forward (4) direction. In our flame calculations, reverse rates are determined from equilibrium constants and forward rates ($k_r = k_f/K_{eq}$); this fact causes the thermochemistry to have a direct effect on kinetics. Furthermore, from the best available thermochemical data, one could determine reaction (-4) to be approximately 0.5 kcal/mol endothermic. This is not consistent with such a large rate coefficient. Later, in 1992, Oser et al. [21] performed direct measurements of the methyl reaction with OH for a range of temperatures from 300 to 480 K. They investigated the ${}^1CH_2$ product channel by measuring the increase in water signal upon reaction. To avoid counting the water formation through OH recombination, they used OD instead of OH so that water from recombination would show up as D_2O, and water from (4) would appear as HDO. By combining the results from Hack et al. [5] for the reverse reaction and their own observation for the forward path, Oser et al. [21] concluded that the heat of formation of ${}^1CH_2$ should be $\Delta H_{f^1CH_2} =$ 103.9 kcal/mol. This conclusion motivated us to test several values of the heat of formation for ${}^1CH_2$ because, although the separation energy for ${}^3CH_2 \rightarrow {}^1CH_2 \sim 9$ kcal/mol is fairly reliable and accepted [22], the error limit for the heat of formation of triplet methylene is subject to some uncertainty [23,24]. The three values used are (1) the currently accepted value of $\Delta H_{f^1CH_2} = 101.5$ kcal/mol, (2) a high value of $\Delta H_{f^1CH_2} = 104.5$ kcal/mol, and (3) an intermediate value of $\Delta H_{f^1CH_2} = 102.5$ kcal/mol. The heats of formation used for triplet methylene (${}^3CH_2$) were

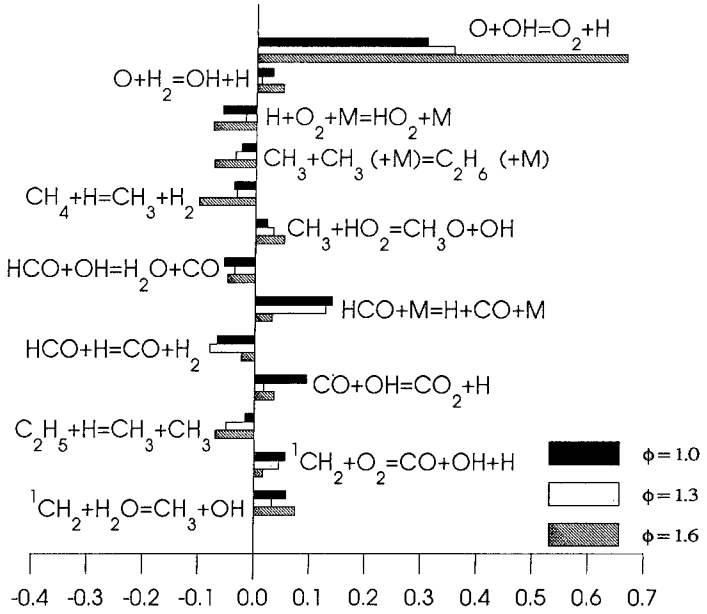

FIG. 3. Normalized sensitivity for the mass burning rate of freely propagating methane-air premixed flames (defined as $(\varepsilon_i/\dot{M})(\partial\dot{M}/\partial\varepsilon_i)$, where ε_i is a temperature- and pressure-independent factor in the ith rate coefficient.

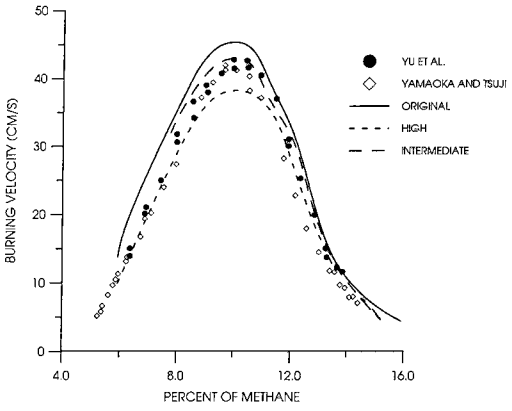

FIG. 4. Burning velocity as a function of equivalence ratio ϕ for freely propagating methane-air premixed flames: ● Yu et al.; ◇ Yamaoka and Tsuji; --- calculated results using $\Delta H_{f^1CH_2}$ = 104.5 kcal/mol; * calculated results using $\Delta H_{f^1CH_2}$ = 102.5 kcal/mol; —— calculated results using $\Delta H_{f^1CH_2}$ = 101.5 kcal/mol.

appropriately changed to correspond with those of singlet methylene using the separation energy of ~9 kcal/mol.

Figure 4 represents the burning velocity as a function of equivalence ratio ϕ. Theoretical predictions are compared with experimental data from Yu et al. [6] (denoted by ●) and Yamaoka and Tsuji [7] (denoted by ◇). The smooth line (——) represents calculations using $\Delta H_{f^1CH_2}$ = 101.5 kcal/mol and $\Delta H_{f^3CH_2}$ = 92.5 kcal/mol; the dotted line (---) represents a higher value of the heat of formation for $\Delta H_{f^1CH_2}$ = 104.5 kcal/mol and $\Delta H_{f^3CH_2}$ = 95.5 kcal/mol. From this plot, it is easily observed that the low heat of formation of singlet methylene produces methane-air flames that are too robust and that a higher value (slightly higher than that recommended by Oser et al.) was tested to yield burning velocities that are too low. Therefore, an intermediate value (denoted by *) of $\Delta H_{f^1CH_2}$ = 102.5 kcal/mol and $\Delta H_{f^3CH_2}$ = 93.5 kcal/mol were used and, as shown in Fig. 4, yield the best agreement with available experimental data. From this plot, it is abundantly clear that there is a direct relationship between the burning velocity of methane-air flame and $\Delta H_{f^1CH_2}$ from lean to rich conditions and that the intermediate value of $\Delta H_{f^1CH_2}$ results in the best match with experimental data. Given the uncertainty in determining this quantity, it is worthwhile to entertain the possibility that $\Delta H_{f^1CH_2}$ ~ 102.5 kcal/mol. This value is closer to that suggested by Oser et al. [21] and is well within the uncertainty reported by Börland et al. [23].

Flammability Limit:

Although the definition of the flammability limit is clear, i.e., the state at which steady propagation of the one-dimensional, planar premixed flame in the doubly infinite domain fails to be possible [25], the theoretical determination of such a limit remains problematical. It is not clear when and if such a limit even exists theoretically. In this work, we compare limits based on two different criteria:

1. The critical composition that produces a burning velocity of 5 cm/s: because the model is adiabatic,

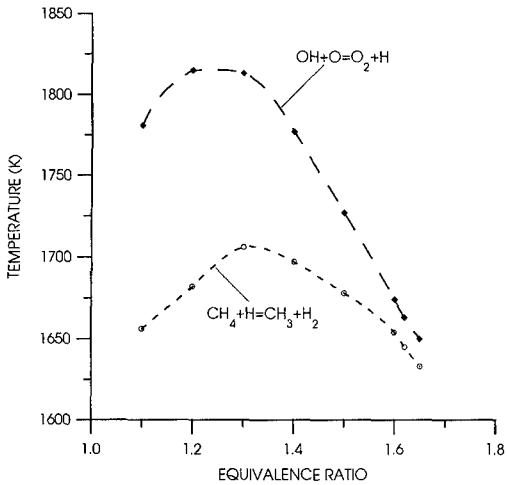

FIG. 5. Temperature at maximum branching and termination rate as a function of equivalence ratio.

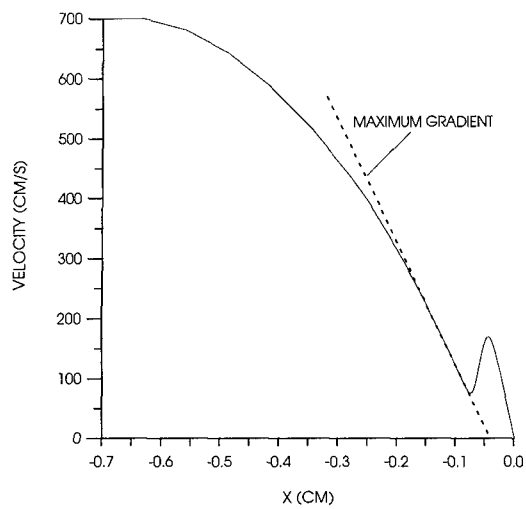

FIG. 6. Axial velocity profile of a strained premixed flame; the stretch parameter K is defined as the maximum axial velocity gradient.

it continues to calculate flame propagation at any equivalence ratio, although the burning velocity is small; Westbrook [8] reported a qualitative rule that $V_u < 5$ cm/s corresponds to a nonflammable mixture, and

2. The critical composition where the rate of the primary chain-termination reaction is equal to that of the chain-branching reaction (Law and Egolfopoulos [9]).

Using the above criteria, we observe from Fig. 4 (*) that $\phi = 1.68$ renders a burning velocity of 5 cm/s. To use Law and Egolfopoulos' criterion, which is based on the concept that competition between branching and termination reactions must be important for the weakly reacting flames close to the flammability limits, a sensitivity analysis was conducted for a rich condition ($\phi = 1.6$) to establish the most important chain-branching and chain-termination reactions. Figure 3 shows that these reactions are $H + O_2 \rightarrow OH + O$ and $CH_4 + H \rightarrow CH_3 + H_2$, respectively. Once the dominant branching and termination paths are identified, it is found that their respective rate profiles approach each other at the flammability limit; this was also reported by Law and Egolfopoulos [9]. This behavior can be seen in Fig. 5, which presents the temperature at the maximum rate of each reaction as a function of equivalence ratio. In order to establish a quantitative critical composition, a parameter a (termed the "flammability exponent") was proposed by Law and Egolfopoulos [9] to be $a = \partial(\ln \omega_T)/\partial(\ln \omega_B)$, where $\omega \equiv$ net rate and T and B denote termination and branching, respectively. The critical composition, where $a = 1$, represents the flammability limit, and from our calculations, $a = 1$ at $\phi = 1.62$. This value agrees very well with Law's experiments ($\phi = 1.67$) and calculations ($\phi = 1.69$). It is interesting to note that the two different definitions yield very similar results; it is safe to say at $\phi > 1.68$, methane-air flames do not propagate at atmospheric pressure.

Extinction Limits:

For the opposed-flow, strained premixed flame computations, a stretch parameter K is defined as the maximum axial velocity gradient $-du/dx$, as shown in Fig. 6. The velocity profile in Fig. 6 is initially that of a stagnation flow characterized by the specified negative slope. It reaches a minimum, then increases because of thermal expansion, and finally, when heat release is complete, it decreases in accordance with the stagnation flow requirement. Figure 7 shows maximum flame temperature as a function of the reciprocal stretch rate, $1/K$, where a vertical tangent can be drawn at extinction. Table 1 summarizes extinction results for different heats of formation of singlet methylene and gives values of $K_{ex} = 2700\ s^{-1}$ and $T_{max} = 1763$ K for a stoichiometric methane-air flame and $K_{ex} = 2600\ s^{-1}$ and $T_{max} = 1814$ K for $\phi = 1.1$, using $\Delta H_{f^1CH_2} = 101.5$ kcal/mol and $\Delta H_{f^3CH_2} = 92.5$ kcal/mol, while $\Delta H_{f^1CH_2} = 102.5$ kcal/mol and $\Delta H_{f^3CH_2} = 93.5$ kcal/mol yield $K_{ex} = 2250\ s^{-1}$ and $T_{max} = 1775$ K for $\phi = 1.0$, $K_{ex} = 2000\ s^{-1}$ and $T_{max} = 1824$ K for $\phi = 1.1$, and $K_{ex} = 1400\ s^{-1}$ and $T_{max} = 1854$ K for $\phi = 1.2$. Comparison of the present model with experiments conducted by Law et al. [4], which give values of $K_{ex} = 1650\ s^{-1}$ for methane-air flame at $\phi = 1.0$, $K_{ex} = 1250\ s^{-1}$ at $\phi = 1.1$, and $K_{ex} = 750\ s^{-1}$ at $\phi = 1.2$, shows better agreement for the higher heats of formation. In comparing with previous calculations

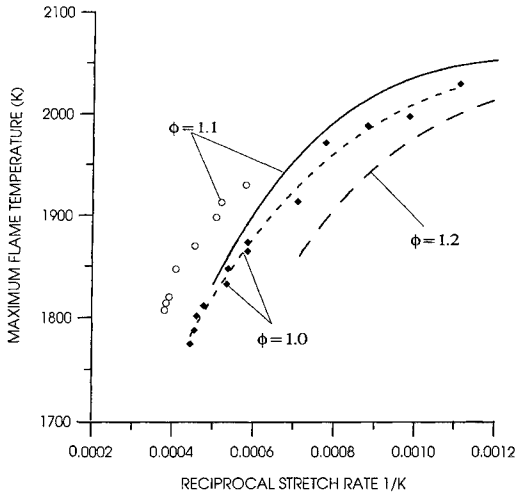

FIG. 7. Maximum flame temperature as a function of the reciprocal stretch rate, $1/K$, for ϕ = 1.0, 1.1, and 1.2 methane-air premixed flames. The symbols represent calculated results using $\Delta H_{f^1CH_2}$ = 101.5 kcal/mol and $\Delta H_{f^3CH_2}$ = 92.5 kcal/mol, and the lines represent calculated results using $\Delta H_{f^1CH_2}$ = 102.5 kcal/mol and $\Delta H_{f^3CH_2}$ = 93.5 kcal/mol.

made by Kee et al. [1], our model gives basically the same results, except that our extinction stretch rate is slightly higher at ϕ = 1.0, and the location of the maximum extinction stretch rate in our calculations matches that of experiments better. An interesting point to note here is that the peak burning velocity for a freely propagating premixed methane-air flame occurs at about ϕ = 1.1 and the peak K_{ex} for an opposed-flow, strained flame occurs at a slightly leaner condition; this observation was found for both experiments and calculations.

Judging from the comparisons, one can observe that although there is good qualitative agreement, there is still a quantitative difference. Kee et al. [1] proposed several possibilities for the discrepancy. The first is that the experimental measurements are made for varying nozzle separations, which are not specifically reported, and this may not be modeled accurately in our calculations since our separation distance was fixed at 7 mm. A second reason may be that we have modeled the flow exiting the nozzles as a simple plug flow where, in reality, there may be some radial spreading at the nozzle exit. A third reason for the discrepancy may lie in the method of calculating K_{ex}; this method is used in both experiments and models and requires some judgment to decide exactly where to define the axial velocity gradient. In the simulations, we observe that there can be a $\geqslant$100 s^{-1} variation in the velocity gradients depending on exactly where they are evaluated. Thus, some disagreement seems inevitable in this comparison.

Concluding Remarks

In the present investigation, we have reported our efforts in developing a reliable kinetic representation that can accurately predict the extinction limits of rich methane/air flames. During this process, we observed that the heat formation of singlet methylene significantly influences the determination of the burning velocity; an increase of only 1–3 kcal/mol of this quantity results in an average decrease of 2–7 cm/s in burning velocity from lean to rich conditions. In comparing with existing experimental burning velocity data, we established that values of $\Delta H_{f^1CH_2}$ = 102.5 kcal/mol and $\Delta H_{f^3CH_2}$ = 93.5 kcal/mol give the best agreement between modeling and experiments. Thus, this change was incorporated into our mechanism. Our predictions of the extinction limit for three equivalence ratios, ϕ = 1.0, ϕ = 1.1, and ϕ = 1.2, reveal better agreement with experiments if this intermediate value of the heat of formation of $^1CH_2$ is used, although there is still a discrepancy in the quantitative comparison that requires further investigation. Flammability limits were also determined using two different criteria, and both yield values that are essentially the same; what this means is that at $\phi \geqslant 1.68$, methane-air flames will not propagate under atmospheric pressure.

Acknowledgments

This research is supported by the Department of Energy through the Office of Basic Energy Sciences, Division of Chemical Sciences. The authors would like to thank Ms. Fran Rupley for her assistance with the computer codes.

TABLE 1
Summary of calculated and experimental extinction results for methane-air flames

$\Delta H_{f,298K^1CH_2}$	ϕ = 1.0	ϕ = 1.1	ϕ = 1.2
101.5 kcal/mole	K_{ex} = 2700 s^{-1} T_{ex} = 1763 K	K_{ex} = 2600 s^{-1} T_{ex} = 1814 K	
102.5 kcal/mole	K_{ex} = 2250 s^{-1} T_{ex} = 1775 K	K_{ex} = 2000 s^{-1} T_{ex} = 1824 K	K_{ex} = 1400 s^{-1} T_{ex} = 1854 K
Law et al.	K_{ex} = 1650 s^{-1}	K_{ex} = 1250 s^{-1}	K_{ex} = 750 s^{-1}

REFERENCES

1. Kee, R. J., Miller, J. A., Evans, G. H., and Dixon-Lewis, Graham, *Twenty-Second Symposium (International) on Combustion*, The Combustion Institute, Pittsburgh, 1988, p. 1479.
2. Miller, J. A., and Bowman, C. T., *Prog. Energy Combust. Sci.* 287 (1989).
3. Frenklach, M., Wang, H., and Rabinowitz, M. J., *Prog. Energy Combust. Sci.* 47 (1992).
4. Law, C. K., Zhu, D. L., and Yu, G., *Twenty-First Symposium (International) on Combustion*, The Combustion Institute, Pittsburgh, 1986, p. 1419.
5. Hack, W., Wagner, H. G., and Wilms, A., *Ber. Bunsenges. Phys. Chem.* 620 (1988).
6. Yu, G., Law, C. K., and Wu, C. K., *Combust. Flame* 63:339 (1986).
7. Yamaoka, I., and Tsuji, H., *Twentieth Symposium (International) on Combustion*, The Combustion Institute, Pittsburgh, 1983, p. 1883.
8. Westbrook, C. K., *Nineteenth Symposium (International) on Combustion*, The Combustion Institute, Pittsburgh, 1982, p. 127.
9. Law, C. K., and Egolfopoulos, F. N., *Twenty-Third Symposium (International) on Combustion*, The Combustion Institute, Pittsburgh, 1990, p. 413.
10. Miller, J. A., and Melius, C. F., *Combust. Flame* 91:21 (1992).
11. Masten, D. A., Hanson, R. K., and Bowman, C. T., *J. Phys. Chem.* 7119 (1990).
12. Du, H., and Hessler, J. P., *J. Chem. Phys.* 96:1077 (1992).
13. Miller, J. A., unpublished results.
14. Tsang, W., *J. Phys. Chem. Ref. Data* 471 (1987).
15. Grotheer, H., Kelm, S., Driver, H. S. T., Hutcheon, R. J., Lockett, R. D., and Robertson, G. N., *Ber. Bunsenges. Phys. Chem.* 1360 (1992).
16. Choudhury, T. K., He, Y., Sanders, W. A., and Lin, M. C., *J. Phys. Chem.* 2394 (1990).
17. Smooke, M. D., Miller, J. A., and Kee, R. J., *Combust. Sci. Technol.* 34:79 (1983).
18. Grcar, J. F., Kee, R. J., Smooke, M. D., and Miller, J. A., *Twenty-First Symposium (International) on Combustion*, The Combustion Institute, Pittsburgh, 1988, p. 1773.
19. Kee, R. J., Dixon-Lewis, G., Warnatz, J., Coltrin, M. E., and Miller, J. A., Sandia Report, SAND86-8246, 1986, reprinted July 1992.
20. Walch, S. P., *J. Chem. Phys.* 98:3163 (1993).
21. Oser, N. D., Stothard, N. D., Humper, R., Grotheer, H. H., and Just, T., *Twenty-Fourth Symposium (International) on Combustion*, The Combustion Institute, Pittsburgh, 1992, p. 597.
22. Leopold, D. G., Murray, K. K., Stevens Miller, A. E., and Lineberger, W. C., *J. Chem. Phys.* 83:4849 (1985).
23. Böhland, T., Temps, F., and Wagner, H. G., *J. Phys. Chem.* 91:1205 (1987).
24. Zabarnick, S., Fleming, J. W., and Lin, M. C., *J. Chem. Phys.* 85:4373 (1986).
25. Spalding, D. B., *Proc. R. Soc. London A* 240:83 (1957).

Twenty-Fifth Symposium (International) on Combustion/The Combustion Institute, 1994/pp. 1317–1323

LAMINAR FLAME SPEEDS AND EXTINCTION STRAIN RATES OF MIXTURES OF CARBON MONOXIDE WITH HYDROGEN, METHANE, AND AIR

C. M. VAGELOPOULOS AND F. N. EGOLFOPOULOS
Department of Mechanical Engineering
University of Southern California
Los Angeles, CA 90089–1453, USA

The effect of hydrogen and methane addition on the propagation and extinction of atmospheric CO/air flames was investigated experimentally and numerically. Experiments were conducted by using the counterflow, twin-flame technique and laser-Doppler velocimetry for the determination of laminar flame speeds and extinction strain rates. The simulation was conducted by using the one-dimensional flame code, and by solving the conservation equations of mass, momentum, energy, and species along the stagnation streamline of the counterflow. In both cases, detailed description of the chemistry and transport was used. Results indicate that the addition of small amounts of hydrogen and methane to CO flames increases the laminar flame speeds and extinction strain rates by accelerating the main CO oxidation reaction. The sensitivity of the mass burning rate to this reaction is particularly high when trace amounts of hydrogen and methane are added. For large amounts of additives, the chemistry shifts toward that of the additive, and the advantages of the CO kinetic simplicity are lost. The experimental data were closely predicted by the numerical calculations for both propagation and extinction, indicating that existing CO, hydrogen, and methane kinetics can be used with confidence for similar studies. Detailed analysis of the flame structure revealed that, when CO and methane are both supplied as reactants, the CO oxidation follows that of methane, and that, for methane-rich mixtures, the supplied CO remains unreacted until the intermediate CO has been completely formed.

Introduction

The accurate knowledge of fundamental properties of laminar flames is very important for practical purposes, as well as for the modeling of chemical kinetics and turbulent combustion. The one property that has been the subject of extensive investigations is the laminar flame speed, which contains essential information regarding the mixture's exothermicity, diffusivity, and reactivity. However, its accurate experimental determination has been a source of controversy since reported data appear to have substantial scatter [1] that cannot be explained by simply considering experimental uncertainties.

Recently, it has been realized that, in many of the existing techniques, the flames are not one-dimensional, and they are strained [2]. Subsequently, Law and coworkers [2,3] introduced the counterflow, twin-flame technique, which systematically accounts for the strain effect and subtracts it out. The counterflow technique has also been criticized [4,5] for overpredicting the true laminar flame speed because of finite-domain effects, given that the experiments are conducted by using two opposing nozzles at a finite distance. However, further studies [6,7], which were conducted by using asymptotic analysis, detailed numerical modeling, and experiments, unambiguously demonstrated that, even though there are finite-domain effects, the technique is indeed viable and leads to values very close to the true laminar flame speed for large values of the ratio between the flame thickness and the nozzle separation distance. The detailed numerical modeling and experiments show that, for atmospheric hydrogen/air and hydrocarbon/air mixtures, the true laminar flame speeds can be closely determined for nozzle separation distances larger than about 14 mm and by obtaining data at the lowest possible strain rates.

While the counterflow technique has been extensively used for the determination of laminar flame speeds of a wide range of mixtures and pressures [3,6–9], CO flames have not been studied systematically. The knowledge of the properties of CO flames is of particular interest because it is a practical fuel, and it is also widely used for modeling purposes because of its kinetic simplicity. Furthermore, the dynamics of the CO flames, in which a small amount of hydrogen-containing species has been added, are dominated by the $CO + OH = CO_2 + H$ reaction, the rate of which is well known. Therefore, they are ideal environments for kinetic studies of additives that can effectively perturb the rate of the CO oxi-

dation reaction, and this approach is extensively followed by Dryer, Yetter, and coworkers [10–12] in homogeneous, low- to intermediate-temperature flow reactors. These kinetic studies can be enhanced by further validating proposed kinetic models against data determined in flames in which the kinetics are also sensitive to species diffusion and to large temperature gradients.

In view of the above considerations, the main objective of the present study was to experimentally determine the laminar flame speeds and extinction strain rates of CO/air flames with the addition of hydrogen and methane by using the counterflow technique, and through comparisons with detailed numerical calculations to assess the validity of existing kinetics. The experimental data on propagation and extinction will be the first to be derived from strained flames, and they are expected to be of particular interest for practical and modeling purposes, given that the hydrogen/CO and methane/CO systems are among the simplest ones in terms of CO oxidation. Furthermore, since CO is an important intermediate of methane oxidation, their mixtures will be of practical relevance in terms of their possible mixing in turbulent environments in which either fuel-rich combustion locally prevails or partial extinction and subsequent reignition have occurred.

Experimental Methodology

The counterflow opposed jet technique for the determination of laminar flame speeds and extinction strain rates is well documented [2,3,8,9]. It involves the establishment of two symmetrical, planar, nearly adiabatic flames in a nozzle-generated counterflow configuration, and the subsequent determination of the axial velocity profile along the centerline of the flow by laser-Doppler velocimetry. A typical velocity profile has a near zero gradient at the nozzle exit, and it gradually develops an increasing slope, which becomes maximum just before the minimum velocity point at which the heating starts. This maximum velocity gradient in the hydrodynamic zone is defined as the imposed strain rate, K, and the minimum velocity as a reference upstream flame speed, $S_{u,\mathrm{ref}}$, as has been proposed by Law and coworkers [2,3]. For a given mixture, the variation of $S_{u,\mathrm{ref}}$ with K is monitored, and by linearly extrapolating to zero K, the laminar flame speed, S_u°, is determined. The K variation is obtained by keeping the mixture equivalence ratio constant and varying the amount of flow rate to the burners through a bypass valve. In the present study, a nozzle separation distance, L, equal to 22 mm was chosen for the experimental determination of all S_u°'s in order to minimize finite-domain effects, as mentioned in the Introduction. Furthermore, in all experimental runs, every possible effort was made to obtain data at the lowest possible strain rates in order to assure reliable linear extrapolations.

By increasing the nozzle exit velocities, K increases, and the flames are pushed toward the stagnation plane, and for further increase of K, extinction is eventually obtained. For selected mixtures, the extinction strain rates, K_{ext}, were also determined by using $L = 14$ mm. The accurate knowledge of L is important for the comparisons with the numerical simulations, since, in one of our studies [13], it has been found that the values of K_{ext} can be affected by the magnitude of L.

The volume flow rates of the gases were determined by flowing them through sonic orifices, which were calibrated by using a wet test meter. For the cases in which very low flow rates of either hydrogen or methane were added to CO, a small-scale flowmeter was used that was calibrated by using the soap bubble technique. The addition of trace amounts of hydrogen and methane resulted in flow rates as low as 1–3 cm^3/s, and the lower limit of addition was restricted by the accuracy of the laser-Doppler velocimeter for flame speeds below 6–7 cm/s.

Numerical Methodology

The laminar flame speeds were calculated by using the one-dimensional code of Kee and coworkers [14]. Numerical simulation of the counterflow configuration was conducted by solving the conservation equations of mass, momentum, species concentrations, and energy for the stagnation streamline. The formulation of the stagnation-point flow has been the subject of extensive investigations for the past 10 years [15,16], and the governing equations and the appropriate boundary conditions are now reasonably well established. Under the assumption that the axial velocity, temperature, and species concentration profiles are uniform in the radial direction, the original stagnation code [16,17] uses the radial pressure curvature and the velocity gradient at the exit of the nozzle as the two parameters characterizing the flow. The code was further modified for more efficient convergence, more accurate calculation of the mass diffusion velocities, and the ability to obtain solutions through continuation for increasing and decreasing nozzle separation distance.

Both codes were integrated to the Chemkin-II [18] and Transport [19] subroutine packages, which provide the detailed chemistry and transport information. The kinetic scheme used was a hierarchically developed C_2 mechanism [8,20] that satisfactorily predicts a wide range of oxidation properties of hydrogen, methane, ethane, ethylene, acetylene, and methanol.

The calculations of the laminar flame speeds using the one-dimensional code were conducted by using the upwind difference for the convective terms since

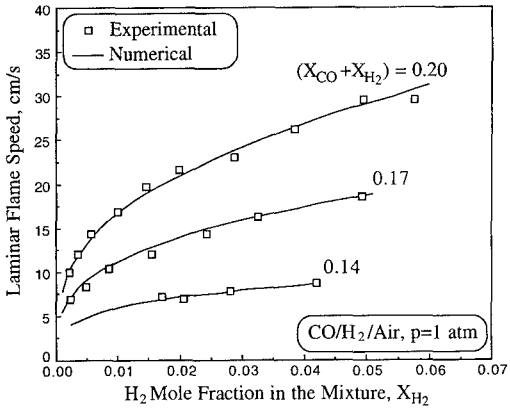

FIG. 1. Experimentally and numerically determined laminar flame speeds, S_u°, as a function of $X_{CO} + X_{CH_4}$ and X_{CH_4} for atmospheric CO/hydrogen/air mixtures.

convergence with the central difference is not possible in our computational facilities. However, the numerical diffusivity that is introduced by using the upwind difference can affect S_u° [7], and it can be minimized by further refining the computational mesh. The reported data were obtained by plotting S_u° vs $1/N$ and extrapolating to $1/N = 0$, which corresponds to the limit of infinitely large number of grid points, N.

Results and Discussions

CO/Hydrogen/Air Mixtures:

The effect of hydrogen addition to CO/air mixtures can be seen in Figs. 1 through 3. The data were determined for total fuel ($CO + H_2$) mole fraction in the mixture, $X_{CO} + X_{H_2}$, equal to 12, 14, 17, and 20%, and for each case, the amount of mole fraction in the mixture of the added H_2, X_{H_2}, was varied to the lowest possible concentration. In Fig. 1, the laminar flame speeds, S_u°, are shown for $X_{CO} + X_{H_2}$ = 14, 17, and 20%, and it can be seen that S_u° decreases as, for fixed X_{H_2} the $X_{CO} + X_{H_2}$ is reduced and, as for fixed $X_{CO} + X_{H_2}$, the X_{H_2} is reduced. The reduction with $X_{CO} + X_{H_2}$ is due to the fact that the flames studied herein are overall fuel lean, and the reduction with X_{H_2} is due to the kinetic effect that the H_2 addition has on the overall branching of the system and that directly affects the rate of the CO main oxidation reaction:

$$CO + OH = CO_2 + H. \qquad \text{(R24)}$$

For a fixed $X_{CO} + X_{H_2}$, it is interesting that the S_u° reduction is quite gradual for the larger values of X_{H_2}, and it becomes more noticeable as $X_{H_2} \to 0$, indicating that the sensitivity of the CO system to the H_2 addition is heightened in this regime. This is due to the fact that, when $X_{H_2} \to 0$, any small H_2 addition noticeably accelerates the rate of reaction (R24), which critically controls the rate of the overall reaction progress [12]. This can be further seen in Fig. 2a, in which the normalized sensitivity [14] of the most important reactions on the mass burning rate is shown for the $X_{CO} + X_{H_2} = 20\%$ case and for various values of X_{H_2}; the results were obtained by detailed numerical calculations. The dominance of reaction (R24) on the mass burning rate is apparent for all cases, and for low X_{H_2} values, the sensitivity of the mass burning rate on reaction (R24) increases with X_{H_2}. However, as X_{H_2} further increases, the hydrogen chemistry starts becoming more important, and the sensitivity of the mass burning rate on reaction (R24) starts reducing. It is also of interest to note the reduced, compared to hydrocarbon flames, sensitivity on the main branching reaction

$$H + O_2 = OH + O, \qquad \text{(R1)}$$

the somehow greater sensitivity on the branching reaction

$$O + H_2 = OH + H, \qquad \text{(R2)}$$

the dominant termination effect of the three-body reaction

$$H + O_2 + M = HO_2 + M, \qquad \text{(R9)}$$

and the increasing role of the HO_2 chemistry at the higher X_{H_2} values, through reactions

$$H + HO_2 = OH + OH \qquad \text{(R18)}$$

$$H + HO_2 = H_2 + O_2 \qquad \text{(R19)}$$

$$OH + HO_2 = H_2O + O_2. \qquad \text{(R20)}$$

The termination effect of reaction (R20) is due to its effect on the OH radical pool, which is crucial for the progress of reaction (R24).

In Fig. 1, numerical results are also shown as independently obtained by using the one-dimensional flame code, and it can be seen that the agreement is very close. This indicates that the CO/H_2 chemistry used in the present investigation, which is mainly based on the work of Yetter et al. [10], is quite accurate in predicting properties of flames, which are inherently diffusive and variable-temperature systems.

Extinction strain rates, K_{ext}, were also obtained for $X_{CO} + X_{H_2}$ = 12 and 14% and various X_{H_2} values, and the results are shown in Fig. 3, along with numerical results obtained by using the counterflow code. It can be seen that K_{ext} decreases as both X_{CO}

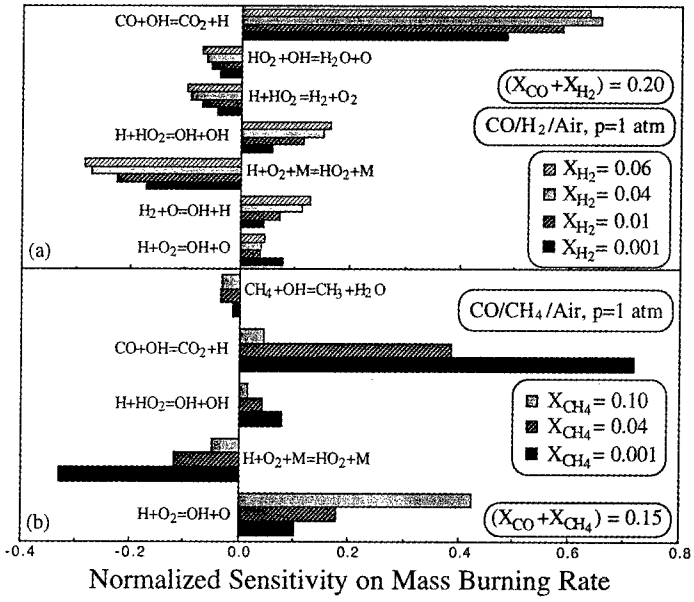

FIG. 2. Normalized sensitivity on the mass burning rate as a function of (a) X_{CH_4} for atmospheric CO/hydrogen/air mixtures and $X_{CO} + X_{H_2} = 0.20$, (b) X_{CH_4} for atmospheric CO/methane/air mixtures and $X_{CO} + X_{CH_4} = 0.15$.

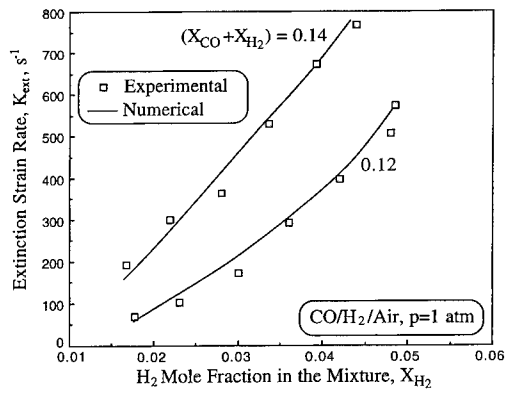

FIG. 3. Experimentally and numerically determined extinction strain rates, K_{ext}, as a function of $X_{CO} + X_{H_2}$ and X_{H_2} for atmospheric CO/hydrogen/air mixtures.

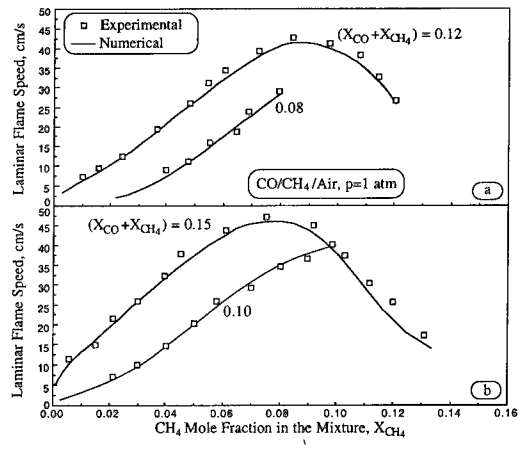

FIG. 4. Experimentally and numerically determined laminar flame speeds, S_u^o, as a function of $X_{CO} + X_{CH_4}$ and X_{CH_4} for atmospheric CO/methane/air mixtures.

$+ X_{H_2}$ and X_{H_2} decrease, which is reasonable since the $X_{CO} + X_{H_2}$ reduction leads to fuel-leaner, weaker mixtures, and the X_{H_2} reduction leads to a lower rate of reaction (24) and, therefore, lower heat release rate and lower flame resistance to extinction. It is also of interest to note the very close agreement between the numerical simulations and the experiments, which further validates the CO/H_2 kinetics used herein. This agreement becomes even more important by considering the fact that our experiments were conducted in a finite-domain configuration, with nozzle separation distance of $L = 14$ mm, and this value was used in the numerical simulations. For a given kinetic scheme, disagreements can be obtained by using a value of L that is not close to the experimental one [13].

CO/Methane/Air Mixtures

The effect of methane addition to CO/air mixtures can be seen in Figs. 4 through 7. The data were taken for total fuel ($CO + CH_4$) mole fraction in the mixture, $X_{CO} + X_{CH_4}$, of 8, 10, 11.6, 12, 14.6, and 15%, and for each case, the amount of mole fraction in the mixture of the added CH_4, X_{CH_4}, was varied. In these experiments, the amount of methane addition was

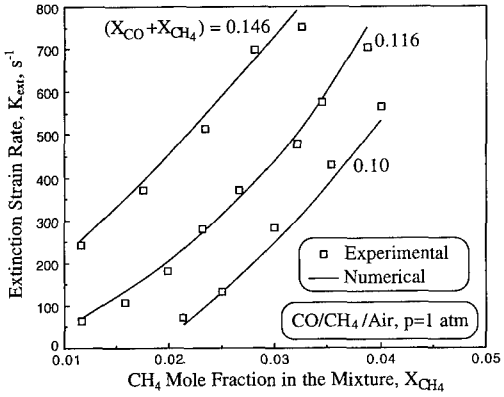

FIG. 5. Experimentally and numerically determined extinction strain rates, K_{ext}, as a function of $X_{CO} + X_{CH_4}$ and X_{CH_4} for atmospheric CO/methane/air mixtures.

varied from trace amounts up to 100% methane in the fuel mixture. This was done because there are no safety considerations as compared to large hydrogen additions, and in order to assess the effect of CO addition to methane, given that CO is a significant intermediate of the methane oxidation.

In Fig. 4, the laminar flame speeds, S_u°, are shown for the $X_{CO} + X_{CH_4} = 8$, 10, 12, and 15% cases. For the $X_{CO} + X_{CH_4} = 8$ and 10% cases, it can be seen that S_u° decreases as, for fixed X_{CH_4}, the $X_{CO} + X_{CH_4}$ is reduced and as, for fixed $X_{CO} + X_{CH_4}$, the X_{CH_4} is reduced. In the limit of $X_{CO} \to 0$, these two cases correspond to fuel-lean and near-stoichiometric methane/air mixtures, respectively, and the corresponding values of S_u° are reached, which are higher compared with the mixtures with finite values of X_{CO}. The monotonic increase of S_u° with X_{CH_4} is due to the increase of the rate of reaction (R24) as a result of the H addition through CH_4.

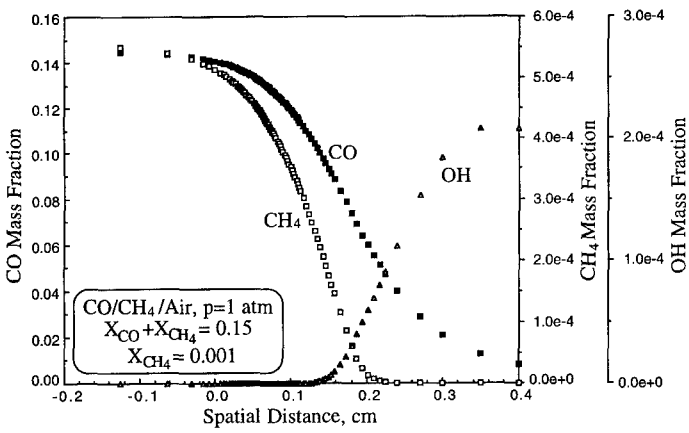

FIG. 6. Spatial variation of the numerically determined mass fractions of CO, methane, and OH for atmospheric CO/methane/air mixture with $X_{CO} + X_{CH_4} = 0.15$ and $X_{CH_4} = 0.001$.

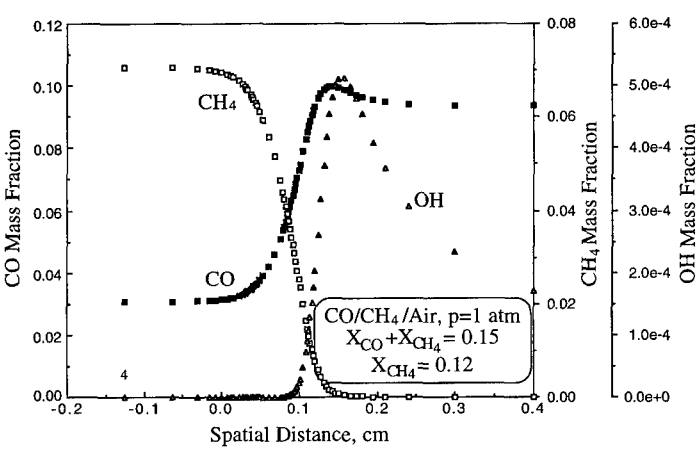

FIG. 7. Spatial variation of the numerically determined mass fractions of CO, methane, and OH for atmospheric CO/methane/air mixture with $X_{CO} + X_{CH_4} = 0.15$ and $X_{CH_4} = 0.12$.

For the $X_{CO} + X_{CH_4} = 12$ and 15% cases, it can be seen that there is a nonmonotonic variation of S_u° with X_{CH_4}. More specifically, at low values of X_{CH_4}, S_u° increases with X_{CH_4}, and then it reaches a maximum and eventually decreases toward the S_u° values of the pure methane/air mixtures at the limit of $X_{CO} \rightarrow 0$; in both cases, the methane/air mixtures are fuel rich. This behavior is due to the fact that, in the low X_{CH_4} regime, the CH_4 addition increases the rate of reaction (R24), which has a significant effect on the mass burning rate. However, in the higher X_{CH_4} regime, the flames start behaving more like rich methane flames, and analysis shows that the sensitivity of the mass burning rate on reaction (R24) reduces rapidly with X_{CH_4}. Physically, this happens because there is not enough oxygen to oxidize CO, which eventually becomes an abundant species, and its rate of destruction is not crucial anymore on the overall reaction progress.

Furthermore, it can be seen that the sensitivity of S_u° to the CH_4 addition for low X_{CH_4}'s, and for flame speeds as low as 2 cm/s, is clearly heightened only for the $X_{CO} + X_{CH_4} = 15\%$ case, for which the values of S_u° are well in the range of 5–10 cm/s, and the numerical calculations are possible. It is expected that, even for the other cases, such an effect would be seen at the very low S_u° regime.

The normalized sensitivity of the mass burning rate on the most important reactions is shown in Fig. 2b for $X_{CO} + X_{CH_4} = 15\%$ and for various X_{CH_4} values ranging from trace to large amounts of added CH_4. It can be seen that, for small X_{CH_4}, the mass burning rate is dominated by the rate of reaction (R24), but this sensitivity is rapidly reduced for large X_{CH_4}, for which the mixture behaves like rich methane/air. It is also seen that, as X_{CH_4} increases, the sensitivity on the main branching reaction (R1) is substantially heightened, while the termination effect of reaction (R9) is reduced. Furthermore, the HO_2 chemistry plays only a minor role, while the termination effect of the added CH_4 through the OH-consuming reaction

$$CH_4 + OH = CH_3 + H_2O \qquad \text{(R82)}$$

is not as strong for any X_{CH_4}. That indicates that results on flame speeds might not be appropriate for the validation of the rate of such a reaction which can potentially perturb the rate of reaction (R24).

In Fig. 4, the experimental results are also compared with the numerical results independently obtained by using the one-dimensional flame code, and it can be seen that the agreement is close. This agreement was anticipated because the existing kinetic scheme has been extensively validated against various properties of CH_4/air flames, and as already mentioned, its CO subset is also considered to be well known.

Extinction strain rates, K_{ext}, were also obtained for $X_{CO} + X_{CH_4} = 10$, 11.6, and 14.6% and various X_{CH_4} values, and the results are shown in Fig. 5 along with numerical results obtained by using the counterflow code. It can be seen that, similarly to the CO/H_2/air flames, K_{ext} decreases as both $X_{CO} + X_{CH_4}$ and X_{CH_4} decrease, which is reasonable since the $X_{CO} + X_{CH_4}$ reduction leads to fuel-leaner, weaker mixtures, and the X_{CH_4} reduction, for fixed $X_{CO} + X_{CH_4}$ values, leads to a lower rate of reaction (R24) and, therefore, lower heat release rate. Similarly to the CO/H_2/air flames, there is also close agreement between the experimental data and the results of the numerical simulations. This further provides confidence to the kinetics used in this study.

The effect of CH_4 addition to the flame structure was also examined numerically, and results are shown in Figs. 6 and 7, in which the mass fraction profiles of CO, CH_4, and OH are plotted vs the spatial distance. In Fig. 6, the results correspond to an overall fuel-lean case with $X_{CO} + X_{CH_4} = 15\%$ and $X_{CH_4} = 0.1\%$, and it can be seen that the CO oxidation follows the CH_4 oxidation and that the OH radical pool starts increasing after the CH_4 has been completely consumed. Analysis showed that CH_4 is consumed basically by OH via reaction (R82), which has a faster rate compared to the CO oxidation reaction (R24). Therefore, only after CH_4 has been consumed to a large extent will the OH radicals be readily available for reaction (R24). These results are also in agreement with the findings of Ref. 12. In Fig. 7, the results correspond to an overall fuel-rich case with $X_{CO} + X_{CH_4} = 15\%$ and $X_{CH_4} = 12\%$, and it can be seen that, similarly to Fig. 6, the OH radical pool starts increasing after the CH_4 has been completely consumed. However, in this fuel-rich case, the CO, which is also supplied as reactant, does not have a chance to be oxidized during the CH_4 oxidation stage in which intermediate CO is also produced. Therefore, the CO mass fraction keeps increasing up to the point that the OH pool reaches a maximum, and a gradual consumption commences. In the case of Fig. 7, the supplied in the initial mixture CO behaves practically as an inert, and it follows the fate of the CO that is produced by the CH_4 oxidation.

Concluding Remarks

In the present study, the effect of hydrogen and methane addition to CO/air flames was examined both experimentally and numerically. The experiments included the use of the counterflow, twin-flame technique, and laser-Doppler velocimetry for the determination of laminar flame speeds and extinction strain rates. The data are expected to be valuable for practical and modeling purposes. The simulations included the use of detailed description of chemical kinetics and molecular transport for both the one-dimensional flame and the counterflow

codes. The latter was used for the integration of the conservation equations in finite-domain configurations that closely describe the actual experiments.

Results show that the addition of small amounts of hydrogen and methane results in the increase of the laminar flame speeds and extinction strains since the added H radicals lead to increased branching and accelerate the rate of the CO oxidation reaction. This increase is more profound when trace amounts of hydrogen and methane are added, and sensitivity analysis shows that the response of the CO/air system is dominated by the CO oxidation reaction. However, for large amounts of additives, the chemistry can shift toward the kinetics of the additive, and the rate of the CO oxidation reaction is not as crucial for the overall reaction rate. It was also found that the experimental results were closely predicted by the numerical calculations, which provides increased confidence to existing CO, hydrogen, and methane kinetics.

Finally, analysis of the detailed flame structure for the case of methane addition shows that the oxidation of the CO is slow until the methane has been consumed to a large extent, since during the methane oxidation stage, the OH radicals react with the methane through a faster reaction compared to the reaction of CO oxidation. For the case of substantial methane addition and under overall fuel-rich conditions, it was found that the supplied as reactant CO remains unreacted until a substantial amount of OH radicals has been reached, and the intermediate CO has been completely formed from the methane oxidation.

Acknowledgments

This study was supported by the National Science Foundation under Grant No. NSF CTS-9211844.

REFERENCES

1. Andrews, G. E., and Bradley, D., *Combust. Flame* 18:133–153 (1972).
2. Law, C. K., *Twenty-Second Symposium (International) on Combustion,* The Combustion Institute, Pittsburgh, 1988, pp. 1381–1402.
3. Egolfopoulos, F. N., Zhu, D. L., and Law, C. K., *Twenty-Third Symposium (International) on Combustion,* The Combustion Institute, Pittsburgh, 1990, pp. 471–478.
4. Tien, J. H., and Matalon, M., *Combust. Flame* 84:238–248 (1991).
5. Dixon-Lewis, G., *Twenty-Third Symposium (International) on Combustion,* The Combustion Institute, Pittsburgh, 1990, pp. 305–324.
6. Chao, B. H., Egolfopoulos, F. N., and Law, C. K., "Structure and Propagation of Counterflow Premixed Flames in a Finite Domain," submitted (1993).
7. Vagelopoulos, C. M., Egolfopoulos, F. N., and Law, C. K., *Twenty-Fifth Symposium (International) on Combustion,* The Combustion Institute, Pittsburgh, 1994, pp. 1341–1347.
8. Egolfopoulos, F. N., Du, D. X., and Law, C. K., *Combust. Technol.* 83:33–75 (1992).
9. Egolfopoulos, F. N., Du, D. X., and Law, C. K., *Twenty-Fourth Symposium (International) on Combustion,* The Combustion Institute, Pittsburgh, 1992, pp. 833–841.
10. Yetter, R. A., Dryer, F. L., and Rabitz, H., *Combust. Sci. Technol.* 79:97 (1991).
11. Yetter, R. A., Dryer, F. L., and Rabitz, H., *Combust. Sci. Technol.* 79:129 (1991).
12. Yetter, R. A., and Dryer, F. L., *Twenty-Fourth Symposium (International) on Combustion,* The Combustion Institute, Pittsburgh, 1992, pp. 757–767.
13. Egolfopoulos, F. N., "Geometric and Radiation Effects on Steady and Unsteady Strained Laminar Flames," Paper 25-629, *Twenty-Fifth Symposium (International) on Combustion,* The Combustion Institute, Pittsburgh, 1994, pp. 1375–1381.
14. Kee, R. J., Grcar, J. F., Smooke, M. D., and Miller J. A., *A Fortran Program for Modeling Steady Laminar One-Dimensional Premixed Flames.* Sandia Report SAND85–8240, 1985.
15. Miller, J. A., Kee, R. J., Smooke, M. D., and Grcar, J. F., "The Computation of the Structure and Extinction Limit of a Methane-Air Stagnation Point Diffusion Flame," Spring Meeting of the Western States Section of The Combustion Institute, Paper WSS/CI 84–10, 1984.
16. Kee, R. J., Miller, J. A., Evans, G. H., and Dixon-Lewis, G., *Twenty-Second Symposium (International) on Combustion,* The Combustion Institute, Pittsburgh, 1988, pp. 1479–1494.
17. Kee, R. J., personal communications.
18. Kee, R. J., Rupley, F. M., and Miller J. A., *Chemkin-II: A Fortran Chemical Kinetics Package for the Analysis of Gas-Phase Chemical Kinetics,* Sandia Report SAND89–8009, 1989.
19. Kee, R. J., Warnatz, J., and Miller, J. A., *A FORTRAN Computer Code Package for the Evaluation of Gas-Phase Viscosities, Conductivities, and Diffusion Coefficients,* Sandia Report SAND83–8209, 1983.
20. Egolfopoulos, F. N., and Law, C. K., "Further Considerations on the Methanol Oxidation Kinetics," in preparation.

Twenty-Fifth Symposium (International) on Combustion/The Combustion Institute, 1994/pp. 1325–1332

ASPECTS OF LAMINAR PREMIXED FLAME EXTINCTION LIMITS

GRAHAM DIXON-LEWIS
Department of Fuel and Energy University of Leeds Leeds LS2 9JT, UK

Numerical methods have been used to examine (1) the combined effects of stretch and upstream heat loss on the properties of a stoichiometric, laminar, pre-mixed methane-air flame, and (2) the combined effects of stretch and an extended, radiative heat loss on the properties of a fuel-lean methane-air flame, equivalence ratio $\phi = 0.57$. Appropriate opposed flow configurations were investigated in both cases. In the first case, fresh gas was discharged towards the stagnation plane from identical, coaxial, plug flow nozzles maintained at constant temperature and separated by a fixed distance. Continuation methods were used in tandem with Newton solutions to study the flame behaviour as the stretch rate (or nozzle inlet velocity) was varied. High and low stretch extinction limits were observed as positions of vertical tangency on the steady-state solution curves of flame property vs stretch rate. The complete series of solutions between these positions formed a limit cycle with both stable and unstable branches. The chemical behaviour at the limits and along the unstable branch is discussed.

The effect of radiative losses on the fuel-lean flame was studied in the unburnt-to-unburnt (UTU) configuration as above, but also in the unburnt-to-burnt (UTB) configuration where the ignited unburnt stream is opposed by a stream of its own equilibrium combustion products. If the flame is adiabatic, the product stream is input at the adiabatic equilibrium flame temperature. Such a system shows no abrupt extinction limits. On the other hand, if the radiative "sink" temperature is below some critical value, then, irrespective of the magnitude of the heat loss rate on a volumetric basis, the unburnt-to-burnt system will show abrupt extinctions if the stretch rate is increased sufficiently. Because of extremely slow numerical convergence, the numerical investigation of these limits for the methane-air system is not yet complete. However, such an investigation is in progress, and this combination of stretch and radiative loss effects is clearly of importance in relation to behaviour at composition limits of flammability.

Introduction

A still insufficiently explored topic in laminar flame propagation is that of the abrupt extinction of single premixed flame fronts, such as is observed at composition limits of flammability. It is well known that such abrupt limits are not predicted by theoretical treatments of unstrained planar one-dimensional adiabatic premixed flames, and effects of stretch alone in the relevant adiabatic unburnt-to-burnt counterflow configuration also fail to predict such limits [1–9]. As was discussed some 30 years ago by Mayer [10] and Spalding [11], by far the most likely cause is nonadiabaticity in the form of extended, radiative heat losses from the flame and burnt gases. Such heat losses impose a residence time criterion, independently of flame stretch, in the high-temperature region of the flame. The idea has recently received strong support from the extensive experimental and theoretical studies of spherically expanding, near-limit flames, under microgravity conditions, by Ronney and coworkers [12–17]; from numerical studies of such flames by Lakshmisha et al. [18,19] and Sibulkin and Frendi [20,21]; and further from studies of unstrained planar flames by Law and Egolfopoulos [22].

In the context of the commonly occurring flames of hydrogen or hydrocarbons in air, important insights into the chemical and physical mechanisms governing the low-temperature limits are likely to be gained by consideration of the combined interactions of heat loss and stretch effects with the detailed flame chemistry. This paper deals with two such situations. Firstly, a continuation method is employed to examine numerically the effect of a nonextended, upstream heat loss on the behaviour of a planar, steady-state, laminar stoichiometric premixed methane-air flame in the back-to-back (or unburnt-to-unburnt), axisymmetric, opposed flow configuration. For the single composition, the combination of possible stretch and heat loss conditions, as the flames are made to move between the nozzles and the stagnation plane, leads to a series of solutions that form a limit cycle with stable and unstable branches, and with both high and low stretch rate extinction limits. The use of the detailed multistep reaction mechanism allows identification of the more important chemical processes controlling these limits. Secondly, for a single low stretch rate, results are presented that illustrate the effect of radiative heat loss on the thermal structure of a fuel-lean ($\phi = 0.57$), laminar premixed methane-air flame in both the un-

burnt-to-unburnt (UTU) and unburnt-to-burnt (UTB) opposed flow configurations.

Counterflow (droplet) diffusion flames with (1) upstream heat loss on the fuel side plus radiative loss from the droplet, and (2) radiative heat loss from the flame itself, have been examined previously by T'ien [23] and Chao et al. [24], respectively, by use of high activation energy asymptotics. Provided that, as the temperature falls, the rate of heat loss diminishes more slowly than the rate of heat generation by combustion, both situations are shown to lead to heat loss induced extinction phenomena, and to possibilities of closed loop response curves.

Mathematical Formulation

We consider first the general case of coaxial, opposed flow nozzles, each with uniform exit velocity. With the use of density-weighted axial distance $\eta = \int_0^x \rho dx$, where x represents the physical distance, the equations governing a steady-state flow system become [25]

$$\frac{dU}{d\eta} + F = 0 \tag{1}$$

$$2U\frac{dF}{d\eta} = \frac{d}{d\eta}\left(\rho\mu\frac{dF}{d\eta}\right) - \frac{J}{\rho} - F^2 \tag{2}$$

$$2U\frac{dh}{d\eta} = -\frac{d}{d\eta}(Q_D + Q_T) + \frac{q_h}{\rho} \tag{3}$$

$$2U\frac{d\sigma_i}{d\eta} = -\frac{d}{d\eta}\left(\frac{j_i}{m_i}\right) + \frac{R_i}{\rho} \quad (i = 1, 2, \ldots, N). \tag{4}$$

Here $U = \rho\mu/2$ and $F = K/2$, where u is the axial velocity and K is the strain rate in the axisymmetric flow, h is the specific enthalpy of the mixture, $\sigma_i = Y_i/m_i$, where Y_i, is the mass fraction and m_i the molecular mass of the ith component, and R_i is the molar volumetric rate of formation of the species. For nonadiabatic flames with extended (radiative) heat losses, q_h similarly represents a volumetric rate of receipt of heat from the surroundings. The density ρ and the enthalpy h are given by

$$\rho^{-1} = \frac{RT}{p}\sum_{i=1}^{N}\sigma_i \tag{5}$$

$$h = \sum_{i=1}^{N}\sigma_i H_i \tag{6}$$

where the molar enthalpies H_i are polynomial functions of the temperature T and p is the pressure. The diffusive flux j_i and the energy fluxes Q_D and Q_T are calculated as described elsewhere [26,27]. Mixture viscosities μ are calculated by Buddenberg and Wilke's formula [28]. We note here that for planar flames lying in the radial coordinate direction, all these quantities are functions of axial distance alone. It should be added that viscous dissipation and pressure work have both been neglected in the derivation of Eq. (3).

For any specific flat flame, the quantity J in Eq. (2) is an eigenvalue pressure curvature or stretch rate that controls the particular condition [25]. The eigenvalue J may also be expressed as a velocity gradient $a_e = (-J/\rho_e)^{1/2}$, where ρ_e is the unburnt free stream density. With the introduction of this relation, and the nondimensionalization of η, U, and F by

$$\hat{\eta} = \{a_e/(\rho\mu)_e\}^{1/2}\,\eta \tag{7}$$

$$\hat{U} = U/\{(\rho\mu)_e\, a_e\}^{1/2} \tag{8}$$

$$\hat{F} = F/a_e \tag{9}$$

Eqs. (1) through (4) become

$$\frac{d\hat{U}}{d\hat{\eta}} + \hat{F} = 0 \tag{1a}$$

$$2\hat{U}\frac{d\hat{F}}{d\hat{\eta}} = \frac{d}{d\hat{\eta}}\left(C\frac{d\hat{F}}{d\hat{\eta}}\right) + \frac{\rho_e}{\rho} - \hat{F}^2 \tag{2a}$$

$$2\hat{U}\frac{dh}{d\hat{\eta}} = -\{(\rho\mu)_e\, a_e\}^{-1/2}\frac{d}{d\hat{\eta}}(Q_D + Q_T) + \frac{q_h}{\rho a_e} \tag{3a}$$

$$2\hat{U}\frac{d\sigma_i}{d\hat{\eta}} = -\{(\rho\mu)_e\, a_e\}^{-1/2}\frac{d}{d\hat{\eta}}\left(\frac{j_i}{m_i}\right) + \frac{R_i}{\rho a_e} \quad (i = 1, 2, \ldots, N) \tag{4a}$$

where $C = (\rho\mu)/(\rho\mu)_e$.

All stretch rates in this paper are quoted as velocity gradients a_e. It is important [25] to note the distinction between stress (or stretch) and strain.

Finally, Eqs. (1) and (2) arise as a consequence of the conservation of radial momentum in the system. The corresponding Navier–Stokes equation for axial momentum leads to an expression for the normal pressure gradient across the flame. Although these pressure gradients are very small in slower burning flames, so that the assumption of constant thermodynamic pressure remains valid, the gradients are nevertheless essential for the acceleration of the gases through the flame front. A necessary consequence of this combination of circumstances is that all real flames other than stationary spherical flames are subject to some degree of strain.

Boundary Conditions

Symmetric Unburnt-to-Unburnt (UTU) Configurations:

Since the configurations are symmetrical about the stagnation plane at $x = 0$, the boundary conditions there are

$$x = 0: \eta = 0, \quad U = 0, \quad \frac{dF}{d\eta} = 0, \quad \frac{dT}{d\eta} = 0, \quad \frac{d\sigma_i}{d\eta} = 0. \tag{10}$$

For these UTU computations, the nozzles are assumed to be separated by a fixed distance $2L$. The state of flow at the nozzles is defined by an axial velocity U_L and a strain rate F_L. Here $F_L = 0$ corresponds with plug flow, and $F_L = (\rho_e/\rho_L)^{1/2} a_e$ [or $\hat{F}_L = (\rho_e/\rho_L)^{1/2}$] corresponds with potential flow conditions at $x = \pm L$. Diffusive conditions are assumed for both species and energy at the boundaries. The adiabatic "free" upstream boundary conditions are thus

$$\begin{gathered} x = \pm L: \eta_L = \int_0^L \rho dx, \\ U = U_L, \qquad F = F_L \\ 2U_L\left(\sum_i G_{iu}H_{iu}/m_i - \sum_i \sigma_{i,L}H_{i,L}\right) = (Q_D + Q_T)_L \\ 2U_L(G_{iu}/m_i - \sigma_{i,L}) = (j_i/m_i)_L \quad (i = 1, 2, \ldots, N) \end{gathered} \tag{11}$$

where the G_{iu} are the mass fractions of the respective components i in the input stream and the subscript u refers to input stream conditions at $\pm\infty$. The quantity η_L is the mass of fluid contained between 0 and L in a cylinder of unit cross-sectional area that lies along the central axis of flow. If L is fixed, η_L becomes a further dependent variable.

Upstream heat losses are introduced by the assumption of a fixed temperature T_u at the upstream boundary, together with zero concentrations of free radicals there. The new boundary conditions are

$$\begin{gathered} x = \pm L: \eta_L = \int_0^L \rho dx, \\ U = U_L, \qquad F = F_L, \qquad T = T_u \\ 2U_L(G_i/m_i - \sigma_{i,L}) = (j_i/m_i)_L \\ \qquad - R_{i,L}, \quad (i = 1, 2, \ldots, N) \\ \sigma_{i,L} = 0 \text{ for all radicals} \end{gathered} \tag{11a}$$

where the $R_{i,L}$ are rates of formation of species due to diffusive arrival and instantaneous reaction of radicals, if necessary with a species already present at the boundary, to give some combination of H_2, H_2O or CO. In this circumstance, the upstream heat loss Z at the boundary is given by

$$Z = Q_{T,L} + \Sigma_i R_{i,L} H_{iu}. \tag{12}$$

Unburnt-to-Burnt (UTB) Configuration:

There is now no symmetry condition, and in the absence of "upstream" heat losses at the ends of the computational domain, the boundary conditions at each end are of the type of Eq. (11). For the radiative loss problem, there is the added condition that the domain must be large enough for the diffusive fluxes at its ends to be small. At the burnt end of the UTB domain, the boundary conditions, at distance L_b from the stagnation plane, are

$$\begin{gathered} x = L_b: \eta_{L_b} = \int_0^{L_b} \rho dx, \\ U = U_{L_b}, \qquad F = F_{L_b} \\ 2U_{L_b}(\Sigma_i G_{ib}H_{ib}/m_i - \Sigma_i \sigma_{i,L_b}H_{i,L_b}) = (Q_D + Q_T)_{L_b} \\ 2U_{L_b}(G_{ib}/m_i - \sigma_{i,L_b}) = (j_i/m_i)_{L_b} \quad (i = 1, 2, \ldots, N). \end{gathered} \tag{13}$$

It remains to define the G_{ib} and H_{ib}. If the radiative exchange is with the surroundings at T_u, it follows that $T_b = T_u$, $H_{ib} = H_{iu}$, and that the G_{ib} can be determined straightforwardly.

Method of Solution

Solution was by an implicit finite-domain procedure. Discretization of Eqs. (1a) through (4a) into mass intervals was performed on a new independent variable ω, defined so that $\eta = \eta_L\omega$. The cell boundary between nodes at ω_j and $\omega_j + 1$ was located at $1/2\ (\omega_j + \omega_{j+1})$. On the assumption of linear variation of F, T, σ_i, R_i/ρ, and q_h/ρ with ω between nodes, Eqs. (1a) through (4a) may be integrated analytically across individual cells to give a large set of algebraic equations of the form

$$f(T, \sigma_i, F, U, \eta_L, a_e) = 0 \tag{14}$$

where the arguments are the solution vectors. The terms η_L and L are related by

$$\eta_L = L/\sum_j \left\{\int_{\omega_j}^{\omega_{j+1}} \rho^{-1}\, d\omega\right\} \tag{15}$$

where, again between nodes, ρ^{-1} can be expressed as a product of two linear functions of ω [see Eq. (5)]. The physical distance intervals remaining in the

discretized expressions for the transport fluxes may be evaluated by use of similar equations.

Both initial and continuation solutions of Eq. (14) were obtained by Newton's method, with grid adaptation by an equidistribution procedure between each continuation solution, before computing the following predictor. For stable flames where Newton's method failed, adaptive time steps were used to bring the solution into the method's domain of convergence. The strategy broadly follows that outlined by Smooke [29], Giovangigli and Smooke [30], and Kee et al. [31]. Details will not be given here.

The reaction mechanism and rate parameters for the methane-air flames were those used by Dixon-Lewis and Islam [32]. They have previously been used successfully for the computation of the structures and properties of lean and slightly rich methane-air flames. Enthalpies were expressed as functions of temperature by way of the NASA fifth-order polynomials. On the assumption that the flames were optically thin, radiative losses ($-q_h$) were calculated by use of Eq. (16):

$$q_h = -4a_p\sigma(T^4 - T_u^4) \tag{16}$$

where σ is the Stefan–Boltzmann constant, T_u is the ambient temperature, and a_p is the total Planck's mean absorption coefficient of the gas. It is related to the mean absorption coefficients a_i belonging to the pure components by

$$a_p = \sum_i a_i p_i \tag{17}$$

where p_i is the partial pressure of the component i. Here CO_2 and H_2O are assumed to be the sole emitters, and mean absorption coefficients for these are given as a function of temperature by Hubbard and Tien [33].

Result and Discussion

Stretched, Stoichiometric UTU Methane-Air Flame with Upstream Heat Loss:

The specific input conditions for these computations were as follows: $L = 3.5$ mm, $F_L = 0$, $T_u = 295$ K, $p = 1$ atm, $G_{CH_4,u} = 0.05515$, $G_{N_2,u} = 0.72485$, and $G_{O_2,u} = 0.22002$. The computational domain for each flame contained between 80 and 90 nodes, and the limit cycle was made up from full Newton solutions for several hundred flames.

Perhaps the most important single chemical feature of the flames of hydrogen and hydrocarbon fuels in air, certainly near the low-temperature extinction limits, is the temperature T_i, akin to an ignition temperature, at which radical production commences in the flame. Values of T_i as a function of stretch rate

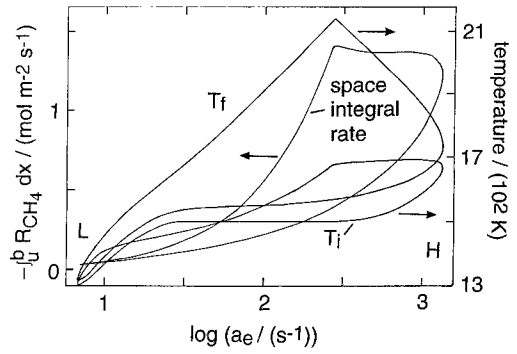

FIG. 1. Variation of T_f, T_i, and the space integral rate $-\int_0^L R_{CH_4}dx$, with stretch rate a_e, for stoichiometric methane-air flame in UTU opposed flow configuration with plug flow ($F = 0$) at $T_u = 295$ K from nozzles with fixed separation $2L = 7$ mm.

are shown in Fig. 1 for the specific boundary conditions. The T_i were computed on the assumption of a radical pool consisting of (H + 2O + OH + CH_3 + C_2H_5 + HO_2 + HCO). Also shown in Fig. 1 are the computed maximum (stagnation plane) temperatures T_f achieved in the flames, and the space integral rates $-\int_0^L R_{CH_4}dx$ for methane removal. The notional burning velocities calculated from these space integral rates vary from near 36 cm s^{-1} for a stretch rate of 10^3 s^{-1} to almost precisely 1 cm s^{-1} near the low stretch rate extinction limit at L.

The extinction limits are at the points of vertical tangency, L and H in Fig. 1. Between these positions, the upper branches of the solution curves refer to stable flames and the lower branches to properties of unstable steady-state solutions. The high stretch rate limit is entirely strain induced, and the flame here is adiabatic. By contrast, the low stretch limit L is certainly not adiabatic. It is determined by a balance between decreasing stretch and increasing upstream heat loss per unit volume of combustible mixture, as the flames move towards the nozzle exits at T_u. We note that the limits L and H are each near a local minimum in the temperature difference ($T_f - T_i$). However, even at the low stretch rates and low temperatures near L, T_f is always above T_i by some 16 K. The frequently made assumption that the low-temperature limits are determined by equality of T_f and T_i is therefore an oversimplification. For constant T_i combined with a sufficiently low concentration of either fuel or oxidizer between T_i and T_f, the temperature difference ($T_f - T_i$) is notionally a measure of the high-temperature radical source strength in the flame. Thus, given the necessity for the prevention of fuel or oxidizer breakthrough under prevailing conditions, the single chemical factor controlling the limits is the further necessity for a balance between the high-temperature radical

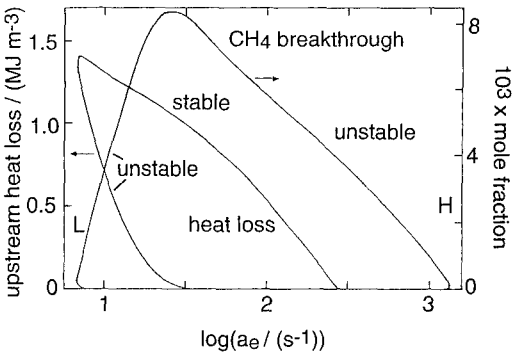

FIG. 2. Variation of heat loss per unit volume at nozzles, and methane breakthrough to the stagnation plane, in flames of Fig. 1.

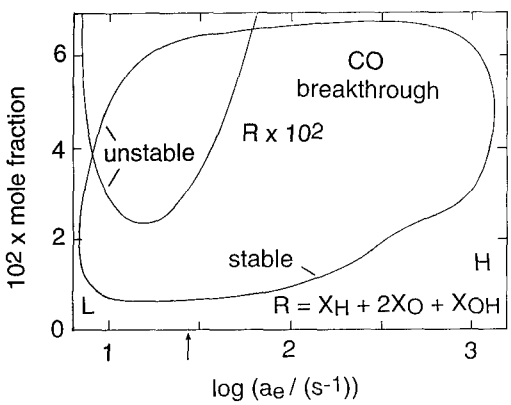

FIG. 3. Variation of CO breakthrough to the stagnation plane, and maximum radical pool concentration (H + 2O + OH) near the low-temperature extinction limit, in flames of Fig. 1.

source strength and the radical removal rates over the whole flame. This feature is of crucial importance in the search for efficient chemically active flame inhibitors and fire suppressants.

Figure 2 shows the methane breakthrough to the stagnation plane and the upstream heat loss, for both the stable and unstable branches of the solution curve. These branches show zero upstream heat loss at stretch rates above 300 and 40 s^{-1}, respectively.

Figure 3 shows the breakthrough of CO to the stagnation plane in the various circumstances, while Figs. 3 and 4 show the maximum radical concentrations achieved in the flames. The vertical arrow below the abscissa in each case denotes the position of maximum CH_4 breakthrough on the unstable branch of the solution curve. Of particular interest overall are the behaviours of the temperature and the intermediate species concentrations along this unstable branch. It is here, at the ridge which divides ignited

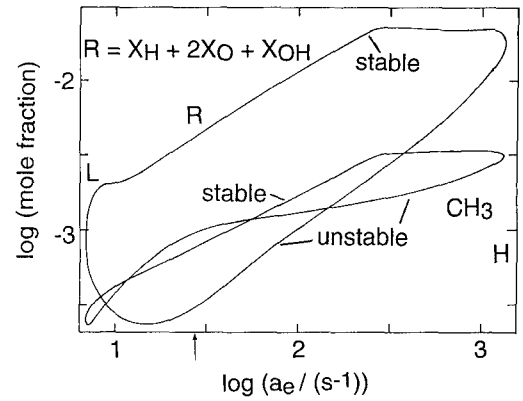

FIG. 4. Variation of maximum radical pool concentration (H + 2O + OH) and maximum CH_3, in flames of Fig. 1.

from nonignited states, that detailed chemical rate interactions are dominant in determining the behaviour. The CH_3 concentration, T_i, and T_f curves all show minima very close to, but not at, the low stretch extinction limit at 6.9 s^{-1}. On increasing the stretch rate from this limit, the (H + 20 + OH) radical pool continues to decrease towards a minimum at around 20 s^{-1}, before the maximum CH_4 breakthrough at about 30 s^{-1}. Finally, the CO breakthrough does not maximize until a stretch rate of about 300 s^{-1}. Note also the very considerable CO breakthrough on the stable branch near each extinction limit, but particularly at H.

The T_i curves of Fig. 1 and the CH_3 mole fraction curve of Fig. 4 are both "twisted," in that between stretch rates of about 12 and 50 s^{-1}, the unstable branch lies above the stable branch. The high values of T_i on the unstable branch in this region are caused by the chain-terminating capability of the CH_3 radical and are thus an indirect consequence of the hydrocarbon fuel breakthrough.

Effects of Radiative Heat Loss on the Thermal Structure of a Weakly Stretched, Fuel-Lean, Premixed Methane-Air Flame:

A specific radial stretch rate $a_e = 2.5\ s^{-1}$ was used in the computations of the structure of a methane-air flame with equivalence ratio $\phi = 0.57$, $T_u = 295$ K, $p = 1$ atm, and zero upstream heat loss. An important part of the early computation is the estimation of a satisfactory length of computational domain. To simplify matters in this connection, as well as to avoid complications in comparisons of flame profiles due to fluid dynamic effects near nozzles, the potential flow boundary conditions $\hat{F}_{Lu} = (\rho_e/\rho_{Lu})^{1/2}$ and $\hat{F}_{Lb} = (\rho_e/\rho_{Lb})^{1/2}$ were used.

For the fixed radial stretch rate of 2.5 s^{-1}, Fig. 5 shows the temperature profiles computed on the ba-

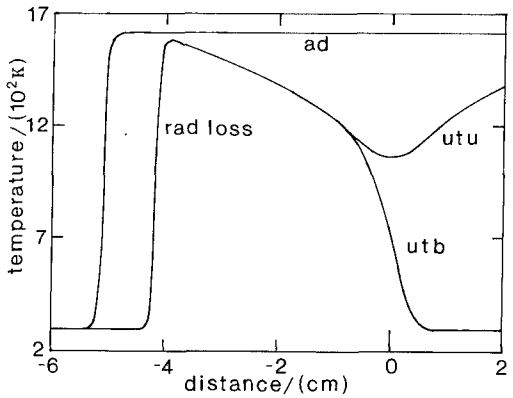

FIG. 5. Temperature profiles of fuel-lean methane-air flame (ϕ = 0.57) at radial stretch rate a_e = 2.5 s^{-1} in adiabatic UTU configuration, and in UTU and UTB configurations with radiative loss.

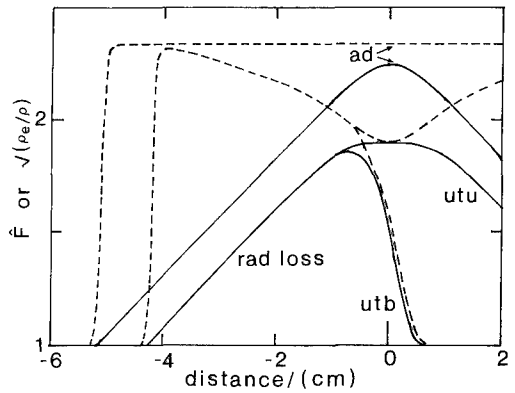

FIG. 6. Dimensionless strain (full lines) and "stretch" (dashed lines) rate profiles for flame of Fig. 5. The stretch rate profiles are simply profiles of $(\rho_e/\rho)^{1/2}$ (see text).

sis of (1) an adiabatic UTU configuration, (2) a UTU configuration with radiative heat loss, and (3) a UTB configuration with radiative heat loss. It should be added that, within the range of distances shown in Fig. 5, the *adiabatic* UTB curve (not calculated) will be indistinguishable from the adiabatic UTU profile. However, whereas the adiabatic UTU profile is symmetrical about the stagnation plane at $x = 0$, the adiabatic UTB curve will continue indefinitely at the high temperature on moving in the direction of positive x.

The main flame zone in all the above cases was represented by upwards of 110 grid intervals, with a further 30 or so intervals to represent the burnt gas region up to the stagnation plane in the UTU cases, and some 50 intervals for the burnt gas in the UTB configuration. In order properly to accommodate the curvatures in the UTU profiles near the stagnation plane, the distance intervals in the region were progressively decreased to 0.07 mm at the symmetry plane itself. Otherwise, by fixing maximum values of $\delta\omega$ in the unburnt and burnt gases, maximum distance intervals of approximately 0.2 and 3 mm were enforced in these regions. The maximum temperature difference across a grid interval on the far burnt side of the UTB flame was held at less than 60 K by a special interpolation procedure, and the temperature intervals in the cooler regions (T < 1000 K) of all the flames were similarly restricted to less than 30 K. Within the reaction zones and in the near burnt gas regions, the temperature intervals were much less than this, and the adaptive gridding there was by the normal equidistribution procedure.

To digress briefly, Libby and Williams [2] and Libby et al. [4] have investigated theoretically the UTB system for situations where the burnt temperature T_b may be above, equal to, or below the adiabatic equilibrium temperature for the corresponding unstrained flame. Abrupt extinction limits were found for sufficiently subadiabatic conditions ($T_b < T_{ad}$). Darabiha et al. [7] also numerically examined the extinction behaviour of a lean propane-air flame in the same configuration, and again observed abrupt ignition and extinction transitions when the product stream was sufficiently cool (T_b < ca. 1500 K). The flame had T_{ad} = 1965 K.

In this context, the present UTB result demonstrates some far-reaching consequences of radiative or similar extended heat losses from flames. If such losses can bring the product temperature below some critical value, then, no matter how small the rate of loss on a volumetric basis, an abrupt extinction limit will be observed if the stretch rate is increased sufficiently. This in turn implies that, although a radiative or similar loss is an essential ingredient of the extinction mechanism, observed flammability limits are also stretch-related phenomena—a feature that may contribute both to the observed variation in limit composition with direction of propagation, and to the fact that, for methane in air, the limit burning velocity in a gravitationally affected environment is greater than that observed for spherically expanding limit flames at zero gravity [12].

A novel feature of the result described in the preceding paragraph is that, in the limit of low radiative heat loss on a volumetric basis, the flame and burnt gas profiles become indistinguishable from those of the otherwise identical adiabatic UTB configuration (that is, the configuration having $T_b = T_u$). However, the extreme slowness of computational convergence for the flames has meant that the details of behaviour near the extinction limits have still to be worked out. For the adiabatic UTU flame with ϕ = 0.57, the computed extinction limit is at a stretch rate of 229 s^{-1}.

The unbroken lines in Fig. 6 show the dimensionless strain rate profiles for the three configurations.

Also shown in Fig. 6, as the dashed lines, are the corresponding profiles of $(\rho_e/\rho)^{1/2}$. Since the eigenvalue $J = \rho a^2 = \rho_e a_e^2$, these latter profiles are in effect "fully developed" dimensionless strain rate profiles that would apply if the systems were devoid of hysteresis effects. It is interesting that, although marked hysteresis effects are observed when a flame is present, the strain rate on the burnt side of the UTB configuration adjusts almost instantaneously to the density changes there.

Yet another property shown by Figs. 5 and 6 is the movement of the flame towards the stagnation plane when radiative losses are included in the computation. Some of this movement is undoubtedly associated with the changes in density and strain rate structure between these and the adiabatic flame. However, the radiative loss causes also a change in the space integral rate across the flame, and hence of notional burning velocity. For the unstrained methane-air flame with $\phi = 0.57$, the computed space integral rate for methane consumption is 0.1814 mol m^{-2} s^{-1}, and the corresponding burning velocity is 7.7 cm s^{-1}. For the adiabatic UTU flame with radial $a_e = 2.5$ s^{-1}, the integral increases slightly, to 0.1841 mol m^{-2} s^{-1}, with the small increase probably due to preferential diffusion effects. The space integral rates for both the UTU and UTB flames with radiative loss were 0.1721 mol m^{-2} s^{-1}, a fall of some 7% compared with the adiabatic flames. In connection with the effect of strain rate history on the flame location, it is observed that, of these two flames with the same space integral rates, the UTB flame is approximately 0.4 mm nearer to the stagnation plane than the UTU.

Conclusions

Abrupt premixed flame extinction limits arise as a result of a failure of the flame chemistry to match residence time conditions that may be imposed on the reaction zone by external factors, so that no solution of the governing equations can be obtained. For a fixed thermodynamic state inside the flammable region, such extinction limits may arise as a result of flame stretch, or a combination of flame stretch and heat losses. In the case of the UTU opposed flow configuration, an abrupt extinction condition may be realized purely by increasing the stretch rate. By forcing two flames together back-to-back, this particular configuration ensures that, at high enough stretch rate, a residence time condition is imposed specifically in the high-temperature region. However, in those UTB situations where the unburnt mixture is opposed by its own hot, adiabatic, equilibrium combustion products, no such high-temperature residence time condition exists, and no abrupt extinction limits are observed. In such cases, it is necessary to invoke also some loss mechanism that ensures that the burnt stream is below some critical temperature. In practice, for single, isolated laminar flames, such a mechanism is always provided by extended, radiative heat losses from the flame and combustion products. Radiative loss is capable of cooling the burnt gas right down to ambient temperature, and a mechanism is thus restored for the production of stretch-induced limits. The magnitude of the limiting stretch rate will of course depend on the magnitude of the volumetric rate of extended heat loss, but in principle, so long only as such loss can reduce the temperature of the burnt stream sufficiently, there will always be a stretch rate at which an abrupt extinction will occur.

We note also that the above arguments apply for a UTB system having a fixed unburnt thermodynamic state within the flammable range. By the same reasoning, a composition extinction limit, or in particular circumstances a composition limit of flammability, may be defined for any fixed combination of stretch rate and nonzero extended heat losses that satisfies the temperature conditions outlined.

For the commonly occurring flames of hydrogen or hydrocarbons burning in air or oxygen-containing atmospheres, the most important single chemical factor controlling the flame is the temperature T_i at which net radical production commences. This temperature and the interval $(T_f - T_i)$ vary with unburnt composition and with the conditions of burning. At the low stretch extinction limit for the (otherwise adiabatic) stoichiometric methane-air flame in the UTU configuration with upstream heat losses, T_i = 1306 K and $(T_f - T_i) = 16.5$ K. Similar values will probably apply at low-temperature extinction limits for other hydrocarbon-air flames. Given the necessity for prevention of fuel or oxidizer breakthrough under prevailing conditions, the single chemical feature controlling the extinction limits is the further necessity for a balance between the high-temperature radical source strength and the radical removal rates over the whole flame.

REFERENCES

1. Libby, P. A., and Williams, F. A., *Comb. Flame* 44:287 (1982).
2. Libby, P. A., and Williams, F. A., *Comb. Sci. Technol.* 31:1 (1983).
3. Libby, P. A., and Williams, F. A., *Comb. Sci. Technol.* 37:221 (1984).
4. Libby, P. A., Liñán, A., and Williams, F. A., *Comb. Sci. Technol.* 34:257 (1983).
5. Darabiha, N., Candel, S. M., and Marble, F. E., *Lecture Notes in Physics*, Springer-Verlag, Berlin, 1985, Vol. 241, p. 218.
6. Darabiha, N., Candel, S. M., and Marble, F. E., *Comb. Flame* 64:203 (1986).

7. Darabiha, N., Candel, S. M., Giovangigli, V., and Smooke, M. D., *Comb. Sci. Technol.* 60:267 (1988).
8. Rogg, B., *Comb. Flame* 60:267 (1988).
9. Dixon-Lewis, G., in *Dynamics of Reactive Systems*, Part 1 (A. L. Kuhl, J. R. Bowen, J. C. Leyer, and A. Borisov, Eds.), *Progress in Astronautics and Aeronautics*, AIAA Inc., New York, 1988, Vol. 113, p. 166.
10. Mayer, E., *Comb. Flame* 1:438 (1957).
11. Spalding, D. B., *Proc. Ry. Soc. London A* 240:83 (1957).
12. Ronney, P. D., and Wachman, H. Y. *Comb. Flame* 62:107 (1985).
13. Ronney, P. D., *Comb. Flame* 62:121 (1985).
14. Ronney, P. D., *Comb. Sci. Technol.* 59:123 (1988).
15. Ronney, P. D., *Twenty-Second Symposium (International) on Combustion*, The Combustion Institute, Pittsburgh, 1988, p. 1615.
16. Abbud-Madrid, A., and Ronney, P. D., *Twenty-Third Symposium (International) on Combustion*, The Combustion Institute, Pittsburgh, 1990, p. 423.
17. Farmer, J. R., and Ronney, P. D., *Comb. Sci. Technol.* 73:555 (1990).
18. Lakshmisha, K. N., Paul, P. J., Rajan, M. K. S., Goyal, G., and Mukunda, H. S., *Twenty-Second Symposium (International) on Combustion*, The Combustion Institute, Pittsburgh, 1988, p. 1573.
19. Lakshmisha, K. N., Paul, P. J., and Mukunda, H. S., *Twenty-Third Symposium (International) on Combustion*, The Combustion Institute, Pittsburgh, 1990, p. 433.
20. Sibulkin, M., and Frendi, A., *Comb. Flame* 82:334 (1990).
21. Frendi, A., and Sibulkin, M., *Comb. Flame* 86:185 (1991).
22. Law, C. K., and Egolfopoulos, F. N., *Twenty-Fourth Symposium (International) on Combustion*, The Combustion Institute, Pittsburgh, 1992, p. 137.
23. T'ien, J. S., *Comb. Flame*, 65:31 (1986).
24. Chao, B. H., Law, C. K., and T'ien, J. S., *Twenty-Third Symposium (International) on Combustion*, The Combustion Institute, Pittsburgh, 1990, p. 523.
25. Dixon-Lewis, G., *Twenty-Third Symposium (International) on Combustion*, The Combustion Institute, Pittsburgh, 1990, p. 335.
26. Dixon-Lewis, G., *Proc. Ry. Soc. London A* 307:111 (1968).
27. Dixon-Lewis, G., "Computer Modelling of Combustion Reactions in Flowing Systems with Transport," *Combustion Chemistry*, Chap. 2 (W. C. Gardiner, Jr., Ed.), Springer-Verlag, New York, 1984.
28. Buddenberg, J. W., and Wilke, C. R., *Ind. Eng. Chem.* 41:1345 (1949).
29. Smooke, M. D., *Comb. Sci. Technol.* 48:72 (1982).
30. Giovangigli, V., and Smooke, M. D., *Appl. Num. Math.* 5:305 (1989).
31. Kee, R. J., Miller, J. A., Evans, G. H., and Dixon-Lewis, G., *Twenty-Second Symposium (International) on Combustion*, The Combustion Institute, Pittsburgh, 1988, p. 1479.
32. Dixon-Lewis, G., and Islam, S. M., *Nineteenth Symposium (International) on Combustion*, The Combustion Institute, Pittsburgh, 1983, p. 283.
33. Hubbard, G. L., and Tien, C. L., *ASME J. Heat Transfer* 100:235 (1978).

COMMENTS

F. A. Williams, University of California, San Diego, USA. The isola is quite reasonable for the back to back (unburnt against unburnt) flames. Experiments (by S. H. Schrub, I think) show about a 50-K temperature minimum in this configuration as a result of radiant heat loss. Your calculations seem to show a difference closer to 500 K, although at a lower strain rate. Is the difference explicable entirely by the lower strain rate of the calculation? Are emissivities known well enough to make accurate calculations? What are the estimated error bars?

Author's Reply. The radiative loss computations described in the paper are of an exploratory nature, and used the thin flame approximation with an added correction term (insignificant in the region of most interest) so that the loss became identically zero at a "sink" temperature $T = T_u$. Only radiation from CO_2 and H_2O was considered, and mixture emissivities were computed from the Planck total mean absorption coefficients given in Ref. 33 of the paper. These last were obtained by integration across the whole spectrum to give effective "grey body" absorption coefficients for the two species. The procedure may be open to some question, but it is unlikely that the errors will much exceed $\pm 20\%$, with the primary line absorption coefficients being much better known.

It should be added that decreasing stretch rate in the UTU configuration is accompanied by increased flame separation, and thus by an increased residence time in the radiative loss region. This will automatically lead to a deeper temperature well at the lower stretch rate. Conversely, little or no temperature well is to be expected at the extinction limit in this configuration. One notes that buoyancy effects will not permit experimental achievement of the $a_e = 2.5\ s^{-1}$ condition in a normal gravitational environment. However, measured and computed burnt gas temperature profiles at higher stretch rates should provide data from which the appropriate grey body emissivities can be independently estimated.

Twenty-Fifth Symposium (International) on Combustion/The Combustion Institute, 1994/pp. 1333–1339

EFFECTS OF PRESSURE AND DILUTION ON THE EXTINCTION OF COUNTERFLOW NONPREMIXED HYDROGEN-AIR FLAMES

P. PAPAS, I. GLASSMAN AND C. K. LAW
Department of Mechanical and Aerospace Engineering
Princeton University Princeton, NJ 08544, USA

To increase the understanding of the critical phenomena of ignition and extinction in high-speed propulsion devices, an experimental and computational study has been conducted on the strain-induced extinction of nonpremixed counterflow flames of diluted hydrogen against air. The study reports laser-Doppler velocimetry- (LDV-) determined local extinction strain rates of these flames, with various amounts of dilution and at pressures of 0.5 and 1.0 atm. The measured data compare well with results obtained from computational simulations with detailed chemistry and transport. Additional computational study on the effects of dilution and pressure shows that the extinction flame temperatures and strain rates exhibit a nonmonotonic variation with increasing pressure, which is characteristic of the explosion limits of homogeneous hydrogen-oxygen mixtures. This behavior is explained on the basis of the intrinsic chain branching-termination kinetics of hydrogen oxidation. The similarity in the dominant kinetic steps responsible for both the ignition/explosion and extinction phenomena is discussed.

Introduction

Recent interests in high-speed aeropropulsion have led to considerable research on hydrogen-oxygen chemistry [1,2] and its coupling to fluid flows. Because of the high-speed nature of the flow, the available residence time for mixing and chemical reactions is significantly reduced, leading to extreme difficulties in achieving ignition and preventing extinction. Consequently, studies of the ignition and extinction phenomena involving hydrogen-air mixtures are of importance to the development of high-speed aeropropulsion.

Recent studies on hydrogen-air flames have mostly been theoretical in nature, involving analyzing the structure and extinction limits of counterflow nonpremixed flames. Prominent contributions include Dixon-Lewis's detailed computational study [3] of the chemical flame structure and extinction limits in terms of the strain rate and oxygen concentrations, Gutheil and coworker's [4,5] computational and asymptotic analysis with emphasis on reduced mechanisms, and Darabiha and Candel's [6] computational study of the temperature effects on the ignition and extinction limits. Experimentally, Pellett and coworkers [7,8] have determined the extinction strain rates of diluted counterflow hydrogen-air flames based on global experimental parameters such as the average air velocity and nozzle diameter.

The present investigation aims to complement the previous studies along the following directions. Since the experimental extinction strain-rate data of Pellett et al. [7,8] are based on global parameters, there has been substantial uncertainty in comparing these data with results from computational studies based on local strain rates. Thus, there exists the need for systematic, benchmark experimental data on hydrogen-air flame extinction based on local measurements. Consequently, local near-extinction strain rates of hydrogen-air counterflow flames with different extent of dilution, and at 0.5 and 1 atm pressure, were measured using laser-Doppler velocimetry (LDV). Comparisons of these experimental data with results obtained from computational simulations utilizing detailed transport and chemistry are then appropriate. When making these comparisons, the effect of the imposition of the various boundary conditions at the reactant stream exits in the computational simulation will be addressed.

Furthermore, computational simulations permit the study of the influence of pressure on the extinction states of hydrogen-oxygen flames. In this regard, it is to be noted that the combustion chamber within aeroengines will not only operate at different pressures, but the chamber pressure can also undergo strong fluctuations. Very few studies have been conducted on the effect of pressure on hydrogen-air flame extinction. Gutheil and Williams [5] have shown that the extinction strain rate increases with pressure. Because of the inherent chain nature of the hydrogen-oxygen chemistry, however, the explosion limits of homogeneous hydrogen-oxygen mixtures exhibit a nonmonotonic behavior with pressure, as shown in Fig. 4. Similar behavior has also been recently observed for the counterflow ignition of a hydrogen jet by a heated air jet [9]. Thus, it is of both

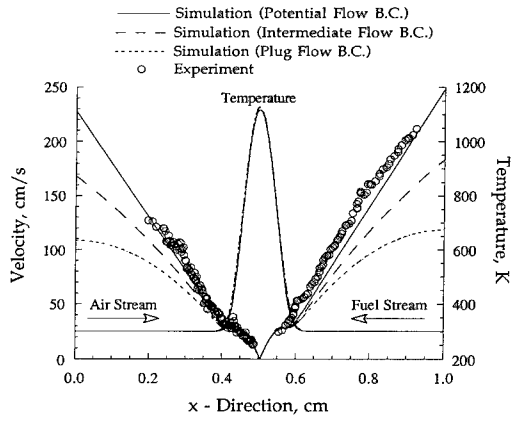

FIG. 1. Axial velocity profiles near extinction for a 16% hydrogen-84% nitrogen mixture impinging air at 1 atm. Reactant stream exit temperatures are 300 K.

fundamental and practical interest to explore if nonmonotonic behavior also exists for flame extinction of counterflow nonpremixed flames.

In the next two sections, the experimental and computational aspects of this study are discussed and the results of the investigation reported.

Experimental

The extinction conditions of nonpremixed hydrogen-air flames were experimentally determined in a nozzle- or tube-generated counterflow configuration [10]. The fuel streams consisted of 12.0–18.5 mole% hydrogen in nitrogen, and the oxidizer stream was air. The diameters of the converging nozzles and tubes were between 0.7 and 1.4 cm. The separation distance between the nozzle and tube exits ranged from 0.6 to 1.4 cm. For each fuel concentration studied, extinction was accomplished by gradually increasing the velocities of both streams. Near-extinction strain rates were determined by LDV from axial velocity profiles obtained along the centerline [10]. In this study, the strain rate, K, is defined as half of the measured axial velocity gradient upstream of the flame on the air side. Typical experimental measurements of axial velocities near extinction are given in Fig. 1. The case depicted is for a 16% hydrogen mixture impinging onto an air stream at 1 atm pressure and room temperature, where x is the axial coordinate, with $x = 0$ and 1 cm corresponding to the air and fuel stream exits, respectively. The open circles in this figure represent the average of many dual-beam LDV measurements (usually 30) at a particular axial location along the stagnation streamline. The accuracy of these experimental measurements is within 10%, with measurements near the stagnation plane having a higher degree of inaccuracy. As will be discussed, experimental axial velocity gradients were determined by fitting a straight line through the LDV measurements.

Computational

In order to allow for comparison with experimental data, numerical simulations were conducted using a quasi-one-dimensional opposed jet nonpremixed laminar flame model along the stagnation point streamline of the axis of symmetry. The corresponding steady-state mass, species, momentum, and energy conservation equations are solved using detailed chemical and transport schemes. The numerical code employed in this work is based on the scheme of Smooke and coworkers, which has been extensively described elsewhere [11]. Boundary conditions are applied at the air and fuel exits. The mass conservation that applies at the exit boundaries is $2b = -(du/dx)$, where u is the axial velocity. Conventionally, the outer frozen fields are assumed to be described by potential flow. The strain rate at the air boundary, $K = b_0$, then describes the constant axial velocity gradient. Another boundary condition commonly applied at the exit is that of plug flow ($b_0 = 0$), where the radial velocity is zero. Typically, the experimental boundary conditions of counterflow burners lie between those of potential and plug flows [10]. The boundary condition imposed in such cases would be determined from the experimental axial velocity gradient at the exits, namely, $b_0 = -(du/dx)_0/2$ and $b_1 = -(du/dx)_1/2$. The potential and plug flow boundary conditions may, therefore, be viewed as limiting cases [10]. The choice of boundary conditions for the outer frozen flow fields will be discussed further in the course of this paper.

The detailed hydrogen-oxygen reaction mechanism used consists of 19 elementary reaction steps with reverse reaction rates determined from equilibrium [1,2,12]. This mechanism is based on the scheme of Yetter et al. [1,2], which has been used to predict a variety of experimental data over a wide range of conditions [1,12]. The scheme utilized in this study, listed in Table 1, includes pressure falloff for the reaction $H_2O_2 + M = 2OH + M$. Thermochemical properties of the nine species in the reaction mechanism are also taken from Yetter et al. [2]. The molecular parameters used in the numerical simulation to evaluate the transport properties were obtained from the CHEMKIN data base [13].

Numerical simulations were conducted for various total pressures of a nitrogen-diluted hydrogen stream impinging an air stream. In particular, the steady-state condition just prior to extinction is examined. Figure 2 represents the variation of the maximum flame temperature of several mixtures as a function of the inverse of the air-side strain rate, $1/K$. The numerical simulation shown in Fig. 2 utilizes poten-

TABLE 1
Hydrogen/oxygen reaction mechanism[a]

	A_f (mole cm^3 s)	n_f	E_{af} (KJ/mole)	T_{range} (K)	Reference
Chain reactions:					
1. $H + O_2 = OH + O$	1.92×10^{14}	0.00	68.78	962–2,577	15
2. $H_2 + O = OH + H$	5.08×10^{04}	2.67	26.33	297–2,495	16
3. $H_2 + OH = H + H_2O$	2.16×10^{08}	1.51	14.35	250–2,581	17
4. $OH + OH = H_2O + O$	1.23×10^{04}	2.62	−7.86	250–2,000	18
Formation and consumption of HO_2:					
5. $H + O_2 + M = HO_2 + M^c$	6.70×10^{19}	−1.42	0.00	200–2,000	19
6. $HO_2 + H = OH + OH$	1.69×10^{14}	0.00	3.66	298–773	20
7. $HO_2 + H = H_2 + O_2$	6.63×10^{13}	0.00	8.89	298–773	20
8. $HO_2 + OH = H_2O + O_2$	1.45×10^{16}	−1.00	0.00	298–1,400	20
9. $HO_2 + O = O_2 + OH$	1.81×10^{13}	0.00	−1.66	200–400	20
Recombination/dissociation reactions:					
10. $H_2 + M = H + H + M^c$	4.57×10^{19}	−1.40	436.80	600–2,000	20
11. $O + O + M = O_2 + M^c$	6.17×10^{15}	−0.50	0.00	2,000–10,000	20
12. $H + OH + M = H_2O + M^c$	2.25×10^{22}	−2.00	0.00	1,000–3,000	20
13. $O + H + M = OH + M^c$	4.72×10^{18}	−1.00	0.00		20
Formation and consumption of HOOH:					
14. $HO_2 + HO_2 = H_2O_2 + O_2$				300–1,100	21
$k = 4.20 \times 10^{14} \exp(-50.13/RT), + 1.30E11 \exp(6.816/RT)$					
15. $H_2O_2 + M = OH + OH + M^{b,c}$					22
$k_o = 1.20 \times 10^{17} \exp(-190.37/RT), \quad F_c = 0.5$					
$k_\infty = 2.95 \times 10^{14} \exp(-202.65/RT), \quad N = 1.13$					
16. $H_2O_2 + OH = H_2O + HO_2$				250–1,250	23
$k = 1.00 \times 10^{12} + 5.80 \times 10^{14} \exp(-39.99/RT)$					
17. $H_2O_2 + H = H_2 + HO_2$	4.82×10^{13}	0.00	33.25	283–800	20
18. $H_2O_2 + H = H_2O + OH$	1.00×10^{13}	0.00	15.02	283–800	24
19. $H_2O_2 + O = OH + HO_2$	9.55×10^{06}	2.00	16.61	250–800	20

[a] $k = AT^n \exp(-E_a/RT)$; f denotes forward rate value.

[b] $k_{15} = k_\infty \left[\frac{k_o/k_\infty}{[1 + (k_o/k_\infty)]}\right] F_c^X$, $X = \{1 + [\log(k_o/k_\infty)/N]^2\}^{-1}$.

[c] $[M] = [N_2] + [O_2] + 2.5[H_2] + 12[H_2O] + [H] + [O] + [OH] + [H_2O_2] + [HO_2]$.

tial flow boundary conditions at the exits (300 K). It is seen that, for a given mixture and stream exit temperatures, as the inverse strain rate, $1/K$, is decreased, the maximum flame temperature decreases until the characteristic extinction turning point is exhibited. Extinction is then identified as the state of the turning point.

Results

Figure 3 shows the experimental and numerical density-weighted near-extinction strain rates, ρK_{ext}, plotted as a function of the fuel-stream hydrogen mole fraction, where ρ is the exit air density and K_{ext} is half the air axial velocity gradient. Overall, the experimentally and numerically determined near-extinction strain rates agree well. The only other experimental values for hydrogen-air extinction were reported by Pellett and coworkers [7,8]. Their value for the extinction strain rate of a 21% mole fraction hydrogen (79% nitrogen) mixture (622/s), shown in Fig. 3, was obtained with global experimental parameters, U_{air}/D_c, where U_{air} is the average air exit velocity and D_c represents an empirically selected weighting factor used to achieve agreement between opposed jet tubular and nozzle exit extinction results. Therefore, there is considerable uncertainty concerning this result.

Also shown in Fig. 3 are the computed results of Gutheil and Williams [5] and Darabiha and Candel [6], using the potential flow boundary condition. The

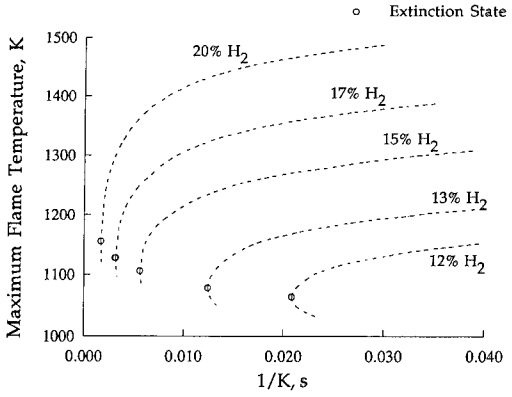

FIG. 2. Maximum flame temperature as a function of inverse strain rate for 20, 17, 15, 13, and 12% hydrogen-nitrogen mixtures impinging and an air stream at 1 atm. Reactant stream exit temperatures are 300 K.

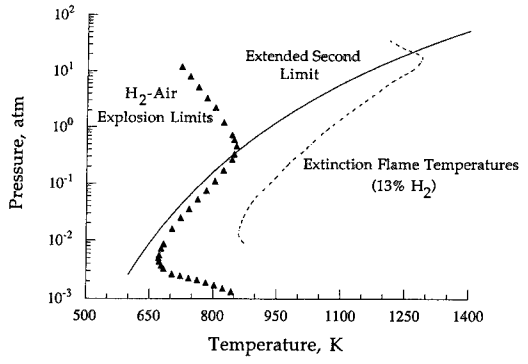

FIG. 4. Explosion limits for a stoichiometric hydrogen-air mixture, the "extended second limit," and extinction temperatures of a nonpremixed 13% hydrogen/87% nitrogen-air flame as a function of pressure.

extinction strain rates calculated by Gutheil and Williams [5] are in close agreement with the calculated results of this study. Darabiha and Candel's extinction strain rate for 16% mole fraction hydrogen in nitrogen, denoted by an arrow, is about 20% lower than the present value. Since the transport descriptions utilized by Darabiha and Candel and the current study are similar, the difference in the calculated extinction strain rates may be attributed to differences in the reaction schemes used.

At this point, it is necessary to examine the sensitivity of the results to the boundary conditions adopted. As stated previously, the experimental boundary conditions lie between those of potential and plug flows. Plotted in Fig. 1 are the near-extinction axial velocity profiles for a 16% hydrogen mixture issuing from a converging nozzle with diameter of 1.4 cm. The numerical simulations are the near-extinction axial velocity profiles using potential, plug, and an intermediate boundary condition. The intermediate boundary condition in Fig. 2 represents the extinction state for exit velocity values that are the average of the plug and potential flow cases. The strain rate defined from the experimental velocity profile over a region extending about 0.2 cm upstream from the reaction zone ($x \approx 0.4$ cm) is 200/s. Similarly, a strain rate of 245/s can be defined for the potential flow boundary condition. The extinction strain rates defined in the potential flow cases are

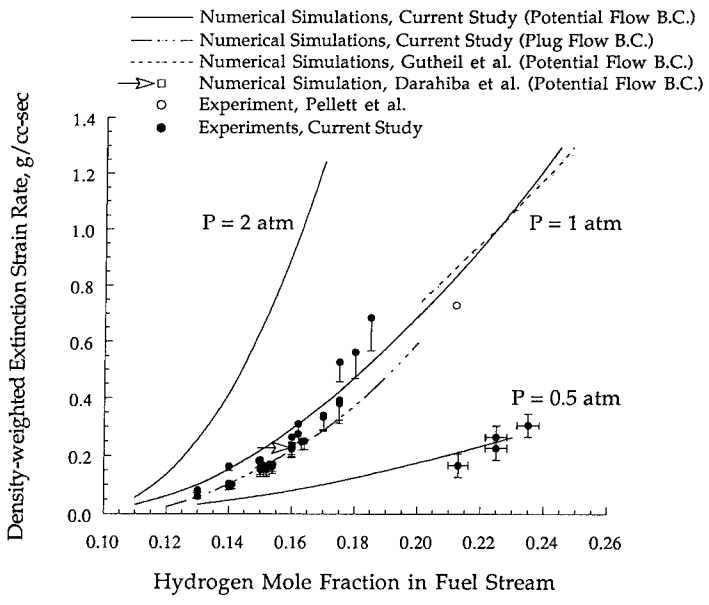

FIG. 3. Experimental and numerical values of air density-weighted extinction strain rates as a function of hydrogen mole fraction in nitrogen in the fuel stream. Reactant stream exit temperatures are 300 K. Unless specified otherwise, numerical simuulations incorporate potential flow boundary conditions.

independent of the axial coordinate in the outer frozen flow field. Moreover, numerical simulations performed in this study have also demonstrated that the definition of the extinction strain rate for the potential flow is, to a great extent, also independent of the stagnation point location. For the plug and intermediate flows, however, the axial velocity gradient varies throughout the domain between the boundaries. Essentially, the strain rate defined for these cases just upstream of the reaction zone on the air side is represented by the maximum strain rate over the air-side axial domain. The maximum strain rate defined for the plug flow case of 185/s is 25% lower than the potential flow extinction strain rate. The flame temperature profiles near extinction of the numerical simulations for the case represented in Fig. 1, however, are largely independent of the type of boundary condition at the frozen reactant exits.

Maximum density-weighted extinction strain rates at 1 atm, obtained with plug flow boundary conditions, are plotted in Fig. 3 as a function of the hydrogen mole fraction in the fuel stream. The stagnation point locations for these plug flow cases are midway between the exits (0.5 cm). As expected, the experimental extinction strain-rate results of this study lie between those obtained with the potential and plug flow boundary conditions.

It is also important to realize that, similar to the computational results, the experimentally defined extinction strain rates also depend on several secondary factors and, therefore, are not unique. These factors include the axial velocity gradients at the nozzle exits, the location of the stagnation plane, and the region over which strain is defined. Consequently, the extinction strain rates reported here should be treated as approximate values. The experimental strain rates in Fig. 3 are based on local definitions obtained from least-squares fits of the experimental data immediately upstream of the reaction zone on the air side. These data have an uncertainty of 10% for the 12–16% hydrogen mixtures at 1 atm, 25% for the 17.0 and 18.5% mixtures at 1 atm, and 20% at 0.5 atm. Error bars for the 0.5-atm data also reflect uncertainties in the system pressure. In general, Fig. 3 shows that the experimentally determined strain rates for the dilute mixtures studied herein are characterized well by the numerically calculated values.

The effect of pressure on extinction of diluted hydrogen-air mixtures was also numerically investigated, using the potential flow boundary conditions for simplicity. Calculated maximum flame temperatures at extinction for a 13% hydrogen mixture are shown in Fig. 4 as a function of the system pressure. The temperature at both exits is 300 K. The relationship of extinction temperatures with pressure for this system exhibits the familiar nonmonotonic pressure dependency as observed for the homogeneous hydrogen-oxygen explosion limits. Specifically, the region to the right of this curve represents burning

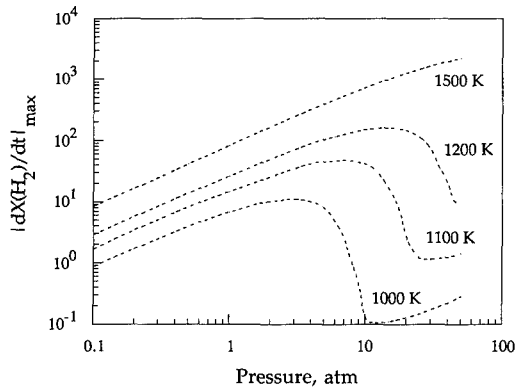

FIG. 5. Maximum reaction rate as a function of pressure for a 1% hydrogen, 0.5% oxygen, and 98.5% nitrogen mixture at initial temperatures of 1000, 1100, 1200, and 1500 K.

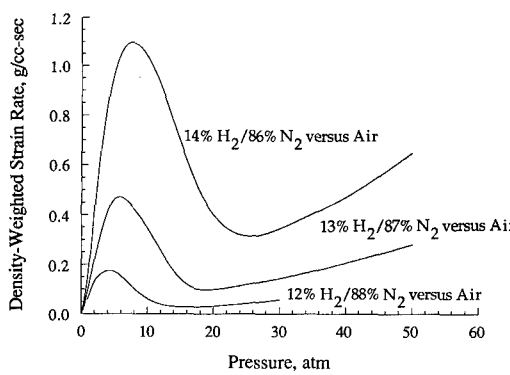

FIG. 6. Air density-weighted extinction strain rates as a function of pressure for 14, 13, and 12% hydrogen-nitrogen mixtures impinging an air stream. Reactant stream exit temperatures are 300 K.

states, while the region to the left represents extinguished states. Thus, an increase in pressure could cause a mixture to change from an extinguished state, to a burning state, and back to an extinguished state.

The above results can best be understood on the basis of the pressure effects on hydrogen oxidation, by examining the maximum hydrogen consumption rate for a *homogeneous* stoichiometric mixture reacting in an adiabatic system *without* mass and heat transport [2]. The maximum reaction rate is defined here as the maximum slope on a hydrogen concentration vs time profile. The computational model describing this closed system at constant pressure is described elsewhere [14]. Figure 5 shows that, for a given initial temperature, the maximum reaction rate, $|dH_2/dt|_{max}$, first rapidly increases with pressure until a pressure is reached that is indicative of the "extended second limit" [2] shown in Fig. 4. At this pressure, the reaction rate decreases rapidly but then

increases again with pressure. The kinetic details for this behavior are well documented [2]. Specifically, as the pressure is increased at a given temperature, the well-known fast reaction proceeds through the bimolecular branching reactions such as $H + O_2 = OH + O$. The subsequent drop in the maximum reaction rate is the result of the slow reaction that proceeds as a consequence of the chain- inhibiting reaction $H + O_2 + M = HO_2 + M$. It is the competition between the chain branching and inhibiting reactions that explains the second explosion limit and defines the extended second limit. The third explosion limit is the result of the production of H_2O_2 via $2HO_2 = H_2O_2 + O_2$ and $HO_2 + H_2 = H_2O_2 + H$ and the decomposition of H_2O_2 via $H_2O_2 + M = 2OH + M$. Thus, for a given temperature, the reaction rate for pressures above the extended second limit increases again as the reaction path $H + O_2 + M = HO_2 + M$ becomes propagating. The pressure dependency of the maximum reaction rate, as shown in Fig. 5, has been quantitatively confirmed in experimental flow reactor studies of near-adiabatic dilute hydrogen-oxygen mixtures [12]. The behavior of the overall reaction rate with pressure explains the explosion peninsula of the hydrogen-air system of Fig. 4.

For the counterflow configuration studied here, the density-weighted strain rate, ρK, defines the characteristic transport rate. Figure 6 shows the variation of the density-weighted strain rate with pressure for a 13% hydrogen mixture impinging onto an air stream. Similar to the overall reaction rate for the homogeneous hydrogen-oxygen system, the density-weighted strain rate initially increases rapidly with pressure, indicating the increase in the burning intensity. It then decreases at about 7 atm, which is relatively close to the extended second limit at the extinction temperature (1225 K), and eventually increases again. Consequently, for a given density-weighted strain rate, increasing pressure from a low value will bring the system from a state of extinction, to burning, to extinction again, and to burning again.

The final point to note is that, since the above nonmonotonic behavior of the explosion limits with pressure is usually associated with low-to-intermediate temperature hydrogen-oxidation kinetics, it may be surprising that it is also observed for burning situations usually associated with high-temperature kinetics. The reason is that, for the highly diluted flames studied here, the flame temperatures are quite low; consequently, a similar change in the rate-controlling steps with pressure responsible for the behavior of the explosion limits is observed. This provides an example where the key reaction steps controlling ignition and extinction events are quite similar.

Summary

In this study, LDV has been employed to experimentally determine the local near-extinction strain rates for counterflow nonpremixed flames of diluted hydrogen against air at 1.0 and 0.5 atm. A numerical model incorporating a detailed hydrogen-oxidation mechanism was used to describe the experimental results and elucidate the important chemical processes near extinction. The predicted extinction strain rates agree with the experimental values to within 20%. A very important observation has been that the calculated extinction flame temperatures (and strain rates) for given hydrogen concentrations exhibit a nonmonotonic pressure dependence, which is similar to the homogeneous hydrogen-oxygen explosion limits, as well as the calculated ignition temperatures of nonpremixed counterflows of hydrogen-nitrogen and air. The effect of pressure on homogeneous hydrogen-oxidation kinetics effectively explains the nonmonotonic pressure dependency.

Acknowledgments

The authors would like to thank Dr. R. A. Yetter for his valuable insights, Dr. T. G. Kreutz for his assistance, Dr. M. Nishioka for helping generate the extinction turning points shown in Fig. 2, and Mr. J. Sivo for his technical assistance in experimentation. This work was supported by the U.S. Air Force Office of Scientific Research, with an AFRAPT Fellowship awarded to PP.

REFERENCES

1. Yetter, R. A., and Dryer, F. L., *Comb. Sci. Technol.* 79:97–128 (1991).
2. Yetter, R., Dryer, F. L., and Golden, D., *Major Research Topics in Combustion* (M. Y. Hussani, A. Kumar, and R. G. Voight,Eds.) ICASE/NASA Series, Springer-Verlag, New York, 1992, p. 309.
3. Dixon-Lewis, G., and Missaghi, M., *Twenty-Second Symposium (International) on Combustion*, The Combustion Institute, Pittsburgh, 1988, pp. 1461–1470.
4. Gutheil, E., Balakrishnan, G., and Williams, F. A., *Reduced Kinetic Mechanisms for Applications in Combustion Systems*, Lecture Notes in Physics (N. Peters and B. Rogg, Eds.), Springer-Verlag, New York, 1992, p. 177.
5. Gutheil, E., and Williams, F., *Twenty-Third Symposium (International) on Combustion*, The Combustion Institute, Pittsburgh, 1990, pp. 513–521.
6. Darabiha, N., and Candel, S., *Combust. Sci. Technol.* 86:67–85 (1992).
7. Pellett, G. L., Northam, G. B., and Wilson, L. G., "Opposed Jet Diffusion Flames of Nitrogen-Diluted Hydrogen vs Air: Axial LDA and CARS Surveys; Fuel/Air Strain Rates at Extinction," AIAA-89-2522, AIAA/ASME/SAE/ASEE 25th Joint Propulsion Conference, Monterey, CA, July 10–12, 1989.
8. Pellett, G. L., and Northam, G. B., "Strain-Induced Extinction of Hydrogen-Air Counterflow Diffusion

Flames: Effects of Steam, CO_2, N_2, and O_2 Additives to Air," AIAA-92-0877, 30th Aerospace Sciences Meeting & Exhibit, Reno, NV, January 6, 1992.

9. Kreutz, T. G., and Law, C. K., "Ignition of Nonpremixed Counterflowing Hydrogen versus Heated Air: Computational Study with Detailed Chemistry," *Combust. Flame*, submitted.
10. Chelliah, H. K., Law, C. K., Ueda, T., Smooke, M. D., and Williams, F. A., *Twenty-Third Symposium (International) on Combustion*, The Combustion Institute, Pittsburgh, 1990, pp. 503–511.
11. Smooke, M. D., Puri, I. K., and Seshadri, K., *Twenty-First Symposium (International) on Combustion*, The Combustion Institute, Pittsburgh, 1988, pp. 1783–1792.
12. Kim, T., Master's Thesis, Princeton University, Princeton, NJ (1993).
13. Kee, R. J., Miller, J. A., and Jefferson, J. H., "CHEMKIN: A General Purpose, Problem Independent, Transportable, Fortran Chemical Kinetic Code Package," Sandia Report, SAND 80–8003, 1980.
14. Lutz, A. E., Kee, R. J., and Miller, J. A., "SENKIN: A Fortran Program for Predicting Homogeneous Gas Phase Chemical Kinetics with Sensitivity Analysis," SAND Report 87–8248, 1991.
15. Pirraglia, A. N., Michael, J. V., Sutherland, J. W., and Klemm, R. B., *J. Phys Chem.* 93:282 (1989).
16. Sutherland, J. W., Michael, J. V., Pirraglia, A. N., Nesbitt, F. L., and Klemm, R. B., *Twenty-First Symposium (International) on Combustion*, The Combustion Institute, Pittsburgh, 1986, pp. 929–941.
17. Michael, J. V., and Sutherland, J. W., *J. Phys. Chem.* 92:3853 (1988).
18. Harding, L. B., and Wagner, A. F., *Twenty-Second Symposium (International) on Combustion*, The Combustion Institute, Pittsburgh, 1988, pp. 983–989.
19. Slack, M. W., *Combust. Flame* 28:241 (1977).
20. Tsang, W., and Hampson, R. F., *J. Phys. Chem. Ref. Data* 15:1987 (1986).
21. Hippler, H., Troe, J., and Willner, J., *J. Chem. Phys.* 93(3):1755 (1990).
22. Brouwer, L., Cobos, C. J., and Troe, J., *J. Chem. Phys.* 86(11):6171 (1987).
23. Hippler, H., and Troe, J., *Chem. Phys. Lett.* 192(4):333 (1992).
24. Warnatz, J., "Survey of Rate Coefficients in C/H/O Systems," in *Combustion Chemistry* (W. C. Gardiner, Jr., Ed.), Springer-Verlag, New York, 1985.

Twenty-Fifth Symposium (International) on Combustion/The Combustion Institute, 1994/pp. 1341–1347

FURTHER CONSIDERATIONS ON THE DETERMINATION OF LAMINAR FLAME SPEEDS WITH THE COUNTERFLOW TWIN-FLAME TECHNIQUE

C. M. VAGELOPOULOS AND F. N. EGOLFOPOULOS
Department of Mechanical Engineering
University of Southern California
Los Angeles, CA 90089-1453, USA

AND

C. K. LAW
Department of Mechanical and Aerospace Engineering
Princeton University
Princeton, NJ 08544, USA

The accuracy of the laminar flame speed determination by using the counterflow twin-flame technique has been computationally and experimentally examined in light of the recent understanding that linear extrapolation of the reference upstream velocity to zero strain rate would yield a value higher than that of the laminar flame speed, and that such an overestimate can be reduced by using either lower strain rates and/or larger nozzle separation distances. A systematic evaluation of the above concepts has been conducted and verified for the ultralean hydrogen/air flames, which have relatively large Karlovitz numbers, even for small strain rates, because of their very small laminar flame speeds. Consequently, the significantly higher values of the previous experimentally measured flame speeds, as compared with the independently calculated laminar flame speeds, can now be attributed to the use of nozzle separation distances that were not sufficiently large and/or strain rates that were not sufficiently small. Thus, by using lower strain rates and larger nozzle separation distances, the experimentally and computationally redetermined values of these ultralean hydrogen/air flames agree well with the calculated laminar flame speeds. The laminar flame speeds of methane/air and propane/air mixtures have also been experimentally redetermined over extensive ranges of the equivalence ratio and are found to be slightly lower than the previously reported experimental values.

Introduction

Because of the fundamental and practical importance of the laminar flame speed, S_u°, commonly known as the laminar burning velocity, extensive efforts have been expended over the years toward achieving accurate determinations of their values. The early efforts, however, have resulted in data with substantial scatter, even for experiments apparently conducted with great care. Furthermore, the extent of scatter also did not improve with time, as demonstrated by the summary plot of Andrews and Bradley [1]. While it was recognized quite early that the laminar flame speeds could be substantially modified by aerodynamic stretch, with or without the additional influence of preferential diffusion [2], it was not until recently that systematic efforts have been mounted toward eliminating these stretch effects either during experimentation or through further data processing. A strong motivation for such efforts was the recent interest in *partially* validating chemical kinetic schemes through numerical simulation of the flame structure and hence the associated S_u°.

One of such efforts was the development of the counterflow twin-flame technique for the determination of S_u° [3,4]. Specifically, a twin-flame configuration is established in counterflow created by impinging two identical, nozzle-generated flows of the combustible mixture of interest onto each other. By mapping the flow field using laser Doppler velocimetry (LDV) and identifying the minimum in the velocity profile as a reference upstream burning velocity, $S_{u,\mathrm{ref}}$, and the velocity gradient ahead of the minimum point as the strain rate experienced by the flame, K, $S_{u,\mathrm{ref}}$ can be plotted for various K (see inset of Fig. 1 for definition). Based on the behavior of the experimental data and the results from theoretical studies, it was suggested that $S_{u,\mathrm{ref}}$ should vary linearly with K, for sufficiently small values of K, such that a linear extrapolation to $K = 0$ should yield the S_u° of the unstrained flame (see Fig. 2 for representative extrapolations). The extrapolated experimental values thus determined appear to agree quite well with those obtained through independent numerical computation of the unstrained planar flame with detailed transport and chemistry, for systems whose

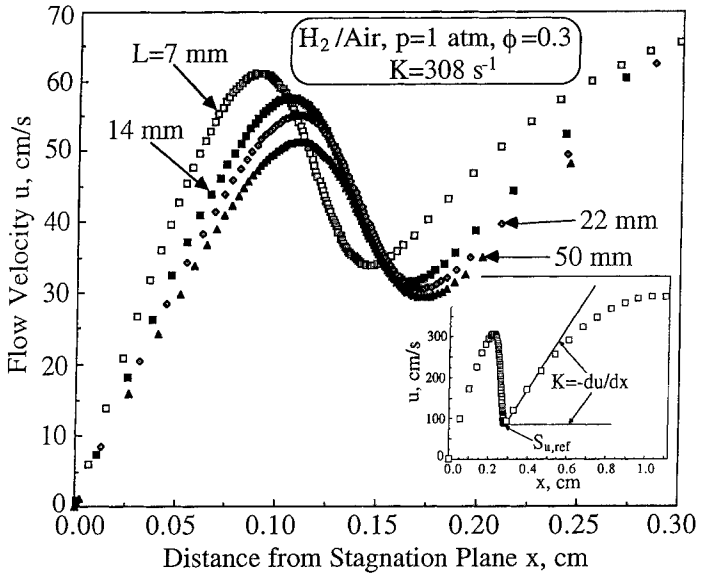

FIG. 1. Spatial variation of the numerically determined flow velocity profiles in the counterflow, for ϕ = 0.3 atmospheric hydrogen/air mixture with K = 308 s^{-1} and L = 7, 14, 22, and 50 mm, and the definition of K and $S_{u,ref}$.

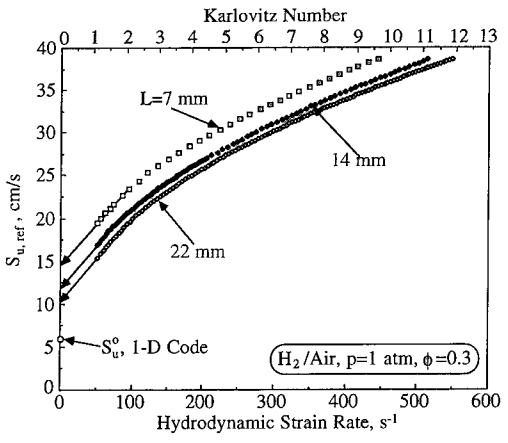

FIG. 2. Variation of the numerically determined $S_{u,ref}$ with K and Karlovitz number for ϕ = 0.3 atmospheric hydrogen/air mixture and L = 7, 14, and 22 mm.

chemistry is considered reasonably well known as far as the computation of S_u° is concerned.

The technique discussed above is based on the assumption of a linear relation between $S_{u,ref}$ and K for small K. Tien and Matalon [5], however, subsequently showed through asymptotic analysis that the relation is actually not linear as $K \to 0$, and that a linear extrapolation would yield a slightly higher value than the true S_u°. This point was further substantiated by Dixon-Lewis [6] through detailed numerical simulation of the counterflow flame with a finite separation distance L between the nozzle exits. The difference observed [6], however, was again small in that, for stoichiometric methane/air flames, the extrapolation yields S_u° = 39.6 cm/s, while direct computation yields 36.7 cm/s. The results of Ref. 6 also did not show any dependence on the separation distance of the nozzle.

Chao et al. [7] subsequently performed an asymptotic analysis of the counterflow problem, allowing for the plug flow boundary condition and a finite nozzle separation distance, L. The solution again yields the nonlinear variation as $K \to 0$, although it also showed that, for a given flame thickness, the overestimate can be reduced by either decreasing K or increasing L such that perturbation of the flow field by the flame is minimized. Note that, since a larger L implies the use of a proportionally larger nozzle if the ratio of L to the nozzle diameter is to be kept fixed, this requirement could have practical experimental limitations due to either inadequate flow rate or safety considerations when working with a large flow rate of combustible gas. Chao et al. [7] further performed detailed numerical simulation and experimentation with methane/air flames of selected stoichiometries. Results demonstrate that, contrary to the finding of Ref. 6, the overestimate indeed can be progressively reduced by using larger values of L. Furthermore, for the mixtures and hence the range of burning velocities studied, results obtained with nozzle separation distances of 14 and 22 mm show little difference, indicating that the use of L within this range should yield laminar flame speeds of reasonable accuracy, at least for methane/air mixtures.

The objectives of the present study are to further explore, computationally and experimentally, the influence of the separation distance on the accuracy of the laminar flame speed determination, and to redetermine the laminar flame speed values for the im-

portant fuel/air mixtures of hydrogen/air, methane/air, and propane/air. Based on the results of Chao et al. [7], we expect the revision from previously reported S_u° to be small for methane/air and propane/air flames. The revision, however, is needed because recent advances in the kinetic database require an increased accuracy for resolution. For hydrogen/air flames, we shall limit our study to ultralean mixtures for safety considerations. For these very weak flames, however, the influence due to the finite separation distance is also expected to be the greatest because they are most susceptible to stretch effects. We are especially interested in resolving the discrepancy observed in our previous work [8] that the experimentally measured S_u° for these flames were substantially higher than the calculated values based on apparently reliable hydrogen oxidation kinetics. In light of the new understanding that linear extrapolation tends to result in overestimates, it is possible that these previous experimental values could indeed be too high. Thus, for these flames, the revision is crucial because of the substantial discrepancy in the earlier data and because of its fundamental implications on the hydrogen oxidation kinetics.

The numerical and experimental methodologies will be presented in the next two sections, which will be followed by results on hydrogen/air, methane/air, and propane/air flames.

Numerical Methodology

Numerical solutions for the one-dimensional and counterflow flames were obtained using well-established formulations and computer codes [6,9–12]. The counterflow code was further modified for more efficient convergence, more accurate calculation of the mass diffusion velocities, and the ability to obtain solutions for increasing and decreasing nozzle separation distance through continuation. Both codes were integrated to the Chemkin-II [13] and Transport [14] subroutine packages, which provide the detailed chemistry and transport information. The kinetic scheme used was a hierarchically developed C_2 mechanism [15,16], which satisfactorily predicts a wide range of oxidation properties of hydrogen, carbon monoxide, methane, ethane, ethylene, acetylene, and methanol [15,16,17–19]. For the numerical determination of the propane/air laminar flame speeds, the C_3 kinetics of Pitz and Westbrook [20] were added to the C_2 mechanism.

In addition to solving the one-dimensional unstrained laminar flames of hydrogen/air, methane/air, and propane/air mixtures, the counterflow flame was also solved for lean hydrogen/air mixtures in order to identify the influence of the separation distance on such weak flames. For the counterflow solutions, zero velocity gradient was used at the nozzle exit, and the nozzle separation distances were 7, 14, 22, and 50 mm.

Typical numerically determined velocity profiles of the counterflow flame are given in Fig. 1 for a fixed strain rate of $K = 308\ s^{-1}$. Upon exiting the nozzle, the velocity gradually develops an increasing slope, which becomes maximum just before the minimum velocity point at which the heating starts. This maximum velocity gradient in the hydrodynamic zone is defined as the imposed strain rate, K, and the minimum velocity is a reference upstream flame speed, $S_{u,\mathrm{ref}}$, as mentioned earlier. Typically, a numerical solution is obtained at the lowest possible strain rate K required for convergence, and then, by using continuation for the nozzle exit velocity, the dependence of $S_{u,\mathrm{ref}}$ on K is determined.

The calculations were performed by using upwind differencing for the convective terms since convergence with the central difference has been found to be difficult in our computational facilities. Similarly, it was found in an earlier study [8] that the effect of numerical diffusivity, introduced by using upwind differencing, can be minimized by further refining the computational mesh. Thus, by increasing the number of grid points, N, the calculated flame speed decreases for the methane/air and propane/air mixtures and increases for the ultralean hydrogen/air mixtures. The reported data were obtained by plotting S_u° vs $1/N$ and extrapolating to $1/N = 0$, which corresponds to the limit of infinitely large N. This approach reduced the stoichiometric S_u° values for methane/air and propane/air mixtures by about 3 cm/s and increased the S_u° value for the $\phi = 0.35$ hydrogen/air mixture by 5 cm/s.

Experimental Methodology

The counterflow opposed-jet technique for the determination of laminar flame speeds and extinction strain rates is well documented [3,4,15,16,21]. In the present study, the nozzle separation distance was varied, and in agreement with our previous study [7], it was found that, by using L larger than about 14 mm, the experimental data on S_u° are minimally affected for methane/air and propane/air mixtures. Thus, the flame speeds for these flames were all obtained with $L = 22$ mm. For lean hydrogen/air flames, values of L equal to 7, 14, and 22 mm were used to demonstrate the influence of the finite separation distance. Efforts were made to obtain data under very low strain rates so as to minimize the stretch effect. Experiments were conducted under atmospheric pressure for the entire flammable range of methane/air and propane/air mixtures, and for lean hydrogen/air flames. For all cases, L was equal to the nozzle diameter, D, although additional measurements with the maximum $D = 22$ mm and $L = 7$, 14 mm indicated no effect on the flame speed data. This is due

to the fact that measurements were taken along the centerline, in the vicinity of which the nozzle diameter effect is not important. Furthermore, formulation of the counterflow equations realistically models our data because these equations represent an asymptotic expansion around the centerline of the system. Deviations would be expected if measurements were taken at radial distances of the same order as the nozzle radius. The uncertainty of the reported experimental data is limited by the accuracy of the LDV, which is estimated to be about ± 1 cm/s.

Results on Ultralean Hydrogen/Air Flames

The effect of the finite domain on S_u° was first numerically examined for the ultralean, $\phi = 0.3$ hydrogen/air mixture at $L = 7$, 14, and 22 mm. This range of the nozzle separation distance is representative of that adopted in previous experiments. We expect that the influence of L is most severe for these mixtures. Figure 1 clearly shows that the reference velocity, $S_{u,\mathrm{ref}}$, increases with decreasing L for the same value of K. That is, since the influence of the finite flame thickness on the flow velocity increases with decreasing L [7], as the freestream flow approaches the flame, the effect of thermal expansion is more readily felt by the flow for small L. This leads to an earlier turnaround in the velocity profile and hence a higher $S_{u,\mathrm{ref}}$, as well as a higher strain rate within the reaction zone [22]. It is further seen that the influence is especially significant for $L = 7$ mm and diminishes for larger values of L.

In Fig. 2, $S_{u,\mathrm{ref}}$ is plotted vs the strain rate K for the three separation distances. It is seen that overall the data show a curved behavior, which becomes more prominent at the lower K values, and that $S_{u,\mathrm{ref}}$ is uniformly higher for smaller separation distances. The dependence on L, however, diminishes with increasing L such that the differences between the results for $L = 14$ and 22 mm appear to be quite small. A linear extrapolation of the $L = 7$ mm and 22 mm data would yield flame speeds of about 15 and 10 cm/s, respectively. Such a significant difference was not observed for the previous study of methane/air flames [7], which showed only about 10% difference. Furthermore, even the 10 cm/s data for $L = 22$ mm substantially overpredict the independently calculated one-dimensional laminar flame speed of 6 cm/s.

In order to identify the observed sensitivity on the separation distance, we have evaluated the Karlovitz number experienced by the flame, defined as $Ka = K\delta/S_u^\circ$, where δ is a characteristic flame thickness. Since Ka represents the ratio of the characteristic residence time in the flame zone to that of the hydrodynamic zone, a smaller Ka implies a thinner flame and hence a correspondingly smaller influence of the finite separation distance. To evaluate δ, the basic laminar flame structure requires that δ be related to S_u° through $\delta(\rho_u S_u^\circ) = (\lambda/c_p)_u$, where ρ_u is the density of the unburned gas, λ the thermal conductivity, and c_p the specific heat, and the subscript "u" designates the unburned mixture. It represents the characteristic diffusion thickness and is well defined once S_u° is given. Alternatively, an empirical flame thickness can also be defined by measuring some effective thicknesses of the experimentally or numerically determined temperature profile across the flame, for example by using the tangent definition [23], which would yield a flame thickness typically larger than the diffusion thickness by a factor of about 3 and more for the present flame. Either definition can be used for the present purpose, as long as it is used consistently in the comparisons. Thus, by using the tangent method, the Karlovitz numbers for the strain rates of Fig. 2 have been evaluated and indicated. It is seen that, even for the lowest strain rate of $K = 50\ \mathrm{s}^{-1}$ obtainable in the experiments, the Karlovitz number is still $O(1)$. This is to be contrasted with the values of 0.1–0.2 (for the same range of strain rates) obtained for methane/air flames [7], for which linear extrapolation yields values close to the independently calculated laminar flame speeds. This exceptionally large Ka is due to the very small flame speeds and larger flame thicknesses for these lean mixtures.

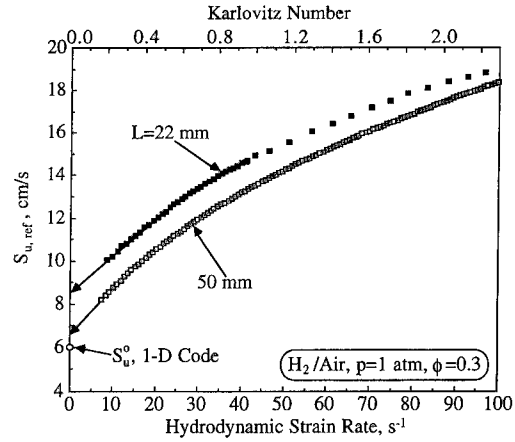

FIG. 3. Variation of the numerically determined $S_{u,\mathrm{ref}}$ for low values of K and Karlovitz number, for $\phi = 0.3$ atmospheric hydrogen/air mixture and $L = 22$ and 50 mm.

In order to further improve the accuracy of the extrapolation, we have extended the calculations for $L = 22$ mm down to lower rates of strain such that Ka is around 0.2, as shown in Fig. 3. It is seen that the extrapolation now places the flame speed to 8.5 cm/s, which is closer to the laminar flame speed of 6 cm/s.

An alternate approach to increase the accuracy is to further increase the separation distance. Hence, by using $L = 50$ mm and very small strain rates, Fig.

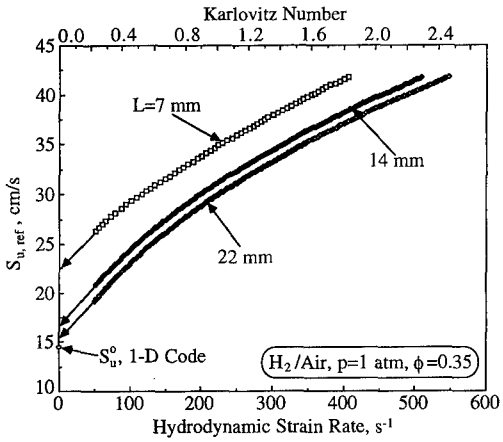

FIG. 4. Variation of the numerically determined $S_{u,ref}$ with K and Karlovitz number for $\phi = 0.35$ atmospheric hydrogen/air mixture and $L = 7$, 14, and 22 mm.

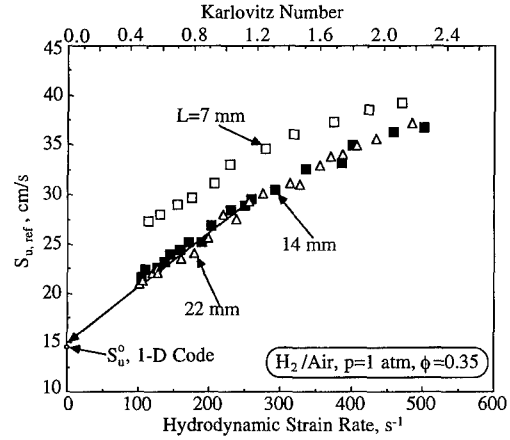

FIG. 6. Variation of the experimentally determined $S_{u,ref}$ with K and Karlovitz number for $\phi = 0.35$ atmospheric hydrogen/air mixture and $L = 7$, 14, and 22 mm.

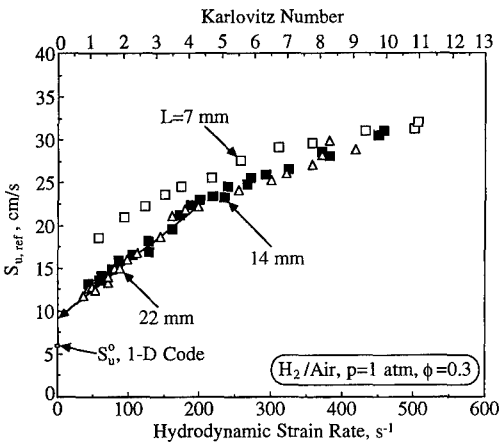

FIG. 5. Variation of the experimentally determined $S_{u,ref}$ with K and Karlovitz number for $\phi = 0.30$ atmospheric hydrogen/air mixture and $L = 7$, 14, and 22 mm.

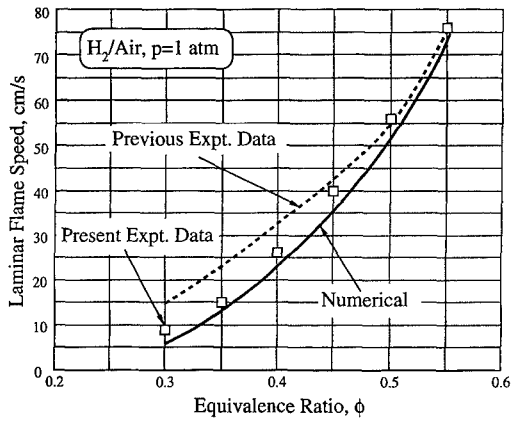

FIG. 7. Experimentally and numerically determined laminar flame speeds, S_u^o, as a function of the equivalence ratio, ϕ, for lean atmospheric hydrogen/air mixtures.

3 shows that the extrapolated value is now 6.6 cm/s, which is within 10% of the laminar flame speed.

Figure 4 shows the corresponding case of $\phi = 0.35$. Here, even though the change in ϕ from 0.3 is slight, the calculated S_u^o increases to 14.5 cm/s. Thus, the Karlovitz number is reduced for the same physical strain rate. A linear extrapolation with $L = 22$ mm and $K = 50\ s^{-1}$ in this case yields 15.5 cm/s, which is close to the laminar flame speed.

Figures 5 and 6 show the experimental results for the $\phi = 0.3$ and $\phi = 0.35$ hydrogen/air mixtures, respectively, with $L = 7$, 14, and 22 mm. The minimum strain rates that could be established for $\phi = 0.3$ and 0.35, with $L = 22$ mm, without inducing flashback in our system were about 50 and 100 s^{-1}, respectively. It is seen that, since the minimum Ka is about 1 for the $\phi = 0.3$ flames, accuracy of the linear extrapolation is not assured. Indeed, extrapolation yields 9 cm/s, which still substantially overpredicts the calculated S_u^o of 6 cm/s. This overprediction was anticipated from the numerical solution of Fig. 2. However, for the $\phi = 0.35$ flame, the minimum Karlovitz number is about 0.4. Consequently, the extrapolation is quite accurate, again in agreement with the numerical results.

Figure 7 compares the experimentally measured laminar flame speeds with the independently computed ones over the range of $\phi = 0.3$–0.55. It is seen that, apart from the $\phi = 0.3$ value, which shows a relatively higher experimental value, comparisons for all the other cases are very close in terms of the rel-

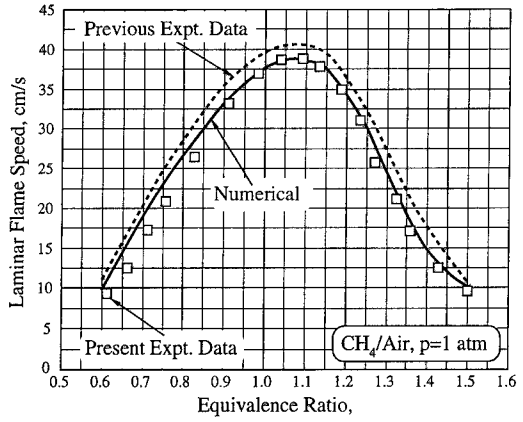

FIG. 8. Experimentally and numerically determined laminar flame speeds, S_u°, as a function of the equivalence ratio, ϕ, for atmospheric methane/air mixtures.

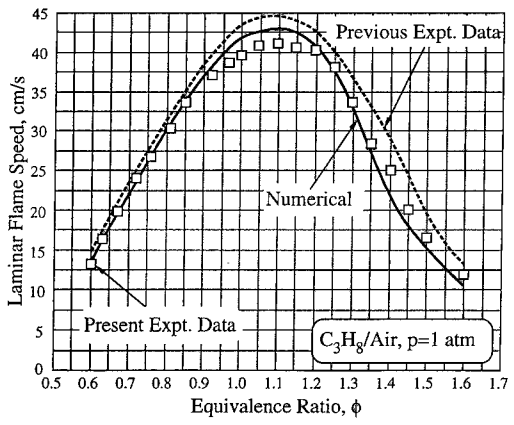

FIG. 9. Experimentally and numerically determined laminar flame speeds, S_u°, as a function of the equivalence ratio, ϕ, for atmospheric propane/air mixtures.

ative extent of deviations. We have also plotted the experimental values determined previously [8] with larger strain rates. It is seen that these values are substantially higher than the calculated values. Thus, the present result provides a satisfactory resolution of this previously observed discrepancy.

Results on Methane/Air and Propane/Air Flames

Figures 8 and 9, respectively, compare the present experimental data, all obtained with a nozzle separation distance of 22 mm, with the previous data [4,15,16,21], obtained mostly with $L = 7$ and 14 mm, for methane/air and propane/air mixtures. The comparison shows that the present experimental flame speeds are indeed lower than the previous values, particularly for rich propane/air mixtures. The differences, however, are much smaller than those for the ultralean hydrogen/air flames. This is reasonable based on considerations of the Karlovitz number for the experimental conditions. In addition, we have also compared the present experimental data with the calculated data by using the one-dimensional flame code. The comparison also shows close agreement, especially for the methane/air flames.

It may be noted that, in our previous studies for the methane and propane flames [4,15,16,21] using smaller separation distances, reasonably good agreements between computed and experimental values were also obtained. Such an agreement is a consequence of the higher experimental flame speeds due to the small L used, and the higher computed flame speeds based on previously accepted kinetic data. Agreement is again found in the present study because, while the experimental flame speeds are now reduced, the computed values obtained by using recent kinetic data and improved numerical accuracy are also reduced. The important points to note are that the computation and experiments were always independently conducted, that the differences between the previous and present values are actually quite small, that the present results are consequences of improvements in chemical kinetics and the experimental and numerical techniques, and that the present agreement also includes the rich propane/air flames.

Concluding Remarks

In this study, we have provided further insight into the accuracy of the linear extrapolation associated with the determination of laminar flame speeds by using the counterflow twin-flame technique, and identified approaches toward minimizing the inaccuracies. Specifically, it is shown that the accuracy of the linear extrapolation increases with decreasing Karlovitz number, that the Karlovitz number needs to be reduced to $O(0.1)$, based on the tangent definition of the flame thickness, in order for the linear extrapolation to be accurate, and that the accuracy can be improved by either reducing the strain rate or increasing the nozzle separation distance. Perhaps the most significant consequence of the above considerations is that our redetermined laminar flame speeds of ultralean hydrogen/air mixtures now agree well with the independently calculated values, thereby satisfactorily resolving the previously observed discrepancy of the much higher values of the experimental data. The redetermined values of the methane/air flames also show closer agreement with the calculated values obtained with the recent kinetic data of methane oxidation.

Under most common situations, the counterflow

technique with linear extrapolation is expected to yield flame speeds of sufficient accuracy, provided the lowest strain rate is not too high while the nozzle separation distance is also not too small. However, since strain rate reduction can be limited by flashbacks while increasing the nozzle separation distance, and hence nozzle diameter can also be complicated by buoyancy-induced flame instability and other experimental difficulties, the accuracy of this technique may decrease for the determination of the laminar flame speeds of very weak flames. We are currently developing nonlinear extrapolation approaches to circumvent such limitations.

Acknowledgments

CMV and FNE were supported by the National Science Foundation under Grant No. NSF CTS-9211844. CKL was supported by the Air Force Office of Scientific Research and the Office of Naval Research.

REFERENCES

1. Andrews, G. E., and Bradley, D. *Combust. Flame* 18:133–153 (1972).
2. Markstein, G., *Nonsteady Flame Propagation*, MacMillan, New York, 1964, pp. 5–73.
3. Wu, C. K., and Law, C. K., *Twentieth Symposium (International) on Combustion*, The Combustion Institute, Pittsburgh, 1984, pp. 1941–1949.
4. Zhu, D. L., Egolfopoulos, F. N., and Law, C. K., *Twenty-Second Symposium (International) on Combustion*, The Combustion Institute, Pittsburgh, 1988, pp. 1537–1545.
5. Tien, J. H., and Matalon, M., *Combust. Flame* 84:238–248 (1991).
6. Dixon-Lewis, G., *Twenty-Third Symposium (International) on Combustion*, The Combustion Institute, Pittsburgh, 1990, pp. 305–324.
7. Chao, B. H., Egolfopoulos, F. N., and Law, C. K., "Structure and Propagation of Counterflow Premixed Flames in a Finite Domain," manuscript in preparation.
8. Egolfopoulos, F. N., and Law, C. K., *Twenty-Third Symposium (International) on Combustion*, The Combustion Institute, Pittsburgh, 1990, pp. 333–340.
9. Kee, R. J., Grcar, J. F., Smooke, M. D., and Miller, J. A., *A Fortran Program for Modeling Steady Laminar One-Dimensional Premixed Flames*, Sandia Report SAND85-8240, 1985.
10. Miller, J. A., Kee, R. J., Smooke, M. D., and Grcar, J. F., "The Computation of the Structure and Extinction Limit of a Methane-Air Stagnation Point Diffusion Flame," Spring Meeting of the Western States Section of The Combustion Institute, Paper WSS/CI 84-10, 1984.
11. Kee, R. J., Miller, J. A., Evans, G. H., and Dixon-Lewis, G., *Twenty-Second Symposium (International) on Combustion*, The Combustion Institute, Pittsburgh, 1988, pp. 1479–1494.
12. Kee, R. J., personal communications.
13. Kee, R. J., Rupley, F. M., and Miller, J. A., *Chemkin-II: A Fortran Chemical Kinetics Package for the Analysis of Gas-Phase Chemical Kinetics*, Sandia Report SAND89-8009, 1989.
14. Kee, R. J., Warnatz, J., and Miller, J. A., *A FORTRAN Computer Code Package for the Evaluation of Gas-Phase Viscosities, Conductivities, and Diffusion Coefficients*, Sandia Report SAND83-8209, 1983.
15. Egolfopoulos, F. N., Cho, P., and Law, C. K., *Combust. Flame* 76:375–391 (1989).
16. Egolfopoulos, F. N., Zhu, D. L., and Law, C. K., *Twenty-Third Symposium (International) on Combustion*, The Combustion Institute, Pittsburgh, 1990, pp. 471–478.
17. Egolfopoulos, F. N., Du, D. X., and Law, C. K., *Combust. Sci. Technol.* 83:33–75 (1992).
18. Vagelopoulos, C. M., and Egolfopoulos, F. N., "Laminar Flame Speeds and Extinction Strain Rates of Mixtures of Carbon Monoxide with Hydrogen, Methane, and Air," *Twenty-Fifth Symposium (International) on Combustion*, The Combustion Institute, Pittsburgh, 1994, pp. 1317–1323.
19. Egolfopoulos, F. N., and Law, C. K., "Further Considerations on the Methanol Oxidation Kinetics," manuscript in preparation.
20. Pitz, W. A., and Westbrook, C. K., *Combust. Flame* 63:113–133 (1986).
21. Law, C. K., Zhu, D. L., and Yu, G, *Twenty-First Symposium (International) on Combustion*, The Combustion Institute, Pittsburgh, 1986, p. 1419.
22. Egolfopoulos, F. N., "Geometric and Radiation Effects on Steady and Unsteady Strained Laminar Flames," *Twenty-Fifth Symposium (International) on Combustion*, The Combustion Institute, Pittsburgh, 1994, pp. 1375–1381.
23. Tsatsaronis, G, *Combust. Flame* 33:217–239 (1978).

Twenty-Fifth Symposium (International) on Combustion/The Combustion Institute, 1994/pp. 1349–1356

LAMINAR FLAME CALCULATIONS USING SIMPLIFIED CHEMICAL KINETICS BASED ON INTRINSIC LOW-DIMENSIONAL MANIFOLDS

U. MAAS
Institut für Technische Verbrennung
Universität Stuttgart
D-70550 Stuttgart, Germany

S. B. POPE
Sibley School of Mechanical and Aerospace Engineering
Cornell University
Ithaca, NY 14853, USA

During the last 10 years, a great success has been achieved in the field of detailed mathematical modeling of combustion processes. However, most detailed models are restricted to the simulation of simple one-dimensional laminar flames, and the extension of detailed kinetic models to general reacting flows of practical importance (e.g., turbulent flow in internal combustion engines) is computationally prohibitive. Thus, simplified kinetic models have to be used. Recently, we presented a mathematical model, the method of intrinsic low-dimensional manifolds (ILDM), which reduces the chemical kinetics automatically. The only inputs to the procedure are the detailed reaction mechanism and the desired number of degrees of freedom. The reduction of the kinetics is performed using the assumption that the fastest timescales are in local equilibrium and can be decoupled. This paper discusses the implementation of the method in reacting flow calculations. The procedure is developed for general three-dimensional reacting flows, which are governed by the system of conservation equations, and the coupling of the reduced chemical kinetics with molecular transport processes and convection is discussed. Then, the mathematical model is verified by sample calculations of structures of laminar premixed flat flames, which provide a simple, but realistic test case. Examples, which verify the approach, are shown for H_2-O_2 and syngas-air flames. Even for these simple examples, a considerable speedup of the computations is observed. However, the method can also be used for other fuels and, thus, will allow an efficient treatment of combustion systems of practical importance.

Introduction

During the last 10 years, the interest in simplified descriptions of chemical reaction systems for the simulation of complex combustion processes has increased considerably, and a variety of different approaches can be found in the literature [1–7]. The main motivation for the use of reduced mechanism is the fact that due to the complexity of the combustion processes usually encountered in practical applications, methods have to be found to describe the chemical reaction by only a small number of species, while still retaining the essential dynamics of the system. Recently, we developed a method, the method of intrinsic low-dimensional manifolds (ILDM), which provides a simplification of the chemical kinetics starting from a detailed reaction mechanism. The method is based on the dynamic systems theory. Besides the detailed reaction mechanism, the only input to the scheme is the desired number of degrees of freedom (i.e., the number of reaction progress variables). Sample calculations for a perfectly stirred reactor [9] have shown that the method yields good results and is able to describe the coupling of chemical reaction with physical processes like mixing or molecular transport.

A nice test case for the application of the ILDM method in reacting flow computations are laminar flames. Although being sufficiently complicated systems with various practical applications, they nevertheless allow a direct comparison with results of detailed calculations. Various investigations over the last few years have shown that up to two-dimensional laminar flame structures can be calculated using detailed reaction and transport models [10–12]. In most cases, the agreement with experimental results is very good. Typical one-dimensional laminar flame calculations take less than 1 h on modern work stations. However, structures of laminar flame calculations are tabulated quite often for use in flamelet models of turbulent flames [13,14]. In this case, many (sometimes more than 1000) flame structures are needed, and the use of detailed kinetics then causes an enormous computational effort. In the sim-

ulation of two-dimensional laminar flames, the computational effort is tremendous [11,12], and reduced mechanisms are desirable anyway. Thus, because laminar flames allow a good comparison between reduced and detailed reaction mechanisms and because their fast simulation is of practical importance, it shall be shown in the following that the concept of intrinsic low-dimensional manifolds can be applied successfully to these systems.

Mathematical Model

Governing Equations:

The dynamic behavior of a chemically reacting flow is governed by the system of conservation equations, namely, the conservation of mass, momentum, energy, and species masses [15,16]. These equations can be rewritten to yield equations for the scalar field of a reacting flow, which is described by the state vector $\underline{\psi} = (h, p, \phi_1, \phi_2, \ldots, \phi_{n_s})^T$. Here, a formal separation into physical processes Ξ and chemical production terms F shall be made. We obtain

$$\frac{\partial h}{\partial t} = F_h + \Xi_h$$

$$\frac{\partial p}{\partial t} = F_p + \Xi_p$$

$$\frac{\partial \phi_i}{\partial t} = F_{\phi_i} + \Xi_{\phi_i} \quad i = 1, 2, \ldots, n_s \tag{1}$$

or in vector formulation

$$\frac{\partial \underline{\psi}}{\partial t} = \underline{F} + \underline{\Xi} \tag{2}$$

with $\underline{F} = (F_h, F_p, F_{\phi_1}, F_{\phi_1}, \ldots, F_{\phi_{n_s}})^T$ and $\underline{\Xi} = (\Xi_h, \Xi_p, \Xi_{\phi_1}, \Xi_{\phi_1}, \ldots, \Xi_{\phi_{n_s}})^T$, and

$$F_h = 0; \qquad \Xi_h = \frac{f_p}{\rho} - \mathbf{v}\,\mathrm{grad}\,h - \frac{1}{\rho}\,\mathrm{div}\,\mathbf{q} - \frac{1}{\rho} \cdot \bar{\bar{p}}\colon \mathrm{grad}\,\mathbf{v} + \frac{1}{\rho}\,\mathrm{div}\,\rho\mathbf{v} + \frac{\omega_h}{\rho}$$

$$F_p = 0; \qquad \Xi_p = f_p$$

$$F_{\phi_i} = \omega_i/\rho; \quad \Xi_{\phi_i} = -\frac{1}{\rho M_i}\,\mathrm{div}\,\mathbf{j}_i - \mathbf{v}\,\mathrm{grad}\,\phi_i; \quad i = 1, 2, \ldots, n_s \tag{3}$$

where t = time, h = specific enthalpy, p = pressure, ρ = density, $\mathbf{v}$ = velocity vector, $\bar{\bar{p}}$ = pressure tensor, $\mathbf{q}$ = heat flux density, ω_h = source term for energy (e.g., radiation), n_s = number of species, ϕ_i = specific mole number of species i ($\phi_i = W_i/M_i$), W_i = mass fraction of species i, M_i = molar mass of species i, $\mathbf{j}_i$ = diffusion flux density of species i, and ω_i = molar rate of formation of species i. The symbol $\otimes$ denotes the dyadic product of two tensors, and : denotes the twofold contraction of two tensors. This choice of the dependent variables is quite arbitrary. Other formulations, like conservative, could be used, too. The term f_p describes the time behavior of the pressure. Because a constant pressure is used quite often in laminar flame calculations ($f_p = 0$), this term shall not be written down explicitly in this paper. Furthermore, note that the Ξ terms are complicated functions of the scalars, the velocity field, and the first and second spatial derivatives.

Coupling of Chemical Kinetics with Convection and Molecular Transport:

The basic assumption of manifold methods for the reduction of chemical kinetics is that the state $\underline{\psi}$ is (at any time and at any point in the flow) close to an attracting low-dimensional manifold (of dimension N). Then the dynamics of the reactive system can be approximated by assuming that the state is confined to those N-dimensional manifolds and is thus a function of N variables only, which describe the dynamics within the manifold. It has been shown in Refs. 8 and 9 that the method of intrinsic low-dimensional manifolds can be used to simplify chemical kinetics. This is done by projecting the governing equation system for the scalar field onto the low-dimensional manifolds. In this way, the $(2 + n_s)$-dimensional equation system 2 is transformed into an equation system of much lower dimension (N) for the variables $\underline{\tau} = (\tau_1, \tau_2, \ldots, \tau_N)^T$. The simplification of the detailed reaction mechanism yields $\underline{\psi}(\underline{\tau})$, which is the equation of the low-dimensional manifold, $\underline{S}$, and, in addition, provides information on how to project the physical processes $\underline{\Xi}$ onto the manifold. The variables $\underline{\tau}$ are, e.g., enthalpy, pressure, variables specifying the element composition, and reaction progress variables. Usually, the results of the mechanism reduction (i.e., the low-dimensional manifolds) are tabulated in terms of the variables $\underline{\tau} = (\tau_1, \tau_2, \ldots, \tau_N)^T$ and stored for subsequent use in other reacting flow codes. This includes, e.g., the storage of the reduced reaction rates $\underline{S}$ (rates of change of the reaction progress variables), the species mass fractions, and information about the local timescales. At this time, we want to emphasize the numerical issue that the reaction rates obtained directly from the reduction procedure are stored and used in the laminar flame calculation. Evaluating the reaction rates from the stored species mass fractions might lead to large errors, as can be shown by some simple examples [21]. Details about the mechanism reduction, the choice of the reaction progress variables, the tabulation pro-

cedure, and the subsequent table lookup and interpolation can be found in Refs. 8 and 9.

Physical perturbations tend to move the system off the intrinsic low-dimensional manifolds. However, if slow physical processes move the system off the manifold, the fast chemical processes cause a relaxation of the system back to the manifold. It can be shown that convection always leads to movements within the manifold. Thus, the only physical perturbation, which tends to move the system off the manifold in the equations above, is molecular transport.

Let the reacting system be described by the $(2 + n_e + n_c)$ parameters $h, p, \chi_1, \ldots, \chi_{n_e}$, and $\underline{\tau}_c = (\tau_{c,1}, \ldots, \tau_{c,n_c})^T$ of the reduced scheme, where χ_j denote the n_e specific element mole numbers ($\chi_j = w_j/M_j$), w_j denote the mass fraction of element j, M_j denote the molar mass of element j, n_e denotes the number of elements in the reaction system, and $\tau_{c,i}$ denote the reaction progress variables. Then the state $\underline{\psi}$ is a known function of these parameters $\underline{\tau} = (h, \overline{p}, \chi_1, \ldots, \chi_{n_e}, \tau_{c,1}, \ldots, \tau_{c,n_c})^T$.

Using the results of Ref. 9, it can be shown (see appendix) that the governing equations of Eq. (1) can be rewritten as follows:

$$\frac{\partial h}{\partial t} = \Xi_h$$

$$\frac{\partial p}{\partial t} = \Xi_p$$

$$\frac{\partial \chi_i}{\partial t} = \mu_i^T \underline{\Xi}_\phi \quad i = 1, 2, \ldots, n_e$$

$$\frac{\partial \underline{\tau}_c}{\partial t} = \underline{S} + Z\Xi \tag{4}$$

where $\underline{\Xi}_\phi = (\Xi_{\phi 1}, \Xi_{\phi 2}, \ldots, \Xi_{\phi n})^T$ and $\underline{S}$ are rates of production of the reaction progress variables and Z is an $n_c \times (n_s + 2)$ projection matrix. The variables $\underline{S}$ and Z are functions of the parameters $\underline{\tau}$, which are calculated in the mechanism reduction and tabulated.

Thus, we have equations for $2 + n_e + n_c$ dependent variables $\underline{\tau}$, namely, for the enthalpy, for the pressure, for each of the specific element mole numbers, and for each of the reaction progress variables. The implementation of the reduced mechanism is now very simple: At each point in the flow, the initial values of the dependent variables are known. Then we know the rates $\underline{S}$ of the reaction progress variables and the thermochemical state $\underline{\psi}$ of the system, which are stored in the tabulation of the manifold. From this, we can compute the physical processes $\underline{\Xi}$ and, using tabulated values for the projection matrix Z, calculate the total rates of change of the reduced variables. It shall be noted that the calculation can be further simplified by rewriting the molecular transport terms in terms of gradients of the variables

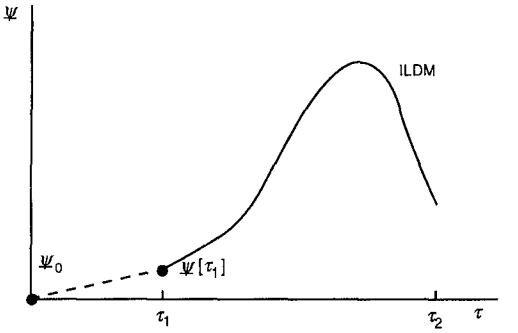

FIG. 1. Intrinsic low-dimensional manifold and its continuation into the domain of negligible chemistry.

of the reduced scheme (this can be done very easily, because the state $\underline{\psi}$ of the system is a known function of the variables of the reduced scheme). In this case, the molecular transport coefficients can be calculated during the mechanism reduction and do not need to be evaluated during the reacting flow calculation [20].

Some complications can arise in the computations due to the fact that initial or boundary values might not correspond to states on the manifolds. A detailed discussion of this problem cannot be given here; however, there are methods to solve it [20]. Here, the basic idea in the case of laminar reacting flows shall be outlined briefly. Suppose that we have a one-dimensional manifold, which is defined in the parameter range $\tau^1 < \tau < \tau^2$ and where the boundary condition is given by ψ_0 (Fig. 1). For $\tau < \tau^1$, chemistry is very slow, and diffusion governs the dynamics of the process. Thus, we have a pure diffusion problem, which is characterized by the two conditions ψ_0 and $\underline{\psi}[\underline{\tau}^1]$. From this, it can be seen that the manifold, which is not defined in the interval $\tau < \tau^1$, can be approximated in this region by assuming a linear shape (corresponding to a linear mixing process). In this way, it is possible to define reasonable initial and boundary conditions for the system. If these conditions lie outside the domain of sufficiently fast chemistry, the dynamics are governed by molecular transport, and the overall process can be viewed as a movement into the domain of sufficiently fast chemistry, relaxation toward the manifold, and finally, a movement within the manifold.

Simulation of One-Dimensional Laminar Premixed Flames

Above, it was shown that the reduced kinetics based on intrinsic low-dimensional manifolds can be used to simulate laminar reacting flows. Although reduced mechanisms are of special interest in multidimensional problems, simple laminar flat premixed

flames shall be considered here. They provide a nice, simple test case for the verification of the model and are usually more sensitive with respect to the reaction mechanism than diffusion flames. The governing equations form a partial differential equation system with the time and one spatial coordinate as the independent variables. Transformation into a moving coordinate system allows the flame front to be fixed such that a stationary solution is obtained for $t \to \infty$. The governing equations form an initial-boundary value problem, which can be solved numerically. However, special properties of the equation system (like its stiffness) require special solution methods, and an implicit method, adaptive in space and time, has been chosen: Spatial discretization using finite differences on a statically adapted mesh leads to large systems of ordinary differential equations, which are solved numerically using an implicit extrapolation method with variable order- and stepsize control. Details on this method and references can be found in Refs. 17 and 19.

An existing program for detailed chemistry calculations of one-dimensional instationary flames [17] has been modified such that the tabulated reduced mechanism can be used in the simulation. The additional subroutines are written in a modular way and can be used in other computational fluid dynamics (CFD) codes, too.

Laminar Premixed H_2-O_2 Flames:

The first example considered here are laminar stationary premixed flat H_2-O_2 flames. The H_2-O_2 system consists of ($n_s = 8$) chemical species (H_2O, H_2, O_2, H, O, OH, HO_2, and H_2O_2). Furthermore, there are ($n_e = 2$) elements (H and O). Thus, a 10-dimensional state space, an 8-dimensional composition space, and a 6-dimensional reaction space are obtained. Two reaction progress variables shall be used, which (for simplicity) shall be given by the specific mole numbers of H_2O and H ($\theta_1 = \phi_{H_2O}$, $\theta_2 = \phi_H$). The notation θ is introduced here to denote those variables τ_i, which change in the reaction system. The other variables τ_j, which do not change, can be treated as constants of the system.

Three cases of different complexity are obtained:

1. Equal diffusivities, $Le = 1$. Although this approximation leads to large errors in the H_2-O_2 system, it shall be considered here, because it is used quite often in the simulation of turbulent flames [18]. Starting from this assumption, the specific enthalpy, as well as the element composition, is constant ($\partial h/\partial t = 0$, $\partial p/\partial t = 0$, and $\partial \chi_i/\partial t = 0$). The system can be described completely by the reaction progress variables, and the scalar field is determined by two partial differential equations for the two variables $\theta_1 = \phi_{H_2O}$ and $\theta_2 = \phi_H$ of the two-dimensional manifold.

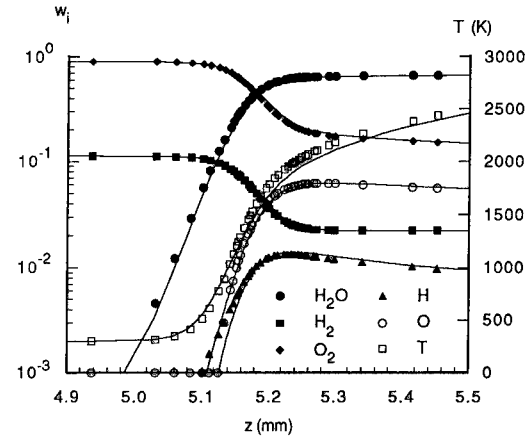

FIG. 2. Calculated structure of a stoichiometric laminar premixed hydrogen-oxygen flame (points: reduced mechanism; lines; detailed reaction mechanism).

2. Equal diffusivities, $Le \neq 1$. In this system the element composition is constant, but the enthalpy changes. In addition to the two equations for the reaction progress variables, a conservation equation for the enthalpy has to be solved ($\partial h/\partial t \neq 0$). The system is described by the three variables $\theta_1 = \phi_{H_2O}$, $\theta_2 = \phi_H$, and $\theta_3 = h$ (corresponding to a three-dimensional manifold).
3. General case. In the general case, differential diffusion changes the element composition. Differential equations are obtained for the specific enthalpy, a specific element mole number (only two elements in the system), and the two reaction progress variables. Thus, the system is governed by the four variables $\theta_1 = \phi_{H_2O}$, $\theta_2 = \phi_H$, $\theta_3 = h$, and $\theta_4 = \chi_H$.

The specific example considered here is a stoichiometric flame at 1 bar and with a temperature of 298 K in the unburnt gas. As an example, Fig. 2 shows the calculated flame structure for equal diffusivities but with a nonunity Lewis number. Good agreement is not only obtained for the stable species but also for the radicals, although only two reaction progress variables are used to describe the whole system. The different transport models are compared in Fig. 3, which shows H-atom profiles for $Le = 1$ as well as for equal diffusivities but with $Le \neq 1$. Plotted is only the small region of the flame front, where the main changes in the profiles occur. It can be seen that the differences between the transport models are larger than the differences between reduced and detailed reaction mechanism. Furthermore, the results of a very detailed transport model (including thermal diffusion) are plotted in the figure. Calculations for this transport model, using the reduced mechanism, can be done too [20]. Other profiles show similar results but are not plotted due to space limitation. Compar-

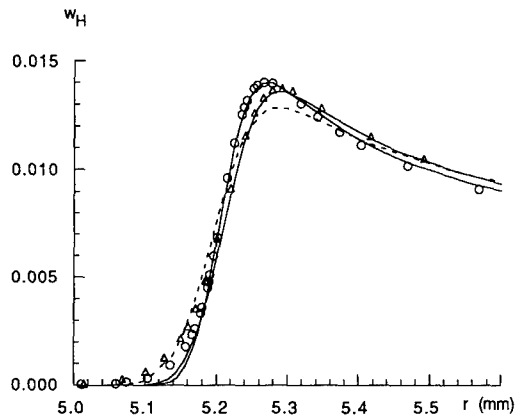

FIG. 3. Calculated profiles of the H-atom mass fractions in a stoichiometric laminar premixed hydrogen-oxygen flame for different transport models. ––: detailed transport model, including thermal diffusion; lines: detailed reaction mechanism; points: reduced mechanism; ○: $Le = 1$; △: $Le \neq 1$.

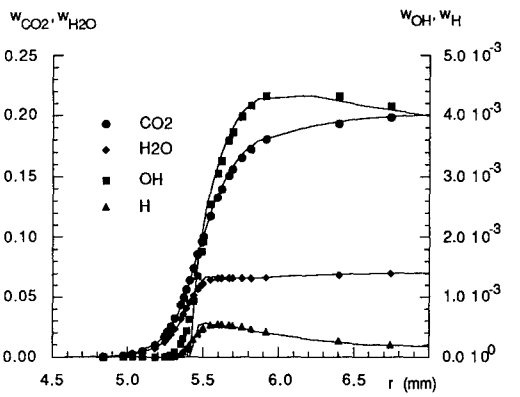

FIG. 4. Calculated structure of a syngas-air flame (points: reduced mechanism, lines: detailed mechanism).

isons of the burning velocities show that the error of the reduced scheme is less than 3% for the specific example considered here. A detailed discussion of burning velocities and flame structures for different fuels (e.g., methane) and stoichiometries is beyond the scope of this work and will be given in a future paper [20].

Laminar Premixed CO-H_2-O_2-N_2 Flames:

The second example is a syngas (40 vol.% CO, 30 vol.% H_2, 30 vol.% N_2)-air system at $p = 1$ bar and with a temperature of 290 K in the unburnt gas. The fuel/air ratio is 6/10. The low-dimensional manifold used for this calculation corresponds to the one used in Ref. 9 for homogeneous systems. The fact that the same manifold is used reflects that the method of intrinsic low-dimensional manifolds yields general reduced mechanisms. An adaptation to the specific problem is not necessary. (Furthermore, this reduced mechanism has been used for the simulation of turbulent jet diffusion flames [23], where the mixture fraction was used as an additional tabulation coordinate for the manifold.)

The influence of simplified transport models has been described in the last section. Here, for the sake of simplicity, only systems with equal diffusivity shall be considered, because this section shall mainly discuss the influence of the tabulation on the results and computational aspects. Figure 4 shows profiles of CO_2, H_2O, OH, and H in the flame both for reduced and detailed kinetics. Good agreement is obtained in the flame front as well as behind the flame front, where the slow equilibration process takes place. Differences are observed at the beginning of the flame front. This is caused by the fact that at the low temperatures ($T < 1000$ K), the decoupled timescales are of the order of the timescales of diffusion and heat conduction. However, if an additional reaction progress variable were used, the results would become much more accurate. The small deviations behind the flame front can be attributed to discretization errors in the numerical simulation (the points reflect directly the mesh used in the computations).

In order to allow a realistic comparison between central processing unit (CPU) times for reduced and detailed chemistry calculations, we performed computations where the initial profiles were assumed as step functions between burnt and unburnt gas composition. Of course, this is an extremely bad initial guess, and it turns out that very small time steps are needed in the detailed chemistry calculations. Surprisingly, those problems do not arise, if the reduced mechanism is used. Because 16 partial differential equations have to be solved for detailed chemistry and only five if reduced chemistry is used, the reduction of the computational effort can be estimated to be a factor of 6 (due to the small number of equations, there is not yet the quadratic dependence of the CPU time on the number of equations, which is typical for implicit methods). However, the comparison of the CPU time shows that the detailed chemistry calculations need 844 CPU seconds on a Silicon-Graphics Indigo, and the calculations with the reduced scheme only 86 CPU seconds, which corresponds to a speedup of a factor of 10. The main reason for this behavior is that much of the stiffness is removed by the mechanism reduction, and large step sizes are chosen by the integrator. Further research will show whether explicit methods can lead to a further speedup of the computation. It is an interesting and promising result that the mechanism generated by the ILDM method does not cause convergence problems in the numerical simulations, which are usually observed, if reduced mechanisms

are used [1]. The reason for this behavior is mainly that the fast timescales are really decoupled locally, whereas the global conditions of other reduced mechanisms do not guarantee this.

One further aspect, which has to be discussed, is the influence of the tabulation procedure on the accuracy of the results. It is evident that the reduced mechanisms are improved, if more reaction progress variables (degrees of freedom) are used. Nevertheless, tables of higher dimension are only possible if coarse grids are used. Thus, following a suggestion of Gran [22], we performed calculations with tables having different levels of refinement (cf. Ref. 9 for the tabulation procedure). The different tables are shown in Fig. 5, and the results obtained with those grids are shown in Fig. 6 for the OH profiles together with the results of the detailed reaction mechanism (the other profiles show a similar-trend, but they show less significant deviations). Only the coarsest grid leads to large errors, especially in the region of the equilibration zone. But even the use of the second coarsest table, which uses only about 100 kbyte of storage, yields good results. From this, it can be seen that even higher dimensional tables can be produced with a reasonable storage requirement. Better refinement strategies and better interpolation methods can further reduce the storage requirement.

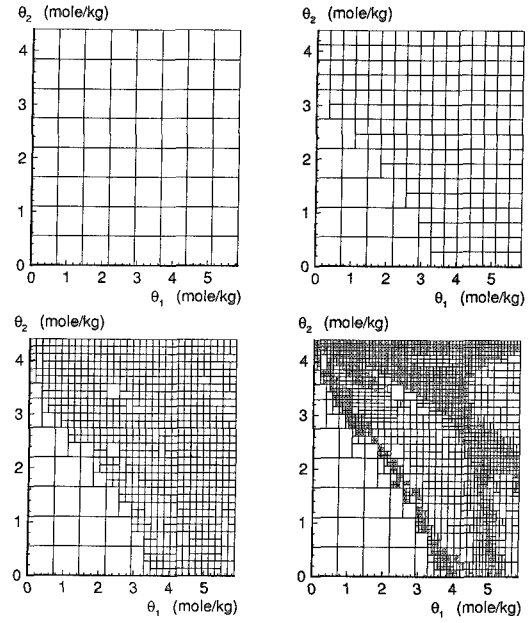

FIG. 5. Structures of the different tables. Upper part: Table 1 (left) and Table 2 (right); lower part: Table 3 (left) and Table 4 (right).

Conclusions

It has been shown that the method of intrinsic low-dimensional manifolds can be used successfully in the simulation of laminar reacting flows. There is in principle no restriction to simplified transport models, but processes like nonunity Lewis number, differential diffusion, or thermal diffusion can be treated by the method very easily. The results are in very good agreement with results from detailed chemistry calculations, which verifies the approach and allows the conclusion that the method can be used in turbulent flame calculations for a reliable description of the chemistry. The computational effort in the laminar flame calculations is reduced considerably. Convergence problems, known from simulations with reduced reaction mechanisms, are not observed, but, to the contrary, the method of intrinsic low-dimensional manifolds yields reduced reaction mechanisms, which simplify the numerical integration to a great extent and might even allow the use of explicit integration methods. It can be estimated that the method can speed up calculations of flames with more complex fuels (like octane) by a factor of much more than 1000.

Acknowledgments

The authors would like to thank I. Gran, D. Schmidt, and J. Warnatz for helpful discussions. Financial support by General Electric and the BMFT (in the frame of the TECFLAM-Project) is gratefully acknowledged.

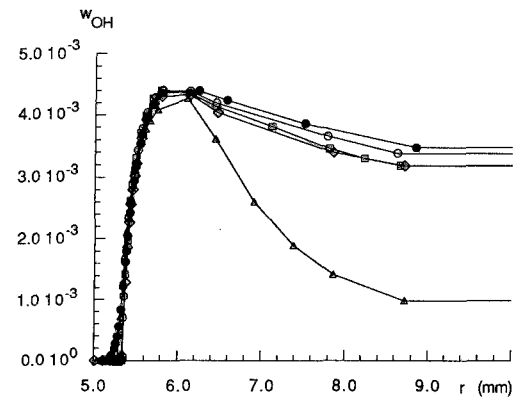

FIG. 6. Comparison of tables with different refinement levels; ●: detailed mechanism; △: Table 1; ◇: Table 2; □: Table 3; ○: Table 4.

Appendix

Within the concept of intrinsic low-dimensional manifolds, a reacting system can be characterized by the $(2 + n_e + n_c)$ parameters $\underline{\tau} = (h,p,\chi,\underline{\tau}_c)^T$; i.e., the system is described by its specific enthalpy, pressure, element composition, and n_c reaction progress variables. Then, the state $\underline{\psi}$ is a known function of the parameters

$$\underline{\psi} = \underline{\psi}(\underline{\tau}[\mathbf{r},t]). \tag{5}$$

Let the parametrization be given by the matrix C,

$$d\underline{\tau} = Cd\underline{\psi}. \tag{6}$$

Then, projection of the $(n = n_s + 2)$-dimensional equation system (2) yields [9]

$$\frac{\partial \underline{\tau}}{\partial t} = C\underline{F} + CP\underline{\Xi}. \tag{7}$$

The projection matrix P is given by [9]

$$P = I - V_f\tilde{V}_f \tag{8}$$

where V_f denotes the $(n \times n_f)$-dimensional matrix of the "fast" right eigenvectors and $\tilde{V}_f$ denotes the corresponding $(n_f \times n)$ matrix of the left eigenvectors (see Ref. 9).

The parametrization matrix can be split into two components, namely, one describing the specific enthalpy, the pressure, and the element composition and another describing the reaction progress variables. Then we obtain

$$C = \begin{pmatrix} C_e \\ C_c \end{pmatrix} \tag{9}$$

where C_c is the $(n_c \times n)$-dimensional matrix for the reaction progress variables and C_e is the $(n_e + 2 \times n)$-dimensional matrix for the remaining variables, which is given by

$$C_e = \begin{pmatrix} 1 & 0 & 0 & \dots & 0 \\ 0 & 1 & 0 & \dots & 0 \\ 0 & 0 & \text{---} & \underline{\mu}_1^T & \text{---} \\ \vdots & \vdots & & \vdots & \\ 0 & 0 & \text{---} & \underline{\mu}_{n_e}^T & \text{---} \end{pmatrix} \tag{10}$$

where $\underline{\mu}_i = (\mu_{1,i}, \mu_{2,i}, \dots, \mu_{n_s,i})^T$ are the element composition vectors and $\mu_{j,i}$, denotes the number of atoms of element i in a species j. It has the property that it allows the direct calculation of the specific element mole numbers from the state vector:

$$C_e\underline{\psi} = (h, p, \chi_1, \chi_2, \dots, \chi_{n_e})^T. \tag{11}$$

It can be shown that the element vectors are orthogonal to the fast eigenvectors, and we can obtain very easily the relation

$$C_eP = C_e - C_eV_f\tilde{V}_f = C_e. \tag{12}$$

This means that physical processes, which change specific enthalpy, pressure, or element composition, do not have to be projected. The physical reason for this is that processes, which perturb in direction of eigenvectors with zero eigenvalue (i.e., which change variables conserved in chemical reaction), have no relaxing component.

Using this property, we obtain from Eq. (1) for the scalar field of a reacting flow

$$\begin{aligned} \frac{\partial h}{\partial t} &= \Xi_h \\ \frac{\partial p}{\partial t} &= \Xi_p \\ \frac{\partial \chi_i}{\partial t} &= \mu_i^T\underline{\Xi}_\phi \quad i = 1, 2, \dots, n_e \\ \frac{\partial \underline{\tau}_c}{\partial t} &= C_c\underline{F} + C_cP\underline{\Xi} \end{aligned} \tag{13}$$

with $\underline{\Xi}_\phi = (\Xi_{\phi 1}, \Xi_{\phi 2}, \dots, \Xi_{\phi n_s})^T$.

Thus, we have obtained equations for specific enthalpy and pressure, n_e equations for the specific element mole numbers, and n_c for the reaction progress variables. Because ψ, and thus also $\underline{F}$, $\underline{\Xi}$, and P are defined by the low-dimensional manifold in terms of h, p, $\underline{\chi}$, and $\underline{\tau}_c$, the equation system can be solved numerically.

REFERENCES

1. Smooke, M. D. (Ed.), "Reduced Kinetic Mechanisms and Asymptotic Approximations for Methane-Air Flames." *Lecture Notes in Physics*, Springer, Berlin, 1991, Vol. 384.
2. Peters, N., and Rogg, B., *Reduced Kinetics Mechanisms for Applications in Combustion Systems*. Springer, Berlin, 1993.
3. Chen, J.-Y., *Combust. Sci. Technol.* 57:89 (1988).
4. Frenklach, M., in *Numerical Approaches to Combustion* (E. S. Oran and J. P. Boris, Eds.), AIAA, Washington, DC, 1991, p. 129.
5. Keck, J. C., *Twenty-Second Symposium (International) on Combustion*, The Combustion Institute, Pittsburgh, 1989, p. 1705.
6. Tomlin, A. S., Pilling, M. J., Turanyi, T., Merkin, J. H., and Brindley, J., *Combust. Flame* 91:107 (1992).
7. Oppenheim, A. K., and Maxson, J. A., *Prog. Astron. Aero.* 152:365 (1993).
8. Maas, U., and Pope, S. B., *Combust. Flame* 88:239 (1992).
9. Maas, U., and Pope, S. B., *Twenty-Fourth Symposium (International) on Combustion*, The Combustion Institute, Pittsburgh, 1992, p. 103.
10. Warnatz, J., *Twenty-Fourth Symposium (International) on Combustion*, The Combustion Institute, Pittsburgh, 1992, p. 553.

11. Smooke, M. D., Mitchell, R. E., and Keyes, D. E., *Combust. Sci. Technol.* 67:85 (1989).
12. Maas, U., and Warnatz, J., *IMPACT Comput. Sci. Eng.* 1(4):394 (1989).
13. Bilger, R. W., in: "Turbulent Flows with Nonpremixed Reactants" P. A. Libby and F. A. Williams, (Hrsg.) Eds., *Turbulent Reactive Flows*, Springer, New York, 1980.
14. Peters, N., *Twenty-first Symposium (International) on Combustion*. The Combustion Institute, Pittsburgh, 1988, p. 1231.
15. Hirschfelder, J. O., and Curtiss, C. F., *Third Symposium on Combustion Flame and Explosion Phenomena*, Williams and Wilkins, Baltimore, 1949.
16. Bird, R. E., Stewart, W. E., and Lightfoot, E. N., *Transport Phenomena*, Wiley Interscience, New York, 1960.
17. Maas, U., and Warnatz, J., *Combust. Flame* 74:53 (1988).
18. Libby, P. A., and Williams, F. A. (ed.), *Turbulent Reactive Flows*, Springer, New York, 1980.
19. Goyal, G., Maas, U., and Warnatz, J., *Proc. 14th ICDERS*, Coimbra, Portugal, 1993.
20. Schmidt, D., Maas, U., Pope, S. B., and Warnatz, J., in preparation.
21. Lam, S. H., private communication, 1992.
22. Gran, I, private communication, 1993.
23. Norris, A., "The Application of PDF Methods to Turbulent Diffusion Flames." Dissertation, Cornell University, Ithaca, NY, 1993.

Twenty-Fifth Symposium (International) on Combustion/The Combustion Institute, 1994/pp. 1357–1364

LAMINAR COUNTERFLOW MIXING OF ACETYLENE INTO HOT COMBUSTION PRODUCTS

H. BREITBACH, J. GOETTGENS, F. MAUSS, H. PITSCH AND N. PETERS
Institut für Technische Mechanik
Rheinisch-Westfälische Technische Hochschule Aachen
52056 Aachen, Federal Republic of Germany

In an axisymmetric counterflow configuration, acetylene was blown against the hot post flame gases of a rich premixed acetylene-air flame stabilized on a sinter metal, thereby creating a broad pyrolysis zone. This one-dimensional configuration has several interesting features for soot formation studies. Temperature, oxygen leakage through the premixed flame, and residence time in the pyrolysis region can be independently controlled by varying the stoichiometry and composition of the premixed flame and the velocity of the fuel counterflow. The thickness of the pyrolysis region, where the soot formation occurs, is large and, thus, experimentally well accessible and resolvable.

Along the axis of symmetry, concentration profiles of various stable species up to C_4 hydrocarbons were measured by gas chromatography. Thermocouples were used for temperature measurements. The soot volume fraction was determined by a laser-light extinction method and Abel's inversion.

The experimental results were compared with one-dimensional calculations using a kinetically based soot model. The reaction mechanism contains 62 species and about 400 reactions. The soot formation mechanism accounts for all possible coagulation processes between polyaromatic hydrocarbons (PAH) and soot particles, namely PAH-PAH coagulation leading to particle inception, PAH-particle coagulation, and particle-particle coagulation, for surface growth by C_2H_2 addition and for oxidation.

The results of the numerical simulation and the experiment show a good agreement for temperature and major species. The prediction for the maximum value of the soot volume fraction is quite good, but deviations in the measured and calculated profiles suggest an underestimated soot particle diffusion, indicating an overprediction of the particle sizes in the soot formation model.

Introduction

Understanding and modeling soot formation in combustion processes is important because soot is a dangerous pollutant due to the carcinogenic effects of the soot particles themselves and the hydrocarbons adsorbed on their surface. Also, soot formation reduces the effectiveness of the combustion and can clog and erode components of the combustion system to an intolerable extent. Soot formation is a major problem in diesel engines, which on the other hand have a high environmental potential due to their high efficiency and thus low CO_2 production.

It is believed that soot formation proceeds through the polymerization of small to large PAHs, which coagulate forming particles [1–4]. In premixed sooting flames, it is observed that in early stages the PAH coagulation is the dominant mechanism forming soot nuclei, whereas at later stages in the hot combustion products, the surface growth rate is mainly due to the addition of C_2H_2 [5–7]. If PAHs are still present at that later stage, they may also contribute to the mass growth rate of soot [5].

In order to differentiate between the two contributions, it is important to control the amount of C_2H_2 and PAHs independently. In premixed flame experiments, the C_2H_2 originates from the fuel, and its concentration in the soot formation region is very sensitive to oxygen concentration and pressure [8]. In the counterflow configuration proposed here for soot formation studies, C_2H_2 may be added into this region by the counterflow stream.

We use an axisymmetric counterflow burner with a rich, premixed acetylene-air flame stabilized on the upper sinter metal nozzle. A pure acetylene flow from the lower nozzle creates a broad pyrolysis region below the premixed flame. Besides being reasonably one-dimensional in the vicinity of the axis of symmetry, this configuration allows to independently control temperature, oxygen leakage through the premixed flame, and residence time in the pyrolysis region by varying the stoichiometry and composition of the premixed flame and the velocity of the fuel counterflow.

Along the axis of symmetry, concentration profiles of various stable species up to C_4 hydrocarbons were measured. The measurements were made by removing gas samples from the reaction zone with a quartz

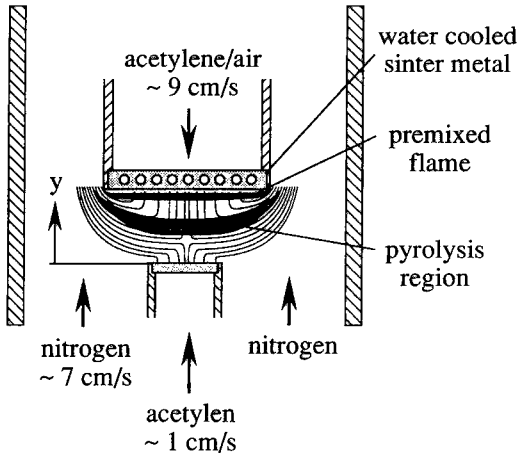

FIG. 1. Burner and flame configuration.

glass probe and analyzing them using a gas chromatograph. Also along the axis temperatures were measured with platinum/platinum-rhodium thermocouples. Using a laser-light extinction method and Abel's inversion, the soot volume fraction on the axis was determined.

For the one-dimensional numerical simulation of the configuration, a recently developed program written in an object-oriented language was used. The conservation equations for energy and momentum in axial direction and the balance equations for mass and species concentration have been solved. The reaction mechanism uses 62 species and about 400 reactions. A detailed soot formation model is used and will be described in the "Numerical Simulation" section.

Apparatus and Procedure

Figure 1 illustrates the flame configuration. The burner consists of two tubes with sinter metal plates at the exit, with the upper sinter metal being water cooled to prevent ignition of the premixed gases on its backside. The diameter of the lower tube is smaller than that of the upper tube, because this and the outer nitrogen flow help to stabilize the pyrolysis region. The mass flow rate of the premixed acetylene-air flow is $1.92 \cdot 10^{-4}$ kg/s; the equivalence ratio is $\phi = 1.47$. The mass flow rate of the pure acetylene is $3.5 \cdot 10^{-6}$ kg/s and that of the outer nitrogen flow is $5.87 \cdot 10^{-4}$ kg/s. Technical grade acetylene was used containing an acetone impurity of 0.8%.

The mass flow rates were measured using rotameters with uncertainties expected to be lower than $\pm$ 3%. The distance between the two nozzles is 22 mm; the diameter of the upper and lower nozzle is 48.5 and 18.5 mm, respectively. To ensure that mere thermal influence of the counterflow does not cause soot formation in the exhaust gases of the premixed flame, the configuration was tested with a pure nitrogen counterflow. This did not lead to soot formation. The counterflow mass flow is about 50 times smaller than that of the premixed flame and, thus, has hardly any influence on the temperature profile in regions where PAHs are still present.

Along the axis of symmetry, gas samples were taken using a quartz microprobe with an outer diameter of about 600 μm and a nozzle diameter of 140 μm. Along a probe length of about 20 mm, the diameter of the capillary increases by a factor of 50 to ensure a rapid expansion and thus cooling of the gas sample. A heated stainless steel tube connects the probe directly with the gas sampling loop of the gas chromatograph. To prevent condensation, the tubing is kept at a temperature of about 380 K. The overall volume of the gas sampling system is about 6 cm^3, ensuring very short sampling times and, thus, preventing blockage of the quartz glass probe by soot. The probe was mounted on a microslide and was introduced into the flame through a sealed vertical slot on the side of the outer tube. The microslide had a positioning accuracy of ± 10 μm, thus making the nozzle diameter of the probe the determining factor for spatial resolution.

A gas chromatograph (equipped with a 3-mL gas sampling loop), a thermal conductivity detector, and a flame ionization detector were used for gas analysis. Packed columns were used, allowing the injection of large amounts of gas sample to ensure a good quantitative detection of light gases like hydrogen, oxygen, or nitrogen. The columns employed in the analysis were a molecular sieve, a porous polymer column, and a column with Bis-2(ethoxyethyl)adiapate on Chromosorb P-AW. Helium was used as carrier gas. The pressure in the sample loop prior to injection was measured with a piezo-resistive pressure sensor, and the temperature was maintained at 380 K. Assuming an ideal gas, the amount of substance in the sample could be determined and used as an external standard to calculate the mole fraction of the detected gases.

The soot volume fraction on the axis was measured with a laser-light extinction method. An argon ion laser beam at 488 nm is split with a semitransparent mirror to obtain a main and a reference beam. The main beam is focussed on the axis of symmetry of the flame configuration, and the transmitted intensity as well as the reference beam intensity are measured using photo multiplier tubes. To diminish the influence of temporal fluctuations in beam intensity, the signals are recorded and averaged over several seconds. An intensity averaging over the beam diameter is achieved by diffusing screens in front of the photo multiplier tubes. Thus, the influence of local inhomogeneities in the beam intensity is diminished. In two successive measurements, with and without soot in

the configuration, the intensities are measured; the reference beam intensity is then used to normalize the transmitted intensity.

For light transmission through a homogeneous particle cloud with the particle number density N along the optical path length L, the Lambert–Beer law is applicable. For spherical particles with a diameter smaller than one-tenth of the wavelength of the light, the following approximation may be used [9]:

$$I_{\text{trans}} = I_0 \cdot e^{LNC_{\text{ext}}} \quad \text{where } C_{\text{ext}} = \frac{k_{\text{ext}}}{N}$$
$$= -\frac{\pi}{2} k d^3 \, Im\left(\frac{m^2 - 1}{m^2 + 2}\right).$$

Here, I_{trans} is the intensity of the transmitted light, C_{ext} is the extinction cross section accounting for incident light absorption and scatter, k_{ext} is the extinction coefficient, $k = 2\pi/\lambda$ is the wave number, and m is the complex refractive index. The soot volume fraction f_v can be written as

$$f_v = \frac{\pi}{6} d^3 N = \frac{k_{\text{ext}}}{C_{\text{ext}}} = \frac{\pi d^3}{6} = \frac{\lambda k_{\text{ext}}}{6\pi Im\left(\frac{m^2 - 1}{m^2 + 2}\right)}.$$

For transmission of the laser light through the radial symmetric flame, one can write

$$F(x) = \ln\left(\frac{I_{\text{trans}}}{I_0}\right) = \int_{z_1}^{z_2} k_{\text{ext}}(z)\, dz$$
$$= 2 \cdot \int_x^{r_0} \frac{r \cdot k_{\text{ext}}(r)}{\sqrt{r^2 - x^2}}\, dr$$

where z is the coordinate along the beam and x is the coordinate in the direction rectangular to beam and axis of symmetry. With Abel's inversion [10], one obtains

$$k_{\text{ext}}(r) = -\frac{1}{\pi} \int_r^{r_0} \frac{F'(x)}{\sqrt{x^2 - r^2}}\, dy$$

Measurements were taken for different values of x to obtain values for $F(x)$, then coefficients for an approximating function were determined, and $F'(x)$ was calculated. With the measured temperature profile and an interpolation of the values of the refractive indices given by Ref. 11, m was calculated as a function of the height y above the lower nozzle. As pointed out in Ref. 11, the refractive index for soot does not differ substantially for different flame conditions. Still, one has to keep in mind that deviations between the conditions m was determined for in Ref. 11, and the present conditions concerning soot structure or size distribution, or concentration of large, absorbing PAH's may lead to different values of m.

Temperature measurements were performed with platinum/platinum-rhodium thermocouples. Both coated and uncoated thermocouples were tested. No catalytic effects were observed with the uncoated thermocouples, and since they have lower radiative losses and better spatial resolution, they were used for measurements. The thermocouple temperatures were corrected, taking into account convective heat transfer and radiative heat losses. The correction was made assuming (1) an ideal spherical shape and (2) an ideal cylindrical shape for the thermocouple. Values for the temperature-dependent emissivity of platinum and platinum-rhodium surfaces were interpolated from values given in Ref. 12. The thermocouple wires had a diameter of 0.1 mm, the bead had one of about 0.2 mm, and thus, a good spatial resolution was possible. Since the bead geometry is neither an ideal cylinder nor an ideal sphere, the corrections assuming ideal shapes are believed to give an upper and a lower temperature estimation for the actual gas temperature.

Numerical Simulation

For the axisymmetric counterflow configuration, a similarity solution exists requiring to solve a set of one-dimensional equations only. Following Ref. 13, the balance equations for mass, transverse momentum, single species, energy, and a mixture fraction variable Z can be written in the limit of low Mach numbers assuming $u = G(y)\, x$ as

$$\frac{d(\rho v)}{dy} = -2\rho G(y) \tag{1}$$

$$\rho v \frac{dG}{dy} = -\rho G(y)^2 + \rho_\infty a^2 + \frac{d}{dy}\left(\mu \frac{dG}{dy}\right) \tag{2}$$

$$\rho v \frac{dY_k}{dy} = \frac{dj_k}{dy} + \dot{m}_k \tag{3}$$

$$\rho v c_p \frac{dT}{dy} = \frac{d}{dy}\left(\lambda \frac{dT}{dy}\right) - \sum_i h_i \dot{m}_i - \sum_i c_{p,i} j_i \frac{dT}{dy} + q_R \tag{4}$$

$$\rho v \frac{dN_i/\rho}{dy} = \frac{d}{dy}\left(\rho D_{p,i} \frac{dN_i/\rho}{dy}\right) + \frac{d}{dy}\left(a \frac{\mu}{T} \frac{N_i}{\rho} \frac{dT}{dy}\right) + \dot{N}_i \qquad i = 1, \ldots, \infty. \tag{5}$$

Closure of the system is the ideal-gas equation of state. The diffusion fluxes j_k were approximated by the Hirschfelder–Curtiss approximation [14], augmented by a simple correction velocity to ensure mass conservation [15]. The chemical production rate $\dot{m}_k$ contains contributions from all reactions:

$$\dot{m}_k = M_k \sum_l \nu_{kl} w_l, \tag{6}$$

where M_k is the molecular weight of species k, ν_{kl} is the matrix of stoichiometric coefficients, and w_l is the vector of reaction rates; q_R denotes the radiation heat loss term, which includes radiation of the gaseous and particle phase. Assuming an optically thin medium, these terms are given by Ref. 16.

In Eq. (5), N_i is the number density of soot particles of size class i, which is defined by $V_i = iV_1$, where V_1 is the volume of the smallest molecule structure occuring in soot particles, which is assumed to be a benzene ring. The diffusion coefficient for the particles $D_{p,i}$ varies in the free molecular regime with d^{-2} [17], where d is the particle diameter. Thus, we can write

$$D_{p,i} = i^{-2/3} D_{p,1}. \tag{7}$$

The second term on the right-hand side of Eq. (5) accounts for thermophoretic transport, where

$$a = \frac{3}{4(1 + \pi \cdot A/8)} \tag{8}$$

and the accommodation coefficient A is usually taken to be 0.9 or 1.0 [17]. To handle the infinite set of equations (5), the method of moments [18] is used. Introducing the size-dependent diffusion coefficient and the definition of the statistical moment,

$$\mu_r = \sum_{i=1}^{\infty} i^r N_i \quad r = 0, \ldots, \infty \tag{9}$$

in Eq. (5) we obtain a transport equation for the statistical moment:

$$\rho v \frac{d\mu_r/\rho}{dy} = \frac{d}{dy}\left(\rho D_{p,1} \frac{d}{dy}(\mu_{r-2/3}/\rho)\right) + \frac{d}{dy}\left(a \frac{\mu}{T} \frac{\mu_r}{\rho} \frac{dT}{dy}\right) + \dot{\mu}_r. \tag{10}$$

The values for the fractional moments appearing in Eq. (10) are determined by logarithmic interpolation.

For the present paper, we did some numerical experiments to test where to truncate the infinite set of equations (10), and we found that there is no need to retain more than the first two statistical moments.

The source term of Eq. (10) is given by a detailed soot formation model, similar to that developed by Frenklach and coworkers [4,19,20]. It accounts for particle inception due to PAH coagulation, condensation of PAHs on the soot particle surface, coagulation of soot particles, and soot growth and oxidation due to surface reactions.

This model is subdivided into three logical parts:

1. The *chemistry of the gas phase* to small PAHs. This part is described using a detailed kinetic mechanism provided by Warnatz and Chevalier [21] for the fuel pyrolysis and oxidation and for the formation of soot precursors up to benzene. This kinetic mechanism was supplemented by reactions from Ref. 22, accounting for the influence of the acetone impurity on the acetylene pyrolysis. The further growth of the small PAHs follows Frenklach and Warnatz [20]. The whole mechanism contains about 400 elementary reactions and 62 chemical species.
2. The *further growth* of PAHs is assumed to be a fast polymerization process. This is based on a steady-state assumption for the PAHs and results in an algebraic equation for each PAH species taken into account [23].
3. The *formation and further growth of soot particles,* including all the above-mentioned coagulation processes and surface reactions. All coagulation processes are assumed to follow Smoluchowski's coagulation equations in the free molecular regime [24]. The evaluation of Smoluchowski's equations follows [18]. Polyaromatic hydrocarbons are allowed to coagulate when they consist of at least four aromatic rings. Coagulated PAHs are counted as soot, thus leading to smallest soot particle sizes of eight aromatic rings. The heterogeneous surface growth and oxidation is described by the H-abstraction/C_2H_2-addition reaction sequence and further O_2 and OH oxidation reactions [4].

The boundary conditions for the velocity were determined from the experimental mass flow rates. The radial velocity components at the nozzles were set to zero. Boundary conditions for species were derived from an interface balance. Complete radical recombination is assumed on the sinter metal surface. The temperature values at the nozzles were taken from the experiments.

The numerical calculations were performed with a newly developed finite difference code. It features a very stable grid refinement technique that derives a weight function for adjusting cell sizes from an approximation of the local truncation error of the computed solution by extrapolating a fine and a coarse grid solution.

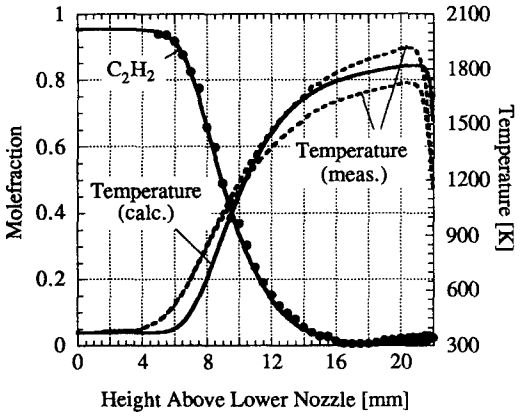

FIG. 2. Comparison of measured and calculated acetylene and temperature profiles.

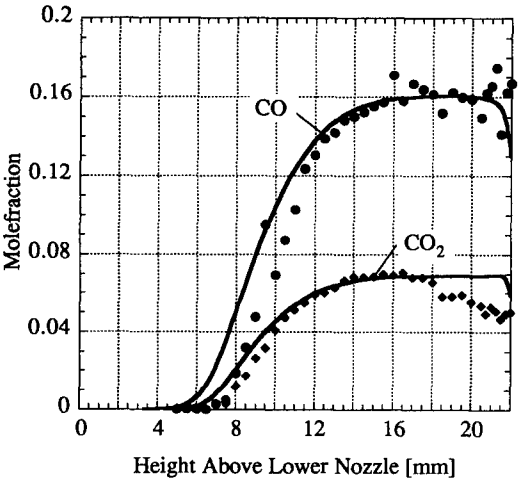

FIG. 3. Comparison of measured and calculated profiles of CO and CO_2.

Results

Figure 2 shows measured and calculated concentration profiles for acetylene and the temperature profiles as function of height y above the surface of the lower sinter metal. The two dashed profiles result from the thermocouple temperature correction assuming cylindrical (higher values) and spherical bead shape. Figure 3 compares carbon monoxide and carbon dioxide profiles.

The burner-stabilized premixed flame burns close to the sinter metal of the upper nozzle. The experimental resolution, approximately given by the diameter of the capillary of the quartz glass probe, does not seem to be sufficient for the thin premixed flame. In addition, the flame is visibly displaced by the probe when sampling in the premixed flame. Below

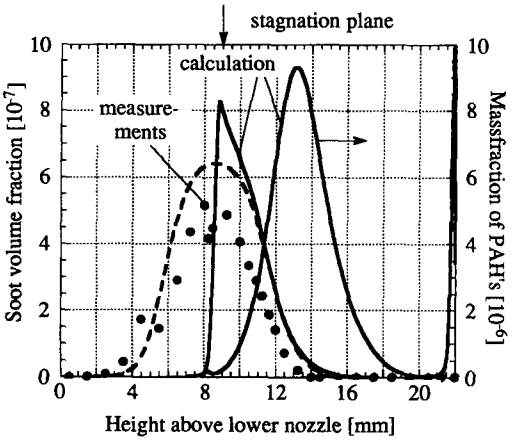

FIG. 4. Comparison of measured and calculated soot volume fraction profiles. The dashed profile shows a calculation where all soot coagulation processes have been suppressed.

the premixed flame, there is a high-temperature region with high concentrations of intermediate species. Acetylene from the lower nozzle is transported across the stagnation point (position marked in Fig. 4) into this region by diffusion. Between 10 and about 16 mm, pyrolysis of the acetylene and formation of higher hydrocarbons and soot occurs. A sensitivity analysis shows that the pyrolysis is considerably enhanced (50% increase in the soot volume fraction) by the presence of the acetone impurity due to the CH_3-radical production during the decomposition of acetone. Since the pyrolysis region is very broad, the spatial resolution of the measurements is sufficient. The agreement between measured and calculated species and temperature profiles in Figs. 2 and 3 is satisfactory, and we can assume that the basic structure of the configuration is sufficiently well described by the numerical simulation.

The soot volume fraction shown in Fig. 4 has a maximum value of about $5 \cdot 10^{-7}$ at $y = 8$ mm. At that height, the temperature is already as low as 900 K. The visible luminous part of the pyrolysis region, as sketched in Fig. 1, is not entirely identical with the soot formation region. Obviously, the temperature in the lower part of the pyrolysis zone is not high enough to lead to visible soot radiation.

The measured and calculated soot volume fraction profiles show good agreement for heights above 9 mm, but there is a steep gradient about 0.5 mm below the stagnation plane in the calculated profile that does not appear in the measurements. As shown in Fig. 5, the profiles for diacetelyene compare fairly well, the maximum value of propadien differs by a factor of about 5 in the pyrolysis region.

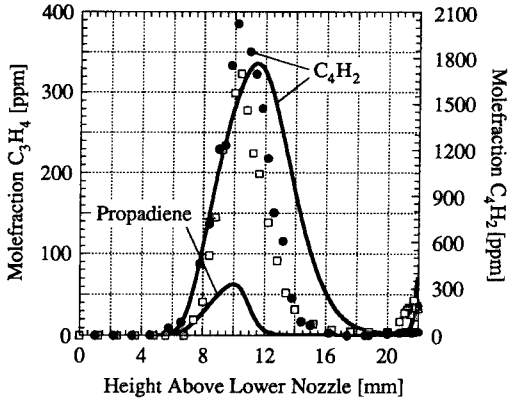

FIG. 5. Comparison of measured and calculated profiles of C_3H_4 and C_4H_2.

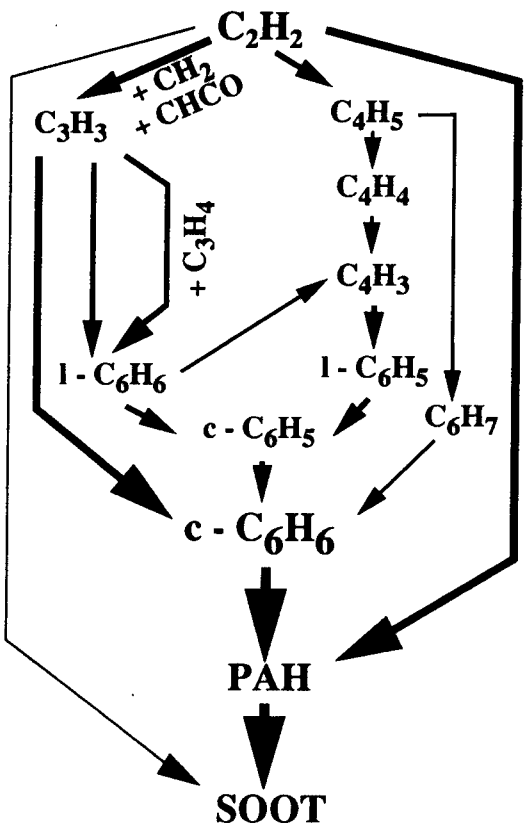

FIG. 6. Schematic illustration of the reaction paths leading to benzene.

Discussion

An analysis of the kinetic soot formation mechanism used in the calculations is illustrated in Fig. 6.

TABLE 1
Important Reactions in This Configuration Leading to Benzene and PAH (Nomenclature according to Ref. 25)

Number	Reaction
1	$C_2H_2 + 3\text{-}CH_2 \rightarrow C_3H_3 + H$
2	$2C_3H_3 \rightarrow A_1$
3	$A_1 \rightarrow A_{1-} + H$
4	$A_{1-} + C_2H_2 \rightarrow A_1C_2H + H$
5	$A_1C_2H + H \rightarrow A_1C_2H^* + H_2$
6	$A_1C_2H^* + C_2H_2 \rightarrow A_1C_2HAC$
7	$A_1C_2HAC \rightarrow A_2\text{-}X$
8	$A_2^- + C_2H_2 \rightarrow A_2R_5 + H$
9	$A_2R_5 + H \rightarrow A_2R_{5-} + H_2$
10	$A_2R_{5-} + C_2H_2 \rightarrow A_2R_5C_2H + H$
11	$A_2R_5C_2H + H \rightarrow A_2R_5C_2H^* + H_2$
12	$A_2R_5C_2H^* + C_2H_2 \rightarrow ANC_2HAC$
13	$ANC_2HAC \rightarrow A_3R_{5-}$
14	$A_3R_{5-} + C_2H_2 \rightarrow A_3R_5AC$

We found that the most important path is via propargyl (C_3H_3), benzene, and PAHs, where C_3H_3 is formed due to CH_2 or CHCO addition to acetylene and combines directly to benzene. This path accounts for more than 60% of the benzene formation. There are some additional, but less important, benzene formation chains via linear C_6H_5 and C_6H_7. Table 1 lists reactions leading to benzene and, beyond that, turned out to be significant in this configuration. Starting from benzene, the formation of PAHs via the H-abstraction/C_2H_2-addition reaction sequence is significant for the soot mass balance, especially between 12 and 16 mm height. This PAH growth occurs up to a PAH size that allows them to coagulate forming soot nuclei, since this then becomes the dominating process. In a similar way, the soot surface growth due to acetylene addition is less important than the coagulation of PAHs. This corresponds to the findings of Ref. [5].

As shown in Fig. 4, the calculated maximum of the PAH volume fraction is located at about 13 mm. Here and slightly lower, particle inception and soot mass production reach peak values. The temperature at this location is about 1600 K, and the acetylene mole fraction is about 5%. At lower heights, PAH formation decreases because of the low temperatures, at higher heights, it decreases because of lower acetylene concentration. The resulting particles are transported by convection toward the stagnation plane, increasing due to coagulation of PAHs with soot and surface growth by the H-abstraction/C_2H_2-addition reaction sequence. As mentioned before, the latter mechanism is not important here, since the radical concentration is very low in this region, and

therefore, there is a low number of active sites on the soot particle surface.

As mentioned above, the profile of the calculated soot volume fraction shows a steep gradient about 0.5 mm below the stagnation plane. The small shift is due to the thermophoretic transport term in Eq. (10). This term can be split into two parts, where one is a diffusive term for ln T, which in our configuration is almost zero in the vicinity of the stagnation plane, and a convective term for the statistical moments of soot μ_r with a convective velocity of $v_s = -avd \ln T/dy$. This leads to an effective stagnation plane for the soot at the location where the effective convective velocity $v + v_s$ is zero. As was discussed earlier, soot nuclei are produced at a height of about 13 mm and are then transported convectively toward the effective stagnation plane. The predicted soot particles in the vicinity of the stagnation plane consist of about 10^5 aromatic rings. Their diffusion coefficient, calculated from Eq. (7) is very small, such that diffusion of these particles cannot balance the convection beneath the effective stagnation plane.

A numerical calculation without consideration of PAH-soot and soot-soot coagulation processes has also been performed. The result is shown in Fig. 4 in comparison with the original calculation. This results in very small soot particles, which are able to diffuse beyond the effective stagnation plane. The better agreement in the shape of the measured and calculated profile for this case suggests that the soot formation mechanism overpredicts the particle sizes. To verify this suggestion, measurements for particle size and soot particle number density would be needed.

Conclusions

The counterflow of acetylene into the hot combustion products of a premixed flame has been used in order to study soot formation. Measured profiles are compared with results from a kinetic soot model. One-dimensional numerical calculations for velocity, temperature, gaseous species, and soot particles have been performed. The agreement is good for the temperature, the acetylene, CO, CO_2, and C_4H_2, while there is a factor of 5 discrepancy for propadiene. The maximum predicted soot volume fraction agrees well with the measurements, but the profile is narrower. This is assumed to be due to the overprediction of the particle size and their consequently smaller diffusivity. When all coagulative mechanisms are suppressed, the overall shape of the soot volume fraction tends to agree better with the experiments. This indicates that the particle size in this configuration should be smaller than in the kinetic model.

Acknowledgment

The measurements for this flame have been carried out by J. Kreye and A. Witthohn.

REFERENCES

1. Wagner, H. G., *Seventeenth Symposium (International) on Combustion,* The Combustion Institute, Pittsburgh, 1979, p. 3.
2. Glassman, I., *Twenty-Second Symposium (International) on Combustion,* The Combustion Institute, Pittsburgh, 1989, p. 295.
3. Bockhorn, H., *Soot Formation during Combustion—Recent Developments in Mechanisms and Models,* Proceedings of the Anglo-German Combustion Symposium, The British Section of the Combustion Institute, 1993.
4. Frenklach, M., and Wang, H., *Twenty-Third Symposium (International) on Combustion,* The Combustion Institute, Pittsburgh, 1990, pp. 1559–1566.
5. McKinnon, J. Th., and Howard, J. B., *Twenty-Fourth Symposium (International) on Combustion,* The Combustion Institute, Pittsburgh, 1992, pp. 965–971.
6. Harris, S. J., and Weiner, A. M., *Combust. Sci. Technol.* 32:267 (1983).
7. Harris, S. J., and Weiner, A. M., *Twenty-Second Symposium on Combustion,* The Combustion Institute, Pittsburgh, 1988, p. 333.
8. Böhm, H., Feldermann, Chr., Heidermann, Th., Jander, H., Luers, B., and Wagner, H. Gg., *Twenty-Fourth Symposium (International) on Combustion,* The Combustion Institute, Pittsburgh, 1992, pp. 991–998.
9. Van de Hulst, H. C., *Light Scattering by Small Particles,* Wiley, New York, 1957.
10. Tourin, R. H., *Spectroscopic Gas Temperature Measurements: Pyrometry of Hot Gases and Plasma,* American Elsevier, New York, 1966.
11. Lee, S. C., and Tien, C. L., *Eighteenth Symposium (International) on Combustion,* The Combustion Institute, Pittsburgh, 1981, p. 1159.
12. Verein, Deutscher, and Ingenieure (Eds.), *VDI-Wärmeatlas,* VDI-Verlag, Düsseldorf, 1991.
13. Peters, N., in *Reduced Kinetic Mechanisms for Applications in Combustion Systems* (N. Peters, and B. Rogg, Eds.), Lecture Notes in Physics, Springer Verlag, Heidelberg, FRG, 1993.
14. Heimerl, J. M., and Coffee, T. P., in *Numerical Methods in Laminar Flame Propagation* (N. Peters, and J. Warnatz, Eds.), Vieweg, Wiesbaden, Federal Republic of Germany, 1982.
15. Oran, E. S., and Boris, J. P., *Proj. Engergy Combust. Sci.* 7:1–71 (1981).
16. Hubbard, G. L., and Tien, C. L., *J. Heat Transfer* 100:235–239 (1978).

17. Friedlander, S. K., *Smoke, Dust and Haze*, Wiley & Sons, New York, 1986.
18. Frenklach, M., and Harris, S. H., *J. Coll. Interf. Sci.* 118:1 (1987).
19. Frenklach, M., Clary, D. W., Gardiner, W. C., and Stein, S. E., *Twentieth Symposium (International) on Combustion*, The Combustion Institute, Pittsburgh, 1985, p. 887.
20. Frenklach, M., and Warnatz, J., *Combust. Sci. Technol.* 51:265 (1987).
21. Warnatz, J., and Chevalier, C., in *Combustion Chemistry*, 2nd ed. (W. C. Gardiner, Jr., Ed.), Springer Verlag, in press.
22. Colket III, M. B., Seery, D. J., and Palmer, H. P., *Comb. Flame* 75:343 (1989).
23. Mauss, F., Trilken, B., Breitbach, H., and Peters, N., in *Mechanism and Models of Soot Formation* (H. Bockhorn, Ed.), Springer Verlag, in press.
24. Friedlander, S. K., *Ann. N. Y. Acad. Sci.* 404:354 (1983).
25. Frenklach, M., Clary, D. W., Yuan, T., Gardiner, W. C., and Stein, S. E., *Combust. Sci. Technol.* 50:79–115 (1986).

Twenty-Fifth Symposium (International) on Combustion/The Combustion Institute, 1994/pp. 1365–1373

DYNAMICS AND STRUCTURE OF UNSTEADY, STRAINED, LAMINAR PREMIXED FLAMES

FOKION N. EGOLFOPOULOS
Department of Mechanical Engineering
University of Southern California
Los Angeles, CA 90089–1453, USA

The influence of unsteadiness on the structure and dynamics of counterflowing, strained, premixed methane/air flames was investigated by conducting a detailed numerical study. The unsteady conservation equations of mass, momentum, energy, and species were solved along the stagnation streamline of the counterflow, in an opposed-jet, finite-domain configuration, by using detailed description of chemistry and transport. The unsteadiness was introduced by imposing sinusoidal variations of the reactant velocity at the exit of the nozzles. Results demonstrate that the flame response is quasi-steady at low frequencies, while at high frequencies it fails to respond to the imposed velocity oscillations. The flame frequency response was physically explained by analyzing the instantaneous flame structure and realizing that the velocity oscillations in the hydrodynamic zone cause reactant concentration oscillations in the diffusion zone. The diffusion processes attenuate these oscillations in a manner analogous to the Stokes' second problem, and the *angular frequency* at which substantial attenuation commences was found to be of the order of $[2(S_u^\circ)^2/a]$, where S_u° is the laminar flame speed and a an average heat diffusivity of the mixture. The validity of the analogy was confirmed by examining flames at a wide range of unsteadiness. The effect of unsteadiness on extinction was also assessed, and the phenomena of partial extinction, reignition, and extinction delay were identified. These phenomena were found to be controlled by the relative magnitudes of the time scales of the imposed oscillations and the time required for permanent extinction.

Introduction

Strained laminar flames have been the subject of extensive investigations over the last 10 to 20 years because of their relevance to turbulent combustion [1–3]. The majority of these studies, however, have been conducted under steady conditions, and the effect of steady strain on the flame structure and dynamics has been extensively assessed (e.g., Refs. 1–6). In a turbulent environment, if laminar flamelets indeed exist, it is expected that they will be embedded into flow fields which are highly nonuniform and also highly unsteady. Under such conditions, the time scales of the flow field disturbances can couple with the time scales of molecular transport and chemical kinetics and lead to phenomena that cannot be predicted from steady analyses.

Although the importance of unsteadiness on laminar flame combustion has been recognized [2], the relevant studies are limited [7–14]. The majority of these studies are theoretical, and the effect of strain oscillations on the flame dynamics was assessed; the only experimental data were reported by Saitoh and Otsuka [9]. Theoretically, the studies were conducted with simplified chemistry and transport, with the exception of the works of Stahl and Warnatz [11] and Darabiha [13] in which detailed modeling was conducted for unsteady premixed and diffusion flames, respectively. In all studies, it has been reported that the amplitude of the flame response to strain oscillations is reduced at high frequencies, but a rigorous physical explanation based on first principles was not provided.

Recently, Egolfopoulos and Campbell [15–17] conducted a detailed numerical simulation of unsteady, counterflowing, strained $CH_4/O_2/N_2$ diffusion flames, and by analyzing the detailed transient flame structure, the physical "attenuation" mechanisms were identified; the unsteadiness was introduced in terms of far-field oscillations of reactant velocity, concentration, and temperature. The central idea of the finding is that velocity oscillations induce reactant concentration oscillations at the beginning of the diffusion zones in a manner analogous to the Stokes' second problem. Furthermore, the flame properties' amplitudes were found to scale very closely with the nondimensional parameter, η, of the Stokes' second problem, which is simply the ratio of the reactant diffusive thickness over a characteristic "penetration" length of the disturbances. In the same studies [15–17], phenomena related to transient extinction were also investigated.

In the present investigation, the main goals were to investigate the effect of flow field velocity unstead-

iness on the structure and dynamics of strained, laminar, premixed CH_4/air flames by conducting detailed numerical modeling and to provide physical insight into the elementary controlling mechanisms.

Numerical Methodology

The numerical simulation of the counterflow was conducted by solving the unsteady conservation equations of mass, momentum, energy, and species concentrations along the stagnation streamline:

$$\frac{\partial \rho}{\partial t} + 2\rho G + \frac{\partial(\rho u)}{\partial x} = 0 \quad \text{(mass conservation)}$$

$$\rho \frac{\partial G}{\partial t} + \rho u \frac{\partial G}{\partial x} + \rho G^2 + J - \frac{\partial}{\partial x}\left(\mu \frac{\partial G}{\partial x}\right) = 0$$

(momentum conservation)

$$\rho \frac{\partial T}{\partial t} + \rho u \frac{\partial T}{\partial x} - \frac{1}{c_p}\frac{\partial}{\partial x}\left(\lambda \frac{\partial T}{\partial x}\right) - \frac{\partial P}{\partial t} + \frac{\rho}{c_p}\sum_{k=1}^{K} Y_k c_{pk} V_k \frac{\partial T}{\partial x} + \frac{1}{c_p}\sum_{k=1}^{K} h_k \omega_k = 0$$

(energy conservation)

$$\rho \frac{\partial Y_k}{\partial t} + \rho u \frac{\partial Y_k}{\partial x} + \frac{\partial}{\partial x}(\rho Y_k V_k) - W_k \omega_k = 0$$

(species conservation)

with $G \equiv \partial v/\partial r = v/r = G(x)$ and $J \equiv (1/r)(\partial P/\partial r)$.

In the above equations, ρ is the density; P is the pressure; μ is the mixture viscosity; λ is the mixture conductivity; c_p is the mixture specific heat; c_{pk} is the specific heat of species k; h_k is the enthalpy of species k; ω_k is the production rate of species k; W_k is the molecular weight of species k; Y_k is the mass fraction of species k; u is the axial velocity component; v is the radial velocity component; K is the total number of species; and V_k is the mass diffusion velocity of species k.

The solutions were obtained in a finite-domain configuration in order to simulate actual experiments that are anticipated in the near future; the present formulation models the region around the centerline of the experimental counterflow configuration. It was also assumed that the gases leaving the nozzles have no radial variations in velocity, temperature, and concentrations. As a consequence, the whole flow field is characterized by a uniform radial pressure curvature, J, which is an eigenvalue of the problem [5,6,11].

The $\partial P/\partial t$ term in the energy equation was neglected for the present study, in which open flames were considered so that the pressure is largely controlled by the far field. This term, however, has to be retained if reacting processes in closed vessels are considered. Furthermore, although a pressure gradient is imposed in the momentum equation as the driving force of the flow, the effects of pressure variation (in space and time) on the density and chemical kinetics were not considered, so that the effect of the unsteadiness on the flame structure and dynamics due solely to the velocity fluctuations was assessed.

The premixed flames studied herein result from the impinging of two identical streams of CH_4/air premixtures emerging from the opposing burner nozzles. Because of the symmetry of the system across the stagnation plane, the equations were formulated and solved between one nozzle and the stagnation plane. As plug flow (zero divergence) boundary conditions at the exit of the nozzles were assumed, the boundary conditions at the exit of the burner ($x = L$) and stagnation plane ($x = 0$) are as follows:

$$x = 0: \quad u = 0, \quad dY_k/dx = 0, \quad dT/dx = 0, \quad dG/dx = 0$$

$$x = L: \quad Y_{O_2} = Y_{O_2,x=L}, \quad Y_{CH_4} = Y_{CH_4,x=L}, \quad Y_{N_2} = Y_{N_2,x=L}, \quad G = 0.$$

The unsteadiness was introduced for the reactant velocity at the exit of the nozzle, u_{exit}, by imposing sinusoidal variations of a given amplitude, $u_{exit,A}$ around a mean value, $u_{exit,O}$ [15–17]. The solution of the equations was obtained by modifying the steady, premixed flame, stagnation-flow code of Kee and coworkers [5,18] and introducing the second-order Crank–Nicolson scheme for the time marching. The code was integrated into the CHEMKIN [19] and transport [20] subroutine packages. The kinetic scheme used is a hierarchically developed C_2 mechanism [21,22].

Results and Discussion

The flame response to far-field velocity unsteadiness was examined for atmospheric CH_4/air flames for three different equivalent ratios, namely $\phi = 0.7$, $\phi = 1.0$, and $\phi = 1.3$, for unburned mixture temperature of 300 K, for various nozzle exit velocities, and for nozzle separation distance $2L = 0.7$ cm. For simplicity, the flames were classified with the Roman numerals I through VI, and their properties will be given the first time they are mentioned.

An examination of a typical flame structure reveals that the temperature rises from its free stream value at the nozzle exit to a maximum value, T_{max}, at the stagnation plane that is in general less than the equilibrium value because of the limited physical space. Furthermore, the velocity decreases as the flame is approached from the nozzle side; then it increases as

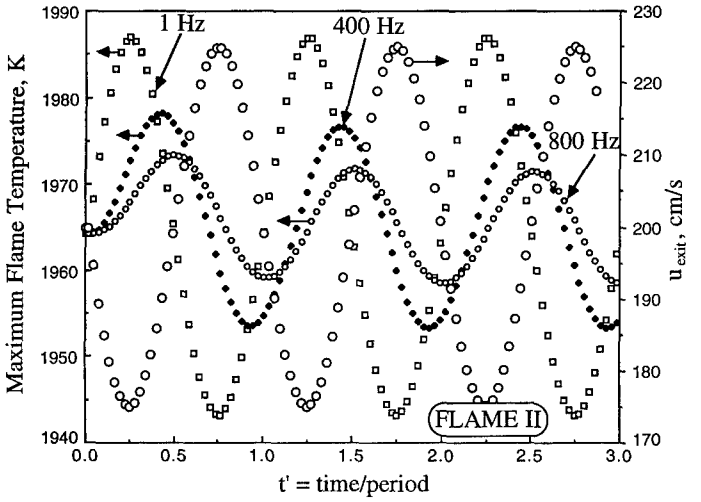

FIG. 1. Variation of u_{exit} and T_{max} with t' for Flame II at different frequencies.

a result of thermal expansion and further decreases toward the zero value at the stagnation plane. The imposed aerodynamic strain rate, K, is determined as the velocity gradient at the quasi-linear part of the profile before the minimum point ahead of the flame. Such definition of the strain rate is consistent with its experimental determination [3,4], and it is a measure of the convective transport in the hydrodynamic zone.

For Flames I (ϕ = 0.7, $u_{exit,O}$ = 70 cm/s, $u_{exit,A}$ = 20 cm/s), II (ϕ = 1.0, $u_{exit,O}$ = 200 cm/s, $u_{exit,A}$ = 25 cm/s), and III (ϕ = 1.3, $u_{exit,O}$ = 60 cm/s, $u_{exit,A}$ = 20 cm/s), the oscillation of u_{exit} induces oscillation of the flame location, since for higher values of u_{exit} the flame moves closer to the stagnation plane in order to be stabilized at a location where its propagation speed will equal the local flow velocity. In Fig. 1, the variation of T_{max}, as induced by the oscillation of the u_{exit}, is shown as a function of a nondimensional time, t', for different frequencies. The peak values of T_{max} occur when u_{exit} is at its trough value and the flame is closer to the nozzle, allowing for more time to reach equilibrium at the stagnation plane. Therefore, T_{max} is a "marker" of the flame location. Figure 1 shows that, for higher frequencies, the amplitude of oscillations decreases and the phase shifts to the right, in agreement with previous observations [7–17]; similar behavior was observed for all flame properties. Furthermore, properties such as the maximum heat release, Q_{max}, and maximum hydrogen radical concentration, $[H]_{max}$, provide a better measure of the burning intensity of the flame with respect to the mixture's Le number. For Flame I (Le < 1), Q_{max} and $[H]_{max}$ peak when the u_{exit} and, therefore, K peak, and the opposite is true for Flame III (Le > 1), in agreement with previous findings [3].

The detailed frequency response of the peak and trough values of T_{max} and its phase shift are shown

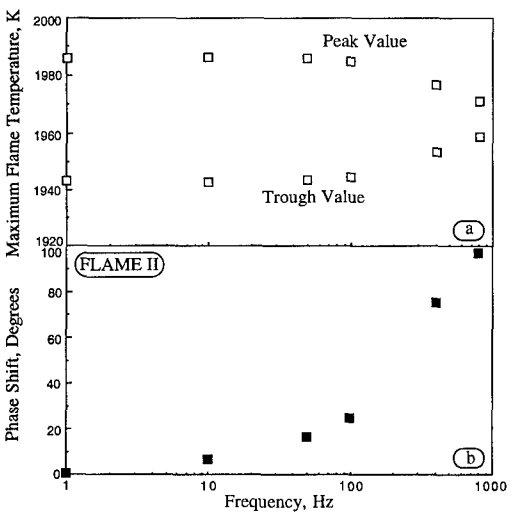

FIG. 2. (a) Frequency response of T_{max} amplitude and (b) phase shift for Flame II.

in Fig. 2. Results indicate that the amplitude of the frequency response is reduced at higher frequencies, while at low frequencies, the flame responds to the u_{exit} oscillations in a quasi-steady manner. Furthermore, while the amplitude reduction occurs symmetrically for T_{max} and all properties for Flames I, II, and III, an asymmetry can be induced as the amplitude of oscillations is increased. More specifically, it was found that, for large amplitudes of u_{exit}, when K is at its peak value, the flame responds to K variations more rapidly compared with the part of the cycle in which K is about its trough value. This is due to the higher sensitivity of the flame to strain rate variations when it is highly strained, as compared to a low strain rate state [15–17].

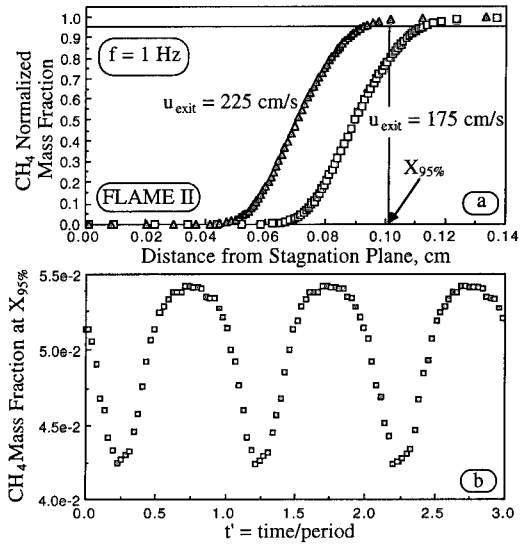

FIG. 3. (a) Variation of the CH_4 mass fraction normalized by its free stream value throughout the flame zone for Flame I and $f = 1$ Hz. (b) Variation of the CH_4 mass fraction with t' at the spatial location $X_{95\%}$, for Flame I and $f = 1$ Hz.

Physical insight into the results of Figs. 1 and 2 was provided after assessing the various processes controlling the instantaneous flame structure. As u_{exit} varies with time, the flow field adjusts nearly instantaneously in the hydrodynamic zone since the disturbances propagate with the speed of sound. These disturbances subsequently will be sensed by the main reaction zone through diffusive processes within the main diffusion zone in which diffusion dominates convection. Therefore, a coupling is expected between the fluid mechanics and the chemical/transport processes of the flame, leading to the distortion of the local velocity field, as will be further explained in a later part of the text. The observed phase shift was found to correspond to the transport time within the diffusion zone, causing a "delay" that is more apparent at higher frequencies.

The mechanisms responsible for the amplitude reduction at high frequencies were identified by realizing that the u_{exit} time variations result in variations of the flame location since the flame is free to move toward the location which satisfies the stabilization criterion. In Fig. 3a, the profiles of the mass fraction of CH_4 (normalized by its free stream value) are plotted vs the spatial location for Flame II at $f = 1$ Hz, for the peak and trough values of u_{exit}. It can be seen that the u_{exit} oscillations result in an effective oscillation of the reactant mass fraction; similar argument can be made for the temperature at the beginning of the diffusion zone. This oscillation has to propagate largely by diffusion into the main reaction zone. A graphic illustration of this point can be seen in Fig. 3b, which shows the mass fraction of CH_4 at a given location, $X_{95\%}$, at the beginning of the diffusion zone. The $X_{95\%}$ spatial location was determined as the mean location of the cycle at which the mass fraction of CH_4 is 95% of its free stream value under quasi-steady conditions.

Similarly to diffusion flames [15–17], a close analogy of this phenomenon is the Stokes' second problem, in which the disturbances caused by an oscillating plate propagate into the stagnant fluid through momentum diffusion. The Stokes' second problem solution scales with a nondimensional spatial coordinate $\eta_z = z\,(\omega/2\nu)^{1/2}$ [23], where z is the dimensional distance from the plate, $\omega = 2\pi f$ the angular frequency, and ν is the kinematic viscosity of the fluid. Results show that attenuation of the signal due to diffusion occurs at large values of η_z (large z or large ω). At high frequencies, the wavelength of the disturbances is reduced so that the diffusive fluxes increase, causing, thus, substantial attenuation, and noticeable amplitude reduction occurs closer to the plate (smaller z's).

In the present problem and similarly to the diffusion flames' response [15–17], the reactant mass fractions oscillate at the beginning of the diffusion zone. The end of the diffusion zone corresponds to the main reaction region at which the mass fractions of both reactants are at fixed values as determined by equilibrium. Therefore, as the frequency increases, the mass fraction oscillations can be attenuated within the diffusion zone when its thickness becomes of the same order with the physical penetration length of the disturbances. This will result in substantial attenuation of the oscillations in the concentration gradients immediately before the main reaction zone, leading to reduced flame response, as the processes inside the main reaction zone are only sensitive to the concentration gradients in its immediate neighborhood.

The frequency responses of Flames I, II, and III can be seen in Fig. 4a, in which the normalized (by their quasi-steady values) amplitudes of T_{max} oscillations are shown as functions of the frequency; the normalization with the quasi-steady amplitude accounts for the amplitude effect of the imposed oscillations. The results show that, at low frequencies, the flame response is quasi steady with values of the normalized amplitude close to 1, while at higher frequencies, the amplitude decreases. However, the amplitude reduction occurs at higher frequencies for the higher burning rates because the flame thickness is reduced, and higher frequencies are required for the attenuation mechanism of Stokes' second problem to work.

The analogy with the Stokes' second problem was demonstrated by quantifying the frequency response of Flames I, II, and III in terms of a nondimensional parameter $\eta = \delta\,(\omega/2a)^{1/2}$ instead of the frequency; η

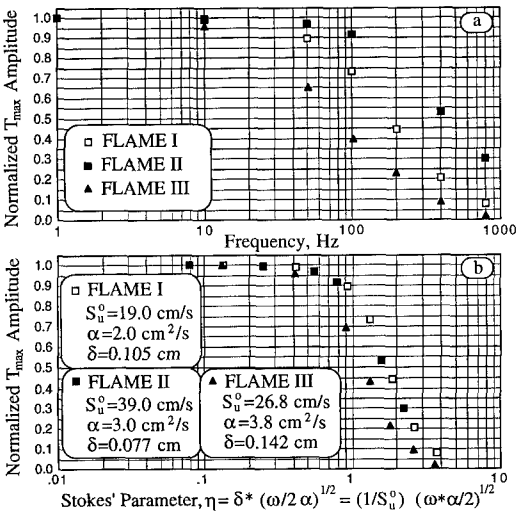

FIG. 4. Variation of the T_{max} amplitude normalized by its quasi-steady value for Flames I, II, and III with (a) frequency and (b) Stokes' parameter, η.

will be referred to for convenience as Stokes' parameter. In this definition, δ is a measure of the thickness of the diffusion zone, and a is a characteristic diffusion coefficient. By further realizing that, for premixed flames, δ scales with the laminar flame speed, S_u°, and a as $\delta \approx a/S_u^\circ$, then $\eta = (1/S_u^\circ)(a\omega/2)^{1/2}$.

In the present analysis, a was chosen to be an average value of the mixture thermal diffusivity; the values of δ, a, and S_u°, determined by detailed numerical calculations, are shown in Fig. 4 for Flames I, II, and III. In Fig. 4b, the variation of the normalized amplitudes of T_{max} oscillations with η are shown, and it can be seen that the data "collapse" close to a single curve. The data of Fig. 4b indicate that η is the appropriate nondimensional parameter controlling the frequency response of the flame. It is also of interest to note that a drastic drop of the normalized temperature amplitude starts for values of η around 1, indicating that, when the characteristic diffusion thickness δ is of the same order with the characteristic penetration length for the oscillations $(2a/\omega)^{1/2}$, the "attenuation" effect starts influencing the structure of the diffusion zone. Therefore, it is proposed that the characteristic *angular frequency* at which substantial attenuation commences is of the order of $[2(S_u^\circ)^2/a]$.

The effect of the frequency on the flame structure is shown in Fig. 5, in which the total (convective + diffusive) mass fluxes of CH_4 are plotted for the conditions corresponding to the peak and trough values of u_{exit} for Flame I, at $f = 1$ Hz and $f = 800$ Hz. At $f = 1$ Hz, there is a distinct "displacement" between the trough and peak flux profiles, indicating that the oscillations propagate through the diffusion zone and are sensed by the reaction zone. On the other hand, while at $f = 800$ Hz the flux profiles are distinctly different in the hydrodynamic zone, they merge within the diffusion zone. Note that "negative" mass flux gradients of CH_4 can be seen in Fig. 5 for the trough value of u_{exit} and $f = 800$ Hz, which suggests that mass is being accumulated.

Mathematically, the mass accumulation can be caused by the $\partial\rho/\partial t$ term in the continuity equation. Since no pressure variation effect on the density was considered in the present analysis, the time variations of the density can be mainly induced through time variations of the mixture temperature; the concentration effect is small in dilute mixtures. By defini-

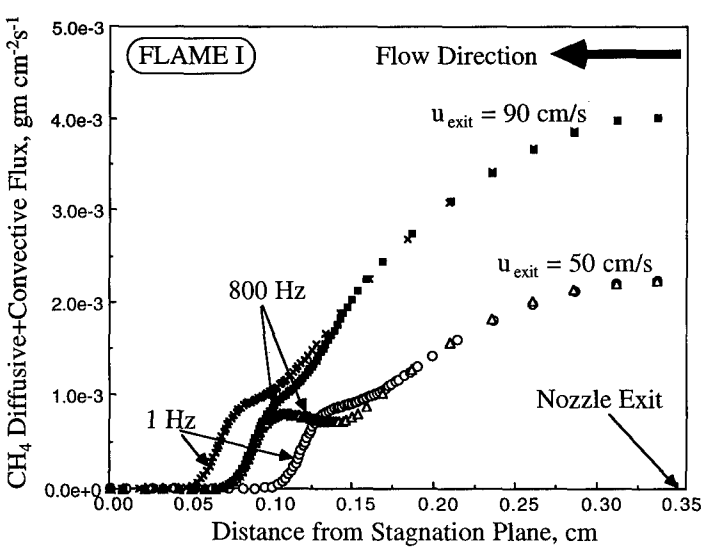

FIG. 5. Variation of the total (diffusive + convective) CH_4 mass flux throughout the flame and hydrodynamic zones for Flame I at $u_{exit} = 50$ cm/s and $u_{exit} = 90$ cm/s, and $f = 1$ Hz and $f = 800$ Hz.

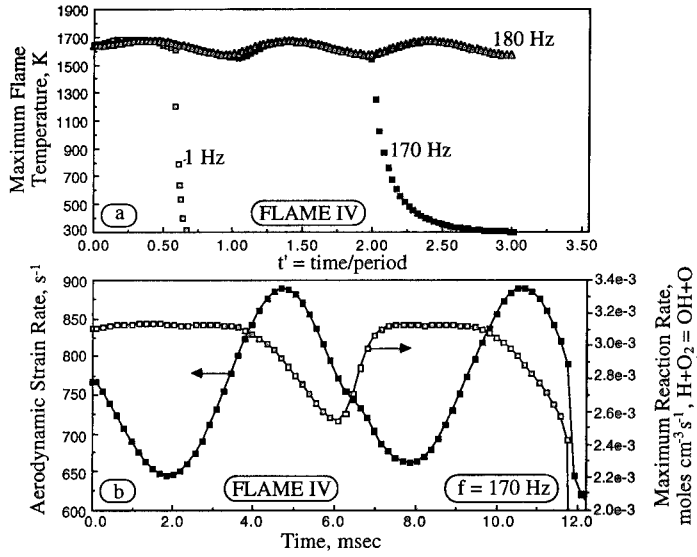

FIG. 6. (a) Transient extinction of Flame IV at various frequencies. (b) Variations of the maximum reaction rate of H + O_2 = OH + O and K with real time for Flame IV at f = 170 Hz.

tion, there are no temperature variations in the hydrodynamic zone, while in the main diffusion zone, substantial attenuation of the temperature amplitude has been induced at high frequencies. At the interface of the two zones, however, strong time variations of the temperature and, therefore, density were identified at high frequencies. Physically, this happens because when u_{exit} is at its peak (trough) value, the flame is stabilized at a nearly fixed location that is closer to the nozzle (stagnation plane) compared with its quasi-steady location, and the convective transport just before the flame substantially varies as the u_{exit} oscillates between its peak and trough value. Therefore, since the amount of heat transfer from the flame is fixed, increased (reduced) convective mass flux results to a lesser (greater) extent of heating, leading to lower (higher) temperatures and eventually to large values of $\partial\rho/\partial t$ at the interface of the hydrodynamic and diffusion zones, especially at high frequencies. This mass accumulation process leads to the modification of the local velocity field just before the diffusion zone.

For Flames I, II, and III, the induced maximum strain rate, K, does not lead to permanent extinction. However, a further increase of u_{exit} and, subsequently, K can cause extinction when K reaches a critical value. In order to study unsteady extinction, the conditions of Flames I, II, and III were modified by allowing for larger values of K, leading to extinction. These will be referred to as Flames IV (ϕ = 0.7, $u_{exit,O}$ = 160 cm/s, $u_{exit,A}$ = 30 cm/s), V (ϕ = 1.0, $u_{exit,O}$ = 330 cm/s, $u_{exit,A}$ = 60 cm/s), and VI (ϕ = 1.3, $u_{exit,O}$ = 70 cm/s, $u_{exit,A}$ = 20 cm/s) respectively. The *steady* extinction strain rates, K_{ext}, for Flames IV, V, and VI were determined in order to compare with the results of transient extinction. It was found that, under unsteady conditions, extinction initiates when the K reaches the K_{ext} value, but whether the extinction will be permanent or not depends on the frequency. The results for the transient extinction of Flame IV are shown in Fig. 6a in terms of T_{max} variation with t' at different frequencies. It can be seen that, while at f = 1 Hz permanent extinction occurs when K reaches the value K_{ext} = 835 s^{-1}, extinction is suppressed at f = 180 Hz, and it is delayed for two periods at f = 170 Hz.

In order to identify the mechanisms responsible for the flame survival at higher frequencies, even though K exceeds K_{ext}, the variations of K and the maximum rate, R_{max}, of the main branching reaction H + O_2 = OH + O (B) are simultaneously shown in Fig. 6b for the case of f = 170 Hz; reaction (B) was chosen because extinction is particularly sensitive to its rate. Results indicate that, when $K = K_{ext}$ = 835 s^{-1}, extinction initiates as shown by the decreasing trend of R_{max}, which is a consequence of reactant leakage and subsequent reduction of T_{max} for the case of the Le < 1 Flame IV [3]. Permanent extinction, however, is not reached instantaneously, and a finite time is required for the complete shutdown of all chemical processes. At low frequencies, the time during which the flame experiences unfavorable straining is greater compared with the required time for extinction, and permanent extinction is observed. At higher frequencies, it is possible that, before the flame reaches permanent extinction, it will experience a favorable straining, and reignition can occur, as can be seen in the first cycle of Fig. 6b. For the case of f = 170 Hz, it was found that, after reignition, the radical pool is reduced compared with the state inducing partial extinction, the flame overall is weaker during the second cycle, a lower favorable

strain rate will not be readily encountered, and permanent extinction occurs. At $f = 180$ Hz, the favorable strain rate is applied well before the flame has been substantially weakened during the partial extinction stage, and reignition occurs, leading to a strongly burning flame that survives all subsequent partial extinction stages. For Flame IV at $f = 170$ Hz, it was found that the flame weakening during the first cycle is due to the accumulation of substantial amounts of O_2 during the partial extinction stage, which during reignition disproportionately deplete the H radicals through reaction (B). Since the supply of H radicals is limited by the fuel consumption, which is reduced during both the partial extinction and reignition stages, it is possible that, under certain conditions, the H radical pool will not completely recover after reignition.

Concluding Remarks

In the present study, the effect of unsteadiness on the structure and dynamics of strained, premixed flames was investigated. The results can be used toward the understanding of turbulent combustion in the laminar flamelet regime and can effectively guide future experimental studies. The analysis included detailed numerical simulation of unsteady, strained, methane/air premixed flames in a finite domain counterflow for various conditions at the nozzle exits. Subsequently, the instantaneous detailed flame structure was examined, and physical insight was provided into the elementary mechanisms controlling the flame frequency response for both vigorous burning and extinction.

For vigorous burning, it was found that, at low frequencies, the flame properties follow the imposed oscillations in a quasi-steady manner, while the amplitudes of the flame properties are reduced at high frequencies. The phenomenon of transient extinction was also investigated, and it was found that extinction occurs as the critical *steady* extinction strain rate, K_{ext}, is reached. At high frequencies, however, the reduction of the time at which the strain rate exceeds K_{ext} can delay extinction for a number of cycles during which the flame experiences partial extinction followed by reignition. At higher frequencies, extinction can be eventually suppressed.

The physical mechanisms responsible for the reduced flame response at high frequencies were also identified. Through detailed flame structure analysis, it was found that the velocity oscillations in the hydrodynamic zone result in reactant concentration oscillations inside the diffusion zones. Similarly to a previous study on diffusion flames, the analogy of the Stokes' second problem was used for the appropriate frequency scaling via the nondimensional parameter $\eta = \delta(\omega/2a)^{1/2}$. The results show that, for all cases studied herein, the amplitude of the flame response scales closely with η, and the angular frequency at which substantial attenuation commences was found to be of the order of $[2(S_u^\circ)^2/a]$.

Finally, the phenomena of partial extinction, reignition, and extinction delay were explained based on the interaction between the processes of aerodynamic straining and chemical kinetics. It was found that, for certain strain rates and frequencies, extinction can be initiated but not completed if the time required for the establishment of favorable straining is small compared with the time required for extinction, so that reignition occurs. Extinction delay occurs when, after reignition, the H radical pool is reduced, leading to gradual flame weakening and permanent extinction after a number of cycles.

Acknowledgments

This study was supported by the National Science Foundation under Grant No. NSF CTS-9211844.

REFERENCES

1. Libby, P. A., and Williams, F. A., *Combust. Flame* 44:287–303 (1982).
2. Peters, N., *Twenty-First Symposium (International) on Combustion,* The Combustion Institute, Pittsburgh, 1986, pp. 1231–1250.
3. Law, C. K., *Twenty-Second Symposium (International) on Combustion,* The Combustion Institute, Pittsburgh, 1988, pp. 1381–1402.
4. Zhu, D. L., Egolfopoulos, F. N., and Law, C. K., *Twenty-Second Symposium (International) on Combustion,* The Combustion Institute, Pittsburgh, 1988, pp. 1537–1545.
5. Kee, R. J., Miller, J. A., Evans, G. H., and Dixon-Lewis, G., *Twenty-Second Symposium (International) on Combustion,* The Combustion Institute, Pittsburgh, 1988, pp. 1479–1494.
6. Dixon-Lewis, G., *Twenty-Third Symposium (International) on Combustion,* The Combustion Institute, Pittsburgh, 1990, pp. 305–324.
7. Strahle, W. C., *Tenth Symposium (International) on Combustion,* The Combustion Institute, Pittsburgh, 1965, pp. 1315–1325.
8. Clarke, J. F., and Stegen, G. R., *J. Fluid Mech.* 34:343–358 (1968).
9. Saitoh, T., and Otsuka, Y., *Combust. Sci. Tech.* 12:135–146 (1976).
10. Rutland, C. J., and Ferziger, J. H., *Combust. Sci. Tech.* 73:305–326 (1990).
11. Stahl, G., and Warnatz, J., *Combust. Flame* 85:285–299 (1991).
12. Cetegen, B. M., and Bogue, D. R., *Combust. Flame* 86:359–370 (1991).
13. Darabiha, N., *Combust. Sci. Tech.* 86:163–181 (1992).
14. Ghoniem, A. F., Soteriou, M. C., Cetegen, B. M., and Knio, O. M., *Twenty-Fourth Symposium (Interna-*

tional) on Combustion, The Combustion Institute, Pittsburgh, 1992, pp. 223–230.
15. Egolfopoulos, F. N., and Campbell, C. S., "On the Structure and Dynamics of Unsteady, Counterflowing, Strained Diffusion Flames," Fall Meeting of the Western States Section of The Combustion Institute, Paper WSS/CI 93–081, 1993.
16. Egolfopoulos, F. N., and Campbell, C. S., "Unsteady, Counterflowing, Strained Diffusion Flames. Part I: Diffusion Limited Frequency Response," *J. Fluid Mech.,* submitted.
17. Egolfopoulos, F. N., and Campbell, C. S., "Unsteady, Counterflowing, Strained Diffusion Flames. Part II: Flame Structure and Extinction," *J. Fluid Mech.,* submitted.
18. Kee, R. J., personal communication.
19. Kee, R. J., Rupley, F. M., and Miller J. A., *Chemkin-II: A Fortran Chemical Kinetics Package for the Analysis of Gas-Phase Chemical Kinetics,* Sandia Report SAND89–8009, 1989.
20. Kee, R. J., Warnatz, J., and Miller, J. A., *A FORTRAN Computer Code Package for the Evaluation of Gas-Phase Viscosities, Conductivities, and Diffusion Coefficients,* Sandia Report SAND83–8209, 1983.
21. Egolfopoulos, F. N., Du, D. X., and Law, C. K., *Combust. Sci. Tech.* 83:33–75 (1992).
22. Egolfopoulos, F. N., and Law, C. K., "Further Considerations on the Methanol Oxidation Kinetics," manuscript in preparation.
23. White, F. M., *Viscous Fluid Flow,* 2nd ed., McGraw-Hill, Inc., New York, 1991.

COMMENTS

A. C. McIntosh, Leeds University, UK. In your numerical study, you are imposing velocity fluctuations and finding that the amplitude of consequent temperature oscillations decreases with frequency. There must be an acoustic field set up by these oscillations. If you were to impose a pressure fluctuation (as against velocity), would you still find that the amplitude of the temperature oscillations decreases with frequency? For a flat flame, there is a growth in amplitude [*Combust. Sci. Technol.* 91:329–346 (see Fig. 1a)].

Author's Reply. Your point is well taken. In the paper, however, it is stated that only the effect due to velocity (strain rate) unsteadiness is assessed. Clearly, effects due to pressure fluctuations can be important if one considers them, and they can couple with the velocity effects. For low frequencies, however, it is not expected that pressure (acoustic) effects will be as important. The experimental data of Ref. 9 show that the frequency response of the flame is reduced at high frequencies. We are currently conducting experiments on unsteady premixed and diffusion flames to examine the validity of the present calculations. We are also in the process of conducting detailed calculations in which the pressure effect will be also included.

•

H. G. Im, Princeton University, USA. Most of the flame responses appear to be sinusoidal in shape, but variation of the CH_4 mass fraction shown in Fig. 3 does not, i.e., the peaks are more blunt than the troughs. Do you have any physical explanation of this nonlinear behavior?

Author's Reply. This asymmetry exists because the profile of the CH_4 mass fraction, Y_{CH_4}, appears to have larger curvature around the peak value compared with the curvature around the trough value at the $X_{95\%}$ location, as can be seen in Fig. 3a. Therefore, by using simple geometric arguments it can be seen that the time variation of Y_{CH_4} will be more gradual around its peak value compared with the variation around its trough value. In any case, there is periodicity in the Y_{CH_4} variation at the beginning of the diffusion zone, which allows for the use of the Stokes' second problem as an analogy.

•

Marios Soteriou, MIT, USA. In your presentation, you suggested that quenching of the flame may take place during the second (or subsequent) cycles of the strain oscillations and that this phenomenon is a consequence of the multistep chemistry as intermediate reactions may quench.

In the work that led to our paper (Ghoniem, Soteriou, Knio, and Cetegen) published in the *Twenty-Fourth Symposium,* we noticed the same phenomenon (i.e., quenching after the first strain cycle) even though we were using a single-step chemistry mechanism. Our explanation was that there was not enough time for the temperature field (which is oscillating out of phase with the strain field) to totally recover after the first cycle and hence quenching was experienced in the second. Could you elaborate on this discrepancy? Are there two mechanisms that may lead to this phenomenon?

Author's Reply. Your observation was unknown to me since it was not included in your paper in the *Twenty-Fourth Symposium.* The assessment of the extinction behavior by using one-step and multistep chemistry may be different since the details of the kinetics become important. The extinction response of any practical flame is highly sensitive to the main branching reaction, $H + O_2 = OH + H$, since it is the main source of radicals, and therefore, it greatly contributes to the overall exothermicity. In the present work, the fate of H radicals and O_2 molecules was monitored during the extinction stage, and the reported trends are physically reasonable. It is not possible

to assess the phenomenon that you have observed and support your explanation since I have not done one-step calculations. Extinction can be captured by using either one-step or multistep chemistry, and I think that different controlling mechanisms can be identified. In one-step calculations, clearly the response of the temperature field is the only parameter that can be used to explain extinction. In my previous work on flammability limits with C. K. Law, as well as in some of my recent unpublished work on extinction using a multistep approach, it has been seen that extinction is controlled by an appropriately formulated sensitivity coefficient between the main branching and main termination reactions; such effects cannot be captured by using one-step solutions. Therefore, it is possible that our conclusions may be different due to the different approaches that we used. It should be realized, however, that there is a direct coupling between temperature field and kinetics.

•

D. Milov, RRA, USA. 1. Does the author need a full kinetic mechanism to solve this problem? A. Ghoniem et al. solved the same problem (for diffusion flames) in a much simpler manner using a one-step reaction.

2. The Stokes' second problem has little to do, except for dimensional analysis, with the present problem. An asymptotic analysis method could provide a much more physical, appropriate, and analytical solution. (See H. G. Im et al., this *Symposium*, Combustion and Flame.)

Author's Reply. 1. The use of detailed description of chemical kinetics and molecular transport for the solution of any combustion problem cannot be underestimated. The present work is a forward step, and Ghoniem et al. in Ref. 14 indicate in their conclusions the need for the detailed solution of the problem. The detailed approach provides results that can be compared with experiments (which are underway at present), and there is no need to assume constant or equal transport coefficients and, more important, to assume values for the activation energy. Such assumptions will depend on arbitrary choices which are clearly not valid in an actual turbulent flow field in which the local conditions, including stoichiometry and pressure, can change in space and time and, therefore, the prevailing overall activation energy can be substantially stratified. Furthermore, only by conducting detailed calculations can the flame structure be meaningfully resolved in terms of intermediate species which can have vastly different time scales of oxidation and which can be important to both the heat release and pollutant formation.

2. I disagree with this point. In no previous work has the physical mechanism of amplitude attenuation with frequency been directly identified and explained from first principles. The phenomenon has been simply reported. The analogy with the Stokes' second problem is an important contribution since besides quantifying the important scaling laws, it provides substantial physical insight into the actual mechanisms of amplitude attenuation, which is a very important phenomenon and possibly the only one that can be accurately quantified in experiments. Furthermore, it is important to know whether or not a flame responds to unsteadiness in a turbulent flow field. Finally, the importance of asymptotic analysis is not underestimated, but it is clear that much can be learned by following different and frequently complementary approaches such as the one of H. G. Im et al. as well as the present one.

Twenty-Fifth Symposium (International) on Combustion/The Combustion Institute, 1994/pp. 1375–1381

GEOMETRIC AND RADIATION EFFECTS ON STEADY AND UNSTEADY STRAINED LAMINAR FLAMES

F. N. EGOLFOPOULOS
Department of Mechanical Engineering
University of Southern California
Los Angeles, CA 90089-1453, USA

A detailed numerical investigation was conducted on the effects of the domain size and radiation on the dynamics of opposed jet, strained, laminar premixed, and diffusion flames. The simulation was performed by solving the conservation equations along the stagnation streamline of the counterflow and by using detailed description of the chemistry, molecular transport, and nonluminous thermal radiation at the optically thin limit. Results indicate that the hydrodynamic extinction strain rate increases with the nozzle separation distance because of the reduction of the values of the strain rate distribution within the main reaction zone. The predictions of extinction strain rates in the present study agree well with available experimental data on premixed flames, after using nozzle separation distances equal to the experimental ones. Furthermore, the inclusion of the Soret effect was found to increase the predicted strain rates for near stoichiometric flames. The effect of radiation was assessed for both steady and unsteady flames. The unsteadiness was introduced through sinusoidal variation of the nozzle exit velocities around some mean values. The results indicate that the effect of the radiation on the flame response and extinction becomes important only for near-limit premixed flames and weakly strained diffusion flames, which are characterized by large thicknesses. An asymmetry was also identified in the response of unsteady diffusion flames for which the trough value of the strain rate is near-zero, while the peak value causes substantial straining. The results were explained based on the competition between the mechanisms of reactant leakage and radiative loss as the strain rate is reduced.

Introduction

Strained laminar flames have been extensively studied over the last 15 years, and it is expected that the results will be useful toward the understanding of turbulent combustion in the laminar flamelet regime [1–7]. Among the various model systems, the opposed flow, stagnation-type configuration offers great mathematical simplicity and well-defined strain rate, and thus, it has been used in the majority of the studies.

A potential problem in this approach is that although the theoretical analyses are typically conducted by assuming potential flow free stream conditions, actual experiments can only be conducted by using opposed nozzles at finite distances. Recently, Kee et al. [4] realized that substantial discrepancies exist when the theoretical results obtained by using the potential flow assumption for the far field are compared with experiments, and the quasi-one-dimensional conservation equations were formulated for finite domain configurations to closely describe actual experimental conditions. By using the new formulation, closer predictions of the experimentally determined extinction strain rates of Law et al. [3] were obtained, although distinct discrepancies were still found for near stoichiometric and fuel-rich mixtures. In addition to the domain effect, the comparison between numerical and experimental data can be further complicated if the radiative heat loss is neglected, especially when the burning is weak. In the majority of the detailed numerical simulations of strained flames, the radiation effect has not been addressed, with the exception of Ref. 8.

The role of the geometry and radiative losses in counterflow configurations can have significant consequences for various reasons. First, when the validation of a chemical kinetic scheme is based on comparisons between experimentally and numerically determined extinction strain rates, it is possible that if the exact experimental nozzle separation distance is not accounted for by the model, then the disagreements can be falsely attributed to the kinetics instead of to the possible finite domain effect. Second, in cases of weakly burning flames, the omission of the radiative heat loss can result to misleading comparisons with experiments, overestimation of the burning intensity of the flame, and false description of the extinction characteristics. The understanding of the mechanisms controlling the response of weakly burning flames is of particular interest in terms of safety and also the coupling between the system losses and crucial chain kinetic mechanisms [9].

In view of the above considerations, the main objectives of the present investigation were to conduct detailed numerical simulations of the counterflow and systematically quantify the effects of the system geometry and thermal radiation on the dynamics of strained laminar flames, both premixed and diffusion. In addition to steady calculations, unsteady calculations were also conducted in order to demonstrate the coupling between the time scales between the imposed oscillations and the thermal loss mechanisms.

Numerical Methodology

The numerical simulation of the counterflow was conducted by solving the steady and unsteady conservation equations of mass, momentum, energy, and species concentrations along the stagnation streamline and by assuming that the gases leaving the nozzles have no radial variations in velocity, temperature, and concentrations. The unsteady equations are reported in detail in Refs. 10 through 12 (this Symposium), with the only difference being the introduction of the radiative heat loss rate per unit volume term, q''', in the energy equation, similarly to the approach of Ref. 9. Assuming that the flames of interest are optically thin, we have [13]

$$q''' = 4a_p\sigma(T^4 - T_u^4)$$

where σ is the Stefan-Boltzmann constant; T is the temperature; T_u is the ambient temperature, which is set to be the unburnt reactant temperature; and a_p is the total Planck's mean absorption coefficient of the gas. In the present calculations, radiative loss from CO_2, H_2O, CO, and CH_4 was included because they are considered to be the primary radiating species in methane flames. The Planck mean absorption coefficient a_i's for the radiating species are given for optically thin conditions by Tien [14] and Hubbard and Tien [15] as functions of temperature. Then, the total mean absorption coefficient, a_p, is given by $a_p = \Sigma a_i p_i$ where p_i is the partial pressure of species i. The assumption of optically thin conditions was chosen in the present work in order to facilitate calculations and still provide meaningful physical insight. The thin limit assumption, however, can lead to distorted results when reabsorption is important, and for these cases, a more rigorous radiation model must be used. In the present investigation, the assumption of the optically thin limit is valid, and it is supported by the detailed calculations of Vranos and Hall [8], who used gas band radiation description and allowed for reabsorption. Calculations for a diffusion methane/air strained flame at 10.5 atm show that reabsorption becomes important only at very low strain rates, and for a strain rate of 30 s^{-1}, a 0.2% correction is required in the maximum flame temperature (5 out of 2400 K) resulting from calculations at the optically thin limit. In the present investigation, the worst case is a similar diffusion flame at the lower pressure of 5 atm, and it is expected that a correction of less than 0.2% in the maximum flame temperature will not critically affect the physical conclusions. Furthermore, the majority of the results will be obtained at a pressure of 1 atm, which further relaxes corrections due to reabsorption. For the premixed flames studied herein, the flame thickness is smaller by at least a factor of 2–4 compared to the low-strain diffusion flames, and therefore, reabsorption is not expected to influence the underlying physics.

The premixed flames studied herein result from the impinging of two identical streams of CH_4/air premixtures emerging from the opposing burner nozzles. Because of the symmetry of the system across the stagnation plane, the equations were formulated and solved between one nozzle and the stagnation plane. As plug flow (zero divergence) boundary conditions at the exit of the nozzles were assumed, the boundary conditions at the exit of the burner ($x = L$) and stagnation plane ($x = 0$) are

$$x = 0: \quad u = 0, \quad dY_k/dx = 0, \quad dT/dx = 0, \quad dG/dx = 0$$

$$x = L: \quad Y_{O_2} = Y_{O_2,x=L}, \quad Y_{CH_4} = Y_{CH_4,x=L}, \quad Y_{N_2} = Y_{N_2,x=L}, \quad G = dv/dr = v/r = 0$$

where u is the axial velocity, v is the radial velocity, Y is the mass fraction, and r is the radius.

The diffusion flames result from the impinging of a fuel stream emerging from the upper burner nozzle onto an oxidizer stream emerging from the lower burner nozzle. The fuel stream was a mixture of CH_4 and N_2 and the oxidizer stream a mixture of O_2 and N_2. Similarly to the premixed flame formulation, the boundary conditions at the exit of the lower ($x = 0$) and upper ($x = L$) burners are

$$x = 0: \quad Y_{O_2} = Y_{O_2,x=0}, \quad Y_{CH_4} = 0, \quad Y_{N_2} = Y_{N_2,x=0}, \quad G = 0$$

$$x = L: \quad Y_{O_2} = 0, \quad Y_{CH_4} = Y_{CH_4,x=L}, \quad Y_{N_2} = Y_{N_2,x=L}, \quad G = 0.$$

The unsteadiness was introduced for the reactant velocity at the exit of the nozzle, u_{exit}, by imposing sinusoidal variations of a given amplitude $u_{exit,A}$ around a mean value $u_{exit,O}$. Details about the solution approach and the handling of the spatial and temporal pressure variations can also be found in Refs. 10 through 12. The code was integrated into

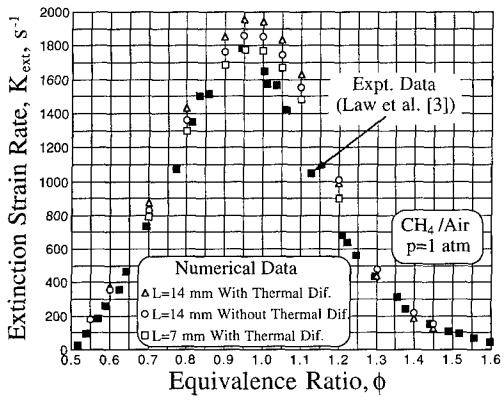

FIG. 1. Comparisons between the numerically determined extinction strain rates, K_{ext}, and the experimental data of Law et al. [3] for atmospheric CH_4/air flames.

the CHEMKIN [16] and transport [17] subroutine packages. The kinetic scheme used is a hierarchically developed C_2 mechanism [18,19].

For both premixed and diffusion flames, the flow exits the nozzles with a zero velocity gradient, it then gradually develops an increasing velocity gradient, which becomes maximum just before the local velocity minimum and is defined as the imposed (hydrodynamic) strain rate, K, which is consistent with its experimental determination [3,5,6]. For the diffusion flames, K was determined by using the velocity profile on the oxidizer side so that it relates to the O_2 leakage through the main reaction zone.

Results and Discussions

Finite Domain Effects:

The effect of the nozzle separation distance, L, on the extinction strain rates, K_{ext}, of atmospheric, premixed, laminar CH_4/air flames can be seen in Fig. 1, in which numerical results are compared with the experimental data of Law et al. [3]. The calculations (adiabatic and steady) were conducted for $L = 7$, 14, and 22 mm, although in Fig. 1, only the results for $L = 7$ and 14 mm are shown, since these are the L's used in the experiments of Ref. 3. Furthermore, in Fig. 1, the effect of the thermal diffusion (Soret effect) on extinction is shown for the $L = 14$ mm case. Results indicate that by increasing L from 7 to 14 mm, the predicted extinction strain increases by about 10%. Although this difference can be considered as minor for weak flames, which are characterized by small K_{ext} values, and it can be well within the experimental uncertainty, it is substantial for near stoichiometric flames by as much as 200 s^{-1}. However, the experiments of Law et al. [3] were conducted with different L's for different equivalence ratios, ϕ, with $L = 14$ mm for $\phi < 0.7$ and $\phi > 1.2$, and $L = 7$ mm for $0.7 \leq \phi \leq 1.2$. Given that in the opposed jet experiments, the L is of the order of the nozzle diameter, d, the choice of the d was based on the requirement that laminar flows must be maintained at the very high values of K near extinction. Comparisons of the experimental results with the numerical results by using the appropriate L show a close prediction of the experimental K_{ext} for the first time, since in previous attempts [4,20] the K_{ext} values of Ref. 3 were overpredicted for near stoichiometric and moderately rich flames. One important feature of the present calculations is that the maximum K_{ext} was found to occur at about $\phi = 0.95$, which is in agreement with the experiments and which was not captured by the calculations of Kee et al. [4]; this behavior has been previously explained based on the Le number effect [3,5]. The close agreement found herein indicates that the present kinetic scheme, which has also been successfully tested against experimental data for laminar flame speeds [21], can be used with confidence in describing at least the dynamic behavior of atmospheric CH_4/air flames. Additional calculations with $L = 22$ mm show a further increase of K_{ext}, which was found to be equal to 2120 s^{-1} for $\phi = 1.0$, and which is substantially larger compared to the experimental value of 1680 s^{-1} [3] and to the numerical value of 1760 s^{-1} for $L = 7$ mm.

The explanation for the finite domain effect on K_{ext} can be provided by considering the strain rate distribution throughout the flame zone for the same K and different L's. The results of such calculations are shown in Fig. 2a in which the density, ρ, weighted strain-rate $\rho^{\circ}G$ is shown throughout the domain for $\phi = 1.0$, $K = 1500$ s^{-1}, and $L = 7$, 14, and 22 mm. While $G = dv/dr$ is a measure of the local straining in terms of the velocity field, $\rho^{\circ}G$ provides a more physical picture by accounting for the radial mass flux gradient that balances the $\partial(\rho u)/\partial x$ term in the continuity equation [12], and therefore, it better relates to the local burning rate. By examining the $\rho^{\circ}G$ profiles throughout the flame, it can be seen that, for the same K, their values are systematically lower inside the main reaction zone for the larger L's. Physically, this happens because for larger L, the flame is located at a greater distance from the stagnation plane, and hence, there is more physical space for the thermal expansion to take place. This leads to lower strain rates inside the main reaction zone, which directly affect the burning intensity by controlling the rate of transport from and to the zone of the major chemical activity. Therefore, as L increases, greater values of K will be required for extinction.

The effect of thermal diffusion (Soret effect) on K_{ext} can also be seen in Fig. 1 for $L = 14$ mm. Results show that the inclusion of the thermal diffusion leads to the increase of K_{ext} by about 5–7% for near-stoichiometric flames, while its effect is minimum for

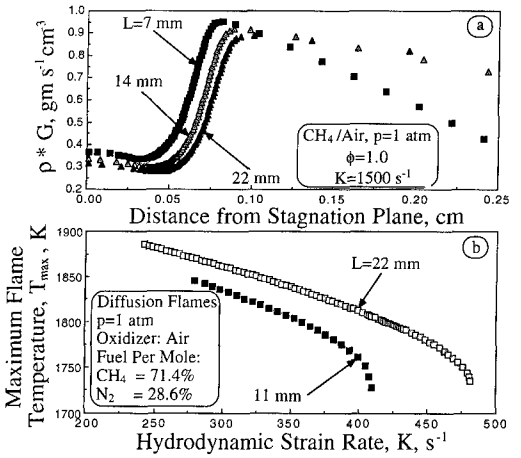

FIG. 2. (a) Spatial variation throughout the flame of the numerically determined density, ρ, weighted radial velocity gradient $\rho^{\circ}G$ for $\phi = 1.0$ CH_4/air counterflow premixed flame under hydrodynamic strain rate $K = 1500$ s^{-1} and for various L's. (b) Variation of the numerically determined maximum flame temperature, T_{max}, with strain rate for counterflow diffusion flames and for various L's.

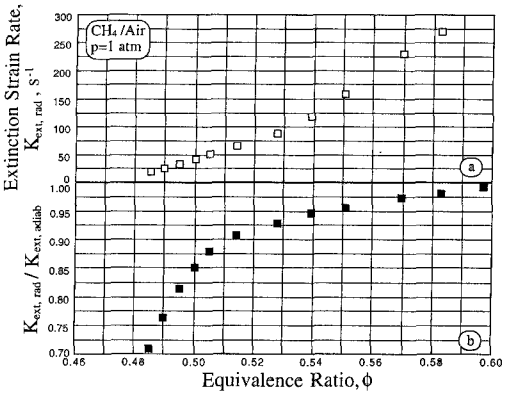

FIG. 3. For near-limit, lean, atmospheric CH_4/air flames: (a) variation of the numerically determined extinction strain rates with radiation, $K_{ext,rad}$, as a function of the equivalence ratio, ϕ and (b) variation of the ratio between the numerically determined extinction strain rates with radiation, $K_{ext,rad}$, and without radiation, $K_{ext,adiab}$, as a function of the equivalence ratio, ϕ.

near-limit flames for which the H radical pool is substantially reduced. This is physically reasonable since the thermal diffusion forces the H radicals toward the hotter region of the flame, and for highly strained flames, the flame temperature at the stagnation plane increases in a way analogous to the Le < 1 strained, premixed flames [3,5]. Therefore, the thermal diffusion results to stronger flames and higher K_{ext} values.

The effect of the domain size on the extinction of strained, laminar diffusion flames is shown in Fig. 2b for $L = 11$ and 22 mm, and a reduction of the K_{ext} from 480 to 410 s^{-1} can be seen as L is reduced from 22 to 11 mm. Similarly to the premixed flames, analysis of the flame structure reveals that, for the same K, the strain rates inside the main reaction zone are lower for the larger L's, and therefore, larger K's will be needed for extinction.

Radiation Effects on Steady, Strained Flames:

The effect of nonluminous radiative loss was assessed for both premixed and diffusion, steady, strained, laminar flames. In general, the inclusion of radiation leads to the reduction of the flame temperature and, therefore, the reduction of the overall reaction rate. This reduction, however, can have a noticeable effect on the flame dynamics, only if the rate of radiative heat loss is comparable to the rate of heat release. While diffusion flames are always stoichiometric, premixed flames can exist at various stoichiometries with various flame temperatures. Previous study [9] has shown that for one-dimensional premixed flames, the burning intensity is significantly influenced by radiation only for stoichiometries close to the flammability limits. For diffusion flames and strains that are low compared to the extinction values, the flame temperature is roughly fixed around its stoichiometric value, and the radiative loss can be enhanced by increasing the flame thickness [8]; the rate of radiative loss directly depends on the gas volume, which is proportional to the flame thickness.

For strained diffusion flames, the flame thickness δ scales with the reactant diffusivity D and strain K as $\delta \approx (D/K)^{1/2}$ and, therefore, can become arbitrarily large for small values of K. This is physically reasonable, since by increasing K, the convective transport balances the diffusive fluxes at spatial locations that are closer to the main reaction zone, and lower δ's are obtained. In contrast, the thickness of premixed flames minimally depends on K for vigorous burning and scales with D and the flame speed, S_u, as $\delta \approx D/S_u$ so that its magnitude is largely determined by the mixture initial conditions and the loss mechanisms via S_u reduction.

The effect of radiation on the extinction of near-limit CH_4/air flames can be seen in Fig. 3. In Fig. 3a, the extinction strain rates calculated with radiation, $K_{ext,rad}$, are shown, and it can be seen that $K_{ext,rad}$ decreases as ϕ decreases since the burning intensity is reduced. In Fig. 3b, the ratio between $K_{ext,rad}$ and the adiabatic extinction strain rates $K_{ext,adiab}$ are shown as a function of ϕ. It can be seen that, in agreement with findings for one-dimensional flames [9], the radiative losses critically affect flame extinction as the lean flammability limit is approached, and

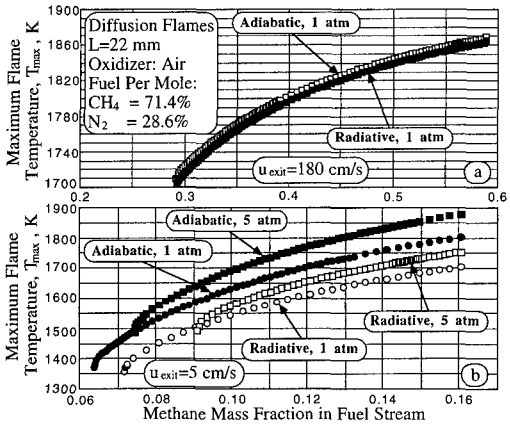

FIG. 4. Comparison of calculated maximum flame temperature, T_{max}, for counterflow diffusion flames under adiabatic and nonadiabatic conditions with (a) $p = 1$ atm and nozzle exit velocity $u_{exit} = 180$ cm/s; (b) $p = 1$ and 5 atm and $u_{exit} = 5$ cm/s.

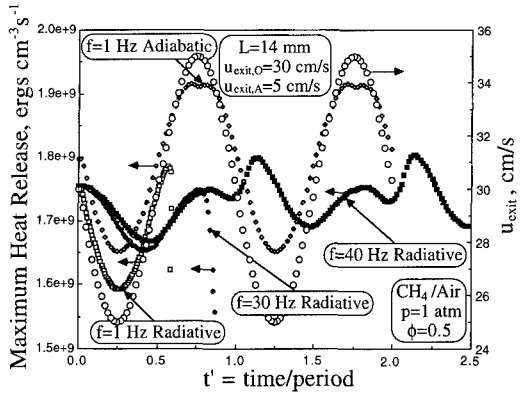

FIG. 5. Variation of the numerically determined maximum heat release Q_{max}, and the imposed u_{exit} with t' and frequency under adiabatic and nonadiabatic conditions for a $\phi = 0.5$ atmospheric CH_4/air flame and $L = 14$ mm. The unsteadiness was introduced by oscillating u_{exit} around a mean value of 30 cm/s with an amplitude of 5 cm/s.

the radiation leads to the substantial reduction of the K_{ext} compared to the adiabatic calculations. However, the inclusion of radiation for ϕ greater than approximately 0.6 has practically no effect on the extinction behavior; flames close to the rich flammability limits were not considered herein. As it has been reported in a previous study [9], as the flammability limit is approached, the sensitivity of the chain mechanism $H + O_2 = OH + O$ (*B*) and $H + O_2 + M = HO_2 + M$ (T) is substantially heightened, the main termination reaction (T) assumes greater importance compared to the main branching reaction (B), and the flame becomes particularly sensitive to loss mechanisms, independently of their magnitude.

The effect of radiation on the extinction of diffusion flames due to the reduction of the methane mass fraction, Y_{CH_4}, in the fuel stream can be seen in Fig. 4 for $L = 22$ mm and fixed nozzle exit velocities. In Fig. 4a, $u_{exit} = 180$ cm/s, which results to large K and therefore, small flame thickness δ. It can be seen that as Y_{CH_4} is reduced, the flame temperature, T_{max}, is reduced and extinction is obtained at sufficiently low Y_{CH_4} values as indicated by the rapid reduction of the T_{max}. However, the overall response of the flame to Y_{CH_4} variations minimally depends on radiation. This indicates that for flames with small thickness, the magnitude of the radiative loss is reduced, and its effect on the flame characteristics and extinction is not crucial.

In Fig. 4b, results similar to Fig. 4a are shown but with $u_{exit} = 5$ cm/s, which results to substantially reduced K and, therefore, increased flame thickness. The results demonstrate that the inclusion of the radiative loss mechanism indeed affects the flame response, as indicated by the substantial reduction of the T_{max}, and the different Y_{CH_4} values at extinction. Such effect is due to the increased magnitude of the radiative loss, as induced by the increased flame thickness and, therefore, volume. In Fig. 4b, results are also shown for 5-atm flames, and it is seen that as the pressure increases, the T_{max} increases and that the temperature reduction due to radiation increases. This is reasonable since the gas emissivity increases directly proportional with pressure. Furthermore, it is seen that the limit Y_{CH_4} values at extinction are higher for the 5-atm case, and this is reasonable because as extinction is approached, the main termination reaction (T) has a gradually increased effect on the overall reaction progress. At higher pressures, the rate of the three-body reaction (T) is favored over the rate of the two-body main branching reaction (B), and extinction is facilitated at larger Y_{CH_4} values. The radiation enhancement at low strain rates has also been reported in Ref. 8.

Radiation Effects on Unsteady Strained Flames:

The effect of radiative loss under the presence of unsteady strain was also examined for both premixed and diffusion flames. For the premixed flames, cases close to the lean flammability limit were studied. For the diffusion flames, conditions allowing for elevated and near-zero strain rates during a cycle were examined.

In Fig. 5, the effects of unsteady strain and radiation on the dynamic response of a $\phi = 0.5$ CH_4/air atmospheric flame are shown in terms of the variation of the value of the maximum heat release, Q_{max}, vs a nondimensional time, t', resulting from the scaling of the real time with the period. It can be seen that by conducting adiabatic calculations, the flame

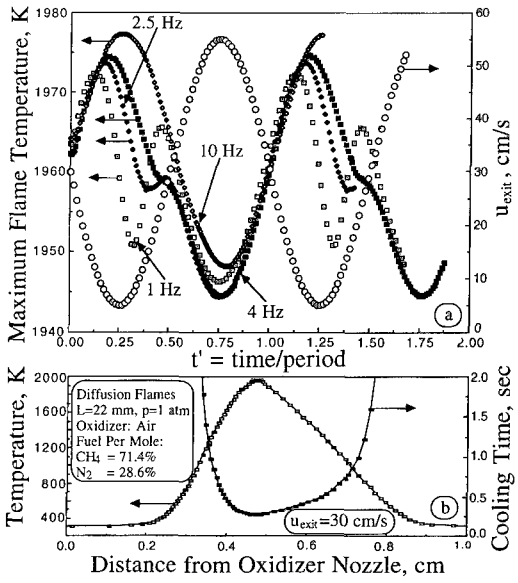

FIG. 6. For a counterflow diffusion flame with $L = 22$ mm under nonadiabatic conditions: (a) variation of the numerically determined maximum flame temperature, T_{max}, and the imposed u_{exit} with t' and frequency; the unsteadiness was introduced by oscillating u_{exit} around a mean value of 30 cm/s with an amplitude of 25 cm/s. (b) Spatial variation of the numerically determined temperature and cooling time due to radiation, t_{cool}, for u_{exit} equal to the mean value of 30 cm/s.

responds in a sinusoidal manner to the imposed sinusoidal u_{exit} variations and permanent extinction does not occur. More specifically, Q_{max}, which is directly proportional to the mass flux under vigorous burning conditions, assumes its peak (trough) value when u_{exit} is at its peak (trough) value. The inclusion of radiation, however, leads to reduced flame strength, and permanent extinction is obtained at low frequencies. At higher frequencies, extinction is either delayed or suppressed, which depends on the relative magnitudes of the time required for extinction and the time during which the flame remains in the "unfavorable" strain regime [10–12]. For the 1-Hz-adiabatic and the 40-Hz-radiative cases, it can be seen that although permanent extinction does not occur, partial extinction and subsequent reignition do occur, as indicated by the reduction and subsequent increase of Q_{max} at the high-strain part of the cycle.

In Fig. 6, the effect of unsteady strain and radiation on the response of a diffusion flame is shown. The results have been obtained for $L = 22$ mm, for a mean $u_{exit,O} = 30$ cm/s and an amplitude $u_{exit,A} = 25$ cm/s, which results to peak and trough values of u_{exit} equal to 55 and 5 cm/s, respectively, and, therefore, to large variations of the flame thickness throughout the cycle. For this reason, it was conjectured that when $u_{exit} = 5$ cm/s, the radiation will be enhanced compared to the $u_{exit} = 55$ cm/s condition. This is indeed shown in Fig. 6a in which the variation of the maximum flame temperature, T_{max}, is shown as a function of t'. It can be seen that, at low frequencies, as the u_{exit} is reduced from its mean value, T_{max} initially increases because of the reduced O_2 leakage through the main reaction zone. This increase, however, is subsequently arrested and a reduction of T_{max} is observed, although u_{exit} keeps decreasing, and this is due to the radiation effect that results from the increased flame thickness as u_{exit} is reduced. Subsequently, T_{max} reaches a local minimum and then starts increasing again at the regime at which u_{exit} starts increasing, leading, therefore, to reduced δ and radiative loss. This T_{max} increase is further arrested at the point at which u_{exit} becomes large enough to cause substantial O_2 leakage and T_{max} reduction. When u_{exit} is at the upper part of its cycle, the asymmetry observed in the lower part of the cycle is not seen anymore, and the flame responds to the u_{exit} variations according to the mechanism of O_2 leakage; the T_{max} values are in all cases lower compared to the ones resulting from adiabatic calculations. As the frequency increases, it can be seen that there is a tendency for "smoothing" of the T_{max} asymmetry in the low part of the u_{exit} cycle, and for frequencies higher than about 5 Hz, the T_{max} variation with t' is controlled by the mechanism of O_2 leakage. This indicates that the characteristic time of oscillations becomes comparable or even smaller compared to the characteristic time for the flame cooling as caused by the thermal radiation loss. Calculations were conducted for the determination of the characteristic cooling time, t_{cool}, of the flame, by dividing the local energy density throughout the flame by the rate of the radiative loss, q'''. Results are shown in Fig. 6b, and it can be seen that at the vicinity of the maximum flame temperature, t_{cool} assumes values at the vicinity of 0.25–0.75 s. This explains the fact that the mechanism of flame cooling due to the radiative loss couples with the imposed oscillations at frequencies of the order of 2–4 Hz.

Concluding Remarks

In the present investigation, the effect of finite size domain and radiation on the dynamics of both steady and unsteady strained laminar flames was numerically assessed. The analysis included the solution of the conservation equations along the centerline of finite domain counterflow configurations, by using detailed description of chemical kinetics and molecular transport. The radiative loss was introduced in the energy equation, and the emissivities of CO_2, H_2O, CO, and CH_4 were calculated at the optically thin limit. The unsteadiness was introduced by sinu-

soidally varying the nozzle exit velocities around a mean value.

Results show that the calculated extinction hydrodynamic strain rates increase with the nozzle separation distance for both premixed and diffusion flames, and the importance of the accurate knowledge of the experimental nozzle separation distance was emphasized. The dependence of the extinction strain rate on the nozzle separation distance was found to be caused by the reduced strain rate distribution within the main reaction zone, as the domain size increases and the hydrodynamic strain rate remains the same. Furthermore, it was found that the inclusion of thermal diffusion has also a noticeable effect on the extinction strain rates of near stoichiometric flames.

The nonluminous radiation effect at the optically thin limit was also investigated for a wide range of flames, and it was found that it becomes important for near-limit premixed flames and for weakly strained diffusion flames, which are characterized by large thicknesses. Unsteady calculations further demonstrated the importance of including radiation when weakly burning flames are investigated, and a distinct asymmetry was identified for the flame temperature of unsteady diffusion flames, for which the strain rate oscillates between a large peak value and a near-zero trough value. This asymmetry was attributed to the competition between the effects of reactant leakage and radiation as the strain is substantially reduced.

Acknowledgment

This study was supported by the National Science Foundation under Grant NSF CTS-9211844.

REFERENCES

1. Libby, P. A., and Williams, F. A., *Combust. Flame* 44:287–303 (1982).
2. Peters, N., *Twenty-First Symposium (International) on Combustion*, The Combustion Institute, Pittsburgh, 1986, pp. 1231–1250.
3. Law, C. K., Zhu, D. L., and Yu, G., *Twenty-First Symposium (International) on Combustion*, The Combustion Institute, Pittsburgh, 1986, p. 1419.
4. Kee, R. J., Miller, J. A., Evans, G. H., and Dixon-Lewis, G., *Twenty-Second Symposium (International) on Combustion*, The Combustion Institute, Pittsburgh, 1988, pp. 1479–1494.
5. Law, C. K., *Twenty-Second Symposium (International) on Combustion*, The Combustion Institute, Pittsburgh, 1988, pp. 1381–1402.
6. Egolfopoulos, F. N., Cho, P., and Law, C. K., *Combust. Flame* 76:375–391 (1989).
7. Dixon-Lewis, G., *Twenty-Third Symposium (International) on Combustion*, The Combustion Institute, Pittsburgh, 1990, pp. 305–324.
8. Vranos, A., and Hall, R. J., *Combust. Flame* 93:230–238 (1993).
9. Law, C. K., and Egolfopoulos, F. N., *Twenty-Fourth Symposium (International) on Combustion*, The Combustion Institute, Pittsburgh, 1992, pp. 137–144.
10. Egolfopoulos, F. N., and Campbell, C. S., "Unsteady, Counterflowing, Strained Diffusion Flames. Part I: Diffusion Limited Frequency Response," submitted to *J. Fluid Mech.* (1993).
11. Egolfopoulos, F. N., and Campbell, C. S., "Unsteady, Counterflowing, Strained Diffusion Flames. Part II: Flame Structure and Extinction," submitted to *J. Fluid Mech.* (1993).
12. Egolfopoulos, F. N., "Dynamics and Structure of Unsteady, Strained, Laminar Premixed Flames," *Twenty-fifth Symposium (International) on Combustion*, The Combustion Institute, Pittsburgh, 1994, pp. 1365–1373.
13. Siegel, R., and Howell, J. R., *Thermal Radiation Heat Transfer*, Hemisphere Publishing Corporation, New York, 1981.
14. Tien, C. L., *Adv. Heat Trans.* 5:253 (1967).
15. Hubbard, G. L., and Tien, C. L., *ASME J. Heat Trans.* 100:235 (1978).
16. Kee, R. J., Rupley, F. M., and Miller, J. A., *Chemkin-II: A Fortran Chemical Kinetics Package for the Analysis of Gas-Phase Chemical Kinetics*, Sandia Report SAND89-8009, 1989.
17. Kee, R. J., Warnatz, J., and Miller, J. A., *A FORTRAN Computer Code Package for the Evaluation of Gas-Phase Viscosities, Conductivities, and Diffusion Coefficients*, Sandia Report SAND83-8209, 1983.
18. Egolfopoulos, F. N., Du, D. X., and Law, C. K., *Combust. Sci. Technol.* 83:33–75 (1992).
19. Egolfopoulos, F. N., and Law, C. K., "Further Considerations on the Methanol Oxidation Kinetics," in preparation.
20. Bui-Pham, M. N., and Miller, J. A., "Theoretical Predictions of the Burning Velocity and Extinction Limit for Methane and Methanol Premixed Flames." Fall Meeting of the Western States Section of The Combustion Institute, Paper WSS/CI 93-105, 1993.
21. Vagelopoulos, C. M., Egolfopoulos, F. N., and Law, C. K., "Further Considerations on the Determination of Laminar Flame Speeds With the Counterflow Twin Flame Technique," *Twenty-Fifth Symposium (International) on Combustion*, The Combustion Institute, Pittsburgh, 1994, pp. 1341–1347.

Twenty-Fifth Symposium (International) on Combustion/The Combustion Institute, 1994/pp. 1383–1390

EFFECTS OF CURVATURE AND UNSTEADINESS IN DIFFUSION FLAMES. IMPLICATIONS FOR TURBULENT DIFFUSION COMBUSTION

B. CUENOT AND T. POINSOT

I.M.F.T. (C.N.R.S.) and C.E.R.F.A.C.S. 42 Av. G. Coriolis, F-31057 Toulouse Cedex, France

Direct numerical simulations (DNS) of flame-vortex interaction are used to study the validity limits of the laminar flamelet assumption (LFA) in diffusion flames. Flame structures measured from DNS are compared with laminar flamelet library predictions obtained from asymptotic analysis performed with similar chemical and transport models (finite rate chemistry and variable density are fully accounted for). Domains where the LFA applies for flame-vortex interaction cases are presented in a (length scale–velocity scale) spectral diagram. Three main effects limit the LFA domain: (1) unsteady effects (the flame structure does not respond fast enough to hydrodynamic excitation), (2) curvature effects (nonlocal effects modify the one-dimensional structure of the flame), and (3) quenching. All these effects are evidenced through numerical simulations and presented on the spectral diagram. As a result, quantitative information is obtained on the exact limits of the LFA for turbulent diffusion combustion. Results show, for example, that quenching is obtained in conditions that are beyond the LFA domain and that, in certain cases, quenching strain rates in turbulent flames may not be obtained from simple laminar flamelet concepts.

Introduction

The validity of flamelet models for turbulent diffusion flames has been the subject of many recent studies [1–5]. Such models are very attractive, as they conveniently separate the combustion problem from the analysis of the turbulent flow field. Various degrees of refinement are possible within the flamelet approach and accordingly a variety of models are currently studied. All flamelet models share the following assumptions: (1) the flame sheet topology—the reaction takes place in relatively thin layers that separate pockets of oxidizer and fuel; (2) the flamelet decomposition—the flame front may be considered as a collection of individual reactive elements and each flame element retains an identifiable structure. Flamelet models differ essentially in the description of the flamelet structure, i.e., in the way the characteristics of the flamelet structure are related to the turbulent flow properties.

Despite their popularity, the exact definition, as well as the usefulness, of the flamelet concepts for turbulent combustion models is still a subject of open discussion. In this paper, we are interested only in the laminar flamelet assumption (LFA), in which we assume that each flamelet in the turbulent diffusion flame behaves like a *laminar* diffusion flame. The derivation of the equations of the laminar flamelet model can be found in Refs. 6 through 8. The structure of this turbulent flamelet corresponds to the structure of the laminar diffusion flame if certain parameters have the same values in both cases. What these "control" parameters should be is still an open question. Fuel and oxidizer concentrations, fuel and oxidizer temperatures, and flame strain are commonly used parameters. However, some authors dispute these choices and argue that reference fuel and oxidizer states are not relevant in turbulent diffusion flames since mixing may lead to different states on both sides of the flame sheet [9,10]. Along the same lines, strain is probably not a good quantity to characterize a diffusion flame, and scalar dissipation should be preferred [1,6]. The exact LFA limits are difficult to provide and are still being discussed. Peters [1] argues that curvature effects are negligible as soon as the Kolmogorov scale is larger than the diffusion thickness, while Bilger [2] proposes that the Kolmogorov scale should be larger than the reaction-zone thickness (which is more restrictive). While these results are mainly based on dimensional analysis and physical intuition, it is of interest to quantify them, as done in the next sections.

Our objective is to perform a direct investigation of the validity of LFA in a simple case where precise diagnostics may be used: a flame-vortex interaction (Fig. 1). We will study the tip of a flame that is curved and strained by a vortex pair in two ways:

1. Perform a direct numerical simulation (DNS) of the interaction to obtain the exact result.
2. Use scalar dissipation at the tip (as measured in the DNS) and a flamelet library (based on the asymptotic approach of Cuenot and Poinsot [6]) to predict flame structure using the LFA.

Comparison between these two techniques will produce a quantitative estimate of the LFA validity in terms of the instantaneous flame structure. More

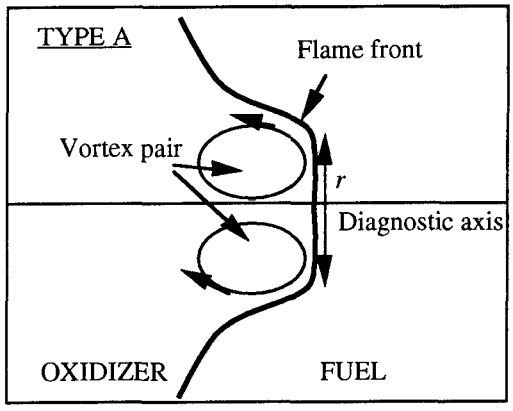

FIG. 1. Configuration A of the simulation.

precisely, we will compare the maximum flame temperature and the total reaction rate, which are important quantities for turbulent models. This information will be used to construct a spectral diagram in which LFA limits will be derived, as well as the quenching limits. Section 2 ("A Spectral Diagram for Flame-Vortex Interaction in Diffusion Flames") will present the parameter controlling flame-vortex interaction and the resulting spectral diagram. Section 3 ("An Asymptotic Flamelet Library for Diffusion Flames with Finite Rate Chemistry") will present the principles of the LFA as used here and describe the parameters that control LFA validity in our situation. Section 4 ("Numerical Method for Flame-Vortex Interaction") will give a brief description of the numerical method. Section 5 ("Results") will present results where LFA is or is not valid and give the validity limits of the LFA in a (vortex length scale–velocity scale) diagram.

A Spectral Diagram for Flame-Vortex Interaction in Diffusion Flames

A classical way of addressing the problem of turbulent combustion regimes is to use turbulent combustion diagrams [1,11,2]. When flame-vortex interactions are studied, diagrams have also been proposed and derived for premixed flames [12,13]. We will first derive similar diagrams for diffusion flames.

Consider a one-step diffusion flame $\nu_F F + \nu_O O \rightarrow P$ where the reaction rate of species F is given by

$$\dot{\omega}_F = \nu_F A^* \rho^{\nu_O + \nu_F} Y_F^{\nu_F} Y_O^{\nu_O} \exp\left(-\frac{T_{\text{act}}}{T}\right) \qquad (1)$$

where A^* is the pre-exponential factor and T_{act} is the activation temperature. The configuration chosen for the flame-vortex interaction is the following (Fig. 1). An unstrained diffusion flame is initialized in the domain: temperature, fuel, and oxidizer mass fractions for this initial flame are obtained from asymptotic analysis [6]. The fuel and oxidizer streams are initially at temperature T_0 and consist of pure fuel and pure oxidizer (initial mass fractions are 1 in both sides). A vortex pair is imposed at time $t = 0$ in front of the flame, in the oxidizer side. This pair corresponds to Oseen vortices of equal radii R separated by a distance l [12,14]. It has a zero circulation in the far field so that the initial vorticity is located only on the oxidizer side. Two flow configurations are considered. In the first (type A), the vortex pair is counter-rotating, and the flow direction along the axis of symmetry is towards the flame. In this interaction, the flame is pushed outward, and the characteristic length is $r = l + 2R$. In the second configuration (type B), the vortex is also counter-rotating, but the flow direction along the axis of symmetry is away from the flame. In this interaction, the flame is pinched, and the characteristic length is $l - 2R$. In both configurations, the characteristic velocity is the absolute value of the maximal initial velocity induced by the pair u'.

The behaviour of the flame-vortex interaction is controlled by three time scales:

1. The intrinsic time scale of the flame (in the absence of vortices) t_i. This time changes slowly compared to the other time scales and may be taken as a constant during the computation, equal to its initial value:

$$t_i = 1/(D_{th}(\nabla z_f)_i^2)$$

where D_{th} is the thermal diffusivity, z is the passive scalar (as defined in Ref. 6), ∇ represents the derivative across the flame front along the axis of symmetry, and the subscripts f and i refer to the stoechiometric point and the initial state, respectively.

2. The chemical time scale τ which takes into account all chemical characteristics of the flame (and is derived from asymptotic analysis [6]).

$$\frac{1}{\tau} = 4\Phi^{\nu_O} A^* \rho_f^{\nu_O + \nu_F - 1} (1 + z_f)^2 \varepsilon^{\nu_O + \nu_F + 1} \cdot \exp\left(-\frac{T_{\text{act}}}{T_{\text{ad}}}\right)$$

where Φ is the stoechiometric ratio, ρ_f, $z_f = (\Phi - 1)/(\Phi + 1)$, and T_{ad} are the values at the flame, respectively, of the density, the passive scalar, and the temperature, and ε is a small parameter characterizing the width of the reaction zone, defined by $\varepsilon = (T_{\text{ad}}^2)/(T_{\text{act}} Q/C_p)$, where Q is the heat release per unit mass of fuel consumed.

3. The flow time scale defined by $t_f = 1/(D_{th}(\nabla z_f)^2)$,

where ∇z_f is the passive scalar gradient imposed by the flow. Note that $(\nabla z_f)^2$ is proportional to the scalar dissipation at the tip of the flame.

The Damköhler number is defined by $Da = (1/\tau)/(1/t_f)$. The length scales to consider are the initial thickness of the flame $\delta_i \simeq 1/(\nabla z_f)_i$ and the vortex size r. The velocity scales are the initial characteristic speed δ_i/τ and the vortex speed u'. The flow time scale t_f is inversely proportional to the vortex strain $\Lambda = u'/\tau$. The proportionality coefficient can be estimated by analogy with a laminar plane flame submitted to a strain Λ. Asymptotic analysis [6] leads to $t_f\Lambda = t_f/(r/u') = \pi \exp(2a^2)/2$, where $a = \mathrm{erf}^{-1}(z_f)$ (erf is the classical error function). From these definitions, we choose r/δ_i and $(u')/(\delta_i/\tau)$ as coordinates for the spectral diagram of Fig. 6.

Three main assumptions are used to support the LFA approach [1,3]:

1. The flame must not be quenched.
2. Unsteady effects inside the flame zone must be negligible (the flame must adjust instantaneously to changes in strain rate).
3. Curvature effects must be negligible.

The previous three effects may be described in the spectral diagram:

1. Quenching will occur for $Da = Da_{\mathrm{ext}}$, where [6,7]

$$Da_{\mathrm{ext}} = \frac{2}{\pi \exp(2a^2)} \left(\frac{(1 - z_f)e}{2\nu_F}\right)^{\nu_F} \cdot \frac{2}{\nu_O!}\left(1 - \frac{1 - z_f}{2}(1 + \nu_O)\right)$$

In the spectral diagram, the quenching limit is therefore represented by the line

$$\frac{u'}{\delta_i/\tau} = \frac{1}{Da_{\mathrm{ext}}}\frac{r}{\delta_i}.$$

2. Unsteady effects will appear when the vortex time scale r/u' is too small compared to the chemical time scale τ: $(r)/(u'\tau) << 1$ or $(u')/(\delta_i/\tau) >> r/\delta_i$, meaning that the flame cannot adjust fast enough to hydrodynamic excitations. Therefore, time derivatives in the final equation cannot be neglected anymore (see Ref. 1). This criterion is essentially equivalent to $Da << Da_{\mathrm{LFA}}$. Whether Da_{LFA} is larger or smaller than Da_{ext} (or in other words, does extinction occur before or after the LFA ceases to apply) is to be determined. In the spectral diagram, the unsteady effects limit is represented by a line

$$\frac{u'}{\delta_i/\tau} = \frac{1}{Da_{\mathrm{LFA}}}\frac{r}{\delta_i}.$$

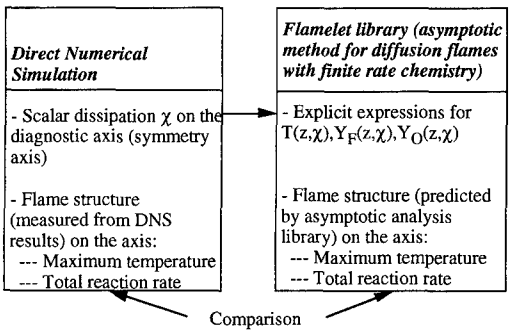

FIG. 2. Correspondence between DNS and asymptotic analysis.

3. Curvature effects will be significant for small vortices $r/\delta_i \leq (r/\delta_i)_{\mathrm{crit}}$, with reasonably large Reynolds numbers (otherwise they will be dissipated by viscous effects). In this case, lateral diffusion becomes significant enough to alter the one-dimensional structure of the flamelet.

Finally, we can measure the ratio of curvature effects with unsteady effects using the Reynolds number of the vortex:

$$Re_{\mathrm{vortex}} = \frac{u'r}{\nu} = \frac{Da_i}{Pr}\frac{u'}{\delta_i/\tau}\frac{r}{\delta_i}$$

where Da_i is the initial Damköhler number: $Da_i = (1/\tau)/(1/t_i)$, ν is the viscosity of the fluid, and Pr is the Prandtl number. This corresponds to a line of slope -1 in the log-log spectral diagram.

We will estimate $(r/\delta_i)_{\mathrm{crit}}$ and Da_{LFA} using DNS of flame-vortex interactions. We will also investigate whether LFA applies close to quenching conditions $Da \simeq Da_{\mathrm{ext}}$.

An Asymptotic Flamelet Library for Diffusion Flames with Finite Rate Chemistry

To compare DNS results and a flamelet library (Fig. 2), we first need to construct the flamelet library. Asymptotic analysis shows that any laminar planar diffusion flame (steady or not, strained or not) is a good prototype of a turbulent diffusion flame if it has the same scalar dissipation [1,6]. As proposed in Refs. 7 and 8, asymptotic techniques have been used in Ref. 6 to predict the response of a laminar flame submitted to a given scalar dissipation. This library is valid for different Lewis numbers in oxidizer and fuel, variable stream temperatures, and finite rate chemistry. The chemistry corresponds to Eq. (1). In this paper we have used unity Lewis numbers for all species so that the binary diffusion coefficients between fuel and mixture D_F, oxidizer and

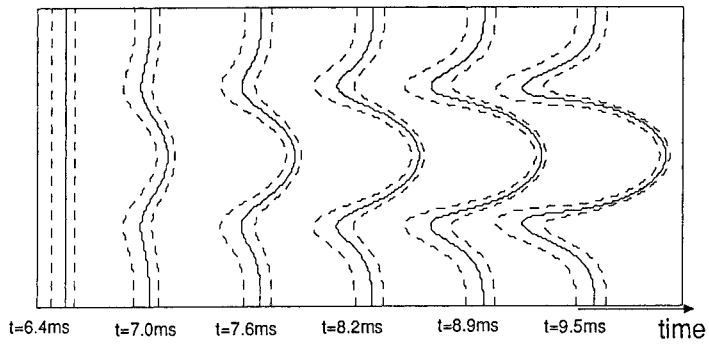

FIG. 3. Passive scalar isolines at different instants for a type A simulation.

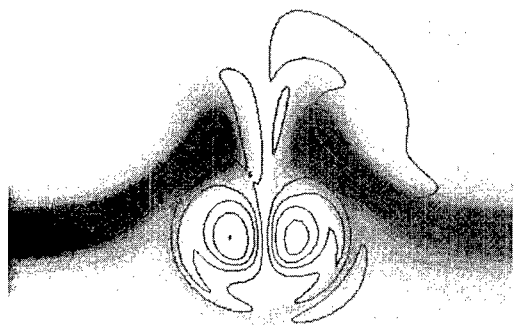

FIG. 4. Temperature and vorticity contours for a type A simulation.

FIG. 5. Reaction rate and vorticity contours for a type A simulation.

mixture D_O, and the viscosity ν are given by $D_F = D_O = \nu_0(\rho_0/\rho_f)^2/Sc$ and $\nu = \nu_0(\rho_0/\rho_f)^2$.

Numerical Method for Flame-Vortex Interaction

A two-dimensional DNS code was used to investigate flame-vortex interaction in diffusion flames. The objective was to create an intrinsically unsteady strained, curved diffusion flame that would be a good prototype of a turbulent diffusion flamelet. A typical time evolution of flame-vortex interaction is given in Fig. 3: passive scalar isolines are plotted at different instants and show how the flame is affected by the pair. Temperature and reaction rate contours are plotted along with vorticity isolines in Figs. 4 and 5. By changing the size and the velocity of the vortex pair, different regimes of combustion may be addressed and the LFA validity may be checked. Now, of course, this configuration does not exhibit all possible situations encountered in real diffusion flames. However, it offers a real quantitative assessment of the LFA. Clearly, the LFA must be valid here if it is to be satisfied in turbulent flames.

The DNS code uses the same assumptions as the asymptotic analysis described above. It solves the full compressible Navier–Stokes equations, including heat release, variable diffusion and viscosity coefficients, and finite rate chemistry. The algorithm is explicit in time (fourth-order Runge-Kutta scheme) and is based on a sixth-order compact scheme [15] for space differencing. The NSCBC boundary conditions are used for inflow and outflow [15]. Periodicity is assumed in the direction parallel to the initial flame.

The DNS code was tested in numerous cases [12,15] and self-consistency between DNS results and asymptotic results was checked by comparing both techniques for a laminar unsteady unstrained flame: in this situation, flame structures and global quantities (such as total reaction rate and maximal temperature) obtained from DNS or asymptotic formula match within 1% [6].

Results

We will first present a case (case A) where the LFA clearly applies, then a second case where curvature effects are evidenced (case B), and last a case where unsteady effects appear (case C). Finally, a case

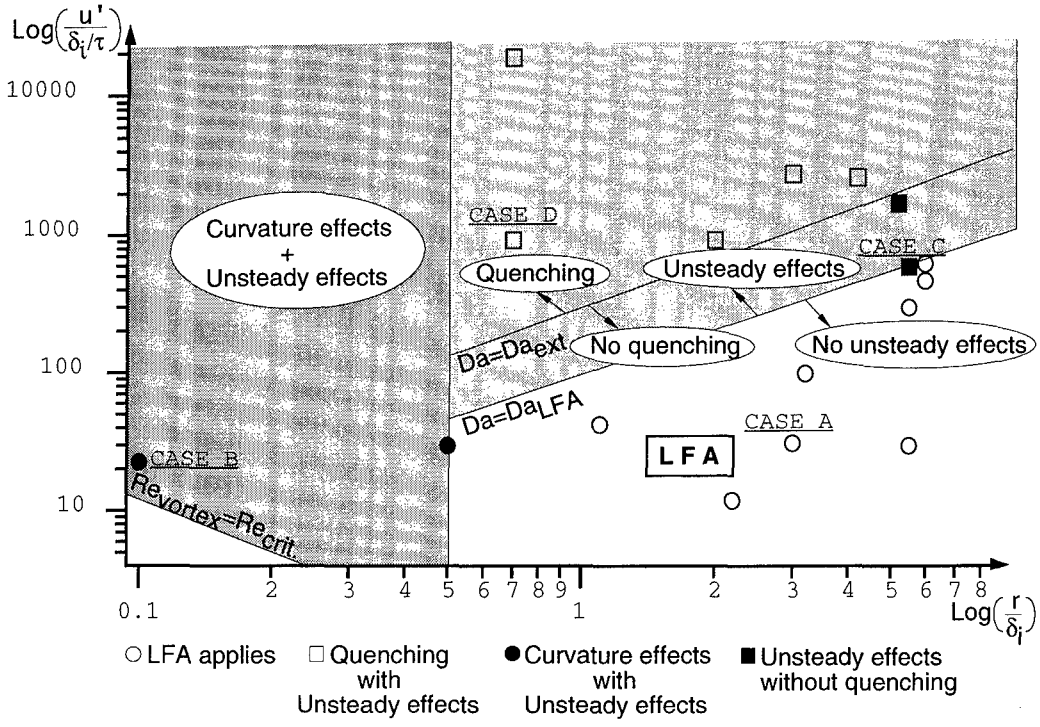

FIG. 6. Spectral combustion diagram for diffusion flames.

where quenching occurs is shown (case D). For each case we will locate corresponding conditions in the spectral diagram of Fig. 2. Parameters that are fixed for the simulation are the following: $\nu_F = 2$, $\nu_O = 1$, $\Phi = 8$, $z_f = 0.778$, $(T_{\text{act}})/(Q/C_p) = 0.9$, $Da_{\text{ext}} = 5.089 \times 10^{-3}$, $Q/C_p = 6000$ K, $Re = 10^4$, $Pr = 0.75$, $(T_0)/(Q/C_p) = 0.05$, $(T_{ad})/(Q/C_p) = 0.161$. To give an estimate of the different critical values of the Damköhler number, other calculations are represented in Fig. 2 for each combustion regime.

Case A: a Situation Where the LFA Applies:

The values of the corresponding coordinates in the spectral diagram and the Damköhler numbers are given in Table 1. They indicate that we are far from quenching. After a short transition phase, we see in Fig. 7 a very good agreement between the numerical values and the one-dimensional laminar flamelet value, as given by asymptotic analysis. We use ∇z_f to measure the hydrodynamic excitation of the flame (for a planar flame, ∇z_f is proportional to flame strain). When far from extinction, the total reaction rate increases with ∇z_f, while the maximal temperature decreases. Both flame temperature and total reaction rate are correctly predicted using only the value of the scalar dissipation at the flame and the library. We do not see any curvature effects, nor any unsteady effects, and conclude that $(r/\delta_i)_{\text{crit}} < 3$ and $Da_{\text{LFA}} < 0.1$.

Case B: Effects of Curvature:

We are here in a type B configuration, leading to a strong curvature of the flame front. Curvature effects appear clearly in Fig. 8: lateral diffusion becomes large enough to make the temperature drop below the LFA value, and the total reaction rate increases as a consequence. Therefore, we can say that $(r/\delta_i)_{\text{crit}} > 0.1$. A limit point gives $(r/\delta_i)_{\text{crit}} \simeq 0.5$.

Curvature effects were never obtained in a type A configuration. When reducing r, and to avoid vanishing of the vortex pair due to a too small Reynolds number, we had to increase u' so much that unsteady effects appeared, completely hiding possible curvature effects.

Case C: Effects of Unsteadiness:

As indicated by the values of the Damköhler numbers in Table 1, this vortex has a high rotation speed but is still far from extinction conditions. The results are shown in Fig. 9. Unsteadiness leads to a maximal temperature that is greater than the predicted value, whereas the total reaction rate is smaller. The temporal evolution of the flame lags the temporal evo-

TABLE 1
Characteristics of the different test cases

Case	Comment	$\frac{u'}{\delta_i/\tau}$	r/δ_i	Da_i	Da
A	LFA applies	32.375	3.158	2.051	9.75×10^{-2}
B	curvature effects	23.564	0.1	2.051	0.134
C	unsteady effects	623.9	5.789	0.102	9.28×10^{-3}
D	extinction	4760	1.76	0.110	3.70×10^{-4}

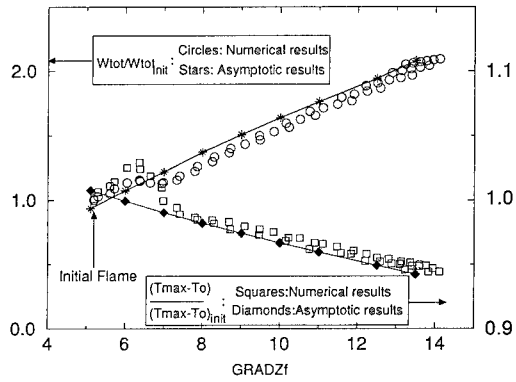

FIG. 7. Nondimensionalized total reaction rate $\dot{\omega}^+_{\text{tot}} = (\dot{\omega}_{\text{tot}})/(\dot{\omega}_{\text{tot}})_{\text{init}}$ and nondimensionalized maximal temperature $T^+_{\max} = (T_{\max} - T_0)/(T_{\max} - T_0)_{\text{init}}$ vs $\nabla z_f^+ = L\nabla z_f$ for case A.

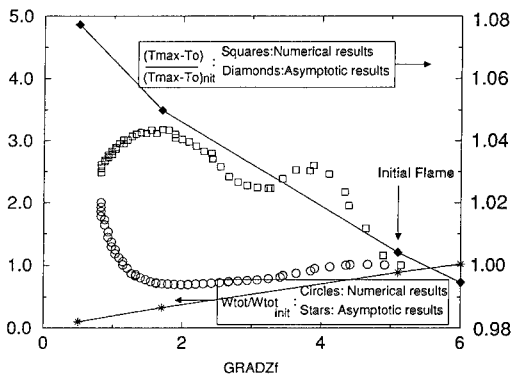

FIG. 8. Nondimensionalized total reaction rate and nondimensionalized maximal temperature vs ∇z_f^+ for case B.

lution of the flow, and an oscillatory regime is installed, due to the trials of the flame to adjust. We do not observe any curvature effect here, as in case A. Therefore, $Da_{\text{LFA}} > 9.28 \times 10^{-3}$. Other points on the diagram lead to $Da_{\text{LFA}} \simeq 9.5 \times 10^{-3}$.

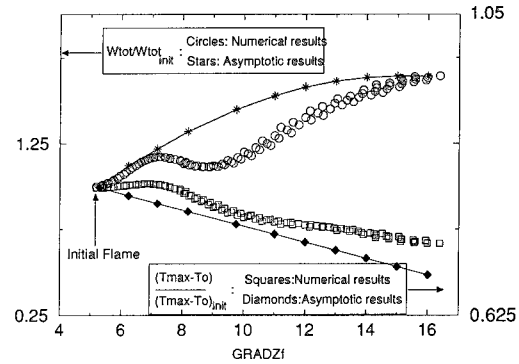

FIG. 9. Nondimensionalized total reaction rate and nondimensionalized maximal temperature vs ∇z_f^+ for case C.

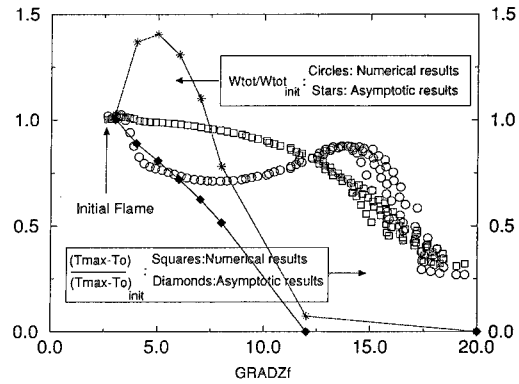

FIG. 10. Nondimensionalized total reaction rate and nondimensionalized maximal temperature vs ∇z_f^+ for case D.

Case D: Quenching Conditions:

In this last case (Fig. 10), we show a quenching of the flame due to a strong strain rate. However, the strain rate at which the flame gets quenched is much larger than the prediction of the flamelet library; this is due to strong unsteady effects that allow the flame to burn beyond the laminar critical Damköhler num-

ber Da_{ext} before quenching. Curvature effects are absent. Several calculations lead to an effective value of $Da_{ext} \simeq 2 \times 10^{-3}$, which is lower than the asymptotic value.

Conclusions

We have derived here the limits of validity of the laminar flamelet assumption in a flame-vortex interaction configuration in terms of two parameters, Da and r/δ_i, that quantify the effects of unsteadiness and curvature, respectively. Numerical simulation is in good agreement with previous asymptotic analysis [6–8], and we were able to locate all test cases on a spectral diagram.

Unsteadiness effects occur when the flow time scale is too small compared to the chemical time scale: the flame does not respond rapidly enough to the fast temporal evolution of the scalar dissipation rate and loses its laminar flamelet structure; the maximal temperature becomes larger than the asymptotic value, and the total reaction rate drops below it accordingly. Curvature effects have an opposite influence on the flame response compared to that of unsteady effects: they lead to a maximal temperature decrease and an increase of the total reaction rate because of lateral diffusion. Quenching by strain has also been evidenced, and compared to the asymptotic quenching limit. Because of unsteady effects, the asymptotic value of Da_{ext} is larger than the effective one.

When the LFA applies, numerical results are in very good agreement with asymptotic results, and flamelet models certainly apply. Quantitative limits for the LFA are given in the spectral diagram.

REFERENCES

1. Peters, N., *Twenty-First Symposium (International) on Combustion*, The Combustion Institute, Pittsburgh, 1986, p. 1231.
2. Bilger, R. W., *Twenty-Second Symposium (International) on Combustion*, The Combustion Institute, Pittsburgh, 1988, pp. 475–488.
3. Montgomery, C., Kosaly, G., and Riley, J., *AIAA Thirty-First Aerospace Sciences Meeting and Exhibit*, AIAA Paper 93-0248, Reno, 1993.
4. Yamashita, H., Kushida, G., and Takeno, T., *Proc. R. Soc. London A* 431:301–314 (1990).
5. Barlow, R. S., and Chen, J. Y., *Twenty-Fourth Symposium (International) on Combustion*, The Combustion Institute, Pittsburgh, 1992, pp. 231–237.
6. Cuenot, B., and Poinsot, T., *Combust. Flame*, submitted.
7. Linan, A., *Acta Astronaut.* 1:1007 (1974).
8. Chung, S. H., and Law, C. K., *Combust. Flame* 52:59–79 (1983).
9. Dahm, W. J. A., *6th Toyota Conference on "Turbulence and Molecular Processes in Combustion,"* Shizuoka-ken, Japan, 1992.
10. Bish, E. S., and Dahm, W. J. A., *1993 Fall Meeting, Western States Section*, The Combustion Institute, Menlo Park, CA, 1993.
11. Borghi, R., J. *Chim. Phys.* 81:361–370 (1984).
12. Poinsot, T., Veynante, D., and Candel, S., *J. Fluid Mech.* 228:561–605 (1991).
13. Roberts, W. L., Driscoll, J. F., Drake, M. C., and Goss, L. P., *Combust. Flame* 94:58–69 (1993).
14. Rutland, C. J., and Ferziger, J., *27th AIAA Aerospace Sciences Meeting*, AIAA Paper 89-0127, Reno, 1989.
15. Poinsot, T., and Lele, S., *J. Comput. Phys.* 101:104–129 (1992).

COMMENTS

V. R. Katta, Systems Research Laboratories, USA. You implemented the finite-rate chemistry effects into the calculations by using a single-step global mechanism. As a consequence, all your results depend on the pre-exponential and activation energy you considered for the reaction rate. For example, if you choose a very high pre-exponential value then all the Damköhler-number effects you indicated will disappear. I feel your results are exaggerating the problems one might see with the laminar-flamelet theory. Do you expect similar results if you use a full-chemistry model?

Author's Reply. It is doubtful that complex chemistry situations may be understood if one does not understand first simple chemistry cases. Asymptotic analysis together with simple chemistry simulations provides unique tools to understand flame-vortex interactions. Actually, asymptotic analysis as used here shows clearly that pre-exponential constant and activation energy values do not play any role in the results. Only reduced numbers (like the Damköhler) are important. There is no doubt that effects described here will appear if the corresponding reduced parameters are reached. Even in the present symposium, experimental evidence of these effects (see paper by Rolon, Aguerre, and Candel) is provided: Quenching will occur if the strain rate is large enough. The value at which this quenching will occur will be different from the flamelet library prediction because unsteady effects will be important. That does not mean that the flamelet approach is not valid. It is valid in a certain range, and we provide limits for this range in our work.

S. Shy, National Central University, Taiwan, R.O.C. The Reynolds number near the flame interaction region was not a constant. What is the effect of R_e on the domain of the laminar flamelet assumption in a length-velocity-scales spectral diagram you presented?

Author's Reply. The only relevant Reynolds number in a flame-vortex interaction is the vortex Reynolds number. This number changes for each point of the diagram as size and velocity are changed.

Twenty-Fifth Symposium (International) on Combustion/The Combustion Institute, 1994/pp. 1391–1398

ON ADIABATIC STABILIZATION AND GEOMETRY OF BUNSEN FLAMES

C. J. SUN, C. J. SUNG AND C. K. LAW
Department of Mechanical and Aerospace Engineering
Princeton University
Princeton, NJ 08544, USA

Two aspects of stretched flame dynamics are investigated via the model problem of the stabilization and geometry of Bunsen flames. Specifically, the possibility of stabilizing a Bunsen flame without heat loss to the burner rim is experimentally investigated by examining the temperature of the rim, the temperature gradient between the rim and the flame base, and the standoff distance of the flame base in relation to the flame thickness. Results show that, while heat loss is still the dominant stabilization mechanism for flames in uniform flows and for strong flames in parabolic flows, adiabatic stabilization and, subsequently, blowoff are indeed possible for weak flames in parabolic flows. The adiabatically stabilized flame is then modeled by using the scalar field formulation and by allowing for the effects of curvature and aerodynamic straining on the local flame speed. The calculated flame configuration agrees well with the experiment for the adiabatically stabilized flame but not for the nonadiabatic flame. Results further show that active modification of the flame curvature is the dominant cause for the flame to maintain adiabatic stabilization. Implications of the present results on turbulent flame modeling are discussed.

Introduction

Recent studies on flame dynamics have led to significant advances in the understanding of flame stretch and its influence on the structure and propagation of laminar flames. Consequently, some of the well-established concepts in flame phenomena have been revised and reinterpreted. One of these is the mechanism through which a Bunsen flame is stabilized over the burner rim.

Conventionally, heat loss is believed to be the stabilization mechanism through which the flame can adjust its local speed to dynamically balance the local flow velocity [1]. However, earlier [2] as well as recent studies [3] have shown that, in addition to heat loss, the flame speed can also be modified by the preferential diffusion of heat and mass as well as flame stretch, which is manifested by flame curvature, flow nonuniformity, and flame motion. Recognizing the potential significance of these additional stabilization mechanisms, Sung et al. [4] recently demonstrated that there indeed exist situations under which flame stabilization can be accomplished without heat loss. Specifically, it was experimentally shown for inverted flames that the flame could be lifted, and still stabilized, sufficiently away from the stabilization rod such that heat loss to the rod became negligible. Theoretically, it was also shown that this adiabatic stabilization was achieved through modification of the flame speed by flame curvature and flow straining. These results on the adiabatic stabilization of inverted flames [4] were further experimentally confirmed by Nomura et al. [5].

The first objective of the present study is to extend the concept of adiabatic flame stabilization, demonstrated for inverted flames, to the more practical situation of the Bunsen flame. Contrary to the axisymmetric inverted flame studied previously [4,5], the base of the Bunsen flame experiences strong concentration asymmetry due to the presence of the ambient gas, and it is not clear a priori whether adiabatic stabilization can still be achieved. Furthermore, we shall also study effects of the mixture strength and flow nonuniformity on stabilization. For the former, we shall scan through the fuel/air equivalence ratio, from lean to rich, and identify the influence of the burning intensity and hence the laminar flame speed on stabilization. For the latter, we shall experiment with both the parabolic and uniform flows, and assess the relative ease with which adiabatic stabilization can be achieved in these flows.

To discuss our second objective, we first recognize that the bulk configuration of the Bunsen flame is expected to be sensitively affected by the configuration of the flame base at the rim because, allowing for the symmetry boundary condition at the flame tip, the flame base provides the second boundary condition for the entire flame. Since the configuration of the flame base is in turn intimately affected by the extent of heat loss to the rim, we would then expect that the entire flame configuration should be influenced by heat loss. Consequently, when this heat loss is eliminated or minimized for an adiabatically stabilized flame, and since the unavoidable downstream heat loss is expected to be of only secondary importance for the flame response sufficiently away

from the extinction state, the entire flame can be considered to be nearly adiabatic. Thus, the second objective of our study is to employ the adiabatically stabilized flame as a prototypical curved and strained flame, and attempt to describe the experimentally determined flame surface configuration through the scalar field formulation [6]. Because of the nonuniform flow field and the fairly complex variation of the flame curvature over the surface of a Bunsen flame, a comparison of the present nature provides a fairly stringent test of the adequacy of the scalar field formulation and the associated description of the dynamics of stretched flames. It is to be noted that such a description is also of relevance to the modeling of turbulent flames through the concept of stretched laminar flamelets [7–9]. Since the effect of turbulence on the laminar flamelets is to wrinkle their surfaces and modify the local burning velocity, it is important to properly describe the flame surface geometry and stretch-affected responses such that the mean turbulent reaction rate can be calculated.

The experimental specifications are given in the next section, which is followed by presentation of the experimental results on flame stabilization. We shall then discuss the scalar field formulation and the flow field description for the present problem, and the comparison between the experimental and calculated flame configurations.

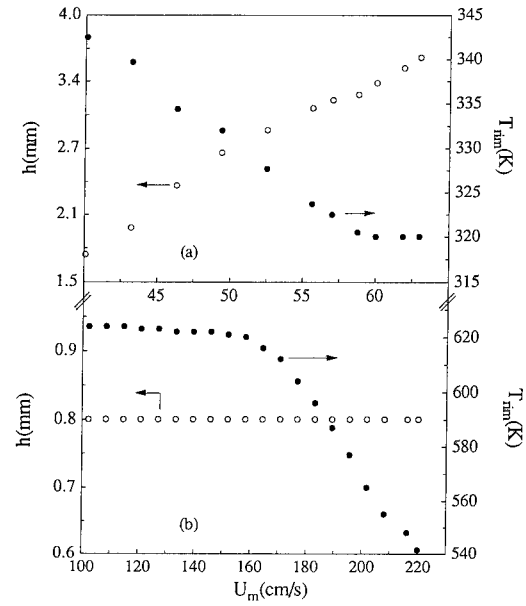

FIG. 1. Standoff distance and burner rim temperature as functions of mean exit velocity for methane/air flame in parabolic flow field: (a) $\phi = 1.33$, (b) $\phi = 1.05$.

Experimental Specifications

Bunsen flames produced by both parabolic and uniform flows were studied. The parabolic flow was generated by a tube burner with 14.5-mm diameter, 0.25-mm tube thickness, and 120-cm length to ensure a fully developed flow. The uniform flow was generated by a contoured nozzle with 13-mm diameter and 0.4-mm wall thickness. The combustible mixture was surrounded by a nitrogen shroud flow. The flow velocity was measured by an Argon-ion LDV system, with 0.3-μm alumina particles and a 0.1-mm-diameter $\times$ 1.0-mm-length measurement volume. The flame shape was recorded by a charge-coupled device (CCD) camera supported by an image-processing system.

Since heat loss to the burner rim is key to the present investigation, the extent of heat loss was determined with two means. Quantitatively, the temperature at the surface of the burner rim was measured by a 0.003-in.-diameter thermocouple. Qualitatively, shearing interferometry [10] was used to examine the temperature gradient, and hence the presence of heat flux, between the flame base and the burner rim. By adjusting the etalon orientation, the setup was arranged such that the fringe shift was caused by the temperature difference between two spatial points that were separated by 0.64 mm normal to the burner. Sensitivity to the temperature difference was 9.75 K.

Results on Flame Stabilization

An extensive number of experiments have been performed as a part of this research program for both methane/air and propane/air flames, although only results on methane/air flames will be presented because of space limitation. Suffice it to note that results on propane/air flames are qualitatively similar to those of the methane/air flames to be reported in the following.

Figure 1a shows a typical behavior of the flame base standoff distance h and the rim temperature T_{rim} as functions of the mean exit velocity U_m, for a rich methane/air flame with equivalence ratio of 1.33. To eliminate transients caused by varying flow velocity, temperature measurement data are taken when the system is in steady state. It is seen that, with increasing U_m, h increases while T_{rim} decreases. However, before the flame is blown off at the state immediately beyond the last data point, there exists a flat regime for T_{rim} at which T_{rim} is about 320 K. The results that T_{rim} is only slightly above the ambient temperature and that it does not further decrease with increasing h strongly suggest that the flame is adiabatically stabilized in this regime. It is also reasonable to expect that, in the absence of con-

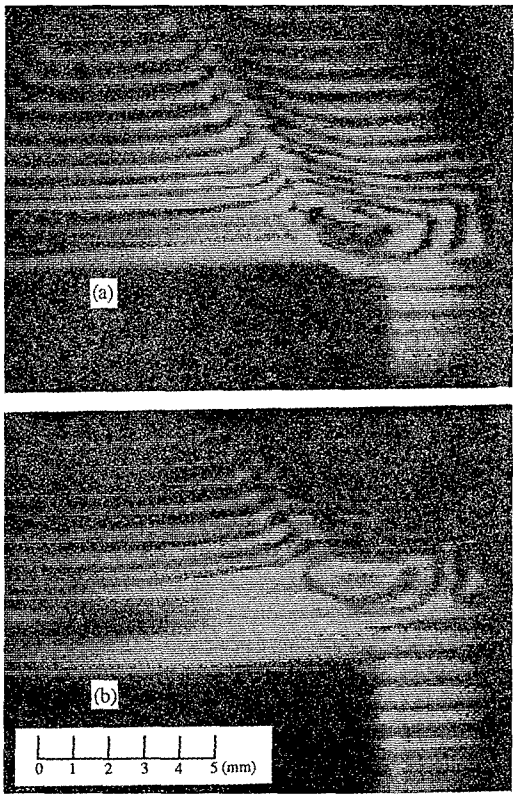

FIG. 2. Interferometer fringe for methane/air flame in parabolic flow field (ϕ = 1.33): (a) U_m = 46.3 cm/s, (b) U_m = 58.8 cm/s.

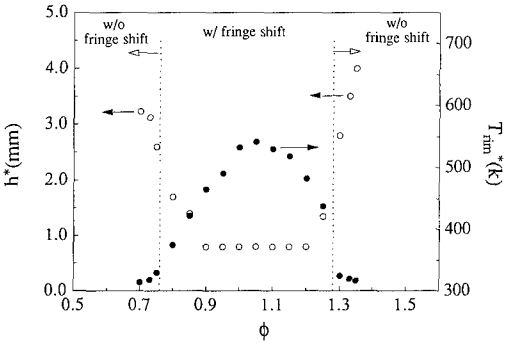

FIG. 3. Standoff distance and burner rim temperature at the state of blowoff as functions of equivalence ratio for methane/air flame in parabolic flow field.

ductive heat transfer, radiative transfer from the flame can contribute to the 20 K increase in the rim temperature from the ambient temperature of about 300 K. Since radiative heat transfer is a long-range process, it is not coupled to the flame stabilization mechanism. The final point to note is that, at blowoff, the flame standoff distance is greater than 3.5 mm, which is well in excess of the flame thickness.

To further demonstrate the absence of conductive heat transfer, the possible existence of a temperature gradient between the flame base and the burner rim was investigated by using shearing interferometry. Figure 2 shows the fringe shift for two values of U_m. It is seen that, when U_m is 46.3 cm/s (Fig. 2a), with the corresponding T_{rim} and h being, respectively, 343 K and 1.7 mm, severe fringe shift is observed, indicating the presence of a temperature gradient. On the other hand, when U_m is 58.8 cm/s (Fig. 2b), the corresponding T_{rim} and h are 320 K and 3.5 mm, and there is no fringe shift near the burner rim. Since the detection sensitivity of temperature gradients for the present interferometer setup is 15 K/mm, and if we use the thermal conductivity of air at 350 K, 3×10^{-4} W/cm-K, as a representative thermal conductivity for the gas between the flame base and the rim, then the maximum conductive heat flux from the flame base to the burner rim can be estimated to be about 0.045 W/cm^2. This is much smaller than the chemical heat flux, 81 W/cm^2, generated by the flame [4,11]. It is therefore reasonable to suggest that the absence of fringe shifts indicates the corresponding absence of significant heat transfer.

Adiabatic flame stabilization and blowoff, however, do not always occur, especially for the strongly burning flames. For these flames, the propagation velocity is so high that they cannot be substantially reduced by stretch. Consequently, the flame will propagate toward the burner rim and eventually become stabilized through heat loss at a distance which is of the order of the flame thickness. This is demonstrated in Fig. 1b for a near-stoichiometric methane/air flame, with ϕ = 1.05. It is seen that, with increasing U_m, while h remains close to the rim at an almost constant distance of about 0.8 mm, T_{rim} first remains almost constant and then decreases rapidly because of the strong convection. The important point to note is that T_{rim} remains at a high value (~540 K) at blowoff. These results, together with those from shearing interferometry, clearly indicate the presence of conductive heat loss and demonstrate that it is the dominant stabilization mechanism.

Figure 3 summarizes the results on T_{rim} and h at blowoff as functions of ϕ for methane/air flame in the parabolic flow, with the superscript * indicating the state of blowoff. The results show that there are basically two kinds of stabilization behavior. For weaker flames with $\phi < 0.76$ and $\phi > 1.28$, adiabatic stabilization is possible, for which the flame standoff distance at blowoff is far from the rim in terms of the flame thickness while the rim temperature is also close to the ambient value. For strong flames with $0.9 < \phi < 1.2$, heat loss is the dominant stabilization mechanism, with the flame standoff distance at blow-

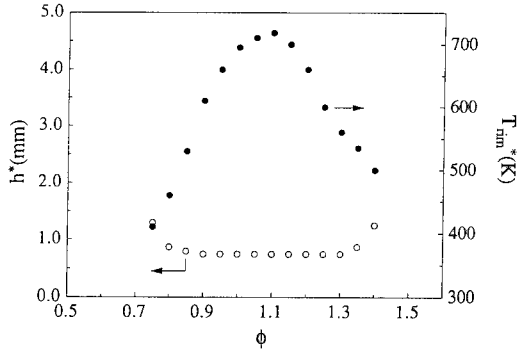

FIG. 4. Standoff distance and burner rim temperature at the state of blowoff as functions of equivalence ratio for methane/air flame in uniform flow field.

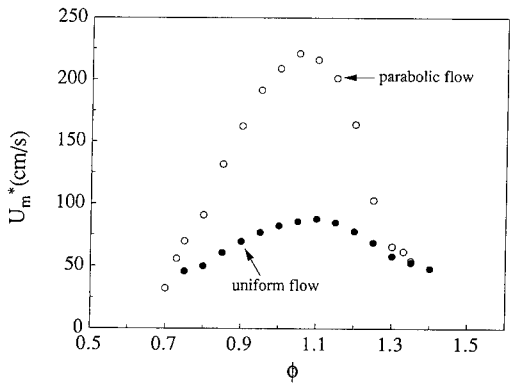

FIG. 5. Mean exit velocity at the state of blowoff as a function of equivalence ratio for methane/air flame in parabolic and uniform flow fields.

off being the same magnitude as the flame thickness and the rim temperature being much higher than the ambient value. Transition from the two modes of stabilization occurs in the intermediate regimes of ϕ.

Heat loss, however, is much stronger for flames situated in the uniform flow. Figure 4 shows that h^* is always very small and that T^*_{rim} is still higher than 400 K, even for the weakest flames that can be stabilized. The results therefore imply that adiabatic stabilization in a uniform flow is not favored.

Figure 5 compares the mean exit velocity at blowoff, U^*_m, for the parabolic and uniform flows. Since a higher U^*_m indicates a stronger stabilization tendency, the results show that stabilization is maximized around the same range of ϕ (1.05–1.1) at which the flame speed is maximized, as is reasonable to expect. Furthermore, it is seen that the parabolic flow has a greater tendency for stabilization than the uniform flow. This is due to the very steep velocity gradient in the radial direction generated in the mixing layer between the uniform flow and the ambient gas [1].

Formulation and Results on Flame Geometry

Having identified regimes in which the flame is adiabatically stabilized, the configurations of these flames have also been determined photographically. Since the flames are very thin as compared to the overall dimension of the flame, such a determination is appropriate and accurate. To obtain a corresponding theoretical description of the flame geometry, we need to specify the dynamics of the flame surface in a flow field, the flow field itself, and the propagation velocity of the stretched flame. These are discussed in the following.

When the thickness of a flame is small compared to the hydrodynamic length scale, the flame can be treated as a surface propagating in the hydrodynamic flow, and its shape can be described by the so-called G equation through the scalar field formulation [6]

$$\frac{\partial G}{\partial t} + \mathbf{v}|_{G=0^-} \cdot \nabla G = s_u |\nabla G| \tag{1}$$

where $\mathbf{v}|_{G=0^-}$ is the flow velocity along the flame front and $G(\mathbf{r},t)$ the scalar field whose zero-value surface represents the flame front, with 0^- designating the unburnt side of the flame. It is noted that the hydrodynamic flow convects the flame front, while the flame front affects the hydrodynamic flow through thermal expansion. Since, for the present flame, the burnt gas is convected into an open atmosphere, we shall assume that the influence of thermal expansion on the upstream flow field is small such that the flame is simply a passive surface convected by an incompressible flow of given $\mathbf{v}$ such that $\mathbf{v}|_{G=0^-}$ can be solved separately. We note that, while previous studies [12] involving strongly burning Bunsen flames ($\phi = 1.1$) have shown deviation of the flow velocity from the cold flow value sufficiently upstream of the flame, the present adiabatically stabilized flames are much weaker, implying that thermal expansion effects are correspondingly weaker.

Further recognizing that the flow is of the boundary-layer type because its radial velocity is expected to be much smaller than its axial velocity, the nondimensional continuity and axial-momentum equations are respectively given by

$$\frac{\partial \tilde{u}}{\partial \tilde{r}} + \frac{\partial \tilde{v}}{\partial \tilde{z}} + \frac{\tilde{u}}{\tilde{r}} = 0 \tag{2}$$

$$\tilde{u}\frac{\partial \tilde{v}}{\partial \tilde{r}} + \tilde{v}\frac{\partial \tilde{v}}{\partial \tilde{z}} = \frac{1}{Re}\left(\frac{\partial^2 \tilde{v}}{\partial \tilde{r}^2} + \frac{1}{\tilde{r}}\frac{\partial \tilde{v}}{\partial \tilde{r}}\right) \tag{3}$$

where $\tilde{u}$ is the radial velocity, $\tilde{v}$ the axial velocity, $\tilde{r}$

the radial coordinate, $\tilde{z}$ the axial coordinate, and Re the Reynolds number based on the burner radius r_0. Furthermore, the spatial coordinates are nondimensionalized by r_0, and the velocities by U_m. The boundary conditions for the tube burner are $\tilde{v} = 2(1 - \tilde{r}^2$ and $\tilde{u} = 0$ at $\tilde{z} = 0$.

A fully implicit scheme is adopted to numerically solve these boundary-layer–type equations. Figure 6 shows typical calculated axial velocity profiles at several axial distances. To further ascertain the validity of the boundary-layer approximation and the accuracy of the calculation, the computed results have been further compared with those obtained from solving the full Navier–Stokes equation [13] and from laser Doppler velocimeter (LDV) measurements. Figure 6 shows close agreement between these three independent means of determining the velocity profile, and hence demonstrates the adequacy of the boundary-layer assumption in the present formulation. It is noted that, at $\tilde{z} = 2.41$, which is roughly the flame tip location, $\tilde{v}(\tilde{r} = 0)$ has only decayed about 2% of its exit value, from 2 to 1.96.

In order to solve the G equation, the weak-stretch flame speed expressions of Chung and Law [14] and Matalon and Matkowsky [15] were used in the calculations and comparisons. Specifically, Chung and Law [14] give

$$\frac{s_u}{s_u^\circ} = 1 + \delta_T^\circ\left[\nabla\cdot\mathbf{n} + \frac{1}{2\varepsilon}\left(\frac{1}{Le} - 1\right)\frac{\kappa}{s_u^\circ}\right] \quad (4)$$

where s_u° is the adiabatic laminar flame speed, δ_T° the corresponding preheat zone thickness, $\mathbf{n}$ the local normal of the flame surface pointing toward the burned mixture, $\varepsilon = (E_a/RT_{\mathrm{ad}})^{-1}$, E_a the activation energy, R the universal gas constant, T_{ad} the adiabatic flame temperature, Le the Lewis number, and κ the stretch rate defined as

$$\kappa = -\mathbf{n}\cdot\nabla \times (\mathbf{v}|_{G=0^-} \times \mathbf{n}) + (\mathbf{V}\cdot\mathbf{n})(\nabla\cdot\mathbf{n}) \quad (5)$$

where $\mathbf{V}$ is the local flame front velocity.

The expression of Matalon and Matkowsky [15] is given by

$$s_u = s_u^\circ\left[1 - a\delta_T^\circ\frac{\kappa}{s_u^\circ}\right] \quad (6)$$

where

$$a = \frac{1 + \tilde{q}_c}{\tilde{q}_c}\ln(1 + \tilde{q}_c) + \frac{T_{\mathrm{ad}}}{T_{-\infty}}\frac{(Le - 1)}{2\varepsilon}\int_{-\infty}^{0}\ln(1 + \tilde{q}_c e^{\zeta})\,d\zeta, \quad (7)$$

$T_{-\infty}$ is the cold reactant temperature, and $\tilde{q}_c = (T_{\mathrm{ad}}/T_{-\infty}) - 1$.

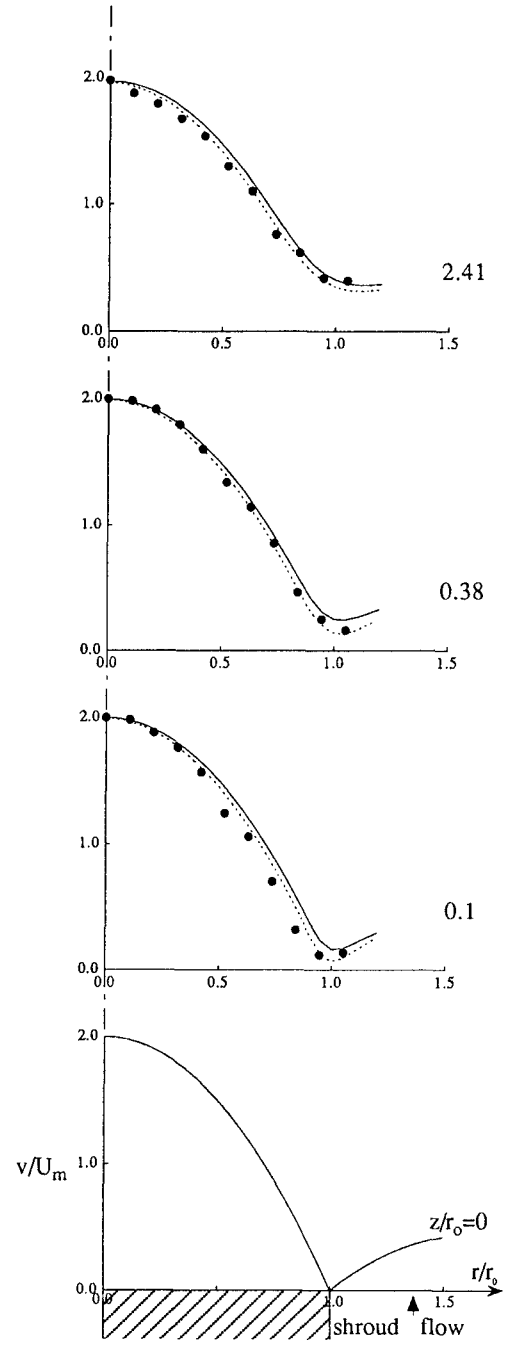

FIG. 6. Axial velocity as a function of radial coordinate at different axial locations. (●: LDV measurements; solid line: results based on boundary-layer assumption; dotted line: results based on solving full Navier–Stokes equation).

For the steady axisymmetric configuration, with $\mathbf{r} = (r,z)$, $\mathbf{v} = (u,v)$, $\mathbf{V} = 0$, and $G(\mathbf{r},t) = z - f(r)$, substituting Eq. (4) into Eq. (1) yields

$$\frac{d\tilde{g}}{d\tilde{r}} = \frac{D^2}{D + (\tilde{u}\tilde{g} - \tilde{v})(1/Le - 1)\beta/2\varepsilon} \cdot \left[\gamma\beta D(\tilde{u}\tilde{g} - \tilde{v}) + \gamma D^2 - \frac{\tilde{g}D}{\tilde{r}} + \frac{\beta}{2\varepsilon}\left(\frac{1}{Le} - 1\right)\left(\tilde{g}^2\frac{\partial\tilde{v}}{\partial\tilde{z}} + \tilde{g}\frac{\partial\tilde{u}}{\partial\tilde{z}} + \tilde{g}\frac{\partial\tilde{v}}{\partial\tilde{r}} + \frac{\partial\tilde{u}}{\partial\tilde{r}} + \frac{\tilde{v}\tilde{g}}{\tilde{r}} + \frac{\tilde{u}}{\tilde{r}}\right)\right] \quad (8)$$

while substituting Eq. (6) into Eq. (1) yields

$$\frac{d\tilde{g}}{d\tilde{r}} = \frac{\gamma}{a(D + \tilde{u}\tilde{g}\beta)}\left[D^2 - \frac{a\beta D^2}{\gamma}\left(\frac{\partial\tilde{u}}{\partial\tilde{r}} + \frac{\tilde{u}}{\tilde{r}}\right) + \beta D(\tilde{u}\tilde{g} - \tilde{v})\right] \quad (9)$$

where $\gamma = r_0/\delta_T^\circ$, $\beta = U_m/s_u^\circ$, $\tilde{g} = df/dr = d\tilde{f}/d\tilde{r}$, and $D = (1 + \tilde{g}^2)^{1/2}$. Coupling $\tilde{z} = \tilde{f}(\tilde{r})$ with either Eq. (8) or Eq. (9), with the symmetry boundary condition $\tilde{g}(\tilde{r} = 0) = 0$, and the flame height information $\tilde{f}(\tilde{r} = 0) = \tilde{f}_0$, the shape of flame front in a given hydrodynamic flow field can be readily calculated. It is to be noted that, because of the uncertainty about the proper boundary condition to be specified on the rim side of the flame, we have used the experimental value of the flame height (at $\tilde{r} = 0$) as an additional boundary condition. We further note that there are two dominant effects in the expression of flame stretch, namely flame curvature, $\tilde{\nabla}\cdot\mathbf{n}$, and the axial velocity gradient in the radial direction, $\partial\tilde{v}/\partial\tilde{r}$, which represents the flow nonuniformity. By evaluating the magnitudes of these two terms near the flame base, we have found that the curvature term has a much larger effect and hence can be considered as having the dominant role in stabilizing the adiabatic Bunsen flame.

In evaluating the above expressions, the Lewis number is taken to be the ratio of thermal diffusivity, D_u, to the controlling mass diffusivity, which is between the deficient species and the abundant inert species, N_2. The preheat zone thickness, δ_T°, is defined as D_u/s_u° according to the definitions [14,15]. The overall activation energy, E_a, is determined from fitting the numerically calculated laminar flame speeds with detailed transport and chemistry [16].

Figure 7 compares the experimental flame configurations with the calculated one by using both flame speed expressions for the adiabatically and nonadiabatically stabilized flames with $\phi = 1.33$. The various thermochemical parameters used are as follows: $Le = 1.1$, $D_u = 0.224$ cm²/s, $s_u^\circ = 28.5$ cm/s, $E_a =$ 71.3 kcal/gmol-K, and $a = 2.638$. Figure 7a shows the comparison for the adiabatic flame, with $U_m =$ 58.8 cm/s. It is seen that both stretched flame speed expressions qualitatively reproduce the overall trend of the flame configuration, especially in capturing the curvature reversal behavior. This demonstrates the importance of properly accounting for stretch effects in the flame speed expression. Figure 7a further shows that the expression of Ref. 14 seems to provide a closer quantitative fit with the experimental data. In this regard, we note that, in studies of the curvature of the Bunsen flame tip, it has been suggested [17,18] that the expression of Ref. 15 would agree more closely with their experimental data if a larger value for the flame thickness were used. We have found that this also holds for the present comparison. However, since the flame thickness is defined through the flame speed and the thermal diffusivity, and since the flame speed is already a given quantity and thermal diffusivity (D_u) a well-defined quantity, we have chosen not to additionally specify/modify the flame thickness.

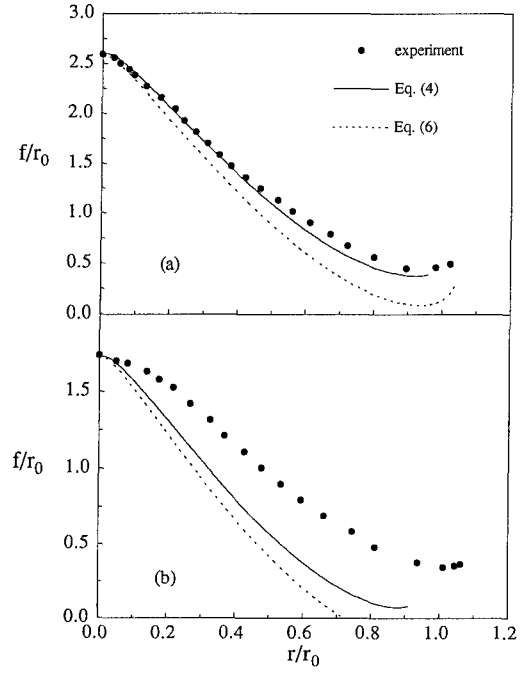

FIG. 7. Computed and experimental flame shape as a function of radial coordinate for methane/air flame ($\phi =$ 1.33) in parabolic flow field: (a) $U_m = 58.8$ cm/s, (b) $U_m =$ 46.3 cm/s.

Figure 7b compares the calculated and experimental configurations for the situation of $\phi = 1.33$ and $U_m = 46.3$ cm/s, for which heat loss is clearly present. It is seen that the calculated flame profile,

which assumes flame adiabaticity, significantly underpredicts the experimental profile such that the experimental flame base is much higher than the calculated value. This is physically reasonable because, with the flame base suffering heat loss, its flame speed is reduced, and it will be blown to a higher position such that heat loss is reduced and dynamic balance can again be achieved.

We close this section by noting that the weak-stretch, linearized flame speed expressions used may require revisions for large stretch rates. The present calculations have shown, however, that the Karlovitz number, defined as $Ka = \kappa\delta_T^\circ/s_u^\circ$, is much smaller than unity over most of the flame shoulder. The stretch correction does become large around the flame tip, although an independent assessment using a nonlinear expression for the stretched flame speed [19] shows that its magnitude is similar to that obtained with the linearized expression. Finally, the linearized solution does break down on the ambient side of the base, where the flow velocity is much smaller than the laminar flame speed such that exceptionally large flame curvatures are needed to slow down the flame. The calculations were thus terminated around the boundary with the ambient.

Concluding Remarks

In the present investigation, we have successfully demonstrated that, for sufficiently weak Bunsen flames in the parabolic flow field, the flame can be lifted above the burner rim to a distance substantially higher than the characteristic flame thickness such that heat loss to the burner rim is negligible and stabilization is achieved through modification of the flame speed by flame curvature and flow straining. However, for Bunsen flames in uniform flows and strong Bunsen flames in parabolic flows, the dominant stabilization mechanism is still heat loss to the burner rim. Since the conventional concept of flame stabilization through heat loss to the rim would lead to flame blowoff when the flame speed over the flame base has been elevated to the laminar flame speed, the potential of extending the blowoff limits through adiabatic flame stabilization is of practical interest. Furthermore, since adiabatic flame stabilization is achieved through flame stretch effects, which in turn depend on aerodynamic straining, flame curvature, and mixture nonequidiffusion, the possibility of manipulating these processes and factors for enhanced stabilization through modifications of the rim configuration, rim processes, and mixture properties is significantly enriched.

Regarding the study on flame geometry, considering the nonuniform nature of the flow and the nonmonotonic variation of the flame curvature, the reasonable agreement between the calculated and measured flame configurations is encouraging. It indicates the potential utility of the scalar field formulation and the stretched flame expressions for the description of wrinkled flame dynamics in nonuniform flows, especially in turbulent flows. As far as calculation of the Bunsen flame configuration is concerned, it may be noted that the present calculation requires input of the experimental flame height as a boundary condition. So far, an appropriate boundary condition to use on the rim side of the flame has not been identified. Further study on this issue is needed toward the formulation of a totally predictive theory for the stabilization and blowoff of adiabatic Bunsen flames.

Acknowledgments

This research was supported by the Office of Basic Energy Sciences of the U.S. Department of Energy. We thank Professor R. H. Yen of the National Taiwan University for providing the Navier–Stokes solution for our flow field.

REFERENCES

1. Lewis, B., and von Elbe, G., *Combustion, Flames and Explosions of Gases*, Academic Press, Orlando, 1987.
2. Markstein, G., *Nonsteady Flame Propagation*, MacMillan, New York, 1964.
3. Law, C. K., *Twenty-Second Symposium (International) on Combustion*, The Combustion Institute, Pittsburgh, 1988, pp. 1381–1402.
4. Sung, C. J., Law, C. K., and Umemura, A., *Twenty-Fourth Symposium (International) on Combustion*, The Combustion Institute, Pittsburgh, 1992, pp. 205–212.
5. Nomura, A., Ishizuka, S., and Hirano, T., *Thirtieth Symposium (Japan) on Combustion*, The Combustion Institute, Nagoya, Japan, 1992, pp. 109–111 (in Japanese).
6. Kerstein, A. R, Ashurst, Wm. T., and Williams, F. A., *Phys. Rev. A* 37:2728–2730 (1988).
7. Peters, N., *Twenty-First Symposium (International) on Combustion*, The Combustion Institute, Pittsburgh, 1986, pp. 1231–1250.
8. Bradley, D., *Twenty-Fourth Symposium (International) on Combustion*, The Combustion Institute, Pittsburgh, 1992, pp. 247–262.
9. Shepherd, I. G., and Ashurst, Wm. T., *Twenty-Fourth Symposium (International) on Combustion*, The Combustion Institute, Pittsburgh, 1992, pp. 485–491.
10. Massie, N. A., *Interferometric Metrology*, SPIE Vol. 816, 1987.
11. Egolfopoulos, F. N., Zhu, D. L., and Law, C. K., *Twenty-Third Symposium (International) on Combustion*, The Combustion Institute, Pittsburgh, 1990, pp. 471–478.
12. Wagner, T. C., and Ferguson, C. R., *Combust. Flame* 56:267–272 (1985).

13. Yen, R. H., personal communication.
14. Chung, S. H., and Law, C. K., *Combust. Flame* 72:325–336 (1988).
15. Matalon, M., and Matkowsky, B. J., *J. Fluid Mech.* 124:239–259 (1982).
16. Egolfopoulos, F. N., and Law, C. K., *Combust. Flame* 80:7–16 (1990).
17. Poinsot, T., Echekki, T., and Mungal, M. G., *Combust. Sci. Technol.* 81:45–73 (1992).
18. Echekki, T., and Mungal, M. G., *Twenty-Third Symposium (International) on Combustion*, The Combustion Institute, Pittsburgh, 1990, pp. 455–461.
19. Chung, S. H., and Law, C. K., *Combust. Flame* 75:309–323 (1989).

Twenty-Fifth Symposium (International) on Combustion/The Combustion Institute, 1994/pp. 1399–1406

EFFECTS OF ROTATION ON THE STABILITY AND STRUCTURE OF TUBULAR FLAME

KAZUHIRO YAMAMOTO, SATORU ISHIZUKA AND TOSHISUKE HIRANO
Department of Chemical System Engineering
Faculty of Engineering
The University of Tokyo
7-3-1 Hongo, Bunkyo-ku, Tokyo 113, Japan

The effect of rotation on the stability and structure of a tubular flame has been experimentally investigated. The concentration field of OH radical has been measured by laser-induced fluorescence, and the temperature field was examined using a fine thermocouple. Results show that, with increasing intensity of rotation, the lean limit of methane flame is decreased, and the stable flame region is expanded. The flame diameter is increased, and the inner flame structure is also changed. Namely, when the rotation is weak, the radial OH distribution takes an M-shaped profile; the concentration is low in the outer region of the unburned gas, increases and takes a local maximum value in the reaction zone, then falls around the center. With decreasing the fuel concentration Ω, the peak positions approach and the profile becomes Π-shaped. With further decreasing Ω, the profile becomes Λ-shaped; eventually, the flame is extinguished. Correspondingly, the peak value is decreased, increased, and decreased with decreasing Ω. However, when the rotation is intensified, the variation of the peak value becomes moderate, and the M-shaped profile is maintained close to extinction. The temperature measurement shows that, with increasing intensity of rotation, a temperature dip appears around the center and its magnitude becomes larger. Although this dip is usually attributed to radiative heat loss, the temperature at the center remains unchanged while the reaction zone temperature is increased; i.e., a protrusion in the reaction zone temperature occurs. This aspect resembles the excess enthalpy flame. Although the details of the extension mechanisms are unclear, these results suggest that the stability of the flame is enhanced by rotation through a mechanism like the excess enthalpy flame.

Introduction

In regard to modeling turbulent combustion in the flamelet regime, the characteristics of elementary flames have been extensively studied. In these studies, there are two important fluid-dynamical factors that influence the flame characteristics. One is stretch and the other is rotation.

Concerning the stretched flames, numerous studies have been made. By using a twin flame established in a counterflow field [1–3], or a tubular flame in an axisymmetric flow field [4], extinction limits and separation distances have been determined. One of the new findings is the Lewis number effect, which is now well known and well understood [1–5].

As for rotation, the flame development in a vortex flow has been numerically simulated [6–9], and the characteristics of the twin flame and the tubular flame around the axis of symmetry have been investigated [4,5,10–12]. However, in the case of the tubular flame, little attention is invested in the effect of rotation on the flame structure [13–15] because it has been found that the rotational flow field is uncoupled from the radial and azimuthal flow fields and does not affect the flame structure [13,14].

However, in studies on plasma jet igniters, the flame stability is enhanced because the radical is encapsulated near the center of the vortex [16]. Also, the radicals play an important role in the vortex-flame interaction [17,18]. The flammable range in a rotating flow field is shifted as a result of nonunity Lewis number and expanded [19]. Hence, the study on the effect of rotation is inadequate in the fundamental field of combustion.

In this study, the effect of rotation on the stability and structure of premixed flame has been investigated. The distribution of OH has been measured with laser-induced fluorescence (LIF) because of its well-known spectroscopic structure [20] and important role in combustion.

Experimental

Figure 1 shows the swirl-type burner used in this study. A combustible mixture is tangentially ejected into a glass (quartz) tube and exits from both ends of the burner; hence, a rotating, stretched flow field is established [4]. The rotational velocity profile is analogous to Rankine's combined vortex, while the radial

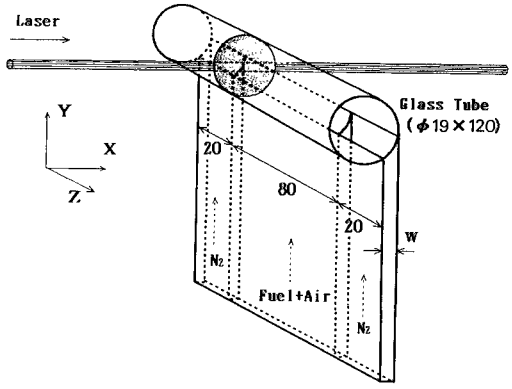

FIG. 1. Experimental setup.

and axial velocity profiles are analogous to those in an axisymmetric stagnation-point flow. The details of the flow field can be found in Ref. 5.

In order to obtain different intensities of rotation, we used three burners of different slit widths (W = 4.5, 3.0, and 1.5 mm) with the same tube diameter (D = 19 mm). The mean tangential ejection velocity V_t is given as $V_t = Q/(W \times L)$, while the mean axial velocity V_a is given as $V_a = Q/2S$ where Q is the volume flow rate of the mixture, L is the inner length of the slit (74 mm), and S is the cross-sectional area of the tube. Thus, by decreasing W, the rotation can be intensified; i.e., $V_t = 1.70V_a$, $2.55V_a$, and $5.11V_a$ in the burners of W = 4.5, 3.0, and 1.5 mm, respectively. Hereafter, the three burners are respectively called the weak, moderate, and strong (rotation) burners. If the flame is rigorously cylindrical and the flow is incompressible, the stretch rate becomes simply proportional to the gradient of V_a [Eq. (8) in Ref. 5]. Actually, the flow field is coupled with the temperature and concentration fields due to combustion, and in addition, a recirculating flow may occur especially in the strong burner, because the estimated swirl numbers [4] are 0.8, 1.3, and 2.9 for the weak, moderate, and strong burners, respectively. However, it is expected that, if V_a is maintained at a constant value, the intensity of rotation will vary, while the stretch rate will remain almost constant in the three burners. The outer length of the center slit is 80-mm long, and those of the side slits are each 20-mm long. Nitrogen, originally for rich mixture experiments [21], is ejected from the side slit at the same value of V_t of the combustible mixture to yield a uniform flow field.

The distribution of OH concentration is measured with laser-induced fluorescence. A Nd:YAG-pumped pulsed dye laser with frequency doubling is used to excite the OH $A^2\Sigma^+(v' = 0) - X^2\Pi(v'' = 0)$ transition. The laser beam is focused to a light spot with a cross section of 2 × 1 mm and is propagated through the flame normal to the longitudinal axis of the vortex tube. The resulting fluorescence I_L from the OH is detected at right angles to the laser beam axis by a gated image-intensified vidicon detector with a spatial resolution of 0.1 × 0.1 mm. To eliminate the reflection of the light at the glass, two rings of inner diameter 14 mm are attached to the burner ends as a beam trap. The laser intensity I_0, which fluctuates pulse-to-pulse, is monitored to calibrate the LIF signals. Fluorescence images obtained from excitation on and off resonance with an OH transition are subtracted to obtain pure OH images. It is important to note that the LIF signals depend on the temperature and the collisional quenching rate [22], which cannot be neglected at atmospheric pressure. However, the population of $N'' = 8$ rotational state has only a small temperature dependence [23]. Furthermore, the variation of the fuel concentration Ω is so small (4.8 ~ 6.0%) in this experiment that the influence of the collision process can be considered to be small. Therefore, LIF images obtained with $P_1(8)$ excitation directly represent the relative OH concentration profiles, and the variation of the LIF signal can be attributed to the variation in the OH concentration.

The fuel is methane. The flame configurations are recorded by direct photography. Temperature measurements are made by using a silica-coated Pt/Pt-13%Rh thermocouple (wire diameter, 0.1 mm); no correction for thermometric error due to radiation is made. The radiative loss estimated is about 60 °C at 1200 °C for emissivity $\varepsilon = 0.22$ [24].

Results

Appearance of Flame:

When a lean mixture is ejected and ignited at the burner end by a torch flame, a tubular flame with a circular cross section is established [4,21]. The flame diameter is almost constant along the axis and decreases with decreasing fuel concentration Ω (%); eventually, the flame extinguishes.

Figures 2(a), 2(b), and 2(c), respectively, show the side views of the tubular flame obtained by the weak, moderate, and strong burners, in which V_t is 2.4, 3.7, and 7.3 m/s, respectively, while V_a (= 1.4 m/s) remains constant. With increasing intensity of rotation, the flame diameter increases while the thickness of the luminous zone becomes thinner.

Extinction Limit:

First, without the beam-trap rings, the extinction limits for the three burners are measured as functions of Ω and V_a. Results are shown in Fig. 3, in which the equivalence ratio ϕ is also indicated. Although Ω at extinction slightly decreases with decreasing V_a in all burners, the value in the moderate

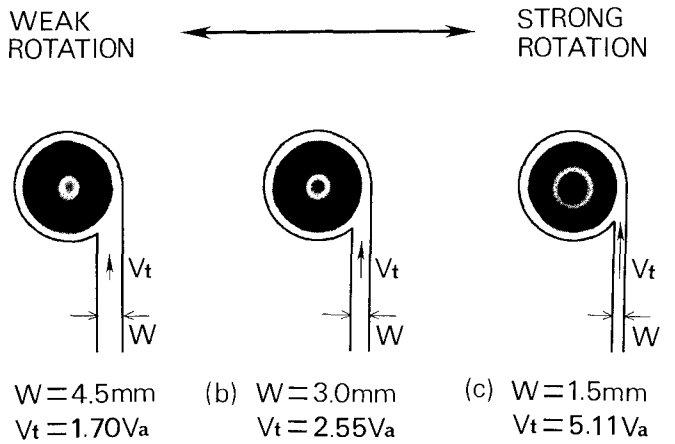

FIG. 2. Configurations of the tubular flames obtained by the three burners of different intensities of rotation: (a) $W = 4.5$ mm, $V_t = 2.4$ m/s, (b) $W = 3.0$ mm, $V_t = 3.7$ m/s, (c) $W = 1.5$ mm, $V_t = 7.3$ m/s; $V_a = 1.4$ m/s, $\Omega = 5.3\%$; with the beam-trap rings, $D_{ring} = 14$ mm.

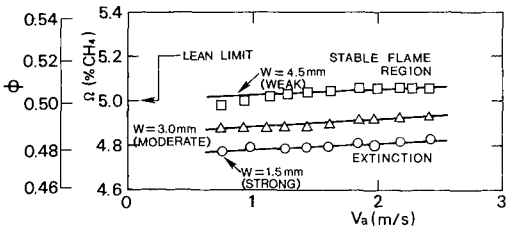

FIG. 3. Extinction limits obtained by the three burners of different intensities of rotation; $D = 19$ mm, without the beam-trap rings.

burner is about 4.9%, which agrees well with the value of 4.9% previously obtained by the burner of 18-mm inner diameter and 3-mm slit width [5]; hence, the reproducibility is good. In the weak and strong burners, the values are about 5.0 and 4.8%, respectively. Therefore, the extinction limit is extended as the rotation is intensified. It is interesting to note that Ω at extinction is smaller than the standard flammability limit (5.0% [25]). When the beam-trap rings are attached (Fig. 5), the values of Ω at extinction increase to about 5.3, 5.1, and 5.0% for the weak, moderate, and strong burners, respectively. This can be understood as follows: When the rings (inner diameter 14 mm) are attached, the effective diameter becomes smaller than the burner inner diameter (19 mm), and as a result, Ω at extinction increases as observed in the experiment with different burner diameters [5].

Radial Distribution of the OH Concentration and Its Peak Value:

To better understand the extension of the stability limit, the OH distributions are measured with varying Ω while maintaining $V_a = 1.4$ m/s. Figure 4 shows the radial distributions of the relative intensity of the OH signal across three representative flames in the moderate burner, determined at a section 30 mm inside from the burner end along the horizontal axis. In this figure, direct photographs are also shown, where x is the distance from the center of the burner. Each profile is obtained with the fluorescence excited by a single laser pulse. The spatial resolution is better than 0.1 mm; thus, the flame zone is well resolved. Above each of the OH profiles, the locations of the luminous flame zone are indicated by hatching.

When Ω is large [Fig. 4(a)], the distance between the luminous flame zones is large. The OH signal is almost zero outside the flame, but increases as the center of the flame is approached and takes its maximum slightly inside the luminous flame zone. Since the right and left peaks are almost the same, the absorption of the laser beam, which is observed in Ref. 26, seems negligible. Then, it decreases and takes a local minimum around the center of the flame. The profile looks "M-shaped."

In the tubular flame, the outside is the unburned gas and the inside is the burned gas [4]. The unburned gas comes from outside, enters the flame zone, and reacts to become a burned gas, which flows in the axial direction and exits from both of the burner ends. Thus, the outside region of zero signal corresponds to the unburned mixture, while the region near the local minimum value corresponds to the burned gas.

When Ω decreases, both the distance between the luminous flame zones and that between the peak positions decrease, and the dip in the OH profile becomes smaller. This results in a Π-shaped profile in which the value around the center is almost constant [Fig. 4(b)]. If Ω is further decreased, the distance between the peak positions becomes completely zero, and the OH profile becomes Λ-shaped with one peak [Fig. 4(c)], although the luminous zones do not completely merge.

Figure 5 shows the variations of the peak value in the OH profile with Ω. The boundaries of M-, Π-,

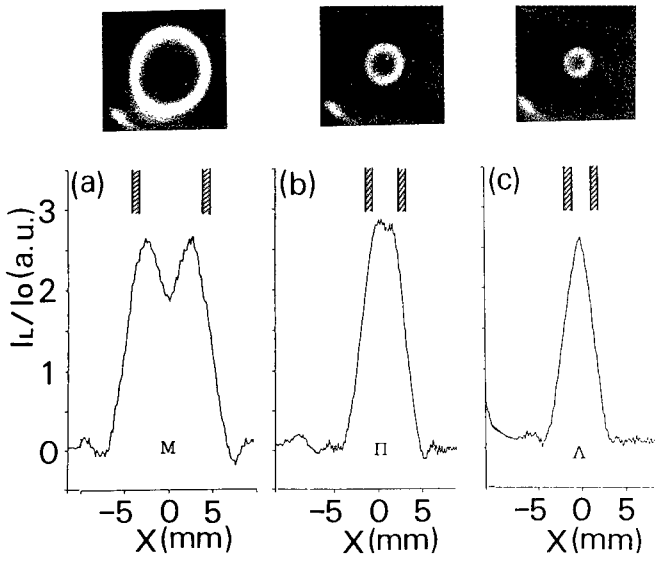

FIG. 4. Radial distributions of the relative intensity of OH signal for different fuel concentrations: (a) $\Omega = 5.8\%$, (b) $\Omega = 5.4\%$, (c) $\Omega = 5.2\%$; $V_a = 1.4$ m/s, $W = 3.0$ mm, $V_t = 3.7$ m/s; with the beam-trap rings; $D_{ring} = 14$ mm.

and Λ-shaped profiles are also indicated. In these measurements, five runs were made, and their results were averaged. The error bars refer to the maximum and minimum values in the five runs.

In the weak burner [Fig. 5(a)], the peak value initially decreases gradually with decreasing Ω. However, when Ω becomes smaller than about 5.42%, the OH profile is converted into the Π-shaped profile, and the peak value steeply increases. When Ω is further reduced to about 5.32%, the OH profile is converted into the Λ-shaped profile, and the peak value decreases again; eventually, the flame extinguishes at $\Omega = 5.26\%$.

In the moderate burner [Fig. 5(b)], the peak value varies as in the weak burner; however, the rate of decrease/increase is slow, and the flame extinguishes at $\Omega = 5.05\%$.

In the strong burner [Fig. 5(c)], the peak value also varies, but the rate of change is much smaller than the previous two, and the M-shaped profile is maintained even close to extinction. By measuring the distances between two peaks, it is found that, when the peak value starts to increase with decreasing Ω, the distance is about 6 mm in the strong and moderate burners, and around 3–6 mm in the weak burner; i.e., the distances are almost the same. The scatter in the last case is due to ambiguity of the local minimum position.

It is interesting to note that the peak value at extinction becomes lower as the rotation is intensified; that is, $I_L/I_0 = 2.8$, 2.0, and 1.8 for the weak, moderate, and strong burners, respectively. Thus, at a condition of intense rotation, the flame is maintained even though the OH concentration is reduced.

Temperature Distribution and Flame Temperature:

Next, the temperature field is examined. Figure 6 shows the radial distribution across the flame ($\Omega = 5.6\%$; $V_a \simeq 1.4$ m/s) in the strong burner. The OH distribution and the luminous flame zones are also indicated.

The temperature distribution is almost symmetrical, and its axis of symmetry is located near $x = 0$ mm, the radial center axis of the burner. The local minimum temperature T_c at the center is smaller than the maximum temperature T_f around the luminous flame zone by 75 °C. Such a temperature dip has not been seen in previous experiments with no rotation [15] or with small swirl number [4], except in the experiment with $D = 19$ mm and $W = 3$ mm [19], in which a very slight temperature hump had been observed. Thus, we measured T_f and T_c as functions of Ω.

The results are shown in Fig. 7. In this figure, the boundaries of the M-shaped, Π-shaped, and Λ-shaped profiles of OH distribution are indicated. For comparison, the value of T_c in the weak rotation burner [Fig. 7(a)] is also plotted (solid triangle) in Figs. 7(b) and 7(c). As seen in Fig. 7, the difference between T_f and T_c increases as the rotation intensifies. At $\Omega = 5.3\%$, the differences are 20 °C, 35 °C, and 40 °C where the observed flame diameters defined by the luminous flame zone are 2.8, 3.4, and

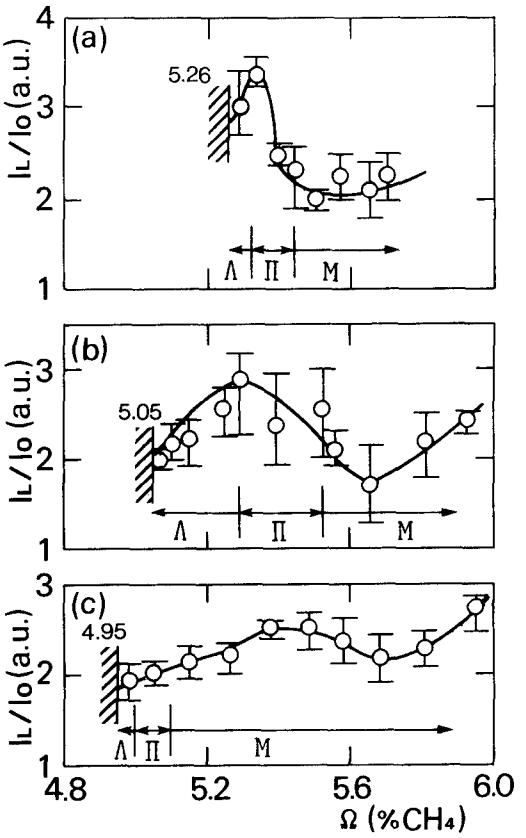

FIG. 5. Variations of the peak value in the radial distributions of OH signal with the fuel concentration: (a) W = 4.5 mm, V_t = 2.4 m/s, (b) W = 3.0 mm, V_t = 3.7 m/s, (c) W = 1.5 mm, V_t = 7.3 m/s; V_a = 1.4 m/s; with the beam-trap rings; D_{ring} = 14 mm.

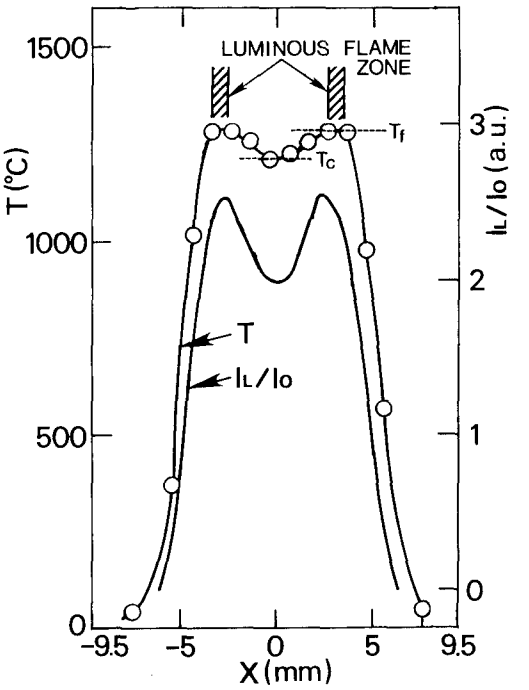

FIG. 6. Temperature distribution across the flame in the strong rotation burner (Ω = 5.6%, V_a = 1.4 m/s, W = 1.5 mm); with the beam-trap rings; D_{ring} = 14 mm..

5.8 mm in the weak, moderate and strong burners, respectively. At Ω = 5.6%, the temperature differences are, 40 °C, 65 °C, and 75 °C, and the corresponding flame diameters are 6.5, 6.5, and 7.2 mm for the forementioned burners.

If there is no heat loss, the temperature profile should be plateau-shaped in the burned gas region. Thus, the temperature fall in the twin-flame geometry is attributed to radiative heat loss [27]. However, it is interesting and important to note that T_c are approximately the same in the three burners, while T_f increases as the rotation intensifies. Thus, the temperature dip cannot be solely explained based on the radiative loss consideration and suggests an alternative extension mechanism of the stability limit in the strong burner.

Another aspect of T_f is that the value abruptly decreases when the OH profile converts into the Λ-shaped profile. This can be seen clearly in the strong burner [Fig. 7(c)] and may indicate that extinction is caused by insufficient residence time for the radical formation reaction, i.e., incomplete reaction [1–4].

Discussion

Before discussing the extension of stability limits by rotation, it may be useful to recognize that the tubular flame has two features. One is stretch; thus, it has aspects similar to the twin flame in a counterflow premixed stream. The difference is whether or not the flame has a curvature. The second feature is rotation. The aspect of stretch is discussed first, followed by the rotational aspect.

In a one-dimensional flame of lean methane mixtures in a uniform stream, the OH concentration increases sharply through the flame front to its maximum nonequilibrium (superequilibrium) concentration and then decreases slowly as a result of recombination reactions to its equilibrium value [17,18,22]. The superequilibrium concentration is highest at ϕ = 0.9 and monotonically decreases with decreasing fuel concentration [28].

In the tubular flame, however, the peak value did not monotonically decrease with decreasing fuel concentration. According to the recent studies by Stahl et al. [29] and by Rogg [30], it is shown that, with

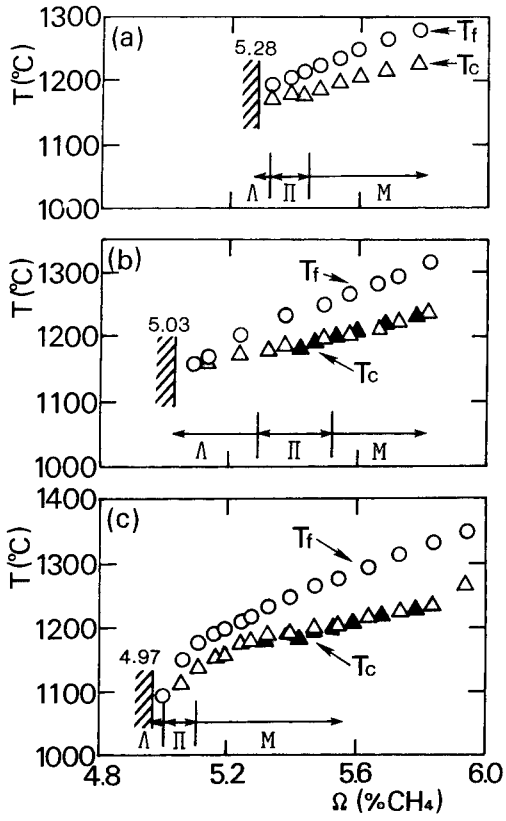

FIG. 7. Variations of the flame temperature T_f (maximum temperature in the reaction zone) and the local minimum temperature T_c at the axis of rotation with the fuel concentration (a) $W = 4.5$ mm, $V_t = 2.4$ m/s, (b) $W = 3.0$ mm, $V_t = 3.7$ m/s, (c) $W = 1.5$ mm, $V_t = 7.3$ m/s; $V_a = 1.4$ m/s; with the beam-trap rings; $D_{ring} = 14$ mm.

increasing strain rate, the twin flames are pushed toward each other, and the two reaction zones of the flame approach the stagnation plane. As a result, peak values of the mass fraction of the H atom (Y_H) slightly increase, but the level of the H atom at the stagnation plane rapidly increases. As a result, the Y_H profile changes from a double-peaked function (M shape), which attains its local minimum at the stagnation plane, to a single-peaked function (Λ shape), which attains its maximum at the stagnation plane. When the strain rate is increased further, instationary flame extinction occurs.

Since the tubular flame is also formed in a stretched flow field, similar behavior may occur. Note that increasing strain rate and decreasing fuel concentration in lean mixtures have the same effect on the flame behavior because both reduce the Damköhler number. Hence, the variations in the shape and the peak value with decreasing Ω (Figs. 4 and 5) can be understood within the work of Refs. 29 and 30. It is important to note that, because of symmetry, there is no radical loss by diffusion behind the flame, resulting in extension of stability limit.

However, when the rotation is intensified, the M-shaped profile in the OH distribution is still maintained even if Ω is reduced [Fig. 5(c)], and the stability is further extended. To account for this, a rotational effect should be taken into consideration.

An interesting feature is the temperature difference, $T_f - T_c$. Usually, such a difference is attributed to radiative heat loss, and in the counterflow twin flame, the magnitude considered is about 20 °C for a 6.18% methane flame, whose separation distance is 11 mm and temperature is 1220 °C. However, in the present strong burner, a temperature fall of 75 °C has been observed in a 5.6% methane flame, whose diameter is 7.2 mm and temperature is 1250 °C. If the radiative mechanism is applied, this 75 °C fall is inconsistent with the 20 °C fall, because the radiating volume of the tubular flame is smaller than that of the twin flame. Also, the values of $T_f - T_c$ at $\Omega = 5.3$ and 5.6% indicated previously do not seem to be simply dependent on the radiating volume of the hot gas cylinder. Therefore, the temperature fall cannot be explained by radiative heat loss alone. It should be remembered that, with increasing intensity of rotation, T_c remains unchanged while T_f increases; namely, a protrusion in the reaction zone temperature occurs. This aspect resembles what is called excess enthalpy flame. In the excess enthalpy flame, heat is recirculated from the back side of the burned gas to the unburned gas, resulting in an increase of the reaction zone temperature while the final burned gas temperature is unchanged. Because of this mechanism, the extinction limit is extended to the equivalence ratio of 0.10 [31,32]. Therefore, it is reasonable to consider that such an excess enthalpy structure may be induced by rotation.

Since the radical concentration field also changes with rotation, a possible mechanism may include the transport of radicals in the flame zone. Namely, the radicals are transported into the reaction zone, deactivated, and their chemical enthalpy is converted into the thermal energy to increase the reaction zone temperature. Next, the heat is convected toward the burned gas side and increases the burned gas temperature, while the thermal energy is converted to the chemical enthalpy to produce the radicals, resulting in a decrease of the burned gas temperature to the original temperature. As a result, the temperature at the center remains unchanged while the temperature in the reaction zone increases. The rotation may act as a promoter in this recirculating system. The change in the rotational flow structure, such as the size of a forced vortex core and the formation of a recirculating flow, may also be coupled with this mechanism.

This mechanism is not conclusive. Since the widening of stability limit by rotation is of practical im-

portance, further studies, focused on the structure study including H radical [29,30], should be conducted.

Conclusions

The effect of rotation on the stability and structure of a tubular flame has been experimentally investigated. The concentration field of the OH radical has been measured by laser-induced fluorescence, and the temperature field has been examined using a fine thermocouple.

Results show that, with increasing intensity of rotation, the lean concentration limit of a methane flame is decreased, and the stable flame region is expanded. The diameter of the flame is increased, and the inner flame structure is also found to change. Namely, when the rotation is weak, the radial OH distribution takes an M-shaped profile; the concentration is low in the outer region of the unburned gas, increases and takes a local maximum (superequilibrium) value in the reaction zone, then falls toward the equilibrium value. With decreasing fuel concentration, the peak positions in the M profile approach each other, and the profile becomes Π-shaped. With a further decrease in the fuel concentration, the profile becomes Λ-shaped, and the flame is eventually extinguished. Correspondingly, the peak value is decreased, increased, and decreased with decreasing fuel concentration. However, when the intensity of rotation is strong, the variation of the peak value becomes moderate, and the M-shaped profile is maintained even close to extinction. The temperature measurement shows that, with increasing intensity of rotation, a temperature dip appears around the center, and its magnitude becomes larger. Although this dip is usually considered to be due to radiative loss, the temperature at the center remains constant, and rather, the temperature in the reaction zone is increased, i.e., a protrusion in the reaction zone temperature occurs. This aspect resembles the temperature profile of the excess enthalpy flame.

Although the details of the extension mechanisms are still unclear, these results suggest that the stability of the flame is increased by rotation through a mechanism like the excess enthalpy flame.

Acknowledgments

The authors would like to thank Professor Hiroyuki Matui and Dr. Atumu Tezaki for helpful discussions on the laser-induced fluorescence measurements.

REFERENCES

1. Tsuji, H., and Yamaoka, I., *Nineteenth Symposium (International) on Combustion*. The Combustion Institute, Pittsburgh, 1982, pp. 1533–1540.
2. Sato, J., *Nineteenth Symposium (International) on Combustion*, The Combustion Institute, Pittsburgh, 1982, pp. 1541–1548.
3. Ishizuka, S., and Law, C. K., *Nineteenth Symposium (International) on Combustion*, The Combustion Institute, Pittsburgh, 1982, pp. 327–335.
4. Ishizuka, S., *Twentieth Symposium (International) on Combustion*, The Combustion Institute, Pittsburgh, 1984, pp. 287–294.
5. Ishizuka, S., *Prog. Energy Combust. Sci.* 19:187–226 (1993).
6. Robert, W. L., and Driscoll, J. F., *Combust. Flame* 87:245–256 (1991).
7. Poinsot, T., Veynante, D., and Candel, S., *Twenty-Third Symposium (International) on Combustion*, The Combustion Institute, Pittsburgh, 1990, pp. 613–619.
8. Ashurst, W. T., and McMurtry, P. A., *Combust. Sci. Technol.* 66:17–37 (1989).
9. Peters, N., and Williams, F. A., *Twenty-Second Symposium (International) on Combustion*, The Combustion Institute, Pittsburgh, 1988, pp. 495–503.
10. Sivashinsky, G. I., and Sohrab, S. H., *Combust. Sci. Technol.* 53:67–74 (1987).
11. Tien, J. H., and Matalon, M., *Combust. Sci. Technol.* 87:257–273 (1992).
12. Smooke, M. D., and Giovangigli, V., *Twenty-Fourth Symposium (International) on Combustion*, The Combustion Institute, Pittsburgh, 1992, pp. 161–168.
13. Takeno, T., and Ishizuka, S., *Combust. Flame* 64:83–98 (1986).
14. Libby, P. A., Peters, N., and Williams, F. A., *Combust. Flame* 75:265–280 (1989).
15. Kobayashi, H., and Kitano, M., *Combust. Flame* 76:285–295 (1989).
16. Weinberg, F., *Combust. Flame* 78:121–127 (1989).
17. Cattolica, R. J., and Vosen, S. R., *Combust. Sci. Technol.* 48:77–87 (1986).
18. Vosen, S. R., Cattolica, R. J., and Weinberg, F., *Proc. R. Soc. Lond. A* 418:313–329 (1988).
19. Sakai, Y., and Ishizuka, S., *Twenty-Fourth Symposium (International) on Combustion*, The Combustion Institute, Pittsburgh, 1992, pp. 153–159.
20. Dieke, G. M., and Crosswhite, H. M., *J. Quant. Spectrosc. Radiat. Transfer* 2:97–199 (1962).
21. Ishizuka, S., *Combust. Flame* 82:176–190 (1990).
22. Cattolica, R. J., and Vosen, S. R., *Twentieth Symposium (International) on Combustion*, The Combustion Institute, Pittsburgh, 1984, pp. 1273–1282.
23. Sick, V., Arnold, A., Dießel, E., Dreier, T., Ketterle, W., Lange, B., Wolfrum, J., Thiele, K. U., Behrendt, F., and Warnatz, J., *Twenty-Third Symposium (International) on Combustion*, The Combustion Institute, Pittsburgh, 1990, pp. 495–501.
24. Kaskan, W. G., *Sixth Symposium (International) on Combustion*, The Combustion Institute, Pittsburgh, 1957, pp. 134–143.
25. Zabetakis, M. G., *Flammability Characteristics of Combustible Gases and Vapors*, U.S. Bureau of Mines, Bulletin 627, 1965.

26. Stepowski, D., Labbaci, K., and Borghi, R., *Twenty-First Symposium (International) on Combustion*, The Combustion Institute, Pittsburgh, 1986, pp. 1561–1568.
27. Liu, G. E., Ye, Z. E., and Sohrab, S. H., *Combust. Flame* 64:193–201 (1986).
28. Cattolica, R. J., *Combust. Flame* 44:43–59 (1982).
29. Stahl, G., Warnatz, J., and Rogg, B., *Progress in Astronautics and Aeronautics*, AIAA, Inc., New York, 1988, Vol. 113, pp. 195–214.
30. Rogg, B., *Combust. Flame* 73:45–65 (1988).
31. Jones, A. R., Lloyd, S. A., and Weinberg, F. J., *Proc. R. Soc. London A* 360:97–115 (1978).
32. Kotani, Y., Benbahani, H. F., and Takeno, T., *Twentieth Symposium (International) on Combustion*, The Combustion Institute, Pittsburgh, 1984, pp. 2025–2023.

Twenty-Fifth Symposium (International) on Combustion/The Combustion Institute, 1994/pp. 1407–1413

THE INITIAL DEVELOPMENT OF A TULIP FLAME

MOSHE MATALON AND JENNIFER L. MCGREEVY*
Department of Engineering Sciences and Applied Mathematics
McCormick School of Engineering and Applied Science
Northwestern University
Evanston, IL 60208-3125, USA

The initial development of a "tulip flame," often observed during flame propagation in closed tubes, is attributed to a combustion instability. The roles of hydrodynamic and of the diffusional-thermal processes on the onset of instability are investigated through a linear stability analysis in which the growth or decay of small disturbances, superimposed on an otherwise smooth and planar flame front, are followed. A range of the Markstein parameter, related to the mixture composition through an appropriately defined Lewis number, has been identified where a tulip flame could be observed. For a given value of the Markstein parameter within this range, a critical wavelength is identified as the most unstable mode. This wavelength is directly related to the minimal aspect ratio of the tube where a tulip flame could be observed. The time of onset of instability is identified as the time when the most unstable disturbance, associated with the critical wavelength, grows at a faster rate than the flame front itself and exceeds a certain threshold. This occurs after the flame has propagated a certain distance down the tube: a value which has been explicitly determined in terms of the relevant parameters. Experimental records on the tulip flame phenomenon support the findings of the analysis. That is, the tulip flame forms after the flame has traveled half the tube's length, it does not form in short tubes, and its formation depends on the mixture composition and on the initial pressure in the tube.

Introduction

This study is concerned with the evolution of premixed flames in closed tubes. In a typical experiment, the combustible mixture is ignited at a point at one end of the tube. During the first phase of the burning process, a spherical flame centered around the ignition point propagates outward, as would be the case in an unbounded domain. It then gradually develops into a hemisphere that continues to grow until it makes contact with the side walls of the tube and subsequently flattens out in the center. At the beginning of the second phase, the flame is nearly planar. In short tubes, of aspect ratio < 2, the flame remains smooth until it reaches the far end of the tube. In longer tubes, however, an instability develops after the flame has reached a certain distance downstream. The flame acquires a peculiar shape in which its center part forms a cusp pointing toward the burned gas.

The first observation of this phenomenon, now referred to as a "tulip flame," was reported by Ellis [1]. This work and the subsequent studies by Guénoche [2] revealed that the formation of the tulip flame depends in part on the mixture composition and on the initial pressure in the tube. Making use of more advanced measurement techniques, recent experiments [3,4] have provided more detailed information on the flow and pressure fields. There have also been several numerical studies aimed at reproducing the tulip flame and possibly clarifying the physical mechanisms responsible for its formation [4–8]. Based on these studies, various possible explanations have been suggested as responsible for the formation of the tulip flame. Although valuable insight has been gained thus far, the actual cause for the formation of the tulip flame has not yet been conclusively determined.

In the present study, a different approach than those undertaken previously is followed. The initial development of a tulip flame is identified as the onset of an instability on an otherwise smooth flame front. By examining the evolution of small disturbances superimposed on an initially planar flame, we have determined explicit conditions for the occurrence of an instability along with the time of its onset. Our results are distinguished from all previous works on two counts. First, we have identified a critical wavelength for the most unstable mode, which is directly related to the minimal aspect ratio of a tube where a tulip flame could be observed. Second, we have identified the role of diffusional-thermal effects on the onset of the instability and have quantified this result in terms of an appropriate range of Markstein length where a tulip flame could be observed. By identifying the role

*Currently at the Department of Mathematics and Physics, Philadelphia College of Pharmacy and Science, Philadelphia, PA 19104, USA.

of the various parameters included in the model, this work sheds additional light on the mechanisms responsible for this initial stage of the phenomenon. The actual development of the tulip flame requires examining the evolution of finite amplitude disturbances, the subject of a future publication.

Formulation

A homogeneous combustible mixture of density ρ_0, pressure p_0, and temperature T_0 occupies the volume of a closed tube of length L. When ignited, a flame propagates to the right throughout the tube. The process is considered to be adiabatic. Furthermore, the analysis assumes that at time $t = 0$, a flat flame has been established at the left end of the tube and follows its evolution thereafter. The model is based on two main assumptions:

1. The flame speed (typically ~50 cm/s) is much smaller than the speed of sound. Hence, the representative Mach number $\mathfrak{M} = S_L(\gamma p_0/\rho_0)^{-1/2}$, with γ being the ratio of specific heats and S_L being the laminar flame speed, is very small.
2. The flame thickness, characterized by the diffusion length $L_D = \lambda/\rho_0 c_p S_L$, with λ and c_p being the thermal conductivity and specific heat of the mixture, respectively, is much smaller than the length of the tube. Typically, $L_D \sim 10^{-2}$ cm, $L \sim 10$ cm, and the ratio $\delta \equiv L_D/L << 1$.

The first assumption implies that acoustic disturbances propagate infinitely fast so that the pressure is almost instantaneously equalized throughout the tube. When scaled with respect to p_0, the pressure may be expressed in the form $P(t) + \gamma\mathfrak{M}^2 p(x,t) + \ldots$, where the small pressure variations from the mean are included here, as they are needed to balance the *small* change in momentum that results as the flame propagates through. The second assumption implies that the flame may be treated as a surface of discontinuity with the flow field obeying the Euler equations on either side. The internal structure of the flame is needed only to determine the propagation speed.

If L, S_L, and L/S_L are used as units of length, speed, and time, respectively, and the state of the fresh unburned gas is used to nondimensionalize the temperature T, density ρ, and pressure p, the governing equations become

$$\frac{1}{\rho}\frac{D\rho}{Dt} + \nabla\cdot\mathbf{v} = 0 \tag{1}$$

$$\rho\frac{D\mathbf{v}}{Dt} = -\nabla p \tag{2}$$

$$\rho\frac{DT}{Dt} = \frac{\gamma - 1}{\gamma}\frac{dP}{dt} \tag{3}$$

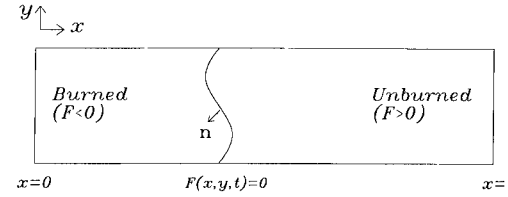

FIG. 1. Schematic representation of a flame propagating in a closed tube.

$$\rho T = P \tag{4}$$

where $\mathbf{v}$ is the velocity field. These equations are to be solved subject to the Rankine–Hugoniot conditions across the flame front, namely,

$$[\rho(\mathbf{v}\cdot\mathbf{n} - V_f)] = 0 \tag{5}$$

$$[\mathbf{v} \times \mathbf{n}] = 0 \tag{6}$$

$$[p + \rho(\mathbf{v}\cdot\mathbf{n} - V_f)^2] = 0 \tag{7}$$

$$[T] = q \tag{8}$$

where $[\cdot] = (\cdot)_{\text{bur}} - (\cdot)_{\text{unb}}$ denotes the jump in the quantity. Here, $\mathbf{n}$ is a unit vector normal to the flame front pointing toward the burned gas, V_f is the velocity of the front measured with respect to the laboratory frame of reference, and $q = Q/c_p T_0$ is the heat release parameter, where Q is the specific heat of combustion. If the flame front is described by $F(\mathbf{x},t) = 0$, such that the unburned gas occupies the region $F > 0$ (see Fig. 1), then

$$\mathbf{n} = -\frac{\nabla F}{|\nabla F|}, \qquad V_f = \frac{1}{|\nabla F|}\frac{\partial F}{\partial t}.$$

The only relevant boundary condition is the requirement that at the walls, the normal velocities vanish. To complete the formulation, one needs equations for V_f, or equivalently for the burning rate $M \equiv \rho(\mathbf{v}\cdot\mathbf{n} - V_f)$, and for the mean pressure P.

Using Eqs. (3) and (4), the continuity Eq. (1) can be rewritten in the form

$$\nabla\cdot\mathbf{v} = -(1/\gamma P)dP/dt. \tag{9}$$

When integrated over the whole volume of the tube, the only contribution from the left side of the equation comes from the surface integrals along the flame front. Using relation (5) and the definition of M, one obtains

$$dP/dt = \gamma q \int_{A_f} M dA \tag{10}$$

where A_f is the flame surface area (per unit area of the tube cross section).

Next, we note that the energy Eq. (3) can be rewritten in the form

$$\frac{D}{Dt}\left(\frac{P^{1/\gamma}}{\rho}\right) = 0. \tag{11}$$

This implies that the state of the unburned gas remains spatially uniform, though it varies in time as the pressure level in the tube increases. Hence,

$$\rho = P^{1/\gamma}, \qquad T = P^{(\gamma-1)/\gamma} \quad \text{for } F > 0. \tag{12}$$

Using condition (8), one also finds that the flame temperature is given by

$$T_f = q + P^{(\gamma-1)/\gamma} \tag{13}$$

where the excess of heat that causes the flame temperature to exceed the adiabatic flame temperature $T_a \equiv 1 + q$ comes from the adiabatic compression process. Note that the entropy, proportional to $S \equiv \rho^{-1}P^{1/\gamma}$, is also conserved along particle paths in the burned gas region. However, as a result of the temperature jump across the flame, the temperature and, hence, the density, are no longer spatially uniform.

The analysis of the flame structure [9] suggests that

$$M = M_0(1 + \mu\nabla\cdot\mathbf{n}) \tag{14}$$

$$M_0 = P^{1/2}(T_f/T_a)^{3/2}\exp(\beta/2T_a - \beta/2T_f) \tag{15}$$

where M_0 is the burning rate of a flat flame, and a Markstein-like model [10] has been assumed for the dependence of M on the local curvature. Note that in free space, where $P = 1$, the burning rate is that of a plane adiabatic flame, $M_0 = 1$, as expected. In a confined environment, M_0 increases due to the increase in pressure and temperature as the flame travels down the tube. The parameter μ, often referred to as the Markstein length, is of the order of the thickness of the flame zone and accounts for diffusive effects within the flame. Since it has been scaled with respect to the length of the tube, $\mu = O(\delta) \sim 10^{-3}$. An expression for the Markstein length has been *derived* for the case of a freely propagating flame [11,12], showing an explicit dependence on the heat release parameter q, the activation energy parameter $\beta = E/RT_0$, where E and R are the overall activation energy of the chemical reaction and the gas constant respectively, and the Lewis number $\mathrm{Le} = \lambda/\rho c_p D$, where D is the mass diffusivity of the deficient component in the mixture. Of particular importance is the finding that μ is proportional to Le $-$ 1. Values of Le sufficiently larger than 1 correspond to lean mixtures of heavy fuels, while values of Le sufficiently less than 1 correspond to rich mixtures of heavy fuels. Thus, μ depends on the mixture composition. Such a dependence is also anticipated in the present case.

The flow in the unburned gas region is homentropic ($S = 1$) and therefore irrotational. The velocity field can therefore be deduced from a potential $\mathbf{v} = \nabla\Phi$, which must satisfy $\nabla^2\Phi = -\dot{P}/\gamma P$, where the "dot" represents differentiation with respect to t. The momentum equations serve only to evaluate the pressure variations p.

On the other hand, the flow in the burned gas region is rotational, as there are two sources of vorticity. First, a curved flame generates vorticity because, as a result of thermal expansion, the flow is refracted on passage through the front. Second, spatial nonuniformity in the density and pressure fields produce a nonzero baroclinic vector $\nabla\rho \times \nabla p$, which appears as a source term in the vorticity equation. In the burned gas, one must, therefore, address the complete Eqs. (1), (2), and (11).

Analysis

The description of a planar flame, which constitutes our basic state, is given in Ref. 9. As the flame propagates down the tube, the fresh mixture is compressed and pushed toward the right end, while the burned products move away toward the left end of the tube. The flame front is located at $x = x_f(t)$, where

$$x_f = P^{-1/\gamma}(P_e - P)/(P_e - 1) \tag{16}$$

with $P_e = 1 + \gamma q$ representing the ending pressure. The pressure is determined by solving Eq. (10). One finds that the pressure, and hence the burning rate M_0, increases continuously in time.

To examine the stability of planar flames, we consider the following initial value problem. *Small* disturbances, characterized by $|\varepsilon| << 1$, are introduced at a sufficiently small time $t = t_s$, and their evolution is followed thereafter. Only two-dimensional disturbances are considered here with u, v and x, y representing axial and transverse velocities and coordinates, respectively. If the basic state is denoted with an "overbar" and the disturbances with "primes," all variables are expressed in the form

$$\begin{aligned}
u &= \bar{u}(x,t) + \varepsilon u'(x,t)e^{iky}\\
p &= \bar{p}(x,t) + \varepsilon p'(x,t)e^{iky}\\
v &= \varepsilon i v'(x,t)e^{iky}\\
\rho &= \bar{\rho}(x,t) + \varepsilon \rho'(x,t)e^{iky}\\
S &= \bar{S}(x,t) + \varepsilon S'(x,t)e^{iky}\\
M &= M_0(t) + \varepsilon M'(t)e^{iky}
\end{aligned}$$

where k is the wave number of the disturbance (made dimensionless with respect to L^{-1}). Similarly, the flame front is given by $x = x_f(t) + \varepsilon A(t)e^{iky}$. Substituting into the governing equations and linearizing about the basic state yields

$$u_x - kv = 0 \tag{17}$$

$$\bar{\rho}(u_t + \bar{u}u_x + \bar{u}_x u) = -p_x + (\bar{p}_x/\bar{\rho})\rho \tag{18}$$

$$\bar{\rho}(v_t + \bar{u}v_x) = -kp \tag{19}$$

$$S_t + \bar{u}S_x + \bar{S}_x u = 0 \tag{20}$$

$$\rho\bar{S} + \bar{\rho}S = 0 \tag{21}$$

where the primes have been dropped for convenience and the subscripts x, t have been used for partial differentiation. It should be noted that upon taking the curl of the momentum equations, Eqs. (18) and (19), the terms on the right-hand side are the ones producing the nonzero baroclinic vector $\sim \bar{\rho}_x p - \bar{p}_x \rho$. The jump conditions of Eqs. (5) through (8), evaluated across the mean position of the flame front $x = x_f(t)$, become

$$[u] = -[\bar{u}_x]A - qP^{-1}M \tag{22}$$

$$[v] = k(\dot{P}/\gamma P)A \tag{23}$$

$$[p] = -[\bar{p}_x]A - 2(\dot{P}/\gamma P)M \tag{24}$$

$$[S] = -[\bar{S}_x]A. \tag{25}$$

In addition, the solution must satisfy the boundary conditions

$$u(0,t) = u(1,t) = 0. \tag{26}$$

Finally, Eq. (14), for the burning rate, yields

$$\dot{A} - \bar{u}_x A = u + P^{-1/\gamma}M \qquad \text{at } x = x_f \tag{27}$$

where $M = -\mu(\dot{P}/\gamma q)k^2 A$.

Since the state of the unburned gas is spatially uniform, it is unaffected by any disturbance; hence, $S = \rho = 0$. The flow and pressure fields in the unburned gas can then be determined explicitly as

$$u = -kC \sinh k(1 - x),$$
$$v = kC \cosh k(1 - x), \tag{28}$$

$$p = -P^{1/\gamma}[\dot{C} \cosh k(1 - x) - (\dot{P}/\gamma P)Ck(1 - x) \sinh k(1 - x)] \tag{29}$$

where the function $C(t)$ remains to be determined. In the burned gas region ($0 < x < x_f(t)$), the problem is solved numerically based on a two-level second-order accurate Crank–Nicolson/Adams–Bashforth scheme. The momentum and energy equations are solved for u, v, and S iteratively with a Poisson equation for the pressure [9]. Since the conditions of Eqs. (22), (23), and (26) are sufficient for the solution of the Euler equations, the additional jump in pressure (Eq. (24)) is used for the determination of $C(t)$. Finally, Eq. (27) is solved for the amplitude $A(t)$.

Results

Due to the unsteady nature of the basic state, several remarks regarding the notion of "stability" are in order [13]. First, since the burning process takes place in a closed tube, the evolution is followed during a *finite* time interval. Consequently, stability/instability reflects the tendency of the planar flame, *at a given moment*, to become more and more or less and less distorted. Second, one must observe the growth/decay of the amplitude of the disturbance relative to the velocity of the advancing flame front. For, if at a given instant in time the disturbance is growing but the flame front is moving more rapidly, a local displacement would appear as decaying in the eye of an observer and the flame would be considered momentarily stable. Conversely, if the disturbance is growing more rapidly then the flame front, a local disturbance would appear as growing in the eye of an observer and the flame would be considered momentarily unstable. Third, since an instability becomes visible in an experiment only after the magnitude of the disturbance has grown sufficiently large, the determination of the critical time t_c for the onset of instability is not obvious. Here, it will be assumed that t_c corresponds to the time when the amplitude of the disturbance, which is now growing more rapidly then the flame itself, reaches the value $A/x_f = 1$. Other definitions of t_c leads to qualitatively equal results; the precise definition can only be made by direct comparison to experimental data.

A small disturbance is introduced at time $t_s = 0.005$ on a nominally flat flame located at $x_f \sim 0.03$. The initial time $t = t_s$ constitutes approximately 1% of the total time of the combustion process and is sufficiently small to ensure numerical stability. The initial amplitude $A(t_s)$ has been chosen so that the disturbed flame front assumes the initial form $x = x_f(t_s)\{1 + \varepsilon \cos ky\}$. The results reported below are based on the following choice of parameters: $\gamma = 1.4$, $q = 6$, and $\beta = 20$.

The growth of the amplitude of a disturbance of wave number k relative to the unperturbed flame is shown in Fig. 2 for the value $\mu = 0.004$. For long wavelength disturbances ($k < 13$), the ratio A/x_f remains small and never exceeds its initial value. The flame reaches the right end of the tube before the perturbations have developed to a significant magnitude. For moderate wavelength disturbances, A/x_f

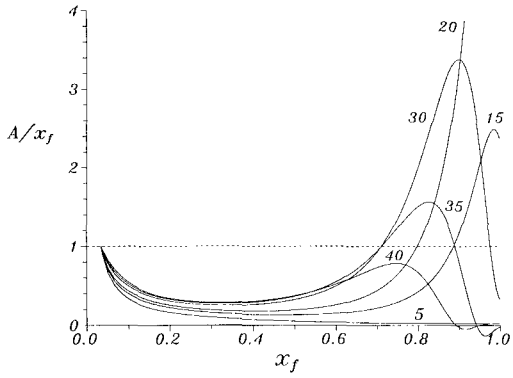

FIG. 2. The growth of the amplitude A relative to the moving flame for selected values of the wave number k and for $\mu = 0.004$.

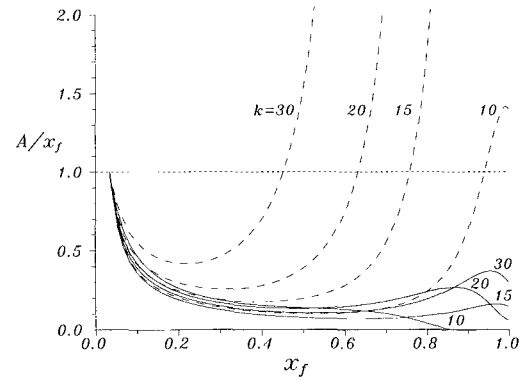

FIG. 3. The growth of the amplitude A relative to the flame position for selected values of the wave number k and for the following two values of the Markstein parameter: $\mu = 0.005$ (solid curves) and $\mu = 0.001$ (dashed curves).

first decreases, reaches a minimum, and then increases rapidly in time. After the flame has reached a certain distance down the tube, flame front disturbances grow at a faster rate than the flame itself, which indicates the onset of an instability. Indeed, as the flame nears the right end of the tube, the perturbations decay because the gas is coming to rest. Before reaching this stage, however, some disturbances have been amplified to an extent that the flame front has been significantly distorted. For example, for $k = 30$, the relative size of the amplitude of a disturbance $A/x_f \sim 3$, whereas for $k = 20$, the value $A/x_f \sim 7$. The assumption of *small disturbances* eventually breaks down, and the inclusion of nonlinear effects (not discussed here) is needed for the description of the new flame structure. For small wavelength disturbances ($k > 40$), the ratio A/x_f decays quite rapidly to zero without exceeding its initial magnitude.

The above results indicate the existence of a range of moderate wave numbers that correspond to growing modes. In particular, a maximum value $k = k_c$ exists ($k_c \sim 30$ in Fig. 2), corresponding to the first growing disturbance. All disturbances with $k > k_c$ are damped out, while those with $k < k_c$ begin to grow at increasingly later times. Thus, k_c identifies the disturbance that is most likely to be manifested first as an instability in an experiment.

The results of Fig. 2 are representative for values of μ in the range $\mu_* < \mu < \mu^\circ$, where $\mu_* \approx 0.001$ and $\mu^\circ \approx 0.006$. Outside of this range, the planar flame is either absolutely stable (for $\mu > \mu^\circ$) or unstable to *all* disturbances (for $\mu < \mu_*$), as exemplified in Fig. 3. Note that when the disturbances are damped out, small wrinkles decay much more rapidly than large wrinkles. But when amplified, small wrinkles begin to grow earlier and at a faster rate than the large wrinkles.

Neutral stability curves are shown in Fig. 4 for $\mu_* < \mu < \mu^\circ$. For a given μ, there exists a band of wave

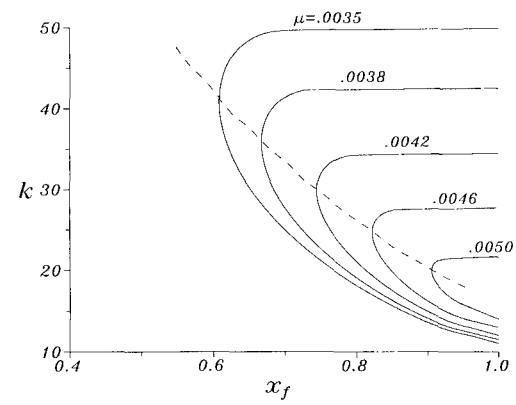

FIG. 4. Neutral stability curves for selected values of μ, indicating the range of the unstable modes along with the position x_f for their onset. The dashed curve represents the critical value k_c vs x_f°.

number of disturbances that start growing, after reaching the position x_f° (the value of x_f at the turning point). The disturbance with wave number $k = k_c$ grows first and is, therefore, the most dangerous mode. The dependence of k_c on x_f° is identified by the dashed curve in Fig. 4, while its dependence on μ is shown in Fig. 5.

Our predictions can be understood as resulting from an interplay between hydrodynamic and diffusional-thermal influences, modified by the effects due to confinement. The density decrease across the flame gives rise to the well-known hydrodynamic instability [14,15]. Accordingly, disturbances of all wave numbers grow; in particular, short waves grow faster than long waves. Under confinement, however, the amplification rate is lower than in open space [9],

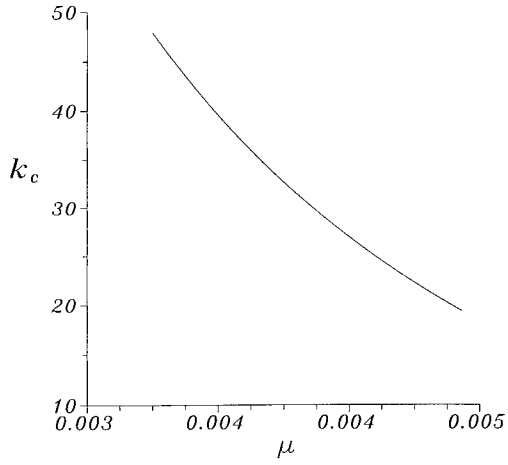

FIG. 5. The dependence of the critical wave number k_c on the Markstein length μ.

because the time for the development of a disturbance is limited and because, relative to an accelerating flame, disturbances grow slower. Hence, the very long waves are not sufficiently amplified to develop into an instability. On the other hand, diffusional-thermal effects within the flame often exert stabilizing influences, thereby stabilizing the small wavelength disturbances. In this case, there will be only a narrow band of growing wavelengths, as predicted. Otherwise, disturbances of all wavelengths are amplified. Diffusional-thermal effects are known to have stabilizing effects in mixtures for which Le $>$ Le$_\circ$, for some Le$_\circ$ slightly below 1 [11,12], or equivalently for $\mu > \mu_\circ$ as our results indicate.

Although the analysis puts no restrictions on the lateral dimension, the results can be applied to a flame propagating in a tube of finite width if one focuses on that portion of the flame surface that exists between two streamlines that are $2\pi/k$ apart. The flow field in the region $-\pi/k < y < \pi/k$ would then correspond to an idealization of that within the tube, because the transverse velocity component Re(v) then vanishes at both sides. Consider now a mixture in a tube of aspect ratio (length to width) AR. Our results suggest that for $\mu > \mu_\circ$, no instability will be observed when AR $< k_c/2\pi$, and the flame will remain planar throughout the propagation. In longer tubes, however, the initially planar flame evolves into a corrugated front identified by a wave number $k_\circ \geq k_c$, where $k_\circ = 2n\pi$ AR, with n being an integer. A one-cell structure indented toward the burned gas at the center of the tube, thus resembling the initial form of the tulip flame, results when $n = 1$ and $\varepsilon < 0$. These results are in complete agreement with the experimental observations referred to earlier [1–4]. First, the predicted critical wave numbers (Figs. 4 and 5) correspond to AR in the range 3–8, which are typical in the reported experiments. Second, as observed, the instability develops after the mean position of the flame exceeds x_f°, with $x_f^\circ > 0.5$. Multicells with $n \geq 2$ may also develop at the onset of the instability in wide tubes. However, as the flame travels farther down the tube, the longer waves ($k > k_\circ$) appear to grow faster (Fig. 2) and will eventually dominate the flame shape. Hence, multicells may quickly disappear in favor of a single-cell structure. Multicells have been reproduced in a numerical study [6] that simulates ignition at the left end of the tube at two points. This situation is effectively similar to a one-point ignition in a wider tube, which is in agreement with our prediction.

The perturbed flow field during the initial development of the tulip flame consists of two recirculation zones in the unburned gas, one on each side of the mid plane. When the intrusion of the flame front at the center of the tube is convex toward the burned gas ($\varepsilon < 0$), the circulation appears clockwise, in agreement with experimental measurements [3]. Although this circulatory motion may not be considered as the main factor in the development of the instability, it probably has an effect on the eventual formation of the tulip flame. As disturbances grow, the perturbed flow, which opposes the gas motion at the center of the tube, may become sufficiently large so as to advect the flame into a shape, whereby its center part becomes increasingly more convex with respect to the burned gas. Consistent with this, one finds that the flame temperature, and hence the burning rate, decreases at the convex portion of the flame front.

It should be pointed out that the linear stability theory is limited to the determination of the conditions for the onset of an instability and does not completely determine the new structure that develops thereafter. Indeed, the present theory suggests that, at the onset of the instability, a flame shape that is convex toward the unburned gas at the center of the tube (i.e., with $\varepsilon > 0$) is equally probable. A nonlinear theory, which accounts for finite amplitude disturbances, is needed to determine the unique flame shape that is observed experimentally as well as the formation of the cusp at the center of the tube.

Conclusions

The initial development of a tulip flame has been identified as the onset of an instability on a nominally planar flame. As the planar front accelerates down the tube, the fresh mixture ahead is compressed and pushed downstream, whereas the burned products expand and move upstream. The density decrease across the flame gives rise to a hydrodynamic instability (the Darrieus–Landau instability). The limitation imposed by the finite duration of the process does not allow the long wavelength disturbances to

significantly develop. Furthermore, a growing disturbance on an accelerating front may not appear as an instability unless its growth rate significantly exceeds the propagation speed. The short wavelength disturbances, on the other hand, can be stabilized by diffusional-thermal effects in mixtures with Lewis numbers $\mathrm{Le} > \mathrm{Le}_*$. Thus, there would be only a certain range of growing modes, corresponding to disturbances of moderate wavelengths. These disturbances will all be excluded if the aspect ratio of the tube is small enough, in which case the flame remains planar as it propagates throughout the tube. In tubes of larger aspect ratio, however, an instability characterized by a wave number $k_* > k_c$, where k_c is the fastest growing mode, develops. The onset of the instability is identified as the location $x = x_f^*$, where the disturbance has grown to a sufficiently large size. It is anticipated that nonlinear effects, which eventually become important, are responsible for the formation of the cusped structure observed in experiments.

Like several previous studies [4,7], our results suggest that the tulip flame phenomenon is a manifestation of the Darrieus–Landau instability. Unlike these studies, however, we find that the roles of diffusion and of flame acceleration due to confinement are equally important. Previous numerical studies have primarily concentrated on reproducing the tulip flame for given conditions. In contrast, our goal has been to determine the conditions under which a tulip flame would be observed in an experiment. We have thus identified a range of values of the Markstein length μ for which a tulip flame may be observed. This range can be also expressed in terms of the Lewis number Le, which is based on the mass diffusivity of the deficient component in the mixture. The formation of the tulip flame, therefore, depends on the mixture composition (via the Lewis number) and on the initial pressure in the tube (because $D \sim$ pressure), as experiments indicate. The analysis also selects the disturbance, which grows first and has the largest growth rate. This, in turn, provides the critical dimensions of the tube where a tulip flame would be observed. In agreement with the experimental records, our analysis shows that typically the tulip flame forms after the flame has traveled half of the length of the tube and does not form in short tubes.

Acknowledgments

This work has been partially supported by the National Science Foundation and by NASA's Microgravity Combustion Science program.

REFERENCES

1. Ellis, O. C. de C., *Fuel Sci. Pract.* 7:502 (1928).
2. Gueńoche H., in *Nonsteady Flame Propagation* (G. H. Markstein, Ed.) The Macmillan Company, New York, 1964, p. 107.
3. Starke, R., and Roth, P., *Combust. Flame* 66:249 (1986).
4. Dunn-Rankin, D., Barr, P. K., and Sawyer, R. F., *Twenty-First Symposium (International) on Combustion,* The Combustion Institute, Pittsburgh, 1986, p. 1291.
5. Rotman, D. A., and Oppenheim, A. K., *Twenty-First Symposium (International) on Combustion,* The Combustion Institute, Pittsburgh, 1986, p. 1303.
6. Gonzalez, M., Borghi, B., and Saouab, A., *Combust. Flame* 88:210 (1992).
7. N'konga, B., Fernandez, G., Guillard, H., and Larrouturou, B., *Combust. Sci. Technol.* 87:69 (1992).
8. Makhviladze, G. M., and Melikhov, V. I., in "Dynamics of Gaseous Combustion," *Prog. Astronautics Aeronautics* 151:307 (1991).
9. McGreevy, J. L., and Matalon, M., "Hydrodynamic Instability of a Premixed Flame under Confinement," *Combust. Sci. Technol.*, to appear.
10. Markstein, G. H., *Nonsteady Flame Propagation,* The Macmillan Company, New York, 1964.
11. Matalon, M., and Matkowsky, B. J., *J. Fluid Mech.* 124:239 (1982).
12. Pelce, P., and Clavin, P., *J. Fluid Mech.* 124:219 (1982).
13. Matalon, M., in *Mathematical Modeling in Combustion Science* (J. D. Buckmaster and T. Takeno, Eds.), Lecture Notes in Physics, 1988, Vol. 299, p. 163.
14. Darrieus, G., Unpublished manuscript presented at the *Sixth International Congress of Applied Mechanics,* 1938.
15. Landau, L. D., *Acta Physicochim. URSS* 19:77 (1944).

Twenty-Fifth Symposium (International) on Combustion/The Combustion Institute, 1994/pp. 1415–1422

FLAME FRONT DISTURBANCE INDUCED BY A WEAK PRESSURE WAVE

RITSU DOBASHI AND TOSHISUKE HIRANO
Department of Chemical System Engineering
The University of Tokyo
Tokyo, Japan

AND

TAKASHI TSURUDA
Environmental Science Center
The University of Tokyo
Tokyo, Japan

An experimental study has been conducted on the effect of unburned mixture properties on flame front disturbance induced by acceleration. Experiments were performed using a rectangular combustion chamber of 80 × 80 × 440 mm. The flame front disturbance was observed in two different directions by high-speed schlieren photography. Mixtures used are of three different concentrations (ϕ = 0.8, 1.0, and 1.25) of methane/air and two different concentrations (ϕ = 1.0 and 1.5) of propane/air. For the methane/air mixture of ϕ = 1.0, experiments were performed at three different initial pressures (P_i = 50, 70, and 101 kPa). The observed disturbance was of a very fine structure of circular spikes, which penetrated into the burned gas. The scales of disturbance were measured and indicated to be in the range of 1.7–4.0 mm. The circular spike shape is a typical structure induced by accelerating the flame front where the density changes steeply. However, the shape of the disturbance observed for a rich propane/air mixture was not of circular spikes but of a net of ridges. For the rich propane/air mixture, the effect by preferential diffusion was remarkable and the disturbance of a different structure was generated. For the methane/air mixtures, the scale was the smallest at ϕ = 1.0 and larger at ϕ = 0.8 and 1.25. The scale for the propane/air mixture of ϕ = 1.0 was slightly larger than that in the methane/air mixture of ϕ = 1.0. The scale became larger with the decrease of the initial pressure. The measured scales were compared with the preheat zone thicknesses of corresponding flames. It was shown that the scale is closely related with the flame thickness. The scale of disturbance is found to be about 15 times as large as the preheat zone thickness.

Introduction

Knowledge of the disturbance appearing on a propagating flame front is indispensable in understanding the behavior of gas explosions [1–3] and the characteristics of reciprocating engines [4,5]. Therefore, it is necessary to study the flame front disturbance for an accurate prediction of gas explosion behavior and an appropriate improvement of reciprocating engines.

Disturbance on a propagating premixed flame front is known to be generated by several causes such as turbulence of the approach flow, hydrodynamic instability, diffusion-thermal instability, and nonuniformity of the unburned mixture [6]. Among these causes, the hydrodynamic instability, especially that induced by an acceleration of the flame front, has been examined in this study. A weak pressure wave was applied to accelerate the flame front in the present experimental study, because it can be easily controlled. Indeed, so many examples can be found of the disturbance appearing on a flame front accelerated by a pressure wave [2,7–15].

This type of flame front disturbance induced by an acceleration has been studied by several researchers who were interested in the instability of the flame front as an interface of different density gases [13] and the interaction of the flame front with acoustic waves [11,12]. In our previous studies [2,10], fine disturbance was found to be generated on a laminar propagating flame front when it was stimulated by a weak pressure wave. Such disturbance was easily enhanced or suppressed, respectively, by accelerating or decelerating the flow field. We have also made simultaneous observation in the two different directions of the flame front disturbance to elucidate its three-dimensional structure [14,15]. As a result, the structure of disturbance was found to be in the shape

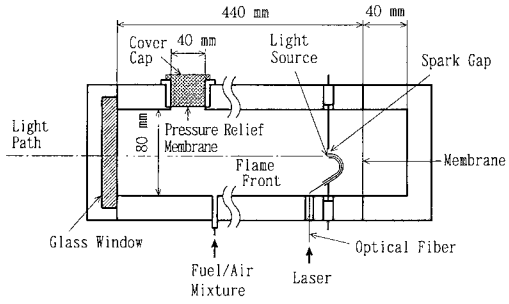

FIG. 1. Schematic of the combustion chamber.

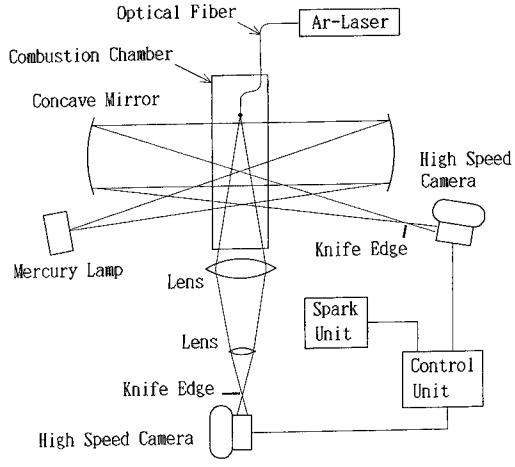

FIG. 2. Schematic of the high-speed schlieren system.

of a circular spike. However, detailed characteristics of the circular spike have not sufficiently elucidated. The objective of the present study is to examine the effects of unburned mixture properties on the behavior of the circular spike. The results will be useful to predict the flame front disturbance induced by acceleration.

Experimental

The combustion chamber used in the present experiments is schematically shown in Fig. 1. It is rectangular, with internal dimensions of 80 × 80 mm in cross section and 440-mm long. On the upper wall, a pressure relief membrane is installed, circular in shape and 40 mm in diameter. Both side walls hold windows, each of which is fitted with an 80- × 180-mm optical glass plate. One end wall of the chamber also holds a window fitted with an 80- × 80-mm optical glass plate. At the other end, a small chamber is connected to the combustion chamber. The cross section of the small chamber is the same as that of the combustion chamber, and its length is 40 mm. A spark gap is installed at the center of the cross section in the combustion chamber 30 mm away from the end of the small chamber.

The combustible gases used were methane and propane. These gases were mixed with air in a mixing tank before each test and subsequently introduced in the pre-evacuated combustion chamber. The initial pressure of the combustion chamber was set to be a prearranged value. At the start of each test, the gas was quiescent and the concentration distribution of the combustible gas was uniform in the combustion chamber. An electrical spark at a spark gap was used to ignite the mixture. The small chamber was used to generate a weak pressure wave. Before starting each test, the small chamber was separated from the combustion chamber by a membrane of paraffin paper and filled with the same mixture at the same initial pressure as the combustion chamber. After ignition, when the pressure in the combustion chamber became about 30 kPa higher than the initial pressure, the paraffin paper sheet broke suddenly. Then, a rarefaction wave started to propagate toward the combustion chamber, and a pressure wave started to propagate in the opposite direction and reflected at the end wall of the small chamber. The part of the flame front propagating toward the glass window of the end wall first decelerated by passing of the rarefaction wave and successively accelerated by passing of the pressure wave. Disturbance on the flame front was generated by the acceleration. The advantage of using such a weak pressure wave as generated by the breakage of paraffin paper is that flame front disturbance can be generated without distorting the whole flame shape [2,10]. At the final stage of each test, the pressure relief membrane failed to provide a vent to prevent the windows from breaking due to an excessive pressure rise.

The flame front disturbance was recorded on high-speed schlieren photographs taken simultaneously in two different directions through the windows of the combustion chamber [14,15]. The schlieren system used in the present experiments is shown schematically in Fig. 2. The schlieren photograph of a flame front observed in the direction normal to it was taken through the glass window of the end wall. The light from the argon laser used as a light source was guided by an optical fiber into the combustion chamber. A point light source at the end of the optical fiber was located near the ignition point. The light emitted from this light source passed the flame and glass window of the end wall and was focused by convex lenses. After being partly cut by a knife edge near a focal point, the light reached a high-speed camera. The camera used in the present experiments was a 16-mm high-speed cine camera operated at a framing rate of 4000 frames/s. The advantage of this system is to reproduce a situation in which (a) the light source is placed inside of the flame sphere and (b)

there is only one objective flame front in the schlieren optical path. At the same time, the schlieren photographs taken in the direction of the tangent line of the leading flame front were taken through the windows installed in both side walls by using a mercury-vapor lamp and concave mirrors with a 3000-mm focal length. This traditional setup of schlieren photography was adopted because the photograph taken by this system and the previous one may give us an image of the three-dimensional structure of flame front disturbance. The schlieren photographs taken in the tangent direction of the leading flame front were recorded by a high-speed 16-mm cine camera synchronized with the camera used to take schlieren photographs in the direction normal to the flame front.

Results and Discussion

Aspects of Disturbance:

Typical results are shown in Fig. 3. The combustible mixture was of methane/air of $\phi = 1.0$, and the initial pressure was 70 kPa. The series of high-speed schlieren photographs shown in Fig. 3 were simultaneously taken in two different directions. The variable t represents the time from ignition. The photographs on the left side in the figure were taken in the normal direction to the flame front (front view) and photographs on the right side were taken in the tangent direction of the leading flame front (side view). Movement of the leading flame front was examined on the schlieren photographs, and the position and velocity of the leading flame front are seen in Fig. 4. The leading flame front is shown to first decelerate by being passed by a rarefaction wave and subsequently accelerate by a weak pressure wave reflected at the end wall of the small chamber. For $t = 27.31$ ms, no disturbance is observed in both the front and side views. Nonuniform images seen in the background of front view photographs were caused by interference of the laser light. In the side view, small-scale disturbance appears at $t = 27.57$ ms. The side view of this disturbance has been observed in our previous studies [2,10,14,15]. This disturbance seems to be caused by penetration of the flame front into the burned gas. Circular images of disturbance suddenly appear in the front view at $t = 28.09$ ms, about 1 ms after the start of acceleration. Individual shapes of disturbance are inferred to be of circular spikes. The scale of these spikes is in the range of 1.7–4 mm. It is shown that very fine disturbance is generated on the flame front within a very short period, less than 1 ms. Pressure variations in the combustion chamber under several conditions are shown in Fig. 5. The pressure increases smoothly at an early stage after ignition and starts to oscillate after the separating paper breaks. The mean pressure increases more rapidly after this point. This rapid pressure increase must be caused by the increase of the flame front area by generated disturbance.

Effect of Mixture Properties on Disturbance:

The flame front disturbance was observed for the cases of five different mixtures of methane/air with $\phi = 0.8$, 1.0, and 1.25 and propane/air with $\phi = 1.0$ and 1.5. In Fig. 6, five pairs of photographs are shown, which represent the flame front disturbance for the above five cases. As pointed out in the previous section, the shapes of disturbance observed in the cases, except for that of a propane/air mixture of $\phi = 1.5$, are seen to be of circular spikes. In the case of the propane/air mixture of $\phi = 1.5$, no circular disturbance can be found but a net composed of thick lines is seen in the front view. In this rich propane/air mixture, the preferential diffusion effect is known to be remarkable. This effect limits the deformation of flame front to a certain amplitude. The deformation caused by the preferential diffusion effect develops to the next point along the flame front. This results in ridge shapes of disturbance, instead of circular spike shape. This should be the reason why circular spike shapes of disturbance were not observed only for the rich propane/air mixture.

The diameters of circles representing the circular spike shapes of disturbance and the distances between the centers of two neighboring circles were measured as representing scales of turbulence. The mean value of the measured diameters and distances are shown in Table 1. The range of the measured values are also listed in the same table. It is seen that the diameter is the smallest for the methane/air mixture of $\phi = 1.0$ (1.7 mm) and the largest for the methane/air mixture of $\phi = 0.8$ (2.6 mm). The distance is also the smallest for the methane/air mixture of $\phi = 1.0$ (2.2 mm) and the largest for the propane/air mixture of $\phi = 1.0$ (2.9 mm). For the methane/air mixtures, the scale is smaller at $\phi = 1.0$ and larger at $\phi = 0.8$ and 1.25. For the propane/air mixtures, the scale is smaller at $\phi = 1.0$ and larger at $\phi = 1.5$. The scale for the propane/air mixture of $\phi = 1.0$ is slightly larger than that for the methane/air mixture of $\phi = 1.0$.

Effect of the Initial Pressure on Disturbance:

Experiments were performed for three different initial pressures of the methane-air mixture of $\phi = 1.0$. The results are shown in Fig. 7. The circles representing circular spike shapes of disturbance are observed in the front views for every initial pressure. The scales (the diameter and the distance) of these circles were measured and listed in Table 1. It is seen that the scale of flame front disturbance becomes larger with the decrease of initial pressure. The largest scales were observed at the lowest initial pressure

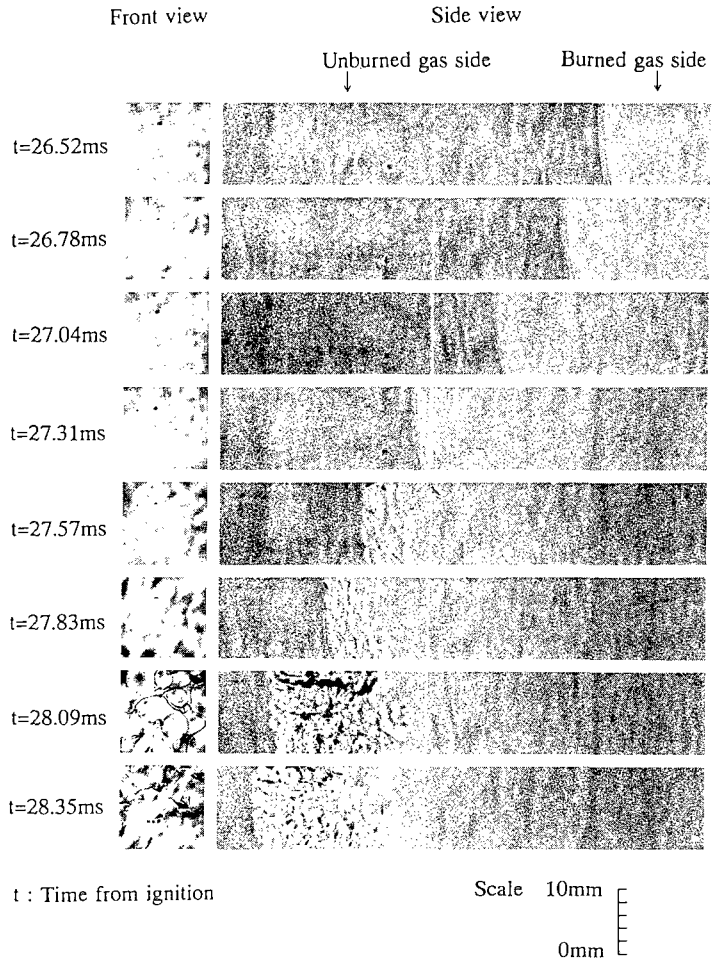

FIG. 3. High-speed schlieren photographs taken in two different directions. Mixture: methane/air of $\phi = 1.0$; initial pressure p_i: 70 kPa.

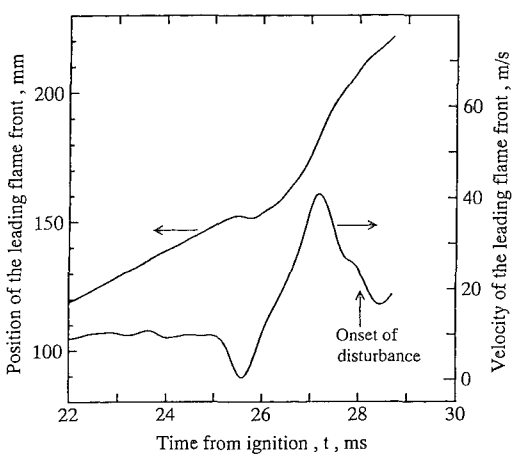

FIG. 4. Position and velocity of the leading flame front. Mixture: methane/air of $\phi = 1.0$; initial pressure p_i: 70 kPa.

(50 kPa), and they are 3.9 mm (diameter) and 4.0 mm (distance).

Discussion:

It has been postulated that the shape of flame front disturbance is closely related to the mechanisms that sustain or enhance the disturbance [7,14,15]. In this study, the flame front disturbance is induced by the acceleration during pressure wave passing. This type of disturbance is understood to be formed by the difference of induced velocities across the flame front where the steep density change exists. The induced velocity can be evaluated by using the following equation [8]:

$$\frac{d\omega}{dt} = 1/\delta(1/\rho_b - 1/\rho_u)\boldsymbol{n} \times (\boldsymbol{n} \times \nabla p) \qquad (1)$$

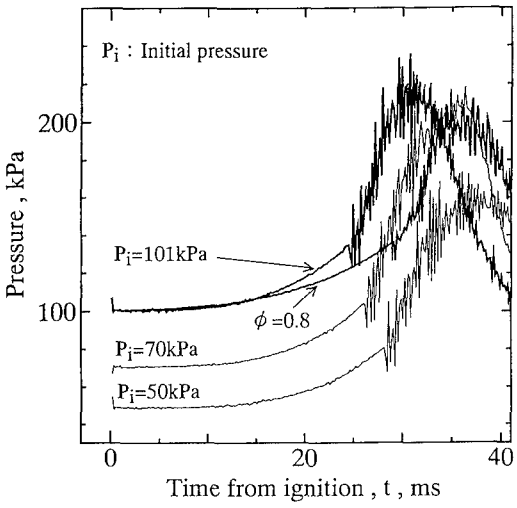

FIG. 5. Pressure variations in the combustion chamber. Mixture: methane/air of $\phi = 1.0$, except for one datum ($\phi = 0.8$).

where $d\omega/dt$ is the rate of vortex generation at the flame front, δ is the flame front thickness across which the density changes from the density of unburned gas ρ_u to that of burned gas ρ_b, $\mathbf{n}$ is the unit vector normal to the flame front and pointing to the unburned gas, and ∇p is the pressure gradient across the pressure wave. The induced velocity along the flame front can be evaluated by the value $d\omega/dt$. If a small fluctuation like a hollow convex to the burned gas side exists, the induced velocity is larger at the point where the angle between the vector $\mathbf{n}$ and ∇p is larger. Thus, the top of the hollow-shaped disturbance develops rapidly in the direction to the burned gas. The small fluctuation is believed to grow to be a spike-shaped disturbance.

In the above discussion, the disturbance grows rapidly as its scale becomes smaller. However, the observed scale of disturbance is finite (1.7–4.0 mm), so that the rate of disturbance growth must be limited. Thus, the mechanism by which the scale of this kind of disturbance is determined seems to be important to predict the rate of disturbance growth but has not been elucidated sufficiently. Searby and Rochwerger [11] studied cellular flames formed in a tube where acoustic standing waves existed and proposed a model to explain the stability limit and the scale of disturbance. In this study, the scale of cellular structure in an acoustic field was determined by the coupling mechanism between the flame and the acoustic field. Whereas, in our study, the disturbance is generated by only one pulse of acceleration, and there is no coupling of periodic phenomena. The scales observed in the present study were much smaller than that observed in the acoustic field.

If the scale of disturbance becomes much smaller, the rate of disturbance growth is considered to decrease because the transport of momentum, heat, and species becomes extremely large. Therefore, the balanced scale might exist in which the disturbances can develop most effectively. It is known that transport occurs effectively in the flame front where the temperature and concentration of species change steeply. Thus, there must be a certain relation between the scale of disturbance and the flame front

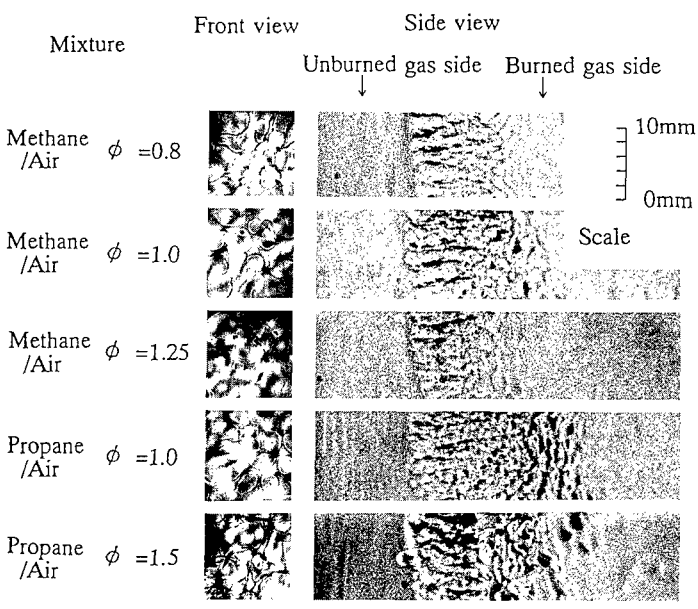

FIG. 6. High-speed schlieren photographs representing the effect of mixture properties on the flame front disturbance. Initial pressure p_i: 101 kPa.

TABLE 1
Measured scale of the flame front disturbance

Mixture	Concentration	Initial pressure p_i (kPa)	Pressure at the onset of disturbance (kPa)	Diameter of circles[a] (mm)	Distance of circles[a] (mm)	Preheat zone thickness δ_{pr} (mm)
Methane/Air	$\phi = 0.8$	101	167	2.6 (2.1–3.1)	2.8 (2.5–3.2)	0.22
	$\phi = 1.0$		192	1.7 (0.8–2.4)	2.2 (1.5–3.0)	0.14
	$\phi = 1.25$		162	2.1 (1.6–2.7)	2.4 (2.2–2.7)	0.17
Propane/Air	$\phi = 1.0$		177	2.3 (1.3–2.8)	2.9 (1.9–3.3)	0.18
	$\phi = 1.5$		167	(not circular)	(not circular)	0.26
Methane/Air	$\phi = 1.0$	70	131	3.1 (2.1–4.8)	3.7 (2.8–4.8)	0.21
		50	103	3.9 (1.4–7.6)	4.0 (2.5–5.7)	0.26

[a]Mean value. The range of the measured values is shown in parentheses.

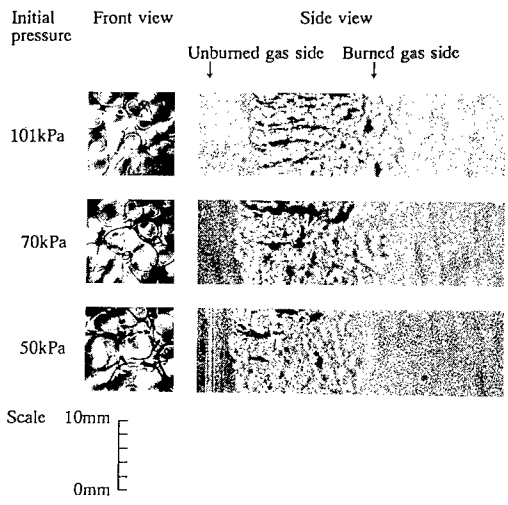

FIG. 7. High-speed schlieren photographs representing the effect of the initial pressure on the flame front disturbance. Mixture: methane/air of $\phi = 1.0$.

thickness. The comparison has been made between the observed scale of disturbance and the preheat zone thickness, which is assumed to represent the flame front thickness. The preheat zone thickness δ_{pr} was calculated by using a simple heat transfer relation given by the following equation [16]:

$$\delta_{pr} = \ln 100 \frac{\lambda}{c_p \rho_u S_u} \qquad (2)$$

where λ is the conductivity, c_p is the specific heat, ρ_u is the density of unburned gas, and S_u is the burning velocity. Here, δ_{pr} was calculated for each test at the same pressure and temperature as the moment when disturbance was observed. The measured value was used for the pressure in the combustion chamber. The temperature was estimated by assuming adiabatic compression of the unburned mixture. The results of experimental measurements [17,18] were used for the burning velocity. The calculated preheat zone thicknesses are listed in Table 1 and plotted in Fig. 8 against the diameter of the circular spike shape of disturbance and the distance between the adjacent circular spike shapes. It is seen that a mutual correlation exists between the scale of disturbance and preheat zone thickness. It is also seen that the scale of disturbance is about 15 times as large as the calculated thickness of the preheat zone.

Conclusions

Detailed structure of flame front disturbance induced by a weak pressure wave has been studied experimentally, and the following conclusions were derived.

The observed disturbance was of a very fine structure of circular spikes, which penetrated into the burned gas. The scales of disturbance were measured and indicated to be in the range of 1.7–4 mm.

The circular spike shape is a typical structure induced by accelerating the flame front where the density changes steeply. However, the shape of the disturbance observed for a rich propane/air mixture was

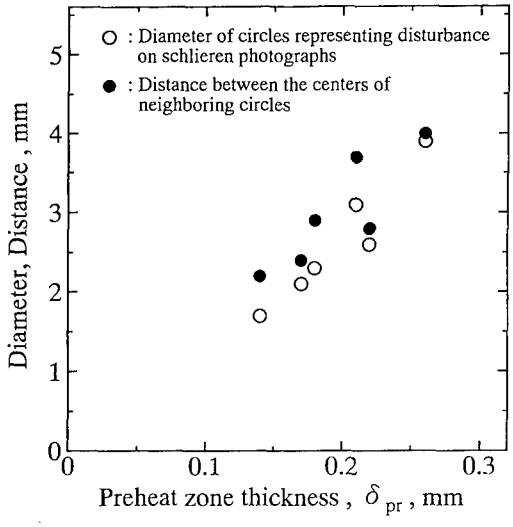

FIG. 8. Correlation between the scale of disturbance and the preheat zone thickness.

not of circular spikes but of a net of ridges. For a rich propane/air mixture, the effect by the preferential diffusion mechanism was remarkable, and the disturbance of different structure was generated.

For the methane/air mixtures, the scale was the smallest at $\phi = 1.0$ and larger at $\phi = 0.8$ and 1.25. The scale for the propane/air mixture of $\phi = 1.0$ was slightly larger than that for the methane/air mixture of $\phi = 1.0$. The scale became larger with the decrease of the initial pressure. The measured scales were compared with the preheat zone thicknesses of corresponding flames, and it was shown that the scale was closely related with the flame thickness. The scale of disturbance was found to be about 15 times as large as the preheat zone thickness.

REFERENCES

1. McCann, D. P. J., Thomas, G. O., and Edwards, D. H., *Combust. Flame* 59:233 (1985).
2. Tsuruda, T., Harayama, M., and Hirano, T., *J. Heat Transfer* 108:877 (1986).
3. Tamanini, F., and Chaffee, J. L., *Twenty-Fourth Symposium (International) on Combustion,* The Combustion Institute, Pittsburgh, 1992, p. 1845.
4. Jones, W. P., and Whitelaw, J. H., *Twentieth Symposium (International) on Combustion,* The Combustion Institute, Pittsburgh, 1984, p. 233.
5. Trautwein, S. E., Grudno, A., and Adomeit, G., *Twenty-Third Symposium (International) on Combustion,* The Combustion Institute, Pittsburgh, 1990, p. 723.
6. Williams, F. A., *Combustion Theory,* Addison-Wesley, Redwood City, CA, 1985.
7. Markstein, G. H., *Nonsteady Flame Propagation,* Pergamon, London, 1964.
8. Tsuruda, T., and Hirano, T., in *Dynamics of Reactive Systems Part II: Modeling and Heterogeneous Combustion* (J. R. Bowen, et al., Eds.), AIAA, Washington, DC, 1986, p. 110.
9. Abdel-Gayed, R. G., Bradley, D., and Lawes, M., *Proc. R. Soc. London A,* 414:389 (1987).
10. Tsuruda, T., and Hirano, T., *Combust. Flame* 84:66 (1991).
11. Searby, G., and Rochwerger, D., *J. Fluid Mech.,* 231:529 (1991).
12. Candel, S. M., *Twenty-Fourth Symposium (International) on Combustion,* The Combustion Institute, Pittsburgh, 1992, p. 1277.
13. Liu, F., McIntosh, A. C., and Brindley, J., *Combust. Sci. Technol.* 91:373 (1993).
14. Dobashi, R., Hirano, T., and Tsuruda, T., *Combust. Sci. Technol.* 96:155 (1994).
15. Dobashi, R., Tsuruda, T., and Hirano, T., *Fourteenth International Colloquium on Dynamics of Explosions and Reactive Systems,* Coimbra, 1993.
16. Gaydon, A. G., and Wolfhard, H. G., *Flames,* Chapman and Hall, London, 1970.
17. Iijima, T., and Takeno, T., *Combust. Flame* 65:35 (1986).
18. Metghalchi, M., and Keck, J. C., *Combust. Flame,* 38:143 (1980).

COMMENTS

A. C. McIntosh, Leeds University, UK. In recent work [1], it has been demonstrated that the Rayleigh–Taylor effect at a flame induced by a pressure gradient interacts with the diffusional-thermal instability (i.e., there is a Lewis number dependence). Thus, for *fuel-rich* hydrocarbons the spikes will occur much more readily than on the fuel-lean side. For a constant value of pressure gradient (burnt to unburnt), you need to plot instability growth against mixture strength to demonstrate this.

Secondly, in the same paper (above) the mushrooming effect was demonstrated as the spikes of unburnt gas protruded into the burnt side. Your paper does not mention this. Did you observe this phenomenon?

REFERENCE

1. Edwards, McIntosh, and Brindley, *Combust. Sci. Technol.* 99:179–200 (1994).

Author's Reply. 1. The objective of this study is to elucidate the characteristics of the structure and scale of disturbance induced by the hydrodynamic instability (the Ray-

leigh–Taylor effect) to understand the initiation of disturbance on the propagating laminar flame front. The dependence of the growth rate on the Lewis number is out of our scope in this study.

The flame front disturbance induced by the Rayleigh–Taylor effect is essentially different from that induced by the diffusion-thermal effect (Lewis number effect). The former must grow more rapidly as the amplitude increases, although the growth of the latter must be balanced at a certain amplitude. Therefore, the structures of these should be quite different (see Ref. 14 in our paper). The structure of the former becomes the spike shape (three-dimensional structure). On the other hand, that of the latter becomes the ridge shape (two-dimensional structure). If these two effects are interacting, the structure of the disturbance can not be a circular spike shape, but a complex shape. In the case for a rich propane/air mixture when the Lewis number effect is efficient, we have observed the front view composed of variously shaped lines (see Fig. 6).

2. We have never observed the formation of the mushroom-shaped structure, although we have performed a lot of experiments in methane/air and propane/air mixtures.

•

Kuldeep Prasad, Yale University, USA. Is there an explanation for flame deceleration before it accelerates under the influence of the pressure wave?

Author's Reply. In our experimental setting, the pressure of the small chamber is lower than that of the combustion chamber when the separating membrane breaks. Therefore, a rarefaction wave passes the flame front before the passage of the weak pressure wave. The passage of the rarefaction wave decelerates the flame front.

•

Bernhard Baüerle, Inst. für Technische Verbreunung, Germany. Do you expect that the flame front disturbances you observed in your flame fronts could also occur in turbulent premixed flame fronts?

Author's Reply. It is expected that the flame front disturbance could develop also on a turbulent flame front when it is accelerated. In this study, small perturbations of laminar flame front grow to be spike-shaped disturbances. In a turbulent flame, convex parts of the distorted flame front will develop and protrude toward the burned gas side. Such phenomena were observed at the final stage of an experiment when disturbance of flame front was fully developed. A spike-shaped disturbance was observed to appear in the side-view high-speed schlieren photographs. However, the shape of the flame front was very complicated and the detailed structure, such as the scale of the disturbance, could not be examined.

•

H. S. Mukunda, Indian Institute of Science, India. The governing instability in the experiments appears to be of Landau–Darries type. Linear stability results are available. Also, some recent computations of linear stability with variable properties seem to indicate most unstable wavelength to flame thickness ratio (for H_2-air system) of 13 for constant properties and 30 for variable properties [see Mukunda and Drummond, "Two Dimensional Linear Stability of Premixed Laminar Flames under Zero Gravity," *Appl. Sci. Res.* 51:687–711 (1993) or NASA TP 3131]. These seem to be in a range similar to the values you are reporting from your experiments.

Author's Reply. The governing instability in our experiments should not be of the Landau–Darries type but of the Rayleigh–Taylor type. The Landau–Darries type instability is a fluid dynamical instability induced by an expansion of gas at a flame front. It must occur without stimulation by a pressure wave; however, no disturbance was observed in our experiments unless a pressure wave was applied. The Rayleigh–Taylor type instability is observed at an interface between two fluids of different densities when the interface is accelerated toward the heavier fluid side. Spike-shaped disturbance was observed to appear not only on a flame front but also on a nonreacting interface where no expansion occurs [1].

REFERENCE

1. Lewis, D. J., *Proc. R. Soc. London, Ser. A* 202:81 (1950).

Twenty-Fifth Symposium (International) on Combustion/The Combustion Institute, 1994/pp. 1423–1437

INVITED TOPICAL REVIEW

POLYMER COMBUSTION AND FLAMMABILITY—ROLE OF THE CONDENSED PHASE*

TAKASHI KASHIWAGI

Building and Fire Research Laboratory
National Institute of Standards and Technology
Gaithersburg, MD 20899, USA

The combustion process of polymers is a complex coupling of energy feedback from a flame to the polymer surface with gasification of the polymer to generate combustible degradation products. Although there are extensive studies of the effects of wind velocity, gas phase oxygen concentration, external thermal radiation, and gravity on the combustion of polymers, the effects of polymer characteristics on combustion and flammability are not nearly as well understood as those in the gas phase. At present, detailed governing equations for continuity, momentum, energy, and chemical species concentration in the gas phase can readily be written with appropriate boundary conditions, and their solutions can be derived for various cases. However, even those governing equations cannot be derived for the condensed phase without understanding of the governing chemical and physical processes that control the gasification of polymers. This paper concentrates on describing various observed phenomena in polymers (which have been often ignored or neglected) during their combustion, some or all of which might have significant effects on the burning rate and flammability properties. Because of a lack of understanding of the basic combustion mechanisms of polymers, theoretical models able to predict combustion phenomena and flammability properties are not available. In order to overcome this problem, global material characteristics are currently measured by well-defined test methods, and the results are used as inputs to fire growth models intended to predict behavior of the materials in specific fire scenarios. To improve the fire performance of polymers, a nonhalogenated char-forming flame-retardant approach is suggested, and its benefits are discussed.

Introduction

Synthetic polymers are a pervasive part of today's society. They can be found in nearly every commercial building, residential house, transportation vehicle, etc.; they permeate our surroundings. Total polymer production in the USA in 1992 was roughly 26 million tons [1] (additional 5 million tons for synthetic rubber and fibers), and it is expected that a similar amount of polymer production will continue. Today, synthetic polymer materials are rapidly replacing more traditional materials such as steel and nonferrous metals and natural polymeric materials such as wood, cotton, natural rubber, and so on, but they also are original materials in their own right, possessing uniquely valuable physical properties. However, one weak aspect of synthetic polymer materials compared with steel and other metals is that these materials are combustible under certain conditions. Thus, the majority of polymer-containing end products (for example, cables, carpets, furniture) must pass some type of regulatory test to help assure public safety from fire. Therefore, it is important to understand how synthetic polymers burn and how to modify the materials to make them less flammable in order to pass such tests without compromising the uniquely valuable physical properties. This paper describes the current understanding of the role of the condensed phase in combustion of synthetic polymers, theoretical modeling in the condensed phase, flammability measurement, and methods to reduce their flammability.

Combustion Process

Combustion of synthetic polymer materials is characterized by a complex coupling between condensed and gas phase phenomena. Furthermore, the phenomena in each phase consist of a complex coupling of chemical reactions with heat and mass transfer processes, as described later. Since the gas phase phenomena, such as chemical reaction, turbulence, soot formation, and so on, have been extensively studied and described elsewhere, this paper concentrates on the less-explored condensed phase phenomena and their role in flammability.

Radiative Heat Transfer:

In order to burn a polymeric material, thermal energy must be added to the material to raise its tem-

*Contribution from the National Institute of Standards and Technology; not subject to copyright.

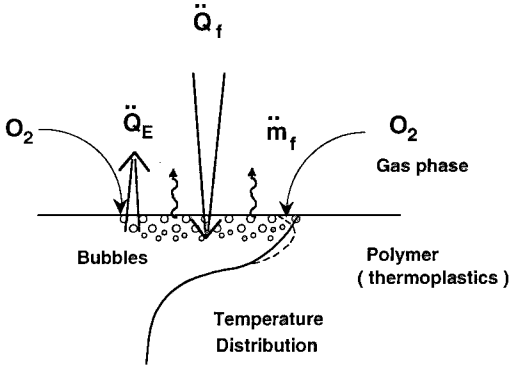

FIG. 1. Schematic illustration of polymer (thermoplastic) gasification. The solid line is the temperature distribution for an opaque material, and the dashed line is for a diathermic material.

perature sufficiently to initiate degradation. This energy could be from an external source, in the case of an ignition event, or from an adjacent flame as energy feedback in the case of flame spread and burning. Thermal radiation is a primary mode of energy transfer from the flame to the polymer surface except for small samples (roughly less than 10-cm diameter) [2–6]. The amount of energy absorbed by the polymeric material depends on the level and the spectral characteristic of the radiant flux, absorption characteristics of the material, and the material surface reflectance with respect to the emission spectrum of the incident radiation [7–10]. Generally, the emission spectra of large flames are continuous in the infrared, as a result of high-temperature soot particles, with additional strong emission bands from H_2O and CO_2 [6]. The absorption spectra of polymeric materials consist of numerous absorption bands in the infrared wavelength region, depending on the vibration modes of the molecular bonds in the polymer structure [11,12]. If the effective absorption coefficient of the material with respect to the external radiation is small, a large amount of the material beneath the surface is heated, which slows the rate at which the material approaches its degradation temperature range. However, if the effective absorption coefficient is large, most of the radiation is absorbed close to the surface, and a thin layer of the material is rapidly heated to its degradation temperature range. In this case, the ignition delay time becomes shorter for the same external radiant flux [13,14]. Also, the maximum temperature in the material is at the surface with an opaque material instead of below the surface with in-depth absorption [9,10,13]. Two different temperature distributions are shown in Fig. 1. The solid line is the temperature distribution for an opaque material, and the dashed line is for a diathermic material. As described below, bubbles are often formed at/near the surface of a thermoplastic sample.** There are no published papers concerning how significantly the bubbles affect the heat transfer process in the sample by modifying heat conduction and/or scattering the incident external radiation, but potential effects could be large.

Degradation Reactions:

When temperatures near the surface become high, thermal degradation reactions occur and evolve small gaseous degradation products. The majority of the evolved products is combustible. Depending on the nature of the polymer, thermal degradation reactions may proceed by various paths. Since there are several recent books and articles describing thermal degradation chemistry in detail [15–17], only an extremely brief discussion is presented here. It has been accepted that the majority of vinyl polymers degrade thermally by a free radical chain reaction path. Free radical chain reactions consist of random or chain-end-initiated scission, depropagation, intermolecular or intramolecular transfer, and termination reactions. Polyethylene (PE) is a typical example of a polymer that undergoes scission at random locations on the main chain to yield many smaller molecular fragments. Polystyrene (PS), polypropylene (PP), and polymethylacrylate (PMA) belong to this group. Polymethylmethacrylate (PMMA) undergoes a reversal of the polymerization reaction after the initial breakage and yields mainly monomer molecules. Polyoxymethylene, poly-α-methylstyrene, and polytetrafluoroethylene belong to this group. These two groups of polymers undergo almost complete degradation while leaving hardly any char (carbonized polymer residue). Polymers with reactive side groups attached to the backbone of a polymer chain may first degrade as a result of interactions or instabilities of these groups; such reactions may then lead to scission of the backbone. Polyvinylchloride (PVC) and polyvinyl alcohol (PVA) are examples of such polymers. This group tends to undergo cyclization, condensation, recombination, or other reactions that ultimately yield some char. Diene polymers, polyacrylonitrile, and many aromatic and heterocyclic backbone polymers also belong to this char-forming group. Common to the pyrolysis of all these polymers is the formation of conjugated multiple bonds, transition from a linear to a cross-linked structure, and an increase of the aromaticity of the polymer residue [18]. For polymers containing aromatic carbon and/or heterocyclic links in the main chain of the polymer structure, general features of their pyrolysis and char

**Most linear or branched polymers can be made to soften and take on new shapes by the application of heat and pressure. These polymers are said to be thermoplastic. The cross-linked polymers (with cross-linkages among different polymer chains) cannot be made to soften and/or melt.

yield have been derived [19,20]. Some features are as follows: (1) the thermal stability and the char yield increase with the relative number of aromatic groups in the main chain per repeat unit of the polymer chain; (2) the thermal stability of heterocyclic polymers increases with the aromatic component of the heterocycles; and (3) pyrolysis begins with the scission of the weakest bonds in the bridging groups connecting the aromatic rings or heterocycles. Char-forming thermoplastics often swell and intumesce during their degradation/combustion, and one recent flame-retardant approach is to promote the formation of such intumescent char, as discussed later in this paper.

Degradation of a polymer is often affected by the presence of abnormal structures that are usually less thermally stable than the regular structures. Some such structures are inherent consequences of the method of polymerization. If a vinyl polymer is polymerized with a free radical initiator, termination reactions yield unsaturated end groups and also a head-to-head linkage within the chain. These abnormal structures were found in PMMA, and it was shown that they lowered the thermal stability of the polymer and reduced ignition delay time and increased burning rate [21,22].

Mass Transport:

As described above, the type of polymer structure, thermal properties, and the amount of heat transferred to the polymer determine the depth over which the polymer is heated sufficiently to degrade. Since the boiling temperatures of some of the degradation products are much less than the polymer degradation temperatures, these products are superheated as they form. They nucleate and form bubbles. Then, these bubbles grow with the supply of more small degradation products to the bubbles by diffusion from the surrounding molten polymer [23]. Since the polymer temperature is higher near the surface than further below, the polymer sample is more degraded there, and its molecular weight, M, is lower. Since the viscosity of the molten polymer, η, depends strongly on molecular weight and temperature (for example, $\eta = cM^{3.4}$ or $\eta = \exp\{-M/(E(T - T_g)\}$ [24]), the viscosity near the surface is much less than that in the interior. The net result is a highly complex generation and transport of bubbles containing small molecules from the interior of the polymer melt outward through a strong viscosity gradient that heavily influences bubble behavior. A qualitative description of this complex transport process and its effect on gasification rate has been given in Ref. 25. These complex effects of the temperature distribution in PMMA and the bubble formation at the time of piloted ignition are clearly seen in Fig. 2 [26].

To avoid the complex coupling between the gas phase and the condensed phase and also to avoid a configuration-dependent energy feedback rate (horizontal vs vertical configuration; also sample size effects), another approach, using a well-controlled external thermal radiation flux simulating the energy feedback from a flame, has been used to study the polymer gasification process [27–33]. Advantages of this approach over a burning polymer configuration are as follows: (1) heat flux can be independently changed, and (2) the surrounding gas composition can be also independently changed. Vovelle et al. [34] and Kashiwagi and Ohlemiller [25] studied the gasification rate of PMMA. They observed an increase in the transient gasification rate after surface temperature reached a constant value and concluded that degradation in the subsurface region of the sample contributes to the rate of gasification. Although it has been assumed that the degradation products generated in the subsurface region are instantaneously transported to the sample surface [34], the transport might become a rate-controlling step particularly at high temperatures [25] and at high heating rates [35]. As discussed above, polymer melt viscosity could have significant effects on bubble transport through a thermoplastic. The effects of *initial* molecular weight of PS (about a factor of 2) on gasification rate were studied at external radiant fluxes of 1.7 and 3.9 W/cm^2. However, here it was found that the effects were not significant, probably because of a rapid reduction in molecular weight by chain scissions, which would reduce the difference in molecular weight between the two samples used [22]. At present, it is clear that the subsurface degradation is important for the gasification, but it is not clear what the main transport process for the small degradation products to the sample surface is and also how rapid this transport is. It appears that diffusion of small molecule gases through a polymer is too slow to be responsible for the transport of the products [36].

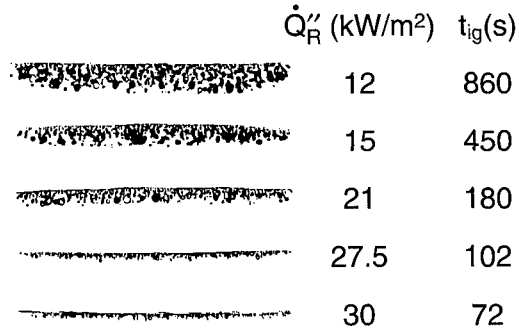

FIG. 2. Cross sections through samples of acrylic sheet that had been ignited at different external radiant fluxes but immediately quenched (Ref. 26).

Oxidative Degradation:

Not only pyrolysis reactions but also oxidative degradations in the condensed phase might significantly affect the gasification rate of a polymer if enough gas phase oxygen is transported to the polymer surface during combustion of the polymer. In order to determine the effects of oxidative degradation on the gasification process, further studies of radiative heating behavior have included measurements of the molecular weight distribution [28,37] and temperature distribution in the sample [34], the oxygen concentration in the sample by elemental analysis [28], bubble sizes (qualitatively) [25], and evolved gas analyses [28]. Brauman [38] concluded that surrounding oxygen does not affect the polymer degradation process in steady-state burning or in steady-state radiative gasification of PS and PMMA. In contrast, in the burning of small-diameter rods of PP, they inferred that condensed phase oxidation occurs, and they suggested that the polymer degrades by oxygen-promoted pyrolysis [28,38]. Stuetz et al. [39] concluded that thermal oxidative reactions at and near the PP surface are the main energy source for the burning process instead of energy feedback rate from the gaseous flame. Their conclusion was based on the measured oxygen concentration (about 26% at the surface) in the quenched sample obtained using neutron activation analysis. However, since oxygen cannot be activated by neutrons, the validity of their measurement is highly questionable. Significant importance of condensed phase oxidation was also found for steady-burning small-diameter rods of PE and PMMA [40] and also for a PE opposed diffusion flame [41]. The latter study estimated that surface oxidation at most accounted for 20% of the energy required for pyrolysis, with the remainder of the energy being delivered to the surface from the flame. These studies measured various gas phase species concentration distributions above the fuel surface, including CO and H_2O, and the importance of the condensed phase oxidation was determined from the gradients of the oxidized species at the sample surface. However, some caution is needed regarding the quantitative accuracy of the gradients, as pointed out by the comments at the end of Ref. 41. These results indicate that oxidative degradation can be of some importance when the gasification rate is relatively low and the evolving gaseous degradation products do not strongly block diffusion of surrounding oxygen into the degrading surface [25]. Such a case is shown in Fig. 3 at an external flux of 1.7 W/cm^2. When the gasification rate becomes high [25] or the heating rate is high [42], oxidation reactions appear to be less important or insignificant; this trend is shown in Fig. 3 at 4 W/cm^2. Still, further careful studies are needed to clarify the potential role of oxidative degradation because the competition between pyrolysis and oxidative degradation depends on attendant oxygen transport, which is affected by the sample orientation and size, and also on the surrounding flow condition; the range of possibilities has been only lightly explored. The contribution of oxidative degradation could be important for ignition processes at low fluxes (low heating rate) as a result of the fact that it increases the gasification rate. Since the surface heating rate of a PMMA sample during surface flame spread is of the order of 5 °C–10 °C/s [43,44], it appears that the effects of oxidative degradation of the PMMA would be negligible under such high heating rates [42]. However, this does not necessarily mean that the contribution of oxidative degradation to flame spread is always negligible. There is some evidence to demonstrate the participation of oxidative degradation in the flame spread process; this includes detection of peroxide and carbonyl moieties on the surface of PP beneath a horizontally traveling flame front [45]. Further studies with PP and other poly-

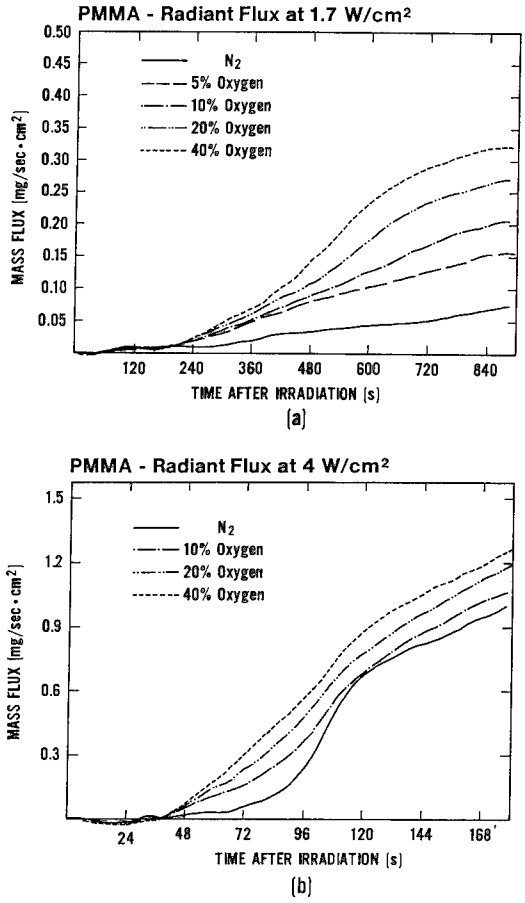

FIG. 3. Histories of mass flux from PMMA (Rohm & Haas Plexiglas G 15-mm thick) after the start of irradiation with various oxygen concentrations in the gas phase: (a) 1.7 W/cm^2, and (b) 4 W/cm^2 (Ref. 25).

mers are needed to determine the extent of the effects of oxidative degradation on flame spread.

Theoretical Models:

Theoretical models describing the above-discussed coupling between the condensed phase and the gas phase are rather limited, although some parts of the processes have been modeled in detail. The details of the thermal degradation of relatively simple polymers such as PE, PS, and PMMA have been studied by using molecular dynamic calculations [46,47], the Monte Carlo method [48,49], and kinetic calculations [50–53]. These studies are able to describe the thermal degradation behavior of polymer chains in a polymer sample and the resulting degradation products, but they are based on imposed spatially uniform temperatures, and no transport processes are included (Some of these calculations were similar to thermogravimetric experiments, i.e., linear temperature increase with time.) Although mass transport of degradation products has been included for wood [54,55] and bubble growth for coal [56,57], these processes are hardly included or even considered for the gasification of synthetic polymers except for Wichman's work [58] on steady-state gasification of PMMA under a specified external flux. A model describing the time-dependent gasification rate of PMMA has been described using a one-step global in-depth degradation reaction (no discussion was given for the kinetic constants used) with heat conduction and with no mass transport process; the numerically calculated results show reasonable agreement with the experimentally measured gasification rates under various external radiant fluxes [34]. Recently, a simple model based on four different chemical reactions, one in the condensed phase and three in the gas phase, was published; but it appears that this model is rather limited because no transport processes are included in either the condensed phase or the gas phase [59].

There are numerous models based on the partial differential equations for conservation of mass, momentum, energy, and chemical species applied to specific aspects of combustion of synthetic polymers such as ignition, flame spread, and extinction. Reviewing these papers is beyond the scope of this paper; excellent review articles are already available [60–63]. However, almost all these models are based simply on condensed phase heat conduction with a one-step global degradation reaction at the surface of the polymer sample or distributed in the sample without any mass transport in the sample. Generally, the gas phase phenomena are treated in much more detail. One of the models is extended to include a detailed description of radiative heat transfer from the flame to the sample surface [64]. It is clear at present that the models for the gas phase are more advanced and include many important physical processes, reflecting a greater understanding of the gas phase phenomena compared with those in the condensed phase.

The most commonly used approach in fire research (for example, Ref. 67) is the use of Spalding's transfer number concept (B number) or the global heat of vaporization concept [65,66], which aims to simplify still further the condensed phase treatment. This approach (sometimes called a thermal model) requires only a few quantities describing the condensed phase: the pyrolysis surface temperature, heat of vaporization, and specific heat of the material. (Basically, it is assumed that the heat transfer characteristic time in the condensed phase is much longer than the degradation reaction time and characteristic time of mass transport through the sample.) Although this approach is very convenient for the relative determination of material combustibility and is often used for engineering analysis of fire growth modeling, this can only apply strictly for the steady-state-burning case [22], and further refinement is needed to extend its application for more common time-dependent cases and also for char-forming materials [68]. This concept has been further extended to charring materials, assuming a constant char-forming degradation temperature and heat of formation of the char. Once the char is formed, it is assumed to be inert, acting only as an insulation layer [69]. A more global approach has been used to express the transient gasification rate of PMMA and particle board, heated by external radiation, as a function of the transient total amount of energy stored in the sample [30–32]. This was demonstrated for the case of a constant external radiant flux [31] and also the case of a variable external radiant flux in a nitrogen atmosphere [30]. Agreement between the model and experimental results for the effect of surrounding oxygen on particle board and the effect of the sample thickness [32] are not as good as in the case for PMMA.

Measurement of Flammability Properties and Their Use

As described above, the theoretical models are not advanced enough to predict flammability characteristics of new polymers. Furthermore, since there is an endless number of polymer products having different molecular weight and additives (often not described in the final products), it is impossible to measure all necessary material characteristics for each of these products in an attempt to predict their flammability characteristics. For this reason, flammability characteristics of commercially available polymer products, including the experimental polymers, are measured by various bench scale test methods (The main reason to measure flammability characteristics is that these materials must meet required fire per-

formance levels, as described in the Introduction.) Such tests do pick up significant effects of compositional changes on flammability, but they cannot be used to predict what these effects may be.

Test Methods:

There are many different tests for assessing the flammability of materials. In general, all of the traditional tests express their results in terms of certain observations or measurements. These are then used to derive a relative ranking scale or index on which to evaluate materials. Unfortunately, the bases of these ranking scales are arbitrary, and therefore, results from one test do not necessarily agree with another [70], nor do they reflect how a material might behave in a real fire.[†] However, more recent test methods tend to measure various flammability properties of materials under well-defined conditions that usually include an external radiant flux, and the results are used as inputs to fire growth models or the results are analyzed using theories of combustion to derive values of critical parameters that determine flammability properties [71]. Here, a brief description is given only of flammability test methods that are commonly used in studies to understand the effects of the polymer chemical structure on flammability. More detailed discussion of many tests can be found, for example, in Refs. 72 and 73.

The oxygen index test (ASTM D 2863, often referred to as the LOI test) measures the minimum concentration of oxygen in a flowing mixture of oxygen and nitrogen that just supports flaming combustion of a sample that burns downward in a candlelike configuration (width 6.5 mm × length 70–150 mm × thickness 3 mm). Problems caused by melting and the results depending on the sample thickness and geometrical configuration were reported for this test [74]. The relevance of this test to real fires has been questioned (the test measures the trend of an extinction limit of a material only under the specific conditions tested), but many chemists have long been using this test since the required equipment is inexpensive and only a small sample size is required.

More modern tests that can measure the flammability characteristics of ignition, heat release rate, and combustion products are the Cone Calorimeter Test (ASTM E 1354) [75] and Factory Mutual Research Corporation's Flammability Apparatus [66]. These tests determine transient heat release rate by measuring transient oxygen consumption rate in the exhaust gases. Since the heat release from the unit mass of oxygen consumed during combustion is nearly a constant (13.4 MJ/kg) for all organic materials [76], the transient heat release rate can be calculated as the product of this constant and the mass consumption rate of oxygen. The development of oxygen consumption calorimetry has made a significant impact on the advancement of fire research, not only because heat release rate is one of the key parameters determining fire characteristics but also because this technique allows measurement of the transient heat release rate of large objects such as furnishings burning by themselves or in a room [77]. This information can be used to predict the gas flow motion induced by the fire and also the transport of combustion products in a building [78].

Another modern test is the LIFT (Lateral Ignition and Flamespread Test, ASTM 1321) [79]. This test is designed to measure lateral (opposed flow) flame spread rates over the range of fluxes or surface preheat temperatures typical of fire. The size of the LIFT flame spread sample is about 15 × 80 cm. The external flux from a gas-fired radiant panel varies from a high value at the end closest to the panel to a low value (a few percent of the high value) at the other end furthest from the panel (the panel is placed at an angle relative to the sample surface instead of parallel to it). Piloted ignition is performed at the high flux end, and arrival times at fixed locations of the traveling flame front along the sample surface from the high flux end to the low flux end are measured. A flammability diagram consisting of ignition delay time and flame spread rate vs external flux can be derived. Three important material characteristics are derived from this test: inferred gasification surface temperature, the product of thermal conductivity, density, and specific heat of the material, $k\rho c$, and energy feedback function from the flame front to the sample surface [79]. These parameters and the models of which they form elements can be used to describe the behavior of the material in the context of a compartment fire.

Upward Flame Spread on a Wall:

Flame spread up a vertical wall is a component of many fire scenarios; it is important to be able to predict whether a flame will spread up the wall or not (and, if so, how fast) when a small ignition source is located at the bottom of the wall. If the flame spreads partially, how far up will it go? There are several relatively simple models to answer such questions using material parameters inferred from the Cone Calorimeter and LIFT or equivalent tests [80–83]. Slightly more detailed models are also available [84,85][‡] but the most simplified model [83] is used

[†]One of such tests is the UL-94 test, which is commonly used in industry. However, the test is only relevant to the fire scenario in which a small sample is ignited by a small external fire source such as a flame.

[‡]There are more detailed models of flame spread, but they are beyond the scope of this paper; generally, however, the increased detail is in the gas phase instead of in the condensed phase. They can be seen in the recent review article [62].

here to demonstrate how the flammability properties measured in the above tests can be used to predict upward flame spread phenomena. The advantages of this most simplified model are that an analytical solution can be derived and the physical factors influencing upward flame spread can be clearly identified. In this model, the movement of the pyrolysis front measured relative to the bottom of the wall, y_p, is expressed as [83]

$$\frac{y_p}{y_0} = \frac{(a+1)}{a} e^{a\tau} - \frac{1}{a} \tag{1}$$

where $a = k_t \dot{Q}''_{avg} - 1$, y_0 is the initial pyrolysis length due to the ignition source, and $y_0 = k_t \dot{Q}'_0$. The parameter k_t is a constant in the relation between flame tip height and total heat release rate per unit width [86], and $\dot{Q}''_{avg}$ is the average heat release rate per unit area of the pyrolyzing material, $\dot{Q}'_0$ is the heat release rate of the ignitor per unit width, and $\tau \equiv t/t_{ig}$, where t_{ig} is ignition delay time of the material at the average flame heat flux. The parameter a must be greater than zero in order for the upward flame spread process to accelerate, as shown in Eq. (1). The values of $\dot{Q}''_{avg}$ and t_{ig} are measured in the above tests.[§] The calculated results show a reasonable agreement with the experimental data in Ref. 83. However, some uncertainty in the measurement procedure for the flammability properties of polymer materials that intumesce during burning was raised [87]. Similar concern was raised for composite materials due to the delamination of the materials and the preferential transport of degradation products through the composite materials, although the comparison of the calculated flame spread behavior agrees reasonably well with the experimental data for a large-size composite panel [88]. This type of approach using a fire growth model in combination with flammability properties measured by well-defined tests as inputs to the model is more scientifically sound for assessing material behavior in fire than the previous ad-hoc-type screen tests. Thus, further refinement of models and analysis of flammability properties are in progress [89].

Effects of Polymer Structure on Flammability

Although values for flammability properties of many synthetic polymers can be found in the published literature, some caution is needed in inferring the effects of polymer structure on this flammability. The same generic name applied to two commercial polymers [90] does not necessarily mean they have the same molecular structure, and there might also be significant differences in additives, molecular weight, branching, copolymers, and so on. Furthermore, sample size, particularly thickness, must be kept the same between the samples if flammability results are to be compared. Although a conventional approach provided useful global trends of materials composition on flammability properties [91], the results obtained from this type of study cannot clearly show what chemical and physical characteristics are most important for flammability behavior. One approach, which chemists use often, is the pyrolysis study, generally a thermogravimetric study [92] or differential scanning calorimetry [93], to elucidate flammability performance of polymers. Van Krevelen [19] combined a thermogravimetric study to determine char residue in wt% at 850 °C with limiting oxygen index data and derived a simple empirical correlation.

Other empirical correlations have been derived between LOI and the heat of combustion of polymers instead of with char yield [94,95]. Although there is some question about the applicability of the LOI data to actual fire performance, as described above, it has been demonstrated that higher char yield polymers have lowered gasification rate [96], and also that physical char structure has significant effects on flammability properties [97,98]. As a latter example, the addition of a small amount of polydimethylsiloxane into polycarbonate does not significantly change char yield but generates a foamy better-insulating char that reduces the peak heat release rate significantly [98].

Since the viscosity of a molten polymer depends strongly on molecular weight [99], the initial molecular weight of a polymer sample might have significant effects on the transport of the degradation products generated by in-depth thermal degradation reactions to the burning surface. In order to determine the effects of molecular weight and thermal stability of polymers on flammability, materials must have almost the same thermal properties to assure their having the same heat transfer characteristics and also almost the same degradation products to insure that the same gas phase reaction characteristics occur. In a study of these issues, two types of polymers, PMMA and PS, were selected because the thermal degradation of PMMA is controlled by weak linkages in the polymer chains [100,101], and the thermal degradation of PS is controlled mainly via intermolecular- and intramolecular-transfer reactions, not by weak linkages [102,103]. Thus, it is expected that the thermal stability of PMMA is sensitive to initial molecular weight because of a change in the number of weak linkages, but the thermal stability of PS is not sensitive to initial molecular weight. Two PS samples with two different initial molecular weights should indicate only the effects of melting characteristics of the sample on flammabil-

[§]There is some uncertainty in the concept of this model regarding under what external flux these values should be measured.

ity. Two PMMA samples with two different initial molecular weights should indicate the combined effects of melting characteristics and thermal stability of the sample on flammability. Using these four different samples, the effects of melt viscosity and thermal stability on piloted ignition [104], flame spread [22], and burning rate [36] were examined. The results indicate that the transport of in-depth degradation products of PS and PMMA through the molten polymer layer inside the sample has a negligible effect on both piloted ignition and burning rate at an external flux of 40 kW/m^2. However, the thermal stability of PMMA has a significant effect on both its ignition delay time (more stable, longer ignition delay time) and its surface temperature at ignition (ignition temperature increased from a range of 260 °C–270 °C to a range of 320 °C–340 °C for the two types of PMMA samples used in Ref. 104) and also on burning rate at an external flux of 40 kW/m^2 [36]. The ignition data are shown in Fig. 4. The initial molecular weight of the samples (both PS and PMMA) has a significant effect on horizontal flame spreading behavior and its rate. The samples with a high initial molecular weight form a thin molten polymer layer near the flame front, and that layer does not significantly affect flame spread. However, the samples with low initial molecular weight form a substantial molten polymer layer that exhibits an opposed, slow flow fluid motion along the *inclined* vaporizing surface against the traveling flame. This phenomenon significantly affects horizontal flame spreading behavior, forming a wall-like step ahead of the flame front and reducing its spread rate [22]. Downward flame spread over the high molecular weight PMMA sample did not show any dripping, and the flame spread steadily. However, the flame spread over the high molecular weight PS sample spread with a much-enhanced rate compared with the rate for horizontal flame spread, as a result of streaking of small molten polymer balls. The flame over the low molecular weight PS and PMMA samples was self-extinguished during downward flame spreading because of heat loss from streaking downward of small burning polymer molten balls to the cold sample surface [22]. Clearly, if the burning sample surface is vertical, the effects of polymer melt viscosity are potentially much greater.

These results indicate that, in certain experimental configurations, the melting of thermoplastics has significant effects on their flammability properties [22,90,105]. However, this phenomenon has been ignored or avoided by using nonmelting or nonflowing polymer samples, with the result that there is little quantitative (or even qualitative) understanding of how melting affects flammability. Since almost all thermoplastics soften above their glass transition temperature, some will exhibit flow motions in the polymer melt. Another interesting recent observation (although this is a sample thickness effect instead of polymer structure) is that a thermally thin material burning on both sides will do so at a rate significantly more than twice the value seen when only one side is burning [106]. Two simplified models demonstrate that this is a consequence of the Arrhenius temperature dependence of the gasification rate of the solid.

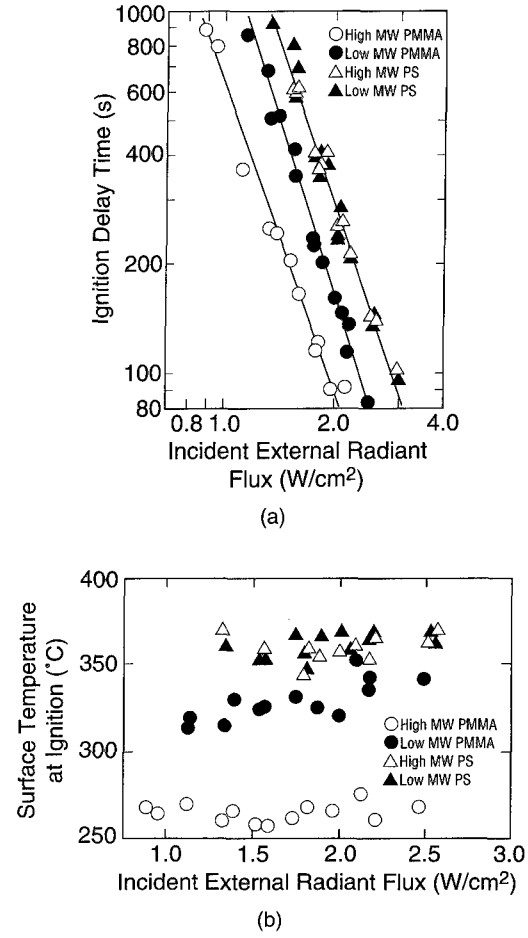

FIG. 4. (a) The relationship between piloted ignition delay time and incident external flux. (b) The relationship between surface temperature at ignition and incident external radiant flux (Ref. 104).

With the advancement of the polymer synthesis field, many new inorganic polymers have been formulated. Their backbone elements are mainly silicon, nitrogen, and phosphorus rather than the carbon of organic polymers. Their combustion behavior could be significantly different from that of the carbon-based polymers. One such example is the combustion of polydimethylsiloxanes, PDMS. PDMS samples having low initial molecular weights burn similarly to hydrocarbons except for the formation of silica particles in the flame [107]. However, PDMS

samples having a high initial molecular weight form a layer at/near the surface consisting mainly of silica (35–45% of original Si), and this layer becomes thicker and has greater mechanical integrity as molecular weight increases. Energy feedback from the flame is inhibited sufficiently by this layer to cause self-extinguishment [108] or to yield a near-constant burning rate even with an increase in external flux [109]. The accumulation of silica at/near the surface of the PDMS samples could be caused either by thermal degradation in the condensed phase or by downward transport (convection/falling/thermophoresis) of silicate particles formed in the flame.

Flame Retardants

The fire safety of materials can be enhanced by increased ignition resistance, reduced flame spread rates, lesser heat release rates, and reduced amounts of toxic and smoke products, preferably simultaneously. The use of more thermally stable polymers, of which many are available, might be a valid solution to these requirements, but generally, the cost of these materials is relatively high, and furthermore, their physical properties or processability may not be as desirable as those of less stable polymers. The most common approach to enhance fire safety performance is the use of flame-retardant additives to inexpensive polymers (large volume commodity polymers such as PE, PP, PS, PVC, and so on). The additives must have a minimum impact on physical properties and product cost. Although halogenated flame retardants are highly effective for reducing the heat release rate of commodity polymers, the future use of these retardants faces some questions. The environmental impact of the processing and combustion of certain halogenated flame retardants has become an issue in Europe. Laboratory and field studies indicate that one class of brominated flame retardants, the brominated diphenyloxides, may serve as precursors for the formation of potentially hazardous polybrominated dibenzo-*p*-dioxins and polybrominated dibenzofurans in yields of up to 16% [110,111]. Furthermore, there is some concern regarding the potential production of bromodioxins and furans from combustion of waste plastics containing such brominated flame retardants during incineration. The environmental effects of the widespread use of chlorinated compounds was debated in a recent publication [112], and concern over the possible corrosion damage to metals by the combustion products from fire in which plastics containing halogenated additives or groups are involved may impact the use of halogenated compounds. As our society becomes more dependent on high technology, the corrosion threat from fire in communication and electronic systems could become a major problem. Because of an increase in public awareness of the potential environmental effects of halogenated compounds and an increase in worldwide legislation on corrosivity of fire products, studies aimed at developing other types of flame-retardant treatments are on-going.

Although there are many possible approaches to nonhalogenated flame retardancy, such as the use of aluminum trihydrate or magnesium hydroxide (both generate water and act as a heat sink), intumescent coatings, and so on [113,114], an interesting and promising approach is the formation of char; only the current status of this latter approach is discussed in this paper. There are three mechanisms whereby the formation of char reduces flammability: (1) part of the carbon (and hydrogen) stays in the condensed phase, thus reducing the amount of gaseous combustible degradation products evolved; (2) the low thermal conductivity of the char layer over the exposed surface acts as thermal insulation to protect the virgin polymer beneath [115]; and (3) a dense char acts as a physical barrier to gaseous combustible degradation products [116]. As described in Ref. 19, some polymers form char when degraded in a fire, but others do not. In order to understand how to form char or increase its amount, it is important to study the chemical and physical structure of char.[#] Reference 18 presents excellent work on detailed analysis of the residues formed from aromatic engineering polymers to determine their chemical structure. Elemental analysis of the chars formed from bisphenol A polycarbonate, BPA-PC, indicates that an increase in pyrolysis temperature increases C/H ratio from an initial value of 1.14 to 1.87 at 591 °C. The Raman spectra and the photoacoustic Fourier transform infrared (FTIR) spectra of the chars show the presence of small graphitic regions in the chars. The infrared spectra of the BPA-PC chars (Fig. 5) show progressive changes in the material, revealing loss of the carbonate group (1775 cm^{-1}) and aliphatic C-H groups (2982 and 1385 cm^{-1}), and the growth or appearance of hydroxyl groups (3580 cm^{-1}), aromatic C-H groups (3012 and 3058 cm^{-1}), ester groups (1740 cm^{-1}), ether groups (1170 and 1260 cm^{-1}), and new aromatic groups (1900, 1610, 752, 820, and 880 cm^{-1}). These results and the solid state ^{13}C NMR results indicate that, when BPA-PC and other aromatic polymers are heated, they lose most of their aliphatic groups, resulting in predominantly protonated and unprotonated aromatic carbons in the residual char. It should be noted that char has no unique structure but rather reflects the starting polymer and its heating rate history.

As noted in the previous section, the physical structure of char has significant effects on polymer

[#]There are numerous publications on the formation and characterization of carbon. Although these publications are relevant to char, this subject is beyond the scope of this paper.

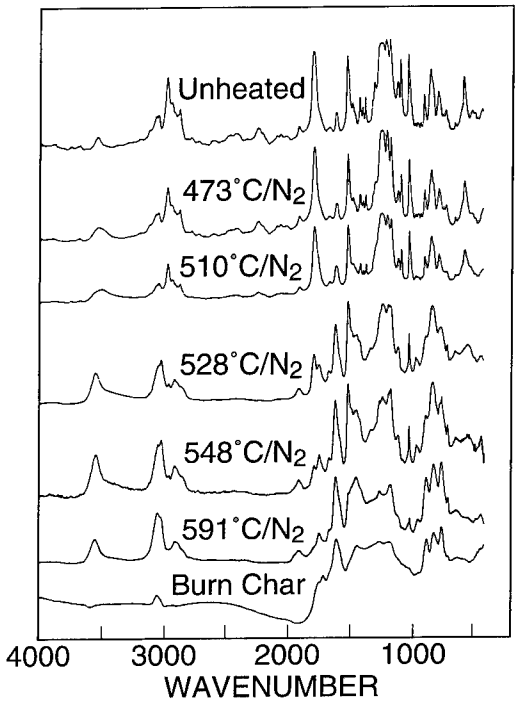

FIG. 5. Photoacoustic FTIR spectra of bisphenol A polycarbonate (Ref. 18).

flammability. It is generally preferable to form an intumescent char (swollen char) having a cellular interior structure consisting of pockets of trapped gas [117]. The dominant protective role of an intumescent char is mainly via its thermal insulating capability [116,117] rather than an obstacle to the passage of volatile and low-viscosity products into the gas phase because low-viscosity polymeric melts can rise through an intumescent char layer as a result of the capillary forces [118].

The majority of commodity polymers do not form char during their combustion, and current research seeks to determine how to form an intumescent char in these polymers. A precise sequence of events is required to form an intumescent char when a polymer is exposed to heat. This is illustrated by the sequence employed in commercial intumescent coating. After the coating sample is sufficiently heated to become softened, a blowing agent must be released. The blowing agent can be released by endothermic decomposition of a hydrated salt that releases water as the blowing agent or the decomposition of an acid salt to yield an anhydrous acid. This anhydrous acid is capable of esterification of polyols. The acid acts as a dehydration agent that, with subsequent heating, leaves a carbonaceous residue. The "timing" (the temperature sequence of each step) is very important [114,117,119,120]. The acid-organic polyol must melt prior to or during esterification so that when the polyol decomposes via dehydration (forming a carbon-inorganic residue), the released blowing agent and the evolution of other nonflammable gases cause the char mass to intumesce and foam. The insulation efficiency of the char depends on the cell structure formed. The structure in turn depends on the staging of the blowing agent relative to the formation of a critical viscosity in the semimolten layers. If the blowing agent action occurs too early, the intumescent action is reduced because the molten material is too viscous. If the action occurs too late, solidification of the char inhibits intumescence. If the molten material becomes too fluid (the viscosity becomes very low), large cells are formed during the blowing process and in the char. These large cells are relatively ineffective as insulators, and the char can become quite fragile. Thus, if any one of the steps does not proceed at the required time, intumescence does not occur or is severely limited. Although a large effort is being carried out by industry to develop new, more highly effective systems, more systematic studies are needed to understand chemical and physical mechanisms of this complex intumescent char-forming process. In order to complement this effort, development of theoretical models to describe the intumescence process is also needed. Previously published models of intumescent char formation [121,122] are rather limited, and further progress is critically needed.

Conclusions and Future Needs

The above discussion clearly shows that fundamental understanding of chemical and physical mechanisms in the condensed phase during combustion of polymers is severely lacking compared with that in the gas phase. Although the overall thermal degradation mechanisms of vinyl polymers are relatively well known compared with those for engineering polymers, available models do not have the capability to predict the evolved rate of degradation products from these polymers except in a few limited cases that exclude any transport processes. Some of the difficulties are a lack of kinetic constants for specific degradation reactions such as intermolecular transfer reactions, which are often not only a function of temperature but also the mobility of polymer chains and the degree of tangling of polymer chains (cage effects). Furthermore, if these kinetic constants are available, generally they are measured at much lower heating rates than those encountered in fire. It is still debatable whether application of kinetic data from low heating rate experiments to high heating rate fire processes is appropriate or not.

The heat and transport processes in the polymers must be better understood, particularly the latter. The roles of bubbles and of oxygen in the gasification

process must be clearly understood. If the gasification is significantly affected by bubbles, the transport mechanism of bubbles through the molten polymer layer to the sample surface must be understood. Another important transport process is polymer melt flow. Using the information available in the field of polymer processing (injection molding), it might be feasible to characterize the polymer melt flow given the distributions of temperature and molecular weight.

Elucidation of char-forming chemical mechanisms and of the chemical and physical structures of chars is needed to permit the enhancement of the formation of char. The thermal properties of char, the heating effects on char yields, and porosity of char must be studied to find the optimum char structure for maximum reduction in flammability.

Acknowledgments

The author is grateful to Dr. Richard G. Gann and Professor Toshisuke Hirano for the invitation to present this paper; to Professors Dougal Drysdale and Giovanni Camino and Dr. Arnold Factor for providing copies of their papers; to Professor A. Carlos Fernandez-Pello for providing his review article (in print); to Dr. Thomas J. Ohlemiller for an extensive, constructively critical review of the manuscript.

REFERENCES

1. *Chemical Engineering News,* American Chemical Society, June 28, 1993, p. 44.
2. Blinov, V. I., and Khudiakov, G. N., *Dok. Akad. Nauk SSSR* 113:1094–1098 (1957); reviewed by Hottel, H. C., *Fire Res. Abstr. Rev.* 1:41–44 (1959).
3. Modak, A. T., and Croce, P. A., *Combust. Flame* 30:251–265 (1977).
4. Orloff, L., Modak, A. T., and Alpert, R. L., *Sixteenth Symposium (International) on Combustion,* The Combustion Institute, Pittsburgh, 1977, pp. 1345–1354.
5. Hamins, A., Klassen, M. E., Gore, J. P., Fischer, S. J., and Kashiwagi, T., "Heat Feedback to the Fuel Surface in Pool Fires," *Combust. Sci. Technol.* 97:37–62 (1994).
6. Choi, M. Y., Hamins, A., Rushmeier, H., and Kashiwagi, T., *Twenty-Fifth Symposium (International) on Combustion,* The Combustion Institute, Pittsburgh, pp. 1471–1480.
7. Hallman, J., Sliepcevich, C. M., and Welker, J. R., *J. Fire Flammab.* 9:353–366 (1978).
8. Kashiwagi, T., *Fire Safety J.* 3:185–200 (1981).
9. Finlayson, E. U., Aung, W., and Kashiwagi, T., "Theoretical Models for Combined Radiation-Conduction in Polymeric Solids Heated by External Radiative Flux," *Proceedings of 1987 ASME/JSME Thermal Engineering Conference,* Vol. 1, ASME, New York, 1987.
10. Manohar, S. S., Kokani, A. K., and Thynell, S. T., "In-Depth Absorption of Externally Incident Radiation in Non-Gray Media," *J. Heat Transfer,* to appear.
11. Comeford, J. J., *Combust. Flame* 18:125–132 (1972).
12. Buckius, R. O., and Tien, C. T., *Int. J. Heat Mass Transfer* 20:93 (1977).
13. Kashiwagi, T., *Combust. Sci. Technol.* 8:225–236 (1974).
14. Ohlemiller, T. J., and Summerfield, M., *Thirteenth Symposium (International) on Combustion,* The Combustion Institute, Pittsburgh, 1971, pp. 1087–1094.
15. Mita, I., "Effects of Structure on Degradation and Stability of Polymers," in *Aspects of Degradation and Stabilization of Polymers,* Chap. 6, (H. H. G. Jellinek, Ed.), Elsevier Scientific, Amsterdam, 1978.
16. Kelen, T., *Polymer Degradation,* Van Nostrand Reinhold, New York, 1983.
17. Grassie, N., and Scott, G., Polymer Degradation and Stabilization, Cambridge University Press, Cambridge, 1985.
18. Factor, A., "Char Formation in Aromatic Engineering Polymers," in *Fire and Polymers* (G. L. Nelson, Ed.), ACS Symposium Series 425, ACS, Washington, DC, pp. 274–287, 1990.
19. Van Krevelen, D. W., *Polymer* 16:615–620 (1975).
20. Aseeva, R. M., and Zaikov, G. E., "Flammability of Polymeric Materials," in *Adv. Polym. Sci.* 70:172–229 (1985).
21. Kashiwagi, T., and Omori, A., *Twenty-Second Symposium (International) on Combustion,* The Combustion Institute, Pittsburgh, 1988, pp. 1329–1338.
22. Kashiwagi, T., Omori, A., and Nanbu, H., *Combust. Flame* 81:188–201 (1990).
23. Clift, R., Grace, J. R., and Weber, M. E., *Bubbles, Drops, and Particles,* Academic Press, New York, 1978.
24. Matsuoka, S., and Kwei, T. K., "Physical Behavior of Macromolecules," in *Macromolecules* (F. A. Bovey and F. H. Winslow, Eds.), Academic Press, New York, 1979, p. 346.
25. Kashiwagi, T., and Ohlemiller, T. J., *Nineteenth Symposium (International) on Combustion,* The Combustion Institute, Pittsburgh, 1982, pp. 815–823.
26. Thompson, H. E., and Drysdale, D. D., *Fire Mater.* 11:163–172 (1987).
27. Brauman, S. K., *J. Polym. Sci., Polym. Chem. Ed.* 15:1507 (1977).
28. Brauman, S. K., Chen, I. J., and Matzinger, D. P., *J. Polym. Sci., Polym. Chem. Ed.* 21:1831 (1983).
29. Brauman, S. K., and Berg, R. A., *Polymer Degradation During Combustion,* SRI Final Report of SRI Project No. 1287, November 1983.
30. Vovelle, C., Akrich, R., and Delfau, J. L., *Twentieth Symposium (International) on Combustion,* The Combustion Institute, Pittsburgh, 1984, p. 1647.

31. Vovelle, C., Akrich, R., and Delfau, J. L., *Combust. Sci. Technol.* 36:1–18 (1984).
32. Vovelle, C., Akrich, R., Delfau, J. L., and Gresillaud, S., *Fire Safety Science—Proceedings of First International Symposium,* Hemisphere, New York, 1986, pp. 473–482.
33. Delichatsios, M. A., and Saito, K., *Fire Safety Science—Proceedings of the Third International Symposium,* Elsevier, London, 1991, pp. 217–226.
34. Vovelle, C., Delfau, J., and Reuillon, M., *Combust. Sci. Technol.* 53:187–201 (1987).
35. Darivakis, G. S., Howard, J. B., and Peters, W. A., *Combust. Sci. Technol.* 74:267–281 (1990).
36. Stannett, V., "Single Gases," in *Diffusion in Polymers,* Chap. 2 (J. Crank, and G. S. Parks, Eds.), Academic Press, New York, 1968.
37. Brown, J., Ohlemiller, T. J., and Kashiwagi, T., paper presented at Symposium on Chemistry of Combustion Processes, 185th ACS National Meeting, Seattle, WA, March 20–25, 1983.
38. Brauman, S. K., *J. Polym. Sci., Part B: Polym. Phys.* 26:1159–1171 (1988).
39. Stuetz, D. E., Diedwardo, A. H., Zitomer, F., and Barnes, B. D. P., *J. Polym. Sci., Chem. Ed.* 13:585–621 (1975).
40. Burge, S. J., and Tipper, C. F. H., *Combust. Flame* 13:495–505 (1969).
41. Pitz, W. J., Brown, N. J., and Sawyer, R. F., *Eighteenth Symposium (International) on Combustion,* The Combustion Institute, Pittsburgh, 1981, pp. 1871–1879.
42. Suuberg, E. M., Dalal, V., and Kelly, T., *Study of the Effects of Oxygen Transport and Temperature History of the Chemistry of PMMA Pyrolysis,* National Bureau of Standards, NBS-GCR-87-523, December 1986.
43. Kashiwagi, T., Inaba, A., and Brown, J. E., *Fire Safety Science—Proceedings of First International Symposium,* Hemisphere, New York, 1986, pp. 483–493.
44. Ito, A., and Kashiwagi, T., *Combust. Flame* 71:189–204 (1988).
45. Jakes, K. A., and Drews, M. J., *J. Polym. Sci., Polym. Chem. Ed.* 19:1921 (1981).
46. Blaisten-Barojas, E., and Nyden, M. C., *Chem.Phys. Lett.* 171:499–505 (1990).
47. Nyden, M. C., and Noid, D. W., *J. Phys. Chem.* 95:940–945 (1991).
48. Guaita, M., and Chiantoe, O., *Polym. Degrad. Stability* 11:167 (1985).
49. Guaita, M., Chiantoe, O., and Costa, L., *Polym. Degrad. Stability* 12:315 (1985).
50. Inaba, A., and Kashiwagi, T., *Macromolecules* 19:2412 (1986).
51. Inaba, A., and Kashiwagi, T., *Eur. Polym. J.* 23:871–881 (1987).
52. Inaba, A., Kashiwagi, T., and Brown, J. E., *Polym. Degrad. Stability* 21:1–20 (1988).
53. Kashiwagi, T., Inaba, A., and Hamins, A., *Polym. Degrad. Stability* 26:161–184 (1989).
54. Kansa, E., Perlee, H. E., and Chaiken, R., *Combust. Flame* 29:311–324 (1977).
55. Di Blasi, C., *Prog. Energy Combust. Sci.* 19:71–104 (1993).
56. Oh, M. S., "Softening Coal Pyrolysis," Dsc, Massachusetts Institute of Technology, Cambridge, MA, March 1985.
57. Hsu, J., "Swelling, Mass Transport, and Chemical Kinetics in Bituminous Coal Pyrolysis," Dsc, Massachusetts Institute of Technology, Cambridge, MA, August 1989.
58. Wichman, I. S., *Combust. Flame* 63:217–229 (1986).
59. Bucsi, A., and Rychly, J., *Polym. Degrad. Stability* 38:33–40 (1992).
60. Kanury, A. M., *The SFPE Handbook for Fire Protection Engineering,* National Fire Protection Association, Quincy, MA, 1988, Vol. 1, p. 326.
61. Fernanandez-Pello, C. A., and Hirano, T., *Combust. Sci. Technol.* 32:1–31 (1983).
62. Fernandez-Pello, C. A., "The Solid Phase," in *Combustion Treatise on Fire,* Chap. 2 (G. Cox, Ed.), Academic Press, to appear.
63. Aseeva, R. M., and Zaikov, G. E., *Combustion of Polymer Materials,* Hanser Publishers, Munich, 1985.
64. Kim, J. S., Balk, S. W., and Kaplan, C. R., *Combust. Sci. Technol.* 88:133–150 (1992).
65. Spalding, D. B., *Fourth Symposium (International) on Combustion,* Williams and Wilkins, Baltimore, 1953, pp. 847–864.
66. Tewarson, A., and Pion, R. F., *Combust. Flame* 26:85–103 (1976).
67. de Ris, J. N., *Twelfth Symposium (International) on Combustion,* The Combustion Institute, Pittsburgh, 1969, pp. 241–252.
68. Sibulkin, M., *Fire Safety Science—Proceedings of the First International Symposium,* Hemisphere, New York, 1986, pp. 391–400.
69. Chen, Y., Delichatsios, M. A., and Motevalli, V., *Combust. Sci. Technol.* 88:309–328 (1993).
70. Emmons, H. W., *Sci. Am.* 231:21–27 (1974).
71. Quintiere, J. G., *J. Res. Nat. Bur. Stand.* 93:61–70 (1988).
72. Hilado, C. J., *Flammability Test Methods Handbook,* Technomic, 1973.
73. *ASTM Fire Test Standards,* 2nd ed., ASTM, Philadelphia, 1988.
74. Stuetz, D. E., Diedward, A. H., Zitomer, F., and Barnes, B. P., *J. Polym. Sci., Polym. Chem. Ed.* 18:967–985 (1980).
75. Barbrauskas, V., *Fire Mater.* 8:81–95 (1984).
76. Huggett, C., *Fire Mater.* 4:61 (1980).
77. Babrauskas, V., *J. Fire Sci.* 1:9–32 (1983).
78. Drysdale, D., *An Introduction to Fire Dynamics,* Chap. 4, John Wiley & Sons, New York, 1985.
79. Quintiere, J. G., and Harklervad, M., "New Concepts for Measuring Flame Spread Properties," in *Fire Safety Science and Engineering* (ASTM STP 882), ASTM, Philadelphia, PA, 1985, pp. 239–267.
80. Hasemi, Y., *Fire Safety Science—Proceedings of the*

First International Symposium, Hemisphere, New York, 1985, pp. 87–96.
81. Mitler, H. E., *Twenty-Third Symposium (International) on Combustion*, The Combustion Institute, Pittsburgh, 1990, pp. 1715–1721.
82. Karlsson, B., and Magnusson, S. E., *Fire Safety Science—Proceedings of the Third International Symposium*, Elsevier, London, 1991, pp. 667–678.
83. Cleary, T. G., and Quintiere, J. G., *Fire Safety Science—Proceedings of the Third International Symposium*. Elsevier, London, 1991, pp. 647–656.
84. Kulkarni, A. K., Kim, C. I., and Kuo, C. H., *Heat Flux, Mass Loss Rate and Upward Flame Spread for Burning Vertical Walls*, NIST-GCR-90-584, NIST, Gaithersburg, MD, November 1990.
85. Chen, Y., Delichatsios, M. A., and Motevalli, V., *Combust. Sci. Technol.* 88:309–328 (1993).
86. Saito, K., Williams, F. A., Wichman, I. S., and Quintiere, J. G., *J. Heat Transfer* 111:438–445 (1989).
87. Kashiwagi, T., and Cleary, T. G., *Fire Safety J.* 20:203–225 (1993).
88. Ohlemiller, T. J., Cleary, T. G., Brown, J. E., and Shields, J. R., *J. Fire Sci.* 11:308–319 (1993).
89. Thomas, P. H. and Karlsson, B., *On Upward Flame Spread on Thick Fuels*, Report LUTVDG/TVBB-3058, Lund University, Sweden, December 1990.
90. Kashiwagi, T., Inaba, A., and Brown, J. E., *Fire Safety Science—Proceedings of the First International Symposium*, Hemisphere, New York, 1986, pp. 483–493.
92. Cullis, C. F., *J. Anal. Appl. Pyrolysis* 11:451–463 (1987).
93. Martel, B., *J. Appl. Polym. Sci.* 35:1213–1226 (1988).
94. Johnson, P. R., *J. Appl. Polym. Sci.* 18:491 (1974).
95. Ohe, H., Matsuura, K., *Textile Res. J.* 45:778 (1975).
96. Brauman, S. K., *J. Fire Retard. Chem.* 6:249–265 (1979).
97. Brauman, S., *J. Fire Retard. Chem.* 6:266–275 (1979).
98. Kashiwagi, T., Cleary, T. C., Davis, G. C., and Lupinski, J. H., *Proceedings of the International Conference for the Promotion of Advanced Fire Resistant Aircraft Interior Materials*. Federal Avaiation Administration, DOT/FAA/93/3, 1993, pp. 175–187.
99. Matsuoka, S., and Kurei, T. K., "Physical Behavior of Macromolecules," in *Macromolecules* (F. A. Bovey and F. H. Winslow, Eds.), Academic Press, New York, 1979, p. 346.
100. Grassie, N., and Melville, H. W., *Proc. Royal Soc. London, Ser. A* 199:14 (1949).
101. Kashiwagi, T., Inaba, A., Brown, J. E., Hatada, K., Kitayama, T., and Masuda, E., *Macromolecules* 19:2160–2168 (1986).
102. Wall, L. A., Straus, S., Flynn, J. H., McIntyre, D., and Simha, R., *J. Phys. Chem.* 70:53 (1970).
103. Guoyt, A., *Polym. Degrad. Stability* 15:219 (1986).
104. Kashiwagi, T., and Omori, A., *Twenty-Second Symposium (International) on Combustion*, The Combustion Institute, Pittsburgh, 1988, pp. 1329–1338.
105. Stuetz, D. E., Diedwardo, A. H., Zitomer, F., and Barnes, B. P., *J. Polym. Sci., Polym. Chem. Ed.* 18:967–985 (1980).
106. Ohlemiller, T. J., and Sheilds, J. R., *Fire Mater.* 17:103–110 (1993).
107. Lipowitz, J., *J. Fire Flammab.* 7:482–503 (1976).
108. Lipowitz, J., and Zremelis, M. J., *J. Fire Flammab.* 7:504–529 (1976).
109. Buch, R. R., *Fire Safety J.* 17:1–12 (1991).
110. Buser, H., *Environ. Sci. Technol.* 20:404–408 (1986).
111. Dumler, R., Lenoir, D., Thomas, H., and Hutzinger, O., *J. Anal. Appl. Pyrolysis* 16:153–158 (1989).
112. *Chemical & Engineering News*, American Chemical Society, April 1993, pp. 11–20.
113. Weil, E. D., Hansen, R. H., and Patel, N., "Prospective Approaches to More Efficient Flame Retardant Systems," in *Fire and Polymers*, (G. Nelson, Ed.), ACS Symposium Series 425, 1990, pp. 97–108.
114. Camino, G., "Fire Retardant Polymeric Materials," in *Atmospheric Oxidation and Antioxidants*, (G. Scott, Ed.), Elsevier, London, 1993, Vol. 2, pp. 461–494.
115. Anderson, C. E., Jr., Ketchum, D. E., and Mountain, W. P., *J. Fire Sci.* 6:390–410 (1988).
116. Camino, G., Costa, L., Casorati, E., Bertelli, G., and Locatello, R., *J. Appl. Polym. Sci.* 35:1863–1876 (1988).
117. Scharf, D., Nalepa, R., Heflin, R., and Wusu, T., *Fire Safety J.* 19:103–117 (1992).
118. Gibov, K. M., Shapovalova, L. N., and Zhubanov, B. A., *Fire Mater.* 10:133–135 (1986).
119. Vandersall, H. L., *J. Fire Flammab.* 2:97–140 (1971).
120. Anderson, C. E., Jr., Dziuk, J., Jr, Mallow, W. A., and Buckmaster, J., *J. Fire Sci.* 3:161–194 (1985).
121. Cagliostro, D. E., Riccitiello, S. R., Clark, K. J., and Shimizu, A. B., *J. Fire Flammab.* 205:221 (1975).
122. Buckmaster, J., Anderson, C., and Nachman, A., *Int. J. Eng. Sci.* 24:263–276 (1986).

COMMENTS

R. H. Essenhigh, Ohio State University, USA. 1. Can you comment on the fragment size of the decomposed polymers, either from measurements or from modeling. Did the polymers degrade to monomer (or were they assumed to do so) and/or did the monomers themselves also degrade? The background to my question is work we reported in 1969 and 1973 [Essenhigh and Dreier, *Fuel* 48:330 (1969) and Waibel and Essenhigh, *International Symposium on Combustion*, 1973, p. 1413] on combustion of a range of thermoplastic polymers. We concluded from analysis of data on flame standoff distance and particle/droplet temperatures that the evaporating fragment was generally

2–10 monomer units in size; the polymers did not degrade to monomer. One associated consequence was that the large molecular weight resulted in smaller diffusion coefficients compared with oils, resulting in smaller flame standoff distances, and hence with steeper temperature gradients the evaporation and thus the burning rates were correspondingly increased. The measured burning rates were roughly three times faster than light oil drops. Is this factor likely to be relevant in your studies?

2. With reference to the thermoplastic nature of the polymers with viscosity, a definable function of temperature, you may know that this is also true for coals. Comparisons with coals might be informative.

Author's Reply. 1. Only a few polymers, such as polymethylmethacrylate (PMMA), poly α-methylstyrene, and polytetrafluoroethylene, generate monomers as the main degradation products. It appears that the effects of higher heating rate on PMMA degradation products are negligible. [Seshadri, K., and Williams, F. A., *J. Polymer Sci: Polymer Chemist Ed.* 16:1755–1778 (1978).] All polymers used in the paper you cited, except PMMA, generate many different sizes of fragments. The pyrolysis occurs at the surface or in depth depending on the heating rate and the thermal stability of the polymers. After reading the two papers you cited, it appears that degradation reactions occurred over some depth in the samples but not necessarily over the entire volume. The competition between polymerization and depolymerization is determined by the ceiling temperature of a polymer. If the polymer temperature is higher than its ceiling temperature, depolymerization exceeds polymerization. This temperature depends on the type of polymer; for PMMA it is 197 °C, and for styrene it is 384 °C [16]. Since the measured polymer temperatures are much higher than these values, the polymerization suggested in the paper appears to be negligible and large fragments are generated directly by degradation reactions. The physical and chemical processes observed in the burning of plastic spheres cited in the two papers by Professor Essenhigh are directly relevant to our studies.

2. The melt viscosity of polymers is well studied and quite definable. A good reference is Brydon, J. A., *Flow Properties of Polymer Melts,* George Godwin Limited, London, 1981. Many different approaches and techniques taken in coal research are quite useful to pursue for polymer combustion research. However, since chemical and physical structures of polymers are much more clearly defined than those of coals, quantitative information about coal might not be as useful as qualitative information.

•

D. Milov, RRA, USA. This was an excellent presentation and review. The author, however, completely ignored an issue: radiation from the flames of pyrolysing gases. This radiation drives the fire growth process. Does the author agree that some (or a lot of) effort should be directed toward formulating new materials that (1) produce char (as the author also proposes) and also (2) reduce (soot) radiation? So, maybe oxygen- or nitrogen-containing materials can be developed that when pyrolysing produce reduced soot amounts (because of oxidation or inerting). The same materials must also have charring or intumescent behavior.

Author's Reply. Although a reduction in the radiative feedback rate from the flame to the fuel surface could be considered as one way to reduce the burning rate of polymers, generally a reduction of soot is more frequently sought due to the need for meeting soot-related regulations. These regulations are set to increase visibility and thus make evacuation from a fire scene easier. Char formation tends to reduce the amount of evolved combustible gases which, in turn, reduces flame height and also radiative feedback rate (shorter radiative path). An increase in the amount of char often requires incorporation of aromatic rings into the polymer chain, which might increase the soot yield. Therefore, the location of these rings in the polymer chain becomes very important to avoid the generation of soot while enhancing the formation of char (Polystyrene does not generate any char, but poly *p*-phenylene generates a lot of char.)

Yes, the addition of oxygen and nitrogen into a polymer chain tends to reduce the generation of soot. The former also reduces the heat of combustion, but the latter might generate HCN.

•

Richard G. Gann, NIST, USA. In this talk, you have shown that improved fire performance can be achieved by chemical changes in the material, changes that have little effect on the material's physical properties. Conventional models of burning and flame spread center on thermophysical properties (e.g., k, ρ, c). What, then, are the implications of these findings for flammability modeling?

Author's Reply. Since there are an endless number of polymer products having different molecular weights and additives (often not described in the commercial products), it is essentially impossible to measure all necessary physical and chemical characteristics for each of these products in an attempt to predict flammability characteristics. Therefore, chemical effects are globally included through the values of gasification (pyrolysis) temperature, ignition temperature, or global heat of vaporization. However, if we want to improve the flammability of a specific polymer or develop a new approach to flame retardancy, we need to model in detail the physical and chemical processes in the condensed phase using the well-defined polymer. Such detailed models serve a research role distinct from more empirical models that attempt to relate small-scale test behavior to full-scale fire performance.

•

A. M. Kanury, Oregon State University, USA. You described clearly the very interesting and important feature that low molecular weight polymers tend to melt more easily and flow ahead of a downward propagating flame and

that such a melt flow can even produce flame quenching. Can you comment on whether this reduction in burning to quenching can be modelled by viewing the drip process as either reducing the effective heat of combustion or increasing the effective latent heat (L_{global}) of phase change?

Author's Reply. Although it could be possible to model these phenomena as you suggested, I would like to see models that describe the observed physical phenomena correctly. Since research on polymer processing such as injection molding and compounding is quite active and has provided much relevant information, it is quite feasible to model polymer melting flow phenomena explicitly.

•

Andreas Hornung, Universitae Kaiserslautern, Germany. How did you calculate the high activation energy of about 700 kJ/mol for the decomposition of C-C double bond systems like polyacetylene and in which temperature range does the decomposition takes place?

Author's Reply. The slide that shows the relationship between bond dissociation energy and external radiant flux was provided by Dr. Richard Lyon at the Technical Center of Federal Aviation Agency, Atlantic City, NJ, and he used the data from *CRC Handbook of Chemistry and Physics,* 63rd ed., The Chemical Rubber Co., Cleveland, 1982/83, p. F-198.

Twenty-Fifth Symposium (International) on Combustion/The Combustion Institute, 1994/pp. 1439–1446

BEHAVIOR OF FIRES SPREADING DOWNWARD OVER THICK PAPER

MASATARO SUZUKI, RITSU DOBASHI AND TOSHISUKE HIRANO
Department of Chemical System Engineering
The University of Tokyo
7-3-1 Hongo, Bunkyo-ku, Tokyo 113, Japan

To explore the flame spread mechanisms over solid fuel sheets, downward flame spread over paper sheets from 0.4 to 10-mm thick have been examined.

The dependence of flame spread rate V on thickness δ indicates that the spreading behavior can be divided into four types observed under conditions in four regions. The flame spread is found to take place for sample thickness $\delta < 8.4$ mm in the present experiments under the conditions of natural convection. Near the limiting thickness, unstable flame spread is observed, and its behavior is examined. The length L of pyrolysis region is measured as a characteristic length representing the pyrolysis area. In the range of $\delta < 7.5$ mm, the value of L increases as δ increases.

A simple heat transfer model is proposed in this paper to examine the heat transfer for charring materials. It is assumed that the heat transferred through the solid surface ahead of the leading edge of the pyrolysis region is constant and that penetrating through the pyrolysis region is proportional to the area of the region. An equation as a function of V and L is derived from this model, which expresses the relation between L and $\rho\delta V$. The heat flux penetrating through the pyrolysis region is estimated much smaller than that through the solid surface ahead of the leading edge of the pyrolysis region. It is also inferred that the flame stagnation is caused by the decrease of the fuel gas ejected from the unit area of the pyrolysis surface.

Introduction

Flame spread over solid fuel is a basic problem in the field of fire research. The flame spread rate depends on the rate of heat transfer from the flame into the preheat region. When the solid fuel is thin, the heat transfer through the solid phase can be neglected compared to that through the gas phase [1,2], but when the solid fuel is thick enough, the heat transfer through the solid phase has been found to become comparable or more [3]. The estimation of the heat transfer through both phases is important for further understanding.

Heat transfer through the solid phase has been discussed based on the results obtained in the experiments of flame spread over noncharring solid fuel such as PMMA sheets [4]. However, it is not clear how to proceed with thermally thick charring materials [5], although many cellulosic materials are used as building materials that are deeply concerned with the characteristics of building fires. Pyrolysis of cellulose involves many steps [6], and its reaction is dependent on a heating rate [7–9]. The process of pyrolysis affects the formation of a char layer, which covers over the surface of the solid and decreases the heat transfer into the solid [10].These characteristics of cellulose should be estimated. In this study, therefore, downward flame spread over paper sheets have been examined for a wide range of thicknesses, and heat transfer mechanisms are discussed.

Experimental

Sample paper sheets are made from filter paper for various thicknesses from 0.4 to 10 mm. The process is as follows: first, a certain amount of filter paper is ground to make its fibers suspended in pure water, and then it is poured into a bucket, whose bottom is made of wire gauze. Pressing and drying processes follow. No glue is used to make up lumps. The density of sample sheets depends on the pressing process and on the density of original filter paper. In this case, the sample sheets of density $2.8(\pm 0.2) \times 10^{-4}$ g/mm^3 are obtained from original filter paper of density 3.2×10^{-4} g/mm^3. The sample sheets have been marked on both surfaces with pencil lines at 10-mm intervals for measurement and have been dried in a desiccator. It is almost impossible to dry out perfectly, and the humidity in the desiccator is controlled within the range of $33 \pm 2\%$.

The arrangement used in this study is shown in Fig. 1. A sample sheet is clamped between pairs of metal straps at both sides and suspended in the air without surroundings that limit the supply of air. Its area of 70×70 mm is exposed to burn. A slit burner is used, igniting a sample sheet on its top edge. To observe unstable spreading behavior, as is described later, both surfaces of the sheet are videotaped during the flame spread. Except for the case of thick sheets which cause flame spread to be unstable, the flame spread rate has become almost constant in a

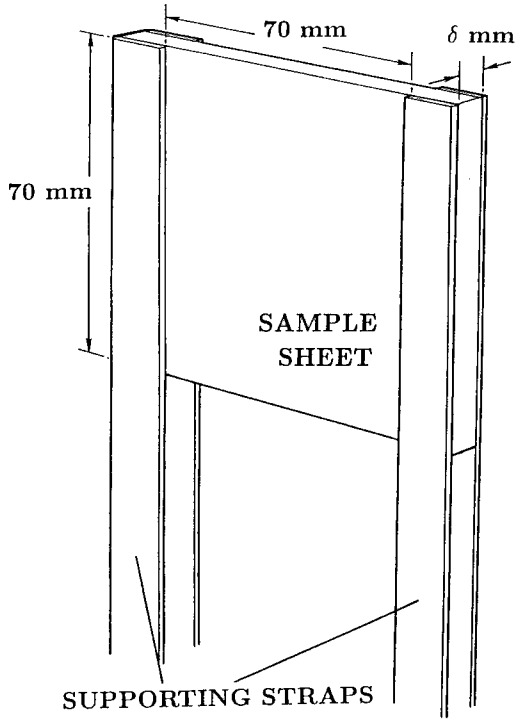

FIG. 1. Experimental arrangement used in this study.

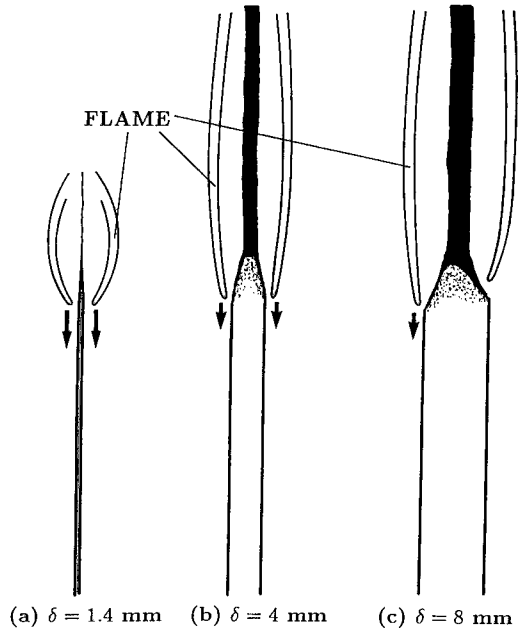

FIG. 2. Sketches of typical flame shapes and sectional pyrolysis structures.

distance of 10 mm from the ignited edge of the sheet. A value of the rate is calculated from the time required to spread between the pencil lines marked beforehand.

After smothering the fire in CO_2, the sheet is cut along a vertical cross section, and the length L of the pyrolysis region is measured, which is schematically shown later (Fig. 6); L is defined as a distance from the middle point of color-change fronts on both surfaces to the point where color changes completely into black. These color changes are sufficiently distinguishable.

Results

Three typical flame shapes and sectional pyrolysis structures, which depend on the sample thickness, are sketched in Fig. 2. If a sample is thin, the leading flame edge extends downward about 1 mm from the pyrolysis front, and the flame front following it is at an angle of a few tens of degrees to the pyrolysis region surface (Fig. 2a). This flame shape is similar to those in previous observations [2,4]. On the other hand, a rather thick sample sheet has a pyrolysis front just underneath the leading flame edge, and the following flame is nearly parallel to the sample surface (Fig. 2b). In the case of a further thick sample, as it is illustrated in Fig. 2c, unstable flame spreading is observed. In this case, flames on both surfaces seem to progress and stagnate alternately. It has also been found that flame spread can take place for the sample thickness $\delta < 8.4$ mm. In the case of the flame spread over a sample of $\delta = 8.4$ mm, stagnation of flames occurs on both surfaces at the same time after the igniting burner has removed, and the flames become small and finally extinction occurs. This fact contrasts to the fact that there is no thick limit for the flame spread over noncharring material such as PMMA [3].

The geometrical configuration of a diffusion flame depends on the balance of mass transfer rates of fuel and oxidizer gases, which are closely related to the flow field, so that it is considered that the profiles of gas flow can be inferred from the flame shape. From the above observations, it can be inferred that the flow rate of combustible gas per unit area is small for thick samples compared to that for thin ones.

Spread Rate:

Figure 3 shows the dependence of flame spread rate V on thickness δ. As indicated in this figure, the spreading behavior can be divided into four types observed under conditions in four regions.

Region I is in the range of $\delta < 1.5$ mm, where flame spreads stably. In this case, the flame spread

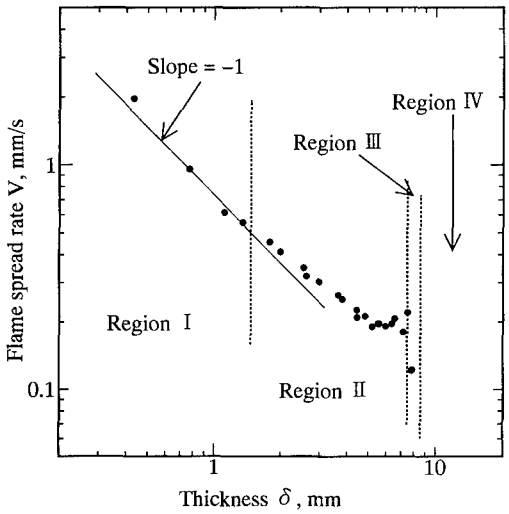

FIG. 3. Dependence of flame spread rate V on thickness δ.

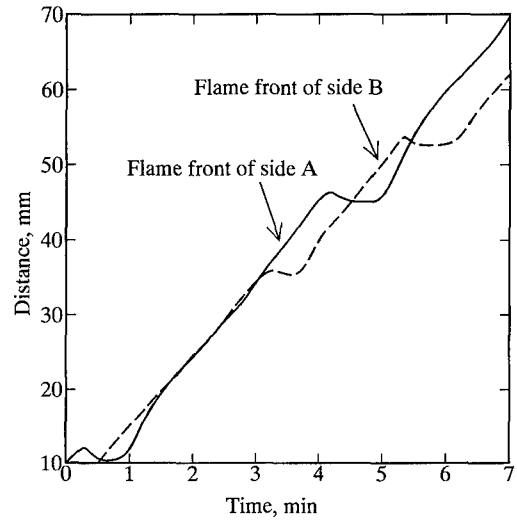

FIG. 4. Typical position-time diagrams of flame front in Region III (δ = 8.1 mm).

rate is inversely proportional to the thickness, as indicated by the solid line in Fig. 3. This region can be called the "thermally thin" region, where spread rate V can be predicted by the relation, namely, $\rho\delta V$ equal to a constant value. Many studies have been done with ordinary paper sheets, the flame spread over which is included in this region. A constant value of $\rho\delta V$ estimated on the basis of the results of measurements in the present study is about 1.9×10^{-4} g/mm s. This value agrees quite well with that for various kinds of filter paper used in the previous studies [1,3].

Region II is in the range of 1.5 mm $\leq \delta <$ 7.5 mm, where the flame spreads stably also, though the decreasing rate of V becomes smaller as the thickness increases. In the range of $\delta >$ 5 mm, the value of V seems to become a constant value, 0.2 mm/s. A similar disposition has been observed for PMMA plates and has been explained that this is because of the growth of internal heat transfer from the pyrolysis region to the preheat region [3].

Region III is in the ranges of 7.5 mm $\leq \delta <$ 8.4 mm, where the flame spreads unstably and the instantaneous value of V fluctuates. The mean value of V is about 0.12 mm/s. This value is appreciably small compared to that in the previous region. Region IV is in the range of $\delta \geq$ 8.4 mm, where continual flame spread cannot progress any longer. These results suggest that 8.4mm is the limiting value of thickness for downward flame spread over paper in the present experiments under the condition of natural convection.

Unstable Behavior in Region III:

The unstable flame spread in Region III is a unique one that has not been investigated in previous studies. It should be helpful to examine the detailed behavior to understand the effect of thickness on flame spread mechanisms. Figure 4 shows typical position-time diagrams, which indicate spread of the leading flame edges on both sides of a sample sheet of thickness δ = 8.1 mm. The variable t is the time after the leading flame edge on one side (side A) passes a marked line that is 10 mm ahead of an ignited edge. Usual forward flame spread proceeds during t from 1.5 to 3 min. Both of the leading flame edges are almost at the same location, spreading at a velocity of 0.16 mm/s. Then, typical unstable behavior is seen to start.

The alternating movements of the leading flame edges on both sides are illustrated in Fig. 5. The preceding leading flame edge on side B stops its progress and moves backward to stagnate at a line behind the leading edge of the pyrolysis region, while the leading flame edge on side A moves downward continuously (Fig. 5a). The stagnating line is about 1.2–2.0 mm behind the color-change front on the surface. The stagnation on side B lasts for 0.5–1.0 min; meanwhile, the leading flame edge of the other side (side A) goes ahead (Fig. 5b). After the leading flame edge on side A precedes, that on side B begins to move again (Fig. 5c), and the situations of both sides change over.

As indicated in Fig. 5b, the flame on side A should overtake that on the side B when the alternating spread cycle goes on. This suggests that heat transfer into the preheat region on side A exceeds to that into side B. This phenomenon seems to be attributable to the difference of the thicknesses of char layers

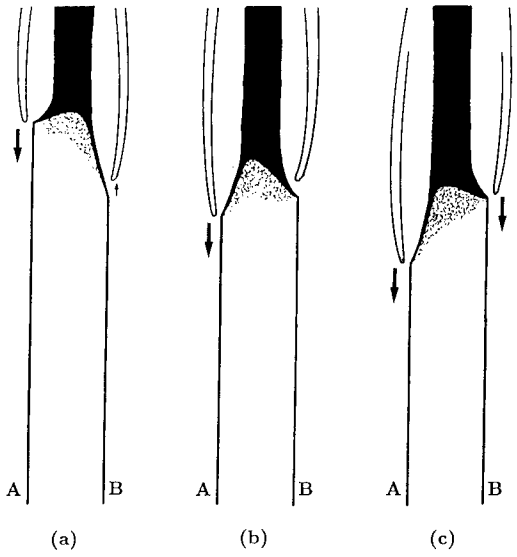

FIG. 5. Illustration of fluctuated movements of the leading flame edges observed in Region III.

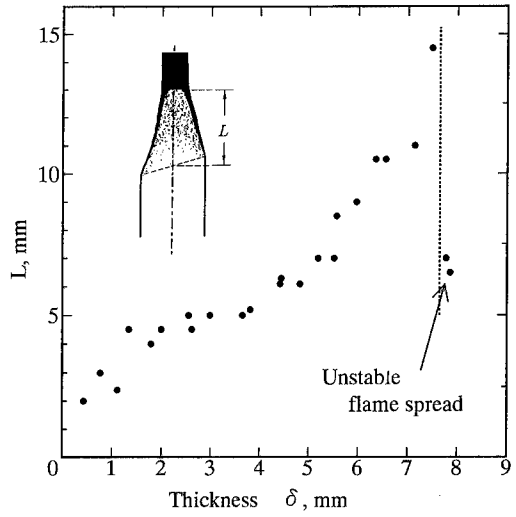

FIG. 6. Variation of pyrolysis region length L with paper thickness δ.

established over the surfaces that hinder heat transfer.

It may also be assumed that preheating by the preceding flame on the other side is needed for the stagnating flame to restart spreading. In other words, if the flames on both surfaces stagnate at the same time, then they will not spread any more. This is just the case in Region IV.

Internal Pyrolysis Structure:

Combustible gas is ejected from the pyrolysis surface, its amount depending on the area of the pyrolysis region. The occurrence of pyrolysis can be distinguished by the color change of cellulosic fibers. Though the color changes gradually at the inside of the sample after the flame passes the surface, the fibrous structure remains until the color becomes completely black. The main pyrolysis layer is assumed to be a narrow layer where the color starts to change to completely black. This layer can be distinguished clearly by observation.

The length L of the pyrolysis region, previously defined, can be considered a characteristic length representing the pyrolysis area. Figure 6 shows the variation of the length L of the pyrolysis region with paper thickness δ. In the range of $\delta < 7.5$ mm, the value of L increases as δ increases. The increasing rate of L is large in the ranges of $\delta < 1.5$ mm and 4 mm $\leq \delta < 7.5$ mm, though it is small in the range of 1.5 mm $\leq \delta < 4$ mm. The data presented in the range of 7.5 mm $\leq \delta < 8.0$ mm are of the unstable flame spread.

Discussion

Heat Flow Model:

Heat transfer to the preheat region has strong influence on flame spread. Several heat transfer models have been proposed for explaining the spread rate [3,12]. However, these models are not practicable to estimate the spread rate if the fuel is not quite thin nor quite thick. Thus, a simple heat flow model should be assumed to interpret the observation.

Figure 7 shows a sketch of an assumed heat flow model. The horizontal distance from the center plane of the sample is represented by y, and x represents the vertical distance from the leading edge of the pyrolysis region. On the x-y coordinate, there is a flow of solid fuel in the positive direction of x at the velocity of V (mm/s). The temperature in the preheat region ranges from the initial temperature T_0 (K) to the pyrolysis temperature T_p. In such a situation, the energy equation for a control volume defined by the central plane and the boundary of virgin material is represented as follows:

$$Q_{\text{tot}} - \frac{1}{2}\rho h \delta V C (T_p - T_0) = 0$$

where the first term, Q_{tot} (J/s), is the total heat input from the flame per unit time, the second term is the convective heat loss by the flow of solid fuel, ρ (g/mm^3) is the density, h (mm) is the horizontal width of the control volume, and C (J/g s) is the heat capacity.

The term Q_{tot} is expressed as

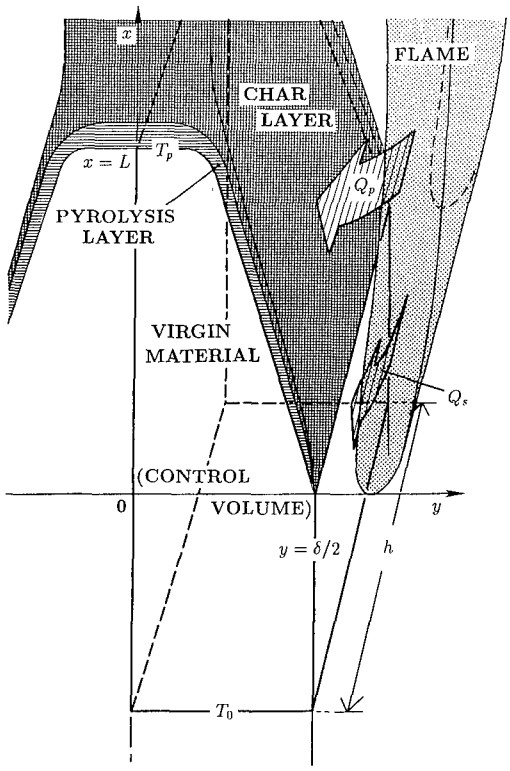

FIG. 7. Sketch of the assumed heat flow into the virgin material.

$$Q_{\text{tot}} = Q_s + Q_p$$

where Q_s (J/s) is the heat transferred through the solid surface ahead of the leading edge of the pyrolysis region and Q_p (J/s) is that penetrating through the pyrolysis layer; Q_s can be regarded as a constant, since the temperature profile near the leading flame edge would not change appreciably for steady downward spread, and Q_p is given as

$$Q_p = -h\lambda \int_0^{S_*} \left(\frac{\partial T}{\partial n}\right)_b dS$$

where λ (J/mm s K) is the thermal conductivity of unburned solid fuel, S is the distance from the line $x = 0, y = \delta/2$ along the boundary of unburned and pyrolysis region, and S_* is S at $x = L$ and $y = 0$, $(\partial T/\partial n)_b$ is the temperature gradient at the boundary in the normal direction to it.

Based on the results of observation and measurement at the cross section of extinguished samples, $(\partial T/\partial n)_b$ is assumed to be constant. Also, S_* is assumed to be approximately equal to L. Then, Q_p can be expressed as $Q_p = hLq_p$, where q_p (J/mm^2 s) is $-\lambda(\partial T/\partial n)_b$.

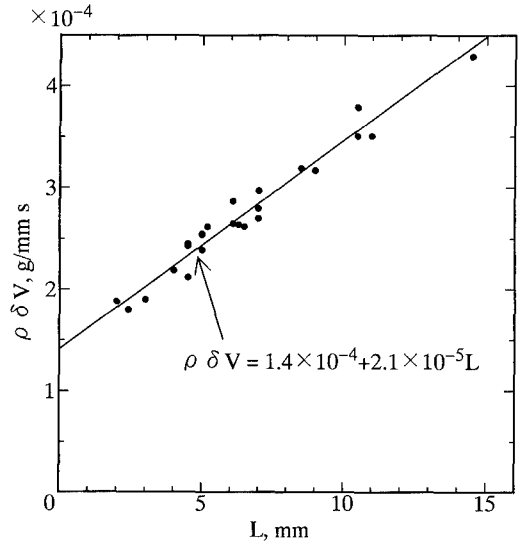

FIG. 8. Relation between L and $\rho\delta V$.

Thus, the relation between spread rate V and L can be written approximately as

$$\rho\delta V = 2(Q_s/h + Lq_p)/C(T_p - T_0). \qquad (1)$$

Figure 8 shows the variation of $\rho\delta V$ with L obtained by the experiments in the range of $\delta < 8.4$ mm and suggests that the relation can be expressed by this simple equation quite accurately. The estimated values from this figure are 7.0×10^{-5} (g/mm s) for $Q_s/hC(T_p - T_0)$ and 1.1×10^{-5} (g/mm^2 s) for $q_p/C(T_p - T_0)$. Main heat flux ahead of the pyrolysis region is supposed to be within 2 mm in the x direction [11] so that the mean value $q_s/C(T_p - T_0)$ per unit length of $Q_s/hC(T_p - T_0)$ is roughly estimated to be 3.5×10^{-5} (g/mm^2 s), where q_s is the heat flux ahead of the pyrolysis region. The value of q_p is much smaller than q_s, though the value of Q_p exceeds Q_s when the sheet is thick enough. This result is reasonable because the heat transferred through the char layer established over the pyrolysis layer is supposed to be small.

Limit Thickness for Downward Spread:

As described before, the stagnating behavior of the flame occurs for a thick sample. To explain the limiting thickness for downward spread, the rate of combustible gas supply seems to be important. The combustible gas is ejected from the pyrolysis region surface. Total mass M_g (g/s) of the generated gas per unit time is expressed as $M_g = aph\delta V$, where a is a mass ratio of the generated gas to consumed virgin material. The mean mass flow rate m_g (g/mm^2 s) per

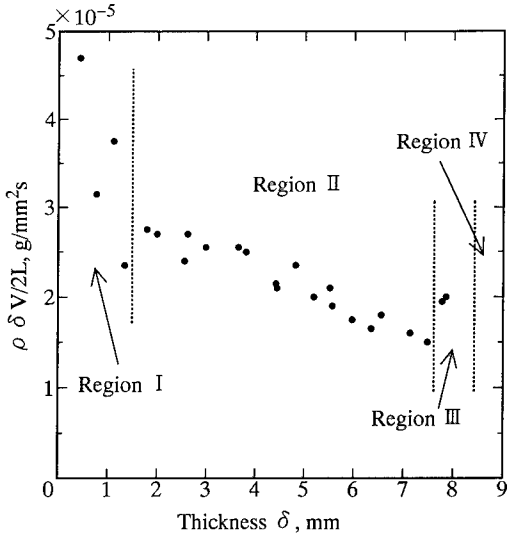

FIG. 9. Variation on mean mass flow rate per unit area $\rho\delta V/2L$ with thickness δ.

unit area is given by dividing M_g by the area $2hL$ of the pyrolysis region surface, i.e.,

$$m_g = M_g/2hL = a\rho\delta V/2L. \quad (2)$$

Equation (1) is substituted into Eq. (2), and the following relation is derived:

$$m_g = \frac{a}{C(T_p - T_0)}\left(\frac{Q_s}{hL} + q_p\right). \quad (3)$$

Equation (3) indicates that m_g decreases with the increase of L and approaches to a constant value, $aq_p/C(T_p - T_0)$.

Figure 9 shows the variation of $\rho\delta V/2L(= m_g/a)$ with δ obtained by the experiments. It is seen that m_g decreases as δ increases in the range of $\delta < 7.5$ mm. In the case of stable downward flame spread, the leading flame edge is usually located in the range of -1 mm $< x < 0$ mm and is separated from the solid surface by the quenching distance. The location of the flame depends on the balance of gas supply rates of fuel and oxidizer. If the fuel gas supply decreases, the flame should move upward to the position where the gas supplies balance, since the leading flame edge cannot approach closer than the quenching distance.

If the value of $aq_p/C(T_p - T_0)$ is small enough, the leading flame edge will move upward to the range of $x > 0$ mm. Once the leading flame edge moves beyond the line $x = 0$, the heat transfer to the preheat region is expected to become extremely small because the heat transfer across the char layer is quite small. This should be the process how the flame stagnation occurs in the case for thick samples.

Conclusions

Downward flame spread over paper sheets of thicknesses from 0.4 to 10 mm have been examined, and the following conclusions are derived.

1. The dependence of flame spread rate V on thickness δ indicates that the spreading behavior can be divided into four types observed under conditions in four regions. The flame spread is found to take place for the sample thickness $\delta < 8.4$ mm in the present experiments under the conditions of natural convection. Near the limiting thickness, unstable flame spread is observed. The flames on both sides stagnate and spread alternately for 7.5 mm $< \delta <$ 8.4 mm.
2. The length L of the pyrolysis region is measured as a characteristic length representing the pyrolysis area. In the range of $\delta < 7.5$ mm, the value of L increases as δ increases.
3. A simple heat transfer model is proposed. It is assumed that the heat transferred through the solid surface ahead of the leading edge of the pyrolysis region is constant and that penetrating through the pyrolysis region is proportional to the area of the region. An equation $\rho\delta V = 2(Q_s/h + Lq_p)/C(T_p - T_0)$ is derived, which expresses the relation between L and $\rho\delta V$ in the present experiments. The heat flux q_p penetrating through the pyrolysis layer is estimated to be much smaller than q_s through the solid surface ahead of the leading edge of the pyrolysis region. It is also inferred that the flame stagnation is caused by the decrease of the fuel gas ejected from the unit area of the pyrolysis surface.

REFERENCES

1. Campbell, A. S., *Combust. Sci. Technol.* 3:103–120 (1971).
2. Parker, W. J., *J. Fire Flammability* 3:254–269 (1972).
3. Hirano, T., Koshida, T., and Akita, K., *Bull. JAFSE* 27:23–39 (1977).
4. Ito, A., and Kashiwagi, T., *Twenty-First Symposium (International) on Combustion,* The Combustion Institute, Pittsburgh, 1986, pp. 65–74.
5. Wichman, I. S., *Prog. Energy Combust. Sci.* 18:553–593 (1992).
6. Di Blasi, C., *Prog. Energy Combust. Sci.* 19:71–104 (1993).
7. Beyler, C., *The SFPE Handbook of Fire Protection Engineering,* SFPE, NFPA, 1988, pp. 165–178.
8. Cullis, C. F., Hirschler, M. M., Townsend, R. P., and Visanuvimol, V., *Combust. Flame* 49:235–248 (1983).

9. Kansa, E. J., Perlee, H. E., and Chaiken, R. F., *Combust. Flame* 29:311–324 (1977).
10. Lee, C. K., Chaiken, R. F., and Singer, J. M., Bureau of Mines Report of Investigations, United States Department of the Interior, 1978.
11. Hirano, T., Noreikis, S. E., and Waterman, T. E., *Combust. Flame* 23:83–96 (1974).
12. de Ris, J. N., *Twelfth Symposium (International) on Combustion*, The Combustion Institute, Pittsburgh, 1969, pp. 241–252.

COMMENTS

Howard D. Ross, NASA Lewis Research Center, USA. 1. For each of the fuel thicknesses, how did the flame curvature vary across the sample width (i.e., was there substantial curvature with the slower spread rate associated with the thick samples)? Did you image the flame both in edge view (as shown in the presentation) and in plan view? With substantial curvature, might transverse flame spread occur at times, and create the irregular spread behavior?

2. What causes the flame extinction with thicker solids in air?

Author's Reply. 1. Because of the heat loss to supporting straps, the flame front near the straps was curved, but the central part of the flame front was almost straight when flame spreading was stable. For the thickness $\delta > 5$ mm, the flame front within 20 mm from each of the straps was observed to curve. For 5 mm $\geq \delta$, the curved part was within 10 mm.

When the spread was unstable, the flame front sometimes curved irregularly because the flame stagnation sometimes occurred partially. In this case, the behavior was not two-dimensional. However, the movement of the flames on both sides along the center line was alternating as indicated in Fig. 5 in the text. The edge views that are shown in Figs. 2 and 5 were not imaged directly since the three-dimensional effects at the edges were not negligible. These sketches were based on the observations of front cross-sectional views.

2. As shown in Fig. 9, the mean mass flow rate per unit area was estimated to decrease as the thickness increases. We suspected that the decrease of fuel evaporation causes the flame stagnation and that the simultaneous stagnation on both sides results in the flame extinction.

•

David N. Schiller, University of California, Irvine, USA. How can an explanation of the cause of unstable flame spread (Region III) be based on an energy balance that does not include either heat conduction from the gas phase to the solid fuel or temperature data? Is a change of governing transport mechanisms (e.g., gas-phase conduction vs solid-phase conduction) responsible for the onset of unstable flame spread, or is the phenomenon due to the proximity of the extinction limit? Is the threshold flame sheet thickness (8.4 mm) for the onset of unstable flame spread related to a critical length scale associated with a change in governing transport mechanisms?

Author's Reply. In this paper, a profile of heat flux from the flame to the solid was assumed to be a step function in which the relation between measured parameters could be expressed. This assumption should be verified in a future study by examining the temperature profile. With the assumption, the explanation of the unstable flame spread was made by considering the decrease of mass flux of evaporated fuel. The estimated value of the mass flux is a function of the thickness δ and the pyrolysis length L in the analysis [Eq. (3)]. However, it should be a function of only δ. The dependence of L on δ should also be cleared by examining the thermal structure in the solid phase.

The causes of the onset of unstable flame spread are considered to be the change of governing transport mechanisms, and the proximity of the extinction limit.

In this case, the critical length scale associated with the change in governing transport mechanism if we define it may be equal to the threshold flame sheet thickness as the commenter pointed out.

•

Takashi Kashiwagi, National Institute of Standards and Technology, USA. 1. Why does the first slowdown of flame spread occur on one side of the surface?

2. Do the unsteady flame spread phenomena occur for a thicker sample or the sample whose back side is quenched?

Author's Reply. 1. There is no doubt that the fluctuating behavior cannot start if the sample sheet is perfectly uniform and the ignited flame is perfectly symmetrical. However, in the actual experiment, the asymmetrical situation is caused by some small disturbances. At first, the sample is excessively heated by the flat burner so that the flame spread on both sides can proceed. As it proceeds, the excessive heat is consumed, and the situation becomes unstable. This would lead to the unsteady behavior.

2. For a sample that was thicker than the limit thickness, the unsteady behavior was seen, though it did not last.

As was described in the paper, the stagnating flame on one side needs additional heat from the preceding flame on the other side to restart spreading. If the back side is quenched, there would be no preceding flame on that side. Thus, the unsteady phenomena would not occur.

•

D. Milov, RRA, USA. How are the different terms defined in the analysis? Is it not that the oscillatory type of spread is due to laboratory-induced flow asymmetry? What is the length of the burnout region?

Author's Reply. In the present analysis, two quantities are defined for heat flow into the control volume. The first question may be asking the definition of these quantities.

The heat flux profile through the surface of the solid fuel has been examined and presented by several researchers [1,2,3]. The flux increases and decreases rapidly as the leading flame edge passes, then becomes almost constant. By a rough estimation, this profile could be expressed by a step function, in which a strong heat flux is followed by a small flux. In the analysis, the location where the heat flux changes was regarded as the location where the pyrolysis starts.

Our experiments were done at natural convection. The sample sheet was fixed by the straps on a table. The distance from the bottom of the sheet to the table surface was 280 mm. Cameras are set at 1 m away from the sample surfaces. There were no other surroundings near the sample sheet. Thus, the induced flow should not depend on the laboratory configuration.

The length of the burnout region is affected not only by the thickness of the sample sheet but also by the igniting condition. It was about 10–20 mm in the case of a 10-mm-thick sample.

REFERENCES

1. Di Blasi, C., *Prog. Energy Combust. Sci.* 19:17–104 (1993).
2. Frey, A. E., and Tien, J. S., *Combust. Flame* 36:263–289 (1979).
3. Kim, J. S., and Back, S. W., *Combust. Sci. Technol.* 88:133–150 (1992).

•

Subrata Bhattacharjes, San Diego State University, USA. Could you comment on whether or not the oscillations you have observed with the flat samples would disappear in a cylindrical configuration?

Author's Reply. It is expected that the flame stagnates partially when the diameter of the fuel cylinder is large enough. However, the diameter for the unsteady-spread condition would be larger than the thickness for region III in this paper, because the cylinder has more flaming area per unit volume than the plate if the diameter and the thickness are the same. This suggests that the stagnating part of the flame is not significantly affected by the part of the flame on the opposite position. Thus, the unstable behavior is supposed not to be oscillating type, but it is expected that the stagnating part of the flame moves along the flame front around the cylinder.

Twenty-Fifth Symposium (International) on Combustion/The Combustion Institute, 1994/pp. 1447–1453

AN INSTRUMENT FOR CHARACTERIZATION OF THE THERMAL AND OPTICAL PROPERTIES OF CHARRING POLYMERIC MATERIALS

MICHAEL A. SERIO, DAVID S. PINES,* ANTHONY S. BONANNO AND PETER R. SOLOMON
Advanced Fuel Research, Inc.
87 Church Street, East Hartford, CT 06108, USA

AND

GIRARD A. SIMONS
Simons Research Associates
3 Juniper Road, Lynnfield, MA 01940, USA

A test instrument was developed and used to characterize the changes in the thermal and optical properties of charring polymeric materials when exposed to radiative heat fluxes. The system is based on a bench-top emissometer apparatus, which was developed originally to simultaneously measure the surface temperature and spectral properties of materials at elevated temperatures and was modified in this work to study charring polymers. An advantage of using a modified emissometer is that the front surface temperature is measured optically instead of with a thermocouple. Time-resolved measurements of the front surface temperature, along with thermocouple measurements of the interior and back surface temperatures can provide information on the changes in thermal conductivity and thermal diffusivity with the extent of charring, assuming that the heat of gasification is known. In addition, this apparatus measures the changes in the material's spectral emissivity and functional group composition as it chars. Data are presented for experiments on two different samples of 3.2-mm-thick polyurethane, heated using radiant fluxes from 22 to 32 kW/m^2. Analysis of the surface temperature and emissivity data indicates that the samples undergo a transition from a volume to a surface absorber during initial irradiation. Quantification of this behavior will be a critical element in predicting the flammability limits of these materials.

Introduction

An important consideration in the combustion of polymers is the pyrolytic degradation processes that lead to the production of volatile fuel, smoke, toxic gases, and char [1,2]. While test methods allow reasonable assessments for noncharring polymers, test methods for charring polymers have not been as well developed, and there is no accepted methodology for prediction of their behavior in a fire [3]. The current polymer decomposition models have also focused primarily on the predictions of relatively simple, noncharring polymers such as PMMA [4–8]. Recently, the study of charring polymers under fire conditions has begun to receive more attention [9–13]. However, there is no currently available model for the pyrolysis of charring polymers that provides a good description of the char physical properties (thermal conductivity, heat capacity, emissivity, and oxygen reactivity). The development of such a model would be of significant benefit in modeling the behavior of charring polymers in fires. These models require input data on the thermal and optical properties at combustion temperatures. This paper describes an apparatus that has been developed to obtain the relevant data for charring polymers.

Experimental

Samples:

The apparatus was developed and tested using two samples of polyurethane (Mobay 110–25) obtained from General Motors in flexible sheets of ~3.2 mm in thickness. The monomeric components of the Mobay 110–25 polyurethane are diphenylmethane diisocyanate and polyether polyol. The samples were cut into discs that were 7.1 mm in diameter. The initial density of the material was estimated to be ~1.08 g/cc. One of the samples was reinforced with 15% mica.

Apparatus:

A bench-top emissometer was developed at Advanced Fuel Research (AFR) to simultaneously mea-

*Current address: Department of Environmental Engineering, University of Massachusetts, Amherst, MA 01002, USA.

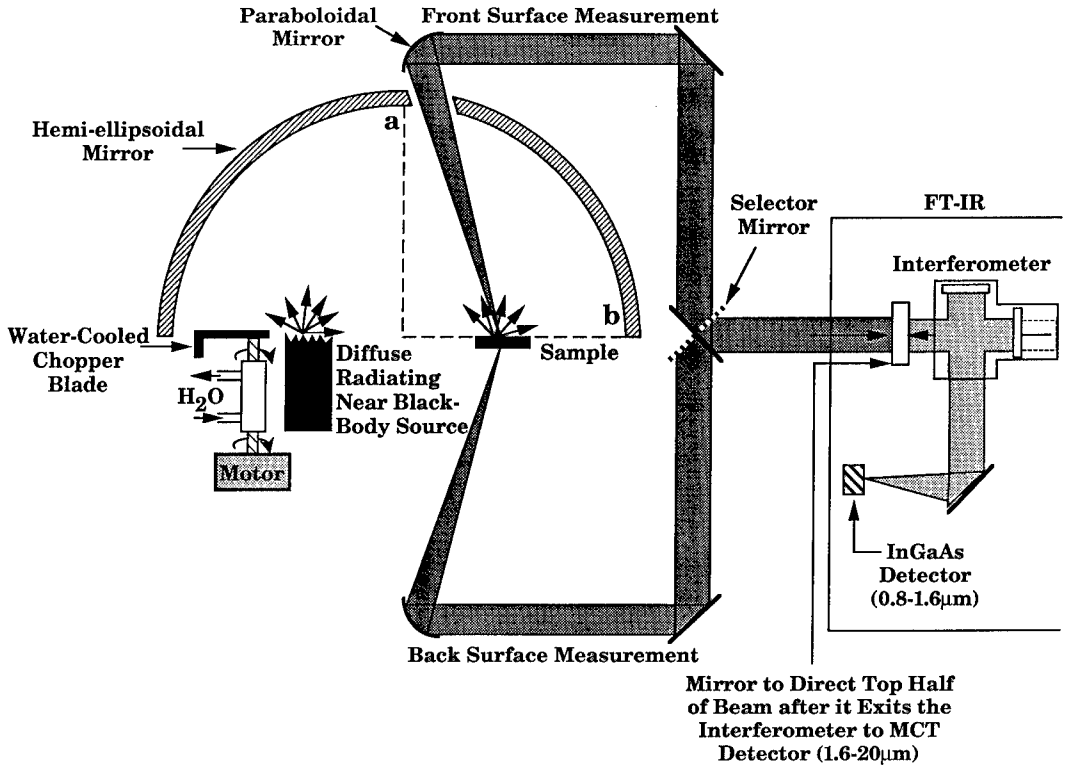

FIG. 1. Schematic diagram of the Bench-top emissometer.

sure the surface temperature and spectral properties of materials at elevated temperatures [14–16]. A schematic of the bench-top emissometer is shown in Fig. 1. The hemiellipsoidal mirror has both foci inside the mirror, with a source located at one of the foci and the sample located at the other focus. This mirror geometry, combined with the radiating characteristics of the blackbody source, provides a means of irradiating the sample both hemispherically and diffusely. Therefore, the measurement of reflected radiation from the front surface in a given direction is that of directional-hemispherical reflectance since the sample is irradiated uniformly from all directions. Likewise, for transmissive samples, the back surface measurement is of directional-hemispherical transmittance.

An integral part of the optics is the rotating chopper system that moves either an aperture or a cold blackbody element in front of the source. The Fourier transform infrared (FT-IR) data collection system is synchronized with these two states and allows for the discrimination of sample radiation from reflected/transmitted radiation as follows. For the reflectance measurement, the IR beam originates at the blackbody source at one focus of the hemiellipsoidal mirror. The radiation reflects from the hemiellipsoidal mirror and is focused onto the sample at the other focus, where it is reflected (scattered) by the sample into the interferometer. The reflectance and the sample radiance are measured together when the aperture on the chopper rotor is in place over the source (chopper open condition). When a cold blackbody is substituted for the aperture over the source (chopper closed condition) it is the sample radiance alone that is measured. Both the radiance and directional-hemispherical reflectance can be obtained from these two spectra and their difference.

For the transmission measurement, radiation from the source is collected by the hemiellipsoidal mirror and directed to the sample. In this case, the radiation directly and diffusely transmitted by the sample is directed by the selector mirror into the FT-IR spectrometer for measurement. Again, the directional-hemispherical transmittance and radiance from the sample's back surface is obtained by comparing the spectra for the two chopper positions.

In the bench-top instrument, two separate detectors are normally utilized to measure the near- and mid-IR energy. A room-temperature indium-gallium-arsenide detector is sensitive to near-IR energy (0.8–1.6 μm), and a liquid nitrogen–cooled mercury-cadmium-telluride detector is used for longer wavelengths (1.6–20 μm). Both spectral regimes are mea-

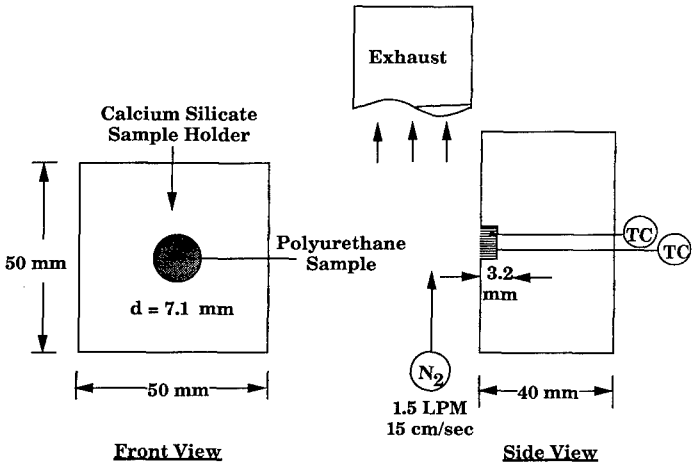

FIG. 2. Configuration of sample holder, thermocouples, and nitrogen purge flow.

sured simultaneously. However, for the work done on the current project, the former detector was not installed.

In order to provide the information required to characterize the properties of a charring polymer that is exposed to a radiant heat source, several changes were made. The emissometer was modified to include an inert gas purge over the sample's front surface, temperature measurements of the interior and back surface using thermocouples and insulation of the sample with a block of calcium silicate to ensure one-dimensional heat transfer. It is planned to include a load cell (for weight loss measurements) and a provision for analysis of evolved gases in the final version of the instrument. The thermocouples used were type K (Omega no. CHAL-005) of 0.13-mm diameter that were inserted through predrilled holes in the calcium silicate block and covered (except at the tip) with a ceramic insulator. A schematic of the sample holder is shown in Fig. 2.

In order to simplify the interpretation of the measured thermal and optical properties, it is desirable to have a uniform heat flux. In a hemiellipsoid mirror, the magnification of an image at one focus onto the other focus depends on the distance between the two foci. In order to determine the heat flux profile of the bench-top emissometer at the sample focus from a 750 °C source furnace (25 × 25 mm), a power gauge with a 3.6-mm aperture was used to measure the heat flux at various locations around the sample's focus [17]. The ellipsoidal shape of the profile was consistent with the experimental and analytical ray tracing done by Neu [18]. The heat flux profile indicates that the energy is more constant in the vertical direction than the horizontal. In order to keep the heat flux over the entire sample within 10% of the average flux, a sample size of approximately 7-mm diameter was selected. To verify the one-dimensional heat-transfer assumption, the temperatures, at the same depth (1.6 mm from the front surface) but at two different radial positions (2 mm right of center and 2.8 mm left of center), were measured using thermocouples for a polyurethane sample with a 750 °C source furnace. Since the measured temperatures were within 2 °C of each other, the one-dimensional assumption was assumed to be valid.

Theoretical Background:

For the front surface sample measurements, the cold blackbody element of the rotor is in place over the cavity radiation source. The measurement M1 will be the sample's directional spectral radiance:

$$\mathrm{M1}_\nu = \varepsilon_\nu(T_s)\, R_\nu^b(T_s) \tag{1}$$

where ε_ν is the emissivity of the sample at temperature, T_s, and R_ν^b is the Planck function at temperature T_s. The subscript ν indicates spectral quantities.

With the aperture of the rotor placed over the blackbody source, the measured radiation, M2, will include that emitted by the sample ($\mathrm{M1}_\nu$) and the blackbody source radiation reflected by the sample in a spectral directional-hemispherical mode,

$$\mathrm{M2}_\nu = \mathrm{M1}_\nu + \rho_\nu(T_s)R_\nu^b(T_{bb}) \tag{2}$$

where T_{bb} is the constant blackbody temperature of the source radiation and ρ_ν is the spectral directional-hemispherical reflectivity. The difference of the two measurements is thus

$$\mathrm{M2}_\nu - \mathrm{M1}_\nu = \rho_\nu(T_s)R_\nu^b(T_{bb}). \tag{3}$$

The constant source radiation is quantified by replacing the sample with a perfect reflector (a gold mirror, $\rho_\nu = 1.0$) and measuring the spectrum in the chopper open condition:

$$\mathrm{M}_\nu^{\mathrm{ref}} = \rho_\nu^{\mathrm{gold}}\, R_\nu^b(T_{bb}) = R_\nu^b(T_{bb}). \tag{4}$$

The ratio of Eq. (3) to Eq. (4) results in the measurement of the directional-hemispherical reflectance of the sample, ρ_ν, at the unknown temperature, T_s:

$$(M2_\nu - M1_\nu)/M_\nu^{ref} = [\rho_\nu(T_s)R_\nu^b(T_{bb})]/R_\nu^b(T_{bb}) = \rho_\nu(T_s). \quad (5)$$

For an opaque sample, the spectral emittance, ε_ν, can now be determined from closure:

$$\varepsilon_\nu = 1 - \rho_\nu \quad (6)$$

Once ε_ν is determined, the precise sample temperature is found by rearrangement of Eq. (1):

$$R_\nu^b(T_s) = [M1_\nu/\varepsilon_\nu(T_s)]. \quad (7)$$

For nonopaque samples, the directional-hemispherical transmittance, τ_ν, is measured by flipping the selector mirror and measuring the back surface radiance ($M3_\nu$) and back surface radiance plus transmittance ($M4_\nu$). The source radiation is quantified with the sample absent, and the analysis to determine τ_ν follows that for ρ_ν. The more extensive closure relationship is then used to determine ε_ν:

$$\varepsilon_\nu = 1 - \rho_\nu - \tau_\nu. \quad (8)$$

Advantages of Emissometer for Charring Polymer Applications:

An advantage of using the modified emissometer for studying the behavior of charring polymers exposed to radiant heat is that the front surface temperature is measured optically instead of with a thermocouple. Front surface temperatures are difficult to measure accurately with a thermocouple because they are affected by the radiant heat source. It is also true that small changes in the placement of the thermocouple (slightly above or below the surface) can give a significant difference in the temperature measurement. In addition to measuring the thermal properties in cases where the heat of gasification is known, this apparatus will measure the change in the material's emissivity as it chars. Knowing the emissivity is necessary in accurately predicting a material's flammability since radiation is usually the main heat-transfer mechanism in a fire.

Results

Preliminary testing of the polyurethane samples was conducted using the existing emissometer prior to making any modifications. The sample without mica reinforcement was tested at blackbody source temperatures ranging from 600 °C to 850 °C, corresponding to radiant heat fluxes ranging from 22 to 32 kW/m^2. The sample was initially heated with a 600 °C blackbody source. When the sample had reached steady state, radiance and radiance plus reflection measurements were taken from the front surface (Fig. 3a). The selector mirror was then flipped, and radiance and radiance plus transmission measurements were taken from the back surface (Fig. 3b). The two back surface measurements were identical below the 4500 cm^{-1} wave number, which indicates that the sample is opaque in this region. By closure $(1 - \rho - \tau)$, the emittance was calculated and is presented in Fig. 3c. Finally, the normalized radiance of the front surface (radiance/emissivity) along with a Planck blackbody curve at 229 °C is presented in Fig. 3d.

These preliminary tests demonstrated the feasibility in using the bench-top emissometer to measure the surface temperature and the spectral changes in a charring polymer. Consequently, the bench-top emissometer was modified to include a nitrogen purge, and a special sample holder was designed and constructed, as described in the experimental section (see Fig. 2). The first tests performed with the modified apparatus were to measure the front, middle, and back surface temperature as well as the spectral properties of the front surface as the sample was being heated at different radiant heat fluxes (22, 26.5, and 32 kW/m^2). The 15% mica-reinforced sample was selected because it is opaque. Therefore, transient temperature measurements can be made using a single scan without having to flip the selector mirror. The front, middle, and back surface temperatures as a function of time at the middle heat flux are shown in Fig. 4. In addition, the average emissivity between 6500 and 500 cm^{-1} wave numbers is shown (right-hand scale). The results at the low (22 kW/m^2) and high (32 kW/m^2) heat fluxes are qualitatively similar [17].

In all three cases, the polyurethane became more reflective as it was charred. The spectral changes in the emissivity as the sample was heated at the 26.5 kW/m^2 heat flux are shown in Fig. 5. Initially, the virgin material is a gray body due to self-absorption. As the surface is charred, it becomes more reflective and exhibits very strong spectral features with an isocyanate peak (N=C=O antisymmetric stretch at 2275 cm^{-1}), a N—H-free stretch at 3350 cm^{-1}, and an O—H stretch at 3625 cm^{-1}. There is initially an aliphatic peak at 2950 cm^{-1}, which then disappears as the polymer becomes charred, with the appearance of a strong aromatic peak at 3079 cm^{-1}. The change from an aliphatic to a more stable aromatic structure is consistent with previous studies involving the pyrolysis of charring polymeric materials [2]. These changes are not only a function of temperature, but are also time dependent, which is consistent with the finite-rate chemistry of the charring process. The ability to see the spectral detail of the char is

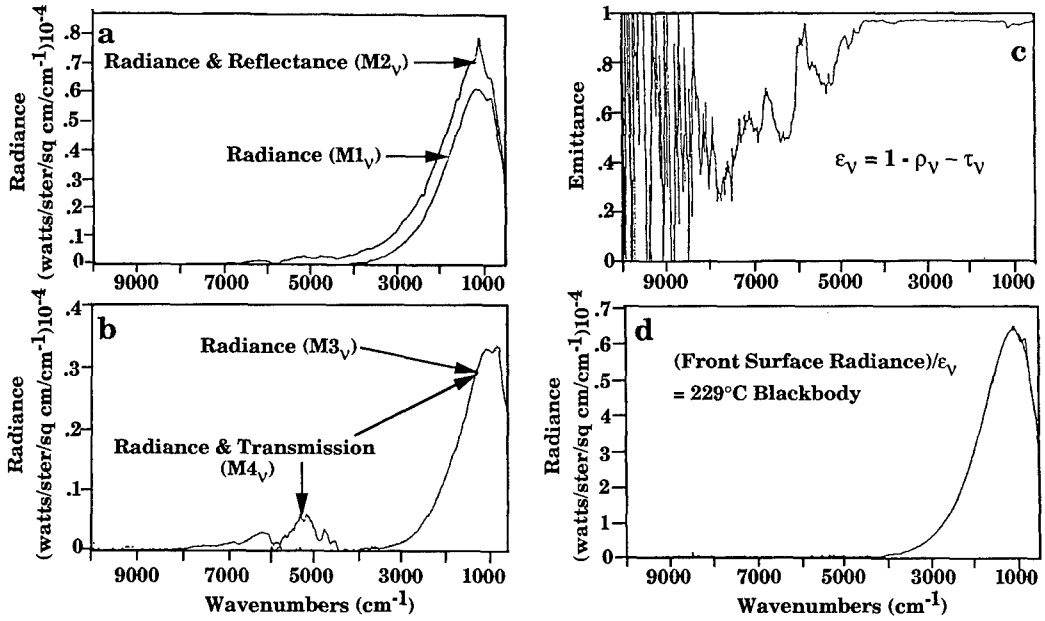

FIG. 3. Spectral emittance and temperature determination of polyurethane: (a) spectral radiance (chopper closed) compared to radiance + reflectance (chopper open); (b) back surface radiance (chopper closed) compared to back surface radiance + transmission (chopper open); (c) spectral emittance by closure, $\varepsilon_v = 1 - \rho_v - \tau_v$; and (d) temperature determination by overlaying normalized radiance with theoretical blackbody temperature curves.

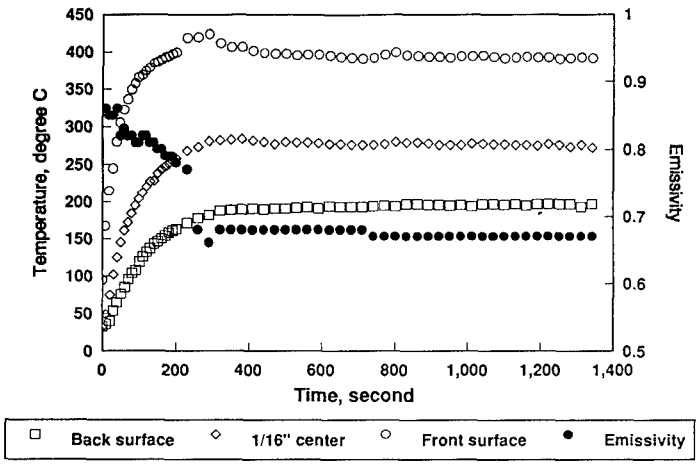

FIG. 4. Polyurethane (15% mica) temperature profile at 26.5 kW/m^2.

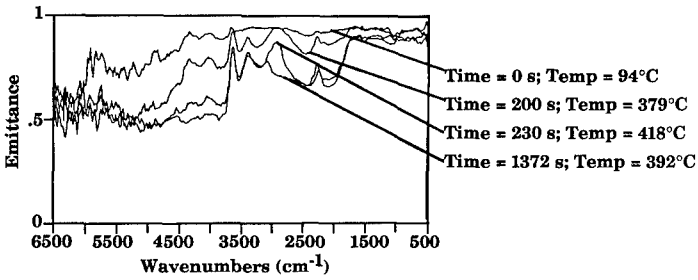

FIG. 5. Spectral emittance of polyurethane (15% mica) exposed to 26.5 kW/m^2.

TABLE 1
Exponential decay constants for temperature profiles in polyurethane slabs

Heat Flux (kW/m^2)	Location		
	Front surface	1/16″ depth	Back surface
22	0.022	0.012	0.008
26.5	0.023	0.013	0.009
32	0.027	0.012	0.008

quite surprising since it was expected that the char would exhibit gray body behavior similar to the virgin material. More work is needed to understand why the spectral features are so strong. However, it is likely that this is related to the change of the material from a volume absorber to a surface absorber as charring proceeds. Further evidence for this phenomenon is obtained from an analysis of the temperature profiles, as discussed below.

This measurement technique provides the important advantage of being able to monitor the chemical changes in the polymer's surface during the charring process. The 25% decrease in the average emissivity indicated in Fig. 4 reduces the radiation absorbed and, therefore, inhibits further pyrolysis of the interior. Knowing how the emissivity changes with charring is an important parameter in being able to accurately predict the behavior of a polymer that is exposed to a radiant heat source.

The temperature profiles of the front, middle, and back surfaces of all three tests showed an exponential decay response from room temperature to an asymptotic maximum temperature. The profiles were fitted using the following formula, and the exponential factors were compared for the three cases:

$$T = (T_{ss} - T_i)\cdot[1 - \exp(-mt)] + T_i \quad (9)$$

where T is the temperature at time t (°C), T_{ss} is the asymptotic steady-state temperature (°C), T_i is the initial temperature at $t = 0$ s (°C), t is time (s), m is the exponential constant.

It is interesting to note that the exponential factors for the interior and back surfaces are approximately the same for the three different heat fluxes. As expected, the exponential factor for the front surface increased as the heat flux increased.

Recent studies conducted on the ignition of solids have treated the optical depth as a constant or as zero for the case of a pure conductor (e.g., see Ref. 11). While in-depth pyrolysis has been described as the source of the combustion products, the subsequent effects of the internal pyrolysis have not been studied extensively. The temperature profiles of the virgin materials, shown in Fig. 4, indicate that temperature overshoot of the front surface temperature is characteristic of the virgin material. However, there is no such observation for the precharred material [17]. The temperature rise of the virgin material is nearly linear, whereas that of the precharred material is approximately the square root of time. This observation suggests that the virgin material is a volume absorber, whereas the precharred material is a surface absorber: relating the heat flux I to the temperature rise $\Delta T\ (t)$, we write

$$It = \rho c_p\ \Delta T\delta \quad (10)$$

where $\rho \approx 1$ g/cc, $c_p \approx 2$ J/g K, and δ is either the optical or the thermal depth of the energy deposition. The surface temperature data for the virgin material ($\Delta T(t) = 4t$) suggests that δ = constant optical depth = 4 mm, while that for the precharred material ($\Delta T(t) = 50\ t^{1/2}$) suggests that δ is a thermal diffusion depth $(4at)^{1/2}$ corresponding to $a = 2 \times 10^{-8}$ m^2/s. A value of 3 mm was independently measured for the optical absorption depth of the virgin material in the near IR (1.5 to 2.7 μm) and a value of 2 to 4 $\times$ 10^{-8} m^2/s for the diffusivity of the char [17]. These data clearly demonstrate that the charring is controlling the evolution of the material from a volume to a surface absorber and a thorough understanding of this aspect of the charring process is necessary to predict the temperature profile and ignition characteristics.

Conclusions

A test instrument was developed and used to characterize the changes in the thermal and optical properties of charring polymeric materials when exposed to radiative heat fluxes. The system is based on a bench-top emissometer apparatus, which was developed originally to simultaneously measure the surface temperature and spectral properties of materials at elevated temperatures and modified in this work to study charring polymers. Time-resolved measurements of the front surface temperature, along with thermocouple measurements of the interior and back

surface temperatures, provide information on the changes in thermal conductivity and thermal diffusivity with the extent of charring, assuming that the heat of gasification is known. These data can be used for characterization of polymeric materials or as inputs to a model of a charring polymer surface. In addition, this apparatus measures the changes in the material's spectral emissivity and functional group composition as it chars. The results for polyurethane indicate that it becomes more reflective as it is charred and that the chemical composition becomes more aromatic. It is relatively straightforward to use the instrument to determine the thermal properties of already charred materials. For the virgin materials, the effects of the heat of gasification and the change in the material from a volume absorber to a surface absorber must be included in the analysis.

Acknowledgments

The authors are grateful for the support of the National Science Foundation under Grant No. III-9101585. The authors also wish to thank Karen Kinsella of Advanced Fuel Research for assistance with the experimental work and Professor Eric Suuberg of Brown University for helpful discussions on the behavior of charring polymers. Professor Mark Petrich of Northwestern University supplied the polyurethane samples, which were obtained from General Motors.

REFERENCES

1. Gann, R. G., and Dipert, R., "Polymer Flammability," *Encyclopedia of Polymer Science and Engineering*, John Wiley and Sons, New York, 1986.
2. Cullis, C. F., and Hirschler, M. M., *The Combustion of Organic Polymers*, Clarendon Press, Oxford, 1981.
3. Di Blasi, C., *Prog. Energy Combust. Sci.* 19:71 (1993).
4. Kashiwagi, T., Inaba, A., Brown, J. E., Hatada, K., Kitayama, T., and Masuda, E., *Macromolecules*, 19:2160 (1986).
5. Inaba, A., Brown, J. E., and Kitayama, T., *Eur. Polym. J.* 23:871 (1987).
6. Kashiwagi, T., and Omori, A., *Twenty-Second Symposium (International) on Combustion*, The Combustion Institute, Pittsburgh, 1329 (1988).
7. Meeki, K., Atreya, A., Agrawal, S., and Wichman, I., *Twenty-Third Symposium (International) on Combustion*, The Combustion Institute, Pittsburgh, 1701 (1990).
8. Hertzberg, M., and Zlochower, I. A., *Twenty-Third Symposium (International) on Combustion*, The Combustion Institute, Pittsburgh, 1247 (1990).
9. Parker, W. J., in *Heat Release from Fires* (V. Babrauskas and S. J. Grayson, Eds.), Elsevier Applied Science, New York, 1992, pp. 333–356.
10. Kashiwagi, T., and Nambu, H., *Combust. Flame* 88:345 (1992).
11. Nakabe, K., Baum, H. R., and Kashiwagi, T., "Ignition and Subsequent Flame Spread over a Thin Cellulosic Material," *Proceedings of the Second International Microgravity Combustion Workshop*, NASA Conference Publication 10113, 1992.
12. Milosavljevic, I., and Suuberg, E. M., *ACS Div. Fuel Chem. Preprints* 37(4):1567 (1992).
13. Ohlemiller, T. J., "Assessment of the NASA Flammability Screening Test and Related Aspects of Material Flammability," Final Report, NASA CR-189226, Aug., 1992.
14. Markham, J. R., Solomon, P. R., and Best, P. E., *Rev. Sci. Instr.* 61:3700 (1990).
15. Markham, J. R., Best, P. E., Solomon, P. R., and Yu, Z. Z., ASME *J. Heat Trans.* 114:458 (1992).
16. Markham, J. R., Kinsella, K., Carangelo, R. M., Brouillette, C. R., Carangelo, M. D., Best, P. E., and Solomon, P. R., *Rev. Sci. Instr.* 64(9):2525 (1993).
17. Serio, M. A., Pines, D. S., Bonanno, A. S, and Solomon, P. R., "Measurements and Modeling of the Behavior of Charring Polymers in Fires," Annual Report for National Science Foundation, Grant No. III-9101585, Dec., 1993.
18. Neu, J. T., NASA CR—73193, 1968.

Twenty-Fifth Symposium (International) on Combustion/The Combustion Institute, 1994/pp. 1455–1462

CARBON MONOXIDE FORMATION IN FIRES BY HIGH-TEMPERATURE ANAEROBIC WOOD PYROLYSIS

WILLIAM M. PITTS, ERIK L. JOHNSSON AND NELSON P. BRYNER
Building and Fire Research Laboratory
National Institute of Standards and Technology
Gaithersburg, MD 20899, USA

Building fire fatalities often occur at locations remote from the room where the fire is actually burning. The majority of these fire deaths are the result of smoke inhalation, primarily due to exposure to carbon monoxide (CO). Although causing nearly 2500 deaths per year in the United States, the mechanisms for the formation of CO in building or enclosure fires remain poorly characterized.

In order to test the hypothesis that high concentrations of CO can be generated by pyrolysis of wood in a high-temperature, vitiated environment, a series of natural gas fires, ranging from 40 to 600 kW in heat release rate, were burned inside a reduced-scale enclosure (RSE). The ceiling and upper walls of the RSE were lined with 6.4-mm-thick plywood. During each burn, the concentrations of CO, CO_2, and O_2 were monitored at two locations within the upper layer. Oxygen calorimetry was used to monitor the total heat release rate for each fire. Vertical temperature profiles for two positions within the enclosure were also recorded.

Much higher levels of CO were generated with the wood-lined upper layer than with comparable fires fueled only by natural gas. Volume concentrations as high as 14% were observed. The fires with wood in the upper layer had higher heat release rates and depressed upper-layer temperatures. The major conclusions of this work based on the experimental findings are (1) the pyrolysis of wood in a highly vitiated, high-temperature environment can lead to the generation of very high concentrations of CO in enclosure fires; (2) the overall wood pyrolysis is endothermic for the experimental conditions studied; and (3) the maximum mass loss rate of wood under the experimental conditions is on the order of 10 gs^{-1} m^{-2} with the majority of released carbon being converted to a roughly 1:1 mixture of CO and CO_2.

Introduction

The majority of fire deaths within buildings [1] occur as the result of smoke inhalation from "flashed over" [2] fires at locations remote from the fire itself. Postmortem analysis of fire victims [3] as well as studies of the causes of fire death reported by medical examiners [4] indicate that roughly two-thirds of all building fire deaths are the direct result of exposure to the carbon monoxide (CO) generated by the fire. Although this represents nearly 2500 deaths per year in the United States [5], very few systematic investigations of CO formation during enclosure fires have been reported, and the mechanism(s) for generating CO in such fires remain poorly characterized.

Earlier idealized experiments [6–8] in which fires burning in an open laboratory were quenched upon entering a hood containing combustion gases showed that concentrations of the combustion gases, including CO and fuel, could be correlated in terms of the global equivalence ratio (GER), ϕ_g, which is defined as the mass of material in the upper layer derived from fuel divided by the mass of material derived from air normalized by the fuel to air ratio required for stoichiometric burning. The existence of these correlations has been termed the "global equivalence ratio concept" [9].

Gottuk et al. [10] demonstrated that the concentrations of combustion species generated within an enclosure carefully designed to create an environment similar to the hood experiments were also well correlated with ϕ_g, even though the correlations differed slightly from the hood results due to higher upper-layer temperatures in the enclosure fires. Work reported by Bryner et al. [11] and discussed by Pitts [12] demonstrated that the GER concept can breakdown when air is entrained directly into the upper layer of an enclosure with a single doorway. Even in the latter case, however, observed CO concentrations for underventilated burning were only 50% higher than predicted by the GER concept.

In 1987 in Sharon, PA, there was a fatal townhouse fire, where deaths occurred on the second floor, even though the fire was essentially localized in a first floor kitchen. One of the victims had an extraordinarily high level of carboxyhemoglobin, suggesting exposure to very high concentrations of CO. Levine and Nelson [13] investigated this fire in detail and

decided to simulate it in the full-scale burn facilities at the National Institute of Standards and Technology (NIST).

In order to simulate the wood paneling and cabinets in the kitchen, a heavy fuel loading of wood, 184 kg, was used. Concentration measurements of CO and other flame gases were made at the soffit of a doorway located at the base of a stairway leading to the second floor as well as in a "bedroom" located on the second floor. Volume concentrations of CO as high as 8% were observed downstairs, while concentrations in the upstairs bedroom exceeded 4%.

Beyler [7] had burned wood in a "hood" experiment and found that CO volume concentrations of 3.2% were generated during underventilated burning. Similar results were reported by Gottuk et al. [10] for their idealized enclosure. Concentrations of CO observed in the Sharon fire test are, therefore, at least 2.5 times higher than predicted by the GER concept. Such a large difference cannot be attributed to a temperature effect or entrainment of air directly into the upper layer. Another mechanism for CO generation must exist.

In this paper, it is shown that direct pyrolysis of wood in highly vitiated (anaerobic), high-temperature flame gases generates very high concentrations of CO, thus providing a likely explanation for the failure of the GER concept to predict the generation of CO during the Sharon fire test. Despite an extensive literature on the pyrolysis and burning behavior of wood and similar substances, we have found no experimental investigations of wood pyrolysis for the conditions of interest to this investigation. However, there are numerous studies in the literature suggesting that wood can be efficiently converted to CO when small particles are exposed to high temperatures under anaerobic conditions.

Milne [14] summarizes a number of experiments in which wood and related substances were rapidly pyrolized at high temperatures in inert environments. Many of these studies reported significant mass conversion to carbon oxides with the CO to CO_2 ratio being generally greater than one. Brink et al. [15] studied wood particle decomposition in a flow reactor over a 300 °C to 900 °C temperature range. The degree of conversion to gas increased with temperature as did the $CO:CO_2$ volume ratio. For 600 °C, this ratio was nearly 1 and increased to 12 by 900 °C. Arpiainen and Lappi [16] reported similar findings for the flash pyrolysis of pine bark with high conversion to carbon oxides and a $CO:CO_2$ ratio of 1 near 600 °C and of 4 for 800 °C.

Experimental

The experiments were performed in the reduced-scale enclosure (RSE) test facility at NIST. This facility is described fully elsewhere [11] and will only be summarized here. The RSE is a two-fifths-scale model of a standard full-scale room widely used for fire testing [17,18]. The RSE has inside dimensions of 0.98-m wide × 0.98-m tall × 1.46-m deep and a single doorway, which is 0.48-m tall × 0.81-m wide. The inside of the enclosure is lined with two layers of 1.27-cm-thick calcium-silicate boards, which are supported by a steel framework.

A 15.2-cm-diameter burner is positioned in the center of the RSE 15.2 cm above the floor. The flow rate of the fuel, natural gas, to the burner is monitored using both a diaphragm test meter and rotameters. The burner is ignited by a small propane pilot flame. Flow rates are adjusted to provide a range of fire sizes (assuming complete combustion and using heats of combustion based on the known composition of the natural gas) up to 600 kW.

Gas concentrations within the RSE are monitored at two locations by continuously extracting samples through 0.95-cm-diameter tubing and, after drying, using nondispersive infrared analyzers (CO and CO_2) and paramagnetic analyzers (O_2). Gas sampling locations are 10 cm from the ceiling (well within the upper layers of the fires). The front sample probe is 10 cm from the front wall that contains the door and 29 cm from a side wall. The rear sample probe is located 29 cm from the side and rear walls. Temperatures are recorded at several heights using two thermocouple trees placed in the front and rear of the enclosure at locations 20.3 cm from the side and end walls.

The RSE is placed under the large hood of the NIST furniture calorimeter [19], which utilizes oxygen calorimetry [20] to measure the heat release rate (HRR) of a fire. Note that measured HRRs reflect burning both inside and outside of the enclosure.

The results of an extensive series of natural gas burns are discussed elsewhere [11,12]. These earlier studies found that the natural gas fires became underventilated for HRRs greater than 200 kW. As the fires became underventilated, the concentration of CO observed in the upper layer increased quickly with fire size, reaching asymptotic values of approximately 2 and 3 vol.% in the rear and front of the enclosure, respectively. Upper-layer temperatures were quite high and also were found to differ in the front and rear of the enclosure (typically 1000 °C in the front and 850 °C in the rear). For underventilated burning, oxygen concentrations were very close to zero as expected for well-mixed rich gases at these temperatures [9,12,21].

For the current study, the ceiling and upper walls (36 cm down from the ceiling) of the RSE were lined with 6.4-mm-thick Douglas fir plywood in order to test the hypothesis that pyrolysis of wood in high-temperature, anaerobic environments can generate high concentrations of CO. The total mass of wood was approximately 10 kg. Natural gas fires of various sizes were then burned, and the concentrations of

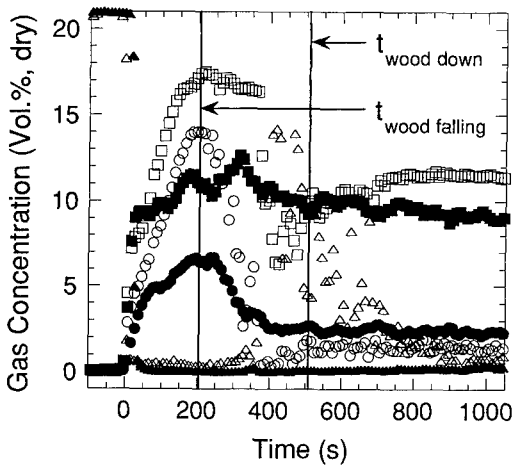

FIG. 1. Volume concentrations (dry) vs time for a fire within the RSE fueled by a natural gas flow corresponding to 400 kW and a plywood lining on the ceiling and upper walls. Results for CO (○, ●), CO_2 (□, ■) and O_2 (△, ▲) are shown. Samples were measured at front (filled symbols) and rear (open symbols) locations. The fire was ignited at time = 0 s. Times for when the wood first began to fall from the ceiling and walls and for when the wood had collapsed are indicated.

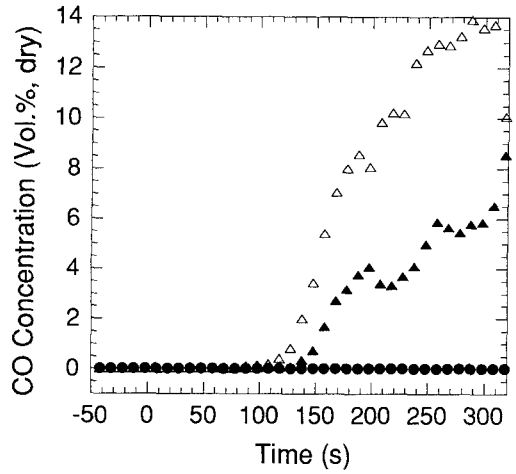

FIG. 2. Volume concentrations (dry) of CO vs time for a 50-kW natural gas fire (○ = rear; ● = front) and for a 50-kW natural gas fire with a plywood lining on the ceiling and upper walls (△ = rear; ▲ = front). The fire was ignited at time = 0 s, and the wood began to fall at 320 s.

CO, CO_2, and O_2 were monitored at the two locations within the upper layer. Vertical temperature profiles for the two positions within the enclosure were recorded. The furniture calorimeter was operated to provide heat release data for the fires. A series of 12 fires were burned in which the size of the natural gas fires was varied from 40 to 600 kW.

Results

Figure 1 shows time histories of CO, CO_2, and O_2 concentrations at the two sampling positions within the upper layer for a nominal 400 kW natural gas fire in the presence of the wood lining. Time zero corresponds to the ignition of the natural gas. For all of the fires in which wood pyrolysis occurred, it was found that the wood lost its structural integrity and fell from the walls and the ceiling to the floor after a period of time. When the wood fell to the floor, it would generally burn intensely with a bright flame for a short period before settling into a smoldering mode. The vertical lines in Fig. 1 indicate when the collapse of the wood began and was completed. Generally, the wood near the doorway of the enclosure collapsed first, but there was only a short delay before nearly all of the wood had fallen.

The most dramatic effect in Fig. 1 is the rapid growth and peak levels of CO observed before the wood collapsed. Dry CO concentrations reached 7% at the front sampling position and 14% in the rear. Note that oxygen concentrations in the upper layer were very nearly zero during this period as expected. Concentrations of CO_2 were also quite high with the higher levels again found in the rear of the enclosure.

It is significant that following the full collapse of the wood, the CO concentrations in the front and rear of the enclosure fell very rapidly, despite the fact that significant combustion of the wood (as determined by the measured heat release rate) was still occurring. Clearly, the high CO levels are associated with the presence of the wood within the upper layer. The time profiles indicate that the burning wood on the floor significantly disrupted the upper layer (e.g., significant O_2 is observed in the rear of the enclosure immediately following the wood collapse). However, as the wood burning eventually died down, the observed concentrations returned to levels typical of a 400 kW natural gas fire in the absence of wood [11].

High CO levels were generated in all cases where natural gas HRRs were greater than 45 kW. For the smallest fires, an induction period was observed following the start of the natural gas fire before the CO concentration began to increase. Note that fires having HRRs less than 200 kW are overventilated in the absence of wood. The observation of high levels of CO requires that the wood generate sufficient fuel to cause the burning to become underventilated.

Figure 2 compares the time behaviors of CO concentration for two 50 kW fires—one with and one without a wood lining. Only the period from just before the start of the fire until the start of the collapse

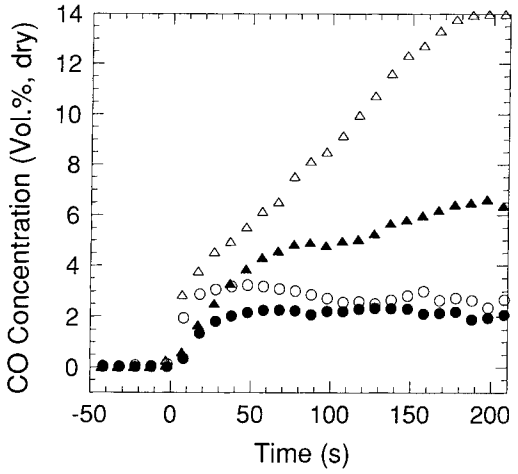

FIG. 3. Volume concentrations (dry) of CO vs time for a 400-kW natural gas fire (○ = rear; ● = front) and for a 400-kW natural gas fire with a plywood lining on the ceiling and upper walls (△ = rear; ▲ = front). The fire was ignited at time = 0 s, and the wood began to fall at 205 s.

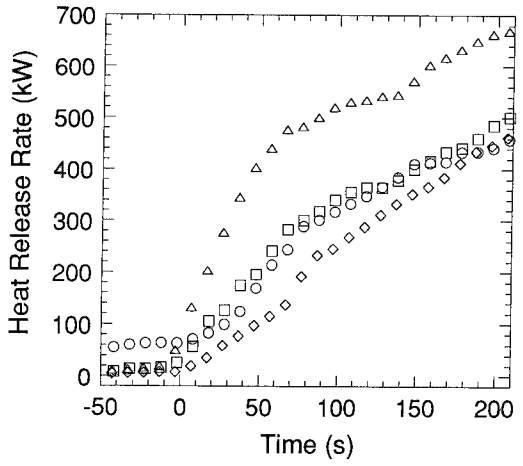

FIG. 4. Heat release rate (kW) vs time for four fires. Each fire was fueled by a plywood lining on the ceiling and upper walls and a natural gas flow corresponding to 50 (○), 100 (◇), 200 (□), or 400 (△) kW. Time zero is defined as the time when the HRR of the fires increased due to the pyrolysis of wood. The wood began to fall at approximately 210 s.

of the wood is shown. The effect of the wood on the observed CO concentrations is obvious, since essentially no CO was detected in the fire without wood. For the wood case, the induction period between the start of the fire and the generation of significant concentrations of CO is apparent.

Similar plots of CO concentration vs time are shown in Fig. 3 for nominally 400 kW natural gas fires. Again, the presence of the wood results in significantly elevated concentrations of CO compared to the fire without a wood lining. Significant CO concentrations are observed in the fire without wood, since this fire is underventilated. Additional CO generated by the wood appears shortly after ignition. Comparison of Figs. 2 and 3 shows that the growth rates of CO concentration with time and the ultimate levels achieved are nearly identical in both cases where wood is present.

Plots of measured HRRs vs time are shown in Fig. 4 for wood-lined enclosure fires in which the heat release rates for the natural gas fires were nominally 50, 100, 200, and 400 kW. It is clear that the wood is contributing significantly to the total HRR of each of these fires.

It is possible to subtract the HRRs for the known flow rates of natural gas from the observed overall values in order to estimate the HRRs due to gases generated by wood pyrolysis as a function of time. If the heat of combustion of the pyrolyzed gases generated by the wood were known, it would now be possible to calculate the mass loss rate of the wood. Unfortunately, the heats of combustion for gases generated from pyrolyzed wood are known to vary, generally increasing with time [22]. Due to the complex nature of the process, these values are also dependent on such experimental parameters as heating rate and pyrolysis temperature [22].

In order to provide an estimate for the mass loss rate, the heat of combustion for a radiatively pyrolyzed sample of the plywood obtained from a Cone Calorimeter [23,24] measurement was utilized. This measurement displayed two distinct temporal regions that are interpreted as corresponding to direct formation of gases by the wood and subsequent pyrolysis of the char that is generated during the direct gasification stage. The average heat of combustion during the gasification stage was 12 MJ/kg, while the pyrolysis of the char stage yielded a much higher value of 25 MJ/kg.

Since the times during which the high concentrations of CO are observed in the current experiments are for the initial wood pyrolysis and the periods are reasonably short, the value of 12 MJ/kg was used to estimate the wood mass loss rate for the period until the wood fell. As a check of the approach, it was assumed that the low HRR applied for the period when the wood was located in the upper layer, and the high value was appropriate after the wood fell. These values, along with estimated HRR data for the wood during the entire burns, allow estimates of the total mass of wood consumed during each burn. The results are within 30% of the initial mass of wood. Figure 5 shows the calculated results for the mass

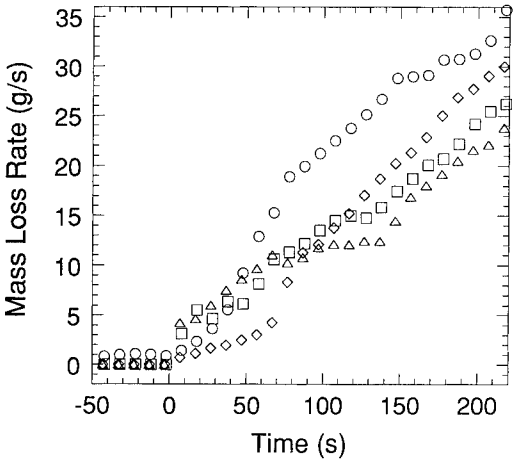

FIG. 5. Mass loss rate of wood (g/s) vs time for the same four fires as in Fig. 4. Each fire was fueled by a plywood lining on the ceiling and upper walls and a natural gas flow corresponding to 50 (○), 100 (◇), 200 (□), or 400 (△) kW. Time zero is defined as the time when the HRR of the fires increased due to the pyrolysis of wood (note the change from earlier figures). The wood began to fall at approximately 210 s.

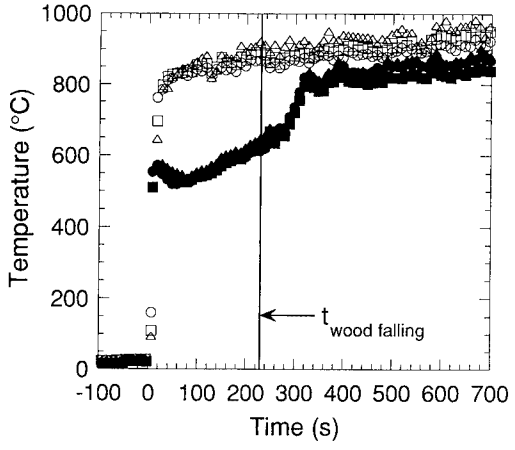

FIG. 6. Temperature vs time for a 360-kW natural gas fire (open symbols) and a 360-kW natural-gas fire with a plywood lining on the ceiling and upper walls (filled symbols). Thermocouples were located 92 cm (○, ●), 88 cm (□, ■), and 84 cm (△, ▲) from the floor. The ceiling is 98 cm from the floor. All of the thermocouples were on the tree located in a front corner of the RSE. The fire was ignited at time = 0 s, and the wood began to fall at 230 s.

loss rate of wood as a function of time over the period before the wood collapses for the 50, 100, 200, and 400 kW natural-gas fires.

A comparison of upper-layer temperature profiles for comparably sized natural gas fires with and without the wood lining allows an assessment of the overall energetics of the wood pyrolysis process for cases when the natural gas fires alone are underventilated. Figure 6 shows temperature-time traces for 360 kW natural gas fires with and without wood at several vertical positions in the front of the enclosure. In the presence of wood, the temperatures are significantly lower. Similar results were found for the other fires having HRRs greater than 200 KW. Assuming that the heat loss mechanisms are not significantly different for the wood-lined and bare enclosures, this requires that the gases generated by the wood pyrolysis cool the combustion gases generated by the natural gas fire, and the overall wood pyrolysis process must, therefore, be endothermic.

Discussion

The hypothesis that the pyrolysis of wood in high-temperature, highly vitiated upper layers results in the generation of very high concentrations of CO is confirmed by the results shown in Figs. 1 through 3. To our knowledge, this is the first demonstration of such a mechanism for the direct formation of CO in enclosure fires. It is likely that this finding provides the explanation for the very high levels of CO observed in the Sharon fire test [13] and for the failure of the GER concept to predict the observed levels of CO.

It is at first glance somewhat surprising that higher concentrations of CO and CO_2 are observed in the rear of the RSE than in the front (Fig. 1). Temperatures in the rear are somewhat cooler than in the front and the wood pyrolysis rate should be slower. The buildup of high concentrations of wood pyrolysis products in the enclosure rear is the result of flow patterns within the enclosure. Gases in the rear of the enclosure have a much longer residence time than the gases flowing out the doorway near the front [12]. As a result, the gases at the front sampling positions are diluted more by gases generated by the natural gas fire plume than the gases in the rear where the gases from the wood pyrolysis accumulate.

The details of the pyrolysis of wood within the RSE are much too complicated to describe in detail. However, the general processes responsible for the generation of gas by wood pyrolysis can be discussed. Here, we adopt the early description of Browne [25].

Pyrolysis is viewed as occurring in four distinct zones:

Zone A (up to 200 °C): Wood is dehydrated and only small amounts of decomposition take place.

Zone B (200–280 °C): A large number of chemical compounds are generated, and charring of the wood begins.

Zone C (280–500 °C): Rapid pyrolysis of wood is initiated, releasing and/or generating a wide range of chemical products, which can undergo secondary reaction, as well as forming charcoal.

Zone D (greater than 500 °C): The surface temperature of the charcoal is sufficient to induce secondary reactions such as

$$C(s) + H_2O(g) \rightarrow CO + H_2 \quad (1)$$

and

$$C(s) + CO_2 \rightarrow 2CO. \quad (2)$$

When the wood in the RSE is exposed to flame gases, it begins to heat from the exposed surface inward. A series of zones develop with the lower-temperature zones moving into the wood and the surface temperature of the wood increasing. If the surface temperature exceeds 500 °C, the fire environment will result in more complicated reactions than simple pyrolysis under inert conditions since significant concentrations of CO_2 and H_2O are present in the flame gases, thus enhancing reactions (1) and (2).

Even though the wood pyrolysis process cannot be studied in detail, it is possible to make checks to see if the results are reasonable. From Fig. 5 and similar results for other fires and using the known surface area of the exposed wood, it is possible to estimate the wood mass loss rate as increasing from 0 to approximately 10 gs^{-1} m^{-2} during the periods before the wood collapsed. The maximum levels are comparable to observed mass loss rates (10–15 gs^{-1} m^{-2}) for samples of the plywood subjected to 50 and 75 kW/m^2 levels of infrared radiation in the cone calorimeter during the period that direct vaporization was occurring. The measured mass loss rate of the wood in the enclosure is consistent with strong heating of a wood sample.

It is not possible to determine the chemical composition of the gases generated by the wood pyrolysis. However, it is clear that large amounts of CO and CO_2 are produced. As a consistency check, it has been assumed that pyrolysis of wood generates only CO, CO_2, and H_2, and the mass production rates have been computed on a global basis using data such as shown in Fig. 5 for the wood mass loss rate as a function of time. Since the flow rates of the natural gas and production rates of CO and CO_2 can be estimated for the natural gas component of the fuel, it is possible to estimate the overall composition of the upper layer by assuming a $CO:CO_2$ mass generation ratio for the wood pyrolysis. Such calculations yield predictions for the observed $CO:CO_2$ concentrations in the front of the enclosure that are consistent with experimental observations. The required $CO:CO_2$ ratio is on the order of 1:1. Based on the ratios for the generation of CO and CO_2 observed for pyrolysis of small particles of wood (see the discussion in the Introduction), this suggests that the average surface temperature for the wood pyrolysis is on the order of 600 °C. The estimated temperature of the pyrolyzing wood surface is considerably lower than the upper-layer gas temperatures (see Fig. 6). This is not too surprising since there are at least two heat loss mechanisms. The wood surface is cooled by heat conduction to the interior, and it has been found experimentally that the wood pyrolysis is overall endothermic, thus requiring heat absorption to proceed.

Final Remarks

The major findings of this study are

1. The pyrolysis of wood in a highly vitiated, high-temperature environment can lead to the production of very high concentrations of CO in enclosure fires.
2. The overall wood pyrolysis is endothermic for the experimental conditions studied.
3. The maximum mass loss rate of wood under the experimental conditions is on the order of 10 gs^{-1} m^{-2}, with the majority of carbon being converted to roughly a 1:1 mixture of CO and CO_2.

These findings have important implications for understanding smoke inhalation deaths that occur in fires. As noted, the conclusions explain the high concentrations of CO generated by the Sharon fire test [13]—a recreation of a fire where CO was known to be responsible for the death of one of the victims. Fire investigations by NIST researchers have provided anecdotal evidence that the generation of CO by wood pyrolysis under conditions similar to those tested for this study is important in numerous multideath fires. Recent examples include the Happyland Social Club fire in the Bronx, NY, which killed 87 persons in 1990 [26], and the Johnson City, TN nursing home fire, which killed 16 people in 1989 [27]. The New York fire resulted from an arson in which gasoline was poured and ignited within a small entryway room lined with plywood and having a fiberboard ceiling. These conditions are very similar to those studied here and would be expected to generate very high concentrations of CO. Most of the fire victims were on the second floor of the building and died as the result of smoke inhalation. The Tennessee fire occurred on the first floor of a multistory building. Victims were found scattered over several floors with the highest being the tenth. Most deaths were again attributed to smoke inhalation. Investigation showed that there was a hidden ceiling above the fire, which consisted of wood fiber tiles attached to wood furring strips and framing members. During the fire, flames broke through the false ceiling and entered air spaces adjacent to the false ceiling. Again, this is a situation similar to the current experiments.

Very high concentrations of CO should have been generated, consistent with casualties far from the fire source.

Additional studies are clearly needed. For instance, it is necessary to determine the conditions for which CO generated within a compartment can exit and be transported without additional reaction. However, as an improved understanding of the conditions responsible for generating dangerous concentrations of CO is obtained, it should be possible to develop predictive methods and strategies for mitigating its effects.

Acknowledgment

The authors would like to thank Dr. Tom Ohlemiller of BFRL for many helpful discussions and for a careful reading of this manuscript.

REFERENCES

1. Babrauskas, V., Levin, B. C., Gann, R. G., Paabo, M., Harris, Jr., R. H., Peacock, R. D., and Yusa, S., *Toxic Potency Measurement for Fire Hazard Analysis*. NIST Special Publication 827, 1991.
2. Babrauskas, V., *J. Fire Sci.* 2:5–19 (1984).
3. Harland, W. A., and Anderson, R. A., *Proceedings, Smoke and Toxic Gases from Burning Plastics*, London, 1982, pp. 15/1–15/19.
4. Harwood, B., and Hall, J. R., *Fire J.* 83:29–34 (1989).
5. Karter, Jr., M. J., *NFPA J.* 87:78–87 (1993).
6. Beyler, C. L., *Fire Safety J.* 10:47–56 (1986).
7. Beyler, C. L., *Fire Safety Science—Proceedings of the First International Symposium*, Hemisphere, New York, 1986, pp. 431–440.
8. Zukoski, E. E., Morehart, J. H., Kubota, T., and Toner, S. J., *Combust. Flame* 83:325–332 (1991).
9. Pitts, W. M., *Twenty-Fourth Symposium (International) on Combustion*, The Combustion Institute, Pittsburgh, 1992, pp. 1737–1746.
10. Gottuk, D. T., Roby, R. J., Peatross, M. J., and Beyler, C. L., *J. Fire Protection Eng.* 4:133–150 (1992).
11. Bryner, N. P., Johnsson, E. L., and Pitts, W. M., *Carbon Monoxide Production in Compartment Fires-Reduced-Scale Enclosure Test Facility*, NIST Internal Report, 1994, in press.
12. Pitts, W. M., *The Global Equivalence Ratio Concept and the Prediction of Carbon Monoxide Formation in Enclosure Fires*, NIST Monograph, 179, 1994.
13. Levine, R. S., and Nelson, H. E., *Full Scale Simulation of a Fatal Fire and Comparison of Results with Two Multi-Room Models*, NIST Internal Report 90-4268, 1990.
14. Milne, T., in *Biomass Gasification. Principles and Technology* (T. B. Reed, Ed.), Noyes Data Corporation, Park Ridge, NJ, 1981, pp. 91–118.
15. Brink, D. L., Massoudi, M. S., and Sawyer, R. F., "A Flow Reactor Technique for the Study of Wood Pyrolysis," 1973 Fall Western States Section/Combustion Institute Meeting, El Segundo, CA, 1973.
16. Arpiainen, V., and Lappi, M., *J. Anal. Appl. Pyrol.* 16:355–376 (1989).
17. "Fire Tests—Full Scale Test for Surface Products," Draft International Standard ISO/DIS 9705.
18. *Proposed Method for Room Fire Test of Wall and Ceiling Materials and Assemblies*, Philadelphia, PA, 1982, pp. 1618–1638.
19. Sensenig, D. L., and Parker, W. J., "New Concept for Rate of Heat Release Measurements by Oxygen Consumption," 1978 Fall Technical Meeting of the Eastern Section Meeting of the Combustion Institute, Miami Beach, FL, 1978.
20. Huggett, C., *Fire Mater.* 4:61–65 (1980).
21. Pitts, W. M., "Application of Thermodynamic and Detailed Chemical Kinetic Modeling to Understanding Combustion Product Generation in Enclosure Fires," *Fire Safety J.*, in press.
22. Drysdale, D., *An Introduction to Fire Dynamics*, John Wiley and Sons, Suffolk, 1985, pp. 176–182.
23. Twilley, W. H., and Babrauskas, V., *User's Guide for the Cone Calorimeter*, National Bureau of Standards Special Publication, NBS SP-745, 1988.
24. Babrauskas, V., *ASTM Standardization News* 18:32–35 (1990).
25. Browne, F. L., *Theories of the Combustion of Wood and Its Control*, Forest Products Laboratory Report No. 2136, 1958.
26. Bukowski, R. W., and Spetzler, R. C., *Fire Arson Invest.* 42:36–47 (1992).
27. Steckler, K., Quintiere, J., and Klote, J., *Johnson City Fire—Key Factors*, unpublished NIST Report, 1990.

COMMENT

Carlos Fernandez-Pello, University of California, Berkeley, USA. Is there experimental evidence of CO production during the pyrolysis of wood in an inert atmosphere such as nitrogen (in a TGA analysis, for example).

Author's Reply. References 14 through 16 describe studies in which wood or related materials were rapidly heated in inert atmospheres to temperatures characteristic of upper layers in underventilated enclosure fires. In each case,

a large fraction of the pyrolyzed material appeared as carbon monoxide for temperatures greater than 900 K. Only one study was identified in which thermogravimetric analysis of wood under inert gases at these temperatures was employed with chemical analysis of pyrolysis products. Hileman et al. [1] found that a Douglas fir sample pyrolyzed at 823 K in helium gave a yield of 21% of its mass as CO. The observed $CO:CO_2$ ratio was 3.7:1.

REFERENCE

1. Hileman, F. D., Wojcik, L. H., Futrell, J. H., and Einhorn, I. N., in *Thermal Uses and Properties of Carbohydrates and Lignins* (F. Shafizadeh, K. V. Sarkanen, and D. A. Tillman, Eds.), Academic Press, New York, 1976, pp. 49–71.

Twenty-Fifth Symposium (International) on Combustion/The Combustion Institute, 1994/pp. 1463–1469

SIMULATION OF SMOKE PLUMES FROM LARGE POOL FIRES

H. R. BAUM, K. B. McGRATTAN AND R. G. REHM
National Institute of Standards and Technology
Gaithersburg, Maryland 20899, USA

A large eddy simulation model of smoke plumes generated by large outdoor pool fires is presented. The plume is described in terms of steady-state convective transport by a uniform ambient wind of heated gases and particulate matter introduced into a stably stratified atmosphere by a continuously burning fire. The Navier–Stokes equations in the Boussinesq approximation are solved numerically with a constant eddy viscosity representing dissipation on length scales below the resolution limits of the calculation. The effective Reynolds number is high enough to permit direct simulation of the large scale mixing over two to three orders of magnitude in length scale. Particulate matter, or any nonreacting combustion product, is represented by Lagrangian particles that are advected by the fire-induced flow field. Background atmospheric motion is described in terms of the angular fluctuation of the prevailing wind and represented by random perturbations to the mean particle paths. Sample computations are presented and compared with plumes generated by large crude oil pool fires. Also presented is an assessment of the potential environmental hazard posed by burning marine oil spills.

Introduction

There is growing interest in the environmental consequences of large fires, since the transport of combustion products by a windblown fire plume can distribute potentially hazardous materials over a wide area. Pools of burning oil and other petroleum products are of particular concern due to the vast flow of these materials through the global economy and because of the fragility of the environment in many regions where oil is extracted or transported. The present work is part of a larger study of a closely related issue, the feasibility of cleaning up oil spills on water through burning [1].

Buoyant windblown plumes have been studied since the early 1960s. A summary of the early work together with a useful bibliography is given by Turner [2]. For summaries of more recent work, see Turner [3] and Wilson [4]. Virtually all the models described in these works are integral models, where the profiles of physical quantities in cross-sectional planes perpendicular to the wind direction are assumed, together with simple laws relating entrainment into the plume to macroscopic features used to describe its evolution. A great many of the models in use for air quality assessment simply use Gaussian profiles of pollutant density. Unfortunately, the plume structures actually observed are too complex to be described in terms of a few simple parameters.

Most of the assumptions required by integral models can be removed by taking advantage of the enormous advances in computational fluid dynamics that have occurred since most of these models were developed. This is especially true if it is assumed that the component of the fluid velocity in the direction of the ambient wind is literally the wind speed. The neglect of streamwise perturbations to the ambient wind is an old idea in aerodynamics, where it has been used to study aircraft wake dynamics since the 1930s [5]. Once this approximation is made, the plume (or wake) can be studied as a two-dimensional, time-dependent entity. The large-scale structure of the plume can then be determined in detail at moderate computational cost. The small-scale "subgrid" mixing and dissipation is represented with a constant eddy viscosity. This permits the mathematical structure of the Navier–Stokes equations to be retained. The effective Reynolds number, defined by the buoyancy-induced velocity, plume height, and eddy viscosity, is chosen to be above 10^4. Thus, at least two orders of magnitude of dynamically active length scales in all coordinate directions are permitted, leaving open the possibility of comparison with laboratory scale experiments (where the Reynolds numbers are low enough to be simulated directly). It is in this sense that the model described here is a large eddy simulation.

This approach was first used to study the settling of a smoke plume in an unstratified atmosphere by Ghoniem et al. [6]. That study was performed using Lagrangian vortex dynamics techniques. More recently, Zhang and Ghoniem have studied plume rise in a linearly stratified atmosphere using this methodology [7]. In these studies, the main emphasis was on the mixing process as it affected the plume structure. The present work uses finite-difference methods to determine the large-scale mixing combined with Lagrangian transport of the smoke or other pol-

lutants. The effect of subgrid scale velocity fluctuations on the dispersion of the smoke is accounted for explicitly, and the ambient temperature profile is subject only to the constraint that it is stable over the altitudes occupied by the plume. In addition, more emphasis is placed in the present study on application of the model to some typical fire scenarios, including large-scale experiments conducted at the U.S. Coast Guard Fire and Safety Test Detachment in Mobile, Alabama [8].

Mathematical Model

The plume is described in terms of steady-state convective transport by a uniform ambient wind of heated gases and particulate matter introduced into a stably stratified atmosphere by a continuously burning fire. As described above, the most important assumption is that the component of the velocity in the direction of the wind is the ambient wind and thus is known. Since the firebed itself is not the object under study, only the overall heat release rate and the fraction of the fuel converted to particulate matter need be specified. The simulation begins several fire diameters downwind of the fire, where the plume is characterized by relatively small temperature perturbations, and minimal radiation effects. In this region the plume gases ascend to a point in the atmosphere of neutral buoyancy and then gradually disperse. The trajectory of the plume is governed by the ambient wind, the atmospheric stratification, and the buoyancy-induced convection. As it is not our objective to calculate the local meteorology, it is assumed that the ambient temperature profile as a function of height is available. The problem can now be reduced to the study of an equivalent two-dimensional unsteady problem in the crosswind plane moving downstream at the ambient wind speed.

Given these assumptions, the mathematical model of a smoke plume consists of the conservation equations of mass, momentum, and energy that govern the temperature T, pressure p, density ρ, and crosswind velocity components (v,w) in a plane (y,z) normal to the direction (x) of the uniform ambient wind. It is convenient to divide the temperature and pressure fields into mean background values $T_0(z)$ and $p_0(z)$ plus perturbations induced by the fire, $\tilde{T}$ and $\tilde{p}$. Similarly, the density ρ is decomposed into an ambient density ρ_0 and a small thermally induced perturbation $\tilde{\rho}$, which is related to the temperature perturbation through the equation of state taken in the small disturbance, low Mach number form appropriate to this problem:

$$\frac{\rho - \rho_0}{\rho_0} = \frac{T - T_0}{T_0}. \tag{1}$$

The ambient density is related to the background pressure through the hydrostatic balance

$$\frac{dp_0}{dz} = -\rho_0 g. \tag{2}$$

Assuming that the perturbations to the background temperature and density are small beyond a few diameters of the fire downwind of the firebed, we can write the conservation equations describing the steady-state plume in the Boussinesq approximation as follows:

Conservation of mass:

$$\frac{\partial v}{\partial y} + \frac{\partial w}{\partial z} = 0. \tag{3}$$

Conservation of lateral and vertical momentum:

$$\rho_0\left(U\frac{\partial v}{\partial x} + v\frac{\partial v}{\partial y} + w\frac{\partial v}{\partial z}\right) + \frac{\partial \tilde{p}}{\partial y} = \mu\left(\frac{\partial^2 v}{\partial y^2} + \frac{\partial^2 v}{\partial z^2}\right) \tag{4}$$

$$\rho_0\left(U\frac{\partial w}{\partial x} + v\frac{\partial w}{\partial y} + w\frac{\partial w}{\partial z}\right) + \frac{\partial \tilde{p}}{\partial z} + \tilde{\rho} g = \mu\left(\frac{\partial^2 w}{\partial y^2} + \frac{\partial^2 w}{\partial z^2}\right). \tag{5}$$

Conservation of energy:

$$\rho_0 c_p\left(U\frac{\partial \tilde{T}}{\partial x} + v\frac{\partial \tilde{T}}{\partial y} + w\frac{\partial \tilde{T}}{\partial z}\right) - \left(\frac{dp_0}{dz} - \rho_0 c_p \frac{dT_0}{dz}\right) w = k\left(\frac{\partial^2 \tilde{T}}{\partial y^2} + \frac{\partial^2 \tilde{T}}{\partial z^2}\right) \tag{6}$$

where c_p is the specific heat of air, k is the thermal conductivity, and μ is the dynamic viscosity. The viscosity and thermal conductivity are to be regarded as "eddy" coefficients whose primary role is to provide sinks of kinetic and thermal energy that are actually the result of subgrid scale dissipative processes. In practice, they are used to set the dynamic range of length scales employed in the simulation. This point is discussed further below. The uniform ambient wind speed U is taken to be constant and larger than the crosswind velocity components. This assumption is quite realistic several flame lengths downwind of the firebed. Since U does not change, there is no need for a windward component of the momentum equations. The details of the firebed are not being simulated, so the only information about the fire required is the overall convective heat release rate Q and the particulate mass flux M. The initial temperature distribution in the plume cross section is as-

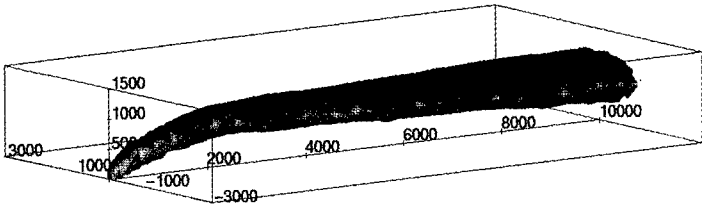

FIG. 1. Three-dimensional view of the 10 $\mu g/m^3$ particulate contour of a computed smoke plume from a 204 MW fire. All lengths are given in meters.

sumed to be Gaussian and satisfies the following integral:

$$\int_{-\infty}^{\infty}\int_{0}^{\infty} \rho_0 c_p U\tilde{T}\, dz\, dy = Q. \tag{7}$$

The particulate matter (or any nonreacting combustion product) is tracked through the use of Lagrangian particles, which are advected with the overall flow. The initial particulate distribution mimics the initial temperature distribution.

The equations of motion are made nondimensional so as to maximize the amount of information that can be extracted from each run. First, the windward spatial coordinate is replaced by a temporal coordinate,

$$\hat{t} = \frac{V}{UL}x \tag{8}$$

where the plume height L is given in terms of the potential temperature of the undisturbed atmosphere $\theta(z)$:

$$L = \left(\frac{Q}{c_p T_0 \rho_0 U \Theta}\right)_{z=0}^{1/3}; \qquad \Theta(z) = \frac{1}{\theta}\frac{d\theta}{dz} \tag{9}$$

The potential temperature is related to the actual temperature through the relation

$$p_0^{-\kappa}(z)T_0(z) = p_0(0)^{-\kappa}\,\theta(z) \tag{10}$$

where $\kappa = R/c_p$ and R is the gas constant for dry air. The characteristic velocity of the fluid is given by

$$V = \left(\frac{Qg}{c_p T_0 \rho_0 UL}\right)_{z=0}^{1/2}. \tag{11}$$

The characteristic length L and velocity V scale the crosswind spatial coordinates $(y,z) = L(\hat{y},\hat{z})$ and velocities $(v,w) = V(\hat{v},\hat{w})$. The temperature perturbation $\tilde{T}$ is made nondimensional by the expression

$$\tilde{T} = \frac{Q}{c_p \rho_0 U L^2}\hat{T}. \tag{12}$$

Finally, the turbulent Reynolds and Prandtl numbers are defined

$$Re = \frac{\rho_0 VL}{\mu}; \qquad Pr = \frac{\mu c_p}{k}. \tag{13}$$

Following this scaling, the three-dimensional, steady-state system of equations above can be considered as a two-dimensional, time-dependent system. We now have an initial value problem in which the solution is initially prescribed in a plane perpendicular to the direction of the prevailing wind. This initial plane is taken to be a few fire diameters downwind of the fire.

The dimensionless form of the conservation laws for the large eddy simulation of a smoke plume trajectory are

$$\frac{\partial \hat{v}}{\partial \hat{y}} + \frac{\partial \hat{w}}{\partial \hat{z}} = 0 \tag{14}$$

$$\frac{\partial \hat{v}}{\partial \hat{t}} + \hat{v}\frac{\partial \hat{v}}{\partial \hat{y}} + \hat{w}\frac{\partial \hat{v}}{\partial \hat{z}} + \frac{\partial \hat{p}}{\partial \hat{y}} = \frac{1}{Re}\left(\frac{\partial^2 \hat{v}}{\partial \hat{y}^2} + \frac{\partial^2 \hat{v}}{\partial \hat{z}^2}\right) \tag{15}$$

$$\frac{\partial \hat{w}}{\partial \hat{t}} + \hat{v}\frac{\partial \hat{w}}{\partial \hat{y}} + \hat{w}\frac{\partial \hat{w}}{\partial \hat{z}} + \frac{\partial \hat{p}}{\partial \hat{z}} - \hat{T} = \frac{1}{Re}\left(\frac{\partial^2 \hat{w}}{\partial \hat{y}^2} + \frac{\partial^2 \hat{w}}{\partial \hat{z}^2}\right) \tag{16}$$

$$\frac{\partial \hat{T}}{\partial \hat{t}} + \hat{v}\frac{\partial \hat{T}}{\partial \hat{y}} + \hat{w}\frac{\partial \hat{T}}{\partial \hat{z}} + \frac{\Theta}{\Theta(0)}\hat{w} = \frac{1}{Re\,Pr}\left(\frac{\partial^2 \hat{T}}{\partial \hat{y}^2} + \frac{\partial^2 \hat{T}}{\partial \hat{z}^2}\right) \tag{17}$$

subject to the initial condition

$$\iint \hat{T}(\hat{y},\hat{z})\, d\hat{y}\, d\hat{z} = 1. \tag{18}$$

The crosswind velocity components $\hat{v}$ and $\hat{w}$ are assumed to be zero initially, although this assumption is not restrictive. No-flux, free-slip boundary conditions are prescribed at the ground, consistent with the assumed uniformity of the prevailing wind and the resolution limits of the calculation. At the outer and upper edges of the computational domain, the perturbation temperature, perturbation pressure, and windward component of vorticity are set to zero. Figure 1 shows the results of a sample computation,

illustrating the position of the initial slice and the extent of the computational domain. The plume is visualized by interpolating the particle locations onto the computational grid and then plotting the isosurface on which the particulate density is a chosen value. This example will be discussed further in the Results section.

Atmospheric turbulence effects mixing on a wide range of scales, extending to scales that are smaller than the resolution of the calculations performed here. There are two sources of turbulence: one due to the fire-induced flow field and the other due to the background atmospheric motion. The small-scale mixing is represented in the model by a constant eddy viscosity μ, which is taken to be three orders of magnitude greater than the actual viscosity of air. The choice is governed by the desire for resolution limits in the 5–15 m range, which are needed to capture the large-scale, fire-induced eddy motions. This requirement, together with the knowledge that the dissipative effects operate at a scale $Re^{-1/2}$ times smaller than the overall geometric scale (the stabilization height of the plume for this problem), translates into Reynolds numbers of the order 10^4. Thermal conductivity is treated in a similar manner to viscosity; thus, the Prandtl number $Pr = c_p\mu/k$ remains of order unity.

The viscosity and thermal conductivity included in Eqs. (3) through (6) does not account for larger scale, background atmospheric motion. For the present purposes, this motion may be expressed in terms of variations of the prevailing wind over time scales of minutes to hours. These deviations can be measured and are introduced into the model through random perturbations to the trajectories of the Lagrangian particles that represent the particulate matter. Thus, the motion of each particle is governed by the fire-induced velocity field (U,v,w), found by solving the conservation equations above, plus a perturbation velocity field $(0,v',w')$, which represents the random temporal and spatial variations of the ambient wind. The perturbation velocity component v' is derived from the recursive relation (the component w' is handled in a similar manner)

$$v'(t + \delta\hat{t}) = R_v(\delta\hat{t})v'(t) + v''. \qquad (19)$$

The term v'' is a random variable with Gaussian distribution whose variance is that of v' multiplied by $(1 - R_v^2)$, ensuring that the variance of the velocity does not change from one time step to another. The function $R_v(\delta\hat{t})$ is a Lagrangian correlation coefficient, taken as exponential

$$R_v(\delta\hat{t}) = e^{-\delta\hat{t}/\tau_v}. \qquad (20)$$

The parameter τ_v is indicative of the period of atmospheric fluctuations. Appropriate values for various meteorological conditions are given by Draxler [11]. Generally speaking, τ_v is on the order of several minutes, and it does not have much of an effect on the outcome of the simulations. The initialization of the recursive relation (19) and the corresponding relation for w' determines the overall level of turbulence in the atmosphere. The initial velocity perturbations $v'(0)$ and $w'(0)$ are randomly assigned from Gaussian distributions with mean zero and standard deviations extracted from anemometer measurements suitably averaged over a timescale appropriate for the problem. Reference 12 has suggested values for these parameters.

Numerical Method

Equations (14) through (17) constitute a mixed system of partial differential equations; i.e., the equations for the temperature and velocity components are parabolic, and the equation for the pressure (which is derived from the incompressibility condition) is elliptic. The equations and the associated boundary conditions are solved using a relatively simple finite-difference technique. The computational domain spanning the crosswind plane is one unit in the vertical direction and (typically) four units in the horizontal direction, representing a physical domain L units high and $4L$ units wide. This area is divided into rectangular cells (preferably square) with a uniform spacing in each direction. The horizontal velocity $\hat{v}$ is taken on the left and right boundaries of each cell; the vertical velocity $\hat{w}$ is taken at the top and bottom, and the perturbation temperature $\hat{T}$ and pressure $\hat{p}$ are taken at cell centers. This placement of the flow variables leads to a very natural and efficient differencing scheme for the equations. Central differences are used for all spatial derivatives, with the momentum equations represented in vector invariant form. The time advancement (i.e., the evolution of the plume downwind) is performed with a second-order Runge–Kutta scheme. The particulate matter or any other pollutant is treated as a passive scalar and represented by Lagrangian elements that are advected with the flow. The pressure is found by applying the divergence-free condition to the momentum equations, which yields a Poisson equation. The Poisson equation is solved using CRAYFISHPAK [9], a package of noniterative Helmholtz equation solvers. The overall scheme is an adaptation of a code developed for enclosure fire convection problems. It is described in detail in Reference [10].

The computational resources required to perform these calculations are modest. For the example shown in Fig. 1, the computational cells are about 8 m on a side in the cross-flow plane, and the time-step size roughly corresponds to 4-m steps in the windward direction. This computation employed a grid of 192 × 768 cells in the cross-flow plane, 2400 "time" steps, and a Reynolds number of 24,000. The

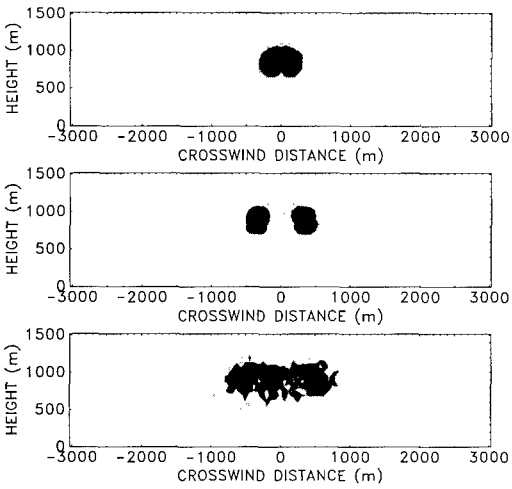

FIG. 2. Cross-sectional slices of the plume shown in Fig. 1, showing contours of particulate concentration. The darker areas correspond to levels above 50 $\mu g/m^3$.

CPU time on an IBM RISC/6000 (model 550) for a 10-km calculation was 2.5 h. Most of the current workstations available can handle these types of calculations very easily.

Results

Two sets of results will be displayed: a simulation of a crude oil burn conducted at the U.S. Coast Guard facility in Mobile, Alabama, for which quantitative plume trajectory data exists, and a calculation performed as part of an environmental hazard assessment. The first permits a comparison with experiment, while the second shows a typical application of the model.

The comparison is made using data from one of a series of mesoscale burn experiments, which are described in Reference 8. Briefly, crude oil was burned in a 15-m square pan, but only a portion of the pan was used. The effective burning diameter was estimated to be 12 m. The heat release rate was estimated to be 204 MW, the mass flux of smoke was 0.5 kg/s. The wind speed was measured to be about 4 m/s; the temperature profile was estimated to be linear with a lapse rate of −9.2 °C/km. The values for the standard deviations of the lateral and vertical wind fluctuations were taken as 5° and 3°, respectively. These values correspond to lightly shifting winds, typical of the coastal region where the experiment was conducted. The computational domain was divided into a rectangular grid 192 cells high and 768 cells wide, which yields cells 8 m on a side. The Reynolds number for the calculation, based on the height of the computational domain, was 24,000. The initial cross section of the plume was assumed to be a circle with a radius of 20 m, centered approximately 40 m off the ground, and located 110 m downwind of the heat source. This is based on the observed plume trajectory reported in Table 18 of Reference 8.

Figure 1 shows the development of the plume in the first 10 km downwind of the source. Shown is an isosurface on which the particulate concentration is 10 $\mu g/m^3$. Of particular interest in this figure are the two main vortices that entrain a large amount of the particulate and surrounding air. In fact, observations from ground observers indicate that a "hole" between the two large swirling vortices develops in the rising plume that allows one to see right through to the sky above. This phenomena is seen more clearly in Fig. 2, which shows computed particulate density cross sections 2, 5, and 10 km downwind of the fire. Figure 3 compares the "centerline" plume trajectory with the observed data. Considering the assumptions of the model and the difficulty in determining the input parameters, the agreement between the experimental data and the calculation is very encouraging. Making this case particularly difficult is the fact that the atmosphere is only slightly stable and, thus, has a relatively small Brunt–Väisällä frequency.

Downstream of the fire, the particulate matter will, in general, rise with the heated plume and later descend after the plume has cooled. Since the combustion products and the particulate matter will produce a cooled plume only slightly more dense than the surrounding air, the descent of the plume will be rather slow compared to its rise. Background atmospheric motion, manifested by fluctuations of the prevailing wind, plays a greater role in dispersing the pollutants at distances greater than a few kilometers from the fire. The balance between the stabilizing

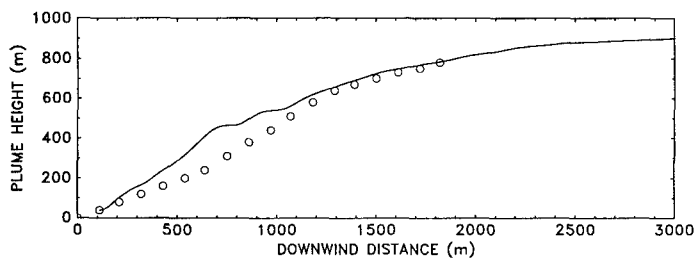

FIG. 3. Centerline plume trajectory for the case shown in Fig. 1. The computational trajectory is denoted by a solid line, the actual observed trajectory by circles.

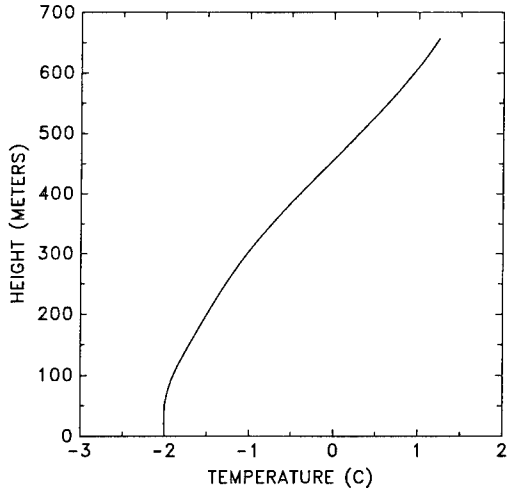

FIG. 4. Atmospheric temperature profile corresponding to an inversion.

effect of the atmospheric stratification and the dispersion induced by wind fluctuations is illustrated in Fig. 2, which shows the breakup of the fire-induced vortices beyond 5 km.

Of concern to the inhabitants of populated areas downwind of a fire is the ground level concentration of smoke and pollutants, particularly in the presence of a temperature inversion. To assess the potential hazards from a fire burning during a period where the temperature of the atmosphere *increases* with height, a simulation was performed for an atmosphere that exhibits a temperature inversion (see Fig. 4), and the resulting particulate density field was analyzed to determine how far downwind one might expect to find high ground-level concentrations. The results are shown in Fig. 5, which displays the hour-averaged ground-level concentrations of particulate matter downwind of a 15 m, 450 MW fire that generates particulate matter at a rate of 1.2 kg/s. This scenario is typical of the type of fire generated during an actual in situ burn. The meaning of "ground level" depends on the resolution of the calculation. For this calculation, it consists of roughly the first 10 m of the atmosphere or the width of a grid cell. It is assumed that the standard deviation of the wind direction distribution is 10° in the lateral direction and 6° in the vertical. These values are appropriate for sampling times on the order of 10 min to an hour for a neutrally stable atmosphere [12]. This case may be considered severe due to the presence of an inversion layer close to the ground. This condition, common over water where warm air flows over the relatively cool surface, tends to trap the plume close to the ground and is of most concern to public health. If in situ burning is adopted as an oil spill mitigation technique, this type of meteorological condition would be least desirable because it can potentially yield dangerous concentrations of pollutants at the ground. For the case shown in Fig. 1, however, the model predicts very little, if any, particulate matter reaching the ground beyond a few hundred meters of the burn site due the relatively high ascent of the plume. In that case, the lapse rate was estimated to be −9.2 °C/km.

Conclusions

The model of plume dispersion presented above is best described as a large eddy simulation valid in an intermediate region downstream from the fire source but close enough to assume that the atmosphere does not change with downwind distance. Nearer to the fire, the temperatures are high, the radiation field intense, and the Boussinesq approximation is not valid. Also, the approximations that allow replacement of a three-dimensional steady plume by a two-dimensional, time-dependent one are not valid near the fire because the buoyant velocity of the plume is comparable to the cross wind. In this region, a fully three-dimensional and time-dependent model of the plume rise in a cross flow must be developed. However, within these limits, the present model offers a high resolution representation of a smoke plume that is consistent with both the

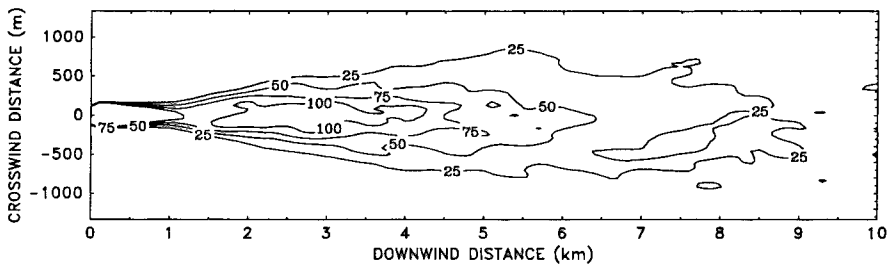

FIG. 5. Hour-averaged, ground-level particulate concentration in units of $\mu g/m^3$ for a 450 MW fire roughly 15 m in diameter. This example shows the effects of a temperature inversion that tends to trap the plume close to the ground, leading to relatively high concentrations of particulate matter.

current understanding of plume dynamics and with such experimental data as is available. Moreover, the computations reported here are well within the range of current generation workstations (where in fact they have been performed). It is hoped that future work will improve the current capabilities of the model.

Acknowledgments

This work was funded by the Technology Assessment and Research Program for Offshore Minerals Operations, Minerals Management Service, U.S. Department of the Interior, managed by J. Gregory and E. Tennyson.

REFERENCES

1. Raloff, J. A., "Burning Issues," *Sci. News* 144:220–223 (1993).
2. Turner, J. S., *Buoyancy Effects in Fluids,* Cambridge University Press, Cambridge, 1973, pp. 165–206.
3. Turner, J. S., *Atmos. Environ.* 19:1215–1218 (1985).
4. Wilson, R. B., *Atmos. Environ.* 27B:41–57 (1993).
5. Batchelor, G. K., *An Introduction to Fluid Dynamics,* Cambridge University Press, Cambridge, 1967, pp. 580–593.
6. Ghoniem, A. F., Zhang, X., Knio, O. M., Baum, H. H., and Rehm, R. G., *J. Hazardous Mater.* 33:275–293 (1993).
7. Ghoniem, A. F., and Zhang, X., "A computational model for the rise and dispersion of wind-blown, buoyancy driven plumes," *Atmos. Environ.* (in press).
8. Evans, D. D., et al., *In-Situ Burning of Oil Spills: Mesoscale Experiments,* Proceedings of the Fifteenth Arctic and Marine Oil Spill Program, Technical Seminar, June 10–12, 1992, Edmonton, Alberta, pp. 593–657.
9. Sweet, R., *CRAYFISHPAK User's Guide, Cray Version 1.1,* Green Mountain Software, Boulder, 1990.
10. McGrattan, K. B., Rehm, R. G., and Baum, H. R., "Fire-Driven Flows in Enclosures," *J. Computational Phys.* 110:2 (1994).
11. Draxler, R. R., "Determination of Atmospheric Diffusion Parameters," *Atmos. Environ.* 10:95–105 (1976).
12. Slade, D. H., (ed.), *Meteorology and Atomic Energy, 1968,* Air Resources Laboratory, Environmental Science Services Administration, United States Department of Commerce, July, 1968 (available through National Technical Information Service (NTIS), Department of Commerce, TID-24190).

COMMENT

A. C. McIntosh, Leeds University, UK. The paper is a very useful numerical simulation of smoke plumes. Could you comment on the dependence of the distance to vortex breakdown on the wind speed for two cases: (1) constant wind speed, (2) wind speed as a function of height (which is more usually the case in the real atmosphere).

Author's Reply. For the case of a constant wind speed, which is the only class of simulations performed to date, the model predicts a linear dependence of distance to vortex breakdown with wind speed. This assumes that the total heat release rate and atmospheric stratification remain unchanged as the wind speed increases. Whether these quantities will remain fixed when the wind speed changes is determined by the local meteorology and the combustion processes in the pool fire, neither of which has been addressed in the present study. We regard these as input parameters which are assumed to be known before the simulation is performed.

Twenty-Fifth Symposium (International) on Combustion/The Combustion Institute, 1994/pp. 1471–1480

SIMULTANEOUS OPTICAL MEASUREMENT OF SOOT VOLUME FRACTION, TEMPERATURE, AND CO_2 IN HEPTANE POOL FIRE

M. Y. CHOI,* A. HAMINS, H. RUSHMEIER** AND T. KASHIWAGI
Building and Fire Research Laboratory
National Institute Of Standards and Technology
Gaithersburg, MD 20899, USA

Detailed measurements of the temperature, soot volume fraction, and CO_2 have been performed for a 10 cm diameter heptane fire. In addition, the concentrations of H_2O and CO were inferred from generalized state relationships. The heat feedback to the surface was calculated by using a reverse Monte-Carlo method in conjunction with RADCAL. The calculated heat fluxes to the surface with and without gas emission indicate that the contributions from the gaseous combustion products to total radiation are significant for heptane due to its mildly sooting nature.

Simultaneous optical measurements using two probes were performed to investigate the importance of temporal correlations on the heat transfer calculations. Measurements made throughout the fire indicate that nonsimultaneous data sets can be used to accurately predict the heat transfer to the fuel surface.

Introduction

For liquid pool fires, the dominant mode of heat feedback to the fuel surface is related to the size of the pool [1,2]. For small fires (less than 10 cm) that produce quasi-laminar flames, conduction and convection are the dominant modes of heat transfer. However, for intermediate to large fires, it has been found that radiation plays a significant role in the heat transfer process. Therefore, detailed examination of the radiative heat transfer mechanism is crucial to the understanding of the burning rate and the flame spread rate. These processes are key factors in assessing potential fire hazards.

Thermal radiation from the fire to the fuel surface is controlled by the emission from the soot and product gases. Radiation analysis using average temperature, average species concentrations and constant cylindrical flame shapes can diminish the turbulent enhancement of the heat flux [3]. Thus, accurate modeling of turbulent radiative heat transfer requires the instantaneous distribution of the local temperature and emissivity within the region between the fuel surface and the flame.

In a previous study that analyzed radiative heat feedback to the surface, the relative importance of gas emission was considered negligible for a flame with high levels of soot concentration [4,5]. Whereas this assumption yields reasonable results for fuels like toluene, for mildly sooting fuels such as heptane, neglecting gas emission may significantly underestimate the overall heat transfer to the surface [6]. Thus, accurate assessment of the surface heat transfer requires radiation contributions from gaseous combustion products.

The goal of this study is to perform a parametric study investigating the importance of the radiative component of the heat transfer to the fuel surface for different fuels and pool dimensions. In this paper, results for a 10-cm-diameter (intermediate sized) heptane pool fire are presented.

The local instantaneous temperature, soot volume fraction, and CO_2 concentrations were measured throughout the flame. The measured CO_2 concentrations were used to estimate the concentrations of H_2O and CO using the generalized state relationship developed by Sivathanu and Faeth [7]. The distributions of T, f_{ve}, CO_2, H_2O, and CO were used to calculate the radiative heat feedback to the surface using a reverse Monte-Carlo heat transfer model that incorporated the RADCAL radiation model developed by Grosshandler [8]. RADCAL is a model that solves the equation of transfer for a nonhomogeneous emitting/absorbing medium composed of soot and gaseous combustion products.

Accurate modeling of the nonsteady heat feedback to the surface requires the instantaneous temperature and emissivity distributions above the pool surface. However, acquiring such information is not practical, considering the turbulent three-dimensional nature of these large fires. In order to understand the importance of simultaneous measurements

*Present Address: Department of Mechanical Engineering, University of Illinois at Chicago, Chicago, IL 60607-7022, USA.

**Computing and Applied Mathematics Laboratory, NIST, Gaithersburg, MD 20899, USA.

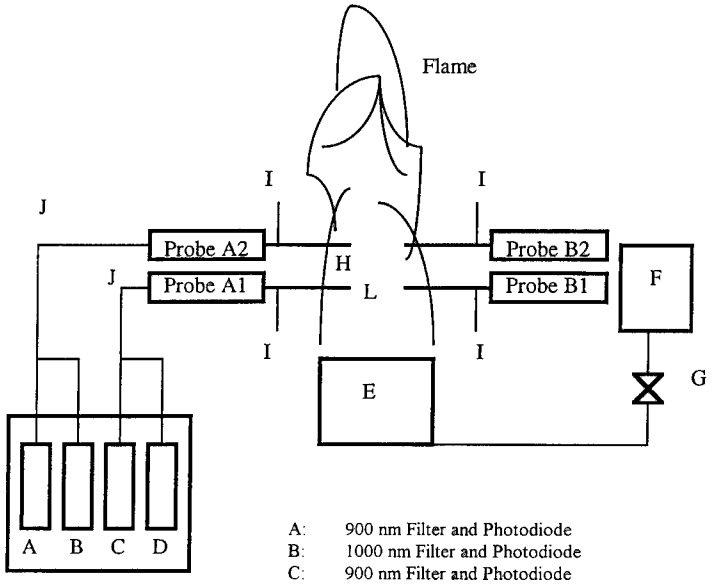

A: 900 nm Filter and Photodiode
B: 1000 nm Filter and Photodiode
C: 900 nm Filter and Photodiode
D: 1000 nm Filter and Photodiode
E: 10 cm Diameter Pool Burner
F: Fuel Reservoir
G: Solenoid Valve
H: Distance between Probes A1 and A2
Distance between Probes B1 and B2
I: Ports for Slow Nitrogen Purge
J: Bifurcated Fiber Optic Bundles
L: Probe Length: Distance between Probes A1 and B1, A2 and B2.

FIG. 1. Diagram of the experimental apparatus.

on the radiative heat transfer calculations, experiments were performed using a dual probe assembly to obtain simultaneous emission information at various locations throughout the fire.

Experimental Technique

The schematic diagram of the experimental apparatus is shown in Fig. 1 [9]. Probes A1 and A2, which were used for temperature and soot volume fraction measurements, consisted of 6.4 mm diameter stainless steel light guides (length 15 cm), and were surrounded by water-cooled jackets. The emission intensity from the luminous path (L in Fig. 1) was carried through two bifurcated fiber optic bundles. The emission intensity was monitored at central wavelengths of 900 and 1000 nm (both with 60 nm half-bandwidths) using two separate biased silicon photodiodes. The use of the fiber optic bundle facilitated the movement of the probes through the fire, circumventing the cumbersome task of moving the burner with respect to the probes. Probe B1 was used to monitor emission from CO_2 and consisted of a 6.4 mm diameter light guide attached to an aluminum box housing a PbSe infrared detector, 4350 nm central wavelength filter (with 180 nm half-bandwidth), a mechanical chopper, and an infrared lens. Nitrogen was purged slowly through ports labeled I (in Fig. 1) at a rate of 2.5 cm^3/min to prevent thermophoretic deposition of soot. The detection systems were calibrated using a high-temperature blackbody source and calibration factors were checked frequently and were found to be constant before and after the experiments. The burner was 10 cm in diameter and was water cooled. The fuel was gravity fed and maintained 0.5 cm below the rim of the burner.

Temperature and f_{ve} Measurements

The temperature and soot volume fraction measurement technique is similar to that used by Klassen and coworkers [4,5]. The emission intensities measured at two wavelengths were simultaneously solved to determine the local soot volume fraction, f_{ve}, and temperature, T.

$$I_{900} = \frac{\int I_{b\lambda} F_{900\lambda} (1 - e^{-K_\lambda f_{ve} L/\lambda})\, d\lambda}{\int F_{900\lambda} d\lambda} \quad (1)$$

$$I_{1000} = \frac{\int I_{b\lambda} F_{1000\lambda} (1 - e^{-K_\lambda f_{ve} L/\lambda})\, d\lambda}{\int F_{1000\lambda} d\lambda} \quad (2)$$

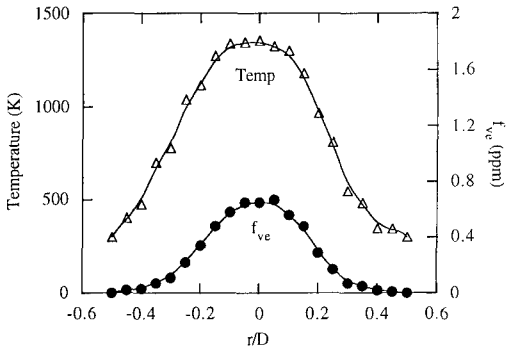

FIG. 2. Average temperature and f_{ve} measurements as a function of radial position at an axial position of 10 cm above the pool surface.

where F_λ is the wavelength-dependent sensitivity of the detection system, K_λ is the dimensionless soot absorption constant, L = 15 mm was the distance maintained between probes A1 and B1, and $I_{b\lambda}$ is Planck's function:

$$I_{b\lambda} = \frac{2hc^2}{\lambda^5(e^{hc/\lambda k_b T} - 1)} \tag{3}$$

where h is Planck's constant, c is the speed of light, k_b is Boltzmann's constant, and T is the temperature of the radiating particles. Equations (1) and (2) were solved iteratively for the two unknowns, temperature, T, and soot volume fraction, f_{ve}.

To be consistent with the practice employed by researchers in the fire community [4,8,12], the dimensionless soot absorption constant used in this work was determined from the indices of refraction of soot reported by Dalzell and Sarofim [10]. The uncertainty in the temperature measurements is approximately 50 °C, and the uncertainty in f_{ve} is approximately 10% [9,11].

Figure 2 displays the measurements of the average temperature and soot volume fraction as a function of radial location at an axial position 10 cm above the pool surface. The data was acquired at 200 Hz for a period of 50 s. The average root-mean-square (rms) values of the temperature and soot volume fraction were 350 K and 0.40 ppm, respectively. The symmetry exhibited by the data in Figure 2 indicates that measurements performed over half the radial domain (from r = 0–5 cm) were sufficient. It was also found that, for fires of this size, positions beyond 30 cm above the pool surface produce only sporadic periods during which the emission from soot or gaseous products can be measured [6]. Thus, most of the thermal radiation emanates from positions below 30 cm.

CO_2 Measurements

For typical temperatures encountered in fires, the CO_2 emission spectra extends from 4100 to 4700 nm [8]. The contributions of the various components to the total emission detected by the PbSe detection system were analyzed using RADCAL for a typical condition: T = 1500 K, f_{ve} = 1 ppm, and mole fractions of CO_2, H_2O, CO, and N_2 equal to 0.1, 0.1, 0.1, and 0.7, respectively. The interference filter (4350-nm central wavelength) was chosen to provide transmission of only the radiation emitted by CO_2 and reject emission from the other species. The contribution from CO_2 emission to the total intensity measured by the present PbSe detection system was approximately 94%, whereas the contributions from CO and H_2O emission were negligible and the contribution from soot emission was only 5%.

The PbSe detection system was calibrated with a blackbody source at various temperatures (150 °C–1000 °C). Using the temperatures determined from emission at 900 and 1000 nm [Eqs. (1) and (2)], the CO_2 concentrations were calculated iteratively until the emission intensity (between 4100 and 4700 nm transmitted through the filter function) predicted by RADCAL was equal to the intensity measured by the PbSe detection system.

Because of the nonsteady nature of fires of this size, the emission data exhibited sporadic periods during which the emission signals at 900 and/or 1000 nm were too low to determine the temperature and soot volume fraction. Typically, "low" emission periods occurred from 5 to 15% of the observation time, depending on location. For these periods, the temperature was set at 1000 K, which is the approximate lower-limit temperature for the detection of soot particle emission [19], and this temperature was used in the RADCAL calculations for determining the CO_2 concentrations. The CO_2 gas temperatures are expected to be somewhat higher than the soot temperatures [20]. Although the choice of temperature affects the calculated CO_2 concentration, calculations show that the impact on the CO_2 radiation intensity is small, typically less than 10%.

Simultaneous Emission Measurements

As mentioned in the Introduction, the calculation of the radiative heat flux to the fuel surface requires the spatial and temporal measurement of the fluctuating temperature and soot volume fraction. The flame for the 10 cm heptane pool exhibits buoyancy-induced fluctuations with an average frequency of approximately 11 Hz [13]. To determine the importance of using nonsimultaneous data for heat transfer calculations, simultaneous information at various locations must be obtained. The sensitivity of the cal-

culated heat transfer to this effect can be determined by uncorrelating the simultaneous data sets.

For this purpose, simultaneous emission measurements were performed using two pairs of identical probes (see Fig. 1). The vertical separation distance between the probes is defined as H. The horizontal distance between the probes was maintained at L = 15 mm. The simultaneous temperature and soot volume fraction information at two discrete locations was determined [from Eqs. (1) and (2)] and was used to calculate the radiative heat transfer (using RADCAL) from the top probe position through the lower probe position to the plane just below the bottom probe.

The effect of temporal correlation of the simultaneous data sets from two locations on the radiative heat transfer was tested by shifting one time series with respect to the other. In effect, the simultaneous (therefore correlated) data sets were effectively uncorrelated. The average of the shifted heat transfer normalized by Q_0 is defined as a:

$$a = \frac{1}{21} \sum_{n=-10,10} \frac{Q_n}{Q_0} \tag{4}$$

which is an indication of the effect of the time shift on the heat transfer calculations. The term Q_0 corresponds to the time-averaged heat transfer calculated with the simultaneous data sets; Q_1 corresponds to the time-averaged heat transfer calculated with a 1 s shift in the time series; and Q_2 corresponds to the time-averaged heat transfer calculated with a 2 s shift in the time series, and so on. The heat transfer was calculated for time shifts between -10 and $+10$ s in 1 s increments. A value of a close to unity suggests only a small change in the heat transfer as a function of the time shift.

Simultaneous emission measurements were performed for the following conditions: L = 15 mm and H = 15, 20, 25, and 30 mm. The center of the probe assembly was placed at x = 10 cm and r = 0 cm. Using the shifted time series modifies the instantaneous heat flux calculations, however, the average value of the heat flux was relatively insensitive to time shifts. For all of the probe separation distances, the calculated a was near unity with a standard deviation less than $\pm 5\%$. Thus, for positions above the pool surface and the various separation distances, uncorrelating the simultaneous data sets had negligible effects on the calculated heat transfer.

Measurements of a were also performed at various locations above the pool surface along the center line using L = 15 mm and H = 30 mm. The center of the assembly was placed at axial positions, x, between 3 and 30 cm (with r = 0 cm) in increments of 3 cm. The calculated a for all positions was near unity with a standard deviation less than $\pm 5\%$. This suggests that there is no effect of correlation between the simultaneous data sets on the calculated heat transfer.

For pool fires, periodic fluctuations (caused by buoyancy) of the outer flame surface occur along both the vertical and horizontal axes. Along the centerline (only vertical fluctuations are present because of the symmetry exhibited by the fire), temporal shifting of the simultaneous data sets does not affect the heat transfer calculations. This was verified by shifting the time series in increments of 0.005 s for a period of 0.5 s (which corresponds to approximately five flame pulsation periods) and calculating the a. Even for the time shifts producing maximum cross correlation between the data sets (H divided by the fluid velocity), the a values varied by only 1%. However, it is unclear how the correlations will affect the radiative heat transfer when both modes of fluctuation are present. Experiments performed for various radial positions (r from 0 to 5 cm) at x locations of 5, 10, and 15 cm also indicated only small changes in heat transfer as a function of time shifting of the data sets.

These findings suggest that, throughout the fire, the heat transfer calculation is relatively insensitive to the temporal correlation between data sets. This is important because it suggests that nonsimultaneous data acquired at different locations can be used to calculate the heat transfer to the pool surface. This practice will be employed for the heat transfer calculations discussed in the next section.

Reverse Monte-Carlo Technique

Because of the complexity of the problem, early attempts at modeling the nonsteady radiative heat feedback mechanism involved several limiting assumptions, including the use of average flame emissivity and constant or mean flame temperatures and absorption/emission coefficients as a function of height and effective flame shapes. However, it has been demonstrated that the use of mean radiative properties to calculate heat feedback can lead to significant differences between the predicted and measured fuel burning rates in these turbulent fires [3,4,5].

In this study, a reverse Monte-Carlo integration technique was used to calculate the incident flux at the fuel surface. The technique is equivalent to the technique described by Carter et al. [14] and Walters and Buckius [15].

The approach has several important advantages. First, it avoids aliasing errors that can be important if the "hot" volumes (localized regions of high temperature or high soot volume fraction) are small. Furthermore, the number of directional rays can automatically be determined by setting acceptable sample standard deviations. The sample standard deviation is an indication of the magnitude of the error in the results.

The incident radiative flux q_i received at area el-

ement dA on the fuel surface is given by the following equation:

$$q_i = \int_{2\pi} i_i(\theta_i,\phi_i) \cos \theta_i \, d\omega_i \tag{5}$$

where the integral is over the hemisphere of incident directions above dA and $i_i(\theta_i,\phi_i)$ is the incident total intensity. The total incident intensity is given by

$$i_i = \int_0^\infty \int_0^s K_\lambda(s^*) i_{b,\lambda}(s^*) \cdot \exp\{-[k_\lambda(s) - k_\lambda(s^*)]\} \, ds^* d\lambda \tag{6}$$

$$k_\lambda(s) = \int_0^s K_\lambda(s^*) \, ds^* \tag{7}$$

and the coordinate s is measured along a path in direction (θ_i,ϕ_i).

Equation (6) can be rewritten as

$$q_i = \int_0^{2\pi} \int_0^{\pi/2} \pi i_i(\theta_i,\phi_i) \cdot [2 \cos \theta_i \sin \theta_i d\theta_i][d\phi_i/(2\pi)]. \tag{8}$$

That is, the flux is equal to $\pi i_i(\theta_i,\phi_i)$ integrated over θ_i and ϕ_i with weighting functions of $2 \cos \theta_i \sin\phi_i$ and $1/2\pi$, respectively. The flux can be estimated then by taking the average of many trial values of $\pi i_i(\theta_i, \phi_i)$ evaluated at random values of θ_i and ϕ_i chosen using the weighting functions as probability density functions (pdfs).

The evaluation of the flux requires the selection of a random direction (θ_i', ϕ_i') and then the evaluation of the incident intensity along that path. Using the appropriate pdfs, the random direction is chosen using

$$\phi_i' = 2\pi R_\phi, \qquad \theta_i' = \arcsin(R_\theta) \tag{9}$$

where R_ϕ and R_θ are random numbers. After N trials using N directions, the estimated q_i' is

$$q_i' = \pi \sum_{j=1}^{N} \frac{i(\theta_j,\phi_j)}{N}. \tag{10}$$

The magnitude of the error in this estimate is indicated by the sample standard deviation:

$$\Delta q_i' = \pi \sqrt{\frac{1}{(N-1)} \sum_{j=1}^{N} (i_j')^2 - \frac{(q_i')^2}{\pi^2 N}}. \tag{11}$$

The line integral in Eq. (7) needs to be evaluated for each trial. For each line integral, a ray is followed through the cylindrical geometry in which T, soot volume fraction, and mole fractions of the gaseous products are known at a set of discrete values of r and x. The integration is performed by considering the cylindrical geometry as a stack of cylindrical rings. For each cylindrical ring, the ray pierces the distance through the ring, and the data for that ring are stored in an array. The array of data is then passed to RADCAL, which performs the integral given in Eq. 6.

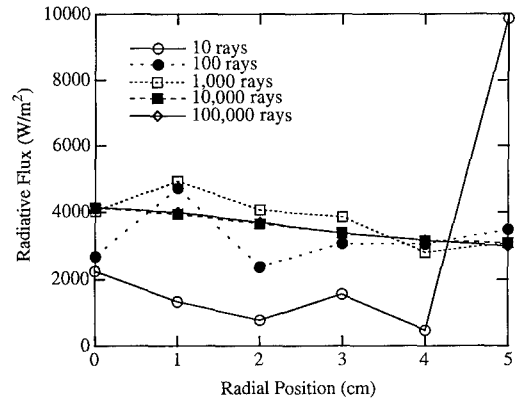

FIG. 3. Calculated heat flux to the pool surface as a function of radial position using 10, 100, 1,000, 10,000, and 100,000 random rays.

Figure 3 displays the irradiance along the pool surface as a function of the number of rays used in the calculations. The use of 10 rays produced very large errors and standard deviations in the heat flux due to aliasing errors. Both the errors and standard deviations decreased as the number of rays increased until the calculation converged for 10,000 rays. For the cases in which 10,000 and 100,000 rays were used, the irradiance decreased smoothly as a function of radial position with the highest value occurring at the pool center. These results indicate that arbitrarily choosing the number of rays can produce large uncertainties in the heat flux calculations.

Generalized State Relationships

In this study, the emission and absorption characteristics of hydrocarbons and pyrolysis gases were not considered. However, in the 10 cm heptane fire, the impact on the total radiative heat transfer calculations is estimated to be modest. The concentrations of hydrocarbons decreased rapidly both as a function of radial and axial positions above the pool surface [18]. Orloff [21] also estimated that the radiation blockage due to pyrolysis gases was not important for fires of this size.

To incorporate the effects of radiation from gaseous combustion products, CO_2 emission at 4350 nm was monitored. CO_2 produces a well-defined emis-

sion band that can be distinguished from the emission of other components [16]. For example, the emission line for H_2O at 2700 nm is difficult to separate from the CO_2 emission at 2700 nm. CO radiation at 4600 nm cannot be extracted from the dominant emission from CO_2.

To estimate the concentrations of H_2O and CO, the generalized state relationships for gas-phase components of diffusion flames [7] were used in conjunction with the measured concentrations of CO_2. However, there are two solutions for the concentrations of H_2O and CO from the CO_2 measurements, depending on whether the local equivalence ratio is lean or rich. In this work, the concentrations were calculated for both the rich and lean conditions.

Figure 4 displays the time-averaged measurements of T, f_{vc}, and CO_2, and inferred values of H_2O and CO distributions calculated assuming rich conditions. Both the average temperature and soot concentration are highest along the centerline above $x \sim 7$ cm. The reduction of the average T and f_{vc} as a function of radial position occur due to the realizations of low emission data. The distributions of the average gaseous species concentrations look similar because the H_2O and CO concentrations were derived from the CO_2 measurements.

Figure 5 compares the instantaneous heat flux integrated over the pool surface using time series of the temperature, soot volume fractions, and species concentrations from all locations above the pool surface for both the rich and lean cases. For the rich case, the average heat flux was approximately 10% greater than the average heat flux calculated for the lean case. This is expected since higher concentrations of gaseous products are formed under rich conditions and therefore can contribute to the total radiation. The difference in the total heat flux was modest, partly because the dominant radiation emanates from soot particles. Thus, in consideration of this small variation in the calculated heat flux between the lean and rich cases, the remainder of the paper will discuss results obtained using the rich conditions.

Contributions from Gas Emission

Figure 6 displays the heat flux integrated over the entire pool surface using the nonsimultaneous T, f_{vc}, CO_2, H_2O and CO data as a function of time step. Figure 6 also displays the running time average. For this case, both gas and soot emissions were considered. There were significant time-varying fluctuations in the instantaneous heat flux to the surface (due to fluctuations in the temperature and/or species concentrations). However, within 400 time steps (corresponding to 2 s), the heat flux reached a steady-state value of 17.7 ± 1 W. The heat flux required to vaporize the fuel (including the heat of vaporization and the energy required for fuel heat-up using the measured fuel consumption rate of 0.08 g/s) is 43.2 W. Thus, the radiative flux to the surface of the 10 cm diameter heptane fire represents 40% of the total heat required for fuel vaporization, which is a significant fraction. The remainder of the heat feedback was attributed to convection, which is important for pool fires of this size [17].

Figure 6 also displays the radiative heat flux calculations for the same condition when gas emissions were suppressed. The average value also asymptoted to a steady-state value within 2 s for this calculation. The steady-state value of 11.6 ± 1 W represents nearly a 40% decrease in the heat flux to the surface compared to the case in which gas emission was included. The radiation from soot represents approximately 60% of the total radiative heat flux to the surface. Thus, for heptane pool fires of this dimension, gas emission represents a significant fraction of the total flame emission and therefore must be included in the heat transfer calculations. This is in contrast to a very sooty fuel like toluene where calculations performed using centerline measurements indicate that the contributions from the gaseous combustion products represent approximately 10% of the total radiation to the surface [4,5].

Average vs Instantaneous Values

Fischer et al. [18] reported a significant difference in the calculated radiant intensities when time-averaged values of the temperature were used instead of the instantaneous values. Using the time-averaged values of T, CO_2, H_2O, CO, and f_{vc} can diminish the effects of turbulent fluctuations of temperature and species concentrations on the radiative heat transfer as a result of the nonlinear dependence of radiation on these parameters. Furthermore, the occurrence of low emission periods will reduce the magnitude of the average values and increase the magnitude of the rms values [19]. Thus, the use of time-averaged values does not provide a true representation of the time-averaged heat transfer.

The radiative heat transfer calculations were also performed for the case using time-averaged values. For this case, the calculated heat flux was approximately 14.0 ± 1 W. As stated earlier, the average heat flux calculated using the instantaneous values was 17.7 ± 1 W. This suggests the importance of using local instantaneous measurements from various locations above the pool surface for calculating the heat transfer to the fuel surface. This finding is in qualitative agreement with the results reported by Fischer et al. [18].

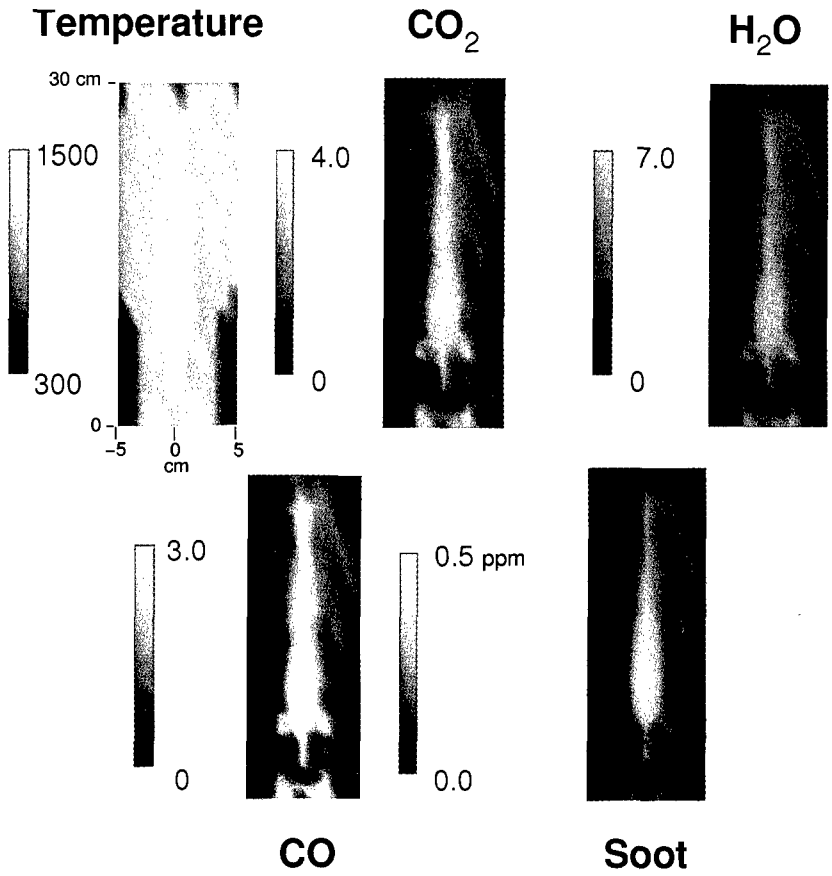

FIG. 4. Time average distributions of temperature, CO_2, H_2O, CO, and f_{ve} above the pool surface.

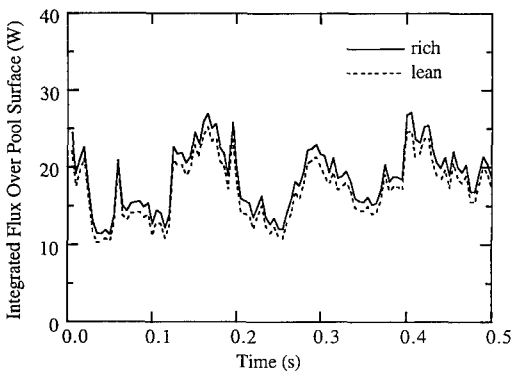

FIG. 5. Comparison of the (calculated) integrated heat flux to the pool surface as a function of time for rich and lean cases.

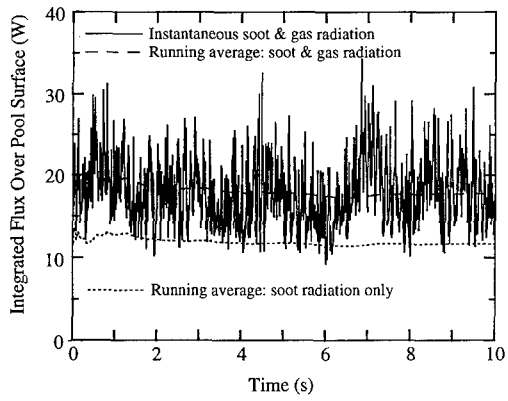

FIG. 6. Calculation of the instantaneous integrated heat flux to the pool surface as a function of time for the case considering gas (rich) and soot emission. The running averages of the cases with and without gas emission are also plotted.

Conclusions

Detailed measurements of the temperature, soot volume fraction, and CO_2 distributions have been made for a 10 cm diameter heptane fire. The emissions from the gaseous combustion products, both measured (in the case of CO_2) and estimated from the generalized state relationship (for H_2O and CO), were calculated using RADCAL in conjunction with the reverse Monte-Carlo method.

Simultaneous emission measurements made for various locations above the pool fire surface indicate relative insensitivity of the heat transfer to the temporal correlation between the data sets. This finding suggests that the use of nonsimultaneous data is adequate to predict the heat transfer to the surface for large fires where simultaneous measurement over the entire flame volume is impractical.

The results indicate that, for the case of a 10 cm diameter pool fire burning heptane (which is a mildly sooting fuel), radiation contributions from the gas phase represent a significant fraction of the total radiative heat transfer to the surface of the pool. However, this fraction is a function of the amount of soot produced by the flame and therefore a function of the fuel structure and pool dimension. The effect of using average values of T, f_{ve}, CO_2, H_2O, and CO indicates that the heat flux was underpredicted when compared to the case in which instantaneous values were used.

Acknowledgments

The authors gratefully acknowledge the helpful discussions and advice provided by Drs. W. L. Grosshandler, C. R. Shaddix, and J. Harrington of NIST and Professor J. P. Gore of Purdue University and technical assistance provided by Mr. A. Hubbard of Princeton University.

REFERENCES

1. Blinov, V. I., and Khudiakov, G. N., *Dok. Akad. Nauk. USSR* 113:241 (1957).
2. Burgess, D., and Hertzberg, M., *Heat Transfer in Flames* (N. H. Afgan and J. M. Beer, Eds.), Hemisphere Press, New York, p. 413, 1974.
3. Hamins, A., Yang, J. C., and Kashiwagi, T., "A Simple Model for Predicting the Burning Rate of Liquid Pool Fires," *Fire Safety J.*; submitted.
4. Klassen, M., Ph.D. Thesis, University Of Maryland, College Park, MD, 1992.
5. Klassen, M., Sivathanu, Y. R., and Gore, J. P., *Combust. Flame* 90:34 (1992).
6. Choi, M. Y., Hamins, A., Rushmeier, H., Hubbard, A., and Kashiwagi, T., "Simultaneous Optical Measurements of Soot Volume Fraction and Temperature in Heptane Pool Fires," Eastern States Section of the Combustion Institute, Princeton, NJ, October 25–28, 1993.
7. Sivathanu, Y. R., and Faeth, G. M., *Combust. Flame* 82:211 (1990).
8. Grosshandler, W. L., "RADCAL: A Narrow-Band Model for Radiation Calculations in a Combustion Environment," NIST Technical Note 1402, 1992.
9. Choi, M. Y., Hamins, A., Mulholland, G. W., and Kashiwagi, T., "Simultaneous Optical Measurements of Soot Volume Fraction and Temperature in Premixed Flames," *Combust. Flame,* in press.
10. Dalzell, W. H., and Sarofim, A. L., *J. Heat Transfer* 91:100 (1969).
11. Choi, M. Y., Mulholland, G. W., Hamins, A., and Kashiwagi, T., "Comparisons of Soot Volume Fraction Measurements Using Optical and Isokinetic Sampling Techniques," Eastern States Section of the Combustion Institute, Princeton, NJ, October 25–28, 1993.
12. Sivathanu, Y. R., and Faeth, G. M., *Combust. Flame* 81:150 (1990).
13. Hamins, A., Yang, J. C., and Kashiwagi, T., *Twenty-Fourth Symposium (International) on Combustion,* The Combustion Institute, Pittsburgh, 1992, p. 1695.
14. Carter, L. L., Horak, H. G., and Sanford III, M. T., *J. Comput. Phys.* 26:119 (1978).
15. Walters, D. V., and Buckius, R. O., *Int. J. Heat Mass Transfer* 35(12):3323 (1992).
16. Sivathanu, Y. R., and Gore, J. P., *Combust. Sci. Technol.* 80:1 (1991).
17. Hottel, H. C., *Fire Res. Abstr. Rev.* 1:41 (1959).
18. Fischer, S. J., Hardouin-Duparc, B., and Grosshandler, W. L., *Combust. Flame* 70:291 (1987).
19. Klassen, M., and Gore, J. P., *Combust. Flame* 93:270 (1993).
20. Best, P. E., Chien, P. L., Carangelo, R. M., Solomon, P. R., Danchak, M., and Ilovici, I., *Comb. Flame* 85:309 (1991).
21. Orloff, L., *Eighteenth Symposium (International) on Combustion,* The Combustion Institute, Pittsburgh, 1981, p. 549.

COMMENTS

Patrick J. Pagni, University of California, Berkeley, USA. Have you compared your soot volume fractions with the pool-fire soot volume fraction measurements in the literature [1,2]?

REFERENCES

1. Bard, S., et al., "Spatial Variation of Soot Volume Fractions in Pool Fire Diffusion Flames," in *Fire Safety Science—Proceedings of the First International Sympo-*

sium (C. Grant et al., Eds.), Hemisphere, New York, 1986, pp. 361–369.
2. Markstein, G. H., "Measurements on Gaseous-fuel Pool Fires with a Fiber-Optic Absorption Probe," *Combust. Sci. Technol.* 39:215 (1984).

Author's Reply. Comparisons with the pool fire results in the literature [1–4] reveal that the time-averaged soot volume fractions measured in the present experiments are of the same order of magnitude. In a previous study performed in a steady-state and homogeneous environment of premixed flames [5], the soot volume fraction measurements were found to be very sensitive to the refractive index used to calculate the soot optical properties. In the present study, the refractive indices of Dalzell and Sarofim [6] were used to be consistent with previous investigations of radiative characteristics of liquid pool fires [3,7].

REFERENCES

1. Bard, S., et al., "Spatial Variation of Soot Volume Fractions in Pool Fire Diffusion Flames," in *Fire Safety Science—Proceedings of the First International Symposium* (C. Grant et al., Eds.), Hemisphere, New York, 1986, pp. 361–369.
2. Bard, S., and Pagni, P. J., *J. Heat Transfer* 103:357 (1981).
3. Klassen, M., Sivathanu, Y. R., and Gore, J. P., *Combust. Flame* 90:34 (1992).
4. Sivathanu, Y. R., and Faeth, G. M., *Combust. Flame* 81:150 (1990).
5. Choi, M. Y., Hamins, A., Mulholland, G. W., and Kashiwagi, T., "Simultaneous Optical Measurement of Soot Volume Fraction and Temperature," *Combust. Flame*, in press, 1994.
6. Dalzell, W. H., and Sarofim, A. L., *J. Heat Transfer* 91:100 (1969).
7. Klassen, M., Ph.D. Thesis, Department of Mechanical Engineering, University of Maryland, 1992.

•

Y. R. Sivathanu and J. P. Gore, Purdue University. You had indicated that the temporal correlation between adjacent points or the spatial correlation does not affect your heat flux calculations. What was the minimum distance between the adjacent points for your measurements? Could you comment on the minimum distance for which your observation is valid? Do your findings essentially agree with those of Kounalakis et al. [1] in that the spatial correlation coefficients have negligible influence on the radiation properties?

REFERENCE

1. Kounalakis, M. E., Gore, J. P., and Faeth, G. M., *J. Heat Transfer* 111:1021–1030 (1989).

Author's Reply. In turbulent fire studies, researchers have to reconstruct the temperature and emissivity distribution using mean values from sets of nonsimultaneous data collected at various locations within the fire [1,2]. The purpose of the present study was to directly measure the effects of using nonsimultaneous data on the radiative heat transfer process without relying on the use of mean temperatures and soot volume fractions and the statistical variation of these parameters. In this work, the radiation characteristics were measured simultaneously in pairs of two spatial locations with separations of H equal to 15, 20, 25, and 30 mm (with the lower limit being determined by the dimensions of the optical probes). These separation distances are of the order of the integral scale lengths reported in the work by Kounalakis et al. [3]. Since the emission data were acquired simultaneously for the top and bottom probes, this study provided a unique opportunity to determine the spatial correlation coefficients as a function of time shift between the data sets. The spatial correlation coefficients were calculated for the H = 30 mm case for heights ranging from 3 to 30 cm above the burner surface. The average coefficient was approximately 0.2 for zero time shift and 0.5 for cases when the time shift was equal to H/u (where u is the local velocity of the flame). Based on measurements at the smaller separation distances, the magnitude of these coefficients is expected to decrease as H is increased beyond the integral scale lengths. The reconstruction of the temperature and emissivity distribution using the data (collected at more than 100 locations above the fire) is equivalent to a random temporal ordering. Although the instantaneous heat transfer between the two locations changes as a function of time shift, the integrated heat transfer varied negligibly with random time shifting.

REFERENCES

1. Klassen, M., Sivathanu, Y. R., and Gore, J. P., *Combust. Flame* 90:34 (1992).
2. Klassen, M., and Gore, J. P., *Combust. Flame* 93:270 (1993).
3. Kounalakis, M. E., Gore, J. P., and Faeth, G. M., *J. Heat Transfer* 111:1021 (1989).

•

J. Gore and Michael Klassen, Purdue University, USA. In previous multiray radiation calculations [1,2], fewer rays were necessary to obtain heat flux values. For example, Klassen et al. (1993) [2] utilized between 22 and 450 rays and 5000 realizations to calculate converged heat feedback in 30-cm toluene pool fires. Please comment on the necessity of using a large number of rays ($\geq$10,000) to obtain converged heat fluxes in your information.

REFERENCES

1. Gore, J. P., Ip, U.-S., and Sivathanu, Y. R., "Coupled Structure and Radiation Analysis of Acetylene/Air

Flames," *J. Heat Transfer Trans. ASME* 114:487–493 (1992).

2. Klassen, M., Gore, J. P., Sivathanu, Y. R., Hamins, A., and Kashiwagi, T., "Radiative Heat Feedback in a Toluene Pool Fire," *Twenty-Fourth Symposium (International) on Combustion*, The Combustion Institute, Pittsburgh, pp. 1713–1719.

Author's Reply. In the present study, the radiative heat transfer characteristics for the 10-cm heptane pool fire were modelled as an aggregate of small emitters and receivers. The turbulent fluctuations of the location of the "hot" emitting volumes above the pool surface required dense sampling using a large number of rays generated in random directions to prevent aliasing errors. The number of rays chosen for these calculations was determined for some initial "pilot" calculations rather than determining the number of rays interactively [1]. To achieve a systematic determinant for convergence, the sample standard deviation was maintained at 1–2%. At a particular time step, the geometry of the radiation field may require less than 10,000 rays to produce a standard deviation less than the determined threshold. However, it has been found that 10,000 rays always provided this level of accuracy for each time step [2].

REFERENCES

1. Kirk, D., and Arvo, J., *Comput. Graphics* 25(4):153 (1991).
2. Rushmeier, H., Hamins, A., and Choi, M. Y., "Volume Rendering of Pool Fire Data," IEEE/ACM Volume Visualization Symposium, Washington, DC, Oct. 1994.

Twenty-Fifth Symposium (International) on Combustion/The Combustion Institute, 1994/pp. 1481–1488

BOILOVER BURNING OF OIL SPILLED ON WATER

J. P. GARO AND J. P. VANTELON
Laboratoire de Chimie Physique de la Combustion
Ecole Nationale Supérieure de Mécanique et d'Aérotechnique
Site du Futuroscope—BP 109 Chasseneuil du Poitou
86960 Futuroscope Cedex, France

AND

A. C. FERNANDEZ-PELLO
Department of Mechanical Engineering
University of California
Berkeley, CA 94720, USA

In-situ burning of fuels spilled on water is of interest as a means for cleaning up these spills. It also is a potential important hazard in unwanted fires. This paper reports the results of small-scale experiments that investigate the combustion of thin layers of heating oil on water, and the events that take place in this complex combustion process, which can lead to the occurrence of explosive burning, normally referred to as boilover. The work concerns primarily the influence of the initial oil-layer thickness and pool diameter on the burning rate, time to the start of boilover, burned mass ratio, boilover intensity, and temperature history of the oil and water. The temperature measurements show that the phenomenon may be due to boiling nucleation near the oil/water interface, in sublayer water that has been superheated. The violent eruptive vaporization of the water bubbles tends to atomize the oil layer above, with subsequent projection of burning droplets. The boilover intensity appears closely related to initial oil-layer thickness and pan diameter. This is discussed in terms of surface tension effects, and growth and expansion of the water bubbles at the nucleation sites.

Introduction

Pollution and fires from accidental liquid fuel spills in open waters are problems of increased concern, and studies of methods to clean up these spills have gained more attention over the past few years. Among the different methods being considered, it appears that in-situ burning may be an interesting alternative, since it avoids the recovering and storage stages of the cleaning process, in addition to eliminating the spilled fuel.

The pool burning of a thin fuel layer on water is similar to that of the single fuel, although it presents the important difference of the heat loss from the fuel to the water underneath. This, together with surface temperature and surface tension effects, is the major reason why the fuel layer must have a minimum thickness to be ignited. Furthermore, the heat transferred to the water can induce water boiling and splashing, a phenomenon referred to as thin-layer boilover.

In general, boilover occurs with fuels whose boiling temperature is higher than that of the water. This phenomenon is often encountered with fires involving large storage tanks containing multicomponent fuels (particularly crude oils or other heavy oils), leading to explosive vaporization of the water often present on the bottom of the tank but it can also occur with the burning of thin layers of these liquids floating on water. The heat transfer through the fuel arises from the phenomenon of hot-zone formation, a zone of practically uniform temperature and composition that propagates through the interior of the fuel. The hot-zone formation in large storage tanks and its extent are normally explained by the generation of continuous and vigorous convective mixing within the liquid, stimulated by selective evaporation of the light ends or by the generation, ascent, and growth of vapors released throughout most of this zone [1–3].

Studies specifically concerning thin-layer boilover of pure or multicomponent fuels are, on the whole, much more recent. Most of these studies have been conducted on small- or medium-scale fires in a laboratory, which helps to reduce the formation of fuel surface waves and ensures calm external conditions, which help the onset of nearly uniform boiling at the fuel/water interface. Twardus and Brzustowski [4] proposed a simple one-dimensional model of the problem that was later improved to include the ab-

sorption of radiation within the fuel layer as well as the effect of wind [5]. Alramadhan et al. [6] extended that work by incorporating into the model buoyant turbulent motion and the explicit effect of the radiation. Petty [7] conducted a series of experiments to simulate large-scale crude oil fires (2 m in diameter), and concluded that fuel surface temperature remains unchanged throughout the burning process, in contradiction to the interpretation of fuel burning as a distillation process. Koseki and Mulholland [8] and Koseki et al. [9] reported that fuel thickness is an important factor in regard to boilover: the thicker the fuel layer, the more violent is boilover. Also, temperature measurements indicate probable superheating of the water when boilover occurs. Arai et al. [10], in studies with simple and multicomponent fuels, brought out some fundamental aspects of the effect of a boiling water sublayer on the behavior of the pool fires.

In spite of extensive studies on the problem, it appears that a complete understanding of boilover is still lacking, most likely because of the complexity of the mechanisms involved. The objective of this work is to investigate the effect of fuel-layer thickness on the burning of this fuel layer spilled on water in the case of test pans of small diameter (≤50 cm). On the basis of the obtained results, the mechanisms that may cause the thin-layer boilover to occur are discussed.

Experiment

To reduce possible experimental complications peculiar to multicomponent fuels, we have selected heating oil for our experiments. Since it is composed of a mixture of C_{14}–C_{21} hydrocarbons, it offers a relatively narrow range of boiling points (250 °C–350 °C), while its burning temperature is high enough to heat the water underneath to its boiling point. Thus, even if it presents a more restricted range of hydrocarbons than the crude oils, it appears well suited for a study of thin-layer boilover.

The pool burning tests of a fuel layer floating on water were conducted in a large-scale test cell vented by natural convection. Stainless-steel pans 6-cm deep and of inner diameters 15, 23, 30, and 50 cm were used in the experiments. The pans were placed on a load cell to measure the consumption of fuel as a function of time. The load cell had a response time of 60 ms and an accuracy within ±0.5 g. It was frequently calibrated to insure reliable measurements.

For each pan diameter, different initial fuel-layer thicknesses were tested (ranging from 2 to 20 mm). Before each test, water was first poured on the pan and next the fuel until it reached 1 mm below the pan lip. During the combustion, the location of the fuel/water interface remained fixed. Therefore, since the height of the burning fuel surface decreases as combustion progresses, the freeboard length increases during the experiment. However, as will be seen later, this freeboard length increase, as well as an observed light increase of the fuel surface temperature (the lighter volatiles tend to burn off first), appeared to have only a minor effect on the measured combustion rate.

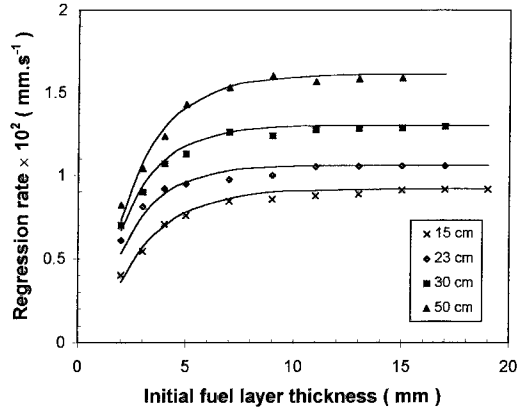

FIG. 1. Regression rate as a function of initial fuel-layer thickness for different pool diameters.

Fuel and water temperature were measured with an array of four, stainless-steel–sheeted, chromel-alumel thermocouples of 0.5-mm diameter inserted horizontally through the side wall of the pan with their junction located along the centerline. Efforts were made to remove from the experiments any significant perturbing influence of their presence and particularly any preferential onset of water boiling at the fuel/water interface.

After a short period of time from ignition, the burning rate reached steady-state, defined here as the pre-boilover burning rate. At the onset of thin-layer boilover, the burning rate increased widely, with intense splashing of water and fuel.

Results

Burning Rate:

Figure 1 shows the surface regression rate as a function of the initial heating-oil-layer thickness, for the different pool diameters tested. It can be observed that the regression rate increases first with increasing initial fuel-layer thickness, and then reaches a constant limiting value that is characteristic of each pan size. This limiting burning rate increases with pool diameter, as has been previously observed for this range of pool sizes [11]. Moreover, the limiting values are in good agreement with those observed for the burning of the same fuel without the water sublayer [11]. The present results seem to in-

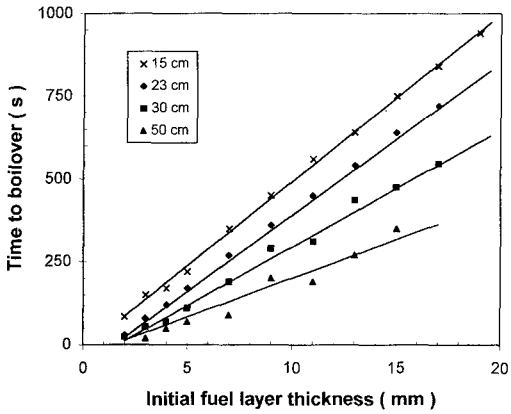

FIG. 2. Pre-boilover time as a function of initial fuel-layer thickness for different pool diameters.

dicate that these limiting values are reached for layer thicknesses around 1 cm or larger. The variation of the combustion rate with the initial fuel-layer thickness is due to heat losses to the water layer underneath. When the fuel thickness is small, the water acts as a heat sink, and the burning rate is reduced. In some specific test, it was observed that, if the fuel layer becomes thin enough (around 0.5 mm), the combustion can be quenched by heat loss to the water. When the fuel thickness is increased, this influence lessens, and there is time for the fuel to reach steady-state burning. A test made with a deeper pan (20 cm instead of 6 cm) showed that the water depth had no significant effect on the boilover characteristics. Thus, the pans used are deep enough so that any effect of water depth is removed from our experiments.

Time to the Start of Boilover:

Figure 2 shows the time to the onset of boilover as a function of the initial fuel-layer thickness. It is seen that the dependence appears practically linear. If, as explained below, it is assumed that thin-layer boilover starts when the temperature at the heating oil/water interface reaches a given value (nucleation temperature), then these straight lines can be considered to be representative of a constant, average, apparent thermal penetration rate (actually, this interface is not really calm and well defined because of the occurrence of some frothing). The larger the pool size, the higher the penetration rate, which is consistent with the increase of burning rate with the pool size. It can also be observed that these lines cut the thickness coordinate, showing that there is a minimum thickness for the combustion to be sustained. Similar experiments are reported by Koseki et al. [9], with crude oil and a larger range of pan diameters (0.3–2.7 m). However, as a result of large scatter in

TABLE 1
Thermal penetration rate results

Pan diameter (cm)	15	23	30	50
Regression rate × 10^2 (mm·s^{-1})	1	1.1	1.3	1.7
Slope of a linear fit to the data × 10^2 (mm·s^{-1})	1.9	2.4	2.7	3.5
Thermal penetration rate × 10^2 (mm·s^{-1})	0.9	1.3	1.4	1.8

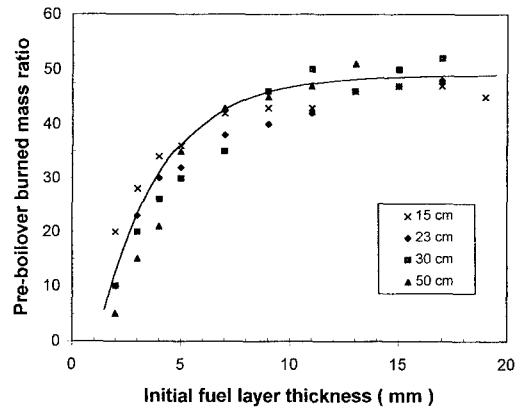

FIG. 3. Burned mass ratio as a function of initial fuel-layer thickness for different pool diameters.

their test results, they only deduced an average thermal penetration rate from a linear fit to the data.

If the regression rate of the fuel surface is known, then it is possible to deduce, by difference from the fitted slope, the effective thermal penetration rate responsible for boilover. The calculated values are reported in Table 1. It is noticed that the thermal penetration rate is of the same order of magnitude as the heating-oil surface regression rate.

Burned Mass Ratio:

The burned mass ratio is defined as the ratio between the amount of fuel burnt before occurrence of boilover and the initial amount of fuel. This ratio can be determined either by comparison of the fuel thicknesses or from the mass loss. Figure 3 shows this ratio as a function of the initial fuel-layer thickness. Independent of the diameter used, a limiting value of about 50% is reached when the initial layer thickness exceeds about 1 cm. This limiting value is consistent with the values of thermal penetration rate, responsible for boilover, and the fuel regression rate, respectively. It is also consistent with the onset of boilover at a constant temperature at the oil/water interface. In the case of initial fuel-layer thicknesses smaller than 1 cm, the comparison between regression rate and thermal penetration rate permits one

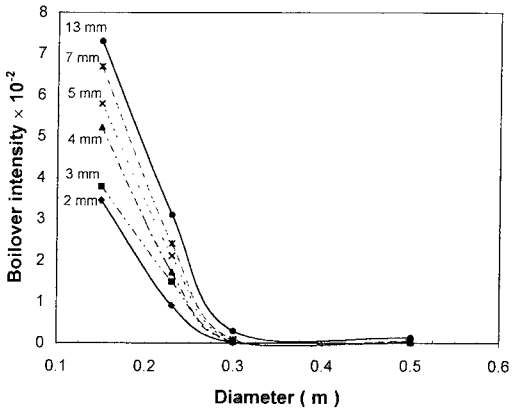

FIG. 4. Boilover intensity as a function of initial fuel-layer thickness for different pool diameters.

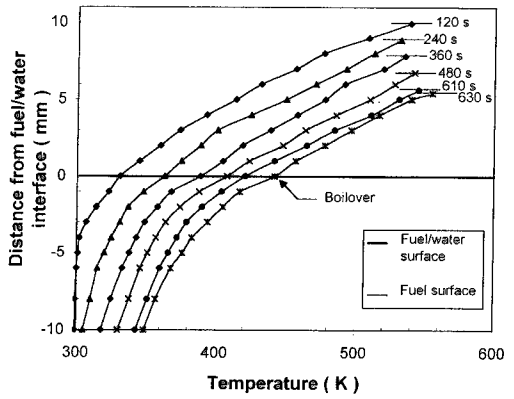

FIG. 5. Development of vertical temperature profile (pan of 15 cm in diameter and initial fuel-layer thickness of 11 mm).

to assess quite well the measured values of burned mass ratio reported in Fig. 3.

Boilover Intensity:

The intensity of boilover is defined here as the ratio between the mass loss rate of fuel during the boilover period and the maximum fuel combustion rate during the pre-boilover period. Note that the load cell signal is very noisy and that the associated uncertainty is within 20%. Moreover, one must be well aware that this corresponds to fuel burnt during eruptive vaporization and also to burning droplets randomly ejected outside the pan, together with an appreciable amount of water. An estimation of the amount of lost water can be made from the difference between the total mass loss recorded and the initial mass of fuel. In any case, the estimation of the boilover intensity is very approximate and only can be viewed as indicative of the intensity of the phenomenon. Figure 4 shows the boilover intensity thus estimated as a function of the initial fuel-layer thickness, for the different pool sizes. It is seen that the intensity increases with the thickness but decreases strongly with the pool diameter. The last observation was previously reported by Koseki et al. [9] with crude oil.

Liquid Temperature History:

Figure 5 shows the variation of the temperature with the distance from the fuel/water interface, for different times after the start of the test (boilover occurs at 630 s), for the case of an initial fuel-layer thickness of 11 mm. Also presented in the figure is the evolution of the fuel surface level for the different periods of time considered. All the temperature measurements presented were made with the smallest pan (15 cm in diameter). Tests conducted to verify the radial temperature variation showed that the variations were not significant whatever the initial fuel-layer thickness. Figure 5 also illustrates the variation of the fuel surface temperature with time in the pre-boilover stage. Contrary to the constant value reported by Petty [7] with crude oils combustion, an appreciable increase in temperature with time is observable here.

Discussion

Previous models of the combustion of a thin fuel layer on water have been formulated incorporating absorption and radiation in depth, in addition to conduction [5,6]. Here a simple one-dimensional steady-state conduction approach has been used to correlate our measurements. As shown below, such analysis is applicable only for the thickest initial fuel layer (more than approximately 8 mm). For thinner layers, a transient treatment is required to describe the results.

If heat transfer from the fuel surface to the liquid phase is assumed to be limited to conduction, and assuming a constant surface regression rate and that both the oil and water have approximately the same thermal diffusivity a, the following conduction equation can be used to predict the spacial temperature variation:

$$\frac{d^2T}{dx^2} = \frac{r}{a}\frac{dT}{dx} \tag{1}$$

where time has been replaced by x/r (where x is the depth from the oil surface and r the regression rate, assumed to be steady). With the boundary conditions that $x = 0$, $T = T_1$ and $x \to \infty$, $T = T_\infty$, solution of Eq. (1) gives the following for the temperature distribution in the liquid phase:

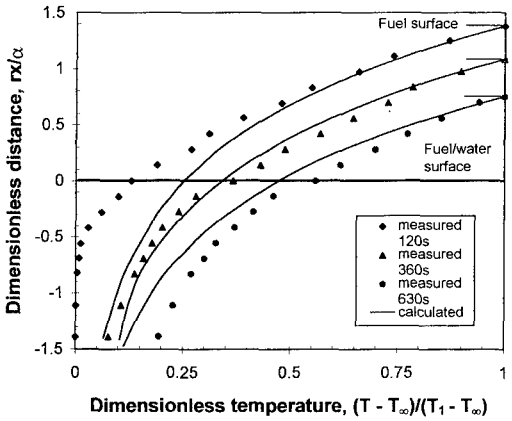

FIG. 6. Correlation of temperature data from measurements of Eq. (2) in terms of rx/a vs $(T - T_\infty)/(T_1 - T_\infty)$.

$$\frac{T - T_\infty}{T_1 - T_\infty} = \exp\left(-\frac{r}{a}x\right). \tag{2}$$

Note that the use of the above formulation gives a simple staggering of the profiles with time that results from the recession of the oil surface. A comparison with measurements obtained at three different time periods during pre-boilover stage is presented in Fig. 6. The agreement appears satisfactory (particularly as the time after the start of the test increases) and shows that a simple treatment, based only on conduction in the fuel layer and steady surface regression, is realistic and may be used to predict the time required to reach boilover.

An interesting result is that boilover appears to occur in all cases when the temperature at the oil/water interface reaches a value of approximately 150 °C. The above-described experimental observation that there is a rapid transition from normal pool burning to disruptive burning, together with the observation that this transition occurs at an approximately fixed temperature that is well above the saturation temperature of the water, indicates that the phenomena may be caused by the boiling nucleation of the water at the water/oil interface.

It is well known [12] that a liquid that is not in contact with a gas phase can be superheated, at constant pressure, to temperatures that are well above the liquid saturation temperature. Under these conditions, bubble nucleation will occur within the liquid at a fixed temperature, called the "limit of superheat." Boiling nucleation can occur at the interior of a liquid (homogeneous nucleation), or at an interface between two liquids of different volatility, or between a liquid and a smooth solid surface (heterogeneous nucleation). Heterogeneous nucleation generally has a lower limit of superheat than homogeneous nucleation. Also, if there are impurities in the liquid, such as solid particulate, the particulate can act as nucleation sites (heterogeneous nucleation) and lower the limit of superheat to values that can be close to the liquid saturation temperature. At the interface between two liquids, one with higher saturation temperature (host liquid) than the other, once nucleate boiling is initiated in the one that is superheated, boiling will occur explosively with an intensity that depends primarily on the surface tensions of the two liquids, the difference between the boiling point of the less volatile liquid and the limit of superheat of the more volatile, and the ambient pressure, among other factors.

Not many studies have been conducted of the bubble nucleation in a water/hydrocarbon interface. Lasheras et al. [13] and Wang and Law [14] observed the explosive burning of droplets of water in hydrocarbon paraffin emulsions and concluded that microexplosions occur if the boiling point of the hydrocarbon is larger than the limit of superheat of the water. This occurs for paraffins with carbon number larger than 14 (tetradecane).

In the present experiments, the fuel (heating oil) has boiling points ranging from 250 °C to 350 °C. As is seen from the results of Fig. 5, the oil temperature at the oil/air interface reaches fairly soon a value close to 350 °C. Thus, heat is transferred from the surface to the liquid interior, causing the temperature at the oil/liquid interface, and at the water interior, to increase to values well above the water saturation temperature at the corresponding pressure (approximately 100 °C); i.e., the water becomes superheated. Under these conditions, bubbles in the superheated water could nucleate, most likely heterogeneously at the oil/water interface, and grow explosively. The violent eruption of the water bubbles will cause the breakup, and possibly the atomization, of the oil layer above, projecting the oil outward. The projected oil burns with the ambient air, increasing the flame extension and, if the explosive nucleation is sufficiently strong, generating a flame-ball–type burning.

The evolution of the oil/water interface temperature with time is shown in Fig. 7, for different initial thicknesses of the oil layer. It is seen that the onset of boilover occurs at an oil/water interface average temperature of approximately 150 °C. Although this temperature is difficult to measure accurately because of liquid motion and, sometimes, foaming at the interface, it appears that the value increases slightly as the oil-layer thickness increases. As described above, it is suggested that the event is caused by the onset of boiling nucleation at the oil/water interface. Also consistent with this process is the observed rapid drop in temperature at the interface, which is due to the liquid motion at the vicinity of the nucleation site, and the rapid exchange of liquid as colder water fills the void left by the water bubbles as they leave the site, or explode. The water temperature at which boilover occurs is lower than that

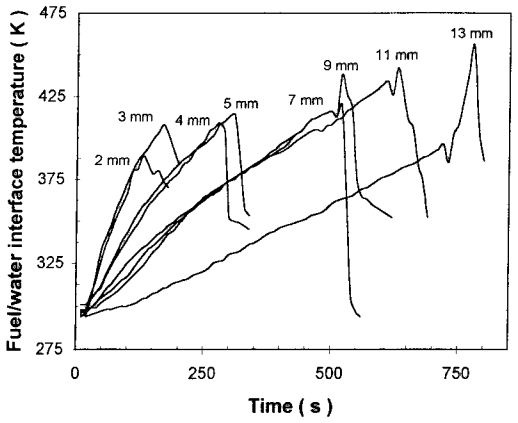

FIG. 7. Fuel/water interface temperature as a function of time for different initial fuel-layer thicknesses.

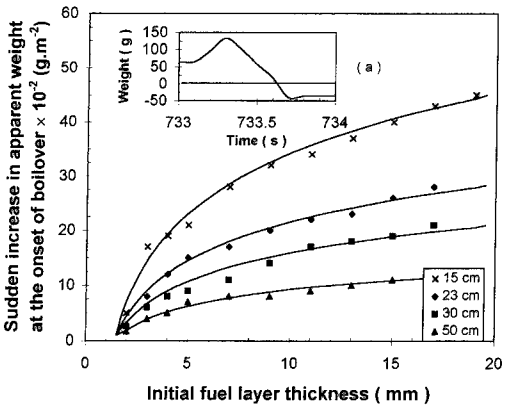

FIG. 8. Apparent increase in pressure at the onset of boilover as a function of initial fuel-layer thickness for different pool diameters. An example of trace recorded by the load cell submitted to this sudden increase is also shown [detail (a)].

measured as the limit of superheat of droplets water/paraffin emulsions (of the order of 250 °C [13]). Although the value of 150 °C could be the actual limit of superheat for water in the oil used in the experiments, it is most likely that the low value indicates that the nucleation is of the heterogeneous type in these experiments, and probably is suppressed somewhat by impurities in the fuel.

The sudden increase in liquid weight observed at the onset of boilover [weight at boilover minus weight before boilover, as shown in Fig. 8, detail (a)] gives further information about the events taking place during this onset. This apparent change of weight may be transformed into change of pressure (Fig. 8). This pressure shock is due to the sudden expansion of water vapor at the nucleation site. The effect is naturally bigger the higher the internal pressure. The effect of pool diameter on the weight increase, and, for that matter, on the intensity of the fire after boilover, is probably due to surface tension effects at the oil surface (oil/air interface). This surface tension will tend to deter the growth of the bubbles underneath, and the subsequent breakup of the oil layer. The smaller the pan diameter, the stronger will be the oil surface tension effect because of the capillary forces at the contact between the oil and the pan edge.

With the hypothesis that boilover will occur when the temperature at the water/oil interface reaches the water nucleation temperature, Eq. (2) can be used to predict the time required to reach boilover by simply setting the temperature equal to the water nucleation temperature, $T = T_n$ (150 °C in this case), and $x = h - r \cdot t_b$, where h is the initial oil-layer thickness, r the surface regression rate, and t_b the time to boilover. The predictions of the analysis agree well (approximately 10%) with the experimental observations for oil-layer thicknesses greater than 8 mm, where the steady-state model applies best.

Conclusion

The present study of the combustion of a fuel spilled on water emphasizes the importance of heat transfer in the direction normal to the fuel and sublayer surfaces. It is shown that the fuel-layer thickness is an important factor in regard to the surface-layer energy balance, the combustion of the fuel, and the possible onset of boilover.

The results show that, at least within the limits of the investigated sizes, the combustion efficiency appears to be independent of the pan diameter and of the initial fuel-layer thickness for layers thicker than 10 mm. It is also observed that the time to the start of boilover corresponds to the time to reach an approximately fixed temperature at the fuel/water interface. This result is particularly verified by the experiments, provided that the burning rate becomes well established.

The characteristics of the boilover intensity lead to consideration of the fundamental aspects that cause this phenomenon to occur. The observations that the transition to boilover is fast and has a violent explosive character, together with the observation that the water temperature reaches approximately 150 °C, well above its saturation temperature, suggest that the event is due to the onset of boiling nucleation in the superheated water at the fuel/water interface. However, the sudden growth and expansion of the water bubbles at the nucleation sites seem to depend greatly on the surface tension forces.

Acknowledgments

The authors express their thanks to the Centre de Documentation de Recherche et d'Expérimentations sur les Pollutions Accidentelles des Eaux, Brest, France, for its interest and help in this study.

REFERENCES

1. Hall, H., *Mech. Eng.* 47(7):540–544 (1925).
2. Burgoyne, J. H., and Katan, L. L., *J. Instit. Pet.* 33:158–191 (1947).
3. Hasegawa, K., *Fire Safety Science—Proceedings of the Second International Symposium*, Hemisphere, New York, 1989, pp. 221–230.
4. Twardus, E. M., and Brzustowski, T. A., *Arch. Combust.* 1:49–60 (1981).
5. Brzustowski, T. A., and Twardus, E. M., *Nineteenth Symposium (International) on Combustion*, The Combustion Institute, Pittsburgh, 1982, pp. 847–854.
6. Alramadhan, M. A., Arpaci, V. S., and Selamet, A., *Combust. Sci. Technol.* 72:233–253 (1990).
7. Petty, S. E., *Fire Safety J.* 5:123–134 (1982).
8. Koseki, H., and Mulholland, G. W., *Fire Technol.* 27(1):54–65 (1991).
9. Koseki, H., Kokkala, M., and Mulholland, G. W., *Fire Safety Science—Proceedings of the Third International Symposium*, Elsevier, London and New York, 1991, pp. 865–874.
10. Arai, M., Saito, K., and Altenkirch, R., *Combust. Sci. Technol.* 71:25–40 (1990).
11. Babrauskas, V., and Grayson, S. J., *Heat Release in Fires*, Elsevier Science Publishers Ltd., London and New York, 1992, pp. 201–206.
12. Blander, M., and Katz, J. L., *AIChE J.* 21(5):834–848 (1975).
13. Lasheras, J. C., Fernandez-Pello, A. C., and Dryer, F. L., *Combust. Sci. Technol.* 21:1–14 (1979).
14. Wang, C. H., and Law, C. K., *Combust. Flame* 59:53–62 (1985).

COMMENTS

R. B. Williamson, University of California at Berkeley, USA. The term "boilover" has usually been applied to a fire scenario in which an open top tank containing burning crude oil, after a long period of quiescent burning, shows a sudden increase in fire intensity associated with the expulsion of burning oil from the tank [1]. It is generally thought that boilover occurs when the residues from the surface burning become denser than the unburned oil and sink below the surface to form a hot layer that progresses downward much faster than the regression rate of the liquid surface. When this isothermal hot layer, or "hot zone," reaches a layer of water or water-in-oil emulsion that almost always exists in crude oil tanks, the water first is superheated and subsequently boils almost explosively, overflowing the tank. Oils subject to this form of boilover are thought to have a wide range of boiling points so that a viscous residue forms after some of the lighter components have burned off, and this allows the formation of the hot zone. Recently, the term boilover has also been applied to the burning of thin layers of oil on the surface of water in order to limit the spread of oil after leakage of oil from a tanker or other spill accident [2]. The research in this paper focuses on the second fire scenario, and it provides useful information for future research. Is there any indication of the formation of a hot zone before the boilover occurs?

REFERENCES

1. Henry, M., and Klem, T., "Scores Die in Tank Fire Boilover," *Fire Service Today*, June 1983, pp. 11–13.
2. Koseki, H., Kokkala, M., and Mulholland, G. W., "Experimental Study of Boilover in Crude Oil Fires," *Fire Safety Science—Proceedings of the Third International Symposium*, 1991, pp. 865–875.

Author's Reply. No, we have not observed any indication of the formation of a hot zone, either visually or through the temperature measurements as shown in the paper. This is due to the nature of the fuel used (narrow range of boiling points) and the small thickness of the fuel layer. Hot zone boilover is normally observed with fuel having a large range of volatilities and large depth, as in crude oil tanks, as you indicate in your comments.

•

Richard G. Gann, NIST/BFRL, USA. In looking at the data here, it appears that the study needs to be extended to larger pan sizes if the real situation is to be well replicated. In Fig. 1, the regression rate is continuing to rise, and in Fig. 2, the time for boilover is still falling as a function of diameter. In addition, Fig. 4 shows the boilover intensity rapidly falling toward 1 at $d \sim 0.5$ m. This is in conflict with the observations by Koseki, Kokkala, and Mulholland (*Third International Symposium on Fire Safety Science*, Elsevier, London, 1991), of vigorous enhancement from 0.3–2.7 m diameters, with crude oil as the fuel. Would you also please comment on how you became assured that the thermocouples were not affecting the boilover behavior?

Author's Reply. We do not think that extending the pan size to larger sizes will change the nature of our results since the present observations are more vigorous at the

smaller sizes. Concerning the observation of Ruchi and Mulholland, at the deadline to reply to this comment, we have not been able to obtain a copy of the work; thus we cannot comment on it. Although the discrepancy in the observations may be due to the difference in fuels (crude oil has a wide range of volatilities vs our fuel, which has a narrow range), we should point out that our observation that the boilover intensity decreases with the diameter is in agreement with observations of Koseki et al. [9].

Regarding the effect of the thermocouples on the boilover behavior, we have made the same observations with and without thermocouples.

Twenty-Fifth Symposium (International) on Combustion/The Combustion Institute, 1994/pp. 1489–1496

EXPERIMENTAL AND COMPUTATIONAL STUDY OF THE EFFECT OF C_2F_6 ON PREMIXED METHANE FLAMES

OUMAR SANOGO, JEAN-LOUIS DELFAU, ROBERT AKRICH AND CHRISTIAN VOVELLE
Laboratoire de Combustion et Systèmes Réactifs
CNRS and Orléans University
1C Avenue de la recherche Scientifique
45071 Orléans Cedex 2, France

The objective of this work was to specify the mechanism of flame inhibition by compounds that do not contain bromine. Mole fraction profiles have been measured by molecular beam-mass spectrometer technique in a stoichiometric $CH_4/O_2/Ar$ low-pressure flame seeded with and without 1% hexafluoroethane (C_2F_6). For both flames, stable and reactive species concentrations have been computed and compared with experimental results in order to validate a detailed mechanism. Extension of the mechanism to atmospheric pressure was carried out by substituting the rate constant of a few reactions by high-pressure values. Mole fraction profiles computed in 1-atm-pressure stoichiometric methane-air flame were in very good agreement with Bechtel's experimental results. Thus validated, the mechanism was used to compute the reduction in flame velocity that results from the addition of increasing amounts of the inhibitor to a methane-oxygen-nitrogen flame. Calculated flame velocities are in very close agreement with experimental values obtained with a premixed flame stabilized on an open tubular burner. This shows that inhibition efficiency of fluorinated compounds can be predicted very accurately.

Introduction

There is a need for new inhibitors that maintain the positive properties of CF_3Br but exhibit null or negligible ozone depletion potential (ODP). One way to reach this objective is to remove bromine from the inhibitors, since this element is responsible for the high ODP.

Derivation of an inhibition index from velocity measurements of flames seeded with compounds containing CF_3 has shown that this radical contributes 25% to the overall efficiency of CF_3Br [1]. Hence, it can be expected that an increase in the number of CF_3 groups contained in a given molecule will increase its inhibition efficiency up to an acceptable value for fire prevention. This assumption is supported by measurements of critical agent concentration required to extinguish a liquid fuel diffusion flame (cup burner test) that lead to values respectively equal to 7.9% and 6.1% for C_2F_6 and C_3F_8 [2]. These values have to be compared with 3.1% for CF_3Br. To a large extent, experimental and computational studies on inhibition mechanisms have focused on bromine and chlorine derivatives [3,4]. Mass spectrometric measurements of species concentration in a stoichiometric methane flame seeded with CF_3Br performed by Biordi et al. [5] give some data on intermediate species formed from the CF_3 group. However, the inhibition effect of this group is hindered by the strong influence exerted by bromine. Some of the consequences of CF_3 addition to a flame can be assessed from the results of Vandooren et al. [6] on the structure of a $CO/H_2/O_2/Ar$ flame seeded with CF_3H, but these results do not refer directly to an hydrocarbon flame.

In this paper, we present results of an experimental study on the structure of a stoichiometric $CH_4/O_2/Ar$ low-pressure flame seeded with and without 1% (molar ratio) hexafluoroethane (C_2F_6). This fluorinated additive is a good representative of CF_3 donor compounds, and it is expected that conclusions drawn in this work can be extended to other CF_3 donors. Mole fraction profiles have been computed as well, and comparison of simulated against experimental profiles was used to validate a detailed mechanism. An atmospheric-pressure version of the mechanism was derived by computing high-pressure values for the kinetic parameters of a few reactions. These changes did not affect reactions involving fluorinated species, so that validation of the atmospheric-pressure mechanism was carried out by comparison of mole fraction profiles computed in a methane-air flame against the experimental results of Bechtel et al. [7]. At the end, and since one main criterion to test an inhibitor is the reduction of flame velocity, a comparative study of measurements and simulation of the effect of C_2F_6 addition on the velocity of a stoichiometric $CH_4/O_2/N_2$ flame stabilized on a tubular burner has been performed.

Experimental

Flame Structure Studies:

Flames were stabilized on a water-cooled flat-flame burner enclosed in a low-pressure chamber. The matrix was made of a brass disc drilled with 1-mm-diameter holes on a 9.0-cm-diameter circular area.

Two premixed flat flames have been stabilized at 4.2 kPa with initial molar composition as follows: flame I: CH_4 (17.0%), O_2 (34.0%), Ar (49.0%); flame II: CH_4 (16.8%), O_2 (33.6%), Ar (48.6%), C_2F_6 (1.0%). For both flames, the unburned gases velocity (at 298 K and 4.2 kPa) was equal to 53.7 cm/s. The burner can be moved vertically, and the flat flames were sampled along the symmetry axis with a quartz cone (aperture diameter 0.1 mm, angle 60°). Sudden expansion across the cone orifice created a supersonic jet that preserves atoms and radicals. After selection of its central part by a skimmer and modulation by a chopper wheel, the jet entered the ionization source of a mass spectrometer. Signal from the mass spectrometer was corrected for residual gas and isotopic contributions and converted into mole fractions by using calibration factors. These factors resulted from direct measurements of mixtures of known composition for stable species and from calculation of ionization cross sections for atoms and radicals. H, O, and OH have been calibrated by assuming partial equilibrium for some reactions of the H_2/O_2 system in the postcombustion region.

Temperature profiles were measured with fine (wire diameter 0.05 mm) Pt-Pt 10% Rh thermocouples coated by a ceramic deposit to prevent catalytic recombination. Heat losses by radiation were eliminated by using the electrical compensation technique. To take account of flame perturbation by the quartz cone, temperature profile measurements were repeated for several distances between the thermocouple bead and the cone tip. A "perturbed-flame" temperature profile was derived from the set of curves thus obtained. This profile reproduces the progressive change from a temperature markedly affected by the cone when samples are withdrawn close to the burner surface up to a temperature that is only slightly perturbed when the cone is far from the burner.

Flame Velocity Measurements:

A conical flame was stabilized at atmospheric pressure at the exit of an open tubular burner (diameter 1.4 cm). Volumetric flow rates for the reference flame were as follows: CH_4: 16.3; O_2: 32.6; N_2: 122.0 cm^3/s. The flame velocity was expressed as the ratio of overall volumetric flow rate to flame area. The latter was derived from photographs of the flame front.

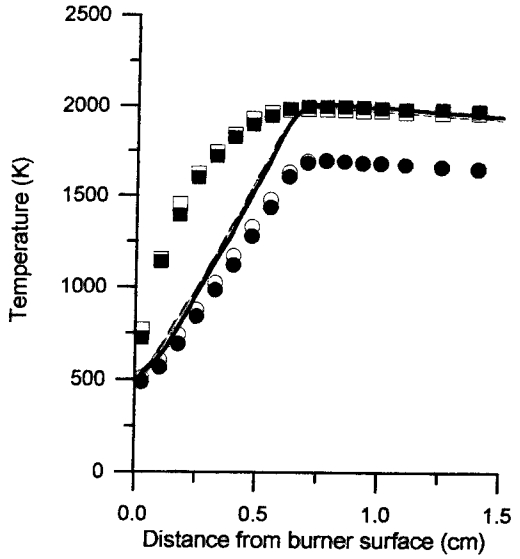

FIG. 1. Temperature profiles in flames I and II (P = 4.2 kPa). (○, ●): T1 thermocouple bead located 0.2 mm under the cone tip; (□, ■): T2 thermocouple bead located 20 mm under the cone tip (open symbol = uninhibited flame; filled symbol = inhibited flame); curves: computed perturbed profiles (---- = uninhibited flame; ——— = inhibited flame).

Modelling

The computation code developed by Warnátz [8] was used for the simulation of the structure of the low-pressure premixed flat flames. Species concentrations were computed with the perturbed-flame temperature profile taken as input data in the code. It has been shown earlier [9] that this procedure most accurately describes the flame in the computation. The free-flame option of the code was used to compute flame velocity of the atmospheric-pressure flames.

Thermodynamic data needed to compute the kinetic parameters of the backward reactions were taken from Kee et al. [10] or JANAF tables [11].

Results and Discussion

Flame Structure of Low-Pressure Flames:

Figure 1 shows that the additive concentration used in this work (1%) is low enough to avoid any change in the temperature profile, so that differences observed between flames I and II can be attributed to chemical effects. Two sets of data points corresponding respectively to measurements performed with the thermocouple located 0.2 (T_1) and 20 mm (T_2) under the cone tip have been plotted on this

TABLE 1
Detailed mechanism for the combustion of methane at 4.2 kPa (units: kJ, mol cm³ s)[a]

No.	Reaction	A	n	E	Ref.
62	$C_2HO + O_2 \rightarrow CO + CO + OH$	$1.46\ 10^{12}$	0.0	10.46	20
119	$CH_4 \rightarrow CH_3 + H$	$1.88\ 10^{20}$	−2.75	403.9	15
120	$CH_2O + H \rightarrow O + CH_3$	$9.25\ 10^{14}$	0.0	291.4	15
121	$C_2H_6 \rightarrow CH_3 + CH_3$	$1.1\ 10^{60}$	−13.6	429.54	16
122	$CHO + H_2 \rightarrow H + CH_2O$	$2.0\ 10^{12}$	0.0	78.1	15
123	$CHO + H_2O \rightarrow OH + CH_2O$	$1.03\ 10^{13}$	0.0	129.0	15
124	$H_2 + C_2H_3 \rightarrow H + C_2H_4$	$9.6\ 10^{12}$	0.0	32.6	15
125	$C_2H_2O + H \rightarrow OH + C_2H_2$	$3.09\ 10^{33}$	−6.75	117.9	15
126	$O_2 + CH_3 = CH_2O + H + O$	$3.0\ 10^{13}$	0.0	120.08	15
128	$O_2 + CH_3 = CH_2O + OH$	$3.31\ 10^{11}$	0.0	37.24	16
130	$OH + CH_3 = CH_2O + H_2$	$8.0\ 10^{12}$	0.0	0.0	17
132	$OH + CH_3 = CH_2O + H + H$	$4.56\ 10^{14}$	0.0	64.8	17
134	$OH + CH_3 = CH_2 + H_2O$	$1.5\ 10^{13}$	0.0	20.93	17
136	$H + CH_3 = CH_2 + H_2$	$1.8\ 10^{14}$	0.0	62.9	15
138	$CH_3 + CH_2O = CHO + CH_4$	$5.54\ 10^{13}$	2.8	24.53	16
140	$CH_2 + CH_2 = C_2H_2 + H_2$	$3.20\ 10^{13}$	0.0	0.0	13
142	$O + C_2H_3 = C_2H_2O + H$	$3.0\ 10^{13}$	0.0	0.0	13
144	$O_2 + C_2H_3 \rightarrow CH_2O + CHO$	$5.4\ 10^{12}$	0.0	0.0	16
145	$C_2HO + OH \rightarrow CHO + CO + H$	$1.0\ 10^{14}$	0.0	0.0	15

[a]Reactions added to Warnatz's [12] mechanism.

figure. The curves represent the perturbed-flame temperature profile and have been derived from T_1 and T_2 values by assuming that cooling by the quartz cone is proportional to the local temperature:

$$T_{per}(z) - 300 = [T_1(z) - 300] \times R$$

with $R = (T_2 - 300)/(T_1 - 300)$ computed at the position corresponding to the maximum T_2 value.

Species detected and analyzed in flame I include CH_4, O_2, Ar, H_2O, CO_2, CO, H_2, C_2H_4, C_2H_2, CH_2O, CH_3, CHO, H, OH, O, and HO_2, and besides these, C_2F_6, HF, CF_2O, CF_2CH_2, CF_2, and CF_3 in flame II. Mole fraction profiles for the former group were computed with a detailed mechanism that we validated recently for a rich acetylene flame [9]. This mechanism is primarily based on the set of reactions proposed by Warnatz [12] to model combustion of alkanes. Reactions 1 through 75 of Ref. 12 were used here, with Reactions 9 through 15, 27, 29 through 40, 43 through 46, 48, 49, 52, 53, 55, 56, 59, 61, 63 through 70, 72, 73, and 75 taken as reversible and Reaction 62 neglected. These changes correspond to an initial version of the mechanism [13] and introduce 43 reverse reactions that are numbered 76 through 118. The mechanism was supplemented by Reactions 62 and 119 through 145, listed in Table 1, while Table 2 mentions the reactions that have been used with new values of the kinetic data.

Part of the mechanism proposed by Westbrook [21] to predict flame inhibition by CF_3Br has been used to compute the mole fraction profiles of the fluorinated species. Reactions B5 through B8, B18 through B20, B25 through B35, B37 through B50, and B52 of Ref. 21 account for the consumption of CF_3 radicals (66 reactions counting the forward and backward reactions as two reactions). They are numbered 146 through 211 in this work. Only one reaction was introduced to form CF_3 from C_2F_6, while 14 additional reactions (here again counting the forward and backward reactions as two reactions) shown in Table 3 were incorporated into the mechanism to improve the agreement with the experimental results. Changes in the kinetic data of six reactions also contributed to improvement of this agreement (Table 3). The overall mechanism involves 225 reactions (145 for methane and 80 for the fluorinated additive) and 32 species.

In Figs. 2 through 4, mole fraction profiles measured in both flames (uninhibited and inhibited) have been compared with the corresponding calculated profiles. Before the accuracy of the model is discussed, these results can be examined to identify the changes introduced by the inhibitor. Comparison of the experimental profiles reveals that the addition of C_2F_6 does not markedly affect the structure of the stoichiometric methane flame. However, slight changes are observed for some species: In the burned gases of the uninhibited flame, H_2O and H have higher mole fractions (respectively, 0.253 and 0.017) than in the inhibited flame (0.223 and 0.014), while

TABLE 2
Detailed mechanism for the combustion of methane at 4.2 kPa (units: kJ, mol cm^3 s)[a]

No.	Reaction	A	n	E	Ref.
5	$OH + H_2 \rightarrow H_2O + H$	$6.38\ 10^{6}$	2.0	12.39	14
6	$H_2O + H \rightarrow OH + H_2$	$6.20\ 10^{7}$	1.9	77.03	15
16	$CO + OH \rightarrow CO_2 + H$	$6.32\ 10^{6}$	1.5	−2.07	16
18	$H + CH_3 \rightarrow CH_4$	$5.11\ 10^{22}$	−3.58	3.67	16
25	$O + CH_3 \rightarrow CH_2O + H$	$8.40\ 10^{13}$	0.0	0.0	16
26	$H + CH_2O \rightarrow CHO + H_2$	$2.3\ 10^{10}$	1.05	13.67	16
34	$CHO + M \rightarrow CO + H + M$	$2.36\ 10^{17}$	−1.0	71.06	18
40	$O_2 + CH = CO + OH$	$4.0\ 10^{13}$	0.0	0.0	15
41	$CH_3 + CH_3 \rightarrow C_2H_6$	$1.51\ 10^{52}$	−12.3	50.32	16
42	$CH_3 + CH_3 \rightarrow C_2H_5 + H$	$3.0\ 10^{13}$	0.0	52.28	16
47	$C_2H_5 + H \rightarrow CH_3 + CH_3$	$3.6\ 10^{13}$	0.0	0.0	16
53	$OH + C_2H_4 = C_2H_3 + H_2O$	$2.05\ 10^{13}$	0.0	24.75	16
54	$H + C_2H_4 \rightarrow C_2H_3 + H_2$	$8.0\ 10^{13}$	0.0	42.7	15
57	$C_2H_3 \rightarrow C_2H_2 + H$	$9.98\ 10^{37}$	−8.53	190.5	16
58	$C_2H_2 + H \rightarrow C_2H_3$	$2.69\ 10^{14}$	−1.0	6.12	16
60	$OH + C_2H_2 \rightarrow C_2H_2O + H$	$1.0\ 10^{32}$	−6.9	23.6	15
64	$H + C_2H_2O = CH_3 + CO$	$1.4\ 10^{13}$	0.0	12.5	15
66	$OH + C_2H_2O = CH_2O + CHO$	$7.0\ 10^{13}$	0.0	0.0	15
68	$C_2H_2 + O = C_2HO + H$	$8.0\ 10^{14}$	0.0	50.7	15
69	$H + C_2HO = CH_2 + CO$	$1.4\ 10^{14}$	0.0	0.0	19
70	$O + C_2HO = CO + CO + H$	$1.0\ 10^{14}$	0.0	0.0	19
71	$H + C_2H_2 \rightarrow H_2 + C_2H$	$5.0\ 10^{12}$	0.0	39.72	15
72	$OH + C_2H_2 \rightarrow H_2O + C_2H$	$2.5\ 10^{13}$	0.0	29.3	15
74	$H_2 + C_2H \rightarrow H + C_2H_2$	$3.70\ 10^{13}$	0.0	12.10	15
75	$C_2H + O_2 \rightarrow CO + CO + H$	$3.0\ 10^{14}$	0.0	6.3	15

[a]Changes in the kinetic data with respect to Warnatz's [12] mechanism.

TABLE 3
Detailed mechanism for the consumption of C_2F_6 (units: kJ, mol cm^3 s)[a]

No.	Reaction	A	n	E	Ref.
212	$F + HO_2 = HF + O_2$	$5.0\ 10^{13}$	0.0	0.0	26
214	$FO + FO = F + F + O_2$	$1.26\ 10^{13}$	0.0	0.0	27
216	$FO + FO \rightarrow F_2 + O_2$	$1.0\ 10^{12}$	0.0	0.0	27
217	$FO + O = O_2 + F$	$3.0\ 10^{13}$	0.0	0.0	28
219	$CF + OH = FCO + H$	$1.0\ 10^{13}$	0.0	0.0	[b]
221	$CF + H \rightarrow CH + F$	$3.7\ 10^{13}$	0.0	78.9	29
222	$CF + O_2 = FCO + O$	$1.0\ 10^{13}$	0.0	0.0	[b]
224	$CF_3 + CF_3 \rightarrow C_2F_6$	$7.08\ 10^{41}$	−9.06	40.56	[b]
225	$C_2F_6 \rightarrow CF_3 + CF_3$	$5.94\ 10^{45}$	−9.40	420.0	[b]
B25	$CF_3 + H = CF_2 + HF$	$5.5\ 10^{13}$	0.0	0.0	22
B41	$CF_2O + O = FCO + FO$	$5.0\ 10^{12}$	0.0	320.8	[b]
B42	$CF_2O + OH = CO_2 + HF + F$	$7.9\ 10^{11}$	0.0	0.0	[b]
B43	$CF_2 + H = CF + HF$	$2.0\ 10^{13}$	0.0	0.0	23
B45	$CF_2 + OH = CF_2O + H$	$5.0\ 10^{12}$	0.0	0.0	24
B39	$CF_2CH_2 + O = CH_2O + CF_2$	$1.51\ 10^{13}$	0.0	0.0	25

[a]212-225 Reactions added to Westbrook's [21] mechanism; B25-B39 changes in the kinetic data with respect to Westbrook's [21] mechanism.

[b]Kinetic data estimated in this work.

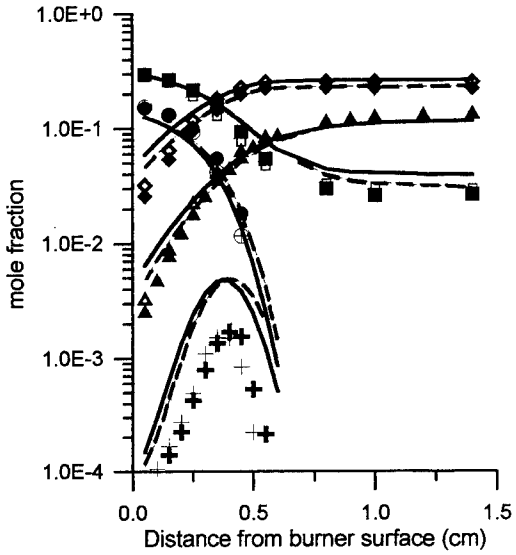

FIG. 2. Comparison of computed (curves) and measured (points) mole fraction profiles in flames I and II (P = 4.2 kPa). (○, ●): CH_4; (□, ■): O_2; (◇, ◆): H_2O; (△, ▲): CO_2; (+, +): CH_3 (open symbol, ——— = uninhibited flame; filled symbol, ---- = inhibited flame).

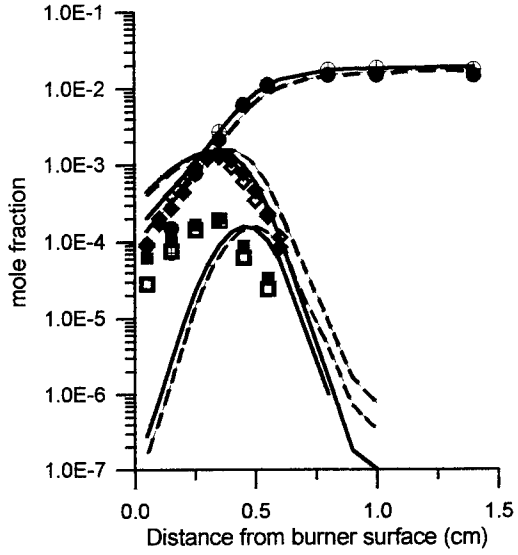

FIG. 4. Comparison of computed (curves) and measured (points) mole fraction profiles in flames I and II (P = 4.2 kPa). (○, ●): H; (□, ■): HCO; (◇, ◆): C_2H_4 (open symbol, ——— = uninhibited flame; filled symbol, ---- = inhibited flame).

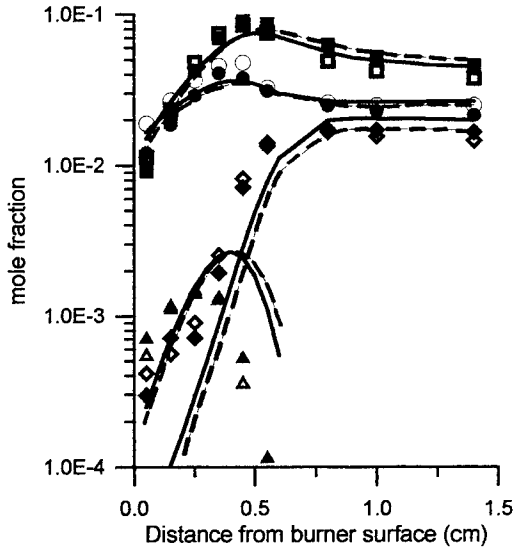

FIG. 3. Comparison of computed (curves) and measured (points) mole fraction profiles in flames I and II (P = 4.2 kPa). (○, ●): H_2; (□, ■): CO; (◇, ◆): OH; (△, ▲): CH_2O (open symbol, ——— = uninhibited flame; filled symbol, ---- = inhibited flame).

CO and OH exhibit an opposite variation (0.037 and 0.014 in flame I; 0.045 and 0.016 in flame II).

For most species, predictions of the model are in close agreement with the measured profiles, and it is especially interesting to note that changes in H_2O, H, and CO concentrations with C_2F_6 addition are well reproduced by the model (mole fractions are respectively 0.262, 0.019, and 0.045 in flame I; 0.231, 0.017, and 0.050 in flame II). Only two discrepancies between computed and experimental profiles have been observed. The first one concerns OH, for which the concentration in the postcombustion zone is predicted to decrease, in contradiction with the experimental result. The second one is related to CH_3, which is overpredicted by the model in both flames. Addition of consumption reactions for this radical (Table 1) was ineffective in improving the agreement with the experimental results. Analyses of the CH_3 radical were carried out with an electron energy adjusted at 12 eV, only 2.2 eV above the ionization potential. Use of so low a value was necessary to avoid methane fragmentation in the ionization source of the mass spectrometer, but it reduces the accuracy of the analyses. Additional measurements of CH_3 concentration were performed, but they all confirmed the results of the previous determinations. To complement this discussion on CH_3, it should be noted that overprediction by a model has been reported as well by Hennessy et al. [30].

Figure 5 compares measured and computed mole fraction profiles for the fluorinated species. A very

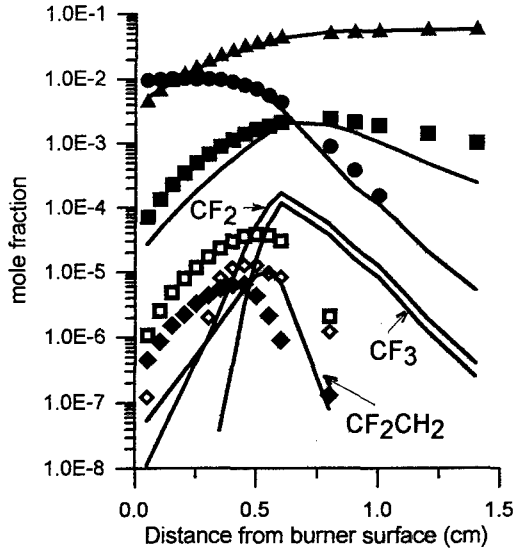

FIG. 5. Comparison of computed (curves) and measured (points) mole fraction profiles in flame II (P = 4.2 kPa). (●): C_2F_6; (■): CF_2O; (◆): CF_2CH_2; (▲): HF; (□): CF_2; (◇): CF_3.

good agreement is obtained for the consumption of the inhibitor and the formation of the main products: HF, CF_2O, and CF_2CH_2. Large discrepancies are observed for CF_3 and CF_2, but here again, very low electron energies (respectively, 12.4 and 11.0 eV) had to be used to prevent fragmentations. However, for these radicals, the accuracy of the experiments is not necessarily the unique cause of the discrepancies and the viability of the kinetic mechanism can be questioned as well. So far, no experimental data are available in the literature on CF_3 concentrations in flames, so the prediction of the mole fraction of this species could not be validated.

Consumption of the inhibitor and formation of intermediate or final fluorinated species can be specified from the reaction rates computed by the model. Decomposition forming two CF_3 radicals (Reaction 225) is the only reaction that has been considered for the consumption of C_2F_6. Its rate constant has been computed from the equilibrium constant and a value calculated by applying Troe formalism [31] for the reverse reaction. It is likely that other reactions (attack by H, O, OH) should have been considered as well, but (1) there is a lack of kinetic data for these reactions, and (2) our interest was not in a detailed description of the very first step of the consumption of C_2F_6 but rather in checking the accuracy of an existing model for the next steps, starting with CF_3 consumption.

Reactions with H and O atoms dominate CF_3 consumption:

$$CF_3 + H = CF_2 + HF \qquad (B25)$$

$$CF_3 + O = CF_2O + F. \qquad (B26)$$

CF_2 consumption occurs by

$$CF_2 + H = CF + HF \qquad (B43)$$

and to a lesser extent by reactions with OH and O that form FCO. CF radicals react with O_2:

$$CF + O_2 = FCO + O. \qquad (222)$$

CF_2O and FCO are consumed by reactions with H and OH:

$$CF_2O + H = FCO + HF \qquad (B40)$$

$$CF_2O + OH = CO_2 + HF + F \qquad (B42)$$

$$FCO + H = CO + HF \qquad (B49)$$

$$FCO + OH = CO_2 + HF. \qquad (B52)$$

Fluorine atoms react with H_2 to form HF.

This mechanism predicts that fluorine and carbon initially present in the inhibitor are entirely converted into HF, CO, and CO_2. These reactions constitute a trap for the chain carriers of the methane combustion mechanism, H and OH. CF_3, CF_2, CF, and FCO are very active intermediates in this conversion, so these four species are in stationary state. This explains why predictions of C_2F_6 consumption and HF formation are in very good agreement with the experimental results in spite of large discrepancies for CF_3 and CF_2.

Extension of the Mechanism to Atmospheric Pressure:

The low-pressure mechanism was used for modelling at atmospheric pressure with only four changes concerning reactions that are in falloff. Troe formalism [31] was used to compute atmospheric values for the kinetic parameters of these reactions, and the results have been compared to the low-pressure values in Table 4. These changes affect only the methane combustion mechanism, so validation of the atmospheric-pressure mechanism was performed by comparison of computed mole fraction profiles against experimental results obtained by Bechtel [7] for a stoichiometric methane-air flame. Predictions of the model are in very good agreement with the experimental profiles for all species analyzed by Bechtel: CH_4, O_2, CO_2, H_2O, CO, H_2, OH. Of course, this comment does not apply to F chemistry that could not be validated at atmospheric pressure.

TABLE 4
Low- and high-pressure values of the kinetic data of reactions in falloff (units: kJ, mol cm³ s)

Reaction	4.2 kPa			101 kPa		
	A	n	E	A	n	E
$CH_3 + H = CH_4$	$5.1\ 10^{22}$	−3.6	3.7	$1.9\ 10^{36}$	−7.0	37.9
$CH_3 + CH_3 = C_2H_6$	$1.5\ 10^{52}$	−12.3	50.3	$1.7\ 10^{53}$	−12.0	81.3
$C_2H_3 = C_2H_2 + H$	$9.9\ 10^{37}$	−8.5	190.5	$1.6\ 10^{32}$	−5.5	193.3
$C_2H_2 + OH = C_2H_2O + H$	$1.0\ 10^{32}$	−6.9	23.6	$1.7\ 10^{34}$	−6.7	41.4

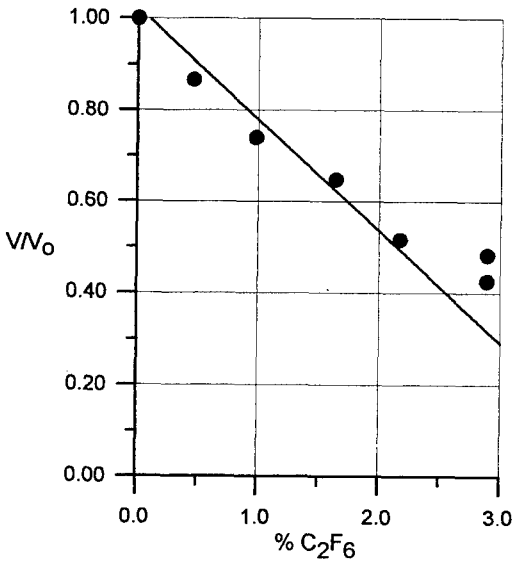

FIG. 6. Comparison of calculation (curve) and measurements (points) of the evolution of flame velocity with the initial concentration of inhibitor CH_4(9.5%)-O_2(19%)-N_2(71.5%) flame stabilized on a tubular burner (P = 101 kPa).

Effect of C_2F_6 on Flame Velocity:

The atmospheric-pressure version of the mechanism was used to calculate the velocity of flames seeded with increasing amounts of the inhibitor. For the uninhibited flame, the model predicts a velocity equal to 40.9 cm/s, in close agreement with the 40.2 cm/s measured by Egolfopoulos et al. [32].

Figure 6 compares the evolution, with the initial content of inhibitor, of the ratio V_{inh}/V_o computed by the model and measured in a flame stabilized on a tubular burner. A very good agreement is observed up to 2% C_2F_6. For higher values, measurements of the flame front area become less accurate, but it is also likely that the model should predict a decrease in the slope of the curve when the inhibitor concentration exceeds 3%. Sensitivity analysis shows that reactions with the highest influence on the flame velocity are as follows: $CF_3 + H = CF_2 + HF$ (B25); $CF_3 + O = CF_2O + F$ (B26); $CF_2O + H = FCO + HF$ (B40); $CF_2O + OH = CO_2 + HF + F$ (B42); and $CF_2 + OH = CF_2O + H$ (B45). [Sensitivities, expressed as $dLn(X_i)/dLn(k_r)$ are respectively −0.037, 0.034, −0.014, 0.013, and 0.012.] For reactions B25 and B26, kinetic data measured recently [23,33], confirm the values used in this work.

So far, we have considered inhibition by C_2F_6 as resulting from a change in the chemistry of the flame. However, physical effects could also contribute to a reduction in the flame velocity. We took advantage of the adiabaticity of the conical flame to measure the evolution of the maximum temperature with the inhibitor concentration. In the range 0–3%, no temperature changes were detected, and this result supports a chemical mechanism of flame inhibition.

Conclusion

A two-step procedure has been adopted to study flame inhibition by C_2F_6. A detailed mechanism was validated by comparison of computed mole fraction profiles against corresponding profiles measured in a low-pressure methane-oxygen-argon flame. Species analysis was carried out by molecular beam-mass spectrometry so that atoms and radicals were analyzed in addition to stable species. The confidence in the predictions of the model is reinforced by its ability to correctly predict mole fraction profiles of active species. Pathway analysis shows that CF_3 radicals formed by decomposition of the inhibitor are consumed by chain reactions with CF_2, CFO, and CF as intermediates. These reactions lead to the formation of stable species CO, CO_2, and HF and constitute a trap for H and OH. In a second step, the mechanism was extended to atmospheric pressure by substituting the kinetic data of four reactions by high-pressure values. This new version of the mechanism was validated by comparison of computed mole fraction profiles in a stoichiometric methane-air flame with Bechtel's experimental results. Thus validated, the mechanism was used to compute flame velocity of a methane-oxygen-nitrogen flame seeded with an increasing amount of the inhibitor. The evolution of

the flame velocity with the initial inhibitor concentration has been measured as well, and the predictions of the model are in very good agreement with the experimental results.

Acknowledgments

The authors are indebted to ATOCHEM and Commission of the European Communities, DG XII (Environment program) for financial support.

REFERENCES

1. Vandermeiren, M., Safieh, H. Y., and Van Tiggelen, P. J., 1st Specialist Meeting of the Combustion Institute, Bordeaux, France, 1981, p. 178.
2. Sheinson, R. S., Penner-Hahn, J. E., and Indritz, D., *Fire Safety J.* 15:437–450 (1989).
3. Wilson, W. E., Jr., O'Donovan, J. T., and Fristrom, R. M., *Twelfth Symposium (International) on Combustion*, The Combustion Institute, Pittsburgh, 1968, p. 829.
4. Day, M. J., Stamp, D. V., Thompson, K., and Dixon-Lewis, G., *Thirteenth Symposium (International) on Combustion*, The Combustion Institute, Pittsburgh, 1971, p. 705.
5. Biordi, J. C., Lazzara, C. P., and Papp, J. F., *J. Phys. Chem.* 81(12):1139 (1977).
6. Vandooren, J., Nelson da Cruz, F., and Van Tiggelen, P. J., *Twenty-Second Symposium (International) on Combustion*, The Combustion Institute, Pittsburgh, 1988, p. 1587.
7. Bechtel, J. H., Blint, R. J., Dasch, C. J., and Weinberger, D. A., *Combust. Flame* 42:197 (1981).
8. Warnatz, J., *Eighteenth Symposium (International) on Combustion*, The Combustion Institute, Pittsburgh, 1981, p. 369.
9. Bastin, E., Delfau, J. L., Reuillon, M., Vovelle, C., and Warnatz, J., *Twenty-Second Symposium (International) on Combustion*, The Combustion Institute, Pittsburgh, 1988, p. 313.
10. Kee, R. J., Rupley, F. M., and Miller, J. A., *The Chemkin Thermodynamic Data Base*, SAND87-8215, VC-4, SANDIA National Laboratory, Livermore, CA, 1988.
11. *JANAF Thermodynamic Tables* (D. R. Stull and H. Prophet, Eds.), U.S. Department of Commerce, Washington DC, 1971.
12. Warnatz, J., *Twenteenth Symposium (International) on Combustion*, The Combustion Institute, Pittsburgh, 1984, p. 845.
13. Warnatz, J., private communication.
14. Cohen, N., and Westberg, K. R., *J. Phys. Chem. Ref. Data* 12(3):531 1983.
15. Bastin, E., "Etude du Mécanisme de Formation des Précurseurs des Particules de Suie dans des Flammes $C_2H_2/O_2/Ar$," Doctoral Thesis, Université Pierre et Marie Curie, Paris, 1989.
16. Baulch, D. L., Cobas, C. J., Cox, R. A., Esser, C., Franck, P., Just, Th., Pilling, M. J., Walker, R.W., and Warnatz, J., "Evaluated Kinetic Data for Combustion Modelling," *J. Phys. Chem. Ref. Data* 21(2) (1992).
17. Paczko, G., Lefdal, F. T. and Peters, N., *Twenty-First Symposium (International) on Combustion*, The Combustion Institute, Pittsburgh, 1986, p. 739.
18. Timonen, R. S., Ratajezak, E., Gutman, D., and Wagner, A. F., *J. Phys. Chem.* 91:5325 (1987).
19. Vinckier, C., Shackers, M., and Peeters, J., *J. Phys. Chem.* 89:508 1985.
20. Miller, J. A., Mitchell., R. E., Smoke, M. D., and Kee, R. J., *Nineteenth Symposium (International) on Combustion*, The Combustion Institute, Pittsburgh, 1982, p. 181.
21. Westbrook, C. K. *Combust. Sci. Technol.* 34:201 1983.
22. Ryan, K. R., and Plumb, I. C., *Plasma Chem. Plasma Process.* 4:141 1978.
23. Tsai, C., and McFadden, D. L., *J. Phys. Chem.* 93:2471 (1989).
24. Biordi, J. C., Lazzara, C. P., and Papp, J. F., *J. Phys. Chem.* 82(2):125 (1978).
25. Westbrook, C. K., *Nineteenth Symposium (International) on Combustion*, The Combustion Institute, Pittsburgh, 1982, p. 127.
26. Walther, C. D., and Wagner, H. Gg., *Ber. Busenges. Phys. Chem.* 87:403 (1983).
27. Atkinson, R., Baulch, D. L., Cox, R. A., Hampson, R. F., Jr., Kerr, J. A., and Troe, J., *Evaluated Kinetic and Photochemical Data for Atmospheric Chemistry*, Supp. III, *J. Phys. Chem. Ref. Data* 18:881 (1989).
28. DeMore, W. B., Golden, D. M., Hampson, R. F., Howard, C. J., Kurylo, M. J., Molina, M. J., Ravishankara, A. R., and Sander, S. P., *Chemical Kinetics and Photochemical Data for Use in Stratospheric Modeling*, Evaluation Number 8 JPL Publication 87–41, 1, 1987.
29. Garret, B. C., and Truhlar, D. J., *J. Am. Chem. Soc.* 101:5207 (1979).
30. Hennessy, J., Robinson, C., and Smith, D. B., *Twenty-First Symposium (International) on Combustion*, The Combustion Institute, Pittsburgh, 1986, p. 761.
31. Troe, J., *Ber. Bunsenges. Phys. Chem.* 78:478 (1974).
32. Egolfopoulos, F. N., Cho, P., and Law, C. K., *Combust. Flame* 76:375 (1989).
33. Tsai, C., Belanger, S. M., Kim, J. T., Lord, J. R., and McFadden, D. L., *J. Phys. Chem.* 93:1916 (1989).

Twenty-Fifth Symposium (International) on Combustion/The Combustion Institute, 1994/pp. 1497–1503

SUPPRESSION OF HIGH-SPEED C_2H_4/AIR FLAMES WITH C_1-HALOCARBONS

GRZEGORZ GMURCZYK AND WILLIAM GROSSHANDLER
National Institute of Standards and Technology
Building and Fire Research Laboratory
Gaithersburg, MD 20899, USA

Experimental investigations of the effect of the presence of five C_1-halocarbons (CF_4, CHF_3, CF_3I, CHF_2Cl, and CF_3Br) on the suppression of premixed high-speed turbulent flames and quasi detonations have been carried out in a 7.5-m long, 50-mm diameter tube. Lean and stoichiometric C_2H_4/air mixtures in the absence of any halocarbon, initially at 100 kPa and 295 K, constitute the reference states. A primary objective of the work has been to determine the relative suppression efficiencies of different agents under highly dynamic situations, without the undue influence of either the ignition event or the mixing of the agent into the flame front. This was accomplished by generating a highly turbulent flame/quasi detonation in the driver section, which contained no suppressant, followed by measurements of the velocity and pressure ratio as the wave front entered the test section of the tube, which contained suppressant premixed with the same fuel/air combination. A turbulence generator in the form of a spiral obstruction was used in the tube to broaden the gas-dynamic conditions attainable by the flame. Flame and shock wave velocities up to 1300 m/s, pressure ratios across the shock fronts over 26:1, and shock wave/flame spacings of the order of 10 cm were measured with piezoelectric pressure transducers and fast photodiodes. The experimental facility was successfully employed to clearly discriminate among the dynamic characteristics of the five compounds, revealing behavior distinct from what was observed in companion studies using atmospheric nonpremixed flames. The suppression process is strongly influenced by the concentration of an agent, the structure and composition of an agent molecule, and the composition of the combustible mixture itself.

Introduction

A shock wave preceding a turbulent flame can occur in a combustible mixture that is confined in space when the mixture composition falls within an appropriate range. Obstructions in the flow can promote the intense mixing of the fresh reactants with the combustion products and can cause pressure waves to interact with the mixing region. Given enough distance, the flame may accelerate dramatically, reaching a supersonic regime of flow. Depending upon the geometric details, the wave can approach its theoretical Chapman–Jouguet velocity and accompanying high-pressure ratio. Even a slight variation in composition of the reactants near the limit of different combustion modes can cause a dramatic change in the wave velocity and destructive pressures to be attained.

An extensive literature describes the kinetics and dynamics of flame/shock wave systems formed within classical detonation tubes [e.g., 1–4]. Chapman and Wheeler [5] noted as far back as 1926 that a methane/air flame could be accelerated to a terminal velocity in a shorter distance within a circular tube by placing obstacles into the flow. Lee, et al. [6] built on this observation to study quasi detonations in hydrogen/air and hydrocarbon/air mixtures. A quasi detonation propagates more slowly than a true detonation as a result of pressure losses in the flow, but its structure is more complex than a true detonation, and the mechanism of its propagation is not fully understood. Although an obstructed flow is more difficult to analyze than the flow in a smooth-walled tube, the former arrangement was chosen for the current study because it more closely simulates a potentially damaging condition that could occur should fuel leak into a confined space aboard an aircraft in the presence of an ignition source. The desire to rapidly suppress a flame and the associated pressure buildup in such a situation is the primary motivation behind this study.

Halon 1301 (CF_3Br) has been used effectively onboard aircraft for a number of years to protect confined spaces called dry bays. However, new production of CF_3Br has ceased because of the deleterious role played by the bromine atom in stratospheric ozone destruction [7]. The work presented here is one part of a comprehensive research program focused on the search for alternatives to CF_3Br for protecting aircraft in flight [8,9].

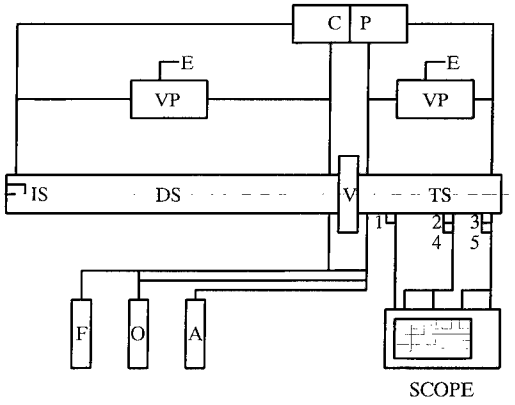

FIG. 1. Schematic of the deflagration/detonation tube facility. DS—driver section, TS—test section, V—vacuum gate valve, CP—dual circulating pump, VP—vacuum pump, E—exhaust, IS—ignition source, F—fuel, O—oxidizer, A—agent, 1—triggering transducer, 2,3—piezoelectric dynamic pressure transducers, 4,5—visible radiation fast photodiodes, SCOPE—collects two signals from pressure transducers plus two signals from photodiodes.

Experimental Facility and Operating Procedure

The effectiveness of a fire-fighting agent in suppressing a high-speed, premixed flame or quasi detonation can be rated by the extent to which it decelerates the propagating wave and simultaneously attenuates the hazardous shock that is always ahead of the flame. Because the fire extinguishant is unlikely to be released prior to the establishment of a turbulent flame, the traditional experiment in which the flame inhibitor is premixed with the fuel and air prior to ignition does not replicate the chemistry critical to the actual situation. Each dry bay on an aircraft has a different geometry, and the release of the agent once a fire is detected is highly variable. The complexities and biases associated with the fluid dynamics of release can be avoided by premixing the agent with the fuel and air in a portion of the tube distinct from where the flame is initiated.

A two-section, deflagration/detonation tube has been designed to produce the desired environment for both the flame initiation and flame suppression regimes. A repeatable, uninhibited turbulent flame is fully established in the driver section, which is based directly upon the design of Peraldi et al. [10]. The driver section, shown to the left in Fig. 1, is 5-m long and is equipped at the closed end with a spark plug. This section was filled with the combustible mixture only. The ignition energy is delivered in a microexplosion of a tin droplet short-circuiting the tips of nichrome electrodes connected to an 80-V power supply. Spiral-shaped obstructions made of 6.4-mm stainless steel rods with a pitch equal to the inner diameter of the tube were inserted into the tube to produce an area blockage ratio of 44%, close to the value shown by Lee et al. [6], to promote a quasi detonation in their facility.

The second section of the deflagration/detonation tube contains the gaseous agent along with the same fuel/air mixture used in the driver section. The diameter is the same, and its length is 2.5 m. An identical spiral insert was used to maintain a high level of mixing. The two sections are separated from each other by a 50-mm inner diameter, stainless steel, high-vacuum gate valve, which remains closed until just before ignition. Two pressure transducers and photodiodes are located 2.2 m beyond the gate valve and 0.3 m from the end of the tube. Their output was recorded on a multichannel, digital, storage oscilloscope.

The whole system was evacuated to 10^{-1} Pa before filling the two sections separately with the desired mixtures, which were attained through the method of partial pressures. The fuel/air ratio and total pressures were held constant across the gate valve. The oxidizer used in all experiments was breathing-grade air. Ethene (CP grade, 99.5% vol. purity) was chosen as the fuel because it has been demonstrated [10] that subsonic flames, quasi detonations, and full detonations all can be obtained in a tube of this geometry simply by varying the stoichiometry. After filling, the gases were homogenized independently using a double, spark-free circulating pump, recirculating the entire tube volume a total of 20 times. The mixtures were left for 5 min to become quiescent. About 10 s prior to ignition, the gate valve was opened manually.

After ignition, the flame propagates through the driver section and accelerates quickly because of the intense turbulence created by the interactions of the flow with the obstacles, generating a shock wave ahead of it. After passing through the open gate valve, the flame/shock system encounters the same combustible mixture and a certain amount of agent in the test section. A rendering of the flame/shock system passing through the gate valve is shown in Fig. 2. Depending on the concentration of the agent, the flame may or may not be extinguished and the pressure wave attenuated.

A protocol was chosen [9] that minimized the impact of any of these parameters and allowed flame/shock speeds to be obtained that were reproducible from run to run within ±2% (maximum deviation). Pressure ratios downstream of the shock wave exhibited a higher variability, ±20% (maximum deviation), because of the complex interactions between the spiral rod insert and the shock wave.

Experimental Results and Discussion

The experiments were conducted for equivalence ratios of 0.75 and 1.00, which correspond to com-

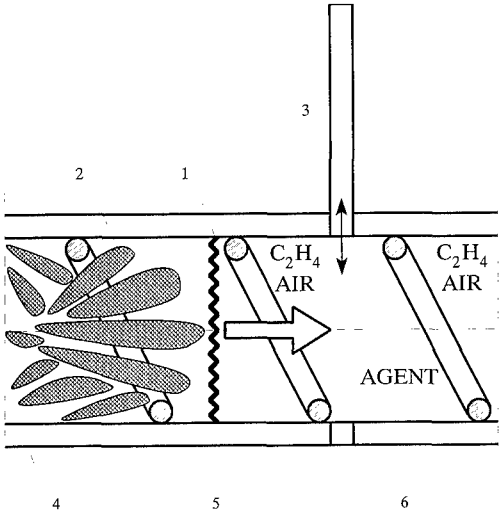

FIG. 2. Schematic of the flame/shock system propagation and suppression/attenuation processes. 1—shock wave, 2—turbulent flame, 3—gate valve, 4—driver section, 5—spiral obstruction, 6—test section.

positions by volume of 5.00 and 6.53% ethene, respectively, in the air plus ethene mixture. The initial reactant temperature was ambient (295 ± 3 K), and the initial total pressure was maintained constant at 100 ± 0.1 kPa.

Three dependent parameters were measured as a means to characterize the extent of flame suppression: Mach number, pressure ratio, and the distance separating the leading shock wave from the radiating flame. The Mach number was based upon the time it took for the pressure wave to travel the distance between the two pressure transducers, normalized by the sonic velocity of the reactant gases in the test section. The pressure ratio was evaluated from the average amplitude of the first pressure pulse to be recorded by each transducer, normalized by the initial pressure (100 kPa). In many cases, the first pressure pulse was less than the maximum measured. Consecutive pressure jumps occurred, possibly indicating that localized explosions in the mixing region between the spirals were present. (An individual experiment was concluded before the arrival of the shock wave reflected from the end plate.) The distance between the leading shock wave and the flame front was quantified by the time lag between the photodiode and pressure transducer response at the identical location.

Table 1 summarizes the results with no suppressant in the test section, and compares the Mach number, pressure ratio, and flame spacing to the situation in a "fully suppressed" flame, in which pure nitrogen was located in the test section. Note that neither the Mach number nor pressure ratio goes to zero for the fully suppressed case because total dissipation of the shock wave would require a substantially longer tube. On the other hand, the flame radiation disappears entirely; hence, the infinite separation distance.

The chemical compounds investigated in this study all contain a single carbon atom covalently bonded to four atoms chosen among fluorine, chlorine, bromine, iodine, and hydrogen. Despite some similarities in structure, the behavior of each chemical as it interacted with the shock wave and flame front was distinct.

Tetrafluoromethane, CF_4:

The distance between the shock wave and flame front increases by more than an order of magnitude with as little as 2% (partial pressure) of CF_4 added to the test section. Figure 3 shows that the separation distance reaches a plateau at 60 mm for the stoichiometric flame. Decreasing the equivalence ratio to 0.75 increases this distance to 80 mm.

The shock Mach number is plotted in Fig. 4 for all five compounds under lean conditions. A 2% partial pressure of CF_4, plotted as ▼, reduces the Mach number from 3.4 to 2.4. Additional tetrafluoromethane further reduces the speed of the shock, until at 12%, the shock has been decelerated to about 1.4. When the fuel/air mixture is stoichiometric, the same behavior is observed; however, the value of the Mach number is uniformly higher over the range of partial pressures examined.

The shock pressure ratio is affected by CF_4 in a manner similar to the Mach number. Under lean conditions, it decreases from its maximum value of

TABLE 1
Summary of flame parameters for ethene/air mixtures under suppression extremes

Equivalence ratio	Amount of N_2 added to test section %	Mach number	Pressure ratio	Flame/shock separation distance (mm)
0.75	0	3.4 ± 0.1	18 ± 2	3 ± 1
0.75	100	1.25 ± 0.05	2.5 ± 0.1	∞
1.00	0	4.1 ± 0.1	26 ± 3	2 ± 1
1.00	100	1.25 ± 0.05	2.5 ± 0.1	∞

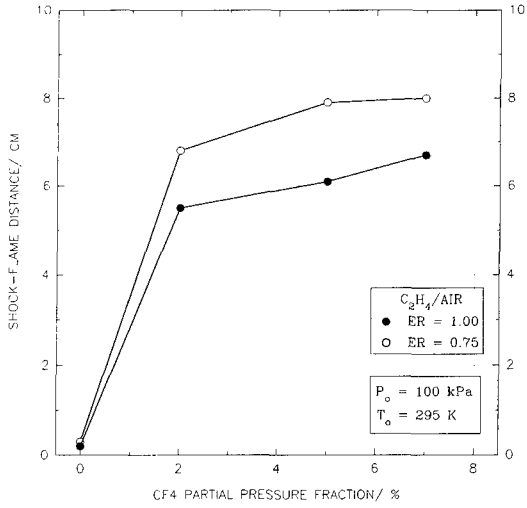

FIG. 3. Effect of the C_2H_4/air mixture equivalence ratio in the presence of CF_4 on the flame/shock distance. Initial conditions: pressure, 100 kPa; temperature 295 K.

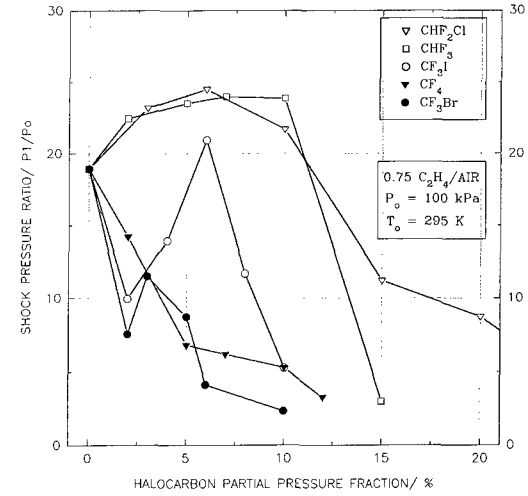

FIG. 5. Suppression/attenuation effect of the C_1-halocarbons based on the shock pressure ratio in the lean 5% vol. C_2H_4/air mixture. Initial conditions: pressure, 100 kPa; temperature, 295 K.

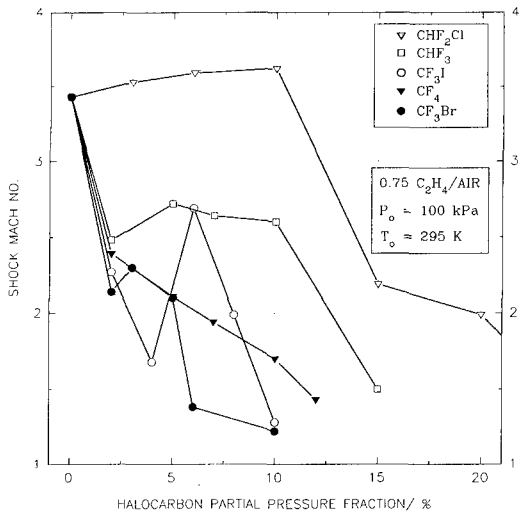

FIG. 4. Suppression/attenuation effect of the C_1-halocarbons based on the flame/shock Mach number in the lean 5% vol. C_2H_4/air mixture. Initial conditions: pressure, 100 kPa; temperature, 295 K.

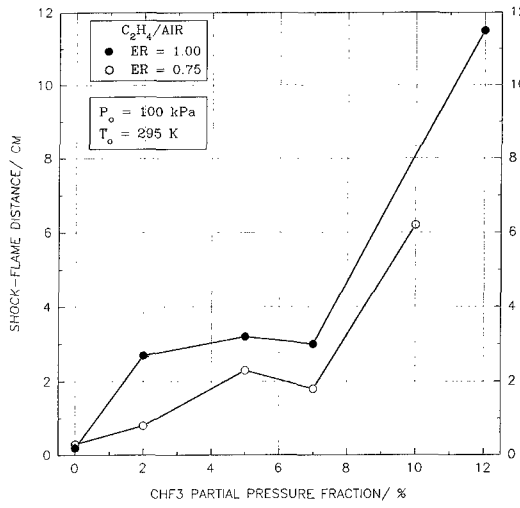

FIG. 6. Effect of the C_2H_4/air mixture equivalence ratio in the presence of CHF_3 on the flame/shock distance. Initial conditions: pressure, 100 kPa; temperature 295 K.

18 when no CF_4 is present to about 3 when a partial pressure fraction of 12% is added to the test section, as can be seen in Fig. 5 (▼ symbols). Experiments with stoichiometric ethene/air revealed nothing unexpected in the behavior of the pressure ratio. The value of P_1/P_0 was greater than that measured for lean combustion conditions, and it decreased monotonically with increasing CF_4.

Trifluoromethane, CHF_3:

The lone hydrogen on trifluoromethane reduces the suppression behavior of this compound. The distance between the flame and the shock wave is about half that of CF_4 when the mixture is stoichiometric. Figure 6 (open circles) shows that the flame begins to lag a substantial distance behind the shock only when the partial-pressure fraction is increased to 10%. The difference in performance between CHF_3

and CF_4 is even more apparent when the lean mixture is used. A 7% partial-pressure fraction of the nonhydrogenated compound leads to a flame separation distance four times that for the hydrogenated compound.

The Mach number is reduced very little when CHF_3 is added to the stoichiometric mixture, until the partial pressure exceeds 7% in the test section. The effect of small amounts of CHF_3 on the lean mixture Mach number is more apparent, as can be seen by the open squares plotted in Fig. 4. As in the flame/shock separation distance, a plateau occurs between about 2 and 10%.

The open squares plotted in Fig. 5 represent the pressure ratio in the lean CHF_3 experiments. This curve differs from the CF_4 not only in magnitude but also in slope. The trifluoromethane in concentrations below 10% (partial pressure) contributes enough hydrogen to the reactants that the shock pressure is substantially enhanced, reaching a maximum of 23:1 in 10% mixtures. An increase in shock pressure ratio does not occur under stoichiometric conditions, but the reduction in P_1/P_0 is modest when compared to the reduction caused by tetrafluoromethane at similar concentrations.

Chlorodifluoromethane, CHF_2Cl:

Replacing an additional fluorine with a chlorine atom further diminishes the agent's ability to suppress the high-speed flame. The shock Mach number (Fig. 4, open triangles) is unaffected by the presence of up to 10% CHF_2Cl. Even when the test mixture contains 20% by partial pressure chlorodifluoromethane, the Mach number remains close to 2. The pressure ratio variation with the addition of CHF_2Cl is similar to what occurs when CHF_3 is added, up to about 10%. Both compounds lead to substantially higher pressure ratios than occur when no agent is added to the ethene/air mixture. For higher partial-pressure fractions, the non–chlorine-containing compound becomes significantly more effective.

Bromotrifluoromethane, CF_3Br:

The bromine atom in CF_3Br is known to inhibit laminar flames by scavenging hydrogen atoms from the chain-branching radical pool. At the lowest concentrations examined in the deflagration/detonation tube, CF_3Br is the most effective in reducing both the Mach number and pressure ratio across the shock wave. The results are plotted with solid circles in Figs. 4 and 5. Bromotrifluoromethane is also the most effective at higher concentrations, suppressing the flame at a partial pressure fraction of 10% to the same extent as if the test section were completely filled with nitrogen. An unusual behavior occurs when the concentration is between 2 and 3%. Both the Mach number and pressure ratio increase with the amount of CF_3Br, followed by the expected decrease for large concentrations. The reversal, while small, is greater than the uncertainty in the data.

Iodotrifluoromethane, CF_3I:

The CF_3I in small concentrations is almost as effective as CF_3Br in attenuating the shock wave. The reversal, which is slight with the bromine-containing compound, becomes obvious with the iodide. The Mach number at a partial pressure fraction of 4% is 1.7, the lowest of all the agents examined. (See the open circles in Fig. 4.) However, an increase in partial pressure to 6% increases the Mach number to 2.7, which is equal to or larger than the Mach numbers measured at that concentration for all the other agents except for CHF_2Cl. The reversal in performance is even more striking in Fig. 5, where the partial pressure ratio more than doubles as the level of CF_3I increases from 2 to 6%. At the latter concentration, the situation is made worse by the presence of the CF_3I than had no agent been added. A similar behavior was observed when iodotrifluoromethane was added to the stoichiometric ethene/air mixture.

Interpretation of Results:

The shock pressure ratio and Mach number yield qualitatively similar results. Effective suppression is accompanied by the reduction of both. The change in one as a function of concentration or equivalence ratio is generally mirrored in the other. An exception is the reduction in Mach number caused by intermediate levels of CHF_3. It is clear that the hydrogen is contributing to the heat release behind the shock wave because the pressure ratio remains high. The mechanism by which this occurs at the same time that the Mach number decreases is not revealed in the experiments.

Increasing the amount of tetrafluoromethane diminishes both the pressure and wave velocity in a manner that suggests the molecule is acting primarily as a thermal sink. This would be expected since CF_4 is known to be extremely stable. The C—H bond is weaker than the C—F bond, so that CHF_3 can thermally decompose to H and CF_3. The hydrogen atom intensifies the combustion for moderate concentrations of CHF_3, but eventually the inhibiting effect of the CF_3 kicks in. This can be observed in the enhanced performance of CHF_3 under stoichiometric conditions, where the additional hydrogen atom has less of a positive effect on the combustion.

Chlorodifluoromethane was observed to be relatively effective in suppressing atmospheric-pressure, nonpremixed flames in another portion of this research program [11]. However, it has also been observed to react violently with air under high pressure [12]. An intermediate behavior has occurred here; however, the complex reaction mechanism

TABLE 2
Performance of C_1-halocarbons relative to CF_3Br in suppressing high-speed flames

Suppressing agent	Equivalence ratio	100% suppression		50% (M)		50% (P_1/P_0)	
		Relative mass	Relative moles	Relative mass	Relative moles	Relative mass	Relative moles
CF_4	0.75	0.80	1.20	0.49	0.75	0.50	0.80
CHF_3	0.75	0.82	1.50	1.41	3.00	1.20	2.70
CHF_2Cl	0.75	1.54	3.00	1.96	3.75	1.87	4.00
CF_3I	0.75	1.18	1.00	1.91	1.75	1.62	1.60

could not be expected to be revealed by the experiments performed.

The bromine- and iodine-carbon bonds are successively weaker than the C—F and C—Cl bonds. The nonmonotonic behavior of both CF_3Br and CF_3I as their concentration was increased suggests competing reactions are present. One can speculate that the shock wave is sufficient to break the iodine bond before the flame arrives, setting up the iodine to scavenge the hydrogen atoms. The separation distance between the flame and shock wave in the CF_3I experiments was twice that measured in CF_4. The iodine is more effective than the bromine at partial-pressure fractions below 5% because it is likely to be present in higher concentrations. At higher partial pressures, the iodine atom may combine to form I_2, which does not interact with the combustion reaction. The fact that the CF_3I works counter to a suppressant in concentrations between 4 and 8% might be in agreement with the observation of Rollefson and Faull [13] that iodine can enter into a catalytic cycle with an organic molecule to actually enhance the overall process.

Rating the Agents:

One objective of the research program was to develop a facility for rating the fire suppression capability of alternatives to CF_3Br. Table 2 ranks the five chemicals in three performance categories: amount required for total suppression (i.e., flame radiation goes to zero, Mach number and pressure ratio approach 100% N_2 values), amount required to diminish the Mach number by 50% of maximum, and amount required for 50% of maximum pressure reduction. In all three cases, the performance of CF_3Br under identical fuel/air conditions is used to normalize the results.

The relative values depend upon whether one chooses the mole fraction of the agent (which is assumed to be identical to the partial-pressure fraction) or the mass fraction of the agent. On a molar basis, CF_3I is equal in performance to CF_3Br if one considers 100% suppression as the appropriate condition. Tetrafluoromethane is superior to all of the other chemicals, including CF_3Br, if one uses a 50% reduction in either the pressure ratio or Mach number as the appropriate criterion. Both the 50% pressure ratio and Mach number reduction approach yield a consistent ranking of agents, whether one uses a mole or mass basis. For the conditions covered in Table 2, the effectiveness of the agents on a mass basis, in decreasing order, is as follows: CF_4, CF_3Br, CHF_3, CF_3I, CHF_2Cl. The ranking is similar on a mole basis, except that trifluoromethane and trifluoroiodomethane exchange places. No experiments were run with CF_3Br under stoichiometric conditions, but the relative effectiveness of CHF_3 increased for an equivalence ratio of unity.

Conclusions

The experimental conditions in the deflagration/detonation tube facility differ significantly from those found in low-speed deflagration flames [8,11,14]. The main qualitative difference is the occurrence of a strong shock wave ahead of the flame. That wave influences the gas-dynamic, thermodynamic, and chemical state of the pure combustible mixture in the driver section and the mixture containing an agent in the test section. Another feature is a high level of turbulence within the flame due to its high speed and the interactions with the spiral obstruction. The quantitative difference is a supersonic regime (relative to the undisturbed mixture) of flame/shock system propagation and strong pressure changes (due to confinement and shock) during the process. Thus, the oxidizer, fuel, and agent molecules undergo preliminary processes before entering the flame zone.

The following statements can be made based upon the results obtained:

1. Suppression of highly dynamic flames can be effectively studied in the two-sectional tube, permitting clear discrimination of performance among various extinguishing compounds.
2. The high-speed turbulent flame and the flame in the quasi detonation wave under suppression strictly follows the shock wave, which is always

ahead of it in such a way that its velocity is the same as the shock velocity. The distance between the flame and the shock increases with the concentration of an extinguishing compound. At extinguishment, the flame disappears, while the residual shock still exists. The distance is dependent on the combustible mixture equivalence ratio and the chemical composition of an agent.

3. The most stable of the compounds, tetrafluoromethane, is the most effective in attenuating the pressure wave, decreasing the flame radiation, and reducing the flame speed. There is evidence of complex chemistry occurring following the arrival of the first shock and prior to the flame front in all of the partially substituted compounds.
4. The presence of hydrogen in the molecule increases the pressure ratio over a large concentration regime. The effect is exacerbated under lean conditions. The chlorine in CHF_2Cl further complicates the chemistry because it can act as an oxidizer and contribute to the exothermic process even under rich conditions.
5. Both the iodine and bromine appear to be released by the passage of the shock wave, and inhibit the flame effectively. The nonmonotonic response of the pressure ratio to increasing the concentration of these compounds (especially CF_3I) suggests that there are competing reactions, with the Br and I either inhibiting or accelerating the combustion depending upon the concentration of the agent.
6. Other than CHF_2Cl, all of the C_1-halocarbons investigated perform well in suppressing turbulent flames and/or quasi detonations under the pressure, temperature, and fuel/air mixtures evaluated. The relatively poorer showing of CF_3I in the deflagration/detonation tube experiments, when compared with suppression studies in constant-pressure flames, is due to the different chemical kinetic pathways that dominate each system.

Acknowledgment

The authors wish to acknowledge the U.S. Air Force, Navy, Army, and Federal Aviation Administration for funding the Agent Screening for Halon 1301 Aviation Replacement project. The program was directed by Mr. Michael Bennett at the Wright Patterson AFB, Flight Dynamics Laboratory, Vehicle Subsystems Division, Survivability Enhancement Branch.

REFERENCES

1. Lee, J. H. S., in *Chemistry of Combustion Processes*, The American Chemical Society, Washington, DC, 1984.
2. Nettleton, M. A., *Gaseous Detonations: Their Nature, Effects and Control*, Chapman and Hall, London, 1987.
3. Westbrook, Ch. K., *Combust. Flame*, 46 (1982).
4. Lefebvre M. H., Nzeyimana, E., and Van Tiggelen, P. J., *Progress in Astronautics and Aeronautics*, AIAA, Inc., New York, 1992, Vol. 115.
5. Chapman, W. R., and Wheeler, R. N. V., *J. Chem. Soc., London* (1926), p. 2139.
6. Lee, J. H., Knystautas, R., and Chan, C. K., *Twentieth Symposium (International) on Combustion*, The Combustion Institute, Pittsburgh, 1984, p. 1663.
7. Gann, R. G. et al., *Preliminary Screening Procedures and Criteria for Replacements for Halons 1211 and 1301*, NIST Technical Note 1278, 1990.
8. Grosshandler, W. L. et al., *Evaluation of Alternative In-flight Fire Suppressants for Full-scale Testing in Simulated Aircraft Engine Nacelles and Dry Bays*, NIST Special Publication No. 861, 1994.
9. Gmurczyk, G., Grosshandler, W., Peltz, M., and Lowe, D., "Chemical and Physical Processes in Combustion," Eastern States Section Conference, The Combustion Institute, Princeton, 1993, p. 487.
10. Peraldi, O., Knystautas, R., and Lee, J. H., *Twenty-First Symposium (International) on Combustion*, The Combustion Institute, Pittsburgh, 1986, p. 1629.
11. Grosshandler, W. L., Lowe, D., Rinkinen, W., and Presser, C., *J. Heat Transfer*, (1995), in press.
12. Fedorko, G., Fredrick, L. G., and Hansel, J. G., *ASHRAE Trans.* 93(3097) (1987).
13. Rollefson, G. K., and Faull, R. F., *J. Am. Chem. Soc.* 59 (1937).
14. Sheinson, R. S., Penner-Hahn, J. E., and Indritz, D., *Fire Safety J.* 15 (1989).

Twenty-Fifth Symposium (International) on Combustion/The Combustion Institute, 1994/pp. 1505–1511

FLUOROMETHANE CHEMISTRY AND ITS ROLE IN FLAME SUPPRESSION

PHILLIP R. WESTMORELAND
University of Massachusetts
Amherst, MA 01003-3110, USA

DONALD R. F. BURGESS, Jr., AND MICHAEL R. ZACHARIAH
Process Measurements Division
Chemical Science and Technology Laboratory
National Institute of Standards and Technology
Gaithersburg, MD 20899, USA

AND

WING TSANG
Chemical Thermodynamics and Kinetics Division
Chemical Science and Technology Laboratory
National Institute of Standards and Technology
Gaithersburg, MD 20899, USA

A detailed reaction set is composed for fluoromethanes in flames, and the competing roles of suppression chemistry, oxidation chemistry, and heat capacity are analyzed. The set is constructed using (1) thermochemistry from the literature, from group additivity, and from BAC-MP4 *ab initio*–based calculations and (2) kinetics from the literature, from simple analogies, from thermochemical kinetics, from BAC-MP4 transition-state calculations, and from Quantum-RRK and RRKM/Master Equation calculations.

Structures of freely propagating laminar flames are then predicted and analyzed. A 6.4% CH_4/air flame (equivalence ratio 0.65) is the base case with dopant CF_4, CHF_3, CH_2F_2, or CH_4 to make up 1 ppm to 2 mol% of the feed. CF_4, which proves to be inert, slows the adiabatic flame speed and reduces the adiabatic flame temperature by dilution and its heat capacity. CHF_3 causes chemical suppression effects, slowing adiabatic flame speed below that with CF_4, despite increasing adiabatic flame temperature. Adding CH_2F_2, CH_3F, or CH_4 increases both flame speed and temperature.

The chemical cause is competition between chain termination, primarily by chemically activated HF elimination, and chain propagation by normal oxidation pathways. Like methane, fluoromethane flame chemistry is dominated by abstraction and by chemically activated reactions. However, abstraction of H is greatly favored over abstraction of F, due to the higher bond strength of C—F, and chemically activated species containing H and F can rapidly eliminate HF. Thus, $OH + CH_3 \rightarrow CH_3OH^*$ slowly forms CH_3OH by third-body stabilization, but $OH + CF_3 \rightarrow CF_3OH^*$ goes rapidly to $CF_2O + HF$. Slow destruction of CF_2O formed by this reaction and by $CF_3 + O$ helps suppress the CHF_3-doped flame, but CH_2F_2 and CH_3F are accelerants because they are oxidized easily.

Introduction

CF_3Br (Halon 1301) has been widely used as a chemical fire extinguisher in ships, aircraft, and computer rooms; however, its production was banned worldwide as of January 1, 1994, because of its potential for depleting stratospheric ozone [1]. To address the need for replacement, 11 alternative agents for flame suppression have been evaluated by experiments and modeling at the National Institute of Standards and Technology [2]. The ozone depletion potential of CF_3Br is caused by bromine, so perfluorocarbons and hydrofluorocarbons are among the candidates.

CF_3Br was experimentally identified in the 1940's as very effective for extinguishing flames, although its mechanism of action was not understood. Being nontoxic made it even more attractive. In the early 1970's, Biordi et al. [3] constructed one of the first flame-sampling molecular-beam mass spectrometers in the U.S. to understand how CF_3Br acted on flames. They mapped radical and stable species in various CF_3Br-containing CH_4 flames and inferred rate constants for some elementary reactions that were involved, culminating in Ref. 3.

In 1984, Westbrook's pioneering work was the first to model CF_3Br chemistry [4]. He showed that bromine suppressed flames by removing H atoms cata-

lytically but that the fluorocarbon part of the molecule also removed H atoms, accounting for the superiority of CF_3Br over CH_3Br or HBr.

The present paper seeks to establish flame chemistry for the fluoromethanes: CH_3F, CH_2F_2, CHF_3, and CF_4. A full set of species and elementary reactions was composed for fluorine-containing C_1/H/O and C_2/H/O species. The general approach was to be comprehensive in developing thermochemistry and kinetics, to predict flame structures for freely propagating flames, to analyze these results identifying the key steps, to re-examine each of these steps using higher levels of molecular or reaction theory, and then to recalculate and reanalyze when indicated.

Developing the Reaction Set

Thermodynamic properties, reaction rate constants, and reaction branching have been measured for relatively few fluorocarbons. Initial values were taken from the literature or estimated from theory. Parameters that proved crucial were then revisited using progressively higher levels of theory.

Species and Reactions:

A species list was composed by considering C/H/O species having up to two carbons and up to two oxygens (35 species), then substituting fluorines for hydrogens to identify possible fluorine-containing species (119 more). This increase is caused by differences in the number of fluorines, as among the fluoromethanes, and in their positions, as in the fluoroethenes.

Hydrocarbon reactions and kinetics were initially taken from the set of Miller and Bowman [5]. Reactions were added for CH_3OH [6,7], and new kinetics were included for $C_2H_5 + O_2$ [8], $C_2H_4 + OH$ [6], and $C_2H_3 + O_2$ [9]. C_2H, C_4H_2, and C_4H_3 (important to fuel-rich flames) proved unimportant in this study and were deleted.

The possible reactions for F-containing species are analogous to C/H/O reactions but have an important difference: thermal or chemically activated species containing H and F can often eliminate HF by 1,1- or 1,2-eliminations. In contrast, such eliminations of H_2 are uncommon. This difference affects thermal decompositions like $CHF_3 \rightarrow {}^1CF_2 + HF$ and, more importantly, chemically activated reactions like $H + CF_3 \rightarrow CHF_3^* \rightarrow {}^1CF_2 + HF$. Flame modeling shows that these channels often dominate the fluorocarbon chemistry.

Thermochemistry:

The literature gives $\Delta_f H^\circ_{298}$, S°_{298}, and $C_p^\circ(T)$ for several fluorinated species of interest here, including fluoromethanes, methyls, ethanes, ethyls, ethenes, and methanals. Values had to be predicted for fluoromethanols, methoxys, hydroxymethylenes, vinyls, acetals, acetyls, ketenes, and ketyl. Generally, group additivity is not applicable to these one- and two-carbon species.

Entropy and specific heat can be often predicted with good accuracy by relatively simple statistical mechanics, using structures and frequencies from analogy [10] or semiempirical molecular-orbital theory. These methods were used when possible. However, often no analogies are available. Furthermore, lower levels of theory do not predict sufficiently accurate heats of formation.

As a consequence, the BAC-MP4 method of Melius [11] was used extensively. Using Gaussian 92 [12] to make Hartree–Fock calculations with a 6–31G* basis set, geometry is optimized and frequencies are calculated. Single-point energies are computed using this geometry: Møller–Plesset fourth-order perturbation theory and a 6–31G** basis set. Finally, internal rotations are identified; entropy, heat capacity, and zero-point energy are computed; and MP4 energy is corrected for type and length of bonds and for spin contamination. C-F bond corrections were all based on $\Delta_f H^\circ_{298}(CF_4) = -934.3$ kJ/mol (-223.3 kcal/mol). For CHF and certain molecular-elimination transition states, a check of the RHF → UHF stability failed, preventing BAC-MP4 corrections [11]. In such crucial cases, G2 calculations [13] were also performed.

Predictions of $\Delta_f H^\circ_{298}$ were compared to literature values where possible (Table 1). The most serious outlier appeared to be CF_2O. JANAF used three similar experimental results to obtain $\Delta_f H^\circ_{298} = (-639.3 \pm 7.1)$ kJ/mol, which was used here. The BAC-MP4 prediction is 40.9 kJ/mol (9.8 kcal/mol) higher. A G2 calculation [15] gives a much closer number, 15.9 kJ/mol higher than the JANAF value. Because the reverse of CF_2O reactions were negligible, this uncertainty has no direct effect.

Kinetics:

The literature on reaction kinetics for these species was reviewed, critically assessed, and used when possible. The NIST Chemical Kinetics Database [6] and the reaction set developed by Westbrook [4] were two important sources. However, for many reactions, data are available only at low temperatures, at low pressures, and/or for reactants with unspecified products.

To extrapolate and to resolve crucial uncertainties, rate constants were estimated by a hierarchy of theoretical methods. Direct analogy is feasible in some cases, such as the high-pressure limit for radical-radical combinations. Estimates of *A* factors were improved for some tight transition states by use of thermochemical kinetics [10], and BAC-MP4 calculations were made for selected transition states.

TABLE 1

Heats of formation $\Delta_f H^\circ_{298}$ (kJ/mol) for C/H/F/O species in the reactions table (Table 2). Values used in modeling are italicized. Predictions are by BAC-MP4 calculations and literature values are from Ref. 14, except as noted.

	Predicted	Literature	Difference
F	79.08	*79.5* ± 4.2	−0.4
HF	−273.30	*−272.4* ± 0.8	−0.9
CH_2F_2	−451.08	*−450.6*	+0.8
CHF_3	−699.44	*−697.1*	−2.4
CHF_2	−247.27	*−247.3*	0.0
CF_3	−471.91	*−470.3* ± 4.2	−1.6
CHF	131.8[a]	*125.5* ± 29 [16]	+6.3
CF_2 ($^1A_1$)	−203.34	*−182.0*[b] [16]	+21.3
CF	236.43	*255.2* ± 8.4	−18.8
CHFO	382.29	*−376.6*	−5.7
CF_2O	−598.40[c]	*−639.3* ± 7.1	+40.9[c]
CFO	−182.88	*−171.5*[d]	−11.4
$CF_2{=}CO$	*−290.45*	—	—
$CH_2{=}CHF$	−139.20	*−138.9* ± 1.7	−0.3
$CH_2{=}CF_2$	−340.12	*−336.8*	+3.0
$CF_2{=}CH$	*−67.66*	—	—

[a] G2 calculation; BAC-MP4 calculation was incomplete because RHF → UHF stability test failed.
[b] Versus −205.0 ± 12.6 [14], −190.0 by G2 calculation [15].
[c] G2 calculation gives −623.4, Δ = +15.9 kJ/mol [15].
[d] Versus −175.7 (Δ = −7.2) in Ref. 16.

Bimolecular Quantum-RRK rate constants [17,18] were calculated for association reactions such as H + CFO → HF + CO via chemically activated CHFO*, and RRKM calculations [19] were made for thermal dissociations such as CHFO → HF + CO.

Rate-constant parameters and their sources are listed (Table 2) for the reactions that were most important for flame predictions with CHF_3 dopant. Many of the reactions are chemically activated associations, and estimates of their rate constants depend on the relative energetics of the association and decomposition channels. If sufficiently exothermic, the association/decomposition reaction proceeds at its high-pressure limit for association (e.g., CF_3 + H → CF_2 + HF). This is the case for many radical-radical combinations forming adducts that can eliminate HF, as is frequently the case for C/H/O/F species.

Reactions of CF_2O with H and H_2O require special comment. Abstraction of strongly bound F from CF_2O is much slower than abstraction of H from CH_2O; BAC-MP4 calculations give $k = 10^{9.15} \cdot T^{1.73} \exp(-72100/T)$ for the F abstraction. Instead, BAC-MP4 calculations identified the most feasible route for H + CF_2O as addition of H to the carbon, followed by chemically activated isomerization (CHF_2O^* → CF_2OH^*) and HF elimination. Biordi et al. [3] had estimated k(H + CF_2O → CFO + HF) from flame data at 1800 K, but their k could be two orders of magnitude too fast. Electronic-structure calculations also identified a direct, concerted transition state for CF_2O + H_2O → CF(O)OH + HF. The fluoroformic acid, formed hot, was assumed to decompose rapidly to CO_2 + HF.

Such calculations were also performed for many species and reactions not included in Table 2, and transport properties were estimated for many fluorinated species. A total of 872 reactions involving 93 species were evaluated or estimated (details in Ref. 2). Many of these reactions proved unimportant in the fuel-lean CH_4/air flames, e.g., reactions involving FO, HOF, F_2O, FO_2, HOOF, and F_2O_2. However, by using a reaction set that was as complete as possible and by then focusing on reactions that proved critical in the flame modeling, a useful, fundamental mechanism has been developed.

Results of Flame Modeling

Freely propagating, adiabatic flames were modeled with the reaction set described above. Decreased adiabatic flame speed corresponds to flame suppression, while an increase is characteristic of acceleration. Flame predictions were made with the Sandia PREMIX code [26] including thermal diffu-

TABLE 2
Kinetics of key reactions for F-containing species in CHF_3-doped CH_4/air flames (ϕ = 0.65); rate constants are in the form $A \cdot T^b \cdot \exp(-C/T)$.

Reaction	A (cm³/mol s)	b	C (K)	Comments
$CHF_3 + H \rightleftarrows CF_3 + H_2$	$1.70 \cdot 10^4$	3.0	4,300	Fit to data for CHF_3 + H [6] with b = 3 as for H + CH_4 [20].
$CHF_3 + OH \rightleftarrows CF_3 + H_2O$	$5.77 \cdot 10^6$	1.8	2,160	Ref. 21.
$CH_2F_2 + H \rightleftarrows CHF_2 + H_2$	$1.65 \cdot 10^3$	3.0	2,800	Fit to data for CHF_3 + H [6] with b = 3 as for H + CH_4 [20].
$CH_2F_2 + OH \rightleftarrows CHF_2 + H_2O$	$2.8 \cdot 10^7$	1.7	1,280	Ref. 21.
$CF_3 + H \rightleftarrows CF_2 + HF$	$5.5 \cdot 10^{13}$	0.	0	Ref. 22, extrapolated with BAC-MP4 and BiQRRK.
$CF_3 + O \rightleftarrows CF_2O + F$	$1.9 \cdot 10^{13}$	0.	0	Est. k_∞, BiQRRK.
$CF_3 + OH \rightleftarrows CF_2O + HF$	$2 \cdot 10^{13}$	0.	0	Est. k_∞ and BAC-MP4 k for decomposition of CF_3OH.
$CF_3 + CH_3 \rightleftarrows CH_2{=}CF_2 + HF$	$5.53 \cdot 10^{19}$	−1.94	1,230	BAC-MP4 for CH_3CHF_2, RRKM.
$CHF_2 + H \rightleftarrows CHF + HF$	$1.49 \cdot 10^{14}$	−0.11	51	BAC-MP4, BiQRRK.
$CHF_2 + O \rightleftarrows CF_2O + H$	$3.7 \cdot 10^{13}$	0.	0	Est. k_∞, BiQRRK.
$CHF_2 + OH \rightleftarrows CHFO + HF$	$2.5 \cdot 10^{13}$	0.	0	Estimated k_∞, BAC-MP4 decomposition k, BiQRRK.
$CHF_2 + CH_3 \rightleftarrows CH_2{=}CHF + HF$	$1.90 \cdot 10^{15}$	−0.586	320	BAC-MP4 for CH_3CHF_2, RRKM.
$CF_2 + H \rightleftarrows CF + HF$	$2 \cdot 10^{14}$	0.	0	Estimate.
$CF_2 + O \rightleftarrows CFO + F$	$5 \cdot 10^{13}$	0.	0	Estimate.
$CHF + H \rightleftarrows CH + HF$	$2 \cdot 10^{14}$	0.	0	Estimate based on k_{300} [22].
$CHF + O \rightleftarrows CO + HF$	$9 \cdot 10^{13}$	0.	0	Estimate based on k_{300} [23].
$CF + O_2 \rightleftarrows CFO + O$	$3 \cdot 10^{13}$	0.	0	Estimate.
$CF + H_2O \rightarrow CHFO + H$	$3 \cdot 10^{13}$	0.	0	Estimate.
$CHFO + M \rightleftarrows CO + HF$	$2.48 \cdot 10^{25}$	−3.0	21,640	Extrapolation/fit of Ref. 24.
$CHFO + H \rightleftarrows CFO + H_2$	$1.10 \cdot 10^8$	1.77	1,510	$k(CH_2O + H)$ [20]/2.
$CHFO + OH \rightleftarrows CFO + H_2O$	$1.72 \cdot 10^9$	1.18	−225	$k(CH_2O + OH)$ [20]/2.
$CF_2O + H \rightleftarrows CFO + HF$	$2.91 \cdot 10^{13}$	−0.03	16,560	BAC-MP4, BiQRRK.
	{$4 \cdot 10^{13}$	0.	10,300	$A = 4 \cdot 10^{13}$ from BAC-MP4 k_∞ for H + CF_2O (to carbon) and k (1800 K) = $1.3 \cdot 10^{11}$ [3].}
$CF_2O + H_2O \rightarrow CO_2 + 2HF$	$3.92 \cdot 10^1$	3.08	13,900	BAC-MP4 transition state to FC(O)OH + HF with fast decomposition assumed.
$CFO + H \rightleftarrows CO + HF$	$1.2 \cdot 10^{14}$	—	—	BAC-MP4, BiQRRK.
$CFO + OH \rightleftarrows CO_2 + HF$	$3 \cdot 10^{13}$	—	—	Estimate.
$CH_2{=}CF_2 + O \rightleftarrows CHF_2 + HCO$	$4.3 \cdot 10^9$	1.0	750	Extrapolation of Ref. 25.
$CH_2{=}CF_2 + OH \rightleftarrows CF_2{=}CH + H_2O$	$2.0 \cdot 10^6$	2.0	1,430	Fit of $k(C_2H_4 + OH \rightarrow C_2H_3 + H_2O)$, corrected for reaction path degeneracy.
$CF_2{=}CH + O_2 \rightleftarrows CF_2O + HCO$	$4.48 \cdot 10^{26}$	−4.55	2,760	BiQRRK, as in Ref. 9.
$CF_2{=}CH + O \rightleftarrows CF_2CO + H$	$3 \cdot 10^{13}$	0.	0	BiQRRK.
$CF_2CO + H \rightleftarrows CHF_2 + CO$	$1.13 \cdot 10^{13}$	0.	1,730	Analogy to Ref. 5.
$F + H_2O \rightleftarrows OH + HF$	$1.30 \cdot 10^9$	1.50	0	Fit of selected data [6].
$F + CH_4 \rightleftarrows CH_3 + HF$	$5.90 \cdot 10^{12}$	0.50	230	Fit of selected data [6].
$F + H_2 \rightleftarrows H + HF$	$2.56 \cdot 10^{12}$	0.50	330	Fit of selected data [6].

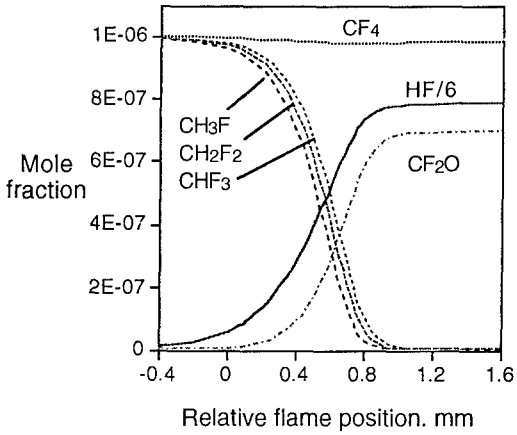

FIG. 1. Principal fluorine-containing species predicted in a freely propagating, lean methane/air flame (ϕ = 0.65 with 1 ppm each of CH_3F, CH_2F_2, CHF_3, and CF_4; 298 K unburned, 1 atm). The zero reference position was at 400 K.

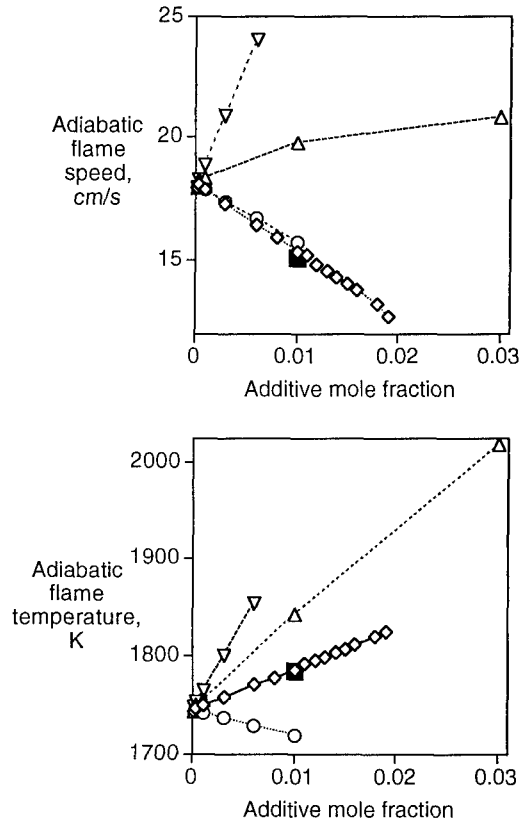

FIG. 2. Effects of additives on adiabatic flame speed (top) and temperature (bottom): CF_4, ○; CHF_3, ◇; CH_2F_2, Δ; CH_4, ∇; and CHF_3 with alternative rate constant for H + CF_2O, ■.

sion (NIST modifications of PREMIX version 2.5 and CHEMKIN II version 3.2; TRANFIT version 1.6). Reaction paths were analyzed with a graphical postprocessor written at NIST.

To assess suppression, CF_4, CHF_3, CH_2F_2, CH_3F, and/or CH_4 were added to a ϕ = 0.65 methane/air blend such that the additive was 1 ppm to 3 mol% of the resulting mixture. Lean conditions were chosen to focus on oxidation and to minimize molecular-weight growth, such as by combination of hydrocarbon and fluorocarbon radicals. The unburned gas was at 298 K, and the flame was isobaric at 0.1 MPa (1 atm).

Figure 1 shows a typical profile of the principal fluorine-containing species for a flame containing 1 ppm each of the fluoromethanes. At these concentrations, fluorine chemistry does not perturb the flame. CF_4 is rather inert, but the other fluoromethanes are rapidly consumed in the flame. The intermediate in highest concentration is CF_2O, followed by CH_2CF_2. All fluorine eventually is converted to HF. Computed adiabatic flame speed is 17.97 cm/s, and adiabatic flame temperature is 1743 K.

Adiabatic flame speeds and temperatures for the flames are shown in Fig. 2. Like CH_4, CH_2F_2 accelerates the flame. It is not as effective a fuel as CH_4, burning to CO_2 + 2HF with a lower, though significant, heat of combustion (488 vs 802 kJ/mol). CF_4 appears to act as an inert, high-C_p diluent to decrease the flame temperature and, consequently, the flame speed. CHF_3 has fuel characteristics, raising the temperature, but it reduces flame speed more than an equal amount of CF_4. Because CHF_3 has lower C_p than CF_4 and is completely consumed in the flame, this observation shows that suppression by CHF_3 must also be caused by chain-terminating or chain-slowing chemistry.

Discussion of Mechanisms

Mechanisms of suppression by CHF_3 and acceleration by CH_2F_2 are established by identifying the key reactions that convert these species to CO_2 (Table 2). Formation and destruction rates are computed and compared for each species at each position in the flame.

Suppression by CHF_3:

CHF_3 suppresses the flame because it burns primarily to CF_2O, which then reacts slowly, and because its oxidation chemistry involves chemically activated HF eliminations, which often are exothermic but chain terminating. Relative importance of the reactions is shown in Fig. 3 (left-hand side).

Abstraction of H from CHF_3 generates CF_3. Even

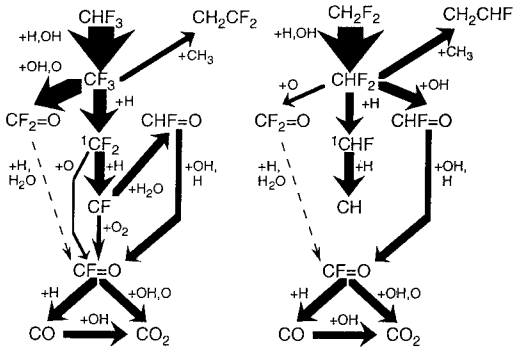

FIG. 3. Reaction paths in lean methane/air flame with 1% CHF_3 (left) or 1% CH_2F_2 (right) added. Thickness of an arrow indicates the relative importance of carbon conversion rates from the starting fluorocarbon.

at this lean condition, CHF_3 is primarily destroyed by H. That reaction proceeds twice as rapidly as OH + CHF_3, mainly because of the faster rate constant for the H-atom reaction. From this point, the chemistry can be used for CF_3Br oxidation, which proceeds with Br and fluorocarbon chemistries that are uncoupled after Br is abstracted [4].

A significant fraction of the CF_3 consumption rate (45%) is CF_2O formation. CF_3 reacts with O-atom by fast radical-radical combination analogously to $CH_3 + O \rightarrow CH_2O + H$, making a chemically activated methoxy that decomposes immediately to CF_2O + F. (Although H reacts with O_2 to cause chain branching, F instead abstracts hydrogens, propagating the chain but removing F from further reaction.) CF_3 reacts with OH in similar fashion, rapidly forming CF_2O by 1,2-elimination of HF from chemically activated CF_3OH^*. A minor contribution is from $CF_3 + CH_3$, again eliminating HF to make CH_2CF_2. These latter two reactions are technically chain-terminating, converting two radicals to two stable species. They are also much faster than the corresponding C/H/O reactions ($CH_3 + OH + M \rightarrow CH_3OH + M$, $CH_3 + CH_3 + M \rightarrow C_2H_6 + M$). However, they are both quite exothermic (−338.9 kJ/mol and −480.3 kJ/mol), which raises the temperature and thus accelerates the H + O_2 chain-branching reaction.

The relative inertness of CF_2O makes it a high-C_p diluent like CF_4. As described above, the fastest theoretical rate constant for CF_2O + H involved addition with chemically activated isomerization and decomposition. Analysis shown in Fig. 3 gives slow, similar rates for this reaction and for $CF_2O + H_2O$. As shown in Fig. 2, an Arrhenius expression based on $k(CF_2O + H, 1800\ K)$ by Biordi et al. [3] (Table 2) caused little change in the predicted suppression or flame temperature. The alternative rate constant used an Arrhenius dependence from the measurement and the BAC-MP4 association A factor.

Nearly as much of the CF_3 consumption rate (42%) is by a faster oxidation route via H + CF_3. From chemically activated CHF_3, CF_2 forms and reacts with H to make CF, again by addition/elimination. Some CF goes to CFO directly, but it mostly proceeds through CHFO (insertion into H_2O with HF elimination).

Some suppression effect is due to CFO oxidation via H and OH. Chemically activated eliminations yield HF + CO and CO_2, respectively, which are very exothermic yet chain-terminating. In contrast to the fast decomposition of CHO, CFO decomposes very slowly because of its strong C—F bond; the rate constant was calculated to be $k(\mathrm{CFO} + \mathrm{M} \rightleftarrows \mathrm{CO} + \mathrm{F}) = 1.89 \cdot 10^{18} \cdot T^{-0.865} \exp(-19{,}600/T)$. This strong bond also prevents fast reaction with O_2, which proceeds rapidly for CHO because internal H abstraction can occur in chemically activated CH(O)OO.

Bromine from CF_3Br participates in homogeneous catalytic cycles of suppression [4], but the fluoromethanes do not. This difference makes the fluoromethanes less effective as flame suppressants. Qualitatively, the prediction that CF_2O is the major flame intermediate agrees with the CF_3 behavior in data from CF_3Br-doped methane flames.

Acceleration by CH_2F_2:

The reactive-flux diagram (Fig. 3, right-hand side) shows that abstraction of H from CH_2F_2 forms CHF_2, but this radical is oxidized to CO_2 more effectively than is CF_3. Most of the CHF_2 consumption is to CHFO and to CHF, and fluoroethene formation is still minor but more important than from CF_3. Only 13% of the CHF_2 consumption forms CF_2O. The increased rate of oxidation raises the temperature much more than with CHF_3 additive, accelerating H + O_2 chain branching. CH_3F accelerates the flame still more by being an even better fuel.

Conclusions and Recommendations

Flame speeds, temperatures, and reaction paths were calculated for adiabatic, freely propagating, lean CH_4/air/fluoromethane flames using a mechanism derived from the literature and a hierarchy of predictive methods. Calculations show that CF_4 suppresses the flames by being an inert diluent. CHF_3 instead has chemical effects through chain-terminating reactions, exothermicity, and generation of CF_2O, which is relatively inert. CH_2F_2 and CH_3F have more fuel behavior, accelerating rather than suppressing the flames.

The reactions that cause these effects are radical-radical combinations with chemically activated HF

eliminations. HF is a strong, favored bond. Its concerted 1,1- or 1,2-elimination usually has a lower barrier than C—H, C—C, or C—O bond breaking, so when the latter bonds form, the chemical activation of the adduct causes fast HF elimination.

Experimental tests of fluoromethane-doped flames are needed to help answer uncertainties in the mechanism. The most serious uncertainty appears to be the destruction chemistry of CF_2O. There are detailed data [3] on CF_3Br-doped flames, so predictions with the larger reaction set are being developed to test the present mechanism. Future modeling will also include the effects of fluoroethane additives.

Acknowledgments

We are particularly grateful to Carl F. Melius, for supplying the BAC-MP4 code and advice. This material is based upon work supported by the United States Army, Air Force, Navy, and Federal Aviation Administration through Wright-Patterson Air Force Base. PRW also gratefully acknowledges support by NIST and by the National Science Foundation under Grant No. CTS-9057406. The Government has certain rights in this material.

REFERENCES

1. Zurer, P. S., *Chem. Eng. News* 71 (46):12–18 (1993).
2. Grosshandler, W. L., Gann, R. G., and Pitts, W. M. (Eds.), *Evaluation of Alternative In-Flight Fire Suppressants for Full-Scale Testing in Simulated Aircraft Engine Nacelles and Dry Bays*, National Institute of Standards and Technology, Special Publication 861 (1994).
3. Biordi, J. C., Lazzara, C. P., and Papp, J. F., *J. Phys. Chem.* 82:125–132 (1978).
4. Westbrook, C. K., *Combust. Sci. Technol.* 34:201–225 (1983).
5. Miller, J. A., and Bowman, C. T., *Prog. Energy Combust. Sci.* 15:287–338 (1989).
6. Mallard, W. G., Westley, F., Herron, J. T., Hampson, R. F., and Frizzell, D. H., *NIST Chemical Kinetics Database—Ver. 5.0*, NIST Standard Reference Database 17, Gaithersburg, MD, 1993.
7. Dean, A. M., and Westmoreland, P.R., *Int. J. Chem. Kin.* 19:207–228 (1987).
8. Bozzelli, J. W., and Dean, A. M., *J. Phys. Chem.* 94:3313–3317 (1990).
9. Westmoreland, P. R., *Combust. Sci. Technol.* 82:151–168 (1992).
10. Benson, S. W., *Thermochemical Kinetics*, Wiley, New York, 1976.
11. Melius, C. F., in *Chemistry and Physics of Energetic Materials*, (S. U. Bulusu, Ed.), Kluwer Academic Publishers, Dorderecht, 1990, p. 21; Ho, P., and Melius, C. F., *J. Phys. Chem.* 94:5120–5127 (1990).
12. Frisch, M. J., et al., *Gaussian 92, Revision E.1*, Gaussian Inc., Pittsburgh, 1992.
13. Curtiss, L. A., Raghavachari, K., Trucks, G. W., and Pople, J. A., *J. Chem. Phys.* 94:7221–7230 (1991).
14. Stein, S. E., Rukkers, J. M., and Brown, R. L., *Structures and Properties Database and Estimation Program—Ver. 1.2*, NIST Standard Reference Database 25, Gaithersburg, MD, 1991.
15. Irikura, K., private communication, 1993.
16. Chase, M. W., Jr., et al., *J. Phys. Chem. Ref. Data*, 14, Suppl. 1 (1985).
17. Dean, A. M., *J. Phys. Chem.* 89:4600–4608 (1985).
18. Westmoreland, P. R., Howard, J. B., Longwell, J. P., and Dean, A. M., *AIChE J.* 32:1971–1979 (1986).
19. Gilbert, R. G., and Smith, S. C., *Theory of Unimolecular and Recombination Reactions*, Blackwell Scientific Publications, Oxford, 1990.
20. Tsang, W., and Hampson, R. F., *J. Phys. Chem. Ref. Data* 15:1087–1279 (1986).
21. Cohen, N., and Benson, S. W., *J. Phys. Chem.* 91:162–170 (1987).
22. Tsai, C., and McFadden, D. L., *J. Phys. Chem.* 93:2471–2474 (1989).
23. Tsai, C., and McFadden, D. L., *J. Phys. Chem.* 94:3298–3300 (1990).
24. Saito, K., Kuroda, H., Kakumoto, T., Munechika, H., and Murakami, I., *Chem. Phys. Lett.* 113:399–402 (1985).
25. Cvetanovic, R. J., *J. Phys. Chem. Ref. Data*, 16:261–326 (1987).
26. Kee, R. J., Grcar, J. F., Smooke, M. D., and Miller, J. A., *A Fortran Program for Modeling Steady Laminar One-Dimensional Premixed Flames*, Sandia National Laboratories, Report No. SAND85–8240, 1985.

Twenty-Fifth Symposium (International) on Combustion/The Combustion Institute, 1994/pp. 1513–1527

COMBUSTION'S IMPACT ON THE GLOBAL ATMOSPHERE

MICHAEL J. PRATHER
Earth System Science
University of California
Irvine, CA 92717-3100, USA

AND

JENNIFER A. LOGAN
Department of Earth & Planetary Sciences
Harvard University
Pierce Hall, 29 Oxford St., Cambridge, MA 02138, USA

The combustion of a hydrocarbon fuel removes molecular oxygen (O_2) from the atmosphere and releases equivalent amounts of water (H_2O) and carbon dioxide (CO_2), almost always with trace amounts of numerous other compounds including hydrocarbons (CH_4, C_2H_2, C_2H_4, C_2H_6, C_3H_8, C_6H_6, CH_3CHO, etc.), carbon monoxide (CO), nitrogen oxides (NO, N_2O) and reduced nitrogen (NH_3 and HCN), sulfur gases (SO_2, OCS, CS_2), halocarbons (CH_3Cl and CH_3Br), and particles. A review of the atmospheric budgets of these gases shows that burning of fossil fuels and recent biomass has led to global alterations in the composition of our atmosphere. Combustion is clearly responsible for most of the enhanced greenhouse forcing to date (through CO_2, tropospheric O_3, soot) and also some counteracting effects (through SO_2). It has had minimal impact on stratospheric O_3 (through CH_3Cl, CH_3Br, CH_4), but has likely changed the tropospheric oxidant levels (through CO, NO_x, NMHC), at least over the northern hemisphere. Most of the important greenhouse gases and tropospheric oxidant gases have significant natural sources, which are not well defined today and may be changing; and thus, quantifying the role of combustion is difficult.

Introduction

The combustion of a hydrocarbon fuel removes molecular oxygen (O_2) from the atmosphere and releases equivalent amounts of water (H_2O) and carbon dioxide (CO_2), often with trace amounts of other species. When recently photosynthesized material is burned, oxidation and decay of biomass are accelerated. When fossil fuel is burned, this activity reverses the geologic process whereby the biosphere has slowly accumulated an oxygenated atmosphere by laying down organic, carbon-rich sediments [1]. In either case, numerous other compounds are emitted in trace amounts, including nitrogen oxides (NO, NO_2, N_2O), sulfur gases (SO_2, OCS, CS_2), carbon monoxide (CO), hydrocarbons (CH_4, C_2H_2, C_2H_4, C_2H_6, C_3H_8, C_6H_6, CH_3CHO, etc.), reduced nitrogen compounds (NH_3 and HCN), halocarbons (CH_3Cl and CH_3Br), and particulate matter. Some of these products are limited by the trace elements in the fuel (e.g., S, Cl, and Br), but overall the emission of trace products depends very much upon the conditions of combustion.

The burning of fossil fuels (coal, oil, and gas) and of recent biomass (savannas, forests, biomass fuels, and agricultural waste) leads to global alteration in the composition of our atmosphere. Concern over such changes focusses on (1) the greenhouse effect, (2) depletion of the ozone layer, and (3) the level of tropospheric oxidants. Arrhenius [2] pointed out that CO_2 would act as a greenhouse gas, and recent scientific assessments [3] show that increases in CO_2 and other greenhouse gases (GHGs) will inevitably lead to a warmer climate. Stratospheric ozone loss associated with halocarbons [4] or with nitrogen oxides from high-altitude aircraft [5] has prompted international treaties (Montreal Protocol on Substances that Deplete the Ozone Layer, Final Act, 1987) controlling ozone-depleting gases (ODGs). Short-lived hydrocarbons and nitrogen oxides can produce unhealthful increases in oxidants (O_3 and NO_2) in polluted urban regions [6], and subsequent understanding of global tropospheric ozone has shown that these oxidant gases (OXGs) have likely increased concentrations of tropospheric O_3 throughout much of the northern hemisphere [7]. Concentration of the hydroxyl radical (OH), the primary sink for most atmospheric compounds, may have been modified by emissions of CO, hydrocarbons, and NO_x from combustion [8,9].

This paper reviews the role of combustion insofar as it changes the composition of the atmosphere on

a global scale, i.e., away from regional pollution in the boundary layer. We estimate how much of this change since preindustrial times can be ascribed to combustion. A summary of atmospheric chemistry given here emphasizes the troposphere and is taken from a chapter one of the authors (MJP) prepared for the new climate assessment [10]. We follow with an examination of how combustion affects the natural levels of each compound. For the consequences of an evolving atmosphere on both chemistry and climate, the reader is referred to recent international assessments [11,3,10] and reference texts [12,13,14].

Atmospheric Chemistry—an Overview

The gases N_2 (78% of dry air), O_2 (21%), and Ar (1%) comprise the bulk of the Earth's atmosphere. Their abundances are controlled over geologic time scales by the biosphere, uptake/release from the crustal material, and degassing of the interior. Water vapor (H_2O) is the next most abundant, but highly variable, species in the lower atmosphere, where the cycles of evaporation and precipitation result in abundances ranging from 4% in the tropical boundary layer to 4×10^{-6} in the lower stratosphere. Of the remaining gases that play a role in the Earth's chemical or radiative balance, all but CO_2 are controlled in one way or another by chemical processes. The cycles of atmospheric aerosols also involve chemical reactions. Atmospheric trace gas composition and its change since the preindustrial era are summarized in Table 1.

The atmospheric abundances of these trace gases, most often designated in volume mixing ratios (e.g., parts per billion = ppb = 10^{-9} vol/vol), are determined by a balance between sources and sinks. The sources are typically surface emissions, such as those associated with combustion, and the sinks are chemical processes in the atmosphere that in general irreversibly oxidize the gas (e.g., CH_4 is oxidized to CO, and then to CO_2). The combined strength of these sinks determines the atmospheric residence time of a gas, i.e., the e-folding of an instantaneous emission. Most of the atmospheric mass, and consequently the mass of most trace gases (except O_3), resides in the troposphere, which comprises on average the lowest 13 km of the atmosphere. The bulk of the remaining atmosphere (~15%) resides in the stratosphere from 13- to 50-km altitude, the region containing most of the ozone (O_3). In the troposphere, the major sink for many gases is through reactions with the hydroxyl radical (OH), while in the stratosphere removal is dominated by ultraviolet photodissociation. Once a constituent becomes "sticky" or soluble, tropospheric removal in clouds and precipitation or surface deposition proceed rapidly.

Photochemical Loss of Trace Gases:

Most chemical cycles in the atmosphere are initiated by ultraviolet sunlight. Since only light with wavelengths greater than 290 nm reaches the troposphere, the number of compounds that can be photodissociated directly is limited. Most of the photochemical chains of interest begin with the dissociation of ozone (O_3) at wavelengths below 320 nm (e.g., Ref. 15).

$$O_3 + \text{UV-sunlight} \rightarrow O_2 + O(^1D). \quad (1)$$

A fraction of this highly reactive, metastable form of atomic oxygen, $O(^1D)$, reacts with water vapor (H_2O) to form the primary source of tropospheric hydroxyl radicals (OH),

$$O(^1D) + H_2O \rightarrow OH + OH. \quad (2)$$

In the troposphere, the OH radical is the most important cleansing agent. It reacts with virtually all molecules containing hydrogen atoms (e.g., CH_4) and also oxidizes species such as carbon monoxide (CO), nitrogen dioxide (NO_2), carbonyl sulfide (OCS), and sulfur dioxide (SO_2). In the unpolluted troposphere, the major reactions of OH are with the molecules:

$$OH + CH_4 + O_2 \xrightarrow{\text{net}} CH_3OO + H_2O \quad (3)$$

$$OH + CO + O_2 \rightarrow CO_2 + HO_2. \quad (4)$$

This loss of OH is followed by production of peroxy radicals (HO_2, CH_3OO). When OH reacts with other, nonmethane hydrocarbons (NMHC) such as ethane, analogous organic peroxy radicals are formed. Subsequent oxidation of CH_3OO and NMHC analogues leads to production of one or more HO_2, which are recycled to OH by the reactions

$$HO_2 + NO \rightarrow OH + NO_2 \quad (5)$$

$$HO_2 + O_3 \rightarrow OH + O_2 + O_2. \quad (6)$$

The reactions (3) or (4) followed by (5) or (6) form a catalytic chain that destroys methane and carbon monoxide but regenerates OH. The cycling of OH and HO_2 is closed off by several reactions involving OH, HO_2, and NO_2. These regenerate H_2O or form hydrogen peroxide that is subsequently removed by clouds and precipitation. In a polluted environment with large concentrations of NO_2, the major loss of OH is through formation of nitric acid (HNO_3).

$$OH + NO_2 \rightarrow HNO_3. \quad (7)$$

This reaction is also the major loss mechanism for

TABLE 1
Radiatively and chemically active gases

Compound	Concentration (10^{-9} vol/vol) Preindustrial	Current	Residence time (yr)	% Change due to combustion	Impact
carbon dioxide					
CO_2	278,000	356,000	120[a]	>90	GHG
methane					
CH_4	700	1,714	14	10	GHG, OXG, ODP
nitrous oxide					
N_2O	270	310	120	20	ODP, GHG
chlorofluorocarbon-11					
$CFCl_3$	0.	0.268	50	0	ODP, GHG
chlorofluorocarbon-12					
CF_2Cl2	0.	0.503	102	0	ODP, GHG
hydrochlorofluorocarbon-22					
CHF_2Cl	0.	0.105	13	0	ODP, GHG
methyl chloroform					
CH_3CCl_3	0.	0.160	5.4	0	ODP, GHG
methyl chloride					
CH_3Cl	<0.600	0.600	1.3	>0	ODP
methyl bromide					
CH_3Br	0.006	0.012	1.4	50	ODP
tetrafluoromethane					
CF_4	0.	0.070	>999	0	GHG
carbon monoxide (northern hemisphere)					
CO	60	120	0.2	>90	OXG
nitric oxides (free troposphere)					
NO_x	?	10–1,000	<0.03	>50	OXG
nonmethane hydrocarbons					
NMHC	?	?	0–0.24	>0	OXG
tropospheric water					
(t)H_2O	10,000,000	same	[a]	0	GHG, OXG
stratospheric water					
(s)H_2O	3,500	5,500	~2	10	GHG, ODG
tropospheric ozone					
(t)O_3	25	50	<0.10	>50	GHG, OXG
stratospheric ozone					
(s)O_3	4,000	3,800	~2	<5	GHG, ODG, OXG
carbonyl sulfide					
OCS	<0.500	0.500	30	>0	anti-GHG, ODP
sulfates					
$SO_2/SO_4^=$	?	>?	[a]	>90	anti-GHG
black carbon aerosols					
soot C	?	>?	[a]	>90	GHG

[a]Variable, see text.

NO_x ($NO + NO_2$) throughout the troposphere, since most of the HNO_3 is washed out of the atmosphere. Like the OH-HO_2 pair above, the NO_x pair is tightly coupled through the reactions

$$NO + O_3 \rightarrow NO_2 + O_2 \quad (8)$$

$$NO_2 + \text{UV-sunlight} \rightarrow NO + O \quad (9)$$

$$O + O_2 + M \rightarrow O_3 + M \quad (10)$$

where M is N_2 or O_2.

In addition to the daytime photochemistry, there

are some nighttime, nonphotolytic reactions that impact O_3 and NO_x. The most important process is the reaction of NO_2 with O_3 to form a nitrate radical (NO_3), which can further react to form nitrate aerosol, thereby removing both ozone and NO_x. Molecules that escape tropospheric oxidation by OH, or removal by clouds and precipitation, will reach the stratosphere where they encounter sunlight with much shorter wavelengths, as low as 180 nm. These photons have sufficient energy to dissociate directly many of the compounds that could not be destroyed in the troposphere. Photolysis initiates the oxidation processes that, for example, turn CFCs into CO_2, HF, and a mix of chlorine compounds. In addition, concentrations of $O(^1D)$ [reaction (1)] are higher in the stratosphere and contribute to the loss of the more stable gases. For gases destroyed primarily in the stratosphere, lifetimes range from 40 to 200 yr and are limited by the rate of transport of air into the stratosphere. A few fluorinated gases (e.g., CFC-115 = CF_3CF_2Cl, CF_4, C_2F_6, SF_6) of concern as GHGs are identified with industrial sources, but not with combustion. They are not easily destroyed in the troposphere or stratosphere and have lifetimes exceeding 1000 yr [16,17].

Ozone:

Sunlight of wavelengths 180–230 nm also dissociates molecular oxygen (O_2), generating O_3 in the process [18]. Because of this absorption by a major atmospheric constituent, these wavelengths do not reach below about 20-km altitude in the atmosphere. The stratospheric column of O_3 is controlled by a balance between this production, atmospheric transport, and the catalytic loss cycles involving Cl and Br species, NO_x, OH, and HO_2. Today about 80% of stratospheric chlorine and a large fraction of the bromine are released from the industrial halocarbons. Stratospheric NO_x is generated by N_2O and has increased by about 15% since preindustrial times, based on data from bubbles trapped in ice cores [19]. Stratospheric H_2O—the source of OH and HO_2—is expected to increase along with the observed increases in atmospheric CH_4. The stratospheric O_3 column is the major absorber of solar UV between 220 and 320 nm, and hence depletion of stratospheric O_3 is likely to change tropospheric chemistry in two ways: (1) by lowering the flux of O_3 into the troposphere, and (2) by increasing tropospheric UV, enhancing production of OH.

The exchange of air from troposphere to stratosphere in the tropics represents a loss for many of the long-lived species, and the return flux in the mid-latitudes brings significant sources of O_3 into the upper troposphere. There are four important contributors to the budget of tropospheric ozone—input from the stratosphere, deposition at the surface of the Earth, chemical production, and chemical loss, all of the same order of magnitude on a globally averaged basis.

Ozone is produced in the oxidation of CO by reactions (4), (5), (9), and (10), with (OH + HO_2) and NO being recycled. If insufficient NO is present, oxidation of CO leads to removal of ozone, reactions (4) and (6), with no effect on OH. Ozone is also produced by oxidation of CH_4 and NMHC. The balance between in situ production and loss of O_3 depends on the NO concentration: Production by reaction (5) is favored over loss by reaction (6) when the NO:O_3 concentration ratio exceeds about 10 ppt:30 ppb. (One ppt, or part per trillion, is 10^{-12} vol/vol mixing ratio.) In most parts of the troposphere, therefore, the addition of NO will induce additional production of O_3, but in the heavily polluted urban environment, with already high concentrations of NO_x, addition of NO can lead to a reduction in local O_3 concentrations. CH_4, CO, NMHC, and NO_x are considered as OXGs.

Atmospheric Chemical Feedbacks and Greenhouse Gases:

The varied chemical and physical couplings in the atmospheric system mean that a perturbation to one gas propagates through a series of feedbacks, perturbing many other species. Methane has an especially large number of identified couplings and is used as an example to illustrate this point. Methane originates primarily through biological processes, both current and ancient (i.e., fossil fuels) and is released near the surface of the Earth. The typical CH_4 molecule travels about 14 years from pole to pole and occasionally into the stratosphere before being destroyed by reaction with OH. During this period, the molecule acts as a GHG, second in importance only to CO_2. When CH_4 is destroyed in the troposphere, its decay products can react with nitrogen oxides to produce additional O_3, another GHG. When NO_x is not present, the CH_4 decay products help to destroy O_3. In addition, the loss of CH_4 removes OH and thus increases indirectly the abundance of other OXGs (e.g., CO, NMHC, NO_x) and some GHGs (e.g., the HCFCs, HFCs, and CH_3CCl_3) that rely on OH for their sink. When CH_4 is destroyed in the stratosphere, it suppresses the chlorine and nitrogen cycles that destroy ozone, thus changing the effectiveness of some ODGs and increasing stratospheric O_3 abundances. The stratosphere is exceptionally dry and the H_2O from CH_4 decay contributes half of the water vapor in the stratosphere today. Even at these low abundances in the stratosphere, H_2O acts as a GHG and, by enhancing catalytic loss through HO_2 and OH reactions, as an ODG. The additional hydrogen that CH_4 carries through the cold trap at the tropopause reaches the highest altitudes of the Earth's atmosphere, the exosphere, where atomic H (half of it from CH_4) is the predominant constituent.

Budgets and Trends of Trace Gases

Our knowledge of the atmospheric budgets of most trace gases (i.e., sources and sinks) is based on a combination of source inventories, atmospheric observations, and chemical models. Rarely does a single approach give a reliable budget. The observed abundance of a compound together with an estimate of the residence time yields the total sink, and consequently the source if the compound is in steady state. Conversely, if the magnitude of the source of a gas and its abundance are well known, the magnitude of the sink can be estimated. The most useful example of this case is methylchloroform (CH_3CCl_3), an industrial solvent, which is removed primarily by OH. The budget of CH_3CCl_3 has been used to infer globally averaged concentration of OH (e.g., Ref. 20) and to test global models of OH (e.g., Ref. 21). A calibrated model for OH can then be used to infer the removal rate of other compounds such as CO, CH_4, NMHC, and HCFCs that are removed by OH. Accurate source inventories are available only for primary compounds of industrial origin (e.g., CFCs). Estimates of emissions from processes such as deforestation, savanna burning, and agriculture practices (e.g., CH_4 from paddy rice and cattle) are uncertain, and constraints on the total source of a gas are particularly useful. For species with large natural sources (e.g., CH_4 and N_2O), it is difficult to partition the total emissions between anthropogenic and natural.

The balance between sources and sinks is most accurately inferred from the observed trends in atmospheric concentration. The long-term changes in many trace gases can also be used to infer the anthropogenic sources, providing natural sources (and sinks) remain constant. Critical data include both recent atmospheric observations [e.g., CO_2 [22]; CH_4 [23] and measurements of the composition of air bubbles trapped in large ice sheets (e.g., Refs. 24, 25, 19). The concentrations of CO_2, CH_4, and N_2O in ice cores that date from the preindustrial period before 1850 are all less than today's levels and consistent with recent atmospheric increases. Further, for the thousand years prior to 1850, the fluctuations in their concentrations (presumably a measure of the natural variations in their sources and sinks) were much smaller than the change from preindustrial to present.

Fuel Burned

Fossil-fuel use is reasonably well documented (e.g., Ref. 26). The total amount of fossil C burned in the 1980s was 5.4 Gt(C)/yr (i.e., 5.4×10^9 metric tonnes of carbon per year), and during 1991 emissions were 6.2 Gt(C)/yr [27]. (Cement production accounts for a small percentage of the CO_2 released from industrial processes and is included in totals of fossil/industrial CO_2 released.) Individual events may seem to be a large perturbation; however, the Kuwaiti oil fires consumed about 4.6 million barrels of crude oil per day, only 3% of the worldwide emissions of CO_2 from fossil fuels at the time [28], and were even less important as sources of N_2O, CH_4, and CO.

The amount of biomass burned each year is much more difficult to estimate. Savanna burning, deforestation, wildfires, burning of agricultural residues, and domestic use of wood and other biomass fuels provide important sources of fuel. The total amount of C burned is 3 to 5 Gt(C)/yr with about 80% of this in the tropics [29,30,31].

Emissions from fossil and biomass fuels depend on the combustion conditions and are typically more variable and less well known for biomass fuels than for fossil fuels. For fossil fuels, the largest yields of reduced gases such as CO and hydrocarbons are from gasoline-powered vehicles, while for biomass fuels, the largest yields are from forest fires [32,33,34]. In contrast to combustion conditions for fossil fuels, temperatures in biomass fires are not usually high enough to produce thermal NO_x.

CO_2 and O_2:

There is currently an observed imbalance in the atmospheric carbon-oxygen cycles with increasing CO_2 [22,3] and a corresponding decrease in O_2 [35]. Although absolute changes are comparable, the relative change in O_2 is inconsequential to chemistry or climate, but the changes in CO_2 are large in terms of potential effects on climate: In the 1980s, CO_2 has changed by +0.5%/yr or +1.6 ppm/yr (ppm = 10^{-6}) or 3.4 Gt(C)/yr. The change in CO_2 is currently the single most important contribution to climate change [36]. Apparently only a little more than half of the fossil-fuel CO_2 [5.4 Gt(C)/yr] remains in the atmosphere; the ocean provides a sink for 2.0 Gt(C)/yr, and it has been proposed that there is an unknown terrestrial sink of 1.2 Gt(C)/yr [37,3]. Combustion of biomass that regrows quickly does not affect the CO_2 balance. However, deforestation releases carbon that has accumulated in the biosphere over decades, and represents a net source of CO_2. Changes in land use are estimated to contribute 1.0 Gt(C)/yr to the atmosphere. The global carbon cycle involves exchange of the atmospheric CO_2 with carbon reservoirs in the ocean and biosphere over several time scales. Some are rapid enough to absorb about half of the fossil CO_2 within a year, but others take much longer to equilibrate. There is no simple lifetime for the decay of a CO_2 perturbation, but time scales are estimated to be about a century (IPCC, 1992).

There is clear evidence that CO_2 concentrations have risen in parallel with, and are caused by, combustion of fossil fuels. The ice-core record shows sta-

ble levels of 278 ± 10 ppm for 1000 years prior to the industrial era [19]. The increase to current levels of 357 ppm has been documented as part of a continuous record of atmospheric concentrations at Mauna Loa since 1957 [22], and at many other locations in recent years. Furthermore, changes in CO_2 isotopes, $^{13}CO_2$ and $^{14}CO_2$, have the same isotopic signature as fossil C. The best current models predict that even a freeze in current emissions would lead eventually to more than a doubling of natural levels [10]. Scientific assessments of climate change note that such CO_2 increases will eventually lead to a warmer surface climate, a colder stratosphere, and possible changes in weather patterns. CO_2 does not impact atmospheric chemistry except indirectly through changes in temperature and circulation.

H_2O:

Water in the form of vapor and clouds is the single most important atmospheric constituent controlling the temperature of the Earth. An increase in water vapor paralleling that of temperature significantly amplifies the expected warming for a doubling of CO_2 (IPCC, 1992). Although H_2O is a major byproduct of combustion, this addition to the lower atmosphere is a small perturbation when compared with the global hydrological cycle of evaporation and precipitation. Emissions of H_2O from aircraft fleet cruising at 10–13 km in the drier regions of the atmosphere have a greater potential to augment natural levels, but recent estimates [38] suggest a minor impact. Similarly, rocket exhaust is expected to lead to minor enhancement in upper stratospheric water [39]. In the future, however, the impact of a proposed fleet of 500 High-Speed Civil Transports (HSCT, supersonic aircraft) cruising at 20-km altitude may be significant. Current assessments predict that a Mach 2.4 HSCT fleet would increase stratospheric H_2O by 10–20% in the lower stratosphere at northern midlatitudes [40].

CH_4:

More than half of current CH_4 emissions, 375 of 550 Mt(CH_4)/, can be attributed to human activities. Many sources of CH_4 have been identified, with wetlands providing the largest natural source [41]. Anthropogenic sources that are associated with biological processes (e.g., rice paddies, cattle, landfills, and waste treatment) make up about 50% of the total; sources related to fossil fuels, about 18%. Most of the fossil-fuel sources are associated with fugitive release of CH_4 from coal mines, natural gas distribution, and petroleum processing. Low-temperature combustion of coal has been identified as a source at the 3% level [42], and combined with a biomass burning source of about 30–40 Tg(CH_4)/yr [43], the total direct contribution of combustion to the global methane budget is about 10%. If the fossil-fuel "industry" were included, this would rise to about 25%, which is consistent with observations of the isotopic abundances of CH_4 from live and fossil sources [44].

N_2O:

Nitrous oxide is important as a GHG and, by supplying the major source of NO to the stratosphere [45], as an ODG. The current imbalance in N_2O is substantial: The atmospheric content is currently increasing at a rate of about 4 Mt(N)/yr [46], and stratospheric losses are about 12 Mt(N)/yr. The change in mixing ratio since preindustrial times is +15%, based on ice-core records, and much of this can be attributed to anthropogenic sources that are not well quantified. Originally, combustion of fuel-N in coal-fired power plants was identified as the major industrial source [47,48,49], but recent work has shown that artifact N_2O was being produced by secondary reactions in the sampling flasks [50]. Current estimates are that combustion is a minor source [51], providing at most 1 Mt(N)/yr, with half from biomass burning and half from fossil fuels [52]. Fluidized-bed combustors emit a significantly higher yield of N_2O than other types of combustion systems [53]. The largest anthropogenic sources of N_2O appear to be agricultural activity and industrial processes involving nitric acid.

Halocarbons

Methyl chloride (CH_3Cl) and methyl bromide (CH_3Br) have long been thought to be the "natural" sources of stratospheric Cl and Br. Volcanic and other soluble sources of Cl/Br do not appear to penetrate the cold condensation trap between the stratosphere and troposphere [54]. The primary emissions of methyl halides were attributed to the oceans, but recent work has shown that biomass burning may contribute to current levels of both species [55,56]. Agricultural use of CH_3Br is an important anthropogenic source of CH_3Br. The atmospheric residence time for both species, about 1.4 yr, is determined by OH, although substantial oceanic uptake reduces the CH_3Br residence time [57]. Preliminary estimates suggest that combustion could provide 10–50% of the source of CH_3Cl and CH_3Br.

The major source of atmospheric chlorine today is from the chlorofluorocarbons (e.g., CFC-11 = $CFCl_3$, CFC-12 = CF_2Cl_2, CFC-113 = $CF_2ClCFCl_2$) and carbon tetrachloride (CCl4). These are industrially produced compounds with long atmospheric residence times (>40 yr) and no known natural sources. Methyl chloroform (CH_3CCl_3) is also an industrial halocarbon with large emissions, with a shorter residence time (5.4 yr). There is no evidence for CFCs

in ice cores, and the current atmospheric abundance and trend are consistent with known production and emissions [58,59,60,61]. Likewise, the bromofluorocarbons (e.g., halon-1211 = CF_2ClBr, halon-1301 = CF_3Br) are also synthetic and emitted only over the last 50 years [62]. All of these compounds are insoluble and relatively long lived. They supply 80% of the Cl and 30% of the Br to the stratosphere today. Solid rocket motors provide an extremely small combustion-related contribution to the atmospheric Cl burden [63]. Ironically, the major use of halons is combustion related, as a fire extinguisher.

The dramatic rise in stratospheric Cl and Br in the past 20 years has led to the formation of the Antarctic ozone hole and is responsible for the extensive ozone depletion over the northern hemisphere today: about 5% loss over the past two decades at 45°N [11,64,65]. (Some of this recent loss may have been accelerated in 1992–1993 by the large enhancement of stratospheric sulfate aerosols from the Mt. Pinatubo volcano). These changes pose a significant environmental threat, and the Montreal Protocol (1987) and its subsequent amendments have led to the international phaseout of these compounds. The CFCs and halons also act as GHGs (e.g., Refs. 66, 67). The CFCs are being replaced by hydrochlorofluorocarbons (HCFCs), which have shorter residence times as they react with OH in the troposphere. Consequently, a much smaller fraction of the Cl reaches the stratosphere. These gases also act as ODGs and GHGs.

CO:

Carbon monoxide is emitted directly into the atmosphere by incomplete combustion, and it is produced in situ by the oxidation of CH_4 and NMHC (e.g., Ref. 15). The predominant sink is tropospheric OH, about 2100 Mt(CO)/yr, with a small additional sink from uptake by soils. Oxidation of atmospheric CH_4 is the largest source of CO, about 33%. The source from biomass burning is hard to quantify accurately, since the combustion conditions determine the yield of CO and NMHC: Smoldering fires can emit several times as much per C atom burned compared to a fast-burning grass fire (e.g., Refs. 68, 31). Estimates range from 12 to 30% of the total source. The burning of fossil fuels, primarily gasoline, is responsible directly for about 14% of the total source, with an additional 3% from the oxidation of NMHCs from technological sources. Thus, combustion as a whole accounts for about 40% of the CO source if we include the secondary sources from CH_4 and NMHC. The fossil-fuel source is most important at northern midlatitudes, while the biomass source is most important in the tropics. Oxidation of isoprene, a natural hydrocarbon, also provides a source of CO, with the yield of CO depending on the local concentration of NO. There are minor sources from the oceans, and vegetation.

Average CO levels are about 50 ppb in the southern hemisphere and about 120 ppb in the northern [69]. This imbalance is consistent with the short residence time of the gas, about 2.5 months, and the preponderance of sources in the northern hemisphere. Through the 1970s and 1980s, increases in CO concentrations of the order of +1%/yr have been observed in northern midlatitudes (e.g., Ref. 70) with no obvious changes in the southern hemisphere. Since 1990, however, CO in the northern hemisphere has decreased, a change caused in part by regulation of vehicular emissions in the U.S. since about 1970, and in Western Europe in the 1980s [68,71]. Overall, combustion has probably increased CO in the northern hemisphere by a factor of 2.

Carbon monoxide is the primary sink for OH in the troposphere. In the northern hemisphere, three times as much OH reacts with CO as with CH_4, while in the southern hemisphere, the ratio is closer to 1:1. Thus, CO controls the level of OH; oxidation of CO in the presence of NO_x also provides an important source of tropospheric O_3 as discussed above.

NMHC/VOC:

The nonmethane hydrocarbons include gaseous compounds of the form C_xH_y. These are short-lived, highly reactive gases whose oxidation also leads to production of tropospheric O_3 in the presence of NO_x. The longest lived NMHC is C_2H_6 with a lifetime similar to CO. Another term used to describe hydrocarbons is volatile organic carbon (VOC), which includes NMHC as well as oxygenated species such as aldehydes and alcohols. A recent estimate of the anthropogenic source of VOC is 110 Mt/yr [72] and includes significant contributions from gasoline vehicles, solvent evaporation, wood fuels, and biomass burning. Natural emissions of isoprene and terpenes from vegetation appear to be much larger than anthropogenic sources, but these estimates are highly uncertain, in the range of 400–800 Mt/yr. Oceanic emissions of C_2H_4 and C_3H_6 are important in remote environments. These biogenic hydrocarbons tend to be very reactive and are usually destroyed in the boundary layer near their source. The hydrocarbons in combination with NO_x (from fossil-fuel combustion) provide a source of ground-level ozone, elevating concentrations in the U.S. and other countries to unhealthful levels in warm, stagnant weather conditions [73]. Similarly, NMHC and NO_x from biomass burning provide an important source of O_3 in the tropics [31].

NO_x:

The nitrogen oxides, NO and NO_2 (NO_x), are essential to the photochemical formation of O_3 in the

troposphere [6]. They are the single most important OXG. The lifetime of NO_x is short, often less than 1 day. Thus, concentrations are highly variable throughout much of the troposphere and depend on the rapidity of transport from distant sources. In the free troposphere away from boundary-layer sources, concentrations range from 0.01 to 1 ppb (e.g., Ref. 74). NO_x is the limiting species for production of ozone in most of the troposphere.

NO_x is emitted primarily as NO by a large variety of sources. Lightning is the largest natural source of NO_x in the free troposphere but is not well quantified: Literature estimates range from 2 to 150 Mt(N)/yr (e.g., Refs. 75, 76), but it is likely that the source is much smaller, in the range 8–16 Mt(N)/yr [77]. Soil emissions represent a natural source of about 12 Mt(N)/yr. Fossil-fuel combustion is the largest source of NO_x, about 24 Mt(N)/yr centered equally in North America, Europe, and East Asia. Biomass burning is smaller, about 8 Mt(N)/yr, centered in the tropics (IPCC, 1994). Emissions from jet aircraft are often considered separately: Although only a fraction of the fossil-fuel source, about 0.4 Mt(N)/yr, they are emitted in the upper troposphere [78,79]. The large surface sources of NO_x are consumed primarily in the boundary layer, and only a small fraction is exported to the free troposphere (e.g., Ref. 80). Thus, aircraft and stratospheric injection [also a small source, <0.2 Mt(N)/yr] may compete with these much larger sources in remote regions. NO_x is converted to PAN (peroxynitric acid) in polluted source regions. Once PAN escapes the boundary layer, it is long lived, and its decomposition may provide a source of NO_x in remote areas.

Combustion has led to a fourfold increase in the source of tropospheric NO_x; however, such increases would not be uniform as emissions near the ground (e.g., automobiles) are more readily oxidized than those aloft (e.g., lightning). The large variability in NO_x concentrations makes it inappropriate to assume an equivalent increase in the "mean" NO_x abundance throughout the free troposphere. Nevertheless, there is indirect evidence of NO_x increases since preindustrial times through the accumulation of nitrate (the end product of NO_x) in Greenland ice [81].

SO_2 and Sulfate Aerosols:

The sulfur in fossil fuel is usually emitted as SO_2. The sulfur content of coal and oil is 0.5–2.5% by weight; in contrast, the sulfur content of biomass is small (e.g., S/C <0.001 in savanna), much smaller than the fuel nitrogen (e.g., N/C = 0.06 in savanna). The atmosphere continues to oxidize this S(IV) to S(VI) and eventually forms sulfates ($SO4^{=}$), which become part of the atmospheric aerosols. The sulfuric acid formed from SO_2 (and to a lesser extent the nitric acid formed from oxidation of NO_x) is the primary source of acid deposition. The life cycle of SO_2 from emission to sulfate to wet or dry deposition at the surface is only a few days.

Combustion of fossil fuels provides a source of SO_2 of about 80 MT/yr (as S), metal smelting about 8 MT(S)/yr, and biomass burning about 2 MT(S)/yr. Natural sources (oceanic emissions, vegetation, soils, and volcanoes) emit about 25 MT(S)/yr of various sulfur compounds (e.g., Ref. 82). Combustion clearly dominates the sulfur budget of the troposphere.

The reflective nature of the sulfate aerosols makes SO_2 an effective anti-GHG [83]. Sulfate aerosols can also impact cloud formation, generally producing more reflective clouds with more small droplets. It has been proposed that the increase in sulfate aerosols since the preindustrial era has offset a large part of the greenhouse forcing from CO_2 increases [84].

Sulfate aerosols in the stratosphere interact strongly with the NO_x chemistry and can greatly enhance catalytic loss of O_3 (e.g., Ref. 85). The large combustion source of SO_2 at the surface is rapidly converted to sulfate and does not reach the stratosphere, but explosive volcanoes can inject SO_2 directly into the stratosphere. Based on a possible decadal trend in background sulfate levels over Wyoming (between large volcanic injections) and a calculation of jet-fuel use, aircraft SO_2 was proposed as the major source of stratospheric sulfate layer [86]; a simple analysis of the stratospheric sulfur budget that includes OCS and simulation of aircraft SO_2 using an atmospheric model [87] ruled out this hypothesis.

OCS:

Carbonyl sulfide is moderately long lived in the troposphere (about 30 years against reaction with OH) with primarily oceanic sources [88]. As an insoluble sulfur compound with an abundance of about 500 ppt, it is believed to be the major source of the stratospheric sulfate layer during volcanically quiescent periods [89]. However, during the past two decades, the median stratospheric sulfate abundance was at least four times this background. Combustion sources of OCS from fossil fuel have been identified [90], but these are not believed to be important globally. There is an indication of possibly larger sources from biomass burning [91]. Significant uncertainty remains in understanding the global OCS budget [92]. It is possible that OCS from biomass burning has increased the nonvolcanic, background sulfate layer and impacted ozone, but we have no strong evidence for a change in OCS since preindustrial times.

Soot

Black carbon aerosols, comprised of graphitic carbon or soot, act as strong absorbers of sunlight in the

atmosphere [93]. Even small amounts of soot within liquid sulfate aerosols or water droplets can decrease the single scattering albedo and reduce the shortwave albedo of clouds [94,95]. Combustion is the only source of soot, and it is possible to distinguish fossil-fuel sources from biomass burning sources [96]. Combustion and subsequent photochemical generation from combustion products (e.g., SO_2, NMHC) generate very fine particles that, once lofted into the upper troposphere, have a long residence time and can be transported globally [97]. Arctic haze consists of graphitic carbon with some other particulate carbon produced in lower temperature combustion or from photochemical oxidation of VOC, but it is the absorbing properties of the soot that are of major concern [98]. Soot from fossil fuels and biomass burning [99] may have global impact as a GHG, but predictions are difficult as the formation of fine black carbon aerosols varies greatly depending on the conditions of combustion. For example, the Kuwaiti oil fires were expected to have a large climatic impact with soot production almost matching current global emissions of about 50 kt/day, but measurements [68] showed that these well fires were relatively efficient (96% as CO_2), and thus soot emissions were much smaller, only 3.4 kt/day.

Tropospheric O_3

Ozone can be produced rapidly by a mix of combustion products and natural emissions in the presence of sunlight (e.g., Refs. 6, 73). In the boundary layer over the U.S. away from cities, empirical evidence shows that between 5 and 8 ozone molecules are produced per NO_x molecule emitted, before the NO_x catalyst is removed by oxidation to nitrate [100]. Surface ozone values commonly exceed 100 ppb in the eastern U.S. in summer under meteorological conditions favorable for photochemical formation of ozone, high temperatures and stagnant air (e.g., Ref. 101). Emissions from biomass burning also produce enhancements of ozone [102]. The impact of massive burns in tropical regions during the southern dry season (August–October) can be seen in satellite data for tropospheric CO and O_3 [103,104,105]. There is a large region over South America, southern Africa, and the south tropical Atlantic Ocean where ozone and CO values are more than twice as high as over the central Pacific Ocean at the same latitudes. In remote marine air, photochemistry provides a net sink for ozone, as concentrations of NO_x are exceedingly low, <10 ppt in the boundary layer.

Combustion emissions, NO_x and NMHC, and products, O_3, are generally short lived in the boundary layer, with a lifetime of less than a few days. Lifetimes are much longer in the upper troposphere. Recent studies have proposed that the direct export of urban O_3 and of NO_x from combustion [80] and the rapid transport of short-lived compounds from the boundary layer to the upper troposphere by cumulus convection [106] are important components of the tropospheric O_3 budget.

There is evidence that the concentrations of surface ozone in Europe, including high mountain sites, have doubled over this century [107,108]. Such are broadly consistent with global model simulations (e.g., Ref. 109). Measurements of the vertical distribution of ozone since the late 1960s show increases in tropospheric ozone over northern midlatitudes of <1–2% per year (e.g., Refs. 110,111). There are significant spatial variations in the trends, and indications that the trend over North America and Europe has levelled off in the last decade [112]. There is no evidence for long-term trends in ozone at southern midlatitudes, based on a 30-year data record. Long-term data for the tropics are lacking.

Nitrogen oxides are the limiting species for ozone formation, and emissions of NO_x from combustion have levelled off in both the US and Western Europe in the past decade, due to a combination of slow growth in fossil-fuel combustion, and regulation of vehicular emissions in the U.S. Emissions are growing rapidly in China and the far East (excluding Japan) because of large increases in consumption of fossil fuels, 5% per year [113]. Aircraft emissions of NO_x from have grown rapidly in the past 20 years, and there is much current interest in possible effects on ozone in the upper troposphere. Ozone is a GHG, and surface temperatures are most sensitive to changes in ozone near the tropopause. The budget of NO_x, and hence of ozone, in the upper troposphere is notwell quantified at present.

Conclusions

Combustion of fossil and recent biomass has clearly changed the composition of the atmosphere. It is responsible for most of the enhanced greenhouse forcing to date (through CO_2, tropospheric O_3, soot) and also some counteracting effects (through SO_2). It has likely changed the tropospheric oxidant levels (through CO_1 NO_x, NMHC) but has had minimal impact on stratospheric O_3 (through CH_3Cl, CH_3Br, CH_4). Most of the important GHG and OXG have significant natural sources, which are not well defined today and may be changing; and thus, quantifying the role of combustion is difficult.

REFERENCES

1. Broecker, W. S., "Man's Oxygen Reserves," *Science* 168:1537–1538 (1970).
2. Arrhenius, S., "On the Influence of Carbonic Acid in the Air upon the Temperature of the ground," *Lon-*

don, Edinburgh, Dublin Philos. Mag. J. Sci. 41:237–276 (1896).

3. Intergovernmental Panel on Climate Change, *Climate Change 1992,* J. T. Houghton, B. A. Callander, and S. K. Varney, (Eds.), Cambridge University Press, 1994, pp. 1–200.
4. Molina M. J., and Rowland, F. S., "Stratospheric Sink for Chlorofluoromethanes: Chlorine Atom Catalyzed Destruction of Ozone," *Nature* 249:810–814 (1974).
5. Johnston, H. J., "Reduction of Stratospheric Ozone by Nitrogen Oxide Catalysts from Supersonic Transport Exhaust," *Science* 173:517–522 (1971).
6. Haagen-Smit, A. J., "Chemistry and Physiology of Los Angeles Smog," *Ind. Eng. Chem.* 44:1342–1346. (1951).
7. Fishman, J., Ramanathan, V., Crutzen, P. J., and Liu, S. C., "Tropospheric Ozone and Climate," *Nature* 282:818–820 (1979).
8. Sze, N. D., "Anthropogenic CO Emissions: Implications for the Atmospheric CO-OH-CH_4 Cycle," *Science* 195:673–675 (1977).
9. Thompson, A. M., "The Oxidizing Capacity of the Earth's Atmosphere: Probable Past and Future Changes," *Science* 256:1157–1165 (1992).
10. IPCC, *Intergovernmental Panel on Climate Change, Radiative Forcing of Climate Change 1994* (J. T. Houghton et al., Eds.), Cambridge University, New York, 1994.
11. World Meteorological Organization, *Scientific Assessment of Ozone Depletion: 1991,* Global Ozone Research and Monitoring Project, Report No. 25, 1992.
12. Finlayson-Pitts, B. J., and Pitts, J. N., Jr., *Atmospheric Chemistry: Fundamentals and Experimental Techniques,* Wiley-Interscience, New York, 1986, pp. 1–1098.
13. Seinfeld, J. H., *Atmospheric Chemistry and Physics of Air Pollution,* Wiley-Interscience, New York, 1986, pp. 1–738.
14. Warneck, P., *Chemistry of the Natural Atmosphere,* Academic Press, New York, 1988, pp. 1–757.
15. Logan, J. A., Prather, M. J., Wofsy, S. C., and McElroy, M. B., "Tropospheric Chemistry: a Global Perspective," *J. Geophys. Res.* 86:7210–7254 (1981).
16. Cicerone, R. J., "Atmospheric CF_4: a Nearly Inert Gas," *Science* 206:59–61 (1979).
17. Ravishankara, A. R., Solomon, S., Turnipseed, A. A., and Warren, R. F., "Atmospheric Lifetimes of Long-Lived Halogenated Species," *Science* 259:194–199 (1993).
18. Chapman, S., "A Theory of Upper Atmospheric Ozone," *Mem. Roy. Met. Soc.* 3:103–125 (1930).
19. Raynaud, D., Jouzel, J., Barnola, J. M., Chappellaz, J., Delmas, R. J., and Lorius, C., "The Ice Record of Greenhouse Gases," *Science* 259:926–934 (1993).
20. Prinn, R., Cunnold, D., Simmonds, P., Alyea, F., Boldi, R., Crawford, A., Fraser, P., Gutzler, D., Hartley, D., Rosen, R., and Rasmussen, R., "Global Average Concentration and Trend for Hydroxyl Radicals Deduced from ALE/GAGE Trichloroethane (Methyl Chloroform) Data for 1978–1990," *J. Geophys. Res.* 97:2445–2461 (1992).
21. Spivakovsky, C. M., Yevich, R., Logan, J. A., Wofsy, S. C., McElroy, M. B., and Prather, M. J., "Tropospheric OH in a 3-D Chemical Tracer Model: an Assessment Based on Observations of CH_3CCl_3," *J. Geophys. Res.* 95:18, 441–18, 471 (1990).
22. Keeling, C. D. et al., "A 3-D Model of Atmospheric CO_2 Based on Observed Winds: 1. Analysis and Observational Data," in *Aspects of Climate Variability in the Pacific and Western Americas* (D. H. Peterson, Ed.), Geophysical Monograph 55, American Geophysical Union, Washington, DC, 1989, pp. 305–363.
23. Dlugokencky, E. J., Masarie, K. A., Lang, P. M., Tans, P. P., Steele, L. P., and Nisbet, E. G., "A Dramatic Decrease in the Growth Rate of Atmospheric Methane in the Northern Hemisphere during 1992, *Geophys. Res. Lett.* (1994), in press.
24. Etheridge, D. M., Pearman, G. I., and Fraser, P. J., "Changes in Tropospheric Methane between 1841 and 1978 from a High Accumulation-Rate Antarctic Ice Core," *Tellus* 44B:282–294 (1992).
25. Chappellaz, J., Blunier, T., Raynaud, D., Barnola, J. M., Schwander, J., and Stauffer, B., "Synchronous Changes in Atmospheric CH_4 and Greenland Climate between 40 and 8 kyr BP," *Nature* 366:443–445 (1993).
26. Marland, G., and Rotty, R. M., "Carbon Dioxide Emissions from Fossil Fuels: a Procedure for Estimation and Results for 1950–1982," *Tellus* 36B:232–261 (1984).
27. Andres, T. J., Marland, G., Boden, T., and Bischoff, S., "Carbon Dioxide Emissions from Fossil Fuel Combustion and Cement Manufacture 1751–1991 and an Estimate of Their Isotopic Composition and Latitudinal Distribution," in *The Carbon Cycle* (T. Wigley, Ed.), Cambridge University Press, 1994 (in press).
28. Ferek, R. J., Hobbs, P. V., Herring, J. A., Laursen, K. K., Weiss, R. E., and Rasmussen, R. A., "Chemical Composition of Emissions from the Kuwaiti Oil Fires," *J. Geophys. Res.* 97:14483–14489 (1992).
29. Crutzen, P. J., and Andreae, M. O., "Biomass Burning in the Tropics: Impact on Atmospheric Chemistry and Biogeochemical Cycles," *Science* 250:1669–1678 (1990).
30. Ward, D. E. et al., "Smoke and Fire Characteristics for Cerrado and Deforestation Burns in Brazil: Base-B Experiment," *J. Geophys. Res.* 97:14601–14619 (1992).
31. Andreae, M. O., in *Biogeochemistry of Global Change: Radiatively Active Trace Gases* (R. S. Oremland, Ed.), Chapman & Hall, New York, 1993, pp. 113–150.
32. Crutzen, P. J., Heidt, L. E., Kranec, J. P., Pollock, W. H., and Seiler, W., "Biomass Burning as a Source of Atmospheric Gases CO, H_2, N_2O, NO, CH_3Cl and COS," *Nature* 282:253–256 (1979).

33. Hurst, D. F., Griffith, D. W. T., Carras, J. N., Williams, D. J., and Fraser, P. J., "Measurements of Trace Gases Emitted by Australian Savanna Fires during the 1990 dry season," *J. Atmos. Chem.* 18:33–56 (1994).
34. Lobert, J. M., Scharffe, D. H., Hao, W. M., Kuhlbusch, T. A., Seuwen, R., Warneck, P., and Crutzen, P. J., "Experimental Evaluation of Biomass Burning Emissions: Nitrogen and Carbon Containing Compounds," in *Global Biomass Burning: Atmospheric, Climatic and Biospheric Implications* (J. S. Levine, Ed.), MIT Press, Cambridge, MA, 1991, pp. 289–304.
35. Keeling, R. F., and Schertz, S. R. "Seasonal and Interannual Variations in Atmospheric Oxygen and Implications for the Global Carbon Cycle," *Nature* 358:723–727 (1992).
36. Shine, K. P., Derwent, R. G., Wuebbles, D. J., and Morcrette, J.-J., "Radiative Forcing of Climate," in *Climate Change. The IPCC Scientific Assessment* (G. J. Jenkins, J. T. Houghton, and J. J. Ephraums, Eds.), Cambridge University Press, Cambridge UK, 1990, pp. 41–68.
37. Dixon, R. K., Brown, S. A., Houghton, R. A., Solomon, A. M., Trexler, M. C., and Wisniewski, J., "Carbon Pools and Flux of Global Forest Ecosystems," *Science* 263:185–190 (1994).
38. Schumann, U., and Wurzel, D., (Eds.), *Impact of Emissions from Aircraft and Spacecraft upon the Atmosphere,* Proceedings of Colloquium, Köln, Germany, April 1994, DLR Mitteilung 94-06.
39. Harwood, R. S., Jackman, C. H., Karol, I. L., and Qiu, L. X., "Predicted Rocket and Shuttle Effects on Stratospheric Ozone," in *Scientific Assessment of Ozone Depletion: 1991*, Chap. 10, World Meteorological Organization, Geneva, 1992, Global Ozone Research and Monitoring Project, Vol. 25, pp. 10.1–10.12.
40. Ko, M. K. W., Douglass, A. R., Grose, W. L., and McElroy, M. B., "Model Calculation of HSCT Effect," in *The Atmospheric Effects of Stratospheric Aircraft: Interim Assessment Report of the NASA High-Speed Research Program.* NASA Ref. Publ. 1333, Washington, DC, June 1993, pp. 103–125.
41. Cicerone, R. J., and Oremland, R. S., "Biogeochemical Aspects of Atmospheric Methane," *Global Biogeochem. Cycles* 2:299–327 (1988).
42. Khalil, M. A. K., Rasmussen, R. A., Shearer, M. J., Ge, S., and Rau, J. A., "Methane from Coal Burning," *Chemosphere* 26:473–477 (1993).
43. Hao, W. M., and Ward, D. E., "Methane Production from Global Biomass Burning," *J. Geophys. Res.* 98:20657–20661 (1993).
44. Quay, P. D. et al., "Carbon Isotopic Composition of Atmospheric CH_4: Fossil and Biomass Burning Source Strengths," *Global Biogeochem. Cycles* 5:25–47 (1991).
45. McElroy, M. B., and McConnell, J. C., "Nitrous Oxide: A Natural Source of Stratospheric NO," *J. Atmos. Sci.* 28:1095–1098 (1971).
46. Prinn, R., Cunnold, D., Rasmussen, R., Alyea, F., Crawford, A., Fraser, P., and Rosen, R., "Atmospheric Emissions and Trends of Nitrous Oxide Deduced from 10 Years of ALE-GAGE Data," *J. Geophys. Res.* 95:18369–18385 (1990).
47. Pierotti, D., and Rasmussen, R. A., "Combustion as a Source of N_2O in the Atmosphere," *Geophys. Res. Lett.* 3:265–267 (1976).
48. Weiss, R. F., and Craig, H., "Production of Atmospheric N_2O by Combustion," *Geophys. Res. Lett.* 3:751–753 (1976).
49. Hao, W. M. et al., "Sources of Atmospheric N_2O from Combustion," *J. Geophys. Res.* 92:3098–3104 (1987).
50. Muzio, L. J., and Kramlich, J. C., "An Artifact in the Measurement of N_2O from Combustion Sources," *Geophys. Res. Lett.* 15:1369–1372 (1988).
51. Linak, W. P. et al., "N_2O Emissions form Fossil Fuel Combustion," *J. Geophys. Res.* 95:7533–7541 (1990).
52. Berges, M. G. M., Hofmann, R. M., Scharffe, D., and Crutzen, P. J., "N_2O Emissions from Motor Vehicles in Tunnels and Their Global Extrapolation," *J. Geophys. Res.* 98:18527–18531 (1993).
53. Environmental Protection Agency, Supplement F to Compilation of Air Pollutant Emission Factors, Vol. 1, Stationary and Point Sources, Rep. AP-42, Research Triangle Park, 1993.
54. Tabazedah, A., and Turco, R. P., "Stratospheric Chlorine Injection by Volcanic Eruptions: HCl Scavenging and Implications for Ozone," *Science* 260:1082–1086 (1993).
55. Tassios, S., and Packham, D. R., "The Release of CH_3Cl from Biomass Burning in Australia," *J. Air Pollution Control. Assoc.* 35:41–42 (1985).
56. Manö, S., and Andreae, M. O., "Emission of Methyl Bromide from Biomass Burning," *Science* 263:1255–1257 (1994).
57. Butler, J. H., "The Potential Role of the Ocean in Regulating Atmospheric CH_3Br," *Geophys. Res. Lett.* 21:185–188 (1994).
58. Lovelock, J. E., "Atmospheric Fluorine Compounds as Indicators of Air Movements," *Nature* 230:379 (1971).
59. Elkins, J., Thompson, T., Swanson, T., Butler, J., Hall, B., Cummings, S., Fisher, D., and Raffo, A., "Decrease in the Growth Rates of Atmospheric Chlorofluorocarbons-11 and -12," *Nature* 364:780–783 (1993).
60. Fisher, D., Duafala, T., Midgley, P., and Niemi, C., "Production and Emissions of CFCs, Halons, and Related Molecules," in *Concentrations, Lifetimes, and Trends of CFCs, Halons, and Related Species* Chap. 2 (J. Kaye and S. Penkett, Eds.), NASA Ref. Publ. 1339, Washington, DC, 1994.
61. Cunnold, D. M., Fraser, P. J., Weiss, R. F., Prinn, R. G., Simmonds, P. G., Miller, B. R., Alyea, F. N., and Crawford, A. J., "Global Trends and Annual Releases of $CFCl_3$ and CF_2Cl_2 Estimated from ALE/GAGE and Other Measurements from July 1978 to June 1991," *J. Geophys. Res.* 99:1107–1126 (1994).

62. McCulloch, A., "Global Production and Emissions of Bromochlorodifluoromethane and Bromotrifluoromethane (Halons 1211 and 1301)," *Atmos. Environ.* 26A:1325–1329 (1992).
63. Prather, M. J., Garcia, M. M., Douglass, A. R., Jackman, C. H., Ko, M. K. W., and Sze, N. D., "The Space Shuttle's Impact on the Stratosphere," *J. Geophys. Res.* 95:18583–18590 (1990).
64. Bojkov, R. D., Zerefos, C. S., Balis, D. S., Ziomas, I. C., and Bais, A. F., "Record Low Total Ozone during Northern Winters of 1992 and 1993," *Geophys. Res. Lett.* 20:1351–1354 (1993).
65. Gleason, J. F., Bhartia, P. K., Herman, J. R., McPeters, R. D., Newman, P., Stolarski, R. S., Flyn, L., Labow, G., Larko, D., Seftor, C., Wellemeyer, C., Komhyr, W. D., Miller A. J., and Planet, W., "Record Low Global Ozone in 1992," *Science* 260:523–526 (1993).
66. Wang, W. C., Yung, Y. L., Lacis, A. A., Mo, T., and Hansen, J. E., "Greenhouse Effect Due to Man-Made Perturbations of Trace Gases," *Science* 194:685–690 (1976).
67. Hansen, J., Lacis, A., and Prather, M., "Greenhouse Effect of Chlorofluorocarbons and Other Trace Gases," *J. Geophys. Res.* 94:16417–16421 (1989).
68. Laursen, K. K., Ferek, R. J., Hobbs, P. V., and Rasmussen, R. A., "Emission Factors for Particles, Elemental Carbon, and Trace Gases from the Kuwaiti Oil Fires," *J. Geophys. Res.* 97:14491–14497 (1992).
69. Novelli, P. C., Masarie, K. A., Tans, P. P., and Lang, P. M., "Recent Changes in Atmospheric Carbon Monoxide," *Science* 263:1587–1590 (1993).
70. Dianov-Klokov, V. I., Yurganov, L. N., Grechko, E. I., and Dzhola, A. V., "Spectroscopic Measurements of Carbon Monoxide and Methane 2: Seasonal Variations and Long Term Trends," *J. Atmos. Chem.* 8:153–164 (1989).
71. Bakwin, P. S., Tans, P. P., and Novelli, P. C., "Carbon Monoxide Budget in the Northern Hemisphere," *Geophys. Res. Lett.* 21:433–436 (1994).
72. Piccot, S. D., Watson, J. J., and Jones, J. W., "A Global Inventory of Volatile Organic Compound Emissions from Anthropogenic Sources," *J. Geophys. Res.* 97:9897–9912 (1992).
73. Seinfeld, J. et al., *Rethinking the Ozone Problem in Urban and Regional Air Pollution*, National Academy Press, Washington, DC, 1991, pp. 1–489.
74. Carroll, M. A., Ridley, B. A., Montzka, D. D., Hubler, G., Walega, J. G., Norton, R. B., and Huebert, B. J., "Measurements of NO and NO_2 during the Mauna Loa Observatory Photochemistry Experiment," *J. Geophys. Res.* 97:10361–10374 (1992).
75. Franzblau, E., and Popp, C. J., "Nitrogen Oxides Produced from Lightning," *J. Geophys. Res.* 94:11089–11104 (1989).
76. Liaw, Y. P., Sisterson, D. L., and Miller, N. L., "Comparison to Field, Laboratory, and Theoretical Estimates of Global Nitrogen Fixation by Lightning," *J. Geophys. Res.* 95:22,489–22,494 (1990).
77. Goldenbaum, G. C., and Dickerson, R. R., "NO Production by Lightning Discharges," *J. Geophys. Res.* 98:18333–18338 (1993).
78. Baughcum, S. L. et al., "Aircraft Emissions Scenarios," in *The Atmospheric Effects of Stratospheric Aircraft: A 3rd Program Report* (R. Stolarksi and H. Wesoky, Eds.), NASA Ref. Publ. 1313, Washington, DC, 1993, pp. 87–208.
79. Hoinka, K. P., Reinhardt, M. E., and Metz, W., "North Atlantic Air Traffic within the Lower Stratosphere: Cruising Times and Corresponding Emissions," *J. Geophys. Res.* 98:23113–23131 (1993).
80. Jacob, D. J., Logan, J. A., Gardner, G. M., Yevich, R. M., Spivakovsky, C. M., Wofsy, S. C., Munger, J. M., Sillman, S., and Prather, M. J., "Factors Regulating Ozone over the United States and Its Export to the Global Atmosphere," *J. Geophys. Res.* 98:14817–14826 (1993).
81. Neftel, A., Beer, J., Oeschger, H. Zurcher, F., and Finkel, R. C., "Sulphate and Nitrate Concentrations in Snow from South Greenland 1895–1978," *Nature* 314:611–613 (1985).
82. Spiro, P. A., Jacob, D. J., and Logan, J. A., "Global Inventory of Sulfur Emissions with 1×1 Degree Resolution," *J. Geophys. Res.* 97:9023–9036 (1992).
83. Hansen, J. E., Lacis, A. A., Lee, P., and Wang, W. C., "Climatic Effects of Atmospheric Aerosols," in *Aerosols Anthropogenic and Natural Sources and Transport* (T. J. Kneip and P. J. Lioy, Eds:), Annals of the NY Academy of Science, New York, 1980, Vol. 338, pp. 575–587.
84. Charlson, R. J., Langner, J., Rodhe, H., Leovy, C. B., and Warren, S. G., "Perturbation of the Northern Hemisphere Radiative Balance by Backscattering from Anthropogenic Sulfate Aerosols," *Tellus* 43AB:152–163 (1991).
85. Hofmann, D. J., and Solomon, S., "Ozone Destruction through Heterogeneous Chemistry following the Eruption of El Chichon," *J. Geophys. Res.* 94:5029–5041 (1989).
86. Hofmann, D. J., "Aircraft Sulfur Emissions," *Nature* 349:659 (1991).
87. Bekki, S., and Pyle, J. A., "Two-Dimensional Assessment of the Impact of Aircraft Sulphur Emissions on the Stratospheric Sulphate Layer," *J. Geophys. Res.* 97:15839–15848 (1992).
88. Ferek, R. J., and Andreae, M. O., "Photochemical Production of OCS in Marine Surface Waters," *Nature* 307:148–150 (1984).
89. Crutzen, P. J., "The Possible Importance of CSO for the Sulfate Layer of the Stratosphere," *Geophys. Res. Lett.* 3:73–78 (1976).
90. Fried, A. et al., "Measurements of OCS in Automotive Emissions and an Assessment of its Importance to the Global Sulfur Cycle," *J. Geophys. Res.* 97:14621–14634 (1992).
91. Bingemer, H. G. et al., "Sulfur Gases and Aerosols in

and above the Equatorial African Rain Forest," *J. Geophys. Res.* 97:6207–6217 (1992).

92. Johnson, J. E., Bandy, A. R., Thornton, D. C., and Bates, T. S., "Measurement of Atmospheric COS during the NASA CITE Project: Implications for the Global COS Budget," *J. Geophys. Res.* 98:23443–23448 (1993).
93. Shaw, G. E., "Perturbation to the Atmospheric Radiation Field from Carbonaceous Aerosols," in *Particulate Carbon, Atmospheric Life Cycle* (G. T. Wolff and R. L. Klimisch, Eds.), Plenum, New York, 1982, pp. 53–73.
94. Twomey, S. A., "The Influence of Pollution on the Short-Wave Albedo of Clouds," *J. Atmos. Sci.* 34:1149–1152 (1977).
95. Ackerman, T. P., and Toon, O. B., "Absorption of Visible Radiation in Atmosphere Containing Mixtures of Absorbing and Non-absorbing Particles," *Appl. Opt.* 20:3661–3668 (1981).
96. Clayton, G. D., Arnold, J. R., and Patty, F. A., "Determination of Sources of Particulate Atmospheric Carbon," *Science* 122:751–753 (1955).
97. Heintzenberg, J., "Size-Aggregated Measurements of Particulate Elemental Carbon and Aerosol Absorption at Remote Locations," *Atmos. Environ.* 16:2461–2469 (1982).
98. Currie, L. A., "Mankind's perturbations of Particulate Carbon," in *Radiocarbon After Four Decades*, Chap. 33 (R. E. Taylor, A. Long, and R. S. Kra, Eds.), Springer-Verlag, New York, 1992, pp. 535–568.
99. Penner, J. E., Dickinson, R. E., and O'Neill, C. A., "Effects of Aerosol from Biomass Burning on the Global Radiation Budget," *Science* 256:1432–1434 (1992).
100. Trainer, M. et al., "Correlation of Ozone with NO_y in Photochemically Aged Air," *J. Geophys. Res.* 98:2917–2925 (1993).
101. Logan, J. A., "Ozone in Rural Areas of the United States," *J. Geophys. Res.* 94:8511–8532 (1989).
102. Evans, L. F., Weeks, I. A., Eccleston, A. J., and Packham, D. R., "Photochemical Ozone in Smoke from Prescribed Burning of Forests," *Environ. Sci. Technol.* 11:896–900 (1977).
103. Reichle, H. et al., "The Distribution of Middle Tropospheric CO during Early October 1984," *J. Geophys. Res.* 95:9845–9856 (1990).
104. Fishman, J., Watson, C. E., Larsen, J. C., and Logan, J. A., "Distribution of Tropospheric Ozone Determined from Satellite Data," *J. Geophys. Res.* 95:3599–3617 (1990).
105. Watson, C. E., Fishman, J., and Reichle, H. G. Jr., "The Significance of Biomass Burning as a Source of CO and O_3 in the Southern Hemisphere Tropics: a Satellite Analysis," *J. Geophys. Res.* 95:16443–16450 (1990).
106. Pickering, K. E., Thompson, A. M., Scala, J. R., Tao, W.-K., Dickerson, R. R., and Simpson, J., "Free Tropospheric Ozone Production following Entrainment of Urban Plumes into Deep Convection," *J. Geophys. Res.* 97:17985–18000 (1992).
107. Volz, A., and Kley, D., "Evaluation of the Montsouris Series of Ozone Measurements Made in the Nineteenth Century," *Nature* 332:240 (1988).
108. Staehelin, J., Thudium, J., Buehler, A., Volz-Thomas, A., and Graber, W., "Trends in Surface Ozone Concentrations at Arosa (Switzerland)," *Atmos. Environ.* 28:75–78 (1994).
109. Isaksen, I. S. A., and Hov, O., "Calculation of Trends in the Tropospheric Concentration of O_3, OH, CO, CH_4, and NO_x," *Tellus* 39B:271–285 (1987).
110. Logan, J. A., "Tropospheric Ozone: Seasonal Behavior, Trends and Anthropogenic Influence," *J. Geophys. Res.* 90:10,463–10,482 (1985).
111. World Meteorological Organization, *Scientific Assessment of Stratospheric Ozone: 1989*, Global Ozone Research and Monitoring Project, Report No. 20, Geneva, 1990.
112. Logan, J. A., "Trends in the Vertical Distribution of Ozone: an Analysis of Ozonesonde Data," *J. Geophys. Res.*, submitted (1994).
113. Kato, N., and Akimoto, H., "Anthropogenic Emissions of SO_2 and NO_x in Asia: Emissions Inventory," *Atmos. Environ.* 26A:2997–3017 (1992).

COMMENTS

P. Wiesen, University of Wuppertal, Germany. You have shown quite nicely the tremendous increase in the concentrations of different atmospheric trace gases during the last 150 years. More recently it was observed, however, that the rates of increase of the concentrations of carbon monoxide and nitrous oxide and, in particular, methane have decreased during the last two years. Could you please comment on that?

Author's Reply. Yes, the growth rates in many trace gases have changed over the past decade. Most species have continued to increase, but their growth has slowed. In some cases, such as the CFCs, we can relate this to the phaseout of production (and hence emissions) as prescribed under the Montreal Protocol and its amendments. Some HCFCs used as CFC substitutes are increasing more rapidly. In the case of CO_2 and CH_4, the slowdown in growth during the period 1991–1993 cannot be easily explained, and measurements into 1994 indicate a return to more rapid growth. The immense injection of stratospheric sulfate by

Mt. Pinatubo changed global temperatures and stratospheric ozone over the two years following eruption in 1991, and may be in part responsible for some of these variations. For CO, the recent data show a dramatic decline in absolute concentrations that is not yet understood. For N_2O, the trend varies from year to year, but has been regular, about 0.25%/yr over the past decade. The record of CO_2, CH_4, and N_2O in ice cores shows that some natural variability in these trace gases preceded global perturbations by humanity.

•

Dr. Hans-Robert Volpp, University of Heidelberg, Germany. I would like to comment on Dr. Wiesen's (University of Wuppertal) question concerning the recently observed stagnation of the tropospheric methane concentration. Could it be possible that this effect is due to an increase in the OH radical concentration in the troposphere in recent years rather than due to an reduction of the global methane release rate?

Author's Reply. The slowdown in CH_4 growth to almost zero in 1992–1993 cannot be explained by increases in the CH_4 sink alone, because the most rapid observed change was in the latitudinal gradient, implying a drop in high northern latitude sources. There are several recent predictions that the decrease in stratospheric ozone driven by Mt. Pinatubo could have contributed to this decline in CH_4 growth, but these cannot explain the change in north-south gradient. Also, with the recent recalibration of the CH_3CCl_3 measurements made by the ALE/GAGE network, there is no longer any evidence for a change in the OH reactivity of the troposphere over the past decade.

•

David R. Crosley, SRI International, USA. You singled out aircraft as a special NO_x emission source because of the altitude at which the emissions occur. Would you comment on the effects of the current subsonic and projected supersonic fleets on the atmosphere?

Author's Reply. The current subsonic fleet is predicted by some models to increase background levels of NO_x in the upper troposphere by as much as 30% in the northern midlatitudes. The ensuing calculations of ozone increases due to this NO_x are typically 5% at the most impacted locations. These predictions need to be re-examined from scratch using three-dimensional models for tropospheric chemistry that are currently being developed, but they are not ready for such assessments. Moreover, we must develop a larger, more coherent database of upper-tropospheric measurements that provide the essential calibration for these models. It will still be difficult to quantitatively determine the role of aircraft NO_x relative to the other natural and anthropogenic sources.

The assessment of supersonic aircraft (High-Speed Civil Transports) cannot rely on a combination of measurements and models for the current atmosphere alone. The models must predict the impact of large effluents of NO_x and H_2O at supersonic cruise levels (15–20 km) in a future stratosphere. The most recent NASA assessment from the High-Speed Research Program (Wesoky and Stolarski, 1994) notes that a large fleet of HSCTs would indeed perturb stratospheric NO_x (by up to 50%) and H_2O (by up to 25%), but that these changes in background trace gases would have only a small impact on stratospheric ozone. The crux of this evaluation is the recent recognition of heterogeneous chemical reactions on the stratospheric sulfate particles that reduce the role of NO_x as an ozone-destroying catalyst in the lower stratosphere.

•

Jan R. Pels, Delft University of Technology, The Netherlands. Fluidised-bed combustion of coal produces N_2O levels much higher than conventional methods. Please comment on the estimations given by G. G. de Soete, who calculates that, if all coal used for power generation would be burnt in FBCs, the emission of N_2O from combustion would be as big as the natural sources.

Do you think that knowing this, FBC should be limited unless it can be applied with strongly reduced N_2O emission?

Author's Reply. This question is appropriate. We have not yet found all of the anthropogenic sources of N_2O that we know are needed to explain the increase since the preindustrial. The original identification of N_2O from coal-fired power plants was erroneous, and only recently has it been shown that these measurements were corrupted (N_2O was produced in the samples before measurement). The role of FBC as a significant N_2O source needs to be confirmed.

•

Bruce W. Gerhold, Phillips Petroleum Company, USA. Atmospheric mixing distributes the "greenhouse" gases (CO_2 for example) at least around a hemisphere. On the other hand, "anti-greenhouse" particulates (SO_x, soot) remain localized around a source, roughly around the continents. Thus, over North America and Europe, incoming solar radiation will be reflected, thereby counteracting part of the greenhouse warming. In contrast, the oceans have little particulate cover and the climate is subject to full greenhouse warming. Do models account for local variations? Might global warming be seen first in remote islands?

Author's Reply. Yes, the long-lived greenhouse gases like CO_2 and CH_4 are well mixed and have a rather uniform radiative forcing of the climate (although this simple view does not take into account that cloud cover and water vapor can dramatically change the regional impact of even these well-mixed gases). The two examples of radiative forcing that is spatially variable are aerosols and ozone (both strat-

ospheric and tropospheric). Several model studies have recently assessed the question of whether the aerosol "cooling" could offset an equivalent CO_2 "warming." The models do include the spotty distribution of aerosols around pollution regions, and do include the effects of clouds and land-ocean differences. Thus far the results are inconclusive, but the recent international climate assessment (IPCC) has strongly warned that equal but opposite radiative forcings may not cancel in terms of regional or even hemispheric climate impacts.

•

Ronald S. Sheinson, Naval Research Laboratory, Washington, DC. Combustion, or rather suppressing combustion via halons (brominated halocarbons), has a profound effect on stratospheric ozone. Halon production has already been stopped in the developed countries under the Montreal Protocol process. Also significant is the effect of environmental concerns on combustion in spurring extensive halon replacement research. While global warming impact of suppression candidates at the quantities required should be very low, the restriction exercised by governments on their implementation in practical systems must be considered. Environment legislation, not the quantified impacts detailed in this paper, frequently dominates.

Author's Reply. Production of halons (used in fire suppression) has been halted. There is still a considerable bank of halons that can be recycled while substitutes are sought. The concentration of the short-lived halon-1211 has already been observed to decline.

Yes, it is the responsibility of the scientific community through national and international assessments to help guide policy so that regulations (which are almost always painful to some community) achieve the desired goal of improving the global environment.

Twenty-Fifth Symposium (International) on Combustion/The Combustion Institute, 1994/pp. 1529–1537

A BIFURCATION ANALYSIS OF HIGH-TEMPERATURE IGNITION OF H_2-O_2 DIFFUSION FLAMES

ANTONIO L. SÁNCHEZ
Center for Energy and Combustion Research
University of California–San Diego, La Jolla, CA 92093-0310, USA

AMABLE LIÑÁN
Universidad Politécnica de Madrid, E. T. S. I. Aeronauticos
Plaza Cardenal Cisneros 3, 28040 Madrid, Spain

AND

FORMAN A. WILLIAMS
Center for Energy and Combustion Research
University of California–San Diego, La Jolla, CA 92093-0310, USA

The form of the ignition branch for steady, counterflow, hydrogen-oxygen diffusion flames, with dilution permitted in both streams, is investigated for two-step reduced chemistry by methods of bifurcation theory. Attention is restricted to fuel-stream temperatures less than or equal to the oxidizer-stream temperature T_∞ and to T_∞ larger than or of the order of the crossover temperature T_c at which the rates of production and consumption of H atoms are equal. Two types of solutions are identified, a frozen solution that always exists in this kinetic approximation because all rates are proportional to the concentration of the intermediate H atom, and an ignited solution, represented by a branch of the curve giving the maximum H concentration in terms of a Damköhler number constructed from the strain rate and the rate of the branching step $H + O_2 \rightarrow OH + O$. For $T_\infty > T_c$, the latter bifurcates from the frozen solution if the Damköhler number is increased to a critical value. For T_∞ larger than a value $T_s > T_c$, the effects of chemical heat release are small, and ignition is always gradual in the sense that the limiting ignited-branch slope is positive (supercritical bifurcation) and there is no S curve. For T_∞ in the range $T_c < T_\infty < T_s$, the heat release associated with the radical-consumption step causes the limiting ignition-branch slope to become negative (subcritical bifurcation), producing abrupt ignition which leads to an S curve. For values of T_∞ below crossover, the ignited branch appears as a C-shaped curve unconnected to the frozen solution. The method of analysis introduced here offers a first step toward analytical description of nonpremixed H_2-O_2 autoignition.

Introduction

Because of interest in applications such as aerospace propulsion, considerable attention has been given in the literature to the study of ignition of hydrogen-oxygen mixtures. Treviño [1] investigated ignition in an isochoric, adiabatic, homogeneous reactor and systematically reduced the well-known detailed reaction mechanism [2–5] to small numbers of global steps for different pressure and temperature regimes. He found that the ignition process is strongly dependent upon the initial temperature of the mixture. A relevant parameter in the description of H_2-O_2 ignition is the so-called crossover temperature T_c, the temperature at which the rates of production and consumption of H radicals are equal. The two determinant reaction rates are those of the chain-branching reaction $H + O_2 \rightarrow OH + O$ and the chain-terminating reaction $H + O_2 + M \rightarrow HO_2 + M$. For initial temperatures on the order of T_c, Treviño [1] deduced a five-step mechanism, which can be further simplified by neglecting the initiation step $H_2 + O_2 \rightarrow HO_2 + H$ and assuming that the hydroperoxyl radical HO_2 is in steady state [6,7]. Reduced chemistry of as few as two steps has been proposed for high-temperature ignition above crossover [8].

Autoignition in practical systems generally occurs during mixing of cool hydrogen with a hot oxidizing gas, leading to the establishment of H_2-O_2 diffusion flames. In such nonpremixed environments, some details of the chemistry may differ from that in homogeneous systems because of complications associated with H_2 diffusion into the O_2 inert mixture.

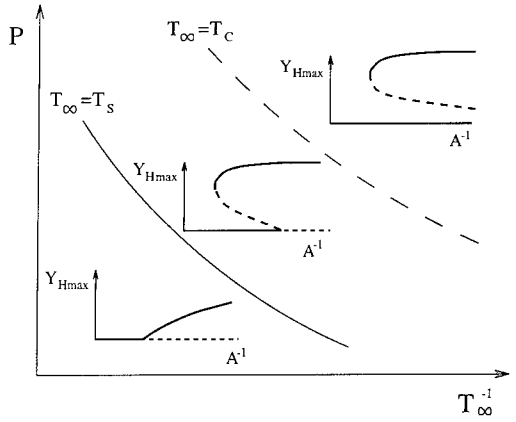

FIG. 1. Ignition behaviors present in high-temperature ignition of H_2-O_2 diffusion flames.

While numerous investigations have been reported on H_2-O_2 ignition histories in homogeneous systems, only a few studies of ignition of H_2-O_2 diffusion flames are available [8,9], and they are purely numerical* and are restricted to steady flows so that ignition times cannot be determined, although critical conditions needed for ignition to occur are obtained. Except for one study [10] including model branched-chain kinetics for a premixed system exposed to a hot inert gas, previously published analytical investigations of the ignition branch of the S curve have been restricted to one-step chemistry.

The main objective of the present paper is to apply the reduced kinetic mechanism derived by Treviño [1] to study the ignition of strained diffusion flames. Steady counterflow systems are addressed, following preliminary ideas developed [11] in considering coflow mixing layers. To simplify the analysis, an inviscid potential solution is adopted to describe the flow field. Although the model retains the physical characteristics of the problem, a more thorough description of the flow field is required if quantitative agreement with numerical results is to be obtained.

For high-temperature H_2-O_2 diffusion flames, Fig. 1 summarizes the different shapes that the ignition curve may exhibit in a plot of the maximum radical concentration as a function of the inverse of the strain rate. For oxidizer-stream temperatures above T_c, the ignited branch bifurcates from the frozen solution at a finite value of the strain rate. The occurrence of ignition as a bifurcation as opposed to a smooth turning point as in conventional one-step asymptotic analyses [12] is a consequence of the autocatalytic character of the kinetic mechanism employed. A limiting temperature $T_s > T_c$ that determines the criticality of the bifurcation will be identified. Above this temperature, the chemical heat release is negligibly small, and a progressive transition from frozen flow to the equilibrium diffusion-flame solution takes place. We shall show that, for stream temperatures below T_s, the exothermicity associated with the radical recombination changes the character of the solution, and an S-shaped curve more typical of diffusion flames is reproduced. As T_c is approached, the strain rate at which ignition occurs decreases, becoming zero at crossover. If the initiation step is neglected in the kinetic mechanism, no chain-branched autoignition is possible below crossover, and the ignited and frozen solutions are unconnected. The ignition behavior shown in Fig. 1 is in qualitative agreement with the numerical results available [8,9].

*An exception is a recent study by activation-energy asymptotics (S. R. Lee and C. K. Law, *Combust. Sci. Technol.*, to appear, 1994) that does not address bifurcation theory.

Kinetic Mechanism and Formulation

The high-temperature ignition of H_2-O_2 mixtures can be described [1] by the reduced kinetic mechanism $H_2 + O_2 \rightarrow HO_2 + H$, $3H_2 + O_2 \rightarrow 2H + 2H_2O$, $H + O_2 + M \rightarrow HO_2 + M$, $2H_2 + HO_2 \rightarrow 2H_2O + H$, $HO_2 + H \rightarrow H_2 + O_2$, where O and OH are assumed to be in steady state. Although the first of these five steps is important at early times during initiation, once trace amounts of radicals are present, its influence becomes negligible, and we neglect it here. A steady state for hydroperoxyl is an excellent approximation [6–8], and since this radical appears in four of the five steps, its steady state reduces the chemistry to a two-step mechanism. If $(a^{-1} - 1)$ denotes the ratio of the rate of the elementary step $HO_2 + H \rightarrow OH + OH$ to that of the step $HO_2 + H \rightarrow H_2 + O_2$, then this two-step mechanism is

$$3H_2 + O_2 \rightarrow 2H + 2H_2O \qquad \text{(I)}$$

$$(2 - 3a)H_2 + (1 - a)O_2 + 2aH \rightarrow 2(1 - a)H_2O \qquad \text{(II)}$$

with rates given, respectively, by those of the elementary reactions $H + O_2 \rightarrow OH + O$ and $H + O_2 + M \rightarrow HO_2 + M$. The specific reaction-rate constants for these two elementary reactions will be denoted by k_1 and k_2, respectively. This same two-step description has been employed in a recent analysis of the premixed H_2-air flame [13] and elsewhere [6]. From the latest data available [8], it can be shown that $a \simeq 1/6$ over the temperature range of interest. Thus, only a small fraction of the HO_2 produced is consumed by $HO_2 + H \rightarrow H_2 + O_2$, partially attenuating, therefore, the chain-terminating effect of reaction II. The overall step I is weakly exothermic, its heat of reaction being roughly an order of magnitude

smaller than that corresponding to II. For values of the mixture temperature sufficiently above T_c, production of HO_2 can be neglected entirely, and the kinetic mechanism reduces to the overall step I. The ignition process is then a typical chain-branching explosion with a fairly small heat release effect. As the temperature of the streams approaches T_c, step II gains importance. The ignition is still characterized as a chain-branching explosion, but now the exothermicity of II as well as its chain-terminating effect play an increasingly important role in the ignition process. Both behaviors will be analyzed in this paper.

Attention will be restricted to stagnation-point counterflow of H_2 and O_2, dilution with an inert being permitted in both feed streams. We shall assume, for the sake of simplicity, that the strain rate, density, specific heat, and transport coefficients are constant; these assumptions are readily removed through suitable well-known transformations. The equations that describe the flow are then given by

$$\zeta \frac{\partial y_H}{\partial \zeta} + \frac{\partial^2 y_H}{\partial \zeta^2} = -\Delta[\exp(\beta_1\theta) - \gamma]\, y_{O_2} y_H \quad (1)$$

$$\zeta \frac{\partial y_{O_2}}{\partial \zeta} + \frac{L_H}{L_{O_2}} \frac{\partial^2 y_{O_2}}{\partial \zeta^2} = s\Delta[\exp(\beta_1\theta) + (1 - a)\gamma/a]\, y_{O_2} y_H \quad (2)$$

$$\zeta \frac{\partial \theta}{\partial \zeta} + L_H \frac{\partial^2 \theta}{\partial \zeta^2} = -\Delta[q_I \exp(\beta_1\theta) + q_{II}\gamma/a]\, y_{O_2} y_H \quad (3)$$

and

$$\zeta \frac{\partial y_{H_2}}{\partial \zeta} + \frac{L_H}{L_{H_2}} \frac{\partial^2 y_{H_2}}{\partial \zeta^2} = 3\Delta[\exp(\beta_1\theta) + (2 - 3a)\gamma/(3a)]\, y_{O_2} y_H \quad (4)$$

where the nondimensional variables are defined as

$$\zeta = y\left(\frac{L_H A}{D}\right)^{1/2}, \qquad y_H = \frac{Y_H}{Y_{H_{2-\infty}}},$$

$$y_{O_2} = \frac{Y_{O_2}}{Y_{O_{2\infty}}}, \quad \theta = \frac{T - T_\infty}{T_\infty}, \quad y_{H_2} = \frac{Y_{H_2}}{Y_{H_{2-\infty}}}$$

$$\Delta = \frac{2B_1 \exp(-\beta_1)\rho Y_{O_{2\infty}}}{W_{O_2} A}, \qquad s = \frac{W_{O_2}}{W_{H_2}} \frac{Y_{H_{2-\infty}}}{Y_{O_{2\infty}}}$$

$$q_i = \frac{q_i'}{c_p T_\infty} \frac{Y_{H_{2-\infty}}}{W_{H_2}}, \qquad \gamma = \frac{A_2}{A_1} \frac{P \exp(\beta_1) a}{R^0 T_\infty^{(1+n_1-n_2)}}. \quad (5)$$

The boundary conditions for the above equations are $y_H \to 0$, $y_{H_2} \to 1$, $y_{O_2} \to 0$, and $\theta \to \theta_{-\infty} \equiv (T_{-\infty} - T_\infty)/T_\infty$ as $\zeta \to -\infty$ and $y_H \to 0$, $y_{H_2} \to 0$, $y_{O_2} \to 1$, and $\theta \to 0$ as $\zeta \to +\infty$.

Here y is the transverse coordinate with origin at the dividing fluid surface, T is the temperature, and Y_H, Y_{H_2}, and Y_{O_2} are the mass fractions of atomic hydrogen, molecular hydrogen, and oxygen, whose Lewis numbers are denoted by L_H, L_{H_2}, and L_{O_2}. Hydrogen is approaching from $-\infty$ with mass fraction $Y_{H_{2-\infty}}$ and temperature $T_{-\infty}$, while the oxidizer flows from $+\infty$, where the oxygen mass fraction is $Y_{O_{2\infty}}$ and the temperature is T_∞. The thermal diffusivity of the mixture is given by $D = \lambda/(\rho c_p)$, where λ is the thermal conductivity, ρ is the fluid density, and c_p is the specific heat at constant pressure, all taken to be constant. The reaction-rate constant, $k_1 = A_1 T^{n_1} \exp(-E_1/R^0 T)$, has been approximated by $k_1 = B_1 \exp(-\beta_1) \exp(\beta_1\theta)$, where B_1 is a new frequency factor given by $B_1 = A_1 T_\infty^{n_1}$ and β_1 is the nondimensional activation temperature $\beta_1 = E_1/(R^0 T_\infty)$. The variation of $k_2 C_M$ with temperature has been neglected, so that $k_2 C_M = A_2 T_\infty^{n_2} P/(R^0 T_\infty)$, C_M being the efficiency-weighted sum of third-body concentrations. Updated values of the reaction-rate constants in mol/cm^3, s^{-1}, K, and cal/mol are [8] $A_1 = 3.52 \times 10^{16}$, $A_2 = 6.76 \times 10^{19}$, $E_1 = 17{,}070$, $n_1 = -0.7$, and $n_2 = -1.42$. The W's are molecular weights, A is the constant strain rate, P is the uniform pressure across the mixing layer, and q_i' is the heat release associated with overall step i. Six parameters appear in the equations, namely, Δ, s, $\theta_{-\infty}$, γ, q_I, and q_{II}, besides the constant a, the Lewis numbers, and the activation-energy parameter β_1. Here Δ is an appropriate nondimensional. Damköhler number, s is an oxygen-to-fuel mass ratio corresponding to the approaching streams, $\theta_{-\infty}$ accounts for the temperature difference between the streams, γ is the ratio of consumption to production rates of H radicals by the two competing reactions evaluated at $T = T_\infty$, and q_I and q_{II} are the nondimensional heats of reaction associated with each global step. The use of T_∞ as the relevant characteristic temperature is dictated later by the location of the reaction region.

The problem defined by Eqs. (1) through (4) admits two types of solutions. The first corresponds to the trivial solution $y_H = 0$, $y_{O_2} = y_{O_2 f}$, $\theta = \theta_f$, $y_{H_2} = y_{H_2 f}$, where $y_{O_2 f}$, θ_f, and $y_{H_2 f}$, are the frozen profiles corresponding to y_{O_2}, θ, and y_{H_2}, respectively. These solutions, which exist for all values of Δ, are given by

$$y_{O_2 f} = \left[1 - \frac{1}{2}\operatorname{erfc}(\zeta/\sqrt{2L_H})\right],$$

$$\theta_f = \frac{\theta_{-\infty}}{2}\operatorname{erfc}(\zeta/\sqrt{2L_H}), \quad y_{H_2 f} = \frac{1}{2}\operatorname{erfc}(\zeta/\sqrt{2}). \quad (6)$$

For Δ sufficiently large, another solution exists as well. Before studying this ignited solution, further constraints, arising from the physics of the problem, must be identified.

A first constraint is that the solution must give positive values of y_H everywhere in the mixing layer. This imposes an upper limit to the range of Δ for which a solution can be found for a given value of y_H, termed $y_{H_{max}}$. A second constraint is that y_{H_2} must be positive for the validity of the two-step kinetic scheme. As a consequence of the reduced mechanism adopted, y_{H_2} does not appear in the chemical production terms on the right-hand sides of Eqs. (1) through (4). Therefore, Eqs. (1) through (3) can be solved separately, and y_{H_2} can be obtained afterward from Eq. (4). When y_{H_2} is calculated in this way, it is found that there exists a value of ζ, termed ζ_d, such that $y_{H_2} < 0$ for $\zeta > \zeta_d$; ζ_d decreases with increasing $y_{H_{max}}$. To avoid negative y_{H_2}, the chemical-reaction model must be modified at sufficiently large ζ to account for H_2 depletion. The kinetic mechanism adopted holds only for values of ζ such that the resultant mixture is not too fuel lean, and for large values of ζ, where y_{H_2} is very small, this mechanism fails and should be replaced by an alternative developed by Treviño and Liñán [11] for lean mixtures. The revised formulation would result in a profile of H_2 smoothly decaying to zero as ζ increases. The approach employed here is simpler in that we assume that the kinetic mechanism for lean and stoichiometric mixtures holds as long as $y_{H_2} > 0$, and for values of ζ larger than the depletion point ζ_d, the chemical reaction is completely frozen. This approximation is motivated by the low rate of the alternative path, controlled by $O + H_2 \rightarrow OH + H$, in the region $\zeta > \zeta_d$, where the concentrations of both H_2 and the radicals are very small. The freezing of the reaction can be introduced formally into Eqs. (1) through (4) by multiplying the chemical production term by a Heaviside function $H(\zeta - \zeta_d)$. The problem defined in this form with the boundary conditions previously stated has a unique nontrivial solution for a given value of the depletion point ζ_d.

Linear and Weakly Nonlinear Analysis for $T_\infty \geq T_c$

The value of the critical Damköhler number for ignition of the autocatalytic reaction, Δ_c, as well as the slope of the bifurcated ignited branch, can be obtained by solving the linearized version of Eqs. (1) through (3) and the equations for the second perturbation. We consider first the problem in which both streams have the same temperature, $\theta_{-\infty} = 0$, and assume that $L_{O_2} = 1$. Since near the bifurcation point $y_{H_{max}} << 1$ and depletion of H_2 occurs far from the stagnation plane, a further simplification can be introduced. For large values of ζ and $\zeta < \zeta_d$, Eq. (1) admits two different types of solutions, whose behaviors as $\zeta \rightarrow \infty$ are given by $\zeta^{[\Delta(1-\gamma)-1]} \exp(-\zeta^2/2)$ and $\zeta^{-\Delta(1-\gamma)}$, respectively. For values of ζ beyond the depletion point, the solution to Eq. (1) is proportional to $\mathrm{erfc}(\zeta/\sqrt{2})$. Matching of the values of the frozen and nonfrozen solutions and their slopes at $\zeta = \zeta_d$ reveals that solutions with algebraic decay are not admissible for $\zeta < \zeta_d$. Therefore, to find the solution for the ignited branch for small values of $y_{H_{max}}$, we can ignore Eq. (4) and replace the Heaviside function on the right-hand side of Eqs. (1) through (3) by the requirements of exponential decay of y_H as $\zeta \rightarrow \infty$ and $y_H > 0$ throughout the mixing layer. It is worth observing that use of this modification causes the solution in the vicinity of the bifurcation point to be independent of the H_2 diffusion coefficient; i.e., the results are independent of the value of L_{H_2}.

For values of $y_{H_{max}} = \varepsilon << 1$, we can introduce the asymptotic expansions

$$\begin{aligned} \Delta &= \phi_1 \Delta_0 + \varepsilon s \phi_1^2 \phi_2 \Delta_1, \\ y_H &= \varepsilon y_{H0} + \varepsilon^2 s \phi_1 \phi_2 y_{H1} \\ y_{O_2} &= y_{O_2 f} - \varepsilon s \phi_1 \phi_2 y_{O_2 0}, \\ \theta &= \varepsilon \phi_1 (q_I + q_{II} \gamma / a)\, \theta_0 \end{aligned} \tag{7}$$

where $\phi_1 = (1 - \gamma)^{-1}$, $\phi_2 = [1 + (1 - a)\gamma/a]$, and $y_{O_2 f}$ is given by Eq. (6). Here y_{H0} is scaled so that its maximum value is unity. Introducing the above expansions into Eqs. (1) through (3) and collecting terms with the same power of ε, we obtain the equations

$$\zeta \frac{\partial y_{H0}}{\partial \zeta} + \frac{\partial^2 y_{H0}}{\partial \zeta^2} = -\Delta_0 y_{O_2 f} y_{H0} \tag{8}$$

$$\zeta \frac{\partial y_{O_2 0}}{\partial \zeta} + L_H \frac{\partial^2 y_{O_2 0}}{\partial \zeta^2} = -\Delta_0 y_{O_2 f} y_{H0} \tag{9}$$

and

$$\zeta \frac{\partial y_{H1}}{\partial \zeta} + \frac{\partial^2 y_{H1}}{\partial \zeta^2} = -\Delta_0 y_{O_2 f} y_{H1} + \Delta_0 [1 - \Omega y_{O_2 f}] y_{O_2 0} y_{H0} - \Delta_1 y_{O_2 f} y_{H0} \tag{10}$$

with boundary conditions that y_{HO}, $y_{O_2 0}$, and y_{H1} approach zero as $\zeta \rightarrow \pm\infty$. The equation that determines θ_0 is simply $\theta_0 = y_{O_2 0}$. The form of the expansions in Eq. (7) is such that the only parameters left in Eqs. (8) through (10) are L_H and $\Omega = \beta_1 (q_I + q_{II}\gamma/a)\phi_1/(s\phi_2)$.

Critical Damköhler Number for Ignition:

For a given value of the Lewis number of the fuel, Eq. (8) with the stated boundary and nonnegativity

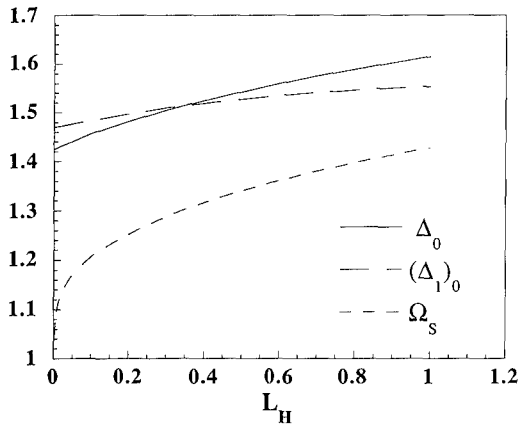

FIG. 2. Variation of the critical Damköhler number, slope of the bifurcation, and criticality condition parameter with the Lewis number of hydrogen.

conditions represents an eigenvalue problem and has a nontrivial solution for only one value of Δ_0. The results obtained for different values of L_H are shown in Fig. 2. The critical Damköhler number for ignition is then given by $\Delta_c = \Delta_0/(1 - \gamma)$. To understand the significance of this result, one must recall that the Damköhler number Δ is constructed from the strain rate and the rate of the branching step $H + O_2 \rightarrow OH + O$, while γ, > 1 for $T_\infty < T_c$, is the ratio of the rate of radical consumption to that of radical production. Therefore, the quantity $(1 - \gamma)\Delta_c$, a constant of order unity for a given value of L_H, represents the ratio of the characteristic strain time to the characteristic chemical time of the two-step kinetic mechanism necessary for ignition to occur. As T_∞ approaches T_c, the chain-terminating character of step II causes the value of γ to increase, which corresponds to an increment of the characteristic chemical time of radical production. Therefore, the lower the temperature is, the lower is the value of the critical strain rate at ignition. A chain-branching explosion is no longer possible for T_∞ below the crossover temperature at which $\gamma = 1$, and the critical Damköhler number becomes infinite. For $T_\infty < T_c$, the frozen and ignited branches are unconnected, and the latter becomes a C-shaped curve standing above $y_{H_{max}} = 0$. Connection between both branches can be recovered if the initiation step $H_2 + O_2 \rightarrow HO_2 + H$ is retained in the kinetic scheme. For sufficiently large values of the Damköhler number, the characteristic residence time A^{-1} becomes a large quantity of the order of the chemical time associated with the initiation step, and production of H radicals by this step is no longer negligible. Ignition in this case is governed by this step that provides a smooth connecting branch between the frozen and ignited curves. For even lower temperatures, ignition occurs as a thermal-runaway process governed by a different kinetic mechanism [1,7].

Bifurcation Character:

The parameter Δ_1, which gives the slope of the bifurcated branch, can be obtained by integrating Eq. (10) or by using the solvability condition

$$\int_{-\infty}^{\infty} y_{H0}^2 \left[\Delta_0 y_{O20}(1 - \Omega y_{O2f}) - \Delta_1 y_{O2f}\right] \exp(\zeta^2/2)\, d\zeta = 0 \quad (11)$$

which can be solved for Δ_1 to give $\Delta_1 = (1 - \Omega/\Omega_s)(\Delta_1)_0$, where

$$\Omega_s = \frac{\int_{-\infty}^{\infty} y_{O20} y_{H0}^2 \exp(\zeta^2/2) d\zeta}{\int_{-\infty}^{\infty} y_{O2f} y_{O20} y_{H0}^2 \exp(\zeta^2/2) d\zeta} \quad (12)$$

and

$$(\Delta_1)_0 = \frac{\int_{-\infty}^{\infty} y_{O20}\, y_{H0}^2 \exp(\zeta^2/2) d\zeta}{\int_{-\infty}^{\infty} y_{O2f}\, y_{H0}^2 \exp(\zeta^2/2)\, d\zeta} \Delta_0. \quad (13)$$

The results of these integrations for different values of the Lewis number of the fuel are shown in Fig. 2.

The criticality of the bifurcation is governed by the parameter Ω that measures the counteracting effects of oxygen consumption and temperature increase resulting from heat release. The behavior of the ignition branch can be explained by considering the right-hand side of Eq. (1). When Ω is larger than Ω_s, the effect of temperature rise dominates the ignition process through the exponential term $\exp(\beta_1\theta)$, causing the Damköhler number to decrease as $y_{H_{max}}$ increases, resulting in a subcritical bifurcation. On the other hand, for small values of Ω, corresponding to large T_∞ and small $Y_{O_{2\infty}}$, the effect of oxygen consumption takes over, giving an overall decreasing $[\exp(\beta_1\theta) - \gamma]y_{O_2}$ term. To balance this effect, as $y_{H_{max}}$ increases Δ must increase, and the bifurcated branch becomes supercritical.

The equation $\Omega = \Omega_s$ determines a limiting temperature T_s that clearly separates abrupt ignition behaviors from smooth transitions to the diffusion-flame solution. For values of T_∞ far above the crossover temperature, γ becomes negligibly small, and Ω reduces to $\beta_1 q_I/s$. Numerical evaluation of this expression reveals that the heat release associated with step I is too small to change the character of the bifurcation, so that it remains supercritical as long as the production of HO_2 is negligible. Since $q_{II}/a >> q_I$, as T_∞ decreases the value of Ω increases signifi-

cantly, and a subcritical character is achieved somewhat above crossover, i.e., $T_s > T_c$. The curves characterizing the ignition behavior sketched in Fig. 1 can be plotted for a given value of $Y_{O_{2\infty}}$ by using the equations $\gamma = 1$ and $\Omega = \Omega_s$. Typically, as P varies from 10^{-1} to 10^2 atm, T_c varies from 800 to 1400 K, and $T_s - T_c$ remains about 200 K, as may be obtained more accurately by the definition of Δ.

Effect of Different Temperatures:

To study the effect of different temperatures of the approaching streams on the values of Δ_c and Δ_1, it is convenient to consider first the physically relevant limiting case $L_H << 1$. We show below that, with the inviscid potential solution adopted for the flow field, the shape and location of the bifurcated branch in this case are independent of the fuel stream temperature. Taking the limit $L_H \to 0$ in Eq. (6) yields the asymptotic frozen profiles $y_{O_2 f} = 0$, $\theta_f = \theta_\infty$ for $\zeta < 0$, and $y_{O_2} = 1$, $\theta_f = 0$ for $\zeta > 0$. The shape of these functions agrees with the fact that the transverse coordinate of the mixing layer, ζ, has been nondimensionalized with the characteristic diffusion length corresponding to H. In the limit $L_H \to 0$, the hydrogen diffusivity is much larger than the oxygen and thermal diffusivities. Therefore, diffusion of O_2 and heat conduction take place in a thin layer located around $\zeta = 0$. The oxidizer is unable to reach the fuel side of the mixing layer. The reaction is frozen for $\zeta < 0$ because of the absence of oxygen. The values of Δ_c and Δ_1 are, therefore, only determined by what occurs on the oxidizer side of the mixing layer and become independent of the temperature of the fuel stream. At this point, it becomes clear that T_∞ is the most relevant temperature for the ignition problem and is properly selected to nondimensionalize the equations. The analysis above indicates that, when the temperatures of the approaching streams are different, Fig. 2 still gives the critical Damköhler number for ignition of the autocatalytic reaction and the slope of the bifurcated branch, provided $L_H << 1$.

To study departures from this result, we consider the case $T_\infty >> T_c$, i.e., $\gamma << 1$, so that $\Delta_c = \Delta_0$ and the effect of $T_{-\infty} < T_\infty$ reduces to the appearance of an additional factor $\exp(\beta_1\theta_f)$ multiplying the right-hand side of Eqs. (8) through (10). Figure 3 shows the ratio $\Delta_c/(\Delta_c)_0$, in which $(\Delta_c)_0$ is the value of Δ_c corresponding to $\theta_{-\infty} = 0$. As can be seen from this graph, although Fig. 2 loses accuracy as L_H increases, it still gives a reasonably good approximation for the critical Damköhler number for ignition.

Solution for Small L_H:

In the limit $L_H << 1$, Eq. (8), modified to account for different stream temperatures, can be solved in the case $T_\infty >> T_c$ to determine Δ_c as an asymptotic

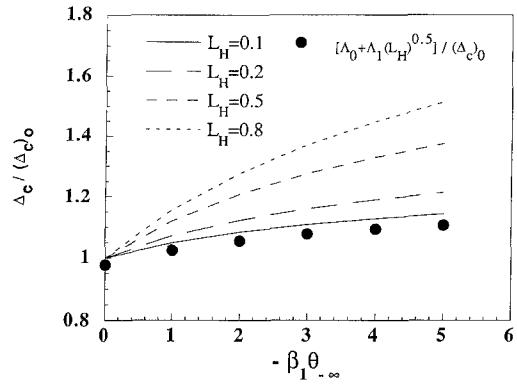

FIG. 3. Effect of the fuel stream temperature on the critical Damköhler number.

expansion in the small parameter $\sqrt{L_H}$ of the form $\Delta_c = \Delta_0 + \sqrt{L_H}\Delta_1 + L_H\Delta_2 + \ldots$. In this limit, the solution can be found by dividing the flow field into three distinct layers, two outer layers on the fuel and oxidizer sides with characteristic nondimensional length of order unity and an inner layer, located around $\zeta = 0$, with characteristic nondimensional length of order $\sqrt{L_H}$. Equation (8) must be solved separately in those three layers, and the value of Δ_c can then be found by matching the different solutions. Let y_l, y_r, and y_i denote the value of y_{H0} in the left outer, right outer, and inner layer, respectively. If one neglects exponentially small terms in Eq. (8), the solutions in the outer layers can be shown to be $y_l = 2[1 - 1/2\,\mathrm{erfc}(\zeta/\sqrt{2})]$ and $y_r = C\exp(-\zeta^2/4)\,U(1/2 - \Delta_c, \zeta)$, where U is the Whittaker's function as defined in Ref. 14. In deriving these expressions, the boundary conditions of Eq. (8) have been used, and the arbitrary value of y_l at $\zeta = 0$ has been chosen to be unity. The value of the constant C must be determined from the matching conditions with the inner layer as an expansion in the small parameter $\sqrt{L_H}$.

To describe this inner layer, a stretched coordinate $\zeta/\sqrt{L_H}$ must be introduced, and the value of y_i has to be expanded in the form $y_i = (y_i)_0 + \sqrt{L_H}(y_i)_1 + \ldots$. This kind of formulation results in a set of equations for the inner layer that must be solved order by order by matching with the solutions for the outer layers given above. Solution to the first three orders provides expressions for Δ_0 and Δ_1, which can be shown to be

$$\sqrt{\pi} = -\frac{\Gamma\left(\frac{1}{2} - \frac{\Delta_0}{2}\right)}{\Gamma\left(1 - \frac{\Delta_0}{2}\right)} \tag{14}$$

$$\Lambda_1 = \frac{\sqrt{2\pi}\,\Lambda_0}{\Psi\left(\frac{1}{2} - \frac{\Lambda_0}{2}\right) - \Psi\left(1 - \frac{\Lambda 0}{2}\right)} \cdot \int_0^\infty F\left(\frac{1}{2}\,\mathrm{erfc}\left(\frac{t}{\sqrt{2}}\right), \beta_1\theta_f\right) dt \qquad (15)$$

where Γ and Ψ are, respectively, the gamma and digamma functions and F is defined as $F(x_1, x_2) = 1 + (x_1 - 1)\exp(x_1x_2) - x_1\exp[(1 - x_1)x_2]$. It can be shown that the only value of Λ_0 that is a solution of Eq. (14) and also satisfies the additional constraint $U(1/2 - \Delta_c, \zeta) > 0$ is given approximately by $\Lambda_0 = 1.4251$. Comparison of the two-term asymptotic expansion for Δ_c with the result obtained by numerical integration is shown in Fig. 3 for the case $L_H = 0.1$. As can be seen, retaining two terms in the expansion suffices to give a good approximation in this case.

The value of Λ_1 becomes zero when the two approaching streams have the same temperature. In that case, the analysis, which is valid for $\gamma \neq 0$, must be carried to a higher order if the effect of $L_H \neq 0$ is to be taken into account. The next two terms in the expansion for Δ_0 were found to be $\Lambda_2 = 2\Lambda_0/[\Psi(1/2 - \Lambda_0/2) - \Psi(1 - \Lambda_0/2)] \simeq 0.3866$ and $\Lambda_3 = -(\sqrt{2}/3)\Lambda_0\Lambda_2 \simeq -0.2597$. The expansion $\Delta_0 = \Lambda_0 + L_H\Lambda_2 + L_H^{1.5}\Lambda_3$ gives the value of Δ_0 for equal stream temperatures within 1% accuracy for values of L_H as large as 0.45.

Nonlinear Analysis of a Simplified Model

Although a simple weakly nonlinear analysis suffices to determine the dependence of the shape of the ignited branch on the different parameters present in the problem, calculation of the solution away from the bifurcation point involves numerical integration of a four-equation boundary-value problem. A significant simplification is obtained if we restrict our attention to the case $T_\infty >> T_c$, i.e., $\gamma << 1$, and also assume that the Lewis numbers of all species present in the mixture are unity. This assumption is clearly inaccurate for hydrogen, whose diffusivity is much higher than that of heat or oxygen. Therefore, the results presented below are not intended to be accurate but rather qualitatively correct. The results would also be quantitatively correct if the chain-branching species were O or OH instead of H.

In this case, the problem reduces to that of solving the differential equation

$$\zeta\frac{\partial y_H}{\partial\zeta} + \frac{\partial^2 y_H}{\partial\zeta^2} = -\Delta\exp(\beta_1\theta_f)\exp(\beta_1 q_1 y_H)(y_{O_2 f} - s y_H)\,y_H \qquad (16)$$

subject to $y_H(-\infty) = 0$, $y_H(\zeta_d) = 1/6\,\mathrm{erfc}(\zeta_d/\sqrt{2})$ and $dy_H/d\zeta(\zeta_d) = -(1/6)\sqrt{2/\pi}\exp(-\zeta_d^2/2)$. In deriving Eq. (16), the boundary conditions of Eqs. (1) through (3) have been used to integrate linear combinations of Eqs. (1) and (2) and of Eqs. (1) and (3), respectively. A similar linear combination of Eqs. (1) and (4) was integrated to obtain $y_{H_2} + 3y_H = 1/2\,\mathrm{erfc}(\zeta/\sqrt{2})$, which was used when determining the boundary conditions at $\zeta = \zeta_d$. The ignited solutions of this problem were obtained by numerical integration using a simple shooting method.* For a given value of ζ_d, integration of the equation starting from $\zeta = \zeta_d$ determines a unique value of Δ for which the solution is positive everywhere and also satisfies the boundary condition at $-\infty$. Different solutions obtained for increasing values of the parameter $\Omega = \beta_1 q_1/s$ are shown in Fig. 4. The bifurcated branch becomes subcritical when the value of Ω exceeds the Ω_s predicted by the weakly nonlinear analysis. Away from the bifurcation point, the consumption of O_2 eventually takes over, and the subcritical bifurcated branches turn around, beginning to reproduce the S-shaped curve typical of diffusion flames.

The asymptotic value approached by the bifurcated branch for large values of Δ was also determined. Since the model employed accounts for H_2 depletion, the limit $\Delta \to \infty$ consistently gives the flame-sheet approximation. In the limit $\Delta \to \infty$, H_2 and O_2 do not coexist, and the chemical reaction is confined in an infinitesimally thin layer located at $\zeta = \zeta_d$. The location of the flame is obtained from the jump condition at the flame sheet,

*We can anticipate the results of the numerical integration of Eq. (16) by using a simple lumped approximation for the equation. In this approximation, attention is restricted to the reaction region, where $y_H \sim y_{H_{max}}$. The differential operator on the left-hand side of the equation, which represents the loss of radicals by diffusion, is replaced by the term $-ay_{H_{max}}$, with a of order unity, and the functions $y_{O_2 f}$ and $\exp(\beta_1\theta_f)$ by their values in the reaction region, $y'_{O_2 f}$ and $\exp(\beta_1\theta'_f)$, both quantities of order unity. With these approximations, Eq. (16) reduces to the simple algebraic equation

$$a y_{H_{max}} = \Delta\exp(\beta_1\theta'_f)\exp(\beta_1 q_1 y_{H_{max}})\,(y'_{O_2 f} - s y_{H_{max}})\,y_{H_{max}}.$$

This equation admits two different solutions, $y_{H_{max}} = 0$ and $\Delta = a[y'_{O_2 f}\exp(\beta_1\theta'_f)]^{-1}\exp(\beta_1 q_1 y_{H_{max}})[1 - (s/y'_{O_2 f})y_{H_{max}}]^{-1}$, corresponding to the frozen and ignited solutions, respectively. Some characteristics of the ignited branch that appear in the numerical results are summarized here. The ignited branch departs from the frozen one at a critical value of the Damköhler number of order unity given by $[y'_{O_2 f}\exp(\beta_1\theta'_f)]^{-1}a$. By linearizing the expression for the ignited branch for small values of $y_{H_{max}}$, it can be seen that the bifurcation is supercritical as long as $\beta_1 q_1/s < [y'_{O_2 f}]^{-1}$, again a quantity of order unity. Away from the bifurcation point, the ignited branch evolves so that the Damköhler number becomes infinite as $y_{H_{max}}$ approaches a value of order s^{-1}.

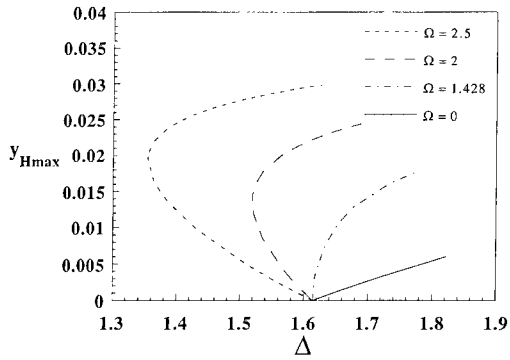

FIG. 4. Effect of heat release on the shape of the ignition branch for $s = 20$ and $L_H = 1$.

$$\left[s \frac{\partial y_H}{\partial \zeta} + \frac{\partial y_{O_2}}{\partial \zeta} \right]_{\zeta_d^-}^{\zeta_d^+} = 0 \tag{17}$$

which can be used to find the asymptotic values of ζ_d and $y_{H_{max}}$,

$$\zeta_d = \sqrt{2}\ \mathrm{erfc}^{-1}\left(\frac{6}{s+3}\right), \qquad y_{H_{max}} = \frac{1}{s+3} \tag{18}$$

where erfc^{-1} is the inverse of the complementary error function.

Discussion and Conclusions

We have seen how the chain-branching process producing hydrogen atoms controls the high-temperature ignition in strained mixing layers of hydrogen and air. The resultant chain-branching process can be described by a two-step reduced kinetic mechanism. It was shown that, in the limit $L_H \to 0$, the ignition process becomes independent of the fuel-stream temperature and is mainly controlled by the oxidizer-stream temperature. Small changes to this result are expected if a more exact description of the flow field is implemented in the analysis.

Because of the particular kinetic mechanism that controls the process, ignition does not take place as a smooth turning point, and three distinctive behaviors were identified. For values of T_∞ above crossover, the solution consists of a bifurcated branch departing from the frozen solution at a critical value of the Damköhler number, Δ_c. From a linear analysis, Δ_c was found as the solution for the eigenvalue in an eigenvalue problem. Also, the slope of the ignition branch in the vicinity of the bifurcation point was calculated as part of the solution, and a limiting temperature T_s was obtained. The bifurcated solution was found for $T_\infty > T_s$ to be supercritical. This corresponds to a smooth transition from a frozen solution to a diffusion flame as the Damköhler number increases. This lack of abrupt ignition for $T_\infty > T_s$ was also observed in the numerical solutions [8,9]. The large heat release associated with the recombination changes the character of the bifurcation to subcritical when $T_\infty = T_s$, and an abrupt type of ignition is obtained below this temperature.

Because of the chain-terminating effect of the principal heat-release step, the value of Δ_c increases significantly as T_∞ approaches T_c, in qualitative agreement with results of previous numerical studies [8,9]. At crossover, Δ_c becomes infinite; i.e., the critical strain rate becomes zero, and below this temperature, the solution consists of a C-shaped curve unconnected to the frozen solution.

Although the kinetic model employed qualitatively reproduces the numerical results shown in previous studies [8,9], further quantitative comparisons with numerical and experimental work are required to test the parametric results presented here. In addition, further analytical study must be given to conditions with $T_\infty << T_c$, where a thermal-explosion character is anticipated, before simple results can be presented that can be used widely in engineering practice.

Acknowledgment

This work was supported by the National Science Foundation through Grant No. CTS-92-14888.

REFERENCES

1. Treviño, C., *Progress in Astronautics and Aeronautics*, AIAA Inc., New York, 1991, Vol. 131, pp. 19–43.
2. Baulch, D. L., Drysdale, D. D., Horne, D. G., and Lloyd, A. C., *Evaluated Kinetic Data for High Temperature Reactions*, Butterworths, London, 1972, Vol. 1.
3. Dixon-Lewis, G., and Williams, D. J., in *Comprehensive Chemical Kinetics* (C. H. Bamford and C. F. H., Tipper Eds.), Elsevier, Oxford, UK, 1977, Vol. 17, pp. 109–144.
4. Warnatz, J., in *Combustion Chemistry* (W. C. Gardiner, Ed.), Springer, New York, 1984, pp. 197–360.
5. Baulch, D. L., Cobos, C. J., Cox, R. A., Esser, C., Frank, P., Just, Th., Kerr, J. A., Philling, M. J., Troe, J., Walker, R. W., and Warnatz, J., *J. Phys. Chem. Ref. Data* 21:411–736 (1992).
6. Clavin, P., *Prog. Energy Combust. Sci.* 11:51 (1985).
7. Treviño, C., and Méndez, F., *Combust. Sci. Technol.* 78:197–216 (1991).
8. Balakrishnan, G., Smooke, M. D., and Williams, F. A., "A Numerical Investigation of Extinction and Ignition Limits in Laminar Nonpremixed Counterflowing Hy-

drogen-Air Streams for Both Elementary and Reduced Chemistry," unpublished, 1993.
9. Darabiha, N., and Candel, S., *Combust. Sci. Technol.* 86:67–85 (1993).
10. Niioka, T., *Combust. Flame* 76:143–149 (1988).
11. Treviño, C., and Liñán, A., "High Temperature Ignition of Hydrogen in Mixing Layers," paper presented at the International Colloquium on Dynamics of Explosions and Reactive Systems in Coimbra, Portugal, August 1–4, 1993.
12. Liñán, A., *Acta Astronaut.* 1:1007–1039 (1974).
13. Seshadri, K., Peters, N., and Williams, F. A., *Combust. Flame* 96:407–427 (1994).
14. Abramowitz, M., and Stegun, A., *Handbook of Mathematical Functions*, Dover, New York, 1965, pp. 686–689.

Twenty-Fifth Symposium (International) on Combustion/The Combustion Institute, 1994/pp. 1539–1545

EFFECT OF THE INITIAL TEMPERATURE AND COMPOSITION OF A HOT TRANSIENT JET ON THE IGNITION OF H_2-AIR-DILUENT MIXTURES

N. DJEBAILI, R. LISBET, G. DUPRE AND C. PAILLARD
Centre National de la Recherche Scientifique
Laboratoire de Combustion et Systèmes Réactifs and Université
1C, Avenue de la Recherche Scientifique
45071 Orléans Cedex 2, France

An original facility has been built, which consists of a shock tube connected to a combustion chamber via an injector, in order to analyze the ignition of a combustible mixture by a subsonic hot gas jet. Using this technique, it is shown that the stagnation temperature, just prior to ejection, of an H_2-Ar mixture heated behind a reflected shock wave between 750 and 3000 K is the main parameter for igniting H_2-air-diluent (CO_2 or H_2O) mixtures. The minimum stagnation temperature to ignite an H_2-air mixture is approximately equal to the self-ignition temperature of this mixture. If CO_2 or H_2O is added to the combustible mixture, the minimum stagnation temperature must be increased. Beyond the critical diluent concentration, the mixture cannot be ignited whatever the initial jet temperature is. The temperature corresponding to the critical composition is called the minimum critical temperature. Under these conditions, the ignition limits by a hot jet constituted of a shock-heated H_2-Ar mixture have been determined for H_2-air-CO_2 and H_2-air-H_2O mixtures. The conditions for which ignition is no longer observed for an H_2-air-H_2O mixture are the following: equivalence ratio $\phi = 0.55$, initial temperature and pressure, respectively, of 403 K and 100 kPa, and mol% $H_2O = 48$. The ignition limits are compared with the classical flammability limits. The influence of the composition of the hot gas jet on the ignition limits of H_2-air-H_2O mixtures has been analyzed and discussed. The present results provide a new assessment, particularly important for nuclear reactor safety.

Introduction

In many practical applications, a hot gas jet is injected into a combustible mixture. Many configurations of this type do exist: For example, in the case of a jet engine combustor, the hot products and unburnt fuel flow from the primary zone and encounter air streams. In this example and in many others, one stream is initially at high temperature, and intuitively, the subsequent combustion and the diffusion flame will be dependent on this temperature. In some scenarios of a severe accident that may occur in nuclear power plants, because of deficient nuclear reactor cooling, a hot hydrogen jet may be injected into an explosive H_2-air-H_2O mixture. The main question is to determine precisely the conditions in which an explosion can be initiated by the hot jet. The ignition mechanism of a fuel jet flowing into an oxidizer stream has been theoretically analyzed by Fendel [1] and Liñan [2]. Darabiha and Candel [3] have shown that the initial temperature of one of the streams has a great influence on the critical conditions of ignition and extinction. In particular conditions, a change in the oxidizer stream temperature from 300 to 1000 K increases the critical strain rate at extinction by a factor of 10. It was also found that a temperature exists beyond which combustion always takes place, whatever the strain rate is. In the case of the ignition of a combustible mixture by a hot fuel jet, the ignition around the jet is followed by a flame propagation. Wolfhard [4] and later Vanpée and Bruszack [5] were among the first who studied the ignition of a combustible mixture by a steady laminar jet of hot gas. Wojcicki [6] has studied the uncontrolled ignition due to hot gas emission in the atmosphere. More recently, Enomoto et al. [7] determined the ability of a hot jet, either air or nitrogen, to ignite an H_2-air mixture with regard to the initial temperature of the hot gas. In these previous studies, the initial temperature, at the jet orifice, did not exceed 1500 K. However, in several hazard applications, the explosion occurs in the early stage of the hot gas flow, and therefore, studies on the ignition by an unsteady flow are more realistic. Phillips [8] carried out experiments and proposed a model of the ignition of a combustible mixture by a jet of hot products, in order to serve as a means of MESG (Maximum Experimental Safety Gap) determination. However, the initial conditions, such as the initial temperature and pressure that generate the jet, were not well defined. Knystautas et al. [9] discovered that a jet of hot products could be used to initiate deto-

nations. Later, Schildknecht et al. [10], Mackay et al. [11], and Shepherd and Krok [12] described the effect of the jet characteristics on the regime of the combustion initiated by a hot gas jet. However, these experiments were carried out with a gas flow generated by a very high pressure ratio, and in some cases, a spherical shock wave could propagate in the combustible mixture and induce changes.

In the present paper, an original method is proposed to generate a subsonic turbulent jet of hydrogen and argon heated to 750–3000 K behind a reflected shock wave and to let it flow downstream into a combustible mixture of H_2-air, either diluted or not by steam or carbon dioxide. In the previous studies cited above, the initial conditions before ejection were not well known since the hot products cooled very rapidly and the pressure drastically decreased. On the other hand, with the shock tube method, the gas parameters heated by the reflected shock wave, prior to ejection, are well defined for several milliseconds. Using a coupling between a shock tube and a combustion chamber, ignition limits by a hot gas jet could be determined and provided new basic information for H_2-air explosion hazards. The importance of both the initial temperature upstream of the jet and the jet composition has also been shown.

Experimental Setup

The main idea of the present experiments is to use a shock tube to heat a gas to a given high temperature before being ejected through an orifice (2.5-mm i.d., 0.4-mm thick) into a combustible mixture contained in a combustion chamber. The experimental setup has been described previously by Djebaili et al. [13,14]. The mixture to be ejected, containing 60% H_2-40% Ar (H_2 can be partially substituted by H_2O or CO_2) is heated by the reflected shock wave to a temperature ranging between 750 and 3000 K and a pressure of 101–520 kPa. The combustion chamber, in which the jet emerges, is filled with an H_2-air mixture, either diluted or not by CO_2 or H_2O, at an initial temperature of 298, 373, or 403 K. The initial pressure of the combustible mixture varies between 100 and 500 kPa. At a given initial pressure of the combustible mixture, the pressure of the shocked gas to be ejected is adjusted behind the reflected shock wave, in such a manner that a subsonic flow is generated. Therefore, the pressure ratio between the shock tube and the combustion chamber does not exceed 1.4. Both premixed mixtures, for the shock tube and the combustion chamber, are prepared using the partial pressure method and stored in two 20-L tanks. To use steam, the whole experimental facility is trace-heated and insulated in order to vary the initial temperature from ambient to 423 ± 2 K. The layout of instrumentation (Fig. 1) consists of four piezoelectric transducers (labelled TC_1–TC_4), mounted flush with the inner surface of the shock tube, and of five transducers (labelled CC_1–CC_5) in the combustion chamber. Coupled to these pressure gages, four optical quartz windows (W) are located across from UV-sensitive photomultipliers (labelled PM_1–PM_4) for the detection of the flame front passage.

The principal advantage of this hot jet production method is that, prior to ejection, the initial parameters such as temperature, pressure, and composition are well known with a 1% accuracy. The hot flow duration, not exceeding a few milliseconds, is a transient flow. For these experiments, an ignition will be considered as positive when the jet induces the ignition of the combustible mixture and the propagation of the flame in the whole combustion chamber. As observed from a fast video camera, a flame can be initiated around the jet without propagating in the combustible mixture. In this case, the ignition is considered as negative.

Results

Determination of the Temperature and Composition of the Hot Gas to be Ejected:

As mentioned above, the shock temperature and pressure remain constant for several milliseconds before they decrease, due to wall heat losses and to the collision between the reflected shock wave and the contact surface. The first parameter to be determined is the *delay of the terphane foil rupture*, τ_{rup}, under the impact of the reflected shock wave—that is, the delay between the shock reflection and the precise time of the foil rupture. The knowledge of this delay provides information on the exact composition and temperature of the gas at the beginning of the flow. The rupture delay is deduced, as shown in Fig. 2, from the recording of the pressure signal delivered by the last pressure gage (TC_4) on the shock tube (from the simultaneous knowledge of the incident and reflected shock wave velocities), and of the emission signal given by the first photomultiplier of the combustion chamber (PM_1). In all experiments, τ_{rup} is found to vary between 10 and 500 μs.

The gas mixture heated by the reflected shock wave will be partially dissociated. However, the equilibrium composition is not instantaneously reached. First, the equilibrium composition is calculated using Stanjan code [15]. Second, a kinetics modeling code [16] is used to determine the concentration profiles' evolution behind the reflected shock wave. It is therefore possible to estimate the composition of the ejected gas as the terphane foil is ruptured. From these profiles, a characteristic time, τ_{eq}, defined as the time necessary to get an H-atom concentration in the ejected gas equal to 90% of the equilibrium value, can be deduced. In Fig. 3, the comparison

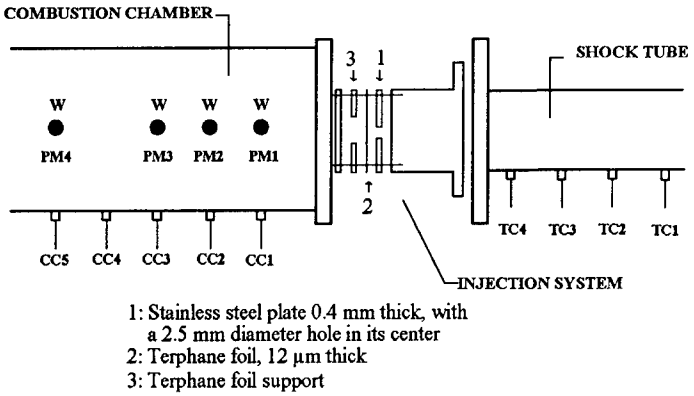

FIG. 1. Schematic of the injection system.

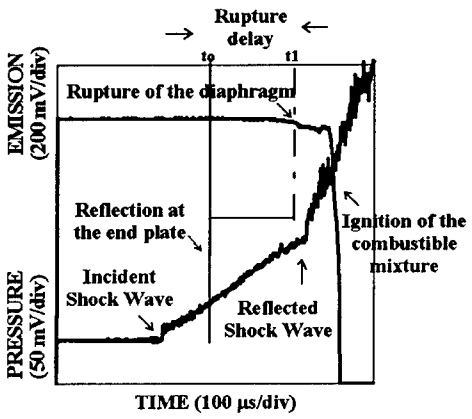

FIG. 2. Pressure signal delivered by the last transducer of the shock tube (TC_4) and emission signal given by the first photomultiplier (PM_1) of the combustion chamber. The ejected mixture is 60% H_2-40% Ar, and the combustible mixture is 18% H_2-82% air, initially at 100 kPa and 298 K.

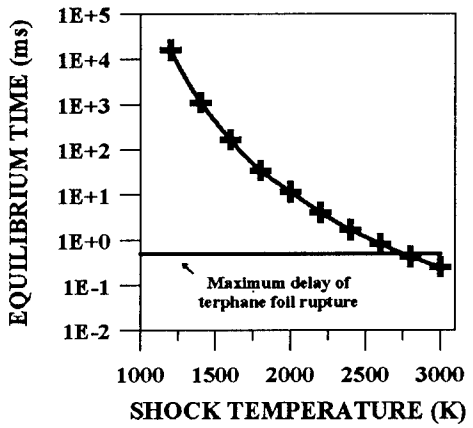

FIG. 3. Evolution of the equilibrium time vs the shock temperature of a 60% H_2-40% Ar mixture at a shock pressure of 113 kPa.

between the rupture delay, τ_{rup}, and the characteristic time, τ_{eq}, for an H_2 + Ar jet shows that the equilibrium state would be reached only at very hot temperatures, higher than 2800 K. Therefore, because of H_2 dissociation, the temperature behind the reflected shock wave (called stagnation temperature) decreases. Thus, the ejected gas temperature depends on rupture time. When the stagnation temperature is of the order of 2000 K, the influence of H_2 dissociation on the temperature of ejected gas is negligible.

Ignition Temperature by a Hot H_2-Ar Jet:

The temperature of the gas, just before its ejection, which represents the stagnation temperature, will constitute an important parameter on which the following discussion is based. The critical stagnation temperature of the hot gas necessary to ignite a combustible mixture is called the *ignition temperature.* In the case of an 18% H_2 in air mixture, initially at 298 ± 2 K and 100 ± 1 kPa, ignited by a shocked 60% H_2-40% Ar mixture, it was shown that the critical stagnation temperature is about 750 K for a subsonic flow. This ignition temperature has to be compared to the autoignition temperature determined by Conti and Hertzberg [17] by another technique, i.e., a furnace. They found that, for lean mixtures, the autoignition temperature decreases slightly from 890 K to reach a value of 750 K as the mixture equivalence ratio tends to 1. If only argon is ejected into the combustible mixture, the ignition becomes more difficult, and the ignition temperature must be higher. The presence of hydrogen in argon makes the ignition easier. This behavior can be due to the high diffusivity of hydrogen atoms and their great reactivity with oxygen. Furthermore, the jet properties are changed if only argon is ejected since, with a heavier component, the entrainment rate and the heat conductivity are not the same.

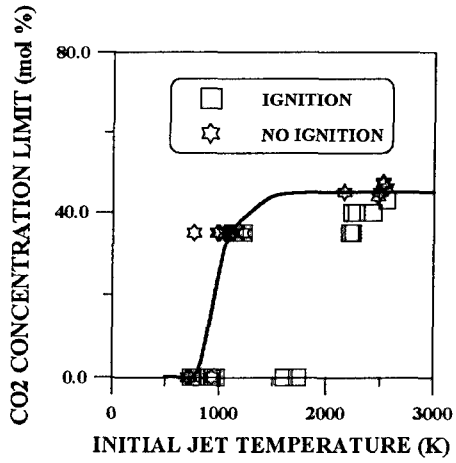

FIG. 4. Concentration limit of CO_2 added to the 18% H_2-82% air mixture, initially at 100 kPa and 298 K, vs the initial jet temperature of the ejected gas containing 60% H_2-40% Ar.

Effect of the Dilution of H_2-Air Mixtures on the Ignition Temperature:

The ignition temperature is noticeably increased when the H_2-air mixture is diluted. For example, the ignition temperature, in the case of the 18% H_2-82% air mixture, is about 750 K. But, if 35% of CO_2 is added to the combustible mixture (that is, for an 11.7% H_2 + 53% air + 35% CO_2 mixture), then the ignition temperature must be at least equal to 1200 K in order to induce a flame propagation in the combustion chamber. As shown in Fig. 4, the required stagnation temperature increases with the CO_2 concentration of the test gas. With a value greater than 45 mol% CO_2, no ignition or flame propagation is observed in the combustible mixture, even if the stagnation temperature of the ejected gas is increased to 2700 K. This CO_2 asymptotic concentration defines both the so-called *ignition limit* for a hot transient gas jet and the corresponding *minimum critical temperature* that is the critical stagnation temperature (required for ignition at this point) close to 2000 K. After ignition, the flame propagates in the combustion chamber.

Ignition Limits by a Hot Transient Gas Jet:

The results concerning the ignition limits by a hot jet of hydrogen and argon are presented in this section. The effects of jet parameters and initial conditions on the flame characteristics have been previously described by Djebaili and coworkers [13,18]; therefore, the sole effect on ignition limits that is described here in detail is the effect of the addition of a diluent (CO_2 or H_2O) to the combustible mixture.

The ignition limit is defined as the minimum concentration of a diluent added to the combustible mixture above which no flame propagation is observed in the combustion chamber, if the stagnation temperature is equal to or higher than the minimum critical temperature previously defined.

In Table 1, a comparison is given between the diluent concentrations at the ignition limit of the combustible mixture, containing initially 18% H_2-82% air and diluted either by CO_2 or by H_2O. These limits are determined for different initial temperatures and pressures of the combustible mixture. The gas jet used to induce ignition is a 60% H_2-40% Ar mixture, heated to 2000–2600 K, that is at a temperature higher than the minimum critical temperature. The ignition limits obtained for H_2-air-CO_2 mixtures can be compared to the classical flammability limits given by Zabetakis [19], who found that 50 mol% CO_2 is needed to avoid combustion in the 18% H_2-82% air mixture; in our case, only 44 mol% CO_2 is needed. If the initial pressure is raised at a given initial temperature, the CO_2 concentration limit remains approximately constant, while the steam concentration limit increases. If the initial temperature is varied from 298 to 403 K at a given initial pressure, the diluent concentration limit is strongly enlarged. At 100 kPa and 403 K, steam is more efficient than carbon dioxide to avoid ignition and the subsequent

TABLE 1
Evolution of the diluent concentration limit added to an 18% H_2-82% air mixture at different initial temperatures, as a function of the initial pressure of the combustible mixture

P_{ini} (kPa)	T_{ini} = 298 K mol% CO_2 lim	T_{ini} = 373 K mol% H_2O lim	T_{ini} = 373 K mol% CO_2 lim	T_{ini} = 403 K mol% H_2O lim	T_{ini} = 403 K mol% CO_2 lim
100	44.0 ± 0.5	39 ± 0.5	50.0 ± 0.5	48 ± 0.5	56.0 ± 0.5
150	47.5 ± 0.5	>(41 ± 0.5)	48.0 ± 0.5	51 ± 0.5	55.0 ± 0.5
200	43.5 ± 0.5	—	50.0 ± 0.5	54 ± 0.5	53.0 ± 0.5
300	43.5 ± 0.5	—	51.0 ± 0.5	60 ± 0.5	51.0 ± 0.5
500	43.5 ± 0.5	—	50.0 ± 0.5	—	51.0 ± 0.5

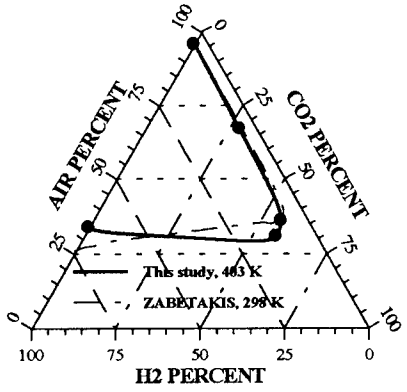

FIG. 5. Ignition limits of H_2-air-CO_2 mixture, initially at 100 kPa and 403 K, by a hot 60% H_2-40% Ar jet ejected through a 2.5-mm-diameter hole at an initial jet temperature ranging from 2300 to 2700 K. Comparison is with Zabetakis [19] flammability limits at 298 K.

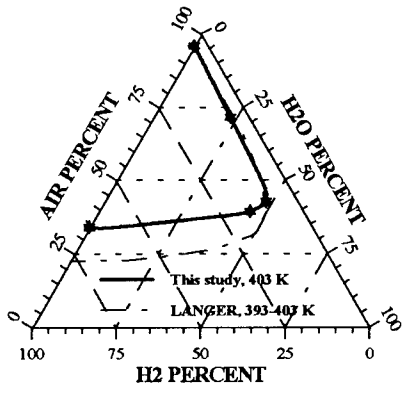

FIG. 6. Ignition limits of H_2-air-H_2O mixture, initially at 100 kPa and 403 K, by a hot 60% H_2-40% Ar jet ejected through a 2.5-mm-diameter hole at an initial jet temperature ranging from 2300 to 2700 K. Comparison is with Langer and Stock [20] flammability limits between 393 and 403 K.

flame propagation, while the behavior is inversed if the initial pressure is increased.

The ignition areas of H_2-air-CO_2 mixtures and H_2-air-H_2O mixtures, at 100 kPa and at 403 K, are given in Figs. 5 and 6, respectively. In both cases, the ignition is produced by a 60% H_2-40% Ar jet ejected at an initial temperature of 2500–2700 K. Three equivalence ratios are chosen: $\phi = 1$, $\phi = 0.55$, and $\phi = 0.25$. The lower ignition limit of the undiluted H_2-air mixtures is found to be equal to 4.5 ± 0.25 mol% H_2 in air. This value agrees well with the lower flammability limit of H_2-air mixtures obtained by Langer and Stock [20]. For rich undiluted H_2-air mixtures, the upper ignition limit is found to be equal to 66.0 ± 0.5 mol% H_2 in air, which is significantly lower than the flammability limit (72 mol% H_2) reported by Langer and Stock in the case of upward propagation. For both H_2-air-CO_2 and H_2-air-H_2O mixtures, the ignition area is smaller than the classical flammability area, with a noticeable reduction on the rich side. For CO_2-diluted mixtures, no data are available at 403 K. For H_2O-diluted mixtures, the ignition area is directly compared with the flammability area determined between 393 and 403 K by Langer and Stock [20]. The discrepancy between ignition and flammability areas can be explained first by the fact that the ignition limits are determined in a horizontal configuration while the flammability limits were determined in an upward one. Second, the ignition by a hot jet is initiated in the near field of the jet where a higher hydrogen concentration exists, due to the mixing with the 60% H_2-40% Ar jet. When both H_2-air-CO_2 and H_2-air-H_2O ignition areas are compared, one observes that the first is situated outside the second ignition area. This result can be surprising, since the molar heat capacity of CO_2 is slightly higher than the molar heat capacity of H_2O. Therefore an inverse effect could be expected, or at least, one could expect that both domains would be the same. Since the H_2-air-CO_2 ignition area is larger than the H_2-air-H_2O area, another phenomenon, that is, a chemical effect, must be taken into account. Steam and carbon dioxide added to the combustible mixture act as a third body in the reaction (1):

$$H + O_2 + M \rightarrow HO_2 + M \qquad (1)$$

This important reaction [with respect to its high exothermicity ($\Delta H^\circ_{298} = -197$ kJ)] competes with the chain-branching reaction (2):

$$H + O_2 \rightarrow OH + O \qquad (2)$$

At moderate initial pressure, CO_2 and H_2O behave like inhibitors. Because of the low reactivity of HO_2, reaction (1) actually behaves as a chain-terminating step, while, at high initial pressure, reaction (1) induces a thermal runaway. So, the rate constant of this reaction is of great importance in the mechanism of ignition and flame propagation. If the values of the collision efficiency of H_2O (6.5) and CO_2 (1.5) relative to H_2 collision efficiency given by Warnatz [21], are taken into account, it is clear that the ignition of an H_2-air mixture becomes more difficult at moderate pressure if the diluent is steam instead of carbon dioxide, since steam is at least four times more efficient than carbon dioxide.

Effect of Diluent Added to the Jet on the Ignition Limits:

The final part of the present paper deals with the effect of a partial substitution of the hydrogen con-

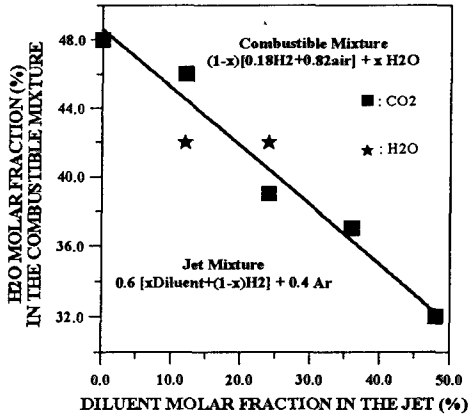

FIG. 7. Steam concentration limit added to the 18% H_2-82% air mixture, initially at 100 kPa and 403 K, vs the molar fraction of the diluent (CO_2 or H_2O) added to the hot gas ejected at an initial temperature close to 2700 K.

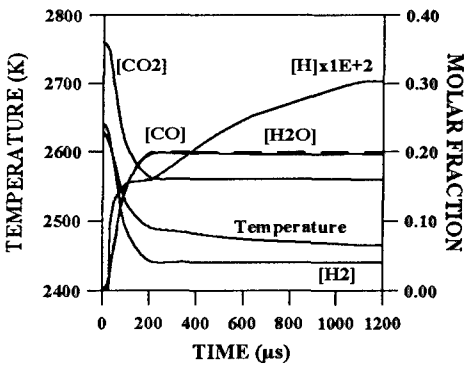

FIG. 8. Evolution of the temperature and the composition of a 36% CO_2-24% H_2-40% Ar mixture behind the reflected shock wave vs time, using the Chemkin code [16]. The initial time corresponds to the shock impact at the shock tube end. Shock temperature and pressure are 2628 K and 113 kPa, respectively (determined by Stanjan code [15]). The combustion chamber is initially at 100 kPa.

tained in the jet by CO_2 or H_2O on the ignition limits of the 18% H_2-82% air mixture diluted by H_2O.

When the stagnation temperature of the hot gas, prior to ejection, is around 2600 K, the substitution of H_2 in the hot gas by CO_2 or H_2O leads to a strong decrease of the steam composition of the combustible mixture at the limit (Fig. 7). For example, if the jet contains 24% CO_2-36% H_2-40% Ar, the ignition limit decreases to 39 mol% H_2O, and it drops to 32 mol% H_2O if the jet contains 48% CO_2-12% H_2-40% Ar. However, if the stagnation temperature is lower, about 2000 K, the ignition limit will decrease as well, since with a jet of 24% CO_2-36% H_2-40% Ar, the ignition limit is equal to 35 mol% H_2O. The same behavior is observed if H_2O is substituted for H_2 in the jet mixture (Fig. 7). The H_2O concentration limit decreases to 37 mol%, as the amount of H_2O in the ejected gas increases to 36 mol%.

The ignition limits of H_2-air-H_2O slightly differ when H_2O or CO_2 is substituted for H_2 in the jet. This result could be expected since, in the case of the H_2-CO_2-Ar mixture heated to 2600 K, the water gas reaction is important and leads to H_2O and CO production. A discussion previously given by Djebaili et al. [18] concerning the exact composition of the ejected gas shows that about half of the initial CO_2 is converted into approximately equal quantities of H_2O and CO because of the water gas reaction (Fig. 8). As a result, a similar diluent effect of H_2O and CO_2 is found.

The present experiments show the importance, in the case of a subsonic jet, of the initial jet temperature on the ability to ignite a combustible mixture, and on the restriction of the ignition area when hydrogen is partially substituted by carbon dioxide or steam.

Conclusions

An original experimental facility has been built to study the ignition of a combustible mixture by a hot gas jet. This device provides good control of the initial parameters of the jet.

The present paper deals with the critical conditions of a transient jet heated to 750–3000 K for igniting a combustible mixture of H_2-air, diluted either by H_2O or by CO_2. From the experimental data, two important parameters emerge:

1. The stagnation temperature is found to be a preponderant parameter that governs the ignition of the combustible mixture by a hot gas jet.
2. The nature and composition of the gas in the hot jet also play an important role in the ignition mechanism.

The ignition limits of H_2-air-CO_2 and H_2-air-H_2O, determined by using the shock-tube–combustion-chamber coupling, constitute a new data base, particularly for the assessment of nuclear power plant safety, since no information is found in the literature with this peculiar hot gas jet.

Acknowledgments

This work was sponsored by Electricité de France (SEPTEN) under Contract No. NC9298. One of the authors (N. Djebaili) acknowledges financial support from E.D.F./S.E.P.T.E.N. Discussions with Professor J. H. Lee were greatly appreciated.

REFERENCES

1. Fendel, F. E., *J. Fluid Mech.* 21:281 (1965).
2. Liñan, A., *Acta Astronaut.* 1:1007 (1974).
3. Darabiha, N., and Candel, S., *Combust. Sci. Technol.* 86:67–85 (1992).
4. Wolfhard, H. G., *Jet Propul.* 798–804 (1958).
5. Vanpée, M., and Bruszak, A. E., *The Ignition of Combustible Mixture by Laminar Jets of Hot Gases*, Bureau of Mines Report 6293, 1963.
6. Wojcicki, St., *Rev. Energ. Primaire* 10:8–13 (1974).
7. Enomoto, K., Furuhama, S., and Kobayachi, Y., *Third World Hydrogen Energy Conference*, Tokyo, 1980, Vol. 2, pp. 1149–1163.
8. Phillips, H., *Combust. Flame* 19:181–186 (1972).
9. Knystautas, R., Lee, J. H., Moen, I. O., and Wagner, H. Gg., *Seventeenth Symposium (International) on Combustion*, The Combustion Institute, Pittsburgh, 1979, pp. 1235–1245.
10. Schildknecht, M., Geiger, W., and Stock, M., in *Dynamics of Shock Waves, Explosions, and Detonations* (J. R. Bowen, N. Manson, A. K. Oppenheim, and R. I. Soloukhin, Eds.), Progress in Astronautics and Aeronautics, AIAA Inc., Washington, DC, 1984, Vol. 94, pp. 474–490.
11. Mackay, D. J., Murray, S. B., Moen, I. O., and Thibault, P. A., *Twenty-Second Symposium (International) on Combustion*, The Combustion Institute, Pittsburgh, 1988, pp. 1339–1353.
12. Shepherd, J. E., and Krok, I. C., *Twentieth Water Reactor Safety Information Meeting*, Bethesda, MD, 1992.
13. Djebaili, N., "Inflammation des Mélanges H_2-Air-H_2O et H_2-Air-CO_2 par un Jet de Gaz Chauds," Ph.D. Thesis, The University of Orléans, Orléans, France, 1993.
14. Djebaili, N., Lisbet, R., Dupré, G., and Paillard, C., *Nineteenth International Symposium on Shock Waves*, Marseille, 1993, to be published by Springer-Verlag in 1995.
15. Reynolds, Wm. C., *Stanjan Chemical Equilibrium Solver*, V. 3.84, IBM-PC, Stanford University, Stanford, CA, 1987.
16. Kee, R. J., Rupley, F. M., and Miller, J. A., *The Chemkin Thermodynamics Data Base*, Sandia National Laboratories, Report No. SAND87-8215B, 1987.
17. Conti, R. S., and Hertzberg, M., *J. Fire Sci.* 6:348–355 (1988).
18. Djebaili, N., Lisbet, R., Dupré, G., and Paillard, C., *Twenty-First Water Reactor Safety Information Meeting*, Bethesda, MD. 1993, to be published.
19. Zabetakis, M. G., *Flammability Characteristics of Combustible Gases and Vapors*, Bureau of Mines, Bull. 627, 1965.
20. Langer, G., and Stock, M., *International Conference on Thermal Reactor Safety*, Avignon, France, 1988.
21. Warnatz, J., in *Combustion Chemistry* (W. C. Gardiner, Jr., Ed.), Springer-Verlag, New York, 1984, p. 187.

COMMENTS

Dr. Gaby Ciccarelli, Brookhaven National Laboratory, USA. In the present study, the authors correlate the hot jet ignition of their test gas with the temperature of the jet. It is well known that the ignition phenomenon is also strongly influenced by gas dynamic effects. The gas dynamic effects manifest themselves in the mixing of the hot jet gas and the test gas and are usually characterized by the jet Reynolds number. Are there any plans to investigate the gas dynamic effects in the future?

Author's Reply. Obviously, the jet temperature is not the sole parameter to affect the ignition process. Indeed, the ignition mechanism by a subsonic hot gas jet is not a purely thermal mechanism. If a jet, constituted of pure argon, is used, a temperature higher than 3000 K has to be reached to ignite an H_2/air mixture. If 2 or 3 mol% H_2 are added to argon in the shock tube, then ignition occurs around 2000 K. At this temperature, the presence of reactive species is necessary to ignite the same mixture by a transient jet whose duration does not exceed 8 ms. Thus, the chemical reaction rate, mostly dependent on temperature, plays the main role in the ignition process of a combustible mixture by a subsonic hot gas jet. However, it is evident that gas dynamic effects must be taken into account in order to model in detail the ignition mechanism. For example, the influence of jet diameter plays a certain role: With a 1-mm-diameter jet, we have found that ignition is much more difficult than with a 2.5-mm-diameter. The influence of the structure of the jet emerging into the combustible mixture and subsequently gas dynamic effects will be investigated in the near future.

Twenty-Fifth Symposium (International) on Combustion/The Combustion Institute, 1994/pp. 1547–1554

DIFFUSION AND PREMIXED FLAME IGNITION DYNAMICS IN A FIELD OF VARIABLE STRAIN RATE

D. THEVENIN* AND S. CANDEL

Laboratoire d'Energétique Moléculaire et Macroscopique, Combustion
UPR 288 du C.N.R.S. and Ecole Centrale Paris
Grande Voie des Vignes, F-92295 Châtenay-Malabry, France

Theoretical studies as well as experimental evidence indicate that the strain rate determines in many cases the structure, consumption rate, and dynamics of diffusion and premixed flames. Large values of the strain rate can lead to extinction of the flame, whereas the level of strain rate controls in many situations the process of ignition. In typical cases of practical interest, a reactive element is transported in a field of variable strain rate. This takes place, for example, when two streams of reactants come into contact and form a mixing layer. In a frame of reference attached to this reactive element, one may describe the external flow field in terms of a time-dependent strain rate, and the response of the reactive element may then be modeled by examining the unsteady behavior of a fixed reactive sheet submitted to a strain rate evolving with time. Combining asymptotic analysis with numerical calculations, systematic studies have been carried out for this generic problem. Comparisons with experimental results relevant to supersonic combustion as well as to the stabilization of premixed flames on flameholders show adequate predictions of the ignition distance and of the stability domain.

Introduction

Problems of ignition in premixed and non-premixed shear flow configurations are of considerable technological importance and have received continuous attention in the past. Many studies have concerned the ignition of a stream of premixed reactants by a stream of hot gases [1–3]. This geometry is typical of that found in the flame stabilization by bluff bodies, and it may be used, for example, to analyze the conditions of flame stability, the standoff distance of the ignition point, and the blowoff phenomenon. The problem of ignition of non-premixed reactants in mixing layers has also been examined in relation with supersonic combustion applications. This problem is equally relevant in diesel engine modeling [4,5]. The non-premixed configuration often gives rise to triple flames, including premixed and diffusion branches, and such structures have been analyzed in many theoretical articles. Much of the recent work extends the classical ideas of Marble and Adamson [1] and the pioneering work of Liñán and coworkers [6,7]. One interesting contribution is due to Niioka [8], who models the ignition of a jet diffusion flame by examining strained flames. The results obtained are then used to describe the process of ignition of a fuel spray in a high-temperature atmosphere. Haworth et al. [9] show the necessity of considering the true time-dependent value of the strain rate at the reactive interface when using flamelet modeling.

Further studies sharing similar lines of reasoning are due, for example, to Liñán and Williams [5,10] and Thévenin and Candel [11]. In the last reference, it is indicated that one may describe the conditions of ignition by examining the nonsteady response of a reactive element in a field of variable strain. It is shown that results obtained for this generic problem may be used to predict the ignition of non-premixed shear flows formed at the confluence of hot and cold streams. This analysis is extended in the present article to premixed as well as partially premixed configurations.

Given a specific aerodynamic flow like a mixing layer, jet, or wake, the spatial distribution of strain rate is first determined. A transformation into a moving frame of reference attached to a reactive element is then carried out (Fig. 1). In this frame, the strain rate appears as a time-dependent parameter. This yields the complete history of the strain rate, which acts on the reactive sheet. An asymptotic analysis then provides the ignition time. Using the convection velocity of the flow being modeled, it is possible to deduce an ignition distance. When the ignition time becomes infinite, the ignition point is rejected to infinity, and this condition defines flame blowoff.

An important advantage of the present analysis is that it is applicable to a variety of shear flows. It is shown in the present article that it may be used to

*Present address: Institut für Technische Verbrennung, Universität Stuttgart, Pfaffenwaldring 12, D-70550 Stuttgart, Germany.

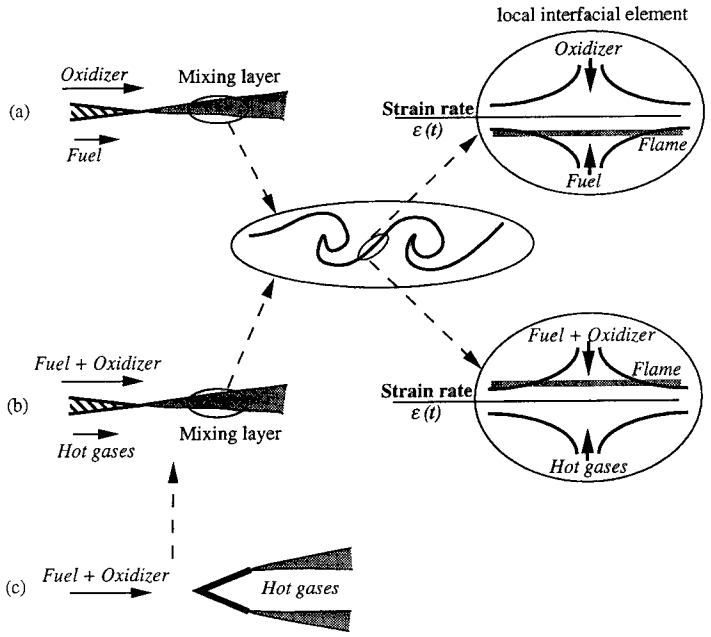

FIG. 1. Principle of the model, showing the relation between a mixing layer and a one-dimensional strained interface between two streams.

deal with non-premixed and premixed situations. Partially mixed flows that are also encountered in practice (for example in afterburners) may be treated as well but will not be considered in this paper.

The problem is formulated in the next section. The numerical procedure and the strain-rate estimation method are briefly described in the third and fourth sections. Examples of application and comparisons with experiments are then provided in the last sections of this paper.

Reduction of the System of Equation

In this analysis, we only consider two different reacting species: one fuel (index F), and one oxidizer (index O). These two species react according to $\nu_F F + \nu_O O \rightarrow \nu_P P$. The kinetics of this single-step reactive process are described by an Arrhenius law. All other species that are or might be present, e.g., the product of the reaction (index P) and possibly a diluent, are grouped under the form of a "global" species (index G).

The thermodiffusive hypothesis [12,13] may be used in this analysis because, during the ignition process, the changes of density due to the reaction are small and may be neglected. One may equally assume that the transverse coordinate is weighted by the density (using the Levy–Lees transformation [14]) so that the governing equations take the constant-density form. Pressure is assumed to be uniform and constant, which is a good approximation in many experimental configurations. We also consider that the thermodynamic properties as well as the diffusion coefficients are constant and identical for all species and that the Lewis number is equal to unity. The viscous dissipation term is also neglected. This term could be important when modeling ignition in boundary layers [15], but it is generally too small in mixing layers to lead to significant changes in temperature [16]. While these hypotheses are quite restrictive, it appears possible to get a good agreement with experiment by working in this frame.

Initial and boundary conditions used in the analysis are as follows. Mass fractions and temperature are kept constant at $z = +\infty$ and $z = -\infty$. At $t = 0$, all parameters are represented by a step function between their value at $z = +\infty$ and $z = -\infty$, the step being located at $z = 0$. Variables with subscript 0 (respectively 1) designate initial values for $z < 0$ (respectively $z > 0$) and, at the same time, boundary values for $z = -\infty$ (respectively $z = +\infty$). In a counterflow configuration with strain rate ε, the system of equations can be written as follows:

$$\frac{\partial Y_F}{\partial t} - \varepsilon z \frac{\partial Y_F}{\partial z} - D \frac{\partial^2 Y_F}{\partial z^2} = -\frac{\nu_F W_F}{\rho_0} \dot{\omega} \quad (1)$$

$$\frac{\partial Y_O}{\partial t} - \varepsilon z \frac{\partial Y_O}{\partial z} - D \frac{\partial^2 Y_O}{\partial z^2} = -\frac{\nu_O W_O}{\rho_0} \dot{\omega} \quad (2)$$

$$\frac{\partial T}{\partial t} - \varepsilon z \frac{\partial T}{\partial z} - D \frac{\partial^2 T}{\partial z^2} = \frac{\nu_F W_F Q}{\rho_0 C_p} \dot{\omega} \quad (3)$$

$$Y_F + Y_O + Y_G = 1. \quad (4)$$

The reaction term $\dot{\omega}$ has the Arrhenius form

$$\dot{\omega} = A\rho_0^{(\nu_F+\nu_O)} Y_F^{\nu_F} Y_O^{\nu_O} T^{\beta} \exp\left(-\frac{T_a}{T}\right). \tag{5}$$

A more compact set of equations may be deduced from the previous system. One first defines $\tilde{Y}_F = Y_F - Y_{F1}$, $\tilde{Y}_O = \sigma(Y_O - Y_{O1})$, and $\tilde{T} = C_p(T - T_1)/Q$, where $\sigma = \nu_F W_F/(\nu_O W_O)$ is the stoichiometric coefficient and Q is the heat released by the reaction per unit mass of fuel. The system becomes

$$\frac{\partial \tilde{Y}_F}{\partial t} - \varepsilon z \frac{\partial \tilde{Y}_F}{\partial z} - D \frac{\partial^2 \tilde{Y}_F}{\partial z^2} = -\dot{\Omega} \tag{6}$$

$$\frac{\partial \tilde{Y}_O}{\partial t} - \varepsilon z \frac{\partial \tilde{Y}_O}{\partial z} - D \frac{\partial^2 \tilde{Y}_O}{\partial z^2} = -\dot{\Omega} \tag{7}$$

$$\frac{\partial \tilde{T}}{\partial t} - \varepsilon z \frac{\partial \tilde{T}}{\partial z} - D \frac{\partial^2 \tilde{T}}{\partial z^2} = \dot{\Omega} \tag{8}$$

with $\dot{\Omega} = \nu_F W_F \dot{\omega}/\rho_0$. The problem can be further simplified by introducing Zeldovich's variables [17] Z_1 and Z_2 defined by

$$Z_1 = \frac{\tilde{T} + \tilde{Y}_F}{\tilde{T}_0 + \tilde{Y}_{F0}} \tag{9}$$

$$Z_2 = \frac{\tilde{T} + \tilde{Y}_O}{\tilde{T}_0 + \tilde{Y}_{O0}}. \tag{10}$$

Considering Eqs. (6) through (8), it is obvious that Z_1 and Z_2 are solutions of the same differential equation, without the source term:

$$\frac{\partial Z_i}{\partial t} - \varepsilon z \frac{\partial Z_i}{\partial z} - D \frac{\partial^2 Z_i}{\partial z^2} = 0, \qquad i = 1, 2. \tag{11}$$

From the definition of the initial and boundary conditions, it can also be seen that the equations for Z_1 and Z_2 are to be solved with the same initial and boundary conditions. It follows that the two variables Z_1 and Z_2 are identical. The frozen temperature T_{fr} corresponding to the same configuration in the absence of chemical reaction is also governed by an equation in the form of Eq. (11). Now, the reduced variable $\tilde{T}_{fr}/\tilde{T}_0$ possesses the same initial and boundary values as Z_1 and Z_2 and, therefore, coincides with these variables at all points and for all times:

$$Z_1(z, t) = Z_2(z, t) = \tilde{T}_{fr}(z, t)/\tilde{T}_0 = Z(z, t). \tag{12}$$

The initial and boundary conditions associated with variable Z are $Z(z = -\infty, t) = 1$ and $Z(z = +\infty, t) = 0$, and at $t = 0$, $Z(z)$ is a jump function that switches from 1 to 0 at $z = 0$. Knowing Z and $\tilde{T}$, it is possible to compute back all the variables of the system. For the mass fractions, one has, e.g.,

$$\tilde{Y}_F = (\tilde{T}_0 + \tilde{Y}_{F0})\, Z - \tilde{T} \tag{13}$$

$$\tilde{Y}_O = (\tilde{T}_0 + \tilde{Y}_{O0})\, Z - \tilde{T}. \tag{14}$$

The system of Eqs. (6) through (8) is therefore equivalent to

$$\frac{\partial Z}{\partial t} - \varepsilon z \frac{\partial Z}{\partial z} - D \frac{\partial^2 Z}{\partial z^2} = 0 \tag{15}$$

$$\frac{\partial \tilde{T}}{\partial t} - \varepsilon z \frac{\partial \tilde{T}}{\partial z} - D \frac{\partial^2 \tilde{T}}{\partial z^2} = \nu_F W_F A \rho_0^{(\nu_F+\nu_O-1)} T^{\beta} \cdot \exp\left(-\frac{T_a}{T}\right)[(\tilde{T}_0 + \tilde{Y}_{F0})\, Z - \tilde{T} + Y_{F1}]^{\nu_F} \cdot \left\{\frac{1}{\sigma}[(\tilde{T}_0 + \tilde{Y}_{O0})\, Z - \tilde{T}] + Y_{O1}\right\}^{\nu_O}. \tag{16}$$

If $\varepsilon(t)$ designates the actual value of the strain rate at the interface ($z = 0$), and ε_1 represents the maximum value of ε, one may define the following dimensionless space and time coordinates as

$$\chi(t) = \frac{1}{t}\int_0^t \varepsilon(\tau)\, d\tau \tag{17}$$

$$\tilde{t} = \chi(t) t \tag{18}$$

$$\tilde{z} = z\left(\frac{\varepsilon_1}{D}\right)^{1/2}. \tag{19}$$

The system thus becomes

$$\frac{\partial Z}{\partial \tilde{t}} - \tilde{z} \frac{\partial Z}{\partial \tilde{z}} - \frac{\varepsilon_1}{\varepsilon} \frac{\partial^2 Z}{\partial \tilde{z}^2} = 0 \tag{20}$$

$$\frac{\partial \tilde{T}}{\partial \tilde{t}} - \tilde{z} \frac{\partial \tilde{T}}{\partial \tilde{z}} - \frac{\varepsilon_1}{\varepsilon} \frac{\partial^2 \tilde{T}}{\partial \tilde{z}^2} = \frac{\nu_F W_F A}{\varepsilon} \rho_0^{(\nu_F+\nu_O-1)} T^{\beta} \cdot \exp\left(-\frac{T_a}{T}\right)[(\tilde{T}_0 + \tilde{Y}_{F0})\, Z - \tilde{T} + Y_{F1}]^{\nu_F} \cdot \left\{\frac{1}{\sigma}[(\tilde{T}_0 + \tilde{Y}_{O0})\, Z - \tilde{T}] + Y_{O1}\right\}^{\nu_O}. \tag{21}$$

It is convenient to define a reduced temperature parameter $T_{\text{red}} = C_p T_1/Q$ as well as a temperature increment above the frozen temperature given by $\theta = (\tilde{T} - \tilde{T}_{fr})/\mu$. The quantity μ is a small parameter and will be defined later. Here, θ is the first-order term in the expansion of the temperature T with respect to the small parameter μ [7], the temperature being written as

$$\tilde{T} = \tilde{T}_{fr} + \mu\theta + \mu^2\theta_2 + \mu^3\theta_3 + \dots \quad (22)$$

We write for convenience $\hat{T}_a = C_p T_a/Q$. Now, as long as the reaction remains weak, $\tilde{T} \sim \tilde{T}_{fr}$. Using these new parameters, one can therefore write at first order, before the thermal runaway,

$$\exp\left(-\frac{T_a}{T}\right) = \exp\left(-\frac{\hat{T}_a}{\tilde{T} + T_{\text{red}}}\right)$$

$$\simeq \exp\left(-\frac{\hat{T}_a}{\tilde{T}_{fr} + T_{\text{red}}}\right)$$

$$\cdot \exp\left(\frac{\mu\hat{T}_a\theta}{(\tilde{T}_{fr} + T_{\text{red}})^2}\right). \quad (23)$$

Neglecting all the terms of higher order in μ, the temperature equation takes the form

$$\frac{\partial\theta}{\partial\tilde{t}} - \tilde{z}\frac{\partial\theta}{\partial\tilde{z}} - \frac{\varepsilon_1}{\varepsilon}\frac{\partial^2\theta}{\partial\tilde{z}^2} = \frac{\nu_F W_F A}{\varepsilon\mu}\rho_0^{(\nu_F+\nu_O-1)}T_{fr}^{\beta}$$

$$\cdot\exp\left(-\frac{\hat{T}_a}{\tilde{T}_{fr} + T_{\text{red}}}\right)\exp\left(\frac{\mu\hat{T}_a\theta}{(\tilde{T}_{fr} + T_{\text{red}})^2}\right)$$

$$[(\tilde{T}_0 + \tilde{Y}_{F0})Z - \tilde{T}_{fr} + Y_{F1}]^{\nu_F}$$

$$\cdot\left\{\frac{1}{\sigma}[(\tilde{T}_0 + \tilde{Y}_{O0})Z - \tilde{T}_{fr}] + Y_{O1}\right\}^{\nu_O}. \quad (24)$$

We already know through Eq. (12) that $\tilde{T}_{fr} = \tilde{T}_0 Z$. It is now adequate to choose $\mu = T_{\text{red}}^2/\hat{T}_a$ as the small temperature expansion parameter, and to define a reduced strain rate $\tilde{\varepsilon} = \varepsilon/\varepsilon_1$ and a Damköhler number given by

$$\Delta = \frac{\nu_F W_F A}{\varepsilon_1\mu}\rho_0^{(\nu_F+\nu_O-1)}T_1^{\beta} \quad (25)$$

The system of equations is now reduced to

$$\frac{\partial Z}{\partial\tilde{t}} - \tilde{z}\frac{\partial Z}{\partial\tilde{z}} - \frac{1}{\tilde{\varepsilon}}\frac{\partial^2 Z}{\partial\tilde{z}^2} = 0 \quad (26)$$

$$\frac{\partial\theta}{\partial\tilde{t}} - \tilde{z}\frac{\partial\theta}{\partial\tilde{z}} - \frac{1}{\tilde{\varepsilon}}\frac{\partial^2\theta}{\partial\tilde{z}^2} = \frac{\Delta}{\tilde{\varepsilon}}\left(\frac{\tilde{T}_0 Z}{T_{\text{red}}} + 1\right)^{\beta}$$

$$\cdot\exp\left(-\frac{\hat{T}_a}{\tilde{T}_0 Z + T_{\text{red}}}\right)\exp\left[\left(\frac{T_{\text{red}}}{\tilde{T}_0 Z + T_{\text{red}}}\right)^2\theta\right].$$

$$[Y_{F0}Z + Y_{F1}(1 - Z)]^{\nu_F}[Y_{O0}Z + Y_{O1}(1 - Z)]^{\nu_O}. \quad (27)$$

The initial solution for Z is a jump function that switches from 1 to 0 at $z = 0$. At $t = 0$, θ is uniformly equal to 0. This system is to be solved with the boundary conditions $Z(z = -\infty, t) = 1$, $Z(z = +\infty, t) = 0$, $\theta(z = -\infty, t) = 0$, and $\theta(z = +\infty, t) = 0$.

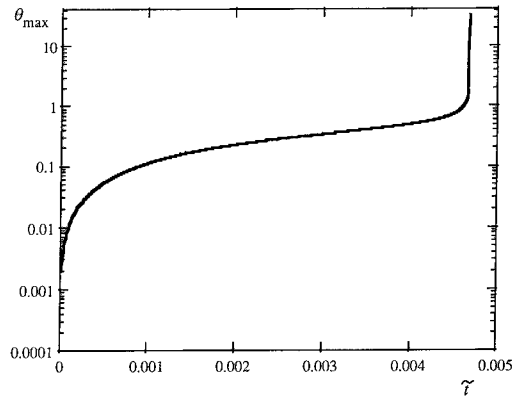

FIG. 2. Example of the evolution of the maximum value of θ with nondimensional time during a typical ignition process.

Numerical Procedure

The simplifying assumptions used in the above analysis yield a system of two uncoupled Eqs. (26) and (27) in place of a system of three fully coupled Eqs. (1) to (3). The solution of the resulting system is straightforward and is obtained with an implicit method, as both equations may be discretized as tridiagonal systems. Knowing the solution at time t_n, the equation for Z is integrated in a first step leading to the value $Z(z, t_{n+1})$. One then uses this new value of Z to integrate the equation in θ. The solution of both tridiagonal systems is obtained with a recursive algorithm [18]. The computing time needed to get a solution is negligible (about 20 s CPU on a standard workstation).

A typical temporal evolution of the maximum value of θ is presented in Fig. 2. At a certain instant in time, $\theta_{\max}$ rises quickly toward infinity, which indicates that ignition is taking place. One may consider that the ignition corresponds to $\theta_{\max} > 50$ and may stop the computation when this criterion is satisfied.

An example of the evolution of the ignition distance when increasing the strain rate is displayed in Fig. 3. This figure corresponds to the stabilization experiment of Scurlock [19] for $\phi = 0.7$, which is described later in this paper. In this case, the strain rate is directly proportional to the inflow velocity. When the velocity is increased, there comes a point where the ignition site moves rapidly toward infinity. The velocity for which this happens will be considered as the blowoff velocity given by the model.

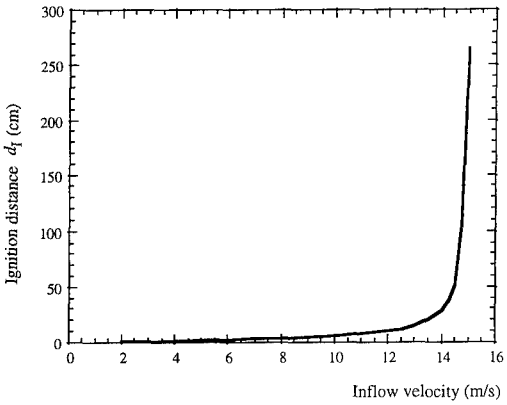

FIG. 3. Evolution of the computed ignition distance with an increasing inflow velocity for $\phi = 0.7$ (experiment described in Ref. 19). Parameters of the computation are listed in Table 2.

Evolution of the Strain Rate

In order to solve Eqs. (26) and (27), one has to specify the time-dependent evolution of the strain rate at the interface between the two streams. This evolution is given by phenomenological considerations based on the principles given in Fig. 1.

For a shear layer, the basic idea consists of computing the spatial evolution of the strain rate in terms of the velocity difference between the two streams $\Delta V = |V_1 - V_2|$ and of the width of the mixed zone between the two streams $w(x)$, leading to

$$\varepsilon(x) = \frac{\Delta V}{w(x)}. \tag{28}$$

This modeling does not allow that $w(x = 0) = 0$. We introduce, therefore, a value w_0, giving the size of the mixed zone between both streams at the level of the first contact point. In the typical case of two coflowing streams separated by a splitter plate, w_0 is the width of this splitter plate. In axisymmetric jet cases, w_0 corresponds to the difference between the inner and outer radii of the inner nozzle.

The spatial evolution of ε is converted into a temporal one by working in a frame of reference attached to a convected interfacial element. This modeling can be used as well in planar two-dimensional cases as in axisymmetric ones. Further details on this phenomenological representation of the strain-rate evolution are given in Ref. 11 and were used without changes here.

Diffusion Flame Cases

The study of the ignition dynamics for diffusion flames submitted to strain is presented in Ref. 11 by using a more restrictive formulation than that derived in this article. Both models are identical for diffusion flames but that of Ref. 11 is unable to deal with premixed situations. As a first test, it is worth showing that the present formulation is equivalent for non-premixed flames to that used previously. For this, we use the new model to obtain predictions of the ignition distance corresponding to four basic experiments pertaining to supersonic combustion [20–23]. A summary of the parameters used for these computations is given in Ref. 11.

TABLE 1
Comparison of computed and experimental ignition distances for four supersonic combustion cases involving diffusion flames

Ref.	Experimental d_I (cm)	Computed d_I (new model)	d_I in Ref. 11
20	$d_I < 6.2$	3.76	3.87
21	$10.32 < d_I < 17.8$	16.95	16.9
22	~5.07	5.28	5.26
23	$10 < d_I < 20$	9.21	9.22

Table 1 shows the experimental ignition distances along with the computed ones given by the present model and by the previous one described in Ref. 11. Computed values given by the new model are, as expected, similar to those found previously. The very slight difference observed corresponds to the modification of the formulation, leading to a small change in the criterion used to stop the computation as θ_{max} goes toward infinity. A good agreement with all four experimental results is observed, which proves that the present model is able to describe the ignition of diffusion flames in supersonic flows.

Premixed Flame Cases

We now consider the problem of flame stabilization in a premixed stream. Numerous experiments were carried out in this configuration [19,24–27]. In what follows, we refer to the experimental results of Fetting et al. [26], concerning the stabilization of a premixed flame on a 5-mm diameter cylindrical bluff body. In this work, the domain of stable combustion is given as a function of the equivalence ratio of the fresh gas. The principle of the transformation into a strained interface model is analogous to the one used for mixing layers and is presented in Fig. 1. We consider that, behind the bluff body, the velocity is zero and that the temperature is equal to 90% of the adiabatic flame temperature of the incoming mixture. Both hypotheses yield fair approximations of the real situation [29]. The adiabatic flame temperature is computed as a function of the equivalence ratio using

TABLE 2
Parameters used to model the experiments described in refs. 19 and 26

Parameter	Value [19]	Value [26]
Equivalence ratio	$\phi = 0.6$ to 1.6	i.d.
Fresh gas composition	given by ϕ	i.d.
Fresh gas temperature	300 K	i.d.
Fresh gas pressure	1 atm	i.d.
Initial mixing width	3×10^{-5} m	2.1×10^{-5} m
Bluff body outer diameter	2.39×10^{-3} m	5×10^{-3} m

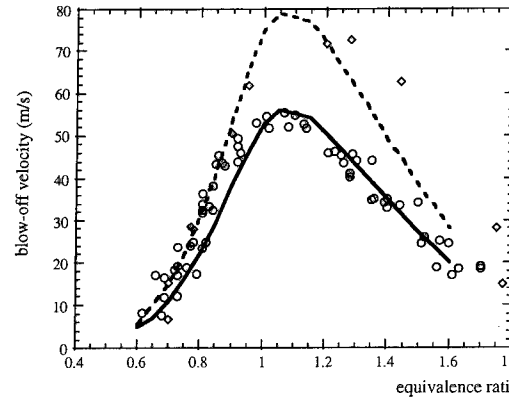

FIG. 4. Comparison of the experimental and computed domains of stable combustion for the experiments described in Refs. 19 and 26. Ref. 19: ◇, experiment; dashed line, computation. Ref. 26: ○, experiment; solid line, computation.

the equilibrium chemistry hypothesis. To describe the reactive process, we take $T_a = 12{,}000$ K [28] and $Q/C_p = 2.7\ 10^4$ K [30]. Writing the chemical reaction as a single-step process would lead to $\nu_F = 1$ and $\nu_O = 5$, which is of course unrealistic, as real reactions can only be bi- or trimolecular. In order to retain partially the dissymetry between the fuel and oxidizer (as it appears also in the experimental results), we choose $\nu_F = 1$ and $\nu_O = 2$. Initial density is computed using a perfect gas law. The value of the pre-exponential factor is not known a priori and is chosen in order to get the correct value of the blowoff velocity at $\phi = 1$, which leads to $A = 1.89 \times 10^{11}$ in SI units.

The experimental parameters needed by the model are listed in Table 2. The computed stability domain is compared in Fig. 4 with the experimental one, showing very good agreement. Using the same set of parameters to describe the chemical process, we now compare predicted values with experimental results given in Ref. 19, also used in Ref. 24. The appropriate maximum blowoff velocity is obtained by slightly changing the value of the parameter w_0, as given in Table 2. It must be mentioned here that it is difficult to clearly define the value of this parameter in the case of cylindrical bluff bodies, as no obvious partially premixed zone exists at the first contact point between fresh gas stream and recirculation zone. The value of w_0 should probably depend also on the turbulence intensity in the fresh gas, and this value is often not given in the original articles. In fact, one also finds a certain scatter in the experimental results obtained by different groups for comparable operating conditions. Using the value of w_0 given in Table 2, the agreement with the experiment described in Ref. 19 is good, with a slight deviation from experimental results for rich mixtures (Fig. 4). These two comparisons show that the present model is applicable to premixed configurations, which was not the case of the original formulation given in Ref. 11.

Conclusion

A model is formulated for ignition and flame stabilization in shear flows. Numerous comparisons with experiments of the predicted ignition distances and blowoff velocities have been carried out. They refer to several experimental results corresponding to various premixed and non-premixed flames (two-dimensional and axisymmetric) and two different fuels (hydrogen and propane). In all cases, the present model predicts the autoignition site and stability domain with good accuracy. This tends to prove that the strain rate is a leading parameter that controls the ignition distance in all the experimental studies used for comparison. This would not be the case if both streams were injected with the same velocities (no strain) or if both temperatures were low (ignition dominated by chemical effects). But, in most self-ignition cases of interest, the proposed model is able to accurately reproduce the evolution of the ignition distance and the stability limits as a function of all major parameters. It requires very short computing times, making it quite attractive for systematic studies.

The results also confirm that flamelet modeling may be used to predict ignition processes, provided that a time-dependent strain rate is included in the computation.

Nomenclature

A pre-exponential factor
C_p heat capacity at constant pressure (J/(kg·K))

D	diffusion coefficient (m^2/s)
d_i	ignition distance (m)
Q	heat released by the reaction by kg fuel (J/kg)
T, $\tilde{T}$	temperature (K) and nondimensional temperature (−)
T_a	activation temperature (K)
$\hat{T}_a$	reduced activation temperature (−)
T_{fr}	frozen temperature (K)
$\tilde{T}_{red}$	reduced temperature parameter (−)
$w(x)$	width of the mixing layer (m)
w_0	initial mixing width (m)
W_i	molar mass of species i (kg/mol)
Y_i $\tilde{Y}_i$	mass fraction of species i and its reduced value (−)
z, $\hat{z}$	coordinate value (m), nondimensional counterpart (−)
Z	Zeldovich variable
β	exponent of the temperature dependence for $\dot{\omega}$ (−)
Δ	Damköhler number
ε	strain rate (1/s)
ε_1	maximal value of the strain rate (1/s)
ϕ	equivalence ratio (−)
μ	small parameter used to expand the temperature (−)
ν	stoichiometric coefficient of species i in reaction (−)
$\dot{\omega}$	production rate of the reaction ($mol/(m^3 \cdot s)$)
ρ_0	density (kg/m^3)
σ	stoichiometric ratio (−)
θ	temperature increase above the frozen value (−)
χ	temporally averaged value of the strain rate (1/s)

REFERENCES

1. Marble, F. E., and Adamson, T. C., *Jet Prop.* Mar.–Apr.:85–94 (1954).
2. Sharma, O. P., and Sirignano, W. A., *Combust. Sci. Technol.* 1:481–494 (1970).
3. Law, C. K., and Law, H. K., *J. Heat Trans.* 104:329–337 (1982).
4. Sato, J., Konishi, K., Okada, H., and Niioka, T., *Twenty-First Symposium (International) on Combustion*, The Combustion Institute, Pittsburgh, 1986, pp. 695–702.
5. Liñan, A., and Williams, F. A., *Combust. Flame* 95:31 (1993).
6. Liñan, A., *Acta Astron.* 1:1007–1039 (1974).
7. Liñan, A., and Crespo, A., *Combust. Sci. Technol.* 14:95–117 (1976).
8. Niioka, T., *Eighteenth Symposium (International) on Combustion*, The Combustion Institute, Pittsburgh, 1981, pp. 1807–1813.
9. Haworth, D. C., Drake, M. C., Pope, S. B., and Blint, R. J., *Twenty-Second Symposium (International) on Combustion*, The Combustion Institute, Pittsburgh, 1988, pp. 589–597.
10. Liñan, A., and Williams, F. E., Fourth IDEA Workshop, April 8–10, 1991, Cambridge, 1991.
11. Thévenin, D., and Candel, S. M., *Combust. Sci. Technol.* 91:73–94 (1993).
12. Marble, F. E., in *Recent Advances in the Aerospace Sciences* (C. Casci Ed.), Plenum Press, New York, 1985, pp. 395–413.
13. Clavin, P., *Prog. Energ. Combust. Sci.* 11 (1985).
14. Lees, L., *J. Heat Trans.* 104:329–337 (1956).
15. da Silva, L. F., Deshaies, B., and Champion, M., *Thirtieth Aerospace Sciences Meeting*, AIAA 92-0338, 1992.
16. Vuillermoz, P., Oran, E., and Kailasanath, K., Thirtieth Aerospace Sciences Meeting, AIAA 92-0337, 1992.
17. Zeldovich, Y. B., Barrenblatt, G. I., Librovich, V. B., and Makhviladze, G. M., *Combustion and Explosions*, Plenum Publishing Corp., New York, 1985.
18. Blottner, F. G., *Introduction to Computational Techniques for Boundary Layers*, SANDIA National Report No. 79-0893, (1981).
19. Scurlock, A. C., Meteor Report No. 19, Fuels Research Laboratory, MIT, Cambridge, 1948.
20. Evans, J. S., Schexnayder, C. J., and Beach, H. L., "Application of a Two-Dimensional Parabolic Computer Program to Prediction of Turbulent Reacting Flows," NASA Technical Paper 1169, NASA Langley, 1978.
21. Cohen, L. S., and Guile, R. N., "Investigation of the mixing and combustion of turbulent, compressible free jets," NASA Technical Paper CR-1473, NASA Langley, 1969.
22. Cheng, T. S., Wehrmeyer, J. A., Pitz, R. W., Jarrett, O., and Northam, G. B., AIAA/ASME/SAE Twenty-Seventh Joint Propulsion Conference, AIAA 91-2320, 1991.
23. Burrows, M., and Kurkov, A. P., "Analytical and experimental study of supersonic combustion of hydrogen," Report NASA TM-2828, NASA, 1973.
24. Williams, G. C., and Shipman, C. W., *Fourth Symposium (International) on Combustion*, The Combustion Institute, Pittsburgh, 1953, pp. 733–742.
25. Longwell, J. P., *Fourth Symposium (International) on Combustion*, The Combustion Institute, Pittsburgh, 1953, pp. 90–97.
26. Fetting, F., Choudury, P. R., and Wilhelm, R. H., *Seventh Symposium (International) on Combustion*, The Combustion Institute, Pittsburgh, 1959, pp. 621–632.
27. Yamaguchi, S., Ohiwa, N., and Hasegawa, T., *Combust. Flame* 62:31–41 (1985).
28. Kundu, K. M., Banerjeee, D., and Bhaduri, D., *Combust. Sci. Technol.* 17:153–162 (1977).
29. Zukoski, E. E., and Marble, F. E., *Gas-Dynamics Symposium on Thermochemistry*, North-Western University, Evanston, IL, 1956, p. 205.
30. Marshall, N., *Gas Encyclopaedia*, Air Liquide Company, Elsevier, New York, 1976.

COMMENTS

H. G. Im, Princeton University, USA. Your asymptotic analysis appears to be inconsistent when T_o is of the same order as T_{red}. In such a case, while z varies from 0 to 1, the exponential factor in the reaction term changes exponentially for large activation energy. What it implies is that in such a case reaction is confined to an asymptotically thin layer near the hot temperature side. If you perform an appropriate local analysis, the problem is reduced to a simple ODE type, and an explicit expression for ignition condition has previously been obtained [1]. Have you tried to compare your numerical result with the previous study?

REFERENCE

1. Liñan and Crespo, *Combust. Sci. Technol.* (1976).

Author's Reply. By making further hypotheses on the relative values of the temperature, it would be possible to simplify further the equations along the lines of Liñan (Refs. 6 and 7 of this paper). We have checked previously that our analysis agrees with the results of Liñan in the case of a constant strain rate. Nevertheless, we do not want to make any hypothesis on the temperature ratio in the general case, and it is in this frame impossible to reduce further the system of equations, which must then be solved numerically.

•

H. S. Mukunda, Indian Institute of Science, India. As you are aware, the ignition dynamics governed by the early roll-up of vertical structures influence the phenomena through curvature tangential (velocity) strain rate and unsteadiness. As you indicate, you are using the simple definition of stretch rate because of simplicity of the approach. This is desirable. For it to be satisfactory, it will be necessary, I believe, to relate the overall stretch rate to the controlling stretch rate and assure that it is monotonic (or perhaps linear, if it so turns out to be). Would you care to comment on this?

Author's Reply. At this point, using the tangential value of the strain rate to model its global effect seems to be the only practical solution. On the other hand, unsteady effects are fully taken into account, and curvative effects are neglected. Further studies are clearly needed to assess the relative importance of these effects, as well as to relate tangential strain rate and controlling stretch (see, e.g., the work of Fichot et al., this symposium).

•

S. K. Aggarwal, University of Illinois at Chicago, USA. 1. Developing an ignition for a time-varying strain rate and applying it to a supersonic shear layer is quite interesting. Have you examined the correlation between ignitability and convective Mach number?

2. Is there any significance of oscillating strain rate in the supersonic shear layer?

Author's Reply. 1. The effect of convective Mach number on the ignition distance was examined in the case of supersonic combustion in our previous work (Ref. 11 in this paper).

2. Trying to model the influence of vortices through oscillating strain rate would certainly be interesting. Flames submitted to sinusoidal strain rates have already been examined (see, e.g., Im et al., this symposium).

Twenty-Fifth Symposium (International) on Combustion/The Combustion Institute, 1994/pp. 1555–1562

SELF-IGNITION OF EXPANDING HIGH-TEMPERATURE H_2-AIR AND CH_4-AIR MIXTURES

H.-J. WEBER, A. MACK AND P. ROTH
Institut für Verbrennung und Gasdynamik
Universität Duisburg
D-47048 Duisburg, Germany

The influence of rarefaction waves on the ignition characteristics of H_2- and CH_4-air mixtures was studied by solving the corresponding conservation equations for mass, species, energy, and momentum in a one-dimensional model. The numerical solution was based on the method of lines and on a dynamic adaptive mesh technique. Because of the stiffness originating from the detailed kinetic mechanism, the resulting system of ordinary differential equations was integrated by a BDF-code.

The rarefaction wave running into the initially homogeneous, quiescent, high-temperature gas was initiated by a piston moving with constant velocity. The wave causes a space- and time-dependent temperature profile resulting in space-dependent ignition processes. Because of the complicated interaction between gas dynamics and induction process, different combustion regimes arise. Nearly constant volume explosion regimes were obtained for low piston velocities. An increased piston velocity resulted in a combustion wave with a peak pressure exceeding the constant volume explosion pressure significantly. This is a quite unexpected result because a stronger expansion wave is associated with a temperature and density decrease. The observed peak pressure increase is a consequence of the wave-induced temperature gradient, creating an ignition wave that in turn interacts with its own pressure wave, resulting in a strong coupling between both waves. This effect was first revealed by Zeldovich for hot-spot temperature gradients and could now be shown to be also valid in the presence of rarefaction waves. A further increased piston velocity reduced the arising peak pressure, because the coupling mechanism failed as a result of the stronger temperature gradient.

Introduction

In recent years, there has been a growing interest in detonation formation due to initial temperature or/and concentration nonuniformities. Zeldovich et al. [1] were the first who investigated numerically the interaction between pressure and combustion waves leading to a detonation. Several years later, Zeldovich [2] introduced the concept of a spontaneous flame arising under conditions close to self-ignition. A series of investigations [3,4] followed this approach. He and Clavin [5] gave a more sophisticated analytical criterion for detonation initiation and failure. Short and Dold [6] extended Zeldovich's concept by including compressibility and expansion effects. Jackson et al. [7] discussed the dynamics of ignition from reaction centers and showed the preeminence of the constant volume thermal explosion as the first event in an ignition sequence. Later, Kapila and Roytburd [8] and Bdzil and Kapila [9] investigated in detail the transition of a shockless weak detonation into a ZND detonation. All these previous studies were using numerical or perturbation techniques assuming one-step chemical kinetics. Recently, Dold and Kapila [10] indicated that significant qualitative differences in detonation initiation arise, depending on global one-step or chain-branching chemical models.

It has previously been established numerically by Goyal et al. [11], Mack et al. [12], Frolov et al. [13], and Weber et al. [14,15] that a detonation can be initiated in a confined combustible mixture by proper temperature or radical concentration gradients in H_2/O_2 and $C_2H_6/O_2/N_2$ mixtures. All models take full transport and detailed reaction mechanisms into account. Those nonuniformities were chosen as initial conditions, but all processes by which they were produced were ignored.

In this work, a rarefaction wave running into an initially homogeneous, quiescent, high-temperature gas mixture was generated by a moving piston. The wave caused a space- and time-dependent temperature profile, thus initiating space-dependent ignition processes. Different combustion regimes were obtained as a result of the complicated interaction between gas dynamics and induction processes. The numerical method applied in this study was based on the method of lines combined with an adaptive moving mesh technique [18,19,20]. Detailed transport and kinetic models for H_2/O_2 and CH_4/O_2 mixtures were incorporated.

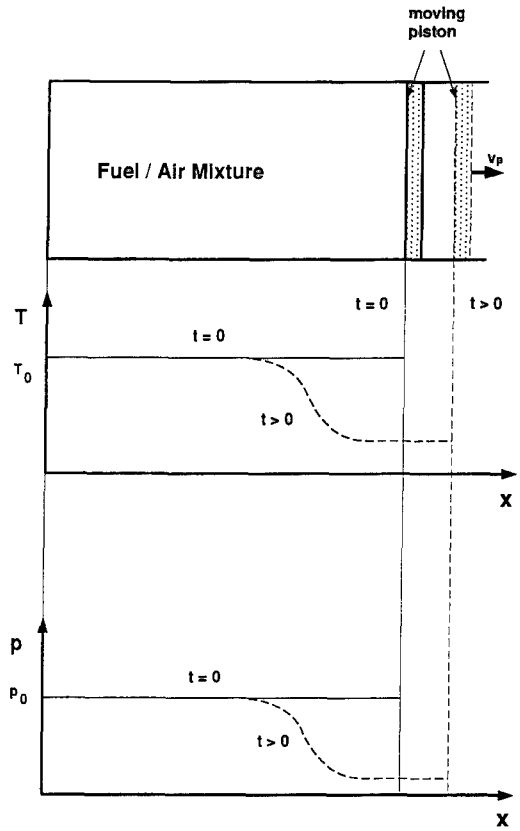

FIG. 1. Initial temperature and pressure distribution for the moving piston problem.

Description of the Model

This study was based on the following one-dimensional model (see Fig. 1). A homogeneous fuel/air mixture is confined in a closed volume at temperatures above autoignition conditions. At $t \geqslant 0$, the piston at the right boundary is accelerated to reach a constant velocity, thus causing a rarefaction wave, which runs into the fuel/air mixture. The resulting space- and time-dependent temperature profile causes a series of space-dependent ignition processes.

The mathematical model used is given by the one-dimensional conservation laws in Lagrangian coordinates for mass, Eq. (1); species, Eq. (2); energy, Eq. (3); and momentum, Eq. (4). Furthermore, the Lagrangian transformation, Eq. (5), and (6), the equation of state for ideal gases, were used.

$$\frac{\partial \rho}{\partial t} + \rho^2 \frac{\partial v}{\partial \psi} = 0 \tag{1}$$

$$\frac{\partial w_i}{\partial t} + \frac{\partial(\rho w_i V_i)}{\partial \psi} = \frac{\dot{r}_i}{\rho} \quad i = 1, \ldots, NST \tag{2}$$

$$\frac{\partial T}{\partial t} - \frac{1}{\rho c_p}\frac{\partial p}{\partial t} + \frac{1}{c_p}\sum_{i=1}^{NST} \rho w_i V_i c_{p_i} \frac{\partial T}{\partial \psi} - \frac{1}{c_p}\frac{\partial}{\partial \psi}\left(\lambda \rho \frac{\partial T}{\partial \psi}\right) - \frac{4}{3}\frac{\rho \mu}{c_p}\left(\frac{\partial v}{\partial \psi}\right)^2 + \frac{1}{\rho c_p}\sum_{i=1}^{NST} \dot{r}_i h_i = 0 \tag{3}$$

$$\frac{\partial v}{\partial t} + \frac{\partial p}{\partial \psi} - \frac{4}{3}\frac{\partial}{\partial \psi}\left(\rho \mu \frac{\partial v}{\partial \psi}\right) = 0 \tag{4}$$

$$\frac{\partial x}{\partial \psi} = \frac{1}{\rho} \tag{5}$$

$$p - R_M \rho T \sum_{i=1}^{NST} \frac{w_i}{M_i} = 0 \tag{6}$$

where $0 \leq \psi \leq \psi_{max}$.

Notation: ψ = Lagrangian mass coordinate, t = time, x = Eulerian coordinate, p = pressure, T = temperature, w_i = mass fraction of species i, ρ = mass density, NST = number of species, M_i = molecular weight of species i, $\dot{r}_i$ = molar rate of formation of species i, c_{p_i} = specific heat capacity at constant pressure of species i, c_p = specific heat capacity at constant pressure of the mixture, λ = thermal conductivity of the mixture, μ = dynamic viscosity, V_i = diffusion velocity of species i, h_i = specific enthalpy of species i, and R_M = universal gas constant. Thermodynamic properties and the mixture-averaged transport properties where evaluated on the basis of CHEMKIN [16] and the corresponding transport subroutine library [17].

Besides the conservation laws, physical boundary and initial conditions are required to state a well-posed problem. The boundary conditions are valid for adiabatic, solid walls. The initial conditions define the initial state of the mixture, which is given by pressure, velocity, composition, and temperature for $t = 0$.

Initial conditions	Boundary conditions	
$T(0,\psi) = T_0(\psi)$	$\frac{\partial T(t,0)}{\partial \psi} = 0$	$\frac{\partial T(t,\psi_{max})}{\partial \psi} = 0$
$w_i(0,\psi) = w_{i,0}$	$\frac{\partial w_i(t,0)}{\partial \psi} = 0$	$\frac{\partial w_i(t,\psi_{max})}{\partial \psi} = 0$
$p(0,\psi) = p_0$	$v(t,0) = 0$	$v(t,\psi_{max}) = v_p(t)$
$v(0,\psi) = 0$	$x(t,0) = 0$	

The piston is accelerated between $t = 0$ and $t = t_a$ and moves for $t > t_a$ with the constant velocity $v_{p_{max}}$. The boundary condition for the piston velocity v_p is

$$t \leq 0: \quad v_p(t) = 0$$

$$0 < t \leq t_a: \quad v_p(t) = 0.5 \cdot v_{p_{\max}}\left(1 - \cos\left(\frac{\pi}{t_a} t\right)\right)$$

$$t > t_a: \quad v_p(t) = v_{p_{\max}}.$$

The nonlinear initial boundary value problem was solved as follows. The discretization of the differential Eqs. (1) through (5) in their spatial coordinate results in a system of nonlinear ordinary differential equations (method of lines). This system is stiff as a result of the nonlinearity in the chemical source terms. It was therefore solved with an implicit BDF-code. Besides the temporal stiffness, the system has very different characteristic length scales; for example, the geometrical vessel length, the flame front thickness, or the pressure wave structure, which result in additional spatial stiffness. Since the propagation of a deflagration wave is driven by transport and reaction processes in the flame region, it is necessary to resolve the spatial structure. This was made possible by applying an adaptive moving grid method [12,19,20], which used a minimum number of grid points to resolve the different moving wave structures.

The main idea of the moving grid method is to equidistribute the arc length of some characteristic physical variables in the $NP + 1$ different intervals. The arc length can be calculated from the distance of the grid points and a function G, which contains the weighted gradients of some physical variables $u_{j,i}$. Here, j denotes the variable (e.g., temperature or pressure) and i the grid point. With

$$G_i = \sqrt{1 + \sum_j c_j(u_{j,i+1}, u_{j,i}) \left(\frac{u_{j,i+1} - u_{j,i}}{\psi_{i+1} - \psi_i}\right)^2} \tag{7}$$

$$n_i = \frac{1}{\psi_{i+1} - \psi_i}, \qquad i = 0, \ldots, NP \tag{8}$$

the equidistribution principle was formulated as follows:

$$\frac{n_{i-1}}{G_{i-1}} = \frac{n_i}{G_i}, \qquad i = 1, \ldots, NP. \tag{9}$$

It can be transformed by some spatial and temporal smoothing into an ordinary differential equation describing the position and movement of the grid points. Details are given in Refs. 12, 19, and 20.

The spatial discretization of Eqs. (1) through (5) together with Eq. (6) and the differential equation of the grid-point movement can be written in the following compact form:

$$\underline{\underline{B}}(\underline{U})\, \dot{\underline{U}} = \underline{F}(\underline{U}), \qquad \underline{U}(0) = \underline{U}_0 \tag{10}$$

In this equation, $\underline{\underline{B}}$ is a singular matrix, because of the discretised Lagrangian transformation (5) and the equation of state (6). It contains the coefficients of the time derivatives of the ordinary differential equations. $\underline{U}$ is the solution vector containing the values of the dependent variables at the $NP + 2$ grid points. The point above $\underline{U}$ indicates the time derivative. The system (10) was solved with the BDF-code DASSL [21].

Computational Results and Discussion

Ignition processes in the presence of rarefaction waves were studied both for stoichiometric H_2-air and CH_4-air mixtures. The reaction mechanism for H_2-air consisting of 18 elementary reactions for nine species was taken from Refs. 22, 23, and 24. The CH_4-air mechanism consisted of 58 elementary reactions for 21 species and was based on works by Warnatz [25] and Skinner et al. [26]. The maximum velocity of the moving piston was varied between 50 m/s $\leq v_{p_{\max}} \leq$ 600 m/s. The acceleration time was always $t_a = 1\ \mu$s. In the following sections, five different examples of calculated self-ignition in expanding mixtures will be presented.

The first two examples deal with simulations of ignition in the presence of weak rarefaction waves. The initial conditions of the stoichiometric hydrogen/air mixture (example 1) are

$$T_0 = 1100 \text{ K} \qquad p_0 = 1.0 \text{ bar}$$

$$x_{m0} = 7 \text{ cm} \qquad v_{p_{\max}} = 50 \text{ m/s}.$$

The corresponding pressure and temperature profiles are shown in Figs. 2 and 3. The sharp decrease of pressure and temperature down to zero indicates the position of the moving piston. At $t = 0$ a rarefaction wave is produced, propagating into the hot hydrogen/air mixture. The pressure decreases from 1.0 bar down to 0.93 bar, see Fig. 2, while the temperature decreases from 1100 K down to 1075 K, see Fig. 3. As a result of the small temperature and pressure difference between the right and the left boundary, the mixture ignites after 100 μs nearly simultaneously in the entire volume. The peak pressure does not exceed the constant volume explosion pressure of 2.4 bar. Only at the end of the ignition process does the reflection of the weak pressure wave lead to an increase of the maximum pressure up to 2.8 bar.

In example 2, the ignition of a methane/air mixture is presented:

$$T_0 = 1850 \text{ K} \qquad p_0 = 1.0 \text{ bar}$$

$$x_{m0} = 7 \text{ cm} \qquad v_{p_{\max}} = 50 \text{ m/s}.$$

In Figs. 4 and 5, results obtained for the develop-

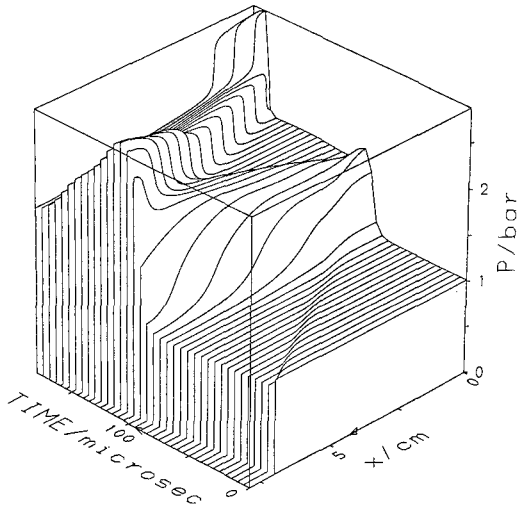

FIG. 2. Time-dependent pressure profile of the igniting hydrogen/air mixture for a piston velocity of 50 m/s.

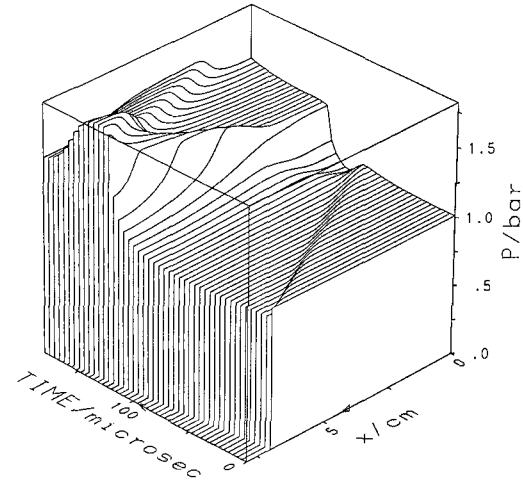

FIG. 4. Time-dependent pressure profile of the igniting methane/air mixture for a piston velocity of 50 m/s.

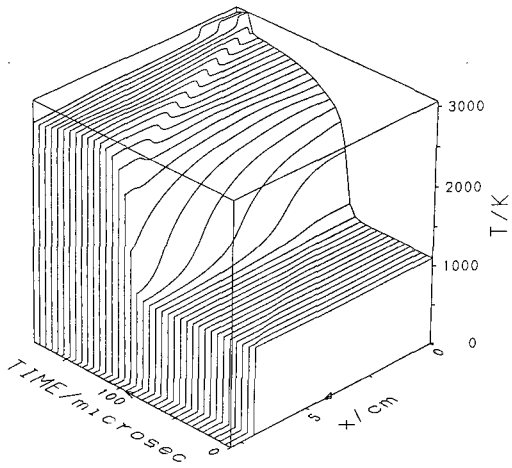

FIG. 3. Time-dependent temperature profile of the igniting hydrogen/air mixture for a piston velocity of 50 m/s.

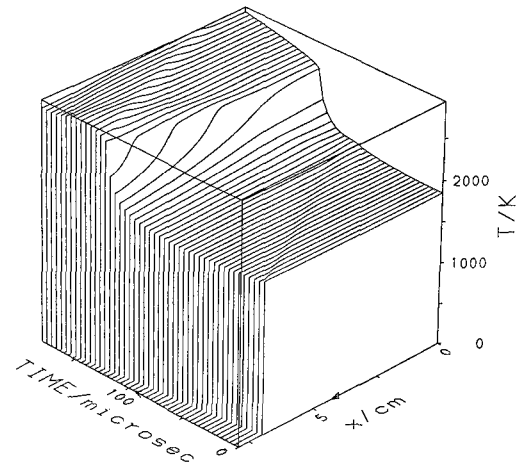

FIG. 5. Time-dependent temperature profile of the igniting methane/air mixture for a piston velocity of 50 m/s.

ment of pressure and temperature structures are summarized. Again, a weak rarefaction wave is produced at $t = 0$, running into the hot fuel/air mixture. Pressure and temperature decrease down to 0.94 bar and 1822 K, respectively. At $t = 100\ \mu s$, the rarefaction wave reaches the left boundary, leading to a sudden pressure decrease. At $t = 125\ \mu s$, ignition occurs, resulting in a pressure and temperature increase. The peak pressure of 1.75 bar is reached after the pressure wave is reflected at the wall.

In the next two examples, the intensity of the rarefaction wave is increased by accelerating the piston to 200 m/s. The stoichiometric hydrogen/air mixture has the following set of initial conditions:

$$T_0 = 1100\ \text{K} \qquad p_0 = 1.0\ \text{bar}$$

$$x_{m0} = 7\ \text{cm} \qquad v_{p_{max}} = 200\ \text{m/s}.$$

The results in Figs. 6 and 7 show a stronger decrease in pressure and temperature compared to examples 1 and 2, and decrease down to 0.71 bar and 1003 K, respectively. The mixture ignites after 100 μs at the hot-temperature boundary, generating a pressure wave. It propagates thru the rarefaction-wave-induced temperature gradient region and focuses the ignition, giving rise to an interaction between combustion and pressure wave. During this process, the intensity of the pressure wave increases to a value of 3.5 bar and exceeds the constant volume explosion

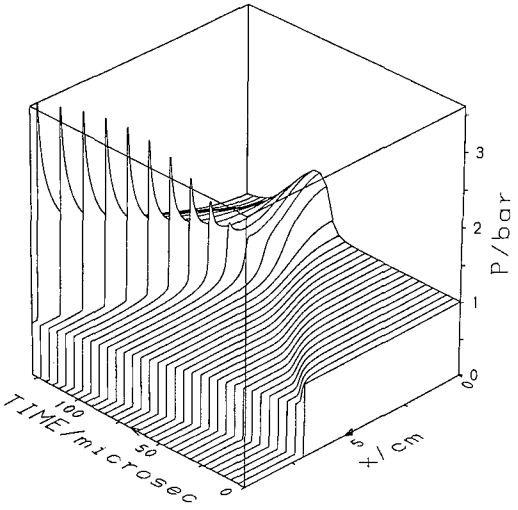

FIG. 6. Time-dependent pressure profile of the igniting hydrogen/air mixture for a piston velocity of 200 m/s.

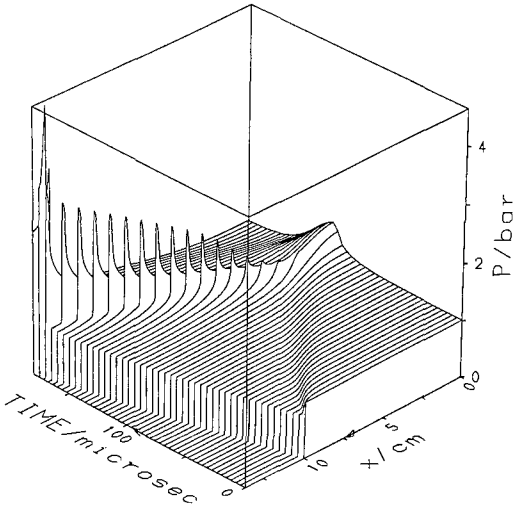

FIG. 8. Time-dependent pressure profile of the igniting methane/air mixture for a piston velocity of 200 m/s.

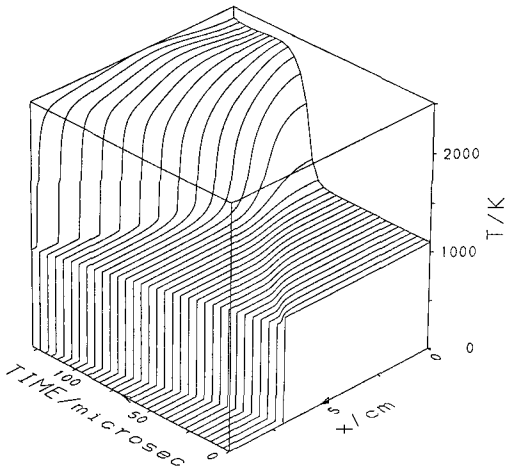

FIG. 7. Time-dependent temperature profile of the igniting hydrogen/air mixture for a piston velocity of 200 m/s.

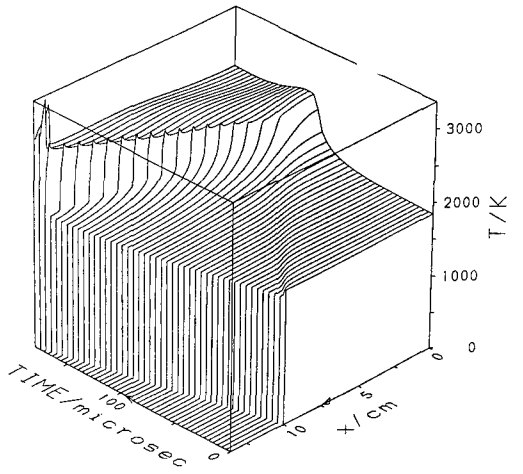

FIG. 9. Time-dependent temperature profile of the igniting methane/air mixture for a piston velocity of 200 m/s.

pressure significantly. This wave shows a detonation-like structure, but peak pressure and velocity of 1550 m/s (with respect to the unburnt gas) are too small for a CJ-detonation (5.3 bar and 1880 m/s) under such conditions.

Example 4 is again a methane/air mixture with the following set of initial conditions:

$$T_0 = 1850 \text{ K} \qquad p_0 = 1.0 \text{ bar}$$

$$x_{m0} = 10 \text{ cm} \qquad v_{p_{\max}} = 200 \text{ m/s}.$$

The initial length of the vessel x_{m0} was increased from 7 to 10 cm. The reason is that the stronger rarefaction wave causes a large temperature drop in the ignition region, thus enlarging the ignition delay time. The pressure in Fig. 8 decreases down to 0.75 bar in the rarefaction wave and results in a temperature decrease from 1850 K down to 1739 K, see Fig. 9. At $t = 110\ \mu$s, ignition occurs in the higher pressure region of the mixture, leading to a pressure increase up to 1.6 bar. Afterwards, a pressure and a combustion wave start to propagate into the unburnt mixture. As a result of the high temperature of the unburnt gas, the pressure wave ignites the gas nearly instantaneously, resulting in a strong coupling between both waves. The pressure wave increases up to 3.2 bar and forms a detonation-like structure that propagates

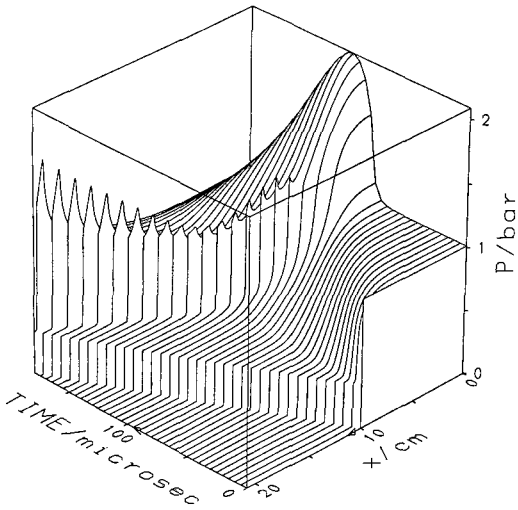

FIG. 10. Time-dependent pressure profile of the igniting hydrogen/air mixture for a piston velocity of 600 m/s.

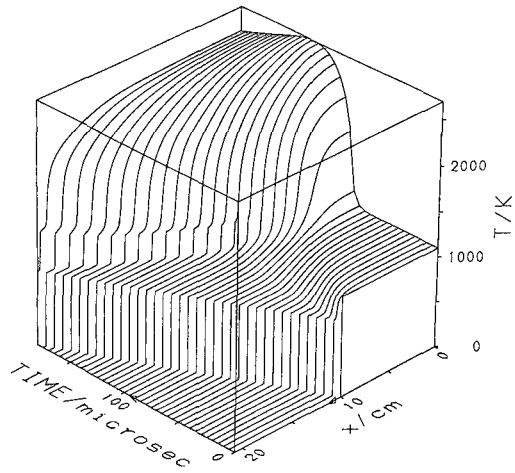

FIG. 11. Time-dependent temperature profile of the igniting hydrogen/air mixture for a piston velocity of 600 m/s.

with a velocity of 1500 m/s with respect to the unburnt gas. The corresponding CJ-detonation would have a velocity of 1700 m/s and a peak pressure of 3.6 bar. During wave reflection at the moving piston, the peak pressure increases again.

The piston velocity $v_{p_{\max}}$ and the associated strength of the rarefaction wave were further increased in the last example. Initial conditions for the stoichiometric hydrogen/air mixture are

$$T_0 = 1100 \text{ K} \qquad p_0 = 1.0 \text{ bar}$$

$$x_{m0} = 10 \text{ cm} \qquad v_{p_{\max}} = 600 \text{ m/s}.$$

According to Figs. 10 and 11, the rarefaction wave causes a strong pressure and temperature drop to 0.33 bar and 819 K, respectively. After ignition at $t = 100\,\mu$s at the hot boundary, the pressure increases up to 2.1 bar. In this case, the resulting pressure wave is steepened up to a shock wave, which moves faster than the reaction wave, leading to a decoupling of both waves, whereby the strength of the wave decreases. At $t = 125\,\mu$s, a new pressure peak behind the existing wave appears, which has its origin in the moving reaction wave. Its interaction with the shock-compressed unburned gas causes an increased intensity of the pressure up to 1.75 bar. The second pressure wave starts to overtake the precursor shock wave, but does not reach it until it is reflected at the moving piston.

The five different examples describe the influence of a rarefaction wave on the ignition of high-temperature fuel/air mixtures. It has been demonstrated that the piston velocity has a strong influence on the resulting combustion regime, which can be classified

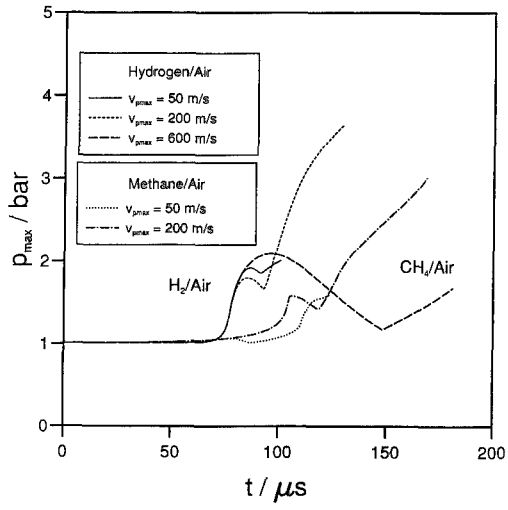

FIG. 12. Peak pressure over time history for different piston velocities.

on the basis of the peak pressure time history, see Fig. 12. For low piston velocities ($v_{p_{\max}} = 50$ m/s), the peak pressure over time diagram shows a value that does not exceed the constant volume explosion pressure of about 2.4 bar for hydrogen/air and 1.7 bar for methane/air mixtures. The constant volume explosion pressure is calculated on the basis of the initial conditions at $t = 0$. The low peak pressure and the nearly simultaneous ignition in the entire volume lead to the conclusion that this ignition process can be considered as a kind of a constant volume explosion.

An increase of the piston velocity to $v_{p_{\max}} = 200$

m/s results in a strong pressure increase after ignition for both mixtures. Both peak pressure profiles have a similar shape: Ignition in the high-pressure part of the mixture leads to a local maximum in the peak pressure. Afterwards, the pressure intensity lowers because the ignition-induced pressure wave propagates through the rarefaction wave. The temperature gradient existing there leads to a coupling of pressure and reaction wave, resulting in an amplification of the peak pressure. This effect is indicated in Fig. 12 by a further increase of the peak pressure, which is still below the value of a CJ-detonation. Under the present conditions, a piston velocity of 200 m/s leads to the formation of an underdriven detonation wave.

An example for a piston velocity of $v_{p_{\max}} = 600$ m/s was shown only for the hydrogen/air mixture. In this case, the ignition process of the higher-pressure region results in a pressure rise up to constant volume explosion conditions. Afterwards, the peak pressure decreases because of the influence of the rarefaction wave and the expansion of the burnt gas. Later on, the intensity of the shock wave originating from self-ignition decreases, but it is still able to induce an ignition process in the shock-heated gas. This results in a further increase of the peak pressure at conditions $t \geqslant 150\ \mu s$. In this case, transition to detonation formation can be seen.

Conclusions

The dynamics of ignition processes in H_2/air and CH_4/air mixtures at high temperatures under the influence of a rarefaction wave was investigated. Depending on the strength of the rarefaction wave, different combustion regimes were obtained as a result of the spatial gradient in the ignition delay time. Under certain conditions, a coupling between the reaction and pressure waves could lead to an amplification of the peak pressure exceeding the constant volume explosion value. The results of this study can be explained by Zeldovich's [2] concept of detonation initiation due to temperature nonuniformities.

Acknowledgment

This work was supported by the Deutsche Forschungsgemeinschaft.

REFERENCES

1. Zeldovich, Y. B., Librovich, V. B., Makhiladze, G. M., and Sivashinsky, G. I., On the Development of Detonation in a Non-Uniformly Preheated Gas, *Astronautica Acta* 15:313–321 (1970).
2. Zeldovich, Y. B., "Regime Classification of an Exothermic Reaction with Nonuniform Initial Conditions" *Combust. Flame* 39:211–214 (1980).
3. Zeldovich, Y. B., Gelfand, B. E., Tsyganov, S. A., Frolov, S. M. and Polenov, A. N., in *Concentration and Temperature Nonuniformities of Combustible Mixtures as Reason for Pressure Wave Generation* (A. L. Kuhl, J.-C. Leyer, A. A. Borisov, and W. A. Sirignano, Eds.), Progress in Astronautics and Aeronautics, AIAA Inc., New York, 1988, Vol. 114, pp. 99–123.
4. Makhviladze, G. M., and Rogatykh, D. I., "Nonuniformities in Initial Temperature and Concentration as a Cause of Explosive Chemical Reactions in Combustible Gases," *Combust. Flame* 87:347–356 (1991).
5. He, L., and Clavin, P., *Twenty-Fourth Symposium (International) on Combustion*, The Combustion Institute, Pittsburgh, 1992, pp. 1861–1867.
6. Short, M., and Dold, J. W., in *Corrections to Zel'dovich's "Spontaneous Flame" and the Onset of Explosion via Nonuniform Preheating* (A. L. Kuhl et al. Eds.), Progress in Astronautics and Aeronautics, AIAA Inc., New York, 1993, Vol. 154, pp. 59–74.
7. Jackson, T. L., Kapila, A. K., and Stewart, D. S., "Evolution of a Reaction Center in an Explosive Material," *SIAM J. Appl. Math.* 49:432–458 (1989).
8. Kapila, A., and Roytburd, V., "Transition to Detonation: A Numerical Study; Numerical Combustion," *Lecture Notes in Physics* (A. Dervieux, and B. Larrouturou Eds.), Springer-Verlag, Berlin, 1989, Vol. 351, pp. 374–382.
9. Bdzil, J. B., and Kapila, A. K., "Shock-to-Detonation Transition: A Model Problem," *Phys. Fluids A* 2:409–418 (1992).
10. Dold, J. W., and Kapila, A. K., "Comparison between Shock Initiations of Detonation Using Thermally-Sensitive and Chain-Branching Chemical Models," *Combust. Flame* 85:185–194 (1991).
11. Goyal, G., Warnatz, J., and Maas, U., "Numerical Studies of Hot Spot Ignition in H_2-O_2 and CH_4-Air Mixtures," *Twenty-Third Symposium (International) on Combustion*, The Combustion Institute, Pittsburgh, 1990, pp. 1767–1773.
12. Mack, A., Weber, H.-J., and Roth, P., "A Numerical Study of Ignition Processes in H2/O2 Mixtures with Initial H Atom Non-Uniformities," presented at the Fifth International SIAM Conference on Numerical Combustion, Garmisch-Patenkirchen, Germany, 1993.
13. Frolov, S. M., Mack, A., and Roth, P., "A Study of Explosion Onset in a Non-Uniformly Preheated H_2/O_2 Mixture," *Conference Proceedings of the 14th ICDERS Conference*, Coimbra, Portugal, 1993.
14. Weber, H.-J., Mack, A., and Roth, P., in *Numerical Simulation of Ignition Processes and Combustion Wave Propagation in H_2O_2 Reaction Systems* (A. L. Kuhl et al., Eds.), Progress in Astronautics and Aeronautics, AIAA Inc., New York, 1993, Vol. 151, pp. 27–38.
15. Weber, H.-J., Mack, A., and Roth, P., *Twenty-Fourth Symposium (International) on Combustion*, The Combustion Institute, Pittsburgh, 1992, pp. 1799–1807.
16. Kee, R. J., Miller, J. A., and Jefferson, T. H., *CHEMKIN: A General Purpose, Problem-Independent*

Transportable FORTRAN Chemical Kinetics Code Package, Sandia Report SAND80-8003, 1980.

17. Kee, R. J., Warnatz, J., and Miller, J. A., *A FORTRAN Computer Code Package for the Evaluation of Gas Phase Viscosities, Conductivities, and Diffusion Coefficients*, Sandia Report SAND83-8209, 1983.
18. Mack, A., Weber, H.-J., and Roth, P., "A Moving Grid Method Applied to One-Dimensional Nonstationary Flame Propagation," *Int. J. Num. Meth. Fluids* 13:869–882 (1991).
19. Furzeland, R. M., Verwer, J. G., and Zegeling, P. A., "A Numerical Study of Three Moving Grid Methods for One-Dimensional Partial Differential Equations Which are Based on the Method of Lines," *J. Comput. Phys.* 89:349–388 (1990).
20. Dorfi, E. A., and O'C. Drury, L., "Simple Adaptive Grids for 1-D Initial Value Problems," *J. Comp. Phys.* 69:175–195 (1987).
21. Petzold, L. R., "A Description of DASSL: A Differential/Algebraic System Solver," in *Scientific Computing*, (R. S. Stepleman, Ed.), North-Holland, Amsterdam, 1983, 65–68.
22. Warnatz, J., in *Numerical Methods in Laminar Flame Propagation, a GAMM-Workshop*, (J. Warnatz, and N. Peters, Eds.), Viehweg, Braunschweig, 1982, pp. 9–64.
23. Warnatz, J., *Ber. Bunsenges. Phys. Chem.* 87:1008–1022 (1983).
24. Warnatz, J., *Ber. Bunsenges. Phys. Chem.* 82:643–649 (1978).
25. Warnatz, J., in 7. ICOGER, Göttingen, AIAA Inc., New York, 1979, pp. 501–521.
26. Skinner, G., Lifshitz, A., Scheller, K., and Burcat, A., *J. Chem. Phys.* 8:3853 (1972).

Twenty-Fifth Symposium (International) on Combustion/The Combustion Institute, 1994/pp. 1563–1569

NATURAL GAS AND BLENDS OXIDATION AND IGNITION: EXPERIMENTS AND MODELING

YEWEN TAN, PHILIPPE DAGAUT, MICHEL CATHONNET AND JEAN CLAUDE BOETTNER
CNRS, LCSR
1C, Avenue de la Recherche Scientifique
45071 Orléans Cedex 2, France

AND

JEAN SYLVAIN BACHMAN AND PATRICK CARLIER
Gaz de France, DETN, CERSTA
361, Avenue du Président Wilson
93210 La Plaine-Saint-Denis, France

The kinetics of the oxidation of natural gas and blends (CH_4/C_2H_6, CH_4/C_3H_8, $CH_4/C_2H_6/C_3H_8$) has been studied in a jet-stirred reactor ($800 \leq T/K \leq 1240$, $1 \leq P/atm \leq 10$, $0.1 \leq$ equivalence ratio ≤ 1.5). The concentration profiles of reactants, intermediates, and products measured in a jet-stirred reactor (JSR) have been used to validate a detailed kinetic reaction mechanism. Literature ignition delay times measured in shock tube have also been modeled. A generally good agreement between the data and the model is found. The same mechanism has also been used to successfully represent the oxidation of methane, ethyne, ethene, ethane, propene, propane, *n*-butane, and 1-butene in various conditions including JSR, shock tube, and flame. The present study clearly shows the importance of trace hydrocarbons in the oxidation of methane. The computations indicate that the oxidation of methane is initiated by its reaction with O_2 when no other hydrocarbon is present. In natural gas and blends, higher hydrocarbons react before methane, leading to the formation of OH, H, and O radicals, which in turn initiate methane oxidation. This work demonstrates that methane cannot be used safely to represent the kinetics of natural gas combustion. However, simple blends like methane-propane or methane-ethane-propane could be used.

Introduction

Natural gas is a major fuel used on earth. In order to sustain and enhance the competitiveness of natural gas use, it is important to provide engineers with predictable tools usable for designing higher performance combustors. One of these is a predictable reaction mechanism. There is a wealth of data concerning methane combustion and ignition. However, very few studies concern the oxidation of natural gas, which is a mixture of methane (typically >90%) with higher hydrocarbons, in various amounts, depending on the source. It is known from previous shock-tube studies that methane ignition is boosted by small quantities of heavier fuels [1–4]. Preliminary interpretations have been proposed [5] but needed further investigation, especially detailed kinetic modeling. It was also interesting to investigate natural gas oxidation at a pressure representative of gas turbine conditions (typically ≈10 atm).

As part of a continuing effort in this laboratory to better understand the kinetics of fuel combustion, a series of experimental and computational studies has been carried out with natural gas and blends in a wide range of conditions. The results of these studies are reported here.

Experiments

The high-pressure jet-stirred reactor (JSR) experimental setup has been presented in detail elsewhere [6,7] and will only be reviewed briefly here. It consists of a 40-mm fused silica sphere (to prevent wall catalytic reactions) equipped with four nozzles of 1-mm diameter for the admission of the gases achieving the stirring. The inside volume of the reactor is 35 cm^3. It is surrounded by a regulated electrical resistance system and located inside a stainless steel pressure-resistant jacket. It can operate at pressures as high as 10 atm. The hydrocarbon and oxygen flow rates are measured and regulated by thermal mass-flow controllers. These gases are diluted by a flow of nitrogen and mixed at the entrance of the injectors after preheating. The pressure inside the reactor is kept constant in time using a pressure regulator on the exhaust line. Good thermal homogeneity was observed for each experiment along the whole vertical

TABLE 1
Experimental conditions in the jet-stirred reactor

			Reactants mole fractions				
τ/s	T/K	P/atm	O_2	CH_4	C_2H_6	C_3H_8	Higher fuels[a]
0.14–1.4	883–1240	1–10	0.006–0.008	0.003–0.004	0.0003–0.0004	none	none
0.14–1.3	903–1213	1–10	0.006–0.008	0.003–0.004	none	0.0003–0.0004	none
0.14–1.2	903–1210	1–10	0.006–0.0053	0.003–0.004	0.0003–0.0004	6.75×10^{-5} to 9×10^{-5}	none
0.14–1.2	883–1225	1–10	0.006–0.0053	0.003–0.004	0.0003–0.0004	6.3×10^{-5} to $8.4\ 10^{-5}$	1.05×10^{-5} to 3.6×10^{-5}

[a]The total mole fraction of higher fuel (other than ethane and propane) concentration is given in the table. It corresponds to n-butane (2.4×10^{-6} to 3.27×10^{-6}), i-butane (3.1×10^{-6} to 4.1×10^{-6}), n-pentane (1.7×10^{-6} to 2.3×10^{-6}), i-pentane (1.7×10^{-6} to 2.3×10^{-6}), n-hexane (1.7×10^{-6} to 2.3×10^{-6}).

axis of the reactor by uncoated chromel-alumel thermocouple (0.16-mm diameter) measurements. Typical gradients of ≤5 K have been measured in the present work. Because of the high dilution of the fuel (0.3–0.5% by volume), the temperature rise due to reaction was less than 20 K. The wall temperature is very close to the reactor gas temperature, so thermocouple heat losses can be neglected. The experimental temperature has been recorded for use in modeling calculations. Low-pressure samples of reacting mixtures have been taken through a sonic quartz probe and stored in 1-L bulbs at ≈25 torr for further gas chromatography (GC) analyses. The sampling procedure has been described previously [8]. The samples are further pressurized at 760 torr using homemade pistons before injection in the GC, in order to increase the sensitivity. Capillary columns of 0.53-mm i.d. (Poraplot U and Q, Molecular sieve 5A) were used with FID and TCD detection for GC measurements of, respectively, hydrocarbons and permanent gases. Carbon balance was checked for every sample and was found good within ≤5%.

In the present work, the JSR oxidation of methane-ethane, methane-propane, methane-ethane-propane, and methane-ethane-propane-butane-i-butane-pentane-i-pentane-hexane mixtures diluted by nitrogen was studied. The evolution of hydrocarbon oxidation from low to high conversion as well as that of intermediates and final products was followed for equivalence ratios, ϕ, of 0.1–1.5, pressures of 1–10 atm, and initial temperatures ranging from 800 to 1240 K (see Table 1).

Modeling and Reaction Mechanism

The computer program developed previously in this laboratory for a JSR [9] operating at steady state was used. The concentration of the gases within the JSR is determined from the balance between the net rate of production of each species by chemical reaction and the difference between the input and the output flow rates of the species. At each mean residence time considered, $\tau = \rho V/\dot{m}$ (where ρ is the mass density, $\dot{m}$ is the overall mass flow rate of the gases, and V is the volume of the reactor), we have to solve the set of nonlinear algebraic equations ($i = 1, 2, \ldots, I$; $j = 1, 2, \ldots, J$):

$$\dot{m}(\sigma_i^* - \sigma_i)/V - \sum_{j=1}^{J} (a_{ij} - \beta_{ij})(R_j - R_{-j}) = 0$$

where σ_i^* and σ_i are the concentrations (mol/g) of species i, respectively, on input and output; a_{ij} and β_{ij} are the stoichiometric coefficients of species i in reaction j; R_j and R_{-j} are the rates of elementary reactions respectively forming and consuming species i. These rates are computed from the kinetic mechanism and the rate constants of the elementary reactions at the experimental temperature, using the modified Arrhenius equation

$$k = A \times T^b \times \exp(-E/RT).$$

The set of nonlinear algebraic equations is solved by the Newton–Raphson method. The rate constants for reverse reactions were computed from forward rate constants and the appropriate equilibrium constants calculated using the Chemkin thermodynamic data base coefficients [10] and Burcat thermochemical data [11,12] for compounds not found in the Chemkin data base.

The computer code [9] employed in this work to model ignition behind reflected shock waves uses the constant density approximation [13]. The integration

method is that of LSODE [14]. In the present work, the ignition delay time is defined as the time at which the rate of temperature rise reaches its maximum (i.e., dT/dt = maximum).

The reaction mechanism base set is the comprehensive mechanism developed for the oxidation of methane, ethane, ethylene, propane, and propene as individual fuels [15,16]. It has been revised and updated to represent acetylene combustion as well as that of natural gas and blends in a wide range of conditions (flow reactor, JSR, flame, shock tube, 0.02–10 atm). The entire mechanism cannot be included in this paper but is presented, as well as the thermochemical data for the reverse rate constant computations, in a recent paper [17]. The pressure dependence of unimolecular reactions and of some pressure-dependent bimolecular reactions was taken into account when information was available [i.e., $k(P,T)$], and modified Arrhenius expressions were derived for particular pressures.

As previously mentioned, the present mechanism has a strong hierarchical structure. Since most of the present mechanism has been presented in detail in recent articles, only the major changes will be presented below.

For reaction

$$H + HO_2 = H_2O + O \qquad (15)$$

we used the rate constant recommended by Baulch et al. [18] [$k_{15} = 3 \times 10^{13} \exp(-866/T)$ cm^3/mole/s].

The kinetics of CH_3 reactions with O_2 have been reevaluated based on several recent studies.

$$CH_3 + O_2 = CH_3O + O \qquad (53)$$

$$CH_3 + O_2 = CH_2O + OH. \qquad (54)$$

The rate constant used for Reaction (53) is that recommended by Baulch et al. [$k_{53} = 1.32 \times 10^{14} \exp(-15{,}830/T)$ cm^3/mole/s). This value is in close agreement with other measurements. Although Reaction (54) has been extensively studied, the rate constant for this reaction remains uncertain, especially in the low-temperature range ($T < 1000$ K). Several recent studies [19,20] suggest that the rate constant for this reaction has a high activation energy, while others proposed a low activation energy for this reaction [21,22]. The rate constant used in our mechanism [$k_{54} = 3.1 \times 10^{10} \exp(-4409/T)$ cm^3/mole/s] was measured by Braun-Unkhoff et al. [22] in shock tube.

The kinetics of Reaction (46) representing a key step for methane ignition has been reinvestigated at high temperature by Troe [23], who found a rate constant of $8 \pm 2 \times 10^{12}$ cm^3 mol^{-1} s^{-1}. A value of 4×10^{12} is used in this mechanism.

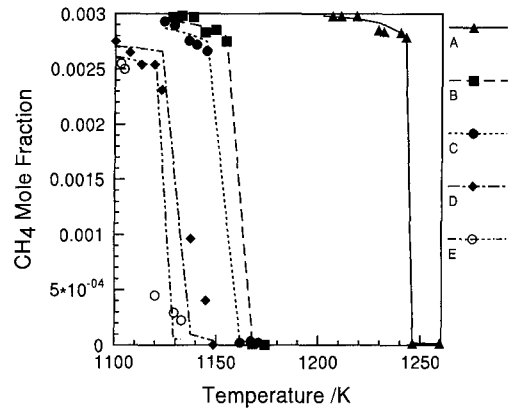

FIG. 1. JSR oxidation of methane and mixtures of methane with higher hydrocarbons (τ = 0.14 s, 1 atm, A: CH_4 0.3%, O_2 1.2%; B: CH_4 0.3%, O_2 1.2%, C_2H_6 0.03%; C: CH_4 0.3%, O_2 1.2%, C_3H_8 0.03%; D: CH_4 0.3%, O_2 1.2%, C_2H_6 0.03%, C_3H_8 0.0046%; E: CH_4 0.3%, O_2 1.2%, C_2H_6 0.033%, C_3H_8 0.0063%, n-C_4H_{10} 0.00024%, iso-C_4H_{10} 0.00031%, n-C_5H_{12} 0.00017%, iso-C_5H_{12} 0.00017%, n-C_6H_{14} 0.00017%). The symbols represent experimental data while the lines are the present computed results.

$$CH_3 + HO_2 = CH_3O + OH \qquad (46)$$

Our rate constants for Reactions (178) and (179) are taken from Michael and Wagner [24] with a branching ratio $k_{179}/(k_{178} + k_{179}) = 0.8$.

$$C_2H_2 + O = CH_2 + CO \qquad (178)$$

$$C_2H_2 + O = HCCO + H \qquad (179)$$

Results and Discussion

Experimental and modeling results for the JSR oxidation of natural gas and blends are presented in Figs. 1 through 5. In order to better evaluate the role of higher hydrocarbons on methane-oxygen oxidation, we present the experimental and modeling results obtained for four mixtures of methane-oxygen-higher hydrocarbon and for a methane-oxygen mixture. In all of these experiments, we kept CH_4 and O_2 initial mole fractions constant. From Fig. 1, it is clear that methane oxidation is boosted by the addition of small quantities of higher hydrocarbons and that the effect increases with the carbon chain length of the additive. In Figs. 2 and 3, we present experimental and computed results obtained for the oxidation at atmospheric pressure of, respectively, a lean CH_4-C_3H_8 mixture, and a slightly rich natural gas mixture. In Figs 4 and 5, we present experimental and computed results for the oxidation of, respectively, a stoichiometric CH_4-C_2H_6 mixture and a stoi-

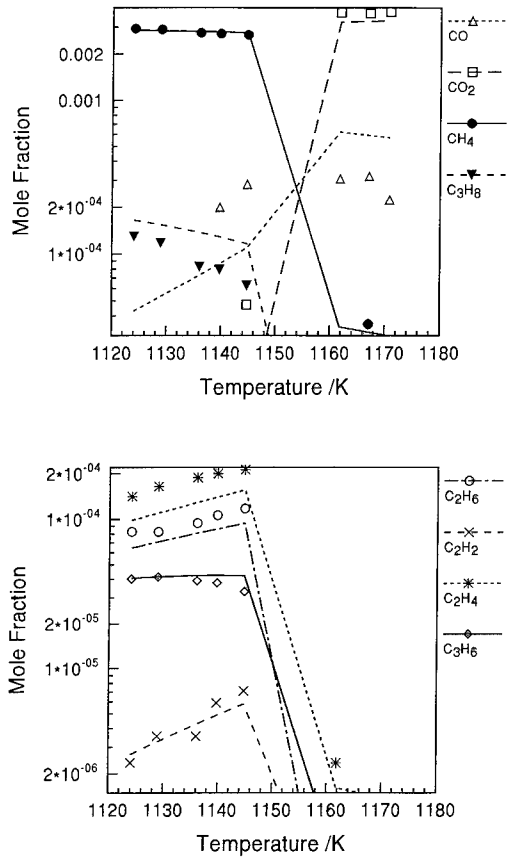

FIG. 2. Comparison between experimental (symbols) and computed (lines) results for the oxidation of a methane-propane mixture in a JSR (τ = 0.14 s, 1 atm, CH_4 0.25%, C_3H_8 0.025%, O_2 1.2%).

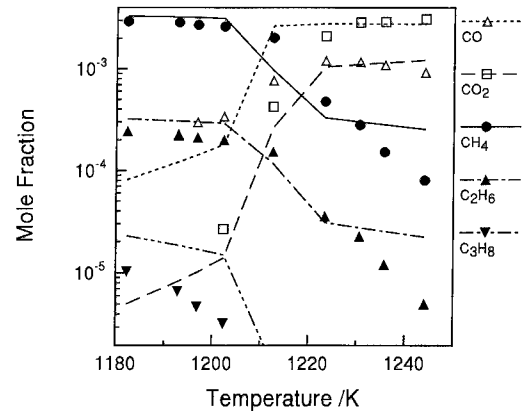

FIG. 3. Comparison between experimental (symbols) and computed (lines) results for the oxidation of a natural gas mixture in a JSR (τ = 0.14 s, 1 atm, CH_4 0.375%, O_2 0.7%, C_2H_6 3.927 × 10^{-6}, C_3H_8 7.497 × 10^{-7}, n-C_4H_{10} 2.83 × 10^{-6}, *iso*-C_4H_{10} 3.64 × 10^{-6}, n-C_5H_{12} 2.02 × 10^{-6}, *iso*-C_5H_{12} 2.02 × 10^{-6}, n-C_6H_{14} 2.02 × 10^{-6}).

chiometric CH_4-C_2H_6-C_3H_8 mixture at 10 atm. As can be seen from these figures, a general good agreement between the data and the modeling is observed. From Figs. 2 through 4, one can see that the higher hydrocarbon oxidation starts first, followed by methane consumption.

In order to interpret the above results, species flux analyses were carried out, showing that the higher hydrocarbons (ethane, propane, . . .) react more readily than methane to produce OH, H, and O radicals that finally contribute significantly to the initiation of methane oxidation, otherwise dominated by $CH_4 + O_2$ reaction. Because of low C—C bond energy found in higher hydrocarbons, primary alkyl radicals are easily formed; their further reactions lead to methane consumption.

When ethane is added to methane, ethane starts to decompose first,

$$C_2H_6 \rightarrow CH_3 + CH_3.$$

Methyl radicals then mainly react with molecular oxygen, ethane, or recombine

$$CH_3 + O_2 \rightarrow CH_2O + OH$$

$$CH_3 + C_2H_6 \rightarrow CH_4 + C_2H_5$$

$$CH_3 + CH_3 \rightarrow C_2H_6.$$

Ethyl radicals mainly decompose and become the major H-atom source.

$$C_2H_5 \rightarrow C_2H_4 + H.$$

Finally, H and OH radicals react with methane, increasing the radical pool

$$OH + CH_4 \rightarrow H_2O + CH_3$$

$$H + CH_4 \rightarrow H_2 + CH_3.$$

Less important is the influence of O atoms formed through

$$CH_3 + O_2 \rightarrow CH_3O + O$$

which further react with methane,

$$O + CH_4 \rightarrow OH + CH_3.$$

When propane is added to methane, the methane consumption scheme is initiated by propane decomposition:

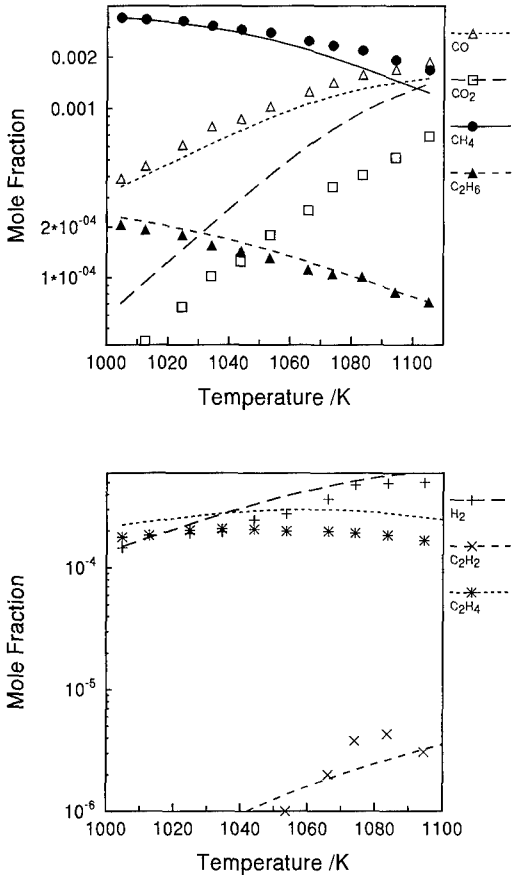

FIG. 4. Comparison between experimental (symbols) and computed (lines) results for the oxidation of a methane-ethane mixture in a JSR (τ = 1.4 s, 10 atm, CH_4 0.4%, C_2H_6 0.04%, O_2 0.8%).

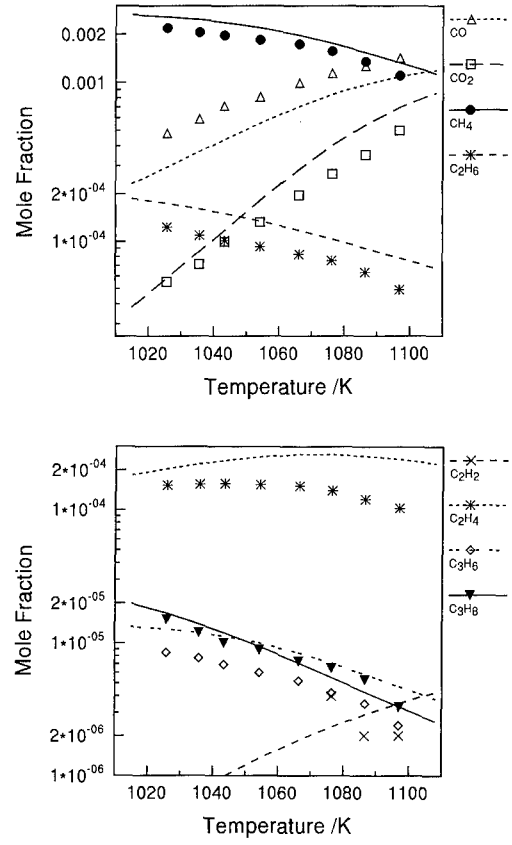

FIG. 5. Comparison between experimental (symbols) and computed (lines) results for the oxidation of a methane-ethane mixture in a JSR (τ = 1.4 s, 10 atm, CH_4 0.3%, C_2H_6 0.03%, C_3H_8 6.76 × 10^{-3}%, O_2 0.6%).

$$C_3H_8 \rightarrow CH_3 + C_2H_5.$$

Methyl radicals mainly recombine to form ethane (≈70%) and to a lesser extent react with O_2,

$$CH_3 + O_2 \rightarrow CH_3O + O$$

$$CH_3 + O_2 \rightarrow CH_2O + OH$$

while ethyl radicals decompose, producing H atoms

$$C_2H_5 \rightarrow C_2H_4 + H.$$

Oxygen atoms are converted into OH radicals by reaction with methane and propane,

$$O + CH_4 \rightarrow CH_3 + OH$$

$$O + C_3H_8 \rightarrow C_3H_7 + OH$$

and methane oxidation is mainly initiated by reactions with H and OH,

$$OH + CH_4 \rightarrow CH_3 + H_2O$$

$$H + CH_4 \rightarrow H_2 + CH_3.$$

It should be noted that ≈50% of methane initial consumption is due to its reaction with OH radicals when ethane or propane are added. The remainder is due to reactions with H and O atoms. This contrasts with the oxidation of methane alone, where the initiation involves O_2.

When higher hydrocarbons are added to methane, the same reaction sequences as above operate, and the radical pool is increased more rapidly and to a higher level with increasing hydrocarbon chain

length. As a result, at 1 atm, the mixture containing ethane will react at 80 K lower than the CH_4-O_2 mixture; when propane is added, a 90-K shift is observed, while, for natural gas, a 125-K shift is obtained (Fig. 1). At 10 atm, the stoichiometric mixtures containing ethane or propane react at a temperature nearly 60 K lower than the CH_4-O_2 mixture.

Sensitivity analyses were carried out for pure methane oxidation and natural gas blends oxidation. They show that the model predictions are influenced by the kinetics of Reactions (133) and (149) when ethane is added and by the kinetics of Reaction (234) when propane is added.

$$C_2H_6 + CH_3 \rightarrow C_2H_5 + CH_4 \qquad (133)$$

$$C_2H_4 + O \rightarrow CH_2 + HCO + H \qquad (149)$$

$$C_3H_8 \rightarrow C_2H_5 + CH_3. \qquad (234)$$

As expected, the sensitivity coefficients for these reactions remain much lower than for the usual important steps of methane oxidation:

$$H + O_2 \rightarrow OH + O \qquad (6)$$

$$CH_4 + H \rightarrow CH_3 + H_2 \qquad (41)$$

$$CH_4 + OH \rightarrow CH_3 + H_2O \qquad (39)$$

$$CH_3 + O_2 \rightarrow CH_2O + OH. \qquad (54)$$

Since general good agreement of the computations with our experimental results was obtained, it appeared interesting to model literature ignition delay times [5,25] of natural gas blends. The present model can well predict ignition delay of natural gas blends measured in shock tube, as depicted in Figure 6.

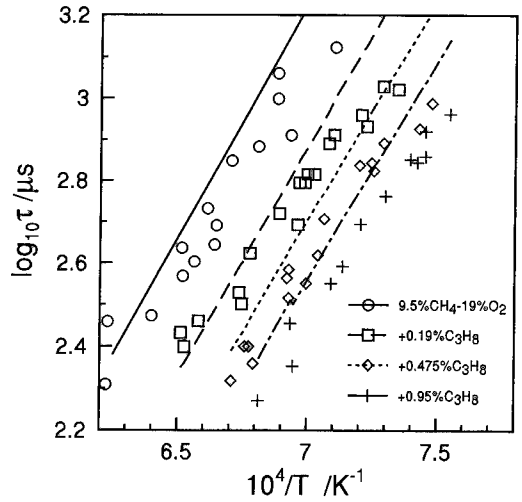

FIG. 6. Comparison between experimental (symbols) and computed (lines) ignition delay times of methane-propane-O_2-Ar mixtures measured by Frenklach and Bornside [25] in shock tube.

Summary

In spite of its wide use and economical importance, very few kinetic studies of natural gas or blends can be found in the literature, where, to date, only ignition delay times had been reported. Methane is frequently used to represent the more complex natural gas in combustion models. This study provides new kinetic data for the oxidation of methane doped with several hydrocarbons in a wide range of conditions and confirms, under controlled conditions, that methane reactivity is significantly enhanced by higher hydrocarbons at a low level of concentration. A detailed kinetic reaction mechanism, tested in a wide range of conditions, is used to interpret the present results. The kinetic modeling clearly demonstrates the activating effect of higher hydrocarbons, which produce radicals more readily than methane, initiating methane consumption at a much lower temperature than observed for pure methane oxidation under the same experimental conditions.

Acknowledgments

Partial financial support by Gaz de France, DETN-CERSTA, is gratefully acknowledged. The authors are grateful to Dr. P. Frank for communicating his results prior to publication.

REFERENCES

1. Lifshitz, A., Scheller, K., Burcat, A., and Skinner, G. B., *Combust. Flame* 16:311 (1971).
2. Crossley, R. W., Dorko, E. A., Scheller, K., and Burcat, A., *Combust. Flame* 19:373 (1972).
3. Higgin, R. M. R., and Williams, A., *Twelfth Symposium (International) on Combustion,* The Combustion Institute, Pittsburgh, 1969, p. 579.
4. Zellner, R., Niemitz, K. J., Warnatz, J., Gardiner, W. C., Eubank, C. S., and Simmie, J., *Progress in Astronautics and Aeronautics,* AIAA Inc., New York, 1983, Vol. 88, p. 252.
5. Eubank, C. S., Rabinowitz, M. J., Gardiner, W. C., and Zellner, R. E., *Eighteenth Symposium (International) on Combustion,* The Combustion Institute, Pittsburgh, 1981, p. 1767.
6. Dagaut, P., "Etude Expérimentale et Modélisation de l'Oxydation de l'Éthylène, du Propane et du Propène en Réacteur Auto-Agité par Jets Gazeux," Ph.D. Thesis, University Pierre et Marie Curie, Paris, (1986).
7. Dagaut, P., Cathonnet, M., Rouan, J. P., Foulatier, R.,

Quilgars, A., Boettner, J. C., Gaillard, F., and James, H., *J. Phys. E: Sci. Instrum.* 19:207 (1986).
8. Dagaut, P., and Cathonnet, M., *J. Chem. Phys.* 87:221 (1990).
9. Boettner, J. C., Cathonnet, M., Dagaut, P., and Gaillard, F., "Kinetic Modeling of Light Hydrocarbons Combustion," in *Mathematical Modeling in Combustion and Related Topics* (C. M. Brauner and C. Schmidt-Lainé (Eds.), Martinus Nijhoff Publishers, Dordrecht, The Netherlands, 1988, NATO ASI Series, Series E: Applied Sciences, Vol. 140, pp. 421–429.
10. Kee, R. J., Rupley, F. M., and Miller, J. A., *The Chemkin Thermodynamic Data Base,* Sandia Technical Report SAND87-8215, 1987.
11. Burcat, A., "Thermochemical Data for Combustion Calculations," in *Combustion Chemistry* (W. C. Gardiner, Jr.), Springer Verlag, New York, 1984, pp. 455–473.
12. Burcat, A., private communication, 1990.
13. Gardiner, W. C., Jr., "Introduction to Combustion Modeling," in *Combustion Chemistry* (W. C. Gardiner, Jr.), Springer Verlag, New York, 1984, pp. 1–19.
14. Hindmarsh, A. C., *SIGNUM Newslett.* 15:10 (1980).
15. Dagaut, P., Boettner, J. C., and Cathonnet, M., *Combust. Sci. Technol.*, 77:127 (1991).
16. Dagaut, P., Cathonnet, M., and Boettner, J. C., *Int. J. Chem. Kinet.* 24:813 (1992).
17. Tan, Y., Dagaut, P., Cathonnet, M., and Boettner, J. C., *Combust. Sci. Technol.*, in press.
18. Baulch, D. L., Cobos, C. J., Cox, R. A., Esser, C., Frank, P., Just, Th., Kerr, J. A., Pilling, M. J., Troe, J., Walker, R. W., and Warnatz, J., *J. Phys. Chem. Ref. Data.* 21:441 (1992).
19. Ohmori, K., Yoshimura, M., Koshi, M., and Matsui, H., *Bull. Chem. Soc. Jpn.* 65:1317 (1992).
20. Frenklach, M., Wang, H., and Rabinowitz, M. J., *Prog. Energy Combust. Sci.* 18:417 (1992).
21. Zellner, R., and Ewig, F., *J. Phys. Chem.* 92:2971 (1988).
22. Braun-Unkhoff, M., Naumann, C., and Frank, P., submitted for publication.
23. Troe, J., private communication, 1992.
24. Michael, J. V., and Wagner, A. F., *J. Phys. Chem.* 94:2453 (1990).
25. Frenklach, M., and Bornside, D. E., *Combust. Flame* 56:1 (1984).

Twenty-Fifth Symposium (International) on Combustion/The Combustion Institute, 1994/pp. 1571–1577

SHOCK-INITIATED IGNITION IN ETHYLENE OXIDE, PROPYLENE OXIDE, 1,2-EPOXYBUTANE, AND 2,3-EPOXYBUTANE

ASSA LIFSHITZ AND AYA SUSLENSKY
Department of Physical Chemistry
The Hebrew University, Jerusalem 91904, Israel

Ignition delay times in ethylene oxide $\underset{\underset{O}{\diagdown\ \diagup}}{CH_2—CH_2}$, propylene oxide $\underset{\underset{O}{\diagdown\ \diagup}}{CH_3CH—CH_2}$, 1,2-epoxybutane $\underset{\underset{O}{\diagdown\ \diagup}}{C_2H_5CH—CH_2}$, and 2,3-epoxybutane $\underset{\underset{O}{\diagdown\ \diagup}}{CH_3CH—CHCH_3}$, in mixtures containing oxygen and a diluent (argon or nitrogen) were measured behind reflected shock waves in a single-pulse shock tube over a wide range of composition, pressure, and temperature. Parametric relation corresponding to the equation

$$\tau = 10^{a} \exp(E/RT)\,[\mathrm{Fuel}]^{\beta_1}[\mathrm{O_2}]^{\beta_2}[\mathrm{M}]^{\beta_3}, \qquad \text{(s)}$$

were deduced for the four fuel molecules. In distinction from hydrocarbon ignition where β_{fuel} is always found to be positive, β_{fuel} in the ignition of the epoxy family of molecules is negative, close to unity, indicating a strong enhancing effect of the fuel. The reason for this enhancement is twofold. Upon subjection to shock heating, the unstable three-membered rings open and undergo exothermic isomerizations to more stable molecules such as ketones, aldehydes, alcohols, and ethers. These isomerizations, which take place during the induction period, release a considerable amount of heat and raise the temperature of the system. The second and more important reason is the high rate of initiation caused by the decomposition of the isomers, which are formed thermally excited with sufficient energy to dissociate into free radicals. The diluent, which is present in large excess, shows a positive power dependence (inhibiting effect) due to its quenching of the thermally excited species and preventing dissociation and due to adsorption of a large amount of heat generated during the induction period.

Introduction

When a mixture of a fuel and an oxidant is suddenly raised to a high temperature, if certain conditions are fulfilled, it ignites, following an induction period known as "ignition delay time." In order that an ignition will occur, the reaction profile (temperature, pressure, free-radical concentration, etc.) must obey an exponential law. Such a profile may result from either chain branching reactions or adiabatic temperature increase during the course of the reaction. If such a profile is then viewed with a linear device, a sensation is obtained that "nothing happens" for a certain period of time and then "everything happens" at a very short time. If the reaction is exothermic and a considerable amount of heat is released, then a phenomenon of ignition occurs.

Many combustion systems have been studied in the past where ignition delay times serve as the basis for computer simulation of the combustion process [1,2]. In view of the high sensitivity of the ignition delay to portions of the kinetic scheme, it is possible on the basis of its measurement to analyze the kinetic behavior of each system.

Although information is available on the ignition of ethylene oxide [3,4], we are not aware of any thorough, comparative investigation of other epoxy compounds. On the other hand, the thermal decomposition of several of these compounds has been studied [5–10]. In view of the instability of the epoxy ring, they tend to isomerize and decompose at rather low temperatures. It is thus of great interest, from a chemical kinetic viewpoint, to examine the incorporation of the decomposition processes in the overall combustion mechanism.

This article presents a detailed investigation of the ignition of four members of the epoxy family of molecules; it deduces parametric relations for the ignition delay, and provides an explanation for the parameters obtained.

Experimental

Apparatus:

The ignition delay times were measured behind reflected shocks in a pressurized driver single-pulse shock tube made of 2-in. id "Double Tough" pyrex tubing. The driven section was 4-m long and the

driver was 2.7 m. A 36-L dump tank was connected to the driven section at 45° angle toward the driver, near the diaphragm holder, in order to prevent reflection of transmitted waves. The driven section was separated from the driver by "Mylar" polyester film of various thickness, depending upon the desired shock strength.

Reflected shock parameters were calculated from the measured incident shock velocities using the three conservation equations and the ideal gas equation of state. The incident shock velocities were measured with two miniature, high-frequency pressure transducers (Vibrometer Model 6QP500) placed 230 mm apart at the downstream end of the driven section. The signals generated by the shock waves passing over the transducers were connected in parallel and were fed through a piezo amplifier to one beam of a Nicolet Model 3091 dual beam digital oscilloscope. Time intervals between the two signals shown on the oscilloscope (approximately 300 μs) were obtained digitally with an accuracy of 2 μs corresponding to 10–15 K, depending upon the shock temperature.

The duration of the induction period was determined from pressure observations with the aid of a third transducer (P.C.B. Model 113A26) located at the center of the end plate of the driven section. It was taken as the time interval between the reflection of the shock wave from the end plate and the sudden increase in pressure caused by the onset of ignition. Reaction dwell times varied between 2.5 and 3 ms, which set an upper limit for the delays that could be measured. The induction times were read from the second beam of the oscilloscope with an accuracy of ~10% at low induction times (around 100 μs) and ~5% at high induction times in which the pressure jumps were sharper. A typical pressure record showing the shock heating and the ignition phenomenon is shown in Figure 1.

Prior to performing an experiment, the tube and the gas handling manifold were pumped down to approximately 2×10^{-5} torr. A more detailed description of the tube has been presented in previous publications [11].

Materials:

Reaction mixtures (except for ethylene oxide) were prepared by injecting a measured volume of the liquid fuel into 12-L glass bulbs, which were then filled with a desired mixture of oxygen in argon to 700 torr. Both the bulbs and the vacuum line were pumped down to better than 10^{-5} torr before the preparation of the mixtures. Mixtures of ethylene oxide and oxygen in argon were prepared manometrically.

Ethylene oxide was obtained from the Matheson gas company and was listed as 97% pure. Propylene oxide (99 + % pure), 1,2-epoxybutane (99%), and 2,3-epoxybutane (96%) were obtained from Aldrich Chemical Company Inc. Argon was Matheson ultra-high-purity grade, listed as 99.9995%, and helium was Matheson pure grade listed as 99.999%. All the materials were used without further purification.

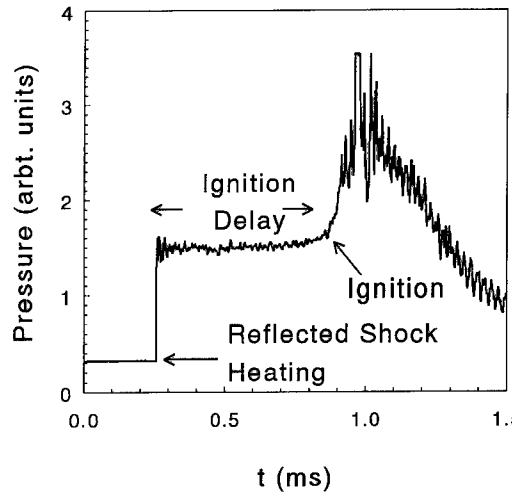

FIG. 1. Pressure record showing shock heating and ignition. The time interval between the two is the ignition delay.

Results

In order to measure ignition delay times and their dependence on the composition, pressure, and temperature, several groups of experiments, in each one of the four molecules studied, were performed. The reaction mixtures were chosen in such a manner that the effect of each one of the components (β_i's) on the induction times could be independently evaluated. More accurate values of the parameters that appear in the equation

$$\tau\ (\mathrm{s}) = 10^{a} \exp(E/RT)[\mathrm{Fuel}]^{\beta_1}[\mathrm{O_2}]^{\beta_2}[\mathrm{M}]^{\beta_3}$$

were later evaluated by least-squares analyses.

The following are three groups of figures showing plots of $\log t_{\mathrm{ign}}$ vs $1/T$ from which the effects of the fuel, the oxygen, and the diluent on the ignition delay times can be seen. Figures 2 and 3 show the results for ethylene oxide. Figure 2 shows the effect of the fuel and oxygen. The upper line (■) corresponds to a stoichiometric mixture of 2% ethylene oxide and 5% oxygen. The oxygen is increased by a factor of two (Δ), and then both the fuel and the oxygen are increased by the same factor (●). Each such increase shortens the ignition delay, indicating that both the fuel and the oxygen have an enhancing effect on the progress of the combustion process. Figure 3 shows a comparison between two groups of experiments

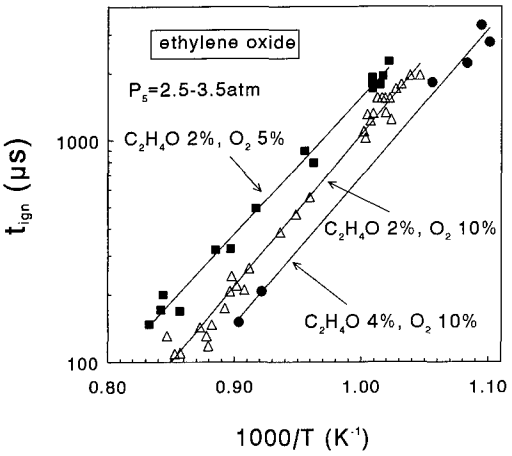

FIG. 2. Logt_{ign} vs $1/T$ for three mixtures of ethylene oxide and oxygen in argon. They show enhancing effects of both fuel and oxygen. The induction times get shorter when both fuel and oxygen concentrations are increased.

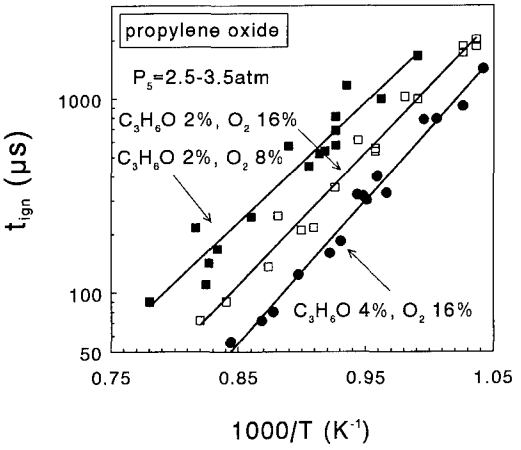

FIG. 4. Ignition delay for three mixtures of propylene oxide and oxygen in argon. They show enhancing effects of both fuel and oxygen. The induction times are shorter when both fuel and oxygen concentrations are increased.

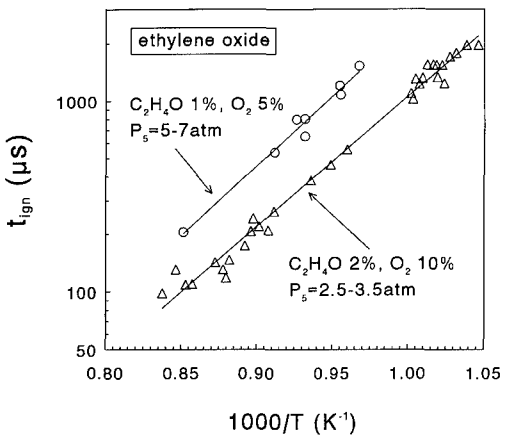

FIG. 3. Ignition delay for two mixtures of ethylene oxide and oxygen in argon. The mixtures differ only in their argon concentration. A strong inhibiting effect of argon can be seen.

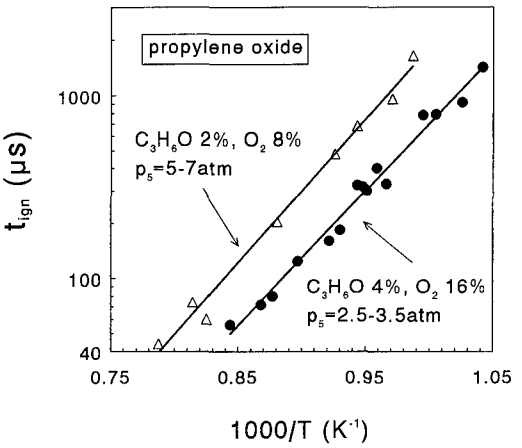

FIG. 5. Ignition delay for two mixtures of propylene oxide and oxygen in argon. The mixtures have the same fuel and oxygen concentrations and differ in their argon concentration. A strong inhibiting effect is demonstrated.

that differ only in the argon concentration. The higher the argon concentration (○), the longer the ignition delay times, indicating that the argon plays the role of an inhibitor. Similar behavior can be seen in the ignition of the other members of the epoxy family. Figures 4 and 5 show similar plots for propylene oxide. Figure 4 shows an even more pronounced enhancing effect of both the fuel and the oxygen. In Fig. 5, we can see the strong inhibiting effect of the argon. The higher the argon concentration (△), the longer the induction times. Figures 6 and 7 show similar behavior for one of the epoxybutanes (the behavior of 1,2- and 2,3-epoxybutane are practically identical).

The quantitative values of the concentration power dependences as well as the temperature dependence are determined by a linear least-squares analysis, which was performed on values of log t_{ign}. The results of these analyses are demonstrated graphically in Figs. 8 through 10 for ethylene oxide, propylene oxide, and 1,2-epoxybutane. They show plots of $\tau/([\mathrm{Fuel}]^{\beta_1}[\mathrm{O_2}]^{\beta_2}[\mathrm{Ar}]^{\beta_3})$ vs $1/T$, where a, E, β_1, β_2, and β_3 are evaluated by the least-squares analyses. As can be seen, the data points from all the series of experiments for each molecule scatter along one line.

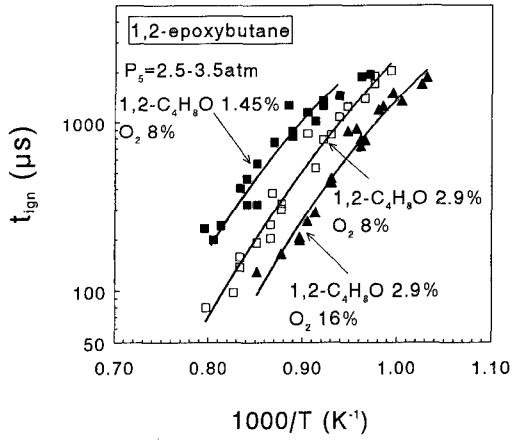

FIG. 6. Ignition delay for three mixtures of 1,2-epoxybutane and oxygen in argon. Strong enhancing effects of both fuel and oxygen can be seen. The induction times are shorter when both fuel and oxygen concentrations are increased.

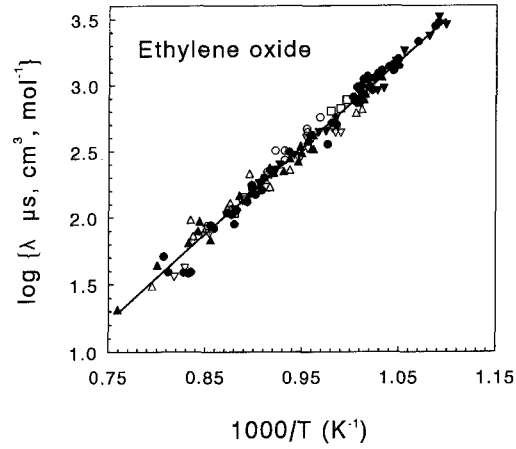

FIG. 8. Logλ vs $1/T$ for the data points obtained in the six series of experiments performed with ethylene oxide-oxygen-argon mixtures; λ is calculated from the correlation $\lambda = \tau/\{[\text{Fuel}]^{-0.44}[O_2]^{-0.72}[\text{Ar}]^{0.78}\}$.

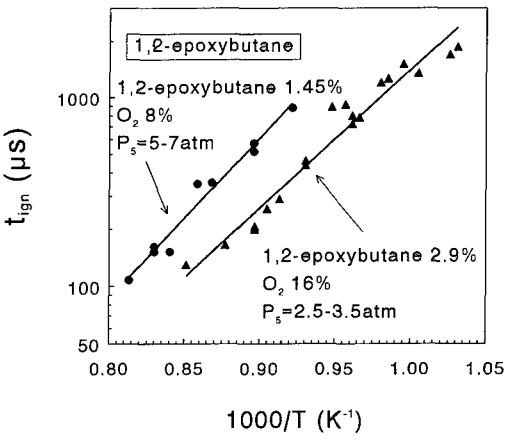

FIG. 7. Ignition delay for two mixtures of 1,2-epoxybutane and oxygen in argon, which differ only in their argon concentration. A strong inhibiting effect is demonstrated.

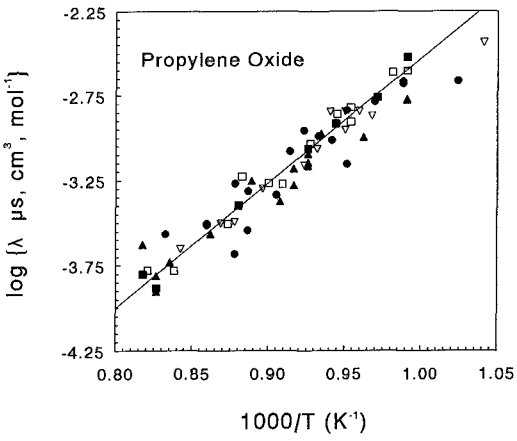

FIG. 9. Logλ vs $1/T$ for the data points obtained in the five series of experiments performed with propylene oxide-oxygen-argon mixtures; λ is calculated from the correlation $\lambda = \tau/\{[\text{Fuel}]^{-1.07}[O_2]^{-0.52}[\text{Ar}]^{0.78}\}$.

The five sets of parameters that were obtained from this evaluation are summarized in Table 1.

Discussion

As can be seen in Table 1, the common features in the ignition of the epoxy group of molecules is the strong enhancing effect of the fuel (a large negative value for β_{fuel}) and the large inhibiting effect of the diluent. This observation is in complete contradiction to the ignition characteristics of hydrocarbon fuels in which β_{fuel} is positive.

The inhibiting effect of the fuel, which is normally observed in hydrocarbons and similar systems, is attributed to the competition reaction $H\bullet + RH \rightarrow H_2 + R\bullet$[2], where a reactive H atom is replaced by an unreactive hydrocarbon residue, a step that takes place on the expense of the major branching reaction $H\bullet + O_2 \rightarrow OH\bullet + O\bullet$. Although this effect does play a role in any C—H system, including the epoxy family of molecules, it is compensated in the present line of fuels by two other phenomena that do not exist in simple hydrocarbons. These phenomena will now be discussed.

The three-membered epoxy rings, being unstable

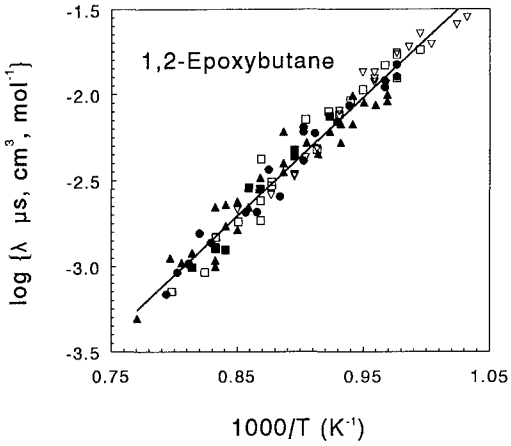

FIG. 10. Logλ vs $1/T$ for the data points obtained in the five series of experiments performed with 1,2-Epoxybutane-oxygen-argon mixtures; λ is calculated from the correlation $\lambda = \tau/\{[\text{Fuel}]^{-0.86}[O_2]^{-0.72}[\text{Ar}]^{0.92}\}$.

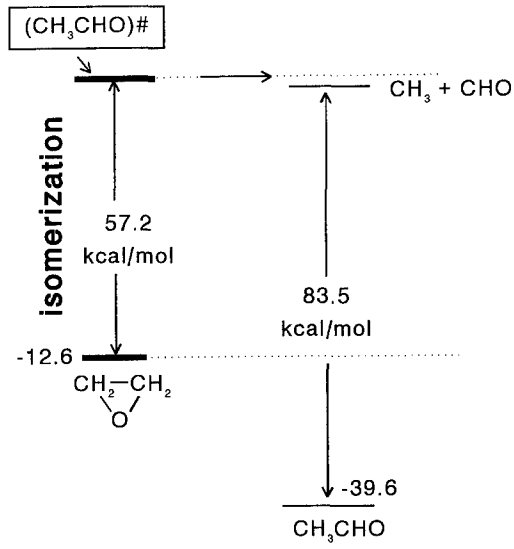

FIG. 11. Energy diagram for the isomerization and decomposition of ethylene oxide.

structures, tend to open and isomerize to more stable molecules such as ketones, aldehydes, alcohols, and ethers. (The isomerization products obtained in ethylene oxide and propylene oxide can be seen in Figs. 11 and 12.) In view of the large differences in the heats of formation of the epoxy molecules and their stable isomers, the latter are produced with large excess of thermal excitation. This excess energy is equal to $E_{act} + \Delta H_r$, where E_{act} is the activation energy of the isomerization process and ΔH_r is the exothermicity of the isomerization reaction (the difference between the heat of formation of the isomers and the epoxy molecule) [12]. Energy diagrams for the isomerizations in ethylene oxide and propylene oxide are shown in Figs. 11 and 12.

The thermally excited products can either lose their energy by collision to produce stable isomers (which is their main reaction) or decompose to produce free radicals that initiate and support the chain reactions in the combustion process. This feature, which is common to all the epoxy molecules, is responsible for the high production rate of free radicals.

Hydrocarbon fuels dissociate from a state of Boltzmann distribution corresponding to the temperature of the reaction mixture. Since this is in most cases a slow process, the contribution of simple fuel dissociation to free-radical production is negligible. Chain branching takes over already at the very early stages of the combustion. The competition reaction $H\bullet + RH \rightarrow H_2 + R\bullet$, which is a fast and important reaction, is not compensated by any enhancing reactions in which the fuel is involved.

In the epoxy line of molecules, the initiation process is very fast compared to a normal hydrocarbon dissociation. Its contribution to the overall production of free radicals is, therefore, important during most of the induction time and can compete with the contribution from the chain-branching processes. This contribution overrides the inhibiting effect of the fuel and leaves an overall enhancing effect. This effect expresses itself experimentally by the high negative power dependence of the induction times on the fuel concentration.

TABLE I
Experimental ignition parameters for various epoxy fuels to fit the equation $\tau = 10^a \exp(E/RT)[\text{Fuel}]^{\beta_1}[O_2]^{\beta_2}[M]^{\beta_3}$

Components	a	E	β_1	β_2	β_3
Ethylene oxide, oxygen, argon	−12.62	29.6	−0.44	−0.72	0.78
Ethylene oxide, oxygen, nitrogen	−12.81	30.8	−0.82	−0.91	1.48
Propylene oxide, oxygen, argon	−14.28	33.6	−1.07	−0.52	0.78
1,2-Epoxybutane, oxygen, argon	−14.56	31.5	−0.86	−0.72	0.92
2,3-Epoxybutane, oxygen, argon	−15.73	34.3	−0.92	−0.76	0.89

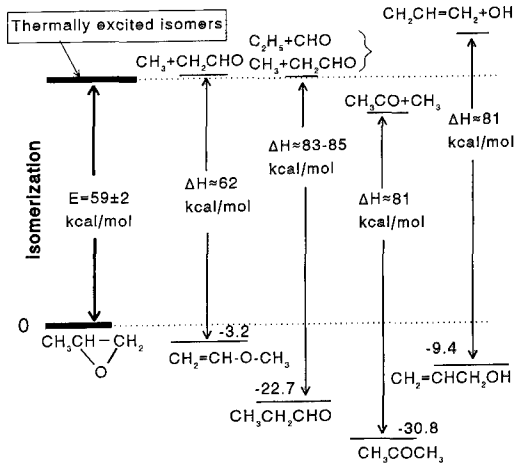

FIG. 12. Energy diagram for the isomerization and decomposition of propylene oxide.

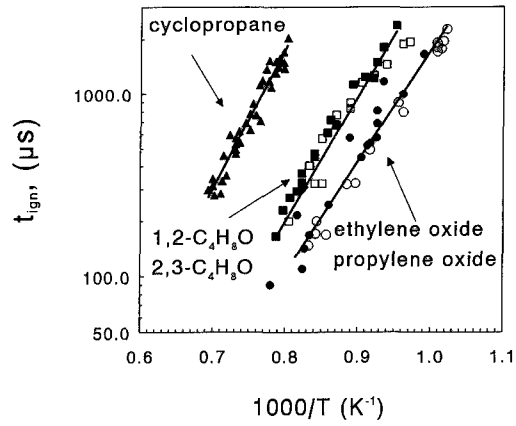

FIG. 13. A comparison of ignition delays for cyclopropane and for the epoxy line of molecules.

Another interesting feature in the epoxy group of fuels is the strong inhibiting effect of the diluent, argon or nitrogen. In simple hydrocarbon ignition, the diluent plays two different roles in the induction period. One is the role of a third body in dissociation-recombination reactions. Due to chain branching reactions, the concentrations of free radicals in the system overshoot their equilibrium concentrations already at the early stages of the reaction. The role of argon or nitrogen as third bodies is thus to enhance recombinations rather than dissociations and to decrease the overall concentration of free radicals. This would normally manifest itself by a positive, although small, power dependence. The second effect of the diluent is a "cooling effect." Since in most cases heat is generated as the reaction proceeds, the temperature and the overall rate increase. An increase in heat capacity for the same amount of heat released, by increasing the diluent concentration, depresses the temperature elevation and thus inhibits the progress of the reaction. In the epoxy line of molecules, a considerable amount of heat is generated in the process of isomerization so that this effect becomes very significant.

A third and perhaps the most significant inhibiting effect in this system is the quenching of the thermally excited species that are formed in the isomerization (Figs. 11 and 12). Since these excited species can lose their excess thermal energy by collisions with argon (or nitrogen), an increase in the diluent concentration will increase the quenching rate and prevent the thermally excited molecule from dissociating to free radicals.

These three roles of the diluent in the epoxy system result in a very high-power dependence of the induction time on its concentration.

Figure 13 shows a comparison of ignition delays in comparable mixtures of the four molecular fuels studied. As can be seen, they are comparable, meaning that the general behavior of the fuels is determined merely by the unstable three-membered epoxy ring and by its characteristic thermal reactions. It should be mentioned that all the C—C bonds in ethylene oxide, propylene oxide, and 2,3-epoxybutane are of sp^2 characteristics, and they are strong bonds. The CH_3—CH_2 bond in 1,2-epoxybutane is of an sp^3 nature and is thus considerably weaker. This fact does not make the 1,2-epoxybutane more reactive (see Fig. 13), which is an additional support for the assumption that initiation does not occur by the dissociation of the reactants but from the thermally excited isomeric products. For comparison, Fig. 13 shows also the ignition delay of cyclopropane for similar initial conditions of pressure and composition [13]. This three-membered ring opens and isomerizes to propylene with an activation energy of ~62 kcal/mol [14], which is not much different from the one required to open the ring in ethylene oxide (57.2 kcal/mol) [3]. However, since there is only a small difference in the heat of formation of cyclopropane ($\Delta H^\circ_{f(298)}$ = 12.8 kcal/mol) [15] and propylene ($\Delta H^\circ_{f(298)}$ = 4.8 kcal/mol) [15], the latter does not have enough energy to dissociate from its thermal excited state and loses its energy before dissociation. As can be seen in Fig. 13, the induction times in cyclopropane are longer than those of the epoxy of molecules at the same temperature by an order of magnitude.

Conclusion

The study of ignition delay times in the four epoxy molecules can be summarized in the following statements:

1. The ignition delay times of molecules containing a three-membered ring epoxy structure are very

similar and are considerably shorter than comparable straight and cyclic hydrocarbons.

2. The epoxy fuel has a strong enhancing effect on the progress of the combustion process (negative β_{fuel}) due to their contribution to production of free radicals.
3. Diluents such as argon and nitrogen have a strong inhibiting effect on the progress of the combustion process (β_{diluent}) due to their absorption of the heat released in the process of the isomerization and quenching of the thermally excited isomers.

REFERENCES

1. Lifshitz, A., *Proceedings of the 14th International Symposium on Shock Tubes and Waves* (R. D. Archer and B. E. Milton Eds.), New South Wales University Press, New South Wales, 1984, pp. 26–40.
2. Tsang, W., and Lifshitz, A., *Ann. Rev. Phys. Chem.* 41:559–599 (1990).
3. Burcat, A., *Comb. Sci. Technol.* 21:169–174 (1980).
4. Yoon, H. M., Yeo, H. G., Yun, S. S., Kim, C. S., and Kang, J. G., *Combust. Flame* 92:481–484 (1993).
5. Lifshitz, A., and Ben Hamou, H., *J. Phys. Chem.* 87:1782–1787 (1983).
6. Flowers, M. C., *J. Chem. Soc. Faraday Trans.* 73:1927–1935 (1977).
7. Zhiwei, Q., Huixing, Y., and Degang, H., *Acta Phys. Chim. Sinica* 1:39–45 (1990).
8. Lifshitz, A., and Tamburu, C., *J. Phys. Chem.* 98:1161–1170 (1994).
9. Flowers, M. C., and Parker, R. M., *J. Chem. Soc.* (*B*, 1980–1988 (1971).
10. Lifshitz, A., and Tamburu, C., *J. Phys. Chem.* in preparation.
11. Lifshitz, A., Tamburu, C., Frank, P., and Just, Th., *J. Phys. Chem.* 97:4085–4090 (1993).
12. Lifshitz, A., *Proceedings of the 19th International Symposium on Shock Tubes and Waves*, 1993, in press.
13. Lifshitz, A., and Barzilai-Gilboa, S., *Twentieth Symposium (International) on Combustion*, The Combustion Institute, Pittsburgh, 1984, pp. 631–638.
14. Westly, F., Herron, J. T., Cvetanovic, R. J., Hampson, R. F., and Mallard, W. G., *NIST-Chemical Kinetics Data Base* 17, Ver 5.0.
15. Stull, D. R., Westrum, E. F., Jr., and Sinke, G. C., *The Chemical Thermodynamics of Organic Compounds*, John Wiley and Sons, New York, 1969.

COMMENT

Laurent Catoire, LCSR-CNRS-Orleans, France. Did you try to correlate your ignition delays with those of Burcat for ethylene-oxide–oxygen–nitrogen mixtures and with those of Yoon et al. for ethylene-oxide–oxygen–argon mixtures? How can you explain the dispersion observed for the propylene-oxide–argon mixtures? Compositions for the six series of experiments performed with ethylene-oxide–argon mixtures are given. What are the two others?

Author's Reply. Burcat's correlation for ignition delay in ethylene-oxide–oxygen–nitrogen mixtures as well as the one of Yoon et al. for ethylene-oxide–oxygen–argon mixtures is, at least qualitatively, similar to ours. All clearly show an enhancing effect of both the fuel and the oxygen and a retarding effect of the diluent. We have not tried to correlate our data with the parameters obtained by Burcat and by Yoon et al. and the parameters that we obtained are the outcome of a least-squares analysis of our results.

I do not have a clear explanation of why our propylene oxide data show such a dispersion using the correlation obtained by least-squares analysis of the data. What we can see in Fig. 9 is that there is no dispersion between the groups and the data of all the groups of experiments mixed together. This is a good indication that the correlation is correct.

The other compositions used in the ethylene oxide experiments were ethylene oxide 4% and oxygen 10% at $p_5 \sim 1$, 1.5, 2, and 3 atm.

Twenty-Fifth Symposium (International) on Combustion/The Combustion Institute, 1994/pp. 1579–1585

SHOCK-TUBE INVESTIGATIONS ON THE SELF-IGNITION OF HYDROCARBON-AIR MIXTURES AT HIGH PRESSURES

K. FIEWEGER, R. BLUMENTHAL AND G. ADOMEIT
Institut für Allgemeine Mechanik, RWTH Aachen
D-52056 Aachen, Germany

The self-ignition behaviour of various fuel-air mixtures has been investigated without inert gas dilution using a high-pressure shock tube. In order to obtain data directly applicable to the modeling of engine combustion, the shock-tube facility was designed to handle fuel-air mixtures up to initial pressures of more than 40 bar and to achieve measuring times up to 10 ms. As typical representatives of engine fuel components, *n*-heptane, benzene, iso-octane, methanol, and methyl-*tert*-butylether (MTBE) were investigated. Two pressure levels for the investigation, 13 bar and nearly 40 bar, have been chosen. The ignition of *n*-heptane begins with a rapid pressure increase, especially at higher temperatures. Benzene, iso-octane, methanol, and MTBE show a slow initiation of the ignition without distinct pressure peak (mild ignition) at low temperatures, which at higher temperatures changes to a rapid pressure increase after a variable time lag (strong ignition). The strong ignition limit depending on temperature, pressure, and fuel was determined. An investigation was made of the dependence of the ignition delay times of iso-octane and benzene on equivalence ratio and temperature at nearly 40 bar. A comparison of the ignition delay times of all the fuels investigated is presented for stoichiometric mixtures and at two pressure levels.

Introduction

Information on the self-ignition of hydrocarbon-air mixtures is of basic importance, as much for the direct implications for practical combustion and ignition processes as for the possibility of deriving kinetic information from these data.

The modeling of the autoignition process, e.g., in engines, is possible if the chemical kinetics of the combustion reactions is known. Hence, a wealth of experimental data has been gathered about this process. The shock tube is a very suitable tool here because of the sufficiently short heating and compression time by the shock wave. The conditions achieved behind the reflected shock wave are homogeneous. The main reaction-determining parameters, such as temperature, pressure, equivalence ratio, additives, kind and degree of dilution, can be adjusted independently.

However, almost all of the data obtained have been gathered making use of a heat bath, i.e., a large fraction of inert gas dilution. A major reason for this is the fact that the final pressures after ignition are drastically decreased by this measure, which reduces considerably the experimental expenditure, as safety measures, etc. The temperature increase caused by the reaction is also reduced, simplifying the kinetic analysis. However, it has various drawbacks. The composition of the heat bath is an influence that has to be considered and is less obvious than may be assumed. Zallen and Wittig [1] have studied this effect specifically. They found that the replacement of an argon heat bath by nitrogen led to a change of the ignition delay of up to a factor of 10. Gasdynamic features of the self-ignition process also change considerably with dilution.

In our case, the desire to obtain data directly applicable to the modeling of engine self-ignition and knock phenomena was the motive to develop a shock-tube facility capable of handling fuel-air mixtures up to initial pressures of more than 40 bar and measuring times up to 10 ms. The ignition delay times obtained in this manner can be used for developing and validating kinetic models, especially for the relatively high pressures and low temperatures occurring in engines [2]. Also, the validation of reduced mechanisms (e.g., Refs. 3 through 6) can be done by adjustment to these data. The gasdynamic features observed in these experiments should also be of direct relevance to corresponding engine phenomena, e.g., knock. Therefore, this work fits well into the rapid compression device investigations, extending their data to smaller values of ignition delay and higher temperatures. In this region, the shock tube has definite advantages concerning compression times, cleanliness, and complete coverage of pressure and temperature range without the necessity to change the composition of the inert fraction of air.

Because commercial fuels consist of a great number of components, typical representatives of different fuel groups were investigated: *n*-heptane and iso-octane (2,2,4-trimethylpentane) for paraffins,

benzene for aromatics, methanol for alcohols, and methyl-tert-butylether (MTBE) for ethers. Mixtures of n-heptane and iso-octane are used as primary reference fuels to determine the octane number. n-Heptane also possesses a cetane number typical for a good diesel fuel. The other possible fuel components, benzene and MTBE, improve knocking properties

Experimental

The experimental device is a single-pulse high-pressure shock tube with an inner diameter of 87 mm, which is described in detail in previous publications [9–12]. The high-pressure part has a length of 5.3 m; the low-pressure part is 6.3 m long. In order to conduct experiments under conditions relevant to engine combustion, the final length of 3.3 m of the driven section used at the moment has been designed for a maximum static pressure of 500 bar.

The measuring plane with 10 radial access ports is located 15 mm in front of the end wall of the low-pressure part. It is equipped with an acceleration compensated piezoelectric PCB 113A pressure transducer, a thin-film heat-transfer gauge, and observation windows. Three more pressure transducers and observation windows are placed at a distance of 100 mm each from the measuring plane. Through the windows, a volume element at the shock-tube axis is focussed on a fused silica fibre optic. The CH-band emission at 431 nm is selected using interference filters and detected by photomultipliers.

Three thin-film heat-transfer gauges are mounted flush to the shock-tube wall along the shock-tube length to measure the velocity of the incident shock wave. With this information, the temperature T_5 behind the reflected shock wave has been calculated by solving the gasdynamic balance equations, considering also real thermodynamics behaviour of the gases (see, e.g., Refs. 13 and 14). Further information and details about the apparatus, the measuring equipment, and the operating modus have been presented in Refs. 10 and 11.

Results and Discussion

Gasdynamic Features of the Self-Ignition Process:

Figure 1 shows two pressure histories of a stoichiometric benzene-air mixture plotted into one diagram. The initial pressure is about 13 bar; the temperatures of the two experiments differ by only 40 K. At lower temperatures (here, 1040 K), the pressure trace shows only a single distinct maximum. Pressure oscillations, which are characteristic of the n-heptane self-ignition process, are not observed here. At a slightly higher temperature (here, 1080 K),

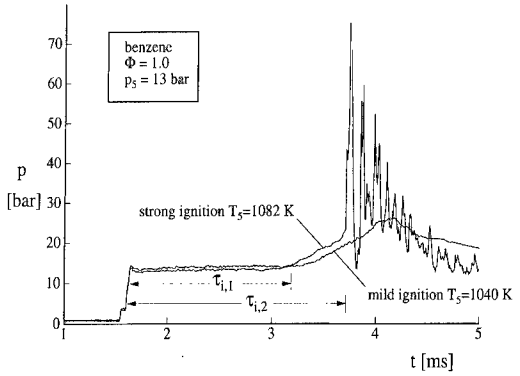

FIG. 1. Pressure histories of a stoichiometric benzene-air mixture; transition from mild to strong ignition.

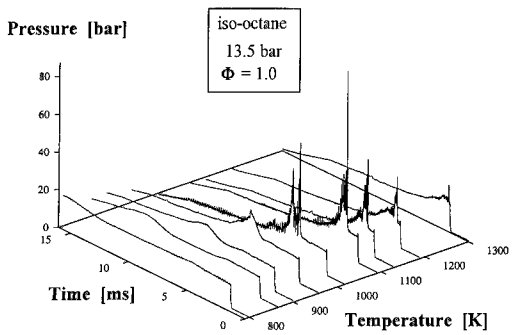

FIG. 2. Pressure histories for various temperatures; iso-octane $\Phi = 1.0$, $p_5 \approx 13$ bar.

the ignition is divided into two parts. A moderate pressure rise occurs at the beginning of the main ignition at $\tau_{i,1}$. After a distinct time, a further rapid pressure increase occurs at $\tau_{i,2}$, which finally shows a sharp peak, followed by pressure oscillations. The time history of the light emission has a similar behaviour and shows definitely that, at $\tau_{i,1}$, the main ignition process begins. No such preignition process as observed for n-heptane [11] occurs for benzene.

Oppenheim and coworkers investigated the gasdynamic processes connected with self-ignition behind the reflected shock wave. They observed the same phenomenon: Two different types of ignition, which they named mild and strong ignition, occur depending upon temperature [15,16]. This phenomenon is not confined to shock-tube experiments. Similar observations have been reported for investigations in rapid compression devices [17].

The development of the pressure traces for a larger range of temperature is illustrated in Fig. 2 at a pressure level of 13 bar for stoichiometric iso-octane–air mixtures. It can be seen that the ignition characteristic of iso-octane is very similar to that of benzene. There is a clear discontinuous transition from mild to strong ignition. The sudden pressure

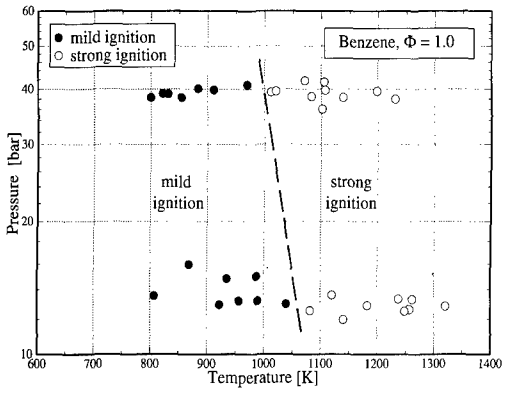

FIG. 3. Summary of the results of stoichiometric benzene-air mixtures on a pressure-temperature diagram delineating the strong ignition limit zone.

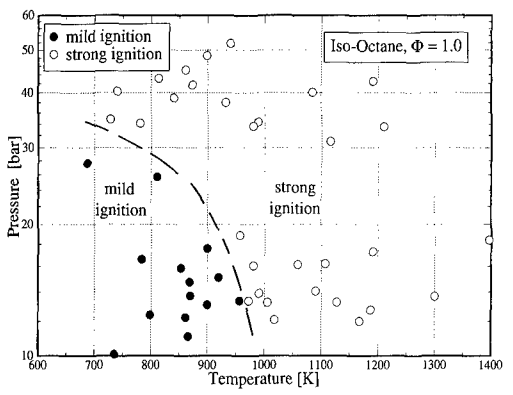

FIG. 4. Summary of the results of stoichiometric iso-octane–air mixtures on a pressure-temperature diagram delineating the strong ignition limit zone.

increase connected with strong ignition (described as $\tau_{i,2}$ in Fig. 1) shifts towards the initial pressure rise of the self-ignition ($\tau_{i,1}$ in Fig. 1). The amplitude of the pressure pulse connected with the strong ignition decreases with increasing temperature.

All experiments with stoichiometric benzene-air mixtures (Fig. 3) and stoichiometric iso-octane–air mixtures (Fig. 4) are summarized in the following two temperature-pressure diagrams. The points with solid circles indicate mild ignition, while at the points marked with a hollow circle, strong ignition occurred. Obviously, there is a distinct demarcation between the two ignition modes, which is named the strong ignition limit [15]. For iso-octane (Fig. 4), this limit shows a marked dependence on pressure, which is not the case for benzene (Fig. 3).

Figures 5 through 7 show histories of pressure and CH emission at 431 nm for different initial temperatures, at an initial pressure of about 30 bar, for stoi-

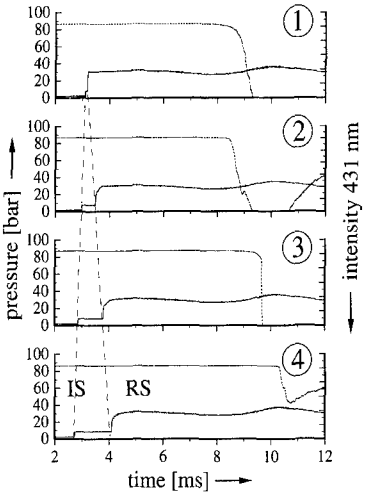

FIG. 5. Pressure and CH-emission signals plotted against time for a mild ignition process (T_5 = 810 K, stoichiometric iso-octane–air mixture). The incident (IS) and the reflected (RS) shock wave are marked with dashed lines. The figure contains the signals measured at four different locations in the driven section of the shock tube.

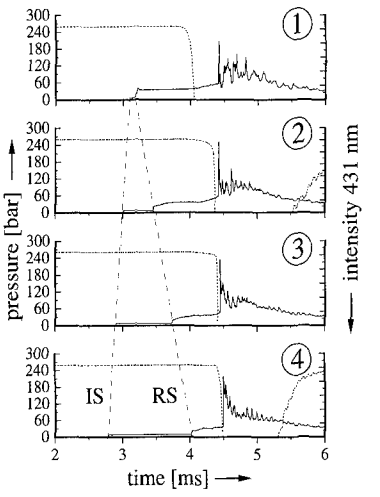

FIG. 6. Pressure and CH-emission signals plotted against time for a strong ignition process (T_5 = 980 K, stoichiometric iso-octane–air mixture). The incident (IS) and the reflected (RS) shock wave are marked with dashed lines. The figure contains the signals measured at four different locations in the driven section of the shock tube.

chiometric iso-octane–air mixtures. Each figure contains the signals measured at four different locations in the driven section of the shock tube. Number 1 (upper plot) stands for the measuring plane 15 mm in front of the end wall; the other measuring planes

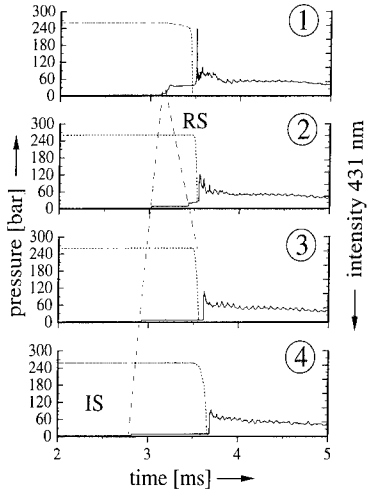

FIG. 7. Pressure and CH-emission signals plotted against time for a strong ignition process (T_5 = 1115 K, stoichiometric iso-octane–air mixture). The incident (IS) and the reflected (RS) shock wave are marked with dashed lines. The figure contains the signals measured at four different locations in the driven section of the shock tube.

2 through 4 are located with a distance of each 100 mm in direction to the high-pressure part.

Figure 5 shows the pressure and CH-emission signals plotted against time for a mild ignition process (T_5 = 810 K). The incident (IS) and the reflected (RS) shock wave are marked with dashed lines. The signals of the CH emission show that, in this experiment, the ignition starts close to the second measurement port 115 mm before the end wall (second plot) and generates a smooth pressure increase, which spreads along the tube axis. The reaction front, indicated by the CH-emission signals, moves more slowly than the pressure wave into the unburned gas.

The plots of an experiment at a higher initial temperature (T_5 = 980 K) are presented in Fig. 6. Self-ignition starts in the measuring plane close to the end wall (signals in the top part of the figure), generating a smooth pressure increase in the same way as the mild ignition process. This pressure wave moves towards the high-pressure part into the unburned gas. At the second measuring location (115 mm in front of the end wall), the temperature increase connected with the pressure rise causes a strong ignition process with a very rapid and strong pressure rise. This pressure wave is coupled with the reaction front. Both move together with very high speed through the tube (measuring points 3 and 4), effecting a very fast oxidation of the fuel.

If the initial temperature is increased further (Fig. 7, T_5 = 1115 K), the behaviour of the self-ignition process reflected in the pressure and CH-emission signals changes again. The self-ignition starts near

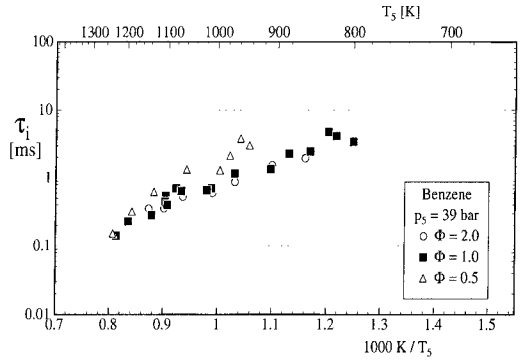

FIG. 8. Ignition delay times of benzene-air mixtures with the equivalence ratio varied; $p_5 \approx 39$ bar.

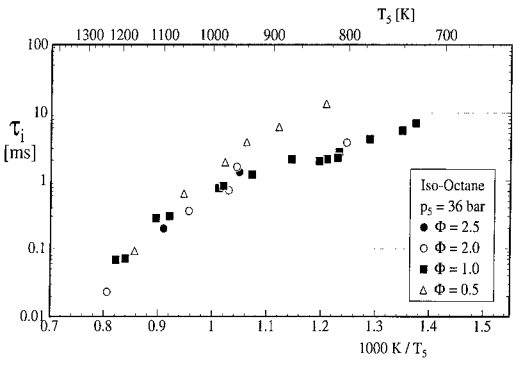

FIG. 9. Ignition delay times of iso-octane–air mixtures with the equivalence ratio varied; $p_5 \approx 36$ bar.

the end wall with a very sharp pressure peak. The reaction front leaves with very high speed from the end wall and catches up with the reflected shock wave between the second and the third measuring planes. The arising shock wave, which is coupled with the reaction front, shows a steplike pressure signal without a single strong peak.

The pressure traces of methanol and MTBE also show features similar to those described for benzene. A slow initiation is followed by a rapid pressure increase and consecutive oscillations at high temperatures. At low temperatures, the trace is smooth and possesses only one maximum.

Ignition Delay Times:

In Fig. 8, the ignition delay times τ_i of benzene for various equivalence ratios are plotted logarithmically vs the inverse of the temperature behind the reflected shock $1000/T_5$. The initial pressure p_5 is kept approximately equal to 39 bar for all the data points. The results of the experiments with iso-octane (p_5 about 36 bar) can be seen in Fig. 9. Both diagrams

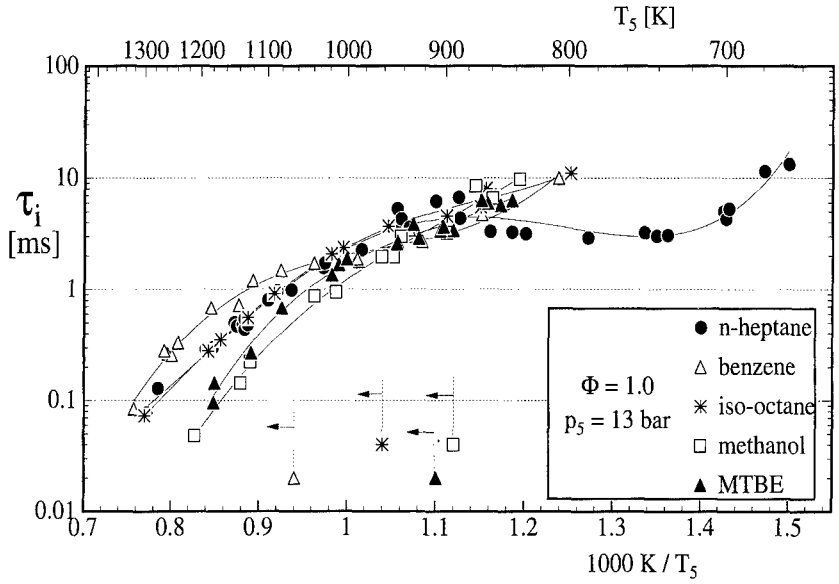

FIG. 10. Ignition delay times of various fuels; $\Phi = 1.0$, $p_5 \approx 13$ bar. The symbols with the arrows indicate the transition from mild to strong ignition. (*n*-Heptane data, see Ref. 11; benzene data, see Ref. 12.)

show that lean mixtures of the two fuels have longer ignition delay times for temperatures smaller than about 1000 K. The results of the rich and the stoichiometric mixtures differ only slightly.

In the last two figures, the results for stoichiometric mixtures of all the fuels investigated are compared. The pressure p_5 is about 13 bar for all the data points in Fig. 10. In Fig. 11, it varies from fuel to fuel but is close to 38 bar, as indicated more accurately in the figure caption.

For *n*-heptane, the ignition delay dependence upon the temperature both in the high- and in the low-temperature region can be expressed approximately by straight lines. In an intermediate range, the dependence becomes strongly nonlinear and is represented by the well-known s-shaped dependence. In this region of negative temperature coefficient, the alkylperoxy radical reactions become dominant (see, e.g., Ref. 2). Increasing the pressure, the s-shaped part is shifted to higher temperatures and lower ignition delay times, which is obvious when Figs. 10 and 11 are compared.

The iso-octane data plotted in Figs. 10 and 11 almost coincide with the *n*-heptane data for temperatures higher than 1000 K at 13 bar and 900 K at 38 bar. Lowering the temperatures, the ignition delay times of iso-octane become longer by a factor of about 10, which explains the large difference of the two fuels in relation to the octane number. The data of iso-octane show a weak s-shaped dependence upon temperature at about 850 K in the Arrhenius diagram at the 38-bar pressure level.

The ignition delay times of benzene show a monotonous dependence upon temperature. At the pressure of 13 bar, the delay times of benzene lie above those of *n*-heptane, except for a small range around 1000 K. This intersection disappears for higher pressures, and the differences between the ignition delay times become larger, as Fig. 11 shows. This becomes particularly pronounced in the important region where *n*-heptane displays the s-shaped dependence, which should be of significance with respect to antiknocking properties.

The MTBE ignition delay shows also the monotonous dependence upon temperature, as observed for benzene. The overall gradient, however, is steeper, which leads to ignition delay times below those of *n*-heptane at high temperatures and low pressures. The data overlap in a region around 900 K. At around 38 bar, the high-temperature values of MTBE and *n*-heptane are close together, differing, however, considerably in the low-temperature transition region. This again is indicative of the MTBE antiknock properties. Comparing the low-pressure data (Fig. 11), methanol shows a very similar behaviour to MTBE. This may be caused by the decomposition of MTBE into methanol and isobutene [18].

The point of transition from strong ignition to mild ignition is marked for every fuel except *n*-heptane in Figs. 10 and 11. This point is located between 1060 K (13 bar) and 990 K (38 bar) for benzene and between 960 K (13 bar) and 700 K (38 bar) for iso-octane. MTBE shows this transition between 910 K (13 bar) and 900 K (38 bar) and methanol at 890 K (13 bar). *n*-Heptane shows strong pressure oscillations at all investigated temperatures [11].

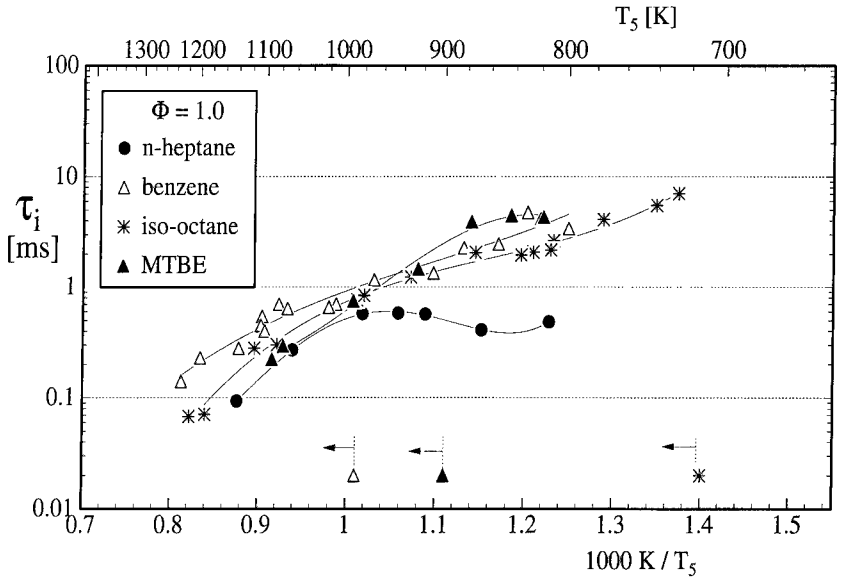

FIG. 11. Ignition delay times of various fuels; $\Phi = 1.0$, *n*-heptane 42 bar, benzene 39 bar, iso-octane 36 bar, MTBE 34 bar. The symbols with the arrows indicate the transition from mild to strong ignition. (*n*-Heptane data, see Ref. 11; benzene data, see Ref. 12.)

Conclusions

The self-ignition behaviour of *n*-heptane, benzene, iso-octane, methanol, and MTBE was investigated under conditions relevant to engine combustion using a high-pressure shock tube.

All fuels investigated except *n*-heptane show a slow initiation of the ignition without distinct pressure peak (mild ignition) at low temperatures, which at higher temperatures changes to a rapid pressure increase after a variable time lag (strong ignition). Optical observations by Oppenheim and coworkers [15,16] reveal that mild ignition at its onset is connected with the formation of flame kernels usually developed in corner eddies. Strong ignition was distinguished by the fact that, at first, a front of a blast wave is formed by the deposition of the exothermic energy in the reactive medium without any prior evidence of flame kernels. The strong ignition limit depending on temperature, pressure, and fuel was determined for iso-octane and benzene.

For *n*-heptane, the well-known s-shaped dependence of the ignition delay time upon the reverse of temperature in the Arrhenius plot, connected with a two-step self-ignition process, was found in our recent investigations [11]. The full kinetic scheme by Chevalier et al. [2] and reduced mechanisms by Müller et al. [3] are able to model this behaviour by the inclusion of peroxide reactions. No mild ignition was observed for *n*-heptane. This may be caused by the fact that the ignition delay times become shorter again at temperatures around 1000 K where the transition between the two modes starts for the other fuels.

The fact that the strong ignition limit of iso-octane is shifted to very low temperatures for higher pressures indicates that, in this region, a behaviour similar to *n*-heptane with negative temperature dependence can be expected. The results of recent rapid compression device investigations, e.g., Ref. 19, for lower pressures show this at low temperatures with long ignition delay times.

Ignition delay times of iso-octane and benzene were obtained in dependence on equivalence ratio and temperature at initial pressures of nearly 40 bar. A comparison of the ignition delay times of all fuels investigated was presented for stoichiometric mixtures and two pressure levels. These results will be helpful for further development, adjusting, and testing of kinetic schemes of iso-octane, benzene, MTBE, and methanol, especially for low temperatures and higher pressures. Without these results, only qualitative conclusions can be drawn from our data.

Detailed simulations of the processes within the shock tube during self-ignition using a Godunov-type method with both detailed and reduced reaction schemes are in progress now. We hope to clarify the interaction of gasdynamic processes with chemical reactions that is expressed in the mild and strong self-ignition processes. These phenomena cannot be explained by usual zero-dimensional kinetic computations.

Acknowledgments

This work was supported by the German Science Foundation DFG as a project of the Sonderforschungsbereich 224 "Motorische Verbrennung."

REFERENCES

1. Zallen, D. M., and Wittig, S. L. K., *Tenth International Symposium on Shock Tubes and Waves,* 1975, p. 640.
2. Chevalier, C., Louessard, P., Müller, U. C., and Warnatz, J., *COMODIA 90,* Kyoto, Japan, 1990.
3. Müller, U. C., Peters, N., and Linan, A., *Twenty-Fourth Symposium (International) on Combustion,* The Combustion Institute, Pittsburgh, 1992.
4. Coward, J. S., Keck, J. C., Heywood, J. B. Westbrook, C. K., and Pitz, W. J., *Twenty-Third Symposium (International) on Combustion,* The Combustion Institute, Pittsburgh, 1990, p. 1055.
5. Cox, R. A., and Cole, J. A., *Combust. Flame* 60:109 (1985).
6. Halstead, M. P., Kirsch, L. J., and Quinn, C. P., *Combust. Flame* 30:45 (1977).
7. Westbrook, Ch. K., Pitz, W. J., and Leppard, W. R., *SAE Paper No. 912314* (1991).
8. Leppard, W. R., *SAE Paper No. 912313* (1991).
9. Ciezki, H., and Adomeit, G., *Seventeenth International Symposium on Shock Tubes and Waves* (Y. W. Kim, Ed.), *AIP Conference Proceedings,* 1989, Vol. 208, p. 707.
10. Ciezki, H., "Untersuchung des Selbstzündverhaltens von n-Heptan/Luft-Gemischen unter hohem Druck," Ph.D. Thesis, RWTH Aachen, Verlag der Augustinus Buchhandlung Aachen, No. 80, ISBN 3 925038 80 9, 1990.
11. Ciezki, H., and Adomeit, G., *Combust. Flame* 93:421–433 (1993).
12. Ciezki, H., and Adomeit, G., VDI-Berichte No. 922, 495–503, VDI-Verlag, Düsseldorf, Germany, 1991.
13. Lee, B. I., and Kesler, M. G., *AIChE J.* 21(3):510 (1975).
14. Gardiner, W. C., Ed., *Combustion Chemistry,* Springer-Verlag, New York, 1984.
15. Oppenheim, A. K., *Phil. Trans. R. Soc. Lond. A* 31(5):471–508 (1985).
16. Vermeer, D. J., Meyer, J. W., and Oppenheim, A. K., *Combust. Flame* 18:327 (1972).
17. Griffith, J. F., and Nimmo, W., *Combust. Flame* 60:215–218 (1985).
18. Norton, T. S., and Dryer, F. L., *Twenty-Third Symposium (International) on Combustion,* The Combustion Institute, Pittsburgh, 1990, pp. 179–185.
19. Halstead, M. P., Kirsch, L. J., Prothero, A., and Quinn, C. P., *Proc. Roy. Soc. London A* 346:515 (1975).

Twenty-Fifth Symposium (International) on Combustion/The Combustion Institute, 1994/pp. 1587–1594

IGNITION AND COMBUSTION OF MAGNESIUM IN CARBON DIOXIDE STREAMS

SABURO YUASA AND APORO FUKUCHI
Tokyo Metropolitan Institute of Technology
Asahigaoka 6-6, Hino-shi, Tokyo 191, Japan

The prospects for using Mg as fuel in a CO_2-breathing engine in Mars atmosphere without oxygen led to this experimental study on the ignition and combustion of Mg performed in pure CO_2 and CO_2/CO streams over a wide range of pressure, velocity, and CO concentration of the streams. The critical ignition temperature of Mg in CO_2 streams decreased with decreasing ambient pressure, and was insensitive to the stream velocity. The ignition temperature in CO_2/CO streams varied little at first, but increased with decreasing CO_2 concentration. Ignition occurred in two distinct stages, the first being surface reactions controlled by chemical kinetics and the second being gas-phase reactions controlled by CO_2 diffusion. The breaking of a thin protective film formed in the first stage played a crucial role in the ignition process, leading to the beginning of the gas-phase reactions and then to ignition.

During combustion, several flames appeared sporadically and intermittently over the swelling sample surface, which was coated with a thick porous layer. The flames produced CO in the gas phase, while, on the nonflame surface, the reactions of Mg with both CO diffusing from the flames and CO_2/CO in the streams generated condensed MgO and C that built the porous layer. The pulsating manner of the flames can be explained in terms of the abrupt breaking of the layer followed by its blockage due to the surface reaction with CO.

Introduction

We have proposed a CO_2-breathing jet engine using metals as fuel for a future aircraft-type vehicle in Mars atmosphere, consisting of CO_2 [1,2]. One of the attractive metal fuels for the engine is Mg. We have performed an experimental study on the ignition and combustion of Mg disks in a CO_2 stream at 1 atm [1]. We found that Mg had easy ignitability and a fast burning rate. During combustion, intermittent flames appeared sporadically over the Mg surface to produce CO by gas-phase reactions. Recently, Shafirovich and Goldshleger [3] have made an experimental study on the combustion of Mg particles introduced into high-temperature CO_2/CO mixtures at 1 atm. They concluded that the heterogeneous reaction of Mg with CO occurred during combustion in CO_2, in addition to the homogeneous reaction of Mg with CO_2. However, detailed experimental knowledge of the ignition and combustion processes, such as the interactions between the homogeneous and heterogeneous reactions and the surface reaction layer structure, has been insufficient. Thus, the ignition and combustion mechanisms still remain obscure. In particular, since the atmospheric pressure of Mars is about 0.6 kPa [4], information about the ignition and combustion of Mg at low pressures will be required to develop a combustor for the engine.

The present experimental study was made to investigate and detail the ignition and combustion process of Mg and to reveal the effects of pressure on it. The experiment was carried out in a stagnation region of CO_2 streams, in the same manner as that of our previous studies of various metals [1,5]. In order to increase understanding of the ignition and combustion mechanism in CO_2, CO_2/CO mixture streams were also used as oxidizers.

Experimental Apparatus and Procedure

Figure 1 shows a schematic of the experimental apparatus [5]. CO_2/CO mixtures at room temperature issued through a nozzle (25-mm diameter) into a combustion chamber. The mixtures impinged on a sample holder of BN (20 mm in diameter), which was situated 17 mm downstream of the nozzle exit. A machined Mg sample (9.5 mm in diameter, 5 mm in height, purity 99.9%) was mounted in a depression of the holder through a thin exchangeable receptacle and a crucible, both of which were made of stainless steel.

In CO_2/CO mixture streams, the experiments were performed at combustion chamber pressures P_m from 8 to 101 kPa, and at the nozzle exit velocities V_m from 0.5 to 5 m/s, with CO_2 mole fractions X_{CO_2} varying from 0 to 1. Before each test, the Mg sample was heated in an Ar stream at a predetermined pressure and flow rate. When the sample tem-

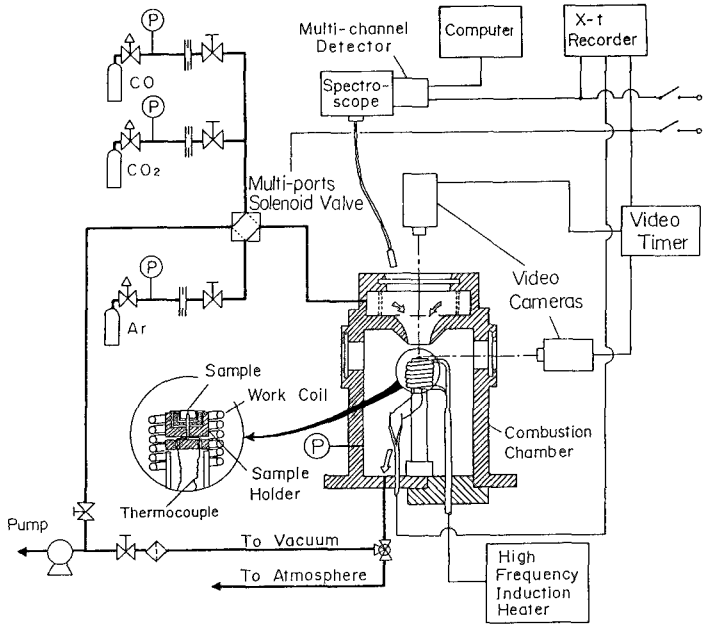

FIG. 1. Schematic of experimental apparatus.

perature reached a predetermined value, the test run was started by changing Ar to a CO_2/CO mixture of the same pressure.

The sample temperature was measured by a chrome-alume thermocouple. Changes in sample appearances were continuously recorded by two video cameras, as shown in Fig. 1. Microphotographic observation was made of samples that were quenched during the ignition and combustion process by injecting Ar into the chamber. Condensed combustion products gathered after the experiment were analyzed chemically and by an x-ray diffractometer.

Experimental Results

Critical Ignition Temperature:

In this study, ignition was defined as a first appearance of a flame on the sample surface. The ignition temperature T_{ig} was the sample temperature at ignition. To determine an ignition limit, the ignition delay time t_d, the interval to ignition after the gas replacement of Ar by a CO_2 stream had taken place, was measured as a function of the initial sample temperature T_{in}, defined as temperature at the gas replacement. Regarding the CO_2 streams, it was found that, at higher pressures, t_d hardly varied with decreasing T_{in} (3–10 s), while, at lower pressures, t_d increased slightly with decreasing T_{in} (up to about 30 s). When T_{in} reached a critical value, ignition did not occur even after an interval of 10 min. The critical ignition temperature T_{cr} was defined as the lowest T_{in} above which a sample heated up by itself to ignition.

Figure 2(1) shows the variation of T_{cr} with P_m in CO_2 streams at V_m = 1.5 m/s. Here T_{cr} decreased with a decrease in P_m. This tendency was different from that in O_2 and air atmospheres [6,7]. Even at the lowest pressure, T_{cr} in CO_2 was higher than that in air at 1 atm [6–8]. Mg in CO_2 streams, as well as in O_2 and air atmospheres [9,10], could burn at sufficiently low pressures. Figure 2(2) shows the effect of V_m on the T_{cr} at P_m = 41.3 kPa in CO_2. Here T_{cr} varied little with V_m. This result suggests that the ignition process of Mg in CO_2 is not controlled by CO_2 diffusion through the boundary layer over the sample surface, but by chemical kinetics. It also suggests that a heat-loss variation with V_m has only a slight influence on T_{cr}. Figure 2(3) shows T_{cr} plotted against X_{CO_2} at P_m = 21.3 kPa and V_m = 1.5 m/s. Here T_{cr} hardly varied when X_{CO_2} decreased from 1.0 to 0.5, but rapidly increased when X_{CO_2} decreased from 0.5 to 0.1. Below X_{CO_2} = 0.1, the sample could not ignite even at the boiling point of Mg (937 °C [11]) at P_m = 21.3 kPa. The dependency of T_{cr} on X_{CO_2} was substantially the same over the P_m range tested, and when X_{CO_2} remained constant, T_{cr} decreased with decreasing P_m.

Ignition and Combustion Process:

Sample appearance and temperature behavior

Figure 3 shows a typical example of the time variation of the sample temperature after the gas replacement at P_m = 41.3 kPa. The sample appear-

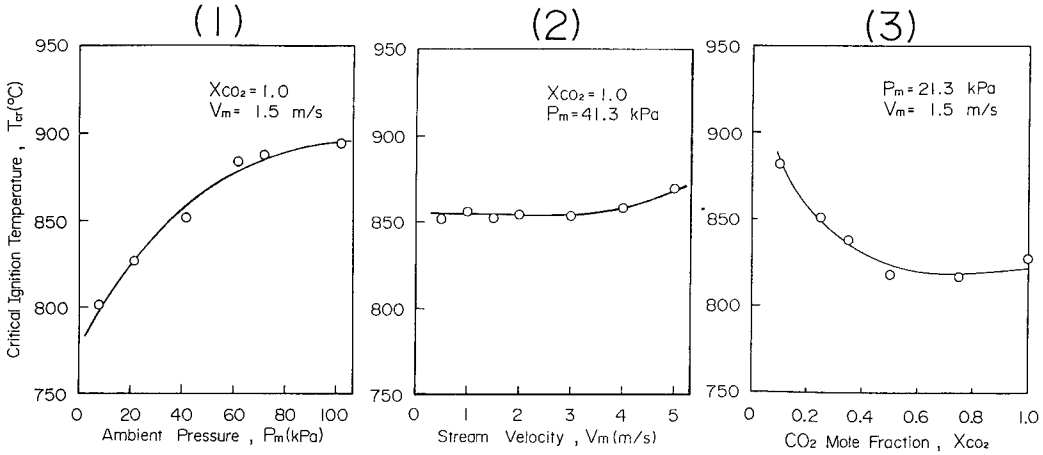

FIG. 2. Variation of critical ignition temperature: (1) with ambient pressure in pure CO_2 streams at V_m = 1.5 m/s, (2) with CO_2 stream velocity at P_m = 41.3 kPa, and (3) with CO concentration in CO_2/CO streams at 21.3 kPa and V_m = 1.5 m/s.

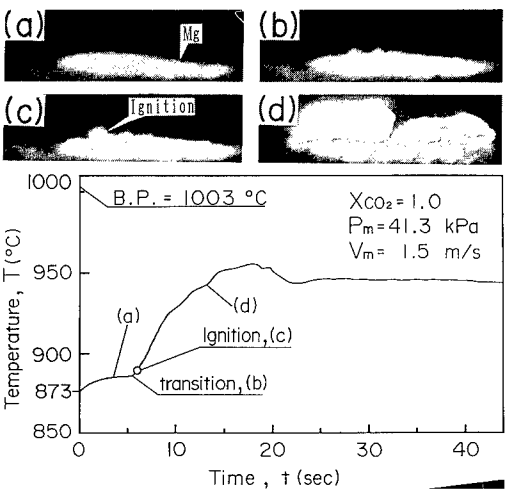

FIG. 3. Time variation of sample temperature and video photographs in a CO_2 stream. T_{in} = 873 °C, P_m = 41.3 kPa, V_m = 1.5 m/s.

ances corresponding to (a) through (d) are also shown in the figure. In an Ar stream, the Mg surface was clean and actively ejected Mg vapor. As soon as the sample was exposed to the CO_2 stream, the surface was uniformly covered with a reaction film that stopped the vapor ejection. Simultaneously, the sample temperature began to increase, and the surface as a whole became red-hot at about (a). As time proceeded, many "bubbles" appeared over the surface at about (b). They further increased in size and number with a corresponding rapid increase in the sample temperature at "transition," where the heat-release mechanism drastically changed. Finally, when one or more of the bubbles burst at (c), incandescent flamelets appeared locally, indicating ignition at T_{ig} = 888 °C. However, when T_{in} was lower than T_{cr}, the temperature increased just after the gas replacement, but this was not followed by the appearance of bubbles, and the sample temperature decreased with time, resulting in nonignition.

The first flamelets at ignition did not spread over the whole sample surface and quenched quickly (about 0.1 s). However, many flamelets continued to appear sporadically and intermittently over the surface with bubbles, repeating the process from ignition to quenching. When the frequency of the appearance increased substantially, stable combustion of the sample was attained at about (d). This behavior is different from that in the air stream, in which a one-dimensional flame appeared over the Mg sample surface without a reaction film [8]. Figure 3 shows that, during stable combustion, the sample temperature remained almost constant at a value close to the boiling point of Mg (1003 °C [11]) at the ambient pressure, in agreement with results for Mg in the air stream [8]. Figure 4 shows a sequence of the developing process of a typical intermittent flamelet that formed during combustion at P_m = 41.3 kPa. Figure 4(a) represents a red-hot bubble that appeared near the top of the surface. As soon as the bubble began to rapidly increase in luminosity, it burst to eject white smoke into the open space, generating an incandescent flamelet like a jet diffusion flame [Figs. 4(b) and 4(c)]. After the flamelet had continued to burn for a while, it was quenched just after (d). The corresponding spectrum of the flamelets showed that

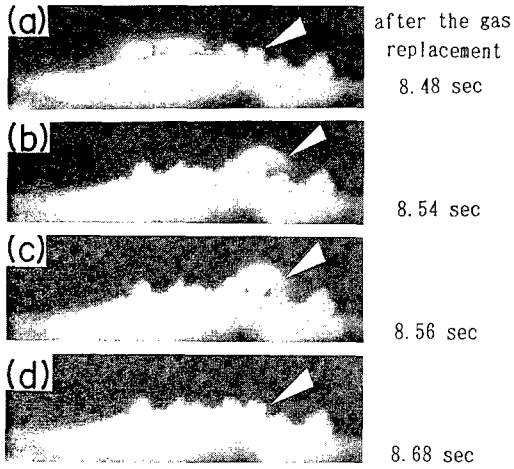

FIG. 4. Video photographs of a flame-developing process in a CO_2 stream. P_m = 41.3 kPa, V_m = 1.5 m/s.

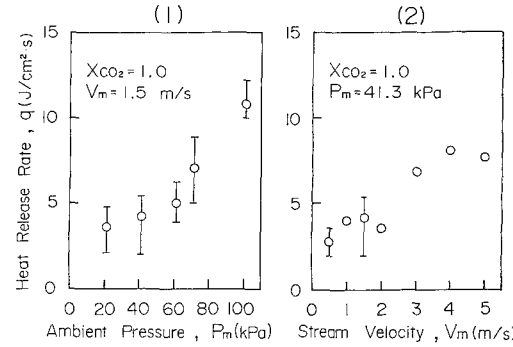

FIG. 5. Variation of heat-release rate in CO_2 streams: (1) with ambient pressure at V_m = 1.5 m/s. (2) with stream velocity at P_m = 41.3 kPa.

Mg lines and MgO bands were visible, in agreement with observations of Mg in O_2 and air atmospheres [8,10]. CO was measured in the gaseous combustion products. It is of interest that the nonflamelet surface area continued to be heated red-hot during combustion. These results indicate that gas-phase reactions of the flamelets produced CO, while surface reactions also occurred on the nonflamelet surface areas. After the stable combustion continued for a few minutes, flamelets vanished and the surface with bubbles became dark, resulting in quenching of a whole sample. A thick black and white shell remained on a quenched sample.

Effects of pressure and velocity

The above-mentioned ignition and combustion process in pure CO_2 streams was found to be essentially similar over the range of pressure tested, except for the case of P_m = 8 kPa. However, pressure has effects on the following characteristics. The T_{ig} scattered in the range of 870–920 °C seems to decrease slightly with decreasing pressure. The averaged heat-release rate q was estimated from the temperature increase rate of the sample between transition and stable combustion by assuming that the sample mass and the reaction surface area were kept constant at original values. Here q was about 3–12 J/(cm^2 · s) and decreased with decreasing pressure from 101 to 21.3 kPa, as shown in Fig. 5(1). Corresponding to this, the total burning time from ignition to quenching increased greatly with pressure: about 50–80 s for 101 kPa and about 100–160 s for 21.3 kPa. With increasing V_m, q also increased, as shown in Fig. 5(2), which implies that, after ignition, CO_2 diffusion through the boundary layer became the rate-limiting step. With a decrease in pressure, the frequency of flamelet appearance decreased, but the scale of bubbles and the height of the swelling surface increased. Individual flamelets continued to burn for about 0.1–0.2 s, and this was observed to be insensitive to the ambient pressure. At P_m = 8 kPa, ignition occurred when a surface film burst extensively without generating bubbles and surface swelling, resulting in a jet diffusion flame.

Effect of CO concentration

Addition of CO to CO_2 led to noticeable changes in the ignition and combustion process. Decreasing X_{CO_2} from 1.0 to 0.25 caused the bubbles to become bigger, and the sample swelled significantly higher. In the range of X_{CO_2} below 0.5, t_d at the ignition limits became much longer than that in CO_2. At lower X_{CO_2}, individual flamelets burned slowly and weakly for a few seconds. Corresponding to this, q was smaller than that in CO_2 streams. The total burning time of the whole sample remarkably increased with decreasing X_{CO_2}; for example, at P_m = 21.3 kPa and V_m = 1.5 m/s, about 100–160 s at X_{CO_2} = 1.0 and about 170–300 s at X_{CO_2} = 0.5. These results suggest that the reaction rate of Mg with CO is considerably slower than that with CO_2. It is noteworthy that pulsating combustion of the whole sample, such as that reported by Shafirovich and Goldshleger [3], was observed over the wide range of X_{CO_2} from 1.0 to 0.5 in the present experiment.

When X_{CO_2} was less than 0.25, the behavior of the sample appearance changed drastically. When ignition took place at lower pressures, an abrupt bursting occurred just after gas replacement, and was followed by a large jet flame of Mg vapor without any flamelets.

Combustion Products and Reaction Film Structure:

Figure 6 shows a typical example of the cross sections of quenched samples at certain intervals after

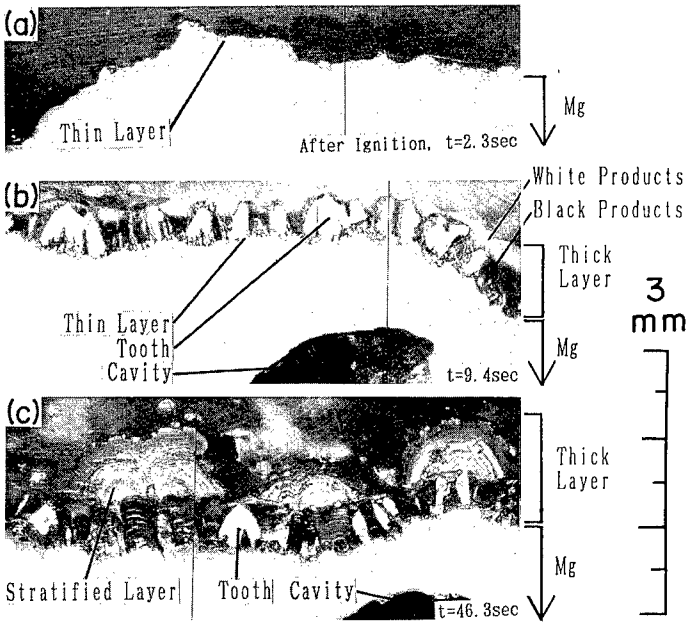

FIG. 6. Cross-section photographs of quenched samples in a CO_2 stream at P_m = 101.3 kPa and V_m = 1.5 m/s: (a) after ignition t = 2.3 s, (b) t = 9.4 s, and (c) t = 46.3 s. T_m = 900 °C.

ignition at 101 kPa in a CO_2 stream. During the ignition stage, a thin gray reaction film about 0.1-mm thick formed and adhered [Fig. 6(a)]. At the next stage, a black product layer was generated over the thin film. It increased in thickness with time, while the thin film maintained an almost constant thickness. As time went on, the unevenness and thickness of the black product layer increased, and many protruding parts, like "teeth", filled with Mg appeared on the rough surface [Fig. 6(b)]. It should be noted that their bottoms attached to the thin gray film, and the black layer was covered with white powder products in spots. All the samples quenched at this stage had cavities inside. They became larger in diameter as combustion proceeded. This observation supports the fact that the sample was boiling during combustion. As combustion continued, the black product layer became more complicated and much thicker. Eventually, several stratified protrusions like "cabbages" formed [Fig. 6(c)]. They consisted of alternately arranged thin metallic layers and thin gray layers and had paths from the Mg sample. The layer number of a stratified protrusion was nearly equal to the pulse number of the corresponding flamelet. This suggests that the protrusions were alternately stratified by Mg and combustion products. The growth of the black product layer indicates that it was appreciably porous and nonprotective, thus allowing further gas-phase reactions to occur close to or inside it. After combustion, the black product layer existed almost entirely clear of white products, remaining as a shell covering the receptacle.

When the ambient pressure was lower, the layer structure was essentially the same as that at high pressures. The differences were that the initial thin film decreased in thickness and that the black product layer, including stratified protrusions, became more complicated and much thicker, for example, up to about 5 mm at P_m = 41.3 kPa. On the other hand, adding CO to the CO_2 streams made the layer both more complicated and thicker. In the quenched layers, stratified protrusions were not observed, but Mg metal existed in a coral formation.

After the test run, the shell of the black product layer was analyzed chemically. It was confirmed that the shell was composed of combustion products, MgO and carbon, and of unburned Mg. The mole fraction of carbon in the combustion products, $X_C = \mathrm{mol}_C/(\mathrm{mol}_C + \mathrm{mol}_{MgO})$, was about 0.15 in CO_2 streams. One possible explanation for the carbon formation is surface reactions, as the gas-phase reactions between Mg vapor and CO_2 produce only CO [1]. Figure 7 shows the variation of X_C with X_{CO_2} in CO_2/CO streams at P_m = 21.3 kPa. With increasing CO concentration, X_C increased. This tendency of X_C on X_{CO_2} remained similar over the range P_m tested. The ST1 curve represents the stoichiometric values for the case when only CO in the mixtures of CO_2/CO is perfectly reduced to C through the heterogeneous reaction Mg (l) + CO = MgO (c) + C (c). The ST2 curve represents the case in which all CO and CO_2 in the mixtures are stoichiometrically converted to C through the heterogeneous reactions Mg (l) + $CO_2/2$ = MgO + C/2 and the above reaction. The difference between the experimental values and the ST1 curve is considered to be equal to the amount of carbon formed from the reaction with CO_2. This consideration may imply that, below ap-

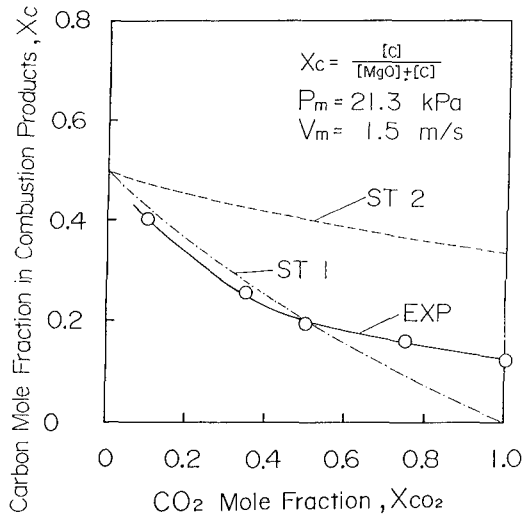

FIG. 7. Carbon mole fraction in combustion products against CO_2 mole fraction in CO_2/CO streams at P_m = 21.3 kPa and V_m = 1.5 m/s.

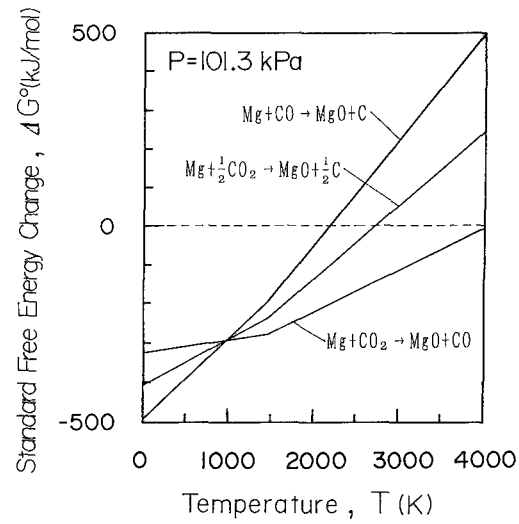

FIG. 8. Standard free energy change as a function of temperature.

proximately X_{CO_2} = 0.5, CO_2 in the mixtures did not take part in the surface reactions to produce carbon. In addition, the amount of carbon corresponding to the difference between ST2 and the experimental values was probably generated as CO without conversion to carbon.

Discussion

Reaction Kinetics:

A proper understanding of the Mg-CO_2/CO reactions will be necessary to make the ignition and combustion process of Mg clear. Possible overall kinetics between Mg and CO_2/CO are as follows:

Reaction 1: $Mg + CO_2 = MgO + CO$

$$\Delta H = -318.9 \text{ [kJ]}$$

Reaction 2: $Mg + CO_2/2 = MgO + C/2$

$$\Delta H = -404.7 \text{ [kJ]}$$

Reaction 3: $Mg + CO = MgO + C$

$$\Delta H = -490.9 \text{ [kJ]}.$$

Figure 8 plots the standard Gibbs free energy change against temperature for Reactions (1) through (3) at 101 kPa. It is known that, if the value is negative, the reaction can proceed spontaneously and that, the lower the position of the line, the more stable the product. At the flame temperature of Mg with CO_2 at stoichiometric ratio (2952 K [1]), only Reaction (1) can take place, but Reactions (2) and (3) cannot. However, below about 2100 K, close to the flame temperature of Mg with CO (2040 K [12]), CO can react with Mg vapor to form carbon. However, the present experimental results related to T_{cr}, the combustion products and the burning time suggest that the reaction rate of CO with Mg was not as fast as that of CO_2. It is interesting to note that, on the burning Mg surface at about 1000 K, Reactions (2) and (3) can occur, producing carbon.

Ignition and Combustion Process:

From the present experimental results and the above considerations, we postulated an ignition and combustion mechanism of Mg in CO_2 as follows. As soon as CO_2 impinges on a clean Mg surface, Reaction (1) occurs in the gas phase to form CO. Part of the CO can diffuse back to the surface to produce MgO and C on the surface because the rate of Reaction (3) is slow in the gas phase. These products form a somewhat protective initial film, inhibiting further gas-phase oxidation. Since the rate of the surface reaction through the film is considered to be much slower than gas diffusion, a kinetic process may control the early ignition stage. As time goes on, at transition, the film will become nonprotective and allow passing of liquid or gaseous Mg. This may be due to the significantly high pressure of Mg. Since the film is not perfectly broken, Reactions (1) and (3) occur only close to the film surface. Thus, the reactions look as if they are pure surface reactions, and produce a porous layer, composed of MgO and C, filled with Mg. When the liquid Mg vaporizes vig-

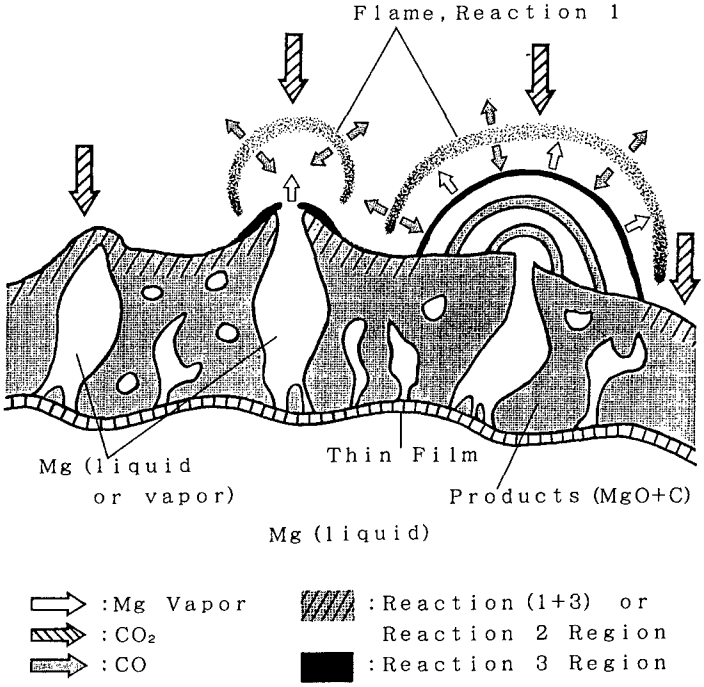

FIG. 9. Schematic representation of a Mg-CO_2 combustion mechanism postulated in this study.

orously inside the layer because of heat caused by the reactions, the unevenness of the layer increases; in particular, it grows into bubbles. If the vapor pressure in a bubble is increased by local heating, the vapor will be ejected into the open space through a hole to form a luminous jet diffusion flame, leading to ignition.

Figure 9 explains schematically the burning of Mg in CO_2. As the vapor pressure of Mg in the bubble decreases, part of the CO produced in the flamelet can diffuse back again to clog its hole with reaction products MgO and C, resulting in quenching. However, at the other nonflamelet parts of the surface, the gas-phase and surface reactions continue to occur in the vacant space near the outer edge of the layer. This is followed by the occurrence of the next flamelets over the surface, leading to the appearance of intermittent and sporadic flamelets. If a flame forms intermittently at the same place, the layer stratifies and the flame appears as pulsating combustion. During combustion, consequently, CO_2 diffusion through the boundary layer over the sample surface becomes a rate-limiting step because it is much slower than the gas-phase reactions.

Effects of Ambient Pressure and Impinging Velocity:

We proposed that the rate-limiting step is changed from chemical kinetics to CO_2 diffusion in the ignition process. The chemically controlled mechanism, supported by the result of Fig. 2(2), leads to the following explanation of the dependency of T_{cr} on P_m. It is known that the oxidation of metals without significant scale cracking proceeds at rates proportional to the $(1/n)$th power of the oxidizer pressure [13]. Generally, n is positive. Thus, the lower the level to which the ambient pressure is decreased, the thinner is the film that forms. This tendency is confirmed by our present observation. If transition from a protective film to a porous one occurs by cracking of the film due to the pressure difference between the external ambient pressure and the internal vapor pressure, a thinner film is more likely to break, and to begin the gas-phase reactions. This consideration could explain how a decrease of P_m facilitates ignition at lower T_{in}. In this case, the heat loss dependent on P_m has only a minor effect because its order is the same as that of V_m, shown in Fig. 2(2).

On the other hand, increasing V_m and P_m causes an increase in mass transfer in the stagnation region due to a decrease in thickness of the boundary layer over the surface. In the diffusion-controlled regime, the decrease effects an increase in the burning rate of Mg, resulting in higher q, as shown in Fig. 5.

Effect of CO Concentration:

The experimental fact concerning the slow gas-phase reaction rate of Mg with CO may allow a preferential reaction of CO_2 with Mg. Thus, the ignition process, controlled by chemical kinetics, should be

essentially insensitive to CO concentration. This is supported by the lack of dependence of T_{cr} on X_{CO_2} in the range from 1.0 to 0.5. Of course, during combustion, the increased CO concentration leads to decreased Mg vapor ejection from the surface because of the additional surface reaction with CO, generating a thicker surface layer. Its growth mechanism is a subject that merits further studies. On the other hand, at higher CO concentrations, probably below $X_{CO_2} = 0.5$, the mass flow rate of CO_2 to the surface decreases substantially. Thus, the gas-phase reactions close to the surface occur inactively, resulting in a higher ignition temperature.

It is interesting to note that, when X_{CO_2} was in the range 1.0–0.5, the whole sample frequently burned in a pulsating manner. In pure CO, however, the sample could not ignite. These results differed from Shafirovich and Goldshleger's experimental observations [3] carried out in CO_2/CO mixtures at 1000 K and 1 atm. This contradiction seems to be the result of the difference of the ambient temperatures. However, our results propose that the pulsating combustion is a fundamental phenomenon attendant on the system in which the gas-phase reactions occur simultaneously with the surface reactions, producing condensed product layer.

Acknowledgments

This work was supported in part by the Grant-in-Aid for Scientific Research of the Ministry of Education, Japan. The authors would like to express their thanks to Mr. C. Nemoto and Mr. T. Yoshida for their cooperation in conducting the experiment.

REFERENCES

1. Yuasa, S., and Isoda, H., *Twenty-Second Symposium (International) on Combustion*, The Combustion Institute, Pittsburgh, 1989, p. 1635.
2. Yuasa, S., and Isoda, H., AIAA 25th Joint Propulsion Conference, AIAA Paper 89-2863, 1989.
3. Shafirovich, E. Ya., and Goldshleger, U. I., *Combust. Sci. Technol.* 84:33–43 (1992).
4. Moore, P., Hunt, G., Nicolson, I., and Cattermole, P., *The Atlas of the Solar System*. Mitchell Beazley Publisher, London, 1983.
5. Yuasa, S., Sogo, S., and Isoda, H., *Twenty-Fourth Symposium (International) on Combustion*. The Combustion Institute, Pittsburgh, 1992, p. 1817.
6. Laurendeau, N. M., and Glassman, I., *Combust. Sci. Technol.* 3:77 (1971).
7. Fassell, W. M., Gulbransen, L. B., Lewis, J. R., and Hamilton, J. H., *J. Met.* 3:522 (1951).
8. Takeno, T., and Yuasa, S., *Combust. Sci. Technol.* 21:109 (1980).
9. Markstein, G. H., *Ninth Symposium (International) on Combustion*. Academic Press, New York, 1963, p. 137.
10. Brzustowski, T. A., and Glassman, I., *Heterogeneous Combustion* (Wolfhard et al., Eds.), Academic Press, New York, 1964, Vol. 15, p. 117.
11. *JANAF Thermochemical Tables*, 2nd ed., The Dow Chemical Company.
12. Gordon, S., and McBride, B., *Computer Program for Calculation of Complex Chemical Equilibrium Compositions, Rocket Performance, Incident and Reflected Shocks, and Chapman-Jouguet Detonations*, NASA SP-273, 1971.
13. Birks, N., and Meier, G. H., *Introduction to High Temperature Oxidation of Metals*, Edward Arnold, London, 1983, pp. 42–58.

Twenty-Fifth Symposium (International) on Combustion/The Combustion Institute, 1994/pp. 1595–1601

MODELING OF PARTIALLY CONFINED HOT FRAGMENT CONDUCTIVE IGNITION

T. H. HUANG
Department of Fuel Science
The Pennsylvania State University
University Park, PA 16802, USA

AND

S. T. THYNELL AND K. K. KUO
Department of Mechanical Engineering
The Pennsylvania State University
University Park, PA 16802

The purpose of this work is to establish a comprehensive theoretical model for studying the degree of vulnerability of nitramine-based propellants subjected to hot fragments within a partially confined enclosure. The model simulates the complicated processes of heat transfer and displacement of the hot fragments, generation of a foam layer caused by liquefaction and decomposition of the propellant, and regression of the propellant. A lumped-parameter analysis is considered for the determination of instantaneous temperature, pressure, and species concentrations of the gas phase within the enclosure. A reduced chemical kinetic scheme for RDX decomposition has been adopted to simulate the chemical reactions at the propellant/foam layer interface, the foam layer, and gas-phase regions. The developed model has been used to study the effects of initial temperature of hot fragment, size of hot fragment, and size of chamber exhaust port on ignition of XM39 propellant. The go/no-go ignition boundary of the highly confined case was found to be lower than that of a partially confined condition by about 150 K and is in good agreement with data obtained from experiments. This is mainly caused by the fact that under highly confined conditions, the accumulation of pyrolysis products and results chamber pressurization significantly enhance the exothermic heat release associated with the gas-phase reactions between CH_2O and NO_2 species.

Introduction

Hot fragment conductive ignition (HFCI) studies help to determine the survivability of weapon systems (such as tanks, ships, etc.) containing stowed ammunition. The hot fragments can be generated during penetration of shaped charge jets or kinetic energy penetrators through armor plates. One way to reduce the threat of propellant ignition by hot fragments is to use a propellant that is resistant to conductive ignition. Considerable effort has been devoted to the development of low vulnerability ammunition (LOVA) and high-energy LOVA (HELOVA) propellants.

Several attempts have been made to model the ignition process encountered in HFCI experiments [1,2]. However, because no gas-phase reaction mechanism was considered and no foam layer reaction was simulated in most of these models of conductive ignition, their validity and usage are limited. In recent years, Hsieh and coworkers developed a comprehensive theoretical model for studying the degree of vulnerability of various solid propellants heated by hot spall fragments [3,4]. The model describes heat transfer and displacement of the hot particle, generation of melt (or foam) layer caused by liquefaction and decomposition of the propellant, regression of propellant, and time variation of its temperature distributions. The model was validated by HFCI test results obtained under constant-pressure environment. However, the model cannot be readily applied to partially confined environments in which the size of exhaust area is limited and, hence, could result in a chamber pressure increase. The main objective of this investigation is to present a modified model for partially confined HFCI (PCHFCI) environment so that the effects of accumulation of pyrolysis products in the enclosure and heat transfer on the ignition behavior of LOVA and HELOVA propellants can be studied. Because of space limitation, only results of the XM39 LOVA propellant are included.

Model Description

A schematic diagram of the physical model considering various processes occurring during the in-

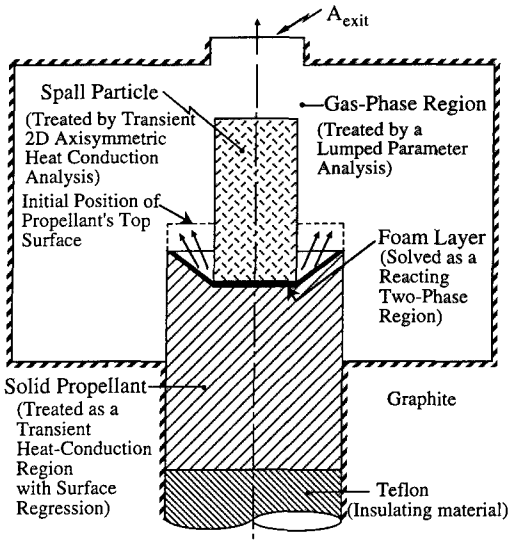

FIG. 1. Schematic diagram of the PCHFCI model.

teraction between the hot spall fragment and the propellant sample is shown in Fig. 1. For mathematical convenience, both the spall fragment and the initial propellant sample are considered as cylinders, whose diameters are 0.63 and 1.27 cm, respectively. The model includes four separate regions in the analysis: the spall particle, the foam layer, the solid propellant, and the gas-phase region. Of these four, the foam layer is the most complex, and the physical and chemical processes occurring in liquid and gas phases within the foam layer are treated separately. In this work, the previous HFCI model is extended in three different areas [3,4]. First, the accumulation of pyrolysis products occurs within the confined region. Second, heat transfer and chemical reactions occurring within the gas-phase region of the partially confined enclosure are described. Finally, a more realistic chemical kinetic scheme of the propellant's thermal decomposition and ignition is incorporated.

In order to predict the occurrence of ignition, it is necessary to include an approximate chemical kinetic scheme. For LOVA propellants, the scheme must consider decomposition of RDX crystals and binder materials. In particular, it is desirable to incorporate the rate of binder decomposition by utilizing results from separate thermal decomposition experiments. Since events leading to ignition are of particular interest to PCHFCI studies, important chemical reactions occurring over the temperature range from 400 to approximately 1000 K must be accounted for. In the case of nitramine-based LOVA propellants, these reactions occur within the foam layer and the fizz zone; that is, reactions occurring within the dark or luminous flame zones are of lesser importance.

The LOVA propellants contain a significant amount of the crystalline cyclic nitramine RDX (cyclotrimethylenetrinitramine). For example, XM39 contains 76% of RDX by weight, and the average crystal size is approximately 5 μm. Table 1 shows the chemical reactions considered at the propellant/foam layer interface, the foam layer, and gas-phase regions. The rate constants for these reactions are listed in Table 2. At the propellant/foam layer interface, the solid RDX filler and binder go through a melting process to form liquid RDX and binder. The decomposition process of RDX has been studied experimentally [5,6] and theoretically [7]. Although the decomposition mechanism appears to be quite complex, it can be split into two general pathways. These two reaction pathways, which differ from RDX evaporation, are shown in Table 1. According to this scheme, the formation of CH_2O and N_2O is favored at the lower temperatures, and the formation of HCN and HONO is favored at the higher temperatures. Because HONO is generally regarded as a short-lived species, it will be assumed that HONO rapidly decomposes into H_2O, NO, and NO_2.

The XM39 propellant contains 12% of cellulose acetate butyrate (CAB), 7.6% of acetyl triethyl citrate (ATEC), 4% of nitrocellulose (NC, 12.45% N), and 0.4% of ethyl centralite (EC). Because of its chemical stability, the effects of EC are assumed to be negligible. Regarding the other binder ingredients, the thermal decomposition behavior of NC has been studied extensively. The thermal decomposition mechanisms of CAB and ATEC have not yet been established. In order to arrive at the assumed decomposition products shown in Table 1, the following aspects have been considered.

First, the decomposition mechanism should be neutral or slightly endothermic [8]. Second, products that are likely to appear and some of which already have been observed in thermolysis experiments must be chosen. Third, the decomposition mechanism must be based on mass conservation. Fourth, since soot formation is observed, both within or at the surface of the foam layer as well as within the dark zone region, precursors to soot formation are likely formed by either CAB or ATEC. Fifth, relatively stable products are formed (e.g., OH is excluded). The decomposition mechanism shown in Table 1 considered these aspects, but it should be stressed that correct mole fractions as well as correct thermal decomposition product species types for CAB and ATEC may not have been selected in this reduced chemical kinetic scheme.

The dissolved gases (including CH_2O, N_2O, HCN, NO, NO_2, H_2O, C_2H_4, CO, C_2H_2, and CH_4) are assumed to desorb from liquid at a rate governed by the pyrolysis rate of the XM39 propellant determined from differential scanning calorimetry (DSC) experiments of Miller [9]. For gas-phase reactions in bubbles, the competing decomposition reactions of RDX are considered together with the major exothermic

TABLE 1
Simplified chemical kinetic scheme for ignition study of XM39 propellant

1. XM39 Solid Propellant / Foam Layer Interface:

$$\text{XM39}\begin{cases}\text{RDX}_{(s)}\\ \text{Binder}_{(s)}\end{cases} \rightarrow \text{RDX}_{(l)} + \text{Binder}_{(l)}$$

2. Foam Layer:

Liquid:

$$\text{RDX}_{(l)} \longrightarrow \begin{cases} \xrightarrow{k_1} 3\ CH_2O_{(dgl)} + 3\ N_2O_{(dgl)} & (\Delta H_r = -894.4\ \text{J/g-RDX}) \\ \xrightarrow{k_2} 3\ HCN_{(dgl)} + 3\ HONO_{(dgl)} \\ \xrightarrow{\text{Fast}} 3\ HCN_{(dgl)} + \frac{3}{2}\ NO_{(dgl)} + \frac{3}{2}\ NO_{2(dgl)} + \frac{3}{2}\ H_2O_{(dgl)} & (\Delta H_r = 587.1\ \text{J/g-RDX}) \end{cases}$$

$$\text{Binder}_{(l)} \xrightarrow{\text{Fast}} \begin{cases} \text{ATEC} \longrightarrow 5\ CH_2O_{(dgl)} + 3\ C_2H_{4(dgl)} + 3\ CO_{(dgl)} \\ \text{NC} \longrightarrow 2.45\ NO_{2(dgl)} + 2\ CH_2O_{(dgl)} + 2\ CO_{(dgl)} + C_2H_{2(dgl)} + H_2O_{(dgl)} \\ \text{CAB} \longrightarrow 6\ CH_2O_{(dgl)} + 3\ C_2H_{2(dgl)} + CH_{4(dgl)} + 2\ CO_{(dgl)} \end{cases}$$

Liquid/Gas Bubble Interface:

$$A_{i(l)} \xrightarrow{k_3} A_{i(g)} \qquad (\Delta H_v = 322.6\ \text{J/g-liq})$$

Where A_i include RDX, CH_2O, N_2O, HCN, NO, NO_2, H_2O, C_2H_4, CO, C_2H_2, and CH_4

Gas Bubbles:

$$\text{RDX}_{(g)} \longrightarrow \begin{cases} \xrightarrow{k_1} 3\ CH_2O_{(g)} + 3\ N_2O_{(g)} & (\Delta H_r = -1318.4\ \text{J/g-RDX}) \\ \xrightarrow{k_2} 3\ HCN_{(g)} + \frac{3}{2}\ NO_{(g)} + \frac{3}{2}\ NO_{2(g)} + \frac{3}{2}\ H_2O_{(g)} & (\Delta H_r = 162.6\ \text{J/g-RDX}) \end{cases}$$

$$NO_{2(g)} + \frac{5}{7}\ CH_2O_{(g)} \xrightarrow{k_4} NO_{(g)} + \frac{2}{7}\ CO_{2(g)} + \frac{3}{7}\ CO_{(g)} + \frac{5}{7}\ H_2O_{(g)} \qquad (\Delta H_r = -4182.5\ \text{J/g-}NO_2)$$

3. Gas-Phase Region:

$$\text{RDX}_{(g)} \longrightarrow \begin{cases} \xrightarrow{k_1} 3\ CH_2O_{(g)} + 3\ N_2O_{(g)} \\ \xrightarrow{k_2} 3\ HCN_{(g)} + \frac{3}{2}\ NO_{(g)} + \frac{3}{2}\ NO_{2(g)} + \frac{3}{2}\ H_2O_{(g)} \end{cases}$$

$$NO_{2(g)} + \frac{5}{7}\ CH_2O_{(g)} \xrightarrow{k_4} NO_{(g)} + \frac{2}{7}\ CO_{2(g)} + \frac{3}{7}\ CO_{(g)} + \frac{5}{7}\ H_2O_{(g)}$$

reaction between NO_2 and CH_2O [10]. These three reactions are also considered for the gas-phase region above the foam layer.

In formulating the theoretical model, four sets of governing equations, as well as their boundary and initial conditions, were derived. These governing equations were formulated by considering the hot spall particle, adequately treated by transient two-dimensional axisymmetric heat conduction; the LOVA propellant, treated as a transient heat-conduction region with surface regression; the foam layer, solved as a reacting two-phase region; and the gas-phase region, treated by a lumped-parameter analysis. Details of this development are available [11,12].

Discussion of Results

Governing equations for heat conduction within spall particle and inert heating of the propellant were recast into ordinary differential equations by integral methods. The overall PCHFCI model consists of a total of 34 ordinary differential equations that were solved simultaneously by Gear's method [13].

TABLE 2
Frequency factors and activation energies of rate constants used in chemical kinetic scheme of XM39 propellant

$k_i = A \exp[-E/RuT]$	A	$E\left(\frac{\text{Kcal}}{\text{g mole}}\right)$	Ref.
k_1	1×10^{13} (1/s)	36.0	7
k_2	2×10^{16} (1/s)	45.0	7
k_3	1.98×10^{14} (1/s)	38.2	9
k_4	10^{12} (cm^3/g mole s)	19.0	10

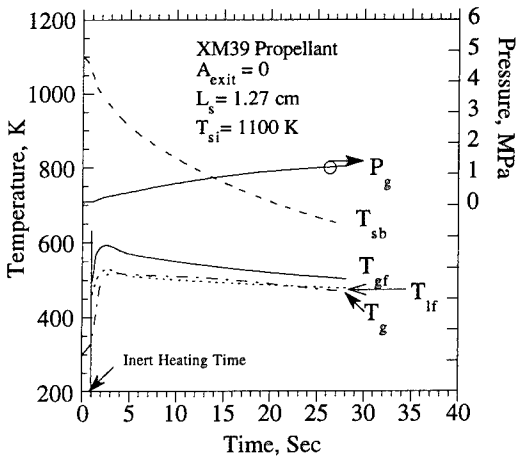

FIG. 2. Variation of temperatures and pressure caused by a spall particle initially at a temperature of 1100 K within a totally confined enclosure ($A_{exit} = 0$).

Species, Temperature, and Pressure Variations:

To study temporal variations of species, temperatures, and pressure for a totally confined enclosure ($A_{exit} = 0$), initial spall temperatures of $T_{si} = 1100$ and 1150 K were considered. For these two cases, a spall of height $L_s = 1.27$ cm and radius $r_s = 0.317$ cm was employed in the numerical simulation. Figure 2 shows the calculated time variations of temperature and pressure for a spall whose initial temperature was 1100 K. Initially, the solid propellant is subjected to an inert heating period of about 1-s duration. Once the inert heating period is complete, both the calculated gas-bubble and liquid-phase temperatures increase rapidly. The initial temperatures of the liquid (T_{lf}) and gas (T_{gf}) in the foam layer were assumed to be 460 K. Peak values of these temperatures occur around 2 s and beyond this peak the foam-layer temperatures gradually decrease. The temperature along the bottom surface of spall, T_{SB}, decreases due to the heat transfer to the foam layer by conduction and to the gas-phase region by both convection and radiation. The thermal response by the gas-phase region, denoted by T_g, is slightly delayed but rapidly reaches a value of about 510 K. This temperature remains fairly steady for about 13 s, because heat losses to chamber walls are balanced by heat gains from an influx of hot gases from foam layer and chemical reactions. Since calculations show a gradual decrease in all temperatures beyond a time of about 15 s, a rapid heat release indicative of ignition was not predicted.

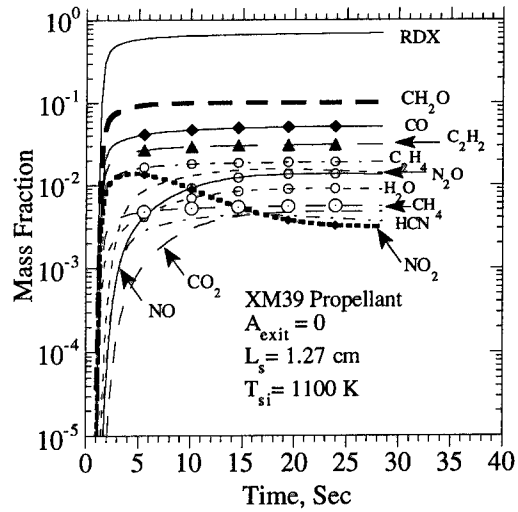

FIG. 3. Composition changes of species in the gas-phase region induced by a spall particle initially at a temperature of 1100 K within a totally confined enclosure ($A_{exit} = 0$).

Figure 3 shows the calculated time variations of species in the gas-phase region. Examination of this figure reveals that there are no significant reactions between CH_2O and NO_2 species which cause an appreciable increase in the temperature of the gas-phase products, as shown in Fig. 2. For the larger times, the spall's temperature becomes too low to promote extensive chemical reactions in the foam layer. The predicted decrease in the mass fraction of NO_2 is believed to be due to two aspects. First, a slow reaction occurs between CH_2O and NO_2 species. Second, the $RDX_{(g)}$ decomposition follows primarily the low-temperature pathway, which does not reduce the total amount of NO_2 gas present in the gas-phase region but reduces only its mass fraction.

An increase in the initial temperature of the spall from 1100 to 1150 K produced an ignition in the gas-phase region. Figures 4 and 5 show the calculated time variations of temperatures and pressure as well

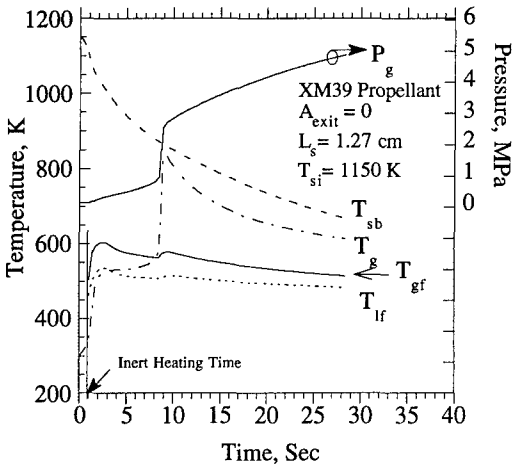

FIG. 4. Variation of temperatures and pressure caused by a spall particle initially at a temperature of 1150 K within a totally confined enclosure (A_{exit} = 0).

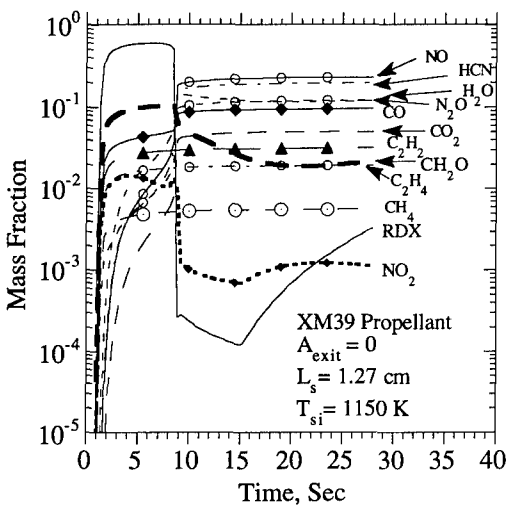

FIG. 5. Composition changes of species in the gas-phase region induced by a spall particle initially at a temperature of 1150 K within a totally confined enclosure (A_{exit} = 0).

as species mass fractions in the gas-phase region, respectively. The ignition event occurs at about 8 s after the spall's initial contact with the propellant. Because of the higher initial temperature of the spall and high gasification rates of the propellant, the temperature of the gas-phase region monotonically increases until ignition occurs. Although gas-bubble temperature is higher than liquid temperature in foam layer, "ignition" does not occur within the gas bubbles, because (1) heat transfer rates to liquid phase are high due to small bubble sizes, (2) the vaporization rate of liquid is limited, and (3) the void fraction is small. Once

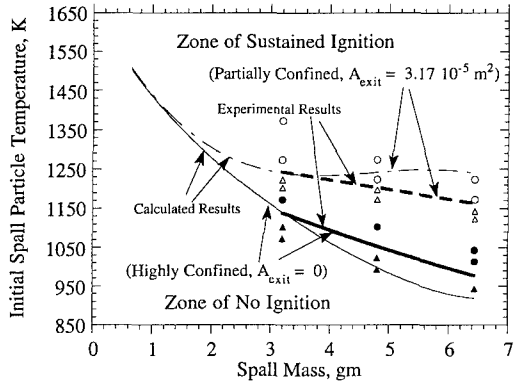

FIG. 6. Comparison of predicted and experimentally determined go/no-go ignition boundaries for XM39 propellant (circles: ignition; triangles: no ignition).

ignition has occurred, the temperature of the gas-phase region decreases rapidly. This decrease is due to heat transfer to the isothermal chamber walls and to the propellant. The effect of heat release from chemical reactions between CH_2O and NO_2 on gas-bubble temperature is relatively small because their mass fractions are relatively small; these species were consumed during ignition, and the rate of replenishment is low, as shown in Fig. 5. It should also be pointed out that the reduced chemical kinetic scheme has been developed to capture the highly exothermic reaction between CH_2O and NO_2 species; subsequent reactions among other species in the gas-phase region would add to the exothermicity of the ignition event.

Figure 4 also shows that almost a fourfold pressure increase occurs due to ignition. However, the pressure continues to rapidly increase after ignition, because of accelerated vaporization of the XM39 propellant and subsequent decomposition of gaseous RDX. Enhanced heat transfer rates by convection to the foam layer take place as density and temperatures rapidly increase. Figure 5 shows the rapid consumption of CH_2O and NO_2. The primary product species are NO and HCN, which are common dark zone species of nitramine-based propellant flames. It is also of interest to observe a combined mass fraction of acetylene and ethylene of about 2%; it is possible that these species are the precursors to soot formation, which has been observed in XM39 propellant flames, as well as in the formation of a carbonaceous residue on the burning surface of the XM39 propellant.

Go/No-Go Ignition Boundaries of XM39 Propellant:

The establishment of a go/no-go ignition boundary for XM39 propellant is of practical interest. Figure 6 illustrates a comparison of experimental data with calculated go/no-go ignition boundaries for XM39

propellant in different confined enclosures. The experimental setup, test procedure, and results are given in Refs. 12 and 14. Although the calculated go/no-go ignition boundaries of XM39 propellant for the range of spall fragment sizes tested are not in perfect agreement with the measured values, both the calculated and experimental results show that the go/no-go ignition boundary of the highly confined case is much lower than that of the partially confined condition. Several interesting ignition characteristics can be observed from Fig. 6. First, the minimum fragment temperature required for conductive ignition decreases with increasing fragment size, since more thermal energy can be stored in larger fragments. Second, ignition is most easily achieved if the system is highly confined with a very limited venting of pyrolyzed gases through a hole in the cartridge or exit port in simulation experiments. The reduction of the observed ignition threshold is believed to be caused mainly by the exothermic reaction between CH_2O and NO_2 species; their concentrations and collision rates are increased under chamber pressurization conditions, as indicated in the model solution. Third, the predicted go/no-go ignition boundaries are in reasonable agreement with experimental data; this implies that the chemical kinetic scheme employed in the calculation is quite adequate. Finally, the convergence of the two sets of ignition boundaries into one for the smaller size spall fragments (upper-left corner region of Fig. 6) corresponds to the ignition induced by chemical reactions occurring within gas bubbles of the foam layer beneath the surface of the hot spall fragment.

Summary and Conclusions

A model for predicting conductive ignition behavior of solid propellant in a confined environment has been developed and presented. The model, utilizing the reduced chemical kinetic scheme suggested by Brill [5] for RDX decomposition and associated kinetic rates by Melius [7], has been applied to study the ignition behavior of a composite nitramine propellant (XM39). The effects of initial temperature of hot fragment, size of hot fragment, and degree of confinement on ignition have been examined. In terms of go/no-go ignition boundaries and their dependency on the degree of confinement, reasonable agreement was obtained between the calculated and experimentally determined results. Major conclusions obtained are given below:

1. Ignition threshold of the highly confined case is significantly lower (by nearly 150 K) than that of the weakly confined case, especially for larger spall fragments.
2. Under a highly confined situation, the accumulation of pyrolysis products, such as NO_2 and CH_2O, can react exothermically in the enclosure, thereby inducing ignition at lower initial spall temperatures.
3. For very small spall fragments, ignition threshold becomes independent of the degree of confinement. This is believed to be caused by the shift of ignition location from the gas-phase region in the enclosure to the gas bubbles in the foam layer beneath the surface of high-temperature spall fragments.
4. The reduced chemical reaction mechanism proposed by Brill [5] appears to be quite adequate, based upon the reasonable agreement between the calculated and measured ignition boundaries.

Acknowledgments

This work was performed under Contract No. DAAL03-92-G-0020 and supported by Dr. D. M. Mann of the U.S. Army Research Office, Research Triangle Park, NC. The authors also gratefully acknowledge the support provided by Dr. J. M. Heimerl of the Army Research Laboratory, Aberdeen Proving Ground, MD.

Nomenclature

A	Arrhenius frequency factor of chemical reaction
A_{exit}	area of chamber exhaust port (m^2)
E	activation energy of chemical reaction (Kcal/g mole)
ΔH_r	heat of reaction (J/g)
L_s	height of spall particle (m)
M_{spall}	mass of spall (kg)
r_s	radius of spall particle (m)
T_g	bulk temperature of gas in chamber (K)
T_{gf}	mean gas-bubble temperature in foam layer (K)
T_{lf}	mean liquid temperature in foam layer (K)
T_{sb}	temperature of bottom surface of spall (K)
T_{si}	initial temperature of spall (K)

REFERENCES

1. Gol'dshleger, U. I., Pribytkova, K. V., and Barzykin, V. V., *Combust. Expl. Shock Waves* 9:99–102 (1973).
2. Tyler, B. J., and Jones, D. R., *Combust. Flame* 42:147–156 (1981).
3. Hsieh, K. C., Hsieh, W. H., Kuo, K. K., and Miller, M. S., *Proceedings of the Twenty-Fourth JANAF Combustion Meeting*, CPIA Publ. 476, Vol. 1, 1987, pp. 309–324.
4. Kuo, K. K., Hsieh, W. H., Hsieh, K. C., and Miller, M. S., *ASME J. Heat Trans.* 110:670–679 (1988).
5. Brill, T. B., in *Third International Symposium on Non-Intrusive Combustion Diagnostics* (K. Kuo and T. Parr, Eds.), Begell House Pub. Co., New York, 1994, to be published.

6. Palopoli, S. F., and Brill, T. B., *Combust. Flame* 87:45–60 (1991).
7. Melius, C. F., in *Chemistry and Physics of Energetic Materials* (S. Bulusu, Ed.), Kluwer Academic Publ., Dordrecht, The Netherlands, 1990, p. 51.
8. Wise, S., and Rocchio, J. J., *Proceedings of the Eighteenth JANAF Combustion Meeting,* CPIA Publ. 347, Vol. 2, 1981, pp. 305–320.
9. Miller, M. S., *Effective Ignition Kinetics for LOVA Propellant,* Ballistic Research Laboratory Report No. BRL-MR-3724, 1988.
10. BenReuven, M., Caveny, L. H., Vichnevetsky, R., and Summerfield, M., *Sixteenth Symposium (International) on Combustion,* The Combustion Institute, Pittsburgh, 1977, pp. 1223–1233.
11. Huang, T. H., Thynell, S. T., and Kuo, K. K., *Proceedings of the Thirtieth JANAF Combustion Subcommittee Meeting,* Monterey, CA, CPIA Publ. 606, Vol. 1, 1993, pp. 387–400.
12. Huang, T. H., "Partially Confined Hot Fragment Conductive Ignition Study of Nitramine-Based Propellants," Ph.D. Dissertation, The Pennsylvania State University, University Park, PA, 1994.
13. Hindmarsh, A. C., *Gear: Ordinary Differential Equations System Solver,* Lawrence Livermore Laboratory Report UCID-30001, Revision 3, 1974.
14. Huang, T. H., Thynell, S. T., and Kuo, K. K., *Proceedings of the Thirtieth JANAF Combustion Subcommittee Meeting,* Monterey, CA, CPIA Publ. 606, Vol. 1, 1993, pp. 401–412.

Twenty-Fifth Symposium (International) on Combustion/The Combustion Institute, 1994/pp. 1603–1608

SOLID-FUEL REGRESSION DURING IGNITION TRANSIENT IN A RAMJET

JING-TANG YANG AND CLIFF YUH-YIH WU*
Department of Power Mechanical Engineering
National Tsing Hua University
Hsinchu, Taiwan 30043, Republic of China

The transient regression and ignition of a solid fuel in a hot-oxidizing flow in a simulated combustor of a solid-fuel ramjet (SFRJ) were experimentally investigated. The local regression of solid fuel was measured at various intervals before ignition, and the controlled variables of the experiments were the inlet flow velocity, gas temperature, oxygen content, and step height. The maximum regression was located at 5.0–5.5 step heights from the entrance. The results of regression tests indicate that the influence of heat transfer was more important than the flow structure of the separated-reattaching flow. The regression rate increased with increasing the flow temperature and mass flow rate but decreased with increasing step height. The oxygen content had no significant influence on the regression before ignition. The transport phenomena in the combustor before ignition were closely related to the ignition mechanisms, which were diffusion control and chemical kinetics control. Diffusion control applied in the region of oxygen concentration greater than 20%, and the ignition delay decreased as pyrolyzed fuel vapor increased during the preignition period. Chemical kinetics control applied in the region of oxygen concentration less than 15%, and the flow feature of flame stabilization was more important than pyrolysis for decreasing the ignition delay.

Introduction

The solid-fuel ramjet (SFRJ) offers significant advantages of economy, simplicity, and good performance. However, it is difficult to control the transient process of solid-fuel ignition in a ramjet combustor because of the complicated flow field and heat transfer. Study of the ignition process thus becomes important for the design and development of a SFRJ.

The SFRJ combustor is simulated by a combustor with a two-dimensional backward-facing step. Sudden expansion of the incoming air generates the flow recirculation zone, which is necessary for flame stabilization. After reattachment of the flow directly behind the recirculation zone, a redeveloping boundary layer starts to build. The solid fuel pyrolyzes, and then the fuel vapor mixes and reacts with the air. Theories of ignition of solid fuel are classified as in the solid, heterogeneous, and gas phases [1]. It is generally agreed that ignition of solid fuels occurs in the gaseous phase [2–4]. Thus, the ignition process is expected to have an intimate relationship with the pyrolysis of solid fuel.

For flow over a backward-facing step, considerable work was reviewed by Eaton and Johnston [5]. The reattachment point was deduced to be 5–8 step heights downstream from the step [5,6]. The maximum rate of heat transfer to the solid surface occurred near the reattachment point [7–9]. Yogesh and Raghunandan [8] reported that the heat flux increased with increasing velocity of the free stream and decreased with increasing step height. Richardson et al. [10] conducted experiments in a SFRJ simulator with mass blowing on the wall behind a backstep and concluded that the size of the recirculation zone diminished with increased blowing. Combustion experiments with polymethylmethacrylate (PMMA) in a SFRJ conducted by Korting et al. [11] showed that the maximum regression was located at 8.5–9.5 step heights from the entrance; the regression rate increased with mass flux, content of oxygen in the oxidizer, temperature of the inlet air, and step height. Temporal data of local fuel regression measured by Zvulony et al. [12] indicated that the local rate of regression was closely related to the local convective heat flux.

Most previous work on combustion in solid-fuel ramjets stressed the global characteristics. Current understanding of local regression of the slid fuel during the ignition transient in a SFRJ is not thorough. The objective of this work is to study the interactions among the flow, heat transfer, regression, and mechanism of ignition in a SFRJ. Experiments were performed on the ignition process in a combustor with a backward-facing step by measurement of the local regression of solid fuel before ignition to relate it to mechanisms of ignition. The ignition of solid fuel by a hot flow was used to simulate the pyrogen igniter.

*Researcher of Mechanical Industry Research Laboratories, Industrial Technology Research Institute, Chutung, Hsinchu, Taiwan, currently a Ph.D. candidate at the Department of Power Mechanical Engineering, National Tsing Hua University.

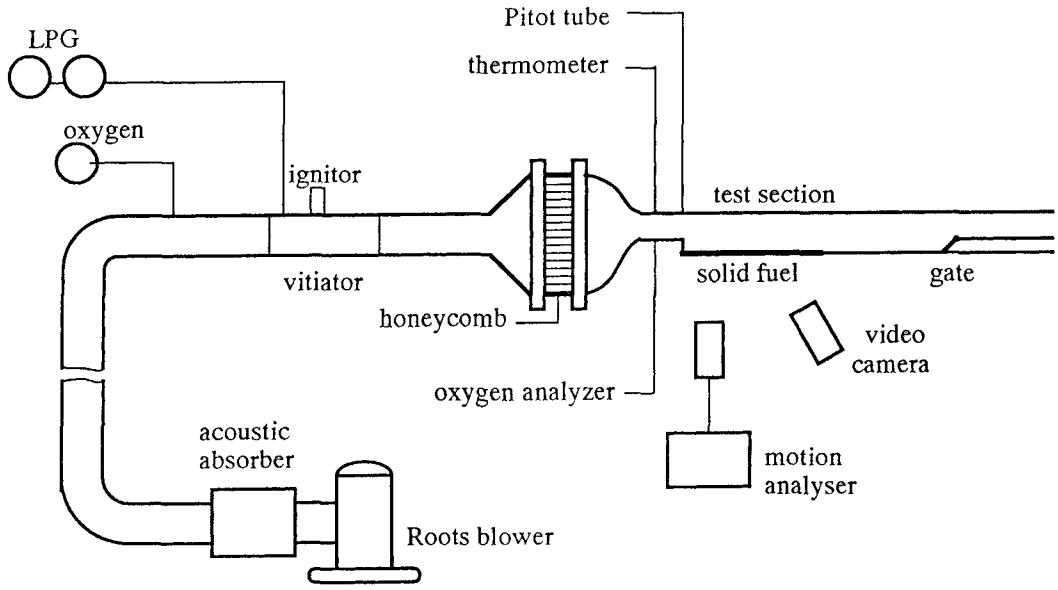

FIG. 1. Schematic diagram of the experimental apparatus.

Experimental Design

Test Rig and Instrumentation:

The experiments were performed in a wind tunnel that supplied a hot-oxidizing flow stream under specified conditions. A schematic diagram of the experimental apparatus appears in Fig. 1. The air flow was supplied by a 75-kW Roots blower with speed controlled by a frequency inverter (HITACHI). The blower provided a maximum flow rate of 50 m^3/min. An acoustic absorber was set behind the Roots blower to minimize pulsation of the flow. The hot-oxidizing gas was generated by burning liquefied petroleum gas (LPG) with air in a specially designed vitiator. Without addition of oxygen, its concentration in the hot flow was 12–15% depending upon the temperature at the inlet of the combustion chamber. The flow rates of LPG and oxygen were adjusted with needle valves and measured with rotameters to control the temperature and the concentration of oxygen in the hot gas. A divergent section, a settling chamber with stainless-steel honeycomb, and a convergent section with a contraction ratio of 13.6 were set before the test section to diminish the turbulence of the flow stream.

The cross section of the combustor entrance was 50-mm high and 200-mm wide. The aspect ratios (channel width to step height) for two step heights, 29 and 20 mm, were 6.9 and 10, respectively. A polymethylmethacrylate (PMMA) slab 10-mm thick, 400-mm long, and 110-mm wide was used as the fuel. The fuel slab was laid in the center of a steel supporter 400-mm long and 196-mm wide. The bottom and two sides of the fuel slab were connected with adiabatic material. Therefore, the difference of the fuel thickness between the centerline and the side was less than 5%. The properties of PMMA are listed in Table 1. Each side of the combustor was fitted with a quartz window to enable visual inspection of the ignition. When the inlet flow remained stable in the specified experimental conditions, the fuel slab with its supporter was slid promptly into the test section through the gate (Fig. 1) and slid out promptly after a prescribed duration of heating. The duration of heating was measured with a stop watch.

TABLE 1
Properties of the polymethylmethacrylate slab (Fernandez-Pello et al., 1981; Ref. 17)

Density	1.19 g/cm^3
Specific heat	2.1 J/(gK)
Thermal conductivity	0.0027 J/(cm s K)
Vaporization temperature	668 K
Effective heat of vaporization	1.6 kJ/g-fuel
Heat of reaction	13.5 kJ/g-oxidant
Activation energy	151 kJ/mol

The inlet velocity was measured with a Pitot tube. The temperature of the inlet gas was measured with a K-type thermocouple and a digital thermometer (FLUKE 2190A). The concentration of oxygen was measured with an oxygen analyzer (SIGNAL Model 8000). All inlet conditions were monitored just before the entrance of the combustion chamber. The

tested fuel slab was cut through the centerline, and the thickness along the centerline was measured with a calipers. The thickness of the fuel slab was uniform before heated, so the local regression could be determined by the variation of the thickness. The ignition delay was recorded by a video camera (SONY CCD-340) operating at 30 frames per second.

Test Conditions and Data Accuracy:

The local regression of solid fuel was determined at various intervals after the solid fuel was exposed to the hot flow in the combustor. In experiments on transient regression, the intervals of exposure were set at 100,200,300,400,500, and 600 s at inlet velocity 25 m/s, step height 29 mm, and gas temperatures 600 °C and 700 °C. At 800 °C, only intervals 100, 200, and 300 s of exposure were tested, because the ignition occurred at an exposure interval longer than 300 s.

The main parameters of the regression tests were the gas temperature (600 °C ~ 800 °C), flow velocity (20 ~ 45 m/s), oxygen concentration (13 ~ 25%, and step height (29 and 20 mm). The corresponding Reynolds numbers based on the inlet velocity and the step height were $3.2 \times 10^3 \sim 13.1 \times 10^3$. The ignition tests were performed at gas temperature 800 °C, oxygen concentrations 13 and 25%, step heights 29 and 20 mm, and various flow velocities. The maximum uncertainties of the ignition delay and the fuel regression were 7.3 and 4.3%, respectively.

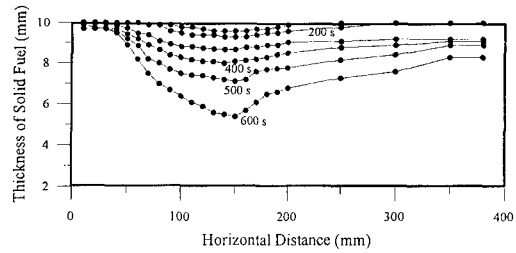

FIG. 2. Thickness of solid-fuel slab after various durations of heating: 100, 200, 300, 400, 500, and 600 s (inlet temperature 600 °C, step height 29 mm, flow velocity 25 m/s; uncertainty in fuel thickness is less than ±4.3%).

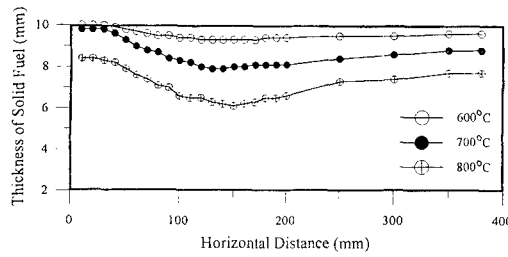

FIG. 3. Thickness of solid-fuel slab after 300 s of heating at inlet temperatures: 600 °C, 700 °C, and 800 °C (step height 29 mm, flow velocity 25 m/s; uncertainty in fuel thickness is less than ±4.3%).

Results and Discussion

Transient of Regression:

The solid fuel was heated from ambient temperature (about 25 °C) to the pyrolysis temperature (about 400 °C); then the rate of regression became larger. As the transport phenomena before a stable flame formed were transient, it is not feasible to take the average transport characteristics, such as rate of regression, species concentration, flow field, or profile of temperature. The instantaneous regression of solid fuel was measured instead, and the amount of fuel regression revealed the extent of pyrolyzed fuel vapor. The instantaneous regression values were obtained by running many repeated tests with various durations of heating. Figure 2 shows the fuel regression after 100–600 s of heating at the inlet temperature 600 °C and flow velocity 25 m/s; the original thickness of the solid fuel was 10 mm. The local convective heat transfer increased gradually from just downstream of the inlet step to a maximum of a few folds greater near the reattachment region. Further downstream, it decreased monotonically along the combustor [12]. The shape of the instantaneous rate of regression on the fuel surface exhibited similar variations along the horizontal direction, as shown in Fig. 2.

The maximum regression was located at 5.0–5.5 step heights from the inlet, which corresponded to the location of the reattachment point determined from the flame configuration after ignition [13]. The reattachment point is a kind of stagnation point, at which the redeveloping boundary layer began and also the convective heat transfer, and hence the regression rate was generally greater than at any other location [14]. In the region near the inlet step, the regression was small because of the locally small temperature and velocity. Downstream from the reattachment point, the growth of the boundary layer hampered the convective heat transfer and hence the rate of regression. This interpretation is consistent with the heat transfer analysis of Sparrow et al. [7].

The inlet temperature had a strong influence on the regression. Variations of the thickness of solid-fuel slab being heated for 300 s at a constant mass flux (91 g/s) of the flow with various temperatures are shown in Fig. 3. The regression at 800 °C was much greater than those at 600 °C and 700 °C, especially in the region near the inlet step. Ignition failed to occur even after the solid fuel was all pyrolyzed when the inlet flow temperature was 600 or 700 °C. The solid fuel was ignited after 621 s of heating, and the

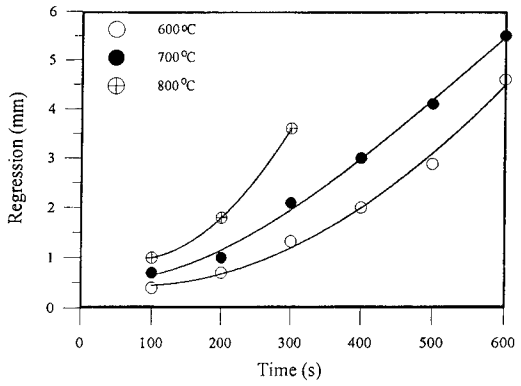

FIG. 4. Time dependence of the maximum regression of solid fuel at inlet temperatures: 600 °C, 700 °C, and 800 °C (step height 29 mm, flow velocity 25 m/s; uncertainty in fuel regression is less than ±4.3%).

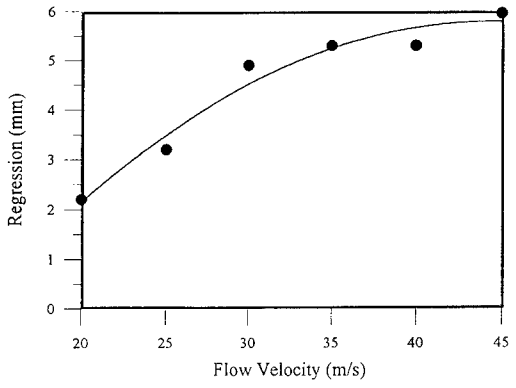

FIG. 5. Effect of flow velocity on the maximum regression of solid fuel at heating duration 400 s (inlet temperature 700 °C, step height 29 mm, flow velocity 25 m/s; uncertainty in fuel regression is less than ±4.3%).

ignition initiated near the step within the recirculation zone at the inlet conditions of temperature 800 °C, velocity 22 m/s, and step height 29 mm. The rate of regression is regarded as the slope of the curve of regression vs time in Fig. 4. In the initial period of heating, the regression rate was small but thereafter increased gradually. The rate of regression was much enhanced at flow temperature 800 °C.

Effect of Inlet Conditions:

Four parameters—flow velocity, gas temperature, oxygen content at the inlet, and step height—were systematically tested. The variation of the maximum regression with flow velocity after heating for 400 s at inlet temperature 700 °C is depicted in Fig. 5. The maximum regression increased with increasing flow

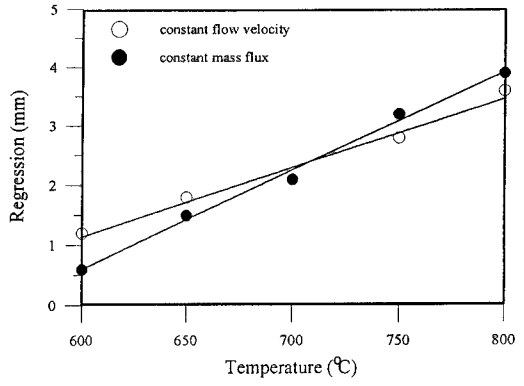

FIG. 6. Effect of inlet temperature on the maximum regression of solid fuel at two different conditions: velocity 25 m/s and mass flux 91 g/s (step height 29 mmm duration of heating 400 s; uncertainty in fuel regression is less than ±4.3%).

velocity. However, the rate of increase diminished as the flow velocity went up.

Figure 6 shows that the maximum regression increased nearly linearly with flow temperature. In addition, the slope of the curve at constant mass flux, which was 91 g/s based on 25 m/s at 700 °C, was greater than that at a constant velocity 25 m/s of flow. Hence, the influence of heat transfer on pyrolysis of solid fuel was more significant than the flow effect in the combustor.

The effect of oxygen concentration on regression was investigated at the inlet conditions of temperature 700 °C and velocity 25 m/s with the step height 29 mm and heating for 400 s. At the oxygen concentrations 15, 17.5, and 29% by volume, the maximum regressions were 3.0, 3.2, and 2.9 mm, respectively. There are no data for greater concentrations of oxygen because the solid fuel invariably ignited before being heated for 400 s. The results indicate that varying the oxygen concentration between 15 °C and 20 °C had no major influence on the regression of solid fuel before ignition. In previous work on combustion [11,15], the regression or rate vaporization generally increased with oxygen concentration because the oxygen stimulated the rate of combustion and hence the heat flux to the fuel. However, the consumption of oxygen was slight before ignition. The oxygen concentration thus did not affect the heat flux and hence the regression of solid fuel.

The effect of step on the regression of solid fuel is depicted in Fig. 7. The maximum regression with step heights 29 and 20 mm was located at 5.5 and 5.3 step heights from the step, respectively. The regression in the reattachment region with step height 20 mm exceeded that with step height 29 mm. At other places, the regressions for these two cases were nearly the same because of the same inlet tempera-

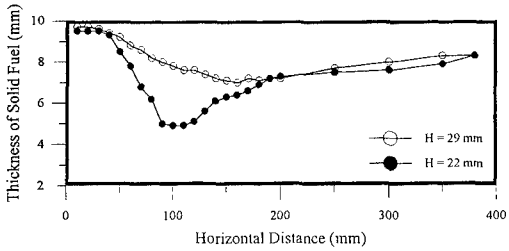

FIG. 7. Thickness of solid-fuel slab after 400 s of heating with step heights 29 and 22 mm (inlet temperature 700 °C, flow velocity 25 m/s; uncertainty in fuel regression is less than ±4.3%).

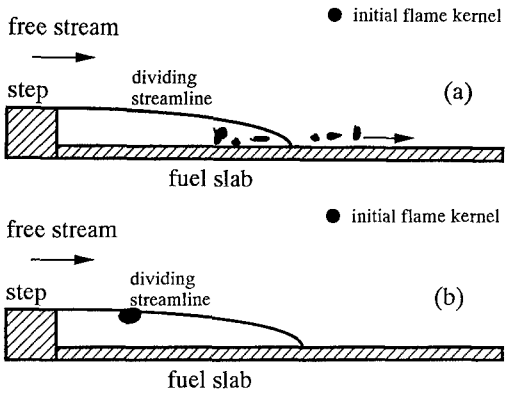

FIG. 8. Schematic diagrams of two controlling mechanisms of ignition: (a) ignition controlled by diffusion, (b) ignition controlled by chemical kinetics.

ture and mass flux. According to Fig. 7, the case of step height 20 mm produced more pyrolyzed fuel vapor in the reattachment region. The large regression with a small step corresponds to the study of heat flux from a hot gas stream to the wall performed by Yogesh and Raghumandan [8]. However, that conclusion conflicts with the result of the regression tests conducted by Korting et al. [11]. The discrepancy might be caused by the test conditions, which for the latter were a cold inlet flow with combustion in the test section.

Ignition Mechanisms:

Two control mechanisms of solid-fuel ignition in a sudden-expansion combustor were observed [13], diffusion control (Fig. 8a) and chemical kinetics control (Fig. 8b). They are identified by the concentration of oxygen in the inlet flow. The ignition with oxygen concentration greater than 20% was controlled by the diffusion process, because of a brief duration of chemical reaction. Diffusion of fuel vapor into the oxidizing gas was the rate-controlling step.

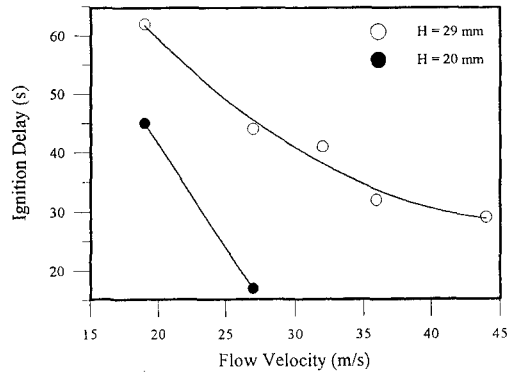

FIG. 9. Ignition delay with two step heights in the region of chemical kinetics control (inlet temperature 800 °C, oxygen concentration 13%; uncertainty in ignition delay is less than ±7.3%).

Consequently, the initial flame kernels formed in the reattachment region in which abundant fuel vapor was pyrolyzed. Conversely, chemical kinetics control applied when the oxygen concentration was less than 15 percent. The residence time was important for a mixture with a small rate of reaction, so the most suitable location for ignition was the recirculation zone.

The larger the step height, the better is the stabilization of the flame and the greater the residence time [16] of mixture in the recirculation zone. In the region of chemical kinetics control, the ignition delay with 29-mm step height was less than that with 20-mm step height (Fig. 9) due to the greater residence time. Decreased flow velocity decreased the ignition delay because it increased the residence time.

In the region of diffusion control, the initial flame kernels formed near the reattachment point, and the ignition delay depended upon the extent of diffusion of fuel vapor into the oxidizing gas. More fuel vapor pyrolyzed in the reattachment region with a 20-mm step height (Fig. 7). Therefore, the ignition delay with a 20-mm step height was shorter than that with a 29-mm step height (Fig. 10). Figure 10 also indicates that increased flow velocity decreased the ignition delay because it enhanced the rate of convective heating and then augmented the pyrolyzed fuel vapor. The maximum fuel regression vs flow velocity depicted in Fig. 5 related well to the ignition delay shown in Fig. 10.

Conditions with large fuel regression, which corresponded to the smaller step height in this experiment, favored ignition in the regime of diffusion control. Conversely, a flow with good flame stabilization, which corresponded to the greater step height, was more important than pyrolysis for ignition in the regime of chemical kinetics control.

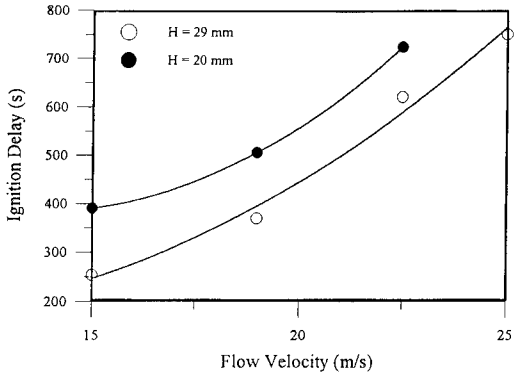

FIG. 10. Ignition delay with two heights in the region of diffusion control (inlet temperature 800 °C, oxygen concentration 25%; uncertainty in ignition delay is less than ±7.3%).

Conclusions

This work showed that the temperature of the inlet flow, mass flux, and step height directly affected the regression of solid fuel before ignition. The regression was slight in the region near the inlet step at which both the local temperature and velocity were small; it then increased to a maximum in the reattachment region, and decreased gradually downstream from that region because of the growth of the redeveloping boundary layer. The regression increased almost linearly with the inlet temperature. The most important factor to influence the regression was heat transfer from the hot flow to the solid fuel, and this was independent of oxygen content before ignition.

Two mechanisms of ignition on were confirmed in this work. Diffusion control applied in the region of oxygen concentration greater than 20%, and the initial flame kernels formed in the reattachment region in which maximum regression occurred. Chemical kinetics control applied in the region of oxygen concentration less than 15%, and the initial flame kernels formed in the recirculation zone in which the residence time of the mixture was great. Conditions with large fuel regression favored ignition in the regime of diffusion control, whereas a flow with good flame stabilization was more important than pyrolysis for ignition in the regime of chemical kinetics control.

Acknowledgments

This work was financially supported by Tsing Hua Fellowship and National Science Council of the Republic of China under Contracts Nos. NSC-82-0401-E-007-305 and CS-82-0210-D-007-013. The authors wish to acknowledge Mr. F. J. Yang and Mr. H. M. Law for their assistance in setting up the experiments.

REFERENCES

1. Price, C. W., Bradley, H. H., Jr., Dehority, G. L., and Ibiricu, M. M., *AIAA J.* 21:1565–1570 (1983).
2. Kumar, M., and Kuo, K. K., in *Fundamentals of Solid-Propellant Combustion* (K. K. Kuo and M. M. Summerfield, Eds.), Progress in Astronautics and Aeronautics, AIAA Inc., New York, 1984, Vol. 90, pp. 305–360.
3. Kashiwagi, T., Macdonald, B. W., Isoda, H., and Summerfield, M., *Thirteenth Symposium (International) on Combustion*, The Combustion Institute, Pittsburgh, 1971, pp. 1073–1085.
4. Kashiwagi, T., and Summerfield, M., *Fourteenth Symposium (International) on Combustion*, The Combustion Institute, Pittsburgh, 1973, pp. 1235–1247.
5. Eaton, J. K., and Johnston, J. P., *AIAA J.* 19:1093–1100 (1981).
6. Shishov, E. V., Roganov, P. S., Grabarnik, S. I., and Zabolotsky, V. P., *Int. J. Heat Mass Transfer* 31:1557–1562 (1988).
7. Sparrow, E. M., Kang, S. S., and Chuck, W., *Int. J. Heat Mass Transfer* 30:1237–1246 (1987).
8. Yogesh, G. P., and Raghunandan, B. N., *Int. J. Heat Mass Transfer* 32:19–28 (1989).
9. Seki, N., Fukusako, S., and Hirata, T., *J. Heat Transfer* 98:588–593 (1976).
10. Richardson, J., de Groot, W. A., Jagoda, J. I., Walterick, R. E., Hubbartt, J. E., and Strahle, W. C., *J. Propulsion* 1:488–493 (1985).
11. Korting, P. A., O. G., van der Geld, C. W. M., Wijchers, T., and Schoyer, H. F. R., *J. Propulsion* 6:263–270 (1990).
12. Zvulony, R., Gany, A., and Levy, Y., *J. Propulsion* 5:32–37 (1989).
13. Wu, C. Y. Y., and Yang, J. T., Paper ST-93-W.2.863, 44th Congress of the IAF, Graz, Austria, October 16–22, 1993.
14. van der Geld, C. W. M. Korting, P. A. O. G., and Wijchers, T., *Combust. Flame* 79:299–306 (1990).
15. Jakes, K. A., and Drews, M. J., *J. Polym. Sci.: Polym. Chem. Ed.* 19:1921–1936 (1981).
16. Bovina, T. A., *Seventh Symposium (International) on Combustion*, The Combustion Institute, Pittsburgh, 1958, pp. 692–696.
17. Fernandez-Pello, A. C., Ray, S. R., and Glassman, I., *Eighteenth Symposium (International) on Combustion*, The Combustion Institute, Pittsburgh, 1981, pp. 579–589.

Twenty-Fifth Symposium (International) on Combustion/The Combustion Institute, 1994/pp. 1609–1618

SUPERCRITICAL AND SUBCRITICAL COMBUSTION OF LOX WITH HYDROGEN IN AN AXISYMMETRIC LAMINAR DIFFUSION FLAME

AN-SHIK YANG, KENNETH K. KUO AND WEN H. HSIEH
Department of Mechanical Engineering
The Pennsylvania State University
University Park, PA 16802, USA

Combustion of liquid oxygen (LOX) with H_2 under super- and subcritical conditions was studied both theoretically and experimentally. In the theoretical work, a comprehensive model was formulated and solved numerically to simulate combustion processes of LOX, supplied from a circular tube at its rate of consumption, with ambient hydrogen gas flowing parallel to the axial direction of LOX-supplying tube. The model was based on the conservation equations for a multicomponent system, with consideration of gravitational body force, solubility of ambient gases in liquid, and variable thermophysical properties. A fugacity-based multicomponent thermodynamic analysis with quantum-gas mixing rules was carried out to characterize the solubility of ambient gas at the LOX surface. A stable onion-shaped LOX/H_2/He diffusion flame was achieved at a pressure of 30 atm. The calculated flame shape agreed well with the shape of the observed luminous flame. Under a supercritical combustion situation at 68 atm, the calculated flame shape exhibited a pearlike contour. From the simulation results, it was found that two counter-rotating vortex structures existed in the flame region due mainly to the combustion-induced baroclinic torque as well as buoyancy-induced flow acceleration and entrainment of the surrounding H_2/He mixture. From the comparison of calculated results using the flame-sheet model and those based upon equilibrium calculations, the flame-sheet model was found to be able to predict the location of the flame front as well as distributions of temperature, velocity, and major constituent species with reasonable accuracy.

Introduction

Liquid oxygen (LOX) and hydrogen have been used in various types of liquid rocket engines because of their high specific impulse and low exhaust pollution.The oxygen and hydrogen are usually injected into a combustion chamber inside a liquid rocket engine. Through the large shear force between the fuel and oxidizer streams, the primary atomization of oxygen is accomplished to form a spray of droplets. The large liquid oxygen droplets then go through secondary atomization, evaporation, and combustion processes at pressures far beyond their thermodynamic critical point. Numerous flow and chemical complexities have attracted significant attention from many researchers [1–9]. Experiments have been carried out to determine the effects of important factors such as droplet size, environmental pressure and temperature, and composition of the ambient gas on the combustion characteristics. Theoretical models have also been presented to elucidate experimental observations and predict burning rate and/or lifetime of droplets. However, the underlying mechanisms in the phenomena associated with liquid jet breakup, atomization, droplet interaction, and droplet evaporation and combustion in high-pressure environments still remain uncertain and need further investigation [10]. Among these unresolved areas, the fundamental study on the evaporation and chemical reaction processes of liquid oxygen droplets with hydrogen under the supercritical condition plays a vital role in advancing the knowledge of overall spray combustion. Therefore, the present research is motivated to explore the transport behavior and structure of a LOX/H_2/He diffusion flame at elevated pressures. There are two reasons for considering H_2/He mixtures: (1) H_2/He is more safe to handle than pure H_2 and (2) the diffusion characteristics of He are close to that of H_2 due to the proximity of their molecular weights.

One of the major obstacles involved in evaporation and combustion studies of a single LOX droplet is that the size of the droplet in a spray is usually too small to allow detailed measurements of flow properties in its neighborhood. To overcome this problem, an alternative liquid strand test setup was employed [11,12]. The basic concept is that the evaporation and combustion processes of oxygen droplets can be studied much more easily by considering a limiting case in which the radius of curvature of a droplet is very large. The limiting condition is achieved by keeping the top surface of a column of liquid oxygen at a fixed location.

Meanwhile, H_2/He mixture is supplied through a

porous plate in the circumferential region surrounding the center tube for LOX. Hence, an axisymmetric diffusion flame can be established above the exit port of the oxygen feeding tube, and the burning behavior of LOX with hydrogen under broad ranges of pressure and temperature can be fully characterized using various combustion diagnostic tools.

In the past, there have been very few fundamental studies on the combustion process of LOX because of the difficulties in handling cryogenic fluids. The overall objective of this investigation is to achieve a better understanding of the combustion process of liquid oxygen with a gaseous hydrogen/helium mixture under high-pressure conditions.

Theoretical Formulation and Numerical Method

Physical Model and Governing Equations:

A comprehensive theoretical formulation has been carried out to study combustion characteristics of LOX with a hydrogen/helium mixture under supercritical conditions. The physical model considers the cylindrical reacting flow field above the porous plate, including the intense reacting diffusion flame formed at the port of the LOX feeding tube (see Fig. 1). Steady-state calculations were performed by considering the LOX being supplied at a certain feeding rate that kept its surface stationary. The gaseous oxygen and hydrogen react and form a diffusion flame anchored near the exit of the inner tube.

The model consists of a set of conservation equations for a multicomponent system with consideration of gravitational body force, ambient gas solubility, and variable thermophysical properties. To allow diffusion in the axial direction, the present approach treats the fully elliptic problem. The governing equations were derived under the following assumptions: (1) flows are steady state, (2) flow field is axisymmetric, (3) viscous dissipation is neglected, (4) Dufour and Soret effects are insignificant, (5) effects of radiative heat transfer and turbulence are negligible, (6) Fick's law of mass diffusion is valid, and (7) the LOX surface is in thermodynamic phase equilibrium. The governing equations are given below.

Continuity equation:

$$\frac{\partial}{\partial x}(\rho u) + \frac{\partial}{r\partial r}(\rho r v) = 0. \tag{1}$$

x-Momentum equation:

$$\frac{\partial \rho u u}{\partial x} + \frac{\partial \rho v r u}{r\partial r} = -\frac{\partial P}{\partial x} - \rho g - \frac{2}{3}\frac{\partial}{\partial x}(\mu \nabla \cdot \mathbf{V}) + \frac{\partial}{\partial x}\left(2\mu \frac{\partial u}{\partial x}\right) + \frac{\partial}{r\partial r}\left[r\mu\left(\frac{\partial u}{\partial r} + \frac{\partial v}{\partial x}\right)\right]. \tag{2}$$

r-Momentum equation:

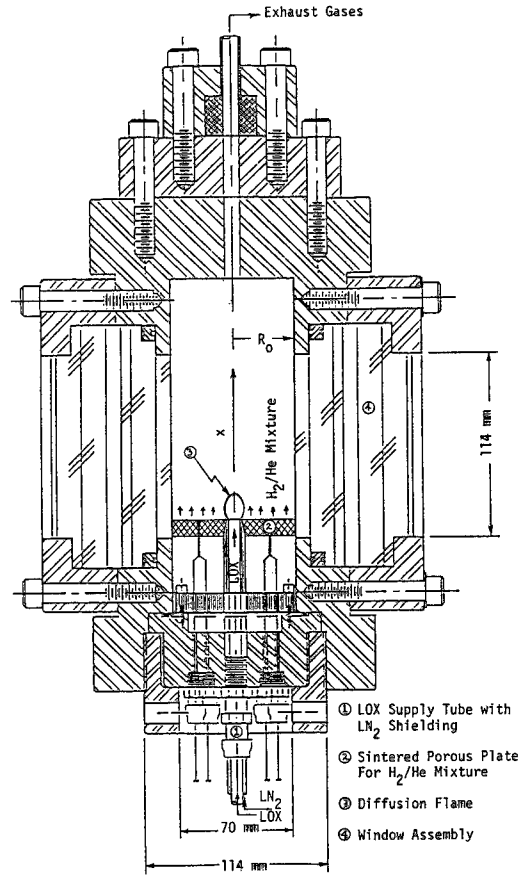

FIG. 1. Cross-sectional view of windowed high-pressure combustor.

$$\frac{\partial \rho u v}{\partial x} + \frac{\partial \rho v r v}{r\partial r} = -\frac{\partial P}{\partial r} - 2\mu\frac{v}{r^2} - \frac{2}{3}\frac{\partial}{\partial r}(\mu \nabla \cdot \mathbf{V}) + \frac{\partial}{\partial x}\left[\mu\left(\frac{\partial u}{\partial r} + \frac{\partial v}{\partial x}\right)\right] + \frac{\partial}{r\partial r}\left(2r\mu\frac{\partial v}{\partial r}\right) \tag{3}$$

where

$$\nabla \cdot \mathbf{V} = \frac{\partial u}{\partial x} + \frac{\partial r v}{r\partial r}. \tag{4}$$

Energy equation:

$$\frac{\partial \rho u h}{\partial x} + \frac{\partial \rho v r h}{r\partial r} = u\frac{\partial P}{\partial x} + v\frac{\partial P}{\partial r} + \rho\sum_{i=1}^{N} g D_{im}\frac{\partial Y_i}{\partial x} + \frac{\partial}{\partial x}\left(\frac{\lambda}{C_p}\frac{\partial h}{\partial x}\right) + \frac{\partial}{r\partial r}\left(r\frac{\lambda}{C_p}\frac{\partial h}{\partial r}\right) + \frac{\partial}{\partial x}\sum_{i=1}^{N}\left(\rho D_{im} - \frac{\lambda}{C_p}\right)h_i\frac{\partial Y_i}{\partial x}$$

$$+ \frac{\partial}{r\partial r} \sum_{i=1}^{N} r\left(\rho D_{im} - \frac{\lambda}{C_p}\right) h_i \frac{\partial Y_i}{\partial r} \quad (5)$$

where h stands for the specific enthalpy of the gas mixture, defined as

$$h = \sum_{i=1}^{N} Y_i h_i = \sum_{i=1}^{N} \left(h_{f,i}^{\circ} + \int_{T_{\text{ref}}}^{T} C_{p,i}\, dT\right) Y_i. \quad (6)$$

ith species equation:

$$\frac{\partial \rho u Y_i}{\partial x} + \frac{\partial \rho v r Y_i}{r\partial r} = \frac{\partial}{\partial x}\left(\rho D_{im} \frac{\partial Y_i}{\partial x}\right) + \frac{\partial}{r\partial r}\left(r\rho D_{im} \frac{\partial Y_i}{\partial r}\right) + \dot{\omega}_i \quad (7)$$

The ideal-gas law was used to solve the gaseous density. However, near the LOX surface, the temperature of the mixture may drop to 90 K. Because the ideal-gas equation could lead to some errors in determining gaseous density at low temperatures, a ninth-order polynomial was used for density calculations in the 90–250 K range [13].

$$\rho = \sum_{n=0}^{9} c_n T^n = c_0 + c_1 T + c_2 T^2 + \ldots + c_9 T^9 \quad (8)$$

where coefficients c_n are functions of pressure.

Combustion Model:

In consideration of the source term in the species equations, the flame-sheet approximation was adopted as one of the options available in describing the laminar diffusion-flame structure. Other options included chemical equilibrium approximation and, if necessary, a set of full-blown detailed H_2/O_2 chemical kinetics model. Although it is fashionable to apply complex chemical kinetics to combustion problems, the authors believe that this is not always necessary for all combustion problems. In this study, the flame zone was mainly characterized by a very low Mach number flow yet having a fast H_2/O_2 reaction rate. Hence, the assumption of infinitely fast chemistry can be considered very reasonable. In the approach of infinitely fast kinetics, the combustion process was modeled by a single irreversible reaction. The following mixture fraction equation was utilized:

$$\frac{\partial \rho u \zeta}{\partial x} + \frac{\partial \rho v r \zeta}{r\partial r} = \frac{\partial}{\partial x}\left(\rho D_{Fm} \frac{\partial \zeta}{\partial x}\right) + \frac{\partial}{r\partial r}\left(r\rho D_{Fm} \frac{\partial \zeta}{\partial r}\right) + \frac{(F/O)_{st}}{(\beta_F - \beta_O)} \left\{\frac{\partial}{\partial x}\left[\rho(D_{Fm} - D_{Om}) \frac{\partial Y_O}{\partial x}\right] + \frac{\partial}{r\partial r}\left[r\rho(D_{Fm} - D_{Om}) \frac{\partial Y_O}{\partial r}\right]\right\} \quad (9)$$

where

$$\beta = Y_F - (F/O)_{st} Y_O \quad (10)$$

and ζ represents the mixture fraction, defined according to Ref. 14 as

$$\zeta = \frac{\beta - \beta_O}{\beta_F - \beta_O} = \frac{[Y_F - (F/O)_{st} Y_O] - [Y_F - (F/O)_{st} Y_O]_O}{[Y_F - (F/O)_{st} Y_O]_F - [Y_F - (F/O)_{st} Y_O]_O}. \quad (11)$$

Solving the transport equations of mixture fraction and the mass fraction of the diluent species (helium) together with other conservation equations, the distributions of thermodynamic and flow properties were determined. The mass fractions of various chemical species were then computed from Eq. (11). The flame front location was also identified.

Boundary Conditions:

Since the conservation equations are elliptical in form, appropriate boundary conditions for each dependent variable must be specified in accordance with experimental conditions. In this study, the flow properties of the LOX surface and the surrounding purge flow at the inlet were set to be uniform and treated as input parameters, based upon flow rate and local temperature measurements.

At inlet plane ($x = 0$), for $r < R_I$:

$$u = u_+, \quad v = 0, \quad h = h_+, \quad Y_i = Y_{i+}, \quad \zeta = \zeta_+. \quad (12)$$

At inlet plane ($x = 0$), for $R_I < r < R_o$:

$$u = u_0, \quad v = 0, \quad h = h_0, \quad Y_i = Y_{i0}, \quad \zeta = \zeta_0. \quad (13)$$

Along the axis of symmetry ($r = 0$):

$$\frac{\partial u}{\partial r} = \frac{\partial h}{\partial r} = \frac{\partial Y_i}{\partial r} = \frac{\partial \zeta}{\partial r} = 0 \quad \text{and } v = 0. \quad (14)$$

At wall ($r = R_O$):

$$u = v = \frac{\partial h}{\partial r} = \frac{\partial Y_i}{\partial r} = \frac{\partial \zeta}{\partial r} = 0. \quad (15)$$

TABLE 1
Methods employed for evaluation of thermodynamic and transport properties

Property	Baseline method[a]	High-pressure correction[b]	Mixing rule[c]
Specific heat	Fourth-order polynomial of temperature[d]	Sychev et al. [13]	Mass fraction weighting
Viscosity	Lucas [15]	Lucas [15]	Lucas [15]
Thermal conductivity	Fourth-order polynomial of temperature[d]	Laesecke et al. [16]	Mole fraction weighting
Diffusion coefficient	Chapman and Cowling [17]	Takahashi [18]	Wilke [19]

[a]For pure component at low-to-moderate pressure.
[b]For pure component.
[c]For mixture.
[d]Coefficients of polynomials are fitted from the data of Daubert and Danner [20] as well as McBride and Zeleznik [21].

At a large distance from the outlet station ($x = L$), the flow field becomes much more uniform than the flame region; therefore, the axial variations of dependent variables are negligible. Also, the radial velocity component becomes negligible at such a large distance; hence,

$$\frac{\partial u}{\partial x} = \frac{\partial h}{\partial x} = \frac{\partial Y_i}{\partial x} = \frac{\partial \zeta}{\partial x} = 0 \quad \text{and } v = 0. \tag{16}$$

Evaluation of Thermodynamic and Transport Properties:

In order to simulate various realistic features involved in the evaporation and combustion processes of LOX, the pressure and temperature dependence of thermophysical properties must be treated properly. In this study, the specific heat of each species was determined from a fourth-order polynomial of temperature. Different sets of coefficients taken from the experimental correlations of Sychev et al. [13] were used for high-pressure correction. The specific heat of the mixture was calculated using the mass-fraction weighted method. Table 1 outlines the methods employed for evaluation of thermodynamic and transport properties. These properties were first calculated as functions of temperature and pressure for each constituent species. Properties for the mixture were subsequently determined by means of appropriate mixing rules.

High-Pressure Phase Equilibrium:

To determine the species-concentration boundary conditions for each species immediately above the liquid surface [Eq. (12)], thermodynamic phase equilibrium is imposed upon the gas/liquid interface. In high-pressure environments, a fugacity-based multicomponent thermodynamic analysis for vapor-liquid phase equilibrium must be conducted to fully account for ambient gas solubility and real gas effects. The high-pressure vapor-liquid equilibrium relationships for each component can be expressed as

$$f_i^{(v)} = f_i^{(l)} \tag{17}$$

$$T^{(v)} = T^{(l)}. \tag{18}$$

The fugacity for species i can be integrated through the following relation [22].

$$P^{(v)} = P^{(l)} \tag{19}$$

$$R_u T \ln\left(\frac{f_i}{X_i P}\right) = \int_V^\infty \left[\left(\frac{\partial P}{\partial n_i}\right)_{T,V,n_j} - \frac{R_u T}{V}\right] dV - R_u T \ln Z \tag{20}$$

To compute the integral term in Eq. (20), the Redlich-Kwong (R-K) equation of state was employed. The two mixture parameters in the cubic-type R-K equation of state were determined from quantum-gas mixing rules [22].

Numerical Algorithm:

The aformentioned governing equations and boundary conditions were solved using an iterative SIMPLE (semi-implicit method for pressure-linked

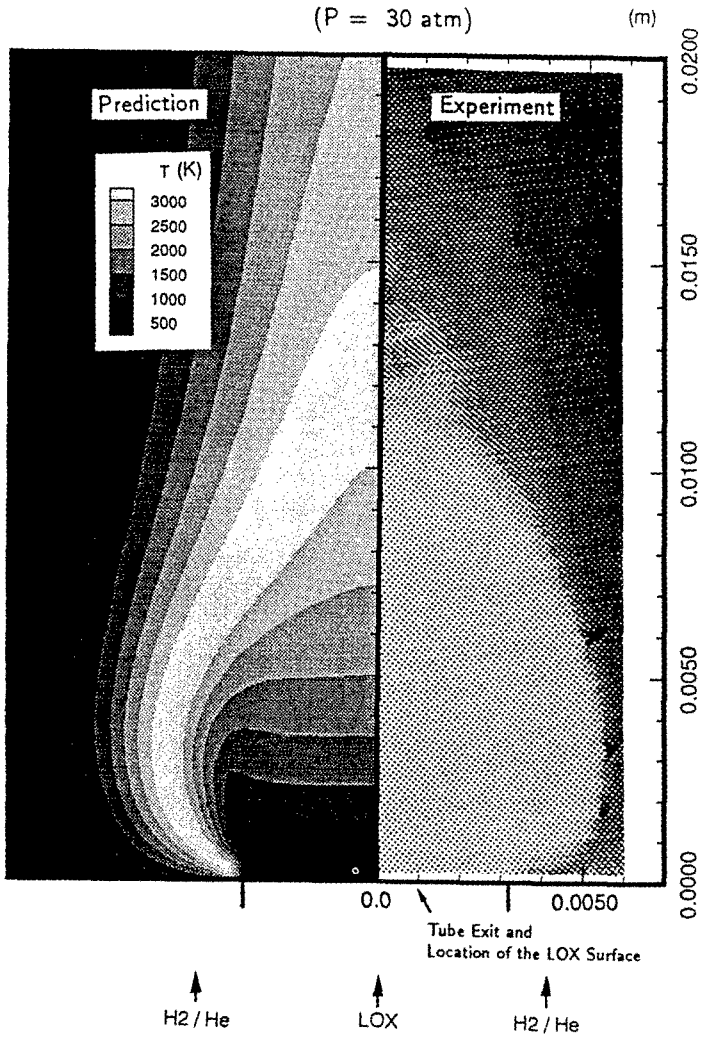

FIG. 2. Predicted and experimentally observed flame shape with an oxygen supply rate of 0.024 gm/s at a pressure of 30 atm (subcritical combustion).

equations) algorithm [23]. To implement a finite control-volume approach, the partial differential equations were first integrated over discrete cells formed by the numerical grids. The line-by-line tridiagonal matrix algorithm (TDMA) method was employed to solve the resulting discretization equations for the entire calculation domain. Because of the staggered grid arrangement, velocity grids were segregated from scalar grids and lie directly on the surfaces of the control volumes. The power-law scheme was applied to model both convective and diffusive fluxes across the faces of two finite-difference cells. The harmonic-mean technique for various transport properties at the interface between cells was incorporated in accurately represent the diffusion-flux terms over adjacent control volumes. To avoid divergence during the iterations, underrelaxation was also adopted, with a factor of 0.6 for pressure and 0.4 for all other dependent variables. A more detailed numerical solution procedure is given in Ref. 12.

Experimental Apparatus

In this study, the experimental setup consists of a (1) a windowed high-pressure test chamber, (2) computerized chamber pressure control system, (3) LOX feeding system, (4) gas supply system, (5) igniter, (6) multichannel data acquisition system, and (7) various safety devices. For the gas-pressurized LOX feeding system, gaseous oxygen was delivered into a cylinder immersed in the liquid nitrogen bath. Cooled by liquid nitrogen, the oxygen was liquefied and eventually filled the interior space of the cylinder serving as a reservoir for LOX. By adjusting the opening of a micrometering valve, the LOX mass consumption rate

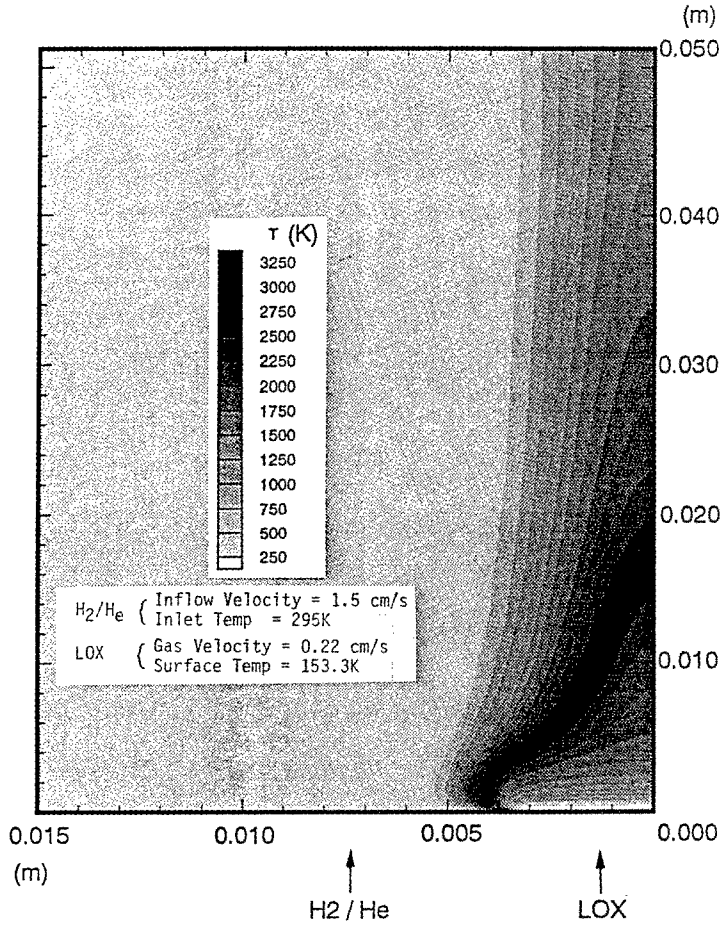

FIG. 3. Temperature contour for the coflowing LOX/hydrogen/helium laminar diffusion flame at a pressure of 68 atm (supercritical combustion).

was controlled to maintain a stable surface at the exit of the LOX feeding tube (6.35-mm diameter) under prespecified steady-state operating conditions. The chamber pressure was maintained at a prespecified level by a computer feedback-controlled gas supply system. A quartz gas-sampling probe was used in conjunction with fast actuating valves to extract samples of combustion products from given locations for GC analysis. Several J-type thermocouples were installed at various locations in the test rig. A detailed description of various components of the experimental setup as well as temperature and oxygen concentration and flow rate measurements can be found in Refs. 11 and 12.

Discussion of Results

In the combustion tests, a stable onion-shaped LOX/H_2/He diffusion flame was achieved at a pressure of 30 atm. The laminar diffusion flame studied had oxygen, hydrogen, and helium supply rates of 0.018, 0.052, and 0.12 gm/s, respectively. The LOX surface was below the exit of the feeding tube by about 1.5 mm. The position of the LOX surface was determined by traversing the thermocouple for surface temperature measurement along the center of the LOX supply tube. To raise the LOX surface to the port of the feeding tube, the oxygen supply rate was gradually increased. When the LOX surface approached the tube exit, the region near the tube rim was cooled down to a greater extent by the LOX. This decrease in temperature caused increase of heat loss from the flame as well as reduction of radical concentrations in chemical reactions, and thus, the flame tended to detach from the tube rim. This quenching effect sometimes even cawed extinguishment of the flame. Due to the sensitive flame holding behavior, establishment of a stable diffusion flame at the exit of the LOX feeding tube was found to be much more difficult than in the case of GOX/H_2/He diffusion flame. Attempts were also made to conduct in situ observation of the LOX surface during combustion; however, due to the brightness of the diffusion flame, the surface region cannot be clearly observed.

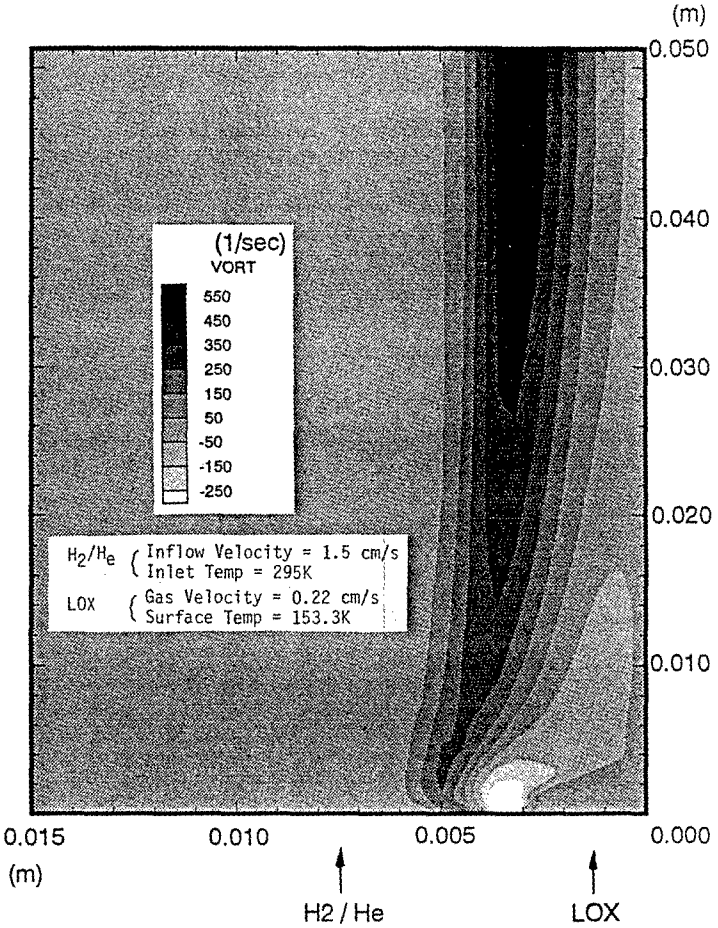

FIG. 4. Vorticity contour for coflowing LOX/hydrogen/helium laminar diffusion flame at a pressure of 68 atm.

To verify the axisymmetric steady-state combustion code, several numerical simulations were conducted; one corresponds to the LOX surface fixed at the exit of the feeding tube. Boundary conditions wed in this case correspond to those given in Eqs. (12) and (13), with the gas velocity above the LOX surface at 0.7 cm/s. Figure 2 presents the predicted and observed flame shape at a pressure of 30 atm. It should be noted that this flame picture represents an image before gradual detachment of the flame from the tube rim. From fine-wire thermocouple measurements, the LOX surface temperature was found to be 136.2 K. The temperature of the surrounding hydrogen/helium mixture was 295 K. In general, the calculated flame shape was in reasonable agreement with the observed luminous flame surface. To study the influence of the LOX surface position on the flame shape, another simulation was carried out for the case in which the LOX surface was maintained 1.5 mm below the exit of the feeding tube. In this case, the gas velocities of the H_2/He mixture and vaporized LOX were 1.5 and 0.523 cm/s, respectively. The oxygen mass fraction at the LOX surface was determined to be 0.981 from phase equilibrium analysis. Comparison between predicted and experimentally observed steady flame shape for the coflowing LOX/H_2/He laminar diffusion flame also showed close agreement [12]. The measured radial hydrogen concentration distributions in the stations beyond the flame height where the quartz probe can survive also matched well with predicted results [12].

In order to explore the flame structure of a LOX/H_2/He laminar diffusion flame, the theoretical model and numerical scheme described in previous sections were adopted to study the combustion process of LOX in the surrounding flow of a hydrogen/helium mixture (with a mass ratio of 30/70) at a pressure of 68 atmospheres. The phase equilibrium analysis was used to determine boundary conditions of species concentration at the LOX surface.

Figure 3 shows temperature contours with respect to both axial and radial coordinates. The calculated peak temperature along the centerline was about 3310 K. The flame height, defined as the location of the peak centerline temperature, was found to be 1.66 cm above the tube exit. Steep axial temperature

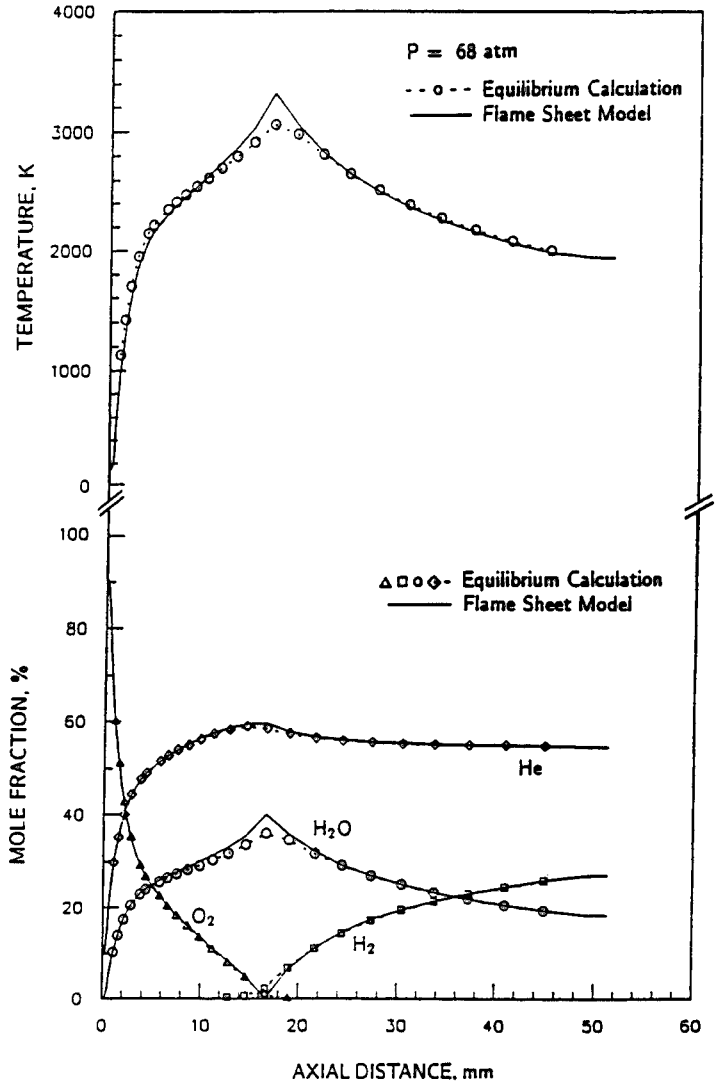

FIG. 5. Comparison between equilibrium calculations and predicted centerline temperature, oxygen (O_2) hydrogen (H_2), water vapor (H_2), and helium (He) profiles (P = 68 atm).

gradients were noted in the vicinity of the LOX surface, indicating a strong heat feedback from the flame to the LOX surface to provide the energy required in the phase change of oxygen from a compressed liquid to a superheated vapor. The buoyancy force accelerates the flow in the reaction zone thereby increasing the entrainment of the surrounding H_2/He mixture. This suctionlike effect induces an inward radial flow motion near the port exit plane to enhance combustion and drive the flame closer to the centerline. Therefore, the flame contour becomes pear-shaped instead of onion-shaped.

The calculated water vapor mass fraction contours (not shown here) are very similar [12] to those shown in Fig. 3. The flame envelope separated oxygen above the LOX feeding tube from the surrounding hydrogen. Oxidizer and fuel diffused in opposite directions toward the flame zone and reacted very near the stoichiometric interface. In the meantime, helium, the diluent species, penetrated through the flame envelope and reached the LOX surface, and as a result, the helium could dissolve in the LOX at high-pressure conditions.

In a diffusion flame, the vorticity field plays an important role in characterizing the mixing and combustion processes. Figure 4 exhibits the vorticity contour for the coflowing LOX/hydrogen/helium laminar diffusion flame at a pressure of 68 atm. Two counterrotation vortex compartments, generated by buoyancy-induced flow acceleration, were distinctly observed inside a center column. The location of the interface boundary of these two compartments was

in accordance with the flame envelope. Originating from the inner side of the tube rim, the negative vortex region displayed a clockwise rotational pattern. Across the flame, the fluid in the positive vortex region tended to flow toward the centerline.

Having described the vortex structure of the flame, the vorticity generation mechanism and transport process were further examined. It was found that the vorticity dilation ($\Omega\nabla\cdot V$) and baroclinic torque ($\nabla\rho \times \nabla P/\rho^2$) terms in the vorticity equation play important roles in the vorticity distribution. The vorticity dilation is related to the effect of variable density in the fluid. A positive value of the vortex dilation leads to a decrease in the magnitude of vorticity. The baroclinic torque represents the generation of vorticity through a nonalignment of the density and pressure gradients; these effects are usually negligible for a nonreacting low Mach-number flow. However, in this combustion problem, these two terms can be significant due to the existence of strong density variations. As reported in Ref. 12, the amplitude of both vorticity dilation and baroclinic torque grew considerably as a consequence of heat release. It was also noted that the magnitude of the baroclinic torque was substantially larger than that of the vorticity dilation. This indicates that the vorticity field is generated mainly by misalignment of density and pressure gradients in the flame.

In order to examine the degree of broadening of the reaction zone resulting from dissociation, the predicted centerline temperature and species-concentration distributions from the flame-sheet model have been compared with those of equilibrium calculations (see Fig. 5). Below 2800 K, the difference was found to be within 2.5%. However, the flame-sheet model overpredicted the peak temperature by 8.5% at the axial location of the flame front (x = 1.66 cm). For species profiles along the centerline, the oxygen and hydrogen were observed to diffuse toward the thin reaction zone where the water vapor concentration attained its maximum value. The rounding of the temperature profile, as well as the coexistence of the oxygen and hydrogen in the narrow flame zone, indicates a reaction-zone broadening due to the dissociation effect at high temperatures.

Conclusions

1. Under a subcritical condition at p = 30 atm, an onion-shaped LOX/H_2/He diffusion flame was observed experimentally. The calculated flame shape was found to agree well with the shape of the observed luminous flame.
2. Under a supercritical condition at p = 68 atm, the calculated flame shape exhibited a pearlike contour. This is caused mainly by the buoyancy-generated entrainment of surrounding fuel mixture toward the centerline of the burner.
3. The chemically reacting flow field was found to be influenced strongly by the vorticity field governed by the combustion-induced baroclinic torque and vorticity dilatation effects.
4. The predicted results using the flame-sheet approach compared very closely with those based upon full equilibrium calculations, except a minor deviation of temperature and water vapor concentration from their equilibrium values in the neighborhood of the flame front due to the effect of high-temperature dissociation.

Nomenclature

C_p	constant-pressure specific heat
D_{im}	effective mass diffusivity of species i
D_{ij}	binary mass diffusivity
f	fugacity
h	enthalpy
h_f	heat of formation
L	length for computational domain
N	total number of species
n_i	number of moles of species i
P	pressure
R_I, R_O	inner and outer radius for computational domain
R_u	universal gas constant
r	coordinate in transverse direction
T	temperature
u, v	velocity components in x and r directions
V	total volume or velocity vector
W	molecular weight
x	coordinate in axial direction
X	mole fraction
Y	mass fraction
Z	compressibility factor
Greek Symbols:	
a	thermal diffusivity
ζ	mixture fraction
Ω	vorticity
Superscripts:	
$(\ )^{(l)}$	liquid phase
$(\ )^{\circ}$	ideal state
$(\ )^{(v)}$	vapor phase
Subscripts:	
$(\ )_i$	species i
$(\ )_0$	gas-phase inlet conditions of surrounding purge flows
$(\ )_s$	surface value
$(\ )_+$,$(\ )_-$	interfacial conditions on gas and liquid sides

Acknowledgments

This research was sponsored by the Marshall Space Flight Center (MSFC), the National Aeronautics and Space Administration, and the Propulsion Engineering Re-

search Center (PERC) of The Pennsylvania State University. The encouragement and support of Mr. Klaus Gross of MSFC are acknowledged.

REFERENCES

1. Williams, A., *Combust Flame* 21:1–31 (1973).
2. Faeth, G. M., *Prog. Energy Combust. Sci.* 3:191–224 (1977).
3. Law, C. K., *Prog. Energy Combust. Sci.* 8:171–201 (1982).
4. Sirignano, W. A., *Prog. Energy Combust. Sci.* 9:291–322 (1983).
5. Hsieh, K. C., Shuen, J. S., and Yang, V., *Combust. Sci. Technol.* 76:111–132 (1991).
6. Shuen, J. S., and Yang, V., "Combustion of Liquid-Fuel Droplets in Supercritical Conditions," AIAA Paper No. 91–78, 1991.
7. Litchford, R. J., and Jeng, S. M., "LOX Vaporization in High-Pressure, Hydrogen-Rich Gas," AIAA Paper No. 90–2191, 1990.
8. Delplanque, J. P., and Sirignano, W. A., "Transient Vaporization and Burning for an Oxygen Droplet at Sub- and Near-Critical Conditions," AIAA Paper No. 91–75, 1991.
9. Yang, V., Lin, N. N., and Shuen, J. S., "Vaporization of Liquid Oxygen (LOX) Droplets at Supercritical Conditions," AIAA Paper No. 92–103, 1992.
10. Chiu, H. H., and Gross, K. W., "Liquid Behavior at Critical and Supercritical Conditions," JANNAF Workshop Summary, Irvine, CA, 1986.
11. Yang, A. S., Hsieh, W. H., Kuo, K. K., and Brown, J. J., "Evaporation of LOX Under Supercritical and Subcritical Conditions," AIAA Paper No. 93–2188, 1993.
12. Yang, A. S., "Combustion of LOX with $H_{2(g)}$ under Subcritical and Supercritical Conditions," Ph.D. Thesis, The Pennsylvania State University, University Park, PA, 1993.
13. Sychev, V. V., et al., *Property Data Update: Official Standards of The National Standard Reference Data Service of the USSR,* Hemisphere Publishing Corporation, Washington, DC, 1987.
14. Kuo, K. K., *Principles of Combustion,* John Wiley & Sons, New York, 1986.
15. Lucas, K., *Phase Equilibria and Fluid Properties in the Chemical Industry,* Dechema, Frankfurt, 1980, pp. 573–587.
16. Laesecke, A., Krauss, R., and Stephan, K., *J. Phys. Chem. Ref. Data* 19:1089–1121 (1990).
17. Chapman, S., and Cowling, T. G., *The Mathematical Theory of Non-uniform Gases,* Cambridge, New York, 1961.
18. Takahashi, S., *J. Chem. Eng. Jpn.* 7:417–420 (1974)
19. Wilke, C. R., *Chem. Eng. Prog.* 46:95–104 (1950).
20. Daubert, T. E., and Danner, R. P., *Physical and Thermodynamic Properties of Pure Chemicals: Data Compilation,* Hemisphere Publishing Corporation, New York, 1989.
21. McBride, B. J., and Zeleznik, F. J., "Computer Program for Calculation of Complex Chemical Equilibrium Compositions and Applications: Supplement I—Transport Properties," NASA TM-86885, 1984.
22. Prausnitz, J. M., Lichtenthaler, R. N., and de Azevedo, E. G., *Molecular Thermodynamics of Fluid-Phase Equilibria,* Prentice-Hall Inc., Englewood Cliffs, NJ, 1986.
23. Patankar, S. V., *Numerical Heat Transfer and Fluid Flows,* Hemisphere Publishing Corporation, New York, 1980.

Twenty-Fifth Symposium (International) on Combustion/The Combustion Institute, 1994/pp. 1619–1625

ANALYSES OF LIQUID ROCKET INSTABILITIES USING A COMPUTATIONAL TESTBED

JEFFREY M. GRENDA, SANKARAN VENKATESWARAN AND CHARLES L. MERKLE
Propulsion Engineering Research Center
The Pennsylvania State University
State College, PA 16802, USA

A synergistic hierarchy of numerical and analytical models is used to simulate three-dimensional combustion instability in liquid rocket engines. Existing phenomenological models for vaporization and atomization are used in quasi-steady form to describe the liquid phase processes. In addition to a complete nonlinear numerical model, linearized numerical and closed-form analytical models are used to validate the numerical solution and to obtain initial estimates of stable and unstable operating regimes. All three models are fully three dimensional. The simultaneous application of these approaches permits computationally inexpensive surveys to be performed in rapid parametric fashion for a wide variety of operating conditions. Stability maps obtained from the computations indicate that, when droplet temperature fluctuations are present, vaporization and atomization can drive instability. The presence of droplet temperature fluctuations introduces areas of instability for smaller drop sizes and colder drop temperatures. The computational procedures are demonstrated to accurately capture the three-dimensional wave propagation within the combustion chamber. The validated results indicate excellent amplitude and phase agreement for properly selected grid resolution. The nonlinear model demonstrates limit cycle behavior for growing waves and wave steepening for large-amplitude disturbances. The current work represents a validated computational testbed upon which more comprehensive physical modeling may be incorporated.

Introduction

Combustion instability continues to be a recurring problem in the development of practical combustion systems. Evidences of instability are encountered in afterburners, dump combustors, ramjets, solid propellant motors, and liquid rocket engines. Although the instabilities in these diverse systems are generically similar, they differ considerably in detail. One characteristic that distinguishes liquid rocket instabilities and which makes their understanding particularly difficult is the inherent multidimensional character of the disturbances. Additional challenges arise from the complex physics of the gas-liquid flow field and the propensity for both linear and nonlinear disturbances. At present, the most pressing issue in liquid instability modeling is the identification of the dominant driving mechanisms for various operating conditions.

Until recently, the multidimensional character of the disturbances prohibited the application of computational fluid dynamic (CFD) techniques to liquid rocket instability problems. Computational methods have recently progressed to the point where the accurate simulation of three-dimensional, unsteady flows is becoming practical. The purpose of the present paper is to assess the prospects for developing a computational testbed for combustion instability that can be used to test the sensitivity to various parameters.

A major issue in applying a CFD instability testbed is that each numerical solution indicates only whether one particular set of conditions is stable or unstable. Voluminous numbers of computations are required to discern trends or to ascertain mechanisms responsible for instability. An equally important issue is the need for validating the accuracy of the CFD solutions. In the present paper, we address both of these requirements by introducing a three-tiered analysis that includes full numerical solutions, linearized numerical solutions, and closed-form analytical solutions. The closed-form solutions and linearized numerical formulation together predict trends in an efficient fashion and serve as a validation standard at small amplitudes, even though the physical modeling is somewhat restricted. The full numerical solution allows more complete physics to be modeled.

Several previous applications of CFD procedures to liquid rocket instabilities have been reported, but none of these has as yet considered the full three-dimensional problem. Habiballah et al. [1] have developed the most complete model and applied it to existing engines with some success; however, this model is two dimensional, and little emphasis has been placed on deducing dominant instability

mechanisms. Similarly, work by Liang et al. [2] has included relatively complete physical submodels but has not been used parametrically to understand instability mechanisms. Less complete models have been reported by Kim et al. [3], Jeng and Litchford [4], Wang et al. [5], and the present authors [6].

Priem and Breisacher [7] have formulated a three-dimensional frequency domain analysis that includes empirical models for atomization and vaporization. This approach provides rapid solutions for single frequencies but is less effective in simulating broadband unsteady disturbances. We follow their approach for modeling atomization and vaporization, but whereas they use the nonlinear models with their linear gas phase solutions, we linearize these models for our linear analyses and retain the complete nonlinear formulations only in our nonlinear simulations.

Governing Equations

The equations that govern liquid rocket instability include conservation laws for both the gas phase and the distributed liquid phase. Each of these includes appropriate source terms that couple the effects of momentum exchange, vaporization, and combustion between the two phases. The Euler equations, with interphase transport terms added, are used to model the gas phase since they provide an accurate description of the wave dynamics and require less computer resources than the Navier–Stokes equations. Further, an accurate, validated Euler solution is a necessary precursor to a full Navier–Stokes solution. In cylindrical coordinates, these can be expressed as,

$$\frac{\partial \mathbf{Q}}{\partial t}+\frac{\partial \mathbf{E}}{\partial x}+\frac{1}{r}\frac{\partial \mathbf{F}r}{\partial r}+\frac{1}{r}\frac{\partial \mathbf{G}}{\partial \theta}=\frac{1}{r}(\mathbf{H}_{\text{gas}}+\mathbf{H}_{\text{liq}}) \qquad (1)$$

where $\mathbf{Q}$ is the vector of primary dependent variables and $\mathbf{E}$, $\mathbf{F}$, and $\mathbf{G}$ are the conservative flux vectors [6]. The source vectors, $\mathbf{H}_{\text{liq}}$ and $\mathbf{H}_{\text{gas}}$, contain the coupling terms between the gas and liquid phases and terms that arise because of cylindrical coordinates. The quantities x, r, and θ are the axial, radial, and azimuthal coordinates. We close the system by the perfect gas relation. The full numerical equations are solved by an explicit four-step Runge–Kutta method using central differencing in space in the axial and radial directions, and a Fourier spectral method in the azimuthal direction. Details of the method are given in Refs. 6 and 13.

The description of the liquid phase must invoke substantial physical modeling to represent the complex processes that occur on the droplet scale. Here, we choose a Lagrangian description and implement available phenomenological models for atomization and vaporization in quasi-steady fashion. This allows experimentally observed effects to be incorporated directly. Until appropriate unsteady models are developed, such quasi-steady models must serve as the basis for instability analyses. Improved physical submodels are an important issue in instability research and one for which the combined application of computational testbeds and experimentation is particularly attractive.

The equations governing a droplet are written as $d\mathbf{Q}_d/dt = \mathbf{H}_d$ where $\mathbf{Q}_d = [m_d, u_i, T_d]^T$ and $\mathbf{H}_d = [-\dot{m}_{\text{vap}}, \Sigma F_i/m_d, \Delta E_s]^T$. The source term, $\mathbf{H}_d$, provides for mass, momentum, and energy exchange with the gas as the droplets traverse the chamber. Summing $\mathbf{H}_d$ contributions from all droplets in a differential volume constitutes the gas phase source, $\mathbf{H}_{\text{liq}}$. Here, m_d and $\dot{m}_{\text{vap}}$ are the droplet mass and vaporization rate, respectively. The drag forces $\mathbf{F}_i$ arise as a result of differences between the gas velocity and droplet velocity, u_i. The determination of the droplet temperature involves an appropriate surface energy balance noted here in symbolic form. The current results utilize an infinite thermal conductivity approximation in the droplet interior as an initial investigative assumption.

Atomization is represented by the Mayer [8], Ingebo [9], and Nurick [10] models, while vaporization is determined by Priem–Heidmann [11] and Abramzon–Sirignano [12] models. The atomization models are implemented as a collapsed zone at the injector face, although distended models are easily accommodated. The entering liquid is partitioned among a number of droplet classes to approximate the droplet distribution function. Since the current work is focused on global understanding, a monodisperse drop size is used in the predictions. Unsteady droplet velocity fluctuations are ignored in the current work such that the local unsteady relative velocity arises from the gas phase perturbation only.

Additional potential instability mechanisms such as chemical reactions, species transport, injector coupling, and droplet collisions and coalescence are omitted here, but can be easily incorporated into a CFD instability testbed from appropriate phenomenological models.

Separation of the Equations into Mean and Disturbance Components

Although the complete equations must serve as the primary approach for combustion instability simulations, a simpler analysis that will provide guidance and qualitative insight, while also serving as a validation procedure for the full numerical solutions, is needed. We obtain such a simplified analysis by linearizing Eq. (1). To do this, we split the vectors into mean and unsteady parts as $\mathbf{Q} = \bar{\mathbf{Q}} + \mathbf{Q}'$, where overbars refer to the mean flow and primes to unsteady perturbations. We then linearize the flux

vectors as $\mathbf{E} = \bar{\mathbf{E}} + \bar{\mathbf{A}}\mathbf{Q}'$, where the matrix $\bar{\mathbf{A}} = \partial\bar{\mathbf{E}}/\partial\bar{\mathbf{Q}}$, etc. [13]. Substituting these expansions into Eq. (1) and restricting the mean flow to axial variations with zero transverse mean velocities allows the perturbation equations to admit a separable solution involving Bessel and trigonometric functions [J_μ and $Z = C_1 \cos(\mu\theta) + C_2 \sin(\mu\theta)$, respectively],

$$\mathbf{Q}' = \begin{bmatrix} \hat{\rho}(x,t)J_\mu Z \\ \widehat{\rho u}(x,t)J_\mu Z \\ \widehat{\rho v}(x,t)J_\mu Z/\lambda \\ \widehat{\rho w}(x,t)J_\mu Z'/\lambda r \\ \hat{e}(x,t)J_\mu Z \end{bmatrix} \tag{2}$$

where primes denote differentiation. The constant λ is determined by the nonpenetration condition at the wall, r_w, namely, $J_\mu(\lambda r_w) = 0$.

These simplifications provide the variables separable expression,

$$\frac{\partial\hat{\mathbf{Q}}}{\partial t} + \frac{\partial\bar{\mathbf{A}}\hat{\mathbf{Q}}}{\partial x} + \bar{\bar{\mathbf{B}}}\hat{\mathbf{Q}} = \bar{\mathbf{D}}_1\hat{\mathbf{Q}} \tag{3}$$

where $\hat{\mathbf{Q}} = (\hat{\rho}, \widehat{\rho u}, \widehat{\rho v}, \widehat{\rho v}, \hat{e})^T$, the matrix $\bar{\mathbf{A}}$ is identical to its standard form, and $\bar{\bar{\mathbf{B}}}$ refers to a slightly modified form of $\bar{\mathbf{B}}$ [13]. This disturbance amplitude equation contains only one spatial variable and can be solved at a small fraction of the computational effort of the fully nonlinear set. The resulting solutions represent meaningful three-dimensional disturbances that can be used effectively for performing exploratory stability surveys prior to attempting complete nonlinear computations.

By further requiring a constant axial mean flow, the disturbance amplitude equation can be solved analytically [13]. This closed-form solution allows numerical accuracy to be verified in the small perturbation limit and provides understanding of the role the various physical processes play in instability. The combination of closed-form models and full CFD solutions provides an effective tool for studying instability characteristics as demonstrated in subsequent sections.

Linearization of Atomization and Vaporization Models

To complete our linear analysis, we must also linearize the atomization and vaporization models. The atomization models can be expressed in the functional form, $d = d(\rho, u; T_l, u_l)$, where the subscript l refers to the liquid phase. For simplicity, we consider constant liquid properties and a fixed droplet velocity to eliminate the dependence on the last two variables. These effects are retained in the full numerical analysis. The atomization response to gas phase oscillations then becomes

$$\frac{d'}{d} = a_d\frac{p'}{\bar{p}} + \beta_d\frac{u'}{\bar{u}}. \tag{4}$$

For the Mayer model [8], the nondimensional coefficients are $a_d = -2/3\gamma$ and $\beta_d = -(4\bar{u}/3\bar{u}_{\text{rel}})$. Values for the Ingebo and Nurick models are given in Ref. 13.

The vaporization correlations can be linearized in similar fashion by expressing the vaporization rate as $\dot{m}_{\text{vap}} = \dot{m}_{\text{vap}}(p, u; T_l)$, where the vapor-pressure dependence has been expressed in terms of the liquid temperature through the Clausius–Clapeyron relation. The dependence on the liquid temperature can then be eliminated by companion linearized expressions for the heat flux to the droplet and the energy balance for the droplet temperature [13]. Because this latter relation is a differential equation, a phase lag is introduced such that the nondimensional vaporization coefficients become complex:

$$\dot{m}'_{\text{vap}} = \bar{\dot{m}}_{\text{vap}}\left[\alpha^*\frac{p'}{\bar{p}} + \beta^*\frac{u'}{\bar{u}}\right] \tag{5}$$

Frequency-dependent expressions for α^* and β^* are given in Ref. 13 for the Priem–Heidmann and Abramzon–Sirignano models.

Results and Discussion

To demonstrate the synergistic application of the numerical solution procedures in simulating instability, a cylindrical combustion chamber of length 0.36 m and radius 0.23 m was used as a baseline geometry. The gas phase composition was taken to be H_2/O_2 combustion products at a nominal temperature of 3000 K and a total flow rate of 1.5 kg/s. To compare the nonlinear, linear, and closed-form analytical solutions, constant mean flow conditions were assumed for the chamber. Unsteady vaporization contributions were considered over a variable fraction of the chamber length fixed by droplet size, relative velocity, and mean vaporization rate. These simplifications are readily removed for the numerical computations. In general, monodisperse liquid oxygen droplets of 110 μm were specified with an inlet temperature of 125 K and velocity of 100 m/s.

Linear Numerical Model and Analytical Solutions:

The linearized vaporization relations express the stability characteristics in terms of the parameters α^* and β^*. The range of α^* and β^* values for the representative liquid rocket operating conditions stated

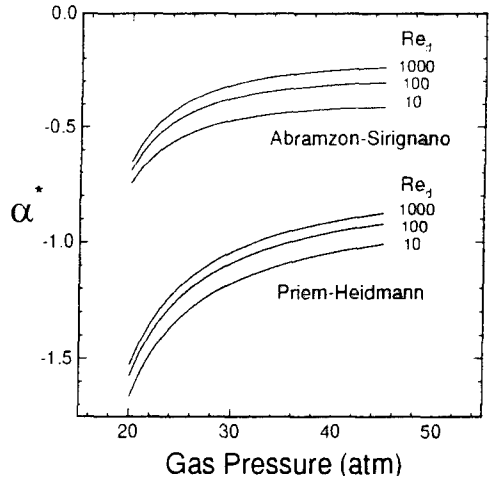

FIG. 1. Comparison of linearized pressure coefficients for Priem–Heidmann and Abramzon–Sirignano vaporization models. T_{gas} = 3000 K, d = 110 μm.

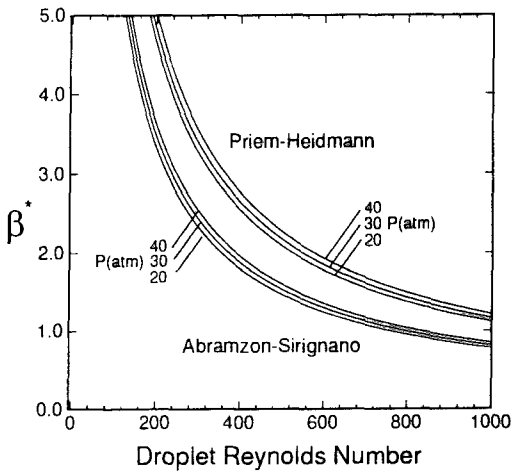

FIG. 2. Comparison of linearized velocity coefficients for Priem–Heidmann and Abramzon–Sirignano vaporization models. T_{gas} = 3000 K, d = 110 μm.

above are given in Figs. 1 and 2 for the case of a constant droplet temperature. For this case, the parameters α^* and β^* are real. Figure 1 shows the variation of the pressure coefficient α^* for chamber pressures ranging between 20 and 45 atm. As can be seen, α^* is negative ($\dot{m}_{vap}$ decreases as pressure increases) and approaches zero as chamber pressure increases for both the Priem–Heidmann and Abramzon–Sirignano models. There is also a weak dependence on droplet Reynolds number. The effects of increasing liquid droplet temperature (not shown) are to drive the pressure coefficients toward more negative values.

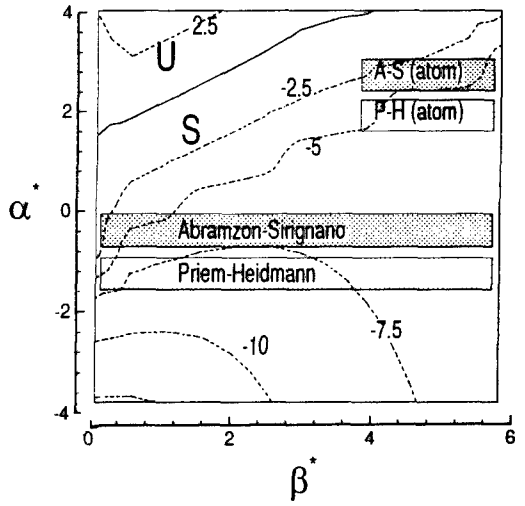

FIG. 3. Stability map as a function of the linearized pressure and velocity coefficients. Models indicate constant temperature droplets $\bar{T}_{liq}$ = 125 K, d = 110 μm, T_{gas} = 3000 K, P_{gas} = 40 atm.

Corresponding results for the velocity coefficient, β^*, are given in Fig. 2 as a function of droplet Reynolds number, $\rho_g|u_{rel}|d/\mu_g$. The velocity coefficient curves for both models have the same functional shape, but the levels differ because of the density used in the Reynolds number definition. As the mean relative velocity approaches zero, the velocity coefficient increases rapidly, indicating a more sensitive dependence on the perturbation velocity. The velocity coefficient is also weakly dependent on the mean chamber pressure.

Figure 3 presents the constant droplet temperature stability domain determined by using both the linearized numerical model and the closed-form analytical solution. This stability domain is presented in terms of the α^* and β^* coefficients. The results correspond to a vaporization zone of 50% of the combustor length, determined by the mean flow vaporization rate. Multiple modes exist at each point on the stability plane, and Fig. 3 indicates the most unstable first tangential, first radial, and arbitrary longitudinal mode (1T, 1R, nL) at each α^*-β^* location (typically n = 1 or 2). The neutral stability curve is indicated by the solid line and separates unstable (U) and stable (S) regions. Positive contour labels indicate unstable growth (percent growth per cycle), while negative values indicate decay. The unstable region lies in the positive α^*-β^* quadrant. Recall that both vaporization models considered give negative values of α^*.

The approximate ranges of the linearized coefficients for the Priem–Heidmann and Abramzon–Sirignano vaporization models for reasonable operating conditions are indicated by the shaded regions on

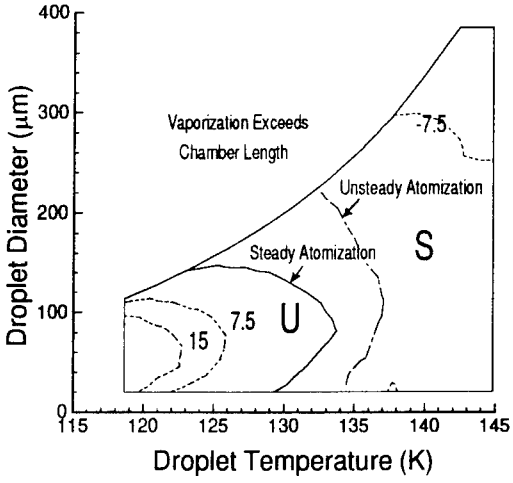

FIG. 4. Stability map as a function of droplet diameter and liquid temperature. Fluctuating-temperature droplets; T_{gas} = 3000 K, P_{gas} = 40 atm.

Fig. 3. Note that both models lie well inside the stable region. This indicates that vaporization coupling is insufficient to drive pressure oscillations for constant temperature droplets. When we combine the effects of atomization with vaporization, the operating domain moves closer to the neutral stability boundary, as indicated by the additional shaded regions. Despite this, no instances of instability were found for constant droplet temperature cases.

As a next step in investigating instability characteristics, we add the effects of unsteady temperature fluctuations in the liquid droplets. Because the α°-β° coefficients are now complex, the stability plane becomes multidimensional and cannot be presented in the manner of Fig. 3. Instead, Fig. 4 presents stability results in terms of the temperature and size of the entering droplets. Again, these results correspond to the most unstable (1T, 1R, nL) mode. The triangular upper bound on the stability map corresponds to an arbitrary constraint that only droplets that vaporize inside the chamber were considered. The lower limit on Fig. 4 represents the minimum drop size considered (20 μm), which resulted in a vaporization length of 14% of the chamber. The neutral stability curve and growth and decay contours are again indicated. The results in Fig. 4 indicate that realistic values of α° and β° result in instability if droplet temperature fluctuations are included. The instabilities occur when the droplets are small, and stability is regained for larger drop sizes. As noted by the dashed contour, the combined effects of unsteady atomization and vaporization again predict a larger unstable region than the effects of vaporization alone. Analogous results for axisymmetric disturbances indicate that the unstable region is considerably smaller than that for three-dimensional disturbances.

Full Euler Equation Solutions—Small Amplitudes:

The previous results have compared the linearized numerical solutions with the analytical results, and investigated representative characteristics of typical stability maps. We now investigate solutions from the full nonlinear analysis, concentrating first on small-amplitude disturbances. To demonstrate the validity of the nonlinear analysis, we begin by comparing predictions of the temporal development of pure mode disturbances with analytical results. A comparison of the pressure oscillation as a function of time at the injector face/wall/zero-degree location is shown in Fig. 5. This computation employs the Priem–Heidmann vaporization model (d = 110 μm and Re_d = 690. This corresponds to a 1T, 1R, 1L mode that grows at approximately 5% per cycle. The grid size chosen was 201 × 51 grid points in the x-r plane by

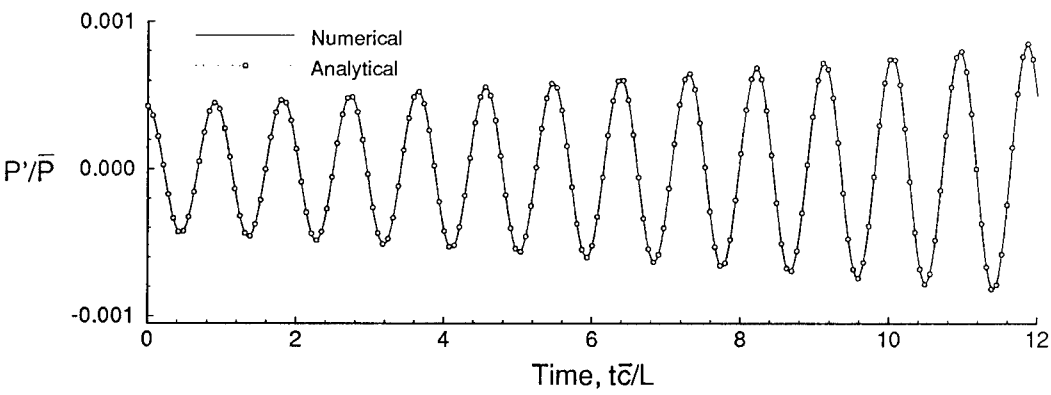

FIG. 5. Comparison of numerical and analytical pressure fluctuation vs. time traces at injector face/wall/zero-degrees location; pure mode initial conditions, fluctuating-temperature droplets $\bar{T}_{liq}$ = 125 K, d = 110 μm.

three Fourier modes in the tangential direction. The agreement between the numerical and analytical pressure oscillations indicated in Fig. 5 demonstrates the accuracy of the numerical solution. The two solutions are nearly indistinguishable over many cycles of oscillation. Similar accuracy is observed for other locations in the combustion chamber.

Numerous other computations over a variety of operating conditions were investigated to verify the physical trends predicted in Figs. 3 and 4. For instance, when the injected drop size is increased to 160 μm, a stable (1T, 1R, 1L) solution is indicated, in agreement with Fig. 4. (This is in contrast with the unstable solution in Fig. 5 for a smaller drop size and shorter vaporization length.) Likewise, if constant-temperature drops are considered with the original 110-μm diameter, decaying pressure oscillations result as predicted in Fig. 3. In all cases, the numerical solutions indicate similar accuracy to the result shown in Fig. 5.

Having established the accuracy of the solution procedure in this low-amplitude regime, the nonlinear numerical results may subsequently be extended to more general cases in which less restrictive mean flow variations and/or finite-amplitude effects may be significant.

Pulsed Mode Pressure Oscillations:

Extensions of the nonlinear calculations to finite-amplitude disturbances are next demonstrated by simulating stability "bombs" like those used for stability rating of liquid motors. Here, we impose a three-dimensional pressure pulse of small amplitude near the injector face as an initial disturbance in a steady-state chamber. The pulse gives rise to a rich variety of multidimensional disturbances. In the longtime limit, we expect the most unstable mode (predicted by the analytical method) to dominate in the absence of nonlinear effects.

The broadband pressure response to a pulse at the chamber wall/injector face/zero degree is shown in Fig. 6. Initially, there is a rapid decay that is later followed by steady growth. Power spectrum analyses of the response show that the short-term solution is dominated by low-frequency stable modes while the long-time spectral analysis indicates that most of the fluctuation energy resides at the most unstable mode of the chamber. Consequently, the nonlinear model faithfully models the broadband amplifier characteristics of these operating conditions. Similar pulsed cases for constant-temperature droplets (not shown) indicate the expected stable oscillating decay back to the mean chamber pressure. Additionally, pulsed pressure responses for axisymmetric modes indicate similar stability characteristics. This is consistent with the stability results obtained earlier.

In the long-time limit, the exponential growth of small-amplitude unstable disturbances must be

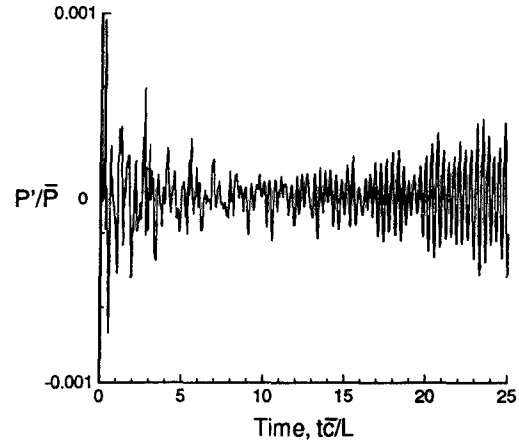

FIG. 6. Numerical pressure fluctuation vs. time trace at injector face/wall/zero-degrees location; pulsed mode initial conditions, fluctuating-temperature droplets $\bar{T}_{liq} = 125$ K, $d = 110\ \mu$m.

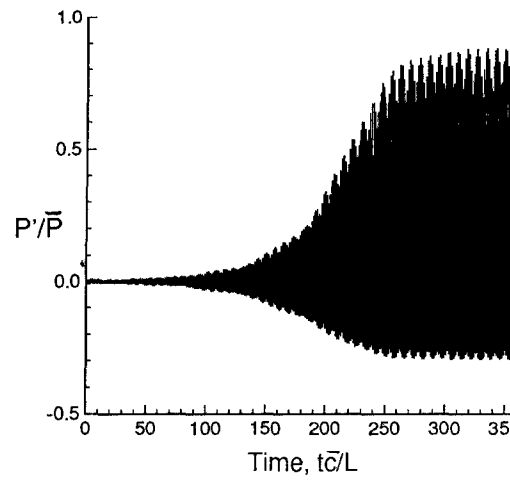

FIG. 7. Limit cycle behavior for strong high-amplitude nonlinear effects.

bounded by physical constraints. An important task of a nonlinear numerical approach is to model such nonlinear effects. Figure 7 demonstrates representative results of this nature. Here, the temporal response to an unstable, single-mode initial condition like those discussed above is shown for long-time solutions. The early-time (linear) response for this case closely matches the corresponding analytical results. The higher amplitudes at long times exhibit strong nonlinear effects that eventually produce a limit cycle in amplitude. Typical solutions exhibit strong wave steepening that results in a propagating triangular wave structure. The entropy losses in the

shocks produce considerably stronger damping than is observed for linear waves.

Conclusions

The use of CFD methods for understanding combustion instability in liquid rocket engines has been investigated using three levels of analysis. These include nonlinear numerical solutions of the complete equations, a linearized numerical procedure that gives rapid, efficient solutions for understanding trends, and an analytical closed-form solution that is used for validation of the numerical methods. Experimentally derived correlations for atomization and vaporization have been used in all three models to provide realistic parametric effects. Both the linear numerical solutions and small-amplitude limit of the nonlinear solutions have been shown to agree closely with the analytical solutions. The nonlinear analysis shows qualitatively realistic behavior in the large-amplitude limit.

Computed stability maps show that, in the absence of temperature fluctuations in the liquid droplets, neither atomization nor vaporization effects drive instability modes if realistic values are chosen for the coupling coefficients. When droplet temperature fluctuations are included, substantial areas of instability are observed, with unstable behavior being enhanced for smaller drop sizes. An important need in instability modeling is for experimental results defining the effects of unsteady pressure and velocity fields on atomization. The current work represents a validated numerical testbed upon which more comprehensive physical modeling may be incorporated.

Acknowledgment

This work was sponsored by NASA Grant No. NAGW-1356.

REFERENCES

1. Habiballah, M., Lourme, D., and Pit, F., "PHEDRE—Numerical Model for Combustion Stability Studies Applied to the Ariane Viking Engine," *J. Propulsion Power*, 7(3):322–329 (1991).
2. Liang, P., Fisher, S., and Chang, Y., "Comprehensive Modeling of a Liquid Rocket Combustion Chamber," *J. Prop. Power* 2(2): 97–104 (1986).
3. Kim, Y., Chen, C., and Ziebarth, J., "Prediction of High Frequency Combustion Instability in Liquid Propellant Rocket Engines," AIAA Paper 92-3763, July 1992.
4. Jeng, S., and Litchford, R., "Liquid Rocket Spray Combustion Stability Analysis," AIAA Paper 92-3227, July 1992.
5. Wang, Z., Yang, H., and Przekwas, A., "Assessment of Total Variation Diminishing Schemes in Combustion Instability Problems," AIAA Paper 93-0111, January 1993.
6. Grenda, J., Venkateswaran, S., and Merkle, C., "Three-Dimensional Analysis of Combustion Instabilities in Liquid Rocket Engines," AIAA Paper 93-0235, January 1993.
7. Priem, R., and Breisacher, K., *Nonlinear Combustion Instability Model in Two- and Three-Dimensions*, Technical Memorandum 102381, NASA, 1989.
8. Mayer, E., "Theory of Atomization in High Velocity Gas Streams," *ARS J.* 31(12):1783–1785 (1961).
9. Ingebo, R. D., *Dropsize Correlation for Cryogen Liquid-Jet Atomization*, NASA TM-102432, March 1990.
10. Nurick, W. M., *A Review of Shear Coaxial Element Atomization*, W. J. Schafer Assoc., Memo #082 to F. Kirby, May 1992.
11. Priem, R., and Heidmann, M., *Propellant Vaporization as a Design Criterion for Rocket-Engine Combustion Chambers*, NASA TR R-67, 1960.
12. Abramzon, B., and Sirignano, W., "Droplet Vaporization Model for Spray Combustion Calculations," *Int. J. Heat Mass Transfer* 32(9):1605–1618 (1989).
13. Grenda, J. M., "Computational Analyses of Combustion Instabilities in Liquid Propellant Rocket Engines," Ph.D. Thesis, The Pennsylvania State University, August 1994.

Twenty-Fifth Symposium (International) on Combustion/The Combustion Institute, 1994/pp. 1627–1634

CHARACTERISTICS OF WATER-BASE FOAM COMBUSTION

V. S. BABKIN, N. A. KAKUTKINA AND V. V. ZAMASCHIKOV
Institute of Chemical Kinetics and Combustion
Siberian Branch of Russian Academy of Sciences
630090 Novosibirsk, Russia

Systematic experimental studies have been carried out to characterize the combustion of water-base foams with various hydrogen- and methane-air mixtures. The dependencies of the combustion wave speed (S) on the expansion ratio of foam (K), concentration of surface-active agent (SAA) in detergent solution, and bubble size of foam have been investigated.

The combustion of foams with hydrogen mixtures has been established to be steady state. The effects of unsteadiness arising from combustion of methane foams are due to sound generation in the system and its interaction with the flame.

The flame speed in foam with rapidly burning gas mixture has been demonstrated to decrease with decreasing expansion ratio and the foams with slowly burning mixtures have demonstrated to be a non-monotonic function of K, including an anomalous region of increasing flame speed with decreasing K.

It has been demonstrated that the increase in both the SAA concentration in a detergent solution and the mean size of foam bubbles have no effect on the form of $S(K)$ dependence but leads, however, to the increase in the flame speed values.

The characteristics of foam combustion have been shown to be due to the effects of heat transfer from the gas to foam films and aerosol droplets forming upon destruction of foams by a flame front. Taking into account the interphase interaction provided the basis for derivation of a simple model of foam combustion and allowed to predict the flame speed dependences on the controlling parameters. The characteristic of combustion predicted by the model are in fair agreement with experimental data.

Introduction

Foams are the variant of two-phase gas-liquid systems that often occur in nature, form in many technological processes, and are used in fire extinction. In some technologies, the water-combustible foams, i.e., water-base foams with a combustible gas phase, can form as basic products or by-products. A principle possibility of deflagration and detonation wave propagation in such foams has been demonstrated in Refs. 1 through 3.

The purpose of this contribution is to study the character of combustion as well as the trends in flame speed in foams as a function of the main system parameters.

Experimental

The scheme of experimental setup is given in Fig. 1. Foam was obtained in foam generator 6 by passing a combustible gaseous mixture through a copper gauze submerged in a foaming solution (sulfonol aqueous solution). Homogeneous methane- and hydrogen-air mixtures for frothing were prepared in mixer 10 and were supplied to the foam generator through reductor 9 and flow meter 8.

The foam was passed through a three-way tap to testing tube 3, filling it up to an open end. Transparent glass tubes with diameters of 55 and 105 mm and lengths of 0.52 and 2.75 m were used. To prevent liquid from flowing out from the foam, the testing tube was rotated with a frequency of 1 Hz by electromotor 5.

Prior to the experiments, the foam expansion ratio and dispersion (the mean size of bubbles) were determined. To this end, the foam sample was taken through three-way tap 1. The foam expansion ratio (K) is the reciprocal of the volume fraction of liquid in foam and is estimated by weighing a selected sample. The expansion ratio was varied by dosed injection of a detergent solution into the foam using peristaltic pump 2 at the inlet of the testing tube; K was varied from 30 to 1600, due to foam stability.

The mean size of foam bubbles (d_m) was varied from 2 to 4 mm by changing the size of holes in the gauze of the foam generator. Here, d_m was measured by replicas of foam left on a special fixing substrate (glass plate covered with aqueous solution of rhodamin-colored gelatin).

The foam was ignited at the open tube end with either electric discharge 4 or open flame. Flame propagation in the tube was recorded by scanning device 11–15. Rotating mirror 11 (rotation period 62

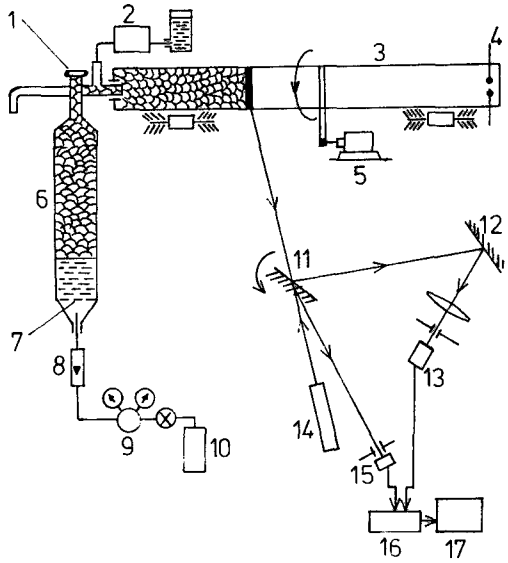

FIG. 1. Scheme of experimental setup.

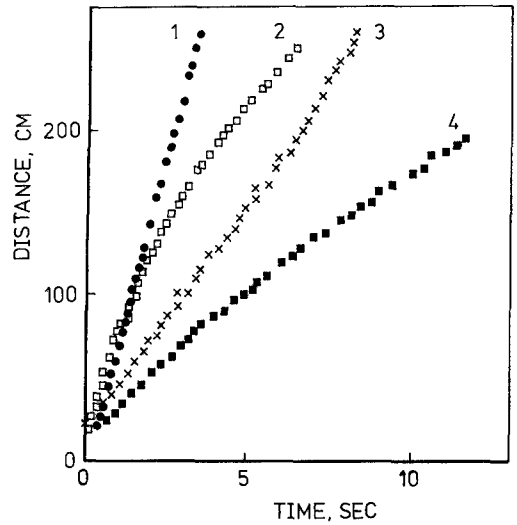

FIG. 2. The typical dependencies of flame front coordinate on time for hydrogen (curve 1, $K = 1400$) and methane (curve 2, $K = 1250$; curve 3, $K = 84$; and curve 4, $K = 350$) foams.

ms), depending on its position, projected the image of the given part of the tube through the diaphragm on photomultiplier 13. Thus, the mirror periodically scanned the whole tube. The sign of the beginning of scanning was created by laser beam 14 reflected from the second mirror situated on the common rotation axis with main mirror 11. The time of tube scanning was 6.5 ms. The signal from photodiode 15 about the beginning of scanning and the signal from photomultiplier from luminous flame front went to amplifier and then to analog-digital transformer 16 and computer 17. Here, the time between the signal of the scanning start and information signal (flame luminescence) was stored.

Experimental Results

The following parameters, defining foam state, were chosen as variable: the type and concentration of combustible gas mixture, surface-active agent (SAA) concentration in foaming liquid, foam expansion ratio, and foam dispersion.

The Character of Flame Propagation:

Figure 2 depicts the typical trajectories $l(t)$ of flame front in foams containing methane- and hydrogen-air mixtures. The character of flame propagation in these foams appears to be quite different. In "hydrogen" foams, the flame propagates in a steady-state way, except for a short start period. The propagation is followed by a weak sound, and flame speeds exceed those of the "methane" foams. Upon combustion of methane foams, the character of flame propagation substantially depends on the expansion ratio. With large K, the flame slows down (curve 2, Fig. 2). In this case, the combustion is accompanied by a strong hum. In the intermediate expansion ratio range ($K \approx 300$), the flame propagates practically in a steady-state mode (curve 4, Fig. 2) and without any sound, and with low K, it propagates in a steady-state way with acceleration at the end of the tube (curve 3, Fig. 2), which is followed by a stronger sound.

Taking this into account, the flame speed was determined as the slope of curve $l(t)$ for the case of steady-state propagation and as the mean rate all the way through the tube in the absence of a steady-state part.

Flame Speed:

The influence of expansion ratio on the flame speed (S) in methane (solid curves 1 through 3) and hydrogen (solid curves 4 through 7) foams is demonstrated in Fig. 3. Upon transition from curve 1 to curve 7, the character of the given dependence is observed to change. Curve 4 includes all the characteristic features of the other curves. Therefore, it should be considered it in detail. Here, the three characteristic sections can be distinguished. In the first one ($K > K_1$), the decrease in K leads to the decrease in flame speed. However, beginning with $K = K_1$, the dependence becomes anomalous: the decrease in expansion ratio leads to the increase of

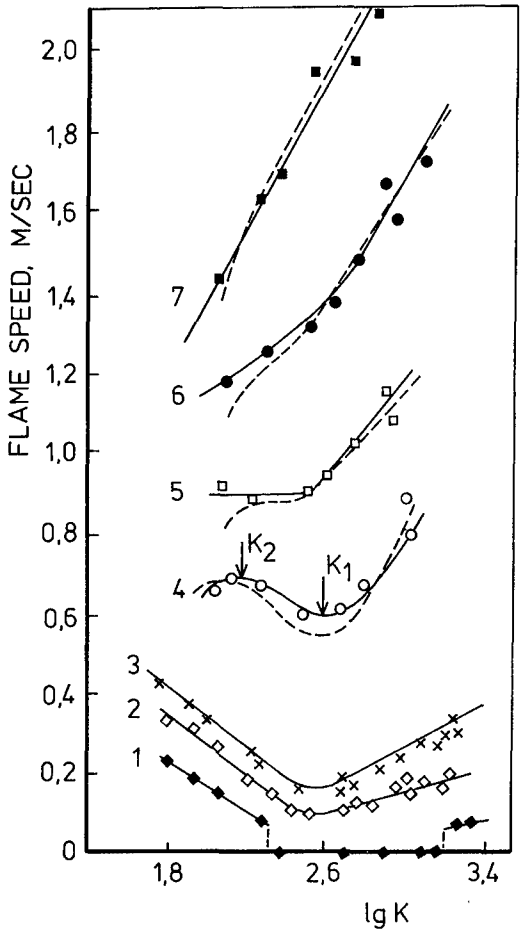

FIG. 3. The dependence of the flame speed in methane (curve 1, 7%; curve 2, 8%; and curve 3, 9.5%) and hydrogen (curve 4, 10%; curve 5, 11.5%; curve 6, 13%; and curve 7, 15%) foams on expansion ratio. Dashed lines are calculated from the model: curve 4, $\beta = 4 \cdot 10^{-4}$; curve 5, $\beta = 1.3 \cdot 10^{-3}$; curve 6, $\beta = 2 \cdot 10^{-3}$; and curve 7, $\beta = 2.8 \cdot 10^{-3}$; $\chi = 2.8$ in all cases.

flame speed (the second section, $K_1 < K < K_2$). In the third section ($K < K_2$), the flame speed decreases with decreasing K.

On the other curves in Fig. 3, some of the sections described are either absent or change. There is no third section in curves 1 through 3. This is due to the fact that for methane foams, K_2 is less than the minimum K value performed in experiments.

The second, anomalous, section regularly transforms upon transition from curve 7 to curve 1. For the foams under discussion, the increase in the reactivity of the gas mixture makes this section less pronounced. When hydrogen content is 11.5%, the second section degenerates into a plateau. With 13%,

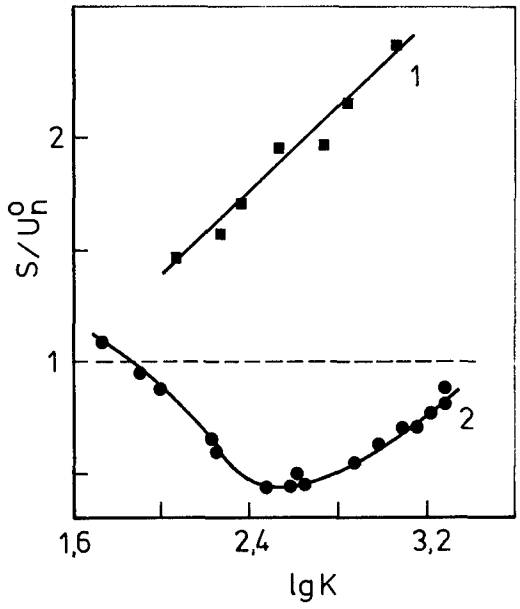

FIG. 4. The S/u_n° dependence on K for foams with a 15% hydrogen-air (curve 1) and 9.5% methane-air (curve 2) mixture.

the curve, in its place, changes the slope, being still monotonic, and with 15%, the character of the dependence is the same within the whole range of K. Thus, it is concluded that the anomalous second section is typical of foams with slowly burning gas mixtures and degenerates with increasing burning velocities of the mixture. Note that the K_1 value, corresponding to the beginning of the second section, remained practically the same upon the change of the combustible gas and varying reactivity of the mixture.

Curve 1, corresponding to the foams with 7% methane mixture, displays the range of expansion ratio at which the foam is incapable of flame propagation. This range lies in the vicinity of the K_1 value, corresponding to the flame speed minimum for the foams with other mixtures. It is noteworthy that the determined value of the expansion ratio limit is in fair agreement with that measured in Ref. 2.

The S value increases with increasing burning velocity of gas mixture (Fig. 3). Flame speed in foams may be less or more than burning velocity of the gas mixture filling the foam. Figure 4 shows the S/u_n° dependencies for 9.5% methane and 15% hydrogen foams (burning velocity data were taken from Refs. 4 and 5). The methane foams are observed to burn mainly more slowly than the gas mixture that fills them up, whereas the hydrogen ones burn faster.

The increase in the mean size of foam bubble d_m fails to cause any change in the character of the $S(K)$

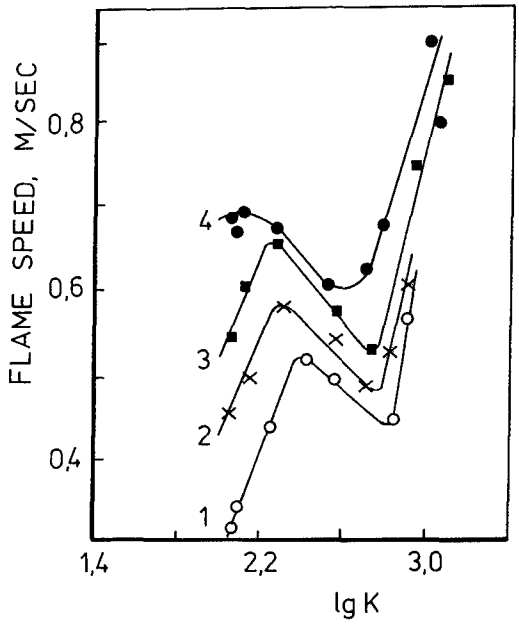

FIG. 5. The $S(K)$ dependence for foams with 10% hydrogen-air mixture with the different sulfonol concentration in liquid phase: curve 1, 0.2%; curve 2, 0.5%; curve 3, 1%; and curve 4, 3%.

dependence but just leads to the increase in the absolute values of flame speed.

Figure 5 demonstrates the influence of sulfonol content in foam on the combustion. With constant K, the S value increases with increasing sulfonol content. A gradual decrease of sulfonol concentration leads to a regular transformation of experimental curves. When concentration decreases, the position of the minimum in the $S(K)$ dependencies noticeably shifts to the higher expansion ratio. In parallel, the position of the maximum shifts.

Discussion

The Nature of Unsteadiness:

Experiments performed have revealed rather complex and sometimes unexpected regularities of foam combustion. Of essence is the question of the existence of steady-state combustion regimes. The character of the combustion of methane and hydrogen foams appeared to be different. The foams with hydrogen-air mixtures burn in a steady-state way. The combustion of methane foams displays the effects of unsteadiness. In this case, the effects are different for different expansion ratios: with high expansion ratios, flames slow down, and with low ones, foams burn with acceleration. The fact that the acceleration and retardation of flame arise only with substantial sound accompaniment suggests an acoustic nature of the unsteadiness. The assumption has been tested by special experiments on the effect of sound on the combustion of hydrogen foams. A dynamic loudspeaker was placed at the open end of the testing tube, and sound was switched on during combustion. According to the experiments, under the action of sound the flame speed of foams with a high expansion ratio decreased, and that with a low expansion ratio increased. Thus, the application of sound to the combustion process of hydrogen foams has given the same effects that are observed upon combustion of the naturally sounded methane foams, which confirmed the acoustic nature of unsteadiness.

The Mechanism of Flame Propagation:

A substantial peculiarity of the combustion of water-base foams is the nonmonotonic dependence of flame speed on expansion ratio, including the range of K values within which the increase in K leads to the decrease in S. Thus, an assumption has been made on the parallel existence of a number of possibly competing elementary processes in the combustion wave. This viewpoint is verified by Fig. 4, testifying to the fact that the foam can lead to both accelerated (in more reactive mixtures) and retarded (in less reactive mixtures) combustion relative to the gas mixture filling the foam.

The important elementary processes include the process of foam destruction, without which combustion is impossible. The combustion of methane foams, as has been mentioned, is followed by sound generation with intensities being no more than 70 dB. Special experiments show that the foams irradiated with sound up to 135 dB do not fail. Therefore, it is assumed that the destruction of foams upon combustion has a thermal rather than mechanical nature.

The destruction of foams results in the formation of liquid aerosol and its heating and evaporation. Since water vapour has no promoting effect on the methane [6] and hydrogen [7,8] flames, aerosol heating and evaporation can only slow down combustion. Therefore, the acceleration of combustion observed in hydrogen foams is, probably, due to a generation of a weak gas turbulence upon the breakage of foam bubbles and the expansion of combustion products in aerosol medium.

It is evident that the process of heat transfer to aerosol and its evaporation are more effective in slowly burning mixtures due to a long residence time of aerosol in the flame zone. According to experiment, just these mixtures display the most anomalous $S(K)$ dependence (Fig. 3, curves 1 through 4) and combustion slow down (Fig. 4, curve 2). Note, however, that a substantial part of aerosol passes the flame zone without evaporation. Indeed, in accord

with Refs. 6 and 9 30–40% water is quite sufficient to extinguish the stoichiometric methane-air flame. The total quantity of water entering the zone of chemical reactions in the form of vapours and aerosol is 60% for $K = 1000$ and 94% for $K = 100$. Nevertheless, flame extinction is not observed within the whole range of K, except for the 7% methane mixture.

To elucidate the role of aerosol and water vapours in combustion, the flame speed was measured together with the aerosol size distribution behind the flame front. To this end, a hole 5 mm in diameter was made in the tube. A plate covered with a fixing staff was put under the hole. Aerosol droplets, resulting from combustion, passed through the hole to the plate and, after drying, left replicates which were examined under a microscope. The rotation of the testing tube was stopped upon sampling of aerosol. The measurements allowed us to determine the mean particle diameter D_1, the mean cubic diameter of droplets D_3, and the number concentration n.

According to the measurements, for all the foams, the decrease in expansion ratio leads to the increase of the mean droplet size. However, these changes are nonuniform: with high expansion ratio, the size remains practically the same, and for the low ones, the changes are rather substantial. When the gas mixture is changed, D_1 and D_3 change little with the given expansion ratio. The increase in either sulfonol concentration in the foaming solution or bubble dispersion causes the increase of D_1 and D_3.

The obtained data have been used to estimate the degree of aerosol particle evaporation in the flame zone. It appeared to be quite low and not to exceed 5% for experimental conditions. On the other hand, the data obtained allowed us to determine the value of heat losses from flame to droplets q_a. As it is known, $q_a = 2\pi\lambda n D_1 (T - T_a)$ [10], and giving n in terms of D_3 and K, we get $q_a = 12\lambda D_1 (T - T_a)/(KD_3^3)$.

Figure 6 gives the value measured for S and calculated for q_a^{-1}. It is seen that the values qualitatively correlate and have the minimum for the close values of K. Thus, it is assumed that the decrease of the flame speed below u_n°, the anomalous behavior of the $S(K)$ curve and the appearance of the limits of flame propagation by K (Ref. 2 and curve 1 in Fig. 3,) are due to the change in aerosol dispersion with the expansion ratio at which the maximum of heat losses in the gas phase is reached and, correspondingly, the temperature minimum in the flame zone.

The lower the burning velocity is, the larger the heat losses from gas and the smaller the flame temperature. On the contrary, the higher the burning velocity is, the weaker the heat transfer at the droplet-gas interface and its influence on the chemical reaction rate.

A detailed mechanism of the thermal destruction of foam is not clear yet. However, it is assumed that

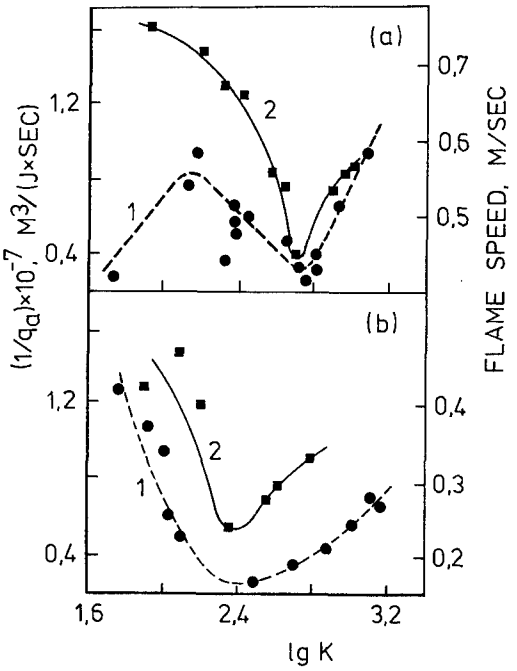

FIG. 6. The $S(K)$ (curve 1) and q_a^{-1} (K) (curve 2) dependencies. (a) 10% H_2 + air, 0.5% sulfonol; (b) 9.5% CH_4 + air, 3% sulfonol.

foam destruction needs irreversible consumption of a certain quantity of heat q_f, which leads to the drop in the maximum temperature in the flame zone. Hence, the thicker the foam film is, the stronger the drop in temperature and the lower the flame speed are. This point of view is in agreement with the $S(K)$ dependence for hydrogen foams in which the influence of heat transfer to liquid aerosol on combustion is comparatively small. Indeed, the smaller K is, the larger the film thickness and the smaller the flame speed (curve 7, Fig. 3).

The physical model of foam combustion under discussion is in agreement with other experimental trends. The increase in sulfonol content for the given value of K, according to measurements, leads to the increase of the mean size of aerosol particles, the decrease in number concentration n, and as a result of these changes, to the decrease of heat losses q_a and the experimentally observed growth of S (Fig. 5).

The increase of d_m causes two opposite tendencies. On the one hand, there is the increase of the foam film thickness and the corresponding increase of q_f, while on the other hand, there is the increase of aerosol particle diameter and the decrease of their number concentration resulting in the decrease of q_a. According to experimental data, the heat losses to droplets dominate in this case.

Phenomenological Model of Foam Combustion:

Foam combustion is modeled as gas combustion with additional heat flow to liquid films and droplets. Consider now, in the one-dimensional approximation, the influence of the evaporation of droplets and films on the parameters of a steady-state combustion wave. Let us take the following simplifying assumptions:

1. The heat consumed by droplets and films is lost by their evaporation. The energy lost by the heating of droplets and films is insignificant for the total heat balance.
2. The relatively large droplets have been considered the evaporation of which in the flame front causes no noticeable changes in the size.
3. Addition of gas mass due to evaporation of droplets and films is not essential for the total balance of gas mass.
4. The flame front in each region is considered to be flat and laminar. The total increase of combustion surface due to the burn out of gas bubbles is taken into account by the empirical factor of turbulence generation χ.
5. The discretely situated foam films are substituted by an imaginary constantly acting film, the heat transfer to which equals the volume-averaged heat transfer to real films.
6. The destruction of foam films is realized by the leading flame front at some distance x_L from the zone of chemical flame reactions. After destruction, the films are spontaneously dispersed to form aerosol. Beginning with coordinate x_L, foam combustion is considered as the gas combustion with distributed water droplets.

Assuming the transfer coefficients to be constant, the equation for energy balance for the system under study is as follows:

$$\rho_0 u_n c \frac{dT}{dx} = \lambda \frac{d^2T}{dx^2} - Q_1 - Q_2 - Q_3 - Q_4 + QW$$

$$x = x_L: \quad T = T_L, \quad \lambda \frac{dT}{dx} = q_f = \chi u_n L \rho \beta / K$$

$$x = 0: \quad T = T_b \qquad (1)$$

where

$$Q_1 = \frac{q_f c_H}{L} \frac{dT}{dx}, \qquad Q_2 = \pi \lambda Nu D_1 n (T - T_a),$$

$$Q_3 = \pi \lambda Nu D_1 n c_H (T - T_a)^2 / L,$$

$$Q_4 = \frac{\pi \lambda Nu D_1 n c_H}{L} \frac{dT}{dx} \int_{x_L}^{x} (T - T_a) dx.$$

Here, Q_1 takes into account the heating of water vapor evaporated from foam films, and Q_4 takes into account those evaporated from droplets; Q_2 is the heat transfer to droplets, and Q_3 takes into account the heating of vapors evaporated from droplets from the temperature of droplet surface T_a to the gas temperature T.

Assuming the Arrhenius dependence of W on temperature and the similarity between the profiles of temperature and fuel concentration and integrating Eq. (1), we get the relations for the maximum flame temperature (T_b) and the flame speed (S):

$$T_b^0 - T_b = [L + (T_b - T_0)c_H] \left\{ \frac{\beta \rho \chi}{K \rho_0 c} + \frac{6D_1}{KD_3^3} \frac{(T_b - T_0)\rho_0 u_n c Nu \chi^2}{L \rho_0 u_n c + q_f c_H} \right\} \qquad (2)$$

$$S = \chi u_n = \chi u_n^\circ \exp[E(T_b - T_b^0)/(2RT_b^{0 2})]. \qquad (3)$$

In order to verify the adequacy of the model proposed for foam combustion, Eqs. (2) and (3) have been solved numerically, and the calculation results (dashed lines in Fig. 3) have been compared with the experimentally measured dependencies of the flame speed on k for various foams. The following values of parameters were used in calculations: $L = 2.26 \cdot 10^3$ J/kg, $c_H = 2 \cdot 10^3$ J/kg K, $c = 1 \cdot 10^3$ J/kg K, $\rho = 10^3$ kg/m^3, $\rho_0 = 1.29$ g/m^3, $E = 1.3 \cdot 10^5$ J/mol for hydrogen, and $E = 1.03 \cdot 10^5$ J/mol for methane. Parameters β and χ were chosen to reach the best agreement with experimental dependencies.

Some qualitative trends can be predicted directly from the analysis of Eq. (2). The two terms in braces in Eq. (2) correspond to the two different components of heat losses. The first one depends on the interaction between flame and foam films, and the second is determined by the interaction with aerosol. With large burning velocities of the gas, filling the foam, the second term becomes negligibly small. In this case, the foam flame speed must monotonically decrease with decreasing expansion ratio, which is actually observed for the foams with rapidly burning hydrogen mixtures (see the data for 15 and 13% mixtures in Fig. 3). For the slowly burning mixtures, the second term in the braces in Eq. (2) becomes the main one, and the character of the $S(K)$ dependence is determined by the heat losses for droplets (q_a) that, as has been shown, are usually the nonmonotonic function of K, which gives the nonmonotonous $S(K)$ dependence (curves 1 through 4 in Fig. 3).

For the medium values of u_n, both of the terms are commensurate, and more complex "mixed" dependencies with the different degree of the expression of the minimum are observed (Fig. 3).

As is evident from the analysis, the model proposed can be used for a qualitative description of all trends observed upon foam combustion. Adjusting

the parameters β and χ, one can reach a quantitative agreement between experimental and calculated $S(K)$ dependencies. The $S(K)$ dependencies calculated by the model for a series of foams are depicted by dotted lines in Fig. 3.

Conclusions

1. A steady-state combustion regime has been established for water-base foams. It is shown that the combustion of foams with hydrogen mixtures is steady state in all the cases. The effects of unsteadiness arising in a number of cases upon combustion of methane foams are caused by the influence of sound on combustion.
2. The dependencies of flame speed on expansion ratio have been studied for foams with different gas compositions, liquid phase composition, and bubble sizes. An anomalous $S(K)$ dependence has been documented for the foams with slowly burning gas mixtures namely, in some K range, flame speed increases while expansion ratio decreases.
3. It has been demonstrated that the anomaly is caused by a unique change with expansion ratio of the degree of dispersion of aerosols that result from destruction of foam by flame front. This leads to a nonmonotonic change with the expansion ratio of heat transfer function.
4. A mechanism for foam combustion has been proposed. It is based on the phenomenon of heat transfer from flame to films and aerosol formed from foam destruction. The constructed elemental model of the process accounts well for the trends observed in foam combustion.

Nomenclature

a	bomb radius
c, c_H	specific heat capacity of gas mixture and water
d_m	mean size of foam bubbles
D_1	mean diameter of droplets
D_3	mean cubic diameter of droplets
E	activation energy of chemical reaction
K	expansion ratio
L	evaporation heat
n	number concentration of droplets
Nu	Nusselt number
S	foam flame speed
T	temperature
T_0	initial temperature
T_b	foam flame temperature
T_b^0	adiabatic temperature of gas mixture burning
T_a	droplet surface temperature
t	time
Q	thermal effect of reaction
q_a	volume rate of heat transfer from gas to droplets
q_f	volume rate of heat transfer from gas to films
u_n°	burning velocity of gas mixture
u_n	burning velocity of foam
W	rate of chemical reaction
ρ_0, ρ	density of gas and liquid
β	empiric coefficient
χ	temperature conductivity
λ	heat conductivity

Acknowledgment

The research described in this publication was made possible in part by a grant from the Russian Foundation of Fundamental Investigations (Grant No. 94-03-08938a).

REFERENCES

1. Saint-Cloud, J. P., Guerraud, C., Moreau, M., and Manson, N., *Acta Astron.* 3:78 (1976).
2. Burgoyne, J. H., and Steel, A. J., *Res. Abstr. Rev.* 4:67–75 (1962).
3. Kudinov, V. M., Palamarchuk, B. I., Lebed, S. I., Borisov, A. A., and Gelfand, B. E., *Dokl. Akad. Nauk USSR* 234:45–47 (1977) (in Russian).
4. Andrews, G. B., and Bradley, D., *Combust. Flame* 20:77–89 (1973).
5. Andrews, G. B., and Bradley, D., *Combust. Flame* 19:275–288 (1972).
6. Babkin, V. S., and Viun, A. V., *Fiz. Gorenija Vzryva*, 7:392–395 (1971) (in Russian).
7. Lui, D. D. S., and Mac Farlane, R., *Combust. Flame* 49:59–71 (1983).
8. Shebeko, Ju. N., Korolchenko, A. Ja., Tsarichenko, S. G., et. al. *Combust., Explosion, Shock Waves* 25:289–291 (1989).
9. Lewis, B., and Elbe, G., *Combust. Flames Explosions Gases*, Academic Press, New York, London, 1961, p. 696.
10. Fuks, N. A., *Droplet Evaporation and Growth in Gases*, AS USSR Press, Moscow, 1958, pp. 1–90 (in Russian).

COMMENTS

R. H. Woodward Waesche, Science Applications International Company, USA. Please amplify the statement (p. 7) that "foams irradiated with sound up to 135 Db do not fail." Was the sound applied directly to the foam (through direct coupling to the wall, then to the foam)? Was the character of the foam altered by the external sound? What frequencies were applied? Did the application of sound affect flame speed?

Author's Reply. The diaphragm of the loudspeaker was placed axially close to the open reaction tube without contacting the foam. The frequency of sound was 20–20,000 Hz. The foam structure was altered by the external sound [see *Colloid J.* 54(2):192 (1992)]. Application of sound affects flame speed in different ways depending on the foam expansion ratio: Flame speed decreases at high expansion ratio and increases at low expansion ratio.

Twenty-Fifth Symposium (International) on Combustion/The Combustion Institute, 1994/pp. 1635–1643

RDX FLAME STRUCTURE

DONNA HANSON-PARR AND TIM PARR
Research Department, Combustion Diagnostics Laboratory
code C02392
Naval Air Warfare Center, Weapons Division
China Lake, CA 93555–6001, USA

Nonintrusive diagnostics were used to measure temperature and species profiles during neat RDX deflagration at 1 atm. UV-visible absorption was measured to obtain absolute concentration profiles of NO, NO_2, CN, NH, H_2CO, and OH. Temperature and species concentrations were obtained by spectral fitting. Planar laser-induced fluorescence (PLIF) of these same species was also measured to obtain two-dimensional (2D) profiles in the flame with excellent spatial resolution. The flame structure is characterized by a "dark zone" close to the surface and a visible flame sheet above the dark zone. For CO_2 laser-assisted deflagration, the narrow flame sheet NH profile peaks 2.3 mm above the surface at a value of 100 ppm. The CN profile is slightly wider and peaks at 2.5 mm at a value of 660 ppm. The OH profile peaks outside the CN/NH flame sheet with a mole fraction of 0.055. The dark zone species studied here were NO_2 and NO. The NO_2 peaks very close to the surface at about 0.17 mole fraction and decays rapidly to 0 at 1.5 mm. Close to the surface, the NO mole fraction is about 0.2 and falls sharply to 0.05 at 2.5 mm as NO is consumed in the CN/NH flame sheet. No formaldehyde was detected. Rotational temperature profiles were measured from OH PLIF and NO absorption spectra. The NO gas temperature near the surface is in good agreement with prior thermocouple measurements. The temperature rises sharply to about 1500 K at 0.3 mm and then turns over to a much more gradual slope in the dark zone. At about 2 mm, it becomes steeper again and finally levels out to 2600 K at 3.0 mm, at the top edge of the CN flame sheet.

Introduction

The purpose of this work was to measure gas phase species concentrations and temperatures as validations to kinetic models of neat RDX deflagration. Nonintrusive diagnostic techniques were used to minimize perturbation of the flame.

Measurements of species concentrations and profiles have been made in nitramine flames using planar laser-induced fluorescence (PLIF), with external CO_2 laser heat flux [1–4], high heating rate thermolysis with Fourier-transform infrared spectroscopy (FTIR) detection [5], time-of-flight mass spectroscopy (TOF-MS) [6], microprobe mass spectroscopy with external CO_2 heat flux [7], absorption spectroscopy [8,9], and coherent anti-Stokes Raman spectroscopy (CARS) [10].

The PLIF measurements [1–4] thus far have mapped out a number of species profiles in HMX monopropellant flames, including CN, NH, NO_2, and OH (and partially NO), during the ignition phase as well as self-deflagration. The current work has extended the PLIF and absorption results to RDX flames at 1 atm.

In the high heating rate thermolysis of RDX with rapid scan Fourier-transform infrared spectroscopy detection [5], the decomposition pathway leading to HCN, NO, and NO_2 was seen to increase with increasing temperature, while that leading to CH_2O and N_2O decreased.

The TOF-MS work [6] was done on flames of RDX at 0.5 atm and led the authors to conclude that the important reaction in the luminous zone is not CH_2O + NO_2, but HCN + NO, and that the overall equation of the decomposition products of RDX is

$$\begin{aligned} RDX_{(s)} \rightarrow\ & 0.35\ CO + 0.55\ CO_2 \\ & + 0.62\ N_2 + 0.35\ N_2O + 1.9\ NO \\ & + 0.19\ NO_2 + 1.95\ H_2O \\ & + 1.9\ HCN + 0.19\ HNCO. \end{aligned}$$

As discussed in Refs. 5 and 7, melt-layer thickness could be a major factor in the profiles obtained. Thick melt layers, as seen with the low burn rates found in atmospheric or subatmospheric deflagration without high external heat fluxes, lead to longer residence times in the melt, higher proportion of decomposition via condensed phase vs gas phase pathways, and more H_2CO + N_2O with less HCN + NO_2. These condensed phase decomposition products may not be seen for the higher burning rates and, therefore, thinner melt layers that are present in rocket motors. The TOF-MS work was done at 0.5

atm without external heat flux, conditions that would give rise to a relatively thick melt layer.

UV-visible absorption measurements have been made in flames of HMX "model" propellants burning in 15 atm of N_2, and both temperature and species profiles were produced for CN, OH, and NH [9]. Flames of neat HMX burning at 1 atm [8] were studied with UV-visible absorption, yielding temperature and species profiles for NO, NO_2, and CN. The CARS measurements were done on HMX model propellants and other propellants [10,11], for which stable species were mapped out. It is difficult to compare neat HMX flames with HMX propellant flames because the binder in the propellants acts as a heat sink and greatly stretches out the flame structure.

Theoretical modeling of nitramine flames using detailed chemical kinetics has been initiated with promising results [6,12,13]. Melius [12] modeled RDX combustion and saw an increase in [NO] with distance from the surface and then a gradual decay, while the [NO_2] rose rapidly to a peak and then decreased farther from the surface, similar to the results of Ref. 5. His model for 17 atm pressure showed a high HCN/N_2O ratio, a peak [NO] of about 0.24 mole fraction, a peak [NO_2] of about 0.056 mole fraction, and a value for [CN] and [NH] of 500 ppm and 260 ppm, respectively. [NO_2] for 0.5 atm was at least 0.1 mole fraction.

Hatch [13] modeled HMX combustion using a set of 77 reaction equations assuming different starting condensed-phase decomposition products. If he chose NO_2 + HCN + H as the sole decomposition pathway, he obtained the correct slope for the burn rate, but values were low by a factor of 2.5. He noted that HCN and NO were the dominant reactive species, with NO_2 and H being consumed mainly through H + $NO_2 \rightarrow$ NO + OH producing slowly reacting NO.

Hatch also tried modeling HMX combustion, assuming that the decomposition products were strictly CH_2O + N_2O, but was not able to achieve convergence. A mix of the decomposition pathways adjusting the relative branching ratios to match the burning rate at 1000 psi did converge. As the branching fraction for the CH_2O + N_2O pathway was increased, the burning rate was found to increase dramatically. The peak [NO_2], [NO], and [CN] obtained were about 0.045, 0.085, and 390 ppm, respectively, these being lower than the values obtained in Ref. 8.

Experimental

Results presented here are for self- and laser-supported deflagration of neat RDX pellets burning at 1 atm. The burn rate for self- and laser-assisted deflagration was measured from the video images to be 0.51 and 1.60 mm/s, respectively.

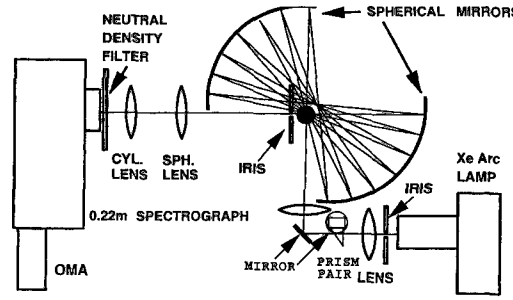

FIG. 1. Apparatus used for UV-visible absorption experiments (multipass configuration shown). The source was a 75 W Xe arc lamp fitted with condensing lens. After passing through an iris at the focal point, the beam was collimated and then rotated with a pair of prisms. The beam was steered toward the pair of spherical mirrors, the five transits of the beam all focussing at two points about equidistant from the two mirrors. The sample was positioned below one of the two foci, and an iris downstream was used to eliminate optical emission from entering the optical multichannel array (OMA) detector.

Absorption:

The experimental layout for the absorption measurements is shown in Fig. 1. The samples used were either 6.4- or 9.5-mm-diameter, 6–10-mm-tall cylinders of RDX formed by pressing neat RDX powder to a density of 96–98% TMD. The samples were ignited at 1 atm in air with a CO_2 laser at a flux of 145 cal/cm^2-s. For species in large concentration (like NO and NO_2), a single-pass absorption configuration was sufficient; for those species of low concentrations in the nitramine flames, a multipass configuration was employed [14].

The spatial resolution in the vertical (flame flow) dimension was directly measured to be 0.05 mm. The spectral resolution was measured as 1.9 A full width at half-maximum (FWHM). The surface was allowed to regress during the burn. The OMA time integration of 0.033 s/frame and aforementioned burning rate of 1.6 mm/s gave an additional equivalent spatial averaging of only 0.05 mm/frame.

The details involved in converting absorption spectra to mole fractions and temperatures have been discussed [8]. Basically, Beer's law is used, and concentrations obtained converted to mole fractions, using the perfect gas law. The parameters used for NO and CN spectral fitting have been given [8]. Wavelengths for the molecular transition databases were obtained from Ref. 15 for NO, Ref. 16 for OH, Ref. 17 for CN, and Ref. 18 for NH. The Hönl–London factors are given by the equations of Earls [17] for NO. A/B in Earls's formulas, as well as rotational energies and transition wavelengths and frequencies for OH, were obtained from Ref. 16. Einstein B factors for OH were available [19] and were

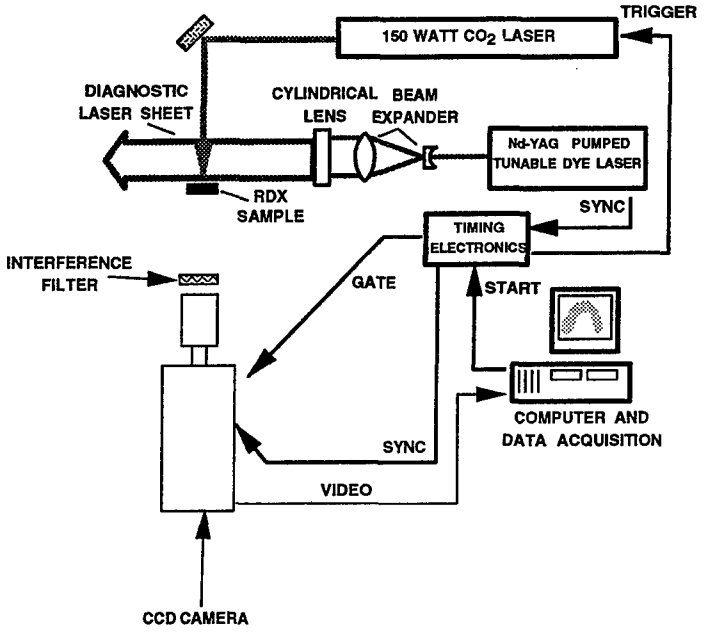

FIG. 2. Apparatus used for laser-induced fluorescence (PLIF) measurements. The probe laser sheet was produced using beam-expanding optics and a cylindrical lens and passed through the center of the flame and into a beam dump. A 150-W CW CO_2 laser was focussed down to produce a flux of 150 cal/cm^2-s at the sample surface for a preset duration, at which time the probe laser fired and the resultant laser-induced fluorescence imaged onto a 752 × 240 pixel array CCD camera fitted with the relevant interference filter. The Nd^{3+}-YAG laser sync controlled the timing during the course of the experiment.

used instead of calculating the line strengths. Hönl–London factors used for CN and NH were found in Ref. 20. The band oscillator strengths for NH were found in Ref. 18.

The collision widths used were obtained from Refs. 14, 21, and 22 for CN, OH, and NH, respectively. Because the broadening parameter obtained for NH with Ar was quite close to that for OH [22], the broadening parameters for OH with H_2O were used for NH. H_2O was assumed to be the major broadening collision partner.

The path lengths used in the simulations were determined from PLIF 2D images and emission images from the current work. Peak concentrations quoted are the result of deconvolution of the absorption spatial resolution over the measured PLIF profile shape.

PLIF:

The PLIF apparatus shown in Fig. 2 has been described previously [1–4]. A high-resolution gated intensified charge coupled device (CCD) camera provided a field-of-view of 6.5 mm (240 pixels) across the pellet and 8.7 mm (752 pixels) above the pellet. For CN, the (B-X) (0,0) band head at 388.3 nm was pumped by the laser and the (0,1) band at 420 nm was monitored. For NH, the (A-X) (1,1) band at 305 nm was pumped and the (0,0) and (1,1) bands were monitored, and for OH, the (A-X) (1,0) band at 281 nm was probed and the (1,1) and (0,0) bands were monitored around 311 nm.

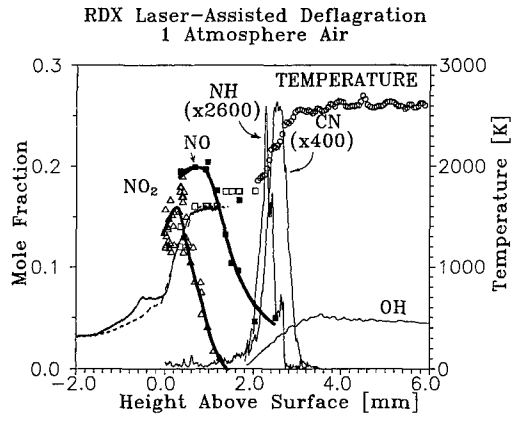

FIG. 3. Species concentrations in a 1-atmosphere laser-assisted combustion flame of RDX.

Results and Discussion

Absorption spectra were measured for NO_2, OH, NO, NH, and CN. The PLIF measurements were also done for laser-assisted deflagration of RDX for CN, NH, OH, and NO as well as for self-deflagrating RDX for CN. The centerline profiles obtained from the PLIF images, calibrated by absorption measurements, are collected in Fig. 3. The flame consists of a dark zone (seen here as NO and NO_2) capped with a thin flame sheet (CN and NH). The temperature profile shown in Fig. 4 was obtained by piecing together the NO and OH rotational temperature re-

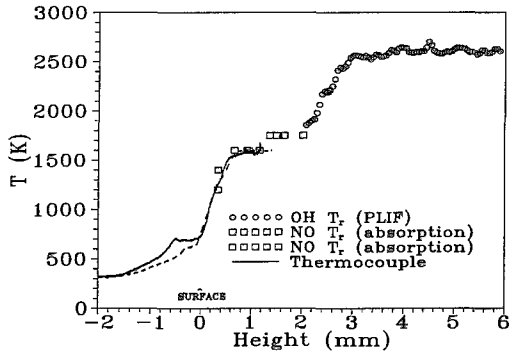

FIG. 4. Temperature in a 1-atmosphere laser-assisted combustion flame of RDX.

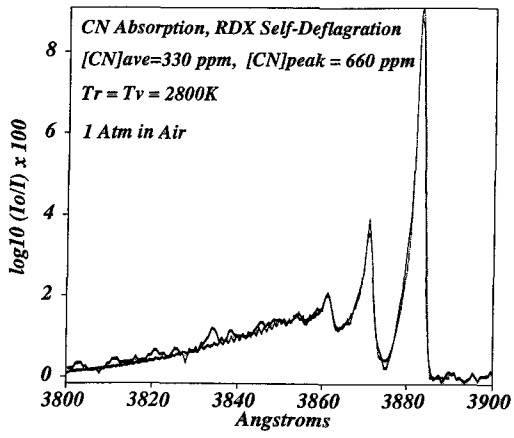

FIG. 5. CN absorption spectrum and spectral fit in a flame of self-deflagrating RDX in air at 1 atmosphere.

sults obtained in this work and previous thermocouple temperature data [1].

CN:

Figure 5 shows an example of a CN absorption spectrum and spectral fit (dashed line). Temperature at the flame front was obtained from the CN fitting process to be between 2600 and 2800 K for self-deflagration of RDX. The differentiation between 2600 and 2800 K in the fits obtained was minor, and the peak value of [CN] was from 595 to 660 ppm using these two temperatures. The [CN] of laser-assisted RDX deflagration was obtained by using temperatures between 2600 and 2800 K, yielding peak values of [CN] from 460 to 510 ppm. For HMX self-deflagration, the peak [CN] was determined for a vibrational and rotational temperature of both 2800 K to be 485 ppm [8].

These values compare favorably with those in the literature. Parr and Hanson-Parr measured an OH

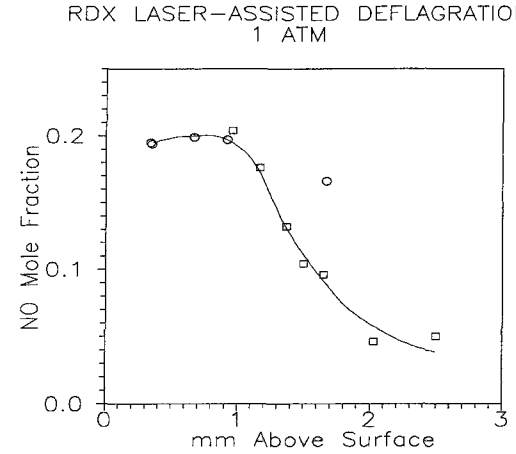

FIG. 6. NO absorption concentration as a function of height off the surface in a laser-assisted RDX flame.

rotational temperature of 2772 K at the peak of the [CN] profile for HMX [1–4] and the PEP thermochemical code [23] yields an equilibrium temperature of 2902 K. The current work (below) yields an OH rotational temperature determined from laser-saturated fluorescence of 2657 ± 109 K. Hatch [13] obtained a value for [CN] of about 330–390 ppm from detailed chemical kinetics calculations for HMX. Melius [12] obtained a peak [CN] of 500 ppm for RDX deflagration at 17 atm.

NO:

[NO] was obtained as a function of distance for laser-assisted RDX deflagration using the single-pass configuration. The [NO] profile and temperature were obtained by fitting with calculated spectra [8]. The concentration profile in Fig. 6 (and Fig. 3) shows the [NO] highest near the pellet surface, nearly constant with distance, and then dropping rapidly with a maximum [NO] of about 0.2 mole fraction, compared with 0.22 mole fraction obtained for HMX [8].

Ermolin et al. [6] measured NO profiles in their TOF-MS and showed the [NO] peaking at the surface and falling off toward higher distances, similar to the [NO_2] profile with peak [NO] of 0.23 mole fraction. Melius [12] obtained a peak [NO] of 0.24 mole fraction at 17 atm. The PLIF measurements (current work and Refs. 1 through 4 for HMX) indicated that [NO] extends out to just below the [CN] peak. Hatch [13] showed a profile similar to the measured one in Fig. 6 with a peak [NO] of almost 0.32 mole fraction, using the decomposition products NO_2 + HCN + H, and 0.085 mole fraction at 100 psi when he added in some CH_2O + N_2O. Therefore, for the conditions of this work, it appears that the major decomposition channel was that of N—

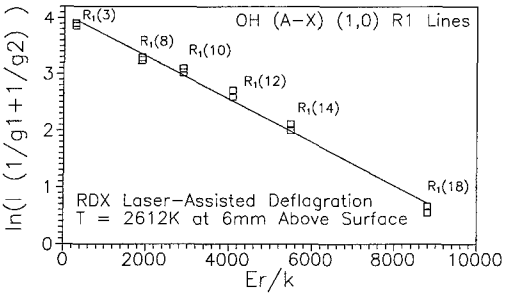

FIG. 7. OH rotational temperature fit for a selected distance off the sample surface. E_r/k is the rotational energy of the lines monitored using laser-saturated PLIF, and g_1 and g_2 are the degeneracies of the upper and lower states of the transition. The negative inverse of the slope yields a temperature of 2653 K.

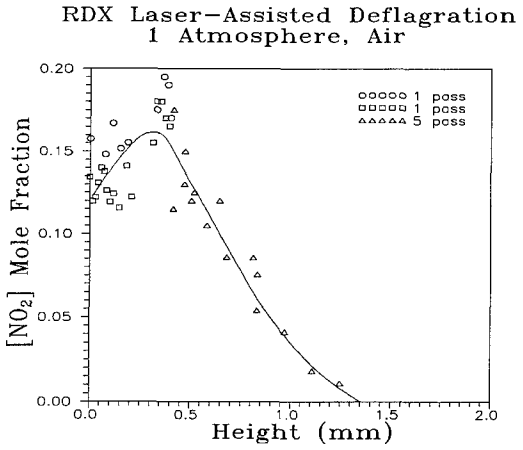

FIG. 8. Absolute $[NO_2]$ profile from RDX laser-assisted deflagration at 1 atmosphere.

NO_2 bond scission, in agreement with the conclusions of Ref. 5. Because the [NO] was nonzero at the surface, it appears that some condensed-phase decomposition occurs. Fetherolf et al. [7] showed a maximum [NO] of about 0.24 mole.

OH:

Laser-saturated PLIF measurements were used to obtain the temperature of OH as a function of distance off the surface of laser-assisted deflagration of RDX at 1 atm. The $R_1(3)$, $R_1(8)$, $R_1(10)$, $R_1(12)$, $R_1(14)$, and $R_1(18)$ transitions of A-X (1,0) band were pumped by the UV laser, and the LIF was imaged using a 311 nm, 5 nm FWHM interference filter in front of the CCD camera. Lines above $K = 18$ were found to not fit a Boltzmann plot; the $R_1(1)$ and $R_1(2)$ lines were left out of the analysis because of serious Lambda-doubling perturbation. Analysis of laser-saturated OH signals has been discussed previously [2,3]. A plot of $\ln(I_{fl}(1/g_1 + 1/g_2))$ vs E_r/k for a selected distance from the RDX surface is shown in Fig. 7, where I_{fl} is the LIF signal, g_1 and g_2 are the degeneracies of the upper and lower levels of the absorption transition, and E_r/k is the rotational energy divided by the Boltzmann constant. Figure 4 shows the temperature profile above the surface of laser-assisted deflagrating RDX.

OH radical absorption measurements were made of burning RDX pellets using the multipass configuration. No concentration information for OH can be obtained below the flame front for the line-of-sight absorption experiments, as there is OH surrounding the flame front "arc." Therefore, only spectra obtained above the flame front were used to obtain [OH] and OH temperature from the absorption measurements. From the PEP code [23], an equilibrium [OH] of 0.0256 mole fraction would be expected in the burnt gas region above the flame front at an adiabatic temperature of 2902 K. Analysis of these spectra verified that a temperature of around 2600 K fit the data, and maximum [OH] of 0.055 mole fraction was obtained, 2.15 times that for thermochemical equilibrium. Vanderhoff [9] has reported a measured [OH] of 1.7 times that for thermochemical equilibrium in a stoichiometric CH_4/N_2O flame and a flame temperature of 2360 K, compared with an adiabatic temperature of 2922 K. No results for [OH] from modeling were available.

NO_2:

Figure 8 (and Fig. 3) shows the concentration profile obtained for NO_2 for laser-assisted deflagration of RDX. Spectra were all obtained for the single-pass configuration close to the surface and with the multipass configuration (five beams at the crossing point) away from the surface where the $[NO_2]$ was small. Several attempts were made to measure $[NO_2]$ for self-deflagrating RDX but were not successful due to the fact that $[NO_2]$ peaks so close to the surface and the self-deflagration flame is compressed with respect to the laser-supported deflagration.

The NO_2 spectrum is much too complex to simulate. Absorption cross sections for the 360–680 nm region were available in the literature [24,25] and were used to obtain the concentration as a function of distance. The absorption cross sections were for room temperature, however. No cross sections for elevated temperatures were available in the literature to the authors' knowledge, so our measurements are in error if the spectrum changes significantly with temperature. The absorbance at three wavelengths (475, 488, and 505 nm—peaks and nearby valleys) were measured for each frame, and then the concentration was calculated using Beer's law and the difference of the absorbances, peak to valley.

Mole fractions of NO_2 in an RDX flame were obtained from the concentrations obtained for room temperature using the perfect gas law and the temperature curve in Fig. 4. The $[NO_2]$ profile in Fig. 8 (and Fig. 3) shows the $[NO_2]$ rising from the surface to a 0.17 mole fraction peak at a distance from the surface corresponding to a plateau in the temperature curve, similar to the [NO] behavior, and then decreases rapidly to zero at about 1.5 mm, at which distance the [NO] starts to decrease rapidly.

Melius [12] shows a peak $[NO_2]$ of at least 0.1 mole fraction for RDX at 0.5 atm and 0.056 at 17 atm. Hatch [13] shows a peak $[NO_2]$ of about 0.1 mole fraction for HMX at 1000 psi for the HCN + NO_2 + H decomposition channel and about half that value when CH_2O + N_2O were added to the decomposition products. Ermolin et al. [6] obtained a maximum concentration (near the surface) of only 0.01 mole fraction. Fetherolf et al. [7] reported a peak $[NO_2]$ of about 0.09 mole fraction for a laser flux of 50 cal/cm^2 s at 1 atm. Because of their presumed thicker melt layer and, therefore, more condensed-phase decomposition, the lower $[NO_2]$ in their work was expected. The fact that the $[NO_2]$ of this work increased initially above the surface indicates that gas phase RDX was present and decomposing above the surface. The large value of $[NO_2]$ seen in our experiments (coupled with the large [NO]) indicates the predominance of the N—NO_2 bond scission channel under our conditions of high heating rate and thinner melt layer. Since actual rocket motor conditions lead to even higher heating rates (i.e., less time spent at lower temperatures) and thinner melt layers, the N—NO_2 bond scission channel will predominate even more.

NH:

NH radical absorption measurements were made for self-deflagrating RDX pellets using the multipass (five beams at crossing point) configuration. Because the spectral resolution was not good enough to resolve rotational lines and the amount of absorption was so small, two simulated spectra were calculated, one for a temperature of 2600 K and the other for 2900 K (adiabatic RDX flame temperature at 1 atm), yielding [NH] of from 97 to 107 ppm (6.4-mm diameter sample). A separate test (9.5-mm diameter) yielded [NH] of from 69 to 76 ppm. Figure 3 shows the profile for [NH] obtained from a PLIF image for laser-assisted deflagration. Thermochemical equilibrium calculations [23] show that [NH] in the burnt gas region should be 0.35 ppm. Melius obtained a peak [NH] of 260 ppm at 17 atm.

H_2CO:

Tests were conducted to measure formaldehyde in the RDX flame since it has been detected with mass spectrometry in some studies [7] and not in others [6]. The CO_2 laser flux level was varied from 12 cal/cm^2-s, which pyrolyzes but does not ignite RDX, up to 50 cal/cm^2-s to match that of Ref. 7. Using literature extinction coefficients [26], as well as absorption measurements of formaldehyde gas from paraformaldehyde, the formaldehyde concentration in the RDX pyrolysis plume was less than 0.005 mole fraction, much below the levels cited in Ref. 7 but closer to the levels calculated in Ref. 12. H_2CO and NO have the same mass and similar appearance potentials [7], leading to difficulty of separation in mass spectrometry studies.

Summary

Nonintrusive diagnostics were used to measure temperature and species profiles during neat RDX deflagration at 1 atm. UV-visible absorption was measured to obtain absolute concentration profiles of NO, NO_2, CN, NH, and OH. Temperature and species concentrations were obtained by spectral fitting. Planar laser-induced fluorescence (PLIF) of these same species was used to obtain 2D profiles in the flame with excellent spatial resolution. The flame structure is characterized by a dark zone close to the surface and a visible flame sheet above. For CO_2 laser-assisted deflagration, the narrow flame sheet NH profile peaks 2.3 mm above the surface at a value of ~100 ppm. The CN profile is wider than the NH profile and peaks slightly further from the surface in agreement with results obtained for HMX [1–4]. The peak is at 2.5 mm with a value of 660 ppm. The OH profile peaks outside the CN/NH flame sheet with a mole fraction of 0.055. The dark zone species studied here were H_2CO, NO_2, and NO. The NO_2 peaks very close to the surface at about 0.17 mole fraction and decays rapidly to zero at 1.5 mm. Very close to the surface, the NO mole fraction is about 0.2 and falls sharply to 0.05 at 2.5 mm as NO is consumed in the CN/NH flame sheet. If formaldehyde is present in the flame, it has a mole fraction less than 0.005. Rotational temperature profiles were measured from OH PLIF and NO absorption spectra. The gas temperature near the surface is in good agreement with prior thermocouple measurements. The temperature rises sharply to about 1500 K at 0.3 mm and then turns over to a much more gradual slope in the dark zone. At about 2 mm, it becomes steeper again and finally levels out to 2600 K at 3.0 mm, at the top edge of the CN flame sheet.

Acknowledgment

The authors gratefully thank Dr. Richard Miller of ONR for funding this work.

REFERENCES

1. Parr, T. P., and Hanson-Parr, D. M., *Twenty-Sixth JANNAF Combustion Subcommittee Meeting*, CPIA Publication 529, 1989, Vol. I, p. 27.
2. Parr, T. P., and Hanson-Parr, D. M., *Twenty-Fourth JANNAF Combustion Subcommittee Meeting*, CPIA Publication 476, 1987, Vol. I, p. 367.
3. Parr, T. P., and Hanson-Parr, D. M., Paper No. 87–14, Western States Section/The Combustion Institute Spring Meeting, Provo, Utah, April 6–7, 1987.
4. Hanson-Parr, D. M., and Parr, T. P., *Twenty-Third JANNAF Combustion Meeting*, CPIA Publication 457, 1986, Vol. I, p. 249.
5. a) Palopoli, S. F., and Brill, T. B., *Combust. Flame* 87:45–60 (1991). b) Oyumi, Y., and Brill, T. B., *Combust. Flame* 62:213–224 (1985). c) Brill, T. B., and Brush, P. J., *Phil. Trans. R. Soc. London A* 339:377–385 (1992).
6. a) Korobeinichev, O. P., *Combust. Expl. Shock Waves* 23:565–576 (1988). b) Ermolin, N. E., Korobeinichev, O. P., Kuibida, L. V., and Fomin, V. M., *Combust. Expl. Shock Waves* 24:400–407 (1989). c) Amosov, K. A., Kuibida, L. V., Korobeinichev, O. P., and Bol'shova, T. A., in *Flame Structure* (O. P. Korobeinichev, Ed.), Vol. 1, Novosibirsk, Nauka, Siberian Branch, 1991, pp. 93–98.
7. Fetherolf, B. L., Liiva, P. M., Litzinger, T. A., and Kuo, K. K., *Twenty-Eighth JANNAF Combustion Committee Meeting*, CPIA Publication 573, Vol. II, 1991, p. 375.
8. Hanson-Parr, D. M., and Parr, T. P., *Twenty-Eighth JANNAF Combustion Committee Meeting*, CPIA Publication 573, Vol. II, 1991, p. 369. (Due to an error in the CN program, the peak CN concentration for HMX should be 485 ppm and not 322 ppm).
9. Vanderhoff, J. A., *Combust. Flame* 84:73–92 (1991). See also the following Army Research Lab technical reports: BRL-MR-3911 (1991), BRL-TR-3098 (1990), and ARL-TR-180 (1993).
10. Stufflebeam, J. H., and Eckbreth, A. C., *Combust. Sci. Technol.* 66:163–179 (1989).
11. Edwards, T., *Twenty-Sixth JANNAF Combustion Committee Meeting*, CPIA Publication 529, Vol. I, 1989, p. 13.
12. Melius, C. F., *Twenty-Fifth JANNAF Combustion Meeting*, CPIA Publication 498, Vol. I, 1988, p. 155.
13. Hatch, R. L., *Twenty-Fourth JANNAF Combustion Meeting*, CPIA Publication 476, Vol. I, 1987, p. 383.
14. Engleman, R., *J. Mol. Spectrosc.* 49:106–116 (1974); Engleman, R., and Rouse, P. E., *J. Quant. Spectrosc. Rad. Trans.* 15:831 (1975).
15. Engleman, R., Rouse, P. E., Peek, H. M., and Baiamonte, V. D., Los Alamos Report LA-4364, October 1969.
16. Dieke, G. H., and Crosswhite, H. M., *J. Quant. Spectrosc. Radiat. Transfer* 2:97 (1962).
17. Earls, L. T., *Phys. Rev.* 48:423–424 (1935); Scheingraber, H., and Vidal, C. R., *J. Chem. Phys.* 83:3873–3877 (1985).
18. Dixon, R. N., *Can. J. Phys.* 37:1171 (1959); see also, Fairchild, P. W., Smith, G. P., Crosley, D. R., and Jeffries, J. B., *Chem. Phys. Lett.* 107:181–186 (1984); Brazier, C. R., Ram, R. S., and Bernath, P. F., *J. Mol. Spec.* 120:381–402 (1986).
19. Copeland, R. A., Jeffries, J. B., and Crosley, D. R., Chem Phys. Lett. 138:425–430 (1987) and Chidsey, I. L. and Crosley, D. R., *J. Quant. Spectrosc. Radiat. Transfer* 23:187–199 (1980).
20. Herzberg, G., *Molecular Spectra and Molecular Structure I. Spectra of Diatomic Molecules*, 2nd ed., Van Nostrand Reinhold Company, New York, 1950.
21. Schmidt, S. C., and Malte, P. C., *J. Quant. Spectrosc. Radiat. Transfer* 16:963–972 (1976); Luck, K. C., and Thielen, W., *J. Quant. Spectrosc. Radiat. Transfer* 20:71–79 (1978); Luck, K. C., and Muller, F. J., *J. Quant. Spectrosc. Radiat. Transfer* 17:403–409 (1977).
22. Chang, A. Y., and Hanson, R. K., *J. Quant. Spectrosc. Radiat. Transfer* 42:207–217 (1989).
23. Cruise, D. R., "Theoretical Computations of Equilibrium Compositions, Thermodynamic Properties, and Performance Characteristics of Propellant Systems," Naval Air Warfare Center, Technical Progress Report NWC-TP-6037.
24. Harker, A. B., Ho, W., and Ratto, J. J., *Chem. Phys. Lett.* 50:394–397 (1977).
25. Hsu, K. D., Monts, D. L., and Zare, R. N., *Spectral Atlas of Nitrogen Oxide*, Academic Press, New York, 1978.
26. McQuigg, R. D., and Calvert, J. G., JACS 91:1590–1599 (1969).

COMMENTS

O. Korobeinichev, Institute of Chemical Kinetics and Combustion, Russia. A very impressive technique has been developed and very interesting research has been done. The results are very important for understanding combustion chemistry of solid propellants. But the chemical mechanism of CO_2 laser assisted combustion may differ from self-sustained deflagration. So it will be very important to perform experiments under conditions of self-sustained deflagration (for example, with slightly preheated RDX or at higher pressures).

Author's Reply. We did do some experiments under self-sustained combustion with RDX. The CN flame sheet under these conditions, even at 1 atm, is only 0.46 mm above the surface, compared to 2.5 mm for laser assisted. This makes resolution of the structure too difficult. Since it is easy to add the extra laser heat flux to computer models,

our data can be used to validate these models with the extra laser flux, which can then easily predict the flame structure *without* the extra flux. Working at elevated pressures reduces the length scales even further (Parr and Hanson-Parr, *Proceedings of the 26th JANNAF Combustion Committee Meeting,* CPIA Publication 529, 1989, Vol. I, p. 27), making resolution of structure even more difficult.

•

H. S. Mukunda, Indian Institute of Science, India. Concerning the differences between the two-stage flame structure and lack of it in theory, it appears to me that while the theory is "clean," the experiment has a liquid bubbly layer with tiny droplets shooting into the flame zone. Depending on the density of the droplets in the flame zone, the phenomena of vaporisation and decomposition will affect the perceived thermal/chemical behavior. The point is that to expect correspondence between the theory and experiment may be too much to ask for.

Author's Reply. This is true, but difficult to overcome. At low pressures, even without external laser flux, the burn rate of nitramines is low and the melt layer quite thick, leading to ejection of droplets from the bubbling liquid. At high pressures, the burn rate is higher, the melt layer much thinner, and droplets are probably no longer ejected. But, at these pressures, the flame length scales are much too small to resolve with any diagnostic technique. Perhaps we can quantify our measured droplet density, size distribution, and spatial distribution and have this information added ad hoc to the theoretical models, allowing the rest of the model to be validated by our species and temperature profiles. This might require some more double pulse images to be taken to measure the evaporation rate versus height in the flame for input into the model.

•

Dieter Bruggemann, ITLR/University of Stuttgart, Germany. At 2.5-mm height above the surface, you measured a NO concentration of 5% while at larger distances no data points are shown. Does this mean that you stopped the measurements at this point or that the NO concentration fell below the detection sensitivity? I would not exclude NO to appear as a major species at larger heights above the surface.

Author's Reply. We mainly concerned ourselves with measuring species concentrations and temperatures in the dark zone and secondary combustion zone up through the CN flame sheet. We have some limited data, however, that indicate that the NO concentration decreases very slowly with distance above the CN flame sheet. We'll do more measurements in the future to quantify this.

•

Michael Page, North Dakota State University, USA. You show two competing pathways for the decomposition of 1/3 RDX: one leading to NO_2 and the other leading to formaldehyde and N_2O. Our calculations indicate a third channel, leading to HONO + HCN, that has a barrier a few kcal/mole below the energy necessary to rupture the NN bond. What role do you see for this channel?

Author's Reply. This channel, i.e., 5 center elimination of HONO and ring fragmentation to HCN, would be indistinguishable in our present results from the (global) NO_2 + H_2CN channel. With the steep temperature rise region close to the surface, HONO would rapidly disproportionate to 1/2 NO + 1/2 NO_2 + 1/2 H_2O while H_2CN would very quickly decompose to H + HCN and the H would react rapidly with the NO_2 to form 1/2 NO + 1/2 NO_2 + 1/2 H_2O. Thus, the products and concentrations are the same in both cases. To distinguish between them, we would have to make HONO measurements very close to the surface. Although HONO cannot be detected via LIF due to predissociation, Wittig [*Chem. Phys. Lett.* 111:25 (1984)] has developed a pump-probe technique that dissociates the HONO to OH and NO and then monitors the product NO or OH by LIF. In our system, where there is an extreme amount of natural NO we would have to monitor OH, which, from our measurements, has a low natural concentration near the surface. We may undertake such experiments in the future and thank Prof. Page for pointing out their importance.

•

Jay Jeffries, SRI International, USA. With the large OH concentration, would you comment on how you avoided optical depth difficulties in the OH PLIF and OH rotational temperature measurements?

Author's Reply. If there were rapid vibrational energy transfer (VET) from the excited $v = 1$ state to the $v = 0$ state, then a significant fraction of the LIF emission would be in the (0,0) band which would suffer from radiation trapping due to the high concentration of $v = 0$ OH in our flames. Several factors conspire to minimize this problem. First, rotational energy transfer (RET) is typically faster than collisional quenching in flames [Crosley and Garland, *Appl. Opt.* 24:4229 (1985)], so no matter what rotational level is pumped, most of the emission comes from a thermalized distribution. Thus, there is little systematic error between various levels pumped, just a constant loss of signal for all levels that is ratioed out in the calculation for temperature. The predominance of RET over quenching was confirmed (in a Bunsen flame with lower [OH]) by a largely thermalized spectral distribution of LIF emission (Parr and Hanson-Parr, Chap. 8, in *Nonsteady Burning and Combustion Stability of Solid Propellants,* Progress in Astronautics and Aeronautics, AIAA Inc., New York, 1992, Vol. 143). The three lines connected to the pumped level were found to be only slightly enhanced over neighboring RET populated lines (although we did not analyze this emission spectrum for thermal distribution). Secondly, VET is typically slower than RET or quenching in 1-atm pressure flames so most of the emission we monitor comes

from the (1,1) band, which is why we use a 315-nm filter rather than a 309 nm. The LIF emission spectrum again verifies that a majority of the detected emission is from (1,1) not (0,0). Since the population of the $v = 1$ level is only 1/8 that of the $v = 0$ level at the measured temperature, it is less susceptible to radiation trapping. Third, the maximum path length for emitted fluorescence is less than 5 mm. Also, there is almost no evidence that the OH PLIF signal from the edges of the flame (short trapping path length). Finally, the facts that the Boltzmann plots were linear and that the PLIF-measured OH peak temperature matches that measured by absorption and is not far below the adiabatic flame temperature give us further confidence in our measurements.

Twenty-Fifth Symposium (International) on Combustion/The Combustion Institute, 1994/pp. 1645–1650

LASER RECOIL, PLUME EMISSION, AND FLAME HEIGHT COMBUSTION RESPONSE OF HMX AND RDX AT ATMOSPHERIC PRESSURE

JERRY C. FINLINSON, TIM PARR AND DONNA HANSON-PARR
Naval Air Warfare Center Weapons Division
Propulsion Research, Code C02392
China Lake, CA 93555, USA

The laser recoil technique was used to measure the combustion response of neat HMX and RDX at atmospheric pressure in air. Heat flux was modulated approximately sinusoidally at frequencies from 2.5 to 1000 Hz and heat fluxes of 8–52 W/cm^2. Thrust, light emission, and flame position were measured simultaneously so that amplitude and phase relationships could be determined as a function of frequency. Thrust was measured using a microforce transducer, light emission was measured by photo diode, and the flame height was photographed using a gated intensified charge coupled device (CCD) camera. The CCD camera recorded CN radical chemiluminescence, which is a measure of flame structure for the final (secondary) flame sheet.

HMX had a broad flat thrust response, suggesting that the recoil technique needs further improvement. HMX had a light emission resonance at 10 Hz. RDX thrust and light emission oscillations were about half the amplitude of HMX. Monopropellant burn rates were 0.080 cm/s and 0.054 cm/s for HMX and RDX, respectively. HMX flame height was found to vary sinusoidally with phase angle, having a response peak between 8 and 50 Hz and crossing from phase lead to phase lag at about 20 Hz. The flame height response function of HMX was similar to light emission response. The resonant peak occurred at approximately the same frequency, the phase reacted the same as a function of frequency, and no unusual effects were seen at high frequency. Based on this data, the flame is reasonably quasi-steady below 40 Hz, in that the difference in phase lag between thrust and flame oscillations is less that 30° with almost no difference at the response peak of 10–20 Hz.

Introduction

To gain insight into the fundamental controlling mechanisms of solid propellant combustion instability, we are studying the response of solid propellant samples to oscillatory CO_2 laser heat flux. The system for laser-driven combustion response measurement was developed in previous work, and similar techniques are used by other researchers [1–12]. Basically, a CO_2 laser is modulated by a sine wave at a chosen frequency to supply the igniting heat flux and an oscillatory heat load to the propellant sample. The resulting sinusoidal thrust oscillations are measured by a force transducer. The phase relation of the imposed heat flux and the propellant thrust signal is determined using cross correlation. A photosensor measures total light output, and a CCD camera records the flame position relative to the sample surface.

Propellant response functions are used to compare the sensitivity of different propellants to combustion instability. The most widely used and accepted experimental method of measuring the pressure-coupled response, R_p, is the T-burner. The term R_p is defined as the ratio of oscillating mass loss component to oscillating pressure component normalized by the steady values, $(m'/\bar{m})/(p'/\bar{p})$. A minimum quantity of 500 g of propellant is required for T-burner testing over a range of frequencies. In combustion response modeling, the problems are nondimensionalized using the equation, $\Omega = 2\pi f a/(\bar{r}^2$, where f = frequency in Hz, a = thermal diffusivity (0.0024 cm^2/s for HMX-pressed pellets at 25 °C, 0.0016 cm^2/s at 106 °C) [13–15], and $\bar{r}$ = mean burn rate (0.08 cm/s for HMX). A thermal diffusivity of 0.0024 cm^2/s was used for both HMX and RDX throughout this paper. T-burner experience suggests that common composite propellants typically have a response peak near a nondimensional frequency, Ω, of 10 [6]. An Ω of 10 corresponds to about 5 Hz for HMX and 2 Hz for RDX at the laser-augmented burn rates studied here. Previous research has verified that both HMX and RDX form melt layers on the surface at pressures below 1000 psi [13–15]. Using the radiative absorption coefficients measured at 10.6 μm, the $1/e$ transmission thickness for HMX is 1 μm and for RDX is 2 μm [19]. The thermal wave thickness, $Xt = a/\bar{r}$, for HMX at these conditions is 200–300 μm. Since the transmission thickness is so small compared to the thermal wave thickness, the

samples are opaque enough to demonstrate measureable response without adding carbon black additive.

The laser recoil technique has the advantage of small sample sizes, which is important for new ingredients that are difficult to obtain. Using sharp pulses and spectral techniques, or more recently a logarithmic frequency sweep, the entire thrust response function has been obtained using a single 0.5-g sample [7]. However, these data were done with a fixed frequency during each test, to allow the CCD camera to synchronize with the oscillations.

The ability to measure phase angle is an added advantage of this technique over T-burner testing. However, instead of measuring the pressure-coupled combustion response, the device measures the radiant heat flux response, $R_q = (m'/\bar{m})/(q'/\bar{q})$, where q' is the oscillating component of heat flux and $\bar{q}$ is the steady component of heat flux. A transfer function between the heat flux response, R_q, and the more useful pressure response, R_p, has been developed and is being verified [6–11].

The response of the gas-phase flame to oscillatory heat loads between very low (~2.5 Hz) and high (~1 KHz) frequencies was investigated. Previous modeling of solid propellant combustion instability [6–12] has nearly universally assumed a quasi-steady-state response of the gas phase; i.e., gas-phase convection and kinetics, and therefore flame height, responds to changes in the propellant burning rate almost immediately, and the resonance is controlled by the lag-lead properties of the condensed-phase temperature profile. It should be noted that the quasi-steady assumption also involves a quasi-steady surface reaction zone [11]. We wished to validate the gas-phase assumption by imaging the gas-phase flame structure using flame chemiluminescence from the CN radicals in the flame front. The frequency and phase angle responses of the flame height were quantified for neat HMX. All data reported in this paper were taken in open atmospheric pressure (13.6 psi).

Apparatus

A schematic of the laser and data acquisition equipment is shown in Fig. 1. A 3.5-L combustion bomb was used at atmospheric pressure with its top cover removed for better exhaust venting [6]. Light emission from the combustion was monitored by a photosensor. The light was gathered by a glass fiber-optic bundle that monitored emission from the surface to 5 cm above. The fiberoptic and silicon photodiode had a spectral bandpass of 400–1050 nm.

A 240 W continuous CO_2 laser (10.6 μm) was modulated sinusoidally by a function generator that controlled the modulation frequency (1–1000 Hz) and amplitude (30–195 W) of the heat flux oscillations.

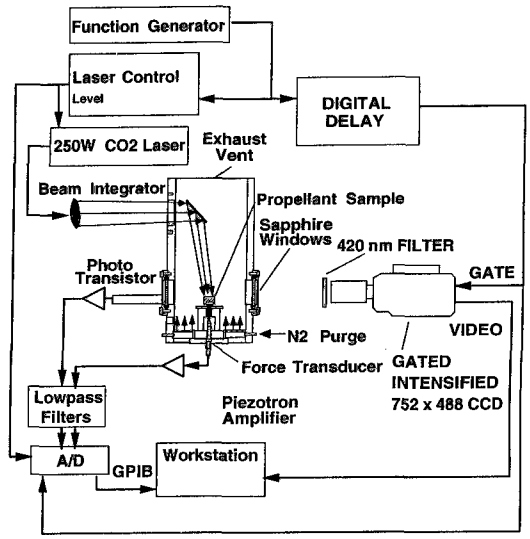

FIG. 1. Schematic of the Laser Recoil Apparatus. Force transducer below sample measures thrust, photo transistor measures light emission, and gated intensified CCD camera measures flame position.

The laser beam had a nonuniform energy profile, and multiple mirror beam integration was used to spread the energy distribution in the laser beam into a top hat profile of a 2.25-cm^2 area [7]. This created a 15-mm square beam that totally covered the samples with a relatively flat heat flux profile. The power transmission loss through the optics was about 33%, and the exhaust plume absorbance was about 10% [7,8]. The mean heat flux delivered to the surface was therefore about 35 W/cm^2. The laser energy was modulated approximately sinusoidally from a minimum of 8 W/cm^2 to a maximum of 52 W/cm^2.

The force magnitude was calibrated by setting small weights on the transducer and removing them to determine the step change in force due to a loss in weight. The resonant frequency of the force transducer system determined by impulse testing was 6900 Hz. Since we operated below 1000 Hz, far from the resonant peak, we expect the phase influence to be small. Laser output was calibrated by using an HgCdTe detector to monitor the beam power as a function of frequency. The laser power amplitude decreased by 50%, and the phase lag increased from 16 to 40 degrees as frequency increased from 10 to 1300 Hz. The data were corrected to account for these effects. Data were sampled at least 20 times the test driving frequency, to allow for at least an 18° phase resolution on the cross-correlation calculation.

The flame structure could be measured either with planar laser-induced fluorescence (PLIF) imaging of radicals [14–17] or by direct imaging of natural flame chemiluminescence. The PLIF imaging monitors the

ground electronic state of flame species, while chemiluminescence comes only from excited electronic states formed in low probability energetic reactions. Chemiluminescence is sometimes a poor choice to monitor flame structure, because it tracks low probability secondary reactions rather than the main flame chemistry pathways. For example, OH chemiluminescence does not track ground state OH radical concentrations at all [18]. We have found that in propellant flames, CN emission tracks CN ground state PLIF very well, so imaging chemiluminescent emission is a good measure of the flame structure. All data reported here are from emission images rather than PLIF images. There is one difference caused by monitoring emission rather than PLIF: here, we report the flame height as being the top of the flame, where CN population has fallen back to a low value beyond its peak. In previous PLIF papers, the flame height was reported as being at the center (peak) of the narrow CN profile, which is a difference of about 0.34 mm.

The CN radical chemiluminescence was monitored using a gated image intensified CCD of 752 by 480 pixel resolution. The gate time was 10 μs, which completely froze the flame structure. The CN emission was selected using a 65-nm bandwidth interference filter centered at 400 nm; this filter passes both $\delta v = 0$ and $\delta v = 1$ bands of the CN B-X transition, yet blocks most other flame radiation, including the 310-nm A-X OH bands. Previous PLIF work on HMX and RDX showed that CN radicals are associated with the final (i.e., secondary) flame sheet where the adiabatic flame temperature is reached. The secondary flame sheet was imaged because the primary flame is much too close to the sample surface to resolve and does not emit chemiluminescence.

Experimental Results and Analysis

Each sample (a pellet of oxidizer 9.5 mm in diameter and 4–6-mm high) burned for up to 8 s at atmospheric pressure. Once ignited, HMX and RDX combust vigorously while subjected to laser radiation, although they tend to smoke profusely until ignition occurs. Ignition delay was reduced by placing a thin sliver of N5-catalyzed double-base propellant on the pellet. Figure 2 shows the laser control, light emission, and total force signals from an HMX combustion test at 7.9 Hz. The three large thrust oscillations near the beginning are due to N5 combustion; also, light emission is initially higher due to N5. The HMX ignited evenly and gave relatively constant thrust and light oscillations until burnout began. The force signal shows a downward trend due to mass loss of the sample (0.731 g/V). Compared to HMX, RDX gave smaller thrust and light oscillations. Because RDX has a lower melting temperature, 205 °C as compared to 280 °C for HMX, it formed a molten

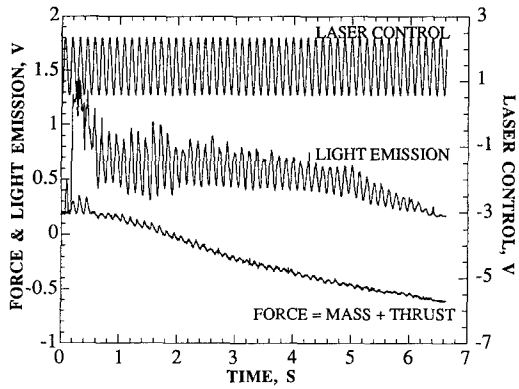

FIG. 2. HMX laser recoil combustion test record. For a 7.9 Hz driving signal, the laser control, light emission, and thrust signals are recorded.

mass as it burned. The molten layer may act as an oscillation damper and modify the thermal profile into the sample. Monopropellant burn rates were 0.080 cm/s and 0.054 cm/s for HMX and RDX, respectively.

The amplitude and phase lead were determined by performing a discrete-time cross correlation of the laser control signal compared to the thrust or photosensor response. This algorithm assumes sinusoidal laser input signals, which is slightly violated, since the power output of the laser is somewhat nonlinear. Root mean square (rms) values were used for signal amplitudes. To reduce data scatter, cycles were analyzed and averaged over half-second time increments. By performing similar tests at various frequencies, the magnitude and phase of the propellant response as a function of frequency was measured.

Figure 3 is a plot of HMX oscillation amplitudes for thrust and light emission as a function of frequency. The thrust response was flat and approaches zero at frequencies above 200 Hz. Ideally, we should compare our results to pressure-coupled T-burner data, but we are unaware of any for pressed HMX or RDX. Error bars indicate standard deviation of data scatter within one test. HMX light emission showed a pronounced response peak from 6 to 25 Hz, with the maximum around 10 Hz, where the light phase changes from lead to lag. Light oscillations were essentially zero at frequencies above 200 Hz. The response peak was much easier to detect using the optical techniques, suggesting that the thrust technique needs further development. The phase has excessive data scatter at high frequencies because of low signal magnitude.

Figure 4 is a plot of the phase lead of the thrust and light emission oscillations as a function of frequency. HMX thrust shows a phase lead at frequencies below 30 Hz and a phase lag approaching 70° at 200 Hz. Since the thrust phase changes from lead to

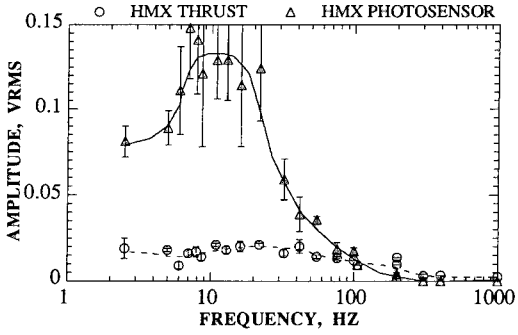

FIG. 3. HMX thrust and light emission amplitude response.

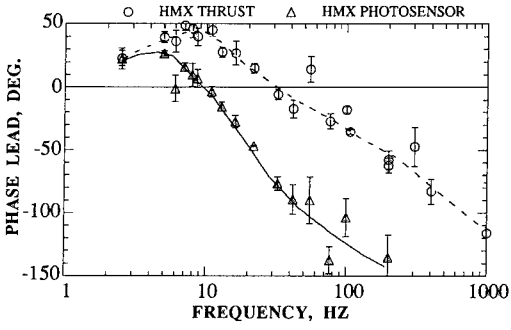

FIG. 4. HMX thrust and light emission phase response.

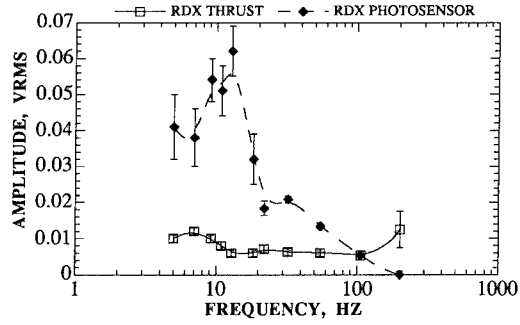

FIG. 5. RDX thrust and light emission amplitude response.

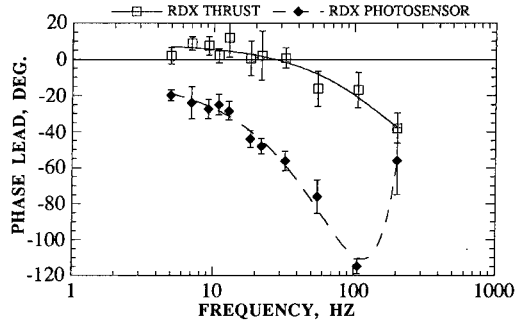

FIG. 6. RDX thrust and light emission phase response.

lag around 28 Hz, the resonance peak should be in that range [12]. From the phase information, we can safely conclude that there was only one resonance peak. Additional resonance peaks would require an additional phase shift from lead to lag.

Note in Fig. 4 that the light phase lagged behind the thrust phase. This is reasonable, because the thrust is produced by the condensed-phase decomposition, $\dot{m}$, and light emission results from gas-phase combustion in the 5-cm plume and, therefore, has a convective delay. Since the photosensor is monitoring a 5-cm plume height, part of the light emission comes from late in the plume rather than from the secondary flame zone. Calculations show that the time constant of the gas-phase light emission decreases as frequency increases. At 7 Hz, the light emission lags 30° behind the thrust, which corresponds to a time delay of 12 ms. At 22 Hz, the light lags 62° or 8 ms behind, and at 42 Hz, it is 72° or 4.8 ms behind. Since the gas velocity coming from the secondary flame is approximately 1400 cm/s, these time delays are larger than expected, strictly from convective delay arguments.

The thrust and light emission responses for RDX are shown in Figs. 5 and 6. The thrust response peak for RDX in Fig. 5 appears to be about 7 Hz. Unfortunately, only one test was performed at frequencies below 7 Hz. The thrust response of HMX is double that of RDX, 20 vs 10 mV rms. Both HMX and RDX thrust crossed from phase lead to lag near 25 Hz. RDX light emission showed a resonant peak from 8 to 15 Hz, at half the magnitude of the HMX peak, and corresponds to Ω values of 38–72. RDX thrust phase lead at low frequencies was smaller than for HMX, which may be due to the thick melt layer. Future plans include tests at higher pressures, where the increased burn rate shifts the resonant peak to a higher frequency.

Flame structure (CN emission) was monitored with the CCD camera at 50-μm resolution. The camera was allowed to free run and the gate pulse digitized so that each image's phase angle could be calculated post test. Test frequencies were selected such that the beat between this frequency and the constant 59.95 Hz framing rate of the camera would map out 12 relatively evenly spaced phase angles. Selected test frequencies used were 2.5, 5.0, 6.0, 7.0, 7.9, 8.6, 10.9, 12.9, 16.1, 21.8, 32.4, 41.6, 55.0, 76.4, 106.0, 200.0, 304.6, 401.2, and 1000 Hz. At the response peak frequency, the HMX flame sheet hopped up and down in response to the varying laser flux. The flame sheet thickness stayed approximately constant through the cycle. In each image, the flame

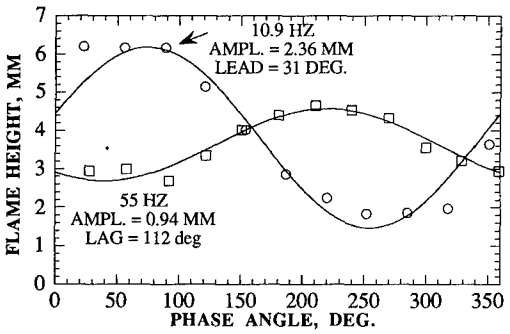

FIG. 7. CN chemiluminescence flame height vs phase angle for HMX at 10.9 and 55 Hz.

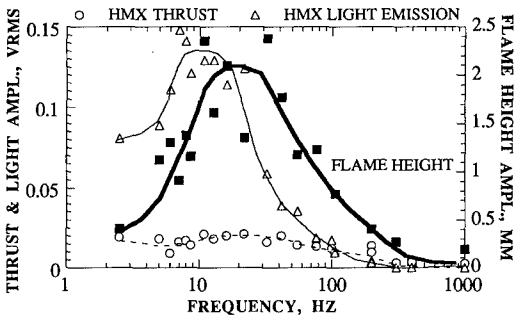

FIG. 8. HMX CN chemiluminescence flame height amplitude response compared with thrust and light emission amplitude response.

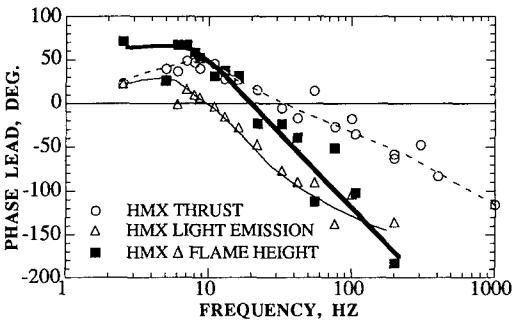

FIG. 9. HMX CN chemiluminescence flame height phase response compared with thrust and light emission phase response.

height was measured at several points across the image field of view on a graphics workstation and the average value reported. Figure 7 shows HMX flame heights plotted vs the phase angle in the forcing cycle for forcing frequencies of 10.9 and 55 Hz. The flame heights were least-square fitted to a sine wave, shown as a solid line. The laser flux would be a sine wave crossing zero at 0° and reaching a peak at 90° on these plots. The 10.9-Hz images show a flame height amplitude variation of 2.36 mm and a phase lead of 31. This is near the resonant peak for HMX under these conditions. For 55 Hz, the amplitude variation is smaller (0.94 mm) and has a phase lag of 112°. At frequencies above 200 Hz, oscillation amplitudes were too small to obtain meaningful data. Similar plots were made at each frequency and the amplitude and phase were determined and summarized in Figs. 8 and 9.

Figures 8 and 9 show the HMX CN chemiluminescence flame height amplitude and phase response compared with the thrust and light emission data from Figs. 3 and 4. We were pleased to measure such a large response peak with the phase changing from lead to lag near the center of the peak. The optical techniques have much better defined peaks than the laser recoil technique, suggesting that the recoil technique needs more improvement. In Fig. 9, it is surprising that the flame height phase is leading the thrust phase at low frequencies. All three techniques cross from lead to lag between 10 and 30 Hz. As frequency increases, the thrust and flame height phases are diverging, indicative of a convective delay. At 50 Hz, the flame lags 54° or 3.0 ms; at 100 Hz, the flame lags 84° or 2.3 ms; and at 200 Hz, the flame lags 110° or 1.5 ms. Since the time delay is getting smaller at higher frequencies, it is not just a constant convective transport delay. Besides, we expected the convective transport delay to be approximately 0.8 ms. Based on a primary flame temperature of 1200 K, the surface gas velocity is about 425 cm/s, and the measured flame height of 3.4 mm yields a convective transport delay of about 0.8 ms. Nothing unusual happened at high frequencies; there was no significant secondary rise in response, as would be expected from another resonant peak or mechanism. To the degree that the flame height oscillation is in phase with the thrust oscillation (or offset only by the convective transport delay), we could say that the combustion is quasi-steady. Based on this data, the flame is reasonably quasi-steady below 40 Hz, in that the difference in phase lag between thrust and flame oscillations is less than 30° with almost no difference at the response peak of 10–20 Hz.

Conclusions

These laser recoil response measurements help validate some theoretical predictions and increase our understanding of oxidizer combustion behavior. Pressed pellets of HMX and RDX were tested at 1 atm in air for laser recoil response over the frequency range 2.5–1000 Hz. RDX thrust and light emission oscillations were about half the amplitude of HMX. Because RDX has a lower melting temperature, 205 °C, it formed a molten mass as it burned, which could

damp thrust oscillations. Monopropellant burn rates were 0.080 cm/s and 0.054 cm/s for HMX and RDX, respectively, using an average heat flux of about 35 W/cm^2. Magnitude and phase of thrust, light emission, and flame position oscillations were measured and reported.

HMX had a broad flat thrust response, suggesting that the recoil technique needs further improvement. RDX thrust response peak appears to be around 7 Hz but was not well defined in these tests. HMX light emission showed a tall resonant peak from 6 to 22 Hz, with maximum around 10 Hz, where the light phase changed from lead to lag. Light oscillations were essentially zero at frequencies above 200 Hz.

CN radical chemiluminescence images recorded on a gated image-intensified CCD camera were used to determine the secondary flame location. HMX flame height oscillations were measured as a function of frequency. HMX flame height was found to vary sinusoidally with phase angle, having a response peak between 8 and 50 Hz and crossing from phase lead to phase lag at about 20 Hz. The flame height response function of HMX was similar to light emission response but at a slightly higher frequency. The resonant peak occurred at approximately the same frequency, the phase reacted the same as a function of frequency, and no unusual effects were seen at high frequency. Based on this data, the flame is reasonably quasi-steady below 40 Hz, in that the difference in phase lag between thrust and flame oscillations is less that 30° with almost no difference at the response peak of 10–20 Hz.

Acknowledgments

The authors would like to thank Richard Stalnaker, the machinist, Professor Merrill Beckstead, Dr. Fred Blomshield, and Dr. Steve Son for helpful discussions and Dr. Richard Miller at ONR for funding Project No. N000149–2-WX-24097.

REFERENCES

1. Mihlfeith, C. M., Baer, A. D., and Ryan, N. W., *AIAA J.* 10 (10):1280–1285 (1972).
2. Mikheev, V. F., Zarko, V. E., Borin, S. M., Kutsenogii, K. P., and Simonenko, V. N., Paper No. AIAA-76–102, *AIAA 14th Aerospace Sciences Meeting*, Washington, DC., Jan. 1976.
3. Simonenko, V. N., Zarko, V. E., and Kutsenogii, K. P., *Fiz. Goreniya Vzryva* 16 (3):60–68 (1980).
4. Zarko, V. E., Simonenko, V. N., and Kiskin, A. B., *Fiz. Goreniya Vzryva* 23 (5):521–530 (1987).
5. De Luca, L., *J. Italian Assoc. Theoretic. Appl. Mech. (Meccanica)* 195–205 (1980).
6. Finlinson, J. C., Hanson-Parr, D., Son, S. F., and Brewster, M. Q., 29th Aerospace Sciences Meeting, Reno, NV, AIAA Paper No. AIAA-91–0204, Jan. 1991.
7. Son, S. F., Burr, R. F., Brewster, M. Q., Finlinson, J. C., and Hanson-Parr, D., 27th Joint Propulsion Conference, AIAA/SAE/ASME/ASEE, Sacramento, CA, No. AIAA-91–2194, June 24–26, 1991.
8. Brewster, M. Q., Hites, M. H., and Son, S. F., *Combust. Flame* 94:178–190 (1993).
9. Son, S. F., "The Unsteady Combustion of Radiant Heat Flux Driven Energetic Solids," Doctoral Thesis, University of Illinois at Urbana-Champaign, October, 1993.
10. Son, S. F., and Brewster, M. Q., *J. Propul. Power* 9 (2):222–232 (1993).
11. Son. S. F., and Brewster, M. Q., *Proceedings of the 30th JANNAF Combustion Committee Meeting*, Monterey, CA, 1993.
12. Culick, F. E. C., *AIAA J.* 6 (12):2241–2254 (1968).
13. Boggs, T. L., "Fundamentals of Solid-Propellant Combustion," in *Progress in Astronautics and Aeronautics* (K. K. Kuo and M. Summerfield, Eds.), AIAA, New York, 1984, Vol. 90.
14. Parr, T. P., and Hanson-Parr, D. M., in *Progress in Astronautics and Aeronautics* (L. De Luca, E. W. Price, and M. Summerfield, Eds.), 1992, Vol. 143, pp. 261–324.
15. Parr, T. P., and Hanson-Parr, D. M., *Proceedings of the 26th JANNAF Combustion Committee Meeting*, CPIA Publication No. 529, 1989, Vol. I, p. 27.
16. Parr, T. P., and Hanson-Parr, D. M., *Proceedings of the 24th JANNAF Combustion Committee Meeting*, CPIA Publication 476, 1987, Vol. I, p. 367.
17. Parr, T. P., and Hanson-Parr, D. M., *Proceedings of the 23rd JANNAF Combustion Committee Meeting*, CPIA Publication 457, 1986, Vol. I, p. 249.
18. Dyer, M. J., and Crosley, D. R., *Opt. Lett.* 9:217 (1984).
19. Nadler, M., and Ashton, P., "Absorption Coefficients at 10.6 micron for AP, RDX, HMX, and HNIW," Naval Weapons Center Memo, Jan. 8, 1991.

Twenty-Fifth Symposium (International) on Combustion/The Combustion Institute, 1994/pp. 1651–1657

COMBUSTION SYNTHESIS OF ZnS IN MICROGRAVITY

S. GOROSHIN, J. H. S. LEE AND D. L. FROST
Department of Mechanical Engineering
McGill University
817 Sherbrook Street West, Montreal, Quebec, H3A 2K6, Canada

The self-heating nature of SHS (Self-propagating High-temperature Synthesis) makes it particularly suitable for microgravity processing of materials where weight and power requirements are severely restricted. The absence of convection, hydrostatic pressure, and phase separation permits the combustion front dynamics and solidification processes of SHS to be studied under controlled conditions. This paper describes recent ground-based and microgravity (NASA KC-135 parabolic flight) experiments on SHS processing of ZnS. A novel technique was used for preparing the precursor mixture of Zn + S by mixing the zinc with molten sulfur, which allows the synthesis of a high-density and high-purity product. The flame speed, quenching diameter, and temperature profile in the flame front and crystal structure of the synthesized samples have been determined. Thermocouple measurement of the temperature profile in the flame front indicates that the thermal thickness of the flame is less than 0.3 mm. The average flame speed is of the order of 7 mm/s, and slightly lower values (~4 mm/s) are observed near the quenching limit. It was found that the flame speed is not stable along the samples with diameters more than 12 mm. The quenching diameter is found to be of the order of 5 mm (in microgravity less than 4 mm). X-ray diffraction data show a wurtzite structure both in ground-based and in-flight synthesized samples, and the lattice's parameters are most similar to the ideal ZnS wurtzite structure in the outer part of samples synthesized in microgravity. The ability to provide containerless SHS processing of molten ZnS in microgravity also has been demonstrated.

Introduction

Access to the microgravity environment provided by the use of drop towers, parabolic trajectories of aircraft and rockets, and shuttle and space station orbits has permitted material scientists to investigate a number of problems associated with gravitational effects on material processing. In the absence of gravity, buoyant convection, hydrostatic pressure, and the separation of phases of different densities are eliminated, providing the ability to synthesize new or improved materials. Conventional methods of material processing require a heat source (i.e., a furnace); thus, the maximum temperature and sample size are severely limited in a microgravity environment as a result of the size and operational limits of the furnace. Combustion synthesis does not require an external energy source; hence, it is particularly advantageous in a microgravity environment where weight, volume, and electrical power requirements must be strictly limited. It is anticipated that containerless material processing and solidification in a microgravity environment will very likely result in the manufacture of materials with a high purity and the possible synthesis of new, unique materials. The use of combustion synthesis eliminates the furnace, allowing for the first time a true containerless environment.

Preliminary studies of Self-propagating, High-temperature Synthesis (SHS) in microgravity have already been initiated by Shteinberg and co-workers [1], who demonstrated that TiC produced in microgravity can have a highly porous (95% porosity) structure. Odawara et al. [2] have reported work on thermite reactions in short-duration microgravity experiments, and Moore [3] has investigated the influence of microgravity on the porosity and structure of combustion-synthesized metal-matrix composites. The present paper describes the SHS studies recently initiated at McGill University on the SHS of ZnS in microgravity.

General Considerations:

The material of interest in our study is ZnS. Zinc sulfide has a variety of luminescent properties (e.g., x-ray, photo-, electro-, as well as triboluminescence) depending on the dopant used, as well as semiconductor and piezoelectric properties. The conventional method of producing fine crystalline or amorphous ZnS powders for luminescent applications is via precipitation from an aqueous solution of zinc sulfate with hydrogen sulfide [4]. Larger single crystals can be obtained from melt or by condensation from the gaseous phase [5,6]. Uniform doping with

small concentrations of impurities and the growth of large crystals are difficult using conventional methods of synthesis [7]; therefore, a suitable industrial technology for fabricating large ZnS single crystals does not currently exist.

Zinc sulfide can also be produced by the SHS process. This was first achieved by the group at Odessa in 1986 [8] where a compacted mixture of zinc and sulfur powders reacted to form ZnS. The SHS-synthesized ZnS was found to have a polycrystalline structure with a density of less than 91% of the theoretical value. The structure of the products depends on the combustion and solidification front dynamics, and the purity of the product was not high enough for electronic applications. Therefore, it is necessary to achieve a better understanding of these processes before the desired structure and purity of ZnS synthesized by SHS can be achieved. Both the combustion and the solidification processes are strongly dependent on temperature, and hence on the mode of heat transport, as well as boundary conditions. In microgravity, convection- and gravity-induced flow of the melt is absent, permitting better observation of the combustion and solidification processes. In addition, in a long-duration microgravity environment, there is the possibility of growing single crystals from SHS-generated ZnS melt.

Experimental Details

Charge Preparation:

High-purity zinc (-325 mesh) and sulfur (-100 mesh) powders (supplied by Aldrich Chemical Company, Milwaukee, WI) were used for preparation of the charges. The powders were mixed in a proportion close to stoichiometric in accordance with the reaction $Zn + S \rightarrow ZnS$. Since part of the Zn in the zinc powder is in the form of an oxide (ZnO), a small empirically determined excess of sulfur (0.01–0.05%) is added in order to compensate for the oxygen. In order to increase the luminescent efficiency of the synthesized samples, some quantity of regular activators such as Cu (0.01–0.05%) or Mn (0.1–1%) was added to the Zn-S powder mixture.

The traditional method of sample preparation in SHS technology is to compact the powder mixture before firing in a steel die by a cylindrical press [9]. This requires a pressing force of up to 50 tons/cm^2, but the final density of the sample for Zn + S is typically less than 85% of the theoretical density [10].

Our innovation in SHS sample preparation is to melt the component with the lowest melting point. For the Zn + S, this corresponds to mixing of molten sulfur with zinc powder. This novelty not only greatly simplifies the preparation of samples of different shape and geometry but eliminates trapped gases, improving the quality of the synthesized product. The difference of the sample structure prepared by cold-pressing and mixing molten sulfur with zinc powder is illustrated in Fig. 1.

Eliminating the gases trapped in the pores of the pressed reactant mixture allows us to produce a final product with a density that is very close to the theoretical value. The synthesized ZnS samples have a density not less than 98.5% of theoretical, compared with the best results of 91% obtained with a cold-pressing method [8]. It can also be seen from Fig. 1 that the zinc particles in a cold-pressed mixture are concentrated along the deformed borders of the initial sulfur particles. This nonuniformity in zinc concentration after cold-pressing decreases the completeness of the chemical reaction and is the cause of the dependence of the purity of the final product on sulfur particle size [10]. Unlike the cold-pressed powders, a mixture prepared from molten sulfur is highly uniform, and completeness of the chemical reaction is higher.

Reactor and Microgravity Experimental Package:

The boiling points of sulfur (717 K) and zinc (1179 K) are less than the temperature in the combustion front (2200 K [8]), and at low pressures, the sublimation temperature of ZnS is lower than the melting point [11]. Therefore, one needs to carry out the process of ZnS-SHS synthesis within a pressurized inert gas environment. The first experiments of ZnS-SHS synthesis [8] showed that the final product could be synthesized in molten form only if the total pressure in the reactor was more than 50 atm. In general, the completeness of the chemical reaction and the quality of the product are also higher for higher pressures [8].

The SHS-ZnS synthesis equipment consists primarily of a high-pressure reactor vessel (Clover Leaf Reactor, Model CL-9, High Pressure Equipment Company, Erie, PA) capable of withstanding a static pressure >1000 atm. The reactor is rated for a working temperature up to 120 °C and includes a quick-opening cover.

A schematic of the experimental flight package and the pneumatic control circuit is given in Fig. 2. The amount of gas in the high-pressure bottle (400 atm) is enough to refill the reactor up to 35 times to the 100 ± 10-atm working pressure. The high-pressure in-line relief valve prevents the high-pressure manifold from overpressurization, and the low-pressure in-line relief valve prevents overpressurization of the plane's overboard vent manifold. The overboard pressure under regular flight conditions is considerably lower than the pressure inside the cabin. Therefore, a special manifold with a low-pressure gauge is used to equalize the pressure in the reactor and cabin before it is opened. An electric ignition circuit and flame-speed measurement circuit are linked to the reactor cover.

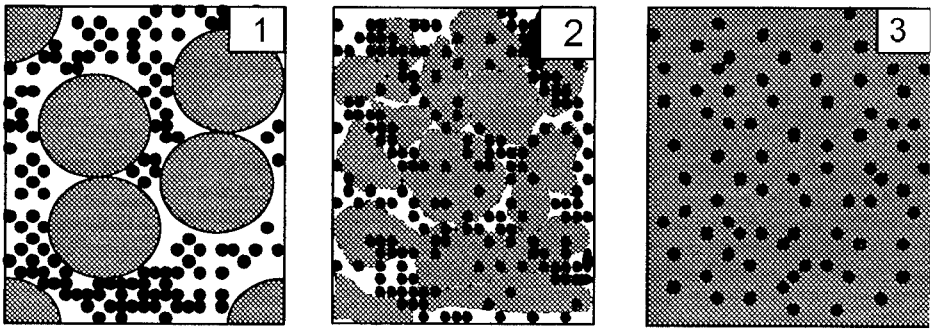

FIG. 1. Schematic illustrations of the structure of the samples prepared by cold-pressing and mixing of the liquid sulfur with the zinc powder: (1) initial powder mixture; (2) compacted powder mixture; (3) melted sulfur mixed with zinc powder.

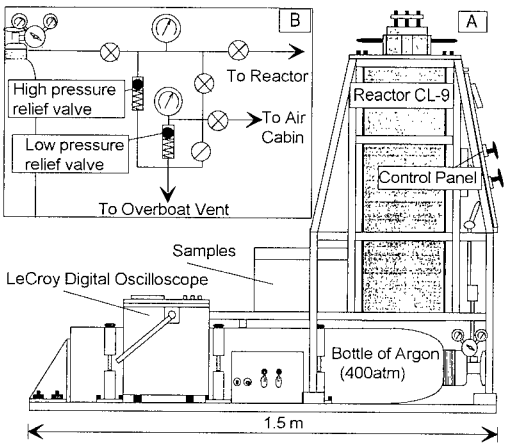

FIG. 2. The schematic of the flight experiment package (A) and the pneumatic circuit (B).

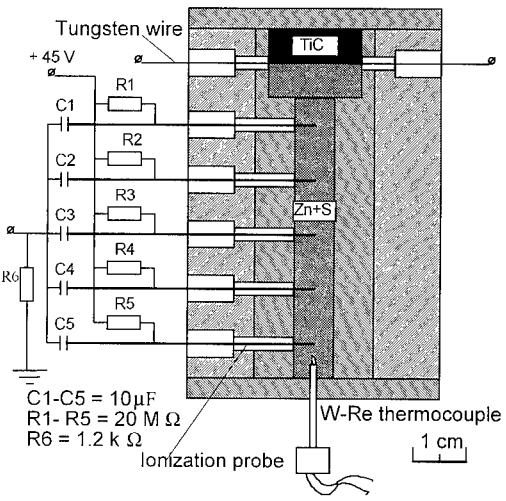

FIG. 3. The arrangement of the sample for flame-speed, temperature, and quenching-distance measurements.

The microgravity flights are carried out on the NASA KC-135 aircraft. Usually, a total of 40–50 parabolas are flown per flight with a 5-minute break in between each set of 10 parabolas. Retrieving the sample and reloading the reactor with a new charge are carried out during the 5-minute break periods. Hence, about 4 or 5 samples are synthesized per flight.

Samples for the Flame-Speed and Quenching-Distance Measurements:

The final temperature of the synthesized sample is close to the adiabatic temperature, i.e., 2200 K. To minimize the heating of the gas inside the reactor, each sample was placed inside a heavy-walled aluminum container (12-cm long, 8.5-cm diameter), as shown in Fig. 3. The container absorbs almost all of the enthalpy of reaction, and its final temperature does not exceed 150 °C. Figure 3 also shows the five "ionization" probes used to measure flame speed and the fine thermocouple embedded into the central axis of the charge used to measure the temperature profile as the flame propagates past the thermocouple. Charges of the mixture of Zn + S of different diameters are placed in an inner aluminum cylinder, which in turn is inserted into the larger heavy-walled aluminum container. At one end of the Zn + S charge is a pressed pellet of Ti + C, which serves as the ignition source. The Ti + C pellet is ignited by a tungsten wire.

The initial Zn + S mixture, because of the very high resistance of sulfur, is an insulator. The final product, ZnS, is a semiconductor at room temperature and has a high resistance of the order of 10^8–10^{10} Ω cm [6]. However, the molten ZnS within the combustion wave apparently has a conductivity that

approaches that of metals.* We used this phenomenon to design the circuit that is similar to the conventional one used for ionization probe flame-speed measurements of detonation and deflagration modes of propagation in a combustible gas. Unlike the ionization probes used in gases, as a result of the high conductivity of the ZnS melt and the low flame speed, the voltage is comparatively low, i.e., 45 V. The 0.5-mm graphite rods are used as probes and allow easy replacement of the sample. Because of the large charging time of the RC circuit, all of the probes are connected to one channel of the digital oscilloscope. The sequential triggering of the ionization probes signaling the arrival of the flame at each of the probe locations is used to determine the flame speed.

For the unconfined charge experiments, the inner aluminum cylinder that surrounds the sample was removed, leaving an air space between the charge and the outer aluminum container wall. In order to synthesize pure samples suitable for x-ray and luminescent analysis, some samples were enclosed in quartz ampoules. The space between the walls of the quartz ampoule and the wall of the aluminum container was filled with 2–3-mm alumina beads.

Results

Flame Speed and Quenching Distance in Confined Charges:

For confined charges in aluminum cylinders where the heat losses are very high, quenching diameters have been measured. In normal gravity, a minimum diameter of about 4.5–5 mm is required for flame propagation. However, in microgravity, self-sustained propagation is observed for charges less than 4 mm.** The absence of convection in the ZnS melt in microgravity may play a role in reduction in the quenching diameter. In particular, the elimination of convection in microgravity will reduce the heat transfer rate and hence reduce the quenching diameter.

The variation of the flame velocity with distance is shown in Fig. 4 for a few charge diameters. For the small-diameter charges, the velocity is found to be very stable, and the flame propagates at 4–5 mm/s. For the larger charge diameters, the velocity fluctuates, indicating a nonsteady flame propagation. In this case, the flame may exhibit a pulsating or spinning instability as observed by other investigators in different SHS systems [9,12]. The phenomena of unstable combustion may be the major source of impurities in the combustion synthesis of ZnS. If the SHS product is solid, it consists after unstable combustion of layers of different chemical composition and structure that can be used to study the parameters of unstable combustion [9]. But this conventional method of studying unstable SHS regimes does not work, of course, if the combustion product is in the liquid phase, as in the case of ZnS-SHS processing. The violent convection that occurs in the nonuniformly cooled high-temperature melt at normal gravity annihilates any footprint of the unstable burning. The fast solidification of the ZnS-SHS melt in microgravity is the only way to have this "footprint" available for study.

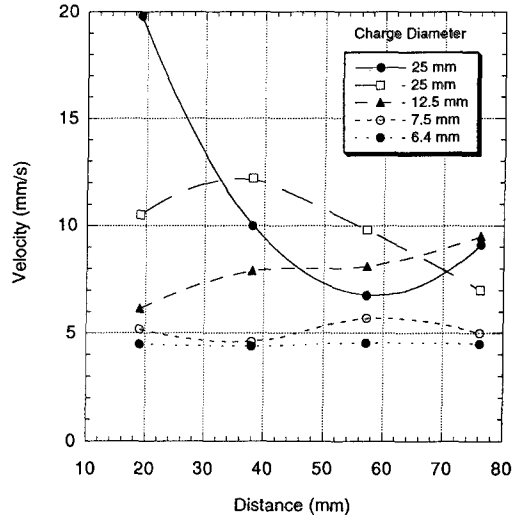

FIG. 4. Changing of the flame speed along the charge.

The variation of the average flame speed with the charge diameter is shown in Fig. 5. In general, a slight increase in the flame speed with charge diameter is observed, indicating the effect of heat losses. The downward-propagating flame in a wide channel ($d > 12$ mm) usually has a speed lower than that of an upward-propagating flame, and the value of the flame speed in microgravity is close to the speed of a downward propagating flame. However, as a result of the limited data available in microgravity as well as the instability of the flame speed itself, this dependence is not clear.

Synthesis of Unconfined Charges:

Since the product of the ZnS combustion synthesis is in the liquid state, in normal gravity it is not possible to carry out experiments with an unconfined charge because of the gravity-induced flow of the melt. In our microgravity experiments, it was found that complete combustion of an unconfined charge was possible. However, as a result of the poor heat

*The conductivity of the molten ZnS has not yet been measured. We did this rough estimation using our own preliminary measurements.

**We did not manage to obtain quenching of the flame in microgravity as yet.

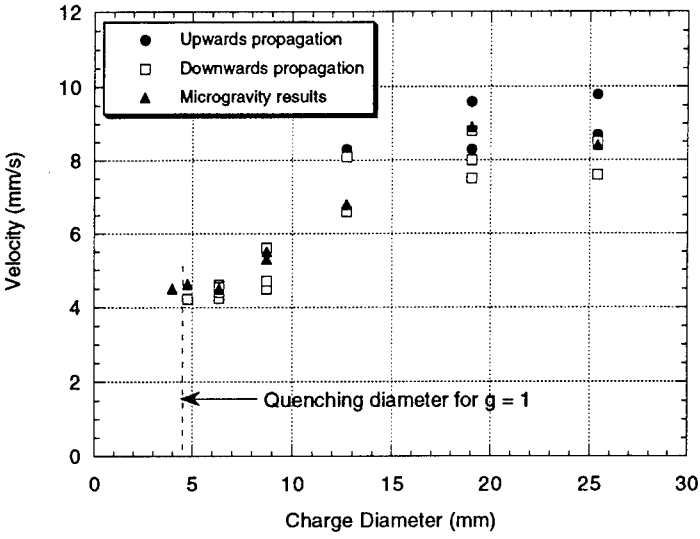

FIG. 5. The variation of the flame speed with the charge diameter.

transfer between the melt and the gaseous environment, the ZnS was still in the molten state upon return to normal gravity. G-jitter and the large acceleration associated with the sudden return of normal gravity at the end of the 20-s microgravity period can introduce significant inertial forces on the melt and cause it to fragment into droplets. Even during the microgravity period, strong Marangoni convection and turbulence effects may also disrupt the melt interface. For the unconfined charge experiments in microgravity, we recovered solid spherical ZnS particles with a wide size spectrum ranging from fractions of a millimeter to 5 mm after the synthesis. If an integral solid sample of ZnS is desired, it is necessary to arrange for rapid quenching within the 20-s parabolic flight microgravity duration.

Temperature Profile in the Flame Front:

The first objective of the thermocouple measurements was to estimate the thickness and temperature profile of the combustion wave. In order to accomplish this, a fine thermocouple was embedded into the central axis of the charge to measure the temperature profile as the flame propagates past the thermocouple. Three types of unsheathed fine-gauge thermocouples were used: type K (chromel-alumel, maximum temperature 1523 K), diameter 25 μm; type S (Pt/Pt-10% Rh, maximum temperature 1723 K), diameter 50 μm; and type C (W/5% Re-W/26% Re, maximum temperature 2593 K), diameter 75 μm. The thermocouple was shielded in a two-hole alumina ceramic tube with outside diameter 1.5 mm and a length of 60 mm. The junction and 5 mm of the thermocouple wire were exposed. The output from the thermocouple was amplified with a 50× DC amplifier and recorded by a digital oscilloscope.

The theoretically estimated adiabatic flame temperature in the Zn-S combustion front is about 2200 K. Only high-temperature thermocouples based on W-Re alloy can cover this temperature range. At the same time, the thickness of the combustion front in our case is very small, so that thermocouples with a very small response time are required to resolve the reaction front. The thermal thickness of the flame is of the order of $L \sim \lambda_s/C_s\rho_s V$, where λ_s, C_s, and ρ_s, are the conductivity, specific heat, and density of the unburned mixture, respectively, and V is the flame speed. Assuming that the thermophysical properties of the mixture are close to those of liquid sulfur, one can estimate for a measured flame speed of 0.5 cm/s that the flame thickness is of the order of 50–100 μm.[†] Correspondingly, the flame passes through the thermocouple in about 10–20 ms. The response time estimated for the 75-μm W-Re thermocouple is about 50 ms. Therefore, the measured value of the flame thickness should be considered as an estimate. The results of the flame structure measurements with the different thermocouples are given in Fig. 6. To plot this graph, the time from the direct temperature measurements was multiplied by the average flame speed in the channel of that diameter (0.7 cm/s), and the point at which the temperature first begins to rise was set to a value of 0.2 mm on the horizontal axis. It is clear that the measured flame thickness shrinks as the thermocouple size decreases, and therefore, the flame thickness is clearly not more than the lowest measured value of about 300 μm.

It was found that the high-temperature Zn-S melt

[†]There are no data available for the sulfur properties at such high temperatures in the literature. We did the estimation by extrapolation of the available data into the high-temperature region.

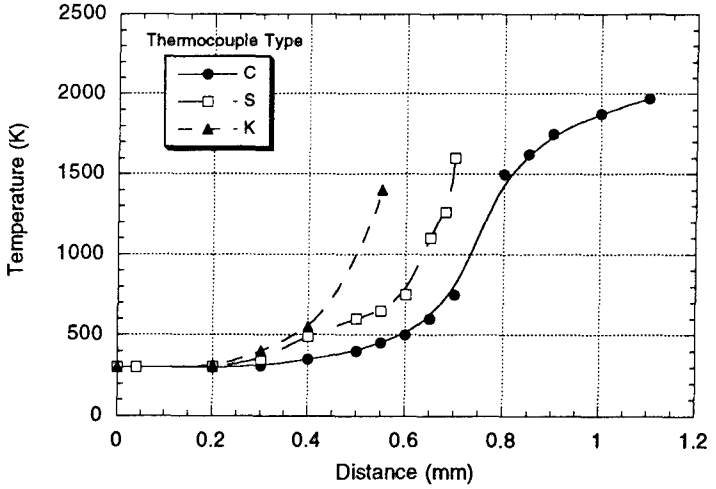

FIG. 6. Temperature profile in the flame front.

is an extremely chemically aggressive environment for all types of thermocouples. It is quite possible, as a result of the chemical reaction with sulfur, that thermocouples usually break at temperatures much lower than the maximum thermocouple temperature limit (see above). The W-Re thermocouples break at temperatures close to 2000 K. Even the Pt-Rh thermocouple, which is usually resistant to the oxidizing environment, breaks at a lower temperature than its theoretical temperature limit.

Crystal Structure and Composition of Synthesized Samples:

Thin polished sections (~50-μm thick) of samples synthesized in the quartz ampoules (i.d. 20 mm) were prepared in order to determine their crystal structure. The sections were studied with an optical microscope under polarized light. The typical structure of the cylindrical sample consists of three zones along the sample's radius, as shown in Fig. 7. The first zone, on the outer boundary of the sample, has a thickness of about 1–2 mm. This zone consists of small (~50–100 μm) crystals of approximately rectangular shape. The borders of the crystals are very close to each other. The bulk of the sample consists of a region containing very long (5–7 mm) radially oriented columnar crystals. The thickness of the crystals increases and reaches about 0.1–0.2 mm near the center of the sample. Columnar crystals are separated by "dark spaces." (the presence of the dark spaces under polarized light usually means the existence of the amorphous phase). As the thickness of the columnar crystals increases, the dark spaces between crystals also become wider. The central third zone has a diameter on the order of 5–7 mm and consists of equiaxial crystals. The size of the crystals is about 0.5–1 mm, and they are separated by wide dark zones.

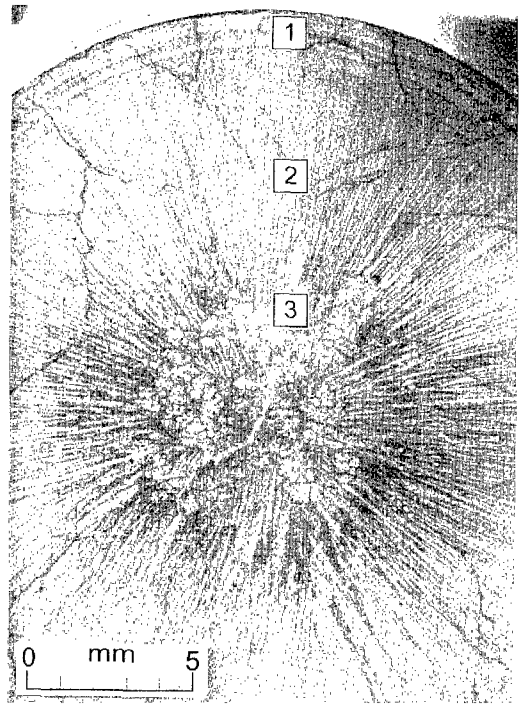

FIG. 7. The typical structure of the synthesized sample: (1) rectangular crystal zone; (2) columnar crystal zone; (3) equiaxial crystal zone.

The samples that were synthesized in microgravity also exhibit the tree zones observed in ground-based samples, although there are a number of differences present. For example, for the microgravity samples, the outer zone 1 is about 30–50% wider and consists of rectangular crystals almost twice as large as the ground-based samples. It is also interesting to note

that the samples synthesized in the flight have a shorter columnar crystal zone. Because the complete solidification time of the cylindrical samples in a quartz ampoule is longer than the microgravity duration, only the outer part of the sample can solidify in microgravity. Therefore, the larger rectangular crystals obtained during microgravity flights may be due to the more uniform cooling of the liquid in the absence of convection. However, the effect of the shrinking of the zone of columnar crystals is probably the consequence of the intense mixing of the melt by the violent convection that starts in the nonuniformly cooled liquid during the "pull down" 2-*g* acceleration.

The x-ray diffraction analysis of the synthesized samples was provided with a Juniaer–Hägg focusing camera and CuK_α radiation. A small amount of $MgAl_2O_4$ (spinel) was added as an internal standard (a = 8.0833 Å at room temperature). In contrast to the results published in Refs. 8 and 10, where it was found that SHS-synthesized ZnS samples have both wurtzite and sphalerite crystal modification, only wurtzite-type crystals were found in our samples. The lattice's parameters for the outer part of the samples (a = 3.8214 Å, c = 6.2657 Å) that were synthesized and presumably solidified in a microgravity environment are closer to the ideal wurzite structure than, for example, the lattice's parameters of standard ZnS industrial powder (Canada Colors and Chemicals Ltd.).

Conclusions

The results reported in this paper are based on ground-based experiments and one KC-135, NASA microgravity parabola flight campaign and have successfully demonstrated the possibility of SHS-ZnS processing in microgravity.

The highlights of the important results are as follows.

1. The novel technique developed for preparing the precursor mixture of Zn-S by mixing the zinc powder in the molten sulfur allowed an increase in the quality of the product. The density of synthesized samples reaches a value of 3.92 g/cm^3 (98.5% of the theoretical density), and the completeness of the chemical reaction was 99%.
2. Average flame speeds are typically of the order of 7 mm/s, and slightly lower values (~4 mm/s) are observed near the quenching limit. The flame speed is not stable along the samples with diameters more than 12 mm.
3. The quenching diameter is found to be of the order of 5 mm in ground-based experiments (and in microgravity less than 4 mm), permitting quite small samples to be studied.
4. Thermocouple measurements of the temperature profile in the flame front indicate that the thermal thickness of the flame is less than 0.3 mm.
5. Containerless processing of ZnS is achieved in microgravity, although the abrupt return to gravity and *G*-jitter cause the melt to break up into a spectrum of drop sizes prior to solidification.
6. X-ray diffraction data show a wurtzite (hexagonal) structure both in ground-based and flight-synthesized samples. The lattice's parameters are the most similar to the ideal ZnS wurtzite structure in the outer part of the sample synthesized in microgravity.

Acknowledgments

This work is supported under CSA Contract No. 9F007-3-6019/01SW, and the authors are grateful for the assistance of Dr. O. Peraldi in designing the microgravity hardware.

REFERENCES

1. Shteinberg, A. S., Sherbakov, V. A., Marttynov, V. V., Mukhoyan, M. Z., and Merzhanov, A. G. *Proceedings of AIAA/IKI Microgravity Science Symposium,* AIAA, Washington, DC, 1991, pp. 268–272.
2. Odawara, O., Mori, K., Tanji, A., and Yoda, S., *J. Mater. Synth. Process.* 1:203–207 (1993).
3. Moore, J. J., 31st Aerospace Meeting and Exhibit, AIAA Paper 93-0830, January 1993.
4. Kane, P., and Larrabee, G., *Characterization of Semiconductor Materials,* McGraw-Hill Book Co., New York, 1970.
5. Shionoya, S., Kobayashi, Y., and Koda, T., *J. Phys. Soc. Jpn.* 20:385–389 (1965).
6. Abricosov, N. Kh., Bankina, V. F., and Poteskaya, L. V., *Semiconducting II-IV, IV-VI and V-VI Compounds,* Plenum Press, New York, 1969, pp. 1–40.
7. Indradev, L. J., Van Ruyven, B., and Williams, F., *Proceedings of the International Conference on Luminescence,* Akademiai Kiado, Budapest, 1968, pp. 1044–1050.
8. Kozitskiy, S. V., Pisarskiy, V. P., and Polischuk, D. D., *Izv. Acad. Nauk SSSR* 10:2472–2475 (1990) (in Russian).
9. Merzhanov, A. G., in *Combustion and Plasma Synthesis of High-Temperature Materials* (L. A. Munir and J. B. Holt, Eds.), VCH, New York, 1990, pp. 1–53.
10. Molodetskaya I. E., and Pisarskiy, V. P., *Combust. Explos. Shock Waves* 28:385–389 (1992).
11. Rubensteine, M., *J. Cryst. Growth* 41:311–316 (1977).
12. Margolis, S., and Matkowski, B. J., in *Combustion and Plasma Synthesis of High-Temperature Materials* (L. A. Munir and J. B. Holt, Eds.), VCH, New York, 1990, pp. 73–83.

Twenty-Fifth Symposium (International) on Combustion/The Combustion Institute, 1994/pp. 1659–1667

PROPAGATION AND DIFFUSION-LIMITED EXTINCTION OF NONADIABATIC HETEROGENEOUS FLAME IN THE SHS PROCESS

ATSUSHI MAKINO
Department of Energy and Mechanical Engineering
Shizuoka University
Hamamatsu 432, Japan

AND

CHUNG K. LAW
Department of Mechanical and Aerospace Engineering
and
Princeton Materials Institute
Princeton University
Princeton, 08544, USA

Nonadiabatic heterogeneous flame propagation and extinction in self-propagating high-temperature synthesis (SHS) are analyzed based on a premixed mode of propagation for the bulk flame supported by the nonpremixed reaction of dispersed nonmetals in the liquid metal. The formulation allows for volumetric heat loss throughout the bulk flame, finite-rate Arrhenius reaction at the particle surface, and temperature-sensitive Arrhenius mass diffusion in the liquid. Results show that, subsequent to melting of the metal, the flame structure consists of a relatively thin diffusion-consumption/convection zone followed by a relatively thick convection-loss zone, that the flame propagation rate decreases with increasing heat loss, that at a critical heat-loss rate the flame extinguishes as indicated by the characteristic turning-point behavior, that the surface reaction is diffusion limited such that the nonlinear, temperature-sensitive nature of the system is actually a consequence of the Arrhenius mass diffusion, and that extinction is sensitively affected by the mixture ratio, the degree of dilution, the initial temperature of the compact, and the size of the nonmetal particles. An explicit expression is derived for the normalized mass burning rate, which exhibits the characteristic turning point and shows that extinction occurs when this value is reduced to $e^{-1/2}$, which is the same as that for the nonadiabatic gaseous premixed flame. It is further shown that the theoretical results agree well with available experimental data, indicating that the present formulation captures the essential features of the nonadiabatic heterogeneous SHS processes and its potential for extension to describe other SHS phenomena.

Introduction

Practical significance of the self-propagating high-temperature synthesis (SHS) process for the combustion synthesis of novel solid materials is well recognized and established [1–3]. An extensive body of theoretical analysis for the various aspects of the SHS phenomena also exists, as was recently reviewed by Margolis [4]. Most of these studies are based on the premise that the synthesis is accomplished through the passage of a premixed flame in a homogeneous medium.

An alternate flame propagation mode was recently proposed [5], suggesting that most SHS processes in solid compacts without external forces could actually involve flame propagation in a two-phase heterogeneous medium consisting of solid nonmetal particles immersed in the fluid phase of the metal which is melted by the approaching flame. In order to describe this inherently heterogeneous mode of flame propagation, especially its dependence on the particle size and the nonpremixed nature of particle consumption, a theory based on spray combustion [6] was formulated [5]. This theory satisfactorily accounts for the premixed mode of the bulk flame propagation supported by the nonpremixed mode of particle consumption. Appropriate flammability limits are also identified, based on considerations of the overall energetics. The theory further allows for a finite surface reaction rate and the inherently Arrhenius nature of the liquid-phase mass diffusion. Predicted burning rates and flammability limits agree well with the experimental results [5,7].

The theory of Ref. 5 is adiabatic and hence is incapable of describing the experimentally observed phenomena of flame extinction due to heat loss from

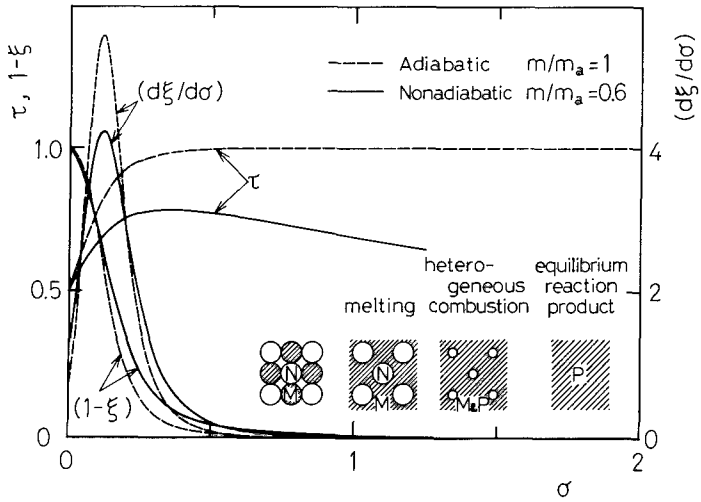

FIG. 1. The representative flame structure for the temperature τ, the solid mass fraction $(1-\xi)$, and the reactant consumption rate $(d\xi/d\sigma)$, along the nondimensional distance; the mixture ratio is $\mu = 1.0$, the degree of dilution $\kappa = 0$, the initial temperature $T_0 = 450$ K, the Lewis number $Le_0 = 100$, the initial Damköhler number $Da_0 = 10^9$, and the adiabatic mass burning-rate eigenvalue $\Lambda_0 = 6.109 \times 10^{-5}$. Solid curves are those with heat loss; $(m/m_a) = 0.6$ and $\tilde{\Psi} = 3.347 \times 10^{-2}$. Dashed curves are those without heat loss; $(m/m_a) = 1$ and $\tilde{\Psi} = 0$.

the high-temperature combustion process. From the practical viewpoint, it is also important that extinction can be properly described and hence controlled in SHS.

In the present study, we have extended the adiabatic theory to allow for volumetric heat loss. This nonadiabatic theory then successfully describes flame extinction and the various parameters that characterize it. Furthermore, the present results show that extinction for the mixture systems studied is actually caused by the temperature-sensitive Arrhenius mass diffusion, not by the surface reaction, which is basically diffusion limited. Predictions from the theory yield satisfactory agreement with the experimental results.

Formulation

The problem of interest, shown as the inset of Fig. 1, is the one-dimensional, planar, heterogeneous flame propagation in the doubly infinite domain of a condensed medium, originally consisting of a mixture of particles of nonmetal (or higher–melting-point metal) N, lower–melting-point metal M, and an inert I that can also be the product P of the reaction between N and M according to:

$$\nu_M M + \nu_N N \rightarrow \nu_P P \qquad \text{(R)}$$

where ν_i is the stoichiometric coefficient of the reaction. For simplicity, we shall assume that the nonmetal particle-size distribution is monodisperse, with an initial radius R_0 and number density n_0. Furthermore, there is no reaction between N and M until the mixture has been heated to the melting point T_m of the metal, at which all the lower–melting-point metal particles instantaneously melt. The reaction between the solid N and molten M then takes place at the particle surface at a finite rate and proceeds until all of the nonmetal particles are consumed. The enthalpy of phase change is neglected because it is much smaller than the heat of combustion. The propagation considered here is nonadiabatic, with heat loss to the ambience occurring throughout the entire flame structure. Consequently, in contrast to the adiabatic theory in which temperature increases monotonically to the adiabatic flame temperature, the temperature would gradually decrease to the ambient value after the maximum "flame temperature."

Conservation equations are as follows [5,6]:

Continuity:

$$(\rho_t u) = (\rho_t u)_0 = m \qquad (1)$$

M Conservation:

$$\left(\frac{\rho_f D}{m}\right)\left(\frac{d\tilde{Y}_M}{dx}\right) = (\tilde{Y}_M + 1)Z - (\tilde{Y}_{M,0} + 1)Z_0 \qquad (2)$$

Energy Conservation:

$$\frac{d}{dx}\left[\left(\frac{\lambda/c}{m}\right)\left(\frac{d\tilde{T}}{dx}\right) - \{(\tilde{T} - \tilde{T}_0) - (Z - Z_0)\}\right] = \frac{L}{m \cdot q} \qquad (3)$$

N Consumption:

$$\left(\frac{dZ}{dx}\right) = \left[\frac{4\pi\rho_N n_0 R_0}{m}\right]\left(\frac{u_0}{u}\chi\right)\left(\frac{1 - Z}{1 - Z_0}\right)^{1/3} \qquad (4)$$

where ρ_f is the fluid density, ρ_s the mass of solid phase per unit spatial volume, $\rho_t = \rho_f + \rho_s$ the total density, $Z = \rho_f/\rho_t$, Y_M the mass fraction of M in the fluid,

T the temperature, u the velocity along the x coordinate, m the mass burning rate (per unit area) of the flame, R the particle radius, λ the thermal conductivity, c the specific heat, $D = D_0 \cdot \exp(-T_d/T)$ the Arrhenius mass diffusivity with an "activation temperature" of T_d, $\tilde{T} = cT/q$, $\tilde{Y}_M = Y_M/f$, $f = (\nu_M W_M/\nu_N W_N)$ the stoichiometric mass ratio, W_i the molecular weight, q the heat of reaction per unit mass of N, L the volumetric heat-loss rate satisfying the requirement that $L \to 0$ as $T \to T_0$, and "0" and "∞" the subscripts respectively designating the unburned and burned states in the adiabatic condition. The surface regression rate χ, defined by $dR/dt = -\chi/R$, is given [5] as

$$\chi = \left(\frac{\rho_M D}{\rho_N}\right)\tilde{\chi}: \qquad \tilde{\chi} = \ln\left[1 + \left(\frac{A}{1 + A}\right)\tilde{Y}_M\right] \tag{5}$$

where $A = Da \cdot \exp(-\tilde{T}_a/\tilde{T})$, $Da = (B \cdot R)/D$, B, and T_a are, respectively, the reduced Damköhler number, the Damköhler number, the frequency factor, and the activation temperature of the surface reaction.

Defining nondimensional variables and parameters as

$$\tau = \frac{\tilde{T} - \tilde{T}_0}{\tilde{T}_\infty - \tilde{T}_0}, \qquad \zeta = \frac{\tilde{Y}_M - \tilde{Y}_{M,0}}{\tilde{Y}_{M,\infty} - \tilde{Y}_{M,0}},$$

$$\xi = \frac{Z - Z_0}{1 - Z_0}, \qquad \sigma = \left[\frac{(1 - Z_0)m_a}{(\lambda/c)}\right]x$$

$$\Lambda_0 = \left[\frac{(1 - Z_0)^2 m_a^2}{4\pi(\rho_M D_0)(\lambda/c)n_0 R_0}\right], \qquad Le_0 = \frac{(\lambda/c)}{(\rho_t D)_0},$$

$$\phi(\tau) = \frac{(\lambda/c)L}{m_a^2 q(\tilde{T}_\infty - \tilde{T}_0)}$$

with

$$\tilde{T}_\infty = 1 - Z_0 + \tilde{T}_0,$$

$$\tilde{Y}_{M,\infty} = (\tilde{Y}_{M,0} + 1)Z_0 - 1$$

the governing equations are reduced to

$$\frac{d\zeta}{d\sigma} = \left[\frac{Le_0(\rho_{t,0}/\rho_t)\exp(\tilde{T}_d/\tilde{T})}{Z}\right]\left(\frac{m}{m_a}\right)\left[\xi\left(\zeta - \frac{1}{1 - Z_0}\right) + \left(\frac{Z_0\zeta}{1 - Z_0}\right)\right] \tag{6}$$

$$\frac{d^2\tau}{d\sigma^2} - \left(\frac{m}{m_a}\right)\frac{d}{d\sigma}\left(\frac{\tau - \xi}{1 - Z_0}\right) = \frac{\phi(\tau)}{(1 - Z_0)^2} \tag{7}$$

$$\frac{d\xi}{d\sigma} = \left[\frac{(1 - \xi)^{1/3}\tilde{\chi}}{(m/m_a)\Lambda_0(\rho_{t,0}/\rho_t)\exp(\tilde{T}_d/\tilde{T})}\right]. \tag{8}$$

In the above, m_a and Λ_0 are, respectively, the mass burning rate and the mass burning-rate eigenvalue in the adiabatic limit.

Equations (6) through (8), together with the mass burning rate m, are to be solved subject to the boundary conditions

$$\sigma = 0: \tau = \tau_m, \qquad \zeta = 0, \qquad \xi = 0 \tag{9}$$

$$\sigma \to \infty: \left(\frac{d\tau}{d\sigma}\right) = -\frac{\phi(\tau)}{(m/m_a)(1 - Z_0)},$$

$$\left(\frac{d\zeta}{d\sigma}\right) = 0, \qquad \left(\frac{d\xi}{d\sigma}\right) = 0. \tag{10}$$

Note that the cold boundary difficulty is eliminated by specifying that the reaction is initiated at the melting point of M. Furthermore, the downstream boundary condition for τ, based on convection-loss balance, requires a short domain of integration.

Computed Results

Values of the physicochemical parameters employed are those for the Ti-C system: $q = 15$ MJ/kg, $c = 1$ kJ/(kg·K), $\rho_M = 4.50 \times 10^3$ kg/m^3, $\rho_N = 2.25 \times 10^3$ kg/m^3, $W_M = 47.9 \times 10^{-3}$ kg/mol, $W_N = 12.0 \times 10^{-3}$ kg/mol, $T_m = 1973$ K, $T_a = 3 \times 10^4$ K. For the mass diffusivity, $D = 2 \times 10^{-7} \cdot \exp(-1.66 \times 10^4/T)$ m^2/s [8] is used. As for the Lewis number, $Le_0 = 100$, because experimental results [9] for various particle radii have been correlated for this value and $B \gtrsim 10^3$ m/s [5]. The total densities before and after the combustion are assumed to be equal. Note that the thermophysical properties used here implicitly account for effects of compact density, gases in void spaces, gas evolution, etc.

We further define the initial molar ratio of N to M divided by the corresponding stoichiometric molar ratio as μ and the initial mass fraction of diluent as κ. These two parameters are commonly used as the controllable variables in experiments to specify the nature of the initial compact, and are related to the initial mass ratio Z_0 through

$$1 - Z_0 = \frac{\mu(1 - \kappa)}{\mu + f}. \tag{11}$$

In the calculations, the heat loss is assumed to be Newtonian such that $\phi(\tau) = \tilde{\Psi} \cdot \tau$. The specific expression approximating radiative heat loss will be given later.

Figure 1 shows representative flame structure for the stoichiometric mixture ($\mu = 1$) with no dilution ($\kappa = 0$). Profiles of the temperature τ, the solid mass fraction $(1 - \xi)$, and the consumption rate $(d\xi/d\sigma)$,

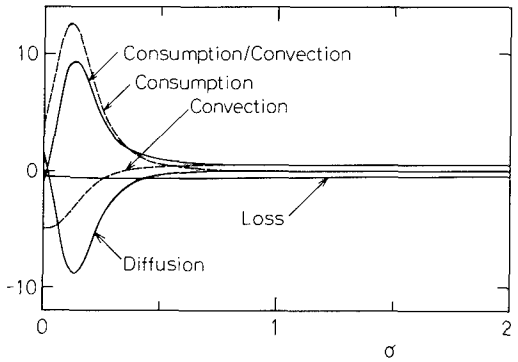

FIG. 2. The representative profiles of the diffusion, consumption, convection, and loss terms in the energy conservation equation, along the nondimensional distance. Conditions are the same as those in the nonadiabatic situation in Fig. 1.

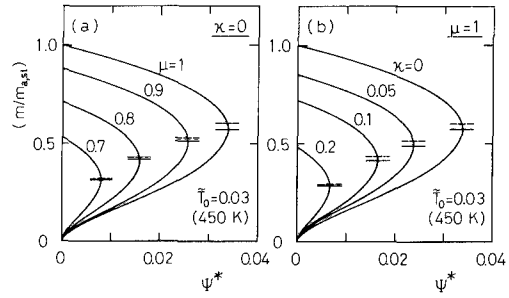

FIG. 3. The nondimensional mass burning rate $(m/m_{a,st})$ as a function of the nondimensional heat loss $\Psi^* = (m_a/m_{a,st})^2 \cdot \tilde{\Psi}$, with the mixture ratio μ and the degree of dilution κ taken as parameters; the initial temperature is $T_0 = 450$ K. The values of numerically obtained $(m/m_{a,st})_{cr}$ corresponding to the turning point are indicated by the horizontal solid lines; those of analytical ones are indicated by the dashed lines.

with and without heat loss, are shown respectively by solid and dashed curves as a function of the nondimensional distance σ. The position at which $\tau = \tau_m$ is set as the origin. In the adiabatic limit, as τ increases from τ_m (melting point of the metal) to 1 (adiabatic flame temperature), the solid mass fraction $(1 - \xi)$ rapidly decreases from 1 to 0. The consumption rate $(d\xi/d\sigma)$ initially increases as a result of the increase in temperature, and consequently decreases as the reactants are depleted. Its profile spans approximately the same range over which τ increases, demonstrating the heterogeneous nature of reactant consumption and hence the flame structure. For the prescribed conditions with $R_0 = 10\ \mu$m, the flame thickness and burning velocity are predicted to be about 1 mm and 10 mm/s, respectively.

The nonadiabatic situation is close to the extinction state. Decrease in τ reduces the consumption rate $(d\xi/d\sigma)$ and hence the normalized burning rate (m/m_a). The reactant consumption zone is also broadened because of heat loss.

To further identify the flame structure for the nonadiabatic case of Fig. 1, we have plotted in Fig. 2 the four terms constituting Eq. (7), that is, $(d^2\tau/d\sigma^2)$, $[(m/m_a)/(1 - Z_0)](d\xi/d\sigma)$, $-[(m/m_a)/(1 - Z_0)](d\tau/d\sigma)$, and $-\phi(\tau)/(1 - Z_0)^2$, which respectively represent diffusion, consumption, convection, and loss. It is clear that the flame consists of a relatively thin zone of diffusion and consumption/convection, which is followed by a much thicker zone of convection and loss. The existence of an extended zone of downstream heat loss is similar to the nonadiabatic homogeneous gaseous flame.

Figure 3 shows variation of the nondimensional mass burning rate $(m/m_{a,st})$ as a function of the nondimensional heat loss $\Psi^* = (m_a/m_{a,st})^2 \cdot \tilde{\Psi}$, with μ and κ taken as parameters. Here, $m_{a,st}$ is the mass burning rate for the stoichiometric mixture in the adiabatic condition. Results exhibit the characteristic extinction turning-point behavior, with the upper branch being the stable solution and the turning point designating the state of extinction. With decreasing μ or increasing κ, the mass burning rate at which extinction occurs gradually decreases. Since both $(m/m_{a,st})$ and $(m_a/m_{a,st})^2 \cdot \tilde{\Psi}$ strongly depend on m, we have used the parameters (m/m_a) and $\tilde{\Psi}$ to obtain the extinction condition, with $\tilde{\Psi}$ being a measure of heat loss to the heat release. It has been found that, depending on μ and κ, the values of $(m/m_a)_{cr}$ corresponding to flame extinction range from 0.57 to 0.70.

Effect of heat loss on the burning velocity is also investigated. Here, we use the following relation [5]:

$$(u_0 \cdot R_0) = D_0\left[3(Le_0 \cdot \Lambda_0)(\rho_M/\rho_N)\frac{\mu + f}{\mu(1 - \kappa)}\right]^{1/2} \tag{12}$$

Figures 4a and 4b respectively show $(u_0 \cdot R_0)$ as functions of μ and κ, with $\tilde{\Psi}$, the heat-loss parameter, taken as a parameter and with $T_0 = 450$ K ($\tilde{T}_0 = 0.03$). Because of the increased amount of volumetric heat release, $(u_0 \cdot R_0)$ significantly increases with either increasing μ or decreasing κ. For a given μ or κ, $(u_0 \cdot R_0)$ decreases with increasing $\tilde{\Psi}$ and reaches the extinction limit shown by the dashed curve. The range for steady flame propagation is contracted because of the heat loss. Although not shown here, the same trends as those in Figs. 4a and 4b are observed for the higher value of $T_0 = 975$ K. For this temperature, the results show that flame propagation can be sustained for higher $\tilde{\Psi}$ as a result of preheating effect.

Figures 5a and 5b respectively show the effect of μ and κ on the critical heat-loss parameter $\tilde{\Psi}_{cr}$, with

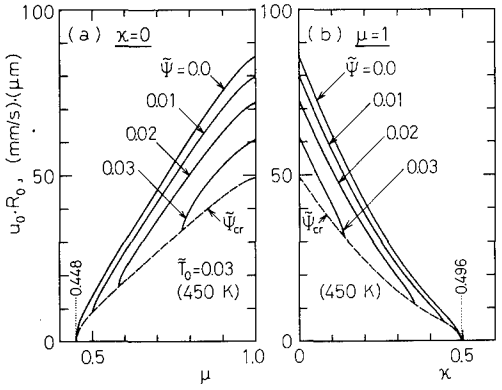

FIG. 4. (a) The combination of $(u_0 \cdot R_0)$ as a function of the mixture ratio μ, with the heat-loss parameter $\tilde{\Psi}$ taken as a parameter; the degree of dilution is $\kappa = 0$ and the initial temperature $T_0 = 450$ K. (b) $(u_0 \cdot R_0)$ as a function of κ, with $\tilde{\Psi}$ taken as a parameter; $\mu = 1.0$ and $T_0 = 450$ K.

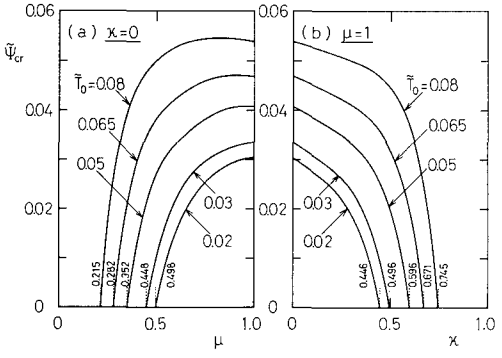

FIG. 5. (a) The critical heat-loss parameter $\tilde{\Psi}_{cr}$ as a function of the mixture ratio μ, with the initial temperature T_0 taken as a parameter; the degree of dilution is $\kappa = 0$. (b) $\tilde{\Psi}_{cr}$ as a function of κ, with T_0 taken as a parameter; $\mu = 1.0$.

the initial temperature T_0 taken as a parameter. We see that the change in $\tilde{\Psi}_{cr}$ is gradual when either μ or κ is away from the flammability limit, and that $\tilde{\Psi}_{cr}$ decreases rapidly as this limit is approached. We also see that $\tilde{\Psi}_{cr}$ increases with increasing T_0 for a given μ or κ. This suggests that, even if there exists heat loss, flame propagation can be sustained when T_0 is high. Note that there exists a maximum in $\tilde{\Psi}_{cr}$ at high T_0.

Further Theoretical Considerations

The heterogeneous SHS flame propagation has some additional features that can be contrasted with the homogeneous gaseous flame propagation. First, we note that because of the very large Lewis number of the condensed phase, with $Le > 10^4$ in the consumption zone, $\tilde{Y}_M$ can be approximated by setting the last term on the right-hand side of Eq. (6) to zero. This yields an explicit relation between ζ and ξ as

$$\zeta \approx \frac{\xi}{Z_0 + (1 - Z_0)\xi}. \tag{13}$$

Equation (13) indicates that, because of the excessively slow rate of diffusion as compared to the rates of thermometric conductivity and reaction, concentration of the molten metal in the compact is affected mainly through consumption instead of diffusion. Numerical results obtained by solving Eq. (13) instead of Eq. (6) for ζ were found to be practically indistinguishable.

We next note that while the surface regression rate χ and hence the reactant consumption rate depend on chemical reactivity through $\tilde{\chi}$ as well as the mass diffusivity, in most SHS processes, the reduced Damköhler number A is sufficiently large such that $\tilde{\chi} \to \ln(1 + \tilde{Y}_M)$, and reactant consumption becomes diffusion limited. Numerical calculations performed in this limit were again found to be indistinguishable from those obtained with finite but large values of A. This result has the following significant implication.

Since extinction in combustion is frequently associated with the nonlinear, highly temperature-sensitive nature of the Arrhenius kinetics, the loss of its influence in the diffusion limit implies that extinction as shown in Fig. 3 is actually caused by an alternate factor that also has a nonlinear influence on flame propagation. This factor is the liquid mass diffusivity, which varies in a sensitive, nonlinear, Arrhenius manner with temperature. Thus, in the present diffusion limit, the particle regression rate is still an Arrhenius function of temperature, with the large activation temperature for diffusion, T_d, exerting the dominant temperature sensitivity.

Finally, an explicit relation can also be derived for the state of extinction. In the thin diffusion-consumption/convection zone, contribution of the loss term is very small. Equation (7) then becomes

$$\frac{d\tau}{d\sigma} \approx \left(\frac{m}{m_a}\right)\left(\frac{\tau - \xi}{1 - Z_0}\right). \tag{14}$$

Eliminating σ from Eq. (14) with Eq. (8) and noting that $(\tilde{T}_d/\tilde{T}) \approx (\tilde{T}_d/\tilde{T}_\infty) + \beta(1 - \tau)$, where $\beta = [\tilde{T}_d(\tilde{T}_\infty - \tilde{T}_0)]/\tilde{T}_\infty^2$, we have

$$\frac{d\tau}{d\xi} = \left(\frac{m}{m_a}\right)^2 A_0\left(\frac{\rho_{t,0}}{\rho_t}\right) \cdot \exp\left(\frac{\tilde{T}_d}{\tilde{T}_\infty}\right) \frac{\tau - \xi}{(1 - Z_0)(1 - \xi)^{1/3}\,\tilde{\chi}\, e^{-\beta(1-\tau)}} + 0\left(\frac{1}{\beta}\right) \tag{15}$$

which upon integration yields

$$\frac{e^{-\beta(1-\tau)}}{\beta} = \left(\frac{m}{m_a}\right)^2 \Lambda_0 \left(\frac{\rho_{t,0}}{\rho_t}\right) \cdot \exp\left(\frac{\tilde{T}_d}{\tilde{T}_\infty}\right) \int_0^\xi \frac{\tau - \xi}{(1 - Z_0)(1 - \xi)^{1/3}\,\tilde{\chi}}\, d\xi. \tag{16}$$

Taking account of the adiabatic condition, that is, $\tau = \xi = \zeta = 1$, and $m = m_a$, we obtain the following relation to the lowest order, evaluated at the edge of the downstream boundary.

$$\left(\frac{m}{m_a}\right)^2 = e^{-\beta(\xi_e - \tau_e)}. \tag{17}$$

Here, use has been made of $\xi_e \approx 1$ because reaction is nearly completed even under the nonadiabatic condition.

Integrating and evaluating Eq. (7) at the downstream edge of the consumption zone, we obtain

$$(\xi_e - \tau_e) = \frac{(\Omega/\beta)}{(m/m_a)^2} \tag{18}$$

where

$$(\Omega/\beta) = \int_0^{\tau_e} \frac{\phi(\tau)}{\tau}\, d\tau + \phi(\tau_e) \tag{19}$$

and use has been made of the upstream relation of $(d\tau/d\sigma) = (m/m_a)[\tau/(1 - Z_0)]$ and the downstream boundary condition of Eq. (10). Equation (17) can then be rewritten as

$$\left(\frac{m}{m_a}\right)^2 \ln\left(\frac{m}{m_a}\right)^2 = -\Omega. \tag{20}$$

It is seen that $(m/m_a)_{cr} = e^{-1/2} = 0.6065$ and that the state of extinction is the same as that for the homogeneous premixed flame [6,15]. Figure 3 shows that this analytical extinction state compares well with the numerical value. Figures 6a and 6b further show $(m/m_a)_{cr}$ as functions of μ and κ, with $\tilde{T}_0$ taken as a parameter. It is seen that the numerical and analytical solutions for $(m/m_a)_{cr}$ differ by 15%. This difference is further reduced to less than 4% in the determination of $\tilde{\Psi}_{cr}$.

Experimental Comparisons

There exist several sources of experimental data that can be compared with calculated results. In comparisons, we tried to keep as many parameters fixed as possible. For the heat loss, only thermal radiation is considered because of the high temperature in the consumption zone, which is typically higher than 2000 K. For a cylindrical compact with radius r, the lateral heat loss can be expressed as $L = (2h_{rad}/r)\cdot(T - T_0)$, where $h_{rad} = \varepsilon\sigma(T^2 + T_0^2)\cdot(T + T_0)$ is a radiative heat-transfer coefficient, ε the emissivity, and σ the Stefan–Boltzmann constant. Then, the heat-loss parameter $\tilde{\Psi}$ can be expressed as

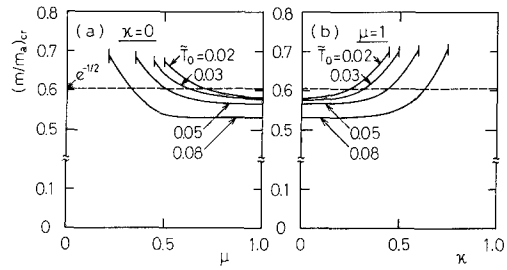

FIG. 6. Comparisons between numerical and analytical solutions for the critical value of the mass burning-rate ratio; (a) $(m/m_a)_{cr}$ as a function of μ, with $\tilde{T}_0$ taken as a parameter; (b) $(m/m_a)_{cr}$ as a function of κ, with $\tilde{T}_0$ taken as a parameter.

$$\tilde{\Psi} = \left(\frac{\lambda}{\rho_t c}\right) \frac{2\varepsilon\sigma(T^2 + T_0^2)(T + T_0)}{(\rho_t c)(u_{0,a}\cdot R_0)^2} \frac{R_0^2}{r} \tag{21}$$

Note that $\tilde{\Psi}$ depends not only on the physicochemical parameters but also on the particle radius R_0 and the compact radius r. Here, $\tilde{\Psi}$ is evaluated at the maximum temperature of the flame.

First, predicted results are compared with experimental data for the Ti-C system. The values of the physicochemical parameters are as follows: $\lambda/(\rho_t c) = 10^{-5}$ m²/s [13], $\varepsilon = 0.4$ [10], $c = 1.0$ kJ/(kg·K), and $\sigma = 5.67 \times 10^{-11}$ kJ/(m²·s·K⁴). In accordance with experimental data [9,11], the compact has a radius $r = 9$ mm and a relative density 0.6.

Figure 7a shows the range of flammability under heat-loss condition; the abscissa is μ and the ordinate the initial particle radius R_0. The initial temperature is $\tilde{T}_0 = 0.03$ (450 K). Extinction is anticipated to occur when $\tilde{\Psi}$ in Eq. (21) reaches the critical heat-loss parameter $\tilde{\Psi}_{cr}$ in Fig. 5a. We see that, while the range of flammability spans from 0.448 to 1 when $R_0 \to 0$, it contracts with increasing R_0. It further shows that the flame front cannot propagate through a compact when R_0 is larger than 21.0 μm. Experimental results [9,11] are also shown in Fig. 7a. Fair agreement is demonstrated for particles that are smaller than 7.5 μm, while discrepancy becomes large for $R_0 = 12.5$ μm. This is attributed to the effect of smaller particles because there exists particle size distribution. Note that the extinction limit obtained here corresponds to that for the steady flame propagation. When the process occurs in an unsteady mode, as a

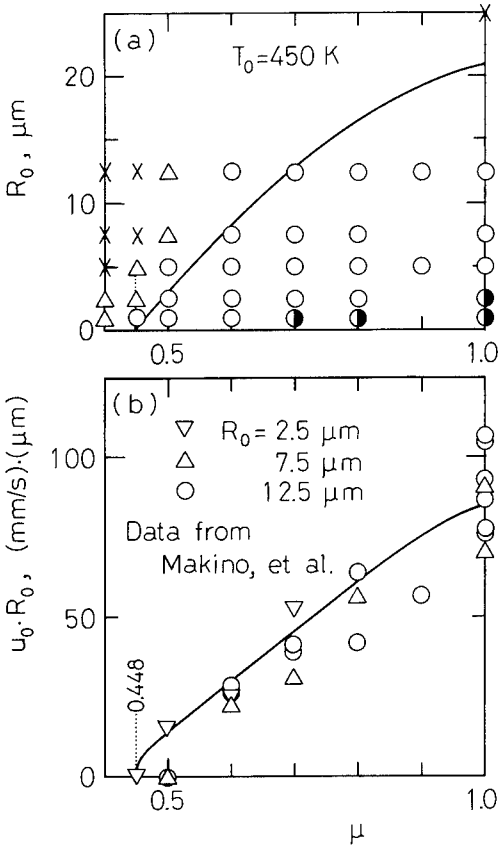

FIG. 7. (a) The range of flammability for the Ti-C system under heat-loss condition as functions of the mixture ratio μ and the initial particle radius R_0; (○) shows the steady propagataion, (◑) the pulsating combustion, (△) the flame extinction during the propagation, and (×) the nonignition; (b) $(u_0 \cdot R_0)$ as a function of μ, with R_0 taken as a parameter. Data points are experimental [9,11].

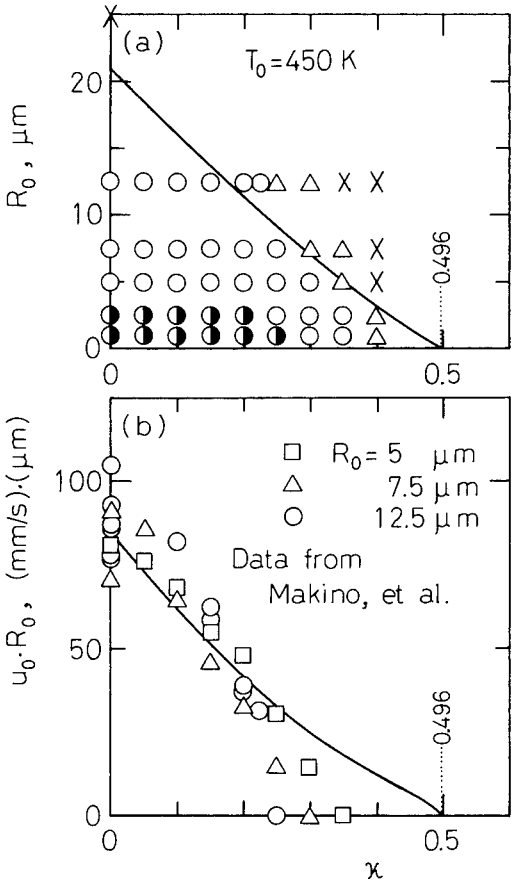

FIG. 8. (a) The range of flammability for the Ti-C system under heat-loss condition as functions of the degree of dilution κ and the initial particle radius R_0; (○) shows the steady propagation, (◑) the pulsating combustion, (△) the flame extinction during the propagation, and (×) the nonignition; (b) $(u_0 \cdot R_0)$ as a function of κ, with R_0 taken as a parameter. Data points are experimental [11].

result of loss of stability of the steady propagation, the limit of self-sustained combustion can be modified accordingly. Figure 7b shows $(u_0 \cdot R_0)$ as a function of μ. The agreement is again fair, as far as the trend and approximate magnitude are concerned. Figure 7b also shows that $(u_0 \cdot R_0)$ is one of the important parameters in correlating experimental results.

The range of flammability with respect to the degree of dilution is also obtained (Fig. 8a). The range of flammability becomes narrow with increasing R_0. Experimental results [11] are also shown in Fig. 8a. Again, fair agreement is demonstrated for particles that are smaller than 7.5 μm, while discrepancy becomes large for R_0 = 12.5 μm. Figure 8b shows $(u_0 \cdot R_0)$ as a function of κ. The same comments as those for Figs. 7a and 7b can be made.

There exists another source of experimental data that can be used for comparison. Munir and Sata [12] measured the boundary of SHS in the boride synthesis of Ti, Zr, and Hf at several ambient (or initial) temperatures. Their test specimen (19 mm in diameter and 0.65 in relative density) is composed of tens of layers, each of which is 5-mm thick and has a certain degree of dilution, which increases gradually. Average size of the boron particles is about 1 μm in diameter. Figure 9a shows the limit of dilution for the Ti-B system. The values of physicochemical parameters are $\lambda/(\rho_t c) = 1.6 \times 10^{-5}$ m^2/s [13], $\varepsilon = 0.6$ [14], and $c = 1.0$ kJ/(kg·K). We see that the range of flame propagation expands with increasing T_0. For a given T_0, the range of flame propagation narrows with increasing radius of boron particle, R_0. Figure 9b shows results for the Hf-B system with $\lambda/(\rho_t c) = 1.8 \times 10^{-5}$ m^2/s [13], ε

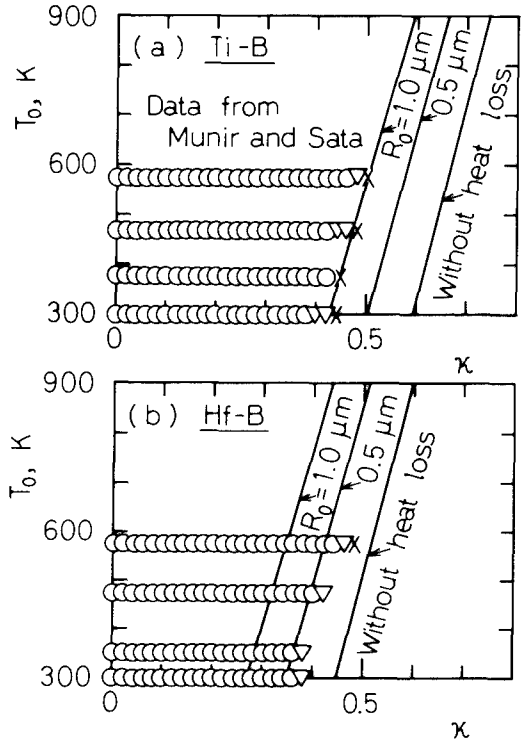

FIG. 9. The range of flammability under heat-loss condition as functions of the degree of dilution κ and the initial temperature T_0, with the initial particle radius R_0 taken as a parameter; (a) for the Ti-B system; (b) for the Hf-B system. Data points are experimental [12]; (○) shows the steady propagation, (▽) the unsteady propagation, and (×) the flame extinction.

$= 0.7$ [14], and $c = 0.45$ kJ/(kg·K). Fair agreement is again observed.

Concluding Remarks

In the present study, we have formulated a nonadiabatic, heterogeneous theory of SHS with volumetric heat loss and have successfully obtained the characteristic extinction turning point. It is of particular significance to note that, since particle consumption is diffusion limited, the process responsible for its temperature sensitivity and ultimate extinguishment is the Arrhenius liquid-phase mass diffusion, which still induces such characteristic Arrhenius behavior as extinction.

It is also of interest to note that analytical solutions have been obtained for the nonadiabatic flame propagation rate, leading to the identification of an explicit criterion governing flame extinction. The normalized extinction burning rate of $e^{-1/2}$ for the present system is the same as that for the gaseous premixed flame.

Finally, the fair agreement between calculated and experimental values, in trend and in approximate magnitude, suggests that the present analysis has captured the essential features of the nonadiabatic heterogeneous flame propagation process in SHS. The analysis therefore forms the basic framework for further studies of other SHS phenomena such as spinning and pulsating combustion, in which heat loss could be important.

Acknowledgments

AM and CKL were respectively supported by the Grant-in-Aid for Scientific Research of the Ministry of Education, Japan, and the Microgravity Materials Program of NASA.

REFERENCES

1. Frankhouser, W. L., Brendley, K. W., Kieszek, M. C., and Sullivan, S. T., *Gasless Combustion Synthesis of Refractory Compounds*, Noyes, Park Ridge, NJ, 1985.
2. Munir, Z. A., and Anselmi-Tamburini, U., *Mater. Sci. Rep.* 3:277–365 (1989).
3. Merzhanov, A. G., *Combustion and Plasma Synthesis of High-Temperature Materials* (Z. A. Munir and J. B. Holt, Eds.), VCH, New York, 1990, pp. 1–53.
4. Margolis, S. B., *Prog. Energy Combust. Sci.* 17:135–162 (1991).
5. Makino, A., and Law, C. K., *Twenty-Fourth Symposium (International) on Combustion*, The Combustion Institute, Pittsburgh, 1992, pp. 1883–1891.
6. Williams, F. A., *Combustion Theory*, 2nd ed., Benjamin/Cummings, Menlo Park, CA, 1985.
7. Makino, A., and Law, C. K., *J. Am. Ceramic Soc.*, 77:778–786 (1994).
8. Hardt, A. P., and Phung, P. V., *Combust. Flame* 21:77–89 (1973).
9. Makino, A., Araki, N., and Kuwabara, T., *Trans. JSME Ser. B* 58:1925–1930 (1992) (in Japanese).
10. Touloukian, Y. S., *Thermophysical Properties of High Temperature Solid Materials*, Thermophysical Properties Research Center, Purdue University, MacMillan, New York, 1967, Vol. 5.
11. Makino, A., Kita, K., and Araki, N., *Nensho no Kagaku to Gijutsu* 1:165–174 (1993) (in Japanese).
12. Munir, Z. A., and Sata, N., *Int. J. SHS* 1:355–365 (1992).
13. Touloukian, Y. S., Powell, R. W., Ho, C. Y., and Nicolaou, M. C., *Thermophysical Properties of Matter*, IFI/Plenum, New York, 1973, Vol. 10.
14. Touloukian, Y. S., and DeWitt, D. P., *Thermophysical Properties of Matter*, IFI/Plenum, New York, 1972, Vol. 8.
15. Kaper, H. S., Leaf, G. K., Margolis, S. B., and Matkowsky, B. J., *Combust. Sci. Technol.* 53:289–314 (1987).

COMMENTS

A. M. Kanury, Oregon State University, USA. 1. What do you assume for the thermal conductivity and its dependence on the degree of compaction of the reaction mixture?

2. Your analysis appears to ignore expansion of the solid upon reaction. Is this realistic?

Author's Reply. 1. In this formulation, what we are concerned about is the conservation in the reaction zone. The thermal conductivity (λ) which always appears in the form of thermometric conductivity ($\lambda/\rho c$) depends on the mixture ratio, degree of dilution, and relative density (degree of compaction). Since its dependence on these parameters is complicated, a representative value is used. In our previous work [5], it has been shown that Lewis number $Le_0 = 100$ correlates well with the experimental data [9] for a Ti-C system whose relative density is about 0.6. Since $Le_0 = 100$ corresponds to $(\lambda/\rho c) \sim 1 \times 10^{-5}$ m²/s, use has been made of this value. Consequently, the experimental data [9,11] for the burning velocity and the flammable range used in the present comparisons are restricted to those with 0.6 relative density.

2. We experimentally observed that there was axial expansion of 30% at the most, depending on the mixture ratio, degree of dilution, relative density, and/or particle size of powder. However, since expansion occurs mostly after the combustion wave has passed, and since flame propagation is primarily controlled by the state of the unburned mixture, the present results are not sensitive to this small amount of expansion.

Twenty-Fifth Symposium (International) on Combustion/The Combustion Institute, 1994/pp. 1669–1675

A DMS KINETIC STUDY OF THE BORON OXIDES VAPOR IN THE COMBUSTION FRONT OF SHS SYSTEM MO + B

OLEG E. KASHIRENINOV AND IGOR A. YURANOV
Institute of Structural Macrokinetics
The Russian Academy of Sciences
142432 Chernogolovka, Moscow Region, Russia

The distribution of the boron oxides vapor in the combustion wave of the SHS system Mo + B has been studied by the dynamic mass spectrometry technique (DMS) to test the thermodynamically based hypothesis for the key role of gas-phase transport in solid-state combustion. The molecular beam sampling of the gases over the burning tablet was performed by a stationary probe cone from the moving combustion wave. Ion currents of boron oxides were recorded at 10–20 ms intervals that afforded spatial resolution of 0.1–0.2 mm. It has been found that the distribution of the boron oxides vapor pressure along the combustion wave corresponds to the known zones of preheating, reaction, and postcombustion. The rapid increase of B_2O_2 pressure takes place in the preheating zone as a result of the reaction $B(s) + B_2O_3(g) \rightarrow B_2O_2(g)$. Boron oxides are not observed over the reaction zone because of their complete decay in the reaction with Mo(s) to form molybdenum boride(s). The appearance of boron oxide vapors over the postcombustion zone is due to the evaporation of $B_2O_3(l)$. The effective kinetic parameters are estimated from the data obtained. The results show that solid-state combustion of the Mo + B system proceeds predominantly through formation of gas-phase boron oxides.

Introduction

Gasless combustion of solid reactant mixtures [1] is usually concerned with the self-propagating high-temperature synthesis (SHS) of inorganic materials [2]. Though much progress has been achieved in SHS over the past few years [3,4], many details of the kinetics and chemical mechanism of the processes remain unstudied. Among other things, one of the key questions not yet clarified is how the fast reactant transport is performed when the adiabatic temperature of the combustion front is lower than melting points of the reactants and possible eutectics. It is quite evident that solid-state diffusion in SHS systems cannot maintain the combustion rates observed [5]. Therefore, it is reasonable either to assume some unknown peculiar mechanism of ultrafast solid-state diffusion, or to accept that reactant transport comes about through the gas phase formed in the combustion wave. The known type of condensed systems combustion with gasification of components is realized in the latter case.

The thermodynamic calculations performed earlier [5,6] for the systems of this type (Mo + B, W + B, Ta + C) show that gas-phase transport of one or both reactants is most probably in the form of volatile oxides. These oxides can a priori exist as a film on the surface of reactant particles and can be formed in the combustion wave through the interaction of reactants with absorbed or occluded oxygen. The typical quantity of oxygen contamination in the starting sample of the above-mentioned systems is more than enough to supply the oxide vapor pressure needed for effective gas-phase transport [7]. Four stages were revealed for the process in the Mo + B system. Redistribution of oxygen between the Mo- and B-subsystems (stages 1 and 2) was determined as a precursor of the main reactions of molybdenum boride formation (stages 3 and 4) that can be presented as

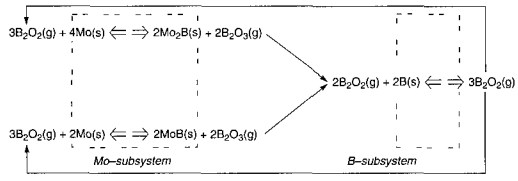

The later stages were assumed to be the cycling process providing the regeneration of oxygen [5]. Estimated gas-phase transport rates can lead to essentially complete reactant conversion in the combustion front [6].

Experimental results obtained by the dynamic mass spectrometry technique (DMS) with molecular beam sampling of high-temperature vapors from various zones of the combustion wave in the Mo + B system are presented in this work.

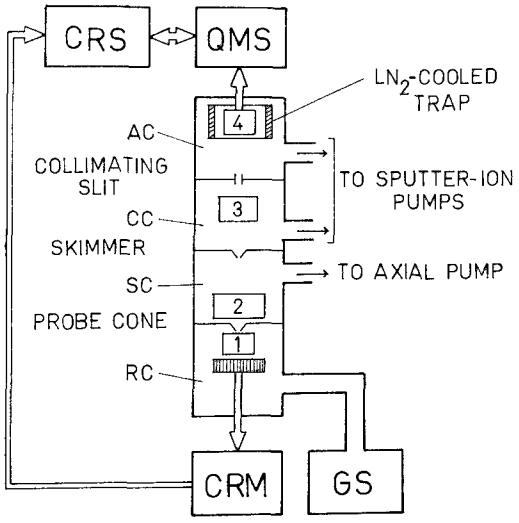

FIG. 1. Schematic of DMS apparatus used: CRS—controlling and recording system; QMS—quadrupole mass spectrometer MS-7303; AC—analyzer chamber; CC—collimator chamber; SC—skimmer chamber; RC—reaction chamber; CRM—system for combustion rate measurement; GS—gas supply and exhaust system; 1—tablet; 2—adjustment system; 3—beam chopper; 4—QMS ion source.

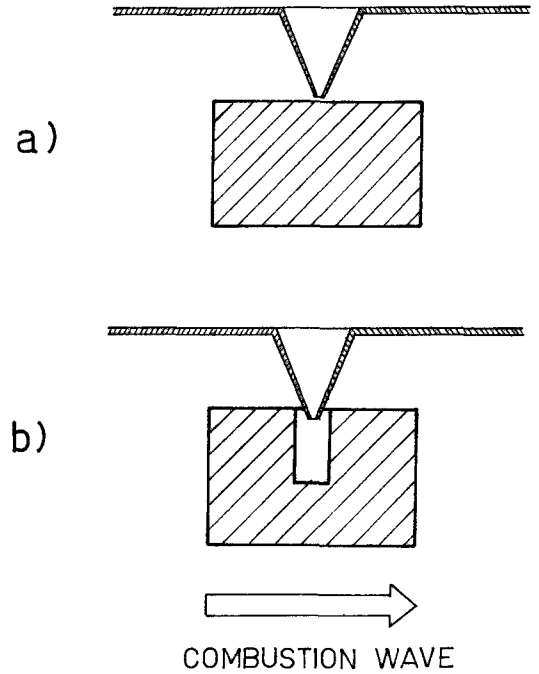

FIG. 2. Relative position of probe cone and tablet during runs with sampling: (a) on surface; (b) from channel.

Technique

The method used was based on the assumption that the gas phase inside the sample (in pores) is related to that on the surface. The observed intensive gas release from the burning "gasless" SHS systems [8,9] is evidence in favor of this. Available data on the thermal structure of the combustion wave in SHS systems indicate that the difference between the temperature in volume and on the surface does not exceed 100 °C [10] for the samples of ordinary size. Therefore, one can consider the gas sampled on the surface as representative of the composition of the gas in the sample.

The installation used is sketched in Fig. 1. Cylindrical tablets 10 mm in diameter and 15–20 mm in length were pressed from equimolecular molybdenum and boron powder mixtures. The sample was placed into the reaction chamber and ignited by a molybdenum coil from the face. The quartz probe cone with a sampling orifice 30–70 μm in diameter was centrally positioned over the sample. Gas was sampled on flat surfaces as well as from cylindrical channels in the sample body with diameters ranging from 2 to 4 mm and about 5 mm in length. In the latter case, the probe and channel were coaxial. The relative positions of probe cone and sample in runs of these types are shown in Fig. 2. The pressure of ambient gas (Ar, 99.98%) in the reaction chamber was equal to 1 bar.

The quadrupole mass spectrometer (QMS) MS-7303 with a mass number range 1–500 was used to analyze the molecular beam. The energy of the ionizing electrons varies from 20 to 100 eV (usually 50 eV). Secondary electron multipliers (SEM) VEU-2 and VEU-6 were used for monitoring the ion currents $\geq 10^{-15}$ and $\leq 10^{-16}$ A, respectively. A computerized control and recording system (CRS) allowed measurement of the ion current for a given mass with a period from 1 ms. The minimum time interval increased to 13 ms if the ion currents for several masses were measured simultaneously.

The system used for molecular beam formation was described elsewhere [11]. In our case, the "sampling spot" (the area of gas composition averaging) for molecular beam formation at the surface is $\Delta = 0.3 \cdot d \cdot a^{1/2}$, where d is the orifice diameter of the probe cone and a is a dimensionless parameter with an order of magnitude of ~100. We can state, therefore, that taking into account the frequency of ion current recording and the rate of combustion front propagation, the spatial resolution in our experiments ranged from 0.09 to 0.21 mm.

Taking into consideration the sensitivity of SEM in use and deterioration of the beam from the probe cone to the ionization area, the pressure sensitivity at the point of sampling was not worse than 0.1 Pa.

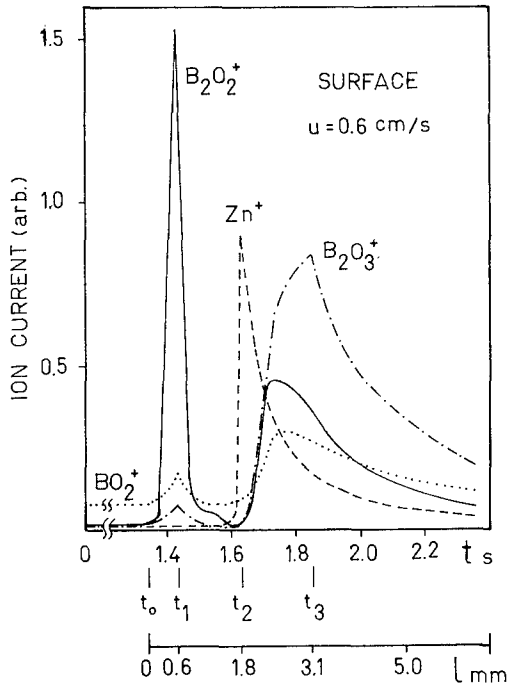

FIG. 3. Time dependence of ion currents and spatial regions of combustion front for the SHS system Mo + B with sampling on the surface.

The combustion rate was measured concurrently with the ion currents, and the sweep of the QMS was initiated by the starting pulse of the CRM (see Fig. 1) with a controlled time delay.

Zinc (99%) powder with a particle size of $\leq 80\ \mu m$ was inserted into the samples in quantities of 0.02–0.03% by mass as a marker to detect the combustion front passing through the probe cone. The samples were prepared from Mo (99.9%) and amorphous B (99.5%) powders with particle size ≤ 5 and $\leq 1\ \mu m$, respectively.

Results

Figure 3 demonstrates the typical time dependence of ion currents obtained by gas sampling from the surface of a burning sample. In the beginning of the process (before the combustion wave reached the probe), only the background ion current for any of the oxide masses is monitored. Some release of H_2 and N_2 (or CO) took place ahead of the combustion wave and was terminated about 200 ms before the wave reached the probe location. When the combustion wave reached the sampling region an ion current from boron oxides appeared. No molybdenum oxides were measured at the highest sensitivity of SEM during the whole period of sample burning, even when ionizing electron energies of up to 100 eV were used.

The ion currents of B^+, BO^+, $B_2O_2^+$, and $B_2O_3^+$ were monitored. According to known data [12], B^+ and BO^+ ions are formed by a complex mechanism involving dissociative ionization. For this reason, the intensities of their ion currents could not be used for quantitative estimations, and therefore, only the time variations of the ion currents of $B_2O_2^+$ + and $B_2O_3^+$ formed from the corresponding molecular precursors are used in the following consideration. The ion current is assumed to be proportional to the partial pressure of the corresponding component of gas phase in the sampling spot.

Structure of Combustion Wave:

The recording of ion current as a function of time at a known and constant combustion rate u allows us to obtain the spatial structure of combustion wave assuming that $l = u \cdot \Delta t$, where l is the distance along the front propagation and $\Delta t = t_i - t_0$. The measured combustion rate of the samples under study ranged from 0.5 to 0.7 $cm \cdot s^{-1}$ and was taken to be 0.6 $cm \cdot s^{-1}$ in the subsequent calculations.

Data obtained reveal four regions in the spatial distribution of gas components over the combustion wave. Vigorous release of boron oxides (B_2O_2, mainly) takes place in the comparatively narrow (0.6 mm) Region I ($t_0 - t_1$; see Fig. 3). Release of boron oxides in a wider (1.2 mm) Region II ($t_1 - t_2$) decreases sharply and then ceases. A noticeable increase of boron oxides is again observed in Region III ($t_2 - t_3 \approx 1.3$ mm). Finally ($t > t_3$), the decrease of all gas components released from the sample, takes place in a wide Region IV (>3.7 mm).

Sampling from Channel:

The spatial distribution of boron oxides from the channel is more complicated and depends on the channel diameter (d_c). The data obtained for d_c = 3.5 m are shown in Fig. 4 and demonstrate the mixing of the gas components released from various regions into the channel when $d_c \geq \delta$, where δ is the width of the combustion wave. In our experiments, the diffusion through the comparatively narrow gap ($\simeq 1$ mm) between the sample and probe cone was not probably fast enough, and boron oxides accumulate to some extent in the channel (their partial pressure is about two times higher than at the sampling on the surface; see Figs. 3 and 4). One can suppose that such accumulation proceeds until the wave leaves the channel. Comparison of Figs. 3 and 4 indicates that the curves for boron oxides release recorded at sampling on the surface and from the channel are quite similar in spite of obvious differences in Region I. The time borders of Region II are also similar.

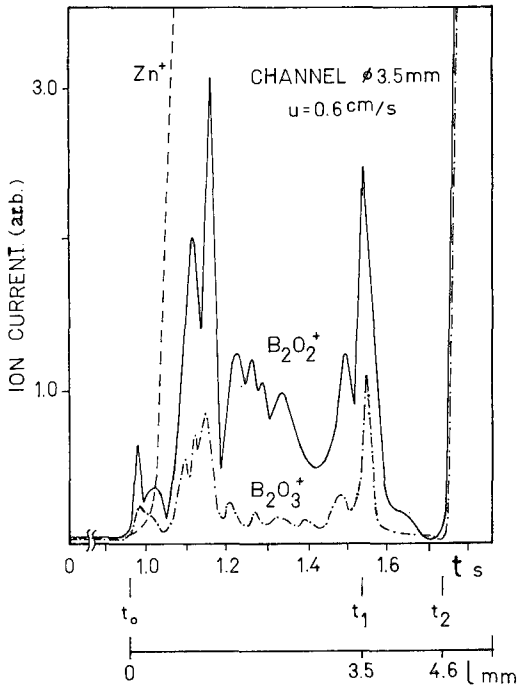

FIG. 4. Time dependence of ion currents and fluctuations of boron oxide pressures in the SHS system Mo + B with sampling from the channel.

Temperature Profile:

As noted above, zinc additives were inserted into the samples as a marker. The ionization potential for Zn (9.39 eV [13]) is considerably lower than for BO, B_2O_2, and B_2O_3 ($\approx$14 eV [13]). The time of zinc ($\sim 10^{-3}$ g·cm^{-3}) heating in the combustion wave from room to adiabatic temperature (T_{ad} = 1800 K [10]) by the heat of reaction Mo(s) + B(s) → MoB(s) + 71 kJ·mol^{-1} does not exceed 0.5 ms. Its complete vaporization at T_{ad} and an external pressure of 1 bar needs at least 0.1 s. This process thus cannot disturb the thermal structure of the combustion wave since the heat of vaporization of zinc is 120 kJ·mol^{-1} [14].

To estimate the possible effect of ZnO presence in the system, the corresponding thermochemical data are needed. Unfortunately, these data are not available. However, the boiling point for Zn ($\approx$1180 K) is about 1000 °C lower than melting point for ZnO ($\approx$2250 K), suggesting that the effect of ZnO is negligible.

Therefore, one can consider the vaporization of zinc from the sample and its corresponding ion current as adequately responding to the temperature change in the combustion wave. The data obtained show (see Fig. 3) the sharp and strong increase of the Zn^+ ion current at the end of Region II. The maximum temperature, which is equal to the adiabatic one, is probably reached there. The decrease of Zn^+ ion current in Regions III and IV can be attributed to depletion of Zn.

TABLE 1
Equilibrium Partial Pressure of the Main Gas Components in the System B + B_2O_3 (Pa)

	1000 K	1800 K
B	—	2.3×10^{-4}
BO	4.0×10^{-9}	0.55
BO_2	2.6×10^{-9}	1.2×10^{-5}
B_2O	—	1.6×10^{-7}
B_2O_2	2.1×10^{-5}	4.5
B_2O_3	2.9×10^{-7}	1.2×10^{-2}

Discussion

It is quite natural to consider the dependencies obtained in terms of the combustion wave structure in SHS systems where the zones of preheating, reaction, and postcombustion are commonly recognized [4].

Region I:

Region I can be identified with the preheating zone. The relatively narrow part of the preheating zone closest to the reaction zone is probably observed in our experiments. The temperature there is high enough to evaporate the boron oxides (see Table 1). Based on the model of the gas-phase reactant transport in the Mo + B system [6], this part of the preheating zone can be considered as "setting the stage" for the main reaction in the system (Stages 1 and 2). The appearance of $B_2O_2^+$ different from the background value could then be taken as the origin of coordinates for the quantitative analysis of the processes in the combustion wave in time as well as in space (t_0).

Maximum pressures of boron oxides in Region I are reached in time $\Delta t = t_1 - t_0$ = 100 ms that corresponds to a width of 0.6 mm in the region. If one assumes that the maximum Zn^+ is detected at the maximum temperature of the combustion front T_{ad} = 1800 K, and the temperature gradient in front is equal to 530 deg·mm^{-1} [10], then the temperature in the beginning (t_0) and in the end (t_1) of Region I is equal to 910 and 1230 K, respectively. These temperatures are rather high. Our estimation shows that the convective flow of the admixed gases from the sample pores through thermal expansion is negligible by the time they are reached. The lack of Zn^+ in Region I is probably due to the fast reaction (k^{1000K}

$\sim 10^{-13}$ $cm^3 \cdot molecule^{-1} \cdot s^{-1}$ [15]) of zinc vapor with oxygen.

From general considerations, it is clear that boron oxides in Region I are mainly evaporated from the binary system B + B_2O_3. The observed relationship of $B_2O_2^+$ and $B_2O_3^+$ ion currents qualitatively corresponds to the data presented in Table 1 ($p_{B_2O_2} >> p_{B_2O_3}$). Besides, these data allow us to consider B_2O_2 as the main component of the gas phase in the combustion wave of the Mo + B system.

In principle, two reactions between the solid boron and B_2O_3 result in B_2O_3(g) formation:

$$B(s) + B_2O_3(l) \rightarrow 1.5\ B_2O_2(g) + 522\ kJ \cdot mol^{-1} \quad (1)$$

$$B(s) + B_2O_3(g) \rightarrow 1.5\ B_2O_2(g) + 147\ kJ \cdot mol^{-1} \quad (2)$$

Reaction (2) is thermodynamically preferred. For kinetic evaluation, it is necessary to determine the rate coefficient for this reaction. Such evaluation based on the data obtained is possible only with some errors originating from the nonisothermicity of Region I and the movement of combustion wave relative to the probe.

The rate coefficient for reaction (2) was estimated assuming the average temperature in the whole Region I to be 1070 K. The ion current of $B_2O_2^+$ in this region increases with a width of <0.3 mm at a reliable spatial resolution of >0.14 mm. Therefore, if one neglects the effect of the combustion wave propagation on such a relatively short length, the rise to the first maximum can be considered as the dependence of $B_2O_2^+$ on time in the sampling spot.

When the process starts, the total surface of boron particles changes insignificantly, and heterogeneous reaction (2) can be described by the first-order kinetic law on B_2O_2(g). Then the treatment of the curve from t_0 to t_1 by

$$k_2 = \ln[I_{B_2O_2^+\,max}/(I_{B_2O_2^+\,max} - I_{B_2O_2^+})]\, t^{-1} \quad (A)$$

where $I_{B_2O_2^+}$ is the ion current of $B_2O_2^+$ in relative units, yields the value $k_2 = 14\ s^{-1}$. Using the known equation [16], the effective rate coefficient for heterogeneous reaction (2) at fully reactive surface can be described by

$$k_2 = S_B \cdot V_r^{-1} \cdot (kT/2\pi m_{B_2O_2})^{1/2} \cdot \exp(-E/RT) \quad (B)$$

where $m_{B_2O_2}$ is the mass of molecule and S_B is the accessible surface of boron particles in the reaction volume V_r. Taking the average radius of boron particles equal to 5×10^{-5} cm and assuming that, in the equimolecular Mo + B mixture, the reactant concentration is equal to 0.043 $mole \cdot cm^{-3}$ at a relative density of 0.6, it is easy to calculate $S_B = 1.8 \times 10^3 \cdot cm^2$ for $V_r = 0.19\ cm^3$. The activation energy estimated from Eq. (B) is equal to 140 $kJ \cdot mol^{-1}$ and unexpectedly fits well the endothermicity of reaction (2). Thus, reaction (2) can be considered as the main source of B_2O_2(g) in the combustion wave of the Mo + B system.

Region II:

The rapid decrease of boron oxide and its absence in a fairly long zone of Region II in the wake of the fast increase in Region I can be caused by the following:

1. the termination of boron oxide formation or vaporization,
2. the decay of boron oxide in the reaction(s) occurring in the sample volume with the rate equal to their formation rate.

The estimate using $k_2 = 14\ s^{-1}$ and the value of equilibrium partial pressure of B_2O_3(g) at 1000 K reveals that boron oxide vapor formation in Region I results in a negligible consumption of B(s). There is no reason to suppose that pores in the sample become closed because of the formation of oxideless liquid phases with the result in arrest of oxide vaporization. Hence, the involving of boron oxides in the reaction(s) with molybdenum can be the only reason for the absence of the detected oxide ion current at high temperature of the combustion front. If one considers B_2O_2(g) as the main component of the equilibrium gas phase in the system, then the following reaction dominates in Region II:

$$B_2O_2(g) + Mo(s) \rightarrow Mo_xB + \ldots \quad (x = 1,2). \quad (3)$$

Figure 3 shows that the ion currents of the boron oxides increase significantly after the passing of Region II. This can be attributed to the Mo(s) vanishing in the system as a result of reaction (3). The relationship between the ion currents of $B_2O_2^+$ and $B_2O_3^+$ changes drastically ($p_{B_2O_3^+} > p_{B_2O_2^+}$) in comparison with Region I and indicates, with the data of Table 2, that B(s) is also converted completely for the period ($t_2 - t_1$). These facts are of particular importance for the following estimates.

The spatial extension of Region II does not allow us to neglect its movement relative to the probe cone and consider the dependence of $B_2O_2^+$ in this region only as a function of time. Besides, the surface of boron particles changes substantially in Region II. Therefore, kinetic equations for two subsequent reactions of pseudo-first-order cannot be used here.

On the assumption of complete boron conversion in Region II during the period of $t_2 - t_1 = 200$ ms and domination of the reaction (3), the specific rate of this reaction is equal to $w_3 = 0.2\ mole \cdot cm^{-3} \cdot s^{-1}$.

TABLE 2
Equilibrium Partial Pressure of the Main Gas Components over B_2O_3(l) (Pa)

	1000 K	1800 K
B	—	2.2×10^{-10}
BO	4.5×10^{-10}	7.2×10^{-2}
BO_2	4.3×10^{-10}	0.22
B_2O	—	—
B_2O_2	6.3×10^{-10}	7.2×10^{-2}
B_2O_3	2.9×10^{-7}	30

According to the data available [5,17], the transfer of boron takes place in the reacting Mo + B system, and MoB formation occurs on the Mo surface. The rate of boride layer growth in towards the particle body is higher than along its surface, and a noticeable part of the molybdenum surface remains uncovered by boride up to the final stage of the process. This allows us to assume that the area of reactive surface of molybdenum particles changes negligible during reaction (3). In such a case, the effective rate coefficient for reaction (3) calculated with a B_2O_2(g) concentration corresponding to the equilibrium partial pressure at T_{ad} = 1800 K [6] is equal in order of magnitude to $k_3 \sim 10^8\ s^{-1}$. Assuming the probability of collisions of B_2O_2 molecules with the surface of molybdenum ($S_{Mo} \approx 6 \times 10^3\ cm^{-1}$) in the volume of Region II (V_r – 0.38 cm^3) as equal to unity, one can estimate the activation energy for reaction (3) using equation (B). The estimate gives the value $E_3 \approx 0$. The absence of an activation barrier in reaction (3) allows the conclusion on the kinetic but not diffusion mode for molybdenum boride formation in the combustion front of the Mo + B system. The widths of Region II (1.2 mm) and combustion front for the Mo + B system measured earlier [10] coincide very closely.

Regions III and IV:

If the reaction of molybdenum boride(s) formation is completed in Region II, it leaves behind the product and B_2O_3(l) with equilibrium vapor as the major contamination. Therefore, the relationship between ion currents of $B_2O_2^+$ and $B_2O_3^+$ in Regions III and IV has to correspond to evaporation of B_2O_3(l) in the absence of B(s). At 1800 K, the equilibrium

$$B_2O_3(l) \Leftrightarrow B_2O_3(g) + B_2O_2(g) + \ldots + 375\ kJ \cdot mol^{-1} \quad (4)$$

is noticeably shifted to the right ($K_P^{1800} \sim 10^9$). Evaporation of B_2O_3(l) is incongruent, and therefore, the rates of B_2O_3(g) and B_2O_2(g) formation have to be described by equal rate coefficient as the experiments verify (see Figs. 3 and 4).

The interval where $B_2O_2^+$ and $B_2O_3^+$ ion currents increase sharply is rather small (like Region I) and allows us to treat the curves $I(t)$ using the kinetic equations for the first-order processes. The calculated value of the rate coefficient for B_2O_3(l) evaporation is equal to $k_4 \approx 20\ s^{-1}$.

According to the theory of evaporation of liquids [18], the equation for the rate coefficient of direct reaction [Eq. (4)] can be represented as

$$k_4 = (kT/2\pi m_{B_2O_3})^{1/2} \cdot (\Omega^{2/3}/\Omega_f) \exp(-E_v/RT) \quad (C)$$

where Ω is the proper volume of molecule, Ω_f is the free volume, and $E_v = \Delta H_v - RT$ (ΔH_v – evaporation heat). Evaluations for T_{ad} = 1800 K using tetrahedral radii of B and O atoms (0.88 and 0.66 A, respectively) to simulate Ω give us the values of E_v = 345 $kJ \cdot mol^{-1}$ and $\Delta H_v \geq 360\ kJ \cdot mol^{-1}$. The latter value fits the tabulated one [14].

The decrease of boron oxides and Zn^+ ion current in Region IV ($t > t_3$) could be explained by the sample cooling.

Sampling from Channel:

Two features attract attention in the data obtained by gas sampling from the channel in the burning tablet. Representative results of such experiments are shown in Fig. 4 for a channel 3.5 mm in diameter. First, the width of Region I, $l = u \cdot \Delta t$, corresponds to the channel diameter. Second, the multiplicity of attainment of the highest peaks on the curves $I(t)$ corresponds to the ratio l/δ = 3. These data are in good agreement with the value of δ obtained at gas sampling from the surface.

The fine structure of the curves $I(t)$ and the corresponding distribution of boron oxide partial pressures correlates with the known oscillations [19] of the combustion front in the SHS system Mo + B. The absence of the fine structure from sampling at the surface (see Fig. 3) is attributable either to their small scale, which is smaller than spatial resolution of the wave, or to the minor (below the sensitivity limits) changes of boron oxide partial pressures in the pulse. The sampling from the channel lifts both restrictions. It is interesting to note that the distance between the peaks of the fine structure coincides with the thickness of layers (0.2 mm) into which the cooled tablet of molybdenum boride breaks down after combustion in the oscillating mode.

Acknowledgments

The authors gratefully acknowledge Dr. V. G. Abramov for his invaluable help in programming of the control system, Mr. A. V. Zharenov and Mr. N. A. Somsikov for tech-

nical assistance, and Mrs. A. G. Mukasyan for preparation of the manuscript.

REFERENCES

1. Merzhanov, A. G., *Arch. Proc. Spalania* 5:17–39 (1974).
2. Merzhanov, A. G., and Borovinskaya, I. P., *Repts. USSR Acad. Sci.* 204:366–369 (1972) (in Russian).
3. Merzhanov, A. G., in *Combustion and Plasma Synthesis of High-Temperature Materials* (Z. A. Munir and J. B. Holt, Eds.), VCH Publishers, New York, 1990, pp. 1–53.
4. Merzhanov, A. G., *Pure Appl. Chem.* 62:861–875 (1990).
5. Kashireninov, O. E., Yuranov, I. A., and Fomin, A. A., *Twenty-Fourth Symposium (International) on Combustion*, The Combustion Institute, Pittsburgh, 1992, pp. 1899–1906.
6. Yuranov, I. A., Fomin, A. A., Shiryaev, A. A., and Kashireninov, O. E., *J. Mater. Synth. Proc.*, in press.
7. Kashireninov, O. E., Fomin, A. A., and Yuranov, I. A., *Chem. Phys.* 10:524–533 (1991) (in Russian).
8. Shcherbakov, V. A., Sytchov, A. E., and Shteinberg, A. S., *Phys. Combust. Explosion* 22:55–61 (1986) (in Russian).
9. Bloshenko, V. N., Bokiy, V. A., and Merzhanov, A. G., *J. Combust. Explosion* 24:102–111 (1988) (in Russian).
10. Zenin, A. A., Merzhanov, A. G., and Nersisyan, G. A., *J. Combust. Explosion* 17:79–80 (1981) (in Russian).
11. Korobeinichev, O. P., and Kuibida, L. V., in *Progress in Astronautics and Aeronautics*, AIAA, New York, 1982, Vol. 88, pp. 197–207.
12. Inghram, M. G., Porter, F., and Chupka, W. A., *J. Chem. Phys.* 25:498–501 (1956).
13. *Bond Energy, Ionization Potential and Electron Affinity* (V. N. Kondratiev, Ed.), Science, Moscow, 1974, pp. 227, 282 (in Russian).
14. *JANAF Thermochemical Tables*, 3rd ed., Parts I and II, *J. Phys. Chem. Ref. Data* 14: Supplement 1 (1985).
15. Kashireninov, O. E., Manelis, G. B., and Repka, L. F., *J. Phys. Chem.* 56:1031–1032 (1982) (in Russian).
16. Emanuel, N. M., and Knorre, V. G., *Comprehensive Chemical Kinetics*, 4th ed., High School Publishers, Moscow, 1984, pp. 132–134 (in Russian).
17. Kashireninov, O. E., Yuranov, I. A., Fomin, A. A., and Lestchev, Yu. A., *Gas-Phase Transport in Reacting SHS Systems*, paper presented at 2nd International Symposium on SHS, Honolulu, Hawaii, November 8–10, 1993, to be published.
18. Hirth, J. P., and Pound, G. M., *Condensation and Evaporation*, Pergamon Press, Oxford-London-Paris-Frankfurt, 1963.
19. Borovinskaya, I. P., Merzhanov, A. G., Novikov, N. P., and Filonenko, A. K., *Phys. Combust. Explosion* 10:4–15 (1974) (in Russian).

Twenty-Fifth Symposium (International) on Combustion/The Combustion Institute, 1994/pp. 1677–1683

THEORY OF SPIN AND SPIRAL GASLESS COMBUSTION

BORIS V. NOVOZHILOV
Institute of Chemical Physics
Russian Academy of Sciences
Moscow, 117977, Russia

Experimental investigations of gasless condensed-system combustion have resulted in the discovery of new interesting regimes of reaction zone propagation. Among them are spin and spiral modes. The former is combustion of a cylindrical sample when a reaction hot spot moves in helical fashion along its surface. The latter represents combustion with a spiral trajectory on a planar sample. From a theoretical point of view, both the spin and spiral combustion are very strongly nonlinear phenomena. An approximate analytical method is formulated for the spin and spiral combustion modes in this paper. Because the surface regimes are considered, one can investigate only a two-dimensional problem, which can be reduced to a one-dimensional one by averaging the temperature over the spin step. The reaction zone is assumed to be infinitely thin in one dimension and of finite length in the other. Finally, it is supposed that two velocity components of the hot spot differ greatly. The conditions for existence of the spin and spiral regimes are obtained. They depend on the cylinder diameter or spiral radius and heat losses. Explicit analytical expressions for various quantities of interest, including the propagation spin and spiral velocity components and the temperature profile, are given. It is possible in the framework of the theory to explain multicenter spin and spiral regimes. Wherever possible, conclusions of the theory are compared with the experimental data.

Introduction

Over the past decades, new interesting wave regimes were discovered in gasless combustion, i.e., when the chemical transformation takes place in solid fuel and when the combustion products are condensed. The most unexpected and puzzling phenomena are spin and spiral combustion modes.

Surface spin burning was first observed by Merzhanov and coworkers [1] in studies of the burning of porous metallic specimens in gaseous oxidizers where only a thin surface layer is consumed during combustion. On igniting the cylindrical sample, a glowing spot of small diameter appears on its lateral surface and spirals along the surface. The spot leaves a bright trace, which gradually merges with a similar trace of the previous turn. There also exists another type of the spinning mode, namely volume spin combustion [2]. In this case, combustion occurs throughout the volume of the cylindrical specimen.

There is only one experimental work devoted to spiral combustion modes [3]. This type of nonsteady burning regime represents combustion with a hot spot spiral trajectory on a thin planar sample.

Besides the spin and spiral modes, other regimes of front propagations in gasless combustion are possible. Recently, a review was published by this author [4] to provide readers with numerous experimental, analytical, and numerical results obtained in this field of the combustion science.

Most theoretical investigations consider mainly the volume spin burning [5–7]. A comprehensive review of these studies, in which the bifurcation theory was used, was given by Margolis [8]. Several mathematical models of spin combustion have been proposed and numerical results were obtained in the instability region of the steady-state regime with very small diameters of samples [9–11].

A real spin observed experimentally is a very strongly nonlinear regime, and its characteristics differ greatly from those obtained in cited theoretical studies. The concept of two types of spin—strong and weak—was advanced Refs. 12 through 14. In the next section, this concept is discussed.

A mathematical theory of the very strong regimes must be strongly nonlinear. In this field, few precise solutions are accessible. The features of the strong spin and spiral phenomena permit one to construct approximate methods to solve the problems. The methods are described in the next three sections of the paper. The paper closes with a comparison of theory with experimental data.

Weak and Strong Nonlinear Combustion Modes

The spin and spiral combustion, as well as other nonlinear nonsteady phenomena observed with solid-phase product systems, are related directly to the existence of stability boundary of a steady-state plane reaction wave. To investigate these burning

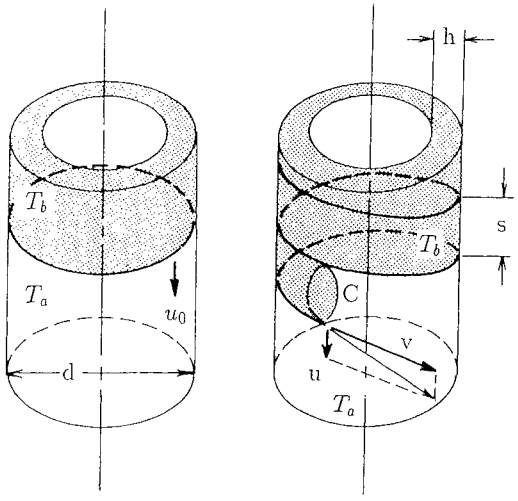

FIG. 1. Schematic drawing of (a) surface planar wave and (b) surface spin combustion. C: hot spinning spot; s: spin step; h: combustion layer thickness; u, v: velocity components.

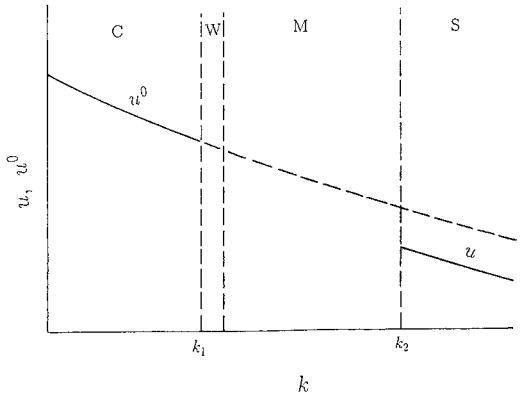

FIG. 2. Different modes of combustion propagation along a cylindrical sample. C: steady-state planar wave; W: weak spin solution; M: multispot unsteady combustion; S: strong spinning regime.

modes, one must study propagation regimes in the instability domain.

It was shown by Makhviladze and Novozhilov [15] that the domains of stability can be expressed in terms of parameter k, defined as

$$k = (T_b^0 - T_a)d \ln u^0/dT_b^0 \qquad (1)$$

whose explicit expression depends on the type of steady-state burning law u^0 (T_b^0). When k exceeds a critical value, k_1, the instability of steady-state regimes with multidimensional perturbations, arises more readily than in the one-dimensional case, and the stability loss is of oscillatory nature. In Eq. (1), T_a and T_b are the initial temperature and adiabatic burning temperature, and the quantities pertaining to the stationary combustion regime are labeled with a zero superscript.

In order to illustrate the stability loss, two cases, a planar stationary wave and a spin-combustion regime, respectively, are shown in Figure 1. If $k < k_1$ ($k_1 \approx 4$—the stability boundary), a steady-state surface planar wave propagates along the cylinder. At $k > k_2 (k_2 > k_1)$, there exists a spin regime. Numerous experiments show nonstationary multispot combustion between k_1 and k_2. The sequence of combustion modes, with increasing k, from steady-state planar wave to the strong spinning regime, is shown in Fig. 2.

To describe the nonsteady modes of combustion on the unstable side of the stability boundary, a nonlinear analysis is needed to calculate the finite amplitudes. As mentioned above, numerous papers were devoted to the searching of the spin problem by means of the bifurcation theory. This theory deals with the determination of perturbation amplitudes only in the vicinity of the stability boundary where the departure of a burning regime from the steady state is a small correction. We called this the weak spin regime [12–14]. There is no experimental evidence of existence of a weak spin. One can say the same about the spiral mode of combustion. The weak spiral problem was discussed theoretically in Ref. 16.

The real spin and spiral combustion regimes observed experimentally are strongly nonlinear. The characteristics of these strong spin and spiral modes differ greatly from those of weak regimes in three ways.

First, it should be emphasized that a flame front in the bifurcation theory is considered as a stationary plane front with a small time-dependent correction. Thus, in such a case, the front is continuous and differs only slightly from the steady-state one. On the contrary, both a strong surface spin and a spiral mode have disrupted fronts (reaction spots). Second, it can be easily shown that the bifurcation theory is able to consider only the case of small sample sizes, $d < 6\chi/u^\circ$, where χ is the thermal diffusivity. Real experiments are run with specimens of much larger sizes. Third, the ratio of the two velocity components v/u in the bifurcation theory is between 3 and 4. These values are not large enough to explain experimental data. In fact, spin and spiral combustion experiments [17] show that the ratio of velocity components v/u ranges from 10 to 30.

Approximate Theory of a Strong Spin

The approximate analytical approach for investigation of a surface spin regime is presented below.

Let us first enumerate the main approximations that can be made in solving the strong surface spin

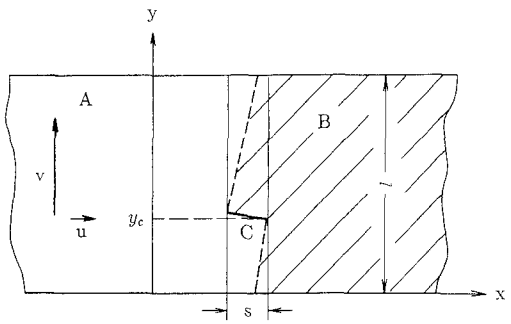

FIG. 3. Sketch of a burning strip. A: initial substance; B: combustion products; C: flame front.

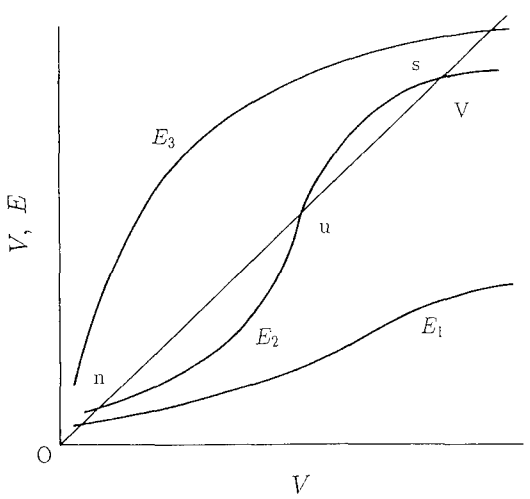

FIG. 4. Graphs of the left (V) and right (E) sides of Eq. (7). *s*: solution corresponding to strong spin combustion; *u*: unstable solution; *n*: physically nonexisting solution.

problem. First, the reaction zone is assumed to be infinitely thin in one dimension and of finite length in the other. This length is equal to a spin step. These approximations are based upon the fact that, as a rule, chemical combustion reactions have large activation energies, so consumption of reactive substances occurs within a very thin layer. Second, it may be supposed that the reaction zone is oriented along the axis of the cylinder. This assumption may be justified by the fact that the ratio of two spin velocity components is large. Dealing with the surface spin regime, one can investigate only the two-dimensional problem. To consider the strong surface spin regime, it is convenient to cut the cylinder surface along the direction parallel to its axis and unroll it. This reduces the geometry one has to consider to an infinite strip whose width equals the length of the circle of the cylinder.

The problem is illustrated by Fig. 3. The process is considered to occur in a strip, infinite in x-direction, and having a width $l = \pi d$, resulting from the unfolding of a cylinder of diameter d. The coordinate system is chosen so that the burning zone is fixed, while the mass flows in x- and y-directions with velocities u and v, respectively.

The width of the combustion zone is equal to spin step s. The law of mass conservation gives $lu = sv$. Taking into account the inequality $l >> s$, the temperature is averaged over the thin substance layer of width s. This layer may be considered as a reactor receiving the flux of unburned mixture in direction x.

Within this layer, we have the stationary heat conductivity equation in the y-direction:

$$\chi \frac{d^2T}{dy^2} - v\frac{dT}{dy} + q_1 - q_2 - q_3 - q_4 = 0 \qquad (2)$$

where

$$q_1 = \frac{u}{s}(T_a - T) \qquad \text{(convective energy flux)}$$

$$q_2 = a\frac{\chi}{s^2}(T - T_a)$$

(heat losses into the green mixture)

$$q_3 = \beta\frac{\chi}{s^2}(T - T_b)$$

(heat losses into the combustion products)

$$q_4 = \frac{\chi}{h^2}(T - T_a)$$

(heat losses into the surroundings).

The values a and β are the corresponding coefficients of heat losses. The effective thickness of the layer in radial direction h is introduced to characterize the heat losses in that direction.

The combustion zone can be conveniently placed at $y = 0$, the corresponding boundary conditions being the following:

$$T|_{y=l} = T|_{y=0}$$

$$\chi\left.\frac{dT}{dy}\right|_{y=l} - \chi\left.\frac{dT}{dy}\right|_{y=0} = v(T_b - T_a). \qquad (3)$$

The combustion zone thickness must be the same order of magnitude as the thickness of the heated layer along the x-axis; $s = b\chi/u$, where b is a coefficient of order unit. From the last correlation and the relationship $s = ul/v$, we have $s = (b\chi l/v)^{1/2}$.

We assume the Arrhenius dependence of burning rate on the temperature of the combustion zone: $v = A\exp(E/R_gT_c)$. Then, let us introduce the dimensionless variables and parameters:

$$V = v/u^0, \quad U = u/u^0, \quad L = lu^0/\chi,$$
$$H = hu^0/\chi, \quad \theta_c = T_c/T_b, \quad \theta_a = T_a/T_b \quad (4)$$

where $u^0 = A \exp(-E/R_gT_b)$ is the burning rate, corresponding to the front temperature T_b.

Equations (2) and (3) can be easily solved to yield the temperature of the combustion zone:

$$\theta_c = \frac{(1 + a/b + L/VH^2)\theta_a + \beta/b}{1 + (a + \beta)/b + L/VH^2} + \frac{(1 - \theta_a)(e_2 - e_1)}{R(1 - e_1)(e_2 - 1)} \quad (5)$$

where

$$e_1 = \exp[-(R + 1)LV/2],$$
$$e_2 = \exp[(R - 1)LV/2],$$
$$R = [1 + 4(b + a + \beta)/bLV + 4/H^2V^2]^{1/2}. \quad (6)$$

The correlation (5) and the relationship between reaction rate and temperature at front

$$V = \exp[k(1 - 1/\theta_c)/(1 - \theta_a)],$$
$$k = (1 - \theta_a)E/2R_gT_b \quad (7)$$

allow us to obtain all the characteristics of spin combustion $V(L)$, $U = (bV/L)^{1/2}$, and $V/U = (L/bV)^{1/2}$.

Figure 4, in which the left part (L) and right part (E) of Eq. (7) are plotted, illustrates the solution of Eqs. (4) and (6). Curves E_1 or E_3 show only one solution. Curve E_2 shows three, but only one of those is a strong spin solution. The other two are either unstable or physically nonexistent.

It is worth pointing out that the model presented above is quite similar to the simplest theory of critical diameter of combustion [18]. However, two major differences should be mentioned. They are, first, the condition of cyclic recurrences (3) that determines the temperature in combustion zone and, second, the fact that heat losses are affected not only by external conditions (through parameter h) but also by internal characteristic of the process, i.e., the burning rate along the x-axis conforming to the burning rate in the perpendicular direction.

The relative width of spin step b as well as the heatloss coefficients a and β depend, obviously, on the actual temperature profile in the x-direction. If it is treated as Michelson's profile, corresponding to burning rate u, then we obtain

$$a = (e - 1)^{-1}, \quad \beta = e, \text{ and } b = 1.$$

These values have been used in calculations, the results of which are given below.

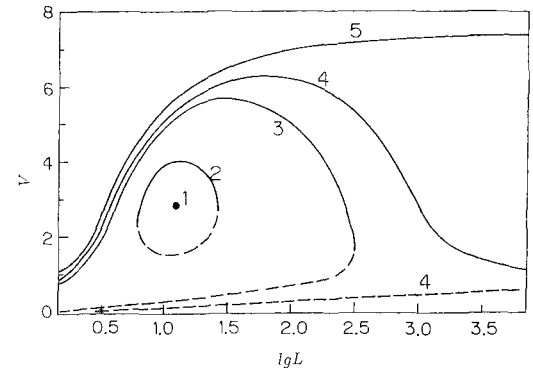

FIG. 5. The dependencies of transversal spin velocity on the cylinder perimeter for $k = 5$, $\theta_a = 0$, and various heat losses. (1) $H = 1.78$; (2) $H = 2.00$; (3) $H = 4.00$; (4) $H = 7.50$; (5) $H = \infty$. The dashed curves show unstable solutions.

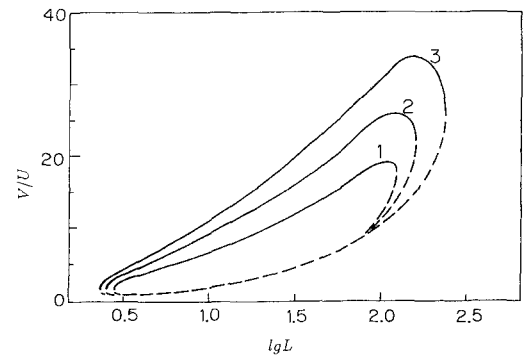

FIG. 6. The ratio of two spin velocity components vs the cylinder perimeter for $H = 3$, $\theta_a = 0$, and various values of the stability parameter, k. (1) $k = 5$; (2) $k = 6$; (3) $k = 7$. The dashed curves show unstable solutions.

Figures 5 and 6 show the dependence of the transverse burning rate, and the ratio of transverse and longitudinal rates on the sample diameter, at different values of the stability parameter and at different intensities of heat losses to the environment. The existence of spin limits both of diameter and heat losses and the values V/U are in agreement with experiment.

It should be noted that conditions for existence and characteristics of multihead spins can be revealed quite easily within the framework of the presented model. It can be shown that $V_n(L) = V_1(L/n)$, where V_n is the velocity of the n-head spin.

Quasi-Stationary Theory of Spiral Combustion

There is a significant difference between the spin and the spiral combustion regimes. The former is a

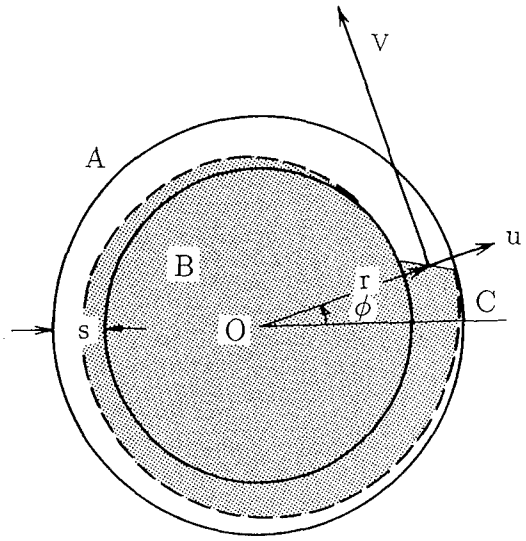

FIG. 7. Sketch of a spiral combustion mode. A: initial substance, B: combustion products, C: flame front.

steady-state regime that can be described in a suitable coordinate system by stationary equations. On the other hand, the latter represents an essentially nonsteady phenomenon. Nevertheless, a quasi-steady spiral burning theory can be formulated based on the above strong spin theory and on the large ratio of two hot spot velocity components.

Figure 7 illustrates spiral combustion. First, one should consider a fast motion of the hot spot around a ring of a constant radius r and width s. A slow expansion of the ring, at this step of solution procedure, is neglected because it is of the order of u/v. It will be readily seen that the solution of this fast part of the spiral combustion problem amounts to solving the set of spin Eqs. (2) and (3), in which the y-coordinate must be replaced by $r\varphi$, where φ is the angular coordinate. Thus, the dependencies of the velocity components on a radius $u(r)$, $v(r)$ can be found from Eqs. (5) through (7).

We next describe the slow radial expansion by the simple kinematic equations

$$\frac{dr}{dt} = u, \qquad \frac{d\varphi}{dt} = \frac{v}{r}, \qquad \frac{dr}{dt} = \frac{ur}{v} \tag{8}$$

with the initial conditions

$$t = t_0, \qquad \varphi = \varphi_0, \qquad r = r_0 \tag{9}$$

where φ_0 and r_0 are the hot spot coordinates at the moment it appears.

The trajectory of the hot reacting zone $r(\varphi)$ and time dependencies $r(t)$ and $\varphi(t)$, therefore, are found from

$$\varphi = \varphi_0 + \int_{r_0}^{r} \frac{v\,dr}{ur}, \qquad t = t_0 + \int_{r_0}^{r} \frac{dr}{u} \tag{10}$$

The explicit expressions for the trajectory and time dependencies of all variables in question can be obtained if we note that the experimental data [3] and the spin theory give the orbital velocity v very close to a constant value v_0. The initial coordinates may be chosen as $t_0 = 0$ and $\varphi_0 = 0$. Then, we obtain

$$u_0 = (b\chi v_0/2\pi r_0)^{1/2}, \qquad u = u_0(r_0/r)^{1/2},$$
$$r(\varphi) = r_0(1 + u_0\varphi/2v_0)^2. \tag{11}$$

The hot spot thus will trace out a trajectory, which is an algebraic spiral (a generalized Archimedian spiral or the special case of a Galileo spiral).

The hot-spot coordinates vary with time as

$$\varphi(t) = (2v_0/u_0)[(1 + 3u_0t/2r_0)^{1/3} - 1],$$
$$r(t) = r_0(1 + 3u_0t/2r_0)^{2/3}. \tag{12}$$

It should be noted in conclusion that, in the framework of this approach, one can also obtain multispot spiral regimes.

Comparison with Experimental Data

Let us now consider experimental data and compare them with the above-described theoretical approach. It should be noted that although spin and spiral combustion modes have been known for about 20 years, these interesting phenomena have been little investigated quantitatively. That is why it is impossible to make an accurate quantitative comparison of theory and experiment at the present time. We can only pose the question whether certain effects predicted by the theory do exist, and if so, whether they are comparable at least in the order of magnitude.

First, the approach presented in this work gives spin and spiral combustion limits both of the perimeter of the sample or the diameter of the spiral and of heat losses. This fact and the order of the ratio of the velocity components v/u are in agreement with the experiment.

The presented model of spin also results in an interesting corollary. It follows from the relations $vs = ul$ and $s = b\chi/u$ that the ratio of the squared velocity along the axis of the cylinder and the frequency of spin $\nu = v/l$ must be constant and of the same order of magnitude as the thermal diffusivity $u^2/\nu = b\chi$. The dependencies of burning rate u and frequency ν on the sample diameter d are given in Ref. 17. It is seen from Table 1 that the frequency decreases approximately threefold and the velocity approximately by a factor of 2 as the diameter varies from

TABLE 1
Experimental dependencies of spin axial burning rate u and frequency ν on the sample diameter d [17] and the ratio u^2/ν calculated from the experimental data

d (cm)	ν (s^{-1})	u (cm s^{-1})	$(u^2/\nu)\ 10^2$ ($cm^2\ s^{-1}$)
0.8	0.70	0.13	2.4
1.0	0.70	0.13	2.4
1.5	0.55	0.11	2.2
1.8	0.20	0.07	2.5

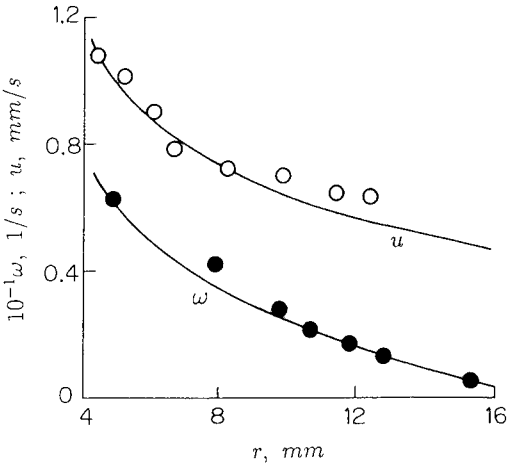

FIG. 8. Comparison of calculated spiral combustion velocities with experimental measurements [3]: $\omega = 2\pi\nu$.

0.8 to 1.8 cm. Meanwhile, the ratio u^2/ν, calculated from the experimental data, remains nearly constant and equal to 2.4×10^{-2} cm^2/s. This value of the thermal diffusivity is quite reasonable [19]. For the spiral burning, we have the relation $2\pi r u^2/v = b\chi$. The experimental data presented in Ref. 3 show that this expression is very close to a constant on the order of 10^{-2} cm^2/s, that is, again in the vicinity of the thermal diffusivity of the mixture investigated [19].

Finally, in Fig. 8, we try to compare quantitatively the theoretical and experimental data concerning the dependencies of the velocity components for the spiral combustion on radius of the spiral. The best agreement is for $E = 50$ kcal/mol, $v(T_b) = 0.15$ cm/s, $T_b = 1350$ K, $T_a = 300$ K, and $h = 0.2$ cm. These values are also quite reasonable [20].

Conclusion

It should be emphasized in conclusion that the theory presented is a very approximate one and cannot claim detailed quantitative description of the processes considered. The simple model adopted in the paper only crudely reflects the real physicochemical processes occurring in gasless processes. Nevertheless, as seen from the previous section, there is qualitative, and in some cases quantitative, agreement between theory and experimental data. The mathematical side of the theory can certainly be improved, for example, by eliminating the temperature averaging over the spin step. However, in our opinion, further progress in the theory of phenomena such as the ones treated in this paper will depend on advances in experimental investigations.

Nomenclature

b	dimensionless spin step
c	specific heat
d	diameter
e_1	function defined by Eq. (6)
e_2	function defined by Eq. (6)
E	activation energy
h	burning layer thickness
H	dimensionless burning layer thickness
k	dimensionless parameter defining dependence of steady-state burning rate on initial temperature
l	perimeter
L	dimensionless perimeter
n	the number of spin heads
q_1	convective energy flux
q_2	energy flux into the green mixture
q_3	energy flux into the combustion products
q_4	energy flux into the surroundings
Q	thermal effect
r	radius
R	function defined by Eq. (6)
R_g	universal gas constant
s	spin or spiral step
t	time
T	temperature
u	axial spin or radial spiral velocity
U	dimensionless axial spin or radial spiral velocity
v	orbital spin or spiral velocity
V	dimensionless orbital spin or spiral velocity
x	space coordinate
y	space coordinate
Z	pre-exponential factor in Arrhenius equation
α	coefficient of heat losses into the green mixture
β	coefficient of heat losses into the combustion products
θ	dimensionless temperature
χ	thermal diffusivity
ν	angular spin velocity
φ	angular coordinate

Subscripts

- a referred to the initial temperature
- b referred to the adiabatic combustion temperature
- c referred to the hot spot
- n the number of the spin head
- 0 initial conditions

Superscripts

- 0 steady state

Acknowledgment

This research was supported by the Russian Foundation of Fundamental Research Grant No. 93-03-4279.

REFERENCES

1. Merzhanov, A. G., Filonenko, A. K., and Borovinskaya, I. P., *Dokl. Akad. Nauk SSSR* 208:892–894 (1973).
2. Maksimov, Yu. M., Merzhanov, A. G., Pak, A. T., and Kuchkin, M. N., *Fiz. Goren. i Vzryva* 4:51–58 (1981).
3. Merzhanov, A. G., Dvoryankin, A. V., and Strunina, A. G., *Dokl. Akad. Nauk SSSR* 267:869–872 (1982).
4. Novozhilov, B. V., *Pure Appl. Chem.* 64:955–964 (1992).
5. Sivashinsky, G. I., *SIAM J. Appl. Math.* 40:432–438 (1981).
6. Volpert, V. A., Volpert, A. I., and Merzhanov, A. G., *Dokl. Akad. Nauk SSSR* 262:642–645 (1982).
7. Aldushin, A. P., Zeldovich, Ya. B., and Malomed, B. A., *Dokl. Acad. Nauk SSSR* 251:1102–1106 (1980).
8. Margolis, S. B., *Prog. Energy Combust. Sci.* 17:135–162 (1991).
9. Ivleva, T. P., Merzhanov, A. G., and Shkadinsky, K. G., *Fiz. Goren. i Vzryva* 2:3–10 (1980).
10. Shcherbak, S. B., *Fiz. Goren. i Vzryva* 5:9–12 (1983).
11. Bayliss, A., Matkovsky, B. J., and Kuske, R., *J. Compos. Phys.* 91:174–196 (1990).
12. Novozhilov, B. V., *Dokl. Russ. Akad. Nauk* 326:485–488 (1992).
13. Novozhilov, B. V., *Pure Appl. Chem.* 65:309–316 (1993).
14. Novozhilov, B. V., *Dokl. Russ. Akad. Nauk* 330:217–219 (1993).
15. Makhviladze, G. M., and Novozhilov, B. V., *Zh. Prikl. Mekh. i Tekh. Fiz.* 5:51–59 (1971).
16. Matkovsky, B. J., and Volpert, V. A., private communication (1992).
17. Filonenko, A. K., and Vershinnikov, V. I., *Fiz. Goren. i Vzryva* 3:353–362 (1975).
18. Zeldovich, Ya. B., *Zhurn. Eksper. i Teoret. Fiziki* 1:159–168 (1941).
19. Butakova, E. A., and Strunina, A. G., *Fiz. Goren. i Vzryva* 1:71–73 (1985).
20. Dvoryankin, A. V., Strunina, A. G., and Merzhanov, A. G., *Fiz. Goren. i Vzryva* 4:44–47 (1985).

COMMENTS

Howard Pearlman, NASA Lewis Research Center, USA. I find your fundamental approach to the spin and spiral instability quite admirable. Could you comment on the mechanism that induces the instability?

Author's Reply. Thank you very much for your kind words. The mechanism that induces gasless combustion when Lewis number equals zero is connected with enthalpy excess in a wave front. The parameter defining stability condition is the Zeldovich number $Z = E/RT_B^2\,(T_B - T_a)$. There is the difference between a "flush-burning of the reactants" and a spin (or spiral) combustion. The former is a one-dimensional phenomenon; the latter may only exist if you have a problem with cylindrical symmetry. In this case, a wave front goes along the heated layer that was made by a previous turn of the spin (or spiral).

•

Robert S. Levine, National Institute of Standards and Technology, USA. There may be similarities between this spinning reaction, which is a function of heat conduction, and sloshing (transverse mode) instability in a rocket thrust chamber. If you drill a large hole through the center of the reactive cylinder, does it make a difference? (Would that prevent thermal diffusion across the cylinder?)

Author's Reply. I think those similarities are not too close because the physical reasons for a spin (or spiral) combustion and transverse mode in a rocket thrust chamber are quite different. The former is connected with heat conduction, the latter with acoustic perturbations. A hole through the center of the cylinder changes heat losses and consequently the characteristics of the spin regime.

Twenty-Fifth Symposium (International) on Combustion/The Combustion Institute, 1994/pp. 1685–1692

BUOYANT DOWNWARD DIFFUSION FLAME SPREAD AND EXTINCTION IN PARTIAL-GRAVITY ACCELERATIONS

KURT R. SACKSTEDER
NASA Lewis Research Center
21000 Brookpark Road, Cleveland, OH 44135, USA

AND

JAMES S. T'IEN
Case Western Reserve University
Cleveland, OH 44106, USA

This paper describes experimental observations of downward, opposed-flow flame spreading made under partial-gravity conditions aboard NASA research aircraft. Special apparatus and techniques for these tests are described, including schlieren imaging of dim near-limit flames. Flame-spreading and flammability limit behaviors of a thin cellulosic fuel, 1×10^{-3} g/cm^2 tested at 1 atm of pressure in oxygen/nitrogen mixtures of 13–21% oxygen by volume, are described for effective acceleration levels ranging from 0.05 to 0.6 times normal earth gravity (1 *g*). Downward-burning flammability increases in partial gravity, with the limiting oxygen fraction falling from 15.6% oxygen in 1 *g* to 13–14% oxygen in 0.05–0.1 *g*. Flame-spread rates are shown to peak in partial gravity, increasing by 20% over the 1-*g* value in air (21% oxygen). Partial-gravity flame-spreading results, corrected for fuel density and thickness, are consistent with results obtained at acceleration levels above 1 *g* in a centrifuge. The results compare qualitatively with predictions of flame spreading in buoyant flow by models that include finite-rate chemical kinetics and surface and gas-phase radiative loss mechanisms. A correlation of experimental buoyant downward flame-spread results is introduced that accounts for radiative heat losses using a dimensionless spread rate, V_f^*, a radiation/conduction number, S_R, and the Damkohler number, *Da*, as parameters. The correlation includes data from 0.05 g to 4.25 *g* and oxygen/nitrogen mixtures from 14% to 50% oxygen.

Introduction

Flame spreading over solid fuels is a phenomena of fundamental interest and of practical value in the study and control of fire. In flame-spread studies, distinctions between flames in flows opposed to and concurrent with the flame-spread direction, between thermally thin and thick fuels, and between flows imposed externally (forced) or by gravity (buoyancy) have been identified. Several reviews articulate the subject [1,2].

Access to microgravity environments motivated theoretical and experimental explorations of low-speed flow regimes in which buoyancy forces could be reduced or eliminated. Numerical modeling quantified surface and gas-phase radiation mechanisms [3–6] and predicted the influence of radiative loss in spread-rate reductions and quenching. Numerical evaluations of velocity-profile effects [7] and predictions that near-wall velocity gradients would correlate spreading behavior [8] led us to suggest separate experimental observations of flames spreading in low-speed purely forced and purely buoyant flows.

Purely forced, opposed-flow, and quiescent studies in microgravity, using drop-tower [9,10] and space shuttle facilities [11], demonstrated the predicted spread rate and quenching effects. In purely buoyant flow, however, downward-burning experiments were limited to normal earth gravity (1 g) and elevated gravity using a centrifuge [12]. While noting a low-gravity, quiescent study perturbed by unsteady accelerations [13], this paper reports the first systematic observations of flames spreading in purely buoyant, low-speed flows induced by accelerations below 1 *g*.

We conducted a series of aircraft-based tests to observe both downward and upward flame-spreading and flammability behavior of thin solid fuels in sustained partial-gravity accelerations between 0.05 and 1 *g*. To obtain these data, special apparatus and techniques were developed. This paper concerns the downward-spreading case only and provides an opportunity to evaluate models of flame spreading in purely buoyant flow.

Experiments

An apparatus was devised to observe flame spread over solid fuels in partial-gravity accelerations aboard

NASA aircraft facilities. The apparatus provides semiautonomous operation, capable of several tests per flight, either attached to the airframe or floated freely in the aircraft cabin. The apparatus includes a 26-liter cylindrical chamber, 25.4 cm in diameter and 50.8 cm in length; simultaneous schlieren and conventional imaging; provisions for atmosphere replacement; thermocouple, ignition, and lighting circuitry; and a flanged end plate with a quick-release binding for rapid specimen replacement.

Test specimens, 8-cm long and 7-cm wide, were made of thin cellulosic tissues (tradename Kimwipes), which were used previously in drop-tower tests [9,10,14]. This material has a half-thickness area density (i.e., mass density × thickness) of 1.0 mg/cm^2 and was used because of its high flame-spread rate compared to other fuels and because it tends to remain flat while burning. The samples were taped across a 25.4 × 5 cm gap in 0.05-cm-thick stainless-steel sample holders that fill a diametrical plane of the cylindrical chamber, thereby exposing fuel, 8 cm in the (axial) burning direction by 5-cm wide, to the atmosphere on both sides.

Control of the fuel moisture content was constrained. Prior to takeoff, premounted samples were stored in vacuum for approximately 1 hour. At altitude, where atmospheric moisture content is low, the samples were exposed to the aircraft cabin. A vacuum exposure in the test chamber before filling and ignition lasted approximately 1 min. Samples were ignited by resistance-heating a thin wire for 0.10 s, releasing 36 j to ignite a strip of nitrocellulose (10.5 mg, +/−1%), releasing an additional 26 j [15] in a flame ball, bathing the ignition region. This technique provided a consistent deposition of ignition energy compared to the hot wire used alone.

The test atmosphere was replaced for each test. After replacing the spent test specimen, the chamber was evacuated to a pressure of less than 0.008 atm and then filled with a commercial oxygen/nitrogen mixture certified to +/−0.03% absolute oxygen content. The residual air after evacuation introduced <0.06% error absolute oxygen content. All experiments were conducted at an initial pressure of 1 atm, measured with a transducer calibrated daily.

Flames were visualized with a color schlieren system [16]. The schlieren system was sensitive to the component of the refractive-index gradient normal to the fuel surface, in a cylindrical detection volume 7.9 cm in diameter. Ray deflections, attributed to flame-induced density variations, were discriminated at the image plane of the schlieren mirror using a color transparency varying linearly in hue with lateral displacement and then imaged with a video camera. Conventional images of the top view of the flames were recorded using a 16-mm motion picture camera operating at 24 frames/s.

The tests were conducted aboard the NASA KC-135 at the NASA Johnson Space Center flying Keplerian trajectories (parabolas) to simulate gravitational accelerations between 0.05 and 0.6 g, including lunar (0.16 g) and martian (0.38 g) levels [17]. The first parabolas ever attempted at 0.05 and 0.6 g were performed for these tests. Local three-axis accelerations were measured with a duplicate of the NASA Space Accelerometer Measurement System [18].

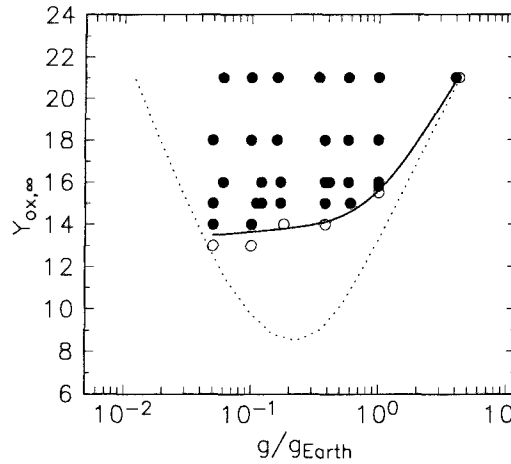

FIG. 1. Flammability map in O_2 mole fraction vs acceleration for thin cellulosic fuels, with downward burning in purely buoyant flows in 1-atm pressure. Solid symbols represent flammable conditions; hollow symbols represent nonflammable conditions. Data near 4 g are from Ref. 12. The solid line estimates experimental flammability boundary; the dotted line is the boundary predicted in Ref. 6. The microgravity limit, not shown, is reported as 21% O_2 [9].

Results

Acceleration Environment:

Wind, atmospheric turbulence, and pilot and aircraft performance introduced continuous variation into the measured acceleration levels. Parabolas at the lowest set points (0.05–0.10 g) were perturbed typically by high-frequency (>1 Hz) variations, often called g-jitter, of about 0.02 g. Higher set points (0.16–0.6 g) were additionally perturbed by lower-frequency variations (≈0.2–1.0 Hz) of about 0.04 g. The average duration of the parabolas increased with partial-gravity level, from about 8 s for the shortest 0.05-g parabola to about 50 s for most 0.6-g parabolas. The parabolas begin and end with a pull-up maneuver at just under 2.0 g acceleration, to which some flames were exposed.

Flammability:

Figure 1 summarizes the test matrix and shows a flammability boundary based on acceleration level

and atmospheric oxygen content. In 1 g, the same apparatus and fuel (5-cm wide) were used to determine the limit using partial-pressure mixtures of the certified 15% and 16% mixtures. In 1 g, the specimens never burned more than 2–3 cm below the ignitor in 15.5% O_2; they usually burned 4–5 cm, but never the full 8 cm, in 15.6% O_2; and they usually, but not always, burned the full 8 cm in 15.7% O_2. Completely burning 0.08 gm of cellulose reduces (by calculation) the oxygen in the chamber from 15.6 to 15.53%, constraining the limit determination to a precision of about 0.1%. Based on the behavior described, a 1-g limit of 15.6% O_2 is shown in Fig. 1.

Obtaining the precision of the 1-g limit criteria was not practical in the aircraft because test opportunities were limited. In 14% O_2 at 0.18 g and 0.38 g, flames propagated 1.4 and 0.4 cm, respectively, and quenched before the onset of high accelerations, while in 15% O_2 (same accelerations), the samples burned completely. In 14% O_2 at 0.05 g and 0.1 g, flames progressed 3.1 and 2.4 cm, respectively, spreading in partial gravity for 8–9 s and then extinguishing during high accelerations. These are interpreted as flammable conditions. Samples ignited in 13% O_2 quickly quenched.

The reported 1-g downward-burning limit of 16.0–16.5% O_2 for 3-cm-wide samples of this fuel [9] was higher than results obtained with 3-cm-wide samples in the aircraft apparatus, where using the above propagation criteria provided a limit of 15.8% O_2. The earlier tests were ignited with a heated wire and may have been influenced by a nearby mirror present to obtain an orthogonal view. The higher flammability limit might be attributed to differences in the useful ignition energy or heat losses to the mirror. This comparison suggests that the quiescent microgravity limit of 21% O_2 (the logical extreme of the buoyant-flow case), obtained in drop-tower tests [9], is reasonable to within 1% O_2. However, because drop-tower accelerations have not been measured, that limit could not be included in Fig. 1. Limiting accelerations between 4.0 and 4.25 g in 21% O_2 for a similar fuel were reported in centrifuge tests [12] and are shown in Fig. 1.

Reducing accelerations from 4 to 0.05 g monotonically enhances downward-burning flammability. The microgravity limit of 21% O_2 implies, however, that the flammability boundary curves upward at smaller accelerations and that a minimally flammable oxygen environment exists for this fuel, for downward burning, at or below 0.05 g. The analogous flammability boundary, predicted by a numerical model [6], is included in Fig. 1 for comparison and later discussion.

Flame Imaging:

Recorded schlieren flame images were fundamentally different from earlier gravity-related flame-spreading results. Visible-light emissions from near-limit flames in microgravity tests are dim and difficult to capture by direct imaging, either by video or by motion picture film [9–11,13,14]. Measures to enhance film images, including forced film processing, low framing rates, and small f/numbers, reduce flame-tracking precision. Short focal-length lenses, typical of compact microgravity experiment designs, introduce spatial distortions from magnification variations across wide flames.

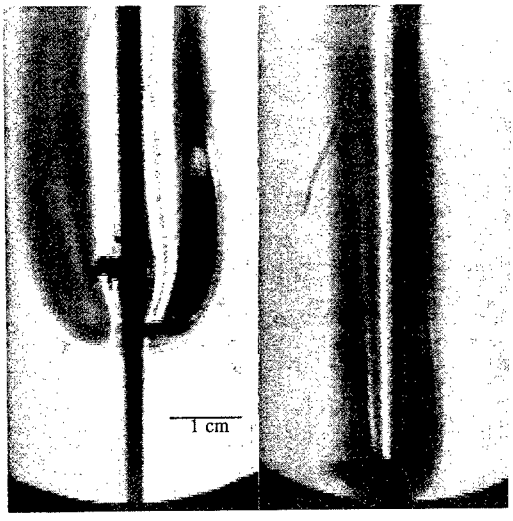

FIG. 2. Rainbow schlieren images of downward-burning thin fuel in 15% O_2: on the left at 0.10 g/g_{earth} on the right near the blowoff limit at 0.6 g/g_{earth}.

Schlieren imaging provided increased dim-flame detection sensitivity and constant image magnification across the flame width. At ignition, an expanding ball of heated gases was visible to the schlieren system, reaching 2–3 cm below (upstream of) the ignitor (for <1 s) before buoyancy displaced it upward. Conventional visible photography showed a smaller flame surrounding the ignitor. Extinguishing flames were clearly defined in the schlieren images, shrinking to ≤2–3 mm in length before disappearing. Figure 2 shows schlieren images of a flame spreading first at 0.1 g in 15% O_2, a nonflammable condition in 1 g, and then, as the flame nears blowoff extinction, at higher accelerations at the end of the test.

Flame Spread:

Flame propagation rates were obtained from the schlieren results. Figure 3 shows the flame displacement with time, synchronized with the component parallel to the flame spreading direction of the instantaneous local acceleration, for a test in 15% O_2, where the slope of the displacement plot indicates flame-spread rate. At the end of the parabola, the increase in local acceleration accompanied a slowed,

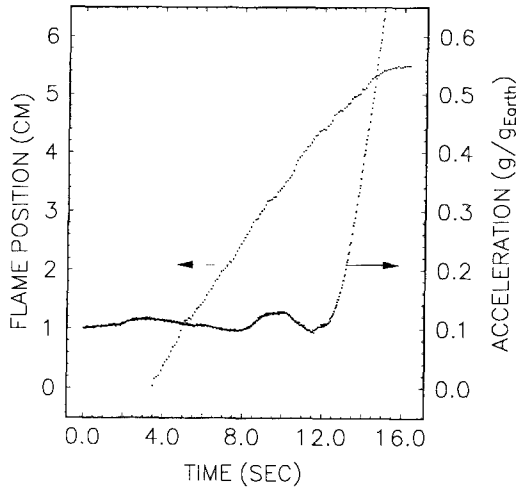

FIG. 3. Synchronized-spreading flame position and local acceleration vs time for downward-burning thin fuel in 15% O_2.

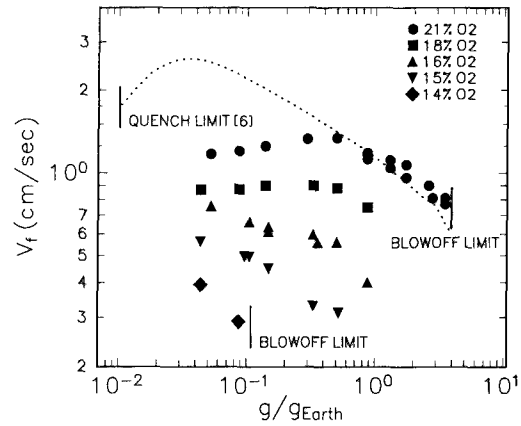

FIG. 4. Flame-spread rates of thin cellulosic fuels in O_2/N_2 mixtures at 1-atm pressure vs local acceleration. Data above 1 g/g_{Earth} are from Ref. 12. The dotted line represents predicted spread rates from Ref. 6. Vertical lines represent flammability limits: blowoff limits at higher accelerations (14% from this work, 21% from Ref. 12) and radiative quenching limit at lower acceleration (theoretical prediction [6]).

then extinguished, flame. Figure 2 shows schlieren images from that test before and during the higher accelerations, illustrating how the flame narrowed as it approached extinction. The flame was extinguished as the local accelerations crossed the flammability boundary of Fig. 1, at about 0.6 g.

Spread rates were influenced by g-jitter to the extent that reporting spread rates averaged over the test time showed unacceptable scatter. The partial-gravity results, shown in Fig. 4, were obtained, instead, by measuring flame displacements during brief time periods, ≥3 s, of smaller g-jitter. This procedure was considered acceptable since flames responded to perturbations in much less than 1 s (e.g., at time 10 s in Fig. 3). Figure 4 also includes 1-g results, obtained in the aircraft, drop-tower [9], and centrifuge [12] test chambers, and centrifuge data in 21% O_2 up to 4.25 g. All spread rates are corrected for fuel area density, ρ_{area}, where $\rho_{area} = \rho_{mass} \cdot \tau$, the mass density times the fuel half-thickness. This correction follows from the assertion in the early heat transfer model [19] that $\rho_{area} \cdot V_f$ = constant for thin fuels and has been used successfully [9,10,12].

Partial-gravity spread rates in 21% O_2 fall naturally along the trend of the centrifuge data, peak at an acceleration level near 0.6 g, then decline with further decreases in acceleration. Spread rates at 1 g from the three different test chambers agree to within 5%. Prediction of spread-rate behavior for a thin fuel in 21% O_2 from a numerical model [6], corrected for ρ_{area}, is included for comparison and later discussion. Spread rates in 18% O_2 show a similar nonmonotonic spread-rate variation with acceleration. Spread rates in 14–16% O_2 show only the downward slope.

Discussion

Comparison with Theory:

Two numerical models predict downward flame-spreading behavior at partial-gravity accelerations [6,8]. Both calculations utilize a one-step, finite-rate, gas-phase chemical reaction model and estimate radiative losses from both the fuel surface and the gas phase. Reference 8 presents calculated spread rates and extinction limits in 50% O_2–50% N_2, at 1.5 atm, from 10^{-6} g to 10 g, and in 21% O_2–79% N_2 at 1–4 g. Reference 6 presents spread rates and extinction limits in 21% O_2–79% N_2, at 1 atm from 0.012 to4.3 g, and a flammability boundary over the same range of accelerations. The data of Ref. 6 are included as the dotted lines in Figs. 1 and 4.

The predictions of spread rate show qualitatively the peak spread-rate feature observed experimentally in 21% and 18% O_2 at intermediate gravity levels. From the peak, falling spread rates at higher gravity are attributed to decreased reactant residence time in the flame zone (compared to the chemical reaction time) and reduced forward heat transfer from flames receding with respect to the pyrolysis front. Falling spread rates at lower gravity are attributed to lower flame temperatures, resulting from an increasing ratio of radiative loss to chemical heat release, and reduced forward heat transfer from cooler flames

farther from the fuel surface. The spread-rate predictions of Ref. 6 for 21% O_2 are higher (Fig. 4) than experimentally observed in partial gravity, though

they agree well with experiments at normal gravity and above. The predictions in Ref. 8 also reproduce the observed experimental results at and above 1 g in 21% O_2, as shown , and also in 50% O_2, at 1.5 atm.

Both models predict a high-gravity extinction limit (*viz.* , a blowoff limit) and a low-gravity extinction limit (*viz.* , a radiative quenching limit). These flammability limits are attributed to the dominance of the flame-retarding mechanisms described above. The flammability boundary predicted in Ref. 6 (Fig. 1) is U-shaped, showing a minimally flammable oxygen concentration between 0.2 g and 0.3 g. The flammability boundary suggested by the experimental data does not show such a minimum, but the reported quiescent microgravity limit for this fuel, 21% O_2 [9], suggests that it exists $\leq$0.05 g. The predicted flammability boundary agrees well with experimental observations above normal gravity but diverges from the observed boundary at normal gravity (13.2 vs 15.6% O_2) and below (21% O_2 limit at 0.012 g vs $\approx$microgravity [9]).

The sources of discrepancy between prediction [6] and observed partial-gravity flammability and spread-rate behavior are not clear but may involve the choice of kinetic and radiation parameters. The spread-rate peak and the (presumed) minimum-oxygen limit arise from competition, under finite kinetics, between the heat-release rate reduction (due to shortened residence time) and the radiative heat-loss rate. An underestimation of the radiative loss rate compared to the chemical reaction rate might explain the differences at 1 g and the partial-gravity levels but would not reconcile the limiting accelerations in 21% oxygen.

Flame Spread-Rate Correlation:

Correlations of measured flame-spread rates have been achieved for purely buoyant flows [12] and for forced-convection flows in normal gravity [20] using formulations of dimensionless spread rate, V_f°, vs Damkohler number, Da. Formulations of Da, nominally a ratio of reactant residence time in the flame to chemical reaction time, have included simple pre-exponential chemical models (without Arrhenius factors) [21,6], models with strong flame temperature dependence [12], and additional provisions for fuel-vapor diffusion from the surface [20]. Velocity characterizations for residence-time estimates have included a buoyant velocity, $V_b \approx (ag(T_f - T_\infty)/T_\infty)^{1/3}$ [21,12,8], where T_f and T_∞ are flame and ambient temperatures, and a is the thermal diffusivity, or the free stream velocity, U_∞, alone [20] or including consideration of the boundary-layer structure [22]. The term V_f°, corrected for ρ_{area}, is a ratio of actual spread rate to the spread rate possible without heat loss in the infinite chemical-rate limit [19]. Where the flame-retarding mechanism is associated with limited residence time, Da correlations of flame-spread rates are successful. This approach neither succeeds with data from microgravity-forced flows nor with partial-gravity data, because it does not account for radiative losses from these flames.

We revisited the formulation of the data correlation for purely buoyant flame-spread data [12], to include the partial-gravity data. We evaluated Da similarly:

$$Da = \frac{B\lambda m_{\text{OX},\infty}}{c_p M_{\text{OX}} V_b^2} \cdot \left[\frac{RT_f}{E} \cdot \frac{T_f}{\left(\frac{\Delta H_c m_{\text{OX},\infty}}{i c_p} \right)} \right]^3 \cdot \exp\left(- \frac{E}{RT_f} \right)$$

where the pre-exponential constant $B = 5.69 \cdot 10^9$ m^3/mole-s; the activation energy $E = 167.35$ Kj/Kg-K; the heat of combustion $\Delta H_c = 16{,}740$ Kj/Kg; $m_{\text{OX},\infty}$ and M_{OX} are the ambient O_2 mass fraction and molecular weight, respectively; the stoichiometric oxygen/fuel mass ratio $i = 1.185$; and λ and c_p are the gas thermal conductivity and specific heat, evaluated for the initial O_2/N_2 mixtures at the fuel vaporization temperature $T_v = 618$ K. We evaluated T_f differently, however, using the STANJAN equilibrium code for a stoichiometric, adiabatic flame temperature, allowing for dissociation, and we evaluated V_b using T_f. The pre-exponential constant, which does not affect the shape of the resulting data presentation, was adjusted from the literature value [12] to bring $Da = 1$ at blowoff extinction. The grouping $(\Delta H_c m_{\text{OX},\infty}/ic_p)$ in the cubic factor is a reference temperature [12] that varies only with the explicit O_2 content.

The dimensionless spread rate, defined [12] as

$$V_f^\circ = \frac{V_f}{V_{f,\infty}} = \rho_{\text{area}} V_f \cdot \frac{c_s (T_v - T_\infty)}{\sqrt{2}\lambda (T_f - T_v)}$$

where $V_{f,\infty}$ is the spread rate in the no-loss, infinite-kinetics limit, and the solid-fuel specific heat $c_s = 1.26$ Kj/Kg-K. A radiation parameter, S_R, derived through a dimensional analysis of the energy equation [3,4,6] as a ratio of radiation to conduction over one thermal length, $S_R = (\sigma T_\infty^4)/[\lambda T_\infty/(a/V_r)] = \sigma T_\infty^3/\rho c_p V_r$, where σ is the Stefan–Boltzmann constant and V_r is the reference velocity for the flow (in the buoyant case, $V_r = V_b$). We have used S_R as a correction to V_f°, suggesting that it estimates the additional spread-rate deficit, due to radiative heat loss, from the no-loss maximum spread rate. Figure 5 shows a plot of $V_f^\circ \cdot S_R$ vs Da for flames spreading in purely buoyant flow, in partial gravity (data of Fig. 4), and in the centrifuge (21% O_2 and 50% O_2 1 atm from 1 g to 4 g [12]).

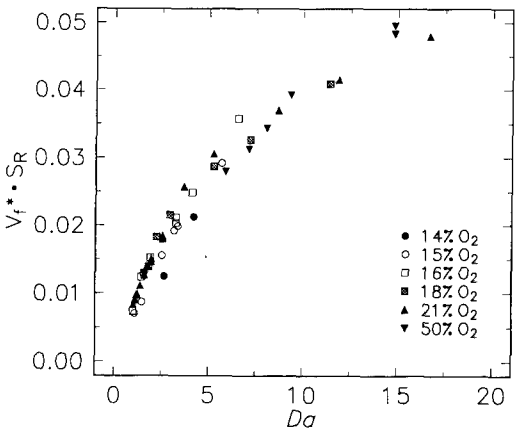

FIG. 5. Dimensionless spread rate corrected using a radiation parameter, $S_R = \sigma T_\infty^4/\rho c_p V_r$ vs Damkohler number for downward burning of thin cellulosic fuels: 50% O_2 data obtained in $g/g_{earth} > 1$ [12], 21% O_2 obtained from $g/g_{earth} = 0.05$–4.25 (>1 g from Ref. 12). Pre-exponential constant in Da adjusted so that $Da = 1$ at blowoff extinction.

We considered that calculating T_f independently, while using c_p and ΔH_c evaluated as in Ref. 12, might suggest an inconsistency in evaluating $V_f^* \cdot S_R$ and Da. The T_f values estimated using ΔH_c, c_p evaluated at T_v for the O_2/N_2 mixture, without dissociation [12], are much higher than ours, which we believe to be more realistic. A correct c_p value is implicit, however, in the equilibrium calculation, allowing dissociation, of T_f. Remaining uncertainty in calculating T_f lies in the chosen value of ΔH_c, which both formulations use. The roles of c_p and λ in $V_f^* \cdot S_R$ and Da are primarily associated with forward heat conduction, so the evaluation for the ambient O_2/N_2 mixture at an intermediate temperature, T_v, is appropriate. The constants ΔH_c, i, and c_p in the reference temperature do not affect the shape of the data presentation.

This presentation smooths the scatter in spread rates seen in Fig. 4. The scatter has no trend attributable to O_2 content. The data in 21% O_2 span the acceleration range of 0.05–4.25 g and also the length of the correlation curve, while the data in 50% O_2 span only 1–4 g and lie within the 21% O_2 data. Near blowoff extinction, $V_f^* \cdot S_R$ vs Da values for 15% O_2 at 0.6 g, 15.6% O_2 at 1 g, and 21% O_2 at 4.25 g lie together at the left-hand end of the curve.

The question arises whether the low-gravity extinction boundary predicted [6] would, like the blowoff extinction, have similar Da for varying g and oxygen contents. Since the predicted low-gravity quenching was not observed in the attainable acceleration range, we cannot determine any quenching values for Da or the nature of the $V_f^* \cdot S_R$ curve at the quenching point. Using an adiabatic T_f, Da increases with oxygen content (i.e., the chemical rate increases faster than V_b) and with decreasing acceleration. Since the flammability boundary prediction [6] suggests that quenching in decreasing accelerations would be observed first in lower O_2 environments, we suggest that a correlation of quenching limits cannot be achieved until the T_f estimate used in Da is altered to represent the cooling effect of radiative loss.

As numerical predictions suggest [8], we attempted to include forced-flow flame-spread data [9,10,20] into this correlation, using the free-stream velocity $V_r = U_\infty$. Generally, the microgravity (low opposed-flow speeds) data [9,10] fell to the right of the curve in Fig. 5, while the normal-gravity (high opposed-flow speeds) data [20] fell to the left. Estimates of the Blasius boundary-layer thickness ahead of the flames in those experiments suggest that they propagated inside a boundary layer (except the quiescent microgravity case, which has none). Mixed forced- and buoyant-flow flames have been characterized using U_∞ plus an estimate of the boundary-layer structure [22], which depended upon the near-wall velocity gradient. It remains unclear whether the flames of Refs. 9, 10, and 20, particularly the microgravity flames, were deep enough in their boundary layers to be affected only by the near-wall gradient or by more of the velocity profile, since the flame standoff distances were not quantified.

We sought to obtain estimates of acceleration levels where quenching of partial-gravity flames would occur. Mindful of the uncertain comparison of forced and buoyant cases we have described, we used the flammability limits observed in forced flows at microgravity to estimate partial-gravity flammability limits. Figure 6 shows an approximate flammability map for opposed-flow flames, including the data of Fig. 1 plus near-limit microgravity data [9,10], where each is characterized by $V_r = V_b$ or U_∞. Adjustments to U_∞ values for boundary-layer influences, even substantial fractional reductions, would not change the position of the flammability curve appreciably. Within the limitations we have discussed, the forced-flow data suggest that quenching of partial-gravity flames should be observable at acceleration levels of $\approx 10^{-3}$–10^{-2} g in 14% oxygen, $\approx 10^{-4}$–10^{-3} g for 15% oxygen, and $\approx 10^{-6}$–10^{-5} g for 21% oxygen.

Conclusions

Using parabolic trajectories in aircraft, we have conducted the first experiments in buoyant diffusion flame spread over a thin solid in a partial-gravity range of 0.05–0.6 times normal earth gravity. Successful operation in this unusual environment required the development of special apparatus and techniques, including a schlieren system for imaging dim near-limit flames, a fast acting and repeatable ignition system, precise acceleration measurements,

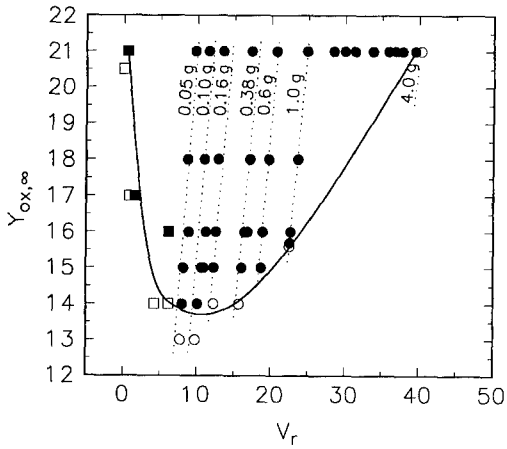

FIG. 6. Estimated flammability map in O_2 mole fraction vs opposed-flow velocity for thin cellulosic fuel. Flow velocities included purely buoyant, V_b, for g/g_{earth} levels shown (circular symbols, >1 g from Ref. 12), and free-stream velocity, U_∞, for microgravity forced-flow tests (square symbols [9,10]). Solid symbols represent flammable conditions; hollow symbols represent nonflammable conditions.

and extending the range of accelerations provided by the aircraft flight crew.

Using gravity as a variable parameter provided a new means to study the effect of convection on flame spread and extinction processes. Unlike experiments in forced flow where the local velocity in front of the flame depends both on the free-stream velocity and the developing boundary layer, the local velocity in front of the flame in buoyant flow depends only on the gravity level.

Downward-spreading flames were observed in partial gravity in O_2/N_2 mixtures between 14% O_2 and 21% O_2 at normal atmospheric pressure, demonstrating peak values of flame-spread rate and increased flammability at local accelerations below normal earth gravity. Flame-spread rates 20% higher than in normal gravity were observed in partial gravity, and flammability increased, with the limiting oxygen fraction falling from 15.6% O_2 in normal gravity to 13–14% O_2 at 0.05–0.1 g.

A data presentation with a radiative correction to dimensionless downward flame-spread rates correlates with Damkohler numbers in purely buoyant flows from 0.05 g to 4.25 g. Comparisons with our data support the qualitative results of theoretical models that include finite-rate chemical kinetics and radiative transport to describe the flame spread and extinction processes. The experimental data provide the basis for improving quantitative predictions from the models.

Acknowledgments

JST would like to gratefully acknowledge the support for his work under NASA Grant No. NAG3-1046. KRS would like to acknowledge the contributions of many associates at the NASA Lewis Research Center, most notably R. Sotos, K. Stambaugh, D. Gotti, D. Griffin, P. Greenberg, and P. Ferkul, and helpful discussions with R. Altenkirch. Finally, both authors would like to acknowledge the support for the work by the Microgravity Science and Applications Division of NASA Headquarters.

REFERENCES

1. Fernandez-Pello, A. C., and Hirano, T., *Combust. Sci. Technol.* 32:1–31 (1983).
2. Di Blasi, C., *Prog. Energy Combust. Sci.* 19:71–104 (1993).
3. T'ien, J. S., *Combust. Flame* 65:1,31–34 (1986).
4. Bhattacharjee, S., and Altenkirch, R. A., Combust. Flame 84:160–169 (1991).
5. Bhattacharjee, S., and Altenkirch, R. A., *Twenty-Third Symposium (International) on Combustion*, The Combustion Institute, Pittsburgh, 1991, p.1627–1633.
6. Chen, C. H., and Cheng, M. C., *Combust. Sci. Technol.* 97:63–83 (1994).
7. Di Blasi, C., Crescitelli, S., Russo, G., and Fernandez-Pello, A. C., *Combust. Sci. Technol.* 64:289–294 (1989).
8. West, J., Bhattacharjee, S., and Altenkirch, R. A., *Combust. Sci. Technol.* 83:233–244 (1992).
9. Olson, S. L., Ferkul, P. V., and T'ien, J. S., *Twenty-Second Symposium (International) on Combustion*, The Combustion Institute, Pittsburgh, 1988, pp. 1213–1222.
10. Olson, S. L., *Combust. Sci. Technol.* 76:233–249 (1991).
11. Bhattacharjee, S., Altenkirch, R. A., and Sacksteder, K. R., *Combust. Sci. Technol.* 91:4–6,225 (1993).
12. Altenkirch, R. A., Eichhorn, R., and Shang, P. C., *Combust. Flame* 37:71 (1980).
13. Weiland, K. J., "Intensified Array Camera Imaging of Solid Surface Combustion Aboard the NASA Learjet," NASA TM-105361, 1992.
14. Grayson, G., Sacksteder, K. R., Ferkul, P. V., and T'ien, J. S., *Microgravity Sci. Technol.* VII:2 (1994).
15. Sarner, Stanley F., *Propellant Chemistry*, Reinhold Pub. Co., New York, 1966, p. 283.
16. Buchele, D. R., and Griffin, D. W., *Appl. Optics* 32:4218–4222 (1993).
17. "JSC Reduced Gravity Program User's Guide," NASA Johnson Space Center Document JSC-22803, 1991.
18. DeLombard, R., Finley, B. D., and Baugher, C. R., "Development of and Flight Results from the Space Acceleration Measurement System (SAMS)," NASA TM-105652, 1992.
19. deRis, J. N., *Twelfth Symposium (International) on*

Combustion, The Combustion Institute, Pittsburgh, 1969, pp. 241–252.
20. Fernandez-Pello, A. C., Ray, S. R., and Glassman, I., *Eighteenth Symposium (International) on Combustion*, The Combustion Institute, Pittsburgh, 1981, pp. 579–589.
21. Frey, A., and T'ien, J. S., *Combust. Flame* 36:33 (1976).
22. Altenkirch, R. A., and Vedha-Nayagam, M., *Twenty-Second Symposium (International) on Combustion*, The Combustion Institute, Pittsburgh, 1988, pp. 1495–1500.

COMMENTS

Paul Ronney, University of Southern California, USA. Your radiation parameter does not include a Planck absorption coefficient, which indicates that you are not considering gas-phase radiation. One then infers that your radiation parameter refers to surface radiation with constant emissivity. Do you believe that the quality of your correlation then suggests that surface radiation is more important than gas-phase radiation?

Author's Reply. The radiation parameter, S_R, indicates the increased importance of radiation losses to the environment as the convecting flow velocity decreases. For the low-speed flow conditions observable only in reduced gravity, we have used S_R to compensate the dimensionless flame spread rate for these radiative losses. Without a third parameter to account for radiative loss, dimensionless spread rates in low-speed flows do not correlate well with Damköhler number, despite the success of this approach for higher-speed flows.

The form of S_R used in the correlation seems to suggest that gas-phase radiation loss is not important in the range of conditions tested. This S_R describes loss from the fuel surface and is proportional (for a 2D flame) to $g^{-1/3}$. Because gas-phase radiation loss grows with the flame volume, a gas-phase S_R is proportional (for a 2D flame) to $g^{-2/3}$. Consequently, while at normal gravity gas-phase loss is much smaller than surface loss, gas-phase loss is amplified with respect to surface loss as gravity becomes small. Numerical modeling (e.g., Ref. 6 in the text) predicts that at sufficiently low gravity, spread rates with gas-phase loss are lower than spread rates with surface loss. We suggest that the lowest partial-gravity level available in the aircraft tests (i.e., 0.05 g_{Earth}) is not low enough for gas-phase loss to dominate spread rate behavior.

•

S. Bhattacharjee, San Diego State University, USA. You evaluated the flame temperature that appears in the deRis/Delichatsios formula using STANJAN, while the original solution requires the use of linearized adiabatic stoichiometric flame temperature. The differences between these two temperatures are quite large, especially at high oxygen concentrations. If the linearized adiabatic temperature was used, how would that affect your correlations?

Author's Reply. In developing the correlation presented in this paper, we first reproduced the correlation of flame spreading presented in Altenkirch et al. [12] in which a calculated stoichiometric, adiabatic flame temperature with no dissociation appeared in the formulation of the Damköhler number, *Da*, and dimensionless spread rate, V_f^*, for purely buoyant flows. These temperatures are very high (e.g., 2822 K at 21% oxygen mole fraction) compared with realistic flame temperatures, but serve to represent the release of all conceivably available energy to maintain the flame reactions and drive the buoyant flow.

In that formulation, V_f^* approaches unity as *Da* increases, in accordance with the scaling of the measured spread rates with the spread rate at the condition of the maximum conceivable forward heat transfer rate, and the data, over a wide range of atmospheric oxygen content, lie along a smooth curve. Modifying Altenkirch's formulation only by allowing for dissociation in the stoichiometric, adiabatic flame temperature calculation (e.g., 2182 K at 21% oxygen) disrupts the smooth curve seen in Ref. 12, creating a family of curves that differ by oxygen content. However, when the partial-gravity data we obtained are included in this formulation a useful property emerges: blowoff extinctions occur at very similar *Da* for 21% oxygen mole fraction at 4.25 times normal Earth gravity (*g*), 15.7% oxygen at 1 *g*, and 15% oxygen at 0.6 *g*. Introducing the radiation parameter, S_R, removes the oxygen-content dependence of the dimensionless spread rate (incidentally, using $1/V_r$ without the gas properties in S_R does not succeed). The combination of using realistic flame temperatures and correcting the dimensionless spread rate for radiation losses provides a correlation that is independent of gravity level and oxygen content over wide ranges of these dimensional parameters.

Twenty-Fifth Symposium (International) on Combustion/The Combustion Institute, 1994/pp. 1693–1699

FLAME PROPAGATION EXPERIMENT OF PMMA PARTICLE CLOUD IN A MICROGRAVITY ENVIRONMENT

HIDEAKI KOBAYASHI, NAOMICHI ONO, YOZO OKUYAMA AND TAKASHI NIIOKA
Institute of Fluid Science
Tohoku University
Katahira, Sendai, Miyagi 980, Japan

The flame propagation experiments on clouds of purely spherical PMMA particles in a microgravity environment were conducted by using the Japan Microgravity Center (JAMIC) drop shaft, where a microgravity condition of 10^{-4} g for 10 s is available. The exact measurement of the burning velocity of the particle cloud was impossible due to the particle sedimentation in normal gravity up to now. The particle cloud was created using a fluidized-bed–type device and suspended in the flame propagation tube. The cloud was ignited at the open end of the tube, and the flame speed was measured by charge coupled device (CCD) video camera images. The flame speed in normal gravity was also measured, and the two groups of results were compared. The results showed that the flame speed in normal gravity was considerably larger than for ordinary gaseous flames, since turbulent combustion occurred due to the residual turbulence of the flow and the turbulence generated by the particle sedimentation. On the other hand, in the microgravity environment, when the cloud was ignited 6 s after the release of the capsule, the particles were quiescent and dispersed with sufficient uniformity, indicating the effectiveness of the long duration microgravity environment on the decay of turbulence. The flame speed decreased drastically in comparison with normal gravity cases, but the dependence of the flame speed on the particle concentration was similar to that in normal gravity.

Introduction

The combustion of solid particle clouds, such as those of coal, solid carbon, metal, and food, has received attention from those interested in the effective use of fossil fuels and in safety engineering. Many experimental and theoretical studies on particle cloud combustion have been made [1–5]. The major problem in measuring the combustion characteristics such as burning velocity, quenching distance, ignition limit, and flame structure for combustible particle clouds is the existence of gravity. Gravity causes particle sedimentation. In normal gravity, the particle has a relative velocity to the surrounding gas, which depends on particle size and makes uniform dispersion of particles difficult.

Recently, the use of microgravity environments for particle cloud combustion research has become of interest. Ballal [6] has measured the burning velocity of coal, carbon, aluminum, and magnesium particle clouds using a drop capsule. A microgravity experiment was also made by Ross et al. [7] and Berlad and Tangirala [8] by using the NASA–Lewis drop tower and aircraft, where the burning velocity was measured for lycopodium, coal, and cellulose particles. However, for comparison with former theoretical analyses or to develop a new model of particle cloud combustion, these particles are not ideal because the physical and chemical properties, i.e., the size, shape, and composition, are not necessarily uniform, and therefore, the vaporization and combustion processes are fairly complicated. In addition, the duration of the microgravity of the drop tower used in the aforementioned research ranging from 1.4 to 2.2 s is insufficient, and the microgravity level for aircraft experiments is relatively high (+/−0.02 g, as reported in Ref. 7). A long duration and high-quality microgravity environment are essential to realize an ideal particle cloud combustion because sufficient time must be allowed for turbulence attenuation before ignition and elimination of the movement of particles relative to the surrounding gas.

The final aim of this study is to establish a more idealized model for particle cloud combustion. To this end, we conducted flame propagation experiments on a polymethylmethacrylate (PMMA) particle cloud by using the Japan Microgravity Center (JAMIC) drop shaft, where a microgravity condition of 10^{-4} g for 10 s is available. The PMMA particle is useful as a model particle because its molecular structure and physical properties are well known. In addition, the particles are perfectly spherical, and the distribution of particle diameters can be successively measured. The JAMIC drop shaft used in this experiment can provide the longest duration of high-quality microgravity of any drop tower in the world.

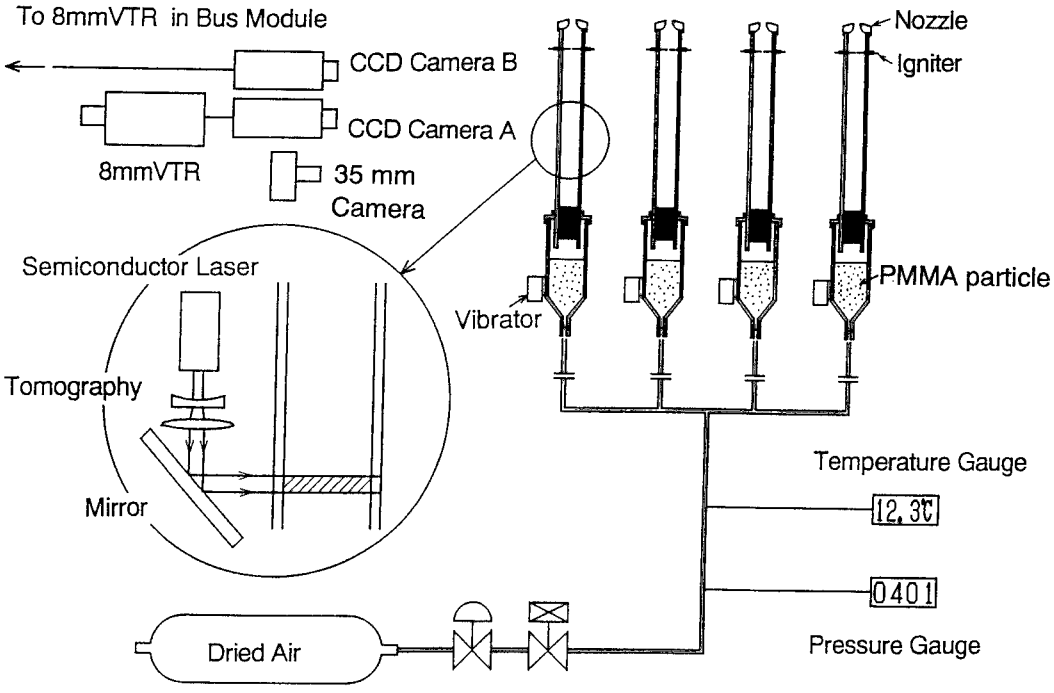

FIG. 1. Schematic diagram of the experimental setup.

Using this facility, we first measured the flame speed of PMMA particle clouds.

Experimental Apparatus

Figure 1 shows the experimental apparatus schematically. Four propagation tubes are made of acrylic, whose length and inner diameter are 500 and 38 mm, respectively. A particle-supplying device using a fluidized bed with a vibrator is installed at the bottom of the tube. At the top of the tube, a nozzle is fitted in order to reduce combustion fluctuation.

Dried air, measured using a critical orifice flow meter, is dispensed into the bottom of the fluidized bed and mixed with PMMA particles. The particle cloud is made in the bed and flows into the propagation tube from the bottom. The relationship between the air flow rate and the mass concentration of particle cloud (mg/L) was calibrated before combustion experiments. When the calibration was made, the amount of wall adhesion, which was related to the air flow rate, was measured and then subtracted from the total particle loaded in order to determine the mass concentration of actually suspended particles. The experimental conditions for the suspended concentrations were determined by using this calibration curve. The particle cloud is ignited by a spark igniter or a heated Nichrome wire installed 100 mm below the outlet of the tube.

The state of the flame propagation was recorded by a charge coupled device (CCD) video camera and a motor-driven 35-mm camera. A time series of the flame front was analyzed using the recorded images. The flame speed v_f ($= dD/dt$, where D and t denote distance and time, respectively) was calculated from the gradient of distance from the plot of the ignition point vs the arrival time, as shown in Fig. 2. In order to observe the motion of particles during the drop, a laser tomographic image using a semiconductor laser as the light source was recorded by another CCD video camera.

All these apparatuses were installed in the experimental container (dimensions of 870-mm long by 425-mm wide by 981-mm high), whose size is one-half of the JAMIC drop shaft payload. Considering the efficiency of drop experiments, four propagation tubes were installed in the container and ignited simultaneously. Air was supplied into the fluidized bed 5 s before the dropping of the capsule in order to fill the tubes with particle clouds. The air was stopped upon release of the capsule, and the particle clouds were ignited 6 s after the release.

Flame propagation experiments were also conducted on the ground in order to investigate the particle motion and flame propagation characteristics of PMMA particles in normal gravity. In this case, the particle cloud was ignited 1 s after the stoppage of the air supply because particles would have sedimen-

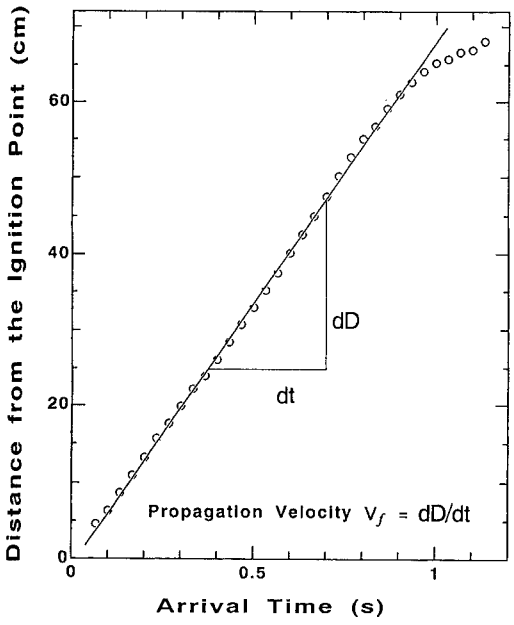

FIG. 2. Relationship between the distance from the ignition point and the arrival time of the flame front (d_p = 7.2 μm; mass concentration: 260 mg/L, in normal gravity).

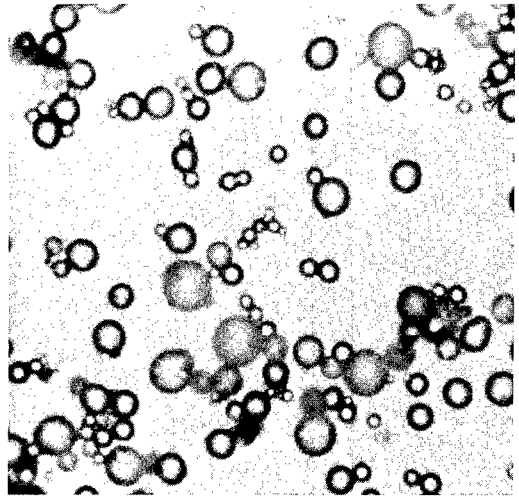

FIG. 3. Photograph of the PMMA particles for 7.2 μm in mean diameter.

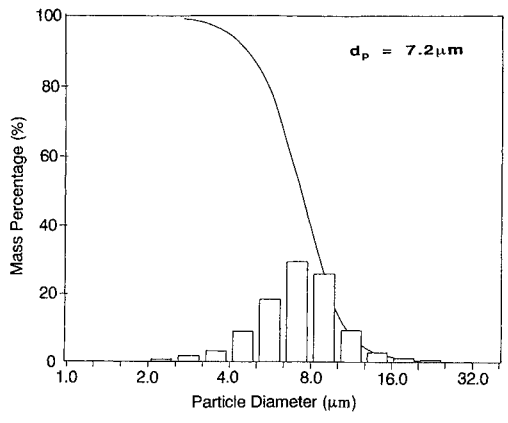

FIG. 4. Distribution of the PMMA particle diameter for 7.2 μm in mean diameter.

tated, and the mass concentration and particle distribution in the tube would have changed if more time had elapsed before ignition. The laser Doppler velocimetry (LDV) measurement of the particle motion was made at a position 150-mm below the ignition point, where the small, flat glass window to introduce laser beams was installed on the tube wall.

Three kinds of PMMA particles, whose mass-averaged mean diameters d_p were 4.8, 7.2, and 18 μm, respectively, were present in this study. Because of the limited number of opportunities for repetition, the microgravity experiment was made only for the particles of mean diameter of 7.2 μm. The shape of the PMMA particle is perfectly spherical, as shown in Fig. 3. The distribution of the particle diameter, whose mean diameter is 7.2 μm, is shown in Fig. 4.

Results and Discussion

Normal Gravity Experiment:

Figure 5 shows the relationship between the flame speed and the mass concentration of PMMA particle clouds for three mean particle diameters. The broken line shown in this figure is the position whose concentration corresponds to an equivalence ratio of unity. We can see that the flame speed has the maximum value in the fuel-rich side for all particle diameters, and the maximum flame speed is larger for small particle diameters than for large diameters. The clouds of larger PMMA particles have the maximum flame speed in the richer side compared to the clouds of smaller particles. For the small particles, i.e., 4.8 μm, the flame speed decreases rapidly in both the rich and the lean side, but for larger particle diameters, i.e., 7.2 and 18 μm, the flame speed decreases gradually in the rich side. For particles with a larger mean diameter, flame propagation is possible even for the considerably large equivalence ratios (Fig. 5). This is because, as pointed out in the analysis by Seshadri et al. [5], the effective gas-phase equivalence ratio in the reaction zone can be small even if the global equivalence ratio based on solid-fuel loading is greater than unity.

Smoot et al. [2] measured the burning velocity of

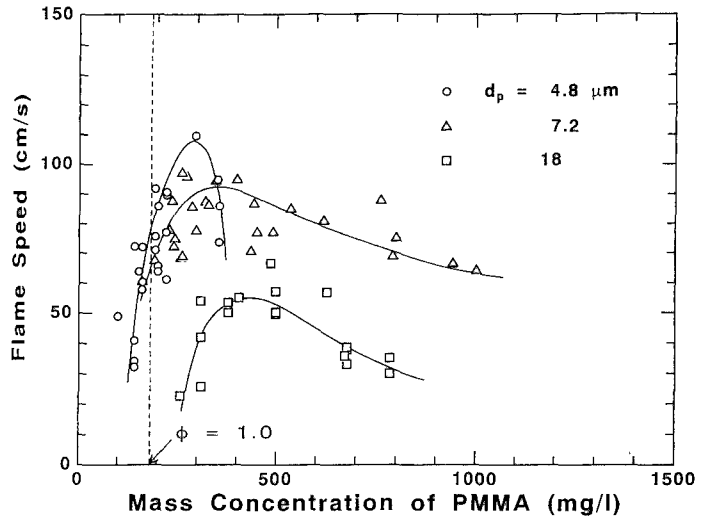

FIG. 5. Relationship between the flame speed and the concentration of PMMA in normal gravity.

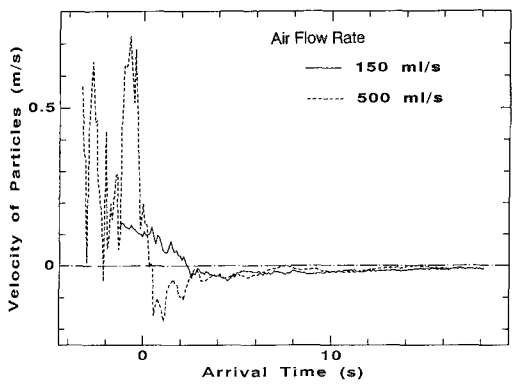

FIG. 6. Time series of axial velocity component of PMMA particles in normal gravity (d_p = 7.2 μm).

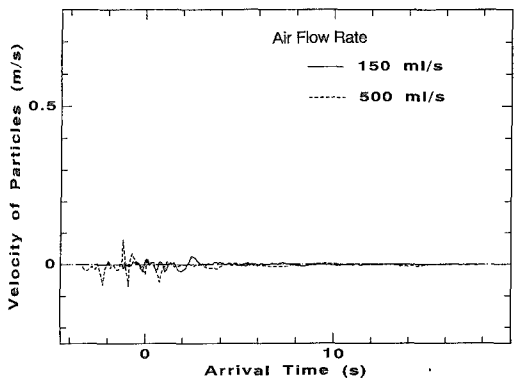

FIG. 7. Time series of radial velocity component of PMMA particles in normal gravity (d_p = 7.2 μm).

coal dust for various particle diameters by using a downward-flowing flat flame burner. The variation of the burning velocity with coal particle concentration and its dependence on the particle diameter has a tendency similar to the one obtained here. However, the propagation velocities measured in this study are considerably larger than the data by Smoot et al., that is, they showed that the burning velocity for 10-μm Pittsburgh coal was 16–33 cm/s, similar to the burning velocity of gaseous fuel and air mixtures. We observed the flame front region using a CCD video camera and a 35-mm camera and found that the region has a blue flame followed by a long yellow luminous zone that may be caused by soot. The flame front was very rough and corrugated.

Figures 6 and 7 show the time series of the axial and radial velocity components of particles in the propagation tube measured by LDV, respectively. The positive velocity in Fig. 6 indicates that the particles move in the upper direction of the tube, and the negative velocity indicates movement in the lower direction. The air supply was stopped at time zero in these figures. The particles began to fall at time zero, after which the particle velocity becomes negative. The velocity components of particles shown in Fig. 6 have a minimum value just after time zero and then the velocity converges to zero while fluctuating. The fluctuation of the axial velocity is the result of nonuniform sedimentation velocity, which is due to both variation in particle size and air turbulence in the propagation tube. On the other hand, it is believed that the fluctuation of the radial velocity component mainly represents the latter (Fig. 7). These results indicate that the particle sedimentation just after the stoppage of the air is of the type where sedimentation interacts with large-scale vortices formed in the propagation tube.

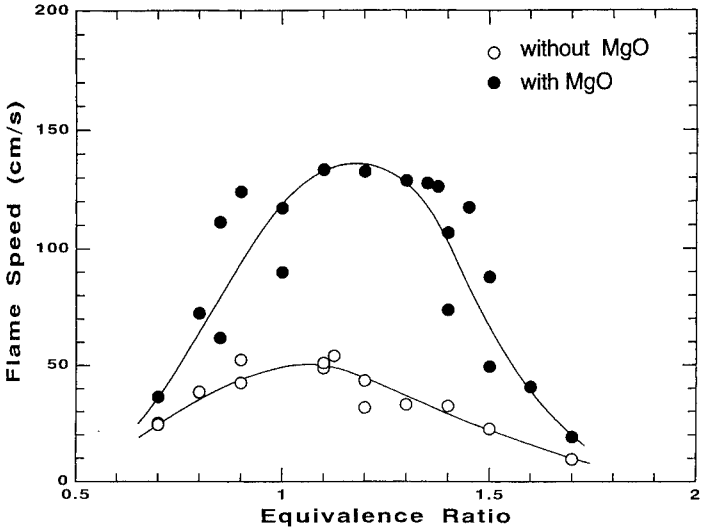

FIG. 8. Effect of the sedimentation of nonreactive particle (MgO) on the flame speed of propane-air mixture.

Based on Figs. 6 and 7, we can say that more than 5 s are necessary to allow for sufficient decay of the intensity of turbulence. Because particle clouds were ignited 1 s after the stoppage of the air supply in the normal gravity experiments, considerable turbulence must remain in the propagation tube, meaning that the roughness of the flame front is due to the turbulent combustion.

The sedimentation velocity is large at first and then gradually decreases, as shown in Fig. 6, since the large particles sediment first, followed by small particles. This gradually makes the average size of the particles in the propagation tube small, and therefore, if ignition were delayed until the turbulence diminished, the concentration and the mean diameter of particles in the propagation tube would change.

Mitani and Niioka [9] have shown that when the nonreactive alumina particles are added to the combustible mixture, the burning velocity decreases with increasing mass concentration of particles due to the thermal effect. However, in that case, the mixture flow is laminar, and the particle velocity relative to the mixture velocity is very small. Concerning the effects of the particle motion on the burning velocity of the gaseous mixture, Klemens [10] conducted experiments on the flame propagation of gases containing neutral particles in a normal gravity environment and found that within a certain range of particle concentration, the gaseous flame accelerated considerably. He concluded that the main reason for this phenomenon is turbulence of the gas mixture caused by falling particles.

In order to know the effect of the particle sedimentation on the gaseous flame propagation, we measured the flame speed of propane-air mixtures by using the same propagation tube. We also measured the flame speed when the MgO particles were dispersed in the mixture and compared the two measurements. Figure 8 shows the effect of the particle sedimentation on the flame speed, indicating that the flame speed is accelerated by the sedimentation of the nonreactive MgO particles.

Although it is difficult to determine which turbulence is the major cause for the turbulent combustion of particle clouds, i.e., the residual turbulence due to the air supply or the turbulence generated by particle sedimentation, it is clear that the particle cloud combustion under normal gravity is highly affected by turbulence.

Microgravity Experiment:

Figure 9 shows the result of microgravity experiments of the flame propagation of PMMA particle clouds, whose mean diameter is 7.2 μm. The data from the normal gravity experiments are also shown in this figure for comparison. The flame speed under microgravity conditions was about 35% lower than that in normal gravity over the whole range of particle concentration, and the maximum flame speed was about 60 cm/s. However, the dependence of the flame speed on the particle concentration has a tendency similar to that in the normal gravity, indicating that the flame speed decreases sharply in the lean side while gradually in the rich side. The concentration at the maximum flame speed, about 350 mg/L, seems to be the same for both gravity conditions.

Particle motion under microgravity was observed using laser tomography during the dropping. Large-scale vortexlike motion was seen just after release, but the motion diminished gradually. When the particle cloud was ignited 6 s after release, it was con-

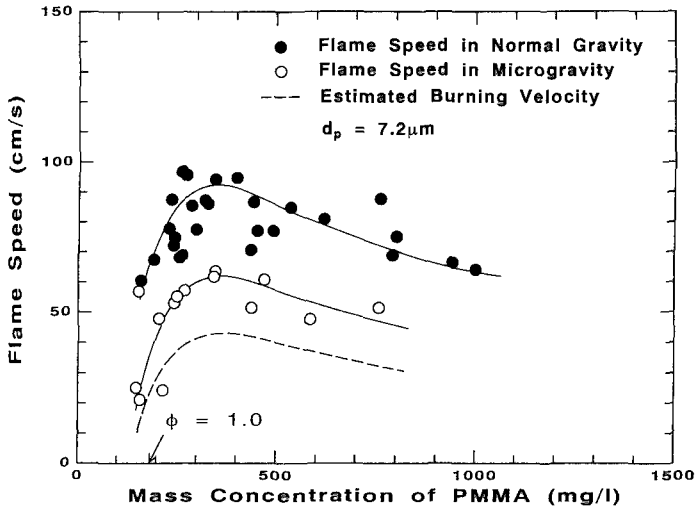

FIG. 9. Relationship between the flame speed and the concentration of PMMA in microgravity.

firmed that the vortexlike motion stopped, and each particle became stationary.

It was very difficult to take clear photographs of the flame front in microgravity because of the attachment of particles on the inner wall of the tube, and so the photographs of the propagating flame front successfully taken were limited. Flame photographs, however, showed that the flame front was sufficiently smooth and slightly convex. The actual area of the flame front was calculated from a few unidirection photographs, assuming the shape of the flame front was axisymmetric with the axis of the flame propagation tube. This showed that the averaged ratio of the cross-sectional area of the flame propagation tube to the area of the flame front was 0.69. Therefore, although the exact determination of the burning velocity and its dependence on the mass concentration is somewhat uncertain, the burning velocity is roughly estimated to be about 0.69 times smaller than the flame speed. The broken line in Fig. 9 illustrates this estimated burning velocity.

The maximum value of the burning velocity in microgravity is equal to or a little bit larger than that of the gaseous hydrocarbon flames. The particle cloud combustion, however, is essentially a heterogeneous combustion. Weak turbulent combustion may occur even if the cloud is quiescent in the propagation tube. Actually, the flame shape often curves and wrinkles during propagation. The existence of this phenomenon is considered to possibly be the result of incomplete dispersion uniformity and/or the agglomeration of particles, but the most plausible reason may be that turbulence is induced by the particles themselves during flame propagation and that turbulent flame propagation is an inherent feature of particle cloud combustion. In order to confirm these hypotheses, more precise measurements of the particle motion and observation of the flame front structure have to be done.

Conclusions

The flame propagation experiments on clouds of spherical PMMA particles in a microgravity environment were conducted using the JAMIC (Japan Microgravity Center) drop shaft, where a microgravity condition of 10^{-4} g for 10 s is available. The particle cloud was formed by a fluidized-bed–type device and suspended in the propagation tube. The cloud was ignited at the open end of the tube, and the flame speed was measured by CCD video camera images. The flame speed in normal gravity was also measured, and the two groups of results were compared.

The experimental results in normal gravity show the clear dependence of the flame speed on the particle size and concentration. However, the flame speed is considerably larger in comparison with ordinary gaseous flames due to the turbulent combustion, resulting from the residual turbulence of the air supply and the turbulence generated by the particle sedimentation, which cannot be avoided in a normal gravity environment.

In the microgravity environment, when the cloud was ignited 6 s after the release of the capsule, the particles were stopped and dispersed almost uniformly, indicating the effectiveness of a comparatively long duration–microgravity environment. The flame speed was about 35% lower than that of the normal gravity case, but the dependence of the flame speed on the particle concentration was similar to that in normal gravity.

Acknowledgments

The authors acknowledge the financial support of NEDO (New Energy and Industrial Technology Development Organization) and JSUP (Japan Space Utilization Promotion Center). The authors also would like to express sincere thanks to Mr. S. Hasegawa for his technical assistance.

REFERENCES

1. Bryant, J. T., *Combust. Sci. Technol.* 2:389 (1971).
2. Smoot, L. D., Horton, M. D., and Williams, G. A., *Sixteenth Symposium (International) on Combustion*, The Combustion Institute, Pittsburgh, 1977, p. 357.
3. Bradley, D., Dixon-Lewis, G., Habik, S. El Din, and Mushi, E. M. J., *Twentieth Symposium (International) on Combustion*, The Combustion Institute, Pittsburgh, 1984, p. 931.
4. Niioka, T., and Mitani, T., *International Symposium on Scale Modeling*, JSME, Tokyo, 1988, p. 129.
5. Seshadri, K., Berlad, A. L., and Tangirala, V., *Combust. Flame* 89:33 (1992).
6. Ballal, D. R., *Proc. R. Soc. London A* 385:21 (1983).
7. Ross, H. D., Facca, L. T., Berlad, A. L., and Tangirala, V., NASA TM-101371, 1989.
8. Berlad, A. L., and Tangirala, V., NASA CR-182299, 1989.
9. Mitani, T., and Niioka, T., *Nineteenth Symposium (International) on Combustion*, The Combustion Institute, Pittsburgh, 1982, p. 869.
10. Klemens, R., *Dynamics of Heterogeneous Combustion and Reacting Systems* (A. L. Kuhl, J. C. Leyer, A. A. Borisov, and W. A. Sirignano, Eds.), AIAA, Washington, 1993, p. 155.

COMMENTS

Kalyan Annamalai, Texas A&M University, USA. Your experiments seem to indicate that introduction of particles (MgO) seems to increase flame velocity, which you attribute to sedimentation and turbulence. However, particles are known to suppress turbulence due to inertia of particles. Is it possible that sedimentation causes combustible gases to be dragged and hence increase flame velocity? Can you comment?

Author's Reply. In microgravity, the inertia of particles may suppress turbulence when the velocity of the particles is smaller than the local turbulence velocity. However, in normal gravity, because particles always have a relative velocity to the surrounding gas due to sedimentation, the turbulence generation effect must be significant in comparison with the suppression of turbulence.

It is considered that the drag of combustible gas induced by particle sedimentation generates turbulence that increases the flame speed in the normal gravity.

Twenty-Fifth Symposium (International) on Combustion/The Combustion Institute, 1994/pp. 1701–1709

THE EFFECT OF GRAVITY ON A LAMINAR DIFFUSION FLAME ESTABLISHED OVER A HORIZONTAL FLAT PLATE

J. L. TORERO, L. BONNEAU, J. M. MOST AND P. JOULAIN
Laboratoire de Chimie Physique de la Combustion
Université de Poitiers—URA872 au CNRS
ENSMA, Site du Futuroscope, BP109 Chasseneuil du Poitou
86960 FUTUROSCOPE CEDEX, France

An experimental study is conducted on a laminar diffusion flame established over a horizontal flat porous burner. The objective of this study is to provide further understanding on the transport mechanisms controlling a diffusion flame, with particular interest on the role of buoyancy. Fuel is injected through the burner and the oxidiser is provided by a forced flow parallel to the surface. The fuel used is ethane and the oxidiser used is air. Experiments are conducted in normal and microgravity conditions, and information about the flame is obtained from video records, temperature measurements, and gas analysing of the global combustion products. The parameters varied are the air-forced flow velocity and the fuel injection velocity. In normal gravity, the flame can be divided in two well-determined regions: a boundary layer region (where inertia dominates) and a plume region (where buoyancy dominates). In the boundary layer region, air entrainment, induced by the plume, adds to the forced flow, resulting in flames closer to the burner and premature extinction. When gravity is eliminated, the plume region disappears; therefore, the overall air flow velocity is reduced to that of the forced flow, and thus, the standoff distance increases and higher air-forced flow velocities are necessary for extinction to occur. The flame is found to establish, both in normal and microgravity, in a line where fuel and oxidiser rates of delivery are in stoichiometric proportions. Experimental results and a scaling analysis of the region close to the flame show that in microgravity, assumptions typical to boundary layer flow, such as stationary regime or neglectable mass transport in the direction perpendicular to the forced flow plane are no longer valid. The good agreement between theory and experiments confirms the important role of gravity in the determination of the characteristics of a diffusion flame.

Introduction

Condensed combustible materials often burn such that a diffusion flame is established over its surface. After ignition occurs, the flame spreads through the material, and if the oxidiser flows parallel to the combustible surface, a stationary diffusion flame will establish in the boundary layer generated over the fuel. Heat transfer from the flame to the surface vaporises the condensed fuel which is transported towards the flame by convection and diffusion. When the fuel reaches the flame, it exothermically reacts with the oxidiser and provides the necessary heat to sustain further pyrolysis. This form of fuel burning is commonly encountered in fires and, thus, is of particular interest in the fire safety field.

Emmons [1] showed that the evaporation rate of the fuel could be expressed as a function of the mass transfer number only. Numerous studies have been conducted on the flat plate, boundary layer, diffusion flame combustion of condensed fuels. The main focus has been to understand the mechanisms controlling heat transfer, reaction chemistry, and surface pyrolysis. The works of Williams [2] and Drysdale [3] provide extensive reviews on the subject.

Limited attention has been given, however, to the aerodynamical structure of the flow and the effect of gravity. Hirano and coworkers [4,5] used a porous plate through which a gaseous fuel was uniformly injected. Velocity overshoots were found near the reaction zone along with pressure distortions near the leading edge. Ramachandra and Raghunandan [6], on a similar burner, studied the effect of injection and free stream velocities on the stability of vaporised n-heptane flames. By substituting the combustible fuel by a porous gas burner, the problem is simplified significantly: Fuel supply is no longer coupled to heat transfer, and therefore, fuel and oxidiser supply to the reaction can be varied independently. Although the similarity solution, obtained by Emmons [1], is no longer possible, this configuration allows for a better study of phenomena such as entrainment due to thermal gradients.

There are very few studies dealing with the effect of gravity on a chemically reacting boundary layer. Fernandez-Pello and Pagni [7] introduced a single

nondimensional parameter to study forced, mixed or free combustion of a vertical fuel surface. Pagni [8] pointed the importance of buoyancy in the determination of the flame length. Kodama et al. [9] and Mao et al. [10] included a buoyancy term in numerical solutions of a burning vertical wall. By using a porous burner, Bonneau et al. [11] obtained some preliminary experimental results on a vertical flame in microgravity. In a horizontal configuration, a buoyantly induced pressure gradient parallel to the wall was discussed by Lavid and Berlad [12]. These studies provide enough information to show that buoyancy has a significant effect on the flame length, ignition, and extinction limits, all of extreme importance for fire prevention and control.

In this work, a porous gas burner is used to determine the effect of gravity on the flow structure of a chemically reacting boundary layer. The parameters varied are the oxidiser flow velocity and fuel injection velocity. Experiments are conducted in normal and microgravity and the results compared to theoretical predictions.

Experimental Apparatus

The experiments are conducted in a small scale, horizontally oriented, combustion tunnel along with the supporting instrumentation. The test section is 270-mm long and has a rectangular cross section 120-mm wide and 90-mm tall. Three of the walls are Pyrex windows to enable visual observation. Ethane, 99.4% pure, is uniformly injected through a porous burner, 200-mm long and 50-mm wide, mounted on the floor of the combustion chamber. Compressed air flows through a settling chamber before entering the test section. The air and fuel velocities are governed with controlled mass flow meters.

Information on the flame is obtained from two CCD video cameras, six Chromel-Alumel thermocouples, and two gas collectors. The video cameras provide a top and a side view of the flame. The thermocouples are placed on a vertical line with their junction located on the plane of symmetry. The thermocouples generate significant perturbations on the flow; therefore, they are placed far away from the leading edge (120 mm). It is important to clarify that the measurements are not representative of the flame temperature but only give a characteristic temperature of the combustion products. Two gas-sampling bottles where placed in the exhaust tanks. Both tanks and bottles remain in a vacuum during normal gravity and are only filled, with the combustion products, in microgravity. The results obtained from these samples only provide a comparative idea of the completeness of the global combustion process and do not attempt to describe the chemical reactions occurring in the chamber.

Experiments under reduced gravity conditions were conducted at the drop tower of the University of Bremen (ZARM) and by using the Caravelle aircraft of CNES. At the drop tower facility, a free fall provided microgravity periods of up to 5 s (gravity levels of 10^{-5} g_0). Following a parabolic trajectory, up to 25 s of reduced gravity were obtained with the Caravelle (gravity levels of 10^{-3} g_0).

A more detailed description of the experimental hardware and procedures can be found in the work of Bonneau et al. [11].

Experimental Results

The description of the experimental results will be divided into three parts: extinction limits, physical characteristics of the flame, and qualitative results obtained from the temperature measurements and gas samples.

To study the effect of gravity on the extinction limits, the flame was established, and then the air flow velocity was increased until extinction occurred. For low air flow velocities, the fuel injection velocity was varied until the flame extinguished. The results are presented in Fig. 1; the data points represent the values of air and fuel velocities at which extinction occurred. In normal gravity, for $U_\infty < 0.03$ m/s, all flames extinguished. Close to the extinction limit, the flames were almost vertical and very close to the leading edge of the plate. For 0.03 m/s $< U_\infty <$ 0.1 m/s, flames extinguished at an almost constant value of V_F. For $U_\infty > 0.1$ m/s, the extinction limit depended on both fuel and oxidiser velocity, with the dependence on the former becoming less significant as U_∞ increased. The extinction curves, in normal and microgravity, were similar with the latter, significantly displaced towards the left. It is important to note that the difference between normal and microgravity extinction limits decreases as U_∞ increases. For $U_\infty < 0.07$ m/s, perturbations in the gravity level become important, rendering the microgravity extinction limits unreliable.

By using an image processing system, boundaries for the yellow and blue zones of the flame are obtained (Fig. 2). The images correspond to a specific flame ($U_\infty = 0.115$ m/s and $V_F = 0.0052$ m/s), but the observations are applicable to most other conditions. Figure 2a shows the flame in normal gravity; close to the leading edge, the flame is blue and established in a boundary layer fashion. Farther upstream, the flame turns yellow, and the boundary layer is substituted by a plume. It is important to observe that the flame propagates opposite to the forced flow in the upper part of the chamber. The transition from normal to microgravity is presented in Fig. 2b. The plume disappears as the flame turns almost entirely yellow, remaining blue only very close to the leading edge. In microgravity, the flame establishes in an almost straight line, and the angle be-

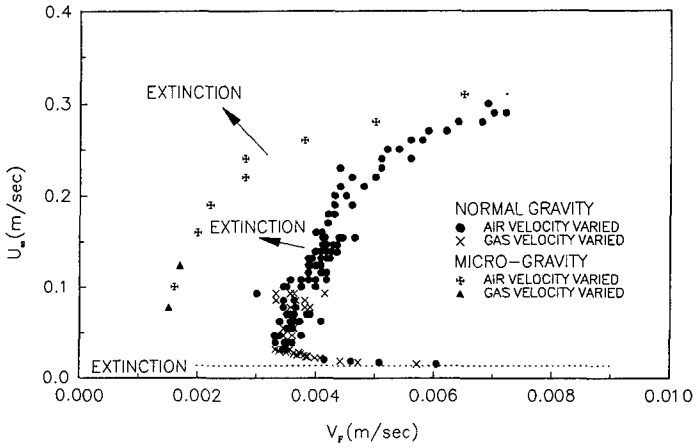

FIG. 1. Effect of the free-stream air velocity and fuel injection velocity on the stability of a boundary layer diffusion flame in normal and microgravity environments.

tween the flame and the burner (θ) increases with time. As θ increases, the flame turns blue (Fig. 2c). Half a second after transition to microgravity, a small yellow spot appears on the flame (Fig. 2d), which expands until it covers the first 60 mm of the flame (Fig. 2e). This expanding reactive zone is convected downstream (Fig. 2f), leaving behind a blue flame similar to that of Fig. 2d.

The sequence explained above will repeat itself periodically; each time the distortion of the flow will be more significant and the characteristics of each structure less obvious. The top view shows that the flame in normal gravity remains on top of the porous burner; when gravity disappears, the flame propagates towards the lateral windows. The characteristic yellow colour of the expanding reactive zone was observed to come mainly from the lateral side of the flame.

The size of the expanding reactive zone was observed to increase with the forced flow velocity and was not affected by the fuel injection velocity. The frequency at which the reactive zones would appear seemed independent from the forced flow and seemed to increase with the fuel injection velocity.

Thermocouple measurements showed that the temperatures decreased on the order of 100 K when the flame makes the transition from normal to microgravity. The magnitude of the temperature change decreases as the flame moves towards extinction. Analysis of the combustion products showed that oxygen consumption is greater in normal gravity. Oxygen consumption was found to decrease when the forced flow and the fuel injection velocity were varied towards extinction. These observations point towards a lower overall combustion completeness in microgravity and close to extinction.

Discussion and Data Correlation

The boundary layer theory and scaling analysis will be used to describe the above observations. The location of the flame will be determined by assuming that the flame is located where the fuel and oxygen rates of delivery are in stoichiometric proportions [13]. The fuel and oxidiser reaching the flame are determined by an overall oxidiser velocity (U_A), the oxygen mass fraction ($Y_{O,i}$), the fuel injection velocity (V_F), and the fuel mass fraction ($Y_{F,i}$). To determine the value of U_A, the combined effects of forced and buoyantly induced flows will be studied. A boundary layer region (where inertia dominates) and a plume region (where buoyancy dominates) will be determined as a function of the distance from the leading edge [13]. An entrainment velocity (U_B), induced by the buoyant plume, will be calculated and superposed to U_∞. Finally, characteristic parameters describing the flame location will be calculated and correlated with experimental values. The finite geometry of the chamber has a slight effect only on the plume; however, the main focus of this work is on the boundary layer region, and the plume region will only be considered in what regards its interaction with the former.

It was observed that extinction limits in normal and microgravity conditions are significantly different. The results of the scaling analysis along with a phenomenological explanation of the extinction process [6,9,14] will be used to explain these differences.

The flame location analysis makes use of the boundary layer theory to describe the problem even though the experimental observations show that in microgravity, assumptions such as stationary regime or neglectable mass transport in the direction perpendicular to the forced flow plane are no longer valid. To provide an explanation of the observed phenomena, a scaling analysis of the region close to the flame is conducted.

At the leading edge, diffusion and convective mass transport are of the same magnitude, and the process can only be described by the solution to the complete two-dimensional Navier–Stokes equations. This complex problem has been previously studied nu-

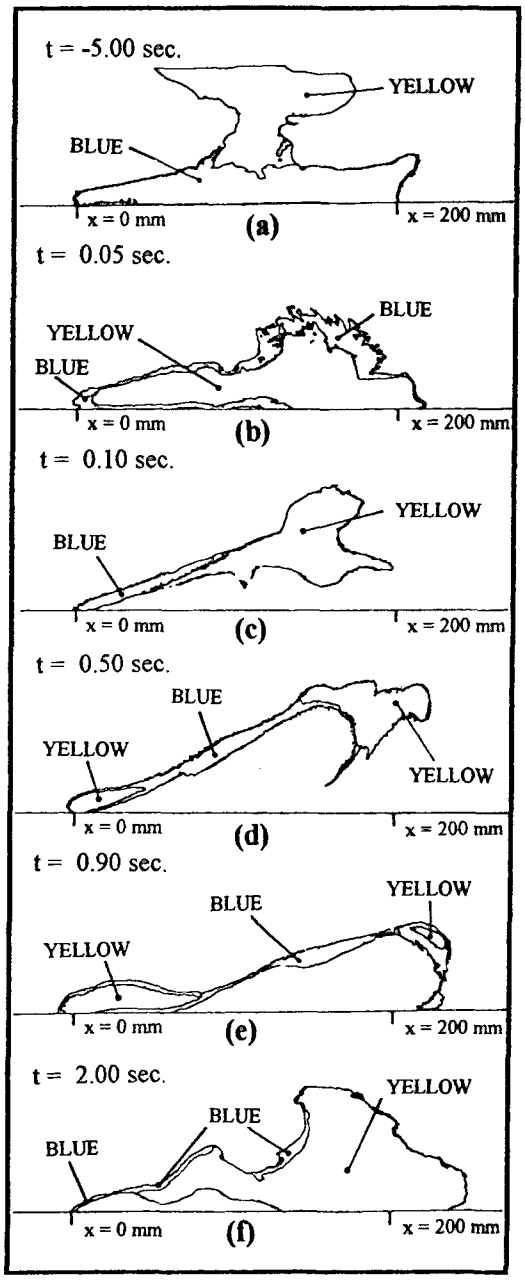

FIG. 2. Processed images of a boundary layer diffusion flame in normal and microgravity (U_∞ = 0.115 m/s and V_F = 0.0052 m/s).

merically and experimentally [9,10,14]. The characteristic scale of the leading edge region was defined by Chen and T'ien [14] as $\delta = a/U_\infty$ and, for all experimental conditions studied, is of the order of 10^{-3} m. The interpretation of the results will not include an analysis of this region, since the resolution of the measurements is not adequate for this length scale.

Flame Location

The stoichiometric line

Away from the leading edge, diffusion mass transfer can be neglected and the oxygen and fuel concentrations considered stationary. Forced convection of the fuel and oxidiser will determine the flame location, and the mass conservation equations for oxygen and fuel can be expressed as follows:

$$\rho U_\infty \frac{\partial Y_O}{\partial x} = -w_O$$

$$\rho V_F \frac{\partial Y_F}{\partial y} = -\frac{w_O}{\phi}.$$

By scaling the oxygen and fuel mass fractions by $Y_{O,i}$ ($Y_{O,i}$ = 0.23) and $Y_{F,i}$ ($Y_{F,i}$ = 1.00), respectively, it can be demonstrated that oxygen and fuel will be delivered in stoichiometric proportions at a straight line that has a slope defined by the following expression:

$$\tan\theta \approx \phi\left(\frac{Y_{F,i}}{Y_{O,i}}\right)\left(\frac{V_F}{U_A}\right). \tag{1}$$

Since the characteristic length scale of the leading edge region is very small, the flame is assumed to be anchored to the upstream edge of the burner (Fig. 3). So if δ_S is the standoff distance, then

$$\delta_S \approx x \cdot \tan\theta.$$

Inherent to this analysis is the assumption that δ_S is greater than the momentum boundary layer (δ_M). To verify this assumption, an approximate value for the momentum boundary layer thickness can be determined by equating inertia and viscous terms in the momentum equation. For all experimental conditions studied, $\delta_M << \delta_S$; thus, the flame will establish outside the momentum boundary layer, and U_A and V_F can be used as characteristic values for the velocity in the x and y directions, respectively.

The role of buoyancy

As it is shown in Fig. 3 and previously observed by Apte et al. [15], in normal gravity, the flame zone can be divided into two different regions: a boundary layer region, controlled by an overall flow parallel to the surface (U_A), and a plume region, where buoyancy dominates. Hot gases in the plume move upward, entraining air at the bottom of the chamber; when the hot gases reach the ceiling, they are forced

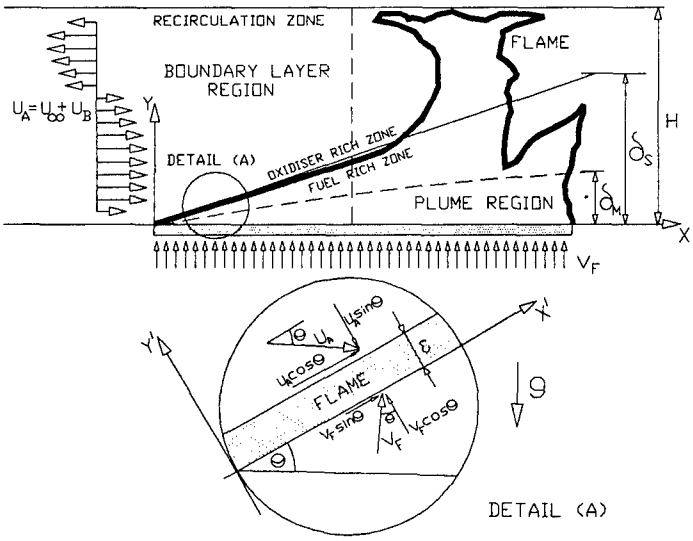

FIG. 3. Schematic diagram of a typical flame in normal gravity.

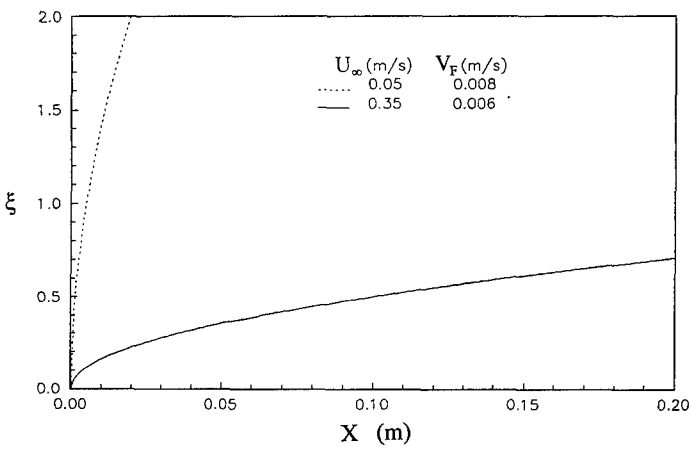

FIG. 4. Nondimensional ratio (ξ) of buoyant forces and inertia as a function of the distance from the leading edge.

upstream and downstream. A recirculation pattern is therefore established upstream of the plume (Fig. 2a). The dimensionless parameter

$$\xi = \frac{\mathrm{Gr}_x}{\mathrm{Re}_x^{5/2}}$$

describes the ratio between buoyant forces and inertia [12]. In general, $\xi < 1$ indicates a predominantly forced convection flow perturbed by natural convection; $\xi > 1$ suggests a predominantly free convection flow perturbed by forced convection. The former is representative of the boundary layer region and the latter of the plume region. A variation of ξ with x is presented in Fig. 4 for two extreme values of U_∞ and V_F. If the magnitude of the forced flow is small and V_F is large, the flame is buoyantly dominated, the boundary layer region will be very small, and an almost vertical plume is observed to appear at a small distance from the leading edge. If U_∞ is large, inertia is always dominant; the plume is hardly noticeable, but gravity and inertia forces are always of comparable magnitudes.

Overall air flow velocity (U_A)

The characteristics of the boundary layer region are determined by the overall flow U_A, where

$$U_A = U_\infty + U_B. \tag{2}$$

The following expression provides an order of magnitude for U_B [16]:

$$U_B \approx \frac{4a}{H} \mathrm{Ra}^{1/4}$$

where

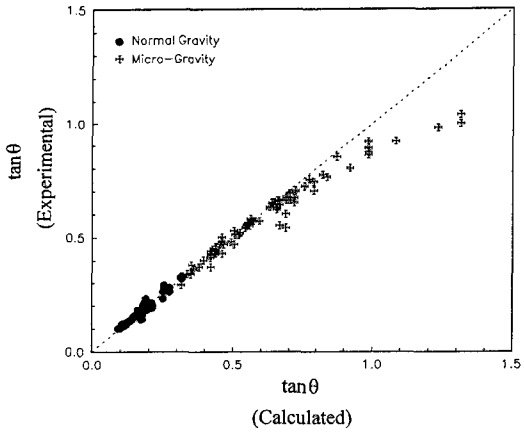

FIG. 5. Comparison of experimental and calculated slopes for the stoichiometric line (the dashed line corresponds to absolute agreement).

$$\mathrm{Ra} = \frac{gH^3}{\alpha v}\left(\frac{T_g - T_a}{T_g}\right).$$

The ceiling of the chamber limits the extension of the plume; thus, the height of the chamber (H) is considered as the characteristic length of the problem. All gas properties are determined at an average temperature ($T = (T_a + T_g)/2$) [14], where T_g is obtained from the thermocouple readings. A characteristic value for U_B is calculated for all experimental conditions and found to be of the order of 0.1 m/s. This value is comparable to the forced flow velocity, which ranges from 0.03 to 0.3 m/s.

Data correlation

The value of tan θ is measured from the video images for normal and microgravity experiments. The results are compared to those predicted by Eq. (1) and presented in Fig. 5. In microgravity conditions, U_B is neglected and $U_A = U_\infty$ (Eq. (2)). For normal and microgravity, Eq. (1) predicts very well the location of the flame for tan $\theta < 0.7$. For tan $\theta > 0.7$, the flame establishes in the fuel-rich zone; this deviation from the stoichiometric line might be due to the effect of the chamber ceiling on the flow.

For equal air-forced flow velocities and fuel injection velocities, flames will be significantly closer to the burner in normal gravity. When transition to microgravity occurs, the flame, located at the stoichiometric line corresponding to $U_A = U_\infty + U_B$, is left in the fuel-rich zone; thus, the flame colour changes towards the yellow (characteristic of a fuel-rich flame). The flame then starts moving towards the oxidiser (θ increases), and the colour changes back to blue (characteristic of a stoichiometric flame). Finally, the flame establishes in the stoichiometric line corresponding to $U_B \approx 0$.

Flame Extinction:

A phenomenological explanation of the extinction process in terms of a critical Damköhler number is provided in the work of Kodama et al. [9]. The Damköhler number is defined as the ratio between the flow (residence) time to the chemical time for the reaction. For a fixed oxygen concentration (fixed chemical time), as the flow velocity increases, the flow time decreases, and consequently, so does the Damköhler number. If the injection velocity increases, the standoff distance increases, and heat losses from the flame to the burner decrease [11]. It can be concluded that increasing U_∞ or decreasing V_F will favour extinction.

Depending on the magnitudes of U_∞ and V_F, the flame will be more sensitive to one of the two mechanisms explained above. In normal gravity, if U_∞ is small, the residence time will be determined by U_B; therefore, it will be almost constant. Under these conditions, extinction will be strongly dependent on V_F. As the magnitude of U_∞ increases and becomes comparable to U_B, extinction will depend on both U_∞ and V_F. Finally, for large values of U_∞, U_B becomes small compared to U_∞; therefore, extinction will be dependent mainly on the magnitude of U_∞.

For a fixed value of U_∞, the total air flow velocity (U_A) is smaller in microgravity; therefore, for each value of V_F, a higher forced flow velocity (U_∞) is needed to extinguish the flame. The difference between normal and microgravity extinction limits will decrease as the magnitude of U_B becomes small compared to that of the forced flow ($U_\infty > 0.2$ m/s).

In normal gravity, extinction was also observed for $U_\infty < 0.03$ m/s; for these fuel and oxidiser velocities, the plume region appeared very close to the leading edge of the burner; the flame establishes almost vertically and downstream of the flame front. Fuel is injected and not burnt; thus, fuel accumulates and extinction follows.

Deviations from the Boundary Layer Regime:

For all experimental conditions, fuel injection velocities are of the same order as diffusion velocities and approximately 50 times smaller than the oxidiser-forced flow velocity. Therefore, a boundary layer is expected to be formed only on top of the burner, and the influence of the air flowing through the sides of the burner is supposed to be negligible.

The video images show a very different scenario. To explain the observations, a new co-ordinate system of (x'-y') anchored to the stoichiometric line is defined (Fig. 3). The flame thickness or characteristic length (ε) is obtained by equating forced convection and diffusion. Forced convection is characterised by

the summation of the y' components of both fuel and oxidiser velocities. Therefore, the expression obtained for the flame thickness is as follows:

$$\varepsilon = \frac{a}{U_A \sin\theta + V_F \cos\theta} = \frac{a}{U_{y'}}.$$

The characteristic reaction time (τ) is defined as the time the fuel and oxidiser need to diffuse in stoichiometric proportions through ε. Therefore,

$$\tau = \frac{\phi\varepsilon^2}{DY_{O,i}}.$$

For all values of fuel and oxidiser velocities studied, $\varepsilon \approx 1$ mm and $\tau \approx 0.15$ s. The reaction between the y'-components of the fuel and oxidiser will then occur in a zone of approximately 1 mm in a period of approximately 0.15 s. In the x' direction, the oxidiser and fuel separate from each other with a velocity given by

$$U_{x'} = U_A \cos\theta - V_F \sin\theta$$

the product of τ and $U_{x'}$ provides a quantitative idea of how much fuel and oxidiser have separated before the reaction can occur. If $\varepsilon/\tau U_{x'} > 1$, the fuel and oxidiser arriving parallel to the x' axis will react; if $\varepsilon/\tau U_{x'} < 1$, the oxidiser will escape before being able to react with the fuel. For all experimental conditions studied $\varepsilon/\tau U_{x'} << 1$; therefore, the oxidiser escapes and fuel accumulates at the stoichiometric line.

The fuel will be convected upstream with a velocity $V_F \sin\theta$, which is comparable to that of diffusion in the z direction; therefore, the accumulated fuel is expected to react with the oxidiser coming from the sides of the burner, generating the previously described reacting zones. It is important to notice that fuel accumulation is independent of U_∞; thus, expanding reactive zones will occur for all values of U_∞. The extent of the accumulation zone is determined by the distance the oxidiser can be convected along the stoichiometric line before it can diffuse a distance ε; therefore, it can be approximately determined by

$$l = (U_A \cos\theta)\tau.$$

The value of l is proportional to U_∞ and ranges from 10 mm, for the smallest air flow velocities, to 50 mm, for the largest air flow velocities studied. The orders of magnitude for l agree well with the experimental observations.

Expanding reactive zones were not observed in normal gravity; oxidiser entrainment by the plume does not allow for diffusion to be the controlling mass transport mechanism in the z direction. Buoyantly induced air flow transports the unburned gas towards the plane of symmetry and then upstream towards the plume. The gas will partially react while convected and complete its oxidation at the plume. A study of the exact mechanisms of local air entrainment induced by buoyancy and thermal gradients at the flame will require local velocity and temperature measurements that escape the possibilities of microgravity facilities and the purpose of this work.

Concluding Remarks

A diffusion flame established over a flat plate porous burner in the presence of a forced flow parallel to the surface was experimentally studied. Experiments conducted in normal and microgravity environments provided further understanding on the effect of gravity on mass transport in a diffusion flame.

In the absence of buoyancy, the flame establishes in the line where the fuel and oxidiser are delivered in stoichiometric proportions. In microgravity, the assumptions of stationary flow and no mass transport in the direction perpendicular to the forced flow plane are no longer valid. Fuel is accumulated in the stoichiometric line until it reacts with the oxidiser transported by diffusion from the sides of the burner. This results in an expanding reactive zone that appears periodically at the stoichiometric line.

In normal gravity, the flame can be divided in a plume region and a boundary layer region. Thermally induced density gradients in the plume region result in the establishment of a recirculation zone upstream of the plume. The magnitude of the entrained velocity is comparable to the air-forced flow velocity for the entire experimental range.

For a constant fuel injection velocity, flames in microgravity extinguish at air-forced flow velocities significantly higher to those in normal gravity due to the previously mentioned entrainment velocity induced by the plume. This observation is of capital importance in any attempt to determine fire risks in spacecraft.

The experimental limitations imposed by microgravity facilities do not allow for better quantitative information on the flame. Due to the lack of quantitative information, the theoretical analysis conducted on the flame only attempted to obtain orders of magnitude that were in very good agreement with the experimental results.

Nomenclature

D	diffusion coefficient
g	gravitational acceleration ($g_o = 9.81$ m/s^2)
$Gr_x = \left(\frac{2T_a}{T_a + T_g}\right)\frac{g \tan\theta \cdot x^3}{\nu^2}$	modified Grashof number

H	chamber height
l	characteristic length of the accumulation zone
$\mathrm{Le} = a/D$	Lewis number (Le = 1)
$\mathrm{Pr} = \nu/a$	Prandtl number (Pr = 1)
Ra	Rayleigh number
$\mathrm{Re}_x = \dfrac{U_\infty x}{\nu}$	Reynolds number
$\mathrm{Sc} = \nu/D$	Schmidt number (Sc = 1)
t	time
$T = (T_a + T_g)/2$	average temperature
T_a	ambient temperature ($T_a \approx$ 300 K)
T_g	average temperature of hot gases ($T_g \approx$ 1100 K)
U	velocity (x direction)
V	velocity (y direction)
$\dot{w}$	reaction rate
x	coordinate parallel to the plate
x'	coordinate parallel to the stoichiometric line
y	coordinate perpendicular to the plate
y'	coordinate perpendicular to the stoichiometric line
Y	mass fraction

Greek symbols:

α	thermal diffusivity ($\alpha = 6.63 \times 10^{-5}$ m^2/s)
δ	characteristic length scale
δ_M	momentum boundary layer thickness
δ_S	standoff distance
ε	characteristic flame thickness
ϕ	stoichiometric ratio ($\phi = 3.5$)
μg	microgravity
ν	kinematic viscosity
ρ	air density ($\rho = 0.503$ Kg/m^3)
θ	angle between the stoichiometric line and the x-axis
τ	characteristic reaction time
ξ	nondimensional parameter

subscripts:

A	air
B	buoyant
F	fuel
i	initial
O	oxidiser
x'	x' direction
y'	y' direction
∞	free stream

Acknowledgments

This research is sponsored by the Centre National d'Etudes Spatiales and by the European Space Agency. Special thanks to Dr. O. Minster (ESA), Dr. B. Zappoli (CNES), and Dipl.-Ing. C. Eigenbrod (ZARM) for their support. The encouragement and numerous technical discussions with Professor Carlos Fernandez-Pello are much appreciated. The authors also wish to thank B. Sztal, J. Baillargeat, and the staff at ZARM and CEV for their invaluable technical support.

REFERENCES

1. Emmons, H., *Z. Angew. Math. Mech.* 36:60–71 (1956).
2. Williams, F. A., *Combustion Theory,* 2nd ed., The Benjamin/Cummings Publishing Company Inc., Menlo Park, CA, 1985, pp. 485–519.
3. Drysdale, D., *An Introduction to Fire Dynamics,* John Wiley and Sons, New York, 1985, pp. 226–252.
4. Hirano, T., Iwai, K., and Kanno, Y., *Astronautica Acta* 17:811–818 (1972).
5. Hirano, T., and Kanno, Y., *Fourteenth Symposium (International) on Combustion,* The Combustion Institute, Pittsburgh, 1973, pp. 391–398.
6. Ramachandra, A., and Raghunandan, B. N., *Combust. Sci. Technol.* 36:109–121 (1984).
7. Fernandez-Pello, A. C., and Pagni, P. J., *Mixed Convective Burning of a Vertical Fuel Surface,* ASME-JSME Thermal Engineering Joint Conference Proceedings, Honolulu, 1983, Vol. 4.
8. Pagni, P. J., *Fire Safety J.* 3:273–285 (1981).
9. Kodama, H., Miyasaka, K., and Fernandez-Pello, A. C., *Combust. Sci. Technol.* 53:37–50 (1987).
10. Mao, C. P., Kodama, H., and Fernandez-Pello, A. C., *Combust. Flame* 57:209–236 (1984).
11. Bonneau, L., Joulain, P., Most, J. M., and Fernandez-Pello, A. C., *Flat Plate Diffusion Flame Combustion in Micro-gravity,* AIAA-93-0826 (1993).
12. Lavid, M., and Berlad, A. L., *Sixteenth Symposium (International) on Combustion,* The Combustion Institute, Pittsburgh, 1977, pp. 1557–1568.
13. Kuo, K. K., *Principles of Combustion,* John Wiley and Sons., New York, 1986, pp. 347–369.
14. Chen, C. H., and T'ien, J. S., *Combust. Sci. Technol.* 50:283–306 (1986).
15. Apte, V. B., Bilger, R. W., Green, A. R., and Quintiere, J. G., *Combust. Flame* 85:169–184 (1991).
16. Bejan, A., *Convection Heat Transfer,* John Wiley and Sons., New York, 1984, pp. 109–201.

COMMENT

Howard D. Ross, NASA Lewis Research Center, USA. How were the cold flow velocities (both fuel and air) characterized experimentally, particularly near the leading edge of the plate?

Author's Reply. Two-dimensional velocity measurements were conducted by using laser-Doppler velocimetry. All measurements were done with cold flow, and in most cases the ethane was substituted by air to avoid unburned fuel mixtures. The measurements close to the floor of the chamber are not of extreme accuracy since the geometry of the chamber and seeding problems did not allow for high-quality measurements. The results show that, upstream of the leading edge, the oxidiser velocity remains almost constant through the entire chamber height and, in the same manner, the fuel injection velocity is also constant along the entire burner. All measurements were conducted in normal gravity, and the results through conclusive, are still preliminary and need further verification.

Twenty-Fifth Symposium (International) on Combustion/The Combustion Institute, 1994/pp. 1711–1718

ON BURNER-STABILIZED CYLINDRICAL PREMIXED FLAMES IN MICROGRAVITY

J. A. ENG, C. K. LAW AND D. L. ZHU
Department of Mechanical and Aerospace Engineering
Princeton University
Princeton, NJ 08544, USA

The structure and response of the curved but unstretched cylindrically symmetric one-dimensional premixed flame generated by a cylindrical porous burner has been studied using (1) activation energy asymptotics with one-step reaction and constant properties, (2) numerical computation with detailed chemistry and transport, and (3) drop-tower microgravity experimentation. The study emphasizes the relative importance of heat loss (to the burner surface) vs flow divergence as the dominant mechanism for flame stabilization, the possibility of establishing a one-dimensional, adiabatic, unstretched, premixed flame in microgravity, the influence of curvature on the upstream and downstream burning rates of the flame, and the relation of these burning rates to those of the inherently nonadiabatic flat-burner flame as well as the freely propagating adiabatic planar flame. Results show that, with increasing flow discharge rate, the dominant flame stabilization mechanism changes from heat loss to flow divergence, hence demonstrating the feasibility of establishing a freely standing, adiabatic, one-dimensional, unstretched flame. It is further shown that, in this adiabatic, divergence-stabilized regime in which the burner discharge flux exceeds that of the adiabatic planar flame, the downstream burning flux is equal to the (constant) burning flux of the adiabatic planar flame while the upstream burning flux exceeds it, and the upstream burning velocity exhibits a maximum with increasing discharge rate. Based on the property of the downstream burning flux, it is also proposed that the laminar burning velocity of a combustible can be readily determined from the experimental values of the burner discharge rate and flame radius. Microgravity results on the flame radius compare favorably with the computed values, while the corresponding laminar burning velocity also agrees well with that obtained from independent numerical computation.

Introduction

The configurational simplicity of the stationary one-dimensional flames renders them intrinsically attractive for fundamental flame structure studies. The possibility and fidelity of studies of such flames on earth, however, have been severely restricted by the unidirectional nature of the gravity vector. To demonstrate these complications, let us consider the stationary, one-dimensional, premixed flame stabilized over the flat-flame burner (Fig. 1a). This flame is inherently nonadiabatic because it is stabilized through heat loss to the burner surface. Furthermore, radicals generated at the flame potentially can also diffuse back to the burner surface and become deactivated. Such loss processes can introduce uncertainties into the study of flame chemistry by using the flat-burner flame. Furthermore, while a nearly adiabatic, planar, quasi-one-dimensional flame can be produced by using the counterflow burner (Fig. 1b), where two symmetrical planar flames are formed in the two-dimensional stagnation field of two opposed jets of premixed gas, the flame is aerodynamically strained by the nonuniform flow field. The associated flame stretch effects can significantly modify the flame properties from the idealized, freely propagating, adiabatic, one-dimensional planar flame in the doubly infinite domain [1].

A class of one-dimensional premixed flames that has the potential of eliminating heat loss and stretch effects is the burner-generated cylindrical and spherical flames, where a premixed gas flows through a porous cylindrical or spherical burner, and the resulting flame is formed at some distance from the burner, as shown in Figs. 1c and 1d. To demonstrate that such flames are curved but not stretched, we consider the general expression for the stretch rate experienced by a flame surface [1,2],

$$\kappa = \frac{1}{A}\frac{dA}{dt} = -\mathbf{n}\cdot\nabla\times(\mathbf{u}_f\times\mathbf{n}) + (\mathbf{s}_f\cdot\mathbf{n})(\nabla\cdot\mathbf{n}) \quad (1)$$

where A is the area of an infinitesimal element of the flame surface, $\mathbf{u}_f$ the flow velocity evaluated at the flame, $\mathbf{s}_f$ the velocity of the flame, and $\mathbf{n}$ the unit normal vector of the surface. Equation (1) shows that, since the flame is stationary ($\mathbf{s}_f \equiv 0$), and the

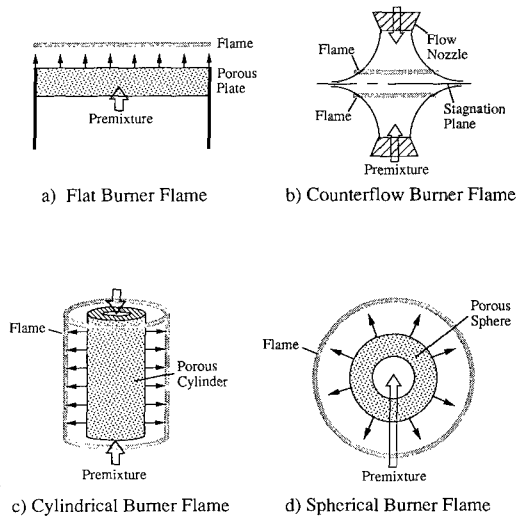

FIG. 1. Various one-dimensional flame configurations: (a) flat-burner flame: planar, nonadiabatic, unstretched; (b) counterflow-burner flame: planar, adiabatic, stretched; (c) and (d) cylindrical and spherical flame: curved, nonadiabatic/adiabatic, unstretched.

flow is normal to the flame surface ($\mathbf{u}_f \times \mathbf{n} \equiv 0$), the stretch rate vanishes identically. Furthermore, while such a flame can be stabilized by heat loss to the burner, the divergent nature of the flow provides an additional stabilization mechanism. That is, as the flow rate is continuously increased, the flame recedes from the burner, and heat loss can be eventually reduced to become negligible as compared with the heat generated at the flame. At this point, the flame temperature is expected to be close to the adiabatic flame temperature. Further increase in the flow rate is then accommodated by an increase in the flame standoff distance to a position where the flame speed again balances the flow velocity. Thus, the cylindrical/spherical geometry offers a unique advantage for the study of adiabatic, one-dimensional, stretch-free flames that is not present in other commonly used experimental systems. Such flames, however, can only be established, and studied, in a microgravity environment because of the distorting nature of the buoyant flow under normal gravity conditions.

In view of the above considerations, an experimental and theoretical program on cylindrical and spherical premixed flames in microgravity has been initiated. We are especially interested in (1) assessing heat loss vs flow divergence as the dominant stabilization mechanism, (2) understanding the effects of flame curvature on the burning intensity, and (3) determining the laminar burning velocity by using this configuration. In the present study, we have performed analytical, computational, and microgravity-experimental investigations of the cylindrical flame. The results are presented in the following sections.

For previous studies on spherical [3–6] and cylindrical [3,7] flames, either burner-stabilized [3,7] or supported by point and line sources [4,6,7], we note the approximate solutions of the gross flame properties [4,5,6], activation energy analysis of flame-front instability [7], and experimental observation of the near-burner flames [3]. Since the present approach and results are quite different from these earlier works, we simply refer the reader to their sources.

Asymptotic Analysis and Qualitative Behavior

The problem analyzed is shown in Fig. 1c. Here a premixture of temperature T_u and mass flow rate m, consisting of a deficient, rate-limiting reactant F (fuel) with mass fraction $Y_{F,u}$ issues from a unit-length, internally cooled porous cylinder that has a radius r_s and surface temperature T_s. From continuity, the mass flow rate $m = 2\pi r\rho u$ is a conserved quantity along the radial distance r, where u is the r velocity and the subscript s designates the burner surface. Upon ignition, a cylindrical flame is established concentric with the burner, with the thin reaction zone located at r_f and the preheat zone extending from the burner surface to r_f, where the subscript f designates the reaction zone. From the experimental point of view, the parameter that can be independently and conveniently controlled is m. Thus, for a given m, the cooling rate of the burner and hence the heat loss rate from the flame, Q_s, can be adjusted to achieve a constant T_s. The flame temperature T_f and flame standoff location r_f will also adjust accordingly for the given m and T_s.

With conventional constant property assumptions, the nondimensional conservation equations for temperature T and mass fraction Y_F of F are, respectively,

$$\tilde{m}\frac{d}{d\tilde{r}}(\tilde{T} + \tilde{Y}_F) - \frac{d}{d\tilde{r}}\left[\tilde{r}\frac{d}{d\tilde{r}}\left(\tilde{T} + \frac{\tilde{Y}_F}{Le}\right)\right] = 0 \quad (2)$$

$$\tilde{m}\frac{d\tilde{T}}{d\tilde{r}} - \frac{d}{d\tilde{r}}\left(\tilde{r}\frac{d\tilde{T}}{d\tilde{r}}\right) = \tilde{w} \quad (3)$$

where

$$\tilde{w} = (Da)\tilde{r}\tilde{\rho}^2\tilde{Y}_F \exp(-\tilde{T}_a/\tilde{T}) \quad (4)$$

is the nondimensional reaction rate for an assumed second-order reaction,

$$Da = \left(\frac{BY_{O,u}}{W_O}\right)\left(\frac{\rho_b^2 r_s^2}{\lambda/c_p}\right) \quad (5)$$

is the Damköhler number, Le is the Lewis number, $\tilde{m} = m/(2\pi\lambda/c_p)$, $\tilde{T} = c_pT/Y_{F,u}q_c$, $\tilde{Y}_F = Y_F/Y_{F,u}$, $\tilde{\rho} = \rho/\rho_b$, $\tilde{r} = r/r_s$, T_a is the activation temperature, ρ the density, Y_O the mass fraction of the abundant species, λ the thermal conductivity, c_p the specific heat, q_c the chemical heat release per unit mass of fuel, and B the frequency factor. The subscripts u and b respectively designate the unburnt and burnt states of the flame. We shall also assume that there is no downstream heat loss such that $T_f \equiv T_b$.

The boundary conditions are

$$\tilde{r} = 1: \tilde{T} = \tilde{T}_s \tag{6}$$

$$\tilde{m}\tilde{Y}_F - \frac{1}{Le}\frac{d\tilde{Y}_F}{d\tilde{r}} = \tilde{m} \tag{7}$$

$$\tilde{r} \to \infty: \tilde{T} = \tilde{T}_b \tag{8}$$

$$\tilde{Y}_F = 0. \tag{9}$$

Thus, for given $\tilde{m}$ and $\tilde{T}_s$, one can solve for the species and temperature profiles as well as the flame response parameters $\tilde{T}_f$, $\tilde{r}_f$ and the specific heat loss per unit length of burner, q_s, which is defined by

$$\left(\frac{d\tilde{T}}{d\tilde{r}}\right)_{\tilde{r}=1} = \tilde{m}\tilde{q}_s \tag{10}$$

where $\tilde{q}_s = [r_s/(Y_{F,u}q_c)]q_s$.

A straightforward application of activation energy asymptotics yields the following flame responses:

$$\left(\frac{\tilde{m}}{\tilde{r}_f}\right)^2 = Le\,\Delta \tag{11}$$

$$\tilde{T}_f = (\tilde{T}_f^\circ + \tilde{T}_s - \tilde{T}_u) - \tilde{q}_s \tag{12}$$

$$\tilde{q}_s = \tilde{r}_f^{-\tilde{m}} \tag{13}$$

with the leading order temperature ($\tilde{T}_0$) and species concentration ($\tilde{Y}_{F,0}$) profiles respectively given by

$$\tilde{r} \le \tilde{r}_f: \frac{(\tilde{T}_0 - \tilde{T}_s)}{(\tilde{T}_f - \tilde{T}_s)} = \frac{(\tilde{r}^{\tilde{m}} - 1)}{(\tilde{r}_f^{\tilde{m}} - 1)} \tag{14}$$

$$(1 - \tilde{Y}_{F,0}) = \frac{\tilde{r}^{Le\tilde{m}}}{\tilde{r}_f^{Le\tilde{m}}} \tag{15}$$

$$\tilde{r} \ge \tilde{r}_f: \tilde{T}_0 = \tilde{T}_f = \tilde{T}_b \tag{16}$$

$$\tilde{Y}_{F,0} = 0 \tag{17}$$

where $\Delta(\tilde{T}_f) = 2Da(\tilde{T}_f^2/\tilde{T}_a)^2\exp(-\tilde{T}_a/\tilde{T}_f)$ is a reduced Damköhler number, $\tilde{T}_f^\circ$ the adiabatic flame temperature, and the superscript "°" designates the adiabatic, one-dimensional planar flame.

For large values of $\tilde{r}_f$, the above solution approaches the adiabatic limit, with $\tilde{q}_s \to 0$, $\tilde{T}_f \to \tilde{T}_f^\circ$, and $\Delta(\tilde{T}_f) \to \Delta(\tilde{T}_f^\circ)$, which is a constant. The last relation, when interpreted in the context of Eq. (11), implies that $(\tilde{m}/\tilde{r}_f)$ becomes a property of the mixture in this limit, being independent of the burning rate $\tilde{m}$ and the flame curvature that is proportional to $\tilde{r}_f^{-1}$. This result has the following implications.

First, since $\tilde{r}_f \sim \tilde{m}$, the flame accommodates an increase in the mass flow rate from the burner by moving to a larger radial distance and hence attaining a larger flame surface area. The flame is therefore stabilized through flow divergence. This stabilization mechanism and hence flexibility do not exist for the flat-burner flame, which loses its planar nature when the burner discharge rate exceeds that of the adiabatic value.

Second, if we evaluate $\tilde{m}$ at the reaction zone, then $(\tilde{m}/\tilde{r}_f) = (\rho_b u_f r_s)/(\lambda/c_p)$ is simply a nondimensional mass flux at $\tilde{r}_f$, say $\tilde{f}_f$, where $\tilde{f} = fr_s/(\lambda/c_p)$ is the nondimensional f. Furthermore, since this quantity is independent of $\tilde{r}_f$, and hence the flame curvature in the adiabatic limit, it must be equal to the (constant) mass flux of the adiabatic planar flame, $\tilde{f}^\circ = \tilde{f}_u^\circ = \tilde{f}_f^\circ$, for which r_s can be considered as an arbitrary length for nondimensionalization. We therefore have the following sequence of identities in the adiabatic limit:

$$\left(\frac{\tilde{m}}{\tilde{r}_f}\right)^2 = (\tilde{f}_f)^2 = (\tilde{f}^\circ)^2 = Le\,\Delta. \tag{18}$$

The invariance of $\tilde{f}_f$ to flame radius variations provides a simple relation for an experimental determination of the laminar burning velocity of the one-dimensional planar flame. That is, since m ($= 2\pi r_f\rho_b u_f$) is given while the flame radius can also be easily measured photographically, the laminar burning flux is simply

$$f^\circ = \frac{m}{2\pi r_f}. \tag{19}$$

Furthermore, since $f^\circ = f_u^\circ = \rho_u u_u^\circ$, the laminar burning velocity is then given by $s_u^\circ = u_u^\circ = f^\circ/\rho_u$. Our experimental result agrees well with Eq. (19), as will be shown later.

Third, since $f_f = f_u^\circ$ while $f_f < f_u$ because of flow divergence, we must have $f_u^\circ < f_u$. Thus, if f_u is identified as the flame propagation rate relative to the freestream, then the concave nature of the present cylindrical flame causes it to have a higher flux and hence propagation rate than the planar flame. This is the same curvature effect that causes the tip of a unity Lewis number Bunsen flame to have a higher burning velocity than its shoulder.

The characteristics of the cylindrical flame can be better demonstrated with the following quantities:

$$\hat{m}_s^2 = \left(\frac{\tilde{m}}{\tilde{m}_s^\circ}\right)^2$$

$$= (\tilde{r}_f)^2\left(\frac{\tilde{T}_f}{\tilde{T}_{\mathrm{ad}}}\right)^4 \exp\left[\tilde{T}_a\left(\frac{1}{\tilde{T}_{\mathrm{ad}}} - \frac{1}{\tilde{T}_f}\right)\right] \quad (20)$$

$$\hat{Q}_s = \left(\frac{\tilde{m}}{\tilde{m}_s^\circ}\right)\tilde{q}_s = \hat{m}_s \tilde{r}_f^{-\tilde{m}} \quad (21)$$

where $\hat{m}_s$ is the ratio of the mass burning rate of the cylindrical flame to that of the adiabatic planar flame with the same cylinder surface area, or $m_s^\circ = 2\pi r_s \rho_s s_u^\circ$. We also define a flame standoff distance $d_f = r_f - r_s$, with $r_s \equiv 0$ for the planar case, and nondimensionalize it by the laminar flame thickness $\delta^\circ = (\lambda/c_p)/f^\circ$ such that $\hat{d}_f = d_f/\delta^\circ$.

For comparison, we note that, for the nonadiabatic planar flame stabilized over a flat burner [8,9,10], $\hat{m}_s = \hat{f} = f/f^\circ$ such that

$$\hat{m}_s^2 = \left(\frac{\tilde{T}_f}{\tilde{T}_{\mathrm{ad}}}\right)^4 \exp\left[\tilde{T}_a\left(\frac{1}{\tilde{T}_{\mathrm{ad}}} - \frac{1}{\tilde{T}_f}\right)\right] \quad (22)$$

$$\hat{Q}_s = \hat{m}_s \exp(-\hat{m}_s \hat{d}_f) \quad (23)$$

while Eq. (12) still holds for the relation between $\tilde{T}_f$ and $\tilde{q}_s$.

Figure 2 shows $\hat{Q}_s$, $\hat{d}_f$, and $\tilde{T}_f/\tilde{T}_f^\circ$ as functions of $\hat{m}_s$ for the planar case as well as the cylindrical case with $r_s = 0.5$ and 5 cm. The solutions were generated with $T_u = T_s = 300$ K, $T_f^\circ = 1800$ K, $T_a = 20{,}000$ K, $f^\circ = 0.022$ g/cm^2-s, and $(\lambda/c_p) = 0.001$ g/cm-s. It is seen that both the planar and cylindrical cases yield a dual solution behavior in that there are two values of the mass burning rate $\hat{m}_s$ for either a given heat loss rate $\hat{Q}_s$ or a given flame standoff distance $\hat{d}_f$. The behavior for the planar case is a well-known observation [11,12,13] that has also been recently explained [9,10] by noting that, by taking $\hat{m}$ as the independent parameter with $\tilde{T}_s$ fixed, the flame responses in terms of $\hat{Q}_s$ and $\hat{d}_f$ are actually unique. By similar reasoning, we then expect that the responses of the cylindrical flame are also unique when $\hat{m}_s$ is the independent parameter.

For the cylindrical flame, it is seen that, when the cylinder radius is large (5 cm), the flame behavior follows closely that of the planar flame up to $\hat{m}_s \approx 1$, as expected. In this regime, heat loss is the dominant flame stabilization mechanism. For $\hat{m}_s > 1$, the planar flame does not exist, while the cylindrical flame can still be maintained because of flow divergence. In this regime, the flame is practically adiabatic, with $\hat{Q}_s \approx 0$ and $\tilde{T}_f \approx \tilde{T}_f^\circ$. For smaller cylinder radius (0.5 cm), the response of the cylindrical flame deviates significantly from that of the planar flame. The flame is almost adiabatic and is stabilized by flow divergence at higher values of $\hat{m}_s$.

In Fig. 3, we compare the mass burning rate of the cylindrical flame, m, with that of the adiabatic planar flame that has the same surface area as the cylindrical flame ($m_f^\circ = 2\pi r_f \rho_u s_u^\circ$), that is, $\hat{m}_f = m/m_f^\circ$, for the $r_s = 0.5$ cm case. It is seen that $\hat{m}_f < 1$ for $\hat{m}_s \lesssim 1.5$, but $\hat{m}_f \to 1$ for larger values of $\hat{m}_s$. This demonstrates that the mass flux in the reaction zone approaches that of the adiabatic planar flame as the flame becomes near adiabatic.

To identify the influence of curvature on the burning flux at the upstream boundary of the flame, in Fig. 3 we have also plotted $\hat{f}_u = f_u/f_u^\circ$, with the unburnt state evaluated at the location of the 1% temperature rise from the freestream temperature according to the suggestion of Tien and Matalon [14]. The results are quite insensitive to the actual state selected as long as it is close to the ambient state. It is seen that, with increasing $\hat{m}_s$, $\hat{f}_u$ initially increases

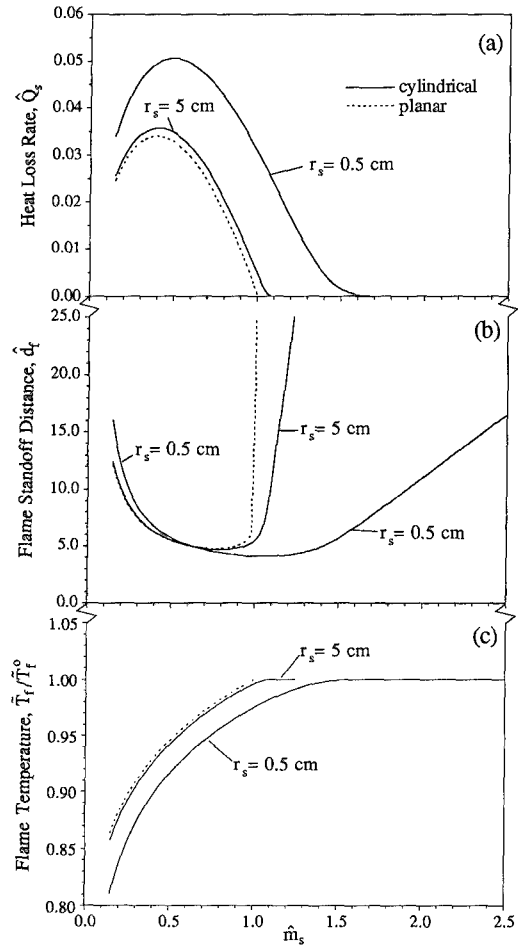

FIG. 2. (a) Heat loss rate to the burner surface, (b) flame standoff distance, and (c) flame temperature as functions of the flow discharge rate for the flat burner and the cylindrical burner with different radii.

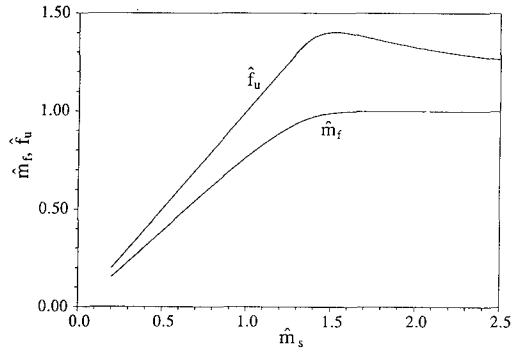

FIG. 3. Normalized mass burning rate and upstream burning flux for the cylindrical flame stabilized by a cylindrical burner with 0.5-cm radius.

to values of $\hat{f}_u > 1$. It then decreases and eventually approaches the adiabatic, planar case of $\hat{f}_u = 1$ as $\hat{r}_f \to \infty$. The important point to note is that f_u can exceed f_u°, in agreement with the previous discussion of curvature-enhanced burning flux and hence burning velocity.

Microgravity Experimentation

The experimental apparatus for the cylindrical flame is shown in Fig. 4. The cylindrical burner was made of a porous bronze tube with 5-μm pore size, 1.25-cm diameter, and 3.76-cm active length. The thickness of the porous wall is 4.7 mm. Since uniformity of the flow through the porous wall depends on the pressure differential across it, the reactant mixture was supplied from both ends of the burner tube so as to minimize the internal pressure gradient in the axial direction of the cylinder. Furthermore, stainless steel tubes with small holes at various locations were positioned inside the burner to further even the axial pressure distribution. A cross-sectional view of the burner with the internal tubes is shown in the inset of Fig. 4. The axial pressure distribution was measured (under normal gravity conditions) by drilling small holes in the porous wall and connecting water manometers to the pressure taps. For the best achieved design of the number and placement of the holes in internal tubes at a typical flow rate, the inlet gage pressure to the burner was 60 cm water and the axial pressure variation was ± 2 cm water, a 10% variation.

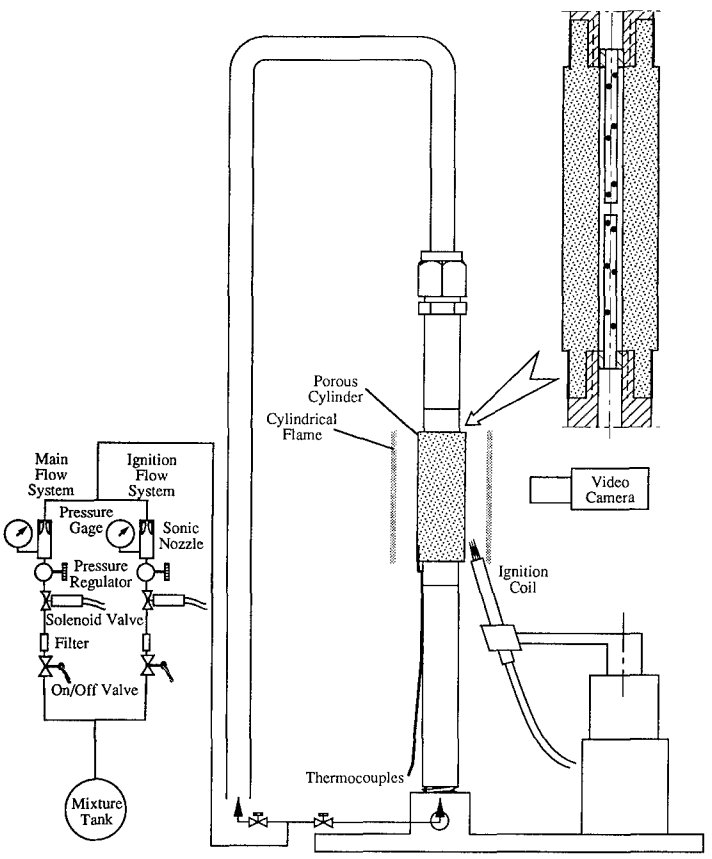

FIG. 4. Schematic of the experimental apparatus. Inset is the cross section of the cylindrical burner.

Because of the small burner size and the limited duration of the microgravity experiments, no cooling was used for the burner. A thermocouple was inserted inside the burner wall to record the burner temperature. A hot wire mounted on a rotary solenoid was used to ignite the mixture. Experiments were performed under microgravity conditions at the NASA-Lewis 2.2-s drop tower. Mass flow rates were measured by using sonic flow nozzles whose upstream pressures were recorded by using pressure transducers. A video camera was used to record the flame shape and standoff distance.

Computational Simulation

The experimental situation was numerically simulated by using the Sandia premixed flame code [15], with modifications to ensure strict mass conservation in the divergent flow field. The program solves the governing equations of mass, energy, and species using finite-difference approximation, allowing for detailed chemical kinetics, multicomponent diffusion, and variable thermal properties. The chemical mechanism used was that developed by Egolfopoulos et al. [16], which has 30 species and 153 reaction steps.

The independent variable for the burner-stabilized flame is the mass flow rate m. The necessary boundary conditions are the burner surface temperature, T_s, and the reactant mixture mass flux fractions. The boundary conditions imposed on the product side are vanishing gradients for species and temperature, dY_i/dr and dT/dr. The program solves the governing equations to determine the temperature profile through the flame, from which the flame location and heat loss to the burner can be found.

Experimental and Computational Results

A mixture of $CH_4 + 2O_2 + 7.52N_2 + 5.665He$, with an effective Lewis number of 1.88, was used for the cylindrical flame experiments. Helium was added to enhance flame-front stability. There are two causes for the enhanced flame stability with helium addition. First, the effective Lewis number of the mixture increases, which reduces the thermal-diffusional instability. Second, the adiabatic flame temperature is reduced, which reduces the density jump across the flame and the propensity to develop the hydrodynamic (Landau) instability. For this mixture, the adiabatic flame temperature for the unburned mixture temperature of 300 K is 1885 K, and the calculated laminar flame speed is 20.8 cm/s, which corresponds to a mass burning flux of 0.016 g/cm^2-s.

Figure 5 compares the calculated and measured flame standoff distance as a function of the normalized mass flow $\hat{m}_s$. The inset shows a typical recorded flame configuration, which exhibits some large-scale,

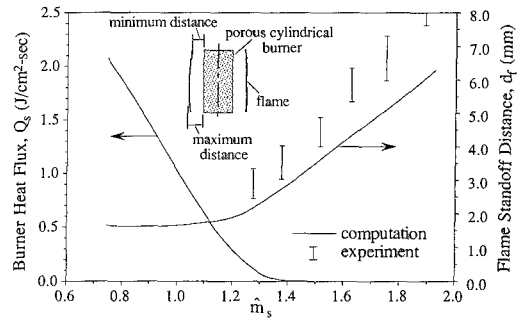

FIG. 5. Computed heat loss flux and flame standoff distance, and experimental flame standoff distance, as functions of the discharge rate. Inset is a representative experimental flame configuration.

weak wrinkling. This wrinkling is believed to be caused by the pressure variation in the burner and leads to a variable standoff distance of $\pm 15\%$ in the axial direction. The spread in the experimental data therefore represents the extent of flame nonuniformity as measured by the minimum and maximum standoff distances. The flame location for the numerical results is taken as that of the maximum CH radical concentration, since this species is chiefly responsible for the luminosity of the flame and assumes its maximum concentration in the active reaction zone of the flame. The heat loss to the burner is also presented for the calculated results and shows that, around a normalized flow rate of $\hat{m}_s \sim 1.4$, the heat loss is essentially zero. At this point, the stabilization mechanism has changed from heat loss to flow divergence. The figure also shows that all the microgravity data are in the regime where the flame is stabilized by flow divergence. This is further substantiated by the experimental result that the thermocouple temperature basically remained at the ambient value during the experiment. The comparison shows that the flame is situated further away than calculated, with about 1–2-mm differences. Overall, the experimental and computational results agree quite well, at least qualitatively, considering the difficulties usually associated with microgravity experimentation.

Figure 6 compares the calculated and observed mass flux through the reaction zone. As discussed, the calculated result in the adiabatic limit should be close to the independently calculated laminar burning flux for the adiabatic planar flame. Exact agreement is not expected because, while the calculated result is a constant for the planar flame, it depends on the present choice of the maximum CH radical location as that of the reaction zone for the cylindrical flame. The uncertainty, however, is not expected to be large because the flame thickness is much smaller than its standoff distance. It is seen that the calculated laminar mass flux attains a value of about

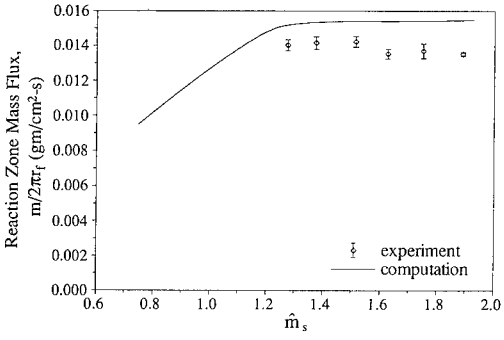

FIG. 6. Computed and reaction zone mass flux as function of the discharge rate.

f_f = 0.0156 g/cm^2-s in the divergence-stabilized regime, which compares very favorably with the independently calculated value of f° = 0.016 g/cm^2-s for the adiabatic planar flame. Figure 6 further shows that the experimentally measured values also agree well with the computed results, being slightly larger. This demonstrates the feasibility of determining the laminar burning flux, and hence the laminar burning velocity, by using the cylindrical/spherical flame as proposed herein.

The difference between the calculated and measured values for the flame location and burning flux can be attributed to the small influence of gas-phase heat loss in the experiment, which is not included in the calculations. Perhaps most importantly, while the calculation assumes an adiabatic downstream, in the experiments, the downstream temperature is that of the ambience. This downstream heat loss reduces the flame burning rate, which in turn causes the slightly weakened flame to move to a larger radial location so that stabilization is achieved with the reduced radial velocity.

Concluding Remarks

In the present investigation, we have demonstrated the usefulness of the stationary cylindrical flame for fundamental flame studies, especially when the flame is stabilized by flow divergence and hence is basically adiabatic. Since these curved flames are stretchless, the influence of curvature on the flame structure and response can be unambiguously studied. Specifically, we have shown that the downstream burning flux of such flames is unaffected by the flame curvature and hence is equal to the constant burning flux of the adiabatic freely propagating planar flame, while the upstream burning flux exceeds it as a result of flow divergence. This understanding is useful to the study of the general nature of stretched flames subjected to the influence of flame curvature, especially within the context of laminar flamelets in the modeling of turbulent flames.

We have also successfully produced a nearly cylindrical and adiabatic flame in the microgravity environment of the drop tower. While the quality of the flame still needs to be improved, the viability of the concept is nevertheless established, especially in light of the favorable agreement between the microgravity results and detailed numerical computation.

A further contribution of the present study is the possibility of determining the laminar burning velocities of combustible mixtures by using the cylindrical flame in the nearly adiabatic regime. While microgravity experiments are fairly complex and possibly also costly in terms of their operation, the simplicity of the experimental configuration and concept renders this methodology a useful substantiating alternative to other approaches for such a determination, at least for reasonably smooth flames.

Finally, we do wish to emphasize again the difficulty in obtaining perfectly cylindrical flames without wrinkles, even with the addition of helium. If such wrinkles are inherent to the flame, as manifestations of some hydrodynamic instabilities [17], then there would exist a limitation on the quantitative accuracy in determining the flame responses such as the burning rate of practical combustion mixtures. Studies are currently underway to assess the nature of such wrinkles. Experiments will also be conducted with spherical flames; it is anticipated that the additional curvature could partially "absorb" the extent of wrinkling.

Acknowledgments

This research was supported by NASA under the Microgravity Combustion Program. We thank Kurt Sacksteder of NASA-Lewis for his invaluable advice and help in the experimentation. JAE also acknowledges the support of an AFRAPT (Air Force Research in Aero Propulsion Technology) Fellowship during the course of this study.

REFERENCES

1. Law, C. K., *Twenty-Second Symposium (International) on Combustion*, The Combustion Institute, Pittsburgh, 1988, pp. 1381–1402.
2. Matalon, M., *Combust. Sci. Technol.* 31:169–181 (1983).
3. Fristrom, R. M., *Combust. Flame* 2:103–105 (1958).
4. Menkes, J., *Combust. Flame* 4:1–7 (1960).
5. Westenberg, A. A., and Favin, S., *Combust. Flame* 4:161–171 (1960).
6. Spalding, D. B., *Combust. Flame* 4:51–58 (1960).
7. Garbey, M., Kaper, H. G., Leaf, G. K., and Matkowsky, B. J., *Quart. Appl. Math.* 47:691–704 (1989).

8. Margolis, S. B., *Combust. Sci. Technol.* 22:143–169 (1980).
9. Chao, B. H., and Law, C. K., *Combust. Sci. Technol.* 62:211–237 (1988).
10. Eng, J. A., Zhu, D. L., and Law, C. K., "On the Structure, Stabilization, and Dual Response of Flat-Burner Flames," *Combust. Flame*, in press.
11. Spalding, D. B., and Yumlu, V. S., *Combust. Flame* 3:553–556 (1959).
12. Ferguson, C. R., and Keck, J. C., *Combust. Flame* 34:85–98 (1979).
13. Yamazaki, S., and Ikai, S., *Trans. Japan Soc. Mech. Eng.* 37.293:121–130 (1971).
14. Tien, J. H., and Matalon, M., *Combust. Flame* 84:238–248 (1991).
15. Kee, R. J., Grcar, J. F., Smooke, M. D., and Miller, J. A., *A Fortran Program for Modeling Steaty Laminar One-Dimensional Premixed Flames,* Sandia National Laboratories Report No. SAND85–8240, 1985.
16. Egolfopoulos, F. N., Du, D. X., and Law, C. K., *Combust. Sci. Technol.* 83:33–75 (1992).
17. McIntosh, A. C., *J. Fluid Mech.* 161:43–75 (1985).

Twenty-Fifth Symposium (International) on Combustion/The Combustion Institute, 1994/pp. 1719–1725

AN EXPERIMENTAL AND NUMERICAL INVESTIGATION ON THE HOT SURFACE IGNITION OF PREMIXED GASES UNDER MICROGRAVITY CONDITIONS

H. NAGATA AND H. M. KIM
University of Tokyo
Hongo, Bunkyo-ku, Tokyo 113, Japan

J. SATO
Ishikawajima-Harima Heavy Industry Co., Ltd.
Toyosu, Koto-ku, Tokyo 135, Japan

AND

M. KONO
University of Tokyo
Hongo, Bunkyo-ku, Tokyo 113, Japan

There have been many studies of hot surface ignition of premixed gases. However, using the experimental results obtained up to this time, it is difficult to understand the basic mechanism of ignition by heated surfaces because these experiments were made under the normal gravity condition, suffering from the effect of natural convection.

In the present study, experiments were made on the ignition of mixtures by heated nickel, tungsten, and platinum wires under normal gravity and microgravity conditions. With a methane-oxygen mixture ignited by a heated tungsten wire, a strong gravity effect on the ignition delay is observed. On the contrary, there is almost no gravity effect observed with a methane-air mixture. Results of calculations show that ignition experiments under the microgravity condition are simulated successfully by this numerical model. It is shown from the numerical results that the ignition point in the methane-oxygen case is apart from the hot-wire surface, while, in the methane-air case, this point exists near the hot-wire surface. Therefore, natural convection has little effect on the ignition delay of a methane-air mixture.

Experimental results of hydrogen-air mixtures ignited by heated platinum wires show that chemical species are supplied to the platinum wire surface by natural convection, and therefore, the surface reaction is promoted under the normal gravity condition. Experimental and numerical results show that the surface reaction is the most energetic when the equivalence ratio of the mixture is 0.3, which conflicts with the result obtained by Coward and Guest that the rate of catalytic reaction attains a maximum at stoichiometric composition. This contradiction may be due partially to the gravity effect in their experiments.

Introduction

There have been many studies of hot surface ignition of premixed gases [1–7]. Coward and Guest [1] measured ignition temperatures of natural gas and air mixtures with heated platinum and nickel bars. They showed that the minimum ignition temperatures of platinum are much higher than those of nickel, and that, when they are plotted against the equivalence ratio, the maximum can be seen near stoichiometric composition. From these results, they concluded that a powerfully catalytic surface requires a higher temperature to ignite the mixture, and the maximum of the platinum temperature curve indicates that the rate of catalytic reaction attains a maximum at stoichiometric composition. These conclusions are generally accepted, and their experimental results have been cited in some textbooks [8]. Ashman and Büchler [4] measured ignition delays and ignition temperatures of hydrogen-air and methane-air mixtures with heated wires. Adomeit [5] measured the temperature field around the igniter of a heated circular rod with a Mach–Zehnder interferometer. Laurendeau [9] reviewed previous work and investigated the influence of surface size, pressure, and flow velocity on the ignition temperature theoretically.

We think that, using these experimental results, it is difficult to explain the basic mechanism of ignition by heated surfaces because these experiments were

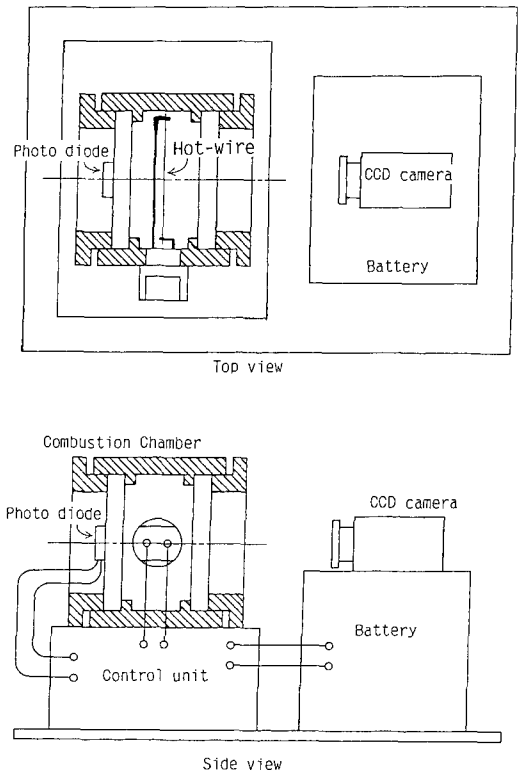

FIG. 1. Schematic diagram of experimental apparatus.

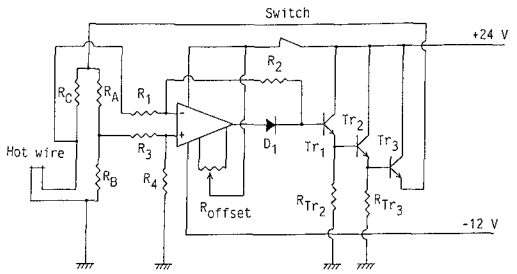

FIG. 2. Ignition circuit diagram.

made under the normal gravity condition, suffering from the effect of natural convection. Additionally, knowledge of the hot surface ignition of combustible mixtures under the microgravity condition is needed to achieve proper designs of space system that should guarantee safe operation and reasonable construction costs.

In the present study, experimental and numerical studies were made on the ignition of mixtures by heated nickel, tungsten, and platinum wires under the microgravity condition. For comparison of the results, experimental studies under the normal gravity condition were also conducted.

Experimental Apparatus

The experimental apparatus is given schematically in Fig. 1. The combustion chamber is a duralmin cylinder, 60 mm in diameter and 16 mm in length, fitted with parallel glass windows. The wire in the chamber is heated electrically up to the desired temperature in a short period (about 10 ms) and maintained at constant temperature thereafter by the ignition circuit, which is shown in Fig. 2. The hot wire plays a function as one resistor of the Wheatstone bridge. The potential difference between the connection of R_A to R_B and R_C to the hot wire drives the OP-amp, whose output current is amplified by transistors. Therefore, the change in resistance of the hot wire yields the desired feedback effect, so that the temperature of the hot wire remains constant. The constant value had been adjusted beforehand by varying resistance R_C. When the hydrogen-air mixture is ignited with the platinum wire, the platinum wire is heated by the heat release due to catalytic reaction on the platinum wire surface (designated as surface reaction), and the platinum wire temperature cannot be kept constant. In this case, the platinum wire is monitored with a charge-coupled device (CCD) camera during the experiments, and the history of the platinum wire temperature is obtained from the light intensity of the wire. The relation between light intensity and the wire temperature measured by the optical pyrometer was obtained in advance. The free-fall method was adopted to obtain the microgravity condition using a drop tower 11 m in height, which can realize about a 1.4-s microgravity condition, at the Department of Aeronautics and Astronautics, University of Tokyo. To minimize the influence of air drag, the experimental apparatus was mounted inside the drag shield.

The experimental apparatus and the drag shield were hung by a steel wire. The initial pressure and the initial temperature of mixtures were atmospheric pressure and room temperature, respectively. Immediately after the wire is cut by a cutter, the switch of the ignition circuit is turned on. It takes some moments from the accomplishment of heating up the wire until the mixture ignites. This is defined as ignition delay. When the mixture around the hot wire ignites, it is detected as a sudden heating of the hot wire and, consequently, in a sharp decrease in OP-amp output voltage. Accordingly, ignition can be determined by change in the OP-amp output voltage.

In the platinum wire case, the OP-amp output voltage sharply decreases to zero because of the heat release due to surface reaction, and ignition of the mixture cannot be detected by this method. Therefore, a photodiode was used to detect the ignition, as shown in Fig. 1. The photodiode and CCD camera

were not used in the nickel and tungsten wire experiments.

Numerical Model Description

Numerical calculations were carried out to simulate the ignition phenomena under the microgravity condition. The numerical model is as follows: A cylindrical heat source, or hot wire, is surrounded with a mixture, and its length is assumed to be infinite. Partial differential equations that govern mass, energy, and species concentrations are stated in one-dimensional cylindrical coordinates. Axial symmetry, zero azimuthal velocity, and no gradient along the axis are assumed. Because of low Mach numbers, constant pressure is assumed, and therefore, momentum equations are not used.

The transport properties such as coefficients of viscosity, diffusion, and thermal conductivity are calculated theoretically [10,11]. The elementary reaction mechanism involves 134 reactions and 29 species for the methane-air and methane-oxygen mixtures and 21 reactions and 9 species for the hydrogen-air mixtures. It is drawn from Kee et al. [12] without any modification. Thermochemical properties are obtained from JANAF tables [13].

The boundary conditions for the case without catalytic effect are given by

$$r = r_w: \quad T = T_w, \quad V = 0, \quad \frac{\partial \rho_k}{\partial r} = 0$$

$$r = \infty: \quad \frac{\partial T}{\partial r} = 0, \quad \frac{\partial V}{\partial r} = 0, \quad \frac{\partial \rho_k}{\partial r} = 0$$

where T_w, r_w, V, and ρ_k are the temperature and the radius of the hot wire, the velocity of radial direction, and the mole fraction of species k, respectively.

When the catalytic effect is included, $(\partial \rho_k/\partial r)_{r=r_w}$ is not zero. Adsorption and desorption of the species and the catalytic reaction mechanism on the platinum surface used here were developed in the study of Ljungström et al. [14].

As the heat balance of the hot wire, heat transfer to the ambient mixture Q_{ht}, radiation Q_{rad}, heat release due to surface reaction Q_{sr}, (for the platinum wire case), and electric power Q_{ep} are considered. Electric power is supplied to the hot wire so as to keep the wire temperature constant, and is given by the following equation:

$$Q_{ep} = Q_{ht} + Q_{rad} - Q_{sr}.$$

When Q_{ep} becomes less than zero, it is set to zero, and the hot-wire temperature does not keep constant in this case.

Ignition occurrence is defined as the appearance of the place where the heat-release rate due to gas-phase chemical reaction takes the local maximum value with time.

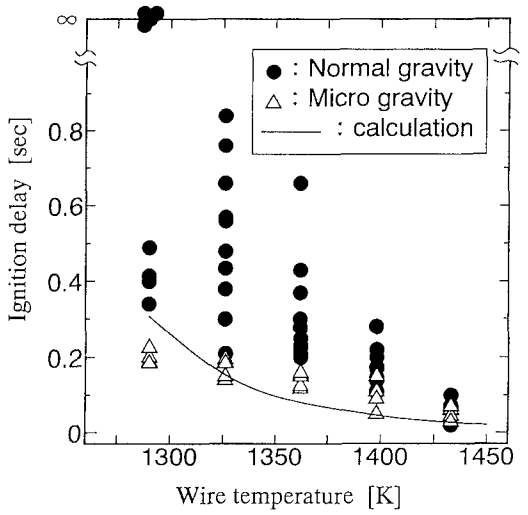

FIG. 3. Ignition delays of stoichiometric methane-oxygen mixture.

Results and Discussion

Methane-Oxygen and Methane-Air Mixtures:

Ignition delays for the stoichiometric mixture of methane-oxygen were measured under normal gravity and microgravity conditions, using tungsten wire 0.15 mm in diameter and 40 mm in length. Their dependence upon the hot-wire temperature is plotted in Fig. 3. The solid line represents the result of calculation. The catalytic effect is not included in the calculation. At lower temperatures, the ignition delays under the microgravity condition are shorter than those under the normal gravity condition, and the difference between them becomes remarkable as the wire temperature decreases. These results may be due to convective cooling, which results in a long ignition delay under the normal gravity condition, and this gravity effect intensifies with the increase in ignition delay.

Ignition experiments on the stoichiometric methane-air mixture give results that differ from the methane-oxygen experiments. That is, the effect of gravity is not observed. Ignition delays obtained under normal gravity and microgravity conditions almost agree with each other, as can be seen in Fig. 4. Generally speaking, the strength of the gravity effect can be estimated with the Grashof number, which is given by

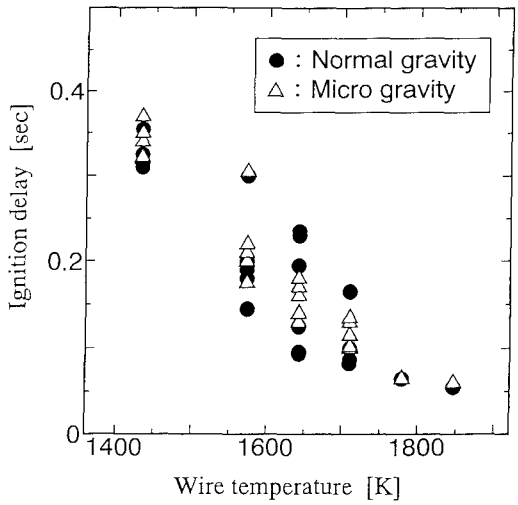

FIG. 4. Variation of ignition delay with wire temperature for stoichiometric methane-air mixture obtained under normal gravity and microgravity conditions.

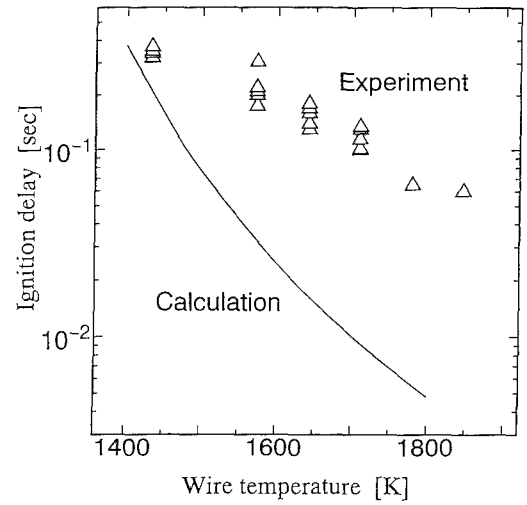

FIG. 5. Ignition delays of stoichiometric methane-air mixture.

$$Gr = \frac{L^3\rho^2 g(T_w - T_g)}{T_m\mu^2}$$

where L, ρ, g, T_w, T_g, T_m, and μ are the diameter of the hot wire, density of the mixture, acceleration of gravity, temperature of the hot wire, temperature of the mixture, the average temperature of T_w and T_g, and viscosity of the mixture, respectively. For example, methane-oxygen and methane-air mixtures ignited by hot-wire temperatures of 1250 and 1450 K show almost equal ignition delay (about 0.3 s) under the microgravity condition and different strengths of the gravity effect. The Grashof numbers in the methane-oxygen case and methane-air case are 0.27 and 0.30, respectively. This result does not explain the difference in the strength of the gravity effect under these two conditions.

The numerical result in Fig. 3 almost agrees with the experimental result obtained under the microgravity condition. This shows that the ignition phenomena under the microgravity condition can be simulated successfully by this model.

Figure 5 shows the calculated ignition delay dependence upon the noncatalytic hot-wire temperature for the stoichiometric methane-air mixture under the microgravity condition. The calculated ignition delay is shorter than the experimental result, and the difference between them increases with increasing wire temperature. This may be due to the oxidation of the tungsten wire, by which the wire diameter decreases gradually. The decrease of the wire diameter causes decrease of the wire temperature, because the resistance of the hot wire is kept constant by the ignition circuit. This effect of oxidation multiplies with increasing wire temperature.

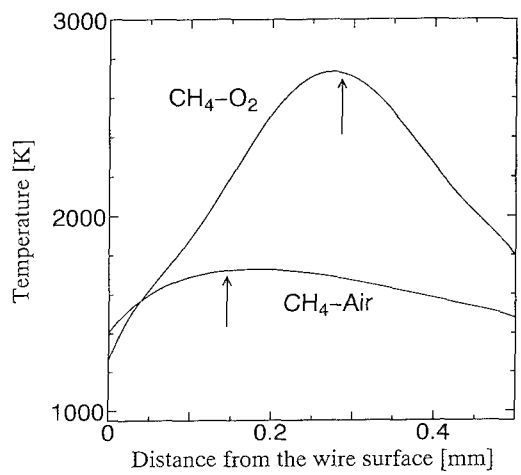

FIG. 6. Calculated temperature profiles at ignition for stoichiometric methane-oxygen mixture with wire temperature 1290 K and stoichiometric methane-air mixture with wire temperature 1414 K.

Figure 6 shows calculated temperature profiles at ignition. Methane-oxygen and methane-air mixtures are ignited by wire temperatures of 1290 and 1414 K, respectively. Ignition delays of both conditions are almost equal to 0.3 s. The difference in the strength of the gravity effect between the methane-oxygen and methane-air experiments can be explained by this figure. Arrows in the figure exhibit the ignition points, which are the places where the heat-release rate due to the chemical reaction have taken the local maximum value with time for the first time. The ignition point in the methane-oxygen case is apart from

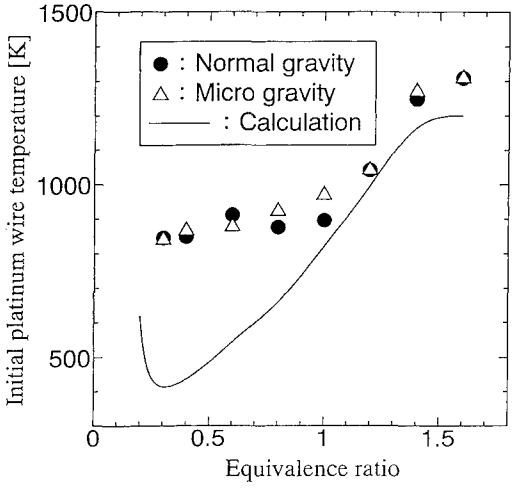

FIG. 7. Numerical and experimental results of initial platinum wire temperature with which ignition delays of hydrogen-air mixtures are 0.3 s.

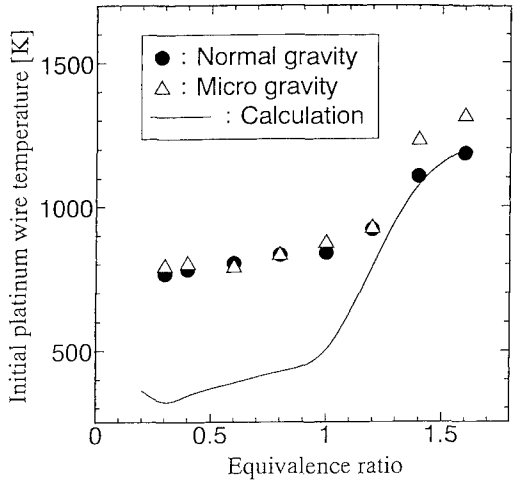

FIG. 8. Numerical and experimental results of initial platinum wire temperature with which ignition delays of hydrogen-air mixtures are 0.6 s.

the hot-wire surface because the hot wire absorbs heat from adjacent gas as the chemical reaction develops. On the other hand, the ignition point in the methane-air case is nearby the hot-wire surface because the hot-wire temperature is so high that the adjacent gas suffers less heat loss to the hot wire. Therefore, natural convection has little effect on the ignition delay in the methane-air case.

Hydrogen-Air Mixtures:

Platinum and nickel wires 0.1 mm in diameter and 40 mm in length were employed as hot wires in this experiment. In the platinum wire case, a surface reaction accompanied by heat release starts soon after the platinum wire is heated up to the arranged temperature. The electrical power is supplied to the platinum wire so as to keep the platinum wire temperature constant. Therefore, the voltage supplied to the platinum wire sharply decreases to zero. Nevertheless, the platinum wire temperature continues to increase, and the heated platinum wire ignites the mixture.

The ignition delay dependencies upon the initial platinum wire temperature were obtained experimentally for mixtures of equivalence ratio 0.3–1.6. Initial platinum wire temperatures by which the mixture is ignited with ignition delays of 0.3 and 0.6 s were obtained from interpolations of those results, which are shown in Figs. 7 and 8. These temperatures are critical initial wire temperatures for ignition when ignition is defined as an ignition delay shorter than 0.3 and 0.6 s. The mixture of equivalence ratio 0.2 cannot be ignited even by a platinum wire temperature near the melting point. The solid lines in

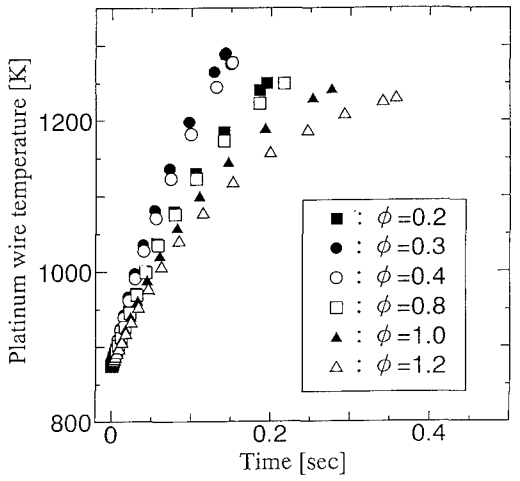

FIG. 9. Histories of platinum wire temperature calculated with initial platinum wire temperature 875 K.

the figures represent the results of calculation. It is shown that the critical initial temperatures under the normal gravity condition are lower than those under the microgravity condition in both cases. This is due to natural convection, which supplies chemical species to the platinum wire surface and promotes the surface reaction. The experimental and numerical results are different from each other especially on the lean side. This may be due to the fact that the activation energy of the surface reaction is different from the real value. On the other hand, they agree with each other on the point that lean mixtures can be ignited by a lower initial platinum wire temperature

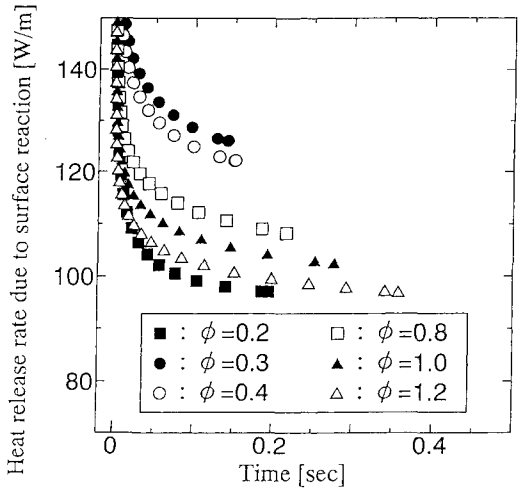

FIG. 10. Histories of heat release due to surface reaction calculated with initial platinum wire temperature 875 K.

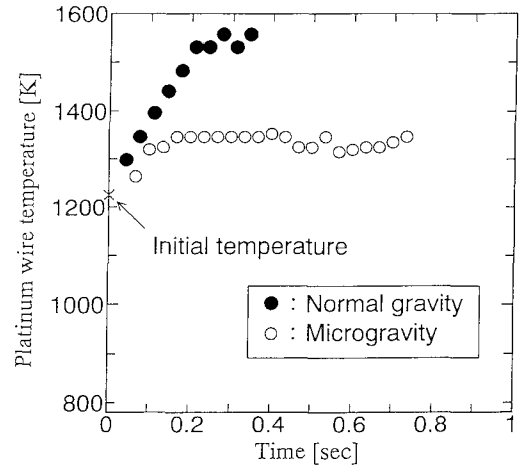

FIG. 12. Histories of platinum wire temperature obtained from the light intensity of the platinum wire with initial platinum wire temperature 1225 K.

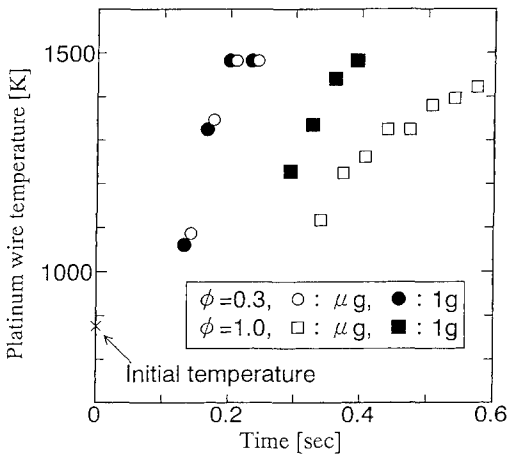

FIG. 11. Histories of platinum wire temperature obtained from the light intensity of the platinum wire with initial platinum wire temperature 875 K.

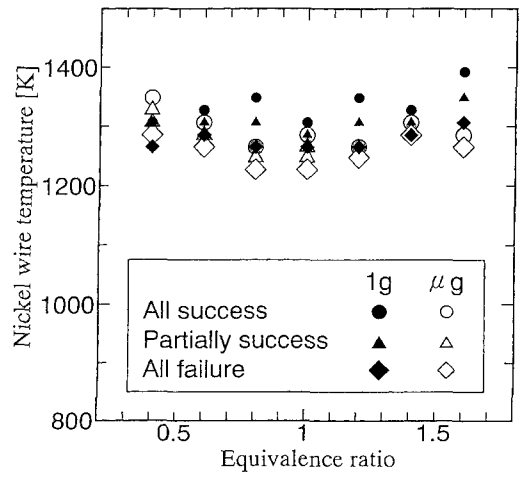

FIG. 13. Results of ignition experiment with nickel wire. Success means that the ignition delay is smaller than 0.3 s.

in comparison with rich or stoichiometric mixture cases.

Figure 9 shows histories of platinum wire temperature calculated with the initial platinum wire temperature of 875 K. The increase rate of the platinum wire temperature becomes high with decreasing equivalence ratio, and highest when the equivalence ratio is 0.3. This is because the surface reaction is the most energetic at this equivalence ratio.

Figure 10 shows the histories of heat-release rate due to surface reaction, calculated with the same conditions as in Fig. 9. It is confirmed by this figure that surface reaction is the most energetic when the equivalence ratio of the mixture is 0.3, This result is explained as follows: The diffusion coefficient of oxygen is smaller than that of hydrogen, and it is generally accepted that hydrogen is easily adsorbed to the platinum surface in comparison with oxygen. Therefore, the rate-controlling step of the surface reaction is the adsorption of oxygen to the platinum surface. When the equivalence ratio is 0.3, the adsorption rate of oxygen matches that of hydrogen, and surface reaction occurs most vigorously. This result conflicts with the conclusion of Coward and Guest [1] that the rate of catalytic reaction attains a maximum at stoichiometric composition. This contradiction may be due partially to the gravity effect in their experiment.

Figures 11 and 12 show the histories of platinum wire temperature that were obtained from the light intensity of the platinum wire. In the rich mixture case of Fig. 12, the platinum wire temperature increases rapidly at first and then remains at almost constant value under the microgravity condition. This shows that the surface reaction is suppressed by the rate of oxygen supply to the platinum wire surface. In the normal gravity case, the platinum wire temperature keeps increasing because oxygen is supplied to the platinum wire surface by natural convection. The increase rate of the platinum wire temperature becomes high with decreasing equivalence ratio, which agrees with the result of calculation.

An ignition experiment with nickel wire was conducted to compare the results with those of the platinum wire case. Because the ignition delay of the nickel wire case scatters extensively, the experiment was carried out five times for each condition. The result is shown in Fig. 13, which differs from the platinum wire results mainly in the two following respects. First, the minimum ignition temperature under the microgravity condition is lower than that under the normal gravity condition. Second, equivalence ratio has little effect on the minimum ignition temperature. Experimental results obtained by Coward and Guest [1] showed that the ignition temperatures of platinum were higher than those of nickel because of the catalytic effect of platinum. On the other hand, our results show that minimum initial temperatures for ignition with platinum are much lower than those of nickel. (In the nickel wire case, wire temperature always equals the initial temperature.) These results are not in conflict with each other because it is shown in Figs. 11 through 13 that the platinum wire temperature at ignition is much higher than the minimum ignition temperatures in the nickel wire case.

Conclusion

Experimental studies were made on the ignition of mixtures by heated nickel, tungsten, and platinum wires under normal gravity and microgravity conditions. With a methane-oxygen mixture ignited by a heated tungsten wire, a strong gravity effect on the ignition delay is observed. On the contrary, there is almost no gravity effect observed with a methane-air mixture. Calculation shows that the ignition point in the methane-oxygen case is apart from the hot-wire surface, while, in the methane-air case, this point exists nearby the hot-wire surface. Therefore, natural convection has little effect on the ignition delay of a methane-air mixture.

Experimental results of hydrogen-air mixtures ignited by heated platinum wire show that chemical species are supplied to the platinum wire surface by natural convection, and therefore, the surface reaction is promoted under the normal gravity condition. Experimental and numerical results show that the surface reaction is the most energetic when the equivalence ratio of the mixture is 0.3, which conflicts with the result obtained by Coward and Guest [1] that the rate of catalytic reaction attains a maximum at stoichiometric composition. This contradiction may be due partially to the gravity effect in their experiments.

REFERENCES

1. Coward, H. F., and Guest, P. G., *J. Am. Chem. Soc.* 49:2479–2486 (1927).
2. Stout, H. P., and Jones, E., *Third Symposium on Combustion, Flame and Explosion Phenomena*, Baltimore, The Williams & Wilkins Co., 1949, pp. 329–337.
3. Kumagai, S., and Kimura, I., *Sixth Symposium (International) on Combustion*, The Combustion Institute, Pittsburgh, 1957, pp. 554–558.
4. Ashman, L. E., and Büchler, A., *Combust. Flame* 5:113–121 (1961).
5. Adomeit, G., *Tenth Symposium (International) on Combustion*, The Combustion Institute, Pittsburgh, 1965, pp. 237–243.
6. Cutler, D. P., *Combust. Flame* 22:105–109 (1974).
7. Detz, C. M., *Combust. Flame* 26:45–55 (1976).
8. Lewis, B., and Elbe, G. V., *Combustion, Flames and Explosions of Gases*, 3rd ed., McGraw-Hill Book Company, 1965, pp. 361–380.
9. Laurendeau, N. M., *Combust. Flame* 46:29–49 (1982).
10. Hirschfelder, J. O., Curtiss, C. F., and Bird, R. B., *Molecular Theory of Gases and Liquids*, John Wiley & Sons, New York, 1964.
11. Monchick, L., and Mason, E. A., *J. Chem. Phys.* 35:1676 (1961).
12. Kee, R. J., Miller, J. A., Evans, G. H., and Dixon-Lewis, G., *Twenty-Second Symposium (International) on Combustion*, The Combustion Institute, Pittsburgh, 1988, pp. 1479–1494.
13. Stull, D. R., and Prophet, H., *JANAF Thermochemical Tables*, 3rd ed., U.S. Department of Commerce, Washington, DC, 1986.
14. Ljungström, S., Kasémo, B., Rosen, A., Wahnström, T., and Fridell, L., *Surf. Sci.* 216:63–92 (1989).

Twenty-Fifth Symposium (International) on Combustion/The Combustion Institute, 1994/pp. 1727–1734

DETERMINATION OF TEMPERATURE FROM N_2 AND O_2 CARS SPECTRA AT VERY HIGH PRESSURE

T. DREIER, M. RIDDER AND G. SCHIFF
Physikalisch Chemisches Institut der Universität Heidelberg
Im Neuenheimer Feld 253, 69120 Heidelberg, Federal Republic of Germany

A. SAUR
Institut für Physikalische Chemie und Elektrochemie
Universität Karlsruhe
Kaiserstr. 12, 76131 Karlsruhe, Federal Republic of Germany

AND

A. A. SUVERNEV
Institute of Cytology and Genetics
630090 Novosibirsk, Russia

Using least-squares routines, temperatures have been obtained from fitting computer-generated spectral shapes of collapsed N_2 and O_2 Q-branch coherent anti-Stokes Raman scattering (CARS) spectra to experimental data at high densities between 120 and 725 amagat (1 amagat = 2.67×10^{19} cm^{-3}) in the temperature range from 300–850 K. Experimental data were obtained from high-pressure gases enclosed in a temperature-controlled vessel that is equipped with sapphire windows for optical access. In the fitting codes, for each temperature iteration step, densities have been readjusted by calculating pVT data from equations of state. Inelastic rotational energy transfer rate constants, necessary for spectral modeling, were calculated from known energy gap scaling laws. Alternatively, temperature-fitting results from the modeling of unresolved Q-branch band shapes using a quasi-classical description of rotational relaxation are presented. Within the pressure range investigated, for nitrogen at 300 K, best agreement is obtained for the polynominal energy gap (PEG) law, whereas the classical model is reasonably good at 700 K. For oxygen at 300 K, the modified exponential gap (MEG) model and, at higher temperatures, the quasi-classical model are preferred.

Introduction

In recent years, there has been growing interest in the field of high-pressure high-temperature kinetics and combustion. In particular, reactive fluid systems at high densities have demonstrated very efficient destruction of liquid and gaseous toxic wastes in aqueous solutions at temperatures and pressures beyond the critical point of water [1–4]. It has been shown recently that, in a mixture of methane, oxygen, and water above the critical point, a diffusion flame can be sustained [5]. On the other hand, there is very limited knowledge about a detailed understanding of the chemical kinetics in such reaction systems. Also, because of the limited availability of experimental data, chemical kinetic modeling still is at its beginning.

One reason for this deficiency is engineering problems in the design of chemical flow reactors for kinetic studies. Probing of these systems for concentration measurements in chemical kinetics investigations mostly has been done by adiabatically expanding the reaction mixture to ambient pressure and temperature and separating gaseous and liquid components for subsequent, e.g., mass spectrometric or gas chromatographic, analysis. For "in situ" optical probing, Raman or infrared spectroscopy has been widely used [6,7]. These methods don't suffer from quenching effects, often a problem in other detection methods, such as laser-induced fluorescence, which rely on prolonged re-emission from excited states.

Being a nonlinear optical method, coherent anti-Stokes Raman scattering (CARS) in addition offers some attractive features in the diagnostics of high-pressure media. One of these is the line-of-sight detection capability through small apertures, whose number and size often limit optical access in high-pressure vessels. Furthermore, in unsteady flow conditions, broadband vibrational or rotational CARS spectroscopy still is one of the few methods for "in situ" single-pulse thermometry [8,9]. The general procedure in this technique is that, in a Raman-en-

hanced four-wave mixing interaction, spectra acquired experimentally from a small probe volume, determined by focused and crossed laser beams, are compared to computer-generated spectral shapes in a least-squares fitting algorithm with temperature as a variable parameter. In this respect, nitrogen CARS thermometry is well characterized in flames at pressures up to 4 MPa [10].

Using stimulated Raman scattering (SRS), a method less often applied for thermometry in practical combusters, similar investigations at medium pressures for N_2 and O_2 have been reported recently by Millot et al. [11]. The purpose of the present paper is to investigate—from experimentally acquired CARS spectra, taken under well-defined conditions of temperature and pressure—the possibilities of vibrational CARS thermometry in high-density nitrogen and oxygen. Calculation of collapsed Q-branch spectral shapes is done by employing various standard empirical scaling-law expressions to determine the elements of the relaxation matrix in the Fourier representation of the spectrum. For the first time, CARS thermometry using a quasi-classical approach [12] for the calculation of unresolved spectral shapes is presented. It is shown—not unexpectedly—that strong discrepancies in the fitted temperature exist between spectra deduced from using the various modeling approaches.

Experimental

The experimental equipment for obtaining nitrogen and oxygen CARS spectra is only briefly described here. A more detailed account of the experimental procedure and the acquired data is given in Ref. 13. A scanning CARS spectrometer is used, consisting of a single-mode Nd: YAG pump laser (Spectra Physics, GCR-3) and a Stokes dye laser (Quanta Ray, PDL-1A) pumped by the same Nd: YAG laser. The optical setup is similar to one described in Ref. 14, except that a planar BOXCARS configuration [15] is realized by splitting the 532-nm pump beam into two parallel beams separated by 14 mm on the focusing lens. Simultaneously with the CARS signal from the high-pressure vessel, a collinear CARS signal in ambient air is generated in a reference channel and detected by a separate photomultiplier tube (Valvo, XP2020) at the exit plane of a filter monochromator. During the dye laser scan, this enables a precise absolute wave number scale to be generated for the collisionally narrowed spectrum by fitting synthetic signatures to the simultaneously recorded rotationally resolved reference N_2/O_2 spectrum.

The pressure cell is made from a high-strength nickel alloy (steel no. 2.4969) and fabricated as a cylindrical 200-mm-long vessel with a 6-mm bore. Optical access is via two 10-mm-thick sapphire windows on each face. Temperature is measured close to the CARS probe volume in the center of the vessel by a chromel-alumel thermocouple, inserted through a 1/4-in. stainless steel T connector (HIP). This tubing also gives access to the high-pressure pump (NOVA) and the gas supply system. Resistive heating wires are wound on bronze sleeves that closely fit around the cell body. Pressures can be read from two Bourdon gauges with a precision of 1% (full scale). To attain the proper final pressure load at higher temperatures, the cell first is filled to a lower pressure and then gradually heated up to the desired temperature with appropriate pressure relief, if necessary.

Theoretical Framework

In the present investigation, the main purpose is to reveal uncertainties that can arise in CARS temperature determinations at high densities when existing theories are used to model collisionally narrowed Q-branch spectra. These effects include broadening and interference of adjacent rotational lines accompanied by the characteristic collisional narrowing of the whole Q-branch manifold at high pressures. This behaviour, verified experimentally for Raman [16] and CARS [17] spectra, can well be described by some of the methods listed below.

Taking the Laplace transform of the time correlation function of the polarizability operator, the spectral response can be calculated, and one obtains for the CARS spectrum [18,19]

$$I_{\mathrm{CARS}}(\omega) \propto \left|\langle 0|\alpha|1\rangle \sum_j \tilde{\alpha}_j(\omega)\right|^2 = \left|\langle 1|\langle 1|\alpha^{(0)}|0\rangle|^2 \sum_{jj'} [G^{-1}(\omega)]_{j'j}\rho_j\right|^2 \quad (1)$$

which can be solved for every frequency interval by inversion of the G Matrix, whose elements are given by

$$G(\omega)_{j'j} = i\left(\omega - \omega_{1j0j} + \Delta_v - \frac{i}{\tau_{dp}}\right)\delta_{jj'} + \Gamma_{j'j} \quad (2)$$

where $[\Gamma_{j'j} + \delta_{j'j}\,(1/\tau_{dp} + i\Delta_v)]$ denotes the matrix element of the relaxation operator (for Q-branch transitions: $|v = 1, j\rangle\langle v = 0, j| \rightarrow |v = 1, j'\rangle\langle v = 0, j'|$). Here δ_{jj} is the Kronecker symbol. The frequency of the respective vibration rotation transition is denoted by ω_{1j0j}, and the sum in Eq. (1) runs over all populated rotational levels. Efficient methods have been employed to diagonalize the dynamic part of the G matrix and perform the inversion only once for each spectrum generation [20]. The unitarity of the relaxation matrix leads to

$$\Gamma_{jj} + \sum_{j' \neq j} \Gamma_{j'j} = 0 \tag{3}$$

which, together with the detailed balance principle for the off-diagonal elements,

$$\frac{\Gamma_{j'j}}{\Gamma_{jj'}} = \frac{2j' + 1}{2j + 1} \exp\left(\frac{E_j - E_{j'}}{kT}\right) \tag{4}$$

determines an inversion method for the development of scaling-law expressions from experimental temperature-dependent line-broadening coefficients [21]. These consist of analytical expressions for the relaxation rates $\Gamma_{jj'}$, that have to be in accord with Eqs. (3) and (4), and whose set of at least three variable parameters is derived from a fit to accurately measured collisional broadening coefficients for nitrogen [19,22] and oxygen [23], or to directly measured state selective relaxation rate constants [24]. We have tested four of the most popular scaling laws for modeling N_2 and O_2 CARS spectra: the modified exponential gap law (MEG) [22,25], the energy-corrected sudden (exponential) power law [ECS-(E)P] [19], the polynomial energy gap law (PEG) [26], and the statistical polynomial energy gap law (SPEG) [27]. As an illustration, in the MEG model, the rate of upward transitions from j to j' ($j' > j$) is given by [22,25]

$$-\Gamma_{jj} = nA_0 \frac{1 - \exp(-m)}{1 - \exp(-mT/T_0)} \left(\frac{T_0}{T}\right)^N \cdot \left(\frac{1 + a\dfrac{E_j}{kT\delta}}{1 + a\dfrac{E_j}{kT}}\right)^2 \exp(-\beta E_{jj}/kT) \tag{5}$$

with the energy gap $E_{j'} - E_j \equiv E_{j'j}$. In this expression, n is the density, a, A_0, N, m, δ, and β are adjustable temperature-independent parameters, and $T_0 = 295$ K is a reference temperature. Their values in the present calculations are those of Rahn and Palmer [25] for N_2-N_2 and of Millot et al. [23] for O_2-O_2 collisions. For the PEG model, various expressions were originally tested by Lavorel et al. [26] for pure nitrogen, and the form that is used here was employed by Sala et al. [28] in reproducing the SRS spectral shape at pressures up to 14 MPa. It reads for the upward rates as follows:

$$-\Gamma_{j'j} = n\left(\frac{T_0}{T}\right)^N \rho_{j'}^I(T) \sum_{l=0}^{5} C_l E_{j'j}^{-l} \tag{6}$$

with fitting parameters C_l and N, $E_{j'j}$ and n as defined in Eq. (5), and $\rho_{j'}^I(T)$ the equilibrium population in the nuclear spin modification I of rotational level j' at temperature T [$\Sigma_{j'=0}^{\infty} \rho_{j'}^I(T) = 1$]. For this expression, suitable parameters for oxygen are not available in the literature. However, its spectral structure and molecular parameters being very similar to nitrogen, we arbitrarily used these values for oxygen. For the ECS-(E)P and SPEG models, parameters for N_2 and O_2 are given in Refs. 29 and 30. A critical review of current scaling laws for nitrogen has been given by Steinfeld et al. [31] and Temkin et al. [30].

Within the framework of the classical approach, the angular momentum j is treated as a continuous variable, and instead of the sums over j', j in Eqs. (1) and (3), corresponding integrals have to be written, e.g.,

$$\Gamma_{jj} + \sum_{j' \neq j} \Gamma_{j'j} \rightarrow \frac{1}{\tau} \int \{\delta(j' - j) - f(j', j)\}\, dj' \tag{7}$$

where τ ($= 1/\Gamma_{jj} =$ const) means the average time between successive collisions and $f(j'j)$ [$\Gamma_{j' \neq j} = -f(j'j)/\tau$] describes the probability density to change the angular momentum from j to j' as the result of a single collision. For this function, one of the most general phenomenological models of f—the Keilson–Storer model [32]—was considered:

$$f_{KS}(j', j) = \frac{j}{d(1 - \gamma^2)} I_0\left[\frac{\gamma j j'}{d(1 - \gamma^2)}\right] \cdot \exp\left[-\frac{j^2 + \gamma^2 j'^2}{2d(1 - \gamma^2)}\right] \tag{8}$$

with the Bessel function of zeroth order I_0 and $d = hkT/8\pi^2 Bc$. Instead of integrating the inverted G operator [Eq. (2)] over all values of the angular momentum in Eq. (1), this expression is evaluated here, as outlined in Ref. 33, by using a continuous fraction form. The temperature dependencies of the cross section of the rotational energy relaxation ($\sigma_E = (1 - \gamma^2)/n\nu\tau$) and the correlation parameter (γ) are determined by the following empirical relations: $\sigma_E = a(300/T)^b$ and $\gamma = c \exp(-d/\sqrt{T})$. The following fitting parameters have been derived from the measured CARS spectra: $a_{N_2} = 35$ A^2, $b_{N_2} = 0.11$, $c_{N_2} = 4.29$, $d_{N_2} = 46.03$, and $a_{O_2} = 28.9$ A^2, $b_{O_2} = 0.41$, $c_{O_2} = 1.96$, $d_{O_2} = 20.55$.

Fitting Codes

Spectral calculations and temperature evaluations using the scaling laws are performed within a standard least-squares Newton fitting algorithm. The program structure is more closely described in Ref. 34.

In a temperature iteration step at high pressure, the corresponding density changes are significant and have to be taken into account. Since the relevant re-

laxation rates, as determined from the scaling laws, are considered to be proportional to density, this density adjustment has a significant influence on the calculated spectral width and shape. Therefore, each new temperature iteration necessitates that the density be recalculated. For this purpose, within a subroutine of the program, densities are derived from an equation of state [35] using second-order virial coefficients of Lennard-Jones–type potentials. The hard sphere diameter is assumed to be slightly temperature dependent. For N_2 and O_2, the calculated values lead to densities within 5% of current literature values [36]. The CARS spectral intensity can then be calculated, whatever the pressure and temperature, provided the relaxation matrix is completely determined (via scaling-law expressions). Intensity convolutions in the spectrum due to correlated CARS pump beam arrangements (cross-coherence effects) are done according to Greenhalgh and Hall [37]. The finite spectral width of the Stokes laser is modeled as a Gaussian with full width at half maximum (FWHM) of 0.14 cm^{-1}. The spectrum then is normalized by the zeroth moment of the sample spectrum, and the peak intensities of calculated and measured spectra are brought into coincidence on the frequency axis by an overall relative frequency shift Δ. Temperature and this shift are fitted iteratively to compensate the uncertainties introduced by the density-dependent overall frequency shift as extrapolated from the low-density linear line-shift data of Ref. 38. The same strategy was followed in Ref. 11. For the quasi-classical model, the sum of least-squares intensity deviations between observed and calculated spectrum was directly minimized during the temperature fit. The calculated spectrum was then obtained as the result of the direct numerical integration of the appropriate convolution expression of susceptibility and laser bandwidths [39].

Results

Figure 1 gives an impression of the appearance of measured oxygen CARS Q bands as a function of pressure and temperature in comparison with a rotationally resolved spectrum at 0.1 MPa from the calibration channel. It is seen that increased temperature is accompanied by a larger FWHM of the collapsed band due to a larger Boltzmann population spread within the rotational levels. In addition, a shift in peak position to lower Raman wave numbers at higher densities can be noticed due to the density-induced shift and a higher population in higher rotational states. Shown as solid lines are calculated best-fit temperature spectral shapes using the MEG model. A similar comparison for nitrogen is presented in Fig. 2 at 300 and 700 K, respectively, with the PEG law employed in the temperature fitting.

The main results of the present temperature-fit-

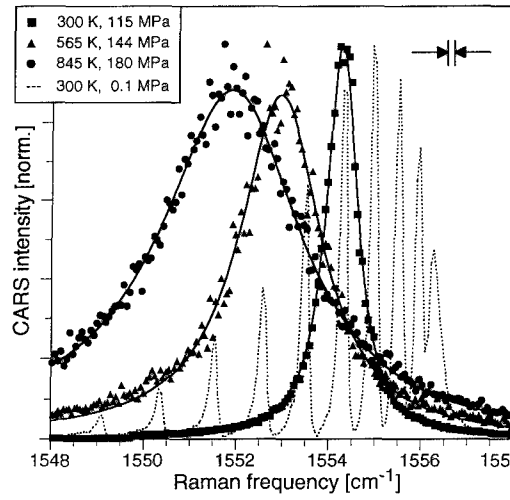

FIG. 1. Experimental O_2 CARS Q-branch spectral profiles at high densities (solid symbols). In addition, a 0.1-MPa room-temperature oxygen spectrum from the calibration channel is shown for comparison (dotted line). The instrumental spectral resolution is indicated by arrows. The result from a temperature fit of the high-pressure spectra using the MEG law is illustrated by solid lines.

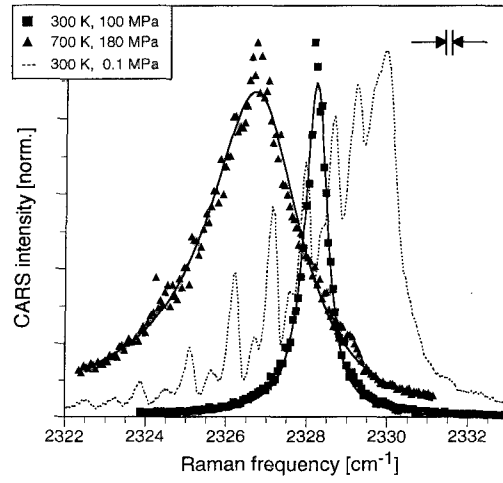

FIG. 2. Experimental N_2 CARS Q-branch spectral profiles at high densities (solid symbols). In addition, a 0.1-MPa room-temperature nitrogen spectrum from the calibration channel is shown for comparison (dotted line). The instrumental spectral resolution is indicated by arrows. The result from a temperature fit of the high-pressure spectra using the PEG law is illustrated by solid lines.

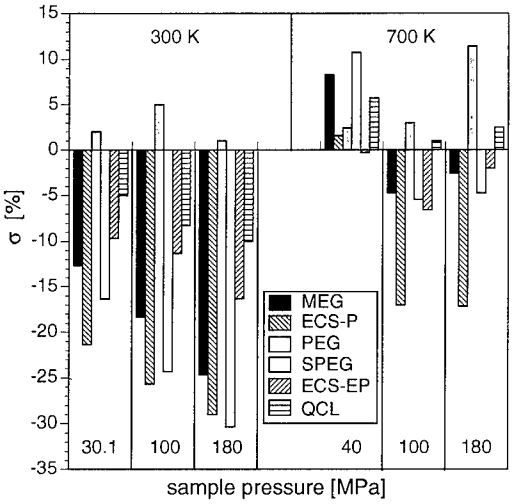

FIG. 3. Relative percentage deviation $\sigma = (T_{fit} - T_m)/T_m$ between calculated (T_{fit}) and measured (T_m) temperatures for nitrogen at 300 and 700 K, respectively, and several pressures. The spectral modeling in the CARS fitting algorithm is done using quantum-mechanical scaling-law expressions and a quasi-classical theory (QCL).

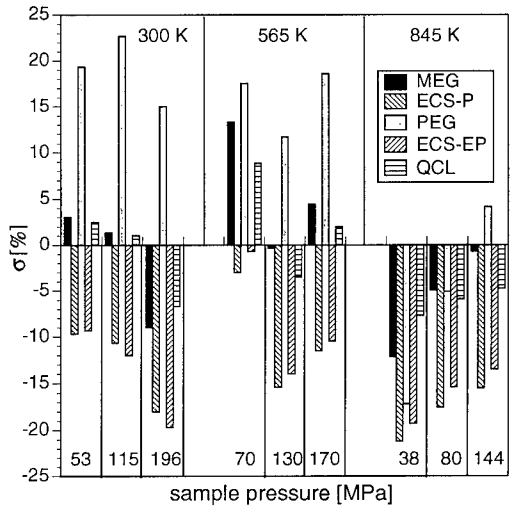

FIG. 4. Relative percentage deviation $\sigma = (T_{fit} - T_m)/T_m$ between calculated (T_{fit}) and measured (T_m) temperatures for oxygen at 300, 565, and 845 K, respectively, and several pressures. The spectral modeling in the CARS fitting algorithm is done using quantum-mechanical scaling-law expressions and a quasi-classical theory (QCL).

ting procedure are summarized in Figs. 3 and 4 for nitrogen and oxygen, respectively. For each temperature investigated, shown on the vertical axis are the relative percentage deviations $\sigma = (T_{fit} - T_m)/T_m$ with T_m from the thermocouple reading, while along the horizontal axis, the given pressures for each temperature setting are indicated. Grouped together for each temperature and pressure reading, the vertical bars indicate the fitting results using the various scaling-law and quasi-classical approaches.

In the case of nitrogen (cf. Fig. 3) at room temperature, all quantum-mechanical scaling laws, except PEG, lead to an underestimation in the given temperature of the gas. The negative deviations $\Delta T = (T_{fit} - T_m)$ between the fitted and measured temperature all increase with pressure, reaching almost 100 K at the highest pressure of 180 MPa when the SPEG law is used. The PEG law, on the other hand, clearly reproduces the thermocouple temperatures at all pressures studied (cf. Fig. 2 for spectral appearance). This finding is in accord with experiments of Lavorel et al. [40] and Bouché et al. [14] that show good agreement to PEG but a corresponding overestimation of measured high-resolution SRS and CARS linewidths in the same order, when ECS and MEG are employed in the calculations.

At higher temperature (i.e., 700 K), trends among the different laws as a function of pressure are less obvious. At lower pressures (40 MPa), most of the laws lead to temperatures above, and at higher pressures (180 MPa), to values below the thermocouple readings. The PEG law, although for this temperature gives best agreement with the thermocouple readings, deviates significantly ($\Delta T \approx 80$ K) at the highest pressures investigated. It should be noted that other causes for line broadening, e.g., vibrational dephasing, that exhibit different temperature dependencies are not taken into account in the calculations and might be the cause for the varying tendency of the fitting results with pressure. This is because the fitting algorithm, in the attempt to minimize the mean squared sum of the residuals, only counteracts by adjusting temperature and density arbitrarily. The classical model at room temperature also shows significant σ values that increase with pressure. At 700 K, the deviations are considerably smaller.

Similar trends and discrepancies are to be noticed for oxygen at room temperature (cf. Fig. 4). This time, however, the MEG law, as already depicted in Fig. 1, gives the best agreement to the thermocouple readings, although deviations in ΔT are larger than for PEG in the case of nitrogen. For the PEG model, it has to be emphasized that, for oxygen, no consistent set of parameters exists, and therefore, the same set as for nitrogen was used. Contrary to nitrogen, the ECS laws give nearly identical deviations that both increase with pressure. The situation at higher temperatures (546 and 845 K, respectively) is more complicated. In general, the deviations between thermocouple readings and fitted temperature increase with increasing temperature, approaching about 150 K ($\Delta T/T_m = 18\%$) with the ECS-P law at 38 MPa and 845 K. Still, the ECS-(E)P fitting results

agree with one another but deviate significantly from the known temperature of the probe volume, generally decreasing with increasing pressure. Similar to the room-temperature results, the MEG law gives the overall best agreement at higher temperatures and higher pressures, although deviations amount to a significant fraction of the measured value. The classical method quite satisfactorily reproduces the temperature readings, the deviations decreasing with increasing pressure.

Discussion/Conclusions

In the previous paragraphs, an attempt was made to estimate the possibilities of nitrogen and oxygen vibrational CARS thermometry of high-pressure gaseous samples. It is shown that the usual practice in the computational CARS spectrum generation—the incorporation of various scaling-law approaches for the determination of relaxation matrix elements—partly leads to significant deviations between known temperatures and the result from the fitting algorithm. The same behaviour is true when a classical analytical model is used in the calculation of the CARS susceptibility for the smoothed Q-branch profile. There is no clear trend with pressure and temperature in using any of the applied calculation methods.

In the following, possible causes of the scatter between the evaluated and measured temperatures are discussed. First of all, it is obvious that the temperature sensitivity of the high-density smoothed Q-branch profile is less than that of the rotationally resolved spectrum at lower densities, where the width and intensity of individual rotational lines vary significantly with temperature. This richness of spectral information within a small bandwidth is one of the key advantages of vibrational CARS thermometry in flames. At high density, only the width and shift of the fully collapsed isotropic Q branch provides temperature-sensitive information. At low temperatures, collisional narrowing of the line can even reduce this sensitivity. Within the pressure range investigated here, this narrowing is less severe at higher temperatures. To still maintain enough sensitivity to temperature variations in the spectral contour, high spectral resolution and low laser-based spectral noise are required if multiplex CARS spectrometers are employed in practical situations. This can be achieved when single-mode pump lasers and, e.g., modeless Stokes dye lasers [41] are used for CARS signal generation. On the detection side, unintensified charge-coupled device cameras with high quantum efficiency and large dynamic range should reduce saturation and pixel cross talk [42]. In the CARS fitting codes, the main problem is in the flexibility and accuracy of the Gauß Newton minimization algorithm. Because of the narrow line shapes of

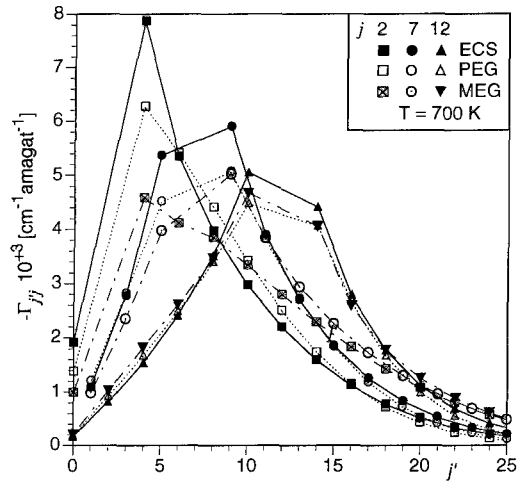

FIG. 5. Calculated rate constants for state-to-state rotational relaxation in nitrogen at 700 K using the ECS-P, MEG, and PEG scaling-law expressions for initial states j = 2, 7, and 12 as a function of final rotational state quantum number j'. The straight lines are shown to guide the eye.

isotropic spectra at high density, the simultaneous fitting of width and shift creates some problems if only first-order derivatives with respect to temperature are considered in the least-squares minimization procedure. To circumvent ambiguities in finding a local minimum, second derivatives have to be included. Furthermore, it has to be emphasized that existing scaling laws and their parameter sets for N_2 and O_2 collisions are optimized to best reproduce measured pressure-broadening coefficients of individual rotational lines in the resolved spectrum. This does not necessarily imply equally precise modeling of the collapsed Q-branch structure at high densities. Figure 5 illustrates the variation in the calculated rate coefficients from some of the employed scaling-law expressions. At high densities, these off-diagonal elements of the relaxation matrix become more important in determining the line shape. For the classical model to be more accurate, the temperature dependence of the energy relaxation cross section σ_E and the correlation parameter γ in Eq. (8) have to be determined more accurately, either by experiment or theory [13,30]. This then enables the development of reliable analytical expressions for interpolation purposes during the temperature-fitting procedure. Finally, rotational CARS thermometry [9] should be a potential alternative since the anisotropic polarizability components of O- and S-branch structures are less influenced by collisional narrowing, the spectral contour is broad compared to otherwise limiting instrumental functions, and some structure still is discernible in the spectrum at high densities.

Acknowledgments

The authors are very thankful to Prof. J. Wolfrum for his current interest in this work. They also acknowledge the fruitful discussions and technical support by Prof. E. U. Franck in planning and setting up the high-pressure equipment. A. A. Suvernev acknowledges the fellowship by the Alexander v. Humboldt foundation. The financial support of the "Stiftung Volkswagenwerk," the "Arbeitsgemeinschaft TECFLAM," and the Deutsche Forschungsgemeinschaft (Grant No. Dr 195/5-1) are gratefully acknowledged.

REFERENCES

1. Modell, M., in *Standard Handbook of Hazardous Waste Treatment and Disposal* (H. M. Freeman, Ed.), McGraw-Hill, New York, 1989.
2. Rofer, C. K., *Kinetics Experiments and Bench-Scale Systems*, Los Alamos Report No. LA-11106-MS, 1987.
3. Webley, P. A., and Tester, J. W., SAE Technical Paper Series No. 881039, 1988.
4. Helling, R. K., and Tester, J. W., *Environ. Sci. Technol.* 22:1319 (1988).
5. Schilling, W., and Franck, E. U., *Ber. Bunsenges. Phys. Chem.* 92:631 (1988).
6. Masten, D. A., Bernard, R. F., Harradine, D. M., and Dyer, R. B., *J. Phys. Chem.* 97:8557 (1993).
7. Frost, M., Bohn, M. A., and Franck, E. U., *Ber. Bunsenges. Phys. Chem.* 93:482 (1989).
8. Peálat, M., Bouchardy, P., Lefebvre, M., and Taran, J. P., *Appl. Opt.* 24:1012 (1985).
9. Aldeń, M., Bengtsson, P.-E., Edner, H., Kröll, S., and Nilsson, D., *Appl. Opt.* 28:3206 (1989).
10. Woyde, M., and Stricker, W., *Appl. Phys. B* 50:519 (1990).
11. Millot, G., Lavorel, B., Fanjoux, G., and Wenger, C., *Appl. Phys. B* 56:287 (1993).
12. Temkin, S. I., and Burshtein, A. I., *Chem. Phys. Lett.* 66:52 (1979).
13. Dreier, T., Schiff, G., and Suvernev, A. A., *J. Chem. Phys.* 100:6275 (1994).
14. Bouché, T., Dreier, T., Lange, B., Wolfrum, J., Franck, E. U., and Schilling, W., *Appl. Phys. B* 50:527 (1990).
15. Eckbreth, A. E., *Appl. Phys. Lett.* 32:421 (1978).
16. May, A. D., Stryland, J. C., and Varghese, G., *Can. J. Phys.* 48:2331 (1970).
17. Kozlov, D. N., Smirnov, V. V., and Volkov, S. Yu., *Appl. Phys. B* 48:273 (1989).
18. Bjarnasson, J. O., Hudson, B. S., and Andersen, H. C., *J. Chem. Phys.* 70:4130 (1979).
19. Bonamy, L., Bonamy, J., Robert, D., Lavorel, B., Saint-Loop, R., Chaux, R., Santos, J., and Berger, H., *J. Chem. Phys.* 89:5568 (1988).
20. Koszykowski, M. L., Farrow, R. L., and Palmer, R. E., *Opt. Lett.* 10:478 (1985).
21. DePristo, A. E., and Rabitz, H., *J. Quant. Spectrosc. Radiat. Transfer* 22:65 (1979).
22. Rahn, L. A., Palmer, R. E., Koszykowski, M. L., and Greenhalgh, D. A., *Chem. Phys. Lett.* 133:513 (1987).
23. Millot, G., Saint-Loup, R., Santos, J., Chaux, R., Berger, H., and Bonamy, J., *J. Chem. Phys.* 96:961 (1992).
24. Sitz, G. O., and Farrow, R. L., *J. Chem. Phys.* 93:7883 (1990).
25. Rahn, L. A., and Palmer, R. E., *J. Opt. Soc. Am. B* 3:1164 (1986).
26. Lavorel, B., Millot, G., Saint-Loup, R., Wenger, C., Berger, H., Sala, J. P., Bonamy, J., and Robert, D., *J. Phys.* 47:417 (1986).
27. Looney, J. P., Rosasco, G. J., Rahn, L. A., Hurst, W. S., and Hahn, J. W., *Chem. Phys. Lett.* 161:232 (1989).
28. Sala, J. P., Bonamy, J., Robert, D., Lavorel, B., Millot, G., and Berger, H., *Chem. Phys.* 106:427 (1986).
29. Millot, G., *J. Chem. Phys.* 93:8001 (1990).
30. Temkin, S., Thuet, J. M., Bonamy, L., Bonamy, J., and Robert, D., *Chem. Phys.* 158:89 (1991).
31. Steinfeld, J. I., Ruttenberg, P., Millot, G., Fanjoux, G., and Lavorel, B., *J. Phys. Chem.* 95:9638 (1991).
32. Keilson, J., and Storer, J. E., *Q. Appl. Math.* 10:243 (1952).
33. Temkin, S. I., and Suvernev, A. A., in *Coherent Raman Spectroscopy* (G. Marowsky and V. V. Smirnov, Eds.), Springer-Verlag, Berlin, 1992.
34. Dießel, E., Dreier, T., Lange, B., and Wolfrum, J., *Appl. Phys. B* 50:39 (1990).
35. Saur, A. M., Behrendt, F., and Franck, E. U., *Ber. Bunsenges. Phys. Chem.* 97:900 (1993).
36. Vargaftik, N. B., *Tables on the Thermophysical Properties of Liquids and Gases*, Hemisphere, Washington, DC, 1975.
37. Greenhalgh, D. A., and Hall, R. J., *Opt. Commun.* 57:125 (1986).
38. Lavorel, B., Millot, G., Bonamy, J., and Robert, D., *Chem. Phys.* 115:69 (1987).
39. Teets, R. E., *Opt. Lett.* 2:226 (1984).
40. Lavorel, B., Oksengorn, B., Fabre, D., Saint-Loup, R., and Berger, H., *Mol. Phys.* 75:397 (1992).
41. Ewart, P., *Opt. Commun.* 55:124 (1985).
42. Plath, I., Meier, W., and Stricker, W., *Opt. Lett.* 17:79 (1992).

COMMENTS

Marcus Alden, Lund Institute of Technology, Sweden. To what degree are stimulated processes influencing the CARS spectrum at these pressures?

Author's Reply. In our experiments, it was always ensured that stimulated Raman and Brillouin scattering were undetectable at the anti-Stokes wave-length by attenuating both pump and Stokes beam intensities below their respective threshold values.

•

P. Ewart, Oxford University, UK. Could you comment on how the degree of cross correlation between pump and Stokes lasers was quantified and on the degree of sensitivity of this correlation at the elevated pressures in your experiments?

Author's Reply. In the modeling codes, cross-coherence effects between pump laser photons were accounted for by the formalism expressions as outlined in Refs. 39 and 37 of the paper. The sensitivity of this correlation with pressure (when the Q-branch profile narrows and thereby the degree of overlap between pump and Stokes modes and the homogeneous Raman line varies) was not investigated. However, the cross correlation between pump photons should be minimized because of the single-mode nature of the Nd:YAG laser.

•

Larry A. Rahn, Sandia National Laboratories, USA. Have you considered the relatively sensitivity to temperature of the width vs the frequency shift of the high-pressure CARS spectrum? As collisional collapse proceeds at very high pressures, the width will be dominated by vibrational dephasing while the frequency will be shifted by collisions as well as the averaged vibrational-rotational interaction. The latter may be more sensitive to temperature at high pressures. The collisional shift, however, will also have a (likely opposite sign) temperature dependence.

Author's Reply. In the current fitting codes, we have not included the variation of a temperature-dependent shift for several reasons: (1) With our currently achievable accuracy of experimental data, the shift of the spectrum is difficult to fit because of the narrow shape of the Q-branch line at high densities in order not to end up in a wrong local minimum. Therefore, higher order fitting procedures have to be employed. We tentatively tried to incorporate measured shift coefficients into the fitting codes, which worked fine for nitrogen but not for oxygen. (2) Within the temperature window investigated in our study, the temperature dependence of the frequency shift is relatively small and can barely be resolved. With higher resolution instruments, however, it should be possible to increase temperature accuracy.

•

Alan Eckbreth, United Technologies Research Center, USA. 1. In performing measurements in actual flames at very high pressures, do you have to worry about variations in background gas composition effects on the Raman linewidths? If so, what would your strategy be for analyzing the CARS signatures to obtain temperature measurements?

2. You mentioned that rotational CARS might be an attractive alternative to vibrational CARS for high-pressure thermometry. At very high pressures, where the rotational lines broaden to the point of significant overlap, wouldn't you need to take collisional narrowing into account as well?

Author's Reply. 1. We found experimentally [1] that for oxygen in argon (12% O_2) or nitrogen (20% O_2) at 300 K, the FWHM of the collapsed Q branch of oxygen varies by less than 20% (with a measurement accuracy of approximately 10%). Also, the shift of the bandhead maximum at 300 K is the same in these gases. But clearly, other collision partners may behave differently and have to be investigated about their effect on broadening and shift of the Q-band shape.

2. For pure rotational CARS, collisional narrowing sets in at much higher pressures than in the vibrational Q branch since spectral exchange takes place across a much larger energy spread determined by ω_Q.

REFERENCE

1. Dreier, T., Schiff, G., and Suvernev, A. A., *J. Chem. Phys.* 100:6275 (1994).

•

Douglas Greenhalgh, Cranfield University, UK. Many years ago when Fiona Porter, Simon Barton, and myself formulated the PEGL model, we chose it because there was essentially no data for the γ_{jk}'s and because the PEGL could be uniquely fit to match the known line widths, Γ_j. Now there are much more data and, for pressures to 40 bar, it is clear that exponential gas models such as MEG are much better. PEGL smears out energy transfer rates away from small Γ_j and small γ_{jk}'s to larger values, which will be less strongly overlapped at a given pressure. Therefore, the difference between PEGL and MEG is rather as if the PEGL is including effects similar to vibrational dephasing. I think the best way forward is to use MEG-like models with improved vibrational dephasing effects.

Author's Reply. It is true, and has recently been investigated theoretically in a comparative study of various scaling laws [1], that vibrational dephasing processes are important to be considered in a correct description of the density dependence of the collapsed Q-branch structure of nitrogen throughout the density range investigated in this study. Dephasing contributions will be considered in future developments of our temperature-fitting codes.

REFERENCES

1. Bulgakov, Yu. I., Storozhev, A. V., and Strekalov, M. L., *Chem. Phys.* 177:145 (1993).

Twenty-Fifth Symposium (International) on Combustion/The Combustion Institute, 1994/pp. 1735–1742

DUAL-BROADBAND ROTATIONAL CARS MEASUREMENTS IN AN IC ENGINE

PER-ERIK BENGTSSON, LARS MARTINSSON AND MARCUS ALDÉN
Department of Combustion Physics, Lund Institute of Technology
P.O. Box 118, S-221 00 Lund, Sweden

AND

BENGT JOHANSSON, BENGT LASSESSON, KARL MARFORIO AND GUNNAR LUNDHOLM
Department of Combustion Engines, Lund Institute of Technology
P.O. Box 118, S-221 00 Lund, Sweden

This is the first report of pure rotational coherent anti-Stokes Raman spectroscopy (CARS) measurements in an internal combustion (IC) engine. Single-shot, dual-broadband rotational CARS (DB-RCARS) spectra were recorded both prior to ignition and in the postcombustion gases. From these spectra, both temperature and relative oxygen concentrations were evaluated. The pressure was registered simultaneously with the CARS measurements in the spark-ignition engine burning natural gas and air. Prior to ignition, normally at temperatures below 1000 K and pressures below 2 MPa, a rotational CARS spectrum is very temperature sensitive, and the technique can be used for temperature measurements with high accuracy. Evaluated temperatures show a negligible dependence on uncertainties in parameters such as the nonresonant susceptibility of the gas and the slit width. Moreover, no collisional narrowing of the lines has to be taken into account. The relative standard deviation of evaluated temperatures and of relative oxygen concentrations from single-shot measurements were as low as 1, and 1.4–1.9%, respectively. In the postcombustion gases at temperatures above 2000 K and pressures above 1.5 MPa, the nonresonant CARS background gave a large contribution to the total spectrum. In this temperature and pressure range, the evaluated values of temperature and nonresonant susceptibility are not independent, and the nonresonant susceptibility had to be fixed at a precalculated value to get a reliable temperature evaluation. The advantages and disadvantages of rotational CARS in comparison with vibrational CARS for IC engine measurements are discussed.

Introduction

To gain a better understanding of fundamental chemical and physical processes in combustion, there is a need for spatially and temporally resolved information on parameters such as temperature and species concentrations. Because of these requirements, laser-based techniques will play an increasing role in combustion diagnostics in the near future. One of the most widely used laser diagnostic techniques is coherent anti-Stokes Raman spectroscopy (CARS), of which different aspects have been reviewed in a number of papers, e.g., Refs. 1 through 4. Over and above high spatial and temporal resolution, the CARS technique has several merits for diagnostics in hostile combustion environments. The CARS signal is generated as a beam of high intensity, and consequently, the isotropic background fluorescence is easily suppressed. Moreover, the CARS signal will appear at wavelengths shorter than the laser wavelengths, whereas potential fluorescence interference usually occurs at longer wavelengths than the exciting wavelengths. Since the temperature and, in many cases, concentrations are evaluated from the shape of a spectrum and not the signal strength, the potential practical problem of attenuation of the signal by contaminated windows is of minor importance.

The most commonly used CARS technique is vibrational CARS, in which the signal originates in transitions between rotational levels of the same rotational quantum number, J, in different vibrational levels of the probed molecule. Nitrogen is the natural choice for thermometry since it has a well-studied spectrum and a high mole fraction (0.60–0.70) in practical air-fed combustion. In the most common setup for vibrational CARS thermometry of nitrogen, a Nd:YAG laser (with laser frequencies ω_p) is used together with a dye laser using a rhodamine dye or a mixture of rhodamine dyes (with frequencies ω_s). The CARS frequencies, ω_{as}, are generated at $\omega_{as} = \omega_p + \omega_R$, where $\omega_R = \omega_p - \omega_s$ are the Raman frequencies.

Several successful temperature measurements have been performed in internal combustion (IC)

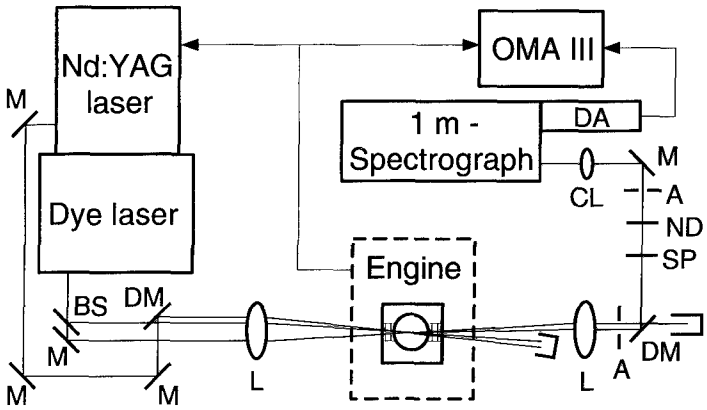

FIG. 1. Experimental arrangement for dual-broadband rotational CARS. M = mirror, DM = dichroic mirror, L = lens, BS = beam splitter, A = aperture, SP = short-pass filter, ND = neutral density filter, CL = cylindrical lens, DA = diode-array detector, OMA = optical multichannel analyser.

engines using vibrational CARS [5–12]. Some studies have been concerned with the problem of engine knock prior to ignition [13–16]. Of relevance for engine knock are the conditions prior to ignition with typical temperatures of 600–1000 K and pressures of 1–2 MPa. In this range of temperatures and pressures, a vibrational nitrogen CARS spectrum has a low temperature sensitivity. The appearance of the hot bands will increase the accuracy of a temperature measurement, but the first hot band will not emerge until the temperature is above ~1000 K. Furthermore, collisional narrowing leads to the collapse of the individual peaks into a single peak [17]. This leads to a decrease in the temperature sensitivity of the spectrum, and an uncertainty in the value of the nonresonant susceptibility of the gas will give a larger uncertainty in the evaluated temperature [18]. It has also been shown that the laser field statistics of the Nd:YAG laser photons affect the CARS intensities in such a way that the ratio between the resonant and the nonresonant CARS signals will depend on the time correlation between the Nd:YAG photons [19]. In the USED CARS phase-matching scheme [20], the time correlation between the pump beams is normally uncontrolled, which leads to uncertainties in the evaluated vibrational CARS temperatures, as discussed in Ref. 12.

Instead of utilising Raman transitions between different vibrational levels as in vibrational CARS, Raman transitions between different rotational levels within a vibrational level are used in pure rotational CARS [21–23]. The vibrational Raman shifts of most molecules are above 1000 cm^{-1}, whereas the rotational Raman transitions present in a rotational CARS spectrum of nitrogen have Raman shifts below 500 cm^{-1} even at flame temperatures. Rotational CARS measurements are normally made using the dual-broadband rotational CARS (DB-RCARS) approach [24,25]. For this technique, a beam from an arbitrary, narrowband laser is used together with the beam from an arbitrary, broadband dye laser split into two beams. The rotational Raman coherences are driven by pairs of photons, one from each of the dye spectral profiles, separated by the Raman frequency of the transition, which are then coupled to the narrowband laser frequency to create the CARS frequencies. DB-RCARS has several merits; most importantly, there is a spectral averaging effect resulting in a high single-shot precision. In addition, red stable dyes can be used, and experiments are easily arranged utilising a planar, BOXCARS, phase-matching scheme even though rotational Raman transitions are probed.

In a previous study, DB-RCARS proved to be an efficient thermometer in the region from ambient temperature and pressure to 870 K and 1.5 MPa in nitrogen [26]. Moreover, the dependence of the evaluated temperature on uncertainties in the nonresonant susceptibility is negligible for rotational CARS in this region, and no effects of collisional narrowing have to be taken into account until pressures of tens of MPa are reached. Motivated by these facts and the inherent problems in vibrational CARS at higher pressures described above, the potential of using DB-RCARS for nitrogen thermometry and oxygen concentration measurements in an IC engine, both before ignition as well as in the burnt gases, has been investigated. The diagnostic aspects of the technique for measurements in IC engines have been critically compared with vibrational CARS.

Experimental Arrangement

The experimental arrangement is shown in Fig. 1. A Nd:YAG laser (YG 681C-10) was used, giving 550 mJ/pulse at 532 nm in a bandwidth of 0.7 cm^{-1} [full width at half maximum (FWHM)] with a duration of ~10 ns. Ten percent of this radiation was used in the CARS-generating process, while the remaining 90% pumped a Quantel TDL 50 HE dye laser. Using a DCM dye, with a FWHM of ~280 cm^{-1}, ~90 mJ was obtained in each laser pulse. The dye laser beam was separated into two beams of equal pulse energy, the beam at 532 nm was superimposed on one of the

dye laser beams using a dichroic mirror, and all three beams propagated parallel to each other towards a focusing lens with a focal length of 300 mm. A planar BOXCARS setup was used, and the distance between the superimposed beams and the single red beam was 14 mm on the focusing lens, giving a probe volume of approximately 30 μm in diameter and 1 mm in length. The maximum laser pulse energy in each of the beams was limited to 30 mJ, because the windows allowing optical access through the cylinder head could be damaged at higher energies.

The CARS signal was recollimated using an f = 500 mm lens. The superimposed primary laser beams were directed to a beam dump before the recollimating lens to minimise stray light reaching the detector. Dichroic mirrors transmitted most of the dye laser energy while reflecting the rotational CARS signal. The CARS signal was focused on the entrance slit of a home-built 1-m spectrograph using an f = 80 mm cylindrical lens. The grating with 600 grooves/mm and a blaze 2.5 μm was used in the fourth order with a dispersion of 10 cm^{-1}/mm. After alignment of the setup, the rest of the dye laser radiation was suppressed using a short-pass filter at 560 nm. Stray light (at 532 nm) from optical components and surfaces was suppressed by several apertures. Neutral density filters were used to attenuate the signal, so that the detector would not be saturated. The CARS signal was detected using a diode-array detector and processed by an optical, multichannel analyser (OMA III, EG&G, PARC). The diode array consists of 1024 pixels, each 25 μm $\times$ 2.5 mm. The detector and the laser were triggered by a pulse from the engine at a certain crank angle position.

The measurements were performed in a six-cylinder Volvo (TD-102) diesel engine, rebuilt as a spark-ignition engine. One of the cylinders was extended by a spacer, through which optical access could be obtained through four rectangular quartz windows positioned orthogonally to each other. The distance between opposite windows was 121 mm. The piston head was elongated to maintain a compression ratio of 10:1.

Measurements

The engine was run at 1200 rpm since this value meant that the Nd:YAG laser was triggered to operate at a repetition frequency of 10 Hz with one measurement for each cycle. The engine was run either continuously or in a skip-fired mode. When using the skip-fire mode, the cycle-to-cycle repeatability will be enhanced since the effect of residual gas from the previous cycle is minimised. The fuel mixture consisted of natural gas (91% methane by volume) and air. This fuel was chosen since it produced only little contamination of the windows. Some oil was deposited on the windows during the measurements but had a negligible effect on the detection of the signal. In this investigation, the probe point was, for most measurements, chosen to be ~3 mm below the spark plug, which is positioned at the centre of the cylinder. Both the crank angle degree and the equivalence ratio of the fuel-air mixture were varied during the measurements.

At each chosen crank angle degree and equivalence ratio, generally 100 single shots were recorded. For each of the cycles, the pressure development during the cycle was recorded. To suppress the image lag of the detector, one readout of the detector was performed between each real measurement. To compensate for the different sensitivity of the diode-array pixels, and for the differences in the available beam energy for generating a CARS photon at different Raman frequencies, the experimental spectral intensity was divided by a nonresonant CARS spectral intensity. Such an accumulated, averaged spectrum was generated in flowing argon with the top of the cylinder removed before the measurements were started. This was an acceptable approach since the nonresonant CARS spectral distribution is very stable using the DB-RCARS approach, and it showed a negligible change during the measurements.

A problem with strong scattering at the Nd:YAG laser wavelength of 532 nm was present over about 30 crank angle degrees around top dead centre (TDC). This stray light "filled" the spectrograph and saturated the detector with a strong background. By using a notch filter in the detection path to suppress light at the wavelength 532 nm, this background was rejected and the signal could be detected, except over a period of about 20 crank angle degrees around TDC, where no rotational CARS signal could be detected at all. This was probably because of strong density fluctuations in the combustion chamber, which disturbed the overlapping of the three primary beams and/or the propagation direction of the CARS signal.

Evaluation Procedure

The temperatures and relative oxygen concentrations were evaluated using a least-squares fitting of a library of calculated spectra to the experimental spectra. The evaluation procedure and computer code are described in Ref. 23. In the evaluations presented here, a straightforward inclusion of oxygen in the calculations of the spectra has been made. The molecular constants for oxygen were taken from Refs. 27 and 28, and the semiclassical, rotational Raman linewidths for nitrogen [29] were used as the oxygen linewidths. The error in the temperature when using this approximation is negligible for temperatures below ~1000 K [30]. The nitrogen Raman linewidths were calculated according to the energy corrected sudden (ECS) model, which has been shown to give the best temperature accuracy [23].

Currently, we are using precalculated linewidths in the temperature range 300–2100 K, in steps of 100 K. Consequently, all temperatures above 2100 K were evaluated with extrapolated linewidths.

The parameters varied in the spectral fitting were, apart from the temperature, also the linear dispersion, and the reference pixel for the Raman shift of a rotational CARS peak, which determines the exact frequency scale of the experimental spectrum. The frequency scale was very stable, the maximum shift of the reference CARS line was 2 pixels ($\sim$0.5 cm^{-1}) in both the spectra recorded before and after combustion. In the spectra recorded before ignition, the nonresonant susceptibility was also fitted, and the resulting values were in good agreement with the theoretical prediction of the nonresonant susceptibility of the natural gas-air mixture. After combustion, the nonresonant susceptibility was fixed at the value 0.89 $\times 10^{-17}$ esu (1.2 times the nitrogen value) [31], since we assume that the gas in the measurement volume is completely combusted. Before ignition, oxygen concentrations were evaluated from least-squares fits of experimental spectra to theoretical spectra at different oxygen concentrations. The oxygen concentration in the theoretical spectra was varied in steps of 0.5%.

Results and Discussion

In Fig. 2, two single-shot spectra recorded at positions prior to ignition are shown. Spectrum A is recorded at -62 crank angle degrees (CAD) before top dead centre (BTDC), and spectrum B at -22 CAD BTDC, just before ignition of the mixture, which occurred at -20 CAD BTDC. Both nitrogen and oxygen lines can be seen in the spectra. The methane does not give rise to any rotational CARS spectrum, because of the symmetry of the molecule, and will contribute only to the nonresonant susceptibility of the mixture. In spectrum B at a pressure of 1.61 MPa, the lines are much broader than in spectrum A at 0.41 MPa as a result of pressure broadening. The higher evaluated temperature for spectrum B of 706 K in comparison with 490 K for spectrum A can be observed as a shift of the maximum intensity towards higher Raman shifts, and a broader spectral envelope. The single-shot peak signal strength was $\sim 4 \times 10^4$ counts for spectrum B; thus, neutral density filters had to be used to get a signal strength within the nonsaturated regime of the detector.

In Table 1, the results are summarised from the evaluation of 100 single-shots at four different crank angle degrees prior to ignition. On the average, two spectra in each series were not evaluated because of spectral interference, possibly originating from laser-induced breakdown of the gas mixture. The compression of the gas in an internal combustion engine

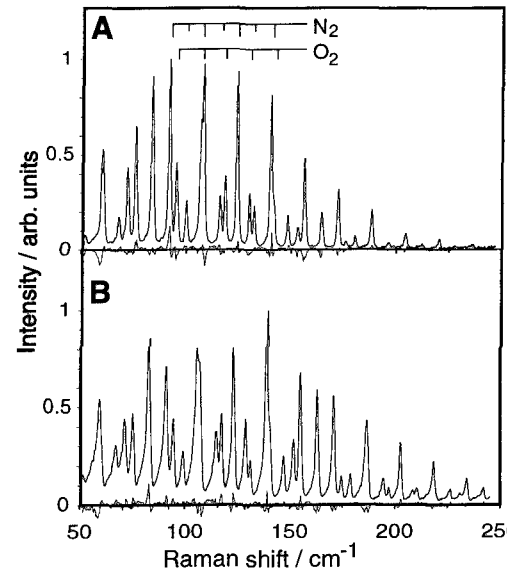

FIG. 2. Single-shot spectra recorded at different crank angle degrees prior to ignition for a mixture of natural gas and air ($\Phi \cong 0.6$). Below the spectra, the difference spectrum between the experimental spectrum and the best-fit theoretical spectrum is displayed. The time, pressure, and evaluated temperature are the following; A: $t = -62$ CAD BTDC, $P = 0.41$ MPa, $T = 490$ K; B: $t = -22$ CAD BTDC, $P = 1.61$ MPa, $T = 706$ K. Both the oxygen and nitrogen peaks are evident in the spectra.

TABLE 1
Results of single-shot precision measurements of temperature and oxygen concentration are shown for four series of 100 single shots recorded prior to ignition at different times.[a]

Time (CAD)	(P) (MPa)	(T) (K)	σ (K)	σ/T (%)	$[O_2]$ (%)	σ (%)	$\sigma/[O_2]$ (%)
−82	0.26	426	4.6	1.1	20.9	0.4	1.9
−62	0.41	490	4.9	1.0	21.0	0.3	1.5
−42	0.78	585	5.9	1.0	21.0	0.3	1.4
−22	1.61	706	7.7	1.1	21.2	0.3	1.4

[a]Column 1: Position in crank angle degrees (CAD); column 2: average pressure (P); column 3: evaluated average temperature (T); column 4: temperature standard deviation (σ); column 5: relative temperature standard deviation (σ/T); column 6: evaluated average oxygen concentration $[O_2]$; column 7: oxygen concentration standard deviation (σ); column 8: relative oxygen concentration standard deviation ($\sigma/[O_2]$)

is considered to occur under adiabatic conditions with a constant value of $p^{\gamma-1}T^{\gamma}$. Using the measured pressures and evaluated average temperatures in Table 1, a γ ($= C_p/C_v$) of 1.38 was calculated, which is equal to the value of the natural gas(methane)-air mixture (at $\Phi = 0.6$) found in the literature, in this temperature range [32]. The relative standard deviation of the pressure of 100 cycles at all four crank angles was ~1%, which for adiabatic conditions gives a cycle-to-cycle variation in temperature of ~0.3%. The relative standard deviation of the evaluated temperatures was at all four crank angles 1.0–1.1%. The oxygen concentration (of the air) was evaluated to be in the range 20.9–21.2% at all four crank angles, with a very high precision for the standard deviation in oxygen concentration, 0.3–0.4%, and a relative standard deviation of 1.4–1.9%. A brief explanation for these low values will be given here. For DB-CARS, mode-amplitude fluctuations (which are the dominating source of noise for vibrational CARS) have a minor influence due to spectral averaging even on a single-shot basis [21]. Instead, according to a model described in Refs. 21 and 33, the noise-to-signal ratio in DB-RCARS is mainly described by

$$\{((2\pi)^{1/2}/T\Gamma_c)(1 + \Gamma_c^2/W^2)^{1/2} + (\Omega_a/2\pi\Gamma_r)\}^{1/2}$$

where T is the duration of the CARS signal, Γ_c and Γ_r are the Nd:YAG laser linewidth and Raman linewidth, respectively, W is the slit width, and Ω_a is the mode spacing of the broadband dye laser. Both terms in the expression are associated with phase-mode fluctuations. For our experimental setup, it turns out that the second term dominates at atmospheric pressure, giving rather poor precision [21]. However, in the present investigation under the conditions prior to ignition, the second term loses its importance (because of increase in Γ_r), and the noise will be determined by the first term, resulting in the low relative standard deviations in Table 1. A consequence of the investigation in Ref. 33 is that use of a single-mode Nd:YAG laser instead of a multimode Nd:YAG laser will (to a first approximation) lead to the disappearance of the first term, and even better precision than the values presented in Table 1 should then be achieved. Modelling of both oxygen and nitrogen slightly reduces the relative standard deviation of evaluated single-shot temperatures in comparison with modelling nitrogen alone, which will be discussed in more detail in Ref. 30.

In Fig. 3, two single-shot spectra from the postcombustion gases are shown. Spectrum A is recorded at 32 CAD after top dead centre (ATDC) at a pressure of 3.20 MPa with a best-fit temperature of 2550 K, and spectrum B was recorded at 56 CAD ATDC at a pressure of 1.55 MPa with a best-fit temperature of 2430 K. As discussed in Ref. 23, our present computer code cannot provide reliable temperatures in the region above 2000 K. It was

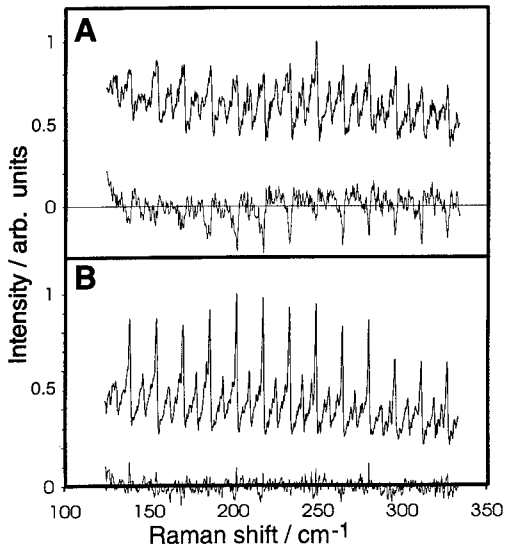

FIG. 3. Single-shot spectra recorded at different crank angle degrees in the postcombustion gases for a stoichiometric mixture of natural gas and air. Below each of the spectra, a difference spectrum between the experimental spectrum and the best-fit theoretical spectrum is shown. The time, pressure, and evaluated temperature are the following; A: t = 32 CAD ATDC, P = 3.20 MPa, T = 2550 K; B: t = 56 CAD ATDC, P = 1.55 MPa, T = 2435 K. The peak single-shot signal strength is ~1000 counts in both spectra.

demonstrated that the difference between evaluated CARS temperatures and temperatures measured with thermocouples in an oven at atmospheric pressure increased for increasing temperatures above 1500 K. An evaluated temperature of 2500 K can, according to Ref. 23, be estimated to be 300–400 K too high. It appears that the lack of knowledge of the correct rotational Raman linewidths for high rotational quantum numbers (J) at high temperatures limits the accuracy of rotational CARS at high temperatures.

Normally, both the temperature and the nonresonant susceptibility are fitted using our code, but for these evaluations at high temperatures and pressures, the best fits (giving lowest values of the sum of squares) resulted both in much too low temperatures, and evaluated nonresonant susceptibilities that were more than twice the value of nitrogen. A reasonable value for the nonresonant susceptibility in the postcombustion gases of a stoichiometric mixture is 1.2 times the value of nitrogen [31], and the nonresonant susceptibility was fixed at this value in the evaluation. Evaluation of 100 single-shot spectra from 32 CAD ATDC (spectrum A) gave a relative standard deviation of the temperature of 2.7%, and an uncertainty in the value of the nonresonant sus-

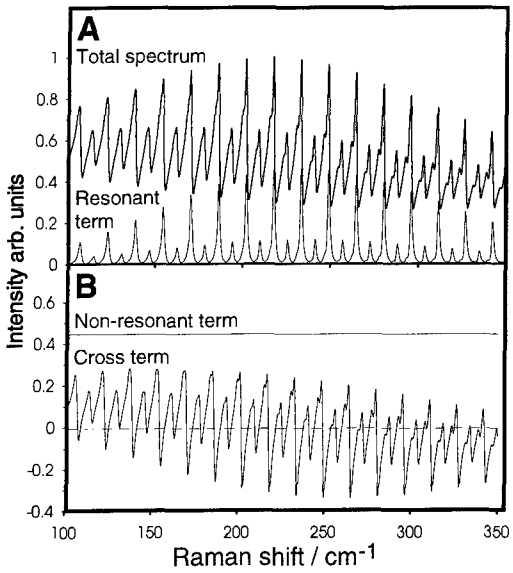

FIG. 4. A: A theoretical rotational CARS spectrum of nitrogen at a temperature of 2100 K and a pressure of 3.2 MPa are shown together with the resonant part of the spectrum under the same conditions. B: The cross-term part and the nonresonant part for the total spectrum shown in A are displayed.

ceptibility of 10% resulted in an uncertainty in the evaluated average temperature from the single shots of ~30 K. For 100 single shots from 56 CAD (spectrum B), the relative standard deviation in temperature was 1.4%, and a 10% uncertainty in the nonresonant susceptibility gave an uncertainty of ~50 K in the evaluated temperature. By inspection of the difference spectra below each figure, the fit of spectrum B is very good, whereas the fit of spectrum A is less good, mostly because the theoretical peaks are much higher than the experimental ones. A possible explanation might be that the focal point of the signal at the entrance slit of the spectrograph was broadened because of beam steering effects in this high-temperature and high-pressure situation. To facilitate the understanding of the spectra in Fig. 3, a theoretical spectrum of nitrogen has been generated for similar conditions, at a temperature of 2100 K and a pressure of 3.2 MPa, and it is shown in Fig. 4. The total CARS spectrum has also been separated into three parts: the resonant part, the nonresonant part, and the cross-term part. Obviously, the nonresonant term has a large impact on the total spectrum and is of the same height as the resonant part under the present conditions. Also, the cross term gives a large contribution to the total spectrum. A way to avoid interference from the nonresonant background is by the use of polarisation suppression techniques [34], albeit at the expense of increased experimental complexity and a severe decrease in signal strength of more than a factor of 64 for rotational CARS.

The main advantage of dual-broadband rotational CARS in comparison with vibrational CARS may be in the temperature and pressure region prior to ignition in IC engines. Although good agreement between experimental spectra and theoretically calculated spectra can be obtained for vibrational CARS for such conditions, the temperature accuracy is critically dependent on parameters such as the nonresonant susceptibility of the gas, the laser linewidth, the slit width, and the theoretical modelling of collisional narrowing. For dual-broadband rotational CARS, the evaluated temperature is almost decoupled from the slit width and the nonresonant susceptibility under conditions prior to ignition. This is an advantageous fact, since the major influence of different practical fuels is to increase the nonresonant susceptibility of the mixture, and spectral lines of fuels generally "drown" in the nonresonant background. An uncertainty in the slit width of 10% gives an uncertainty in the evaluated temperature of as little as less than 0.5%. Another problem for vibrational CARS is the long-term drift in the broadband dye laser spectral profile [14], whereas DB-RCARS is inherently insensitive to spectral changes in the dye profile. These merits of DB-RCARS will be valuable in forthcoming projects aiming at accurate temperature measurements in studies of engine knock, and simultaneous measurements of temperature and oxygen concentrations in studies of the mixing of the fuel-air mixture with exhaust gases.

Conclusions

1. Dual-broadband rotational CARS (DB-RCARS) was successfully used for diagnostics in a spark-ignition engine. Single-shot measurements were performed both prior to ignition and in the postcombustion gases, and temperatures and relative oxygen concentrations were evaluated from the recorded spectra.
2. Prior to ignition at temperatures below 800 K and pressures below 2 MPa, previous studies have revealed a high accuracy for DB-RCARS. The technique showed a very high precision in this temperature and pressure range. The relative standard deviation of single-shot temperatures was found to be as low as ~1%, and the relative standard deviation of single-shot oxygen concentrations was 1.4–1.9%. The temperature and the nonresonant susceptibility are independent variables, implying that reliable temperatures are obtained without the need for a precise knowledge of the nonresonant susceptibility.
3. In the postcombustion gases at temperatures above 2000 K and 1.5 MPa, recorded DB-RCARS spectra showed a large influence from the non-

resonant susceptibility. To obtain reliable temperatures from a spectral fit, the nonresonant susceptibility of the gas had to be assigned a precalculated value; otherwise, the best-fit spectrum resulted in erroneous values for both the evaluated temperature and the nonresonant susceptibility. Evaluated temperatures above 2000 K are at present uncertain, mainly because of uncertainties in the rotational Raman linewidths generally at high temperatures and in particular for high rotational quantum numbers.

4. The greatest experimental problem in the application of DB-RCARS in the engine was the suppression of laser radiation at 532 nm scattered from windows, optical components, and surfaces. Careful alignment of the setup was therefore necessary. Rotational CARS spectra could be registered over the whole engine cycle except over ~20 crank angle degrees around top dead centre during the flame propagation in the cylinder.
5. DB-RCARS has some advantageous features for measurements in engines in comparison with vibrational CARS. Temperature and oxygen concentration measurements can be performed simultaneously using a Nd:YAG and single dye laser system. Under the conditions prior to ignition, DB-RCARS gives a high accuracy in the temperature determination, with negligible influence from parameters such as the slit width and the nonresonant susceptibility. DB-RCARS is inherently insensitive to spectral changes in the dye laser profile that might occur during measurements. Effects of cross coherence and collisional narrowing can be disregarded in the calculation of theoretical spectra.

Acknowledgements

The work was financially supported by the Swedish Board for Industrial and Technical Development, NUTEK, and the Swedish Research Council for Engineering Sciences (TFR). The technical assistance of Bertil Andersson and stimulating discussions with Dr. Stefan Kröll are gratefully acknowledged.

REFERENCES

1. Druet, S. A. J., and Taran, J.-P. E., *Prog. Quant. Electron.* 7:1–72 (1981).
2. Eckbreth, A. C., *Laser Diagnostics for Combustion Temperature and Species*, Abacus Press, Cambridge, MA, 1987.
3. Greenhalgh, D. A., in *Advances of Non-linear Spectroscopy* (R. J. H. Clark and R. E. Hester, Eds.), Wiley, New York, 1988, pp. 193–251.
4. Stricker, W., and Meier, W., in *Trends in Applied Spectroscopy* (Council of Scientific Research Integration, Eds.), Research Trends, Trivandrum, India, 1993.
5. Stenhouse, I. A., Williams, D. R., Cole, J. B., and Swords, M. D., *Appl. Opt.* 18:3819–3825 (1979).
6. Klick, D., Marko, K. A., and Rimai, L., *Appl. Opt.* 20:1178–1181 (1981).
7. Kajiyama, K., Sajiki, K., Kataoka, H., Maeda, S., and Hirose, C., SAE Technical Paper 821036 (1983).
8. Rahn, L. A., Johnston, S. C., Farrow, R. L., and Mattern, P. L., in *Temperature: Its Measurement and Control in Science and Industry* (J. F. Schooley, Ed.), American Institute of Physics, New York, 1982, Vol. 5, pp. 609–613.
9. Alessandretti, G. C., and Violino, P., *J. Phys. D: Appl. Phys.* 16:1583–1594 (1983).
10. Lucht, R. P., Dunn-Rankin, D., Walter, T., Dreier, T., and Bopp, S. C., SAE Technical Paper 910722 (1991).
11. Brüggemann, D., Wies, B., Zhang, X. X., Heinze, T., and Knoche, K.-F., in *Combustion Flow Diagnosics* (D. F. G. Durão, M. V. Heitor, J. H. Whitelaw, and P. O. Witze, Eds.), NATO ASI Series, Kluwer Academic Publishers, Dordrecht, The Netherlands, 1992, pp. 495–511.
12. Porter, F. M., and Williams, D. R., "CARS Thermometry Accuracy in an IC Engine," *Appl. Phys. B*, submitted.
13. Green, R. M., and Lucht, R. P., *Proceedings from International Symposium on Diagnostics and Modeling of Combustion in Reciprocating Engines*, Tokyo, 1985, pp. 259–266.
14. Lucht, R. P., Teets, R. E., Green, R. M., Palmer, R. E., and Ferguson, C. R., *Combust. Sci. Technol.* 55:41–61 (1987).
15. Marie, J.-J., and Cottereau, M.-J., SAE Technical Paper 870458 (1987).
16. Cottereau, M. J., Grisch, F., and Marie, J. J., *Appl. Phys. B* 51:63–66 (1990).
17. Hall, R. J., Verdieck, J. F., and Eckbreth, A. C., *Opt. Comm.* 35:69–75 (1980).
18. Woyde, M., and Stricker, W., *Appl. Phys. B* 50:519–525 (1990).
19. Rahn, L. A., Farrow, R. L., and Lucht, R. P., *Opt. Lett.* 9:223–225 (1984).
20. Davis, L. C., Marko, K. A., and Rimai, L., *Appl. Opt.* 20:1685–1690 (1981).
21. Aldén, M., Bengtsson, P.-E., Edner, H., Kröll, S., and Nilsson, D., *Appl. Opt.* 28:3206–3219 (1989); Erratum: *Appl. Opt.* 29:4434 (1990).
22. Leipertz, A., Magens, E., Seeger, T., and Spiegel, H., in *Aerothermodynamics in Combustors IUTAM Symposium* (R. S. L. Lee, J. H. Whitelaw, and T. S. Wung, Eds.), Springer-Verlag, Berlin, Heidelberg, 1992, pp. 105–117.
23. Martinsson, L., Bengtsson, P.-E., Aldén, M., Kröll, S., and Bonamy, J., *J. Chem. Phys.* 99:2466–2477 (1993).
24. Eckbreth, A. C., and Anderson, T. J., *Opt. Lett.* 11:496–498 (1986).
25. Aldén, M., Bengtsson, P.-E., and Edner, H., *Appl. Opt.* 25:4493–4500 (1986).
26. Martinsson, L., Bengtsson, P.-E., Aldén, M., and Kröll,

S., in *Temperature: Its Measurement and Control in Science and Industry* (J. F. Schooley, Ed.), American Institute of Physics, New York, 1992, Vol. 6, pp. 679–684.
27. Laher, R. R., and Gillmore, F. R., *J. Phys. Chem. Ref. Data* 20:685–712 (1991).
28. Rouillé, G., Millot, G., Saint-Loup, R., and Berger, H., *J. Mol. Spectrosc.* 154:372–382 (1992).
29. Robert, D., and Bonamy, J., *J. Phys. (Paris)* 10:923–943 (1979).
30. Martinsson, L., Bengtsson, P.-E., and Aldén, M., "Oxygen Concentration and Temperature Measurements in N_2–O_2 Mixtures Using Rotational Coherent Anti-Stokes Raman Spectroscopy," *Appl. Phys. B,* submitted.
31. Hall, R. J., and Boedeker, L. R., *Appl. Opt.* 23:1340–1346 (1984).
32. Heywood, J. B., *Internal Combustion Engine Fundamentals,* McGraw-Hill Book Company, New York, 1988.
33. Kröll, S., and Sandell, D., *J. Opt. Soc. Am. B.* 5:1910–1926 (1988).
34. Rahn, L. A., Zych, L. J., and Mattern, P. L., *Opt. Comm.* 30:249–252 (1979).

COMMENTS

Larry A. Rahn, Sandia National Laboratories, USA. How important are photon statistics to the precision of these single-shot measurements? Does this become the limiting problem at higher temperatures?

Author's Reply. Under preignition conditions, a relative standard deviation in temperature as low as ~1% was achieved (see Table 1). This value includes the cycle-to-cycle variation which, however, is believed to contribute with a negligible uncertainty. Since high peak single-shot signal strengths of 5000–10,000 counts were readily obtained on the detector (using neutral density filters), the shot noise contribution to the uncertainty in evaluated single-shot temperatures is small. Thus even for this low relative standard deviation of 1%, it seems that noise due to phase mode fluctuations is the dominating source of uncertainty to evaluated single-shot temperatures. The use of a single-mode Nd:YAG laser instead of a multimode Nd:YAG laser should, according to the model in Ref. 21, further reduce the noise from phase mode fluctuations. The real improvement is uncertain since other parameters such as the detector shot noise may then be the dominating source of error. This will be investigated further both theoretically and in experimental studies under static conditions.

Under the conditions in postcombustion gases dealt with in this paper (at $T > 2000$ K and $P > 1$ MPa), peak single-shot signal strengths of ~1000 counts were obtained. The question of the role of detector shot noise in comparison with phase mode fluctuations for the precision of single-shot temperatures is of minor importance for evaluated single-shot temperatures, since there are several factors that severely affect the possibility of extracting correct temperatures from a single-shot spectrum. In this temperature and pressure range, a rotational CARS spectrum is not so sensitive to changes in temperature, making the evaluated temperature easily affected by experimental uncertainties, such as the nonresonant susceptibility, which can have a large impact on the total spectrum. In addition, present linewidth models lead to evaluated temperatures that are too high at temperatures above 1500 K.

•

Douglas Greenhalgh, Cranfield University, UK. I have two comments, but first let me congratulate you on realising the potential of rotational CARS. First, for 1% uncertainty in temperature I would suspect that detector noise, as evaluated by Fiona Porter and David Snelling, is much more important. Secondly, given that you show that rotational CARS is excellent up to say 1500 K (given that 0-band CARS is good above 1500 K), but poor above this temperature. Perhaps you could arrange the frequency of your dye laser so that both convectional Q-brand CARS and double broad and rotational CARS are generated simultaneously?

Author's Reply. The uncertainty of single-shot temperatures was already discussed in the author reply to the comment by L. Rahn. The second comment is also on a very interesting topic for the application of dual-broadband rotational CARS. Recently, we have published a paper describing the potential of a technique for simultaneous generation of vibrational CARS on the C-H stretch vibration of a fuel and dual-broadband rotational CARS on nitrogen/oxygen [1]. Both signals are generated in the same direction. This study was based on a demonstration of the same technique for nitrogen [2].

REFERENCES

1. Bengtsson, P.-E., Martinsson, L., and Aldén, M., "Combined Vibrational and Rotational CARS for Simultaneous Measurements of Temperature and Concentrations of Fuel, Oxygen, and Nitrogen," *Appl. Spectrosc.,* in press.
2. Aldén, M., Bengtsson, P.-E., and Edner, H., *Appl. Opt.* 25:4493–4500 (1986).

Twenty-Fifth Symposium (International) on Combustion/The Combustion Institute, 1994/pp. 1743–1750

DOUBLE-PULSE IMAGING USING SIMULTANEOUS OH/ACETONE PLIF FOR STUDYING THE EVOLUTION OF HIGH-SPEED, REACTING MIXING LAYERS

JERRY M. SEITZMAN
School of Aerospace Engineering
Georgia Institute of Technology
Atlanta, GA 30332-0150, USA

AND

MICHAEL F. MILLER, TOBIN C. ISLAND AND RONALD K. HANSON
High Temperature Gasdynamics Laboratory
Department of Mechanical Engineering
Stanford University
Stanford, CA 94305, USA

A technique for recording the evolution of large-scale structures in high-speed nonpremixed combustion flows is demonstrated. A single frequency-doubled dye laser system that can produce two pulses separated by tens of microseconds is used to simultaneously excite fluorescence from acetone, seeded into the fuel stream, and from OH, which marks the combustion gases. Thus, four images, an OH/acetone pair for each of the two pulses, are recorded on four separate cameras. The accuracy of the double-pulse technique is examined in a low-speed methane-air flame, which is essentially frozen during the measurement time. The average difference, or error, between corresponding pixels in a double-pulse pair of OH images shows little spatial biasing and primarily results from signal shot-noise fluctuations. The double-pulse OH/acetone technique is demonstrated in a nominally two-dimensional, high-speed reacting mixing layer consisting of an ambient-temperature, low-speed hydrogen-containing fuel stream and a high-temperature, high-speed oxidizing stream. Two mixing layer conditions are presented: a low compressibility case, with convective Mach number $M_c = 0.32$, and a more compressible case, $M_c = 0.70$. Reasonable quality images, having minimum noise levels of 11–14%, were obtained in both cases. The peak OH levels are near 2000 ppm, and the acetone seeding is roughly 3500 ppm. The regions of the flow defined by the interface between the mixing layer and the acetone-seeded fuel stream are relatively stable during the 30–50 μs measurement times and have convective velocities slightly higher than the speed of the fuel stream. The regions of the mixing layer marked by OH move faster and exhibit greater distortion.

Introduction

For high-speed combustion devices in which the fuel and oxidizer are supplied in separate streams, successful operation will often be limited by the rate of mixing between the two streams. In turbulent free shear flows, large-scale motions are responsible for the first step in the mixing process, the entrainment of fuel and oxidizer into the mixing region. Therefore, measurements that shed light on the evolution, e.g., convection, deformation, and chemical transformation, of the large-scale structures should provide insight into the dynamics of entrainment and mixing, and their coupling to the overall combustion process. A logical choice for obtaining such measurements is high-speed planar imaging of the instantaneous spatial structure of the flow [1,2]. A number of digital image processing algorithms could then be employed to quantify the evolution of the flow structures [3]. Among the possible planar imaging techniques, planar laser-induced fluorescence (PLIF) is well suited for combustion measurements, since as a resonant technique, it provides high-quality records of a number of interesting species in reacting flows [4].

Here, we demonstrate a unique double-pulse PLIF visualization technique that requires only a single laser to record the structure of a mixing region at two instants in time separated by tens of microseconds. By tuning the laser to simultaneously excite fluorescence from two gases, acetone and OH, and using four detectors, we separately record regions containing unburned fuel and those containing combustion gases at both instants in time. Measurements are presented for a nominally two-dimensional, supersonic, reacting mixing layer consisting of an ambient-temperature, low-speed hydrogen-containing

fuel stream and a high-temperature, supersonic oxidizing stream. The accuracy of the technique, with respect to correlations between time-delayed image pairs, is experimentally investigated in a low-speed flame.

Description of Experiment

Simultaneous OH/Acetone Imaging:

For studying large-scale structures, we use simultaneous PLIF imaging of two species, one marking the unburned fuel gases and the other marking the combustion gases. The ability to acquire both these quantities with a single laser system greatly reduces the complexity and cost of the measurement system. One such technique, recently demonstrated, is based on the simultaneous excitation of OH, as the combustion gas marker, and acetone vapor, seeded into the fuel stream [5–7]. With this technique, a laser is tuned to simultaneously excite both species, while the fluorescence from the two is captured on separate cameras. While both OH and acetone absorb light in the same ultraviolet (UV) regions (OH has many discrete UV absorption lines, while acetone absorbs continuously over ~225–320 nm), the resulting fluorescence from the two molecules is well separated in wavelength. OH emits primarily in the UV, while acetone emits mostly in the blue (~400–500 nm). Thus, simple optical filters can be used to discriminate the two fluorescence signals.

The previous applications of combined OH and acetone imaging used a XeCl excimer laser at 308 nm (~100–150-mJ pulse energy) to simultaneously excite the $S_1 \leftarrow S_0$ electronic transition of acetone and a rotational line in the $A - X$ (0,0) vibration band of OH [5–7]. In contrast, the current measurements use frequency-doubled, dye laser excitation near 285 nm to excite lines in the OH (1,0) band along with the acetone. The new approach allows for better rejection of laser scattering onto the OH camera and more flexibility in choosing the OH pump transition. While the dye laser system provides less UV energy (~20–40 mJ) than the XeCl laser, the resulting PLIF signals are comparable for the two systems because (1) the acetone absorption coefficient at 285 nm is higher ($\times 3$) than at 308 nm; and (2) the OH line pumped by the XeCl laser is poorly populated at high temperatures, and the resulting fluorescence is partially saturated.

Again, the goal here is to develop a method for studying the evolution of the instantaneous, large-scale spatial structures in a reacting mixing flow. In this light, highly accurate concentration measurements are not required. Still, the interpretation of the OH and acetone fluorescence deserves some attention. For the high-speed flow under consideration, the Damkhler number for OH formation and destruction is on the order of unity [7]; thus, OH is not limited to chemical reaction zones but also marks regions of hot combustion products. Based on a simple mixing analysis between the two streams, the OH fluorescence signal is expected to track the OH concentration within $\pm 20\%$ across most OH-containing regions of the mixing layer. Similarly for acetone, the fluorescence varies nearly linearly with acetone concentration [8], and the chemical removal of acetone is similar to that of hydrogen in the flow [7]. Therefore, acetone fluorescence performs as an adequate marker of unburned hydrogen concentration in these high-speed mixing layers.

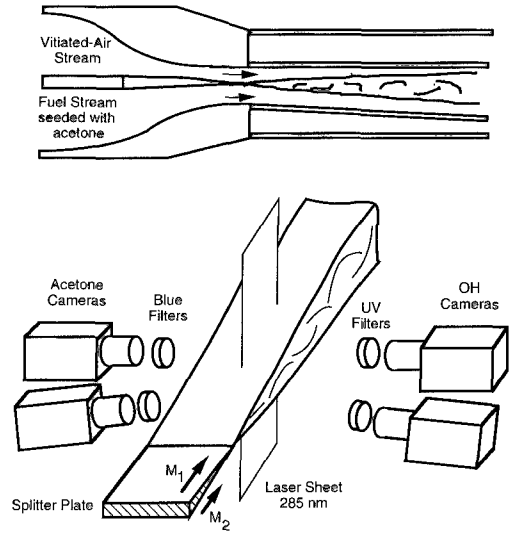

FIG. 1. Schematic of mixing layer facility, and optical arrangement of laser sheet and cameras.

Flow Facilities and Optical Layout:

Double-pulse imaging experiments were performed in two flow facilities. Basic characterization measurements were carried out in a small-scale (10 $\times$ 4 cm) flat flame burner. The burner was operated at atmospheric pressure in a premixed mode, burning a fuel-rich mixture of methane and air. The flow speeds in the resulting lifted flames did not exceed 1 m/s.

As depicted in Fig. 1, the mixing layer experiments were performed in a large-scale blowdown facility, with a rectangular test section (8 $\times$ 10 cm, 45-cm long). The facility is described in detail elsewhere [7]. In brief, a plane mixing layer was formed between a high-speed, high-temperature (1500 K) oxidizing stream and a slower, low-temperature (270 K) fuel stream. The oxidizing stream was produced from the exhaust of a vitiation heater burning oxygen-enriched air and hydrogen in a fuel-lean mixture, which was then expanded through a supersonic nozzle. The ox-

idizing stream constituents were primarily oxygen (23%), water vapor (25%), and nitrogen. The fuel stream consisted of a 1:9 mixture of hydrogen diluted in nitrogen, with a small amount of acetone vapor (2500–3500 ppm). For the measurements presented here, the imaged region was centered near the middle of the test section, approximately 22 cm downstream of the splitter plate.

The optical arrangement of the laser sheet and camera systems for the double pulse is also shown in Fig. 1. Laser-induced fluorescence images of OH and acetone were produced by 8-ns pulses from a single Nd:YAG-pumped, frequency-doubled dye laser (Lumonics: YM-1200, HD-500). The YAG laser was modified by the manufacturer to allow the Q switch to gate twice during each (10 Hz) flashlamp pulse, with a user-variable pulse separation. The sheet was formed with three cylindrical lenses. Two lenses formed a telescope that spread the beam into a collimated, 83-mm-tall sheet, and a third lens focused the laser to a narrow sheet. Real-time laser monitors, similar to those used in an earlier study [9], recorded pulse energies and spectral line shapes.

Each OH/acetone fluorescence imaging system consisted of two fiberoptically coupled, intensified charge-coupled device cameras (Princeton Instruments ICCD576/RB, 578 × 384 pixels) mounted behind commercial photographic lenses. In order to increase the framing rate of the camera systems, and therefore the number of images acquired per run, on-chip binning of the pixels was employed, with each binned superpixel representing the sum of a 2 × 2 subarray. The OH fluorescence images were acquired through f/4.5, 105-mm UV lenses with glass filters to remove the elastic laser scattering (Schott WG305) and the visible acetone fluorescence (Schott UG11). The acetone fluorescence was imaged through a 500-nm low-pass interference filter (Andover 500FL0750) and a glass f/1.2 50-mm lens, neither of which transmitted the UV laser scattering or OH fluorescence. As shown in Fig. 1, the acetone and OH cameras viewed the sheet-illuminated region from opposite sides. The intensifier gates were 400 ns for the OH camera and 200 ns for the acetone camera, with the shorter gate used to reduce the visible emission background.

For the double-pulse measurements, four nearly identical camera systems were employed. One pair of OH/acetone cameras viewed the illuminated plane at right angles; the other pair were placed slightly off-axis. Pixel-to-pixel spatial alignment between the cameras was ensured by simultaneously recording the image of a thin, transparent alignment target with each camera system. Careful attention was paid to the camera positioning during the measurements in order to minimize (or eliminate) postexperiment image processing intended to match the cameras' fields of view. The images were corrected for background signal (dark level, luminosity, and scattering), detection system (spatially) nonuniform response, and (shot-to-shot resolved) laser sheet energy distribution.

Double-Pulse Laser Characterization:

While two separate laser systems could be used to produce the two laser pulses needed for a time-delayed measurement, the use of a single laser simplifies the experimental setup. One potential tradeoff, however, is lower laser energy and, therefore, less fluorescence. With the current laser system, we have been able to produce two pulses (near 285 nm) separated by 20–70 μs and with energies of 2–6 mJ per pulse.

Since double pulsing of a frequency-doubled dye laser with tens of microseconds between pulses is a relatively novel mode of operation [10], a number of tests were performed to compare the characteristics of the UV beams between single- and double-pulse operation. The measurements included pulse energies, center wavelengths, and spectral profiles of the beams, and spatial profiles of the resulting laser sheets. The most significant variation between single- and double-pulse operation is the spectral detuning of the second pulse. For the pulse delays here (30 and 50 μs), the first pulse has the same center wavelength and linewidth ($\sim$0.6 cm^{-1}) as in single-pulse operation, while the second pulse is blue-shifted by approximately 0.006 nm, or 0.75 cm^{-1}, and has a 10–15% broader spectral profile.

Less change was seen in the spatial profile of the laser sheet, measured at the center of the imaged region. The full width of the sheet (at 2% of peak), was 630($\pm$50) μm for single-pulse operation and 560 μm for the first of the (lower energy) double pulses. For the second pulses, the widths were 630 and 700 μm at 30- and 50-μs delays, respectively. The location of the image plane in the flow, as determined by the center of the sheet waist, did not move by more than 23 μm between the various test conditions. In all the measurements reported here, the second pulse was made to have roughly two-thirds of the total energy in order to partially offset the signal loss associated with its detuning. To further compensate for the detuning, the wavelength of the first pulse was slightly red-shifted with respect to the OH transition in the high-speed experiments. For the 30-μs delay, total pulse energies reached 7 mJ, and in the 50-μs case, the maximum total energy was 9 mJ.

Results

As an example of the high-quality images obtainable with the dye laser approach to combined OH/acetone imaging, Fig. 2 shows a single-shot measurement in the compressible reacting mixing layer. The convective Mach number [11], $M_c = (u_1 - u_2)/(a_1$

$+ a_2$), of the layer, which is commonly used to characterize the importance of compressibility, is 0.70. The images shown in Fig. 2 were obtained with nearly 15 mJ of sheet energy (at the image plane) and with the laser tuned to the (1,0) $P_1(7)$ line of OH. Based on calibration measurements with the camera systems in a shock-heated OH flow [9], the peak OH levels in the layer are about 2000 ppm, and the average OH levels in the vitiated air stream are 200–300 ppm. For these data, the peak (seeded free stream) acetone levels are ~2500 ppm.

Based on root-mean-squared variations in regions of nominally uniform signal in the corrected images, the signal-to-noise ratio (SNR) of the single-shot acetone images peaks at 12 in the undiluted free stream. For the OH data, the peak SNR in the mixing layer is between 10 and 12, and in the vitiated air stream, the SNR is 5. These SNR values compare well with the previous XeCl measurements in the same facility, which employed an injection-locked laser tuned to the more temperature-dependent (0,0) $Q_1(3)$ line of OH. With approximately 50–60 mJ reaching the flow in a sheet of nearly the same height, the peak SNR values in the previous measurements were about 15 for both molecules [5].

As mentioned previously, double-pulse measurements were made in a slowly moving methane-air flame (which could be considered frozen for the 30–50-μs measurement times) in order to test the technique's capability to accurately record flow evolution. In order to create distinct spatial structures, a lifted flame was used. Figure 3 illustrates the (corrected) second pulse image from a pair of double-pulse OH images, acquired in the laminar flame with a 50-μs pulse delay and a total sheet energy (at the image plane) of about 5.5 mJ. With a maximum gas velocity of 1 m/s, convective motion during the measurement period should correspond to less than one-quarter of a pixel. Some change, however, in the chemical structure of the flame is possible. The image of Fig. 3 shows one result from a set of 20 double-pulse image pairs. One scaling factor for each image pair was applied to force the average pixel value to be the same for both images. This scaling factor is nearly the same for each image pair; the standard deviation over the 20 pairs is 14% and reduces to 9% if the highest and lowest values are omitted.

Figure 3 also contains an image of the difference between the second and first pulses (2 − 1), normalized by the average of the two. Thus, it represents the per-pixel fractional difference, or error, between the two images. No spatial corrections were applied to these images to improve the experimental camera alignment. In order to reduce the shot-noise fluctuations and highlight any potential systematic errors, however, the OH images were convolved with a 3 × 3 low-pass filter, and the error was conditionally zeroed at pixels with values considered to be in the background noise (~2–3% of peak). While the flame outline is evident (because of the noise thresholding), the error levels are somewhat randomly distributed across the flame. As would be expected for shot noise, the fractional error generally declines with increasing signal, so the errors tend to be larger near the (low signal) edges of the flame. A histogram of the fractional error image (from Fig. 3) shows a somewhat normal distribution of errors with a slight bias toward negative errors. Considering only nonzero error values, the conditioned error distribution has a peak at −2% error, a mean of −0.7% error, and a standard deviation of 12% (99.5% of the nonzero errors fall within a ±35% error range). The other image pairs also show some bias toward the first or second pulse, and the average standard deviation for the complete set is 14%. Combined with the lack of significant spatial biasing, these relatively low errors should allow this technique to accurately record the evolution of the high-speed mixing layer.

For all the double-pulse measurements, the laser was tuned to excite the overlapping $Q_1(9)$ and $Q_2(8)$ lines of OH. Combined, these lines have an absorption coefficient 2.5 times greater (at 1500–1600 K) than the $P_1(7)$ line used for the single-shot data and only a slightly greater temperature dependence. The higher absorption coefficient of the combined lines was used to partially compensate the OH signals for the lower energies available in the double-pulse measurements. For the mixing layer data, the acetone signals were further improved by increasing the acetone seeding in the mixing layer to ~3500 ppm. Double-pulse measurements were obtained for two mixing layer conditions: the same high-compressibility (M_c = 0.70) case described in the single-pulse measurements as well as a lower-compressibility (M_c = 0.32) case. The high-compressibility case has a higher vitiated-air stream velocity (u_1 = 960 m/s) and a lower fuel stream velocity (u_2 = 150 m/s) compared to the low-compressibility case (u_1 = 550 m/s, u_2 = 185 m/s). For visualizing the evolution of these different speed layers, it is convenient to use a shorter pulse separation as the speed of the layer is increased. For the high- and low-compressibility cases, respectively, the pulse separations were 30 and 50 μs, which limit the maximum convective motion (based on the maximum free stream velocity) to ~2.8 cm in both layers.

Figure 4 shows a typical result for the low-compressibility layer, acquired with a total laser energy of ~6 mJ in the measurement plane. In the first pulse image, the peak SNR values are 7 for the acetone PLIF and 9 for the OH. For the second pulse, the peak acetone SNR increases to 9, while the OH SNR decreases to 7. Recall, the second pulse has twice the energy of the first, thus explaining the improved acetone signal, but the second pulse partially detunes from the OH line and therefore produces a weaker OH signal. For the high-compressibility case (Fig. 5), similar SNR values were obtained with ~5 mJ. In

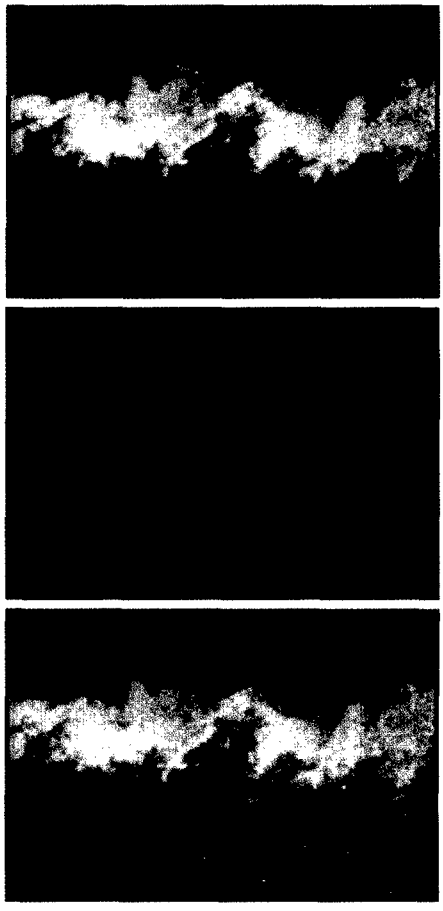

FIG. 2. Single-pulse simultaneous images (200 × 133 pixels, 77 × 50 mm) of OH and acetone in a reacting mixing layer with $M_c = 0.70$: (upper) the OH distribution (yellow), (middle) the acetone distribution (purple), and (lower) the color overlay of the OH and acetone images. Increasing color intensities correspond to increasing concentration for each species. The sheet propagates upward in these side view images of the mixing layer.

both the high- and low-compressibility cases, the acetone signal in the mixing layer quickly drops from its free stream value. The prominent structures in the acetone-bearing fluid are defined by this interface between the layer and the undiluted acetone. Thus, the acetone structures primarily exist in the lower portion of the mixing layer. In the high-compressibility case (Fig. 5), a few acetone features are seen to extend upward, reaching near the middle of the layer. In comparison, the prominent OH structures are found higher in the mixing layer and exist across a larger fraction of the mixing layer.

In Figs. 4 and 5, the relationship between acetone-marked structures in the sequential images is clear,

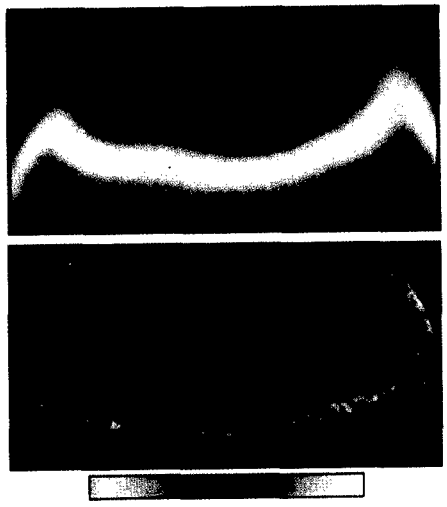

FIG. 3. Images from a double-pulse image pair (281 × 143 pixels, 69 × 35 mm) of OH in the low-speed, premixed methane-air lifted flame: (upper) second pulse OH image (50-μs delay from first pulse) and (lower) fractional difference image, i.e., second pulse minus first pulse normalized by the average of the two. The sheet propagates right-to-left in these side view images of the flame. The OH image uses the same color scale described in Fig. 2, and the lower color bar maps fractional errors from −50% (left) to +50% (right).

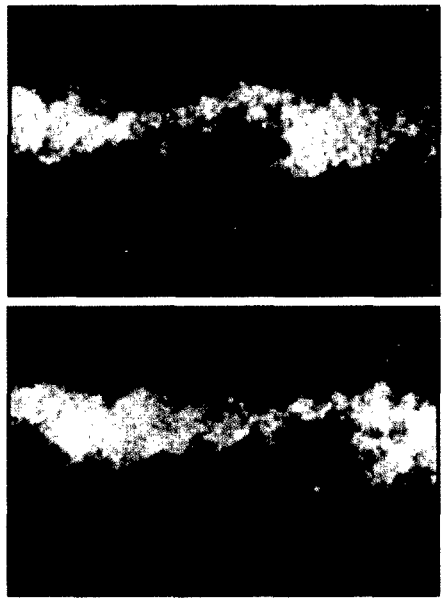

FIG. 4. Overlaid (see Fig. 2), double-pulse side view images (77 × 50 mm) of acetone and OH in the mixing layer with $M_c = 0.32$: (upper) first pulse image and (lower) second pulse image with a 50-μs delay. The color scaling is described in Fig. 2. The images were smoothed with a 3 × 3 low-pass filter.

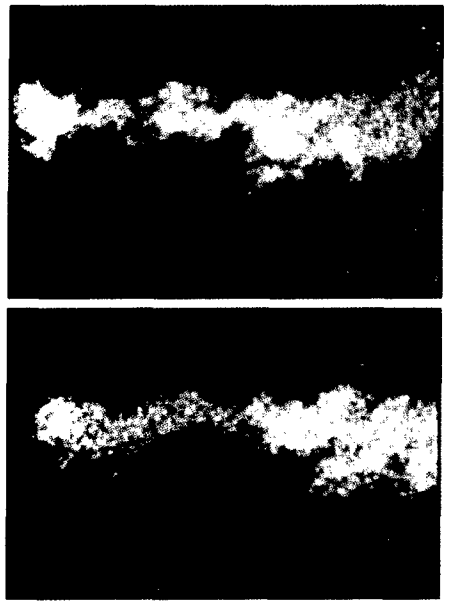

FIG. 5. Overlaid (see Fig. 2), double-pulse side view images (77 × 50 mm) of acetone and OH in the mixing layer with M_c = 0.70: (upper) first pulse and (lower) second pulse with 30-μs delay. The color scaling is described in Fig. 2. The images were smoothed with a 3 × 3 low-pass filter.

and they exhibit little distortion. Using the movement of distinct features in the aceteone/layer interface from 12 double-pulse image pairs, an average convective (axial) velocity (u_{acet}) was determined for each compressibility case. For the low-compressibility layer, $u_{acet} \approx 200$ m/s, and for the high-compressibility layer, $u_{acet} \approx 180$ m/s. For both cases, most of the measurements were within ±10% (±20 m/s) of the average values. These acetone convective velocities are only slightly greater than the low-speed free stream velocities for each case (by ~15–30 m/s). For the OH images shown in Figs. 4 and 5, it is fairly easy to identify and follow the movement of certain distinct features between the sequential images. For the complete data set, however, the (visual) correlation of sequential OH images is more difficult; the OH structures generally exhibit more distortion than the acetone structures. The change in the OH regions may be the result of in-plane deformation effects, out-of-plane motion, or chemical reaction. Still, some flow features can be identified and used to determine an average OH (axial) convective velocity (u_{OH}). For the same set of 12 image pairs, u_{OH} is ~350 m/s for the low-compressibility case and ~650 m/s for the high-compressibility layer. The image-to-image variability for u_{OH} is greater than for u_{acet}, partly because the increased distortion of the OH features leads to larger uncertainties. For the low-compressibility case, the variation in u_{OH} is ±10% (±30 m/s) and increases to ±20% (±130 m/s) for the high-compressibility layer. The measured OH and acetone velocities represent movements in the images of between 20 and 80 (super)pixels (0.39 mm/pixel in the layer).

Comparison can be made with the expression for the overall convective speed (u_c) of large-scale, mixing layer structures developed by Papamoschou and Roshko [11]. While discrepancies with high-compressibility measurements have been reported [1,12], this expression predicts values of 300 and 390 m/s, respectively, for our low- and high-compressibility layers. In both cases, the measured OH and acetone convective velocities, relative to the predicted u_c, are biased by their location in the layer, i.e., toward the velocity of the adjacent free stream. For example, in the low-compressibility layer, the OH convects at a speed 17% higher than the predicted u_c, while the acetone interface scarcely moves faster than the slow-speed stream. This biasing is consistent with recent results from nonreacting studies [2] and highlights a difficulty associated with measurement of overall convective speeds using spatially biased tracers. When such methods are employed and comparisons with u_c are made, variations in convective speed across the layer, for example due to rotation of the structures, must be considered. Tracking the centroids of mixing layer structures may be a more suitable approach [1]; in our measurements, this would require defining the centroid of a combined OH/acetone structure. This approach, however, is also prone to biasing since speeds can be determined only when a suitable structure is identified, and the problem worsens with increasing compressibility since the mixing layer structures become more disorganized. Considering the limited data available, further investigation of these issues must be considered in future work.

Conclusions

We have demonstrated a combined OH/acetone PLIF imaging technique for recording the evolution of large-scale structures in high-speed nonpremixed combustion flows. In this novel approach, a single frequency-doubled dye laser provides sufficient energy to simultaneously record regions containing unburned fuel, marked by acetone, and of combustion gases containing OH, with two pulses separated by tens of microseconds. The spatial and spectral properties of the laser sheets produced by the two pulses were found to be similar, with the exception of a relative spectral shift (−0.006 nm) for the second pulse. The accuracy of the technique was tested in a low-speed methane-air flame. Image pairs of OH obtained in this nominally frozen flow showed average

pixel-to-pixel errors of 15%; much of this error results from signal shot-noise.

The combined OH/acetone technique was demonstrated in a high-speed reacting mixing layer under conditions of high and low compressibility. Reasonable quality images, having minimum noise levels of 11–14%, were obtained in both cases, with peak OH levels near 2000 ppm and acetone seeding levels of roughly 3500 ppm. The structures containing unburned fuel are relatively stable during the measurement periods used here (30–50 μs), while the OH-marked hot combustion gases exhibit more distortion. The measured convective speeds are reasonable; the speed of the acetone/mixing layer interface is only slightly higher than the speed of the acetone free stream, while the OH structures move at speeds closer to (but higher than) the predicted convective speeds of the layers.

The data presented here clearly demonstrate the capabilities of the double-pulse imaging technique; convective motion and structural distortion can be seen in the image pairs. The limited size of our data set, however, does not permit a rigorous investigation of the evolution of large-scale structures in reacting mixing layers. Other views of the mixing layer, e.g., plan views, would also be useful. While the analysis of the mixing layer data presented here consists of qualitative comparisons and average (visual) convective velocities, the high quality of the images, combined with the low systematic errors measured in the laminar flame, suggests that similar double-pulse data can be successfully interrogated by more advanced processing algorithms, and then more complex issues could be addressed.

Acknowledgments

This work was supported by the U.S. Air Force Office of Scientific Research, Aerospace Sciences Directorate, with Dr. J. Tishkoff as the technical monitor.

REFERENCES

1. Fourguette, D. C., Mungal, M. G., and Dibble, R. W., *AIAA J.* 29:1123–1130 (1991).
2. Elliott, G. S., Samimy, M., and Arnette, S. A., "The Evolution of Large Scale Structures in Compressible Mixing Layers," paper presented at the Ninth Symposium on Turbulent Shear Flows, Kyoto, Japan, August 1993.
3. Strickland, R. N., and Sweeney, D. W., *Appl. Opt.* 27:5213–5220 (1988).
4. Hanson, R. K., Seitzman, J. M., and Paul, P. H., *Appl. Phys. B* 50:441–454 (1990).
5. Yip, B., Miller, M. F., Lozano, A., and Hanson, R. K., *Exp. Fluids,* in press.
6. Paul, P. H., and Clemens, N. T., "Planar Laser-Induced Fluorescence Imaging of Lifted H_2-Air Flames," Paper AIAA-93-0800 presented at the 31st AIAA Aerospace Sciences Meeting, Reno, NV, January 1993.
7. Miller, M. F., Island, T. C., Yip, B., Bowman, C. T., Mungal, M. G., and Hanson, R. K., "An Experimental Study of the Structure of a Compressible, Reacting Mixing Layer," Paper AIAA-93-0354 presented at the 31st AIAA Aerospace Sciences Meeting, Reno, NV, January 1993.
8. Lozano, A., Yip, B., and Hanson, R. K., *Exp. Fluids* 13:369–376 (1992).
9. Seitzman, J. M., Hanson, R. K., DeBarber, P. A., and Hess, C. F., *Appl. Opt.* 33:4000–4012 (1994).
10. Dyer, M. J., and Crosley, C. R., *Opt. Lett.* 9:217–219 (1984).
11. Papamoschou, D., and Roshko, A., *J. Fluid Mech.* 7:453–477 (1988).
12. Papamoschou, D., "Structure of the Compressible Turbulent Shear Layer," Paper AIAA-89-0126 presented at the 27th AIAA Aerospace Sciences Meeting, Reno, NV, January 1989.

COMMENTS

Michael Drake, General Motors, USA. Why does the acetone LIF intensity completely disappear in the mixing layers?

Author's Reply. Because the acetone traces only unburned fuel, we expect, and we find, that the acetone fluorescence is absent in the reacting (OH-containing) regions of the mixing layer. The lack of significant levels of recorded acetone fluorescence within some other regions of the layer primarily results from limits of the detection system and the fact that the acetone fluorescence does not scale linearly with mixture fraction.

Recall that the acetone fluorescence is proportional to acetone concentration (rather than mole fraction). Thus, the decrease in density associated with mixing of the hot air and cold fuel causes the acetone signal to decrease more rapidly than mixture fraction as the two fluids mix, even at low dilution levels. Because of the limited dynamic range (or detection sensitivity) of the measurement system, these reduced signals eventually become indistinguishable from the noise in the images. This is why the single-pulse measurements of the high compressibility layer (e.g., Fig. 2) show greater penetration of acetone into the layer than do the double-pulse images (Fig. 5). The higher laser energies, and thus increased sensitivity, available in the single-pulse experiments effectively increase the dynamic range of the measurements.

•

Michael Winter, United Technologies Research Center, USA. In Lozano's thesis, a mechanism is described corre-

sponding to fast photoionization of acetone after excitation at 285 nm. Is there evidence of this in the comparison of the two acetone images?

Author's Reply. Lozano (Ph.D. Thesis, Mechanical Engineering, Stanford University, 1992) described various photodissociation processes that can occur when acetone is illuminated with UV radiation. From the limited data available on the variation in fluorescence efficiency with excitation wavelength, one can estimate that the dissociation rate is only 10–20% greater for 285-nm excitation compared with excitation at 308 nm. In the current double-pulse measurements, photodissociation would result in a lower acetone concentration for the second pulse image compared with the first. Comparing the fluorescence in the fuel free stream for the two pulses with the laser pulse energies recorded with the photodiode, we find no evidence that acetone removal could be greater than a few percent for our laser energies (~5 mJ per pulse).

•

Nigel Tait, Cranfield University, UK. Some of the images presented implied a small overlap between the OH and acetone fields, which seems unlikely given the rapid pyrolysis of acetone at the temperature at which OH exists. Is this real or an artifact of the measurement system?

Author's Reply. The apparent overlap in OH and acetone fields is an artifact produced by low levels of visible flame emission from the layer that is captured on the acetone camera and subsequently amplified by laser sheet nonuniformity corrections to the lower-energy first pulse image. Since the flame emission is well separated from the acetone layer, it is easily discriminated.

•

Paul Ewart, Oxford University, UK. Regarding the measured shift in frequency between the two pulses from the dye laser; if indeed the cause is a refractive index change arising from heating, it would be interesting to use water as the dye solvent to see if the thermal effect on refractive index is reduced. Furthermore, if the water solvent is maintained around 4 °C these thermal effects would be minimized, since at this temperature $dn/dT = 0$ (n = reference index, T = temperature).

Author's Reply. This is an interesting area, both to determine the cause of the frequency shift and possibly to minimize it. It should be noted that refractive index change induced by pump laser absorption and heating in the dye is just one possible explanation of the laser frequency shift.

INDEX OF AUTHORS AND DISCUSSORS

(**Bold face** numbers refer to papers' authors; other numbers refer to papers' discussors)

Abbas, T., **617°**
Adomeit, G., **395°**, **1579**
Adusei, G. Y., **801**
Agarwal, P., 217
Aggarwal, S. K., **767°**, 1554
Aguerre, F., **422°°**
Akanetuk, A. J., 559, 926, 1010, 1222
Akrich, R., **1489**
Al-Fawaz, A. D., **1027**
Aldén, M., **449°**, **1735**, 1734
Aldredge, R. C., 1106
Algermissen, J., **21**
Altenkirch, R. A., **71°°**
Alvarez, J. R., **460°**
An, C., **175**
Anderson, W. R., **323°**
Andrews, G. E., **103**
Annamalai, K., 297, **413°°**, 626, 1699
Antonio, C., 1098
Aoki, H., **493**
Arena, U., **219**, 217
Ashurst, W. T., **1075**
Avedisian, C. T., 268, **353**, 429, 437, 445, 452
Axelbaum, R. L., **350°°**, **367°°**, 600, 607

Babkin, V. S., **1627**
Bachalo, W. D., **333**, **413**
Bachman, J. S., **1563**
Bachmann, M., **635**
Baek, S. W., **1183**
Bains, M., **541°**
Bar-Ziv, E., **519**
Barbella, R., **167**, **679**
Barlow, R. S., **153°°**, **1301**
Baronnet, F., **644°**
Barr, P. K., **460°**
Bartenev, A. M., **61**
Bartholomew, C. H., **94°°**
Bassilakis, R., **553**
Bassin, X., **573°**
Batt, L., **793**
Battin-Leclerc, F., **644°**
Bäuerle, B., **135**, 1421
Bauerle, S., **627**
Baum, H. R., **1463**
Baumann, H., **193**
Baxter, L. L., 473, 491, **511**
Bazile, R., **363**
Bédat, B., **485°°**, 1238
Beér, J. M., **1215**
Behrendt, F., **135**
Bellan, J., 369, **397**
Benari, Y., **519**
Bencsura, Á., **817**
Bengtsson, P. E., **1735**
Benz, P., **1019**
Bérces, T., **775**, 840
Berckmüller, M., **151**
Berghmans, J., **37**
Bermudez, G., **41°°**
Bhattacharaya, S., **511**
Bhattacharjee, S., **71°°**, 1445, 1692
Biede, O., **475**
Bilger, R. W., **347°**, 1106, 1131, **1141**, **1159**, 1230
Bish, E. S., **457°°**
Blasi, C. D., **332°°**
Blumenthal, R., **1579**
Boccio, J., **212°**
Bockhorn, H., 642, **1019**, **697°**
Boettner, J. C., **919**, **1563**
Bonanno, A. S., **1447**
Bonn, B., **193**
Bonneau, L., **1701**
Bool-III, L. E., **262°°**
Borghi, R., **1107**
Boris, J., 1262
Borisov, A. A., 86
Bossard, J. A., 360, 420
Bowman, C. T., **101°°**, **741**, **983**
Bozzelli, J. W., 703, 731, 774, **783**, **965**
Bradley, D., **125**, **562°**, **581°**
Bramlette, T. T., **460°**
Bray, K. N., **440°**
Breitbach, H., **95**, 140, **1099**, **1357**
Brewster, M. Q., **283°°**
Brouillette, M., **292°°**
Brouwer, J., **231°**
Brown, M. J., **1011**
Brown, T. M., **775°**
Brüggemann, D., **21**, 132, 140, 420, 1641
Brüls, H. K., **37**
Bryner, N. P., **1445**
Buermann, D. H., **413**
Bui-Pham, M. N., **1309**
Burgess, D. R., **1505**
Buser, S., **1019**
Buth, R., **841**

°Combustion and Flame, Vol. 99, 1994.
°°Combustion and Flame, Vol. 100, 1995.

Cadou, C., **280°**
Calhoon, W. H., **1125**
Cammarota, A., **219**
Candel, S., **422°°**, 1262, **1273**, **1547**
Carlier, P., **1563**
Carter, C. D., **153°°**, **1301**
Carvalho, M. G., **227**
Cathonnet, M., **919**, **1563**
Catoire, L., **573°**, 1577
Cavaliere, A., **679°**
Cernansky, N. P., 940
Cessou, A., **516°**
Cetegen, B. M., **232°°**, 1281
Chan, C. K., **341°°**
Chan, C., 110
Chan, S. H., **1115**
Chandraratna, M. R., **626°**
Chang, A. Y., **965**
Chang, D. P., **259°°°**
Chao, Y. C., 1189
Chebotko, I. S., **371°**
Chelliah, H. K., **221°**
Chen, H., **177°°**
Chen, J. H., **1091**
Chen, L., **175**
Chen, R. C., 1072
Chen, R. H., 191, 242
Chen, W. Y., 226
Cheng, C. Q., **175**
Cheng, R. K., **485°°**
Cheng, T. S., **1133**
Cheng, W. K., **422°**
Chesworth, S., **259°°°**
Chiang, W. T., **355°**
Chirone, R., **219**
Choi, M. Y., **1471**
Choi, S., **317**
Chomiak, J., 123, 140, 1087, 1113, 1238, 1262, 1272, 1281
Chung, S. H., **1175**
Ciajola, A., **167**
Ciajolo, A., **679**
Ciambelli, P, **413°**
Ciccarelli, G., **212°**, 1545
Clarke, J. F., **465°°**
Clavin, P., **45**
Coelho, P. J., **227**
Coimbra, C. F., 233
Colket, M. B., **883**
Colussi, A. J., **733**
Come, G. M., **644°**
Corcione, F. E., **387°**
Correa, S. M., **1167**, **1293**
Costen, P., **617°**
Cotton, D. F., **422°**
Crocombe, W., **541°**
Crosley, D. R., **261°**, 1525
Cuenot, B., **1383**

D'Alessio, A., **645**
D'Amore, M., **413°**
D'Anna, A., **167**, **645**, **679**
da Silva, L. F., **29**
Dagaut, P., **919**, **1563**
Dahm, W. J., **457°°**
Dally, B. B., **1301**
Dam-Johansen, K., **523°**
Dasappa, S., **569**
Davies, N. H., **211**
Davis, K. A., **31°°**, 429, **561**
Dayton, D. C., **323°**
de, Goey, L. P., **957**
de, Vries, J. E., **1241**
Dean, A. J., **1293**
Dean, A. M., **965**
Dearden, L. M., **1027**
Delfau, J. L., **1489**
Delhaye, B., **1273**
Delichatsios, M. A., **601°**, 1248
Dellinger, B., **11°°**
Denk, V., **389**
Desbordes, D., 44, **53**
Deshaies, B., **29**
Di Julio, S. S., **192°**
Dibble, R. W., **153°°**, **395°°**, 1106
Dixon-Lewis, G., 757, **1325**
Djavdan, E., 259
Djebaili, N., **1539**
Dobashi, R., **1415**, **1439**
Dobbins, R. A., **301°°**
Dobé, S., **775**
Dold, J. W., 102, **359°°**, **450°°**, **465°°**
Dorofeev, S., 51
Doughty, A., 866, **893**
Drake, M. C., **323°°**, 1749
Dreier, T., **1727**
Drennan, S. A., 233, 352
Driscoll, J. F., **323°°**, 1156
Drobot, K., **422°**
Dryer, F. L., **495°°**, **759**, **901**, 940, 948
Du, J., **367°°**
Dubinsky, I. A., **817**
Duclos, J. M., **1249**
DuFaux, D. P., **350°°**
Dugué, J., **235**
Dupre, G., **573°**, **1539**
Durant, J., 972, 1000
Dwyer, H. A., **389**

Eckbreth, A., 132, 1734
Economos, C., **212°**
Edgar, B. L., **395°°**
Egolfopoulos, F. N., **1317**, **1341**, **1365**, **1375**
Eichholtz, M., **859**

°Combustion and Flame, Vol. 99, 1994.
°°Combustion and Flame, Vol. 100, 1995.
°°°Combustion and Flame, Vol. 98, 1994.

Eigenbrod, C., **455**
El-Naggar, M., **679°**
Elghobashi, S., 1262, 1272
Endo, N., **1191**
Eng, J. A., **1711**
Espey, C., 173
Essenhigh, R. H., **262°°**, **269°**, 607, 1435
Ewart, P., 1734, 1749

Faeth, G. M., **310°°**
Faust, C. M., **323°**
Fernandez-Alonso, F., **261°**
Fernandez-Pello, A. C., 1461, **1481**
Fichot, F., **397**, **1273**
Fieweger, K., **1579**
Filtopoulos, E. E., **1223**
Finlinson, J. C., 36, **1645**
Fletcher, R. A., **301°°**
Fletcher, T. H., **94°°**, **463**
Fontijn, A., **801**
Frank, J. H., **347°**, **1159**
Frank, P., **833**
Frenklach, M., **111°°**, 642, **941**
Frisch, S., **254°**
Frost, D. L., **292°°**, **1651**
Froud, D., **407°°**
Fujita, O., **363°**
Fujiwara, T., **85°°**
Fukuchi, A., **1587**
Fureby, C., **1257**
Furukawa, J., **1233**

Gaffuri, P., **201°**
Gale, T. K., **94°°**
Gambi, G., **645**
Gann, R. G., 1435, 1487
Gany, A., 452
Garo, J. P., **1481**
Gelfand, B. E., **61**, **73**
Geratz, K. J., **95**
Gerhold, B. W., **144°°**, 703, 1525
Gerlinger, P., **21**
Ghoniem, A. F., 1072, 1262, **1265**
Gibbs, B. M., **508°**
Gilot, P., 559, **619**
Ginsberg, T., **212°**
Glarborg, P., **475°**, **523°**
Glassman, I., 940, **1333**
Gmurczyk, G., **1497**
Goel, S. K., **1051**
Goettgens, J., **1357**
Goix, P., **516°**
Gökalp, I., 452, **1199**
Golden, D. M., 882
Goldin, G., **1125**
Gonzalez, M., **1107**
Gopalakrishnan, C., **413°°**
Góral, J., **1035**
Gore, J. P., **52°°**, 1478
Goroshin, S., **1651**
Gouldin, F. C., **202°°**, **339°**, 1255
Gradon, B., **1035**
Gran, I. R., **1283**
Greenberg, J. B., **474°°**
Greenhalgh, D. A., 132, **151**, 1734, 1742
Grela, M. A., **733**
Grenda, J. M., **1619**
Griffiths, J. F., 140, **533°**, **541°**, **626°**, **933**
Grinstein, F. F., **2°°**
Grosshandler, W., **1497**
Grotheer, H. H., 288, **721**, 857, 916
Guerraud, C., **53**
Gulati, A., **395°°**, **1167**
Gülder, Ö. L., 132, **371**, 592, 634, 940
Gupta, A. K., **353**, 352
Gupta, R. P., **511**
Gupta, S. B., **585**
Gutman, D., **817**

Hall, M., 1087
Hamins, A., **221°**, 314, 445, **1471**
Hanisch, S., **577**
Hanson, R. K., **741**, **983**, **1743**
Hanson-Parr, D., **1635**, **1645**
Hara, H., **423**
Harb, J. H., **511**
Harper, C. M., **562°**
Harrington, J. E., **723°**
Harstad, K., **397**
Hartinger, K. T., **193**
Hassel, E. P., 1139, 1166
Haug, M., 250, 379
Hayhurst, A. N., **211**
Haynes, B. S., **909**, **1003**
He, L., **45**
Headley, T. J., **31°°**, **131°°**
Heberlein, D. C., **79**
Hedley, J. T., **1027**
Hedman, P. O., **185°°**
Heist, D. K., **339°**
Held, T. J., **901**, 926
Hemberger, R., **660°**
Hernberg, R., 199
Hershberger, J., 1000
Herzler, J., **833**
Hippler, H., **254°**, **875**
Hirano, T., **376°°**, **1233**, **1399**, **1415**, **1439**
Hochgreb, S., **193°°**
Hodges, J. T., **353**
Hoffmann, F., **135**
Homann, K. H., 583, **635**, 668
Hoogendoorn, C. J., **1241**
Hornung, A., 642, 1435
Howard, J. B., **671**
Hoyermann, K., **841**, **851**

°Combustion and Flame, Vol. 99, 1994.
°°Combustion and Flame, Vol. 100, 1995.

Hsieh, W. H., **1609**
Huang, T. H., **1595**
Huang, X. Q., **669°**
Hughes, K. J., **533°**
Humpfer, R., **721**
Hurt, R. H., **31°°**, **131°°**, 501, **561**, 1058
Hwang, P. W., **591°**

Ibrahim, K. M., **413**
Ibrahim, S. S., 1255, 1262, 1290
Im, H. G., **21°°**, 1372, 1554
Ingham, T., **767**
Inkrott, K. E., **144°°**
Ishida, H., **331°**
Ishii, K., **151**
Ishino, Y., **302°**
Ishizuka, S., **1399**
Isia, K., 217
Island, T. C., **1743**
Ito, H., **363°**
Ito, K., **363°**

Jacobs, R. A., **243**
Jagoda, J. I., **251°°**
Jander, H., **577**
Jasuja, A. K., **345**
Jeffries, J. B., **261°**, 1641
Jiang, T. L., **355°**
Johansson, B., **449°**, **1735**
Johnsson, E. L., **1445**
Johnsson, J. E., **523°**
Jokiniemi, J. K., **201**, 583
Jones, A. D., **259°°°**
Jones, H. R., **404°**
Joulain, P., **1701**
Joulin, G., **450°°**
Joyce, R. P., **79**
Ju, Y., **240°**, 948
Just, T., **687**, 712, **721**, **833**, 972

Kailasanath, K., **2°°**, **247°**
Kaiser, E. W., **422°**
Kakutkina, N. A., **1627**
Kalghatgi, G. T., **125**
Kandamby, N. H., **251**, **617°**
Kantorovich, I. I., **519**
Kanury, A. M., 1435, 1667
Kaplan, C. R., **1183**
Kapteijn, F., **499°**
Kapuscinski, M., **742°**
Karagozian, A. R., **280°**
Karasevich, Y., **627**
Karim, H., **299**
Kashireninov, O. E., **1669**
Kashiwagi, T., **1423**, **1471**, 1445
Kato, H., **431**, **439**
Kato, S., **447**
Katoshevski, D., **381**
Katta, V. R., **61°°**, **767°**, 1389
Kauffman, C. W., **505°°**
Kauppinen, E. I., **201**, 583, 634
Kazakov, A., **111°°**, **941**
Keener, H. M., **262°°**
Keller, J. O., **460°**
Kelly, J., **1149**, **1223**
Kelly, P. B., **259°°°**
Kelman, J. B., **1141**, 1156
Kennedy, I. M., **259°°°**, 617, 1166
Kennedy, L. A., **221°°**, 123, 275, 288
Kern, R. D., **177°°**
Kerr, O. S., **359°°**
Kerschl, P., **389**
Kerstein, A. R., **1125**
Khan, M. A., **793**
Kharbat, E., **413°°**
Khina, B. B., **371°**
Khomik, S. V., **73**
Khusid, B. M., **371°**
Kiefer, J. H., **177°°**, 857, 874, 900, 990
Kiger, K. T., **407**
Kim, H. M., **1719**
Kim, J. S., **21°°**, **1175**
Kim, S. K., **317**
Kim, T. J., **759**
Klein, R., **95**, 123, 1272
Klemens, R., **742°**
Kneer, R., **1043**
Knozze, V., 634
Knyazev, V. D., **817**
Knystautas, R., **65**
Kobayashi, H., **447**, **1693**
Koch, R., **1043**
Koenig, J., **455**
Koester, G., **221°°**
Kohse-Hoinghaus, K., 1156
Koizumi, K., **545**
Kollmann, W., **1091**
Kono, M., **431**, **439**, **455**, **1719**
Korobeinichev, O., 1641
Koshland, C. P., **325**
Kowalemicz, A., 437
Köylü, Ü. Ö., **310°°**
Kozinski, J. A., **121°°**, 208, 288
Kramlich, J. C., **440°°**, 1058
Krammer, G., **519**
Kravchik, T., **635°**
Kreutz, T. G., **758°**
Krier, H., 86
Krishenik, P. M., **713°**
Kubitza, C., 685
Kumagai, S., **423**
Kuo, K. K., **1595**, **1609**
Kuramoto, K., **545**

°Combustion and Flame, Vol. 99, 1994.
°°Combustion and Flame, Vol. 100, 1995.
°°°Combustion and Flame, Vol. 98, 1994.

Lallemant, N., **235**
Lasheras, J. C., **407**
Lassesson, B., **1735**
Laughlin, K. M., **211**
Laurendeau, N. M., 1156
Laurs, A., **395°**
Law, C. K., **21°°**, **291**, **758°**, **1333**, **1341**, **1391**, **1659**, **1711**
Lawes, M., **581°**
Lee, B. J., **1175**
Lee, J. G., **161°°**
Lee, J. H., **65**, **292°°**, **1651**
Lee, J. J., **292°°**
Lee, J. S., **317**
Lee, S. T., **484°**
Lee, T. W., **161°°**
Lefebvre, A. H., **345**
Lefebvre, M. H., **37**, **85°°**
Leng, J., **404°**
Levine, R. S., 1683
Levinsky, H. B., **243**
Li, S. C., **1207**
Li, T. X., **291**
Li, T., **749°**
Li, Y. C., **505°°**
Libby, P. A., **1207**
Lien, W. Y., **591°**
Lifshitz, A., 668, 900, **1571**
Lifshitz, C., 890
Lighty, J. S., **121°°**
Lillich, H., **993**
Lim, K. P., **713**, **809**
Lin, J. L., **262°°**
Lin, M. C., **169°°**, 840, 990, 1000, 1010
Lin, W. Y., **669°**
Linak, W. P., **241°°**
Liñán, A., **1529**
Lind, T., **201**
Lindstedt, R. P., **551°**
Lingens, A., **933**
Liou, D., **261**
Liou, S. G., **89**
Liou, T. M., **591°**
Lisbet, R., **1539**
Lockett, R. D., **151**, 132
Lockwood, F. C., **251**, **503**, **617°**
Löfström, C., **1257**
Logan, J. A., **1513**
Long, M. B., **347°**, **1159**
Longwell, J. P., **231°**
Lu, G. Q., **545**
Lu, W., **301°°**
Lucas, D., **325**
Lucas, J. A., **485**
Lundholm, G., **1735**
Luo, W. W., **669°**
Lyon, R. K., 972
Lyons, K. M., **347°**, **1159**

Maas, U., **1349**
Maček, A., 217, 297
Mack, A., **1555**
Mackie, J. C., 882, 890, **893**
Maenhaut, W., **201**
Magnussen, B. F., **1283**
Makino, A., **1659**
Makris, A., **65**, 44
Maloney, D. J., **733°**
Malte, P. C., 259, **440°°**
Maly, R. R., **111**, **143**, 420, 592
Mantashyan, A. A., **927**
Maqsud, L., **11°°**
Marble, F., **1**
Marcuccilli, F., **619**
Marforio, K., **1735**
Margolis, S. B., **311°**
Markatou, P., **299**
Markus, M. W., **705**
Marran, D. F., **1159**
Martin, J., **431°**
Martinsson, L., **1735**
Mascolo, G., **11°°**
Masri, A. R., **1141**, 1248, **1301**
Matalon, M., **1407**
Mauss, F., **1019**, **1357**, **697°**
Maxson, J. A., **157**
May, H., 140
McEnally, C. S., **325**
McGrattan, K. B., **1463**
McGreevy, J. L., **1407**
McIntosh, A. C., 44, **541°**, 1372, 1421, 1469
McLean, I. C., **749**
Medvedev, S. P., **73**
Megaridis, C. M., **593**
Meisl, J., **1043**
Melaaen, M. C., **1283**
Menginc, M. P., 617
Menon, S., **1125**
Merkle, C. L., **1619**
Mertens, J. D., **983**
Michael, J. V., **713**, **809**
Mick, H. J., **610°**
Mikami, M., **431**, **439**
Miles, P. C., **202°°**
Miller, J. A., **475°**, 916, 972, **1309**
Miller, J. H., **430°°**, 1010, 1156
Miller, M. F., **1743**
Milne, A., 44
Milov, D., 1372, 1435, 1445
Minutolo, P., **645**
Mishra, D. P., **379°**
Missaghi, M., **1027**
Mitchell, M., **280°**
Mitchell, R., 576

°Combustion and Flame, Vol. 99, 1994.
°°Combustion and Flame, Vol. 100, 1995.

Mitchell, T. J., **793**
Miura, T., **493**
Modestino, A., **519**
Mokhov, A., **243**
Monazam, E. R., **733***
Monkhouse, P. B., **193**
Moreira, A. L., **227**
Morihara, A., **1051**
Morley, C., **125**
Moss, J. B., **609**
Most, J. M., **1701**
Moulijn, J. A., **499***
Mounaïm-Rousselle, C., **1199**
Mudipalli, P. S., **177****
Mueller, C. J., **323****
Mukunda, H. S., **379***, **569**, 1421, 1554, 1641
Müller, C. M., **1099**
Mungal, G., 1146
Muris, S., **660***
Mushi, E. M., **581***
Musmarra, D., 208

Nader, J. D., **192***
Nagata, H., **1719**
Naik, P. D., **993**
Nakamura, S., **269**
Nakanishi, R., **447**
Namazian, M., **1149**, **1223**
Nandula, S. P., **775***
Naruse, I., **545**
Natarajan, K., **610***
Neij, H., **449***
Nelson, P. F., **1003**
Nguyen, Q. V., **395****
Ni, T., **585**
Nicol, D. G., **440****
Niioka, T., **240***, **447**, **1693**
Nikiforakis, N., **465****
Nikolova, I. P., 268, **359****
Niksa, S., **384****, 473, **537**, 916, 1058
Nirschl, H., **389**
Nishioka, M., **758***
Niwa, M., **439**
Norris, A. T., **211****
Norris, M. G., **193****
Novozhilov, B. V., **1677**
Nye, D. A., **161****

O'Doherty, T., **407****
Obounou, M., **1107**
Oh, T. J., **65**
Ohiwa, N., **302***
Ohtake, K., **545**
Ohtani, H., **376****
Okuyama, Y., **1693**
Ono, N., **1693**
Ooms, A. C., **499***
Oppenheim, A. K., 123, **157**
Oran, E. S., **1183**
Orth, A., **143**
Oser, H., **721**
Ou, J. J., **617***

Padmanabhan, K. T., **101****
Page, M., 1641
Pagni, P. J., 1478
Paillard, C., **573***, **1539**
Palma, V., **413***
Palmer, J. M., **893**
Pan, X. C., **1115**
Papas, P., **1333**
Pape, T., **577**
Park, T. W., **767***
Parr, T., **1635**, **1645**
Patel, D. L., **79**
Patnaik, G., **247***
Paul, P. J., **379***, **569**
Paulicelli, M., **527**
Pearlman, H., 1683
Peck, R. E., **475**
Peeters, T. W., **1241**, 1290
Pels, J. R., **499***, 972, 1525
Pennati, G., **201***
Peters, N., 164, 173, **1099**, 1230, **1357**
Peterson, T. W., **262****
Pfefferle, L. D., **41****, **299**
Phylaktou, H., **103**
Piana, J., **1249**
Pines, D. S., **1447**
Pitsch, H., **1357**
Pitts, W. M., **1445**
Pitz, R. W., **775***, **1133**, 1156
Pitz, W. J., **201***, **783**
Pleban, K. U., **660***
Podvoisky, E. P., **371***
Poinsot, T., 1262, **1383**
Polenov, A. N., **73**
Poletaev, N. I., **706***
Pope, C. J., **671**, 668
Pope, S. B., **211****, 1087, 1146, **1167**, **1349**
Poppe, C., **533***
Pourkashanian, M., **1027**
Powell, J. D., **101****
Prado, G., **619**
Prather, M. J., **1513**
Presser, C., **353**

Qian, C., **331***

Ragucci, R., **167**, 379, **679***
Rahn, L. A., 1734, 1742
Ramachandra, P. A., **71****
Rampp, F., **431***
Ranzi, E., **201***
Rath, H. J., **455**

*Combustion and Flame, Vol. 99, 1994.
**Combustion and Flame, Vol. 100, 1995.

Ravichanran, M., **339°**
Rehm, R. G., **1463**
Reinelt, D., **395°**
Reuillon, M., **919**
Rhodes, M. J., **508°**
Richard, J. R., 972
Richards, G. H., **511**
Richter, H., **825**
Ridder, M., **1727**
Rink, K. K., **121°°**
Roberts, W. L., **323°°**
Rodriguez-Mirasol, J., **499°**
Roegner, E. V., **474°°**
Roekaerts, D. J., **1241**
Roesler, J. F., **495°°**
Röhrig, M., **975**
Rolon, J. C., **422°°**
Ronney, P. D., **474°°**, 1087, 1692
Roquemore, W. M., **61°°**
Ross, H. D., 1445, 1709
Roth, P., **467°**, **610°**, **661**, **705**, **1555**
Rotinian, M., **13**
Rumanov, E. N., **713°**
Rushmeier, H., **1471**
Russo, S., **645**

Sacchi, G., **231°**
Sacksteder, K. R., **1685**
Saito, K., **331°**
Sakak, A. S., **933**
Salatino, P., **527**
Samuelsen, G. S., **307**
Sánchez, A. L., **1529**
Sangiovanni, J., 360
Sankar, S. V., **413**
Sanogo, O., **1489**
Santavicca, D. A., **161°°**, **261**
Santoro, R. J., **585**
Sarofim, A. F., **231°**, **519**, 668, **1051**, **1215**
Sato, J., **376°°**, **431**, **439**, **455**, **1719**
Saur, A., **1727**
Sausa, R. C., **323°**
Sawyer, R. F., **325**
Sayre, A., **235**
Schading, G. N., **467°**
Schadow, K. C., **295°**
Schäfer, T., **697°**
Schefer, R. W., **1149**, **1223**
Schiff, G., **1727**
Schiller, D. N., 1445
Schlegel, A., **1019**
Schmoll, W. J., **183**
Schneider, A., **859**
Schreiber, M., **533°**, **933**
Schuck, A., **993**, **491°**
Schuler, F., **431°**
Scott, M. J., **581°**
Seeba, J., **841**, **851**
Seery, D. J., **883**
Seisel, S., **875**
Seitzman, J. M., 1146, **1743**
Senger, W., **95**
Senkan, S. M., **817**
Serauskas, R. V., 314, 1166
Serio, M. A., **553**, **1447**
Seshadri, K., **221°**
Shaddix, C. R., **723°**
Shah, N., 268
Shaw, B. D., 429
Sheinson, R. S., 1525
Shen, B., **503**
Sheng, H. Z., **175**
Shepherd, I., 1255
Sher, E., **635°**
Shin, D. H., **317**
Shkadinskii, K. G., **713°**
Short, M., **465°°**
Shouse, D. T., **183**
Shrinivasa, U., **569**
Shur, M., **13**
Shurupov, S. V., **653**
Shy, S., 1389
Sichel, M., **505°°**, **742°**, 44, 86
Sick, V., **143**
Sidhu, S. S., **11°°**
Siebers, D. L., **192°**
Siegl, W. O., **422°**
Silva, A. M., **227**
Silva, T. F., **227**
Simmons, G. A., **1447**
Sirignano, W. A., 164
Sivathanu, Y. R., 1478
Skaggs, R. R., **430°°**
Skevis, G., **551°**
Slavov, S., **627**
Smallwood, G. J., **371**
Smith, D. B., **749**, **1011**
Smith, G. P., **261°**
Smith, L. L., **153°°**
Smith, O. I., **280°**
Smooke, M. D., **299**, **323°°**
Smoot, D., 288
Smyth, K. C., 140, 331, **723°**
Snelling, D. R., 132, **371**
Snowden, P., **125**
Sobiesiak, A., 233
Sogaro, A., **201°**
Solomon, P. R., **463**, **553**, **1447**
Somers, L. M., **957**
Son, S. F., **283°°**
Sorensen, L. H., **475**
Soteriou, M. C., **1265**, 1372
Sridhar, H. V., **569**
Srivastava, R. K., **241°°**
St. John, D., **307**

°Combustion and Flame, Vol. 99, 1994.
°°Combustion and Flame, Vol. 100, 1995.

Stanmore, B., **619**
Stårner, S. H., **347***, **1141**, **1159**
Steele, R. C., **440****
Stenberg, J., 1058
Stepowski, D., **363**, **516***
Stewart, C. D., **609**
Strahle, W. C., **89**
Strelets, M., **13**
Stroomer, P. P., **1241**
Stuchen, D. V., **859**
Sugiyama, G., **601**
Sumida, W. K., **79**
Sun, C. J., **1391**
Sunderland, P. B., **310****, 583
Sung, C. J., **1391**
Suslensky, A., **1571**
Suvernev, A. A., **1727**
Suzuki, M., **1439**
Switzer, G. L., **183**
Syred, N., **407****

Tien, J. S., **1685**
Tait, N. P., **151**, 1166, 1749
Takahashi, F., **183**
Takeno, T., **1061**
Talbot, L., **153****
Tambour, Y., **381**
Tan, Y., **1563**
Tanabe, M., **455**
Tang, L., **71****
Tang, Y. M., **251****
Tanke, D., **627**
Tappe, M., **627**
Taylor, S. C., **749**
Temps, F., **775**
Tereza, A. M., **705**
Tesner, P. A., 634, **653**, 1222
Thevenin, D., **1547**
Thienel, T., **627**
Thijssen, J. H., **1215**
Thynell, S. T., **1595**
Tomeczek, J., 559, **1035**
Toqan, M. A., **1215**
Torero, J. L., **1701**
Trees, D., **221***
Tregrossi, A., **679**
Trinker, F. H., **422***
Troe, J., **254***, **875**, 890
Trouvé, A., **687***
Tsai, C. H., **484***
Tsai, G. L., **288***
Tsang, W., 791, **867**, **1505**
Tsuge, H., **493**
Tsuji, H., **1191**
Tsuruda, T., **1415**
Tulis, A. J., **79**
Tullin, C. J., **1051**
Turányi, T., **949**

Umiyama, H., **151**
Underwood, J., **422***
Urata, Y., **151**

Vaccaro, S., **413***
Vagelopoulos, C. M., **1317**, **1341**
Valentino, G., **387***
van der Meij, C. E., **243**
Van Tiggelen, P. J., **825**
Vandooren, J., **825**
Vantelon, J. P., **1481**
Venkateswaran, S., **1619**
Veranth, J., 288
Veynante, D., **1249**, **1273**
Viguier, C., **53**
Vollmer, J. T., **859**
Volpp, H. R., **491***, **993**, 1525
von-Gersum, S., **661**
Vovchuk, J. I., **706***
Vovelle, C., **1489**

Wagner, H. G., **577**, **627**, **775**, **859**, **975**
Wahl, C., **833**
Waibel, R. T., 314
Waldherr, G., **251****
Walker, J. A., **867**
Walker, R. W., **767**, 791, 799, 874
Wall, T. F., **485**, **511**
Walsh, P. M., **749***
Wang, H., **111****, **941**
Wang, X. S., **508***
Warnatz, J., **135**, 916, 1058
Warren, D. L., **185****
Weber, H. J., **1555**
Weber, R., **235**, 233, 314, 1034, 1262
Weinberg, F., **269**
Weiss, Y., **519**
Wendt, J. O., **241****, **262****, **277**
Westblom, U., **261***
Westbrook, C. K., **192***, **201***
Westmoreland, P. R., 703, 712, 890, **1505**
Wiese, W., 297, **635**
Wiesen, P., 1525
Williams, A., **1027**
Williams, F. A., **21****, **1207**, 1332, **1529**
Williamson, R. B., 1487
Willis, J. W., **280***
Winter, M., 452, 1749
Wittig, S., **1043**
Wolanski, P., **742***
Wolfrum, J., **143**, **193**, **431***, **491***, **660***, **993**
Wolinski, M., **742***
Wolverton, M. K., **71****
Woods, I. T., **909**
Woodward, Waesche, R. H., 1634
Wooldridge, M. S., **741**

*Combustion and Flame, Vol. 99, 1994.
**Combustion and Flame, Vol. 100, 1995.

Wooldridge, S. T., **983**
Woolford, R. E., **767**
Wornat, M. J., **131°°**
Wu, C. K., **175**
Wu, C. Y., **1603**
Wu, K. C., **193°°**

Yamaguchi, S., **302°**
Yamamoto, K., **1399**
Yang, A. S., **1609**
Yang, G. S., **259°°°**
Yang, J. T., **288°**, **1603**
Yang, N. Y., **31°°**, **131°°**
Yap, L. T., 288, **1027**
Yen, C. W., **288°**
Yeo, J., **125**
Yetter, R. A., **495°°**, **759**
Yoshida, A., **1191**
Yoshida, K., **151**
Yoshida, T., **493**
Yoshihara, Y., **941**
Young, K. J., **609**
Yu, K., **295°**
Yu, T., **169°°**
Yuasa, S., **1587**
Yuranov, I. A., **1669**

Zachariah, M. R., **1505**
Zahn, M., **143**
Zamansky, V. M., 926, 972
Zamaschikov, V. V., **1627**
Zaslonko, I. S., 668
Zhang, J., **1115**, **593**
Zhang, Y., **474°°**
Zhang, Z. P., **175**
Zhao, H. F., **653°**
Zhao, Y., **553**
Zhdanok, S., **221°°**
Zheng, L. L., **440°**
Zhou, L. X., 233, **669°**
Zhou, X. C., **52°°**
Zhu, D. L., **1711**
Ziemer, H., **775**
Zimbardi, F., **527**
Zinn, B. T., **251°°**

°Combustion and Flame, Vol. 99, 1994.
°°Combustion and Flame, Vol. 100, 1995.
°°°Combustion and Flame, Vol. 98, 1994.

SUBJECT INDEX (Volume XXV)

1.0 AEROSOLS

The Fate of Arsenic in a Laminar Diffusion Flame. S. Chesworth, G. S. Yang, D. P. Y. Chang, A. D. Jones, P. B. Kelly and I. M. Kennedy, 259***

Soot Mass Growth and Coagulation of Soot Particles in C_2H_4/Air Flames at 15 Bar. S. Hanisch, H. Jander, Th. Pape and H. Gg. Wagner, 577

1.2 Solid

A Field Study on the Trace Metal Behavior in Atmospheric Circulating Fluidized-Bed Combustion. T. Lind, E. I. Kauppinen, J. K. Jokiniemi and W. Maenhaut, 201

Sorbent Capture of Nickel, Lead and Cadmium in a Laboratory Swirl Flame Incinerator. W. P. Linak, R. K. Srivastava and J. O. L. Wendt, 241**

Radiative Heat Transfer in Pulverized-Coal-Fired Boilers—Development of the Absorptive/Reflective Character of Initial Ash Deposits. G. H. Richards, J. H. Harb, L. L. Baxter, S. Bhattacharaya, R. P. Gupta and T. F. Wall, 511

Flame Propagation Experiment of PMMA Particle Cloud in a Microgravity Environment. H. Kobayashi, N. Ono, Y. Okuyama and T. Niioka, 1693,

2.0 COAL COMBUSTION

(*Also see* **COMBUSTION IN PRACTICAL SYSTEMS,** *Furnaces and Incinerators;* **HETEROGENEOUS COMBUSTION,** *Dispersed Particles, Multiphase, and Single Solid Particles*)

Evolution of Char Chemistry, Crystallinity, and Ultrafine Structure during Pulverized-Coal Combustion. K. A. Davis, R. H. Hurt, N. Y. C. Yang and T. J. Headley, 31**

Decreases in the Swelling and Porosity of Bituminous Coals during Devolatilization at High Heating Rates. T. K. Gale, C. H. Bartholomew and T. H. Fletcher, 94**

Determination of Flue Gas Alkali Concentrations in Fluidized-Bed Coal Combustion by Excimer Laser Induced Fragmentation Fluorescence. K. T. Hartinger, P. B. Monkhouse, J. Wolfrum, H. Baumann and B. Bonn, 193

Primary and Secondary Fragmentation of Coals in a Circulating Fluidized Bed Combustor. U. Arena, A. Cammarota and R. Chirone, 219

The Partitioning of Iron during the Combustion of Pulverized Coal. L. E. Bool III, T.W. Peterson and J. O. L. Wendt, 262**

Influence of Initial Particle Density on the Reaction Mode of Porous Carbon Particles. R. H. Essenhigh, 269*

Predicting the Devolatilization Behavior of Any Coal From its Ultimate Analysis. S. Niksa, 384**

Impact of Coal Pyrolysis on Combustion. P. R. Solomon and T. H. Fletcher, 463

Volatile Matter Release, Particle/Cloud Ignition and Combustion of Near-Stoichiometric Suspensions of Pulverized Coal. J. A. Lucas and T. F. Wall, 485

Performance Predictions of Pulverized-Coal Flames of Power Station Furnace and Cement Kiln Types. F. C. Lockwood and B. Shen, 503

Evolution of Porosity and Thermal Conductivity during Char Oxidation. Y. Weiss, Y. Benari, I. I. Kantorovich, E. Bar-Ziv, G. Krammer, A. Modestino and A. F. Sarofim, 519

A Transient Kinetics Study of the Combustion Reactivity of a Coal Char. P. Salatino, F. Zimbardi and M. Paulicelli, 527

Predicting the Evolution of Fuel Nitrogen from Various Coals. S. Niksa, 537

Combustion Roles of Bubble and Emulsion Phase in Bubbling Fluidized Bed Coal Combustion Elucidated by Conditional Gas Sampling. I. Naruse, K. Koizumi, K. Kuramoto, G.-Q. Lu and K. Ohtake, 545

A Method of Predicting Coal Devolatilization Behavior Based on the Elemental Composition. Y. Zhao, M. A. Serio, R. Bassilakis and P. R. Solomon, 553

Near-Extinction and Final Burnout in Coal Combustion. R. H. Hurt and K. A. Davis, 561

Application of Multiple Opposed Jets to Coal Flame Stabilization of Precombustor Burner. H. F. Zhao, 653*

Gas-Particle Flows and Coal Combustion in a Burner/Combustor With High-Velocity Jets. L. X. Zhou, W. Y. Lin, W. W.Luo and X. Q. Huang, 669*

Characterization of Mass and Density Distributions of Sized Coal Fractions. E. R. Monazam and D. J. Maloney, 733*

Fragmentation and Attrition of Coal Char Particles Undergoing Collisions during Combustion at Temperatures from 900 to 1100. K. P. M. Walsh and Tong Li, 749*

*Combustion and Flame, Vol. 99, 1994.

**Combustion and Flame, Vol. 100, 1995.

***Combustion and Flame, Vol. 98, 1994.

3.0 COMBUSTION IN PRACTICAL SYSTEMS

A Thermochemical Phase Space for Combustion in Engines. A. K. Oppenheim and J. A. Maxson, 157
Mixing and Chemical Kinetic Constraints on PIC Production during Chlorocarbon Combustion. J. Brouwer, G. Sacchi, J. P. Longwell and A. F. Sarofim, 231*
Effect of Radiation on Nitrogen Oxides Emissions from Non-Sooty Swirling Flames of Natural Gas. A. Sayre, N. Lallemant, J. Dugué and R. Weber, 235
On the Effects of Fuel Leakage on CO Production from Household Burners as Revealed by LIF and CARS. C. E. van der Meij, A. Mokhov, R. A. A. M. Jacobs and H. B. Levinsky, 243
Combustion Science for Incineration Technology. J. Wendt, 277
The Nonlinear Dynamics of Intrinsic Acoustic Oscillations in a Model Pulse Combustor. S. B. Margolis, 311*
The Effect of Hydrogen and Propane Addition on the Operation of a Natural Gas-Fired Pulsed Combustor. H. R. N. Jones and J. Leng, 404*
NO_x Formation in Lean Premixed Non-Catalytic and Catalytically Stabilized Combustion of Propane. A. Schlegel, S. Buser, P. Benz, H. Bockhorn and F. Mauss, 1019

3.1 Diesel Engines

Fuel and Soot Oxidation in Diesel-like Conditions. A. Cavliere, R. Barbella, A. Ciajola, A. D'Anna and R. Ragucci, 167
The Droplet Group Microexplosions in Water-in-Oil Emulsion Sprays and their Effects on Diesel Engine Combustion. H. Z. Sheng, L. Chen, Z. P. Zhang, C. K. Wu, C. An and C. Q. Cheng, 175
Effects of Natural Gas Composition on Ignition Delay under Diesel Conditions. J. D. Naber, D. L. Siebers, S. S. Di Julio and C. K. Westbrook, 192*
The Structure of the Dense Core Region in Transient Diesel Sprays. G. J. Smallwood, Ö. L. Gülder and D. R. Snelling, 371
Analysis of In-Cylinder Flow Processes by LDA. F. E. Corcione and G. Valentino, 387*
Reduced Mechanism of Soot Formation—Application to Natural Gas Fueled Diesel Combustion. Y. Yoshihara, A. Kazakov, H. Wang and M. Frenklach, 941
Shock-Tube Investigation on the Self-Ignition of Hydrocarbon-Air Mixtures at High Pressures. K. Fieweger, R. Blumenthal and G. Adomeit, 1579

*Combustion and Flame, Vol. 99, 1994.
**Combustion and Flame, Vol. 100, 1995.

3.2 Furnaces and Incinerators

The Homogeneous, Gas-Phase Formation of Chlorinated and Brominated Dibenzo-*p*-dioxins from 2,4,6-Trichloro- and 2,4,6-Tribromophenols. S. S. Sidhu, L. Maqsud, B. Dellinger and G. Mascolo, 11**
An Adaptive Optimal Combustion Control Strategy. K. T. Padmanabhan, C. T. Bowman and J. D. Powell, 101**
The Oxidation of Calcium Sulphide at the Temperatures of Fluidised Bed Combustors. N. H. Davies, K. M. Laughlin and A. N. Hayhurst, 211
Primary and Secondary Fragmentation of Coals in a Circulating Fluidized Bed Combustor. U. Arena, A. Cammarota and R. Chirone, 219
Superadiabatic Combustion of Methane Air Mixtures under Filtration in a Packed Bed. S. Zhdanok, L. A. Kennedy and G. Koester, 221**
Comparison of Measurements and Predictions of Wall Heat Flux and Gas Composition in an Oil-Fired Utility Boiler. M. G. Carvalho, P. J. Coelho, A. L. N. Moreira, A. M. C. Silva and T. F. Silva, 227
Mixing and Chemical Kinetic Constraints on PIC Production during Chlorocarbon Combustion. J. Brouwer, G. Sacchi, J. P. Longwell and A. F. Sarofim, 231*
Effect of Radiation on Nitrogen Oxides Emissions from Non-Sooty Swirling Flames of Natural Gas. A. Sayre, N. Lallemant, J. Dugué and R. Weber, 235
Heat Release Timing in a Non-Premixed Helmholtz Pulse Combustor. Y. M. Tang, G. Waldherr, J. I. Jagoda and B. T. Zinn, 251**
The Partitioning of Iron during the Combustion of Pulverized Coal. L. E. Bool III, T. W. Peterson and J. O. L. Wendt, 262**
Fuel Saving by Heat-Recirculating Combustion Using Fibre Mats. S. Nakamura and F. Weinberg, 269
Destruction of Liquid and Gaseous Waste Surrogates in an Acoustically Excited Dump Combustor. J. W. Willis, C. Cadou, M. Mitchell, A. R. Karagozian and O. I. Smith, 280*
Active, Optimal Control of a Model, Industrial, Natural Gas-Fired Burner. D. St. John and G. S. Samuelsen, 307
Cold-Flow Simulation of Municipal Waste Incinerators. S. Choi, J. S. Lee, S. K. Kim and D. H. Shin, 317
In Situ Detection of Hazardous Waste. C. S. McEnally, R. F. Sawyer, C. P. Koshland and D. Lucas, 325
Experimental and Numerical Study of an Incinerator- and Furnace-Related Flow. D. K. Heist, M. Ravichanran and F. C. Gouldin, 339*
Analysis of Droplet Arrival Statistics in a Pressure-

Atomized Spray Flame. J. T. Hodges, C. Presser, A. K. Gupta and C. T. Avedesian, 353
Phase Averaging of the Precessing Vortex Core in a Swirl Burner under Piloted and Premixed Combustion Conditions. D. Froud, T. O'Doherty and N. Syred, 407**
TACCOS—A Thermography-Assisted Combustion Control System for Waste Incinerators. F. Schuler, F. Rampp, J. Martin and J. Wolfrum, 431*
NO_x and CO Emissions from a Pulse Combustor Operating in a Lean Premixed Mode. J. O. Keller, T. T. Bramlette, P. K. Barr and J. R. Alvarez, 460*
The Effect of Pulverized Coal Injection and Volatile Matter Content of Coal on Combustion Characteristics around the Raceway Zone in the Blast Furnace. H. Tsuge, T. Yoshida, H. Aoki and T. Miura, 493
Performance Predictions of Pulverized-Coal Flames of Power Station Furnace and Cement Kiln Types. F. C. Lockwood and B. Shen, 503
Radiative Heat Transfer in Pulverized-Coal-Fired Boilers—Development of the Absorptive/Reflective Character of Initial Ash Deposits. G. H. Richards, J. H. Harb, L. L. Baxter, S. Bhattacharaya, R. P. Gupta and T. F. Wall, 511
The Influence of Burner Injection Mode on Pulverised Coal and Biomass Co-Fired Flames. T. Abbas, P. Costen, N. H. Kandamby, F. C. Lockwood and J. J. Ou, 617*

3.3 *Liquid, Hybrid, and Gas Rockets*

Analyses of Liquid Rocket Instabilities Using a Computational Testbed. J. M. Grenda, S. Venkateswaran and C. L. Merkle, 1619

3.5 *Ramjets and Augmentors*

Gasdynamic Enhancement of Nonpremixed Combustion. F. Marble, 1
An Adaptive Optimal Combustion Control Strategy. K. T. Padmanabhan, C. T. Bowman and J. D. Powell, 101**
Solid-Fuel Regression during Ignition Transient In A Ramjet. J.-T. Yang and C. Y. Y. Wu, 1603

3.6 *Solid Rockets*

RDX Flame Structure. D. Hanson-Parr and T. Parr, 1635

3.7 *Spark Ignition Engines*

Surface Erosion by High Speed Combustion Waves. R. Klein, H. Breitbach, K. J. Geratz and W. Senger, 95
State of the Art and Future Needs in S.I. Engine Combustion. R. R. Maly, 111
Cars Temperature Measurements and the Cyclic Dispersion of Knock in Spark Ignition Engines. D. Bradley, G. T. Kalghatgi, C. Morley, P. Snowden and J. Yeo, 125
Detection of Hot Spots in the End Gas of an Internal Combustion Engine Using Two-Dimensional LIF of Formaldehyde. B. Bäuerle, F. Hoffmann, F. Behrendt and J. Warnatz, 135
Simultaneous 2D-Single Shot Imaging of OH Concentrations and Temperature Fields in a SI Engine Simulator. A. Orth, V. Sick, J. Wolfrum, R. R. Maly and M. Zahn, 143
In-Cylinder Crank Angle Resolved Imaging of Fuel Concentration In a Firing Spark-Ignition-Engine Using Planar Laser-Induced Flourescence. M. Berckmüller, N. P. Tait, R. D. Lockett, D. A. Greenhalgh, K. Ishii, Y. Urata, H. Umiyama and K. Yoshida, 151
Chemical Kinetic Modeling of Exhaust Hydrocarbon Oxidation. K. C. Wu, S. Hochgreb and M. G. Norris, 193**
Hydrocarbon Oxidation in the Exhaust Port and Runner of a Spark Ignition Engine. K. Drobot, W. K. Cheng, F. H. Trinker, E. W. Kaiser, W. O. Siegl, D. F. Cotton and J. Underwood, 422*
Development and Demonstration of 2D-LIF for Studies of Mixture Preparation in SI Engines. H. Neij, B. Johansson and M. Aldén, 449*
Numerical Modeling of Spark Ignition and Flame Initiation in a Quiescent Methane-Air Mixture. T. Kravchik and E. Sher, 635*
Modeling Turbulent Flame Propagation. W. T. Ashurst, 1075
Dual-Broadband Rotational CARS Measurements in an IC Engine, P.-E. Bengtsson, L. Martinsson, M. Aldén, B. Johansson, B. Lassesson, K. Marforio and G. Lundholm, 1735

3.8 *Turbine Combustors*

An Adaptive Optimal Combustion Control Strategy. K. T. Padmanabhan, C. T. Bowman and J. D. Powell, 101**
Structure of a Spray Flame Stabilized on a Production Engine Combustor Swirl Cup. F. Takahashi, W. J. Schmoll, G. L. Switzer and D. T. Shouse, 183
Turbulent Velocity and Temperature Measurements from a Gaseous Fueled Technology Combustor with a Practical Fuel Injector. P. O. Hedman and D. L. Warren, 185**
On the Aero-thermal Characteristics of Gasifier-Fuelled Gas Turbine Combustors with Complex Geometries. N. H. Kandamby and F. C. Lockwood, 251
A Spark Ignition Model for Relight Problems in Air-

*Combustion and Flame, Vol. 99, 1994.
**Combustion and Flame, Vol. 100, 1995.

craft Gas Turbines. D. Liou and D. A. Santavicca, 261
Influence of Ambient Pressure on Drop-Size and Velocity Distributions in Dense Sprays. A. K. Jasuja and A. H. Lefebvre, 345
Numerical Simulation of Local Extinction Effects in Turbulent Combustor Flows of Methane and Air. I. R. Gran, M. C. Melaaen and B. F. Magnussen, 1283

3.9 Fluidized Beds

Biosludge Incineration in FBCs: Behavior of Ash Particles. K. K. Rink, J. A. Kozinski and J. S. Lighty, 121**
Determination of Flue Gas Alkali Concentrations in Fluidized-Bed Coal Combustion by Excimer Laser Induced Fragmentation Fluorescence. K. T. Hartinger, P. B. Monkhouse, J. Wolfrum, H. Baumann and B. Bonn, 193
A Field Study on the Trace Metal Behavior in Atmospheric Circulating Fluidized Bed Combustion. T. Lind, E. I. Kauppinen, J. K. Jokiniemi and W. Maenhaut, 201
The Oxidation of Calcium Sulphide at the Temperatures of Fluidised Bed Combustors. N. H. Davies, K. M. Laughlin and A. N. Hayhurst, 211
Primary and Secondary Fragmentation of Coals in a Circulating Fluidized Bed Combustor. U. Arena, A. Cammarota and R. Chirone, 219
Pyrolysis and Combustion of Corncobs in a Fluidized Bed: Measurement and Analysis of Behavior. J.-L. Lin and H. M. Keener, 271**
Combustion Roles of Bubble and Emulsion Phase in Bubbling Fluidized Bed Coal Combustion Elucidated by Conditional Gas Sampling. I. Naruse, K. Koizumi, K. Kuramoto, G.-Q. Lu and K. Ohtake, 545
Fragmentation and Attrition of Coal Char Particles Undergoing Collisions during Combustion at Temperatures From 900 to 1100 K. P. M. Walsh and T. Li, 749*
Effect of NO and O_2 Concentration on N_2O Formation during Coal Combustion in a Fluidized Bed Combustor: Modeling Results. S. K. Goel, A. Morihara, C. J. Tullin and A. F. Sarofim, 1051

DEFLAGRATION
(*See* **FLAMES**)

4.0 DETONATIONS

Theoretical and Numerical Analysis of the Photochemical Initiation of Detonations in Hydrogen-Oxygen Mixtures. L. He and P. Clavin, 45
Critical Diameter for the Transmission of a Detonation Wave into a Porous Medium. A. Makris, T. J. Oh, J. H. S. Lee and R. Knystautas, 65
Detonation Cell Size Measurements and Predictions in Hydrogen-Air-Stream Mixtures at Elevated Temperatures. G. Ciccarelli, T. Ginsberg, J. Boccio, C. Economos, K. Sato and M. Kinoshita, 212*
Effect of Diethylenetriamine Sensitization on Detonation of Nitromethane in Porous Media. J. J. Lee, M. Brouillette, D. L. Frost and J. H. S. Lee, 292**

4.1 Condensed-Phase

Effect of Diethylenetriamine Sensitization on Detonation of Nitromethane in Porous Media. J. J. Lee, M. Brouillette, D. L. Frost and J. H. S. Lee, 292**

4.2 Gas-Phase

On Deviations from Ideal Chapman-Jouguet Detonation Velocity. H. K. Brüls, M. H. Lefebvre and J. Berghmans, 37
Critical Diameter for the Transmission of a Detonation Wave into a Porous Medium. A. Makris, T. J. Oh, J. H. S. Lee and R. Knystautas, 65
Numerical Modeling of Combustion Processes Induced by a Supersonic Conical Blunt Body. M. H. Lefebvre and T. Fujiwara, 85**
Detonation Cell Size Measurements and Predictions in Hydrogen-Air-Stream Mixtures at Elevated Temperatures. G. Ciccarelli, T. Ginsberg, J. Boccio, C. Economos, K. Sato and M. Kinoshita, 212*
Accumulating Sequence of Ignitions from a Propagating Pulse. J. W. Dold, M. Short, J. F. Clarke and N. Nikiforakis, 465**
Shock Tube Study of Ignition Delays and Detonation of Gaseous Monomethylhydrazine/Oxygen Mixtures. L. Catoire, X. Bassin, G. Dupre and C. Paillard, 573*

4.3 Failure

Critical Diameter for the Transmission of a Detonation Wave into a Porous Medium. A. Makris, T. J. Oh, J. H. S. Lee and R. Knystautas, 65

4.4 Initiation

Theoretical and Numerical Analysis of the Photochemical Initiation of Detonations in Hydrogen-Oxygen Mixtures. L. He and P. Clavin, 45
Weak and Strong Ignition within the Scope of Spontaneous Flame Concept. A. M. Bartenev and B. E. Gelfand, 61
Collision of a Shock Wave with Obstacles in a Combustible Mixture. C. K. Chan, 341**
Self Ignition of Expanding High Temperature H_2-

*Combustion and Flame, Vol. 99, 1994.
**Combustion and Flame, Vol. 100, 1995.

Air and CH_4-Air Mixtures. H.-J. Weber, A. Mack and P. Roth, 1555

4.5 Limits

Effect of Diethylenetriamine Sensitization on Detonation of Nitromethane in Porous Media. J. J. Lee, M. Brouillette, D. L. Frost and J. H. S. Lee, 292**
Shock-Tube Investigation on the Self-Ignition of Hydrocarbon-Air Mixtures at High Pressures. K. Fieweger, R. Blumenthal and G. Adomeit, 1579

4.6 Multiphase

Phenomenological Aspects in Explosive Powder/Gas Two-Phase Detonations. A. J. Tulis, W. K. Sumida, R. P. Joyce, D. C. Heberlein and D. L. Patel, 79
An Experimental Study of Deflagration to Detonation Transition Supported by Dust Layers. Y.-C. Li, C. W. Kauffman and M. Sichel, 505**
Investigation of Organic Dust Detonation in the Presence of Chemically Inert Particles. R. Klemens, M. Kapuscinski, M. Wolinski, P. Wolanski and M. Sichel, 742*

4.7 Structure

H_2-Air and CH_4-Air Detonations and Combustions behind Oblique Shock Waves. C. Viguier, C. Guerraud and D. Desbordes, 53
Detonation Cell Size Measurements and Predictions in Hydrogen-Air-Stream Mixtures at Elevated Temperatures. G. Ciccarelli, T. Ginsberg, J. Boccio, C. Economos, K. Sato and M. Kinoshita, 212*

4.9 Transition to Detonation

Theoretical and Numerical Analysis of the Photochemical Initiation of Detonations in Hydrogen-Oxygen Mixtures. L. He and P. Clavin, 45
Weak and Strong Ignition within the Scope of Spontaneous Flame Concept. A. M. Bartenev and B. E. Gelfand, 61
Critical Diameter for the Transmission of a Detonation Wave into a Porous Medium. A. Makris, T. J. Oh, J. H. S. Lee and R. Knystautas, 65
Initiation of Upstream-Directed Detonation Induced by the Venting of Gaseous Explosion. S. P. Medvedev, A. N. Polenov, S. V. Khomik and B. E. Gelfand, 73
Numerical Modeling of Combustion Processes Induced by a Supersonic Conical Blunt Body. M. H. Lefebvre and T. Fujiwara, 85**
Collision of a Shock Wave with Obstacles in a Combustible Mixture. C. K. Chan, 341**
An Experimental Study of Deflagration to Detonation Transition Supported by Dust Layers. Y.-C. Li, C. W. Kauffman and M. Sichel, 505**
Investigation of Organic Dust Detonation in the Presence of Chemically Inert Particles. R. Klemens, M. Kapuscinski, M. Wolinski, P. Wolanski and M. Sichel, 742*
Shock-Tube Investigation on the Self-Ignition of Hydrocarbon-Air Mixtures at High Pressures. K. Fieweger, R. Blumenthal and G. Adomeit, 1579

5.0 DIAGNOSTIC METHODS

Laser Ionization Time-Of-Flight Mass Spectrometry Combined With Residual Gas Analysis for the Investigation of Moderate Temperature Benzene Oxidation. G. Bermudez and L. Pfefferle, 41**
Phenomenological Aspects in Explosive Powder/Gas Two-Phase Detonations. A. J. Tulis, W. K. Sumida, R. P. Joyce, D. C. Heberlein and D. L. Patel, 79
2D Laser Diagnostics of Liquid Methanol for Investigation of Atomization and Vaporization Dynamics in a Burning Spray Jet. R. Bazile and D. Stepowski, 363
Clarification of the Flame Structure of Droplet Burning Based on Temperature Measurement in Microgravity. M. Mikami, M. Niwa, H. Kato, J. Sato and M. Kono, 439
Determination of Temperature From N_2 and O_2 Cars Spectra at Very High Pressure. T. Dreier, M. Ridder, G. Schiff, A. Saur and A. A. Suvernev, 1727

5.1 CARS (Coherent Anti Stokes Raman Spectroscopy)

Cars Temperature Measurements and the Cyclic Dispersion of Knock in Spark Ignition Engines. D. Bradley, G. T. Kalghatgi, C. Morley, P. Snowden and J. Yeo, 125
Turbulent Velocity and Temperature Measurements from a Gaseous Fueled Technology Combustor with a Practical Fuel Injector. P. O. Hedman and D. L. Warren, 185**
NO_x and N_2O in Lean-Premixed Jet-Stirred Flames. R. C. Steele, P. C. Malte, D. G. Nicol and J. C. Kramlich, 440**
Large Eddy Simulations of Bluff Body Stabilized Flames. C. Fureby and C. Löfström, 1257
Determination of Temperature From N_2 and O_2 Cars Spectra at Very High Pressure. T. Dreier, M. Ridder, G. Schiff, A. Saur and A. A. Suvernev, 1727
Dual-Broadband Rotational CARS Measurements in an IC Engine. P.-E. Bengtsson, L. Martinsson,

*Combustion and Flame, Vol. 99, 1994.
**Combustion and Flame, Vol. 100, 1995.

M. Aldén, B. Johansson, B. Lassesson, K. Marforio and G. Lundholm, 1735

5.3 Fluorescence

Detection of Hot Spots in the End Gas of an Internal Combustion Engine Using Two-Dimensional LIF of Formaldehyde. B. Bäuerle, F. Hoffmann, F. Behrendt and J. Warnatz, 135

Simultaneous 2D-Single Shot Imaging of OH Concentrations and Temperature Fields in a SI Engine Simulator. A. Orth, V. Sick, J. Wolfrum, R. R. Maly and M. Zahn, 143

In-Cylinder Crank Angle Resolved Imaging of Fuel Concentration In a Firing Spark-Ignition-Engine Using Planar Laser-Induced Flourescence. M. Berckmüller, N. P. Tait, R. D. Lockett, D. A. Greenhalgh, K. Ishii, Y. Urata, H. Umiyama and K. Yoshida, 151

Lewis Number Effects on Premixed Flames Interacting with Turbulent Kármán Vortex Streets. J. G. Lee, T.-W. Lee, D. A. Nye and D. A. Santavicca, 161**

Determination of Flue Gas Alkali Concentrations in Fluidized-Bed Coal Combustion by Excimer Laser Induced Fragmentation Fluorescence. K. T. Hartinger, P. B. Monkhouse, J. Wolfrum, H. Baumann and B. Bonn, 193

Laser-Induced Fluorescence Study of Manganese Fuel Additive Effects in a Propane/Air Flame. U. Westblom, F. Fernandez-Alonso, G. P. Smith, J. B. Jeffries and D. R. Crosley, 261*

In Situ Detection of Hazardous Waste. C. S. McEnally, R. F. Sawyer, C. P. Koshland and D. Lucas, 325

Develoment and Demonstration of 2D-LIF for Studies of Mixture Preparation in SI Engines. H. Neij, B. Johansson and M. Aldén, 449*

Flame Stabilization and OH Fluorescence Mapping of the Combustion Structures in the Near Field of a Spray Jet. D. Stepowski, A. Cessou and P. Goix, 516*

Kinetic Studies of the Reactions $NH(X^3\Sigma^-) + NO$ and $NH(X^3\Sigma^-) + O_2$ at Elevated Temperatures. H. Lillich, A. Schuck, H.-R. Volpp, J. Wolfrum and P. D. Naik, 993

Simultaneous NO and Temperature Imaging Measurements in Turbulent Nonpremixed Flames. M. Namazian, J. Kelly and R. Schefer, 1149

Mixture Fraction Imaging in Turbulent Nonpremixed Hydrocarbon Flames. J. H. Frank, K. M. Lyons, D. F. Marran, M. B. Long, S. H. Stårner and R. W. Bilger, 1159

RDX Flame Structure. D. Hanson-Parr and T. Parr, 1635

Double-Pulsed Imaging Using Simultaneous OH/Acetone PLIF for Studying the Evolution of High-Speed, Reacting Mixing Layers. J. M. Seitzman, M. F. Miller, T. C. Island and R. K. Hanson, 1743

5.4 Laser

Air Entrainment Flow Field Induced by a Pool Fire. X. C. Zhou and J. P. Gore, 52**

Detection of Hot Spots in the End Gas of an Internal Combustion Engine Using Two-Dimensional LIF of Formaldehyde. B. Bäuerle, F. Hoffmann, F. Behrendt and J. Warnatz, 135

In-Cylinder Crank Angle Resolved Imaging of Fuel Concentration in a Firing Spark-Ignition-Engine Using Planar Laser-Induced Flourescence. M. Berckmüller, N. P. Tait, R. D. Lockett, D. A. Greenhalgh, K. Ishii, Y. Urata, H. Umiyama and K. Yoshida, 151

Laser Raman Scattering Measurements of Differential Molecular Diffusion in Turbulent Nonpremixed Jet Flames of H_2/CO_2 Fuel. L. L. Smith, R. W. Dibble, L. Talbot, R. S. Barlow and C. D. Carter, 153**

The Droplet Group Microexplosions in Water-in-Oil Emulsion Sprays and Their Effects on Diesel Engine Combustion. H. Z. Sheng, L. Chen, Z. P. Zhang, C. K. Wu, C. An and C. Q. Cheng, 175

On the Effects of Fuel Leakage on CO Production from Household Burners as Revealed by LIF and CARS. C. E. van der Meij, A. Mokhov, R. A. A. M. Jacobs and H. B. Levinsky, 243

Laser-Induced Fluorescence Study of Manganese Fuel Additive Effects in a Propane/Air Flame. U. Westblom, F. Fernandez-Alonso, G. P. Smith, J. B. Jeffries and D. R. Crosley, 261*

Flame Stabilization in the Wake Flow behind a Slit V-Gutter. J.-T. Yang, C.-W. Yen and G.-L. Tsai, 288*

Laser Microprobe Analysis of Soot Precursor Particles and Carbonaceous Soot. R. A. Dobbins, R. A. Fletcher and W. Lu, 301**

In Situ Detection of Hazardous Waste. C. S. McEnally, R. F. Sawyer, C. P. Koshland and D. Lucas, 325

Injection, Dispersion, and Combustion of Liquid Fuels. W. D. Bachalo, 333

Influence of Ambient Pressure on Drop-Size and Velocity Distributions in Dense Sprays. A. K. Jasuja, A. H. Lefebvre, 345

Conserved Scalar Measurements in Turbulent Diffusion Flames by a Raman and Rayleigh Ribbon Imaging Method. S. H. Starner, R. W. Bilger, K. M. Lyons, J. H. Frank and M. B. Long, 347*

Analysis of Droplet Arrival Statistics in a Pressure-Atomized Spray Flame. J. T. Hodges, C. Presser, A. K. Gupta and C. T. Avedesian, 353

The Structure of the Dense Core Region in Tran-

*Combustion and Flame, Vol. 99, 1994.

**Combustion and Flame, Vol. 100, 1995.

sient Diesel Sprays. G. J. Smallwood, Ö. L. Gülder and D. R. Snelling, 371
Analysis of In-Cylinder Flow Processes by LDA. F. E. Corcione and G. Valentino, 387*
Experimental and Numerical Comparison of Extractive and In-Situ Laser Measurements of Non-Equilibrium Carbon Monoxide in Lean-Premixed Natural Gas Combustion. Q. V. Nguyen, B. L. Edgar, R. W. Dibble and A. Gulati, 395**
Application of an Integrated Phase Doppler Interferometer/Rainbow Thermometer/Point Diffraction Interferometer for Characterizing Burning Droplets. S. V. Sankar, D. H. Buermann, K. M. Ibrahim and W. D. Bachalo, 413
Experiments on the Interaction between a Vortex and a Strained Diffusion Flame. J. C. Rolon, F. Aguerre and S. Candel, 422**
A Study of Carbon Monoxide in a Series of Laminar Ethylene/Air Diffusion Flames using Tunable Diode Laser Absorption Spectroscopy. R. R. Skaggs and J. H. Miller, 430**
Suppression of Soot Formation in Ethene Laminar Diffusion Flames by Chemical Additives. T. Ni, S. B. Gupta and R. J. Santoro, 585
Experimental Identification of Mixing Regimes in the Analysis of Turbulent Diffusion Flames. A. Cavaliere, M. El-Naggar and R. Ragucci, 679*
Quantitative Measurements of Enhanced Soot Production in a Flickering Methane/Air Diffusion Flame. C. R. Shaddix, J. E. Harrington and K. C. Smyth, 723*
A Shock Tube Study of the $CO + OH \rightarrow CO_2 + H$ Reaction. M. S. Wooldridge, R. K. Hanson and C. T. Bowman, 741
Measurements of Scalar Dissipation in the Reaction Zones of Turbulent Nonpremixed H_2-Air Diffusion Flames. S. P. Nandula, T. M. Brown and R. W. Pitz, 775*
The Reactions of $NH(X^3\Sigma^-)$ with the Water Gas Components CO_2, H_2O and H_2. M. Röhrig and H. Wagner, 975
A Shock Tube Study of the Reactions of CN and NCO with NO_2. S. T. Wooldridge, J. D. Mertens, R. K. Hanson and C. T. Bowman, 983
Kinetic Studies of the Reactions $NH(X^3\Sigma^-) + NO$ and $NH(X^3\Sigma^-) + O_2$ at Elevated Temperatures. H. Lillich, A. Schuck, H.-R. Volpp, J. Wolfrum and P. D. Naik, 993
Simultaneous Measurement of Conserved and Reactive Scalars in Turbulent Diffusion Flames for Assessment of PDF Models. T. S. Cheng and R. W. Pitz, 1133
Mixture Fraction Imaging in Turbulent Nonpremixed Hydrocarbon Flames. J. H. Frank, K. M. Lyons, D. F. Marran, M. B. Long, S. H. Stårner and R. W. Bilger, 1159
Raman Measurements and Joint PDF Modeling of a Non-Premixed Bluff-Body-Stabilized Methane Flame. S. M. Correa, A. Gulati and S. B. Pope, 1167
Strain Effects on the Structure of Counterflowing Turbulent Premixed Flames. C. Mounaïm-Roussel and I. Gökalp, 1199
Experimental Analysis of Flamelet Models for Premixed Turbulent Combustion. D. Veynante, J. M. Duclos and J. Piana, 1249
Double-Pulsed Imaging using Simultaneous OH/Acetone PLIF for Studying the Evolution of High-Speed, Reacting Mixing Layers. J. M. Seitzman, M. F. Miller, T. C. Island and R. K. Hanson, 1743

5.5 *Photographic*

Interactions Between Nonsymmetrical Wake Structure and Turbulent Diffusion Flames behind a Rear-Facing Semicircular Cylinder. N. Ohiwa, Y. Ishino and S. Yamaguchi, 302*
The Structure of the Dense Core Region in Transient Diesel Sprays. G. J. Smallwood, Ö. L. Gülder and D. R. Snelling, 371
Near-Extinction and Final Burnout in Coal Combustion. R. H. Hurt and K. A. Davis, 561

5.6 *Probes*

Comparison of Measurements and Predictions of Wall Heat Flux and Gas Composition in an Oil-Fired Utility Boiler. M. G. Carvalho, P. J. Coelho, A. L. N. Moreira, A. M. C. Silva and T. F. Silva, 227
Flame Structure Studies of a Lean $H_2/N_2O/Ar$ Flame Employing Molecular Beam Mass Spectrometry and Modeling. D. C. Dayton, C. M. Faust, W. R. Anderson and R. C. Sausa, 323*
Experimental and Numerical Comparison of Extractive and In-Situ Laser Measurements of Non-Equilibrium Carbon Monoxide in Lean-Premixed Natural Gas Combustion. Q. V. Nguyen, B. L. Edgar, R. W. Dibble and A. Gulati, 395**
Clarification of the Flame Structure of Droplet Burning Based on Temperature Measurement in Microgravity. M. Mikami, M. Niwa, H. Kato, J. Sato and M. Kono, 439
NO_x and N_2O in Lean-Premixed Jet-Stirred Flames. R. C. Steele, P. C. Malte, D. G. Nicol and J. C. Kramlich, 440**
Combustion Roles of Bubble and Emulsion Phase in Bubbling Fluidized Bed Coal Combustion Elucidated by Conditional Gas Sampling. I. Naruse, K. Koizumi, K. Kuramoto, G.-Q. Lu and K. Ohtake, 545
The Reactions of Phenylacetylenes With $O(^3P)$ in

*Combustion and Flame, Vol. 99, 1994.
**Combustion and Flame, Vol. 100, 1995.

the Gas Phase. M. Eichholtz, A. Schneider, D.-V. Stuchen, J.-T. Vollmer and H. G. Wagner, 859

5.8 Pyrometric

TACCOS—A Thermography-Assisted Combustion Control System for Waste Incinerators. F. Schuler, F. Rampp, J. Martin and J. Wolfrum, 431°

5.9 Spectroscopic

Laser Ionization Time-Of-Flight Mass Spectrometry Combined with Residual Gas Analysis for the Investigation of Moderate Temperature Benzene Oxidation. G. Bermudez and L. Pfefferle, 41°°
In Situ Detection of Hazardous Waste. C. S. McEnally, R. F. Sawyer, C. P. Koshland and D. Lucas, 325
Volatile Matter Release, Particle/Cloud Ignition and Combustion of Near-Stoichiometric Suspensions of Pulverized Coal. J. A. Lucas and T. F. Wall, 485
Radiative Heat Transfer in Pulverized-Coal-Fired Boilers—Development of the Absorptive/Reflective Character of Initial Ash Deposits. G. H. Richards, J. H. Harb, L. L. Baxter, S. Bhattacharaya, R. P. Gupta and T. F. Wall, 511
The Thermal Reactions of CH_3. K. P. Lim and J. V. Michael, 713
Determination of Flue Gas Alkali Concentrations in Fluidized-Bed Coal Combustion by Excimer Laser Induced Fragmentation Fluorescence. K. T. Hartinger, P. B. Monkhouse, J. Wolfrum, H. Baumann and B. Bonn, 193

6.0 ELECTRICAL PROPERTIES OF FLAMES

ENGINE KNOCK

(*See* **COMBUSTION IN PRACTICAL SYSTEMS**, *SI Engines*)

7.0 EXPERIMENTAL METHODS

Fragmentation and Attrition of Coal Char Particles Undergoing Collisions during Combustion at Temperatures from 900 to 1100 K. P. M. Walsh and T. Li, 749°
Wide Field Conserved Scalar Imaging in Turbulent Diffusion Flames by a Raman and Rayleigh Method. J. B. Kelman, A. R. Masri, S. H. Stårner and R. W. Bilger, 1141
Buoyant Downward Diffusion Flame Spread and Extinction in Partial-Gravity Accelerations. K. R. Sacksteder and J. S. T'ien, 1685

7.1 Burners

An Adaptive Optimal Combustion Control Strategy. K. T. Padmanabhan, C. T. Bowman and J. D. Powell, 101°°
Nonoxide Ceramic Powder Synthesis. B. W. Gerhold and K. E. Inkrott, 144°°
Chemical Closure and Burning Rates in Premixed Turbulent Flames. F. C. Gouldin and P. C. Miles, 202°°
Superadiabatic Combustion of Methane Air Mixtures under Filtration in a Packed Bed. S. Zhdanok, L. A. Kennedy and G. Koester, 221°°
Effect of Radiation on Nitrogen Oxides Emissions from Non-Sooty Swirling Flames of Natural Gas. A. Sayre, N. Lallemant, J. Dugué and R. Weber, 235
Fuel Saving by Heat-Recirculating Combustion Using Fibre Mats. S. Nakamura and F. Weinberg, 269
Interactions between Nonsymmetrical Wake Structure and Turbulent Diffusion Flames behind a Rear-Facing Semicircular Cylinder. N. Ohiwa, Y. Ishino and S. Yamaguchi, 302°
Active, Optimal Control of a Model, Industrial, Natural Gas-Fired Burner. D. St. John and G. S. Samuelsen, 307
Conserved Scalar Measurements in Turbulent Diffusion Flames by a Raman and Rayleigh Ribbon Imaging Method. S. H. Starner, R. W. Bilger, K. M. Lyons, J. H. Frank and M. B. Long, 347°
Nanoscale Unagglomerated Nonoxide Particles from a Sodium Coflow Flame. D. P DuFaux and R. L. Axelbaum, 350°°
Analysis of Droplet Arrival Statistics in a Pressure-Atomized Spray Flame. J. T. Hodges, C. Presser, A. K. Gupta and C. T. Avedesian, 353
Agglomeration of Soot Particles in Diffusion Flames under Microgravity. H. Ito, O. Fujita and K. Ito, 363°
The Effect of Hydrogen and Propane Addition on the Operation of a Natural Gas-Fired Pulsed Combustor. H. R. N. Jones and J. Leng, 404°
Phase Averaging of the Precessing Vortex Core in a Swirl Burner under Piloted and Premixed Combustion Conditions. D. Froud, T. O'Doherty and N. Syred, 407°°
An Experimental Study of High-Temperature, Oxidative Pulverized Coal Devolatilization. L. H. Sorensen, O. Biede and R. E. Peck, 475
Experimental Study of Premixed Flames in Intense Isotropic Turbulence. B. Bédat and R. K. Cheng, 485°°
Thermal and Chemical Influences on the Soot Mass Growth. M. Bachmann, W. Wiese and K. H. Homann, 635

°Combustion and Flame, Vol. 99, 1994.
°°Combustion and Flame, Vol. 100, 1995.

Quantitative Measurements of Enhanced Soot Production in a Flickering Methane/Air Diffusion Flame. C. R. Shaddix, J. E. Harrington and K. C. Smyth, 723*
Influence of Gasodynamics on NO_x Emission from Large Diffusion Natural Gas Flames. J. Tomeczek, J. Góral and B. Gradon, 1035
Partially Premixed Turbulent Flame Propagation in Jet Flames. C. M. Müller, H. Breitbach and N. Peters, 1099
Mixture Fraction Imaging in Turbulent Nonpremixed Hydrocarbon Flames. J. H. Frank, K. M. Lyons, D. F. Marran, M. B. Long, S. H. Stårner and R. W. Bilger, 1159
Raman Measurements and Joint PDF Modeling of a Non-Premixed Bluff-Body-Stabilized Methane Flame. S. M. Correa, A. Gulati and S. B. Pope, 1167
On Burner-Stabilized Cylindrical Premixed Flames in Microgravity. J. A. Eng, C. K. Law and D. L. Zhu, 1711

7.2 Combustion Bombs

The Droplet Group Microexplosions in Water-in-Oil Emulsion Sprays and Their Effects on Diesel Engine Combustion. H. Z. Sheng, L. Chen, Z. P. Zhang, C. K. Wu, C. An and C. Q. Cheng, 175
Effects of Natural Gas Composition on Ignition Delay Under Diesel Conditions. J. D. Naber, D. L. Siebers, S. S. D. Julio and C. K. Westbrook, 192*
Pressure and Concentraion Dependences of the Autoignition Temperature for Normal Butane + Air Mixtures in a Closed Vessel. M. R. Chandraratna and J. F. Griffiths, 626*
The Use of Carbon Monoxide/Hydrogen Burning Velocities to Examine the Rate of the CO + OH Reaction. I. C. McLean, D. B. Smith and S. C. Taylor, 749

7.3 Explosion Vessels

Suppression of High-Speed C_2H_4/Air Flames with C_1-Halocarbons. G. Gmurczyk and W. Grosshandler, 1497

7.4 Plug Flow Reactors

Experimental and Numerical Comparison of Extractive and In-Situ Laser Measurements of Non-Equilibrium Carbon Monoxide in Lean-Premixed Natural Gas Combustion. Q. V. Nguyen, B. L. Edgar, R. W. Dibble and A. Gulati, 395**
Mechanism and Modeling of Hydrogen Cyanide Oxidation in a Flow Reactor. P. Glarborg and J. A. Miller, 475*
Kinetic Interactions of CO, NO_x, and HCl Emissions in Post-Combustion Gases. J. F. Roesler, R. A. Yetter and F. L. Dryer, 495**
New Results on Moist CO Oxidation: High Pressure, High Temperature Experiments and Comprehensive Kinetic Modeling. T. J. Kim, R. A. Yetter and F. L. Dryer, 759
The Reactions of Phenylacetylenes With $O(^3P)$ in the Gas Phase. M. Eichholtz, A. Schneider, D.-V. Stuchen, J.-T. Vollmer and H. G. Wagner, 859
An Experimental and Computational Study of Methanol Oxidation in the Intermediate and High Temperature Regimes. T. J. Held and F. L. Dryer, 901
Hydrocarbon-NO_x Interactions at Low Temperatures −1. Conversion of NO to NO_2 Promoted by Propane and the Formation of HNCO. P. F. Nelson and B. S. Haynes, 1003

7.5 Shock Tubes

H_2-Air and CH_4-Air Detonations and Combustions behind Oblique Shock Waves. C. Viguier, C. Guerraud and D. Desbordes, 53
Phenomenological Aspects in Explosive Powder/Gas Two-Phase Detonations. A. J. Tulis, W. K. Sumida, R. P. Joyce, D. C. Heberlein and D. L. Patel, 79
Thermal Decomposition of Propargyl Bromide and the Subsequent Formation of Benzene. R. D. Kern, H. Chen, J. H. Kiefer and P. S. Mudipalli, 177**
Thermal Decomposition of HCl Measured by ARAS and IR Diode Laser Spectroscopy. G. N. Schading and P. Roth, 467*
Shock Tube Study of Ignition Delays and Detonation of Gaseous Monomethylhydrazine/Oxygen Mixtures. L. Catoire, X. Bassin, G. Dupre and C. Paillard, 573*
Soot Formation at Elevated Pressures and Carbon Concentrations in Hydrocarbon Pyrolysis. S. Bauerle, Y. Karasevich, S. Slavov, D. Tanke, M. Tappe, T. Thienel and H. G. Wagner, 627
High Temperature Pyrolsis and Oxidation of Fullerene C_{60} behind Shock Waves. S. von Gersum and P. Roth, 661
The Thermal Reactions of CH_3. K. P. Lim and J. V. Michael, 713
A Shock Tube Study of the $CO + OH \rightarrow CO_2 + H$ Reaction. M. S. Wooldridge, R. K. Hanson and C. T. Bowman, 741
Thermal Decomposition of CH_2Cl_2. K. P. Lim and J. V. Michael, 809
Kinetics of the Thermal Decomposition and Isomerisation of Pyrazine (1,4 Diazine). A. Doughty, J. C. Mackie and J. M. Palmer, 893
The Reactions of $NH(X^3\Sigma^-)$ with the Water Gas Components CO_2, H_2O and H_2. M. Röhrig and H. Wagner, 975

*Combustion and Flame, Vol. 99, 1994.
**Combustion and Flame, Vol. 100, 1995.

A Shock Tube Study of the Reactions of CN and NCO with NO_2. S. T. Wooldridge, J. D. Mertens, R. K. Hanson and C. T. Bowman, 983
Effect of the Initial Temperature and Composition of a Hot Transient Jet on the Ignition of H_2-Air-Diluent Mixtures. N. Djebaili, R. Lisbet, G. Dupre and C. Paillard, 1539
Shock-Tube Investigation on the Self-Ignition of Hydrocarbon-Air Mixtures at High Pressures. K. Fieweger, R. Blumenthal and G. Adomeit, 1579

7.6 Stirred Reactors

Experimental and Numerical Comparison of Extractive and In-Situ Laser Measurements of Non-Equilibrium Carbon Monoxide in Lean-Premixed Natural Gas Combustion. Q. V. Nguyen, B. L. Edgar, R. W. Dibble and A. Gulati, 395**
NO_x and N_2O in Lean-Premixed Jet-Stirred Flames. R. C. Steele, P. C. Malte, D. G. Nicol and J. C. Kramlich, 440**
Kerosene Combustion at Pressures up to 40 Atm: Experimental Study and Detailed Chemical Kinetic Modeling. P. Dagaut, M. Reuillon, J.-C. Boettner and M. Cathonnet, 919
Natural Gas and Blends Oxidation and Ignition: Experiments and Modeling. Y. Tan, P. Dagaut, M. Cathonnet, J. C. Boettner, J. S. Bachman and P. Carlier, 1563

8.0 EXPLOSIONS

Physical and Chemical Observations in Underwater Explosion Bubbles. W. C. Strahle and S. G. Liou, 89
Prediction of the Maximum Turbulence Intensities Generated by Grid-Plate Obstacles in Explosion-Induced Flows. H. Phylaktou and G. E. Andrews, 103
The Development of Instabilities in Laminar Explosion Flames. D. Bradley and C. M. Harper, 562*
Afterburning in Spherical Premixed Turbulent Explosions. D. Bradley, M. Lawes, M. J. Scott and E. M. J. Mushi, 581*
Pressure and Concentraion Dependences of the Autoignition Temperature for Normal Butane + Air Mixtures in a Closed Vessel. M. R. Chandraratna and J. F. Griffiths, 626*
Flame Front Disturbance Induced by a Weak Pressure Wave. R. Dobashi, T. Hirano and T. Tsuruda, 1415

8.3 Inhibition

Suppression of High-Speed C_2H_4/Air Flames with C_1-Halocarbons. G. Gmurczyk and W. Grosshandler, 1497

8.7 Venting

Initiation of Upstream-Directed Detonation Induced by the Venting of Gaseous Explosion. S. P. Medvedev, A. N. Polenov, S. V. Khomik and B. E. Gelfand, 73

9.0 FIRE

Ignition Process of Heated Iron Blocks in High Pressure Oxygen Atmosphere. J. Sato, H. Ohtani and T. Hirano, 376**
Autoignition of Combustible Fluids in Porous Insulation Materials. A. C. McIntosh, M. Bains, W. Crocombe and J. F. Griffiths, 541*
Carbon Monoxide Formation in Fires by High-Temperature Anaerobic Wood Pyrolysis. W. M. Pitts, E. L. Johnsson and N. P. Bryner, 1445
An Instrument for Characterization of the Thermal and Optical Properties of Charring Polymeric Materials. M. A. Serio, D. S. Pines, A. S. Bonanno, P. R. Solomon and G. A. Simmons, 1447
Simultaneous Optical Measurement of Soot Volume Fraction, Temperature, and CO_2 in Heptane Pool Fire. M. Y. Choi, A. Hamins, H. Rushmeier and T. Kashiwagi, 1471

9.1 Buoyant Flames and Wakes

Air Entrainment Flow Field Induced by a Pool Fire. X. C. Zhou and J. P. Gore, 52**
Buoyant Downward Diffusion Flame Spread and Extinction in Partial-Gravity Accelerations. K. R. Sacksteder and J. S. T'ien, 1685
The Effect of Gravity on a Laminar Diffusion Flame Established over a Horizontal Flat Plate. J. L. Torero, L. Bonneau, J. M. Most and P. Joulain, 1701

9.2 Fire Dynamics

The Behavior of Flames Spreading over Thin Solids in Microgravity. P. A. Ramachandra, R. A. Altenkirch, S. Bhattacharjee, L. Tang, K. Sacksteder and M. K. Wolverton, 71**
Simulation of Smoke Plumes from Large Pool Fires. H. R. Baum, K. B. McGrattan and R. G. Rehm, 1463
Boilover Burning of Heating Oil Spilled on Water. J. P. Garo, J. P. Vantelon and A. C. Fernandez-Pello, 1481

9.3 Flame Spread

The Behavior of Flames Spreading over Thin Solids in Microgravity. P. A. Ramachandra, R. A. Altenkirch, S. Bhattacharjee, L. Tang, K. Sacksteder and M. K. Wolverton, 71**
Upward Flame Spread along PMMA Vertical Corner Walls. Part II: Mechanism of "M" Shape Py-

*Combustion and Flame, Vol. 99, 1994.
**Combustion and Flame, Vol. 100, 1995.

rolysis Front Formation. C. Qian, H. Ishida and K. Saito, 331*
Predictions of Wind-Opposed Flame Spread Rates and Energy Feed Back Analysis for Charring Solids in a Microgravity Environment. C. Di Blasi, 332**
Flame Spread over Thin Solid Fuels in Partially Premixed Atmospheres. P. D. Ronney, J. B. Greenberg, Y. Zhang and E. V. Roegner, 474**
Creeping Flame Spread: Some New Results and Interpretation for Material Flammability Characterization. T. Chen and M. A. Delichatsios, 601*
Behavior of Fires Spreading Downward over Thick Paper. M. Suzuki, R. Dobashi and T. Hirano, 1439
Buoyant Downward Diffusion Flame Spread and Extinction in Partial-Gravity Accelerations. K. R. Sacksteder and J. S. T'ien, 1685

9.4 Safety

Suppression of High-Speed C_2H_4/Air Flames with C_1-Halocarbons. G. Gmurczyk and W. Grosshandler, 1497

9.6 Radiation

Predictions of Wind-Opposed Flame Spread Rates and Energy Feed Back Analysis for Charring Solids in a Microgravity Environment. C. Di Blasi, 332**
Two-Dimensional Non-Stationary Causal Stochastic Model for Turbulence/Radiation Interactions in Flames. S. H. Chan, X. C. Pan and J. Zhang, 1115
Simultaneous Optical Measurement of Soot Volume Fraction, Temperature, and CO_2 in Heptane Pool Fire. M. Y. Choi, A. Hamins, H. Rushmeier and T. Kashiwagi, 1471

10.0 FLAMES

Numerical Simulations of Burner-Stabilized Hydrogen-Air Flames in Microgravity. G. Patnaik and K. Kailasanath, 247*
Effect of Unsteady Stretch Rate on OH Chemistry During a Flame-Vortex Interaction: To Assess Flamelet Models. C. J. Mueller, J. F. Driscoll, D. J. Sutkus, W. L. Roberts, M. C. Drake and M. D. Smooke, 323**
Flame Propogation through Periodic Vortices. J. W. Dold, O. S. Kerr and I. P. Nikolova, 359**
Flame Spread over Thin Solid Fuels in Partially Premixed Atmospheres. P. D. Ronney, J. B. Greenberg, Y. Zhang and E. V. Roegner, 474**
Soot Mass Growth and Coagulation of Soot Particles in C_2H_4/Air Flames at 15 Bar. S. Hanisch, H. Jander, T. Pape and H. G. Wagner, 577
Optical Characterization of Rich Premixed CH_4/O_2 Flames Across the Soot Formation Threshold. A. D'Alessio, G. Gambi, P. Minutolo, S. Russo and A. D'Anna, 645
Kinetic Parameters for the Initiation Reaction RH + $O_2 \rightarrow$ R + HO_2. T. Ingham, R. W. Walker and R. E. Woolford, 767
Two-Dimensional Non-Stationary Causal Stochastic Model for Turbulence/Radiation Interactions in Flames. S. H. Chan, X. C. Pan and J. Zhang, 1115
Fine Structure of Small-Scale and High-Intensity Turbulent Premixed Flames. J. Furukawa and T. Hirano, 1233
Laminar Flame Speeds and Extinction Strains Rates of Mixtures of Carbon Monoxide with Hydrogen, Methane, and Air. C. M. Vagelopoulos and F. N. Egolfopoulos, 1317
Further Considerations on the Determination of Laminar Flame Speeds With the Counterflow Twin Flame Technique. C. M. Vagelopoulos, F. N. Egolfopoulos and C. K. Law, 1341
Laminar Flame Calculations using Simplified Chemical Kinetics Based on Intrinsic Low-Dimensional Manifolds. U. Maas and S. B. Pope, 1349
Laminar Flame Calculations using Simplified Chemical Kinetics Based on Intrinsic Low-Dimensional Manifolds. U. Maas and S. B. Pope, 1349
Dynamics and Structure of Unsteady, Strained, Laminar Premixed Flames. F. N. Egolfopoulos, 1365
Geometric and Radiation Effects on Steady and Unsteady Strained Laminar Flames. F. N. Egolfopoulos, 1375

10.1 Burning Velocity

Chemical Closure and Burning Rates in Premixed Turbulent Flames. F. C. Gouldin and P. C. Miles, 202**
Flame Propogation through Periodic Vortices. J. W. Dold, O. S. Kerr and I. P. Nikolova, 359**
Stretch Effects Extracted from Propagating Spherical Premixed Flames with Detailed Chemistry. D. P. Mishra, P. J. Paul and H. S. Mukunda, 379*
Phase Averaging of the Precessing Vortex Core in a Swirl Burner under Piloted and Premixed Combustion Conditions. D. Froud, T. O'Doherty and N. Syred, 407**
Experimental Study of Premixed Flames in Intense Isotropic Turbulence. B. Bédat and R. K. Cheng, 485**
The Production of Premixed Flame Surface Area in Turbulent Shear Flow. A. Trouvé, 687*
The Use of Carbon Monoxide/Hydrogen Burning Velocities To Examine the Rate of the CO + OH

*Combustion and Flame, Vol. 99, 1994.
**Combustion and Flame, Vol. 100, 1995.

Reaction. I. C. McLean, D. B. Smith and S. C. Taylor, 749
Aspects of Nitrogen Flame Chemistry Revealed by Burning Velocity Modelling. M. J. Brown and D. B. Smith, 1011
Rich Methane/Air Flames: Burning Velocities, Extinction Limits and Flammability Limit. M. N. Bui-Pham and J. A. Miller, 1309
Laminar Flame Speeds and Extinction Strains Rates of Mixtures of Carbon Monoxide with Hydrogen, Methane, and Air. C. M. Vagelopoulos and F. N. Egolfopoulos, 1317
Further Considerations on the Determination of Laminar Flame Speeds With the Counterflow Twin Flame Technique. C. M. Vagelopoulos, F. N. Egolfopoulos and C. K. Law, 1341
On Adiabatic Stabilization and Geometry of Bunsen Flames. C. J. Sun, C. J. Sung and C. K. Law, 1391
Flame Propagation Experiment of PMMA Particle Cloud in a Microgravity Environment. H. Kobayashi, N. Ono, Y. Okuyama and T. Niioka, 1693
On Burner-Stabilized Cylindrical Premixed Flames in Microgravity. J. A. Eng, C. K. Law and D. L. Zhu, 1711

10.2 Cool

Cars Temperature Measurements and the Cyclic Dispersion of Knock in Spark Ignition Engines. D. Bradley, G. T. Kalghatgi, C. Morley, P. Snowden and J. Yeo, 125
Effects of Natural Convection on Two Stage Ignition of an n-Dodecane Droplet. M. Tanabe, M. Kono, J. Sato, J. Koenig, C. Eigenbrod and H. J. Rath, 455
Kinetic Parameters for the Initiation Reaction RH + $O_2 \rightarrow R + HO_2$. T. Ingham, R. W. Walker and R. E. Woolford, 767
Cool Flames and Oscillations in Hydrocarbon Oxidation. A. A. Mantashyan, 927

10.4 Diffusion

Gasdynamic Enhancement of Nonpremixed Combustion. F. Marble, 1
Three-Dimensional Numerical Simulations of Unsteady Reactive Square Jets. F. F. Grinstein and K. Kailasanath, 2**
Navier-Stokes Numerical Simulation of Supersonic Hydrogen-Flourine Combustion in CW Chemical Lasers. M. Rotinian, M. Shur and M. Strelets, 13
Response of Counterflow Diffusion Flames to Oscillating Strain Rates. H. G. Im, C. K. Law, J. S. Kim and F. A. Williams, 21**
On the Structure of Stretched/Compressed Laminar Flamelet—Influence of Preferential Diffusion. V. R. Katta and W. M. Roquemore, 61**
The Behavior of Flames Spreading over Thin Solids in Microgravity. P. A. Ramachandra, R. A. Altenkirch, S. Bhattacharjee, L. Tang, K. Sacksteder and M. K. Wolverton, 71**
Modeling of Extinction in Turbulent Diffusion Flames by the Velocity-Dissipation-Composition PDF Method. A. T. Norris and S. B. Pope, 211**
Extinction of Nonpremixed Flames with Halogenated Fire Suppressants. A. Hamins, D. Trees, K. Seshadri and H. K. Chelliah, 221*
Interactions between Nonsymmetrical Wake Structure and Turbulent Diffusion Flames behind a Rear-Facing Semicircular Cylinder. N. Ohiwa, Y. Ishino and S. Yamaguchi, 302*
Soot Formation in Weakly Buoyant Acetylene-Fueled Laminar Jet Diffusion Flames Burning in Air. P. B. Sunderland, Ü. Ö. Köylü and G. M. Faeth, 310**
Predictions of Wind-Opposed Flame Spread Rates and Energy Feed Back Analysis for Charring Solids in a Microgravity Environment. C. Di Blasi, 332**
Conserved Scalar Measurements in Turbulent Diffusion Flames by a Raman and Rayleigh Ribbon Imaging Method. S. H. Starner, R. W. Bilger, K. M. Lyons, J. H. Frank and M. B. Long, 347*
Nanoscale Unagglomerated Nonoxide Particles from a Sodium Coflow Flame. D. P DuFaux and R. L. Axelbaum, 350**
Agglomeration of Soot Particles in Diffusion Flames under Microgravity. H. Ito, O. Fujita and K. Ito, 363*
Effect of Flame Structure and Soot-Particle Inception in Diffusion Flames. J. Du and R. L. Axelbaum, 367**
Similarity Analysis of Spray Diffusion Flames in a Unidirectional Shear-Layer Flow. Y. Tambour and D. Katoshevski, 381
Experiments on the Interaction between a Vortex and a Strained Diffusion Flame. J. C. Rolon, F. Aguerre and S. Candel, 422**
A Study of Carbon Monoxide in a Series of Laminar Ethylene/Air Diffusion Flames using Tunable Diode Laser Absorption Spectroscopy. R. R. Skaggs and J. H. Miller, 430**
The Application of New Combustion and Turbulence Models to H_2-Air Non-premixed Supersonic Combustion. L. L. Zheng and K. N. C. Bray, 440*
Strained Dissipation and Reaction Layer Analyses of Nonequilibrium Chemistry in Turbulent Reacting Flows. E. S. Bish and W. J. A. Dahm, 457**
Experimental Identification of Mixing Regimes in the Analysis of Turbulent Diffusion Flames. A. Cavaliere, M. El-Naggar and R. Ragucci, 679*
Temperature Field on a Laminar Diffusion Dust Flame. J. I. Vovchuk and N. I. Poletaev, 706*
Quantitative Measurements of Enhanced Soot Pro-

*Combustion and Flame, Vol. 99, 1994.
**Combustion and Flame, Vol. 100, 1995.

duction in a Flickering Methane/Air Diffusion Flame. C. R. Shaddix, J. E. Harrington and K. C. Smyth, 723*
Effect of Gravity on the Structure of an Unsteady Spray Diffusion Flame. T. W. Park, S. K. Aggarwal and V. R. Katta, 767*
Measurements of Scalar Dissipation in the Reaction Zones of Turbulent Nonpremixed H_2-Air Diffusion Flames. S. P. Nandula, T. M. Brown and R. W. Pitz, 775*
Transition and Structure of Jet Diffusion Flames. T. Takeno, 1061
A Lagrangian Model For Predicting Turbulent Diffusion Flames with Chemical Kinetic Effects. M. Obounou, M. Gonzalez and R. Borghi, 1107
Effects of Molecular Transport on Turbulence-Chemistry Interactions in a Hydrogen-Argon-Air Jet Diffusion Flame. S. Menon, W. H. Calhoon, Jr., G. Goldin and A. R. Kerstein, 1125
Simultaneous Measurement of Conserved and Reactive Scalars in Turbulent Diffusion Flames for Assessment of PDF Models. T. S. Cheng and R. W. Pitz, 1133
Wide Field Conserved Scalar Imaging in Turbulent Diffusion Flames by a Raman and Rayleigh Method. J. B. Kelman, A. R. Masri, S. H. Stårner and R. W. Bilger, 1141
Stabilization Mechanism of Lifted Jet Diffusion Flames. C. R. Kaplan, E. S. Oran and S. W. Baek, 1183
The Effect of Turbulence on Extinction of Counterflow Diffusion Flame. H. Tsuji, A. Yoshida and N. Endo, 1191
Temporal Evolution of Turbulence/Chemistry Interactions in Lifted, Turbulent-Jet Flames. R. W. Schefer, M. Namazian, E. E. J. Filtopoulos and J. Kelly, 1223
Comparative Experimental and Numerical Investigation of a Piloted Turbulent Natural-Gas Diffusion Flame. T. W. J. Peeters, P. P. J. Stroomer, J. E. de Vries, D. J. E. M. Roekaerts and C. J. Hoogendoorn, 1241
The Vorticity Dynamics of an Exothermic, Spatially-Developing, Forced, Reacting Shear Layer. M. C. Soteriou and A. F. Ghoniem, 1265
Strain Rate Modelling for a Flame Surface Density Equation with Application to Non-premixed Turbulent Combustion. F. Fichot, B. Delhaye, D. Veynante and S. M. Candel, 1273
Numerical Simulation of Local Extinction Effects in Turbulent Combustor Flows of Methane and Air. I. R. Gran, M. C. Melaaen and B. F. Magnussen, 1283
The Structure of the Recirculation Zone of a Bluff-Body Combustor. A. R. Masri, B. B. Dally, R. S. Barlow and C. D. Carter, 1301
Effects of Pressure and Dilution on the Extinction of Counterflow Nonpremixed Hydrogen-Air Flames. P. Papas, I. Glassman and C. K. Law, 1333
Geometric and Radiation Effects on Steady and Unsteady Strained Laminar Flames. F. N. Egolfopoulos, 1375
Effects of Curvature and Unsteadiness in Diffusion Flames. Implications for Turbulent Diffusion Combustion. B. Cuenot and T. Poinsot, 1383
A Bifurcation Analysis of High-Temperature Ignition of H_2-O_2 Diffusion Flames. A. L. Sánchez, A. Liñán and F. A. Williams, 1529
Supercritical and Subcritical Combustion of LOX with Hydrogen in an Axisymmetric Laminar Diffusion Flame. A.-S. Yang, K. K. Kuo and W. H. Hsieh, 1609
The Effect of Gravity on a Laminar Diffusion Flame Established over a Horizontal Flat Plate. J. L. Torero, L. Bonneau, J. M. Most and P. Joulain, 1701

10.5 Extinction

Navier-Stokes Numerical Simulation of Supersonic Hydrogen-Flourine Combustion in CW Chemical Lasers. M. Rotinian, M. Shur and M. Strelets, 13
Modeling of Extinction in Turbulent Diffusion Flames by the Velocity-Dissipation-Composition PDF Method. A. T. Norris and S. B. Pope, 211**
Extinction of Nonpremixed Flames with Halogenated Fire Suppressants. A. Hamins, D. Trees, K. Seshadri and H. K. Chelliah, 221*
The Effect of Initial Diameter on Free Droplet Combustion with Spherical Flame. H. Hara and S. Kumagai, 423
Experimental Identification of Mixing Regimes in the Analysis of Turbulent Diffusion Flames. A. Cavaliere, M. El-Naggar and R. Ragucci, 679*
A Lagrangian Model for Predicting Turbulent Diffusion Flames with Chemical Kinetic Effects. M. Obounou, M. Gonzalez and R. Borghi, 1107
The Effect of Turbulence on Extinction of Counterflow Diffusion Flame. H. Tsuji, A. Yoshida and N. Endo, 1191
Numerical Simulation of Local Extinction Effects in Turbulent Combustor Flows of Methane and Air. I. R. Gran, M. C. Melaaen and B. F. Magnussen, 1283
Rich Methane/Air Flames: Burning Velocities, Extinction Limits and Flammability Limit. M. N. Bui-Pham and J. A. Miller, 1309
Laminar Flame Speeds and Extinction Strains Rates of Mixtures of Carbon Monoxide with Hydrogen, Methane, and Air. C. M. Vagelopoulos and F. N. Egolfopoulos, 1317
Aspects of Laminar Premixed Flame Extinction Limits. G. Dixon-Lewis, 1325

*Combustion and Flame, Vol. 99, 1994.
**Combustion and Flame, Vol. 100, 1995.

Effects of Pressure and Dilution on the Extinction of Counterflow Nonpremixed Hydrogen-Air Flames. P. Papas, I. Glassman and C. K. Law, 1333
Dynamics and Structure of Unsteady, Strained, Laminar Premixed Flames. F. N. Egolfopoulos, 1365
Geometric and Radiation Effects on Steady and Unsteady Strained Laminar Flames. F. N. Egolfopoulos, 1375

10.6 Holding

Flame Stabilization in the Wake Flow Behind a Slit V-Gutter. J.-T. Yang, C.-W. Yen and G.-L. Tsai, 288*
Nanoscale Unagglomerated Nonoxide Particles from a Sodium Coflow Flame. D. P DuFaux and R. L. Axelbaum, 350**
Effect of Dilution on the Liftoff of Non-Premixed Jet Flames. B. J. Lee, J. S. Kim and S. H. Chung, 1175
On Adiabatic Stabilization and Geometry of Bunsen Flames. C. J. Sun, C. J. Sung and C. K. Law, 1391

10.7 Inhibition

Extinction of Nonpremixed Flames with Halogenated Fire Suppressants. A. Hamins, D. Trees, K. Seshadri and H. K. Chelliah, 221*
Decay Mechanism of CF_3H or CF_2HCl In $H_2/O_2/Ar$ Flames. H. Richter, J. Vandooren and P. J. Van Tiggelen, 825
Experimental and Computational Study of the Effect of C_2F_6 on Premixed Methane Flames. O. Sanogo, J.-L. Delfau, R. Akrich and C. Vovelle, 1489
Suppression of High-Speed C_2H_4/Air Flames with C_1-Halocarbons. G. Gmurczyk and W. Grosshandler, 1497

10.8 Laminar

Extinction of Nonpremixed Flames with Halogenated Fire Suppressants. A. Hamins, D. Trees, K. Seshadri and H. K. Chelliah, 221*
On the Effects of Fuel Leakage on CO Production from Household Burners as Revealed by LIF and CARS. C. E. van der Meij, A. Mokhov, R. A. A. M. Jacobs and H. B. Levinsky, 243
Soot Formation in Weakly Buoyant Acetylene-Fueled Laminar Jet Diffusion Flames Burning in Air. P. B. Sunderland, Ü. Ö. Köylü and G. M. Faeth, 310**
Nanoscale Unagglomerated Nonoxide Particles from a Sodium Coflow Flame. D. P DuFaux and R. L. Axelbaum, 350**
Agglomeration of Soot Particles in Diffusion Flames under Microgravity. H. Ito, O. Fujita and K. Ito, 363*
Effect of Flame Structure and Soot-Particle Inception in Diffusion Flames. J. Du and R. L. Axelbaum, 367**
Stretch Effects Extracted from Propagating Spherical Premixed Flames with Detailed Chemistry. D. P. Mishra, P. J. Paul and H. S. Mukunda, 379*
Similarity Analysis of Spray Diffusion Flames in a Unidirectional Shear-Layer Flow. Y. Tambour and D. Katoshevski, 381
Experiments on the Interaction between a Vortex and a Strained Diffusion Flame. J. C. Rolon, F. Aguerre and S. Candel, 422**
An Experimental Study of High-Temperature, Oxidative Pulverized Coal Devolatilization. L. H. Sorensen, O. Biede and R. E. Peck, 475
Suppression of Soot Formation in Ethene Laminar Diffusion Flames by Chemical Additives. T. Ni, S. B. Gupta and R. J. Santoro, 585
Thermal and Chemical Influences on the Soot Mass Growth. M. Bachmann, W. Wiese and K. H. Homann, 635
Inception and Growth of Soot Particles in Dependence on the Surrounding Gas Phase. F. Mauss, T. Schäfer and H. Bockhorn, 697*
Temperature Field on a Laminar Diffusion Dust Flame. J. I. Vovchuk and N. I. Poletaev, 706*
C_1/C_2 Chemistry in Fuel-Rich Post-Flame Gases: Detailed Kinetic Modelling. I. T. Woods and B. S. Haynes, 909
Analysis of a Systematical Reduction Technique. L. M. T. Somers and L. P. H. de Goey, 957
Effect of Dilution on the Liftoff of Non-Premixed Jet Flames. B. J. Lee, J. S. Kim and S. H. Chung, 1175
Laminar Flame Speeds and Extinction Strains Rates of Mixtures of Carbon Monoxide with Hydrogen, Methane, and Air. C. M. Vagelopoulos and F. N. Egolfopoulos, 1317
Aspects of Laminar Premixed Flame Extinction Limits. G. Dixon-Lewis, 1325
Effects of Pressure and Dilution on the Extinction of Counterflow Nonpremixed Hydrogen-Air Flames. P. Papas, I. Glassman and C. K. Law, 1333
Further Considerations on the Determination of Laminar Flame Speeds with the Counterflow Twin Flame Technique. C. M. Vagelopoulos, F. N. Egolfopoulos and C. K. Law, 1341
Laminar Counterflow Mixing of Acetylene Into Hot Combustion Products. H. Breitbach, J. Goettgens, F. Mauss, H. Pitsch and N. Peters, 1357
Dynamics and Structure of Unsteady, Strained, Laminar Premixed Flames. F. N. Egolfopoulos, 1365

*Combustion and Flame, Vol. 99, 1994.
**Combustion and Flame, Vol. 100, 1995.

Geometric and Radiation Effects on Steady and Unsteady Strained Laminar Flames. F. N. Egolfopoulos, 1375
On Adiabatic Stabilization and Geometry of Bunsen Flames. C. J. Sun, C. J. Sung and C. K. Law, 1391
Effects of Rotation on the Stability and Structure of Tubular Flame. K. Yamamoto, S. Ishizuka and T. Hirano, 1399
Flame Front Disturbance Induced by a Weak Pressure Wave. R. Dobashi, T. Hirano and T. Tsuruda, 1415
Experimental and Computational Study of the Effect of C_2F_6 on Premixed Methane Flames. O. Sanogo, J.-L. Delfau, R. Akrich and C. Vovelle, 1489
Supercritical and Subcritical Combustion of LOX with Hydrogen in an Axisymmetric Laminar Diffusion Flame. A.-S. Yang, K. K. Kuo and W. H. Hsieh, 1609
The Effect of Gravity on a Laminar Diffusion Flame Established over a Horizontal Flat Plate. J. L. Torero, L. Bonneau, J. M. Most and P. Joulain, 1701
On Burner-Stabilized Cylindrical Premixed Flames in Microgravity. J. A. Eng, C. K. Law and D. L. Zhu, 1711

10.9 Limits

Fuel Saving by Heat-Recirculating Combustion Using Fibre Mats. S. Nakamura and F. Weinberg, 269
Aspects of Laminar Premixed Flame Extinction Limits. G. Dixon-Lewis, 1325
Effects of Rotation on the Stability and Structure of Tubular Flame. K. Yamamoto, S. Ishizuka and T. Hirano, 1399
Effect of the Initial Temperature and Composition of a Hot Transient Jet on the Ignition of H_2-Air-Diluent Mixtures. N. Djebaili, R. Lisbet, G. Dupre and C. Paillard, 1539

10.10 Premixed

H_2-Air and CH_4-Air Detonations and Combustions behind Oblique Shock Waves. C. Viguier, C. Guerraud and D. Desbordes, 53
Detailed Modeling of Soot Formation in Laminar Premixed Ethylene Flames at a Pressure of 10 Bar. A. Kazakov, H. Wang and M. Frenklach, 111**
Lewis Number Effects on Premixed Flames Interacting with Turbulent Kármán Vortex Streets. J. G. Lee, T.-W. Lee, D. A. Nye and D. A. Santavicca, 161**
Chemical Closure and Burning Rates in Premixed Turbulent Flames. F. C. Gouldin and P. C. Miles, 202**
Flame Structure Studies of a Lean $H_2O/N_2O/Ar$ Flame Employing Molecular Beam Mass Spectrometry and Modeling. D. C. Dayton, C. M. Faust, W. R. Anderson and R. C. Sausa, 323*
Stretch Effects Extracted from Propagating Spherical Premixed Flames with Detailed Chemistry. D. P. Mishra, P. J. Paul and H. S. Mukunda, 379*
NO_x and N_2O in Lean-Premixed Jet-Stirred Flames. R. C. Steele, P. C. Malte, D. G. Nicol and J. C. Kramlich, 440**
An Evolution Equation Modelling Inversion of Tulip Flames. J. W. Dold and G. Joulin, 450**
NO_x and CO Emissions from a Pulse Combustor Operating in a Lean Premixed Mode. J. O. Keller, T. T. Bramlette, P. K. Barr and J. R. Alvarez, 460*
Numerical Investigation of Steady Laminar Flame Propagation in a Circular Tube. S. T. Lee and C. H. Tsai, 484*
Experimental Study of Premixed Flames in Intense Isotropic Turbulence. B. Bédat and R. K. Cheng, 485**
Detailed Kinetic Modelling of Premixed Benzene Flames. R. P. Lindstedt and G. Skevis, 551*
Optical Characterization of Rich Premixed CH_4/O_2 Flames Across the Soot Formation Threshold. A. D'Alessio, G. Gambi, P. Minutolo, S. Russo and A. D'Anna, 645
The Formation of Aromatic Carbon in Sooting Ethylene Flames. A. Ciajolo, A. D'Anna, R. Barbella and A. Tregrossi, 679
Analysis of a Systematical Reduction Technique. L. M. T. Somers and L. P. H. de Goey, 957
Modeling Turbulent Flame Propagation. W. T. Ashurst, 1075
Strain Effects on the Structure of Counterflowing Turbulent Premixed Flames. C. Mounaïm-Rousel and I. Gökalp, 1199
Experimental Investigation of a Premixed Flame in an Impinging Turbulent Stream. S. C. Li, P. A. Libby and F. A. Williams, 1207
Fine Structure of Small-Scale and High-Intensity Turbulent Premixed Flames. J. Furukawa and T. Hirano, 1233
Experimental Analysis of Flamelet Models for Premixed Turbulent Combustion. D. Veynante, J. M. Duclos and J. Piana, 1249
Rich Methane/Air Flames: Burning Velocities, Extinction Limits and Flammability Limit. M. N. Bui-Pham and J. A. Miller, 1309
Laminar Flame Speeds and Extinction Strains Rates of Mixtures of Carbon Monoxide with Hydrogen, Methane, and Air. C. M. Vagelopoulos and F. N. Egolfopoulos, 1317
Aspects of Laminar Premixed Flame Extinction Limits. G. Dixon-Lewis, 1325
Further Considerations on the Determination of Laminar Flame Speeds With the Counterflow

*Combustion and Flame, Vol. 99, 1994.
**Combustion and Flame, Vol. 100, 1995.

Twin Flame Technique. C. M. Vagelopoulos, F. N. Egolfopoulos and C. K. Law, 1341
Dynamics and Structure of Unsteady, Strained, Laminar Premixed Flames. F. N. Egolfopoulos, 1365
Geometric and Radiation Effects on Steady and Unsteady Strained Laminar Flames. F. N. Egolfopoulos, 1375
On Adiabatic Stabilization and Geometry of Bunsen Flames. C. J. Sun, C. J. Sung and C. K. Law, 1391
Effects of Rotation on the Stability and Structure of Tubular Flame. K. Yamamoto, S. Ishizuka and T. Hirano, 1399
The Initial Development of a Tulip Flame. M. Matalon and J. L. McGreevy, 1407
Flame Front Disturbance Induced by a Weak Pressure Wave. R. Dobashi, T. Hirano and T. Tsuruda, 1415
Diffusion and Premixed Flame Ignition Dynamics in a Field of Variable Strain Rate. D. Thevenin and S. Candel, 1547
On Burner-Stabilized Cylindrical Premixed Flames in Microgravity. J. A. Eng, C. K. Law and D. L. Zhu, 1711
An Experimental and Numerical Investigation on the Hot Surface Ignition of Premixed Gases Under Microgravity Conditions. H. Nagata, H. M. Kim, J. Sato and M. Kono, 1719

10.12 Stretch

On the Structure of Stretched/Compressed Laminar Flamelet—Influence of Preferential Diffusion. V. R. Katta and W. M. Roquemore, 61**
Lewis Number Effects on Premixed Flames Interacting with Turbulent Kármán Vortex Streets. J. G. Lee, T.-W. Lee, D. A. Nye and D. A. Santavicca, 161**
Stretch Effects Extracted from Propagating Spherical Premixed Flames with Detailed Chemistry. D. P. Mishra, P. J. Paul and H. S. Mukunda, 379*
The Effect of Turbulence on Extinction of Counterflow Diffusion Flame. H. Tsuji, A. Yoshida and N. Endo, 1191
Strain Effects on the Structure of Counterflowing Turbulent Premixed Flames. C. Mounaïm-Roussel and I. Gökalp, 1199
Aspects of Laminar Premixed Flame Extinction Limits. G. Dixon-Lewis, 1325
Effects of Pressure and Dilution on the Extinction of Counterflow Nonpremixed Hydrogen-Air Flames. P. Papas, I. Glassman and C. K. Law, 1333
On Adiabatic Stabilization and Geometry of Bunsen Flames. C. J. Sun, C. J. Sung and C. K. Law, 1391
Effects of Rotation on the Stability and Structure of Tubular Flame. K. Yamamoto, S. Ishizuka and T. Hirano, 1399
Diffusion and Premixed Flame Ignition Dynamics in a Field of Variable Strain Rate. D. Thevenin and S. Candel, 1547
On Burner-Stabilized Cylindrical Premixed Flames in Microgravity. J. A. Eng, C. K. Law and D. L. Zhu, 1711

10.13 Structure

Three-Dimensional Numerical Simulations of Unsteady Reactive Square Jets. F. F. Grinstein and K. Kailasanath, 2**
Lewis Number Effects on Premixed Flames Interacting with Turbulent Kármán Vortex Streets. J. G. Lee, T.-W. Lee, D. A. Nye and D. A. Santavicca, 161**
Structure of a Spray Flame Stabilized on a Production Engine Combustor Swirl Cup. F. Takahashi, W. J. Schmoll, G. L. Switzer and D. T. Shouse, 183
Flame Stabilization in the Wake Flow behind a Slit V-Gutter. J.-T. Yang, C.-W. Yen and G.-L. Tsai, 288*
Effect of Flame Structure and Soot-Particle Inception in Diffusion Flames. J. Du and R. L. Axelbaum, 367**
Experiments on the Interaction between a Vortex and a Strained Diffusion Flame. J. C. Rolon, F. Aguerre and S. Candel, 422**
Strained Dissipation and Reaction Layer Analyses of Nonequilibrium Chemistry in Turbulent Reacting Flows. E. S. Bish and W. J. A. Dahm, 457**
Experimental Study of Premixed Flames in Intense Isotropic Turbulence. B. Bédat and R. K. Cheng, 485**
Flame Stabilization and OH Fluorescence Mapping of the Combustion Structures in the Near Field of a Spray Jet. D. Stepowski, A. Cessou and P. Goix, 516*
Temperature Field on a Laminar Diffusion Dust Flame. J. I. Vovchuk and N. I. Poletaev, 706*
Decay Mechanism of CF_3H or CF_2HCl In $H_2/O_2/Ar$ Flames. H. Richter, J. Vandooren and P. J. Van Tiggelen, 825
Analysis of a Systematical Reduction Technique. L. M. T. Somers and L. P. H. de Goey, 957
Fine Structure of Small-Scale and High-Intensity Turbulent Premixed Flames. J. Furukawa and T. Hirano, 1233
Effects of Rotation on the Stability and Structure of Tubular Flame. K. Yamamoto, S. Ishizuka and T. Hirano, 1399
RDX Flame Structure. D. Hanson-Parr and T. Parr, 1635

*Combustion and Flame, Vol. 99, 1994.
**Combustion and Flame, Vol. 100, 1995.

10.14 Theory

Response of Counterflow Diffusion Flames to Oscillating Strain Rates. H. G. Im, C. K. Law, J. S. Kim and F. A. Williams, 21**
Chemical Closure and Burning Rates in Premixed Turbulent Flames. F. C. Gouldin and P. C. Miles, 202**
Analysis of a Systematical Reduction Technique. L. M. T. Somers and L. P. H. de Goey, 957
Modeling Turbulent Flame Propagation. W. T. Ashurst, 1075
Dynamics of the Flame Surface Area in Turbulent Non-Premixed Combustion. W. Kollmann and J. H. Chen, 1091
Two-Dimensional Non-Stationary Causal Stochastic Model for Turbulence/Radiation Interactions in Flames. S. H. Chan, X. C. Pan and J. Zhang, 1115

10.15 Turbulent

Three-Dimensional Numerical Simulations of Unsteady Reactive Square Jets. F. F. Grinstein and K. Kailasanath, 2**
Prediction of the Maximum Turbulence Intensities Generated by Grid-Plate Obstacles in Explosion-Induced Flows. H. Phylaktou and G. E. Andrews, 103
Laser Raman Scattering Measurements of Differential Molecular Diffusion in Turbulent Nonpremixed Jet Flames of H_2/CO_2 Fuel. L. L. Smith, R. W. Dibble, L. Talbot, R. S. Barlow and C. D. Carter, 153**
Lewis Number Effects on Premixed Flames Interacting with Turbulent Kármán Vortex Streets. J. G. Lee, T.-W. Lee, D. A. Nye and D. A. Santavicca, 161**
Turbulent Velocity and Temperature Measurements from a Gaseous Fueled Technology Combustor with a Practical Fuel Injector. P. O. Hedman and D. L. Warren, 185**
Chemical Closure and Burning Rates in Premixed Turbulent Flames. F. C. Gouldin and P. C. Miles, 202**
Modeling of Extinction in Turbulent Diffusion Flames by the Velocity-Dissipation-Composition PDF Method. A. T. Norris and S. B. Pope, 211**
On the Aero-thermal Characteristics of Gasifier-Fuelled Gas Turbine Combustors with Complex Geometries. N. H. Kandamby and F. C. Lockwood, 251
Cavity-Actuated Supersonic Mixing and Combustion Control. K. Yu and K. C. Schadow, 295*
Interactions Between Nonsymmetrical Wake Structure and Turbulent Diffusion Flames behind a Rear-Facing Semicircular Cylinder. N. Ohiwa, Y. Ishino and S. Yamaguchi, 302*
Conserved Scalar Measurements in Turbulent Diffusion Flames By a Raman and Rayleigh Ribbon Imaging Method. S. H. Starner, R. W. Bilger, K. M. Lyons, J. H. Frank and M. B. Long, 347*
Phase Averaging of the Precessing Vortex Core in a Swirl Burner Under Piloted and Premixed Combustion Conditions. D. Froud, T. O'Doherty and N. Syred, 407**
The Application of New Combustion and Turbulence Models to H_2-Air Non-premixed Supersonic Combustion. L. L. Zheng and K. N. C. Bray, 440*
An Evolution Equation Modelling Inversion of Tulip Flames. J. W. Dold and G. Joulin, 450**
Strained Dissipation and Reaction Layer Analyses of Nonequilibrium Chemistry in Turbulent Reacting Flows. E. S. Bish and W. J. A. Dahm, 457**
Experimental Study of Premixed Flames in Intense Isotropic Turbulence. B. Bédat and R. K. Cheng, 485**
Performance Predictions of Pulverized-Coal Flames of Power Station Furnace and Cement Kiln Types. F. C. Lockwood and B. Shen, 503
The Development of Instabilities in Laminar Explosion Flames. D. Bradley and C. M. Harper, 562*
Afterburning in Spherical Premixed Turbulent Explosions. D. Bradley, M. Lawes, M. J. Scott and E. M. J. Mushi, 581*
Large-Eddy Simulations of Turbulent Reacting Flows in a Chamber With Gaseous Ethylene Injecting through the Porous Wall. T. M Liou, W. Y. Lien and P. W. Hwang, 591*
Soot Formation in Turbulent Non-Premixed Kerosine-Air Flame Burning at Elevated Pressure: Experimental Measurement. K. J. Young, C. D. Stewart and J. B. Moss, 609
The Production of Premixed Flame Surface Area in Turbulent Shear Flow. A. Trouvé, 687*
Measurements of Scalar Dissipation in the Reaction Zones of Turbulent Nonpremixed H_2-Air Diffusion Flames. S. P. Nandula, T. M. Brown and R. W. Pitz, 775*
Transition and Structure of Jet Diffusion Flames. T. Takeno, 1061
Modeling Turbulent Flame Propagation. W. T. Ashurst, 1075
Dynamics of the Flame Surface Area in Turbulent Non-Premixed Combustion. W. Kollmann and J. H. Chen, 1091
Partially Premixed Turbulent Flame Propagation in Jet Flames. C. M. Müller, H. Breitbach and N. Peters, 1099
A Lagrangian Model For Predicting Turbulent Diffusion Flames with Chemical Kinetic Effects. M. Obounou, M. Gonzalez and R. Borghi, 1107
Two-Dimensional Non-Stationary Causal Stochastic

*Combustion and Flame, Vol. 99, 1994.
**Combustion and Flame, Vol. 100, 1995.

Model for Turbulence/Radiation Interactions in Flames. S. H. Chan, X. C. Pan and J. Zhang, 1115
Effects of Molecular Transport on Turbulence-Chemistry Interactions in a Hydrogen-Argon-Air Jet Diffusion Flame. S. Menon, W. H. Calhoon, Jr., G. Goldin and A. R. Kerstein, 1125
Simultaneous Measurement of Conserved and Reactive Scalars in Turbulent Diffusion Flames for Assessment of PDF Models. T. S .Cheng and R. W. Pitz, 1133
Wide Field Conserved Scalar Imaging in Turbulent Diffusion Flames by a Raman and Rayleigh Method. J. B. Kelman, A. R. Masri, S. H. Stårner and R. W. Bilger, 1141
Simultaneous NO and Temperature Imaging Measurements in Turbulent Nonpremixed Flames. M. Namazian, J. Kelly and R. Schefer, 1149
Mixture Fraction Imaging in Turbulent Nonpremixed Hydrocarbon Flames. J. H. Frank, K. M. Lyons, D. F. Marran, M. B. Long, S. H. Stårner and R. W. Bilger, 1159
Raman Measurements and Joint PDF Modeling of a Non-Premixed Bluff-Body-Stabilized Methane Flame. S. M. Correa, A. Gulati and S. B. Pope, 1167
Effect of Dilution on the Liftoff of Non-Premixed Jet Flames. B. J. Lee, J. S. Kim and S. H. Chung, 1175
Stabilization Mechanism of Lifted Jet Diffusion Flames. C. R. Kaplan, E. S. Oran and S. W. Baek, 1183
The Effect of Turbulence on Extinction of Counterflow Diffusion Flame. H. Tsuji, A. Yoshida and N. Endo, 1191
Strain Effects on the Structure of Counterflowing Turbulent Premixed Flames. C.Mounaïm-Rousel and I. Gökalp, 1199
Experimental Investigation of a Premixed Flame in an Impinging Turbulent Stream. S. C. Li, P. A. Libby and F. A. Williams, 1207
The Formation and Destruction of Aromatic Compounds in a Turbulent Flame. J. H. Thijssen, M. A. Toqan, J. M. Beér and A. F. Sarofim, 1215
Temporal Evolution of Turbulence/Chemistry Interactions in Lifted, Turbulent-Jet Flames. R. W. Schefer, M. Namazian, E. E. J. Filtopoulos and J. Kelly, 1223
Fine Structure of Small-Scale and High-Intensity Turbulent Premixed Flames. J. Furukawa and T. Hirano, 1233
Comparative Experimental and Numerical Investigation of a Piloted Turbulent Natural-Gas Diffusion Flame. T. W. J. Peeters, P. P. J. Stroomer, J. E. de Vries, D. J. E. M. Roekaerts and C. J. Hoogendoorn, 1241
Experimental Analysis of Flamelet Models for Premixed Turbulent Combustion. D. Veynante, J. M. Duclos and J. Piana, 1249
Large Eddy Simulations of Bluff Body Stabilized Flames. C. Fureby and C. Löfström, 1257
Strain Rate Modelling for a Flame Surface Density Equation with Application to Non-premixed Turbulent Combustion. F. Fichot, B. Delhaye, D. Veynante and S. M. Candel, 1273
Numerical Simulation of Local Extinction Effects in Turbulent Combustor Flows of Methane and Air. I. R. Gran, M. C. Melaaen and B. F. Magnussen, 1283
The Structure of the Recirculation Zone of a Bluff-Body Combustor. A. R. Masri, B. B. Dally, R. S. Barlow and C. D. Carter, 1301
Effects of Curvature and Unsteadiness in Diffusion Flames. Implications for Turbulent Diffusion Combustion. B. Cuenot and T. Poinsot, 1383
Flame Front Disturbance Induced by a Weak Pressure Wave. R. Dobashi, T. Hirano and T. Tsuruda, 1415

11.0 FLUID DYNAMICS

Prediction of the Maximum Turbulence Intensities Generated by Grid-Plate Obstacles in Explosion-Induced Flows. H. Phylaktou and G. E. Andrews, 103
Mixing Characteristics of Compressible Vortex Rings Interacting with Normal Shock Waves. B. M. Cetegen and J. C. Hermanson, 232**
Vortex Pairing and Droplet Dispersion in a Turbulent, Free Shear Layer. K. T. Kiger and J. C. Lasheras, 407
Numerical Investigation of Steady Laminar Flame Propagation in a Circular Tube. S. T. Lee and C. H. Tsai, 484*
Large-Eddy Simulations of Turbulent Reacting Flows in a Chamber with Gaseous Ethylene Injecting Through the Porous Wall. T. M Liou, W. Y. Lien and P. W. Hwang, 591*
The Production of Premixed Flame Surface Area in Turbulent Shear Flow. A. Trouvé, 687*
Measurements of Scalar Dissipation in the Reaction Zones of Turbulent Nonpremixed H_2-Air Diffusion Flames. S. P. Nandula, T. M. Brown and R. W. Pitz, 775*
Theory of Spin and Spiral Gasless Combustion. B. V. Novozhilov, 1677

11.1 Atomization of Liquids

The Droplet Group Microexplosions in Water-in-Oil Emulsion Sprays and their Effects on Diesel Engine Combustion. H. Z. Sheng, L. Chen, Z. P. Zhang, C. K. Wu, C. An and C. Q. Cheng, 175
Injection, Dispersion, and Combustion of Liquid Fuels. W. D. Bachalo, 333

*Combustion and Flame, Vol. 99, 1994.
**Combustion and Flame, Vol. 100, 1995.

Influence of Ambient Pressure on Drop-Size and Velocity Distributions in Dense Sprays. A. K. Jasuja and A. H. Lefebvre, 345
2D Laser Diagnostics of Liquid Methanol for Investigation of Atomization and Vaporization Dynamics in a Burning Spray Jet. R. Bazile and D. Stepowski, 363
The Structure of the Dense Core Region in Transient Diesel Sprays. G. J. Smallwood, Ö. L. Gülder and D. R. Snelling, 371
Analysis of In-Cylinder Flow Processe by LDA. F. E. Corcione and G. Valentino, 387*
Vortex Pairing and Droplet Dispersion in a Turbulent, Free Shear Layer. K. T. Kiger and J. C. Lasheras, 407

11.2 Blast Waves

Numerical Modeling of Spark Ignition and Flame Initiation in a Quiescent Methane-Air Mixture. T. Kravchik and E. Sher, 635*

11.3 Boundary Layer Phenomena

The Influence of Equivalence Ratio and Sorêt Effect on the Ignition of Hydrogen-Air Mixtures in Supersonic Boundary Layers. L. F. F. da Silva and B. Deshaies, 29

11.4 Jets

Gasdynamic Enhancement of Nonpremixed Combustion. F. Marble, 1
Three-Dimensional Numerical Simulations of Unsteady Reactive Square Jets. F. F. Grinstein and K. Kailasanath, 2**
Cavity-Actuated Supersonic Mixing and Combustion Control. K. Yu and K. C. Schadow, 295*
Transition and Structure of Jet Diffusion Flames. T. Takeno, 1061
Effects of Molecular Transport on Turbulence-Chemistry Interactions in a Hydrogen-Argon-Air Jet Diffusion Flame. S. Menon, W. H. Calhoon, Jr., G. Goldin and A. R. Kerstein, 1125
Wide Field Conserved Scalar Imaging in Turbulent Diffusion Flames by a Raman and Rayleigh Method. J. B. Kelman, A. R. Masri, S. H. Stårner and R. W. Bilger, 1141
Effect of Dilution on the Liftoff of Non-Premixed Jet Flames. B. J. Lee, J. S. Kim and S. H. Chung, 1175
Temporal Evolution of Turbulence/Chemistry Interactions in Lifted, Turbulent-Jet Flames. R. W. Schefer, M. Namazian, E. E. J. Filtopoulos and J. Kelly, 1223
Effect of the Initial Temperature and Composition of a Hot Transient Jet on the Ignition of H_2-Air-Diluent Mixtures. N. Djebaili, R. Lisbet, G. Dupre and C. Paillard, 1539

11.5 Mixing

Gasdynamic Enhancement of Nonpremixed Combustion. F. Marble, 1
Navier-Stokes Numerical Simulation of Supersonic Hydrogen-Flourine Combustion in CW Chemical Lasers. M. Rotinian, M. Shur and M. Strelets, 13
Numerical Simulation of Supersonic Mixing and Combustion. P. Gerlinger, D. Brüggemann and J. Algermissen, 21
Air Entrainment Flow Field Induced by a Pool Fire. X. C. Zhou and J. P. Gore, 52**
In-Cylinder Crank Angle Resolved Imaging of Fuel Concentration In a Firing Spark-Ignition-Engine Using Planar Laser-Induced Flourescence. M. Berckmüller, N. P. Tait, R. D. Lockett, D. A. Greenhalgh, K. Ishii, Y. Urata, H. Umiyama and K. Yoshida, 151
Laser Raman Scattering Measurements of Differential Molecular Diffusion in Turbulent Nonpremixed Jet Flames of H_2/CO_2 Fuel. L. L. Smith, R. W. Dibble, L. Talbot, R. S. Barlow and C. D. Carter, 153**
Mixing Characteristics of Compressible Vortex Rings Interacting with Normal Shock Waves. B. M. Cetegen and J. C. Hermanson, 232**
Cavity-Actuated Supersonic Mixing and Combustion Control. K. Yu and K. C. Schadow, 295*
Injection, Dispersion, and Combustion of Liquid Fuels. W. D. Bachalo, 333
Experimental and Numerical Study of an Incinerator- and Furnace-Related Flow. D. K. Heist, M. Ravichanran and F. C. Gouldin, 339*
Phase Averaging of the Precessing Vortex Core in a Swirl Burner under Piloted and Premixed Combustion Conditions. D. Froud, T. O'Doherty and N. Syred, 407**
Vortex Pairing and Droplet Dispersion in a Turbulent, Free Shear Layer. K. T. Kiger and J. C. Lasheras, 407
Strained Dissipation and Reaction Layer Analyses of Nonequilibrium Chemistry in Turbulent Reacting Flows. E. S. Bish and W. J. A. Dahm, 457**
NO_x and CO Emissions from a Pulse Combustor Operating in a Lean Premixed Mode. J. O. Keller, T. T. Bramlette, P. K. Barr and J. R. Alvarez, 460*
Experimental Identification of Mixing Regimes in the Analysis of Turbulent Diffusion Flames. A. Cavaliere, M. El-Naggar and R. Ragucci, 679*
Raman Measurements and Joint PDF Modeling Of a Non-Premixed Bluff-Body-Stabilized Methane Flame. S. M. Correa, A. Gulati and S. B. Pope, 1167
The Vorticity Dynamics of an Exothermic, Spatially-

*Combustion and Flame, Vol. 99, 1994.
**Combustion and Flame, Vol. 100, 1995.

Developing, Forced, Reacting Shear Layer. M. C. Soteriou and A. F. Ghoniem, 1265
Double-Pulsed Imaging Using Simultaneous OH/Acetone PLIF For Studying the Evolution of High-Speed, Reacting Mixing Layers. J. M. Seitzman, M. F. Miller, T. C. Island and R. K. Hanson, 1743

11.6 Nozzle Flow

Navier-Stokes Numerical Simulation of Supersonic Hydrogen-Flourine Combustion in CW Chemical Lasers. M. Rotinian, M. Shur and M. Strelets, 13

11.7 Particle Trajectories

Air Entrainment Flow Field Induced by a Pool Fire. X. C. Zhou and J. P. Gore, 52**
Injection, Dispersion, and Combustion of Liquid Fuels. W. D. Bachalo, 333
Analysis of Droplet Arrival Statistics in a Pressure-Atomized Spray Flame. J. T. Hodges, C. Presser, A. K. Gupta and C. T. Avedesian, 353
Vortex Pairing and Droplet Dispersion in a Turbulent, Free Shear Layer. K. T. Kiger and J. C. Lasheras, 407
The Effect of Pulverized Coal Injection and Volatile Matter Content of Coal on Combustion Characteristics around the Raceway Zone in the Blast Furnace. H. Tsuge, T. Yoshida, H. Aoki and T. Miura, 493

11.8 Plumes

Air Entrainment Flow Field Induced by a Pool Fire. X. C. Zhou and J. P. Gore, 52**
Cavity-Actuated Supersonic Mixing and Combustion Control. K. Yu and K. C. Schadow, 295*
Simulation of Smoke Plumes from Large Pool Fires. H. R. Baum, K. B. McGrattan and R. G. Rehm, 1463

11.9 Supersonic Flow

Gasdynamic Enhancement of Nonpremixed Combustion. F. Marble, 1
Navier-Stokes Numerical Simulation of Supersonic Hydrogen-Flourine Combustion in CW Chemical Lasers. M. Rotinian, M. Shur and M. Strelets, 13
Numerical Simulation of Supersonic Mixing and Combustion. P. Gerlinger, D. Brüggemann and J. Algermissen, 21
The Influence of Equivalence Ratio and Sorêt Effect on the Ignition of Hydrogen-Air Mixtures in Supersonic Boundary Layers. L. F. F. da Silva and B. Deshaies, 29
H_2-Air and CH_4-Air Detonations and Combustions behind Oblique Shock Waves. C. Viguier, C. Guerraud and D. Desbordes, 53
Numerical Modeling of Combustion Processes Induced by a Supersonic Conical Blunt Body. M. H. Lefebvre and T. Fujiwara, 85**
Mixing Characteristics of Compressible Vortex Rings Interacting with Normal Shock Waves. B. M. Cetegen and J. C. Hermanson, 232**
Reduced Kinetic Mechanism of Ignition for Non-Premixed Hydrogen/Air in a Supersonic Mixing Layer. Y. Ju and T. Niioka, 240*
Cavity-Actuated Supersonic Mixing and Combustion Control. K. Yu and K. C. Schadow, 295*
The Application of New Combustion and Turbulence Models to H_2-Air Non-Premixed Supersonic Combustion. L. L. Zheng and K. N. C. Bray, 440*
Double-Pulsed Imaging Using Simultaneous OH/Acetone PLIF For Studying the Evolution of High-Speed, Reacting Mixing Layers. J. M. Seitzman, M. F. Miller, T. C. Island and R. K. Hanson, 1743

11.10 Others

Experimental and Numerical Study of an Incinerator- and Furnace-Related Flow. D. K. Heist, M. Ravichanran and F. C. Gouldin, 339*
Heat, Mass, and Momentum Transfer about Arbitrary Groups of Particles. H. A. Dwyer, H. Nirschl, P. Kerschl and V. Denk, 389
Experiments on the Interaction between a Vortex and a Strained Diffusion Flame. J. C. Rolon, F. Aguerre and S. Candel, 422**
Large Eddy Simulations of Bluff Body Stabilized Flames. C. Fureby and C. Löfström, 1257
The Vorticity Dynamics of an Exothermic, Spatially-Developing, Forced, Reacting Shear Layer. M. C. Soteriou and A. F. Ghoniem, 1265

FLUIDIZED-BED COMBUSTION
(*See* **COMBUSTION IN PRACTICAL SYSTEMS,** *Furnaces and Incinerators;* **HETEROGENEOUS COMBUSTION,** *Dispersed Particles*)

12.0 HEAT TRANSFER

A Thermochemical Phase Space for Combustion in Engines. A. K. Oppenheim and J. A. Maxson, 157
Effect of Unsteady Stretch Rate on OH Chemistry During a Flame-Vortex Interaction: To Assess Flamelet Models. C. J. Mueller, J. F. Driscoll, D. J. Sutkus, Wm. L. Roberts, M. C. Drake and M. D. Smooke, 323**
Boilover Burning of Heating Oil Spilled on Water.

*Combustion and Flame, Vol. 99, 1994.
**Combustion and Flame, Vol. 100, 1995.

J. P. Garo, J. P. Vantelon and A. C. Fernandez-Pello, 1481
Buoyant Downward Diffusion Flame Spread and Extinction in Partial-Gravity Accelerations. K. R. Sacksteder and J. S. T'ien, 1685

12.1 Conduction

Evolution of Porosity and Thermal Conductivity during Char Oxidation. Y. Weiss, Y. Benari, I. I. Kantorovich, E. Bar-Ziv, G. Krammer, A. Modestino and A. F. Sarofim, 519

12.2 Convection

Heat, Mass, and Momentum Transfer About Arbitrary Groups of Particles. H. A. Dwyer, H. Nirschl, P. Kerschl and V. Denk, 389
Effects of Natural Convection on Two Stage Ignition of an n-Dodecane Droplet. M. Tanabe, M. Kono, J. Sato, J. Koenig, C. Eigenbrod and H. J. Rath, 455
Evolution of Porosity and Thermal Conductivity during Char Oxidation. Y. Weiss, Y. Benari, I. I. Kantorovich, E. Bar-Ziv, G. Krammer, A. Modestino and A. F. Sarofim, 519

12.3 Radiation

Effect of Radiation on Nitrogen Oxides Emissions From Non-Sooty Swirling Flames of Natural Gas. A. Sayre, N. Lallemant, J. Dugué and R. Weber, 235
Fuel Saving by Heat-Recirculating Combustion Using Fibre Mats. S. Nakamura and F. Weinberg, 269
The Effect of Pulverized Coal Injection and Volatile Matter Content of Coal on Combustion Characteristics Around the Raceway Zone in the Blast Furnace. H. Tsuge, T. Yoshida, H. Aoki and T. Miura, 493
Radiative Heat Transfer in Pulverized-Coal-Fired Boilers—Development of the Absorptive/Reflective Character of Initial Ash Deposits. G. H. Richards, J. H. Harb, L. L. Baxter, S. Bhattacharaya, R. P. Gupta and T. F. Wall, 511
Two-Dimensional Non-Stationary Causal Stochastic Model for Turbulence/Radiation Interactions in Flames. S. H. Chan, X. C. Pan and J. Zhang, 1115

13.0 HETEROGENEOUS COMBUSTION

Structural and Compositional Transformations of Biomass Chars During Combustion. M. J. Wornat, R. H. Hurt, N. Y. C. Yang and T. J. Headley, 131**
Influence of Initial Particle Density on the Reaction Mode of Porous Carbon Particles. R. H. Essenhigh, 269*
Vaporization of a Dense Spherical Cloud of Droplets at Subcritical and Supercritical Conditions. T. L. Jiang and W.-T. Chiang, 355*
Ignition Process of Heated Iron Blocks in High Pressure Oxygen Atmosphere. J. Sato, H. Ohtani and T. Hirano, 376**
Interactive Combustion of Two Droplets in Microgravity. M. Mikami, H. Kato, J. Sato and M. Kono, 431
Clarification of the Flame Structure of Droplet Burning Based on Temperature Measurement in Microgravity. M. Mikami, M. Niwa, H. Kato, J. Sato and M. Kono, 439
NO and N_2O Decomposition over Coal Char at Fluidized-Bed Combustion Conditions. J. Rodriguez-Mirasol, A. C. Ooms, J. R. Pels, F. Kapteijn and J. A. Moulijn, 499*
Impact of Air Staging on the Fate of NO and N_2O in a Circulating Fluidized-Bed Combustor. X. S. Wang, B. M. Gibbs and M. J. Rhodes, 508*
Gas-Particle Flows and Coal Combustion in a Burner/Combustor With High-Velocity Jets. L. X. Zhou, W. Y. Lin, W. W. Luo and X. Q. Huang, 669*
Modeling of Combustion Wave Propagation in Carbon Dust/Gas Mixture. P. M. Krishenik, E. N. Rumanov and K. G. Shkadinskii, 713*
Effect of NO and O_2 Concentration on N_2O Formation during Coal Combustion in a Fluidized Bed Combustor: Modeling Results. S. K. Goel, A. Morihara, C. J. Tullin and A. F. Sarofim, 1051
Ignition and Combustion of Magnesium in Carbon Dioxide Streams. S. Yuasa and A. Fukuchi, 1587

13.1 Catalytic Combustion

Modeling Heterogeneous/Homogeneous Reactions and Transport Coupling for Catalytic Combustion of Methyl Chloride over a Mn-based Catalyst. H. Karim, L. D. Pfefferle, P. Markatou and M. Smooke, 299
Catalytic Oxidation of an Amorphous Carbon Black. P. Ciambelli, M. D'Amore, V. Palma and S. Vaccaro, 413*
NO_x Formation in Lean Premixed Non-Catalytic and Catalytically Stabilized Combustion of Propane. A. Schlegel, S. Buser, P. Benz, H. Bockhorn and F. Mauss, 1019
An Experimental and Numerical Investigation on the Hot Surface Ignition of Premixed Gases Under Microgravity Conditions. H. Nagata, H. M. Kim, J. Sato and M. Kono, 1719

*Combustion and Flame, Vol. 99, 1994.
**Combustion and Flame, Vol. 100, 1995.

13.2 Dispersed Particles

Phenomenological Aspects in Explosive Powder/Gas Two-Phase Detonations. A. J. Tulis, W. K. Sumida, R. P. Joyce, D. C. Heberlein and D. L. Patel, 79
Biosludge Incineration in FBCs: Behavior of Ash Particles. K. K. Rink, J. A. Kozinski and J. S. Lighty, 121**
Ignition and Combustion of Isolated and Binary Arrays of Coal Particles. E. Kharbat, K. Annamalai and C. Gopalakrishnan, 413**
The Effect of Pulverized Coal Injection and Volatile Matter Content of Coal on Combustion Characteristics around the Raceway Zone in the Blast Furnace. H. Tsuge, T. Yoshida, H. Aoki and T. Miura, 493
On the Combustion of Wood-Char Spheres in O_2/N_2 Mixtures—Experiments and Analysis. S. Dasappa, H. V. Sridhar, P. J. Paul, H. S. Mukunda and U. Shrinivasa, 569
Gas-Particle Flows and Coal Combustion in a Burner/Combustor With High-Velocity Jets. L. X. Zhou, W. Y. Lin, W. W. Luo and X. Q. Huang, 669*
Temperature Field on a Laminar Diffusion Dust Flame. J. I. Vovchuk and N. I. Poletaev, 706*
Modeling of Combustion Wave Propagation in Carbon Dust/Gas Mixture. P. M. Krishenik, E. N. Rumanov and K. G. Shkadinskii, 713*
Flame Propagation Experiment of PMMA Particle Cloud in a Microgravity Environment. H. Kobayashi, N. Ono, Y. Okuyama and T. Niioka, 1693

13.3 Multiphase

Superadiabatic Combustion of Methane Air Mixtures under Filtration in a Packed Bed. S. Zhdanok, L. A. Kennedy and G. Koester, 221**
Ignition Process of Heated Iron Blocks in High Pressure Oxygen Atmosphere. J. Sato, H. Ohtani and T. Hirano, 376**
Interactive Combustion of Two Droplets in Microgravity. M. Mikami, H. Kato, J. Sato and M. Kono, 431
Clarification of the Flame Structure of Droplet Burning Based on Temperature Measurement in Microgravity. M. Mikami, M. Niwa, H. Kato, J. Sato and M. Kono, 439
The Effect of Pulverized Coal Injection and Volatile Matter Content of Coal on Combustion Characteristics around the Raceway Zone in the Blast Furnace. H. Tsuge, T. Yoshida, H. Aoki and T. Miura, 493
Performance Predictions of Pulverized-Coal Flames of Power Station Furnace and Cement Kiln Types. F. C. Lockwood and B. Shen, 503
An Experimental Study of Deflagration to Detonation Transition Supported by Dust Layers. Y.-C. Li, C. W. Kauffman and M. Sichel, 505**
The Influence of Burner Injection Mode on Pulverised Coal and Biomass Co-Fired Flames. T. Abbas, P. Costen, N. H. Kandamby, F. C. Lockwood and J. J. Ou, 617*
Investigation of Organic Dust Detonation in the Presence of Chemically Inert Particles. R. Klemens, M. Kapuscinski, M. Wolinski, P. Wolanski and M. Sichel, 742*
Ignition and Combustion of Magnesium in Carbon Dioxide Streams. S. Yuasa and A. Fukuchi, 1587
Characteristics of Water-Base Foam Combustion. V. S. Babkin, N. A. Kakutkina and V. V. Zamaschikov, 1627

13.4 Single Droplet

Burning Rate Enhancement and Soot Reduction Through Blending in Chlorinated Waste Incineration. T. X. Li and C. K. Law, 291
Application of an Integrated Phase Doppler Interferometer/Rainbow Thermometer/Point Diffraction Interferometer for Characterizing Burning Droplets. S. V. Sankar, D. H. Buermann, K. M. Ibrahim and W. D. Bachalo, 413
The Effect of Initial Diameter on Free Droplet Combustion with Spherical Flame. H. Hara and S. Kumagai, 423
Clarification of the Flame Structure of Droplet Burning Based on Temperature Measurement in Microgravity. M. Mikami, M. Niwa, H. Kato, J. Sato and M. Kono, 439
Ignition Experiment of a Fuel Droplet in High-Pressure High-Temperature Ambient. R. Nakanishi, H. Kobayashi, S. Kato and T. Niioka, 447
Effects of Natural Convection on Two Stage Ignition of an n-Dodecane Droplet. M. Tanabe, M. Kono, J. Sato, J. Koenig, C. Eigenbrod and H. J. Rath, 455

13.5 Single Solid Particle

Evolution of Char Chemistry, Crystallinity, and Ultrafine Structure during Pulverized-Coal Combustion. K. A. Davis, R. H. Hurt, N. Y. C. Yang and T. J. Headley, 31**
Decreases in the Swelling and Porosity of Bituminous Coals during Devolatilization at High Heating Rates. T. K. Gale, C. H. Bartholomew and T. H. Fletcher, 94**
Structural and Compositional Transformations of Biomass Chars during Combustion. M. J. Wornat, R. H. Hurt, N. Y. C. Yang and T. J. Headley, 131**
The Oxidation of Calcium Sulphide at the Temper-

*Combustion and Flame, Vol. 99, 1994.
**Combustion and Flame, Vol. 100, 1995.

atures of Fluidised Bed Combustors. N. H. Davies, K. M. Laughlin and A. N. Hayhurst, 211
Influence of Initial Particle Density on the Reaction Mode of Porous Carbon Particles. R. H. Essenhigh, 269*
Pyrolysis and Combustion of Corncobs in a Fluidized Bed: Measurement and Analysis of Behavior. J.-L. Lin and H. M. Keener, 271**
Evolution of Porosity and Thermal Conductivity during Char Oxidation. Y. Weiss, Y. Benari, I. I. Kantorovich, E. Bar-Ziv, G. Krammer, A. Modestino and A. F. Sarofim, 519
A Transient Kinetics Study of the Combustion Reactivity of a Coal Char. P. Salatino, F. Zimbardi and M. Paulicelli, 527
Near-Extinction and Final Burnout in Coal Combustion. R. H. Hurt and K. A. Davis, 561
Characterization of Mass and Density Distributions of Sized Coal Fractions. E. R. Monazam and D. J. Maloney, 733*
Laser Recoil, Plume Emission, and Flame Height Combustion Response of Oxidizers HMX and RDX at Atmospheric Pressure. J. C. Finlinson, T. Parr and D. Hanson-Parr, 1645

13.6 Solid Propellants

Unsteady Combustion of Homogeneous Energetic Solids Using the Laser-Recoil Method. S. F. Son and M. Q. Brewster, 283**
Modelling of Partially Confined Hot Fragment Conductive Ignition. T. H. Huang, S. T. Thynell and K. K. Kuo, 1595
Solid-Fuel Regression During Ignition Transient In A Ramjet. J.-T. Yang and C. Y. Y. Wu, 1603
RDX Flame Structure. D. Hanson-Parr and T. Parr, 1635
Laser Recoil, Plume Emission, and Flame Height Combustion Response of Oxidizers HMX and RDX at Atmospheric Pressure. J. C. Finlinson, T. Parr and D. Hanson-Parr, 1645

13.7 Solid-Solid

Stochastic Modeling of Multi-State Combustion of Condensed Heterogeneous Systems. B. M. Khusid, B. B. Khina, E. P. Podvoisky and I. S. Chebotko, 371*
Catalytic Oxidation of an Amorphous Carbon Black. P. Ciambelli, M. D'Amore, V. Palma and S. Vaccaro, 413*

13.8 Sprays

Fuel and Soot Oxidation in Diesel-like Conditions. A. Cavliere, R. Barbella, A. Ciajola, A. D'Anna and R. Ragucci, 167
The Droplet Group Microexplosions in Water-in-Oil Emulsion Sprays and Their Effects on Diesel Engine Combustion. H. Z. Sheng, L. Chen, Z. P. Zhang, C. K. Wu, C. An and C. Q. Cheng, 175
Structure of a Spray Flame Stabilized on a Production Engine Combustor Swirl Cup. F. Takahashi, W. J. Schmoll, G. L. Switzer and D. T. Shouse, 183
Injection, Dispersion, and Combustion of Liquid Fuels. W. D. Bachalo, 333
Influence of Ambient Pressure on Drop-Size and Velocity Distributions in Dense Sprays. A. K. Jasuja and A. H. Lefebvre, 345
Analysis of Droplet Arrival Statistics in a Pressure-Atomized Spray Flame. J. T. Hodges, C. Presser, A. K. Gupta and C. T. Avedesian, 353
2D Laser Diagnostics of Liquid Methanol for Investigation of Atomization and Vaporization Dynamics in a Burning Spray Jet. R. Bazile and D. Stepowski, 363
The Structure of the Dense Core Region in Transient Diesel Sprays. G. J. Smallwood, Ö. L. Gülder and D. R. Snelling, 371
Similarity Analysis of Spray Diffusion Flames in a Unidirectional Shear-Layer Flow. Y. Tambour and D. Katoshevski, 381
Heat, Mass, and Momentum Transfer About Arbitrary Groups of Particles. H. A. Dwyer, H. Nirschl, P. Kerschl and V. Denk, 389
Entrainment and Evaporation of Drops in the Laminar Part of a Two-Dimensional Developing Mixing Layer. F. Fichot, J. Bellan and K. Harstad, 397
Interactive Combustion of Two Droplets in Microgravity. M. Mikami, H. Kato, J. Sato and M. Kono, 431
Flame Stabilization and OH Fluorescence Mapping of the Combustion Structures in the Near Field of a Spray Jet. D. Stepowski, A. Cessou and P. Goix, 516*
Effect of Gravity on the Structure of an Unsteady Spray Diffusion Flame. T. W. Park, S. K. Aggarwal and V. R. Katta, 767*

14.0 IGNITION

The Influence of Equivalence Ratio and Sorêt Effect on the Ignition of Hydrogen-Air Mixtures in Supersonic Boundary Layers. L. F. F. da Silva and B. Deshaies, 29
Weak and Strong Ignition within the Scope of Spontaneous Flame Concept. A. M. Bartenev and B. E. Gelfand, 61
Heat Release Timing in a Non-Premixed Helmholtz Pulse Combustor. Y. M. Tang, G. Waldherr, J. I. Jagoda and B. T. Zinn, 251**
Ignition Process of Heated Iron Blocks in High Pressure Oxygen Atmosphere. J. Sato, H. Ohtani and T. Hirano, 376**
Ignition and Combustion of a Packed Bed in a Stag-

*Combustion and Flame, Vol. 99, 1994.
**Combustion and Flame, Vol. 100, 1995.

nation Point Flow. D. Reinelt, A. Laurs and G. Adomeit, 395*
Ignition and Combustion of Isolated and Binary Arrays of Coal Particles. E. Kharbat, K. Annamalai and C. Gopalakrishnan, 413**
Effects of Natural Convection on Two Stage Ignition of an n-Dodecane Droplet. M. Tanabe, M. Kono, J. Sato, J. Koenig, C. Eigenbrod and H. J. Rath, 455
Accumulating Sequence of Ignitions from a Propagating Pulse. J. W. Dold, M. Short, J. F. Clarke and N. Nikiforakis, 465**
Volatile Matter Release, Particle/Cloud Ignition and Combustion of Near-Stoichiometric Suspensions of Pulverized Coal. J. A. Lucas and T. F. Wall, 485
Autoignition of Combustible Fluids in Porous Insulation Materials. A. C. McIntosh, M. Bains, W. Crocombe and J. F. Griffiths, 541*
Pressure and Concentration Dependences of the Autoignition Temperature for Normal Butane + Air Mixtures in a Closed Vessel. M. R. Chandraratna and J. F. Griffiths, 626*
Numerical Modeling of Spark Ignition and Flame Initiation in a Quiescent Methane-Air Mixture. T. Kravchik and E. Sher, 635*
The Role of Kinetic Versus Thermal Feedback in Nonpremixed Ignition of Hydrogen versus Heated Air. T. G. Kreutz, M. Nishioka and C. K. Law, 758*
A Reduced Thermokinetic Model For The Autoignition of Fuels With Variable Octane-Ratings. M. Schreiber, A. Sadat Sakak, A. Lingens and J. F. Griffiths, 933
A Bifurcation Analysis of High-Temperature Ignition of H_2-O_2 Diffusion Flames. A. L. Sánchez, A. Liñán and F. A. Williams, 1529
Diffusion and Premixed Flame Ignition Dynamics in a Field of Variable Strain Rate. D. Thevenin and S. Candel, 1547
Ignition and Combustion of Magnesium in Carbon Dioxide Streams. S. Yuasa and A. Fukuchi, 1587

14.1 Delay

Cars Temperature Measurements and the Cyclic Dispersion of Knock in Spark Ignition Engines. D. Bradley, G. T. Kalghatgi, C. Morley, P. Snowden and J. Yeo, 125
Effects of Natural Gas Composition on Ignition Delay Under Diesel Conditions. J. D. Naber, D. L. Siebers, S. S. Di Julio and C. K. Westbrook, 192*
A New Comprehensive Reaction Mechanism for Combustion of Hydrocarbon Fuels. E. Ranzi, A. Sogaro, P. Gaffuri, G. Pennati, C. K. Westbrook and W. J. Pitz, 201*
Reduced Kinetic Mechanism of Ignition for Non-Premixed Hydrogen/Air in a Supersonic Mixing Layer. Y. Ju and T. Niioka, 240*
Ignition Experiment of a Fuel Droplet in High-Pressure High-Temperature Ambient. R. Nakanishi, H. Kobayashi, S. Kato and T. Niioka, 447
Turbulent Broadening of Autoignition Limits. S. M. Correa and A. J. Dean, 1293
Shock Initiated Ignition in Ethylene Oxide, Propylene Oxide. 1,2-Epoxybutane and 2,3-Epoxybutane. A. Lifshitz and A. Suslensky, 1571
Shock-Tube Investigation on the Self-Ignition of Hydrocarbon-Air Mixtures at High Pressures. K. Fieweger, R. Blumenthal and G. Adomeit, 1579
Solid- Fuel Regression During Ignition Transient In A Ramjet. J.-T. Yang and C. Y. Y. Wu, 1603
An Experimental and Numerical Investigation on the Hot Surface Ignition of Premixed Gases under Microgravity Conditions. H. Nagata, H. M. Kim, J. Sato and M. Kono, 1719

14.3 Gases

A Spark Ignition Model for Relight Problems in Aircraft Gas Turbines. D. Liou and D. A. Santavicca, 261
Application of Repro-Modeling for the Reduction of Combustion Mechanisms. T. Turányi, 949
Effect of the Initial Temperature and Composition of a Hot Transient Jet on the Ignition of H_2-Air-Diluent Mixtures. N. Djebaili, R. Lisbet, G. Dupre and C. Paillard, 1539
Self Ignition of Expanding High Temperature H_2—Air and CH_4—Air Mixtures. H.-J. Weber, A. Mack and P. Roth, 1555

15.0 INHIBITION

15.2 Homogeneous

Extinction of Nonpremixed Flames with Halogenated Fire Suppressants. A. Hamins, D. Trees, K. Seshadri and H. K. Chelliah, 221*
The Inhibiting Effect of CF_3Br on the Reaction CH_4 + O_2 at 1070 K. F. Battin-Leclerc, G. M. Come and F. Baronnet, 644*
Decay Mechanism of CF_3H or CF_2HCl In $H_2/O_2/Ar$ Flames. H. Richter, J. Vandooren and P. J. Van Tiggelen, 825
Suppression of High-Speed C_2H_4/Air Flames with C_1-Halocarbons. G. Gmurczyk and W. Grosshandler, 1497
Fluoromethane Chemistry and Its Role in Flame Suppression. P. R. Westmoreland, D. R. F. Burgess, M. R. Zachariah and W. Tsang, 1505

16.0 INSTABILITY

The Development of Instabilities in Laminar Explosion Flames. D. Bradley and C. M. Harper, 562*
Laser Recoil, Plume Emission, and Flame Height

*Combustion and Flame, Vol. 99, 1994.
**Combustion and Flame, Vol. 100, 1995.

Combustion Response of Oxidizers HMX and RDX at Atmospheric Pressure. J. C. Finlinson, T. Parr and D. Hanson-Parr, 1645

16.1 Acoustic

Response of Counterflow Diffusion Flames to Oscillating Strain Rates. H. G. Im, C. K. Law, J. S. Kim and F. A. Williams, 21**
Destruction of Liquid and Gaseous Waste Surrogates in an Acoustically Excited Dump Combustor. J. W. Willis, C. Cadou, M. Mitchell, A. R. Karagozian and O. I. Smith, 280*
The Nonlinear Dynamics of Intrinsic Acoustic Oscillations in a Model Pulse Combustor. S. B. Margolis, 311*
NO_x and CO Emissions from a Pulse Combustor Operating in a Lean Premixed Mode. J. O. Keller, T. T. Bramlette, P. K. Barr and J. R. Alvarez, 460*
Analyses of Liquid Rocket Instabilities Using a Computational Testbed. J. M. Grenda, S. Venkateswaran and C. L. Merkle, 1619

16.2 Fluid Dynamic

Three-Dimensional Numerical Simulations of Unsteady Reactive Square Jets. F. F. Grinstein and K. Kailasanath, 2**
Physical and Chemical Observations in Underwater Explosion Bubbles. W. C. Strahle and S. G. Liou, 89
Quantitative Measurements of Enhanced Soot Production in a Flickering Methane/Air Diffusion Flame. C. R. Shaddix, J. E. Harrington and K. C. Smyth, 723*
Effect of Gravity on the Structure of an Unsteady Spray Diffusion Flame. T. W. Park, S. K. Aggarwal and V. R. Katta, 767*
Transition and Structure of Jet Diffusion Flames. T. Takeno, 1061
The Initial Development of a Tulip Flame. M. Matalon and J. L. McGreevy, 1407
Flame Front Disturbance Induced by a Weak Pressure Wave. R. Dobashi, T. Hirano and T. Tsuruda, 1415

16.3 Nonlinear

The Nonlinear Dynamics of Intrinsic Acoustic Oscillations in a Model Pulse Combustor. S. B. Margolis, 311*
Stochastic Modeling of Multi-State Combustion of Condensed Heterogeneous Systems. B. M. Khusid, B. B. Khina, E. P. Podvoisky and I. S. Chebotko, 371*
Bifurcation Analysis of Methyl Radical Oxidation in Open Systems. The Low Pressure Regime. M. A. Grela and A. J. Colussi, 733

16.4 Others

Unsteady Combustion of Homogeneous Energetic Solids Using the Laser-Recoil Method. S. F. Son and M. Q. Brewster, 283**
The Effect of Hydrogen and Propane Addition on the Operation of a Natural Gas-Fired Pulsed Combustor. H. R. N. Jones and J. Leng, 404*

17.0 KINETICS

Kinetics of the Phenyl Radical Reaction with Ethylene: An RRKM Theoretical Analysis of Low and High Temperature Data. T. Yu and M. C. Lin, 169**
Thermal Decomposition of HCl Measured by ARAS and IR Diode Laser Spectroscopy. G. N. Schading and P. Roth, 467*
Mechanism and Modeling of Hydrogen Cyanide Oxidation in a Flow Reactor. P. Glarborg and J. A. Miller, 475*
Kinetic Investigation of the Reactions of NCO Radicals With Alkanes in the Temperature Range 294 K to 1113 K. A. Schuck, H.-R. Volpp and J. Wolfrum, 491*
Kinetics of Homogeneous Nitrous Oxide Decomposition. P. Glarborg, J. E. Johnsson and K. Dam-Johansen, 523*
A Shock Tube Study of the Reaction $H_2 + NO \rightarrow HNO + H$. K. Natarajan, H. J. Mick, D. Woiki and P. Roth, 610*
The Inhibiting Effect of CF_3Br on the Reaction $CH_4 + O_2$ at 1070 K. F. Battin-Leclerc, G. M. Come and F. Baronnet, 644*
An Experimental and Modeling Study of the Selective Noncatalytic Reduction of NO by Ammonia in the Presence of Hydrocarbons. R. Hemberger, S. Muris, K.-U. Pleban and J. Wolfrum, 660*
Multichannel Reactions in Combustion. Th. Just, 687
Thermal Decomposition of CH_2 Verified by Product Concentration Measurements of C, H, and CH. M. W. Markus, A. M. Tereza and P. Roth, 705
Kinetic Parameters for the Initiation Reaction $RH + O_2 \rightarrow R + HO_2$. T. Ingham, R. W. Walker and R. E. Woolford, 767
The Unimolecular Decomposition of 1-Chloroethyl Radical. V. D. Knyazev, A. Bencsura, I. A. Dubinsky, D. Gutman and S. M. Senkan, 817
Reactions of Phenoxy Radicals in the Gas Phase. R. Buth, K. Hoyermann and J. Seeba, 841
A Direct Study of the Reaction of Benzyl Radicals With Molecular Oxygen: Kinetics and Thermochemistry. K. Hoyermann and J. Seeba, 851
Hydrogen Atom Attack on 1-Phenylpropene at High Temperatures. W. Tsang and J. A. Walker, 867

*Combustion and Flame, Vol. 99, 1994.
**Combustion and Flame, Vol. 100, 1995.

Kinetics of the Thermal Decomposition and Isomerisation of Pyrazine (1,4 Diazine). A. Doughty, J. C. Mackie and J. M. Palmer, 893
Cool Flames and Oscillations in Hydrocarbon Oxidation. A. A. Mantashyan, 927
Laminar Flame Calculations Using Simplified Chemical Kinetics Based on Intrinsic Low-Dimensional Manifolds. U. Maas and S. B. Pope, 1349

17.1 Elementary Reactions

Kinetics of the Phenyl Radical Reaction with Ethylene: An RRKM Theoretical Analysis of Low and High Temperature Data. T. Yu and M. C. Lin, 169**
Thermal Decomposition of Propargyl Bromide and the Subsequent Formation of Benzene. R. D. Kern, H. Chen, J. H. Kiefer and P. S. Mudipalli, 177**
Reduced Kinetic Mechanism of Ignition for Non-Premixed Hydrogen/Air in a Supersonic Mixing Layer. Y. Ju and T. Niioka, 240*
Shock Wave Study of the Thermal Decomposition of Benzyl Alcohol. S. Frisch, H. Hippler, H. Neunaber and J. Troe, 254*
Multichannel Reactions in Combustion. Th. Just, 687
Thermal Decomposition of CH_2 Verified by Product Concentration Measurements of C, H, and CH. M. W. Markus, A. M. Tereza and P. Roth, 705
The Thermal Reactions of CH_3. K. P. Lim and J. V. Michael, 713
The Reaction System CH_3 + OH at Intermediate Temperatures. Appearance of a New Product Channel. R. Humpfer, H. Oser, H.-H. Grotheer and Th. Just, 721
A Shock Tube Study of the CO + OH → CO_2 + H Reaction. M. S. Wooldridge, R. K. Hanson and C. T. Bowman, 741
The Use of Carbon Monoxide/Hydrogen Burning Velocities To Examine the Rate of the CO + OH Reaction. I. C. McLean, D. B. Smith and S. C. Taylor, 749
Kinetic Parameters for the Initiation Reaction RH + O_2 → R + HO_2. T. Ingham, R. W. Walker and R. E. Woolford, 767
Formation of Methoxy and Hydroxymethyl Free Radicals in Selected Elementary Reactions. S. Dóbé, T. Bérces, F. Temps, H. Gg. Wagner and H. Ziemer, 775
The Reaction of Hydroperoxy-Propyl Radicals with Molecular Oxygen. J. W. Bozzelli and W. J. Pitz, 783
Experimental Studies of Cl-Atom Reactions at High Temperatures: Cl + H_2 → HCl + H from 291 to 1283 K. G. Y. Adusei and A. Fontijn, 801
Thermal Decomposition of CH_2Cl_2. K. P. Lim and J. V. Michael, 809
The Unimolecular Decomposition of 1-Chloroethyl Radical. V. D. Knyazev, A. Bencsura, I. A. Dubinsky, D. Gutman and S. M. Senkan, 817
High Temperature Reactions of Phenyl Oxidation. P. Frank, J. Herzler, Th. Just and C. Wahl, 833
Reactions of Phenoxy Radicals in the Gas Phase. R. Buth, K. Hoyermann and J. Seeba, 841
A Direct Study of the Reaction of Benzyl Radicals With Molecular Oxygen: Kinetics and Thermochemistry. K. Hoyermann and J. Seeba, 851
The Reactions of Phenylacetylenes With $O(^3P)$ in the Gas Phase. M. Eichholtz, A. Schneider, D.-V. Stuchen, J.-T. Vollmer and H. Gg. Wagner, 859
Pyrolysis of p-Xylene and of 4-Methylbenzyl Radicals. H. Hippler, S. Seisel and J. Troe, 875
Analysis of the Reactions H + N_2O and NH + NO: Pathways and Rate Constants over a Wide Range of Temperature and Pressure. J. W. Bozzelli, A. Y. Chang and A. M. Dean, 965
The Reactions of $NH(X^3\Sigma^-)$ with the Water Gas Components CO_2, H_2O and H_2. M. Röhrig and Hg. Wagner, 975
A Shock Tube Study of the Reactions of CN and NCO with NO_2. S. T. Wooldridge, J. D. Mertens, R. K. Hanson and C. T. Bowman, 983
Kinetic Studies of the Reactions $NH(X^3\Sigma^-)$ + NO and $NH(X^3\Sigma^-)$ + O_2 at Elevated Temperatures. H. Lillich, A. Schuck, H.-R. Volpp, J. Wolfrum and P. D. Naik, 993
Rich Methane/Air Flames: Burning Velocities, Extinction Limits and Flammability Limit. M. N. Bui-Pham and J. A. Miller, 1309
Fluoromethane Chemistry and Its Role in Flame Suppression. P. R. Westmoreland, D. R. F. Burgess, M. R. Zachariah and W. Tsang, 1505

17.2 Heat Release Rates

An Experimental and Numerical Investigation on the Hot Surface Ignition of Premixed Gases Under Microgravity Conditions. H. Nagata, H. M. Kim, J. Sato and M. Kono, 1719

17.4 Modeling

The Homogeneous, Gas-Phase Formation of Chlorinated and Brominated Dibenzo-*p*-dioxins from 2,4,6-Trichloro- and 2,4,6-Tribromophenols. S. S. Sidhu, L. Maqsud, B. Dellinger and G. Mascolo, 11**
Detailed Modeling of Soot Formation in Laminar Premixed Ethylene Flames at a Pressure of 10 Bar. A. Kazakov, H. Wang and M. Frenklach, 111**
Cars Temperature Measurements and the Cyclic

*Combustion and Flame, Vol. 99, 1994.
**Combustion and Flame, Vol. 100, 1995.

Dispersion of Knock in Spark Ignition Engines. D. Bradley, G. T. Kalghatgi, C. Morley, P. Snowden and J. Yeo, 125
Effects of Natural Gas Composition on Ignition Delay Under Diesel Conditions. J. D. Naber, D. L. Siebers, S. S. Di Julio and C. K. Westbrook, 192*
Chemical Kinetic Modeling of Exhaust Hydrocarbon Oxidation. K. C. Wu, S. Hochgreb and M. G. Norris, 193**
A New Comprehensive Reaction Mechanism for Combustion of Hydrocarbon Fuels. E. Ranzi, A. Sogaro, P. Gaffuri, G. Pennati, C. K. Westbrook and W. J. Pitz, 201*
Modeling Heterogeneous/Homogeneous Reactions and Transport Coupling for Catalytic Combustion of Methyl Chloride over a Mn-based Catalyst. H. Karim, L. D. Pfefferle, P. Markatou and M. Smooke, 299
Experimental and Numerical Comparison of Extractive and In-Situ Laser Measurements of Non-Equilibrium Carbon Monoxide in Lean-Premixed Natural Gas Combustion. Q. V. Nguyen, B. L. Edgar, R. W. Dibble and A. Gulati, 395**
NO_x and N_2O in Lean-Premixed Jet-Stirred Flames. R. C. Steele, P. C. Malte, D. G. Nicol and J. C. Kramlich, 440**
Kinetic Interactions of CO, NO_x, and HCl Emissions in Post-Combustion Gases. J. F. Roesler, R. A. Yetter and F. L. Dryer, 495**
Thermal and Chemical Influences on the Soot Mass Growth. M. Bachmann, W. Wiese and K. H. Homann, 635
Further Testing of the Fullerene Formation Mechanism With Predictions of Temperature and Pressure Trends. C. J. Pope and J. B. Howard, 671
Multichannel Reactions in Combustion. Th. Just, 687
Inception and Growth of Soot Particles in Dependence on the Surrounding Gas Phase. F. Mauss, T. Schäfer and H. Bockhorn, 697*
The Thermal Reactions of CH_3. K. P. Lim and J. V. Michael, 713
The Reaction System CH_3 + OH at Intermediate Temperatures. Appearance of a New Product Channel. R. Humpfer, H. Oser, H.-H. Grotheer and Th. Just, 721
Bifurcation Analysis of Methyl Radical Oxidation in Open Systems. The Low Pressure Regime. M. A. Grela and A. J. Colussi, 733
The Use of Carbon Monoxide/Hydrogen Burning Velocities to Examine the Rate of the CO + OH Reaction. I. C. McLean, D. B. Smith and S. C. Taylor, 749
New Results on Moist CO Oxidation: High Pressure, High Temperature Experiments and Comprehensive Kinetic Modeling. T. J. Kim, R. A. Yetter and F. L. Dryer, 759
Kinetic Parameters for the Initiation Reaction RH + $O_2 \rightarrow$ R + HO_2. T. Ingham, R. W. Walker and R. E. Woolford, 767
High Temperature Reactions of Phenyl Oxidation. P. Frank, J. Herzler, Th. Just and C. Wahl, 833
Reaction Mechanisms for Toluene Pyrolysis. M. B. Colket and D. J. Seery, 883
Kinetics of the Thermal Decomposition and Isomerisation of Pyrazine (1,4 Diazine). A. Doughty, J. C. Mackie and J. M. Palmer, 893
An Experimental and Computational Study of Methanol Oxidation in the Intermediate and High Temperature Regimes. T. J. Held and F. L. Dryer, 901
C_1/C_2 Chemistry in Fuel-Rich Post-Flame Gases: Detailed Kinetic Modelling. I. T. Woods and B. S. Haynes, 909
Kerosene Combustion at Pressures up to 40 Atm: Experimental Study and Detailed Chemical Kinetic Modeling. P. Dagaut, M. Reuillon, J.-C. Boettner and M. Cathonnet, 919
A Reduced Thermokinetic Model For The Autoignition of Fuels With Variable Octane-Ratings. M. Schreiber, A. Sadat Sakak, A. Lingens and J. F. Griffiths, 933
Application of Repro-Modeling For the Reduction of Combustion Mechanisms. T. Turányi, 949
Analysis of the Reactions H + N_2O and NH + NO: Pathways and Rate Constants Over a Wide Range of Temperature and Pressure. J. W. Bozzelli, A. Y. Chang and A. M. Dean, 965
Aspects of Nitrogen Flame Chemistry Revealed By Burning Velocity Modelling. M. J. Brown and D. B. Smith, 1011
Effect of NO and O_2 Concentration on N_2O Formation during Coal Combustion in a Fluidized Bed Combustor: Modeling Results. S. K. Goel, A. Morihara, C. J. Tullin and A. F. Sarofim, 1051
A Lagrangian Model For Predicting Turbulent Diffusion Flames With Chemical Kinetic Effects. M. Obounou, M. Gonzalez and R. Borghi, 1107
The Formation and Destruction of Aromatic Compounds in a Turbulent Flame. J. H. Thijssen, M. A. Toqan, J. M. Beér and A. F. Sarofim, 1215
Turbulent Broadening of Autoignition Limits. S. M. Correa and A. J. Dean, 1293
Rich Methane/Air Flames: Burning Velocities, Extinction Limits and Flammability Limit. M. N. Bui-Pham and J. A. Miller, 1309
Fluoromethane Chemistry and Its Role in Flame Suppression. P. R. Westmoreland, D. R. F. Burgess, M. R. Zachariah and W. Tsang, 1505
Natural Gas and Blends Oxidation and Ignition: Experiments and Modeling. Y. Tan, P. Dagaut, M. Cathonnet, J. Cl. Boettner, J. S. Bachman and P. Carlier, 1563
Modelling of Partially Confined Hot Fragment Con-

*Combustion and Flame, Vol. 99, 1994.
**Combustion and Flame, Vol. 100, 1995.

ductive Ignition. T. H. Huang, S. T. Thynell and K. K. Kuo, 1595

17.5 Overall Rates

A Unified Approach to the Reduced Kinetic Modelling of Alkane Combustion. J. F. Griffiths, K. J. Hughes, M. Schreiber and C. Poppe, 533*
Near-Extinction and Final Burnout in Coal Combustion. R. H. Hurt and K. A. Davis, 561
Soot Formation at Elevated Pressures and Carbon Concentrations in Hydrocarbon Pyrolysis. St. Bauerle, Y. Karasevich, St. Slavov, D. Tanke, M. Tappe, Th. Thienel and H. Gg. Wagner, 627
High Temperature Pyrolsis and Oxidation of Fullerene C_{60} Behind Shock Waves. S. von Gersum and P. Roth, 661
A DMS Kinetic Study of the Boron Oxides Vapor in the Combustion Front of SHS System Mo + B. O. E. Kashireninov and I. A. Yuranov, 1669
Hydrogen Atom Attack on 1-Phenylpropene at High Temperatures. W. Tsang and J. A. Walker, 867

18.0 MODELING AND SCALING

Numerical Simulations of Burner-Stabilized Hydrogen-Air Flames in Microgravity. G. Patnaik and K. Kailasanath, 247*
A Spark Ignition Model for Relight Problems in Aircraft Gas Turbines. D. Liou and D. A. Santavicca, 261
Modeling Heterogeneous/Homogeneous Reactions and Transport Coupling for Catalytic Combustion of Methyl Chloride over a Mn-based Catalyst. H. Karim, L. D. Pfefferle, P. Markatou and M. Smooke, 299
Mechanism and Modeling of Hydrogen Cyanide Oxidation in a Flow Reactor. P. Glarborg and J. A. Miller, 475*
Kinetics of Homogeneous Nitrous Oxide Decomposition. P. Glarborg, J. E. Johnsson and K. Dam-Johansen, 523*
A Unified Approach to the Reduced Kinetic Modelling of Alkane Combustion. J. F. Griffiths, K. J. Hughes, M. Schreiber and C. Poppe, 533*
Detailed Kinetic Modelling of Premixed Benzene Flames. R. P. Lindstedt and G. Skevis, 551*
Shock Tube Study of Ignition Delays and Detonation of Gaseous Monomethylhydrazine/Oxygen Mixtures. L. Catoire, X. Bassin, G. Dupre and C. Paillard, 573*
The Influence of Burner Injection Mode on Pulverised Coal and Biomass Co-Fired Flames. T. Abbas, P. Costen, N. H. Kandamby, F. C. Lockwood and J. J. Ou, 617*
Effects of Molecular Transport on Turbulence-Chemistry Interactions in a Hydrogen-Argon-Air Jet Diffusion Flame. S. Menon, W. H. Calhoon, Jr., G. Goldin and A. R. Kerstein, 1125
Laminar Flame Calculations Using Simplified Chemical Kinetics Based on Intrinsic Low-Dimensional Manifolds. U. Maas and S. B. Pope, 1349
Laminar Flame Calculations Using Simplified Chemical Kinetics Based on Intrinsic Low-Dimensional Manifolds. U. Maas and S. B. Pope, 1349
Simultaneous Optical Measurement of Soot Volume Fraction, Temperature, and CO_2 in Heptane Pool Fire. M. Y. Choi, A. Hamins, H. Rushmeier and T. Kashiwagi, 1471

18.1 Empirical

A Method of Predicting Coal Devolatilization Behavior Based on the Elemental Composition. Y. Zhao, M. A. Serio, R. Bassilakis and P. R. Solomon, 553
NO_x Formation in Geometrically Scaled Gas-Fired Industrial Burners. A. D. Al-Fawaz, L. M. Dearden, J. T. Hedley, M. Missaghi, M Pourkashanian, A. Williams and L. T. Yap, 1027
Behavior of Fires Spreading Downward Over Thick Paper. M. Suzuki, R. Dobashi and T. Hirano, 1439

18.2 Fundamental

On the Structure of Stretched/Compressed Laminar Flamelet—Influence of Preferential Diffusion. V. R. Katta and W. M. Roquemore, 61**
The Behavior of Flames Spreading over Thin Solids in Microgravity. P. A. Ramachandra, R. A. Altenkirch, S. Bhattacharjee, L. Tang, K. Sacksteder and M. K. Wolverton, 71**
Detailed Modeling of Soot Formation in Laminar Premixed Ethylene Flames at a Pressure of 10 Bar. A. Kazakov, H. Wang and M. Frenklach, 111**
A New Comprehensive Reaction Mechanism for Combustion of Hydrocarbon Fuels. E. Ranzi, A. Sogaro, P. Gaffuri, G. Pennati, C. K. Westbrook and W. J. Pitz, 201*
The Partitioning of Iron during the Combustion of Pulverized Coal. L. E. Bool III, T. W. Peterson and J. O. L. Wendt, 262**
The Nonlinear Dynamics of Intrinsic Acoustic Oscillations in a Model Pulse Combustor. Stephen B. Margolis, 311*
Experimental and Numerical Study of an Incinerator- and Furnace-Related Flow. D. K. Heist, M. Ravichanran and F. C. Gouldin, 339*
Stochastic Modeling of Multi-State Combustion of Condensed Heterogeneous Systems. B. M. Khu-

*Combustion and Flame, Vol. 99, 1994.
**Combustion and Flame, Vol. 100, 1995.

sid, B. B. Khina, E. P. Podvoisky and I. S. Chebotko, 371*
Heat, Mass, and Momentum Transfer About Arbitrary Groups of Particles. H. A. Dwyer, H. Nirschl, P. Kerschl and V. Denk, 389
Performance Predictions of Pulverized-Coal Flames of Power Station Furnace and Cement Kiln Types. F. C. Lockwood and B. Shen, 503
A Transient Kinetics Study of the Combustion Reactivity of a Coal Char. P. Salatino, F. Zimbardi and M. Paulicelli, 527
On the Combustion of Wood-Char Spheres in O_2/N_2 Mixtures—Experiments and Analysis. S. Dasappa, H. V. Sridhar, P. J. Paul, H. S. Mukunda and U. Shrinivasa, 569
Bifurcation Analysis of Methyl Radical Oxidation in Open Systems. The Low Pressure Regime. M. A. Grela and A. J. Colussi, 733
Effect of Gravity on the Structure of an Unsteady Spray Diffusion Flame. T. W. Park, S. K. Aggarwal and V. R. Katta, 767*
Reduced Mechanism of Soot Formation—Application to Natural Gas Fueled Diesel Combustion. Y. Yoshihara, A. Kazakov, H. Wang and M. Frenklach, 941
Analysis of the Reactions H + N_2O and NH + NO: Pathways and Rate Constants Over a Wide Range of Temperature and Pressure. J. W. Bozzelli, A. Y. Chang and A. M. Dean, 965
Modeling Turbulent Flame Propagation. W. T. Ashurst, 1075
Partially Premixed Turbulent Flame Propagation in Jet Flames. C. M. Müller, H. Breitbach and N. Peters, 1099
A Lagrangian Model For Predicting Turbulent Diffusion Flames With Chemical Kinetic Effects. M. Obounou, M. Gonzalez and R. Borghi, 1107
Stabilization Mechanism of Lifted Jet Diffusion Flames. C. R. Kaplan, E. S. Oran and S. W. Baek, 1183
Experimental Analysis of Flamelet Models for Premixed Turbulent Combustion. D. Veynante, J. M. Duclos and J. Piana, 1249
Strain Rate Modelling for a Flame Surface Density Equation with Application to Non-premixed Turbulent Combustion. F. Fichot, B. Delhaye, D. Veynante and S. M. Candel, 1273
Turbulent Broadening of Autoignition Limits. S. M. Correa and A. J. Dean, 1293
Modelling of Partially Confined Hot Fragment Conductive Ignition. T. H. Huang, S. T. Thynell and K. K. Kuo, 1595
Supercritical and Subcritical Combustion of LOX with Hydrogen in an Axisymmetric Laminar Diffusion Flame. A.-S. Yang, K. K. Kuo and W. H. Hsieh, 1609
An Experimental and Numerical Investigation on the Hot Surface Ignition of Premixed Gases Under Microgravity Conditions. H. Nagata, H. M. Kim, J. Sato and M. Kono, 1719

*Combustion and Flame, Vol. 99, 1994.
**Combustion and Flame, Vol. 100, 1995.

18.3 Others

Comparison of Measurements and Predictions of Wall Heat Flux and Gas Composition in an Oil-Fired Utility Boiler. M. G. Carvalho, P. J. Coelho, A. L. N. Moreira, A. M. C. Silva and T. F. Silva, 227
Comparative Experimental and Numerical Investigation of a Piloted Turbulent Natural-Gas Diffusion Flame. T. W. J. Peeters, P. P. J. Stroomer, J. E. de Vries, D. J. E. M. Roekaerts and C. J. Hoogendoorn, 1241

19.0 OXIDATION
(*Also see* **KINETICS**)

Laser Ionization Time-Of-Flight Mass Spectrometry Combined With Residual Gas Analysis for the Investigation of Moderate Temperature Benzene Oxidation. G. Bermudez and L. Pfefferle, 41**
Chemical Kinetic Modeling of Exhaust Hydrocarbon Oxidation. K. C. Wu, S. Hochgreb and M. G. Norris, 193**
Influence of Initial Particle Density on the Reaction Mode of Porous Carbon Particles. R. H. Essenhigh, 269*
An Experimental Study of High-Temperature, Oxidative Pulverized Coal Devolatilization. L. H. Sorensen, O. Biede and R. E. Peck, 475
Kinetic Interactions of CO, NO_x, and HCl Emissions in Post-Combustion Gases. J. F. Roesler, R. A. Yetter and F. L. Dryer, 495**
On the Combustion of Wood-Char Spheres in O_2/N_2 Mixtures—Experiments and Analysis. S. Dasappa, H. V. Sridhar, P. J. Paul, H. S. Mukunda and U. Shrinivasa, 569
High Temperature Pyrolsis and Oxidation of Fullerene C_{60} Behind Shock Waves. S. von Gersum and P. Roth, 661
Bifurcation Analysis of Methyl Radical Oxidation in Open Systems. The Low Pressure Regime. M. A. Grela and A. J. Colussi, 733
New Results on Moist CO Oxidation: High Pressure, High Temperature Experiments and Comprehensive Kinetic Modeling. T. J. Kim, R. A. Yetter and F. L. Dryer, 759
An Experimental and Computational Study of Methanol Oxidation in the Intermediate and High Temperature Regimes. T. J. Held and F. L. Dryer, 901
Kerosene Combustion at Pressures up to 40 Atm: Experimental Study and Detailed Chemical Ki-

netic Modeling. P. Dagaut, M. Reuillon, J.-C. Boettner and M. Cathonnet, 919
Cool Flames and Oscillations in Hydrocarbon Oxidation. A. A. Mantashyan, 927
Hydrocarbon-NO_x Interactions at Low Temperatures-1. Conversion of NO to NO_2 Promoted by Propane and the Formation of HNCO. P. F. Nelson and B. S. Haynes, 1003
Natural Gas and Blends Oxidation and Ignition: Experiments and Modeling. Y. Tan, P. Dagaut, M. Cathonnet, J. Cl. Boettner, J. S. Bachman and P. Carlier, 1563

PARTICULATES
(*See* **AEROSOLS**)

20.0 PHASE CHANGES

Vaporization of a Dense Spherical Cloud of Droplets at Subcritical and Supercritical Conditions. T. L. Jiang and W.-T. Chiang, 355*
Interactive Combustion of Two Droplets in Microgravity. M. Mikami, H. Kato, J. Sato and M. Kono, 431
Ignition and Combustion of Magnesium in Carbon Dioxide Streams. S. Yuasa and A. Fukuchi, 1587

20.1 Condensation

A Field Study on the Trace Metal Behavior in Atmospheric Circulating Fluidized Bed Combustion. T. Lind, E. I. Kauppinen, J. K. Jokiniemi and W. Maenhaut, 201

20.2 Evaporation

2D Laser Diagnostics of Liquid Methanol for Investigation of Atomization and Vaporization Dynamics in a Burning Spray Jet. R. Bazile and D. Stepowski, 363
Interactive Combustion of Two Droplets in Microgravity. M. Mikami, H. Kato, J. Sato and M. Kono, 431
Ignition Experiment of a Fuel Droplet in High-Pressure High-Temperature Ambient. R. Nakanishi, H. Kobayashi, S. Kato and T. Niioka, 447
Flame Stabilization and OH Fluorescence Mapping of the Combustion Structures in the Near Field of a Spray Jet. D. Stepowski, A. Cessou and P. Goix, 516*

20.3 Nucleation

Sorbent Capture of Nickel, Lead and Cadmium in a Laboratory Swirl Flame Incinerator. W. P. Linak, R. K. Srivastava and J. O. L. Wendt, 241**
Boilover Burning of Heating Oil Spilled on Water. J. P. Garo, J. P. Vantelon and A.C. Fernandez-Pello, 1481

21.0 POLLUTANTS

The Fate of Arsenic in a Laminar Diffusion Flame. S. Chesworth, G. Yang, D. P. Y. Chang, A. D. Jones, P. B. Kelly and I. M. Kennedy, 259***
Combustion Roles of Bubble and Emulsion Phase in Bubbling Fluidized Bed Coal Combustion Elucidated by Conditional Gas Sampling. I. Naruse, K. Koizumi, K. Kuramoto, G.-Q. Lu and K. Ohtake, 545
The Influence of Burner Injection Mode on Pulverised Coal and Biomass Co-Fired Flames. T. Abbas, P. Costen, N. H. Kandamby, F. C. Lockwood and J. J. Ou, 617*
Combustion's Impact on the Global Atmosphere. M. J. Prather and J. A. Logan, 1513

21.1 HC (Hydrocarbons) and CO

Chemical Kinetic Modeling of Exhaust Hydrocarbon Oxidation. K. C. Wu, S. Hochgreb and M. G. Norris, 193**
On the Effects of Fuel Leakage on CO Production from Household Burners as Revealed by LIF and CARS. C. E. van der Meij, A. Mokhov, R. A. A. M. Jacobs and H. B. Levinsky, 243
Hydrocarbon Oxidation in the Exhaust Port and Runner of a Spark Ignition Engine. K. Drobot, W. K. Cheng, F. H. Trinker, E. W. Kaiser, W. O. Siegl, D. F. Cotton and J. Underwood, 422*
TACCOSA—Thermography-Assisted Combustion Control System for Waste Incinerators. F. Schuler, F. Rampp, J. Martin and J. Wolfrum, 431*
C_1/C_2 Chemistry in Fuel-Rich Post-Flame Gases: Detailed Kinetic Modelling. I. T. Woods and B. S. Haynes, 909
Hydrocarbon-NO_x Interactions at Low Temperatures −1. Conversion of NO to NO_2 Promoted by Propane and the Formation of HNCO. P. F. Nelson and B. S. Haynes, 1003

21.2 NO_x

On the Structure of Stretched/Compressed Laminar Flamelet—Influence of Preferential Diffusion. V. R. Katta and W. M. Roquemore, 61**
Effect of Radiation on Nitrogen Oxides Emissions From Non-Sooty Swirling Flames of Natural Gas. A. Sayre, N. Lallemant, J. Dugué and R. Weber, 235
On the Aero-thermal Characteristics of Gasifier-Fuelled Gas Turbine Combustors with Complex Geometries. N. H. Kandamby and F. C. Lockwood, 251
Laser-Induced Fluorescence Study of Manganese

*Combustion and Flame, Vol. 99, 1994.
**Combustion and Flame, Vol. 100, 1995.
***Combustion and Flame, Vol. 98, 1994.

Fuel Additive Effects in a Propane/Air Flame. U. Westblom, F. Fernandez-Alonso, G. P. Smith, J. B. Jeffries and D. R. Crosley, 261*
Active, Optimal Control of a Model, Industrial, Natural Gas-Fired Burner. D. St. John and G. S. Samuelsen, 307
Flame Structure Studies of a Lean $H_2/N_2O/Ar$ Flame Employing Molecular Beam Mass Spectrometry and Modeling. D. C. Dayton, C. M. Faust, W. R. Anderson and R. C. Sausa, 323*
NO_x and CO Emissions from a Pulse Combustor Operating in a Lean Premixed Mode. J. O. Keller, T. T. Bramlette, P. K. Barr and J. R. Alvarez, 460*
Mechanism and Modeling of Hydrogen Cyanide Oxidation in a Flow Reactor. P. Glarborg and J. A. Miller, 475*
Kinetic Investigation of the Reactions of NCO Radicals With Alkanes in the Temperature Range 294 K to 1113 K. A. Schuck, H.-R. Volpp and J. Wolfrum, 491*
NO and N_2O Decomposition Over Coal Char at Fluidized-Bed Combustion Conditions. J. Rodriguez-Mirasol, A. C. Ooms, J. R. Pels, F. Kapteijn and J. A. Moulijn, 499*
Impact of Air Staging on the Fate of NO and N_2O in a Circulating Fluidized-Bed Combustor. X. S. Wang, B. M. Gibbs and M. J. Rhodes, 508*
Kinetics of Homogeneous Nitrous Oxide Decomposition. P. Glarborg, J. E. Johnsson and K. Dam-Johansen, 523*
Predicting the Evolution of Fuel Nitrogen From Various Coals. S. Niksa, 537
A Shock Tube Study of the Reaction $H_2 + NO \rightarrow HNO + H$. K. Natarajan, H. J. Mick, D. Woiki and P. Roth, 610*
An Experimental and Modeling Study of the Selective Noncatalytic Reduction of NO by Ammonia in the Presence of Hydrocarbons. R. Hemberger, S. Muris, K.-U. Pleban and J. Wolfrum, 660*
Analysis of the Reactions $H + N_2O$ and $NH + NO$: Pathways and Rate Constants Over a Wide Range of Temperature and Pressure. J. W. Bozzelli, A. Y. Chang and A. M. Dean, 965
The Reactions of $NH(X^3\Sigma^-)$ with the Water Gas Components CO_2, H_2O and H_2. M. Röhrig and Hg. Wagner, 975
Hydrocarbon-NO_x Interactions at Low Temperatures −1. Conversion of NO to NO_2 Promoted by Propane and the Formation of HNCO. P. F. Nelson and B. S. Haynes, 1003
Aspects of Nitrogen Flame Chemistry Revealed By Burning Velocity Modelling. M. J. Brown and D. B. Smith, 1011
NO_x Formation in Lean Premixed Non-Catalytic and Catalytically Stabilized Combustion of Propane. A. Schlegel, S. Buser, P. Benz, H. Bockhorn and F. Mauss, 1019
NO_x Formation in Geometrically Scaled Gas-Fired Industrial Burners. A. D. Al-Fawaz, L. M. Dearden, J. T. Hedley, M. Missaghi, M Pourkashanian, A. Williams and L. T. Yap, 1027
Influence of Gasodynamics on NO_x Emission From Large Diffusion Natural Gas Flames. J. Tomeczek, J. Góral and B. Gradon, 1035
Study of NO_x Emission Characteristics In Pressurized Staged Combustor Concepts. J. Meisl, R. Koch, R. Kneer and S. Wittig, 1043
Effect of NO and O_2 Concentration on N_2O Formation during Coal Combustion in a Fluidized Bed Combustor: Modeling Results. S. K. Goel, A. Morihara, C. J. Tullin and A. F. Sarofim, 1051
Simultaneous NO and Temperature Imaging Measurements in Turbulent Nonpremixed Flames. M. Namazian, J. Kelly and R. Schefer, 1149

21.4 PAH (Polycyclic Aromatic Hydrocarbons)

Detailed Modeling of Soot Formation in Laminar Premixed Ethylene Flames at a Pressure of 10 Bar. A. Kazakov, H. Wang and M. Frenklach, 111**
Sorbent Capture of Nickel, Lead and Cadmium in a Laboratory Swirl Flame Incinerator. W. P. Linak, R. K. Srivastava and J. O. L. Wendt, 241**
Combustion Science for Incineration Technology. J. Wendt, 277
Laser Microprobe Analysis of Soot Precursor Particles and Carbonaceous Soot. R. A. Dobbins, R. A. Fletcher and W. Lu, 301**
A Study of Carbon Monoxide in a Series of Laminar Ethylene/Air Diffusion Flames using Tunable Diode Laser Absorption Spectroscopy. R. R. Skaggs and J. H. Miller, 430**
Thermal and Chemical Influences on the Soot Mass Growth. M. Bachmann, W. Wiese and K. H. Homann, 635
Further Testing of the Fullerene Formation Mechanism With Predictions of Temperature and Pressure Trends. C. J. Pope and J. B. Howard, 671
The Formation of Aromatic Carbon in Sooting Ethylene Flames. A. Ciajolo, A. D'Anna, R. Barbella and A. Tregrossi, 679
High Temperature Reactions of Phenyl Oxidation. P. Frank, J. Herzler, T. Just and C. Wahl, 833
The Reactions of Phenylacetylenes With $O(^3P)$ in the Gas Phase. M. Eichholtz, A. Schneider, D.-V. Stuchen, J.-T. Vollmer and H. G. Wagner, 859
Reaction Mechanisms for Toluene Pyrolysis. M. B. Colket and D. J. Seery, 883
The Formation and Destruction of Aromatic Compounds in a Turbulent Flame. J. H. Thijssen, M. A. Toqan, J. M. Beér and A. F. Sarofim, 1215

*Combustion and Flame, Vol. 99, 1994.
**Combustion and Flame, Vol. 100, 1995.

21.5 Particulates (also see AEROSOLS)

Biosludge Incineration in FBCs: Behavior of Ash Particles. K. K. Rink, J. A. Kozinski and J. S. Lighty, 121**

21.6 Soot (also see SOOT)

Burning Rate Enhancement and Soot Reduction Through Blending in Chlorinated Waste Incineration. T. X. Li and C. K. Law, 291
Laser Microprobe Analysis of Soot Precursor Particles and Carbonaceous Soot. R. A. Dobbins, R. A. Fletcher and W. Lu, 301**
Effect of Flame Structure and Soot-Particle Inception in Diffusion Flames. J. Du and R. L. Axelbaum, 367**
Catalytic Oxidation of an Amorphous Carbon Black. P. Ciambelli, M. D'Amore, V. Palma and S. Vaccaro, 413*
Detailed Kinetic Modelling of Premixed Benzene Flames. R. P. Lindstedt and G. Skevis, 551*
Suppression of Soot Formation in Ethene Laminar Diffusion Flames by Chemical Additives. T. Ni, S. B. Gupta and R. J. Santoro, 585
Iron/Soot Interaction in a Laminar Ethylene Nonpremixed Flame. J. Zhang and C. M. Megaridis, 593
Nonluminous Diffusion Flame of Diluted Acetylene in Oxygen Enriched Air. G. Sugiyama, 601
Soot Formation in Turbulent Non-Premixed Kerosine-Air Flame Burning at Elevated Pressure: Experimental Measurement. K. J. Young, C. D. Stewart and J. B. Moss, 609
Experimental and Theoretical Study of Diesel Soot Reactivity. F. Marcuccilli, P. Gilot, B. Stanmore and G. Prado, 619
Some Physico-Chemical Parameters of Soot Formation During Pyrolysis of Methane and Methane-Acetylene and Methane-Benzene Mixtures. P. A. Tesner and S. V. Shurupov, 653
Reduced Mechanism of Soot Formation—Application to Natural Gas Fueled Diesel Combustion. Y. Yoshihara, A. Kazakov, H. Wang and M. Frenklach, 941
The Formation and Destruction of Aromatic Compounds in a Turbulent Flame. J. H. Thijssen, M. A. Toqan, J. M. Beér and A. F. Sarofim, 1215
Laminar Counterflow Mixing of Acetylene Into Hot Combustion Products. H. Breitbach, J. Goettgens, F. Mauss, H. Pitsch and N. Peters, 1357

21.7 SO_x

The Oxidation of Calcium Sulphide at the Temperatures of Fluidised Bed Combustors. N. H. Davies, K. M. Laughlin and A. N. Hayhurst, 211,

*Combustion and Flame, Vol. 99, 1994.
**Combustion and Flame, Vol. 100, 1995.
***Combustion and Flame, Vol. 98, 1994.

21.8 Metals

A Field Study on the Trace Metal Behavior in Atmospheric Circulating Fluidized Bed Combustion. T. Lind, E. I. Kauppinen, J. K. Jokiniemi and W. Maenhaut, 201
Sorbent Capture of Nickel, Lead and Cadmium in a Laboratory Swirl Flame Incinerator. W. P. Linak, R. K. Srivastava and J. O. L. Wendt, 241**
The Fate of Arsenic in a Laminar Diffusion Flame. S. Chesworth, G. Yang, D. P. Y. Chang, A. D. Jones, P. B. Kelly and I. M. Kennedy, 259***
Combustion Science for Incineration Technology. J. Wendt, 277

21.9 Chloro- and Chloro-fluoro Carbons

The Homogeneous, Gas-Phase Formation of Chlorinated and Brominated Dibenzo-*p*-dioxins from 2,4,6-Trichloro- and 2,4,6-Tribromophenols. S. S. Sidhu, L. Maqsud, B. Dellinger and G. Mascolo, 11**
Burning Rate Enhancement and Soot Reduction Through Blending in Chlorinated Waste Incineration. T. X. Li and C. K. Law, 291
In Situ Detection of Hazardous Waste. C. S. McEnally, R. F. Sawyer, C. P. Koshland and D. Lucas, 325
Thermal Decomposition of HCl Measured by ARAS and IR Diode Laser Spectroscopy. G. N. Schading and P. Roth, 467*
Thermal Decomposition of CH_2Cl_2. K. P. Lim and J. V. Michael, 809
Decay Mechanism of CF_3H or CF_2HCl In $H_2/O_2/Ar$ Flames. H. Richter, J. Vandooren and P. J. Van Tiggelen, 825

21.10 Others

Experimental Studies of Cl-Atom Reactions at High Temperatures: $Cl + H_2 \rightarrow HCl + H$ from 291 to 1283 K. G. Y. Adusei and A. Fontijn, 801
Effect of NO and O_2 Concentration on N_2O Formation during Coal Combustion in a Fluidized Bed Combustor: Modeling Results. S. K. Goel, A. Morihara, C. J. Tullin and A. F. Sarofim, 1051
Boilover Burning of Heating Oil Spilled on Water. J. P. Garo, J. P. Vantelon and A. C. Fernandez-Pello, 1481

22.0 PROPAGATION RATES

Buoyant Downward Diffusion Flame Spread and Extinction in Partial-Gravity Accelerations. K. R. Sacksteder and J. S. T'ien, 1685
Flame Propagation Experiment of PMMA Particle Cloud in a Microgravity Environment. H. Kobayashi, N. Ono, Y. Okuyama and T. Niioka, 1693

22.1 Detonations

Numerical Modeling of Combustion Processes Induced by a Supersonic Conical Blunt Body. M. H. Lefebvre and T. Fujiwara, 85**

22.2 Laminar Flames

Fluoromethane Chemistry and Its Role in Flame Suppression. P. R. Westmoreland, D. R. F. Burgess, M. R. Zachariah and W. Tsang, 1505

22.3 Liquids

Boilover Burning of Heating Oil Spilled on Water. J. P. Garo, J. P. Vantelon and A. C. Fernandez-Pello, 1481

22.4 Solids

Behavior of Fires Spreading Downward over Thick Paper. M. Suzuki, R. Dobashi and T. Hirano, 1439
Combustion Synthesis of ZnS in Microgravity. S. Goroshin, J. H. S. Lee and D. L. Frost, 1651

22.5 Turbulent Flames

H_2-Air and CH_4-Air Detonations and Combustions behind Oblique Shock Waves. C. Viguier, C. Guerraud and D. Desbordes, 53
The Production of Premixed Flame Surface Area in Turbulent Shear Flow. A. Trouvé, 687*

23.0 PROPERTY MEASUREMENTS

Characterization of Mass and Density Distributions of Sized Coal Fractions. E. R. Monazam and D. J. Maloney, 733*
Comparative Experimental and Numerical Investigation of a Piloted Turbulent Natural-Gas Diffusion Flame. T. W. J. Peeters, P. P. J. Stroomer, J. E. de Vries, D. J. E. M. Roekaerts and C. J. Hoogendoorn, 1241
An Instrument for Characterization of the Thermal and Optical Properties of Charring Polymeric Materials. M. A. Serio, D. S. Pines, A. S. Bonanno, P. R. Solomon and G. A. Simmons, 1447

23.1 Composition

A Field Study on the Trace Metal Behavior in Atmospheric Circulating Fluidized Bed Combustion. T. Lind, E. I. Kauppinen, J. K. Jokiniemi and W. Maenhaut, 201
Soot Formation in Turbulent Non-Premixed Kerosine-Air Flame Burning at Elevated Pressure: Experimental Measurement. K. J. Young, C. D. Stewart and J. B. Moss, 609

23.3 Species Identification

RDX Flame Structure. D. Hanson-Parr and T. Parr, 1635

23.4 Spectra

Interactions Between Nonsymmetrical Wake Structure and Turbulent Diffusion Flames behind a Rear-Facing Semicircular Cylinder. N. Ohiwa, Y. Ishino and S. Yamaguchi, 302*
Determination of Temperature From N_2 and O_2 Cars Spectra at Very High Pressure. T. Dreier, M. Ridder, G. Schiff, A. Saur and A. A. Suvernev, 1727

23.5 Temperature

Simultaneous 2D-Single Shot Imaging of OH Concentrations and Temperature Fields in a SI Engine Simulator. A. Orth, V. Sick, J. Wolfrum, R. R. Maly and M. Zahn, 143
Turbulent Velocity and Temperature Measurements from a Gaseous Fueled Technology Combustor with a Practical Fuel Injector. P. O. Hedman and D. L. Warren, 185**
Application of an Integrated Phase Doppler Interferometer/Rainbow Thermometer/Point Diffraction Interferometer for Characterizing Burning Droplets. S. V. Sankar, D. H. Buermann, K. M. Ibrahim and W. D. Bachalo, 413
TACCOS—A Thermography-Assisted Combustion Control System for Waste Incinerators. F. Schuler, F. Rampp, J. Martin and J. Wolfrum, 431*
Temperature Field on a Laminar Diffusion Dust Flame. J. I. Vovchuk and N. I. Poletaev, 706*
Simultaneous NO and Temperature Imaging Measurements in Turbulent Nonpremixed Flames. M. Namazian, J. Kelly and R. Schefer, 1149
Mixture Fraction Imaging in Turbulent Nonpremixed Hydrocarbon Flames. J. H. Frank, K. M. Lyons, D. F. Marran, M. B. Long, S. H. Stårner and R. W. Bilger, 1159
Determination of Temperature From N_2 and O_2 Cars Spectra at Very High Pressure. T. Dreier, M. Ridder, G. Schiff, A. Saur and A. A. Suvernev, 1727
Dual-Broadband Rotational CARS Measurements in an IC engine. P.-E. Bengtsson, L. Martinsson, M. Aldén, B. Johansson, B. Lassesson, K. Marforio and G. Lundholm, 1735

*Combustion and Flame, Vol. 99, 1994.
**Combustion and Flame, Vol. 100, 1995.

23.6 Velocity; Pressure; Flow Direction

Turbulent Velocity and Temperature Measurements from a Gaseous Fueled Technology Combustor with a Practical Fuel Injector. P. O. Hedman and D. L. Warren, 185**
Heat Release Timing in a Non-Premixed Helmholtz Pulse Combustor. Y. M. Tang, G. Waldherr, J. I. Jagoda and B. T. Zinn, 251**
Analysis of In-Cylinder Flow Processes by LDA. F. E. Corcione and G. Valentino, 387*
Experimental Analysis of Flamelet Models for Premixed Turbulent Combustion. D. Veynante, J. M. Duclos and J. Piana, 1249

23.7 Others

Evolution of Char Chemistry, Crystallinity, and Ultrafine Structure during Pulverized-Coal Combustion. K. A. Davis, R. H. Hurt, N. Y. C. Yang and T. J. Headley, 31**
Simultaneous 2D-Single Shot Imaging of OH Concentrations and Temperature Fields in a SI Engine Simulator. A. Orth, V. Sick, J. Wolfrum, R. R. Maly and M. Zahn, 143
Application of an Integrated Phase Doppler Interferometer/Rainbow Thermometer/Point Diffraction Interferometer for Characterizing Burning Droplets. S. V. Sankar, D. H. Buermann, K. M. Ibrahim and W. D. Bachalo, 413
Experimental Analysis of Flamelet Models for Premixed Turbulent Combustion. D. Veynante, J. M. Duclos and J. Piana, 1249
Dual-Broadband Rotational CARS Measurements in an IC Engine. P.-E. Bengtsson, L. Martinsson, M. Aldén, B. Johansson, B. Lassesson, K. Marforio and G. Lundholm, 1735

PYROLYIS
(*See* **THERMAL DECOMPOSITION**)

24.0 REACTION MECHANISMS

Impact of Coal Pyrolysis on Combustion. P. R. Solomon and T. H. Fletcher, 463
Further Testing of the Fullerene Formation Mechanism With Predictions of Temperature and Pressure Trends. C. J. Pope and J. B. Howard, 671
Reaction of Hydroperoxy *t*-Butyl Radicals and *t*-Butyl Peroxy *t*-Butyl Radicals in Relation to Chain Propagation in Combustion. L. Batt, M. A. Khan and T. J. Mitchell, 793
High Temperature Reactions of Phenyl Oxidation. P. Frank, J. Herzler, T. Just and C. Wahl, 833
Hydrogen Atom Attack on 1-Phenylpropene at High Temperatures. W. Tsang and J. A. Walker, 867
Reaction Mechanisms for Toluene Pyrolysis. M. B. Colket and D. J. Seery, 883
Aspects of Nitrogen Flame Chemistry Revealed By Burning Velocity Modelling. M. J. Brown and D. B. Smith, 1011
A Bifurcation Analysis of High-Temperature Ignition of H_2-O_2 Diffusion Flames. A. L. Sánchez, A. Liñán and F. A. Williams, 1529
Ignition and Combustion of Magnesium in Carbon Dioxide Streams. S. Yuasa and A. Fukuchi, 1587

24.1 Identification of Intermediates and Products

Nonoxide Ceramic Powder Synthesis. B. W. Gerhold and K. E. Inkrott, 144**
Thermal Decomposition of Propargyl Bromide and the Subsequent Formation of Benzene. R. D. Kern, H. Chen, J. H. Kiefer and P. S. Mudipalli, 177**
Kinetic Interactions of CO, NO_x, and HCl Emissions in Post-Combustion Gases. J. F. Roesler, R. A. Yetter and F. L. Dryer, 495**
The Formation of Aromatic Carbon in Sooting Ethylene Flames. A. Ciajolo, A. D'Anna, R. Barbella and A. Tregrossi, 679
New Results on Moist CO Oxidation: High Pressure, High Temperature Experiments and Comprehensive Kinetic Modeling. T. J. Kim, R. A. Yetter and F. L. Dryer, 759
Reaction of Hydroperoxy *t*-Butyl Radicals and *t*-Butyl Peroxy *t*-Butyl Radicals in Relation To Chain Propagation in Combustion. L. Batt, M. A. Khan and T. J. Mitchell, 793
Reaction Mechanisms for Toluene Pyrolysis. M. B. Colket and D. J. Seery, 883
An Experimental and Computational Study of Methanol Oxidation in the Intermediate and High Temperature Regimes. T. J. Held and F. L. Dryer, 901
Hydrocarbon-NO_x Interactions at Low Temperatures −1. Conversion of NO to NO_2 Promoted by Propane and the Formation of HNCO. P. F. Nelson and B. S. Haynes, 1003
Carbon Monoxide Formation in Fires By High-Temperature Anaerobic Wood Pyrolysis. W. M. Pitts, E. L. Johnsson and N. P. Bryner, 1445

24.2 Reaction Pathways

Fuel and Soot Oxidation in Diesel-like Conditions. A. Cavliere, R. Barbella, A. Ciajola, A. D'Anna and R. Ragucci, 167
Thermal Decomposition of Propargyl Bromide and the Subsequent Formation of Benzene. R. D. Kern, H. Chen, J. H. Kiefer and P. S. Mudipalli, 177**
Influence of Initial Particle Density on the Reaction

*Combustion and Flame, Vol. 99, 1994.
**Combustion and Flame, Vol. 100, 1995.

Mode of Porous Carbon Particles. R. H. Essenhigh, 269°
An Experimental Study of High-Temperature, Oxidative Pulverized Coal Devolatilization. L. H. Sorensen, O. Biede and R. E. Peck, 475
Kinetic Interactions of CO, NO_x, and HCl Emissions in Post-Combustion Gases. J. F. Roesler, R. A. Yetter and F. L. Dryer, 495°°
Multichannel Reactions in Combustion. Th. Just, 687
New Results on Moist CO Oxidation: High Pressure, High Temperature Experiments and Comprehensive Kinetic Modeling. T. J. Kim, R. A. Yetter and F. L. Dryer, 759
The Reaction of Hydroperoxy-Propyl Radicals with Molecular Oxygen. J. W. Bozzelli and W. J. Pitz, 783
Kinetics of the Thermal Decomposition and Isomerisation of Pyrazine (1,4 Diazine). A. Doughty, J. C. Mackie and J. M. Palmer, 893
An Experimental and Computational Study of Methanol Oxidation in the Intermediate and High Temperature Regimes. T. J. Held and F. L. Dryer, 901
Analysis of the Reactions H + N_2O and NH + NO: Pathways and Rate Constants Over a Wide Range of Temperature and Pressure. J. W. Bozzelli, A. Y. Chang and A. M. Dean, 965
Laminar Counterflow Mixing of Acetylene Into Hot Combustion Products. H. Breitbach, J. Goettgens, F. Mauss, H. Pitsch and N. Peters, 1357
Fluoromethane Chemistry and Its Role in Flame Suppression. P. R. Westmoreland, D. R. F. Burgess, M. R. Zachariah and W. Tsang, 1505
Shock Initiated Ignition in Ethylene Oxide, Propylene Oxide, 1,2-Epoxybutane and 2,3-Epoxybutane. A. Lifshitz and A. Suslensky, 1571
Reaction of Hydroperoxy *t*-Butyl Radicals and *t*-Butyl Peroxy *t*-Butyl Radicals in Relation To Chain Propagation in Combustion. L. Batt, M. A. Khan and T. J. Mitchell, 793

25.0 REVIEW PAPERS

Gasdynamic Enhancement of Nonpremixed Combustion. F. Marble, 1
State of the Art and Future Needs in S.I. Engine Combustion. R. R. Maly, 111
Combustion Science for Incineration Technology. J. Wendt, 277
Injection, Dispersion, and Combustion of Liquid Fuels. W. D. Bachalo, 333
Impact of Coal Pyrolysis on Combustion. P. R. Solomon and T. H. Fletcher, 463
Multichannel Reactions in Combustion. Th. Just, 687
Transition and Structure of Jet Diffusion Flames. T. Takeno, 1061
Modeling Turbulent Flame Propagation. W. T. Ashurst, 1075
Polymer Combustion and Flammability—Role of the Condensed Phase. T. Kashiwagi, 1423
Combustion's Impact on the Global Atmosphere. M. J. Prather and J. A. Logan, 1513

SAFETY

(*see* **FIRE**, *safety*)

26.0 SOOT

Agglomeration of Soot Particles in Diffusion Flames under Microgravity. H. Ito, O. Fujita and K. Ito, 363°
Nonluminous Diffusion Flame of Diluted Acetylene in Oxygen Enriched Air. G. Sugiyama, 601
Optical Characterization of Rich Premixed CH_4/O_2 Flames Across the Soot Formation Threshold. A. D'Alessio, G. Gambi, P. Minutolo, S. Russo and A. D'Anna, 645
High Temperature Pyrolsis and Oxidation of Fullerene C_{60} Behind Shock Waves. S. von Gersum and P. Roth, 661

26.1 Control

Effect of Flame Structure and Soot-Particle Inception in Diffusion Flames. J. Du and R. L. Axelbaum, 367°°
Catalytic Oxidation of an Amorphous Carbon Black. P. Ciambelli, M. D'Amore, V. Palma and S. Vaccaro, 413°
Suppression of Soot Formation in Ethene Laminar Diffusion Flames by Chemical Additives. T. Ni, S. B. Gupta and R. J. Santoro, 585

26.2 Formation

Detailed Modeling of Soot Formation in Laminar Premixed Ethylene Flames at a Pressure of 10 Bar. A. Kazakov, H. Wang and M. Frenklach, 111°°
Laser Microprobe Analysis of Soot Precursor Particles and Carbonaceous Soot. R. A. Dobbins, R. A. Fletcher and W. Lu, 301°°
Soot Mass Growth and Coagulation of Soot Particles in C_2H_4/Air Flames at 15 Bar. S. Hanisch, H. Jander, T. Pape and H. G. Wagner, 577
Suppression of Soot Formation in Ethene Laminar Diffusion Flames by Chemical Additives. T. Ni, S. B. Gupta and R. J. Santoro, 585
Soot Formation in Turbulent Non-Premixed Kerosine-Air Flame Burning at Elevated Pressure: Experimental Measurement. K. J. Young, C. D. Stewart and J. B. Moss, 609

°Combustion and Flame, Vol. 99, 1994.
°°Combustion and Flame, Vol. 100, 1995.

Soot Formation at Elevated Pressures and Carbon Concentrations in Hydrocarbon Pyrolysis. S. Bauerle, Y. Karasevich, S. Slavov, D. Tanke, M. Tappe, T. Thienel and H. G. Wagner, 627
Thermal and Chemical Influences on the Soot Mass Growth. M. Bachmann, W. Wiese and K. H. Homann, 635
Some Physico-Chemical Parameters of Soot Formation During Pyrolysis of Methane and Methane-Acetylene and Methane-Benzene Mixtures. P. A. Tesner and S. V. Shurupov, 653
The Formation of Aromatic Carbon in Sooting Ethylene Flames. A. Ciajolo, A. D'Anna, R. Barbella and A. Tregrossi, 679
Inception and Growth of Soot Particles in Dependence on the Surrounding Gas Phase. F. Mauss, T. Schäfer and H. Bockhorn, 697*
Quantitative Measurements of Enhanced Soot Production in a Flickering Methane/Air Diffusion Flame. C. R. Shaddix, J. E. Harrington and K. C. Smyth, 723*
Reduced Mechanism of Soot Formation—Application to Natural Gas Fueled Diesel Combustion. Y. Yoshihara, A. Kazakov, H. Wang and M. Frenklach, 941
Laminar Counterflow Mixing of Acetylene Into Hot Combustion Products. H. Breitbach, J. Goettgens, F. Mauss, H. Pitsch and N. Peters, 1357

26.3 Morphology

Iron/Soot Interaction in a Laminar Ethylene Nonpremixed Flame. J. Zhang and C. M. Megaridis, 593
Experimental and Theoretical Study of Diesel Soot Reactivity. F. Marcuccilli, P. Gilot, B. Stanmore and G. Prado, 619

26.4 Oxidation

Fuel and Soot Oxidation in Diesel-like Conditions. A. Cavliere, R. Barbella, A. Ciajola, A. D'Anna and R. Ragucci, 167
Catalytic Oxidation of an Amorphous Carbon Black. P. Ciambelli, M. D'Amore, V. Palma and S. Vaccaro, 413*
Soot Formation in Turbulent Non-Premixed Kerosine-Air Flame Burning at Elevated Pressure: Experimental Measurement. K. J. Young, C. D. Stewart and J. B. Moss, 609
Experimental and Theoretical Study of Diesel Soot Reactivity. F. Marcuccilli, P. Gilot, B. Stanmore and G. Prado, 619
Reduced Mechanism of Soot Formation—Application to Natural Gas Fueled Diesel Combustion. Y. Yoshihara, A. Kazakov, H. Wang and M. Frenklach, 941

26.5 Precursors

Thermal Decomposition of Propargyl Bromide and the Subsequent Formation of Benzene. R. D. Kern, H. Chen, J. H. Kiefer and P. S. Mudipalli, 177**
Laser Microprobe Analysis of Soot Precursor Particles and Carbonaceous Soot. R. A. Dobbins, R. A. Fletcher and W. Lu, 301**
Optical Characterization of Rich Premixed CH_4/O_2 Flames Across the Soot Formation Threshold. A. D'Alessio, G. Gambi, P. Minutolo, S. Russo and A. D'Anna, 645
Further Testing of the Fullerene Formation Mechanism With Predictions of Temperature and Pressure Trends. C. J. Pope and J. B. Howard, 671
The Formation of Aromatic Carbon in Sooting Ethylene Flames. A. Ciajolo, A. D'Anna, R. Barbella and A. Tregrossi, 679
Laminar Counterflow Mixing of Acetylene Into Hot Combustion Products. H. Breitbach, J. Goettgens, F. Mauss, H. Pitsch and N. Peters, 1357
The Formation and Destruction of Aromatic Compounds in a Turbulent Flame. J. H. Thijssen, M. A. Toqan, J. M. Beér and A. F. Sarofim, 1215

27.0 THERMAL DECOMPOSITION

Impact of Coal Pyrolysis on Combustion. P. R. Solomon and T. H. Fletcher, 463
Hydrogen Atom Attack on 1-Phenylpropene at High Temperatures. W. Tsang and J. A. Walker, 867

27.1 Gas

A New Comprehensive Reaction Mechanism for Combustion of Hydrocarbon Fuels. E. Ranzi, A. Sogaro, P. Gaffuri, G. Pennati, C. K. Westbrook and W. J. Pitz, 201*
Shock Wave Study of the Thermal Decompostion of Benzyl Alcohol. S. Frisch, H. Hippler, H. Neunaber and J. Troe, 254*
Soot Formation at Elevated Pressures and Carbon Concentrations in Hydrocarbon Pyrolysis. S. Bauerle, Y. Karasevich, S. Slavov, D. Tanke, M. Tappe, T. Thienel and H. G. Wagner, 627
High Temperature Pyrolsis and Oxidation of Fullerene C_{60} Behind Shock Waves. S. von Gersum and P. Roth, 661
Thermal Decomposition of CH_2Cl_2. K. P. Lim and J. V. Michael, 809
Pyrolysis of *p*-Xylene and of 4-Methylbenzyl Radicals. H. Hippler, S. Seisel and J. Troe, 875
Reaction Mechanisms for Toluene Pyrolysis. M. B. Colket and D. J. Seery, 883
Kinetics of the Thermal Decomposition and Iso-

*Combustion and Flame, Vol. 99, 1994.
**Combustion and Flame, Vol. 100, 1995.

merisation of Pyrazine (1,4 Diazine). A. Doughty, J. C. Mackie and J. M. Palmer, 893

27.3 Solid

Decreases in the Swelling and Porosity of Bituminous Coals during Devolatilization at High Heating Rates. T. K. Gale, C. H. Bartholomew and T. H. Fletcher, 94**
Pyrolysis and Combustion of Corncobs in a Fluidized Bed: Measurement and Analysis of Behavior. J.-L. Lin and H. M. Keener, 271**
Predicting the Devolatilization Behavior of Any Coal From its Ultimate Analysis. S. Niksa, 384**
An Experimental Study of High-Temperature, Oxidative Pulverized Coal Devolatilization. L. H. Sorensen, O. Biede and R. E. Peck, 475
Volatile Matter Release, Particle/Cloud Ignition and Combustion of Near-Stoichiometric Suspensions of Pulverized Coal. J. A. Lucas and T. F. Wall, 485
Predicting the Evolution of Fuel Nitrogen From Various Coals. S. Niksa, 537
A Method of Predicting Coal Devolatilization Behavior Based on the Elemental Composition. Y. Zhao, M. A. Serio, R. Bassilakis and P. R. Solomon, 553
Carbon Monoxide Formation in Fires By High-Temperature Anaerobic Wood Pyrolysis. W. M. Pitts, E. L. Johnsson and N. P. Bryner, 1445
An Instrument for Characterization of the Thermal and Optical Properties of Charring Polymeric Materials. M. A. Serio, D. S. Pines, A. S. Bonanno, P. R. Solomon and G. A. Simmons, 1447
Modelling of Partially Confined Hot Fragment Conductive Ignition. T. H. Huang, S. T. Thynell and K. K. Kuo, 1595

28.0 THERMOCHEMISTRY AND THERMODYNAMICS

Nonoxide Ceramic Powder Synthesis. B. W. Gerhold and K. E. Inkrott, 144**
A Thermochemical Phase Space for Combustion in Engines. A. K. Oppenheim and J. A. Maxson, 157
Shock Wave Study of the Thermal Decompostion of Benzyl Alcohol. S. Frisch, H. Hippler, H. Neunaber and J. Troe, 254*
High Temperature Reactions of Phenyl Oxidation. P. Frank, J. Herzler, Th. Just and C. Wahl, 833

*Combustion and Flame, Vol. 99, 1994.
**Combustion and Flame, Vol. 100, 1995.

29.0 TRANSPORT PROPERTIES

On the Structure of Stretched/Compressed Laminar Flamelet—Influence of Preferential Diffusion. V. R. Katta and W. M. Roquemore, 61**

29.1 Diffusion

Laser Raman Scattering Measurements of Differential Molecular Diffusion in Turbulent Nonpremixed Jet Flames of H_2/CO_2 Fuel. L. L. Smith, R. W. Dibble, L. Talbot, R. S. Barlow and C. D. Carter, 153**
Effects of Molecular Transport on Turbulence-Chemistry Interactions in a Hydrogen-Argon-Air Jet Diffusion Flame. S. Menon, W. H. Calhoon, Jr., G. Goldin and A. R. Kerstein, 1125

29.2 Thermal Conductivity

Evolution of Porosity and Thermal Conductivity during Char Oxidation. Y. Weiss, Y. Benari, I. I. Kantorovich, E. Bar-Ziv, G. Krammer, A. Modestino and A. F. Sarofim, 519

29.4 Viscosity

Modeling Heterogeneous/Homogeneous Reactions and Transport Coupling for Catalytic Combustion of Methyl Chloride over a Mn-based Catalyst. H. Karim, L. D. Pfefferle, P. Markatou and M. Smooke, 299

30.0 COMBUSTION SYNTHESIS

Nonoxide Ceramic Powder Synthesis. B. W. Gerhold and K. E. Inkrott, 144**
Nanoscale Unagglomerated Nonoxide Particles from a Sodium Coflow Flame. D. P. DuFaux and R. L. Axelbaum, 350**
Stochastic Modeling of Multi-State Combustion of Condensed Heterogeneous Systems. B. M. Khusid, B. B. Khina, E. P. Podvoisky and I. S. Chebotko, 371*
Further Testing of the Fullerene Formation Mechanism With Predictions of Temperature and Pressure Trends. C. J. Pope and J. B. Howard, 671
Combustion Synthesis of ZnS in Microgravity. S. Goroshin, J. H. S. Lee and D. L. Frost, 1651
Propagation and Diffusion Limited Extinction of Nonadiabatic Heterogeneous Flame in the SHS Process. A. Makino and C. K. Law, 1659
A DMS Kinetic Study of the Boron Oxides Vapor in the Combustion Front of SHS System Mo + B. O. E. Kashireninov and I. A. Yuranov, 1669

AIR FORCE OF SCIENTIFIC RESEARCH (AFSC)
NOTICE OF [illegible] DTIC
This [illegible] has been reviewed and is
approved [illegible] release IAW AFR 190-12
Distribution [illegible] unlimited.
Joan Boggs
STINFO Program Manager

Distribution unlimited release.

THE COMBUSTION INSTITUTE

5001 BAUM BOULEVARD PITTSBURGH, PENNSYLVANIA 15213-1851
Telephone: (412) 687-1366
Facsimile: (412) 687-0340

These volumes provide a unique collection of research results from many countries where important combustion research and development is done. The contributions cover material of interest to Physical Chemists, Fuel Technologists, Fluid Dynamicists, Combustion Engine Designers, Furnace Designers, Fire Scientists, Environmental Scientists, and others interested in the fundamentals and applications of Combustion Science.

First/Second Symposia on Combustion (1928/1937) 361 pp.

Third Symposium on Combustion, Flame and Explosion Phenomena (1948) 761 pp. University of Wisconsin

Fourth Symposium (International) on Combustion—Combustion and Detonation Waves (1952) 946 pp. Massachusetts Institute of Technology

Fifth Symposium (International) on Combustion—Combustion in Engines and Combustion Kinetics (1954) 826 pp. University of Pittsburgh

Sixth Symposium (International) on Combustion (1956) 968 pp. Yale University

Seventh Symposium (International) on Combustion (1958) 992 pp. Oxford University

Eighth Symposium (International) on Combustion (1960) 1188 pp. California Institute of Technology

Ninth Symposium (International) on Combustion (1962) 1112 pp. Cornell University

Tenth Symposium (International) on Combustion (1964) 1514 pp. University of Cambridge

Eleventh Symposium (International) on Combustion (1966) 1221 pp. University of California, Berkeley

Twelfth Symposium (International) on Combustion (1968) 1312 pp. University of Poitiers

Thirteenth Symposium (International) on Combustion (1970) 1209 pp. University of Utah

Fourteenth Symposium (International) on Combustion (1972) 1451 pp. The Pennsylvania State University

Fifteenth Symposium (International) on Combustion (1974) 1564 pp. Tokyo, Japan

Sixteenth Symposium (International) on Combustion (1976) 1570 pp. Massachusetts Institute of Technology

Seventeenth Symposium (International) on Combustion (1978) 1496 pp. University of Leeds

Eighteenth Symposium (International) on Combustion (1980) 1974 pp. University of Waterloo

Nineteenth Symposium (International) on Combustion (1982) 1563 pp. Technion Institute of Technology, Israel

Twentieth Symposium (International) on Combustion (1984) 2123 pp. The University of Michigan

Twenty-First Symposium (International) on Combustion (1986) 2023 pp. The Technical University of Munich

Twenty-Second Symposium (International) on Combustion (1988) 2099 pp. University of Washington, Seattle

Twenty-Third Symposium (International) on Combustion (1990) 1972 pp. University of Orléans

Twenty-Fourth Symposium (International) on Combustion (1992) 2017 pp. University of Sydney

Twenty-Fifth Symposium (International) on Combustion (1994) 1840 pp. University of California, Irvine

SPECIAL PRICE FOR COMPLETE SET (Vols. 1 through 25).
DISCOUNT PRICES TO MEMBERS, LIBRARIES, AND BOOKDEALERS.

The Twenty-Sixth Symposium (International) on Combustion will be held July 28–August 2, 1996, in Naples, Italy.